Polyhedron 28 (2009) 1–6

Contents lists available at ScienceDirect

Polyhedron

journal homepage: www.elsevier.com/locate/poly

Copper(II) complexes of tetradentate N2S2 donor sets: Synthesis, crystal structure characterization and reactivity

S. Sarkar [a], A. Patra [a], M.G.B. Drew [b], E. Zangrando [c], P. Chattopadhyay [a,*]

[a] Department of Chemistry, Burdwan University, Golapbag, Burdwan 713 104, India
[b] Department of Chemistry, Reading University, Reading RG 66AD, Berks, UK
[c] Dipartimento di Scienze Chimiche, Via Licio Giorgieri 1, 34127 Trieste, Italy

ARTICLE INFO

Article history:
Received 14 July 2008
Accepted 19 August 2008
Available online 23 September 2008

Keywords:
Copper(II) complex
Copper(I) complex
Nitrogen–sulphur ligands
Crystal structure

ABSTRACT

Two mononuclear and one dinuclear copper(II) complexes, containing neutral tetradentate NSSN type ligands, of formulation $[Cu^{II}(L^1)Cl]ClO_4$ (**1**), $[Cu^{II}(L^2)Cl]ClO_4$ (**2**) and $[Cu^{II}_2(L^3)_2Cl_2](ClO_4)_2$ (**3**) were synthesized and isolated in pure form [where L^1 = 1,2-bis(2-pyridylmethylthio)ethane, L^2 = 1,3-bis(2-pyridylmethylthio)propane and L^3 = 1,4-bis(2-pyridylmethylthio)butane]. All these green colored copper(II) complexes were characterized by physicochemical and spectroscopic methods. The dinuclear copper(II) complex **3** changed to a colorless dinuclear copper(I) species of formula $[Cu^{I}_2(L^3)_2](ClO_4)_2{,}0.5H_2O$ (**4**) in dimethylformamide even in the presence of air at ambient temperature, while complexes **1** and **2** showed no change under similar conditions. The solid-state structures of complexes **1, 2** and **4** were established by X-ray crystallography. The geometry about the copper in complexes **1** and **2** is trigonal bipyramidal whereas the coordination environment about the copper(I) in dinuclear complex **4** is distorted tetrahedral.

© 2008 Elsevier Ltd. All rights reserved.

1. Introduction

The potential role played by copper ions in the active sites of a large number of metalloproteins has stimulated efforts to design and characterize copper complexes as models for providing better understanding of biological systems and for assisting in the development of new homogeneous catalysts for selective oxidation. Particularly, the coordination chemistry and reactivity of copper complexes involving nitrogen–sulfur donor ligands has received considerable attention as models [1]. In particular the CuN_2S_2 chromophore is present in blue copper proteins such as plastocyanine [2] and copper(II) chelates of SNNS ligands have been found to have antineoplastic activities and to interact with biological systems [3].

Pursuing our continuous interest on nitrogen–sulphur polydentate chelators [4] and in addition of the importance of nitrogen–sulphur donor sets in the coordination chemistry of copper complexes, herein we report an account on the coordination properties of three neutral tetradentate ligands containing two pyridyl-N and two thioether-S donors. The mononuclear complexes **1** and **2** show penta-coordinated copper(II) ion with distorted trigonal bipyramid coordination geometry and the trigonality index (τ) of the solid-state structure increases (from 0.619 to 0.716) with the number of carbon atoms in the backbone of the ligands. The penta-coordinated copper(II) in the dinuclear green colored complex (**3**) is reduced to tetra-coordinated copper(I) species with concomitant change of color (colorless (**4**)) in dimethylformamide (DMF) even in the presence of air at ambient temperature within few days, while other complexes **1** and **2** show no change after several days. The single crystal X-ray structural analysis of **1, 2** and **4** are discussed and compared.

2. Experimental

2.1. Materials and physical measurements

All chemicals and reagents were obtained from commercial sources and used as received, unless otherwise stated. Tetra-*n*-butylammoniumperchlorate was prepared by addition of sodium perchlorate to a hot solution of tetra-*n*-butylammoniumbromide (Aldrich). The product was recrystallized from aqueous ethanol and tested for the absence of bromide. Solvents were distilled from an appropriate drying agent [5].

The C, H, N elemental analyses were performed on a Perkin Elmer model 2400 elemental analyzer. Copper analysis was carried out by Varian atomic absorption spectrophotometer (AAS) model-AA55B, GTA using graphite furnace. Electronic absorption spectra were recorded on a JASCO UV-Vis/NIR spectrophotometer model V-570 in the range of 1100–200 nm. IR spectra were obtained by JASCO FT-IR spectrometer model 460 *plus* using KBr disk. ^{1}HNMR spectra were recorded on a Bruker AC300 spectrometer

* Corresponding author. Tel.: +91 342 2558339; fax: +91 342 2530452.
E-mail address: pabitracc@yahoo.com (P. Chattopadhyay).

0277-5387/$ - see front matter © 2008 Elsevier Ltd. All rights reserved.
doi:10.1016/j.poly.2008.08.004

using TMS as an internal standard in $CDCl_3$. The room temperature magnetic susceptibility measurements were performed by using a vibrating sample magnetometer PAR 155 model. Molar conductance (Λ_M) were measured in a systronics conductivity meter 304 model using $\sim 10^{-3}$ mol L^{-1} solutions in acetonitrile. The measurement of pH of the reaction mixture was done with a systronics digital pH meter (Model 335). The separation and detection of the species in the reaction mixture were carried out using the hyphenated GC–MS system (Schimadzu, model GCMS-QP5050A). Electrochemical measurements were recorded on a computer controlled EG & G PAR model 270 VERSTAT electrochemical instruments using Ag/AgCl electrodes with TBAP as supporting electrolyte. All the measurements were made at 298 K with acetonitrile as solvent for complexes **1** and **2** and dimethylformamide for 3, using a concentration ca. 10^{-3}–10^{-4} M purged with dry nitrogen for 3–4 min in order to remove dissolved oxygen.

2.2. Preparation of the ligands

The syntheses of the ligands were carried out following the reported procedure [6] with slight modification. A common procedure has been performed to obtain the ligands. The procedure for the preparation of 1,2-bis(2-pyridylmethylthio)ethane, (L^1) is here described. An ethanolic solution of 2-picolyl chloride, hydrochloride (1.64 g, 10.0 mmol) was added to 1,2-ethandithiol (0.47 g, 5.0 mmol) in dry ethanol containing sodium ethoxide (0.46 g 20.0 mmol) at low temperature (0–5 °C). Then this mixture was allowed to stir at room temperature for 0.5 h and then it was refluxed for 2 h. The mixture was cooled to room temperature, water was added and finally the ethanol was off by rotary evaporator. The product was extracted into dichloromethane and dried by using $NaHSO_3$. The product, 1,2-bis(2-pyridylmethylthio)ethane (L^1) was obtained as a yellow oil by removing the dichloromethane by rotary evaporator. The other products were also obtained as liquids. Finally the products were verified by ^1H NMR spectroscopy.

2.3. Preparation of the copper(II) complexes

The copper(II) complexes were synthesized following a common procedure as described below, using copper(II) perchlorate hexahydrate and the respective organic compounds in equimolar ratio. For complex **1**, L^1 (276.0 mg, 1.0 mmol), for complex **2**, L^2 (292.0 mg, 1.0 mmol) and for complex **3**, L^3 (306.0 mg, 1.0 mmol) were mixed with 1.0 mmol of copper(II) perchlorate hexahydrate, and the mixture was stirred for 4 h in methanol. Then sodium chloride (1.0 mmol) was added to the resulting mixture and stirred for another 1 h at room temperature. The green coloured complexes were precipitated out and the solid complexes were filtered, washed with water, cold methanol and dried in vacuo. Yield: 84–85%.

$[Cu(L^1)Cl]ClO_4$ (**1**): *Anal.* Calc. for $C_{14}H_{16}Cl_2CuN_2O_4S_2$: C, 35.37; H, 3.37; N, 5.90, Cu, 13.37. Found: C, 35.52; H, 3.46; N, 5.74, Cu, 13.21%. IR0020(cm^{-1}): $\nu_{C=N}$, 1476; ν_{C-S}, 758; ν_{ClO_4}, 1090 and 621. Magnetic moment (μ, B.M.): 1.81. Conductivity (Λ_o, Ω^{-1} cm^2 mol^{-1}) in acetonitrile: 145.

$[Cu(L^2)Cl]ClO_4$ (**2**): *Anal.* Calc. for $C_{15}H_{18}Cl_2CuN_2O_4S_2$: C, 36.82; H, 3.68; N, 5.73, Cu, 12.99. Found: C, 37.22; H, 3.77; N, 5.81, Cu, 13.11%. IR (cm^{-1}): $\nu_{C=N}$, 1465; ν_{C-S}, 758; ν_{ClO4}, 1088 and 624. Magnetic moment (μ, B.M.): 1.79. Conductivity (Λ_o, Ω^{-1} cm^2 mol^{-1}) in acetonitrile: 140.

$[Cu_2(L^3)_2Cl_2](ClO_4)_2$ (**3**): *Anal.* Calc. for $C_{32}H_{40}Cl_4Cu_2N_4O_8S_4$: C, 38.18; H, 3.98; N, 5.57, Cu,12.63. Found: C, 37.82; H, 4.02; N, 5.79, Cu, 12.47%. IR (cm^{-1}): $\nu_{C=N}$, 1478; ν_{C-S}, 760, ν_{ClO4}, 1088 and 622. Magnetic moment (μ, B.M.): 1.45 per Cu atom. Conductivity (Λ_o, Ω^{-1} cm^2 mol^{-1}) in DMF: 150.

2.4. Preparation of the copper(I) complex of 1,4-bis(2-pyridylmethylthio)butane (**4**)

The solution of complex **3** in DMF was stirred for 1 h at room temperature in presence of air. After few days, the colorless single crystals of complex **4** were collected by slow evaporation of this solution

$[Cu_2(L^3)_2](ClO_4)_2,0.5H_2O$ (**4**): *Anal.* Calc. for $C_{32}H_{41}Cl_2Cu_2N_4O_{8.5}S_4$: C, 40.68; H, 4.34; N, 5.93, Cu, 13.45. Found: C, 40.01; H, 4.21; N, 5.88; Cu, 13.34%. IR (cm^{-1}): $\nu_{C=N}$, 1479; ν_{C-S}, 758; ν_{ClO4}, 1092 and 623.

2.5. X-ray crystal structure analysis

Single crystals suitable for X-ray diffraction analysis were grown by slow evaporation of acetonitrile solutions of complex **1** and **2** at ambient temperature, while crystals of complex **4** were obtained from dimethylformamide solution of copper(II) complex **3** by slow evaporation at room temperature in presence of air.

Crystal data and details of data collections and refinements for the structures reported are summarized in Table 1. Diffraction data of **1** and **2** were collected at 150(2) K on Oxford Diffraction X-Calibur CCD System, data collection of **4** were carried out, at room temperature, on a Nonius DIP-1030H system, by using Mo Kα radiation, $\lambda = 0.71073$ Å in both cases. Cell refinement, indexing and scaling of all the data sets were performed using programs Crys Alis [7], Denzo and Scalepack [8]. All the structures were solved by direct methods and subsequent Fourier analyses and refined by the full-matrix least-squares method based on F^2 with all observed reflections [9]. A residual in the difference Fourier map of **4**, located on a two-fold axis, was assigned to a water oxygen with occupancy 0.25. The contribution of hydrogen atoms at calculated positions were included in final cycles of refinement. All the calculations were performed using the WinGX System, Ver 1.70.01 [10].

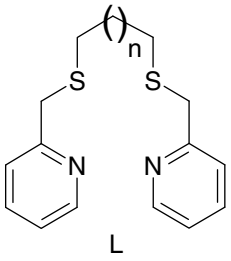
3. Result and discussion

3.1. Synthesis and characterization

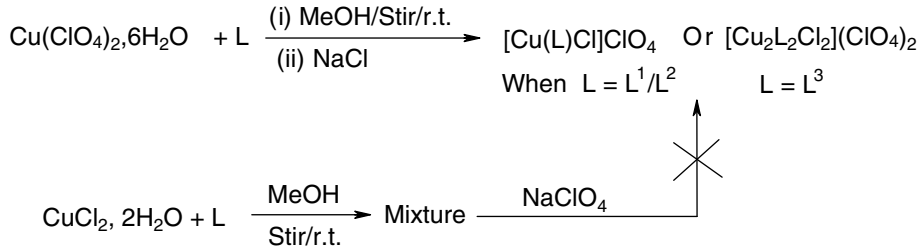
The organic compounds (L) were synthesized by the reaction of the respective alkyl dithiol compound with 2-picolyl chloride in

Table 1
Crystal data and details of refinements for **1**, **2** and **4**

	1	**2**	**4**.0 · $5H_2O$
Empirical formula	$C_{14}H_{16}Cl_2CuN_2O_4S_2$	$C_{15}H_{18}Cl_2CuN_2O_4S_2$	$C_{32}H_{41}Cl_2Cu_2N_4O_{8.5}S_4$
Formula weight	474.85	488.87	943.91
Crystal system	triclinic	monoclinic	orthorhombic
Space group	$\overline{P}$	$P2_1/a$	*Iba*2
a (Å)	8.2345(9)	8.5188(5)	20.331(4)
b (Å)	10.2758(10)	24.783(3)	21.310(4)
c (Å)	12.1620(11)	9.0438(12)	9.988(3)
α (°)	109.456(9)	90.00	90.00
β (°)	96.603(8)	92.586(7)	90.00
γ (°)	111.400(9)	90.00	90.00
Volume (Å^3)	870.03(15)	1907.4(3)	4327.3(18)
Z	2	4	4
ρ_{calc} (g/cm^3)	1.813	1.702	1.449
F(000)	482	996	1940
θ Range (°)	2.74–30.00	2.40–30.00	2.97–25.02
μ (Mo Kα) (mm^{-1})	1.825	1.668	1.349
Independent reflections	4824	5519	3598
Reflections with $I > 2\sigma(I)$	3343	2129	2454
R_1	0.0570	0.0418	0.0664
wR_2	0.1469	0.0760	0.1728
Goodness-of-fit	1.028	0.764	0.975



n	0	1	2
L	L^1	L^2	L^3



Scheme 1. Ligands and the reaction procedure.

presence of sodium ethoxide. These organic moieties have been confirmed by ^{1}H NMR spectral analyses. The five coordinated Cu(II) complexes with NSSN donor centers of these ligands and one chloride ion (**1, 2** and **3**) were obtained in good yield from the reaction of copper(II) perchlorate with equimolar amounts of the respective organic moieties in the methanol medium followed by the addition of aqueous sodium chloride solution at ambient temperature according to Scheme 1. Here, the sequence of the addition of anions along with Cu(II) ions to the ligand solutions is crucial. In the preparation of the complexes, it was found that the identity of the anion used was important. Thus the present complexes were obtained only when copper(II) perchlorate was used. A different series of copper(II) complexes were formed containing the decomposed product of these organic moieties and precipitated out from the reaction mixture when the organic moieties were allowed to react with copper(II) chloride in the first step. Characterization of these copper(II) complexes is in progress.

Here both monomeric **1** and **2** complexes are soluble in acetonitrile and DMF but sparingly soluble in methanol, ethanol and dichloromethane, while **3** is dimeric and soluble in DMF. At room temperature the magnetic moment (μ) of **1** and **2** is 1.81 and 1.79 B.M., respectively, while for **3** it is 1.40 B.M. per copper atom. The conductivity measurement of complexes **1** and **2** in acetonitrile shows the conductance values of 145 and 140 Λ_o mol^{-1} cm^{-1} respectively and while that of **3** in DMF is 150 Λ_o mol^{-1} cm^{-1} at 300 K. These values suggest that complexes **1** and **2** exist as 1:1 electrolytes and **3** as a 1:2 electrolyte in solution.

3.2. Structures of the Cu(II) complexes *1* and *2*

The ORTEP views of **1** and **2** with the atom numbering schemes are illustrated in Figs. 1 and 2, respectively, and a selection of bond distances and angles are listed in Table 2. In both mononuclear complexes, the copper center is coordinated by the tetradentate donor organic moiety and by a monodentate chloride ligand, but with a different geometrical disposition of the NSSN ligand in **1** and **2**. In fact, the highly distorted trigonal bipyramidal geometry about copper (II) shows axial positions occupied by the pyridyl-N donors in **1**, with chlorine and both thioether sulphur in the equatorial plane. On the other hand, in **2**, a pyridyl-N and a thioether-S reside at the axial positions, the equatorial plane consisting of the chlorine, the other pyridyl-N and thioether-S atoms. The almost

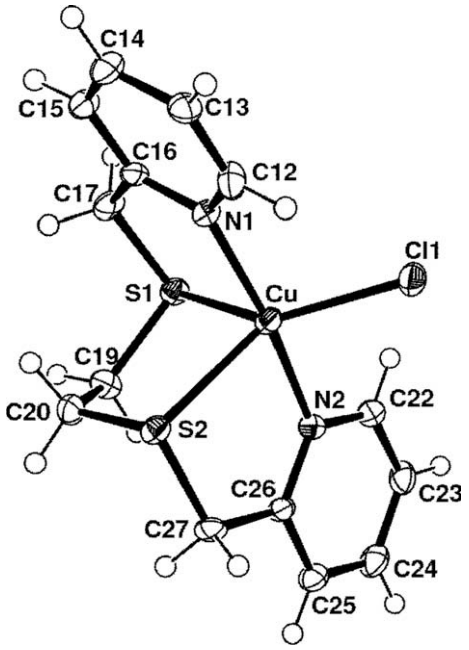


Fig. 1. ORTEP view of the cation in [Cu(L^1)Cl]ClO$_4$ (**1**) with labeling scheme.

trigonal bipyramid geometry present in complexes **1** and **2** is demonstrated by the trigonality index [11] τ of 0.619 and 0.716, respectively.

Coordination bond angles listed in Table 2 indicate large variation from the ideal geometry, especially for the atoms in the equatorial plane, indicating the strained suffered by the ligand coordinating the metal ion. In **1**, both axial bond distances Cu–N1 and Cu–N2 are comparable with their s.u. (2.006(3) and 1.994(3) Å, respectively), but in **2**, the axial Cu–N2 bond length (1.992(3) Å) is significantly shorter than the equatorial one (Cu–N1 of 2.076(3) Å) as the two pyridyl-N donors occupy different positions in the copper coordination sphere. It is worth noting that the Cl atom, located in equatorial position both in **1** and **2**, shows Cu–Cl bond length of 2.270(1) Å in **1**, and significantly longer in **2** (2.441(1) Å). The trend in Cu–Cl bond lengths follows

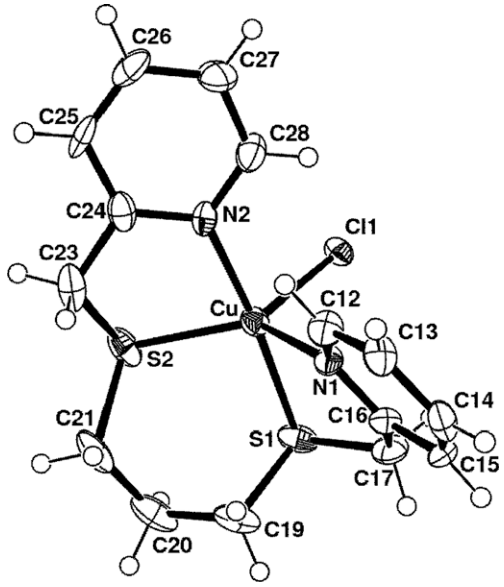


Fig. 2. ORTEP view of the molecular cation in $[Cu(L^2)Cl]ClO_4$ (**2**) with labeling scheme.

Table 2
Selected bond distances (Å) and bond angles (°) for **1**, **2** and **4**

	1	2		4
Bond distances				
Cu–S(1)	2.387(1)	2.274(1)	Cu–S(1)	2.344(2)
Cu–S(2)	2.486(1)	2.287(1)	Cu–S(2′)	2.402(3)
Cu–N(1)	2.006(3)	2.076(3)	Cu–N(1)	2.032(6)
Cu–N(2)	1.994(3)	1.992(3)	Cu–N(2′)	2.008(6)
Cu–Cl(1)	2.270(1)	2.441(1)		
Bond angles				
S(1)–Cu–S(2)	91.45(3)	92.94(4)	S(1)–Cu–S(2′)	119.47(8)
N(1)–Cu–N(2)	172.57(12)	100.85(11)	N(1)–Cu–N(2′)	129.2(2)
N(1)–Cu–S(1)	84.58(9)	81.98(8)	N(1)–Cu–S(1)	85.88(16)
N(1)–Cu–S(2)	92.03(9)	131.57(8)	N(1)–Cu–S(2′)	118.08(17)
N(2)–Cu–S(1)	89.64(9)	174.52(8)	N(2′)–Cu–S(1)	123.48(17)
N(2)–Cu–S(2)	83.44(9)	81.66(8)	N(2′)–Cu–S(2′)	84.88(17)
Cl(1)–Cu–S(1)	135.41(4)	89.32(3)		
Cl(1)–Cu–S(2)	132.99(4)	120.05(3)		
N(1)–Cu–Cl(1)	95.53(9)	108.07(7)		
N(2)-Cu-Cl(1)	91.86(9)	94.22(8)		

Symmetry code in **4** (′) $-x+1, -y+1, z$.

a reverse order with respect to the Cu–S bond distances (Table 2), which average to 2.436 Å in **1** and 2.280 Å in **2**. The Cu–Cl distance in **1** is within the range found in complexes $[Cu(L)Cl]^+$ [12], where L ligand is close comparable to L^1 by replacing pyridine by imidazolyl rings. Thus the addition of a methylene group inside the ligand leads to different donor atom arrays in **1** and **2** with a significant change in the structural geometry, likely attributable to steric constraint. This feature has been already observed by Reedijk for analogous NSSN ligands containing imidazolyl rings [11,12].

3.3. Reactivity of *3* and structure of the Cu(I) complex *4*

A colourless dinuclear copper(I) complex of formula $[Cu^I_2(L^3)_2](ClO_4)_2$, $0.5H_2O$ (**4**) was obtained from the solution of copper(II) complex (**3**) in DMF at ambient temperature in presence of air or in nitrogen atmosphere. On the other hand, the monomeric copper(II) complexes **1** and **2** in DMF showed no change *via* this type of reduction in nitrogen atmosphere even at elevated temperature. Here, 1,4-bis(2-pyridylmethylthio)butane (L^3) plays key role in DMF as no change has been observed in case of **1** and **2** under the same condition. This behavior is quite different from the observations where the ligand itself behaved as reducing agent [13,14].

Here, at the first step, DMF was hydrolysed in presence of the dimeric copper(II) complex (**3**) and in this reaction, formic acid and dimethylamine are formed as the hydrolytic products of DMF. Then formic acid as reducing agent, reacts with $[Cu_2^{II}(L^3)_2Cl_2](ClO_4)_2$ (**3**) to produce $[Cu_2^{I}(L^3)_2](ClO_4)_2$ (**4**), CO_2 and HCl. The other hydrolytic product dimethylamine reacts with HCl to form $[Me_2NH_2]Cl$. The proposed path was established following the pH decreasing of the reaction mixture associated with a colour change from blue to colourless. This observation indicates that the production of H^+ takes place in the reaction mixture and after 24 h, the pH of the solution remained unaltered. The steps of the reactions are as follows:

$$2Me_2NCHO + 2H_2O \rightarrow 2HCOOH + 2Me_2NH$$
$$2HCOOH + [Cu_2^{II}(L^3)_2Cl_2]^{2+} \rightarrow 2CO_2 + [Cu_2^{I}(L^3)_2]^{2+} + 2HCl$$
$$2Me_2NH + 2HCl \rightarrow 2\,[Me_2NH_2]Cl$$
$$2Me_2NCHO + [Cu_2^{II}(L^3)_2Cl_2]^{2+} + 2H_2O \rightarrow 2CO_2 + [Cu_2^{I}(L^3)_2]^{2+} + 2\,[Me_2NH_2]Cl$$

The presence of the HCOOH and $[Me_2NH_2]Cl$ was confirmed through GC–MS by injecting the reaction mixture into GC and detecting by mass spectrometry. Again the presence of chloride ion in the reaction mixture was confirmed as we got the precipitation of AgCl by adding a silver nitrate solution and the production of CO_2 was detected using saturated $Ca(OH)_2$ solution. The complex **4** was characterized by physicochemical tools and the molecular structure was established by single-crystal X-ray crystallography.

The reduction of the other copper(II) complexes (**1** and **2**) was observed when these species were allowed to react with formic acid but the first step of hydrolysis in DMF was not observed.

An ORTEP view of the cation of **4** with the atom numbering scheme is illustrated in Fig. 3, while a selection of bond distances and angles is listed in Table 2. The crystal structure consists of dinuclear complexes, located about a crystallographic two fold axis, and perchlorate anions. Thus the flexible NSSN ligand acts as a bis chelating agent towards the symmetry related metal ions which are separated by 8.089(2) Å. The copper exhibits a highly distorted tetrahedral coordination geometry, as evident from the coordination bond angles reported in Table 2. The Cu–S bond lengths are 2.344(2) and 2.402(3) Å, within the range measured in **1** and **2**, while the Cu–N distances are 2.032(6) and 2.008(6) Å. The chelating angles N–Cu–S (85.88(6) and 84.88(7)°) are comparable to those observed in **1** (84.58(9), 83.44(9)°), but larger than the values of **2** (81.98(8), 81.66(8)°), likely induced by the different coordination geometry in the latter species. The torsion angle of 162.6(9)° along the alkyl C atoms (anti conformation) indicates no strain in ligand L^3.

3.4. Spectral properties

Infrared spectra of all the complexes **1–4** exhibit an intense band at approximately 1090 cm^{-1} along with a weak band at 624 cm^{-1}, which have been assigned to $\nu_{s(ClO4)}$ and $\nu_{as(ClO4)}$ respectively. The $\nu_{C=N}$ band is observed at 1465–1478 cm^{-1} for all the complexes, in addition to the ν_{C-S} at 760 cm^{-1}.

The electronic absorption spectra of the complexes **1, 2** and **3** were recorded at room temperature using acetonitrile (for **1** and **2**) and dimethylformamide (for **3**) as solvent and the data has been

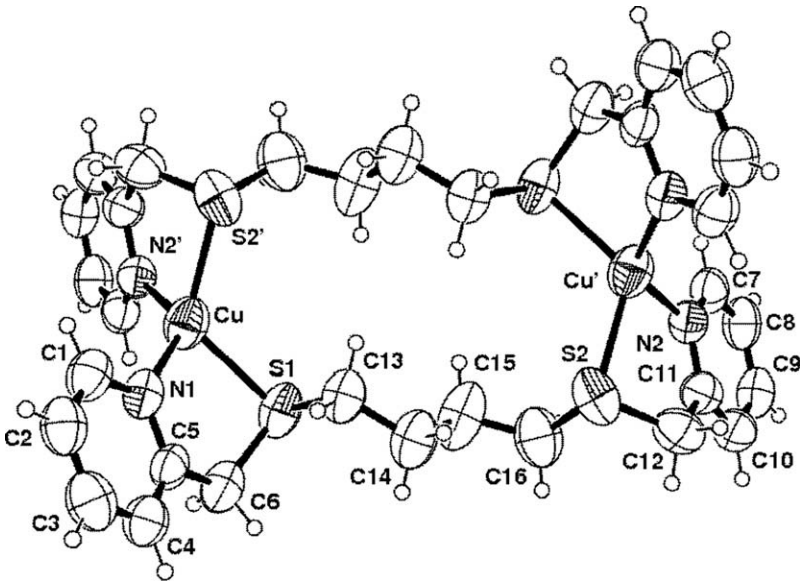


Fig. 3. ORTEP drawing of the molecular cation in $[Cu_2(L^3)_2](ClO_4)_2 \cdot 0.5H_2O$ (**4**) with labeling scheme of the crystallographic independent atoms.

tabulated in Table 3. All the spectra exhibit a band around 360 nm assignable to the $S(\sigma) \rightarrow Cu(II)$ charge transfer (LMCT) transition [15] along with the transition at high energy region corresponding to intramolecular $\pi \rightarrow \pi^*$ and $n \rightarrow \pi^*$ transitions [16]. A characteristic d-d absorption band (above 640 nm) has been also observed in the electronic spectra of these complexes. In the electronic spectra of complex **2,** a high-energy shoulder at 626 nm along with the characteristic d–d band at 667 nm is present and this result emphasizes that the stereochemistry of the complex **2** in the solution state shows a typical trigonal bypyramidal geometry, as in many cases it has been shown that the presence of a single d–d band with high energy (low wave length) shoulder is typical of this stereochemistry for copper [17].

3.5. Electrochemistry

Redox properties of complexes **1**, **2** and **3** were examined by cyclic voltammetry using a Pt-disk working electrode and a Pt-wire auxiliary electrode in dry MeOH and in presence of $[n\text{-}Bu_4N]ClO_4$ as supporting electrolyte. The potentials (Table 3) are expressed with reference to Ag/AgCl electrodes. In solution all compounds displayed a quasi-reversible voltammogram having $i_{pc}/i_{pa} \approx 1$ in the range of −340 mV to −387 mV with ΔE = 132–294 mV. Only one quasi-reversible Cu(II)/Cu(I) redox couple at negative potential was observed and it indicates that the similar chemical environment of the two copper ions in dinuclear complex **3** towards the electrochemical properties.

Table 3
UV–Vis spectral and electrochemical data[a]

Compound	λ nm (ε) (ε, $dm^3\ mol^{-1}\ cm^{-1}$)	Electrochemical data[b] $E^{o\prime}$, mV (ΔE_p, mV) (E_{pa} mV E_{pc} mV)
1	212 (s, 9,322), 261 (s, 8,442), 364 (s, 3,076), 672 (b, 238),	−340 (294) (−193, −487)
2	210 (s, 11,061), 257 (s, 8,302), 359 (s, 3,045), 626 (sh, 122), 667 (b, 249)	−387 (132) (−321, −453)
3	210 (s, 12,227), 258 (s, 8,432), 362 (s, 3,971), 646 (b, 316)	−378 (182) (−287, −469)

[a] **1** and **2** in acetonitrile, **3** in DMF.
[b] Scan rate of 100 mV s^{-1}.

4. Conclusion

Here, three tetradentate N_2S_2 neutral ligands (where L^3 is hitherto new) have been used to synthesize copper(II) complex having CuN_2S_2 chromophore. The addition of methylene group inside the ligand backbone leads to a significant change in the structural geometry and the chemistry of the organic moieties with copper. When the four methylene groups are present between the thioether-S donor atoms (in case of L^3), the chemistry of L^3 with copper is different from that of L^1 and L^2. The reduction of copper(II) in **3** resulted a new colorless dinuclear copper(I) complex of formula $[Cu^I_2(L^3)_2](ClO_4)_2$, $0.5H_2O$ (**4**) in DMF at ambient temperature in presence of air, where the complex **3** plays a key role in DMF as the complex is dimeric complex of L^3. On the other hand, the monomeric copper(II) complexes **1** and **2** in DMF showed no change *via* this type of reduction in nitrogen atmosphere even at elevated temperature.

Acknowledgements

Financial support from Council of Scientific and Industrial Research (CSIR), New Delhi, India is gratefully acknowledged. M.G.B. Drew thanks EPSRC and the University of Reading for funds for the Oxford X-Calibur system. E. Zangrando thanks MIUR-Rome, PRIN N° 2005035123 for financial support.

Appendix A. Supplementary material

CCDC 694636, 694637 and 694638 contain the supplementary crystallographic data for **1**, **2** and **4**. These data can be obtained free of charge via http://www.ccdc.cam.ac.uk/conts/retrieving.html, or from the Cambridge Crystallographic Data Centre, 12 Union Road, Cambridge CB2 1EZ, UK; fax: (+44) 1223-336-033; or e-mail: deposit@ccdc.cam.ac.uk. Supplementary data associated with this article can be found, in the online version, at doi:10.1016/j.poly.2008.08.004.

References

[1] (a) R.H. Holm, E.I. Solomon, Chem. Rev. 104 (2004) 347;
(b) T.C. Harrop, P.K. Mascharak, Acc. Chem. Res. 37 (2004) 253. and references therein;
(c) T.S. Lobana, K. Isobe, H. Kitayama, T. Nishioka, I. Kinoshita, Angew. Chem., Int. Engl. 43 (2004) 213;

(d) D. Sellmann, R. Prakash, F.W. Heinemann, Eur. J. Inorg. Chem. (2004) 1847;
(e) P.A.N. Reddy, B.K. Santra, M. Nethaji, A.R. Chakravarty, J. Inorg. Biochem. 98 (2004) 377;
(f) S. Dhar, D. Senapati, P.K. Das, P. Chattopadhyay, M. Nethaji, A.R. Chakravarty, J. Am. Chem. Soc. 125 (2003) 12118;
(g) B.K. Santra, P.A.N. Reddy, M. Nethaji, A.R. Chakravarty, J. Chem. Soc., Dalton Trans. (2001) 3553;
(h) J.J. Wilker, S.J. Lippard, J. Am. Chem. Soc. 117 (1995) 8682.

[2] (a) R.H. Holm, P. Kennepohl, E.I. Solomon, Chem. Rev. 96 (1996) 2239;
(b) M.A. Ali, S.M.G. Hossain, S.M.M.H. Majumder, M. Nazimuddin, M.T.H. Tarafder, Polyhedron 6 (1987) 1653.

[3] (a) D.T. Minkel, A.L. Saryan, D.H. Petering, Cancer Res. 38 (1978) 124;
(b) D.T. Minkel, C.H. ChanStier, D.H. Petering, Mol. Pharmacol. 12 (1976) 1036;
(c) C.H. ChanStier, D.T. Minkel, D.H. Petering, Bioinorg. Chem. 5 (1976) 203.

[4] (a) P.K. Dhara, S. Pramanik, T.H. Lu, M.G.B. Drew, P. Chattopadhyay, Polyhedron 23 (2004) 2457;
(b) P.K. Dhara, S. Pramanik, T.H. Lu, P. Chattopadhyay, J. Coord. Chem. 58 (2005) 985;
(c) P.K. Dhara, B. Das, J.M. Lo, P. Chattopadhyay, Appl. Radiat. Isot. 62 (2005) 729;
(d) P.K. Dhara, M.G.B. Drew, P. Chattopadhyay, Polyhedron 25 (2006) 1945;
(e) P.K. Dhara, M.G.B. Drew, P. Chattopadhyay, Trans.Met.Chem. 31 (2006) 740;
(f) P.K. Dhara, M.G.B. Drew, P. Chattopadhyay, J. Coord. Chem. 60 (2007) 627;
(g) P.K. Dhara, S. Sarkar, M.G.B. Drew, M. Nethaji, P. Chattopadhyay, Polyhedron 27 (2008) 2447;
(h) S. Sarkar, P.K. Dhara, M. nethaji, P. Chattopadhyay, J. Coord. Chem., in press.

[5] D.D. Perrin, W.L.F. Armarego, D.R. Perrin, Purification of Laboratory Chemicals, Pergamon Press, Oxford UK, 1981.

[6] S.E. Livingstone, J.D. Nolan, Aust. J. Chem. 23 (1970) 1553.

[7] Crys Alis, Oxford Diffraction Ltd., Version 1, 2005.

[8] Z. Otwinowski, W. Minor, Processing of X-ray diffraction data collected in oscillation mode, in: C.W. Carter Jr., R.M. Sweet (Eds.), Methods in Enzymology, vol. 276, Academic Press, New York, 1997, pp. 307–326.

[9] G.M. Sheldrick, SHELX97 Programs for Crystal Structure Analysis (Release 97-2), University of Göttingen, Germany, 1998.

[10] L.J. Farrugia, J. Appl. Crystallogr. 32 (1999) 837–838.

[11] A.W. Addision, T.N. Rao, J. Reedijk, J. van Rijn, G.C. Verschoor, J. Chem. Soc., Dalton Trans. (1984) 1349.

[12] (a) W.G. Haanstra, W.L. Driessen, R.A.G. de Graaff, J. Reedijk, Y.F. Wang, C.H. Stam, Inorg. Chim. Acta 186 (1991) 215;
(b) E. Bouwman, R. Day, W.L. Driessen, W. Tremel, B. Krebs, J.S. Wood, J. Reedijk, Inorg. Chem. 27 (1988) 4614;
(c) E. Bouwman, A. Burik, J.C.T. Hove, W.L. Driessen, J. Reedijk, Inorg. Chim. Acta 150 (1988) 125;
(d) P.J.M.W.L. Birker, J. Helder, G. Henkel, B. Krebs, J. Reedijk, Inorg. Chem. 21 (1982) 357.

[13] S. Banthia, A. Samanta, Polyhedron 25 (2006) 2269.

[14] S. Banthia, A. Samanta, Inorg. Chem. 43 (2004) 6890.

[15] T. Kita, I. Miura, N. Nakayama, T. Kawata, K. Kano, S. Hirota, M. Kodera, J. Am. Chem. Soc. 123 (2001) 7715.

[16] B.H. Chen, H.H. Yao, W.T. Huang, P. Chattopadhyay, J.M. Lo, T.H. Lu, Solid State Sci. 1 (1999) 119.

[17] (a) J. Zubieta, K.D. Karlin, J.C. Hayes, in: K.D. Karlin, J. Zubieta (Eds.), Copper Coordination Chemistry: Biochemical and Inorganic Perspectives, Adenine Press, Albany, NY, 1983, p. 97;
(b) Y. Nakao, M. Onoda, T. Sakurai, A. Nakahara, I. Kinoshita, S. Ooi, Inorg. Chim. Acta 151 (1988) 55;
(c) K.D. Karlin, J.C. Hayes, S. Juen, J.P. Hutchinson, J. Zubieta, Inorg. Chem. 21 (1982) 4106.

Polyhedron 28 (2009) 7–12

Contents lists available at ScienceDirect

Polyhedron

journal homepage: www.elsevier.com/locate/poly

Photophysical properties of copper(I) and zinc(II) complexes containing phosphinoquinoline ligands

Toshiaki Tsukuda *, Chikamine Nishigata, Kodai Arai, Taro Tsubomura *

Department of Applied Chemistry, Faculty of Engineering, Seikei University, Musashino, Tokyo 180-8633, Japan

ARTICLE INFO

Article history:
Received 15 May 2008
Accepted 28 August 2008
Available online 18 November 2008

Keywords:
d10 Transition metal complexes
Phosphinoquinoline ligand
X-ray crystal structures
Luminescent properties

ABSTRACT

Several copper(I) and zinc(II) complexes with 8-(diphenylphosphino)quinoline (PPh_2qn) or 8-diphenylphosphinoquinaldine (PPh_2qna) have been prepared. These ligands contain both imine and phosphine moieties, which can act as coordinating groups. X-ray analysis of the Cu(I) complexes reveals that $[Cu(PPh_2qn)_2]PF_6$ (**Cu-1**) and $[Cu(PPh_2qn)_2]PF_6$ (**Cu-2**), coordinated by two PPh_2qn and PPh_2qna ligands respectively, are obtained. In the Zn(II) complexes, a structural study shows that $[ZnCl_2(PPh_2qn)]$ (**Zn-1**), $[ZnBr_2(PPh_2qn)]$ (**Zn-2**) and $[ZnI_2(PPh_2qn)]$ (**Zn-3**) are coordinated by one PPh_2qn ligand and two of the corresponding halogeno ligands (Cl^-, Br^- and I^-). In the solid state **Cu-1** and **Cu-2** show luminescence which is assigned to a ^{3}MLCT transition involving π^* of the quinoline group, as shown in the $[Cu(dmp)(diphosphine)]^+$ complexes; due to the reduced bulkiness of the coordination sphere around the copper atom, no emission is observed in solution. **Zn-1** shows a similar emission band to that of free PPh_2qn at both room temperature and 77 K. It suggests the emission bands should be assigned to a ligand-centered (LC) transition. In the solid state, it is found that the emissive energy of the complexes shift to lower energy and the energy depends on the halogeno ligands in the zinc complexes.

© 2008 Elsevier Ltd. All rights reserved.

1. Introduction

Much attention has been paid to emissive copper(I) complexes containing polypyridine and/or phenanthroline ligands as candidates for practical components for chemical sensors, display devices and solar-energy conversion schemes [1]. In contrast to the hitherto reported heavy metal complexes, the copper-based system is promising due to the comparative cost advantage. Recently, extensive studies of some mixed-ligand copper(I) complexes involving both imines and phosphines have been reported [2–6]. $[Cu(dmp)(DPEphos)]^+$ (DPEphos = bis[2-(diphenylphosphino)-phenyl]ether) exhibits an unprecedented high quantum yield and a long lifetime in CH_2Cl_2 at room temperature [3,4]. Armaroli et al. and our group have also studied the emissive properties of the mixed-ligand $[Cu(dimine)(diphosphine)]^+$ type complexes coordinated by a diimine ligand such as dmp and several types of diphosphine ligand [5,6]. As other alternatives to heavy metal complexes, several zinc(II) complexes with quinoline groups are potentially promising as luminescent probes and as emissive compounds in electroluminescent devices [7,8].

8-Quinolylphosphine derivatives, which have both imine and phosphine moieties, can act as bidentate ligands. Structural studies of several transition metal complexes with 8-diphenylphosphinoquinoline(PPh_2qn) (Chart 1, left) have been reported [9–11]. Photochemical and photophysical properties of several mixed-ligand ruthenium(II) polypyridine complexes with 8-quinolylphosphines have been investigated [12]. It is expected that copper(I) complexes containing this type of ligand can also behave as good emitters, because the ligands have both diimine and phosphine character. As a similar system, dinuclear copper(I) complexes bridged by 2-(diphenylphosphino)pyridine (PPh_2py) ligands have been reported [13]. However, the dinuclear complexes do not keep a rigid structure in solution due to coordination of donor solvent as well as a PPh_2py exchange process. In contrast, PPh_2qn, which can coordinate to a metal center in a chelate fashion, appears to provide discrete compounds even in solution.

We found that the $[Cu(PPh_2qn)_2]^+$ complex is readily prepared and shows emission in the solid state. In this study, the luminescence of such copper(I) complexes with phosphinoquinoline derivatives has been examined. In addition, treatment of zinc

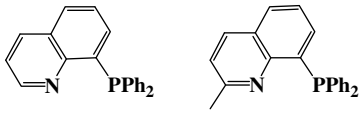


Chart 1. PPh_2qn (left) and PPh_2qna (right).

* Corresponding authors. Tel.: +81 422373759; fax: +81 422373871 (T. Tsukuda), tel.: +81 422373752; fax: +81 422373871 (T. Tsubomura).
E-mail addresses: tsukuda@st.seikei.ac.jp (T. Tsukuda), tsubomura@st.seikei.ac.jp (T. Tsubomura).

0277-5387/$ - see front matter © 2008 Elsevier Ltd. All rights reserved.
doi:10.1016/j.poly.2008.08.028

halogenide with PPh_2qn readily gave the corresponding [ZnX_2-(PPh_2qn)] complexes (X = Cl, Br and I). Zinc complexes coordinated by phosphorus atoms are rare. The luminescence of these complexes are observed in both CH_2Cl_2 solution and in the solid state. In this work, the photophysical properties of the complexes are described in detail.

2. Experimental

2.1. General

8-(Diphenylphosphino)quinoline (PPh_2qn) [14] and [$Cu(CH_3CN)_4$]PF_6 [15] were prepared by the literature methods. 8-(Diphenylphosphino)quinaldine (PPh_2qna) (Chart 1, right) was synthesized by a similar method to that of PPh_2qn, with the use of 8-chloroquinaldine [16]. Each zinc halogenide was purchased from WAKO Chemical Co. Ltd. All reactions were carried under an argon atmosphere using Schlenk techniques until air-stable solid complexes were obtained. Elemental analyses of the complexes were performed on a Perkin Elmer model 2400 CHN analyzer. NMR spectra were obtained using a JEOL Λ-400 spectrometer, in which the chemical shifts are referenced to tetramethylsilane (^1H; as internal) or 85% H_3PO_4 ($^{31}P\{^1H\}$; as external). Absorption and emission spectra were measured with an Agilent 8453 spectrometer and a Shimadzu RF-5000 fluorometer, respectively.

2.2. General procedure to prepare the Cu complexes

PPh_2qn (58 mg, 0.184 mmol) or PPh_2qna (60 mg, 0.183 mmol) was added to a solution of [$Cu(CH_3CN)_4$]PF_6 (34 mg, 0.092 mmol) in $CHCl_3$ (10 ml). The mixture was continuously stirred for 1 h, then the solution was evaporated to a small volume. Addition of diethyl ether to the solution afforded a pale orange precipitate.

[Cu(PPh_2qn)$_2$]PF_6 (Cu-1): Yield: 51 mg (66%). *Anal.* Calc. for [$Cu(C_{21}H_{16}NP)_2$]PF_6 C, 60.40; H, 3.86; N, 3.25. Found: C, 60.22; H, 3.70; N, 3.22%. ^1H NMR ($CDCl_3$) δ 8.49 (d, 1H), 8.18 (d, 2H), 7.96 (d, 1H), 7.79 (t, 1H), 7.31–7.48 (m, 11H). ^{31}P NMR ($CDCl_3$): δ −16.1 (br).

[Cu(PPh_2qna)$_2$]PF_6 (Cu-2): Yield: 48 mg (56%). *Anal.* Calc. for [$Cu(C_{22}H_{18}NP)_2$]PF_6: C, 61.22; H, 4.20; N, 3.25. Found: C, 59.77; H, 4.04; N, 3.07%. ^1H NMR ($CDCl_3$) δ 8.42 (d, 1H), 8.16 (d, 1H), 7.83–7.87 (m, 1H), 7.72 (t, 1H), 7.47 (d, 1H), 7.14–7.20 (m, 10H), 2.0 (s, 3H). ^{31}P NMR ($CDCl_3$): δ −19.2 (br).

2.3. General procedure to prepare the Zn complexes

A solution of $ZnCl_2$, $ZnBr_2$ or ZnI_2 (1.0 mmol) in ethanol (5 ml) was dropped into a solution of PPh_2qn (0.157 g, 0.5 mmol) dissolved in 5 ml $CHCl_3$. The precipitated white powder was filtered and washed with a small amount of ethanol.

[$ZnCl_2$(PPh_2qn)] (Zn-1): Yield 0.15 g (67%). *Anal.* Calc. for [$ZnCl_2(C_{21}H_{16}NP)$]: C, 56.10; H, 3.59; N, 3.12. Found: C, 55.30; H, 3.34; N, 2.96%. ^1H NMR ($CDCl_3$) δ 9.21 (d, 1H), 8.54 (d, 1H), 8.16 (d, 1H), 7.99 (t, 1H), 7.80 (br, 2H), 7.66–7.70 (m, 4H), 7.47–7.53 (m, 6H). ^{31}P NMR ($CDCl_3$): δ −34.3

[$ZnBr_2$(PPh_2qn)] (Zn-2): Yield 0.18 g (67%). *Anal.* Calc. for [$ZnBr_2(C_{21}H_{16}NP)$]: C, 46.84; H, 2.99; N, 2.60. Found: C, 55.30; H, 3.34; N, 2.96%. ^1H NMR ($CDCl_3$) δ 9.23 (d, 1H), 8.54 (d, 1H), 8.17 (d, 1H), 7.99 (t, 1H), 7.79–7.83 (m, 2H), 7.66–7.70 (m, 4H), 7.46–7.53 (m, 6H). ^{31}P NMR ($CDCl_3$): δ −36.0.

[ZnI_2(PPh_2qn)] (Zn-3): Yield 0.12 g (38%). *Anal.* Calc. for [$ZnI_2(C_{21}H_{16}NP)$]: C, 39.88; H, 2.55; N, 2.21. Found: C, 55.30; H, 3.34; N, 2.96%. ^1H NMR ($CDCl_3$): δ 9.29 (d, 1H), 8.55 (d, 1H), 8.18 (d, 1H), 7.98 (t, 1H), 7.81–7.84 (m, 2H), 7.65–7.70 (m, 4H), 7.45–7.53 (m, 6H). ^{31}P NMR ($CDCl_3$): δ −37.3.

2.4. X-ray measurements

X-ray crystallographic measurements were made on a Rigaku AFC-5S (for **Cu-1**, **Cu-2** and **Zn-1** at 296 K) or a Rigaku Saturn 70 CCD area detector (for **Zn-2** and **Zn-3** at 123 K) with graphite-monochromated Mo Kα radiation. Absorption corrections were made by the numerical method. Each structure was solved by direct methods (SIR92 [17]) and refined by full matrix least square procedures (SHELXL-97 [18]). The non-hydrogen atoms were refined anisotropically and the hydrogen atoms were fixed at calculated positions. All calculations were carried out by CRYSTAL STRUCTURE software.[1]

3. Results and discussion

3.1. Preparation and characterization of the Cu(I) complexes

Since PPh_2qn has both phosphine-P and imine-N donor atoms, the coordination of two PPh_2qn ligands to the copper(I) ion leads to a similar structure to that of mixed-ligand complexes with diphosphine and diimine ligands. The reaction of [$Cu(CH_3CN)_4$]PF_6 with a two equivalent molar amount of PPh_2qn in $CHCl_3$ readily gave a pale yellow powder of the bis-PPh_2qn copper(I) complex **Cu-1**. The product was identified by elemental analysis and ^1H and $^{31}P\{^1H\}$ NMR spectra. The ^1H NMR spectrum of **Cu-1** shows a symmetric signal set; *e.g.* only one doublet assigned to the proton in the 2-position on a quinoline ring at δ 8.5 appeared The ^{31}P NMR spectrum of **Cu-1** shows a relatively broad signal at δ −16.1, whereas the signal of free PPh_2qn is sharp at δ −17.0. If the signal broadening results from a rapid exchange between the coordination and dissociation of a PPh_2qn ligand in solution, lowering the temperature may cause further broadening based on the splitting of signals assigned to the coordinated and the free ligand. However, the measurement of the ^{31}P NMR spectrum at −40 °C shows a slight sharpening of the signal. So the signal broadening could result from quadrapolar relaxation arising from the copper nucleus, which has been observed for $[Cu(dmpe)]^+$ (dmpe = 1,2-bis(dimethylphosphino)ethane) [19].

Single crystals suitable for X-ray analysis were obtained by slow diffusion of diethylether into an acetone solution of the complex. The molecular structure of [$Cu(PPh_2qn)_2$]PF_6 is illustrated in Fig. 1, and detailed crystallographic data are shown in Table S1. In this complex, the copper atom is coordinated by two bidentate PPh_2qn ligands and has a four-coordinate structure with tetrahedral geometry. Selected bond lengths and angles are summarized in Table 1. The bond lengths of Cu–P are 2.220(1) and 2.229(1) Å. The bite angles for the chelate ring formed by the two PPh_2qn ligands are 87.4(1)° and 86.4(1)°, which are comparable to the other complexes containing PPh_2qn [12b]. The chelate rings are almost planar, as is evident from the torsion angles of Cu–P(1)–C(7)–C(8) (2.4(3)°) and Cu–N(1)–C(8)–C(7) (0.3(5)°). The P–Cu–P bond angle is 131.12(5)°, which is similar to that of [Cu(dmp)(DPEphos)]BF_4. One quinoline ring is arranged parallel to the quinoline ring on an adjacent molecule, and the interplanar distance between the quinoline rings is 3.6 Å.

The reaction of PPh_2qna instead of PPh_2qn with [$Cu(CH_3CN)_4$]PF_6 gave **Cu-2**. This product was also identified by elemental analysis and ^1H and $^{31}P\{^1H\}$ NMR spectra. Just as the case of **Cu-1**, a symmetrical signal set for **Cu-2** in the ^1H NMR spectrum was obtained. A methyl singlet of **Cu-2** was observed at δ 2.00, which is shifted to higher field compared to that of free PPh_2qna (δ 2.57)

[1] CrystalStructure, ver.3.60: Single Crystal Structure Analysis Software, Molecular Structure Corporation.

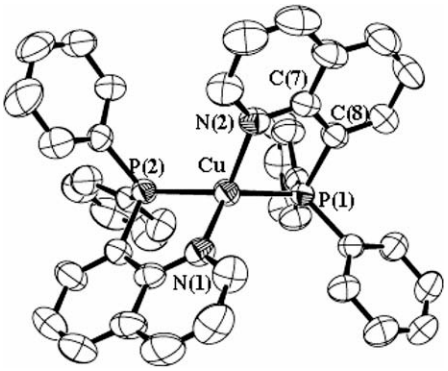


Fig. 1. ORTEP structure of **Cu-1**.

Table 1
Selected bond lengths (Å) and angles (°) for **Cu-1** and **Cu-2**.

Cu-1		**Cu-2**	
Cu–P(1)	2.220 (1)	Cu–P(1)	2.227 (2)
Cu–P(2)	2.229 (1)		
Cu–N(1)	2.071 (4)	Cu–N(1)	2.081 (3)
Cu–N(2)	2.073 (4)		
P(1)–Cu–P(2)	131.12 (5)	P(1)–Cu–P(1)*	118.27 (8)
N(1)–Cu–N(2)	112.1 (1)	N(1)–Cu–N(1)*	112.7 (2)
P(1)–Cu–N(1)	125.4 (1)	P(1)–Cu–N(1)	87.7 (1)
P(2)–Cu–N(2)	116.2 (1)		
P(1)–Cu–N(2)	87.4 (1)	P(1)–Cu–N(1)*	127.5(1)
P(2)–Cu–N(1)	86.4 (1)		

on coordination. The ^{31}P NMR spectrum of **Cu-2** shows a relatively broad signal at δ −19.23.

The crystals of **Cu-2** for X-ray analysis were obtained by slow diffusion of diethylether into a chloroform solution of the complex. The structure of $[Cu(PPh_2qna)_2]PF_6$ is illustrated in Fig. 2. Just as in the case of **Cu-1**, the copper atom coordinated by two PPh_2qna ligands has a four-coordinate structure with a tetrahedral geometry, however the crystal of **Cu-2** has different space group, *C*2/*c*, compared to $P2_1/c$ for **Cu-1**, as shown in Table 1. A twofold axis goes through the copper atom. Selected bond lengths and angles are summarized in Table 2. The Cu–P and Cu–N bond lengths are 2.227(2) and 2.081(3) Å, respectively, which are similar to those of **Cu-1**. The P–Cu–P bond angle is 118.27(8)°.

3.2. Preparation and characterization of the Zn(II) complexes

The treatment of $ZnCl_2$, $ZnBr_2$ and ZnI_2 with PPh_2qn readily afforded **Zn-1**, **Zn-2** and **Zn-3**, respectively. Unlike $[Cu(PPh_2qn)_2]^+$,

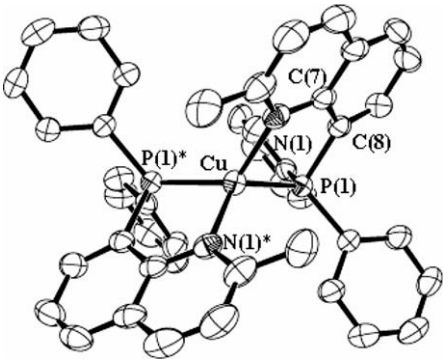


Fig. 2. ORTEP structure of **Cu-2**.

Table 2
Selected bond lengths (Å) and angles (°) for **Zn-1**, **Zn-2** and **Zn-3**.

	Zn-1 (X = Cl)	**Zn-2** (X = Br)	**Zn-3** (X = I)
Zn–X(1)	2.218(2)	2.3601(8)	2.5388(6)
Zn–X(2)	2.201(2)	2.3377(6)	2.5509(6)
Zn–P	2.395(2)	2.395(1)	2.390(1)
Zn–N	2.104(5)	2.096(5)	2.094(3)
X(1)–Zn–X(2)	116.53(6)	115.17(3)	11.9.92(2)
P(1)–Zn–N(1)	82.0(1)	82.4(1)	83.30(9)
P(1)–Zn–X(1)	112.71(6)	113.03(4)	112.53(3)
P(1)–Zn–X(2)	122.95(5)	123.98(4)	117.7(4)
N(1)–Zn–X(1)	106.9(1)	106.8(1)	114.0(1)
N(1)–Zn–X(2)	108.5(1)	108.7(1)	102.6(1)

only one PPh_2qn ligand is coordinated to the zinc(II) ion in these complexes. Attempts to prepare $[Zn(PPh_2qn)_2]$ by treatment of $Zn(PF_6)_2$ without halides failed. Preparation of the $[ZnF_2(PPh_2qn)]$ complex by treatment with ZnF_2 was also unsuccessful. The products were identified by elemental analysis and ^{1}H and ^{31}P{^{1}H} NMR spectra. In the ^{31}P NMR spectra of the complexes, a sharp singlet signal was observed between δ −34 and −39, which shifted to higher field on coordination. Such higher field shifts are hardly ever observed in other Zn(II) complexes containing phosphines [20]. It suggests that the electron density around the phosphorus atom is considerably increased by either the zinc atom or the coordinated halides.

Recrystallization of the zinc complexes did not give single crystals available for X-ray analysis, whereas they were directly obtained by slowly mixing both solutions of PPh_2qn in $CHCl_3$ and ZnX_2 in CH_3OH. The molecular structures of **Zn-1**, **Zn-2** and **Zn-3** are illustrated in Fig. 3. It was found that the PPh_2qn ligand coordinates to the zinc center with two halide ions. Selected bond lengths and angles are summarized in Table 2. and crystallographic data are described in Table S2. The Zn–P bond lengths in these complexes range from 2.390(1) to 2.395(1) Å. Especially, **Zn-3** has the shortest bond length of the reported zinc complexes containing aryl phosphine derivatives [21–23]. The Zn–X bond lengths increase in the order of the following halide ions, Cl, Br and I, however there are no notable differences in the other bond lengths (*e.g.* Zn–N bonds) and bond angles in the three complexes. So the three complexes have a similar coordination environment with regard to PPh_2qn.

3.3. Photophysical properties of the complexes containing phosphinoquinoline ligands

The absorption spectra of **Cu-1** and **Cu-2** in CH_2Cl_2 are shown in Fig. 4. Each complex shows an absorption ranging from 380 to 450 nm, which is not observed for the corresponding free phosphinoquinoline ligand. The Cu–diimine MLCT bands are known to be observed in the region 400–360 nm, with an absorption coefficient of the order of 1.0×10^3 mol^{-1} dm^3 cm^{-1} for mononuclear Cu–P_2N_2 complexes [3–6]. It suggests that the absorption bands of **Cu-1** and **Cu-2** are assigned to the MLCT transition from the Cu(I) center to the quinoline moiety. The enhancement of the absorption intensity in the region from 300 to 340 nm for each complex stems from the coordination of the two ligands in one complex molecule. The bands are assigned to the quinoline-based intraligand π–π^* transition, as reported for the ruthenium(II) complexes containing PPh_2qn [12].

Cu-1 and **Cu-2** show emission in the solid state as shown in Fig. 5. The emission maximum of **Cu-1** is located at *ca.* 640 nm. The emission lifetime is estimated at 0.33 μs from the emission decay curve fitted with a single exponential function. The luminescent properties, which are comparable to that of $[Cu(dmp)(diphosphine)]^+$, suggests that the emission band is assigned to

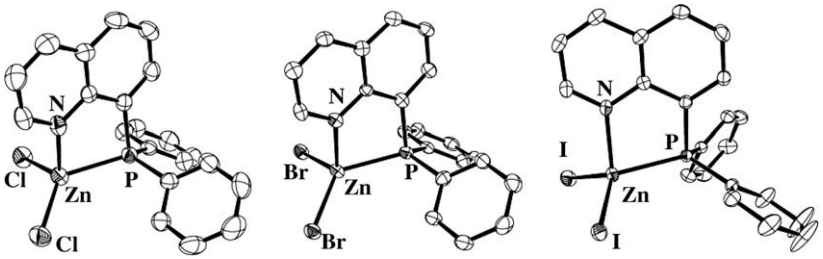


Fig. 3. ORTEP structures of **Zn-1** (left), **Zn-2** (middle) and **Zn-3** (right).

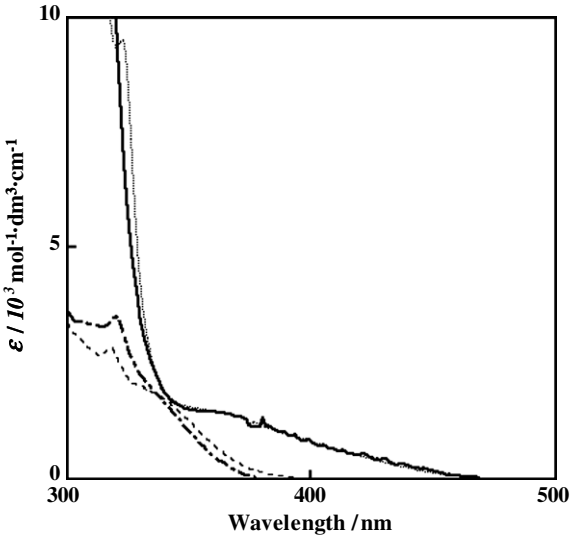


Fig. 4. Absorption spectra of **Cu-1** (solid line), **Cu-2** (dotted line), PPh_2qn (dashed line) and PPh_2qna (dashed-dotted line) in CH_2Cl_2.

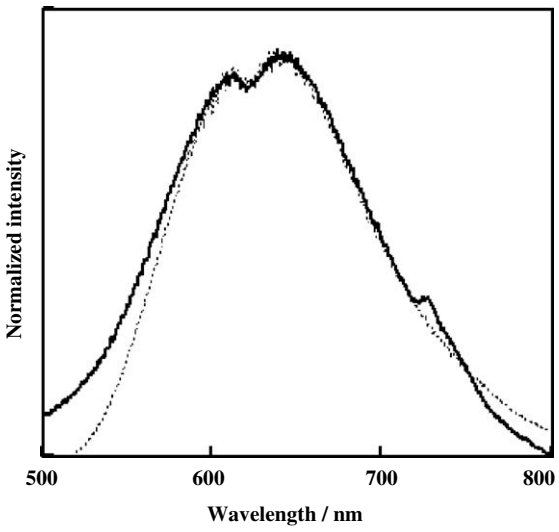


Fig. 5. Emission spectra (uncorrected) of **Cu-1** (solid line) and **Cu-2** (dotted line) in the solid state.

^{3}MLCT transition involving π^* of the quinoline group. The assignment is consistent with the suggestion that no emission is observed in solution because of the lower bulkiness of the coordination sphere around the copper atom in the complex structure, facilitating a tetragonal flattening distortion of the excited luminophore and/or attack of solvent molecules to the excited one in solution. The emission maximum of **Cu-2** is similar to that of **Cu-1**. However, the emission lifetime of **Cu-2** is ca. 1.0 μs, which is three times longer than that of **Cu-1**. In the case of copper(I) complexes containing dmp, it has already been shown that the steric effect of methyl-substituted groups usually results in a higher quantum yield and a longer emission lifetime [2–5]. However, as described in the X-ray structure, the coordination sphere around copper in **Cu-2** is not bulky enough to inhibit quenching of the excited states to emit in solution, even in the presence of the methyl-substituted group in PPh_2qna.

The absorption spectra of the zinc complexes are shown in Fig. 6. All the zinc complexes show similar absorption spectra. Although the free PPh_2qn ligand has an absorption band ranging from 330 to 370 nm, the zinc complexes show smaller intensity in this region. It suggests that the band is assigned to the n–π^* charge transfer transition from the lone pair on the phosphorus atom to the quinoline ring. This type of transition for some metal complexes was reported to have character similar to a protonated aryl phosphine, involving a shift to higher energies compared to the free phosphine [24].

Among the three Zn complexes, only **Zn-1** shows luminescence in CH_2Cl_2 solution at room temperature. As shown in Fig. 7, the emission spectrum of **Zn-1** is similar to that of free PPh_2qn. Therefore, the emission bands are assigned to the ligand-centered (LC) transition. Dissociation of PPh_2qn from **Zn-1** is not suggested because the ^{31}P NMR spectrum of **Zn-1** shows a sharp singlet, as described above. The emission lifetime of **Zn-1** is too short to be measured (<20 ns). It suggests that the emission is fluorescent.

The emission spectra in frozen CH_2Cl_2 at 77 K of **Zn-1** and free PPh_2qn show emission maxima at 535 and 530 nm, respectively (Fig. 7). The spectra were independent of the excitation wave-

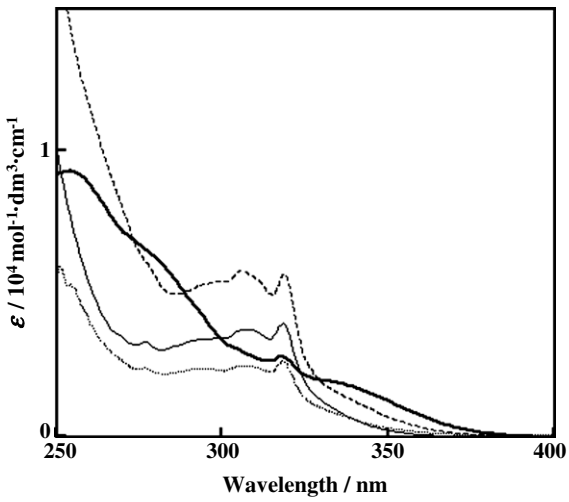


Fig. 6. Absorption spectra of PPh_2qn (bold solid line), **Zn-1** (solid line), **Zn-2** (dotted line) and **Zn-3** (dashed line) in CH_2Cl_2 solution.

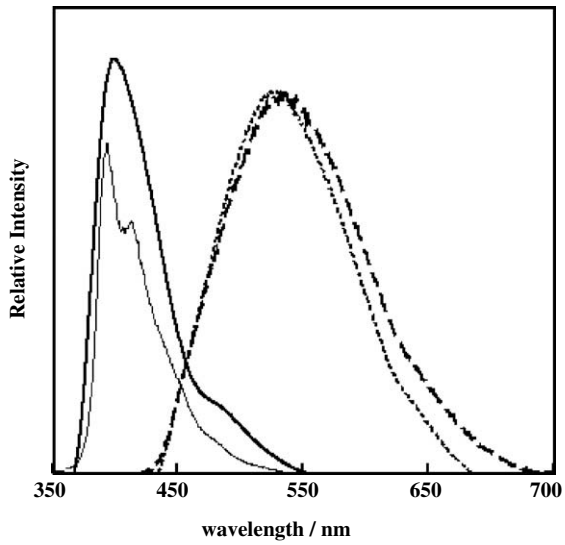


Fig. 7. Emission spectra (uncorrected) of **Zn-1** and PPh_2qn in CH_2Cl_2; **Zn-1** at 298 K (solid line), PPh_2qn at 298 K (bold solid line), **Zn-1** at 77 K (dashed line) and PPh_2qn at 77 K (dotted line).

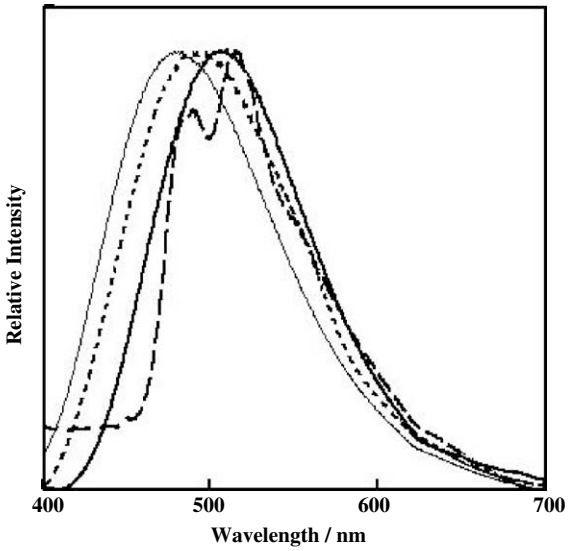


Fig. 8. Emission spectra of PPh_2qn (bold solid line) **Zn-1** (solid line), **Zn-2** (dotted line), **Zn-3** (dashed line) in the solid state at room temperature.

length, over the range 330–350 nm. Fife et al. have reported that the emission spectrum of $[ZnCl_2(PPh_2Me)]$ in diethylether–isopentane–ethanol glass at 77 K show a slightly higher energy emission maximum, at *ca.* 420 nm, than that of free PPh_2Me [24]. The emission band of **Zn-1** is also similar to that of $[Ru(bpy)_2(PPh_2qn)]$ observed in EtOH/MeOH glass at 77 K, which is assigned to a quinoline based $^3(\pi-\pi^*)$ transition [12]. In the case of zinc(II) complexes, a high promotion energy does not result in low-energy MLCT excited states [24]. Thus unlike the Cu(I) complexes, the emission band is assigned to not a metal-to-ligand but to a ligand-centered transition, maybe typically the $(\pi-\pi^*)$ transition in the quinoline ring. One more possibility is a $(n-\pi^*)$-like charge transfer from the Zn–P σ-bond orbital to the π^* orbital on the quinoline ring. However, such a CT emission should be observed at higher energy than that of the corresponding free phosphine [24]. The slight low-energy shift of the emission on coordination to the Zn center suggests that the emission is originates from $\pi-\pi^*$ states.

The emission spectra of the zinc complexes and the free ligand have been obtained in the solid state and are shown in Fig. 8. The emission band of **Zn-1** at *ca.* 500 nm is shifted to lower energy than that in solution, whereas the lifetime is very short (<20 ns). The emission maxima of **Zn-1** and **Zn-2** are slightly shifted to higher energy compared to that of the free PPh_2qn, whereas that of **Zn-3** is observed in the lower energy region and involves vibrational structure; thus the heavier the halogen in the zinc complex, the lower the energy of the emission. The emission energy dependence on the coordinated halogenide ions and structural similarity involving the Zn-PPh_2qn moiety between the complexes suggest that the halogen-to-ligand charge transfer (XLCT) from halogenide to quinoline ring may contribute to the emissive excited states. However, it should be noted that the absorption bands ranging from 300 to 330 nm hardly show any dependence on the halogenide ion, so the character of the excited states associated with the absorption, which may be $\pi-\pi^*$ of the quinoline ring, may differ from that of the emissive excited states.

4. Conclusion

The utilization of PPh_2qn or PPh_2qna, containing both imine and phosphine moieties, successfully gives the new copper complexes **Cu-1** and **Cu-2**, respectively. Both complexes have similar structures to those of mixed-ligand complexes with a P_2N_2 donor set. In the solid state, both Cu(I) complexes show an emission assigned to ^{3}MLCT. However, no emission is observed in solution, even for **Cu-2** coordinated by PPh_2qna which has a bulkier group than PPh_2qn. The bulkiness in the coordination sphere around the copper atom should be smaller than that of the reported mixed-ligand [Cu(dmp)(diphosphine)]-type complexes.

Meanwhile, a series of Zn(II) complexes coordinated by only one PPh_2qn ligand and two halogenide ions was also prepared. All the complexes are stable in solution, and each sharp singlet signal was shifted to amazingly higher field on coordination. Structural characterization shows the similarity of the coordination environment around the PPh_2qn ligand for the three complexes. **Zn-1** shows a similar emission band to that of free PPh_2qn at both room temperature and 77 K. It suggests the emission bands are assigned to a ligand-centered (LC) transition. In the solid state, it is found that the emissive energy of the complex is shifted to lower energy for the series, $Cl^- > Br^- > I^-$. A contribution of the halogenide orbitals in the emissive states is suggested Chart 1.

Appendix A. Supplementary data

CCDC 683537, 683538, 683539, 683540 and 683541 contain the supplementary crystallographic data for **Cu-1**, **Cu-2**, **Zn-1**, **Zn-2** and **Zn-3**. These data can be obtained free of charge via http://www.ccdc.cam.ac.uk/conts/retrieving.html, or from the Cambridge Crystallographic Data Centre, 12 Union Road, Cambridge CB2 1EZ, UK; fax: (+44) 1223-336-033; or e-mail: deposit@ccdc.cam.ac.uk. X-ray crystallographic data of the Cu(I) and Zn(II) complexes are shown in Figs. S1 and S2, respectively. Supplementary data associated with this article can be found, in the online version, at doi:10.1016/j.poly.2008.08.028.

References

[1] (a) See reviews as follows: D.R. McMillin, K.M. McNett, Chem. Rev. 98 (1998) 1201;
(b) N. Armaroli, Chem. Soc. Rev. 30 (2001) 113;
(c) D.V. Scaltrito, D.W. Thompson, J.A. O'Callaghan, G.J. Meyer, Coord. Chem. Rev. 208 (2000) 243.
[2] (a) C.E.A. Palmer, D.R. McMillin, Inorg. Chem. 26 (1987) 3837;
(b) R.A. Rader, D.R. McMillin, M.T. Buckner, T.G. Matthews, D.J. Casadonte, R.K. Lengel, S.B. Whittaker, L.M. Darmon, F.E. Lytle, J. Am. Chem. Soc. 103 (1981) 5906;

(c) J.R. Kirchhoff, D.R. McMillin, W.R. Robinson, D.R. Powell, A.T. McKenzie, S. Chen, Inorg. Chem. 24 (1985) 3928.
[3] (a) S.-M. Kuang, D.G. Cuttell, D.R. McMillin, P.E. Fanwick, R.A. Walton, Inorg. Chem. 41 (2002) 3313;
(b) D.G. Cuttell, S.-M. Kuang, P.E. Fanwick, D.R. McMillin, R.A. Walton, J. Am. Chem. Soc. 124 (2002) 6.
[4] N. Armaroli, G. Accorsi, G. Bergamini, P. Ceroni, M. Holler, O. Moudam, C. Duhayon, B.D. Nicot, J.F. Nierengarten, Inorg. Chim. Acta 360 (2007) 1032.
[5] (a) K. Saito, T. Arai, T. Tsukuda, T. Tsubomura, J. Chem. Soc., Dalton Trans. (2006) 4444;
(b) K. Saito, T. Tsukuda, T. Tsubomura, Bull. Chem. Soc. Jpn. 79 (2006) 437;
(c) T. Tsukuda, A. Nakamura, T. Arai, T. Tsubomura, Bull. Chem. Soc. Jpn. 79 (2006) 288;
(d) T. Tsubomura, N. Takahashi, K. Saito, T. Tsukuda, Chem. Lett. 33 (2004) 678.
[6] (a) A. Barbieri, G. Accorsi, N. Armaroli, Chem. Commun. (2008) 2185;
(b) N. Armaroli, G. Accorsi, M. Holler, O. Moudam, J.-F. Nierengarten, Z. Zhou, R.T. Wegh, R. Welter, Adv. Mater. 18 (2006) 1313.
[7] M. Ghedini, M. La Deda, I. Aiello, A. Grisolia, J. Chem. Soc., Dalton Trans. (2002) 3409.
[8] L.S. Sapochak, F.E. Benincasa, R.S. Schofield, J.L. Baker, K.K.C. Riccio, D. Fogarty, H. Kohlmann, K.F. Ferris, P.E. Burrows, J. Am. Chem. Soc. 124 (2002) 6119.
[9] H.A. Hudali, J.V. Kingston, H.A. Tayim, Inorg. Chem. 18 (1979) 1391.
[10] K. Issleib, M. Haftendorn, Z. Anorg. Allg. Chem. 389 (1972) 263.
[11] P. Wehman, H.M.A. van Donge, A. Hagos, P.C.J. Kamer, P.W.N.M. van Leeuwen, J. Organomet. Chem. 535 (1997) 183.
[12] (a) T. Suzuki, T. Kuchiyama, S. Kishi, S. Kaizaki, H.D. Takagi, M. Kato, Inorg. Chem. 42 (2003) 785;
(b) T. Suzuki, T. Kuchiyama, S. Kishi, S. Kaizaki, M. Kato, Bull. Chem. Soc. Jpn. 75 (2002) 2433.
[13] E. Lastra, M.P. Gamasa, J. Gimeno, M. Lanfranchi, A. Tiripicchio, J. Chem. Soc., Dalton Trans. (1989) 1499.
[14] R.D. Feltham, H.G. Metzger, J. Orgnomet. Chem. 33 (1971) 347.
[15] G.J. Kubas, Inorg. Synth. 19 (1979) 90.
[16] V.I. Minkin, J. Gen. Chem. (USSR) 30 (1960) 2742.
[17] SIR-92 A. Altomare, M.C. Burla, M. Camalli, M. Cascarano, C. Giacovazzo, A. Guagliardi, G.J. Polidori, Appl. Crystallogr. 27 (1994) 435.
[18] G.M. Sheldrick, SHELXL-97, Program for crystal determination and refinement, University of Göttingen, Germany, 1997.
[19] B. Mohr, E.E. Brooks, N. Rath, E. Deutsch, Inorg. Chem. 30 (1991) 4541.
[20] M. Bochmann, G.C. Bwembya, R. Grinter, A.K. Powell, K.J. Webb, M.B. Hursthouse, K.M.A. Abdul Malik, M.A. Mazid, Inorg. Chem. 33 (1994) 2290.
[21] D. Ellis, L.J. Farrugia, D.T. Hickman, P.A. Lovatt, R.D. Peacock, Chem. Commun. (1996) 1817.
[22] F.A. Cotton, S.A. Duraj, W.J. Roth, C.D. Schmulbach, Inorg. Chem. 24 (1985) 525.
[23] R.E. Desimone, G.D. Stucky, Inorg. Chem. 24 (1985) 525.
[24] D.J. Fife, W.M. Moore, K.W. Morse, Inorg. Chem. 23 (1984) 1545.

Polyhedron 28 (2009) 13–26

Contents lists available at ScienceDirect

Polyhedron

journal homepage: www.elsevier.com/locate/poly

Investigations of bis(methyltetrazolyl)triazenes as nitrogen-rich ingredients in solid rocket propellants – Synthesis, characterization and properties

Thomas M. Klapötke *, Norma K. Minar, Jörg Stierstorfer

Ludwig-Maximilian University Munich, Energetic Materials Research, Department of Chemistry and Biochemistry, Butenandtstr. 5-13, D-81377 Munich, Germany

ARTICLE INFO

Article history:
Received 4 September 2008
Accepted 25 September 2008
Available online 1 November 2008

Keywords:
Solid rocket propellants
Tetrazoles
Bis(tetrazolyl)triazenes
Crystal structures
Detonation parameter
Sensitivities

ABSTRACT

The energetic nitrogen-rich compounds 1,3-bis(1-methyltetrazol-5-yl)triaz-1-ene (**4**) and 1,3-bis(2-methyltetrazol-5-yl)triaz-1-ene (**5**) were synthesized by diazotation of 1-methyl-5-aminotetrazole (**2**) and 2-methyl-5-aminotetrazole (**3**), respectively, by using half an equivalent of sodium nitrite. The reaction of **4** and **5** with diluted ammonia solution yields ammonium bis(1-methyltetrazol-5-yl)triazenate (**6**) and ammonium bis(2-methyl-tetrazol-5-yl)triazenate (**7**). Treating of **4** and **5** with aqueous sodium hydroxide solution yields sodium bis(1-methyltetrazol-5-yl)triazenate (**8**) and sodium bis(2-methyltetrazol-5-yl)triazenate (**9**) almost quantitative. Compounds **8** and **9** were methylated using methyl iodide and dimethyl sulfate, respectively, originating bis(1-methyltetrazol-5-yl)-3-methyltriaz-1-ene (**10**) and bis(2-methyltetrazol-5-yl)-3-methyltriaz-1-ene (**11**). The products **4**–**11** were characterized by Raman, IR, multinuclear NMR and UV–Vis spectroscopy, mass spectrometry, elemental analysis and differential scanning calorimetry. The structures of the crystalline state of **4** · H_2O, **5**, **8** · MeOH, **10** and magnesium bis(2-methyltetrazol-5-yl)triazenate (**12**) were determined by low temperature single crystal X-ray diffraction. The heats of formation $\Delta_f H^\circ$ of **4**–**7**, **10** and **11** were calculated using energies of combustion $\Delta_c U^\circ$ determined by bomb calorimetry, resulting in strongly endothermic values. With these data and by using calculated (**4**, **5**, **10**) as well as measured (**6**, **7**, **11**) crystal densities, several detonation parameter (heats of explosion, detonation pressure, detonation velocity, explosion temperature) were calculated by the EXPLO5 software. In addition, the specific impulse of different propellant mixtures of the most promising compound **6** with ammonium dinitramide (ADN) were computed. Furthermore the *n*-octanol/water partition coefficients of **4**, **5**, **6** and **7** were determined and the long-term stability of **6** was tested by thermal safety calorimetry. Lastly the sensitivities toward impact and friction as well as electrical discharge were determined by the BAM drophammer, friction tester and a small scale electrical discharge tester.

© 2008 Elsevier Ltd. All rights reserved.

1. Introduction

In contrast to high explosives, propellants need to release their energy in form of deflagration. In this way they produce high pressure without fracturing the containment chamber. Black powder [1] was one of the first propellants used in guns and motors. Today it is still used in pyrotechnic goods, especially small rockets. However the use of black powder as propellant for larger objects like missiles and space rockets contain too much disadvantages. There is a certain unpredictability of the behavior and development of extremely dirty gases [2]. Rocket propellants need to fulfill a couple of requirements: (i) The explosives must have a high energy content and slow burning rate to sustain impulse over a period of time. (ii) The substance additionally needs to be stable over a long time period and in a wide as possible temperature range. To compare different propellants in their performance the specific impulse I_{sp} is used. It is defined as the thrust divided by the mass flow rate of the explosive (Eq. (1)):

$$I_{sp} = \frac{\text{thrust of motor}}{\text{mass flow rate through nozzle}} \quad (1)$$

The specific impulse is also a function of the temperature in the combustion chamber and the average molar mass of the gases:

$$I_{sp} \approx \sqrt{\frac{\text{temperature of combustion chamber}}{\text{average molar mass of gaseous products}}} \quad (2)$$

Therefore I_{sp} depends on the properties of the propellant, on the design of the combustion chamber and the rocket motor, respectively [3]. The two main types of solid rocket propellant are double-base propellants and composite propellants. Double-base propellants are homogenous and composed of nitrocellulose with nitroglycerine or other nitroglycols as energetic plasticizers. Because the dimension of propellant grains based on this type of mixture is

* Corresponding author.
E-mail address: tmk@cup.uni-muenchen.de (T.M. Klapötke).

0277-5387/$ - see front matter © 2008 Elsevier Ltd. All rights reserved.
doi:10.1016/j.poly.2008.09.015

limited, composite propellants were developed during the second world war. The most important composite propellant today is a mixture of aluminum as fuel and ammonium perchlorate as oxidizer. As binding agent serves a polymer, e.g. hydroxy- or carboxy-terminated polybutadiene. This type of mixture is used for example as solid rocket boosters at the US Space Shuttle (and also in Ariane rockets ESA). Depending on the kind of binder and other additives used the specific impulse reaches about 2400–2600 Ns/kg (engl. (I_{sp}/g): 245–265 s) and the flame temperature is about 2850–3500 K [3].

Although the performance of ammonium perchlorate is highly suitable as rocket propellant, it has one big disadvantage. As it can be seen from the decomposition Eq. (3) a high amount of HCl is produced.

$$2NH_4ClO_4 \rightarrow N_2 + 3H_2O + 2HCl + 2.5O_2 \quad (3)$$

With the fact of 500 kg propellant per booster for the Space Shuttle there is a total output of 217 tons of HCl per launch. With the humidity in the air a huge quantity of acid mist is released, which leads to acid rain. In addition the resulting Al_2O_3 is harmful for living creatures and plants. Some endeavors were made to reduce the environmental pollution, especially, concerning the HCl impact. One possibility is to add $NaNO_3$ to build up NaCl [4]:

$$NH_4ClO_4 + NaNO_3 \rightarrow NH_4NO_3 + NaClO_4$$
$$\rightarrow \text{production of NaCl} \quad (4)$$

The simplest way to reduce the environmental pollution would be using propellants which contain no chloride and do not produce any other harmful residues. Many scientists today are searching for new energetic materials with good performance and at the same time having environmental friendly properties. Examples for this new class of energetic materials are 5,5′-bis(1*H*-tetrazolyl)amine (H_2BTA) [5] and salts of 5,5′-bis(1*H*-tetrazolyl)hydrazine (BTH) [6] as well as 5,5′-azotetrazolates (ATZ), which syntheses are illustrated in Scheme 1.

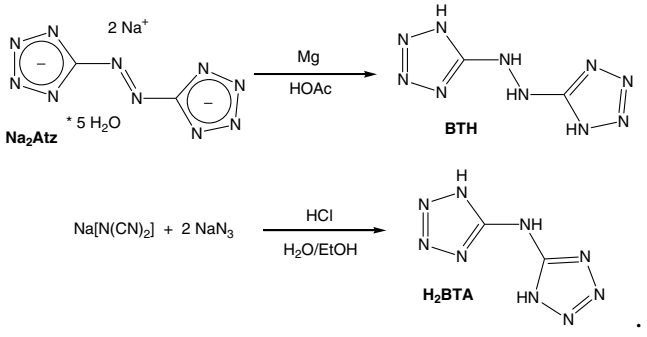
Compounds containing the 5,5′-azotetrazolate anion are particularly suitable target molecules, since these salts have a considerable nitrogen content and are expected to have appropriate stabilities toward friction, impact and heat. Metal salts of 5,5′-azotetrazolates have been extensively studied [7] and also N-rich guanidinium derivatives of 5,5′-azotetrazolate are described in literature as possible additives in solid propellants [8]. The main disadvantage is the incompatibility toward acids. Suitable alternatives for 5,5′-azotetrazolates are derivatives of bis-tetrazolyl-triazenes, which are also stable toward acid conditions. Derivates of bis-tetrazolyl-triazenes have also high-nitrogen contents and a very high positive heat of formation. Due to their high-nitrogen content the main decomposition product is also dinitrogen. In 1910, Hofmann and Hock synthesized bis(1*H*-tetrazol-5-yl)triaz-1-ene for the first time [9], which decomposes slowly by simple exposure to air but can be used as precursor producing 5-tetrazolylhydrazones. A great deal better are the methylated derivatives of bis(1*H*-tetrazol-5-yl)triaz-1-ene since they are thermally stable and show lower sensitivities. toward outer stimuli. These properties can be still improved by deprotonation of the triazene group forming triazenates. Bis(1-methyl-tetrazol-5-yl)-triazene is unknown in literature. Bis(2-methyltetrazol-5-yl)triaz-1-ene was synthesized accidentally by Hattori et al. during the attempt producing methylated 5-hydroxytetrazole, but was not further described [10]. It has been also mentioned in literature as intermediate in synthesis of arylidene-2-methyl-2*H*-tetrazol-5-yl-hydrazones [11] and 1,3,4,6-tetrakis(2-methyltetrazol-5-yl)hexaaza-1,5-diene [12]. In the work of A. Lyakhov deprotonated bis(2-methyltetrazol-5-yl)triaz-1-ene was used as a chelate ligand for Ni(II) [13]. In this work we present facile synthetic routes to several bis(methyltetrazolyl)-triazenes, bis(methyltetrazolyl)-triazenates and bis(methyltetrazolyl)-methyltriazenes, which were fully characterized and also tested with regard to their energetic properties.

2. Results and discussion

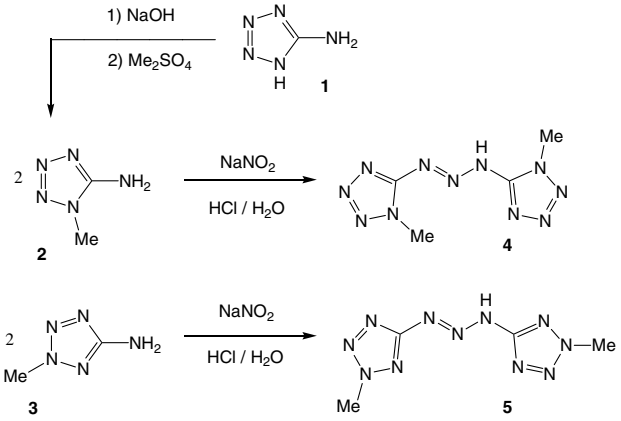
2.1. Synthesis

1-Methyl-5-aminotetrazole (**2**) and 2-methyl-5-aminotetrazole (**3**) were synthesized by methylation of 5-aminotetrazole (**1**) using dimethyl sulfate according to the literature [14]. The diazotation of **2** was carried out in water, according to Scheme 2. A matter of particular interest is the sequence of addition. In this case a solution of 1-methyl-5-aminotetrazole in diluted hydrochloric acid is slowly dropped to an ice cold solution of half an equivalent of sodium nitrite. Bis(1-methyltetrazolyl)triazene (**4**) starts to precipitate after a few minutes (from this solution) and was isolated by filtration. Recrystallization from hot water yielded single crystals of the monohydrate suitable for XRD. Bis(2-methyltetrazolyl)triazene (**5**) can also be synthesized via this route, but also, due to its solubility in organic solvents, by the reaction in THF as solvent and *i*-pentylnitrite as the diazotation agent. Recrystallization from hot water yielded also light yellow single crystals. A small amount of single crystals of magnesium bis(2-methyl-tetrazolyl)triazenate dodecahydrate (**12**) was accidentally obtained on working up one of the reactions originally carried out to establish the reaction conditions toward **5** using $MgSO_4$ as drying agent.

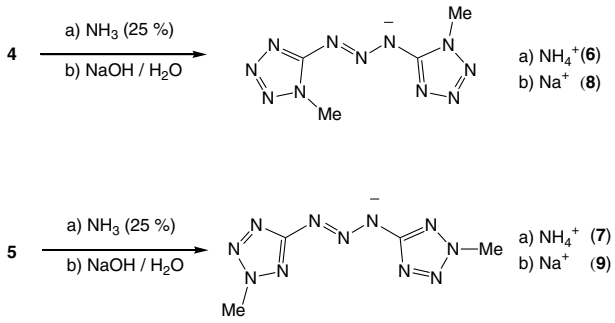
Deprotonation (Scheme 3) of **4** and **5** can be performed in water by adding common bases e.g metal hydroxides or carbonates. The reactions with conc. ammonia solution yielded the water free salts



Scheme 1. Syntheses of the nitrogen-rich materials 5,5′-bis(1*H*-tetrazolyl)amine (H2BTA) and salts of 5,5′-bis(1*H*-tetrazolyl)hydrazine (BTH).



Scheme 2. Synthesis of bis(1-methyltetrazolyl)triazene (**4**) and bis(2-methyltetrazolyl)-triazene (**5**).



Scheme 3. Deprotonation of **4** and **5** using aqueous NH_3 and NaOH solution.

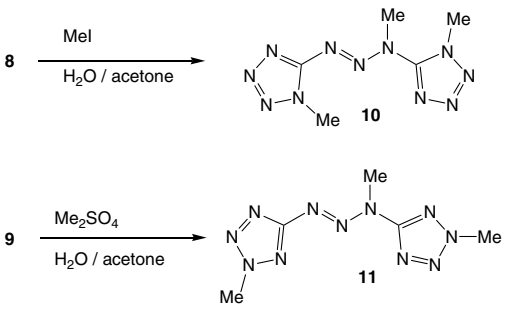
ammonium bis(1-methyltetrazolyl)triazenate (**6**) and ammonium bis(2-methyl-tetrazolyl)triazenate (**7**). Both compounds are low soluble in water below ca. 50 °C and crystallize as microcrystalline materials. Many attempts to obtain single crystals for X-ray determination failed. To obtain other crystals containing the bis(methyltetrazolyl)triazenate anions the salts sodium bis(1-methyltetrazolyl)triazenate (**8**) and sodium bis(2-methyl-tetrazolyl)triazenate (**9**) were synthesized by the reaction of **4** and **5** with aqueous sodium hydroxide solutions. Suitable single crystals could be obtained of **8** by recrystallization from water or a H_2O/MeOH mixture, whereby only the methanol adduct could be determined by X-ray diffraction.

The triazenate unit can be alkylated by common alkylation reagents at one of the marginal nitrogen atoms. This was proofed by the reactions of **8** and **9** with methyl iodide and dimethyl sulfate, respectively, yielding bis(1-methyltetrazol-5-yl)-3-methyl-1-triazene (**10**) and bis(2-methyltetrazol-5-yl)-3-methyl-1-triazene (**11**) depicted in Scheme 4. The products are insoluble in water, slightly soluble in solvents like MeCN, THF, acetone and good soluble in DMF or DMSO. Compounds **10** and **11** could be recrystallized from hot EtOH.

2.2. Structures

2.2.1. X-ray diffraction studies

Suitable single crystal of **5** and **12** were picked from the crystallization mixture, mounted in Kel-F oil and transferred to the N_2 stream of Oxford Xcalibur3 diffractometer with a Spellman generator (voltage 50 kV, current 40 mA) and a KappaCCD detector. The data collection was performed using the CRYSALIS CCD software [15], the data reduction with the CRYSALIS RED software [16]. The data for compounds **4** · H_2O, **8** · MeOH and **10** were collected on a Nonius Kappa CCD diffractometer under a N_2 stream as well. Data collections and reductions were done by the Bruker "COLLECT" and the "HKL DENZO and SCALEPACK" software [17]. The structures were solved



Scheme 4. Methylation of **8** and **9** yielding bis(1-methyltetrazolyl)-3-methyl-1-triazene (**10**) and bis(2-methyltetrazolyl)-3-methyl-1-triazene (**11**).

with SIR-92 (**4** · H_2O, **5** and **10**) [18], and SHELXS-97 (**8** · MeOH, **12**) [19], refined with SHELXL-97 [20] and finally checked using the PLATON software [21], integrated in the WINGX software suite [22]. The non-hydrogen atoms were refined anisotropically. The hydrogen atoms of the methyl groups were partly fixed while the hydrogen atoms bonded ate nitrogen or oxygen atoms were located and freely refined. The absorption of **5** and **12** was corrected by a SCALE3 ABSPACK multi-scan method [23]. All relevant data and parameters of the X-ray measurements and refinements are given in Table 1. Further information on the crystal-structure determinations have been deposited with the Cambridge Crystallographic Data Centre[1].

The monohydrate of **4** crystallizes in the orthorhombic space group *Pnma* with four molecules in the unit cell. The density was calculated to be 1.529 g cm^{-3} which is low in comparison to other 5-*N* substituted tetrazoles in the literature, such as 5-amino-1*H*-tetrazole [24], 5-nitro-2*H*-tetrazole [25], 5-azido-1*H*-tetrazole [26–28] and 5-nitriminotetrazole [29–31]. The molecular moiety, which is shown in Fig. 1 is affected by a planar setup. All non-hydrogen atoms lie on the mirror plane in the a–c layer. The water molecule is coordinated via a strong hydrogen bond to the nitrogen atom N5. The geometry of the triazene unit follows that expected by the "Lewis structure". The distance between the atoms N6–N7 of 1.264(2) Å corresponds with the bond length of a N=N double bond (1.20 Å), while the N6–N5 distance of 1.331(2) is significantly longer, but also shorter than a N–N single bond (1.48 Å) [32]. The geometries of the two tetrazole rings differ considerably. In 5-*N* substituted tetrazoles, usually the shortest N–N distances are observed between the atoms N2 and N3 (1.297(2) Å) as well as N9 and N10 1.294(3) which is also the case in the structure of **4**. The other ring shows an opposed trend. In this the N9–N10 distance is found to be the longest (1.354(3) Å). The bond lengths to the external methyl groups have typical values (1.46 Å) found for C–N single bonds.

The packing of **4** is characterized by a layer structure along the c–a plane (Fig. 2a). The layers have distances of 3.15 Å. Within the layers, strong hydrogen bonds involving the NH group and water molecules, are observed (Fig. 2b). On this account columns along the *c* axes are formed.

Compound **5** crystallizes in the monoclinic space group *I*2/*a* with eight molecules in the unit cell and a slightly higher density of 1.532 g cm^{-3} in comparison to **4**. The molecular geometry in terms of the bond lengths is similar to that observed for **4**. Exact bond distances can be found in Table 2. However, **5** is not completely planar. While the triazene unit is planar (torsion angle C1–N5–N6–N11 = 179.7(2)°), the tetrazole rings are slightly out of phase, which can be seen on the N10–C3–C1–N4 torsion angle of 12.3(4)° (Fig. 3).

On inspection along the *a axes* wave like pattern can be detected (Fig. 4a). The discrete layers are connected by two kinds of interactions. On the one hand dimers are formed by the O1–H1···N7^{i} hydrogen bond (0.79(3) Å, 2.05(3) Å, 2.838(2) Å, 178(3)°; (i) $-1-x, y, 0.5-z$), on the other hand hydrophobic areas are build by the interaction of the methyl groups (marked in Fig. 4b).

8 · MeOH crystallizes in the monoclinic space group $P2_1/c$ with four molecules in the unit cell and a calculated density of 1.327 g cm^{-3}. The sodium cations are coordinated sixfold by a distorted pentagonal-pyramidal coordination sphere. The bis(1-methyl-tetrazolyl)triazenate anions act as tridentate ligands by the coordination of its atoms N4, N6, and N11. The fourth coordination position is filled by the methanol oxygen atom O1, while the fifth and sixth positions are filled by the nitrogen atoms N2 and N11 of two neighbored bis(1-methyl-tetrazolyl)triazenate molecules. Here dimers (Fig. 5) can be detected as a structural motive.

[1] See Supplementary data.

Table 1
Crystallographic data and parameter

	4 · H_2O	**5**	**8** · MeOH	**12**	**10**
Formula	$C_4H_9N_{11}O$	$C_4H_7N_{11}$	$C_5H_{10}N_{11}NaO$	$C_8H_{36}N_{22}MgO_{12}$	$C_5H_9N_{11}$
Formula mass (g/mol)	227.19	209.21	263.23	656.90	223.20
Crystal system	orthorhombic	monoclinic	monoclinic	triclinic	orthorhombic
Space group	*Pnma* (62)	*I*2/*a*(15)	$P2_1/c$(14)	$P\bar{1}$	$Pca2_1$ (29)
Color/habit	colorless needles	colorless needles	yellow rods	colorless rods	colorless needles
Size (mm)	0.03 × 0.10 × 0.11	0.04 × 0.13 × 0.17	0.07 × 0.08 × 0.15	0.10 × 0.14 × 0.17	0.11 × 0.14 × 0.23
a (Å)	23.548(5)	13.9626(5)	6.905(1)	8.2922(5)	10.395(2)
b (Å)	6.309(1)	6.7239(3)	9.177(2)	9.1757(6)	12.313(3)
c (Å)	6.649(1)	19.3318(7)	20.919(4)	10.0013(6)	14.865(3)
α (°)	90.0	90.0	90.0	87.597(5)	90.0
β (°)	90.0	91.750(3)	96.32(3)	89.622(5)	90.0
γ (°)	90.0	90.0	90.0	78.714(5)	90.0
V (Å^3)	987.90(4)	1814.1(1)	1317.5(5)	745.59(8)	1902.6(7)
Z	4	8	4	1	8
ρ_{calc} (g cm^{-3})	1.528	1.532	1.327	1.463	1.559
μ (mm^{-1})	0.121	0.117	0.130	0.148	0.117
F(000)	472	864	544	346	928
$\lambda_{Mo K\alpha}$ (Å)	0.71073	0.71073	0.71073	0.71073	0.71073
T (K)	173	200	200	200	200
$\tau_{min-max}$ (°)	3.2, 26.5	3.7, 26.0	3.0, 26.0	3.7, 26.0	3.2, 26.4
Dataset *h*; *k*; *l*	−30:30; −8:8; −8:8	−17:17; −8:8; −23:23	−8:8; −10:10; −25:25	−10:10; −11:11; −12:12	−12:12; −15:15; −18:17
Reflections collected	1938	8764	4817	7614	11948
Independent reflections	1118	1778	2512	2929	2015
R_{int}	0.026	0.047	0.024	0.028	0.044
Reflection observed	894	1130	1902	1794	1748
Number of parameters	108	164	170	268	361
R_1 (obs.)	0.0405	0.0376	0.0424	0.0309	0.0505
wR_2 (all data)	0.1056	0.1028	0.1196	0.0728	0.1391
Goodness-of-fit	1.15	0.99	1.05	0.90	1.06
Residual density (e Å^{-3})	−0.21, 0.32	−0.21, 0.23	−0.29, 0.21	−0.19, 0.19	−0.31, 0.48
Device type	Nonius Kappa CCD	Oxford Xcalibur3 CCD	Nonius Kappa CCD	Oxford Xcalibur3 CCD	Nonius Kappa CCD
Solution	SIR-92	SIR-92	SHELXS-97	SHELXS-97	SIR-92
Refinement	SHELXL-97	SHELXL-97	SHELXL-97	SHELXL-97	SHELXL-97
Absorption correction	multi-scan	multi-scan	multi-scan	multi-scan	multi-scan
CCDC	699132	699130	699133	699134	699131

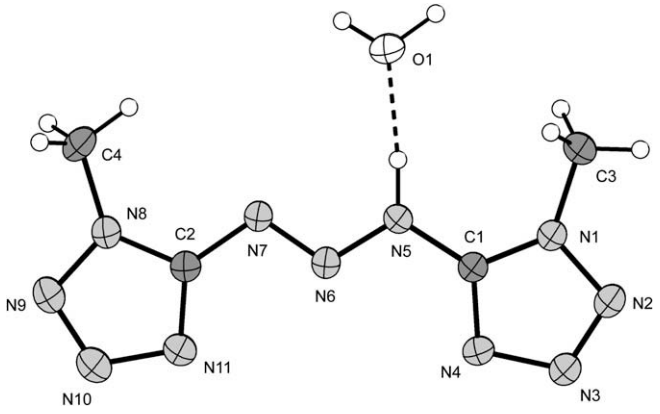


Fig. 1. Molecular moiety of **4** · H_2O. Ellipsoids of non-hydrogen atoms are drawn at the 50% probability level.

Single crystals of **8** recrystallized from hot water could also be obtained, measured at our diffractometer but only insufficiently refined. This may be a reason that the methyl groups are partly disordered and also huge amounts of partly strong disordered crystal water are included in the packing. Therefore a discussion of this structure with a sum formula $C_{12}H_{48}N_{33}Na_3O_{15}$ is abdicated. However the wR_2 value could be lowered to ca. 14% and the coordination of two of the sodium atoms representing a distorted octahedron is depicted in Fig. 6.

Single crystals of **9** could not have been measured since the crystal size was too small for reaching an adequate dataset. However, suitable crystals of magnesium bis(2-methyl-tetrazolyl)triazenate dodecahydrate (**12**) were accidentally obtained on a different work up procedure of **5** using $MgSO_4$ as drying agent. Compound **12** crystallizes with one molecular moiety in the unit cell in the triclinic space group $P\bar{1}$. The bis(2-methyl-tetrazolyl)triazenate anions do not participate in the coordination of the magnesium cations. These are surrounded by six water molecules building a regular octahedral coordination sphere with distances between 2.05 and 2.10 Å (Fig. 7).

Compound **10** crystallizes in the orthorhombic space group $Pca2_1$ with eight molecules in the unit cell. For better clearness only one molecule of the asymmetric unit is shown in Fig. 8. Although no hydrogen bonds can be formed the highest density of 1.559 g cm^{-3} is be observed. The methyl group bonded at the nitrogen atom N5 does not influence the geometry of the triazene unit. The distances N5–N6 (1.324(5) Å) and N6–N7 (1.269(5) Å) are similar to the other structures discussed in this work. Also the C–N bonds of the triazene group to the tetrazole rings are not affected. While the atoms C1, N5, N6 N7 and C2 lie in one plane, the tetrazole rings are twisted 16.1° (torsion angle N5–C2–C1–N4 molecule a) as well as 33.9° (b) to each other.

A view on the unit cell along the *b* axes is shown in Fig. 9. Thereby alternating columns can be found, which are mainly connected by "Van der Waals" forces.

2.3. Spectroscopy

2.3.1. Multinuclear NMR spectroscopy

NMR spectroscopy is a valuable method to identify bis(methyl-tetrazolyl)triazenes. All Shifts are given with respect to TMS (^{1}H, ^{13}C) and CH_3NO_2 (^{14}N, ^{15}N) as external standards. DMSO-d_6 (**4**, **5**, **6**, **7** and **9**), D_2O (**8**) and $CDCl_3$ (**10**, **11**) were used as solvents. The ^{1}H NMR spectra of **4** and **5** measured in DMSO-d_6 show sing-

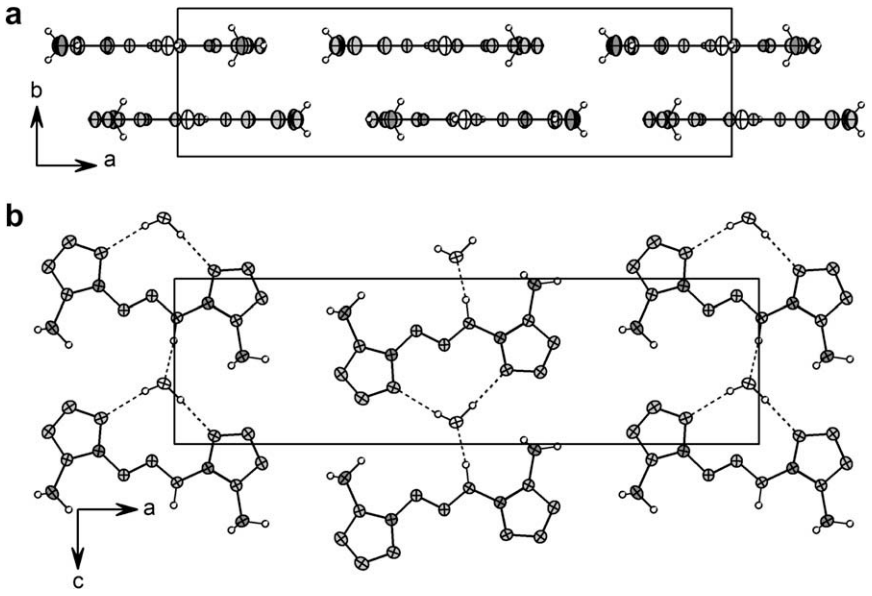


Fig. 2. View on the unit cell of **4** · H_2O along (a) the *c* axes showing the layers, (b) the *b* axes showing the connections within the layers. Hydrogen bonds: O1–H1a···N11 = 0.81(3) Å, 2.10(3) Å, 2.902(3) Å, 172(3)°; N5–H5···O1 = 0.94(3), 1.76(3), 2.703(2), 175(3); O1–H1b···N1 = 0.94(4), 1.99(4), 2.934(3), 178(4).

Table 2
Bond distances (Å) of **4**·H_2O, **5**, **8**·MeOH, **10** and **12**

Atoms	**4**·H_2O	**5**	**8**·MeOH	**10** (a)	**10** (b)	**12**
N1–N2	1.354(2)	1.340(2)	1.362(2)	1.360(5)	1.357(5)	1.333(2)
N2–N3	1.297(2)	1.308(2)	1.372(2)	1.277(6)	1.292(5)	1.311(2)
N3–N4	1.364(2)	1.329(2)	1.378(2)	1.359(5)	1.364(5)	1.333(2)
N5–N6	1.331(2)	1.336(2)	1.352(2)	1.343(5)	1.328(5)	1.309(2)
N6–N7	1.264(2)	1.263(2)	1.313(2)	1.282(5)	1.270(5)	1.305(2)
N8–N9	1.351(2)	1.318(2)	1.412(2)	1.341(4)	1.355(5)	1.337(2)
N9–N10	1.294(3)	1.330(2)	1.311(2)	1.307(5)	1.293(5)	1.312(2)
N10–N11	1.354(3)	1.330(2)	1.394(2)	1.364(5)	1.356(5)	1.322(2)
N1–C1	1.334(3)	1.325(2)	1.396(2)	1.330(5)	1.348(5)	1.338(2)
N4–C1	1.325(3)	1.345(2)	1.380(2)	1.313(5)	1.300(5)	1.356(2)
N5–C1	1.372(3)	1.375(2)	1.385(2)	1.400(5)	1.389(5)	1.382(2)
N7–C2	1.395(3)	1.404(2)	1.430(2)	1.383(5)	1.399(5)	1.386(2)
N8–C2	1.329(3)	1.329(3)	1.345(2)	1.347(6)	1.346(5)	1.334(2)
N11–C2	1.323(3)	1.347(2)	1.383(2)	1.333(5)	1.314(5)	1.358(2)
N1(2)–C3	1.458(3)	1.462(3)	1.539(3)	1.468(5)	1.460(5)	1.455(3)
N8(9)–C4	1.452(3)	1.458(3)	1.487(2)	1.447(5)	1.448(5)	1.446(2)
N5–C5				1.455(5)	1.465(4)	

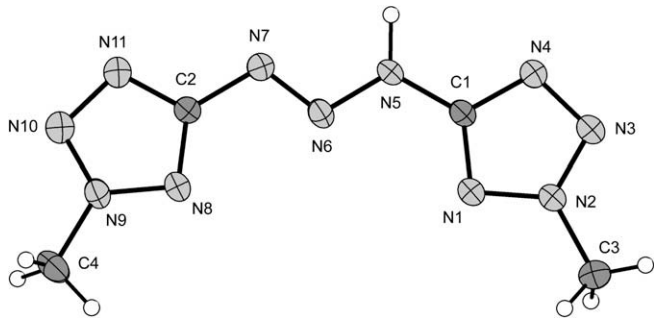


Fig. 3. Molecular moiety of **5**. Ellipsoids of non-hydrogen atoms are drawn at the 50% probability level.

lets at 4.04 ppm and 4.32 ppm, respectively. The hydrogen atom at the triazene unit in **4** provides no visible signal, because of fast proton exchange in polar solvents like DMSO [33]. In **5** it is found weakly at 14.10 ppm. Deprotonation of the triazene unit decrease the hydrogen resonances to higher fields (**6**: 3.86, **7**: 4.20 ppm).

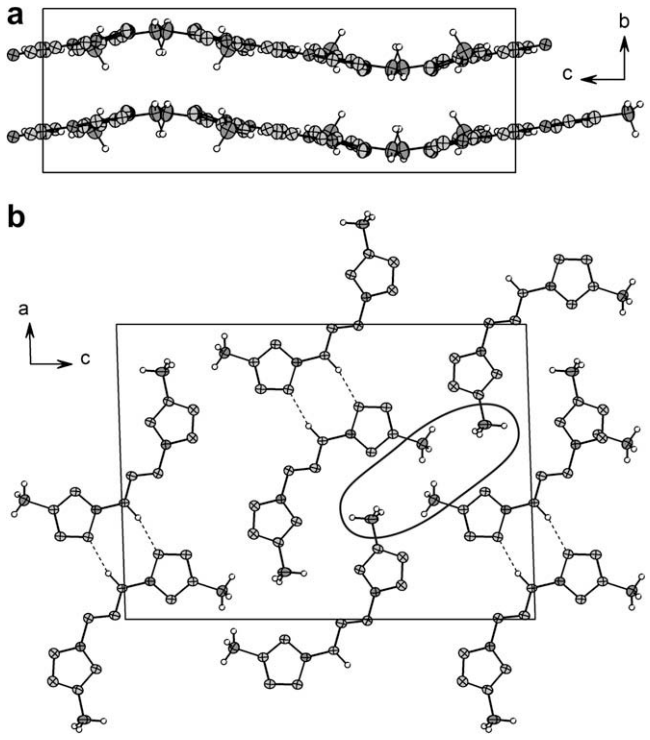


Fig. 4. View on the unit cell of **5** along (a) the *a* axes; (b) the *b* axes illustrating the formation of dimers.

Methylation affords a down field shift and also a split into two resonances (**6**: 4.12, 4.11 ppm, **7**: 4.38, 4.39 ppm). The ^{13}C NMR resonances of the methyl carbon atoms and the tetrazole carbon in **4** and **5** are found at 34.9 ppm and 155.2 ppm (**4**) as well as 40.5 and 162.9 ppm (**5**). In the ammonia salts the methyl resonances are found at higher fields (**6**: 33.1, **7**: 39.7 ppm) while the tetrazole carbon shifts significantly increase to 161.9 (**6**) and 173.7 ppm (**7**). In the case of the methylated compounds **10** and **11**, two signals are observed for the tetrazole carbon atoms (**10**: 157.9, 154.2; **11**: 169.5 and 165.0 ppm) whereby the higher ones can be assigned

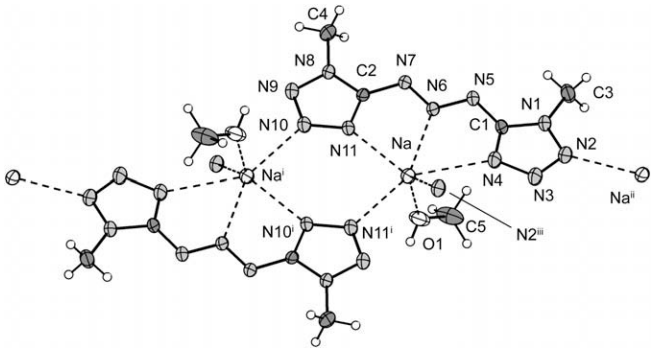


Fig. 5. View on the dimers in **8** · MeOH. Selected distances (Å): Na–O1 = 2.475(2), Na– N11 = 2.498(2), Na–N6 = 2.640(2), Na–N4 = 2.766(2), Na–N2^{iii} = 2.668(2), O1–C5 = 1.561(3); (i) $2-x$, $-y$, $1-z$; (ii) $2-x$, $0.5+y$, $1.5-z$; (iii) $2-x$, $-0.5+y$, $1.5-z$.

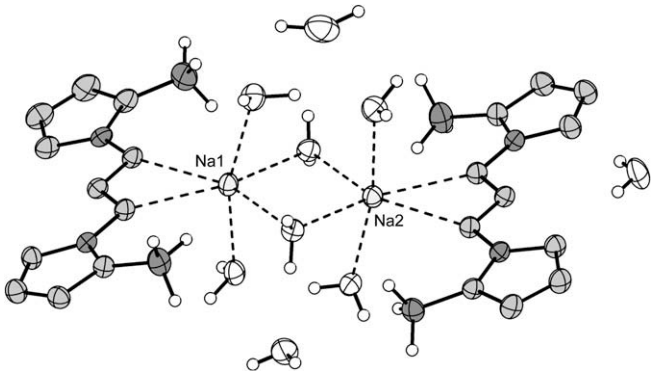


Fig. 6. A selected view on the coordination sphere of the sodium atoms of **8** · $5H_2O$. Several water molecules and one anion and cation were removed for better clearness. Selected crystallographic data: $a = 6.865(1)$ Å, $b = 11.929(2)$ Å, $c = 27.155(5)$ Å, $\alpha = 80.87(3)°$, $\beta = 88.48(3)°$, $\gamma = 76.45(3)°$, $V = 2134.5(7)$, $Z = 2$, Å^3, $\rho = 1.50$ g cm^{-3}.

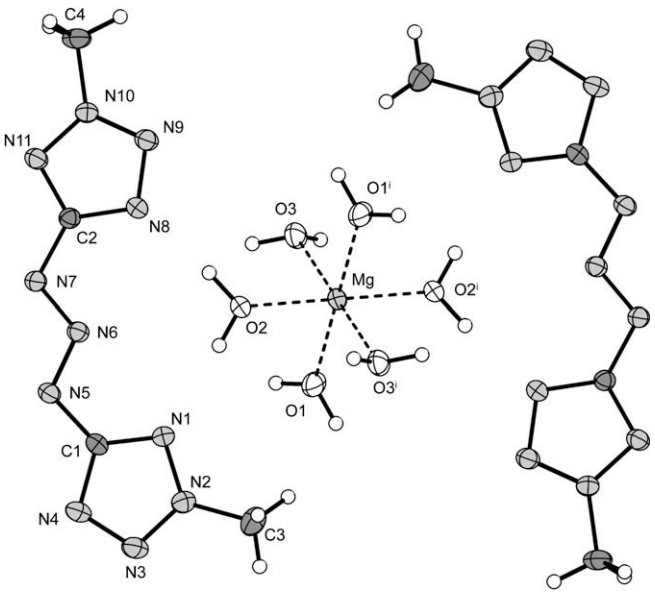


Fig. 7. View on the molecular moiety of **12**. Non-coordinated crystal water was removed for better clearness. Selected distances (Å): Mg–O1 = 2.050(1), Mg–O2 = 2.097(1), Mg–O3 = 2.071(1); selected angles (Å): O1–Mg–O2 = 90.04(5), O1–Mg–O3 = 89.66(6), (i) $1-x$, $-y$, $-z$.

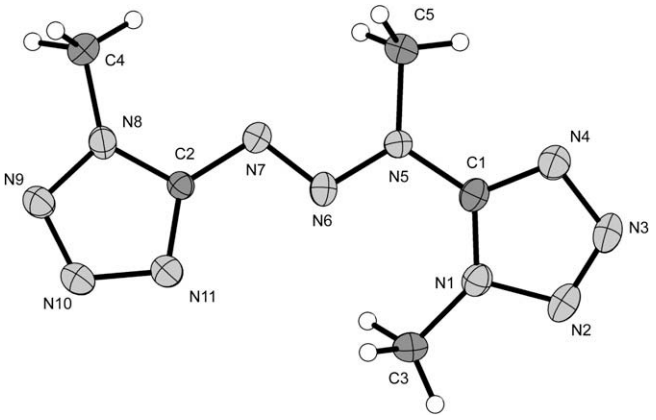


Fig. 8. Molecular moiety of **10**. Ellipsoids of non-hydrogen atoms are drawn at the 50% probability level.

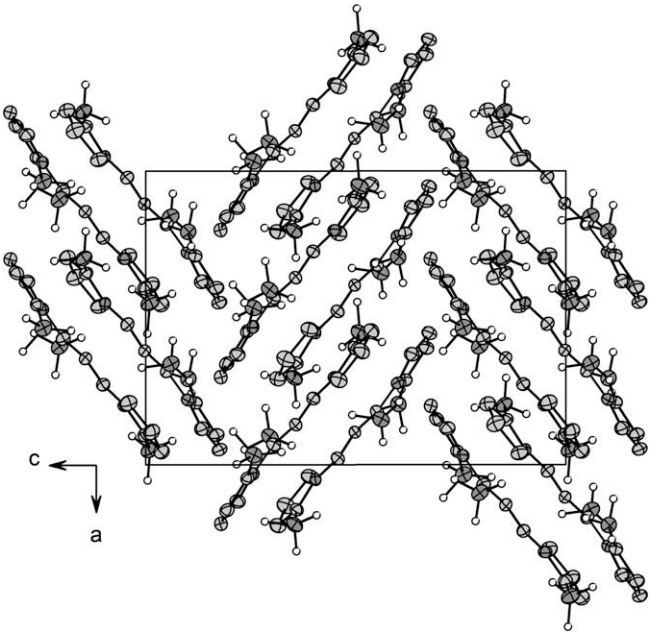


Fig. 9. View on the unit cell of in **10** along the *b* axes.

to the carbon atoms closer to the introduced methyl group. ^{14}N NMR spectroscopy of bis(methyltetrazolyl)triazenes yields uninterpretable spectra due to the quadrupole moment of the ^{14}N core. Solely in the ^{14}N spectra of **6** and **7** the ammonia nitrogen atoms could be detected at −358 ppm (**6**) and −359 ppm (**7**). ^{15}N NMR spectroscopy yields sharp signals, however, it is hard to measure due to the low frequency of the ^{15}N core (0.3%). Therefore high concentrations are required, which is hard to fulfill for the investigated compounds due to their low solubility. To exemplify, the proton coupled ^{15}N NMR spectra of compound **5** and **11** are shown in Fig. 10. The assignments are based on the analysis of the ^{15}N, ^{1}H coupling constants and on comparison with literature [32].

2.3.2. Vibrational spectroscopy

The investigated compounds **4–11** can be easily identified using IR and Raman spectroscopy. The Raman spectra of **4** and **5** are dominated by the asymmetric stretching mode $\nu_{asym}(N{=}N_{triazene})$ providing signals in the range of 1430–1460 cm^{-1}. This vibration is lower in energy in the spectra of the deprotonated triazenes **6–9**. The IR spectra contain more vibrations with high intensities.

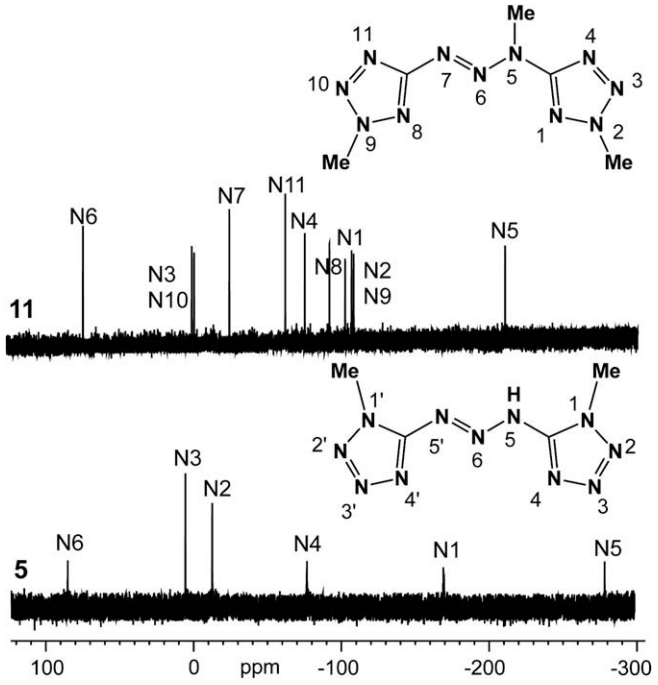


Fig. 10. ^{15}N NMR spectra of **5** and **11**. (δ, ppm): (**5**): 85.2 (N6), 5.54 (N3/N3′), − 76.6 (N4), −12.7 (N2/N2′, q, $^{3}J_{NH}$ = 1.8 Hz), −168.7 (N1, q, $^{2}J_{NH}$ = 2.1 Hz), −265.0 (N5/N5′); δ (**11**): 72.6 (N6), −0.6 (N3, q, $^{3}J_{NH}$ = 1.8 Hz), −2.2 (N10, q, $^{3}J_{NH}$ = 1.8 Hz), −25.8 (N7), −63.5 (N11), −76.6 (N4), −93.2 (N8, q, $^{3}J_{NH}$ = 1.8 Hz), −103.7 (N1, q, $^{3}J_{NH}$ = 1.8 Hz), −108.1 (N9, q, $^{2}J_{NH}$ = 2.2 Hz), −109.5 (N2, q, $^{2}J_{NH}$ = 2.3 Hz), −211.3 (N5, q, $^{2}J_{NH}$ = 2.4 Hz).

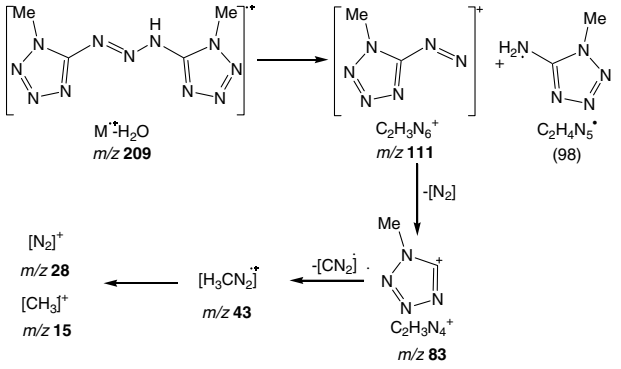
Of course the O–H vibration caused by the crystal water in **4**, **8** and **9** and the symmetric bending mode of the ammonia cations in **6** and **7** can be observed as broad signals above 3150 cm^{-1}. The vibrational spectra contain further vibrations: 3080–2980 cm^{-1} [$\nu_{sym}(CH_3)$], 3430–3140 cm^{-1} [$\nu_{sym/asym}$ (NH_4^+)], 1680–1550 [ν(N–H)], 1550–1350 [ν, tetrazole ring, $\nu_{as}(CH_3)$], ~1380 [$\nu(CH_3)$], 1350–700 [ν(N1–C1–N4), ν(N–N), ν(N–H), ν, tetrazole ring], <700 [ν, δ_{oop}(N–H)].

2.3.3. UV–Vis spectroscopy

The UV–Vis spectra of compounds (**4**–**11**) were measured in diluted methanol solutions. In general the observed resonances are n → π^* transitions. All substances show absorptions below the visible wavelength region. These results are consistent with the visible impressions since all substances are colorless or slightly yellow colored. The UV–Vis spectrum of **4** contains one absorbtion at 315 nm. The two corresponding salts **6** and **8** show both a maximum peak red shifted about 15 nm. In addition, the spectra of **6** and **8** include a shoulder at 240 nm. The resonance of the methylated compound **10** is blue shifted toward 299 nm. Compound **5** shows a maximum value for the absorption at 291 nm, whereby a shoulder can be found at 244 nm. The spectrum of salts **7** and **9** is nearly equal to this observed for **5**. The resonance of **11** is blue shifted to 281 nm.

2.3.4. Mass spectrometry

In all DEI$^+$ mass spectra of the neutral compounds (**4**, **5**, **10** and **11**) the mass peaks at *m*/*z* 209 and 223, respectively, could have been detected. In the spectra of the 1-methyl-tetrazolylderivatives the 1-methyl-5-azotetrazolyl radical was observed with a peak at *m*/*z* 111 as a main fragmentation product. In Scheme 5, one possible fragmentation pathway is shown, which is comparable to that of azotetrazoles [34].



Scheme 5. Possible fragmentation pathway of **4**.

Compound **5** shows analogue fragmentation than that of **4** (Scheme 5). An additional peak at 181 *m*/*z* was detected, which is generated by the loss of dinitrogen (M^+-N_2). Again ($NH_2^{\cdot+}$) (28 *m*/*z*) and CH_3^+ (15 *m*/*z*) arise as further intensive fragmentation products. The ammonium salts were measured in the FAB$^-$ mode, where the mass *m*/*z* 208 of the anion was detected.

2.4. Energetic properties

2.4.1. Differential scanning calorimetry

DSC measurements to determine the melt- and decomposition temperatures of **4**–**11** were performed in covered Al-containers containing a hole in the lid with a nitrogen flow of 20 mL/min on a Linseis PT10 DSC [35], calibrated by standard pure indium and zinc at a heating rate of 5 °C min^{-1}. The DSC plots in Fig. 11 show the thermal behavior of ca. 1.5 mg energetic material in the 50–400 °C temperature range. Temperatures are given as onset temperatures. In general it can be seen that the position of the methyl group does not influence the thermal behavior a lot. The neutral compounds **4** and **5** melt under exothermic decomposition at

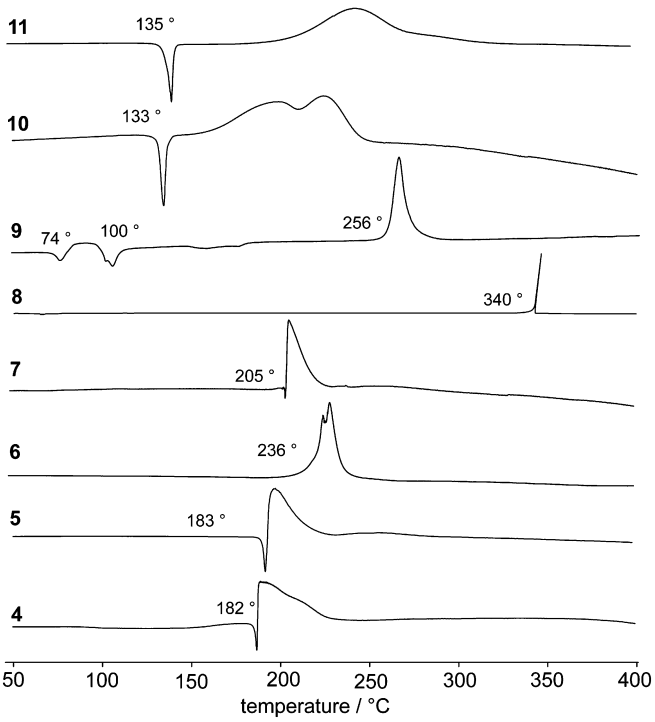


Fig. 11. DSC thermograms of compounds **4**–**11** (heating rate of 5 deg min^{-1}).

temperatures of 182 °C and 183 °C, respectively. Deprotonation increase the decomposition temperatures, which can be seen on the curves of **6**–**9**. Compound **6** decomposes without melting above a temperature of 236 °C. On the other hand ammonium salt **7** decomposes at lower temperatures of 205 °C. However, both nitrogen-rich salts decomposes above 200 °C, which is one of the most important criteria of new energetic materials for use in technical applications. The sodium salt **8** even decomposes not until 340 °C, which is more than 100 °C higher comparing with the corresponding ammonium salt. However, sodium salt **9** looses its five crystal water molecules in two steps at 74 and 100 °C followed by the decomposition above 256 °C. The methylation products **10** and **11** show discrete melting points at 133 °C and 135 °C, respectively, followed by a broad decomposition area starting at 160 °C (**10**) as well as 200 °C (**11**). These thermal behaviors are caused by that no classical hydrogen bonds could be formed in the structures of **10** and **11**.

2.4.2. Bomb calorimetry

The heats of combustion of compounds **4**–**7**, **10** and **11** were determined experimentally using a Parr 1356 bomb calorimeter (static jacket) equipped with a Parr 1108CL oxygen bomb [36]. To achieve better combustion, the samples (ca. 200 mg) were pressed with a defined amount of benzoic acid (ca. 800 mg) forming a tablet, and a Parr 45C10 alloy fuse wire was used for ignition. In all measurements, a correction of 2.3 cal cm^{-1} wire burned has been applied and the bomb was examined for evidence of non-combusted carbon after each run. A Parr 1755 printer was furnished with the Parr 1356 calorimeter to produce a permanent record of all activities within the calorimeter. The reported values are the average of three separate measurements. The calorimeter was calibrated by combustion of certified benzoic acid (SRM, 39i, NIST) in an oxygen atmosphere at a pressure of 3.05 MPa. The experimental results of the constant volume combustion energy ($\Delta_c U$) of the salts are summarized in Table 3. The standard molar enthalpy of combustion ($\Delta_c H^\circ$) was derived from $\Delta_c H^\circ = \Delta_c U + \Delta nRT$ ($\Delta n = \Delta n_i$ (products, g) $- \Delta n_i$ (reactants, g); Δn_i is the total molar amount of gases in the products or reactants). The enthalpy of formation, $\Delta_f H^\circ$, for each of the compounds was calculated at 298.15 K using Hess' law and the following combustion reactions.

$$\mathbf{4}: C_4H_9N_{11}O\ (s) + 5.75O_2\ (g) \rightarrow 4CO_2\ (g) + 4.5H_2O\ (l) + 5.5N_2\ (g)$$

$$\mathbf{5}: C_4H_7N_{11}\ (s) + 5.75O_2\ (g) \rightarrow 4CO_2\ (g) + 3.5H_2O\ (l) + 5.5N_2\ (g)$$

$$\mathbf{6},\mathbf{7}: C_4H_{10}N_{12}\ (s) + 6.5O_2\ (g) \rightarrow 4CO_2\ (g) + 5H_2O\ (l) + 6N_2\ (g)$$

$$\mathbf{10},\mathbf{11}: C_5H_9N_{11}\ (s) + 7.25O_2\ (g) \rightarrow 5CO_2\ (g) + 4.5H_2O\ (l) + 5.5N_2\ (g)$$

All investigated tetrazoles are strongly endothermic, which was expected by comparison with the literature ($\Delta_f H^\circ$ **4** · H_2O: +514, **5**: +792, **6**: +650, **7**: +647, **10**: +686, **11**: +586 kJ mol^{-1}). The influence of crystal water can be seen at the lower $\Delta_f H^\circ$ of **4** · H_2O, in comparison with **5**.

The enthalpies of energetic materials are governed by the molecular structure of the compounds and, therefore, heterocycles with a higher nitrogen content (e.g. imidazole ($\Delta_f H^\circ_{cryst}$ = 14.0 kcal/mol) [37]; 1,2,4-triazole ($\Delta_f H^\circ_{cryst}$ = 26.1 kcal/mol); ($\Delta_f H^\circ_{cryst}$ = 56.7 kcal/mol)) [38] show higher heats of formation. From the experimentally determined heats of formation and densities obtained from single crystal structure X-ray diffraction, various thermochemical properties have been calculated using the EXPLO5 software (see below) and are summarized in Table 4.

2.4.3. Sensitivities

Since the investigated bis(methyltetrazolyl)triazenes **4**–**7**, **10** and **11** are energetic compounds with high-nitrogen contents, the sensitivities toward friction and impact were tested [39]. The impact sensitivity (IS) tests were carried out according to STANAG 4489 [40] and were modified according to instruction [41] using a BAM (Bundesanstalt für Materialforschung, [42]) drophammer [43]. The friction sensitivity (FS) tests were carried out according to STANAG 4487 [44] and were modified according to instruction [45] using the BAM friction tester. Powdered **4** and **5** are sensitive toward impact (**4**: 3 J, **5**: 2.5 J). However, monohydrate **4** is only very weak sensitive toward friction (360 N), while **5** is very friction sensitive (70 N). The ammonium salts **6** (IS: 7.5 J, FS: 360 N) and **7** (IS: 4 J, FS: >360 N) are lower sensitive than their corresponding neutral derivatives. Interestingly also the methyl derivatives **10** and **11** containing a higher carbon and hydrogen content are very sensitive toward impact (**10**: 3 J, **11**: 3 J). Again only the 2-methyltetrazolyl derivative **11** is very sensitive toward friction (20 N) while **10** is nearly insensitive (360 N). According to the UN Recommendations on the Transport of Dangerous Goods,[2] compounds **4** · H_2O, **5**, **10** and **11** are classified as "very sensitive" regarding the impact sensitivity, while **6** and **7** are classified "only" as sensitive. Regarding the friction sensitivities **7** is classified as insensitive, **4**, **6** and **10** are less sensitive and **5** and **11** are classified as "very sensitive". Therefore all derivatives should only be handled with care and appropriate precaution. Thus compound **6** is not only most promising in terms of the thermal stability but also in terms of the sensitivities.

Electrostatic sensitivity tests of **6** were carried out using an electric spark tester ESD 2010EN (OZM Research) operating with the "WINSPARK 1.15 software package" [46]. The electrical spark sensitivity of microcrystalline (1–50 μm particle size) **6** was determined to be 1.2 (±0.1) J.

2.4.4. Detonation parameter

Some detonation parameters such as pressure, temperature, velocity, the heat of explosion, and the amount of gaseous decomposition products were calculated with the EXPLO5 V5.02 software [47,48]. This program is based on the steady-state model of equilibrium detonation and uses BKW E.O.S for gaseous detonation products and Cowan-Fickett E.O.S. for solid carbon [49]. The calculations were performed using the BKWN set of constants, the maximum densities, the molecular masses and the experimentally determined heats of formations. The results are given in Table 4. The most useful values for classifying new explosives are the detonation pressure and detonation velocity. In comparison with common explosives such as TNT (trinitrotoluene, p = 202 kbar, D = 7150 m s^{-1}), compounds **4**–**7**, **10** and **11** show higher detonation pressures (**4** · H_2O: 209, **5**: 221, **6**: 248, **7**: 248, **10**: 220, **11**: 215 kbar). Due to the correlation of the detonation pressure and velocity, the same trend can be found in the detonation velocities. (**4** · H_2O: 7825, **5**: 7982, **6**: 8484, **7**: 8484, **10**: 8014, **11**: 7961 m s^{-1}). Unfortunately all compounds show lower values than those of commonly used RDX (hexogen, p = 340 kbar, D = 8882 m s^{-1}). This may be a reason of the lower densities and that the compounds contain no oxygen resulting in a strongly negative oxygen balance. Therefore their use as solid propellants was investigated by calculating the specific impulse.

2.4.5. Specific impulse

Whereas the performance of HEs can be related to heat of explosion (Q), detonation pressure (p) and detonation velocity (D), the performance of rocket/missile propellants is best characterized by their specific impulse (I_{sp}), as mentioned in Section 1

[2] Impact: Insensitive > 40 J, less sensitive ⩾ 35 J, sensitive ⩾ 4, very sensitive ⩽ 3 J; friction: Insensitive > 360 N, less sensitive = 360 N, sensitive < 360 N, a > 80 N, very sensitive ⩽ 80 N, extreme sensitive ⩽ 10 N; According to the UN Recommendations on the Transport of Dangerous Goods (+) indicates: not safe for transport.

Table 3
Physico-chemical properties of **4**–**7**, **10** and **11**

	4	**5**	**6**	**7**	**10**	**11**
Formula	$C_4H_9N_{11}O$	$C_4H_7N_{11}$	$C_4H_{10}N_{12}$	$C_4H_{10}N_{12}$	$C_5H_9N_{11}$	$C_5H_9N_{11}$
Molecular Mass (g mol^{-1})	227.19	209.17	226.20	226.20	223.20	223.20
Impact sensitivity[a] (J)	3	2.5	7.5	4	3	3
Friction sensitivity[b] (N)	360	70	360	>360	360	20
N[c] (%)	67.82	73.66	74.31	74.31	69.03	69.03
Ω[d] (%)	−80.99	−87.97	−91.95	−91.95	−103.94	−103.94
Combustion	good	good	good	good	moderate	moderate
$T_{dec.}$[e] (°C)	182	183	236	205	200	195
Density[f] (g cm^{-3})	1.528	1.532	1.6 (exp.)	1.6 (exp.)	1.559	1.50 (est.)
$-\Delta U_{comb}$[g] (cal g^{-1})	3556	3861	3867	3864	4225	4206
$-\Delta H^{\circ}_{comb}$[h] (kJ mol^{-1})	3375	3367	3654	3651	3940	3922
$\Delta_f H^{\circ}_m$[i] (kJ mol^{-1})	514	792	650	647	686	668
Calculated values using EXPLO5						
$-\Delta_E U^{\circ}_m$[j] (kJ kg^{-1})	3934	4450	3714	3701	3840	3759
T_E[k] (K)	2843	3136	2626	2620	2704	2673
p[l] (Pa)	209	221	248	248	220	215
D[m] (m s^{-1})	7825	7982	8484	8484	8014	7961
Gas volume[n] (L kg^{-1})	799	760	816	816	757	757

[a,b] BAM methods.
[c] Nitrogen content.
[d] Oxygen balance.
[e] Temperature of decomposition by DSC (β = 5 °C).
[f] Estimated from a structure determination.
[g] Experimental (constant volume) combustion energy.
[h] Experimental molar enthalpy of combustion.
[i] Molar enthalpy of formation.
[j] Energy of explosion.
[k] Explosion temperature.
[l] Detonation pressure
[m] Detonation velocity.
[n] Assuming only gaseous products.

Table 4
Computed propulsion parameters for formulations of **6** with ADN and for single-, double- and triple-base propellants for comparison

O[a]	F[b]	ρ (g cm^{-3})	Ω (%)	T_c (K)	I_{sp} (s)	N_2/CO
ADN[c]	**6**					
10	90	1.621	−80.17	1843	207	7.96
20	80	1.642	−68.40	1853	208	3.81
30	70	1.662	−56.62	1865	209	2.43
40	60	1.683	−44.85	2016	214	2.16
50	50	1.704	−33.08	2384	231	2.61
60	40	1.725	−21.30	2741	243	3.43
70	30	1.746	−9.53	3037	251	5.82
80	20	1.766	2.25	3035	244	21.19
90	10	1.787	14.02	2649	227	316.60
NC[d]		1.66	−30.2	2750	232	0.3
NC[d]/NG (50:50)		1.63	−13.3	3287	248	0.7
NC[d]/NG[e]/NQ[f] (25:25:50)		1.70	−22.0	2663	235	1.4

[a] Oxidizer.
[b] Fuel.
[c] ADN, ammonium dinitramide.
[d] NC-13.3 (N content 13.3%).
[e] NG, nitroglycerine.
[f] NQ, nitroguanidine.

[50]. Moreover, for gun-propellants, erosivity is an additional concern. Also lower reaction temperatures and a high N_2/CO ratio of the reaction gases are desirable [51]. Equally important, an increase of the I_{sp} of only 20 s would be expected to increase the payload or range by ca. 100%. Moreover, smokeless combustion, which is an inherent feature of high-nitrogen compounds, is not only of environmental but particularly of strategic interest since localization of the gun, missile or rocket is much more difficult.

In order to evaluate the properties of the most suitable compound **6** as potential energetic component in gun or missile propellants we calculated the specific impulses and combustion temperatures under isobaric conditions at 45 and 70 bar, representative for rocket and gun-propellants, using the EXPLO5 code [48,49]. Table 4 summarizes the computed isobaric combustion temperatures (T_c, the lower the better for gun-propellants), the specific impulses (I_{sp}) and the molar N_2/CO ratios for mixtures of **6** with ADN and three typical conventional gun-propellants (single-, double-, triple-base) at 70 bar.

Whereas single-base propellants are used in all guns from pistols to artillery weapons, the more powerful (see I_{sp}) double-base propellants are commonly used in pistols and mortars [52]. The disadvantage of double-base propellants is the excessive erosion of the gun barrel (see N_2/CO ratio) by the much higher flame temperatures, and the presence of a muzzle flash (fuel–air explosion of the combustion products). In order to reduce erosion and muzzle flash, triple-base propellants with up to 50% nitroguanidine are used in tank guns, large calibre guns and naval guns. However, the performance of triple-base propellants is lower than that of double-base propellants. A formulation of **6** with ADN (**6**: ADN = 30:70) shows a suitable combustion temperature (3037 K, between single and double-based propellants), with an excellent molar N_2/CO ratio of 5.82 (which are usually 0.5 for conventional propellants). The computed specific impulse of 251 s for such a mixture make a possible application of **6** as promising energetic component in erosion-reduced gun-propellants very interesting. Table 5 summarized the propulsion parameters for formulations of **6** with ADN at 45 bar pressure and for a stoichiometric formulation of AP/Al which is presently used in large booster motors (e.g. ARIANE5, Space Shuttle).

2.4.6. Decomposition experiments

A specially equipped IR cell was loaded each with 50 mg of **4**, **5** and their corresponding ammonia salts **6** and **7**. After heating the cell to 300 °C, the resulting combustion products were analyzed via IR spectroscopy.

Table 5
Computed propulsion parameters for formulations of **6** with ADN and for an AP/Al formulation for comparison

O	F	ρ (g cm^{-3})	Ω (%)	T_c (K)	I_{sp} (s)
ADN[a]	**6**				
10	90	1.621	−80.17	1835	200
20	80	1.642	−68.40	1845	201
30	70	1.662	−56.62	1857	203
40	60	1.683	−44.85	2016	214
50	50	1.704	−33.08	2383	224
60	40	1.725	−21.30	2735	235
70	30	1.746	−9.53	3016	241
80	20	1.766	2.25	2706	236
90	10	1.787	14.02	2640	218
AP[b]	Al[c]				
70	30	2.178	−2.9	4199	232

[a] ADN, ammonium dinitramide
[b] Ammonium perchlorate.
[c] Aluminum.

As it can be seen in Fig. 12 the IR active gaseous decomposition products are hydrogen cyanide (HCN), methane (CH_4) and ammonia (NH_3). The IR spectrum of **4** shows intensive resonances of HCN at 3300–3400 cm^{-1} and 1300–1500 cm^{-1}. In the region of 750 cm^{-1}, the signals are broadened due to a superposition with vibrational bands of methane.

This effect is even more obvious in the spectrum of **5**. Furthermore, signals at 1300 cm^{-1} and in the range of 3100–2900 cm^{-1} confirm the existence of methane in the explosion products.

In the spectrum of **6**, the vibrational resonances of methane in the low frequency area (750 cm^{-1}) appear almost without interference. In this spectrum only traces of HCN could be detected. The main products seem to be NH_3 and methane.

Interestingly, in the spectrum of the ammonia salt **7** only vibrational signals originating from NH_3 are visible. This contradicts with the expectation of seeing additional methane and HCN as explosion products. One possible reason could be an incomplete combustion because of insufficient heating. From the mass spectroscopic analysis of **4** and **5** of course N_2 arises as the main decomposition product.

2.4.7. Long-term stabilities

The long-term stability test of **6** was performed using a Systag FlexyTSC [53] (Thermal Safety Calorimetry) in combination with a RADEX V5 oven and the SYSGRAPH software. The test was undertaken as long-term isoperibolic evaluation in a glass test vessel at atmospheric pressure with 400 mg of **6**. It was previously shown that tempering a substance for 48 h at 40° under the decomposition point results in storage periods about over 50 years at room temperature. Initially for **6** a temperature of 190 °C was chosen and possible occurrences of exo- or endothermic behavior were investigated over period of 48 h. Compound **6** was completely stable during this period. It can therefore be reasoned, that **6** is long-term stable even at higher temperatures, which is a basic requirement for possible applications.

2.4.8. n-Octanol/water partition coefficient

With regard to environmental compatibility of new energetic materials the *n*-octanol/water partition coefficient [54] of **4–7** were tested. The partition coefficient of a substance between water and a lipophilic solvent (*n*-octanol) is one model variable which may be used to describe the transfer of a substance from the aquatic environment into an organism and the potential bioaccumulation of the substance. Studies show a highly significant relationship between the partition coefficient of different substances in the system water/*n*-octanol and their bioaccumulation in fish described in the literature [55]. It has also been shown to be a useful parameter in other forms of biological activity. The partition coefficient (P) is defined as the ratio of the equilibrium concentrations (C_i) of a dissolved substance in a two-phase system consisting of two largely immiscible solvents. In the case *n*-octanol and water: $P_{ow} = C_{n\text{-octanol}}/C_{water}$. The partition coefficient (P) therefore is the quotient of two concentrations and is usually given in the form of its logarithm to base ten ($\log P$). The tests were carried out with a mixture of analytical grade *n*-octanol and distilled water at 22 °C (±1 °C). The partition coefficients of **4** and **5** could not be determined, since the compounds are not soluble either in *n*-octanol or water. This represents the ideal case of new compounds. The partition coefficients (P) of **6** and **7** were determined to be 0.081 ($\log P = -1.09$, **6**) and 0.078 ($\log P = -1.11$, **7**). This is a appropriate value (comparable to that of urea (0.062, $\log P = -1.21$)) for a new compound, which could be upscaled in future times.

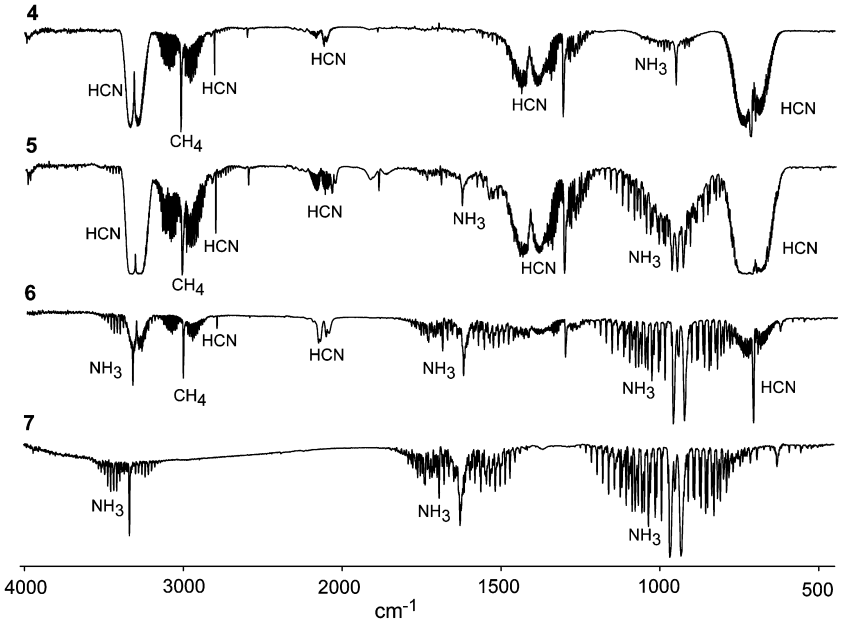


Fig. 12. Gas IR spectra of thermal decomposition products.

3. Experimental

All reagents and solvents were used as received (Sigma–Aldrich, Fluka, Acros Organics) if not stated otherwise. 5-Aminotetrazole (97%) was purchased from Aldrich. Melting points were measured with a Perkin–Elmer Pyris6 DSC, using heating rates of 5°/min. Otherwise melting points were determined with a Büchi Melting Point B-450 apparatus and are not corrected. ^{1}H and ^{13}C spectra were recorded with a Jeol Eclipse 270, Jeol EX 400 or a Jeol Eclipse 400 instrument. All chemical shifts are quoted in ppm relative to TMS (^{1}H, ^{13}C). Infrared (IR) spectra were recorded using a Perkin–Elmer Spektrum One FT-IR instrument. Raman spectra were measured using a Perkin–Elmer Spektrum 2000R NIR FT-Raman instrument equipped with a Nd:YAG laser (1064 nm). Mass spectrometric analyses were obtained with a JOEL JMS 700. Elemental Analyses were performed with a Netsch STA 429 simultaneous thermal analyzer. Bomb Calorimetry was done, using a Parr 1356 Bomb calorimeter with a Parr 1108CL oxygen bomb. The sensitivity data were performed using a BAM drophammer and a BAM friction tester. The ESD test was performed using a OZM small scale electrostatic discharge tester.

Caution! The prepared compounds **4**–**11** are energetic compounds with increased sensitivities against heat, impact and friction. Although we had no problems in synthesis, proper protective measures (safety glasses, face shield, leather coat, earthened equipment and shoes, Kevlar® gloves and ear plugs) should be used during work on **4**–**11**.

3.1. Bis(1-methyl-tetrazol-5-yl)-triazene monohydrate (*4*)

1-Methyl-5-aminotetrazole (19.82 g, 200 mmol) was elutriated in 100 mL water and cooled to 0 °C. After adding concentrated HCl (21.24 g, 200 mmol), 1-methyl-5-aminotetrazole was solved completely. A solution of $NaNO_2$ (6.90 g, 10 mmol) in 40 mL water was added drop wise within 20 min. Thereafter the solution was stirred for 24 h, the resulting colorless solid was isolated by filtration and washed with water. Single crystals were obtained from a wet methanol solution (11.0 g, yield 52.6%). M.p.: 160 °C, 182 °C (dec.); IR (KBr, cm^{-1}): $\overline{\nu}$ = 3375 (m), 3270 (m), 3081 (w), 3031 (w), 2662 (m), 2554 (m), 1664 (m), 1631 (s), 1530 (m), 1502 (m), 1458 (m), 1437 (s), 1396 (m), 1308 (m), 1268 (s), 1247 (m), 1226 (m), 1194 (s), 1102 (w), 1036 (m), 1003 (w), 983 (w), 936 (m), 806 (m), 747 (m), 729 (m), 699 (s), 666 (m), 641 (m), 605 (m), 482 (w); Raman (1064 nm, 200 mW, 25 °C, cm^{-1}) $\overline{\nu}$ = 2987 (59), 1619 (17), 1531 (54), 1453 (43), 1429 (100), 1306 (8), 1284 (28), 1246 (12), 1250 (8), 1221 (11), 1113 (24), 938 (9), 697 (15), 485 (10), 421 (11), 393 (9), 220 (28), 184 (10); ^{1}H NMR (DMSO-d_6, 25 °C, ppm) δ: 4.04 (s, 6*H*, CH_3); ^{13}C NMR (DMSO-d_6, 25 °C, ppm) δ: 34.9 (s, CH_3), 155.2 (tetrazole); ^{15}N NMR (DMSO-d_6, 25 °C, ppm) δ: −265.0 (s, N5, N7), −168.7 (d, $^{2}J_{NH}$ = 2.1 Hz, N1), −76.59 (s, N4), −12.72 (d, $^{3}J_{NH}$ = 1.8 Hz, N2), 5.54 (s, N3), 85.20 (s, N6); EA ($C_4H_9N_{11}O$, 227.19): calc.: C, 21.15; H, 3.99; N, 67.82; O, 7.04. Found: C, 21.18; H, 3.89; N, 67.48%; *m/z* (DEI^+): 209 [M^+-H_2O] (11), 111 [$(C_2H_3N_6^+)$] (100), 83 [$(C_2H_3N_4^+)$] (12), 53 (19), 43 [$(CH_3N_2^+)$] (45), 28 [(N_2^+)] (64); UV–Vis (MeOH): λ_{max} = 315 nm; ΔU_c: −3556 cal g^{-1}; BAM drophammer: 3 J; friction tester: 360 N.

3.2. Bis(2-methyl-tetrazol-5-yl)-triazene (*5*)

2-Methyl-5-aminotetrazole (8.72 g, 88 mmol) was solved in 80 mL THF and cooled to 0 °C. After adding concentrated HCl (4.58 g, 44 mmol), the formation of a colorless solid could be observed. Within 30 min 5.9 mL *i*-pentylnitrite (5.15 g, 44 mmol) were added drop wise, the suspension turned into light yellow and was stirred for 24 h at room temperature afterwards. The resulting solid was recrystallized from methanol to obtain the colorless product (15.1 g, 82%). M.p.: 183 °C (dec.); IR (KBr, cm^{-1}) $\overline{\nu}$ = 3445 (m), 3190 (m), 3136 (m), 3060 (m), 2995 (m), 2920 (m), 2857 (m), 2686 (w), 2384 (w), 1598 (s), 1521 (m), 1468 (s), 1409 (m), 1389 (m), 1349 (m), 1285 (m), 1205 (s), 1100 (w), 1063 (w), 1040 (m), 1018 (m), 949 (m), 808 (m), 758 (m), 744 (m), 705 (m), 686 (m), 672 (m), 661 (m), 590 (w), 491 (w); Raman (1064 nm, 200 mW, 25 °C, cm^{-1}) $\overline{\nu}$ = 2980 (4), 2963 (8), 1601 (12), 1528 (24), 1455 (100), 1413 (8), 1361 (5), 1291 (7), 1193 (4), 1100 (7), 1079 (6), 1049 (9), 942 (6), 703 (4), 489 (3), 434 (2), 376 (3), 174 (5); ^{1}H NMR (DMSO-d_6, *25 °C, ppm)* δ: 4.32 (s, 6*H*, CH_3), 14.10 (s, 1*H*, NH); ^{13}C NMR (DMSO-d_6, 25 °C, ppm) δ: 40.5 (CH_3), 162.9 (tetrazole); EA ($C_4H_7N_{11}$, 209.17): calc.: C, 22.97; H, 3.37; N, 73.66. Found: C, 22.78; H, 3.31; N, 73.17%; *m/z* (DEI^+): 209 [M^+] (5), 181 [M^+-N_2] (18), 111 [$C_2H_3N_6^+$] (39), 83 [$C_2H_3N_4^+$] (3), 55 (8), 42 (11), 43 [$CH_3N_2^+$] (100), 28 [N_2^+] (37), 15 [CH_3^+] (16); UV–Vis (MeOH): λ_{max} = 291 nm; ΔU_c: −3861 cal g^{-1}; BAM drophammer: 2.5 J; friction tester: 70 N.

3.3. Ammonium bis(1-methyl-tetrazol-5-yl)-triazenate (*6*)

Bis(1-methyl-tetrazol-5-yl)-triazene monohydrate (2.27 g, 10.0 mmol) was elutriated in 20 mL water. The suspension was heated to 80 °C and an excess of concentrated ammonia (25%, 25 mL) was added until the reactant was completely dissolved. The ammonium salt crystallized after cooling down to room temperature, was washed with ethanol and diethyl ether and finally dried using high vacuum (1.58 g, 70% yield). M.p.: 236 °C (dec.); IR (KBr, cm^{-1}) $\overline{\nu}$ = 3425 (m), 3158 (m), 3062 (m), 2956 (m), 2857 (m), 2760 (m), 2197 (w), 2125 (w), 1971 (w), 1720 (w), 1612 (w), 1519 (s), 1478 (s), 1451 (s), 1313 (s), 1229 (m), 1209 (m), 1119 (w), 1105 (w), 1047 (w), 1009 (w), 807 (w), 749 (m), 705 (m), 666 (m), 613 (m), 498 (w); Raman (1064 nm, 200 mW, 25 °C, cm^{-1}) $\overline{\nu}$ = 2987 (5), 2962 (6), 1529 (100), 1478 (14), 1467 (16), 1415 (7), 1327 (35), 1290 (14), 1204 (18), 1127 (14), 1007 (3), 948 (6), 707 (12), 498 (15), 422 (5), 405 (4), 221 (22); ^{1}H NMR (DMSO-d_6, 25 °C, ppm) δ: 3.86 (s, 6H, 2 × CH_3), 7.42 (s, 4H, NH_4^+); ^{13}C NMR (DMSO-d_6, 25 °C, ppm) δ: 33.1 (CH_3), 161.9 (tetrazole); ^{14}N NMR (DMSO-d_6, 25 °C, ppm) δ: −358 NH_4^+; EA ($C_4H_{10}N_{12}$, 226.2): calc.: C, 21.24; H, 4.46; N, 74.31. Found: C, 21.16; H, 4.39; N, 73.86%; *m/z* (FAB^-): 208 [anion]; UV–Vis (MeOH): λ_{max} = 329 nm; ΔU_c: −3867 cal g^{-1}; BAM drophammer: 7.5 J; friction tester: 360 N.

3.4. Ammonium bis(2-methyl-tetrazol-5-yl)-triazenate (*7*)

Bis(2-methyl-tetrazol-5-yl)-triazene (2.09 g, 10 mmol) was elutriated in 20 mL water. The suspension was heated to 80 °C and concentrated ammonia (25%, 27.3 g, 0.4 mol) was added until the reactant was completely dissolved. The ammonium salt crystallized after cooling down to room temperature, was washed with ethanol and diethyl ether and afterwards dried in vacuum (1.63 g, 72% yield). M.p.: 205 °C (dec.); IR (KBr, cm^{-1}) $\overline{\nu}$ = 3434 (w), 3137 (m), 3063 (m), 2910 (m), 2756 (m), 2554 (m), 2115 (w), 1183 (w), 1701 (w), 1599 (w), 1563 (w), 1511 (m), 1461 (s), 1423 (m), 1408 (m), 1382 (m), 1322 (s), 1272 (s), 1205 (m), 1052 (m), 1030 (m), 812 (m), 767 (m), 710 (m), 671 (w), 519 (w), 432 (w); Raman (1064 nm, 200 mW, 25 °C, cm^{-1}) $\overline{\nu}$ = 2961 (4), 1509 (100), 1469 (5), 1410 (5), 1259 (12), 1259 (6), 1106 (7), 1050 (3), 1037 (3), 964 (11), 520 (5), 185 (4); ^{1}H NMR (DMSO-d_6, 25 °C, ppm) δ: 4.20 (s, 6*H*, CH_3), 6.10 (s br, 4H, NH_4^+); ^{13}C NMR (DMSO-d_6, 25 °C, ppm) δ: 39.7 (CH_3), 173.7 (tetrazole); ^{14}N NMR (DMSO-d_6, 25 °C, ppm) δ: −359 (NH_4^+); EA ($C_4H_{10}N_{12}$, 226.2): calc.: C, 21.24; H, 4.46; N, 74.31. Found: C, 21.27; H, 4.48; N, 74.31%; *m/z* (FAB^-): 208 [anion]; UV–Vis (MeOH):

λ_{max} = 292 nm; ΔU_c: −3864 cal g^{-1}; BAM drophammer: 4 J; friction tester: >360 N.

3.5. Sodium bis(1-methyltetrazol-5-yl)-triazenate (**8**)

Bis(1-methyltetrazol-5-yl)-triazene monohydrate (2.27 g, 10 mmol) was deprotonated using 100 mL of an aqueous NaOH (0.40 g, 10 mmol) solution. After stirring for 5 min at 80 °C, the solution was cooled while the product started to precipitate. The light yellow micro crystals were filtered off and washed with ethanol and diethyl ether. The elemental analysis fits to the monohydrate (2.39 g, 96% yield). The raw product could be recrystallized either from a small amount of water including five water molecules or from a water/methanol mixture co crystallizing with one molecule methanol. M.p.: 135 °C, 195 °C (dec.); IR (KBr, cm^{-1}) $\overline{v}$ = 3445 (m), 3203 (w), 1622 (w), 1519 (s), 1474 (m), 1456 (w) 1323 (vs), 1284 (m), 1218 (m), 1205 (w), 707 (w); Raman (1064 nm, 200 mW, 25 °C, cm^{-1}) $\overline{v}$ = 2987 (7), 2965 (7), 1546 (100), 1473 (11), 1402 (6), 1338 (22), 1288 (15), 1206 (24), 1129 (15), 1012 (5), 711 (10), 500 (22), 412 (9), 222 (22); ^{1}H NMR (D_2O-*d*, 25 °C, ppm) δ: 3.94 (s, 6*H*, tetrazole-C*H*$_3$); ^{13}C NMR (D_2O, 25 °C, ppm) δ: 161.0 (tetrazole-C), 33.0 (*C*H$_3$); EA ($C_4H_8N_{11}NaO$, 249.2): calc.: C, 19.28; H, 3.24; N, 61.84. Found: C, 19.27; H, 3.27; N, 61.32%; UV–Vis (MeOH): λ_{max} = 330 nm.

3.6. Sodium bis(2-methyl-tetrazol-5-yl)-triazenate pentahydrate (**9**)

To bis(2-methyltetrazol-5-yl)-triazene (2.09 g, 10 mmol) 20 mL of an 0.5 M NaOH (10 mmol) solution was added. After stirring for 10 min at 80 °C, the solution was evaporated. The raw product was recrystallized from hot ethanol, isolated by filtration and washed with small amounts of diethyl ether (3.08 g, 96% yield). M.p.: 74 °C (–H_2O), 100 °C (–H_2O), 256 °C (dec.); **IR** (KBr, cm^{-1}) $\overline{v}$ = 3588 (m), 3479 (s), 3422 (s), 3180 (s), 2163 (w), 1735 (w), 1682 (m), 1630 (m), 1517 (m), 1469 (vs), 1441 (m), 1419 (m), 1388 (m), 1340 (vs), 1274 (s), 1252 (s), 1212 (m), 1056 (m), 1031 (w), 820 (w), 767 (m), 710 (m), 669 (m), 594 (w), 505 (w); Raman (1064 nm, 200 mW, 25 °C, cm^{-1}) $\overline{v}$ = 3025 (1), 2961 (3), 1512 (100), 1463 (10), 1415 (7), 1372 (2), 1334 (2), 1250 (8), 1200 (1), 1107 (7), 962 (10), 712 (1), 503 (3), 420 (2), 316 (2), 211 (2); ^{1}H NMR (DMSO-d_6, 25 °C, ppm) δ: 4.18 (s, 6*H*, CH_3), 3.46 (s, 10*H*, H_2O); ^{13}C NMR (DMSO-d_6, 25 °C, ppm) δ: 174.8 (tetrazole), 39.7 (*C*H$_3$); EA ($C_4H1_6N_{11}NaO_5$, 321.23): calc.: C, 14.96; H, 5.02; N, 47.96. Found: C, 14.91; H, 5.36; N, 46.53%; UV–Vis (MeOH): λ_{max} = 295 nm.

3.7. Bis(1-methyl-tetrazol-5-yl)-3-methyltriaz-1-ene (**10**)

Bis(1-methyltetrazol-5-yl)-triazene monohydrate (4.54 g, 20 mmol) was stirred in 200 mL of an aqueous NaOH (800 mg, 20 mmol) solution for 5 min at 60 °C. Then 1.1 equivalent of methyl iodide (1.4 mL) was added drop wise and the solution was stirred for 2 h at 80 °C. The light yellow precipitate was filtered off and washed with water and a small amount of ethanol (3.04 g, 68% yield). Single crystals were obtained by recrystallization from hot ethanol. M.p.: 140 °C, 200 °C (dec.); IR (KBr, cm^{-1}) $\overline{v}$ = 3431 (w, br), 1574 (s), 1519 (m), 1491 (m), 1473 (m), 1454 (s), 1423 (vs), 1393 (m), 1322 (w), 1281 (s), 1263 (w), 1231 (m), 1194 (m), 1155 (s), 1098 (w), 991 (m), 914 (w), 742 (w), 731 (m), 723 (m), 701 (w), 688 (w), 649 (m), 570 (m), 499 (w); Raman (1064 nm, 200 mW, 25 °C, cm^{-1}) $\overline{v}$ = 2950 (11), 1573 (100), 1518 (44), 1490 (20), 1449 (54), 1422 (38), 1396 (42), 1322 (5), 1265 (25), 1230 (6), 1100 (18), 1033 (4), 991 (7), 916 (6), 724 (11), 708 (12), 568 (7), 501 (7), 421 (10); ^{1}H NMR ($CDCl_3$, 25 °C, ppm) δ: 4.12 (s, 3*H*, CH_3), 4.11 (s, 3*H*, CH_3), 3.83 (s, 3*H*, CH_3); ^{13}C NMR ($CDCl_3$, 25 °C, ppm) δ: 157.9 (tetrazole), 154.2 (tetrazole), 37.6 (CH_3), 35.9 (CH_3), 34.0 (CH_3); EA ($C_5H_9N_{11}$, 223.2): calc.: C, 26.91; H, 4.06; N, 69.03. Found: C, 26.90; H, 3.97; N, 68.54%; *m/z* (DEI$^+$): 43 [$CH_3N_2^+$] (100), 83 [$C_2H_3N_4^+$] (20), 111 [$C_2H_3N_6^+$] (17), 223 [M]$^+$ (38); UV–Vis (MeOH): λ_{max} = 299 nm; ΔU_c: −4225 cal g^{-1}; BAM drophammer: 3 J; friction tester: 360 N.

3.8. Bis(2-methyltetrazol-5-yl)-3-methyltriaz-1-ene (**11**)

Bis(2-methyl-tetrazol-5-yl)-triazene (2.09 g, 10 mmol) was stirred in 100 mL of an aqueous NaOH (400 mg, 10 mmol) solution for 5 min at 60 °C. Then 0.65 equiv. of Me_2SO_4 (0.62 mL) were added drop wise and the solution was stirred for 2 h at 80 °C. The light yellow precipitate was filtered off and washed with water and a small amount of ethanol (1.29 g, 58% yield). M.p.: 135 °C, 195 °C (dec.); IR (KBr, cm^{-1}) $\overline{v}$ = 3446 (w), 3038 (w), 1613 (w), 1569 (vs), 1476 (vs), 1422 (m), 1398 (vs), 1292 (w), 1234 (s), 1218 (s), 1175 (m), 1071 (m), 1032 (m), 980 (m), 916 (w), 801 (w), 761 (w), 745 (m), 713 (m), 631 (w), 590 (w), 99 (w); Raman (1064 nm, 200 mW, 25 °C, cm^{-1}) $\overline{v}$ = 3041 (3), 1964 (10), 1563 (85), 1478 (100), 1399 (20), 1360 (6), 1293 (10), 1207 (4), 1179 (3) 1083 (3), 1034 (15), 982 (10), 915 (4), 762 (2), 746 (2), 717 (7), 638 (2), 501 (7), 444 (6), 345 (3), 183 (5); ^{1}H NMR ($CDCl_3$, 25 °C, ppm) δ: 3.74 (s, 3*H*, triazene-CH_3), 4.38 (s, 3*H*, C*H*$_3$), 4.39 (s, 3*H*, tetrazole-CH_3); ^{13}C NMR ($CDCl_3$, 25 °C, ppm) δ: 169.5 (tetrazole), 165.0 (tetrazole), 40.2 (CH_3), 40.1 (CH_3), 33.7 (triazene-CH_3); ^{15}N NMR ($CDCl_3$, 25 °C, ppm) δ: 72.6 (s, N7), −0.57 (s, N3), −2.20 (s, N3′), −25.8 (s, N6), −63.5 (s, N4), −76.6 (s, N4′), −93.2 (s, N1), −103.7 (s, N1′), −108.1 (s, N2), −109.5 (d, $^2J_{NH}$ = 2.3 Hz, N2′), −211.3 (s, N8); EA ($C_5H_9N_{11}$, 223.1): calc.: C, 26.91; H, 4.06; N, 69.03. Found: C, 26.90; H, 3.97; N, 68.54%; *m/z* (DEI$^+$): 43 [$CH_3N_2^+$] (100), 55 (17), 83 [$C_2H_3N_4^+$] (8), 111 [$C_2H_3N_6^+$] (86), 223 [M]$^+$ (7); UV–Vis (MeOH): λ_{max} = 281 nm; ΔU_c: −4491 cal g^{-1}; BAM drophammer: 3 J; friction tester: 20 N.

4. Conclusion

From this experimental study the following conclusions can be drawn:

- Bis(1-methyltetrazolyl)triazene (**4**) and bis(2-methyltetrazolyl)triazene (**5**) were synthesized by diazotation of 1-methyl-5-aminotetrazole (**2**) and 2-methyl-5-aminotetrazole (**3**), respectively, by using half an equivalent of sodium nitrite. The sodium and ammonium salts of **4** and **5** were synthesized by aqueous ammonia as well as sodium hydroxide solution. These triazenate salts can be methylated yielding bis(1-methyltetrazolyl)-3-methyltriaz-1-ene (**10**) and bis(2-methyltetrazolyl)-3-methyltriaz-1-ene (**11**). All syntheses could be performed via facile routes in good yields using cheap available precursors.
- The molecular structures of **4** · H_2O, **5**, sodium bis(1-methyl-tetrazolyl)triazenate (**8**), magnesium bis(2-methyl-tetrazolyl)triazenate (**12**) and **10** were determined using low temperature single crystal X-ray diffraction and a detailed description is given in this work.
- All compounds were characterized by Raman, IR, multinuclear NMR and UV–Vis spectroscopy, mass spectrometry, elemental analysis and differential scanning calorimetry. The decomposition temperature of the investigated compounds range from 182 to 340 °C.
- All substances show desirable high positive heat of formation (514–792 kJ mol^{-1}) determined in bomb calorimetric measurements. With these values and densities either obtained by X-ray or pycnometry several detonation parameter were computed by the EXPLO5 program, resulting in values much higher than those of TNT but lower than those of RDX. In addition promising specific impulses of mixtures of ammonium

dinitramide (AND) and ammonium bis(1-methyl-tetrazolyl)triazenate (**6**) with good N_2/CO ratios were calculated.
- The sensitivities toward impact and friction were determined by the BAM drophammer and friction tester varying from very sensitive comparable to those of primary explosives to completely insensitive.
- The most promising new energetic material is ammonium bis(1-methyl-tetrazolyl)triazenate (**6**), which combine a high decomposition temperature and high heat of formation with low sensitivities and a long-term stability.

Acknowledgements

Financial support of this work by the Ludwig-Maximilian University of Munich (LMU), the Fonds der Chemischen Industrie (FCI), the European Research Office (ERO) of the U.S. Army Research Laboratory (ARL) and ARDEC (Armament Research, Development and Engineering Center) under Contract Nos. N 62558-05-C-0027, R&D 1284-CH-01, R&D 1285-CH-01, 9939-AN-01 and W911NF-07-1-0569 and the Bundeswehr Research Institute for Materials, Explosives, Fuels and Lubricants (WIWEB) under Contract Nos. E/E210/4D004/X5143 & E/E210/7D002/ 4F088 is gratefully acknowledged. The authors acknowledge collaborations Dr. M. Krupka (OZM Research, Czech Republic) in the development of new testing and evaluation methods for energetic materials and with Dr. M. Sucesca (Brodarski Institute, Croatia) in the development of new computational codes to predict the detonation parameters of high-nitrogen explosives. We are indebted to and thank Dr. Betsy M. Rice (ARL, Aberdeen, Proving Ground, MD) for many helpful and inspired discussions and support of our work. The authors are indebted to and would like to thank the research group of Prof. Dr. P. Klüfers for their generous allocation of time at the Nonius Kappa CCD diffractometer.

Appendix A. Supplementary data

CCDC 699132, 699130, 699133, 699134 and 699131 contain the supplementary crystallographic data for **4** · H_2O, **5**, **8** · MeOH, **10** and **12**. These data can be obtained free of charge via http://www.ccdc.cam.ac.uk/conts/retrieving.html, or from the Cambridge Crystallographic Data Centre, 12 Union Road, Cambridge CB2 1EZ, UK; fax: (+44) 1223-336-033; or e-mail: deposit@ccdc.cam.ac.uk. Supplementary data associated with this article can be found, in the online version, at doi:10.1016/j.poly.2008.09.015.

References

[1] (a) R. Escales, Schwarzpulver und Sprengsalpeter, 1st ed., Survival press, 2008. p. 1;
(b) M. Baetz, Schwarzpulver für Survival, 1st ed., Books on Demand, 2004.;
(c) J.P. Agrawal, R. Hodgson, Organic Chemistry of Explosives, 1st ed., Wiley, 2007. p. 1;
(d) J. Akhavan, The Chemistry of Explosives, 2nd ed., RSC, 2004. p. 1.
[2] P. Folly, P. Mäder, Chimia 58 (2004) 374.
[3] J. Akhavan, The Chemistry of Explosives, 2nd ed., RSC, Cambridge, 2004. p. 154.
[4] N. Kubota, Propellants and Explosives, 2nd ed., Wiley-VCH, Weinheim, 2007. p. 360.
[5] T.M. Klapötke, P. Mayer, J. Stierstorfer, J.J. Weigand, J. Mater. Chem., in press, doi:10.1039/6811273h.
[6] T.M. Klapötké, Carles Miró Sabaté, Chem. Mater. 20 (2008) 3629.
[7] (a) M.A. Hiskey, D.E. Chavez, D.L. Naud, S.F. Son, H.L. Berghout, C.A. Bolme, Proc. Int. Pyrotech. Semin. 27 (2000) 3;
(b) M.A. Hiskey, N. Goldman, J.R. Stine, J. Energ. Mater. 16 (1998) 119;
(c) A. Hammerl, T.M. Klapötke, H. Nöth, M. Warchhold, G. Holl, M. Kaiser, U. Ticmanis, Inorg. Chem. 40 (2001) 3570;
(d) A. Hammerl, G. Holl, T.M. Klapötke, P. Mayer, H. Nöth, H. Piotrowski, M. Warchhold, M. Eur. J. Inorg. Chem. 4 (2002) 834;
(e) H. Ang, W. Frank, K. Karaghiosoff, T.M. Klapötke, H. Nöth, J. Sprott, M. Suter, M. Vogt, M.Z. Warchhold, Anorg. Allg. Chem. 628 (2002) 2901;
(f) Y. Peng, C. Wong, U.S. Patent 5,877,300, 1999; Chem. Abstr. 130 (1999) 196656.;
(g) M. Tremblay, Can. J. Chem. 42 (1964) 1154;
(h) A. Hammerl, G. Holl, M. Kaiser, T.M. Klapötke, P. Mayer, H. Piotrowski, M. Vogt, Z. Naturforsch. 56 (2001) 847;
(i) A. Hammerl, G. Holl, M. Kaiser, T.M. Klapötke, P. Mayer, H. Nöth, H. Piotrowski, M. Suter, Z. Naturforsch. 56 (2001) 857.
[8] A. Hammerl, M.A. Hiskey, G. Holl, T.M. Klapötke, K. Polborn, J. Stierstorfer, J.J. Weigand, Chem. Mater. 17 (2005) 3784.
[9] (a) J. Reilly, J. Teegan, M. Carey, Nature 159 (1947) 643;
(b) V.P. Shchipanov, A.I. Zabolotskaya, R.A. Badryzlova, Chem. Heterocycl. Compd. 6 (1975) 850.
[10] K. Hattori, E. Lieber, J.P. Horwitz, J. Am. Chem. Soc. 78 (1956) 411.
[11] R.N. Butler, F.L. Scott, J. Org. Chem. 32 (1967) 1224.
[12] R.N. Butler, V.C. Garvin, C. Victor, J. Chem. Res. Synopses 7 (1982) 183.
[13] A.S. Lyakhov, P.N. Gaponik, D.S. Pytleva, S.V. Voitekhovich, L.S. Ivashkevich, Acta Crystallogr., Sect. C 60 (2004) 421.
[14] R.A. Henry, W.G. Finnegan, J. Am. Chem. Soc. 76 (1954) 923.
[15] CRYSALIS CCD, Oxford Diffraction Ltd., Version 1.171.27p5 beta (release 01-04-2005 CrysAlis171 .NET).
[16] CRYSALIS RED, Oxford Diffraction Ltd., Version 1.171.27p5 beta (release 01-04-2005 CrysAlis171 .NET).
[17] Z. Otwinowski, W. Minor, Processing of X-ray diffraction data collected in oscillation mode, in: C.W. Carter Jr., R.M. Sweet (Eds.), Methods in Enzymology, Macromolecular Crystallography, Part A, vol. 276, Academic Press, New York, 1997, p. 307.
[18] A. Altomare, G. Cascarano, C. Giacovazzo, A. Guagliardi, J. Appl. Crystallogr. 26 (1993) 343.
[19] G.M. Sheldrick, SHELXS-97, Program for Crystal Structure Solution, Universität Göttingen, 1997.
[20] G.M. Sheldrick, SHELXL-97, Program for the Refinement of Crystal Structures, University of Göttingen, Germany, 1997.
[21] A.L. Spek, PLATON, A Multipurpose Crystallographic Tool, Utrecht University, Utrecht, The Netherlands, 1999.
[22] L.J. Farrugia, J. Appl. Crystallogr. 32 (1999) 837.
[23] SCALE3 ABSPACK – An Oxford Diffraction program (1.0.4,gui:1.0.3) (C) 2005 Oxford Diffraction Ltd.
[24] (a) J. Thiele, Liebigs Ann. 270 (1892) 1;
(b) D.D. Bray, J.G. White, Acta Crystallogr., Sect. B 35 (1979) 3039;
(c) V. Ernst, T.M. Klapötke, J. Stierstorfer, Z. Anorg. Allg. Chem. 633 (2007) 879.
[25] (a) T.M. Klapötke, C.M. Sabaté, J. Stierstorfer, New J. Chem., in press;
(b) G.I. Koldobskii, D.S. Soldatenko, E.S. Gerasimova, N.R. Khokhryakova, M.B. Shcherbinin, V.P. Lebedev, V.A. Ostrovskii, Russ. J. Org. Chem. (Engl. Trans.) 33 (1997) 1771.
[26] J. Stierstorfer, T.M. Klapötke, A. Hammerl, B. Chapman, Z. Anorg. Allg. Chem. 634 (2008) 1051.
[27] A. Hammerl, T.M. Klapötke, Inorg. Chem. 41 (2002) 906.
[28] A. Hammerl, T.M. Klapötke, P. Mayer, J.J. Weigand, Propellants, Explos., Pyrotechn. 30 (2005) 17.
[29] T.M. Klapötke, J. Stierstorfer, Helv. Chim. Acta 90 (2007) 2132.
[30] T.M. Klapötke, J. Stierstorfer, New trends in research of energetic materials, in: Proceedings of the Seminar, 10th, Pardubice, Czech Republic, vol. 2, 2007, p. 674.
[31] A.M. Astakhov, R.S. Stepanov, L.A. Kruglyakova, A.A. Nefedov, Russ. J. Org. Chem. 37 (2001) 577.
[32] N. Wiberg, in: A.F. Holleman, E. Wiberg (Eds.), Lehrbuch der anorganischen Chemie, 101st ed., Walter de Gryter, Berlin, 1995, p. 1842.
[33] H. Günther, in: NMR-Spektroskopie, 3rd ed., Georg Thieme Verlag, Stuttgart, 1991.
[34] J.J. Weigand, Dissertation, Ludwig-Maximilians-Universität München, 2005.
[35] http://www.linseis.com.
[36] http://www.parrinst.de/.
[37] R.C. West, R.M. Selby, Handbook of Chemistry and Physics, 48th ed., The Chemical Rubber Co., Cleveland, OH, 1967–1968. p. D22.
[38] V.A. Ostrovskii, M.S. Pevzner, T.P. Kofman, I.V. Tselinskii, Targets Heterocycl. Syst. 3 (1999) 467.
[39] (a) M. Sućeska, Test Methods for Explosives, Springer, New York, 1995. p. 21 (impact)/p. 27 (friction);
(b) http://www.bam.de.
[40] NATO standardization agreement (STANAG) on explosives,impact sensitivity tests, no. 4489, Ed. 1, September 17, 1999.
[41] WIWEB-Standardarbeitsanweisung 4-5.1.02, Ermittlung der Explosionsgefährlichkeit, hier der Schlagempfindlichkeit mit dem Fallhammer, November 8, 2002.
[42] http://www.bam.de.
[43] http://www.reichel-partner.de/.
[44] NATO standardization agreement (STANAG) on explosive, friction sensitivity tests, no. 4487, Ed. 1, August 22, 2002.
[45] WIWEB-Standardarbeitsanweisung 4-5.1.03, Ermittlung der Explosionsgefährlichkeit oder der Reibeempfindlichkeit mit dem Reibeapparat, November 8, 2002.
[46] (a) S. Zeman, V. Pelikán, J. Majzlík, Cent. Eur. J. Energ. Mater. 3 (2006) 45;
(b) 60 D. Skinner, D. Olson, A. Block-Bolten, Propellants Explos. Pyrotech. 23 (1997) 34;
(c) http://www.ozm.cz/testing-instruments/small-scale-electrostatic-discharge-tester.htm.
[47] (a) M. Sućeska, Propellants Explos. Pyrotech. 16 (1991) 197;
(b) M. Sućeska, Propellants Explos. Pyrotech. 24 (1999) 280.

[48] (a) EXPLO5.V2, M. Sućeska, in: Proc. of 32nd Int. Annual Conference of ICT, July 3–6, Karlsruhe, German, 2001, p. 110/1 (a software for determining detonation parameter, 2006);
(b) M. Suceska, in: Proc. of 30th Int. Annual Conference of ICT, June 29–July 2, Karlsruhe, Germany, 1999, p. 50/1.
[49] M.L. Hobbs, M.R. Baer. Calibration of the BKW-EOS with a large product species data base and measured *C–J* properties, in: Proc. of the 10th Symp. (International) on Detonation, ONR 33395-12, Boston, MA, July 12–16, 1993, p. 409.
[50] T.M. Klapötke, Nachr. Chem. 56 (2008) 645.
[51] R.M. Doherty, Novel energetic materials for emerging needs, in: 9th-IWCP on Novel Energetic Materials and Applications, Lerici (Pisa), Italy, September 14–18, 2003.
[52] J. Akhavan, The Chemistry of Explosives, 2nd ed., RSC Press, Cambridge, 2004.
[53] http://www.systag.ch.
[54] A. Leo, C. Hantsch, D. Elkins, Chem. Rev. 71 (1971) 525.
[55] W.B. Neely, D.R. Branson, G.E. Blau, Environ. Sci. Technol. 8 (1974) 1113.

Polyhedron 28 (2009) 27–32

Contents lists available at ScienceDirect

Polyhedron

journal homepage: www.elsevier.com/locate/poly

Multinuclear NIR luminescent 1,4-BDC bridged Schiff-base complexes of Nd(III)

Xingqiang Lü [a,*], Weiyu Bi [a], Wenli Chai [a], Jirong Song [a], Jianxin Meng [b], Wai-Yeung Wong [b], Wai-Kwok Wong [b,*], Xiaoping Yang [c], Richard A. Jones [c,*]

[a] Department of Chemical Engineering, Shaanxi Key Laboratory of Physico-inorganic Chemistry, Northwest University, Xi'an 710069, Shaanxi, PR China
[b] Department of Chemistry, Hong Kong Baptist University, Waterloo Road, Kowloon Tong, Hong Kong, PR China
[c] Department of Chemistry and Biochemistry, The University of Texas at Austin, 1 University Station A5300, Austin, TX 78712-0165, United States

ARTICLE INFO

Article history:
Received 19 May 2008
Accepted 25 September 2008
Available online 30 October 2008

Keywords:
NIR luminescence
3d–4f complex
X-ray crystallography
1,4-Benzenedicarboxylate
Nd(III)
Schiff-base

ABSTRACT

Solvent and reaction stoichiometry dictate the products isolated from reactions of the dinuclear precursor complex $[ZnNdL(H_2O)(NO_3)_3]$ (H_2L = *N*,*N*′-bis(3-methoxy-salicylidene)ethylene-1,2-diamine) with the anionic multidentate linker 1,4-benzenedicarboxylate (1,4-BDC). With a 2:1 molar ratio of ZnNd:$Na_2$1,4-BDC in CH_3CN–EtOH the tetranuclear complex $[Zn_2Nd_2L_2(1,4\text{-BDC})(NO_3)_4(EtOH)_2] \cdot 2MeCN$ (**1**) is produced while hexanuclear $[Zn_4Nd_2L_4(1,4\text{-BDC})_2] \cdot (NO_3)_2 \cdot 2Et_2O \cdot 4H_2O$ (**2**) can be isolated from a DMF–EtOH mixture. A 4:1 mole ratio in DMF–EtOH gave the unusual polynuclear complex $[Zn_4Nd_2L_4(1,4\text{-BDC})_2] \cdot [ZnNdL(NO_3)_3(OAc)]_2$ (**3**). The NIR photophysical properties of the new compounds are reported.

© 2008 Elsevier Ltd. All rights reserved.

1. Introduction

Much recent attention has been focused on the near-infrared (NIR) emission properties of complexes of Nd(III), Yb(III) and Er(III), because of their potential applications in bioassays and laser systems [1]. However, this is limited by the low absorption coefficients of the lanthanide ions due to parity forbidden f–f transitions for these lanthanide ions [2]. This has led to considerable interest in the exploration of suitable chromophores [3] to sensitize the NIR emission of lanthanide ions in complex systems. One feasible way to solve this problem is to use organic dyes [4] or d-block metal complexes (Cr(III) [5], Ru(II) [6], Pt(II) [7], Re(I) or Os(II) [8]), with intense and tunable absorption maximum in the visible region, to act as sensitizers for NIR luminescence from lanthanides.

Our research has focused on the use of Zn(II) complexes of a variety of different Schiff-base ligands as possible chromophores and antennae for the sensitization of lanthanide ions [9]. We recently showed that by changing the electronic properties of the Schiff-base ligands (spacers or substituents on the phenyl rings), it is possible to influence the emissive properties of the lanthanide ions [9e]. Of relevance to the work described in this communication is our recent report of a luminescent Zn_4Nd_2 complex, in which the multidentate dianion, 1,4-benzenedicarboxylate (1,4-BDC) linked two 3d–4f moieties via axial sites to form a hexanuclear complex [10]. The compound appeared to have enhanced NIR luminescent properties over those of simple dinuclear 3d–4f complexes [9,11]. In this paper, we further demonstrate that by varying the solvent system used for crystallization and the stoichiometry of the self-assembly components, it is possible to control the nuclearity of the resultant isolated supramolecules (Scheme 1). Photophysical studies of the new compounds show that the structural variations cause modifications in the NIR luminescence of the Nd(III) ions.

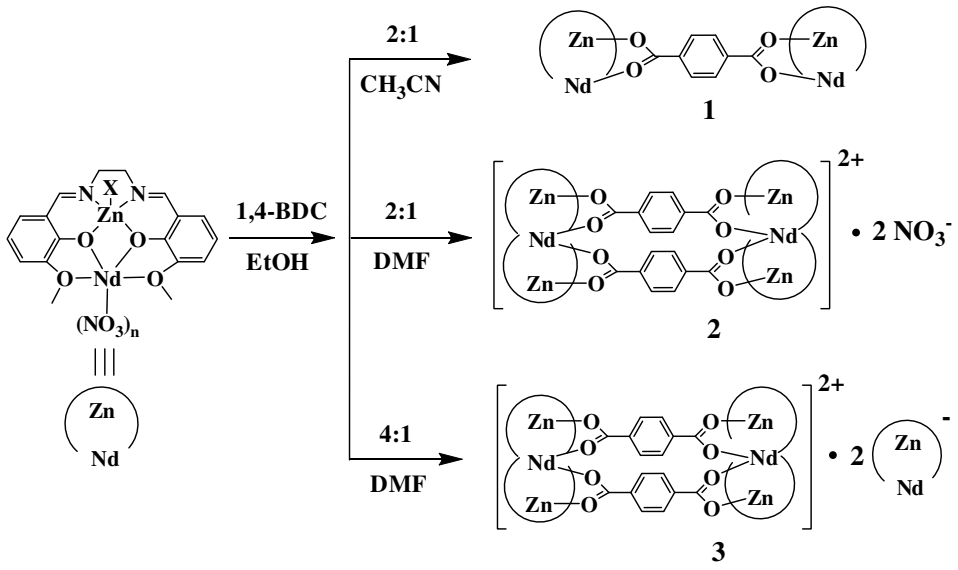
2. Results and discussion

2.1. Synthesis of metal complexes

Reaction of the dinuclear precursor complex $[ZnNdL(H_2O)(NO_3)_3]$, generated in situ from the reaction of equimolar amounts of $Zn(OAc)_2 \cdot 2H_2O$, H_2L (H_2L = *N*,*N*′-bis(3-methoxy-salicylidene)ethylene-1,2-diamine) and $Nd(NO_3)_3 \cdot 6H_2O$ in ethanol, with sodium 1,4-benzenedicarboxylate ($Na_2$1,4-BDC) in a 2:1 molar ratio followed by the addition of MeCN gave the tetranuclear complex $[Zn_2Nd_2L_2(1,4\text{-BDC})(NO_3)_4(EtOH)_2] \cdot 2MeCN$ (**1**) (Scheme 1). In contrast the hexanuclear complex $[Zn_4Nd_2L_4(1,4\text{-BDC})_2] \cdot (NO_3)_2 \cdot 2Et_2O \cdot 4H_2O$ (**2**) was obtained when the reaction mixture was treated with DMF. The solid state structures of **1** and **2** were determined by single crystal X-ray crystallography. Fig. 1 shows the molecular structure of **1**. Two crystallographically equivalent

* Corresponding author. Tel.: +1 512 471 1706.
E-mail address: rajones@mail.utexas.edu (R.A. Jones).

0277-5387/$ - see front matter © 2008 Elsevier Ltd. All rights reserved.
doi:10.1016/j.poly.2008.09.014



Scheme 1. Routes to polynuclear heterometallic 3d–4f complexes.

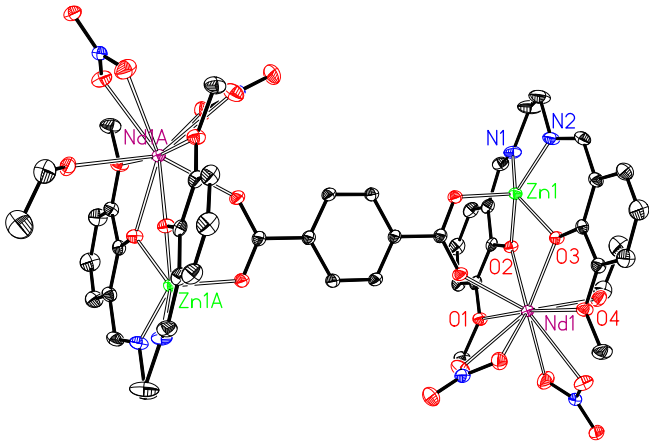


Fig. 1. A view of the molecular structure of **1**. H atoms and solvates have been omitted for clarity. Atoms are shown at the 25% probability level. Atoms whose labels are appended by an A are related by $2 - x, -y, 1 - z$.

Zn–Nd moieties lie about the inversion center, and are linked by one 1,4-BDC group. The Zn(II) ions have a distorted square pyramidal geometry, coordinated to the inner N_2O_2 cores of each Schiff-base ligand and one O atom of 1,4-BDC in the axial position. Each Nd(III) ion is 10-coordinate and surrounded by 10 O atoms, four from the outer O_2O_2 set of the Schiff-base ligand, four from the two bidentate nitrate ligands, one from the 1,4-BDC and one from an EtOH solvate. A view of the hexanuclear complex **2** is shown in Fig. 2. Two trimetallic Zn_2NdL_2 fragments are linked by two 1,4-BDC dianions to give the dicationic unit $[Zn_4Nd_2L_4(1,4\text{-BDC})_2]^{2+}$, in which the Nd(III) ions are also ten-coordinate, with eight O atoms from two outer O_2O_2 sets of two Schiff-base ligands and two O atoms from two 1,4-BDC linkers. The central core structure of **2** is similar to that found in $[Zn_4Nd_2L'_4(1,4\text{-BDC})_2] \cdot [Nd(NO_3)_5(H_2O)] \cdot 2EtOH \cdot 3H_2O$ (H_2L' = *N*,*N*′-bis(5-bromo-3-methoxysalicylidene)propylene-1,3-diamine), where the +2 charge is balanced by the dianion $[Nd(NO_3)_5(H_2O)]^{2-}$, not by the two NO_3^- ions as in **2**. [10] A somewhat related hexanuclear complex $[Cu_4Sm_2L''_4(fum)_2](OH)_2$ (H_2fum = fumaric acid; H_2L'' = *N*,*N*′-bis(3-methoxy-salicylidene)ethylene-1,3-diamine) has also been reported recently [12]. When the dinuclear precursor complex $[ZnNdL(H_2O)(NO_3)_3]$ and $Na_2$1,4-BDC were allowed to react in a 4:1 molar ratio in EtOH followed by treatment with DMF, the unusual polynuclear species $[Zn_4Nd_2L_4(1,4\text{-BDC})_2] \cdot [ZnNdL(NO_3)_3(OAc)]_2$ (**3**) was obtained in 30% yield. The solid state structure of **3**, determined by X-ray crystallography revealed the presence of one $[Zn_4Nd_2L_4(1,4\text{-BDC})_2]^{2+}$ dicationic unit (Fig. 3). The +2 charge is now balanced by the presence of two anionic $[ZnNdL(NO_3)_3(OAc)]^-$ groups instead of two NO_3^-. The anionic ZnNd moieties have structures typical of dinuclear Zn–Nd salen-type Schiff-base complexes. The Zn(II) ion adopts a distorted square-based pyramidal geometry and is five-coordinate being bound to the inner N_2O_2 cavity of the Schiff-base and to one O atom from the OAc^- group. The Nd(III) ion is 10-coordinate and bound by the outer O_2O_2 donor set of the Schiff-base ligand and six O atoms from the three bidentate NO_3^- anions. A detailed examination of the crystal stacking of complexes **1**–**3** (see Supplementary data) reveals that supramolecular interactions involving complimentary C–H···O hydrogen bonds (**1** and **2**), and electrostatic interactions (**3**) generate closely packed 3D frameworks for these compounds. Both solvent and nitrate anions in **1** and **2** were located inside the cavities of the 3D frameworks and appear to exhibit no strong interactions with the host structure.

2.2. Spectroscopy

The ^{1}H NMR spectra of all three compounds in CD_3OD solution are complex and span the range from δ *−8.38* to 14.66 ppm (see Supplementary data). There are no changes in the spectra for up to one month at room temperature.

At room temperature, complexes **1**–**3** and the precursor complex exhibit similar ligand-centered solution absorption spectra (Fig. S4) in the UV–Vis region (λ_{max} = 203, 230, 267 and 348 nm), which are red-shifted compared to the free Schiff-base (λ_{max} = 248, 337 nm) at the same concentration in degassed absolute MeOH. Complex **2** shows higher molar absorption coefficients than the other three compounds. The NIR emission spectra of all four compounds at room temperature in MeOH solution are shown in Fig. 4, and are typical for the NIR emission bands of Nd^{3+} ($^4F_{3/2} \rightarrow {}^4I_{j/2}$, j = 9, 11, 13). The emissions centered at 863, 1060 and 1328 nm can be assigned to the $^4F_{3/2} \rightarrow {}^4I_{9/2}$, $^4F_{3/2} \rightarrow {}^4I_{11/2}$ and $^4F_{3/2} \rightarrow {}^4I_{13/2}$ transitions of Nd^{3+}, respectively; while the free H_2L ligand and 1,4-BDC do not exhibit any NIR luminescence under similar conditions. At a con-

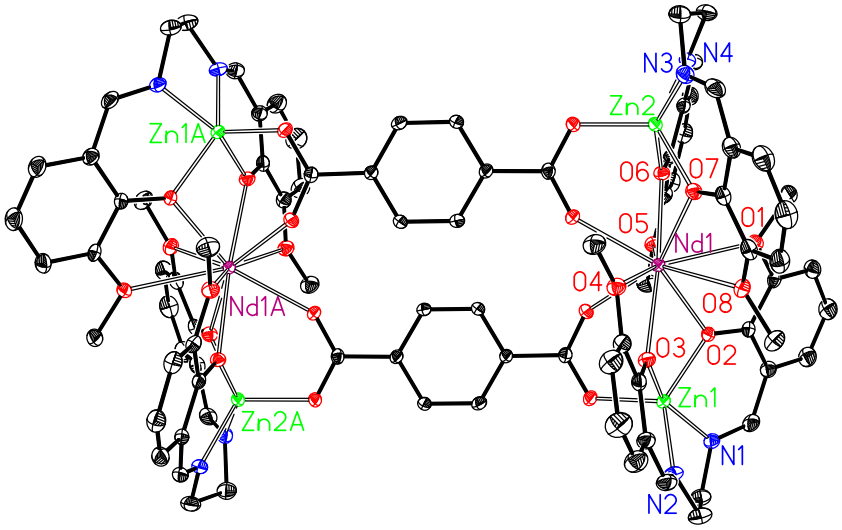


Fig. 2. A view of the cationic hexanuclear moeity of **2**. H atoms, nitrate anions and solvates have been omitted for clarity. Atoms are shown at the 30% probability level. Atoms whose labels are appended by an A are related by $2 - x, -y, 1 - z$.

centration of 4×10^{-5} M NIR Nd(III) emission was not observed for $Nd(NO_3)_3$ under the same experimental conditions.

In solution the relative emission intensities of the tetranuclear complex **1** (Zn_2Nd_2) and the hexanuclear complex **2** (Zn_4Nd_2) at 1060 nm were estimated to be *ca.* 1.13 and 2.74 times that of the dinuclear Zn–Nd precursor, respectively. Complex **3** has a relative emission intensity which is greater than that of the precursor (*ca.* 1.45 times), but significantly weaker than that of complex **2.** In solution complex **3** no doubt exists as a mixture of $Zn_4Nd_2^{2+}$ cations plus two $[ZnNd]^-$ anions, so that direct comparison of the relative emission intensities of **3** versus **2** is less reliable [11]. In the solid state structure of **1** there is one coordinated EtOH molecule, which can assist in the quenching of the luminescence of Nd^{3+} ions. In contrast there are no coordinated solvent molecules in **2** which also exhibits a higher molar absorption coefficient than **1**. This may partly explain the emission enhancement of **2** versus that of **1**. [13] The solution NIR emission spectra of the four complexes are almost identical to their solid state spectra (Fig. S5) with similar relative intensities.

In conclusion, luminescent compounds of varying stoichiometries can be isolated by controlling the mole ratios and solvent systems used in the preparation and isolation of Schiff-base stabilized 3d–4f units linked with 1,4-BDC groups.

3. Experimental

All operations were performed under a dry oxygen-free dinitrogen atmosphere using standard Schlenk techniques. Solvents and starting materials were all purchased commercially and used without further purification unless otherwise stated. Elemental analyses were performed on a Perkin–Elmer 240C elemental analyzer. Infrared spectra were recorded on a Nicolet Nagna-IR 550 spectrophotometer in the region 4000–400 cm^{-1} using KBr pellets. ^1H NMR spectra were recorded on a JEOL EX270 spectrometer with $SiMe_4$ as internal standard in CD_3OD at room temperature. Electronic absorption spectra in the UV/Vis region were recorded with a Hewlett Packard 8453 UV/Vis spectrophotometer, and NIR emission was detected by a liquid nitrogen cooled INSb IR detector (EG & G) with a preamplifier and recorded by a lock-in amplifier system. The third harmonics, 337-nm line of a Nd-YAG laser (Quantel Brilliant B), was used as the excited light source. Melting points

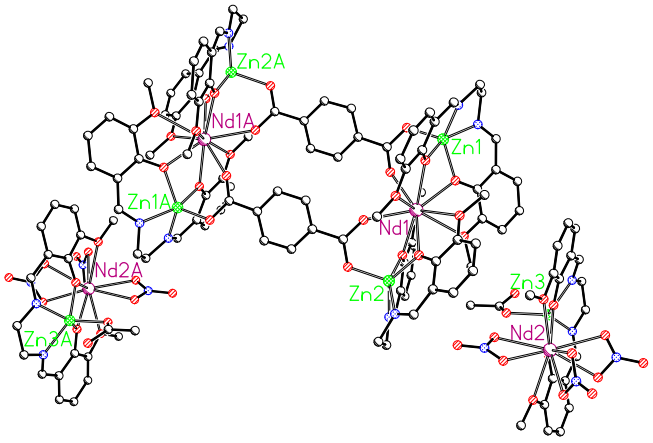


Fig. 3. A view of the structure of **3** showing both anions and cations. H atoms have been omitted for clarity. Atoms whose labels are appended by an A are related by $-x, 1 - y, -z$.

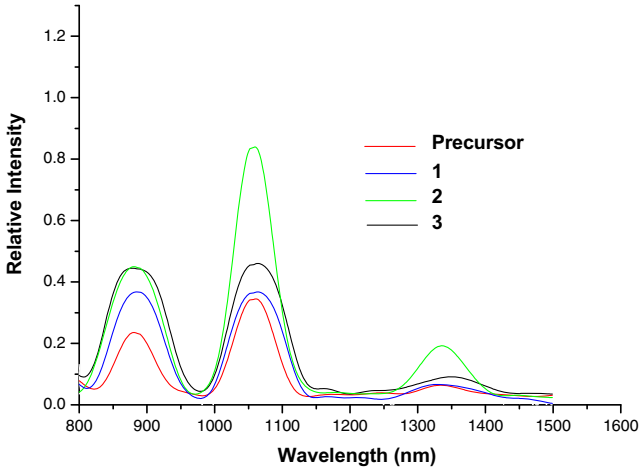


Fig. 4. NIR emission spectra of the four compounds in MeOH solution at 2×10^{-5} M at room temperature. λ_{ex} = 337 nm.

Table 1
Crystal data and structure refinement for complexes **1**–**3**

	1	**2**	**3**
Formula	$C_{52}H_{58}N_{10}O_{26}Zn_2Nd_2$	$C_{96}H_{108}N_{10}O_{36}Zn_4Nd_2$	$C_{128}H_{122}N_{18}O_{54}Zn_6Nd_4$
F_w	1658.30	2527.88	3745.62
Crystal system	monoclinic	monoclinic	monoclinic
Space group	*P*2(1)/*c*	*C*2/*c*	*C*2/*c*
a (Å)	12.2121(9)	27.3694(17)	53.246(3)
b (Å)	15.1642(11)	24.5347(17)	13.9411(8)
c (Å)	17.1667(12)	20.1567(13)	22.5571(13)
β (°)	100.5240(10)	127.337(2)	94.2200(10)
V (Å^3)	3125.6(4)	10761.6(12)	16698.8(17)
Z	2	4	4
D_{calc} (g cm^{-3})	1.762	1.560	1.490
T (K)	293(1)	293(1)	293(1)
F(000)	1656	5128	7472
μ (mm^{-1})	2.482	1.910	2.147
θ Range (°)	2.16–25.00	1.87–25.00	1.91–25.00
Reflection meads	15204	26629	40364
Reflection used	5492	9453	14596
Parameters	417	678	952
R^a ($I > 2\sigma(I)$)	R_1 = 0.0295	R_1 = 0.0424	R_1 = 0.0564
	wR_2 = 0.0765	wR_2 = 0.1202	wR_2 = 0.1342
R^a (all data)	R_1 = 0.0352	R_1 = 0.0797	R_1 = 0.1199
	wR_2 = 0.0812	wR_2 = 0.1420	wR_2 = 0.1698
S	1.144	1.035	1.008

[a] $R_1 = \sum|F_o| - |F_c|\sum|F_o|$. $wR_2 = [\sum w[(F_o^2 - F_c^2)^2]/\sum[w(F_o^2)^2]]^{1/2}$. $w = 1/[\sigma^2(F_o^2) + (0.075P)^2]$, where $P = [\max(F_o^2,0) + 2F_c^2]/3$.

were obtained in sealed glass capillaries under dinitrogen and are uncorrected.

3.1. Synthesis

3.1.1. In situ generation of [ZnNdL(H$_2$O)(NO$_3$)$_3$] (precursor)

To a stirred suspension of H_2L (0.033 g, 0.10 mmol) in absolute ethanol (5 ml), $Zn(OAc)_2 \cdot 2H_2O$ (0.022 g, 0.10 mmol) was added and the mixture was refluxed for 5 h. Upon cooling to room temperature, a solution of $Nd(NO_3)_3 \cdot 6H_2O$ (0.044 g, 0.10 mmol) in absolute ethanol (2 ml) was added to the reaction solution, and then further refluxed for another 3 h. The yellow clear solution was then cooled to room temperature and used as the starting material for further reactions.

3.1.2. [Zn$_2$Nd$_2$L$_2$(1,4-BDC)(NO$_3$)$_4$(EtOH)$_2$] · 2MeCN (**1**)

To an ethanol solution (7 ml) of [ZnNdL(H$_2$O)(NO$_3$)$_3$] (0.10 mmol), generated in situ as above, was added half an equivalent of sodium 1,4-benzenedicarboxylate ($Na_2$1,4-BDC, 0.011 g, 0.05 mmol) and the mixture was refluxed for 2 h. The reaction solution was cooled down to room temperature and then 2 ml of anhydrous CH_3CN was added to give a clear yellow solution. Diethyl ether was allowed to diffuse slowly into this solution at room temperature and pale yellow single crystals were obtained in two weeks. Yield: 34 mg (41%). *Anal.* Calc. for $C_{52}H_{58}N_{10}O_{26}Zn_2Nd_2$: C, 37.66; H, 3.53; N, 8.45. Found: C, 37.38; H, 3.45; N, 8.73%. ^{1}H NMR (270 MHz, CD_3OD): 14.66 (1H), 14.06 (1H), 13.80 (1H), 11.60 (1H), 11.50 (1H), 10.68 (1H), 8.55 (1H), 8.12 (1H), 8.02 (1H), 3.64 (1H), 3.61 (6H), 2.66 (6H), 1.20 (4H), −1.06 (2H), −2.46 (1H), −3.64 (1H), −8.24 (2H). IR (KBr, cm^{-1}): 3444b, 1637vs, 1606m, 1560s, 1467vs, 1396s, 1287s, 1240m, 1217vs, 1169w, 1076m, 1037m, 956m, 885m, 818w, 783w, 759m, 738s, 639m, 592m, 536w, 506w, 441w.

Table 2
Selected bond lengths (Å) and angles (°) for **1**

Nd(1)–O(2)	2.401(3)	O(12)–Nd(1)–O(5)	145.73(12)
Nd(1)–O(3)	2.425(3)	O(2)–Nd(1)–O(11)	144.54(11)
Nd(1)–O(12)	2.427(3)	O(3)–Nd(1)–O(11)	106.82(12)
Nd(1)–O(5)	2.484(3)	O(12)–Nd(1)–O(11)	69.94(12)
Nd(1)–O(11)	2.560(4)	O(5)–Nd(1)–O(11)	137.48(12)
Nd(1)–O(9)	2.581(4)	O(2)–Nd(1)–O(9)	114.67(13)
Nd(1)–O(8)	2.638(4)	O(3)–Nd(1)–O(9)	141.94(12)
Nd(1)–O(6)	2.673(4)	O(12)–Nd(1)–O(9)	69.29(13)
Nd(1)–O(1)	2.735(3)	O(5)–Nd(1)–O(9)	141.53(13)
Nd(1)–O(4)	2.737(3)	O(11)–Nd(1)–O(9)	48.75(13)
Nd(1)–N(4)	2.989(4)	O(2)–Nd(1)–O(8)	143.48(11)
Zn(1)–O(13)	1.988(3)	O(3)–Nd(1)–O(8)	115.94(12)
Zn(1)–O(3)	2.010(3)	O(12)–Nd(1)–O(8)	141.75(12)
Zn(1)–O(2)	2.021(3)	O(5)–Nd(1)–O(8)	69.16(12)
Zn(1)–N(2)	2.030(4)	O(11)–Nd(1)–O(8)	71.83(13)
Zn(1)–N(1)	2.039(4)	O(9)–Nd(1)–O(8)	86.42(14)
O(2)–Nd(1)–O(3)	65.92(9)	O(2)–Nd(1)–O(6)	109.02(13)
O(2)–Nd(1)–O(12)	74.75(11)	O(3)–Nd(1)–O(6)	145.39(13)
O(3)–Nd(1)–O(12)	74.88(11)	O(12)–Nd(1)–O(6)	138.79(13)
O(2)–Nd(1)–O(5)	76.61(11)	O(5)–Nd(1)–O(6)	69.18(15)
O(3)–Nd(1)–O(5)	76.52(12)		

3.1.3. [Zn$_4$Nd$_2$L$_4$(1,4-BDC)$_2$](NO$_3$)$_2$ · 2Et$_2$O · 4H$_2$O (**2**)

To an ethanol solution (7 ml) of [ZnNdL(H$_2$O)(NO$_3$)$_3$] (0.10 mmol), generated in situ as above, was added half an equivalent of $Na_2$1,4-BDC (0.011 g, 0.05 mmol) and the mixture was refluxed for 2 h. The resultant solution was cooled down to room temperature and then 2 ml of anhydrous DMF was added to give a clear yellow solution. Diethyl ether was allowed to diffuse slowly into this solution at room temperature and pale yellow single crystals were obtained in two weeks. Yield: 21 mg (31%). *Anal.* Calc. for $C_{96}H_{108}N_{10}O_{36}Zn_4Nd_2$: C, 45.61; H, 4.31; N, 5.54. Found: C, 45.08; H, 3.82; N, 5.65%. ^{1}H NMR (270 MHz, CD_3OD): δ (ppm) 14.64 (2H), 13.98 (2H), 13.76 (2H), 11.57 (2H), 11.45 (2H), 10.62 (2H), 8.52 (2H), 8.03 (2H), 3.71 (2H), 3.57 (2H), 1.29 (3H), −1.06 (6H), −2.47 (2H), −3.69 (2H), −8.38 (6H). IR (KBr, cm^{-1}): 3446b, 1656s, 1637vs, 1606m, 1561m, 1454s, 1389s, 1287m, 1240m, 1217s, 1167m, 1074m, 955m, 850m, 819w, 783w, 736w, 670w, 638m, 590w, 533w, 505w, 440w.

3.1.4. [Zn$_4$Nd$_2$L$_2$(1,4-BDC)$_2$] · [ZnNdL(NO$_3$)$_3$(OAc)]$_2$ (**3**)

To an ethanol solution (7 ml) of [ZnNdL(H$_2$O)(NO$_3$)$_3$] (0.10 mmol), generated in situ as above, was added $Na_2$1,4-BDC (0.005 mg, 0.024 mmol) and the mixture was refluxed for 2 h. The resultant solution was cooled down to room temperature and then 2 ml of anhydrous DMF was added to give a clear yellow

Table 3
Selected bond lengths (Å) and angles (°) for **2**

Nd(1)–O(2)	2.410(4)	O(10)–Nd(1)–O(11)	74.12(14)
Nd(1)–O(10)	2.435(4)	O(10)–Nd(1)–O(7)	152.37(15)
Nd(1)–O(11)	2.437(5)	O(2)–Nd(1)–O(6)	117.48(14)
Nd(1)–O(7)	2.439(5)	O(11)–Nd(1)–O(6)	71.58(14)
Nd(1)–O(6)	2.462(5)	O(2)–Nd(1)–O(3)	65.16(14)
Nd(1)–O(3)	2.466(4)	O(11)–Nd(1)–O(3)	104.46(15)
Nd(1)–O(1)	2.714(4)	O(6)–Nd(1)–O(3)	175.60(14)
Nd(1)–O(8)	2.748(5)	O(10)–Nd(1)–O(1)	123.01(15)
Nd(1)–O(5)	2.828(5)	O(7)–Nd(1)–O(1)	79.13(14)
Nd(1)–O(4)	2.880(5)	O(3)–Nd(1)–O(1)	116.51(14)
Zn(1)–O(9)	1.994(4)	O(10)–Nd(1)–O(8)	138.87(15)
Zn(1)–O(2)	2.025(4)	O(10)–Nd(1)–O(11)	74.12(14)
Zn(1)–O(3)	2.035(4)	O(10)–Nd(1)–O(7)	152.37(15)
Zn(1)–O(2)	2.035(4)	O(2)–Nd(1)–O(6)	117.48(14)
Zn(1)–N(2)	2.042(6)	O(11)–Nd(1)–O(6)	71.58(14)
Zn(1)–N(1)	2.050(6)	O(2)–Nd(1)–O(3)	65.16(14)
Zn(2)–O(12)	1.967(4)	O(11)–Nd(1)–O(3)	104.46(15)
Zn(2)–O(6)	2.006(4)	O(6)–Nd(1)–O(3)	175.60(14)
Zn(2)–O(7)	2.020(5)	O(10)–Nd(1)–O(1)	123.01(15)
Zn(2)–N(3)	2.046(6)	O(7)–Nd(1)–O(1)	79.13(14)
Zn(2)–N(4)	2.050(6)	O(3)–Nd(1)–O(1)	116.51(14)
O(2)–Nd(1)–O(10)	78.72(14)	O(10)–Nd(1)–O(8)	138.87(15)
O(2)–Nd(1)–O(11)	152.84(15)		

Table 4
Selected bond lengths (Å) and angles (°) for **3**

Nd(1)–O(2)	2.409(6)	O(1)–Nd(1)–O(4)	135.4(2)
Nd(1)–O(10)	2.413(6)	O(8)–Nd(1)–O(4)	159.6(2)
Nd(1)–O(6)	2.420(6)	O(9)–Zn(1)–O(3)	99.2(3)
Nd(1)–O(12a)	2.451(7)	O(9)–Zn(1)–O(2)	113.4(3)
Nd(1)–O(7)	2.474(7)	O(3)–Zn(1)–O(2)	80.5(3)
Nd(1)–O(3)	2.506(7)	O(9)–Zn(1)–N(2)	109.9(4)
Nd(1)–O(5)	2.695(6)	O(3)–Zn(1)–N(2)	90.6(4)
Nd(1)–O(1)	2.707(6)	O(2)–Zn(1)–N(2)	136.6(3)
Nd(1)–O(8)	2.861(8)	O(9)–Zn(1)–N(1)	108.3(3)
Nd(1)–O(4)	2.881(8)	O(3)–Zn(1)–N(1)	152.5(3)
Zn(1)–O(9)	1.970(7)	O(2)–Zn(1)–N(1)	88.8(4)
Zn(1)–O(3)	2.009(7)	N(2)–Zn(1)–N(1)	79.9(4)
Zn(1)–O(2)	2.017(7)	O(11a)–Zn(2)–O(6)	112.4(3)
Zn(1)–N(2)	2.049(10)	O(11a)–Zn(2)–O(7)	100.6(3)
Zn(1)–N(1)	2.054(10)	O(6)–Zn(2)–O(7)	81.2(3)
Zn(2)–O(11a)	1.960(7)	O(11a)–Zn(2)–N(3)	105.8(4)
Zn(2)–O(6)	2.018(6)	O(6)–Zn(2)–N(3)	88.4(4)
Zn(2)–O(7)	2.027(8)	O(7)–Zn(2)–N(3)	153.6(3)
Zn(2)–N(3)	2.038(10)	O(11a)–Zn(2)–N(4)	109.0(4)
Zn(2)–N(4)	2.074(12)	O(6)–Zn(2)–N(4)	138.6(3)
O(7)–Nd(1)–O(4)	122.5(2)	O(7)–Zn(2)–N(4)	90.6(4)
O(3)–Nd(1)–O(4)	56.4(2)	N(3)–Zn(2)–N(4)	81.2(5)
O(5)–Nd(1)–O(4)	65.4(2)		

Symmetry operator ($-x$, $1-y$, $-z$) generates equivalent atoms marked with "a".

solution. Diethylether was allowed to diffuse slowly into this solution at room temperature and pale yellow single crystals were obtained in two weeks. Yield: 0.018 g (30%). *Anal.* Calc. for $C_{128}H_{122}N_{18}O_{54}Zn_6Nd_4$: C, 41.04; H, 3.28; N, 6.73. Found: C, 41.48; H, 3.46; N, 6.23%. ^{1}H NMR (270 MHz, CD_3OD): δ (ppm) 14.46 (2H), 13.82 (2H), 13.44 (3H), 11.39 (2H), 11.18 (3H), 10.45 (2H), 8.46 (2H), 8.01 (2H), 3.88 (2H), 3.58 (6H), 1.94 (2H), 1.50 (4H), 1.12 (6H), −0.06 (8H), −0.98 (4H), −2.36 (2H), −3.41 (2H), −8.11 (4H). IR (KBr, cm^{-1}): 1637vs, 1606m, 1560s, 1467s, 1395s, 1287s, 1240m, 1217s, 1169m, 1075m, 1036m, 955m, 884m, 819w, 783w, 738w, 639w, 592w, 536w, 506w, 442w.

3.2. X-ray crystallographic studies

Details of crystallographic parameters, data collection and refinements are listed in Table 1. Selected bond lengths (Å) and angles (°) for **1–3** are listed in Tables 2–4, respectively. Reflection intensity data single crystals of **1–3** with suitable dimensions were mounted onto thin glass fibers. All the intensity data were collected at on a Bruker SMART 1K CCD diffractometer (Mo Kα radiation, λ = 0.71073 Å) in φ and ω scan modes. Structures were solved by the direct method followed by difference Fourier syntheses, and then refined by full-matrix least squares refinement on F^2 using SHELXL. [14]. All the non-hydrogen atoms were refined with anisotropic parameters while H atoms were placed in calculated positions and refined using a riding model. The OAc^- groups in **3** were found to exhibit disorder and refined with fractional occupancies. Neutral atom scattering factors were taken from Cromer and Waber [15].

Acknowledgments

We thank the Robert A. Welch Foundation (Grant F-816), the Texas Higher Education Coordinating Board (ARP 003658-0010-2006), the Petroleum Research Fund, administered by the American Chemical Society (47014-AC5), the Hong Kong Research Grants Council (HKBU 202407) and the Talent Foundation of Northwest University for financial support.

Appendix A. Supplementary data

Views of the solid state packing arrangements, ^{1}H NMR and UV–Vis and solid state emission spectra for **1–3**. CCDC 652078, 652079 and 652080 contain the supplementary crystallographic data for **1, 2 and 3**. These data can be obtained free of charge via http://www.ccdc.cam.ac.uk/conts/retrieving.html, or from the Cambridge Crystallographic Data Centre, 12 Union Road, Cambridge CB2 1EZ, UK; fax: (+44) 1223-336-033; or e-mail: deposit@ccdc.cam.ac.uk. Supplementary data associated with this article can be found, in the online version, at doi:10.1016/j.poly.2008.09.014.

References

[1] (a) S. Tanabe, Comp. Rend. Chim. 5 (2002) 815;
(b) G.R. Motson, J.S. Fleming, S. Brooker, Adv. Inorg. Chem. 55 (2004) 361;
(c) G.A. Kumar, R. Riman, E. Snitzer, J. Ballato, J. Appl. Phys. 95 (2004) 40.
[2] W.T. Carnall, in: K.A. Gschneidner Jr., L. Eyring (Eds.), Handbook on the Physics and Chemistry of Rare Earths, vol. 3, Elsevier, Amsterdam, 1987, p. 171.
[3] (a) J.-C.G. Bünzli, C. Piguet, Chem. Soc. Rev. 34 (2005) 1048;
(b) S. Comby, J.-C.G. Bünzli, in: K.A. Gschneidner Jr., J.-C.G. Bünzli, V.K. Pecharsky (Eds.), Handbook on the Physics and Chemistry of Rare Earths, vol. 37, Elsevier, Amsterdam, 2007, p. 217.
[4] (a) A. Beeby, R.S. Dickins, S. Faulkner, D. Parker, J.A.G. Williams, Chem. Commun. (1997) 1401;
(b) S.I. Klink, G.A. Hebbink, L. Grave, F.C.J.M. van Veggel, D.N. Reinhoudt, L.H. Slooff, A. Polman, J.W. Hofstraat, J. Appl. Phys. 86 (1999) 1181;
(c) A. Beeby, R.S. Dickins, S. FitzGerald, L.J. Govenlock, C.L. Maupin, D. Parker, J.P. Riehl, G. Siligardi, J.A.G. Williams, Chem. Commun. (2000) 1183.
[5] (a) D. Imbert, M. Cantnuel, J.-C.G. Bünzli, G. Bernardinelli, C. Piguet, J. Am. Chem. Soc. 125 (2003) 15698;
(b) S. Torelli, D. Imbert, M. Cantuel, G. Bernardinelli, S. Delahaye, A. Hauser, J.-C.G. Bünzli, C. Piguet, Chem. Eur. J. 11 (2005) 3228.
[6] (a) S.I. Klink, H. Keizer, F.C.J.M. van Veggel, Angew. Chem., Int. Ed. 39 (2000) 4319;
(b) D. Guo, C.-Y. Duan, F. Lu, Y. Hasegawa, Q.-J. Meng, S. Yanagida, Chem. Commun. (2004) 1486.
[7] (a) N.M. Shavaleev, L.P. Moorcraft, S.J.A. Pope, Z.R. Bell, S. Faulkner, M.D. Ward, Chem. Commun. (2003) 1134;
(b) N.M. Shavaleev, L.P. Moorcraft, S.J.A. Pope, Z.R. Bell, S. Faulkner, M.D. Ward, Chem. Eur. J. 9 (2003) 5283;
(c) P.B. Glover, P.R. Ashton, L.J. Childs, A. Rodger, M. Kercher, R.M. Williams, L.D. Cola, Z. Pikramenou, J. Am. Chem. Soc. 125 (2003) 9918;
(d) H.-B. Xu, L.-X. Shi, E. Ma, L.-Y. Zhang, Q.-H. Wei, Z.-N. Chen, Chem. Commun. (2006) 1601.
[8] S.J.A. Pope, B.J. Coe, S. Faulkner, R.H. Laye, J. Chem. Soc., Dalton Trans. (2005) 1482.
[9] (a) W.-K. Wong, H. Liang, W.-Y. Wong, Z. Cai, K.-F. Li, K.-W. Cheah, New J. Chem. 26 (2002) 275;
(b) X.-P. Yang, R.A. Jones, V. Lynch, M.M. Oye, A.L. Holmes, J. Chem. Soc., Dalton Trans. (2005) 849;
(c) X.-P. Yang, R.A. Jones, J. Am. Chem. Soc. 127 (2005) 7686;
(d) W.-K. Wong, X.-P. Yang, R.A. Jones, J.H. Rivers, V. Lynch, W.-K. Lo, D. Xiao, M.M. Oye, A.L. Holmes, Inorg. Chem. 45 (2006) 4340;

(e) W.-K. Lo, W.-K. Wong, W.-Y. Wong, J.-P. Guo, K.-T. Yeung, Y.-K. Cheng, X.-P. Yang, R.A. Jones, Inorg. Chem. 45 (2006) 9315.
[10] X.-P. Yang, R.A. Jones, W.-K. Wong, M.M. Oye, A.L. Holmes, Chem. Commun. (2006) 1836.
[11] (a) M.P. Hogenheide, J. Boersma, G.V. Konten, Coord. Chem. Rev. 155 (1996) 87;
(b) N. Sabbatini, M. Guardigli, M.L. Lehn, Coord. Chem. Rev. 123 (1993) 201;
(c) P. Guerriero, S. Tamburini, P.A. Vigato, Coord. Chem. Rev. 139 (1995) 17.
[12] (a) R. Gheorghe, P. Cucos, M. Andruh, J.P. Costes, B. Donnadieu, S. Shova, Chem. Eur. J. 12 (2006) 187–203;
(b) M. Andruh, Chem. Commun. (2007) 2565–2577.
[13] (a) G.A. Hebbink, S.I. Klink, L. Grave, P.G.B. Oude Alink, F.C.J.M. van Veggel, Chem. Phys. Commun. 3 (2002) 104;
(b) M. Iwamura, Y. Wada, T. Kitamura, N. Nakashima, S. Yanagida, Phys. Chem. Chem. Phys. 2 (2000) 2291.
[14] G.M. Sheldrick, SHELX 97, A Software Package for the Solution and Refinement of X-ray Data, University of Göttingen, Göttingen, Germany, 1997.
[15] D.T. Cromer, J.T. Waber, International Tables for X-ray Crystallography, vol. 4, Kynoch Press, Birmingham, 1974. Table 2.2A.

Polyhedron 28 (2009) 33–42

Contents lists available at ScienceDirect

Polyhedron

journal homepage: www.elsevier.com/locate/poly

Synthesis and electrochemistry of tetrakis(7-coumarinthio-4-methyl)-phthalocyanines, and preparation of their cinnamic acid and sodium cinnamate derivatives

Aliye Aslı Esenpınar, Ali Rıza Özkaya, Mustafa Bulut *

Marmara University, Department of Chemistry, Faculty of Art and Science, 34722 Goztepe, Istanbul, Turkey

ARTICLE INFO

Article history:
Received 13 May 2008
Accepted 29 September 2008
Available online 6 November 2008

Keywords:
Phthalocyanines
Cinnamic acid
Coumarin (*2H*-1-benzopyran-2-one)
Cobalt
Zinc
Spectroelectrochemistry

ABSTRACT

Novel water soluble free-base, Zn(II) and Co(II) metallo phthalocyanines with four cinnamic acid moieties were prepared from the corresponding tetrakis(7-coumarinthio-4-methyl)-phthalocyanine by the lactone ring opening reaction. The new compounds were purified and characterized by elemental analysis, ^{1}H NMR, Maldi-TOF, FT-IR and UV–Vis spectral data. Cyclic and differential pulse voltammetry and *in situ* spectroelectrochemistry of the 2,9,16,23-tetrakis(7-coumarinthio-4-methyl) substituted free-base **1a**, Zn(II) **1b** and Co(II) **1c** phthalocyanines, employed as the starting compounds have been studied. This allowed us not only to identify metal- and phthalocyanine ring-based redox processes of the complexes, but also the effect of aggregation on these processes.

© 2008 Elsevier Ltd. All rights reserved.

1. Introduction

Since their accidental synthesis in 1928, phthalocyanines (Pcs) have enjoyed considerable industrial importance for use in dyes, paints, color for metal surfaces, fabrics and plastics. Accordingly, in recent years, various Pc complexes have been synthesized, characterized and investigated in terms of their properties. Various investigations have concerned the potential utility of metallo phthalocyanines (MPcs) as solar cell functional materials [1], sensing elements in chemical sensors [1,2], optical storage vehicles and nonlinear optical limiting devices [1–3], photoconducting agents in photocopying machines [1–4], electrocatalysts [1–5], and photodynamic reagents for cancer therapy and for other medical applications [1–10]. Water-soluble Pcs are the most promising materials as photosensitizers in photodynamic therapy (PDT), due to their intense absorption in the red region of the optical spectrum (ca. 700 nm) and superior photophysical properties [11]. Therefore, the synthesis of water-soluble MPcs is of great theoretical and practical significance. The solubility of Pcs in water provides additional advantage despite the fact that the aggregation tendency in such polar medium, in particular, is very high [6]. It is well known that due to their extended π-systems, macrocyclic Pc compounds exhibit an high aggregation tendency forming dimeric and oligomeric species, and thus cause a decrease in light absorptions. On the other hand, the formation of Pc aggregates is useful in materials applications where the self-assembly of Pc cores in close proximity is beneficial. The aggregation process of Pcs can be monitored using electronic spectroscopy since the coupling between the electronic states of individual monomeric Pc units causes significant spectral perturbations upon formation of higher order complexes.

Cinnamic acid (3-phenyl-2-propenoic acid) a derivative of phenylalanine, composed of relatively large family of organic acid isomers and possesses antibacterial, antifungal and parasite fighting abilities. In nature, cinnamic acid derivatives are important metabolic building blocks in the production of lignins for higher plants. Carboxyl groups in cinnamic acid molecules are separated from aromatic rings by a C=C double bond, linked with styryl substituents, and thus conjugated with the extended delocalized π-electronic systems. These compounds possess antitumor activity and behave as an important class of pharmaceuticals for high blood pressure and stroke prevention [12]. On the other hand, it is well known that coumarin (2*H*-1-benzopyran-2-one) and its derivatives are biologically active substances with numerous metabolites, and widespread in nature [13]. Some coumarin derivatives were used as anticoagulants, additives in food and cosmetics, reagents in the preparation of insecticides, optical brighteners, dispersed fluorescent, and laser dyes [14–19]. Coumarin and its derivatives are one kind of significant organic fluorescent chromophores and widely used in synthesizing laser dyes, fluorescent whiteners, the organic nonlinear optical materials and so on [20].

* Corresponding author. Tel.: +90 216 3479641/1370; fax: +90 216 3478783.
E-mail addresses: mbulut@marmara.edu.tr, mustafabulut50@gmail.com (M. Bulut).

0277-5387/$ - see front matter © 2008 Elsevier Ltd. All rights reserved.
doi:10.1016/j.poly.2008.09.021

We report herein the synthesis and characterization of new highly water soluble free-base and MPcs (Zn and Co) bearing 2-alkoxycinnamic acid and their sodium salts. Pcs coupled with the cinnamic acid moiety may exhibit biological activities. The introduction of carboxy or amino groups enhances their solubility in water. Moreover, soluble Pcs synthesized in this study may provide new optical, electronic, redox and magnetic properties, and thus increase possible applications. The functions of metal Pcs and their derivatives are based mainly on their redox or electron transfer reactions. The understanding of the redox properties of the Pc complexes is important in terms of their applications in many areas. These processes occur at either the Pc ring or the metal center. However, it is not possible to distinguish such processes by voltammetry alone. Spectroelectrochemistry provide additional support for the assignment of the redox processes. Moreover, spectroelectrochemical studies of Pcs are also important in identifying the aggregation–deaggregation equilibrium of Pcs which is known to affect their redox behavior. Taking into consideration these purposes in this study, we also report voltammetry and *in situ* spectroelectrochemistry of **1a**, **1b** and **1c**.

2. Experimental

Routine IR spectra were recorded on a Shimadzu Fourier Transform FTIR-8300 Infrared Spectrometer using KBr pellets, electronic spectra on a Shimadzu UV-1601 UV–Vis Spectrometer, ^{1}H NMR spectra on a Varian Unity Inova 500 MHz NMR Spectrometer using TMS as internal reference at Erzurum University Laboratory. Mass spectra were performed on a Bruker Daltonic Autoflex MALDI-TOF spectrometer at Marmara University.

2,9,16,23-Tetrakis(7-coumarinthio-4-methyl)-phthalocyanine (**1a**), 2,9,16,23-tetrakis(7-coumarinthio-4-methyl)-phthalocyaninatozinc (**1b**) and 2,9,16,23-tetrakis(7-coumarinthio-4-methyl)-phthalocyaninatocobalt (**1c**) were synthesized according to reported procedure [21]. All reagents and solvents were of reagent-grade quality obtained from commercial suppliers. All solvents were purified and stored over molecular sieves (4 Å). The homogeneity of the products was checked at each stage in their synthesis by TLC (SiO_2).

The cyclic voltammetry, differential pulse voltammetry, and controlled potential chronocoulometry (CPC) measurements were carried out with a Princeton Applied Research Model Versostat II potentiostat/galvanostat controlled by an external PC and utilizing a three-electrode configuration at 25 °C. The working electrode was a Pt plate with a surface area of 0.10 cm^2. The surface of the working electrode was polished with H_2O suspension of Al_2O_3 before each run. The last polishing was done with a particle size of 50 nm. A Pt wire served as the counter electrode. A saturated calomel electrode (SCE) was employed as the reference electrode and separated from the bulk of the solution by a double bridge. Electrochemical grade tetrabutylammonium perchlorate (TBAP) in extra pure DMSO was employed as the supporting electrolyte at a concentration of 0.10 mol dm^{-3}. High purity N_2 was used for deoxygenating the solution at least 20 min prior to each run and to maintain a nitrogen blanket during the measurements. For CPC studies, a Pt gauze working electrode (10.5 cm^2 surface area), a Pt wire counter electrode separated by a glass bridge, and a SCE as reference electrode were used. Spectroelectrochemical measurements were carried out by an Agilent Model 8453 diode array spectrophotometer equipped with the potentiostat/galvanostat and utilizing an optically transparent thin layer (OTTLE) cell with three-electrode configuration at 25 °C. The working electrode was transparent Pt gauze. A Pt wire counter electrode and a SCE reference electrode separated from the bulk of the solution by a double bridge were used.

*2.1. General procedure for the synthesis of 2,9,16,23-tetrakis[(E)-3-(2-(hexyloxy)-4-mercaptophenyl)but-2-enoic acid] phthalocyanine (**2a**), 2,9,16,23-tetrakis[(E)-3-(2-(hexyloxy)-4-mercaptophenyl)but-2-enoic acid] phthalocyaninatozinc (**2b**), their sodium salts and 2,9,16,23-tetrakis[(E)-3-(2-(hexyloxy)-4-mercaptophenyl)but-2-enoic acid] phthalocyaninatocobalt (**2c**)*

To a solution of each 2,9,16,23-tetrakis(7-coumarinthio-4-methyl) substituted Pc [(0.075 g, 0.06 mmol H_2Pc, **1a**) (0.050 g, 0.03 mmol ZnPc, **1b**) (0.050 g, 0.03 mmol CoPc, **1c**)] in dry DMSO (10 ml) was added NaOH pallets (0.024 g, 0.60 mmol for **1a**; 0.015 g, 0.37 mmol for **1b** and 0.015 g, 0.37 mmol for **1c**). Each mixture was held at 50 °C for two days and then cooled to room temperature. 1-Bromohexane (0.05 ml) was added to each mixture and it was stirred at room temperature in a sealed tube for two days. Each product poured into 2 M HCl ice-water. Each precipitate was collected by filtration, washed with water and finally dried. The products were purified by extraction with ethylacetate, ethanol, methanol, acetone, THF and $CHCl_3$. The compounds **2a** and **2b** were soluble in DMF, DMSO and 5% NaOH. Compound **2c** was soluble in DMF and DMSO, but insoluble in 5% NaOH.

Sodium salts of **2a** and **2b** were obtained by dissolving these compounds in 5% NaOH, and then precipitating with MeOH.

*2.1.1. Compound **2a***

Yield: 0.060 g (60%). M.p.: > 300 °C. IR γ_{max} (cm^{-1}): 3053 (aryl CH), 2858–2925 (alkyl CH), 3276 (NH), 2950–3400 (OH), 1718 (C=O acid), 1595 (C=C), 1242 (Ar–O–C). ^{1}H NMR δ_H (DMSO): 7.22–8.09 (m, 24H, Ar–H), 6.24 (s, 4H, C=C*H*), 4.30–4.40 (t, 8H, OCH_2Ar), 3.65–3.70 (t, 8H, OCH_2), 2.40 (s, 12H, CH_3), 1.74–2.10 (t, 8H, C$H_2$$CH_2$OAr), 0.85–1.43 (m, 72H, alkyl CH), 11.0 (b, OH). UV–Vis (DMF) λ_{max} (nm) ($\log\varepsilon$): 689 (4.66), 641 (4.37), 343 (4.80). *Anal.* Calc. for $C_{96}H_{98}N_8O_{12}S_4$ (1682): C, 68.48; H, 5.82; N, 6.65; S, 7.60. Found: C, 68.17; H, 5.02; N, 6.58; S, 6.62%. MS (MALDI-TOF) *m/z*: 1682 $[M]^+$, 1680 $[M-2]^+$.

*2.1.2. Compound **2a** sodium salt*

IR γ_{max} (cm^{-1}): 3040 (aryl CH), 2850–2902 (alkyl CH), 3272 (NH), 1639 (C=O acid), 1598 (C=C), 1249 (Ar–O–C), 3396 (moisture peak). UV–Vis (5% NaOH) λ_{max} (nm) ($\log\varepsilon$): 703 (4.39), 664 (4.38), 324 (4.70). *Anal.* Calc. for $C_{96}H_{94}N_8O_{12}S_4Na_4$ (1770): C, 65.08; H, 5.31; N, 6.32; S, 7.23. Found: C, 64.98; H, 5.15; N, 6.42; S, 7.04%. MS (MALDI-TOF) *m/z*: 1770 $[M]^+$, 1768 $[M-2]^+$.

*2.1.3. Compound **2b***

Yield: 0.025 g (38%). M.p.: > 300 °C. IR γ_{max} (cm^{-1}): 3058 (aryl CH), 2858–2918 (alkyl CH), 2940–3450 (OH), 1718 (C=O acid), 1595 (C=C), 1242 (Ar–O–C). ^{1}H NMR δ_H (DMSO): 7.48–8.14 (m, 24H, Ar–H), 6.12 (s, 4H, C=C*H*), 4.30–4.421 (t, 8H, OCH_2Ar), 3.59–3.70 (t, 8H, OCH_2), 2.36 (s, 12H, CH_3), 1.68–2.18 (t, 8H, C$H_2$$CH_2$OAr), 0.82–1.40 (m, 72H, alkyl CH), 11.27 (b, OH). UV–Vis (DMF) λ_{max} (nm) ($\log\varepsilon$): 691 (4.96), 624 (4.22), 341 (4.98). *Anal.* Calc. for $C_{96}H_{96}N_8O_{12}S_4Zn$ (1745): C, 66.01; H, 5.50; N, 6.41; S, 7.33. Found: C, 67.98; H, 5.45; N, 6.28; S, 7.24%. MS (MALDI-TOF) *m/z*: 1745 $[M]^+$.

*2.1.4. Compound **2b** sodium salt*

IR γ_{max} (cm^{-1}): 3043 (aryl CH), 2852–2902 (alkyl CH), 1650 (C=O acid), 1465 (C=C), 1249 (Ar–O–C), 3425 (moisture peak). UV–Vis (5% NaOH) λ_{max} (nm) ($\log\varepsilon$): 701 (4.41), 657 (4.63.), 357 (4.60). *Anal.* Calc. for $C_{96}H_{92}N_8O_{12}S_4ZnNa_4$ (1833): C, 62.84; H, 5.01; N, 6.11; S, 6.98. Found: C, 62.04; H, 4.98; N, 6.01; S, 6.78%. MS (MALDI-TOF) *m/z*: 1833 $[M]^+$.

*2.1.5. Compound **2c***

Yield: 0.027 g (41%). M.p.: > 300 °C. IR γ_{max} (cm^{-1}): 3058 (aryl CH), 2858–2933 (alkyl CH), 2950–3400 (OH), 1718 (C=O acid), 1595 (C=C), 1242 (Ar–O–C). UV–Vis (DMF) λ_{max} (nm) ($\log\varepsilon$): 691 (4.84), 627 (4.37), 305 (4.94). *Anal.* Calc. for $C_{96}H_{96}N_8O_{12}S_4Co$ (1739): C, 66.24; H, 5.52; N, 6.44; S, 7.36. Found: C, 65.17; H, 5.50; N, 6.36; S, 7.01%. MS (MALDI-TOF) *m/z*: 1739 $[M]^+$.

*2.2. General procedure for the 2,9,16,23-tetrakis[(E)-3-(2-(2-(dimethylamino)ethoxy)-4-mercaptophenyl)but-2-enoic acid] phthalocyanine (**3a**) and 2,9,16,23-tetrakis[(E)-3-(2-(2-(dimethylamino)ethoxy)-4-mercaptophenyl)but-2-enoic acid] phthalocyaninatozinc (**3b**) and their sodium salts*

To a solution of each 2,9,16,23-tetrakis(7-coumarinthio-4-methyl) substituted Pc [(0.050 g, 0.04 mmol H_2Pc, **1a**) (0.050 g, 0.04 mmol ZnPc, **1b**) in dry DMSO (10 ml) was added NaOH pallets (0.015 g, 0.40 mmol for **1a** and 0.015 g, 0.40 mmol for **1b**). Each mixture was stirred at room temperature in vacuo for two days, and then 2-(dimethylamino)chloroethanhydrochloride salt (0.058 g, 0.40 mmol for **1a** and 0.058 g, 0.40 mmol for **1b**) was added. Each mixture was stirred at room temperature in a sealed tube for two days in vacuo and each product was poured into acetone (10 ml). Each precipitate was collected by filtration, washed with 2 M HCl for removing excess NaOH and water, and finally dried. The green products **3a** and **3b** were purified by extraction with ethylacetate, ethanol, methanol, acetone, THF and $CHCl_3$. The compounds were soluble in DMF, DMSO and 8% NaOH.

Sodium salts of **3a** and **3b** were obtained by dissolving these compounds in 8% NaOH, and then precipitating with MeOH.

*2.2.1. Compound **3a***

Yield: 0.040 g (63%). M.p.: > 300 °C. IR γ_{max} (cm^{-1}): 3053 (aryl CH), 2819–2931 (alkyl CH), 3278 (NH), 2950–3400 (OH), 1639 (C=O acid), 1596 (C=C), 1242 (Ar–O–C). ^1H NMR δ_H (DMSO): 7.36–8.14 (m, 24H, Ar–H), 6.32 (s, 4H, C=C*H*), 4.36–4.45 (t, 8H, OCH_2Ar), 3.66–3.74 (t, 8H, OCH_2), 2.46 (s, 12H, CH_3), 1.78–2.15 (t, 8H, CH_2CH_2OAr), 0.90–1.46 (m, 72H, alkyl CH); 11,96 (b, OH), UV–Vis (DMF) λ_{max} (nm) ($\log\varepsilon$): 691 (4.33), 651 (4.07), 343 (4.39). *Anal.* Calc. for $C_{88}H_{86}N_{12}O_{12}S_4$ (1630): C, 64.78; H, 5.27; N, 10.30; S, 7.85. Found: C, 63.26; H, 4.93; N, 9.97; S, 7.82%. MS (MALDI-TOF) *m/z*: 1630 $[M]^+$, 1628 $[M-2]^+$.

*2.2.2. Compound **3a** sodium salt*

IR γ_{max} (cm^{-1}): 3042 (aryl CH), 2914–2950 (alkyl CH), 3275 (NH), 1642 (C=O acid), 1597 (C=C), 1245 (Ar–O–C), 3390 (moisture peak). UV–Vis (8% NaOH) λ_{max} (nm) ($\log\varepsilon$): 702 (3.58), 661 (4.08), 327 (4.40). *Anal.* Calc. for $C_{88}H_{82}N_{12}O_{12}S_4Na_4$ (1718): C, 61.46; H, 4.77; N, 9.77; S, 7.45. Found: C, 61.48; H, 4.68; N, 8.96; S, 7.04%. MS (MALDI-TOF) *m/z*: 1718 $[M]^+$, 1716 $[M-2]^+$.

*2.2.3. Compound **3b***

Yield: 0.020 g (32%). M.p.: > 300 °C. IR γ_{max} (cm^{-1}): 3055 (aryl CH), 2892–2934 (alkyl CH), 2950–3400 (OH), 1704 (C=O acid), 1596 (C=C), 1234 (Ar–O–C); ^1H NMR δ_H (DMSO): 7.34–8.13 (m, 24H, Ar–H), 6.30 (s, 4H, C=C*H*), 4.30–4.40 (t, 8H, OCH_2Ar), 3.62–3.72 (t, 8H, OCH_2), 2.40 (s, 12H, CH_3), 1.74–2.10 (t, 8H, CH_2CH_2OAr), 0.91–1.42 (m, 72H, alkyl CH); 11,90 (b, OH). UV–Vis (DMF) λ_{max} (nm) ($\log\varepsilon$): 690 (4.98), 626 (4.40), 341 (4.85). *Anal.* Calc. for $C_{88}H_{84}N_{12}O_{12}S_4Zn$ (1693): C, 62.37; H, 4.96; N, 9.92; S, 7.56. Found: C, 61.26; H, 4.93; N, 9.97; S, 7.42%. MS (MALDI-TOF) *m/z*: 1693 $[M]^+$, 1691 $[M-2]^+$.

*2.2.4. Compound **3b** sodium salt*

IR γ_{max} (cm^{-1}): 3040 (aryl CH), 2859–2916 (alkyl CH), 1654 (C=O acid), 1469 (C=C), 1245 (Ar–O–C), 3430 (moisture peak). UV–Vis (8% NaOH) λ_{max} (nm) ($\log\varepsilon$): 703 (4.64), 658 (4.48), 319 (4.72). *Anal.* Calc. for $C_{88}H_{80}N_{12}O_{12}S_4ZnNa_4$ (1781): C, 59.29; H, 4.49; N, 9.43; S, 7.18. Found: C, 58.16; H, 4.45; N, 9.26; S, 7.08%. MS (MALDI-TOF) *m/z*: 1781 $[M]^+$, 1779 $[M-2]^+$.

3. Result and discussion

3.1. Synthesis and characterization

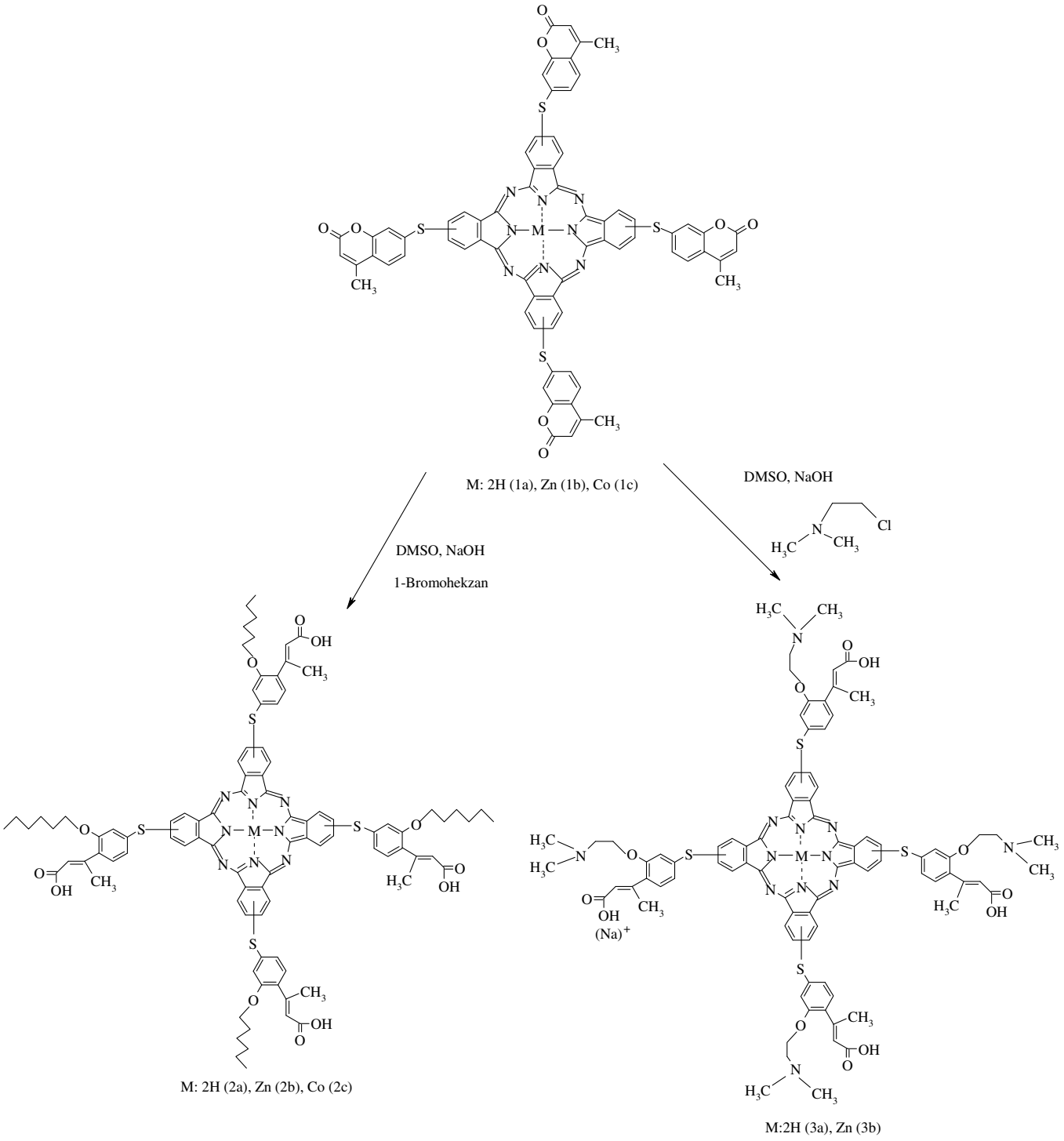
Novel free-base and metallo Pcs containing four 7-phenylthio-4-methylcoumarin moieties were synthesized according to the reported procedure [21]. The coumarin substituents on the periphery of the Pc bring out a vast number of possibilities for binding with different nucleophiles. Opening all of the four lactone rings in **1a**, **1b** and **1c** with NaOH in DMSO, then concomitant reaction of formed hydroxy group with 1-bromohexane or 2-(dimethylamino)chloroethane gave Pcs **2a**, **2b** and **2c** or **3a** and **3b**. These compounds were purified by extraction with ethylacetate, ethanol, methanol, acetone, THF and $CHCl_3$. The products **2a** and **2b** show good solubility in organic solvents such as DMF, DMSO and 5% $NaOH_{(aq)}$. Compound **2c** was soluble in DMF and DMSO, but insoluble in 5% $NaOH_{(aq)}$. For this reason, sodium salt of **2c** could not be prepared. Compounds **3a** and **3b** were soluble in DMF, DMSO and 8% NaOH.

Starting from 2,9,16,23-tetrakis(7-coumarinthio-4-methyl)-phthalocyanine (**1a**), 2,9,16,23-tetrakis(7-coumarinthio-4-methyl)-phthalocyaninatozinc (**1b**) and 2,9,16,23-tetrakis(7-coumarinthio-4-methyl)-phthalocyaninatocobalt (**1c**), the derived novel cinnamic acid substituted Pcs **2a**, **2b**, **2c**, **3a** and **3b** were prepared according to the route shown in Scheme 1. The characterization of the products involved a combination of methods including, ^1H NMR, FT-IR, UV–Vis, elemental analysis and MALDI-TOF spectrometer.

In the IR spectra, N–H stretching peaks in the core of free-base Pcs (**2a**, and **3a**) were monitored at around 3280 cm^{-1}. The increase in the intensity of alkyl CH peaks and the appearance of C–OH stretching bands in the range of 2940–3400 cm^{-1} for **2a**, **2b** and **2c**, as compared with that of starting compounds (**1a**, **1b** and **1c**) [21], confirmed the formation of cinnamic acid substituted Pcs with long alkyl chains. C–OH stretching bands for **3a** and **3b** were observed in a similar range. Additionally, C–N stretching for **3a** and **3b** were also recorded around 1020–1420 cm^{-1}. All these IR data clearly proved the opening of the lactone ring of coumarin substituted starting compounds.

^1H NMR spectra of the compounds synthesized were almost identical except for small shifts. These spectra exhibited vinilic protons at 6.24 ppm for **2a**, 6.12 ppm for **2b**, 6.32 ppm for **3a** and 6.30 ppm for **3b**. The aromatic protons of all compounds appeared at 7.22–8.09 ppm for **2a**, 7.48–8.14 ppm for **2b**, 7.36–8.14 ppm for **3a** and 7.34–8.13 ppm for **3b**. The acid protons were observed at 11.0 ppm for **2a**, 11.27 ppm for **2b**, 11.96 ppm for **3a** and 11.90 ppm for **3b**. A common feature of these spectra is the broad signals probably caused by the aggregation of Pcs.

A closer investigation of the mass spectra of the Pcs confirmed the proposed structures. In the mass spectra of the compounds, the $[M^+]$ peaks were identified easily, as shown as an example in Fig. 1 for **3a**. The MALDI-TOF-MS spectra provided definitive characterization of the structures of all complexes. Linear mode positive ion MALDI mass spectra could be obtained in 7-hydroxycoumarin (umbelliferone) MALDI matrix. The protonated molecular ion peak of the complexes were observed at 1682 Da for **2a**, at 1745 Da for **2b**, at 1339 Da for **2c**, at 1630 Da for **3a** and at 1693 Da for **3b**. These mass values corresponded to the theoretical calculated mass values for the molecular ion of all the complexes.



Scheme 1. Synthesis of the free-base and metallo phthalocyanines with four cinnamic acid moieties.

The Pcs synthesized in this study show typical electronic spectra with two absorption regions, one of them in the UV region at about 300–350 nm (B band) and the other in the visible part of the spectrum around 600–700 nm (Q band). Fig. 2A exemplifies the UV–Vis spectra of the Pcs involving cinnamic acid (**2a**, **2b** and **2c**) in DMF. The absorption bands around 700 nm correspond to characteristic $a_{1u}(\pi) \rightarrow e_g(\pi^*)$ transitions while the B bands are assigned to $a_{2u}(\pi) \rightarrow e_g(\pi^*)$ transitions of the complexes with fully conjugated 18π electron system. Free-base derivative, **2a** showed a splitted Q band absorption in the visible region, as expected, due to its D_{2h} symmetry. On the other hand, the weak bands around 641 nm, as satellite, at the blue side of the main Q band, observed for **2b** and **2c** are known as "vibrionic Q_m band". The absence of an additional absorption band around 630–640 nm at the blue side of the main Q band shows that complexes **2b** and **2c** are mainly in the form of monomers in DMF. The UV–Vis spectral behavior of tetra substituted coumarin Pcs (**1a**, **1b** and **1c**) and involving 2-(dimethylamino)ethyloxy tetra substituted cinnamic acid Pcs (**3a**, **3b**) were considerably similar to those of **2a**, **2b** and **2c**, except small shifts due to different substituent effects (Fig. 2B). However, the UV–

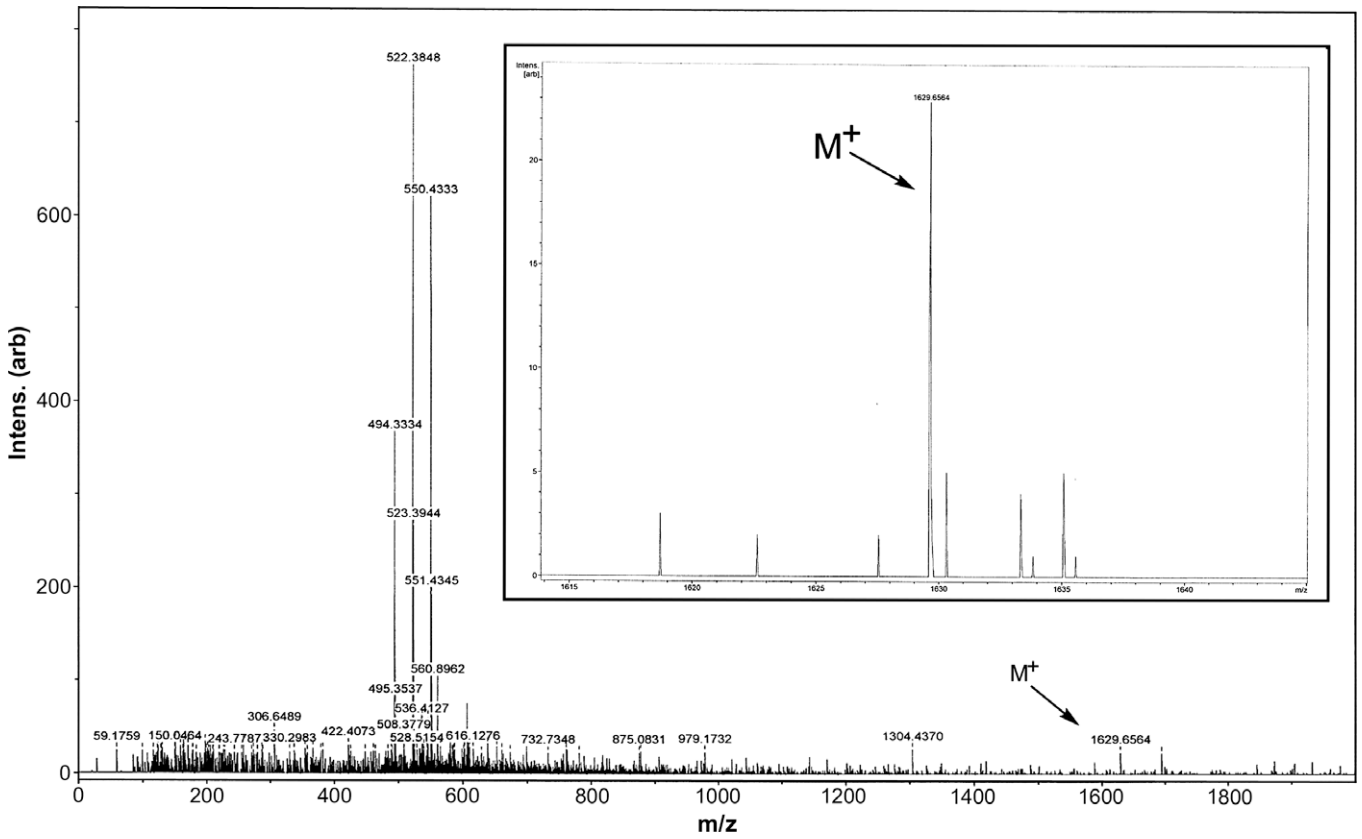


Fig. 1. The positive ion and linear mode MALDI-TOF MS spectrum of **3a** in 7-hydroxycoumarin (umbelliferone) MALDI matrix using nitrogen laser accumulating 50 laser shots. Inset spectrum shows expanded molecular mass region of the complex.

Vis spectra of the Pc compounds in DMSO and especially in water are remarkably different from those of in DMF. Typical spectra of some Pc compounds in various solvents are shown in Fig. 3. As shown in Fig. 3A for **2b**, the appearance of a new band around 656 nm, at the blue side of the main Q band absorption, in DMSO and water suggests clearly the presence of aggregated species. Aggregation is usually depicted as a coplanar association and strongly dependent on the concentration and nature of the solvent. Generally, it results in a decrease in intensity in the components of the Q band corresponding to the monomeric species, in the mean time a new broader and blue-shifted band is observed to increase in intensity. This shift to lower wavelengths corresponds to H-type aggregates. At the high concentrations or with solvents of high polarity, it is usually more pronounced. Fig. 3B indicates the effect of increasing concentration on the UV–Vis spectra of 1×10^{-6} mol dm^{-3} **3b** in DMSO, as an example. At the beginning (for 1×10^{-6} mol dm^{-3} **3b**), the intensities of two bands are approximately equal to each other. As the concentration of **3b** is increased, the band with the lower wavelength becomes higher in intensity as compared with the other band. This clearly suggests that the band with the higher energy corresponds to the aggregated species, and provides additional support for H-type aggregation. The other complexes also displayed a similar behavior in the same solvents.

3.2. Electrochemistry and spectroelectrochemistry

Voltammetry and spectroelectrochemistry of the complexes **1a**, **1b** and **1c** were performed in de-aerated DMSO containing TBAP. The half-wave potentials ($E_{1/2}$) are listed in Table 1. Controlled potential coulometry studies at the peak potentials suggested that the number of electrons transferred for all redox processes of the complexes are one with deviation from unity for some couples at the end of potential window. Anyway, in Pcs, multi-electron processes occurring in one step are not common. Thus, all the complexes displayed three reductions and one oxidation signal. The ratio of anodic to cathodic peak currents for the redox couples were near unity and anodic to cathodic peak separation, ΔE ranged 60–200 mV, thus suggesting reversible to quasi-reversible behavior, ΔE of 90 mV at 0.100 V s^{-1} was obtained for the ferrocene internal standard.

Fig. 4 shows the cyclic voltammogram (CV) in (A) and differential pulse voltammogram (DPV) in (B) of 5.00×10^{-4} mol dm^{-3} **1a** in DMSO/TBAP, with three reduction processes (labelled II–IV) and an oxidation process (labelled I). These processes are clearly ligand-based. The rounded shape of the reduction couples, II and III, are probably due to the aggregation of the complex which is known to occur usually at high concentrations employed for voltammetric studies. Fig. 5 shows the cyclic and differential pulse voltammograms (CV in A and DPV, in B) of 5.00×10^{-4} mol dm^{-3} **1b** in DMSO/TBAP. The redox potentials of **1a** and **1b** are similar to each other except half-wave potentials of **1b** are usually more negative as compared with those of **1a**. This can be attributed to the difference in the polarizing effects of Zn(II) and 2H. The similarity between the redox potentials of **1a** and **1b** suggests that the redox processes of **1b** are also ligand-based. Anyway, the central Zn metal in ZnPc complexes is electro-inactive [22]. Reduction of the Pc ligand is associated to the position of the lowest occupied molecular orbital (LUMO) whereas oxidation of the ligand is associated to the position of the highest occupied molecular orbital (HOMO). Thus, the difference between the potentials of the first oxidation and the first reduction processes ($\Delta E_{1/2}$) reflects the

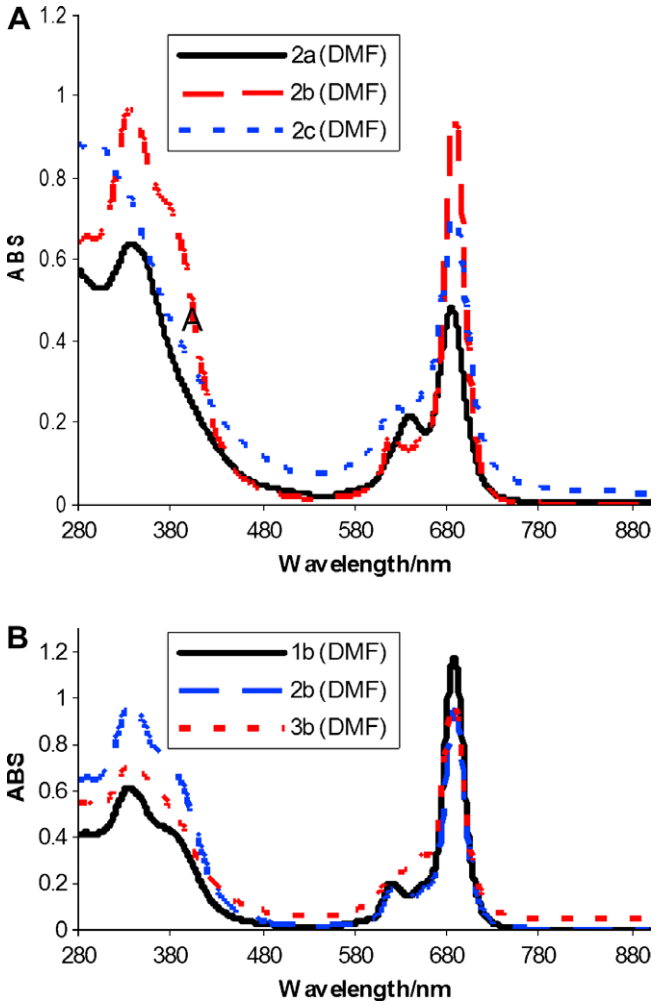


Fig. 2. UV–Vis spectra of 1×10^{-5} mol dm^{-3} **2a**, **2b** and **2c** (A) and **1b**, **2b** and **3b** (B) in DMF.

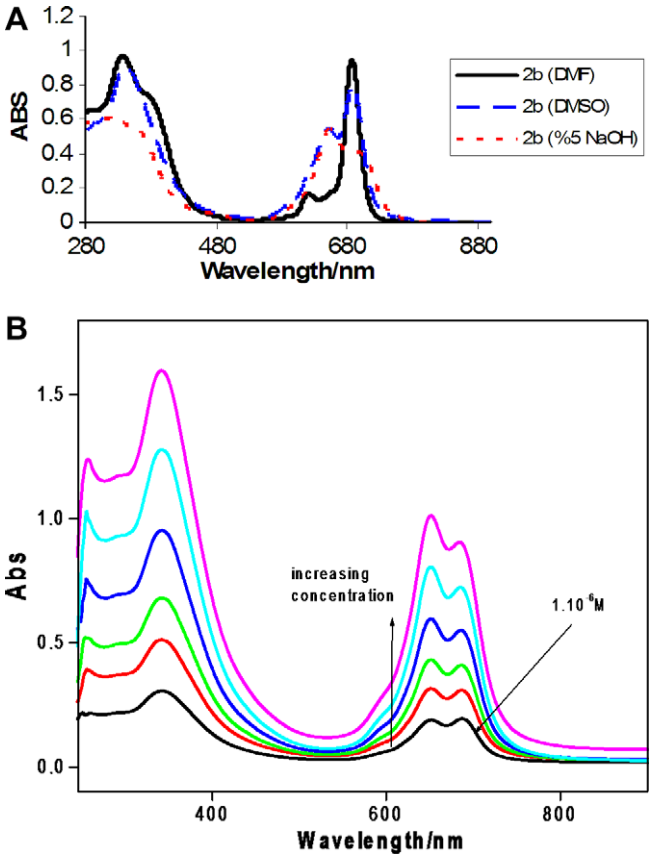


Fig. 3. UV–Vis spectra of 1×10^{-5} mol dm^{-3} **2b** in various solvents (DMF, DMSO and 5% NaOH) (A), and the effect of increasing concentration on the UV–Vis spectra of 1×10^{-6} mol dm^{-3} **3b** in DMSO (B).

homo–lumo gap for free-base Pcs and it is closely related with the homo–lumo gap in MPc species involving redox-inactive metal center. $\Delta E_{1/2}$ values recorded for **1a** (1.35 V) and **1b** (1.47 V) in this study are in agreement with the values reported previously for the relevant Pcs involving redox-inactive metal center [22–26].

Fig. 6 shows the cyclic and differential pulse voltammograms (CV in A and DPV in B) of 5.00×10^{-4} mol dm^{-3} 1 c in DMSO/TBAP. The redox potentials of **1c** are highly different in comparison with those of **1a** and **1b** (Table 1). As compared with **1a** and **1b**, the first reduction of Co(II) complex, **1c** occurs at a potential less negative (−0.40 V versus SCE), and the first oxidation at a potential less positive (0.43 V versus SCE) (Table 1). This difference in the voltammetric behavior is due to the fact that MPcs, such as MnPc, CoPc and FePc, having a metal that possesses energy levels lying between the HOMO and the LUMO of the Pc ligand, in general exhibit redox processes centered on the metal [22,25–28]. For CoPc complexes, the first oxidation and first reduction processes occur on the metal center in polar solvents such as DMF and DMSO, however the first oxidation process occurs on the Pc ring in nonpolar solvents such as DCM and THF. Therefore, the first reduction (couple II) and the first oxidation (couple I) processes of **1c** could be assigned to the $[Co(II)Pc(-2)]/[Co(I)Pc(-2)]^{-}$ and $[Co(II)Pc(-2)]/[Co(III)Pc(-2)]^{+}$ redox couples, respectively. The second and third reduction processes (couples III and IV) are probably ligand-based and can be assigned to $[Co(I)Pc(-2)]^{-}/[Co(I)Pc(-3)]^{2-}$ and $[Co(I)Pc(-3)]^{2-}/[Co(I)Pc(-4)]^{3-}$. The separation between the first oxidation and the first reduction potentials of the metal center for the Co(II) complex, **1c** (0.83 V) is comparable with the relevant values in the literature [22,25–28], and does not reflect the HOMO–LUMO gap.

Table 1
The electrochemical data for **1a**, **1b** and **1c**.

Complex	Redox processes		$E_{1/2}$[a] (V versus SCE)	ΔE_p[b] (V)	ΔE_{12}[c] (V)
1a	$[H_2Pc(-1)]^{-}/H_2Pc(-2)$	I	0.72	0.06	1.35
	$H;Pc(-2)/[H_2Pc(-3)]^{-}$	II	−0.63	0.10	
	$[H:Pc(-3)]^{-}/[H_2Pc(-4)]^{2-}$	III	−0.88	0.20	
	$[H:Pc(-4)]^{2-}/[H:Pc(-5)]^{3-}$	IV	−1.64	0.20	
1b	$[Zn(II)Pc(-1)^{-}/Zn(II)Pc(-2)$	I	0.67	0.06	1.47
	$Zn(II)Pc(-2)/[Zn(II)Pc(-3)]^{-}$	II	−0.80	0.10	
	$[Zn(H)Pc(-3)]^{-}/$ $[Zn(II)Pc(-4)]^{-}$	III	−1.19	0.06	
	$[Znai)Pc(-4)]^{2-}/$ $[Zn(II)Pc(-5)]^{3-}$	IV	−1.45	0.08	
1c	$[Co(III)Pc(2)]^{-}/Co(II)Pc(2)$	I	0.13	0.11	0.83
	$Co(II)Pc(-2)/[Co(I)Pc(-2)]^{-}$	II	−0.40	0.20	
	$[Coa)Pc(-2)]^{-}/$ $[Co(I)Pc(-3)]^{-}$	III	−1.30	0.08	
	$[Co(I)Pc(-3)]^{-}/$ $[Co(I)Pc(-4)]^{3-}$	IV	1.65	0.10	

[a] $E_{1/2} = (E_{pa} - E_{pc})/2$ at 0.100 V s^{-1}.
[b] $\Delta E_p = E_{pa} - E_{pc}$ at 0.100 V s^{-1}.
[c] $\Delta E_{1/2} = E_{1/2}$ (first oxidation) − $E_{1/2}$ (first reduction). This value reflects the HOMO–LUMO gap for **Ia** and **Ib** but does not for **Ic**.

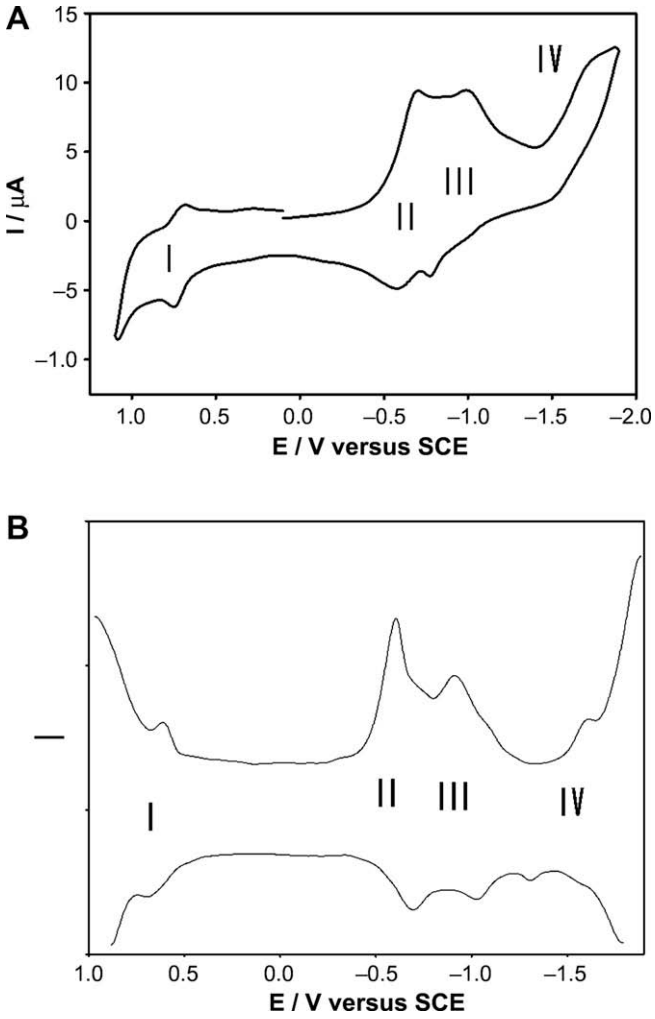


Fig. 4. Cyclic (A) and differential pulse (B) voltammograms of 2.5×10^{-4} mol dm^{-3} **1a** in DMSO/TBAP.

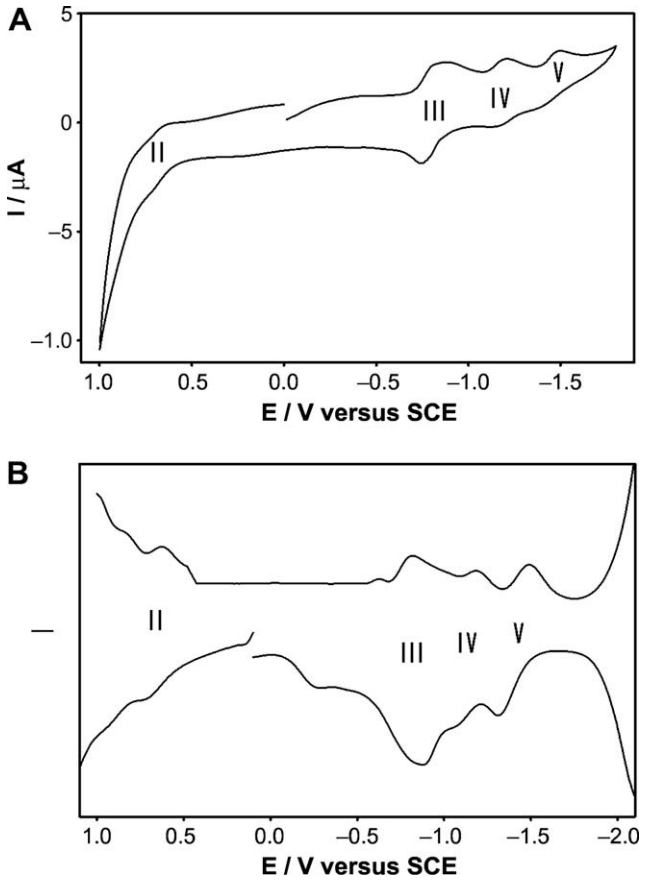


Fig. 5. Cyclic (A) and differential pulse (B) voltammograms of 2.5×10^{-4} mol dm^{-3} **1b** in DMSO/TBAP.

Spectroelectrochemical measurements in solution have a vital importance in confirming the assignment of the redox processes. Thus, *in situ* spectroelectrochemistry of MPcs, **1b** and **1c**, during the controlled potential electrolysis of the complexes was employed to further provide information on the nature of the redox processes observed in Figs. 5 and 6, respectively. The spectral changes during the redox processes of **1b** are shown in Fig. 7. Aggregation in MPc complexes is typified by a broadened or split Q band, with the high energy band being due to the aggregate and the low energy band due to the monomer. Thus, the starting spectrum with the split Q band reflects clearly the presence of an equilibrium between the aggregated and monomer species (Fig. 7A). Upon first reduction at −1.00 V versus SCE, two different types of subsequent spectral changes are observed (Fig. 7A and B). These spectral changes are accompanied by a very slight increase in absorption at around 500 nm. It appears that monomer-aggregate equilibrium shifts toward monomer species just before the first reduction process, since the band at 650 nm decreases and the other at 680 nm increases with a red shift. Normally, the shift in the Q band absorption is not observed during the reduction of Pc ligand. The formation of deaggregated species is confirmed by well-defined isosbestic points appeared at 560, 676 and 724 nm during the former spectral changes. The slight increase in absorption at around 500 nm may be due to the reduction of some aggregated species. The former spectral changes in Fig. 7A are followed by a decrease in both the Q band absorptions at 650 and 690 nm without shift, and the appearance of a new band at 580 nm (Fig. 7B). Well-defined isosbestic points are observed at 472, 615 and 735 nm. These spectral changes probably correspond to the reduction of disaggregated species [29,30]. The new band at 580 nm and the decrease in the Q band absorption without shift are characteristic for Pc ring reduction, and thus the formation of Zn(II)Pc(−3) species, confirming the CV assignment of couple II to Pc(−2)/Pc(−3) redox process [31,32]. In the mean time, two new bands with low intensity at 828 and 974 nm form in the near IR region, during the latter changes. These bands are usually observed in dinuclear Pcs and attributed to the some conformational changes during the redox processes [33], but also observed for some mononuclear Pcs [34,35]. The well-defined UV–Vis spectral changes during the second reduction of **1b** with applied potential of −1.25 V in OTTLE cell are shown in Fig. 7C. A decrease in the absorption of the bands at 650, 680 and 690 nm without shift are observed while a new band (at 746 nm) at the red side of the Q band appears. In the mean time, the absorption of the band at 828 nm increases with disappearance of the one at 974 nm. The decrease in the Q band absorption without shift and the appearance of a new band in the Q band region are characteristic for ligand reduction. The first and second reduction processes were chemically reversible on the spectroelectrochemical time scale and the nearly original spectrum of compound **1b** was obtained upon reoxidation at a positive potential of the first reduction potential. Thus, the species produced during the first and second reduction processes remained stable throughout the measurement. The subsequent third reduction is also expected to be on the ring in comparison with literature [22]. The UV–Vis spectral

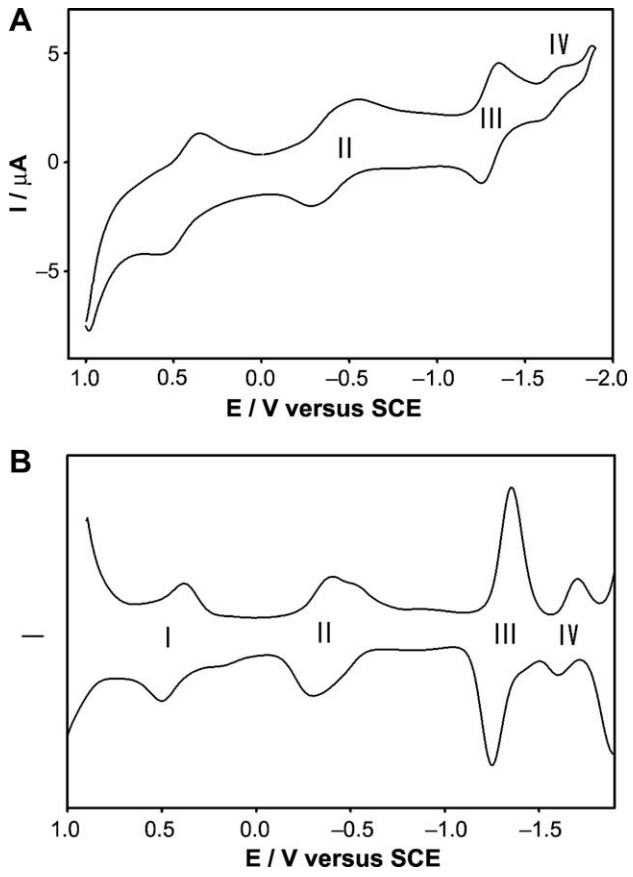


Fig. 6. Cyclic (A) and differential pulse (B) voltammograms of 2.5×10^{-4} mol dm^{-3} **1c** in DMSO/TBAP.

changes recorded during the first oxidation process of **1b** are shown in Fig. 7D. There is a continuous decrease in the absorption of all bands. In addition, re-reduction of oxidized species did not generate the compound **1b** with its original spectrum. This is probably due to the fact that the first oxidation process occurs at considerably positive potentials, and decomposition of the complex may occur when the potential is held constant at a potential considerably positive.

Fig. 8 shows the UV–Vis spectra of **1c** and its electrochemically generated species. The broad blue-shifted Q band at 670 nm in the starting spectrum of **1c** implies that the complex is mainly in aggregated form. Fig. 8A shows the UV–Vis spectral changes of **1c** during its first reduction at −0.90 V versus SCE. Upon the first reduction, the Q band absorption at 670 nm decreases considerably at first with a red shift and then increases slightly. This spectral change is accompanied by the formation of two newly formed absorption bands at 483 and 715 nm. The position of the isosbestic points is not clear during these spectral changes. when the spectral changes in Fig. 8A are divided in two parts accordingly, we obtained the spectral changes in Fig. 9A and B. In Fig. 9A, the first reduction process has well-defined isosbestic points at 412, 550 and 742 nm. The new band at 483 nm is typical for Co(I)Pc(−2) species, and thus clearly suggests that the first reduction of **1c** (couple II in Fig. 6) occurs at the metal center [36,37]. On the other hand, as shown in Fig. 9B, both Q and B band absorptions increase continuously without formation of isosbestic points after the changes at the beginning. These two different spectral changes during the first reduction imply that the former changes are due to the metal-based reduction of aggregated CoPc species while the latter changes result from deaggregation of reduced species. During the second reduction process, a new band appears at 677 nm (Fig. 8B). There is also a remarkable increase in the absorption within the range of 525–600 nm, while the spectral changes

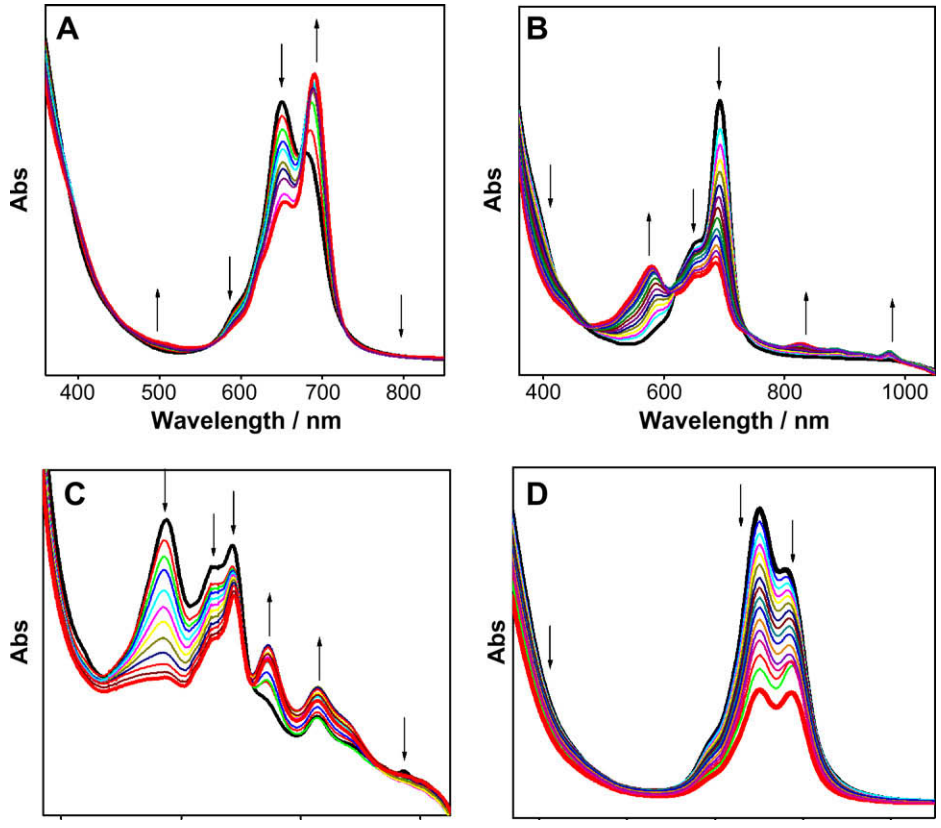


Fig. 7. *In situ* UV–Vis spectral changes during the first reduction (A) and (B), the second reduction (C) and the first oxidation (D) of **1b**.

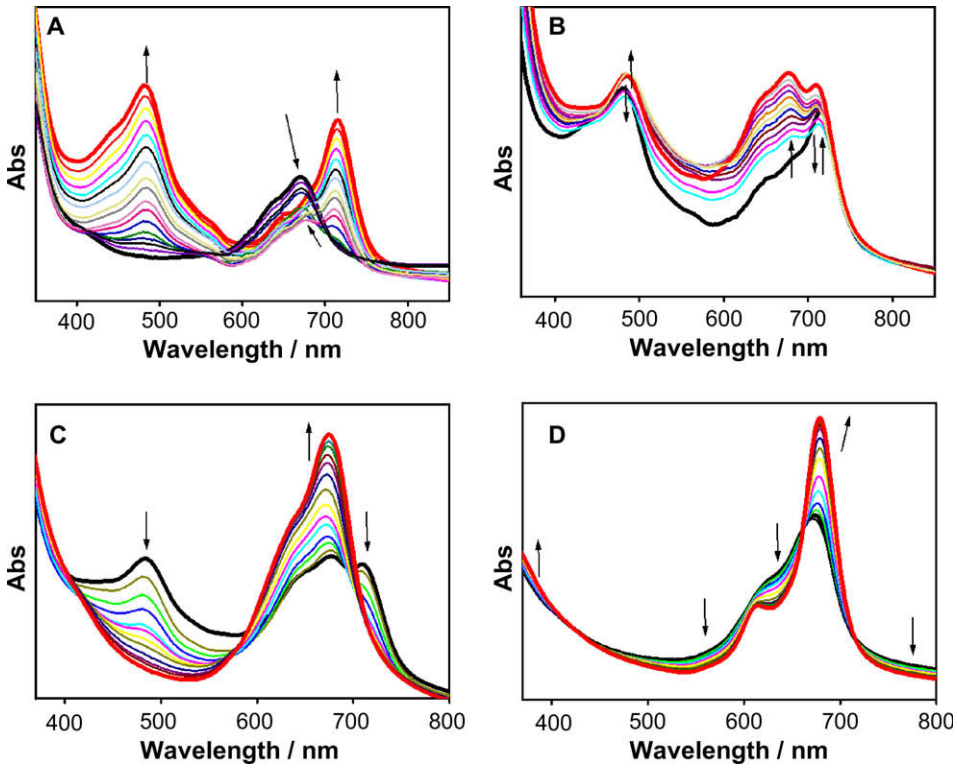


Fig. 8. *In situ* UV–Vis spectral changes during the first reduction (A), the second reduction (B), the third reduction (C) and the first oxidation (D) of **1c**.

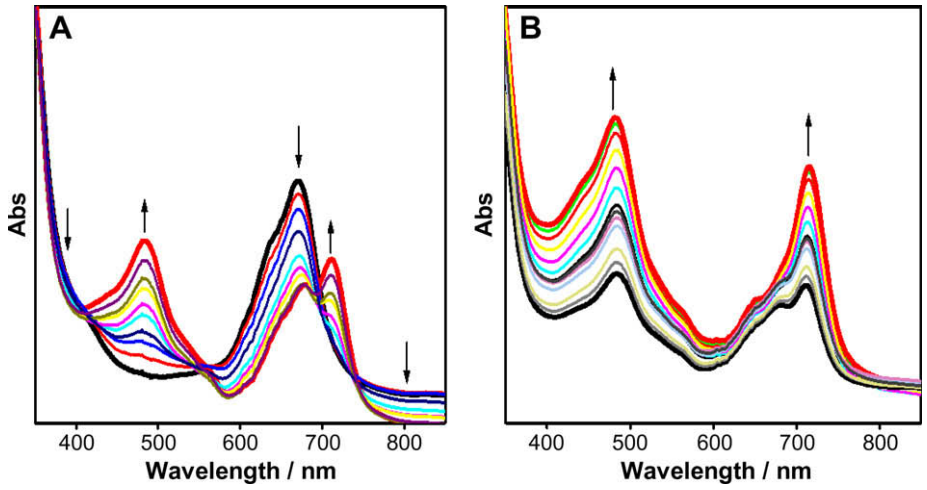


Fig. 9. *In situ* UV–Vis spectral changes during the first reduction processes of **1c** deaggregation process (A), reduction of deaggregated species (B).

are very limited at around the band at 483 nm. Thus, these changes are probably due to ring-based reduction in Pc complexes [30,36,37]. In most of the studies in literature [29,33,38,39], it was reported that a decrease in the Q band intensity and a decrease or increase in absorption at around 480 nm occurred during the ligand-based second reduction process of a Co(II)Pc. The broad split band observed in this study may suggest that aggregation still affects the electron transfer process during the second reduction process. On the other hand, nearly all studies in literature about the spectroelectrochemistry of MPcs do not report on the spectral changes during the third reduction process. The third reduction in this study results in disappearance of the band at around 715 nm and the narrowing of the Q band absorption due to completely deaggregated reduced species resulting from high negative charge on the Pc ring as shown in Fig. 8C. In the mean time, the band at around 483 nm disappears. Fig. 8D shows the spectral changes observed when potentials corresponding to first oxidation process were applied to solution of **1c**. There is a shift in wavelength of the Q band from 670 to 677 nm as the electrolysis progressed. This is typical of a metal-based oxidation in CoPc complexes [29,30,36]. The final spectrum in Fig. 8D is therefore belong to Co(III)Pc(−2), confirming CV assignment.

Acknowledgements

We are thankful to The Scientific and Research Council of Turkey (TUBITAK) (Project Nos. 107T347 and 107T834) and Marmara

University, The Commission of Scientific Research Project under grant FEN-BGS-120707-0149.

References

[1] H. Eichhorn, J. Porphyr. Phthalocyan. 4 (2000) 88.
[2] C.C. Leznoff, A.B.P. Lever, Phthalocyanines Properties and Applications, VCH, Weinheim, 1989–1996. p. 1.
[3] M. Hanack, M. Lang, Adv. Mater. 6 (1994) 819.
[4] C.S. Frampton, J.M. O'Conner, J. Retevson, J. Silver Displays (1988) 174.
[5] J.H. Zagal, Coord. Chem. Rev. 119 (1992) 89.
[6] A.C.H. Ng, X. Li, D.K.P. Ng, Macromolecules 32 (1999) 5292.
[7] H. Ali, J.E. van Lier, Chem. Rev. 99 (1999) 2379.
[8] M.C. Derosa, R. Crutchely, J. Coord. Chem. Rev. 233 (2002) 351.
[9] P. Tau, T. Nyokong, Inorg. Chim. Acta 360 (2007) 2615.
[10] N.S. Lebedeva, O.V. Petrova, A.I. Vyugin, V.E. Maizlish, G.P. Shaposhnikov, Thermochim. Acta 417 (2004) 127.
[11] Y. Pan, W. Chen, S. Lu, Y. Zhang, Dyes Pigments 66 (2005) 115.
[12] M.G.L. Hertog, D. Kromhout, C. Aravanis, et al., Arch. Intern. Med. 155 (1995) 381.
[13] A. Kotali, I.S. Lafazanis, P.A. Haris, Tetrahedron Lett. 48 (2007) 7181.
[14] R.D.H. Murray, J. Mendez, S.A. Brown, The Natural Coumarins: Occurrence, Chemistry and Biochemistry, Wiley & Sons, New York, 1982.
[15] J.H. Fentem, J.R. Fry, Comp. Biochem. Physiol. 104C (1) (1993) 1.
[16] D. Bogdal, J. Chem. Res. (S) (1998) 468.
[17] M.C. Laufer, H. Hausmann, W.F. Hölderich, J. Catal. 218 (2003) 315.
[18] D.S. Bose, A.P. Rudradas, M.H. Babu, Tetrahedron Lett. 43 (2002) 9195.
[19] G.P. Romanelli, D. Bennardi, D.M. Ruiz, G. Baronetti, H.J. Thomas, J.C. Autino, Tetrahedron Lett. 45 (2004) 1.
[20] F.F. Ye, J.R. Gao, W.J. Sheng, J.H. Jia, Dyes Pigments 77 (2008) 556.
[21] A.A. Esenpınar, M. Bulut, Dyes Pigments 76 (1) (2008) 249.
[22] A.B.P. Lever, E.R. Milaeva, G. Speier, in: C.C. Leznoff, A.B.P. Lever (Eds.), Phthalocyanines: Properties and Applications, vol. 3, VCH Publishers, Weinheim, 1993, p. 1.
[23] A.R. Özkaya, A. Gürek, A. Gül, Ö. Bekaroğlu, Polyhedron 16 (1997) 1877.
[24] A.R. Özkaya, I. Yılmaz, Ö. Bekaroğlu, J. Porphyr. Phthalocyan. 2 (1998) 483.
[25] A.R. Özkaya, E. Hamuryudan, Z.A. Bayır, Ö. Bekaroğlu, J. Porphyr. Phthalocyan. 4 (2000) 689.
[26] M. Kandaz, A.R. Özkaya, Ö. Bekaroğlu, Monatsh. Chem. 132 (2001) 1013.
[27] M. Özer, A. Altindal, A.R. Özkaya, M. Bulut, Ö. Bekaroglu, Polyhedron 25 (2006) 3593.
[28] D. Kulaç, M. Bulut, A. Altındal, A.R. Özkaya, B. Salih, Ö. Bekaroglu, Polyhedron 26 (2007) 5432.
[29] B. Agboola, K.I. Ozoemena, T. Nyokong, Electrochim. Acta 51 (2006) 4379.
[30] J. Obirai, T. Nyokong, Electrochim. Acta 50 (2005) 3296.
[31] J. Mack, M.J. Stillman, J. Am. Chem. Soc. 116 (1994) 1292.
[32] T. Nyokong, Z. Gasyna, M.J. Stillman, Inorg. Chem. 26 (1987) 548.
[33] N. Kobayashi, H. Lam, W.A. Nevin, P. Janda, C.C. Leznoff, T. Koyama, A. Monden, H. Shirai, J. Am. Chem. Soc. 116 (1994) 879.
[34] H. Homborg, Z. Anorg. Allg. Chem. 507 (1983) 35.
[35] H. Homborg, C.L. Teske, Z. Anorg. Allg. Chem. 527 (1985) 45.
[36] M.J. Stillman, T. Nyokong, in: C.C. Leznoff, A.B.P. Lever (Eds.), Phthalocyanines: Properties and Applications, VCH Publishers, New York, 1989, p. 1.
[37] J. Obirai, N.P. Rodrigues, F. Bedioui, T. Nyokong, J. Porphyr. Phthalocyan. 7 (2003) 508.
[38] I. Yılmaz, M.B. Koçak, Polyhedron 23 (2004) 1279.
[39] T. Nyokong, Z. Gasyna, M.J. Stillman, Inorg. Chim. Acta 112 (1986) 11.

Polyhedron 28 (2009) 43–48

Contents lists available at ScienceDirect

Polyhedron

journal homepage: www.elsevier.com/locate/poly

The effect of water-miscible organic solvents on the substitution reaction of Keggin-type heteropolysilicates and -germanates with vanadium(V) ion

Tadaharu Ueda *, Jun-ichi Nambu, Hirofumi Yokota, Masashi Hojo

Department of Material Science, Faculty of Science, Kochi University, Kochi 780-8520, Japan

ARTICLE INFO

Article history:
Received 31 March 2008
Accepted 26 September 2008
Available online 20 November 2008

Keywords:
Polyoxometalate
Keggin
Substitution
Vanadium
Organic solvent
Permittivity

ABSTRACT

The substitution reaction of Keggin-type polyoxometalates, $[XM_{12}O_{40}]^{n-}$ (*X = Si,* Ge, P, or As; M = Mo or W), with vanadium(V) ion was investigated with cyclic voltammetry, Raman spectroscopy, and ^{31}P NMR. The effect of organic solvents, such as acetonitrile (ACN), tetrahydrofuran (THF), formamide (FA), N-methylformamide (NMF), and N-methylacetoamide (NMA) on their substitution reactions was examined. In aqueous and aqueous-FA, -NMF, and -NMA solutions, the molybdenum or tungsten unit in the Keggin-anions was substituted with vanadium(V) ion to form V(V)-substituted polyoxometalates, while no substitution reaction occurred in aqueous-ACN and -THF solutions. It is suggested that this results from the relationship between the total anion charge and the permittivity of organic solvents.

© 2008 Elsevier Ltd. All rights reserved.

1. Introduction

Many kinds of polyoxometalates have been prepared and characterized since the first report on the formation of 12-molybdophosphate in 1826 [1]. Polyoxometalates with Keggin structure, whose formulas are denoted as $XM_{12}O_{40}^{n-}$ (X = Si, P, etc.; M = Mo and W), have been applied to various fields such as analytical chemistry, biochemistry, and catalysis [1,2]. It has been well known that one or three addenda units are generally removed from the Keggin-type polyoxometalate to form so-called lacunary anions as $XM_{11}O_{39}^{n-}$ and A-$XM_9O_{34}^{n-}$ and that the other metal ions are incorporated to the vacant sites of these lacunary anions to form metal-substituted polyoxometalates. The structures of these polyoxometalates are not only Keggin-type but also sandwich-type. Metal-substituted polyoxometalates are attracting interest because of their use in specific catalysis rather than non-substituted polyoxometalates. Though much attention has been directed toward the preparation and the application of polyoxometalates, their formation mechanisms still remain ambiguous.

In general, many polyoxometalates have been prepared in aqueous solution, while some new polyoxometalates with new types of structures have been also reported to be formed under specific conditions such as non-aqueous, mixed media, and hydrothermal condition [1–4]. Novel polyoxometalates containing diphosphate, phosphonate, arsenite, selenite, or tellurite as hetero ions were synthesized from aqueous organic solutions [5–9]. Even though in aqueous solution $[PMo_{12}O_{40}]^{3-}$ does not form as the main species and $[AsMo_{12}O_{40}]^{3-}$ does not form at any appreciable concentrations, the addition of water-miscible organic solvents, such as acetonitrile and acetone, makes the formation of these complexes more stable and their likelihood greater [10]. Recently, the vanadium(V)-substitution reactions of Keggin-type molybdophosphates, tungstophosphates, and arsenate analogues were examined in aqueous and aqueous-ACN solutions, and it was found that water-miscible organic solvents played important roles on their substitution reactions [11,12]. The Pettersson group also reported the detailed formation conditions of molybdovanadophosphates in aqueous solution obtained through ^{31}P and ^{51}V NMR and potentiometry [13].

The V(V)-substituted molybdosilicates and tungstosilicates, and the corresponding germanates, were prepared in aqueous solution and characterized with various methods, such as cyclic voltammetry, IR, UV–Vis, and NMR. There has been, however, no report on the formation of these complexes in aqueous solution and mixed media. Therefore, in the present study, to obtain a detailed examination of the effect of organic solvent on the formation of V(V)-substituted polyoxometalates, the V(V)-substitution reactions with Keggin-type molybdosilicate and tungstosilicate, and the corresponding germanates were investigated in aqueous solution and mixed media.

* Corresponding author. Tel.: +81 88 844 8299; fax: +81 88 844 8359.
E-mail address: chuji@kochi-u.ac.jp (T. Ueda).

0277-5387/$ - see front matter © 2008 Elsevier Ltd. All rights reserved.
doi:10.1016/j.poly.2008.09.028

2. Experimental

2.1. Apparatus and materials

Voltammetric measurements were made with a microcomputer-controlled system. A glassy carbon electrode (BAS GC-30S) with a surface area of 0.071 cm^2 was used as a working electrode and a platinum wire served as a counter electrode. The reference electrode was an Ag/AgCl (saturated KCl) electrode. Prior to the measurement, the GC electrode was polished with 0.1 μm diamond slurry and washed with distilled water. The voltammograms were recorded at 25 ± 0.1 °C, and the voltage scan rate was set at 100 mV s^{-1}. Raman spectra were recorded with a Jobin Yvon Model HR-800 spectrophotometer. The argon line at 514.5 nm was used for excitation. The Raman measurements were made at 25 °C. The Raman intensity was normalized by the Raman band of each of the organic solvents used: 922 cm^{-1} for ACN, 914 cm^{-1} for THF, 1093 cm^{-1} for FA, 962 cm^{-1} for NMF, and 885 cm^{-1} for NMA, and the 1048 cm^{-1} band due to NO_3^- (50 mM $NaNO_3$) in aqueous solution. IR spectra were obtained on a Jasco FT/IR-460 plus spectrophotometer by the KBr pellet method.

A stock solution of V(V) was prepared by dissolving 22.735 g of V_2O_5 and 15.0 g of NaOH in 250 mL of water. Other reagents were of analytical grade and were used as received.

2.2. Preparation of heteropolymolybdates and -tungstates and vanadium(V) derivatives

Tetrabutylammonium (n-Bu_4N^+) salts of $SiW_{12}O_{40}^{4-}$ (SiW_{12}), $GeW_{12}O_{40}^{4-}$ (GeW_{12}), $SiMo_{12}O_{40}^{4-}$ ($SiMo_{12}$), and $GeMo_{12}O_{40}^{4-}$ ($GeMo_{12}$) were prepared according to the reported procedures and recrystallized from ACN [14]. The n-Bu_4N^+ salts of $SiVW_{11}O_{40}^{5-}$ ($SiVW_{11}$), $GeVW_{11}O_{40}^{5-}$ ($GeVW_{11}$), $SiVMo_{11}O_{40}^{5-}$ ($SiVMo_{11}$), and $GeVMo_{11}O_{40}^{5-}$ ($GeVMo_{11}$) were prepared according to both the formation conditions reported in the present study and described procedures with modifications [15–18]. They were recrystallized from acetonitrile and cross checked by FT-IR spectra and elemental analysis [19].

3. Results and discussion

3.1. IR and Raman spectra and cyclic voltammograms of XM_{12} and XVM_{11} (X = Si, Ge; M = Mo, W)

Table 1 shows the vibrational frequencies of XM_{12} and XVM_{11} in their IR and Raman spectra. All spectra of XVM_{11} were very similar to those of the corresponding XM_{12}, though each of frequencies was slightly shifted. From these results, we can interpret that all of the XVM_{11} retained a Keggin structure. It has been reported that counter cations, especially small cations, affect the vibrational frequencies of polyoxometalates in the solid state [14]. In general, the Raman band of the Mo–O_d bond in non-substituted Keggin anions is at a higher wavenumber than that in vanadium-substituted ones in solutions under the same conditions [11,12]. The Raman bands of the n-Bu_4N salts of $GeMo_{12}$ and $SiMo_{12}$, however, are at a lower wavenumber than those of the n-Bu_4N salts of $GeVMo_{11}$ and $SiVMo_{11}$ in the solid state. This is because $GeVMo_{11}$ and $SiVMo_{11}$ contain a proton as a counter cation, which interacts with a proton to shift the Raman band to a higher wavenumber [14]. In fact, the Raman bands of $GeVMo_{11}$ and $SiVMo_{11}$ anions are at a lower wavenumber than those of $GeMo_{12}$ and $SiVMo_{12}$ anions in the reaction mixtures, as shown below. The Raman peaks observed in the reaction mixtures were assigned on the basis of the Raman bands of the complex in the solid state.

Fig. 1 shows the cyclic voltammograms of GeV_xMo_{12-x} and GeV_xW_{12-x} (x = 0, 1) in 95% (v/v) CH_3CN containing 0.1 M $HClO_4$, respectively. The $GeMo_{12}$ and $GeVMo_{11}$ complexes exhibit reversible step waves with E_{mid} of 505, 400, 155, and 15 mV, and 670, 480, 340, 150, and 5 mV, respectively, where $E_{mid} = (E_{pc} + E_{pa})/2$; E_{pc} and E_{pa} are the cathodic and the anodic peak potential, respectively. Each wave was diffusion controlled. Coulometric analysis and normal-pulse voltammetric measurements confirmed that the four-step reduction waves of the $GeVMo_{11}$ complex corresponded to one- and three two-electron transfers, and those of the $GeMo_{12}$ complex corresponded to four two-electron transfers, respectively. The first wave in curve (a) and (c) in Fig. 1 indicates the reduction (V → IV) of vanadium atom in each of complexes, as with $[XV_xW_{12-x}O_{40}]^{(3+x)-}$ and $[XV_xMo_{12-x}O_{40}]^{(3+x)-}$, while other waves are ascribed to the reduction (VI → V) of molybdenum or tungsten atoms. Unfortunately, the oxidation peak at ca. 300 mV in Fig. 1(a) could not be assigned, although no peak at ca. 300 mV appeared when switching potential was set at −150 mV. The oxidation peak at ca. 300 mV should be indicated to be an

Table 1
Mid-point potentials[a] (E_{mid}/mV) of redox of $XVM_{11}O_{40}^{5-}$ and $XM_{12}O_{40}^{4-}$ (X = Si and Ge; M = Mo and W)[b].

Compounds	Redox processes[c]				
	$V^V \rightarrow V^{IV}$	0M → IIM	IIM → IVM	IVM → VIM	VIM → VIIIM
$SiVMo_{11}$	630	455	320	105	−45
$SiMo_{12}$		465	360	105	40
$GeVMo_{11}$	670	480	340	150	5
$GeMo_{12}$		505	400	155	15
$SiVW_{11}$	513	−340	−408		
SiW_{12}		−346	−444		
$GeVW_{11}$	583	−280	−366		
GeW_{12}		−294	−390		

[a] $E_{mid} = (E_{pc} + E_{pa})/2$, where E_{pc} and E_{pa} indicate cathodic and anodic peak potentials, respectively.
[b] All samples were measured in 95% (v/v) CH_3CN containing 0.1 M $HClO_4$.
[c] II, IV, VI, and VIII indicate the number of the molybdenum or tungsten sites reduced from +6 into +5 in anions.

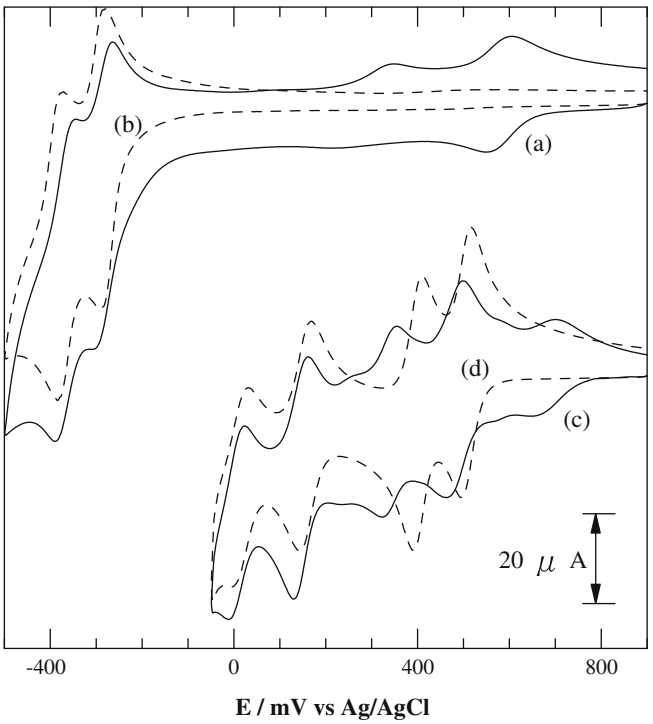


Fig. 1. Cyclic voltammograms of (a) $GeVW_{11}$, (b) GeW_{12}, (c) $GeVMo_{11}$, and (d) $GeMo_{12}$ in 95% (v/v) CH_3CN containing 0.1 M $HClO_4$.

Table 2
IR and Raman peak frequencies of $XVM_{11}O_{40}^{5-}$ and $XM_{12}O_{40}^{4-}$ (X = Si and Ge; M = Mo and W).

Compounds	ν^{IR}(M–O_d[d])	ν^{IR}(M–O_b[b]–M)	ν^{IR}(M–O_c[c]–M)	ν^{IR}(X–O_a[a])	ν^{Raman}(M–O_d)
$SiMo_{12}$	945, 940	868	795	899	968(970[e], 988[f])
$SiVMo_{11}$	942		793	898	975[e]
$GeMo_{12}$	939	873	778	812	968(970[e], 988[g])
$GeVMo_{11}$	942	876	775	808	974[e]
SiW_{12}	967	883	797	920	987(994[e])
$SiVW_{11}$	957	877	793	909	979(988[e])
GeW_{12}	965	895, 885	780	830	986(994[e])
$GeVW_{11}$	961	882	776	821	980(988[e])

[a] O_a: oxygen bonded with silicon or germanium atom.
[b] O_b: octahedral corner-sharing oxygen.
[c] O_c: octahedral edge-sharing oxygen.
[d] O_d: terminal oxygen.
[e] Measured the solution dissolved the compound in ACN.
[f] $H_4SiMo_{12}O_{40}$ in Ref. [14].
[g] $H_4GeMo_{12}O_{40}$ in Ref [14].

adsorption wave. Cyclic voltammograms of the other XVM_{11} and XM_{12} anions were also measured in acidic aqueous-CH_3CN solution under the same conditions as in Fig. 1, and E_{mid} values obtained are listed in Table 2. Each of the E_{mid} values of the redox waves for $GeVMo_{11}$ and $GeVW_{11}$ is ca. 50 mV more positive than each of those for $SiVMo_{11}$ and $SiVW_{11}$, respectively. This behavior is similar to that seen for other complexes in that each of the E_{mid} potentials of AsV_xM_{12-x} (x = 0, 1; M = Mo, W) is more positive than each of those of the corresponding PV_xM_{12-x}. On the basis of these voltammetric manners, the occurrence of vanadium substitution reaction can be determined from the appearance of new peak at more positive potential than redox potentials of Mo or W parts in polyoxometalates after the addition of V(V) into the reaction mixtures.

3.2. V(V)-substitution reaction of heteropolysilicates and heteropolygermanates

Fig. 2A and B shows the cyclic voltammograms and Raman spectra for a 50 mM Mo(VI)–5 mM Ge(IV)–0.5 M HCl–40% (v/v) FA system. Three-step voltammetric waves at E_{pc} = 180, 15, and −115 mV corresponding to two-electron transfers, respectively, and Raman band at 980 cm^{-1} were observed (Fig. 2(a)). These reduction waves and Raman peak indicate the formation of the $GeMo_{12}$ anion. After the addition of 5 mM V(V), new reduction peaks at 335 and −70 mV and a new Raman band at 974 cm^{-1} appeared, while three reduction peaks and a Raman band at 980 cm^{-1} disappeared (Fig. 2(b)). Simultaneously, the color of the solution changed to yellow from colorless. These new reduction peaks and Raman bands were due to the formation of the $GeVMo_{11}$. The changes of voltammograms and Raman spectra indicate that the $GeMo_{12}$ anion was substituted with V(V) to form the $GeVMo_{11}$ anion in aqueous-FA solution. When the same experiments were carried out with 20% (v/v) NMF and NMA, instead of FA, in aqueous-NMF and -NMA, a new redox wave appeared at more positive potential than the redox waves of $GeMo_{12}$ as well as a new Raman band at around 974 cm^{-1} after the addition of 5 mM V(V) and heating at 80 °C for 1 day. These voltammetric and Raman spectroscopic changes are the same as those obtained in the aqueous-FA solution, indicating that the $GeMo_{12}$ anion was also substituted with V(V) ion to form the $GeVMo_{11}$ anion in respective aqueous-organic solution. If, after the addition of 5 mM V(V), the solution was not heated or >40% (v/v) NMF or NMA was added, there was no voltammetric and Raman spectroscopic change.

To investigate the V(V)-substitution reaction in aqueous solution, cyclic voltammograms and Raman spectra for a 50 mM Mo(VI)–5 mM Ge(IV)–pH 2.0 system were recorded (Fig. 3A and B). In the absence of V(V), two voltammetric waves at E_{pc} = 290 and 185 mV and a Raman band at 980 cm^{-1} were observed. After

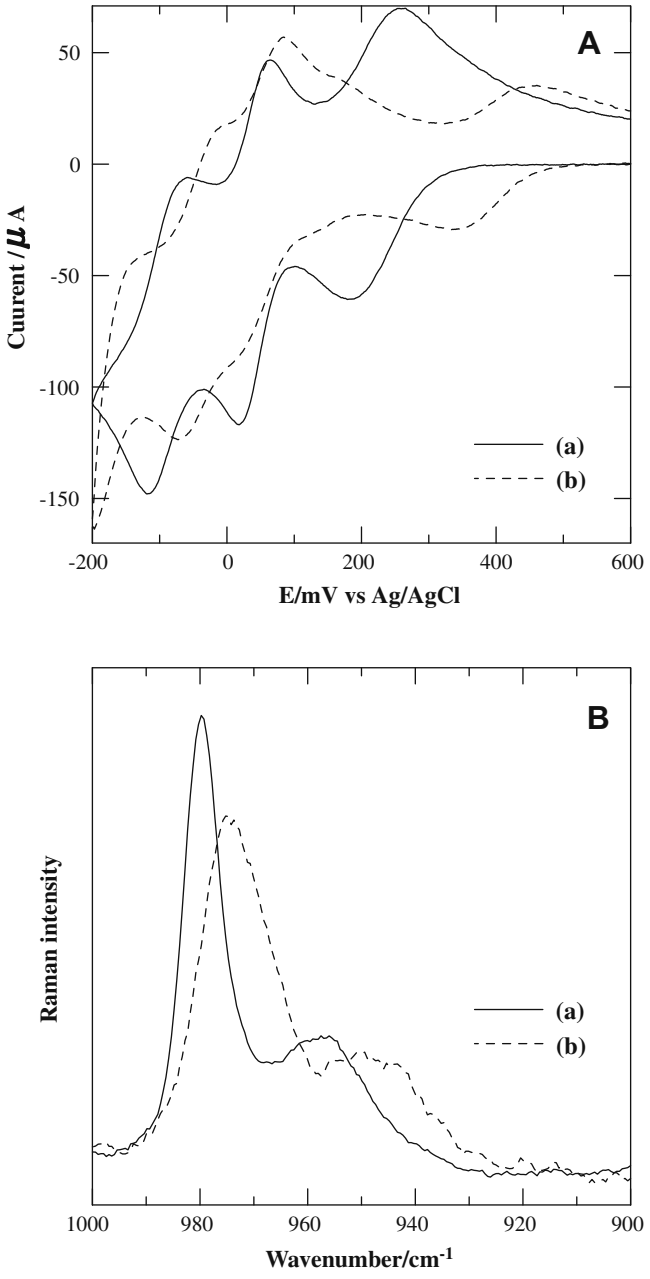


Fig. 2. Cyclic voltammograms (A) and Raman spectra (B) for a 50 mM Mo(VI)–5 mM Ge(IV)–0.5 M HCl–50% (v/v) FA system without (a) and with (b) 5 mM V(V).

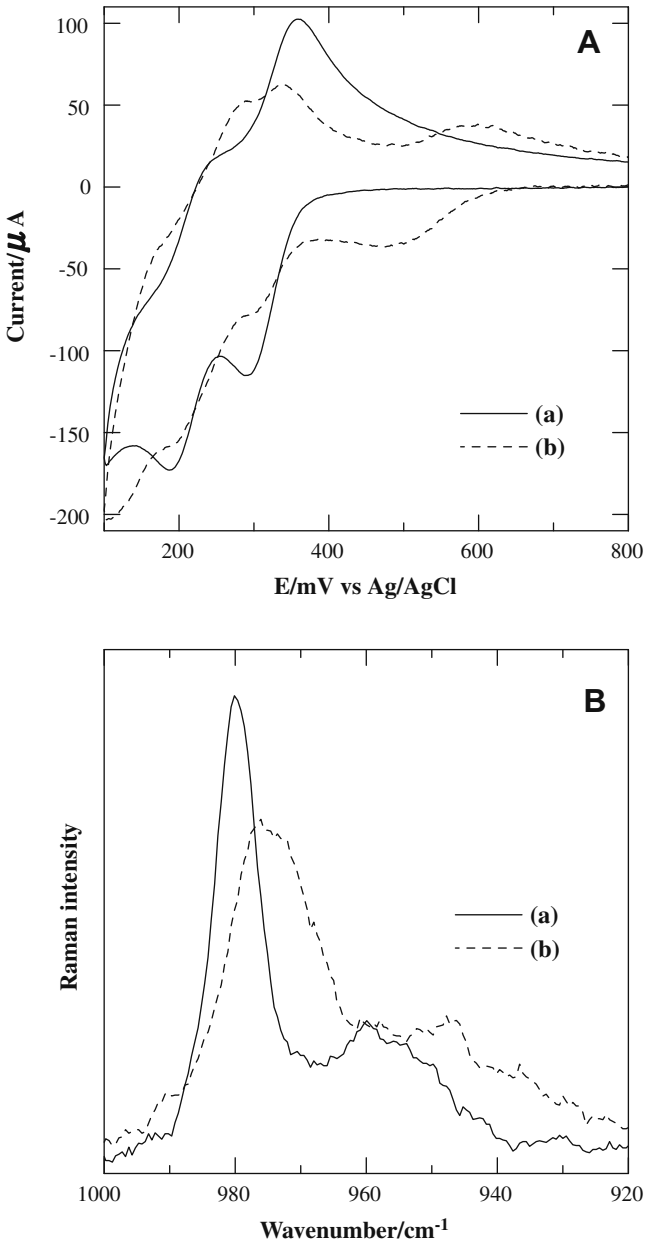


Fig. 3. Cyclic voltammograms (A) and Raman spectra (B) for a 50 mM Mo(VI)–5 mM Ge(IV)–pH 2.0 system without (a) and with (b) 5 mM V(V).

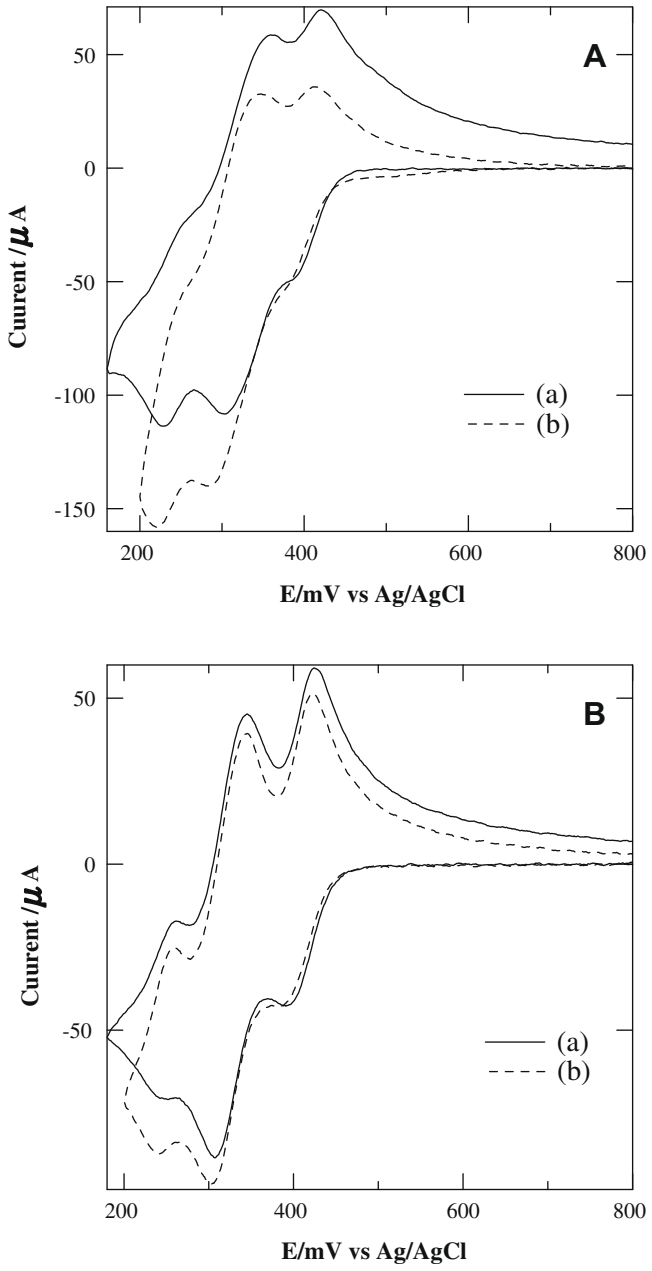


Fig. 4. Cyclic voltammograms for 50 mM Mo(VI)–5 mM Ge(IV)–0.5 M HCl–50% (v/v) ACN (A) and THF (B) systems without (a) and with (b) 5 mM V(V).

the addition of 5 mM V(V), the readjustment of pH at 2.0 by a small amount of HCl, and heating at 80 °C for 1 day, a new reduction peak at 475 mV and a new Raman band at 974 cm^{-1} appeared, though the reduction waves at 290 and 185 mV and the Raman peak at 980 cm^{-1} did not completely disappear. In aqueous solution, the $GeMo_{12}$ anion was substituted with V(V) to form the $GeVMo_{11}$ anion in systems similar to aqueous-FA, -NMF and -NMA, but not all of the $GeMo_{12}$ anion was transformed into the $GeVMo_{11}$ anion.

Furthermore, the vanadium-substitution reaction of the $GeMo_{12}$ anion was investigated in aqueous-CH_3CN and -THF solution. Fig. 4A and B shows cyclic voltammograms for 50 mM Mo(VI)–5 mM Ge(IV)–0.5 M HCl–40% (v/v) CH_3CN and THF systems. Before the addition of V(V), reduction waves were observed at 385, 305 and 230 mV in aqueous-CH_3CN solution and at 390, 305, and 240 mV in aqueous-THF solution. Cyclic voltammograms for a Mo(VI)–P(V)–HCl system in aqueous-CH_3CN solution gave three redox waves: the first and second reduction waves are due to the formation of β-PMo_{12}, and the second and third ones are due to the formation of α-PMo_{12}. It is thought that the first and second waves in Fig. 4 are ascribed to the formation of the β-$GeMo_{12}$ anion and that the second and third waves are ascribed to that of the α-$GeMo_{12}$ anion. After the addition of 5 mM V(V), no peak appeared at a more positive potential than the 1st reduction wave of β-$GeMo_{12}$, while the currents of the second and third waves increased without the shifts of peak potentials. This may indicate that the V(V) ion gives rise to catalytic waves, similar to Mo(VI)–P(V)–V(V), in aqueous-ACN solution [11]. Even though the 5 mM V(V) containing solution was heated at 80 °C for aqueous-ACN, or 50 °C for aqueous-THF for 1 day, no new reduction peak appeared as was seen for the aqueous-NMF and -NMA systems. In aqueous-ACN or -THF solution, no substitution reaction of $GeMo_{12}$ with V(V) occurred.

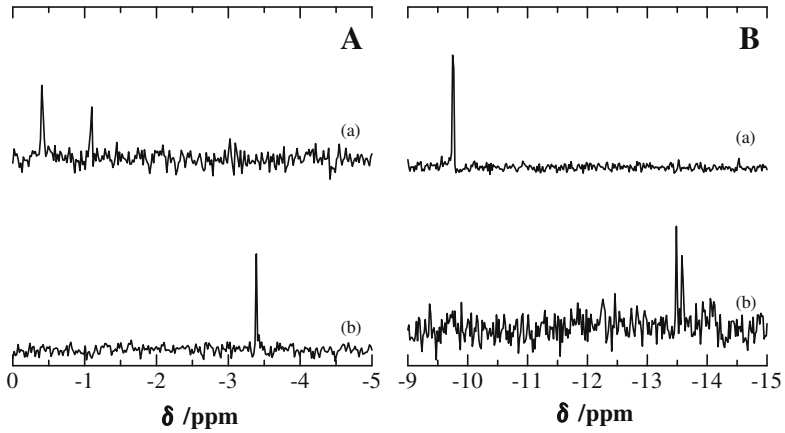


Fig. 5. ^{31}P NMR for 50 mM Mo(VI)–5 mM Ge(IV)–0.5 M HCl–50% (v/v) NMF (A) and 50 mM W(VI)–5 mM Ge(IV)–0.5 M HCl–50% (v/v) NMF (A) systems without (a) and with (b) 5 mM V(V).

Similarly to the Mo(VI)–Ge(IV) systems, the vanadium(V) substitution reaction in the W(VI)–Ge(IV) systems was also investigated. For a 50 mM W(VI)–5 mM Ge(IV)–0.2 M HCl–20% (v/v) NMF or NMA system, two reduction waves at $E_{pc} = -200$ and -440 mV for aqueous-NMF system, and -235 and -485 mV for the aqueous-NMF system, and a Raman band at 997 cm^{-1} were observed after the solution was heated at 80 °C for 3 days. After the addition of 5 mM V(V) and heating again at 80 °C for 1 day, new reduction peaks at $E_{pc} = 470$ mV for the aqueous-NMF system, 430 mV for the aqueous-NMF system, and a Raman band at 991 cm^{-1} appeared, while the original reduction peaks and Raman band disappeared. These results indicate that the GeW_{12} anion was substituted with V(V) to form the $GeVW_{11}$ anion. In aqueous-FA solution, however, no new reduction wave at a more positive potential than the redox of tungsten, and only a Raman peak at around 990 cm^{-1} were obtained before and after the addition of V(V), even though reaction mixtures containing various concentrations of HCl and FA were measured. This indicates that no Keggin anion exists and no vanadium substitution reactions occur.

The vanadium substitution reactions for Mo(VI)–Si(IV) and W(VI)–Si(IV) systems were also examined with CV and Raman at the same conditions as Mo(VI)–Ge(IV) and W(VI)–Ge(IV) systems, respectively. The results for Mo(VI)–Si(IV) and W(VI)–Si(IV) systems were very similar to the ones for Mo(VI)–Ge(IV) and W(VI)–Ge(IV) systems.

3.3. V(V)-substitution reaction of heteropolyphosphates and heteropolyarsenates in aqueous-FA, -NMF and -NMA solution

Recently, V(V)-substitution reactions were investigated in aqueous solution and aqueous-organic solutions for M(VI)–X(V) (M = Mo, W; X = P, As) systems [11,12]. In aqueous solution, the PMo_{12} and PW_{12} are substituted with V(V) to form PV_xMo_{12-x} and PV_xW_{12-x}, respectively, while no substitution reaction occurs for M(VI)–As(V) systems, though small amounts of AsV_xMo_{12-x} and AsV_xW_{12-x} form. In aqueous organic solution, such as ACN and THF, however, all types of Keggin anions are substituted with V(V) to form XV_xM_{12-x}, though PM_{12} is not perfectly substituted due to the stability of the anion. In the present study, the substitution reactions of XM_{12} (X = P, As; M = Mo, W) with V(V) were investigated in aqueous-FA, -NMF and -NMA solution. Fig. 5 shows the ^{31}P NMR spectra for 50 mM Mo(VI) or W(VI)–5 mM P(V)–0.5 M HCl–50 (v/v)% NMF systems with and without 5 mM V(V). In the absence of V(V), NMR peaks appeared at -0.40 and -1.10 ppm for the Mo(VI) system (Fig. 5A(a)) and -9.75 ppm for the W(VI) system (Fig. 5B(a)), but no peaks appeared at around -3.1 and -14.6 ppm corresponding to PMo_{12} and PW_{12}, respectively. The PMo_9 and PW_9 complexes form in each of the studied solutions. After the addition of 5 mM V(V), new peaks appeared at -3.39 ppm (Fig. 5A(b)), -13.49, and -13.58 ppm (Fig. 5B(b)). These peaks indicate the formation of $PVMo_{11}$ and PV_xW_{12-x} ($x = 2, 3$) [11,20], but these reactions are not substitution reactions but mere formation reactions of PM_9 and V(V). The vacant sites of PM_9 were fulfilled with V(V) and M(VI), which were decomposed from PM_9 or from an excess of M(VI), to form stable Keggin-type vanadium-substituted heteropolyphosphates. For M(VI)–P(V) systems in aqueous-FA solution and a W(VI)–P(V) system in aqueous-NMA, no PM_{12} anion was detected, though the PVM_{11} anion formed after the addition of V(V), as seen for M(VI)–P(V) systems in aqueous-NMF. For a 50 mM Mo(VI)–5 mM P(V)–0.5 M HCl–50% (v/v) NMA system, however, in the absence of V(V), a ^{31}P NMR peak at -3.11 ppm was obtained. After the addition of V(V), this peak diminished, and a new peak appeared at -3.45 ppm, indicating that PMo_{12} was substituted with V(V) to form $PVMo_{11}$.

The substitution reactions for As(V)–Mo(VI) and –W(VI) systems in aqueous-FA, -NMF, and -NMA solutions were investigated. No reversible redox waves, which were assigned to the formation of AsW_{12}, were observed for 50 mM Mo(VI) (or W(VI))–5 mM As(V)–0.5 M HCl systems in aqueous-NMF and -FA solutions, though redox waves due to the formation of $AsVMo_{11}$ and $AsVW_{11}$ were obtained after the addition of V(V). These results were ascribed to the formation of $AsVMo_{11}$ and $AsVW_{11}$ by incorporation of V(V) and M(VI) into the vacant sites of lacunary species similar to those seen in P(V) systems. Based on the results of voltammetric and Raman spectroscopic measurements, a large number of AsM_{12} anions do not form in aqueous-NMA solution, those that undergo substitution form the $AsVM_{11}$ anions, as seen for the Mo(VI)–P(V) system in aqueous-NMA solution.

4. Conclusion

The substitution reactions of Keggin-type heteropolysilicates and heteropolygermanates with V(V) were investigated in aqueous and mixed media and compared with those of heteropolyphosphates and heteropolyarsenates. For heteropolysilicates and heteropolygermanates, substitution reactions occurred when the media were water or aqueous-FA, -NMF, and -NMA, while they did not occur when the media were aqueous-ACN and -THF. In contrast, for heteropolyphosphates and heteropolyarsenates, the V(V)-substituted species formed in aqueous-FA, -NMF, and -NMA, while Keggin-type PMo_{12} and $AsMo_{12}$ did not form at any appreciable concentration. The corresponding lacunary species occurred in

Table 3
Physical properties of solvents [21–23].

Solvent	DN	AN	Permittivity
THF	20.0	8.0	7.6
ACN	14.1	18.9	35.9
Water	18(33)	54.8	78.4
FA	(24)	39.8	111
NMF	49	32.1	182.4
NMA			191.3

solution, and the V(V) ion incorporated into their vacant site to form the vanadium-substituted species. Table 3 shows the physical properties of the solvents used in the present study [21–23]. The relative permittivity of FA, NMF, and NMA is higher than that of water, while that of ACN and THF is lower. The size of all of the Keggin-type heteropolymolybdates and -tungstates, respectively, is nearly the same. Their radius has been reported as ca. 5.6 Å, independent of the kind of hetero atoms and the substitution of vanadium, while only the total charge of anions is different [1,24–27]. The change in the total charge by vanadium substitution reactions ranges from −4 (non-substituted species) to −5 (substituted species) for Keggin-type heteropolysilicates and -germanates, while it ranges from −3 to −4 for Keggin-type heteropolyphosphates and -arsenates. It is well known that Keggin-type heteropolysilicates and -germanates form stable complexes in aqueous solution, while Keggin-type heteropolyphosphates and -arsenates do so in aqueous-organic solution, such as ACN and THF. Therefore, it is certain that Keggin anions with a total charge of over −4 are favorable in media with a higher permittivity than water. Unfortunately, no reason has been elucidated for why PM_{12} and AsM_{12} form in aqueous-NMA, and substitution reactions did not occur for W(VI)–Ge(IV) and –Si(IV) systems in aqueous-FA solution. Though no direct dependence has been thought to exist between the vanadium-substitution reactions and AN or DN of organic solvents, it has been suggested that whether or not vanadium-substitution reactions occur should depend on the permittivity of the solvents used.

Acknowledgments

This work is supported in part by a Grant-in-aid for Young Scientists (B) (No. 15750146) and Scientific Research (C) (No. 20550079) from the Ministry of Education, Culture, Sports, Science and Technology of Japan, a Special Research Grant for Green Science and the Kochi University President's Discretionary Grant from Kochi University, and the Kogin regional economy promotion foundation.

References

[1] (a) M.T. Pope, Heteropoly and Isopoly Oxometalates, Springer, Berlin, 1983;
(b) C.L. Hill (Ed.), Chem. Rev. 98 (1998) 1;
(c) M.T. Pope, A. Müller (Eds.), Polyoxometalate Chemistry from Topology via Self-Assembly to Applications, Kluwer Academic Publishers, 2001;
(d) T. Yamase, M.T. Pope (Eds.), Polyoxometalate Chemistry for Nano-Composite Design, Kluwer Academic/Plenum Publishers, 2002;
(e) J.J. Borrás-Almenar, E. Coronado, A. Müller, M.T. Pope (Eds.), Polyoxometalate Molecular Science, Kluwer Academic Publishers, 2003;
(f) P. Mialane, A. Dolbecq, F. Sécheresse, Chem. Commun. (2006) 3477;
(g) D.-L. Long, E. Burkholder, L. Cronin, Chem. Soc. Rev. 36 (2007) 105;
(h) A. Proust, R. Thouvenot, P. Gouzerh, Chem. Commun. (2008) 1837.
[2] (a) C.L. Hill (Ed.), J. Mol. Catal. A: Chem. 262 (2007) 1;
(b) T. Ueda, H. Kotsuki, Heterocycles 76 (2008) 73.
[3] M. Higashijima, Chem. Lett. (1999) 1093.
[4] G. Luan, Y. Li, E. Wang, Z. Han, C. Hu, N. Hu, H. Jia, Inorg. Chem. Commun. 5 (2002) 509.
[5] S. Himeno, A. Saito, T. Hori, Bull. Chem. Soc. Jpn. 63 (1990) 1602.
[6] S. Himeno, T. Kubo, A. Saito, T. Hori, Inorg. Chim. Acta 236 (1995) 167.
[7] T. Ueda, K. Sano, S. Himeno, T. Hori, Bull. Chem. Soc. Jpn. 70 (1997) 1093.
[8] K. Maeda, S. Himeno, A. Saito, T. Hori, Bull. Chem. Soc. Jpn. 66 (1993) 1693.
[9] S. Himeno, K. Sano, H. Niiya, Y. Yamazaki, T. Ueda, Inorg. Chim. Acta 281 (1998) 214.
[10] S. Himeno, M. Hashimoto, T. Ueda, Inorg. Chim. Acta 284 (1999) 237.
[11] T. Ueda, K. Wada, M. Hojo, Polyhedron 20 (2001) 83.
[12] T. Ueda, M. Komatsu, M. Hojo, Inorg. Chim. Acta 344 (2003) 77.
[13] A. Selling, I. Andersson, J.H. Grate, L. Pettersson, Eur. J. Inorg. Chem. (2000) 1509.
[14] C. Rocchiccioli-Deltcheff, M. Fournier, R. Franck, R. Thouvenot, Inorg. Chem. 22 (1983) 207.
[15] W.G. Klemperer, Inorg. Synth. 27 (1990) 71.
[16] J.J. Altenau, M.T. Pope, R.A. Prados, H. So, Inorg. Chem. 14 (1975) 417.
[17] J. Gong, Z.-M. Su, Z.-M. Dai, R.-S. Wang, L.-Y. Qu, Synth. Met. 101 (1999) 751.
[18] Q. Wu, G. Meng, Mater. Res. Bull. 35 (2000) 85.
[19] *Anal.* Calc. for $(n\text{-}Bu_4N)_{4.5}H_{0.5}SiVW_{11}O_{40}$: Si, 0.73; V, 1.33; W, 52.76; C, 22.56; H, 4.27; N, 1.64. Found: Si, 0.78; V, 1.35; W, 53.31; C, 22.66; H, 4.75; N, 1.71%. *Anal.* Calc. for $(n\text{-}Bu_4N)_4HSiVMo_{11}O_{40}$: Si, 1.02; V, 1.86; Mo, 38.44; C, 28.00; H, 5.32; N, 2.04. Found: Si, 1.37; V, 2.30; Mo, 37.89; C, 28.22; H, 5.94; N, 2.02%. *Anal.* Calc. for $(n\text{-}Bu_4N)_{4.5}H_{0.5}GeVW_{11}O_{40}$: Ge, 1.87; V, 1.31; W, 52.15; C, 22.30; H, 4.22; N, 1.63. Found: Ge, 1.76; V, 1.76; W, 52.55; C, 22.46; H, 4.68; N, 1.70%. *Anal.* Calc. for $(n\text{-}Bu_4N)_4HGeVMo_{11}O_{40}$: Ge, 2.60; V, 1.83; Mo, 37.83; C, 27.55; H, 5.24; N, 2.01. Found: Ge, 2.51; V, 2.58; Mo, 35.97; C, 27.56; H, 5.70; N, 2.00%.
[20] P.J. Domaille, J. Am. Chem. Soc. 106 (1984) 7677.
[21] C. Reichardt, Solvents and Solvent Effects in Organic Chemistry, 2nd ed., VCH, 1988.
[22] V. Gutmann, The Donor–Acceptor Approach to Molecular Interactions, Plenum, 1978.
[23] J.A. Riddick, W.B. Bunger, T.K. Sakano, Organic Solvents, Physical Properties and Methods of Purification, 4th ed., Wiley, 1986.
[24] M.C. Baker, P.A. Lyons, S.J. Singer, J. Am. Chem. Soc. 77 (1955) 2011.
[25] T. Kurucsev, A.M. Sargeson, B.O. West, J. Phys. Chem. (1957) 1567.
[26] L.C.W. Baker, M.T. Pope, J. Am. Chem. Soc. 82 (1960) 4176.
[27] M.T. Pope, G.M. Varga Jr., Inorg. Chem. 5 (1966) 1249.

Polyhedron 28 (2009) 49–56

Contents lists available at ScienceDirect

Polyhedron

journal homepage: www.elsevier.com/locate/poly

New polyaza macrobicyclic binucleating ligands and their binuclear copper(II) complexes: Electrochemical, catalytic and DNA cleavage studies

S. Anbu [a], M. Kandaswamy [a,*], Pon. Sathya Moorthy [b], M. Balasubramanian [b], M.N. Ponnuswamy [b]

[a] Department of Inorganic Chemistry, School of Chemical Sciences, University of Madras, Guindy Campus, Chennai 600 025, India
[b] Centre of Advanced Study in Crystallography and Biophysics, University of Madras, Guindy Campus, Chennai 600 025, India

ARTICLE INFO

Article history:
Received 28 July 2008
Accepted 23 September 2008
Available online 6 November 2008

Keywords:
Tetraldehyde
Macrobicyclic ligands
Binuclear Cu(II) complexes
DNA cleavage

ABSTRACT

A new symmetrical polyaza macrocyclic binucleating ligand $\mathbf{L^1}$ and its permethylated derivative ligand $\mathbf{L^2}$ have been synthesized by using the precursor compound 2-[2-(2,6-diformyl-4-methylphenoxy)propoxy]-5-methylisophthalaldehyde and bis(aminoethyl) amine. The molecular structure of the precursor compound and the ligand $\mathbf{L^2}$ were determined by the single crystal XRD method. The ligands $\mathbf{L^1}$ and $\mathbf{L^2}$ were treated with two equivalents of $Cu(ClO_4)_2 \cdot 6H_2O$ to afford the new binuclear complexes $[Cu_2L^1(\mu\text{-}OH)(ClO_4)_2](ClO_4)$ (**1**) and $[Cu_2L^2(\mu\text{-}OH)(ClO_4)_2](ClO_4)$ (**2**), respectively. Both the complexes were characterized by elemental and spectral methods. A cyclic voltammetric investigation of these Cu(II) complexes show a quasireversible followed by an irreversible one electron reduction processes around $E^1_{pc} = -0.59$ V, -0.55 V and $E^2_{pc} = -1.07$ V, -1.02 V. ESR spectra of the copper(II) complexes **1** and **2** show a broad signal at $g = 2.08$ and 2.10, and μ_{eff} values of 1.43 and 1.46 BM, respectively, which convey a spin–spin interaction between the two copper(II) ions. The initial rate (V_{in}) for the oxidation of 3,5-di-*tert*-butylcatechol to *o*-quinone by the binuclear Cu(II) complexes **1** and **2** are 1.15×10^{-4} and 1.66×10^{-4} Ms^{-1} respectively. Both the complexes remarkably promote the hydrolytic cleavage of supercoiled plasmid DNA under physiological conditions in the presence of H_2O_2 at pH 7.2 and 37 °C. The reaction profile for the complex **1** mediated reaction displayed approximately pseudo-first-order kinetic behavior, with $k_{obs} \sim 0.07$ min^{-1} and $R^2 = 0.984$.

© 2008 Elsevier Ltd. All rights reserved.

1. Introduction

Polyaza macrocyclic Schiff bases have been studied as potential inorganic and organic cation receptors [1], electron transfer agents, homogeneous catalysts and DNA, RNA interacting agents [2]. Because of their unique and selective complexing properties [3], macrocyclic ligands are particularly suited for the synthesis of such complexes as they are more stable than their acyclic counterparts and the two metal ions are fixed in close proximity which has important implications for metal–metal interactions and binuclear metal reactivity [4]. They are smaller than enzymes, which allows them to attack macromolecular regions that are inaccessible to enzymes, and also their specificity and efficiency may be modulated. These properties have turned chemical nucleases into useful tools as adjuvants in PCR diagnostics [5], nucleic acid attacking and cleaving agents [6]. These polyaza copper(II) complexes are a beacon in modelling, and they serve as bioinorganic model compounds not only in enzymatic reactions, but also in catalytic synthetic oxidation reactions [7,9]. Hence, binuclear copper(II) complexes are of interest for availing magnetostructural correlations and as useful model systems for catalysis. Catechol oxidases are ubiquitous plant enzymes belonging to the oxidoreductase class that contain a dinuclear Cu center in their site, which catalyses the two-electron oxidation of a broad range of *o*-diphenols (catechol) to the corresponding quinones, coupled with the reduction of molecular oxygen to water [7]. Further, catechol oxidases exclusively catalyze the oxidation of catechols to quinones without tyrosine [10]. This reaction is of great importance in medical diagnosis for the determination of the hormonally active catecholamine adrenaline, noradrenalin and dopa [11]. The synthesis and investigation of functional model complexes for metalloenzymes with oxidize or oxygenase activity is therefore of great promise for the development of new and efficient catalysts for oxidation reactions [12]. Further, compounds showing the property of cleaving double stranded DNA under physiological conditions are of importance since these could be used as diagnostic agents in medicinal and genomic research [13]. Several efficient cleaving agents have been developed over the course of time, however, most of the studies deal with macrocyclic mononuclear Cu(II) complexes [14–16]. It has been noticed that macrocyclic binuclear copper(II) complexes show greater DNA cleaving efficiency than mononuclear complexes [17,18]. For these reasons, we aimed to design new polyaza macrocyclic binuclear Cu(II) complexes, which are suitable to

* Corresponding author. Tel./fax: +91 44 22300488.
E-mail address: mkands@yahoo.com (M. Kandaswamy).

0277-5387/$ - see front matter © 2008 Elsevier Ltd. All rights reserved.
doi:10.1016/j.poly.2008.09.022

cleave DNA significantly. As a consequence, the design of the binucleating ligand has to satisfy a number of conditions: metal–metal distance, steric, electronic and bridging ligand features, etc. A new aromatic tetraldehyde is used to function as a precursor in the preparation of polydentate ligands which can form binuclear complexes. The above features can be altered by condensing the precursor compound with various amines. The tetraldehyde is readily condensed with aliphatic α,ω-diamines and subsequent reduction of the intermediate imine compounds provides many macrocyclic ligands [19]. In this paper, we report the synthesis and characterization of new symmetrical macrobicyclic ligands and their dicopper(II) complexes. We describe here two macrocyclic binucleating ligands $\mathbf{L^1}$ and $\mathbf{L^2}$ (Scheme 1) by employing the new precursor compound, 2-[2-(2,6-diformyl-4-methylphenoxy)propoxy]-5-methylisophthalaldehyde and α,ω-diamines.

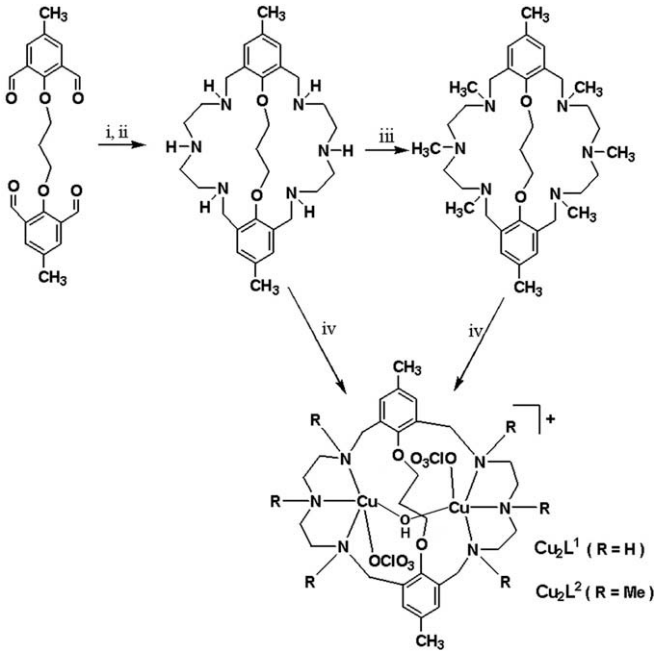
2. Experimental

2.1. Materials

2,6-Diformyl-4-methylphenol [20] and the binucleating macrobicyclic ligands $\mathbf{L^1}$ and $\mathbf{L^2}$ were prepared by a modified procedure of the literature methods [21]. Tetra(*n*-butyl)ammonium perchlorate (TBAP), used as the supporting electrolyte in electrochemical measurements, was purchased from Fluka and recrystallized from hot methanol (Caution! All perchlorate salts are potentially explosive; hence, care should be taken in handling TBAP and complexes containing the perchlorate anion). All the solvents were purified by reported procedures [22]. The supercoiled pBR322 DNA was purchased from Bangalore Genei (India). Superoxide dismutase (SOD), ethidium bromide (EB) and L-histidine were obtained from Sigma (USA). Tris(hydroxymethyl)aminomethane–HCl (Tris–HCl) buffer solution was prepared by using deionized, sonicated triple distilled water.

2.2. General methods

Elemental analysis was carried out on a Carlo Erba model 1106 elemental analyzer. FT-IR spectra were obtained on a Perkin Elmer FTIR spectrometer with the samples prepared as KBr pellets. UV–Visible spectra were recorded using a Perkin Elmer Lambda 35 spectrophotometer operating in the range 200–1400 nm with quartz cells and ε values are given in $M^{-1}\,cm^{-1}$. NMR spectra were recorded in $CDCl_3$, using TMS as an internal standard, on a BRUKER 300 instrument. EI mass spectra were recorded on a JEOL DX-303 EI mass spectrometer. Electrospray ionization mass spectral measurements were done using a Thermo Finnigan LCQ-6000 Advantage Max-ESI mass spectrometer. Cyclic voltammograms were obtained on a CH11008 Electrochemical analyzer using a three-electrode set-up comprising of a glassy carbon working, platinum wire auxiliary and a saturated Ag/AgCl reference electrode under oxygen free conditions. The concentration of the complexes was 10^{-3} M. TBAP (Tetra(butyl)ammonium perchlorate) (10^{-1} M) was used as the supporting electrolyte. The FAB mass spectra of the complexes were recorded on a JOEL SX 102/DA 6000 mass spectrometer using 3-nitrobenzyl alcohol as the matrix solvent. EPR spectra were recorded on powdered samples of **1** and **2** using a JEOL TES 100 ESR spectrometer. Low temperature measurements were made using a liquid nitrogen Dewar.



Scheme 1. (i) $NH(CH_2CH_2NH_2)_2$, CH_2Cl_2–EtOH(high dilution); (ii) $NaBH_4$; (iii) HCHO, HCOOH; (iv) $Cu(ClO_4)_2 \cdot 6H_2O$.

2.3. Synthesis

2.3.1. Synthesis of the precursor compound (2-[2-(2,6-diformyl-4-methylphenoxy)propoxy]-5-methylisophthalaldehyde)

A mixture of 2,6-diformyl-4-methylphenol (3 g, 18.2 mmol), 1,3-dibromopropane (1.73 g, 9.1 mmol) and K_2CO_3 (1.26 g, 9.1 mmol) was stirred in dry DMF at 90 °C for 2 h. The resulting solution was cooled to room temperature and poured onto crushed ice. A white solid separated by filtration and was dried. Colorless crystals suitable for XRD analysis were obtained by slow evaporation of a dichloromethane solution of this solid. Yield: 5.5 g (81%). Mp 210 °C. Elemental *Anal.* Calc. for $C_{21}H_{20}O_6$ (L^1) C, 68.5; H, 5.4. Found: C, 68.4; H, 5.5%. EI Mass: $[M^+ + 1] = 369$. ^1H NMR ($CDCl_3$, 300 MHz): 2.36 ($2CH_3$, s, 6H), 2.43 (CH_2, quintet, 2H), 4.28 ($2CH_2$, t, 4H, J = 6.3 Hz), 7. 84 (Ar H, s, 4H), 10.28 (CHO, s, 4H). ^{13}C NMR ($CDCl_3$, 75 MHz): 20.5 (CH_3), 29.6 (CH_2), 75.9 (CH_2), 129.8, 136.0 (ArH), 188.5 (CHO). IR (cm^{-1}, KBr pellet): 2925 (CH stretching), 1669 (CO stretching), 1435 (O–CH_2).

2.3.2. Synthesis of the macrobicyclic binucleating ligand ($\mathbf{L^1}$)

The precursor compound (3.68 g, 10 mmol) in chloroform (100 ml) and diethylenetriamine (2.06 g, 20 mmol) in ethanol were added simultaneously over a period of 8 h to a mixture of chloroform (300 ml) and ethanol (100 ml). After complete addition, the reaction mixture was stirred at room temperature for 24 h. The chloroform was then removed at reduced pressure and a solution of sodium borohydride (3.03 g, 80 mmol) in ethanol (100 ml) was added. After stirring at room temperature for 2 h, the reaction mixture was acidified to pH 1 with conc. hydrochloric acid and the resulting colorless suspension was evaporated to dryness. Water (100 ml) and chloroform (200 ml) were added to the residue, the pH of the aqueous phase was adjusted to 13 with 3 M aqueous potassium hydroxide, and the heterogeneous mixture was stirred vigorously for 1 h. The aqueous phase was extracted with chloroform and dried over sodium sulfate. Evaporation of the solvent gave $\mathbf{L^1}$ as a colorless foamy solid. Yield: 4.3 g (84%). M.p. 173 °C. Elemental *Anal.* Calc. for $C_{29}H_{46}N_6O_2$ ($\mathbf{L^1}$) C, 68.2; H, 9.0; N, 16.5. Found: C, 68.1; H, 9.2; N, 16.7%. ESI-MS in CH_3OH: *m*/*z* 511.47 $[M+H]^+$. ^1H NMR ($CDCl_3$, 75 MHz): 2.09 (CH_3, s, 6H), 2.29 (–CH_2–, t, 2H, J = 6.6 Hz), 2.69 (–CH_2–, s, 16H), 3.67 (–CH_2–, s, 8H), 4.18 (–CH_2–, t, 4H, J = 6.6 Hz), 4.54 (NH, s, 2H), 4.72 (NH, br s, 4H), 6.90 (ArH, s, 4H). ^{13}C NMR $CDCl_3$, 75 MHz): 19.6 ($2CH_3$), 30.6 (CH_2), 48.1 ($4CH_2$), 48.5 ($4CH_2$), 71.5 ($2CH_2$), 129.7, 132.0, 132.5, 153.4 (ArC). IR (cm^{-1}, KBr pellet): 3235 (NH stretching), 2916 (CH stretching), 1517 (NH bending), 1215 (O–C stretching).

2.3.3. Synthesis of the macrobicyclic binucleating ligand (L^2)

The binucleating macrobicyclic ligand L^1 (5.1 g, 10.0 mmol) was dissolved in formic acid (20 mL). To the above warm solution, aqueous formaldehyde (37%, 20 mL) was added. The reaction mixture was heated under reflux for 24 h, then concentrated in vacuo to about 10 mL. Water (50 mL) and dichloromethane (100 mL) were added to the sticky residue, the pH of the aqueous phase was adjusted to 13 by the addition of 3 M aqueous potassium hydroxide solution and the heterogeneous mixture was stirred vigorously for 30 min. The layers were separated and the aqueous phase was extracted with dichloromethane (3 × 100 mL). The combined organic fractions were dried over K_2CO_3 and filtered. Methanol (100 mL) was added to the clear solution. On evaporation of the dichloromethane, the permethylated macrocycle **L^2** was obtained as colorless crystals. Yield: 5.2 g (87%). M.p. 120 °C. Elemental *Anal.* Calc. for $C_{35}H_{58}N_6O_2$ (**L^2**) C, 70.7; H, 9.8; N, 14.1. Found: C, 70.8; H, 9.5; N, 14.3%. ESI-MS in CH_3OH: *m/z* 595.53 $[M+H]^+$. ^1H NMR ($CDCl_3$, 300 MHz): 2.24 (N–CH_3, s, 18H), 2.28 (Ar–CH_3, s, 6H), 2.76 (–CH_2–, quintet, 2H), 2.66 (8CH_2, s, 16H), 3.52 (–CH_2–, s, 8H), 4.32 (–CH_2–, t, 4H, J = 6.6 Hz), 6.99 (ArH, s, 4H). ^{13}C NMR ($CDCl_3$, 75 MHz): 20.7 (2CH_3), 31.7 (1CH_2), 42.0 (4N–CH_3), 54.8 (CH_2), 55.2 (8CH_2), 57.5 (8CH_2), 72.18 (2CH_2), 131.2, 132.2, 132.4, 155.11 (Ar-C). IR (cm^{-1}, KBr pellet): 2946 (CH stretching), 1224 (O–C stretching).

*2.3.4. Synthesis of the binuclear Cu(II) complex (**1**) [Cu_2L^1 (μ-OH)(ClO_4)$_2$] (ClO_4)*

The binuclear Cu(II) complex **1** was synthesized by refluxing a methanolic solution of the ligand **L^1** (1 g, 1.96 mmol) and a methanolic solution of $Cu(ClO_4)_2 \cdot 6H_2O$ (1.45 g, 3.92 mmol). A blue colored solid was separated on evaporating the solution at room temperature and the resulting compound was washed with cold methanol and dried. Yield: (77%). Elemental *Anal.* Calc. for $C_{29}H_{47}Cl_3Cu_2N_6O_{15}$ (**1**) C, 36.5; H, 4.9; N, 8.8. Found: C, 36.2; H, 4.6; N, 8.3%. FAB-MS in NBA: *m/z* 837 $[L^1 + 2Cu + 2ClO_4 + H]^+$; 738 $[L^1 + 2Cu + ClO_4 + H]^+$. Λ_M, S $m^2\,M^{-1}$ in CH_3CN at 25 °C: 81. IR (cm^{-1}, KBr pellet): 3431, 3221w ν(N–H), 2926w, 2879 ν(C–H), 1635m, 1458w, 1209s (C–O), 1105vs, 1085vs $\nu(ClO_4)$, 624m, 420s. UV–Visible [λ/nm ($\epsilon/M^{-1}\,cm^{-1}$)] in CH_3CN: 633 (380), 272 (84,000). g = 2.081. μ_{eff}, μ_B at 298 K: 1.43.

*2.3.5. Synthesis of the binuclear Cu(II) complex (**2**) [Cu_2L^2 (μ-OH)(ClO_4)$_2$] (ClO_4)*

The complex **2** was prepared by following the above method using ligand **L^2** (1 g, 1.68 mmol) and $Cu(ClO_4)_2 \cdot 6H_2O$ (1.24 g, 3.36 mmol), which resulted in a bluish green colored solid. Yield: (56%). Elemental *Anal.* Calc. for $C_{35}H_{59}Cl_3Cu_2N_6O_{15}$ (**2**) C, 40.5; H, 5.7; N, 8.1. Found: C, 40.9; H, 5.4; N, 8.4%. FAB-MS in NBA: *m/z* 921 $[L^2 + 2Cu + 2ClO_4 + H]^+$; 822 $[L^2 + 2Cu + ClO_4 + H]^+$. Λ_M, S $m^2\,M^{-1}$ in CH_3CN at 25 °C: 85. IR (cm^{-1}, KBr pellet) 3462br, 2931m, 2860m ν(C–H), 1685, 1637, 1463, 1212s ν(C–O), 1105vs, 1088vs $\nu(ClO_4)$, 627m, 420s. UV–Visible [λ/nm ($\epsilon/M^{-1}\,cm^{-1}$)] in CH_3CN: 657 (260), 283 (3,90,000). g = 2.102. μ_{eff}, μ_B at 298 K: 1.46.

2.4. X-ray data collection and reduction

Crystals of the precursor compound and ligand **L^2** were colorless and could be sorted using a polarizing microscope (Leica DMLSP). Crystals were cut to a suitable size (less than the collimator cross section diameter) and mounted on a Kappa Apex 2 CCD diffractometer equipped with graphite monochromatic Mo(Kα) radiation (λ = 0.71073 Å). The unit cell parameters were obtained using 36ω-frames of 0.5° width and scanned from three different zones of the reciprocal lattice. The intensity data were collected using ω and φ scans with a frame width of 0.5°. The frame integration and data reduction were performed using Bruker SAINT-PLUS (Version 7.06a) software [23]. The multi-scan absorption corrections were applied to the data using the SADABS [24] program. Both samples were stable at room temperature. The structures were solved using SIR92 [25]. Full matrix least squares refinement was performed using SHELXL-97 [26] programs. All the non-hydrogen atoms were refined with anisotropic displacement parameters. All the hydrogen atoms could be located in the Difference Fourier map. However, they were relocated at chemically meaningful positions and were given riding model refinement with following restraints: tertiary CH_3 groups (C–H = 0.96 Å, U_{iso} = 1.5U_{eq} of parent carbon), secondary CH_2 group (C–H = 0.97 Å, U_{iso} = 1.2U_{eq} of the parent carbon), aromatic C–H group (C–H = 0.93 Å U_{iso} = 1.2U_{eq} of the parent carbon). Selected crystallographic data of the precursor compound and ligand **L^2** are depicted in Table 1.

2.5. Kinetic studies of oxidation of catechol (catecholase activity)

The catalytic oxidation of 4,5-ditertiarybutyl catechol (DTBC) to the corresponding *o*-quinone (DTBQ-ditertiary butyl quinone) was studied using 10^{-3} M of the copper(II) complexes as a biomimetic catalyst in acetonitrile solution. The reaction was followed spectrophotometrically by choosing the strongest absorbance of the product, DTBQ, around 395 nm and monitoring the increase in the absorbance at this wavelength over time intervals of 10 min. Initial rates (d*c*/d*t*) (<2% conversion of DTBC into DTBQ) were determined by a spectrophotometric method. The initial reaction rate values were obtained from the slope of the trace at 395 nm during the first 30 min of the reactions, when the absorption at 395 nm increases linearly.

2.6. DNA cleavage experiments

The cleavage of supercoiled pBR322DNA by the complexes was studied by agarose gel electrophoresis. The gel electrophoresis experiments were performed as follows: pBR322DNA (0.2 μg, 33 μM) was treated with the copper(II) complexes **1** and **2** in 50 mM Tris–HCl/NaCl buffer (pH 7.2) and H_2O_2 followed by dilution with Tris–HCl buffer to a total volume of 18 μL. All the samples were incubated for 30 min at 37 °C followed by their addition to

Table 1
Selected crystallographic data of the precursor compound and the ligand **L^2**.

Parameters	Precursor compound	L^2
Empirical formula	$C_{21}H_{20}O_6$	$C_{35}H_{58}N_6O_2$
Formula weight	368.37	594.87
T (K)	293(2)	293(2)
Wavelength (Å)	0.71073	0.71073
Crystal system	monoclinic	triclinic
Space group	*C*2	$P\bar{1}$
a (Å)	15.8317(11)	9.2656(3)
b (Å)	4.1407(3)	13.1391(4)
c (Å)	14.3460(11)	14.9542(5)
α (°)	90	81.354(2)
β (°)	103.443(5)	84.839(2)
γ (°)	90	76.139(2)
V (A^3)	914.73(12)	1744.69(10)
Z	2	*2*
D_{calc} (Mg/m^3)	1.337	1.132
Absorption coefficient (mm^{-1})	0.098	0.071
Crystal size (mm)	0.26 × 0.16 × 0.16	0.16 × 0.12 × 0.12
θ Range for (data collection (°)	3.37–25.00	2.65–19.34
Maximum and minimum transmission	0.9749–0.9845	0.988–0.9915
Data/restraints/parameters	2636/1/137	2972/0/390
Final *R* indices [$I > 2\sigma(I)$]	R_1 = 0.0498 (2170)	R_1 = 0.0688 (2392)
R indices (all data)	wR_2 = 0.1525 (2636)	wR_2 = 0.2127 (2972)

the loading buffer containing 25% bromophenol blue, 0.25% Xylene cyanol, 30% glycerol (3 μL). The solution was finally loaded on 0.8% agarose gel containing ethidium bromide (1 μg/mL^{-1}). Electrophoresis was done for 1 h at 50 V in TBE (45 mM Tris, 45 mM H_3BO_3, 1 mM-EDTA, pH 8.3) buffer. Bands were visualized by UV light and photographed. Quantification of closed circular and nicked DNA was made by densitometric analysis of ethidium bromide containing agarose gels. Quantification was performed by fluorescence imaging by the use of a Gel-Doc 1000 (BioRad) and data analysis with MULTIANALYSIS software (version 1.1) provided by the manufacturer, using the volume quantification method. In all cases, background fluorescence was subtracted by reference to a lane containing no DNA. A correction factor of 1.47 was used for supercoiled DNA since the ability of ethidium bromide to intercalate into supercoiled DNA (form I) decreased relative to the nicked circular (form II). The fraction of each form of DNA was calculated by dividing the intensity of each band by the total intensities of all the bands in the lane. All results were obtained from experiments that were performed at least in triplicate.

3. Result and discussion

The precursor compound and the ligand **L^1** were prepared by using a modified literature procedure of Clark et al. [27]. We synthesized two macrocyclic binucleating ligands by employing the new precursor compound, 2-[2-(2,6-diformyl-4-methylphenoxy)propoxy]-5-methylisophthalaldehyde and α,ω-diamines. The macrocycle **L^1** was obtained by a (2+1) condensation between the precursor compound and bis(aminoethyl)amine in ethanol-dichloromethane, followed by reduction with $NaBH_4$ (Scheme 1). Reductive methylation of **L^1** with formaldehyde and formic acid under Eschweiler–Clarke conditions gave the permethylated derivative **L^2**. The structure of **L^2** was derived from that of ligand **L^1** by replacing the six NH hydrogen atoms by methyl groups. Synthetic pathways for the complexes are shown in Scheme 1. The molar conductivity measurements of the copper(II) complexes **1** and **2** in CH_3CN resulted in Λ_M values of 81 and 85 S m^2 M^{-1} respectively, which indicate that the complexes are 1:1 electrolytes [28]. The FAB mass spectrum of complex 1, $[Cu_2L^1(\mu\text{-}OH)(ClO_4)_2]$ (ClO_4), showed a peak at $m/z = 837$, corresponding to the $[L^1 + 2Cu + 2\text{-}ClO_4 + H]^+$ ion, and the complex **2**, $[Cu_2L^2(\mu\text{-}OH)(ClO_4)_2]$ (ClO_4), showed a peak at $m/z = 920$, corresponding to the $[L^2 + 2Cu + 2\text{-}ClO_4 + H]^+$ ion. The FAB mass spectral data of the copper(II) complexes confirm the proposed formula of the complexes.

3.1. Crystal structures

The precursor compound crystallizes in the monoclinic system with the space group C2 and half of the molecule in the asymmetric unit. The molecule has twofold symmetry with a two fold axis passing through at C11. The tetraldehyde molecule and its twofold equivalents are linked through C10–H10B···O2 hydrogen bonds (2.58 Å, 143.25°, Symm: 1.5 − x, ½ + y, −z). The hydrogen bonding extends through a-translation to form a one dimensional chain. The packing is further stabilized through Van der Waals interactions. The ORTEP diagram of the precursor compound is given in Fig. 1. The permethylated macrocyclic ligand **L^2** crystallizes in the triclinic space group $P\bar{1}$ with one molecule in the asymmetric unit. The molecules are stabilized by Van der Waals interactions, weak intramolecular C–H···O, C–H···N bonds and intermolecular C–H (π) interactions. Fig. 2 represents the ORTEP diagram of the macrocyclic ligand **L^2**.

3.2. Spectral studies

The IR spectra of the two complexes showed a strong band in the region around 1000–1100 cm^{-1} and a sharp band in the region around 626 cm^{-1}, which could be due to the antisymmetric stretch and antisymmetric bend of perchlorate ions, respectively. The perchlorate peak around 1100 cm^{-1} splits in to two peaks around 1105 and 1085 cm^{-1}, indicating that the perchlorate ions present in the complexes are coordinated to the Cu(II) ions. Complex **1** has another prominent feature of a sharp but weak band at 3221 cm^{-1}, a frequency typical for the N–H stretching vibration of a coordinated secondary amine group. The disappearance of the band around 3220 cm^{-1} and the increasing intensity of the band at 2925 cm^{-1} for complex **2** confirms the N-methylation of the ligand **L^2**. The important strong band observed at around 3460 cm^{-1} for both of the macrocyclic Cu(II) complexes are assignable to OH vibrations. The electronic spectra of an acetonitrile solution of complexes **1** and **2** show three intense intraligand bands in the UV region. In the visible region the copper(II) complexes **1** and **2** exhibit absorption maxima at 633 and 657 nm (Fig. 3), respectively. This strongly suggests that the coordination geometry around the metal ion might be distorted square pyramidal [29]. An increase in λ_{max} (red shift) of complex **2** may be due to the weaker field strength of ligand **L^2** and larger distortion of the coordination geometry around the Cu(II) ion than for complex **1**. The EPR spectra of the solid com-

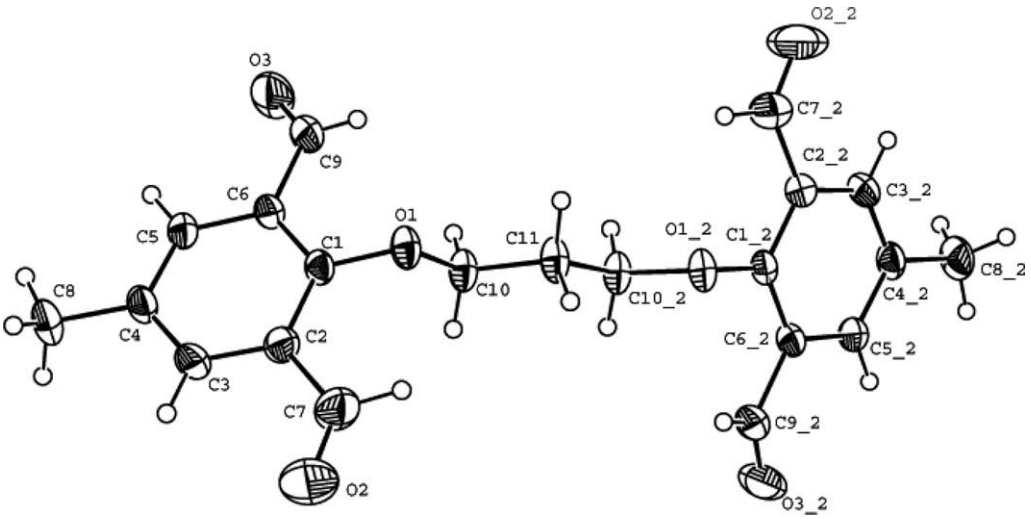


Fig. 1. ORTEP diagram of precursor compound **I**. Displacement ellipsoids are drawn at the 50% probability level.

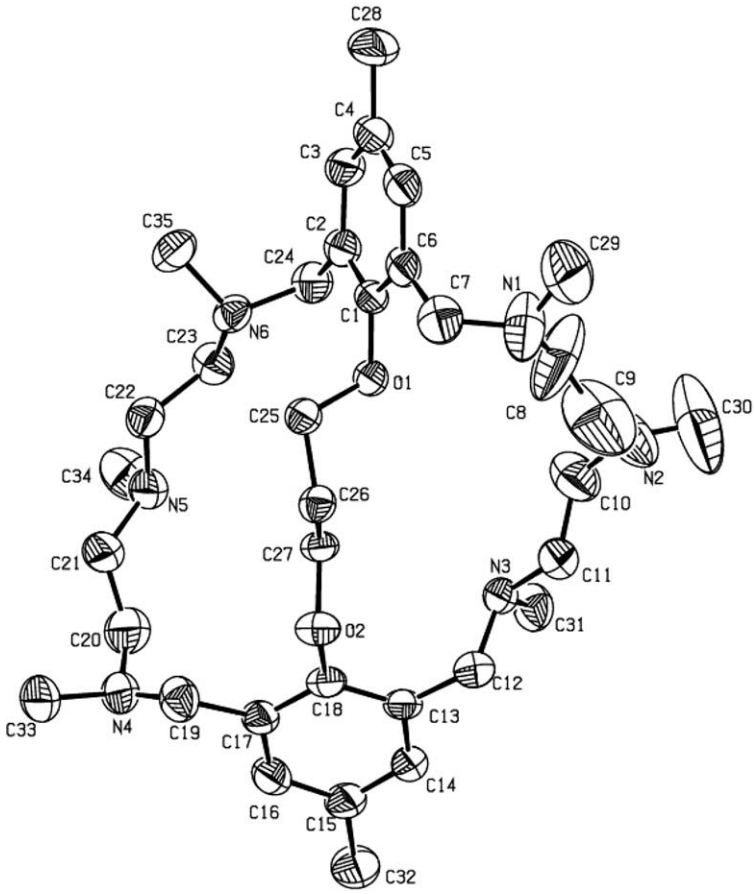


Fig. 2. ORTEP diagram of ligand L^2. Displacement ellipsoids are drawn at the 50% probability level.

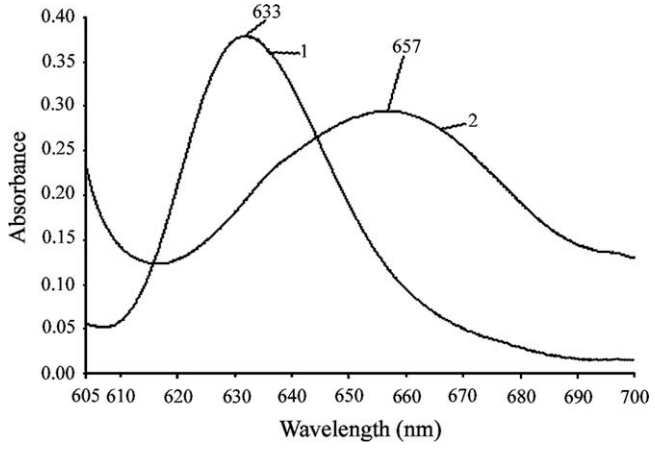


Fig. 3. Electronic spectra of complexes **1** and **2** in CH_3CN.

plexes **1** and **2** were recorded at liquid nitrogen temperature (LNT). Both the binuclear complexes showed a single broad-band resonance at ca. $g = 2.06–2.10$, with the half field signal at 1500G ($M = \pm 2$), which suggest magnetic interactions between the two copper ions through the hydroxyl bridge (Fig. 4). The probe room temperature magnetic studies of the binuclear copper(II) complexes **1** and **2** resulted in magnetic moment values of 1.43 and 1.46 BM, respectively, which suggest the presence of an antiferromagnetic interaction between the two Cu(II) ions.

3.3. Electrochemistry

The cyclic voltammograms of complexes **1** and **2** (Fig. 5) were recorded in CH_3CN solution. Both complexes display in the negative region of potentials a quasireversible redox wave followed by an irreversible cathodic peak at a lower potential. The first reduction potentials are observed at (E^1_{pc}) −0.59 V and −0.55 V for complexes **1** and **2**, respectively. Coulometric titrations by potentiostatic exhaustive electrolysis performed at 100 mV more negative to the first reduction wave consumed approximately one electron ($n \approx 0.96$). This indicates that each process corresponds to a single electron transfer process, and this can be assigned to the redox couple $Cu^{II}Cu^{II}/Cu^{II}Cu^{I}$. The second reduction potentials for complexes **1** and **2** are irreversible and are observed at $E^2_{pc} = -1.07$ and −1.02 V versus Ag/AgCl, respectively. These can be attributed to the transformation $Cu^{II}Cu^{I} \rightarrow Cu^{I}Cu^{I}$. The fact that this process is completely irreversible for both complexes suggests a fast decomposition of the $Cu^{I}Cu^{I}$ species, as evidenced by Neves et al. [7]. Complex **2** reduces at less negative potentials than the complex **1**. This suggests that the geometry around the copper ions with ligand $\mathbf{L^2}$ is more distorted than the copper ions with ligand $\mathbf{L^1}$. The ligands are structurally different in that the amine donor nitrogens of $\mathbf{L^2}$ contain bulky methyl groups, whereas the ligand $\mathbf{L^1}$ has hydrogen atoms. The deviation of the metal from its coordination plane should be larger for the $\mathbf{L^2}$ complex in order to destabilize the Cu(II) oxidation state. Thus, the electron density on the copper ions of complex **2** is less and the copper coordination geometry may also be more distorted due to the steric effect of the bulky methyl group substituents. It has been suggested [30,31] that reduction in electron density on the copper ions and distortion in

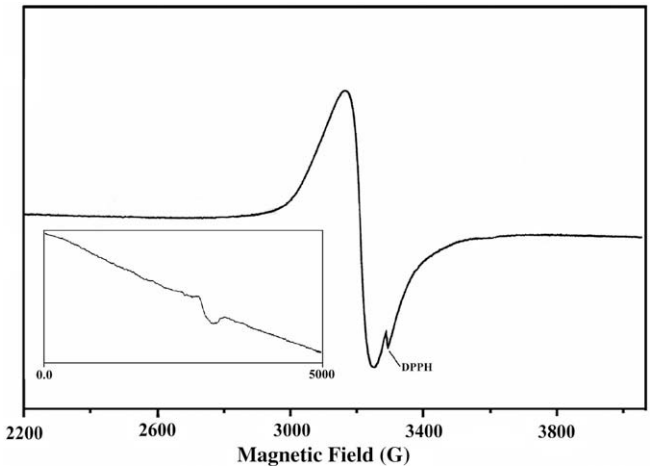


Fig. 4. X- band EPR spectrum of frozen solid (**1**) at 77 K. Inset gives the EPR showing the $\Delta M_s = \pm 2$ transition.

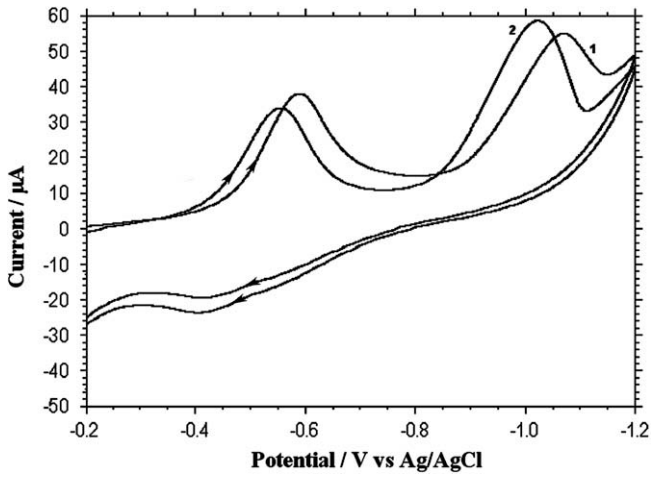


Fig. 5. Cyclic voltammograms of complexes **1** and **2** in CH_3CN.

geometry favors the reduction process ($Cu^{II} \rightarrow Cu^{I}$) at less negative potentials, as observed in the complex of the ligand $\mathbf{L^2}$ relative to the ligand $\mathbf{L^1}$.

3.4. Catalytic studies

The catecholase activity of the polyaza binuclear copper(II) complexes **1** and **2** has been studied, with the help of electronic spectroscopy, by monitoring the appearance of the absorbance maximum of the substituted quinone [(DTBQ) ditertiary butyl quinone] (λ_{max} = 395 nm). The time dependent formation of DTBQ in the presence of **1** and **2** is shown in Fig. 6. The initial rate values for the binuclear copper(II) complexes **1** and **2** are 1.15×10^{-4} and $1.66 \times 10^{-4}\,Ms^{-1}$ respectively. The oxidation of catechol to *o*-quinone requires the presence of two metal ions in close proximity; hence, the initial rate values for binuclear complexes are comparatively high. The intrinsic flexibility of the ligand $\mathbf{L^2}$ makes the metal ion reduce easily and bind with the substrate; this facilitates the better catalytic activity of complex **2** compared to complex **1**. It has been assumed that the geometry around the copper ions and the intermetallic distance are the two key factors that determine the catalytic activity of the complexes. The Cu(II) ions may be in close proximity when coordinated by the ligand $\mathbf{L^2}$, and the bridging catechol coordination is compatible with the distance between

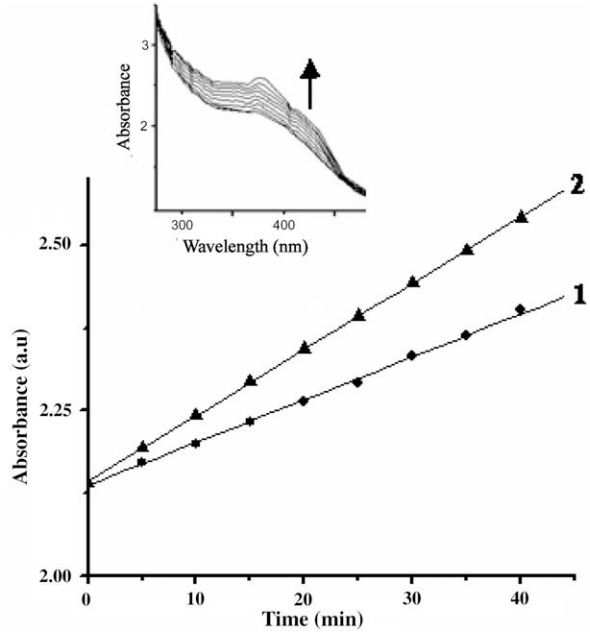


Fig. 6. Time-dependent formation of DTBQ in the presence of complexes **1** and **2**. Inset shows oxidation of 3,5-DTBC by the binuclear copper(II) complex **2**.

the two *o*-diphenol oxygen atoms [32]. The presence of the bulky *N*-methyl group of ligand $\mathbf{L^2}$ makes the coordination geometry around the copper(II) ions more distorted than with the macrocycle ligand $\mathbf{L^1}$. It is evident from the literature [33,34] that the initial rate values for more distorted complexes are higher than those of less distorted complexes.

3.5. DNA cleavage studies

As evident from the literature, complexes of polyamine ligands play an important role due their good nuclease activity [35,36]. In order to assess any cleavage of DNA as a result of the binding of complexes **1** and **2**, agarose gel electrophoresis has been performed with the supercoiled form of plasmid DNA. This method using supercoiled pBR322 DNA in the presence of the macrocyclic Cu(II) complexes **1** and **2** was carried out in a medium of 50 mM Tris–HCl/NaCl Buffer (pH 7.2). Both complexes showed remarkable cleavage in the presence of H_2O_2 (40 μM) as an oxidizing agent. Fig. 7a shows the gel electrophoretic results of the interaction of complexes **1** and **2** with plasmid pBR322 DNA. Under similar conditions, no cleavage of pBR322 DNA occurred for free H_2O_2 (Fig. 7b; lane 2) or free complex (lane 4). The control DNA (lane 1) itself shows two bands [Form I, SC $\geqslant$ 90%; Form II, NC $\leqslant$ 10%]. The Cu(II) complex/H_2O_2 treated DNA also results in two bands, which are exactly parallel to the bands of lane 1, and the band intensity corresponding to Form I (SC DNA) is diminished whilst the band

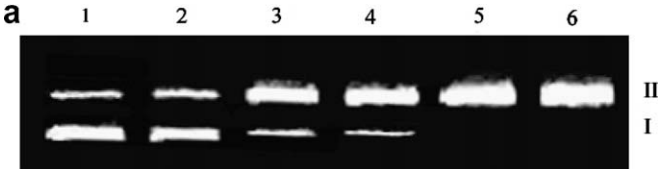


Fig. 7a. Cleavage of SC pBR322 DNA (0.2 μg, 33 μM) by the Cu(II) complexes **1** and **2** (30–50 μM) in the presence of reducing agent H_2O_2 (40 μM) in 50 mM Tris–HCl/NaCl buffer (pH 7.2). Lane 1, DNA control; Lane 2, DNA + 40 μM H_2O_2; Lanes 3–4, DNA + 40 μM H_2O_2 + **1** and **2** (30 μM), respectively; Lanes 5–6, DNA + 40 mM H_2O_2 + **1** and **2** (50 μM), respectively.

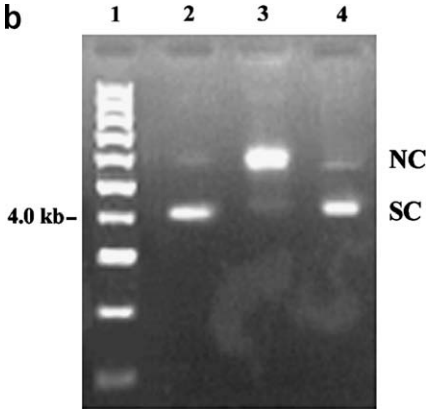


Fig. 7b. Lane 1, Molecular weight markers (1 kb); lane 2, DNA control, lane 3, DNA + 40 μM H_2O_2 + Complex **1** (50 μM); lane 4, DNA + Complex **1** (50 μM). SC – supercoiled, NC – Nicked circular.

intensity of Form II (NC DNA) is increased (lanes 3–4), confirming the formation nicked DNA. At a slightly higher concentration of the binuclear complexes (50 μM), the cleavage is found to be much more efficient in lane 5 and 6. The amount of Form I (supercoiled) decreases, whereas that of Form II (nicked circular) increases with the increase in complex concentration. It is clear that the cleavage of pBR322 DNA is highly dependent on the concentration of the complexes. The cleavage mechanism of pBR322 DNA induced by complexes **1** and **2** was investigated (Fig. 8) and clarified in the presence of a hydroxyl radical scavenger, 1 mM DMSO (lanes 1–2), superoxide scavenger (SOD) (lanes 3–4) and singlet oxygen quencher L-histidine (lanes 5–6) [37]. Only a slight inhibition of DNA cleavage was observed in the presence of the scavengers, which suggests that hydroxyl radical, superoxide and singlet oxygen might not occur in the reaction. The binuclear Cu(II) complexes were found to be highly active in cleaving DNA in the presence of hydrogen peroxide. The H_2O_2 is coordinated to the copper ions of the complexes, affording a peroxo-dicopper species [38]. This coordinated peroxide ion attacks the DNA phosphate bond via a nucleophilic mechanism and hydrolyzes the P–O bond [39–41]. The polyamine groups of the ligand also have the ability to promote the performance of the metal complex in the cleavage of DNA under physiological conditions [17]. The reactions of SC (Form I) plasmid DNA with complex **1** were carried out in the presence of H_2O_2. Typical results from this set of experiments are shown in Fig. 9a and 9b. The disappearance of SC versus time followed pseudo first-order kinetics. The reaction profile for the complex **1** mediated reaction displayed approximately pseudo-first-order kinetic behavior (Fig. 9b), with $k_{obs} \sim 0.07\ min^{-1}$ and $R^2 = 0.984$. On comparison of the cleavage property with some reported results [42,43] of Cu(II) complexes, we note that a lesser amount of oxidizing agents (here hydrogen peroxide) and complex are required in our case for maximum cleavage of DNA. This is well reflected from the cleavage data which show more than 80% of cleavage occurs with a very low

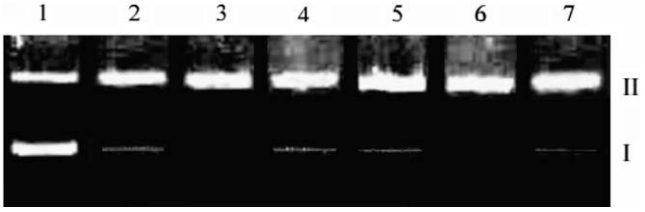


Fig. 8. Lane 1, DNA control; lanes 2–3, DNA + 40 μM H_2O_2 + DMSO (0.1 mM) + **1** and **2** (50 μM), respectively; lanes 4–5, DNA + 40 μM H_2O_2 + SOD (4 units) + **1** and **2** (50 μM) respectively; lanes 6–7, DNA + 40 μM H_2O_2 + L-histidine (0.21 mM) + 1 and 2 (50 μM), respectively.

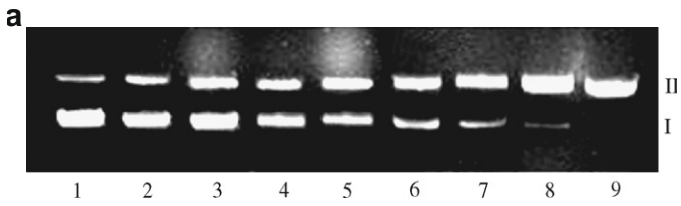


Fig. 9a. Cleavage activity of **1** monitored by 0.8% agarose gel electrophoresis, where [DNA] 0.2 μg, 33 μM (complex 1) 50 μM, and [H_2O_2] 40 μM. Time course measured in 10 mM Tris buffer, pH 7.4, 37 °C, showing the disappearance of supercoiled DNA (I) at (1) 0 min, (2) 2 min, (3) 4 min, (4) 6 min, (5) 10 min, (6) 15 min, (7) 20 min, (8) 25 min, (9) 30 min. (Gel image showing supercoiled (Form I) and circular relaxed (Form II) DNA).

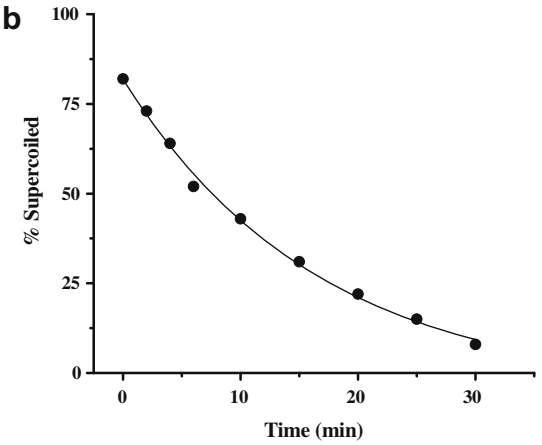


Fig. 9b. Reaction curve, showing a pseudo-first-order kinetic profile (R^2) 0.974, $k_{obs} \sim 0.04\ min^{-1}$.

amount of complex concentration (50 μM). Meanwhile, due to the cyclic nature of the ligands, the two Cu(II) ion centers display an appropriate distance and angle in the cleavage process, so a synergistic effect might exist in the system. Further studies on the macrocyclic ring size effect on DNA molecules as well as on the sequence selectivity of the copper(II) complexes are in progress.

4. Conclusions

Two symmetrical polyaza macrobicyclic binuclear Cu(II) complexes have been synthesized from the new macrocyclic ligand $\mathbf{L^1}$ and its permethylated derivative ligand $\mathbf{L^2}$ and subsequently characterized. Both ligands were prepared using a new tetraldehyde as a precursor compound. Both complexes show good catalytic activity for the catechol oxidation reaction and remarkably promote the hydrolytic cleavage of supercoiled plasmid DNA under physiological conditions in the presence of H_2O_2 at pH 7.2 and 37 °C.

Acknowledgement

The authors gratefully acknowledge DST-FIST, India for financial assistance.

Appendix A. Supplementary data

CCDC 673462 and 688536 contain the supplementary crystallographic data for compounds **I** and $\mathbf{L^2}$. These data can be obtained free of charge via http://www.ccdc.cam.ac.uk/conts/retrieving.html, or from the Cambridge Crystallographic Data Centre, 12 Union Road, Cambridge CB2 1EZ, UK; fax: (+44) 1223-336-033; or e-mail: deposit@ccdc.cam.ac.uk.

References

[1] E. Kimura, Tetrahedron 48 (1992) 6175.
[2] B. Sarkar, P. Mukhopadhyay, P.K. Bharadwaj, Coord. Chem. Rev. 236 (2003) 1.
[3] R.M. Izatt, K. Pawlak, J. Bradshaw, S. Bruening, Chem. Rev. 91 (1991) 1721.
[4] M.H. Klingle, G. Steinfeld, B. Kersting, Z. Naturforsch. 56b (2001) 901.
[5] (a) M. Wu, D. Stoermer, T.D. Tullius, C.A. Townsend, J. Am. Chem. Soc. 122 (2000) 12884;
(b) M.C.B. Oliveira, M.S.R. Couto, P.C. Severino, T. Foppa, G.T.S. Martins, B. Szpoganicz, R.A. Peralta, A. Neves, H. Terenzi, Polyhedron 24 (2005) 495.
[6] H.A. Avila, D.S. Sigman, L.M. Cohen, R.C. Millikan, L. Simpson, Mol. Biochem. Parasitol. 48 (1991) 211.
[7] N.A. Rey, A. Neves, A. Bortoluzzi, C.T. Pich, H. Terenzi, Inorg. Chem. 46 (2007) 348.
[8] M.R. Malachowski, B.R. Dorsey, M.R. Parker, M.E. Adams, R.S. Kelly, Polyhedron 17 (1998) 1289.
[9] M.S. Niasari, A. Amiri, J. Mol. Catal. A: Chem. 235 (2005) 114.
[10] M. Tremolieres, J.B. Bieth, Phytochemistry 23 (1984) 501.
[11] D. Meiwes, B. Ross, M. Kiesshauer, K. Cammann, H. Witzel, M. Knoll, M. Borchardt, C. Sandermaier, Lab. Med. 15 (1992) 24.
[12] P. Gentschev, N. Moller, B. Krebs, Inorg. Chim. Acta 300–302 (2000) 442.
[13] D. Koushik, J. Ratha, M. Manassero, X-Y. Wang, S. Gao, P. Banerjee, J. Inorg. Biochem. 101 (2007) 95.
[14] E.L. Hegg, J.N. Burstyn, Inorg. Chem. 35 (1996) 7474.
[15] E.L. Hegg, K.A. Deal, L.L. Kiessling, J.N. Burstyn, Inorg. Chem. 36 (1997) 1715.
[16] Y.G. Fang, J. Zhang, S.Y. Chen, N. Jiang, H.H. Lin, Y. Zhang, X.-Q. Yu, Bioorg. Med. Chem. 15 (2007) 696.
[17] M.C.B. Oliveira, M.S.R. Couto, P.C. Severino, T. Foppa, G.T.S. Martins, B. Szpoganicz, R.A. Peralta, A. Neves, H. Terenzi, Polyhedron 24 (2005) 495.
[18] K.G. Ragunathan, H.-J. Schneider, Angew. Chem., Int. Ed. 35 (1996) 1219.
[19] B. Kersting, G. Steinfeld, Chem. Commun. (2001) 1376.
[20] N.V. Verani, E. Rentschler, T. Weyhermuller, E. Bill, P. Chaudhuri, J. Chem. Soc., Dalton Trans. (2000) 251.
[21] G. Siedle, B. Kersting, Z. Anorg. Allg. Chem. 629 (2003) 2083.
[22] M. Thirumavalavan, P. Akilan, M. Kandaswamy, Inorg. Chem. 42 (2003) 3308.
[23] Bruker-Nonius (2004). APEX-II and SAINT-Plus (Version 7.06a), Bruker AXS Inc., Madison, Wisconsin, USA.
[24] G.M. Sheldrick, SADABS, University of Göttingen, Germany, 2001.
[25] A. Altomare, G. Cascarano, C. Giacovazzo, A. Guagliardi, J. Appl. Crystallogr. 26 (1993) 343.
[26] G.M. Sheldrick, Acta Crystallogr., Sect. A 64 (2008) 112.
[27] B.P. Clark, J.R. Harris, G.H. Timms, Tetrahedron Lett. 36 (1995) 3889.
[28] W.J. Geary, Coord. Chem. Rev. 7 (1971) 81.
[29] A.B.P. Lever, Inorganic Electronic Spectroscopy, second ed., Elsevier, Amsterdam, 1984.
[30] J. Zubieta, J. C. Hayes, K. D. Karlin, Copper coordination chemistry, biochemical and inorganic perspective (eds) (1983) 97.
[31] H.B. Gray, B.G. Malstrom, Inorg. Chem. 5 (1983) 203.
[32] C.T. Yang, M. Vetrichelvan, X. Yang, B. Moubaraki, K.S. Murray, J.J. Vittal, J. Chem. Soc., Dalton Trans. (2004) 113.
[33] P. Zanello, S. Tamburini, P.A. Vigato, A. Mazzocchin, Coord. Chem. Rev. 77 (1987) 165.
[34] B. Bosnich, Inorg. Chem. 38 (1999) 2554.
[35] Q.L. Li, J. Huang, Q. Wang, N. Jiang, C.Q. Xia, H.H. Lin, J. Wu, X.Q. Yu, Bioorg. Med. Chem. 14 (2006) 4151.
[36] Q.X. Xiang, J. Zhang, P.Y. Liu, C.Q. Xia, Y.Z. Zhou, R.G. Xie, X.Q. Yu, J. Inorg. Biochem. 99 (2005) 1661.
[37] N. Grover, N. Gupta, P. Singh, H.H. Thorp, Inorg. Chem. 31 (1992) 2014.
[38] N. Kitajima, K. Fujisawa, Y. Moro-oka, J. Am. Chem. Soc. 111 (1989) 8975.
[39] L.M.T. Schnaith, R.S. Hanson, L. Que Jr., Proc. Natl. Acad. Sci. U.S.A. 91 (1994) 569.
[40] W.E. Gao, G. Bu, D. Yang, Z. Liao, S. Jiang, G. Yan, J. Way, J. Chem. Soc., Dalton Trans. (2000) 1431.
[41] S. Nishinoa, T. Kobayashia, H. Matsushimab, T. Tokiib, Y. Nishida, Z. Naturforsch. 56c (2001) 138.
[42] R. Cejudo, G. Alzuet, M.G. Alvarez, J.L.G. Gimenez, J. Borras, M.L. Gonzalez, J. Inorg. Biochem. 100 (2006) 70.
[43] M.G. Alvarez, G. Alzuet, J. Borras, B. Macıas, A. Castineiras, Inorg. Chem. 42 (2003) 2992.

Polyhedron 28 (2009) 57–62

Contents lists available at ScienceDirect

Polyhedron

journal homepage: www.elsevier.com/locate/poly

Novel η^1-allyl– and acyliridium(III)/pybox complexes

Paloma Paredes, Josefina Díez, M. Pilar Gamasa *

Departamento de Química Orgánica e Inorgánica, Instituto Universitario de Química Organometálica "Enrique Moles" (Unidad Asociada al CSIC), Facultad de Química, Universidad de Oviedo, 33071 Oviedo, Spain

ARTICLE INFO

Article history:
Received 23 July 2008
Accepted 1 October 2008
Available online 10 November 2008

Keywords:
Iridium complexes
Enantiopure pybox ligands
Allyl complexes
Acyl complexes

ABSTRACT

The complex [IrCl(η^1-$CH_2CH{=}CH_2$)(η^2-$MeO_2CC{\equiv}CCO_2Me$){κ^3-*N,N,N*-(*S,S*)-^{i}Pr-pybox}][PF_6] (**1**) has been prepared by oxidative addition of allyl chloride to a solution of the complex [Ir(η^2-$MeO_2CC{\equiv}CCO_2Me$)$_2$){κ^3-*N,N,N*-(*S,S*)-^{i}Pr-pybox}][PF_6] in acetone. The treatment of the complexes [Ir(η^2-C_2H_4)$_2$(κ^3-*N,N,N*-R-pybox)][PF_6] (R-pybox = 2,6-bis[4′-(*S*)-isopropyloxazolin-2′-yl]pyridine, 2,6-bis[4′-(*R*)-phenyloxazolin-2′-yl]pyridine) with (*E*)-3-chloro-1-phenyl-1-propene (cinnamyl chloride) (1:1 molar ratio) in methanol at −40 °C, followed by warming to room temperature, affords stereoselectively the complexes [IrCl(η^1-$CH_2CH{=}CHPh$)(η^2-C_2H_4)(κ^3-*N,N,N*-R-pybox)][PF_6] (R = (*S,S*)-^{i}Pr (**2**), (*R,R*)-Ph (**3**)). Warming of acetonitrile solutions of complexes **2** or [IrCl(η^3-C_3H_5){κ^3-*N,N,N*-(*S,S*)-^{i}Pr-pybox}][PF_6] gives the complexes [IrCl(η^1-$CH_2CH{=}CHPh$)(MeCN){κ^3-*N,N,N*-(*S,S*)-^{i}Pr-pybox}][PF_6] (**4**) and [IrCl(η^1-$CH_2CH{=}CH_2$)(MeCN){κ^3-*N,N,N*-(*S,S*)-^{i}Pr-pybox}][PF_6] (**5**). Complex [Ir(η^2-C_2H_4)$_2$){κ^3-*N,N,N*-(*S,S*)-^{i}Pr-pybox}][PF_6] undergoes the oxidative addition of RCOCl (R = Me, Ph) in acetonitrile leading stereoselectively to the complexes [IrCl(COR)(MeCN){κ^3-*N,N,N*-(*S,S*)-^{i}Pr-pybox}][PF_6] (R = Me (**6**), Ph (**7**)). The structure of the complex **7** · CH_2Cl_2 has been determined by an X-ray monocrystal study.

© 2008 Elsevier Ltd. All rights reserved.

1. Introduction

Iridium allyl-complexes display a rich chemistry and are widely used as synthetic reagents [1] as well as in catalysis [2]. Thus, the reaction of a π-allyl-iridium intermediate with nucleophiles is recognized as a useful reaction from a synthetic point of view [2a,b]. Helmchen reported, in 1997, the first iridium-catalyzed asymmetric allylic substitution and since then this field has experienced a pronounced growth [3]. Regarding the asymmetric iridium/pybox-catalyzed processes, the allylic substitution with nitrogen nucleophiles (e.g. oximes, amines, hydroxylamines) [4a–c] and the catalytic reductive aldol [4d] reactions catalyzed by mixtures of [Ir(μ-Cl)(cod)]$_2$/phenyl-pybox and [Ir(μ-Cl)(cod)]$_2$/indane-pybox, respectively, are the sole examples reported.

In this context, we have recently prepared η^3- and η^1-allyl complexes, [IrCl(η^3-C_3H_5)(κ^3-*N,N,N*-R-pybox)][PF_6] and [IrCl(η^1-$CH_2CH{=}CH_2$)(CO)(κ^3-*N,N,N*-R-pybox)][PF_6] (R = ^{i}Pr, Ph) [5], by oxidative addition of allyl chloride to the complexes [Ir(η^2-C_2H_4)$_2$(κ^3-*N,N,N*-R-pybox)][PF_6] and [Ir(CO){κ^3-*N,N,N*-*R*-pybox}][Y] (R = ^{i}Pr, Ph), respectively. We have observed that the coordination mode of the allyl group in the new complexes is highly dependent on the nature of the auxiliary ligands in the precursor complex.

On the ground of these results, we found interesting to explore the synthesis of novel allyliridium(III)–pybox complexes using different iridium(I) precursors and allyl and cinnamyl chloride ($RHC{=}CHCH_2Cl$, R = H, Ph). Unravelling the factors that favour the coordination mode of the allyl group (either η^1 or η^3) for discovering new precatalysts for enantioselective allylic substitution reactions. Moreover, the preparation of allyliridium– and acyliridium–pybox complexes having acetonitrile as a labile ligand is also reported.

2. Experimental

2.1. General procedure

The reactions were performed under an atmosphere of dry nitrogen using vacuum-line and standard Schlenk techniques. All reagents were obtained from commercial suppliers and used without further purification. Solvents were dried by standard methods and distilled under nitrogen before use. The complexes [Ir(η^2-C_2H_4)$_2$(κ^3-*N,N,N*-R-pybox)][PF_6] (R = (*S,S*)-^{i}Pr, (*R,R*)-Ph), [Ir(η^2-$MeO_2CC{\equiv}CCO_2Me$)$_2$){κ^3-*N,N,N*-(*S,S*)-^{i}Pr-pybox}][PF_6] and [IrCl(η^3-C_3H_5){κ^3-*N,N,N*-(*S,S*)-^{i}Pr-pybox}][PF_6] were prepared by previously reported methods [5]. Infrared spectra were recorded on a Perkin–Elmer 1720-XFT spectrometer. The conductivities were measured at room temperature, in ca. 5×10^{-4} mol L^{-1} acetone solutions, with a Jenway PCM3 conductimeter. The C, H and N analyses were carried out with a Perkin–Elmer 240-B microanalyzer

* Corresponding author. Tel.: +34 985103460; fax: +34 985103446.
E-mail address: pgb@uniovi.es (M.P. Gamasa).

0277-5387/$ - see front matter © 2008 Elsevier Ltd. All rights reserved.
doi:10.1016/j.poly.2008.10.002

(inconsistent analyses was found for complex **4** due to incomplete combustion). Electrospray mass spectra (ESI-MS) were recorded on a Bruker MicroTof-Q instrument, operating in the positive mode and using methanol solutions. NMR spectra were recorded on a Bruker AC300 (DPX-300 or AC-300) instrument at 300 MHz (^{1}H) or 75.4 MHz (^{13}C) or a Bruker AMX-400 instrument at 400 MHz (^{1}H) or 100.6 MHz (^{13}C) and using $SiMe_4$ as standard. DEPT experiments were carried out for whole of the complexes reported. 2D-NMR (COSY, HSQC) were performed in selected complexes (AMX-400). Coupling constants *J* are given in Hertz. Abbreviations used: s, singlet; d, doublet; dd, doublet of doublets; t, triplet; m, multiplet; q, quartet; br, broad; pt, pseudotriplet.

2.2. Synthesis

2.2.1. Synthesis of complex [IrCl(η^1-$CH_2CH{=}CH_2$)(η^2-$MeO_2CC{\equiv}CCO_2Me$){κ^3-*N,N,N*-(*S,S*)-^{i}Pr-pybox)][PF_6] (**1**)

To a solution of complex [Ir(η^2-$MeO_2CC{\equiv}CCO_2Me$)$_2${κ^3-*N,N,N*-(*S,S*)-^{i}Pr-pybox}][PF_6] (0.092 g, 0.1 mmol) in 10 mL of acetone, allyl chloride (0.016 mL, 0.2 mmol) was added. The resulting solution was stirred for 1 h at room temperature and the solvent was then removed under vacuum. The residue was extracted with dichloromethane and the resulting red solution was filtered and concentrated to ca. 2 mL. The addition of 30 mL of a mixture diethyl ether/hexane (1:1) afforded **1** as an orange solid, which was washed with hexane (3 × 5 mL) and vacuum-dried. Yield: 0.062 g (72%). IR (KBr, cm^{-1}): *ν* 843 vs (PF_6^-). ^{1}H NMR (acetone-d_6, 293 K, 300 MHz): *δ* 8.47 (t, J_{HH} = 7.9 Hz, 1H, H^4 C_5H_3N), 8.35 (d, J_{HH} = 7.9 Hz, 1H, H^{3,5} C_5H_3N), 8.30 (d, J_{HH} = 7.9 Hz, 1H, H^{3,5} C_5H_3N), 5.20 (m, 5H, *H*C=CH_2, OCH_2), 4.75 (dd, J_{HH} = 9.8 Hz, J_{HH} = 2.5 Hz, 1H, HC=C*H*$_2$), 4.52 (m, 1H, HC=C*H*$_2$), 4.36 (m, 1H, C*H*^{i}Pr), 4.22 (m, 1H, C*H*^{i}Pr), 3.95 (s, 3H, CO_2*Me*), 3.91 (s, 3H, CO_2*Me*), 2.76 (m, 1H, $IrCH_2$), 2.49 (m, 1H, C*H*Me_2), 2.24 (m, 1H, $IrCH_2$), 2.00 (m, 1H, C*H*Me_2), 0.97 (d, J_{HH} = 6.9 Hz, 6H, CH*Me*$_2$), 0.84 (d, J_{HH} = 6.9 Hz, 3H, CH*Me*$_2$), 0.68 (d, J_{HH} = 6.9 Hz, 3H, CH*Me*$_2$) ppm. ^{13}C{^{1}H} NMR (acetone-d_6, 293 K, 75.5 MHz): *δ* 181.2 (s, *C*O_2Me), 179.7 (s, *C*O_2Me), 174.3 (s, OCN), 174.0 (s, OCN), 145.8 (s, C^{2,6} C_5H_3N), 143.0 (s, C^{4}H C_5H_3N), 141.4 (s, HC=CH_2), 129.0 (s, *C*CO_2Me), 128.2 (s, C^{3,5}H C_5H_3N), 111.0 (s, *C*CO_2Me), 110.4 (s, HC=*C*H_2), 74.3 (s, OCH_2), 74.2 (s, OCH_2), 70.9 (s, *C*H^{i}Pr), 69.3 (s, *C*H^{i}Pr), 56.1 (s, CO_2*Me*), 52.0 (s, CO_2*Me*), 30.0 (s, *C*HMe_2), 28.4 (s, *C*HMe_2), 19.6 (s, CH*Me*$_2$), 19.0 (s, CH*Me*$_2$), 14.9 (s, CH*Me*$_2$), 13.9 (s, CH*Me*$_2$), −4.6 (s, $IrCH_2$) ppm. Molar conductivity (acetone, Ω^{-1} cm^2 mol^{-1}): 117. *Anal.* Calc. for $C_{26}H_{34}ClF_6IrN_3O_6P$: C, 36.43; H, 4.00; N, 4.90. Found: C, 36.05; H, 3.79; N, 5.03%.

2.2.2. Synthesis of complexes [IrCl(η^1-$CH_2CH{=}CHPh$)(η^2-C_2H_4)(κ^3-*N,N,N*-R-pybox)][PF_6] (R = (*S,S*)-^{i}Pr (**2**), (*R,R*)-Ph (**3**))

To a solution of complexes [Ir(η^2-C_2H_4)$_2$(κ^3-*N,N,N*-R-pybox)][PF_6] (R = (*S,S*)-^{i}Pr, (*R,R*)-Ph). (0.1 mmol) in MeOH (10 mL) at −40 °C, cinnamyl chloride (0.017 mL, 0.1 mmol) was added. After stirring for 40 min at room temperature, diethyl ether (100 mL) was added and the resulting orange solid was filtered, washed with hexane (3 × 5 mL) and then vacuum-dried.

Complex **2**: Yield: 0.070 g (86%). IR (KBr, cm^{-1}): *ν* 842 vs (PF_6^-). ^{1}H NMR (acetone-d_6, 293 K, 300 MHz): *δ* 8.61 (t, J_{HH} = 8.0 Hz, 1H, H^4 C_5H_3N), 8.49 (d, J_{HH} = 8.0 Hz, 1H, H^{3,5} C_5H_3N), 8.21 (d, J_{HH} = 8.0 Hz, 1H, H^{3,5} C_5H_3N), 7.20–7.00 (2 × m, 5H, Ph), 6.00 (m, 1H, HC=C*H*Ph), 5.75 (m, 1H, *H*C=CHPh), 5.50, 5.25, 5.15, 5.02, 4.85, 4.75 (m, 10H, C_2H_4, OCH_2, C*H*^{i}Pr), 2.61 (m, 1H, $IrCH_2$), 2.46 (m, 2H, C*H*Me_2), 2.17 (m, 1H, $IrCH_2$), 1.19 (d, J_{HH} = 7.1 Hz, 3H, CH*Me*$_2$), 1.08 (d, J_{HH} = 7.1 Hz, 3H, CH*Me*$_2$), 1.04 (d, J_{HH} = 6.7 Hz, 3H, CH*Me*$_2$), 0.87 (d, J_{HH} = 6.7 Hz, 3H, CH*Me*$_2$) ppm. ^{13}C{^{1}H} NMR (acetone-d_6, 293 K, 75.5 MHz): *δ* 172.0 (s, OCN), 171.3 (s, OCN), 143.8 (s, C^{2,6} C_5H_3N), 143.5 (s, C^{2,6} C_5H_3N), 142.7 (s, C^{4}H C_5H_3N), 138.7 (s, C^{ipso} Ph), 134.8 (s, H*C*=CHPh), 129.6, 129.3, 129.0, 127.8, 127.5, (s, C^{3,5}H C_5H_3N, Ph), 125.9 (s, HC=*C*HPh), 75.2 (s, OCH_2), 74.7 (s, OCH_2), 72.0 (s, C_2H_4), 71.4 (s, *C*H^{i}Pr), 71.2 (s, *C*H^{i}Pr), 30.9 (s, *C*HMe_2), 19.1 (s, CH*Me*$_2$), 18.7 (s, CH*Me*$_2$), 14.8 (s, CH*Me*$_2$), 14.7 (s, CH*Me*$_2$), 3.8 (s, $IrCH_2$) ppm. Molar conductivity (acetone, Ω^{-1} cm^2 mol^{-1}): 130. *Anal.* Calc. for $C_{28}H_{36}ClF_6IrN_3O_2P$: C, 41.05; H, 4.43; N, 5.13. Found: C, 40.95; H, 4.19; N, 5.20%.

Complex **3**: Yield: 0.078 g (88%). IR (KBr, cm^{-1}): *ν* 841 vs (PF_6^-). ^{1}H NMR (acetone-d_6, 293 K, 300 MHz): *δ* 8.63 (m, 2H, H^4, H^{3,5} C_5H_3N), 8.27 (dd, J_{HH} = 7.7 Hz, J_{HH} = 1.3 Hz, 1H, H^{3,5} C_5H_3N), 7.79 (m, 2H, Ph), 7.53 (m, 5H, Ph), 7.42 (m, 3H, Ph), 7.20 (m, 3H, Ph), 7.07 (m, 2H, Ph), 6.00 (m, 2H, HC=C*H*Ph, OCH_2), 5.78 (m, 3H, *H*C=CHPh, OCH_2), 5.62 (m, 1H, OCH_2), 5.22 (m, 1H, *CH*Ph), 4.99 (m, 1H, *CH*Ph), 4.50 (m, 2H, C_2H_4), 3.96 (m, 2H, C_2H_4), 2.50 (m, 1H, $IrCH_2$), 1.83 (m, 1H, $IrCH_2$) ppm. ^{13}C{^{1}H} NMR (acetone-d_6, 293 K, 75.5 MHz): *δ* 172.9 (s, OCN), 143.9 (s, C^{2,6} C_5H_3N), 143.7 (s, C^{2,6} C_5H_3N), 142.5 (s, C^{4}H C_5H_3N), 139.2, 138.8 and 138.7 (s, C^{ipso} Ph), 135.0 (s, *C*H=CHPh), 130.6, 130.3, 130.0, 129.8, 129.6, 129.4 and 128.9 (s, Ph), 127.4 (s, C^{3,5}H C_5H_3N), 127.3 (s, C^{3,5}H C_5H_3N), 126.0 (s, CH=*C*HPh), 82.2 (s, OCH_2), 81.9 (s, OCH_2), 72.1 (s, C_2H_4), 70.3 (s, *C*HPh), 70.2 (s, *C*HPh), 3.8 (s, $IrCH_2$) ppm. Molar conductivity (acetone, Ω^{-1} cm^2 mol^{-1}): 112. *Anal.* Calc. for $C_{34}H_{32}ClF_6IrN_3O_2P$: C, 46.02; H, 4.00; N, 4.74. Found: C, 45.63; H, 3.87; N, 4.64%.

2.2.3. Syntheses of complexes [IrCl(η^1-$CH_2CH{=}CHPh$)(MeCN){κ^3-*N,N,N*-(*S,S*)-^{i}Pr-pybox}][PF_6] (**4**) and [IrCl(η^1-$CH_2CH{=}CH_2$)(MeCN){κ^3-*N,N,N*-(*S,S*)-^{i}Pr-pybox}][PF_6] (**5**)

A solution of the complex [IrCl(η^3-C_3H_5){κ^3-*N,N,N*-(*S,S*)-^{i}Pr-pybox}][PF_6] or [IrCl{η^1-$CH_2CH{=}CHPh$}(η^2-C_2H_4){κ^3-*N,N,N*-(*S,S*)-^{i}Pr-pybox}][PF_6] (**1**) (0.1 mmol) in acetonitrile (6 mL) was stirred at 60 °C for 3 h. A (1:1) diethyl ether/hexane mixture (50 mL) was added and the resulting red solid was filtered, washed with diethyl ether (3 × 5 mL) and then vacuum-dried.

Complex **4**. Yield: 0.060 g (72%). IR (KBr, cm^{-1}): *ν* 844 vs (PF_6^-). ^{1}H NMR (acetone-d_6, 293 K, 300 MHz): *δ* 8.28 (t, J_{HH} = 8.0 Hz, 1H, H^4 C_5H_3N), 8.19 (d, J_{HH} = 8.0 Hz, 1H, H^{3,5} C_5H_3N), 7.97 (d, J_{HH} = 8.0 Hz, 1H, H^{3,5} C_5H_3N), 7.16, 7.11 (2 × m, 5H, Ph), 5.93 (m, 2H, HC=C*H*Ph and *H*C=CHPh), 5.28 (m, 2H, OCH_2), 5.14 (dd, J_{HH} = 9.6 Hz, J_{HH} = 6.1 Hz, 1H, OCH_2), 5.00 (m, 1H, OCH_2), 4.55 (m, 2H, C*H*^{i}Pr), 3.05 (s, 3H, MeCN), 2.99 (pt, J_{HH} = 9.3 Hz, 1H, $IrCH_2$), 2.54 (m, 1H, $IrCH_2$), 2.50 (m, 2H, C*H*Me_2), 1.15 (d, J_{HH} = 7.0 Hz, 3H, CH*Me*$_2$), 1.06 (m, 9H, CH*Me*$_2$) ppm. ^{13}C{^{1}H} NMR (acetone-d_6, 293 K, 100.6 MHz): *δ* 174.2 (s, OCN), 173.5 (s, OCN), 148.6 (s, C^{2,6} C_5H_3N), 148.5 (s, C^{2,6} C_5H_3N), 142.0 (s, C^{4}H C_5H_3N), 140.7 (s, C^{ipso} Ph), 137.4 (s, H*C*=CHPh), 131.0, 129.3, 128.6, 127.8, 127.5, 127.3 (s, C^{3,5}H C_5H_3N, Ph, HC=CHPh), 124.7 (s, MeCN), 76.1 (s, OCH_2), 75.9 (s, OCH_2), 72.2 (s, *C*H^{i}Pr), 71.8 (s, *C*H^{i}Pr), 30.3 (s, *C*HMe_2), 29.5 (s, *C*HMe_2), 21.1 (s, CH*Me*$_2$), 20.4 (s, CH*Me*$_2$), 17.6 (s, CH*Me*$_2$), 17.2 (s, CH*Me*$_2$), 5.2 (s, *Me*CN), 3.7 (s, $IrCH_2$) ppm. Molar conductivity (acetone, Ω^{-1} cm^2 mol^{-1}): 133. MS (ESI+): *m/z* = 646 ([IrCl(C_3H_4Ph)(^{i}Pr-pybox)]$^+$, 100%), 687 ([IrCl(C_3H_4Ph)(^{i}Pr-pybox)(NCMe)]$^+$, 18%).

Complex **5**: Yield: 0.067 g (89%). IR (KBr, cm^{-1}): *ν* 842 vs (PF_6^-). ^{1}H NMR (acetone-d_6, 293 K, 300 MHz): *δ* 8.33 (m, 1H, H^4 C_5H_3N), 8.21 (m, 2H, H^{3,5} C_5H_3N), 5.42 (m, 1H, *H*C=CH_2), 5.23 (m, 4H, OCH_2), 4.70 (dd, J_{HH} = 9.9 Hz, J_{HH} = 2.6 Hz, 1H, HC=C*H*$_2$), 4.57 (m, 1H, HC=C*H*$_2$), 4.51 (m, 2H, C*H*^{i}Pr), 3.08 (s, 3H, MeCN), 2.78 (pt, J_{HH} = 9.3 Hz, 1H, $IrCH_2$), 2.42 (m, 2H, C*H*Me_2), 2.20 (pt, J_{HH} = 9.3 Hz, 1H, $IrCH_2$), 1.06 (m, 12H, CH*Me*$_2$) ppm. ^{13}C{^{1}H} NMR (acetone-d_6, 293 K, 75.5 MHz): *δ* 171.6 (s, OCN), 171.0 (s, OCN), 146.2 (s, C^{2,6} C_5H_3N), 146.0 (s, C^{2,6} C_5H_3N), 142.2 (s, C^{4}H C_5H_3N), 139.8 (s, H*C*=CH_2), 127.2 (s, C^{3,5}H C_5H_3N), 127.1 (s, C^{3,5}H C_5H_3N), 122.2 (s, MeCN), 109.1 (s, HC=*C*H_2), 74.2 (s, OCH_2), 73.6 (s, OCH_2), 69.8 (s, *C*H^{i}Pr), 69.2 (s, *C*H^{i}Pr), 29.9 (s, *C*HMe_2), 29.1 (s, *C*HMe_2), 18.7 (s, CH*Me*$_2$), 18.0 (s, CH*Me*$_2$), 15.2 (s, CH*Me*$_2$), 14.7 (s, CH*Me*$_2$), 2.8 (s, *Me*CN), 1.7 (s, $IrCH_2$) ppm. Molar conductivity (acetone, Ω^{-1} cm^2 mol^{-1}): 137. *Anal.* Calc. for $C_{22}H_{31}ClF_6IrN_4O_2P$: C, 34.95; H, 4.13; N, 7.41. Found: C, 35.13; H, 4.02; N, 7.32%.

*2.2.4. Syntheses of complexes [IrCl(COMe)(MeCN){κ³-N,N,N-(S,S)-ⁱPr-pybox}][PF₆] (**6**) and [IrCl(COPh)(MeCN){κ³-N,N,N-(S,S)-ⁱPr-pybox}][PF₆] (**7**)*

To a solution of complex [Ir(η²-C_2H_4)₂{κ³-N,N,N-(S,S)-ⁱPr-pybox}][PF_6] (0.069 g, 0.1 mmol) in acetonitrile (5 mL), acetyl chloride or benzyl chloride (0.1 mmol) was added. The resulting solution was stirred at room temperature for 5 min and concentrated in vacuo to 2 mL. A (1:1) diethyl ether/hexane mixture (60 mL) was added and the resulting orange solid was filtered, washed with diethyl ether (3 × 5 mL) and then vacuum-dried.

Complex **6**: Yield: 0.064 g (85%). IR (KBr, cm^{-1}): *ν* 842 vs (PF_6^-). ^{1}H NMR (acetone-d_6, 293 K, 300 MHz): *δ* 8.54 (t, J_{HH} = 7.9 Hz, 1H, H^4 C_5H_3N), 8.32 (d, J_{HH} = 7.9 Hz, 1H, $H^{3,5}$ C_5H_3N), 8.24 (d, *J* = 7.9 Hz, 1H, $H^{3,5}$ C_5H_3N), 5.27 (m, 4H, OCH_2), 4.70 (m, 1H, C*H*ⁱPr), 4.47 (m, 1H, C*H*ⁱPr), 3.15 (s, 3H, MeCN), 2.58 (m, 1H, C*H*Me_2), 2.34 (s, 3H, COMe), 2.29 (m, 1H, C*H*Me_2), 1.13 (d, J_{HH} = 7.1 Hz, 6H, CH*Me*$_2$), 1.07 (d, J_{HH} = 7.1 Hz, 3H, CH*Me*$_2$), 0.83 (d, J_{HH} = 7.1 Hz, 3H, CH*Me*$_2$) ppm. ^{13}C{^{1}H} NMR (acetone-d_6, 293 K, 75.5 MHz): *δ* 200.9 (s, *C*OMe), 172.1 (s, OCN), 147.0 (s, $C^{2,6}$ C_5H_3N), 146.4 (s, $C^{2,6}$ C_5H_3N), 142.0 (s, C^4H C_5H_3N), 128.1 (s, $C^{3,5}H$ C_5H_3N), 127.3 (s, $C^{3,5}H$ C_5H_3N), 123.7 (s, Me*C*N), 74.4 (s, OCH_2), 73.9 (s, OCH_2), 70.5 (s, C*H*ⁱPr), 69.5 (s, C*H*ⁱPr), 39.2 (s, CO*Me*), 30.3 (s, *C*HMe_2), 29.4 (s, *C*HMe_2), 18.8 (s, CH*Me*$_2$), 18.6 (s, CH*Me*$_2$), 15.5 (s, CH*Me*$_2$), 14.1 (s, CH*Me*$_2$), 3.4 (s, *Me*CN) ppm. Molar conductivity (acetone, Ω^{-1} cm^2 mol^{-1}): 132. *Anal.* Calc. for $C_{21}H_{29}ClF_6IrN_4O_3P$: C, 33.27; H, 3.86; N, 7.39. Found: C, 33.01; H, 4.00; N, 7.48%.

Complex **7**: Yield: 0.068 g (83%). IR (KBr, cm^{-1}): *ν* 841 vs (PF_6^-). ^{1}H NMR (acetone-d_6, 293 K, 300 MHz): *δ* 8.60 (t, J_{HH} = 8.0 Hz, 1H, H^4 C_5H_3N), 8.42 (d, J_{HH} = 8.0 Hz, 1H, $H^{3,5}$ C_5H_3N), 8.24 (d, J_{HH} = 8.0 Hz, 1H, $H^{3,5}$ C_5H_3N), 7.45 (m, 5H, Ph), 5.25 (m, 4H, OCH_2), 4.58 (m, 1H, C*H*ⁱPr), 4.45 (m, 1H, C*H*ⁱPr), 2.97 (s, 3H, MeCN), 2.60 (m, 1H, C*H*Me_2), 2.06 (m, 1H, C*H*Me_2), 1.13 (m, 6H, CH*Me*$_2$), 1.01 (d, 3H, J_{HH} = 7.1 Hz, CH*Me*$_2$), 0.86 (d, J_{HH} = 6.6 Hz, 3H, CH*Me*$_2$) ppm. ^{13}C{^{1}H} NMR (acetone-d_6, 293 K, 75.5 MHz): *δ* 201.1 (s, *C*OPh), 174.3 (s, OCN), 174.2 (s, OCN), 149.2 (s, $C^{2,6}$ C_5H_3N), 148.3 (s, $C^{2,6}$ C_5H_3N), 144.5 (s, C^4H C_5H_3N), 132.7, 130.5, 129.7, 129.5 and 128.4 (s, Ph and $C^{3,5}H$ C_5H_3N), 126.0 (s, Me*C*N), 76.2 (s, OCH_2), 72.9 (s, C*H*ⁱPr), 71.3 (s, C*H*ⁱPr), 30.3 (s, *C*HMe_2), 29.3 (s, *C*HMe_2), 20.8 (s, CH*Me*$_2$), 17.7 (s, CH*Me*$_2$), 16.3 (s, CH*Me*$_2$), 5.2 (s, *Me*CN) ppm. Molar conductivity (acetone, Ω^{-1} cm^2 mol^{-1}): 137. *Anal.* Calc. for $C_{26}H_{31}ClF_6IrN_4O_3P$: C, 38.07; H, 3.81; N, 6.83. Found: C, 37.68; H, 3.69; N, 6.85%.

*2.2.5. X-ray structure determination of **7** · CH_2Cl_2*

Crystals suitable for X-ray diffraction analysis were obtained by slow diffusion of hexane into a saturated solution of the complex **7** in dichloromethane. Data collection, crystal and refinement parameters are collected in Table 1. Diffraction data were recorded at 150(2) K on a Nonius Kappa CCD single crystal diffractometer, using Mo Kα radiation (*λ* = 0.71073 Å). Crystal–detector distance was fixed at 29 mm, and images were collected using the oscillation method, with 2° oscillation and 50 s exposure time per image. Data collection strategy was calculated with the program COLLECT [6]. Data reduction and cell refinement were performed using the programs HKL DENZO and SCALEPACK [7]. A semi-empirical absorption correction was applied using the program SORTAV [8].

The software package WINGX was used for space group determination, structure solution and refinement [9]. The space group determination was based on a check of the Laue symmetry and systematic absences, and ascertained from the structure solution. The structure was solved by Patterson interpretation and Phase expansion using DIRDIF [10]. Isotropic least-squares refinement on F^2 using SHELXL-97 [11]. During the final stages of the refinements, all positional parameters and the anisotropic temperature factors of all non-H atoms were refined. Hydrogen atoms were geometrically placed riding on their parent atoms with isotropic displacement parameters set to 1.2 times the Ueq of the atoms to which they are attached (1.5 for methyl groups). The function minimized was $([\sum wF_o^2 - F_c^2)/\sum w(F_o^2)]^{1/2}$ where $w = 1/[\sigma^2(F_o^2) + (0.0678P)^2 + 0.3718P]$ with $\sigma(F_o^2)$ from counting statistics and $P = (\text{Max}(F_o^2, 0) + 2F_c^2)/3$. The maximum residual electron density is located near to heavier atoms and to the solvent molecule. Atomic scattering factors were taken from International tables for X-ray Crystallography [12]. The crystallographic plots were made with PLATON [13].

Table 1
Crystal data and structure refinement for complex **7** · CH_2Cl_2.

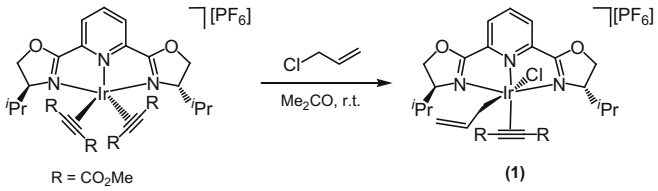
Empirical formula	$C_{27}H_{33}Cl_3F_6IrN_4O_3P$
Fw	905.09
Temperature (K)	150(2)
Wavelength (Å)	0.71073
Crystal system	monoclinic
Space group	$P2_1$
a (Å)	10.7502(1)
b (Å)	11.8183(1)
c (Å)	14.1307(2)
β (°)	109.456(1)
V (Å³)	1692.78(3)
Z	2
D_{calcd} (g cm^{-3})	1.776
Absorption coefficient (mm^{-1})	4.296
F(000)	888
Crystal size (mm)	0.17 × 0.15 × 0.05
θ Range for data collection (°)	2.01–25.24
Index ranges	$-12 \leqslant h \leqslant 12$ $-14 \leqslant k \leqslant 13$ $0 \leqslant l \leqslant 16$
Number of reflections collected	11 726
Number of independent reflections (R_{int})	5508 (0.0283)
Completeness to *θ* = 25.24	96.2%
Absorption correction	multi-scan
Refinement method	full-matrix least-squares on F^2
Number of data/restraints/parameters	5508/1/411
Goodness-of-fit on F^2	1.263
Final *R* indices ($I > 2\sigma(I)$)[a]	R_1 = 0.0310, wR_2 = 0.0844
R indices (all data)	R_1 = 0.0372, wR_2 = 0.1101
Absolute structure parameter	−0.030(9)
Largest difference in peak and hole (e Å^{-3})	1.266 and − 2.177

[a] $R_1 = \sum(|F_o| - |F_c|)/\sum|F_o|$; $wR_2 = \{\sum[w(F_o^2 - F_c^2)^2]/\sum[w(F_o^2)^2]\}^{1/2}$.

3. Results and discussion

*3.1. Synthesis of complex [IrCl(η¹-$CH_2CH{=}CH_2$)(η²-$MeO_2CC{\equiv}CCO_2Me$){κ³-N,N,N-(S,S)-ⁱPr-pybox}][PF_6] (**1**)*

The reaction of complex [Ir(η²-$MeO_2CC{\equiv}CCO_2Me$)₂{κ³-N,N,N-(S,S)-ⁱPr-pybox}][PF_6] with allyl chloride (2 eq.) in acetone at room temperature produces stereoselectively the allyliridium(III) complex **1** isolated as an orange solid in 72% yield (Scheme 1). Its analytical and spectroscopic NMR data support the proposed formulation (see Section 2 for details). In particular the following data can be pointed: (a) the ^{1}H and ^{13}C NMR resonances of the allyl group are in accordance with a σ-coordination mode. The ^{1}H NMR spectrum shows the three olefinic hydrogens at 5.20 (m), 4.75 (dd,



Scheme 1.

J_{HH} = 9.8 Hz, J_{HH} = 2.5 Hz) and 4.52 (m) ppm and the $IrCH_2$ protons as two multiplets at 2.76, 2.24 ppm. Moreover, the $^{13}C\{^1H\}$ NMR spectrum shows the expected singlet resonances at 141.4, 110.4 and - 4.6 for the C_β, C_γ and C_α nuclei, respectively, of the η^1-allyl group. (b) The $MeO_2CC{\equiv}CCO_2Me$ (DMAD) ligand shows two singlets at 3.95 and 3.91 ppm (CO_2Me) in the ^1H NMR spectrum as well as six singlets [181.2 and 179.7 (CO_2Me); 129.9 and 111.0 (CCO_2Me); 56.1 and 52.0 (CO_2CH_3)] in the $^{13}C\{^1H\}$ NMR spectrum.

The reaction involves decoordination of one DMAD ligand and oxidative addition of allyl chloride to the iridium center to give **1** in which the allyl group participates as a monodentate ligand. Similar coordination of the allyl group has been recently found in the complexes $[IrCl(\eta^1\text{-}CH_2CH{=}CH_2)(CO)(\kappa^3\text{-}N,N,N\text{-R-pybox})][PF_6]$ (R = (*S,S*)-^{i}Pr, (*R,R*)-Ph) [5b] resulting from the reaction of complexes $[Ir(CO)(\kappa^3\text{-}N,N,N\text{-R-pybox})][PF_6]$ and allyl chloride. These η^1-allyl complexes do not evolve into the corresponding η^3-allyl complexes by loss of DMAD or CO. On the contrary, we reported recently that the complexes $[IrCl(\eta^3\text{-}C_3H_5)(\kappa^3\text{-}N,N,N\text{-R-pybox})][PF_6]$ [5a] are rapidly formed at room temperature from complexes $[Ir(\eta^2\text{-}C_2H_4)_2(\kappa^3\text{-}N,N,N\text{-R-pybox})][PF_6]$ and allyl chloride. Probably, the higher π-acceptor capability of either alkyne or CO ligands than that of the alkene makes their dissociation disfavoured and consequently the η^3-coordination of the allyl group is not observed.

An X-ray analysis to determine the real stereoisomer could not be performed since all attempts to crystallize complex **1** have been unsuccessful.

3.2. Synthesis of complexes [IrCl(η^1-$CH_2CH{=}CHPh$)(η^2-C_2H_4)(κ^3-N,N,N-R-pybox)][PF_6] (R = (S,S)-^{i}Pr (**2**), (R,R)-Ph (**3**))

The reaction of equimolecular amounts of the complexes $[Ir(\eta^2\text{-}C_2H_4)_2(\kappa^3\text{-}N,N,N\text{-R-pybox})][PF_6]$ (R-pybox = (*S,S*)-^{i}Pr-pybox, (*R,R*)-Ph-pybox) and (*E*)-3-chloro-1-phenyl-1-propene (cinnamyl chloride) (methanol, −40 °C to room temperature) produces the iridium(III) complexes $[IrCl(\eta^1\text{-}CH_2CH{=}CHPh)(\eta^2\text{-}C_2H_4)(\kappa^3\text{-}N,N,N\text{-R-pybox})][PF_6]$ (R = (*S,S*)-^{i}Pr (**2**), (*R,R*)-Ph (**3**)) in a stereoselective manner (Scheme 2). These complexes have been isolated as orange solids (86 and 88% yield, respectively) and characterized by elemental analyses, molar conductivity and NMR spectroscopy (see Section 2 for details). Significant spectroscopic data are: (a) the ^1H NMR spectrum shows two multiplets for the ethylene ligand [4.50 and 3.96 ppm (**3**)] while the corresponding carbon atoms are observed in the $^{13}C\{^1H\}$ NMR spectra as a singlet [ca. 72.0 ppm (**2**); 72.1 ppm (**3**)], (b) the ^1H and ^{13}C NMR resonances of the allyl group are in accordance with a σ-coordination mode. The ^1H NMR spectra show the olefinic hydrogens as two multiplets [6.00 and 5.75 ppm (**2**); 6.00 and 5.78 (**3**), the last ones being overlapped with the resonances of the oxazoline OCH_2] and the $IrCH_2$ protons as two multiplets [2.61 and 2.17 ppm (**2**); 2.50 and 1.83 ppm (**3**)]. In addition, the $^{13}C\{^1H\}$ NMR spectra show singlet signals at 134.8 (HC=CHPh), 125.9 (HC=CHPh) and 3.8 ($IrCH_2$) ppm for complex (**2**) and at 135.0 (HC=CHPh), 126.0 (HC=CHPh) and 3.8 ($IrCH_2$) ppm for complex (**3**).

Although three stereoisomers can be expected, a single reaction product was obtained in both cases according to the NMR data of the reaction crude. Unfortunately, an X-ray analysis could not be performed since all attempts to crystallize complexes **2** and **3** have been unsuccessful.

Attempts have been undertaken to obtain the cinnamyl complexes with η^3-coordination by warming methanol or acetone solutions of complexes **2** or **3** at 50 °C. In all cases, the analysis of the resulting solution reveals the presence of a η^3-coordination complex along with unidentified compounds. Probably, the tridentate coordination mode would be hampered in this case because of the sterically more demanding nature of the cinnamyl ligand.

3.3. Synthesis of complex [IrCl(η^1-$CH_2CH{=}HPh$)(MeCN){κ^3-N,N,N-(S,S)-^{i}Pr-pybox}][PF_6] (**4**)

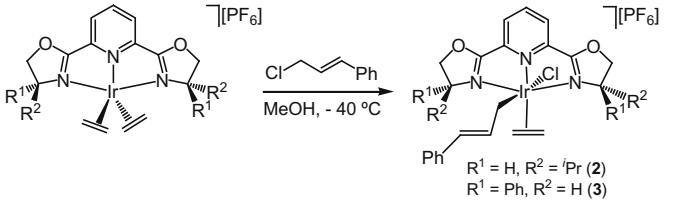
Warming a solution of complex **2** in acetonitrile at 60 °C during 3 h allows for the ethylene-acetonitrile ligand exchange leading to the complex $[IrCl(\eta^1\text{-}CH_2CH{=}CHPh)(MeCN)\{\kappa^3\text{-}N,N,N\text{-}(S,S)\text{-}^i\text{Pr-pybox}\}][PF_6]$ (**4**) which is isolated as red solid in 89% yield (Scheme 3). Its analytic and spectroscopic NMR data support the proposed formulation (see Section 2 for details). In particular the following data can be pointed: (a) The resonance of the acetonitrile ligand appears as a singlet at 3.05 ppm in the ^1H NMR spectrum. In addition the $^{13}C\{^1H\}$ NMR spectrum shows singlet signals for the acetonitrile carbons at 124.7 (CN) and 5.2 ppm (*Me*CN). (b) The resonance signals of the allyl ligand are in accordance with a η^1-coordination mode as it was found in the case of its precursor **2** (see Section 2 for details).

3.4. Synthesis of complex [IrCl(η^1-$CH_2CH{=}CH_2$)(MeCN){κ^3-N,N,N-(S,S)-^{i}Pr-pybox}][PF_6] (**5**)

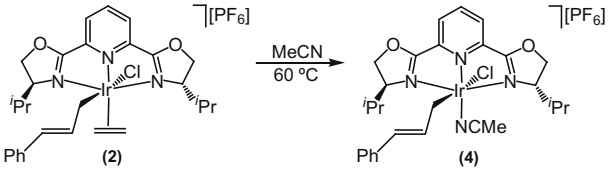
When a solution of complex $[IrCl(\eta^3\text{-}C_3H_5)\{\kappa^3\text{-}N,N,N\text{-}(S,S)\text{-}^i\text{Pr-pybox}\}][PF_6]$ [5c] in acetonitrile is warmed at 60 °C during 3 h the complex **5** is isolated as a red solid in 72% yield (Scheme 4). Its analytic and spectroscopic NMR data support the proposed formulation (see Section 2 for details). In particular the following data can be pointed: (a) the ^1H and ^{13}C NMR resonances of the allyl group are in accordance with the η^1-coordination mode. Thus, the ^1H NMR spectrum shows the three olefinic hydrogens at 5.42 (m), 4.70 (dd, J_{HH} = 9.9 Hz, J_{HH} = 2.6 Hz) and 4.57 (m) ppm and the $IrCH_2$ protons as two pseudotriplets at 2.78 and 2.20 ppm (J_{HH} = 9.3 Hz). The $^{13}C\{^1H\}$ NMR spectrum shows the expected singlet resonances at 139.8, 109.1 and 1.7 ppm assigned to the C_β, Cγ, and C_α nuclei, respectively, of the η^1-allyl group. (b) The resonances of the acetonitrile ligand appear as singlets at 3.08 ppm (^1H NMR) and at 122.2 (CN) and 2.8 (*Me*CN) ppm (^{13}C NMR). The formation of the complex **5** presumably proceeds via the η^3-allyl-to-η^1-allyl isomerization reaction followed by coordination of acetonitrile to the resulting unsaturated iridium complex.

3.5. Synthesis of complexes [IrCl(COR)(MeCN){κ^3-N,N,N-(S,S)-^{i}Pr-pybox}][PF_6] (R = Me (**6**), Ph (**7**))

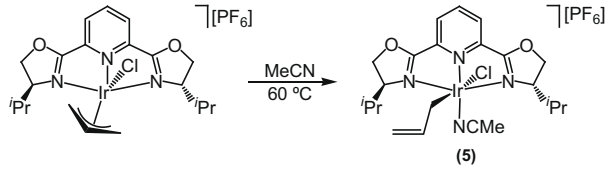
The oxidative addition of acetyl and benzoyl chloride to complex $[Ir(\eta^2\text{-}C_2H_4)_2\{\kappa^3\text{-}N,N,N\text{-}(S,S)\text{-}^i\text{Pr-pybox}\}][PF_6]$ has been also performed. Thus, the reaction of equimolecular amounts of that



Scheme 2.



Scheme 3.



Scheme 4.

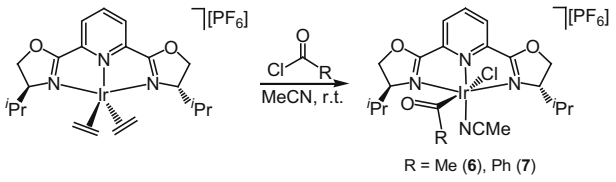
complex and acetyl or benzyl chloride in acetonitrile at room temperature produces stereoselectively the complexes **6** and **7**, respectively (Scheme 5). These complexes have been isolated as orange solids in 83–85% yield. Their analytic and spectroscopic data (IR and ^{1}H, ^{13}C{^{1}H} NMR) support the proposed formulations (see Section 2 for details).

Significant spectroscopic data are given: (a) the carbonyl carbon of the acyl ligand appears in the ^{13}C{^{1}H} NMR spectra at low field as singlet signals (200.9 (**6**) and 200.1 (**7**) ppm); (b) the methyl group of the MeCN ligand is observed as a singlet at 3.15 (**6**) and 2.97 (**7**) ppm in the ^{1}H NMR spectra. In addition the ^{13}C{^{1}H} NMR spectra show singlet signals for the acetonitrile carbons at 123.7 (CN) and 3.4 (*Me*CN) ppm for complex (**6**) and at 126.0 (CN) and 5.2 ppm (*Me*CN) for complex (**7**). The reaction presumably involves the formation of a non-detected monoolefin acyliridium(III) complex, which in turn evolves by ethylene displacement and acetonitrile coordination to thus provide complexes **6** and **7**. When this reaction was carried out in less coordinating solvents a complex mixture of unidentified products was obtained.

3.6. Characterization structural: X-ray structure of complex [IrCl(COPh)(MeCN){κ^3-*N,N,N*-(*S,S*)-^{i}Pr-pybox}][PF$_6$] · CH_2Cl_2

Since the NMR data do not allow the unambiguous assignment of the stereochemistry of complexes **6**, **7** a single-crystal X-ray analysis of complex **7** has been performed. An ORTEP view of the molecular structure is shown in Fig. 1. The more significant bond length and angle values are collected in Table 2. The structure exhibits a distorted octahedral geometry around the iridium atom, and shows the bonding of iridium to the three nitrogen atoms of the ^{i}Pr-pybox ligand, the chlorine atom, the acetonitrile, and the benzoyl group. The chlorine atom and the benzoyl group are located in a *trans* arrangement. The distances Ir–N(1) (2.075(7) Å), Ir–N(2) (1.975(7) Å) and Ir–N(3) (2.039(6) Å), as well as the bond angles N–Ir–N (79.6(3)°, 78.3(3)° and 157.7(3)°) fall in the range observed for the related complexes [Ir(η^2-C_2H_4)$_2$(κ^3-*N,N,N*-(*S,S*)-^{i}Pr-pybox)][PF$_6$] and [IrCl(η^3-C_3H_5)(κ^3-*N,N,N*-(*S,S*)-^{i}Pr-pybox)][PF$_6$] [5a]. The Ir-benzoyl distances [Ir–C(18) (2.054(8) Å) and C(18)–O(3) (1.204(11) Å)] are in the range found for other acyliridium(III) complexes [14]. The acetonitrile group is almost linearly coordinated to iridium, as indicated by the C(25)–N(4)–Ir angle of 175.9(10)°; the distance Ir–N(4) is 2.024(8) Å.

We assume that the stereochemistry of complex **7** is maintained in complexes **1**–**5**, with the chloride and the allyl ligands *trans* to each other. A similar stereochemical environment was reported for the complex [IrCl(η^1-$CH_2CH{=}CH_2$)(CO)(κ^3-*N,N,N*-(*R,R*)-Ph-pybox)][PF$_6$] [5b].



Scheme 5.

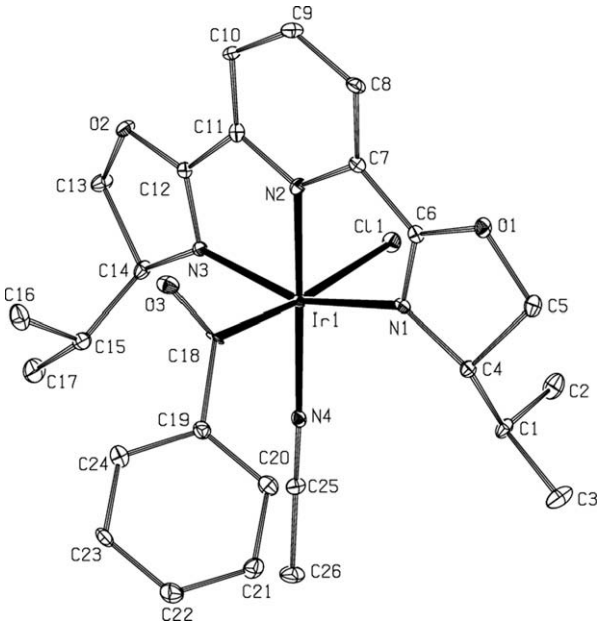


Fig. 1. An ORTEP type view of the molecular structure of the cation of complex [IrCl(COPh)(MeCN){κ^3-*N,N,N*-(*S,S*)-^{i}Pr-pybox}][PF$_6$] · CH_2Cl_2 (**7** · CH_2Cl_2); drawn at 10% probability level. Hydrogen atoms have been omitted for clarity.

Table 2
Selected bond distances (Å) and angles (°) for complex **7** · CH_2Cl_2.

Bond	Distance	Bond	Distance
Ir–N(2)	1.975(7)	C(18)–Ir	2.054(8)
Ir–N(1)	2.075(7)	C(18)–O(3)	1.204(11)
Ir–N(3)	2.039(6)	N(4)–C(25)	1.131(11)
Ir–N(4)	2.024(8)	C(25)–C(26)	1.450(13)
Ir–Cl(1)	2.495(2)		
Angle	**Value**	**Angle**	**Value**
N(1)–Ir–N(3)	157.7(3)	N(4)–Ir–N(3)	99.4(3)
N(1)–Ir–N(2)	78.3(3)	N(2)–Ir–N(4)	179.0(3)
N(2)–Ir–N(3)	79.6(3)	N(4)–Ir–N(1)	102.8(3)
C(18)–Ir–Cl(1)	173.6(2)	N(4)–Ir–C(18)	91.9(3)
N(3)–Ir–Cl(1)	86.7(2)	N(1)–Ir–C(18)	93.5(3)
N(1)–Ir–Cl(1)	89.9(2)	N(3)–Ir–C(18)	88.0(3)
N(2)–Ir–Cl(1)	87.4(2)	N(2)–Ir–C(18)	88.0(4)
N(4)–Ir–Cl(1)	92.6(2)	O(3)–C(18)–Ir	119.2(6)
O(3)–C(18)–C(19)	118.8(8)	Ir–N(4)–C(25)	174.4(7)
N(4)–C(25)–C(26)	175.9(10)		

4. Conclusions

In summary, we have accomplished the synthesis of enantiopure η^1-allyl and acyliridium(III) complexes of the types [IrCl(η^1-$CH_2CH{=}CHR$)(L)(κ^3-*N,N,N*-^{i}Pr-pybox)][PF$_6$] (R = H, L = $MeO_2CC{\equiv}C$-CO_2Me, MeCN; R = Ph, L = C_2H_4, MeCN), [IrCl(η^1-$CH_2CH{=}CHPh$)(η^2-C_2H_4)(κ^3-*N,N,N*-Ph-pybox)][PF$_6$] and [IrCl(COR)(MeCN)(κ^3-*N,N,N*-^{i}Pr-pybox)][PF$_6$] (R = Me, Ph) by the stereoselective oxidative addition of allyl or acyl chloride to the iridium(I) precursors or by ligand exchange on the allyliridium(III) complexes. The X-ray crystal structure of complex **7** · CH_2Cl_2 is reported and shows a *trans* disposition of the chlorine and benzoyl ligands. Although we have recently described the synthesis of complexes [IrCl(η^3-C_3H_5)(κ^3-*N,N,N*-R-pybox)][PF$_6$] from [Ir(η^2-C_2H_4)$_2$(κ^3-*N,N,N*-R-pybox)][PF$_6$] (R = (*S,S*)-^{i}Pr, (*R,R*)-Ph) and allyl chloride [5a], the results reported in this paper suggest that a η^1-coordination of allyl group is favoured in the presence of DMAD, MeCN and CO [5b]. On the other hand, the tridentate coordination is disfavoured for the cinnamyl group in comparison with the allyl group.

Acknowledgements

This work was supported by the Ministerio de Educación y Ciencia of Spain (Project CTQ2006-08485 and Consolider Ingenio 2010 (CSD2007-00006)). P.P. thanks the Ministerio de Educación y Ciencia (MEC) of Spain for a Ph.D. fellowship.

Appendix A. Supplementary data

CCDC 695931 contains the supplementary crystallographic data for **7** · CH_2Cl_2. These data can be obtained free of charge via http://www.ccdc.cam.ac.uk/conts/retrieving.html, or from the Cambridge Crystallographic Data Centre, 12 Union Road, Cambridge CB2 1EZ, UK; fax: (+44) 1223-336-033; or e-mail: deposit@ccdc.cam.ac.uk. Supplementary data associated with this article can be found, in the online version, at doi:10.1016/j.poly.2008.10.002.

References

[1] (a) A. Sivaramakrishna, E. Hager, F. Zheng, H. Su, G.S. Smith, J.R. Moss, J. Organomet. Chem. 692 (2007) 5125;
(b) K. Osakada, M. Kimura, J.-Ch. Choi, J. Organomet. Chem. 602 (2000) 144. and references therein;
(c) J.D. John, K.V. Salazar, B.L. Scott, R.T. Baker, A.P. Sattelberger, Organometallics 20 (2001) 296;
(d) K.E. Schwiebert, J.M. Stryker, J. Am. Chem. Soc. 117 (1995) 8275;
(e) E.B. Tjaden, J.M. Stryker, J. Am. Chem. Soc. 112 (1990) 6420.
[2] (a) Review: R. Takeuchi, S. Kezuka, Synthesis 20 (2006) 3349;
(b) L.S. Hegedus, Transition Metals in the Synthesis of Complex Organic Molecules, 2nd ed., University Science Books, Mill Valley, 1999.
[3] (a) J.P. Janssen, G. Helmchen, Tetrahedron Lett. 38 (1997) 8025;
(b) Review: G. Helmchen, A. Dahnz, P. Dübon, M. Schelwies, R. Weihofen, Chem. Commun. (2007) 675.
[4] (a) H. Miyabe, A. Matsumura, K. Motiyama, Y. Takemoto, Org. Lett. 6 (2004) 4631;
(b) H. Miyabe, K. Yoshida, M. Yamauchi, Y. Takemoto, J. Org. Chem. 70 (2005) 2148;
(c) Review: H. Miyabe, Y. Takemoto, Synlett (2005) 1641;
(d) C.-X. Zhao, M.O. Duffey, S.J. Taylor, J.P. Morken, Org. Lett. 3 (2001) 1829.
[5] (a) J. Díez, M.P. Gamasa, J. Gimeno, P. Paredes, Organometallics 24 (2005) 1799;
(b) D. Cuervo, J. Díez, M.P. Gamasa, J. Gimeno, P. Paredes, Eur. J. Inorg. Chem. (2006) 599;
(c) P. Paredes, J. Díez, M.P. Gamsa, Organometallics 27 (2008) 2597.
[6] Bruker 2004: COLLECT data collection software, Bruker AXS, Delft, The Netherlands, 2004.
[7] Z. Otwinowski, W. Minor, Methods Enzymol. 276 (1997) 307.
[8] R.H. Blessing, Acta Crystallogr., Sect. A 51 (1995) 33.
[9] L.J. Farrugia, J. Appl. Crystallogr. 32 (1999) 837.
[10] P.T. Beurskens, G. Admiraal, G. Beurskens, W.P. Bosman, S. García-Granda, R.O. Gould, J.M.M. Smits, C. Smykalla, The DIRDIF Program System; Technical Report of the Crystallographic Laboratory, University of Nijimegen: Nijimegen, The Netherlands, 1999.
[11] G.M. Sheldrick, SHELXL-97: Program for the Refinement of Crystal Structures, University of Göttingen, Göttingen, Germany, 1997.
[12] International Tables for X-ray Crystallography; Kynoch Press, Birmingham, UK, 1974, vol. IV (present distributor: Kluwer Academic Publishers, Dordrecht, The Netherlands).
[13] L. Spek, PLATON: A Multipurpose Crystallographic Tool, University of Utrecht, Utrecht, The Netherlands, 2007.
[14] (a) X. Song, K.S. Chan, Organometallics 26 (2007) 965;
(b) F. Acha, M.A. Garralda, R. Hernández, L. Ibarlucea, E. Pinilla, M.R. Torres, M. Zarandona, Eur. J. Inorg. Chem. (2006) 3893.

Polyhedron 28 (2009) 63–68

Contents lists available at ScienceDirect

Polyhedron

journal homepage: www.elsevier.com/locate/poly

Attainment of new Te^{II} and Te^{IV} iodides by unexpected removal of the mesityl group of $[mesTeI_2]^-$: Synthesis and structural features of $[TeI_4][Co(en)_3] \cdot I$, $[TeI_6][Co(en)_3] \cdot I$, $[\{TeI_6\}\{Te_2I_{10}\}][Co(NH_3)_6]_2 \cdot 2I \cdot 6H_2O$ and $[(mesTeI_2)_2(\mu\text{-}I_2)][Co(bpy)_3] \cdot I_3 \cdot 2CHCl_3$ (mes = 2,4,6-trimetylphenyl; *en* = ethylenediamine; bpy = bipyridine)

Eliandro Faoro, Gelson Manzoni de Oliveira *, Ernesto Schulz Lang

Departamento de Química, Laboratório de Materiais Inorgânicos, Universidade Federal de Santa Maria, 97105-900 Santa Maria, RS, Brazil

ARTICLE INFO

Article history:
Received 29 August 2008
Accepted 2 October 2008
Available online 5 November 2008

Keywords:
Organyltellurium iodides
Supramolecular assemblies
Secondary interactions

ABSTRACT

$(MesTe)_2$ reacts with I_2 and $[CoL_n]I_3$ {L = $(NH_3)_6$, $(en)_3$} in a biphasic system (chloroform and water) to give, in the interface of the two phases, crystals of $[TeI_4][Co(en)_3] \cdot I^-$ (**1**), $[TeI_6][Co(en)_3] \cdot I^-$ (**2**) and $[\{TeI_6\}\{Te_2I_{10}\}]$ $[Co(NH_3)_6]_2 \cdot 2I^- \cdot 6H_2O$ (**3**), in a high yield. If the crystallization is carried out with $[Co(bpy)_3]I_3$ under addition of THF, the mesityl groups are retained and the final product is $[(mesTeI_2)_2(\mu\text{-}I_2)][Co(bpy)_3] \cdot I_3^- \cdot 2CHCl_3$ (**4**), which crystallizes in the organic phase. The already known species {mesTeI···I(mes)Te–Te(mes)$_2$} appears as subproduct in the syntheses of **1**, **2** and **3**, in the organic phase.

The X-ray structural characterization of the new complexes is discussed, together with some synthetic features related with the abstraction of the mesityl groups in the three first syntheses.

© 2008 Elsevier Ltd. All rights reserved.

1. Introduction

It is not an overstatement when we classify the chemistry of organochalcogene halides, this subject of considerable current interest, as the "chemistry of the secondary bonds". The bonding in these compounds get away from simple description, and concepts like hypervalence, multicenter bonding, charge transfer interactions and secondary bonds have been arisen in the understanding of their structural and chemical features [1–5]. Intermolecular bonding effects of the type E···X and X···X (E = Se, Te; X = Cl, Br, I) of various strengths, together with hydrogen bonding (especially if pyridinium counter ions occur), lead to the formation of one, bi and three-dimensional polymeric chains, dimeric structures or monomers with fairly strong intermolecular interactions. Many of these halogen compounds lie close to the ionic/covalent borderline, and several identified species have been found to be dependent on variables like the substituents R, the donor atom, the identity of the halogen, and, in some cases, also on the dielectric constant of the solvent in which they have been prepared [6–9].

Newly we have described [10] the synthesis and the X-ray characterization of the new T-shaped [9,11] organotellurium dihalides (PyH)[mesTeI$_2$] (**A**), (PyH)[mesTeIBr] (**B**) and (PyH)[mesTeICl] (**C**), which were prepared starting from $(mesTe)_2$, with insertion – in **B** and **C** – of two different halogen atoms on tellurium and without the participation of ethylenethiourea, a coordinating solvent commonly used to mediate this type of reactions [12]. The anions [mesTeI$_2$] and [mesTeIBr] build dimers by reciprocal, secondary Te···X interactions and are also linked to the pyridinium cations through NH···X bonding; the anion [mesTeICl] do not interact with neighboring anionic moieties, but attains as well secondary NH···Cl bonding with the pyridinium cation. Following these experimental studies we have reported further [13] the analogous T-shaped organotellurium(II) dihalides (PyH)[mesTeBr$_2$], (PyH)[mesTeClBr] and (PyH)[mesTeCl$_2$], which do not reproduce the assembling of the above mentioned parent dihalides, e.g., there is no dimeric association of the anions, although the secondary NH···X bonds of the anionic moieties toward the pyridinium cations are maintained.

If the reaction milieu – in the synthesis of the two series of compounds described above – is anyway disturbed by using appropriated reagents, the final products can be essentially different, chemically and structurally. We have demonstrated [14] the effects of these controlled "disturbances" on the intermediary mesTeI, with the syntheses of the organotellurium iodides $[mesTeI(\mu\text{-}I)_2(TeImes)_2]_n$, $(C_5H_6N)_4[mesTeI_2]_2(I_3)_2$ and $\{(C_5H_6N)_3[(mesTeI_3)(\mu\text{-}I^-)(TeI_3mes)](I_3)_2\}_n$. All these compounds show unusual compositions and configurations, attaining secondary, interanionic $I_3^-\cdots I\text{–}Te^-$ bonds, $N^+\text{–}H\cdots I\text{–}Te^-$ interactions and $N^+\text{–}H\cdots I_3^-$ contacts. The last compound presents the tellurium atoms with mixed valence states, Te^{II} and Te^{IV}.

* Corresponding author. Tel.: +55 55 3220 8757; fax: +55 55 3220 8031.
E-mail address: manzoni@quimica.ufsm.br (Gelson Manzoni de Oliveira).

0277-5387/$ - see front matter © 2008 Elsevier Ltd. All rights reserved.
doi:10.1016/j.poly.2008.10.001

Because of the structural importance (multicenter and secondary bonding) and chemical properties of T-shaped organochalcogene dihalides [15–18], as well as their charge transfer interactions, we have attempted the recrystallization in two phases of an excess of [mesTeI](CHCl$_3$) plus I_2 with [CoL$_n$]I$_3$(H$_2$O) {L = (NH$_3$)$_6$, (*en*)$_3$} to obtain products related to **A**, but containing a Co^{III} complex as counter ion, as well as the already observed I_3^- interactions, with different stoichiometric relations. Instead, the obtained crystalline products, $[TeI_4][Co(en)_3]\cdot I^-$ (**1**), $[TeI_6][Co(en)_3]\cdot I^-$ (**2**) and $[\{TeI_6\}\{Te_2I_{10}\}][Co(NH_3)_6]_2\cdot 2I^-\cdot 6H_2O$ (**3**), are quite different of those expected, and all of them present a common feature: the absence of the mesityl group. When the reaction is carried out with [Co(bpy)$_3$]I$_3$, under addition of THF, the mesityl groups are retained and the final product is $[(mesTeI_2)_2(\mu\text{-}I_2)][Co(bpy)_3]\cdot I_3^-\cdot 2CHCl_3$ (**4**), which presents an iodine bridge between the two (mesTeI$_2$) anions. The already known [19], neutral species {mesTeI···I(mes)Te–Te(mes)$_2$} appears as subproduct in the syntheses of **1**, **2** and **3**.

We discuss now the synthetic procedures and the structural characterization of the title complexes, as well as possible reasons for the surprising withdrawal of the mesityl group in **1**, **2** and **3**.

2. Results and discussion

2.1. Structural features of *1*, *2*, *3* and *4*

The X-ray crystal data and the experimental conditions for the analyses of the complexes $[TeI_4][Co(en)_3]\cdot I^-$ (**1**), $[TeI_6][Co(en)_3]\cdot I^-$ (**2**), $[\{TeI_6\}\{Te_2I_{10}\}]\ [Co(NH_3)_6]_2\cdot 2I^-\cdot 6H_2O$ (**3**) and $[(mesTeI_2)_2(\mu\text{-}I_2)][Co(bpy)_3]\cdot I_3^-\cdot 2CHCl_3$ (**4**), are given in Table 1. Table 2 summarizes selected bond distances and angles for the title compounds. Figs. 1 and 2 represent the molecular structures of compounds **1** and **2** with their multiple secondary interactions (identified by dashed lines), which lead to the one-dimensional assembling of both compounds. Fig. 3 shows the two-dimensional assembly of the molecules in compound **3** (without the solvate molecules), with the secondary interactions also represented by dashed lines. Fig. 4 displays the structural composition of **4** (not including the chloroform molecules), with the iodine bridge as dotted lines, and Fig. 5 shows the one-dimensional assembly of **4**, attained by all the compound-forming entities.

In the complex $[TeI_4][Co(en)_3]\cdot I^-$ (**1**), the octahedral $[Co(en)_3]^{3+}$ ions are linked through angular (105.7°) NH···I$^-$···HN secondary bonding, with distances of 2.726(2) and 2.721(1) Å. Each octahedral moiety is connected to one semi planar $[TeI_4]^{2-}$ ion through a secondary NH···I bond, measuring 2.775(1) Å. The Te–I bonds are not symmetrical, ranging from 2.894(2) to 3.064(2) Å. The association of the ionic species through secondary interactions yields a one-dimensional chain along the bisector of the ac axes (see Fig. 1).

The complex $[TeI_6][Co(en)_3]\cdot I^-$ (**2**) presents two kinds of NH···I$^-$ interactions, H(2)″···I(7) {2.834(0)} and H(4)···I(7) {2.809(0) Å}, (see Fig. 2). The secondary iodine interactions of the tipe Te–I···I$^-$ {I(2)···I(7)} exhibit a distance of 3.934(1) Å, whereas the Te–I···I–Te contacts {I(2)···I(3′)} are somewhat shorter {3.907(0) Å}. The octahedral $[TeI_6]^{2-}$ ions are linked through iodine interactions, alternating $[Co(en)_3]^{3+}$ and I$^-$ ions in a zigzag configuration, which leads also to the assembly of the ionic species in a one-dimensional chain.

The unusual structure of the two-dimensional lattice of $[\{TeI_6\}\text{-}\{Te_2I_{10}\}]\ [Co(NH_3)_6]_2\cdot 2I^-\cdot 6H_2O$ (**3**) appears as a result of the transversal interlacement (in the same plane) of two kinds of chains: along a direction close on 20° to the *b* axis the ionic species $[TeI_6]^{2-}$ and $[Te_2I_{10}]^{2-}$ build parallel single chains through two I···I interactions {I(2)···I(7′)} with 3.930(2) Å. The $[Te_2I_{10}]^{2-}$ species attain also secondary bonding with two I$^-$ ions {I(6)···I(9)}, 3.674(2) Å}. With these shorter I···I$^-$ contacts, each two I$^-$ ions assemble a parallelogram with one $[Te_2I_{10}]^{2-}$ moiety, in the

Table 1
Crystal data and structure refinement for **1**, **2**, **3** and **4**.

	1	**2**	**3**	**4**
Empirical formula	$C_6H_{24}N_6CoI_5Te$	$C_6H_{24}N_6CoI_7Te$	$H_{24}N_6O_3CoI_9Te_{1.50}$	$C_{50}H_{48}N_6Cl_6CoI_9Te_2$
Formula weight	1001.34	1255.14	1548.68	2401.87
T (K)	293(2)	293(2)	293(2)	293(2)
Radiation, λ (Å)	0.71073	0.71073	0.71073	0.71073
Crystal system, space group	triclinic, $P\bar{1}$	monoclinic, $P2_1/n$	triclinic, $P\bar{1}$	monoclinic, $C2/c$
Unit cell dimensions a, b, c (Å)	a = 8.4679(2)	a = 8.4705(10)	a = 8.4665(2)	a = 12.3930(4)
	b = 8.6754(2)	b = 26.2899(5)	b = 11.4469(2)	b = 20.3038(7)
	c = 14.9450(3)	c = 11.5526(2)	c = 16.2735(3)	c = 27.2267(9)
α, β, γ (°)	α = 89.7150(10)	α = 90	α = 74.8210(10)	α = 90
	β = 83.4430(10)	β = 101.680(10)	β = 76.9250(10)	β = 97.015(2)
	γ = 81.1510(10)	γ = 90	γ = 68.6100(10)	γ = 90
V (Å^3)	1077.64(4)	2519.36(7)	1402.20(5)	6799.6(4)
Z, $D_{Calc.}$ (g cm^{-3})	2, 3.086	4, 3.309	2, 3.654	4, 2.346
Absorption coefficient (mm^{-1})	9.284	10.397	12.059	5.453
F(000)	892	2208	1332	4400
Crystal size (mm)	0.205 × 0.079 × 0.06	0.301 × 0.162 × 0.085	0.49 × 0.195 × 0.188	0.112 × 0.099 × 0.057
θ range (°)	1.37–32.20	1.96–29.99	1.95–30.10	1.94–24.79
Index ranges	$-12 \leqslant h \leqslant 12$	$-11 \leqslant h \leqslant 11$	$-11 \leqslant h \leqslant 11$	$-14 \leqslant h \leqslant 14$
	$-12 \leqslant k \leqslant 12$	$-36 \leqslant k \leqslant 36$	$-16 \leqslant k \leqslant 15$	$-23 \leqslant k \leqslant 23$
	$-22 \leqslant l \leqslant 22$	$-16 \leqslant l \leqslant 16$	$-22 \leqslant l \leqslant 21$	$-31 \leqslant l \leqslant 32$
Reflections collected	28758	29353	33670	26803
Reflections unique (R_{int})	7353 (0.0485)	7209 (0.0308)	8157 (0.0437)	5809 (0.1331)
Completeness to theta max. (%)	96.7	98.4	98.9	99.5
Absorption correction	Gaussian	Gaussian	Gaussian	Gaussian
Maximum and minimum transmission	0.573 and 0.419	0.413 and 0.144	0.746 and 0.398	0.745 and 0.618
Refinement method	Full-matrix	Full-matrix	Full-matrix	Full-matrix
	least-squares on F^2	least-squares on F^2	least-squares on F^2	least-squares on F^2
Data/restraints/parameters	7353/0/173	7209/0/191	8157/0/177	5809/0/336
Goodness-of-fit on F^2	1.036	1.110	1.093	0.951
Final R indices [$I > 2\sigma(I)$]	R_1 = 0.0497, wR_2 = 0.1226	R_1 = 0.0324, wR_2 = 0.0773	R_1 = 0.0333, wR_2 = 0.0854	R_1 = 0.0602, wR_2 = 0.1523
R indices (all data)	R_1 = 0.0834, wR_2 = 0.1365	R_1 = 0.0466, wR_2 = 0.0906	R_1 = 0.0421, wR_2 = 0.0985	R_1 = 0.1512, wR_2 = 0.2338
Largest difference in peak and hole (e Å^{-3})	2.249 and −1.392	2.088 and −1.382	3.362 and −1.897	1.241 and −1.191

Table 2
Selected bond lengths (Å) and angles (°) for the compounds **1**, **2**, **3** and **4.**

1		**2**		**3**		**4**	
Bond lengths		*Bond lengths*		*Bond lengths*		*Bond lengths*	
Te(1)–I(1)	3.034(8)	Te(1)–I(1)	2.946(6)	Te(1)–I(1)	2.9428(4)	Te(1)–C(1)	2.21(2)
Te(1)–I(2)	3.064(8)	Te(1)–I(2)	2.866(5)	Te(1)–I(2)	2.9559(4)	Te(1)–I(2)	2.900(1)
Te(1)–I(3)	2.894(8)	Te(1)–I(3)	2.857(5)	Te(1)–I(3)	2.9435(4)	Te(1)–I(1)	3.006(2)
Te(1)–I(4)	2.911(8)	Te(1)–I(4)	2.934(6)	Te(2)–I(4)	2.8203(6)	I(3)–I(4)	2.9142(17)
N(1)–Co(1)	1.971(7)	Te(1)–I(5)	3.066(5)	Te(2)–I(5)	3.1480(5)	I(5)–I(5)′	2.847(4)
N(3)–Co(1)	1.978(7)	Te(1)–I(6)	3.023(5)	Te(2)–I(6)	2.8225(5)	N(11)–Co(1)	1.932(17)
N(2)–Co(1)	1.959(6)	N(1)–Co(1)	1.970(5)	Te(2)–I(7)	3.1720(6)	N(21)–Co(1)	1.931(16)
N(4)–Co(1)	1.961(6)	N(2)–Co(1)	1.963(5)	Te(2)–I(8)	2.7839(6)	N(31)–Co(1)	1.925(17)
N(5)–Co(1)	1.973(6)	N(3)–Co(1)	1.974(5)	N(1)–Co(1)	1.952(5)	Te(1)···I(5)	3.225(1)
N(6)–Co(1)	1.962(7)	N(4)–Co(1)	1.965(5)	N(2)–Co(1)	1.984(2)	Cl(1)‴···I(2)⁗	3.855(11)
H(2a)···I(1)	2.775(1)	N(5)–Co(1)	1.981(5)	N(3)–Co(1)	1.953(5)	Cl(3)‴···I(4)	3.862(8)
H(2b)···I(5)	2.721(1)	N(6)–Co(1)	1.983(5)	N(4)–Co(1)	1.969(5)	*Bond angles*	
H(4a)′···I(5)	2.726(2)	I(2)···I(3)′	3.907(0)	N(5)–Co(1)	1.961(5)	C(1)–Te(1)–I(1)	88.4(5)
Bond angles		I(2)···I(7)	3.934(1)	N(6)–Co(1)	1.957(5)	C(1)–Te(1)–I(2)	88.8(5)
I(1)–Te(1)–I(4)	175.42(3)	H(2)″···I(7)	2.834(0)	I(2)···I(7)′	3.930(2)	C(1)–Te(1)–I(5)	123.44(0)
I(2)–Te(1)–I(3)	174.40(2)	H(4)···I(7)	2.809(0)	I(6)···I(9)	3.674(2)	I(1)–Te(1)–I(2)	174.87(8)
N(1)–Co(1)–N(5)	173.90(3)	*Bond angles*		H(6)···I(9)	2.800(3)	I(4)–I(3)–I(4)″	177.28(11)
N(2)–Co(1)–N(4)	172.60(3)	I(1)–Te(1)–I(4)	175.464(19)	H(1)‴···I(9)	2.843(1)	Te(1)···I(5)–I(5)′	171.74(0)
N(3)–Co(1)–N(6)	174.60(3)	I(2)–Te(1)–I(5)	177.969(18)	*Bond angles*		N(11)–Co(1)–N(31)	176.2(8)
		I(3)–Te(1)–I(6)	174.816(19)	I(1)–Te(1)–I(1)″	180.0(17)	N(21)–Co(1)–N(21)″	177.8(11)
		N(1)–Co(1)–N(5)	175.4(2)	I(2)–Te(1)–I(2)″	180.0(17)	N(11)–Co(1)–N(21)	82.7(9)
		N(2)–Co(1)–N(3)	175.8(2)	I(3)–Te(1)–I(3)″	180.0(16)	N(31)–Co(1)–N(31)″	82.6(12)
		N(4)–Co(1)–N(6)	175.3(2)	I(4)–Te(2)–I(5)	176.674(19)		
				I(6)–Te(2)–I(7)	178.287(19)		
				I(8)–Te(2)–I(5)′	177.561(2)		
				Te(2)–I(5)–Te(2)′	93.021(1)		
				N(1)–Co(1)–N(2)	178.42(18)		
				N(3)–Co(1)–N(6)	178.6(2)		
				N(4)–Co(1)–N(5)	178.7(2)		

Symmetry transformations used to generate equivalent atoms: **1** {(′) = 1 − *x*, 1 − *y*, 1 − *z*}; **2** {(′) = −*x*, −*y*, 1 − *z*; (″) = −1−*x*, −*y*, 1 − *z*}; **3** {(′) = 1 − *x*, 2 − *y*, 1 − *z*; (″) = −*x*, 1 − *y*, −*z*; (‴) = 1 + *x*, *y*, *z*}; **4** {(′) = −*x*, 1 − *y*, −*z*; (″) = 1 − *x*, *y*, 0.5 − *z*; (‴) −*x*, *y*, 0.5 − *z*; (⁗) = 0.5 − *x*, 0.5 + *y*, 0.5 − *z*}.

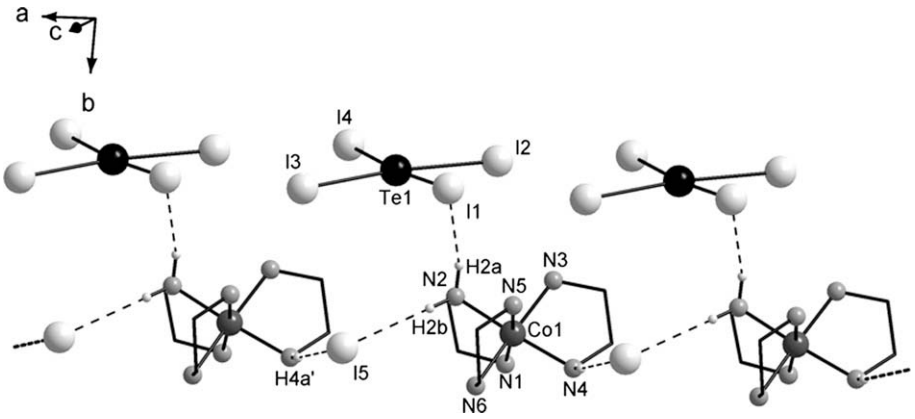


Fig. 1. Molecular/ionic structure and one-dimensional assembly of $[TeI_4][Co(en)_3]\cdot I^-$ (**1**). The dashed lines represent secondary interactions. Symmetry transformations used to generate equivalent atoms: (′) = 1 − *x*, 1 − *y*, 1 − *z*.

equatorial plane of the two octahedrons. An inversion center is located in the middle of the ring formed by the four Te(2) and I(5) atoms. The second set of chains crosses over the first one along the *a* axis, and is formed by $[Co(NH_3)_6]^{3+}$ octahedral moieties linked through NH···I$^-$ interactions. These non-symmetrical hydrogen bridges, H(1)‴···I(9) and I(9)···H(6), have distances of 2.843(1) and 2.800(3) Å, respectively (see Fig. 3).

The ionic species $[Te_2I_{10}]^{2-}$, counterbalanced by *N*,*N*-dimethylanilinium cations – with secondary I···I bonds building up a 3D network – was described for the first time by Ryan and Xu [20]. Also the analogous $[Te_2Cl_{10}]^{2-}$ ion is already known [21].

Complex **4**, $[(mesTeI_2)_2(\mu\text{-}I_2)][Co(bpy)_3]\cdot I_3^-\cdot 2CHCl_3$, the only product which retains the mesityl rings, is a typical T-shaped tellurium diiodide. The Te–I bonds show distances of 2.900(1) {Te(1)–I(2)} and 3.006(2) Å) {Te(1)–I(1)}. The I(1)–Te(1)–I(2) angle is 174.87(8)°, and the C(1)–Te(1)–I(1)/C(1)–Te(1)–I(2) angles measure 88.4(5) and 88.8(5)°, respectively. These angles characterize the classical T configuration of this type of compounds. As shown in Fig. 4, the two ($mesTeI_2$) ions are linked by a symmetrical iodine bridge of 3.225(1) Å.

The solvate I_3^- accomplishes the charge balance of **4** and shows identical I(4)–I(3)–I(4)″ interatomic distances, an uncommon feature in the case of poli-iodides {I(4)–I(3) = 2.9142(17) Å; the position of I(4)″ is obtained from I(4) through the symmetry transformation (″) = 1 − *x*, *y*, 0.5 − *z*}; the two bonds are virtually linear, with an angle of 177.28(11)° (see Table 2).

Also in the compound **4** secondary interactions produce a one-dimensional arrangement of the lattice, as shown in Fig. 5. The chain increases in a zigzag configuration along the direction which forms an angle of nearly 45° with the *a* axis. The molecules of the

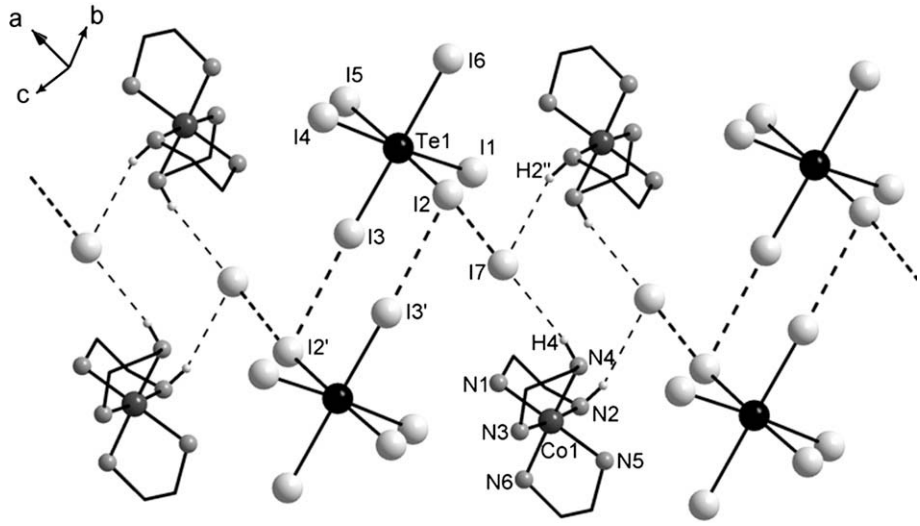


Fig. 2. Molecular/ionic structure and one-dimensional assembly of $[TeI_6][Co(en)_3] \cdot I^-$ (**2**). Secondary interactions are represented by dashed lines. Symmetry transformations used to generate equivalent atoms: (′) = −*x*, −*y*, 1 − *z*; (″) = −−1−*x*, −*y*, 1 − *z*.

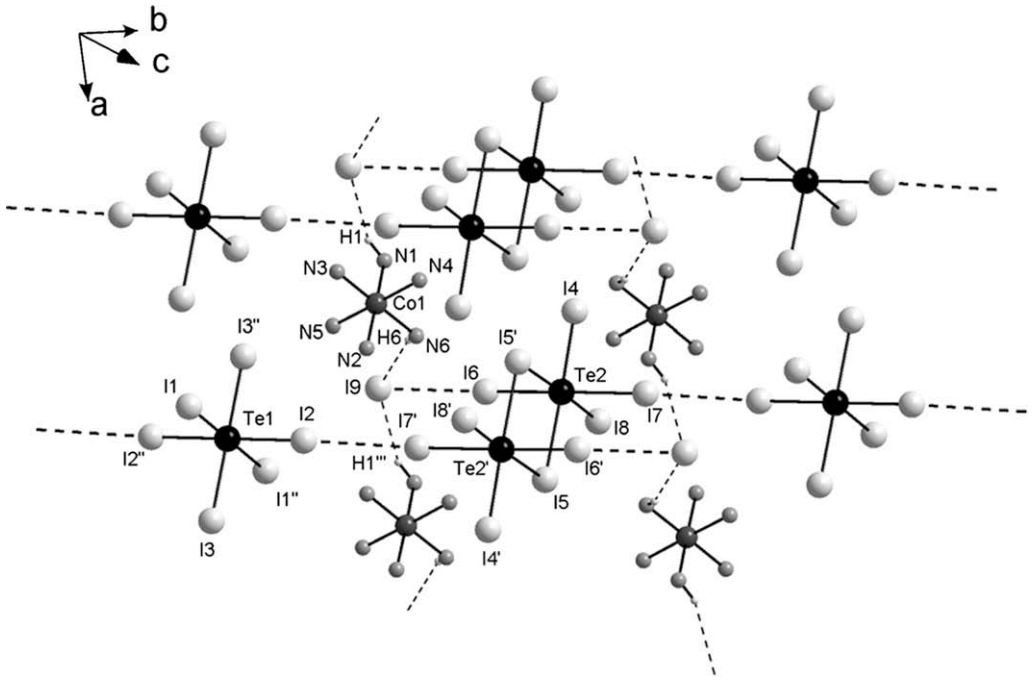


Fig. 3. The two-dimensional assembly of the species in $[\{TeI_6\}\{Te_2I_{10}\}][Co(NH_3)_6]_2 \cdot 2I^- \cdot 6H_2O$ (**3**). For clarity the water molecules are not displayed. The dashed lines represent secondary interactions. Symmetry transformations used to generate equivalent atoms: (′) = 1 − *x*, 2 − *y*, 1 − *z*; (″) = −*x*, 1 − *y*, −*z*; (‴) = 1 + *x*, *y*, *z*.

solvate $CHCl_3$ attain symmetrical, secondary interactions with I_3^- {Cl(3)‴···I(4), 3.862(8) Å} and with the single $(mesTeI_2)^-$ units {Cl(1)‴···I(2)⁗, 3.855(11) Å}, these last also connected through I_2 bridges. Each chain is delimited by two series of linear standing $[Co(bpy)_3]^{3+}$ ions, which do not interact ostensibly with any species.

2.2. Synthetic considerations

The syntheses of **1, 2**, **3** and **4** were carried out with basis on the formation of the intermediary {**mesTeI**} (see Section 3) and its further reactions and rearrangements.

The obtained products allow the conclusion that in the three first reactions (synthesis of **1**, **2** and **3**) has occurred partial decomposition of the intermediary mesTeI in the water/chloroform interface, due to the high difference of polarity. The action of the water dipoles probably has lead to the cleavage of C−Te bonds, what should explain the formation and crystallization, in the $H_2O/CHCl_3$ interface, of products without mesityl rings. Rearrangement reactions of mesityl rings and chemically altered mesTeI should also explain the crystallization, in the organic phase (for all the three first procedures), of the already known compound {mesTeI···I(mes)Te−Te(mes)$_2$} [19]. The preparation of **4** differs only in the addition of 5 mL of THF to the aqueous solution, together with iodine, in the second step of the synthesis. Since 5 mL of THF is the halve of the amount of water (10 mL) in the system, and THF and water are miscible in good extent, the addition of THF has reduced the polarity of the milieu, attenuating also the

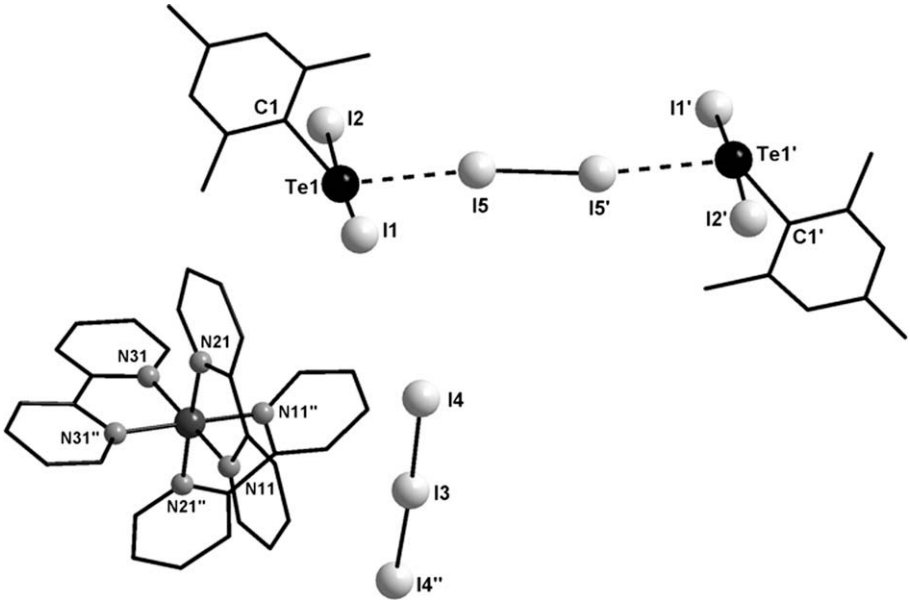


Fig. 4. Structural composition of $[(mesTeI_2)_2(\mu\text{-}I_2)][Co(bpy)_3] \cdot I_3^- \cdot 2CHCl_3$ (**4**), not including the chloroform solvate molecules. The dashed lines represent the iodine bridge. Symmetry transformations used to generate equivalent atoms: (′) = −*x*, 1−*y*, −*z*; (″) = 1 − *x*, *y*, 0.5 − *z*.

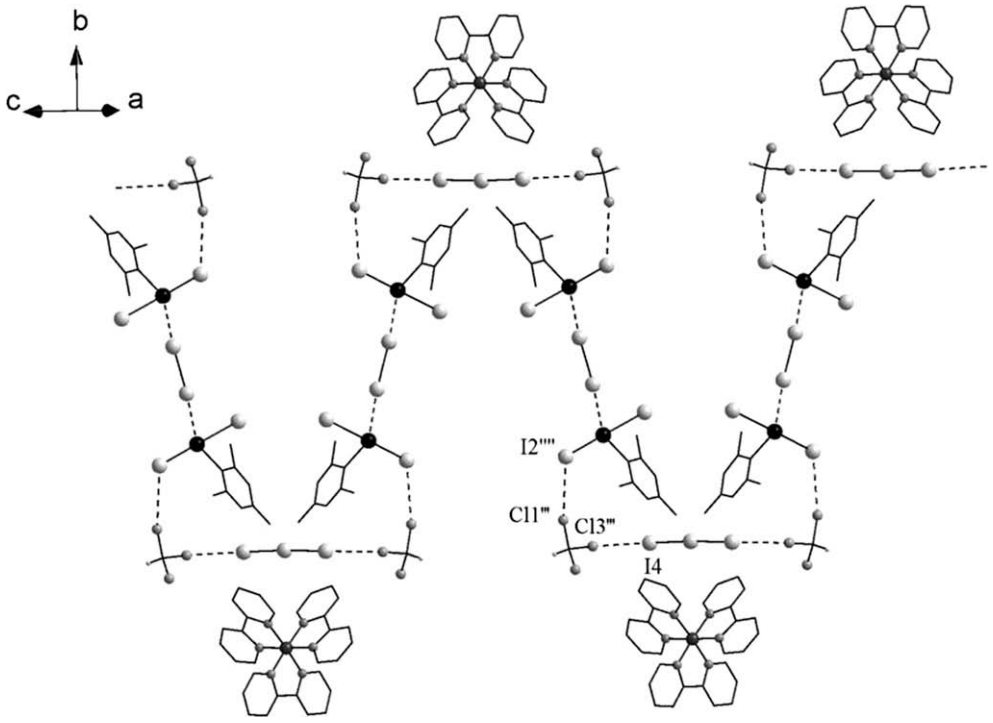


Fig. 5. Zigzag chain of **4**, delimited by the $[Co(bpy)_3]^{3+}$ ions, involving secondary interactions of the solvate molecules/ions and iodine bridges, in dashed lines. Symmetry transformations used to generate equivalent atoms: (‴) −*x*, *y*, 0.5 − *z*; (⁗) = 0.5 − *x*, 0.5 + *y*, 0.5 − *z*.

decomposition power of the water. This allowed the formation of compound **4** in the (mild) interface of the system and its resettlement to the organic phase, where the crystallization has occurred. From these considerations can be easily inferred that the solubility of these compounds is a strongly limiting factor for the availability of structural analytical methods. For example, the possibility of use of ^{125}Te NMR spectroscopy is remarkable reduced.

Finally, the title compounds here discussed represent also examples of supramolecular compounds. This is typical for a large amount of organotellurium halides, in which multiple secondary interactions are able to build chemical nets whose interpretation can be sometimes troublesome to puzzle out.

3. Experimental

3.1. Synthesis of $[TeI_4][Co(en)_3] \cdot I^-$ (**1**) and $[TeI_6][Co(en)_3] \cdot I^-$ (**2**)

To a solution of $(MesTe)_2$ (0.148 g, 0.3 mmol) in 5 mL $CHCl_3$, resublimed I_2 (0.077 g, 0.3 mmol) was added. The solution was

stirred by 30 min and the color turned blue, making evident the formation of the intermediary {mesTeI}. Over this solution 10 mL of an *aqueous* solution of $[Co(en)_3]I_3$ (0.125 g, 0.2 mmol) plus I_2 (0.052 g, 0.2 mmol) was added, remaining a biphasic system. After a few days, in the interface of the system arose the crystallization of two distinct crystalline products, **1** and **2**. In the organic phase occurs the crystallization of the adduct {(mes)2Te–TeI(mes)}-(mesTeI) [19]. Yield: 25% (**1**), 65% (**2**) based on $[Co(en)_3]I_3$.

$[TeI_4][Co(en)_3]\cdot I^-$ (**1**): red crystalline substance. $C_6H_{24}N_6CoI_5Te$ (1001.34). Melting point: 159.5–160.8 °C. *Anal.* Calc.: C, 7.20; H, 2.42; N, 8.39. Found: C, 7.24; H, 2.38; N, 8.43%.

IR (KBr): 3016.4 [ν(N–H)], 2917.2 [ν(C–H)], 1591.3 [δ(C–N–H)], 1438.8 [δ(C–C–H)], 849.8 cm^{-1} [$\delta_{out\,pl.}(NH_2)$].

$[TeI_6][Co(en)_3]\cdot I^-$ (**2**): black crystals. $C_6H_{24}N_6CoI_7Te$ (1255.14). Melting point: 105.5–106.2 °C. *Anal.* Calc.: C, 5.74; H, 1.93; N, 6.70. Found: C, 5.69; H, 1.96; N, 6.76%.

IR (KBr): 3014.2 [ν(N–H)], 2915.5 [ν(C–H)], 1592.5 [δ(C–N–H)], 1433.4 [δ(C–C–H)], 851.7 cm^{-1} [$\delta_{out\,pl.}$ (NH_2)].

3.2. Synthesis of $[\{TeI_6\}\{Te_2I_{10}\}][Co(NH_3)_6]_2\cdot 2I^-\cdot 6H_2O$ (**3**) and $[(mesTeI_2)_2(\mu\text{-}I_2)][Co(bpy)_3]\cdot I_3^-\cdot 2CHCl_3$ (**4**)

According to the former synthesis (**1** and **2**), under addition of $[Co(NH_3)_6]I_3$ (0.108 g, 0.2 mmol) (**3**), and $[Co(bpy)_3]I_3$ (0.181 g, 0.2 mmol) (**4**), in lieu of $[Co(en)_3]I_3$. In the preparation of **4** the second addition of iodine (to the aqueous solution) was preceded by its (I_2) dissolution in 5 mL of THF. The single product **3** crystallizes also in the interface of the biphasic system, while the crystallization of **4** occurs in the organic phase. In the case of **3**, crystalline {$(mes)_2$Te–TeI(mes)}(mesTeI) [19] was identified in the organic phase as well. Yield: 80% based on $[Co(NH_3)_6]I_3$ (**3**), 82% based on $[Co(bpy)_3]I_3$ (**4**).

$[\{½TeI_6\}\{½Te_2I_{10}\}][Co(NH_3)_6]\cdot I^-\cdot 3H_2O$ (**3**): black crystalline substance. $H_{24}N_6O_3CoI_9Te_{1.50}$ (1548.68). Melting point: 168.5–169.9 °C. *Anal.* Calc.: H, 1.55; N, 5.52; O, 3.17. Found: H, 1.51; N, 5.48; O, 3.14%.

IR (KBr): 3449.4 [ν(O–H)], 3147.7 [ν(N–H)], 1324.1 [$\delta(NH_2)$], 818.7 cm^{-1} [$\delta_{out\,pl.}(NH_2)$].

$[(mesTeI_2)_2(\mu\text{-}I_2)][Co(bpy)_3]\cdot I_3^-\cdot 2CHCl_3$ (**4**): dark red crystals. $C_{50}H_{48}N_6Cl_6CoI_9Te_2$ (2401.87). Melting point: 104.1–105.2 °C. *Anal.* Calc.: C, 25.00; H, 2.01; N, 3.50. Found: C, 25.04; H, 2.05; N, 3.56%.

IR (KBr): 3074.0 [$\nu(C–H)_{Ar.}$], 2958.4 [$\nu(C–H)CH_3$], 1601.0 [ν(C=C)], 1562.8 [ν(C=N)], 1445.1 [δ(C=C–H)], 758.4 cm^{-1} [$\delta_{out\,pl.}(NH)_2$].

3.3. X-ray structure determinations

Data were collected with a Bruker APEX II CCD area-detector diffractometer and graphite-monochromatized Mo Kα radiation. The structures were solved by direct methods using SHELXS [22]. Subsequent Fourier-difference map analyses yielded the positions of the non-hydrogen atoms. Refinements were carried out with the SHELXL package [22]. All refinements were made by full-matrix least-squares on F^2 with anisotropic displacement parameters for all non-hydrogen atoms. Hydrogen atoms were included in the refinement in calculated positions. Crystal data and more details of the data collections and refinements are contained in Table 1.

Acknowledgment

This work was supported with funds from PRONEX-CNPq/FAPERGS (Brazil).

Appendix A. Supplementary data

CCDC 698816, 698817 and 698818 contain the supplementary crystallographic data for 1, 2 and 4. These data can be obtained free of charge via http://www.ccdc.cam.ac.uk/conts/retrieving.html, or from the Cambridge Crystallographic Data Centre, 12 Union Road, Cambridge CB2 1EZ, UK; fax: (+44) 1223-336-033; or e-mail: deposit@ccdc.cam.ac.uk.

The supplementary crystallographic data for 3 were deposited with FIZ Karlsruhe receiving the number CSD 419781. The data can be obtained free of charge via http://www.fiz-karlsruhe.de/obtaining_crystal_structure_data.html.

References

[1] N.W. Alcock, Adv. Inorg. Chem. Radiochem. 15 (1972) 1.
[2] B. Krebs, F.-P. Ahlers, Adv. Inorg. Chem. 35 (1990) 235.
[3] W.-W. Du Mont, J. Jeske, P.G. Jones, Phosphorous, Sulfphur Silicon 136–138 (1998) 305.
[4] M.C. Aragoni, M. Arca, A.J. Blake, F.A. Devillanova, W.W. du Mont, A. Garau, F. Isaia, V. Lippolis, G. Verani, C. Wilson, Angew. Chem., Int. Ed. 40 (2001) 4229.
[5] M.C. Aragoni, M. Arca, F. Demartin, F.A. Devillanova, A. Garau, P. Grimaldi, F. Isaia, F. Lelj, V. Vippolis, G. Verani, Eur. J. Inorg. Chem. (2004) 2363.
[6] P.D. Boyle, W.I. Cross, S.M. Godfrey, C.A. McAuliffe, R.G. Pritchard, S.J. Teat, J. Chem. Soc., Dalton Trans. (1999) 2845.
[7] E. Schulz Lang, R.M. Fernandes Jr., E.T. Silveira, U. Abram, E.M. Vázquez-López, Z. Anorg. Allg. Chem. 625 (1999) 1401.
[8] P.D. Boyle, W.I. Cross, S.M. Godfrey, C.A. McAuliffe, R.G. Pritchard, S. Sarwar, J.M. Sheffield, Angew. Chem. 112 (2000) 1866.
[9] P.D. Boyle, W.I. Cross, S.M. Godfrey, C.A. McAuliffe, R.G. Pritchard, S. Sarwar, J.M. Sheffield, Angew. Chem., Int. Ed. Engl. 39 (2000) 1796.
[10] G. Manzoni de Oliveira, E. Faoro, E. Schulz Lang, G.A. Casagrande, Z. Anorg. Allg. Chem. 632 (2006) 659.
[11] E. Schulz Lang, G. Manzoni de Oliveira, E.T. Silveira, R.A. Burrow, E.M. Vázquez-López, J. Organomet. Chem. 664 (2002) 306.
[12] E. Schulz Lang, G. Manzoni de Oliveira, G.A. Casagrande, J. Organomet. Chem. 691 (2006) 59.
[13] E. Faoro, G. Manzoni de Oliveira, E. Schulz Lang, Z. Anorg, Allg. Chem. 632 (2006) 2049.
[14] E. Faoro, G. Manzoni de Oliveira, E. Schulz Lang, J. Organomet. Chem. 691 (2006) 5867.
[15] J. Konu, T. Chivers, J. Chem. Soc., Dalton Trans. (2006) 3941.
[16] S.M. Godfrey, S.L. Jackson, C.A. McAuliffe, R.G. Pritchard, J. Chem. Soc., Dalton Trans. (1998) 4201.
[17] C.G. Hrib, F. Ruthe, E. Seppälä, M. Bätcher, C. Druckenbrodt, C. Wismach, P.G. Jones, W.-W. du Mont, V. Lippolis, F.A. Devillanova, M. Bühl, Eur. J. Inorg. Chem. (2006) 88.
[18] A.K.S. Chauhan, Anamika, A. Kumar, R.C. Srivastava, R.J. Butcher, J. Beckmann, A. Duthie, J. Organomet. Chem. 690 (2005) 1350.
[19] L. Copolovici, C. Silvestru, V. Lippolis, R.A. Varga, Acta Crystallogr. C63 (2007) o528.
[20] J.M. Ryan, Z. Xu, Inorg. Chem. 43 (2004) 4106.
[21] J. Beckmann, S. Heitz, M. Hesse, Inorg. Chem. 46 (2007) 3275.
[22] G.M. Sheldrick, Acta Crystallogr. A64 (2008) 112.

Polyhedron 28 (2009) 69–76

Contents lists available at ScienceDirect

Polyhedron

journal homepage: www.elsevier.com/locate/poly

A novel dinuclear double-stranded helical complexes of bis(terdentate) N_4O_2 donor ligand with silver(I) and zinc(II) d^{10} metal ions

Abdurrahman Şengül [a,*], Wen-Jwu Wang [b,*], Simon J Coles [c]

[a] Department of Chemistry, Faculty of Arts and Sciences, Zonguldak Karaelmas University, Zonguldak, TR-67100, Turkey
[b] Department of Chemistry, Tamkang University, 25137 Taipei, Taiwan
[c] School of Chemistry, University of Southampton, Southampton, SO17 1BJ, UK

ARTICLE INFO

Article history:
Received 18 September 2008
Accepted 3 October 2008
Available online 17 November 2008

Keywords:
Self-assembly
Supramolecular chemistry
Helical structures
Silver
Zinc
N,O-ligands

ABSTRACT

Reaction of the hexadentate N_4O_2-donor ligand 6,6′-bis(3-hydrazonobutan-2-one)-2,2′-bipyridine (**L**) with $Ag^{(I)}$ and $Zn^{(II)}$ affords a dinuclear double stranded helicate species $[Ag_2\mathbf{L}_2]^{2+}$ (**1a**) and $[Zn_2\mathbf{L}_2]^{2+}$ (**1b**), in which partitioning of the ligand into two bis-tridentate pyridyl-ketoimine chelating units allow each ligand to bridge both metal centres. X-ray crystallography, ESI-MS and UV–Vis spectrophotometric titration experiments reveal that the complex (**1a**) retains its solid-state structure in solution. The crystal structure of (**1a**) provides the first example of dinuclear silver(I) complex in which both of the metal centres can be approximated as a seven coordinate distorted mono-capped trigonal prism in which the Ag···Ag close contact of 3.034(4) Å is taken into account and forms the cap. The counter-ions do not interact with metal centres but hydrogen bond to N–H protons of the hydrazonic arms from the separate strands. The adjacent helical units are cross-linked together via NH···O_{keto} hydrogen bonding to maintain the supramolecular structure.

© 2008 Elsevier Ltd. All rights reserved.

1. Introduction

Helical metal complexes [1–8] occupy a privileged position in metallosupramolecular chemistry. The basic principles of the formation of polynuclear helicates with a wide variety of metals and ligands have been well established. The development of new polydentate ligands which give optimized supermolecules upon complexation to two or more metal ions is thus a theme of considerable interest in supramolecular chemistry [9,10]. Particular interest has been shown in double-helical structures which may be generated by complexation of two ligands twisted around metal ions lying on the helical axis [11–14].

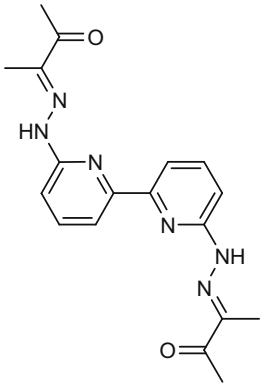
Oligo-bipyridine ligands containing 6,6′-disubstituted-bipyridyl (bpy) units, bridged by suitable spacers, and coordinated to a metal ion show a preference for tetrahedral geometry (such as Cu(I) or Ag(I)) to form double-stranded helicates [4–6,15–18]. However, in self-assembled polymeric Ag(I) complexes, the full diversity in coordination geometries exhibited by silver(I) is commonly observed. It has been shown that Ag(I) can adopt a range of coordination numbers between two and six, and exhibit coordination geometries from linear through trigonal to tetrahedral, square-planar, trigonal pyramidal and octahedral, and also very rarely in the case of coordination chemistry (there are numerous high coordination number Ag complexes known in cluster chemistry – some 150 in the Cambridge Crystallographic Database) seven- and eight-coordinate complexes [19–22]. On the other hand, a metal ion which has no fixed preference such as Zn(II) gives a triple helix at high ligand:metal ratios and a double helix at lower ratios [23]. There are some structurally characterised dizinc helical complexes described in the literature [24–31], but only two helicates (one triple and one double-stranded) contain Schiff bases. NMR spectroscopic studies have shown that Schiff bases with flexible spacers (e.g., 2,9-bis[(6-methyl-2,2′-bipyridin-6′-yl)methyleneoxymethylen-yl]-1,10-phenanthroline) can generate double-stranded zinc(II) helicates [8].

A considerable body of research now exists and has been reviewed in detail by Piguet et al. [4] and others [2,3]. Many such systems were reported by Lehn and his collaborators [32,33], who synthesized a series of oligo-bipyridyl ligands which form double-helicates containing as many as five Cu(I) ions, and by Dietrich-Bucheker and Sauvage [34,35] who used the double-helical complexes formed by Cu(I) with two oligo-phenanthroline ligands as precursor for the synthesis of the first molecular knot. In these systems, the coordinating possibilities of the ligand should match the stereochemical preferences of the metal ion. Thus, the reaction of the two binucleating ligands with cations favouring tetrahedral coordination can lead to a double-helical structure [10,23].

* Corresponding authors. Tel.: +90 372 2574010; fax: +90 372 2574181 (A. Şengül), tel.: +886 226224096; fax: +886 226224096 (W.-J. Wang).
E-mail addresses: abdurrahmans2002@yahoo.co.uk (A. Şengül), wjw@mail.tku.edu.tw (W.-J. Wang).

0277-5387/$ - see front matter © 2008 Elsevier Ltd. All rights reserved.
doi:10.1016/j.poly.2008.10.011

For oligobipyridine ligands, several spacers have been used to connect 2,2′-bipyridine or 1,10-phenanthroline units [1,4,6,36]. The binding of the linker is crucial in determining the nature of the resulting coordination. The linker must be short enough so that tetrahedral binding does not occur with one bpy unit of the same strand, yet sufficiently flexible that inter-strand coordination can occur without undue strain [6]. The formation of helicates is not only controlled by the coordination geometry of the metal ions and the flexibility of the spacer groups, but also by the linkage mode of the spacer units [37]. Following these criteria, a novel dinucleating ligand, 6,6′-bis(3-hydrazonobutan-2-one)-2,2′-bipyridine (**L**) presenting two N_2O-donor sites was designed and synthesized (*vide infra*).



The well-established coordination ability of the bpy ligand [38–40] suggests that the bulky substituents at the 6,6′-positions repel each other and prevent the ligand adopting a planar conformation to facilitate the self-assembly of mono-, double-, or triple-stranded helicates containing one or more transition metal cations with a variety of coordination geometries [5]. In such systems the metal centres will be organized in a well-defined array.

Early interest in the coordination chemistry of acylhydrazones led to the synthesis and structural characterization of a number of metal complexes of 2,6-diacetylpyridine aroylhydrazones (aroyl = benzoyl, picolinoyl, salicyloyl and thenoyl) [41–48]. These ligands were shown to be able to assume different conformations due to flexibility, and form mono-and bi-nuclear metal complexes.

A point of significant interest relating to the self-assembly of polynuclear complexes is to ascertain whether the double-helical structure found in the solid state is maintained in solution [3,5,7,49–51]. Thus, by means of classical spectrophotometric titrations and electrospray mass spectrometric (ESI-MS) measurements, we have investigated the nature of the species that **L** forms with $Ag^{(I)}$ and $Zn^{(II)}$. From these measurements stability constants and absorption spectra were used to gain insight into the distribution of the different species at a given [*M*]/[*L*] ratio and into the physicochemical features of their self-assembly process. A similar behaviour has been observed for both metal ions. Solution studies and X-ray analysis proved that the present ligand is a good helicant for Ag(I) and Zn(II) ions. Since, the keto oxygen atoms seem weakly interact with the metal centres, the double-helical structures may conveniently be transformed into molecular knots by condensation with simple diamine ligands. This will be addressed as an extension of the present study in future work. The zinc complex did not provide a suitable crystal for diffraction studies, but solution studies by ESI-MS and UV–Vis spectroscopy data show $[Zn_2\mathbf{L}_2]^{2+}$ that the idealized dinuclear double-stranded helical structure is maintained in solution.

2. Results and discussion

2.1. Synthesis of the ligand (*L*)

The bis(3-hydrazonobutan-2-one)-2,2′-bipyridine ligand was synthesized in high yield by condensation of 6,6′-dihydrazine-2,2′-bipyridine [52,53] with excess of butandione in dry thf in the presence of catalytic amount of glacial acetic acid under dry nitrogen atmosphere over molecular sieves. It is quite soluble in common organic solvents and acidic aqueous solutions. The ESI-MS of the free ligand in acetonitrile displays the expected singly charged species $[\mathbf{L}+H]^+$ and $[2L + CH_3CN + H_2O]^+$ adducts at *m*/*z* 353.4 and 763.3, respectively, (Fig. S1). The ^1H NMR spectrum measured in DMSO-d_6 confirmed the chemical structure as having C_2-symmetry (Fig. S2). In the aromatic region of the spectrum the NH proton appears as a singlet at 11.6 ppm, and the three distinguished bipyridinyl protons in the expected range (8.23–7.52 ppm), and two singlets in the aliphatic region at 2.5 and 2.3 ppm attributed to the methyl protons having different chemical environments due to having different electronegative atoms (N and O), adjacent to them.

2.2. Syntheses of the metal complexes

The metal complexes were prepared in similar manner with high yield: to a solution of **L** in dichloromethane was added equimolar AgOTf or $Zn(OTf)_2$ in MeCN at 40 °C with vigorous stirring under inert atmosphere for 12 h over molecular sieves (0.4 nm). The solutions were concentrated under vacuum and filtered from *Celite* into the test tubes and allowed to stand for crystallisation at r.t. The single crystals of **1a** were obtained by slow ether diffusion into the concentrated MeCN–CH_2Cl_2 solution in a well-isolated system at room temperature. These cationic d^{10} metal complexes are stable in the solid state and in solution, and are soluble in polar organic solvents such as DMF, DMSO, MeCN and MeOH. The physicochemical characterization proved that the hydrazonic ligand forms dinuclear complexes with AgOTf and $Zn(OTf)_2$, which well agrees with the general formulae $[M_2\mathbf{L}_2]^{2+}$.

2.3. Qualitative ESI-MS and spectrophotometric titration studies

The ESI-MS spectrum of the crystals of $[Ag_2\mathbf{L}_2][OTf]_2$ (**1a**) dissolved in MeCN revealed a peak at *m*/*z* 1068 which corresponds to the cationic fragment $[Ag_2\mathbf{L}_2(OTf)]^+$. The simulated isotopic pattern is in good agreement with the measured spectrum (Fig. S3). The isotopic pattern was also used for the characterization of the self-assembled dinuclear double-helical complexes in MeCN which represent typical cases for supramolecular complexes where the monomer $[M\mathbf{L}]^+$ and the dimer $[M_2\mathbf{L}_2]^{2+}$ display the same *m*/*z* ratio [54]. So, the elegant choice of alternative is to use of the isotopic pattern obtained by increasing resolution. The observation of singly charged peaks at *m*/*z* = 460 and 813 may be attributed to $[Ag\mathbf{L}]^+$ and $[Ag\mathbf{L}_2]^+$ species in solution. However, the formation of $[Ag_2\mathbf{L}_2]^{2+}$ can also not be excluded, since the resolution of the mass spectra is not good enough to discriminate between these two species with our experimental setup.

It is worthnoting that $[Ag_2\mathbf{L}_2]^{2+}$ displays a helical double-stranded structure in solution similar to that found for its Zn(II) analogue (*vide infra*). Such process was studied by UV–Vis spectrophotometric titration of **L** with AgOTf in MeCN (Fig. S4). Analysis of the titration data, using the SPECFIT/32 Global Analysis System [55–58] which performs a nonlinear best fit of the spectrophotometric data should provide the thermodynamic parameters for double-helicate formation. This programme calculates the binding constants β_{ml} for each M_mL_l species of a proposed chemical model by iterative comparison of calculated with experimental

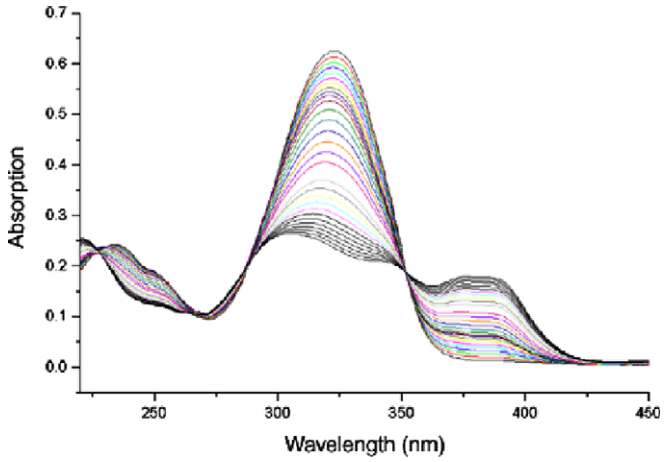


Fig. 1. Variation of the absorption spectra observed during the spectrophotometric titration of **L** with varying concentration of $Zn(OTf)_2$ in MeCN.

absorbance values, searching for the global minimum of the error function. The spectroscopic data can be satisfactorily fitted with the following equilibria (1)–(3), described by three stability constants β_{ml}.

$$Ag^+ + \mathbf{L} \rightleftharpoons [AgL]^+ \quad \log\beta_{11} = 3.5(1) \tag{1}$$

$$Ag^+ + 2\mathbf{L} \rightleftharpoons [Ag\mathbf{L}_2]^+ \quad \log\beta_{12} = 15(3) \tag{2}$$

$$2Ag^+ + 2\mathbf{L} \rightleftharpoons [Ag_2\mathbf{L}_2]^{2+} \quad \log\beta_{22} = 21(3) \tag{3}$$

These data allow the computation of the distribution diagram for the M_mL_l species and provide the basis for investigating the process of the formation of the $[Ag_2\mathbf{L}_2]^{2+}$ helicate **1a** (Fig. S5). The overall stability constant, β_{ml} values, towards silver(I) for the helicate compares quite well with the similar processes available in the literature [32]. The present equilibrium intermediates compare well to those observed in the ESI-MS spectrum. The helicate is also the stable form in the solid, as confirmed by X-ray analysis.

The ESI-MS spectrum of the zinc(II) complex (**1b**) measured in MeCN-CH_2Cl_2 solution (Fig. S6), shows peaks at $m/z = 208.2$, 415.2, 564.9 and 1283.5, which may be attributed to species $[Zn\mathbf{L}]^{2+}$, $[Zn\mathbf{L}_2]^{2+}$ adducts of MeCN and H_2O, singly charged $[Zn\mathbf{L}(OTf)]^+$ or doubly charged $[Zn_2\mathbf{L}_2(OTf)_2]^{2+}$, and finally the singly charged dimer $[Zn_2\mathbf{L}_2(OTf)_3]^+$. However, the peaks at 415.2 and 1146.7 demonstrate the additional coordination of keto oxygen atoms to form a pseudo-octahedral geometry at the $Zn^{(II)}$ centres, where the ligands are coordinated in the monoanionic form to reduce the overall positive charge on the complex ions. This occurs due to deprotonation after enolization as usually observed for similar kind of ligands possessing N_3O_2 [13] and N_2O or N_4O coordination modes [59–62]. It has been suggested that the effect of charge on the cation is important in the hydrolysis process of carbonyl ligands coordinated to metal centres, where the electron withdrawing effect of the metal ion will increase the polarisation of the carbonyl bond upon coordination [63,64]. Thus, the $Zn^{(II)}$ cations have an octahedral N_4O_2 coordination sphere assembled by using the two N_2O-donor set of **L** in the monoanionic form.

The formation of **1b** was followed by the spectrophotometric titration of **L** with $Zn(OTf)_2$ (Fig. 1). The data which allow the computation of the distribution diagram (Fig. 2) for the M_mL_l species indicate that upon increasing the metal ion concentration the dinuclear species becomes the major product in the final solution, as revealed by the qualitative ESI-MS studies. The calculated binding constants for the M_mL_l species can be satisfactorily fitted with the following equilibria (4)–(6):

$$Zn^{2+} + \mathbf{L} \rightleftharpoons [Zn\mathbf{L}]^{2+} \quad \log\beta_{11} = 1.6(1) \tag{4}$$

$$Zn^{2+} + 2\mathbf{L} \rightleftharpoons [Zn\mathbf{L}_2]^{2+} \quad log\beta_{12} = 13.9(1) \tag{5}$$

$$2Zn^{2+} + 2\mathbf{L} \rightleftharpoons [Zn_2\mathbf{L}_2]^{2+} \quad \log\beta_{22} = 19.5(2) \tag{6}$$

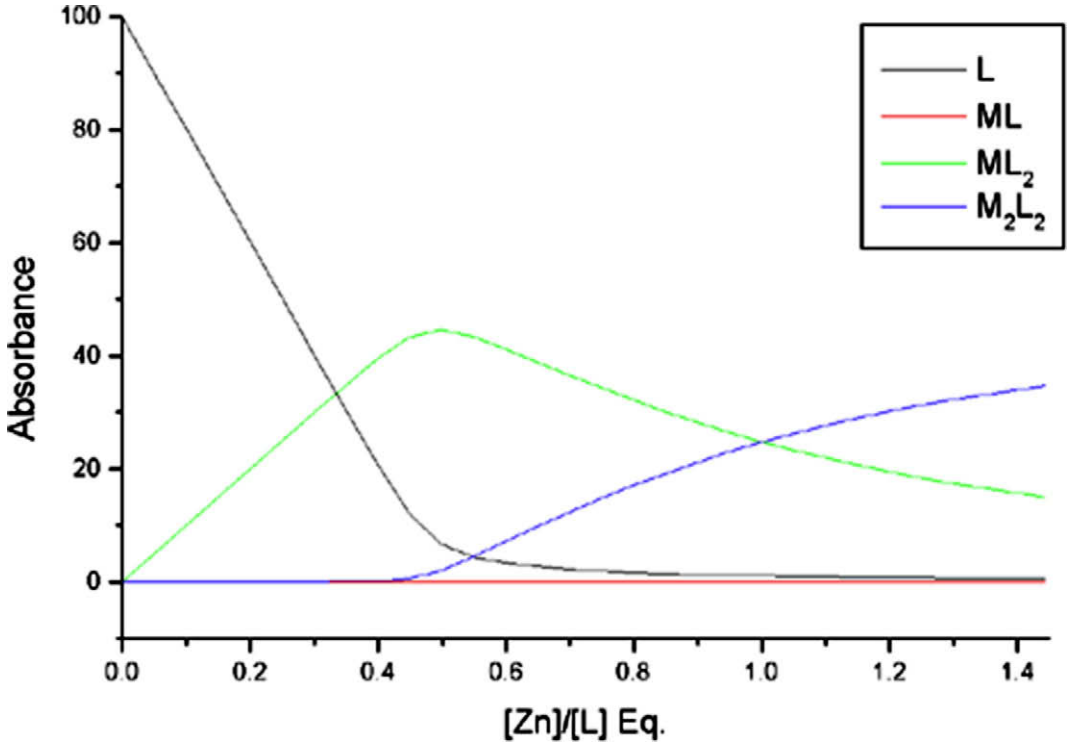


Fig. 2. Distribution curves predicted for the complexation of Zn(II) by **L**.

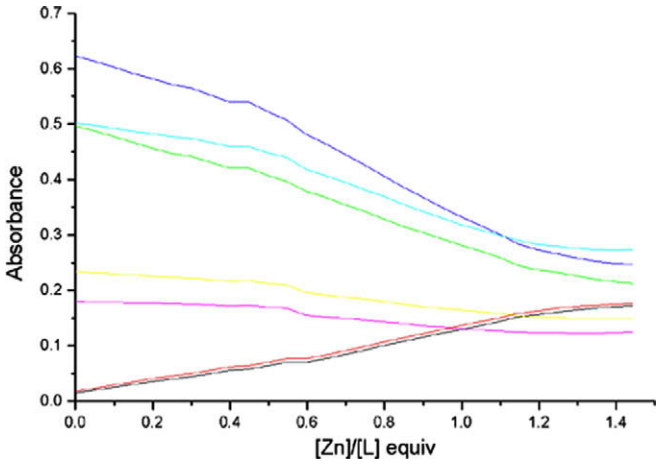


Fig. 3. EA plot, variation of observed absorbance during spectrophotometric titration of **L** with $Zn(OTf)_2$ in MeCN.

These data allow the computation of the distribution diagram for the M_mL_l species and provide the basis for investigating the process of the formation of the $[Zn_2\mathbf{L}_2]^{2+}$ helicate **1b**. The present equilibrium intermediates parallel to those observed in the ESI-MS spectrum. Furthermore, the excess absorbance diagrams (EA) [32] for several wavelengths shown in Fig. 3 confirms the existence of only two absorbing species, the ratio between which is less than 1.2. These features indicate the generation of the double-helical structure of **1b** [5].

2.4. X-ray crystal structure of *1a*

The double-helical structure of **1a** is depicted in Fig. 4. The crystal structure of **1a** shows the double helical cation $[Ag_2\mathbf{L}_2]^{2+}$, and two uncoordinated triflate anions (Fig. S7). Both these anions exhibit disorder; in one there is an overlay of a second fractionally occupied molecule over the original such that CF_3 moiety nearly overlaps with a SO_3 group; in the second there is a rotation about a 2-fold axis which generates two orientations where the C–S bonds cross each other with an angle of about 15°, which results in two O atoms in the SO_3 group overlapping directly with a symmetry generated pair and in the third case with a F atom, whilst the remaining F atoms in the CF_3 group nearly overlap with their symmetry related counterparts. As a result the triflate atoms exhibit high atomic displacement parameters and have been constrained to an idealised geometry.

In the dinuclear cation $[Ag_2\mathbf{L}_2]^{2+}$, the ligands act as neutral bis(terdentate) units bound to the silver atoms and wrap around a helical axis. This leads to a double-helical structure with a pseudo-C_2 axis defined by the Ag(I) atoms which are separated by 3.034(4) Å. It is noteworthy that this Ag···Ag separation is significantly shorter than the sum of the van der Waals radii of two silver atoms (3.44 Å) [65,66], indicating the presence of ligand supported Ag···Ag interactions which are often observed in $Ag^{(I)}$ complexes

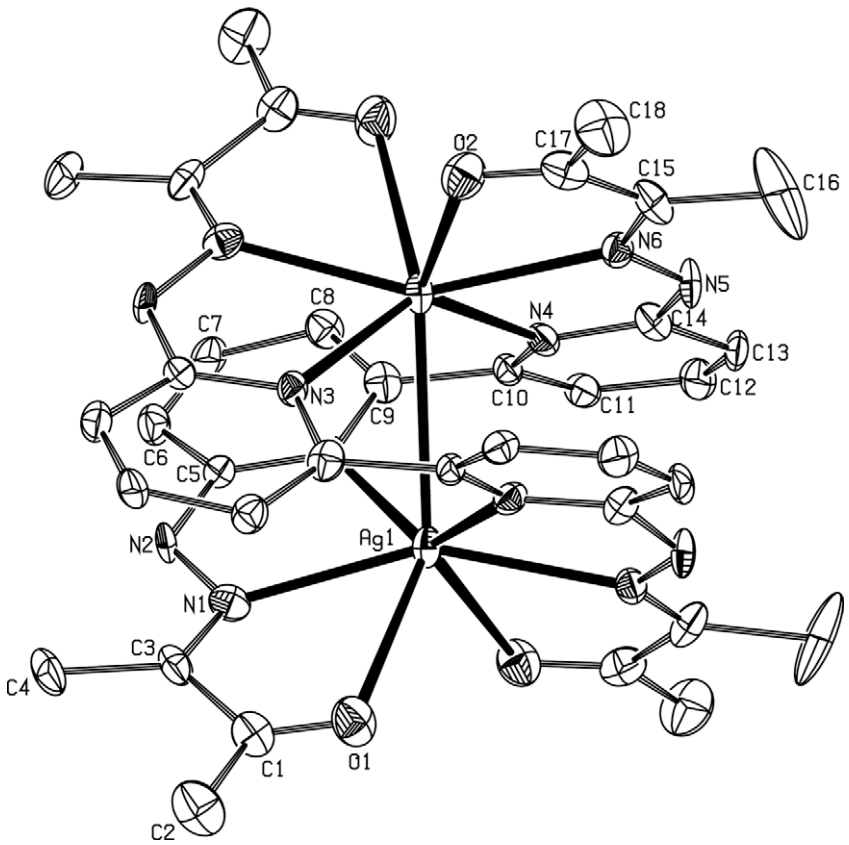


Fig. 4. ORTEP view of $[Ag_2L_2][OTf]_2$ (**1a**). Triflate ions and hydrogens have been omitted for clarity. Selected bond lengths (Å) and angles (°): Ag1–N3 2.389(1); Ag1–$N4^i$ 2.389(2); Ag1–N1 2.428(2); Ag1–N6 2.437(2); Ag1–O1 2.720(2); Ag1–O 2 2.722(2); Ag1–$Ag1^i$ 3.034(4); N3–Ag1–$N4^i$ 138.26(7); N3–Ag1–N1 67.88(5); $N4^i$–Ag1–N1 120.80(5); N3–Ag1–N6 124.43(5); $N4^i$–Ag1–N6 68.319(6); N1–Ag1–N6 153.14(7); $N4^i$–Ag1–O1 79.01(7); N3–Ag1–O1 129.01(7); N1–Ag1–O1 61.52(7); N6–Ag1–O1 98.99(7); N1–Ag1–O2 101.27(7); N3–Ag1–O2 80.31(7); N6–Ag1–O2 62.20(7); O1–Ag1–O2 100.94(7); N3–Ag1–$Ag1^i$ 70.48(5); $N4^i$–Ag1–$Ag1^i$ 67.84(5); N1–Ag1–$Ag1^i$ 104.29(5); N6–Ag1–$Ag1^i$ 102.47(5); O1–Ag1–$Ag1^i$ 129.59(5). Symmetry code for generated atoms with label = $-x+1, y, -z+1/2$.

[67–72]. The double helix nature of the complex gives rise to two ligands binding in an antiparallel fashion, with the angle between the mean planes of the two ligand strands (i.e., between the two moieties coordinated through N4, N6, O2 and the other two moieties coordinated through N1, N3, O1) averaging to approximately 13.3(2)° and separated by 3.55(3) Å. This suggests a significant π–π stacking interaction between the py ring from one ligand and the hydrazonic unit from the other (Fig. 5a). This is typical of π–π stacking interactions which along with hydrogen bonding and argentophilic interactions control the formation of the secondary double strand structure [73]. Despite OTf^- disorder in the lattice, the crystal structure provides no evidence of interaction between the $Ag^{(I)}$ centre and the remote OTf^- counter-ion. However, the triflate ions hold two strands in close proximity by intermolecular N–H···O, C–H···O and C–H···F weak interactions (Fig. S8). Further, the two hydrazonic NH groups of each strand also interact with the keto oxygen atoms of the adjacent helical cations to give rise to its supramolecular structure.

The ligand is a symmetrically substituted bpy incorporating two ketoiminohydrazone units at 6,6′-positions. These arms contain two donor atoms: one imine *N* atom and one keto oxygen atom. Although, Datta and his co-authors [74,75] have speculated that 'the keto oxygen atoms do not bind $Ag^{(I)}$ even in the solid' and the Cambridge Structural Database (January 2008)[1] contains no structures based on the AgN_4O_2 chromophore with an $Ag^{(I)}$–keto oxygen bond. There are also a very limited number of examples of structurally characterized $Ag^{(I)}$ complexes with aliphatic and aromatic ketones [64,76,77], di-2-pyridyl ketone [63] or 4-acyl-5-pyrazolone [78]. The carbonyl form is favoured in the $Ag^{(I)}$ complexes whereas in the $Zn^{(II)}$ complexes polarization of carbonyl bond is affected by the electron-withdrawing nature of the doubly charged ion [63].

It is clear from the X-ray structural analysis that the two ligand strands adopt a head-to-tail configuration. The twisting of the ligand strand (essential for helicate formation) takes place primarily about the central bond between the pyridine rings (dihedral angle = 52.5(2)°), and the planarity of the hydrazonic arms is significantly constrained by the Ag–O1 and the Ag–O2 interactions. The maximum deviation from the mean plane O1–C1–C3–N1–N2–C5 is 0.027 Å (for atom N2), and O2–C15–N6–N5–C14 is 0.062 Å (for atom C16). The former plane makes an angle of 9.81(9)° with the py ring C5–C9–N3, and the latter one an angle of 9.54(9)° with C10–C14–N4 py ring. The structure shows that the assembly of the helicate adopts an arrangement in which the steric hindrance is minimised. In this structure the bonds to the imino nitrogens (2.428(2), 2.437(2) Å) are significantly longer than those to the pyridyl nitrogens (2.392(2), 2.389(2) Å). The $Ag^{(I)}$–O_{keto} distances 2.720(2) and 2.722(2) Å are significantly greater than the sum of ionic radii (2.66 Å) [64] suggesting a weak bonding interactions between the $Ag^{(I)}$ and keto oxygen atoms O(1) and O(2). If these bonds are included [20–22], the $Ag^{(I)}$ centres could be considered to have a distorted mono-capped trigonal prismatic geometry as shown in Fig. 5b. Thus, the ligands which form four five-membered chelate rings around each metal atom resemble the complexes of bis[6,6′-(*N*-2″-pyridylmethylidenehydrazino)][2,2′-bipyridine] N_6-donor ligand [79,80] with a range of transition metal cations. A similarity may also be drawn with a polymeric silver(I) complex [81] in which one $Ag^{(I)}$ centre is in a distorted octahedral geometry coordinating to one thio-ether sulphur atom and one quinoline nitrogen atom of the ligand, and four oxygen atoms of three nitrate groups with two in monodentate and one in a bidentate coordination forms. However, the presence of a ligand supported argentophilic interaction in **1a** implies a weak binding and leads to the coordination geometry around Ag(I) best being described as a distorted mono-capped trigonal prism. As shown in Fig. 5b, the cap is formed through coordination to another silver centre (angles to N3, N4 and N6 = 70.48(5)°, 67.84(5)° and 102.47(5)°, respectively) and the prism is composed of the pyramidal coordination of N1, N3, O2 (angles about Ag of 67.88(5)°, 101.27(7)° and 80.31(7)°) and N4, N6, O1 (angles about Ag of 68.32(6)°, 98.99(7)° and 79.01(7)°, respectively).

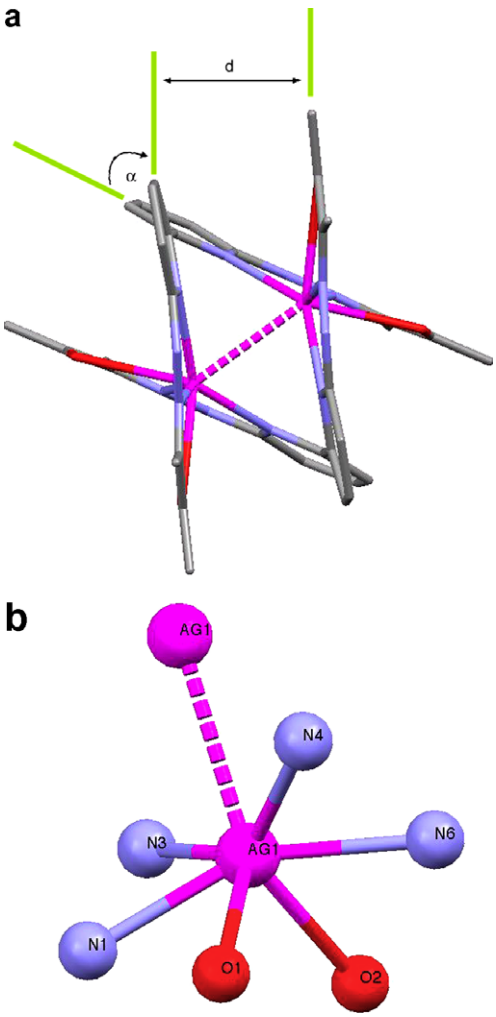


Fig. 5. (a) The Ag···Ag separation of 3.034(4) Å, the dihedral angles [α = 52.5(2)°] between the py rings and the aromatic π–π stacking interactions between the py rings [*d* = 3.5(3) Å]. (b) Depicting the spatial arrangements of the octahedral environment around the each silver(I) centre.

As the compound crystallises in a centrosymmetric space group, the crystal contains both left and right-handed helical cations. The helical structure is reminiscent of those reported by Schröder [79,80] and Wang [67,68]. A recent survey by Ziessel [5] proposed that the presence of two additional donor atoms in the vicinity of the central bipyridine frame will cause the conventional chelating coordination mode of the bipyridine to be that of a non-conventional character, where the ligand bridges two metal centres. The crystallographic structures of the helicates of imino-bipyridine ligands with Cu(I) cation clearly indicate that incorporation of imine groups at the α,α′-positions of a bpy causes the central unit to become non-chelating and, to adopt a bridging role. In those reported complexes, the bpy units was found to be twisted by 33° about the exocyclic central C–C bond, and in contradiction to the

[1] CSD version 5.29 (November 2007) has no hits for N_4O_2Ag–AgN_4O_2 motif with Ag–O_{keto} bond, but contains 18 hits for N_2O_2Ag–AgN_2O_2 motif (only two cases contain Ag–O_{keto} bonds derived from hexafluoropentane-2,4-dione and 2-pyridyl-3-methyl-4-trifluoroacetylpyrazol-5-one), and also shows 16 hits for the N_4Ag–AgN_4 query.

case presented here, the copper(I) centre was shown to be significantly closer to the imino *N* atom than to the adjacent pyridine unit. The unprecedented helicate **1a** is the first example to reveal the ability of the hexadentate ligand presenting two N_2O coordination sites to act selectively as a bridging ligand with d^{10} metal ions such as Ag(I) and Zn(II) ions.

3. Experimental

3.1. General

All commercially available chemicals were of reagent grade and used without further purification, unless otherwise stated. Tetrahydrofuran and diethyl ether were distilled from sodium benzophenone ketyl immediately prior to use. Dichloromethane was distilled over calcium hydride. Methanol and ethanol were of HPLC grade. Melting points were recorded on a Bushi Melting Points B-540 apparatus. The CHN microanalyses were performed with a Heraeus Rapid CHNO elemental analyzer. The electrospray ionisation mass spectral (ESI-MS) measurements were carried out on a LCQ (Finnegan MAT, USA) using MeCN as the mobile phase. The samples for ESI-MS measurements were prepared by redissolving the final isolated compounds in MeCN or methanol. Solutions containing **1a** and **1b** in MeCN (1.2×10^{-4} M) were injected into the mass spectrometer source with a syringe pump at a flow rate of 10 μL/min. ^{1}H NMR spectra were measured in DMSO-d_6 with a Bruker AC300 300 MHz spectrometer at room temperature. Chemical shifts are given in parts per million with reference to TMS. Abbreviations are as follows: s, singlet; d, doublet; dd, doublet of doublets; t, triplet; and m, multiplet. Spectrophotometric titrations were performed with a Shimadzu UV-1601 UV–Visible spectrophotometer connected to an external computer. In a typical experiment, 50 mL of ligand **L** in acetonitrile (1.05×10^{-5} M) was titrated with a 2.6×10^{-3} M solution of the trifluoromethanesulfonate salt of the appropriate metal ion [silver(I) and zinc(II)] in MeCN. Each addition (0.01 mL increments of the salt solution at 5 min. intervals) was carried out by using a precision micropipette at 25 °C. The absorbances at ten different wavelengths were recorded using a 1 cm quartz cell and transferred to the computer. The spectrophotometric data were analysed with SPECFIT programme [54], by which the absorptivities and the stability constants of the species formed at equilibrium were adjusted. The SPECFIT programme uses factor analysis (which confirms the number of different absorbing species) to reduce the absorbance matrix and to extract the eigenvalue prior to the multiwavelength fit of the reduced data set according to the MARQUARD algorithm [57,58]. The synthesis of the silver(I) complex was carried out in the dark.

3.2. Synthesis of bis(3-hydrazonobutan-2-one)-2,2′-bipyridine **L**

6,6′-Dihydrazine-2,2′-bipyridine (0.43 g, 2 mmol) was dissolved in dry thf (5 mL) containing molecular sieves (4 Å), and followed by addition of glacial acetic acid (5 mL). After dropwise addition of 2,3-butandione (0.173 g, 20 mmol, in excess) under nitrogen, the solution was set to reflux at 60 °C with vigorous stirring for 12 h. The off white precipitate was collected by filtration and washed with methanol and ether, and air-dried to give **L** (0.52 g, 74%), mp 286–288 °C (decomp.). ESI-MS: 353.3 $[\mathbf{L}+H]^+$ $C_{18}H_{20}N_6O_2$ requires 352.2; 763.3 $[2\mathbf{L}+CH_3CN+H_2O]^+$ $C_{38}H_{45}N_{13}O_5$ requires 763.4; 778.9 $[2\mathbf{L}+CH_3CN+2H_2O]^+$ $C_{38}H_{47}N_{13}O_6$ requires 781.4; δ_H (300 MHz; DMSO-d_6; Me_4Si): 2.03 (3H, s, CH_3), 2.41 (3H, s, CH_3), 7.40 (2H, d, H5,5′), 7.90 (4H, m, H3,3′ and H4,4′), 10.38 (2H, s, NH); *Anal.* Calc. for $C_{18}H_{22}N_6O_3$ ($\mathbf{L}+H_2O$) (370.41): C, 58.37; H, 5.99; N, 22.69. Found: C, 58.54; H, 5.76; N, 22.70%.

3.3. Synthesis of $[Ag_2L_2][OTf]_2$ **1a**

All procedures for synthesis and recrystallization were carried out in the dark. A degassed solution (10 mL) of CF_3SO_3Ag (72.9 mg, 0.28 mmol) in MeCN was added dropwise to a stirred solution of **L** (100 mg, 0.28 mmol) in dichloromethane (25 mL) at room temperature under N_2 atmosphere and stirred for over night at 40 °C. The solution was cooled to room temperature and filtered. Ether vapour diffusion into this solution gave yellow-orange crystals of **1a**. The synthesis of **1a** was repeated three times and recrystallisation by ether diffusion or slow evaporation of the solution for each time yielded the same type of crystals with identical diffraction data **1a** (0.128 mg, 75%). ESI-MS: 459.1 $[Ag\mathbf{L}]^+$ $C_{18}H_{20}N_6O_2Ag$ requires 459.1; 461.1 $[Ag_2\mathbf{L}_2]^{2+}$ $C_{36}H_{40}N_{12}O_4Ag_2$ requires 460.6; 812.7 $[Ag\mathbf{L}_2]^+$ $C_{36}H_{40}N_{12}O_4Ag$ requires 813.2; 1068.6 $[Ag_2\mathbf{L}_2(OTf)]^+$ $C_{37}H_{40}N_{12}SO_7F_3Ag_2$ requires 1069.1. *Anal.* Calc. for $Ag_2C_{41}H_{46}N_{14}O_{10}S_2F_6$: C, 38.21; H, 3.59; N, 15.21. Found: C, 38.02; H, 3.65; N, 15.10%.

3.4. Synthesis of $[Zn_2\mathbf{L}_2][OTf]_4$ **1b**

L (57 mg, 016 mmol) was dissolved in dichloromethane (10 mL) under inert atmosphere. A solution (25 mL) of $Zn(CF_3SO_3)_2$ (58 mg, 0.16 mmol) was added dropwise with continuous stirring. The colour was initially orange-red, and finally turned to yellow upon stirring. The filtered yellowish solution was bubbled wit N_2 for 10 min, and left for crystallization to afford **1b** (0.09 mg, 78%). ESI-MS: 208.2 $[Zn\mathbf{L}]^{2+}$ $C_{18}H_{20}N_6O_2Zn$ requires 208.1; 415.2 $[Zn\mathbf{L}]^+$ $C_{18}H_{20}N_6O_2Zn$ requires 416.1; 565.0 $[Zn\mathbf{L}(OTf)]^+$ $C_{19}H_{20}N_6SO_5F_3Zn$ requires 565.0; 566.9 $[Zn_2\mathbf{L}_2(OTf)_2]^{2+}$ $C_{38}H_{40}N_{12}S2O_8F_6Zn_2$ requires 567.6; 1146.7 $[Zn_2\mathbf{L}_2(OTf)_2]^+$ $C_{39}H_{40}N_{12}S_2O_{10}F_6Zn_2$ requires 1146.1; 1282.4 $[Zn_2\mathbf{L}_2(OTf)_3]^+$ $C_{39}H_{40}N_{12}S_3O_{13}F_9Zn_2$ requires 1283.0. *Anal.* Calc. for $Zn_2C_{40}H_{42}N_{12}O_{18}S_4F_{12}$: C, 32.77; H, 2.89; N, 11.47. Found: C, 32.7; H, 3.3; N, 11.3%.

Table 1
Crystallographic data for **1a**.

Complex	**1a**
Formula	$C_{38}H_{40}Ag_2F_6N_{12}O_{10}S_2$
M_r	1218.68
T (K)	120(2)
λ (Å)	0.71073
Crystal system	monoclinic
Space group	*C*2/*c*
a (Å)	19.8367(5)
b (Å)	19.9704(5)
c (Å)	13.6569(3)
α (°)	90.00(2)
β (°)	125.30(2)
γ (°)	90.00(2)
V (Å^3)	4415.30(18)
Z	4
D_{calc} (g cm^{-3})	1.833
μ (mm^{-1})	1.079
F(000)	2448
Crystal size (mm^3)	0.06 × 0.05 × 0.03
θ Range (°)	2.92–27.49
Index range (h, k, l)	$-25 \leqslant h \leqslant 23$, $-25 \leqslant k \leqslant 25$, $-17 \leqslant l \leqslant 17$
Independent reflections (R_{int})	5063 (0.0502)
Reflections collected	23982
Maximum and minimum transmission	0.9683 and 0.9381
Data/restraints/parameters	5063/57/383
Goodness-of-fit on F^2	1.218
Final R indices [$I > 2\sigma(I)$]	R_1 = 0.0973, wR_2 = 0.2089
R indices (all data)	R_1 = 0.1062, wR_2 = 0.2134
Largest difference in peak and hole (e Å^{-3})	3.452 and −3.361

Table 2
Hydrogen bond data (Å and °) for **1a**.

D–H···A	d(D–H)	d(H···A)	d(D···A)	∠(DHA)
N(2)–H(2)···O(2)#1	0.86	2.31	3.020(2)	140
N(5)–H(5)···O(6)#2	0.86	2.24	3.024(8)	154
C(2)–H(2C)···O(7)#3	0.98	2.58	3.058(7)	110
C(6)–H(6)···F(2)#1	0.95	2.50	3.287(4)	140
C(6)–H(6)···O(2)#1	0.95	2.59	3.325(4)	134
C(7)–H(7)···O(5)#1	0.95	2.41	3.104(9)	129
C(8)–H(8)···O(6)#1	0.95	2.57	3.427(8)	152
C(12)–H(12)···O(1)#4	0.95	2.49	3.213(8)	133
C(13)–H(13)···O(6)#2	0.95	2.50	3.264(4)	138
C(16)–H(16B)···O(7)#5	0.98	2.57	3.213(8)	123
C(18)–H(18A)···O(4)#6	0.98	2.48	3.248(5)	135

[a]Symmetry transformations used to generate equivalent atoms: #1: $x, -y, -1/2+z$, #2: $½-x, 1/2+y, 1/2-z$, #3: $1-x, -y, 1-z$, #4: $-1/2+x, 1/2-y, -1/2+z$, #5: $½+x, 1/2+y, z$, #6: $1-x, y, 3/2-z$.

3.5. Crystal structure determination of complex *1a*

Data were collected at 120K on a Nonius KappaCCD area detector situated at the window of a rotating anode (λ Mo kα = 0.71073 Å). The structure was solved by direct methods, SHELXS-97, and refined using SHELXL-97 [82]. Hydrogen atoms were included in the refinement, but thermal parameters and geometry were constrained to ride on the atom to which they are bonded. The data were corrected for absorption effects using SADABS [83]. The two trifluoromethanesulfonate anions exhibit positional disorder where two molecules occupy the same space in the crystal lattice (geometric constraints were applied for one case where a molecule inverted about the centre of the C–S bond lies almost on top of another and a second case where a two fold axis produces two partially overlapping orientations such that oxygen and fluorine atoms F(4) and O(7) nearly overlap). The crystallographic details of **1a** are summarised in Table 1. Selected bond lengths and angles are displayed in the caption of Fig. 4, and hydrogen bonds are displayed in Table 2.

4. Conclusions

This study shows that the reactions of a multidentate Schiff-based bipyridine ligand **L** with d^{10} metal ions such as $Ag^{(I)}$ and $Zn^{(II)}$ can afford dinuclear double-stranded helical complexes. These are characterized in solution by means of ESI-MS spectrometry and UV–Vis spectrophotometry. The spectrophotometric measurements allowed the calculation of binding constants for the complexes and indicate that the helicate formation process is through a $[M\mathbf{L}_2]^{2+}$ intermediate. Furthermore, the molecular structure of the $Ag^{(I)}$ complex **1a** was also investigated by X-ray crystallography, which confirmed that it indeed has a dimeric helical structure with a head-to-tail configuration where the silver(I) ion is coordinated to two pyridyl nitrogen atoms, two imino nitrogen atoms and weakly to two keto oxygen atoms from two ligands to afford a pseudo octahedral geometry about each $Ag^{(I)}$ centre which shares a short Ag···Ag contact to accomplish a seven coordinated mono-capped trigonal prismatic geometry. The triflate anions are not involved in coordination but form hydrogen bonds with the hydrazonic NH groups of the two ligands to stabilize the double stranded helical structure. The neighbouring units are cross-linked together by hydrogen bonding between the carbonyl groups and NH groups. The supramolecular structure is stabilised by N–H···O, C–H···O and C–H···F interactions (Table 1). In the solid state, the electrostatic forces, π–π stacking interactions and metal···metal contacts seem to control the secondary structure involving the double strand formation. On the other hand, the ESI-MS of the zinc(II) complex **1b** reveals that **L** is in the monoanionic form by deprotonation on coordination to $Zn^{(II)}$ to form a distorted octahedral geometry at each zinc centre. This is very much akin to those zinc(II) complexes with N_4O_2 donor ligands reported by McMorran [84] and with N_6-donor ligand by Schröder [79,80]. The importance of structural factors can be seen by comparing the formation constants for the helicate **1a** ($\log\beta_{22} = 21$) and **1b** ($\log\beta_{22} = 19.5$). Since two complexes are likely to contain comparable binding sites and be subject to similar electrostatic energies. The novel N_4O_2 coordination mode offers **L** as a building block for interesting frame works through self-assembly, and may find use in the design of molecular devices due to the stability in silver(I) and zinc(II) complexation.

Acknowledgments

The authors are grateful to the Turkish Scientific and Technical Research Council [TBAG-2450 (104T060)], the UK Engineering and Physical Sciences Research Council and also to the National Science Council of Taiwan [95-2113-M-032-007].

Appendix A. Supplementary data

CCDC 664817 contains the supplementary crystallographic data for **1a**. These data can be obtained free of charge via http://www.ccdc.cam.ac.uk/conts/retrieving.html, or from the Cambridge Crystallographic Data Centre, 12 Union Road, Cambridge CB2 1EZ, UK; fax: (+44) 1223-336-033; or e-mail: deposit@ccdc.cam.uk. Supplementary data associated with this article can be found, in the online version, at doi:10.1016/j.poly.2008.10.011.

References

[1] J.-M. Lehn, Supramolecular Chemistry, VCH, Weinheim, 1995 (Chapter 9).
[2] J.-M. Lehn, Angew. Chem., Int. Ed. Engl. 27 (1988) 89.
[3] J.S. Lindsey, New J. Chem. 15 (1991) 153.
[4] C. Piguet, G. Bernardinelli, G. Hopfgartner, Chem. Rev. 97 (1997) 2005.
[5] R. Ziessel, Coord. Chem. Rev. (2001) 216.
[6] R. Ziessel, Coord. Chem. Rev. (2001) 195.
[7] J.-M. Lehn, A. Rigault, J. Siegel, J. Harrowfield, B. Chevrier, D. Moras, Proc. Natl. Acad. Sci. USA 84 (1987) 2565.
[8] R.F. Carina, A.F. Williams, C. Piguet, Helv. Chim. Acta 81 (1998) 548.
[9] M. Greenwald, D. Wessely, I. Goldberg, Y. Cohen, New J. Chem. (1999) 337.
[10] E.C. Constable, Nature 346 (1990) 314.
[11] S. Ruttiman, C. Piguet, G. Bernardinelli, B. Bocquet, A.F. Williams, J. Am. Chem. Soc. 114 (1992) 4230.
[12] C. Piguet, G. Bernardinelli, A.F. Williams, Inorg. Chem. 28 (1989) 2920.
[13] C. Piguet, G. Bernardinelli, B. Bocquet, O. Schaad, A.F. Williams, Inorg. Chem. 33 (1994) 4112.
[14] A.F. Williams, Pure Appl. Chem. 68 (1996) 1285.
[15] G. Dong, H. Cheng, D. Chun-Ying, Q. Chun-Qi, M. Qing-Jin, New J. Chem. 26 (2002) 796.
[16] M.-H. Shu, W.-Y. Sun, C.-Y. Duan, W.-X. Tang, Transition Met. Chem. 24 (1999) 628.
[17] A. Pfeil, J.-M. Lehn, J. Chem. Soc., Chem. Commun. (1992) 838.
[18] C.R. Woods, M. Benaglia, F. Cozzi, J.S. Seigel, Angew. Chem., Int. Ed. 35 (1996) 1830.
[19] T.M. Garret, U. Koert, J.-M. Lehn, A. Rigault, D. Meyer, J. Fischer, J. Chem. Soc., Chem. Commun. (1990) 557.
[20] G.K. Patra, I. Goldberg, New J. Chem. 27 (2003) 1124.
[21] H. Oshio, T. Ito, Coord. Chem. Rev. 198 (2000) 329.
[22] A.N. Khlobystov, A.J. Blake, N.R. Champness, D.A. Lemenovskii, A.G. Majouga, N.V. Zyk, M. Schroder, Coord. Chem. Rev. 222 (2001) 155.
[23] A.G. Young, L.R. Hanton, Coord. Chem. Rev. 252 (2008) 1346.
[24] C. Piguet, G. Bernardinelli, B. Bocquet, A. Quattropani, A.F. Williams, J. Am. Chem. Soc. 114 (1992) 7440.
[25] Y. Yoshida, K. Ichikawa, Chem. Commun. (1997) 1091.
[26] N. Yoshida, K. Ichikawa, M. Shiro, J. Chem. Soc., Perkin Trans. 2 (2000) 17.
[27] G. Struckmeier, U. Thewalt, J.H. Furhop, J. Am. Chem. Soc. 98 (1976) 278.
[28] D. Wester, G.J. Palenik, Inorg. Chem. 15 (1976) 755.
[29] C. Lorenzini, C. Pelizzi, G. Predieri, J. Chem. Soc., Dalton Trans. (1983) 2155.
[30] R. Chotalia, E.C. Constable, M. Neuburger, D.R. Smith, M. Zehnder, J. Chem. Soc., Dalton Trans. (1996) 4207.
[31] Y. Zhang, A. Thompson, S.J. Rettig, D. Dolphin, J. Am. Chem. Soc. 120 (1998) 13537.
[32] M. Vazquez, M.R. Bermejo, M. Fondo, A. Garcia-Deibe, A.M. Gonzalez, R. Pedrido, Eur. J. Inorg. Chem. (2002) 465.
[33] A. Pfeil, J.-M. Lehn, J. Chem. Soc., Chem. Commun. (1992) 838.
[34] T.M. Garrett, U. Koert, J.-M. Lehn, J. Phys. Org. Chem. 5 (1992) 529.

[35] J.P. Sauvage, Acc. Chem. Res. 23 (1990) 319.
[36] C.O. Dietrich-Buchecker, J. Guilhem, C. Pascard, J.P. Sauvage, Angew. Chem., Int. Ed. Engl. 29 (1990) 1154.
[37] M.-T. Youinou, R. Ziessel, J.-M. Lehn, Inorg. Chem. 30 (1991) 2144.
[38] M.-H. Shu, W.-Y. Sun, C.-Y. Duan, Y.-J. Fu, W.-J. Zhang, W.-X. Tang, J. Chem. Soc., Dalton Trans. (1999) 729.
[39] W.W. Brandt, F.P. Dwyer, E.C. Gyarfas, Chem. Rev. 54 (1954) 959.
[40] G.R. Newkome, J.D. Sauer, J.M. Roper, D.C. Hager, Chem. Rev. 77 (1977) 513.
[41] N.F. Curtius, Coord. Chem. Rev. 3 (1968) 3.
[42] C. Lorenzini, C. Pelizzi, G. Pelizzi, G. Predieri, J. Chem. Soc., Dalton Trans. (1983) 721.
[43] M. Nardelli, C. Pelizzi, G. Pelizzi, Transition Met. Chem. 2 (1977) 35.
[44] C. Pelizzi, G. Pelizzi, J. Chem. Soc., Dalton Trans. (1980) 1970.
[45] C. Pelizzi, G. Pelizzi, G. Predieri, S. Resola, J. Chem. Soc., Dalton Trans. (1982) 1349.
[46] C. Lorenzini, C. Pelizzi, G. Pelizzi, G. Predieri, J. Chem. Soc., Dalton Trans. (1983) 2155.
[47] A. Bonardi, C. Carini, C. Merlo, C. Pelizzi, G. Pelizzi, P. Tarasconi, F. Vitali, J. Chem. Soc., Dalton Trans. (1990) 2771.
[48] A. Bonardi, S. Ianelli, C. Pelizzi, G. Pelizzi, C. Solinas, Inorg. Chim. Acta 232 (1995) 211.
[49] N.F. Rouge, S. Blanc, A. Pfeil, A. Rigault, A.-M.A. Gary, J.-M. Lehn, Helv. Chim. Acta 84 (2001) 1694.
[50] J. Hamacek, M. Borkovec, C. Piguet, Dalton Trans. (2006) 1473.
[51] C. Piguet, M. Borkovec, J. Hamacek, K. Zeckert, Coord. Chem. Rev. 249 (2005) 705.
[52] J.P. Schneider, R.S. Topgi, J.W. Kelly, Synth. Commun. 22 (1992) 1033.
[53] J. Lewis, K.P. Wainwright, J. Chem. Soc., Dalton Trans. (1977) 734.
[54] G. Hopfgartner, C. Piguet, J.D. Henion, A.F. Williams, Helv. Chim. Acta 76 (1993) 1759.
[55] H. Gampp, M. Maeder, C.J. Meyer, A.D. Zuberbuhler, Talanta 32 (1985) 257.
[56] H. Gampp, M. Maeder, C.J. Meyer, A.D. Zuberbuhler, Talanta 32 (1985) 1133.
[57] D.W. Marquardt, J. Soc. Ind. Appl. Math. 11 (1963) 431.
[58] M. Maeder, A.D. Zuberbuhler, Anal. Chem. 62 (1990) 2220.
[59] E.P. Manoj, M.R. Panicker, P. Kurup, H.-K. Fun, Inorg. Chem. Commun. 10 (2007) 324.
[60] K. Andelkovic, D. Sladic, A. Bacchi, G. Pelizzi, N. Filipovic, M. Rajkovic, Transition Met. Chem. 30 (2005) 243.
[61] S. Pal, J. Pushparaju, N.R. Sangeetha, S. Pal, Transition Met. Chem. 25 (2000) 529.
[62] S. Pal, S. Pal, J. Chem. Soc., Dalton Trans. (2002) 2102.
[63] G. Yang, S.-L. Zheng, X.-M. Chen, H.K. Lee, Z.-Y. Zhou, T.C.W. Mak, Inorg. Chim. Acta 303 (2000) 86.
[64] D.R. Crist, Z.-H. Hsieh, C.O. Quicksall, M.K. Sun, J. Org. Chem. 49 (1984) 2478.
[65] N.B.N. Greenwood, A. Earnshaw, Chemistry of the Elements, Pergamon, Oxford, UK, 1989.
[66] Y.-B. Xie, X.-H. Bu, J. Cluster Sci. 14 (2003) 471.
[67] C.-C. Cheng, S.-M. Hung, C.-Y. Yeh, C.-S. Chang, W.-J. Wang, J. Chin. Chem. Soc. 50 (2003) 189.
[68] J.-P. Zhang, Y.-B. Wang, X.-C. Huang, Y.-Y. Lin, X.-M. Chen, Chem. Eur. J. 11 (2005) 552.
[69] J.E. Aguado, M.J. Calhorda, P.J. Costa, O. Crespo, V. Felix, M.C. Gimeno, P.G. Jones, A. Laguna, Eur. J. Inorg. Chem. (2004) 3038.
[70] A.M. Stadler, N. Kyritsakas, G. Vaughan, J.-M. Lehn, Chem. Eur. J. 13 (2007) 59.
[71] T. Riis-Johannessen, J.C. Jeffery, A.P.H. Robson, C.R. Rice, L.P. Harding, Inorg. Chim. Acta 358 (2005) 2781.
[72] P. Pyykkö, Chem. Rev. 97 (1997) 597.
[73] T.J. Burchell, R.J. Puddephatt, Inorg. Chem. 45 (2006) 650.
[74] M.G.B. Drew, J.P. Naskar, S. Chowdhury, D. Datta, Eur. J. Inorg. Chem. (2005) 4834.
[75] S. Chowdhury, M.G.B. Drew, D. Datta, New J. Chem. 27 (2003) 831.
[76] L. Zanotto, F. Benetollo, M. Natali, G. Rossetto, P. Zanella, S. Kaciulis, A. Mezzi, Chem. Vap. Deposition 10 (2004) 207.
[77] X.-D. Chen, T.C.W. Mak, J. Mol. Struct. 743 (2005) 1.
[78] A.C. Effendy, F. Marchetti, C. Pettinari, R. Pettinari, B.W. Skelton, A.H. White, Inorg. Chem. 43 (2004) 4387.
[79] C.J. Horn, A.J. Blake, N.R. Champness, A. Garau, V. Lippolis, C. Wilson, M. Schröder, Chem. Commun. (2003) 312.
[80] C.J. Horn, A.J. Blake, N.R. Champness, V. Lippolis, C. Wilson, M. Schröder, Chem. Commun. (2003) 1488.
[81] S. Liao, C.-Y. Su, C.-H. Yeung, A.-W. Xu, H.-X. Zhang, H.-Q. Liu, Inorg. Chem. Commun. 3 (2000) 405.
[82] G.M. Sheldrick, SHELX-97, A Programs for Crystal Structure Solution and Refinement, University of Gottingen, Germany, 1997.
[83] G.M. Sheldrick, SADABS Version 2007/2, Bruker AXS Inc., Wisconsin, USA, 1997.
[84] D.A. McMorran, P.J. Steel, Inorg. Chem. Commun. 10 (2007) 324.

Polyhedron 28 (2009) 77–84

Contents lists available at ScienceDirect

Polyhedron

journal homepage: www.elsevier.com/locate/poly

Cyclopalladation of enantiopure oxazolines having the prochiral CMe_2 moiety at position 2 of the heterocycle

Relindis Y. Mawo, Irina P. Smoliakova *

Chemistry Department, University of North Dakota, 151 Cornell St., Grand Forks, ND 58202-9024, USA

ARTICLE INFO

Article history:
Received 24 July 2008
Accepted 3 October 2008
Available online 19 November 2008

Keywords:
Cyclopalladated complexes
Diastereoselective cyclopalladation
Oxazolines
Exo and endo palladacycles

ABSTRACT

(*R*)-4-Ethyl-2-(1,1-dimethylpropyl)-2-oxazoline (**1**) and (*S*)-4-*tert*-butyl-2-(1,1-dimethylbutyl)-2-oxazoline (**2**) were synthesized in two steps from the corresponding enantiopure amino alcohols and acid chlorides in a total yield of 95% and 72%, respectively. (*S*)-2-(1-Adamantyl-1-methylethyl)-4-isobutyl-2-oxazoline (**3**) was obtained from adamantyl bromide and L-leucinol in five steps in a total yield of 82%. Reactions of oxazolines **1**–**3** with $Pd(OAc)_2$ in AcOH or CH_2Cl_2 followed by treatment with LiCl afforded the corresponding μ-Cl dimeric cyclopalladated complexes **15**, **17**, and **20** in good yield. Compounds **15**, **17**, and **20** reacted with PPh_3 to furnish the corresponding mononuclear complexes **16**, **19**, and **21**. The ^{31}P NMR spectra of trans(*N*,*P*) adducts **16**, **19**, and **21** contained signals of two diastereomers in a ratio of ca. 1.3:1.

© 2008 Elsevier Ltd. All rights reserved.

1. Introduction

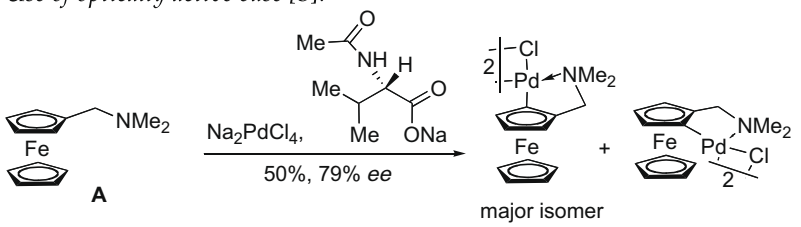
Cyclopalladated complexes have been postulated as intermediates in some highly efficient Pd-catalyzed asymmetric reactions; therefore, understanding the factors governing stereoselectivity of cyclopalladation is of high importance [1,2]. There have been a number of reports on both enantio- and diastereoselective cyclopalladation. Three approaches have been used for enantioselective cyclopalladation (Chart 1). In the first method, prochiral substrates reacted with a source of Pd(II) in the presence of an optically active base. This approach was used by Sokolov et al. for enantioselective metalation of (dimethylamino)methylferrocene (**A**) using Na_2PdCl_4 in the presence of optically active salts of carboxylic acids [3]. The same group used this idea for enantioselective cyclopalladation of (dimethylamino)methylruthenocene [4], 6-ferrocenyl-2,2′-bipyridine [5], 2-ferrocenyl-1,10-phenanthroline [5], and ruthenocene-derived imines [6]. A second approach, the use of optically active Pd coordination complexes, *cis*-$PdCl_2L_2$ (L = (*R*)-methyl *p*-tolyl sulfoxide), was tested in cyclopalladation of (dimethylamino)methylferrocene **A**; however, no chiral induction was observed [7]. The third method is a cyclopalladated ligand exchange reaction (transcyclopalladation) between a substrate having prochiral groups and an enantiopure cyclopalladated complex, whose ligands play the chiral auxiliary role. This approach was effectively used by Dunina's group for preparation of optically active *CP*-palladacycles from prochiral phosphines, e.g. **B** [8,9]. In the reported studies of enantioselective cyclopalladation, almost exclusively, either planar or central chirality has been induced as a result of aromatic (sp^2)C–H bond activation. A few studies of enantioselective benzylic (sp^3)C–H bond activation have also been published. In one of them, transcyclopalladation of 8-ethylquinoline with an optically active cyclopalladated complex of *N*,*N*-dimethyl-α-methylbenzylamine proceeded with no asymmetric induction [10]. However, trans metalation of *tert*-butyldi(*o*-tolyl)phosphine using cyclopalladated α-*tert*-butylbenzylamine afforded the corresponding *CP*-complex in 91% *ee* [8].

The majority of the studies of diastereoselective cyclopalladation have been reported for substrates with the ferrocene backbone or compounds in which planar chirality can arise after metalation (Chart 2). As a rule, the chirality source was a stereogenic center in the ligand to be palladated and complexes with a (sp^2)C–Pd bond were formed. For example, Sokolov et al. used optically active 1-(dimethylamino)ethylferrocene (**C**) to obtain the corresponding cyclopalladated dimer with 70% de [11]. Similar results for the same substrate were reported by the López group [12]. Optically active ferrocene-derived imidozolines [13], hydrazones [14], and imines [15] also underwent cyclopalladation with very high or complete diastereoselectivity. Direct palladation of racemic ferrocene-based phosphinites by $(PhCN)_2PdCl_2$ was not diastereoselective [16], whereas reaction of racemic di-*tert*-butyl-1-ferrocenylethylphosphine with $Pd(OAc)_2$ proceeded with complete diastereoselectivity [17]. Diastereoselective cyclopalladation through (sp^3)C–H bond activation in the prochiral CMe_2 fragment was reported for a number of steroids and terpenoids, e.g. oxime **D** [18]. The only enantiopure oxazoline used for diastereoselective cyclopalladation was a (4*S*)-derivative with the prochiral (η^5-C_6H_4)(η^4-C_4Ph_4)Co fragment (**E**); it reacted with $Pd(OAc)_2$ to form

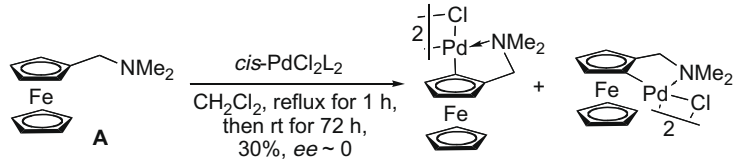
* Corresponding author. Tel.: +1 701 777 3942; fax: +1 701 777 2331.
E-mail address: ismoliakova@chem.und.edu (I.P. Smoliakova).

0277-5387/$ - see front matter © 2008 Elsevier Ltd. All rights reserved.
doi:10.1016/j.poly.2008.10.010

Use of optically active base [3]:



Use of optically active $PdCl_2L_2$, L = (R)-methyl p-tolyl sulfoxide [7]:



Enantioselctive transcyclopalladation [8,9]:

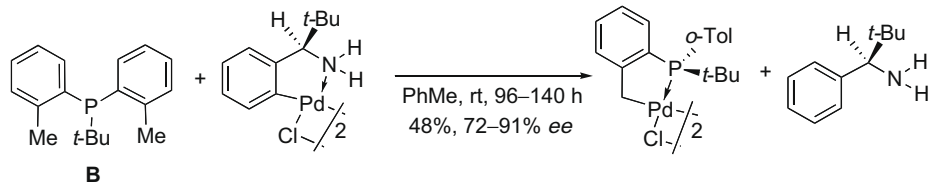


Chart 1. Examples of reported enantioselective cyclopalladation reactions [3,7–9].

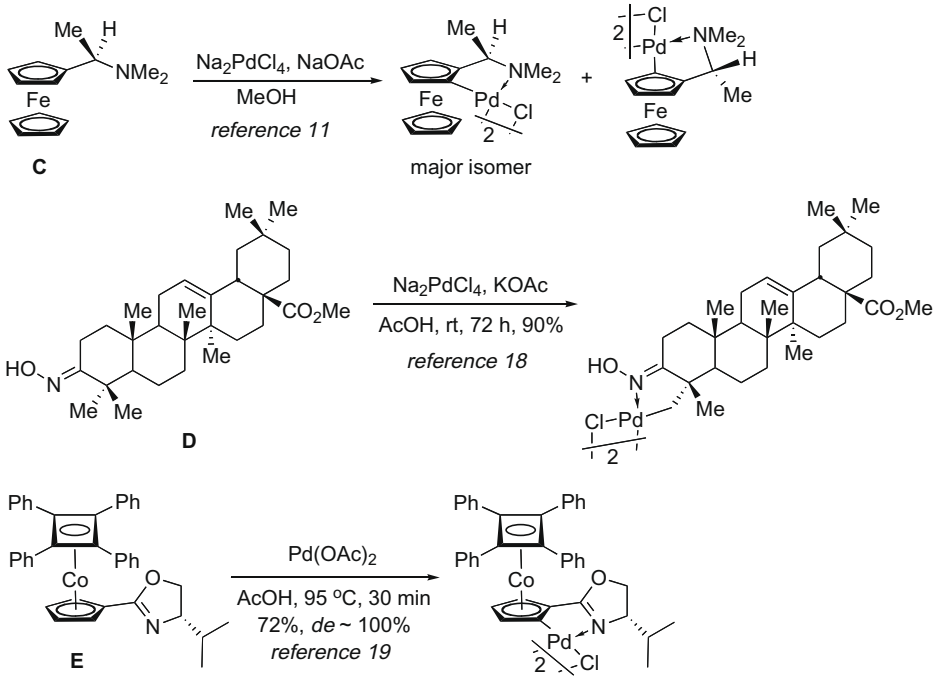


Chart 2. Examples of reported diastereoselective cyclopalladation reactions [11,18,19].

the corresponding palladacycle with complete diastereoselectivity [19].

In line with our interest in the study of cyclopalladated oxazolines [20–24], we report direct palladation of enantiopure oxazolines **1**–**3** having a chiral center at the 4-position and the prochiral CMe_2 fragment in the substituent at the 2-position of the heterocycle (Chart 3). We were interested in determining diastereoselectivity of these reactions and analyzing the effects of different factors on stereoselectivity.

2. Experimental

2.1. Materials

All reactions were carried out using standard bench top techniques. HPLC grade acetone and acetonitrile, as well as ACS reagent grade acetic acid were used without further purification. Other solvents were dried by distillation over CaH_2. Prior to use, $Pd(OAc)_2$ was dissolved in hot benzene followed by filtration and solvent

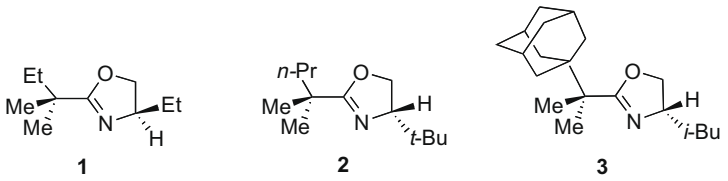


Chart 3. Enantiopure oxazolines **1**–**3** with the prochiral CMe_2 fragment.

removal in vacuum. All other chemicals were used as purchased from commercial sources (Sigma–Aldrich, Acros Organics or Alfa Aesar).

2.2. Chromatography

Column and preparative thin layer chromatography (TLC) was performed using Natland silica gel 60 (230–400 mesh). Analytical TLC was carried out on Whatman silica gel 60 (F_{254}) 250 μm precoated plates. Compounds on TLC plates were visualized using UV light (254 nm) and iodine stain (complexes) or vanillin/heat (ligands).

2.3. Physical measurements

Acquisition of ^1H (500 MHz), ^{13}C (126 MHz), ^{31}P NMR (202 MHz), DEPT, COSY, and HSQC spectra was performed in $CDCl_3$ using a Bruker AVANCE 500 spectrometer. Chemical shifts are reported in ppm relative to $SiMe_4$ as the internal standard (^1H and ^{13}C) or $P(OEt)_3$ as the external reference (^{31}P). Spin–spin coupling constants, *J*, are given in Hz. IR spectra were recorded on an ATI Mattson Genesis Series FT-IR. Melting points were determined on a Laboratory Devices Mel-Temp apparatus and are uncorrected. Optical rotations were measured in a 1 dm cell using an Autopol III automatic polarimeter. High resolution mass spectra were obtained on an Agilent 6200 LCTOF mass spectrometer at the Mass Spectrometry Facility, University of California Riverside, Riverside, CA, USA. Elemental analyses were performed by Atlantic MicroLabs Inc., Norcross, GA, USA.

2.4. Synthesis

2.4.1. Preparation of (R)-N-(1-hydroxybutan-2-yl)-2,2-dimethylbutanamide (**8**)

Compound **8** was obtained as a yellow solid in quantitative yield from (*R*)-(−)-amino-1-butanol (0.60 mL, 0.0063 mmol) and 2,2-dimethylbutyryl chloride (1.3 mL, 0.0095 mmol) according to a literature procedure reported for related compounds [25]. Mp 40–43 °C; R_f 0.35 (2:3 pet. ether–EtOAc); IR (thin film of $CHCl_3$ soln, *v*, cm^{-1}): 3342–3347 (OH, NH), 1640 (N–C=O); $[\alpha]_{633}^{25}$ +33.8, $[\alpha]_D^{25}$ +49.7 (*c* 0.208, CH_2Cl_2); ^1H NMR (δ, ppm): 0.86 (t, 3H, ^3J = 7.5, CMe_2CH_2Me), 0.95 (t, 3H, ^3J = 7.5, $NCHCH_2Me$), 1.17 (s, 6H, CMe_2), 1.49 (m, 1H, $NCHCH^AMe$), 1.56 (q, 2H, CMe_2CH_2Me), 1.62 (m, 1H, $NCHCH^BMe$), 3.40 (br. s, 1H, OH), 3.58 (dd, 1H, $^2J_{AB}$ = 10.9, ^3J = 5.8, OCH^A), 3.67 (dd, 1H, ^3J = 3.3, OCH^B), 3.86 (m, 1H, NCH), 5.84 (br. s, 1H, NH); ^{13}C NMR (δ, ppm): 9.2 (CMe_2CH_2Me), 10.6 ($NCHCH_2Me$), 24.2 ($NCHCH_2Me$), 25.0 and 25.1 (CMe_2), 33.9 (CMe_2CH_2Me), 42.5 (CMe_2), 53.4 (NCH), 65.8 (OCH_2), 179.0 (OCN). *Anal. Calc.* for $C_{10}H_{21}NO_2$: C, 64.13; H, 11.30; N, 7.48. Found: C, 63.66; H, 11.31; N, 7.26%.

2.4.2. Preparation of (S)-N-(1-tert-butyl-2-hydroxyethyl)-2,2-dimethylpentanamide (**9**)

Compound **9** was obtained as a cream-white solid from (*S*)-*tert*-leucinol (441.5 mg, 3.767 mmol) and 2,2-dimethylvaleroyl chloride (837.7 mg, 5.636 mmol) in 96% yield following a procedure reported for similar compounds [25]. Mp 94–97 °C; R_f 0.46 (2:3 pet. ether–EtOAc); IR (thin film of $CHCl_3$ soln, *v*, cm^{-1}): 3354 (NH), 3288 (OH), 1624 (N–C=O); $[\alpha]_D^{22.5}$ −22.9, $[\alpha]_{546}^{22.5}$ −27.6 (*c* 0.274, CH_2Cl_2); ^1H NMR (δ, ppm): 0.90 (t, 3H, ^3J = 7.3, CH_2Me), 0.96 (s, 9H, *t*-Bu), 2.21 and 2.22 (two s, 6H, CMe_2), 1.28 (m, 2H, CH_2Me), 1.52 (m, 2H, CH_2CMe_2), 3.54 (dd, 1H, $^3J_1$ = 7.9, $^3J_2$ = 10.7, OCH^A), 3.82–3.89 (m, 2H, NCH and OCH^B); ^{13}C NMR (δ): 14.6 (CH_2Me), 18.2 (CH_2Me), 25.49 and 25.54 (CMe_2), 27.0 (CMe_3), 33.3 (CMe_3), 42.6 (CMe_2), 43.7 (CH_2CMe_2), 59.7 (NCH), 63.8 (OCH_2), 179.8 (N–C=O). HRMS (TOF): calcd. for $[MH^+]$ 230.2120, found 230.2120.

2.4.3. Preparation of (R)-4-ethyl-2-(1,1-dimethylpropyl)-2-oxazoline (**1**)

Compound **1** was obtained from amide **8** (0.47 g, 2.5 mmol) and (diethylamino)sulfur trifluoride (0.36 mL, 2.8 mmol) as a colorless liquid in 89% (after distillation) using a procedure reported for other oxazolines [25]. Bp 82 °C/22 mm Hg; R_f 0.47 (6:1 pet. ether–EtOAc); IR (neat, *v*, cm^{-1}): 1658 (C=N); $[\alpha]_{633}^{23}$ +57.3, $[\alpha]_D^{23}$ +75.7, $[\alpha]_{546}^{23}$ +87.3, $[\alpha]_{435}^{23}$ +164.5, $[\alpha]_{365}^{23}$ +270.6 (*c* 0.210, CH_2Cl_2); ^1H NMR (δ, ppm): 0.84 (t, 3H, ^3J = 7.5, CMe_2CH_2Me), 0.90 (t, 3H, ^3J = 7.5, $NCHCH_2Me$), 1.17 (s, 6H, CMe_2), 1.49 (m, 1H, $NCHCH^AMe$), 1.54, (q, 2H, CMe_2CH_2Me), 1.65 (m, 1H, $NCHCH^BMe$), 3.86 (dd, 1H, ^3J = 7.2, $^2J_{AB}$ = 8.2, OCH^A), 4.02 (m, 1H, NCH), 4.23 (dd, 1H, ^3J = 9.4, OCH^B); ^{13}C NMR (δ, ppm): 9.1 (CMe_2CH_2Me), 9.5 ($NCHCH_2Me$), 25.5 (CMe_2), 28.4 ($NCHCH_2Me$), 33.4 (CMe_2CH_2Me), 36.8 (CMe_2), 67.0 (NCH), 71.5 (OCH_2), 172.7 (OCN); HRMS (TOF): calcd. for $[MH^+]$: 170.1543, found 170.1545.

2.4.4. Preparation of (S)-4-tert-butyl-2-(1,1-dimethylbutyl)-2-oxazoline (**2**)

Using a known procedure for related compounds [25], cyclization of amide **9** (3.113 g, 0.01357 mol) in the presence of (diethylamino)sulfur trifluoride (2.1 mL, 0.016 mol) afforded oxazoline **2** as a colorless liquid in 73% yield (after distillation). Bp 58–65 °C/1 mm Hg; R_f 0.64 (7:1 pet. ether–EtOAc); IR (neat, *v*, cm^{-1}): 1662 (C=N); $[\alpha]_{633}^{21}$ −54.8, $[\alpha]_D^{21}$ −64.3, $[\alpha]_{546}^{21}$ −77.1, $[\alpha]_{435}^{21}$ −140.2 (*c* 0.441, CH_2Cl_2); ^1H NMR (δ, ppm): 0.87–0.91 (m, 12H, 9H s of *t*-Bu and 3H of CH_2Me), 1.18 and 1.19 (two s, 6H, CMe^A and CMe^B), 1.27 (m, 2H, CH_2Me), 1.48 (m, 2H, CH_2CMe_2), 3.79 (dd, 1H, $^3J_1$ = 7.1, $^3J_2$ = 10.0, NCH), 4.03 (dd, 1H, $^2J_{AB}$ = 8.6, OCH^A), 4.09 (dd, 1H, OCH^B); ^{13}C NMR (δ): 14.7 (CH_2Me), 18.0 (CH_2Me), 25.8 (CMe_3), 25.9 and 26.3 (CMe^A and CMe^B), 33.7 and 36.6 (CMe_3, CMe_2), 43.2 (CH_2CMe_2), 68.3 (OCH_2), 75.4 (NCH), 172.7 (OCN). HRMS (TOF): calcd. for $[MH^+]$ 212.2014, found 212.2014.

2.4.5. Synthesis of methyl 2-adamantyl-2-methylpropanoate (**11**)

Compound **11** was obtained in 97% yield following a modified literature procedure [26]. $ZnCl_2$ (416 mg, 3.05 mmol) was sublimed under N_2 in a Schlenk flask, cooled to rt, and then agitated vigorously in CH_2Cl_2 (5.0 mL) before adding methyl trimethylsilyl dimethylketene acetal (2.0 mL, 9.8 mmol) via a syringe. The mixture was cooled to 0 °C in an ice-bath and a solution of 1-bromoadamantane (2.1242 g, 9.8736 mmol) in CH_2Cl_2 (10.0 mL) was added. The reaction mixture was stirred at rt for 28 h and then washed with distilled water (120 mL × 3). The combined aqueous

layers were extracted with CH_2Cl_2 (100 mL × 3). The combined organic solutions were dried over anhydrous $MgSO_4$. After solvent removal in vacuum, the product was isolated as a white solid. Mp 57–59 °C (lit. data [26] 58–59 °C); R_f 0.71 (9:1 benzene–EtOAc); IR (thin film of CH_2Cl_2 soln, ν, cm^{-1}): 1718 (C=O) [lit. data [26] 1710 (KBr)]; ^1H NMR (δ, ppm): 1.12 (s, 6H, CMe_2), 1.59–1.68 (m, 12H, CH_2 of Ad), 1.98 (br. s, 3H, CH of Ad), 3.64 (s, 3H, OMe); ^{13}C NMR (δ): 20.2 (CMe_2), 28.8 (CH of Ad), 36.6 (CMe_2), 36.95 and 36.97 (two s, two CH_2 groups of Ad), 48.8 (quat. C of Ad), 51.1 (OMe), 177.5 (C=O).

2.4.6. Synthesis of 2-adamantyl-2-methylpropionic acid (**12**)

Ester **11** (1.2366 g, 5.2321 mmol) was suspended in DMSO (21 mL) and NaSMe (0.8801 g, 12.56 mmol) was added. The mixture was stirred under N_2 at 84 °C (bath temp.) for 12 h. The yellowish slurry was treated with distilled water (140 mL) and extracted with Et_2O (100 mL × 3). Conc. H_2SO_4 was added dropwise to the aqueous solution to pH 3. The precipitated product (1.0609 g, 91%) was filtered off and dried under vacuum at rt. Mp 194–195 °C [lit. data [26] (164 °C)]; R_f 0.50 (4:1 benzene–EtOAc); IR (thin film of $CHCl_3$ soln, ν, cm^{-1}): 3500–2500 (OH), 1692 (C=O) [lit. data [26] 3300–2500 (OH), 1690 (C=O) (KBr)]; ^1H NMR (δ, ppm): 1.12 (s, 6H, CMe_2), 1.61–1.69 (m, 12H, CH_2 of Ad), 2.0 (br. s, 3H, CH of Ad), 11.34 (br. s, 1H, OH); ^{13}C NMR (δ): 20.4 (CMe_2), 29.2 (CH of Ad), 36.8 (CMe_2), 37.25 and 37.32 (two s, two CH_2 groups of Ad), 49.1 (quat. C of Ad), 183.4 (C=O).

2.4.7. Preparation of 2-adamantyl-2-methylpropionyl chloride (**13**)

A mixture of acid **12** (545.4 mg, 2.453 mmol) and $SOCl_2$ (0.27 mL, 3.7 mmol) was heated at 78 °C (bath temp.) under N_2 for 3 h. After removal of excess $SOCl_2$ in vacuum, the product was obtained as a pale-yellowish solid in quantitative yield. IR (thin film of CH_2Cl_2 soln, ν, cm^{-1}): 1788 (C=O); ^1H NMR (δ, ppm): 1.25–1.75 (m, 18H, CMe_2 and CH_2 of Ad), 2.03 (br. s, 3H, CH of Ad); ^{13}C NMR (δ): 21.7 (CMe_2), 28.7 (CH of Ad), 36.7 and 36.9 (two CH_2 groups of Ad), 37.9 (CMe_2), 59.3 (quat. C of Ad), 180.1 (C=O).

2.4.8. Synthesis of (S)-N-(1-isobutyl-2-hydroxyethyl)-2-adamantyl-2-methylpropanamide (**14**)

The synthesis of compound **14** was achieved according to a literature procedure for other amides [25]. Acyl chloride **13** (590.7 mg, 2.453 mmol) was added dropwise over 40 min to L-leucinol (**10**, 0.21 mL, 1.6 mmol) dissolved in a 1:1 mixture of CH_2Cl_2/H_2O containing K_2CO_3 (6.56 g, 0.0474 mol). The reaction proceeded at rt for 39 h. The product was obtained as a white solid in quantitative yield after crystallization from $CHCl_3$–pentane. Mp 113–115 °C; R_f 0.44 (3:2 pet. ether–EtOAc); IR (thin film of $CDCl_3$ soln, ν, cm^{-1}): 3456 (NH), 3386 (OH), 1633 (NC=O); $[\alpha]^{21}_{633}$ −39.8, $[\alpha]^{21}_{D}$ −49.3, $[\alpha]^{21}_{546}$ −62.3, $[\alpha]^{21}_{435}$ −105, $[\alpha]^{21}_{365}$ −153 (*c* 0.166, CH_2Cl_2); ^1H NMR (δ, ppm): 0.92 and 0.95 (two d, 6H, ^3J = 6.6, CHMe_2), 1.12 (s, 6H, CMe_2), 1.36 (m, 2H, CH_2CHMe$_2$), 1.59–1.69 (m, 13H, overlapping signals of C*H*Me$_2$ and CH_2 of Ad), 1.99 (br. s, 3H, CH of Ad), 2.59 (br. s, 1H, OH), 3.54 (dd, 1H, $^2J_{AB}$ = 10.9, ^3J = 6.4, OCH^A), 3.68 (dd, 1H, ^3J = 3.2, OCH^B), 4.03 (m, 1H, NCH), 5.63 (d, 1H, ^3J = 6.7, NH); ^{13}C NMR (δ): 20.3 and 20.4 (two s, CMe_2), 22.0 and 23.1 (two s, CHMe_2), 25.0 ($CHMe_2$), 28.8 (CH of Ad), 36.4 (CMe_2), 36.9 and 37.0 (two s, two CH_2 groups of Ad), 40.2 (CH_2CHMe_2), 48.2 (quat. C of Ad), 50.4 (NCH), 67.4 (OCH_2), 178.0 (C=O). Anal. Calc. for $C_{20}H_{35}NO_2$: C, 74.72; H, 10.97; N, 4.36. Found: C, 74.91; H, 11.11; N, 4.37%.

2.4.9. Synthesis of (S)-2-(1-adamantyl-1-methylethyl)-4-isobutyl-2-oxazoline (**3**)

Oxazoline **3** was obtained in quantitative yield as a viscous light yellow oil by the cyclization of amide **14** (494.8 mg, 1.539 mmol) with (diethylamino)sulfur trifluoride (0.22 mL, 1.7 mmol) according to a published procedure for other oxazolines [25]. The reaction mixture was stirred at −78 °C for 15.5 h and then slowly (11 h) warmed up to +5 °C. R_f 0.60 (5:1 pet. ether–EtOAc); IR (thin film of CH_2Cl_2 soln, ν, cm^{-1}): 1643 (C=N); $[\alpha]^{21}_{633}$ −37.9, $[\alpha]^{21}_{D}$ −43.9, $[\alpha]^{21}_{546}$ −53.6, $[\alpha]^{21}_{435}$ −92.4, $[\alpha]^{21}_{405}$ −114 (*c* 0.383, CH_2Cl_2); ^1H NMR (δ, ppm): 0.92 and 0.95 (two d, 6H, ^3J = 6.4, CHMe_2), 1.14 and 1.16 (two s, 6H, CMe_2), 1.28 (m, 1H, C*H*^{A}CHMe$_2$), 1.55–1.75 (m, 14H, overlapping signals of C*H*Me$_2$, C*H*^{B}CHMe$_2$ and CH_2 of Ad), 1.99 (br. s, 3H, CH of Ad), 3.91 (t, 1H, J = 7.7, OCH^A), 4.21 (m, 1H, NCH), 4.37 (t, 1H, J = 8.8, OCH^B); ^{13}C NMR (δ): 20.7 and 20.8 (CMe_2), 22.3 and 23.3 (CHMe_2), 25.4 ($CHMe_2$), 28.8 (CH of Ad), 36.9 (CMe_2), 37.0 and 37.03 (two CH_2 groups of Ad), 43.0 (C of Ad), 45.4 (CH_2CHMe_2), 63.2 (NCH), 73.0 (OCH_2), 173.8 (C=N); HRMS (TOF): calcd. for [MH^+] 304.2636, found 304.2640.

2.4.10. Synthesis of di-μ-chlorobis-[2-methyl-2-(4-ethyl-2-oxazolin-2-yl)butyl-C,N]dipalladium(II) (**15**)

Oxazoline **1** (79.7 mg, 0.471 mmol) was dissolved in MeCN (2.0 mL) and the solution was added to a suspension of $Pd(OAc)_2$ (107 mg, 0.476 mmol) and NaOAc (45.5 mg, 0.555 mmol) in MeCN (1.5 mL). The reaction mixture was stirred under N_2 at reflux for 4 h. The mixture was allowed to cool to rt and filtered through celite. After solvent removal, the crude μ-OAc dimer was dissolved in acetone (3 mL) and LiCl (22.0 mg, 0.519 mmol) was added. The mixture was stirred at rt for 24 h, then the solvent was evaporated and the crude μ-Cl dimer was purified by column chromatography using benzene and 98:2 benzene–EtOAc as the eluents. The pure product was isolated as a yellow powder in 77% yield. Data for a mixture of isomers: Mp 131–133 °C; R_f 0.52 (19:1 benzene–EtOAc); IR (thin film of $CDCl_3$ soln, ν, cm^{-1}): 1648 (C=N); ^1H NMR (δ, ppm): 0.87 (td, 3H, $J \approx 7.3$, $J \approx 2.9$, NCHCH$_2$*Me*), 0.87 and 0.94 (two t, 3H, ^3J = 7.5, PdCH$_2$C(Me)CH$_2$*Me*), 1.11 and 1.18 (two s, 3H, CMe), 1.44 (m, 1H, C(Me)C*H*^{A}Me), 1.51, (q, 1H, J = 7.6, C(Me)C*H*^{B}Me), 1.65 (m, 1H, NCHC*H*^{A}Me), 1.77–1.89 (m, 2H, NCHC*H*^{B}Me and PdCH^A), 2.10 and 2.11 (two d, 1H, ^2J = 7.7, PdCH^B), 3.96 (br. s, 1H, NCH), 4.17 (m 1H, OCH^A), 4.37 (m, 1H, OCH^B); ^{13}C NMR (δ, ppm): 8.2 and 8.6 (NCHCH$_2$*Me*), 9.2 and 9.5 (PdCH$_2$C(Me)CH$_2$*Me*), 25.1 and 25.6 (C*Me*), 25.7 and 26.0 (PdCH$_2$), 26.8 and 27.0 (NCH*C*H$_2$Me), 32.4 and 32.7 (C(Me)*C*H$_2$Me), 45.1 (*C*Me), 63.5 and 63.8 (NCH), 72.7 and 72.8 (OCH_2), 182.5 (OCN). *Anal. Calc.* for $C_{20}H_{36}Cl_2N_2O_2Pd_2$: C, 38.73; H, 5,85; N, 4.52. Found: C, 38.74; H, 5.95; N, 4.54%.

2.4.11. Synthesis of chloro-[2-methyl-2-(4-ethyl-2-oxazolin-2-yl)butyl-C,N](triphenylphosphine)palladium(II) (**16**)

The μ-chloro dimer **15** (52.0 mg, 0.0838 mmol) was dissolved in benzene (3 mL). PPh_3 (43.7 mg, 0.167 mmol) was added and the mixture was stirred under N_2 at rt for 24 h. After solvent removal, the crude product was purified by preparative TLC using 4:1 benzene–EtOAc as the eluent. Compound **16** was obtained as a white powder (73.9 mg, 77%) and as a 1:1 mixture (^{31}P NMR data) of diastereomers. Data for a 1:1 mixture of two diastereomers: Mp 145–148 °C; R_f 0.49 (4:1 benzene–EtOAc); IR (thin film of $CDCl_3$ soln, ν, cm^{-1}): 1649 (C=N); ^1H NMR (δ, ppm): 0.72 and 0.77 (two t, 3H, ^3J = 7.5, C(Me)CH$_2$*Me*), 0.86 (m, 1H, PdCH^A), 0.91 (td, 3H, J = 7.3, J = 1.7, NCHCH$_2$*Me*), 0.98 and 1.09 (two s, 3H, CMe), 1.26 (m, 1H, C(Me)C*H*^{A}Me), 1.43, (m, 2H, PdCH^B and C(Me)C*H*^{B}Me), 1.79 (m, 1H, NCHC*H*^{A}Me), 2.11 (m, 1H, NCHC*H*^{B}Me), 4.28 (m 1H, OCH^A), 4.40–4.49 (m, 2H, overlapping signals of OCH^B and NCH) 7.36–7.43 (m, 9H, *m*- and *p*-CH of PPh_3), 7.73 (m, 6H, *o*-CH of PPh_3); ^{13}C NMR (δ, ppm): 8.3 and 8.7 (NCHCH$_2$*Me*), 8.6 and 9.4 (C(Me)CH$_2$*Me*), 25.4 and 26.7 (C*Me*), 27.1 and 27.2 (NCH*C*H$_2$Me), 32.9 and 33.4 (PdCH$_2$), 33.9 and 34.1 (C(Me)*C*H$_2$Me), 45.05 and 45.11 (*C*Me), 62.7 and 63.0 (two d, $^3J_{CP}$ = 2.3 and 2.1, NCH), 73.5

and 73.7 (two d, $^4J_{CP}$ = 3.4, OCH_2), 128.1 (d, $^3J_{CP}$ = 10.6, *m*-CH of PPh_3), 130.2 (d, $^4J_{CP}$ = 2.0, *p*-CH of PPh_3), 131.5 and 131.6 (two d, $^1J_{CP}$ = 48.8 and 48.3, *ipso*-C of PPh_3), 134.7 (two d, $^2J_{CP}$ = 11.4, *o*-CH of PPh_3), 182.86 and 182.92 (two d, $^3J_{CP}$ = 2.8, OCN). ^{31}P NMR (δ, ppm): 32.91 and 32.94. *Anal. Calc.* for $C_{28}H_{33}ClNOPPd$: C, 58.75; H, 5.81; N, 2.45. Found: C, 58.62; H, 5.92; N, 2.49%.

*2.4.12. Synthesis of di-μ-chlorobis-[2-methyl-2-(4-tert-butyl-2-oxazolin-2-yl)pentyl-C,N]dipalladium(II) (**17**)*

$Pd(OAc)_2$ (73.2 mg, 0.326 mmol) and NaOAc (53.4 mg, 0.651 mmol) were added to a CH_2Cl_2 (5.2 mL) solution of oxazoline **2** (68.6 mg, 0.325 mmol). The mixture was stirred at rt for 5 days. The solvent was evaporated and the resulting μ-OAc dimer was reacted overnight at rt with LiCl (27.5 mg, 0.649 mmol) in acetone (5.7 mL). The acetone was removed and the residue was dissolved in CH_2Cl_2 and filtered. Evaporation of the solvent afforded a dark-yellow residue, which was purified by column chromatography using gradient elution with benzene and 95:5–1:1 benzene–CH_2Cl_2. This led to the isolation of 69 mg (61%) of compound **17** as a yellow powder. Data for the mixture of isomers: R_f 0.56 (19:1 benzene–EtOAc); IR (neat, *v*, cm^{-1}): 1639 (C=N); ^{1}H NMR (δ, ppm) 0.85 and 0.96 (two t, 3H, *J* = 6.9 and 7.3, CH_2*Me*), 1.00 (s, 9H, *t*-Bu), 1.02 (s, 3H, C*Me*), 1.12–1.27 (m, 1H, C*H*^{A}Me), 1.40 and 1.81 (m, 1H, C*H*^{B}Me), 1.62 (m, 2H, [C(Me)C*H*$_2$CH$_2$Me]), 1.81 and 2.17 (two d, 2H, ^2J = 8.3, $PdCH_2$), 3.63 (m, 1H, NCH), 4.18 and 4.23 (two t, 1H, *J* = 9.2, OCH^A), 4.41 (dd, 1H, $^2J_{AB}$ = 9.2, ^3J = 3.5, OCH^B); ^{13}C NMR (δ, ppm): 14.6 (CH_2*Me*), 17.2 and 18.7 (*C*H$_2$Me), 24.8 and 25.9 (C*Me*$_3$), 25.5 and 26.0 ($PdCH_2$), 26.0 and 26.9 ($PdCH_2$C*Me*), 34.2 and 34.4 (*C*Me$_3$), 41.1 and 42.9 [C(Me)*C*H$_2$CH$_2$Me], 44.7 and 45.0 ($PdCH_2$*C*Me), 70.4 and 70.7 (NCH), 70.5 and 71.0 (OCH_2), 181.9 and 182.5 (OCN). *Anal. Calc.* for $C_{26}H_{48}Cl_2N_2O_2Pd_2$: C, 44.33; H, 6.87; N, 3.98. Found: C, 44.90; H, 6.98; N, 4.07%.

*2.4.13. Synthesis of di-μ-chlorobis-{2-methyl-2-[2-(2-methylbutan-2-yl)-2-oxazolin-4-yl]propyl-C,N}dipalladium(II) (**18**)*

Compound **18** was isolated from the reaction of oxazoline **2** with $Pd(OAc)_2$ and NaOAc in AcOH (68 °C, 90 h) followed by treatment with LiCl in acetone in 11% yield (along with 28% of compound **17**). ^{1}H NMR (δ, ppm): 0.88 and 0.89 (two t, 3H, *J* = 7.25, CH_2C*H*$_3$), 0.96 (s, 6H, C(C*H*$_3$)$_2$), 1.15, 1.16, 1.17 (three s, 6H, C(C*H*$_3$)$_2$), 1.25 (m, 3H from CH_2CH_2), 1.47 (m, 2H from $PdCH_2$ and 1H from CH_2CH_2), 4.09 (m, 3H, OCH_2CHN); ^{13}C NMR (δ, ppm): 14.9 and 15.0 (*C*H$_3$CH$_2$), 18.5 and 18.6 (CH$_3$C*H*$_2$), 25.48, 25.50, 25.86 and 25.96 (C(*C*H$_3$)$_2$), 27.4 (C(*C*H$_3$)$_2$), 34.2 (*C*(CH$_3$)$_2$), 42.38 and 42.41 (*C*(CH$_3$)$_2$), 43.06 ($PdCH_2$), 43.63 ($CH_3CH_2CH_2$), 55.0 (NCH), 64.1 (OCH_2), 171.1 and 178.1 (OC=N).

*2.4.14. Preparation of chloro-[2-methyl-2-(4-tert-butyl-2-oxazolin-2-yl)pentyl-C,N](triphenylphosphine)palladium(II) (**19**)*

Complex **19** is obtained using a procedure described for compound **16** from pure dimer **17** in 95% yield. Data for a mixture of two diastereomers: R_f 0.27 (96:4 benzene–EtOAc); IR (thin film of $CDCl_3$ soln, *v*, cm^{-1}): 1643 (C=N); ^{1}H NMR (δ, ppm): ^{1}H NMR: 0.67 and 0.80 (two m, 4H, CH_2*Me* and PdCH^A), 1.06 and 1.07 (two s, 9H, *tert*-Bu), 0.94 and 1.22 (two s, 3H, Me), 1.00–1.45 (m, 4H, CH_2CH_2), 1.65 and 1.86 (two d, 1H, *J* = 9.45, PdCH^B), 4.29 (m, 2H, OCH_2), 4.49 (m, 1H, NCH), 7.35–7.40 (m, 9H, *m*- and *p*-CH of PPh_3), 7.71–7.74 (m, 6H, *o*-CH of PPh_3). ^{13}C NMR (δ, ppm): 14.5, 14.6 (CH_3), 25.9, 26.1 (*tert*-Bu), 28.6 (CH_3), 17.2, 18.7, 42.4 and 44.1 (CH_2CH_2), 34.3, 34.6, 45.1, 45.3 (*C*Me$_3$ and $PdCH_2$*C*), 34.5 and 35.4 ($PdCH_2$), 68.7 and 68.9 (two d, $^3J_{CP}$ = 2.8, OCH_2), 71.6 and 72.1 (two d, $^3J_{CP}$ = 2.8, NCH), 127.9 and 128.1 (*m*-CH of PPh_3), 130.13 and 130.14 (*p*-CH of PPh_3), 131.6 and 131.9 (two d, $^1J_{CP}$ = 4.0, *ipso*-C of PPh_3), 134.6 and 134.7 (*o*-CH of PPh_3), 181.8 and 182.2 (two d, $^3J_{CP}$ = 2.8, C=N); ^{31}P NMR (δ, ppm): 34.06 and 34.32.

*2.4.15. Synthesis of di-μ-chlorobis-[2-adamantyl-2-(4-isobutyl-2-oxazolin-2-yl)propyl-C,N]dipalladium(II) (**20**)*

A solution of oxazoline **3** (88.0 mg, 0.290 mmol) in acetic acid (4.0 mL) was added to a suspension of $Pd(OAc)_2$ (81.8 mg, 0.364 mmol) and NaOAc (26.2 mg, 0.319 mmol) in acetic acid (2 mL). The reaction mixture was stirred under N_2 at 80 °C (bath temp.) for 16 h. The solvent was evaporated and the resulting dark-brown residue was reacted under N_2 at rt for 22 h with a solution of LiCl (22.0 mg, 0.519 mmol) in acetone. The mixture was filtered through celite and the solvent was evaporated. Purification of the crude product by column chromatography with benzene as the eluent afforded the pure product (75% yield) as a yellow powder. Data for a mixture of isomers: Mp 180–184 °C; R_f 0.51 (benzene); IR (thin film of $CDCl_3$ soln, *v*, cm^{-1}): 1637 (C=N); ^{1}H NMR (δ, ppm): 0.83–2.37 (m, 29H, CH*Me*$_2$, CMe, $PdCH_2$, C*H*Me$_2$, C*H*$_2$CHMe$_2$, CH_2 and CH of Ad), 3.90 (m, NCH), 4.15 (m, 1H, OCH^A), 4.34 and 4.40 (two t, 1H, *J* = 9.1 and 8.9, OCH^B); ^{13}C NMR (δ, ppm): 20.0, 20.3, 21.6 and 21.8 (C*Me*$_2$), 23.6 and 23.7 (C*Me*), 24.3 and 24.5 ($PdCH_2$), 25.2, 25.4, 28.6 and 28.7 (*C*HMe$_2$ and CH of Ad), 36.4, 36.5, 36.6, 37.0 and 37.02 (CH_2 and C of Ad), 43.4 and 44.4 (*C*H$_2$CHMe$_2$), 50.8 and 51.1 (*C*Me), 61.0 and 61.2 (NCH), 72.9 and 73.9 (OCH_2), 181.6 and 181.7 (OCN). *Anal. Calc.* for $C_{40}H_{64}Cl_2N_2O_2Pd_2$: C, 54.06; H, 7.26; N, 3.15. Found: C, 54.30; H, 7.31; N, 3.21%.

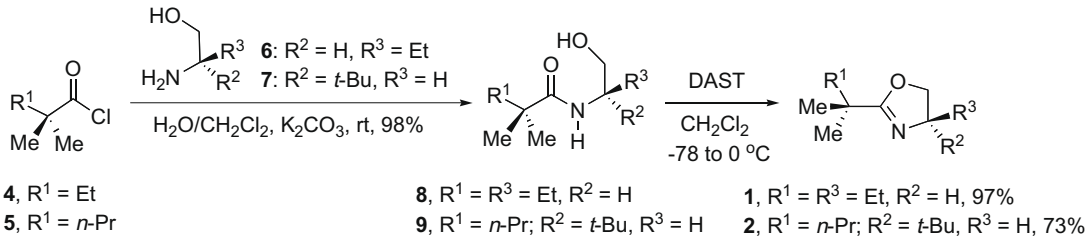
*2.4.16. Preparation of chloro-[2-adamantyl-2-(4-isobutyl-2-oxazolin-2-yl)propyl-C,N](triphenylphosphine)palladium(II) (**21**)*

A solution of the μ-Cl dimer **20** (68.2 mg, 0.0767 mmol) and PPh_3 (42.8 mg, 0.163 mmol) in benzene (5.0 mL) was stirred under N_2 at rt for 43 h. The solvent was evaporated and the residue was purified by preparative TLC using 95:5 benzene–EtOAc as the eluent. The product (101.8 mg, 94%) was isolated as a white solid and as a 1:1 mixture of two isomers (^{31}P NMR data). Mp 123–128 °C; R_f 0.57 (4:1 benzene–EtOAc); IR (thin film of $CDCl_3$ soln, *v*, cm^{-1}): 1639 (C=N); ^{1}H NMR (δ, ppm, a mixture of two isomers): 0.70 and 1.48 (dd and m, $^2J_{HH}$ = 10.0, $^3J_{HP}$ = 7.2, PdCH^A and PdCH^B of one isomer), 0.99 and 1.15 (m and d, $^2J_{HH}$ = 10.0, PdCH^A and PdCH^B of the other isomer), 0.90–1.7 (m, 23H, CH_2 of Ad, C*H*^{B}C*HMe*$_2$ and $PdCH_2$C*Me*), 1.87 (br. s, 3H, CH of Ad), 2.34 (m, 1H C*H*^{A}CHMe$_2$), 4.25 (m, OCH^A), 4.40–4.51 (m, 2H, OCH^B and NCH); ^{13}C NMR (δ, ppm): 20.7 and 21.2 (C*Me*$_2$), 21.6, 21.7, 23.8 and 23.9 (CH*Me*$_2$), 25.3 and 25.5 (*C*HMe), 28.6 and 28.8 (CH of Ad), 32.4 and 32.6 ($PdCH_2$), 36.5, 36.9, 37.0 and 37.6 (two CH_2 groups of Ad), 36.7 and 37.5 (*C*Me$_2$), 43.5 and 44.3 (*C*H$_2$CHMe$_2$), 50.9 and 51.6 (C of Ad), 60.6 and 60.8 (two d, $^3J_{CP}$ = 2.4 and 2.1, NCH), 73.6 and 74.6 (two d, $^4J_{CP}$ = 3.0, OCH_2), 128.1 (d, $^2J_{CP}$ = 10.4, *o*-CH of PPh_3), 130.1 (d, $^4J_{CP}$ = 2.4, *p*-CH of PPh_3), 131.6 and 131.7 (two d, $^1J_{CP}$ = 47.6 and 47.9, *ipso*-C of PPh_3), 134.7 and 134.8 (two d, $^3J_{CP}$ = 7.5, *m*-CH of PPh_3), 181.9 and 182.5 (two d, ^3J = 2.3 and 2.7, OCN). ^{31}P NMR (δ, ppm): 32.7 and 32.3. *Anal. Calc.* for $C_{38}H_{47}ClNOPPd_2$: C, 64.59; H, 6.70; N, 1.98. Found: C, 64.39; H, 6.72; N, 2.09%.

3. Results and discussion

3.1. Oxazoline synthesis

(*R*)-4-Ethyl-2-(1,1-dimethylpropyl)-2-oxazoline, **1,** and (*S*)-4-*tert*-butyl-2-(1,1-dimethylbutyl)-2-oxazoline, **2**, were obtained from the corresponding acid chlorides **4** and **5** and commercially available optically enantiopure amino acids (*R*)-**6** and (*S*)-**7** following a two-step published procedure (Scheme 1). First, acid chlorides **4** and **5** were converted to the corresponding hydroxy amides **8** and **9** in quantitative yield. Then, compounds **8** and **9**



Scheme 1.

were subjected to the (diethylamino)sulfur trifluoride (DAST)-mediated cyclization [25] to afford oxazolines **1** and **2** in 97% and 73%, respectively.

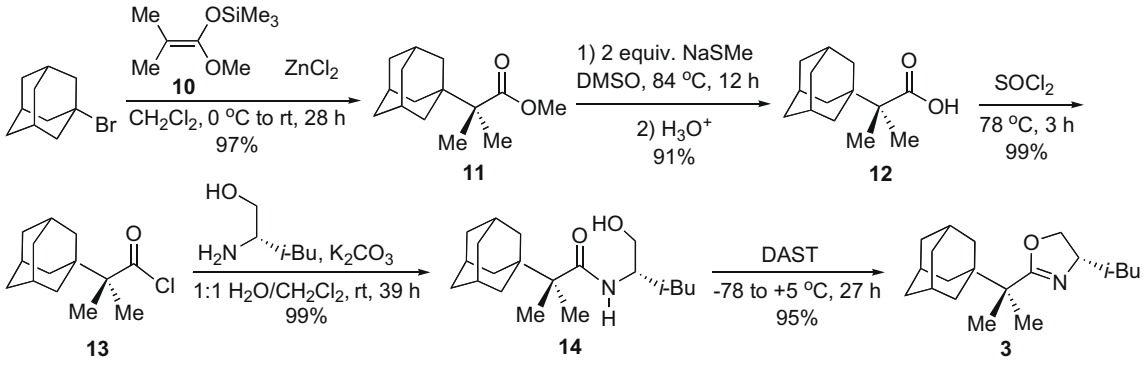
Synthesis of (*S*)-2-(1-adamantyl-1-methylethyl)-4-isobutyl-2-oxazoline, **3**, was achieved from adamantyl bromide in five steps in 82% overall yield (Scheme 2). First, adamantyl bromide was converted to carboxylic ester **11** using methyl trimethylsilyl dimethylketene acetal **10** and $ZnCl_2$ in 97% yield [26]. The treatment of ester **11** with 2 equiv. of NaSMe in DMSO, followed by aqueous workup, afforded the corresponding acid **12** in 91% yield. The reaction of acid **12** with excess $SOCl_2$ provided acyl chloride **13** in quantitative yield. The acylation of commercially available (*S*)-leucinol by acyl chloride **13** furnished amide **14** in quantitative yield. In the last step, the DAST-mediated cyclization [25] of **14** afforded oxazoline **3** in quantitative yield.

3.2. Cyclopalladation of oxazolines *1–3*

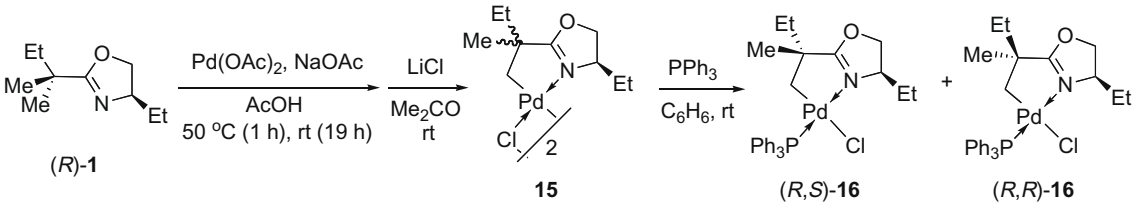
Direct cyclopalladation of oxazoline **1** using $Pd(OAc)_2$ in acetic acid in the presence of NaOAc, followed by treatment of the crude product with LiCl, afforded dimer **15** in 68% yield after purification (Scheme 3). According to ^1H and ^{13}C NMR data, compound **15** was a complex mixture of two major isomers in a ratio of 1.3:1, with a trace amount of other isomers. It was impossible to assign the structures of two major isomers, because dimeric cyclopalladated complexes can exhibit trans/cis isomerism and each of these geometrical isomers contains two palladacycles with the same or opposite configuration of the new chiral center. Attempts to separate the isomers by column chromatography or preparative TLC on silica gel were unsuccessful. Reaction of dimer **15** with PPh_3 resulted in the formation of two diastereomeric mononuclear complexes, (*R,R*)-**16** and (*R,S*)-**16**. The ^{31}P NMR spectrum of complex **16** obtained from compound **15** contained two signals (δ 32.91 and 32.94 ppm) in a ratio of 1.3:1. All known PPh_3 adducts of cyclopalladated oxazolines have the trans(*N,P*) geometry [20–24,27]. The chemical shift of δ 32.9 ppm for the ^{31}P NMR signal of compound **16** is the same or very similar, δ 32.4, compared to the values reported for two PPh_3 mononuclear cyclopalladated complexes with a (sp^3)C–Pd bond and the trans(*P,N*) geometry proven by X-ray crystallographic analysis of solid samples [21,28]. Assuming that both signals in the spectrum of **16** belong to trans(*N,P*) isomers, the 1.3:1 signal ratio must correspond to the ratio of two diastereomers of **16**, which differ by the configuration of the chiral center created upon the cyclopalladation.

To investigate the solvent effect on the isomer ratio, cyclopalladation of oxazoline **1** using $Pd(OAc)_2$/NaOAc was also carried out in MeCN. The reaction was performed at reflux during 4 h and yielded 77% of dimer **15.** The diastereomer ratio of the corresponding PPh_3 adducts **16** obtained from a crude mixture of isomers **15** was similar, ca. 1.2:1 (^{31}P NMR data). Cyclopalladation of oxazoline **1** using $Pd(OAc)_2$/NaOAc in MeCN at room temperature (12 h) followed by treatment with LiCl, provided only traces of dimer **15** (TLC data). When heterocycle **1** reacted with Na_2PdCl_4 in MeOH in the presence of NaOAc at room temperature, the desired complex **15** was not detected (^1H NMR data) and the coordination complex $PdCl_2(\mathbf{1})_2$ was isolated in 62% yield.

The poor diastereoselectivity observed with oxazoline **1** prompted us to test heterocycle **2** with the much bulkier *tert*-butyl group at the chiral center than the ethyl group in compound **1**. Reaction of compound **2** in acetic acid (68 °C, 90 h) provided two complexes, **17** and **18**, in a ratio of 5:2 and a total yield of 39%. Compounds **17** and **18** had completely different ^1H and ^{13}C NMR spectra. This suggests that the complexes have two different palladacycles, endo and exo. Previously, we reported that oxazolines have a strong tendency to form endo-cyclic complexes with the C=N bond within a palladacycle [21,23,24]. For example, cyclopalladation of (*S*)-2-*tert*-butyl-4-phenyl-2-oxazoline using $Pd(OAc)_2$ provided two products with the endo and exo metalacycles in a ratio of 13:1 in spite of the fact that the formation of the major endo complex required the (sp^3)C–H bond activation versus the usually more preferable (sp^2)C–H bond activation for the minor exo derivative [21]. Assuming the endo palladation preference in the reaction of oxazoline **2**, the major isomer **17** was assigned the endo structure of the palladacycle, while the minor isomer **18** must be the exo derivative. To support this assignment, ^{13}C NMR spectra of known oxazoline-based exo and endo palladacycles were com-



Scheme 2.



Scheme 3.

pared with those of complexes **17** and **18**. For the reported endo palladacycle obtained from 2-*tert*-butyl-4-phenyl-2-oxazoline, the ^{13}C NMR chemical shift of the $PdCH_2$ signal was δ 28.2 ppm [21]. The ^{13}C NMR signals of the same fragment in complexes **15**, **17**, and **20** (*vide infra*) appeared at δ 25.7, 25.5, and 24.3 ppm, respectively. For comparison, the only reported exo palladacycle with the $PdCH_2$ moiety exhibited a signal at δ 40.9 ppm [22]; this value is close to that for the signal at δ 43.06 ppm assigned to the same group in the spectrum of complex **18** (Scheme 4).

Cyclopalladation of oxazoline **2** using $Pd(OAc)_2$ in MeCN (76 °C, 11 h) also furnished a mixture of two types of complexes, **17** and **18**, in a ratio of 7:2 and a total yield of 58%. Unfortunately, the ^1H and ^{13}C NMR spectra of mixtures of **17** and **18**, as well as mixtures of the corresponding PPh_3 adducts, were too complicated for the analysis of possible stereoisomers. After many purifications, a pure sample of **17** was obtained; however, it could not be used for estimation of diastereoselectivity in reactions of oxazoline **2** with $Pd(OAc)_2$ in AcOH and MeCN.

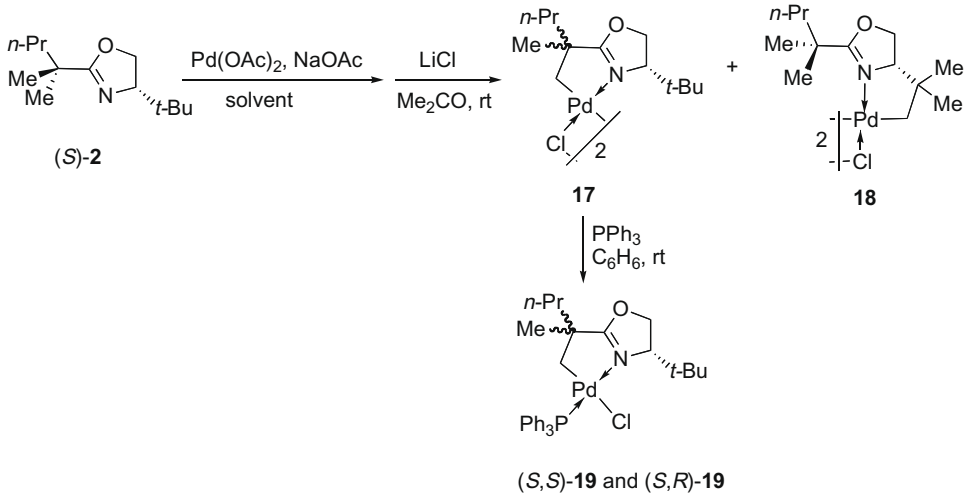
When the reaction of oxazoline **2** with $Pd(OAc)_2$ was carried out in CH_2Cl_2 (rt, 120 h), only one cyclopalladated complex **17** was obtained (61% yield). For estimation of cyclopalladation diastereoselectivity, crude dimer **17** was converted to the corresponding PPh_3 adduct **19**. According to ^{31}P NMR data, the obtained complex **19** was a mixture of two diastereomers in a ratio of 1.3:1.

Reaction of oxazoline **2** with Na_2PdCl_4 in MeOH at rt was also tested; however, it produced no traces of either **17** or **18**. The corresponding coordination complex $PdCl_2(\mathbf{2})_2$ was isolated in 17% yield.

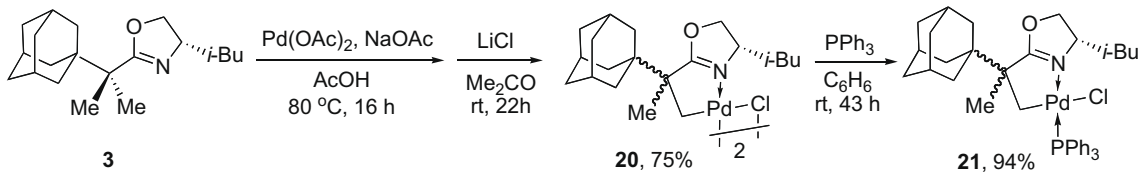
Since the replacement of the ethyl group at the chiral center in oxazoline **1** for the bulkier *tert*-Bu group in oxazoline **2** did not improve diastereoselectivity of cyclopalladation, reactions of heterocycle **3** were also investigated. In oxazoline **3**, a bulky adamantyl group was placed next to the prochiral CMe_2 center instead of the ethyl and *n*-propyl groups in compounds **1** and **2**, respectively. To avoid the exo palladacycle formation, the *tert*-butyl fragment in heterocycle **2** was replaced by the *iso*-Bu group in oxazoline **3**.

Cyclopalladation of oxazoline **3** with $Pd(OAc)_2$ in AcOH (80 °C, 16 h) followed by treatment with LiCl in acetone, provided complex **20** in 75% (Scheme 5). To estimate diastereoselectivity of the metalation, dimer **20** was converted to the PPh_3 adduct **21**. According to the ^{31}P NMR data, a ratio of two diastereomers of **21** was close to 1.3:1. Cyclopalladation of the adamantyl derivative **3** at rt in CH_2Cl_2 (65 h) followed by transformation of dimer **20** to mononuclear complex **21**, provided a diastereomeric mixture of the PPh_3 adduct of the same ratio.

The observed stereoselectivity for metalation of oxazolines **1**–**3** is significantly lower from that reported for palladation of ferrocenyl derivatives and structurally related compounds having the oxazoline [19], imidozoline [13], imine [15], or hydrazone [14] moiety with a N atom in the β-position to the prochiral metallocene fragment. The reason for excellent results in cyclopalladation of such systems is the possibility of only one rotamer of the Pd-coordinated ligand leading to the C–H bond activation [13–15,19]. Interestingly enough, excellent stereoselectivity for such systems was observed regardless the conditions used: Na_2PdCl_4 at rt [15] or $Pd(OAc)_2$ at 95 °C [19]. The reported highly diastereoselective palladation of the prochiral CMe_2 group in steroids and terpenoids [18] can be explained by a rigid polycyclic structure of the ligands. Such structures are expected to have preferred conformations with two prochiral Me groups positioned in two distinctly different faces of the chiral molecule. In the studied oxazolines **1**–**3**, there is unrestricted rotation around the $C^{ox}(2)$–CMe_2 bond; therefore, there is neither a preferred conformation of the $RCMe_2$ substituent relative to the Pd-coordinated oxazoline fragment nor a significant difference for the Pd atom to react with a C–H bond in either pro(*S*)-Me or pro-(*R*)-Me groups.



Scheme 4.



Scheme 5.

4. Conclusions

We have presented the synthesis of three enantiopure oxazolines **1**–**3** and their cyclopalladation using $Pd(OAc)_2$. The diastereoselectivity of cyclopalladation was estimated using ^{13}P NMR spectra of the corresponding PPh_3 adducts. It was found that, under the conditions used, cyclopalladation of enantiopure oxazolines **1**–**3** occurred with low diastereoselectivity. Neither the introduction of the bulky *tert*-butyl group at the chiral center in oxazoline **2**, nor the presence of the large adamantyl group next to the prochiral CMe_2 in compound **3** affected diastereoselectivity.

Acknowledgments

We are grateful to NSF and ND EPSCoR (Grant No. EPS-0814442) for financial support.

References

[1] (a) R. Giri, X. Chen, J.-Q. Yu, Angew. Chem., Int. Ed. 44 (2005) 2112;
(b) R. Giri, X. Chen, X.-S. Hao, J.-J. Li, J. Liang, Z.-P. Fan, J.-Q. Yu, Tetrahedron: Asymmetry 16 (2005) 3502;
(c) X. Chen, J.-J. Li, X.-S. Hao, C.E. Goodhue, J.-Q. Yu, J. Am. Chem. Soc. 128 (2006) 78;
(d) J.-Q. Yu, R. Giri, X. Chen, Org. Biomol. Chem. 4 (2006) 4041.
[2] (a) A.R. Dick, M.S. Remy, J.W. Kampf, M.S. Sanford, Organometallics 26 (2007) 1365;
(b) N.R. Deprez, M.S. Sanford, Inorg. Chem. 46 (2007) 1924;
(c) K.L. Hull, M.S. Sanford, J. Am. Chem. Soc. 129 (2007) 11904;
(d) D. Kalyani, A.R. Dick, W.Q. Anani, M.S. Sanford, Tetrahedron 62 (2006) 11483;
(e) L.V. Desai, K.L. Hull, M.S. Sanford, J. Am. Chem. Soc. 126 (2004) 9542.
[3] (a) V.I. Sokolov, L.L. Troitskaya, Chimia 32 (1978) 122;
(b) V.I. Sokolov, L.L. Troitskaya, O.A. Reutov, J. Organomet. Chem. 182 (1979) 537.
[4] I.A. Mamedyarova, M.N. Nefedova, V.I. Sokolov, J. Organomet. Chem. 524 (1996) 181.
[5] L.A. Bulygina, V.I. Sokolov, I.A. Utepova, V.L. Rusinov, O.N. Chupakhin, O.N. Russ, Chem. Bull. Int. Ed. 56 (2007) 1080.
[6] L.L. Troitskaya, S.T. Ovseenko, V.I. Sokolov, M. Gruselle, Russ. Chem. Bull. 47 (1998) 1382.
[7] A.D. Ryabov, I.M. Panyashkina, G.M. Kazankov, V.A. Polyakov, L.G. Kuz'mina, J. Organomet. Chem. 601 (2000) 51.
[8] V.V. Dunina, O.N. Gorunova, E.D. Kuznetsova, E.I. Turubanova, M.V. Livantsov, Y.K. Grishin, L.G. Kuz'mina, A.V. Churakov, Russ. Chem. Bull. Int. Ed. 55 (2006) 2193.
[9] V.V. Dunina, E.D. Razmyslova, O.N. Gorunova, M.V. Livantsov, Y.K. Grishin, Tetrahedron: Asymmetry 14 (2003) 2331.
[10] A.D. Ryabov, G.M. Kazankov, Vestn. Mosk. Univ., Ser. 2: Khim. 29 (1988) 220.
[11] V.I. Sokolov, L.L. Troitskaya, O.A. Reutov, J. Organomet. Chem. 133 (1977) C28.
[12] C. López, R. Bosque, X. Solans, M. Font-Bardia, Tetrahedron: Asymmetry 7 (1996) 2527.
[13] R. Peters, Z. Xin, D.F. Fischer, W.B. Schweizer, Organometallics 25 (2006) 2917.
[14] G. Zhao, Q.-G. Wang, T.C.W. Mak, J. Chem. Soc., Dalton Trans. (1998) 3785.
[15] (a) G. Zhao, Q.-C. Yang, T.C.W. Mak, Organometallics 18 (1999) 3623;
(b) G. Zhao, Q.-G. Wang, T.C.W. Mak, Polyhedron 18 (1999) 577;
(c) G. Zhao, Q.-G. Wang, T.C.W. Mak, Organometallics 17 (1998) 3437;
(d) G. Zhao, F. Xue, Z.-Y. Zhang, T.C.W. Mak, Organometallics 16 (1997) 4023.
[16] L.L. Troitskaya, S.T. Ovseenko, Y.L. Slovokhotov, I.S. Neretin, V.I. Sokolov, J. Organomet. Chem. 642 (2002) 191.
[17] V.V. Dunina, O.N. Gorunova, M.V. Livantsov, Y.K. Grishin, L.G. Kuz'mina, N.A. Kataeva, A.V. Churakov, Inorg. Chem. Commun. 3 (2000) 354.
[18] A. García-Granados, P.E. López, E. Melguizo, A. Parra, Y. Simeó, J. Org. Chem. 72 (2007) 3500. and references cited therein.
[19] A.M. Stevens, C.J. Richards, Organometallics 18 (1999) 1346.
[20] (a) R.Y. Mawo, D.M. Johnson, J.L. Wood, I.P. Smoliakova, J. Organomet. Chem. 693 (2008) 33;
(b) I.P. Smoliakova, K.J. Keuseman, D.C. Haagenson, D.M. Wellmann, P.B. Colligan, N.A. Kataeva, A.V. Churakov, L.G. Kuz'mina, V.V. Dunina, J. Organomet. Chem. 603 (2000) 86.
[21] R.Y. Mawo, S. Mustakim, V.G. Young Jr., M.R. Hoffmann, I.P. Smoliakova, Organometallics 26 (2007) 1801.
[22] K.J. Keuseman, I.P. Smoliakova, V.V. Dunina, Organometallics 24 (2005) 4159.
[23] O.N. Gorunova, K.J. Keuseman, B.M. Goebel, N.A. Kataeva, A.V. Churakov, L.G. Kuz'mina, V.V. Dunina, I.P. Smoliakova, J. Organomet. Chem. 689 (2004) 2382.
[24] D.L. Peterson, K.J. Keuseman, N.A. Kataeva, L.G. Kuz'mina, J.A.K. Howard, V.V. Dunina, I.P. Smoliakova, J. Organomet. Chem. 654 (2002) 66.
[25] P. Lafargue, P. Guenot, J.-P. Lellouche, Heterocycles 41 (1995) 947.
[26] M.T. Reetz, K. Schwellnus, F. Huebner, W. Massa, R.E. Schmidt, Chem. Ber. 116 (1983) 3708.
[27] (a) T. Izumi, H. Watabe, A. Kasahara, Bull. Chem. Soc. Jpn. 54 (1981) 1711;
(b) A. Moyano, M. Rosol, R.M. Moreno, C. López, M.A. Maestro, Angew. Chem., Int. Ed. 44 (2005) 1865;
(c) G. Balavoine, J.C. Clinet, P. Zerbib, J. Organomet. Chem. 389 (1990) 259;
(d) C. Bolm, K. Wenz, G. Raabe, J. Organomet. Chem. 66 (2002) 23;
(e) G. Balavoine, J.C. Clinet, J. Organomet. Chem. 390 (1990) C84;
(f) A.R. Cowley, R.I. Cooper, E. Capito, J.M. Brown, A. Ricci, Acta Crystallogr., Sect. E 60 (2005) m582.
[28] V.V. Dunina, O.N. Gorunova, E.B. Averina, Y.K. Grishin, L.G. Kuz'mina, J.A.K. Howard, J. Organomet. Chem. 603 (2000) 138.

Polyhedron 28 (2009) 85–90

Contents lists available at ScienceDirect

Polyhedron

journal homepage: www.elsevier.com/locate/poly

Synthesis and characterization of adducts of bis(*O,O′*-ditolyl/dibenzyl dithiophosphato)cobalt(II) with pyridine: Crystal structures of $[Co\{S_2P(OC_6H_4Me\text{-}p)_2\}_2(C_5H_5N)_2]$ and $[Co\{S_2P(OC_6H_4Me\text{-}p)_2\}_2(NH_3)]$

Subhash C. Bajia [a], John E. Drake [b], Mark E. Light [c], Manisha Nirwan [a], Sushil K. Pandey [d], Raju Ratnani [a,*]

[a] Department of Pure and Applied Chemistry, M.D.S. University, Jaipur Road, Ajmer 305 009, Rajasthan, India
[b] Department of Chemistry and Biochemistry, University of Windsor, Windsor, Ont., Canada N9B 3P4
[c] Department of Chemistry, University of Southampton, Highfield, Southampton SO17 1BJ, UK
[d] Department of Chemistry, Jammu University, Jammu 180 006, India

ARTICLE INFO

Article history:
Received 24 July 2008
Accepted 29 September 2008
Available online 17 November 2008

Keywords:
Cobalt(II) complexes
O,O′-Ditolyl/dibenzyl dithiophosphates
Nitrogen base adducts
Crystal structures

ABSTRACT

Bis(*O,O′*-ditolyl/dibenzyl dithiophosphato)cobalt(II) complexes with pyridine ligands of the type $[Co\{S_2P(OR)_2\}_2(C_5H_5N)_2]$ (R = *o*-, *m*-, *p*-C_6H_4Me, CH_2Ph) have been synthesized by the reaction of $CoCl_2(C_5H_5N)_2$ and the corresponding ammonium salt of *O,O′*-ditolyl/dibenzyl dithiophosphate in methanol. These newly synthesized adducts were characterized by elemental analysis, IR, UV–Vis spectroscopy, magnetic susceptibility measurements and single crystal X-ray diffraction. These structures confirm that in the pyridine complex the geometry around the cobalt metal centre is distorted octahedral, and in the amine complex it is distorted trigonal bipyramidal.

© 2008 Elsevier Ltd. All rights reserved.

1. Introduction

The 1,1-dithiolate ligands, viz. *O,O′*-dialkyl/alkylene dithiophosphates, are versatile in nature and coordination complexes with cobalt have been reported in the literature [1–13]. In these complexes, the dithiophosphate ligand moieties are normally bidentate. X-ray crystal structures have been reported for a number of cobalt compounds with *O,O′*-dialkyl dithiophosphates including $Co[S_2P(OMe)_2]_3$ [14], $Co[S_2P(i\text{-}OPr)_2]_3$ [15], $[Co\{S_2P(OMe)_2\}_2 \cdot PPh_3]$ [16], $[NMe_4][CoCl\{S_2P(OMe)_2\}_2]$ [17], $Co[S_2P(OEt)_2]_3 \cdot 1/2H_2O$ [18], $[Co\{S_2P(OEt)_2\}_2(C_5H_5N)_2]$ [19], $[Co\{S_2P(OCy)_2\}_2(C_5H_5N)_2]$ [20] and $[Co\{S_2P(OEt)_2\}_2(C_{24}H_{26}O_2N_4)]$ [21]. Reports on metal complexes containing *O,O′*-ditolyl dithiophosphate ligands are relatively few [22–24]. Recently, we have used *O,O′*-ditolyl/dibenzyl dithiophosphate to examine the influence of bulkier groups on phosphorus and have reported the syntheses, spectroscopic studies and single crystal X-ray structures of $Ni[S_2P(OC_6H_4CH_3\text{-}o)_2]_2$ [25], $Ni[S_2P(OC_6H_4CH_3\text{-}m)_2]_2$ [25], $Ni[S_2P(OCH_2Ph)_2]_2$ [25], $[Ni\{S_2P(OC_6H_4Me\text{-}p)_2\}_2(N_2C_{10}H_8)]$ [26], $[Ni\{S_2P(OC_6H_4Me\text{-}o)_2\}_2(N_2C_{14}H_{12})] \cdot C_6H_6$ [26] $Me_2Sn[S_2P(OC_6H_4Me\text{-}o)_2]_2$ [27], $Bu_2Sn[S_2P(OC_6H_4Me\text{-}o)_2]_2$ [27], $Mo_2O_3[S_2P(OC_6H_4Me\text{-}o)_2]_4$ [28], $Mo_2O_3[S_2P(OC_6H_4Me\text{-}m)_2]_4$ [28] and $MoO_2[S_2P(OC_6H_4Me\text{-}p)_2]_2$ [28].

In continuation of this interest, we report here the synthesis, and spectroscopic characterization of pyridine adducts of bis(*O,O′*-ditolyl/dibenzyl dithiophosphato)cobalt(II) complexes and a bis(*O,O′*-dibenzyl dithiophosphato)cobalt(II) complex. We also report the single crystal X-ray structures of $[Co\{S_2P(OC_6H_4Me\text{-}p)_2\}_2(C_5H_5N)_2]$ and $[Co\{S_2P(OC_6H_4Me\text{-}p)_2\}_2(NH_3)]$.

2. Results and discussion

The reactions of cobalt chloride hexahydrate with ammonium salts of *O,O′*- ditolyl dithiophosphates in a 1:2 molar ratio were carried out in methanol. Initially a blue solution of bis(*O,O′*-ditolyl dithiophosphato)cobalt(II) was obtained, which soon turned green, indicating oxidation of Co(II) to Co(III), and finally turned brown. Various methods were adopted to avoid decomposition, such as carrying out the reaction in a foil wrapped flask at low temperature, but all failed, with the solid obtained slowly decomposing into a brown solid. Attempts were also made to avoid oxidation by carrying out the reactions with $CoCl_2 \cdot 6H_2O$ and the sodium salts of the *O,O′*-ditolyl dithiophosphates, but these again yielded the oxidized brown solids. However, the oxidation reactions were comparatively slow as compared to when the ammonium salts were used. Reactions were also carried out at lower temperature (5 °C), which again yielded cobalt(III) complexes. However, in one of these attempts plate-like blue crystals of $[Co\{S_2P(OC_6H_4Me\text{-}p)_2\}_2(NH_3)]$ were isolated, which were relatively stable.

An indirect method was used to prepare adducts of bis(*O,O′*-ditolyl dithiophosphato)cobalt(II) with pyridine, This route readily

* Corresponding author. Tel.: +91 11 145 2640059.
E-mail address: ratnaniraju@yahoo.co.uk (R. Ratnani).

0277-5387/$ - see front matter © 2008 Elsevier Ltd. All rights reserved.
doi:10.1016/j.poly.2008.09.025

produced the expected compounds in good yields. Initially, the blue solid bispyridine cobalt(II) chloride was prepared and then a stoichiometric amount of ligand was added in situ, to give the purple pyridine adducts of the (*O,O′*-ditolyldithiophosphato)cobalt(II) complexes.

$$CoCl_2 \cdot 6H_2O + 2C_5H_5N \rightarrow CoCl_2(C_5H_5N)_2$$
$$CoCl_2(C_5H_5N)_2 + 2NH_4S_2P(OR)_2 \rightarrow [Co\{S_2P(OR)_2\}_2(C_5H_5N)_2]$$
$$(R = o-, m-, p- C_6H_4Me, CH_2Ph)$$

However, the cobalt(II) complex with dibenzyl dithiophosphate was prepared by the one step stoichiometric reaction of cobalt chloride hexahydrate with the ammonium salt of dibenzyl dithiophosphate in methanol on stirring at room temperature to give a blue solid product in good yield. This blue solid, on further reaction with pyridine, gave a purple coloured adduct.

$$CoCl_2 \cdot 6H_2O + 2NH_4S_2P(OCH_2Ph)_2 \rightarrow [Co\{S_2P(OCH_2Ph)_2\}_2]$$
$$[Co\{S_2P(OCH_2Ph)_2\}_2] + 2C_5H_5N \rightarrow [Co\{S_2P(OCH_2Ph)_2\}_2(C_5H_5N)_2]$$

In the case of the *O,O′*-dibenzyl dithiophosphate cobalt(II) complex, the decomposition rate to the brown coloured cobalt(III) complex is quite slow, giving enough time to isolate the tetrahedral blue coloured cobalt(II) complex at room temperature. The fact that the oxidation rate for the bis(*O,O′*-ditolyl dithiophosphato)cobalt(II) complexes is comparatively fast is probably because of the electron withdrawing effect due to the conjugation of the tolyl moiety which makes the phosphorous have a lower electron density and in turn withdraw electrons from the sulfur, giving rise to weaker bonding between the Co and S atoms, which aids the oxidation of Co(II) to Co(III). This conjugation effect is absent for the dibenzyl derivative.

All these pyridine adducts of the bis(*O,O′*-ditolyl/dibenzyl dithiophosphato)cobalt(II) complexes are soluble in common organic solvents such as benzene, chloroform and acetone. The products were characterized by elemental analysis, IR, UV–Vis spectroscopy and magnetic susceptibility measurements, along with the X-ray crystal structure determination of $[Co\{S_2P(OC_6H_4Me\text{-}p)_2\}_2(C_5H_5N)_2]$ and $[Co\{S_2P(OC_6H_4Me\text{-}p)_2\}_2(NH_3)]$.

2.1. IR spectra

The relevant assignments of the IR bands (Table 1) have been made by a comparison with the spectra of the ammonium salts of the *O,O′*-ditolyl/dibenzyl dithiophosphates [29] and analogous adducts of cobalt(II) complexes [9]. The two strong to medium intensity bands present in the regions 1030–1068 and 897–993 cm^{-1} are assigned to ν[(P)–O–C] and ν[P–O–(C)] stretching vibrations, respectively. Bands due to ν(P=S) or $\nu(P–S)_{asymm}$ and ν(P–S) or $\nu(P–S)_{symm}$ are observed in the ranges 669–702 and 591–602 cm^{-1}. The metal sulfur ν(Co–S) weak bands in the 405–439 cm^{-1} region indicate coordination of the dithiophosphate ligands through the sulfur atoms. Weak to medium intensity bands due to ν(Co–N) are also seen in the region 351–388 cm^{-1}. Further, in the case of the pyridine adducts **1–4**, additional medium intensity bands in the region 1579–1634 cm^{-1} are due to the C–N vibrations of the aromatic ring, indicating the presence of the nitrogen base donors in the adducts.

2.2. Electronic absorption spectra

The electronic spectra of the pyridine adducts of the bis(*O,O′*-ditolyl/dibenzyl dithiophosphato)cobalt(II) complexes and the bis(*O,O′*-dibenzyl dithiophosphato)cobalt(II) complex were carried out in pyridine and CH_2Cl_2 solvents, respectively. The electronic spectra suggest a tetrahedral configuration for $[Co\{S_2P(OCH_2Ph)_2\}_2]$ which is supported by the presence of a strong absorption band at 613 nm [2]. This band is caused by the $^4A_2 \rightarrow {}^4T_1(F)$ transition whereas, the band at 579 nm is due to the $^4A_2 \rightarrow {}^4T_1(P)$ transition. Splitting is also observed in the main band at 613 nm due to spin–orbital coupling.

In the case of the octahedral adducts, the peaks corresponding to the transitions $^4T_{1g}(F) \rightarrow {}^4T_{1g}(P)$, $^4T_{1g}(F) \rightarrow {}^4A_{2g}(F)$ and $^4T_{1g}(F) \rightarrow {}^4T_{2g}(F)$ are seen in the ranges 500–524, 574–746 and 1026–1138 nm, respectively. Almost identical electronic transitions for the pyridine adducts of bis(diethyldithiocarbamato) cobalt(II) [30] and benzathiazole and benzimidazole adducts of bis(diethyldithiophosphato)cobalt(II) [9] were observed, indicating an octahedral coordination.

2.3. Magnetic measurements

The conclusion about the tetrahedral and octahedral coordination in the complexes is further supported by the magnetic moment for $[Co\{S_2P(OCH_2Ph)_2\}_2]$ of 4.34 B.M., as compared with those of the pyridine adducts which range from 4.87 to 5.0 B.M.

2.4. Crystal Structures of $[Co\{S_2P(OC_6H_4Me\text{-}p)_2\}_2(C_5H_5N)_2]$ and $[Co\{S_2P(OC_6H_4Me\text{-}p)_2\}_2(NH_3)]$

$[Co\{S_2P(OC_6H_4Me\text{-}p)_2\}_2(C_5H_5N)_2]$ (**3**) and $[Co\{S_2P(OC_6H_4Me\text{-}p)_2\}_2(NH_3)]$ (**6**) crystallize in the monoclinic space groups $P2_1/c$ (centrosymmetric) and $P2_1/n$, respectively. The ORTEP diagram of the molecular structure of **3** in Fig. 1 displays a distorted octahedral geometry with the pyridine molecules occupying *trans* positions. In contrast, the ORTEP diagram of the molecular structure of **6** in Fig. 2 displays distorted trigonal bipyramidal geometry with N(1), S(1) and S(3) occupying the equatorial plane and S(2) and S(4) in the axial positions, similar to the structure of $[Co\{S_2P(OMe)_2\}_2 \cdot PPh_3]$ [16], with a phosphine electron donor instead of a nitrogen base. The Co–N bond distance of (2.162(2) Å) in **3** is essentially the same as that in $[Co\{S_2P(OEt)_2\}_2(C_5H_5N)_2]$ (2.164(3) Å) [19], which also has *trans* Co–N bonds. The shorter Co–N bond length of 2.052(2) Å in **6**, is closer to the average Co–N bond length of 2.041(7) Å in $[Co\{S_2P(OEt)_2\}_2(C_{24}H_{26}N_4O_2)]$ [21] where the Co–N bonds are *cis*.

In **6**, as is to be expected for a trigonal pyramidal structure, the $Co–S_{axial}$ bonds (ave. 2.567(5) Å) are longer than the $Co–S_{equatorial}$ bonds (ave. 2.3421(7) Å), as was found in $[Co\{S_2P(OMe)_2\}_2 \cdot PPh_3]$ [16]. The longer axial Co–S bonds are accompanied by relatively shorter S(2)–P(1) and S(4)–P(2) bonds (ave. 1.960(2) Å) than the

Table 1
IR spectral data (cm^{-1}) for the pyridine adducts of the bis(*O,O′*-ditolyl/dibenzyl dithiophosphato)cobalt(II) complexes[a] and the bis(dibenzyl dithiophosphato)cobalt(II) complex.

No.	Compound	ν[(P)–O–C]	ν[P–O–(C)]	ν(P=S)	ν(P–S)	ν(Co–S)	ν(C–N)	ν(Co–N)
1	$Co[S_2P(OC_6H_4Me\text{-}o)_2]_2(2C_5H_5N)$	1038s	915m	669s	601m	439w	1599m	351w
2	$Co[S_2P(OC_6H_4Me\text{-}m)_2]_2(2C_5H_5N)$	1039s	945s	690s	591m	414w	1579m	356w
3	$Co[S_2P(OC_6H_4Me\text{-}p)_2]_2(2C_5H_5N)$	1036m	897s	688s	599m	428w	1596m, 1628m	388w
4	$Co[S_2P(OC_6H_5CH_2)_2]_2(2C_5H_5N)$	1030s	990m	702s	602s	405w	1597m, 1634m	360w
5	$Co[S_2P(OC_6H_5CH_2)_2]_2$	1068s	993m	697m	592m	402w		

[a] *Key*: s = strong, m = medium, w = weak.

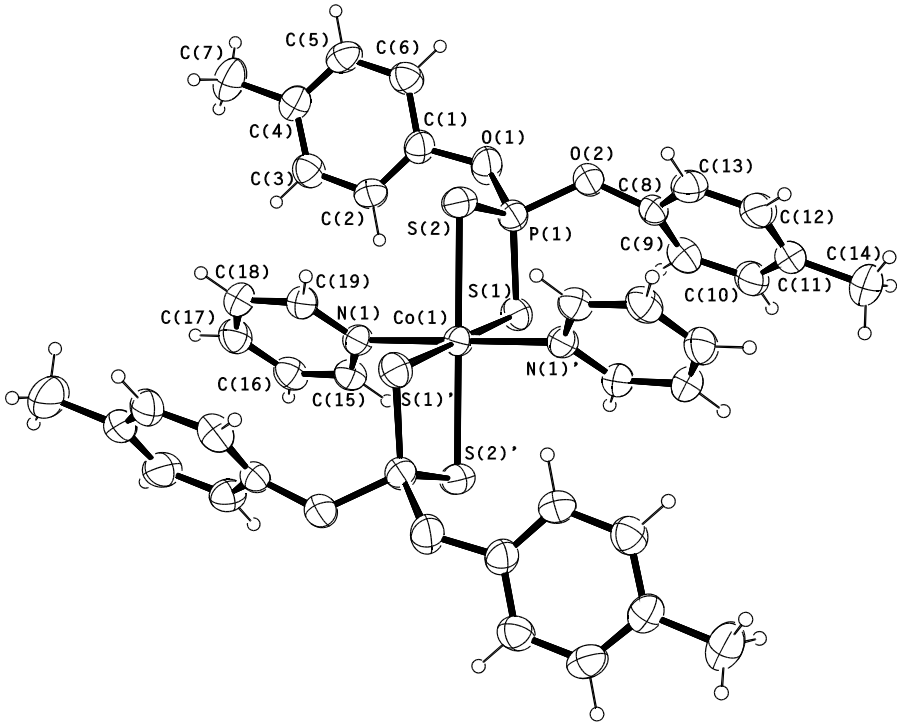


Fig. 1. ORTEP plot of the molecule $[Co\{S_2P(OC_6H_4Me\text{-}p)_2\}_2(C_5H_5N)_2]$. The non-hydrogen atoms are drawn with 30% probability ellipsoids.

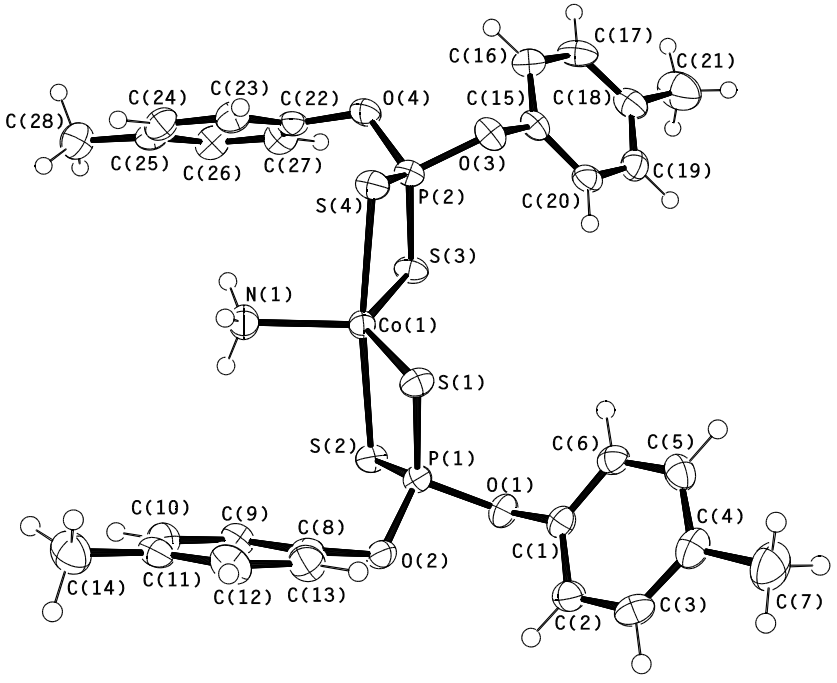


Fig. 2. ORTEP plot of $[Co\{S_2P(OC_6H_4CH_3\text{-}p)_2\}_2(NH_3)]$. The non-hydrogen atoms are drawn with 50% probability ellipsoids.

S(1)–P(1) and S(3)–P(2) bonds (ave. 1.994(9) Å) that accompany the shorter Co–S equatorial bonds. Similar trends were observed in $[Co\{S_2P(OMe)_2\}_2 \cdot PPh_3]$ [16].

When a monodentate coordinating moiety is sterically hindered, 5-coordinated Co(II) adduct formation is seen, viz. $[Co\{S_2P(OMe)_2\}_2 \cdot PPh_3]$ [16], as observed in **6**. NH_3 is a very small molecule but it may need considerable space for its coordination sphere. However, two molecules of monodentate coordinating ligands can be attached to Co(II) complexes when the coordinating moiety is planar (as in pyridine), viz. $[Co\{S_2P(OEt)_2\}_2(C_5H_5N)_2]$ [19].

In the octahedral complex **3**, there are again two sets of Co–S bonds, Co(1)–S(1) and Co(1)–S(1)′ (2.5053(8) Å) and Co(1)–S(2) and Co(1)–S(2)′ (2.5735(8) Å), although the differences are much smaller. There are no obvious signs of secondary interactions involving the sulfur atoms to account for the difference, so possibly it is indicative of a slight tetragonal distortion along the S(2)–Co(1)–S(2)′ axis; the one with the weakest bonds. The average

distance of all four Co–S bonds of 2.54(5) Å is comparable with the average Co–S distance of 2.52(2) Å reported in $[Co\{S_2P(OEt)_2\}_2(C_5H_5N)_2]$ [19].

In **3**, not unexpectedly, the longer Co(1)–S(2) bonds, are accompanied by relatively shorter S(2)–P(1) bonds (1.970(1) Å) and the shorter Co(1)–S(1) bonds by longer P(1)–S(1) bonds (1.974(1) Å). The P–O distances in **3** (ave. 1.599(2) Å), **6** (ave. 1.598(4) Å), $[Co\{S_2P(OEt)_2\}_2(C_5H_5N)_2]$ [19] (ave. 1.593(1) Å) and $[Co\{S_2P(OEt)_2\}_2(C_{24}H_{26}N_4O_2)]$ [21] (ave. 1.596(9) Å) are similar, regardless of their environment.

In **6**, the three angles in the equatorial plane, N(1)–Co(1)–S(1), N(1)–Co(1)–S(3) and S(1)–Co(1)–S(3) of 112.42(6)°, 112.96(6)° and 134.58(3)°, respectively, sum to exactly 360° as expected. The S(2)–Co(1)–S(4) angle of 172.23(2)° is not so far from 180°, given the planarity of the equatorial bonds and the requirements of the bite angles of the ligands, S(1)–Co(1)–S(2) and S(3)–Co(1)–S(4) of 83.88(2)° and 83.48(2)°, respectively In **3**, with the three 180° angles required by symmetry, the S(1)–Co(1)–S(2) and S(1)′–C(1)–S(2)′ bite angles (80.18(3)°) and the S(1)–Co(1)–S(2)′ and S(1′–Co(1)–S(2)′ (99.82(3)°) inter-ligand angles show the greatest deviation from 90°, the N–Co–S bond angles in the range of 88.82(6)–91.23(6)° showing only slight variation from a regular octahedral geometry.

3. Experimental

All chemicals (Emerk) were used after purification and solvents were dried before use by standard methods. $CoCl_2(C_5H_5N)_2$ was prepared by the reported method [30]. Literature methods were used for the preparation of the *O,O′*-ditolyl dithiophosphoric acids [29]. *O,O′*-dibenzyl dithiophosphoric acid was prepared by the reaction of P_2S_5 and benzyl alcohol in a 1:4 molar ratio. The ammonium salts of these dithiophosphoric acids were prepared by the reaction of the parent acids with an equimolar amount of ammonia in benzene. Cobalt and Sulfur were estimated by pyridine thiocyanate and Messenger's methods, respectively. Electronic spectra were recorded on a Perkin–Elmer UV–Vis–NIR spectrometer in pyridine (**1–4**) and dichloromethane (**5**). Infrared spectra were recorded on a Perkin–Elmer 983G spectrometer as Nujol mulls between CsI discs over the range 4000–180 cm^{-1}.

3.1. Preparations

3.1.1. $[Co\{S_2P(OC_6H_4Me\text{-}o)_2\}_2(C_5H_5N)_2]$ (**1**)

Typically, $CoCl_2(C_5H_5N)_2$ (0.254 g, 0.882 mmol) was dissolved in methanol (30 mL) and then a solution of $NH_4S_2P(OC_6H_4Me\text{-}o)_2$ (0.579 g, 1.825 mmol) in methanol (20 mL) was added, followed by refluxing for 1 h. The dark-pink precipitate that formed was filtered, washed and dried in vacuo. Yield: 0.644 g (87%); Calc. for $C_{38}H_{38}O_4N_2P_2S_4Co$: N, 3.35; S, 15.35; Co 7.05. Found: N, 3.40; S, 15.12; Co 6.94%; UV–Vis electronic absorption spectral data [$\lambda_{max.}$, nm(A); ε(L mol^{-1})] in 0.01 M pyridine solution 525(44), 653(42), 746(25), 915(31), 1126(22); μ_{eff} 4.91 B.M.

3.1.2. $[Co\{S_2P(OC_6H_4Me\text{-}m)_2\}_2(C_5H_5N)_2]$ (**2**)

Prepared as for $[Co\{S_2P(OC_6H_4Me\text{-}o)_2\}_2(C_5H_5N)_2]$. Yield: 0.544 g (71%); Calc. for $C_{38}H_{38}O_4N_2P_2S_4Co$: N, 3.35; S, 15.35; Co 7.05. Found: N, 3.23; S, 15.11; Co 7.14%; UV–Vis electronic absorption spectral data [$\lambda_{max.}$, nm(A); ε(L mol^{-1})] in 0.004 M pyridine solution 522(155), 574(147), 610(143), 642(135), 1138(120); μ_{eff} 4.87 B.M.

3.1.3. $[Co\{S_2P(OC_6H_4Me\text{-}p)_2\}_2(C_5H_5N)_2]$ (**3**)

Prepared as for $[Co\{S_2P(OC_6H_4Me\text{-}o)_2\}_2(C_5H_5N)_2]$. Yield: 0.531 g (76%); Calc. for $C_{38}H_{38}O_4N_2P_2S_4Co$: N, 3.35; S, 15.35; Co 7.05. Found: N, 3.44; S, 15.53; Co 7.22%; UV–Vis electronic absorption spectral data [$\lambda_{max.}$, nm(A); ε(L mol^{-1})] in 0.008 M pyridine solution 520(87), 568(80), 632(77), 715(60), 1033(57); μ_{eff} 5.0 B.M.

3.1.4. $[Co\{S_2P(OCH_2C_6H_5)_2\}_2(C_5H_5N)_2]$ (**4**)

Prepared as for $[Co\{S_2P(OC_6H_4Me\text{-}o)_2\}_2(C_5H_5N)_2]$. Yield: 0.531 g (76%); Calc. for $C_{38}H_{38}O_4N_2P_2S_4Co$: N, 3.35; S, 15.35; Co 7.05. Found: N, 3.29; S, 15.49; Co 7.12%; UV–Vis electronic absorption spectral data [$\lambda_{max.}$, nm(A); ε(L mol^{-1})] in 0.0057 M pyridine solution 500(135), 523(133), 668(98), 1038(114). μ_{eff} 4.95 B.M.

3.1.5. $[Co\{S_2P(OCH_2C_6H_5)_2\}_2]$ (**5**)

$CoCl_2 \cdot 6H_2O$ (0.289 g, 1.215 mmol) and $NH_4S_2P(OCH_2C_6H_5)_2$ (0.798 g, 2.437 mmol) were added to toluene (30 mL) and the solution was stirred for 30 min to give a blue solution which was concentrated before the addition of hexane (10 mL). The blue solid that formed was filtered, washed with hexane and dried in vacuo. Yield 0.539 g, (66%). Calc. for $C_{28}H_{28}O_4P_2S_4Co$; S, 18.93; Co, 8.70. Found: S, 18.64; Co, 8.57%; UV–Vis electronic absorption spectral data [$\lambda_{max.}$, nm(A); ε(L mol^{-1})] in 0.01 M in dichloromethane solution 579(57), 613(55), 635(49), 1043(35); μ_{eff} 4.34 B.M.

3.2. Crystallography

A purple block crystal of $[Co\{S_2P(OC_6H_4Me\text{-}p)_2\}_2(C_5H_5N)_2]$ (**3**), and a blue block crystal of $[Co\{S_2P(OC_6H_4Me\text{-}p)_2\}_2(NH_3)]$ **6** were mounted on glass fibres. Data for **3** were collected on a Siemens SMART System CCD diffractometer with the collection of a hemisphere of data in 1329 frames with 10 s exposure times. Data for **6** were collected on a Bruker-Nonius Kappa CCD area detector diffractometer, with ϕ and ω scans chosen to give a complete asymmetric unit. Cell refinements [31] gave cell constants corresponding to monoclinic cells for both, whose dimensions

Table 2
Crystal data and structure refinements for $[Co\{S_2P(OC_6H_4Me\text{-}p)_2\}_2(C_5H_5N)_2]$ and $[Co\{S_2P(OC_6H_4Me\text{-}p)_2\}_2(NH_3)]$.

Empirical formula	$C_{38}H_{38}O_4N_2P_2S_4Co$	$C_{28}H_{31}O_4N_1P_2S_4Co$
Formula weight	835.81	694.65
Temperature (K)	296(2)	120(2)
Wavelength (Å)	0.71073	0.71073
Crystal system	monoclinic	monoclinic
Space group	$P2_1/c$	$P2_1/n$
a (Å)	12.215(1)	9.9460(7)
b (Å)	15.123(2)	16.2434(8)
c (Å)	11.575(1)	19.610(1)
β (°)	114.573(1)	95.187(7)
Volume (Å^3)	1944.6(3)	3155.2(3)
Z	2	4
D_{calc} (g/cm^3)	1.427	1.462
Absorption coefficient (mm^{-1})	0.780	0.944
F(000)	866	1436
Crystal size (mm)	0.60 × 0.20 × 0.20	0.18 × 0.10 × 0.08
θ Range for data collection (°)	1.83–25.00	3.06–27.48
Index ranges	$-14 \le h \le 14$, $-17 \le k \le 17$, $-13 \le l \le 13$	$-12 \le h \le 12$, $-21 \le k \le 19$, $-25 \le l \le 25$
Reflections collected	18315	13504
Independent reflections (R_{int})	3418 (0.0324)	7184 (0.0383)
Minimum and maximum transmission	0.8595 and 0.6517	0.9283 and 0.8484
Refinement method	full-matrix least-squares on F^2	full-matrix least-squares on F^2
Data/restraints/parameters	3418/0/234	7184/0/365
Goodness-of-fit on F^2	1.047	0.990
Final R indices [$F^2 > 4\sigma(F^2)$]	R_1 = 0.0423, wR_2 = 0.1066	R_1 = 0.0411, wR_2 = 0.0893
R indices (all data)	R_1 = 0.0561, wR_2 = 0.1166	R_1 = 0.0771, wR_2 = 0.1014
Largest difference in peak and hole (e Å^{-3})	0.386 and −0.162	0.342 and −0.452

are given in Table 2 along with other experimental parameters. An absorption correction was applied [32].

The structures were solved by direct methods [33] and were refined using the WINGX version [34] of SHELX-97 [35]. All of the non-hydrogen atoms were treated anisotropically. Hydrogen atoms were included in idealized positions with isotropic thermal parameters set at 1.2 times that of the carbon atoms to which they were attached. The final cycle of full-matrix least-squares refinement was based on 3418 (for **3**) and 7184 (for **6**) observed reflections, 2629 with $F^2 > 4\sigma(F^2)$ for **3** and 4823 with $F^2 > 4\sigma(F^2)$ for **6** and 234 (for **3**) and 365 (for **6**) variable parameters, and converged (the largest parameter shift was 0.001 times its esd).

The structure **6** is pseudo symmetric with a possible higher symmetry space group of $C2/c$. However refinement in $C2/c$ leads to physically less reasonable thermal parameters and the structure has therefore been left in $P2_1/n$. Selected distances and bond angles are given in Tables 3 and 4 and the molecules are displayed as an ORTEP diagrams in Figs. 1 and 2, respectively.

Table 3
Bond distances (Å) and angles (°) for $[Co\{S_2P(OC_6H_4Me\text{-}p)_2\}_2(C_5H_5N)_2]$.[a]

Co(1)–S(1)	2.5053(8)	Co(1)–S(1)′	2.5053(8)
Co(1)–S(2)	2.5735(8)	Co(1)–S(2)′	2.5735(8)
Co(1)–N(1)	2.162(2)	Co(1)–N(1)′	2.162(2)
S(1)–P(1)	1.974(1)	S(2)–P(1)	1.970(1)
P(1)–O(1)	1.597(2)	P(1)–O(2)	1.600(2)
O(1)–C(1)	1.399(4)	O(2)–C(8)	1.397(3)
N(1)–C(15)	1.342(3)	N(1)–C(19)	1.335(4)
N(1)–Co(1)–N(1)′	180.0		
S(1)–Co(1)–S(1)′	180.0	S(2)–Co(1)–S(2)′	180.0
S(1)–Co(1)–S(2)	80.18(3)	S(1)′–Co(1)–S(2)′	80.18(3)
S(1)–Co(1)–S(2)′	99.82(3)	S(1)′–Co(1)–S(2)	99.82(3)
N(1)–Co(1)–S(1)	88.77(6)	N(1)′–Co(1)–S(1)′	88.77(6)
N(1)–Co(1)–S(1)′	91.23(6)	N(1)′–Co(1)–S(1)	91.23(6)
N(1)–Co(1)–S(2)′	88.82(6)	N(1)′–Co(1)–S(2)	88.82(6)
N(1)–Co(1)–S(2)	91.18(6)	N(1)′–Co(1)–S(2)′	91.18(6)
Co(1)–N(1)–C(15)	121.7(2)	Co(1)–N(1)–C(19)	121.2(2)
Co(1)–S(1)–P(1)	84.51(4)	Co(1)–S(2)–P(1)	82.76(4)
S(1)–P(1)–O(1)	113.5(1)	S(2)–P(1)–O(2)	113.1(1)
S(1)–P(1)–O(2)	112.3(1)	S(2)–P(1)–O(1)	112.4(1)
S(1)–P(1)–S(2)	112.07(5)	O(1)–P(1)–O(2)	92.0(1)
P(1)–O(1)–C(1)	127.6(2)	P(1)–O(2)–C(8)	127.9(2)

[a] Symmetry equivalent position $(-x, -y+1, -z)$ given by a prime.

Table 4
Bond distances (Å) and angles (°) for $[Co\{S_2P(OC_6H_4CH_3\text{-}p)_2\}_2(NH_3)]$.

Co(1)–N(1)	2.052(2)		
Co(1)–S(1)	2.3423(7)	Co(1)–S(3)	2.3419(7)
Co(1)–S(2)	2.5632(7)	Co(1)–S(4)	2.5705(7)
S(1)–P(1)	1.9937(9)	S(3)–P(2)	1.9949(9)
S(2)–P(1)	1.9616(9)	S(4)–P(2)	1.9589(9)
P(1)–O(1)	1.595(2)	P(2)–O(3)	1.593(2)
P(1)–O(2)	1.602(2)	P(2)–O(4)	1.602(2)
O(1)–C(1)	1.409(3)	O(3)–C(15)	1.409(3)
O(2)–C(8)	1.407(3)	O(4)–C(22)	1.403(3)
N(1)–Co(1)–S(1)	112.42(6)	N(1)–Co(1)–S(3)	112.96(6)
N(1)–Co(1)–S(2)	95.37(6)	N(1)–Co(1)–S(4)	92.40(6)
S(1)–Co(1)–S(2)	83.88(2)	S(3)–Co(1)–S(4)	83.48(2)
S(1)–Co(1)–S(3)	134.58(3)	S(2)–Co(1)–S(4)	172.23(2)
S(2)–Co(1)–S(3)	93.60(2)	S(1)–Co(1)–S(4)	93.02(2)
S(1)–Co(1)–S(2)	83.88(2)	S(3)–Co(1)–S(4)	83.48(2)
Co(1)–S(1)–P(1)	84.48(3)	Co(1)–S(3)–P(2)	84.95(3)
Co(1)–S(2)–P(1)	79.37(3)	Co(1)–S(4)–P(2)	79.69(3)
S(1)–P(1)–S(2)	112.19(4)	S(3)–P(2)–S(4)	111.84(4)
S(1)–P(1)–O(1)	111.94(7)	S(3)–P(2)–O(3)	112.27(7)
S(2)–P(1)–O(1)	107.90(7)	S(4)–P(2)–O(3)	107.87(7)
S(1)–P(1)–O(2)	110.49(7)	S(3)–P(2)–O(4)	110.29(8)
S(2)–P(1)–O(2)	114.59(7)	S(4)–P(2)–O(4)	114.67(7)
O(1)–P(1)–O(2)	99.01(8)	O(3)–P(2)–O(4)	99.29(9)
P(1)–O(1)–C(1)	122.9(2)	P(2)–O(3)–C(15)	124.6(2)
P(1)–O(2)–O(8)	121.6(1)	P(2)–O(4)–C(22)	121.7(1)

4. Conclusion

We have prepared and characterized the following complexes, $[Co\{S_2P(OC_6H_4Me\text{-}p)_2\}_2(C_5H_5N)_2]$ (R = *o*-, *m*-, *p*-C_6H_4Me, $CH_2C_6H_5$) and $Co[S_2P(OCH_2C_6H_5)_2]_2$. The IR and UV–Vis spectra and magnetic moments of these compounds are consistent with the proposed distorted octahedral structure. The molecular structures of $[Co\{S_2P(OC_6H_4Me\text{-}p)_2\}_2(C_5H_5N)_2]$ (**3**) and $[Co\{S_2P(OC_6H_4Me\text{-}p)_2\}_2(NH_3)]$ (**6**) were determined to have distorted octahedral and distorted trigonal bipyramidal geometries, respectively, around the central cobalt atom.

Acknowledgements

S.B. and M.N. are grateful to UGC and CSIR, New Delhi, respectively, for financial support. M.E.L. thanks the UK Engineering and Physical Sciences Council for support of the X-ray facilities at Southampton University.

Appendix A. Supplementary data

CCDC 686208 and 686209 contain the supplementary crystallographic data for $[Co\{S_2P(OC_6H_4Me\text{-}p)_2\}_2(C_5H_5N)_2]$ and $[Co\{S_2P(OC_6H_4Me\text{-}p)_2\}_2(NH_3)]$. These can be obtained free of charge via http://www.ccdc.cam.ac.uk/conts/retrieving.html, or from the Cambridge Crystallographic Data Centre, 12 Union Road, Cambridge CB2 2EZ, UK (fax: +44 1223 336033; email: deposit@ccdc.cam.ac.uk. Supplementary data associated with this article can be found, in the online version, at doi:10.1016/j.poly.2008.09.025.

References

[1] L. Malatesta, R. Pizzotti, Chim. Ind. 27 (1945) 6.
[2] R.G. Cavell, E.D. Day, W. Byers, P.M. Watkins, Inorg. Chem. 11 (1972) 1759.
[3] J.D. Lebedda, R.A. Palmer, Inorg. Chem. 10 (1971) 2704.
[4] R. Micu-Semeniuc, L. Dumitrescu-Silaghi, I. Haiduc, Inorg. Chim. Acta 33 (1979) 281.
[5] C.K. Jorgensen, Acta Chem. Scand. 16 (1962) 2017.
[6] U.N. Tripathi, M.S. Singh, J. Indian Chem. Soc. 76 (1999) 360.
[7] V.F. Toropova, R.A. Cherkasova, N.I. Savel'eva, E.J. Petrova, Zh. Obsh. Khim. 44 (1974) 531.
[8] V.V. Ovchinnikov, V.I. Galkin, A.R. Garifzyanov, V.F. Toropova, R.A. Cherkasov, Zh. Obsh. Khim. 55 (1985) 357.
[9] Y. Yamada, M. Shimoi, A. Quchi, S. Sato, Y. Saito, Chem. Lett. (1978) 867.
[10] V.N. Kirichenko, S.V. Larionov, Zh. Neorgan. Khim. 24 (1979) 3064.
[11] I.M. Oglezneva, V.N. Kirichenko, Zh. Strukt. Khim. 25 (1984) 164.
[12] B.F. Hoskins, R. Robson, G.A. Willaims, Inorg. Chim. Acta 16 (1976) 121.
[13] B.F. Hoskins, G.A. Willaims, Aust. J. Chem. 28 (1975) 2593.
[14] J.F. McConnell, A. Schwartz, Acta Crystallogr., Sect. B 28 (1972) 1546.
[15] B.H. Zu, S.T. Liu, B.F. Wu, X. Hu, Huaxue Yanjiu Yu Yingyong 14 (2002) 671.
[16] M. Shimoi, A. Quchi, S. Sato, Y. Saito, Chem. Lett. (1979) 319.
[17] K. Kirschbaum, U. Bonnighausen, E. Gesing, K. Greiwe, U. Kuhlmann, H. Strasdeit, B. Krebs, G. Henkel, Z. Naturforsch. 45B (1990) 245.
[18] Hu. Sheng-Zhi, Jiegou Huaxue 18 (1999) 476.
[19] Z. Xhu, J.H. Lin, Y.P. Yu, J. Xu, X.Z. You, S.X. Liu, C.C. Lin, Huaxue Xuebao 7 (1989) 623.
[20] M.Q. He, X.P. Shen, W.L. Zhang, Y.L. Wu, X.N. Cheng, Y.P. Yu, Wuji Huaxue, Xuebao Chin, J. Inorg. Chem. 18 (2002) 739.
[21] G.A. Williams, R. Robson, Aust. J. Chem. 34 (1981) 65.
[22] A. Kumar, D. Kumar, S.K. Pandey, Synth. React. Inorg. Metal-Org. Nano-Metal Chem. 37 (2007) 697.
[23] S. Wu, Z. Liu, Y. Zhang, P. Li, Gaz. Chim. Ital. 123 (1993) 647.
[24] Q. Hao, H.K. Fun, S.L. Chantrapromma, A. Razak, F. Jian, X. Yang, L. Lu, X. Wang, Acta Crystallogr. 57 (2001) 717.
[25] A.L. Bingham, J.E. Drake, M.E. Light, M. Nirman, R. Ratnani, Polyhedron 25 (2006) 945.
[26] A.L. Bingham, J.E. Drake, M.B. Hursthouse, M.E. Light, M. Nirman, R. Ratnani, Polyhedron 26 (2007) 2672.
[27] J.E. Drake, C. Gurnani, M.B. Hursthouse, M.E. Light, M. Nirman, R. Ratnani, Appl. Organomet. Chem. 21 (2007) 539.
[28] L. Aawal, R. Kumar, J.E. Drake, M.B. Hursthouse, M.E. Light, R. Ratnani, K. Saraswat, Polyhedron 26 (2007) 3973.

[29] J.E. Drake, C.L.B. Macdonald, A. Kumar, S.K. Panday, R. Ratnani, J. Chem. Crystallogr. 35 (6) (2005) 447.
[30] K.S. Siddiqi, S.A.A. Nami, Lutfullah, Y. Chebude, Synth. React. Inorg. Metal-Org. Nano-Metal Chem. 35 (2005) 445.
[31] A.J.M. Duisenberg, J. Appl. Crystallogr. 25 (1992) 92.
[32] G.M. Sheldrick, SADABS V2.10, University of Gottingen, Germany, 2003.
[33] G.M. Sheldrick, Acta Crystallogr., Sect. A 46 (1990) 467.
[34] L.J. Farrugia, J. Appl. Crystallogr. 32 (1999) 837.
[35] G.M. Sheldrick, SHELXL97, Structure Determination Software, University of Gottingen, Germany, 1997.

Polyhedron 28 (2009) 91–94

Contents lists available at ScienceDirect

Polyhedron

journal homepage: www.elsevier.com/locate/poly

Chiral molybdenum(0) and tungsten(0) carbonyl diimine complexes

Mehmet Karakus [a,*], Gulnihal Davulga [a], Santiago Gómez-Ruiz [b], Steffen Tschirschwitz [b], Evamarie Hey-Hawkins [b,*]

[a] Department of Chemistry, Faculty of Arts and Sciences, Pamukkale University, Kinikli, 20017 Denizli, Turkey
[b] Institut für Anorganische Chemie der Universität Leipzig, Johannisallee 29, D-04103 Leipzig, Germany

ARTICLE INFO

Article history:
Received 19 August 2008
Accepted 6 October 2008
Available online 14 November 2008

Keywords:
Chiral diimine ligand
Molybdenum
Tungsten
Carbonyl complexes

ABSTRACT

The chiral diimine ligand C_5H_4N-2-C(C_6H_5)=N{(1*S*,2*S*)-C_5H_8-2-$OCH_2C_6H_5$)} (**1**) was prepared via the reaction of 2-benzoyl pyridine and (1*S*,2*S*)-(+)-2-benzyloxycyclopentylamine. **1** (=L) reacts with $M(CO)_6$ in toluene to give the respective metal(0) complexes [$M(CO)_4$(L-κ *N*,*N*′)] (M = Mo (**2**) and W(**3**)). **1**–**3** were fully characterized by elemental analyses, IR, multinuclear NMR spectroscopy and MS. The complexes **2** and **3** are isostructural and crystallize in the chiral hexagonal space group $P3_1$ with three molecules in the unit cell.

© 2008 Elsevier Ltd. All rights reserved.

1. Introduction

The chemistry of Mo^0 and W^0 diimine complexes has attracted much attention due to the catalytic role of these compounds in allylic alkylations, metal–ligand charge transfer transitions, and due to their luminescence properties [1–7]. Especially molybdenum(0)-catalyzed allylic alkylations which show excellent chemoselectivity due to the high coordination number of molybdenum have been widely studied [7], and several Mo^0 and W^0 carbonyl diimine complexes have already been described [1,8–23]. A series of *meso* and C_2-symmetric tetracarbonyl Mo^0 and W^0 diimines was also reported [24], but the number of enantiomerically pure complexes is still small. Thus, the chiral molybdenum(0) and tungsten(0) carbonyl diimine complexes [$M(CO)_4C_5H_4NC(R)$=NCH(Me)Ph] (M = Mo, W; R = H, Me) and [$Mo(CO)_4C_9H_7NCH$=NCH(Me)Ph] were prepared, but their stereochemistry was discussed only on the basis of NMR data, and no X-ray data are available [1]. Examples of enantiomerically pure, structurally characterized complexes include (μ_2-*trans*-1,2-bis(2-pyridylmethylimine)cyclohexane-*N*,*N*′,*N*″,*N*‴)octacarbonyldimolybdenum dichloromethane solvate [25], tetracarbonyl-(*N*-(2-pyridylmethylene)-β-alanylvaline methyl ester-*N*,*N*′)tungsten [9] and piperidinium (*N*-(2-pyridylmethylene)-L-alanato)tetracarbonylmolybdenum [26].

In this paper, we report the synthesis and molecular structures of molybdenum(0) (**2**) and tungsten(0) (**3**) tetracarbonyl complexes containing the new chiral diimine ligand C_5H_4N-2-C(C_6H_5)=N{(1*S*,2*S*)-C_5H_8-2-$OCH_2C_6H_5$)} (**1**).

2. Results and discussion

2.1. Synthesis and characterization of the diimine ligand and its Mo^0 and W^0 complexes

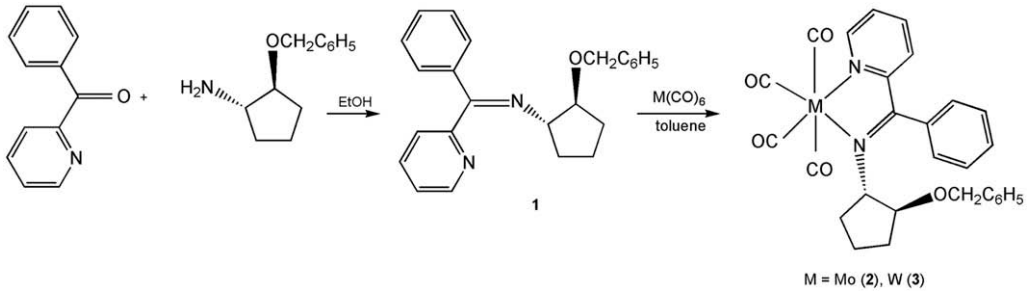
The ligand C_5H_4N-2-C(C_6H_5)=N{(1*S*,2*S*)-C_5H_8-2-$OCH_2C_6H_5$)} (**1**) has been synthesized by condensation of 2-benzoyl pyridine and (1*S*,2*S*)-(+)-2-benzyloxycyclopentylamine in ethanol (Scheme 1). **1** was obtained as a pure yellow oil which was characterized by elemental analyses, IR, multinuclear NMR spectroscopy and MS (see Section 3). The ^1H and ^{13}C NMR spectrum of **1** confirm the formation of the diimine ligand, but exhibit two sets of signals corresponding to the *cis* and *trans* isomer. The EI mass spectrum shows the molecular ion peak at m/z = 356, and in the IR spectrum the characteristic C=N band is observed at 1665 cm^{-1}. These results are in good agreement with the experimental data reported before for similar compounds [13,27,28].

The corresponding Mo^0 and W^0 complexes were prepared by reaction of **1** with $M(CO)_6$ (M = Mo and W) in toluene (Scheme 1).

Complexes **2** and **3** were obtained as dark purple or blue crystals, respectively, in 55% or 46% yield. The ^1H NMR spectra show six multiplets between 1.4 and 2.8 ppm corresponding to the protons of the cyclopentyl ring. Three multiplets between ca. 4.0 and 5.0 ppm were assigned to the methine groups of the cyclopentyl ring and to the methylene group of the benzyl ligand, and a set of several multiplets between ca. 7.0 and 9.3 ppm corresponds to the aromatic protons of the phenyl and pyridyl groups. The carbonyl region of the ^{13}C NMR spectra exhibits four signals due to

* Corresponding authors. Tel.: +90 (0) 258/2134030; fax: +90 (0) 258/2125546 (M. Karakus); tel.: +49 (0) 341/9736151; fax: +49 (0) 341/9739319 (E. Hey-Hawkins)
E-mail addresses: mkarakus@pamukkale.edu.tr (M. Karakus), hey@rz.uni-leipzig.de (E. Hey-Hawkins).

0277-5387/$ - see front matter © 2008 Elsevier Ltd. All rights reserved.
doi:10.1016/j.poly.2008.10.004



Scheme 1.

the presence of four inequivalent CO groups (203.5, 203.8, 222.3, 223.5 ppm for **2** and 199.1, 199.4, 214.7, 215.9 ppm for **3**). The chemical shift of Mo–CO resonances is typically observed at lower field than in the corresponding W–CO complexes [10,11]. The IR spectra of **2** and **3** display the characteristic absorption bands attributed to ν(CN) and the four CO stretching frequencies which are expected for these chiral molecules. The mass spectra (FAB) show the molecular ion peaks of **2** (m/z = 566) and **3** (m/z = 652).

2.2. Molecular structure of *2* and *3*

Complexes **2** and **3** crystallize in the chiral hexagonal space group $P3_1$ with three molecules in the unit cell. A disordered toluene molecule is also present in the asymmetric unit. The crystal structures of **2** and **3** are isotypical and isostructural (Fig. 1). In **2** and **3** the central atom (Mo or W) has an octahedral coordination with a chelating *cis*-diimine ligand and four carbonyl ligands. Due to the observed yields of 55% (**2**) and 46% (**3**) we assume that only the *cis* isomer of the diimine reacts and that isomerization of *trans* to *cis* is probably slow.

The M–N bond lengths (225.7(4) and 222.9(4) pm for **2** and 221.2(3) and 224.2(3) pm for **3**) are in the range observed for similar molybdenum and tungsten complexes [12,29], and the M–C

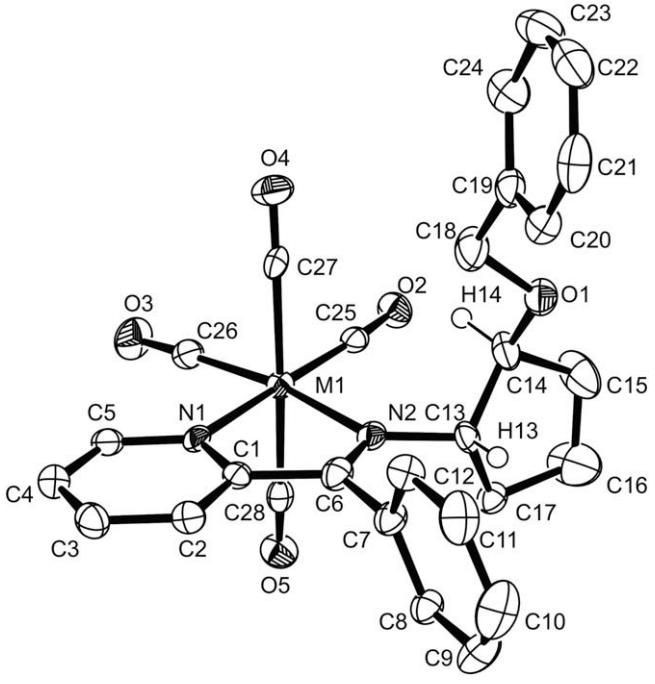
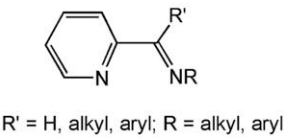


Fig. 1. Molecular structure of complex **2** with thermal ellipsoids at 50% probability level, hydrogen atoms, except at chiral centres, and a toluene molecule have been omitted for clarity. The tungsten complex **3** is isostructural and isotypical.



Scheme 2.

bond lengths (194.0(5), 194.6(6), 202.5(5) and 204.8(5) pm for **2** and 194.5(6), 195.3(5), 200.8(5) and 204.0(5) pm for **3**) are, as expected, similar to those observed in related molybdenum and tungsten carbonyl complexes [1]. The carbonyl ligands are nearly linear with M–C–O bond angles close to 180°. The five-membered MN_2C_2 ring (M1, N1, C1, C6 and N2) is almost planar (max. deviations from plane ca. 6 pm). The C–M–C bond angles of *cis*-CO groups are close to 90°, the C–M–C bond angle for the *trans* CO ligands deviate slightly from linearity (C27–Mo1–C28 171.3(2)° for **2** and C27–W1–C28 171.1(2)° for **3**). The short N1–C1 (135.4(5) for **2** and 136.0(5) for **3**) and N2–C6 bonds (132.0(5) for **2** and 129.9(5) for **3**) indicate multiple bond character, while the C1–C6 bond length (147.1(6) for **2** and 146.8(5) pm for **3**) is typical for a C–C single bond.

Several other pyridyl-based diimine molybdenum and tungsten tetracarbonyl complexes with the type of diimine ligand shown in Scheme 2 have been structurally characterized and have similar structural features as complexes **2** and **3** [8,9,14–23,25,26,29].

3. Experimental

3.1. General remarks

When necessary, experiments were performed under an atmosphere of dry nitrogen using standard Schlenk techniques. The NMR spectra were recorded on a Bruker AVANCE DRX 400 spectrometer. ^{1}H NMR (400.13 MHz): internal standard solvent, external standard TMS; ^{13}C NMR (100.16 MHz): external standard TMS; IR spectra: KBr pellets were prepared in a nitrogen-filled glove box and the spectra were recorded with a Perkin–Elmer System 2000 FTIR spectrometer in the range 350–4000 cm^{-1}. FAB MS spectra were recorded with a MASPEC II spectrometer with 3-nitrobenzyl alcohol as matrix. EI MS spectra were recorded with a MAT-8230. All solvents were purified by distillation, dried and saturated with nitrogen. Elemental analyses were determined with a VARIO EL (Heraeus) and LECO-CHNS-O. Melting points (Gallenkamp) are uncorrected. $Mo(CO)_6$, $W(CO)_6$ and 2-benzoyl pyridine and (1*S*,2*S*)-(+)-2-benzyloxycyclopentylamine are commercially available.

3.2. X-ray crystallography

Data for **2** and **3** were collected on a CCD Oxford Xcalibur S (λ(Mo Kα) = 0.71073 Å) in ω and ϕ scans mode. Semi-empirical

from equivalents absorption corrections were carried out with SCALE3 ABSPACK [30]. The structures were solved with direct methods [31]. The structure refinements were carried out with SHELXL-97 [32]. All non-hydrogen atoms were refined anisotropically; H atoms were located in difference maps and refined isotropically. Crystallographic data for **2** and **3** are given in Tables 1 and 2.

3.3. Synthesis of C_5H_4N-2-$C(C_6H_5)$=N{(1S,2S)-C_5H_8-2-$OCH_2C_6H_5$)} (**1**)

2-Benzoyl pyridine (1.83 g, 10.00 mmol) was dissolved in EtOH (25 mL) and (1*S*,2*S*)-(+)-2-benzyloxycyclopentylamine (1.91 g, 10.00 mmol) was added dropwise via syringe. The reaction mixture was refluxed for 2 h. The solvent was then removed under vacuum to yield a yellow oily product. Yield 3.14 g (88%). *Anal.* Calc. for $C_{24}H_{24}N_2O$: C, 80.87; H, 6.79; N, 7.86. Found: C, 79.89; H, 6.17; N, 7.39%. IR (cm^{-1}): ν(C=N) 1665 (s). ^1H NMR ($CDCl_3$) (only the signals of the predominant isomer are given): δ 8.71 (d, 1H, $^3J(^1H–^1H)$ = 5.4 Hz, pyridyl), 8.05 (br m, 1H, pyridyl), 7.97 (d, 1H, $^3J(^1H–^1H)$ = 7.8 Hz, pyridyl), 7.89 (m, 1H, pyridyl), 7.74–7.23 (m, 10H, Ph), 4.64 (m, 1H, CHO), 4.44 (m, 2H, OCH_2), 4.11 (m, 1H, NCH), 2.16, 1.90, 1.88 (m, 3H, CH_2 of cyclopentyl ring), 1.86–1.71 (m, 3H, CH_2 of cyclopentyl ring) ppm. ^{13}C NMR ($CDCl_3$) (mixture of isomers): δ 21.7, 22.0, 29.8, 31.2, 32.5, 32.6 (CH_2 of cyclopentyl), 68.8, 68.9 (OCH_2–), 71.2, 71.4, (C–O of cyclopentyl), 86.9, 87.0 (C–N of cyclopentyl), 122.3, 123.1, 123.7, 123.8, 124.6, 126.2, 126.9, 127.3, 127.5, 127.6, 127.7, 128.1, 128.2, 128.3, 128.4, 128.4, 128.5, 129.9, 131.0, 132.9, 136.2, 136.4, 137.1 (pyridyl and phenyl rings), 148.5, 149.0, 156.0, 157.8 (C1 and C5 of pyridine), 165.2, 167.3 (Py–C=N) ppm. EI MS: *m*/*z* (int.): 356 (37%) $[M]^+$, 265 (5%) $[M\text{-}CH_2Ph]^+$, 182 (18%) $[M\text{-}C_5H_8OCH_2Ph]$.

Table 1
Crystal data and structure refinement for complexes **2** and **3**.

	2	**3**
Empirical formula	$C_{35}H_{32}MoN_2O_5$	$C_{35}H_{32}N_2O_5W$
Formula weight	656.57	744.48
Temperature	130(2)	130(2)
Crystals system	hexagonal	hexagonal
Space group	$P3_1$	$P3_1$
Unit cell dimensions		
a (pm)	1717.37(3)	1714.30(2)
b (pm)	1717.37(3)	1714.30(2)
c (pm)	918.36(2)	918.98(2)
α (°)	90	90
β (°)	90	90
γ (°)	120	120
V (nm^3)	2.34569(8)	2.33889(6)
Z	3	3
D_{calc} (Mg/m^3)	1.394	1.586
Absorption coefficient (mm^{-1})	0.464	3.748
F(000)	1014	1110
Crystal size (mm^3)	0.6 × 0.02 × 0.02	0.4 × 0.1 × 0.1
Θ range for data collection (°)	2.61–26.37	2.61–30.49
Index ranges	$-20 \leqslant h \leqslant 21$ $-21 \leqslant k \leqslant 20$ $-11 \leqslant l \leqslant 11$	$-18 \leqslant h \leqslant 24$ $-24 \leqslant k \leqslant 20$ $-12 \leqslant l \leqslant 13$
Reflections collected	25868	15937
Independent reflections	6419 [*R*(int) = 0.0602]	8038 [*R*(int) = 0.0395]
Completeness to Θ_{max}	99.9%	99.7%
Data/restraints/parameters	6419/15/353	8038/20/397
Goodness-of-fit on F^2	0.968	0.899
Absolute structure parameter	0.05(3)	−0.017(6)
Final *R* indices [$I > 2\sigma(I)$]	R_1 = 0.0387, wR_2 = 0.0779	R_1 = 0.0295, wR_2 = 0.0447
R indices (all data)	R_1 = 0.0585, wR_2 = 0.0841	R_1 = 0.0439, wR_2 = 0.0471
Largest difference in peak and hole ($e/Å^3$)	0.814 and −0.785	3.344 and −1.144

Table 2
Selected bond lengths (pm) and angles (°) in **2** and **3**.

	2	**3**
O2–C25	118.4(6)	117.3(5)
O3–C26	115.2(5)	116.7(6)
O4–C27	113.5(6)	115.4(6)
O5–C28	114.4(5)	114.9(5)
M1–C26	194.0(5)	194.5(6)
M1–C25	194.6(6)	195.3(5)
M1–C27	202.5(5)	200.8(5)
M1–C28	204.8(5)	204.0(5)
M1–N1	222.9(4)	221.2(3)
M1–N2	225.7(4)	224.2(3)
O2–C25–M1	176.5(4)	177.2(4)
O3–C26–M1	177.3(4)	177.2(4)
O4–C27–M1	172.2(4)	173.2(4)
O5–C28–M1	173.7(4)	173.8(4)
C27–M1–C28	171.3(2)	171.1(2)
C25–M1–N1	175.8(2)	175.6(2)
C27–M1–N1	94.1(2)	93.5(2)
C28–M1–N1	91.9(2)	92.6(1)
C26–M1–N2	167.8(2)	166.7(2)
C25–M1–N2	103.6(2)	103.6(2)
N1–M1–N2	72.6(2)	72.5(2)

3.4. Synthesis of $[Mo(CO)_4\{C_5H_4N$-2-$C(C_6H_5)$=N{(1S,2S)-C_5H_8-2-$OCH_2C_6H_5$)}-κ N,N′] (**2**)

C_5H_4N-2-$C(C_6H_5)$=N{(1*S*,2*S*)-C_5H_8-2-$OCH_2C_6H_5$)} (**1**) (3.56 g, 10.00 mmol) was dissolved in 50 mL toluene and $Mo(CO)_6$ (2.64 g, 10.00 mmol) was added under N_2. The mixture was refluxed for 4 h and a dark red solution was obtained. The solution was then stored under nitrogen at room temperature. After two days, dark purple crystals were obtained, which were isolated by filtration and dried under vacuum. Yield 3.10 g (55%), m.p. 116–117 °C. *Anal.* Calc. for $C_{28}H_{24}N_2O_5Mo$: C, 59.58; H, 4.29; N, 4.96. Found: C, 60.32; H, 4.29; N, 4.33%. IR (cm^{-1}): 1630 (w) (C=N), 2013 (s), 1894 (s), 1876 (s), 1823 (s) (CO). ^1H NMR ($CDCl_3$): δ 9.21 (d, 1H, $^3J(^1H–^1H)$ = 5.4 Hz, pyridyl), 7.69 (t, 1H, $^3J(^1H–^1H)$ = 7.2 Hz, pyridyl), 7.52 (m, 2H, pyridyl), 7.44–7.05 (m, 10H, Ph), 4.89 (m, 1H, CHO), 4.51 (m, 2H, OCH_2), 4.19 (m, 1H, NCH), 2.52, 2.33, 2.02, 1.81, 1.76, 1.55 (m, 6H, CH_2 of cyclopentyl ring) ppm. ^{13}C NMR ($CDCl_3$): δ 21.1, 30.4, 32.1 (CH_2 of cyclopentyl), 72.1 (OCH_2), 73.6, (C–O of cyclopentyl), 86.8 (C–N of cyclopentyl), 125.8, 127.2, 127.4, 127.5, 128.2, 128.9, 129.0, 129.1, 129.3 129.9, 134.0, 136.9, 138.8 (pyridyl and phenyl rings), 152.8, 156.5 (C1 and C5 of pyridine), 171.6 (Py–C=N), 203.5, 203.8, 222.3, 223.5 (CO) ppm. FAB MS: *m*/*z* (int.): 566 (76%) $[M]^+$, 538 (26%) $[M\text{-}CO]^+$, 482 (84%) $[M\text{-}3CO]^+$, 454 (100%) $[M\text{-}4CO]^+$, 359 (6%) $[M\text{-}Mo(CO)_4]^+$.

3.5. Synthesis of $[W(CO)_4\{C_5H_4NC(C_6H_5)$=$NC_5H_8OCH_2C_6H_5$-κ N,N′}] (**3**)

C_5H_4N-2-$C(C_6H_5)$=N{(1*S*,2*S*)-C_5H_8-2-$OCH_2C_6H_5$)} (**1**) (1.78 g, 5 mmol) was dissolved in 50 mL toluene and $W(CO)_6$ (1.75 g, 5 mmol) was added. The mixture was refluxed for 16 h and a dark blue solution was obtained. The solvent was reduced to 10 mL and the solution was then stored under nitrogen at room temperature. After one day blue crystals of **3** were obtained. The crystals were isolated and dried under vacuum. Yield 1.49 g (46%), m.p. 127 °C. *Anal.* Calc. for $C_{28}H_{24}N_2O_5W$: C, 51.55; H, 3.71; N, 4.29. Found: C, 52.95; H, 3.55; N, 4.22%. IR (cm^{-1}): 1637 (m) (C=N), 2005 (s), 1884 (sh), 1870 (br), 1815 (s) (CO). ^1H NMR ($CDCl_3$): δ 9.35 (d, 1H, $^3J(^1H–^1H)$ = 4.6 Hz, pyridyl), 7.70 (t, 1H, $^3J(^1H–^1H)$ = 7.8 Hz, pyridyl), 7.53 (m, 2H, pyridyl), 7.45–7.09 (m, 10H, Ph), 4.93 (m, 1H, CHO), 4.51 (m, 2H, OCH_2), 4.21 (m, 1H, NCH), 2.55, 2.34, 2.03, 1.82, 1.72, 1.55 (m, 6H, CH_2 of cyclopentyl ring) ppm. ^{13}C NMR ($CDCl_3$): δ 21.1, 30.3 32.7 (CH_2 of cyclopentyl), 72.1 (OCH_2), 74.6,

(C–O of cyclopentyl), 87.3 (C–N of cyclopentyl), 126.2, 127.1, 127.3, 127.5, 128.1, 128.9, 129.1, 129.4, 130.0 130.9, 132.9, 134.0, 136.2, 137.0, 138.9 (pyridyl and phenyl rings), 152.7, 157.8 (C1 and C5 of pyridine), 173.4 (Py–C=N), 199.1, 199.4, 214.7, 215.9 (CO) ppm. FAB MS: *m*/*z* (int.): 652 (22%) $[M]^+$, 624 (11%) $[M\text{-}CO]^+$, 568 (36%) $[M\text{-}3CO]^+$, 540 (22%) $[M\text{-}4CO]^+$, 357 (81) $[M\text{-}W(CO)_4]^+$.

Supplementary data

CCDC 699013 and 699014 contain the supplementary crystallographic data for **2** and **3**. These data can be obtained free of charge via http://www.ccdc.cam.ac.uk/conts/retrieving.html, or from the Cambridge Crystallographic Data Centre, 12 Union Road, Cambridge CB2 1EZ, UK; fax: (+44) 1223-336-033; or e-mail: deposit@ccdc.cam.ac.uk.

Acknowledgements

This work was supported by TUBITAK (Grant No: TBAG 106T034), Turkey and the IPP (*Research at the Frontiers of Chemistry*, DAAD) of Universität Leipzig, Germany.

References

[1] C.E. Alyea, V.K. Jain, Polyhedron 15 (1996) 1723.
[2] D.A. Boga, S. Ozkar, J. Organomet. Chem. 691 (2006) 3293.
[3] A. Mentes, R.D.W. Kemmitt, J. Fawcett, D.R. Russell, J. Organomet. Chem. 660 (2002) 91.
[4] B.M. Trost, C.A. Merlic, J. Am. Chem. Soc. 112 (1990) 9590.
[5] B.M. Trost, M. Lautens, J. Am. Chem. Soc. 109 (1987) 1469.
[6] S. Tamagaki, R.J. Card, D.C. Neckers, J. Am. Chem. Soc. 100 (1978) 6635.
[7] B.M. Trost, M. Lautens, J. Am. Chem. Soc. 104 (1982) 5543.
[8] A. Mentes, R.D.W. Kemmitt, J. Fawcett, D.R. Russell, Acta Crystallogr. C55 (1999) 48.
[9] R.S. Herrick, J. Dupont, I. Wrona, J. Pilloni, M. Beaver, M. Benotti, F. Powers, C.J. Ziegler, J. Organomet. Chem. 692 (2007) 1226.
[10] T. Ederer, R.S. Herrick, W. Beck, Z. Anorg. Allg. Chem. 633 (2007) 235.
[11] P. Datta, C. Sinha, Polyhedron 26 (2007) 2433.
[12] R.S. Herrick, C.J. Ziegler, M. Precopio, K. Crandall, J. Shaw, R.M. Jarret, J. Organomet. Chem. 693 (2008) 619.
[13] D.M. Boghaei, S. Mohedi, Tetrahedron 58 (2002) 5357.
[14] B.P. Buffin, P.J. Squattrito, A.O. Ojewole, Inorg. Chem. Commun. 7 (2004) 14.
[15] A. Mentes, O. Buyukgungor, Acta Crystallogr. E60 (2004) m530.
[16] L.A. Garcia-Escudero, D. Miguel, J.A. Turiel, J. Organomet. Chem. 691 (2006) 3434.
[17] E.C. Alyea, G. Ferguson, V.K. Jain, Acta Crystallogr. C50 (1994) 854.
[18] N. Cosquer, B. Le Gall, F. Conan, J.-M. Kerbaol, J. Sala-Pala, M.M. Kubicki, E. Vigier, Inorg. Chim. Acta 359 (2006) 4311.
[19] M. Shamsudin, M.A. Affan, R. Hitam, B.M. Yamin, H.-K. Fun, A.R. Ibrahim, Z. Kristallogr. 214 (1999) 499.
[20] R.S. Herrick, K.L. Houde, J.S. McDowell, L.P. Kiczek, G. Bonavia, J. Organomet. Chem. 589 (1999) 29.
[21] Shijie Lu, J. Selbin, Inorg. Chim. Acta 134 (1987) 229.
[22] K. Heinze, J. Chem. Soc., Dalton Trans. (2002) 540.
[23] K. Heinze, V. Jacob, J. Chem. Soc., Dalton Trans. (2002) 2379.
[24] R.S. Herrick, C.J. Ziegler, H. Bohan, M. Corey, M. Eskander, J. Giguere, N. McMicken, I.E. Wrona, J. Organomet. Chem. 687 (2003) 178.
[25] D. Morales, J. Perez, L. Riera, V. Riera, R. Corzo-Suarez, S. Garcia-Granda, D. Miguel, Organometallics 21 (2002) 1540.
[26] R. Garcia-Rodriguez, D. Miguel, Dalton Trans. (2006) 1218.
[27] L. Gonsalvi, J.A. Gaunt, H. Adams, A. Castro, G.J. Sunley, A. Haynes, Organometallics 22 (2002) 1047.
[28] J.R. Dilworth, S.D. Howe, A.J. Hutson, J.R. Miller, J. Silver, R.M. Thompson, M. Harman, M.B. Hursthouse, J. Chem. Soc., Dalton Trans. (1994) 3553.
[29] J. Burgess, J. Fawcett, D.R. Russell, J. Sawbridge, H. Yu, Transition Met. Chem. 25 (2000) 547.
[30] SCALE3 ABSPACK: Empirical absorption correction, CRYSALIS – Software package, Oxford Diffraction Ltd., 2006.
[31] G.M. Sheldrick, SHELXS-97, Program for Crystal Structure Solution, Göttingen, 1997.
[32] G.M. Sheldrick, SHELXL-97, Program for the Refinement of Crystal Structures, Göttingen, 1997.

Polyhedron 28 (2009) 95–100

Contents lists available at ScienceDirect

Polyhedron

journal homepage: www.elsevier.com/locate/poly

Spectroscopic and structural studies of the 2D Mn(II) coordination polymer from a bridging N_{oxa}, N_{py} bidentate ligand; tetra-*n*-butylammonium[5-(3-pyridyl)-1,3,4-oxadiazole-2-thiolate]

M. Singh [a], R.J. Butcher [b], N.K. Singh [a,*]

[a] Department of Chemistry, Banaras Hindu University, Varanasi 221005, India
[b] Department of Chemistry, Howard University, 525 College Street NW, Washington, DC 20059, USA

ARTICLE INFO

Article history:
Received 13 June 2008
Accepted 8 October 2008
Available online 17 November 2008

Keywords:
Mn(II) complex
Coordination polymer
Bridging bidentate 1,3,4-oxadiazole ligand
X-ray crystallography

ABSTRACT

A coordination polymer $\{[Mn(3\text{-pyt})_2(H_2O)_2][N(n\text{-Bu})_4]^+[3\text{-pyt}]^-\}_n$ (**3**) has been synthesized from the reaction of tetra-*n*-butylammonium[5-(3-pyridyl)-1,3,4-oxadiazole-2-thiolate] $\{[N(n\text{-Bu})_4]^+[3\text{-pyt}]^-\}$ and $Mn(OAc)_2 \cdot 4H_2O$. The ligand and the Mn(II) complex **3** have been characterized by elemental analyses, IR, ^1H and ^{13}C NMR spectroscopy, in addition **3** has also been studied crystallographically. The single crystal X-ray structure of the **3** shows that the ligand is bonded to Mn(II) via its pyridyl and oxadiazole nitrogen atoms. This bonding pattern connects the Mn(II) centres to afford an uniform two dimensional coordination frame work where the $[Mn(3\text{-pyt})_2(H_2O)_2]_n$ molecules are stacked in a parallel layers. The overall arrangement of molecules in crystal lattice results in open channels in which the enclosed tetra-*n*-butylammonium cations are stabilized by anionic oxadiazole molecules through $N^+\cdots S^-$ ionic interactions.

© 2008 Elsevier Ltd. All rights reserved.

1. Introduction

There has been a considerable interest in the coordination polymers of 1,3,4-oxadiazole-2-thione because of their interesting role in supramolecular chemistry and crystal engineering [1–3]. This type of metal–organic framework with intriguing network structures [4–6] find potential applications in catalysis [7], gas storage [8] and photoluminescence [9,10]. Recently, pyridyl oxadiazoles have been systematically explored for their potential biological activities [11] and also as promising bridging ligands in coordination chemistry [12–14]. The design and assembly of supramolecular architectures with variable cavities or channels are currently of great interest owing to their novel topologies [15–17]. There are a few reports on the metal complexes of 5-phenyl-1,3,4-oxadiazole-2-thione [18–21], 5-(4-pyridyl)-1,3,4-oxadiazole-2-thione [12–14,22], 5-(2-pyridyl)-1,3,4-oxadiazole-2-thione [10] and 5-(3-pyridyl)-1,3,4-oxadiazole-2-thione [23]. The reported works mostly describe the coordination chemistry of symmetric bridging ligands used in the construction of network structures leading to porous coordination polymers [24]. Contrary to symmetrical bridging ligands, there is scanty of information on the coordination polymers of unsymmetrical organic ligands [12–14]. These unsymmetrical bridging ligands may show four types of binding modes involving monodentate (N_{oxo}) (I), bidentate (N_{py}, N_{oxo} or N_{py}, S) (II), tridentate (N_{py}, N_{oxo}, S) (III) and tetradentate (N_{py}, N_{oxo},S, S) (IV) as shown in Fig. 1. Such a type of multidentate module has been envisaged as useful building block for constructing coordination polymers [12]. As a part of our ongoing studies on metal complexes of unsymmetrical 1,3,4-oxadiazoles [18,23], we report herein the preparation, spectroscopic characterization of a new unsymmetrical heterocyclic oxadiazole bridging ligand $\{[N(n\text{-Bu})_4]^+[3\text{-pyt}]^-\}$ (**2**) and its Mn(II) complex **3**. Molecular structure of **3** has also been elucidated by X-ray crystallography.

2. Experimental

2.1. Materials and methods

All commercially available starting materials (analytical grade) were used as received and all experiments were carried out in open atmosphere. Nicotinamide was purchased from Sigma Aldrich and used as such. Carbon disulfide and hydrazine hydrate (SD fine Chemicals, India) and the solvents (Merck Chemicals, India) were used in the syntheses. Nicotinic acid hydrazide was synthesized according to the reported method [25].

2.2. Synthesis

2.2.1. Synthesis of potassium[N-(pyridine-3-carbonyl)-hydrazinecarbodithioate] $K^+(H_2L^-)$ (*1*)

$K^+(H_2L^-)$ was synthesized by the dropwise addition of CS_2 (4 ml, 53 mmol) to a solution of nicotinic acid hydrazide (7 g, 51 mmol)

* Corresponding author. Tel.: +91 542 2318529; fax: +91 542 2368127.
E-mail address: singhnk_bhu@yahoo.com (N.K. Singh).

0277-5387/$ - see front matter © 2008 Elsevier Ltd. All rights reserved.
doi:10.1016/j.poly.2008.10.008

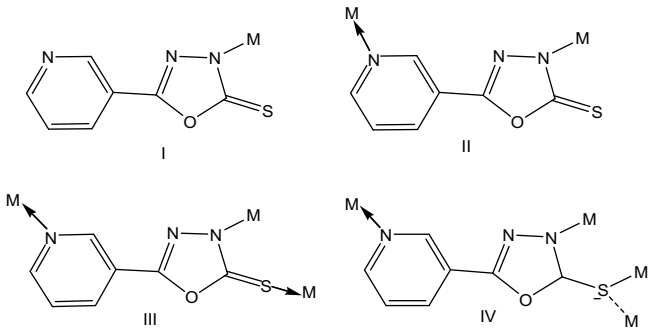


Fig. 1. Possible bonding modes of unsymmetrical 3-pyridyl oxadiazole.

and KOH (2.86 g, 51 mmol) in 35 ml of methanol (MeOH). The mixture was stirred continuously for 2 h at room temperature, thereafter the precipitated product was filtered off, washed twice with diethyl ether, m.p. 525 K. The analytical and spectroscopic data of **1** were identical to that reported previously [23].

*2.2.2. Synthesis of {[N(n-Bu)$_4$]$^+$[3-pyt]$^-$} (**2**)*

Potassium[N-(pyridine-3-carbonyl)-hydrazinecarbodithioate] (5.6 g, 22.5 mmol) was dissolved in a EtOH–H_2O mixture (75:25 v/v) (30 ml) and to it was added an EtOH solution (30 ml) of tetra-*n*-butylammonium bromide (7.2 g, 22.5 mmol). The resulting dirty yellow solution was concentrated at room temperature to afford the solid product. The separated solid was dissolved in a minimum amount of EtOH (25 ml) and water was added drop wise until the impurities settled down. The solution was decanted off and after evaporation of the solvent, a white solid product was obtained, m.p. 343 K (yield 3.60 g, 64%). Anal. Calc. for $C_{23}H_{40}N_4OS$ (420.66): C, 65.67; H, 9.58; N, 13.32; S, 7.62. Found: C, 65.73; H, 9.55; N, 13.46; S, 7.50%. IR (KBr, ν cm^{-1}): 1591 ν(C=N), 1188 ν_{as}(C–O–C), 1134 ν_s(C–O–C), 1035 ν(N–N), 905 ν(C–S); pyridine ring 626; ^{1}H NMR ($CDCl_3$, δ ppm): 7.35, 8.22, 8.59, 9.19 (4H, pyridine ring), 2.14 (m, 8H, CH_2 of N(*n*-Bu)$_4$), 1.63 (m, 8H, CH_2 of N(*n*-Bu)$_4$), 1.46 (m, 8H, CH_2 of N(*n*-Bu)$_4$), 0.97 (12H, CH_3 of N(*n*-Bu)$_4$); ^{13}C NMR ($CDCl_3$, δ ppm): 180.38 (C1), 160.21 (C2), 123.41 (C3), 132.66 (C4), 122.16 (C5), 146.93 (C6), 149.99 (C7), 58.97 (C11, C21, C31,C41), 24.06 (C12, C22, C32, C42A), 20.80 (C13, C23, C33, C43), 13.70 (C14, C24, C34, C44) (Ref. Fig. 4). UV–Vis [λ_{max}, MeOH, nm]: 322, 224. The tentative structure of the ligand based on the physico-chemical studies is shown in Fig. 2.

*2.2.3. Synthesis of the complex {[Mn(3-pyt)$_2$(H$_2$O)$_2$][N(n-Bu)$_4$]$^+$[3-pyt]$^-$}$_n$ (**3**)*

A methanolic solution (10 ml) of [$Mn(OAc)_2 \cdot 4H_2O$] (.249 g, 1 mmol) was mixed with the ethanolic solution (10 ml) of {[N(*n*-Bu)$_4$]$^+$[3-pyt]$^-$} (1.26 g, 3 mmol). The resulting yellow solution was filtered off and kept for crystallization. After 10 days, yellow crystals of **3** suitable for an X-ray crystallographic study were obtained.

Yellow crystals. *Anal.* Calc. for $C_{37}H_{52}MnN_{10}O_5S_3$ (868.01): C, 51.20; H, 6.04; N, 16.14; S, 11.08; Mn, 6.33. Found: C, 51.28; H, 6.10; N, 16.20; S, 11.12; Mn, 6.29%. μ_B = 5.93 BM. M.p. 413 K. IR data for [Mn(3-pyt)$_2$(H$_2$O)$_2$]$_n$ (KBr, ν cm^{-1}); ν(OH) 3442; ν(C=N) 1612; ν_{as}(C–O–C) 1196; ν_s(C–O–C) 1156; ν(N–N) 1084; ν(C=S) 942; pyridine ring 642. IR data for co-crystallized {[N(*n*-Bu)$_4$]$^+$[3-pyt]$^-$} (KBr, ν cm^{-1}): ν(C=N) 1584; ν_{as}(C–O–C) 1196; ν_s(C–O–C) 1156; ν(N–N) 1034; ν(C=S) 901; pyridine ring 642. UV–Vis [λ_{max}, MeOH, nm]: 834, 434, 342, 298.

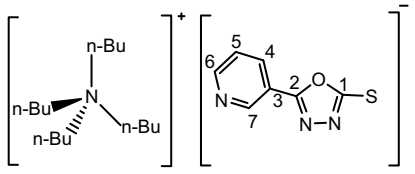


Fig. 2. Tentative structure of the ligand {[N(*n*-Bu)$_4$]$^+$[3-pyt]$^-$} (**2**).

3. Analyses and physical measurements

Carbon, hydrogen, nitrogen and sulfur contents were estimated on a CHN Model CE-440 Analyzer and on an Elementar Vario EL III. Magnetic susceptibility measurement was performed at room temperature on a Cahn Faraday balance using Hg[Co(NCS)$_4$] as the calibrant and the electronic spectra were recorded on a UV-1700 Pharmaspec spectrophotometer. By following standard procedures, the complex was analyzed for its manganese content, after decomposition with a mixture of conc. HNO_3 and HCl, followed by conc. H_2SO_4 [26]. IR spectra were recorded in the 4000–400 cm^{-1} region as KBr pellets on a Varian 3100 FT-IR Excalibur series. ^{1}H and ^{13}C NMR spectra were recorded in $CDCl_3$ on a JEOL AL300 FT NMR spectrometer using TMS as an internal reference.

4. Crystal structure determination

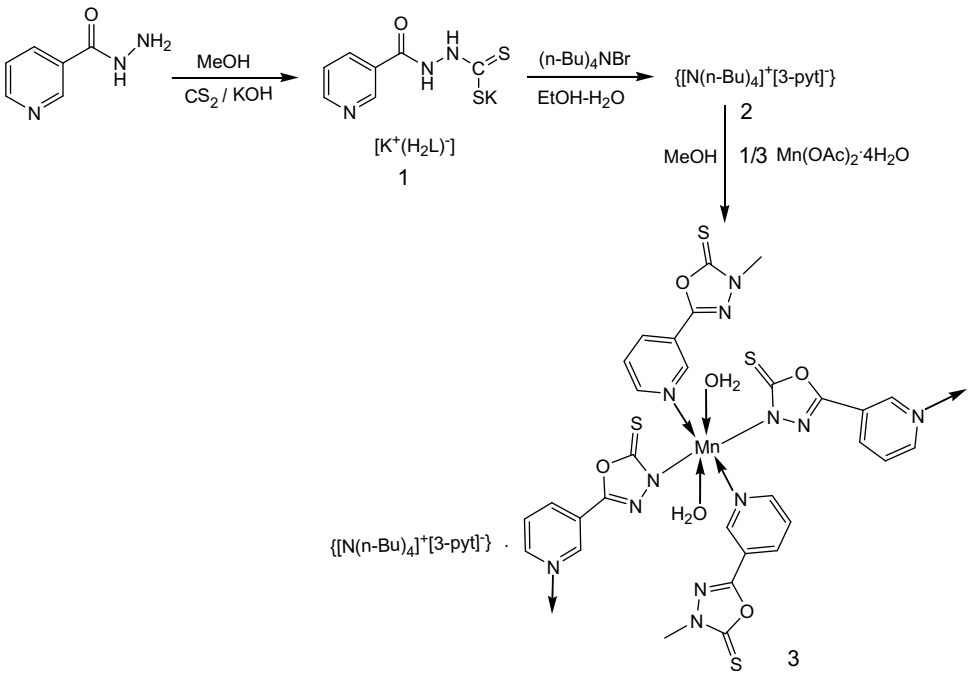
X-ray single crystal refinement, diffraction data collection and data reduction for complex **3** were performed at 295(2) K with a graphite monochromated Mo Kα (λ = 0.71073 Å) radiation source using standard methods [27].

The structure was solved by direct methods (SHELX-97) and refined against all data by full-matrix least-squares on F^2 using anisotropic displacement parameters for all non-hydrogen atoms. All H atoms attached to C atoms were fixed geometrically and treated as riding with C–H = 0.98 Å (methyl), 0.97 Å (methylene) and 0.93 Å (aromatic) with U∼iso∼(H) = 1.2U∼eq∼(C) or 1.2U∼eq∼(methyl). H atoms of water molecules were initially located in difference Fourier maps and included in the subsequent refinement using restraints (O–H = 0.82(1) Å and H···H = 1.38(2) Å with U∼iso∼(H) = 1.5U∼eq∼(O). In the last stages of refinement they were treated as riding on their parent O atoms. One of the propyl groups is disordered over two positions with occupancy factors in the ratio 0.57/0.43. The occupancy factor has been determined by refining, in the first stage of refinement, a free variable fixing the two occupancies factor to sum to 1.0 and attributing all the disordered atoms a dummy isotropic temperature factor (2nd free variable). The atomic positions were refined using distances and angles restraints with the tools (PART and SAME) available in SHELXL-97. Once the occupancy factors were determined, they were fixed and the isotropic temperature factors were freely refined. In the last stages of refinement, the atomic positions were refined with anisotropic temperature factors. The refinement of the Flack's parameter gives a value of 0.55(2). Inverting the absolute structure gave a value of 0.45(2). In such a case, one may consider that the crystal is twinned by inversion and then the two domains were refined using the TWIN instruction in SHELXL-97.

MERCURY package was used for molecular graphics [28]. Crystal structure diagrams were generated by use of the ORTEP-3 for Windows program [29].

5. Results and discussion

The reaction of tetra-*n*-butylammonium[5-(3-pyridyl)-1,3,4-oxadiazole-2-thiolate] {[N(*n*-Bu)$_4$]$^+$[3-pyt]$^-$} (**2**) with $Mn(OAc)_2 \cdot 4H_2O$ in a 3:1 molar ratio generates a polymeric complex with



Scheme 1. Preparation of the ligand **2** and its Mn(II) complex.

the general formula $\{[Mn(3\text{-pyt})_2(H_2O)_2][N(n\text{-}Bu)_4]^+[3\text{-pyt}]^-\}_n$ (Scheme 1) which has been confirmed by X-ray crystallography. The X-ray data show that the ligand is bridged between two Mn(II) centres via one pyridyl nitrogen and one oxadiazole nitrogen forming a novel coordination polymer. The ligand $\{[N(n\text{-}Bu)_4]^+[3\text{-pyt}]^-\}$ (**2**) and the Mn(II) complex **3** are soluble in common organic solvents and are air stable.

5.1. IR spectra

The IR spectrum of compound **3** reveals five characteristics bands due to ν(C=N), ν(N–N), ν_{as}(C–O–C), ν_s(C–O–C) and ν(C–S) at 1612, 1084, 1196, 1156 and 942 cm^{-1} respectively. The IR spectra of **2** and **3** are devoid of any peak in the region of 3300–3200 cm^{-1} indicating the absence of –NH group.

The IR spectrum of compound **3** shows a positive shift of 49 cm^{-1} in ν(N–N) region due to the bonding of oxadiazole nitrogen atom to the metal ion. A further positive shift of 37 cm^{-1} in thioamide IV indicates a change of the C–S bond to C=S during complex formation. Thus ligand **2** adopts thiolato form in the free state but is present in the thione form in complex **3.** A band occurring at 3442 cm^{-1} shows the presence of water molecule(s) in the complex. A positive shift of 16 cm^{-1} in the pyridine ring vibration of the complex in comparison to the free ligand **2** suggests involvement of pyridine nitrogen in bonding with Mn(II).

The above IR data clearly indicates the participation of oxadiazole and pyridine nitrogens in bonding, conversion of the thiolato form of the ligand **2** to the thione form and the presence of water molecule(s), all of which are supported by X-ray analysis. The IR spectral bands of the co-crystallized part of the complex **3** are observed at 1584 ν(C=N), 1196 and 1134 ν(C–O–C), 1034 ν(N–N) and 901 cm^{-1} ν(C–S) which are very close to the corresponding bands of $[3\text{-pyt}]^-$ except that of the pyridine ring vibration. The pyridine ring vibration of co-crystallized $\{[N(n\text{-}Bu)_4]^+[3\text{-pyt}]^-\}$ observed at 642 cm^{-1} shows a positive shift of 16 cm^{-1} in comparison to **2** due to the presence of hydrogen bonding between the pyridine nitrogen and hydrogen of water molecule.

5.2. Electronic spectra and magnetic moment

The UV–Vis spectrum of $\{[N(n\text{-}Bu)_4]^+[3\text{-pyt}]^-\}$ (**2**) exhibits bands at 322 and 224 nm attributed to intraligand transitions. The magnetic moment and electronic spectrum of complex **3** suggests its distorted octahedral geometry. The complex $\{[Mn(3\text{-pyt})_2(H_2O)_2][N(n\text{-}Bu)_4]^+[3\text{-pyt}]^-\}_n$ exhibits a μ_{eff} of 5.93 BM and shows two bands at 834 nm (11 990 cm^{-1}) and 434 nm (23 042 cm^{-1}) assigned to the $^5B_{1g} \rightarrow {}^5A_{1g}$ and $^5T_{2g}$ transitions, respectively, for high spin distorted octahedral Mn(II). The additional high intensity bands at 342 nm (29 240 cm^{-1}) and 298 nm (33 558 cm^{-1}) are tentatively assigned to charge transfer/intraligand transitions [30].

5.3. ^1H and ^{13}C NMR spectra

The ^1H NMR spectrum of $\{[N(n\text{-}Bu)_4]^+[3\text{-pyt}]^-\}$ exhibits no signals between 10.5 and 13.5 ppm, indicating the absence of NH protons. The protons due to pyridine ring appear as multiplets between 9.19 and 7.35 ppm. The aliphatic protons for $-CH_2$ of tetra-*n*-butylammonium ion are observed at 2.14, 1.74 and 1.68 ppm while those of $-CH_3$ are located at 0.96 ppm. The ^{13}C NMR spectrum of $\{[N(n\text{-}Bu)_4]^+[3\text{-pyt}]^-\}$ shows 11 peaks for 23 carbon atoms, out of which the signal due to >C–S appears at 180.38 ppm. The signals between 160.21 and 122.16 ppm are assigned the pyridine ring and oxadiazole carbons. The peaks appearing at δ 58.97, 24.06, 19.72 and 13.61 ppm are due to aliphatic carbons of tetra-*n*-butylammonium cation [31].

6. Crystal structure description of $\{[Mn(3\text{-pyt})_2(H_2O)_2][N(n\text{-}Bu)_4]^+[3\text{-pyt}]^-\}_n$

The crystal structure refinement data related to complex **3** are given in Table 1 and the main bond distances and bond angles of **3** are given in Table 2. The hydrogen bonds are listed in Table 3. The various possible binding sites of the ligand are represented in Fig. 1.

Table 1
Crystal refinement parameters of complex **3**.

Parameters	complex **3**
Empirical formula	$C_{37}H_{52}MnN_{10}O_5S_3$
Formula weight	868.01
Space group	*Pca*21
Crystal system	orthorhombic
T (K)	295(2)
λ, Mo Kα (Å)	0.71073
a (Å)	16.6730(2)
b (Å)	10.54060(10)
c (Å)	25.1940(4)
$\alpha = \beta = \gamma$ (°)	90
V (Å^3)	4427.68(10)
Z	4
ρ_{calcd} (Mg/m^3)	1.302
μ (mm^{-1})	0.491
F(000)	1828
Crystal size (mm)	0.45 × 0.39 × 0.28
θ Range for data collection (°)	4.65–26.37
Index ranges	$-20 \leqslant h \leqslant 20$ $-13 \leqslant k \leqslant 13$ $-31 \leqslant l \leqslant 31$
Reflections collected	96617
Independent reflections	8998
Data/restraints/parameters	8998/14/536
Goodness-of-fit on F^2	1.258
R_1, wR_2 [$I > 2\sigma(I)$]	0.0344, 0.0158
R_1, wR_2 (all data)	0.0288, 0.0806
Largest difference in peak and hole (e Å^{-3})	0.330 and −0.277

Table 2
Selected bond lengths and bond angles for complex **3** [Å and (°)].

Bond length of [Mn(3-pyt)$_2$(H$_2$O)$_2$]$_n$			
Mn–O(2W)	2.1854(19)	Mn–N(1A)	2.2671(18)
Mn–O(1W)	2.2055(19)	Mn–N(1B)	2.2680(19)
Mn–N(3B)#1	2.265(2)	Mn–N(3A)#2	2.2703(19)
S(1A)–C(1A)	1.674(3)	S(1B)–C(1B)	1.681(3)
N(1A)–C(1A)	1.322(3)	N(1A)–N(2A)	1.402(3)
N(1B)–C(1B)	1.321(3)	N(1B)–N(2B)	1.408(3)
N(2A)–C(2A)	1.283(3)	O(1A)–C(2A)	1.361(3)
N(2B)–C(2B)	1.283(3)	O(1A)–C(1A)	1.390(3)
O(1B)–C(2B)	1.356(3)	O(1B)–C(1B)	1.384(3)
Angles [°]			
O(2W)–Mn–O(1W)	174.74(8)	O(2W)–Mn–N(3B)#1	90.18(8)
O(1W)–Mn–N(3B)#1	84.57(7)	O(2W)–Mn–N(1A)	90.41(7)
O(1W)–Mn–N(1A)	89.68(7)	N(3B)#1–Mn–N(1A)	92.58(7)
O(2W)–Mn–N(1B)	90.61(8)	O(1W)–Mn–N(1B)	89.36(8)
N(3B)#1–Mn–N(1B)	88.13(7)	N(1)–Mn–N(1B)	178.75(9)
O(2W)–Mn–N(3A)#2	88.94(8)	O(1W)–Mn–N(3A)#2	96.32(8)
N(3B)#1–Mn–N(3A)#2	178.95(9)	N(1A)–Mn–N(3A)#2	88.01(7)
N(1B)–Mn–N(3A)#2	91.30(7)	N(2)–N(1A)–Mn	122.16(14)
C(1A)–N(1A)–Mn	129.68(16)	C(7)–N(3A)–Mn#3	121.01(16)
C(6A)–N(3A)–Mn#3	121.15(16)	N(2B)–N(1B)–Mn	118.67(15)
C(1B)–N(1B)–Mn	133.28(17)	C(7B)–N(3B)–Mn#4	119.34(16)
C(6B)–N(3B)–Mn#4	122.81(16)		
Bond lengths of [3–pyt]$^-$			
S–C(1)	1.683(4)	N(1)–N(2)	1.408(4)
N(1)–C(1)	1.295(4)	O–C(1)	1.400(4)
N(2)–C(2)	1.288(4)	O–C(2)	1.350(4)
Bond lengths of [N(n–Bu)$_4$]$^+$			
N–C(31)	1.516(5)	N–C(41)	1.518(4)
N–C(11)	1.516(4)	N–C(21)	1.522(5)

Symmetry transformations used to generate equivalent atoms: #1: $x - 1/2$, $-y + 2$, z; #2: $x + 1/2$, $-y + 1$, z; #3: $x - 1/2$, $-y + 1$, z; #4: $x + 1/2$, $-y + 2$, z.

The X-ray study of complex **3** indicates the following characteristics of the ligand: (i) it exists in thione and thiolato forms (ii) it shows two preferential binding sites i.e. N_{py} (pyridyl nitrogen) and N_{ox} (oxadiazole nitrogen) and (iii) it has strong capability of forming hydrogen bonding i.e. O–H···N(3), O–H···S(1B), O–H···S(1A) and O–H···S#5 (Fig. 3). Single crystal X-ray analyses reveal that the complex **3** possesses a two dimensional (2-D) framework constructed of Mn(II) centres and two [3-pyt]$^-$ ligands. It is very interesting that the [3-pyt]$^-$ part of the ligand adopts a bidentate bridging mode (nitrogen atoms from pyridyl and oxadiazole groups, Fig. 4a). As evident from the bond angles [trans angles ranging from 174.74(8)° to 178.75(9)° and cis angles ranging from 84.57(7)° to 96.32(8)°], the Mn(II) is in a slightly distorted six coordinated octahedral environment formed by two identical oxadiazole N donors [2.265(2) and 2.2703(19) Å for Mn–N(3B) and Mn–N(3A)], and two pyridine N-donors [2.2671(18) and 2.2680(19) Å for Mn–N(1A) and Mn–N(1B)] in equatorial positions, two water molecules [2.1854(19) Å for Mn–O(2W) and 2.2055(18) Å for Mn–O(1W)] in the axial positions (Fig. 4). The two [3-pyt]$^-$ ligands in complex **3** act as bridging ligands, alternately employing oxadiazole or pyridine nitrogen donors to bond to a Mn(II) centre. The [3-pyt]$^-$ ligand is thus bonded in a N_{py}, N_{oxa} bidentate bridged coordination mode. The dihedral angle between the pyridyl plane and the oxadiazole ring is 13.65(2)°. Since all the bonding sites of 3-pyt occupy equatorial positions in the coordination sphere of each Mn, the result is a 2-D sheet in which the molecules are stacked in parallel layers, forming a supramolecular metal–organic framework (Fig. 4b). The coordinated axial water molecules, above and below this sheet, from hydrogen bonds [O–H···S#5 and O–H···N(3) with the occluded [N(*n*-Bu)$_4$]$^+$ and [3-pyt]$^-$ moieties (Fig. 4b). The tetra-*n*-butylammonium cation and oxadiazole anion are enclosed and stabilized in this rectangular cavity through ionic interactions ($N^+ \cdots S^+$) (Fig. 4b). The rectangular cavity formed by one dimensional chain of the complex molecules have a dimension of 9.823 × 13.650 Å^2 [adjacent Mn···Mn separation between inter (13.650 Å) and intra (9.823 Å) chain] (Fig. 4a). The enclosed {[N(*n*-Bu)$_4$]$^+$[3-pyt]$^-$} is stabilized by two types of C–H···π interactions occurring between C–H of tetra-*n*-butylammonium cation [N(*n*-Bu)$_4$]$^+$] and centroid (Cg) of pyridine ring and oxadiazole ring of [3-pyt]$^-$ at the distance of 3.430 Å and 3.334 Å, respectively. There are two types of intermolecular hydrogen bonding, C21-H21B···S#5 = 2.973 Å and C41-H41B···N1 = 2.326 Å which provide stability to the occluded [N(*n*-Bu)$_4$]$^+$ and [3-pyt]$^-$ (Fig. 4b).

The pyridine nitrogen and thiolato sulfur of occluded {[N(*n*-Bu)$_4$]$^+$[3-pyt]$^-$} are also involved in strong intermolecular hydrogen bonding [O–H···N_{py} and O(2W)–H(2W1)···S#5, 1.98 and 2.43 Å, respectively]. Further, the intramolecular hydrogen bonding O(1W)–H(1W1)···S(1B and O(2W)–H(2W2)···S(1A) having the distances of 2.38 and 2.33 Å, respectively, are also observed. These hydrogen bonding interactions add further stability to the overall structure.

A comparison of Mn–N_{py}, Mn–O_{water}, C=S and C=N bond lengths with similar systems show that the values are in good agreement with those reported in literature [32]. The bond lengths of 1,3,4-oxadiazole-2-thione/thiolate are intermediate between single and double bonds and provide evidence for a high degree of delocalization in the ring. The π-electron delocalization in the oxadiazole ring and inter/intra molecular hydrogen bonding interactions contribute to the stabilization of the molecular structure of

Table 3
Hydrogen bonds for complex **3** [Å and °].

D–H···A	*d*(D–H)	*d*(H···A)	*d*(D···A)	∠(DHA)
O(1W)–H(1W1)···S(1B)	0.82	2.33	3.133(2)	166.5
O(1W)–H(1W2)···N(3)	0.82	1.98	2.794(4)	168.9
O(2W)–H(2W1)···S#5	0.83	2.43	3.246(2)	172.3
O(2W)–H(2W2)···S(1A)	0.82	2.38	3.148(2)	156.4

Symmetry transformations used to generate equivalent atoms: #1: $x-1/2$, $-y$, z; #2: $x + 1/2$, $-y + 1$, z; #3: $x + 1/2$, $-y$, z; #4: $x - 1/2$, $-y + 1$, z; #5: $-x + 1$, $-y + 1$, $z - 1/2$.

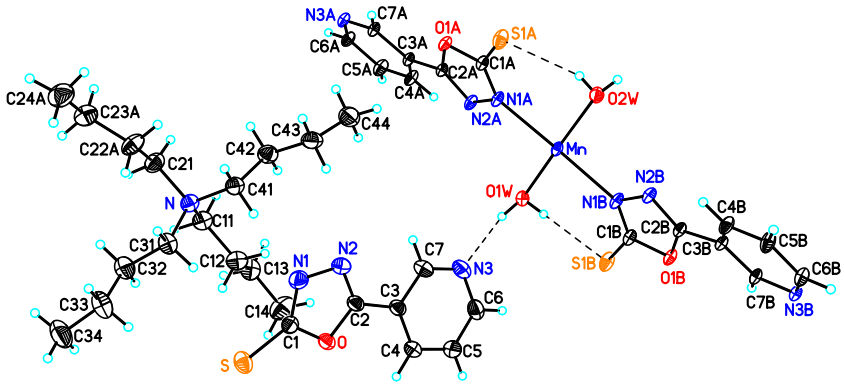


Fig. 3. Structure of the asymmetric formula unit of the complex $\{[Mn(3\text{-pyt})_2(H_2O)_2][N(n\text{-Bu})_4]^+[3\text{-pyt}]^-\}_n$ with the atom numbering scheme, showing O–H···N and O–H···S hydrogen bonding.

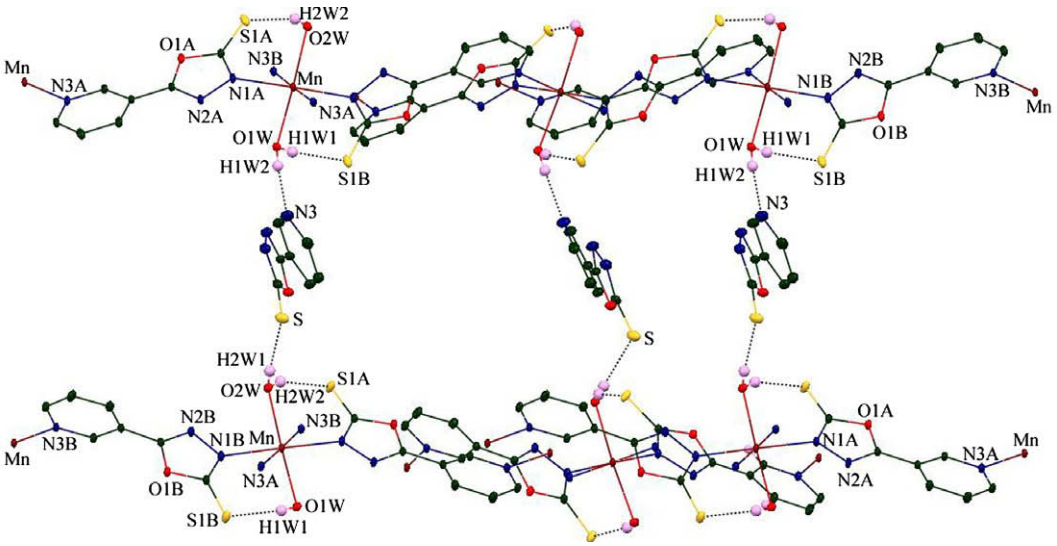


Fig. 4a. Mercury view of the crystal packing of complex **3**, showing O(1W)–H(1W1)···S(1B), O(2W)–H(2W1)···S(1A) intramolecular and O(1W)–H(1W2)···N(3), O(2W)–H(2W1)···S#5 intermolecular hydrogen bonding. Hydrogen atoms are omitted for clarity except those involved in hydrogen bonding.

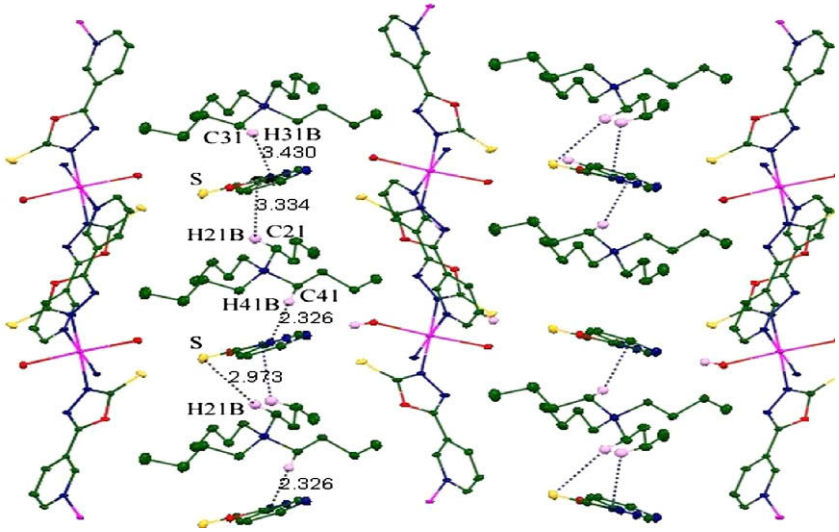


Fig. 4b. The supramolecular architecture of the complex **3,** view along *b* axis. Hydrogen atoms are omitted for clarity. Figure shows C–H···π interaction and C21–H21B···S#5 and C41–H41B···N1 intermolecular hydrogen bonding.

3. The specific arrangement of molecules along the *b* axis, gives rise to the 2-D sheet linked by strong hydrogen bonds formed between the axial water molecules and the occluded $N(n\text{-}Bu)_4]^+$ and $[3\text{-}pyt]^-$ moieties, resulting in a supramolecular architecture.

7. Conclusion

A new polymeric distorted octahedral Mn(II) complex $\{[Mn(3\text{-}pyt)_2(H_2O)_2][N(n\text{-}Bu)_4]^+[3\text{-}pyt]^-\}_n$ is synthesized from an unique ambidentate tetra-*n*-butylammonium [5-(3-pyridyl)-1,3,4-oxadiazole-2-thiolate] in which $[3\text{-}pyt]^-$ adopts the N_{py}, N_{oxa} coordination mode. The hydrogen bonding and arrangement of $[Mn(3\text{-}pyt)_2(H_2O)_2]_n$, along the *b* axis generates a rectangular cavity where tetra-*n*-butylammonium ion is enclosed and stabilized by anionic oxadiazole-2-thiolate through $N^+\cdots S^-$ ionic interaction.

Acknowledgements

Authors are thankful to Prof. J.-C. Daran, Laboratoire de Chimie de Coodination, UPR-CNRS 8241, 205, route de Narbonne, 31077 – Toulouse cedex 04, France for his help in further refinement of .cif of the complex. This work was supported by CSIR Grant No. 01(2152)07/EMR-II. One of the authors (M. Singh) is thankful to CSIR, New Delhi, India for the award of SRF, supported by Grant No. 9/13(160)2008/EMR-I.

Appendix A. Supplementary data

CCDC 677285 contains the supplementary crystallographic data for **3**. These data can be obtained free of charge via http://www.ccdc.cam.ac.uk/conts/retrieving.html, or from the Cambridge Crystallographic Data Centre, 12 Union Road, Cambridge CB2 1EZ, UK; fax: (+44) 1223-336-033; or e-mail: deposit@ccdc.cam.ac.uk. Supplementary data associated with this article can be found, in the online version, at doi:10.1016/j.poly.2008.10.008.

References

[1] Z.H. Zhang, C.-P. Li, Y.-L. Tian, Y.-M. Guo, Inorg. Chem. Commun. 11 (2008) 326.
[2] G. Mahmoudi, A. Morshli, CrystEngCommun. 9 (2007) 1062.
[3] X.-X. Zhao, J.-P. Ma, Y.-B. Dong, R.Q. Huang, T. Lai, Cryst. Growth & Design 7 (2007) 1058.
[4] S.R. Batten, R. Robson, Angew. Chem., Int. Ed. 37 (1998) 1461.
[5] N.W. Ockwig, O. Delgado- Friedrichs, M. O′ Keefe, O.M. Yaghi, Acc. Chem. Res. 38 (2005) 176.
[6] N. Atoub, G. Mohmoudi, A. Morsali, Inorg. Chem. Commun. 10 (2007) 166.
[7] R.-Q. Zhou, H. Sakurai, Q. Xu, Angew, Chem., Int. Ed. 45 (2006) 2542.
[8] S. Kitagawa, R. Kitaura, S. Nora, Angew. Chem., Int. Ed. 43 (2004) 250.
[9] G.M. Abou-Elenien, N.A. Ismail, A.A. El-Maghraby, G.M. Al-Abdallah, Electroanalysis 13 (2001) 1022.
[10] Y.-T. Wang, G.-M. Tang, Z.-W. Quang, Polyhedron 26 (2007) 4542.
[11] Z.M. Nofal, H.H. Fahmy, H.S. Mohamed, Arch. Pharm. Res. 25 (2002) 250.
[12] M. Du, Z.H. Zhang, X.-J. Zhao, Q. Xu, Inorg. Chem. 45 (2006) 5785.
[13] Z.-H. Zhang, Y.-L. Tian, Y.-M. Guo, Inorg. Chim. Acta 360 (2007) 2783.
[14] H. Liu, B.-H. Zhong, L.P. Liu, S.-T. Han, J. Chemical Cryst. 34 (2004) 259.
[15] Y.-T. Wang, H.-H. Fan, H.-Z. Wang, X.-M. Chen, Inorg. Chem. 44 (2005) 4148.
[16] Y.-T. Wang, H.-H. Fan, H.-Z. Wang, X.-M. Chen, J. Mol. Struct. 740 (2005) 61.
[17] Y.-T. Wang, G.-M. Tang, W.-Y. Ma, W.-Z. Wan, Polyhedron 26 (2007) 782.
[18] P. Tripathi, A. Pal, V. Jancik, A.K. Pandey, J. Singh, N.K. Singh, Polyhedron 26 (2007) 2597.
[19] O.H. Amin, L.J. Al-Hayaly, S.A. Al-Jiboori, T.A.K. Al-Allaf, Polyhedron 23 (2004) 2013.
[20] C.-L. Ma, G.-R. Tian, R.-F. Zhang, Polyhedron 24 (2005) 1773.
[21] C. Ma, G. Tian, R. Zhang, Inorg. Chim. Acta 360 (2007) 1762.
[22] Y.-T. Wang, G.-M. Tang, Inorg. Chem. Commun. 10 (2007) 53.
[23] M. Singh, R.J. Butcher, N.K. Singh, Polyhedron 27 (2008) 3151.
[24] A.V. Robin, K.M. Fromm, Coord. Chem. Rev. 250 (2006) 2127.
[25] T. Curtius, J. Prakt. Chem. 50 (1894) 278.
[26] A.I. Vogel, A Text Book of Quantitative Inorganic Analysis, 3rd ed., ELBS, Longman, London, 1969.
[27] Oxford Diffraction, CRYSALIS RED and CRYSALIS CCD Versions 1.171.31.8, Oxford Diffraction Ltd., Abingdon, Oxafordshire, England, 2007.
[28] I.J. Bruno, J.C. Cole, P.R. Edgington, M. Kessler, C.F. Macrae, P. Mc. Cabe, J. Pearson, R. Taylor, Acta Crystallogr., Sect. B 58 (2002) 389.
[29] L.J. Farrugia, J. Appl. Crystallogr. 30 (1997) 565.
[30] A.B.P. Lever, Inorganic Electronic Spectroscopy, 2nd ed., Elsevier, Amsterdam, 1984.
[31] N.K. Singh, R.J. Butcher, A.K. Pandey, M. Singh, M.K. Bharty, Acta Crystallogr., Sect. E 63 (2007) o4327.
[32] Y.-T. Wang, G.-M. Tang, J. Coord. Chem. 60 (2007) 2139.

Polyhedron 28 (2009) 101–106

Contents lists available at ScienceDirect

Polyhedron

journal homepage: www.elsevier.com/locate/poly

Copper(I) complexes of a thioether-functionalized short-bite aminobis(phosphonite), [PhN{P(–$OC_{10}H_6$(μ-S)$C_{10}H_6O$–)}$_2$]

Benudhar Punji [a], Joel T. Mague [b], Shaikh M. Mobin [c], Maravanji S. Balakrishna [a,*]

[a] Phosphorus Laboratory, Department of Chemistry, Indian Institute of Technology Bombay, Powai, Mumbai 400 076, India
[b] Department of Chemistry, Tulane University, New Orleans, LA 70118, USA
[c] National Single Crystal X-ray Facility Center, Indian Institute of Technology Bombay, Powai, Mumbai 400 076, India

ARTICLE INFO

Article history:
Received 5 June 2008
Accepted 14 October 2008
Available online 20 November 2008

Keywords:
Aminobis(phosphonite)
π–π stacking interactions
Metallophilic interactions
Copper complexes
Short-bite ligands

ABSTRACT

Copper(I) complexes of short-bite aminobis(phosphonite), PhN{P(–$OC_{10}H_6$(μ-S)$C_{10}H_6O$–)}$_2$ (**1**) have been synthesized. Reactions of **1** with an excess of CuX (X = Cl, Br, and I) afforded the ligand-bridged binuclear complexes, [PhN(PR-κ*P*)$_2${Cu(μ-X)(MeCN)}$_2$] (**2**, X = Cl; **3**, X = Br; **4**, X = I; R = –$OC_{10}H_6$(μ-S)$C_{10}H_6O$–), whereas treatment with 0.5 equiv. of [Cu(MeCN)$_4$]PF_6 produces the mononuclear bischelated cationic complex, [{PhN(PR-κ*P*)$_2$}$_2$Cu](PF_6) (**5**). Single crystal X-ray structures of complexes **3** and **4** are reported. Complex **3** shows strong π–π stacking interactions between the naphthyl moieties, whereas complex **4** shows ligand-supported Cu···Cu metallophilic interactions.

© 2008 Elsevier Ltd. All rights reserved.

1. Introduction

Short-bite ligands have drawn considerable attention over the last three decades owing to their novelty in organometallic chemistry and catalytic applications [1]. In such bidentate ligands, the donor atoms are generally separated by a single atom fragment such as CR_2, NR, O or S and can coordinate to metal centers in monodentate, chelating or bridging modes. In mononuclear chelate complexes, the ligand forms a highly strained four-membered ring with conformational rigidity whereas the bridging coordination mode brings the two metal centers into close proximity to facilitate a cooperative metallophilic interaction between two or more metal centers [2f]. Both of these factors, either conformational rigidity or metallophilic interaction, can activate the substrate molecules during catalysis [2]. Among the short-bite ligands, the P–C–P framework *i.e.* bis(diphenylphosphino)methane (dppm) and similar diphosphines has been widely investigated and achieved considerable success [1c,3]. In contrast, although the coordination chemistry of P–N–P framework ligands *i.e.* diphosphazane (or diphosphinoamine) has been well documented [1d,4], their catalytic applications have been much less explored. Recently, Faraone and co-workers have prepared diphosphazane ligands containing a dinaphthyl backbone between the phosphorus centers and used them in the enantioselective palladium-catalyzed allylic substitution reactions and the rhodium catalyzed hydroformylation of styrene [5]. However, diphosphazanes with donor atoms such as O, N or S incorporated into the ligand framework are less well known [6]. The development of such hybrid ligands is of particular significance because they can generate interesting coordination chemistry mainly for the synthesis of heterobimetallic and high-nuclearity complexes. In this context, we have recently synthesized a thioether-functionalized aminobis(phosphonite), PhN{P(–$OC_{10}H_6$(μ-S)$C_{10}H_6O$–)}$_2$ (**1**) and reported its reactivity with platinum metals where it exhibits interesting coordination behaviors producing neutral, cationic and anionic complexes (Chart 1) which show excellent catalytic activities [7].

Here we sought to examine the reactivity of this thioether-functionalized aminobis(phosphonite) with copper(I) derivatives as their complexes can be ideal candidates for luminescence studies. The dinaphthyl moiety was chosen as it is well known for exhibiting aromatic–aromatic π-stacking interactions which in turn can contribute to self assembly or molecular recognition processes [8].

As a part of our research in organometallic chemistry [9] and catalytic investigation [10] of phosphorus-based ligands, we report in this paper the copper(I) complexes of thioether-functionalized aminobis(phosphonite) (**1**).

2. Results and discussion

2.1. Copper derivatives

In our recent investigation on the coordination behavior of thioether-aminobis(phosphonite) **1** with platinum metal precursors, interesting anionic complexes with phosphorus and sulfur coordi-

* Corresponding author. Tel.: +91 22 2576 7181; fax: +91 22 2576 7152/2572/3480.
E-mail addresses: krishna@chem.iitb.ac.in, msb_iitb@yahoo.com (M.S. Balakrishna).

0277-5387/$ - see front matter © 2008 Elsevier Ltd. All rights reserved.
doi:10.1016/j.poly.2008.10.014

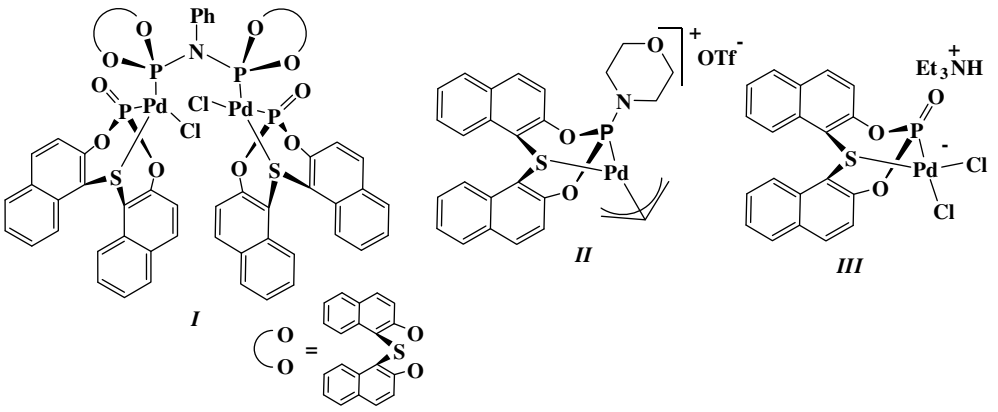


Chart 1.

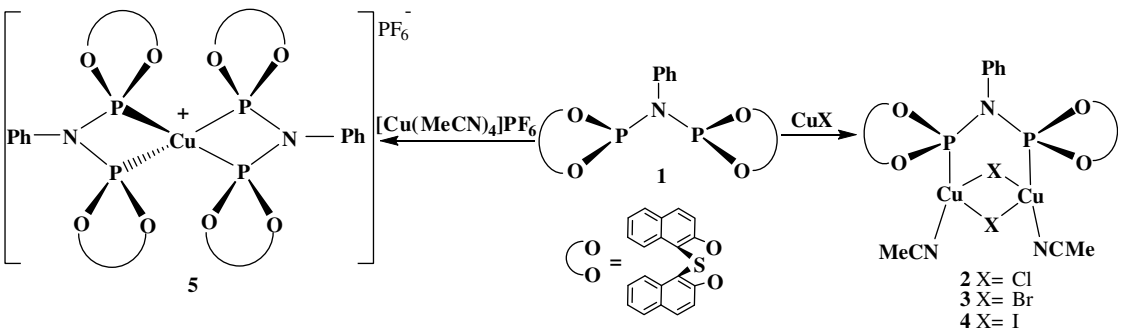
nation as well as neutral platinum complexes with highly strained four-membered chelate rings were produced and their catalytic applications were explored [7]. However, the reactivity of aminobis(phosphonite) with group 11 metal precursors is considerably different. Thus the reaction of **1** with an excess of CuX (X = Cl, Br, and I) in dichloromethane and acetonitrile afforded the corresponding binuclear complexes, [PhN(PR-κP)$_2${Cu(μ-X)(MeCN)}$_2$], (**2**, X = Cl; **3**, X = Br; **4**, X = I; R = −OC$_{10}$H$_6$(μ-S)C$_{10}$H$_6$O−) (Scheme 1). The bromo and iodo derivatives are highly soluble in dichloromethane whereas the chloro derivative is only partially soluble in dichloromethane. The ^{31}P NMR spectra of complexes **2**–**4** show single resonances at 102.9, 94.9 and 91.8 ppm, respectively. In the ^{1}H NMR spectra of all these complexes, a singlet is observed in the region 2.01–2.16 ppm which is assigned to the protons of the coordinated acetonitrile groups. Treatment of CuX with 1 equiv. of **1** did not give the four-membered chelate complexes; instead the same binuclear complexes **2–4** are obtained in excellent yield. The reaction of **1** with 0.5 equiv. of [Cu(MeCN)$_4$]PF$_6$ produces the mononuclear bischelated cationic complex, [{PhN(PR-κP)$_2$}$_2$Cu](PF$_6$) (**5**) in good yield. The ^{31}P NMR spectrum of complex **5** shows a single resonance at 100.7 ppm for the phosphorus of the aminobis(phosphonite) and a septet at −145.9 ppm for the PF_6^- group with a $^{1}J_{PF}$ coupling of 713 Hz. The structures of **3** and **4** are confirmed by single crystal X-ray diffraction studies.

2.2. Crystal structures of complexes *3* and *4*

Perspective views of the molecular structures of complexes **3** and **4** with the atom numbering schemes are shown in Figs. 1 and 2, respectively. The crystallographic data and details of the structure determinations are given in Table 1 while selected bond lengths and bond angles appear in Table 2.

In the molecular structures of **3** and **4**, the molecules consist of two copper atoms linked by one bridging aminophosphonite ligand and two bridging halides (bromide or iodide) with one acetonitrile coordinated to each copper center. Complex **3** has crystallographically-imposed mirror symmetry with all Cu, P, S and N atoms lying on the mirror. In both the complexes, the copper centers display distorted tetrahedral geometry with internal angles in the range 99.04(2)–115.13(2)° for complex **3** and 97.17(1)–127.82(1)° for complex **4**. The Cu–P distances (Cu1–P1 = 2.185(1), Cu2–P2 = 2.194(1) Å for **3** and Cu1–P1 = 2.214(1), Cu2–P2 = 2.220(1) Å for **4**) are shorter than those shown by other polynuclear copper (I) complexes containing dppm (Cu–P ≈ 2.277(6) Å) and dppf (Cu–P ≈ 2.306(7) Å) ligands [11]. The Cu···Cu distance in **3** (2.800(1) Å) is significantly longer than that in **4** (2.638(7) Å) with the latter somewhat shorter than the value of 2.695(1) Å found in [(PhN(PR$_2$)$_2$Cu$_2$(μ-Br)$_2$(L)]$_n$ (R = *o*-MeOC$_6$H$_4$O; L = 4,4'-bipy) [12a].

However, the span of Cu···Cu separations in {Cu(μ-X)$_2$Cu} moieties containing P–N–P type ligands is rather large and includes values of 2.742(2) Å in [(MeCN)$_2$(Cu(μ-Br)$_2$Cu)((R$_2$P)$_2$NC$_6$H$_4$N(PR$_2$)$_2$) (Cu(μ-Br)$_2$Cu) (MeCN)$_2$] and 2.920(3) and 2.941(3) Å in [(L)$_2$(Cu(μ-I)$_2$Cu)((R$_2$P)$_2$NC$_6$H$_4$N(PR$_2$)$_2$)(Cu(μ-I)$_2$Cu)(L)$_2$] (R = *o*-MeOC$_6$H$_4$O; L = HNC$_5$H$_9$C$_3$H$_3$N$_2$ [12b]. These last compare favorably with those found in trinuclear complexes of the type [Cu$_3$(μ^3-η^1-C≡CR)(μ-dppm)$_n$] (Cu···Cu = 2.997(3) Å) [11a]. In the case of complex **3**, the eight-membered ring containing phosphorus and sulfur atoms is in the *anti* chair-like conformation and the sulfur atom lies far away from the copper center thus preventing any S···Cu interaction. In contrast, the phosphorus- and



Scheme 1.

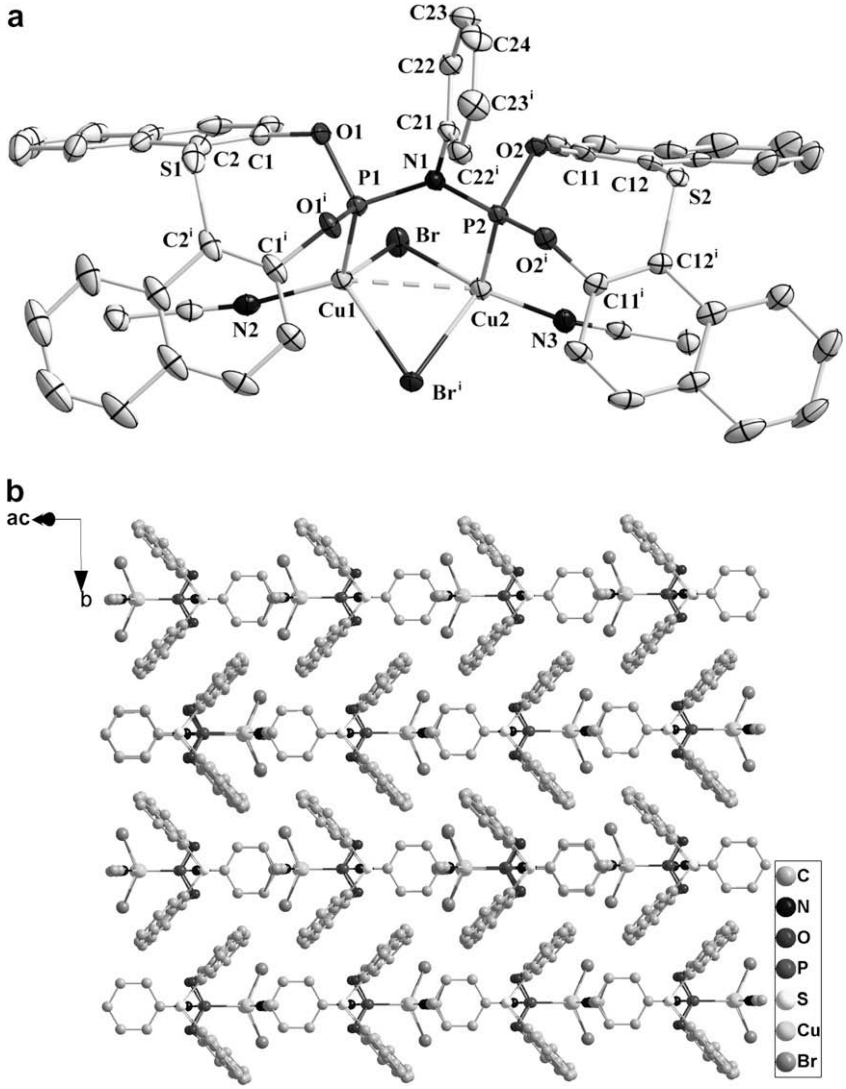


Fig. 1. (a) Molecular structure of **3**. For clarity, solvent and all hydrogen atoms have been omitted. (b) Molecular structure of **3** showing π–π stacking interactions.

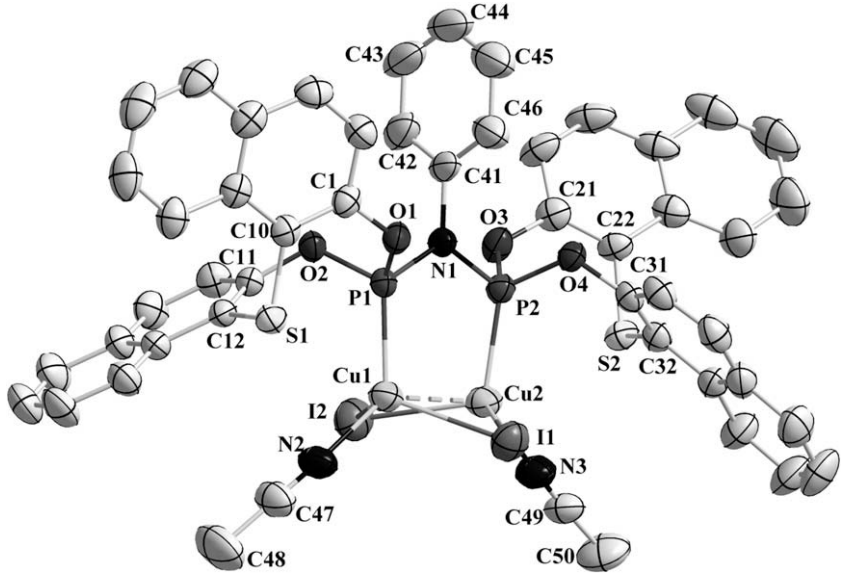


Fig. 2. Molecular structure of **4**. For clarity, solvent and all hydrogen atoms have been omitted.

Table 1
Crystallographic data for complexes **3** and **4**.

	3	**4**
Formula	$C_{50}H_{35}Br_2Cu_2N_3O_4P_2S_2$ .CH_3CN	$C_{50}H_{35}I_2N_3O_4P_2S_2Cu_2$
Mol. wt.	1195.9	1248.8
Crystal system	monoclinic	monoclinic
Crystal size (mm)	0.06 × 0.07 × 0.12	0.35 × 0.28 × 0.21
Space group	$P2_1/m$ (no. 11)	$P2_1/n$
a (Å)	12.482(1)	13.722(1)
b (Å)	14.214(1)	29.801(5)
c (Å)	13.847(1)	14.010(2)
β (°)	98.965(1)	114.947(8)
V (Å^3)	2426.7(3)	5194.3(2)
Z	2	4
$\rho_{calc.}$ (g cm^{-3})	1.662	1.643
μ (Mo Kα), (mm^{-1})	2.754	2.199
F(000)	1215	2536
Temperature (K)	100	293(2)
$\theta_{min-max}$ (°)	1.5, 28.3	3.00, 25.00
Goodness-of-fit (F^2)	0.72	0.993
R_1[a]	0.0467	0.0492
wR_2[b]	0.1274	0.0921

[a] $R_1 = \sum|F_o| - |F_c|/\sum|F_o|$.
[b] $wR_2 = \{\sum w[(F_o^2 - F_c^2)^2]/\sum[w(F_o^2)^2]\}^{1/2}$.

Table 2
Selected bond distances (Å) and bond angles (°) for complexes **3** and **4**.

Complex **3**		Complex **4**	
Cu1–Br	2.513(6)	Cu1–I1	2.641(6)
Cu2–Br	2.502(5)	Cu1–I2	2.750(7)
Cu1–P1	2.185(1)	Cu2–I2	2.660(6)
Cu2–P2	2.194(1)	Cu2–I1	2.700(7)
Cu1–N2	1.996(4)	Cu1–P1	2.214(1)
Cu2–N3	1.995(5)	Cu2–P2	2.220(1)
P1–N1	1.679(4)	Cu2–N3	1.997(4)
P2–N1	1.681(4)	Cu1–N2	1.995(3)
Cu1···Cu2	2.801	P1–N1	1.698(3)
		P2–N1	1.695(3)
		Cu1···Cu2	2.638(7)
Cu1–Br–Cu2	67.89(2)	Cu1–I1–Cu2	59.171(2)
Br–Cu1–P1	110.43(3)	Cu2–I2–Cu1	58.330(2)
Br–Cu1–N2	110.33(8)	I1–Cu1–I2	114.01(2)
Br–Cu1–Br^i	99.04(2)	P1–Cu1–I1	109.62(3)
P1–Cu1–N2	115.13(2)	P1–Cu1–I2	101.22(3)
Br–Cu2–P2	108.67(3)	N2–Cu1–P1	127.73(1)
Br–Cu2–N3	112.76(7)	N2–Cu1–I2	97.17(1)
Br–Cu2–Br^i	99.62(2)	I1–Cu2–I2	115.04(2)
P2–Cu2–N3	113.42(1)	P2–Cu2–I1	103.71(3)
P1–N1–P2	116.5(2)	P2–Cu2–I2	105.77(3)
P1–N1–C21	122.7(3)	N3–Cu2–P2	127.82(1)
P2–N1–C21	120.7(3)	N3–Cu2–I1	102.19(1)
		P1–N1–P2	120.02(2)
		P1–N1–C41	120.1(2)
		P2–N1–C41	119.8(2)

sulfur-containing eight-membered rings in complex **4** are in a *syn* boat-like conformation which places the sulfur atoms *syn* to the four-membered Cu_2I_2 ring. As the Cu1···S1 (3.459(8) Å) and Cu2···S2 (3.438(8) Å) separations are noticeably less than the sum of the corresponding van der Waals radii (4.12 Å), attractive Cu···S interactions are likely present. In the solid state **3** shows a strong π-π stacking interaction-ring involving the C1–C3;C8–C10 portion of one naphthyl group and the C11–C13;C18–C20 portion of the one in the molecule at $1-x, -y, 1-z$. There is a 9.91° dihedral angle between the mean planes of these two rings and the distance between their centroids (Cg) is 3.489(2) Å while the perpendicular distance from the Cg of the latter ring to the mean plane of the former is 3.299(3) Å [13]. In addition, there are C–H···Cg (π-ring) interactions involving the acetonitrile attached to Cu1 and the C3–C8 portion of one naphthyl group (C26–H26c···Cg(ring) = 2.71 Å; 151° (intramolecular) and C26–H26a···Cg (ring at $x, ½-y, z$) = 2.67 Å; 158°) as well as weak C–H···Br interactions (C6–H6···Br (at $1-x, -y, -z$) = 2.90 Å; 177° and C16–H16···Br (at $-x, -y, 1-z$) = 2.91 Å; 157°). Complex **4** shows a weak C37–H37···O1 (at $1-x, 1-y, -z$) interaction (2.67 Å; 162°) as well as intermolecular C–H···I interactions with the acetonitrile ligands in two adjacent molecules (I1···H48c–C48 (at $1-x, 1-y, 1-z$) = 3.05 Å; 176° and I1···H50b–C50b (at $2-x, 1-y, 1-z$) = 3.14 Å; 157°.

3. Conclusion

Copper(I) complexes of a thioether-functionalized aminobis(phosphonite) ligand have been synthesized. The aminobis(phosphonite) **1**, which contains a hemilabile thioether functionality, shows versatile coordination properties. By choosing appropriate metal reagents and reaction conditions both mononuclear and bridged binuclear complexes are obtained. In the solid state complex **3** shows strong π–π stacking interactions while in complex **4** there is a significant ligand-supported metallophilic interactions.

4. Experimental

All experimental manipulations were carried out under an atmosphere of dry nitrogen or argon using Schlenk techniques. Solvents were dried and distilled prior to use by conventional methods. Aminobis(phosphonite) (**1**) [7a], CuX (X = Cl, Br) [14] and $[Cu(MeCN)_4PF_6]$ [15] were prepared according to the published procedures. Other reagents were obtained from commercial sources and used after purification. The ^{1}H and ^{31}P{^{1}H} NMR (δ in ppm) spectra were obtained on a Varian VRX 400 spectrometer operating at frequencies of 400 and 162 MHz, respectively. The spectra were recorded in $CDCl_3$ (or DMSO-d_6) solutions with $CDCl_3$ (or DMSO-d_6) as an internal lock; TMS and 85% H_3PO_4 were used as internal and external standards for ^{1}H and ^{31}P{^{1}H} NMR, respectively. Positive shifts lie downfield of the standard in all of the cases. Microanalyses were carried out on a Carlo Erba (Model 1106) elemental analyzer. Melting points of all compounds were determined on Veego melting point apparatus and were uncorrected.

4.1. Synthesis of [PhN(PR-κP)$_2${Cu(μ-Cl)(MeCN)}$_2$] (**2**, R = –OC$_{10}$H$_6$(-S)C$_{10}$H$_6$O–)

A solution of CuCl (0.030 g, 0.303 mmol) in acetonitrile (4 ml) was added dropwise to a solution of **1** (0.059 g, 0.076 mmol) in dichloromethane (10 ml) and the reaction mixture was stirred for 1 h. The suspension was filtered to remove unreacted CuCl and the mother liquor was concentrated under vacuum, to give a crystalline product **2** at −25 °C. Yield: 85% (0.069 g), m.p.: 194–196 °C (dec.). ^{1}H NMR (400 MHz, DMSO-d_6): δ 8.70 (d, 4H, $^3J_{HH}$ = 9.2 Hz, Ar), 7.51–7.95 (m, 20H, Ar, 5H, Ph), 2.10 (s, 6H, CH_3CN). ^{31}P{^{1}H} NMR (121.4 MHz, DMSO-d_6): δ 102.9 (s). *Anal.* Calc. for $C_{50}H_{35}Cl_2N_3O_4P_2S_2Cu_2$: C, 56.34; H, 3.31; N, 3.94; S, 6.02. Found: C, 56.31; H, 3.29; N, 3.92; S, 5.99%.

4.2. Synthesis of [PhN(PR-κP)$_2${Cu(μ-Br)(MeCN)}$_2$] (**3**)

This was synthesized by a procedure similar to that for **2** using CuBr (0.050 g, 0.348 mmol) and **1** (0.068 g, 0.087 mmol). Yield: 87% (0.087 g), m.p.: 210 °C (dec.). ^{1}H NMR (400 MHz, $CDCl_3$): δ 8.51 (d, 4H, $^3J_{HH}$ = 8.8 Hz, Ar), 7.11–7.56 (m, 16H, Ar, 5H, Ph), 7.01 (d, 4H, $^3J_{HH}$ = 8.8 Hz, Ar), 2.16 (s, 6H, CH_3CN). ^{31}P{^{1}H} NMR (162 MHz, $CDCl_3$): δ 94.9 (s). *Anal.* Calc. for $C_{50}H_{35}Br_2N_3O_4P_2S_2Cu_2$: C, 52.00; H, 3.05; N, 3.64; S, 5.55. Found: C, 51.97; H, 2.99; N, 3.62; S, 5.51%.

4.3. Synthesis of [PhN(PR-κP)$_2${Cu(μ-I)(MeCN)}$_2$] (**4**)

This was synthesized by a procedure similar to that for **2** using CuI (0.050 g, 0.315 mmol) and **1** (0.062 g, 0.079 mmol). Yield: 91% (0.09 g), m.p.: 174 °C (dec.). ^{1}H NMR (400 MHz, $CDCl_3$): δ 8.87 (d, 4H, $^3J_{HH}$ = 9.2 Hz, Ar), 6.67–7.86 (m, 20H, Ar, 5H, Ph), 2.01 (s, 6H, CH_3CN). $^{31}P\{^1H\}$ NMR (162 MHz, $CDCl_3$): δ 91.8 (s). *Anal.* Calc. for $C_{50}H_{35}I_2N_3O_4P_2S_2Cu_2$: C, 48.09; H, 2.82; N, 3.36; S, 5.14. Found: C, 48.02; H, 2.79; N, 3.34; S, 5.11%.

4.4. Synthesis of [{PhN(PR-κP)$_2$}$_2$Cu](PF$_6$) (**5**)

To a solution of **1** (0.084 g, 0.107 mmol) in dichloromethane (12 ml) $Cu(MeCN)_4PF_6$ (0.020 g, 0.054 mmol) was added and the reaction mixture was stirred for 2 h. The colorless solution obtained was concentrated and diethyl ether (8 ml) was added to precipitate out the white product. This was then filtered off and dried under vacuum. Yield: 89% (0.085 g), m.p.: 180 °C (dec.). ^{1}H NMR (400 MHz, $CDCl_3$): δ 8.49 (d, 8H, $^3J_{HH}$ = 7.6 Hz, Ar), 7.14–8.23 (m, 40H, Ar, 10H, Ph). $^{31}P\{^1H\}$ NMR (162 MHz, $CDCl_3$): δ 100.7 (s, 4 P), −145.9 (septet, 1P, PF_6, $^1J_{PF}$ = 713 Hz). *Anal.* Calc. for $C_{92}H_{58}F_6N_2O_8P_5S_4Cu$: C, 62.07; H, 3.28; N, 1.57; S, 7.21. Found: C, 62.01; H, 3.25; N, 1.53; S, 7.18%.

5. X-ray crystallography

A crystal of **3** which proved to be twinned was mounted in a Cryoloop™ with a drop of Paratone oil and placed in the cold nitrogen stream of the Kryoflex™ attachment of the Bruker APEX CCD diffractometer. A full sphere of data was collected using 606 scans in ω (0.3° per scan) at Φ = 0°, 120° and 240° using the SMART software package [16]. The raw data were reduced to F^2 values using the SAINT+ software [17] and a global refinement of unit cell parameters using 9500 reflections chosen from the full data set was performed. Multiple measurements of equivalent reflections provided the basis for an empirical absorption correction as well as a correction for any crystal deterioration during the data collection (TWINABS [18]). The structure was solved by direct methods and refined by full-matrix least-squares procedure using the SHELXTL program package [19]. Hydrogen atoms were placed in calculated positions and included as riding contributions with isotropic displacement parameters tied to those of the attached non-hydrogen atoms.

A crystal of **4** was mounted on a OXFORD DIFFRACTION XCALIBUR-S CCD system equipped with graphite monochromated Mo Kα radiation (0.71073 Å). The data were collected in the ω–2θ scan mode and an absorption correction was applied by using multiscan techniques. The structure was solved by direct methods (SHELXS 97) and refined by full-matrix least-squares against F^2 using the SHELXL 97 software [19b]. Non-hydrogen atoms were refined with anisotropic thermal parameters. All hydrogen atoms were geometrically fixed and allowed to refine using a riding model.

Acknowledgments

We are grateful to the Department of Science and Technology (DST), New Delhi for funding through Grant SR/S1/IC-02/2007. B.P. thanks CSIR for Research Fellowship (JRF and SRF). We also thank Department of Chemistry Instrumentation Facilities, Bombay, for spectral and analytical data and the Louisiana Board of Regents through Grant LEQSF (2002-03)-ENH-TR-67 for purchase of the CCD diffractometer and the Chemistry Department of Tulane University for support of the X-ray laboratory. National Single Crystal X-ray Facility Center, IIT Bombay is acknowledged for solving one of the structures.

Appendix A. Supplementary data

CCDC 673994 and 673995 contain the supplementary crystallographic data for **3** and **4**. These data can be obtained free of charge via http://www.ccdc.cam.ac.uk/conts/retrieving.html, or from the Cambridge Crystallographic Data Centre, 12 Union Road, Cambridge CB2 1EZ, UK; fax: (+44) 1223-336-033; or e-mail: deposit@ccdc.cam.ac.uk. Supplementary data associated with this article can be found, in the online version, at doi:10.1016/j.poly.2008.10.014.

References

[1] (a) G. Wilkinson, F.G.A. Stone, E.W. Abel (Eds.), Comprehensive Organometallic Chemistry, Pergamon Press, Oxford, 1982;
(b) L.H. Pignolet (Ed.), Homogeneous Catalysis with Metal Phosphine Complexes, Plenum, New York, 1983, p. 167;
(c) B. Chaudret, B. Delavaux, R. Poilblanc, Coord. Chem. Rev. 86 (1988) 191;
(d) M.S. Balakrishna, V.S. Reddy, S.S. Krishnamurthy, J.F. Nixon, J.C.T.R.B. St. Laurent, Coord. Chem. Rev. 129 (1994) 1;
(e) M. Witt, H.W. Roesky, Chem. Rev. 94 (1994) 1163.
[2] (a) D.J. Anderson, K.W. Kramarz, R. Eisenberg, Inorg. Chem. 35 (1996) 2688;
(b) G. Francio, R. Scopelliti, C.G. Arena, G. Bruno, D. Drommi, F. Faraone, Organometallics 17 (1998) 338;
(c) A. Scrivanti, V. Beghetto, E. Campagna, M. Zanato, U. Matteoli, Organometallics 17 (1998) 630;
(d) J.R. Torkelson, F.H. Antwi-Nsiah, R. Mc Donald, M. Cowie, J.G. Pruis, K.J. Jalkanen, R.L. DeKock, J. Am. Chem. Soc. 121 (1999) 3666;
(e) Y. Gao, J.K. Kuncheria, H.A. Jenkins, R.J. Puddephatt, G.P.A. Yap, J. Chem. Soc., Dalton Trans. (2000) 3212;
(f) G.A. Bowmaker, J.V. Hanna, R.D. Hart, P.C. Healy, A.H. White, J. Chem. Soc., Dalton Trans. (1994) 2621 and references cited therein.
[3] R.J. Puddephatt, Chem. Soc. Rev. 12 (1983) 99.
[4] (a) R.B. King, Acc. Chem. Res. 13 (1980) 243;
(b) T. Appleby, J.D. Woollins, Coord. Chem. Rev. 235 (2002) 121.
[5] (a) G. Calabrò, D. Drommi, G. Bruno, F. Faraone, Dalton Trans. (2004) 81;
(b) G. Calabrò, D. Drommi, C. Graiff, F. Faraone, A. Tiripicchio, Eur. J. Inorg. Chem. (2004) 1447.
[6] (a) R.P. Kamalesh Babu, S.S. Krishnamurthy, M. Nethaji, J. Organomet. Chem. 454 (1993) 157;
(b) R.P. Kamalesh Babu, S.S. Krishnamurthy, M. Nethaji, Tetrahedron: Asymmetry 6 (1995) 427;
(c) R.P. Kamalesh Babu, K. Aprna, S.S. Krishnamurthy, M. Nethaji, Phosphorus, Sulfur Silicon Relat. Elem. 103 (1995) 39.
[7] (a) B. Punji, J.T. Mague, M.S. Balakrishna, Inorg. Chem. 46 (2007) 11316;
(b) B. Punji, J.T. Mague, M.S. Balakrishna, Inorg. Chem. 46 (2007) 10268;
(c) B. Punji, J.T. Mague, M.S. Balakrishna, Inorg. Chem. 45 (2006) 9454.
[8] (a) For example see: P.J. Stang, B. Olenyuk, Acc. Chem. Res. 30 (1997) 502;
(b) D. Ranganathan, V. Haridas, R. Gilardi, I.L. Karle, J. Am. Chem. Soc. 120 (1998) 10793;
(c) M. Mazik, D. Blaser, R. Boese, Tetrahedron 55 (1999) 7835;
(d) I.S. Lee, D.M. Shin, Y.K. Chung, Cryst. Growth Des. 3 (2003) 521;
(e) T.Q. Nguyen, R. Martel, P. Avouris, M.L. Bushey, L. Brus, C. Nuckolls, J. Am. Chem. Soc. 126 (2004) 5234;
(f) D.S. Li, Y.Y. Wang, X.J. Luan, P. Liu, C.H. Zhou, H. Ma, Q.H. Shi, Eur. J. Inorg. Chem. (2005) 2678.
[9] (a) P. Chandrasekaran, J.T. Mague, M.S. Balakrishna, Organometallics 24 (2005) 3780;
(b) P. Chandrasekaran, J.T. Mague, M.S. Balakrishna, Inorg. Chem. 44 (2005) 7925;
(c) B. Punji, M.S. Balakrishna, Indian J. Chem. A 45 (2006) 1390;
(d) B. Punji, J.T. Mague, M.S. Balakrishna, Eur. J. Inorg. Chem. (2007) 720;
(e) P. Chandrasekaran, J.T. Mague, M.S. Balakrishna, Inorg. Chem. 45 (2006) 5893;
(f) P. Chandrasekaran, J.T. Mague, M.S. Balakrishna, Inorg. Chem. 44 (2006) 6678;
(g) D. Suresh, M.S. Balakrishna, K. Rathinasamy, D. Panda, J.T. Mague, Dalton Trans. (2008) 2285;
(h) S. Priya, M.S. Balakrishna, J.T. Mague, Inorg. Chem. Commun. 4 (2001) 437.
[10] (a) B. Punji, M.S. Balakrishna, J. Organomet. Chem. 692 (2007) 1683;
(b) R. Venkateswaran, J.T. Mague, M.S. Balakrishna, Inorg. Chem. 46 (2007) 809;
(c) B. Punji, J.T. Mague, M.S. Balakrishna, J. Organomet. Chem. 691 (2006) 4265;
(d) B. Punji, J.T. Mague, M.S. Balakrishna, Dalton Trans. (2006) 1322;
(e) B. Punji, C. Ganesamoorthy, M.S. Balakrishna, J. Mol. Catal. A: Chem. 259 (2006) 78;
(f) B. Kaboudin, M.S. Balakrishna, Synth. Commun. 31 (2001) 2773.
[11] (a) J. Diez, M.P. Gamasa, J. Gimeno, E. Lastra, A. Aguirre, S. Garcfa-Granda, Organometallics 12 (1993) 2213;
(b) I.D. Salter, S.A. Williams, T. Adatia, Polyhedron 14 (1995) 2803;

(c) J. Diez, M.P. Gamasa, J. Gimeno, A. Aguirre, S. Garcia-Granda, J. Holubova, L.R. Falvello, Organometallics 18 (1999) 662.
[12] (a) C. Ganesamoorthy, M.S. Balakrishna, P.P. George, J.T. Mague, Inorg. Chem. 46 (2007) 848;
(b) C. Ganesamoorthy, M.S. Balakrishna, J.T. Mague, H.M. Tuononen, Inorg. Chem. 47 (2008) 2764;
(c) C. Ganesamoorthy, M.S. Balakrishna, J.T. Mague, H.M. Tuononen, Inorg. Chem. 47 (2008) 7035.
[13] C. Janiak, J. Chem. Soc., Dalton Trans. (2000) 3885.
[14] B.S. Furniss, A.J. Hannaford, P.W.G. Smith, A.R. Tatchell, Vogel's Textbook of Practical Organic Chemistry, 5th ed., ELBS, England, 1989, p. 428.
[15] G.J. Kubas, Inorg. Synth. 28 (1990) 68.
[16] Bruker-AXS, SMART, Version 5.625, Madison, WI, 2000.
[17] Bruker-AXS, SAINT+, Version 6.35A, Madison, WI, 2002.
[18] G.M. Sheldrick, TWINABS, Version 1.02, University of Göttingen, Germany, 2005.
[19] (a) Bruker-AXS, SHELXTL, Version 6.10, Madison, WI, 2000;
(b) G.M. Sheldrick, SHELXS97 and SHELXL97, University of Göttingen, Germany, 1997.

Polyhedron 28 (2009) 107–112

Contents lists available at ScienceDirect

Polyhedron

journal homepage: www.elsevier.com/locate/poly

Synthesis, characterization and spectroscopic studies of a new ligand [N′-(2-methoxybenzoyl)hydrazinecarbodithioate] ethyl ester and its Mn(II) and Cd(II) complexes: X-ray structural study of Mn(II) complex

Mamata Singh [a,*], Vaibhave Aggarwal [b], Udai P. Singh [b], Nand K. Singh [a,*]

[a] Department of Chemistry, Banaras Hindu University, Varanasi 221 005, UP, India
[b] Department of Chemistry, Indian Institute of Technology, Roorkee 247 667, Uttarakhand, India

ARTICLE INFO

Article history:
Received 1 September 2008
Accepted 14 October 2008
Available online 27 November 2008

Keywords:
Carbodithioic acid ester
ONS donor ligand
Crystal structure
Coordination polymer

ABSTRACT

A new dithioligand [N′-(2-methoxybenzoyl)hydrazinecarbodithioate] ethyl ester (H_2mbhce, **1**) formed complexes $[M(Hmbhce)_2]_n$ {M = Mn(II), Cd(II)} which have been characterized with the help of elemental analyses, magnetic susceptibility measurements, IR, UV–Vis, ^{1}H and ^{13}C NMR and mass spectrometry. $[Mn(Hmbhce)_2]_n$ (**2**) crystallized in monoclinic system with space group P_{21}/n. In the polymeric structure of **2**, the ligand acts as an uninegative tridentate N(1), O(1), S(3) donor and forms a five membered chelate ring with N(1), C(2) and O(1). The intermediate bond lengths (between single and double bond distances) O(1)–C(2) = 1.241(3), N(2)–C(2) = 1.325(3), N(1)–N(2) = 1.393(2), N(1)–C(8) = 1.311(3) Å and C(8)–S(3) = 1.704(2) Å suggest considerable delocalization of charge which develops slightly aromatic character in the chelate ring.

© 2008 Elsevier Ltd. All rights reserved.

1. Introduction

Dithioligands are very promising compounds from the view point of coordination chemistry because of their ability toward complexation and involvement in a wide range of biological [1,2] and non-biological processes [3,4]. The metal dithiocomplexes frequently undergo facile and reversible one electron redox reaction and have been used as sensitizers in photoelectrochemical solar cells [5,6]. They also show solid state electrical conductivities and can be used as molecular conductors [7,8]. Some transition metal chelates of the derivatives of N and S substituted dithiocarbazates [9,10] such as S-alkyldithiocarbazates [11] and their Schiff's bases [12–16] have been widely studied for their unique antitumor, antibacterial and antifungal activities. The interest in these ligand systems is also stimulated by their unusual physicochemical [17,18] and chemotherapeutic properties [9]. Although N′-acylhydrazinecarbodithioates are structurally similar to the dithiocarbazates, not much data is available on the synthesis, characterization and biological activity of these ligands and their complexes. Following our interest in the study of the coordination properties of the ligands containing the HN–C(=S) group, we have recently reported synthesis and X-ray studies of N′-(pyridine-3-carbonyl)hydrazine carbodithioate (H_2pchc) and their Mn(II) complex [19]. Keeping in view the above points and with the aim of elucidating the coordination geometry of the complexes of this class of ligand, [N′-(2-methoxybenzoyl)hydrazine]carbodithioic acid ethyl ester (H_2mbhce) and its Mn(II) and Cd(II) complexes were synthesized and characterized by X-ray.

2. Experimental

2.1. Materials and methods

Commercial reagents were used without further purification and all experiments were carried out in open atmosphere. Methyl 2-methoxy-benzoate was purchased from Sigma Aldrich and used as such. Carbon disulfide and hydrazine hydrate (SD Fine Chemicals, India) and the solvents (Merck Chemicals, India) were used in the syntheses.

2.1.1. Preparation of the ligand $[K^+(H_2L)^-]$

The preparation and characterization of potassium [N′-(2-methoxybenzoyl)hydrazinecarbodithioate] ethyl ester $[K^+(H_2L)]$ has been published elsewhere [20].

2.1.2. Preparation of the ligand (H_2mbhce) (**1**)

The [N′-(2-methoxy-benzoyl)-hydrazine]-carbodithioic acid ethyl ester (H_2mbhce) was synthesized by drop wise addition of ethyl iodide (1.5 ml, 25.64 mmol) to a suspension of freshly prepared potassium [N′-(2-methoxybenzoyl)hydrazinecarbodithioate] ethyl ester $[K^+(H_2L)^-]$ (4 g, 14.29 mmol) in methanol (25 ml)

* Corresponding authors. Tel.: +91 542 2318529; fax: +91 542 2368127 (N.K. Singh).
E-mail addresses: mamatasingh6@gmail.com (M. Singh), nksingh@bhu.ac.in, singhnk_bhu@yahoo.com (N.K. Singh).

0277-5387/$ - see front matter © 2008 Elsevier Ltd. All rights reserved.
doi:10.1016/j.poly.2008.10.015

and stirring the reaction mixture continuously for 2 h at room temperature. On evaporation of the solvent and acidification of the product with CH_3COOH (20% v/v), white precipitate was obtained. This was suction filtered, washed with water, dried in vacuo and recrystallized from methanol–chloroform mixture (50:50 v/v).

*2.1.2.1. Compound (**1**).* White recrystalline compound of **(1)** suitable for spectroscopic analyses was obtained by slow evaporation of its MeOH–$CHCl_3$ solution. Yield (67%); m.p. 162 °C. *Anal.* Calc. for $C_{11}H_{14}N_2O_2S_2$ (270.36): C, 48.87; H, 5.22; N, 10.36; S, 23.72. Found: C, 48.38; H, 5.22; N, 10.01; S, 23.50.

IR data (ν cm^{-1}, KBr): ν(NH) 3244m, 3120m; ν(C=O) 1645s; thioamide I [β(NH) + ν(CN)] 1469s; thioamide II [ν(CN) + β(NH)] 1248s; ν(N–N) 1086m; ν(C=S) 968; (CH_3) 2929; (CH_2) 2873. ^{1}H NMR (DMSO-d_6; δ ppm): 11.46, 10.49 (2H, –NH), 2.50 (m, 2H, >CH_2), 1.30 (m, 3H, –CH_3), 3.88 (m, 3H, –OCH_3), 7.89–7.22 (4H, multiplets, benzene ring). ^{13}C NMR (DMSO-d_6, δ ppm): 202.96 (>C=S), 164.52 (>C=O), 28.28 (>CH_2), 14.38 (–CH_3), 120.85 (C1), 161.63 (C3), 130.70 (C4), 121.18 (C5), 133.46 (C6), 112.34 (C7), 56.27 (–OCH_3). UV–Vis [λ_{max}, DMSO, nm]: 307, 258. MS(FAB) m/z = 271 $[M]^+$. Based on the above data the tentative structure of the ligand is depicted in Fig. 1.

*2.1.3. Preparation of complexes (**2**–**3**)*

A solution of H_2mbhce (0.540 g, 2 mmol) in MeOH–$CHCl_3$ (8 ml) was added to a MeOH solution (10 ml) of $Mn(OAc)_2 \cdot 4H_2O$ (0.249 g, 1 mmol) and stirred the mixture for 2 h at room temperature. The resulting clear yellow solution of complex **2** was filtered off and kept for crystallization.

Complex **3** was prepared by adding a MeOH–$CHCl_3$ solution of H_2mbhce (2 mmol) to a MeOH solution (10 ml) of $Cd(OAc)_2 \cdot 2H_2O$ (1 mmol) and stirring the mixture for 3–4 h. The resulting precipitate was filtered off, washed thoroughly with ethanol and chloroform, dried at room temperature and stored in desiccators.

*2.1.3.1. [Mn(Hmbhce)$_2$]$_n$ (**2**).* Light yellow single crystals of **(2)** suitable for X-ray analyses were obtained by slow evaporation of the above methanol: chloroform solution over a period of 7 days.

Yield 58%; m.p. 230 °C, μ_{eff} = 5.98 BM. *Anal.* Calc. for $C_{22}H_{26}MnN_4O_4S_4$ (593.43): C, 44.51; H, 4.41; N, 9.44; S, 21.60; Mn, 9.25. Found: C, 44.12; H, 4.37; N, 9.04; S, 21.70; Mn, 9.20%. IR(ν cm^{-1}, KBr): ν(NH) 3162m; ν(>C=O) 1603s; thioamide I [β(NH) + ν(CN)] 1514s; thioamide II [ν(CN) + β(NH)] 1297s; ν(N–N) 1101m; ν(>C=S) 905; (CH_3) 2922; (CH_2) 2858. UV–Vis [λ_{max}, DMSO, nm]: 629, 393, 220. MS(FAB) m/z = 594 $[M]^+$.

*2.1.3.2. [Cd(Hmbhce)$_2$]$_n$ (**3**).* Yellowish white; Yield 65%; m.p. 175 °C; *Anal.* Calc. for $C_{22}H_{26}CdN_4O_4S_4$ (651.12): C, 40.58; H, 4.02; N, 8.60; S, 19.70; Cd, 17.26. Found: C, 40.77; H, 4.07; N, 8.24; S, 20.03; Cd, 17.63%. IR(ν cm^{-1}, KBr): ν(NH) 3166m; ν(>C=O) 1605s; thioamide I [β(NH) + ν(CN)] 1510s; thioamide II [ν(CN) + β(NH)] 1295s; ν(N–N) 1100m; ν(>C=S) 900; (CH_3) 2920; (CH_2) 2861. ^{1}H NMR (DMSO-d_6; δ ppm): 13.01, (1H, –NH), 3.00 (m, 2H, >CH_2), 1.07 (m, 3H, –CH_3), 3.34 (m, 3H, –OCH_3), 8.09–7.12 (4H, multiplets, benzene ring). ^{13}C NMR (DMSO-d_6, δ ppm): 180.65 (>C=S), 159.52 (>C=O), 27.41 (>CH_2), 14.86 (–CH_3), 120.03 (C1), 157.47 (C3), 130.91 (C4), 121.38 (C5), 133.64 (C6), 112.38 (C7), 56.55 (–OCH_3). UV–Vis spectrum [λ_{max}, DMSO, nm]: 304, 254. MS(FAB) m/z = 650 $[M]^+$.

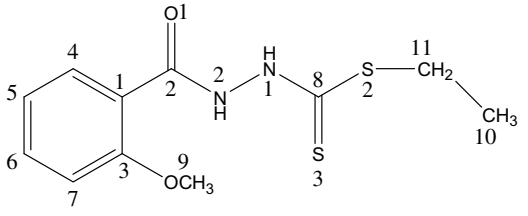


Fig. 1. [N′-(2-methoxybenzoyl)hydrazinecarbodithioate] ethyl ester (H_2mbhce).

2.1.4. Physical measurements

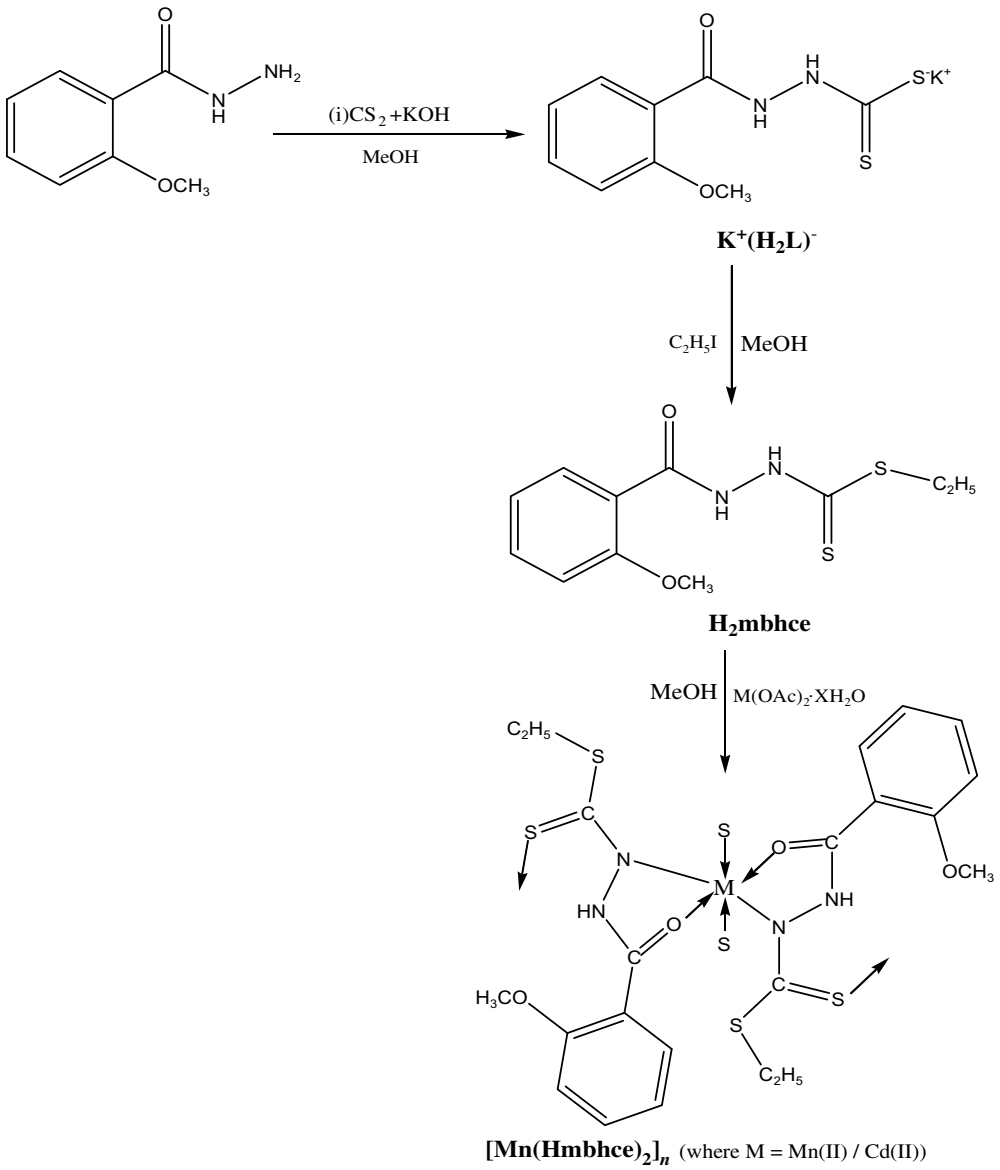
Carbon, hydrogen, nitrogen and sulfur contents were estimated on a CHN Model CE-440 Analyzer and on an Elementar Vario EL III Carlo Erbo 1108. By following standard procedure, the complexes were analyzed for their metal content, after decomposition with a mixture of conc. HNO_3 and HCl, followed by conc. H_2SO_4 [21]. Magnetic susceptibility measurements were performed at room temperature on a Cahn Faraday balance using $Hg[Co(NCS)_4]$ as the calibrant and electronic spectra were recorded on an UV-1700 Pharmaspec spectrophotometer. IR spectra were recorded in the 4000–400 cm^{-1} region as KBr pellets on a Varian Excalibur 3100 FT-IR spectrophotometer. ^{1}H and ^{13}C NMR spectra were recorded in DMSO-d_6 on a JEOL AL300 FT NMR spectrometer using TMS as an internal reference. The FAB mass spectra were recorded on a Jeol SX 102/Da-600 mass spectrometer/data system using Argon/Xenon (6 kV, 10 m A0) as the FAB gas m-nitro benzyl alcohol (NBA) was used as the matrix.

3. Crystal structure determination

The X-ray data collection and processing for **2** were performed on Bruker Kappa Apex-CCD diffractometer by using graphite monochromated Mo Kα radiation (λ = 0.71070 Å) at 100 K. Crystal structures were solved by direct methods. Structure solution, refinement and data output were carried out with the SHELXTL program [22,23]. All non-hydrogen atoms were refined anisotropically. Hydrogen atoms were placed at geometrically calculated positions by using a riding model. Diagrams were created with the DIAMOND program [24]. Hydrogen bonding interactions in the crystal lattice were calculated with both SHELXTL and MERCURY [25].

4. Results and discussion

With an aim to obtain N′-acylhydrazine carbodithioic acid ester, H_2mbhce was synthesized by the reaction of freshly prepared $[K^+(H_2L)^-]$ with C_2H_5I in equivalent molar ratio in methanolic solution. The synthetic route for the complexes **2** and **3** are given in Scheme 1. H_2mbhce having multidentate donor sites are expected to coordinate in neutral or anionic form. Owing to the presence of amide and thioamide functional groups, it can exhibit keto-enol and thione-thiol tautomerism [26]. But the IR (KBr) and ^{1}H NMR (DMSO-d_6) spectra of H_2mbhce are devoid of any peak to be attributed to SH for the thiol form indicating that it exists in thione form in solid (also by XRD) as well as in solution. Due to the more acidic character of HN(C=S), this proton undergoes deprotonation during complexation. It is seen that, H_2mbhce loses a proton directly from the nitrogen of HN(C=S) moiety to metal ion to fulfill the neutralization of positive charge of the metal ion. Thus, the ligand gets monodeprotonated to facilitate the formation of metal complexes **2**–**3.** Complex **2** has been obtained as single crystals and analyzed, which shows that the carbonyl oxygen, thione sulfur and hydrazinic nitrogen (after deprotonation) participate in bonding. The ligand and complexes are air-stable and can be kept in desiccators over a prolonged period without sign of decomposition. The complex 2 is soluble in DMF, DMSO, $CHCl_3$–MeOH mixture and other polar solvents while the Cd(II) complex is sparingly soluble in DMSO-d_6.



Scheme 1. Preparation of H_2mbhce and $[Mn(Hmbhce)_2]_n$.

4.1. IR spectra

The ligand H_2mbhce **(1)** contains the thioamide HN(C=S) group which should give rise to characteristic bands associated with thioamide I, thioamide II and thioamide IV having contributions from [β(NH) + *ν*(CN)], [*ν*(CN) + β(NH)], *ν*(C=S), modes of vibrations, respectively. The IR spectrum of H_2mbhce displays two bands at 3244 and 3120 cm^{-1} arising from two –NH groups attached to >C=O and >C=S groups, respectively, present in the ligand. The peaks at 1645, 1469, 1248, 1086, 968 cm^{-1} are assigned to *ν*(C=O), thioamide I [β(NH) + *ν*(CN)], thiamide II [*ν*(CN) + β(NH)], *ν*(N–N) and *ν*(C=S), respectively. The bands at 2929 and 2873 cm^{-1} correspond to *ν*(C–H) of ($–CH_3$) and $–CH_2$ groups, respectively, of H_2mbhce.

Comparison of the main vibrational bands of H_2mbhce (**1**) is used to establish its ligating behavior in the complexes **2**–**3**. Disappearance of one of the bands due to *ν*(NH) adjacent to thione sulfur in complexes **2**–**3** suggests loss of a proton from HN(C=S) group and participation of the deprotonated nitrogen in bonding with the metal ion. The *ν*(N–N) shows a positive shift of 14–15 cm^{-1} indicating bonding through hydrazinic nitrogen. The IR spectra of both complexes (**2**–**3**) show a strong band in 1594–1605 cm^{-1} region for amide I [mainly due to *ν*C(=O)]. A negative shift of 40–42 cm^{-1} in *ν*(C=O) indicates the involvement of carbonyl oxygen in bonding. A negative shift of 63–68 cm^{-1} in the *ν*(C=S) in the complexes **2** and **3** indicate involvement of the thione sulfur in bonding which is further supported by positive shifts of 41–45 and 47–49 cm^{-1} in thioamide I and II bands, respectively. Thus H_2mbhce behaves as uninegative tridentate O, N, S donor in the complexes **2** and **3**.

4.2. Magnetic moment and electronic spectra

The UV–Vis spectrum of H_2mbhce exhibits bands at 307 and 258 nm attributed to the intraligand transitions. $[Mn(Hmbhce)_2]_n$ exhibits a μ_{eff} of 5.98 B.M., indicating the presence of five unpaired electrons in the complex and shows three electronic bands at 629, 393 and 220 nm. The band at 629 nm is assigned to the $^6A_{1g} \rightarrow {}^4T_{1g}$, transition for a high spin octahedral geometry around Mn(II) [27]. The high energy bands at 393 and 220 nm may be assigned to the

intraligand/charge transfer transition. The high energy bands at 329 and 246 nm in the diamagnetic complex Cd(II) may be due to intraligand/charge transfer transitions [28].

4.3. ^1H and ^{13}C NMR spectra

The ^1H NMR spectrum of H_2mbhce exhibits signals at δ 10.49 and 11.46 ppm for the amide –NH(CO) and thioamide –NH(CS) protons, respectively. The protons due to the benzene ring appear as multiplets between δ 7.89, 7.70, 7.58, 7.22 ppm. The ^{13}C NMR spectrum of H_2mbhce shows 11 signals for 11 carbon atoms, out of which the signals at δ 202.96, 164.52 and 56.27 ppm are due to the >C=S, >C=O and $-OCH_3$ carbons, respectively. The expected structure of H_2mbhce is shown in Fig. 1. Due to the paramagnetic nature of **2** the ^1H and ^{13}C NMR spectra could not be studied. The ^1H and ^{13}C NMR spectra of $[Cd(Hmbhce)_2]_n$ in DMSO-d_6 was interpreted by comparing its spectra with that of H_2mbhce. The ^1H NMR of Cd(II) complex shows a signal at 13.01 ppm showing the presence of one hydrazinic proton while the signal due to another is found absent indicating deprotonation of the thioamide proton. The peaks at 3.34, 3.00 and 1.07 ppm corresponding to the $-OCH_3$, $-CH_3$, $-CH_2$ groups show slight variation during complexation as compared to the ligand. The signals due to the 2-methoxybenzene ring protons appear at 8.09, 7.62, 7.27, and 7.12 as multiplets. In the case of Cd(II), the peaks due to >C=S and >C=O appear at 180.65 and 159.52 ppm as compared to 202.96 and 164.52 ppm in the H_2mbhce, which suggests bonding through the thione sulfur and carbonyl oxygen.

4.4. Mass spectrometry

The ligand H_2mbhce is identified by FAB mass spectrum which shows many peaks due to various fragments. The molecular ion peak for $[H_2mbhce]^{+\cdot}$ is observed at m/z = 271. Other three important peaks at m/z = 242 (50% intensity), 209 (52% intensity) and 237 (35% intensity) correspond to fragments formed from H_2mbhce after the release of $-C_2H_5$, $-SC_2H_5$ and H_2S, respectively.

Table 1
Crystallographic data and structure refinements for **2**.

Parameters	Complex **2**
Color	Colorless
Crystal size (mm)	0.25 × 0.21 × 0.19
Empirical formula	$C_{22}H_{26}MnN_4O_4S_4$
Formula weight	593.65
Space group	$P21/n$
Crystal system	monoclinic
T (K)	100(2)
λ (Mo Kα)	0.71073
a (Å)	13.470(2)
b (Å)	5.5379(9)
c (Å)	18.222(3)
β (°)	108.051(1)
V (Å^3)	1292.3 (4)
Z	2
ρ_{calc} (g/cm^3)	1.525
M (mm^{-1})	0.871
F(000)	614
θ Range for data collection	2.25–28.36
Index ranges	$-17 \leqslant h \leqslant 17$ $-7 \leqslant k \leqslant 7$ $-24 \leqslant l \leqslant 23$
Reflections collected	20677
Independent reflections	3206
Data/restraints/parameters	3206/0/162
Goodness-of-fit on F^2	1.059
R_1, wR_2 [$I > 2\sigma(I)$]	0.0366, 0.0870
R_1, wR_2 (all data)	0.0718, 0.0997
Largest difference in peak and hole (e Å^{-3})	0.379 and −0.299

FAB mass spectral analyses of $[Mn(Hmbhce)_2]_n$ and $[Cd(Hmbhce)_2]_n$ show the presence of corresponding molecular ion peaks at m/z = 594 and 650, respectively, which correspond to the mol. wt. of one unit of the polymer. Other peaks at higher m/z values indicate their polymeric nature. Complex **2** gave four important peaks at m/z = 413 (50% intensity), 470 (90% intensity), 532 (50% intensity) and 560 (65% intensity) corresponding to the fragments formed from the $[Mn(Hmbhce)_2]_n$ after release of $2H_2S$, $2C_2H_5SH$, C_2H_5SH and H_2S, respectively. The fragmentation pattern of the Cd(II) complex shows peaks at m/z = 582 (25% intensity), 513 (25% intensity), 307 (30% intensity) and 268 (12.5% intensity) corresponding to fragments formed from

Table 2
Selected bond lengths (Å) and angle (°) for **2**.

Bond length (Å)			
Mn(1)–O(1)	2.1280(15)	Mn(1)–S(3)#2	2.7053(7)
Mn(1)–N(1)	2.2474(18)	S(2)–C(8)#2	1.768(3)
O(1)–C(2)	1.241(3)	S(2)–C(11)	1.799(3)
N(1)–N(2)	1.393(2)	S(3)–C(8)	1.704(2)
C(8)–S(2)#2	1.766(2)	N(1)–C(8)	1.311(3)
N(2)–C(2)	1.325(3)		
Angles (°)			
O(1)–Mn(1)–O(1)#1	180	O(1)#1–Mn(1)–N(1)	105.40(6)
O(1)–Mn(1)–N(1)	74.60(7)	O(1)–Mn(1)–N(1)#1	105.40(6)
O(1)#1–Mn(1)–N(1)#1	74.60(7)	N(1)–Mn(1)–N(1)#1	180
O(1)–Mn(1)–S(3)#2	90.14(5)	O(1)#1–Mn(1)–S(3)#2	89.86(5)
N(1)–Mn(1)–S(3)#2	97.48(5)	N(1)#1–Mn(1)–S(3)#2	82.52(5)
O(1)–Mn(1)–S(3)#3	89.86(5)	O(1)#1–Mn(1)–S(3)#3	90.14(5)
N(1)–Mn(1)–S(3)#3	82.52(5)	N(1)#1–Mn(1)–S(3)#3	97.48(5)
S(3)#2–Mn(1)–S(3)#3	180	C(8)#2–S(2)–C(11)	103.76(11)
C(8)–S(3)–Mn(1)#4	98.00(8)	C(2)–O(1)–Mn(1)	116.52(14)
N(2)–N(1)–Mn(1)	108.00(12)	C(2)–N(2)–N(1)	118.93(18)
O(1)–C(2)–N(2)	121.5(2)	N(1)–C(8)–S(3)	125.70(16)
N(1)–C(8)–S(2)#2	111.64(16)	S(3)–C(8)–S(2)#2	122.66(12)
C(10)–C(11)–S(2)	114.1(2)		
Torsional angles (°)			
N(1)–Mn(1)–O(1)–C(2)	4.93(15)	O(1)–Mn(1)–N(1)–N(2)	−5.40(13)
N(1)#1–Mn(1)–O(1)–C(2)	−175.07(15)	O(1)#1–Mn(1)–N(1)–N(2)	174.60(13)
S(3)#2–Mn(1)–O(1)–C(2)	−92.80(15)	S(3)#2–Mn(1)–N(1)–N(2)	82.68(13)
S(3)#3–Mn(1)–O(1)–C(2)	87.19(18)	S(3)#3–Mn(1)–N(1)–N(2)	97.32(13)
Mn(1)–N(1)–N(2)–C(2)	6.0(2)	N(1)–N(2)–C(2)–O(1)	−2.2(3)
Mn(1)–O(1)–C(2)–N(2)	−3.4(3)	N(2)–N(1)–C(8)–S(3)	−7.0(3)
Mn(1)–N(1)–C(8)–S(3)	159.64(13)	Mn(1)#4–S(3)–C(8)–N(1)	−20.8(3)
N(2)–N(1)–C(8)–S(2)#2	172.61(14)	Mn(1)–N(1)–C(8)–S(2)#2	−81.95(2)
Mn(1)#4–S(3)–C(8)–S(2)#2	98.51(13)	C(8)#2–S(2)–C(11)–C(10)	−82.2(3)

Symmetry transformations used to generate equivalent atoms: #1: $-x+1$, $-y+1$, $-z+1$; #2: $-x+1$, $-y+2$, $-z+1$; #3: x, $y-1$, z; #4: x, $y+1$, z.

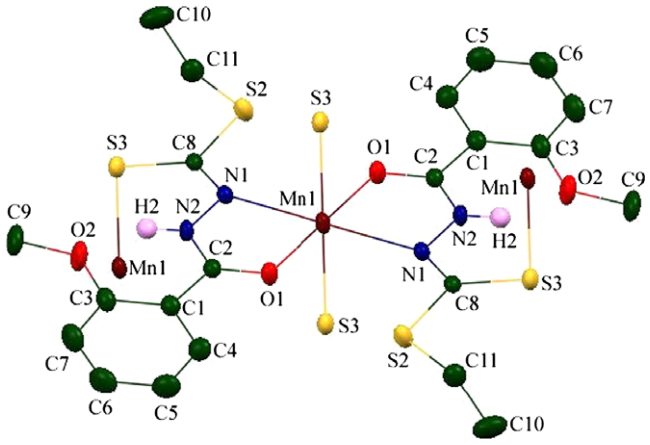


Fig. 2. Thermal ellipsoidal view of $[Mn(Hmbhce)_2]_n$ at 30% probability with atom numbering scheme. The hydrogen atoms are omitted for clarity.

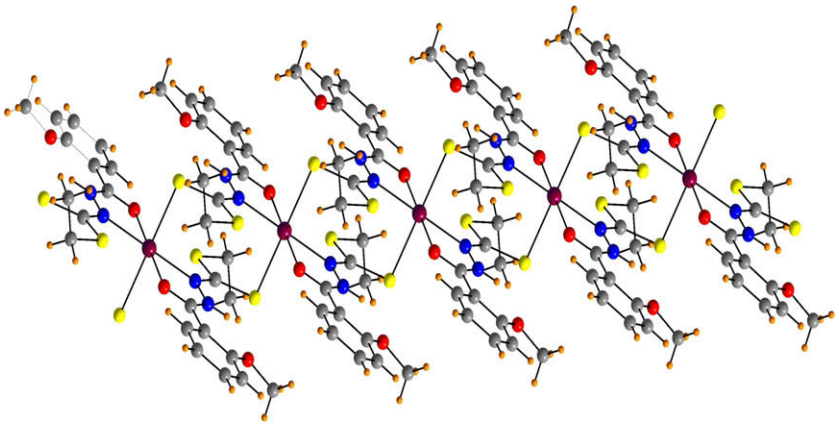


Fig. 3. One dimensional layer view of molecular packing in DIAMOND package for $[Mn(Hmbhce)_2]_n$.

$[Cd(Hmbhce)_2]_n$ after release of $2H_2S$, H_3CO–(C_6H_5CO)–, H_3CO–(C_6H_5CO)–NH and NH–N–C(S)SC_2H_5, respectively.

5. Structural description of $[Mn(Hmbhce)_2]_n$ (2)

The crystallographic data and structural refinement details of complex **2** are given in Table 1 whereas the important bond distances and bond angles are listed in Table 2. Compound **2** crystallized in monoclinic system with space group P_{21}/n and its thermal ellipsoidal view at 30% probability level is shown in Fig. 2. As shown in Fig. 2, the Mn(II) center is bonded to the ligand through the deprotonated hydrazinic nitrogen, carbonyl oxygen and thione sulfur forming a five membered chelate ring with oxygen and nitrogen atoms. The geometry around the Mn(II) ion is approximately octahedral. The H_2mbhce coordinates to Mn(II) center in meridonial configuration i.e. the carbonyl oxygen and hydrazinic nitrogen are *cis* to each other and thione sulfur *trans*. The Mn–N and Mn–O bond lengths are 2.2474(18) and 2.1280(15) Å, respectively. These values are in the ranges found for octahedrally coordinated Mn(II) with ONS donor ligands [29]. The Mn–S bond distance of 2.7053(7) Å is longer as compared to those found for $[Mn\{SSi(oBu^t)_3\}_2(o\text{-phen})]$, $[Mn\{SSi(oBu^t)_3\}_2(bpy)]$, $Mn(L_1)_2$ {L_1 = S-methyl-3-(2-S-methyl-6-methyl-4-pyrimidyl)methyl)dithiocarbazate} and $Mn(L_2)_2$ {L_2 = S-benzyl-3-(2-S-methyl-6-methyl-4-pyrimidyl)methyl)dithiocarbazate} [Mn–S = 2.4777(5)–2.555(2) Å] indicating that the Mn–S bond in the present complex is weaker than those cited above [29,30]. The C–S bond distances of 1.768(2) Å and 1.704(2) Å are intermediate between single C–S (1.82 Å) and double C=S (1.56 Å) bond distances. The lengthening of the C=S and shortening of the C–S bond may be caused due to the deprotonation of hydrazinic proton adjacent to the dithio group {–C(=S)S} and subsequent development of the negative charge on the nitrogen which is delocalized during complexation. The C–O, C–N and N–N bond distances are 1.241(3) Å, 1.325(3) Å and 1.392(2) Å, respectively, which are also intermediate between single and double bond character [31]. All these intermediate distances suggest extensive delocalization of charge in the five membered chelate ring of complex **2**, similar to the complexes of a few dithiocarbazates [32–34]. An angle of 180° is subtended at the Mn(II) ion {viz. the S(3)#2–Mn(1)–S(3)#3 angle} which is equivalent to the theoretical value. The angles N(1)–Mn(1)–O(1) and O(1)–Mn(1)–N(1) formed by two equatorial donors N(1) and O(1) at Mn(II) center are 74.60(6)° and 105.40(6)°, respectively, which shows deviation from an ideal value of 90° for an ideal octahedral structure. The metal center is bonded through two uninegative tridentate sites (N2O2S2) of $(Hmbhce)^-$ utilizing deprotonated hydrazinic nitrogen, carbonyl oxygen and thione sulfur, forming two five remembered chelate rings. The mean plane formed by O1C2N2N1Mn1 in the complex structure reveal the planar nature of both chelate rings. This chelate ring and the 2-methoxybenzene ring lie in the same plane and make an extended coplanar system (Fig. 3).

5.1. Crystal packing of complex 2

Fig. 3 shows the formation of one dimensional layer structure of polymeric complex $[Mn(Hmbhce)_2]_n$ due to the presence of weak interactions. The intramolecular N(2)–H(2)···O(2) (1.942 Å), C(4)–H(4)···O(1) (2.389 Å), C(11)–H(11B)···S(3) (2.686 Å) and N(2)–H(2)···S(3) (2.430 Å) hydrogen bonding in the molecule provide stability to complex **2**. The hydrogen of methyl group [$C(sp^3)$–H(s)] of one molecule shows weak van der Waals' interaction with the hydrogen of another methyl group causing the superimposition of molecules over each other. The crystal packing shows a special type of interaction between C2 and S2 with a distance of 3.402 Å and intermolecular hydrogen bonding O1···H11B (2.698 Å). There is no face to face (π–π) interaction and edge to face (C–H···π) interaction between two 2-methoxyphenyl rings in the crystal structure of **2**.

6. Conclusion

A new [N′-(2-methoxybenzoyl)hydrazinecarbodithioate] ethyl ester (**1**) and its Mn(II) (**2**) and Cd(II) (**3**) complexes have been synthesized. In the complex **2,** the chelate ring and the 2-methoxybenzene ring lie in the same plane making an extended coplanar system with the two chelate ring.

Acknowledgement

One of the authors (M. Singh) is thankful to CSIR, New Delhi, India for the award of Direct SRF, supported by Grant No. 9/13(160)2008/EMR-I.

Appendix A. Supplementary data

CCDC 679569 contains the supplementary crystallographic data for **2**. These data can be obtained free of charge via http://www.ccdc.cam.ac.uk/conts/retrieving.html, or from the Cambridge Crystallographic Data Centre, 12 Union Road, Cambridge CB2 1EZ, UK; fax: (+44) 1223-336-033; or e-mail: deposit@ccdc.cam.ac.uk. Supplementary data associated with this article can be found, in the online version, at doi:10.1016/j.poly.2008.10.015.

References

[1] M.T.H. Tarafdar, N. Sarvanan, K.A. Crouse, M.A. Ali, Transition Met. Chem. 26 (2001) 613.
[2] P.K. Bharadwaj, W.K. Musker, Inorg. Chem. 26 (1987) 1453.
[3] E. Emmet Reid, Organic Chemistry of Bivalent Sulfur, vol. IV, Chemical Publishing Co., New York, 1962 (Chapters 1, 2 and 3).
[4] R.P. Burns, C.A. Mc Auliffe, Adv. Inorg. Radiochem. 22 (1979) 303.
[5] L. Bahadur, J.P. Pandey, J. Electrochem. Soc. 137 (1990) 3755.
[6] N. Singh, N.K. Singh, P.P. Agrawal, Transition Met. Chem. 15 (1990) 325.
[7] N. Singh, S. Gupta, Synth. React. Inorg. Met.-Org Nano-metal Chem. 30 (2000) 1429.
[8] N. Singh, S. Gupta, Synth. React. Inorg. Met.-Org. Nano-metal Chem. 32 (1) (2002) 189.
[9] M.A. Ali, S.E. Livingston, Coord. Chem. Rev. 13 (1974) 101.
[10] M. Das, S.E. Livingstone, Inorg. Chim. Acta 19 (1976) 5.
[11] M. Das, S.E. Livingstone, Br. J. Cancer 37 (3) (1978) 463.
[12] D.L. Kalaymann, J.P. Scovill, J.F. Bartosevich, J. Bruce, J. Med. Chem. 26 (1983) 35. and references cited therein.
[13] D.L. Kalaymann, J.P. Scovill, C.F. Franchino, J. Med. Chem. 25 (1982) 1261.
[14] D.L. Kalaymann, J.F. Bartosevich, T.S. Griffin, C.J. Mason, J.P. Scovill, J. Med. Chem. 22 (1979) 855.
[15] D.L. Kalaymann, J.P. Scovill, C. Lambros, G.K. Childs, J.D. Nortsh, J. Med. Chem. 27 (1984) 87.
[16] S. Gou, Z. Yu, K. Xu, Z. Zou, Polyhedron 9 (1990) 2981.
[17] N. Singh, S. Gupta, Int. J. Inorg. Mater. 2 (2000) 427.
[18] N. Singh, S.K. Rai, J. Organomet. Chem. 605 (2000) 102.
[19] M. Singh, R.J. Butcher, N.K. Singh, Polyhedron 27 (2008) 3451.
[20] N.K. Singh, M. Singh, R.J. Butcher, Acta Crystallogr., Sect. E 63 (2007) o4405.
[21] A.I. Vogel, A Text Book of Quantitative Inorganic Analysis, 3rd ed., ELBS, Longman, London, 1969.
[22] G.M. Sheldrick, Acta Crystallogr., Sect. A 46 (1990) 467.
[23] G.M. Sheldrick, SHELXTL-NT 2000 Version 6.12, Reference Manual, University of Göttingen, Göttingen, Germany.
[24] B. Klaus, DIAMOND, Version 1.2c, University of Bonn, Germany, 1999.
[25] I.J. Bruno, J.C. Cole, P.R. Edgington, M. Kessler, C.F. Macrae, P. McCabe, J. Pearson, R. Taylor, Acta Crystallogr., Sect. B 58 (2002) 389.
[26] K.A. Crouse, K.-B. Chew, M.T.H. Tarafder, A. Kasbollah, A.M. Ali, B.M. Yamin, H.-K. Fun, Polyhedron 23 (2004) 161.
[27] A.B.P. Lever, Inorganic Electronic Spectroscopy, Elsevier, Amsterdam, 1984.
[28] M.K. Ali, A.H. Mirza, C.W. Voo, A.L. Tau, P.V. Bernhardt, Polyhedron 22 (2003) 3433.
[29] A. Kropidłowska, J. Chojnacki, B. Becker, Polyhedron 25 (2006) 2142.
[30] S. Roy, T.N. Mandal, A.K. Barik, S. Gupta, R.J. Butcher, M. Nethaji, S.K. Kar, Polyhedron 27 (2008) 593.
[31] D.-H. Wu, C. He, C.-Y. Duan, X.-Z. You, Acta Crystallogr., Sect. C 56 (2000) 1336.
[32] M.A. Ali, A.H. Mirza, M.T.H. Tarafder, M.A. Ali, R.J. Butcher, Inorg. Chim. Acta 320 (2001) 1.
[33] M.T.H. Tarafder, M.A. Ali, D.J. Wee, K. Azahari, S. Silong, K.A. Crouse, Transition Met. Chem. 25 (2000) 456.
[34] S. Bhattacharjee, R. Bhattacharjee, J. Chem. Soc., Dalton Trans. (1992) 1357.

Polyhedron 28 (2009) 113–120

Contents lists available at ScienceDirect

Polyhedron

journal homepage: www.elsevier.com/locate/poly

Photocatalytic self-assembled solid porphyrin microcrystals from water-soluble porphyrins: Synthesis, characterization and application

Walid M. Hikal *, H. James Harmon

Department of Physics, Oklahoma State University, Stillwater, OK 74078, USA

ARTICLE INFO

Article history:
Received 25 April 2008
Accepted 16 October 2008
Available online 25 November 2008

Keywords:
Porphyrins
Solid porphyrin crystals
Self-assembly
2,4,6-Trinitrotoluene

ABSTRACT

In this article, we report on the formation of a photocatalytic porphyrin crystalline structure using two oppositely charged commercially available low cost porphyrins, [*meso*-tetra(*N*-methy-4-pyridyl)porphyrin tetratosylate (TMPyP) and zinc-tetrakis(4-sulfonatophenyl)porphyrin (Zn-TPPS)], by self-assembly at room temperature without acidification. Using optical microscopy, the crystals were determined to have a length of 30–55 μm and width of 2–50 μm, depending on the molar ratio of the porphyrins in the starting solution. The porphyrin crystals were characterized by means of powder X-ray diffraction and UV–Vis, fluorescence, and optical microscopic techniques. The UV–Vis absorbance spectrum of the crystalline structure is different than those of the monomer solutions, involving a broadened Soret band that is split into two blue-shifted and red-shifted peaks and broadened red-shifted Q-bands. The crystals exhibit a different emission spectrum from those of the porphyrin solutions in that they are red-shifted, split, and show a dramatic decrease in intensities. A hypothetical model for the crystal structure of the porphyrin crystals is developed. Illumination of the crystals in a 2,4,6-trinitrotoluene solution with a tungsten lamp results in TNT reduction to 1,3,5-trinitrobenzene and 4-amino-2,6-dinitrotoluene.

© 2008 Elsevier Ltd. All rights reserved.

1. Introduction

Porphyrins and their derivatives possess particular photophysical and photochemical properties that depend on the substituents attached to the tetrapyrrolic ring as well as the metal linked to the nitrogen atoms in the core of the porphyrin ring [1,2]. Porphyrins play a principle role in many biochemical reactions including photosynthesis, drug detoxification, oxidation, and electron transfer [3]. Molecular self-assembly is a stratagem for the fabrication of many new materials involving the spontaneous aggregation of small molecular entities into specific structures in liquid or solid environments by a variety of cooperative and directional intermolecular interactions. Molecular self-assembly accomplishes the ordering of molecular components in space to form supramolecular entities with predefined dimensionality and connectivity [4]. Self-assembled, self-organized, and covalently-bound porphyrin arrays are of importance as attractive building blocks for the modular construction of tailored field-responsive materials and provide a versatile tool for potential applications in the design of sensors, catalysts, electronic and photonic devices, molecular sieves, and solar energy conversion devices [5,6]. Porphyrins have been used for the detection and degradation of hazardous, toxic gases, environmental pollutants, nitroaromatic compounds, insecticides, pesticides, and weapons of mass destruction [7–12]. Effort has been expanded in our laboratory to study the interaction between porphyrins and 2,4,6-trinitrotoluene to design efficient, low cost, and reusable photocatalytic porphyrin-based catalysts as well as sensitive detectors for explosives [13].

The nitroaromatic explosive 2,4,6-trinitrotoluene has been widely used in detonators, mines, rocket boosters, and plastic explosives [14]. 2,4,6-trinitrotoluene is found in the soil, ground water, and surface waters at the sites where it was manufactured [15]. TNT is toxic and is classified as priority EPA pollutant at concentrations above 2 μg/L [16].

Binding of 2,4,6-trinitrotoluene to porphyrins [17] as well as the degradation of TNT by porphyrins solutions using means of illumination [18] have been previously reported. Free base porphyrin and metalloporphyrin solutions have been shown to be a photocatalytic agent for TNT degradation [18]. The fact that porphyrins are inseparable from the solution after the degradation process such that they cannot be easily recovered and reused is a disadvantage of using porphyrin solutions in TNT degradation process. There is a need for a solid porphyrin-based catalyst for TNT degradation.

In this work we report on the formation of highly stable microscale solid porphyrin crystals using commercially available water-soluble porphyrins at room temperature without pH control. The ease of preparation, low cost, and speed of formation are three advantages of making these crystals. The solid crystalline structures reported in this article overcome the disadvantages of using porphyrin solutions in the TNT degradation process. The crystalline structure was investigated and characterized by light microscopy,

* Corresponding author. Tel.: +1 405 744 9692; fax: +1 405 744 6811.
E-mail address: walid.hikal@okstate.edu (W.M. Hikal).

0277-5387/$ - see front matter © 2008 Elsevier Ltd. All rights reserved.
doi:10.1016/j.poly.2008.10.026

UV–Vis spectroscopy, fluorescence spectroscopy, and powder X-ray diffraction to determine the chemical structure and the nature of binding between the two different porphyrin molecules in the crystals. Prior to use as a photocatalyst, the porphyrin crystals were immobilized on microscope slides and used as a photocatalyst for aqueous 2,4,6-trinitrotoluene (TNT) degradation using light in the visible portion of the spectrum.

2. Experimental

2.1. Materials

meso-Tetra(*N*-methy-4-pyridyl)porphyrin tetratosylate (TMPyP) and zinc-tetrakis(4-sulfonatophenyl)porphyrin (Zn-TPPS), shown in Fig. 1, were obtained from Frontier Scientific (Logan, UT) and used without further purification. Porphyrin solutions were prepared at 1 mM stock concentration in 18 mΩ de-ionized water, stored refrigerated, and used within two weeks of preparation.

TNT (weapon grade) was obtained as a saturated water solution from the US Army Defense Ammunition Center at McAlester, OK.

2.2. Spectroscopic techniques

Absorbance spectra of the porphyrin monomers in pH 7.0 phosphate buffer and the absorbance spectra of the immobilized porphyrin crystals were collected using a Cary 5E UV–Vis spectrophotometer at 0.5 nm resolution using de-ionized water or a microscope slide as a reference depending on the sample being measured.

Fluorescence measurements were carried out with a SPEX FluoroMax-3 (Jobin-Yvon, Inc. Edison, NJ). Very dilute solutions (1 μM) were used to avoid spectral distortions due the inner filter effect and emission re-absorption. Before measuring fluorescence spectra of TMPyP, the cuvettes were first cleaned with nitric acid since TMPyP has a marked tendency to adhere on the cuvette walls.

Crystals were immobilized on a ProbeOn™ microscope slides obtained from Fisher Scientific. The immobilized crystals in aqueous 2,4,6-trinitrotoluene solution were illuminated at room temperature using an automotive headlamp (Osram HLX 46610, 50 W at 12 V) mounted with a flat rear reflector; the bulb was situated 2 cm from the lamp assembly. The total distance from the filament to the sample was 6 cm. The TNT aqueous solution was in a 16 mm diameter Pyrex test tube and stirred with a magnetic stirrer during illumination. The intensity of light at the sample was 5.1 mW/cm^2 as measured with an Optronics 740A photometer with the detector traceable to NIST standard no. 844/D-2 (Optronics Laboratories, Inc., Orlando, FL).

2.3. Chemical analysis

Organic intermediates and 2,4,6-trinitrotoluene were detected by HPLC chromatography using a Varian Prostar 210 HPLC with model 330 PDA detector fitted with a Supelcosil LC-18 column. A 40% acetonitrile/60% water solution was used as eluent at 0.7 mL/min flow rate. Identification of intermediates was performed by comparison of their UV–Vis spectra to the spectra of known specific compounds.

3. Results

3.1. Formation of porphyrin crystals

The porphyrin crystals were made by mixing 1:1 molar ratios of Zn-TPPS and TMPyP in 18 mΩ de-ionized water solutions at room temperature. The pH of the solution was not controlled or monitored. Crystals start forming immediately after mixing the two porphyrin monomers. The aqueous mixture of the two porphyrins solution was kept undisturbed in the dark for 24 h. After crystals formed in solution, the solid (dark purple color) crystals were filtered and washed three times with de-ionized water, ethanol, and pH 7.0 sodium phosphate (NaPi) buffer. Different porphyrin concentrations were used to make the crystals to study the effect of the porphyrin concentrations on the size and morphology of the crystals. The resulting crystals have a rod-like or needle-like structure using concentrations up to about 100 μM of each porphyrin in the formation process. The crystal length is 30–55 μm and the thickness is 2–3 μm as shown in Fig. 2a At porphyrin concentrations between 100 μM and 0.5 mM, the rod-like crystals have split ends. The length of the crystals is also 30–55 μm but the thickness increases to 3–4 μm as shown in Fig. 2b. At 0.5 mM porphyrin concentration, the crystals have a 'star-like' shape with length ranging from 30 μm to 40 μm, width ranging between 10 μm and 25 μm, and thickness 3–5 μm as shown in Fig. 2c.

3.2. UV–Vis spectroscopy

The absorbance spectra of *meso*-tetra(*N*-methy-4-pyridyl)porphyrin tetratosylate (TMPyP) in a 50 mM pH 7.0 phosphate buffer at room temperature exhibits an absorbance peak in the Soret region at 422 nm and four Q-bands at 519 nm, 553 nm, 585 nm, and 640 nm. The absorbance spectrum of zinc-tetrakis(4-sulfonatophenyl)porphyrin (Zn-TPPS) in 50 mM pH 7.0 phosphate buffer at room temperature exhibits a Soret absorbance peak at 421 nm and two Q-bands at 556 nm and 597 nm as seen in Fig. 3. The locations of the peaks were determined from the second derivatives of the absorbance spectra using Grams/32 (Galactic Industries, Salem,

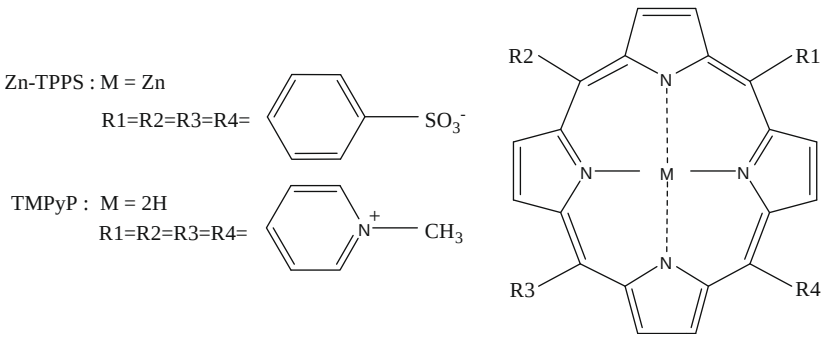


Fig. 1. Chemical structures of porphyrins used in making the porphyrin crystals.

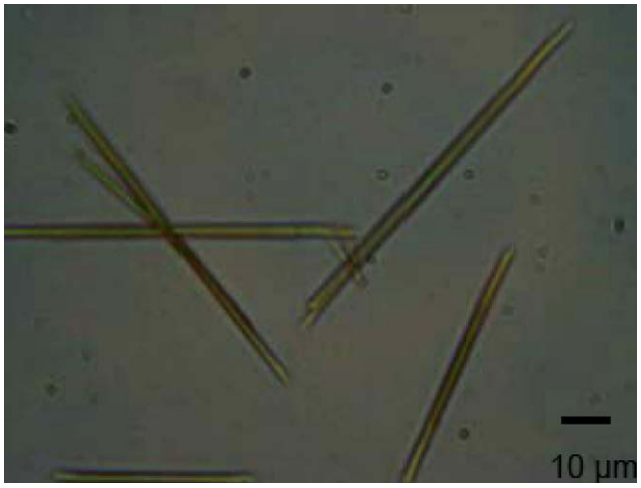


Fig. 2a. Optical microscope micrograph of porphyrin crystals: porphyrin concentration = 100 μM.

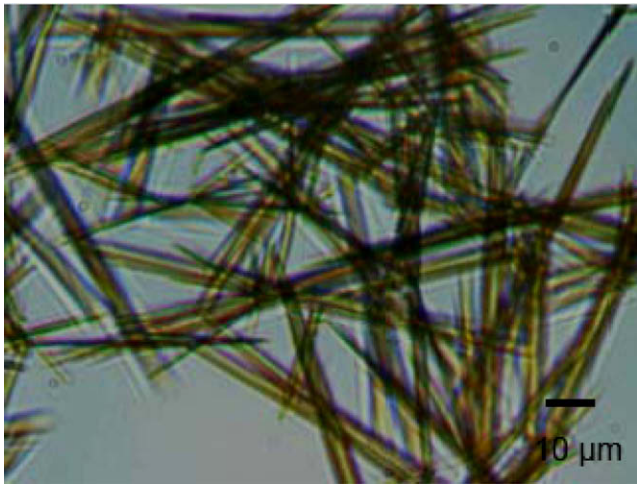


Fig. 2b. Optical microscope micrograph of porphyrin crystals: porphyrin concentration = 200 μM.

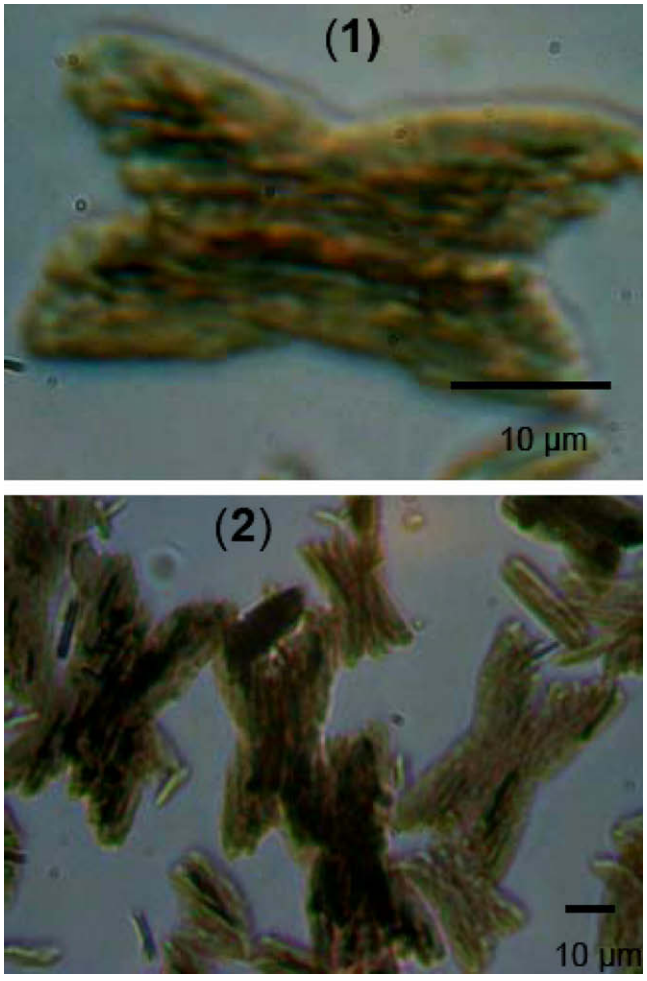


Fig. 2c. Optical microscope micrograph of porphyrin crystals: porphyrin concentration = 0.5 mM.

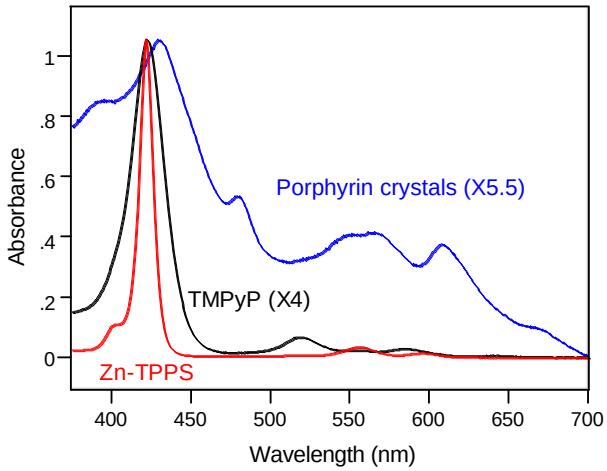


Fig. 3. Absorbance spectra of 1.6 μM *meso*-tetra(*N*-methy-4-pyridyl)porphyrin (TMPyP) and 1.6 μM zinc-tetrakis(4-sulfonatophenyl)porphyrin (Zn-TPPS) in 50 mM sodium phosphate (NaPi) buffer compared to the absorbance spectrum of the solid porphyrin crystals at room temperature (note the different scale).

NH). The Soret band of the porphyrin crystals is broadened and split into a blue-shifted band at 398 nm and a red-shifted band at 431 nm with a shoulder at 450 nm. The Q-bands of the porphyrin crystals are located at 486 nm, 548 nm, 552 nm, 577 nm, 612 nm, and 677 nm. The shape of the spectrum and the locations of the absorbance peaks are independent of the crystals size.

To determine the amount of porphyrins incorporated into the crystal structures, the absorbance spectrum of the solution remaining after crystal formation was measured and the intensity of the Soret peak was compared to those of the absorbance spectra of 1.6 μM of Zn-TPPS and TMPyP porphyrins in solutions at pH 7.0 sodium phosphate (NaPi) buffer at room temperature. The results indicate that 100% of TMPyP and 96% of Zn-TPPS starting solutions are incorporated into crystals (data not shown). The microcrystals are highly stable; crystals dissolve only in a 4 M HCl solution at room temperature for about 24 h or in a 2 M NaCl at 60 °C.

3.3. Fluorescence spectroscopy

The fluorescence spectra of TMPyP and Zn-TPPS are shown in Fig. 4 along with that of the crystalline structure with excitation at 422 nm, 421 nm, and 431 nm (Soret peak absorbance wavelengths), respectively. The positions of the emission peaks were determined from the second derivatives of the fluorescence spectra using Grams/32. The fluorescence spectrum of TMPyP consists of two broad and overlapping emission peaks centered at 654 nm

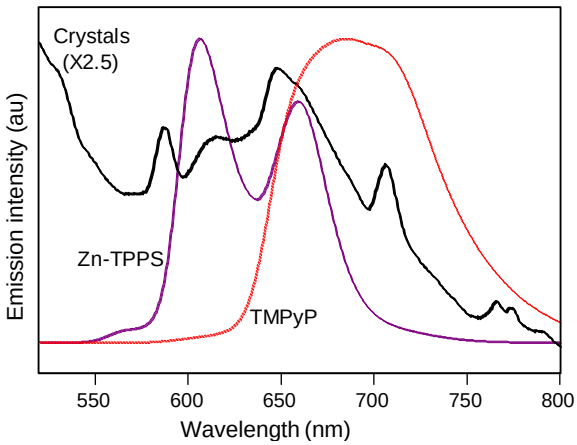


Fig. 4. Normalized emission spectra of Zn-TPPS, TMPyP, and crystals excited at 421 nm, 422 nm, and 431 nm, respectively.

with a shoulder at 683 nm and 713 nm. The fluorescence spectrum of Zn-TPPS consists of two well-defined emission peaks at 603 nm and 660 nm. The fluorescence spectrum of the porphyrin crystals is quenched and consists of seven emission peaks centered at 587 nm, 610 nm, 646 nm with a shoulder at 661 nm, 707 nm, 765 nm, 774 nm, and 791 nm. The three crystalline structures have similar fluorescence spectra.

3.4. Powder X-ray diffraction

Powder X-ray diffraction patterns of the two porphyrins, Zn-TPPS and TMPyP, used in making the solid porphyrin crystals have been obtained (data not shown). The porphyrin powders were used as supplied by the manufacturer. The X-ray diffraction patterns indicate that while Zn-TPPS is not in a crystalline form, TMPyP porphyrin is crystallized. We did not attempt to determine the crystal structure of the starting porphyrins since there is no standard procedure for crystallizing porphyrins. The crystal structure of the two monomer porphyrins could not be found in the literature.

The powder X-ray diffraction pattern of the porphyrin crystals is shown in Fig. 5. The diffraction pattern of the solid porphyrin crystals consists of only five peaks, which indicates that porphyrin crystals exist in a single phase. The diffraction pattern of porphyrin crystals is different from those of the monomer porphyrins suggesting the complexation of the two porphyrins to form the porphyrin crystals. The X-ray crystallography study reveals that the porphyrin crystals belong to the orthorhombic ($\alpha = \beta = \gamma = 90°$) system with unit cell dimensions of $a = 16.9416$ Å, $b = 14.5787$ Å, and $c = 4.8935$ Å. The volume of the unit cell is $V = a * b * c = 1208.616$ Å^3. Zinc porphyrins have been reported to crystallize in the orthorhombic system, for example, zinc(II)-tetrakis(4-methoxycarbonylphenyl)porphyrin–pyridine complex [30]. Crystal structure of multi-porphyrin structures could not be found in the literature. Since the negative charge on the anionic Zn-TPPS is held by the positive charge on the sodium ions (Na^+) and the positive charge on the cationic TMPyP porphyrin is held by the negative charge on the tosylate ions (Tos^-), sodium tosylate (or sodium toluene sulfonate) is formed in the process of developing the porphyrin crystals. This raises the possibility that sodium tosylate might be incorporated in the porphyrin crystals or exist side-by-side with the porphyrin crystals if has not been removed in washing/rinsing the crystals. Thus, for comparison reasons, a powder X-ray diffraction pattern of sodium tosylate crystals was obtained. The diffraction pattern of sodium tosylate is completely different from that of the porphyrin crystals (data not shown). The three prominent peaks of sodium tosylate XRD pattern at $\theta = 5°$, $\theta = 40°$, and $\theta = 45.5°$ do not exist in the porphyrin crystals XRD pattern which indicates that sodium tosylate is not incorporated in the porphyrin crystals and was removed in the washing/rinsing process of the porphyrin crystals.

3.5. 2,4,6-Trinitrotoluene degradation

The loss of 2,4,6-trinitrotoluene over time in presence of the immobilized star-like porphyrin crystalline structure is shown in

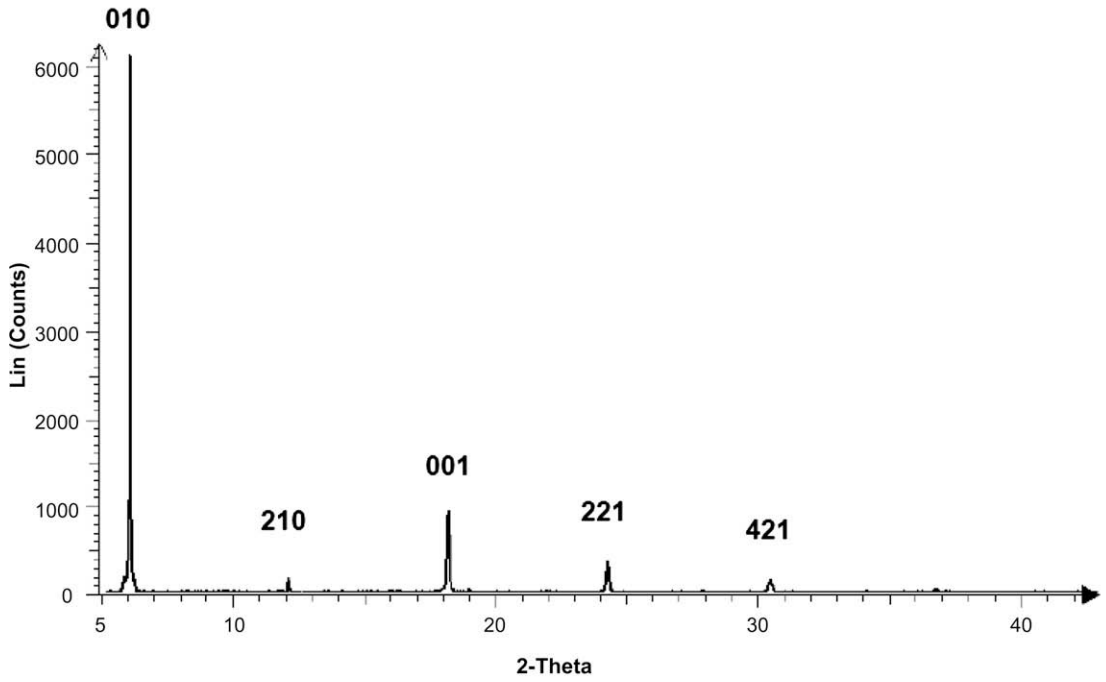


Fig. 5. Powder X-ray diffraction pattern of porphyrin crystals.

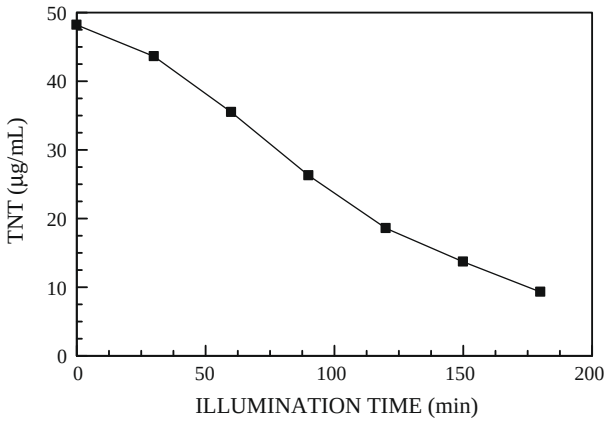


Fig. 6a. Time-dependent degradation of aqueous TNT solution using tungsten illumination in the presence of porphyrin crystals.

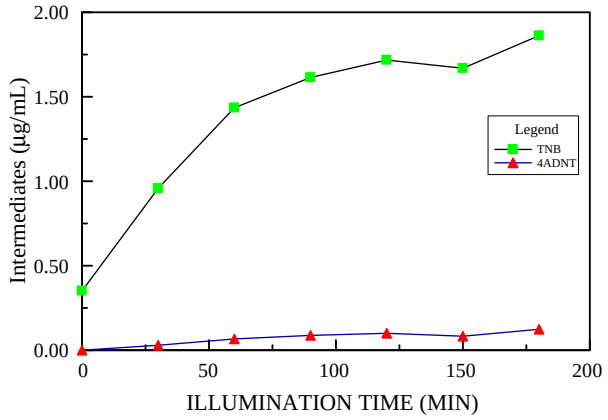


Fig. 6b. Time-dependent appearance of the TNT degradation products using tungsten illumination in the presence of porphyrin crystals.

Fig. 6a. Twenty percent of the original concentration (48 µg/mL) of TNT remained after 3 h of visible light exposure. The loss of TNT results in only two degradation products, 1,3,5-trinitrobenzene (TNB) and 4-amino-2,6-dinitrotoluene forming over time as shown in Fig. 6b, which were identified as such to greater than 99.9% probability on the basis of comparison of HPLC retention times and UV–Vis light spectra of pure standard compounds chromatographed under the same experimental conditions. Formation of other compounds was not observed. The degradation products seem to level off after 90 min of illumination even though the amount of TNT continues to decrease, possibly indicates that these intermediates are at a steady state level as they are degraded. After 90 min, intermediates are degraded as fast as or faster than they are generated. TNT degradation does not occur in the absence of light or the absence of crystals. The solid porphyrin crystals do not degrade over the course of the experiment.

4. Discussion

The formation of porphyrin aggregates can involve electrostatic forces between porphyrins molecules, hydrogen bonding, van der Waals, axial coordination, or other weak intermolecular interactions. These forces enhance the structural stability of the formed structures [19,20].

1:1 mixtures of tetrakis(4-methylpyridyl)porphyrin (TMPyP) and tetrakis(4-sulfonatophenyl)porphyrin (TPPS) in water results in the formation of precipitates that do not have a specific shape or structure [21]. This is in agreement with our results of mixing the same non-metallated porphyrins and confirms that zinc is needed for the production of the porphyrin crystals being reported in this article. We have attempted to make porphyrin crystals using different matalloporphyrins such as Cu-TPPS, Ni-TPPS, and Fe-TPPS instead of Zn-TPPS in de-ionized water. Mixing these porphyrins with TMPyP under the same experimental conditions results in the formation of non-crystalline precipitates (aggregates) with no specific morphology. Zinc in Zn-TPPS porphyrin solution exists as Zn^{2+} ions which makes it readily available for axial coordination with other species. Zinc is a good candidate for the use in making our porphyrin crystals in de-ionized water since it has high affinity for axial coordination bonding with water molecules than iron, copper, tin, and nickel.

Nanoporous metalloporphyrin crystalline solids as possible size- and shape-selective oxidation catalysts and zinc-porphyrin-doped polymethylmethacrylate (PMMA) used as a photochromic recording medium have been studied [22]. Fluorescent micro-scaled needle-shaped zinc–porphyrin crystals have been made via hydrothermal synthesis [23]. Porphyrin polymers have been previously reported to form by coordination bonding between a Zn^{2+} ion embedded in 5,15-di(4-nitrophenyl)-10,20-di(*p*-tolyl)porphyrin core and one of the oxygen atoms of the nitro groups on two neighboring molecules [24]. Homogeneous coordination polymers composed of metal chromophores without exocyclic linkers have also been reported [4,25] where the metal ion inserted in the core of the porphyrin exhibits a high propensity for octahedral coordination to the pyrrole groups of the porphyrin ligand at the four equatorial positions and to two adjacent porphyrin entities at the axial sites. Zn-TMPyP is a suitable example, in which the resulting assemblies represent two-dimensional nets composed of hexa-coordinated porphyrins that are nearly orthogonal with respect to one another. The negatively charged $[H_4TPPS_4]^{2-}$ porphyrin and the positively charged $[Sn–TPyP]^{4+/5+}$ porphyrin have been reported to form porphyrin nanotubes [26] in aqueous solution by ionic binding of the oppositely charged substituent groups with the aid of acidification. Porphyrin nanotubes form only at pH 2.0 and dissolve into monomeric porphyrins at pH 12.0. At pH 2.0, the anionic $[H_4TPPS_4]^{2-}$ porphyrin is protonated (the four nitrogen atoms in the core of the TPPS porphyrin molecule are bound to four hydrogen atoms), but the sulfonate groups (p*K*a = 1.6) are not. This would prevent the hydrogen bonding between the water molecules that are axially bonded to the metal ions embedded in $[Sn-TPyP]^{4+/5+}$ porphyrin, allowing only the formation of two-dimensional structures (sheets that roll into tubes) by the ionic binding of the oppositely charged substituents.

The two oppositely charged porphyrins (Zn-TPPS and TMPyP) used in the current study each possess four symmetrical substituent groups. Since the crystals were made in de-ionized water without acidification, deprotonation of the sulfonate groups ($pK \approx 1.6$) on the Zn-TPPS porphyrin could allow ionic binding of negatively charged sulfonate groups to the positively charged methylpyridinium groups of TMPyP porphyrin. As we mentioned above the Zn^{2+} ion in the core of Zn-TPPS could bind axially to two atoms of higher electronegativity above and below the plane of Zn-TPPS porphyrin. These two facts suggest the binding of the two porphyrins via at least two different types of chemical bonds that allow three-dimensional crystalline structures formation.

The absorbance spectrum of the porphyrin crystals is rather complicated than those of the porphyrin monomers. The Soret band of the porphyrin crystals is broadened and split into a blue-shifted band at 398 nm and a red-shifted band at 431 nm with a shoulder at 450 nm. The Q-bands are broadened and red-shifted. The large shifts, peak splitting, and the broadening in the absorbance peaks are expected for porphyrin architectures and multi-

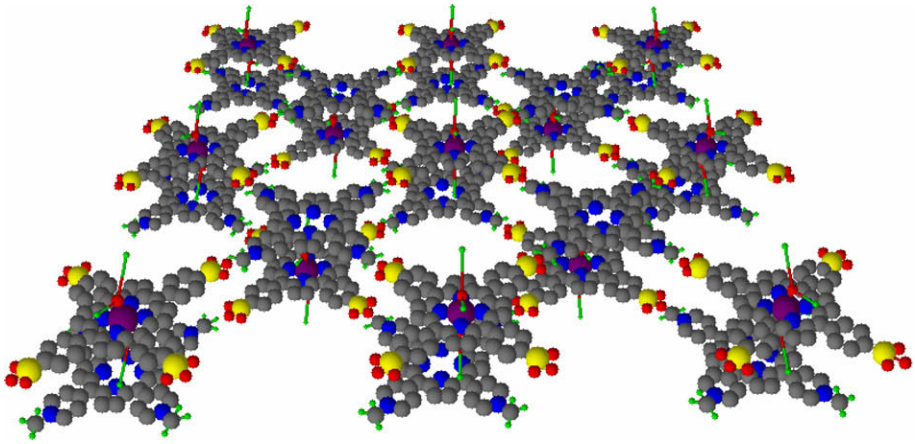


Fig. 7. Crystal packing of the solid porphyrin crystals showing the offset stacking mode between two neighboring layers. The axial water ligands of one layer protrude into the hydrogen bonding sites of the next layer to facilitate interlayer hydrogen bonding.

porphyrin systems [27,28]. The locations of both the Soret band and the Q-bands of the absorbance spectrum of the porphyrin crystals are different from those of the original porphyrin monomers consistent with the complexation of the two porphyrins to form the solid porphyrin crystals; if complexation had not occurred the spectrum of the crystals would be a simple additive combination of the two porphyrins spectra. The broadening, blue-shift, and red-shift in the Soret band in addition to the broadening and red-shift in the Q-bands of the porphyrin crystals absorbance spectrum indicate strong intermolecular and π–π interactions (marked orbital overlap) between the monomer porphyrins in forming the solid crystals [29–31]: This suggests the presence of both side-by-side (J-aggregation) and face-to-face (H-aggregation) interactions.

The different locations of the fluorescence peaks of the porphyrin crystals further suggest the complexation of the two monomer porphyrins to form the solid crystals. Furthermore, the fluorescence of the porphyrin crystals is quenched compared to those of the porphyrin monomers. This could be explained by the fact that in a composite molecule the internal conversion between the split singlet states is expected resulting in preventing fluorescence from the allowed excited state to the ground state [29]. The quenching of the fluorescence spectrum of the porphyrin crystals indicates the occurrence of π–π interactions [31].

The complexation of the Zn-TPPS and TMPyP porphyrins to form the porphyrin crystals is also highly suggested by the crystalline nature of the X-ray diffraction pattern of the porphyrin crystals which is different from those of the monomer porphyrins. Based on the crystallographic data and the chemical nature of the two porphyrins used in making the solid porphyrin crystals, we speculate that the formation of the crystals is achieved by the ionic bonding of the cationic and anionic porphyrins supported by the π–π interactions between *meso*-substituents (the phenyl group on the Zn-TPPS porphyrin and the methylpyridinium group on the TMPyP porphyrin) and the pyrrole rings of the two porphyrins.

The size of the porphyrin crystals is not suitable for performance of single-crystal X-ray diffraction in order to determine, to some extent, the exact crystal structure of these crystals. However, the dimensions of the unit cell, determined from the powder X-ray diffraction measurements, along with the chemical nature of the two porphyrins, suggest the ionic bonding between the two oppositely charged porphyrins resulting in the development of two-dimensional sheets of the two porphyrins with 1:1 stoichiometry. The dimensions of the unit cell (a = 16.9416 Å and b = 14.5787 Å) are of the order of the dimensions of a single porphyrin molecule. The small value of the third dimension of the unit cell (c = 4.8935 Å) suggests the co-facial offset stacking of the porphyrin sheets assisted by the axial coordination bonding of Zn^{2+} ions to two oxygen atoms of two water molecules (Zn^{2+}–O coordination) which in turn could bind to two unprotonated nitrogen atoms in the pyrrole ring of two TMPyP porphyrin molecules above and below the plane of this specific Zn-TPPS molecule via hydrogen bonding. This allows for formation of multiple interlayer links from the axial water ligands as shown in Fig. 7. Stacking of oppositely charged porphyrins in an alternated face-to-face geometry in porphyrin aggregates is well-known and has been reported by Lauceri et al. [31]. However in their study the cationic porphyrins are metallated (M-TMPyP) and the anionic porphyrin (TPPS) is protonated hindering the H-aggregation even though the metal ion in the cationic porphyrin is axially coordinated with two water molecules. This agrees well with our system and further suggests the growth of the porphyrin crystals by the mechanisms discussed above. The zinc atom at the center of porphyrins have been reported to lie out of the zinc porphyrins plane by 0.16–0.425 Å [32,33]. The oxygen atom has also been reported to form Zn–O bond in 5,10,15,20-tetrakis(4-(2-hydroxyethoxy)ethoxy)phenyl)porphyrin with a bond length of 2.124 Å [34] which is also similar to the bond length of Zn–N bond when zinc porphyrins bind to a pyridyl groups (Zn–N = 2.1 Å) [35]. The molecular diameter of a water molecule is 2.6–2.75 Å which is coincidentally is similar to a hydrogen bond [36]. The sum of the lengths of these bonds lies in the range from 4.88 Å to 5.299 Å. The value of the interplanar distance between the sheets in the porphyrin crystals (c = 4.89 Å) lies within the range of the sum of the lengths of the bonds mentioned above. Similar unit cell dimensions have been reported for single crystals of monomer porphyrin crystalline structures implicating the involvement of water molecules in the axial coordination of metlloporphyrins [33,37]. We suggest that the porphyrin crystals are likely formed via different bonding mechanisms: ionic bonding, π–π interactions, and hydrogen bonding in addition to the expected hydrophobic interaction of the aromatic macrocycles concur in holding the individual constituents together. All of these forces would result in a very stable complex (porphyrin crystals) formed with close face-to-face geometry. Porphyrin crystals were soaked in 95% ethanol, 1 M NaOH, 1 M NaCl, and 8 M urea for 24 h in order to examine their stability. The crystals did not dissolve in any of the listed solutions. However, the crystals dissolve completely by soaking them in 4 M HCl at room temperature for 24 h or in 2 M NaCl at 60 °C for 24 h further suggesting the involvement of both hydrogen and ionic bonds in making the crystals and the unusual stability of the solid crystals porphyrin reported in this work.

The increase of the size (rod-like or needle-like crystals to rod-like or needle-like with split ends and larger dimensions crystals to star-like with even larger dimensions crystals) of the porphyrin crystals with increasing porphyrin concentration in the solution may be explained by the higher binding probability at higher porphyrin concentrations. This is due to the relatively large electrostatic forces exerted by the neighboring porphyrin molecules at higher concentrations: increasing the concentration of porphyrins in the solution results in a smaller value of the intermolecular separation and in turn a greater electrostatic force. The different shapes of the crystals at different concentrations indicate the effect of the concentration on shaping the crystals; higher concentrations give rise to a specific binding mechanism (probably the ionic bonding between the porphyrin molecules) over the others as a result of decreasing the molecular spacing giving rise to crystalline structure with a flatter surface (star-like crystals). At low porphyrin concentrations, the ionic bonding between Zn-TPPS and TMPyP porphyrins is expected to be slower than that at high concentration allowing the porphyrin sheets to roll into tubes. However, the axial hydrogen coordination bonding of zinc with water in Zn-TPPS still can take place on the surface of these tubes resulting in rod-like or needle-like crystals that consist of numerous concentric tubes (rod-like or needle-like crystals).

Porphyrins have been previously used in 2,4,6-trinitrotoluene photodegradation. Harmon [18] reported on degrading diluted TNT solution using both free-base and metalloporphyrin solutions and showed that free-base porphyrin (TPPS) degrade TNT faster than metalloporphyrins with trinitrobenzene and trinitrobenzoic acid as degradation products and 37% of the original TNT concentration remained after 3.5 h of illumination. White et al. [38] have also reported on sunlight catalyzed conversion of TNT using porphyrin-embedded periodic mesoporous organosilica and showed that 32% of the original concentration of the diluted TNT solution remained after 5 h of illumination.

In the current work, 2,4,6-trinitrotoluene degradation data show that porphyrin solid crystals are able to degrade TNT when illuminated by visible light without addition of additional reductants. Only twenty percent of the original concentration of TNT solution remained after illumination with visible light for 3 h with trinitrobenzene (TNB) and 4-amino-2,6-DNT the only observed intermediates. The TNT degradation products suggest that the degradation of TNT occurs via two steps. First is the oxidation of the methyl group of TNT, which results in removing the methyl group, to yield TNB and second is the reduction of the 4-nitro group of TNT to an amino group to yield 4ADNT.

The immobilized porphyrin crystals used in the HPLC experiment were dissolved in 4 M HCl. The Soret band of the absorbance spectrum of the dissolved crystals was compared to the Soret band of a 1:1 molar ratio solution of the two monomer porphyrins in 4 M HCl to determine the concentration of porphyrin used in this specific run. The comparison revealed that 23 μM of each porphyrin was incorporated in theses crystals. Thus, in our system the porphyrins exist in approximately 1:8 mol/mol with respect to 2,4,6-trinitrotoluene (approximately 400 μM). The porphyrin crystals hydrolyze water resulting in production of protons and electrons. Thus the water molecules serve as the sacrificial electron donor [39–41].

Usually π-electron structure of porphyrin monocation is unstable [39] but the electron structure can be stabilized in the ground state in the case of dimeric form by coordination of the neighboring porphyrin molecule with the formation of water-porphyrin dimeric complex (donor–acceptor complex) via hydrogen bonds of two water molecules involved in the complex [40,41]. The stability of the porphyrin crystals is achieved via the donation of protons to the complexed porphyrin monomers by the water molecules as a result of formation of donor–acceptor complex.

We have previously reported on the binding of 2,4,6-trinitrotoluene to porphyrin by hydrogen bond(s) between a pyrrole-N(s) in the core of the porphyrin and a nitro-oxygen(s) of TNT at room temperature [13]. We suggest that the binding of TNT to the porphyrin crystals occurs by the same mechanism since the crystals will have both types of porphyrins, Zn-TPPS and TMPyP, which will provide larger number of binding sites for TNT that are closely packed. Based on the preferred reduction of the 4-nitro group of TNT to a 4-amino group [42] and that the reduction will occur via the pyrrole core of the porphyrin [43], we suggest that the hydrogen bond(s) form between the 4-nitro group of TNT and the pyrrole nitrogen atoms as O–H–N hydrogen bonds. Once the TNT binds to the crystals surface the degradation process takes place by either the demethylation of TNT (removal of the methyl group) [18] which will yield trinitrobenzene (TNB) or the reduction of one of the nitro group(s) of TNT to form amino group(s) to yield 4-amino-2,6-dinitrotoluene which has been previously reported [43,44].

5. Conclusion

The formation of highly stable micro-scale crystalline structures using two oppositely charged water-soluble porphyrins (TMPyP and Zn-TPPS) was investigated by means of optical microscopy, UV–Vis spectroscopy, fluorescence spectroscopy, and powder X-ray diffraction. The porphyrin crystals have different absorbance and fluorescence spectra from the porphyrin monomers used in making them which suggests the complexation of the two monomer porphyrins used in making the crystals. Porphyrin crystals photocatalytically degrade aqueous 2,4,6-trinitrotoluene solution upon illumination with a tungsten lamp (visible light). The porphyrin solid crystals do not dissolve or degrade over the course of the experiment.

Acknowledgements

This research was funded by contract #F42620-00-D-0036 from the US Army. We would like to thank Dr. A. Apblett at the Department of Chemistry at Oklahoma State University for conducting the powder X-ray diffraction experiment. The cooperation and support of Dr. S.W. Kwak at the US Army Defense Ammunition Center, McAlester, OK is appreciated.

References

[1] J.B. Birks, Organic Molecular Photophysics, vol. 1, John Wiley, New York, 1973.
[2] S. Bargdonas, R. Rotomskis, Lithuanian J. Phys. 38 (1998) 75.
[3] K.M. Kadish, K.M. Smith, R. Guilard, The Porphyrin Handbook, Academic, New York, 2000.
[4] I. Goldberg, Chem. Commun. (2005) 1243.
[5] J.-M. Lehn, Angew. Chem., Int. Ed. Engl. 29 (1990) 1304.
[6] G.M. Whitesides, J.P. Mathias, C.T. Seto, Science 254 (1991) 1312.
[7] R.L. Homstead, J. Agric. Food Chem. 24 (1976) 620.
[8] S. Khalifa, R.L. Holmstead, J.E. Casida, J. Agric. Food Chem. 24 (1976) 277.
[9] T.S. Marks, J.D. Allpress, A. Maule, Appl. Environ. Microbiol. 55 (1989) 1258.
[10] S. Hasan, J.-G. Cho, K.L. Sublette, D. Pack, A. Maule, J. Biotechnol. 24 (1992) 195.
[11] J.-G. Cho, W.T. Potter, K.L. Sublette, Appl. Biochem. Biotechnol. 45 (1994) 861.
[12] A.M. Awawdeh, H.J. Harmon, Sens. Actuators, B-Chem. 106 (2005) 234.
[13] W.M. Hikal, H.J. Harmon, J. Hazard. Mater. 154 (2008) 826.
[14] J. Yinon, Toxicity and Metabolism of Explosives, CRC Press, Ann Arbor, 1990.
[15] S.D. Comfort, P.J. Shea, L.S. Hundal, Z.M. Li, B.L. Woodbury, J.L. Martin, W.L. Powere, J. Environ. Qual. 24 (1995) 1174.
[16] US EPA, Health Advisory on Trinitrotoluene, Office of Drinking Water, Washington, DC, 1998.
[17] M. Rahman, H.J. Harmon, Spectrochim. Acta, Part A 65 (2006) 901.
[18] H.J. Harmon, Chemosphere 63 (2006) 1094.
[19] N. Micali, A. Romeo, R. Lauceri, R. Purrello, F. Mallamace, L.M. Scolaro, J. Phys. Chem. B 104 (2000) 9416.
[20] R. Lauceri, S. Gurrieri, E. Bellacchio, A. Contino, L.S. Monsu, A. Romeo, A. Tuscano, R. Purrello, Supermol. Chem. 12 (2000) 193.
[21] A. Iosif, U.-W. Grummt, J. Prakt. Chem. 339 (1997) 420.
[22] O.V. Khodykin, S.J. Zilker, D. Haarer, B.M. Kharlamov, Opt. Lett. 24 (1999) 513.

[23] R. Brunner, M.E. Kosal, K.S. Suslick, R. Lamche, O. Marti, J.O. White, Ultramicroscopy 84 (2000) 149.
[24] S. Adilov, V. Thalladi, Cryst. Growth Des. 7 (3) (2007) 481.
[25] R.K. Kumar, S. Balasubramanian, I. Goldberg, Chem. Commun. (1998) 1435.
[26] Z. Wang, C.J. Medforth, J.A. Shelnutt, J. Am. Chem. Soc. 126 (2004) 15954.
[27] X. Gong, T. Milic, C. Xu, J.D. Batteas, C.M. Drain, J. Am. Chem. Soc. 124 (2002) 14290.
[28] Z. Wang, Z. Li, C.J. Medforth, J.A. Shelnutt, J. Am. Chem. Soc. 129 (2007) 2440.
[29] M. Kasha, H.R. Rawls, M.A. El-Bayoumi, Pure Appl. Chem. 11 (1965) 371.
[30] Z.-M. Ou, H. Yao, K. Kimura, J. Photochem. Photobiol. A: Chem. 189 (2007) 7.
[31] R. Lauceri et al., Supramol. Chem. 12 (2000) 193.
[32] P.D.W. Boyd, A. Hosseini, Acta Crystallogr., Sect. E 62 (2006) m1542.
[33] S. Muniappan, S. Lipstman, I. Goldberg, Acta Crystallogr., Sect. C 62 (2006) m477.
[34] S.J. Langford, C.P. Woodward, Polyhedron 26 (2007) 338.
[35] S. George, I. Goldberg, Cryst. Growth Des. 6 (2006) 755.
[36] J. Sun, H. Viadiu, A.K. Aggarawal, A. Weinstein, Biophys. J. 84 (2003) 3317.
[37] H.-J. Kim, H.J. Jo, J. Kim, S.-Y. Kim, D. Kim, K. Kim, CrystEngCommun 7 (2005) 417.
[38] B.J. White, M. Zeinali, A.P. Malanoski, M.A. Dinderman, Catal. Commun. 8 (2007) 1052.
[39] P. Hambright, E.B. Fleischer, Inorg. Chem. 9 (1970) 1757.
[40] A.V. Udal'tsov, A.A. Churin, Int. Photochem. Photobiol. (1998). <http://www.photobiology.com/IUPAC98?Udaltsov/index.htm>.
[41] A.V. Udal'tsov, Y.V. Kovalev, J. Photochem. Photobiol. A: Chem. 135 (2000) 193.
[42] C.E. Castro, M. Jamin, W. Yokoyama, R. Wade, J. Am. Chem. Soc. 108 (1986) 4179.
[43] O. Munro, P.S. Madala, R.A.F. Warby, T.B. Seda, G. Hearne, Inorg. Chem. 38 (1999) 4724.
[44] M.J. Huang, J. Leszczynski, Theochem 592 (2002) 105.

Polyhedron 28 (2009) 121–125

Contents lists available at ScienceDirect

Polyhedron

journal homepage: www.elsevier.com/locate/poly

Reactivity of triazolyl Schiff bases with Ru(II)-2,2′-bipyridyl: Synthesis, spectroscopic characterization of isomers and their photo-physical properties

Vinod K. Yadav [a], Sanjib Kar [b], L. Mishra [a,*]

[a] Department of Chemistry, Faculty of Science, Banaras Hindu University, Varanasi 221 005, India
[b] National Institute of Science Education and Research, Bhubaneswar, India

ARTICLE INFO

Article history:
Received 25 June 2008
Accepted 18 September 2008
Available online 29 October 2008

Keywords:
3-Amino-1H-1,2,4-triazole
Schiff bases
Ru(II)2,2′-bipyridyl complexes
Isomers
Photo-physical properties

ABSTRACT

The condensation of 3-amino-1*H*-1,2,4-triazole with benzaldehyde and terephthalaldehyde provides the bidentate and tetradentate Schiff bases 1,2,4-triazolo-3-imino-benzene L^1H and 1,4-bis(1,2,4-triazolo-3-imino)benzene L^2H_2, respectively. The well characterized Schiff bases were allowed to react with *cis*-$Ru(bpy)_2Cl_2 \cdot 2H_2O$. Isomers of the mononuclear complexes $Ru(bpy)_2L^1]PF_6 \cdot NH_4PF_6$ (**1a**, N4) and $[Ru(bpy)_2L^1]PF_6 \cdot 0.5NH_4PF_6$ (**1b**, N2), and the dinuclear Ru(II) complexes $[Ru(bpy)_2L^2Ru(bpy)_2](PF_6)_2 \cdot NH_4PF_6$ (**2a**, N4N4), $[Ru(bpy)_2L^2Ru(bpy)_2](PF_6)_2 \cdot NH_4PF_6 \cdot 2H_2O$ (**2b**, N2N2) and $[Ru(bpy)_2L^{2-}Ru(bpy)_2](PF_6)_3 \cdot NH_4PF_6$ (**2c**, Ru(II)-Ru(III)) were separated by column chromatography and characterized by their elemental analysis, FAB mass and spectral (IR, NMR, UV–Vis) data. The data obtained suggest that the ligands are bound to the metal centre via the N4 and N2 atoms of the triazole moiety along with the N (imine) atom. The complexes display metal-to-ligand charge-transfer (MLCT) transitions in the visible region from the $d\pi(Ru^{II}) \rightarrow \pi^*L$ transition. Highly intense ligand-based $\pi \rightarrow \pi^*$ transitions are observed in the UV region. A dual emission occurs from the N2 and N2N2 isomers.

© 2008 Elsevier Ltd. All rights reserved.

1. Introduction

Ruthenium(II) polypyridyl complexes are at the centre of research owing to their well defined spectroscopic, photo-physical, photochemical and electrochemical properties [1]. These properties are exploited in the construction of supramolecular systems [2] as well as in the development of molecular devices [3]. Their incorporation into multinuclear structures capable of directing and modulating electron and or energy transfer processes has been extensively studied [3,4]. The ability of these complexes to tune their excited state properties lies in centre of their potential applications. In this context, a detailed and interesting investigation on the synthesis and characterization of multinuclear ruthenium(II) and osmium(II) polypyridyl complexes using negatively charged triazole based ligands have been reported [5,6]. Relatively strong interactions can be obtained between metal centres mediating both electron transfer and energy transfer processes efficiently [7]. Thus the synthesis and characterization of dinuclear complexes specifically with Schiff bases which are considered potential candidates to facilitate thermal and photon induced energy transfer processes [8], is considered as a challenging and interesting research area.

Recently, Vos et al. have extended these studies with the complex of *cis*-$Ru(bpy)_2Cl_2 \cdot 2H_2O$ with the ligand 3-(pyrazin-2-yl)-5-(pyridin-2-yl)-1,2,4-triazole (Hppt) [9]. The asymmetry of the ligand may result in the formation of four different mononuclear coordination isomers (N2 and N4). As expected, the reaction of one equivalent of the bridging ligand with two equivalents of a $[M(bpy)_2]$ precursor leads to the formation of a mixture of different coordination isomers. Hence identification of the different isomers is found challenging. However, it has been reported for several 1,2,4-triazoles that the presence of bulky substituents in the 5-position of the 1,2,4-triazole ring leads to the preferential formation of the N2 isomer. Thus, the amount of N4 bound isomers varies from 50% (5 position occupied by hydrogen) [10] to less than 5% (5 position occupied by Br) [11].

Based on these precedences and our earlier interest on triazole systems [12], an attempt has been made to synthesize, purify and characterize some mononuclear and dinuclear complexes of bidentate (L^1H) and tetradentate (L^2H_2) triazole based Schiff bases (Fig. 1) with the $Ru(bpy)_2$ unit. The different isomers obtained from complexes **1** and **2** are separated using column chromatography. The separated complexes are characterized using spectroscopic techniques.

In the present system, the 5-position of the triazole ring bears only a hydrogen atom, so equal amounts of N2 and N4 isomers are found.

* Corresponding author. Tel.: +91 542 6702449; fax: +91 542 2368174.
E-mail address: lmishrabhu@yahoo.co.in (L. Mishra).

0277-5387/$ - see front matter © 2008 Elsevier Ltd. All rights reserved.
doi:10.1016/j.poly.2008.09.012

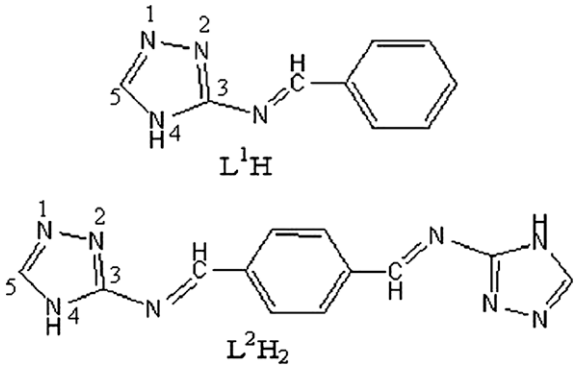


Fig. 1. Structure of the ligands.

2. Experimental

2.1. Materials and methods

All the preparations were carried out in a N_2 gas atmosphere at ambient temperature and pressure. All the solvents purchased from E. Merck were used without further distillation. However, $RuCl_3 \cdot 3H_2O$, 2,2′-bipyridine, 3-amino-1*H*-1,2,4-triazole and terephthalaldehyde purchased from Sigma–Aldrich were used as supplied. *cis*-$[Ru(bpy)_2Cl_2] \cdot 2H_2O$ [13] was prepared using the reported method. For electrochemical studies, HPLC-grade acetonitrile was used.

FAB mass data were obtained from SAIF-CDRI, Lucknow, India, using a JEOL SX-102/DA-6000 mass spectrometer and nitrobenzyl alcohol (NBA) as a matrix. IR spectra were recorded on a JASCO FT/IR 5300 or a Varian 3100 FTIR. ^{1}H NMR/^{13}C NMR spectra (in DMSO-d_6) were recorded on a JEOL-AL-300 MHz NMR spectrometer using $Si(CH_3)_4$ as an internal reference. UV–Vis spectra were recorded on a SHIMADZU UV-1601 spectrophotometer, whereas luminescence measurements were recorded on a LS-45 spectrophotometer (Perkin Elmer).

2.2. Synthesis of the ligands

The ligands L^1H and L^2H_2 were synthesized by the condensation of 3-amino-1*H*-1,2,4-triazole (10 mmol, 0.84 g) with benzaldehyde (10 mmol, 1.06 g) and terephthalaldehyde (5 mmol, 0.67 g), respectively, in methanol, containing a few drops of acetic acid. After refluxing for 4–6 h, the corresponding solid compounds thus obtained were filtered, washed with methanol, diethylether and dried in vacuo. The ligands were then characterized by IR, ^{1}H NMR, ^{13}C NMR, elemental analysis and FAB mass data. L^1H: A pure white powder. Yield = 1.049 g, 61%. M.p.: 212 °C. Elemental *Anal.* Calc. for $C_9H_8N_4$ (L^1H): C, 62.79; H, 4.65; N, 32.55. Found: C, 62.45; H, 4.41; N, 32.97%. IR (KBr pellet, cm^{-1}): 3245 (ν_{N-H}), 1595 ($\nu_{N=CH}$), 1335 cm^{-1} ($\nu_{triazole\ ring}$). ^{1}H NMR (DMSO-d_6, δ ppm): 14.05 (s, 1H; NH), 9.23 (d, 1H; HC=N), 8.33 (s, 1H; triazole CH), 8.00 (d, 2H; Ar-H), 7.57 (t, 3H; Ar-H). ^{13}C NMR (DMSO-d_6, δ ppm): 163.6 (N=*C*H), 144.9 (N–*C*N_2, triazole), 135.2 (N–*C*H, triazole), 132.3, 129.4, 129.1, 128.8 (aromatic). FAB-MS: *m/z:* 173 $[M+1]^+$. L^2H_2: A pure light yellow powder. Yield = 0.839 g, 73%. Elemental *Anal.* Calc. for $C_{12.5}H_{12}N_8O_{0.5}$ ($L^2H_2 \cdot 0.5CH_3OH$): C, 53.19; H, 4.25; N, 39.71. Found: C, 53.41; H, 4.01; N, 40.09%. IR (KBr pellet, cm^{-1}): 3152 (ν_{N-H}), 1608 ($\nu_{N=CH}$), 1271, 1219 ($\nu_{triazole\ ring}$). ^{1}H NMR (DMSO-d_6, δ ppm): 14.05 (s, 2H; NH), 9.30 (d, 2H; N=CH), 8.38 (s, 2H; trizole CH), 8.15 (d, 4H; Ar-H). ^{13}C NMR (DMSO-d_6, δ ppm): 163.1 (N=CH), 138.3 (N–CH, triazole), 129.8, 129.5 (aromatic). FAB-MS: *m/z:* 267 $[M+1]^+$.

2.3. Synthesis of the complexes

2.3.1. Mononuclear complexes: $[Ru(bpy)_2L^1] \cdot PF_6 \cdot NH_4PF_6$, **1a** and $[Ru(bpy)_2L^1] \cdot PF_6 \cdot 0.5NH_4PF_6$, **1b**

The ligand L^1H (1 mmol, 0.172 g) was mixed with *cis*-$Ru(bpy)_2Cl_2 \cdot 2H_2O$ (1 mmol, 0.520 g) in ethylene glycol and then refluxed for 13 h. A solution of the reaction mixture was then cooled to room temperature, followed by addition of an aqueous solution of NH_4PF_6, and then it was kept for 24 h. The crystalline solid thus obtained was filtered, washed with water followed by a few drops of methanol and diethylether, then dried in vacuo. The yield of the crude product was found to be 0.408 g (56%). After column chromatography on an alumina column using acetonitrile as the eluent, the complex was separated into two products after removing a light yellow band from the column. The second light brown band (isomer **1a**) was then collected followed by another dark brown fraction (**1b**) which was eluted using a mixture of acetonitrile, a saturated aqueous solution of KNO_3 and water in a 7:1:0.5 ratio (v/v). The last two fractions were then reprecipitated separately by the addition of an aqueous solution of NH_4PF_6. The corresponding crystalline solids thus obtained were then filtered, washed with water and methanol, and dried in vacuo. Both parts were further crystallized by dissolving them separately in acetonitrile containing a few drops of water, and kept for 5 days. The crystalline products were then collected, washed with water and dried. Fraction I was characterized as the N4 isomer and was designated as **1a**. Yield = 0.160 g, 22%. Elemental *Anal.* Calc. for $C_{29}H_{27}N_9P_2F_{12}Ru$ ($[Ru(bpy)_2L^1] \cdot PF_6 \cdot NH_4PF_6$): C, 39.01; H, 3.02; N, 14.12. Found: C, 38.69; H, 3.20; N, 14.50%. Λ_M (Ω^{-1} cm^2 mol^{-1}) 367.0. IR (KBr pellet, cm^{-1}): 1603 ($\nu_{N=CH}$), 1218 ($\nu_{triazole\ ring}$), 1465–1415 (ν_{bpy}), 557 (ν_{Ru-N}), 843 ($\nu_{PF_6^-}$); ^{1}H NMR (DMSO-d_6, δ ppm): 9.35 (N=CH), 8.10 (triazole N–CH), 8.02 (Ar-H), 7.80 (Ar-H), 8.70–7.35 (bpy-H); ^{13}C NMR (DMSO-d_6, δ ppm): 156.9 (N=*C*H), 151.4, 149.7, 127, 126, 122 (bpy-C), 137.9, 135.9 (triazole N–*C*), 126.1, 125.5, 123.6 (aromatic). FAB-MS: *m/z*: 729 $[M]^+$, 497, 413.

The second fraction **1b** was identified as the N2 isomer. Yield = 0.182 g 25%. Elemental *Anal.* Calc. for $C_{29}H_{25}N_{8.5}P_{1.5}F_9Ru$ ($[Ru(bpy)_2L^1] \cdot PF_6 \cdot 0.5NH_4PF_6$): C, 42.92; H, 3.08; N, 14.67. Found: C, 43.52; H, 3.00; N, 14.06%. Λ_M (Ω^{-1} cm^2 mol^{-1}) 257.0. IR (KBr pellet, cm^{-1}): 1606 ($\nu_{N=CH}$), 1224 ($\nu_{triazole\ ring}$), 1463, 1447 (ν_{bpy}), 557 (ν_{Ru-N}), 840 ($\nu_{PF_6^-}$). 1H NMR (DMSO-d_6, δ ppm): 9.37 (N=CH), 8.29 (triazole N–CH), 7.83, 7.43 (aromatic), 8.65, 8.20, 7.97, 7.33 (bpy). ^{13}C NMR (DMSO-d_6, δ ppm): 157.5 (N=CH), 153.1, 151.5, 138, 127, 120 (bpy), 137.8, 136 (triazole N–CN_2), 127.1, 124.2, 123.7 (aromatic). FAB-MS: *m/z*: 729 $[M]^+$, 497, 413.

2.3.2. Dinuclear complexes: $[Ru(bpy)_2L^2Ru(bpy)_2](PF_6)_2 \cdot NH_4PF_6$ (**2a**), $[Ru(bpy)_2L^2Ru(bpy)_2](PF_6)_2 \cdot NH_4PF_6 \cdot 2H_2O$ (**2b**) and $[Ru^{II}(bpy)_2L^2Ru^{III}(bpy)_2](PF_6)_3 \cdot NH_4PF_6$ (**2c**)

These complexes were prepared using the procedure as adopted for the synthesis of complex **1**, condensing the ligand L^2H_2 (1 mmol, 0.272 g) with $Ru(bpy)_2Cl_2 \cdot 2H_2O$ (2 mmol, 1.040 g) in ethylene glycol. The reaction mixture was then refluxed for 16 h in a N_2 gas atmosphere. After cooling to room temperature, an aqueous solution of NH_4PF_6 was added and then it was kept for 24 h. The crystalline solid thus obtained was then filtered, washed with water, methanol and diethylether, and dried in vacuo. The yield of the crude products was found to be 0.843 g (61%). The initial yellow solution, separated using column chromatography on an alumina column, was rejected. The next two bands, light and deep dark brown fractions, were separated using acetonitrile as the eluent. The third black fraction was separated using a mixture of acetonitrile, a saturated aqueous solution of KNO_3 and water in a ratio of 7:1:0.5, respectively. These three fractions were identified as N4N4, N2N2 and Ru(II)–Ru(III) isomers, symbolized as **2a**, **2b** and **2c**, respectively. These isomers were further purified

separately by the addition of an aqueous solution of NH_4PF_6 into their corresponding solutions in acetonitrile. The crystallized solids thus obtained were filtered, washed with water and dried in vacuo. Suitable crystals of both mononuclear and dinuclear complexes could not be obtained even after trying for many months.

Complex **2a**: Yield = 0.212 g, 16%. Elemental *Anal.* Calc. for $C_{52}H_{44}N_{17}P_3F_{18}Ru_2$ ($[Ru(bpy)_2L^2Ru(bpy)_2](PF_6)_2 \cdot NH_4PF_6$): C, 40.44; H, 2.85; N, 15.42. Found: C, 40.43; H, 3.13; N, 15.72%. Λ_M (Ω^{-1} cm^2 mol^{-1}) 541.0. IR (KBr pellet, cm^{-1}): 1605 ($\nu_{N=CH}$), 1282 cm^{-1} ($\nu_{triazole\ ring}$), 1459–1383 (ν_{bpy}), 556 (ν_{Ru-N}), 843 ($\nu_{PF_6^-}$). ^{1}H NMR (DMSO-d_6, δ ppm): 8.80 (N=CH), 8.02 (triazole N–CH), 7.95, 7.66 (aromatic), 8.86, 8.18, 7.74, 7.54, 7.46 (bpy). ^{13}C NMR (DMSO-d_6, δ ppm): 157.6 (N=CH), 153.1, 151.5, 137.8, 127.8, 123 (bpy), 137.5, 137.3 (triazole N–CH), 127.2, 126.8 (aromatic). FAB-MS: *m/z*: 1090 [M]$^+$, 413.

Complex **2b**: Yield = 0.186 g 14%. Elemental *Anal.* Calc. for $C_{52}H_{48}N_{17}O_2P_3F_{18}Ru_2$ ($[Ru(bpy)_2L^2Ru(bpy)_2](PF_6)_2 \cdot NH_4PF_6 \cdot 2H_2O$): C, 39.51; H, 3.03; N, 15.07. Found: C, 39.34; H, 2.81; N, 15.55%. Λ_M (Ω^{-1} cm^2 mol^{-1}) 493.0. IR (KBr pellet, cm^{-1}): 1603 ($\nu_{N=CH}$), 1217 cm^{-1} ($\nu_{triazole\ ring}$), 1459–1377 (ν_{bpy}), 557 (ν_{Ru-N}), 844 ($\nu_{PF_6^-}$). ^{1}H NMR (DMSO-d_6, δ ppm): 9.34 (N=CH), 8.42 (N–CH), 8.24, 8.09 (aromatic), 8.78, 8.58, 7.72, 7.35 (bpy). ^{13}C NMR (DMSO-d_6, δ ppm): 157.8 (N=CH), 151.3, 137.0, 127.3, 123, 122 (bpy), 145.8, 137.5 (triazole N–C), 127.1, 125.7 (aromatic). FAB-MS: *m/z*: 1090 [M]$^+$, 413.

Complex **2c**: Yield = 0.265 g, 21%. Elemental *Anal.* Calc. for $C_{52}H_{44}N_{17}P_4F_{24}Ru_2$, ($[Ru(bpy)_2L^2Ru(bpy)_2](PF_6)_3 \cdot NH_4PF_6$): C, 36.96; H, 2.60; N, 14.09. Found: C, 36.48; H, 2.80; N, 13.82%. Λ_M (Ω^{-1} cm^2 mol^{-1}) 584.0. IR (KBr pellet, cm^{-1}): 1604 ($\nu_{N=CH}$), 1223 ($\nu_{triazole\ ring}$), 1458–1383 (ν_{bpy}), 557 (ν_{Ru-N}), 844 ($\nu_{PF_6^-}$). ^{1}H NMR (DMSO-d_6, δ ppm): (broad spectrum) 8.89 (N=CH), 8.09 (N–CH), 8.06, 7.55 (Ar-H), 8.62-7.30 (bpy). FAB-MS: *m/z*: 1090 [M]$^+$, 413.

3. Results and discussion

All the complexes were found to be thermally stable at room temperature and were soluble in acetone, acetonitrile, DMSO and DMF. All the complexes contain NH_4PF_6, even after several washings with water, and are of an electrolytic nature in solution. The physicochemical and electronic properties of the complexes are shown in Table 1.

3.1. IR spectra

It is only νNH and νCH (both of triazole rings) together with νN=CH vibrations that can be used as diagnostics for the characterization of the binding pattern of the ligands with the metal ion. The peak observed at 1216–1285 cm^{-1} is assigned to the triazole ring skeletal vibration in view of an earlier report [14]. However the peak observed at ~1602–1606 cm^{-1} in the spectra of the complexes indicates that a change in the peak position of νN=CH of the free ligands (1595 and 1608 cm^{-1}) occurs upon complexation. The νNH (triazole) vibration observed at 3245 and 3152 cm^{-1} for free ligands L^1 H and L^2H_2, respectively, disappeared in the infrared spectra of their corresponding complexes, indicating that the ligands get deprotonated during their coordination with the metal ion. In this context, it is worth mentioning that it is only the change in the νCH (triazole ring) vibration which could be exploited as a diagnostic to distinguish the N2 and N4 isomers. For the N4 isomer, a change in the νCH vibration is supposed to occur while for the N2 isomer no significant change in νCH is expected. Additionally, peaks observed at 557 cm^{-1} in the spectra of all the isomers were assigned to νRu–N vibrations in view of an earlier report [15]. The peak observed at ~840–844 cm^{-1} was assigned to the $\nu_{PF_6^-}$ vibration. These assignments are further substantiated by the ^{1}H NMR spectra of the complexes.

Table 1
Electronic[a] data of the complexes

Complexes	λ_{max} in nm ($\varepsilon \times 10^4$ M^{-1} cm^{-1})	λ_{em} (nm) at 300 K
1a	465 (1.78), 346 (2.18), 290 (3.99),	520 (0.62)
1b	438 (1.70), 290 (4.00), 236 (3.98),	518 (0.59), 606 (0.86),
2a	456 (0.28), 344 (0.37), 288 (2.08), 245 (1.12)	603 (2.31)
2b	476 (0.35), 343 (0.53), 289 (2.41), 242 (1.32)	635 (1.52), 518 (0.84)
2c	471 (0.52), 343 (0.62), 289 (3.46), 244 (1.74)	675 (0.12)
$[Ru(bpy)_3]^{2+}$	451 (1.29)	608

[a] In acetonitrile at 298 K.

3.2. ^{1}H NMR spectra

The peak observed at δ 14.1 ppm in the spectra of the free ligands and assigned to the NH (triazole ring) proton disappears in the spectra of the complexes. Thus, it supports the proposal that the ligands have coordinated with the metal ion in the deprotonated form. However, a peak observed at δ 8.80–9.37 ppm and assigned to imine protons, also supports that the imine nitrogen of the ligands coordinates with the metal ion. As shown in the ^{1}H NMR spectrum of a representative complex **2a**, (Fig. 2a), the N–*CH* (triazole ring) proton appears at δ 8.02 ppm, whereas the same proton appears at 8.38 ppm in the spectrum of the free ligand L^2H_2. This difference in N–C*H* peak position could arise due to coordination of its neighbouring nitrogen atom. Hence complex **2a** is identified as the N4N4 isomer. However, in the spectrum of complex **2b**, the δ N–*CH* (triazole) proton appears at δ 8.42 ppm, which supports that the triazole rings coordinate via the N2 atom, and hence identifies it as the N2N2 isomer. However, in complex **2c**, the ^{1}H NMR spectral pattern was broad, with the N–*CH* proton of the triazole ring centred at δ = 8.09 ppm. Therefore, coordination via N4 of both triazole rings is considered and hence it is assigned as the N4N4 isomer. However in view of the broad NMR peak, combined with the elemental analysis, complex **2c** is proposed to be the mixed metal (Ru^{II}–Ru^{III}) isomer. For further support, the ^{13}C NMR spectra of the complexes have also been recorded and a representative spectrum of complex **2a** is shown in Fig. 2b.

3.3. ^{13}C NMR spectra

The peak observed at δ 163 ppm in the spectra of the free ligands is assigned to the carbon of the CH=N group which shifts to δ ~157 ppm in the spectra of the complexes (Fig. 2b). Thus, comparison of their ^{13}C NMR spectra directly support the participation of the nitrogen of CH=N in coordination with the metal ion.

3.4. Electronic properties

3.4.1. UV–Vis

UV–Vis spectral data recorded for all isomers in CH_3CN solution (10^{-4} M) are listed in Table 1 and the spectra are shown in Figs. 3a and 3b. The absorption peaks observed in the UV region at λ_{max} 285–346 nm are assigned to ligand-based π–π^* transitions. These bands are very intense in nature. The overall spectral properties are found to be similar to ruthenium bipyridyl as well as Ru-triazole, consistent with an earlier report [2]. The lowest energy MLCT band of $[Ru(bpy)]_3$ appears at 451 nm. The replacement of one bpy ligand by a symmetric coordination (N2N2 and N4N4) results in a red-shift of the same transition (456–476 nm). Since in these complexes, Ru^{II} is in the low-spin t_{2g}^6 state, the observed visible bands

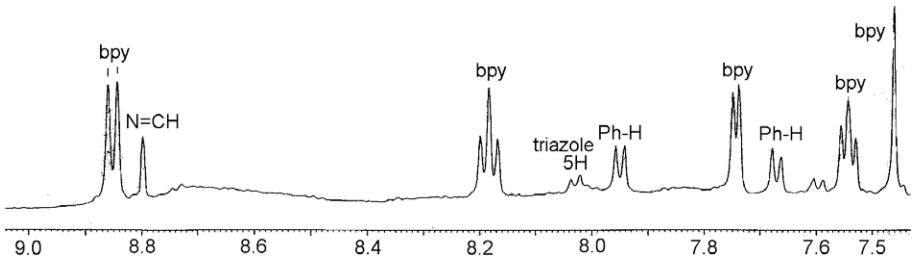


Fig. 2a. ^{1}H NMR spectrum of the representative dinuclear complex **2a**.

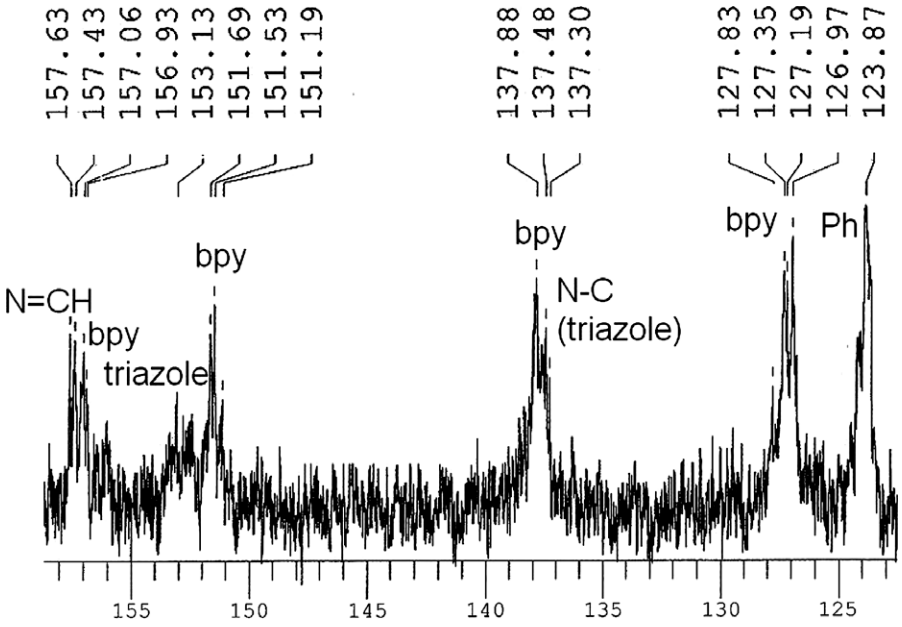


Fig. 2b. ^{13}C NMR spectrum of the representative dinuclear complex **2a**.

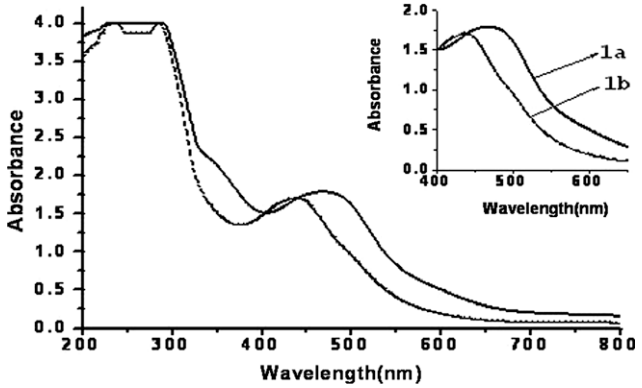


Fig. 3a. UV–Vis spectra of the complexes **1a** and **1b** in acetonitrile at 298 K.

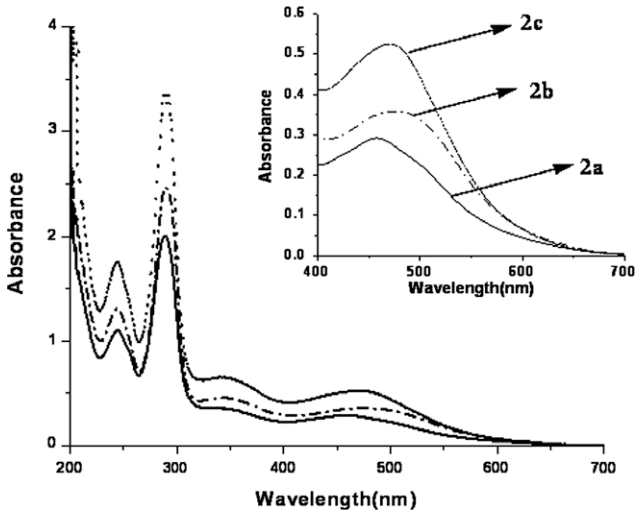


Fig. 3b. UV–Vis spectra of the complexes **2a**, **2b** and **2c** in acetonitrile at 298 K.

are considered to be metal-to-ligand charge-transfer (MLCT) transitions. The lowest energy band is assigned to the $d\pi(Ru^{II}) \rightarrow \pi^{*}(L)$ transition. This explains the observed shifts in this transition with the change in the bridging ligand in the complexes.

Since isomeric coordination compounds have also been distinguished from their emission behaviour, an attempt has been made to study the emission properties of both the mononuclear and dinuclear complexes. Thus, based on the elemental analysis and spectroscopic data, the structures of the complexes are shown in Fig. 4.

3.4.2. Luminescence

The emission spectra of the complexes, excited at λ_{ex} 450 nm and recorded in 10^{-4} M acetonitrile solution, are shown in Fig. 5. From the emission spectra, it is noticed that a dual emission arises at 518 and 606 nm from complex **1b**, whereas complex **2b** emits at 518 and 635 nm. Other isomers show a single emission, except

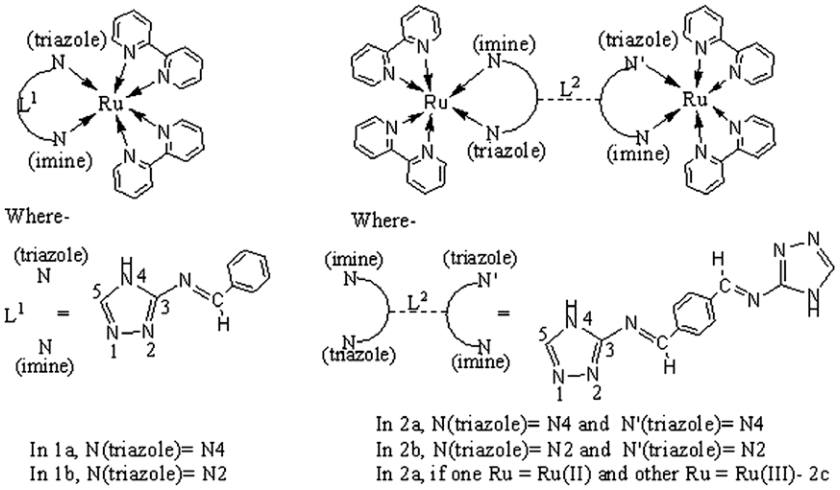


Fig. 4. Proposed structure of the complexes.

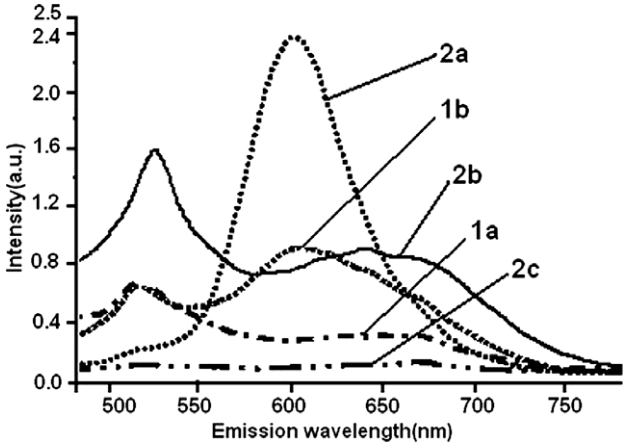


Fig. 5. Emission spectra of the complexes, λ_{ex} = 450 nm, in acetonitrile at 298 K.

complex **2c** which does not emit. Although dual emission is very rare, it has been reported earlier [16,17] in the region 518 and 625 nm, especially arising from triazole complexes with the ruthenium metal ion.

4. Conclusion

Triazolyl Schiff bases, upon their reaction with Ru(II)-2,2′-bipyridyl, provide isomeric metal complexes which are separated by column chromatography. These isomers are characterized by their spectroscopic properties. Dual emissions from metal complexes are rarely observed but the **1b** and **2b** isomers in the present system show dual emissions even at room temperature.

Acknowledgements

Authors are grateful to the authorities of CSIR, New Delhi, India, for the financial support and to Professor J.G. Vos Dublin City University, Ireland for reading the manuscript and giving useful suggestions in its preliminary stage of preparation.

Appendix A. Supplementary data

Cyclic voltametric measurements of the complexes in acetonitrile (5×10^{-4} M) containing tetrabutylammonium perchlorate as the supporting electrolyte were carried out using a CHI620c electrochemical analyzer. A glassy carbon working electrode, a platinum wire auxiliary electrode and an Ag/AgCl reference electrode were used in a three electrode configuration. The cyclic voltammograms thus obtained are shown as supporting informations (S1). Supplementary data associated with this article can be found, in the online version, at doi:10.1016/j.poly.2008.09.012.

References

[1] (a) V. Balzani, A. Juris, M. Venturi, S. Campagna, S. Serroni, Acc. Chem. Res. 31 (1998) 26;
(b) A. Slate, D.R. Striplin, J.A. Moss, P. Chen, B.W. Erickson, T.J. Meyer, J. Am. Chem. Soc. 120 (1998) 4885;
(c) Y.Z. Hu, S. Tsukiji, S. Shinkai, S. Oishiand, I. Hamachi, J. Am. Chem. Soc. 122 (2000) 241;
(d) V. Balzani, A. Juris, M. Venturi, S. Campagna, S. Serroni, Chem. Rev. 96 (1996) 759.
[2] (a) A. Juris, V. Balzani, F. Barigelletti, S. Campagna, P. Belser, A. von Zelewsky, Coord. Chem. Rev. 84 (1988) 85;
(b) T.J. Meyer, Acc. Chem. Res. 22 (1989) 163;
(c) L.D. Cola, P. Belser, Coord. Chem. Rev. 177 (1998) 301.
[3] V. Balzani (Ed.), Supramolecular Photochemistry, Reidel, Dordrecht, 1997.
[4] L. Mishra, A.K. Yadav, Indian J. Chem. A 42 (2003) 1797.
[5] (a) R. Hage, R. Prins, J.G. Haasnoot, J. Reedijk, J.G. Vos, J. Chem. Soc., Dalton Trans. (1987) 1389;
(b) H.A. Nieuwenhuis, J.G. Haasnoot, R. Hage, J. Reedijk, T.L. Snoeck, D.J. Stufkens, J.G. Vos, Inorg. Chem. 30 (1990) 48;
(c) B.E. Buchanan, R. Wang, J.G. Vos, R. Hage, J.G. Haasnoot, J. Reedijk, Inorg. Chem. 29 (1990) 3263;
(d) W.R. Browne, C.M. O'Connor, C. Villani, J.G. Vos, Inorg. Chem. 40 (2001) 5461.
[6] (a) R. Hage, A.H.J. Dijkhuis, J.G. Haasnoot, R. Prins, J. Reedijk, B.E. Buchanan, J.G. Vos, Inorg. Chem. 27 (1988) 2185;
(b) F. Barigelletti, L.D. Cola, V. Balzani, R. Hage, J.G. Haasnoot, J.G. Vos, Inorg. Chem. 28 (1989) 4344.
[7] R. Hage, J.G. Haasnoot, H.A. Nieuwenhuis, J. Reedijk, D.J.A. De Ridder, J.G. Vos, J. Am. Chem. Soc. 112 (1990) 9249.
[8] L. Mishra, K. Bindu, S. Bhattacharya, Inorg. Chem. Commun. 7 (2004) 777.
[9] W.R. Browne, C.M. O'Connor, H.P. Hughes, R. Hage, O. Walter, M.F. Doering, J.F. Gallagher, J.G. Vos, J. Chem. Soc., Dalton Trans. (2002) 4048.
[10] (a) H.A. Nieuwenhuis, J.G. Haasnoot, R. Hage, J. Reedijk, T.L. Snoeck, D.J. Stufkens, J.G. Vos, Inorg. Chem. 30 (1991) 48;
(b) S. Fanni, T.E. Keyes, C.M. O'Connor, H. Hughes, R. Wang, J.G. Vos, Coord. Chem. Rev. 208 (2000) 77;
(c) S. Fanni, C.D. Pietro, S. Serroni, S. Campagna, J.G. Vos, Inorg. Chem. Commun. 3 (2000) 42.
[11] L. Mishra, A.K. Yadaw, Transition Met. Chem. 25 (2000) 579.
[12] B.P. Sullivan, D.J. Salmon, T.J. Meyer, Inorg. Chem. 17 (1978) 3334.
[13] V. Krisnakumar, R.J. Xavier, Spectrochim. Acta, Part A 60 (2004) 709. and references cited therein.
[14] Kazuo. Nakamoto, Infrared and Raman Spectra of Inorganic and coordination Compounds, third ed., John Wiley & Sons, New York, 1978. 374.
[15] T.E. Keyes, C. O'Conner, J.G. Vos, Chem. Commun. (1998) 889.
[16] R.L. Blakley, M.K. DeArmond, J. Am. Chem. Soc. 109 (1987) 4895.
[17] S. Chakraborty, R.H. Laye, P. Munshi, R.L. Paul, M.D. Ward, G.K. Lahiri, J. Chem. Soc., Dalton Trans. (2002) 2348.

Polyhedron 28 (2009) 126–130

Contents lists available at ScienceDirect

Polyhedron

journal homepage: www.elsevier.com/locate/poly

Synthesis of oleylamine capped copper nanocrystals via thermal reduction of a new precursor

Masoud Salavati-Niasari [a,b,*], Zeinab Fereshteh [a], Fatemeh Davar [b]

[a] Institute of Nano Science and Nano Technology, University of Kashan, Kashan, P.O. Box 87317-51167, Islamic Republic of Iran
[b] Department of Chemistry, Faculty of Science, University of Kashan, Kashan, P.O. Box 87317-51167, Islamic Republic of Iran

ARTICLE INFO

Article history:
Received 5 August 2008
Accepted 18 September 2008
Available online 10 November 2008

Keywords:
Nanocrystalline materials
Copper
Capping agent
Thermal reduction

ABSTRACT

The present investigation reports the novel synthesis of copper nanocrystals using thermal reduction, and their physicochemical characterization. The copper nanocrystal powder has been prepared using [bis(2-hydroxyacetophenato)copper(II)] as a precursor. The effect of oleylamine and triphenylphosphine on the particle morphology has been investigated. Transmission electron microscopy (TEM) analysis has demonstrated that the copper nanocrystals have an average diameter of about 3 nm. The as-prepared copper nanocrystals were characterized by XRD, SEM, TEM, EDX, UV–Vis and FTIR.

© 2008 Elsevier Ltd. All rights reserved.

1. Introduction

Synthesis of metal nanoparticles other than those of silver and gold is often difficult due to the possibility of surface oxidation of the metal particles. Surface oxidation can be prevented by protecting the outer surface by the use of a suitable surfactant. The surfactant can also control the nucleation of particles and act as a particle growth terminator. Thus the surfactant has a dual role, i.e., to prevent surface oxidation of the particles and to control the growth of the particles. The study of nanoparticles of metals has been an extremely active area of research in recent years because of their unusual properties which are different from those of bulk materials. Since heterogeneous catalysis is a surface phenomenon and the surface to volume ratio increases with decreasing particle diameter, nanoparticles are vital for high catalytic activity. Copper metal has great significance in all industries, particularly in the electrical sector due to low cost. Copper nanoparticles have potential applications as fillers in polymers, as lubricants and they are used as ink and metallic coating [1,2]. For their application in electronics, the stability of the nanoparticles and their reactivity are two important factors. In addition, colloidal copper is also useful as an antibacterial agent.

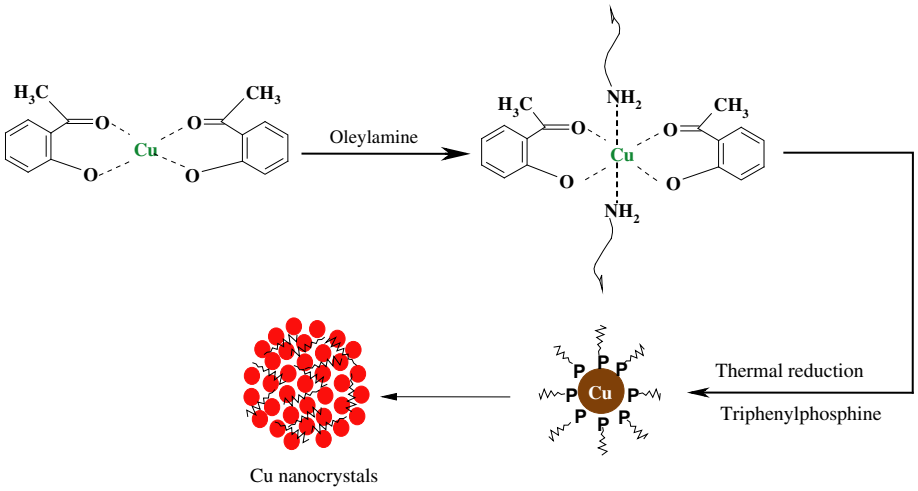
Cu nanoparticles have been synthesized through different methods such as thermal decomposition [3–6], metal salt reduction [7], microwave heating [8], radiation methods [9], micro emulsion techniques [10], laser ablation [11], the polyol method [12], the solvothermal method [13], thermal and sonochemical reduction [14].

Among the various techniques developed for the synthesis of copper and copper oxide nanoparticles, thermal decomposition is a novel method to produce stable monodispersed species [15] and it is a rapidly developing research area. As compared to conventional methods, it is much faster, cleaner and economical. However, improvement in the thermal reduction process should be made in preparing copper nanoparticles with controllable size and shape in order to extend the application areas and to satisfy the needs of fundamental research.

The current synthetic procedure is a modified version of the method developed by the Hyeon group for the synthesis of various nanoparticles of metals and oxides, which employs the thermal decomposition of metal–surfactant complexes in hot surfactant solution [16]. More recently, our group reported the synthesis of metal oxide nanoparticles via thermal decomposition [17,18]. Fischer and coworkers synthesized monodisperse copper nanoparticles from the thermal decomposition of $Cu(OCH(Me)CH_2NMe_2)_2$ [19]. Hyeon and co-workers have reported the synthesis of copper nanoparticles by thermal decomposition of $[Cu(acac)_2]$ (acac = acetylacetonate) in oleylamine [20]. A major interest at the moment is in the development of organometallic or inorganic compound for preparation of nanoparticles. Using novel compounds opens a new way for preparing nanomaterials whilst controlling the nanocrystal size, shape and distribution size. We synthesized Cu nanoparticles by the thermal decomposition of the new precursor copper 2-hydroxyacetophenato in oleylamine (Scheme 1). In this process, oleylamine was used as both the medium and the

* Corresponding author. Address: Institute of Nano Science and Nano Technology, University of Kashan, Kashan, P.O. Box 87317-51167, Islamic Republic of Iran. Tel.: +98 361 5555333; fax: +98 361 5552935.
E-mail address: salavati@kashanu.ac.ir (M. Salavati-Niasari).

0277-5387/$ - see front matter © 2008 Elsevier Ltd. All rights reserved.
doi:10.1016/j.poly.2008.09.027



Scheme 1. Schematic depiction of the selective formation of Cu nanocrystals.

stabilizing reagent. To the best of our knowledge, this is the first report on the synthesis of Cu nanoparticles from [Cu(aceto)$_2$] (aceto = 2-hydroxyacetophenato). The aim of the present work is to prepare copper nanocrystals using the thermal reduction method, and their physicochemical characterization.

2. Experimental

2.1. Materials

The precursor complex, [bis(2-hydoxyacetophenato)copper(II)], was prepared according to the procedure described previously [21]. Oleylamine, triphenylphosphine (TPP), toluene, hexane and ethanol were purchased from Aldrich and were used as received.

2.2. Characterization

XRD patterns were recorded on a Rigaku D-max C III, X-ray diffractometer using Ni-filtered Cu Kα radiation. Elemental analyses were obtained on a Carlo ERBA Model EA 1108 analyzer. Scanning electron microscopy (SEM) images were obtained on a Philips XL-30ESEM equipped with an energy dispersive X-ray spectroscope. Transmission electron microscopy (TEM) images were obtained on a Philips EM208 transmission electron microscope with an accelerating voltage of 200 kV. The compositional analysis was done by energy dispersive X-ray (EDX, Kevex, Delta ClassI). Thermogravimetric–differential thermal analyses (TG–DTA) were carried out using a thermal gravimetric analysis instrument (Shimadzu TGA-50H) with a flow rate of 20.0 mL min^{-1} and a heating rate of 10 °C min^{-1}. X-ray photoelectron spectroscopy (XPS) measurements of the as-prepared products were measured on an ESCA-3000 electron spectrometer with a non-monochromatized Mg Kα X-ray excitation source. Fourier transform infrared (FT-IR) spectra were recorded on a Shimadzu Varian 4300 spectrophotometer in KBr pellets. The electronic spectra of the complexes were taken on a Shimadzu UV–Vis scanning spectrometer (Model 2101 PC).

2.3. Synthesis of the Cu nanocrystals

In this synthesis, Cu nanocrystals were prepared by the thermal reduction of the [Cu(aceto)$_2$]–oleylamine complex as a precursor. The [Cu(aceto)$_2$]–oleylamine complex was prepared by the reaction of 0.5 g of [Cu(aceto)$_2$] with 5 mL of oleylamine. The mixed solution was placed in a 50 mL three-neck distillation flask and heated to 140 °C for 60 min under an argon atmosphere. The resulting metal-complex solution was injected into 5 g of triphenylphosphine, TPP, at 245 °C. As the thermal reduction proceeded, the dark green solution turned to red, indicating the formation of metallic copper. The reddish solution was aged at 245 °C for 35 min, and then cooled to room temperature. The reddish nanoparticles were precipitated by adding excess ethanol to the solution. The final product was washed with ethanol at least three times to remove impurities, if any, and dried at 100 °C. This product could easily be re-dispersed in non-polar organic solvents, such as hexane or toluene (Scheme 1).

3. Results and discussion

The thermal behaviour of the as-prepared precursor was investigated by thermal gravimetric analysis (TGA). Fig. 1 shows that [Cu(aceto)$_2$] starts to decompose at 195 °C and the weight loss occurs in the temperature range 195–330 °C. The weight loss may be ascribed to the decomposition of [Cu(aceto)$_2$]. The weight loss is about 25.58%, which is close to the theoretical value.

The X-ray powder diffraction (XRD) pattern of the Cu nanocrystals at room temperature is shown in Fig. 2. The XRD pattern is consistent with the spectrum of copper, and no peak attributable to possible impurities is observed. The peaks are very sharp due to the high nanocrystalline nature of copper. The peak positions are consistent with metallic copper. All possible peaks of copper

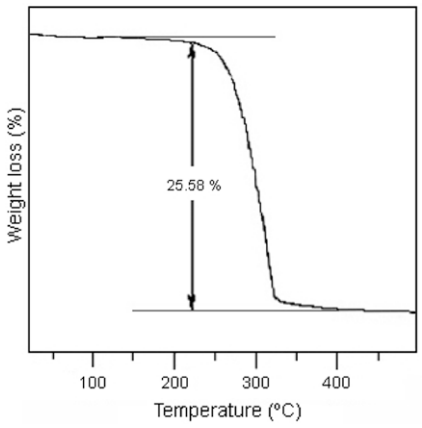


Fig. 1. TGA of the copper oxalate precursor, [Cu(aceto)$_2$].

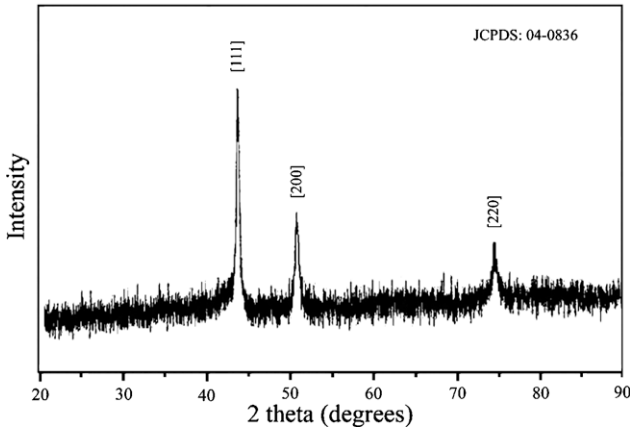


Fig. 2. XRD pattern of the copper nanoparticles.

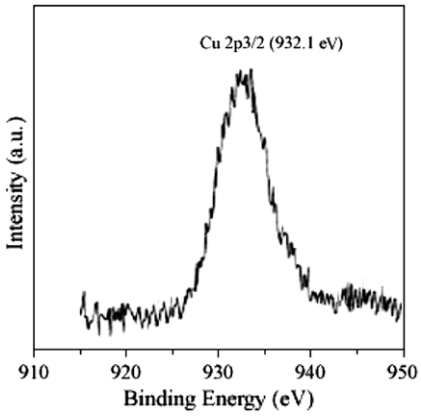


Fig. 4. XPS spectrum of the Cu nanocrystals.

are observed, which indicates the polycrystalline nature of the product. Bragg's reflections for the Cu nanocrystals are observed in the XRD pattern at 2θ values of 43.4°, 50.5° and 74.2°, representing [1 1 1], [2 0 0] and [2 2 0] planes of the *fcc* structure of copper with the space group *Fm3m* (JCPDS No. 04–0836). The size of the nanoparticles was estimated from the full width at half maxima (FWHM) of the [1 1 1] diffraction peak on the basis of the Scherrer formula: $D = 0.9\lambda/\beta\cos\theta$, and this gives a value of about 2 nm for the nanoparticles synthesized. Fig. 3 shows the EDX spectrum of the copper nanoparticles excited by an electron beam (24 kV). Peaks for the elements Cu, C and O were observed at 0.5469 (O_{ka}), 0.9698 (Cu_{La}), 0.9678 (Cu_{Lb}), 8.0977 (Cu_{ka}), 8.9050 (Cu_{kb}) and 0.2874 (C_{ka}).There is no impurity atom in the nanoparticles except oleylamine capped copper. Accordingly, from the EDX spectrum we could confirm that the nanoparticles in the TEM images are pure copper [22,23].

Surface information of the freshly obtained sample as shown in Fig. 4 can be properly provided by XPS analysis. The binding energies obtained in the XPS analysis were corrected with reference to C1s (284.6 eV). The spectrum of Cu 2p, Fig. 4, illustrates that the observed value of the binding energy for Cu $2p^{3/2}$ (932.1 eV) is consistent with the reported data for Cu^0 [24].

FT-IR spectroscopy is a useful tool to understand the functional group of any organic molecule (Fig. 5a and b). The presence of the oleylamine group on the Cu nanocrystals (Fig. 5b) is indicated by the N–H wagging mode from 650 to 900 cm^{-1}, NH_2 bending modes at 909, 964 and 993 cm^{-1}, and NH_2 scissor mode at 1568 cm^{-1} [25]. The spectrum, shown in Fig. 5b, also reveals the characteristic peak of the C–N stretch at 1042 cm^{-1} which suggests that the C–N bonds in the amine groups, and therefore the oleylamine ligands, remain intact, capping the Cu nanocrystals. The peak at 1468 cm^{-1} is associated with the C–H bending mode and the three peaks at 2865, 2921 and 2955 cm^{-1} represent the C–H stretching

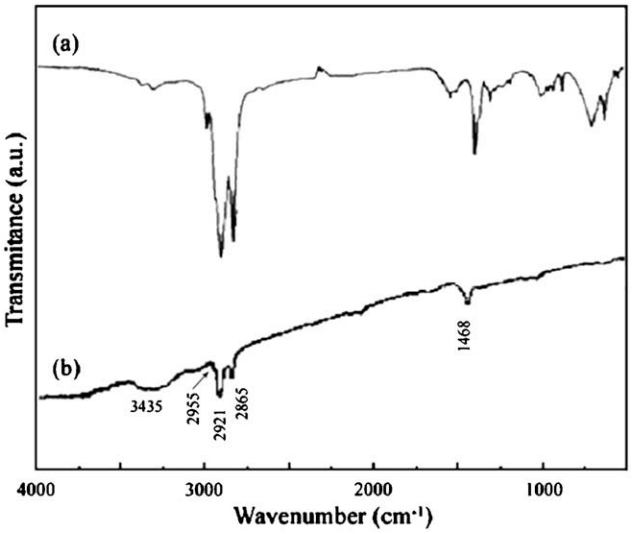


Fig. 5. FTIR spectra of (a) oleylamine and (b) Cu nanocrystals.

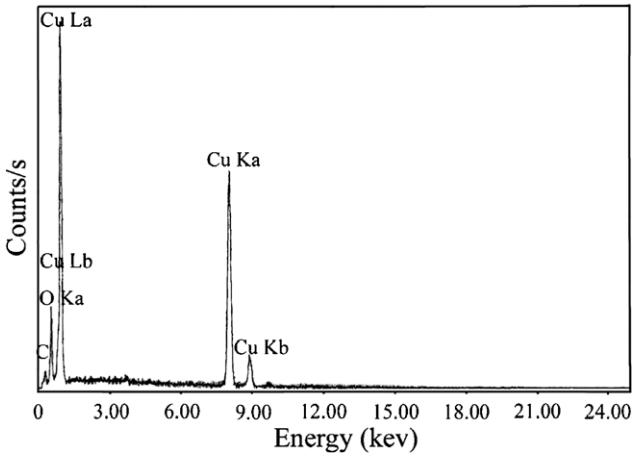


Fig. 3. EDX spectrum of the copper nanocrystals.

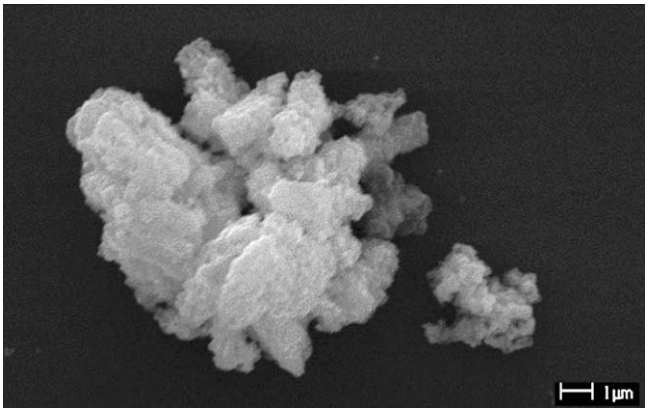


Fig. 6. SEM image of the Cu nanocrystals.

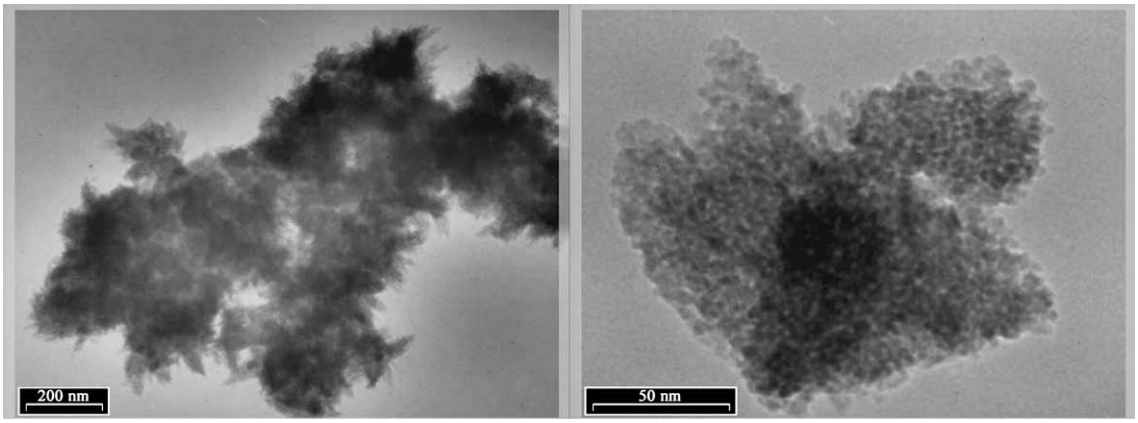


Fig. 7. TEM image of the Cu nanocrystals.

modes of the oleylamine carbon chain. The presence of various N–H peaks suggests that the amines are bound to the surface of the Cu nanocrystals. Based on the FTIR data, we deduce the following reaction mechanism. Upon injection of [Cu(aceto)$_2$] and oleylamine into hot TPP solution, the Cu–O bond is cleaved by the oleylamine group and Cu is subsequently reduced. The weak peak at 3435 cm^{-1} has been assigned to the EtOH used in the separation step. There was no evidence of the free precursor, copper 2-hydroxyacetophenato, in the sample, because the stretch vibration of C=O ($\upsilon_{C=O}$) and C–O (υ_{C-O}) disappeared. So the oleylamine serves as the capping ligand that controls growth.

The morphology of the product is examined by SEM. Fig. 6 depicts the SEM pictures of a sample of Cu nanoparticles. From the micrograph, it was observed that the nanoparticles are agglomerated. The transmission electron microscopic (TEM) photographs of the product are given in Fig. 7. The size of the nanocrystals obtained from the XRD diffraction patterns are in close agreement with the TEM studies which show sizes of 2–4 nm (Fig. 7). These sizes are nearly spherical. Some loose spheres formed by aggregation of small particles can be observed in the TEM images. We may consider that when the reaction was carried out at 245 °C, most organic molecules decomposed. Since only a few oleylamine molecules were adsorbed on the Cu nanocrystals, a loose solid flower-like morphology was finally produced.

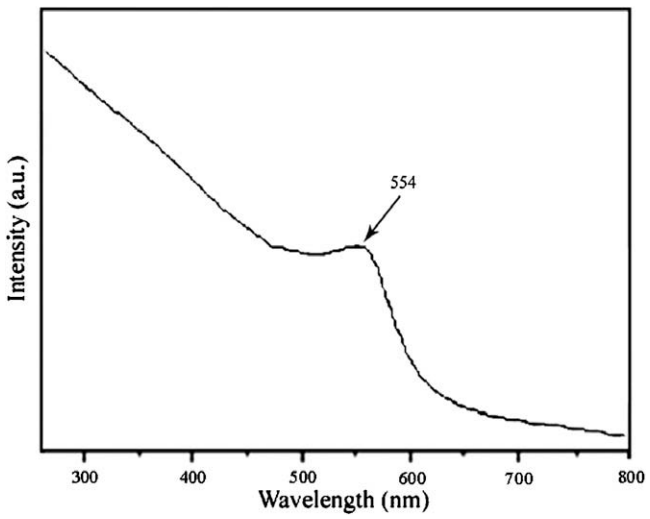


Fig. 8. The UV–Vis absorption spectrum of the Cu nanocrystals.

Since the surface areas of metal nanocrystals are enormously relative to their masses, they have an excess free energy surface comparable to the lattice energy, making them thermodynamically unstable. Protective agents are therefore essential in order to be able to outweigh the attractive van der Waals forces by repulsive steric forces. To achieve sufficient inter-particle separation, it can be helpful to use sterically demanding substituents [26]. In this work we have used TPP as a ligand stabilizing agent to make the nanocrystals stable and prevent their agglomeration. TPP is a high-boiling point surfactant with a patulous long-chain structure providing great steric hindrance. So, this agent might slow down the addition rate of materials to the nanoparticles during their growth, resulting in much smaller nanocrystals. Also we have used oleylamine as an additional surfactant in order to reduce the particle size much further and this resulted in uniform size (Fig. 7). Oleylamine has been known as a ligand that binds tightly to metal nanoparticle surfaces. The combined effects of TPP and oleylamine were much more profound than those of the individual contributions.

Nanosized particles exhibit unique optical properties with an exponential-decay Mie scattering profile with decreasing photon energy. Some transition metal nanoparticles show a distinct surface-plasmon resonance (SPR). The SPR is very sensitive to the metal size, dielectric constant of the metal and embedding medium (here it is oleylamine) [27,14]. For instance, Cu nanoparticles typically exhibit SPR at around 600 nm [28], however the fresh Cu nanocrystals synthesized here show an absorption peak at around 554 nm (2.24 eV) (Fig. 8). This peak can be assigned to the absorption of nanoparticles of copper [28]. A modest blue shift (about 46 nm) of the absorption edge relative to that of bulk copper powder is observed. This observation alludes to the size effect to the Cu nanoparticles. The synthesized particles were stable for ~12 days. This kind of stabilization of Cu nanocrystals is due to the capping of particles by oleylamine on thermal treatment. The arrangement of the capping agent, oleylamine, surrounding the nanoparticles is size dependent.

4. Conclusion

In summary, we have shown that a new simple, low cost thermal reduction precursor is particularly suited for the synthesis of copper nanocrystals. Because of the simplicity of the method, many opportunities may exist to further control the size and shape of the Cu nanoparticles. Furthermore, we suggest as a general principle that other organometallic decomposition precursors may be very good choices for the synthesis of nanometals.

Acknowledgement

Authors are grateful to council of University of Kashan for providing financial support to undertake this work.

References

[1] J.G. Yang, Y.L. Zhou, T. Okamoto, T. Bessho, S. Satake, R. Ichino, M. Okido, Chem. Lett. 35 (2006) 1190.
[2] S. Panigrahi, S. Kundu, S.K. Ghosh, S. Nath, S. Praharaj, S. Basu, T. Pal, Polyhedron 25 (2006) 1263.
[3] X. Liu, B. Geng, Q. Dua, J. Ma, X. Liu, Mater. Sci. Eng. A 448 (2007) 7.
[4] Y.H. Kim, D.K. Lee, B.G. Jo, J.H. Jeong, Y.S. Kang, Colloid Surf. A: Physicochem. Eng. Aspect 284–285 (2006) 364.
[5] A.G. Nasibulin, P.P. Ahonen, O. Richard, E.I. Kauppinen, I.S. Altman, J. Nanoparticle Res. 3 (2001) 383.
[6] L. Daroczi, M.T. Beck, D.L. Beke, M. Kis-Varga, L. Harasztosi, N. Takacs, Mater. Sci. Forum. 319 (1998) 269.
[7] S. Chen, J.M. Sommers, J. Phys. Chem. B 105 (2001) 8816.
[8] H. Zhu, C. Zhang, Y. Yin, Nanotechnology 16 (2005) 3079.
[9] S.S. Joshi, S.F. Patil, V. Iyer, S. Mahumuni, Nanostruct. Mater. 10 (1998) 1135.
[10] M.P. Pileni, B.W. Ninham, T. Gulik-Krzywicki, J. Tanori, I. Lisiecki, A. Filankembo, Adv. Mater. 11 (1999) 1358.
[11] R.G. Song, M. Yamaguchi, O. Nishimura, M. Suzuki, Appl. Surf. Sci. 253 (2007) 3093.
[12] B.K. Park, S. Jeong, D. Kim, J. Moon, S. Lim, J.S. Kim, J. Colloid Interface Sci. 311 (2007) 417.
[13] T. Xin-ling, R. Ling, S. Ling-na, I. Wei-guo, C. Min-hua, H. Chang-wen, Chem. Res. Chin. U 22 (2006) 547.
[14] N.A. Dash, C.P. Raj, A. Gedanken, Chem. Mater. 10 (1998) 1446.
[15] M. Yin, C.-K. Wu, Y. Lou, C. Burda, J.T. Koberstein, Y. Zhu, S. O'Brien, J. Am. Chem. Soc. 127 (2005) 9506.
[16] T. Hyeon, S.S. Lee, J. Park, Y. Chung, H.B. Na, J. Am. Chem. Soc. 123 (2001) 12798.
[17] M. Salavati-Niasari, F. Davar, M. Mazaheri, M. Shaterian, J. Magn. Magn. Mater. 320 (2008) 575.
[18] M. Salavati-Niasari, F. Davar, M. Mazaheri, Mater. Lett. 62 (2008) 1890.
[19] J. Hambrock, R. Becker, A. Birkner, J. Wei, R.A. Fischer, Chem. Commun. (2002) 68.
[20] S.U. Son, I.K. Park, J. Park, T. Hyeon, Chem. Commun. (2004) 778.
[21] M. Salavati-Niasari, M. Shaterian, M.R. Ganjali, P. Norouzi, J. Mol. Catal. A: Chem. 261 (2007) 147.
[22] E.N. Kang, J.N. Park, Y.S. Hwang, M.S. Kang, J.G. Park, T.H. Hyeon, J. Phys. Chem. B 108 (2004) 13932.
[23] D.K. Lee, Y.H. Kim, Y.S. Kang, P. Stroeve, J. Phys. Chem. B 109 (2005) 14939.
[24] W.-T. Yao, S.-H. Yu, Y. Zhou, J. Jiang, Q.-S. Wu, L. Zhang, J. Jiang, J. Phys. Chem. B 109 (2005) 14011.
[25] C. Mui, J. Han, G. Wang, C. Musgrave, S. Bent, J. Am. Chem. Soc. 124 (2002) 4027.
[26] B. Corain, G. Schmid, N. Toshima (Eds.), Metal Nanoclusters in Catalysis and Materials Science: The Issue of Size Control, Elsevier Publishers, Oxford, 2008, p. 21.
[27] S. Chen, J.M. Sommers, J. Phys. Chem. B 105 (2001) 8816.
[28] J.A. Creighton, D.G. Eadon, J. Chem. Soc., Faraday Trans. 87 (1991) 3881.

Polyhedron 28 (2009) 131–137

Contents lists available at ScienceDirect

Polyhedron

journal homepage: www.elsevier.com/locate/poly

Synthesis, spectral, thermal and structural study of bis(2-bromobenzoato-*O,O′*)-bis(methyl-3-pyridylcarbamate-*N*)-zinc(II)

Annamária Erdélyiová [a,*], Katarína Győryová [a], Róbert Gyepes [b], Ladislav Halás [a], Jana Kovářová [c]

[a] Department of Inorganic Chemistry, P. J. Šafárik University, Moyzesova 11, 041 54 Košice, Slovak Republic
[b] Department of Inorganic Chemistry, Charles University, Albertov 8, 128 43 Praha 2, Czech Republic
[c] Institute of Macromolecular Chemistry, AV ČR, Heyrovského nám. 2, 162 06 Praha 6, Czech Republic

ARTICLE INFO

Article history:
Received 29 May 2008
Accepted 17 September 2008
Available online 5 November 2008

Keywords:
Zinc
Methyl-3-pyridylcarbamate
Spectral, thermal and structural study
DFT calculations

ABSTRACT

The new complex bis(2-bromobenzoato-*O,O′*)-bis(methyl-3-pyridylcarbamate-*N*)-zinc(II), [Zn(2-$BrC_6H_4COO)_2mpc_2$] (**1**), has been prepared and characterized by elemental analysis, IR spectroscopy, thermal analysis and single-crystal X-ray diffraction. The bonding between the ligands and the central atom was investigated by DFT studies. The theoretical infrared spectrum of **1** was compared with the experimental data. The complex proved to be thermally stable up to 165 °C. Volatile intermediate products of its thermal decomposition were identified by mass spectrometry. The coordination environment of the zinc atom consists of two nitrogen atoms of two methyl-3-pyridylcarbamate ligands and is chelated by four oxygen atoms of two 2-bromobenzoate ligands (ZnO_4N_2 – chromophore).

© 2008 Elsevier Ltd. All rights reserved.

1. Introduction

Several aromatic carboxylic acids (e.g. benzoic acid, salicylic acid) are known to have antibacterial and antifungal properties [1,2]. For metal carboxylate complexes it has been found that their antibacterial activity is higher than that of the parent carboxylic acid [3].

Our interest is aimed at studying compounds of halogenobenzoic acids with zinc, which can have a considerable effect on many biological processes. Zinc(II) complexes with organic ligands have proved to be useful in clinical medicine, e.g. for acne therapy [4]. Moreover, organic ligands can contribute to a better transport of metal ions through the lipophylic regions of cell membranes [5]. In addition, heterocyclic compounds play a significant role in many biological systems, e.g. vitamins. Therefore heterocyclic compounds such as nicotinamide, methyl-3-pyridylcarbamate and theophylline, incorporated in complexes as ligands have been investigated by many authors and their biological activities have been examined [6]. The thermal behaviour of several aliphatic zinc(II) carboxylate complexes with methyl-3-pyridylcarbamate was investigated by Szunyogová et al. [7]. Győryová et al. studied the thermal, spectral and structural properties of aliphatic zinc(II) carboxylates and halogenocarboxylates [8–11], and zinc(II) halogenosalicylates [12] with different bioactive ligands.

For the preparation of effective antimicrobial species it is important to gain information about the structure of the compound. It has been observed that the antibacterial effect can be enhanced when the ligands are chelated to the metal [13]. Zeleňák et al. [14] investigated Zn(II) benzoate complexes with pyridine based ligands. They found that for the zinc(II) benzoate complex with methyl-3-pyridylcarbamate, the metal atom is tetrahedrally coordinated by two monodentate benzoate and two heterocyclic ligands. Intermolecular hydrogen bonds connect the molecules to form a two-dimensional network. Maroszová et al. [15] studied the structural properties of a zinc(II) 2-chlorobenzoate complex with methyl-3-pyridylcarbamate. They found that the zinc atom is coordinated by two nitrogen atoms from two methyl-3-pyridylcarbamate ligands and four oxygen atoms from two bidentate 2-chlorobenzoate anions in a pseudo-octahedral geometry. The molecules are linked into a chain by hydrogen bonds.

The present work deals with the structural and bonding characterization, thermal and spectral properties of the new monomeric complex [Zn(2-$BrC_6H_4COO)_2mpc_2$].

2. Experimental

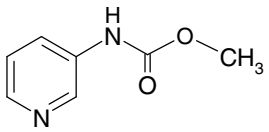
2.1. Materials and instrumentation

The following A. R. grade chemicals were used for the preparation of the studied compound: $ZnCl_2$ (Fluka), Na_2CO_3 (Mikrochem a.s. Pezinok), 2-bromobenzoic acid 97% (Aldrich), methyl-3-pyridylcarbamate (Merck) (Scheme 1).

The carbon, hydrogen and nitrogen content in the newly synthesised compound was determined on a CHN analyser PERKIN EL-

* Corresponding author. Tel.: +421 55 234 2345.
E-mail address: annamaria.erdelyiova@student.upjs.sk (A. Erdélyiová).

0277-5387/$ - see front matter © 2008 Elsevier Ltd. All rights reserved.
doi:10.1016/j.poly.2008.09.017



Scheme 1. Methyl-3-pyridylcarbamate (mpc).

MER 2400. The zinc content was determined by complexometry using Complexone III as an agent and Eriochrome black T as an indicator. The IR spectrum of the prepared zinc complex compound was recorded on an AVATAR 330 FT-IR Thermo Nicolet spectrometer using KBr pellets (2 mg/200 mg KBr), operating in the range 4000–400 cm^{-1}. The thermal measurements were carried out in air using ceramic crucibles under dynamic conditions on a NETZSCH STA 409 PC/PG Thermoanalyzer (heating rate 9 °C min^{-1}) with a sample mass of 24.970 mg, in the temperature range 26–900 °C. A GC/MS Agilent 7890A mass spectrometer (heating rate 30 °C min^{-1} from 100 °C up to 280 °C) was used for determination of volatile intermediate products of the thermal decomposition.

2.2. Synthesis

Compound **1** was synthesised as follows: $ZnCO_3$ was prepared by the reaction of an aqueous solutions of 1.35 g (10 mmol) $ZnCl_2$ and 1.06 g (10 mmol) Na_2CO_3. The freshly prepared aqueous suspension of $ZnCO_3$ was added in excess to the methanol solution of 2.58 g 97% 2-bromobenzoic acid under continual stirring. The reaction mixture was stirred for 1 h at 70 °C. Excess $ZnCO_3$ was filtered off using an S4 frit and the filtrate was left for crystallization at room temperature. After several days a white powdery compound of $[Zn(2\text{-}BrC_6H_4COO)_2]$ was formed (2.46 g, 5 mmol, yield: 83%). Afterwards, 1.61 g (10 mmol) of methyl-3-pyridylcarbamate was dissolved in methanol and added gradually to the methanol solution of zinc(II) 2-bromobenzoate. The reaction mixture was stirred for 2 h at 50 °C and the solution was reduced in volume at 70 °C in a water bath and left to crystallise at room temperature. After a few days colourless crystals of **1** were formed (2.69 g, 3.5 mmol, yield: 70%).

Anal. Calc. for $C_{28}H_{24}O_8N_4Br_2Zn$ (MW: 769.70): C, 43.66; H, 3.14; N, 7.28; Zn, 8.49. Found: C, 43.93; H, 3.13; N, 7.25; Zn, 8.46%.

IR (KBr, cm^{-1}): 3310s [ν(N–H)]; 3098m, 3066m [ν_{ar}(C–H)]; 2951 m [$\nu(C-H)_{-CH_3}$]; 1732 s [ν(C=O)]; 1613s [δ(N–H)]; 1593s, 1491s, 1467m [ν(C=C, C=N)]; 1542s [$\nu_{as}(COO^-)$]; 1437s [$\delta_{as}(C-H)_{-CH_3}$]; 1398s [$\nu_s(COO^-)$]; 1335m [$\delta_s(C-H)_{-CH_3}$]; 1028s, 641m [ν(C–Br)]; 756s [γ(C–H)]; 709m [γ(N–H)]; 695s [$\delta(COO^-)$].

GC/MS (*m*/*z*): 152 [$C_7H_8N_2O_2$], 120 [$C_6H_4N_2O$], 107 [$C_5H_4N_2O$], 92 [$C_5H_4N_2$], 78 [$\cdot C_5H_4N$], 51 [$C_4H_3^+$], 42 [$\cdot NCO$], 32 [CH_3OH], 28 [CO], 27 [HCN].

2.3. X-ray crystallographic study

Diffraction data for a suitable single crystal of **1** were collected on a Nonius Kappa CCD diffractometer (Mo Kα radiation, $\lambda = 0.71073$ Å) and processed by the HKL program package [16]. The phase problem was solved by direct methods (SIR97) [17], and refined by full-matrix least-squares on F^2 (SHELX97) [18]. Hydrogen atoms were refined isotropically, while all the other atoms anisotropically. The hydrogen atom on N17 was located from difference Fourier maps and refined without any constraints. Hydrogen atoms on the aromatic rings were included in ideal positions with C–H bonds fixed to 0.95 Å and U_{iso}(H) assigned to $1.2U_{eq}$ of the adjacent carbon atom; terminal methyl group hydrogen atoms were included in ideal positions with C–H bonds fixed to 0.98 Å and U_{iso}(H) assigned to $1.5U_{eq}$ of the pivot atom (Table 1).

Table 1
Crystal data and structure refinement for **1**

Empirical formula	$C_{28}H_{24}Br_2N_4O_8Zn$
Formula weight	769.70
Temperature (K)	150(2)
Wavelength (Å)	0.71073
Crystal system, space group	orthorhombic, *Pccn* (No. 56)
Unit cell dimensions	
a (Å)	15.8880(4)
b (Å)	13.2252(3)
c (Å)	13.4622(2)
V (Å^3)	2828.70(10)
Z, D_{calc} (Mg/m^3)	4, 1.807
Absorption coefficient (mm^{-1})	3.752
F(000)	1536
Crystal size (mm^3)	0.48 × 0.08 × 0.05
θ Range for data collection	2.00–27.47
Refinement method	full-matrix least-squares on F^2
Data/restraints/parameters	3237/0/200
Final *R* indices [$I > 2\sigma(I)$]	$R_1 = 0.0300$, $wR_2 = 0.0581$
R indices (all data)	$R_1 = 0.0491$, $wR_2 = 0.0640$
Largest difference peak and hole (e Å^{-3})	0.435 and −0.413

2.4. Computational details

DFT studies have been carried out at the fermi cluster at the J. Heyrovský Institute of Physical Chemistry, Academy of Sciences of Czech Republic, using GAUSSIAN 03, Revision E.01 [19]. All calculations used the Becke exchange [20] and the Perdew/Wang 91 correlational [21] functionals. For a proper elucidation of the theoretical infrared spectrum, the solid-state structure has been optimized using the 6-311+G(3d,p) basis set [22] employed for all atoms and an analytical Hessian determined before the first step of the optimization procedure. Numerical integration was done on a pruned grid having 99 radial shells each of 590 angular points. The IR spectrum was computed after the optimization step yielded a proper stationary point where no imaginary frequencies were present. No scaling was employed for the obtained bands. Natural bonding analysis [23] was carried out by the NBO 3.1 [24] program integrated in Gaussian. To remove any side effects of possible near linear dependencies in the basis set due to the incorporation of diffuse functions, the NBO analysis and Mayer bond order [25] determination were carried out employing only the 6-311G(3d,p) basis set on the optimized geometry. Visualization and examination of molecular orbitals was accomplished by MOLDEN [26].

3. Results and discussion

3.1. Synthesis and properties of the prepared compound

Several methods of preparing zinc(II) carboxylate compounds are described in the literature [14,27,28]. Methods involving either the reaction of the sodium salt of the carboxylic acid with zinc sulfate, or the reaction between carboxylic acid and zinc(II) carbonate can be used.

The compound **1** was synthesised according to the following reactions:

$$ZnCl_2 + Na_2CO_3 \rightarrow ZnCO_3 \downarrow + 2NaCl$$

$$ZnCO_3 + 2(2\text{-}BrC_6H_4COOH) \rightarrow [Zn(2\text{-}BrC_6H_4COO)_2] + H_2O + CO_2 \uparrow$$

$$[Zn(2\text{-}BrC_6H_4COO)_2] + 2\ mpc \rightarrow [Zn(2\text{-}BrC_6H_4COO)_2mpc_2]$$

The prepared complex, $[Zn(2\text{-}BrC_6H_4COO)_2mpc_2]$, is colourless, and is stable to light and air at ambient temperature. It exhibits a very good solubility in methanol, acetone and DMSO, and is insoluble in chloroform and water.

3.2. Crystallographic characterization

Compound **1** crystallized with an orthorhombic lattice (space group *Pccn*) and with an exact molecular twofold symmetry, thus only one half of the molecule is located in the asymmetric part of the unit cell. The symmetrically dependent part of the molecule is generated by a twofold rotation around the axis passing through the central atom. The whole molecule is depicted in Fig. 1; selected bond distances and angles are listed in Table 2.

The coordination environment of the zinc atom consists of two nitrogen atoms from the mpc ligand and four oxygen atoms from the two 2-bromobenzoate carboxylate groups, making up an octahedral environment. This octahedron is however significantly distorted. Although the two least-squares planes, both containing one nitrogen and three oxygen atoms (cf. Table 3) do not suffer from large deviances of their constituent atoms, the geometry constrains imposed by the presence of the rather rigid carboxylate group leads to a large deflection of the oxygen atoms from the ideal positions at the octahedron vertices.

The driving force of the solid state packing is the presence of an infinite network of hydrogen bridges, chaining the hydrogen atom of one mpc NH group and one carboxylate oxygen atom from one neighbouring molecule (Table 4, Fig. 2).

Table 2
Selected bond lengths [Å] and angles [°] for **1**

Zn(1)–N(11); Zn(1)–N(11)^{i}	2.1151(19)
Zn(1)–O(9); Zn(1)–O(9)^{i}	2.1389(17)
Zn(1)–O(8); Zn(1)–O(8)^{i}	2.2208(17)
Zn(1)–C(7); Zn(1)–C(7)^{i}	2.508(2)
C(7)–O(8); C(7)^{i}–O(8)^{i}	1.256(3)
C(7)–O(9); C(7)^{i}–O(9)^{i}	1.263(3)
N(11)–Zn(1)–N(11)^{i}	95.37(10)
N(11)–Zn(1)–O(9); N(11)^{i}–Zn(1)–O(9)^{i}	97.89(7)
N(11)^{i}–Zn(1)–O(9); N(11)–Zn(1)–O(9)^{i}	90.98(7)
O(9)–Zn(1)–O(9)^{i}	166.83(9)
N(11)^{i}–Zn(1)–O(8); N(11)–Zn(1)–O(8)^{i}	150.91(7)
N(11)–Zn(1)–O(8); N(11)^{i}–Zn(1)–O(8)^{i}	91.86(7)
O(8)–Zn(1)–O(9); O(8)^{i}–Zn(1)–O(9)^{i}	60.09(6)
O(8)^{i}–Zn(1)–O(9); O(8)–Zn(1)–O(9)^{i}	110.14(6)
O(8)–Zn(1)–O(8)^{i}	95.38(9)
N(11)^{i}–Zn(1)–C(7); N(11)–Zn(1)–C(7)^{i}	121.21(8)
N(11)–Zn(1)–C(7); N(11)^{i}–Zn(1)–C(7)^{i}	93.29(7)
O(9)–Zn(1)–C(7)^{i}	139.99(7)
O(8)–Zn(1)–C(7)^{i}	106.88(7)
C(7)–Zn(1)–C(7)^{i}	129.39(11)

Symmetrically equivalent atoms generated by:
(^{i}): $-x + 1/2, -y + 1/2, z$.

3.3. Spectroscopic and thermal properties

In the case of carboxylate compounds, the values of the asymmetric and symmetric vibrations of COO^{-} are important. In the prepared compound, $[Zn(2\text{-}BrC_6H_4COO)_2mpc_2]$, the stretching vibrations of the aromatic rings of 2-bromobenzoate and the heterocyclic ligand fall in the same region of the spectrum as the stretching vibrations of the carboxylate group, therefore the IR spectrum of $[Zn(2\text{-}BrC_6H_4COO)_2mpc_2]$ has been compared with the spectrum of $[Zn(2\text{-}BrC_6H_4COO)_2]$ and methyl-3-pyridylcarba-

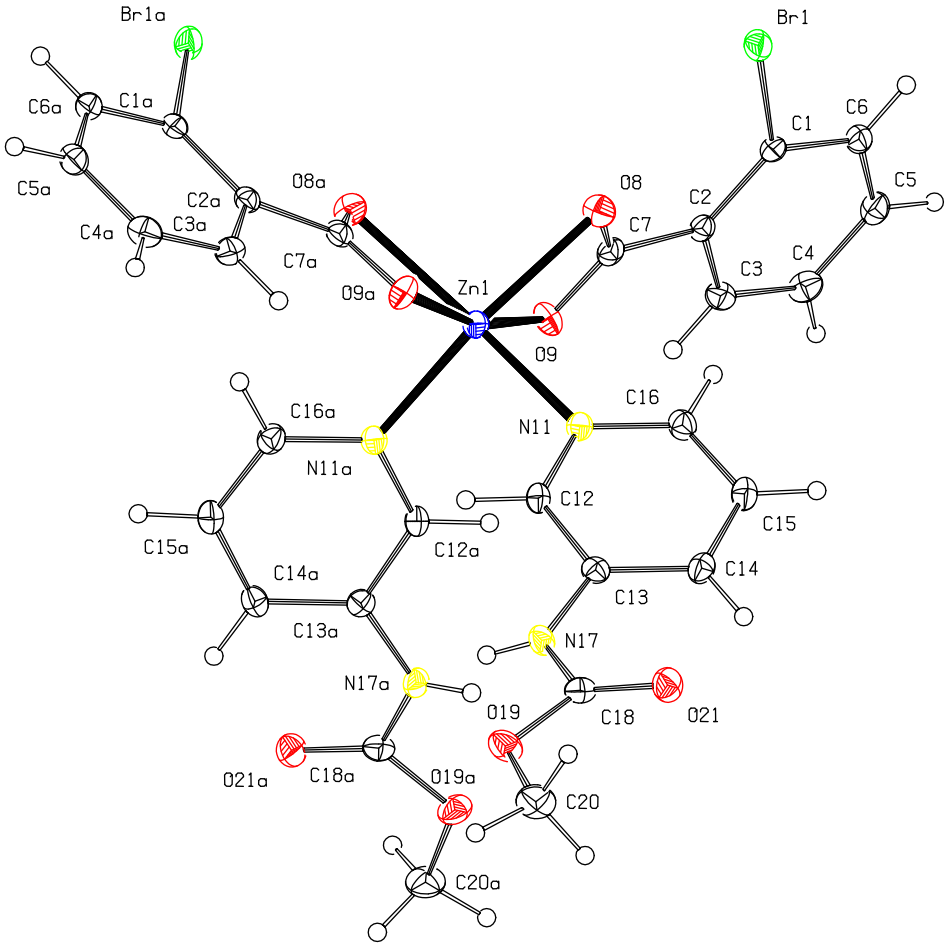


Fig. 1. Solid state structure of **1**. Displacement ellipsoids are drawn at the 30% probability level. Symmetrically dependant atoms are labelled with a terminal 'a'.

Table 3
Least-squares planes and deviations of individual atoms from them

Plane 1		Plane 2	
Atom	Deviation	Atom	Deviation
O9	0.0251(6)	$O9^{i}$	0.0251(6)
N11	−0.0308(7)	$N11^{i}$	−0.0308(7)
$O8^{i}$	−0.0383(10)	O8	0.0383(10)
$O9^{i}$	0.0440(11)	O9	0.0440(11)

The distance of Zn1 from both planes is 0.1379(9) Å, the angle between the two planes is 89.39(4)°.

Table 4
Hydrogen bonds with H···A < r(A) + 2.000 Å and DHA > 110° in solid state

D–H	d(D–H)	d(H···A)	∠DHA	d(D···A)	A
N17–H17	0.774 Å	2.115 Å	150.12°	2.813 Å	O8 [$-x+1/2, y, z-1/2$]

D denotes the donor and A the acceptor atom.

mate. The vibration observed at 1541 cm^{-1} was assigned as $\nu_{as}(COO^{-})$ and that at 1397 cm^{-1} as $\nu_{s}(COO^{-})$.

The strong absorption band of the carbonyl ν(C=O) vibration at 1732 cm^{-1} is slightly shifted to a higher wavenumber as compared with the free methyl-3-pyridylcarbamate (1727 cm^{-1}). This is in agreement with the results of Bellamy and Akbar Ali [29,30]. It can be explained by the fact that the pyridine nitrogen of methyl-3-pyridylcarbamate ligand is involved in coordination with zinc, therefore the electron density in the ligand is shifted towards the pyridine nitrogen, leading to the increase in the double bond character of the carbonyl group and shift the stretching vibration ν(C=O) to a higher value.

The most significant stretching and deformation vibrations are listed in Section 2.

Table 5
Comparison of the experimental and the theoretical values of the IR absorption bands

Assignment	Experimental (KBr) [cm^{-1}]	Theoretical [cm^{-1}]
ν(N–H)	3310s	3530
ν_{ar}(C–H)	3098m, 3066m	3164–3102
(ν(C–H)$_{-CH_3}$)	2951m	2990
ν(C=O)	1732s	1749
ν(C=C, C=N)	1593s, 1491s, 1467m	1596, 1527, 1476
$\nu_{as}(COO^{-})$	1542s	1563
(δ_{as}(C–H)$_{-CH_3}$)	1437s	1456
$\nu_{s}(COO^{-})$	1398s	1376
ν(C–Br)	1028s, 641m	1008, 637
$\delta(COO^{-})$	695s	697

The experimentally obtained and calculated IR spectra of [Zn(2-$BrC_6H_4COO)_2mpc_2$] are in good agreement (Table 5), with the notable exception of the N–H vibration. However, this particular hydrogen atom is part of a hydrogen bridge in the solid state (see above), which leads to a prolongation of the N–H bond. The latter phenomenon could not be reflected by the computational studies as these were performed on one single molecule only.

The results of thermogravimetric analysis are presented in Fig. 3. It was found that the studied complex compound is thermally stable up to 165 °C. Above this temperature the thermal decomposition is accompanied by the loss of methyl-3-pyridylcarbamate and CO_2 (calc. mass loss 51.07%, exp. 51.44%). The released methyl-3-pyridylcarbamate was confirmed by mass spectrometry (Fig. 4). The next step of the thermal decomposition is the release of bromobenzene (calc. mass loss 40.79%, exp. 42.67%). Zinc is the solid product of the thermal decomposition (calc. 8.49%, exp. 7.75%). The following reaction is proposed for the thermal decomposition of the investigated compound:

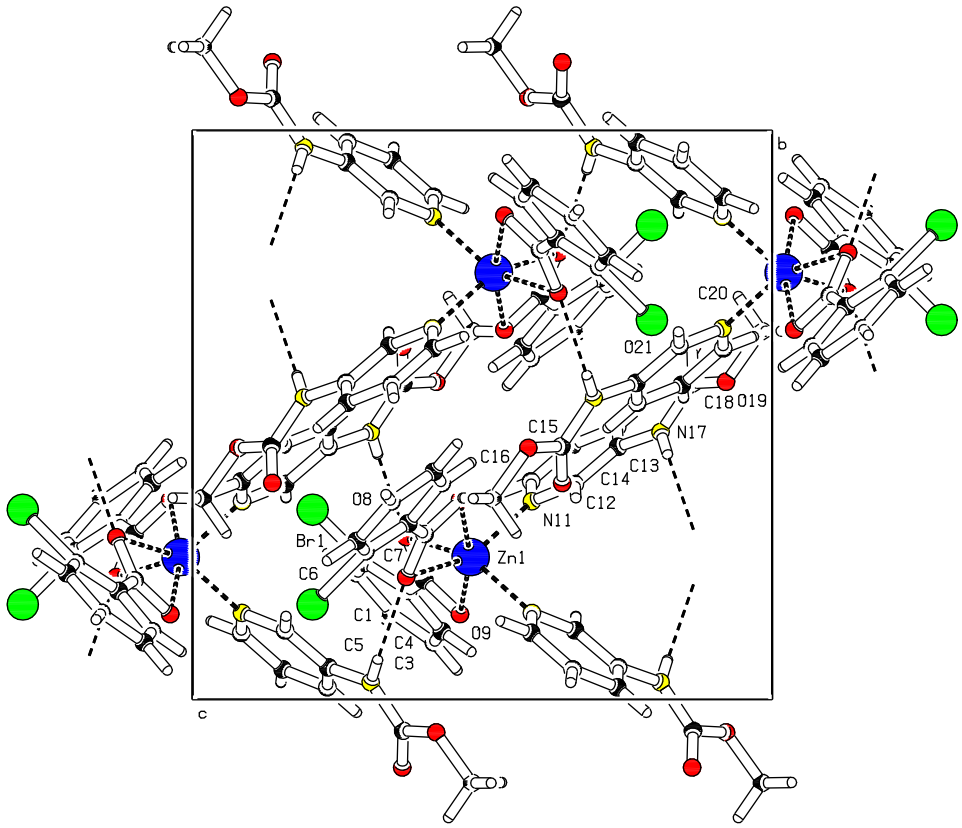


Fig. 2. Solid state packing of **1**. View along [100].

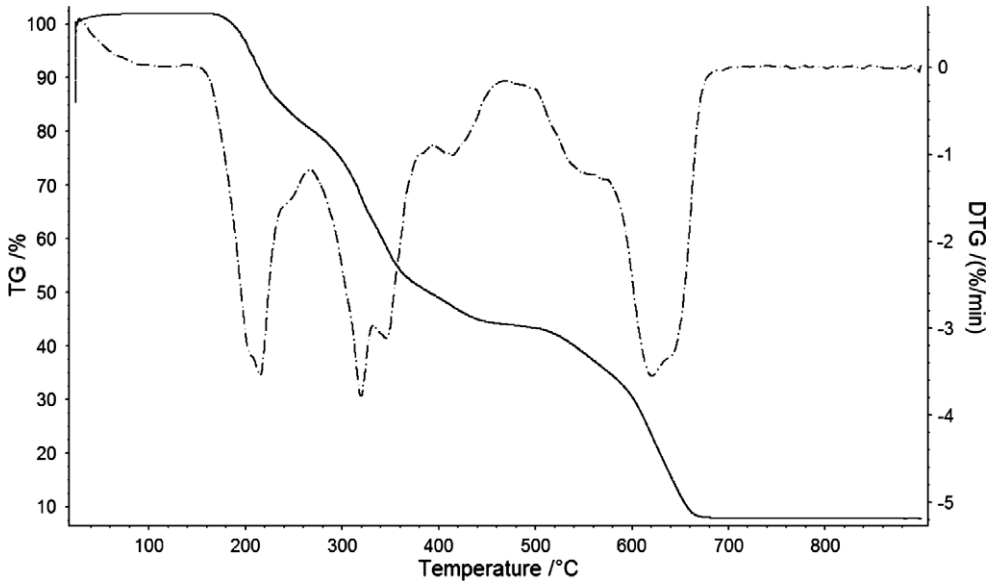


Fig. 3. Thermal decomposition of $[Zn(2\text{-}BrC_6H_4COO)_2mpc_2]$.

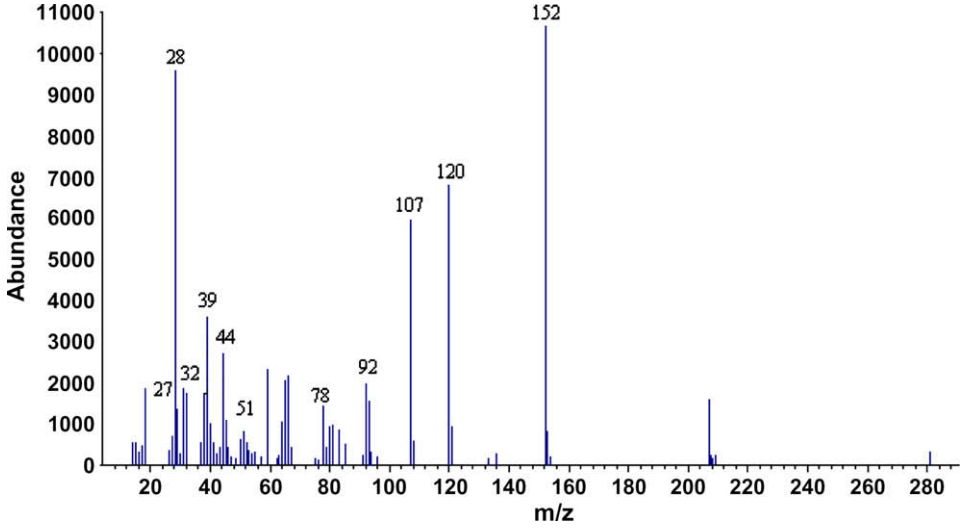
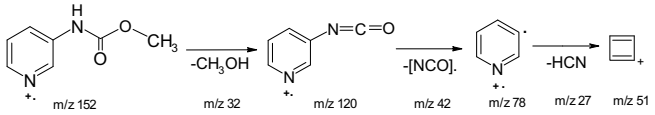


Fig. 4. Mass spectrum of $[Zn(2\text{-}BrC_6H_4COO)_2mpc_2]$ heated up to 280 °C.

$$[Zn(2\text{-}BrC_6H_4COO)_2mpc_2] \rightarrow 2\ mpc + 2\ CO_2 + 2\ C_6H_5Br + Zn$$

Based on the mass spectrum pattern, we propose the following fragmentation scheme for methyl-3-pyridylcarbamate:



This assumption is in a good agreement with the results of pyridine fragmentation proposed by Smith [31].

3.4. Computational studies

The IR spectrum of **1** (discussed above) and the nature of the bonding between the central atom and its ligands was investigated by DFT calculations. As expected for a Zn(II) compound, the calculations suggest a predominantly ionic character of the ligand coordination, with only a slight covalent contribution. The overall low ratio of the covalent contribution from the ligands can be conveniently deduced by examination of the crystal orbital overlap population (COOP) diagram (Fig. 5), depicting the value of the overlap integral between the ligands and the central atom versus orbital energies. In accordance with their lower electronegativity, an increased covalency ratio was observed for the two nitrogen atoms, since the total contribution from the 2-bromobenzoate ligand has to be partitioned among four oxygen atoms.

The apparent proximity of the carboxylate carbon atom and the central zinc atom could suggest a partial (covalent) bonding between them; however, Mayer bond order [25] analysis disproved any such possibility (Table 6). The carboxylate oxygen atoms thus coordinate as separate entities and the coordination environment of the central atom cannot be described as pseudotetrahedral by considering the centre of gravity of the carboxylate group only.

According to the results of natural bonding analysis [23], the electronic configuration of the central zinc atom is [Ar] $4s^{0.42}3d^{9.96}4p^{0.02}$, proving the presence of a zinc divalent cation, calling for primarily electrostatic interactions with the ligands.

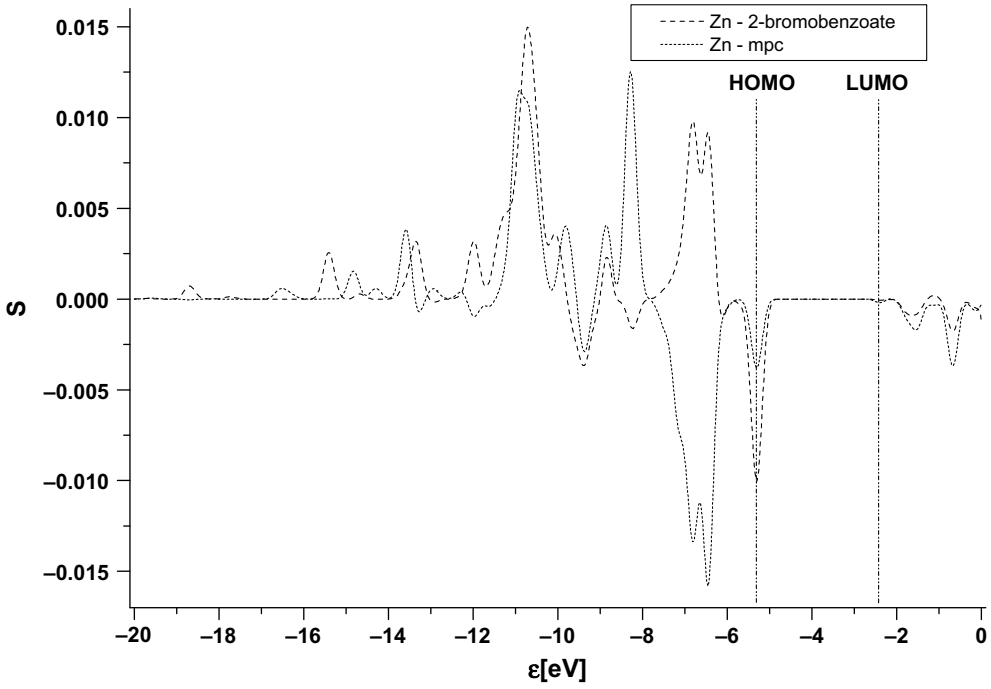


Fig. 5. The COOP diagram of **1**.

Table 6
Mayer bond orders between the central zinc atom and selected donors

Atoms	Mayer bond order(s)
Carboxylate oxygens	0.222, 0.204
Carboxylate carbons	0.015
mpc nitrogens	0.223

4. Conclusion

The present work describes the synthesis and characterization of $[Zn(2\text{-}BrC_6H_4COO)_2mpc_2]$. It was found out that the zinc is coordinated by two nitrogen atoms from two methyl-3-pyridylcarbamate ligands and by four oxygen atoms from two bidentate 2-bromobenzoates in a pseudo-octahedral geometry. The molecules are linked into a chain by hydrogen bridges between the NH group of methyl-3-pyridylcarbamate and one carboxylate oxygen atom from a neighbouring molecule.

According to our computational studies, the prevalence of an electrostatic interaction between the zinc divalent cation and two carboxylate anions of 2-bromobenzoate ligands was proved. A somewhat greater covalent contribution was observed only for the two nitrogen atoms of the methyl-3-pyridylcarbamate ligands. A notable bonding interaction between the two carboxylate carbon atoms and the central atom was disproved.

Acknowledgements

This work was supported by the Slovak Ministry of Education (VEGA project 1/0122/08). The financial support is gratefully acknowledged.

Appendix A. Supplementary data

CCDC 686772 contains the supplementary crystallographic data for this paper. These data can be obtained free of charge via http://www.ccdc.cam.ac.uk/conts/retrieving.html, or from the Cambridge Crystallographic Data Centre, 12 Union Road, Cambridge CB2 1EZ, UK; fax: (+44) 1223-336-033; or e-mail: deposit@ccdc.cam.ac.uk. Supplementary data associated with this article can be found, in the online version, at doi:10.1016/j.poly.2008.09.017.

References

[1] H. Kluge, J. Broz, K. Eder, J. Anim. Physiol. Nutr. 90 (2006) 316.
[2] M. de Silva, C.M.C.S. Menezes, E.I. Ferreira, C.Q.F. Leite, D.N. Sato, C.C. Correia, C.P. Pimenta, K.C.A. Botelho, Chem. Biol. Drug Design 71 (2008) 167.
[3] C. Dendrinou-Samara, G. Tsotsou, L.V. Ekateriniadou, A.H. Kortsaris, C.P. Raptopoulou, A. Terzis, D.A. Kyriakidis, D.P. Kessissoglou, J. Inorg. Biochem. 71 (1998) 171.
[4] C.L. Freucht, B.S. Allen, D.K. Chalker, J. Am. Acad. Dermatol. 3 (1980) 483.
[5] R.B. Martin, in: H. Sigel (Ed.), Metal Ions in Biological Systems, vol. 20, Marcel Dekker, New York and Basel, 1986.
[6] D.B. Christianson, Adv. Protein Chem. 42 (1991) 281.
[7] E. Szunyogová, K. Győryová, J. Kovářová, E. Juhászová, J. Therm. Anal. Cal. 71 (2003) 967.
[8] K. Győryová, V. Balek, V. Zeleňák, Thermochim. Acta 234 (1994) 221.
[9] K. Győryová, V. Balek, J. Kovářová, Thermochim. Acta 269/270 (1995) 425.
[10] V. Zeleňák, K. Győryová, J. Simon, J. Therm. Anal. Cal. 46 (1996) 573.
[11] V. Zeleňák, I. Císařová, M. Sabo, P. Llewellyn, K. Győryová, J. Coord. Chem. 57 (2004) 87.
[12] K. Győryová, J. Chomič, J. Kovářová, J. Therm. Anal. Cal. 80 (2005) 375.
[13] Z.H. Chohan, S.K.A. Sherazi, Metal-Based Drugs 4 (1997) 327.
[14] V. Zeleňák, M. Sabo, W. Massa, P. Llewellyn, Inorg. Chim. Acta 357 (2004) 2049.
[15] J. Maroszová, L. Findoráková, K. Győryová, J. Moncol, M. Melník, Acta Crystallogr., Sect. E 63 (2007) m1520.
[16] Z. Otwinowski, W. Minor, HKL DENZO and SCALEPACK program package by Nonius BV, Delft, 1997. For a reference see: Z. Otwinowski, W. Minor, Methods Enzymol. 276 (1997) 307.
[17] A. Altomare, M.C. Burla, M. Camalli, G. Cascarano, C. Giacovazzo, A. Guagliardi, G. Polidori, J. Appl. Crystallogr. 27 (1994) 435.
[18] G.M. Sheldrick, SHELXL97: Program for Crystal Structure Refinement from Diffraction Data, University of Gottingen, Gottingen, Germany, 1997.
[19] M.J. Frisch, G.W. Trucks, H.B. Schlegel, G.E. Scuseria, M.A. Robb, J.R. Cheeseman, J.A. Montgomery Jr., T. Vreven, K.N. Kudin, J.C. Burant, J.M. Millam, S.S. Iyengar, J. Tomasi, V. Barone, B. Mennucci, M. Cossi, G. Scalmani, N. Rega, G.A. Petersson, H. Nakatsuji, M. Hada, M. Ehara, K. Toyota, R. Fukuda, J. Hasegawa, M. Ishida, T. Nakajima, Y. Honda, O. Kitao, H. Nakai, M. Klene, X. Li, J.E. Knox, H.P. Hratchian, J.B. Cross, V. Bakken, C. Adamo, J. Jaramillo, R. Gomperts, R.E. Stratmann, O. Yazyev, A.J. Austin, R. Cammi, C. Pomelli, J.W. Ochterski, P.Y. Ayala, K. Morokuma, G.A. Voth, P. Salvador, J.J. Dannenberg, V.G. Zakrzewski, S. Dapprich, A.D. Daniels, M.C. Strain, Ö. Farkas, D.K. Malick, A.D. Rabuck, K. Raghavachari, J.B. Foresman, J.V. Ortiz, Q. Cui, A.G. Baboul, S. Clifford, J. Cioslowski, B.B. Stefanov, G. Liu, A. Liashenko, P. Piskorz, I. Komaromi, R.L. Martin, D.J. Fox, T. Keith, M.A. Al-Laham, C.Y. Peng, A. Nanayakkara, M.

Challacombe, P.M.W. Gill, B. Johnson, W. Chen, M.W. Wong, C. Gonzalez, J.A. Pople, GAUSSIAN 03, Revision E.01, Gaussian, Inc., Wallingford CT, 2004.
[20] A.D. Becke, Phys. Rev. A 38 (1988) 3098.
[21] J.P. Perdew, K. Burke, Y. Wang, Phys. Rev. B 54 (1996) 16533.
[22] A.D. McLean, G.S. Chandler, J. Chem. Phys. 72 (1980) 5639.
[23] J.E. Carpenter, F. Weinhold, J. Mol. Struct. (Theochem) 41 (1988) 169.
[24] E.D. Glendening, J.K. Badenhoop, A.E. Reed, J.E. Carpenter, F. Weinhold, NBO Version 3.1, Theoretical Chemistry Institute, University of Wisconsin, Madison.
[25] A.J. Bridgemann, G. Cavigliasso, L.R. Ireland, J. Rothery, J. Chem. Soc., Dalton Trans. (2001) 2095.
[26] G. Schaftenaar, J.H. Noordik, J. Comput.-Aided Mol. Des. 14 (2000) 123.
[27] E. Szunyogová, D. Mudroňová, K. Győryová, R. Nemcová, J. Kovářová, L. Piknová-Findoráková, J. Therm. Anal. Cal. 88 (2007) 355.
[28] K. Győryová, J. Chomič, E. Szunyogová, L. Piknová, V. Zeleňák, Z. Vargová, J. Therm. Anal. Cal. 84 (2006) 727.
[29] L.J. Bellamy, The Infrared Spectra of Complex Molecules, Methuen and Co., London, 1958.
[30] M. Akbar Ali, Hjh Junaidah, Abu Bakar, A.H. Mirza, S.J. Smith, L.R. Gahan, P.V. Bernhardt, Polyhedron 27 (2008) 71.
[31] R. Martin Smith, Understanding Mass Spectra: A Basic Approach, 2nd ed., John Wiley & Sons, New Jersey, 2004.

Polyhedron 28 (2009) 138–144

Contents lists available at ScienceDirect

Polyhedron

journal homepage: www.elsevier.com/locate/poly

Synthesis, structure and biological properties of several binary and ternary complexes of copper(II) with ciprofloxacin and 1,10 phenanthroline

J. Hernández-Gil [a], L. Perelló [a,*], R. Ortiz [a], G. Alzuet [a], M. González-Álvarez [a], M. Liu-González [b]

[a] Departamento de Química Inorgánica, Facultad de Farmacia, Universidad de Valencia, Avda. Vicent Andrés Estellés s/n, 46100 Burjassot, Valencia, Spain
[b] SCSIE, Universidad de Valencia, Dr. Moliner 50, 46100 Burjassot, Valencia, Spain

ARTICLE INFO

Article history:
Received 27 June 2008
Accepted 26 September 2008
Available online 3 November 2008

Keywords:
Copper(II)
Quinolone complexes
Ciprofloxacin
Nuclease activity

ABSTRACT

In this study, a new binary complex $[Cu(HCip)_2](NO_3)_2 \cdot 6H_2O$ (**1**) has been synthesized and then characterized by X-ray structure analyses. In this compound, each ciprofloxacin acts as a bidentate ligand resulting in a crystallographically planar configuration; the nitrate anions are located in apical positions with an axial distance significantly larger than the equatorial distances, which would be consistent with a very weak metal ion interaction due to the Jahn–Teller effect. In addition, both the synthesis and characterization of two new ternary complexes of ciprofloxacin–copper(II)–1,10-phenanthroline, $[Cu(phen)(Cip)](NO_3) \cdot 4H_2O$ (**2**) and $Cu(phen)(HCip)(NO_3)_2 \cdot H_2O$ (**3**), have been accomplished. We have also undertaken the single crystal structural determination of **2**, in which the ciprofloxacin acts as tridentate bridging ligand; the complex exhibits a five-coordinated motif in a distorted square pyramidal environment around the metal center. The chemical nuclease activity of compounds **2** and **3** has also been studied, revealing that both compounds behave as efficient chemical nucleases in the presence of ascorbate. Mechanistic studies, with various radical oxygen scavengers, indicate that the DNA cleavage reaction is mediated by hydroxyl radicals, singlet oxygen, and the superoxide anion.

© 2008 Elsevier Ltd. All rights reserved.

1. Introduction

The biological activity of copper, a physiologically metal element that plays an important role in many biological processes [1], has been the subject of numerous studies [2–4]. Since Sigman et al. [5] discovered in 1979 that copper ions complexed to 1,10-phenanthroline were capable of cleaving DNA [6], copper complexes with a nitrogen donor heterocyclic ligand have been used widely to improve nuclease activity [6–11], mostly because their high nucleolytic efficiency is able to break the DNA chain in the presence of H_2O_2 and reducing agents [12]. In recent years, the study of quinolones–copper–1,10-phenanthroline complexes has become an increasingly important field due to the antibacterial properties of these compounds [13–19]. Quinolones, a commonly used term for the quinolone–carboxylic acids or 4-quinolones, are a group of synthetic antibacterial agents containing a 4-oxo-1,4-dihydroquinoline skeleton [20] which act by inhibiting the enzymes (topoisomerases) necessary for DNA synthesis. The spectrum of activity of these compounds has become increasingly broad, especially since the introduction of a fluorine atom at position 6 (fluoroquinolones) [21]. In 2002, Turel [22] reviewed the synthesis, physico-chemical properties, and structural characteristics of several binary and ternary fluoroquinolone compounds, together with their biological activity. Ciprofloxacin [HCip, 1-cyclopropyl-6-fluoro-1,4-dihydro-4-oxo-7-(1-piperazinil)-3-quinolone carboxylic acid], is a second generation fluoroquinolone that was synthesized for first time in 1987 [21]. A well known antibacterial drug with a wide spectrum of activity, it is extremely useful for the treatment of a variety of infections [22,23]. Over the past few years many studies have examined both the structure and chemical behavior of several complexes of cinoxacin and ciprofloxacin in which the bonding of the quinolones to the copper has been through the ring carbonyl group oxygen atom and one of the carboxylic atoms [24–28]. In addition, ciprofloxacin contains a nitrogen atom in its piperazinil group which is capable of attaching to the metal centers in a silver complex, as reported by Chen et al. [29]. Ternary complexes of copper(II), quinolones and 1,10-phenanthroline have also been isolated and characterized with the aid of X-ray diffraction methods. All of these ternary complexes have been found to be mononuclear species with a five-coordinate environment and a square pyramidal geometry around the copper center [4,30–35].

The DNAase activity of copper phenanthroline has been widely documented [36,37]. The $[Cu(phen)(nal)]^+$ compound likewise

Abbreviations: DMSO, dimethyl sulfoxide; EDTA, ethylenediaminetetraacetic acid; ESI, electrospray ionization; HCip, ciprofloxacin; HNor, norfloxacin; Nal, nalidixic acid; Phen, *o*-phenanthroline; SOD, superoxide dismutase; TBE, Tris, boric acid, EDTA; Tris, Tris(hydroxymethyl)aminomethane.

* Corresponding author. Tel.: +34 963544522; fax: +34 963544960.
E-mail address: Lourdes.Perello@uv.es (L. Perelló).

0277-5387/$ - see front matter © 2008 Elsevier Ltd. All rights reserved.
doi:10.1016/j.poly.2008.09.018

acts as a powerful nuclease capable of degrading plasmid DNA under reductive conditions, and has an even stronger activity than that of the chemical nuclease copper phenanthroline [Cu(phen)$_2$]$^{2+}$ [38]. In the past few years, we have reported on the ability of two Cu(II)–norfloxacin–phenanthroline compounds to cleave DNA. Mechanistic studies with various inhibiting reagents indicate that hydroxyl radicals, singlet oxygen, and superoxide radicals are all involved in the DNA scission process mediated by these compounds [30]. In addition, several ternary copper(II)–quinolone–phenanthroline complexes have been screened for their activity against different strains of bacteria, exhibiting a higher inhibitory capacity than their individual components [32,34,39].

In this paper, we describe the synthesis, characterization and X-ray crystallographic structure of a new binary Cu(II) complex of ciprofloxacin. In addition, we report on the synthesis and characterization of two new ternary ciprofloxacin–copper(II)–1,10-phenanthroline complexes along with the crystal structure of [Cu(Cip)(phen)](NO$_3$) · 4H$_2$O. Data on the activity of the synthesized ternary compounds of ciprofloxacin as artificial nucleases is also included.

2. Experimental

Ciprofloxacin hydrochloride was provided by Sigma. Plasmid pUC18 (0.25 μg/μL in 10 mM Tris and 1 mM EDTA, pH 8.0) was purchased from Roche Diagnostics, Germany. Solutions of the metal complexes and other reagents for DNA strand scission were prepared fresh daily. All reagents used were of analytical grade.

2.1. Analyses

Cu was determined by means of atomic absorption spectroscopy with a Perkin–Elmer spectrometer model 2380. Elemental chemical analyses for C, H, N were performed on a Carlo Erba instruments EA 1110.

2.2. Physical measurements

Infrared spectra were recorded on a Satellite FTIR Mattson spectrophotometer with KBr pellets in the 4000–600 cm^{-1} range. UV–Vis absorption spectra were obtained on a Shimadzu 2101 PC spectrophotometer with the aid of the diffuse reflectance technique. Magnetic susceptibilities were measured on a Faraday magnetometer with Hg[Co(SCN)$_4$] as a standard; diamagnetic corrections were made with Pascal's constants. The electrospray ionization mass spectra of aqueous solutions of compounds **2** and **3** were obtained in positive mode [ESI$^+$] with an ESQUIRE 3000-plus Brucker ion trap mass spectrometer.

2.3. Synthesis of the complexes

2.3.1. [Cu(HCip)$_2$](NO$_3$)$_2$ · 6H$_2$O (**1**)

Adenine (34.29 mg, 0.25 mmol) was dissolved in 0.5 mL of 1 M HCl and the minimum amount of water. To this solution, an aqueous suspension of sodium ciprofloxacinate (102.24 mg, 0.25 mmol) was added and then stirred until total solution was achieved (pH 2.28). Next, a solution of 0.5 mmol (121.76 mg) of Cu(NO$_3$)$_2$ · 3H$_2$O in water was added. The final pH of the reaction mixture was approximately 5.45 for a final volume of 50 mL. The resulting blue solution was left to stand at room temperature. Pale blue crystals suitable for X-ray analysis formed after ca. 8 days.

Calc. for C$_{34}$H$_{48}$N$_8$O$_{18}$F$_2$Cu (**1**): C, 42.58; H, 5.01; N, 11.69; Cu, 6.63. Found: C, 42.08; H, 4.93; N, 11.62; Cu, 6.52%.

2.3.2. [Cu(Cip)(phen)](NO$_3$) · 4H$_2$O (**2**)

A solution of 1,10-phenantroline (49.6 mg, 0.25 mmol) was added to a suspension of sodium ciprofloxacinate (102.5 mg, 0.25 mmol). After 10 min of vigorous stirring, a solution of Cu(NO$_3$)$_2$ · 3H$_2$O (60.5 mg, 0.25 mmol) was added. The solvent used was a mixture of MeOH:H$_2$O (1:1) and the final volume was 50 mL. The pH was adjusted to 7.84 with 1 M NaOH and the resulting solution was stirred and filtered off. Green crystals suitable for X-ray structure determination formed after 10–15 days.

Calc. for C$_{29}$H$_{33}$N$_6$O$_{10}$FCu (**2**): C, 49.15; H, 4.66, N, 11.86; Cu, 8.97. Found: C, 48.58; H, 4.89; N, 11.80; Cu, 8.82%.

2.3.3. Cu(HCip)(phen)(NO$_3$)$_2$ · H$_2$O (**3**)

To an aqueous solution of 1,10-phenantroline (99.12 mg, 0.5 mmol), 0.5 mmol (204.18 mg) of sodium ciprofloxacinate and 0.5 mL of 1 M HNO$_3$ were added. After several minutes of stirring, an aqueous solution of Cu(NO$_3$)$_2$ · 3H$_2$O (120.8 mg, 0.5 mmol) was added to the mixture. The blue solution was stirred vigorously for approximately 10 min, after which a solution of 1 M NaOH was added. The final volume was 50 mL with a pH of 5.52. The resulting suspension was stirred and removed through filtration. After 8 days, the blue crystals that had formed were filtered off and air-dried.

Calc. for C$_{29}$H$_{28}$N$_7$O$_4$FCu (**3**): C, 48.52; H, 3.90; N, 13.66; Cu, 8.86. Found: C, 48.09; H, 4.16; N, 13.62; Cu, 8.74%.

2.4. X-ray structure determination

A summary of the crystallographic data for **1** and **2** is given in Table 1. First, green single-crystals of both **1** and **2** were selected. Data collection was performed at 293 K on a Nonius Kappa-CCD single-crystal diffractometer with Mo Kα radiation (λ = 0.7173 Å). The data collection strategy was determined with the aid of the program COLLECT [40]. Data reduction and cell refinement were car-

Table 1
Crystal data of the compounds: [Cu(HCip)$_2$](NO$_3$)$_2$ · 6H$_2$O (**1**), [Cu(phen)(Cip)](NO$_3$) · 4H$_2$O (**2**).

Compound	**1**	**2**
Empirical formula	$C_{34}H_{48}CuF_2N_8O_{18}$	$C_{29}H_{33}CuFN_6O_{10}$
Formula weight	958.34	708.15
Temperature (K)	293(2)	293(2)
Crystal system	triclinic	monoclinic
Space group	$P\bar{1}$	$P2_1/c$
Unit cell dimensions		
a (Å)	9.280(5)	8.9330(2)
b (Å)	9.347(5)	18.2790(4)
c (Å)	11.785(5)	19.9570(4)
α (°)	89.564(5)	90
β (°)	78.594(5)	111.1560(12)
γ (°)	89.721(5)	90
Volume (Å^3)	1002.0(9)	3039.07(11)
Z	1	4
D_{calc} (Mg/m^3)	1.588	1.548
Absorption coefficient (mm^{-1})	0.643	0.793
F(000)	499	1468
Crystal size (mm)	0.15 × 0.15 × 0.20	0.2 × 0.2 × 0.18
θ Range (°)	1.76–25.41	1.56–27.47
h, k, l Ranges	−8 11, −11 11, −14 14	−11 11, −23 23, −25 25
Reflections collected/unique	5263/3624	11584/6759
Data /restraints/parameters	3624/0/382	6759/0/428
Goodness-of-fit on F^2	1.089	1.107
R indices [$I > 2\sigma(I)$]	R_1 = 0.0667 wR_1 = 0.1659	R_1 = 0.0558 wR_1 = 0.1491
R indices (all data)	R_2 = 0.0988 wR_2 = 0.1927	R_2 = 0.0969 wR_2 = 0.1769
Largest difference in peak and hole (e Å^{-3})	0.871 and −1.011	0.576 and −0.597

ried out with the HKL DENZO and SCALEPACK programmes [41]. Unit cell dimensions were determined from 2745 reflections between $\theta = 0.998°$ and 25.485° for **1** and 5857 reflections between $\theta = 0.998°$ and 27.485° for **2**. The crystal structures were solved by means of direct methods, with the program SIR-97 [42]. Anisotropic least-squares refinement was carried out with SHELXL-97 [43]. All non-hydrogen atoms were anisotropically refined. For compound **1**, some hydrogen atoms were located in a difference Fourier map and others located geometrically; the nitrate and water molecules how some kind of disorder. For compound **2**, all hydrogen atoms were located geometrically.

Geometrical calculations were made with PARST [44] and the crystallographic plots were made with ORTEP [45] (Figs. 1 and 2).

2.5. Cleavage of pUC18 by complexes [Cu(Cip)(phen)](NO$_3$) · 4H$_2$O (**2**) and Cu(HCip)(phen)(NO$_3$)$_2$ · H$_2$O (**3**)

Reactions were carried out in a total volume of 20 μL by mixing 7 μL of 0.1 M cacodylate buffer (pH 6), 6 μL of 10, 20, 30, or 40 μM complex solutions of **2** or **3** in 0.1 M cacodylate buffer (pH 6), 1 μL of 0.25 μg/μL pUC18; and 6 μL of ascorbate (2-fold molar excess relative to the concentration of the complexes) in 0.1 M cacodylate buffer (pH 6.0). The resulting mixtures contain 3, 6, 9, or 12 μM complex **2** or **3**, 0.012 μg/μL pUC18 (3.5 μM in nucleotides) and 6, 12, 18, or 24 μM ascorbate. The samples were then incubated at 37 °C for 60 min, after which 3 μL of a quench buffer solution (0.25% bromophenolblue, 0.25% xylene cyanole, and 30% glycerol) was added. The samples were then loaded on agarose gel (0.8%) containing 2 μL/100 mL of a solution of ethidiumbromide (10 mg/mL). Electrophoresis was carried out at 80 V for 2 h in 0.5 × TBE buffer (0.045 M Tris, 0.045 M boric acid and 1 mM EDTA). The gel was photographed on a capturing system gel printer plusTDI. To study mechanistic aspects of the DNA cleavage reaction performed by both compounds, scavengers of reactive oxygen intermediates [DMSO (0.4 M), sodium formate (0.4 M), sodium azide (20 mM), 2,2,6,6-tetramethyl-4-piperidone (0.4 M), SOD (15 units), tiron (10 mM)] and catalase (6.5 units) were added to the reaction mixtures. Assays in the presence of the minor groove binder distamycin (8 μM) and the major groove binder methyl green (2.5 μL of a 0.01 mg/mL solution) were also performed. The reduction of Cu(II) to Cu(I) was tested by adding 120 μM neocuproine, a ligand that chelates strongly to copper(I). Samples were treated as described above.

3. Results and discussion

3.1. Description of the structure of [Cu(HCip)$_2$] (NO$_3$)$_2$ · 6H$_2$O (**1**)

The structure of the complex is shown in Fig. 1 while selected bond lengths and angles are given in Table 2.

The structure consists of cationic monomeric units of [Cu(HCip)$_2$]$^{2+}$, two nitrate anions which neutralize the charge, and six lattice water molecules that provide crystalline stability through a network of hydrogen bond interactions. As in other previously reported ciprofloxacin compounds [27,46–51], the molecule of the ligand is zwitterionic in form with two hydrogen atoms attached to a nitrogen atom N(3). These hydrogen atoms are clearly visible in the difference Fourier map, and both form donor hydrogen bonds with water molecules. The Cu(II) ion is coordinated to two ciprofloxacin ligands that are related through an inversion center. Each ciprofloxacin acts as a bidentate ligand bonded to the cation through both its carboxylic oxygen atom and its carbonyl oxygen atom; this results in a CuO_4 chromophore in a crystallographically planar configuration (Σ(angles) = 360°). The nitrate anions are located in apical positions [O(1)–Cu(1)–O(13) 84.51(19)° and O(3)–Cu(1)–O(13) 79.13(19)°], with an axial distance Cu–O(13) (2.672(7)) Å. This is significantly larger than the equatorial distances, which would be consistent with a very weak metal ion interaction due to the Jahn–Teller effect. These equatorial bond Cu–O lengths (1.926(3) and 1.931(3) Å) are similar to those observed in related compounds [28,48]. The difference in the carboxylate distances O(1)–C(1) (1.265(6) Å) and O(2)–C(1) (1.245(6) Å) indicates the formation of a bond between the anionic carboxylate oxygen atom and the copper ion; these bond lengths are virtually identical in the uncomplexed ciprofloxacin ligand [49]. The quinolone moiety is practically planar with the exception of the cyclopropyl group sticking out of the plane, and the piperazine ring system is in the normal chair conformation [28,52]. The terminal nitrogen atom is protonated which explains why this atom fails to coordinate with the metallic ion.

Three interstitial water molecules complete the asymmetric unit. They are connected via hydrogen bonds with the protonated external nitrogen atom (N(3)) of the piperazine group as well as with the O(11) and O(13) from the nitrate group, the O(3)$_{keto}$ and the two *O*-carboxylate moieties. This bonding pattern contributes to the stability of the structure.

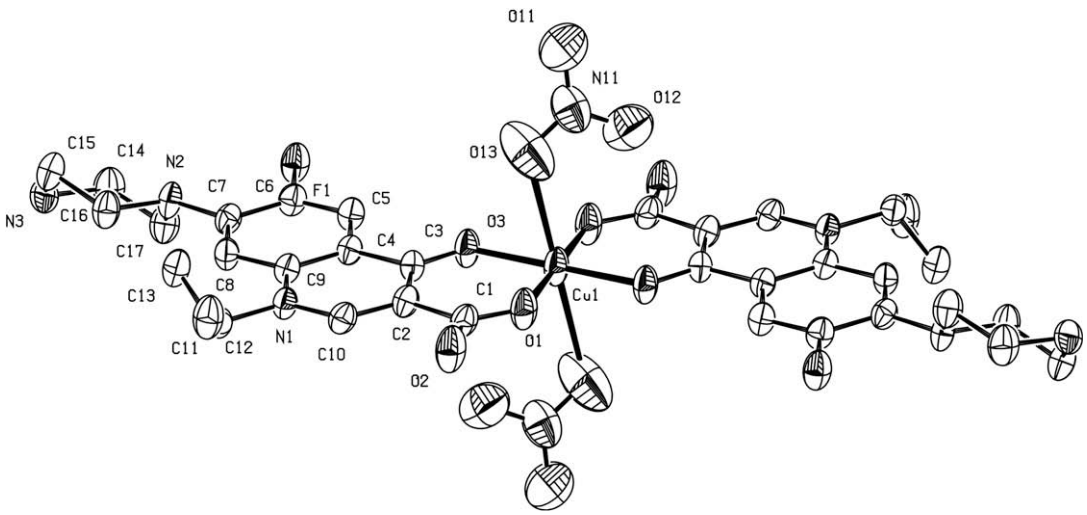


Fig. 1. Crystal structure of compound [Cu(HCip)$_2$](NO$_3$)$_2$ (**1**).

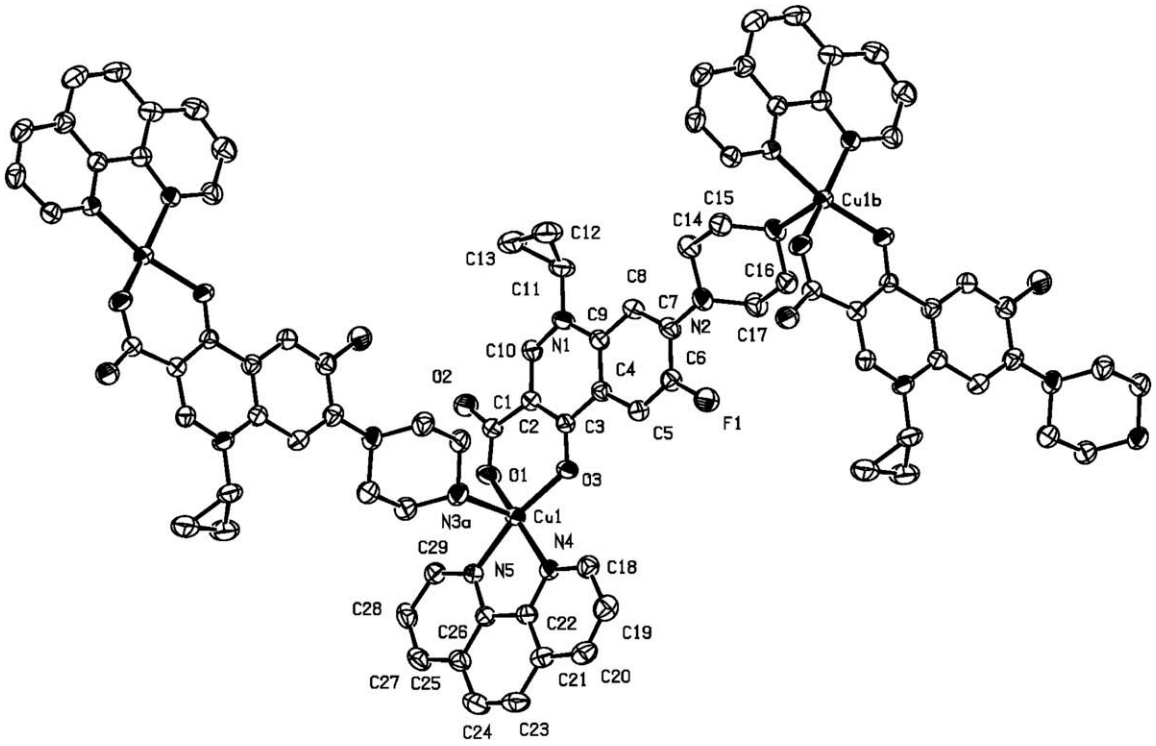


Fig. 2. Crystal structure of compound $[Cu(Cip)(phen)]^+$ (**2**).

Table 2
Selected bond lengths (Å) and angles (°) for compound $[Cu(HCip)_2](NO_3)_2 \cdot 6H_2O$ (**1**).

Cu(1)–O(1)	1.926(3)	O(11)–N(11)	1.245(8)
Cu(1)–O(3)	1.931(3)	O(12)–N(11)	1.248(8)
Cu(1)–O(13)	2.672(8)	O(13)–N(11)	1.209(8)
O(1)–C(1)	1.265(6)	C(1)–C(2)	1.506(6)
O(2)–C(1)	1.245(6)	C(2)–C(3)	1.428(6)
O(3)–C(3)	1.266(5)		
O(1)–Cu(1)–O(3)#1	85.91(14)	O(1)–Cu(1)–O(13)	84.51(19)
O(1)–Cu(1)–O(3)	94.09(14)	O(3)–Cu(1)–O(13)	79.13(19)

Symmetry transformation used to generate equivalent atoms: #1 $-x, -y+1, -z+2$.

Table 3
Selected bond lengths (Å) and angles (°) for compound $[Cu(phen)(Cip)](NO_3) \cdot 4H_2O$ (**2**).

Cu(1)–O(1)	1.923(3)	O(3)–C(3)	1.286(4)
Cu(1)–O(3)	1.931(2)	N(4)–C(22)	1.360(4)
Cu(1)–N(5)	2.013(3)	N(5)–C(26)	1.353(4)
Cu(1)–N(4)	2.012(3)	C(22)–C(26)	1.435(5)
Cu(1)–N(3)#1	2.337(3)	C(1)–C(2)	1.507(5)
O(1)–C(1)	1.282(4)	C(2)–C(3)	1.413(5)
O(2)–C(1)	1.231(4)	C(11)–C(13)	1.496(6)
O(3)–Cu(1)–O(1)	92.66(10)	O(3)–Cu(1)–N(3)#1	98.31(10)
O(1)–Cu(1)–N(5)	91.08(11)	O(1)–Cu(1)–N(3)#1	97.05(11)
O(3)–Cu(1)–N(4)	91.77(10)	N(5)–Cu(1)–N(3)#1	93.03(10)
N(5)–Cu(1)–N(4)	81.80(11)	N(4)–Cu(1)–N(3)#1	96.24(11)

Symmetry transformation used to generate equivalent atoms: #1 $-x, y+1/2, -z+3/2$.

3.2. Description of the structure of $[Cu(Cip)(phen)](NO_3) \cdot 4H_2O$ (**2**)

Bond distances and angles for the compound **2** are given in Table 3 while Fig. 2 shows the ORTEP diagram for this copper complex.

Each crystallographically independent unit contains one copper(II) atom, one quinolone ligand in its anionic form (Cip^-), and one 1,10-phenanthroline, which together form cationic units $[Cu(Cip)(phen)]^+$, as well as one nitrate counteranion and four water molecules. The complex exhibits a five-coordinated motif in a distorted square pyramidal environment around the metal center. In the equatorial plane the metallic ion is coordinated by two nitrogen atoms (N(4) and N(5)) from a 1,10-phenanthroline molecule and by two oxygen atoms (O(1) and O(3)) from its quinolone ligand. The apical position is occupied by a third piperazinil nitrogen atom from a second ciprofloxacinate ligand, resulting in a CuN_3O_2 chromophore. It should be emphasised, that this ternary complex is the first time a quinolone has been found to act as a bridge-ligand by attaching two metallic centers.

The metal ion deviates from the mean least-squares basal plane in the direction of the apical piperazinil coordinated nitrogen atom by 0.2128(4) Å. The equatorial bond lengths between the copper ion and the two nitrogen atom (2.012(3) and 2.013(3) Å, respectively) are similar to those found in analogous compounds [53]. Furthermore, the axial distance Cu(1)–N(3)#1 (2.337(3) Å) is longer than those of the equatorial nitrogens. The equatorial oxygen bond lengths (1.923(3) and 1.931(2) Å) are similar to those found in previously reported structures of mixed copper–ciprofloxacin ternary complexes [28,33,48,54]. The O(1)–C(1) distance (1.282(4) Å) is longer than the O(2)–C(1) distance (1.231(4) Å) due to the formation of the Cu(1)–O(1) bond. The angles in the basal plane vary from 81.80(11)° to 92.66(10)°; these ranges are similar to those found in other previously described mixed copper–quinolone–1,10-phenantroline compounds [33,53]. In the apical direction, the Cu(1)–N(3)#1 vector is nearly perpendicular to the basal plane; the bond angles O_{basal}–Cu(1)–N(3)#1 and N_{basal}–Cu(1)–N(3)#1 are between 98.31(10)° and 93.03(10)°, respectively. The two basal ligands are planar with a dihedral angle between them of 7.75(07)° while the piperazinil ring, which is non-coplanar

with the quinolone ring, adopts a normal chair conformation [28,52].

The four interstitial water molecules are connected via hydrogen bonds, as well as with the two oxygen atoms of the nitrate anions, which helps stabilize the structure.

3.3. Spectroscopic properties

The IR spectra of the three compounds show a broad split band between 3600 and 2300 cm^{-1} which can be assigned to the O–H stretching vibrations of water molecules as well as to the N–H stretching vibration of the piperazinil moiety [28,51,55,56]. The latter signal appears between 2750 and 2300 in the IR spectra of complexes **1** and **3,** in which the ligand is in a neutral zwitterionic form (ν(N–H) of the NH_2^+ group). Furthermore, all the compounds present a slightly split band between 1640 and 1620 cm^{-1} which can be assigned to the ν(CO) vibrations of the ketonic group and ν_a(OCO) of the carboxylate group. At around 1383 cm^{-1} an intense band assigned to ν_s(OCO) + ν_3 (NO_3^-) is also visible, thereby confirming the presence of the nitrate group [49,57]. None of the IR spectra exhibit a band around 1730 cm^{-1} which would be assigned to the ν(C=O) vibration of the carboxylic group; this indicates the deprotonation of this moiety and its probable interaction with the metal ion [5,30,51,55]. The spectra of compounds **2** and **3** exhibit two new bands between 1610 and 1514 cm^{-1} which can be assigned to the vibrations ν(C=N) and ν(arC–C) of the phenantroline aromatic rings [30].

The diffuse reflectance spectra of the Cu(II)–ciprofloxacin complexes exhibit one asymmetric broad band centered around 15 000 cm^{-1} for compounds **2** and **3** and at 14368 cm^{-1} for compound **1**. These spectra suggest that compounds **2** and **3** have a distorted square-pyramidal geometry or tetragonal arrangement of the ligands donor atoms around the cupric ion while compound **1** presents a distorted octahedral arrangement [58].

At room temperature, the magnetic moments of all the complexes lie in the range 1.80–1.99 B.M., which is higher than the spin-only value of 1.73 B.M. Such divergence is not uncommon in mononuclear Cu(II) complexes due to the mixing-in of some angular moment from nearby excited states via spin–orbit coupling [59].

3.4. Nuclease activity of the complexes [Cu(Cip)(phen)] $(NO_3) \cdot 4H_2O$ (**2**) and Cu(HCip)(phen)$(NO_3)_2 \cdot H_2O$ (**3**)

The ability of [Cu(Cip)(phen)]$(NO_3)] \cdot 4H_2O$ (**2**) and Cu(HCip)-(phen)$(NO_3)_2 \cdot 3H_2O$ (**3**) to perform DNA cleavage has been investigated by means of gel electrophoresis with supercoiled pUC18 DNA in cacodylate buffer (pH 6.0). Reactions were carried out with ascorbate activation. Assays were also performed with Cu(II) due to the fact that Cu(II) ions in the presence of ascorbate are able to produce DNA damage. In addition, the DNA cleavage efficiency of **2** and **3** was compared with that of $[Cu(phen)_2]^{2+}$.

Fig. 3 shows the agarose gel electrophoresis of the oxidative cleavage of pUC18 plasmid DNA by the copper complexes, the Cu(II), and $[Cu(phen)_2]^{2+}$.

The DNA cleavage activity of the complexes was measured as the ability to convert supercoiled (form I) DNA to nicked circular (form II) or linear (form III) DNA.

The nuclease activity of the complexes was found to be dependent on complex concentration; thus, the activity of **2** and **3** increased at higher complex concentrations. At the lowest concentration assayed (3 μM), neither **2** nor **3** caused any damage to the DNA (lanes 8 and 12). However, at 6, 9 and at 12 μM, the compounds behaved as efficient chemical nucleases. At 6 μM, both **2** and **3** partially transformed the supercoiled DNA into its nicked circular form (lanes 9 and 13). At higher concentrations, the cleavage efficiency of complex **3** was found to be greater than that of **2**. Thus, at 9 μM, [Cu(Cip)(phen)]$(NO_3)] \cdot 4H_2O$ (**2**) promoted the partial conversion of form I DNA into nicked circular (form II) and a small amount of linear (form III) DNA (lane 10) while at the same concentration, Cu(HCip)(phen)$(NO_3)_2 \cdot 3H_2O$ (**3**) completely transformed the supercoiled DNA into its circular and linear forms (lane 14). The higher nuclease activity of **3** was even more evident at 12 μM, for at this concentration the compound was able to degrade form I DNA into linear DNA and small linear fragments that appeared as a smear (lane 15). The difference in the nuclease activity of the complexes is probably related to the difference in the amount of active copper species in solution able to promote DNA strand scission [60]. These species have been identified from the ESI^+ mass spectra of **2** and **3** as $[Cu(Cip)(phen)]^+$ (m/z = 573.2) and $[Cu(HCip)(phen)]^{2+}$ (m/z = 287.1), respectively. The presence of both species in solution is in good agreement with previous studies on the stability of ternary Cu:quinolone:phenantroline (1:1:1) compounds [61] which have concluded that Cu(HL)phen and Cu(L)phen are the predominant species under physiological conditions. We suggest that a higher amount of the active copper species is more easily produced in the monomeric compound **2** than in the polymeric compound **3,** which would explain the difference in cleavage activity. No cleavage was found with free Cu(II) (lanes 4–7). It is worth noting that the efficiency of compounds **2** and **3** at 12 μM was higher than that of $[Cu(phen)_2]^{2+}$ which, under identical reaction conditions, converted partially supercoiled DNA into circular and a small amount of linear DNA (lane 16). Similar results have been obtained for the [Cu(nal)-(phen)]$^+$ compound [38] and for the related [Cu(Nor)(phen)-(H_2O)](NO_3) and [Cu(HNor)(phen)(NO_3)]$(NO_3) \cdot 3H_2O$ compounds, which were all found to be more potent nucleases than $[Cu(phen)_2]^{2+}$ [30]. This fact clearly indicates that substituting

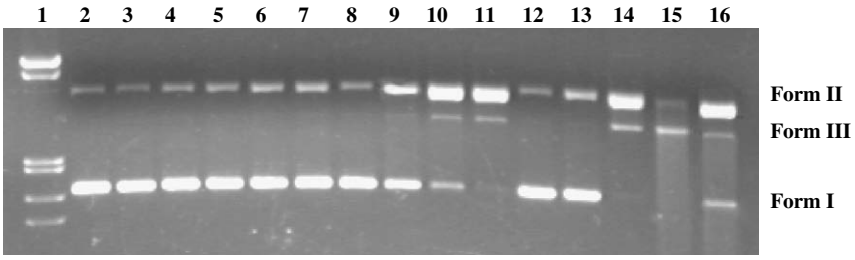


Fig. 3. Agarose gel electrophoresis of pUC18 plasmid DNA treated with [Cu(Cip)(phen)]$(NO_3)] \cdot 4H_2O$ (**2**) and Cu(HCip)(phen)$(NO_3)_2 \cdot 3H_2O$ (**3**) in the presence of ascorbate. [ascorbate]:[tested compound] = 2:1. Incubation time: 60 min (37 °C). Lane 1: λDNA/EcoRI + Hind III. Marker, 3, lane 2: supercoiled DNA, lane 3: supercoiled DNA with 24 μM ascorbate, lane 4: $Cu(NO_3)_2$ 3 μM, lane 5: $Cu(NO_3)_2$ 6 μM, lane 6: $Cu(NO_3)_2$ 9 μM, lane 7: $Cu(NO_3)_2$ 12 μM, lane 8: **2** 3 μM, lane 9: **2** 6 μM, lane 10: **2** 9 μM, lane 11: **2** 12 μM, lane 12: **3** 3 μM, lane 13: **3** 6 μM, lane 14: **3** 9 μM, lane 15: **3** 12 μM, lane 16: $[Cu(phen)_2]^{2+}$ 12 μM.

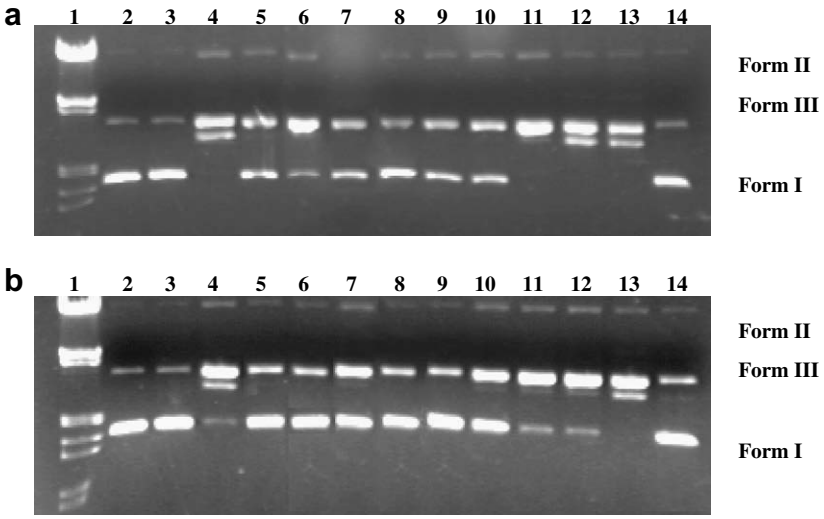


Fig. 4. (a) Agarose gel electrophoresis of pUC18 plasmid treated with 12 μM [Cu(Cip)(phen)](NO$_3$)] · 4H$_2$O (**2**) and 24 μM ascorbate in the presence of potential inhibitors. Incubation time: 60 min h (37 °C). (b) Agarose gel electrophoresis of pUC18 plasmid treated with 12 μM and Cu(HCip)(phen)(NO$_3$)$_2$ · 3H$_2$O (**3**) and 24 μM ascorbate in the presence of potential inhibitors. Incubation time: 60 min (37 °C). Lane 1: λDNA/EcoRI + Hind III. Marker, 3, lane 2: supercoiled DNA, lane 3 supercoiled DNA with ascorbate, lane 4: complex, lane 5: complex + DMSO (0.4 M), , lane 6: complex + sodium formate (0.4 M), lane 7: complex + NaN_3 (20 mM), lane 8: complex + 2,2,6,6-tetramethyl-4-piperidone (0.4 M), lane 9: complex + tiron (10 mM), lane 10: complex + SOD (15 units), lane 11: complex + neocuproine (120 μM), lane 12: complex + methyl green (2.5 μL of a 0.01 mg/mL solution), lane 13: complex + distamycin (8 μM), lane 14: catalase (6.5 units).

one phenanthroline with a quinolone ligand gives rise to a significant increase in nuclease activity.

In order to identify the reactive oxygen species that mediate the DNA strand scission brought about by compounds **2** and **3**, we decided to investigate the influence of different potentially inhibiting agents (Fig. 4).

The hydroxyl radical scavengers, dimethylsulfoxide and sodium formate both inhibited the scission reaction, which suggests that hydroxyl radicals are involved in the cleavage mechanism (lanes 5 and 6). Sodium azide and 2,2,6,6-tetramethyl-4-piperidone ($^1O_2$ scavengers) were also effective in blocking the DNA strand scission promoted by compounds **2** and **3** (lanes 7 and 8), indicating that either $^1O_2$ or a singlet-oxygen-like entity is one of the active oxygen intermediates responsible for the cleavage. In contrast, the presence of the superoxide radical scavengers tiron and SOD (lanes 9 and 10) attenuated the chemical nuclease activity of the complexes. These points to a cleavage pathway involving the formation of the reactive superoxide radical. Catalase (lanes 14) also inhibited the nucleolytic process, which confirms that hydrogen peroxide is also necessary for the DNA strand scission. With the Cu(I) chelator neocuproine, DNA damage was also significantly reduced (lanes 11); this suggests that the reduction of Cu(II) to Cu(I) is an important step in the cleavage process.

In summary, these results indicate that the cleavage reaction involves various oxygen species, including hydroxyl radicals, singlet-oxygen-like entities (e.g. Cu(I)–OOH) [62], and superoxide radicals. As is the case for other related compounds with nuclease activity, either a Fenton-type or a Haber–Weiss reaction leads to the formation of these oxygen active species, which, in turn, cleave the DNA [30,60].

$$(L)Cu^{2+} + Hasc^- \rightarrow (L)Cu^+ + acs^{\cdot -} + H^+$$
$$(L)Cu^+ + O_2 \rightarrow (L)Cu^{2+} + O_2{}^{\cdot -}$$
$$2O_2{}^{\cdot -} + 2H^+ \rightarrow H_2O_2$$
$$\text{Fenton}: (L)Cu^+ + H_2O_2 \rightarrow (L)Cu^{2+} + OH^- + {\cdot}OH$$
$$(L)Cu^+ + H_2O_2 \rightarrow (L)Cu^+ - OOH^- + H^+$$
$$\text{Haber–Weiss}: O_2{}^{\cdot -} + H_2O_2 \rightarrow {}^1O_2 + OH^- + OH$$

$(L)Cu^{2+}$ represents the active complex in solution.

The involvement of hydroxyl radicals in the DNA cleavage mechanism mediated by **2** and **3** suggests that the mode of action of these compounds differs from that of the Cu–phenanthroline compound [63].

In order to study how the complexes actually bind to DNA, the major groove binder methyl green and the minor groove binder distamycin were used. Treatment of pUC18 DNA with distamycin or methyl green prior to the addition of the complexes had no significant effect on the cleavage reaction, which indicate a lack of major or minor groove binding preferences for the complexes (lanes 12 and 13). Considering the cationic nature of the complexes in solution ($[Cu(Cip)(phen)]^+$ and $[Cu(HCip)(phen)]^{2+}$), their interaction with DNA must be primarily through electrostatic interactions with the phosphate backbone, although an intercalation involving the phenantroline and/or the ciprofloxacin ligands should not be ruled out.

4. Supplementary data

CCDC 702889 and 702890 contains the supplementary crystallographic data for compounds **1** and **2**, respectively. These data can be obtained free of charge via http://www.ccdc.cam.ac.uk/conts/retrieving.html, or from the Cambridge Crystallographic Data Centre, 12 Union Road, Cambridge CB2 1EZ, UK; fax: (+44) 1223-336-033; or e-mail: deposit@ccdc.cam.ac.uk.

Acknowledgements

The authors acknowledge financial support from the Spanish CICYT (CTQ2004-03735) and CICYT (CTQ2007-63690).

References

[1] J.R.J. Sorenson, Prog. Med. Chem. 26 (1989) 437.
[2] M. Kato, Y. Muto, Coord. Chem. Rev. 92 (1988) 45.
[3] J.E. Weder, C.T. Dillon, T.W. Hambley, B.J. Kennedy, P.A. Lay, J.R. Biffin, H.L. Regtop, N.M. Davies, Coord. Chem. Rev. 232 (2002) 95.
[4] G. Psomas, A. Tarushi, E.K. Efthimiadou, Y. Sanakis, C.P. Raptopoulou, N. Katsaros, J. Inorg. Biochem. 100 (2006) 1764.
[5] D.S. Sigman, D.R. Graham, V.D. Aurora, A.M. Stern, J. Biol. Chem. 254 (1979) 12269.

[6] F.Q. Liu, Q. Wang, K. Jiao, F. Jian, G. Liu, R. Li, Inorg. Chim. Acta 359 (2006) 1524.
[7] M.M. Meijler, O. Zelenko, D.S. Sigman, J. Am. Chem. Soc. 119 (1997) 1135.
[8] S.A. Ross, M. Pitié, B. Meunier, Eur. J. Inorg. Chem. 3 (1999) 557.
[9] G. Psomas, C.P. Raptopoulou, L. Iordanidis, C. Dendrinou-Samara, V. Tangoulis, D.P. Kessissoglou, Inorg. Chem. 39 (2000) 3042.
[10] C. Dendrinou-Samara, G. Psomas, C.P. Raptopoulou, D.P. Kessissoglou, J. Inorg. Biochem. 83 (2001) 7.
[11] B.K. Santra, P.A.N. Reddy, G. Neelakanta, S. Mahadevan, M. Nethaji, A.R. Chakravartym, J. Inorg. Biochem. 89 (2002) 91.
[12] L.Z. Li, C. Zhao, T. Xu, H. Ji, Y. Yu, G. Guo, H. Chao, J. Inorg. Biochem. 99 (2005) 1076.
[13] C. Dendrinou-Samara, G. Psomas, K. Christophorou, V. Tangolius, V.P. Raptopoulou, A. Terzis, D.P. Kessissoglou, J. Chem. Soc., Dalton Trans. (1996) 3737.
[14] J. Alós, Enferm. Infec. Microbiol. Clin. 21 (2003) 261.
[15] E.Y. Bivián-Castro, F. Cervantes-Lee, G. Mendoza-Díaz, Inorg. Chim. Acta 357 (2004) 349.
[16] D. Skrzypek, B. Szymanska, D. Kovala-Demertzi, J. Wiecek, E. Talik, Mavroudis A. Demertzis, J. Phys. Chem. Solids 67 (2006) 2550.
[17] P.R. Reddy, K.S. Rao, B. Satyanarayana, Tetrahedron Lett. 47 (2006) 7315.
[18] E.K. Efthimiadou, Y. Sanakis, C.P. Raptopoulou, A. Karaliota, N. Katsaros, G. Psomas, Bioorg. Med. Chem. Lett. 16 (2006) 3864.
[19] E.K. Efthimiadou, H. Thomadaki, Y. Sanakis, C.P. Raptopoulou, N. Katsaros, A. Scorilas, A. Karaliota, G. Psomas, J. Inorg. Biochem. 101 (2007) 64.
[20] D.T.W. Chu, P.B. Fernandes, in: B. Testa (Ed.), Advances in Drug Research, vol. 21, Academic Press, London, 1991, p. 39.
[21] O. Paulsen, Drugs Today 23 (1987) 269.
[22] I. Turel, Coord. Chem. Rev. 232 (2002) 27.
[23] H.C. Neu, J. Am. Med. 82 (1987) 196.
[24] M. Ruíz, L. Perelló, R. Ortiz, A. Castiñeiras, C. Maichle-Mössmer, E. Cantón, J. Inorg. Biochem. 59 (1995) 801.
[25] M. Ruíz, R. Ortiz, L. Perelló, J. Latorre, J. Server-Carrió, J. Inorg. Biochem. 65 (1997) 87.
[26] M. Ruiz, L. Perelló, J. Server-Carrió, R. Ortiz, S. García-Granda, M.R. Diaz, E. Canton, J. Inorg. Biochem. 69 (1998) 231.
[27] M. Ruíz, R. Ortiz, L. Perelló, A. Castiñeiras, Acta Crystallogr., C 55 (1999) 878.
[28] N. Jiménez-Garrido, L. Perelló, R. Ortiz, G. Alzuet, M. González-Álvarez, E. Cantón, M. Liu-González, S. García-Granda, M. Pérez-Priede, J. Inorg. Biochem. 99 (2005) 677.
[29] Z. Chen, L. Yu, D. Zhong, H. Liang, X. Zhu, Z. Zhou, Inorg. Chem. Commun. 9 (2006) 839.
[30] P. Ruiz, R. Ortiz, L. Perelló, G. Alzuet, M. González-Álvarez, M. Liu-González, F. Sanz-Ruíz, J. Inorg. Biochem. 101 (2007) 831.
[31] G. Mendoza-Díaz, L.M.R. Martinez-Aguilera, R. Moreno-Esparza, K.H. Pannell, F. Cervantes-Lee, J. Inog. Biochem. 50 (1993) 65.
[32] D.K. Saha, S. Padhye, C.E. Anson, A.K. Powell, Transition Met. Chem. 28 (2003) 579.
[33] P. Drevensek, I. Laban, I. Turel, G. Giester, E. Tillmanns, Acta Crystallogr., Sect. C 59 (2003) m376.
[34] D.K. Saha, U. Sandbhor, K. Sirias, S. Padhye, D. Dobagkar, C.E. Anson, A.K. Powell, Bioorg. Med. Chem. Lett. 14 (2004) 3027.
[35] E.K. Efthimiadou, Y. Sanakis, M. Katsarou, C.P. Raptopoulou, A. Karaliota, N. Katsaros, G. Psomas, J. Inorg. Biochem. 100 (2006) 1378.
[36] P. Schaeffer, J. Mollet, J.P. Aubert, Proc. Natl. Acad. Sci. 54 (1965) 704.
[37] D.S. Sigman, A. Mazumder, D.M. Perrin, Cem. Rev. 93 (1993) 2295.
[38] N. Ramírez-Ramírez, G. Mendoza-Díaz, F. Gutiérrez-Corona, M. Pedraza-Reyes, J. Biol. Inorg. Chem. 3 (1998) 188.
[39] S. Arias-Negrete, M. Nieto-Gómez, F. Anaya-Velázquez, R.M. García-Nieto, G. Mendoza-Díaz, Rev. Soc. Quim. 37 (1993) 3.
[40] B.V. Nonius, Collect (1997–2000).
[41] Z. Otwinowski, W. Minor, Methods Enzymol. 276 (1997) 307.
[42] SIR97 A. Altomare, M.C. Burla, M. Camalli, G.L. Cascarano, G. Giacovazzo, A. Guagliardi, A.G.G. Moliterni, G. Polidori, R. Spagna, J. Appl. Crystallogr. 32 (1999) 115.
[43] G.M. Sheldrick, SHELX97. Programs for Crystal Structure Analysis (Release 97-2), University of Göttingen, Germany, 1997.
[44] Parst M. Nardelli, J. Appl. Crystallogr. 28 (1995) 659.
[45] L.J. Farrugia, J. Appl. Crystallogr. 30 (1997) 565.
[46] I. Turel, I. Leban, N. Bukovec, J. Inorg. Biochem. 56 (1994) 273.
[47] S.C. Wallis, L.R. Gahan, B.G. Charles, T.W. Hambley, Polyhedron 14 (1995) 2835.
[48] S.C. Wallis, R. Lawrencem, L.R. Gahan, B.G. Charles, T.W. Hambley, P.A. Duckworth, J. Inorg. Biochem. 62 (1996) 1.
[49] I. Turel, P. Bukovec, M. Quirós, Int. J. Pharm. 152 (1997) 59.
[50] I. Turel, L. Golič, O.L. Ruiz Ramírez, Acta Chim. Slov. 46 (1999) 203.
[51] M.P. López-Gresa, R. Ortiz, L. Perelló, J. Latorre, M. Liu-González, S. García-Granada, M. Pérez-Priede, E. Cantón, J. Inorg. Biochem. 92 (2002) 65.
[52] D. Cremer, J.A. Pople, J. Am. Chem. Soc. 97 (1975) 1354.
[53] G. Mendoza-Díaz, L.M.R. Martínez-Aguilera, R. Pérez-Alonso, X. Solans, R. Moreno-Esperanza, Inorg. Chim. Acta 138 (1987) 41.
[54] D.K. Saha, S. Pradhye, C.E. Anson, A.K. Powell, Transition Met. Chem. 28 (2003) 579.
[55] M. Ruíz, R. Ortíz, L. Perelló, A. Castiñeiras, M. Quirós, Inorg. Chim. Acta 211 (1993) 133.
[56] J.R. Anacona, C. Toledo, Thermochim. Acta (2000).
[57] K. Nakamoto, Infrared and Raman Spectra of Inorganic and Coordination Compounds, John Wiley and Sons, New York, 1986.
[58] A.B.P. Lever, Inorganic Electronic Spectroscopy, second ed., Elsevier, Amsterdam, 1984.
[59] B.N. Figgis, J. Lewis, R.G. Wilkins (Eds.), Modern Coordination Chemistry: Principles and Methods, Interscience, New York, 1960.
[60] P. Drevenšenk, T. Zupančič, B. Pihlar, R. Jerala, U. Kolitsch, A. Plaper, I. Turel, J. Inorg. Biochem. 99 (2005) 432.
[61] P. Gameiro, C. Rodrigues, T. Baptista, I. Sousa, B. De Castro, Int. J. Pharm. 334 (2007) 129.
[62] B. Macias, M.V. Villa, B. Gómez, J. Borrás, G. Alzuet, M. González-Álvarez, A. Castiñeiras, J. Inorg. Biochem. 101 (2007) 444.
[63] D.S. Sigman, Acc. Chem. Res. 19 (1986) 180.

Polyhedron 28 (2009) 145–149

Contents lists available at ScienceDirect

Polyhedron

journal homepage: www.elsevier.com/locate/poly

Syntheses, structures and bioactivities of silver(I) complexes with a tridentate heterocyclic N- and S-ligand

Jing-An Zhang [a,b], Mei Pan [a,*], Jian-Yong Zhang [a], Hai-Ke Zhang [c], Zhi-Jin Fan [c], Bei-Sheng Kang [a], Cheng-Yong Su [a,*]

[a] MOE Laboratory of Bioinorganic and Synthetic Chemistry, School of Chemistry and Chemical Engineering, Sun Yat-Sen University, Guangzhou 510275, PR China
[b] School of Pharmacy, Guangdong Pharmaceutical University, Guangzhou 510006, PR China
[c] State Key Laboratory of Elemento-Organic Chemistry, Nankai University, Tianjin 300071, PR China

ARTICLE INFO

Article history:
Received 19 August 2008
Accepted 18 September 2008
Available online 14 November 2008

Keywords:
Quinoline
Pyridine
Thioether
Complex
Bioactivity

ABSTRACT

Three silver(I) complexes of the asymmetric tridentate ligand 8-((pyridin-3-yl)methylthio)quinoline (TQMP3), namely $[Ag_2(TQMP3)_2(NO_3)_2]$ (**1**), $[Ag_2(TQMP3)_2(CF_3CO_2)_2]$ (**2**) and $\{[Ag_2(TQMP3)_2](CF_3SO_3)_2(H_2O)\}_n$ (**3**), have been prepared by the method of layering and diffusing of diethyl ether. The structures of the complexes have been identified by elemental analysis (EA), infrared spectra (IR) and single-crystal diffraction, and are composed of discrete binuclear rings in complexes **1** and **2**, with π–π interactions or H-bonds further extending the structures into 2D nets, while in complex **3**, Ag···Ag interactions between the rings result in a 1D polymer chain. The antibacterial, antifungal and pesticide activities of the three complexes were tested.

© 2008 Elsevier Ltd. All rights reserved.

1. Introduction

Ligands containing thioether or quinolinyl groups are well-established sources for structurally diverse and biologically active supramolecular complexes. Yuchi, Su, Luciano and Oh et al., have reported a series of transition metal complexes with symmetrical or asymmetrical thioether ligands containing quinolinyl groups [1–12]. Reports on the bioactivities of these kinds of complexes have also increased in recent years, and they show considerable antibactererial, antifungal and pesticide activities [13–15].

Referring to some reported heterocyclic N- and S-ligands [16–18], we designed a new kind of semi-rigid monothioether ligand, 8-((pyridin-3-yl)methylthio) quinoline (TQMP3) (Chart 1), and some discrete binuclear Ag(**I**) complexes were obtained using this ligand. We report herein the synthesis of the ligand and the structures of its three Ag(**I**) complexes. The antibacterial, antifungal and pesticide activities of the complexes have been tested.

2. Experimental

2.1. Materials and general methods

Silver nitrate, silver trifluoroacetate and silver trifluoromethylsulfonate were purchased from Aldrich Chemical Co. Inc., while sodium 8-mercaptoquinoline [19] and 3-chloromethylpyridine hydrochloride [20,21] were prepared according to reported procedures. All the other reagents and solvents were commercially available and employed as received or purified by standard methods prior to use. All reactions involving thiols were carried out under a nitrogen atmosphere. Elemental analyses were performed on a Germany Vario EL analyzer (Elementar) and IR spectra on an Avatar 330 FT-IR (Thermo Nicolet) spectrometer with KBr pellets. ^{1}H NMR spectra were recorded on a Mercury-Plus 300 spectrometer (VARIAN, 300 MHz) at 25 °C in $CDCl_3$ with tetramethylsilane as the internal reference. The UV–Vis spectra were recorded on a CARY-300 spectrometer (VARIAN).

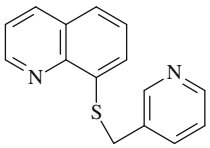
2.2. Syntheses of the ligand and the complexes

2.2.1. Preparation of the ligand 8-[(pyridin-3-yl)methylthio]quinoline (TQMP3)

Sodium hydroxide (1.800 g, 45 mmol) and potassium iodide (0.322 g, 2 mmol) were dissolved in anhydrous ethanol (100 mL) in a 250 mL three-neck flask with a magnetic stirrer, a reflux condenser and an isobaric drop tundish. Sodium 8-mercaptoquinoline (4.045 g, 20 mmol) was added to the above mixture and dissolved by stirring under nitrogen. 3-Chloromethylpyridine hydrochloride (3.418 g, 21 mmol) in anhydrous ethanol (50 mL) was dropped into the mixed solution under nitrogen and heated in an oil bath at 80 °C for 8 h. Then it was cooled to room temperature, filtrated and washed with anhydrous ethanol (10 mL × 2). The filtrate was

* Corresponding authors. Tel.: +86 20 8411 0539; fax: +86 20 8411 5178 (M. Pan).
E-mail address: panm@mail.sysu.edu.cn (M. Pan).

0277-5387/$ - see front matter © 2008 Elsevier Ltd. All rights reserved.
doi:10.1016/j.poly.2008.09.029



TQMP$_3$

Chart 1. Structure of the ligand.

concentrated and dropped into petroleum ether (60–90 °C), stirred strongly and then cooled to 4 °C. Yellow-white crystals were recrystallized in ethanol in 65.3% yield (3.435 g). IR (KBr pellet, cm^{-1}): 3028 (w), 2923 (w), 1583 (m), 1445 (vs), 1371 (m), 1301 (w), 1196 (w), 1082 (w), 1028 (w), 982 (m), 821 (m), 714 (m), 655 (w). ^{1}H NMR ($CDCl_3$, 300 MHz): 8.95–8.97 (q, 1H, Ha), 8.60–8.61 (d, 1H, Hj), 8.47–8.49 (q, 1H, Hc), 7.75–7.79 (m, 1H, Hh), 7.61–7.64 (q, 1H, Hf), 7.44–7.51 (m, 3H, Hd, e, i), 7.20–7.24 (q, 1H, Hb), 4.32 (s, 2H, Hg). UV (CH_3CN, λ, nm): 215.0 ($\varepsilon = 3.5 \times 10^3$ dm^3 mol^{-1} cm^{-1}), 250.0 (1.5×10^4), 330.0 (3.6×10^3). *Anal.* Calc. for $C_{15}H_{12}N_2S$: C, 71.40; H, 4.79; N, 11.10. Found: C, 71.04; H, 4.92; N, 10.91%.

2.2.2. Syntheses of the complexes

$[Ag_2(TQMP3)_2(NO_3)_2]$ (**1**). The linear tridentate ligand 8-[(pyridin-3-yl)methylthio]quinoline (TQMP3) (25 mg, 0.10 mmol) was dissolved in chloroform (3 mL) and acetone (2 mL), and the mixture was filtered into the bottom of a tube, then chloroform (1 mL) and acetonitrile (3 mL) were added very slowly onto the mixture, and silver nitrate (23 mg, 0.14 mmol) in absolute acetonitrile (3 mL) was layered on the top. The tube was sealed with film and put in dark for some days, and thus colorless crystals were obtained. The crystals were filtered and washed several times in anhydrous diethyl ether and then dried in vacuum. Yield 59% (25 mg). IR (KBr pellet, cm^{-1}): 3027 (w), 2923 (w), 1594 (m), 1575 (m), 1489 (m), 1456 (m), 1381 (vs), 1302 (m), 1190 (w), 1071 (w), 1027 (w), 985 (m), 822 (m), 788 (m), 754 (m), 711 (w), 657 (w). ^{1}H NMR (DMSO-d_6, 300 MHz): 8.86–8.88 (q, 1H), 8.58–8.59 (d, 1H), 8.41–8.42 (d, 1H), 8.38–8.39 (q, 1H), 7.81–7.82 (m, 2H), 7.79–7.80 (d, 1H), 7.73–7.75 (d, 1H), 7.58–7.62 (q, 1H), 7.52–7.55 (d, 1H), 7.29–7.33 (q, 1H), 4.38 (s, 2H). UV (CH_3CN, λ, nm): 250.0 ($\varepsilon = 8.5 \times 10^4$ dm^3 mol^{-1} cm^{-1}), 325.8 (2.4×10^4). *Anal.* Calc. for $C_{15}H_{12}AgN_3O_3S$: C, 42.67; H, 2.86; N, 9.95. Found: C, 42.42; H, 2.89; N, 10.04%.

$[Ag_2(TQMP3)_2(CF_3CO_2)_2]$ (**2**). The ligand 8-[(pyridin-3-yl)methylthio]quinoline (TQMP3) (25 mg, 0.10 mmol) was dissolved in chloroform (3 mL) and acetone (2 mL), and the mixture was filtered into the bottom of a tube, then chloroform (1 mL) and acetonitrile (3 mL) were added very slowly onto the mixture, and silver trifluoroacetate (28 mg, 0.13 mmol) in absolute acetonitrile (3 mL) was layered on the top. The tube was sealed with film and put in dark for some days, and thus colorless crystals were obtained. The crystals were filtered and washed several times in anhydrous diethyl ether, and then dried in vacuum. Yield 70% (33 mg). IR (KBr pellet, cm^{-1}): 3039 (w), 2917 (w), 1686 (vs), 1582 (w), 1484 (w), 1426 (m), 1369 (w), 1206 (s), 1130 (s), 987 (w), 802 (w), 718 (w), 652 (w). ^{1}H NMR (DMSO-d_6, 300 MHz): 8.85–8.87 (q, 1H), 8.62 (s, 1H), 8.41–8.42 (d, 1H), 8.35–8.38 (q, 1H), 7.82–7.85 (d, 1H), 7.74–7.77 (q, 1H), 7.66–7.68 (d,1H), 7.55–7.60 (m, 1H), 7.50–7.52 (d, 1H), 7.30–7.34 (q, 1H), 4.37 (s, 1H). UV (CH_3CN, λ, nm): 249.8 ($\varepsilon = 5.1 \times 10^4$ dm^3 mol^{-1} cm^{-1}), 329.0 (1.3×10^4). *Anal.* Calc. for $C_{34}H_{24}Ag_2F_6N_4O_4S_2$: C, 43.15; H, 2.56; N, 5.92. Found: C, 43.18; H, 2.56; N, 6.01%.

$\{[Ag_2(TQMP3)_2](CF_3SO_3)_2(H_2O)\}_n$ (**3**). A solution of $AgCF_3SO_3$ (28 mg, 0.11 mmol) in CH_3CN (3 mL) was added to a solution of TQMP3 (25 mg, 0.10 mmol) in $CHCl_3$ (3 mL) and CH_3COCH_3 (2 mL). Slow diffusion of diethyl ether into the resulting solution yielded colorless single crystals of **3**, which were filtered and washed several times in anhydrous diethyl ether, and then dried in vacuum. Yield 69% (36 mg) based on TQMP3. IR (KBr pellet, cm^{-1}): 3438 (w), 3028 (w), 2925 (w), 1596 (m), 1489 (m), 1457 (m), 1425 (m), 1375 (m), 1251 (vs), 1169 (s), 1048 (s), 985 (m), 820 (m), 788 (m), 712 (m), 657 (s), 579 (m), 520 (m). ^{1}H NMR (DMSO-d_6, 300 MHz): 8.85–8.87 (q, 1H), 8.63–8.64 (d, 1H), 8.41–8.43 (m, 1H), 8.33–8.36 (q, 1H), 7.84–7.86 (d, 1H), 7.71–7.74 (d, 1H), 7.62–7.65 (t, 1H), 7.54–7.59 (m, 1H), 7.48–7.51 (d, 1H), 7.30–7.34 (q, 1H), 4.37 (s, 2H). UV (CH_3CN, λ, nm): 250.4 ($\varepsilon = 3.9 \times 10^4$ dm^3 mol^{-1} cm^{-1}), 331.0 (9.4×10^3). *Anal.* Calc. for $C_{16}H_{13}AgF_3N_2O_{3.50}S_2$: C, 37.08; H, 2.53; N, 5.41. Found: C, 37.31; H, 2.48; N, 5.50%.

2.3. Antimicrobial assay

The complexes were dissolved in DMSO (dimethylsulfoxide) and tested against five aerobic reference strains for their inhibitory activities. The antimicrobial assays were performed using a modified version of the 2-fold serial dilution method of R.A. Fromtling (1993), in which two starting yeast inoculum sizes ($5 \times 10(4)$ and $2.5 \times 10(3)$ cells per ml) were compared, and readings were taken after 24 and 48 h of incubation. All other test conditions were standardized. The resultant turbidities in all tubes were estimated visually on a scale from 0 to ++++ turbidity, and MIC-0, MIC-1 and MIC-2 were defined as the lowest drug concentrations that reduced the growth to 0, + or ++ turbidity, respectively [22].

2.4. X-Ray diffraction analyses

Single-crystal X-ray diffraction measurements of complexes **1**–**3** were carried out on an Oxford Gemini S Ultra CCD diffractometer equipped with a graphite monochromator at 150 K. The determination of unit cell parameters and data collection were performed with Mo Kα radiation ($\lambda = 0.71073$ Å). The unit cell parameters were obtained with least-squares refinements and all structures were solved by direct methods [23]. The Ag atoms in each complex were located from *E*-maps. The other non-hydrogen atoms were located in successive difference Fourier syntheses. The final refinement was performed by full matrix least-squares methods with anisotropic thermal parameters for non-hydrogen atoms against F_0^2 [24]. Hydrogen atoms were added in calculated positions.

3. Results and discussion

3.1. Spectral analyses

3.1.1. ^{1}H NMR spectra

The ^{1}H NMR spectrum of the ligand is shown in Fig. 1 and the main data for both the ligand and the three complexes are listed in part 2. From the ^{1}H NMR data, we can see that in the complexes, the proton resonances on the $-CH_2$ linking group and the –CH groups far from the N atom on the heterocyclic rings shift to lower fields as compared to those in the free ligand (4.32 → 4.37–4.38 (s, 2H, Hg), 7.20–7.24 → 7.29–7.34 (q, 1H, Hb), 7.44–7.51 → 7.48–7.55 (m, 3H, Hd, e, i), which could be explained by the fact that upon coordination these groups are further shielded by another heterocyclic ring. In contrast, the other proton resonances on the heterocyclic rings shift to higher field as compared to those in the free ligand, which can be attributed to the packing effects amongst the rings.

3.1.2. IR spectra

The IR data for the ligand and the three complexes are listed in part 2. We can see that in the complexes, except for the peaks

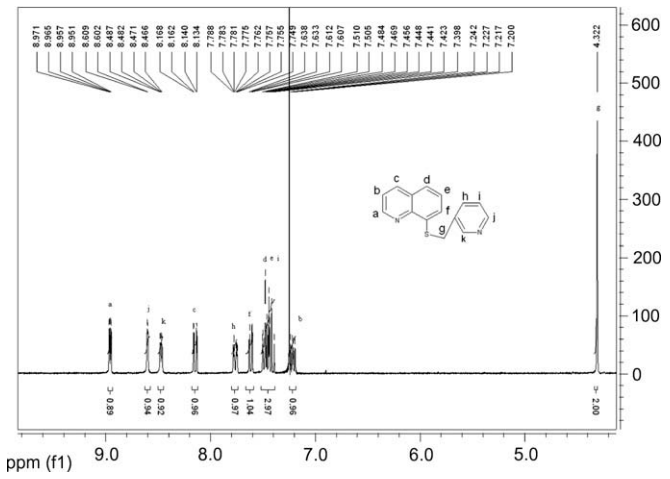


Fig. 1. ^{1}H NMR spectra of the ligand.

relevant to the ligand, they also show the typical peaks of the corresponding anions, i.e., 1575, 1381, 754 cm^{-1} for NO_3^- in complex **1**, 1686, 1484, 1206, 802, 718 cm^{-1} for $CF_3CO_2^-$ in complex **2**, and 1251, 1169, 1048, 657 cm^{-1} for $CF_3SO_3^-$ in complex **3**. These data prove the formation of coordination complexes.

3.1.3. UV spectra

The UV data for the ligand and the three complexes are also listed in part 2. We can see that in complexes **1** and **2**, the two absorbance peaks are caused by the characteristic $\pi \rightarrow \pi^*$ transition in the ligand, but they both show slight blue-shifts compared to those in the free ligand, which is due to strengthening in the π conjugate systems after coordination. In contrast, the two peaks in complex **3** show slight red-shifts, which can be attributed to the infinite polymer chain structure of the complex.

3.2. Crystal structures

The unit structures of complexes **1** and **2** are basically the same, composed of a dimetallic ring, as shown in Fig. 2. In the asymmetry unit, the Ag(I) center is in a distorted tetrahedral geometry, which is coordinated by two N atoms from one quinoline ring (Ag–N = 2.366(3) Å in **1** and 2.383(5) Å in **2**) and one pyridine moiety (Ag–N = 2.225(8) Å in **1** and 2.243(5) Å in **2**) from two different ligands. The remaining coordinated sites are occupied by a S atom from one ligand (Ag–S1 = 2.519(9) Å in **1** and 2.569(6) Å in **2**) and one O atom from NO_3^- (Ag–O1 = 2.366(3) Å) in **1** or the $CF_3CO_2^-$ anion (Ag–O1 = 2.539(6) Å) in **2**. In the $[Ag_2L_2(X)_2]$ ($X = NO_3^-$ or $CF_3CO_2^-$) unit, a twelve-membered ring is formed by the two Ag1 centers and the corresponding atoms on the two ligands.

In complex **1**, each molecular ring piles up with bordering rings by strong π-π interactions between the quinoline rings and pyridine rings, extending into a 2D structure in the *ac* plane. The central distance between the quinoline rings is 3.539 Å and that between the pyridine rings is 3.535 Å. While in complex **2**, the oxygen atoms in the $CF_3CO_2^-$ anion and hydrogen atoms on the quinoline ring form O1···H–C11 (Qui) and O2···H–C6 (CH_2) hydrogen bonds (3.312 and 3.370 Å), and a fluorine atom in the $CF_3CO_2^-$ anion

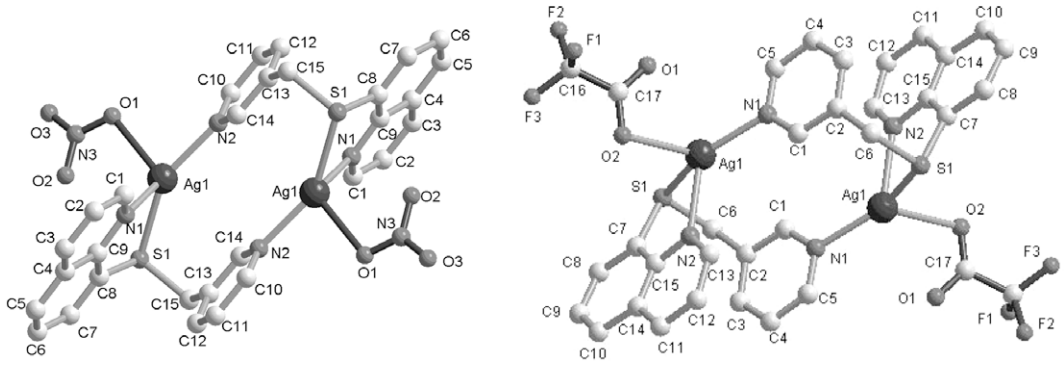


Fig. 2. Unit structures of complexes **1** (left) and **2** (right) (H atoms are omitted).

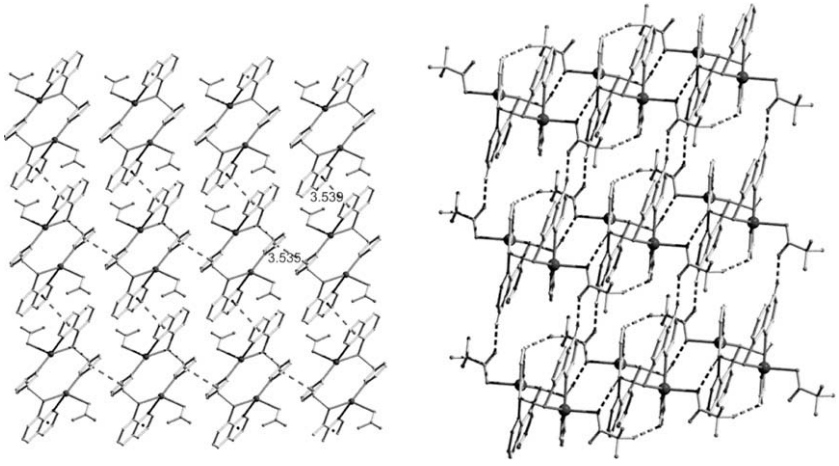


Fig. 3. Weak interactions and packing modes in complexes **1** (left) and **2** (right) (H atoms are omitted).

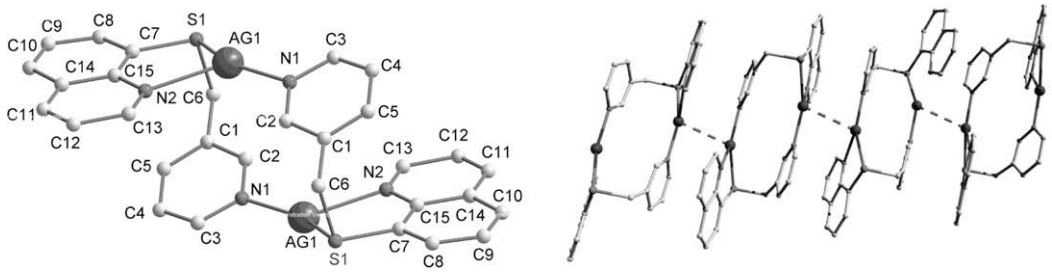


Fig. 4. Unit structure (left) and weak interactions (right) in complex **3** (H atoms and anions are omitted).

and a hydrogen atom on the pyridine ring form the F1···H–C5 (Py) hydrogen bond (3.243 Å), and thus a 2D net is formed along the *c* axis, as shown in Fig. 3.

In complex **3**, the self-assembly of Ag(I) ions and TQMP3 ligands gives the binuclear $[Ag_2(TQMP3)_2]$ $(CF_3SO_3)_2$ unit. Different from the above two complexes, the central Ag(I) is three coordinated by one S atom (d_{Ag-S} = 2.554(2) Å), one quinoline N atom (d_{Ag-N} = 2.347(2) Å) from one ligand, and one pyridyl N atom (d_{Ag-N} = 2.199(2) Å) from another ligand, forming a T-shaped configuration (Fig. 4 left). The $CF_3SO_3^-$ anions do not participate in the coordination and only act as counter anions for charge equilibrium. In the crystals, there exist Ag···Ag interactions between neighboring binuclear rings (d_{Ag-Ag} = 3.123(3) Å) and a 1D polymer chain is formed (Fig. 4 right). The data of the main bond lengths (Å) and angles (°) for complexes **1**–**3** are listed in Tables 1–3 and the crystallographic data and structure refinement summary are listed in Table 4.

3.3. The antibacterial, antifungal and pesticide activities of the three complexes

From the antibacterial results listed in Table 5, we can see that the three complexes show different inhibition activities against various kinds of bacteria. All of them have good efficiency in inhibiting *P. aeruginosa* and *Sarcina ureae*, while all are poor against *Escherichia coli*. Among them, complex **2** appears to be the most powerful one, showing quite good MIC values ($\leqslant$0.25 μg mL^{-1})

Table 1
Selected bond lengths (Å) and angles (°) for complex **1**.

Ag(1)–N(2a)	2.225(3)	Ag(1)–O(1)	2.494(3)
Ag(1)–N(1)	2.366(3)	Ag(1)–S(1)	2.519(1)
N(2*a*)–Ag(1)–N(1)	121.3(1)	O(1)–Ag(1)–S(1)	109.2(7)
N(2*a*)–Ag(1)–O(1)	87.2(1)	C(8)–S(1)–C(15)	100.2(1)
N(1)–Ag(1)–O(1)	113.1(1)	C(8)–S(1)–Ag(1)	98.4(1)
N(2*a*)–Ag(1)–S(1)	148.1(1)	C(15)–S(1)–Ag(1)	107.1(1)
N(1)–Ag(1)–S(1)	78.2(1)		

Symmetry code: (a) $-x+1, -y+1, -z+1$.

Table 2
Selected bond lengths (Å) and angles (°) for complex **2**.

Ag(1)–N(1)	2.244(4)	Ag(1)–O(2*b*)	2.539(4)
Ag(1)–N(2*a*)	2.383(4)	Ag(1)–S(1*a*)	2.569(1)
xN(1)–Ag(1)–N(2*a*)	118.3(1)	N(1)–Ag(1)–S(1*a*)	142.0(1)
N(1)–Ag(1)–O(2*b*)	116.1(1)	N(2*a*)–Ag(1)–S(1*a*)	77.0(1)
N(2*a*)–Ag(1)–O(2*b*)	86.7(1)	O(2*b*)–Ag(1)–S(1*a*)	98.4(1)

Symmetry code: (a) $-x+1, -y+1, -z$, (b) $x-1, y, z-1$.

Table 3
Selected bond lengths (Å) and angles (°) for complex **3**.

Ag(1)–N(1*a*)	2.199(5)	Ag(1)–S(1)	2.555(2)
Ag(1)–N(2)	2.347(6)	Ag(1)–Ag(1*b*)	3.124(1)
N(1*a*)–Ag(1)–N(2)	128.8(2)	N(1*a*)–Ag(1)–Ag(1*b*)	78.3(1)
N(1*a*)–Ag(1)–S(1)	150.1(1)	N(2)–Ag(1)–Ag(1*b*)	96.4(1)
N(2)–Ag(1)–S(1)	77.6(2)	S(1)–Ag(1)–Ag(1*b*)	116.6(5)

Symmetry code: (a) $-x+1, -y+1, -z+1$, (b) $-x+1, y, -z+1/2$.

Table 4
Crystallographic data and structure refinement summary for complexes **1**–**3**.

Identification code	**1**	**2**	**3**
Chemical formula	$C_{15}H_{12}AgN_3O_3S$	$C_{34}H_{24}Ag_2F_6N_4O_4S_2$	$C_{16}H_{13}AgF_3N_2O_{3.50}S_2$
Formula weight	422.21	946.43	518.27
Crystal system	monoclinic	triclinic	monoclinic
Space group	*P*2(1)/*n*	$P\bar{1}$	*C*2/*c*
a (Å)	8.5615(3)	7.141(2)	16.2829(16)
b (Å)	15.4789(8)	10.396(3)	16.779(2)
c (Å)	11.4205(4)	11.745(2)	13.5178(14)
α (°)	90.00	93.28(2)	90.00
β (°)	94.353(3)	101.85(2)	91.148(10)
γ (°)	90.00	99.64(3)	90.00
V (Å^3)	1509.11(11)	837.5(4)	3692.5(7)
Z	4	1	8
ρ_{calc} (g cm^{-3})	1.858	1.877	1.865
Stability	good	good	good
Solubility	soluble in DMF/DMSO	soluble in DMF/DMSO	soluble in DMF/DMSO
(Mo Kα) (mm^{-1})	1.492	1.374	1.37
F(000)	840	468	2056
T (K)	150(2)	150(2)	150(2)
Reflections collected	2545	2868	2216
Data/restrains/parameters	2545/6/208	2868/18/235	3041/26/252
Final *R* indexes [$I > 2\sigma(I)$]	R_1 = 0.0292, wR_2 = 0.0587	R_1 = 0.0460, wR_2 = 0.1205	R_1 = 0.0634, wR_2 = 0.1758
Final *R* indexes [all data]	R_1 = 0.0477, wR_2 = 0.0631	R_1 = 0.0535, wR_2 = 0.1256	R_1 = 0.0912, wR_2 = 0.1817
Unique reflections (R_{int})	6739/2545 (0.0295)	5849/2868 (0.0502)	8585/4259 (0.0389)

Table 5
Tests of MIC (μg/mL) of the compounds against four bacterial and three fungal strains[a].

Strains	Compounds					
	1	**2**	**3**	Amp[b]	Str[b]	Nys[b]
Staphylococcus aureus ATCC 27154 (G$^+$)	>50	0.25	25	12.5	1.56	NT
Escherichia coli ATCC 25922 (G$^-$)	>50	>50	>50	6.25	3.13	NT
P. aeruginosa (G$^-$)	0.06	0.06	6.25	3.13	1.56	NT
Sarcina ureae (G$^+$)	12.5	0.25	6.25	3.13	3.13	NT
Aspergillus niger	125	>125	>125	NT	NT	3.9
Saccharomyces cerevisiae	31.25	125	125	NT	NT	3.9
Fusarium oxysporum f. sp. cubense	31.25	62.5	62.5	NT	NT	7.8

[a] The results are expressed as the minimum inhibitory concentration (MIC).
[b] Ampicillin (Amp), Streptomycin sulfate (Str), Nystatin (Nys): positive control; NT, not tested.

Table 6
Tests of pesticide activities of the complexes against five botanic bacteria.

Bacteria code	1		2		3	
	Percentage	Grade	Percentage	Grade	Percentage	Grade
C	38.18		52.73	+	56.36	+
F	11.11		77.78	++	55.56	+
U	52.94	+	82.35	++	52.94	+
I	67.09	+	82.28	++	51.90	+
D	52.00	+	68.00	+	60.00	+

Notes: (1) Biological activity is shown with killing or restraining percentage.
(2) Grades of biological activity to insect bacteria are +++ is ⩾90%; ++ is ⩾70–89%; + is ⩾50–69%; s- is <50%.
(3) C is cucumber fusarium wilt (*Fusarium oxysporum f. cucumerinum*); F is tomato early blight (*A. solani*); U is watermelon anthracnose (*C. lagenarium*); I is apple ring rot (*Physalospora piricola*); D is peanut brown spot (*Cercospora rachidicola*).

against both the bacteria with G^+ (*Staphylococcus aureus* and *S. ureae*) and those with G^- (*P. aeruginosa*), except for *E. coli*, providing potential applications in the broad spectrum of the anti-bacteria field.

The antifungal activities of the three complexes show that only complex **1** has considerable effect against *Saccharomyces cerevisiae* (*S. c*) and *Fusarium oxysporum f.sp.cubense* (*F. o*) (MIC = 31.25 μg mL^{-1}). The effects of the other complexes were poor in inhibiting fungal activities. The experimental results are also listed in Table 5.

The pesticidal activities of the three complexes against five botanic bacteria show that complexes **1**–**3** have distinct effects to inhibit cucumber fusarium wilt (*Fusarium oxysporum f. cucumerinum*, *C*), tomato early blight (*Alternaria solani*, F), watermelon anthracnose (*Colletotrichum lagenarium*, *U*), apple ring rot (*Physalospora piricola*, *I*) and peanut brown spot (*Cercospora rachidicola*, *D*), except that complex **1** has no effect against *C* and *F*. Complex **2** has the most powerful effect against *F*, *U* and *I*. The experimental results are listed in Table 6.

From the above results, we can see that for complexes **1** and **2**, with discrete binuclear rings aligned together by hydrogen bonds and π–π interactions, the bioactivities are comparatively better than complex **3** with a polymeric structure. This may be due to the fact that the relatively crowded packing of the heterocyclic rings in complex **3** makes it difficult to insert into the DNA helical chains in the bacterial or fungal molecules, and therefore makes it show worse inhibition results.

4. Conclusions

Three silver complexes from the ligand 8-((pyridin-3-yl)methylthio)quinoline (TQMP3) have been prepared and characterized, and they have been shown to have discrete or connected binuclear subunit rings in the crystal structures. Different kinds of intermolecular interactions, such as H-bonds, π–π interactions or Ag···Ag interactions, extend the structures into a 1D chain or 2D net. The antibacterial activity tests show that the three complexes are quite efficient at inhibiting certain bacteria, such as *P. aeruginosa* and *S. ureae*, while their antifungal activities are not quite so good. As for the pesticide activities, complexes **1**–**3** have distinctly inhibited several kinds of botanic bacteria, with complex **2** being the most powerful one against *A. solani* (F), *C. lagenarium* (U) and *P. piricola* (I). In general, complexes **1** and **2**, with discrete binuclear structures, show more efficient bioactivities than the polymeric complex **3**.

Supplementary data

CCDC 694468–694470 contain the supplementary crystallographic data for complexes **1**–**3**. These data can be obtained free of charge via http://www.ccdc.cam.ac.uk/conts/retrieving.html, or from the Cambridge Crystallographic Data Centre, 12 Union Road, Cambridge CB2 1EZ, UK; fax: (+44) 1223-336-033; or e-mail: deposit@ccdc.cam.ac.uk.

Acknowledgements

This work has been supported by the Outstanding Youth Foundation of NSFC (No. 20673147). We also thank the Natural Science Foundation of China (20673147 and 20672062), the Natural Science Foundation of Tianjin (07JCYBJC01200) and the starting-up foundation for young teachers in Sun Yat-Sen University.

References

[1] A. Yuchi, M. Shipo, H. Wada, G. Nakagawa, Bull. Chem. Soc. Jpn. 65 (1992) 2275.
[2] C.Y. Su, B.S. Kang, J. Sun, Chem. Lett. 8 (1997) 821.
[3] C.Y. Su, D.K. Li, W.Z. Zeng, B.S. Kang, Acta Sci. Nat. Univ. Sun Yat-Seni 37 (1998) 122 (in Chinese).
[4] C. Luciano, V. Fabiano, C. Gavino, U. Paolo, L. Carlo, D. Alessandro, B. Giuliano, Organometallics 25 (2006) 5355.
[5] Y.J. Zhao, M.C. Hong, Y.C. Liang, W.P. Su, R. Cao, Z.Y. Zhou, A.S.C. Chan, Polyhedron 20 (2001) 2619.
[6] C.L. Chen, C.Y. Su, Y.P. Cai, H.X. Zhang, A.W. Xu, B.S. Kang, H.C. zur Loye, Inorg. Chem. 42 (2003) 3738.
[7] C.Y. Su, S. Liao, H.L. Zhu, B.S. Kang, X.M. Chen, H.Q. Liu, J. Chem. Soc., Dalton Trans. (2000) 1985.
[8] S. Liao, C.Y. Su, H.X. Zhang, J.L. Shi, Z.Y. Zhou, H.Q. Liu, A.S.C. Chan, B.S. Kang, Inorg. Chim. Acta 336 (2002) 151.
[9] M. Oh, C.L. Stern, C.A. Mirkin, Chem. Commun. 23 (2004) 2684.
[10] M. Oh, C.L. Stern, C.A. Mirkin, Inorg. Chem. 44 (2005) 2647.
[11] Adeline Y. Robin, Katharina M. Fromm, Coord. Chem. Rev. 250 (2006) 2127.
[12] Katharina M. Fromm, Jorge L. Sagué Doimeadios, Adeline Y. Robin, Chem. Commun. 36 (2005) 4548.
[13] J.L. Liu, Master Thesis of Qufu Normal University, 2006.
[14] J. Zhang, Master Thesis of Qufu Normal University, 2005.
[15] J. Gao, Master Thesis of Zhengzhou University, 2003.
[16] C. Luciano, V. Fabiano, C. Gavino, U. Paolo, L. Carlo, D. Alessandro, B. Giuliano, Organometallics 25 (2006) 5355.
[17] R.F. Song, Y.B. Xie, J.R. Li, X.H. Bu, J. Chem. Soc., Dalton Trans. (2003) 4742.
[18] R.F. Song, Y.B. Xie, J.R. Li, X.H. Bu, CrystEngComm 7 (2005) 249.
[19] S. Liao, Doctor Thesis of Sun Yat-Sen University, 2000.
[20] Y. Wang, L.W. Liu, L. Alexandre, L. Olivier, P. Diane, US 5942625, 19990824.
[21] W.E. Bay, M.A. Brown, D.R. Kilanowski, WO 9532186, 19951130.
[22] R.A. Fromtling, J.N. Galgiani, M.A. Pfaller, A. Espinel-Ingroff, K.F. Bartizal, M.S. Bartlett, B.A. Body, C. Frey, G. Hall, G.D. Roberts, F.B. Nolte, E.C. Odds, M.G. Rinaldi, A.M. Suger, K. Villareal, Antimicrob. Agents Chemother. 37 (1993) 39.
[23] G.M. Sheldrick, SHELXS-97, Program for Solution of Crystal Structures, University of Göttingen, Germany, 1997.
[24] G.M. Sheldrick, SHELXL-97, Program for Refinement of Crystal Structures, University of Göttingen, Germany, 1997.

Polyhedron 28 (2009) 150–156

Contents lists available at ScienceDirect

Polyhedron

journal homepage: www.elsevier.com/locate/poly

Coordination polymers of Mn(II) and Cu(II) orotate with 2-methylimidazole and *N,N,N′,N′*-tetramethylethylenediamine ligands: Syntheses, spectroscopic and thermal analyses and crystal structures of *mer*-$[Mn(\mu\text{-}HOr)(H_2O)(2\text{-}meim)_2]_n$ and thermochromic $\{[Cu(\mu\text{-}HOr)(tmen)] \cdot 1.5H_2O\}_n$ complexes

Okan Zafer Yeşilel [a,*], Hakan Erer [a], Aylin Mutlu [a], Orhan Büyükgüngör [b]

[a] Eskişehir Osmangazi University, Faculty of Arts and Sciences, Department of Chemistry, 26480 Eskişehir, Turkey
[b] Ondokuz Mayıs University, Faculty of Arts and Sciences, Department of Physics, 55139 Samsun, Turkey

ARTICLE INFO

Article history:
Received 23 May 2008
Accepted 26 September 2008
Available online 17 November 2008

Keywords:
Orotate complexes
Coordination polymers
Thermochromism
2-Methylimidazole complexes
N,N,N′,N′-Tetramethylethylenediamine complexes

ABSTRACT

The syntheses, FT-IR and UV–Vis spectra, thermal analyses and crystal structures of Mn(II) and Cu(II) orotate coordination polymers with 2-methylimidazole (2-meim) and *N,N,N′,N′*-tetramethylethylenediamine (tmen) ligands are described. The orotate ligand acts as a bridging ligand with two different coordination modes, the $\{mer\text{-}[Mn(\mu\text{-}HOr)(H_2O)(2\text{-}meim)_2]\}_n$ (**1**) complex displays an linear chain structure in which each Mn(II) ion exhibits a distorted octahedral coordination by a tridentate orotate, two 2-meim and one aqua ligand. In $\{[Cu(\mu\text{-}HOr)(tmen)] \cdot 1.5H_2O\}_n$ (**2**), the Cu(II) ion is coordinated by a tridentate orotate and one bidentate tmen ligand, and exhibits a square pyramidal geometry. These polymer chains are linked by hydrogen-bond interactions forming a three-dimensional network. Complex **2** exhibits an irreversible thermochromic effect. After dehydration, the color of the complex changes from blue to green.

© 2008 Elsevier Ltd. All rights reserved.

1. Introduction

The construction of novel supramolecular coordination polymers has been of increasing interest in recent years due to their potential applications in material sciences [1–5]. Organic molecules containing carboxylic acid have been used as building blocks in crystal engineering and many coordination polymers [6–8]. Orotic acid (2,6-dioxo-1,2,3,6-tetrahydropyrimidine-4-carboxylic acid, vitamin B13, and H_3Or) is a well-known versatile ligand able to chelate as well as to bridge metal ions, leading to the formation of polynuclear complexes [9–13], and it has been widely studied in recent years as a polyfunctional ligand because of its significance in the biosynthesis of pyrimidine bases, with antitumour activity displays for Ni(II), Pt(II), and Pd(II) complexes. The orotate ligand coordinates to metal ions by means of its four oxygen atoms of carboxyl or carbonyl groups and two nitrogen atoms, forming monodentate [14,15], bidentate [16–19], bis(bidentate) [20–22], tridentate bridging [23,24,7], tetradentate bridging [12] and mixed chelating-bridging coordination modes [25–27]. Until now, the crystal structures of two polynuclear Mn(II)–orotate complexes, $[Mn_2(HOr)_2(H_2O)_6]_n$ [12] and $[Mn(HOr)(H_2O)(bipy)]_n$ [13], and two mononuclear Mn(II)–orotate complexes, $[Mn(HOr)(H_2O)(phen)]$ [28] and $(enH_2)[Mn(HOr)_2(H_2O)_2]$ [20], have been reported, in which the orotate ligand acts as a tridentate bridging ligand and a bidentate ligand (N1, O1). Although there are many copper(II)–orotate complexes with mononuclear structures, $[Cu(HOr)(phen)]$ [29], $[Cu(HOr)(mea)_2]$ [30], $[Cu(HOr)(H_2O)(en)] \cdot H_2O$ [19], $[Cu(HOr)(tea)] \cdot H_2O$ [31], $[Cu(HOr)(bipy)(H_2O)] \cdot H_2O$ [32], and $[Cu(HOr)(etpy)]_2$ [33], only one polynuclear orotate complex of the Cu(II) ion has been reported, by Ha et al. [9].

Recently, we have reported the synthesis and structures of orotate complexes with different amines [19–22,30–47]. In the present study, we describe the preparation, spectral, thermal (TG, DTG, and DTA) and crystal structures of two novel supramolecular coordination polymers of Mn(II) and Cu(II) orotate with 2-methylimidazole and *N,N,N′,N′*-tetramethylethylenediamine ligands (Scheme 1.): *mer*-$[Mn(\mu\text{-}HOr)(H_2O)(2\text{-}meim)_2]_n$ (**1**) and $\{[Cu(\mu\text{-}HOr)(tmen)] \cdot 1.5H_2O\}_n$ (**2**).

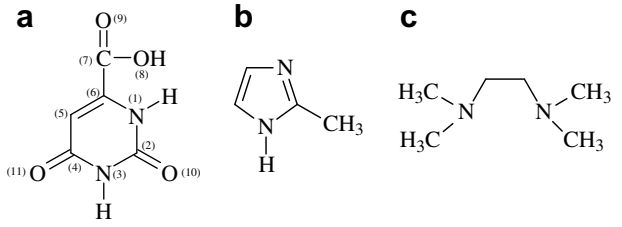
2. Experimental

2.1. Preparation of the complexes

A solution of orotic acid monohydrate (0.871 g, 5 mmol) in water (50 mL) was added dropwise with stirring at 50 °C to a solution of $Mn(CH_3COO)_2 \cdot 4H_2O$ (1.23 g, 5 mmol) or $Cu(CH_3COO)_2 \cdot H_2O$ (1.00 g, 5 mmol) in distilled water (25 mL). The

* Corresponding author.
E-mail address: yesilel@ogu.edu.tr (O.Z. Yeşilel).

0277-5387/$ - see front matter © 2008 Elsevier Ltd. All rights reserved.
doi:10.1016/j.poly.2008.09.024



Scheme 1. (a) Orotic acid, (b) 2-methylimidazole, (c) *N,N,N′,N′*-tetramethylethylene diamine.

solution immediately became a suspension and was stirred for 4 h at 50 °C. Then 2-methylimidazole (1.65 g, 20 mmol) for **1** and *N,N,N′,N′*-tetramethylethylenediamine (1.16 g, 10 mmol) for **2** in water (10 mL) was added dropwise to this suspension. The clear solution that formed was stirred for 2 h at 50 °C and then cooled to room temperature. The crystals that formed were filtered and washed with 10 mL of water and were dried in air.

2.2. Materials and measurements

All chemicals used were analytical reagents and were commercially purchased. IR spectra were obtained with a Perkin Elmer 100 FT-IR spectrometer using KBr pellets in the 4000–400 cm^{-1} range. The UV–Vis spectrum was obtained for an aqueous solution of the complex (10^{-3} M) with a Shimadzu UV-3150 spectrometer in the range 900–190 nm. Magnetic susceptibility measurements at room temperature were performed using a Sherwood Scientific MXI model Gouy magnetic balance. A Perkin Elmer Diamond TG/DTA Thermal Analyzer was used to record simultaneous TG, DTG and DTA curves in static air atmosphere at a heating rate of 10 °C min^{-1} in the temperature range 20–600 °C using platinum crucibles.

2.3. Crystallographic analyses

Diffraction experiments were carried out at 296 K on a Stoe IPDS diffractometer. The structures were solved by direct methods and refined using the programs SHELXS97 and SHELXL97 [48]. All non-hydrogen atoms were refined anisotropically by full-matrix least-squares methods [48]. The hydrogen atoms were placed in geometrically idealized positions and refined as riding atoms. Data collection: X-AREA, cell refinement: X-AREA, data reduction: X-RED [49]; program(s) used for molecular graphics: ORTEP-3 for Windows [50]; software used to prepare material for publication: WINGX [51].

3. Results and discussion

3.1. UV–Vis spectrum and magnetic properties

The electronic spectrum of an aqueous solution of complex **2** displays a broad absorption band at 653 ($\varepsilon = 82$ L mol^{-1} cm^{-1}), which is assigned to the $a_1 \rightarrow b_1$ transition [52]. The strong absorption bands below 300 nm are due to $n \rightarrow \pi^*$ and $\pi \rightarrow \pi^*$ transitions of the ligands in the complex.

The complexes exhibit magnetic moment values of 5.92 BM for **1** and 1.68 BM for **2**, which corresponds to five and one unpaired electrons, respectively.

3.2. IR spectra

The IR spectra of complexes **1** and **2** exhibit a medium intensity and broad band in the range of 3233–3133 cm^{-1} for **1** and 3109 cm^{-1} for **2**, which can be attributed to the N–H stretching vibration of 2-meim or/and HOr ligands. The presence of coordinated water molecules in **1** caused the appearance of a strong and broad absorption band with a maximum at 3342 cm^{-1}. The IR spectrum of **2** shows sharp bands at 3515 and 3453 cm^{-1}, the characteristic stretching of crystal water molecules. The weak bands observed in the 3085–2744 cm^{-1} region are due to CH/CH_2/CH_3 stretching vibrations. The separation $\Delta\upsilon$, defined as υ_{as}(COO)–υ_s(COO), provides some useful information on the bonding mode of the carboxylate groups [53]. The strong and broad bands appearing in the ranges 1683–1600 and 1408–1387 cm^{-1} for **1** and 1643–1558 and 1407–1337 cm^{-1} for **2** are ascribed to the asymmetric and symmetric stretching vibrations of the carboxylate group of the orotate ligand, respectively. The observed Δ values for the complexes are 306 and 264 cm^{-1}, respectively. This result indicates that the coordination mode of the carboxylate group is monodentate for **1** and bridging for **2**. These conclusions are also supported from the results obtained from X-ray diffraction measurements. The weak bands observed in the regions 427–569 cm^{-1} for **1** and 458–598 cm^{-1} for **2** are due to M–N and M–O stretching vibrations [53].

Table 1
Crystal data and structure refinement parameters for **1** and **2**.

	1	**2**
Empirical formula	$C_{13}H_{14}N_6O_5Mn$	$C_{22}H_{42}N_8O_{11}Cu_2$
Formula weight	389.24	721.72
Temperature (K)		293 (2)
Wavelength (Å)		0.71073 Mo–Kα
Crystal system	orthorhombic	monoclinic
Space group	*Pna*21	*C*2/*c*
a (Å)	13.6808 (10)	23.936 (5)
b (Å)	8.3378 (6)	8.079 (5)
c (Å)	14.5273 (8)	17.441 (5)
β (°)	90	112.980 (5)
V (Å^3)	1657.1 (2)	3105 (2)
Z	4	4
Absorption coefficient (mm^{-1})	0.84	1.44
D_{calc} (Mg m^{-3})	1.560	1.544
θ Range for data collection (°)	2.04–27.87	1.79–27.97
Measured reflections	13738	26024
Independent reflections	3148	3055
Absorption correction	integration Stoe X–RED ([49])	
Refinement method	full-matrix least-squares on F^2	
Final *R* indices [$I > 2\sigma(I)$] (R_{int})	(0.073)	(0.067)
Final *R* indices (all data)	$R_1 = 0.086$	$R_1 = 0.028$
	$wR_2 = 0.220$	$wR_2 = 0.080$
Goodness-of-fit on F^2	1.15	1.06
$\Delta\rho_{max}$ (e Å^{-3})	0.68	0.27
$\Delta\rho_{min}$ (e Å^{-3})	−0.87	−0.56

Table 2
Selected geometric parameters (Å, °) for **1**.

N1–Mn1	2.319 (7)	O3–Mn1^{i}	2.136 (6)
N3–Mn1	2.265 (10)	O5–Mn1	2.192 (9)
N5–Mn1	2.288 (9)	Mn1–O3^{ii}	2.136 (6)
O1–Mn1	2.131 (6)		
O1–Mn1–O3^{ii}	101.8 (3)	O5–Mn1–N5	91.1 (3)
O1–Mn1–O5	159.1 (3)	N3–Mn1–N5	169.3 (3)
O3^{ii}–Mn1–O5	98.1 (4)	O1–Mn1–N1	75.6 (3)
O1–Mn1–N3	96.8 (3)	O3^{ii}–Mn1–N1	173.6 (4)
O3^{ii}–Mn1–N3	85.8 (3)	O5–Mn1–N1	83.9 (3)
O5–Mn1–N3	90.9 (4)	N3–Mn1–N1	100.3 (4)
O1–Mn1–N5	84.9 (3)	N5–Mn1–N1	90.4 (3)
O3^{ii}–Mn1–N5	83.5 (3)		

D–H···A	D–H	H···A	D···A	<D–H···A
Hydrogen-bond geometry (Å, °)				
N2–H2···O2^{iii}	0.86	2.09	2.92	161
N4–H4···O2^{iv}	0.86	2.00	2.86	172
N6–H6A···O4^{v}	0.86	2.08	2.91	164

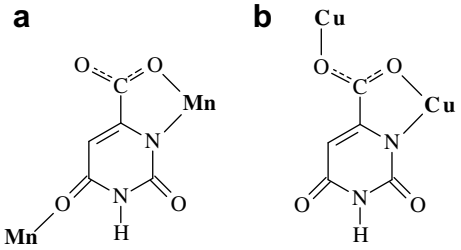
Symmetry codes: (i) *x*, *y* + 1, *z*, (ii) *x*, *y* − 1, (iii) *x* + 1/2, −*y* + 1/2 + 1, +*z*, (iv) −*x* + 1/2, +*y* − 1/2, +*z* − 1/2, (v) −*x* + 1, −*y* + 1, +*z* + 1/2.

Table 3
Selected geometric parameters (Å, °) for **2**.

N1–Cu1	1.95	O3–Cu1^{i}	2.00
N3–Cu1	2.02	O4–Cu1	2.26
N4–Cu1	2.10	Cu1–O3^{ii}	2.00
N1–Cu1–O3^{ii}	94.72 (6)	N3–Cu1–N4	85.56 (7)
N1–Cu1–N3	175.76 (6)	N1–Cu1–O4	77.96 (6)
O3^{ii}–Cu1–N3	86.71 (6)	O3^{ii}–Cu1–O4	105.28 (6)
N1–Cu1–N4	94.55 (7)	N3–Cu1–O4	97.82 (6)
O3^{ii}–Cu1–N4	157.30 (6)	N4–Cu1–O4	96.90 (7)

D–H···A	D–H	H···A	D···A	<D–H···A
Hydrogen-bond geometry (Å, °)				
N2–H2···O1^{iii}	0.86	1.96	2.816 (2)	172
O5–H5A···O1^{iii}	0.798 (17)	2.19 (3)	2.870 (2)	144 (3)
O5–H5B···O2	0.840 (17)	2.03 (2)	2.857 (3)	168 (3)
O6–H6···O2^{iv}	0.834 (19)	2.28 (4)	2.907 (2)	132 (5)

Symmetry codes: (i) $-x+3/2, y+1/2, -z+3/2$; (ii) $-x+3/2, y-1/2, -z+3/2$; (iii) $-x+3/2, -y+1/2, -z+1$; (iv) $x-1/2, -y+3/2, z-1/2$.



Scheme 2. Coordination modes of the orotate ligand (a) complex **1**, (b) complex **2**.

$$mer\text{-}[Mn(\mu\text{-HOr})(2\text{-meim})(H_2O)] \xrightarrow{164-211^{\circ}C} [Mn(\mu\text{-HOr})(im)_2] + 2CH_3 + H_2O$$

$$[Mn(\mu\text{-HOr})(im)2] \xrightarrow{211-322^{\circ}C} [Mn(\mu\text{-HOr})] + 2im$$

$$[Mn(\mu\text{-HOr})] \xrightarrow{322-450^{\circ}C} MnO + HOr$$

3.3. Thermal analyses

Thermal analyses of the complexes were performed in static atmosphere air in the temperature range 20–600 °C.

3.3.1. *mer*-[Mn(μ-HOr)(H_2O)(2-meim)$_2$]$_n$

This complex shows a three stage decomposition process. Although the complex contains the aqua ligand, it is stable up to 164 °C. In the first stage, the complex starts to lose the aqua ligand and two CH_3 radicals between 164 and 207 °C, with an experimental mass loss of 11.98% (calc. mass loss 12.28%). This type of behavior of methylimidazole ligands in the complexes [Zn(Han)$_2$(4-Meim)$_2$] (Han = *o*-aminobenzoate, 4-Meim = 4-methylimidazole) [54] and [Co(HOr)(H_2O)(4-Meim)$_3$] [41] has been reported earlier. The IR spectrum of the complex heated just to the end of this weight loss show no evidence of CH_3 bands. The second stage is related to the release of the remaining two imidazole ligands, giving an endothermic effect (calc. = 34.80, found = 34.02%). In the last extremely exothermic stage between 322 and 450 °C, the orotate ligand is abruptly burnt (DTA = 446 °C). The total mass loss of all the decomposition processes is 79.60% (calc. 81.86%), suggesting that MnO is the end product.

3.3.2. {[Cu(μ-HOr)(tmen)] · 1.5H_2O}$_n$

This complex exhibits four decomposition stages. In the first stage, endothermic removal of crystal water molecules occurs between 47 and 104 °C (calc. 7.60, found 7.48%, DTA$_{max}$ = 96 °C). The anhydrous complex is thermally stable up to about 234 °C and then undergoes complete exothermic decomposition after melting at 235 °C. The second stage in the temperature range 235–273 °C is related to the decomposition of the tmen ligand by exothermic effects (calc. 32.20, found 32.69%, DTA$_{max}$ = 262 °C). The exothermic effect between 273 and 360 °C is likely due to the release of CO_2 from the HOr ligand (calc. 12.19, found 11.92%). Similar behavior has been reported earlier [36,41,42]. The strong exothermic peak is associated with the decomposition of the uracil ligand in the range of 360–436 °C. The final decomposition product, namely CuO, was identified by IR spectroscopy by

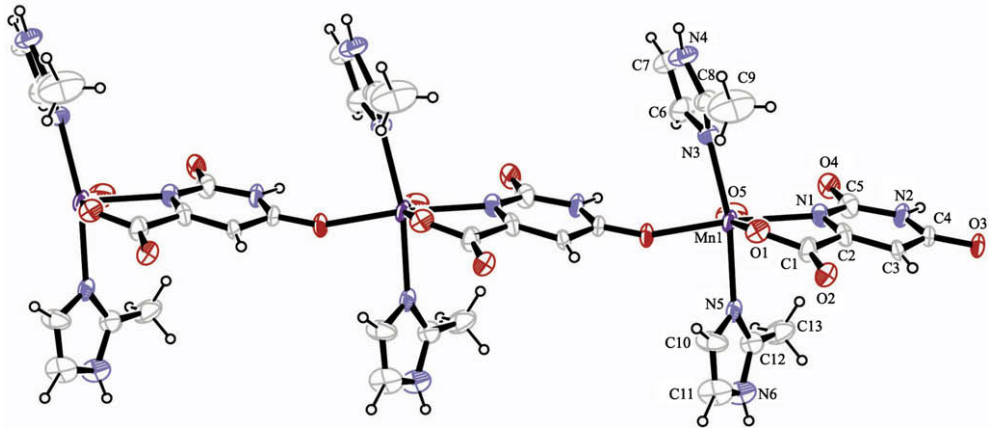


Fig. 1. The molecular structure of **1** showing the atom numbering scheme. The thermal ellipsoids are plotted at the 50% probability level.

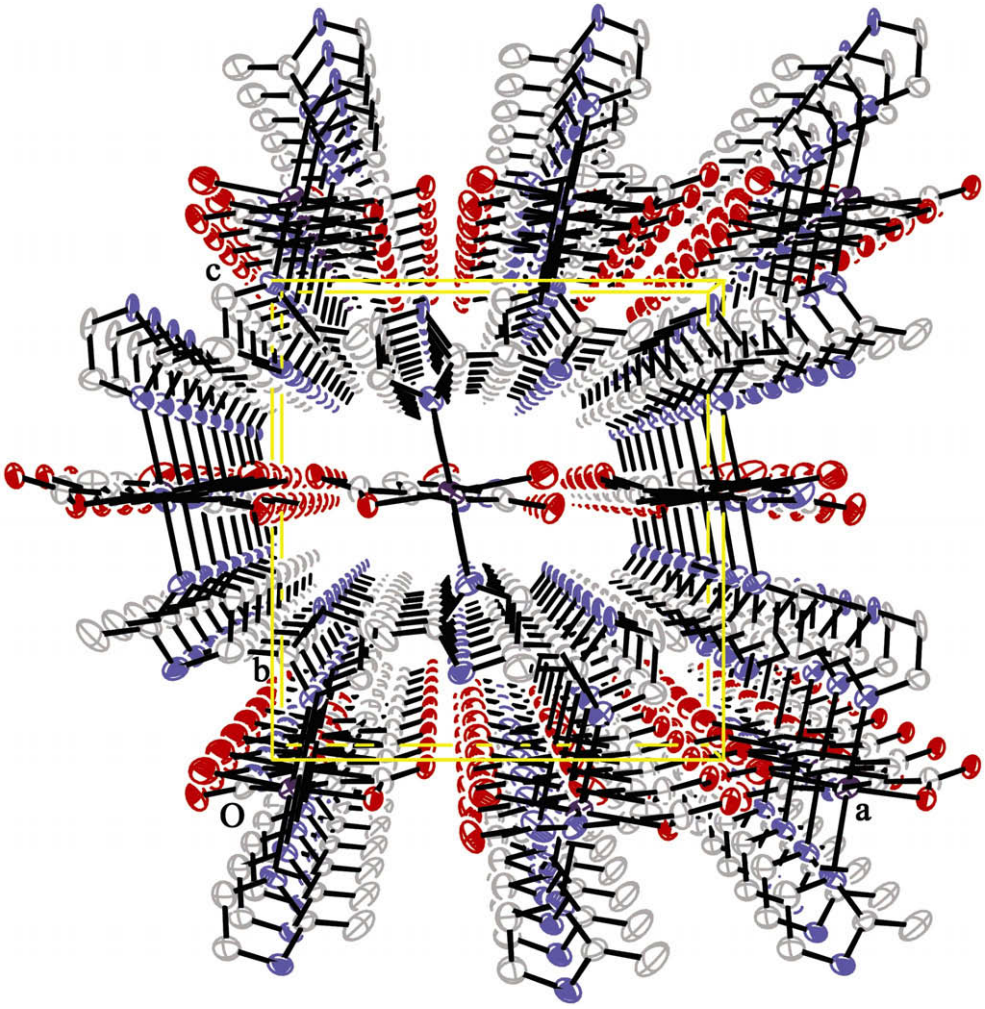


Fig. 2. Packing diagram of **1**.

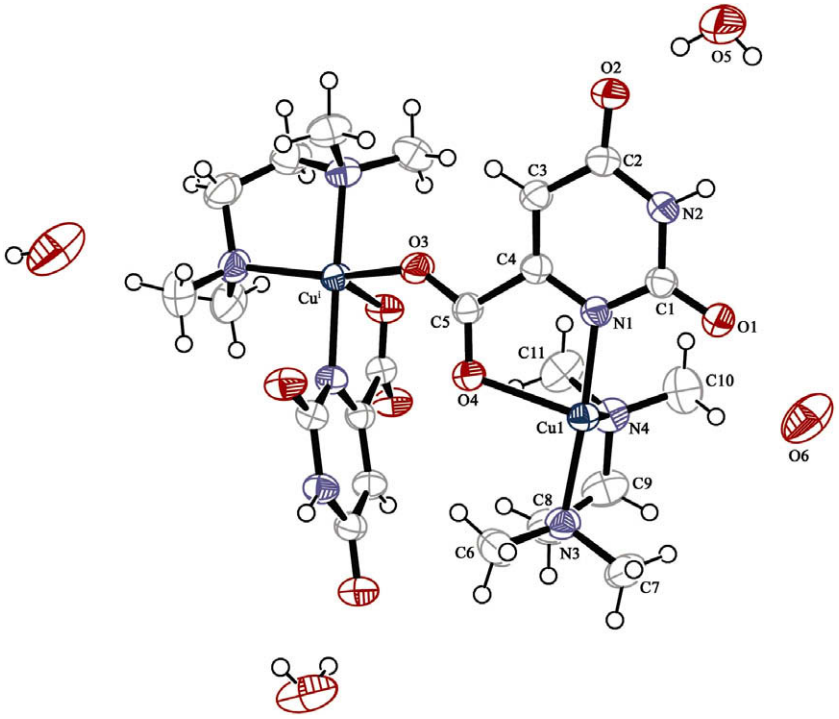


Fig. 3. The molecular structure of **2** showing the atom numbering scheme. The thermal ellipsoids are plotted at the 50% probability level.

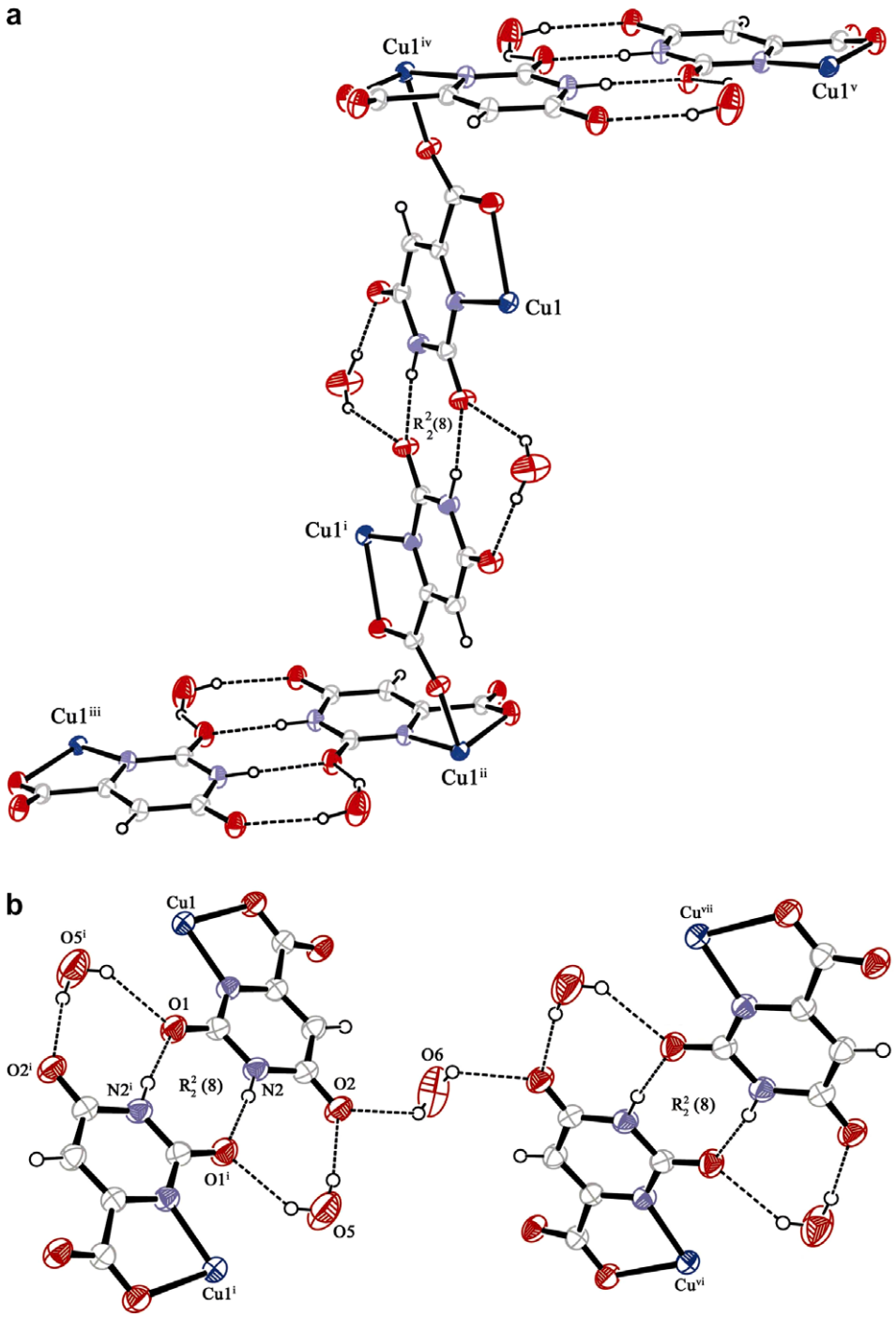


Fig. 4. Intermolecular hydrogen-bonding geometry between the chains of complex **2** (a) DA:AD (b) water bridge interactions. (symmetry codes: (i) 1.5 − *x*, ½ − *y*, 1-*z*; (ii) *x*, 1 − *y*, ½ + *z*; (iii) 1.5 − *x*, −½ + *y*, ½ − *z*; (iv) *x*, −*y*, −½ + *z*; (v) 1.5 − *x*, ½ − *y*, 1 − *z*; (vi) 2 − *x*, *y*, 1.5 − *z*; (vii) ½ + *x*, ½ − *y*, ½ + *z*).

comparison to the corresponding spectrum obtained under the same conditions with the pure oxide. The total weight loss is found to be 78.82% (calc. 77.96%).

$$[Cu(\mu\text{-HOr})(tmen)]\cdot 1.5H_2O \overset{47-104^{\circ}C}{\rightarrow} [Cu(\mu\text{-HOr})(tmen)] + 1.5H_2O$$
$$[Cu(\mu\text{-HOr})(tmen)] \overset{234-273^{\circ}C}{\rightarrow} [Cu(\mu\text{-HOr})] + tmen$$
$$[Cu(\mu\text{-HOr})] \overset{273-360^{\circ}C}{\rightarrow} [Cu(uracil)] + CO_2$$
$$[Cu(uracil)] \overset{360-436^{\circ}C}{\rightarrow} CuO + uracil$$

Thermochromic complexes showed abrupt color changes on heating in the solid state and these complexes are very important owing to their applicability as temperature sensors. Complex **1** exhibits irreversible thermochromism and on dehydration the color of the complex changes from blue to green. The thermochromism is proposed to be due to a decrease of the in-plane ligand field strength resulting from conformational changes of the diamine chelate rings.

3.4. Crystal structures of the complexes

The relevant crystal data and experimental conditions along with the final parameters are summarized in Table 1. Selected bond lengths and angles together with the hydrogen bonding geometries are given in Tables 2 and 3.

3.4.1. mer-[Mn(μ-HOr)(H$_2$O)(2-meim)$_2$]$_n$

The molecular structure of **1** with the atom labelling is shown Fig. 1. Selected bond lengths and angles are collected in Table 2. The crystallographic analyses reveal that the crystal structure of **1** is a one dimensional linear chain polymer along the *b* axis. The Mn(II) ion is coordinated by one orotate, two *trans*-2-methylimidazole and one aqua ligand, and is a *mer* isomer. The orotate ligand behaves as a tridentate bridging ligand through the oxygen atom of the carboxylate group and deprotonated nitrogen atom of the pyrimidine ring in a chelate manner, and the oxygen atom of another carbonyl group (Scheme 2a). The distorted octahedral geometry is completed with two nitrogen atoms of 2-methylimidazole and one aqua ligand. One carbonyl oxygen atom (O3) of a neighboring complex molecule and three nitrogen atoms (N1, N3, and N5) from the HOr and 2-meim ligands comprise the equatorial plane [N1–Cu1–N3 = 100.3 (4)°, N3–Cu1–N5 = 169.3 (3)°], while one oxygen atom of a carboxylate group (O1) of the HOr ligand and an oxygen atom (O5) of an aqua ligand occupy the axial positions. The Mn1–O1, Mn–O3 and Mn1–O5 bond distances are 2.131(6), 2.136(6), and 2.192(9) Å, and the Mn1–N1, Mn1–N3 and Mn1–N5 bond distances are 2.319(7), 2.265(10), and 2.288(9) Å, respectively. The Mn1–O$_{HOr}$ and Mn1–N$_{HOr}$ bond distances are significantly longer than that found in [Ni(HOr)(H$_2$O)$_3$]$_n$ (Ni–O = 2.064(2), 2.083(2) Å and Ni–N = 2.056(2) Å) [33] and [Co(HOr)(H$_2$O)$_3$]$_n$ (Co–O = 2.092(2), 2.133(5) Å and Co–N = 2.103(6) Å) [33]. However these bond distances are similar to the corresponding values found in the reported [Mn(HOr)(phen)-(H$_2$O)$_2$] [28], (enH$_2$)[Mn(HOr)$_2$(H$_2$O)$_2$] · 2.5H$_2$O [20], [Mn$_2$(HOr)$_2$-(H$_2$O)$_6$] [12], and [Mn(HOr)(bipy)(H$_2$O)] [13] complexes. The intermolecular Mn1–Mn1^{i} and Mn1–Mn1^{ii} ((i) $-1/2+x$, $1/2-y$, z; (ii) $1-x$, $1-y$, $1/2+z$) distances are 6.843 and 8.767 Å, respectively, and the intramolecular Mn1–Mn1^{iii} ((iii) x, $-1+y$, z) distance is 8.338 Å.

The crystal packing of the complex is stabilized through strong intermolecular hydrogen bonding (i) between the N atom of the 2-meim ligand and the uncoordinated oxygen atom of a carboxylate group [N(4)···O(2): 2.86 Å] and (ii) among the aqua ligand, coordinated and uncoordinated carboxylate oxygen atoms [O5···O(1): 2.944 and O5–O2 = 2.971 Å]. As a result of all these interactions, each chain is linked to other chains by hydrogen-bond interactions, forming a three dimensional network (Fig. 2).

3.4.2. {[Cu(μ-HOr)(tmen)] · 1.5H$_2$O}$_n$

A view of the molecule and its atom-numbering scheme are shown in Fig. 3 and selected bond lengths and bond angles are given in Table 3. Each Cu(II) center displays a square pyramidal coordination environment with two oxygen atoms and three nitrogen atoms: one oxygen atom (O4) of a carboxylate group and its adjacent nitrogen (N1) atom from the HOr ligand, one carbonyl oxygen atom from neighboring HOr ligand (Scheme 2b), and two nitrogen atoms from the tmen ligand (Fig. 3). One carboxylate oxygen atom (O3^{i}, (i) $-x+3/2$, $y+1/2$, $-z+3/2$) and three nitrogen atoms (N1, N3, and N4) from the HOr and tmen ligands comprise the equatorial plane [N1–Cu1–N4 = 169.95 (11)°, N3–Cu1–N4 = 90.06 (12)°], while one oxygen atom of a carboxylate group, O4, occupies the axial position. The Cu1–N1, Cu1–O4, Cu1–O3^{i}, Cu1–N3 and Cu1–N4 bond distances are 1.95, 2.26, 2.00, 2.02 and 2.10 Å, respectively. The Cu1–N1$_{HOr}$ bond distance is comparable to those reported for [Cu(HOr)(H$_2$O)$_2$]$_n$ *[1.975(2) Å]* [9], but the Cu1–O4 and Cu1–O3^{i} bonds distances are significantly different from the

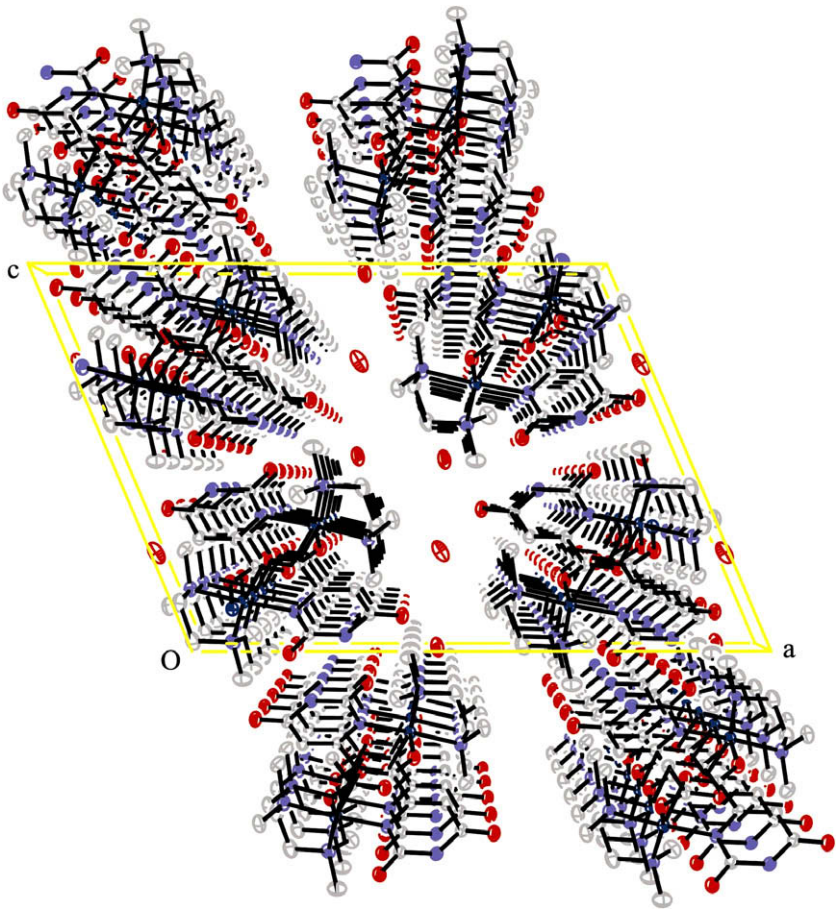


Fig. 5. Packing diagram of **2**.

corresponding distances of 1.948(2) and 2.337(2) Å, respectively. The intermolecular Cu1–Cu1^{i} = 8.622, ((i) $1.5 - x$, $1.5 - y$, $1 - z$) and Cu(1)–Cu(1)^{ii} = 7.828 Å ((ii) $1 - x$, $1 - y$, $1 - z$)] distances are longer than the intramolecular distance Cu1–Cu1^{iii} = 5.663 Å ((iii) = $1.5 - x$, $-1/2 + y$, $1.5 - z$).

The orotate ligand is essentially planar with a r.m.s. deviation of −0.0009 Å and the largest deviation from the mean plane is 0.0118 Å for the C4 atom. Of all the N–C bonds in the uracil ring of the orotato ligand, C1–N1 (1.357(2) Å), C1–N2 (1.373(2) Å) and C4–N1 (1.354(2) Å) are the shortest. This indicates significant π-electron delocalization within the uracil ring.

The details of the hydrogen bonding geometries are given in Table 3. The orotate anions can align to form a tail-to-tail cyclic dimer through strong N2–H···O1 hydrogen bonds, forming a DA:AD dimer [N2···O1^{iii} = 2.816 (2) Å, N2–H2···O1^{iii} = 172°, (iii) $-x + 3/2$, $-y + 1/2$, $-z + 1$]. This property establishes orotate as a significant candidate for designing supramolecular structures based on metal ion complexes [20]. In complex **1**, each of the HOr ligands are doubly hydrogen bonded to a corresponding HOr ligand of a neighboring complex, forming a cyclic dimer (Fig. 4a) and these motifs are linked to each other by water bridges (O5–H5···O2), generating a two dimensional network (Fig. 4b). These arrangement gives rise to eight membered rings that can be described as R_2^2 (8) and, R_3^3, respectively, in Etter's notation [55]. The two dimensional networks are linked to each other by water bridges (O6–H6···O2) (Fig. 4b). All these intermolecular interactions result in the formation of a three dimensional network (Fig. 5).

4. Conclusion

In this study, we have synthesized and structurally characterized two new Mn(II) and Cu(II) orotate coordination polymers with 2-methylimidazole and *N,N,N′,N′*-tetramethylethylenediamine ligands. In the *mer*-[Mn(μ-HOr)(H_2O)(2-meim)$_2$]} (**1**) and {[Cu(μ-HOr)(tmen)] · 1.5H_2O}$_n$ (**2**) complexes, the orotate dianion acts as a bridge between the metal ions forming one-dimensional polymeric chains, its coordination sites being the carboxylate oxygen atom (O8), nitrogen atom (N1) of the pyrimidine ring and oxygen atom O(11) for **1** and carboxylate oxygen atoms (O8 and O9) and nitrogen atom (N1) of the pyrimidine ring for **2**. These polymer chains are linked by hydrogen-bond interactions to form a three-dimensional network. The Cu(II) complex exhibits irreversible thermochromism and on dehydration the color of the complex changes from blue to green.

Appendix A. Supplementary data

CCDC 676222 and 676223 contain the supplementary crystallographic data for **1** and **2**. These data can be obtained free of charge via http://www.ccdc.cam.ac.uk/conts/retrieving.html, or from the Cambridge Crystallographic Data Centre, 12 Union Road, Cambridge CB2 1EZ, UK; fax: (+44) 1223-336-033; or e-mail: deposit@ccdc.cam.ac.uk. Supplementary data associated with this article can be found, in the online version, at doi:10.1016/j.poly. 2008.09.024.

References

[1] H.P. Jia, W. Li, Z.F. Ju, J. Zhang, Eur. J. Inorg. Chem. (2006) 4264.
[2] H.T. Zhang, X.Z. You, Acta Crystallogr., Sect. C 59 (2003) m313.
[3] A. Demessence, G. Rogez, R. Welter, P. Rabu, Inorg. Chem. 46 (2007) 3423.
[4] L. Gao, B. Zhao, G. Li, Z. Shi, S. Feng, Inorg. Chem. Commun. 6 (2003) 1249.
[5] Y.C. Liang, M.C. Hong, J.C. Liu, R. Cao, Inorg. Chim. Acta 328 (2002) 152.
[6] H.D. Yin, F.H. Li, C.H. Wang, Inorg. Chim. Acta 360 (2007) 2797.
[7] H. Yin, S.X. Liu, Polyhedron 26 (2007) 3103.
[8] X.H. Li, Q. Shi, M.L. Hu, H.P. Xiao, Inorg. Chem. Commun. 7 (2004) 912.
[9] T.T.B. Ha, A.M. Larsonneur-Galibert, P. Castan, J. Jaud, J. Chem. Crystallogr. 29 (1999) 565.
[10] D. Sun, R. Cao, Y. Liang, M. Hong, Y. Zhao, J. Weng, Aust. J. Chem. 55 (2002) 681.
[11] I. Mutikainen, Finn. Chem. Lett. (1985) 193.
[12] F. Nepveu, N. Gaultier, N. Korber, J. Jaud, P. Castan, J. Chem. Soc., Dalton Trans. (1995) 4005.
[13] M.J. Plater, M.R.J. Foreman, J.M.S. Skakle, R.A. Howie, Inorg. Chim. Acta 332 (2002) 135.
[14] D. Mentzafos, N. Katsaros, A. Terzis, Acta Crystallogr., Sect. C 43 (1987) 1905.
[15] D.A. Köse, B. Zümreoglu-Karan, O. Şahin, O. Büyükgüngör, J. Mol. Struct. 789 (2006) 147.
[16] T. Solin, K. Matsumoto, K. Fuwa, Bull. Chem. Soc. Jpn. 54 (1981) 3731.
[17] T.S. Khodashova, M.A. Porai-Koshits, N.K. Davidenko, N.N. Vlasova, Koord. Khim. 10 (1984) 262.
[18] A. Karipides, B. Thomas, Acta Crystallogr., Sect. C 42 (1986) 1705.
[19] H. Icbudak, H. Ölmez, O.Z. Yesilel, F. Arslan, P. Naumov, G. Jovanovski, A.R. Ibrahim, A. Usman, H.K. Fun, S. Chantrapromma, S.W. Ng, J. Mol. Struct. 657 (2003) 255.
[20] O.Z. Yeşilel, O. Büyükgüngör, Solid State Sci. 9 (2007) 485.
[21] O.Z. Yeşilel, H. Ölmez, C. Arıcı, Polyhedron 26 (2007) 3669.
[22] O.Z. Yeşilel, H. Paşaoğlu, K. Akdağ, O. Büyükgüngör, Polyhedron 26 (2007) 2761.
[23] C.P. Raptopoulou, V. Tangoulis, V. Psycharis, Inorg. Chem. 39 (2000) 4452.
[24] I. Bach, O. Kumberger, H. Schmidbaur, Chem. Ber. 123 (1990) 2267.
[25] I. Mutikainen, Recl. Trav. Chim. Pays-Bass 106 (1987) 438.
[26] X. Li, R. Cao, D. Sun, Q. Shi, W. Bi, M. Hong, Inorg. Chem. Commun. 6 (2003) 815.
[27] A.Q. Wu, F.K. Zheng, X. Liu, G.C. Guo, L.Z. Cai, Z.C. Dong, Y. Takano, J.S. Huang, Inorg. Chem. Commun. 9 (2006) 347.
[28] R. Wu, Y. Huo, J. Li, Z. Zheng, Acta Crystallogr., Sect. E 64 (2008) m500.
[29] X. Li, R. Cao, W. Bi, D. Sun, M. Hong, Acta Crystallogr., Sect. E 59 (2003) m228.
[30] O.Z. Yeşilel, E. Şahin, Z. Anorg. Allg. Chem. 633 (2007) 1087.
[31] H. Ölmez, H. Icbudak, O.Z. Yesilel, C. Arıcı, D. Ülkü, Z. Kristallogr. 219 (2004) 300.
[32] O.Z. Yesilel, H. Olmez, H. Icbudak, O. Büyükgüngör, Z. Naturforsch. 60b (2005) 1138.
[33] O.Z. Yeşilel, A. Mutlu, C. Öğretir, O. Büyükgüngör, J. Mol. Struct. 889 (2008) 415.
[34] O.Z. Yeşilel, N. Dege, C. Darcan, O. Büyükgüngör, Z. Naturforsch. 62b (2007) 1590.
[35] O.Z. Yeşilel, H. Paşaoğlu, K. Akdağ, O. Büyükgüngör, Z. Anorg. Allg. Chem. 633 (2007) 1731.
[36] O.Z. Yeşilel, H. Olmez, H. İçbudak, J. Therm. Anal. Calorim. 89 (2007) 555.
[37] O.Z. Yeşilel, H. Olmez, J. Therm. Anal. Calorim. 89 (2007) 261.
[38] O.Z. Yeşilel, G. Kaştaş, O. Büyükgüngör, Inorg. Chem. Commun. 10 (2007) 936.
[39] O.Z. Yeşilel, K. Akdağ, H. Paşaoğlu, O. Büyükgüngör, Z. Naturforsch. 62b (2007) 818.
[40] O.Z. Yeşilel, H. Olmez, C. Arıcı, Acta Crystallogr., Sect. C 63 (2007) m240.
[41] O.Z. Yeşilel, M.S. Soylu, H. Olmez, O. Büyükgüngör, Polyhedron 25 (2006) 2985.
[42] O.Z. Yeşilel, H. Olmez, J. Therm. Anal. Calorim. 86 (2006) 211.
[43] O.Z. Yeşilel, I. Uçar, A. Bulut, H. Olmez, O. Büyükgüngör, Z. Naturforsch. 61b (2006) 147.
[44] O.Z. Yeşilel, H. Ölmez, I. Uçar, A. Bulut, C. Kazak, Z. Anorg. Allg. Chem. 631 (2005) 3100.
[45] O.Z. Yeşilel, F. Tezcan, H. Ölmez, H. Paşaoğlu, O. Büyükgüngör, Z. Anorg. Allg. Chem. 631 (2005) 2497.
[46] I. Uçar, A. Bulut, O.Z. Yeşilel, H. Ölmez, O. Büyükgüngör, Acta Crystallogr., Sect. C 60 (2004) m563.
[47] A. Bulut, H. Icbudak, O.Z. Yeşilel, H. Olmez, O. Büyükgüngör, Acta Crystallogr., Sect. E 59 (2003) m736.
[48] G.M. Sheldrick, SHELXS-97 and SHELXL-97. Program for Refinement of Crystal Structures, University of Göttingen, Germany, 1997.
[49] Stoe & Cie (2002). X?Area (Version 1.18) and X?Red32 (Version 1.04). Stoe & Cie, Darmstadt, Germany, 2001.
[50] L.J. Farrugia, J. Appl. Crystallogr. 30 (1997) 565.
[51] L.J. Farrugia, J. Appl. Crystallogr. 32 (1999) 837.
[52] F.A. Cotton, Advanced Inorganic Chemistry, Wiley-Interscience, New York, 1980. p. 642.
[53] K. Nakamoto, Infrared and Raman Spectra of Inorganic and Coordination Compounds, fifth ed., Wiley-Interscience, New York, 1997. p. 59.
[54] M. Olczak-Kobza, Thermochim. Acta 419 (2004) 67.
[55] M.C. Etter, Acc. Chem. Res. 23 (1990) 120.

Polyhedron 28 (2009) 157–161

Contents lists available at ScienceDirect

Polyhedron

journal homepage: www.elsevier.com/locate/poly

Interaction of colloidal $AgTiO_2$ nanoparticles with bovine serum albumin

A. Kathiravan [a], R. Renganathan [a,*], S. Anandan [b]

[a] School of Chemistry, Bharathidasan University, Tiruchirappalli 620 024, Tamil Nadu, India
[b] Nanomaterials and Solar Energy Conversion Lab, Department of Chemistry, National Institute of Technology, Tiruchirappalli 620 015, Tamil Nadu, India

ARTICLE INFO

Article history:
Received 5 July 2008
Accepted 26 September 2008
Available online 27 November 2008

Keywords:
Colloidal $AgTiO_2$
Fluorescence quenching
BSA

ABSTRACT

The interaction between colloidal $AgTiO_2$ nanoparticles and bovine serum albumin (BSA) was studied by using absorption, steady state, time resolved and synchronous fluorescence spectroscopy measurements. Absorption spectroscopy proved the formation of a ground state BSA···$AgTiO_2$ complex. Upon excitation of BSA, colloidal $AgTiO_2$ nanoparticles effectively quenched the intrinsic fluorescence of BSA. The number of binding sites ($n = 1.06$) and apparent binding constant ($K = 3.71 \times 10^5\ M^{-1}$) were calculated by the fluorescence quenching method. A static mechanism and conformational changes of BSA were observed.
© 2008 Elsevier Ltd. All rights reserved.

1. Introduction

One of the most important biological functions of albumins is their ability to carry drugs as well as endogenous and exogenous substances [1]. The binding capacity and sites of albumins have been characterized [2]. Serum albumins are the most abundant proteins in plasma [3]. As the major soluble protein constituents of the circulatory system, they have many physiological functions [4]. Among the serum albumins, BSA has a wide range of physiological functions involving binding, transport and delivery of fatty acids, porphyrins, bilirubin and steroids, etc. It is home to specific binding sites for metals and pharmaceutical dyes [5]. The binding properties of BSA with various drugs have been fully investigated by many researchers [6–10], which are useful for understanding the reaction mechanism as well as for providing guidance for the application and design of new drugs [11].

Bovine serum albumin (BSA) has been selected as our protein model due to its water-soluble nature which is important for interaction studies [12,13]. It contains 582 amino-acid residues with a molecular weight of 69,000, and two tryptophan moieties at positions 134 and 212 as well as tyrosine and phenylalanine [14]. The intrinsic fluorescence of BSA is due to aromatic amino-acid residues. Nanoparticle probes act as biosensors in the chemical and biochemical fields, and their applications are becoming more extensive. These probes have been applied to ultrasensitive detection of proteins, DNA sequencing, clinical diagnostics etc. Recently we reported the interaction of colloidal TiO_2 with bovine serum albumin using fluorescence spectroscopy [15].

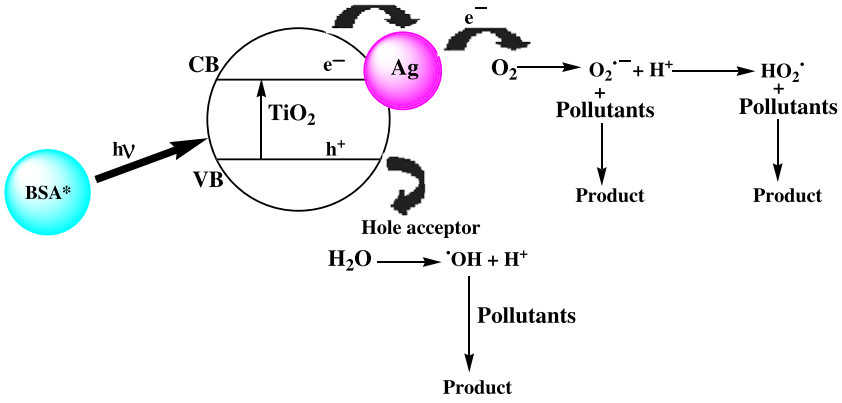
Metal semiconductor nanoparticles have become an attractive topic of research because of their potential applications in different fields, such as charge-transfer processes [16], optoelectronics [17] and medicine [18]. Among such nanocomposite structures, $AgTiO_2$ has more attention paid to it because silver is an extremely attractive noble metal on the nanoscale due to its remarkable catalytic activity [19], size and shape-dependent optical properties, promising applications in chemical and biological sensing [20], and also due to its antimicrobial activity [21]. Elechiguerra et al. studied metal nanoparticle interactions with the human immunodeficiency virus-1 (HIV-1), and silver nanoparticles of the size 1–10 nm were attached to HIV-1, and this prevented the virus from binding to host cells [22].

Based on the above strategy we have investigated the interaction of BSA with colloidal $AgTiO_2$ nanoparticles (Scheme 1). This is the first challenge made to investigate the mode of interaction of colloidal $AgTiO_2$ nanoparticles with BSA.

BSA absorbs light energy around 280 nm, which is not absorbed by TiO_2. The excited state energy of BSA is transferred to the ground state TiO_2, thus TiO_2 gets excited and generates conduction band electrons and valence band holes (Scheme 1). The conduction band electrons are transferred to the metal core, and then the electrons in the metal and holes in the valence band of TiO_2 take part in subsequent redox reactions with the surface adsorbed molecules to yield the ultimate products. The photogenerated electrons have sufficient electronegativity to reduce dioxygen to superoxide/hydroperoxide radicals, effecting the deep oxidation of a wide range of organic pollutants to degraded products. In addition, the photogenerated holes are highly oxidizing which can split water into H^+ and $OH^{\bullet}$, and then the produced $OH^{\cdot}$ radicals can oxidize the organic pollutants.

* Corresponding author. Tel.: +91 431 2407053; fax: +91 431 2407045.
E-mail address: rrengas@gmail.com (R. Renganathan).

0277-5387/$ - see front matter © 2008 Elsevier Ltd. All rights reserved.
doi:10.1016/j.poly.2008.09.023



Scheme 1. Interaction of colloidal $AgTiO_2$ nanoparticles with BSA.

2. Experimental

2.1. Materials

Bovine serum albumin and titanium-(triethanolaminato) isopropoxide were purchased from Aldrich. All measurements were performed at ambient temperature.

2.2. Methods

2.2.1. Preparation of colloidal $AgTiO_2$ nanoparticles

The method of preparation of colloidal $AgTiO_2$ nanoparticles in water is similar to the one reported earlier [23]. Colloidal $AgTiO_2$ nanoparticles were prepared by a one pot synthesis that involved reduction of metal ions and hydrolysis of titanium-(triethanolaminato)isopropoxide [TTEAIP] in dimethylformamide. The solvent, DMF, plays an important role in reducing the Ag^+ ions first, followed by the slow hydrolysis of TTEAIP to form colloidal $AgTiO_2$ nanoparticles.

2.2.2. Instrumentation

Samples for spectroscopic measurements were prepared by dissolving bovine serum albumin in water and administering the appropriate concentration of colloidal $AgTiO_2$ nanoparticles. The samples were carefully degassed using pure nitrogen gas for 15 min. Quartz cells (4 x 1 × 1 cm) with high vacuum Teflon stopcocks were used for degassing.

The fluorescence quenching measurements were carried out in a JASCO FP-6500 spectrofluorimeter. The slit width (each 5 nm) and scan rate (500 nm/min) were constantly maintained for all measurements. Absorption spectral measurements were recorded using a Cary 300 UV–Vis spectrophotometer. Fluorescence lifetime measurements were carried out in a picosecond time correlated single photon counting (TCSPC) spectrometer. The excitation source was the tunable Ti-sapphire laser (TSUNAMI, Spectra Physics, USA). The fluorescence decay was analyzed by using the software provided by IBH (DAS-6). The particle size of the prepared $AgTiO_2$ nanoparticles were analyzed by transmission electron microscopy (recorded using TECNAI G^2 model).

3. Results and discussion

3.1. Characterization of the $AgTiO_2$ nanoparticles

Transmission electron microscope pictures have been taken for the prepared Ag–TiO_2 nanoparticles (Fig. 1) to give an idea about the particle size and surface modifications effected during doping of the metal on TiO_2 nanoparticles. The TEM pictures permit easy differentiation of metal nanoparticles (small dark areas) and TiO_2 (large bright areas), that is, an Ag nanoparticle is seen on the surface of a TiO_2 particle as a dark dot. Also, there is the possibility of metal particles to be incorporated into the interstitial positions of the semiconductor particles. Further, it is observed that the average size of silver in the Ag–TiO_2 particles is in the range 10–20 nm.

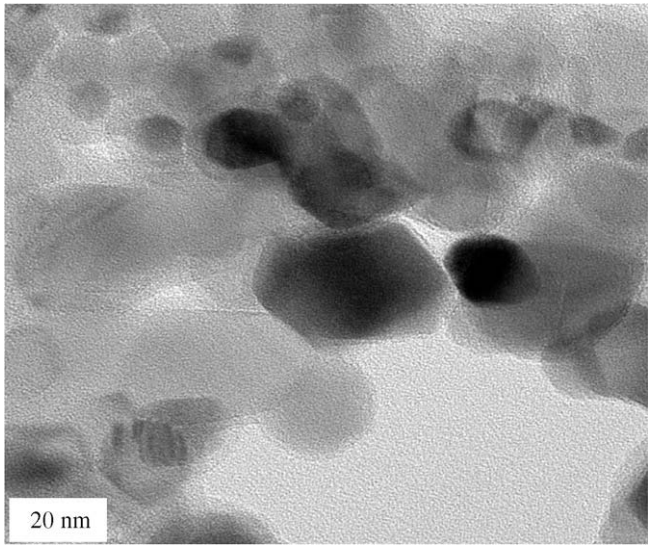


Fig. 1. TEM image of $AgTiO_2$ nanoparticles.

3.2. XRD characterization of $AgTiO_2$ nanoparticles

Fig. 2 shows the XRD spectrum of $AgTiO_2$ nanoparticles. Diffractions that are attributable to the anatase phase of TiO_2 crystals (101) are clearly detectable at $2\theta = 25°$ (JCPDS 21-1272) in Fig. 2. Peaks at $2\theta = 38.4°$, 44.5° and 64.6° in $AgTiO_2$ are assigned to (111), (200) and (220) planes of silver (JCPDS), which proves that the TiO_2 surfaces are covered with metal particles.

3.3. Absorption characteristics of BSA–$AgTiO_2$ nanoparticles

Fig. 3 shows the absorption spectra of BSA in the presence and absence of colloidal $AgTiO_2$ nanoparticles at different concentrations. From this study we observed that upon increasing the concentration of colloidal $AgTiO_2$ the absorption of BSA increases regularly with the peak shift of around 5 nm. It is due to the

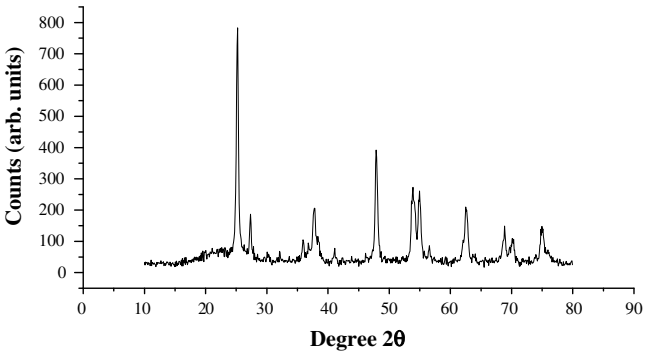


Fig. 2. XRD pattern of $AgTiO_2$ and nanoparticles.

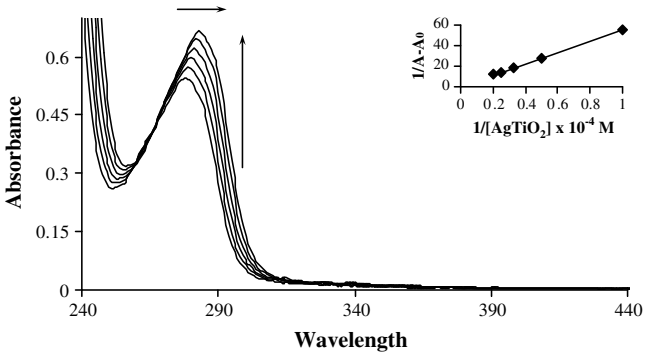


Fig. 3. Absorption spectrum of BSA in the presence of colloidal TiO_2 in the concentration range 0–5 × 10^{-4} M. Inset is the linear dependence of $1/A - A_0$ on the reciprocal concentration of colloidal $AgTiO_2$.

adsorption of BSA on the surface of colloidal $AgTiO_2$ nanoparticles, supported by similar observations reported earlier [24].

The equilibrium for the formation of complex between BSA and colloidal $AgTiO_2$ nanoparticles can be given by Eq. (1), where K_{app} represents the apparent association constant:

$$\mathrm{BSA} + \mathrm{AgTiO_2} \overset{K_{app}}{\rightleftharpoons} \mathrm{BSA}\cdots\mathrm{AgTiO_2} \quad (1)$$

$$K_{app} = \frac{[\mathrm{BSA}\cdots\mathrm{AgTiO_2}]}{[\mathrm{BSA}]\cdot[\mathrm{AgTiO_2}]}$$

The change in intensity of the absorption peak (280 nm) as a result of the formation of the surface complex were utilized to obtain K_{app} according to Benesi and Hildebrand [25]:

$$A_{obs} = (1-\alpha)C_0\varepsilon_{BSA}1 + \alpha C_0\varepsilon_c 1 \quad (2)$$

where A_{obs} is the observed absorbance of the solution containing different concentrations of colloidal $AgTiO_2$ at 280 nm, α is the degree of association between BSA and $AgTiO_2$, ε_{BSA} and ε_c are the molar extinction coefficients at the defined wavelength (λ = 280 nm) of BSA and the formed complex, respectively, in water. Eq. (2) can be expressed as Eq. (3), where A_0 and A_c are the absorbances of BSA and the complex at 280 nm, respectively, with a concentration of C_0:

$$A_{obs} = (1-\alpha)A_0 + \alpha A_c \quad (3)$$

At relatively high $AgTiO_2$ concentrations, α can be equated to $(K_{app}[AgTiO_2])/(1 + K_{app}[AgTiO_2])$. In this case, Eq. (3) can be changed to Eq. (4):

$$\frac{1}{A_{obs}-A_0} = \frac{1}{A_c-A_0} + \frac{1}{K_{app}(A_c-A_0)[\mathrm{AgTiO_2}]} \quad (4)$$

The enhancement of absorbance at 280 nm was due to absorption of the surface complex, based on the linear relationship between $1/(A_{obs} - A_0)$ vs reciprocal concentration of colloidal $AgTiO_2$ with a slope equal to $1/K_{app}(A_c - A_0)$ and an intercept equal to $1/(A_c - A_0)$ (Fig. 3, insert). The value of the apparent association constant (K_{app}) determined from this plot is 5.58 × 10^5 M^{-1}. Further, the reason for the higher association constant of $AgTiO_2$ compared to that reported for TiO_2 [15] may be due to the larger surface area of the $AgTiO_2$ nanoparticles.

3.4. Fluorescence quenching of BSA by colloidal $AgTiO_2$ nanoparticles

The fluorescence quenching is described by the Stern–Volmer relation:

$$I_0/I = 1 + K_{sv}[Q] = 1 + K_q\tau_0[Q] \quad (5)$$

where I_0 and I are the fluorescence intensities of BSA in the absence and presence of quencher, K_{SV} is Stern–Volmer constant, k_q is the bimolecular quenching rate constant, and τ_0 is the average lifetime of BSA, 10^{-8} s [26], [Q] is the concentration of quencher. Fig. 4 shows the effect of increasing the concentration of colloidal $AgTiO_2$ on the fluorescence emission spectrum of BSA. Addition of colloidal $AgTiO_2$ resulted in the quenching of BSA fluorescence emission and there is no peak shift and no new peak was observed. It is noted that a complex formed between colloidal $AgTiO_2$ and BSA is responsible for the quenching of BSA. According to Eq. (5), a linear plot [Inset, Fig. 4] between I_0/I against [$AgTiO_2$] was obtained and from the slope we calculated the quenching rate constant (k_q) as 1.64 × 10^{15} $M^{-1}s^{-1}$. In general, the maximum collisional quenching constant (k_q) of various kinds of quenchers to biopolymers is 2.0 × 10^{10} $M^{-1}s^{-1}$ [26], but for the BSA–$AgTiO_2$ system a higher quenching rate constant (1.64 × 10^{15} $M^{-1}s^{-1}$) was obtained. This shows that the quenching is not dynamic in nature, it depends on the formation of a complex between $AgTiO_2$ and BSA (Scheme 2). Further the type of interaction between BSA and colloidal $AgTiO_2$ was also confirmed by time resolved spectroscopy.

3.5. Fluorescence lifetime measurements

Fig. 5 shows the fluorescence decay of BSA in the absence and presence of colloidal $AgTiO_2$ nanoparticles. BSA exhibits single exponential decay not only in dilute solutions but also in the pres-

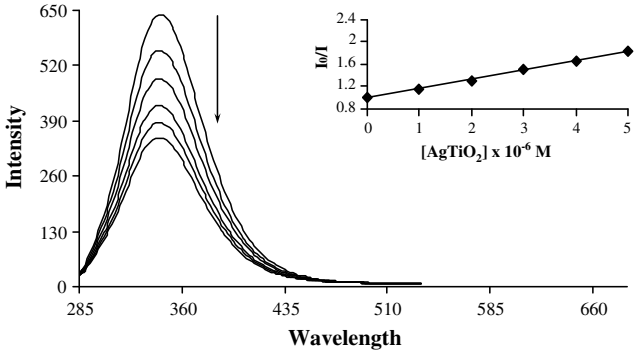


Fig. 4. Fluorescence Quenching of BSA in the presence of various concentrations of colloidal $AgTiO_2$ nanoparticles, [TiO_2] = 0, 1, 2, 3, 4 and 5 × 10^{-6} M. Insert shows the Stern–Volmer plot.

$$\mathrm{BSA} + \mathrm{AgTiO_2} \rightleftharpoons \mathrm{BSA}.....\mathrm{AgTiO_2}$$

$$\mathrm{BSA}.....\mathrm{AgTiO_2} \xrightarrow{h\nu} \mathrm{BSA}^{*}.....\mathrm{AgTiO_2}$$

Scheme 2. Mechanism of complex formation.

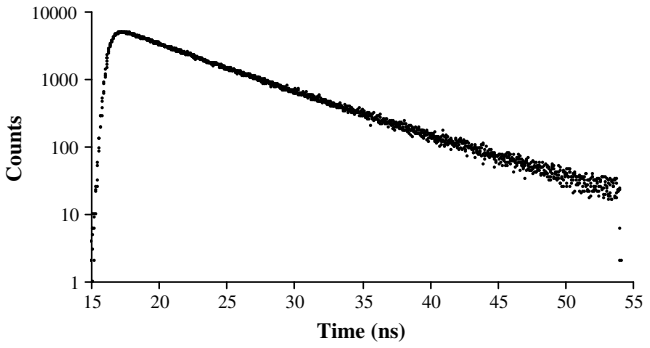


Fig. 5. Fluorescence decay curve of BSA in the absence and presence of colloidal $AgTiO_2$ in the concentration range 0–5 × 10^{-6} M.

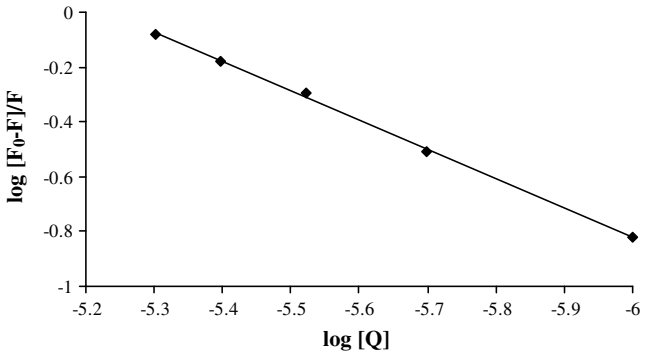


Fig. 6. Plot of $\log[(F_0 - F)/F]$ vs. log[Q].

ence of colloidal $AgTiO_2$ nanoparticles. On increasing the concentration of colloidal $AgTiO_2$ there is no change in the lifetime of BSA. This observation shows that the quenching follows a static mechanism. It also supports the formation of a ground state surface complex. (In Fig. 5 although the decay traces of BSA in the absence and presence of colloidal $AgTiO_2$ were actually plotted, the lifetime of BSA remained the same under both conditions, hence merging of the kinetic traces was observed, and the plot looks like a single decay curve.) For static quenching, we can deduce the binding constant (K) resulting from the formation of a ground state complex between fluorophore and the quencher.

3.6. Binding constant and number of binding sites

The relationship between the fluorescence intensity and quenching medium can be deduced from the following formula:

$$n\mathrm{Q} + \mathrm{B} \overset{K}{\rightleftharpoons} \mathrm{Q}_n \cdots \mathrm{B} \tag{6}$$

where B is the biomolecule with the fluorophore, Q is the quencher molecule, $Q_n \cdots B$ is the quenched biomolecules and the resultant constant K is given by

$$K = \frac{[\mathrm{Q}_n \cdots \mathrm{B}]}{[\mathrm{Q}]^n \cdot [\mathrm{B}]} \tag{7}$$

If the overall amount of biomolecules (bound or unbound with the quencher) is B_0, then $[B_0] = [Q_n \cdots B] + [B]$, here [B] is the concentration of unbound biomolecules. Thus the relationship between fluorescence intensity and the unbound biomolecule is $[B]/[B_0] = F/F_0$, that is

$$\log\left[\frac{F_0 - F}{\mathrm{F}}\right] = n\log[\mathrm{Q}] + \log K \tag{8}$$

where K is the binding constant of $AgTiO_2$ with BSA, which can be determined from the plot of $\log[(F_0 - F)/F]$ versus log[Q] as shown in Fig. 6. Thus we obtained the binding constant "K" as $3.71 \times 10^5\ M^{-1}$ and binding sites "n" (1.06) for $AgTiO_2$ with BSA from the intercept and slope of Fig. 5. The value of K obtained from the data of fluorescence quenching matches well with that determined from the absorption spectral changes. The good agreement between these values of K highlights the validity of assumption proposed for the association between BSA and colloidal $AgTiO_2$ nanoparticles.

3.7. Characteristics of synchronous fluorescence spectra

To explore the structural changes of BSA by the addition of colloidal $AgTiO_2$, we measured the synchronous fluorescence spectra of BSA with the concentrations of colloidal $AgTiO_2$ used for the fluorescence quenching study. Synchronous fluorescence spectra provide information on the molecular microenvironment, particularly in the vicinity of fluorophore functional groups [27]. The fluorescence of BSA is due to the presence of tyrosine, tryptophan and phenylalanine residues. Hence spectroscopic methods are usually applied to study the conformation of the serum protein. In synchronous fluorescence spectroscopy, according to Miller [28], the difference between the excitation and emission wavelength ($\Delta\lambda = \lambda_{emi} - \lambda_{exc}$) reflects the spectra of chromophores with the different natures. With larger $\Delta\lambda$ values, such as 60 nm, the synchronous fluorescence of BSA is characteristic of the tryptophan residue, and smaller $\Delta\lambda$ values, such as 15 nm, are characteristic of tyrosine [29]. The synchronous fluorescence spectra of BSA with various concentrations of colloidal $AgTiO_2$ were recorded at $\Delta\lambda$ = 15 nm (Fig. 7) and $\Delta\lambda$ = 60 nm (spectra not shown here). With an increasing concentration of colloidal $AgTiO_2$ the intensity of tyrosine decreased, and a red-shift of the emission wavelength (Fig. 7) was observed. At the same time, the tryptophan fluorescence emission decreased regularly, but no significant change in wavelength was observed. It suggests that the interaction of colloidal $AgTiO_2$ with BSA affects the conformation of the tyrosine region, but not the tryptophan micro-region. The tyrosine fluorescence spectrum may represent that the conformation of BSA has changed, leading to a strengthening of the polarity around the tyrosine residues and a weakening of the hydrophobicity [30]. It is important to note that colloidal $AgTiO_2$ affects only the tyrosine residues in the BSA moiety. This is because tyrosine contains one aromatic hydroxyl group, unlike tryptophan.

In our previous study, riboflavin was used as a sensitizer for colloidal TiO_2 [31] and it was observed that riboflavin interacted through the hydroxyl group of colloidal TiO_2. In addition, tyrosine can undergo an excited state ionization, resulting in the loss of a proton from the aromatic hydroxyl group. Hence it is clear that the presence of a hydroxyl group in the tyrosine residues may be

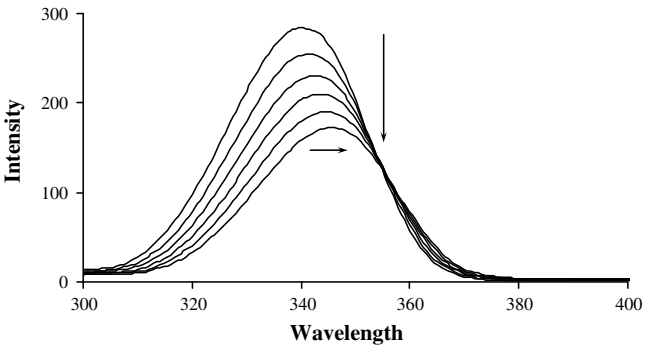
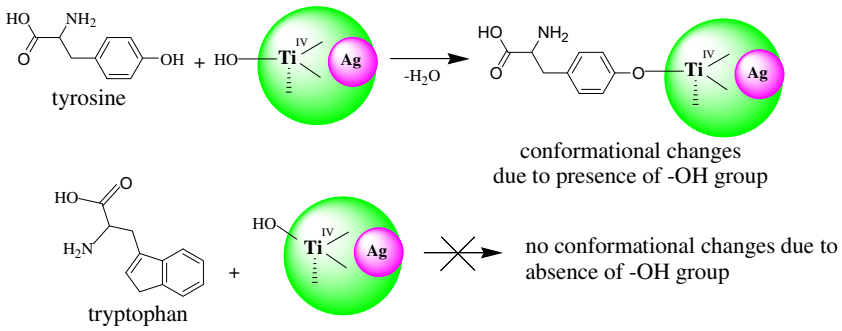


Fig. 7. Synchronous fluorescence spectrum of BSA with $\Delta\lambda$ = 15 nm in the absence and presence of colloidal $AgTiO_2$ nanoparticles.



Scheme 3. Mechanism for the interaction of $AgTiO_2$ nanoparticles with BSA.

responsible for the interaction of BSA with $AgTiO_2$, similar to 2,3-diazabicyclo [2.2.2] oct-2-ene (DBO) interacting with the aromatic hydroxyl group of tyrosine in BSA [32], as reported by Anbazhagan and Renganathan (Scheme 3).

4. Summary

The interaction between colloidal $AgTiO_2$ nanoparticles and BSA has been studied by various spectroscopic measurements. The results presented clearly indicate that colloidal $AgTiO_2$ nanoparticles quench the fluorescence emission of BSA through a static mechanism, which is further confirmed by the unaltered lifetime of BSA by time resolved measurements. The quenching rate constant, binding constant and number of binding sites were calculated according to the relevant fluorescence quenching data. From the synchronous fluorescence spectra, it is shown that the conformational change of BSA is induced by the interaction of colloidal $AgTiO_2$ nanoparticles with the tyrosine micro-region of the BSA molecules. The binding study of drugs with nanoparticles is of great importance in pharmacy, pharmacology and biochemistry. This study is expected to provide important insight into the interactions of the physiologically important protein BSA with metal nanoparticles. Information is also obtained about the effect of the environment on the BSA structure, which may be correlated to its physiological activity.

Acknowledgements

R.R. thanks DST (SR/NM/NS-16/2007, dt. 26-09-2008) (Government of India) for the NSTI Project. R.R. and A.K. thank CSIR (Ref: No. 01(2217)/08/EMR-II, dt. 06/05/2008) for the Project and Fellowship respectively. We are thankful to Prof. P. Ramamoorthy, NCUFP, University of Madras, Chennai for lifetime measurements. The author, S.A. thanks CSIR, New Delhi for the sanction of a major research fund (CSIR Reference No. 01(2197)/07/EMR-II dated 26th November, 2007).

References

[1] F. Moreno, M. Cortijo, J.G. Jimenez, Photochem. Photobiol. 70 (1999) 695.
[2] M. Kessler, O. Wolfbeis, Anal. Biochem. 200 (1992) 254.
[3] D.D. Carter, J.X. Ho, Adv. Protein Chem. 45 (1994) 153.
[4] R.E. Olson, D.D. Christ, Ann. Rep. Med. Chem. 31 (1996) 327.
[5] S. Ashoka, J. Seetharamappa, P.B. Kandagal, S.M.T. Shaikh, J. Lumin. 121 (2006) 179.
[6] D. Gao, Y. Tian, F. Liang, D. Jin, Y. Chen, H. Zhang, Aimin Yu, J. Lumin. 127 (2007) 515.
[7] N. Zhou, Y.Z. Liang, P. Wang, J. Photochem. Photobiol. A: Chem. 185 (2006) 271.
[8] B. Zhou, Z. Qi, Q. Xiao, J.X. Dong, Y.Z. Zhang, Y. Liu, J. Biochem. Biophys. Meth. 70 (2007) 743.
[9] Z. Hongwei, G. Min, Z. Zhaoxia, W. Wenfeng, W. Guozhong, Spectrochim. Acta, Part A 65 (2006) 811.
[10] Y.B. Yin, Y.N. Wang, J.B. Ma, Spectrochim. Acta, Part A 64 (2006) 1032.
[11] Y.J. Hu, Yi. Liu, R.M. Zhao, J.X. Dong, S.S. Qu, J. Photochem. Photobiol. A: Chem. 179 (2006) 324.
[12] J. Valanciunaite, S. Bagdonas, G. Streckyte, R. Rotomskis, Photochem. Photobiol. Sci. 5 (2006) 381.
[13] U.K. Hansen, Pharmacol. Rev. 33 (1981) 17.
[14] L.A. Sklar, B.S. Hudson, R.D. Simoni, Biochemistry 16 (1977) 5100.
[15] A. Kathiravan, R. Renganathan, Colloids Surf. A 324 (2008) 176.
[16] K. Vinodgopal, S. Hotchandani, P.V. Kamat, J. Phys. Chem. 97 (1993) 9040.
[17] T. Hirakawa, P.V. Kamat, Langmuir 20 (2004) 5645.
[18] V. Alt, T. Bechert, P. Steinrucke, M. Wagener, P. Seidel, E. Dingeldein, U. Domann, R. Schnettler, Biomaterials 25 (2004) 4383.
[19] A. Roucoux, J. Schulz, H. Patin, Chem. Rev. 102 (2002) 3757.
[20] A. Tao, F. Kim, C. Hess, J. Goldberger, R. He, Y. Sun, Y. Xia, P. Yang, Nano Lett. 3 (2003) 1229.
[21] C. Hu, Y. Lan, J. Qu, X. Hu, A. Wang, J. Phys. Chem. B 110 (2006) 4066.
[22] J.L. Elechiguerra, J.L. Burt, J.R. Morones, A. Camacho-Bragado, X. Gao, H.H. Lara, M.J. Yacaman, J. Nanobiotechnol. 3 (2005).
[23] P.K. Sudeep, K. Takechi, P.V. Kamat, J. Phys. Chem. C 111 (2007) 488.
[24] C. Chen, X. Qi, B. Zhou, J. Photochem. Photobiol. A: Chem. 109 (1997) 155.
[25] H.A. Benesi, J.H. Hildebrand, J. Am. Chem. Soc. 71 (1949) 2703.
[26] J.R. Lakowicz, G. Weber, Biochemistry 12 (1973) 4161.
[27] G.Z. Chen, X.Z. Huang, J.G. Xu, Z.Z. Zheng, Z.B. Wang, Methods of Fluorescence Analysis, 2nd ed., Science Press, Beijing, 1990.
[28] J.N. Miller, Proc. Anal. Div. Chem. Soc. 16 (1979) 203.
[29] J.H. Tang, F. Luan, X.G. Chen, Bioorg. Med. Chem. 14 (2006) 3210.
[30] B. Klajnert, M. Bryszewska, Bioelectrochemistry 55 (2002) 33.
[31] A. Kathiravan, R. Renganathan, Spectrochim. Acta A 71 (2008) 1080.
[32] V. Anbazhagan, R. Renganathan, J. Lumin. 128 (2008) 1454.

Polyhedron 28 (2009) 162–166

Contents lists available at ScienceDirect

Polyhedron

journal homepage: www.elsevier.com/locate/poly

Syntheses, crystal structures and magnetic properties of three new binuclear Ni(II) complexes derived from tripodal tetradentate (N_4) ligands

Sadegh Salehzadeh [a,*], Reza Golbedaghi [a], Ian. S. Tidmarsh [b], Lorenzo Sorace [c], Harry Adams [b], Michael D. Ward [b]

[a] Faculty of Chemistry, Bu-Ali Sina University, Hamedan, Iran
[b] Department of Chemistry, University of Sheffield, Sheffield, S3 7HF, UK
[c] Dipartimento di Chimica, UniVersita' di Firenze, and UdR INSTM, Sesto Fiorentino, Italy

ARTICLE INFO

Article history:
Received 11 September 2008
Accepted 29 September 2008
Available online 18 November 2008

Keywords:
Crystal structure
Magnetic properties
Ferromagnetic
Binuclear nickel complexes
Bridging

ABSTRACT

Three new binuclear Ni(II) complexes [{Ni(L_{22py})Cl}$_2$](ClO_4)$_2$ (**1**), [{Ni(L_{23py})Cl}$_2$](ClO_4)$_2$ (**2**), and [{Ni(L_{33py})Cl}$_2$](ClO_4)$_2$ (**3**), {L_{22py} = *N*-(2-pyridylmethyl)-*N*-(2-aminoethyl)-1,2-diaminoethane, L_{23py} = *N*-(2-pyridylmethyl)-*N*-(2-aminoethyl)-1,3-diaminopropane, L_{33py} = *N*-(2-pyridylmethyl)-*N*-(3-aminopropyl)-1,3-diaminopropane} have been synthesized. Single crystal X-ray structure analysis showed that in each complex two distorted octahedral Ni(II) ions are bridged asymmetrically by a pair of chloride anions. Variable temperature magnetic susceptibility measurements of **1** and **3** revealed dominant ferromagnetic exchange interactions.

© 2008 Elsevier Ltd. All rights reserved.

1. Introduction

The discovery that individual molecules can display a magnetic memory effect (such molecules are termed a Single Molecule Magnet or SMM) has perhaps been one of the biggest driving forces towards the synthesis of new polynuclear coordination complexes [1]. Many varied synthetic routes are employed to achieve such complexes, but most have a common feature: the use of bridging ligands for the assembly of transition metal ions into individual species. Such ligands are often simple mono or bidentate anions (Cl^-, HO^-, RO^-, N_3^-, $RCOO^-$ for example), and although uncomplicated in themselves, they can yield elaborate coordination complexes displaying numerous topologies [2,3]. One topology of particular current interest is composed of two metal ions bridged so as to form a diamond arrangement of metal ions and ligands ({ML}$_2$) [4]. From a magnetic stand point, Ni(II) clusters have received extensive recent interest [5]. When Ni(II) is five-coordinate, the magnetic coupling observed between the metal ions is usually dominantly antiferromagnetic in nature [6]. However, when the Ni center is six coordinate the situation is more complicated. In cases where there is pronounced tetragonal distortion, the degeneracy of the e_g level is removed and the coupling is therefore dominantly antiferromagnetic [7]. In cases where the metal center is octahedral or pseudo-octahedral, the degeneracy of the e_g level is maintained and the coupling is always dominantly ferromagnetic [8–13].

We have been involved in the synthesis of new tripodal tetraamine ligands [14–19], their macrocyclic [15,16] and macroacyclic [17–19] Schiff base complexes, determination of their stability constants [20] and their gas phase proton affinities [21,22]. In this work we set out to establish how the chelate sizes in a series of chloro-bridged binuclear Ni(II) complexes with tripodal ligands would affect their molecular structure and/or their magnetic properties. Thus we have used two ligands with pairs of identical alkyl-amino arms (L_{22py} and L_{33py}) and one with two different arms (L_{23py}) (Fig. 1) to prepare three bridged binuclear Ni(II) complexes with tetradentate ligands; [{Ni(L_{22py})Cl}$_2$](ClO_4)$_2$ (**1**), [{Ni(L_{23py})Cl}$_2$](ClO_4)$_2$ (**2**), and [{Ni(L_{33py})Cl}$_2$](ClO_4)$_2$ (**3**). We are reporting the single crystal X-ray structures of all three complexes, **1**–**3**, and the magnetic properties of **1** and **3**. To the best of our knowledge the Ni(II) complexes composed of the ligands L_{22py} and L_{23py} are previously unreported, with **2** being the first complex composed of the ligand L_{23py}, while a mononuclear Ni(II) complex of L_{33py}, [NiL(MeCN)$_2$]$^{2+}$, has been reported previously [23].

2. Experimental

2.1. General Information

$Ni(ClO_4)_2 \cdot 4H_2O$ was obtained from Aldrich and was used without further purification. The asymmetrical tripodal ligands were

* Corresponding author. Fax: +98 811 8257407.
E-mail addresses: saleh@basu.ac.ir, ssalehzadeh@gmail.com (S. Salehzadeh).

0277-5387/$ - see front matter © 2008 Elsevier Ltd. All rights reserved.
doi:10.1016/j.poly.2008.09.026

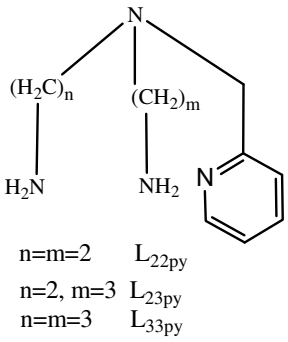


Fig. 1. Structure of the tripodal tetradentate ligands investigated here.

prepared as their hydrochloride salts *via* literature methods [14,24]. IR spectra were measured on a Perkin Elmer FT-IRGX spectrophotometer. Variable-temperature magnetic data were measured with a Cryogenic S600 SQUID magnetometer on polycrystalline samples in **1** (**300–35** K) and 0.1 (<35 K) T fields. Low temperature (1.5 K), variable-field (up to 12 T) magnetization measurements were measured on an Oxford Instruments vibrating-sample magnetometer. The data were corrected for the contribution of the sample holder and for the diamagnetism of the sample estimated from Pascal's constants.

2.2. X-ray crystal structure determination

A summary of the details of the crystal data, data collection and refinement details is given in Table 1. All structural determinations were carried out using a Bruker SMART-1000 CCD diffractometer equipped with Mo Kα X-radiation ($\lambda = 0.71073$ Å for all compounds) at 150(2) K for **1** and 100(2) K for **2** and **3**. In all cases, absorption corrections were applied using SADABS [25], and structure solution and refinement was carried out using SHELXS-97 and SHELXL-97, respectively, [26]. The structures were solved by direct methods and refined by full-matrix least-squares methods on F^2. Hydrogen atoms were placed geometrically and refined with a riding model, with U constrained to be 1.2 (1.5 for methyl groups) times U of the carrier atom. The lattice of **2** contained a disordered perchlorate anion that has been split over two sites (Cl2, O1–O4; 50:50 occupancy). The oxygen atoms of this residue have been left isotropic. All other non-hydrogen atoms were refined anisotropically.

2.3. Synthesis

2.3.1. Preparation of the complex $[\{Ni(L_{22py})Cl\}_2](ClO_4)_2$ (**1**)

A mixture of $L_{22py} \cdot 3HCl$ (0.1 g, 0.33 mmol) and NaOH (0.039 g, 0.99 mmol) in EtOH (15 cm^3) was heated under reflux for 1 h, allowed to cool and then filtered. A solution of $Ni(ClO_4)_2 \cdot 4H_2O$ (0.12 g, 0.37 mmol) in MeOH (5 ml) was added to the filtrate. The mixture was stirred at 50–60 °C for 1 h, during which time it turned blue in color. The solution was filtered and the filtrate reduced to ca. 10 cm^3. X-ray quality crystals were obtained by slow diffusion of Et_2O vapor into the latter solution. Yield: 0.15 g (57%). *Anal.* Calc. for $C_{20}H_{36}Cl_4N_8Ni_2O_8 \cdot CH_3OH$: C, 31.2; H, 5.0; N, 13.9. Found C, 31.8; H, 4.7; N, 13.4%. IR (Nujol, cm^{-1}): 3355 and 3302 (υ(N–H) stretching), 1605 and 1573 (υ(C=N and/or υ(N–H) bending), 1090 (υ(Cl–O) stretching).

2.3.2. Preparation of the complex $[\{Ni(L_{23py})Cl\}_2](ClO_4)_2$ (**2**)

Complex **2** was prepared in an analogous manner. Yield: 0.1 g (38%). *Anal.* Calc. for $C_{22}H_{40}Cl_4N_8Ni_2O_8 \cdot CH_3OH$: C, 33.0; H, 5.3; N, 13.4. Found C, 32. 4; H, 5.2; N, 12.6%. IR (Nujol, cm^{-1}): 3340 and 3290 (υ(N–H) stretching), 1606 and 1573 (υ(C=N and/or υ(N–H) bending), 1087 (υ(Cl–O) stretching).

Table 1
Crystal data and structure refinement for complexes **1**–**3**.

	1	**2**	**3**
Empirical formula	$C_{20}H_{36}Cl_4N_8Ni_2O_8$	$C_{22}H_{40}Cl_4N_8Ni_2O_8$	$C_{24}H_{44}Cl_4N_8Ni_2O_8$
Formula weight	775.79	803.84	831.89
Crystal system	monoclinic	monoclinic	triclinic
Space group	$P2(1)/n$	$P2(1)/n$	$P\bar{1}$
Unit cell dimensions			
a (Å)	8.2808(7)	9.1185(12)	9.2119(9)
b (Å)	16.7236(15)	18.832(2)	9.2188(9)
c (Å)	10.9301(9)	10.0768(13)	10.6890(10)
α (°)	90	90	72.688(3)
β (°)	90.143(4)	113.414(5)	80.973(4)
γ (°)	90	90	77.004(4)
V (Å^3)	1513.6(2)	1587.9(4)	840.46(14)
Z	2	2	1
D_{calc} (Mg/m^3)	1.702	1.681	1.644
Absorption coefficient (mm^{-1})	1.654	1.580	1.496
$F(000)$	800	832	432
Crystal size (mm^3)	0.18 × 0.14 × 0.11	0.40 × 0.30 × 0.30	0.60 × 0.40 × 0.10
θ Range for data collection (°)	2.23–27.64	2.45–28.28	2.28–25.03
Index ranges	$-10 \leqslant h \leqslant 10$, $-21 \leqslant k \leqslant 21$, $-14 \leqslant l \leqslant 14$	$-12 \leqslant h \leqslant 12$, $-25 \leqslant k \leqslant 25$, $-13 \leqslant l \leqslant 13$	$-10 \leqslant h \leqslant 10$, $-10 \leqslant k \leqslant 10$, $-12 \leqslant l \leqslant 12$
R_{int}	0.0245	0.0631	0.0202
Completeness to $\theta = 25.00°$ (%)	100.0	99.9	99.3
Absorption correction	semi-empirical from equivalents	semi-empirical from equivalents	semi-empirical from equivalents
Maximum and minimum transmission	0.8390 and 0.7550	0.5054 and 0.5054	0.7541 and 0.4207
Refinement method	full-matrix least-squares on F^2	full-matrix least-squares on F^2	full-matrix least-squares on F^2
Data/restraints/parameters	3501/0/190	3935/36/197	2937/0/224
Goodness-of-fit on F^2	1.337	1.069	1.056
Final R indices	$R_1 = 0.0365$	$R_1 = 0.0350$	$R_1 = 0.0248$
$[I > 2\sigma(I)]$	$wR_2 = 0.0954$	$wR_2 = 0.0910$	$wR_2 = 0.0658$
R indices (all data)	$R_1 = 0.0371$, $wR_2 = 0.0956$	$R_1 = 0.0401$, $wR_2 = 0.0939$	$R_1 = 0.0255$, $wR_2 = 0.0663$
Largest difference in peak and hole (e Å^{-3})	0.424 and −0.492	0.756 and −0.739	1.498 and −0.397

*2.3.3. Preparation of the complex [{Ni(L_{33py})Cl}$_2$](ClO$_4$)$_2$ (**3**)*

Complex **3** was prepared in an analogous manner. Yield: 0.14 g (51%). *Anal.* Calc. for $C_{24}H_{44}Cl_4N_8Ni_2O_8 \cdot CH_3OH$: C, 34.8; H, 5.6; N, 13.0. Found C, 35.2; H, 5.4; N, 12.6%. IR (Nujol, cm^{-1}): 3335 and 3285 (υ(N–H) stretching), 1605 and 1573 (υ(C=N and/or υ(N–H) bending), 1092 (υ(Cl–O) stretching).

3. Results and discussion

Complexes **1**–**3** were readily synthesized by neutralization of the hydrochloric salts of the L_{22py}, L_{23py} and L_{33py} tripodal ligands with sodium hydroxide, followed by reaction with Ni(II) perchlorate, respectively. The IR spectra and analytical data are consistent with their structure and formulation. In the IR spectra of all the complexes a pair of sharp υ(N–H) bands at about 3200–3300 cm^{-1} correspond to the coordinated primary amine groups [27]. The stretching bands of the pyridine C=N groups and bending bands of primary amine groups appear, as expected, at about 1573–1606 cm^{-1}. A broad intense band at *ca.* 1100 cm^{-1} due to ClO_4^- shows no splitting, indicating the absence of anion coordination. This is consistent for all complexes.

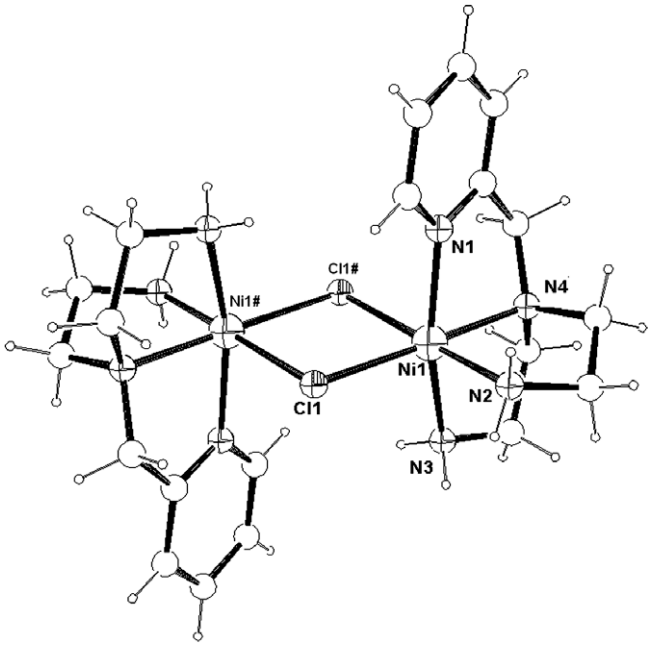


Fig. 2. Crystal structure of complex **1**. Perchlorate anions are omitted for clarity.

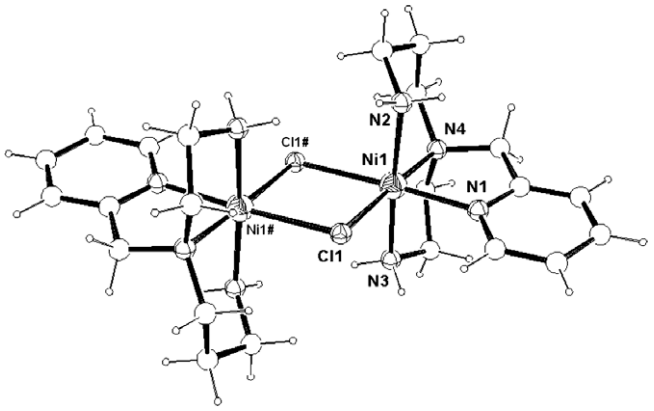


Fig. 3. Crystal structure of complex **2**. Perchlorate anions are omitted for clarity.

3.1. X-ray crystal structure analysis

Suitable crystals of **1**–**3** were obtained by slow diffusion of diethyl ether vapor into methanol–ethanol solutions. The structures of these compounds with the atomic numbering schemes are shown in Figs. 2–4, respectively. Single crystal X-ray structure analysis shows that all complexes have a solid state binuclear geometry, where two bridging chloride ions complete the octahedral coordination environments at the nickel atoms. Selected bond lengths and bond angles are given in Table 2. The Ni–N bond lengths are in the expected range from 2.0720(3) to 2.1110(3) Å (**1**), 2.0651(18) to 2.1212(19) Å (**2**) and 2.0727(18) to

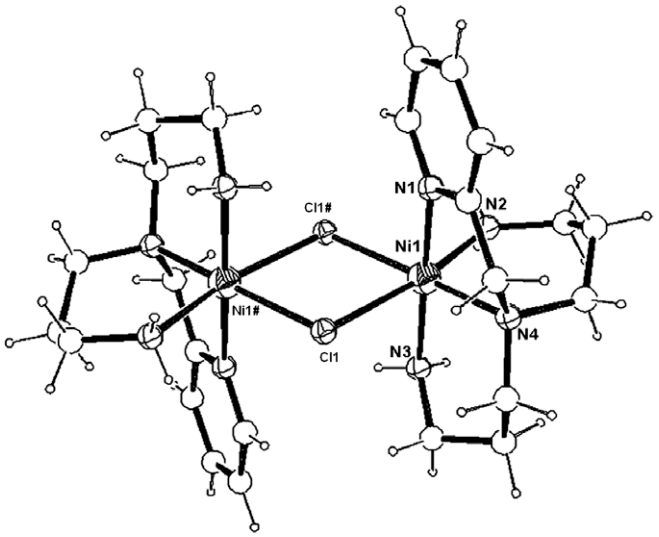


Fig. 4. Crystal structure of complex **3**. Perchlorate anions are omitted for clarity.

Table 2
Selected bond lengths (Å) and bond angles (°) for compounds **1**–**3**.

	1	2	3
Bond lengths (Å)			
Ni(1)–N(1)	2.072(3)	2.065(18)	2.075(17)
Ni(1)–N(3)	2.111(3)	2.091(2)	2.073(18)
Ni(1)–N(2)	2.078(3)	2.098(2)	2.098(18)
Ni(1)–N(4)	2.076(3)	2.121(19)	2.124(17)
Ni(1)–Cl(1)	2.374(9)	2.452(6)	2.543(6)
Ni(1)–Cl(1)#	2.522(9)	2.480(6)	2.490(5)
Bond angles (°)			
N(1)–Ni(1)–N(3)	162.98(11)	87.55(8)	175.18(7)
N(1)–Ni(1)–N(4)	80.21(11)	82.58(7)	81.39(7)
N(3)–Ni(1)–N(4)	83.47(12)	84.58(8)	94.90(7)
N(1)–Ni(1)–N(2)	90.84(11)	91.16(8)	90.13(7)
N(3)–Ni(1)–N(2)	92.69(11)	173.38(8)	93.44(8)
N(4)–Ni(1)–N(2)	85.50(11)	88.81(8)	98.00(7)
C(6)–N(4)–Ni(1)	106.15(11)	108.45(13)	104.29(12)
C(8)–N(4)–Ni(1)	107.63(11)		
C(10)–N(4)–Ni(1)	106.75(11)		
C(9)–N(4)–Ni(1)		114.42(14)	114.82(13)
C(11)–N(4)–Ni(1)		104.26(14)	
C(12)–N(4)–Ni(1)			113.83(13)
N(1)–Ni(1)–Cl(1)	98.52(8)	95.64(5)	89.04(5)
N(3)–Ni(1)–Cl(1)	97.83(9)	94.27(6)	87.99(6)
N(4)–Ni(1)–Cl(1)	179.05(9)	177.92(5)	91.55(5)
N(2)–Ni(1)–Cl(1)	94.01(8)	92.31(6)	170.18(5)
N(1)–Ni(1)–Cl(1)#	88.27(8)	175.73(6)	95.21(5)
N(3)–Ni(1)–Cl(1)#	88.07(9)	88.30(5)	88.25(6)
N(4)–Ni(1)–Cl(1)#	94.06(8)	96.02(5)	174.55(5)
N(2)–Ni(1)–Cl(1)#	178.65(8)	92.84(6)	86.23(5)
Cl(1)–Ni(1)–Cl(1)#	86.41(3)	85.677(19)	84.107(17)
Ni(1)–Cl(1)–Ni(1)#	93.59(3)	94.323(19)	95.893(17)

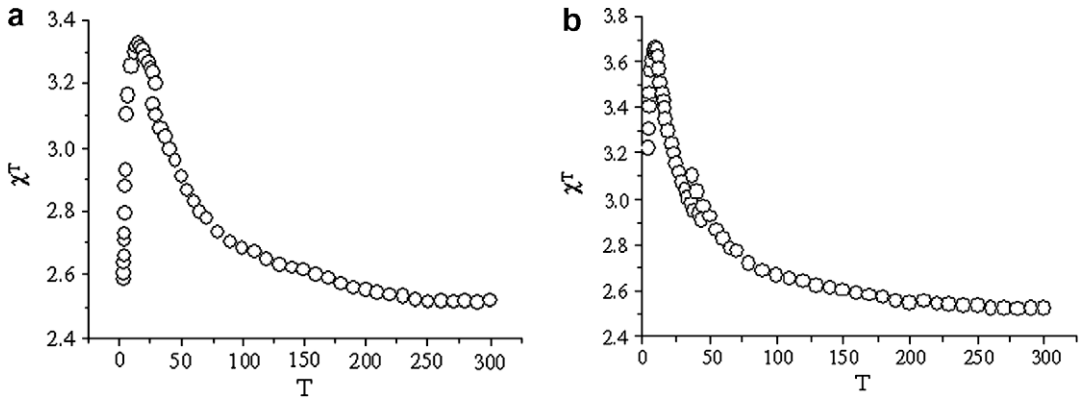


Fig. 5. Temperature-dependence of the magnetic properties for complexes **1**, (a), and **3**, (b), in the form of χT vs. T.

2.1237(17) Å (**3**). The N–Ni–N, Cl–Ni–N, and Cl–Ni–Cl bond angles in all three complexes are different, indicating a distorted octahedral coordination environment for each Ni atom.

The Ni–Cl bridges are asymmetric, (2.3739(9) and 2.5223(9) Å (**1**), 2.4518(6) and 2.4802(6) Å (**2**) and 2.5428(6) and 2.4904(5) Å (**3**)). In **1**, the bond to the monodentate ligand *trans* to N_{tert} [Ni–Cl1 2.3739(9) Å] is shorter than that to the ligand *cis* to N_{tert} [Ni–Cl1# 2.5223(9) Å]. The same situation can be seen in **2** and **3**, 2.4518(6) compared to 2.4802(6) Å and 2.4904(5) compared to 2.5428(6) Å, respectively. A similar observation has been reported for a binuclear Ni(II) complex of an asymmetric tripodal tetramine [28]. The distances between the nickel atoms in **1**, **2**, and **3** are 3.570, 3.616, and 3.737 Å, respectively, indicating the metal–metal distance increases with increasing ligand size. In complex **1** the bond length between a Ni atom and one of the primary amine groups, Ni(1)–N(3) [2.1110(3) Å], is the longest bond distance, but in both **2** and **3** the Ni(1)–N_{tert} bond length [2.1212(19) and 2.1237(17) Å, respectively] is longer than the other bond distances. On the other hand, in both **1** and **2** Ni(1)–$N_{pyridine}$ is the shortest bond distance, while for complex **3** the Ni(1)–N(3) distance is smaller than the other bond lengths. It is interesting that the variations of the Ni–N bond lengths in compounds **2** and **3** are very similar and are different to those of compound **1**. This may be related to the fact that in compound **1** all the chelates are five-membered rings. It should be noted that compounds **1** and **3** have the pyridine donors *trans* to a primary amino donor atom while compound **2** has the primary amino group *trans* to another primary amino donor.

We note that there are a number of isomeric possibilities for these complexes, especially for compound **2** which is an asymmetric compound. In addition to the observed structures for compounds **1**–**3** we can consider several different structures for the present binuclear complexes. Note that in each complex each of the three arms of the tripodal ligand can be located in a *trans* position relative to the other arms or relative to the bridging-chlorine atoms. Furthermore the present binuclear complexes are all centro-symmetric, but we can also consider some centro-asymmetric structures. We have no evidence to confirm that other possible isomers have been formed in our reaction system.

The N_{tert}–Ni–N bond angles for the five-membered chelate rings, as expected, are smaller than corresponding angles for the six-membered chelate rings in both complexes **2** and **3**.

3.2. Magnetic studies

The magnetic properties of compounds **1** and **3** are similar in nature. The room temperature values of χT are 2.52 and 2.53 emu K mol^{-1} respectively, in good agreement with that expected for two uncoupled Ni(II) spins [6,8] (Fig. 5). In both complexes χT increases with decreasing T, indicative of dominant ferromagnetic exchange interactions within the cluster. Further cooling from 3 to 8 K gives a sharp decrease of χT, suggesting a weak antiferromagnetic interaction at low temperature; this can be accounted for using the Weiss correction. In **1** χT reaches a maximum of 3.27 at 8 K before dropping to 2.59 at 3 K, and in **3** χT reaches a maximum of 3.67 at 8 K before dropping to 3.23 at 3 K. Using a simple exchange spin Hamiltonian we have modeled the magnetic data and obtain excellent fits with the parameters $J = 9.3$ cm^{-1}, $D = -12.9$ cm^{-1} and $g = 2.19$ for **1**, and $J = 6.8$ cm^{-1}, $D = -6.9$ cm^{-1} and $g = 2.2$ for **3**. The obtained values are consistent with those presented for related complexes [10].

In all the complexes, in spite of the differences in ring size, the magnetic properties are similar. The complex $[\{Ni(L_{22py})Cl\}_2]^{2+}$ has five-membered chelating rings whereas $[\{Ni(L_{33py})Cl\}_2]^{2+}$ has six-membered chelating rings, but both complexes display ferromagnetic coupling. $[\{Ni(_{L23py})Cl\}_2]^{2+}$ has five and six-membered chelating rings and we would also expect this complex to display similar magnetic properties.

4. Conclusion

The synthesis and characterization of three binuclear Ni(II) complexes (**1**–**3**) with tripodal tetradentate ligands are reported. The molecular structures of complexes **1**–**3** have been determined by single crystal X-ray diffraction studies and have been shown to exhibit distorted octahedral-coordinated nickel ions. In all the compounds the Ni(II) centers are bridged by two chlorides. The magnetic properties of **1** and **3** have been investigated and reveal dominant ferromagnetic interactions between the metal centers down to 8 K. The magnitude of these interactions has shown them to be ferromagnetic.

Acknowledgment

We are grateful to the Bu-Ali Sina and Sheffield universities for financial support.

Appendix A. Supplementary data

CCDC 699256, 699258, and 699257 contain the supplementary crystallographic data for complexes **1**, **2,** and **3** respectively. These data can be obtained free of charge via http://www.ccdc.cam.ac.uk/conts/retrieving.html, or from the Cambridge Crystallographic Data Centre, 12 Union Road, Cambridge CB2 1EZ, UK; fax: (+44) 1223-336-033; or e-mail: deposit@ccdc.cam.ac.uk. Supplementary

data associated with this article can be found, in the online version, at doi:10.1016/j.poly.2008.09.026.

References

[1] S. Sain, S. Bid, A. Usman, H.K. Fun, G. Aromi, X. Solans, S.K. Chandra, Inorg. Chim. Acta 358 (2005) 3362.
[2] R.E.P. Winpenny, Adv. Inorg. Chem. 52 (2001) 1.
[3] G. Aromi, S.M.J. Aubin, M.A. Bolcar, G. Christou, H.J. Eppley, K. Folting, D.N. Hendrickson, J.C. Huffman, R.C. Squire, H.L. Tsai, S. Wang, M.W. Wemple, Polyhedron 17 (1998) 3005.
[4] Y. Yamamoto, T. Suzuki, S. Kaizaki, J. Chem. Soc., Dalton Trans. (2001) 2943.
[5] F. Meyer, S. Demeshko, G. Leibling, B. Kersting, E. Kaifer, H. Pritzkow, Chem. Eur. J. 11 (2005) 1518.
[6] J.C. Jansen, H.V. Koningsveld, J.A.C.V. Ooijen, J. Rerdijk, Inorg. Chem. 19 (1980) 170.
[7] K.K. Nanda, R. Das, L.K. Thompson, K. Vankastsubramanian, P. Paul, K.K. Nag, Inorg. Chem. 33 (1994) 1188.
[8] A.P. Gisberg, R.L. Martin, R.W. Brokes, R.C. Sherwood, Inorg. Chem. 11 (1972) 2884.
[9] D. Knetsch, W.L. Groenveld, Inorg. Nucl. Chem. Lett. 12 (1976) 27.
[10] K.O. Joung, C.J. Oconnor, E. Sinn, R.L. Carlin, Inorg. Chem. 18 (1979) 804.
[11] Y. Journaux, O. Kahn, J. Chem. Soc., Dalton Trans. (1979) 1575.
[12] C.P. Landee, R.D. Willitt, Inorg. Chem. 20 (1981) 2521.
[13] I. Bkouche-Waksman, Y. Journaux, O. Kahn, Transition Met. Chem. 6 (1981) 176.
[14] S. Salehzadeh, R. Golbedaghi, J. Chem. Res. (2007) 94.
[15] H. Keypour, S. Salehzadeh, R.G. Pitchard, R.V. Parish, Inorg. Chem. 39 (2000) 5787.
[16] H. Keypour, S. Salehzadeh, Transition Met. Chem. 25 (2000) 204.
[17] H. Keypour, S. Salehzadeh, R.G. Pitchard, R.V. Parish, Polyhedron 19 (2000) 633.
[18] S. Salehzadeh, S.M. Nouri, H. Keypour, M. Bagherzadeh, Polyhedron 24 (2005) 478.
[19] S. Salehzadeh, S.A. Javarsineh, H. Keypour, J. Mol. Struct. 54 (2006) 785.
[20] H. Keypour, M. Dehdari, S. Salehzadeh, K.P. Wainwright, Transition Met. Chem. 28 (2003) 425.
[21] S. Salehzadeh, M. Bayat, Chem. Phys. Lett. 427 (2006) 455.
[22] S. Salehzadeh, M. Bayat, M. Hashemi, J. Phys. Chem. A 111 (2007) 8188.
[23] R.W. Hay, T. Clifford, P. Lightfoot, Polyhedron 17 (1998) 4347.
[24] T.H. Cheng, Y.M. Wang, W.T. Lee, G.C. Liu, Polyhedron 19 (2000) 2027.
[25] G.M. Sheldrick, SADABS Version 210, University of Gottingen, 2003.
[26] G.M. Sheldrick, SHELXS-97 and SHELXL-97, University of Gottingen, 1997.
[27] S.S. Massoud, F.A. Mautner, M.A.M. Abu-yossef, N.M. Shuaib, Polyhedron 18 (1999) 2061.
[28] C. Ochs, F.E. Hahn, T. Lügger, Eur. J. Inorg. Chem. (2001) 1279.

Polyhedron 28 (2009) 167–171

Contents lists available at ScienceDirect

Polyhedron

journal homepage: www.elsevier.com/locate/poly

Synthesis and coordination chemistry of new tetradentate N_2S_2 donor Schiff-base ligand ca_2-dapte: Mononuclear and dinuclear copper(I) complexes $[Cu(ca_2dapte)]ClO_4$ and $[\{Cu(PPh_3)(X)\}_2(ca_2dapte)]$ (X = I and Br)

Mahbod Morshedi [a], Mehdi Amirnasr [a,*], Alexandra M.Z. Slawin [b], J Derek Woollins [b], Aliakbar Dehno Khalaji [c,*]

[a] Department of Chemistry, Isfahan University of Technology, Isfahan 84156-83111, Iran
[b] Department of Chemistry, University of St. Andrews, St. Andrews, Fife KY16 9ST, United Kingdom
[c] Department of Science, Gorgan University of Agricultural Sciences and Natural Resources, Gorgan 49189-43464, Iran

ARTICLE INFO

Article history:
Received 27 May 2008
Accepted 7 October 2008
Available online 27 November 2008

Keywords:
N/S donor
Copper(I) complexes
Mononuclear
Dinuclear
Single-crystal X-ray diffraction

ABSTRACT

A mononuclear copper(I) complex, $[Cu(ca_2dapte)]ClO_4$ (**1**), and two dinuclear copper(I) complexes, $[\{Cu(PPh_3)(X)\}_2(ca_2dapte)]$ (X = I (**2**) and Br (**3**)), of a new tetradentate N_2S_2 donor Schiff-base ligand ca_2dapte have been prepared (ca_2dapte = *N*,*N*′-bis(*trans*-cinnamaldehyde)-1,2-di(o-iminophenylthio)ethane). These compounds have been characterized by elemental analyses (CHN), FT-IR, UV–Vis and ^{1}H NMR spectroscopy. The crystal structures of these copper(I) complexes have been determined by single-crystal X-ray diffraction. The coordination geometry around Cu(I) centers in these complexes is a distorted tetrahedron. The ca_2dapte is coordinated to Cu(I) as a tetradentate ligand in **1**, while it acts as a bis-bidentate bridging ligand in **2** and **3**.

© 2008 Elsevier Ltd. All rights reserved.

1. Introduction

There has been a growing interest in recent years toward the crystal structures and properties of copper(I) complexes with multidentate ligands [1–5], particularly in view of their potential applications in metallosupramolecular assemblies [6–10], bioinorganic chemistry [11] and catalysis [12]. Many efforts have been devoted to the design and synthesis of new multidentate ligands that are able to control the crystal structure and properties of copper(I) complexes [13–16]. With flexible ligands, the competition between bridging and chelating coordination modes is an important factor in producing mono, di, and polynuclear metal complexes [17,1,18,19]. We have recently studied the coordination behavior of the Schiff-base ligands such as ca_2en, Phc$a_2$en, and (Me-pk)$_2$en [20–29]. While ca_2en and Phc$a_2$en act as simple bidentate chelates [20–27], (Me-pk)$_2$en acts as a bidentate bridging ligand between two metal ions [28,29]. In this paper, we describe the synthesis and coordination behavior of the new Schiff-base ligand ca_2dapte (Scheme 1).

2. Experimental

2.1. General

All solvents and chemicals were of commercial reagent grade and used as received from Aldrich and Merck. 1,2-di(o-aminophenylthio)ethane (dapte) was prepared using the reported procedure [30]. Infrared spectra as KBr pellets were obtained on a FT-IR JASCO 680 PLUS spectrophotometer in the range 4000–400 cm^{-1}. UV–Vis absorption spectra were recorded on a JASCO V-570 spectrophotometer; λ_{max} (log ε) in nm. ^{1}H NMR spectra were measured with Bruker ACP-500 spectrometer at 500 MHz, and chemical shifts δ are reported in parts per million (ppm) relative to an internal standard of Me_4Si. Elemental analyses were performed using a Perkin–Elmer 2400II CHNS-O elemental analyzer.

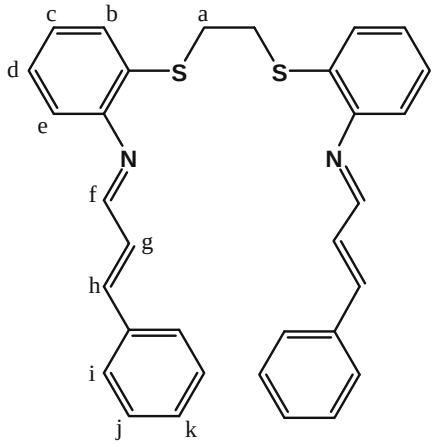
2.2. Synthesis

2.2.1. Synthesis of the ligand ca_2dapte

To a solution of dapte (0.276 g, 1 mmol) in EtOH (20 ml) was added, with continuous stirring, cinnamaldehyde (0.264 g, 2 mmol). The mixture was stirred for about 30 min to give a yellow precipitate. The product was then filtered off and washed with EtOH. Yield 84%. M.p. 181 °C; *Anal.* Calc. for $C_{32}H_{28}N_2S_2$: C, 76.15; H, 5.59; N, 5.55. Found: C, 74.52; H, 5.38; N, 5.49%. IR (KBr pellet,

* Corresponding authors. Tel.: +98 311 3912351; fax: +98 311 3912350 (M. Amirnasr).
E-mail address: amirnasr@cc.iut.ac.ir (M. Amirnasr).

0277-5387/$ - see front matter © 2008 Elsevier Ltd. All rights reserved.
doi:10.1016/j.poly.2008.10.018



Scheme 1.

ν/cm^{-1}) 1624s (C=N). UV–Vis [chloroform; λ_{max} in nm ($\log\varepsilon$ in L mol^{-1} cm^{-1})] 357 (24772), 301 (76924). ^{1}H NMR ($CDCl_3$), δ (ppm) = 3.17(s, 4H$_a$), 6.92 (dd, 2H$_g$), 7.10–7.40 (m, 16H$_{b,c,d,e,h,j,k}$), 7.52 (dd, 4H$_i$), 8.14 (d, 2H$_f$).

2.2.2. Synthesis of [Cu(ca$_2$dapte)]ClO$_4$ (**1**)

To a solution of [Cu(CH$_3$CN)$_4$]ClO$_4$ (32 mg, 0.1 mmol) in CH$_3$CN (5 ml) was added, with continuous stirring, a solution of ca$_2$dapte (50 mg, 0.1 mmol) in the minimum amount of chloroform. The mixture was stirred at room temperature for about 10 min to give a clear dark-red solution. Dark-red single crystals suitable for X-ray analysis were obtained by diffusion of diethyl ether into the filtrate. Yield 79%. *Anal.* Calc. for $C_{32}H_{28}N_2S_2CuClO_4$: C, 57.56; H, 4.23; N, 4.20. Found: C, 57.43; H, 3.91; N, 4.20%. IR (KBr pellet, ν/cm^{-1}) 1613s (C=N), 1089 m (ClO$_4$). UV–Vis [chloroform; λ_{max} in nm ($\log\varepsilon$ in L mol^{-1} cm^{-1})] 340 (52164). ^{1}H NMR ($CDCl_3$), δ (ppm) = 2.95 (s, 4H$_a$), 7.00 (br d, 2H$_g$), 7.19–7.37 (m, 16H$_{b,c,d,e,h,j,k}$), 7.57 (d, 4H$_i$), 8.23 (d, 2H$_f$).

2.2.3. Synthesis of [{Cu(PPh$_3$)(I)}$_2$(ca$_2$dapte)] (**2**)

To a solution of PPh$_3$ (52 mg, 0.2 mmol) in CH$_3$CN (5 ml) was added a solution of CuI (38 mg, 0.2 mmol) in CH$_3$CN (5 ml) and the mixture was stirred at room temperature for about 10 min to give a clear colorless solution. The ligand ca$_2$dapte (50 mg, 0.1 mmol) was then added and a clear orange-red solution was obtained. Orange-red single crystals suitable for X-ray analysis were obtained by diffusion of diethyl ether into the filtrate. Yield 77%. *Anal.* Calc. for $C_{68}H_{58}N_2P_2S_2Cu_2I_2$: C, 57.92; H, 4.15; N, 1.99. Found: C, 57.48; H, 3.84; N, 2.15%. IR (KBr pellet, ν/cm^{-1}) 1620s (C=N). UV–Vis [chloroform; λ_{max} in nm ($\log\varepsilon$ in L mol^{-1} cm^{-1})] 332 (54889), 300 (64457). ^{1}H NMR ($CDCl_3$), δ (ppm) = 3.05 (s, 4H$_a$), 7.01 (br d, 2H$_g$), 7.11–7.42 (m, 46H$_{b,c,d,e,h,j,k}$, PPh$_3$), 7.57, 7.98 (d, 4H$_i$), 8.41 (d, 2H$_f$).

2.2.4. Synthesis of [{Cu(PPh$_3$)(Br)}$_2$(ca$_2$dapte)] (**3**)

This complex was prepared by a procedure similar to that for complex **2** except that CuI was replaced with CuBr. Orange-red single crystals suitable for X-ray analysis were obtained by diffusion of diethyl ether into the filtrate. Yield 84%. *Anal.* Calc. for $C_{68}H_{58}N_2P_2S_2Cu_2Br_2$: C, 62.05; H, 4.44; N, 2.13. Found: C, 61.49; H, 4.17; N, 2.23%. IR (KBr pellet, ν/cm^{-1}) 1622s (C=N). UV–Vis [chloroform; λ_{max} in nm ($\log\varepsilon$ in L mol^{-1} cm^{-1})] 332 (66740), 311 (71440). ^{1}H NMR ($CDCl_3$), δ (ppm) = 3.08 (s, 4H$_a$), 7.04–7.45 (m, 48H$_{b,c,d,e,g,h,j,k}$, PPh$_3$), 7.59, 8.018 (m, 4H$_i$), 8.33 (d, 2H$_f$).

2.3. Crystal structure determination

Data were collected using a Rigaku MM007 rotating anode/confocal optics (Mo Kα radiation λ = 0.71073 Å) and a Mercury CCD at 93(2) K. Data were corrected for Lorentz polarization and absorption effects. The structures were solved by direct methods and refined on F^2 (SHELXL). All non-hydrogen atoms were refined anisotropically. Crystal data and structure refinement are listed in Table 1.

3. Results and discussion

3.1. General characterization of ligand and corresponding complexes

The new tetradentate N_2S_2 donor Schiff-base ligand ca$_2$dapte was prepared by condensation reaction of 2 equiv. of cinnamaldehyde with 1 equiv. of dapte [30] in EtOH. The product precipitated and was readily isolated in approximately 80% yield; the ligand was characterized by CHN, FT-IR, UV–Vis and ^{1}H NMR spectroscopy. The IR spectrum of the free ligand ca$_2$dapte exhibits the characteristic band of the imine group, which appears at 1624 cm^{-1}.

Table 1
Crystallographic data for the three crystal structures.

Compound	**1**	**2**	**3**
Empirical formula	$C_{32}H_{28}ClCuN_2O_4S_2$	$C_{68}H_{58}Cu_2I_2N_2P_2S_2$	$C_{68}H_{58}Cu_2Br_2N_2P_2S_2$
Formula weight	667.67	1410.10	1316.12
Crystal system	monoclinic	triclinic	triclinic
Space group	$P2_1/n$	$P\bar{1}$	$P\bar{1}$
a (Å)	23.761(3)	8.6428(18)	8.654(3)
b (Å)	19.440(2)	11.221(3)	11.145(4)
c (Å)	27.823(3)	15.579(4)	15.527(5)
α (°)	90.00	80.282(13)	79.407(16)
a (°)	110.699(3)	88.237(11)	87.818(15)
β (°)	90.00	86.483(12)	88.150(17)
V (Å^3)	12023(2)	1486.0(6)	1470.5(8)
Z	16	1	1
D_{calc} (Mg/m^3)	1.457	1.576	1.486
μ (mm^{-1})	0.995	1.922	2.251
Crystal size (mm)	0.12 × 0.12 × 0.12	0.10 × 0.10 × 0.03	0.10 × 0.10 × 0.03
Reflections collected	7682	8653	8314
R_{int}	0.1303	0.0423	0.1229
Data/restraints/parameters	21715/0/1514	5121/0/353	5090/0/353
Final R indices [$I > 2\sigma(I)$]	R_1 = 0.0683, wR_2 = 0.1645	R_1 = 0.0424, wR_2 = 0.1116	R_1 = 0.0866, wR_2 = 0.2161
R indices (all data)	R_1 = 0.1071, wR_2 = 0.1908	R_1 = 0.0446, wR_2 = 0.1148	R_1 = 0.1172, wR_2 = 0.2402
Largest difference in peak and hole (e Å^{-3})	0.817 and −0.688	1.099 and −2.618	0.904 and −0.808

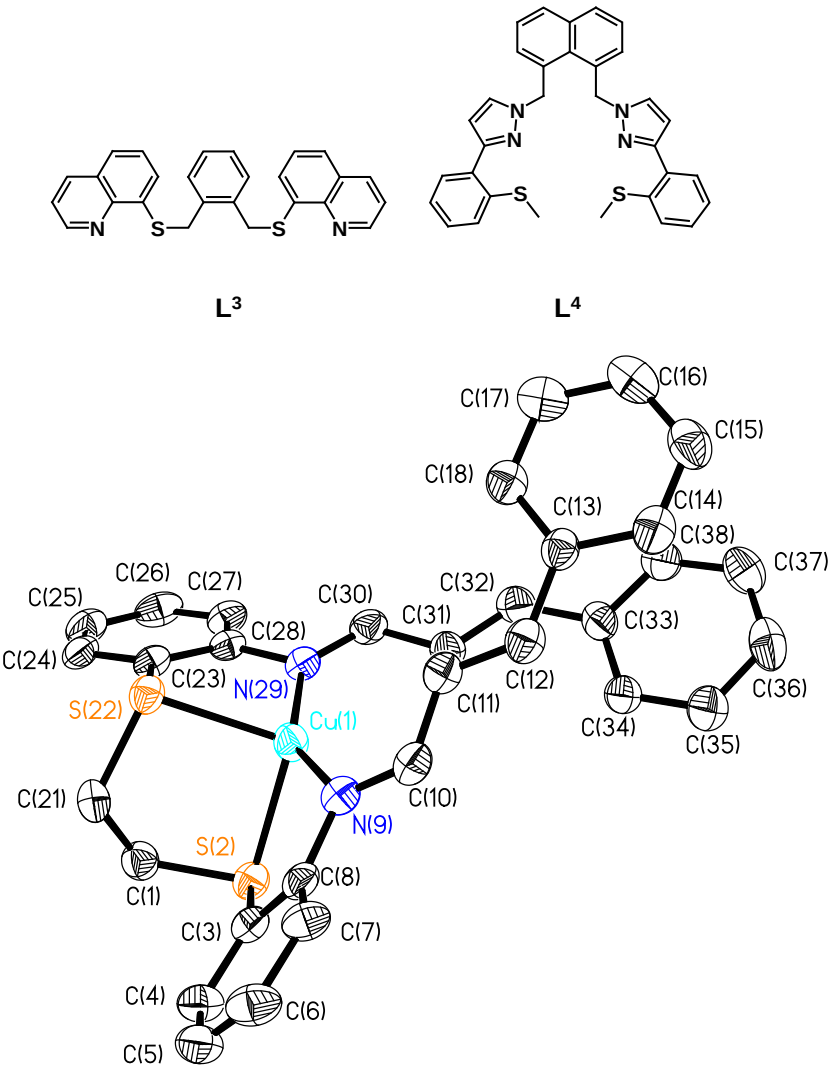


Fig. 1. View of the structure of $[Cu(ca_2dapte)]^+$ cation showing 50% probability ellipsoids.

This band is shifted to lower frequencies in the IR spectra of the corresponding complexes due to the coordination of the imine nitrogen [31], and appears at 1613 cm^{-1} in **1**, but at 1621 cm^{-1} in **2** and at 1622 cm^{-1} in **3** presumably due to weaker electron back donation by Cu(I) to the imine π^* in **2** and **3**. A strong band at about 1089 cm^{-1} in the spectrum of **1** is characteristic of the asymmetric Cl–O stretching mode of the perchlorate [32]. Since no d–d transitions are expected for d^{10} complexes, the UV–Vis bands are assigned to metal to ligand charge transfer (MLCT) or ligand-centered $\pi \rightarrow \pi^*$ transitions (Section 2) [33].

The ^1H NMR data and peak assignment are presented in Section 2. The ^1H signals of the coordinated ligand are commonly observed in all complexes, however, the aromatic H atoms of the coordinated PPh_3 ligands overlap to some extent with those of the phenyl H atoms of ca_2dapte. The two imine protons (H_f) appear as a doublet at 8.23 ppm in **1**, 8.41 ppm in **2** and 8.33 ppm in **3**. The downfield shift of iminic protons relative to the corresponding signals in the free ligand (8.14 ppm) can be attributed to the deshielding effect resulting from the coordination of the imine nitrogens.

3.2. Mononuclear copper(I) complex $[Cu(ca_2dapte)]ClO_4$ (*1*)

The crystal structure of the mononuclear $[Cu(ca_2dapte)]ClO_4$ (**1**) is shown in Fig. 1, and selected bond distances and angles are listed in Table 2. There are four similar but independent complex units in the asymmetric unit, one of which is only shown in Fig. 1. The complex is mononuclear and the central Cu(I) ion has the common irregular pseudo-tetrahedral geometry arising from the restricting bite angles of the chelating ligand (Table 2). In the absence of other coordinating ligands the ca_2dapte acted as a tetradentate ligand (*vide infra*). However, $[Cu(ca_2dapte)NCS]$ complex is formed in the presence of NCS [34] indicating that the ca_2dapte is capable of coordinating as a tridentate ligand leaving a free site for the NCS to coordinate. The Cu–N (1.982(4) and 1.996(4) Å) and Cu–S (2.3485(14) and 2.3489(13) Å) bond distances are similar to those found in $[Cu(L^3)][PF_6]$ [10] and $[Cu(L^4)][PF_6]$ [9].

Table 2
Selected bond distances (Å) and angles (°) for $[Cu(ca_2dapte)]ClO_4$ (**1**).

Cu(1)–N(29)	1.981(4)	Cu(1)–S(2)	2.3485(14)
Cu(1)–N(9)	1.996(4)	Cu(1)–S(22)	2.3489(13)
N(9)–C(10)	1.296(6)	N(29)–C(30)	1.285(6)
N(9)–Cu(1)–S(2)	86.55(12)	N(9)–Cu(1)–S(22)	114.27(1)
N(29)–Cu(1)–S(22)	86.93(11)	N(9)–Cu(1)–N(29)	149.10(16)
N(29)–Cu(1)–S(2)	115.78(12)	S(22)–Cu(1)–S(2)	93.11(5)
C(8)–N(9)–C(10)	121.6(4)	C(28)–N(29)–C(30)	120.2(4)

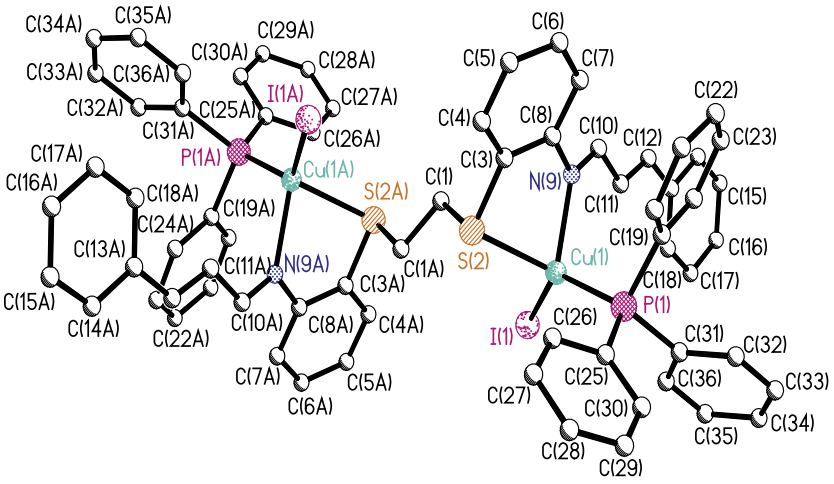


Fig. 2. View of the structure of $[\{Cu(PPh_3)(I)\}_2(ca_2dapte)]$ (**2**) complex.

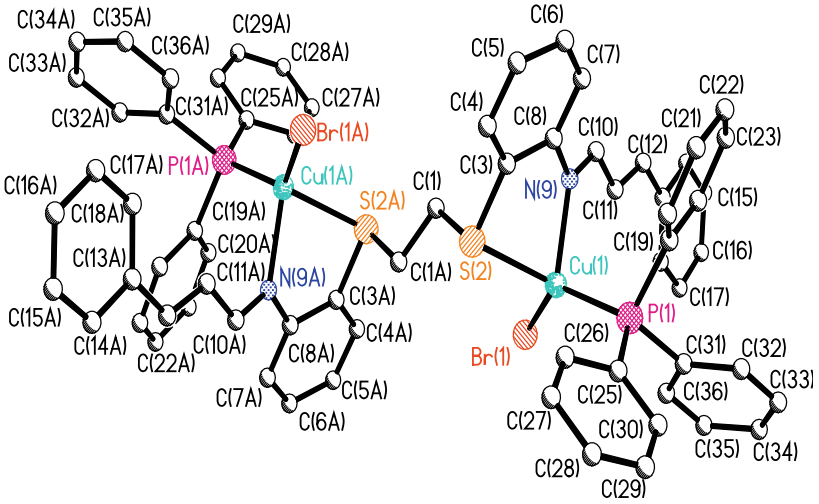


Fig. 3. View of the structure of $[\{Cu(PPh_3)(Br)\}_2(ca_2dapte)]$ (**3**) complex.

*3.3. Dinuclear copper(I) complexes $[\{Cu(PPh_3)(I)\}_2(ca_2dapte)]$ (**2**) and $[\{Cu(PPh_3)(Br)\}_2(ca_2dapte)]$ (**3**)*

Complexes **2** and **3** were readily obtained by reactions of CuI or CuBr and PPh_3 with ca_2dapte in a molar ratio 2:2:1 under mild conditions. Elemental analyses (CHN) and spectroscopic data were consistent with the formation of the dinuclear species $[\{Cu(PPh_3)(I)\}_2(ca_2dapte)]$ **2** and $[\{Cu(PPh_3)(Br)\}_2(ca_2dapte)]$ (**3**). X-ray quality crystals of **2** and **3** were grown by diffusion of diethyl ether into a concentrated acetonitrile solution; the crystal structure of $[\{Cu(PPh_3)(I)\}_2(ca_2dapte)]$ **2** and $[\{Cu(PPh_3)(Br)\}_2(ca_2dapte)]$ (**3**) are shown in Figs. 2 and 3, respectively, and selected bond distances and angles are listed in Table 3. These complexes are centrosymmetric dimmers with pairs of $Cu(PPh_3)(X)$ (X = I, Br) units bridged by ca_2dapte. The central Cu(I) ion has the common irregular pseudo-tetrahedral geometry arising from the low intraligands N(9)–Cu(1)–S(2) chelate angles (80.72(8)° in (**2**) and 80.54(19)° in **3**. The Cu–N and Cu–S bond distances are larger than those found in $[Cu(L^3)][PF_6]$ [10] and $[Cu(L^4)][PF_6]$ [9]. The Cu–X (X = I and Br) and Cu–P are similar to those reported for similar copper(I) complexes [6,35,36].

Table 3
Selected bond distances (Å), and angles (°) for $[\{Cu(PPh_3)(I)\}_2(ca_2dapte)]$ (**2**) and $[\{Cu(PPh_3)(Br)\}_2(ca_2dapte)]$ (**3**).

Complex	**2**	**3**
Cu(1)–N(9)	2.119(3)	2.117(6)
Cu(1)–P(1)	2.2169(10)	2.214(2)
Cu(1)–S(2)	2.3881(10)	2.397(2)
Cu(1)–X	2.5724(6)	2.4055(13)
N(9)–C(10)	1.285(4)	1.277(10)
N(9)–Cu(1)–P(1)	103.69(8)	102.24(18)
N(9)–Cu(1)–S(2)	80.72(8)	80.54(19)
P(1)–Cu(1)–S(2)	117.27(3)	117.74(8)
N(9)–Cu(1)–X	113.98(3)	112.61(17)
P(1)–Cu(1)–X	126.17(3)	127.41(7)
S(2)–Cu(1)–X	105.91(3)	106.16(6)
C(10)–N(9)–C(8)	119.0(3)	119.1(7)

4. Conclusion

This paper describes the synthesis of a new versatile tetradentate S_2N_2 Schiff-base ligand, ca_2dapte, with varying coordination capability, and three of its Cu(I) complexes. A mononuclear copper(I) complex with ca_2dapte acting as simple tetradentate ligand and two dinuclear complexes with ca_2dapte acting as a bis-bidentate bridging ligand was prepared.

Acknowledgments

Partial support of this work by the Isfahan University of Technology Research Council is gratefully acknowledged. A.D.K. would like to acknowledge the Gorgan University of Agricultural Sciences and Natural Resources for financial support.

Appendix A. Supplementary data

CCDC 679700, 679701, and 679702 contain the supplementary crystallographic data for **1**, **2** and **3**. These data can be obtained free of charge via http://www.ccdc.cam.ac.uk/conts/retrieving.html, or from the Cambridge Crystallographic Data Centre, 12 Union Road, Cambridge CB2 1EZ, UK; fax: (+44) 1223-336-033; or e-mail: deposit@ccdc.cam.ac.uk. Supplementary data associated with this article can be found, in the online version, at doi:10.1016/j.poly.2008.10.018.

References

[1] M. Gennari, M. Lanfranchi, R. Cammi, M.A. Pellinghelli, L. Marchio, Inorg. Chem. 46 (2007) 10143.
[2] C.-H. Chou, W.-Y. Yeh, G.-H. Lee, S.-M. Peng, Inorg. Chim. Acta 359 (2006) 4139.
[3] M. Glockle, K. Hubler, H.-J. Kummerer, G. Denninger, W. Kaim, Inorg. Chem. 40 (2001) 2263.
[4] S. Panja, S. Chowdhury, M.G.B. Drew, D. Datta, Inorg. Chem. Commun. 5 (2002) 304.
[5] W.L. Jia, T. McCormick, Y. Tao, J.-P. Lu, S. Wang, Inorg. Chem. 44 (2005) 5706.
[6] X.-H. Zhou, T. Wu, D. Li, Inorg. Chim. Acta 359 (2006) 1442.
[7] Z.R. Bell, L.P. Harding, M.D. Ward, Chem. Commun. (2003) 2432.
[8] R.l. Paul, S.P. Argent, J.C. Jeffery, L.P. Harding, J.M. Lynam, M.D. Ward, Dalton Trans. (2004) 3453.
[9] T.K. Ronson, H. Adams, M.D. Ward, Eur. J. Inorg. Chem. (2005) 4533.
[10] S. Tavacoli, T.A. Miller, R.L. Paul, J.C. Jeffery, M.D. Ward, Polyhedron 22 (2003) 507.
[11] R.M. Kretzer, R.A. Ghiladi, E.L. Lebeau, H.-C. Liang, K.D. Karlin, Inorg. Chem. 42 (2003) 3016.
[12] E.I. Solomon, P.M. Jones, J.A. Maj, Chem. Rev. 93 (1993) 2623.
[13] S.-M. Kuang, D.G. Cuttell, D.R. McMillin, P.E. Fanwick, R.A. Walton, Inorg. Chem. 41 (2002) 3313.
[14] Y.-C. Liu, C.-I. Li, W.-Y. Yeh, G.-H. Lee, S.-M. Peng, Inorg. Chim. Acta 359 (2006) 2361.
[15] E. Cariati, D. Roberto, R. Ugo, P.C. Foed, S. Galli, A. Sironi, Inorg. Chem. 44 (2005) 4077.
[16] C.-C. Chou, C.-C. Su, A. Yeh, Inorg. Chem. 44 (2005) 6122.
[17] H. Wang, M.-X. Li, M. Shao, X. He, Polyhedron 26 (2007) 5171.
[18] C. Ganesamoorthy, M.S. Balakrishna, P.P. George, J.T. Mague, Inorg. Chem. 46 (2007) 848.
[19] B.-J. Liaw, T.S. Lobana, Y.-W. Lin, J.-C. Wang, C.W. Liu, Inorg. Chem. 44 (2007) 9921.
[20] A.D. Khalaji, M. Amirnasr, K. Aoki, Anal. Sci. 22 (2006) x149.
[21] A.D. Khalaji, M. Amirnasr, K.J. Schenk, Acta Crystallogr., Sect. E 63 (2007) m1684.
[22] A.D. Khalaji, K. Aoki, M. Amirnasr, J. Coord. Chem. 60 (2007) 201.
[23] M. Amirnasr, A.D. Khalaji, L.R. Falvello, T. Soler, Polyhedron 25 (2006) 1967.
[24] G. Kickelbick, M. Amirnasr, A.D. Khalaji, S. Dehghanpour, Aust. J. Chem. 56 (2003) 323.
[25] G. Kickelbick, M. Amirnasr, A.D. Khalaji, S. Dehghanpour, Acta Crystallogr., Sect. E 58 (2002) m381.
[26] A.D. Khalaji, R. Welter, Inorg. Chim. Acta 359 (2006) 4403.
[27] A.D. Khalaji, M. Amirnasr, J.-C. Daran, Acta Crystallogr., Sect. E 62 (2006) m3183.
[28] A.D. Khalaji, M. Amirnasr, R. Welter, Acta Crystallogr., Sect. E 62 (2006) m2950.
[29] A.D. Khalaji, M. Amirnasr, R. Welter, Anal. Sci. 22 (2006) x151.
[30] S. Chandra, R. Kumar, Transition Met. Chem. 29 (2004) 269.
[31] C.T. Cunningham, J.J. Moore, K.L.H. Cunningham, P.E. Fanwick, D.R. McMillin, Inorg. Chem. 39 (2000) 3638.
[32] K. Nakamoto, Infrared and Raman Spectra on Inorganic and Coordination Complexes, 4th ed., John Wiley & Sons, USA, 1992.
[33] A.A. Del Paggio, D.R. McMillin, Inorg. Chem. 22 (1983) 691.
[34] M. Morshedi, M. Amirnasr, A.M.Z. Slawin, J.D. Woollins, A.D. Khalaji, submitted for publication.
[35] D.-H. Wang, L.-Q. Song, J.-H. Chen, Y. Chen, W.-F. Fu, Acta Crystallogr., Sect. E 63 (2007) m474.
[36] J.-H. Chen, L.-Q. Song, D.-H. Wang, J.-F. Zhang, W.-F. Fu, Acta Crystallogr., Sect. E 63 (2007) m34.

Polyhedron 28 (2009) 172–180

Contents lists available at ScienceDirect

Polyhedron

journal homepage: www.elsevier.com/locate/poly

Palladium(II)–rare-earth metal(III) paddlewheel carboxylate complexes: Easy total acetate to pivalate metathesis

Sergei E. Nefedov, Natalia Yu. Kozitsyna, Michael N. Vargaftik *, Ilya I. Moiseev

N.S. Kurnakov Institute of General and Inorganic Chemistry, Russian Academy of Sciences, 119991 Moscow, Russian Federation

ARTICLE INFO

Article history:
Received 26 August 2008
Accepted 7 October 2008
Available online 18 November 2008

Keywords:
Palladium carboxylates
Rare-earth metals
Heterometallic paddlewheel complexes
X-ray structure
H-bonding

ABSTRACT

Bis-paddlewheel heterobimetallic complexes in which palladium(II) is connected to the rare-earth metals(III) $[Pd(\mu\text{-}OOCMe)_4Ln(OH_2)(\mu,\eta^2\text{-}OOCMe)]_2 \times 2HOOCMe$ (Ln = Nd, Sm, Eu, Yb and Tm) by four acetate bridges were synthesised by the reaction of $Pd_3(\mu\text{-}OOCMe)_6$ with the Ln^{III} acetates. The tetraacetate-bridged complexes were unexpectedly found to be readily transformed by the stoichiometric amount of pivalic acid into the mono-paddlewheel tetrapivalate-bridged analogues in which the paddlewheel structure $[Pd(\mu\text{-}OOCR)_4Ln]$ maintains as established by X-ray crystallography. The role of the intra- and intermolecular H-bonding in these complexes is discussed.

© 2008 Elsevier Ltd. All rights reserved.

1. Introduction

Palladium-based mixed-metal materials, such as palladium–lanthanide alloys and catalysts present academic and industrial interest for material science and catalysis [l,2]. Traditional techniques of making palladium–lanthanide materials are based on direct fusion of the metallic components [1] or coimpregnation of a catalyst support with the constituent metal salts followed by redox treatments [2].

Recently we have synthesised in high yields and X-ray structurally characterised Pd^{II}-based heterobimetallic acetate-bridged complexes containing the complementary transition (Mn^{II}, Co^{II}, Ni^{II}), post-transition (Zn^{II}), alkaline earth (Ca^{II}, Sr^{II}, Ba^{II}) and rare-earth (Ce^{IV}, Sm^{III}, Nd^{III}, Eu^{III}) metals [3a–d]. These molecular systems in which the Pd^{II} and co-metal atoms are strongly linked by four acetate bridges (and in some cases possible metal–metal interactions[1]) seem to be favorable for keeping together the metal atoms during the deposition and redox treatments, giving promise for the preparation of heterometallic nanoclusters and catalysts.

For instance, the complex $Pd(\mu\text{-}OOCMe)_4Zn(OH_2)$ was readily reduced with H_2 under fairly mild conditions (150–250 °C, 5–10% H_2/He) both in the crystalline and carbon-supported states to afford a PdZn 1:1 nanoparticles as evidenced by ICP elemental analysis, EXAFS, XANES and XRD [4a]. The supported PdZn 1:1 nanoalloy prepared by this way from the heterobimetallic complex is an efficient and highly selective catalyst for acetylene to ethylene hydrogenation [4b].

The above heterobimetallic complexes were found to maintain the general shape of the Pd–co-metal moiety and nearly invariable metal–metal distance upon the attack of rather strong nucleophilic agents, as shown by the reactions of the complex $Pd(\mu\text{-}OOCMe)_4Co(NCMe)$ with such N-bases as 1,10-phenanthroline [5a] and pyridine [5b].

In this paper we report studies of the reaction of the tetraacetate-bridged Pd^{II}–Ln^{III} complexes with a weaker O-base, trimethylacetic (pivalic) acid. For this purpose we synthesised new heterobimetallic Pd^{II}-based carboxylate complexes with the early (Sm^{III}, Eu^{III}) and late (Tm^{III}, Yb^{III}) rare-earth metals whose distinctive features are the easy change of the Ln^{III}–Ln^{II} oxidation states in redox reactions and different atomic radii due to the lanthanide contraction. For comparison, the Pd^{II}–Nd^{III} acetate and pivalate complexes also were studied.

We unexpectedly found that all the tetraacetate-bridged complexes readily undergo total bridging acetate to pivalate metathesis, while the paddlewheel Pd–Ln motif remains practically unchanged.

2. Results and discussion

The reaction of palladium(II) acetate $Pd_3(\mu\text{-}OOCMe)_6$ with trivalent rare-earth metal acetates $Ln(OOCMe)_3 \times nH_2O$ (M = Nd^{III}, n = 1.5; Eu^{III}, Tm^{III}, Yb^{III}, n = 4) in hot acetic acid followed by concentration and slow cooling of the reaction solution to room temperature afforded in high yield the single-crystalline heterobimetallic complexes $[Pd(\mu\text{-}OOCMe)_4Ln(OH_2)(\mu,\eta^2\text{-}OOCMe)]_2 \times 2HOOCMe$

* Corresponding author. Tel.: +7 (495) 9554865; fax: +7 095 954 1279.
E-mail address: wahr36@mail.ru (M.N. Vargaftik).

[1] Quantum chemical calculations of the metal–metal bonding in these molecular systems are in progress now.

0277-5387/$ - see front matter © 2008 Elsevier Ltd. All rights reserved.
doi:10.1016/j.poly.2008.10.006

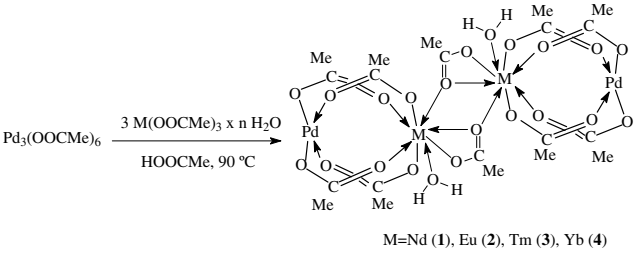
(Ln = Nd^{III} (**1**), Eu^{III} (**2**), Tm^{III} (**3**), Yb^{III} (**4**)) with a bis-paddlewheel structure (Scheme 1).

According to X-ray diffraction study (Fig. 1, Tables 1–5), molecules **1**–**4** containing different rare-earth metals consist of two tetraacetate-bridged fragments $Pd(\mu\text{-}OOCMe)_4Ln$ (Pd–O 1.995 (3)–2.002(4) Å, Nd–O 2.391(4)–2.416(3) Å for **1**; Pd–O 1.995(11)–2.003(8) Å, Eu–O 2.340(9)–2.361(8) Å for **2**; Pd–O 1.997 (3)–2.003(3) Å, Tm–O 2.282(2)–2.305(2) Å for **3**; Pd–O 1.993(5)–2.001(4) Å, Yb–O 2.265(4)–2.289(5) Å for **4**) linked by a pair of μ,η^2-acetate bridges (for **1**: Nd···Nd 4.1721(19) Å, Nd(1)–O(9) 2.558(3) Å, Nd(1)–O(10) 2.501(4) Å; for **2**: Eu···Eu 4.0764(15) Å; Eu(1)–O(9) 2.488(8) Å, Eu(1)–O(10) 2.433(7) Å; for **3**: Tm···Tm 3.9923(7) Å, Tm(1)–O(9) 2.433(2) Å, Tm(1)–O(10) 2.388(2) Å; for **4**: Yb···Yb 3.9823(6) Å, Yb(1)–O(9) 2.424(4) Å, Yb(1)–O(10) 2.382(5) Å).

The metal–metal distances Pd···Ln in the paddlewheel fragments (Pd···Nd 3.221(2) Å in **1**, Pd···Eu 3.1983(12) Å in **2**, Pd···Tm 3.1783(4) Å in **3**, Pd···Yb 3.1834(7) Å in **4**) are much shorter that the sum of the van der Waals radii of the corresponding metals, being close to the sum of the corresponding covalent radii (Pd–Nd 2.92 Å, Pd–Eu 3.13 Å, Pd–Tm 2.84 Å, Pd–Yb 3.02 Å). The coordination sphere of the rare-earth metal atoms is complemented with H_2O ligand, and the coordination number of these atoms is eight under suggestion of the absence of the direct Pd^{II}—Ln^{III} bond (Nd(1)–O(11) 2.462(3) Å, Eu(1)–O(11) 2.378(8) Å, Tm(1)–O(11) 2.310(2) Å, Yb(1)–O(11) 2.296(4) Å).

The Pd–O bond lengths in all complexes **1**–**4** are nearly the same, while the Ln^{III}–O distances are shortened with a decrease in the atomic radius of the Ln^{III} atom. Meanwhile, the Ln^{III}–O(9) bond length is noticeably longer compared to the other Ln^{III}–O distances likely due to the strong H-bonding between this atom belonging to η^2-acetate anion and the H atom of the solvate acetic acid molecule ((O(9)···O(12) 2.698(4), 2.671(7), 2.666(3), 2.665(4) Å, in **1**–**4**, respectively). However, the Ln^{III}–O(9) bond is slightly shorter than one bond of the bridging oxygen atom O(10) of the μ,η^2-coordinated acetate ligand (Nd(1)–O(10A) 2.570(3) Å, Eu(1)–O(10A) 2.500(9) Å, Tm(1)–O(10A) 2.446(2) Å, Yb(1)–O(10A) 2.427(4) Å).

Earlier we synthesised the relative bis-paddlewheel tetraacetate-bridged complexes $[Pd(\mu\text{-}OOCMe)_4Ln(THF)(\mu,\eta^2\text{-}OOCMe)_2]_2 \times 2THF$ (Ln = Eu, Nd; Pd···$Nd_{av.}$ 3.227, Nd···Nd_{av} 4.156 Å, Pd···Eu_{av} 3.208 Å, Eu···Eu 4.089 Å in two independent molecules) [3c] using the similar synthetic procedure, with the only exception that water and acetic acid were thoroughly removed from the primary reaction product by distillation with benzene followed by recrystallisation from hot THF [3c]. In contrast to crystals **1**–**4**, the crystals of these complexes have no intermolecular H-bonds and seemingly due to this fact, the metal–oxygen distances in the fragment $Ln(\mu,\eta^2\text{-}OOCMe)_2Ln$ are noticeably redistributed. The Ln–O(9) and Ln–O(10) bond lengths are close to each other (Nd–$O(9)_{av}$ 2.512 Å, Eu–$O(9)_{av}$ 2.472 Å Nd–$O(10)_{av}$ 2.553 Å, Eu–$O(10)_{av}$ 2.506 Å), while the Ln–O(10A) distances are shortened (Nd–$O(10A)_{av}$ 2.445 Å Eu–$O(10A)_{av}$ 2.401 Å) compared to those found in the H-bonded complexes **1** and **2** (Table 6).



Scheme 1.

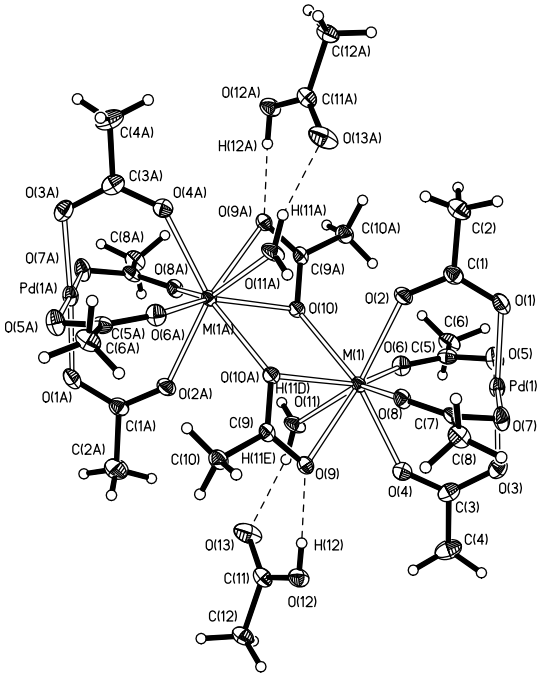


Fig. 1. Molecular structure of the bis-paddlewheel complexes $[Pd(\mu\text{-}OOCMe)_4\text{-}Ln(OH_2)(\mu,\eta^2\text{-}OOCMe)]_2 \times 2HOOCMe$ (Ln = Nd^{III} (**1**), Eu^{III} (**2**), Tm^{III} (**3**), Yb^{III} (**4**)) drawn with displacement ellipsoids at the 50% probability level.

The second O atom of the HOOCMe solvate molecule in **1**–**4** is linked to H atoms of the coordinated water molecules belonging to two adjacent complexes (O(13)···O(11)(11A) 2.819(4), 2.757(4) Å; 2.749(8), 2.787(9) Å; 2.789(3), 2.741(3) Å; 2.744(4), 2.798(5) Å for **1**–**4**, respectively), forming 1D polymeric chain (Fig. 2).

The geometry of molecules **1**–**4** is practically the same as that of the earlier synthesised complex $[Pd(\mu\text{-}OOCMe)_4Sm(OH_2)(\mu,\eta^2\text{-}OOCMe)]_2 \times 2HOOCMe$ [3a].

Complexes **1**–**4** and the earlier synthesised similar Pd^{II}-based acetate complexes are soluble and stable in water but poorly soluble in low-polarity organic solvents. To improve their solubility, it would desirable to change the acetate anions for the more lyophilic trimethylacetate (pivalate) ligands. The acetate-bridged palladium(II) acetate $Pd_3(\mu\text{-}OOCMe)_6$ is known to maintain its trinuclear structure upon changing all the acetate bridges by pivalate ligands [6a]. Meanwhile, the analogous acetate-bridged tetranuclear platinum(II) acetate $Pt_4(\mu\text{-}OOCMe)_8$ was transformed by pivalic acid or pivalate salts to the mixed-ligand complex $Pt_4(OOCBu^t)_4(OOCMe)_4$ only [6b].

In this context, we attempted to transform complexes **1**–**4** and the earlier synthesised [3b] complex $[Pd(\mu\text{-}OOCMe)_4Sm(OH_2)\text{-}(\mu,\eta^2\text{-}OOCMe)]_2 \times 2HOOCMe$ to the corresponding pivalates by refluxing in benzene solution of pivalic acid Bu^tCOOH. It was unexpectedly found that not only the solvate acetic acid and two μ,η^2-acetate bridges but also all the μ-acetate bridges undergo total ligand substitution by the reaction with a stoichiometric amount of pivalic acid to give the purely pivalate complexes in high yield:

$$[Pd(\mu\text{-}OOCMe)_4M]_2L + 4HOOCBu^t \rightarrow Pd(\mu\text{-}OOCBu^t)_4ML' + 4MeCOOH,$$

$$L = OOCMe^-,\ H_2O;\ L' = OOCBu^{t-},\ HOOCBu^t$$

which are well soluble in low-polarity organic solvents, including benzene and *n*-pentane.

Table 1
Crystal data and structure refinement for compounds **1**–**9**.

	1	**2**	**3**	**4**	**5**	**6**	**7**	**8**	**9**
Empirical formula	$C_{24}H_{42}Nd_2O_{26}Pd_2$	$C_{24}H_{42}Eu_2O_{26}Pd_2$	$C_{24}H_{42}O_{26}Pd_2Tm_2$	$C_{24}H_{42}O_{26}Pd_2Yb_2$	$C_{40}H_{75}O_{16}PdNd$	$C_{40}H_{75}O_{16}PdSm$	$C_{40}H_{75}EuO_{16}Pd$	$C_{40}H_{75}O_{16}PdTm$	$C_{40}H_{75}O_{16}PdYb$
Fw	1247.86	1263.30	1297.24	1305.46	1062.64	1068.75	1070.36	1087.33	1091.44
Colour	orange	yellow	yellow	yellow	yellow	yellow-orange	yellow-orange	yellow-orange	yellow-orange
Temperature (K)	295(2)	295(2)	200(2)	200(2)	295(2)	295(2)	295(2)	200(2)	160(2)
Diffractometer	Smart Apex II	Siemens P4	Smart Apex II	Smart Apex II	Smart Apex II	Smart	Smart Apex II	Smart Apex II	Smart
Crystal system	monoclinic	monoclinic	monoclinic	monoclinic	triclinic	triclinic	triclinic	triclinic	triclinic
Space group	$P2(1)/n$	$P2(1)/n$	$P2(1)/n$	$P2(1)/n$	$P\bar{1}$	$P\bar{1}$	$P\bar{1}$	$P\bar{1}$	$P\bar{1}$
Unit cell dimensions									
a (Å)	8.856(9)	8.854(5)	8.7250(7)	8.7262(8)	11.5212(18)	11.4949(15)	11.4787(12)	11.0892(18)	11.108(2)
b (Å)	19.98(2)	19.822(6)	19.3676(16)	19.3632(16)	11.7569(18)	11.7480(15)	11.7377(13)	11.8066(18)	11.833(2)
c (Å)	11.922(12)	11.740(4)	11.5976(9)	11.5855(9)	21.527(3)	21.537(3)	21.506(2)	19.557(3)	19.611(5)
α (°)	90	90	90	90	88.090(3)	88.126(3)	88.187(1)	96.418(3)	96.426(9)
β (°)	90.730(13)	90.76(4)	90.852(2)	90.850(2)	88.848(3)	88.825(3)	88.865(1)	96.606(3)	96.586(12)
γ (°)	90	90	90	90	63.596(2)	63.650(3)	63.614(1)	92.115(4)	92.060(6)
V (Å^3)	2109(4)	2060.2(14)	1959.6(3)	1957.4(3)	2610.2(7)	2604.7(6)	2594.4(5)	2524.3(7)	2541.6(10)
Z (Z')	2 (0.5)	2 (0.5)	2 (0.5)	2 (0.5)	2 (1)	2 (1)	2 (1)	2(1)	2 (1)
d_{calc} (Mg/m^3)	1.965	2.036	2.199	2.215	1.352	1.363	1.370	1.431	1.426
Absorption coefficient (mm^{-1})	3.344	3.948	5.477	5.729	1.386	1.519	1.602	2.162	2.242
$F(000)$	1212	1224	1248	1252	1098	1102	1104	1116	1118
Crystal size (mm)	0.16 × 0.14 × 0.14	0.16 × 0.14 × 0.14	0.18 × 0.16 × 0.16	0.18 × 0.16 × 0.16	0.14 × 0.12 × 0.10	0.20 × 0.18 × 0.16	0.18 × 0.14 × 0.12	0.17 × 0.14 × 0.12	0.24 × 0.22 × 0.20
θ Range for data collection (°)	2.85–27.00.	2.02–25.00	2.05–29.00	2.05–25.00	1.93–26.00	1.89–26.00	3.33–27.00	1.74–27.00	1.73–29.00
Index ranges	$-11 \leqslant h \leqslant 11$, $-22 \leqslant k \leqslant 25$, $-14 \leqslant l \leqslant 15$	$0 \leqslant h \leqslant 10$, $-23 \leqslant k \leqslant 0$, $-13 \leqslant l \leqslant 13$	$-6 \leqslant h \leqslant 11$, $-25 \leqslant k \leqslant 26$, $-15 \leqslant l \leqslant 15$	$-10 \leqslant h \leqslant 8$, $-23 \leqslant k \leqslant 12$, $-12 \leqslant l \leqslant 12$	$-14 \leqslant h \leqslant 14$, $-14 \leqslant k \leqslant 14$, $-26 \leqslant l \leqslant 26$	$-14 \leqslant h \leqslant 14$, $-14 \leqslant k \leqslant 14$, $-26 \leqslant l \leqslant 26$	$-14 \leqslant h \leqslant 14$, $-14 \leqslant k \leqslant 14$, $-27 \leqslant l \leqslant 27$	$-14 \leqslant h \leqslant 11$, $-13 \leqslant k \leqslant 15$, $-24 \leqslant l \leqslant 22$	$-15 \leqslant h \leqslant 15$, $-16 \leqslant k \leqslant 16$, $-26 \leqslant l \leqslant 26$
Reflections collected	17430	5716	14310	7191	22744	22722	22006	15806	27916
Independent reflections (R_{int})	4528 (0.0452)	3624 (0.0789)	5172 (0.0337)	3248 (0.0394)	10123 (0.0523)	10045 (0.0399)	11204 (0.0268)	10821 (0.0318)	13350 (0.0288)
Data/restraints/parameters	4528/0/249	3624/0/250	5172/0/250	3248/102/254	10123/289/521	10045/288/539	11204/0/487	10821/288/547	13350/288/547
Goodness-of-fit on F^2	0.951	1.046	0.953	1.000	0.998	1.010	1.025	1.101	1.030
Final R indices [$I > 2\sigma(I)$][a]	$R_1 = 0.0293$, $wR_2 = 0.0543$	$R_1 = 0.0475$, $wR_2 = 0.0856$	$R_1 = 0.0269$, $wR_2 = 0.0563$	$R_1 = 0.0345$, $wR_2 = 0.0693$	$R_1 = 0.0610$, $wR_2 = 0.1571$	$R_1 = 0.0513$, $wR_2 = 0.1343$	$R_1 = 0.0472$, $wR_2 = 0.1150$	$R_1 = 0.0552$, $wR_2 = 0.1191$	$R_1 = 0.0454$, $wR_2 = 0.1139$
R indices (all data)[a]	$R_1 = 0.0464$, $wR_2 = 0.0580$	$R_1 = 0.0893$, $wR_2 = 0.0997$	$R_1 = 0.0392$, $wR_2 = 0.0600$	$R_1 = 0.0487$, $wR_2 = 0.0740$	$R_1 = 0.0988$, $wR_2 = 0.1721$	$R_1 = 0.0722$, $wR_2 = 0.1508$	$R_1 = 0.0607$, $wR_2 = 0.1243$	$R_1 = 0.0795$, $wR_2 = 0.1291$	$R_1 = 0.0566$, $wR_2 = 0.1213$
Largest difference in peak and hole[b] (e A^{-3})	0.746 and −0.666	1.262 and −0.847	1.034 and −0.579	1.026 and −0.760	1.095 and −1.927	2.435 and −1.328	1.597 and −0.868	2.024 and −1.896	2.031 and −1.132

[a] $R_1 = \sum||F_o| - |F_c||/\sum|F_o|$; $wR_2 = \{\sum[w(F_o^2 - F_c^2)^2]/\sum w(F_o^2)^2\}^{1/2}$.
[b] In all structures the largest difference in peak is observed in the vicinity of heavy atom.

Table 2
Selected bond lengths (Å) and angles (°) for complex **1**.

Nd(1)–Pd(1)	3.221(2)	Pd(1)–O(1)	2.002(4)
Pd(1)–O(3)	1.996(4)	Pd(1)–O(5)	1.995(3)
Pd(1)–O(7)	2.001(3)	Nd(1)–O(2)	2.416(3)
Nd(1)–O(4)	2.412(4)	Nd(1)–O(6)	2.413(3)
Nd(1)–O(8)	2.391(4)	Nd(1)–O(11)	2.462(3)
O(1)–Pd(1)–O(3)	175.51(14)	O(1)–Pd(1)–O(5)	89.99(14)
O(1)–Pd(1)–O(7)	90.61(14)	O(1)–Pd(1)–Nd(1)	92.01(10)
O(3)–Pd(1)–Nd(1)	92.45(11)	O(5)–Pd(1)–Nd(1)	91.08(12)
O(7)–Pd(1)–Nd(1)	91.79(12)	O(2)–Nd(1)–Pd(1)	63.42(8)
O(4)–Nd(1)–Pd(1)	62.88(9)	O(6)–Nd(1)–Pd(1)	63.79(9)
O(8)–Nd(1)–Pd(1)	63.52(9)	O(9)–Nd(1)–Pd(1)	119.79(9)
O(10)–Nd(1)–Pd(1)	127.77(7)	O(11)–Nd(1)–Pd(1)	131.16(8)
O(9)–Nd(1)–O(10)#1	50.32(10)	Nd(1)–O(10)–Nd(1)#1	110.70(10)

Symmetry transformations used to generate equivalent atoms: #1 $-x+1$, $-y+2$, $-z+2$.

Table 3
Selected bond lengths (Å) and angles (°) for complex **2**.

Eu(1)–Pd(1)	3.1983(12)	Pd(1)–O(1)	2.000(10)
Pd(1)–O(3)	1.995(11)	Pd(1)–O(5)	1.978(9)
Pd(1)–O(7)	2.003(8)	Eu(1)–O(2)	2.340(9)
Eu(1)–O(4)	2.361(8)	Eu(1)–O(6)	2.328(9)
Eu(1)–O(8)	2.352(8)	Eu(1)–O(11)	2.378(8)
O(1)–Pd(1)–O(3)	176.1(4)	O(1)–Pd(1)–O(5)	91.0(4)
O(1)–Pd(1)–O(7)	90.2(4)	O(1)–Pd(1)–Eu(1)	91.1(3)
O(3)–Pd(1)–Eu(1)	92.7(3)	O(5)–Pd(1)–Eu(1)	91.0(3)
O(7)–Pd(1)–Eu(1)	90.6(2)	O(2)–Eu(1)–Pd(1)	64.0(2)
O(4)–Eu(1)–Pd(1)	63.2(2)	O(6)–Eu(1)–Pd(1)	64.0(2)
O(8)–Eu(1)–Pd(1)	64.2(2)	O(9)–Eu(1)–Pd(1)	119.33(17)
O(10)–Eu(1)–Pd(1)	128.2(2)	O(11)–Eu(1)–Pd(1)	130.2(2)
O(9)–Eu(1)–O(10)#1	51.9(2)	Eu(1)–O(10)–Eu(1)#1	111.5(3)

Symmetry transformations used to generate equivalent atoms: #1 $-x+1$, $-y+2$, $-z+2$.

Table 4
Selected bond lengths (Å) and angles (°) for complex **3**.

Tm(1)–Pd(1)	3.1783(4)	Pd(1)–O(1)	2.003(3)
Pd(1)–O(3)	2.003(3)	Pd(1)–O(5)	1.997(3)
Pd(1)–O(7)	1.998(3)	Tm(1)–O(2)	2.303(2)
Tm(1)–O(4)	2.293(3)	Tm(1)–O(6)	2.282(2)
Tm(1)–O(8)	2.305(2)	Tm(1)–O(9)	2.433(2)
Tm(1)–O(10)	2.388(2)	Tm(1)–O(10)#1	2.446(2)
Tm(1)–O(11)	2.310(2)		
O(1)–Pd(1)–O(3)	176.74(10)	O(1)–Pd(1)–O(5)	90.73(11)
O(1)–Pd(1)–O(7)	89.85(11)	O(1)–Pd(1)–Tm(1)	90.72(7)
O(3)–Pd(1)–Tm(1)	92.43(8)	O(5)–Pd(1)–Tm(1)	90.81(8)
O(7)–Pd(1)–Tm(1)	90.31(7)	O(2)–Tm(1)–Pd(1)	64.65(7)
O(4)–Tm(1)–Pd(1)	62.93(6)	O(6)–Tm(1)–Pd(1)	64.45(6)
O(8)–Tm(1)–Pd(1)	64.46(6)	O(9)–Tm(1)–Pd(1)	118.21(6)
O(10)–Tm(1)–Pd(1)	128.78(6)	O(11)–Tm(1)–Pd(1)	131.11(7)
O(9)–Tm(1)–O(10)#1	52.77(8)	Tm(1)–O(10)–Tm(1)#1	111.34(9)

Symmetry transformations used to generate equivalent atoms: #1 $-x+1$, $-y+2$, $-z+2$.

Table 5
Selected bond lengths (Å) and angles (°) for complex **4**.

Yb(1)–Pd(1)	3.1834(7)	Pd(1)–O(1)	2.001(4)
Pd(1)–O(3)	1.998(4)	Pd(1)–O(5)	1.996(5)
Pd(1)–O(7)	1.993(5)	Yb(1)–O(2)	2.286(4)
Yb(1)–O(4)	2.284(4)	Yb(1)–O(6)	2.265(4)
Yb(1)–O(8)	2.289(5)	Yb(1)–O(9)	2.424(4)
Yb(1)–O(10)	2.382(5)	Yb(1)–O(10)#1	2.427(4)
Yb(1)–O(11)	2.296(4)		
O(1)–Pd(1)–O(3)	177.00(19)	O(1)–Pd(1)–O(5)	88.6(2)
O(1)–Pd(1)–O(7)	90.60(19)	O(1)–Pd(1)–Yb(1)	92.40(14)
O(3)–Pd(1)–Yb(1)	90.50(13)	O(5)–Pd(1)–Yb(1)	90.73(14)
O(7)–Pd(1)–Yb(1)	90.21(14)	O(2)–Yb(1)–Pd(1)	62.61(12)
O(4)–Yb(1)–Pd(1)	64.58(12)	O(6)–Yb(1)–Pd(1)	64.37(12)
O(8)–Yb(1)–Pd(1)	64.36(12)	O(9)–Yb(1)–Pd(1)	118.09(11)
O(10)–Yb(1)–Pd(1)	129.10(11)	O(11)–Yb(1)–Pd(1)	130.88(12)
O(9)–Yb(1)–O(10)#1	53.13(14)	Yb(1)–O(10)–Yb(1)#1	111.83(17)

Symmetry transformations used to generate equivalent atoms: #1 $-x+1$, $-y+2$, $-z+2$.

Table 6
Comparison of geometries of the fragments Ln(μ,η^2-OOCMe)$_2$Ln in the bis-paddlewheel complexes [Pd(μ-OOCMe)$_4$Ln(OH$_2$)(μ,η^2-OOCMe)]$_2$ × 2HOOCMe (**1**,**2**) and [Pd(μ-OOCMe)$_4$Ln(THF)(μ,η^2-OOCMe)$_2$]$_2$ × 2THF (Ln = Eu, Nd).

	1	Ln = Nd (in two independent molecules) [3c]	**2**	Ln = Eu (in two independent molecules) [3c]
Ln(1)–O(9) (Å)	2.558(3)	2.512(5), 2.495(5); 2.520(5), 2.520(5)	2.488(8)	2.496(7), 2.469(8); 2.442(8), 2.480(7)
Ln(1)–O(10) (Å)	2.501(4)	2.561(5), 2.557(5); 2.547(5) 2.547(5)	2.433(7)	2.509(8), 2.495(7); 2.525(7), 2.497(7)
Ln(1)–O(10A) (Å)	2.500(9)	2.399(7), 2.423(5); 2.445(5), 2.420(7).	2.570(3)	2.449(5), 2.404(7); 2.382(7), 2.445(5)

The detailed geometry of the pivalate complexes depends on the size of the rare-earth metal atom. The early lanthanides form the complexes Pd(μ-OOCBu^t)$_4$Ln(OOCBu^t)(HOOCBu^t)$_3$ (Ln = Nd (**5**), Sm (**6**), Eu (**7**)) (Scheme 2).

According to X-ray diffraction data (Fig. 3, Tables 7–9) the Pd–co-metal distances in complexes **5**, **6** and **7** (3.2584(9) Å in **5**; 3.2548(6) Å in **6** and 3.2506(5) Å in **7**) are only slightly elongated compared to the corresponding bis-paddlewheel acetate complexes (*cf.* 3.221(2) Å in the Pd–Nd complex, 3.2047(9) Å in the Pd–Sm complex [3b] and 3.1983(12) Å in the Pd–Eu complex). The Pd–O distances are also nearly the same (1.998(6)–2.008(6) Å in **5**, 2.004(4)–2.008(4) Å in **6** and 1.996(4)–2.004(4) Å in **7**).

The coordination sphere of the Nd^{III}, Sm^{III} and Eu^{III} atoms is complemented with three coordinated molecules of pivalic acid and one terminal pivalate anion (Fig. 3, Tables 1 and 6–8). A special feature of this structure is the short intramolecular bonds between the H atoms of two axially coordinated molecules of pivalic acid and O atoms of two bridging pivalate anions, resulting in a noticeable (0.12–0.15 Å) loosing of two Nd(Sm,Eu)–O bonds, while all the H-bonded O···O distances have close values O(2)···O(10) (2.695(6), 2.678(4), 2.672(4) Å; O(4)···O(12) 2.660(6), 2.668(4), 2.657(4) Å) in complexes **5**, **6** and **7**, respectively). The H atom of the third pivalic acid forms a very short H bond with the O atom of the terminal pivalate anion (O(14)···O(16) 2.453(7) in **5** 2.455(4) Å in **6** and 2.434(4) Å in **7**).

The late lanthanides form the mono-paddlewheel complexes Pd(μ-OOCBu^t)$_4$Ln(η-OOCBu^t)(HOOCBu^t)$_2$ × HOOCBu^t (Ln = Tm (**8**), Yb (**9**) (Scheme 3).

When complexes **8**–**9** are formed, one of the coordinated pivalic acid ligands is displaced to become a solvate molecule because of the reduced atomic radii of the late lanthanides (Fig. 4, Tables 10 and 11). The coordinated pivalate anion becomes a η^2-terminal ligand, one of its O atoms being H-bonded with the O atom of the coordinated pivalic acid molecule. The H-bonding of the second coordinated pivalic acid molecule remains unchanged (O(2)···O(14) 2.657(4), 2.663(4) Å; Ln–O(2) 2.338(5), 2.334(3) Å in **8** and **9**, respectively). The metal–metal and metal–oxygen distances in

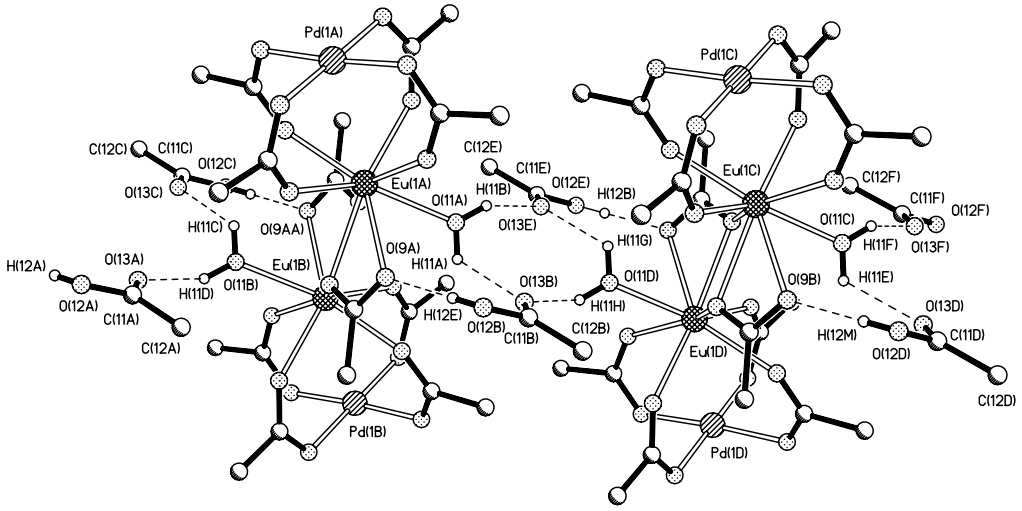
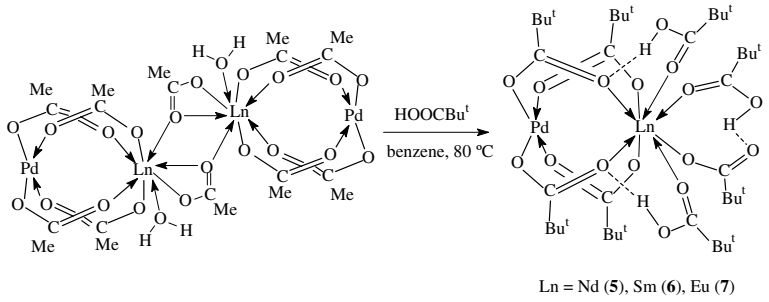


Fig. 2. Fragment of the linear 1D polymeric chain in the crystal packing of the complexes $[Pd(\mu\text{-}OOCMe)_4Ln(OH_2)(\mu,\eta^2\text{-}OOCMe)]_2 \times 2HOOCMe$ exemplified by complex **2**.



Scheme 2.

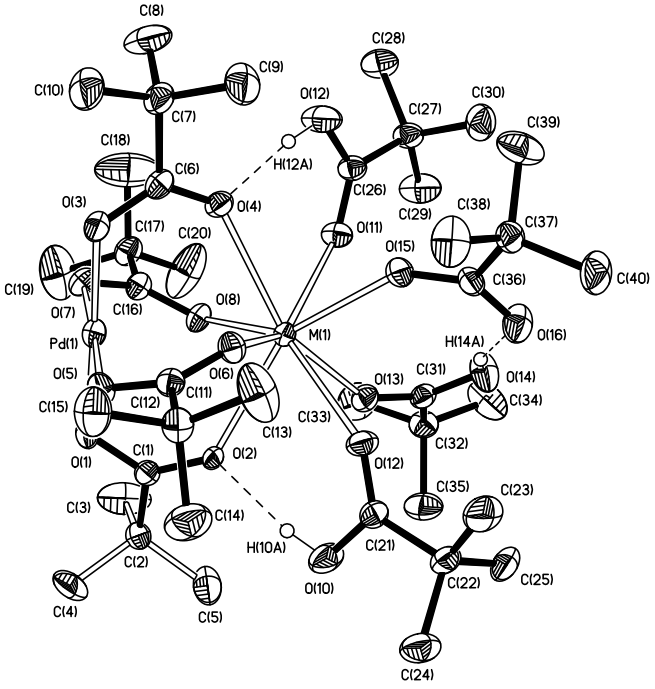


Fig. 3. Molecular structure of the tetrapivalate-bridged complexes with the early lanthanides $Pd(\mu\text{-}OOCBu^t)_4Ln(OOCBu^t)(HOOCBu^t)_3$ (Ln = Nd^{III} (**5**), Sm^{III} (**6**), Eu^{III} (**7**) drawn with displacement ellipsoids at the 30% probability level.

Table 7
Selected bond lengths (Å) and angles (°) for complex **5**.

Nd(1)–Pd(1)	3.2584(9)	Pd(1)–O(1)	1.998(6)
Pd(1)–O(3)	2.008(6)	Pd(1)–O(5)	2.002(6)
Pd(1)–O(7)	1.997(6)	Nd(1)–O(2)	2.480(5)
Nd(1)–O(4)	2.517(6)	Nd(1)–O(6)	2.418(6)
Nd(1)–O(8)	2.412(6)	Nd(1)–O(9)	2.562(6)
Nd(1)–O(11)	2.534(6)	Nd(1)–O(13)	2.370(6)
Nd(1)–O(15)	2.355(6)		
O(1)–Pd(1)–O(3)	177.7(2)	O(1)–Pd(1)–O(5)	92.4(3)
O(1)–Pd(1)–O(7)	88.0(3)	O(1)–Pd(1)–Nd(1)	90.50(17)
O(3)–Pd(1)–Nd(1)	91.34(17)	O(5)–Pd(1)–Nd(1)	91.28(17)
O(7)–Pd(1)–Nd(1)	91.33(18)	O(2)–Nd(1)–Pd(1)	62.42(14)
O(4)–Nd(1)–Pd(1)	62.09(13)	O(6)–Nd(1)–Pd(1)	60.61(14)
O(8)–Nd(1)–Pd(1)	60.80(15)	O(9)–Nd(1)–Pd(1)	116.21(15)
O(11)–Nd(1)–Pd(1)	118.51(16)	O(13)–Nd(1)–Pd(1)	133.52(16)
O(15)–Nd(1)–Pd(1)	133.96(15)	O(13)–Nd(1)–O(15)	92.5(2)

complexes **8** and **9** are almost the same as those in the corresponding bis-paddlewheel acetate complexes (Pd···Ln 3.1673(7), 3.1781(7) Å; Pd–O 1.992(5)–2.004(5) Å, 1.999(4)–2.006(3) Å; Ln–O 2.266(5)–2.291(5), 2.262(4)–2.285(4) Å in **8** and **9**, respectively).

However, unlike bis-paddlewheel acetates **1**–**4**, the solvate molecules of pivalic acid in **8** and **9** do not form H-bonds with the O atoms of the coordinated anions and acid molecules, but produce dimeric associates (O···O 2.654(5) and 2.660(4) Å for **8** and **9**, respectively) (Fig. 5).

Hence, the complete replacement of the bridging and terminal acetate ligands in the Pd^{II}–Ln^{III} heterobimetallic complexes by

Table 8
Selected bond lengths (Å) and angles (°) for complex **6**.

Sm(1)–Pd(1)	3.2545(6)	Pd(1)–O(1)	2.004(4)
Pd(1)–O(3)	2.008(4)	Pd(1)–O(5)	2.007(4)
Pd(1)–O(7)	2.003(4)	Sm(1)–O(2)	2.478(4)
Sm(1)–O(4)	2.500(4)	Sm(1)–O(6)	2.381(4)
Sm(1)–O(8)	2.393(4)	Sm(1)–O(9)	2.534(4)
Sm(1)–O(11)	2.534(4)	Sm(1)–O(13)	2.322(4)
Sm(1)–O(15)	2.344(4)		
O(1)–Pd(1)–O(3)	178.06(17)	O(1)–Pd(1)–O(5)	92.34(19)
O(1)–Pd(1)–O(7)	87.97(18)	O(1)–Pd(1)–Sm(1)	90.48(12)
O(3)–Pd(1)–Sm(1)	90.96(12)	O(5)–Pd(1)–Sm(1)	90.76(13)
O(7)–Pd(1)–Sm(1)	91.54(12)	O(2)–Sm(1)–Pd(1)	62.53(10)
O(4)–Sm(1)–Pd(1)	62.50(10)	O(6)–Sm(1)–Pd(1)	60.61(10)
O(8)–Sm(1)–Pd(1)	61.12(10)	O(9)–Sm(1)–Pd(1)	116.92(11)
O(11)–Sm(1)–Pd(1)	119.03(11)	O(13)–Sm(1)–Pd(1)	133.31(11)
O(15)–Sm(1)–Pd(1)	133.15(11)	O(13)–Sm(1)–O(15)	93.53(16)

Table 9
Selected bond lengths (Å) and angles (°) for complex **7**.

Eu(1)–Pd(1)	3.2506(5)	Pd(1)–O(1)	2.004(4)
Pd(1)–O(3)	2.005(4)	Pd(1)–O(5)	2.000(4)
Pd(1)–O(7)	1.996(4)	Eu(1)–O(2)	2.460(3)
Eu(1)–O(4)	2.480(3)	Eu(1)–O(6)	2.376(3)
Eu(1)–O(8)	2.374(3)	Eu(1)–O(9)	2.524(4)
Eu(1)–O(11)	2.511(4)	Eu(1)–O(13)	2.318(3)
Eu(1)–O(15)	2.337(3)		
O(1)–Pd(1)–O(3)	178.08(15)	O(1)–Pd(1)–O(5)	92.53(16)
O(1)–Pd(1)–O(7)	88.30(16)	O(1)–Pd(1)–Eu(1)	90.62(10)
O(3)–Pd(1)–Eu(1)	90.98(10)	O(5)–Pd(1)–Eu(1)	91.15(10)
O(7)–Pd(1)–Eu(1)	91.31(11)	O(2)–Eu(1)–Pd(1)	62.64(8)
O(4)–Eu(1)–Pd(1)	62.62(8)	O(6)–Eu(1)–Pd(1)	60.73(9)
O(8)–Eu(1)–Pd(1)	60.91(9)	O(9)–Eu(1)–Pd(1)	117.09(9)
O(11)–Eu(1)–Pd(1)	119.26(9)	O(13)–Eu(1)–Pd(1)	132.81(9)
O(15)–Eu(1)–Pd(1)	132.94(10)	O(13)–Eu(1)–O(15)	94.24(13)

the more basic pivalate ones does not change the paddlewheel structural motif of the complexes. The detailed structure of the molecules formed is determined by both the nature of the co-metal and the electronic and steric features of the carboxylate anions. The smaller acetate anions, unlike the larger pivalate anions, are prone to form bis-paddlewheel complexes and intermolecular H-bonds with the solvate carboxylic acid molecules. The bis-paddlewheel acetate complexes are formed from two mono-paddlewheel fragments due to a donor–acceptor bonding of the bridging oxygen atom of the η^2-acetate anion. Meanwhile, this structure remains unchanged upon refluxing in polar and donor solvents, such as THF, water and acetic acid.

The composition and structure of complexes **5**–**9** convey the suggestion on a plausible mechanism of the easy acetate to pivalate substitution observed in the complexes under question. When the molecule of pivalic acid approaches to the tetraacetate-bridged complex, it can be first coordinated to the rare-earth metal atom at the axial position; the subsequent formation of an intramolecular

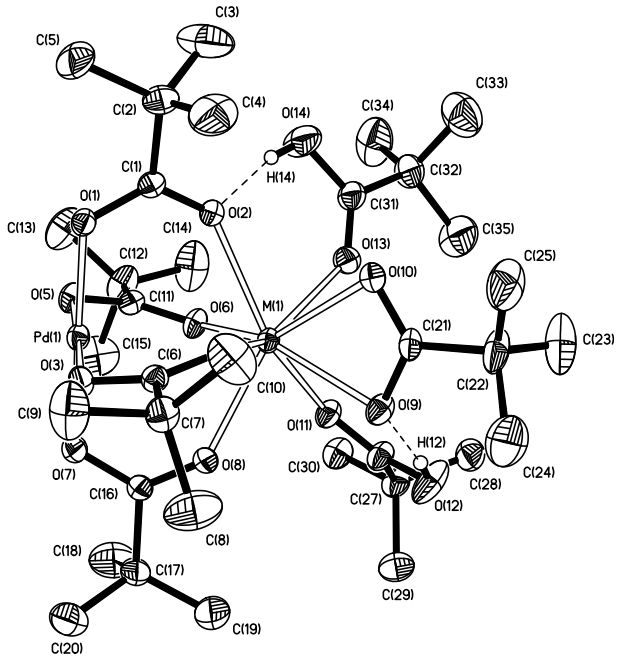


Fig. 4. Molecular structure of the tetrapivalate-bridged complexes with the late lanthanides $Pd(\mu\text{-}OOCBu^t)_4Ln(\eta\text{-}OOCBu^t)(HOOCBu^t)_2 \times HOOCBu^t$ (Ln = Tm^{III} (**8**), Yb^{III} (**9**)) drawn with displacement ellipsoids at the 30% probability level.

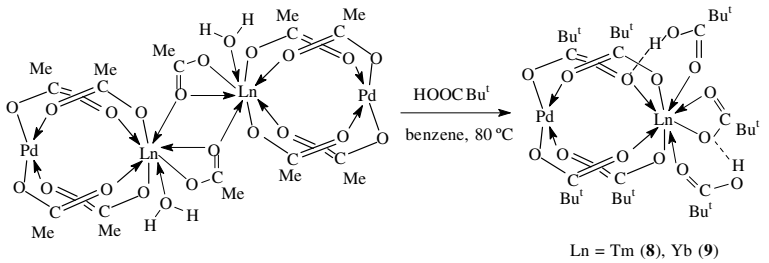
hydrogen bond with the bridging acetate ligand followed by proton transfer [7a–d] releases a molecule of acetic acid and produces a pivalate bridge (Scheme 4).

It is not inconceivable that the intra- and intermolecular bonds found in the crystals of complexes **1**–**9** are formed in intermediates during acetate to pivalate ligand metathesis, facilitating the removal of acetic acid.

3. Experimental

3.1. Reagents and solvents

Palladium(II) acetate $Pd_3(OOCMe)_6$ was prepared from $PdCl_2$ (purchased from Reakhim, Russia) by reduction with $NaBH_4$ followed by the oxidation of the Pd black that formed with concentrated HNO_3 in glacial acetic acid according to a procedure [8] and recrystallisation of $Pd_3(OOCMe)_6$ from hot acetic acid. Other chemicals (pivalic acid, $Sm(OOCMe)_3 \times 4H_2O$, $Eu(OOCMe)_3 \times 4H_2O$, $Nd(OOCMe)_3 \times 1.5H_2O$, $Tm(OOCMe)_3 \times 4H_2O$, $Yb(OOCMe)_3 \times 4H_2O$, all reagent grade, purchased from Reakhim, Russia) and solvents (glacial acetic acid, benzene, pentane and hexane, all reagent grade, purchased from Acros, Belgium) were purified by standard procedures [9].



Scheme 3.

Table 10
Selected bond lengths (Å) and angles (°) for complex **8**.

Tm(1)–Pd(1)	3.1674(7)	Pd(1)–O(1)	2.001(5)
Pd(1)–O(3)	1.994(5)	Pd(1)–O(5)	1.996(5)
Pd(1)–O(7)	2.005(5)	Tm(1)–O(2)	2.339(5)
Tm(1)–O(4)	2.274(5)	Tm(1)–O(6)	2.294(5)
Tm(1)–O(8)	2.263(5)	Tm(1)–O(9)	2.360(5)
Tm(1)–O(10)	2.431(5)	Tm(1)–O(11)	2.421(5)
Tm(1)–O(13)	2.364(5)		
O(1)–Pd(1)–O(7)	177.9(2)	O(1)–Pd(1)–O(3)	92.4(2)
O(1)–Pd(1)–O(5)	87.9(2)	O(1)–Pd(1)–Tm(1)	89.59(14)
O(3)–Pd(1)–Tm(1)	91.07(15)	O(5)–Pd(1)–Tm(1)	91.22(14)
O(7)–Pd(1)–Tm(1)	90.08(15)	O(2)–Tm(1)–Pd(1)	64.27(12)
O(4)–Tm(1)–Pd(1)	63.23(13)	O(6)–Tm(1)–Pd(1)	62.61(13)
O(8)–Tm(1)–Pd(1)	63.86(13)	O(9)–Tm(1)–Pd(1)	135.48(14)
O(10)–Tm(1)–Pd(1)	126.83(12)	O(11)–Tm(1)–Pd(1)	122.63(13)
O(13)–Tm(1)–Pd(1)	129.54(14)	O(9)–Tm(1)–O(10)	54.05(18)

Table 11
Selected bond lengths (Å) and angles (°) for complex **9**.

Yb(1)–Pd(1)	3.1781(7)	Pd(1)–O(1)	2.006(3)
Pd(1)–O(3)	1.999(4)	Pd(1)–O(5)	2.003(4)
Pd(1)–O(7)	1.998(4)	Yb(1)–O(2)	2.334(3)
Yb(1)–O(4)	2.285(4)	Yb(1)–O(6)	2.278(4)
Yb(1)–O(8)	2.262(4)	Yb(1)–O(9)	2.357(4)
Yb(1)–O(10)	2.425(4)	Yb(1)–O(11)	2.412(4)
Yb(1)–O(13)	2.355(4)		
O(1)–Pd(1)–O(7)	177.62(15)	O(1)–Pd(1)–O(3)	87.72(15)
O(1)–Pd(1)–O(5)	92.56(15)	O(1)–Pd(1)–Yb(1)	89.58(10)
O(3)–Pd(1)–Yb(1)	91.27(10)	O(5)–Pd(1)–Yb(1)	90.94(11)
O(7)–Pd(1)–Yb(1)	89.80(11)	O(2)–Yb(1)–Pd(1)	64.20(9)
O(4)–Yb(1)–Pd(1)	62.55(9)	O(6)–Yb(1)–Pd(1)	63.34(10)
O(8)–Yb(1)–Pd(1)	63.57(9)	O(9)–Yb(1)–Pd(1)	135.64(11)
O(10)–Yb(1)–Pd(1)	126.65(10)	O(11)–Yb(1)–Pd(1)	122.80(10)
O(13)–Yb(1)–Pd(1)	129.94(10)	O(9)–Yb(1)–O(10)	54.17(13)

3.2. Physical measurements

The elemental C,H,N analysis was performed on an automated C,H,N-analyzer (Carlo Erba Strumentazione, Italy). The IR spectra were recorded on a Nicolet Nexus spectrometer in KBr pellets.

3.2.1. X-ray diffraction analysis

Details of the data collection and structure refinement for complexes **1**–**9** are presented in Table 1. Single-crystal X-ray diffraction experiments were carried out on Siemens P4 (for complex **2**) and Bruker SMART and Bruker SMART APEX II diffractometers with a CCD area detector (graphite monochromator, Mo Kα radiation, $\lambda = 0.71073$ Å, ω-scans). The semi-empirical method SADABS [10] was applied for the absorption correction. The structures were solved by direct methods and refined by the full-matrix least-squares technique against F^2 with the anisotropic displacement parameters for all non-hydrogen atoms. All the hydrogen atoms in the complexes were placed geometrically and included in the structure factors calculation in the riding motion approximation. All the data reduction and further calculations were performed using the SAINT [11] and SHELXTL-97 [12] program packages.

3.3. Syntheses

3.3.1. [Pd(μ-OOCMe)$_4$Nd(OH$_2$)(μ,η^2-OOCMe)]$_2$ × 2HOOCMe (**1**)

In 50 ml water-jacketed flask equipped with reflux condenser and magnetic stirrer, $Pd_3(OOCMe)_6$ (100 mg, 0.45 mmol based on Pd atom), $Nd(OOCMe)_3 \times 1.5H_2O$ (156 mg, 0.45 mmol) and glacial acetic acid (15 ml) were stirred at 90 °C in an oil bath for ~40 min (more prolonged heating of the reaction mixture results in partial Pd^{II} to Pd^0 reduction). The light-yellow reaction solution was concentrated to 5 ml and slowly cooled in the bath to room temperature for crystallisation. Yellow crystals of complex **1** (194 mg) suitable for X-ray diffraction study were separated by decantation, washed with diethyl ether and dried in Ar flow. An additional amount of the smaller crystals were obtained by precipitation with ether from the mother liquid. Total yield of **1** was 250 mg (90% based on Pd). *Anal.* Calc. for $Pd_2Nd_2C_{24}O_{26}H_{42}$: C, 23.10; H, 3.39. Found: C, 22.76; H, 3.47%. IR spectrum (KBr, ν/cm^{-1}): 3420br, s, 3267w, 2940w, 2634w, 2553w, 1688m, 1628br, vs, 1546m, 1438s, 1415vs, 1346w, 1285m, 1050m, 1022m, 958w, 695s, 627m, 587w, 460w.

3.3.2. [Pd(μ-OOCMe)$_4$Eu(OH$_2$)(μ,η^2-OOCMe)]$_2$ × 2HOOCMe (**2**)

Compound **2** was prepared and crystallised by analogous procedure (see above) from $Pd_3(OCOMe)_6$ (100 mg, 0.45 mmol) and $Eu(OOCMe)_3 \times 4H_2O$ (177 mg, 0.45 mmol). Total yield of **2** was 253 mg (90% based on Pd). *Anal.* Calc. for $Pd_2Eu_2C_{24}O_{26}H_{42}$: C, 22.82; H, 3.35. Found: C, 22.69; H, 3.27%. IR spectrum (KBr, ν/cm^{-1}): 3419br, s, 3267w, 2938w, 2632w, 2552w, 1688m, 1627br, vs, 1544m, 1437s, 1413vs, 1346w, 1284m, 1049m, 1020m, 957w, 694s, 625m, 587w, 460w.

3.3.3. [Pd(μ-OOCMe)$_4$Tm(OH$_2$)(μ,η^2-OOCMe)]$_2$ × 2HOOCMe (**3**)

Compound **3** was prepared and crystallised by analogous procedure (see above) from $Pd_3(OCOMe)_6$ (100 mg, 0.45 mmol) and $Tm(OOCMe)_3 \times 4H_2O$ (188 mg, 0.45 mmol). Yield of crystals **3** was 257 mg (89% based on Pd). *Anal.* Calc. for $Pd_2Tm_2C_{24}O_{26}H_{42}$: C, 22.22; H, 3.26. Found: C, 21.98; H, 3.19%. IR spectrum (KBr,

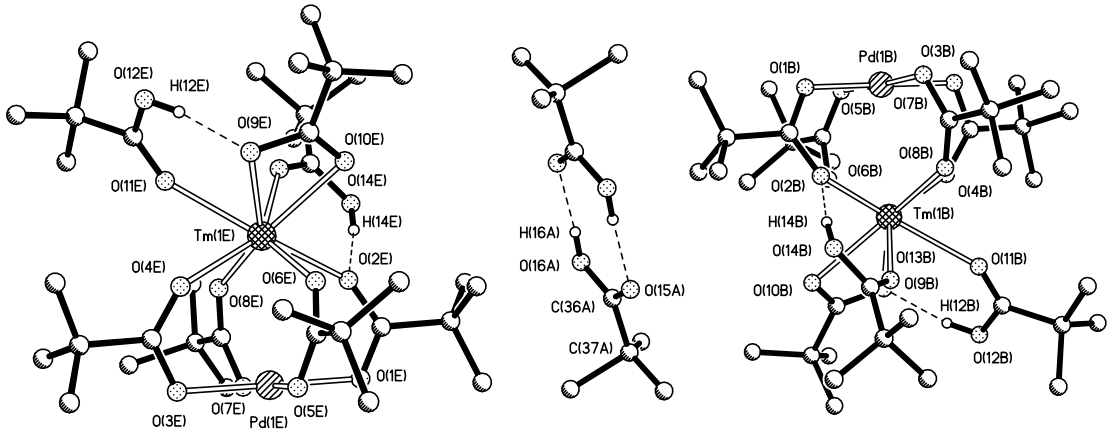
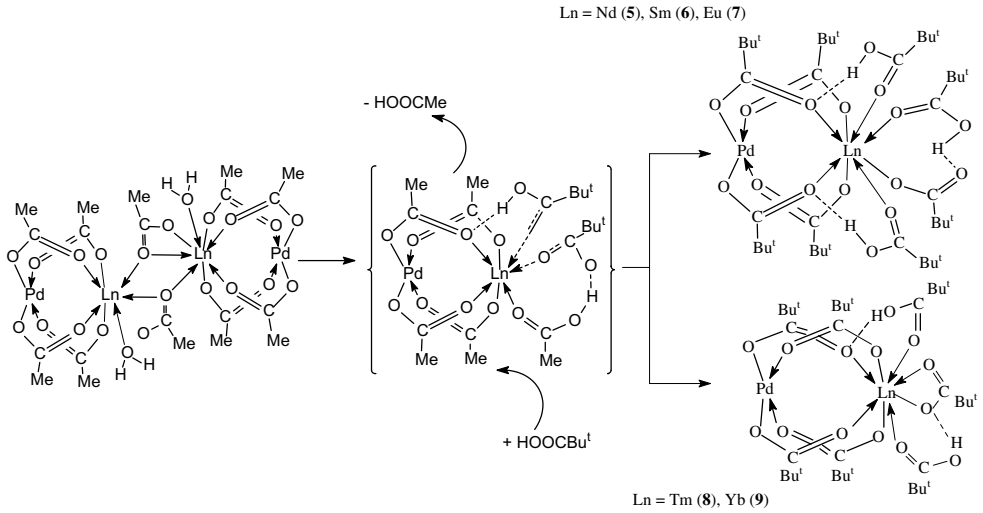


Fig. 5. Fragment of the crystal packing of the complex Pd(μ-OOCBu^t)$_4$Tm(η-OOCBu^t)(HOOCBu^t)$_2$ × HOOCBu^t.



Scheme 4.

ν/cm^{-1}): 3419br, s, 3268w, 2938w, 2632w, 2550w, 1687m, 1627br, vs, 1544m, 1437s, 1413vs, 1346w, 1284m, 1049m, 1020m, 957w, 694s, 625m, 585w, 460w.

*3.3.4. [Pd(μ-OOCMe)$_4$Yb(OH$_2$)(μ,η^2-OOCMe)]$_2$ × 2HOOCMe (**4**)*

Compound **4** was prepared and crystallised by analogous procedure (see above) from $Pd_3(OCOMe)_6$ (100 mg, 0.45 mmol) and $Yb(OOCMe)_3 \times 4H_2O$ (190 mg, 0.45 mmol). Yield of yellow crystals **4** was 265 mg (91% based on Pd). *Anal.* Calc. for $Pd_2Yb_2C_{24}O_{26}H_{42}$: C, 22.08; H, 3.24. Found: C, 21.89; H, 3.18%. IR spectrum (KBr, ν/cm^{-1}): 3417br, 3268w, 2929w, 2630w, 2550w, 1687m, 1628br, vs, 1545s, 1438s, 1413vs, 1346m, 1284m, 1049w, 1020m, 957w, 694 s, 625m, 590w, 461w.

*3.3.5. Pd(μ-OOCBu^t)$_4$Nd(OOCBu^t)(HOOCBu^t)$_3$ (**5**)*

A suspension of $Pd_3(OOCMe)_6$ (100 mg, 0.45 mmol) and $Nd(OOCMe)_3 \times 1.5H_2O$ (156 mg, 0.45 mmol) in 15 ml of glacial acetic acid was stirred at 90 °C for 40 min, cooled to room temperature and evaporated to dryness on a rotary evaporator (temperature of the water bath should be at most 60 °C). The dry residue was dissolved in warm benzene (10 ml), the solution was evaporated to dryness, and this operation was twice repeated to completely remove water and acetic acid. To the obtained dry yellow-orange powder was added a solution of pivalic acid (363 mg, 3.6 mmol) in benzene (15 ml) and refluxed for 0.5 h. The solution formed was evaporated to produce a yellow oil, which was thoroughly dried on a rotary evaporator to remove acetic acid formed by the acetate to pivalate metathesis. For the completion of the metathesis reaction a new portion of benzene (10 ml) was added and the solution was refluxed for 15 min followed by solvent evaporation. The oil residue was dissolved in 1 ml of warm pentane and stayed for 1–2 h for crystallisation either at room temperature or in a fridge at −10 °C. The yellow-orange crystals of **5** suitable for X-ray diffraction study were separated by decantation and dried in vacuum. Yield of **5** was 374 mg (79% based on Pd). *Anal.* Calc. for $PdNdC_{40}O_{16}H_{75}$: C, 45.21; H, 7.11. Found: C, 44.98; H, 6.93%. IR spectrum (KBr, ν/cm^{-1}): 3447br, m, 2969m, 2932w, 2877w, 1699s, 1596ws, 1575w, 1485m, 1461w, 1416s, 1374br, m, 1308w, 1229m, 1203w, 1031w, 869w, 788w, 647w, 452w.

*3.3.6. Pd(μ-OOCBu^t)$_4$Sm(OOCBu^t)(HOOCBu^t)$_3$ (**6**)*

Compound **6** was prepared and crystallised by analogous procedure (see above) from $Pd_3(OCOMe)_6$ (100 mg, 0.45 mmol), $Sm(OOCMe)_3 \times 4H_2O$ (178 mg, 0.45 mmol) and HOOCBu^t (363 mg, 3.6 nmmol). Yield of **6** was 390 mg (82% based on Pd). *Anal.* Calc. for $PdSmC_{40}O_{16}H_{75}$: C, 44.95; H, 7.07. Found: C, 44.73; H, 6.92%. IR spectrum (KBr, ν/cm^{-1}): 3441br, m, 2967m, 2933w, 2875w, 1697s, 1595ws, 1573w, 1484m, 1459w, 1413s, 1372br, m, 1306w, 1227m, 1200w, 1030w, 869w, 787w, 647w, 450w.

*3.3.7. Pd(μ-OOCBu^t)$_4$Eu(OOCBu^t)(HOOCBu^t)$_3$ (**7**)*

Compound **7** was prepared and crystallised by analogous procedure (see above) from $Pd_3(OCOMe)_6$ (100 mg, 0.45 mmol), $Eu(OOCMe)_3 \times 4H_2O$ (177 mg, 0.45 mmol) and HOOCBu^t (363 mg, 3.6 nmmol). Yield of **7** was 343 mg (72% based on Pd). *Anal.* Calc. for $PdEuC_{40}O_{16}H_{75}$: C, 44.88; H, 7.06. Found: C, 44.59; H, 7.01%. IR spectrum (KBr, ν/cm^{-1}): 3453br, m, 2961m, 2931w, 2875w, 1697s, 1596vs,1572m, 1484m, 1460w, 1412s, 1376m, 1364m, 1308w, 1226s, 1199w, 1029w, 896w, 786w, 648w, 449w.

*3.3.8. Pd(μ-OOCBu^t)$_4$Tm(η-OOCBu^t)(HOOCBu^t)$_2$ × HOOCBu^t (**8**)*

Compound **8** was prepared and crystallised by analogous procedure (see above) from $Pd_3(OCOMe)_6$ (100 mg, 0.45 mmol), $Tm(OOCMe)_3 \times 4H_2O$ (188 mg, 0.45 mmol) and HOOCBu^t (363 mg, 3.6 mmol). Yield of **8** was 377 mg (86% based on Pd). *Anal.* Calc. for $PdTmC_{40}O_{16}H_{75}$: C, 44.18; H, 6.95. Found: C, 44.32; H, 7.07%. IR spectrum (KBr, ν/cm^{-1}): 3427br, m, 2963s, 2929m, 2874w, 1703w, 1684w, 1618vs, 1572s, 1484s, 1459w, 1415vs, 1377m, 1363w, 1304w, 1227m, 1205w, 1031w, 899w, 787w, 648w, 456w.

*3.3.9. Pd(μ-OOCBu^t)$_4$Yb(η-OOCBu^t)(HOOCBu^t)$_2$ × HOOCBu^t (**9**)*

Compound **9** was prepared and crystallised by analogous procedure (see above) from $Pd_3(OCOMe)_6$ (100 mg, 0.45 mmol), $Yb(OOCMe)_3 \times 4H_2O$ (190 mg, 0.45 mmol) and HOOCBu^t (363 mg, 3.6 mmol). Yield of **9** was 348 mg (79% based on Pd). *Anal.* Calc. for $PdYbC_{40}O_{16}H_{75}$: C, 44.02; H, 6.93. Found: C, 44.16; H, 6.96%. IR spectrum (KBr, ν/cm^{-1}): 3443 (br, m), 2971s, 2932m, 2879w, 1711w, 1691w, 1622vs, 1579s, 1492s, 1464w, 1419vs, 1382m, 1367w, 1309w, 1230m, 1209w, 1035w, 899w, 788w, 649w, 455w.

4. Conclusion

This and previous our studies [3a–d] showed that irrespectively of the complementary metal (transition, post-transition, alkaline earth or rare earth) acetates, palladium(II) readily forms similar Pd^{II}-based heterobimetallic complexes in high yields. The structure

of the complexes formed seems to be governed by the square planar palladium(II) atom that can be treated as a sort of a tetradentate chelating ligand towards the co-metal carboxylate to form a tetrabridged paddlewheel moiety $Pd(\mu\text{-}OOCR)_4M$ with rather short Pd–M distances.

Notwithstanding an apparent simplicity of the synthetic procedure, the reaction mechanism is rather complicated, as was shown by our recent kinetic study [13]. Therefore, it is somewhat surprising that the reaction products are such similar over a wide range of the complementary metals.

Unlike the mono-paddlewheel acetate complexes containing divalent transition, post-transition, alkali-earth metal, the trivalent rare-earth metal acetates form bis-paddlewheel heterobimetallic complexes. Meanwhile, when acetate ligands in the Ln^{III}-containing complexes are changed by pivalate anions, mono-paddlewheel compounds are formed.

A peculiarity of the Pd^{II}-based paddlewheel carboxylates is their ability to form intra- and intermolecular H-bonds in the crystals, which is particularly typical of the rare-earth metal complexes under study. The H-bonding induces the loosing of one or several Ln–O bonds with the bridging carboxylate ligands. It is possible that this bonding plays a significant role in the bridging acetate to pivalate metathesis. Although the reaction mechanism needs additional studying, we can note now that the tetraacetate-bridged Pd^{II}–Ln^{III} complexes readily react with a rather weak O-base, pivalic acid, resulting in the complete substitution of all $MeCOO^-$ anions by Bu^tCOO^- ones.

Acknowledgements

We thank for financial support the Russian Foundation for Basic Research (projects Nos. 06-03-32578, 06-03-08173, 06-03-33005, 08-03-01063 and 08-03-01150), the Foundation of President of the Russian Federation (program for support of leading Russian scientific schools NSh-1733.2008.3) and the Foundation of the Russian Academy of Sciences (programs for Basic Research "Purposeful synthesis of inorganic substances and creation of related functional materials" and "Theoretical and experimental investigation of the nature of chemical bonding and mechanisms of important reactions and processes").

Appendix A. Supplementary data

CCDC 695866, 695867, 695868, 695869, 695870, 695871, 695872, 695873 and 698647 contain the supplementary crystallographic data for this paper. These data can be obtained free of charge via http://www.ccdc.cam.ac.uk/conts/retrieving.html, or from the Cambridge Crystallographic Data Centre, 12 Union Road, Cambridge CB2 1EZ, UK; fax: (+44) 1223-336-033; or e-mail: deposit@ccdc.cam.ac.uk. Supplementary data associated with this article can be found, in the online version, at doi:10.1016/j.poly.2008.10.006.

References

[1] (a) M.L. Doyle, I.R. Harris, Platinum Metals Rev. 32 (1988) 130;
(b) Y. Ning, Platinum Metals Rev. 46 (2002) 108.
[2] (a) J.M. Thomas, W.J. Thomas, Principles and Practice of Heterogeneous Catalysis, VCH, New York, 1997;
(b) Do Heui Kim, Seong Ihl Woo, Jin Man Lee, O-Bong Yang, Catal. Lett. 70 (2000) 35.
[3] (a) N.Yu. Kozitsyna, S.E. Nefedov, N.V. Cherkashina, V.N. Ikorsky, M.N. Vargaftik, I.I. Moiseev, Russ. Chem. Bull. 54 (2005) 2215;
(b) N.Yu. Kozitsyna, S.E. Nefedov, M.N. Vargaftik, I.I. Moiseev, Mendeleev Commun. 15 (2005) 223;
(c) N.Yu. Kozitsyna, S.E. Nefedov, F.M. Dolgushin, N.V. Cherkashina, M.N. Vargaftik, I.I. Moiseev, Inorg. Chim. Acta 359 (2006) 2072;
(d) N.Yu. Kozityna, S.E. Nefedov, I.A. Yakushev, Z.V. Dobrokhotova, M.N. Vargaftik, I.I. Moiseev, Mendeleev Commun. 17 (2007) 261.
[4] (a) O.P. Tkachenko, A.Yu. Stakheev, L.M. Kustov, I.V. Mashkovsky, M. van den Berg, W. Grünert, N. Yu. Kozitsyna, Zh.V. Dobrokhotova, V.I. Zhilov, S.E. Nefedov, M.N. Vargaftik, I.I. Moiseev, Catal. Lett. 112 (2006) 155;
(b) M.N. Vargaftik, I.V. Mashkovsky, A.Yu. Stakheev, O.P. Tkachenko, G. N. Baeva, L.M. Kustov, M. van den Berg, W. Grünert, N.Yu. Kozitsyna, S.E. Nefedov, I.I. Moiseev, EUROPA CAT VIII, Turku/Abo, Finland 2007, Books of theses, P-2-138.
[5] (a) S.E. Nefedov, M.N. Vargaftik, I.I. Moiseev, Inorg. Chim. Commun. 9 (2006) 755;
(b) S.E. Nefedov, I.A. Yakushev, N.Yu. Kozityna, Zh.V. Dobrokhotova, V.N. Ikorsky, M.N. Vargaftik, I.I. Moiseev, Inorg. Chem. Commun. 10 (2007) 948.
[6] (a) A.S. Batsanov, G.A. Timko, Yu.T. Struchkov, N.V. Gerbeleu, K.M. Indrichan, G.A. Popovich, Koordinat. Khim. (Russ. Coord. Chem.) 15 (1989) 688;
(b) N.V. Cherkashina, N.Yu. Kozitsyna, G.G. Aleksandrov, M.N. Vargaftik, I.I. Moiseev, Mendeleev Commun. 12 (2002) 49.
[7] (a) S.E. Nefedov, Russ. J. Inorg. Chem. 51 (Suppl. 1) (2006) S49;
(b) E.V. Amel'chenkova, T.O. Denisova, S.E. Nefedov, Russ. J. Inorg. Chem. 51 (2006) 1763;
(c) T.O. Denisova, Zh.V. Dobrokhotova, V.N. Ikorskii, S.E. Nefedov, Russ. J. Inorg. Chem. 51 (2006) 1363;
(d) E.V. Amel'chenkova, T.O. Denisova, S.E. Nefedov, Russ. J. Inorg. Chem. 51 (2006) 1218.
[8] T.A. Stephenson, S.M. Morehouse, A.R. Powell, J.P. Heffer, G. Wilkinson, J. Chem. Soc. (1965) 3632.
[9] D.D. Perrin, W.L.F. Armarego, Purification of Laboratory Chemicals, 3rd ed., Pergamon, Oxford, 1988.
[10] G.M. Sheldrick, SADABS, Bruker AXS Inc., Madison, WI-53719, USA, 1997.
[11] SMART V5.051 and SAINT V5.00, Area detector control and integration software, Bruker AXS Inc., Madison, WI-53719, USA, 1998.
[12] G.M. Sheldrick, SHELXTL-97 V5.10, Bruker AXS Inc., Madison, WI-53719, USA, 1997.
[13] N.S. Akhmadullina, N.V. Cherkashina, N.Yu. Kozitsyna, I.P. Stolarov, E.V. Perova, A.E. Gekhman, S.E. Nefedov, M.N. Vargaftik, I.I. Moiseev, Inorg. Chim. Acta, in press.

Polyhedron 28 (2009) 181–187

Contents lists available at ScienceDirect

Polyhedron

journal homepage: www.elsevier.com/locate/poly

Surface layer-by-layer chemical deposition reaction for thin film formation of nano-sized metal 8-hydroxyquinolate complexes ☆

Mohamed E. Mahmoud [a,*], Sawsan S. Haggag [b], Tarek M. Abdel-Fattah [c]

[a] Faculty of Sciences, Chemistry Department, University of Malaya, Kuala Lumpur 50603, Malaysia
[b] Faculty of Sciences, Chemistry Department, Alexandria University, P.O. Box 426, Alexandria 21321, Egypt
[c] Department of Biology, Chemistry and Environmental Science, Christopher Newport University, Newport News, VA 23606, USA

ARTICLE INFO

Article history:
Received 7 May 2008
Accepted 29 September 2008
Available online 17 November 2008

Keywords:
Nano-sized
8-Hydroxyquinoline
Metal complexes
Layer-by-layer
Chemical deposition
Thin film

ABSTRACT

The feasibility of a novel and simple layer-by-layer chemical deposition method for the preparation of nano-sized metal 8-hydroxyquinolate complexes has been investigated and reported. Uniform nanocrystalline films have been synthesized via dipping a substrate alternately in metal ion solution followed by ligand solution. The stoichiometry of the as-grown anhydrous Fe(III), Co(II), Ni(II), Cu(II) and Zn(II) complex crystals were confirmed from the metal analysis and molar stoichiometric ratio of metal ion to 8-hydroxyquinoline. This was characterized as 1:2 for the Co(II), Ni(II), Cu(II) and Zn(II)–quinolate complexes. The Fe(III)–quinolate thin film was found to exhibit a 1:3 ratio. Electron impact-mass spectra (EI-MS) of all the synthesized thin film metal quinolate complexes were recorded and the results refer to the existence of the molecular ion peak at the corresponding *m*/*z* values. Confirmation of such stoichiometric 1:2 and 1:3 ratios were also evident from the (EI-MS) study. The deposited thin films were also subjected to analysis by a scanning electron microscope (SEM) and a particle size $\geqslant$50 nm was detected. FT-IR and UV–Vis spectroscopy were further used to confirm the structure of the metal 8-hydroxyquinolate complexes. Thermal gravimetric analysis (TGA) was also used to follow up the possible thermal decomposition steps and to calculate the thermodynamic parameters of the nano-sized metal complexes.
© 2008 Elsevier Ltd. All rights reserved.

1. Introduction

Recently, more research efforts have been focused on the beneficial applications of the layer-by-layer deposition technique. This methodology has emerged and been found a more economic alternative for the direct preparation of thin films [1–3]. The highly sophisticated gas-phase layer deposition method can be easily replaced by this simple and direct liquid-phase solution-based layer-by-layer technique for thin film formation [4,5]. The formation of a variety of important compounds was successfully synthesized via the layer-by-layer thin film deposition approach. Polyelectrolyte thin films were prepared via alternately dipping the substrate into polycation and polyanion solutions to form polyelectrolyte multilayer films [6] as well as polymer-nanoclay multilayers [7]. The application of the layer-by-layer deposition method for the formation of various metal oxide [8–10] and metal sulfide thin films [11–13] have been reported and their optical properties investigated.

8-Hydroxyquinoline, 8HQ, also known as oxine, its derivatives as well as related metal complexes, are playing a uniquely important role in different disciplines of chemical research and applications. 8HQ, as a complexone or sequestering reagent, is considered second to EDTA and its analogues in binding with metal ions [14]. 8HQ was mainly applied for analytical purposes and separation techniques as an excellent reagent for the extraction of metal ions due to its extraordinary coordinating capabilities [15–20]. However, in coordination chemistry, versatile synthetic approaches for the formation of metal complexes of 8HQ and its derivatives were extensively used to open a wide range of di and tri-valent metal complexes that can be used as an arsenal for various impacts and applications in different fields. Among these applications are the utilization of 8-hydroxyquinoline as an interesting chelating agent for the formation of luminescent coordination compounds as light emitting devices. A review covering the applications of metal complexes of 8-hydroxyquinoline derivatives to obtain new supramolecular sensors, emitting devices or self-assembled aggregates was recently published [21]. Moreover, tris(8-hydroxyquinoline) aluminum (Alq3) is widely used in modern organic light emitting diodes (OLEDs) due to its excellent stability and electroluminescent properties via the high dependence on the injection behavior of the metallic contacts [22–24]. Most recent research efforts have also been focused on the synthesis of quinolate metal

☆ This work was partially presented in The 235th ACS National Meeting, New Orleans, USA April 6–10, 2008.

* Corresponding author.
E-mail addresses: memahmoud10@yahoo.com (M.E. Mahmoud), fattah@cnu.edu (T.M. Abdel-Fattah).

0277-5387/$ - see front matter © 2008 Elsevier Ltd. All rights reserved.
doi:10.1016/j.poly.2008.09.030

complex nanomaterials by physical vapor deposition [25,26] and adsorbent assisted physical vapor deposition [27] techniques, with positive results at the end.

The strong necessity to fabricate thin films of various metal derivatives in the form of oxides, sulfides and complexes to desired shapes and sizes by an easy and simple technique has been previously reported [28]. Therefore, we present and describe in this work a simple and rapid method for the synthesis of nanomaterials derived from quinolate complexes of Fe(III), Co(II), Ni(II), Cu(II) and Zn(II) based on the application of a layer-by-layer technique via successive and alternative deposition of metal ions and ligand molecules from their aqueous and methanolic solutions, respectively, for the formation of a thin film loaded on a glass substrate. The structures of the thin film synthesized metal quinolate complexes were confirmed on the basis of scanning electron microscopy (SEM), electron impact-mass spectrometry (EI-MS) UV–Vis spectroscopy, Fourier Transform infrared spectroscopy (FT-IR) and thermal gravimetric analysis (TGA).

2. Experimental

2.1. Layer-by-layer thin film formation of 8HQ metal complexes

The formation of the 8HQ metal complexes was carried out by a chemical dipping method according to the following procedure. In this method, a clean glass micro-slide of the size 76.2 mm by 25.4 mm by 1 mm was used as the solid substrate. A solution of 0.1 M metal acetate or chloride was prepared in double distilled water and the 8HQ solution was also prepared (0.1 M) in methanol. The clean substrate was vertically immersed into the metal ion solution for a 30 s period to deposit the corresponding metal ion on the substrate surface. The substrate was then immersed in the ligand solution for another 30 s, where the pre-adsorbed metal ion on the glass substrate was allowed to react with the ligand. A colored and uniform thin film of the metal complex was formed after a few dipping cycles. The reaction substrate was rinsed with distilled water after each reaction cycle. This procedure was repeated several times (15–50 times) to increase the film thickness and homogeneity.

2.2. Instrumentation

A Shimadzu gas chromatography–mass spectrometer (GCMS-QP2010S) interfaced with a direct insertion probe (DIP) was used to acquire the electron impact-mass spectra (EI-MS) of the metal quinolate complexes, viz. Fe(III), Co(II), Ni(II), Cu(II) and Zn(II), by the application of 70-eV as the ionization energy. The heating temperature programming of the DIP was performed at 20 °C min^{-1} for all the metal quinolate complexes. The maximum temperature was set to 350 °C and the run time was completed in 20.0 min. The collected mass spectrum of each metal quinolate complex was library searched to obtain the best possible match.

Scanning electron microscopes (JSM-6360LA, JEOL Ltd.), (JSM-5300, JEOL Ltd.) and an ion sputtering coating device (JEOL-JFC-1100E) were used to examine the deposited thin film of the metal quinolate complexes. SEM specimens were coated with gold to increase the conductivity. The thermal gravimetric analysis (TGA) and thermoanalytical curves were obtained using a Perkin–Elmer TGA7 Thermobalance at Moubarak City, Egypt. The operating conditions were as follows: a temperature heating range of 20–1000 °C with a heating rate of 10 °C min^{-1}, a flow rate of 20 ml min^{-1} in a pure nitrogen atmosphere and a sample mass in the range 5–12 mg. The FT-IR spectra of the metal quinolate complexes were measured on a Shimadzu Fourier Transform infrared spectrophotometer (FTIR-8400S) in the range 4000–200 cm^{-1}. The metal contents of the quinolate complexes were determined on a Shimadzu (AA-6650) atomic absorption spectrophotometer after acid decomposition and suitable dilution. UV–Vis spectra of the metal quinolate complexes were measured on a Perkin–Elmer UV–Vis Spectrometer Lambda EZ210.

2.3. Chemical and materials

The metal salts were all of analytical grade and were purchased from Aldrich Chemical Company, USA and BDH limited, Poole, England. The acetate salts were cobalt acetate, $Co(OAc)_2 \cdot 4H_2O$, nickel acetate, $Ni(OAc)_2 \cdot 4H_2O$, copper acetate, $Cu(OAc)_2 \cdot H_2O$ and zinc acetate, $Zn(OAc)_2 \cdot 2H_2O$. Only iron was in the chloride form, $FeCl_3$. 8-Hydroxyquinoline (8HQ) and methanol were obtained from BDH limited, Poole, England and were used as received. The metal ion solutions (0.1 M) were prepared from doubly distilled water by dissolving the appropriate mass of the metal salt in a 500 ml flask. A 0.1 M methanolic solution of 8HQ was also prepared and used. The glass micro-slide glass substrate, of the size 76.2 mm by 25.4 mm by 1 mm, was cleaned as previously reported [10].

3. Results and discussion

3.1. SEM of the metal 8HQ complexes

Fig. 1 shows the SEM images of an 8HQ deposited thin film on a glass substrate for simple comparison with the thin film metal 8-quinolate complexes. It is evident that the 8HQ molecules are distributed into nano-sized tubes upon direct deposition on the glass substrate and the SEM images of 8HQ are somewhat similar to the SEM image of a carbon nanotube structure [29,30]. The diameter of the 8HQ-nanotube was found to be in the range 33–43 nm, as measured from the SEM images.

The detected SEM images of the various metal complexes were found to be completely different from that of 8HQ. Fig. 2(i)–(iii) shows the SEM images of the $Co(8HQ)_2$ complex deposited thin film on a glass substrate after 50 times of alternate dipping in metal ion solution and 8HQ ligand counter part solution. The $Co(8HQ)_2$ complex was observed to start forming uniform complex particles after only a few dipping cycles, indicating that a fast complex reaction is taking place for the formation of the desired thin films. Fig. 2(i) is a 30,000-times magnified image of the $Co(8HQ)_2$ complex particle, showing a number of deposited molecules under one particle aggregate. Fig. 2(ii) is a 7500 times magnified image of the $Co(8HQ)_2$ complex and clearly refers to the existence of several particles with different contributions of nano-sized aggregates.

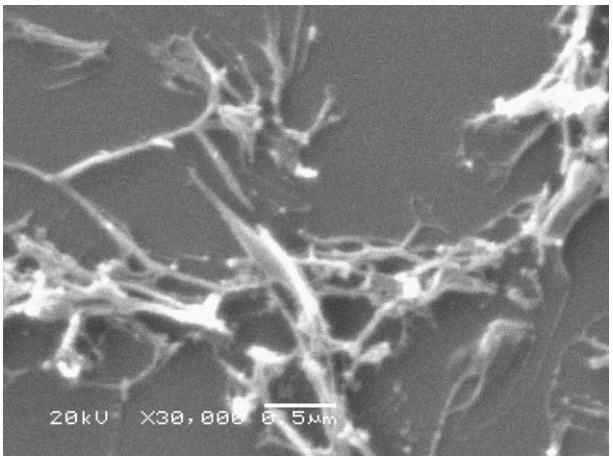


Fig. 1. SEM image of the 8HQ deposited thin film.

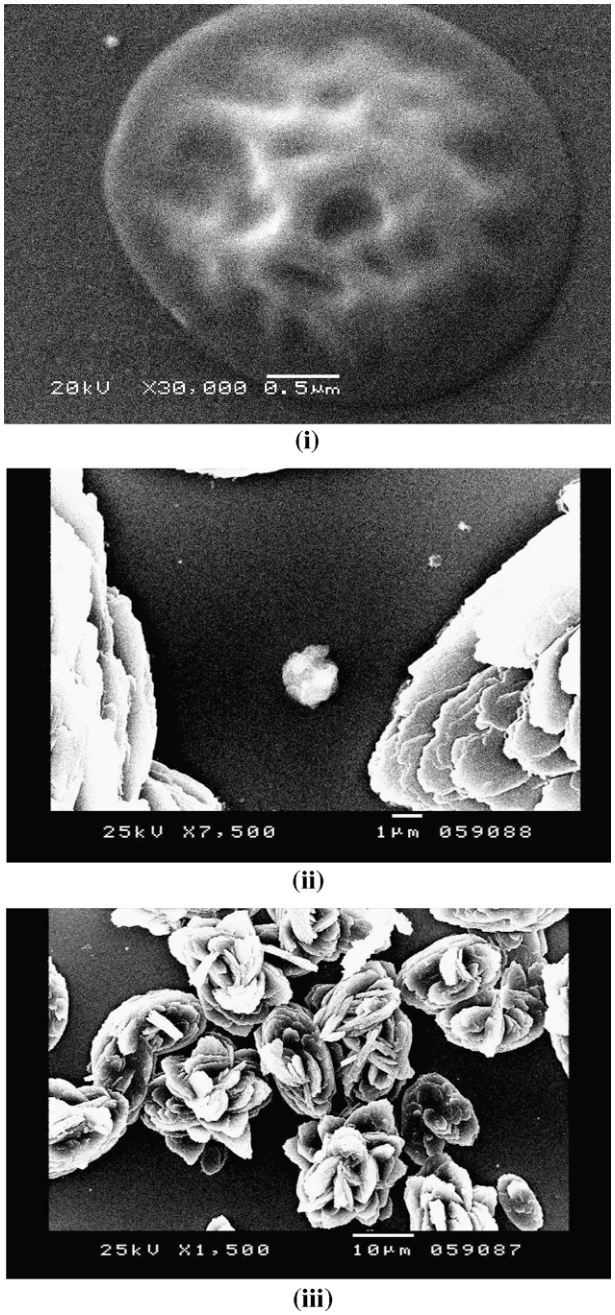


Fig. 2. SEM images of the thin film $Co(8HQ)_2$ complex on glass substrate based on 50-dipping cycles.

Finally, Fig. 2(iii) represents a 1500-times magnified SEM image of the $Co(8HQ)_2$ complex deposited thin film and refers to the high homogeneity and similarity in the $Co(8HQ)_2$ crystal growth based on layer-by- layer complex formation.

Fig. 3(i) and (ii) shows the SEM images of the deposited thin film of the $Fe(8HQ)_3$ complex after 50-dipping cycles in metal ion and 8HQ ligand solutions. Fig. 3(i) shows a homogeneous particle size distribution of the formed $Fe(8HQ)_3$ complex with 10,000-times magnification. Most of the $Fe(8HQ)_3$ complex particle sizes were identified as being under 200 nm. In a similar fashion to the thin film formation of the $Co(8HQ)_2$ complex, a fast complex formation reaction of $Fe(8HQ)_3$ thin film was characterized after only a few dipping cycles. Fig. 3(ii) represents a SEM image of the $Fe(8HQ)_3$ complex deposited thin film with a homogeneous

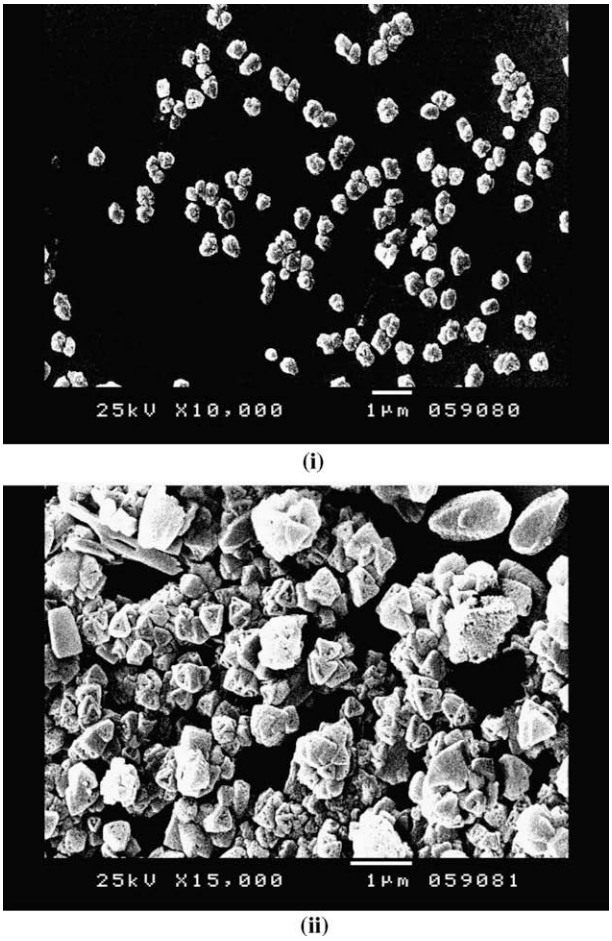


Fig. 3. SEM image of thin film $Fe(8HQ)_3$ complex on glass substrate based on 50-dipping cycles.

distribution of $Fe(8HQ)_3$ crystal growth based on layer-by-layer complex formation. The SEM images of the other metal complexes synthesized based on layer-by-layer thin film formation are shown in Figs. 4–6 for the $Ni(8HQ)_2$, $Cu(8HQ)_2$ and $Zn(8HQ)_2$ complexes, respectively. The numbers of dipping cycles are 30, 15 and 15 for the three tested complexes, respectively.

It is evident from the SEM study that all the synthesized metal quinolate complex crystals were found to grow up from just a single molecule to several molecules in an aggregate distribution with particle sizes starting from a few nanometers to several hundred nanometers. In addition, various characteristic shapes of metal

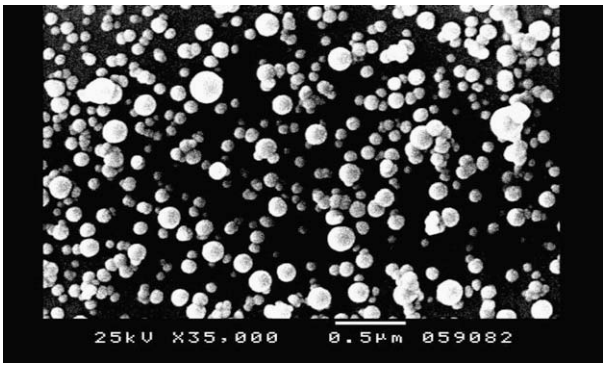


Fig. 4. SEM image of the thin film $Ni(8HQ)_2$ complex on glass substrate based on 30-dipping cycles.

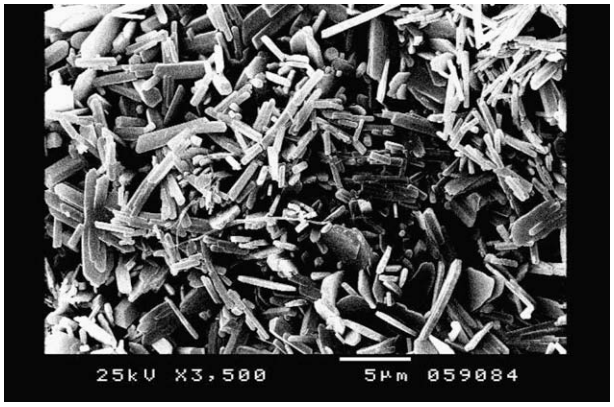


Fig. 5. SEM image of the thin film $Cu(8HQ)_2$ complex on glass substrate based on 15-dipping cycles.

quinolate complexes were identified and these SEM images are quite different from that of 8HQ alone. The shape difference of the metal quinolate complex crystal aggregates deposited on the thin films is mainly dependent on the reacted metal ions.

3.2. Stoichiometry based on metal analysis and EI-MS of the metal quinolate complexes

The molar stoichiometric ratios of the synthesized metal complexes, determined on the basis of the metal analysis, are listed in Table 1. The metal analysis of the characterized layer-by-layer thin film formation of the Co(II), Ni(II), Cu(II) and Zn(II) complexes proved a good similarity to the reactions with 8HQ providing a 1:2 stiochiometric ratio. It is important to report here that the two reaction species, metal ion and 8HQ, were prepared as 0.1 M and

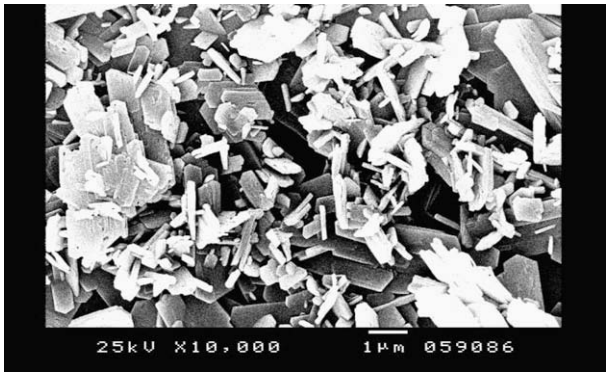


Fig. 6. SEM image of the thin film $Zn(8HQ)_2$ complex on glass substrate based on 15-dipping cycles.

Table 1
Some characteristic data of thin film metal quinolate complexes.

Structure	FW	Color	% Theoretical	% Experimental	Film (mg/cm^2)	Dipping cycles
$Co(8HQ)_2$	346.93	Orange	% Co = 16.99	% Co = 16.79	4.569	50×
$Ni(8HQ)_2$	347.01	Yellowish green	% Ni = 16.91	% Ni = 16.87	4.194	30×
$Cu(8HQ)_2$	351.87	Olive green	% Cu = 18.07	% Cu = 18.06	4.869	15×
$Zn(8HQ)_2$	353.39	Yellowish green	% Zn = 18.50	% Zn = 18.66	4.469	15×
$Fe(8HQ)_3$	488.33	Black	% Fe = 11.44	% Fe = 11.35	4.328	50×

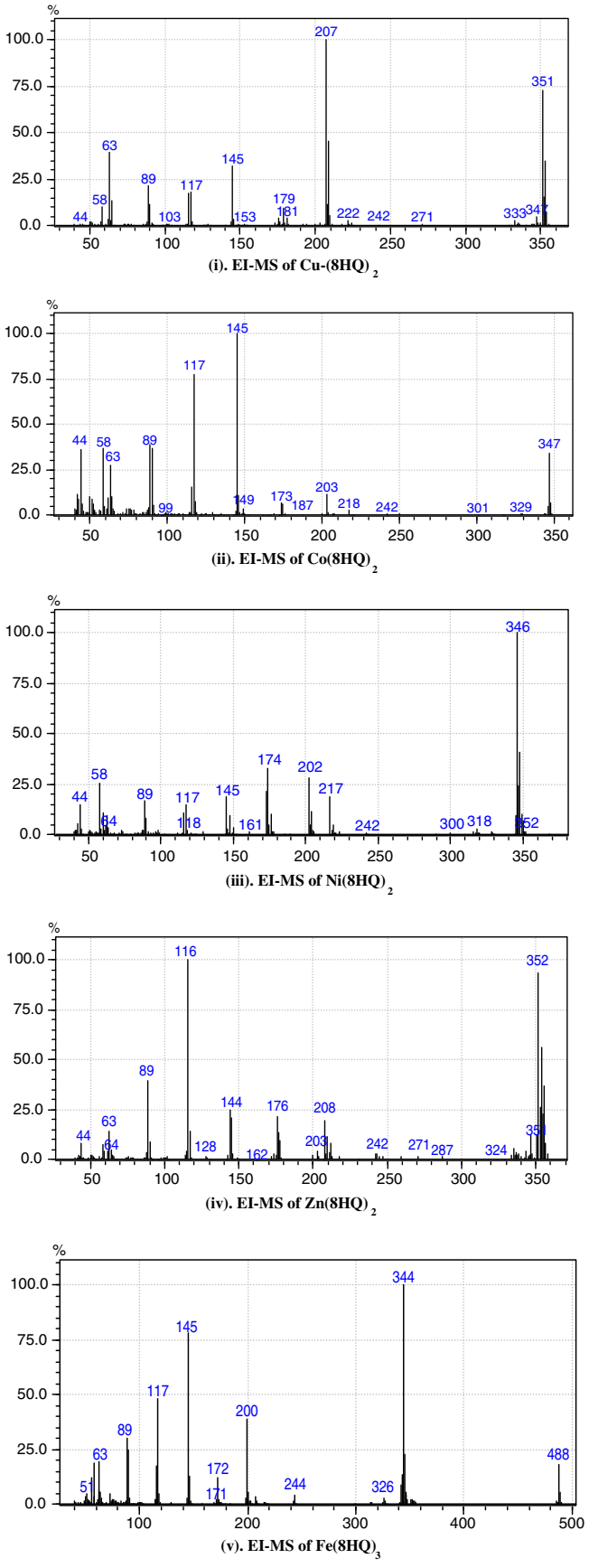


Fig. 7. EI-MS of layer-by-layer thin films of metal quinolate complexes.

when the glass substrate was first dipped in metal ion solution followed by the ligand solution, a rapid complexation reaction took place between the metal ion and 8HQ in a 1:2 ratio, respectively. Thus, the relative concentration of the two reacting species is considered of less importance when layer-by-layer thin film metal quinolate complexes are formed. In the same manner, the Fe(III) ion was characterized by its reaction with 8HQ in a 1:3 ratio based on the metal analysis of Fe(III) in the layer-by-layer thin film $Fe(8HQ)_3$ complex. The same observation of concentration independence can be also assigned in this case.

Electron impact-mass spectra (EI-MS) were also acquired to confirm the molecular masses of all the metal quinolate complexes. The collected spectra of the metal complexes were library searched for the best possible fit. The EI-MS of the $Cu(8HQ)_2$ complex, shown in Fig. 7(i), was found to exhibit a few characteristic ion peaks. A molecular ion peak at m/z 351 (rel. int. = 75%) was detected assuming ^{63}Cu as the most abundant copper isotope. The base peak in the EI-MS of the $Cu(8HQ)_2$ complex, m/z 207, is related to a loss of 144 amu as the deprotonated 8HQ ligand from the molecular ion peak. Some other fragment ion peaks were characterized in the EI-MS of the $Cu(8HQ)_2$ complex and these are directly related to direct and possible successive losses from the ligand ion. These ion peaks were identified at m/z 145, 117, 89 and 63, with relative abundances of 35%, 20%, 23% and 40%, respectively. The library search for the acquired EI-MS of the $Cu(8HQ)_2$ complex was found to strongly fit with the stored mass spectra of the copper 8-hydroxyquinoline complex.

Similar EI-MS of $Co(8HQ)_2$, $Ni(8HQ)_2$ and $Zn(8HQ)_2$ to that of $Cu(8HQ)_2$ were characterized. The molecular ion peaks of these metal quinolate complexes were characterized at m/z 347 (rel. int. = 100%), 346 (rel. int. = 35%) and 352 (rel. int. = 95%) assuming ^{59}Co, ^{58}Ni, ^{64}Zn as the most abundant isotopes of cobalt, nickel and zinc, respectively. These metal quinolate complexes were found to exhibit a loss of 144 amu, for the deprotonated 8HQ ligand, from the molecular ion peak, similar to $Cu(8HQ)_2$. In addition, the same characteristic ion peaks that are derived from 8HQ at m/z 145, 117, 89 and 63 are evident in the EI-MS of these metal complexes, as represented in Fig. 7(ii)–(iv).

The EI-MS of $Fe(8HQ)_3$ exhibited a molecular ion peak at m/z 488 (rel. int. = 20%). Two successive losses of 144 amu were identified and characterized in the mass spectrum of $Fe(8HQ)_3$ due to elimination of two deprotonated 8HQ ligand molecules from the molecular ion peak. These two fragment ion peaks are recorded at m/z 344 (rel. int. = 100%) and 200 (rel. int. = 40%). Fragment ion peaks at m/z 145, 117, 89 and 63 were also characterized in the EI-MS of the $Fe(8HQ)_3$ complex based on fragmentation parts of 8HQ as described above for $Cu(8HQ)_2$, $Co(8HQ)_2$, $Ni(8HQ)_2$ and $Zn(8HQ)_2$. The EI-MS of the $Fe(8HQ)_3$ complex is shown in Fig. 7(v).

Table 2
FT-IR assignments of major peaks.

Compound	Peak (cm^{-1})	Assignment
8HQ [18]	3410	ν_{OH}
	3090	ν_{CH}
	1570	ν_{CO}
	1380	ν_{ring}
	1223	ν_{CN}
$Co(8HQ)_2$		ν_{OH}
	3057	ν_{CH}
	1574	ν_{CO}
	1338	ν_{ring}
	1277	ν_{CN}
$Ni(8HQ)_2$		ν_{OH}
	3058	ν_{CH}
	1577	ν_{CO}
	1340	ν_{ring}
	1284	ν_{CN}
$Zn(8HQ)_2$		ν_{OH}
	3053	ν_{CH}
	1569	ν_{CO}
	1348	ν_{ring}
	1278	ν_{CN}
$Cu(8HQ)_2$		ν_{OH}
	3053	ν_{CH}
	1570	ν_{CO}
	1339	ν_{ring}
	1279	ν_{CN}
$Fe(8HQ)_3$		ν_{OH}
	3055	ν_{CH}
	1570	ν_{CO}
	1378	ν_{ring}
	1271	ν_{CN}

3.3. FT-IR and UV–Vis spectrophotometric analysis of thin film metal 8HQ complexes

The FT-IR spectrum of 8HQ exhibited characteristic absorption peaks for ν(C=N) and ν(OH). In the FT-IR spectra of the five thin film complexes, the absorption peak ν(OH) disappeared with deprotonation of the H-atom of $C_{8\text{-OH}}$ while the ν(C=N) was shifted, indicating that coordination of 8HQ to the various metal ions has taken place via the nitrogen atom of the imine group and oxygen atom of the $C_{8\text{-OH}}$ group, consistent with the results outlined in Section 3.2. A comparison of the FT-IR spectra with

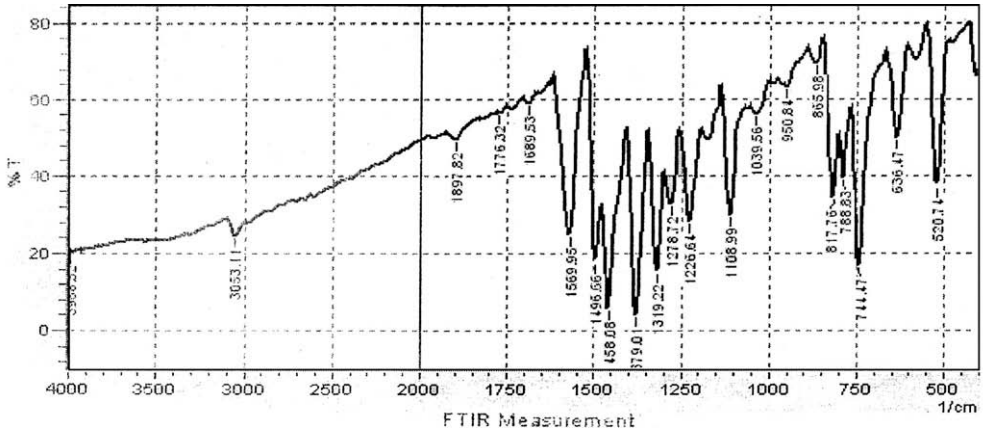


Fig. 8. FT-IR of Cu(II)–quinolate complex.

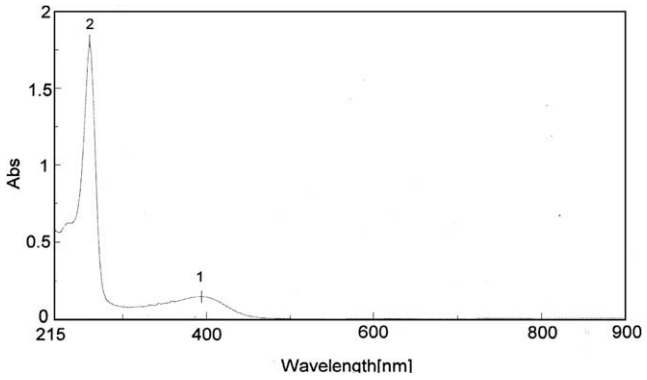


Fig. 9. UV–Vis of Cu(II)–quinolate complex in ethanol.

the molar stoichiometric ratio, metal analysis data and the EI-MS of the metal complexes revealed that 8HQ is behaving as a monobasic bidentate ligand in the process of layer-by-layer thin film formation of all the tested complexes. The metal ions are coordinated through two N,O metal-chelate rings in the case of Co(II), Ni(II), Cu(II) and Zn(II), indicating that these complexes have similar structures, and three N,O metal-chelate rings in $Fe(8HQ)_3$, proving the structure assigned for these thin film complexes by the stoichiometric metal analysis and the EI-MS. Fig. 8 is given as a representative FT-IR spectrum of the Cu(II)-8-hydroxyquinolate complex and the FT-IR assignments of the major peaks are given in Table 2.

The UV–Vis electronic spectra of the layer-by-layer thin film of metal quinolate complexes were also studied and proved to exhibit characteristic d–d transition bands. This band was centered at a wavelength of ~381 nm, with a shoulder band at ~433 nm, for the $Co(8HQ)_2$ complex. The $Zn(8HQ)_2$ complex showed a d–d transition band centered at a wavelength of ~371 nm with a shoulder band at ~427 nm. The d–d transition bands of the $Ni(8HQ)_2$ complex were centered at a wavelength of ~386 nm with a shoulder band at ~427 nm. The $Cu(8HQ)_2$ complex showed d-d transition bands at a wavelength of ~391 nm and two shoulder bands at ~235 and 427 nm. Finally, the $Fe(8HQ)_3$ complex exhibited three d–d transition bands centered at ~363, 461 and 578 nm. Fig. 9 shows a representative UV–Vis spectrum for the Cu(II)–8-hydroxyquinolate complex.

3.4. Thermal gravimetric analysis of the metal 8HQ complexes

Thermal gravimetric analysis of the layer-by-layer synthesized thin film metal quinolate complexes was performed and the thermal parameters are compiled in Table 3. Several thermal degradation steps were identified and are mainly due to the direct decomposition of 8HQ from the metal complexes. The $Co(8HQ)_2$ and $Zn(8HQ)_2$ complexes showed three possible degradation steps, with the final stable product expected to be the metal oxide at $\geqslant$985 K and $\geqslant$965 K, respectively. $Cu(8HQ)_2$ was found to decompose via two degradation steps in the temperature ranges 586–701 K and 765–977 K, due to the possible loss of 8HQ from the complex. The final product formed from the $Cu(8HQ)_2$ complex is also expected to be the metal oxide species at a temperature $\geqslant$977 K. On the other hand, $Ni(8HQ)_2$ and $Fe(8HQ)_2$ were characterized by their thermal gravimetric decomposition via four various degradation steps. These steps also refer to the direct decomposition of the bound 8HQ molecule from these two metal quinolate complexes, leaving the corresponding metal oxide at temperatures $\geqslant$919 K and $\geqslant$1018 K for the $Ni(8HQ)_2$ and $Fe(8HQ)_2$ complexes, respectively. The assigned temperature range of the metal oxide formations is very important if the study of the optical or electric applications of these layer-by-layer thin films of nano-sized particles is targeted, as previously reported for similar oxides [8–10].

4. Conclusion

The outlined results in this work directly refer to the suitability and applicability of the layer-by-layer chemical dipping method as a simple, efficient, low cost and rapid technique for the formation of nano-sized metal 8-hydroxyquinolinate complexes based on crystal growth and thin film formation. The reaction between the metal ion and 8HQ is very fast and a uniform thin film can be observed after only a few dipping cycles. The stoichiometry of the metal quinolate thin film is complete regardless of the concentration of these two interacting species. In addition, the assigned temperature for metal oxide formation is another dimension in this work owing to the possible extension of the presented method for such thin film oxide formation by simply annealing the metal complexes.

Several factors are considered to be of great importance upon application of the layer-by-layer thin film formation of metal complexes that must be explored in order to identify the optimum conditions and generalize the presented method for the formation of nano-sized metal complexes. These include the effect of (i) metal and ligand concentration on the stoichiometry of the metal complex and the particle size, (ii) number of dipping cycles on the particle size, (iii) immersion time on the particle size, (iv) pH of the metal and ligand solutions on the complex formation and (v) sol-

Table 3
Thermal gravimetric data of the layer-by-layer metal quinolate complexes.

Compound	Step	Temperature range (K)	DTG_{max} (K)	Wt. loss (% calculated)	n	E_a (J mol^{-1})	ΔS (J mol^{-1} K^{-1})	R	Ln(A)
$Co(8HQ)_2$	1	394–455	433	8.40	1	69.66	−91.69	0.97753	18.80
	2	685–743	725	11.45	1	186.47	0.53	0.98484	30.41
	3	959–985	893	34.40	1	208.26	−35.62	0.98775	26.27
$Ni(8HQ)_2$	1	381–437	413	10.38	1	76.29	−68.87	0.98504	21.50
	2	621–719	701	42.39	1	176.67	−3.52	0.99419	29.89
	3	719–832	739	18.36	1	103.05	−129.9	0.96222	14.73
	4	832–919	881	16.16	zero	28.76	−249.4	0.47928	0.54
$Cu(8HQ)_2$	1	586–701	636	45.65	1	107.08	−95.39	0.95730	18.74
	2	765–977	863	31.70	1	98.99	−155.8	0.97669	11.78
$Zn(8HQ)_2$	1	387–429	413	8.19	1	58.03	−110.3	0.95632	16.51
	2	629–731	708	23.84	zero	173.73	−11.33	0.94297	28.96
	3	765–965	843	45.21	1	139.51	−108.3	0.99169	17.48
$Fe(8HQ)_2$	1	622–650	643	5.33	0.5	283.81	188.87	0.92750	52.94
	2	652–677	663	6.66	0.5	140.75	−43.46	0.94548	25.03
	3	768–868	824	22.20	1	178.75	−45.74	0.97676	24.97
	4	967–1018	983	10.65	1	274.36	19.95	0.93071	33.05

vent on the particle size and complex formation. An evaluation study of these important factors is now underway.

References

[1] P.K. Arcot, J. Luo, Surf. Coat. Technol. 202 (2008) 2690.
[2] P.K. Arcot, J. Luo, Mater. Lett. 62 (2008) 117.
[3] G. Bhagavannarayana, S.K. Kushwaha, S. Parthiban, G. Ajitha, S. Meenakshisundaram, J. Cryst. Growth 310 (2008) 2575.
[4] T.P. Niesen, M.E.D. Guire, J. Electroceram. 6 (2001) 169.
[5] T.P. Niesen, M.E.D. Guire, Solid State Ion. 151 (2002) 61.
[6] P.T. Hammond, Adv. Mater. 16 (2005) 1271.
[7] M. Rubner, Nature 423 (2003) 925.
[8] S.G. Kandalkar, C.D. Lokhande, R.S. Mane, Sung-Hwan Han, Appl. Surf. Sci. 253 (2007) 3952.
[9] T.P. Gujar, V.R. Shinde, C.D. Lokhande, Mater. Chem. Phys. 103 (2007) 142.
[10] V.R. Shinde, T.P. Gujar, C.D. Lokhande, Sol. Energy Mat. Sol. Cells 91 (2007) 1055.
[11] R.S. Patil, T.P. Gujar, C.D. Lokhande, R.S. Mane, S.H. Han, Sol. Energy 81 (2007) 648.
[12] G.D. Bagde, S.D. Sartale, C.D. Lokhand, Thin Solid Films 445 (2003) 1.
[13] R.S. Patil, C.D. Lokhande, R.S. Mane, T.P. Gujar, S.H. Han, J. Non-Cryst. Solids 353 (2007) 1645.
[14] K. Soroka, R.S. Vithanage, D.A. Phillips, B. Walker, P.K. Dasgupta, Anal. Chem. 59 (1967) 629.
[15] R.G.W. Hollingshead, Oxine and its Derivatives, Butterworths, London, 1954.
[16] M.E. Mahmoud, Encyclopedia of Chromatography, second ed., March 2006, pp. 1–14, 10.1081/E-ECHR-120042798.
[17] M.E. Mahmoud, E.M. Soliman, J. Liq. Chromatogr. Rel. Technol. 26 (2003) 3045.
[18] B. Wen, X.Q. Shan, Anal. Bioanal. Chem. 374 (2002) 948.
[19] A. Goswami, A.K. Singh, B. Venkataramani, Talanta 60 (2003) 1141.
[20] M.L. Firdaus, K. Norisuye, T. Sato, S. Urushihara, Y. Nakagawa, S. Umetani, Y. Sohrin, Anal. Chim. Acta 583 (2007) 296.
[21] M. Albrecht, M. Fiege, O. Osetska, Coord. Chem. Rev. (2007). in press.
[22] C.W. Tang, S.A. Van Slyke, J. Appl. Phys. 65 (1989) 3610.
[23] S. Meloni, A. Palma, J. Schwartz, A. Kahn, R. Car, J. Am. Chem. Soc. 125 (2003) 7808.
[24] R.H. Friend, R.W. Gymer, A.B. Holmes, J.H. Burroughes, R.N. Marks, C. Taliani, D.A. Dos Santos, J.L. Bredas, M. Logdlund, W.R. Salaneck, Nature 397 (1999) 121.
[25] F. Qian, Y. Li, S. Gradecak, D. Wang, C.J. Barrelet, C.M. Lieber, Nano Lett. 4 (2004) 1975.
[26] S.C. Lyu, Y. Zhang, C.J. Lee, Chem. Mater. 15 (2003) 3294.
[27] Y.S. Zhao, C. Di, W. Yang, G. Yu, Y. Liu, J. Yao, Adv. Funct. Mater. 16 (2006) 1985.
[28] K. Ueda, G. Tanaka, T. Suzuki, R. Kita, S. Kokado, Polyhedron 24 (2005) 2533.
[29] K. Kanetoa, M. Tsurutaa, G. Sakaia, W.Y. Chob, Y. Ando, Synth. Met. 103 (1999) 2543.
[30] C.Y. Lin, W.T. Tsai, Mater. Chem. Phys. 82 (2003) 929.

Polyhedron 28 (2009) 188–194

Contents lists available at ScienceDirect

Polyhedron

journal homepage: www.elsevier.com/locate/poly

Structure and emission spectra of dinuclear lanthanide(III) β-diketonate complexes with a bridging 2,2′-bipyrimidine ligand

Madelyn H. Baker [a], Jason D. Dorweiler [a], Amanda N. Ley [b], Robert D. Pike [b], Steven M. Berry [a,*]

[a] Department of Chemistry and Biochemistry, University of Minnesota Duluth, 1039 University Dr., Duluth, MN 55812-3020, USA
[b] Department of Chemistry, College of William and Mary, P.O. Box 8795, Williamsburg, VA 23187-8795, USA

ARTICLE INFO

Article history:
Received 28 July 2008
Accepted 16 October 2008
Available online 21 November 2008

Keywords:
Dinuclear
Bipyrimidine
β-Diketonate
Lanthanide
Luminescence

ABSTRACT

The 2,2′-bipyrimidine (bpm) adducts of the β-diketonate complexes of Eu(III), Sm(III), or Yb(III) with 2,2′,6,6′-tetramethyl-2,4-heptanedione (tmhd) resulted in the formation of dinuclear species. The synthesis and X-ray structure of these three new dinuclear lanthanide complexes are found to be similar. Each lanthanide ion is eight coordinate, bound to six O-atoms from the β-diketonates and 2N atoms from the bridging bpm ligand. They exhibit Ln–Ln distances (Sm(III): 6.935 Å, Eu(III): 6.901 Å, Yb(III): 6.679 Å) and Ln–ligand distances that are consistent with the decrease in radii across the lanthanide series. Absorption spectra of the complexes are dominated by ligand absorptions. Both the solution and solid state emission spectra of the complexes resemble ordinary monomeric lanthanide species, indicating independent ions in the dinuclear species. Cyclic voltammetry of all the complexes appear almost identical with discernable ligand centered redox reactions. The complex with Eu(III) ions, having the lowest possible lanthanide redox potential, was not found to display a signal corresponding to metal reduction.

© 2008 Elsevier Ltd. All rights reserved.

1. Introduction

Many intriguing fundamental properties of the f-electron compounds arise from their electronic structure which leads to broad applications. The lanthanide (Ln) elements have been exploited for such commercial uses as lasers, phosphors, luminescent biological probes, MRI contrast reagents, NMR shift reagents, magnets, and medicines [1–3]. In addition, it is important to note the utilization of 4f electron compounds for magnetic materials and their potential use as high temperature superconductors [4]. The development of these and other Ln technologies is dependent on the elucidation of fundamental Ln properties, such as electronic and magnetic interactions. Electronic and magnetic inter-ion communications have been noted between Ln ions of a common oxidation state in dinuclear complexes [5,6], as well as extended solids in superconductors, lasers, and phosphors [4,7,8]. We are interested in generating dinuclear lanthanide complexes with bridging ligands that allow possible communication between lanthanide elements and thus provide insight into electron interactions in these f-electron ions. Elucidation of f-electron interactions can foster further development of Ln technologies [4].

Synthesizing dinuclear or polynuclear species with lanthanide ions is challenging due to the cationic repulsions. Coordination chemistry of the lanthanides is driven by ionic interactions between the ligands and the generally trivalent Ln ions. Furthermore, lanthanides typically adopt high coordination numbers and coordination geometries are heavily influenced by sterics [9]. The use of chelating ligands and hard donor atoms is important for generating stable complexes of the Ln ions.

The 2,2′-bipyrimidine (bpm) ligand has been used successfully in numerous transition metal complexes to bridge metal ions and functions as a channel for energy and electron transfer [10–16]. Bpm has also been used to form heterodinuclear metal complexes between Ln and transition metals [17–19]. In these studies, energy transfer was found to occur efficiently between the transition metal and the lanthanide ion [17]. Finally, there have been a few recent reports of crystallographically characterized dinuclear lanthanide complexes with bpm as the bridge [20–23]. Interestingly, there are still few examples of these dinuclear lanthanide species, and many complexes form mononuclear rather than the desired dinuclear structure.

We report the successful synthesis of more examples of dinuclear β-diketonate adducts of lanthanide complexes using bpm as the bridging ligand. Complexes of Eu(III), Sm(III), and Yb(III) ions with the β-diketone 2,2′,6,6′-tetramethyl-2,4-heptanedione (tmhd) were formed. The β-diketone was chosen to ensure complex solubility in organic solvents, a problem found with at least one β-diketonate complex [24]. Also, the higher electron donating ability of the β-diketone *tert*-butyl groups was hypothesized to encourage the formation of dinuclear complexes.

* Corresponding author. Tel.: +1 218 726 7087; fax: +1 218 726 7394.
E-mail address: smberry@d.umn.edu (S.M. Berry).

0277-5387/$ - see front matter © 2008 Elsevier Ltd. All rights reserved.
doi:10.1016/j.poly.2008.10.019

2. Experimental

2.1. Materials

Solvents and reagents were of commercial grade and used without further purification. Hexahydrates of the lanthanide chloride salts (Eu(III), Sm(III), and Yb(III)), 2,2′,6,6′-tetramethyl-2,4-heptanedione (tmhd) and 2,2′-bipyrimidine (bpm) were obtained from Strem Chemicals, ACROS, and Aldrich, respectively, without further purification. Elemental analysis data were collected by Atlantic Microlabs, Norcross, GA. bpm: IR (KBr): $\nu\sim$ = 508, 637, 668, 686, 766, 819, 986, 1097, 1140(m), 1194(w), 1237(w), 1257(w), 1406(s), 1433(w), 1557(s), 1653(m), 2973(w), 3027(w), 3060(w), 3126(w), 3436(br) cm^{-1}.

2.2. Synthesis

Powders of the dinuclear lanthanide complexes were all obtained by the same method of mixing Ln(III), bpm and β-diketone in ratios of 2:1:6, as described below. Sodium hydroxide in distilled and deionized water (8.4 mL of 0.0974 M solution, 0.82 mmol) was added drop-wise with stirring to a solution of absolute ethanol (7.1 mL), bpm (0.136 mmol) and tmhd (0.82 mmol) at room temperature (21 °C) in a 25 mL Erlenmeyer flask. The resulting solution was clear. A 3 mL solution of $LnCl_3 \cdot 6H_2O$ in absolute ethanol (0.272 mmol) was added a drop at a time with stirring every 1–2 min over the course of 45 min. With the first drop of Ln(III) salt solution, the solution became cloudy. A light-yellow colored precipitate formed upon further addition of metal. After the final drop of Ln(III) salt solution was added, the cloudy mixture was allowed to stir for another 30 min at room temperature. The light yellow precipitate was collected by filtration through a fine porcelain fritted funnel. The powder was washed with ~10 mL of cold absolute ethanol, dried under vacuum for 12–16 h, and weighed to determine yields. The powdered samples were further purified by dissolution in a minimum volume of room temperature $CHCl_3$ (~3 mL), immediately filtered to remove insoluble particulates with a fine-fritted porcelain funnel, and then re-precipitated by the addition of cold absolute ethanol (~10 mL). The precipitated solution was again filtered with a fine porcelain fritted funnel and dried under vacuum for 12–16 h. For all three Ln (Eu(III), Sm(III), and Yb(III)), diffraction quality crystals were formed by dissolving the complex in $CHCl_3$ with various amounts of CH_3OH as a precipitating co-solvent (from 1:1 to 1:10 $CHCl_3$:CH_3OH by volume). All solutions were clear initially and crystals formed in 1 to 10 days by allowing slow evaporation. Crystals removed from the mother liquor turned from clear and colorless to opaque over the course of 2–4 days. For this reason, crystals were left in solution until immediately before X-ray diffraction analysis or luminescence studies, whereupon they were quickly frozen in liquid nitrogen.

2.2.1. $[Eu(tmhd)_3]_2bpm$ (**1**)

A pale yellow powder was obtained in 91% average yield. Powder M.P.: 300 °C, crystal M.P.: 290 °C. Powder *Anal.* Calc. for $C_{74}H_{120}N_4O_{12}Eu_2$: C, 56.91; H, 7.75; N, 3.59. Found: C, 56.63; H, 7.65; N, 3.57%. IR (KBr): $\nu\sim$ = 474, 603, 659, 736, 758, 792, 815, 869, 961, 1020, 1065, 1139(m), 1181, 1226, 1246, 1284, 1359(s), 1388(sh), 1419(s), 1453(s), 1506(s), 1540(s), 1576(br), 2866(m), 2962(s) cm^{-1}.

2.2.2. $[Sm(tmhd)_3]_2bpm$ (**2**)

A pale yellow powder was obtained in 81% average yield. Powder M.P.: 306 °C, crystal M.P.: 303 °C. Powder *Anal.* Calc. for $C_{74}H_{120}N_4O_{12}Sm_2$: C, 57.03; H, 7.76; N, 3.59. Found: C, 57.15; H, 7.73; N, 3.42%. IR (KBr): $\nu\sim$ = 474, 602, 659, 735, 759, 793, 815, 868, 960, 1020, 1065, 1139(m), 1182, 1227, 1246, 1277, 1358(s), 1388(sh), 1418(s), 1452, 1506(s), 1539(s), 1575(br), 2866(m) 2954(s) cm^{-1}.

2.2.3. $[Yb(tmhd)_3]_2bpm$ (**3**)

A pale yellow powder was obtained in 78% average yield. Powder M.P.: 305 °C, crystal M.P.: 305 °C. Powder *Anal.* Calc. for $C_{74}H_{120}N_4O_{12}Yb_2$: C, 55.42; H, 7.54; N, 3.49. Found: C, 55.21; H, 7.49; N, 3.43%. IR (KBr): $\nu\sim$ = 478, 605, 662, 737, 758, 792, 816, 870, 963, 1023, 1065, 1143(s), 1182, 1228, 1246, 1286, 1358(s), 1388(sh), 1430(s), 1455(s), 1508(s), 1540(s), 1580(br), 2866(m), 2954(s) cm^{-1}.

2.3. Methods

UV–Vis absorption spectra were recorded on a Shimadzu UV2401 PC UV–Vis recording spectrophotometer at room temperature. Purified powder samples were run in $CHCl_3$ solution with 1 cm quartz cuvettes. Solution fluorescence spectra and emission decay curves were obtained with a Cary Eclipse Fluorescence Spectrophotometer equipped with a Cary Peltier temperature controller. Purified powder samples were run in $CHCl_3$ solution with 1 cm quartz cuvettes with excitation and emission slit widths of 5 nm. Solid state fluorescence data was recorded with a McPherson RS-10 spectrophotometer. Crystals of the complexes were placed in a 3 mm i.d. quartz tube and immersed in liquid N_2 held in a Wilmad quartz cold finger Dewar flask. The excitation source was the 365 nm line from a 100 W Osram mercury vapor lamp, selected by a glass filter. The spectrophotometer was calibrated before use with Hg emission lines. Electrochemistry measurements were obtained using a CH-Instruments 620B electrochemical analyzer with faraday cage. The working electrode was a 3 mm diameter glassy carbon disk purchased from CH-Instruments. The reference electrode was a Ag/AgCl electrode made with the same solvent and supporting electrolyte as the sample. Furthermore, ferrocene was added to each sample after initial data collection as an internal reference and displayed a midpoint potential of +0.750 V versus our Ag/AgCl electrode in DMF with 0.02 M tetrabutylammonium hexafluorophosphate ($TBAPF_6$). Purified powder samples and crystals of the homodinuclear complexes were dissolved in DMF solvent at 1 mM concentration with 0.02 M $TBAPF_6$ as supporting electrolyte. Solutions were added to a 2 mL cell with a Pt counter electrode, the reference electrode, and the working electrode. Anhydrous (<5 ppm H_2O) and degassed DMF was used and the sample was continuously bubbled with Argon during sample measurement. IR spectra were obtained on KBr pellets of purified powder samples with a Perkin Elmer Spectrum RX FT-IR spectrophotometer.

2.4. X-ray analysis

Single-crystal determinations were carried out using a Bruker SMART Apex II diffractometer using graphite-monochromated Cu Kα radiation [25]. The data were corrected for Lorentz and polarization [26] effects and absorption using SADABS [27]. The structures were solved by use of direct methods or Patterson map. Least squares refinement on F^2 was used for all reflections. Structure solution, refinement, and the calculation of derived results were performed using the SHELXTL [28] software package. The non-hydrogen atoms were refined anisotropically. The hydrogen atoms were located and then placed in theoretical positions. Images of molecular structures were created using ORTEP III [29].

3. Results and discussion

3.1. Synthesis

The Ln complexes were synthesized by mixing solutions of the lanthanide chloride salts of Eu(III), Sm(III), or Yb(III) with the β-diketonate and bpm in a 2:6:1 molar proportion. Precipitates

formed immediately and the resulting light-yellow powders were obtained in good yield. Elemental analyses of the powders indicated that the isolated complexes were dinuclear. These results parallel those of others [21,23], and represent a general way of synthesizing dinuclear lanthanide complexes with bridging bpm. This procedure differs slightly from an alternative procedure used to make dimers where bpm displaces water ligands of preformed mononuclear lanthanide(III) tris(β-diketonate) hydrates through ligand displacement reactions [20].

There are instances however where dinuclear species do not form and only mononuclear β-diketonate species assemble [30,31], or cases that go beyond the formation of dinuclear complexes with the formation of linear polymers of repeating Ln–bpm units [32,33]. The larger lanthanide ions have been observed to tend toward mononuclear complexes [21,24,30]. It is also apparent that the nature of the β-diketone makes a significant difference. β-diketones with groups capable of π–π interactions have been observed in crystal structures to stabilize dinuclear structures in the solid state by interacting above and below the bpm bridge [21–23].

The β-diketone tmhd was chosen for our studies based on the electron donating ability of *tert*-butyl groups versus other groups such as highly fluorinated alkyl groups. Tmhd was expected to encourage the formation of dinuclear complexes for two reasons. First, the greater charge neutralization of +3 lanthanide ions helps to minimize charge repulsions as the ions come in close proximity in the dimer. Second, the greater donating ability of the β-diketone allows less polarization of the bpm bridge and thus ensures the bpm can donate equally well from either side of the ligand. Stronger σ bonding on one side of bpm could withdraw charge density from the ligand and make the non-bonding electrons on the other side of bpm less available for complexation [31].

3.2. X-ray structures

Ready growth of X-ray quality crystals was accomplished from $CHCl_3$:CH_3OH solutions for all three lanthanide ions. The crystals were found to contain $CHCl_3$ solvent molecules trapped in the crystal lattice which evaporated over the course of days resulting in opaque crystals. For diffraction, crystals were removed from the mother liquor and quickly frozen in a cold stream of nitrogen to prevent solvent loss from the lattice.

All three crystallized lanthanide complexes were found to have dinuclear structures. The Eu(III) and Sm(III) structures were isomorphic, crystallizing in the chiral monoclinic $P2_1$ space group and having a single $CHCl_3$ solvate molecule. Both showed evidence of racemic twinning, with the Flack parameters being 0.503(2) and 0.121(2), respectively. The Yb(III) complex crystallized in the orthorhombic *Pbca* group with two $CHCl_3$ molecules in the lattice. Some minor rotational disorder was observed in the *tert*-butyl groups of the β-diketone ligand for all complexes. The Yb(III) complex contains a crystallographic center of symmetry at the bpm ligand. The crystal data (Table 1) and selected bond lengths and angles (Table 2) are reported for all three structures.

3.2.1. $[Eu(tmhd)_3]_2bpm$ (**1**) structure

The Eu complex crystallized as the dinuclear species bridged by a single bpm molecule (Fig. 1). In addition to the two Ln–N bonds to bpm, each Eu(III) center has six Ln–O bonds to three β-diketonate ligands. The resulting 8-coordinate structures adopt distorted square antiprismatic geometries for each Eu(III) ion, based on the method of Porai-Koshits and Aslanov (Table 3) [34]. The polyhedra exhibit slight distortion towards the bicapped trigonal prism. This coordination number and geometry is commonly found in many Ln(III) β-diketonate complexes [9]. The top square face of the antiprisms are defined by O1, O2, O3, O4 for Eu1 and N2,N4,O11,O12 for Eu2, with all four chelating rings spanning *s* edges [34]. Furthermore, the chelating ligands span *s* edges in a fashion such that the β-diketone ligands on either side of the bpm bridge are parallel and facing each other, thus minimizing steric conflicts. The average Eu–O distance is 2.339 Å, while the average Eu–N distance is 2.642 Å (Tables 2 and 4). Other reported dinuclear bpm bridged Eu(III) β-diketonate complexes exhibit very similar bond distance averages for Eu–O (2.355 [20], 2.354 [23], 2.370 [23], 2.343 [21], and 2.394 Å [21]) and Eu–N (2.610 [20], 2.609 [23], 2.646 [23], 2.677 [21], and 2.687 Å [21]). The Eu–Eu distance was found to be 6.901 Å, which is intermediate between other known bpm bridged Eu(III) dimers (6.8035 [23], 6.856 [20], 6.9212 [23], 6.993 [21], and 7.011 Å [21]).

It has been observed that the two rings of the bridging bpm ligand can be twisted from co-planarity in some complexes [21–23] while remaining co-planar in others [20,21,23]. Those complexes with co-planar bpm rings have crystallographic centers of symmetry centered on the bpm ligand. The two mean planes of

Table 1
Crystal data, collection and structure refinement parameters for complexes **1**, **2**, and **3**.

Parameters	**1**	**2**	**3**
Empirical formula	$C_{74}H_{120}Eu_2N_4O_{12} \cdot CHCl_3$	$C_{74}H_{120}N_4O_{12}Sm_2 \cdot CHCl_3$	$C_{74}H_{120}N_4O_{12}Yb_2 \cdot 2CHCl_3$
Formula weight	1681.03	1677.81	1842.56
Crystal system	monoclinic	monoclinic	orthorhombic
Space group	$P2_1$	$P2_1$	*Pbca*
Crystal size (mm^3)	$0.23 \times 0.16 \times 0.15$	$0.34 \times 0.09 \times 0.06$	$0.23 \times 0.19 \times 0.15$
Temperature (K)	100(2)	100(2)	100(2)
a (Å)	10.7788(2)	10.7544(2)	19.9428(3)
b (Å)	29.4774(4)	29.5209(5)	20.9030(3)
c (Å)	13.8407(2)	13.9030(2)	20.9908(3)
α (°)	90	90	90
β (°)	106.8600(10)	106.9430(10)	90
γ (°)	90	90	90
V ($Å^3$)	4208.59(11)	4222.33(12)	8750.3(2)
Z	2	2	4
ρ_{calc} ($g\ cm^{-3}$)	1.327	1.320	1.399
μ (mm^{-1})	11.88	11.65	5.97
F(000)	1744	1740	3776
$R_1[I > 2\sigma(I)]$	0.0260	0.0255	0.0367
$wR_2[I > 2\sigma(I)]$	0.0555	0.0584	0.0836
R_1 (all data)	0.0275	0.0270	0.0427
wR_2 (all data)	0.0559	0.0591	0.0875
Goodness-of-fit	1.06	1.00	1.03

Table 2
Selected bond lengths (Å) and angles (°) for complexes **1**, **2**, and **3**.

1		**2**		**3**	
Eu1–O1	2.335(2)	Sm1–O1	2.363(2)	Yb1–O1	2.253(2)
Eu1–O2	2.357(2)	Sm1–O2	2.345(3)	Yb1–O2	2.278(2)
Eu1–O3	2.288(2)	Sm1–O3	2.347(3)	Yb1–O3	2.220(2)
Eu1–O4	2.339(2)	Sm1–O4	2.292(3)	Yb1–O4	2.261(2)
Eu1–O5	2.341(2)	Sm1–O5	2.355(3)	Yb1–O5	2.295(2)
Eu1–O6	2.358(2)	Sm1–O6	2.376(3)	Yb1–O6	2.272(2)
Eu1–N1	2.647(3)	Sm1–N1	2.703(3)	Yb1–N1	2.556(3)
Eu1–N3	2.680(3)	Sm1–N3	2.661(3)	Yb1–N2	2.527(3)
Eu2–O7	2.383(2)	Sm2–O7	2.340(3)	Yb1′–O1′	2.253(2)
Eu2–O8	2.333(2)	Sm2–O8	2.391(2)	Yb1′–O2′	2.278(2)
Eu2–O9	2.338(3)	Sm2–O9	2.357(3)	Yb1′–O3′	2.220(2)
Eu2–O10	2.308(2)	Sm2–O10	2.328(3)	Yb1′–O4′	2.261(2)
Eu2–O11	2.360(2)	Sm2–O11	2.366(3)	Yb1′–O5′	2.295(2)
Eu2–O12	2.324(2)	Sm2–O12	2.338(3)	Yb1′–O6′	2.272(2)
Eu2–N2	2.627(3)	Sm2–N2	2.630(3)	Yb1′–N1′	2.556(3)
Eu2–N4	2.613(3)	Sm2–N4	2.639(3)	Yb1′–N2′	2.527(3)
O1–Eu1–O2	71.62(8)	O2–Sm1–O1	71.19(9)	O1–Yb1–O2	73.97(9)
O3–Eu1–O4	73.33(9)	O4–Sm1–O3	73.20(10)	O3–Yb1–O4	75.00(9)
O5–Eu1–O6	71.84(9)	O5–Sm1–O6	71.35(9)	O5–Yb1–O6	73.51(9)
N1–Eu1–N3	60.62(9)	N3–Sm1–N1	60.10(10)	N1–Yb1–N2	63.85(9)
O7–Eu2–O8	71.42(8)	O7–Sm2–O8	70.99(9)	O1′–Yb1–O2′	73.97(9)
O9–Eu2–O10	72.26(9)	O10–Sm2–O9	71.49(10)	O3′–Yb1–O4′	75.00(9)
O11–Eu2–O12	72.18(9)	O12–Sm2–O11	72.03(10)	O5′–Yb1–O6′	73.51(9)
N2–Eu2–N4	62.00(9)	N2–Sm2–N4	61.44(10)	N1′–Yb1–N2′	63.85(9)

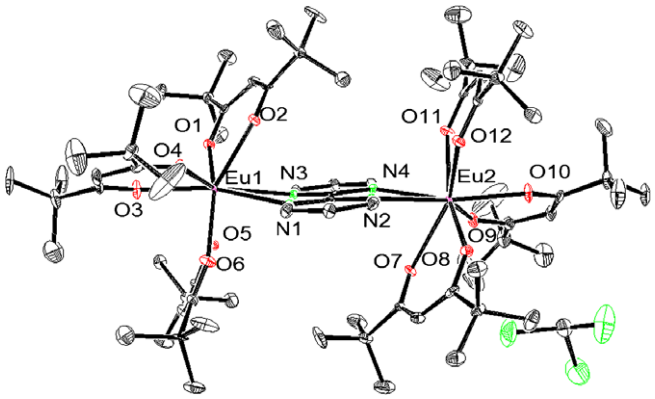


Fig. 1. Structure of $[Eu(tmhd)_3]_2$bpm, **1**. Thermal ellipsoids are shown at the 50% level.

Table 3
Angles defining the polyhedra of complexes **1**, **2**, and **3**, based on the method of Porai-Koshits and Aslanov [34].

	b Edge δ angles (°)				Trapezoid φ angles (°)	
Ideal dodecahedron	29.5	29.5	29.5	29.5	0.0	0.0
Ideal bicapped trigonal prism	21.8	0.0	48.2	48.2	14.1	14.1
Ideal square antiprism	0.0	0.0	52.4	52.4	24.5	24.5
1, Eu1	4.6	0.1	49.6	47.0	23.8	24.1
1, Eu2	5.1	4.4	46.5	47.3	22.4	22.4
2, Sm1	4.3	0.5	49.5	46.8	23.5	24.3
2, Sm2	4.7	5.1	47.0	47.5	22.6	22.7
3, Yb1 and Yb1′	1.6	5.8	55.7	52.3	23.9	25.9

Table 4
Average Ln–O, Ln–N, and Ln–Ln bond lengths (Å) for complexes **1**, **2**, and **3**.

1		**2**		**3**	
Eu–O	2.339	Sm–O	2.350	Yb–O	2.263
Eu–N	2.642	Sm–N	2.658	Yb–N	2.542
Eu–Eu	6.901	Sm–Sm	6.935	Yb–Yb	6.679

the bridging bpm ligand in our complex were only slightly twisted from co-planarity by 0.63°. In addition, the bridging bpm ligand binds to each Eu(III) ion in a bidentate fashion, however each Eu(III) ion is not in the same plane as the bpm ligand. Eu1 and Eu2 bind to the bpm ligand above and below the mean plane defined by the bpm ligand by 0.518 and 0.373 Å, respectively. This results in a chair-like conformation for the six-membered ring defined by Eu1–N3–N4–Eu2–N2–N1 (Fig. 1).

3.2.2. $[Sm(tmhd)_3]_2$bpm (*2*) structure

The structure of **2** (Fig. 2) is largely similar to that of **1**. Both molecules crystallize in the same space group and contain a single solvent molecule. The Sm(III) ions are 8-coordinate with six Sm–O bonds to the three β-diketone ligands and two Sm–N bonds to the bridging bpm ligand. The geometry around each Sm(III) center is square antiprismatic with distortion towards a bicapped trigonal prism (Table 3) [34]. All chelating ligands span the *s* edges of the square antiprism. The angles defining the polyhedra are very similar to and parallel those of the complex **1**. The average Sm–O and Sm–N bond lengths are 2.350 and 2.658 Å, respectively (Table 2). Again, these are very similar to the average bond lengths for the Eu complex (Table 4). The slightly longer averages for the bond lengths in **2** however, are consistent with the well known decrease in ionic radii across the row. Finally, the Sm–Sm distance of 6.935 Å is longer than that in complex **1**.

The binding of the bridging bpm ligand is very similar between complexes **2** and **1**. The rings of the bpm ligand in **2** are slightly offset from co-planarity by 0.34°. Also, the Sm atoms are bound to the bpm ligand slightly above and below the plane defined by the bpm rings (Sm1: 0.527 Å, Sm2: 0.373 Å), creating a chair-like conformation. To our knowledge, there are no other published structures of dinuclear Sm(III) complexes with bridging bpm however this structure is not believed to be unusual due to its high similarity to the other known dinuclear complexes.

3.2.3. $[Yb(tmhd)_3]_2$bpm (*3*) structure

Complex **3** (Fig. 3) crystallizes in a different crystal system than the other dinuclear complexes reported here even though it has a similar ligand set and structure. The complex contains a crystallographic inversion center located at the center of the bridging bpm ligand and thus only half of the dimer is crystallographically independent. The Yb(III) center is a distorted square antiprism (Table 3) with six β-diketonate O atoms and two bpm N atoms chelating the *s* edges [34]. The average Yb–O and Yb–N bond distances are 2.263 and 2.542 Å, respectively. These distances are shorter than both **1** and **2** as expected from the contraction in radii across the

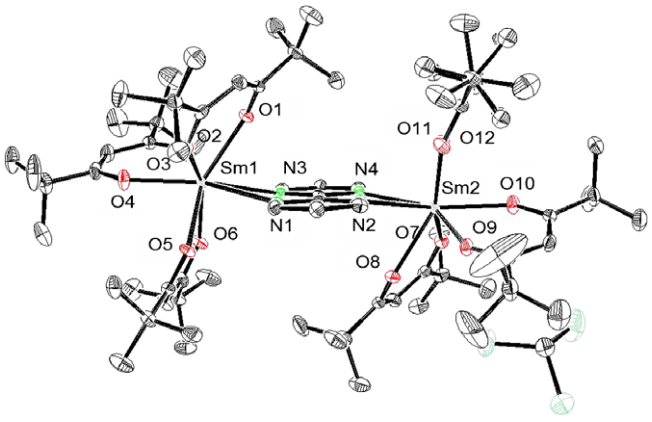


Fig. 2. Structure of $[Sm(tmhd)_3]_2$bpm, **2**. Thermal ellipsoids are shown at the 50% level.

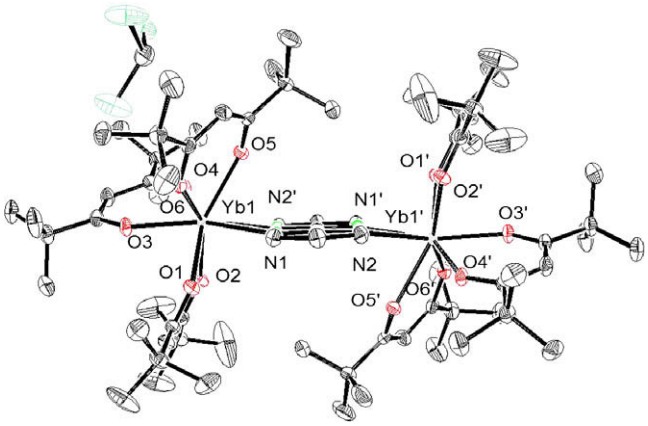


Fig. 3. Structure of $[Yb(tmhd)_3]_2$bpm, **3**. Thermal ellipsoids are shown at the 50% level.

lanthanide series. In addition, the Yb–Yb distance of 6.679 Å is shorter than in **1** and **2**. As required by symmetry, the bpm ligand is perfectly planar. However, the Yb(III) ions are coordinated to bpm 0.339 Å above and below the plane defined by bpm, resulting in the similar chair-like conformation seen with complexes **1** and **2**.

3.3. Absorbance and Luminescence spectroscopy

The UV–Vis absorption spectra of the complexes in $CHCl_3$ solution are dominated by the absorption of the β-diketonate and bpm ligands (Fig. 4). The spectra of all complexes are similar and have maxima around 280 nm. They exhibit higher energy absorption peaks and slightly smaller intensities than those observed in complexes utilizing aromatic side groups on the β-diketone ligands [21,23,30].

Solution luminescence spectra of the complexes in $CHCl_3$, with excitation into the 280 nm absorption band, result in spectra typical of the individual lanthanide ions (Fig. 5). The red-colored emission from the Eu(III) $^5D_0$ to the $^7F_0$, $^7F_1$, $^7F_2$, $^7F_3$, and $^7F_4$ states are observed near 580, 590, 612, 655, and 705 nm, respectively

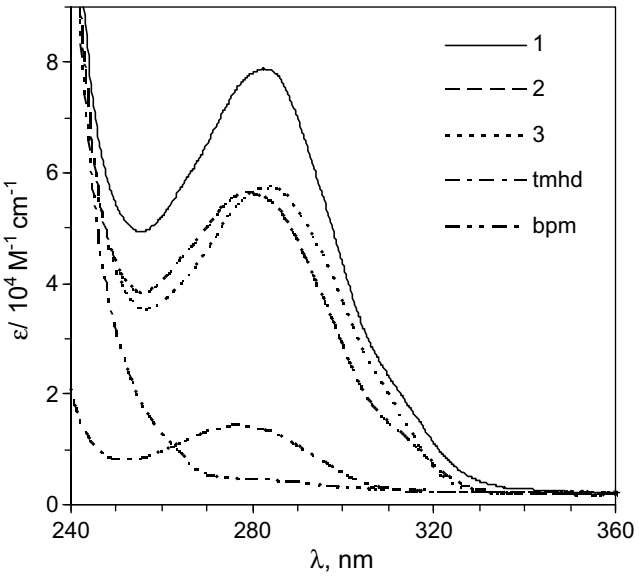


Fig. 4. The UV–Vis absorption spectra of 20 μM solutions of **1**, **2**, **3**, tmhd, and bpm in $CHCl_3$ at 22 °C.

(Fig. 5a). Lifetime measurements (data not shown) at 25 °C was fit closely with a first order, single exponential decay curve with rate constant value of 2.265 ms^{-1}. This decay rate constant is comparable to other mononuclear Eu(III) species as well as the few known dinuclear ones [23] when they are dissolved in solution. The Sm(III) complex, **2**, has four major emission peaks at 568, 607, 649, and 715 nm corresponding to transitions between its $^4G_{5/2} \rightarrow {}^6H_{5/2-11/2}$ levels (Fig. 5b) [35,36]. The NIR emissions from the Yb(III) ions $^2F_{5/2} \rightarrow {}^2F_{7/2}$ transitions [37] were not found, possibly due to inefficient energy transfer from ligand to metal. The emission peaks observed in **1** and **2** are similar to others observed from solutions of dissolved monomeric [35,37,38] and dimeric [36] complexes indicating that the bpm ligand has no significant effect on the luminescence. Furthermore, the labile nature in general of lanthanide coordination complexes precludes the conclusion that

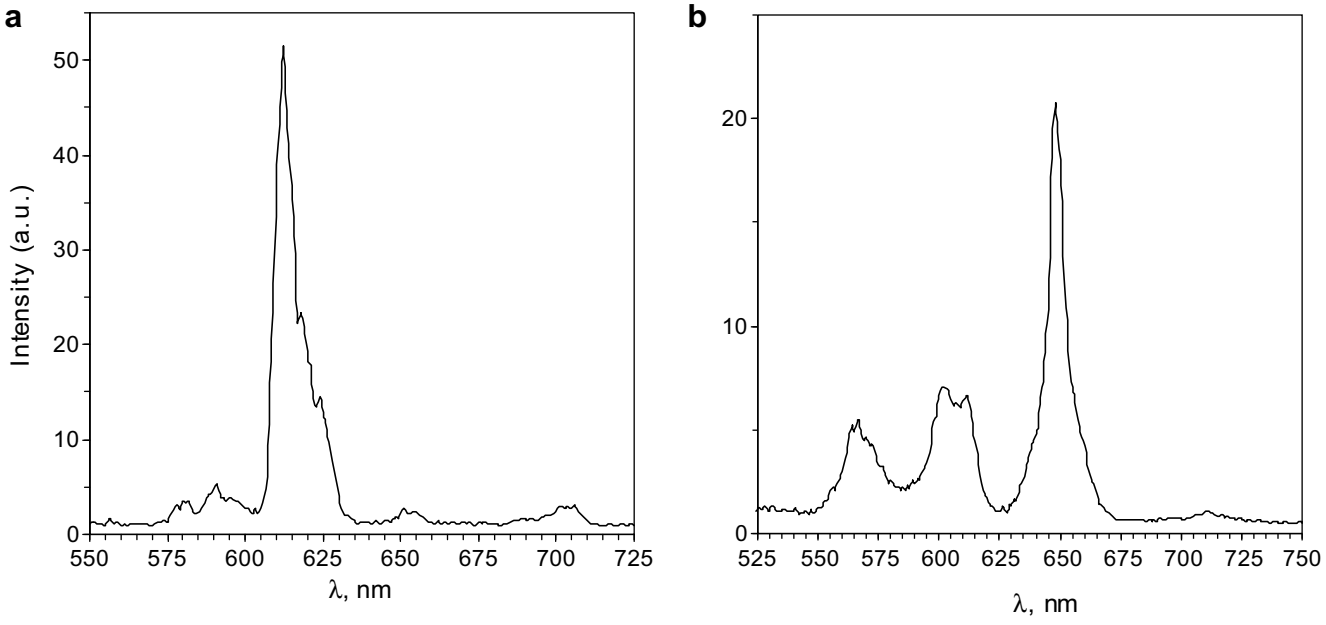


Fig. 5. The solution state luminescence spectra of *ca.* 20 μM solutions of (a) **1** and (b) **2** in $CHCl_3$.

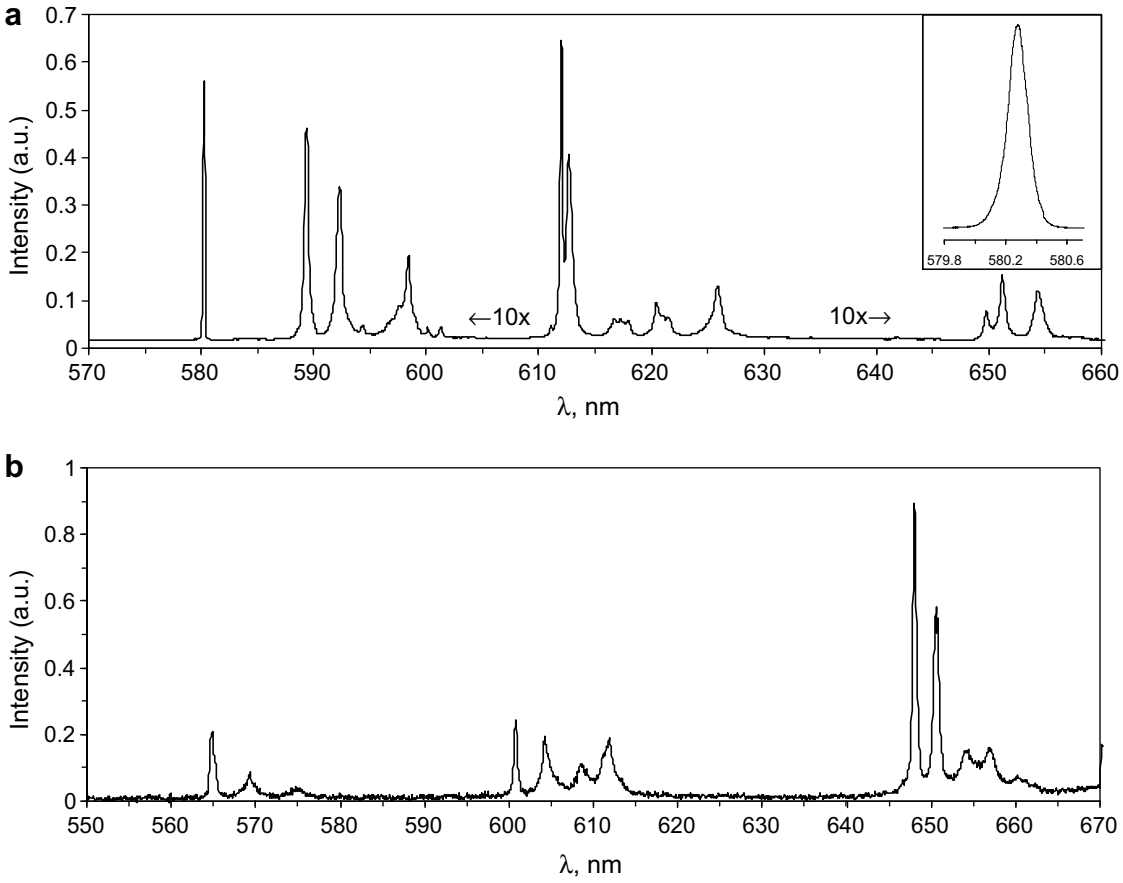


Fig. 6. The emission spectra for crystals of (a) **1** (inset view of the $^5D_0 \rightarrow {}^7F_0$ transition) and (b) **2** at 77 K.

dissolving dinuclear complexes in solution necessarily results in dinuclear solution species.

The solid state emission spectrum of crystals of **1** displays very sharp peaks for the $^5D_0$ to $^7F_{0-3}$ transitions (Fig. 6). The singly degenerate $^5D_0 \rightarrow {}^7F_0$ transition should have one peak for each Eu(III) center. The crystal structure indicates two different Eu centers, however the spectrum of the sample shows only one peak at 580.3 nm implying that both Eu(III) centers are located in similar ligand environments (Fig. 6, inset). Examination of the $^5D_0 \rightarrow {}^7F_0$ peak does reveal a small shoulder on the low energy side. The different Eu(III) environments must be similar enough to result in unresolved emission lines. The transitions from $^5D_0$ to the $^7F_{1\text{-}3}$ manifolds appear around 590, 615, and 650 nm, respectively. The clear splitting of these manifolds into their Stark components suggests low symmetry of the Eu(III) centers and is consistent with the structure. Crystals of the Sm(III) complex, **2**, gave similar results. Three major emission manifolds beginning near 565, 600, and 648 nm corresponding to transitions between its $^4G_{5/2} \rightarrow {}^6H_{5/2-11/2}$ levels (Fig. 5b). The NIR emissions from the Yb(III) ions were outside the range of our instrument.

3.4. Electrochemistry

The cyclic voltammograms of complexes **1**, **2**, and **3** in DMF solution are illustrated in Fig. 7. Three irreversible reduction waves are observed for each complex, with cathodic peak potentials *ca.* $E_{pc} = -1.24$, -1.5, and -2.0 V. To elucidate the origin of these peaks, we also studied cyclic voltammograms of solutions of 2,2′-bipyrimidine or deprotonated β-diketone with various molar equivalents Eu(III), Sm(III), and Yb(III) chloride (data not shown). It is interesting that complexes **1**, **2**, and **3** all yield very similar voltammograms. The peaks present in these data arise from the ligands, and no metal centered redox processes are apparent. The cathodic peaks at -1.24 and -1.5 V in complexes **1**, **2**, and **3** corresponds to bpm ligand reductions, which are shifted to more positive potentials relative to the free bpm (-1.64 V). Our studies

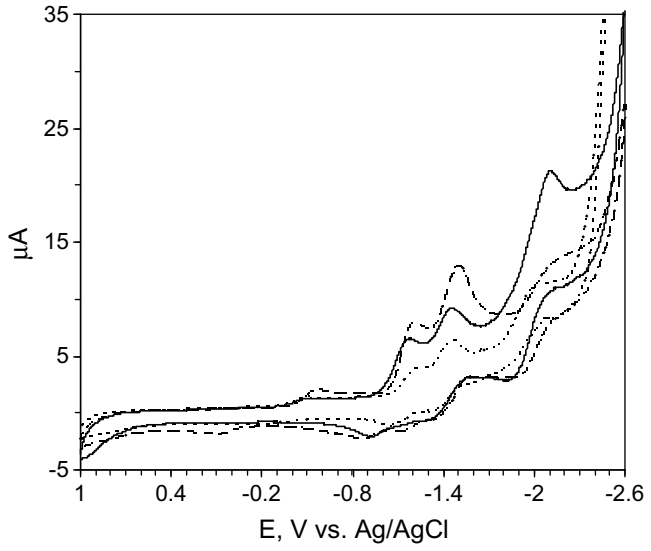


Fig. 7. Cyclic voltammograms for DMF solutions of 1 mM **1** (—), **2** (·····), and **3** (- - - -). All samples contain 0.02 M $TBAPF_6$ as electrolyte.

suggest that the peak at −1.24 V arises from the bpm ligand and not from the Eu(III) center [30]. All three of our complexes display this cathodic peak at ∼ −1.24 V and it is unlikely that all lanthanide centers are reduced here, given that the reported reduction potentials for ions of Eu(III) (−0.34 V versus NHE), Yb(III) (−1.05 V) and Sm(III) (−1.55 V) span more than a volt [3]. Furthermore, both of these peaks are present in the same ratio in solutions of bpm with 1–10 equiv. of added $LnCl_3$ and likely represent coordinated bpm reductions. The peak at −2.0 V in the complexes arises from the β-diketonate with a small contribution from the bpm ligand. Both bpm with $LnCl_3$ and the mixture of deprotonated tmhd with $LnCl_3$ were found to display peaks near −2.0 V.

4. Conclusions

We report the structures and spectroscopic properties of three new dinuclear lanthanide complexes using Sm(III), Eu(III), and Yb(III). The three β-diketonate complexes successfully assemble in the solid state as dimeric species through a bridging 2,2′-bipyrimidine ligand. The lanthanide ions are all 8-coordinate with square antiprismatic geometries, typical of such complexes. In addition, the fluorescence of the complexes in solution exhibits behavior similar to solutions of other known mononuclear and dinuclear complexes. The solid state fluorescence spectrum of the dinuclear Eu(III) complex indicates a single Eu(III) environment. Finally, cyclic voltammograms of the species in solution were dominated by cathodic peaks corresponding to ligand centered reductions and no peaks corresponding to the lanthanide ions were apparent. All the characterizations were consistent with independent lanthanide ions in the dimer and the bridging bpm ligand did not provide sufficient means for fostering M–M interactions.

Acknowledgments

The authors are grateful to the Research Corporation (Grant No. CC6396) for financially supporting this research and providing M.H.B with a summer stipend. M.H.B. and S.M.B. would like to thank the Swenson Family Foundation and UMD for a summer stipend and research support. J.D.D. thanks the UMD Department of Chemistry for the Moses Passer Fellowship. R.D.P. is indebted to NSF (CHE-0443345) and the College of William and Mary for the purchase of the X-ray diffraction equipment.

Appendix A. Supplementary data

CCDC 696334, 696335, and 696336 contain the crystallographic data for the reported complexes **1**, **2**, and **3**, respectively. These data can be obtained free of charge via http://www.ccdc.cam.ac.uk/conts/retrieving.html, or from the Cambridge Crystallographic Data Centre, 12 Union Road, Cambridge CB2 1EZ, UK; fax: (+44) 1223-336-033; or e-mail: deposit@ccdc.cam.ac.uk. Supplementary data associated with this article can be found, in the online version, at doi:10.1016/j.poly.2008.10.019.

References

[1] G.F. de Sá, O.L. Malta, C. de Mello Donegá, A.M. Simas, R.L. Longo, P.A. Santa-Cruz, E.F. da Silva Jr., Coord. Chem. Rev. 196 (2000) 165.
[2] N. Kaltsoyannis, P. Scott, The f Elements, 1999.
[3] S. Cotton, Lanthanides and Actinides, Oxford University Press, New York, 1991.
[4] W. Suski, Phys. Solid State 41 (1999) 733.
[5] R.C. Howell, K.V.N. Spence, I.A. Kahwa, D.J. Williams, J. Chem. Soc., Dalton Trans. (1998) 2727.
[6] A. Panagiotopoulos, T.F. Zafiropoulos, S.P. Perlepes, E. Bakalbassis, I. Masson-Ramade, O. Kahn, A. Terzis, C.P. Raptopoulou, Inorg. Chem. 34 (1995) 4918.
[7] M.B. Maple, J. Alloys Compd. 303–304 (2000) 1.
[8] D.S. Kumar, V.A.J. Aruna, V. Alexander, Polyhedron 18 (1999) 3123.
[9] L.C. Thompson, Handb. Phys. Chem. Rare Earths 3 (1979) 209.
[10] A. Inagaki, S. Yatsuda, S. Edure, A. Suzuki, T. Takahashi, M. Akita, Inorg. Chem. 46 (2007) 2432.
[11] J.-M. Herrera, S.J.A. Pope, H. Adams, S. Faulkner, M.D. Ward, Inorg. Chem. 45 (2006) 3895.
[12] S. Swavey, Z. Fang, K.J. Brewer, Inorg. Chem. 41 (2002) 2598.
[13] R.A. Pavinato, J.A. Walk, M.E. McGuire, Inorg. Chem. 32 (1993) 4982.
[14] D.B. MacQueen, J.D. Petersen, Inorg. Chem. 29 (1990) 2313.
[15] R. Sahai, D.P. Rillema, R. Shaver, S. Van Wallendael, D.C. Jackman, M. Boldaji, Inorg. Chem. 28 (1989) 1022.
[16] E.V. Dose, L.J. Wilson, Inorg. Chem. 17 (1978) 2660.
[17] N.M. Shavaleev, G. Accorsi, D. Virgili, Z.R. Bell, T. Lazarides, G. Calogero, N. Armaroli, M.D. Ward, Inorg. Chem. 44 (2005) 61.
[18] N.M. Shavaleev, Z.R. Bell, M.D. Ward, J. Chem. Soc., Dalton Trans. (2002) 3925.
[19] T. Lazarides, H. Adams, D. Sykes, S. Faulkner, G. Calogero, M.D. Ward, J. Chem. Soc., Dalton Trans. (2008) 691.
[20] J.A. Fernandes, R.A. Sa Ferreira, M. Pillinger, L.D. Carlos, J. Jepsen, A. Hazell, P. Ribeiro-Claro, I.S. Goncalves, J. Lumin. 113 (2005) 50.
[21] H. Jang, C.-H. Shin, B.-J. Jung, D.-h. Kim, H.-K. Shim, Y. Do, Eur. J. Inorg. Chem. (2006) 718.
[22] K. Kirschbaum, A. Fratini, S. Swavey, Acta Crystallogr., Sect. C: Cryst. Struct. Commun. C62 (2006) m186.
[23] S. Swavey, J.A. Krause, D. Collins, D. D'Cunha, A. Fratini, Polyhedron 27 (2008) 1061.
[24] D. D'Cunha, D. Collins, G. Richards, G.S. Vincent, S. Swavey, Inorg. Chem. Commun. 9 (2006) 979.
[25] Smart Apex ii, Data Collection Software, Version 2.1; Bruker AXS Inc.: Madison, WI, 2005.
[26] Saint Plus, Data Reduction Software, Version 7.34a; Bruker AXS Inc.: Madison, WI, 2005.
[27] G.M. Sheldrick, SADABS, University of Göttingen, Göttingen, Germany, 2005.
[28] G.M. Sheldrick, Acta Crystallogr., Sect. A A64 (2008) 112.
[29] L.J. Farrugia, J. Appl. Crystallogr. 30 (1997) 565.
[30] R. Sultan, K. Gadamsetti, S. Swavey, Inorg. Chim. Acta 359 (2006) 1233.
[31] Q. Jaradat, T. Akasheh, Polyhedron 6 (1987) 175.
[32] A. Fratini, G. Richards, E. Larder, S. Swavey, Inorg. Chem. 47 (2008) 1030.
[33] A. Fratini, S. Swavey, Inorg. Chem. Commun. 10 (2007) 636.
[34] M.A. Porai-Koshits, L.A. Aslanov, Zhur. Strukt. Khim. 13 (1972) 266.
[35] E. Bakier, M.S.A. Abdel-Mottaleb, Int. J. Photoen. 7 (2005) 51.
[36] F.R. Gonçalves e Silva, O.L. Malta, C. Reinhard, H.-U. Güdel, C. Piguet, J.E. Moser, J.-C.G. Bünzli, J. Phys. Chem. A 106 (2002) 1670.
[37] A. Beeby, R.S. Dickins, S. Faulkner, D. Parker, J.A.G. Williams, Chem. Commun. (1997) 1401.
[38] G.E. Khalil, K. Lau, G.D. Phelan, B. Carlson, M. Gouterman, J.B. Callis, L.R. Dalton, Rev. Sci. Instrum. 75 (2004) 192.

Polyhedron 28 (2009) 195–199

Contents lists available at ScienceDirect

Polyhedron

journal homepage: www.elsevier.com/locate/poly

Synthesis, spectroscopic and crystal structure investigation of $[Cu(bzsmp)_2Cl_2]$; {bzsmp = 2-benzylsulfanyl-5-(2-methoxyphenyl)-1,3,4-oxadiazole}: cyclization of N^2-[bis(benzylsulfanyl)methylene]-2-methoxybenzohydrazide to 2-benzylsulfanyl-5-(2-methoxyphenyl)-1,3,4 -oxadiazole during complexation

M. Singh [a], V. Aggarwal [b], U.P. Singh [b], N.K. Singh [a,*]

[a] Department of Chemistry, Banaras Hindu University, Varanasi 221 005, Uttar Pradesh, India
[b] Department of Chemistry, Indian Institute of Technology, Roorkee 247 667, Uttarakhand, India

ARTICLE INFO

Article history:
Received 30 July 2008
Accepted 16 October 2008
Available online 25 November 2008

Keywords:
Cu(II) complex
X-ray
1,3,4-Oxadiazole
C–H···π interactions
Cyclization

ABSTRACT

The ligand N^2-[bis(benzylsulfanyl)methylene]-2-methoxybenzohydrazide (N^2-bmbh) (**1**) on reaction with $CuCl_2.2H_2O$ yielded the mononuclear complex $[Cu(bzsmp)_2Cl_2]$ (**2**) (2-benzylsulfanyl-5-(2-methoxyphenyl)-1,3,4-oxadiazole, bzsmp). Complex **2** has been characterized by analytical, spectroscopic and X-ray data. X-ray study of **2** reveals that the cyclized ligand 2-benzylsulfanyl-5-(2-methoxyphenyl)-1,3,4-oxadiazole (bzsmp) acts as neutral bidentate ligand to form six membered chelate ring and the presence of C–H···π (face to edge) and C–H···S and two type of C–H···Cl weak interactions.

© 2008 Elsevier Ltd. All rights reserved.

1. Introduction

The 1,3,4-oxadiazoles have found applications in several areas [1,2] such as anti tuberculostatic, anti-inflammatory, analgesic, antipyretic, anticonvulsant and medicine [3–6]. The syntheses of this type of heterocyclic compounds have attracted considerable attention and a number of methods have been used for their syntheses [7–9]. The widely used strategy involves the dehydrative cyclization of diacylhydrazides usually with strong acids [10–13]. The cyclization of potassium salt of 3-benzoyldithiocarbazate into the corresponding 5-phenyl-1,3,4-oxadiazole-2-thiol was first reported by Hoggarth [14]. The cyclization of 3-acyldithiocarbazates esters, N-aroyldithiocarbazates and their salts to 1,3,4-oxadiazoles in the presence of a base is also reported in the literature [15–18]. Several other methods are reported for the synthesis of oxadiazoles from acyclic precursor which includes oxidative cyclization of acylhydrazones [19], acylthiourea [20–22] and acylthiosemicarbazides [23–26]. Platinum assisted cyclization of S-methyl 3-acyl-2-methyldithiocarbazates under mild conditions was reported by Bergamini and co-workers [27]. Earlier we have reported the metal assisted cyclization of N-benzoyldithiocarbazate to 5-phenyl-1,3,4-oxadiazole-2-thiol and potassium[N′-(pyridine-3-carbonyl) hydrazine to 5-(3-pyridyl)-1,3,4-oxadiazole-2-thione in the presence of an excess ethylenediamine (en) [28,29]. A few papers are available on the syntheses and X-ray studies of [bis(benzylsulfanyl)methylene]-2-acidhydrazide [30,31] and (benzylsulfanyl)-1,3,4-oxadiazole [32,33], but for the first time we report here the metal complex of 2-benzylsulfanyl-5-(2-methoxyphenyl)-1,3,4-oxadiazole obtained from the cyclization of N^2-[bis(benzylsulfanyl)methylene]benzohydrazide (N^2-Hbmbh) during complexation. The cyclization of N^2-Hbmbh to 2-benzylsulfanyl-5-(2-methoxyphenyl)-1,3,4-oxadiazole has been performed under normal condition without the use of any other reagents viz. base or acid as already described in the case of other oxadiazoles. The spectroscopic and single crystal X-ray studies of the resulting Cu(II) complex obtained by the reaction of Cu(II)chloride and N^2-[bis(benzylsulfanyl)methylene]-2-methoxy-benzohydrazide [N^2-Hbmbh] is reported in the present paper.

2. Experimental

2.1. Materials and methods

Commercial reagents were used without further purification and all experiments were carried out in open atmosphere. Methyl 2-methoxy benzoate (Sigma Aldrich, USA) and hydrazine hydrate (S.D. Fine Chemicals, India) were used as such. All solvents were purchased from Merck Chemicals, India and used after purification.

* Corresponding author. Tel.: +91 542 2318529; fax: +91 542 2368127.
E-mail addresses: nksingh@bhu.ac.in, singhnk_bhu@yahoo.com (N.K. Singh).

0277-5387/$ - see front matter © 2008 Elsevier Ltd. All rights reserved.
doi:10.1016/j.poly.2008.10.016

2.2. Preparation of the ligand N^2-Hbmbh (**1**)

The ligand N^2-Hbmbh was synthesized as described previously [30].

2.3. Preparation of the complex $[Cu(bzsmp)_2Cl_2]$ (**2**)

A solution of N^2-Hbmbh (**1**) (2 mmol) in MeOH (15 ml) was added to a solution of $CuCl_2 \cdot 2H_2O$ (1 mmol) in 10 ml of MeOH and the mixture was stirred for 2 h at room temperature. The resulting green color solution was filtered off and kept for crystallization. Green Crystals of **2** suitable for X-ray analyses were obtained by slow evaporation of its methanolic solution over a period of 21 days. Yield 64%; m.p. 145 °C. *Anal.* Calc. for $C_{32}H_{28}N_4CuO_4S_2Cl_2$ (731.17): C, 52.57; H, 3.86; N, 7.66. Found: C, 52.42; H, 4.12; N, 7.60%. I.R. data (ν cm^{-1} KBr) ν(C=N) 1603 s; ν(C–O–C) 1254 w; ν(N–N) 1133 s; ν(C–S) 869 m; $\nu(CH_2)$ 2979; ν(Cu–N) 478, ν(Cu–O) 420, ν(Cu–Cl) 325.

2.4. Physical measurements

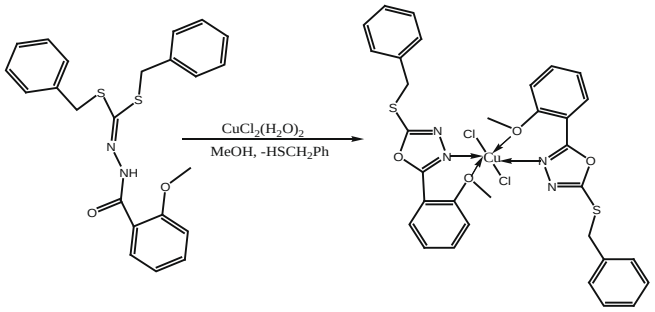
Carbon, hydrogen and nitrogen contents were estimated on a CHN Analyser Model CE-440. Magnetic susceptibility measurement was performed at room temperature on a Cahn Faraday balance using $Hg[Co(NCS)_4]$ as the calibrant and electronic spectra were recorded on UV-1700 Pharmaspec spectrophotometer. IR spectra were recorded in the 4000–400 cm^{-1} region as KBr pellets on a Varian Excalibur 3100 FT-IR spectrophotometer.

3. Crystal structure determination

The X-ray data collection and processing for **2** were performed on Bruker Kappa Apex-CCD diffractometer by using graphite monochromated Mo Kα radiation (λ = 0.71070 Å) at 273(2) K. Crystal structure was solved by direct methods. Structure solution, refinement and data output were carried out with the SHELXTL program [34,35]. All non-hydrogen atoms were refined anisotropically. Hydrogen atoms were placed in geometrically calculated positions by using a riding model. Images were created with the DIAMOND program [36]. Hydrogen bonding interactions in the crystal lattice were calculated with both SHELXTL and MERCURY [37].

4. Results and discussion

The $[Cu(bzsmp)_2Cl_2]$ [bzsmp = 2-benzylsulfanyl-5-(2-methoxyphenyl)-1,3,4-oxadiazole] was obtained by stirring the methanolic solution of N^2-Hbmbh (**1**) and $CuCl_2 \cdot 2H_2O$ in a 2:1 molar ratio at room temperature. A ring closure reaction takes place due to cleavage of C–S bond followed by elimination of $PhCH_2SH$ during complexation resulting in the formation of complex **2** (Scheme 1). The green solution obtained after the reaction was filtered off and on



Scheme 1. Preparation of complex $[Cu(bzsmp)_2Cl_2]$.

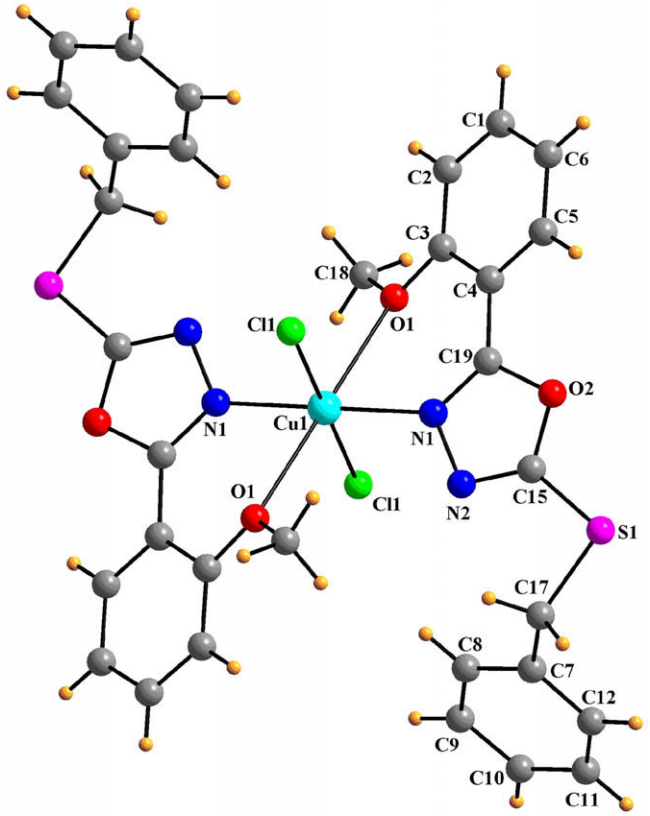


Fig. 1. Molecular structure of $[Cu(bzsmp)_2Cl_2]$ with atomic numbering scheme. Color code: C, grey; H, orange; N, blue; O, red; S, purple; Cl, green; Cu, cyan. (For interpretation of the references to color in this figure legend, the reader is referred to the web version of this article.)

Table 1
Crystal refinement parameters of $[Cu(bzsmp)_2Cl_2]$ (**2**).

Parameters	$[Cu(bzsmp)_2Cl_2]$
Color	Green
Crystal size (mm)	0.24 × 0.21 × 0.18
Empirical formula	$C_{32}H_{30}N_4CuO_4S_2Cl_2$
Formula weight	733.19
Space group	$P21/n$
Crystal system	monoclinic
T (K)	273(2)
λ (Mo Kα)	0.71073
a (Å)	13.0027(17)
b (Å)	8.2990(12)
c (Å)	15.634(2)
α (°)	90
β (°)	93.496(9)
γ (°)	90
V (Å^3)	1683.9(4)
Z	16
ρ_{calc} (Mg/m^3)	1.442
M (mm^{-1})	0.973
$F(000)$	1344
θ Range for data collection	1.98–40.01
Index ranges	$-22 \leqslant h \leqslant 23$, $-13 \leqslant k \leqslant 15$, $-24 \leqslant l \leqslant 28$
Reflections collected	38 153
Independent reflections	10 340
Data/restraints/parameters	10 340/0/206
Goodness-of-fit on F^2	0.817
R_1, wR_2	0.0353, 0.1017
R_1, wR_2, (all data)	0.0736, 0.1367
Largest difference in peak and hole (e Å^{-3})	0.533 and −0.714

slow evaporation of the solvent the resulting complex **2** crystallized. Crystals of complex **2** were obtained after three weeks in 64% yield. Complex **2** has been structurally characterized by single crystal X-ray. The molecular structure of **2** is shown in Fig. 1. The physical and analytical data of compound **2** supports the X-ray structure.

4.1. IR spectra

A comparative study of the IR spectral data of the complex with ligand **1** gives meaningful information regarding bonding sites and its cyclization during complexation. The IR spectrum of **1** shows bands at 3252, 2969, 1658, 1071, 1598 and 877 which correspond to ν(NH), δ(CH_2), ν(CO), ν(N–N), ν(C=N) and ν(C–S), respectively [30]. The bands due to ν(NH) and ν(CO) are absent in **2** and a new band appears at 1254 cm^{-1} due to ν(C–O–C) which suggests cyclization [28,29] of acyclic {–C(O)–NH–N=C=} moiety by elimination of $HSCH_2C_6H_4$ during complexation with Cu(II). Thus I.R. data of **2** supports cyclization of **1** and formation of 1,3,4-oxadiazole moiety in the complex. A positive shift of 62 cm^{-1} in ν(N–N) as compared to the ligand suggests the involvement of this group as a bonding site.

Table 2
Selected bond lengths for the complex [Cu(bzsmp)$_2$Cl$_2$] (Å) and angles (°).

Copper coordination sphere			
Bond length			
Cu(1)–N(1)	1.9999(10)	Cu(1)–O(1)	2.5080(4)
Cu(1)–Cl(1)	2.2830(4)	C(4)–C(19)	1.4532(18)
O(1)–C(3)	1.3612(16)	N(1)–C(19)	1.3013(15)
C(3)–C(4)	1.4018(18)		
Angles			
O(1)–C(3)–C(4)	116.41(12)	C(19)–N(1)–Cu(1)	132.65(8)
N(1)–C(19)–C(4)	131.88(10)	C(3)–C(4)–C(19)	121.30(11)
C(3)–O(1)–Cu(1)	124.18(12)		
Oxadiazole ring			
Bond lengths			
O(1)–C(18)	1.4280(17)	O(2)–C(15)	1.3607(17)
N(1)–N(2)	1.3986(14)	O(2)–C(19)	1.3631(14)
N(1)–C(19)	1.3013(15)	N(2)–C(15)	1.2929(15)
S(1)–C(15)	1.7268(12)	S(1)–C(17)	1.8285(17)
Angles			
N(2)–C(15)–S(1)	129.42(11)	C(7)–C(17)–S(1)	114.95(11)
C(15)–S(1)–C(17)	99.99(7)	O(2)–C(15)–S(1)	117.10(9)
N(1)–Cu(1)–N(1)#1	180.00(6)	N(1)–Cu(1)–Cl(1)#1	89.31(3)
Cl(1)–Cu(1)–Cl(1)#1	180.00(12)	N(1)#1–Cu(1)–Cl(1)#1	90.69(3)
		N(1)#1–Cu(1)–Cl(1)	89.31(3)

Symmetry transformations used to generate equivalent atoms: #1 $-x+2$, $-y+1$, $-z+1$.

Table 3
Hydrogen bonds for Cu(bzsmp)$_2$Cl$_2$ (Å and °).

D–H···A	d(D–H)	d(H···A)	d(D···A)	∠(DHA)
C(6)–H(6)···S(1)	0.93	2.970(3)	3.766(3)	144.57
C(17)–H(17A)···Cl(1)	0.97	2.900(12)	3.710(12)	141.70

4.2. UV spectra

The electronic spectrum of the ligand N^2-Hbmbh shows bands at 337, 252 and 213 nm assigned to the $n\rightarrow\pi^*$ and $\pi\rightarrow\pi^*$ transitions. The magnetic moment of 1.82 B.M. for **2** is normal as expected for the presence of one unpaired electron. The complex [Cu(bzsmp)$_2$Cl$_2$] displays electronic bands at 557, 316, 297, 257 nm. A Cu(II) complex with d^9 configuration is expected to experience Jahn–Teller distortion which leads to further splitting of the ^{2}Eg and $^2T_{2g}$ levels and give rise to the $^2B_{1g}\rightarrow{}^2A_{1g}$ (ν_1), $^2B_{2g}$(ν_2), ^2E_g (ν_3) transitions which is expected to be close in energy and generally appear as a broad band. Therefore the broad band at 557 nm is assigned to the envelope of $^2B_{1g}\rightarrow{}^2A_{1g}$, $^2B_{2g}$ and ^2E_g transitions [38]. The strong absorptions found for complex **2** in the range 316–257 nm is due to the ligand to copper(II) charge transfer and intraligand transitions.

4.3. Crystal structure of complex *2*

The crystal structure refinement data related to complex **2** are given in Table 1 and the main bond distances and bond angles of **2** are given in the Table 2. The hydrogen bonds are listed in Table 3. In the centrosymmetric mononuclear [Cu(bzsmp)$_2$Cl$_2$], each Cu(II) ion is located at the inversion center. The six membered [CuO1C3C4C19N1] chelate ring is not coplanar (rms deviation from mean plane = 0.207 Å) but the two six membered chelate rings are parallel to each other separating a distance of 0.532 Å. Two ligands coordinate to Cu(II) center in meridonial fashion i.e. the carbonyl oxygen and hydrazinic nitrogen are cis to each. The bite angle for both C_3NCuO chelate rings is 75.28°. Cu(II) is bonded octahedrally with two methoxy oxygens, two oxadiazole nitrogens and two chlorine atoms with Cu–N, Cu–O and Cu–Cl distances of 1.9999(10) Å, 2.5080(4) Å, 2.2830(4) Å}, respectively (Fig. 1). Thus the ligand behaves as a neutral bidentate chelating ligand (Scheme 1). The Cu–N bond length in complex **2** agrees well with those

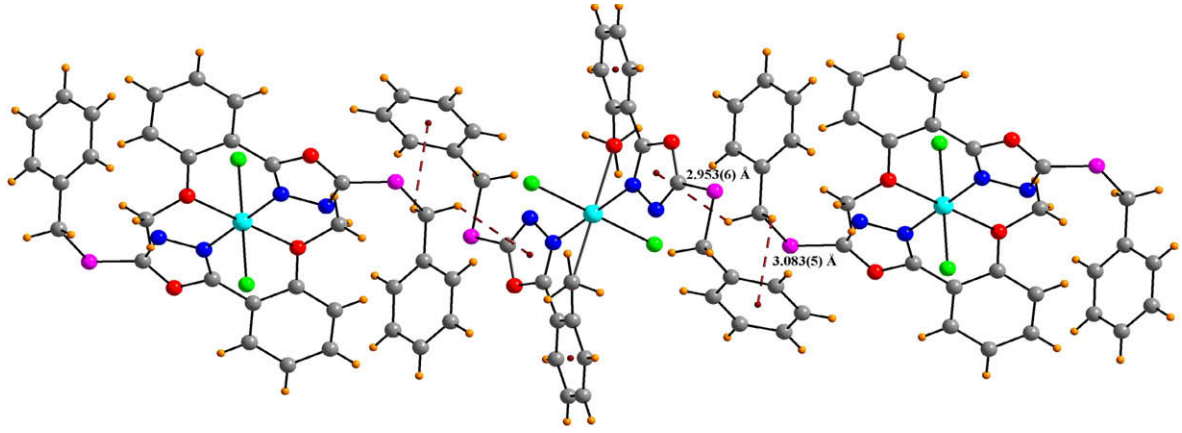


Fig. 2. One dimensional chain formed by C–H···π interaction (brown dotted) in the complex. Color code: C, grey; H, orange; N, blue; O, red; S, purple; Cl, green; Cu, cyan. (For interpretation of the references to color in this figure legend, the reader is referred to the web version of this article.)

found for compounds e.g. [Cu(2-PBZM)MoO_4] {2-PBZM = 2-(2-pyridyl)benzimidazole) [39] and [Cu_2(EGTA)$(Him)_2]_n$, [Cu_2(EGTA)$(Him)_4] \cdot 4H_2O$ {Him = imidazole, EGTA = ethylenebis(oxyethylnitrilo)tetraaceticacid)}. The Cu–O bond length is comparably shorter than the sum of van der Waal's radii of oxygen and copper atoms (1.50 + 1.40 = 2.90 Å), indicating comparatively strong Cu–O bonding [40]. The 2-methoxybenzene and oxadiazole rings make a dihedral angle of 23.57°. Similarly, the dihedral angle between benzyl and oxadiazole rings is 57.46°. The plane containing the oxadiazole ring equally divides the 2-methoxy benzene ring in equal halves.

The crystal packing of **2** reveals the existence of C–H···π, C–H···S and C–H···Cl intermolecular interactions. There are two C–H···π interactions, one occurring between a hydrogen atom of the methylene group and the π-electrons of the oxadiazole ring and the second one between other hydrogen of the same methylene group and the π-electrons of benzyl group from the adjacent molecule with a distance of 2.953(6) and 3.083(5) Å, respectively. These two C–H···π interactions provide one dimensional chain (Fig. 2). Additionally, two molecules of the complex are also linked by C–H···S interaction (2.970(3) Å) formed between C–H of 2-methoxy phenyl

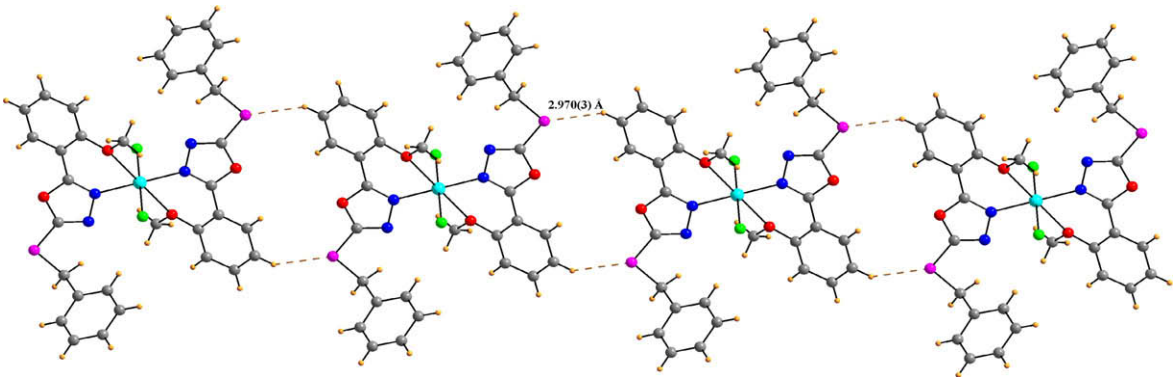


Fig. 3. One dimensional chain formed by C–H···S interaction (orange dotted) in complex. Color code: C, grey; H, orange; N, blue; O, red; S, purple; Cl, green; Cu, cyan. (For interpretation of the references to color in this figure legend, the reader is referred to the web version of this article.)

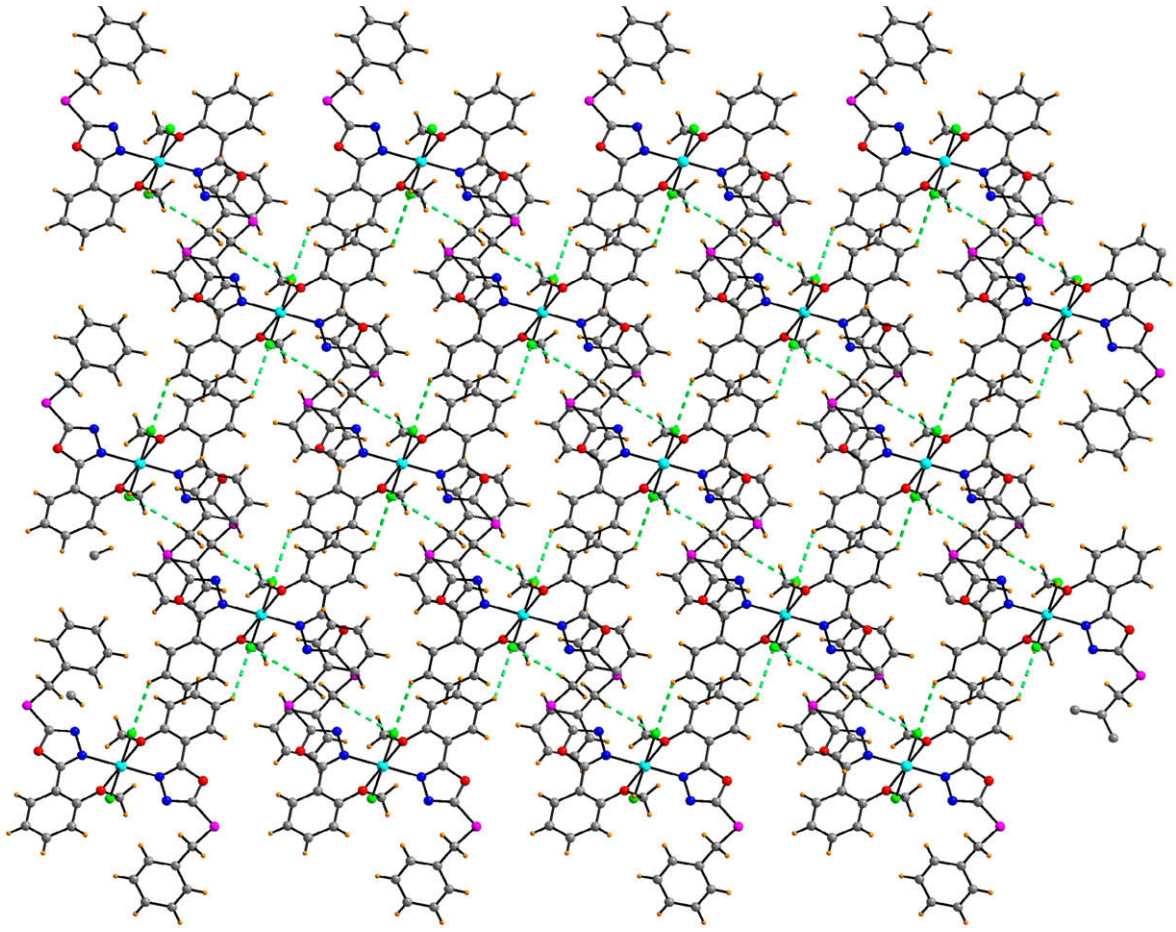


Fig. 4. Three-dimensional packing of complex [$Cu(bzsmp)_2Cl_2$] showing C–H···Cl interactions (green dotted). Color code: C, grey; H, orange; N, blue; O, red; S, purple; Cl, green; Cu, cyan. (For interpretation of the references to color in this figure legend, the reader is referred to the web version of this article.)

ring and sulfur atom which extend in one dimensional chain (Fig. 3). The three dimensional packing in the complex is also stabilized by two types of C–H···Cl interactions (one between hydrogen atom of methoxy phenyl ring and chlorine atom and other between hydrogen atom of benzyl ring and chlorine atom) with a distances of 2.951(6) and 2.900(12) Å, respectively (Fig. 4).

5. Conclusion

We have reported that acyldithocarbazates derivatives undergo cyclization during complex formation in the presence of en [13]. The present work indicates that the presence of Cu(II) is required for the cleavage of C–S bond leading to the elimination of $C_6H_5CH_2SH$ and cyclization of the cleaved product. As a conclusion of this work we describe a very facile route to obtain 2-benzylsulfanyl-1,3,4-oxadiazole as a stable Cu(II) complex.

Acknowledgment

Financial support [01(2152)07/EMR-II] from Council of Scientific and Industrial Research (CSIR), New Delhi, India is gratefully acknowledged. One of the authors (M. Singh) is thankful to CSIR, New Delhi, India for the award of SRE, supported by Grant No. 9/13(160) 2008/EMR-I and [01 (2152) 07/EMR-II].

Appendix A. Supplementary data

CCDC 685385 contains the supplementary crystallographic data for **1**. These data can be obtained free of charge via http://www.ccdc.cam.ac.uk/conts/retrieving.html, or from the Cambridge Crystallographic Data Centre, 12 Union Road, Cambridge CB2 1EZ, UK; fax: (+44) 1223-336-033; or e-mail: deposit@ccdc.cam.ac.uk. Supplementary data associated with this article can be found, in the online version, at doi:10.1016/j.poly.2008.10.016.

References

[1] C. Chen, C.H. Senanayake, T.J. Bill, R.D. Larsen, T.R. Verhoeven, P.J. Reider, J. Org. Chem. 59 (1994) 3738.
[2] J. Saunders, M. Cassidy, S.B. Freedmen, E.A. Harley, L.L. Iversen, C. Kneen, A.M. MacLeod, K.J. Merchant, R.J. Snow, R.J. Baker, Med. Chem. 33 (1990) 1128.
[3] Y.D. Kulkarni, A. Rowhani, J. Indian Chem. Soc. 66 (1989) 492.
[4] K. Obi, A. Kojima, H. Fukunda, K. Hirai, Bioorg. Med. Chem. Lett. 5 (1995) 2777.
[5] A. Hetzheim, K. Möckel, Adv. Heterocycl. Chem. 7 (1966) 183.
[6] B.L. Sharma, S.K. Tandon, Pharmazie 39 (H-12) (1984) 858.
[7] B. Rigo, D. Fassuer, P. Cauliez, D. Couturier, Synth. Commun. 19 (1989) 2321.
[8] S.P. Singh, R. Naithani, H. Batra, O. Prakash, D. Sharma, Indian J. Heterocycl. Chem. 8 (1998) 103.
[9] Y.-H. Yang, M. Shi, Tetrahedron Lett. 46 (2005) 6285.
[10] A.-S.S. Hamad, H.I. Hashem, J. Heterocycl. Chem. 39 (2002) 1325.
[11] V.N. Kerr, D.G. Ott, F.N. Hayes, J. Am. Chem. Soc. 82 (1960) 186.
[12] S. Borg, R.C. Vollinga, M. Labarre, K. Payza, L. Terenius, K. Luthman, J. Med. Chem. 42 (1999) 4331.
[13] C.K. Reddy, P.S.N. Reddy, C.V. Ratnam, Synthesis (1983) 842.
[14] E. Hoggarth, J. Chem. Soc. (1952) 4811.
[15] R.W. Young, K.H. Wood, J. Am. Chem. Soc. 77 (1955) 400.
[16] J.R. Reid, N.D. Heindel, J. Heterocycl. Chem. 13 (1976) 925.
[17] H. Foks, J. Mieczkowska, M. Janowiec, Z. Zwolska, Z. Andrzejczyk, Chem. Heterocycl. Comp. 38 (2002) 810.
[18] C. Ainsworth, J. Am. Chem. Soc. 78 (1956) 4475.
[19] E. Jedlovska, J. Lesko, Synth. Commun. 24 (1994) 1879.
[20] S.P. Hiremath, V.N. Sonar, K.R. Sekhar, M.G. Purohit, Indian J. Chem. 28B (1989) 626.
[21] D.-J. Che, G. Li, Z. Yu, D.-P. Zou, C.-X. Du, Inorg. Chem. Commun. 3 (2000) 537.
[22] A. Tadjarodi, F. Adhami, Y. Hanifehpour, M. Yazdi, Z. Moghaddamfard, G. Kickelbick, Polyhedron 26 (2007) 4609.
[23] F.A. Omar, N.M. Mahfouz, M.A. Rahman, Eur. J. Med. Chem. 31 (1996) 819.
[24] B.S. Vashi, D.S. Mehta, V.H. Shah, Indian J. Chem. B 35 (1996) 111.
[25] V.I. Kelarev, R.A. Karakhanov, S.S. Gasanov, G.V. Morozova, K.P. Kuatbekova, Russ. J. Org. Chem. 29 (1993) 323.
[26] K. Raman, H.K. Singh, S.K. Salzman, S.S. Parmar, J. Pharm. Sci. 82 (1993) 167.
[27] G. Annibale, P. Bergamini, V. Bertolasi, M. Cattabriga, A. Lazzaro, A. Marchi, G. Vertuani, J. Chem. Soc., Dalton Trans. (1999) 3877.
[28] P. Tripathi, A. Pal, V. Jancik, A.K. Pandey, J. Singh, N.K. Singh, Polyhedron 26 (2007) 2597.
[29] N.K. Singh, M. Singh, R.J. Butcher, Polyhedron 27 (2008) 3151.
[30] N.K. Singh, M. Singh, R.J. Butcher, Acta Crystallogr., Sect. E 63 (2007) 4405.
[31] R.J. Butcher, J.P. Jasinski, S.K. Kushwaha, M.K. Bharty, N.K. Singh, Acta Crystallogr., Sect. E 63 (2007) 4590.
[32] N.K. Singh, R.J. Butcher, M.K. Bharty, A.K. Shrivastava, P. Tripathi, Acta Crystallogr., Sect. E 62 (2006) 3473.
[33] M. Zareef, R. Iqbal, J.H. Zaidi, M. Arfan, M. Parvez, Acta Crystallogr., Sect. E 62 (2006) 2449.
[34] G.M. Sheldrick, Acta Crystallogr., Sect. A 46 (1990) 467.
[35] G.M. Sheldrick, SHELXTL-NT 2000 Version 6.12, Reference Manual, University of Göttingen, Germany.
[36] B. Klaus, DIAMOND, Version 1.2c, University of Bonn, Germany, 1999.
[37] I.J. Bruno, J.C. Cole, P.R. Edgington, M. Kessler, C.F. Macrae, P. McCabe, J. Pearson, R. Taylor, Acta Crystallogr., Sect. B 58 (2002) 389.
[38] A.B.P. Lever, Inorganic Electronic Spectroscopy, 2nd ed., Elsevier, Amsterdam, 1984.
[39] L.-J. Chen, X. He, Q.-Z. Zhang, X.-Y. Wu, C.-z. Lu, Inorg. Chem. Commun. 9 (2006) 740.
[40] C.A. Payer, E.B. Altamirano, D.C. Lazarte, A. Castiñeiras, J.M. Gonzàlez-Pérez a, J.N. Gutiérrez, Inorg. Chem. Commun. 9 (2006) 903.

Polyhedron 28 (2009) 200–204

Contents lists available at ScienceDirect

Polyhedron

journal homepage: www.elsevier.com/locate/poly

X-ray diffraction study of bisphosphonate metal complexes: Mg, Sr and Ba complexes of (dichloromethylene)bisphosphonic acid *P*,*P*′-dibenzoyl anhydride

Susan Kunnas-Hiltunen [a,*], Mervi Matilainen [a], Jouko J. Vepsäläinen [b], Markku Ahlgrén [a]

[a] Department of Chemistry, University of Joensuu, Yliopistokatu 7, P.O. Box 111, FI-80101 Joensuu, Finland
[b] Department of Chemistry, University of Kuopio, P.O. Box 1627, FI-70211 Kuopio, Finland

ARTICLE INFO

Article history:
Received 18 September 2008
Accepted 16 October 2008
Available online 27 November 2008

Keywords:
Bisphosphonate
Clodronate
Clodronic acid dianhydrides
Crystal structures

ABSTRACT

The first alkaline earth metal complexes of a dibenzoyl derivative of clodronic acid were prepared and characterised by X-ray crystallography, elemental analysis and infrared spectroscopy. The complexes were $[Mg\{[Cl_2C(PO_2O(C(O)C_6H_5))_2](H_2O)_5\}\cdot H_2O]$ (**1**), $[Sr_2\{[Cl_2C(PO_2O(C(O)C_6H_5))_2]_2(H_2O)_9\}\cdot H_2O]_n$ (**2**) and $[Ba\{Cl_2C(PO_2O(C(O)C_6H_5))_2\}(H_2O)_2]_n$ (**3**). The monomeric units of **1** and the polymeric chains of **2** and **3** form 2D layer-like structures through intermolecular hydrogen bonds. The $Cl_2C(PO_2O(C(O)C_6H_5))_2^{2-}$ ligand acts as a bridging and chelating ligand, forming six- and eight-membered chelate rings with metal atoms. In addition, the previously determined polymeric calcium complex of clodronate, $[Ca_2\{Cl_2C(PO_3)_2\}(H_2O)_6\cdot 4.5H_2O]_n$ (**4**), was synthesised by hydrolysis method from the dibenzoyl derivative of clodronic acid.

© 2008 Elsevier Ltd. All rights reserved.

1. Introduction

The research on metal phosphonates has resulted in many interesting structures and applications in the field of solid state chemistry. Applications have been found in sorption, catalysis and ion exchange [1–4]. The investigation of metal bisphosphonates is an interesting extension of this work. In general, metal bisphosphonates adopt two-dimensional (2D) layered [5–14] or three-dimensional (3D) pillared layered structures [8,12–23], though one-dimensional (1D) chain structures [9–14,24–26] are also reported. In addition, bisphosphonates and other polyfunctional phosphonates enable the formation of 3D crystalline structures with open frameworks, containing predominantly 1D pores [13,14,16–23,27]. The structures of metal bisphosphonates typically include an inorganic hydrophilic part, in which metal atoms are bonded to the organobisphosphorus ligand by the phosphonate oxygens, whilst the hydrophopic organic part projects to the interlayer section. The dimensionality depends on the number of donor atoms of the ligand, on the length and structure of the organic tether between the phosphonate groups and on the degree of protonation of the phosphonate groups. However, prediction of metal bisphosphonate structures is not straightforward [2].

Bisphosphonates (BPs) have important pharmaceutical applications [28]. One of the best known methylenebisphosphonate derivatives is disodium (dichloromethylene)bisphosphonate tetrahydrate, clodronate, which is used to inhibit the bone resorption [29]. Several metal complexes of clodronate [30–34], its symmetrical diethyl [34,35] and diisopropyl ester [36,37] derivatives, and the methyl ester of piperidine derivative of clodronate [38] have been prepared and characterised to study the properties of solid materials. Clodronate and its derivatives form molecular compounds and polymeric chain and layer structures [30–38]. 3D structures are formed when the Na^+ cation participates in structure formation [32,37]. Few metal complexation studies on derivatives of clodronate have been published. We recently reported the hydrolysis product of the polymeric Mg complex of the clodronic acid dianhydride *P*,*P*′-diacetyl(dichloromethylene)bisphosphonate disodium salt $Na_2Cl_2C[PO_3(COMe)]_2$ [32], and the results have encouraged us to study in more detail the metal complexes of clodronic acid dianhydrides and their metal complexation behaviour.

In this paper we present the metal complexation properties of the clodronic acid dianhydride *P*,*P*′-dibenzoyl(dichloromethylene)bisphosphonate disodium salt $Na_2Cl_2C[PO_3(COC_6H_5)]_2$ (**L1**). Magnesium, strontium and barium complexes of this dianhydride, namely, monomeric $[Mg\{[Cl_2C(PO_2O(C(O)C_6H_5))_2]\}(H_2O)_5\}\cdot H_2O]$ (**1**), polymeric $[Sr_2\{[Cl_2C(PO_2O(C(O)C_6H_5))_2]_2(H_2O)_9\}\cdot H_2O]_n$ (**2**) and polymeric $[Ba\{Cl_2C(PO_2O(C(O)C_6H_5))_2\}(H_2O)_2]_n$ **(3)** were crystallised under carefully controlled conditions by gel and liquid crystallisation methods. In addition, the previously published [33] polymeric calcium complex of clodronate, $[Ca_2\{Cl_2C(PO_3)_2\}(H_2O)_6\cdot 4.5H_2O]_n$ **(4)**, was synthesised by hydrolysis method from the dibenzoyl derivative. The structures of the complex crystals were determined by single-crystal X-ray methods.

* Corresponding author. Tel.: +358 13 251 3377; fax: +358 13 251 3390.
E-mail address: Susan.Kunnas-Hiltunen@joensuu.fi (S. Kunnas-Hiltunen).

0277-5387/$ - see front matter © 2008 Elsevier Ltd. All rights reserved.
doi:10.1016/j.poly.2008.10.030

2. Experimental

2.1. General

All reagents used for the synthesis and characterisation of compounds **1–4** were of analytical reagent grade. The synthesis and characterisation of *P*,*P*′-dibenzoyl (dichloromethylene)bisphosphonate disodium salt $Na_2Cl_2C[PO_3(COC_6H_5)]_2$ (**L1**) have been reported earlier [39]. Infrared spectra were recorded on a Nicolet Magna-IR™ spectrometer 750 by the KBr pellet technique. The metal complexes of **L1** were crystallised by gel crystallisation method, and, additionally, compound **1** was prepared by liquid crystallisation method. In the gel crystallisation, carefully weighed amounts of **L1** and the metal salt were separately dissolved in water (2×0.45 ml) and the **L1** solution was warmed to 40 °C in a water bath. The solutions were mixed together, the TMOS (0.1 ml) was added, and the two-phase system was shaken until homogeneous. After the gel formation, organic precipitant was added. Exceptionally, in the preparation of **2**, a pure 20% supplemental TMOS layer (0.225 ml) was placed above the gel and allowed to gelate before the precipitant was added.

2.2. Syntheses of complexes

2.2.1. $[Mg\{[Cl_2C(PO_2O(C(O)C_6H_5))_2](H_2O)_5\} \cdot H_2O]$ (**1**)

Compound **1** was prepared by mixing the water solutions of **L1** (0.0101 mmol/0.45 ml, pH 4.01) and $Mg(NO_3)_2 \cdot 6H_2O$ (0.0101 mmol/0.45 ml, pH 5.17) with TMOS (0.1 ml). After the gel (pH 3.92) was formed, ethanol was added above the gel. Colourless and plate-like crystals were formed in the gel (pH 4.00) in one day. After two weeks the crystals dissolved in the gel through the effect of ethanol. In air atmosphere the dried crystals degraded during a few hours, probably due to the loss of water molecules. The crystals of **1** were also grown by liquid crystallisation method in 4/9:5/9 acetone/water solution (4.5 ml) of the ligand (0.050 mmol) and the metal salt (0.050 mmol) at 5 °C. *Anal.* Calc. for $C_{15}H_{22}MgCl_2O_{14}P_2$ (583.48): C, 30.88; H, 3.80; Mg, 4.17. Found: C, 30.97; H, 4.24; Mg, 3.91%. IR/cm^{-1} (KBr pellet, characteristic region): 1735 (s), 1604 (m), 1592 (m), 1505 (w), 1454 (s), 1273 (vs), 1181 (m), 1147 (m), 1105 (m), 1087(s), 1062 (s), 1026 (s), 1002 (m), 858 (s), 764 (s), 698 (s), 682 (s).

2.2.2. $[Sr_2\{[Cl_2C(PO_2O(C(O)C_6H_5))_2]_2(H_2O)_9\} \cdot H_2O]_n$ (**2**)

In the preparation of **2** the water solutions of **L1** (0.0019 mmol/0.45 ml, pH 4.00) and $SrCl_2 \cdot H_2O$ (0.0019 mmol/0.45 ml, pH 4.95) were mixed with TMOS (0.1 ml). A pure 20% TMOS layer (0.225 ml) was placed above the gel and allowed to gelate before the precipitant, 1:1 acetone/water solution, was added above the gel (pH 3.95). The plank-like and colourless crystals were formed in the gel (pH 4.60) in two days. *Anal.* Calc. for $C_{15}H_{20}SrCl_2O_{13}P_2$ (628.80): C, 28.65; H, 3.21; Sr, 13.94. Found: C, 28.71; H, 3.10; Sr, 13.72%. IR/cm^{-1} (KBr pellet, characteristic region): 1721 (s), 1601 (m), 1587 (m), 1494 (w), 1452 (m), 1281 (vs), 1181 (m), 1132 (s), 1107 (s), 1083 (s), 1061 (s), 1060 (s), 1027 (s), 1002 (m), 858 (s), 770 (s), 765 (sh), 755 (sh), 701 (s), 684 (s).

2.2.3. $[Ba\{Cl_2C(PO_2O(C(O)C_6H_5))_2\}(H_2O)_2]_n$ (**3**)

Compound **3** was prepared by mixing water solutions of **L1** (0.0010 mmol/0.45 ml, pH 4.05) and $Ba(NO_3)_2$ (0.0010 mmol/0.45 ml, pH 5.00) with TMOS (0.1 ml). After the gel (pH 3.90) was formed, ethanol was added above it. Colourless and thin plate-like crystals were formed in the gel (pH 4.69) in few days. Like the crystals of **1**, the crystals of **3** degraded in air atmosphere within a few hours. *Anal.* Calc. for $C_{15}H_{14}BaCl_2O_{10}P_2$ (624.44): C, 28.85; H, 2.26; Ba, 21.99. Found: C, 28.50; H, 2.41; Ba, 21.80%. IR/cm^{-1} (KBr pellet, characteristic region): 1721 (vs), 1714 (s), 1602 (m), 1588 (w), 1498 (w), 1455 (m), 1281 (vs), 1182 (m), 1136 (s), 1089 (s), 1066 (s), 1027 (s), 1110 (s), 1001 (w), 860 (s), 768 (s), 750 (sh), 700 (s), 685 (s).

2.2.4. $[Ca_2\{Cl_2C(PO_3)_2\}(H_2O)_6 \cdot 4.5H_2O]_n$ (**4**)

The preparation of **4** from the clodronate ligand has been described earlier [33], but now **4** was prepared by mixing water solutions of **L1** (0.0013 mmol/0.45 ml, pH 4.08) and $CaCl_2 \cdot 2H_2O$ (0.0026 mmol/0.45 ml, pH 5.40) with TMOS (0.1 ml). After the gelation (pH 4.10), acetone was added. Colourless, plank-like crystals formed above the gel during one month (pH 4.75). *Anal.* Calc. for $CH_{21}Ca_2Cl_2O_{16.5}P_2$ (510.18): C, 2.35; H, 4.15; Ca, 15.71. Found: C, 2.11; H, 3.90; Ca, 15.62%.

2.3. X-ray crystallographic study

X-ray diffraction data were collected with a Nonius Kappa CCD diffractometer using Mo–Kα-radiation ($\lambda = 0.71073$ Å). DENZO and SCALEBACK [40] programs were used for cell refinements and data reduction. The structures were solved by direct methods with SHELXS 97 [41], and structural refinements were carried out with SHELXL 97 [42]. The H_2O hydrogen atoms of the structures **1** and **3** were located from the difference Fourier map but constrained to ride on their parent atom, with $U_{iso} = 1.5$. The H_2O hydrogen atoms of the structure **2** are disordered and therefore they are omitted from the structure. The other hydrogen atoms of the structures **1–3** were positioned geometrically and were also constrained to ride on their parent atoms, with $U_{iso} = 1.2 \cdot U_{eq}$ (parent atom). Crystallographic data of compounds **1–3** are summarised in Table 1.

3. Results and discussion

3.1. Complex synthesis

Moderately stable crystals of metal complexes of dibenzoyl derivative of clodronic acid (**L1**) were formed by gel and liquid crystallisation methods. Because the rate of the hydrolysis of the ligand is dependent on the pH [39], the pH was followed in every step of the crystallisation: at the beginning when the water solutions of ligand and metal salt were mixed together, after gelation

Table 1
Experimental data for the crystallographic analyses (Kappa CCD) of compounds **1**– **3**.

	1	**2**	**3**
Empirical formula	$C_{15}H_{22}Cl_2MgO_{14}P_2$	$C_{15}H_{20}Cl_2SrO_{13}P_2$	$C_{15}H_{14}Cl_2BaO_{10}P_2$
Formula weight	583.48	628.77	624.44
Temperature (K)	120(2)	120(2)	120(2)
λ (Å)	0.71073	0.71073	0.71073
Crystal system	monoclinic	monoclinic	triclinic
Space group	$P2/c$	$P2/m$	$P\bar{1}$
a (Å)	18.2000(4)	6.957(1)	6.5430(2)
b (Å)	7.1740(2)	33.053(7)	10.8789(4)
c (Å)	20.2440(5)	10.561(2)	15.2653(6)
α (°)	90	90	82.64(2)
β (°)	114.849(2)	18.28(3)	89.277(2)
γ (°)	90	90	72.723(2)
V (Å^3)	2398.48(10)	2305.9(8)	1028.56(6)
Z	4	4	2
ρ_{calc} (g cm^{-3})	1.616	1.811	2.016
μ(Mo Kα) (mm^{-1})	1.149	2.773	2.398
Number of reflections	27673	23711	18248
Unique reflections	4701	4607	4038
R_{int}	0.0581	0.0622	0.0625
R_1[a] ($I \geqslant 2\sigma$)	0.0371	0.0456	0.0351
wR_2[b] ($I \geqslant 2\sigma$)	0.0834	0.1397	0.0847

[a] $R_1 = \Sigma||F_o| - |F_c||/\Sigma|F_o|$.
[b] $wR_2 = [\Sigma[w(F_o^2 - F_c^2)^2]/\Sigma[w(F_o^2)^2]]^{1/2}$.

with tetramethoxysilane TMOS and after the crystals were formed. The pH values of all syntheses were in the range where the ligand should not hydrolyse fast. The results established that there were no significant difference in the pH change in the syntheses of compounds **1–3** and the hydrolysis product **4**. In all cases, the pH decreased slightly when the water solutions of ligand and metal salt were mixed together, and the pH rose during the formation of the crystals. Thus, the crystallisation time is the most important factor in the syntheses. The crystals of the clodronate dianhydride complexes need to form within a few days, or otherwise the hydrolysis product may form instead. The crystallisation tests were done by varying the precipitant and the ratio of the concentrations of the metal salt and the ligand.

3.2. Crystal structures

Compound **1** consists of monomeric units. The asymmetric unit contains one independent Mg^{2+} atom, one $Cl_2C(PO_2O(C(O)C_6H_5))_2^{2-}$ ligand, five aqua ligands and one lattice water molecule (see Fig. 1a). The geometry around the six-coordinated magnesium atom is a distorted octahedron having Mg–O bond lengths of 2.010(2)–2.139(2) Å. The $Cl_2C(PO_2O(C(O)C_6H_5))_2^{2-}$ ligand is coordinated to the Mg atom monodentately via the phosphonate O11 atom, and the remaining coordination sites of the Mg atom are occupied by aqua ligands. The other phosphonate oxygen atoms of the ligand are unprotonated. Intramolecular hydrogen bond contacts are formed between the O1···O21, O2···O6 and O6···O22 having the distances 2.684(3), 2.748(3) and 2.854(2) Å, respectively, and the angles 150.8–174.5°. The monomeric units of **1** form parallel to the (010) plane a 2D layer-like structure where the units are placed with hydrophilic parts against each other (see Fig. 1b). The monomeric units are held together by intermolecular hydrogen bonds involving all aqua ligands and lattice water molecules as donors and O atoms of $Cl_2C(PO_2O(C(O)C_6H5))_2^{2-}$ as acceptors. The O4···O12^{i}, O5···O6^{i}, O1···O12^{i}, O2···O22^{ii}, O6···O21^{ii}, O5···O24^{ii}, O3···O5^{iii}, O3···O14^{iv}, O1···O22^{i}, O4···O24^{v}, O6···O1^{ii} distances are 2.615(3)–3.254(2) Å (symmetry code: i, *x*, y + 1, *z*; ii, −*x*, y + 1/2, −*z* + 1/2; iii, −*x*, −*y* + 2, −*z*; iv, −*x*, −*y* + 1, −*z*; v, *x*, −*y* + 1/2, *z* − 1/2) and the angles 123.5–172.8°. The benzene rings and chlorine atoms point out from the layers making the external parts hydrophobic with no intermolecular hydrogen bonds between the layers.

Compounds **2** and **3** consist of polymeric chains. The asymmetric unit of compound **2** contains two Sr^{2+} atoms on the mirror plane, one $Cl_2C(PO_2O(C(O)C_6H_5))_2^{2-}$ ligand, 4.5 aqua ligands and 0.5 lattice water molecules (see Fig. 2a). The $Cl_2C(PO_2O(C(O)C_6H_5))_2^{2-}$ ligand acts as a bridging ligand bonding to the Sr1 atom via phosphonate oxygen O11 and to the Sr2 atom via phosphonate oxygen O21 leaving two phosphonate oxygen atoms unprotonated. The other coordination sites of the Sr1 and Sr2 atoms are occupied by aqua ligands and by the bridge oxygen μ-O1 between the Sr atoms. The hydrogen atoms of the aqua ligands O3, O4, O4A, O6 and O7 and the lattice water molecule O8 are in disorder, therefore they are omitted from the structure **2**. The Sr1–O bond distances vary from 2.555(3) to 2.827(5) Å, but there exists the Sr1–O5A distance of 3.049(5) Å. This indicates a strong interaction between the Sr1 and O5A atoms, thus the Sr1 atom has a sphere with a coordination character of nine. The Sr2–O distances of the eight-coordinated Sr2 atom vary from 2.530(7) to 2.679(4) Å. According to the preceding indication, the polymeric chains consist of dimeric units linked together via one monoatomic bridge O5/O5A and two μ-aqua bridges (O2/O2B and O2A/O2C) between Sr atoms. The geometry around the Sr1 atom can be described as tricapped trigonal prism and around the Sr2 atom as distorted bicapped trigonal prism. The chains are formed parallel to the *a*-axis and are bonded together in the direction of the *a*- and *c*-axis by intermolecular hydrogen bonds between the lattice water molecules, aqua ligands and phosphonate oxygen atoms (see Fig. 2b). The O8···O6^{i}, O2···O12^{ii}, O5···O2^{ii}, O6···O22^{iii}, O7···O3^{iv}, O4···O24^{v}, O2···O21^{ii}, O8···O4^{vi}, O6···O2^{vi}, O8···O7^{v} and O8···O21^{vi} distances are estimated to be 2.7050(5), 2.7635(5), 2.7967(5), 2.8012(6), 2.838(10), 2.892(5), 2.9611(9), 2.962(8), 2.9877(6), 3.003(10) and 3.0200(8) Å (symmetry code: i, 1 + *x*, 1/2 − *y*, −1 + *z*; ii, −1 + *x*, 1/2 − *y*, *z*; iii, 1 + *x*, 1/2 − *y*, *z*; iv, *x*, *y*, 1 + *z*; v, *x*, *y*, −1 + *z*; vi, −1 + *x*, *y*, *z*), respectively. In addition, the phosphonate oxygen atoms, aqua ligands, lattice water molecule and carbonyl oxygen atoms form intramolecular hydrogen bonds. The O3···O14, O2B/O2C···O21/O21A, O5···O11, O8···O4/O4A, O7···O21, O7···O24, O3···O11, O1···O2 and O1···O5 distances are 2.902(4), 2.957(4), 2.9586(4), 2.962(8), 3.0868(5),

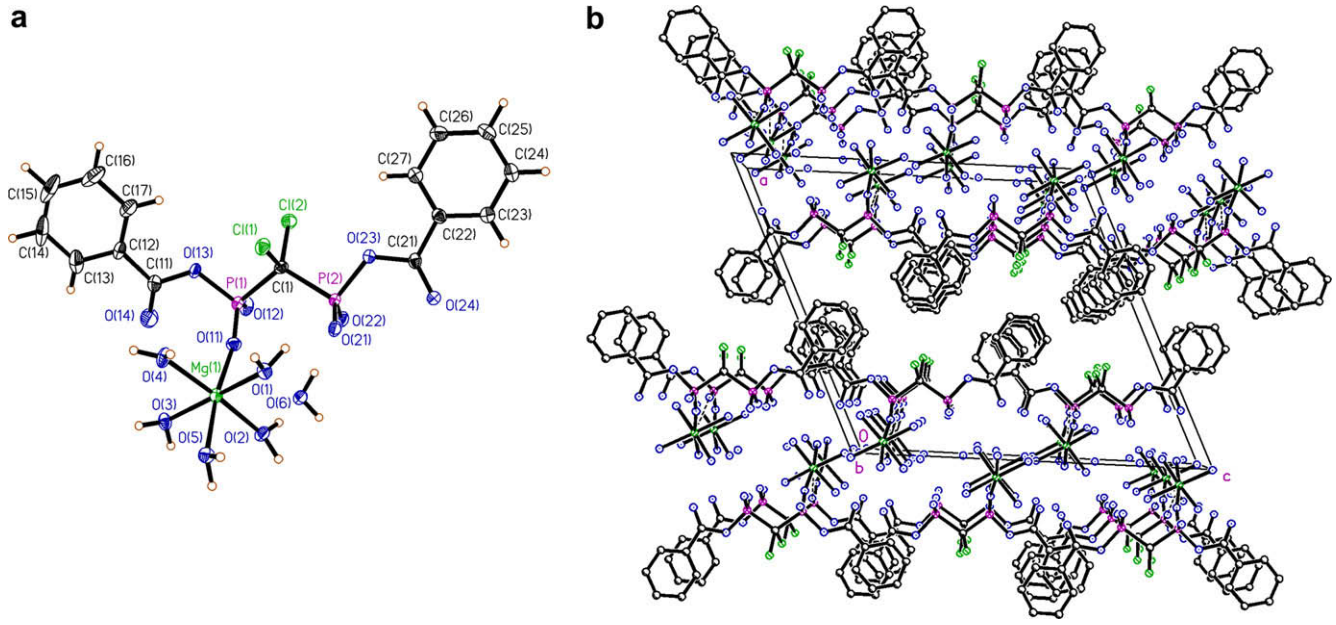


Fig. 1. (a) The structure of **1** with numbering scheme and thermal ellipsoids (50%) and (b) packing of the monomeric units of **1**. Hydrogen atoms are omitted for clarity. Selected bond distances (Å): Mg–O1 2.079(2), Mg–O2 2.034(2), Mg–O3 2.052(2), Mg–O4 2.066(2), Mg–O5 2.139(2), Mg–O11 2.010(2).

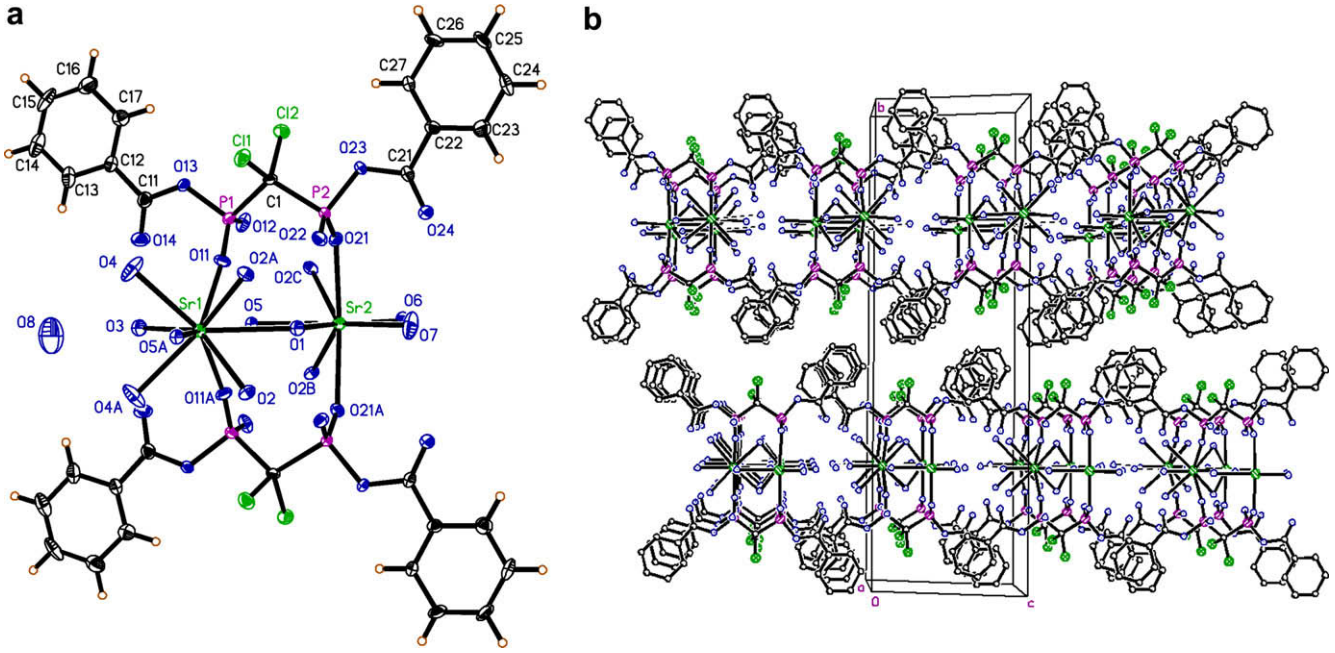


Fig. 2. (a) Part of the polymeric structure of **2** with numbering scheme and thermal ellipsoids (50%). The H_2O hydrogen atoms are disordered and thus omitted. (b) Packing of the chains of **2**. Hydrogen atoms are omitted for clarity. Selected bond distances: Sr1–O11 2.555(3), Sr1–O11A 2.555(3), Sr1–O3 2.621(5), Sr1–O4 2.628(3), Sr1–O4A 2.628(3), Sr1–O2 2.633(3), Sr1–O2A 2.633(3), Sr1–O1 2.827(4), Sr1–O5A^{i} 3.049(5), Sr2–O7 2.530(7), Sr2–O6 2.574(7), Sr2–O21 2.612(3), Sr2–O21A 2.612(3), Sr2–O5 2.668(4), Sr2–O2B 2.675(3), Sr2–O2C 2.675(3), Sr2–O1 2.679(4). In the figure, A refers to atoms at ($x-1, y, z$), A^{i} to atoms at ($x+1, y, z$), B to atoms at ($x-1, -y+1/2, z$) and C to atoms at ($x-1, y, z$).

3.0960(6), 3.1211(5), 3.1801(5) and 3.232(1) Å, respectively. The inner space between the 2D layers is filled by hydrophobic benzene rings and chlorine atoms of the ligands.

The asymmetric unit of compound **3** consists of one independent Ba^{2+} atom, one $Cl_2C(PO_2O(C(O)C_6H_5))_2^{2-}$ ligand and two aqua ligands (see Fig. 3a). The geometry around the eight-coordinated Ba atom can be described as a distorted square antiprism where three independent $Cl_2C(PO_2O(C(O)C_6H_5))_2^{2-}$ ligands are bidentately coordinated to the Ba atom through their phosphonate oxygen atoms forming six- and eight-membered chelate rings. The phosphonate oxygen O11 also acts as a bridging atom between two Ba atoms. The remaining two coordination sites of the Ba atom are occupied by aqua ligands O1 and O2. The Ba–O bond lengths range from 2.682(3) to 2.850(3) Å. The polymer chains are formed in the direction of the crystallographic *a*-axis (see Fig. 3b). Intramolecular hydrogen bonds are formed between the aqua ligand oxygen O1, carbonyl oxygen O24 and phosphonate oxygen O21. The hydrogen atoms of the aqua ligand O1 are disordered having the population parameter 0.5. In every second molecule the intramolecular hydrogen bond interaction from the aqua ligand oxygen O1 is directed towards the phosphonate oxygen O21, with shortest O1···O21 distance 2.680(4) Å and smallest angle 110.8°, and towards the carbonyl oxygen O24 having the O1···O24 distance 3.917(5) Å and angle 163.8°, whilst in the other molecules the intramolecular hydrogen bonds do not exist. Intermolecular hydrogen bonds formed between aqua ligand oxygens O1 hold the polymer chains together in the direction of the *b*-axis and, in addition, there are intermolecular hydrogen bonds between the aqua ligand oxygen O2, the carbonyl oxygen O24 and the phosphonate oxygen O12. The O2···O24^{i}, O2···O12^{ii}, O1···O1^{iii}, O1···O24^{i} distances are 2.808(4), 2.817(4), 2.823(4) and 3.073(5) Å (symmetry code: i, $-x+1, -y, -z$; ii, $-x, -y+1, -z$; iii, $-x+2, -y, -z$), respectively, and the angles are 148.4–171.0°. There are no intermolecular hydrogen bonds between the polymer chains in the direction of *c*-axis, only benzene rings, and the chlorine atoms point towards each other.

3.3. Spectroscopic properties

The characteristic absorption region and bands of the ligand **L1** and the compounds **1–3** were determined by IR spectroscopy. The assignments are based on published values for similar compounds and IR tables [43–45]. For all compounds the characteristic region was at 1735–700 cm^{-1}. The significant difference between the IR spectrum of **L1** and the IR spectra of its metal complexes were the bands for the water molecules. Strong, broad bands of $\nu(H_2O)$ around 3300 cm^{-1} and weaker absorptions of δ(H–O–H) in the region 1653–1623 cm^{-1} were present in the spectra of the metal complexes **1–3**, but were lacking in the spectrum of **L1**. Otherwise the absorptions and their intensities in the spectra of **L1** and **1–3** were closely similar.

A C=O stretching vibration overtone appeared around 3550 cm^{-1} for all compounds, and a very strong absorption band due to the stretching vibration of the carbonyl group, ν(C=O), appeared in the region 1735–1720 cm^{-1}. There was a strong asymmetric C–O stretching vibration, with weak shoulder at 1281 cm^{-1}, the symmetric ν(C–O) vibration appeared at 1130–1150 cm^{-1}. A series of strong bands in the 1300–1000 cm^{-1} region was attributed to the stretching vibrations of phosphonate PO_3 groups, and strong absorptions in the region 861–847 cm^{-1} to asymmetric and symmetric ν(P–C–P) vibrations. The aromatic ring carbon carbon stretching vibrations, ν(C=C), occurred at 1602 cm^{-1}, 1587 cm^{-1}, 1494 cm^{-1} and 1454 cm^{-1} and the stretching vibrations of the ring C–H bonds appeared with four weak peaks at around 3080–3010 cm^{-1}. The strongest absorptions for the monosubstituted aromatic ring, due to the out-of-plane C–H vibrations were at ca. 750 cm^{-1} and 700 cm^{-1}.

4. Conclusion

The dibenzoyl derivative of clodronic acid forms typical metal bisphosphonate complexes with alkaline earth metals. The

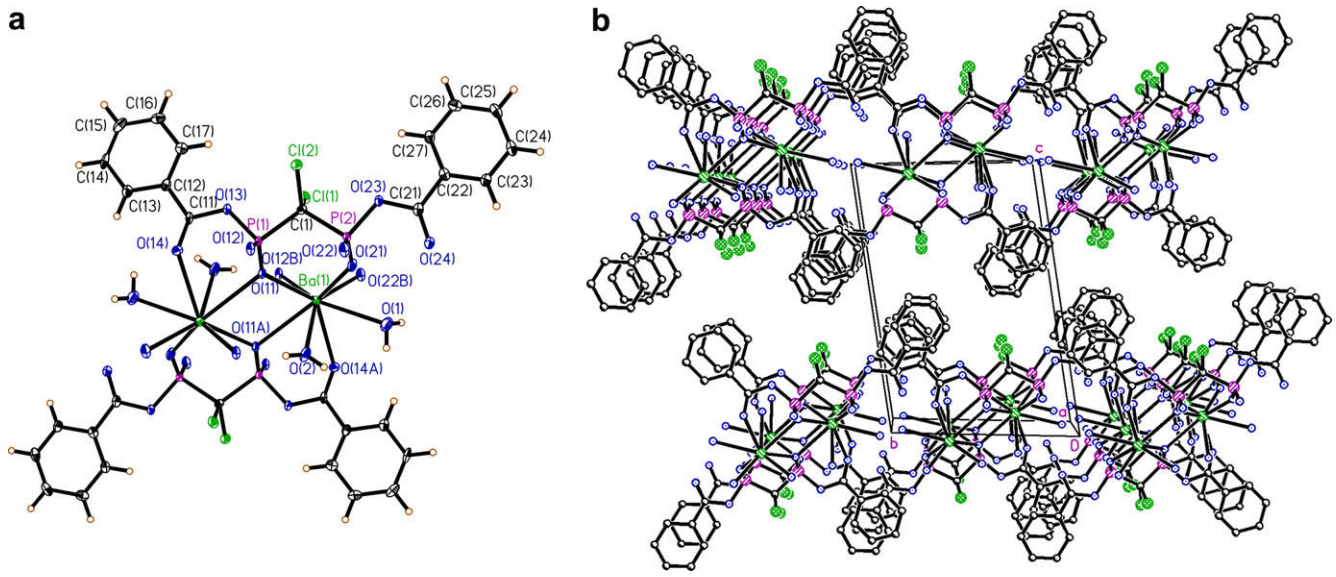


Fig. 3. (a) Part of the polymeric structure of **3** with numbering scheme and thermal ellipsoids (50%) and (b) packing of the chains. Hydrogen atoms are omitted for clarity. Selected bond distances: Ba1–O21 2.682(3), Ba1–O2 2.728(3), Ba1–O22B 2.732(3), Ba1–O1 2.795(3), Ba1–O14A 2.814(3), Ba1–O12B 2.758(3), Ba1–O11 2.840(3), Ba1–O11A 2.850(3). In the figure, A refers to atoms at $(-x+1, -y+1, -z)$ and B to atoms at $(x+1, y, z)$.

monomeric units of **1** and the polymer chains of **2** and **3** form 2D layer-like structures through intermolecular hydrogen bonds. In all structures the benzene rings and chlorine atoms of the ligand point to the interlayer part making the outer surfaces of the layers hydrophopic. The structures are packed efficiently and there are no porous channels. The $Cl_2C(PO_2O(C(O)C_6H_5))_2^{2-}$ ligand acts as both a bridging and a chelating ligand. It forms six- and eight-membered chelate rings with metal atoms via the four available phosphonate oxygens and via two carbonyl oxygens of the dibenzoyl groups. Studies on the complexing properties of other dianhydride derivatives of clodronate are in progress.

5. Supplementary data

Crystallographic data for the structural analysis have been deposited with the Cambridge Crystallographic Data Centre, CCDC Nos. 702609 (**1**), 702610 (**2**) and 702611 (**3**). These data can be obtained free of charge from The Cambridge Crystallographic Data Centre via www.ccdc.cam.ac.uk/data_request/cif.

Acknowledgement

The assistance of Professor Matti Haukka and Mrs. Tarja Virrantalo (Dept. Chem., Univ. Joensuu) are gratefully acknowledged.

References

[1] K.M. Fromm, Coord. Chem. Rev. 252 (2008) 856.
[2] A. Clearfield, Progress in Inorganic Chemistry: Metal–Phosphonate Chemistry, John Wiley & Sons, Inc., New York, 1998. p. 373.
[3] G. Alberti, M. Casciola, U. Constantino, R. Vivani, Adv. Mater. 8 (1996) 291.
[4] P.M. Forster, A.K. Cheetham, Top. Catal. 24 (2003) 79.
[5] R.C. Finn, J. Zubieta, J. Chem. Soc., Dalton Trans. (2000) 1821.
[6] L.-M. Zheng, S. Gao, H.-H. Song, S. Decurtins, A.J. Jacobson, X.-Q. Xin, Chem. Mater. 14 (2002) 3143.
[7] D.-K. Cao, S. Gao, L.-M. Zheng, J. Solid State Chem. 177 (2004) 2311.
[8] R.C. Finn, R. Lam, J.E. Greedan, J. Zubieta, Inorg. Chem. 40 (2001) 3745.
[9] L.-M. Zheng, H.-H. Song, C.-Y. Duan, X.-Q. Xin, Inorg. Chem. 38 (1999) 5061.
[10] R.C. Finn, R.S. Rarig Jr., J. Zubieta, Inorg. Chem. 41 (2002) 2109.
[11] R.C. Finn, J. Zubieta, Inorg. Chem. 40 (2001) 2466.
[12] Y. Gong, W. Tang, W. Hou, Z. Zha, C. Hu, Inorg. Chem. 45 (2006) 4987.
[13] H.-H. Song, L.-M. Zheng, Z. Wang, C.-H. Yan, X.-Q. Xin, Inorg. Chem. 40 (2001) 5024.
[14] A. Distler, D.L. Lohse, S.C. Sevov, J. Chem. Soc., Dalton Trans. (1999) 1805.
[15] K. Barthelet, M. Nogues, D. Riou, G. Férey, Chem. Mater. 14 (2002) 4910.
[16] C. Serre, G. Férey, J. Mater. Chem. 12 (2002) 2367.
[17] P. Yin, Y. Peng, L.-M. Zheng, S. Gao, X.-Q. Xin, Eur. J. Inorg. Chem. (2003) 726.
[18] H.-H. Song, P. Yin, L.-M. Zheng, J.D. Korp, A.J. Jacobson, S. Gao, X.-Q. Xin, J. Chem. Soc., Dalton Trans. (2002) 2752.
[19] L.-M. Zheng, H.-H. Song, C.-H. Lin, S.-L. Wang, Z. Hu, Z. Yu, X.-Q. Xin, Inorg. Chem. 38 (1999) 4618.
[20] S. Bauer, H. Müller, T. Bein, N. Stock, Inorg. Chem. 44 (2005) 9464.
[21] Z.-G. Sun, L.-Y. Cui, Z.-M. Liu, L. Meng, H. Chen, D.-P. Dong, L.-C. Zhang, Z.-M. Zhu, W.-S. You, Inorg. Chem. Commun. 9 (2006) 999.
[22] P. Yin, L.-M. Zheng, S. Gao, X.-Q. Xin, Chem. Commun. (2001) 2346.
[23] H.G. Harvey, S.J. Teat, M.P. Attfield, J. Mater. Chem. 10 (2000) 2632.
[24] H.-H. Song, L.-M. Zheng, C.-H. Lin, S.-L. Wang, X.-Q. Xin, S. Gao, Chem. Mater. 11 (1999) 2382.
[25] H.-H. Song, L.-M. Zheng, G. Zhu, Z. Shi, S. Feng, S. Gao, Z. Hu, X.-Q. Xin, J. Solid State Chem. 164 (2002) 164. 367.
[26] H.-H. Song, L.-M. Zheng, Y.-J. Liu, X.-Q. Xin, A.J. Jacobson, S. Decurtins, J. Chem. Soc., Dalton Trans. (2001) 3274.
[27] A.K. Cheetham, G. Férey, T. Loiseau, Angew. Chem., Int. Ed. 38 (1999) 3268.
[28] J.H. Lin, Bone 18 (1996) 75.
[29] R. Hannuniemi, L. Laurén, H. Puolijoki, Drugs Today 27 (1991) 375.
[30] M. Kontturi, S. Peräniemi, J.J. Vepsäläinen, M. Ahlgrén, Acta Crystallogr., Sect. E 60 (2004) m1060.
[31] M. Kontturi, S. Peräniemi, J.J. Vepsäläinen, M. Ahlgrén, Acta Crystallogr., Sect. C 60 (2004) m592.
[32] M. Kontturi, S. Kunnas-Hiltunen, J.J. Vepsäläinen, M. Ahlgrén, Solid State Sci. 8 (2006) 1098.
[33] M. Kontturi, S. Peräniemi, J.J. Vepsäläinen, M. Ahlgrén, Eur. J. Inorg. Chem. (2004) 2627.
[34] M. Kontturi, E. Vuokila-Laine, S. Peräniemi, T.T. Pakkanen, J.J. Vepsäläinen, M. Ahlgrén, J. Chem. Soc., Dalton Trans. (2002) 1969.
[35] M. Kontturi, S. Peräniemi, J.J. Vepsäläinen, M. Ahlgrén, Acta Crystallogr., Sect. E 61 (2005) m638.
[36] M. Kontturi, S. Peräniemi, J.J. Vepsäläinen, M. Ahlgrén, Polyhedron 24 (2005) 305.
[37] M. Kontturi, E. Laurila, R. Mattsson, S. Peräniemi, J.J. Vepsäläinen, M. Ahlgrén, Inorg. Chem. 44 (2005) 2400.
[38] J. Jokiniemi, E. Vuokila-Laine, S. Peräniemi, J. Vepsäläinen, M. Ahlgrén, CrystEngCommun 9 (2007) 158.
[39] M. Ahlmark, J. Vepsäläinen, H. Taipale, R. Niemi, T. Järvinen, J. Med. Chem. 42 (1998) 1473.
[40] Z. Otwinowski, W. Minor, in: C.W. Carter, R.M. Sweet (Eds.), Methods in Enzymology, Macromolecular Crystallography, Part A, vol. 276, Academic Press, New York, 1997, p. 307.
[41] G.M. Sheldrick, SHELXS 97 Program for Crystal Structure Determination, University of Göttingen, Germany, 1997.
[42] G.M. Sheldrick, SHELXL 97 Program for Crystal Structure Refinement, University of Göttingen, Germany, 1997.
[43] J. Kivikoski, J.M. Garcia-Ruiz, J. Vepsäläinen, F. Higes, E. Pohjala, J. Välisaari, J. Phys. D: Appl. Phys. 26 (1993) B172.
[44] K. Moedritzer, J.R.R. Irani, J. Inorg. Nucl. Chem. 22 (1961) 297.
[45] G. Socrates, Infrared and Raman Characteristic Group Frequencies, John Wiley & Sons, Ltd., Chichester, 2001.

Polyhedron 28 (2009) 205–208

Contents lists available at ScienceDirect

Polyhedron

journal homepage: www.elsevier.com/locate/poly

Potassium and lithium pyrazolates: The interplay of electronic and steric factors on the hapticity of the pyrazolate ligand and the influence of Lewis bases on nuclearity

Miguel-Ángel Velázquez-Carmona, Alejandro-José Metta-Magaña, Sara-Angélica Cortés-Llamas, Virginia Montiel-Palma, Miguel-Ángel Muñoz-Hernández *

Centro de Investigaciones Químicas, Universidad Autónoma del Estado de Morelos, Av. Universidad 1001, Col. Chamilpa, Cuernavaca, Morelos 62209, Mexico

ARTICLE INFO

Article history:
Received 19 July 2008
Accepted 17 October 2008
Available online 6 December 2008

Keywords:
Alkali metal complexes
Pyrazolates
Crown ethers

ABSTRACT

The oligomeric potassium complex $[(Me_2pzH)(Me_2pz)_2(18\text{-crown-6})(THF)K_2]_2$ (**1**) and the lithium dimer $[(^tBu_2pz)(THF)Li]_2$ (**2**) were synthesized. Both complexes were fully characterized by spectroscopic methods and single crystal X-ray diffraction. Complex **1** crystallized in the triclinic space group $P\bar{1}$, the structure shows an oligomer capped with 18-crown-6 and THF in both ends. This oligomer may be thought as the result of exscind an infinite single ladder structure in which η^2-coordinated pyrazolate ligands to potassium ions are the steps of the stair, and the crown ether acting as a scissor. The potassium ions that form the truncated stair are coordinated in a η^5-fashion to one pyrazolate ligand and in a η^1-fashion to one pyrazolate and one pyrazolyl ligand, respectively. The potassium ions in the cavity of the 18-crown-6 ligand complete their coordination spheres with η^5-coordination to one pyrazolate ligand and one THF molecule. Complex **2** is formed from the nucleophilic addition of THF to the lithium pyrazolate tetramer, $[(^tBu_2pz)Li]_4$. Complex **2** crystallized in the monoclinic space group *C*2/*c*. The molecular structure shows a dimer in which the pyrazolate ligands are coordinated in a $\mu\text{-}\eta^1{:}\eta^1$ fashion to two Li ions. These ions complete their respective coordination spheres with THF.

© 2008 Elsevier Ltd. All rights reserved.

1. Introduction

It is currently being recognized that the cation-π interactions of alkali metals with aromatic rings are an important class of non-covalent binding modes that should play an important role in molecular biology and could have repercussions even in the design of new materials and molecular devices [1]. Alkali and other Main Group cyclopentadienyl complexes have recently been the subject of intense experimental and theoretical work [2]. These results have advanced our understanding of the nature of the bonding and the factors that prompt Cp to bind a Main Group metal in a high hapticity fashion [3]. The Main Group coordination chemistry of its heterocyclic analogues such as the pyrazolyls has attracted considerable attention due to the discovery of several coordination modes to alkali and alkaline ions, including the $\pi\text{-}\eta^5$ coordination mode [4–11]. 18-crown-6 complexes that incorporate pyrazolates and alkali ions should favor the expression of the η^5-coordination mode, due the fact, that the crown ether blocks in plane coordination sites without a high demand of steric bulk, leaving the pyrazolate ligand coordinate the ion axially in the best circumstances. The known examples with Na and K show the pyrazolate ligand coordinating the ion in a η^2 fashion, more likely as a consequence of big alkyl groups on the pyrazolate and/or competition for the same coordination site occupied by the pyrazolate by another ligand [4,7–9]. On this vein, the structure of the complex previously reported by us $[(^tBu_2pz)K]_\infty$ [8] that shows η^5 coordination of potassium in a 1D extended chain, inspired us to use 18-crown-6 ligand as a scissor and a small pyrazolate, expecting to witness the highest possible hapticiy of the ligand in a olygomeric or monomeric structure. On the other hand, the isolation of the dimeric lithiumpyrazolates $[(^tBu_2pzH)(^tBu_2pz)Li]_2$ [8] and $[(Ph_2pz)(OEt_2)Li]_2$ [9], rise the question if a similar structure may be obtained from nucleophilic addition of THF to $[(^tBu_2pz)Li]_4$. The results obtained are presented herein.

2. Results and discussion

From the mixture of $pzMe_2K$ with 18-crown-6 in THF, it was isolated a colorless crystalline complex with a formulation $[(Me_2pzH)(Me_2pz)_2(18\text{-crown-6})(THF)K_2]_2$ (**1**), which was established with spectroscopic methods and single crystal X-ray diffraction analysis (crystal data and structural parameters are shown in Table 1). The incorporation of the pyrazol, Me_2pzH, to complex **1** may be due to the introduction of adventitious water into the potassium pyrazolate, Me_2pzK.

* Corresponding author. Tel./fax: +52 777 3297997.
E-mail address: mamund2@buzon.uaem.mx (M.-Á. Muñoz-Hernández).

0277-5387/$ - see front matter © 2008 Elsevier Ltd. All rights reserved.
doi:10.1016/j.poly.2008.10.041

Table 1
Crystal data and refinement parameters for complexes **1** and **2**.

	1	2
Formula	$C_{27}H_{46}K_2N_6O_6$-$0.5C_4H_8O$	$C_{30}H_{54}Li_2N_4O_2$
Formula weight	664.95	487.42
Crystal system	Triclinic	Monoclinic
Space group	$P\bar{1}$	$C2/c$
a (Å)	11.274(3)	25.897(2)
b (Å)	12.521(3)	17.0953(15)
c (Å)	14.981(4)	19.1351(17)
α (°)	100.764(4)	90.00
β (°)	97.964(4)	128.1070(10)
γ (°)	116.178(4)	90.00
V (Å^3)	1804.9(7)	6665.9(10)
Z	2	8
$\rho_{calc.}$ (g cm^{-3})	1.223	1.030
μ(Mo Kα) (mm^{-1})	0.310	0.063
F(000)	712	2272
Crystal size (mm^3)	0.32 × 0.27 × 0.24	0.26 × 0.19 × 0.16
Temperature (K)	173(2)	100(2)
Θ range for data collection (°)	1.43–25.00	1.55–25.00°
Index ranges: $-h \leqslant h$, $-k \leqslant k$, $-l \leqslant l$	$-12 \leqslant 13$, $-14 \leqslant 14$, $-17 \leqslant 17$	$-30 \leqslant 30$, $-20 \leqslant 20$, $-22 \leqslant 22$
Total number reflections	11 354	31 548
Independent reflections [$R_{(int)}$]	6198 [0.0330]	5887 [0.0333]
Refinement methods	Full matrix least square on F^2	Full matrix least square on F^2
Data/restraints/parameters	6198/56/433	5887/147/356
Goodness-of-fit (GOF) on F^2	1.094	1.035
R_1 [$I > 2\sigma(I)$]	0.1051	0.0952
Largest difference in peak and hole (e/Å^{-3})	0.66 and −0.55	1.07 and −0.60

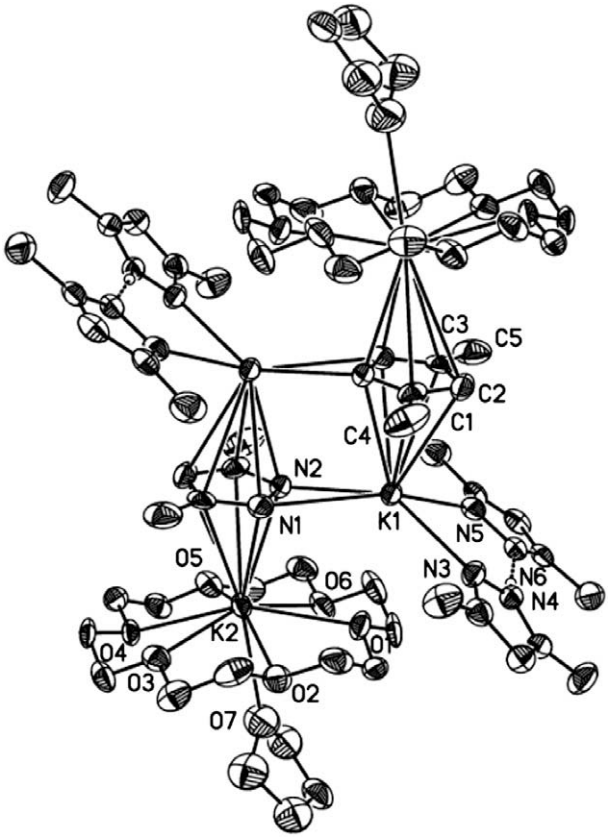


Fig. 1. Perspective view of complex [(Me$_2$pzH)(Me$_2$pz)$_2$(18-crown-6)(THF)K$_2$]$_2$ (**1**), showing thermal ellipsoids at the 50% probability level. Most hydrogen atoms were omitted for clarity. Symmetry transformation used to generate equivalent atoms: $-x+1$, $-y+2$, $-z+1$.

Complex **1** crystallized in the triclinic $P\bar{1}$ space group, the structure, which is presented in Fig. 1, shows an oligomer capped with 18-crown-6 and THF in both ends (Fig. 1). Apart from the intramolecular interactions described below (selected bond lengths and angles are given in Table 2), there are no significant intermolecular contacts in the crystal structure. The molecular structure of **1** is somehow related to the crystal structure of the potassium pyrazolate [(^{t}Bu$_2$pz)K]$_\infty$ [8] that has an infinite single ladder like structure. For **1** the single ladder structure is truncated as the result of the action of the crown ether and hydrogen bonded pyrazolate-pyrazol moiety acting as the scissors. The potassium ions that form the truncated stair (K1A and K1B) are coordinated in a η^5-fashion to one pyrazolate ligand and in a η^1-fashion to one pyrazolate and one pyrazolyl ligand, respectively. These η^1-coordinated pyrazolyl and pyrazolate ligands are bonded by unsymmetrical hydrogen bonding (N4–H100 0.87(2) Å, N6···H100 1.84(2) Å, N4···N6 2.712(7) Å, N4–H100···N6 176(7)). The potassium ions in the cavity of the 18-crown-6 ligand (K2A and K2B) are above by 0.603 Å to the best-fit plane formed by the oxygen atoms of the crown ether toward a η^5-coordinated pyrazolate ligand, and complete their coordination spheres with one THF molecule. Interestingly, both K1 and K2 ions are π-bound to one pyrazolate ring in a η^5-fashion. Both ions are oriented to the C_3N_2 ring centroid (distance K-ring centroid 2.922 Å), but marginally slipped toward the two nitrogen atoms as reflected by the shorter K–N bond lengths compared to the K–C bond lengths of 2.723(5)–2.989(5) and 3.181(6)–3.365(7) Å, respectively. These bond lengths are in the range observed for the π-bound potassium complexes [Tp^{CF3,CH3}CuK(CO$_3$)KTp^{CF3,CH3}]$_2$ (K–N 3.277(2)–3.339(3), K–C 3.339(3)–3.424(4) Å) [5], and [(^{t}Bu$_2$pz)K]$_\infty$ (K–N 2.803(2)–2.967(3), K–C 3.177(4)–3.431(3) Å) [8]. Moreover, the π-bound pyrazolate ligands further coordinate the K1 ions in a η^2-fashion resulting in an unusual binding mode μ_3-η^5:η^5:η^2, which to our knowledge has not been previously observed. The pyrazolate ring best-fit plane compared to the best-fit plane formed by the 18-crown-6 ligand with K2 in the cavity is almost coplanar (tilted by 10.5°). Comparison of the same angle in the related complexes [K(η^2-3,5-Ph$_2$pz)(η^6-18-crown-6)] 85.0° [12], [K(η^2-3,5-Me$_2$pz)(H$_2$O)(η^6-18-crown-6)] 25.4° [12], and [(^{t}Bu$_2$pz)Na(18-crown-6)] 52.3° [8] suggests that electronic and steric factors are operating in the perpendicular or coplanar orientation of the pyrazolate ligand in these complexes. In a previous report we showed with *ab initio* calculations at the MP2 level of theory that η^5-coordination of the C3N2 ring in simple alkalipyrazolates (C_s symmetry) is more favored with K in the series Li, Na, K [8]. In addition, the smaller steric requirements of the Me groups on the C3N2 ring versus the requirements of the ^{t}Bu and Ph groups should favor also in

Table 2
Selected bond lengths (Å) and angles (°) for complex **1**.

K(1)–N(1)	2.984(6)	K(2)–O(1)	2.827(5)
K(1)–N(2)	2.723(5)	K(2)–O(2)	2.828(4)
K(1)–N(3)	2.924(5)	K(2)–O(3)	2.845(5)
K(1)–N(5)	2.900(5)	K(2)–O(4)	2.877(5)
K(2)–N(1)	2.961(5)	K(2)–O(5)	2.938(5)
K(2)–N(2)	2.989(5)	K(2)–O(6)	2.939(5)
K(1)–N(1)#1	3.122(5)	K(2)–O(7A)	2.979(11)
K(1)–N(2)#1	3.118(5)	N(3)–K(1)–N(5)	83.00(15)
K(1)–O(1)	3.309(5)	C(1)–K(1)–O(1)	153.52(16
K(1)–C(1)	3.135(6)	O(7A)–K(2)–N(2)	152.2(3)
K(1)–C(2)	3.189(7)		
K(1)–C(3)	3.158(6)		
C(1)–K(2)#1	3.250(6)		
C(2)–K(2)#1	3.365(6)		
C(3)–K(2)#1	3.181(6)		

#1 $-x+1$, $-y+2$, $-z+1$.

the former case a C_s symmetry. Both factors appear to favor in **1** the observed η^5-coordination of the pyrazolate ligand to the K2 ions. In contrast, it is the steric hindrance of the phenyl groups attached to the pyrazolate ligand in [K(η^2-3,5-Ph_2pz)(η^6-18-crown-6)] that may favor the observed perpendicular configuration. Thus, the intermediate perpendicular-coplanar configuration observed in [(^{t}Bu_2pz)Na(18-crown-6)] accounts again for the interplay of both the electronic and steric factors previously discussed.

The ^{1}H and ^{13}C NMR spectra of complex **1** in benzene-d_6 account partially with the formulation found in the solid state by X-ray diffraction. In particular the resonance signals ascribed to THF by NMR are most likely due to uncoordinated THF (^{1}H δ 1.43 and 3.58 ppm, ^{13}C δ 68.2 and 26.3 ppm). It appears that complex **1** easily release coordinated solvent as evidenced by the crystal structure obtained by X-ray, which shows partial occupancy of THF (0.5). In the ^{1}H NMR, a broad singlet resonance at considerably low field δ 16.25 ppm is ascribed to the N–H proton of the hydrogen bonded pyrazolate-pyrazol moiety (*cf.* free Me_2pzH 12.29 ppm).

Dimeric complex [(^{t}Bu_2pz)Li(THF)]$_2$ (**2**) was obtained by the opening of the lithium pyrazolate tetramer [(^{t}Bu_2pz)Li]$_4$ via nucleophilic addition of THF (Scheme 1). Similar nucleophilic additions were previously reported using the pyrazol ^{t}Bu_2pzH and diethyl ether affording complexes [(^{t}Bu_2pz)Li(^{t}Bu_2pzH)]$_2$ [8] and [(Ph_2pz)Li(OEt_2)]$_2$ [9], respectively. The spectroscopic and X-ray analysis (crystal data and structural parameters are shown in Table 1) evidence is consistent with the formulation proposed for **2**.

Complex **2** crystallized in the monoclinic space group C2/c, selected bond lengths and angles are given in Table 3. The molecular structure presented in Fig. 2, shows a dimer in which the pyrazolate ligands (^{t}Bu_2pz) are coordinated in a μ-η^1:η^1 fashion to two Li ions. These ions complete their respective coordination spheres with THF in a pyramidal coordination geometry around the lithium atom. The related complexes [(^{t}Bu_2pz)Li(^{t}Bu_2pzH)]$_2$ [8] and [(Ph_2pz)Li(OEt_2)]$_2$ [9] show μ-η^2:η^1 coordination of the pyrazolate ligand to Li. As a consequence of the lower hapticity of the pyrazolate ligand in **2,** a six-membered ring Li_2N_4 in a chair conformation is formed. The THF moieties occupy anti-axial positions of the chair, which in turn minimize steric bulk in the complex. Although the torsion angles Li–N–N–Li (50.8 and −49.1°) in **2** are more acute than those of [(^{t}Bu_2pz)Li(^{t}Bu_2pzH)]$_2$ and [(Ph_2pz)Li(OEt_2)]$_2$ (69.3 and 60.2°, respectively),[8–9] the chair conformation adopted by Li_2N_4 ring prevents steric crowding of the ^{t}Bu groups. The Li–N bond length values found in **2** (1.942(5) and 1.952(5) Å) are statistically similar compared to the sum of covalent radii of Li and N (1.99 Å)[1] [13] and those found in [(Ph_2pz)Li(OEt_2)]$_2$ (1.945(3)–1.954(3) Å) [9], but somehow shorter than those reported in [(^{t}Bu_2pz)Li(^{t}Bu_2pzH)]$_2$ (2.009(4)–2.048(4) Å) [8]. Although in the pyrazolates [(^{t}Bu_2pz)Li(^{t}Bu_2pzH)]$_2$ and [(Ph_2pz)Li(OEt_2)]$_2$ there is η^2 coordination, in **2** is precluded due to rather long Li···N contacts (2.471(2)–2.820(1) Å) if compared to the sum of covalent radii of Li and N (0.48–0.83 Å difference).

Table 3
Selected bond lengths (Å) and angles (°) for complex **2**.

N(1)–N(2)	1.387(3)	N(1)–Li(1)–N(4)	125.0(3)
N(3)–N(4)	1.382(3)	O(1)–Li(1)–N(1)	115.2(3)
N(1)–Li(1)	1.943(6)	O(1)–Li(1)–N(4)	112.5(3)
N(4)–Li(1)	1.952(6)	N(2)–Li(2)–N(3)	121.4(3)
N(2)–Li(2)	1.952(6)	O(2)–Li(2)–N(2)	111.6(3)
N(3)–Li(2)	1.932(6)	O(2)–Li(2)–N(3)	115.6(3)
O(1)–Li(1)	1.914(6)		
O(2)–Li(2)	1.918(6)		

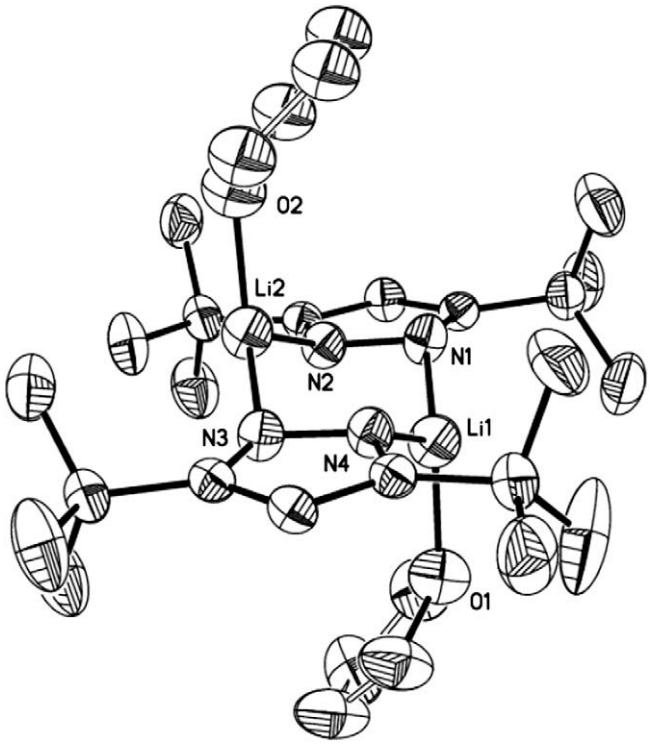
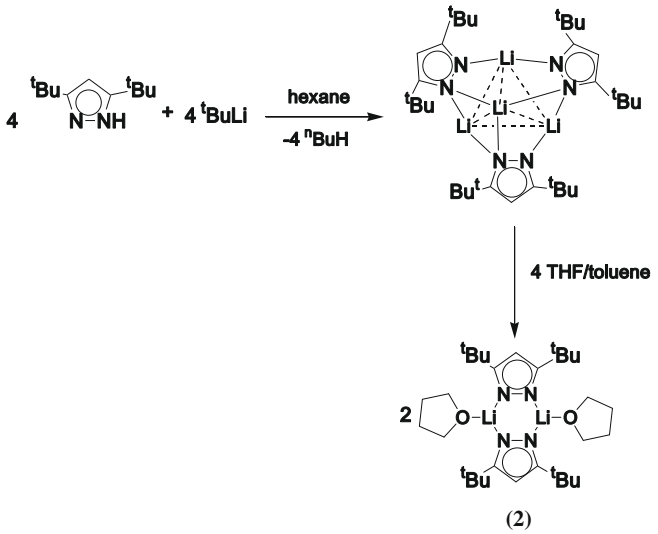


Fig. 2. Perspective view of complex [(^{t}Bu_2pz)Li(THF)]$_2$ (**2**), showing thermal ellipsoids at the 50% probability level. Hydrogen atoms were omitted and only one component of the disordered THF is shown for clarity.



Scheme 1.

2.1. Conclusions

We have prepared the oligomeric complex **1** that can be envisioned as the result of exscind the parent compound [(Me_2pz)K]$_\infty$ [8] with 18-crown-6 ether and the hydrogen bonded pyrazolyl-pyrazolate moiety. Complex **1** shows strong π binding in a η^5 fashion between pyrazolate rings and potassium, which in strength is comparable to what it has been observed for [η^5-CpK]$_\infty$ (K–C bond lengths: 2.995(5)–3.080(7) Å; K-ring centroid: 2.816 Å) [14].

[1] Covalent radii of Li and N: 1.28(7) and 0.71(1) Å, respectively. Data from Ref. [13].

Additionally, the structure of **1** display a new binding mode of the pyrazolate ligand to potassium of the type μ_3:η^5:η^5: η^2.

The crystal structure of **2** and others related reported elsewhere, demonstrate that coordination of a better nucleophile is highly favored in the tetramer $[(R_2pz)Li]_4$, resulting in dimeric structures with the nucleophile coordinating the lithium atom.

3. Experimental

3.1. General methods

All experiments were carried out under argon using standard Schlenk techniques in a dual argon/vacuum line in conjunction with an inert atmosphere glovebox. THF and toluene were distilled from Na/benzophenone and stored under N_2 prior to use. [^{t}Bu$_2$pzLi]$_4$ and ^{t}Bu$_2$pzK were prepared as described in the literature [8]. All other chemicals were purchased from Aldrich and used as received.

3.1.1. Instrumentation

The ^{1}H, ^{13}C{^{1}H}, and ^{7}Li{^{1}H} NMR (δ in ppm) were obtained on a Varian Gemini-200 MHz spectrometer (200 MHz for ^{1}H, 50.30 MHz for ^{13}C, and 77.7 MHz for ^{7}Li) at ambient probe temperature (293 K). ^{1}H and ^{13}C NMR chemical shifts were determined by reference to the residual solvent peaks. ^{7}Li NMR chemical shifts are reported versus LiCl in D_2O. IR data were recorded as KBr pellets on a FT-IR Bruker spectrometer and are reported in cm^{-1}.

3.2. Single crystal X-ray diffraction analysis

Crystals of **1** and **2** were mounted directly from solution under argon using an inert oil, which protects them from atmospheric oxygen and moisture. X-ray intensity data were collected using the program SMART [15] on a Bruker APEX CCD diffractometer with monochromatic Mo Kα radiation (λ = 0.71073 Å). Cell refinement and data reduction were carried out with the use of the program SAINT, the program SADABS was employed to make incident beam, decay and absorption corrections in the SAINT-PLUS v. 6.0 suite [16]. Then, the structures were solved by direct methods with the program SHELXS and refined by full-matrix least-squares techniques with SHELXL in the SHELXTL v. 6.1 suite [17]. Crystals of **1** show half a molecule of THF that was refined accordingly with an occupancy of 0.5. Statistical disorder was found for the two THF molecules of **2**, refinement of each molecule into two split positions gave an occupancy factor level of 0.48. Except for H100, all hydrogen atoms in complex **1** were generated in calculated positions and constrained with the use of a riding model. H100 was located by the difference Fourier synthesis and refined isotropically restraining the N4-H100 distance to a target value of 0.88 Å. The final models involved anisotropic displacement parameters for all non-hydrogen atoms. Further details of the structure analyses are given in Table 1.

3.2.1. Synthesis of bis[(η^1:η^6-18-crown-6)(μ_3:η^5:η^5:η^2-Me$_2$pz)(η^1-Me$_2$pz)(η^1-Me$_2$pzH)(η^1-THF)K$_2$] (**1**)

A Schlenk flask was charged with a solution of [^{t}Bu$_2$pzK] (0.26 g, 1.39 mmol) in toluene (20 mL) and THF (5 mL). Then, 18-crown-6 was added (0.18 g, 0.7 mmol) and the reaction mixture was stirred 1 h at ambient temperature. The solution was concentrated to 10 mL and stored under argon at −20 °C. Once the compound crystallized, it was isolated by cannula filtration and dried under vacuum. Yield: 50 mg (10.64%). ^{1}H NMR (benzene-d_6, 25 °C): δ 16.24 (bs, 1H, N*H*), 6.07 (s, 3H, C*H*), 3.58 (m, 4H, THF), 3.17 (s, 24H, 18-crown-6), 2.59 (s, 18H, C-C*H*$_3$), 1.43 (m, 4H, THF). ^{13}C NMR (benzene-d_6, 25 °C): δ 145.84 (s, *C*-CH$_3$), 102.06 (s, *C*H), 70.49 (s, 18-crown-6), 68.24 (s, THF), 26.27 (s, THF), 14.81 (s, C-*C*H3).

3.2.2. Synthesis of bis[(μ:η^1:η^1-^{t}Bu$_2$pz)(η^1-THF)-Li] (**2**)

A Schlenk flask was charged with a solution of (^{t}Bu$_2$pz)Li (0.26 g, 1.39 mmol) in toluene (20 mL) and THF was added (0.1 g, 1.39 mmol). The reaction mixture was stirred 30 min at ambient temperature. The solution was then concentrated until the solution shows signs of precipitation. After this, it was stored under argon at −20 °C for several days. Upon crystallization, **2** was isolated by cannula filtration and dried under vacuum leaving a white solid residue (0.34 g, 97%). M.p. >350 °C, ^{1}H NMR (benzene-d_6, 25 °C): δ 6.084 (s, 1H, C*H*), 3.50 (m, 4H, O-C*H*$_2$), 1.35 (m, 4H, O-CH$_2$-C*H*$_2$), 1.02 (s, 18H, C*H*$_3$). ^{13}C NMR (THF, 25 °C): δ 163.72 (s, *C*-^{t}Bu), 97.15 (s, *C*H), 67.41 (s, O-*C*H$_2$), 31.74 (s, *C*-CH$_3$), 31.37 (s, C-*C*H$_3$), 25.55 (s, O-CH$_2$-*C*H$_2$). ^{7}Li NMR (THF, 25 °C): δ −0.88 (s). IR (KBr, cm^{-1}): 2960 (s), 2902 (m), 2866 (m), 1565 (w), 1503 (m), 1462 (m), 1402 (w), 1360 (m), 1308 (w), 1250 (m), 1208 (w), 1047 (m), 1024 (m), 1001 (m), 896 (w), 782 (w), 730 (w), 473 (m), 432 (m).

Acknowledgments

We are indebted to CONACYT-México (Grant UI-54151) for generous financial support of this work, Ph.D. scholarships to S.A.C.L. and M.-A.V.-C. (165618 and 186755, respectively), and a postdoctoral grant to A.J.M.-M (050287).

Appendix A. Supplementary data

CCDC 695529 and 695530 contain the supplementary crystallographic data for **1** and **2**. These data can be obtained free of charge via http://www.ccdc.cam.ac.uk/conts/retrieving.html, or from the Cambridge Crystallographic Data Centre, 12 Union Road, Cambridge CB2 1EZ, UK; fax: (+44) 1223-336-033; or e-mail: deposit@ccdc.cam.ac.uk. Supplementary data associated with this article can be found, in the online version, at doi:10.1016/j.poly.2008.10.041.

References

[1] (a) A few leading references are: W. Schmitt, C.E. Anson, J.P. Hill, A.K. Powell, J. Am. Chem. Soc. 125 (2003) 11142;
(b) G.W. Gokel, L.J. Barbour, R. Ferdani, J. Hu, Acc. Chem. Res. 35 (2002) 878;
(c) J.C. Ma, D.A. Dougherty, Chem. Rev. 97 (1997) 1303.
[2] (a) P. Jutzi, N. Burford, Chem. Rev. 99 (1999) 969;
(b) J.D. Smith, Adv. Organomet. Chem. 43 (1996) 267;
(c) P. Jutzi, Adv. Organomet. Chem. 26 (1986) 267;
(d) V.M. Rayón, G. Frenking, Chem. Eur. J. 8 (2002) 4693.
[3] P.H.M. Budzelaar, J.J. Engelberts, J.H. Lenthe, Organometallics 22 (2003) 1562.
[4] C. Yélamos, M.J. Heeg, C.H. Winter, Inorg. Chem. 37 (1998) 3892.
[5] Z. Hu, S.M. Gorun, Inorg. Chem. 40 (2001) 667.
[6] G.B. Deacon, E.E. Delbridge, C.M. Forsyth, Angew. Chem., Int. Ed. Engl. 38 (1999) 1766.
[7] W. Zheng, M.J. Heeg, C.H. Winter, Eur. J. Inorg. Chem. (2004) 2652.
[8] S.Á. Cortés-Llamas, R. Hernández-Lamoneda, M.Á. Velázquez-Carmona, M.Á. Muñoz-Hernández, R.A. Toscano, Inorg. Chem. 45 (2006) 286.
[9] S. Beani, G.B. Deacon, A.P. Erven, P.C. Junk, D.R. Turner, Chem. Asian J. 2 (2007) 539.
[10] A.Y. O'Brien, J. Hitzbleck, A. Torvisco, G.B. Deacon, K. Ruhlandt-Senge, Eur. J. Inorg. Chem. (2008) 172.
[11] F. Blanco, I. Alkorta, J. Elguero, J. Phys. Chem. A 112 (2008) 7682.
[12] W. Zheng, M.J. Heeg, C.H. Winter, Eur. J. Inorg. Chem. (2004) 2652.
[13] B. Cordero, V. Gómez, A.E. Platero-Prats, M. Revés, J. Echeverría, E. Cremades, F. Barragán, S. Alvarez, Dalton Trans. (2008) 2832.
[14] R.E. Dinnebier, U. Behrens, F. Olbrich, Organometallics 16 (1997) 3855.
[15] G.M. Sheldrick, SMART, Bruker AXS, Inc., Madison, WI, USA, 2000.
[16] G.M. Sheldrick, SAINT-PLUS 6.0, Bruker AXS, Inc., Madison, WI, USA, 2000.
[17] G.M. Sheldrick, SHELXTL 6.10, Bruker AXS, Inc., Madison, WI, USA, 2000.

Polyhedron 28 (2009) 209–214

Contents lists available at ScienceDirect

Polyhedron

journal homepage: www.elsevier.com/locate/poly

Substitution kinetics of biphenol at dichlorobis(acetylacetonato-*O*,*O*′)titanium(IV): Isolation, characterization, crystal structure and enhanced hydrolytic stability of the product bis(acetylacetonato-*O*,*O*′)(biphenyldiolato-*O*,*O*′)titanium(IV)

Tsietsi A. Tsotetsi, Annemarie Kuhn, Alfred Muller, Jeanet Conradie *

Department of Chemistry, University of the Free State, Nelson Mandela Drive, Bloemfontein 9301, South Africa

ARTICLE INFO

Article history:
Received 13 October 2008
Accepted 21 October 2008
Available online 4 December 2008

Keywords:
Acetylacetone
Titanium
Substitution
Kinetics

ABSTRACT

Novel bis(acetylacetonato-*O*,*O*′)(biphenyldiolato-*O*,*O*′)titanium(IV) is synthesized and characterized by 'X-ray crystallography and other physical methods. The kinetics of substitution of bidentate 2,2′-biphenyldiolato for the two monodentate Cl^- ligands in $Ti(CH_3COCHCOCH_3)_2Cl_2$ proceeds *via* a 7-coordinated transition state according to an associative mechanism. The $Ti(CH_3COCHCOCH_3)_2$biphen complex exhibits high hydrolytic stability.

© 2008 Elsevier Ltd. All rights reserved.

1. Introduction

Complexes of titanium(IV) are widely studied for a variety of purposes, mainly serving as a catalyst in different organic reactions as well as for antitumor activity [1,2]. Titanium alkoxides are excellent precursors for the deposition of metal oxides used in optoelectronics, high-T_c superconductors and ceramic materials [3,4]. Titanium alkoxy systems are, for example, effective catalysts in a variety of processes such as the Diels–Alder reaction [5], C–C bond forming reactions [6], esterification reactions including ones involved in the production of dialkyl phthalate plasticisers [7], polymerization of alkenes and alkynes [8,9], asymmetric and enantioselective reactions [10–12] and many more [12–14]. However, since titanium alkoxides are very sensitive to hydrolysis, a problem frequently encountered when used as catalysts, is that as the catalytic reaction commences, there is some cleavage of the Ti–OR bonds due to the reaction with water that is produced as by-product in the reaction, for example in esterification reactions [15]. Studies on sol–gel systems involving $[Ti(OR)_4]$ have shown that the rate of hydrolysis of the metal alkoxide can be significantly reduced by the presence of bulky [16], or chelating ligands as acetylacetonate and glycols [17]. Thus, producing titanium(IV) complexes exhibiting enhanced water resistance, is extremely valuable. Electron-rich oxygen-based ligands may lead to resistance towards hydrolysis. The *O*,*O*′-chelate bidentate 1,1-bi-2-naphthol ligand in the (BINOLate)TiX_2 catalysts have resulted in development of an impressive number of highly enantioselective processes [18] such as the cyanosylation of aldehydes [19], Diels–Alder cycloadditions [20] hetero Diels–Alder cycloaddition [21], carbonyl-ene reaction [22], Mukaiyama aldol condensation [23] and asymmetric addition of alkyl groups to aldehydes, to name a few [24]. In this paper we describe the synthesis of a remarkably hydrolytically stable catalytic complex containing three electron donating *O*,*O*′-chelate bidentate ligands: bis(acetylacetonato-*O*,*O*′)(biphenyldiolato-*O*,*O*′)titanium(IV).

2. Results and discussion

2.1. Reactivity of $Ti(acac)_2Cl_2$ with 2,2′-biphenyldiol

The complex $Ti(acac)_2Cl_2$ **1** (Hacac = acetylacetone = $CH_3COCHCOCH_3$) was prepared by treating $TiCl_4$ with two equivalents of acetylacetone and isolated and purified by recrystallization before use [25,26]. Reaction of complex **1** with 2,2′-biphenyldiol in 1:1 ratio in CH_3CN yielded the mixed ligand complex, $Ti(acac)_2$(biphen) **2** (H_2biphen = 2,2′-biphenyldiol = $HOC_6H_4C_6H_4OH$). Even with the use of higher ligand ratios, 1:2 or 1:3, the reaction yielded **2** rather than a product possessing more than one biphenolato ligand in the coordination sphere of Ti. This is similar to what was found for the reaction between $Ti(acac)_2Cl_2$ and 1,1′-methylenedi-2-naphtol [27]. Stoichiometric amounts of $Ti(acac)_2Cl_2$ and H_2biphen (representing second-order reaction conditions), stirred at room temperature for 25 h under an inert atmosphere, generated the product $Ti(acac)_2$(biphen) **2** in low yields (<10%).

* Corresponding author. Tel.: +27 51 4012194; fax: +27 51 4446384.
E-mail address: conradj.sci@ufs.ac.za (J. Conradie).

0277-5387/$ - see front matter © 2008 Elsevier Ltd. All rights reserved.
doi:10.1016/j.poly.2008.10.025

2.2. Spectral study of Ti(acac)$_2$(biphen) **2**

The proton NMR spectrum of **2** showed methyl protons of acac as a singlet at 2.05 ppm and the methine proton of acac also as a singlet at 5.81 ppm. The biphenolato ring protons were arranged in a 2:2:2:2 ratio (d; t; t; d pattern) at 6.88; 7.00; 7.21; 7.39 ppm, compared to the 4:4, m; m pattern at 7.07; 7.33 ppm in the uncoordinated ligand. The disappearance of the phenolic–OH protons in the spectrum of **2**, compared to the uncoordinated ligand, suggests that the bidentate ligand is chelated through the two oxygens to the Ti(IV) centre. The methine proton of the chelated ring in both Ti(acac)$_2$biphen (5.81 ppm) and parent complex, Ti(acac)$_2$Cl$_2$ (6.00 ppm) is slightly downfield shifted relative to the uncoordinated Hacac (5.50 ppm). This is due to the formation of the six-membered, planar *pseudo*-aromatic system when acetylacetone coordinates to the Ti(IV) centre.

2.3. X-ray structure of (**2**)

A molecular diagram showing the numbering scheme of the title compound Ti(acac)$_2$biphen, **2**, is presented in Fig. 1a. Crystal data and details for data collections and refinements are summarized in Table 1. Selected bond lengths and angles for **2** and for comparison, also of **1**, are displayed in Fig. 1b and c, respectively.

The Ti(acac)$_2$biphen, **2**, structure consists of an octahedrally coordinated titanium atom with all three ligands acting as bidentate. The octahedral coordination around titanium is distorted to accommodate the three chelated ligands, *i.e.*, the two six-membered acetonato and seven-membered biphenolato rings. The bond angles vary from 83° to 103° compared to 90° in a perfect octahedron. Due to the strain in the ring, the ligand O–Ti–O angle increases from 82.8° for the six-membered acetonato chelated ligand to 89.9° for the seven-membered biphenolato ring, which is in the same trend as the angle of 94.0° found for an eight-membered 1,1′-methylenedi-2-naphtol (mbinaph) ring in the structure of Ti(acac)$_2$mbinaph [27]. The Ti–O bond lengths in **2** are in the order Ti–O$_{biphen}$ (1.860 Å) < Ti–O$_{acac\ axial}$ (1.985 Å) < Ti–O$_{acac\ equatorial}$ (2.013 Å) as illustrated in Fig. 1b. The formal Ti–O single bond is 1.94–1.99 Å (Ti–O distances found in rutile, TiO$_2$ [28]) and Ti=O double bond is 1.61–1.68 Å [29]. Therefore the shortest Ti–O distance is clearly shorter than one expected for a single bond, suggesting that this Ti–O bond possesses partial double bond character arising from donation of the electrons from the p_y and p_z filled oxygen orbitals to the empty titanium *d* orbitals [30]. The Ti–O$_{acac}$ bonds *trans* to another acac oxygen, are shorter (*ca.* 1.99 Å) than those *trans* to the oxygen of the chelated dianion biphenalato ligand (*ca.* 2.01 Å). The Ti–ligand bond lengths in **1** are in the order Ti–O$_{acac\ axial}$ (1.924–1.936 Å) < Ti–O$_{acac\ equatorial}$ (1.967–1.978 Å) < Ti–Cl (2.277 Å) as illustrated in Fig. 1c. Both Ti–O$_{acac\ axial}$ and Ti–O$_{acac\ equatorial}$ are slightly longer in **2** than in **1**, but the Ti–O$_{biphen}$ bond in **2** is considerably shorter than any Ti–O$_{acac}$ bond in either 1 or 2. Therefore, a strong electron donation to the titanium centre is expected due to the short Ti–O$_{biphen}$ bond.

Table 1
Crystal and structure refinement data for Ti(acac)$_2$biphen (**2**).

Formula	$C_{22}H_{22}O_6Ti$
Formula weight	430.30
Crystal colour/habit	orange, cuboid
Crystal system	monoclinic
Space group	C_2/c
Unit cell dimension	
a (Å)	15.8796(13)
b (Å)	9.7062(6)
c (Å)	13.2038(11)
α (°)	90
β (°)	93.097(2)
γ (°)	90
Volume (Å^3)	2032.1(3)
Z	4
D_{calc} (Mg m^{-3})	1.406
Temperature (°C)	−173
Wavelength (Å)	0.71073
Absorption coefficient (mm^{-1})	0.457
F(000)	896
Crystal size (mm)	0.46 × 0.34 × 0.21
θ Range for data collection (°)	2.46–28.00
Index ranges	$-20 \le h \le 20$, $-7 \le k \le 12$, $-17 \le l \le 16$
Reflections collected	6844
Independent reflections (R_{int})	2358 (0.0307)
Completeness to θ = 28.35 (%)	96.1
Absorption correction	semi-empirical from equivalents
Max. and min. transmission	0.9101 and 0.8173
Refinement method	full-matrix least-squares on F^2
Data/restraints/parameters	2358/0/134
Goodness-of-fit on F^2	1.188
Final R indices [$I > 2\sigma(I)$]	R_1 = 0.0395, wR_2 = 0.1213
R indices (all data)	R_1 = 0.0538, wR_2 = 0.1544
Largest difference in peak and hole (e Å^{-3})	0.567 and −0.752

The compound Ti(acac)$_2$biphen, **2**, crystallizes in the monoclinic centrosymmetric space group $C2/c$ with Z = 4, resulting in only half the molecule necessary for the asymmetric unit as it is situated on a twofold rotational axis. Intermolecular π–π stacking of the chelated β-diketonato acac moieties is clearly observed in Ti(acac)$_2$biphen (Fig. S1a Supplementary material). The planes of the π–π stacked rings are parallel with the rings displaced from each other in a slipped or offset alignment resulting in a centroid–centroid

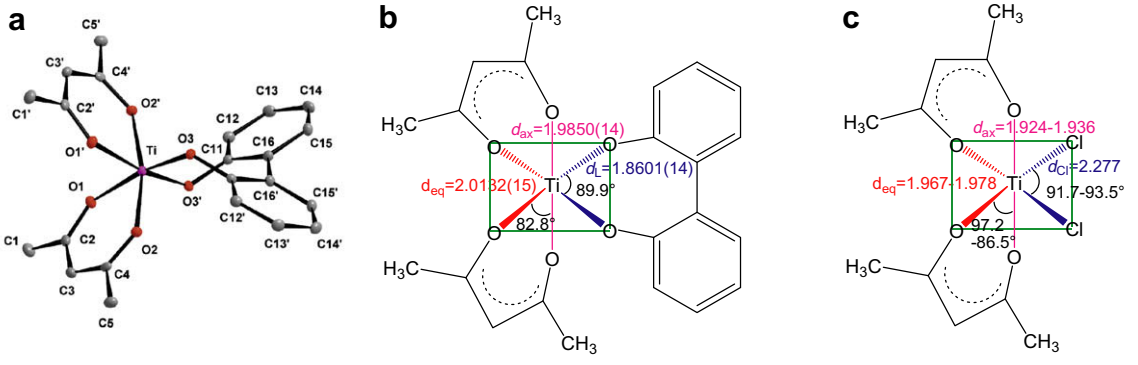


Fig. 1. (a) The molecular structure (30% probability displacement ellipsoids) of Ti(acac)$_2$biphen (**2**) showing the numbering scheme (primed labels indicate atoms generated by symmetry operations). Diagram indicating coordination, distances (Å) and angles (°) around the titanium centre of (b) Ti(acac)$_2$biphen (**2**) and (c) Ti(acac)$_2$Cl$_2$ (**1**).

separation of the acetylacetono backbones of 3.619 Å and a centre-normal angle θ of 8.6°. The geometrical parameters describing π–π stacking [31,32] are given in Supplementary material Fig. S1b.

2.4. Hydrolytic stability of (**2**)

Complex **1** is extremely moisture sensitive and hydrolyzes easily [33]. The final stage of hydrolysis is the formation of TiO_2. Keppler and Heim [33] evaluated the rate of hydrolysis, showing that complex **1** precipitates within 5 s when dissolved in dry acetonitrile treated with 0.01% water. Complex **2**, however, exhibits a high hydrolytic stability and is "air stable" for more than 3 years. The solution stability was tested under the same conditions as Keppler and Heim, *i.e.*, 0.01% water/CH_3CN, and it was found that **2** does not precipitate within 6 weeks. The strong electron donation to the titanium centre observed in the form of a short Ti–O_{biphen} bond may contribute to the enhanced hydrolytic stability of **2** relative to **1**.

2.5. Substitution kinetics

The kinetics of substitution of bidentate 2,2-biphenyldiolato for the two monodentate Cl^- ligands in $Ti(CH_3COCHCOCH_3)_2Cl_2$ takes place in two kinetically distinct steps, including a solvent pathway.

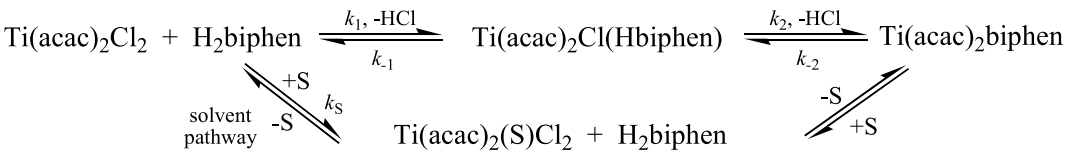
Table 2
Kinetic data and activation parameters for the substitution of 2,2′-biphenyldiolato for the two monodentate Cl^- ligands in $Ti(acac)_2Cl_2$.

T (°C)	k_1 ($dm^3\ mol^{-1}\ s^{-1}$)	$10^3\ k_S$ (s^{-1})	$\Delta H^{\#}$ (kJ mol^{-1})	$\Delta S^{\#}$ (J $mol^{-1}\ K^{-1}$)	$\Delta G^{\#}$ (kJ mol^{-1})
15.0	0.062(2)	0.12(3)			
25.0[a]	0.153(4)	4.61(7)	59.6	−60.8	77.7
36.2	0.365(5)	13.3(1)			

[a] $k_2 = 0.0015(2)\ s^{-1}$ for the second step at 25°.

are given in Table 2 and the results plotted as a function of the incoming H_2biphen concentration in Fig. 2b.

The general rate law applicable to the first [H_2biphen] dependent step is given by Rate = $\{k_S + k_1[H_2biphen]\}[Ti(acac)_2Cl_2] = k_{obs}[Ti(acac)_2Cl_2]$ [35,36] with the pseudo-first-order rate constant $k_{obs} = k_S + k_1[H_2biphen]$ and k_1 the second-order rate constant for the substitution process and k_S the first-order rate constant for a solvent pathway. A noticeable solvent path is observed, *e.g.* $k_S = 0.00461(7)\ s^{-1}$ at 25 °C. That $Ti(CH_3COCHCOCH_3)_2Cl_2$ **1** indeed forms a solvent coordinated species is also confirmed on ^1H NMR. ^1H NMR in $CDCl_3$ (a non-coordinating solvent) showed one set of proton signals corresponding to the signals of the protons of the methyl groups and the methine protons of the acac ligand coordinated to $Ti(CH_3COCHCOCH_3)_2Cl_2$, but in CD_3CN solution (a coordinating solvent), two sets of signals were observed, see Supporting material Fig. S2. Since the ^1H NMR spectrum in $CDCl_3$ confirmed the purity of **1**, the second species in CD_3CN must correspond to the seven-coordinate $[Ti(CH_3COCHCOCH_3)_2(Cl_2)(CD_3CN)]$ solvent coordinated species. Each signal of the solvent coordinated species split since the methyl and methine groups are not chemical equivalent in $[Ti(CH_3COCHCOCH_3)_2(Cl_2)(CD_3CN)]$.



(1)

Both reaction steps were observed when following the reaction on a UV–Vis spectrophotometer, see Fig. 2a. The rate constant for the second step (0.0015(2) s^{-1} at 25 °C) is *ca.* 10 times slower than that of the first step (0.153(4) $dm^3\ mol^{-1}\ s^{-1}$ at 25 °C). The first step was followed at 340 cm^{-1} where the second reaction did not have a change in absorbance. The two stages and the rate constants were determined independently. The H_2biphen was in excess, so first-order kinetics in [H_2biphen] was observed for the first step. The second step was [H_2biphen] independent, consistent with the second step being rate-limiting ring closure [34]. Rate constants for the first and second stages of substitution at $Ti(acac)_2Cl_2$

The activation parameters, the entropy of activation, $\Delta S^{\#}$, and activation enthalpy, $\Delta H^{\#}$, were determined from a temperature dependence study. The large negative activation entropy of

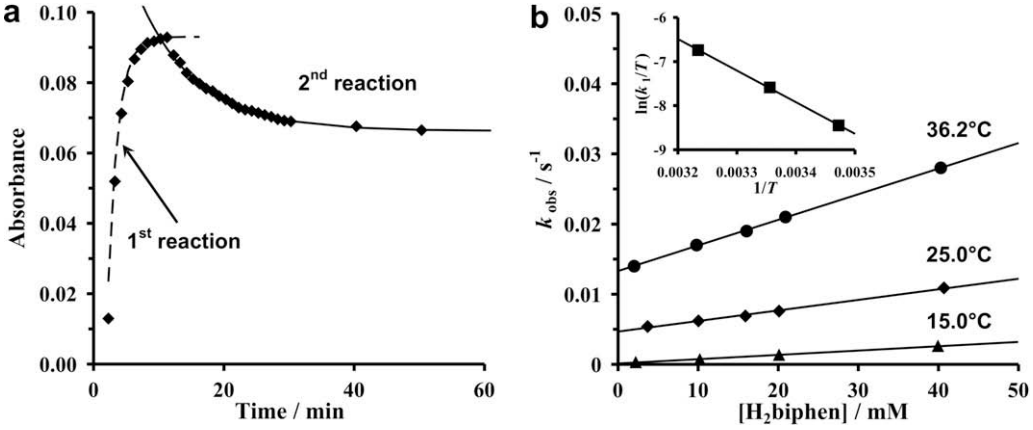
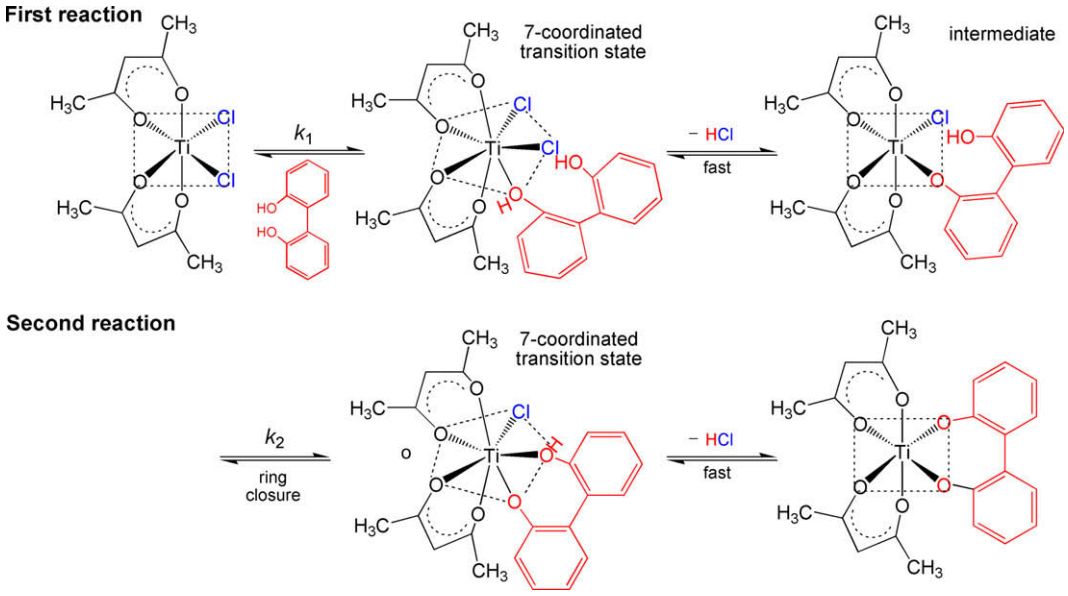


Fig. 2. (a) Absorbance *vs.* time data of the UV monitoring of the reaction between 0.0002 mol dm^{-3} $Ti(CH_3COCHCOCH_3)_2Cl_2$, **1**, and 0.040 mol dm^{-3} H_2biphen at 336 nm illustrating the two reaction steps observed. (b) Temperature and H_2biphen concentration dependence of the first reaction step of the substitution of 2,2-biphenyldiolato for the two monodentate Cl^- ligands in $Ti(CH_3COCHCOCH_3)_2Cl_2$. Inset: linear dependence between $\ln(k_1/T)$ and $1/T$, as predicted by the Eyring equation (k_1 is the second-order rate constant for the first reaction step in Eq. (1)).



Scheme 1. Schematic presentation of the proposed associative mechanism of the substitution reaction between Ti(acac)Cl_2 (**1**) and H_2biphen to afford Ti(acac)$_2$(biphen) (**2**).

−60.8 J mol^{-1} K^{-1}, suggests that the substitution process proceeds *via* an associative mechanism. This is expected, since octahedral complexes of Ti^{IV} (d^0) are coordinatively unsaturated, *i.e.*, Ti(acac)$_2Cl_2$ is a 12-electron species, and therefore would prefer an associatively activated pathway. The incoming H_2biphen ligand is thus expected to compete with the solvent to form a 7-coordinated transition state. When considering the nature of the transition state of the first reaction, an activated complex in which the biphenolato binds to the Ti nucleus through only one of the O-atoms, is expected to form first. This transition state may then convert to another transition state in which the biphenol ligand becomes bidentate. Stable Ti(IV) complexes with coordination numbers greater than six, for example, 7- and 8-coordination, are known [37]. The common geometry for 7-coordinated Ti(IV) complexes is pentagonal bipyramidal, as in the case of Ti(dithioacetato)$_3$Cl [38] and Ti(N,N-diethyldithiocarbamato)$_4$ [39]. In a dissociative mechanism, the 5-coordinated cationic species, [Ti(acac)$_2$Cl]$^+$, formed by breaking the first Ti–Cl bond, is considerably less likely. The proposed reaction pathway for the substitution the reaction between Ti(acac)$_2Cl_2$ and H_2biphen may thus be presented as in Scheme 1 where the first [H_2biphen] dependent step is the formation of a 7-coordinated [Ti($CH_3COCHCOCH_3$)$_2$(Cl_2)(H_2biphen)] complex, and the second [H_2biphen] independent step being rate-limiting ring closure.

3. Conclusions

The substitution of bidentate 2,2-biphenyldiolato for the two monodentate Cl^- ligands in Ti($CH_3COCHCOCH_3$)$_2Cl_2$ proceeded *via* a 7-coordinated transition state according to an associative mechanism. The product of the substitution reaction, Ti($CH_3COCHCOCH_3$)$_2$biphen, is "air stable" and also exhibits high resistance towards hydrolysis.

4. Experimental

4.1. Materials and apparatus

Solid reagents used in preparations (Merck, Aldrich and Fluka) were used without further purification. Liquid reactants and solvents were distilled prior to use; water was doubly distilled. Organic solvents were dried according to published methods [40].

4.2. Synthesis of **2**

Complex **1** was synthesized according to published methods [25,26]. To 15 ml CH_3CN, 2,2′-biphenyldiol (0.186 g, 1 mmol) was added and stirred at RT. Complex **1** (0.317 g, 1 mmol) in 15 ml CH_3CN was added drop by drop to give an orange red solution which was refluxed for 4–6 h. The reaction mixture was then cooled to RT and filtered. The precipitate was washed in MeOH to remove unreacted biphenol, filtered, dried and stored under N_2 atmosphere. Yield: 0.333 g (77.5%). M.p. >250 °C. ^{1}H NMR (δ/ppm, $CDCl_3$): 2.05 (s, 12H, 4 × CH_3); 5.81 (s, 2H, acacH); 6.88 (d, 2H, biphenH); 7.00 (t, 2H, biphenH); 7.21 (t, 2H, biphenH); 7.39 (d, 2H, biphenH). λ_{max}(CH_3CN)/nm 334 (ε/dm^{+3} mol^{-1} cm^{-1} 4890(30)). Elemental *Anal.* Calc. for $C_{22}H_{22}O_6Ti$: C, 61.4; H, 5.2. Found: C, 61.2; H, 5.1%.

4.3. Spectroscopy and spectrophotometry

NMR measurements at 25 °C were recorded on a Bruker Advance II 600 NMR spectrometer [1H(600.130 MHz)]. The chemical shifts were reported relative to $SiMe_4$ (0.00 ppm). Positive values indicate downfield shift. IR spectra were recorded from neat samples on a Digilab FTS 2000 infrared spectrophotometer. UV–Vis spectra were recorded on a Cary 50 Probe UV–Vis spectrophotometer.

4.4. Kinetic measurements

The substitution reaction was monitored on the UV–Vis (by monitoring the change in absorbance at the indicated wavelength) spectrophotometer. All kinetic measurements were monitored under pseudo-first-order conditions with [H_2biphen] 10–200 times the concentration of the Ti(acac)$_2Cl_2$ complex in CH_3CN solution. The concentration Ti(acac)$_2Cl_2$ ≅ 0.0002 mol dm^{-3}. Kinetic measurements, under pseudo-first-order conditions for different concentrations of Ti(acac)$_2Cl_2$ at a constant [H_2biphen], confirmed that the concentration of Ti(acac)$_2Cl_2$ did not influence the value of the observed kinetic rate constant. A linear relationship between

UV absorbance, A, and concentration, *C*, confirmed the validity of the Beer–Lambert law ($A = \varepsilon Cl$ with l = path length = 1 cm) for the complexes **1** and **2** at experimental wave lengths λ_{max} = 340 nm (ε/dm^3 mol^{-1} cm^{-1} is 1830(20) for **1** and 4890(30) for **2**). The observed first-order rate constants were obtained from least-square fits of absorbance *versus* time data [41].

4.5. Calculations

Pseudo-first-order rate constants, k_{obs}, were calculated by fitting kinetic data [41] to the first-order equation [42] $[A]_t = [A]_0 e^{(-kobs\ t)}$ with $[A]_t$ and $[A]_0$ the concentration of the indicated species at time t and at $t = 0$ (UV–Vis). The experimentally determined pseudo-first-order rate constants were converted to second-order rate constants, k_1, by determining the slope of the linear plots of k_{obs} against the concentration of the incoming biphenolato ligand. Non-zero intercepts implied that $k_{obs} = k_1[\text{biphen}] + k_{-1}$ and that the first-order rate constant for a solvent pathway, k_{-1}, in the proposed reaction mechanism exists. All kinetic mathematical fits were done utilizing the fitting program MINSQ [41]. The error of all the data are presented according to crystallographic conventions, for example $k_{obs} = 0.0236(1)\ s^{-1}$ implies $k_{obs} = (0.0236 \pm 0.0001)\ s^{-1}$. The activation parameters were determined from the Eyring relationship [42] and the activation free energy $\Delta G^{\#} = \Delta H^{\#} - T\Delta S^{\#}$.

4.6. X-ray crystal structure determination

Crystals of Ti(acac)$_2$biphen (**2**) were obtained from recrystallization in chloroform. X-ray intensity data for **2** was measured on a Bruker X8 Apex II 4K CCD area detector, equipped with a graphite monochromator and Mo Kα fine-focus sealed tube (λ = 0.71073 Å) operated at 1.5 kW power (50 kV, 30 mA). The detector was placed at a distance of 3.75 cm from the crystal. Sample temperature was kept constant at 100(2) K using an Oxford 700 series cryostream cooler.

The initial unit cell and data collection of **2** were achieved by the Apex2 software [43] utilizing COSMO [44] for optimum collection of more than a hemisphere of reciprocal space. A total of 948 frames were collected with a scan width of 0.5° in φ and ω with an exposure time of 20 s per frame. The frames were integrated using a narrow frame integration algorithm and reduced with the Bruker SAINTPLUS and XPREP software [45] packages respectively. Analysis of the data collections showed no significant decay during the data collection. Data were corrected for absorption effects using the multi-scan technique SADABS [46].

The structure was solved by the direct methods package SIR97 [47] and refined using the WINGX software package [48] incorporating SHELXL [49]. The largest peaks on the final difference electron densities and the deepest holes were all within 1 Å from non-hydrogen atoms which presented no physical meaning in the final refinements. Aromatic protons were placed in geometrically idealized positions (C–H = 0.95 Å) and constrained to ride on their parent atoms with *U*iso(H) = 1.2 *U*eq(C). Initial positions of the methyl protons were obtained from a Fourier difference map and refined as fixed rotors with *U*iso(H) = 1.5 *U*eq(C) and C–H = 0.98 Å.

Atomic scattering factors were taken from the International Tables for Crystallography Volume C [50]. The molecular plot was drawn using the DIAMOND program [51] with a 30% thermal envelope probability for non-hydrogen atoms. Hydrogen atoms were drawn as arbitrary sized spheres with a radius of 0.135 Å.

Acknowledgements

Financial assistance by the South African National Research Foundation under Grant No. 2067416 and the Central Research Fund of the University of the Free State is gratefully acknowledged.

Appendix A. Supplementary data

CCDC 705149 contains the supplementary crystallographic data for Ti(acac)$_2$biphen. These data can be obtained free of charge via http://www.ccdc.cam.ac.uk/conts/retrieving.html, or from the Cambridge Crystallographic Data Centre, 12 Union Road, Cambridge CB2 1EZ, UK; fax: (+44) 1223-336-033; or e-mail: deposit@ccdc.cam.ac.uk. Text and figures giving further explanations is provided in the supplementary data. Supplementary data associated with this article can be found, in the online version, at doi:10.1016/j.poly.2008.10.025.

References

[1] E. Meléndez, Crit. Rev. Oncol. Hematol. 42 (2002) 309.
[2] B.K. Keppler, C. Friesen, H.G. Moritz, H. Vongerichten, E. Vogel, Struct. Bond. 78 (1991) 97.
[3] D.C. Bradley, Chem. Rev. 89 (1989) 1317.
[4] A. Braunemann, M. Hellwog, A. Varede, R.K. Bhakta, M. Winter, S.A. Shivashankar, R.A. Fisher, A. Devi, Dalton Trans. (2006) 3485.
[5] Y. Chen, S. Yekta, A.K. Yudir, Chem. Rev. 103 (2003) 3155.
[6] D. Kitamoto, H. Imma, T. Nakai, Tetrahedron Lett. 36 (1995) 1861.
[7] N.J. Hinde, C.D. Hall, J. Chem. Soc., Perkin Trans. 2 (1998) 1249.
[8] V.C. Gibson, S.K. Spitzmesser, Chem. Rev. 103 (2003) 283.
[9] K. Akagi, K. Mochiznki Y. Aoki, H. Shirakawa, Bull. Chem. Soc. Jpn. 66 (1993) 3444.
[10] P. Kocovsky, S. Vyskocil, M. Smrcina, Chem. Rev. 103 (2003) 3213.
[11] A. van der Linden, C.J. Schaverien, N. Meijboom, C. Ganter, A.G. Orpen, J. Am. Chem. Soc. 117 (1995) 3008.
[12] J. Balsells, T.J. Davis, P. Caroll, P.J. Walsh, J. Am. Chem. Soc. 124 (2002) 10336.
[13] G.E. Keck, K.H. Tarbet, L.S. Geraci, J. Am. Chem. Soc. 115 (1993) 8467.
[14] J.W. Faller, D.W. Sams, X. Liu, J. Am. Chem. Soc. 118 (1995) 1217.
[15] J.P. Corden, W. Errington, P. Moore, M.G. Partridge, M.G.H. Wallbridge, Dalton Trans. (2004) 1846.
[16] T.J. Boyle, A.T. Pearson, R.W. Schwartz, Ceram. Trans. 43 (1993) 79.
[17] M. Aizwa, Y. Nosaka, N. Fujii, J. Non-Cryst. Solids 128 (1991) 77.
[18] (a) C. Rosini, L. Franzini, A. Raffaelli, P. Salvadori, Synthesis (1992) 503;
(b) L. Pu, Chem. Rev. 98 (1998) 2405;
(c) K. Mikami, in: L.A. Paquette (Ed.), Encyclopedia of Reagents for Organic Synthesis, vol. 1, John Wiley and Sons, New York, 1995, p. 403;
(d) K. Mikami, Y. Motoyama, in: L.A. Paquette (Ed.), Encyclopedia of Reagents for Organic Synthesis, vol. 1, John Wiley and Sons, New York, 1995, p. 397;
(e) H. Yamamoto, A. Yanagisawa, K. Ishihara, S. Saito, Pure Appl. Chem. 70 (1998) 1507;
(f) M. Shibasaki, H. Sasai, T. Arai, Angew. Chem., Int. Ed. Engl. 36 (1997) 1237.
[19] M. Mori, H. Imma, T. Nakai, Tetrahedron Lett. 38 (1997) 6229.
[20] (a) S. Matsukawa, K. Mikami, Tetrahedron: Asymmetry 8 (1997) 815;
(b) G.H. Posner, H. Dai, D.S. Bull, J.-K. Lee, F. Eydoux, Y. Ishihara, W. Welsh, N. Pryor, S.J. Petr, J. Org. Chem. 61 (1996) 671;
(c) L.C. Dias, J. Braz. Chem. Soc. 8 (1997) 289.
[21] (a) S. Kobayashi, S. Komiyama, H. Ishitani, Angew. Chem., Int. Ed. 37 (1998) 979;
(b) S. Kobayashi, K.-I. Kusakabe, H. Ishitani, Org. Lett. 2 (2000) 1225;
(c) K.B. Simonsen, N. Svenstrup, M. Roberson, K.A. Jorgensen, Chem. Eur. J. 6 (2000) 123.
[22] (a) K. Mikami, M. Terada, Tetrahedron 48 (1992) 5671;
(b) K. Mikami, Y. Motoyama, M. Terada, Inorg. Chim. Acta 222 (1994) 71;
(c) K. Mikami, S. Matsukawa, T. Volk, M. Terada, Angew. Chem., Int. Ed. Engl. 36 (1997) 2768;
(d) L.C. Dias, Curr. Org. Chem. 4 (2000) 305.
[23] (a) S. Matsukawa, K. Mikami, Tetrahedron: Asymmetry 6 (1995) 2571;
(b) G.E. Keck, D. Krishnamurthy, J. Am. Chem. Soc. 117 (1995) 2363.
[24] (a) M. Mori, T. Nakai, Tetrahedron Lett. 38 (1997) 6233;
(b) F.-Y. Zhang, C.-W. Yip, R. Cao, A.S.C. Chan, Tetrahedron: Asymmetry 8 (1997) 585;
(c) K. Mikami, R. Angelaud, K.L. Ding, A. Ishii, A. Tanaka, N. Sawada, K. Kudo, M. Senda, Chem. Eur. J. 7 (2001) 730;
(d) K. Ding, A. Ishii, K. Mikami, Angew. Chem., Int. Ed. 38 (1999) 497.
[25] R.C. Fay, R.N. Lowry, Inorg. Chem. 6 (1967) 1512.
[26] N. Serpone, R.C. Fay, Inorg. Chem. 6 (1967) 1835.
[27] P.V. Rao, C.P. Rao, E.K. Wegelius, E. Kolehmainen, K. Rissanen, J. Chem. Soc., Dalton Trans. (1999) 4470.
[28] W.H. Baier, Acta Crystallogr. 9 (1956) 515.
[29] A. Bodner, P. Jeske, T. Weyhermuller, K. Wieghardt, E. Dubler, H. Schmalle, B. Nuber, Inorg. Chem. 31 (1992) 3737.
[30] P. Corradini, S. Allegra, J. Am. Chem. Soc. 81 (1959) 5510.
[31] C. Janiak, J. Chem. Soc., Dalton Trans. (2000) 3885.
[32] G.B. McGaughey, M. Gagne, A.K. Rappe, J. Biol. Chem. 273 (1998) 15458.
[33] B.K. Keppler, M.E. Heim, Drugs Future 3 (1988) 638.
[34] J. Burgess, S.a. Parson, Appl. Organomet. Chem. 7 (1993) 343.

[35] F. Basolo, R. Pearson, Mechanism of Inorganic Reactions, 2nd ed., Wiley, New York, 1965 (K.F. Purcell, J.C. Kotz, Inorganic Chemistry, International Edition, Saunders, London, 1977, p. 697).
[36] R.G. Wilkins, Kinetics and Mechanism of Reactions of Transition Metal Complexes, 2nd thoroughly revised ed., VCH, Weinheim, 1991. p. 103, 232.
[37] C.A. McAuliffe, D.S. Barratt, in: G. Wilkinson, R.D. Gillard, J.A. McCleverty (Eds.), Comprehensive Coordination Chemistry, vol. 3, Pergamon Press, Oxford, 1987, p. 323.
[38] L. Gastaldi, L. Scaramuzza, Cryst. Struct. Commun. 9 (1980) 469.
[39] M. Colapietro, A. Vaciago, D.C. Bradley, M.B. Hursthouse, I.F. Rendalln, J. Chem. Soc., Dalton Trans. (1972) 1052.
[40] B.S. Furniss, A.J. Hannaford, P.W.G. Smith, A.R. Tatchell, Vogel's Textbook of Practical Organic Chemistry, 5th ed., John Wiley & Sons, New York, 1994. p. 409.
[41] L. Helm, MINSQ, Non-linear Parameter Estimation and Model Development, Least Squares Parameter Optimization V3.12, MicroMath Scientific Software, Salt Lake City, UT, 1990.
[42] J.H. Espenson, Chemical Kinetics and Reaction Mechanisms, 2nd ed., McGraw-Hill, New York, 1995. p. 15, 49, 70, 156.
[43] APEX2 (Version 1.0-27), Bruker AXS Inc., Madison, Wisconsin, USA, 2005.
[44] COSMO (Version 1.48), Bruker AXS Inc., Madison, Wisconsin, USA, 2003.
[45] SAINT-PLUS (Version 7.12 including XPREP), Bruker AXS Inc., Madison, Wisconsin, USA, 2004.
[46] SADABS (Version, 2004/1), Bruker AXS Inc., Madison, Wisconsin, USA, 1998.
[47] A. Altomare, M.C. Burla, M. Camalli, G.L. Cascarano, C. Giacovazzo, A. Guagliardi, A.G.G. Moliterni, G. Polidori, R. Spagna, J. Appl. Crystallogr. 32 (1999) 115.
[48] L.J. Farrugia, J. Appl. Crystallogr. 32 (1999) 837 (WinGX 1.70.01).
[49] G.M. Sheldrick, SHELXL97, Program for Crystal Structure Refinement, University of Göttingen, Germany, 1997.
[50] International Tables for Crystallography, vol. C, Kluwer Academic Publishers, Dordecht, The Netherlands, 2006, p. 1002.
[51] K. Brandenburg, H. Putz, DIAMOND Release 3.1a, Crystal Impact GbR, Bonn, Germany, 2005.

Polyhedron 28 (2009) 215–220

Contents lists available at ScienceDirect

Polyhedron

journal homepage: www.elsevier.com/locate/poly

Synthesis, structure and magnetism of a one-dimensional silicotungstate array: $K_3H_4Cu_{0.5}\{Cu[Cu_{7.5}Si_2W_{16}O_{60}(H_2O)_4(OH)_4]_2\} \cdot 9H_2O$

Zhen Luo [a], Paul Kögerler [b], Rui Cao [a], Craig L. Hill [a,*]

[a] Department of Chemistry, Emory University, Atlanta, GA 30322, USA
[b] Institut für Anorganische Chemie, RWTH Aachen University, D-52074 Aachen, Germany

ARTICLE INFO

Article history:
Received 8 January 2008
Accepted 8 September 2008
Available online 8 December 2008

Keywords:
Multi-copper
Polyoxometalate
Polymer
Ferromagnetism

ABSTRACT

A structurally distinct, multi-copper(II)-substituted silicotungstate $K_3H_4Cu_{0.5}\{Cu[Cu_{7.5}Si_2W_{16}O_{60}(H_2O)_4(OH)_4]_2\} \cdot 9H_2O$ (**1**) has been synthesized and characterized by FT-IR spectroscopy, elemental analysis, variable-temperature magnetic measurements, electron spin resonance, and X-ray diffraction. Green crystalline plates of **1** were obtained by the reaction of $K_8[\gamma\text{-}SiW_{10}O_{36}] \cdot 12H_2O$ with 8 equiv. of Cu(II) in a 50% ethylene glycol solution. A cationic copper center connects the terminal oxygen atoms of neighboring polyanions, resulting in a one-dimensional structure. Magnetic susceptibility measurements indicate weak ferromagnetic superexchange between the Jahn–Teller-distorted $S = 1/2$ Cu(II) centers.

© 2008 Elsevier Ltd. All rights reserved.

1. Introduction

Polyoxometalates (POMs) substituted with one or more d-electron metal centers constitute a large class of electronically highly tunable and structurally robust multinuclear compounds [1–3] with applications in catalysis [2,4–11] and potential applications in electroactive materials [12–14], magnetism [15–20], medicine (diagnostics or therapeutics) [21–27], and other fields. The incorporation of transition metals into lacunary POM precursors is generally simple and straightforward; however, the exact mechanisms by which metal-substituted POMs are formed are complex and not well understood. Most frequently, the d-electron metals fill the vacant positions of the lacunary POM forming a saturated (or plenary) structure. Complicating plenary structure reconstitution is the fact that multi-vacant (di-lacunary or tri-lacunary) POM precursors can isomerize under different synthetic conditions, leading to a range of metal-substituted structures. The di-vacant silicotungstate, $[\gamma\text{-}SiW_{10}O_{36}]^{8-}$, readily isomerizes to α and β structures in aqueous solution [28–30], and these processes result in the formation of a diverse set POM structures [31–42] upon reaction with transition metals.

Several research groups have investigated the reactions of $[\gamma\text{-}SiW_{10}O_{36}]^{8-}$ with first-row transition metal salts [31–48]. Early work to prepare disubstituted $\{\gamma\text{-}M_2SiW_{10}\}$ (M = V, Cr, Mn), where the γ-isomer polyoxoanion structure is retained, was performed by Pope and co-workers [32,33,44]. These di-metal substituted structures contain the two d metals in adjacent positions as either "in-pocket" or "out-of-pocket" isomers. The in-pocket isomers contain bonds between the central heteroatom oxygens and the incorporated d-electron centers. In contrast, the out-of-pocket isomers do not contain this bond, and consequently the d-electron metals are displaced from the center of the polyanion and frequently multiply bonded to other adjacent polyanions or distinct structural units. Subsequently $\{\gamma\text{-}M_xSiW_{10}\}$ structures were reported by the research groups of Mizuno [43,45,46], Mialane [39], Peng [47], and others. By slightly changing the synthetic conditions, Kortz and co-workers [36] prepared a series of sandwich dimers, $[\beta\text{-}(M_2SiW_9O_{34})_2]^{(2n+4)-}$ (M = Mn, Cr, Zn). Further investigation of the reactions of d-electron-metals with $[\gamma\text{-}SiW_{10}O_{36}]^{8-}$ by this group afforded several other d-electron-metal-substituted silicotungstates [37,38,40,41,48,49]. Meanwhile, Mialane and co-workers [39,50,51] reported several different metal-substituted silicotungstates with complicated structures by adding azide and/or other ligands to the reaction system. Peng and co-workers [47] described dimers, $[\{K(H_2O)\}_2\{(\mu_3\text{-}H_2O)M(H_2O)\}(\gamma\text{-}Si_2W_{20}O_{70})]^{8-}$ (M = Mn^{2+}, Co^{2+}, and Ni^{2+}), prepared in acidic aqueous solution, that retain the $\{\gamma\text{-}SiW_{10}\}$ unit of the precursor.

Recently, we obtained a di-copper substituted dimeric silicotungstate complex, $K_9Na_2Cu_{0.5}[\gamma\text{-}Cu_2(H_2O)SiW_8O_{31}]_2 \cdot 38H_2O$ from the reaction of a copper(II) salt with $K_8[\gamma\text{-}SiW_{10}O_{36}] \cdot 12H_2O$ in an acetate-buffered 50% ethylene glycol solution [52]. This copper substituted silicotungstate cluster contains two pseudo-planar Cu_2O_2 motifs, and strong ferromagnetic superexchange between the $S = 1/2$ Cu(II) centers was observed. Simultaneously, Peng and co-workers obtained a similar complex via a different synthetic

* Corresponding author. Tel.: +1 404 727 6611; fax: +1 404 727 6076.
E-mail address: chill@emory.edu (C.L. Hill).

0277-5387/$ - see front matter © 2008 Elsevier Ltd. All rights reserved.
doi:10.1016/j.poly.2008.09.031

approach [53]. We report here that reaction of $[\gamma\text{-}SiW_{10}O_{36}]^{8-}$ and $Cu(NO_3)_2$ in unbuffered aqueous solution followed by crystallization out of water:ethylene glycol (1:1) produces a one-dimensional polymeric structure comprising $\{Cu_{16}Si_4W_{32}\}$ polyanions interlinked by additional individual Cu(II) centers, $K_3H_4Cu_{0.5}\{Cu[Cu_{7.5}Si_2W_{16}O_{60}(H_2O)_4(OH)_4]_2\}\cdot 9H_2O$ (**1**). Magnetic susceptibility and ESR measurements of **1** show that this multi-copper substituted silicotungstate exhibits more complicated magnetic properties. As we were reporting our work, Su and co-workers [53] reported a similar multi-copper polyanion, $Na_{16}[Cu_{14}(OH)_4(H_2O)_{16}(SiW_8O_{31})_4]\cdot 20.5H_2O$, but here the structure features discrete polyanion units, and no magnetic data were reported. Herein, we describe the synthesis, structure, and magnetic properties of **1**.

2. Experimental

2.1. General methods and materials

$K_8[\gamma\text{-}SiW_{10}O_{36}]\cdot 12H_2O$ was prepared according to literature procedure [30] and the purity was checked by infrared spectroscopy. Copper nitrate, acetonitrile and ethylene glycol were obtained from Aldrich and used without further purification. Elemental analyses for K, Cu, Si and W were performed by Galbraith Laboratories (Knoxville, Tennessee). The infrared spectrum (2 weight% sample in KBr pellet) was recorded on a Nicolet 6700 FT-IR spectrometer. Thermogravimetric data were collected on an ISI TGA 1000 instrument. ESR measurements were performed on a powder sample at 290 K using a Magnettech Miniscope MS-100 spectrometer and DPPH as an external standard. Magnetic susceptibility measurements were performed at 0.1–5.0 T for $T = 1.8$–290 K using a Quantum Design MPMS-5S SQUID magnetometer. Experimental susceptibility data were corrected for diamagnetic and (significant) temperature-independent paramagnetic contributions that were determined from measurements on a range of diamagnetic γ-Keggin polyoxotungstate compounds ($\chi_{dia/TIP}$(**1**) = -1.10×10^{-3} emu/mol).

2.2. Synthesis of $K_3H_4Cu_{0.5}\{Cu[Cu_{7.5}Si_2W_{16}O_{60}(H_2O)_4(OH)_4]_2\}\cdot 9H_2O$ (**1**)

A 5 mL aliquot of acetonitrile solution containing 0.5 g (2.66 mmol) of $Cu(NO_3)_2$ was dissolved in 20 mL of deionized water. To this solution 1.0 g (0.33 mmol) of $K_8[\gamma\text{-}SiW_{10}O_{36}]\cdot 12H_2O$ was added with stirring. After stirring for 20 min, the undissolved residues were removed from the solution by a medium frit and the filtrate (25 mL) was collected. A 5 mL portion of the filtrate was transferred to a 15 mL vial and 5 mL of ethylene glycol was added. The mixture was stirred for an additional 5 min and then placed into a dark cabinet. Green plate-like diffraction quality crystals of **1** grew from this 1:1 water:ethylene glycol mixed solution after two weeks (0.12 g, yield 14.4%). IR (2% KBr pellet, 1200–400 cm^{-1}): 1082 (w), 1039 (w), 990 (w, sh), 950 (m), 878 (s, sh), 787 (w), 736 (s), 696 (w), and 519 (w, sh), 491 (w). Elemental composition *Anal.* Calc. for $K_3H_4Cu_{0.5}\{Cu[Cu_{7.5}Si_2W_{16}O_{60}(H_2O)_4(OH)_4]_2\}\cdot 9H_2O$: Cu, 11.00; K, 1.23; Si, 1.18; W, 61.75. Found: Cu, 11.9; K, 1.07; Si, 1.22; W, 58.2%. [MW = 9527.6 g/mol].

2.3. X-ray crystallography of **1**

A green plate crystal of **1** with dimensions of $0.19\times0.17\times0.04$ mm^3 coated in Paratone-N oil was mounted on a small fiber loop for index and intensity data collection. The data were collected at 30 K under a helium stream on a Bruker-AXS SMART 1000 CCD single-crystal diffractometer using Mo K_α (0.71073 Å) radiation. Indexing, and initial cell refinements of the collected data were performed by the SMART [54] program. The frame integration and final cell refinements were carried out by using the SAINT [55] program. The final cell parameters were determined from the least-squares refinement of 79 664 reflections. From these unique reflections ($2\theta_{max} = 46.52°$), 13 924 reflections ($R_{int} = 0.2197$) were considered to be observed. The structure was determined through direct methods (SHELXS97) via locating the tungsten atoms and difference Fourier maps (SHELXL97). The hydrogen atoms of the water molecules were not located in the difference Fourier maps. The final cycle of refinement resulted at $R = 0.0979$ and $R_w = 0.1513$ ($I > 2\sigma(I)$) (Table 1). In the final difference map, a residual electron density maximum of 3.954 e $Å^{-3}$ and a minimum of -3.304 e $Å^{-3}$ were observed.

Table 1
Crystallographic data and structure refinement for **1**.

	1
Empirical formula	$Cu_{16.5}H_{46}K_3O_{145}Si_4W_{32}$
Formula weight (g mol^{-1})	9527.6
Temperature (K)	173(2)
Wavelength (Å)	0.71073
Crystal system	monoclinic
Space group	*C2/c* (#15)
Unit cell	
a (Å)	27.268(8)
b (Å)	22.895(6)
c (Å)	33.304(9)
β (°)	111.070(9)
V ($Å^3$)	19402(9)
Z	4
D_{calc} (g cm^{-3})	3.350
Absorption coefficient (mm^{-1})	20.778
Goodness-of-fit	1.034
final R_1[a] [$I > 2\sigma(I)$]	0.0979
final wR_2[b] [$I > 2\sigma(I)$]	0.2524

[a] $R_1 = \sum||F_0| - |F_c||/\sum|F_0|$.
[b] $wR_2 = \sum[w(F_0^2 - F_c^2)]/\sum[w(F_0^2)^2]^{1/2}$.

3. Results and discussion

3.1. Synthesis

The potassium salt of **1** was prepared by mixing 8:1 mole ratio of $Cu(NO_3)_2$ and $K_8[\gamma\text{-}SiW_{10}O_{36}]\cdot 12H_2O$ in a 1:1 water–ethylene glycol solution. Green crystalline plates of **1** were obtained after two weeks in ca. 14% yield. If the same synthetic procedure is followed but without the addition of ethylene glycol, small green needle-like crystals appear after several hours in significantly higher yield (ca. 46%). The FT-IR spectrum of these needles are very similar to that of **1** except that there is an absence of two peaks at 1082 and 1039 cm^{-1}, which are attributed to the C–O stretch of ethylene glycol. Unfortunately, the needles diffracted X-rays poorly providing commensurately low quality datasets. Complex **1** was synthesized in an acidic environment (pH 4.2) without buffer and the blue needle-like crystals were obtained when HOAc/NaOAc buffer was used to maintain the same pH value. X-ray diffraction established that the blue crystals are a dimeric silicotungstate which contains a $\{\gamma\text{-}Cu_2(H_2O)SiW_8O_{31}\}$ motif in each subunit. Both **1** and the dimeric POM contain the tetra-vacant $\{B\text{-}\beta\text{-}SiW_8O_{31}\}$ fragment in their structures. The appearance of this $\{B\text{-}\beta\text{-}SiW_8O_{31}\}$ fragment in both multi-copper-containing POM products may indicate that Cu^{2+} ions facilitate conversion of the di-vacant $[\gamma\text{-}SiW_{10}O_{36}]^{8-}$ into $\{B\text{-}\beta\text{-}SiW_8O_{31}\}$ *in situ* and/or stabilize the latter unit via coordination. It is reasonable that the excess acetate from the buffer and the polytungstate intermediates compete to coordinate to the hydrated Cu^{2+} ions, and this competition leads to the formation of the recently reported dimeric cluster [52,56] which contains fewer copper centers per polyanion.

Kortz and co-workers [38,48] recently reported several POM structures that contain the {B-β-SiW_8O_{31}} unit in their study of the Co(II)/[γ-$SiW_{10}O_{36}$]$^{8-}$ system, where a large excess $CoCl_2$ was reacted with [γ-$SiW_{10}O_{36}$]$^{8-}$ in aqueous solution buffered at pH 5.5 and heated to 50 °C for 30 min. This procedure resulted in the cobalt-substituted silicotungstate trimer [{$Co_9Cl_2(OH)_3(H_2O)_9$(β-$SiW_8O_{31})_3$}]$^{5-}$ of D_{3h} symmetry. Each subunit of this trimer contains a {B-β-SiW_8O_{31}} unit, which coordinates with three cobalt atoms and forms a {M_3SiW_8} motif. By changing the pH to 4.8 and the molar ratio of Co:[γ-$SiW_{10}O_{36}$]$^{8-}$ to 2:1, another cobalt-substituted silicotungstate, [{Co_3(B-β-SiW_9O_{33})(OH))(B-β-SiW_8O_{29}-$(OH)_2$}$_2$]$^{22-}$, was obtained which also contains the {M_3SiW_8} motif [38,48].

Mialane and co-workers [39,51,57] have investigated the reaction of transition metals and [γ-$SiW_{10}O_{36}$]$^{8-}$ in the presence of azide and documented several instances where azide interacts with metal centers, resulting in the formation of new POM structures. They obtained a copper-substituted trimer, [{$SiW_8O_{31}Cu_3$-$(OH)(H_2O)_2(N_3)$}$_3(N_3)$]$^{19-}$, that is structurally analogous to the Co-substituted trimer obtained by Kortz and co-workers when an excess of azide was used. Their study of the Co/[γ-$SiW_{10}O_{36}$]$^{8-}$ system afforded several different cobalt-substituted silicotungstates, including the dimer polyanion [{(B-β-SiW_9O_{33})(OH)(β-SiW_8O_{29}-$(OH)_2$)$Co_3(H_2O)$}$_2$$Co(H_2O)_2$]$^{20-}$. Each subunit of this dimer contains a {B-β-SiW_8O_{31}} and a {B-β-SiW_9O_{34}} motif connected by three cobalt atoms, and the {B-β-SiW_8O_{31}} motif in each subunit is linked to another by a six-coordinated cobalt center. The general polyanion framework of this Co-substituted POM is similar to our sixteen-copper-containing polyanion, **1**. Very recently, Zhang et al. [53] reported a 14-copper-containing silicotungstate by the reaction of 12 mol equiv. of copper salt with [γ-$SiW_{10}O_{36}$]$^{8-}$ in a pH 5.5 boiling aqueous solution containing D-proline for 2 h. This Cu_{14} silicotungstate is structurally analogous to **1** but contains less copper since the polyanions are not linked by Cu centres into a one-dimensional material as it is the case in **1** (*vide infra*).

3.2. Structural features

The new polymeric multi-copper-substituted silicotungstate, **1**, crystallizes in the monoclinic space group, *C2/c*. The polyanion unit contains 2 equiv. [$Cu_7Si_2W_{16}O_{60}(H_2O)_4(OH)_4$]$^{6-}$ subunits related by a four-coordinate copper located on the C_2 axis (C_2 local symmetry; Fig. 1). The inversion center is not located at this copper, but lies in the center of the unit cell. Each subunit contains two multi-copper substituted {B-β-SiW_8O_{31}} motifs (Fig. 2). The two motifs connect to each other via three five-coordinate copper atoms: Cu2, Cu3 and Cu4. O30 is a μ_3-oxo bridging Cu3, Cu4 and Si1; O35 is a μ_4-oxo bridging Cu2, Cu3, Cu4 and Si2. In the {B-β-SiW_8O_{31}} motif containing Si1, two of the copper atoms, Cu3 and Cu4, exist as a {Cu_2O_6} unit which resides in the position of the conventional {W_2O_6} group, thus forming a {γ-$Cu_2SiW_8O_{31}$} unit that maintains the γ isomerism of the [γ-$SiW_{10}O_{36}$]$^{8-}$ precursor. Alternatively, the {B-β-SiW_8O_{31}} motif with Si2 contains these three copper atoms, Cu2, Cu3 and Cu4, as a {Cu_3O_5} unit that defines a β-Keggin structure, {β-$Cu_3SiW_9O_{34}$}. The remaining lacunary (vacant) position of the {β-$Cu_3SiW_9O_{34}$} motif is filled by Cu6. Two more copper atoms, Cu5 and Cu7, are also five coordinate each forming a pyramidal unit linked to Cu6. The three copper atoms linked via four μ_3-oxo groups form a nearly planar Cu_3O_4 motif. The pyramidal units share the terminal O1 and O7 with the {γ-$Cu_2SiW_8O_{31}$} motif located on the other subunit, thus connecting the β and γ motifs in different subunits to form the large cluster. Cu1, the only four-coordinate copper in the structure which is located on the C_2 axis, fills the lacunary position opposite to Cu3 and Cu4 on each γ motif. In each subunit, a copper atom, Cu8, is bonded to three oxygens on the outside (away from the central multi-copper region) of the γ motif. One more cationic copper, Cu9, connects to the terminal oxygen of W15 and W15′ located on two neighboring molecules thereby linking the clusters to form the one-dimensional array (Fig. 3).

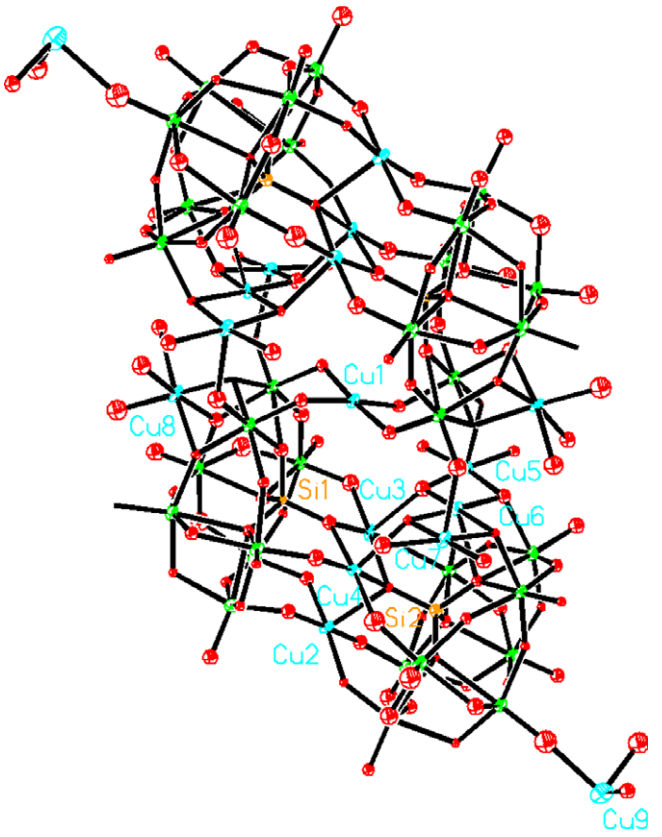


Fig. 1. Ball and stick representation of [$Cu\{Cu_{7.5}Si_2W_{16}O_{60}(H_2O)_4(OH)_4\}_2$]$^{8-}$ (**1a**, the polyanion of **1**) showing 50% probability ellipsoids and selected atomic labels. Cu: blue; O: red; Si: orange; W: green. (For interpretation of the references to colour in this figure legend, the reader is referred to the web version of this article.)

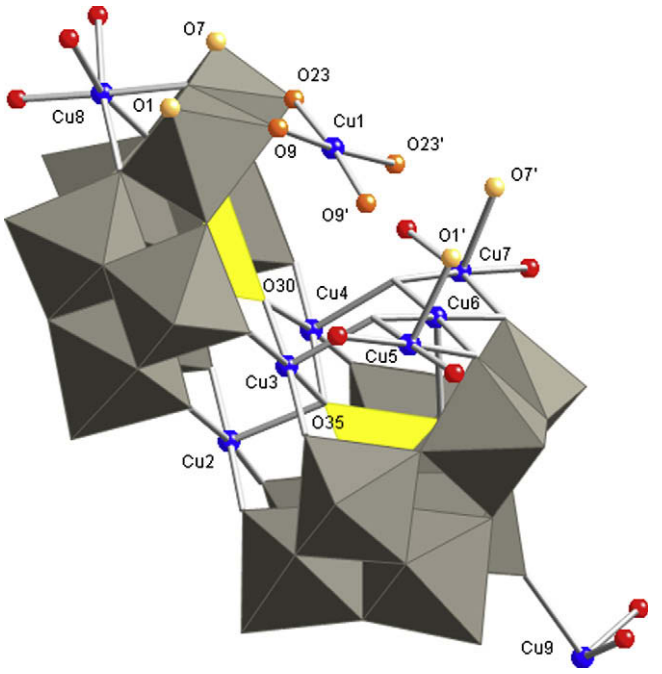


Fig. 2. A combination polyhedral/ball-and-stick representation of the {Cu_9Si_2-$W_{16}O_{60}(H_2O)_4(OH)_4$} subunit of **1**.

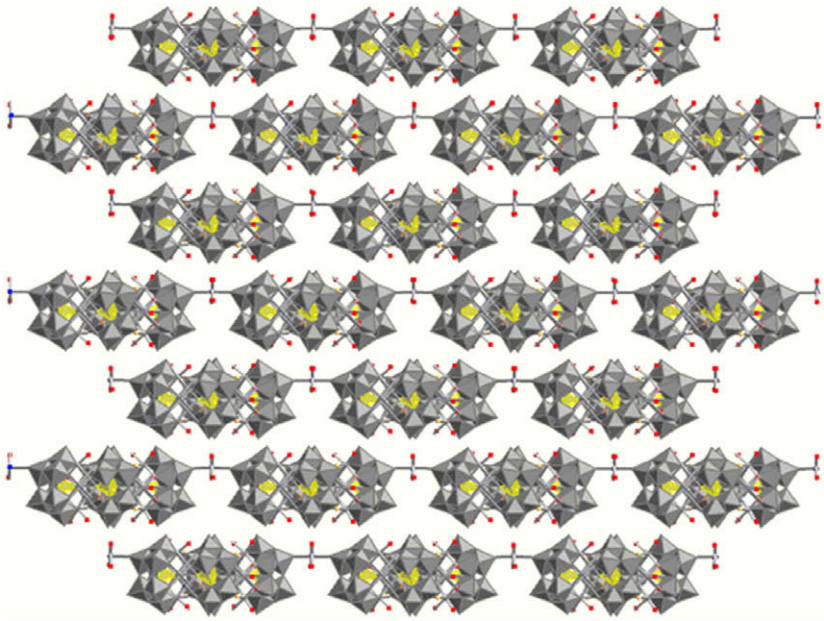


Fig. 3. Structural view of the one-dimensional array of **1** from *c* axis direction.

3.3. Electron spin resonance

The X-band ESR spectrum of **1**, measured as a powder, displays an overlay of several different Cu(II) environments, resulting in a very broad signal (Fig. 4). The resulting convoluted response can be understood as an average of Jahn–Teller-distorted Cu(II) signals characterized by vertical and parallel g tensor components, $g_{\perp} = (g_{xx} + g_{yy})/2$ and $g_{||} = g_{zz}$, characteristic for Cu(II) centers in such distorted environments. From the average values $g_{\perp} = 2.04$ and $g_{||} = 2.48$, an average isotropic $g_{iso} = 2.19$ is derived. Note that limited solubility of **1** in polar and nonpolar solvents prevented recording of an ESR spectrum of **1** in solution of possibly higher resolution.

3.4. Magnetic properties

The low-field (0.1 T) magnetism of compound **1** indicates dominating weak ferromagnetic intramolecular superexchange between the Jahn–Teller-distorted $s = 1/2$ Cu(II) centers that are spaced apart less than 3 Å (Table 2). Note that ferromagnetic interactions of comparable strength are also observed in Cu(II)-substituted polyoxometalates such as $\{Mo_{57}Cu_6\}$-type clusters [58] in which the spin centers are bridged by O–Mo–O fragments and where the orthogonality of the magnetic Cu(3d) orbitals necessary for ferromagnetic exchange is achieved by rotation of their colinear local orbital coordinate frameworks by 60° around the local z axis, i.e. the elongated Jahn–Teller axis. In **1** the coupling within a subunit (characterized by the exchange energy J_1 between Cu3 and Cu4) is mediated via a μ_3-oxo group (O30) and a μ_4-oxo group (O35), whereby the Cu(II) centers form a nearly planar Cu_2O_2 motif with oxo groups in the equatorial coordination plane. Very similar and coplanar Cu_2O_2 motifs result for the triad formed by Cu5, Cu6, and Cu7. The geometry of the $Cu_2(\mu\text{-}O)_2$ fragments are expected to result in ferromagnetic exchange based on the empirical correlation studies of oxo-bridged Cu(II) dimer compounds [59–62]. We expect that both of these effects, the rotation of the coordinate systems and the Cu–O–Cu bond angles in the subunits, are the primary source for the observed ferromagnetic coupling. However, additional weaker antiferromagnetic coupling is likely to be present, too, e.g. for contacts involving O–W–O exchange pathways such as Cu1–Cu8. On the other hand, we expect Cu9, interlinking the POM units, to be magnetically isolated as any pathways to other Cu centers involve at least five non-magnetic centers. Furthermore, also Cu2 has to be assumed to be magnetically isolated: the magnetic Cu(3d) orbital will be of $d_{x^2-y^2}$ character due to the observed Jahn–Teller distortion so that virtually no exchange will be active via the apical oxo center (O35), and exchange with any

Table 2
Select bond distances (Å) and bond angles (°) for **1**.

Cu3–Cu4	2.930(6)	Cu6–O37	1.92(2)
Cu5–Cu6	2.954(6)	Cu6–O38	1.85(3)
Cu6–Cu7	2.927(6)	Cu3–O30–Cu4	95.9(12)
Cu1–O9	1.90(3)	Cu3–O35–Cu4	92.5(10)
Cu3–O30	1.95(3)	Cu5–O37–Cu6	101.9(15)
Cu3–O35	2.05(2)	Cu5–O50–Cu6	97.1(13)
Cu4–O30	2.00(3)	Cu6–O38–Cu7	97.4(12)
Cu4–O35	2.01(2)	Cu6–O9–Cu7	94.9(11)

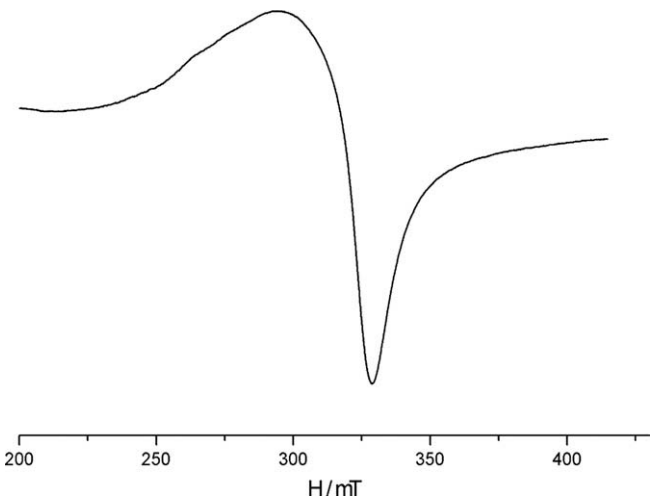


Fig. 4. X-band ESR spectrum of compound **1**, measured as a microcrystalline powder at 290 K.

adjacent Cu centers via the equatorial oxo ligands will, on the other hand, again involve more than five non-magnetic centers. For the same reasons, the interaction between the Cu3/Cu4 dimer and the Cu5/Cu6/Cu7 triad will be very weak as well. In summary, in terms of magnetic interactions **1** can be approximated as several independent entities: magnetically isolated centers, Cu2 and Cu9, a weakly antiferromagnetically coupled symmetric trimer, Cu8–Cu1–Cu8′, a ferromagnetically coupled dimer, Cu3–Cu4, and a ferromagnetically coupled trimer, Cu5–Cu6–Cu7. The high nuclearity and the large number of intramolecular exchange contacts in **1** precludes, however, the unambiguous determination of coupling constants J_n based on the susceptibility data, even if only a simple isotropic Heisenberg-type model Hamiltonian is employed.

The high-temperature limit of χT of 7.6 emu K/mol (at 290 K) corresponds to the spin-only moment of 16.9 spin-1/2 centers (assuming the ESR-derived $g_{iso} = 2.19$). This value indicates an additional fraction of approx. 0.9 isolated Cu(II) centers per formula unit in the cationic lattice. Below ca. 100 K, χT rises continually, and even at 1.8 K (15.3 emu K/mol) the χT versus T graph does not show any signs of approaching a maximum (Fig. 5). This steep increase is, however, quenched at higher fields. At 5.0 Tes/a, χT reaches a maximum at ca. 12 K.

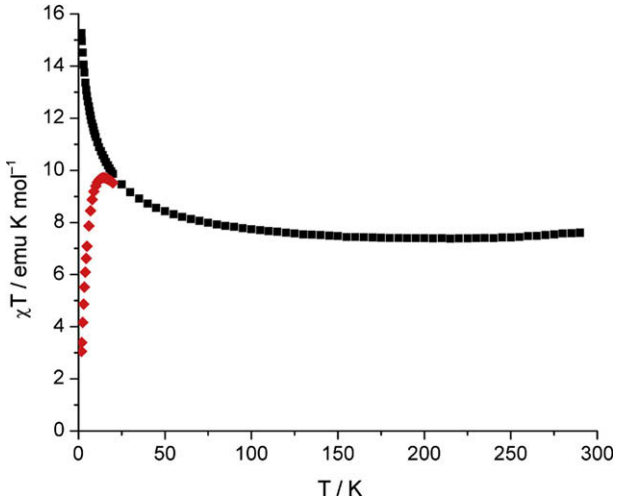


Fig. 5. Temperature dependence of χT of **1** at 0.1 T (black squares) and at 5.0 T (red carets, the data follows the 0.1 T curve for higher temperatures). (For interpretation of the references to colour in this figure legend, the reader is referred to the web version of this article.)

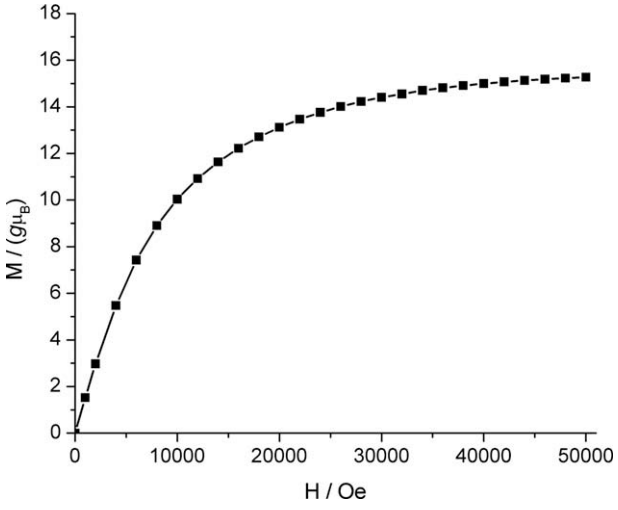


Fig. 6. Field dependence of the magnetization, M, of **1** at 1.8 K.

Field-dependent magnetization measurements at 1.8 K (Fig. 6) indicate the expected magnetic saturation. However, the aforementioned magnetically isolated entities all contribute to the low-temperature magnetization; therefore, the spin ground state of an individual POM cluster unit cannot be determined with certainty from these data. In addition, as evident from the very broad ESR spectrum, the coordination environments of the Cu(II) centers differ significantly and thus contribute to the overall magnetization to a different extent. We are currently working to characterize this system using large-scale simulation techniques (Quantum Monte Carlo simulations) and will present a more detailed description of the magnetism of **1** in forthcoming work.

Supplementary data

CSD 418999 contains the supplementary crystallographic data for **1**. Further details of the crystal structure investigation may be obtained from Fachinformationszentrum Karlsruhe, 76344 Eggenstein-Leopoldshafen, Germany (fax: (+49)7247-808-666; e-mail: crysdata@fiz-karlsruhe.de, http://www.fiz-karlsruhe.de/request_for_deposited_data.html) on quoting the appropriate CSD number.

Acknowledgments

C.L.H. thanks TDA Research Corporation (W911NF-04-C-0136), the US Army Research Office (W911NF-05-1-0200), and the National Science Foundation (CHE-0553581) for funding this work and Dr. Joseph Reibenspies at Texas A&M University for collection of the low temperature X-ray dataset.

References

[1] M.T. Pope, Heteropoly and Isopoly Oxometalates, Springer-Verlag, Berlin, 1983.
[2] C.L. Hill, C.M. Prosser-McCartha, Coord. Chem. Rev. 143 (1995) 407.
[3] C.L. Hill, Chem. Rev. 98 (1998) 1.
[4] E. Coronado, C.J. Gómez-García, Chem. Rev. 98 (1998) 273.
[5] I.V. Kozhevnikov, Chem. Rev. 98 (1998) 171.
[6] T. Okuhara, N. Mizuno, M. Misono, Adv. Catal. 41 (1996) 113.
[7] N. Mizuno, M. Misono, Chem. Rev. 98 (1998) 199.
[8] R. Neumann, Prog. Inorg. Chem. 47 (1998) 317.
[9] D.E. Katsoulis, Chem. Rev. 98 (1998) 359.
[10] W.G. Klemperer, C.G. Wall, Chem. Rev. 98 (1998) 297.
[11] A. Müller, S.K. Das, C. Kuhlmann, H. Bögge, M. Schmidtmann, E. Diemann, E. Krickemeyer, J. Hormes, H. Modrow, M. Schindler, Chem. Commun. (2001) 655.
[12] M. Kozik, L.C.W. Baker, J. Am. Chem. Soc. 112 (1990) 7604.
[13] M. Kozik, L.C.W. Baker, in: M.T. Pope, A. Müller (Eds.), Polyoxometalates: From Platonic Solids to Anti-retroviral Activity, Kluwer Academic Publishers, Dordrecht, 1994, p. 191.
[14] I.A. Weinstock, Chem. Rev. 98 (1998) 113.
[15] I.M. Mbomekalle, B. Keita, L. Nadjo, P. Berthet, K.I. Hardcastle, C.L. Hill, T.M. Anderson, Inorg. Chem. 42 (2003) 1163.
[16] N.M. Okun, T.M. Anderson, C.L. Hill, J. Am. Chem. Soc. 125 (2003) 3194.
[17] C.J. Gómez-García, N. Casañ-Pastor, E. Coronado, L.C.W. Baker, G. Pourroy, J. Appl. Phys. 67 (1990) 5995.
[18] N. Casañ-Pastor, J. Bas-Serra, E. Coronado, G. Pourroy, L.C.W. Baker, J. Am. Chem. Soc. 114 (1992) 10380.
[19] J.R. Galan-Mascaros, C.J. Gomez-Garcia, J.J. Borras-Almenar, E. Coronado, Adv. Mater. 6 (1994) 221.
[20] J.M. Clemente-Juan, E. Coronado, Coord. Chem. Rev. 193–195 (1999) 361.
[21] M.T Pope, A. Müller, in: Polyoxometalates From Platonic Solids to Anti-retroviral Activity, Kluwer Academic Publishers., Dordrecht, Netherlands, 1993.
[22] T. Yamase, H. Fujita, K. Fukushima, Inorg. Chim. Acta 151 (1988) 15.
[23] C. Hill, M. Weeks, M. Hartnup, J.-P. Sommadossi, R. Schinazi, Ann. N.Y. Acad. Sci. 616 (1990) 528.
[24] C.L. Hill, M.S. Weeks, R.F. Schinazi, J. Med. Chem. 33 (1990) 2767.
[25] J.T. Rhule, C.L. Hill, D.A. Judd, R.F. Schinazi, Chem. Rev. 98 (1998) 327.
[26] J.T. Rhule, C.L. Hill, Z. Zheng, R.F. Schinazi, in: M.J. Clarke, P.J. Sadler (Eds.), Topics in Biological Inorganic Chemistry, Springer-Verlag, Heidelberg, 1999, p. 117.
[27] T. Yamase, in: J.C. Salamone (Ed.), Polymeric Materials Encyclopedia, CRC Press, Boca Raton, 1996, p. 365.

[28] A. Tézé, J. Canny, L. Gurban, R. Thouvenot, G. Hervé, Inorg. Chem. 35 (1996) 1001.
[29] J. Canny, A. Tézé, R. Thouvenot, G. Hervé, Inorg. Chem. 25 (1986) 2114.
[30] A. Tézé, G. Hervé, in: A.P. Ginsberg (Ed.), Inorg. Synth., John Wiley and Sons, New York, 1990, p. 85.
[31] B. Botar, Y.V. Geletii, P. Kögerler, D. Musaev, G.K. Morokuma, I.A. Weinstock, C.L. Hill, Dalton Trans. (2005) 2017.
[32] K. Wassermann, H.-J. Lunk, R. Palm, J. Fuchs, N. Steinfeldt, R. Stosser, M.T. Pope, Inorg. Chem. 35 (1996) 3273.
[33] J. Canny, R. Thouvenot, A. Tézé, G. Hervé, M. Leparulo-Loftus, M.T. Pope, Inorg. Chem. 30 (1991) 976.
[34] F. Xin, M.T. Pope, Inorg. Chem. 35 (1996) 5693.
[35] F. Xin, M.T. Pope, G.J. Long, U. Russo, Inorg. Chem. 35 (1996) 1207.
[36] U. Kortz, S. Isber, M.H. Dickman, D. Ravot, Inorg. Chem. 39 (2000) 2915.
[37] U. Kortz, S. Matta, Inorg. Chem. 40 (2001) 815.
[38] B.S. Bassil, U. Kortz, A.S. Tigan, J.M. Clemente-Juan, B. Keita, P.d. Oliveira, L. Nadjo, Inorg. Chem. 44 (2005) 9360.
[39] P. Mialane, A. Dolbecq, J. Marrot, E. Rivière, F. Sécheresse, Chem. Eur. J. 11 (2005) 1771.
[40] B.S. Bassil, M.H. Dickman, U. Kortz, Inorg. Chem. 45 (2006) 2394.
[41] B.S. Bassil, M.H. Dickman, M. Reicke, U. Kortz, B. Keita, L. Nadjo, Dalton Trans. (2006) 4253.
[42] Z. Zhang, Y. Li, E. Wang, X. Wang, C. Qin, H. An, Inorg. Chem. 45 (2006) 4313.
[43] Y. Goto, K. Kamata, K. Yamaguchi, K. Uehara, S. Hikichi, N. Mizuno, Inorg. Chem. 45 (2006) 2347.
[44] X. Zhang, C.J. O'Connor, G.B. Jameson, M.T. Pope, Inorg. Chem. 35 (1996) 30.
[45] C. Nozaki, K. Kiyoto, Y. Minai, M. Misono, M. Mizuno, Inorg. Chem. 38 (1999) 5724.
[46] S. Yamaguchi, Y. Kikukawa, K. Tsuchida, Y. Nakagawa, K. Uehara, K. Yamaguchi, N. Mizuno, Inorg. Chem. 46 (2007) 8502.
[47] H. Liu, J. Peng, Z. Su, Y. Chen, B. Dong, A. Tian, Z. Han, E. Wang, Eur. J. Inorg. Chem. (2006) 4827.
[48] B.S. Bassil, S. Nellutla, U. Kortz, A.C. Stowe, J.v. Tol, N.S. Dalal, B. Keita, L. Nadjo, Inorg. Chem. 44 (2005) 2659.
[49] U. Kortz, Y.P. Jeannin, A. Tézé, G. Hervé, S. Isber, Inorg. Chem. 38 (1999) 3670.
[50] P. Mialane, A. Dolbecq, J. Marrot, E. Rivière, F. Sécheresse, Angew. Chem., Int. Ed. 42 (2003) 3523.
[51] L. Lisnard, P. Mialane, A. Dolbecq, J. Marrot, J.M. Clemente-Juan, E. Coronado, B. Keita, P.d. Oliveira, L. Nadjo, F. Sécheresse, Chem. Eur. J. 13 (2007) 3525.
[52] Z. Luo, P. Kögerler, R. Cao, I. Hakim, C.L. Hill, Dalton Trans. (2008) 54.
[53] Z. Zhang, Y. Qi, C. Qin, Y. Li, E. Wang, X. Wang, Z. Su, L. Xu, Inorg. Chem. 46 (2007) 8162.
[54] Bruker AXS, Inc., Madison, 2000.
[55] Bruker AXS, Inc., Madison, 1999.
[56] H. Liu, C.J. Gomez-Garcia, J. Peng, Y. Feng, Z. Su, J. Sha, L. Wang, Inorg. Chem. 46 (2007) 10041.
[57] P. Mialane, C. Duboc, J. Marrot, E. Rivière, A. Dolbecq, F. Sécheresse, Chem. Eur. J. 12 (2006) 1950.
[58] P. Kögerler, A. Müller, J. Appl. Phys. 93 (2003) 7101.
[59] B.H. Chiari, J.H. Piovesana, O. Tarantelli, T.P.F. Sanáis, P.F. Zanazzi, Inorg. Chem. 25 (1986) 2213.
[60] O. Kahn, Angew. Chem., Int. Ed. Engl. 24 (1985) 834.
[61] M. Kato, Y. Muto, Coord. Chem. Rev. 92 (1988) 45.
[62] M. Melnik, Coord. Chem. Rev. 42 (1982) 259.

Polyhedron 28 (2009) 221–226

Contents lists available at ScienceDirect

Polyhedron

journal homepage: www.elsevier.com/locate/poly

Unreported coordination behaviour of a bis(semicarbazone) ligand in a lead(II) complex

Elena López-Torres [a,*], M. Antonia Mendiola [a], César J. Pastor [b]

[a] Departamento de Química Inorgánica, Avenida Francisco Tomás y Valiente, 7, Universidad Autónoma de Madrid, Cantoblanco, 28049-Madrid, Spain
[b] Servicio Interdepartamental de Investigación, Avenida Francisco Tomás y Valiente, 7, Universidad Autónoma de Madrid, 28049-Madrid, Spain

ARTICLE INFO

Article history:
Received 30 September 2008
Accepted 23 October 2008
Available online 8 December 2008

Keywords:
Lead(II) complex
Bis(semicarbazone) complexes
Crystal structure

ABSTRACT

A novel lead(II) complex with the Schiff base benzil bis(semicarbazone), $[Pb(LH_2)_2(NO_3)]NO_3 \cdot 1/2H_2O$, has been synthesised and structurally characterized as well as the free ligand. The coordination number of Pb(II) is seven provided by two neutral ligand molecules and one nitrato group. The most interesting characteristic of this complex is the different behaviour observed in the two bis(semicarbazone) molecules. One of them is a N_2O_2 chelate ligand, whereas the other one is bonded to the lead ion only through one of the semicarbazone branches. The seventh position in the lead coordination sphere is provided by one oxygen atom from a nitrato ligand.

© 2008 Elsevier Ltd. All rights reserved.

1. Introduction

In the course of our studies on the coordination ability of ligands derived from 1,2-diphenylethanedione (benzil) with thiosemicarbazides to bind to transition and main group metals, we have established the importance of the working conditions and the preferred coordination geometries of the metal ion in the structure of the final complexes. A combination of both factors permits the synthesis of mono, binuclear, hexanuclear or extended coordination polymers [1–5]. Control of the structural properties is essential, since they will determine the potential applications of the metal complexes [6–8].

Relatively less attention has been devoted to the synthesis and biological properties of their structurally analogous semicarbazones and their metal complexes, and excluding derivatives from 2,6-diacetylpyridine there is almost nothing reported with bis(semicarbazones), despite the fact that, some of these compounds have shown considerable anticonvulsant, antimicrobial and antitumor activities and some VO_2^+ complexes can act as insulin-mimetic agents [9–12]. The great advantage of semicarbazone derivatives over their thiosemicarbazone analogues seems to be their lower toxicity. One reason for the lack of complexes containing bis(semicarbazone) ligands might be the fact that they frequently undergo cyclization reactions, particularly in the presence of metal ions. This has also been observed for benzil bis(semicarbazone) LH_2, which even in the absence of metal cyclises when heated [13]. With rhenium at room temperature it readily loses one of its semicarbazone arms to yield a triazine-3-one, which forms complexes with different triazine binding modes depending on the precursor used [14].

On the other hand, the Pb(II) ion is a heavy p-block metal that possess variable coordination behaviours, coordination numbers ranging from 2 to 10 and diverse coordination geometries, caused by the stereo-chemical active lone pair [15–21]. With respect to the large number of thiosemicarbazone complexes with many main group and transition metals, the number of structurally characterized lead complexes with such ligands is relatively small [22–26] and as far as we know, only five crystal structures of lead semicarbazones have been reported [27–30]. In order to compare the reactivity of benzil bis(semicarbazone) with the analogous benzil bis(thiosemicarbazone) [2,31], we have explored the reaction of LH_2 with lead nitrate and here we report its lead derivative, which has been crystallographically characterized, as well as the crystal structure of the free ligand.

2. Experimental

2.1. Physical measurements

Microanalyses were carried out using a Perkin-Elmer 2400 II CHNS/O Elemental Analyser. IR spectra in the 4000–400 cm^{-1} range were recorded as KBr pellets on a Jasco FT/IR-410 spectrophotometer. Fast atom bombardment mass spectra were recorded on a VG Auto Spec instrument using Cs as the fast atom and *m*-nitrobenzylalcohol (*m*NBA) as the matrix. ^1H spectrum was recorded on a Bruker AMX-300 spectrometer using THF-d_8 and CD_3CN as solvents; chemical shifts are expressed on the δ scale relative to TMS as internal reference. ^{13}C CP/MAS NMR spectra

* Corresponding author.
E-mail address: elena.lopez@uam.es (E. López-Torres).

0277-5387/$ - see front matter © 2008 Elsevier Ltd. All rights reserved.
doi:10.1016/j.poly.2008.10.058

were recorded at 298 K in a Bruker AV400WB spectrometer equipped with a 4 mm MAS NMR probe (magic-angle spinning) and obtained using cross-polarization pulse sequence. For the recorded spectra a contact time of 4 ms were used and recycle delays of 4 s were used. Chemical shifts are reported relative to TMS, using the CH group of adamantano as a secondary reference (29.5 ppm).

2.2. Synthesis of benzil bis(semicarbazone), LH_2

This was prepared by reaction between benzil and semicarbazide hydrochloride in the presence of $LiOH \cdot H_2O$ [13]. Selected spectroscopic data for LH_2: IR (KBr): ν = 3411(s), 3325(s), 3255(s), 3158(s) ν(N–H), 1682(s) amide I, 1584(w) ν(CN), 1569(s) $\delta(NH_2)$ cm^{-1}. ^1H NMR (25 °C, DMSO-d_6, 300 MHz): δ = 9.09 (s, 2H, NH), 7.65 (m, 4H, Ph), 7.51–7.25 (m, 6H, Ph), 6.59 (s, 4H, NH_2) ppm. ^{13}C CP/MAS NMR (300 MHz): δ = 158.9 (CO), 141.1 (CN), 128.9 (Ph) ppm. Crystals suitable for X-ray studies were obtained by recrystallization in methanol.

2.3. Synthesis of $[Pb(LH_2)_2(NO_3)]NO_3$ (**1**)

A solution of $Pb(NO_3)_2$ (165 mg, 0.5 mmol) in distilled water (5 mL) was mixed with a suspension of LH_2 (324 mg, 1 mmol) and $LiOH{\cdot}H_2O$ (42 mg, 1 mmol) in methanol (50 mL). The mixture was stirred for 6 h under reflux. A crystalline yellow material was formed after partial evaporation of the yellow solution (389 mg, 80%). *Anal.* Calc. for $C_{32}H_{32}N_{14}O_{10}Pb$ (979.45): C, 39.21; H, 3.29; N, 20.02. Found: C, 39.45; H, 3.08; N, 19.87%. IR (KBr): ν = 3398(s), 3335(s), 3231(s), 3188(s) ν(N-H), 1691(s), 1667(s) amide I, 1614(m) ν(CN), 1539 (s) $\delta(NH_2)$ cm^{-1}. MS(FAB+): *m/z*: 855.3 $[Pb(LH_2)(LH)]^+$, 594.1 $[Pb(LH_2)(NO_3)]^+$, 531.1 $[Pb(LH)]^+$. ^1H NMR (25 °C, THF-d_8, 300 MHz): δ = 10.84 (s, 1H, NH), 9.79 (s, 3H, NH), 7.67–7.65 (m, 8H, Ph), 7.30–7.26 (m, 12H, Ph), 6.32 (s, 6H, NH_2), 4.74 (s, 2H, NH_2) ppm. ^1H NMR (25 °C, CD_3CN, 300 MHz): δ = 9.48 (s, 1H, NH), 8.05 (s, 3H, NH), 7.70–7.68 (m, 8H, Ph), 7.44–7.42 (m, 12H, Ph), 7.19 (s, 2H, NH_2), 5.81 (s, 6H, NH_2) ppm. ^{13}C CP/MAS NMR (25 °C, 300 MHz): 159.8, 150.5 (CO), 147.6, 145.4 (CN), 130.4, 126.3 (Ph) ppm. Single crystals suitable for X-ray analysis were grown from THF.

2.4. X-ray crystallography

Crystal data and refinement results are listed in Table 1. Data for LH_2 were collected on a Bruker SMART 6K CCD area-detector three-circle diffractometer with a MAC Science Co., Ltd. Rotating Anode (Mo Kα radiation, λ = 1.54178 Å) and for **1** on a Bruker AXS Kappa Apex-II diffractometer equipped with an Apex-II CCD area detector using a graphite monochromator (Mo Kα radiation, λ = 0.71073 Å). The substantial redundancy in data allows empirical absorption corrections (SADABS) [32] to be applied using multiple measurements of symmetry-equivalent reflections. The raw intensity data frames were integrated with the SAINT program, which also applied corrections for Lorentz and polarization effects [33].

The software package SHELXTL version 6.10 was used for space group determination, structure solution and refinement. The structures were solved by direct methods (SHELXS-97) [34], completed with difference Fourier syntheses, and refined with full-matrix least squares using SHELXL-97 minimizing $\omega(F_0^2 - F_c^2)$. Weighted *R* factors (R_w) and all goodness of fit *S* are based on F^2; conventional *R* factors (*R*) are based on *F* [35], All non-hydrogen atoms were refined with anisotropic displacement parameters and hydrogen atoms were located by difference maps although were positioned geometrically after each cycle refinement .All scattering factors and anomalous dispersions factors are contained in the SHELXTL 6.10 program library.

Table 1
Crystal data and structure refinement for $LH_2 \cdot 2CH_3OH$ and **1** $\cdot$ $1/2H_2O$.

	$LH_2 \cdot 2CH_3OH$	$1 \cdot 1/2H_2O$
Formula	$C_{18}H_{24}N_6O_2$	$C_{32}H_{33}N_{14}O_{10.5}Pb$
M	388.43	988.91
Temperature (K)	100(2)	100(2)
Wavelength (Å)	1.54178	0.71073
Crystal system	orthorhombic	trigonal
Space group	*Pccn*	*R*-3
a (Å)	7.9278(4)	32.8193(10)
b (Å)	15.2611(7)	32.8193(10)
c (Å)	17.1644(9)	19.4458(12)
α (°)	90	90
β (°)	90	90
γ (°)	90	120
U (Å^3)	2076.67(18)	18139.1(14)
Z	4	18
D_{calc} (Mg m^{-3})	1.236	1.630
Absorption coefficient (mm^{-1})	0.749	4.258
F(000)	824	8802
Goodness of fit on F^2	1.030	1.049
Reflections collected	11334	55737
Independent reflections (R_{int})	1994 (0.0840)	8884 (0.0569)
Completeness to θ (%)	98.6	99.5
Absorption correction	SADABS	SADABS
Refinement method	full-matrix least-squares on F^2	full-matrix least-squares on F^2
Final $R_1$and $wR_2[I > 2\sigma(I)]$	R_1 = 0.0455, wR_2 = 0.1072	R_1 = 0.0471, wR_2 = 0.1269
R indices (all data)	R_1 = 0.0828, wR_2 = 0.1259	R_1 = 0.0771, wR_2 = 0.1386

In complex **1** the hydrogen atoms of the molecule of water could not be located in the difference Fourier map, presumably as a result of disorder. In addition, the difference Fourier map showed a number of peaks of additional electron density, which were identified as the N and O of half a nitrate anion, but as a consequence of the disorder they could not be satisfactorily modelled. Its contribution was removed from the observed data using SQUEEZE in the software program PLATON [36], but the atom count from this $1/2NO_3$ is included in the empirical formula. The water hydrogen atoms and the half a nitrate molecule have been omitted from the model, but included in calculations of the formula, weight etc. The other half a nitrate is also disordered, but only over two sites, so it could be modelled.

3. Results and discussion

The crystal structure of the bis(semicarbazone) consists of discrete molecules of LH_2 with two molecules of methanol (Fig. 1). Both semicarbazone branches are identical due to a crystallographically imposed symmetry, with the bond distances and angles corresponding to an imine–ketone disposition, which is supported by the presence of hydrazinic hydrogens (Table 2). To difference with the analogue thiosemicarbazone ligand [1], the two semicarbazone arms are not *trans* with respect to the single bond C(2)–C(2A), and the angle between them is 75.5°, being close to be perpendicular. The angle between the aromatic rings is 73.4°, so they are in a perpendicular disposition, thus minimizing the phenyl intramolecular interaction. The semicarbazone core can be considered planar with a maximum deviation of 0.02 Å for C(2) and forms an angle of 22.5° with the phenyl ring. The molecular conformation of the oxygen atom and the hydrazinic hydrogen H(2) is *cis* with respect to C(1)–N(2). Starting from the free ligand the N_2O_2 chelate formation can only take place via 180° rotation about the C–$N_{hydrazinic}$ single bond, which is in an *E* disposition, and an additional rotation around the C(2)–C(2A) bond. The ligand molecules are held together in the crystal packing through hydrogen bonds involving the amine nitrogen atom N(1) and the oxygen atom O(1) (Table

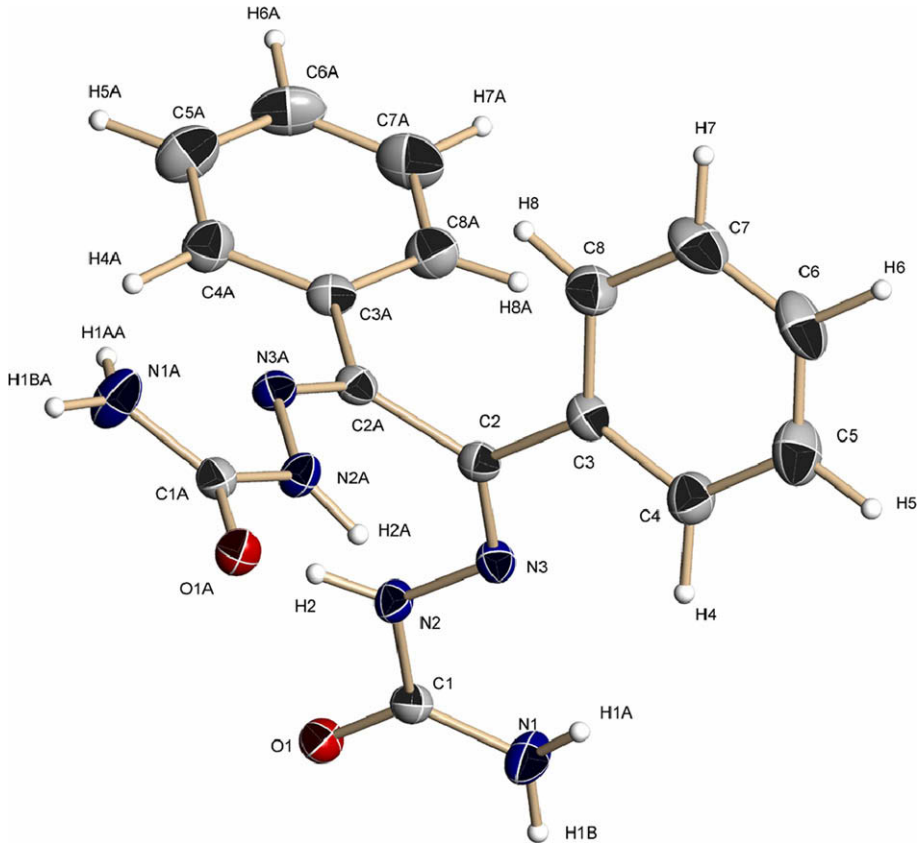


Fig. 1. Representation of the crystal structure of $LH_2 \cdot 2CH_3OH$, with thermal ellipsoids at 50% probability. Solvent molecules have been omitted for clarity.

Table 2
Selected bond lengths (Å) and angles (°) for $LH_2 \cdot 2CH_3OH$.

C(1)–O(1)	1.243(2)	C(2)–N(3)	1.290(3)
C(1)–N(1)	1.329(3)	C(2)–C(2)#1	1.501(4)
C(1)–N(2)	1.365(3)	N(2)–N(3)	1.374(2)
O(1)–C(1)–N(1)	123.15(18)	N(3)–C(2)–C(2)#1	122.73(19)
O(1)–C(1)–N(2)	119.45(18)	C(3)–C(2)–C(2)#1	118.57(18)
N(1)–C(1)–N(2)	117.39(18)	C(1)–N(2)–N(3)	118.44(16)
N(3)–C(2)–C(3)	118.62(17)	C(2)–N(3)–N(2)	118.02(16)

Symmetry transformations used to generate equivalent atoms: #1 $-x + 1/2$, $-y + 3/2$, z.

Table 3
Hydrogen bonds for $LH_2.2CH_3OH$ (Å and °).

D–H···A	d(D–H)	d(H···A)	d(D···A)	<(DHA)
O(2)–H(2A)···O(1)	0.84	1.92	2.745(2)	166.7
N(2)–H(2)···O(2)#2	0.88	2.08	2.894(2)	153.3
N(1)–H(1B)···O(1)#3	0.88	2.02	2.849(2)	157.1

Symmetry transformations used to generate equivalent atoms: #1 $-x + 1/2$, $-y + 3/2$, z #2 $x + 1/2$, $-y + 1$, $-z + 1/2$ #3 $x - 1/2$, $-y + 1$, $-z + 1/2$.

3, Fig. 2). This forms zigzag chains running along the *b* axis. The chains are also linked through hydrogen bonds running in the direction of *a* and through C(7)–H(7)···O(1) interactions (3.333 Å, 159.5°) along *c*, leading a 3D network. It seems that along *c* there are some π–π interactions, although the distance of 3.999 Å between centroids avoids π–π stacking. The methanol molecules are also connected through hydrogen bonds acting both as donor and acceptor, with the hydrazinic nitrogen N(2) and O(1) (Table 3), reinforcing the 3D structure, although they are not necessary for the formation of the 3D network.

The lead complex $[Pb(LH_2)_2(NO_3)]NO_3$ was prepared by reaction of LH_2 and $Pb(NO_3)_2$. Its analytical data indicate a 2:1 ligand:Pb ratio, as well as the presence of two NO_3^-. The mass spectrum does not show a peak corresponding the cationic part $[Pb(LH_2)_2(NO_3)]^+$, but peaks corresponding to the loss of LH_2 and/or NO_3^- are observed. The infrared spectrum shows the same number of bands corresponding to the N–H stretching vibrations, suggesting the ligand is not deprotonated, although they are shifted with respect to LH_2. There are two bands corresponding to the amide I, one almost in the same place than in the free bis(semicarbazone) and another shifted to lower wavenumber, suggesting that there exist both free and coordinated C=O groups. This is also observed in the case of the C=N moieties. The presence of NO_3^- is confirmed by a strong band at 1386 cm^{-1}. ^1H NMR spectrum in THF-d_8 or CD_3CN shows that the ligands are not deprotonated, as well as the presence of semicarbazone arms with different behaviour. Due to the low solubility of $[Pb(LH_2)_2(NO_3)]NO_3$, which is only soluble in an amount enough for ^{13}C studies in DMSO-d_6, but with decomposition, ^{13}C/CP MAS spectrum of the complex and the free ligand were recorded. In the complex there are two signals corresponding to C=O and two to C=N, confirming the presence of two types of CO and CN groups, as was deduced form the IR.

The crystal structure of **1** shows an asymmetric unit containing one $[Pb(LH_2)_2(NO_3)]^+$ cation, one nitrate and half a molecule of water (Fig. 3). In the cation the lead atom is in a hepta-coordinate geometry formed by one N_2O_2 tetradentate ligand, one NO bidentate and the oxygen of one nitrato in a distorted capped octahedron arrangement and represents, as far as we know, the first complex containing two bis (semicarbazone) ligands with a different coordination mode and the second containing one coordinated and

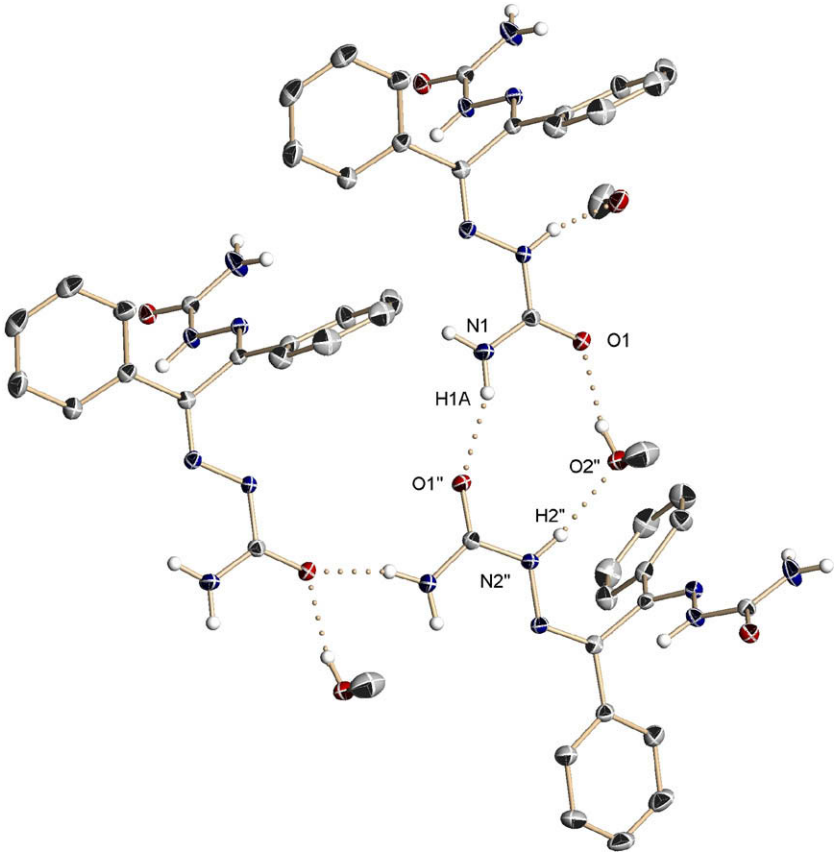


Fig. 2. View of the hydrogen bonds involving LH_2 and the methanol molecules. C–H hydrogen atoms have been omitted for clarity.

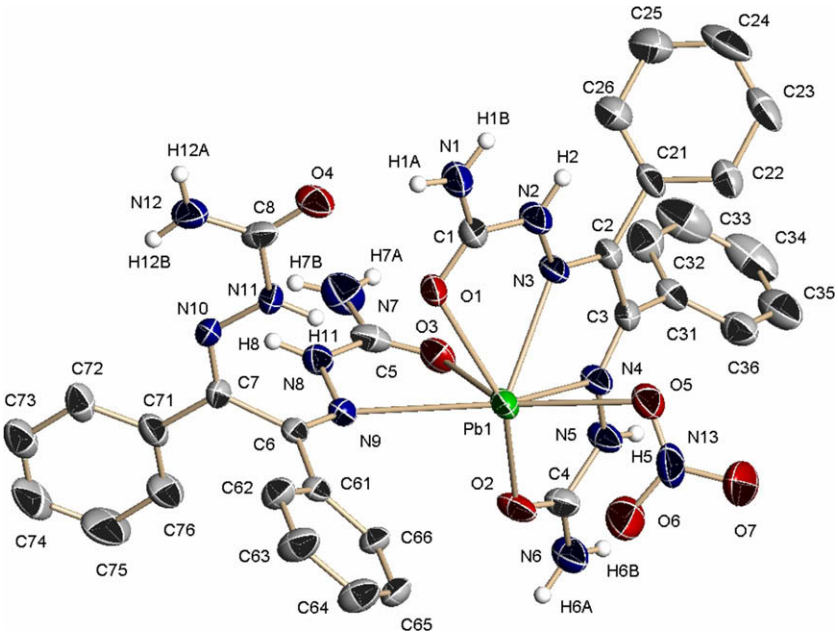


Fig. 3. Representation of the crystal structure of $[Pb(LH_2)_2(NO_3)]NO_3 \cdot 1/2H_2O$ with thermal ellipsoids at 40% probability. Water and nitrate molecules have been omitted for clarity.

one free arm [37]. The difference between our complex and the one previously described is that in those the two bis(semicarbazone) ligands act as tridentate monodeprotonate molecules. The N(1)–C(1)–N(2)–N(3)–C(2)–C(3)–N(4)–N(5)–C(4)–N(6) core of the tetradentate ligand is almost flat, with a maximum deviation of 0.15 Å for N(4). The Pb(II) is 0.50 Å over this plane and the oxygens O(2) and O(1) are 0.19 Å over and 0.26 Å under the plane respectively. The dihedral angle between the phenyl rings in this ligand

is 64.4°. In the bidentate ligand, where one semicarbazone arm is coordinated and the other is free, the branches have a similar disposition than the free ligand and are virtually perpendicular, 89.3°. Whereas in the free arm the semicarbazone, including the aromatic ring (dihedral angle 3.3°), is flat, in the bidentate one the phenyl ring is canted 29.2°. This difference in the position of the phenyl rings makes that they are not exactly perpendicular and form an angle of 80.3° Another difference is that in the free arm the imine nitrogen N(10) and O(4) are in a *trans* disposition, as well as in the free ligand, whilst in the coordinated one they are *cis*.

Within both ligands bond distances and angles correlate well with an imine-ketone form (Table 4), and as a consequence of their behaviour as neutral molecules, there is not a great deal of electronic delocalization, being quite similar to those of the free bis(semicarbazone). Pb–N bond distances with the tetradentate ligand are almost identical [2.551(5) and 2.557(5) Å], whilst N(9) is significantly larger [2.870(5)]. Although this bond is long, is supported by the *cis* disposition of O(3) and N(9). In contrast, Pb–O bond distances with the N_2O_2 LH_2 are quite different [2.497(4) and 2.643(4) Å]. The distance with the bidentate branch is significantly the shortest [2.427(5) Å] and the one with the nitrato the largest [2.701(5) Å].

All of the NH and NH_2 groups participate in hydrogen bonding with both the nitrato and the modelled nitrate groups, as well as with and the oxygen atoms of the water molecules, acting as acceptors to give a 3D network (Table 5). This 3D network can be obtained only through the hydrogen bonds existing between the $[Pb(LH_2)NO_3]^+$ units. The water molecules also have additional short non-bonded contacts, presumably also indicative of hydrogen bonding, although as their H atoms could not be located, these are ambiguous.

Table 4
Selected bond lengths (Å) and angles (°) for **1**.1/H_2O.

Pb(1)–O(3)	2.427(5)	N(9)–C(6)	1.299(7)
Pb(1)–O(2)	2.497(4)	N(10)–C(7)	1.288(7)
Pb(1)–N(4)	2.551(5)	N(10)–N(11)	1.364(7)
Pb(1)–N(3)	2.557(5)	N(11)–C(8)	1.379(8)
Pb(1)–O(1)	2.643(4)	N(12)–C(8)	1.296(10)
Pb(1)–O(5)	2.701(5)	N(13)–O(5)	1.201(8)
Pb(1)–N(9)	2.870(5)	N(13)–O(6)	1.255(8)
N(1)–C(1)	1.341(8)	N(13)–O(7)	1.288(8)
N(2)–N(3)	1.341(7)	O(1)–C(1)	1.240(7)
N(2)–C(1)	1.380(8)	O(2)–C(4)	1.220(7)
N(3)–C(2)	1.289(8)	O(3)–C(5)	1.231(8)
N(4)–C(3)	1.275(8)	O(4)–C(8)	1.238(8)
N(4)–N(5)	1.342(7)	C(2)–C(3)	1.489(9)
N(5)–C(4)	1.384(8)	C(6)–C(7)	1.501(8)
N(6)–C(4)	1.319(8)	N(14)–O(10)	1.127(13)
N(7)–C(5)	1.335(9)	N(14)–O(9)	1.204(10)
N(8)–C(5)	1.369(9)	N(14)–O(8)	1.348(8)
N(8)–N(9)	1.368(7)		
O(3)–Pb(1)–O(2)	75.75(16)	O(2)–Pb(1)–N(9)	90.78(14)
O(3)–Pb(1)–N(4)	69.75(17)	N(4)–Pb(1)–N(9)	127.43(16)
O(2)–Pb(1)–N(4)	63.55(14)	N(3)–Pb(1)–N(9)	112.60(15)
O(3)–Pb(1)–N(3)	74.71(16)	O(1)–Pb(1)–N(9)	65.69(13)
O(2)–Pb(1)–N(3)	123.87(15)	O(5)–Pb(1)–N(9)	162.96(14)
N(4)–Pb(1)–N(3)	61.78(16)	C(2)–N(3)–Pb(1)	121.9(4)
O(3)–Pb(1)–O(1)	82.29(15)	N(2)–N(3)–Pb(1)	116.2(4)
O(2)–Pb(1)–O(1)	153.94(15)	C(3)–N(4)–Pb(1)	122.9(4)
N(4)–Pb(1)–O(1)	121.28(15)	N(5)–N(4)–Pb(1)	115.8(3)
N(3)–Pb(1)–O(1)	61.45(14)	C(6)–N(9)–Pb(1)	128.3(4)
O(3)–Pb(1)–O(5)	136.49(15)	N(8)–N(9)–Pb(1)	108.3(3)
O(2)–Pb(1)–O(5)	99.24(15)	C(1)–O(1)–Pb(1)	114.5(4)
N(4)–Pb(1)–O(5)	69.59(16)	C(4)–O(2)–Pb(1)	120.9(4)
N(3)–Pb(1)–O(5)	73.00(16)	C(5)–O(3)–Pb(1)	126.3(4)
O(1)–Pb(1)–O(5)	106.36(14)	N(13)–O(5)–Pb(1)	104.5(4)
O(3)–Pb(1)–N(9)	59.37(14)		

Symmetry transformations used to generate equivalent atoms: #1 $-x, -y+1, -z$.

Table 5
Hydrogen bonds for **1**.1/H_2O (Å and °).

D–H···A	d(D–H)	d(H···A)	d(D···A)	<(DHA)
N(12)–H(12B)···O(2)#2	0.86	2.13	2.854(8)	141.3
N(8)–H(8)···O(9)#3	0.86	1.97	2.702(11)	141.6
N(7)–H(7B)···O(9)#3	0.86	1.89	2.666(13)	150.3
N(6)–H(6A)···O(8)#4	0.86	2.20	3.035(10)	162.8
N(6)–H(6B)···O(4)#5	0.86	1.97	2.779(7)	155.7
N(5)–H(5)···O(4)#5	0.86	2.16	2.903(7)	144.9
N(2)–H(2)···O(5)#6	0.86	2.06	2.834(7)	149.0
N(1)–H(1B)···O(7)#6	0.86	2.17	3.000(9)	161.7
N(11)–H(11)···O(1)	0.86	2.31	3.048(6)	143.5
N(1)–H(1A)···O(4)	0.86	1.95	2.791(7)	163.7

Symmetry transformations used to generate equivalent atoms: #1 $-x, -y+1, -z$ #2 $y-1/3, -x+y+1/3, -z+1/3$ #3 $x-y+2/3, x+1/3, -z+1/3$ #4 $-y+1, x-y+1, z$ #5 $y, -x+y, -z$ #6 $-x+1/3, -y+2/3, -z-1/3$.

4. Conclusions

In this paper we have synthesised and structurally characterised a lead(II) bis(semicarbazone) complex, which represents the first complex containing two bis(semicarbazone) ligands with different behaviour. This structure points out the preference of lead to bind to oxygen instead of to sulphur, since the complex obtained with benzil bis(thiosemicarbazone), under the same reaction conditions, leads a 1:1 complex with the lead atom in a tetracoordinated arrangement and with the ligand doubly deprotonated [2].

In this reaction, the pH does not seem to determine the ligand behaviour on the contrary to the analogue bis(thiosemicarbazone) ligand.

Acknowledgement

We thank to DGICYT for financial support (Project CT2005-07788/BQU).

Appendix A. Supplementary data

CCDC the supplementary crystallographic data.

CCDC 696037 and 696038 contain the supplementary crystallographic data for $LH_2 \cdot 2CH_3OH$ and $[Pb(LH_2)_2(NO_3)]NO_3 \cdot 1/2H_2O$. These data can be obtained free of charge via http://www.ccdc.cam.ac.uk/conts/retrieving.html, or from the Cambridge Crystallographic Data Centre, 12 Union Road, Cambridge CB2 1EZ, UK; fax: (+44) 1223-336-033; or e-mail: deposit@ccdc.cam.ac.uk. Supplementary data associated with this article can be found, in the online version, at doi:10.1016/j.poly.2008.10.058.

References

[1] E. López-Torres, M.A. Mendiola, C.J. Pastor, B. Souto Pérez, Inorg. Chem. 43 (2004) 5222. and reference therein.
[2] D.G. Calatayud, E. López-Torres, M.A. Mendiola, Inorg. Chem. 46 (2007) 10434. and references therein.
[3] E. López-Torres, M.A. Mendiola, C.J. Pastor, Inorg. Chem. 45 (2006) 3103.
[4] E. López-Torres, M.A. Mendiola, Polyhedron 24 (2005) 1435.
[5] D.G. Calatayud, E. López-Torres, M.A. Mendiola, C.J. Pastor, J.R. Procopio, Eur. J. Inorg. Chem. (2005) 4401.
[6] J. Ruipérez, M.A. Mendiola, M.T. Sevilla, J. Rodríguez-Procopio, L. Hernández, Electroanalysis 14 (2002) 532.
[7] M. Colilla, M.A. Mendiola, J.R. Procopio, M.T. Sevilla, Electroanalysis 17 (2005) 933.
[8] H. Behmadi, H.A. Zamani, M.R. Ganjali, P. Norouzi, Electrochim. Acta 53 (2007) 1870.
[9] P. Yogeeswari, J.V. Ragavendran, D. Sriram, Y. Nageswari, R. Kavya, N. Sreevatsan, K. Vanita, J. Stables, J. Med. Chem. 50 (2007) 2459.
[10] N.C. Kasuga, K. Onodera, S. Nakano, K. Hayashi, K. Nomiya, J. Inorg. Biochem. 100 (2006) 1176.
[11] Z. Afrasiabi, E. Sinn, W. Lin, Y. Ma, C. Campana, S. Padhye, J. Inorg. Biochem. 99 (2005) 1526.

[12] P. Noblía, E.J. Baran, L. Otero, P. Draper, H. Cerecetto, M. González, O.E. Piro, E.E. Castellano, T. Inohara, Y. Adachi, H. Sakurai, D. Gambino, Eur. J. Inorg. Chem. (2004) 322.
[13] A. Arquero, M. Cañadas, M. Martínez-Ripoll, M.A. Mendiola, A. Rodríguez, Tetrahedron 54 (1998) 11271.
[14] E. López-Torres, U. Abram, Inorg. Chem. 47 (2008) 2890.
[15] D-Q. Li, X. Liu, J. Zhou, Inorg. Chem. Commun. 11 (2008) 367.
[16] B. Ding, E-C. Yang, J-H. Guo, X-J. Zhao, X-G. Wang, Inorg. Chem. Commun. 11 (2008) 509.
[17] E. S Claudio, H.A. Godwin, J.S. Magyar, Prog. Inorg. Chem. 51 (2003) 1.
[18] R.D. Hancok, in: A.F. Williams, C. Floriani, A.E. Merbach (Eds.), Perspectives in Coordination Chemistry, VCHA:VCH, Basel, 1992.
[19] L. Shimoni-Livny, J.P. Glusker, C.W. Bock, Inorg. Chem. 37 (1998) 1853.
[20] R.D. Hancock, J.H. Reibenspies, H. Maumela, Inorg. Chem. 43 (2004) 2981.
[21] D. Esteban-Gómez, C. Platas-Iglesias, T. Enríquez-Pérez, F. Avecilla, A. de Blas, T. Rodríguez-Blas 45 (2006) 5407.
[22] J.S. Casas, M.S. García-Tasende, J. Sordo, Coord. Chem. Rev. 209 (2000) 197.
[23] R. Pedrido, M.R. Bermejo, M.J. Romero, M. Vázquez, A.M. Gónzalez-Noya, M. Maneiro, M.J. Rodríguez, M.I. Fernández, Dalton Trans. (2005) 572.
[24] M.R. Bermejo, A.M. Gónzalez-Noya, M. Martínez-Calvo, R. Pedrido, M. Maneiro, M.I. Fernández, E. Gómez-Fórneas, Z. Anorg. Allg. Chem. 633 (2007) 1911.
[25] J.S. Casas, E.E. Castellano, J. Ellena, M.S. García-Tasende, A. Sánchez, J. Sordo, A. Touceda, S. Vázquez Rodríguez, Polyhedron 26 (2007) 4228.
[26] R. Pedrido, M.J. Romero, M.R. Bermejo, A.M. Gónzalez-Noya, I. García-Lema, G. Zaragoza, Chem. Eur. J. 14 (2008) 500.
[27] H. Aghabozorg, R.C. Palenik, G.J. Palenik, Inorg. Chim. Acta 111 (1986) L53.
[28] H. Aghabozorg, R.C. Palenik, G.J. Palenik, Iranian Chem. Chem. Eng. 7 (1986) 3.
[29] A.E. Koziol, R.C. Palenik, G.J. Palenik, Inorg. Chim. Acta 116 (1986) L51.
[30] L.P. Battaglia, M.B. Ferrari, R. Boggia, Inorg. Chim. Acta 215 (1994) 85.
[31] E. López-Torres, D.G. Calatayud, C.J. Pastor, M.A. Mendiola, Polyhedron 27 (2008) 2507.
[32] G.M. Sheldrick, SADABS Version 2.03, Program for Empirical Absorption Corrections, Universität Göttingen, Göttingen, Germany, 1997–2001.
[33] G.M. Sheldrick, SAINT+NT (Version 6.04) SAX Area-Detector Integration Program, Bruker AXS, Madison, WI, 1997–2001.
[34] G.M. Sheldrick, SHELXTL (Version 6.10) Structure Determination Package, Bruker AXS, Madison, WI, 2000.
[35] G.M. Sheldrick, Acta Crystallogr., Sect. A 46 (1990) 467.
[36] A.L. Spek, PLATON, The University of Utrecht, The Netherlands, 2004.
[37] M. Carcelli, S. Ianelli, P. Pelagatti, G. Pelizzi, Inorg. Chim. Acta 292 (1999) 121.

Polyhedron 28 (2009) 227–232

Contents lists available at ScienceDirect

Polyhedron

journal homepage: www.elsevier.com/locate/poly

Bimetallic Pt(II)-bipyridyl-diacetylide/Ln(III) tris-diketonate adducts based on a combination of coordinate bonding and hydrogen bonding between the metal fragments: Syntheses, structures and photophysical properties

Nawal K. Al-Rasbi [a], Sofia Derossi [a], Daniel Sykes [b], Stephen Faulkner [b], Michael D. Ward [a,*]

[a] Department of Chemistry, University of Sheffield, Sheffield S3 7HF, UK
[b] Department of Chemistry, University of Manchester, Oxford Road, Manchester M13 9PL, UK

ARTICLE INFO

Article history:
Received 9 July 2008
Accepted 28 October 2008
Available online 4 December 2008

Keywords:
Platinum
Lanthanides
Crystal structure
Luminescence
Energy-transfer

ABSTRACT

The luminescent Pt(II) complex [Pt(4,4′-^{t}Bu$_2$-bipy){CC-(5-pyrimidinyl)}$_2$] (**1**) was prepared by coupling of [Pt(4,4′-^{t}Bu$_2$-bipy)Cl$_2$] with 5-ethynyl-pyrimidine, and contains two pyrimidinyl units pendant from a Pt(II) bipyridyl diacetylide core; it shows luminescence at 520 nm which is typical of Pt(II) luminophores of this type. Reaction with [Ln(hfac)$_3$(H$_2$O)$_2$] (hfac = anion of hexafluoroacetylacetone) affords as crystalline solids the compounds [**1** · {Ln(hfac)$_3$(H$_2$O)}{Ln(hfac)$_3$(H$_2$O)$_2$}] (Ln = Nd, Gd, Er, Yb), in which the {Ln(hfac)$_3$(H$_2$O)} unit is coordinated to one pyrimidine ring *via* an N atom, whereas the {Ln(hfac)$_3$(H$_2$O)$_2$} unit is associated with two N atoms, one from each pyrimidine ring of **1**, *via* N···HOH hydrogen-bonding interactions involving the coordinated water ligands on the lanthanide centre. Solution spectroscopic studies show that the luminescence of **1** is partly quenched on addition of [Ln(hfac)$_3$(H$_2$O)$_2$] (Ln = Er, Nd) by formation of Pt(II)/Ln(III) adducts in which Pt(II)→Ln(III) photoinduced energy-transfer occurs to the low-lying f–f levels of the Ln(III) centre. Significant quenching occurs with both Er(III) and Nd(III) because both have several f–f states which match well the ^{3}MLCT emission energy of **1**. Time-resolved luminescence studies show that Pt(II)→Er(III) energy-transfer (7.0×10^7 M^{-1}) is around three times faster than Pt(II)→Nd(III) energy-transfer ($\approx 2 \times 10^7$ M^{-1}) over the same distance because the luminescence spectrum of **1** overlaps better with the absorption spectrum of Er(III) than with Nd(III). In contrast Yb(III) causes no significant quenching of **1** because it has only a single f–f excited level which is a poor energy match for the Pt(II)-based excited state.

© 2008 Elsevier Ltd. All rights reserved.

1. Introduction

There has been extensive recent interest in the preparation and photophysical properties of d–f dinuclear complexes in which d-block chromophores, generally with long-lived MLCT excited states, are used as energy-donors to generate sensitised near-infrared luminescence from lanthanide(III) ions such as Nd(III) and Yb(III) which have low-lying emissive f–f states [1–4]. The intense and fully allowed ^{1}MLCT absorptions of the d-block unit allow light to be absorbed at a range of wavelengths in the visible region, overcoming the inability of lanthanide(III) ions to absorb light themselves due to the f–f transitions being Laporte-forbidden. Two recent results of particular significance are (i) that d→f energy-transfer occurs by the Dexter mechanism over long distances (up to 20 Å) when conjugated bridging ligands are used to link the d-block and f-block components [3], and (ii) there is a clear correlation of energy-transfer rate with donor/acceptor spectroscopic overlap [4], which is to be expected but was nonetheless clearly demonstrated in some Pt(II)/Ln(III) dyads in which the ^{3}MLCT energy of the Pt(II) unit varied [4].

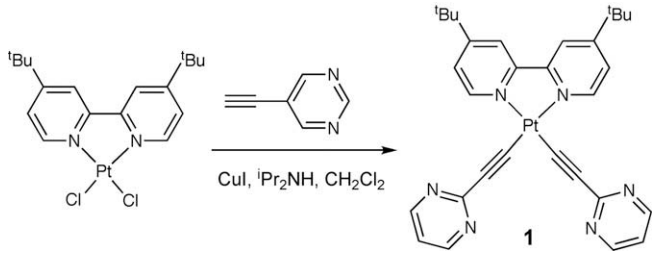
In this paper we report a new series of Pt(II)/Ln(III) dyads based on a luminescent Pt(II)-diimine-diacetylide chromophore [4,5] which bears two pendant pyrimidinyl groups. These groups in turn provide four N-donor sites which could potentially act as sites of attachment to {Ln(diketonate)$_3$} centres to allow buildup of polynuclear Pt(II)/Ln(III) assemblies. We describe the synthesis and structure of the new Pt(II) unit, the unexpected structure of a trinuclear PtEr$_2$ adduct, and the photophysical properties of some 1:1 Pt/Ln assemblies (Ln = Gd, Er, Nd, Yb) in solution, in which Pt→Ln energy-transfer occurs to varying extents depending on the nature of the Ln(III) centres.

2. Results and discussion

The new Pt(II) complex **1** (Scheme 1) was prepared from the Cu(I)-catalysed coupling of 4-ethynylpyrimidine with [Pt(^{t}Bu$_2$bipy)Cl$_2$] according to the literature method [5], followed by

* Corresponding author. Tel.: +44 0114 2229484; fax: +44 0114 2229346.
E-mail address: m.d.ward@sheffield.ac.uk (M.D. Ward).

0277-5387/$ - see front matter © 2008 Elsevier Ltd. All rights reserved.
doi:10.1016/j.poly.2008.10.046



Scheme 1.

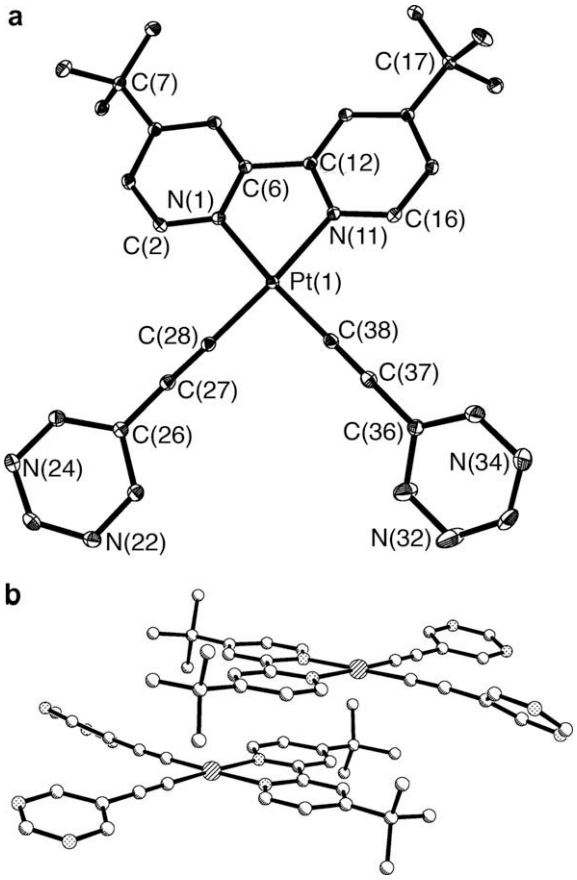


Fig. 1. (a) An ORTEP view of a molecule of complex **1**, with thermal ellipsoids at the 30% level; (b) a view showing stacking of adjacent molecules into pairs. H atoms are not shown for clarity.

chromatographic purification to give pure **1** in 64% yield. Satisfactory spectroscopic and analytical data were obtained (see Section 3). X-ray quality crystals were grown by slow evaporation of a CH_2Cl_2 solution of **1**; the crystal structure is shown in Fig. 1. The Pt(II) ion is in the usual square planar coordination environment, with the Pt–N(py) bond lengths being significantly longer than the Pt–C bond lengths, as is typical for complexes of this type. One pyrimidine ring [containing N(32) and N(34)] is twisted out of the plane of the ^{t}Bu$_2$bipy ligand by 30°; this deviation of a ring from overall planarity prevents the molecules from forming well-defined columnar stacks. Stacking between adjacent molecules involves the {Pt(bipy)} cores, separated by (on average) 3.4 Å and is shown in Fig. 1(b); there are no short Pt···Pt contacts.

The UV–Vis absorption spectrum of **1** in CH_2Cl_2 shows absorption maxima at 378 nm (ε, 8.7×10^3 M^{-1} cm^{-1}) and 287 nm (ε, 44×10^3 M^{-1} cm^{-1}) which can be assigned to ^{1}MLCT and ligand-centred π–π^* transitions, respectively. Excitation of the complex into the ^{1}MLCT absorption band generates typical strong luminescence at 520 nm with t = 105 ns and ϕ = 3.7% (in air-equilibrated CH_2Cl_2) which may be ascribed to a ^{3}MLCT process [4,5]. Thus, the complex has the potential to act as an energy-donor to Ln(III) ions whose f–f states are lower in energy than the ^{3}MLCT energy of **1** [1–4].

Reaction of **1** with [Ln(hfac)$_3$(H$_2$O)$_2$] (Ln = Gd, Nd, Er, Yb) in CH_2Cl_2 solution, followed by layering heptane on to the reaction mixture and leaving the solutions to stand for several days, afforded reasonable yields of orange crystalline products for which elemental analysis was consistent with a 1:2 association of Pt(II) complex **1** and {Ln(diketonate)$_3$} units, respectively. This reaction exploits the lability of the two water ligands of [Ln(hfac)$_3$(H$_2$O)$_2$] units and their tendency to be replaced by N-heterocyclic donors [1–4].

We had expected that the pyrimidine rings might act as bridging ligands, each spanning two Ln(III) centres to generate network structures. However the crystal structure of [**1** · {Er(hfac)$_3$(H$_2$O)}{Er(hfac)$_3$(H$_2$O)$_2$}] (Figs. 2 and 3) reveals a trinuclear PtEr$_2$ species in which the {Er(hfac)$_3$} units interact with the pyrimidine rings of **1** by a combination of conventional N–Er dative bonds, and N···HOH hydrogen bonds to the water molecules that are in turn coordinated to the Er(III) centres. Thus Er(1) is 8-coordinate from three diketonate ligands, one water ligand, and one directly coordinated pyrimidine N atom [N(4)]. Er(2) is also 8-coordinate, from three diketonate and two water ligands, and is associated with both pyrimidine rings of **1** by a pair of N···HOH hydrogen-bonding interactions: effectively complex **1** behaves as a chelating bidentate H-bond acceptor to this {Er(hfac)$_3$(H$_2$O)$_2$} unit. The non-bonded N···O distances in these hydrogen bonds are N(2)···O(2 W), 2.764(7) Å and N(12)···O(3 W), 2.770(7) Å. The N···H–O angles are 168.8° and 161.8°, respectively. The

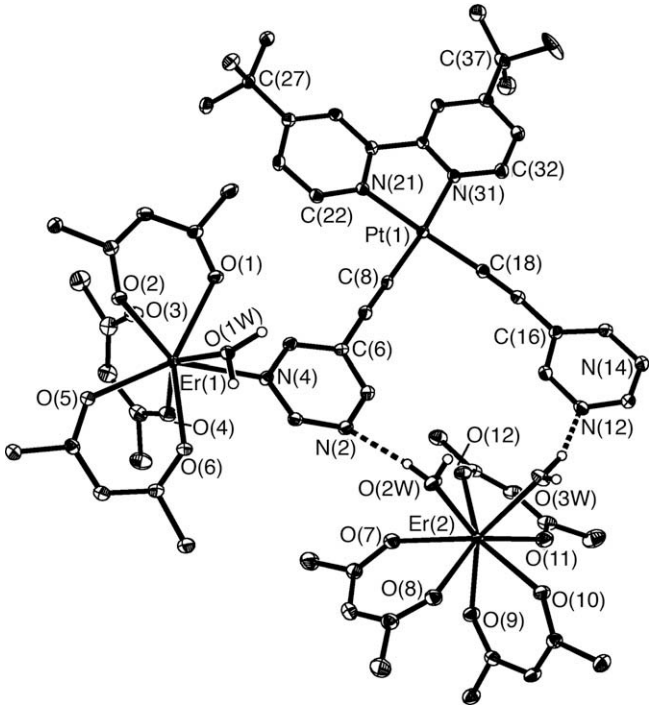


Fig. 2. An ORTEP view of a molecule of [**1** · {Er(hfac)$_3$(H$_2$O)}{Er(hfac)$_3$(H$_2$O)$_2$}], with thermal ellipsoids at the 30% level. The dashed lines are hydrogen bonds between pyrimidine N atoms and water molecules coordinated to Er(2). H atoms (apart from those on the water ligands), F atoms on the hfac ligands, and the minor disorder component of the methyl groups on the ^{t}Bu substituents, ate not shown for clarity.

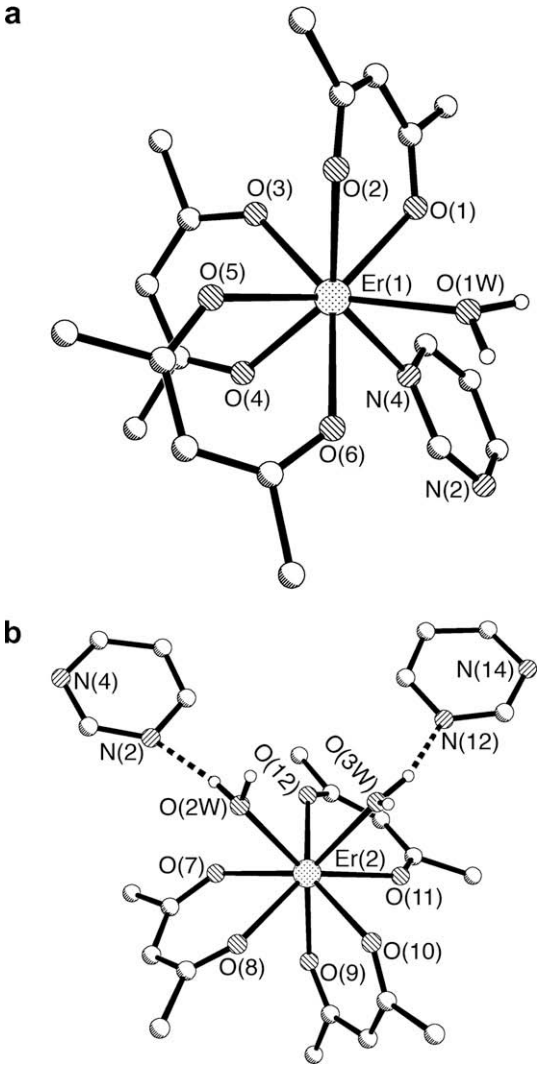


Fig. 3. Coordination environments around (a) Er(1) and (b) Er(2) in the structure of [**1** · {Er(hfac)$_3$(H$_2$O)}{Er(hfac)$_3$(H$_2$O)$_2$}]. The dashed lines are hydrogen bonds between pyrimidine N atoms and water molecules coordinated to Er(2).

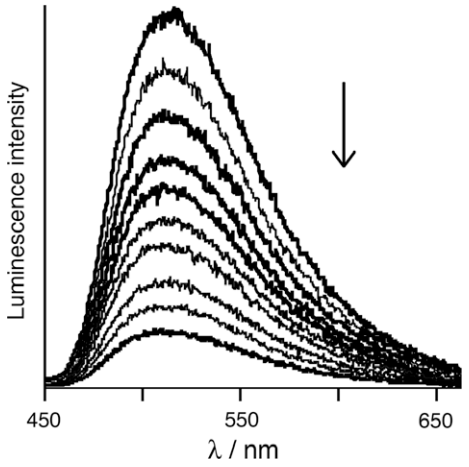


Fig. 4. Steady decrease in the luminescence intensity of **1** (0.6 μM solution in CH_2Cl_2) as portions of [{Er(hfac)$_3$(H$_2$O)$_2$}] (up to 9 equiv) are added. Excitation was at 345 nm, a wavelength at which the absorbance of the solution did not change significantly during the titration.

arrangement of this pair of pyrimidine N atoms [N(2) and N(12)], both oriented inwards towards the same cavity, makes an ideal hydrogen-bond accepting site for the {Er(hfac)$_3$(H$_2$O)$_2$} unit. We have seen a similar hydrogen-bonding interaction between a coordinated water ligand and a weakly basic N-heterocyclic donor, in which the heterocycle does not coordinate directly to the Ln(III) centre, in previous work [6].

The geometry around both Er(III) centres is approximately square antiprismatic, as shown in Fig. 3 which emphasises their immediate coordination environments. For Er(1) the two square planes consist of O(1)/O(3)/O(4)/N(4) and O(2)/O(5)/O(6)/O(1 W); for Er(2) the two planes consist of O(8)/O(10)/O(3 W)/O(2 W) and O(7)/O(9)/O(11)/O(12). The two Er(III) units are 8.99 Å apart; the Pt···Er separations are 8.67 Å to Er(1) and 8.81 Å to Er(2). The tendency we see in this complex of the pyrimidine N atoms not to coordinate fully to the Ln(III) centres presumably reflects the poorer basicity of pyrimidine compared to pyridine.

Spectroscopic titrations were then performed in which small portions of [Ln(hfac)$_3$(H$_2$O)$_2$] were added to a solution of **1** (5×10^{-5} M) in CH_2Cl_2. This addition resulted in no perceptible change to the position or intensity of the ^{1}MLCT absorption band at 378 nm, but resulted in significant changes in luminescence intensity depending on the nature of Ln(III). The decrease in luminescence during the titration when Ln = Er is shown in Fig. 4. During this titration the luminescence intensity from **1** was slightly blue-shifted from 520 to 510 nm, and steadily diminished in intensity. The blue-shift is consistent with the energy of the ^{3}MLCT state being increased by the coordinated Er(III) centre attached to a pyrimidine ring (*cf.* the crystal structure). This arises because of the electron-withdrawing effect of the electropositive Er(III) ion, which inductively stabilises the Pt(II) d(π) orbitals and slightly increases the Pt(II)→bipy MLCT energy gap [4]. The steady reduction in luminescence intensity during the titration, on the other hand, must arise from Pt(II)→Er(III) energy-transfer which quenches the Pt(II)-based excited state by generation of an f–f excited state at Er(III).

A plot of decrease in luminescence intensity of **1** *versus* amount of added [Er(hfac)$_3$(H$_2$O)$_2$] produced a curve which fitted well to a 1:1 binding isotherm, from which an association constant of 7×10^3 M^{-1} could be calculated. We do not know what the solution structure of the adduct (denoted **1** · Er) is: it may differ significantly from what was observed in the solid state (a kinetic species) although adduct formation is clearly occurring. The most likely behaviour – based on extensive previous work [4,7] – is that an {Er(hfac)$_3$} fragment is bound to **1** *via* one of the weakly basic pendant pyrimidine N atoms, *cf.* atom Er(1) in Fig. 2. An association constant of 7×10^3 M^{-1} involving binding of an {Er(hfac)$_3$} fragment to a single pyrimidine ring is reasonable given that we have obtained association constants of the order of 10^5 M^{-1} for binding to a chelating 2,2′-bipyrimidine site in a neutral complex [7b]. We could not find any evidence for a 1:2 Pt:Er adduct (*cf.* the crystal structure) in which a second {Ln(hfac)$_3$} fragment is associated *via* hydrogen bonding. Presumably the second association constant is too low to have any noticeable effect at the low concentrations used for photophysical studies.

As a control experiment we performed the same titration of **1** with [Gd(hfac)$_3$(H$_2$O)$_2$]. Gd(III) cannot quench the excited state of **1** because its lowest energy f–f excited state is at 32 000 cm^{-1}, in the UV region. Thus Gd(III) behaves the same as other Ln(III) ions in terms of electrostatic and steric effects, but without being able to cause quenching by energy-transfer. In this experiment, addition of portions of [Gd(hfac)$_3$(H$_2$O)$_2$] to a solution of **1** resulted in a slight *increase* in emission intensity – consistent with the increase in energy of the ^{3}MLCT state – and a corresponding increase in emission lifetime to 141 ns. This lifetime of 141 ns for the ad-

duct between **1** and {Gd(hfac)$_3$} is then used as the basis for comparison with other **1** · Ln$_2$ adducts in solution.

$$k_{EnT} = 1/\tau_1 - 1/\tau_2 \quad (1)$$

At the end of the titration of **1** with [Er(hfac)$_3$(H$_2$O)$_2$], the partially-quenched Pt(II)-based emission of **1** displayed dual-exponential decay with lifetimes of 96 ns (major component) and 13 ns (minor component). Given that the titration did not go to completion, because of the relatively low association constant of 7×10^3 M^{-1}, we assign the 96 ns component to luminescence from free **1** which was measured as 105 ns in the absence of any added [Er(hfac)$_3$(H$_2$O)$_2$] (the slight reduction from 105 ns to 96 ns may be ascribed to collisional quenching between **1** and increasing amounts of [Er(hfac)$_3$(H$_2$O)$_2$] even when adduct formation is not occurring). The 13 ns component may be ascribed to nearly-quenched emission from the Pt(II) centre in the adduct **1** · Er. From Eq. (1) [in which k_{EnT} is the energy-transfer rate, and τ_1 (13 ns) and τ_2 (141 ns) are the partially-quenched and unquenched Pt(II)-based luminescence lifetimes, respectively], we can determine the Pt(II)→Er(III) energy-transfer rate to be 7.0×10^7 s^{-1}.

An exactly similar experiment with [Yb(hfac)$_3$(H$_2$O)$_2$] resulted in no significant quenching, with **1** · Yb$_2$ showing essentially identical properties to **1** · Gd$_2$ with a final lifetime of 137 ns. Application of Eq. (1) gives $k_{EnT} \approx 2 \times 10^5$ s^{-1}, although given the very small difference between the values of τ_1 (137 ns) and τ_2 (141 ns), each individually having a margin of error of at least 2%, this calculation is of little significance and we can just say that there is essentially no Pt(II)→Yb(III) energy-transfer.

When [Nd(hfac)$_3$(H$_2$O)$_2$] was used in the titration, the luminescence from **1** was again steadily, but not completely, quenched. At the end of the titration – after addition of 10 equiv. of [Nd(hfac)$_3$(H$_2$O)$_2$] – the decay curve showed signs of dual-exponential decay, although it this was difficult to deconvolute into two components with confidence. If we fixed one component at 105 ns, being unchanged luminescence from the substantial amount of free **1**, the second component refined to being *ca.* 30–40 ns from several independent measurements. If we take an estimate of 35 ns for the partially-quenched luminescence of **1** · Nd we get from Eq. (1) a Pt(II)→Nd(III) energy-transfer rate constant of *ca.* 2×10^7 s^{-1}, about one-third the value of the value Pt(II)→Er(III) energy-transfer rate constant (7.0×10^7 s^{-1}).

The ability of these different lanthanide(III) ions to accept energy from the ^{3}MLCT state of **1** is therefore in the order Er > Nd > Yb, which agrees with what we have seen before in Pt(II)/Ln(III) dyads where the Pt(II) emission is quite high in energy [4]. The results can be rationalised on the basis of overlap between the donor's emission spectrum and the acceptor's absorption spectrum. Yb(III) only has a single f–f absorption at 10200 cm^{-1} which has negligible overlap with the tail end of the luminescence spectrum of **1**. Nd(III) is much richer in f–f excited states in the relevant region (Figs. 5 and 6), with 10 f–f levels lying between 11000 and 20000 cm^{-1} (910 and 500 nm) spanning the region where the Pt-based emission occurs; however, the Nd(III)-based f–f absorptions are weak in the area where the Pt(II) emission is at its most intense (Figs. 4 and 6). In contrast, the region of maximum f–f absorption intensity for Er(III) – between 520 and 530 nm (Fig. 6) – exactly matches the emission maximum of **1** (Fig. 4), giving good donor/acceptor overlap which results in Er(III) being the best energy acceptor from complex **1** from this set of Ln(III) ions.

We note also that the absolute values of these energy-transfer rates are slower than we observed before in other Pt(II)–Ln(III) dyads [4], despite the inter-metallic distances being shorter. This is likely to be a consequence of the bridging pathway which provides the necessary electronic coupling for Dexter energy-transfer [3]. In the crystal structure of **1** · Er$_2$ we can see that one {Er(hfac)$_3$} unit is only connected to **1** *via* hydrogen bonding, through which

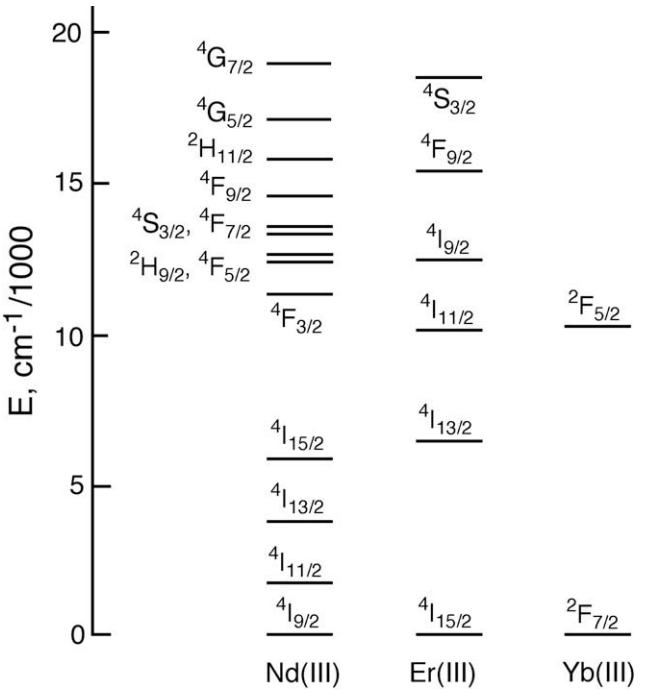


Fig. 5. Excited f–f levels of Nd(III), Er(III) and Yb(III).

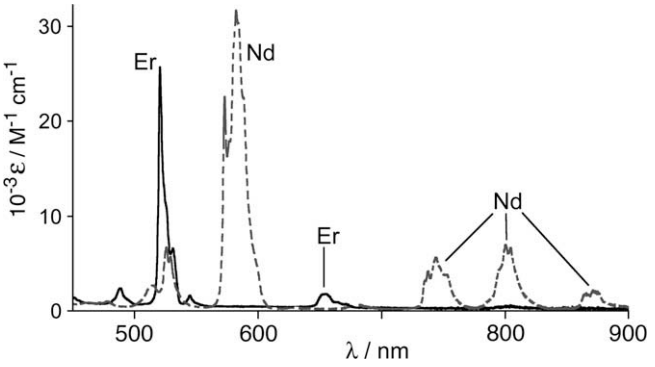


Fig. 6. Absorption spectra of [Ln(hfac)$_3$(phen)] in CH_2Cl_2 (Ln = Nd, Er). Note the exact correspondence of the strong Er(III)-based absorption maximum in the 520–530 nm region with the ^{3}MLCT emission maximum of **1** at 520 nm.

electronic coupling will necessarily be weak, and the other is connected to the N atoms of a pyrimidine ring which has a *meta* relationship to the acetylide 'wire'. The relative weakness of electronic couplings across *meta*-substituted aromatic rings compared to *para* linkages is well known [8].

Even though it is relatively slow, Pt(II)→Ln(III) energy-transfer is clearly occurring to Nd(III) and Er(III). We attempted therefore to see if we could see sensitised Ln(III)-based emission from these centres following excitation of the MLCT absorption of **1** at 450 nm. We could not detect any significant sensitised Nd(III)-based or Er(III)-based luminescence under these conditions however, which is likely to be a consequence of (i) slow energy-transfer leading to only a fraction of the Ln(III) centres being excited by this mechanism, (ii) the relatively low absorbance of the adducts at 450 nm, and (iii) the presence of water molecules in the coordination spheres of these ions (according to the crystal structure) which will make any luminescence weak and short-lived. It is well known that directly coordinated OH oscillators are very effective at quenching low-energy luminescence from lanthanide(III) ions [9].

We could however detect weak Nd(III)-based emission using 337 nm excitation which directly excites the Ln(III) centres *via* the diketonate π–π^* absorptions in a region where the extinction coefficient is much higher, and in this case we could detect weak luminescence from Nd(III) at its characteristic wavelengths of 1060 and 1340 nm; this emission clearly showed dual-exponential decay with lifetimes of *ca.* 1.0 and 0.2 μs, in agreement with the presence of two environments for Nd(III), one with two coordinated water molecules (to which can be ascribed the shorter-lived lifetime component) [4] and the other with only one coordinated water molecule (to which can be ascribed the longer-lived lifetime component). Similarly, direct excitation of the {Er(hfac)$_3$} centre in **1** · Er$_2$ using 337 nm excitation revealed very weak luminescence at 1530 nm characteristic of Er(III) (too weak for lifetime measurements to be reliable, due to the coordinated water ligands).

In conclusion, the new luminescent complex **1**, with two pendant pyrimidinyl units, forms adducts with {Er(hfac)$_3$(H$_2$O)$_n$} fragments (n = 1, 2) which in the solid state are associated by a combination of direct Pt–Er dative bonds, and N···HOH hydrogen bonds between pyrimidine rings and the water molecules coordinated to Er(III). This association results in Pt→Ln photoinduced energy-transfer to lanthanide(III) ions having low-lying f–f states, with energy-transfer rates in the order Pt→Er > Pt→Nd > Pt→Yb, in agreement with expectations based on the availability of f–f states on these lanthanide ions which can act as energy-acceptors and how well they overlap with the luminescence from **1**. The presence of coordinated water molecules still attached to the Ln(III) centres however means that the resulting sensitised near-infrared luminescence is very weak.

3. Experimental

3.1. General details

The following were prepared using the literature methods: [Ln(hfac)$_3$(H$_2$O)]$_2$ [10], [Pt(^{t}Bu$_2$bipy)Cl$_2$] [4]. The following instruments were used for routine spectroscopic measurements: UV–Vis spectra, a Cary 50 spectrophotometer; luminescence spectra, a Perkin–Elmer LS-50 fluorimeter; luminescence lifetimes in the visible region, an Edinburgh Instruments 'mini-τ' time-resolved fluorimeter equipped with a 405 nm pulsed diode laser excitation source; EI mass spectra, a VG AutoSpec magnetic sector instrument; ^{1}H NMR spectra, a Bruker AC-250 spectrometer. Lanthanide-based luminescence lifetimes in the near-infrared region were measured using a setup described previously [11].

3.2. X-ray crystallography

X-ray crystallographic data are summarised in Table 1. For each compound a suitable crystal was coated with hydrocarbon oil and attached to the tip of a glass fibre and transferred to a Bruker-SMART 1000 or APEX-2 CCD diffractometer (graphite-monochromated Mo Kα radiation, λ = 0.71073 Å) under a stream of cold N$_2$. Data were corrected for Lorentz and polarisation effects and for absorption by semi-empirical methods (SADABS) [12] based on symmetry-equivalent and repeated reflections. The structures were solved by direct methods or heavy atom Patterson methods and refined by full-matrix least-squares methods on F^2. Hydrogen atoms were placed geometrically and refined with a riding model and with U_{iso} constrained to be 1.2 (1.5 for methyl groups) times U_{eq} of the carrier atom. Structures were solved and refined using the SHELX suite of programs [13]. Significant bond distances and angles for the structures of the metal complexes are in Tables 2 and 3. The structure determination of **1** presented no significant problems. In [**1** · {Er(hfac)$_3$(H$_2$O)$_2$} {Er(hfac)$_3$(H$_2$O)}] however there was rotational disorder involving both some of the CF$_3$ groups of the hfac ligand, and some of the ^{t}Bu groups of the ^{t}Bu$_2$bipy ligands. Specifically the CF$_3$ groups involving C atoms C(55), C(61), C(65) and C(85) exhibited disorder of the attached F atoms, with two or three F atoms at each of these CF$_3$ groups disordered over two positions with site occupancies of 51% and 49%. Likewise the methyl groups C(38) and C(39) were disordered over two sites each with the same fractional occupancies. These disordered atoms, with fractional site occupancies, were refined with isotropic displacement parameters.

Table 1
Crystallographic data for the two new structures.

Compound	**1**	[**1** · {Er(hfac)$_3$(H$_2$O)} {Er(hfac)$_3$(H$_2$O)$_2$}]
Formula	$C_{30}H_{30}N_6Pt$	$C_{60}H_{42}Er_2F_{36}N_6O_{15}Pt$
Formula weight	669.69	2270.01
T (K)	100(2) K	100(2) K
Crystal system, space group	monoclinic, $P2(1)/c$	monoclinic, $P2(1)/n$
a (Å)	14.3009(10)	15.9945(14)
b (Å)	11.1471(7)	17.2734(14)
c (Å)	18.0535(12)	28.924(2)
b (°)	113.046(3)	97.966(4)
V (Å^3)	2648.3(3)	7914.0(11)
Z	4	4
D_{calc}	1.680	1.905
μ (mm^{-1})	5.329	3.476
Crystal size (mm)	0.15 × 0.09 × 0.06	0.16 × 0.07 × 0.04
Reflections collected	55334	121054
Independent reflections (R_{int})	6135 (0.0288)	18083 (0.0447)
Data/restraints/parameters	6135/0/334	18083/22/1072
Final R indices[a]	R_1 = 0.0161wR_2 = 0.0355	R_1 = 0.0358wR_2 = 0.0854
Largest difference in peak and hole (e Å^{-3})	0.953 and −0.489	1.883 and −2.298

[a] The value of R_1 is based on selected data with $I > 2\sigma(I)$; the value of wR_2 is based on all data.

Table 2
Selected bond distances (Å) and angles (°) for the structure of **1**.

Pt(1)–C(38)	1.946(2)
Pt(1)–C(28)	1.947(2)
Pt(1)–N(1)	2.0528(17)
Pt(1)–N(11)	2.0610(18)
C(38)–Pt(1)–C(28)	87.52(9)
C(38)–Pt(1)–N(1)	175.49(8)
C(28)–Pt(1)–N(1)	96.95(8)
C(38)–Pt(1)–N(11)	97.15(8)
C(28)–Pt(1)–N(11)	175.33(8)
N(1)–Pt(1)–N(11)	78.38(7)

Table 3
Selected bond distances (Å) and angles (°) in the structure of [**1** · {Er(hfac)$_3$(H$_2$O)}{Er(hfac)$_3$(H$_2$O)$_2$}].

Er(1)–O(3)	2.281(4)	Er(2)–O(9)	2.286(3)
Er(1)–O(5)	2.311(3)	Er(2)–O(10)	2.307(4)
Er(1)–O(4)	2.320(3)	Er(2)–O(7)	2.311(4)
Er(1)–O(6)	2.326(3)	Er(2)–O(12)	2.325(3)
Er(1)–O(2)	2.342(3)	Er(2)–O(3W)	2.334(3)
Er(1)–O(1W)	2.343(3)	Er(2)–O(8)	2.343(4)
Er(1)–O(1)	2.365(3)	Er(2)–O(2W)	2.343(4)
Er(1)–N(4)	2.532(4)	Er(2)–O(11)	2.357(4)
Pt(1)–C(8)	1.951(5)	Pt(1)–N(21)	2.055(4)
Pt(1)–C(18)	1.959(5)	Pt(1)–N(31)	2.065(4)
C(8)–Pt(1)–C(18)	85.73(19)	C(8)–Pt(1)–N(31)	174.54(17)
C(8)–Pt(1)–N(21)	95.93(17)	C(18)–Pt(1)–N(31)	99.44(18)
C(18)–Pt(1)–N(21)	177.44(18)	N(21)–Pt(1)–N(31)	78.84(16)

3.3. Preparation of 5-ethynylpyrimidine

This is based on a literature method [14] but with some modifications. To a mixture of 5-bromopyrimidine (5.03 g, 31.6 mmol), $Pd(PPh_3)_2Cl_2$ (150 mg) and CuI (25 mg) in THF (15 mL) under N_2, was added 2-methyl-3-butyn-2-ol (2.60 g, 31.0 mmol) and diethylamine (30 mL). After stirring for 5 h at room temperature, the solvent was evaporated to dryness. Recrystallisation from ethylacetate/diethylether afforded yellow microcrystalline needles of 2-methyl-4-(5-pyrimidine)-3-butyn-2-ol in 84% yield. EI-MS: *m*/*z* 162 [M^+]. ^{1}H NMR (250 MHz, $CDCl_3$): δ 9.10 (s, 1H; pyrimidine H^2), 8.75 (d, 2H; pyrimidine H^4/H^6), 1.60 (s, 6H; $2CH_3$): the OH peak could not be observed.

To a solution of 2-methyl-4-(5-pyrimidine)-3-butyn-2-ol (3.50 g, 33.7 mmol) in a mixture of toluene (30 mL) and diethylether (15 mL), was added finely powdered NaOH (0.80 g, 20 mmol). The mixture was refluxed for 3 h and was then cooled to room temperature and filtered. The solvent was concentrated in vacuum to 10 mL and cooled in the fridge. Pale yellow microcrystalline needles were isolated in 80% yield. EI-MS: *m*/*z* 104 [M^+]. ^{1}H NMR (250 MHz, $CDCl_3$): δ 9.15 (s, 1H; pyrimidine H^2), 8.80 (s, 2H; pyrimidine H^4/H^6) and 3.40 (s, 1H; CH).

3.4. Preparation of complex **1**

A mixture of [Pt(4,4-^{t}Bu$_2$bipy)Cl_2] (0.63 g, 1.20 mmol), anhydrous CuI (175 mg, catalyst), and dry iPr$_2$NH (30 mL) in dry, degassed dichloromethane (150 mL) under N_2 was stirred for 10 min, after which time 4-ethynylpyrimidine (0.63 g, a large excess) was added. The resulting suspension was stirred under N_2 at room temperature for 5 days whilst being protected from light. The solvent was evaporated and the solid residue was dried *in vacuo* to remove traces of ^{i}Pr$_2$NH. The product was purified by column chromatography (2% MeOH–CH_2Cl_2/alumina) to give 0.53 g (64%) of the desired product. EI-MS: *m*/*z* 669 [M^+]. ^{1}H NMR (250 MHz, $CDCl_3$): δ (ppm) 9.50 (2H, d; bpy H^6), 8.90 (2H, s; pym H^2), 8.74 (4H, s; pym $H^{4,6}$), 7.96 (2H, d; bpy H^3), 7.58 (2H, dd; bpy H^5) and 1.41 (18H, s; $C(CH_3)_3$). $PtC_{30}H_{30}N_6$ requires C, 53.8; H, 4.5; N, 12.5. Found: C, 53.3; H, 4.3; N, 12.2%. X-ray quality crystals were grown by slow evaporation of a CH_2Cl_2 solution.

3.5. Preparation of trinuclear complexes *[1 · {Ln(hfac)$_3$(H$_2$O)$_2$}{Ln(hfac)$_3$(H$_2$O)}] (1 · Ln$_2$)*

A solution of complex **1** (50 mg, 0.07 mmol) in CH_2Cl_2 was added to a solution of the appropriate [Ln(hfac)$_3$(H$_2$O)$_2$] (2 equiv.) in CH_2Cl_2 and the mixture was stirred overnight. A small layer of heptane was placed over the solution and the system left to evaporate slowly until orange needles of the desired compounds grew in a few days. The crystals were filtered off, washed with hexane and dried.

Data for [**1** · {Nd(hfac)$_3$(H$_2$O)$_2$}{Nd(hfac)$_3$(H$_2$O)}]. Yield: 50%. $C_{60}H_{42}N_6O_{15}F_{36}PtNd_2$ requires C, 32.0; H, 1.9; N, 3.7. Found: C, 32.2; H, 1.8; N, 3.8%.

Data for [**1** · {Er(hfac)$_3$(H$_2$O)$_2$}{Er(hfac)$_3$(H$_2$O)}]. Yield: 53%. $C_{60}H_{42}N_6O_{15}F_{36}PtEr_2$ requires C, 31.3; H, 1.8; N, 3.7. Found: C, 31.8; H, 1.9; N, 3.9%.

Data for [**1** · {Yb(hfac)$_3$(H$_2$O)$_2$}{Yb(hfac)$_3$(H$_2$O)}]. Yield: 44%. $C_{60}H_{42}N_6O_{15}F_{36}PtYb_2$ requires C, 31.2; H, 1.8; N, 3.6. Found: C, 31.3; H, 1.8; N, 3.7%.

Data for [**1** · {Gd(hfac)$_3$(H$_2$O)$_2$}{Gd(hfac)$_3$(H$_2$O)}]. Yield: 48%. $C_{60}H_{42}N_6O_{15}F_{36}PtGd_2$ requires C, 31.6; H, 1.8; N, 3.7. Found: C, 31.8; H, 1.9; N, 3.7%.

Supplementary data

CCDC 694403 and 694404 contain the supplementary crystallographic data for this paper. These data can be obtained free of charge via http://www.ccdc.cam.ac.uk/conts/retrieving.html, or from the Cambridge Crystallographic Data Centre, 12 Union Road, Cambridge CB2 1EZ, UK; fax: (+44) 1223-336-033; or e-mail: deposit@ccdc.cam.ac.uk.

Acknowledgements

We thank the Government of the Sultanate of Oman and EPSRC for financial support, and Mr. William S. Perry for assistance with the near-IR luminescence measurements.

References

[1] M.D. Ward, Coord. Chem. Rev. 251 (2007) 1663.
[2] (a) S. Torelli, D. Imbert, M. Cantuel, G. Bernardinelli, S. Delahaye, A. Hauser, J.-C.G. Bünzli, C. Piguet, Chem. Eur. J. 11 (2005) 3228;
(b) S.J.A. Pope, B.J. Coe, S. Faulkner, R.H. Laye, Dalton Trans. (2005) 1482;
(c) P.D. Beer, F. Szemes, P. Passaniti, M. Maestri, Inorg. Chem. 43 (2004) 3965;
(d) P.B. Glover, P.R. Ashton, L.J. Childs, A. Rodger, M. Kercher, R.M. Williams, L. De Cola, Z. Pikramenou, J. Am. Chem. Soc. 125 (2003) 9918;
(e) H.-B. Xu, L.-X. Shi, E. Ma, L.-Y. Zhang, Q.-H. Wei, Z.-N. Chen, Chem. Commun. (2006) 1601;
(f) M. Mehlstäubl, G.S. Kottas, S. Colella, L. De Cola, Dalton Trans. (2008) 2385;
(g) J.W. Stouwdam, M. Raudsepp, F.C.J.M. van Veggel, Langmuir 21 (2005) 7003;
(h) S.I. Klink, H. Keizer, F.C.J.M. van Veggel, Angew. Chem., Int. Ed. 39 (2000) 4319.
[3] T. Lazarides, D. Sykes, S. Faulkner, A. Barbieri, M.D. Ward, Chem. Eur. J. 14 (2008) 9389.
[4] T.K. Ronson, T. Lazarides, H. Adams, S.J.A. Pope, D. Sykes, S. Faulkner, S.J. Coles, M.B. Hursthouse, W. Clegg, R.W. Harrington, M.D. Ward, Chem. Eur. J. 12 (2006) 9299.
[5] (a) S.L. James, M. Younus, P.R. Raithby, J. Lewis, J. Organomet. Chem. 542 (1997) 233;
(b) E.C. Whittle, J.A. Weinstein, M.W. George, K.S. Schanze, Inorg. Chem. 40 (2001) 4053;
(c) M. Hissler, M. Connick, D.K. Geiger, J.E. McGarrah, D. Lipa, R.J. Lachiotte, R. Eisenberg, Inorg. Chem. 39 (2000) 447.
[6] Z.R. Reeves, K.L.V. Mann, J.C. Jeffery, J.A. McCleverty, M.D. Ward, F. Barigelletti, N. Armaroli, J. Chem. Soc., Dalton Trans. (1999) 349.
[7] (a) T. Lazarides, H. Adams, D. Sykes, S. Faulkner, G. Calogero, M.D. Ward, Dalton Trans. (2008) 691;
(b) N.M. Shavaleev, G. Accorsi, D. Virgili, Z.R. Bell, T. Lazarides, G. Calogero, N. Armaroli, M.D. Ward, Inorg. Chem. 44 (2005) 61.
[8] (a) J.A. McCleverty, M.D. Ward, Acc. Chem. Res. 31 (1998) 842;
(b) M.D. Ward, Chem. Soc. Rev. 24 (1995) 121.
[9] (a) A. Beeby, S. Faulkner, Chem. Phys. Lett. 266 (1997) 116;
(b) A. Beeby, I.M. Clarkson, R.S. Dickins, S. Faulkner, D. Parker, L. Royle, A.S. de Sousa, J.A.G. Williams, M. Woods, J. Chem. Soc., Perkin Trans. 2 (1999) 493.
[10] Y. Hasegawa, Y. Kimura, K. Murakoshi, Y. Wada, J. Kim, N. Nakashima, T. Yamanaka, S. Yanagida, J. Phys. Chem. 100 (1996) 10201.
[11] N.M. Shavaleev, S.J.A. Pope, Z.R. Bell, S. Faulkner, M.D. Ward, Dalton Trans. (2003) 808.
[12] G.M. Sheldrick, SADABS Version 2.10, University of Göttingen, 2003.
[13] G.M. Sheldrick, SHELXS-97 and SHELXL-97, University of Göttingen, 1997.
[14] L. Yu, J.S. Lindsey, J. Org. Chem. 66 (2001) 7402.

Polyhedron 28 (2009) 233–238

Contents lists available at ScienceDirect

Polyhedron

journal homepage: www.elsevier.com/locate/poly

Synthesis, characterization and fluorescence behavior of new fluorescent probe phthalocyanines bearing coumarin substituents

Meryem Çamur [a], Mustafa Bulut [a,*], Mehmet Kandaz [b,*], Orhan Güney [c]

[a] Department of Chemistry, Marmara University, 34722 Kadıköy-Istanbul, Turkey
[b] Department of Chemistry, Sakarya University, 54140 Esentepe, Sakarya, Turkey
[c] Department of Chemistry, Istanbul Technical University, 34469 Maslak, Istanbul, Turkey

ARTICLE INFO

Article history:
Received 14 March 2008
Accepted 22 October 2008
Available online 11 December 2008

Keywords:
Phthalocyanines
Fluorescence
Coumarin derivatives
Aggregation
Cobalt
Zinc

ABSTRACT

In this study, we report a new ligand, 6-hexyloxy-3-[*p*-(3′,4′-dicyanophenoxy)phenyl]coumarin, and its fluorescent tetrasubstituted phthalocyanines {M[Pc(OBzCou)$_4$], M = 2H, Zn(II), Co(II); Bz: Benzene}. The effect of the coumarin derivative on the intensity of the fluorescence spectra of the metal-free (H_2Pc) and zinc phthalocyanine (ZnPc) derivatives was investigated. The change of the emission properties of both the coumarin moieties and the phthalocyanine core in the presence of the metal ion and the ring-opening reaction of the coumarin were studied by means of steady-state fluorescence spectroscopy. The radiative decay of the Pcs and the treated coumarin substituents bound to the Pcs was examined. The novel chromogenic compounds were characterized by elemental analysis, ^{1}H NMR, ^{13}C NMR, Maldi-TOF, IR and UV–Vis spectral data. The photophysical properties of the Pcs are extensively affected by their state of aggregation: in particular, dimerization and aggregation result in a remarkable modification of the absorption and emission bands and may induce significant quenching of the usually strong Pc fluorescence. The electronic spectra exhibit a band of coumarin identity together with characteristic Q and B bands of the phthalocyanine core.

© 2008 Elsevier Ltd. All rights reserved.

1. Introduction

Phthalocyanines have been discovered to be versatile functional materials and have been applied in biological as well as electronic areas for many years [1–4]. The benefits of phthalocyanines (Pc's) in terms of technological applications is beyond question, such as sensing elements in chemical sensors, photoconducting agents in photocopying machines, carrier generation materials in near-IR, etc. [5–10]. They exhibit excellent chemical and photochemical properties, but poor fluorescent properties [11–13]. On the other hand, coumarins (2*H*-1-benzopyran-2-one), found naturally in many higher plants and essential oils including tonka beans, sweet clover and lavender [14,15], are used as anticoagulants, additives in food and cosmetics, in the preparation of insecticides, optical brighteners and dispersed fluorescent, laser dyes, anti-HIV activities, etc. [16–18]. The family of functional phthalocyanines has been an interesting target for chemists for the development of further chemical reactions on phthalocyanine complexes [19–23]. Therefore in this paper we have, in particular, combined these two functional materials into a single compound via synthetic methodology to obtain soluble fluorescent phthalocyanines. The experimental results demonstrate that the introduction of coumarin derivatives into the peripheral ring of phthalocyanines increases the fluorescent properties of phthalocyanines. Phthalocyanines coupled with the coumarin moiety may exhibit biological activities and, after cleavage of the lactone ring of the peripheral 2*H*-1-benzopyran-2-one (coumarin), the solubility can also be increased.

In this study, the phthalocyanines {M[Pc(OBzCou)$_4$], M = 2H, Zn(II), Co(II)}, with four peripheral 6-hexyloxy-3-(4-oxyphenyl)-coumarin substituents, were prepared via cyclotetramerization from the 6-hexyloxy-3-[*p*-(3′,4′-dicyanophenoxy)phenyl]coumarin and the products resulting from lactone ring-opening reactions on the periphery of H_2Pc (**3**) and ZnPc (**4**) were synthesized. In addition, we report here the effect of the coumarin substituent on intensity of the fluorescence emission spectra of **3**, **3a**, **4** and **4a**, as well as the effect of the phthalocyanine core on the coumarin emission.

2. Experimental

Chloroform ($CHCl_3$), tetrahydrofuran (THF), $Zn(O_2CMe)_2 \cdot 2H_2O$, $CoCl_2 \cdot 6H_2O$, 1,8-diazabicyclo-[5,4,0]undec-7-ene (DBU) were purchased from Merck and Alfa Aesar, and were used as received. All other reagents were obtained from Fluka, Aldrich Chemical Co.

* Corresponding authors. Tel.: +90 216 3479641/1370; fax: +90 216 347 87 83 (M. Bulut); tel./fax: +90 264 295 59 50 (M. Kandaz).
E-mail addresses: mbulut@marmara.edu.tr (M. Bulut), mkandaz@sakarya.edu.tr (M. Kandaz).

0277-5387/$ - see front matter © 2008 Elsevier Ltd. All rights reserved.
doi:10.1016/j.poly.2008.10.066

and were used without purification. *p*-(3,4-Dicyanophenoxy)-phenylacetic acid [21] and 4-nitro-1,2-dicyanobenzene [24] were prepared according to reported procedures. The purity of the products was tested in each step by TLC (silica gel: $CHCl_3$ and MeOH). Routine IR spectra were recorded on a Shimadzu Fourier Transform FTIR-8300 Infrared spectrophotometer using KBr pellets, and electronic spectra on a Shimadzu UV-1601 UV–Vis spectrophotometer. ^{1}H NMR and ^{13}C NMR spectra were recorded on a Bruker 300 spectrometer instrument using TMS as an internal reference at Sakarya University. Elemental analysis was performed by the Instrumental Analysis Laboratory of TUBITAK Ankara Test and Analysis Laboratory. Mass spectra were performed on a Bruker Autoflex III mass spectrometer. Fluorescence excitation and emission spectra were recorded on a Jasco FP-750 spectrofluorimeter. Fluorescence measurements utilized 10 μM samples, 5-nm band-pass in both excitation and detection paths, and right-angle geometry.

2.1. 6-Hydroxy-3-[p-(3′,4′-dicyanophenoxy)phenyl]coumarin (**1**)

A mixture of *p*-(3,4-dicyanophenoxy)phenylacetic acid (2.00 g, 7.19 mmol), 2,5-dihydroxybenzaldehyde (0.99 g, 7.19 mmol), sodium acetate (2.95 g, 36 mmol), anhydrous acetic anhydride (15 mL) was heated and stirred at reflux temp. in a sealed glass tube for 8 h under N_2. After cooling to room temperature, water was added and the mixture stirred overnight. The resulting solid, 6-acetoxy-3-[*p*-(3′,4′-dicyanophenoxy)phenyl]coumarin, was filtered, washed with water and dried. The crude product 6-acetoxy-3-[*p*-(3′,4′-dicyanophenoxy)phenyl]coumarin was suspended in methanol. 10% HCl was added until the pH of the solution was 3 and the mixture was heated and stirred at 60 °C for 4 h under N_2. At the end of the reaction, the resulting powder, 6-hydroxy-3-[*p*-(3′,4′-dicyanophenoxy)phenyl]coumarin, was filtered, washed with water and dried. It was purified by silica gel column chromatography with chloroform as the eluent.

Yield: 1.61 g (59%); m.p. 284–286 °C. IR ν(cm^{-1}): 3440 (OH), 3105–3044 (Ar-H), 2924–2843 (alkyl-CH), 2229 (–C≡N), 1709 (C=O lactone), 1626 (C=C), 1589–1488 (Ar C=C), 1258 (Ar-O-Ar). ^{1}H NMR (DMSO-d_6) δ (ppm): 9.78 (s, Ar-OH, 1H, deuterium exchangeable), 8.22 (s, 1H, *meta* to lactone, Cou-H), 8.12 (d, 1H, *ortho* to CN, Phenyl H2), 7.84 (d, isomer, 1H, *ortho* to CN; H3), 7.42 (Bz_2; dd, 4H, Ar-H), 7.27 (d, 1H, *meta* to Cou-OH), 7.06 (d, 1H, *ortho* to Cou-OH), 7.05 (Bz_1; dd, 1H, *meta* to CN; H2), 7.02 (dd, 1H, *ortho* to Cou-OH). ^{13}C NMR (300 MHz, DMSO-d_6) δ (ppm): 164.32 (Ar-C=O), 160.55 (Ar-H, *ortho* to Ar-OH), 145.23, 141.80 (Cou), 140.65 (Bz_1), 136.11 (Bz_2), 135.58, 134.44, 133.92, 131.16, 128.42, 127.34, 125.65 (Cou), 123.85, 123.10, 116.57 (Bz_1), 115.78, 115.09, 114.63, 40.45 (DMSO). *Anal.* Calc. for $C_{23}H_{12}N_2O_4$ (380 g/mol): C, 72.63; H, 3.16; N, 7.37. Found: C, 72.56; H, 3.32; N, 7.43%. UV–Vis (DMF): λ_{max} (nm) (log ε): 326 (4.22), 380 (3.90 Coumarin).

2.2. 6-Hexyloxy-3-[p-(3′,4′-dicyanophenoxy)phenyl]coumarin (**2**)

6-Hydroxy-3-[*p*-(3′,4′-dicyanophenoxy)phenyl]coumarin **1** (1.61 g, 4.24 mmol) and 1-bromohexane (0.70 g, d 1.11 g/ml, 4.24 mmol) were dissolved in dry DMF (50 mL), and K_2CO_3 (0.60 g, 4.34 mmol) and tetrabutylammoniumbromide (0.02 g, excess) as a catalyst were added. After refluxing for 5 days under nitrogen the reaction mixture was poured into iced water and acidified with aq. HCl solution. The precipitate that formed was filtered, washed with water and the crude product dried. It was purified on silica gel column chromatography with chloroform as the eluent.

Yield: 1.76 g (89%); m.p. 164–166 °C. IR ν(cm^{-1}): 3090–3044 (Ar-H), 2962–2858 (alkyl-CH), 2226 (–C≡N), 1701 (C=O lactone), 1607 (C=C), 1585–1496 (Ar C=C), 1281 (Ar-O-Ar), 1242–1130 (Ar-O-C). ^{1}H NMR (DMSO-d_6) δ (ppm): 8.23 (s, 1H, *meta* to lactone, Cou-H), 8.12 (d, 1H, *ortho* to CN, Phenyl H2), 7.83 (d, isomer, 1H, *ortho* to CN; H3), 7.80 (d, 1H, *meta* to Cou-OR), 7.43 (Bz_2; dd, 4H, Ar-H), 7.36 (d, 1H, *ortho* to Cou-OR), 7.26 (Bz_1; dd, 1H, *meta* to CN; H2), 7.20 (dd, 1H, *ortho* to Cou-OR), 3.98 (t, 2H, OCH_2–), 1.74–1.69 (m, 2H, –OCH_2CH_2–), 1.42–1.21 (m, 6H, $CH_2CH_2CH_2CH_3$), 0.90 (t, 3H, CH_3). ^{13}C NMR (300 MHz, DMSO-d_6) δ (ppm): 162.11 (Ar-C=O), 160.06 (Ar-H, ortho to Ar-OH), 144.98, 140.40 (Cou), 140.07 (Bz_1), 135.77 (Bz_2), 134.34, 133.70, 130.28, 129.40, 127.62, 126.08 (Cou), 123.85, 122.01, 116.18 (Bz_1), 115.95, 115.24, 114.04, 66.38 (CH_2O–), 40.45 (DMSO) 29.67 ($CH_2CH_2CH_3$), 28.43 (OCH_2CH_2), 25.66 ($OCH_2CH_2CH_2$), 23.47 (CH_3CH_2) 14.70 (CH_3). *Anal.* Calc. for $C_{29}H_{24}N_2O_4$ (464 g/mol): C, 75.00; H, 5.17; N, 6.03. Found: C, 75.21; H, 5.12; N, 6.08%. UV–Vis ($CHCl_3$): λ_{max} (nm) (log ε): 308 (4.30), 362 (4.01 Coumarin).

2.3. 2,9,16,23-Tetrakis[6-hexyloxy-3-(4-oxyphenyl)coumarin] metal-free-phthalocyanine (**3**)

Compound **2** (0.10 g, 0.22 mmol) and anhydrous *N*,*N*-dimethylaminoethanol (1.0 mL) were refluxed with stirring for 48 h in a sealed glass tube under N_2. After cooling to room temperature, methanol (2 mL) was added in order to precipitate the product. The green product was filtered and washed with water, MeOH, CH_3CN, EtOH, acetone, ethyl acetate and diethyl ether, and dried.

Yield: 0.025 g (25%); m.p. > 300 °C. IR ν(cm^{-1}): 3283 (N–H), 3067–3044 (Ar-H), 2932–2851 (alkyl-CH), 1713 (C=O lactone), 1593 (C=C), 1573–1431 (Ar C=C), 1269–1234 (Ar-O-Ar), 1169–1095 (Ar-O-C). ^{1}H NMR (DMSO-d_6) δ (ppm): 8.37–7.60 (Bz_1, Bz_3(coum); br, 16H), 7.40–6.80 (Bz_2, br, 16H), 6.70–6.57 (Coum, br, 12H), 3.96 (t, OCH_2–, 8H), 1.77–1.74 (m, –OCH_2CH_2–, 8H), 1.42–1.22 (m, $CH_2CH_2CH_2CH_3$, 24H), 0.98 (t, CH_3, 12H), -3.43 (s, br, NH, inner). *Anal.* Calc. for $C_{116}H_{98}N_8O_{16}$ (1858 g/mol): C, 74.92; H, 5.27; N, 6.03. Found: C, 74.44; H, 5.30; N, 5.72%. UV–Vis (DMSO): λ_{max} (nm) (log ε): 336 (5.26), 642 (4.76), 675 (4.88), 703 (4.77). MS Maldi-TOF, α-cyano-4-hydroxycinnamic acid as matrix, α-CHCA) *m*/*z*: 1858.73 [M+H]$^+$.

2.3.1. 2,9,16,23-Tetrakis[(E)-hexyl-3-(2,5-bis(hexyloxy)phenyl-2-(4-oxyphenyl)acrylate] metal-free-phthalocyanine (**3a**)

To a solution of 2,9,16,23-tetrakis[6-hexyloxy-3-(4-oxyphenyl)coumarin] metal-free-phthalocyanine (**3**) (0.025 g, 0.014 mmol) in dry DMF (5 mL), hexanol (5 mL) and lithium metal (0.0012 g, 0.17 mmol) were added. The mixture was refluxed for 24 h, and then it was cooled to room temperature. 1-Bromohexane (0.3 mL) was added to the reaction mixture and it was heated at 50 °C for 3 days under N_2. After cooling to room temperature, the mixture was treated with 2 M HCl under ice-cooling. The precipitate that formed was collected by filtration, washed with H_2O, MeOH, EtOH, CH_3CN, acetone, ethyl acetate and diethyl ether, and dried.

Yield: 0.015 g (43%); m.p. > 300 °C. IR ν(cm^{-1}): 3298 (N–H), 3058–3074 (Ar-H), 2916–2851 (alkyl-CH), 1710 (C=O ester), 1597 (C=C), 1504–1466 (Ar C=C), 1269–1227 (Ar-O-Ar), 1165–1092 (Ar-O-C). ^{1}H NMR (DMSO-d_6) δ (ppm): 8.33–7.50 (Bz_1, br, 12H), 7.40–7.10 (Bz_2, br, 16H), 6.90–6.50 (br, 16 H, Coum and –C=CH–), 4.30–4.10 (t, OCOCH_2, 8H) 3.98–3.80 (t, OCH_2–, 16H), 1.80–1.65 (m, –OCH_2CH_2–, 24H), 1.40–1.25 (m, $CH_2CH_2CH_2CH_3$, 72H), 0.96 (t, CH_3, 36H), −3.45 (s, br, NH, inner, 2H). *Anal.* Calc. for $C_{164}H_{202}N_8O_{20}$ (2602 g/mol): C, 75.63; H, 7.76; N, 4.30. Found: C, 74. 98; H, 7.33; N, 4.11%. UV–Vis (DMSO): λ_{max} (nm) (log ε): 340 (5.26), 643 (agg 4.91), 673 (5.04), 702 (4.96). MS (Maldi-TOF, α-CHCA as matrix) *m*/*z*: 2603.54 [M+H]$^+$.

2.4. 2,9,16,23-Tetrakis[6-hexyloxy-3-(4-oxyphenyl)coumarin]phthalocyaninatozinc(II) (**4**)

A mixture of compound **2** (0.10 g, 0.22 mmol), $Zn(O_2CMe)_2$ (0.012 g, 0.055 mmol) and 1,8-diazobicyclo[5.4.0]undec-7-ene (DBU) (0.07 mL, 0.04 mmol) in hexanol (1.5 mL) was heated and stirred at 160 °C for 24 h under N_2. The resulting green mixture was cooled to room temperature and then methanol (2 mL) was added in order to precipitate the product. The product was filtered and washed with water, methanol, acetonitrile, ethanol, acetone, ethyl acetate and diethyl ether, and dried.

Yield: 0.031 g (30%); m.p. > 300 °C; IR $\nu(cm^{-1})$: 3059–3044 (Ar-H), 2916–2866 (alkyl-CH), 1717 (C=O lactone), 1601 (C=C), 1477–1331 (Ar C=C), 1261–1231 (Ar-O-Ar), 1172–1092 (Ar-O-C). ^1H NMR (DMSO-d_5) δ (ppm): 8.35–7.50 (Bz_1, Bz_3 (coum); br, 16H), 7.35–7.00 (Bz_2; br, 16H), 6.95–6.55 (coum; br, 12H), 3.98 (t, OCH_2–, 8H), 1.76–1.72 (m, –OCH_2CH_2–, 8H), 1.44–1.22 (m, $CH_2CH_2CH_2CH_3$, 24H), 0.96 (t, CH_3, 12H). *Anal.* Calc. for $C_{116}H_{96}N_8O_{16}Zn$ (1921 g/mol): C, 72.46; H, 4.99; N, 5.83. Found: C, 72.10; H, 5.31; N, 5.45%. UV–Vis (DMSO): λ_{max} (nm) ($\log\varepsilon$): 355 (5.22), 630 (sh, 4.63), 685 (5.22). MS (Maldi-TOF; α-CHCA as matrix) *m*/*z*: 1922.69 $[M+H]^+$, 1958.64 $[M+2H_2O]^+$.

2.4.1. 2,9,16,23-Tetrakis[(E)-hexyl-3-(2,5-bis(hexyloxy)phenyl-2-(4-oxyphenyl)acrylate]phthalocyaninatozinc(II) (**4a**)

To a solution of 2,9,16,23-tetrakis[6-hexyloxy-3-(4-oxyphenyl)coumarin]phthalocyaninatozinc(II) (**4**) (0.030 g, 0.0135 mmol) in dry DMF (5 mL), hexanol (5 mL) and lithium metal (0.0012 g, 0.17 mmol) were added. The mixture was refluxed for 24 h, and then it was cooled to room temperature. 1-Bromohexane (0.3 mL) was added to the reaction mixture and it was heated at 50 °C for 3 days under N_2. After cooling to room temperature, the mixture was treated with 2 M HCl under ice-cooling. The precipitate was collected by filtration, washed with water, methanol, acetonitrile, ethanol, acetone, ethyl acetate and diethyl ether, and dried.

Yield: 0.009 g (22%); m.p. > 300 °C. IR $\nu(cm^{-1})$: 3036–3074 (Ar-H), 2932–2866 (alkyl-CH), 1711 (C=O ester), 1601 (C=C), 1501–1474 (Ar C=C), 1269–1231 (Ar-O-Ar), 1165–1096 (Ar-O-C). ^1H NMR (DMSO-d_6) δ (ppm): 8.38–7.70 (Bz_1; br, 12H), 7.65–7.45 (br, 16H, Bz_2), 7.35–6.40 (br, 16H, coum and –C=CH–), 4.30–4.12 (t, $OCOCH_2$, 8H), 3.90 (t, OCH_2–, 16H), 1.86–1.55 (m, superimposed, br, –OCH_2CH_2–, 24H), 1.42–1.20 (m, br, CH_2CH_2 CH_2CH_3, 72H), 0.95 (t, CH_3, 36H). *Anal.* Calc. for $C_{164}H_{200}N_8O_{20}Zn$ (2665 g/mol): C, 73.85; H, 7.51; N, 4.20. Found: C, 73.29; H, 7.43; N, 4.10%. UV–Vis (DMSO): λ_{max} (nm) ($\log\varepsilon$): 356 (5.23), 630 (4.49), 684 (4.98). MS (Maldi-TOF, α-CHCA as matrix) *m*/*z*: 2666.22 $[M+H]^+$.

2.5. 2,9,16,23-Tetrakis[6-hexyloxy-3-(4-oxyphenyl)coumarin]phthalocyaninatocobalt (II) (**5**)

A mixture of compound **2** (0.10 g, 0.215 mmol), $CoCl_2$ (0.0134 g, 0.054 mmol) and 1,8-diazobicyclo[5.4.0]undec-7-ene (DBU) (0.07 mL, 0.04 mmol) in hexanol (1.5 mL) was heated and stirred at 160 °C for 24 h under N_2. The resulting green mixture was cooled to room temperature and then methanol (2 mL) was added in order to precipitate the product. The product was filtered and washed with water, methanol, acetonitrile, ethanol, acetone, ethyl acetate and diethyl ether, and dried.

Yield: 0.031 g (30%); m.p. > 300 °C. IR $\nu(cm^{-1})$: 3067–3036 (Ar-H), 2932–2858 (alkyl-CH), 1713 (C=O lactone), 1601 (C=C), 1506–1469 (Ar C=C), 1323–1234 (Ar-O-Ar), 1191–1096 (Ar-O–C); *Anal.* Calc. for $C_{116}H_{96}N_8O_{16}Co$ (1915 g/mol): C, 72.69; H, 5.01; N, 5.85. Found: C, 72.15; H, 5.22; N, 5.54%. UV–Vis (DMSO): λ_{max} (nm) ($\log\varepsilon$): 358 (4.84), 470 (4.23), 606 (4.62), 668 (4.97). MS (Maldi-TOF, α-CHCA as matrix) *m*/*z*: 1916.12 $[M+H]^+$, 1935.05; $[M+H_2O]^+$.

3. Results and discussion

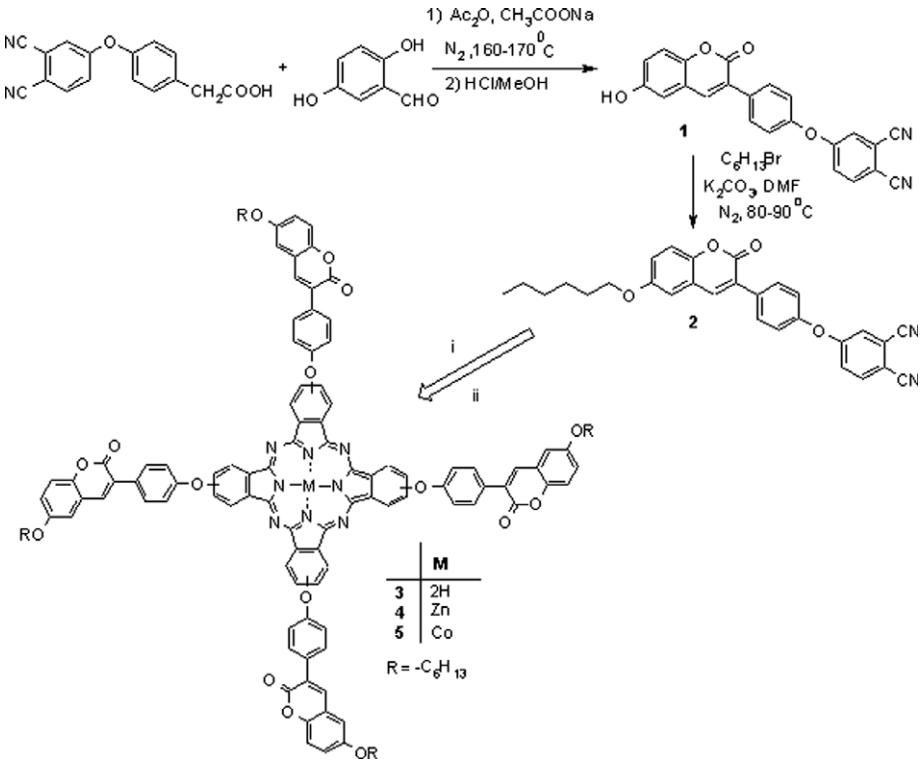
Fluorescence functional metallophthalocyanines (**3**–**5**) bearing coumarin were accomplished by heating a mixture of 6-hexyloxy-3-[*p*-(3′,4′-dicyanophenoxy)phenyl]coumarin with anhydrous $Zn(O_2CMe)_2$ and $CoCl_2$ salts at ca. 170–180 °C under a N_2 atmosphere in the presence of 1,8-diazabicyclo[5.4.0]undec-7-ene (DBU) in hexanol, while metal-free (**3**) was obtained in anhydrous *N*,*N*-dimethylaminoethanol solvent (Scheme 1). In addition, the lactone ring of the synthesized 2,9,16,23-tetrakis[6-hexyloxy-3-(4-oxyphenyl)coumarin] metal-free-phthalocyanine (**3**) and 2,9,16,23-tetrakis[6-hexyloxy-3-(4-oxyphenyl)coumarin]phthalocyaninatozinc(II) (**4**) was opened and the released hydroxyl group was hexylated (Scheme 2). The yields of **3**–**5** were rather low (25% for **3**, 30% for **4** and **5**). The structures of the phthalocyanines **3**–**5** were verified by FTIR, ^1H NMR, UV–Vis and MALDI-TOF MS spectroscopic methods, as well as by elemental analysis. All the analytical and spectral data are consistent with the predicted structures.

Cyclotetramerization of the dinitrile derivative, 6-hexyloxy-3-[*p*-(3′,4′-dicyanophenoxy)phenyl]coumarin to the phthalocyanines **3**–**5** was confirmed by the disappearance of the sharp –C≡N vibration at 2226 cm^{-1} in compound **2**. The strong C=O (lactone) vibration at 1701, Ar-H and Aliph-H at above and below 3000 cm^{-1} together with the Ar-O-Ar band at ca. 1240 cm^{-1} in the compound **2** underwent small shifts. The ester stretching bands in the FTIR spectra of **3a** and **4a** at ca. 1710 cm^{-1} are evidence for the formation of **3a** and **4a**.

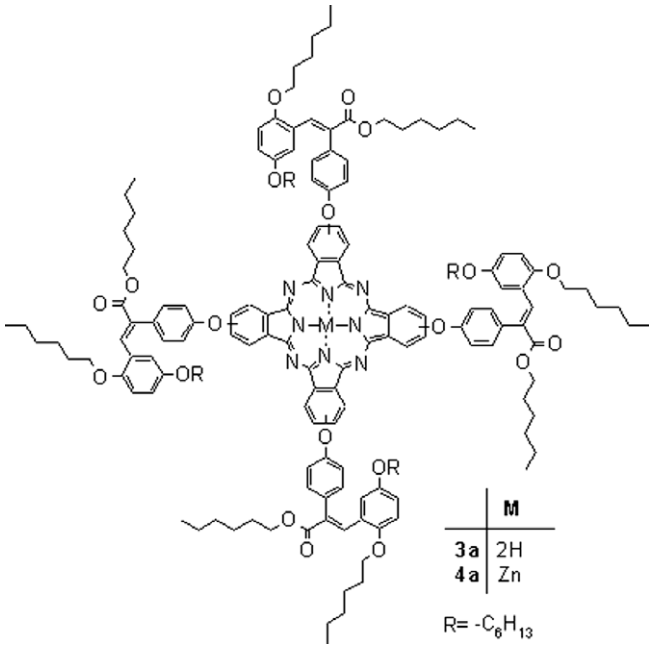
The ^1H NMR spectra of compounds **3**–**4** are somewhat broader than the corresponding signals in the starting dinitrile derivative. This broadening is likely due to chemical exchange caused by aggregation–disaggregation equilibria and the fact that the product obtained in these reactions is a mixture of positional isomers which are expected to show chemical shifts that differ slightly from each other. The inner NH protons of **3** and **3a** were also identified in the ^1H NMR spectra with a broad chemical shift, $\delta = -3.43$ and −3.45 ppm, respectively, as a consequence of the 18π-electron systems of the planar molecule, and this signal disappears on deuterium oxide (D_2O) exchange [12]. The other resonances related to aliphatic and aromatic (OCH_2, CH_2, CH_3, Ar-H) protons in the ^1H NMR spectra of **3** and **3a** are similar to each other, except for the esteric protons. The ^1H NMR spectra of **3a** and **4a** indicated characteristic aromatic protons (Bz_1, Bz_2 and Bz_3) at 8.33–6.75 and 8.38–6.92 ppm, ethilenic protons at 6.60 and 6.75 ppm and aliphatic ester protons at 4.30–4.10 and 4.30–4.12 ppm, respectively. The signals belonging to aromatic protons in the downfield region of the spectra for **3**, **3a**, **4** and **4a** are broader than the aliphatic ones in the highfield region of the spectra.

3.1. UV–Vis absorption spectra

UV–Vis spectra of the phthalocyanine complexes exhibit characteristic Q and B bands, one in the visible region at ca. 600–750 nm (Q-band) attributed to the π–π^* transition from the HOMO to the LUMO of the Pc^{2-} ring, and the other in the UV region at ca. 300–400 nm (B-band) arising from deeper π–π^* transitions [25]. While the zinc and cobalt phthalocyanines (**4**, **4a** and **5**) gave a single Q-band of high intensity due to a single π–π^* transition, as expected as a result of D_{4h} symmetry, H_2Pc (**3** and **3a**) displayed a split Q-band as a result of D_{2h} symmetry with shoulders at the slightly higher energy side of the Q-band for each phthalocyanine in addition to B-bands in the UV region [12,18,25]. The Q-band absorptions of **3**, **4** and **5** were observed at 703, 675 (Qx and Qy), 685 and 668 nm, respectively, with shoulders at the slightly higher energy side of the Q band for each phthalocyanine (Fig. 1). The shoulder between 400 and 450 nm may be due to a charge transfer



Scheme 1. Synthetic route to **3**, **4** and **5**, {M[Pc(OBzCou)$_4$], M = 2H, Zn(II) and Co(II)}. (i) *N*,*N*-Dimethylaminoethanol and (ii) anhydrous $Zn(O_2CMe)_2$, $CoCl_2$, hexanol and dbu.



Scheme 2. Schematic representation of 2,9,16,23-tetrakis[(*E*)-hexyl-3-(2,5-bis(hexyloxy)phenyl-2-(4-oxyphenyl)acrylate]metal-free (**3a**), and zinc(II) phthalocyanine (**4a**).

from the electron-rich ring to the electron-poor acceptor metal. The B bands are broad due to the superimposition of the B1 and B2 bands in the 330–350 nm region in the case of compound **2** [25]. Therefore the B bands are more intense than the Q bands because of the absorption contribution of the coumarin derivatives peripherally substituted on Pc.

The protonated molecular ion peak for **3** (α-cyano-4-hydroxycinnamic acid matrix, α-CHCA) was observed at 1858 Da from the monoisotopic masses of the elements in compound **3** (H_2Pc), with the other isotopic peaks (between 1857 and 1460 with about 1 Da mass differences) mainly resulting from the isotopic distribution of carbon, which exactly overlapped with the mass of the ligand calculated theoretically from the elemental composition of the ligand. The mass spectrum of compound **3a** also confirmed the proposed structure, giving MS (Maldi-TOF (α-cyano-4-hydroxycinnamic acid matrix) at *m*/*z*: 2603.54 $[M+H]^+$. The protonated molecular ion peaks were identified at *m*/*z*: 1922.69 $[M+H]^+$ for **4**, at *m*/*z*: 2666.22 $[M+H]^+$ for **4a** and at *m*/*z*: 1916.12 $[M+H]^+$, 1935.05 $[M+H_2O]^+$ for **5**, by using α-cyano-4-hydroxycinnamic acid matrix in MS Maldi-TOF. Isotopic peaks resulting from the isotopic distribution of the protonated molecular ion of the **4** were observed between 1922 and 1927 Da with 1 Da increments in the high mass range (Fig. 2). Following the protonated molecular ion peak, a peak group was observed at 36 Da mass higher than the protonated molecular ion peak group, with almost the same pattern. This peak is the result of two moles of H_2O adduct on the neutral molecule of **4**.

3.2. Fluorescence spectra and quantum yields

Excitation and emission spectra of the phthalocyanine derivatives substituted with coumarin groups were obtained in DMSO solution. The reason for using DMSO as the solvent for spectral measurement is that DMSO, with a relatively high dipole moment of 3.96, more easily dissolved the compounds synthesized in our work. Also, we could not observe enough aggregation behavior in different solvents such as THF, $CHCl_3$ and DMF, showing that a hypsochromic shift with increasing solvent polarity was not a pronounced effect for the Q band maxima of the Pc derivatives.

The excitation spectra of the coumarin substituted phthalocyanine derivatives (**3**, **3a**, **4** and **4a**) at 460 nm emission wavelength are shown Fig. 3A. As seen from the figure, the Pc derivatives exhibit excitation maximum wavelength at 380 nm where the couma-

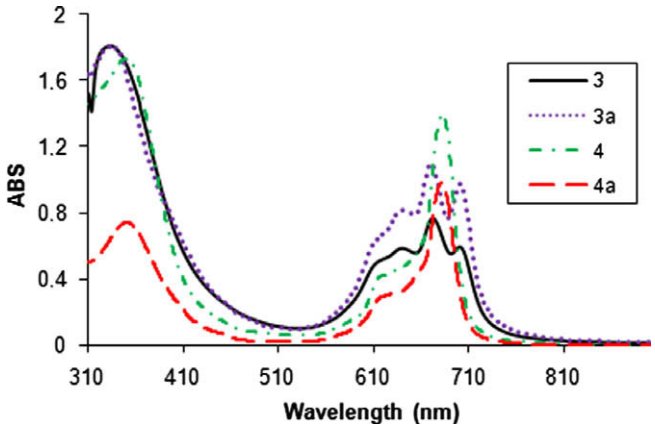


Fig. 1. UV–Vis spectra of 10 μM **3**, **3a**, **4** and **4a** in DMSO.

rin moiety shows high excitation intensity alone (spectrum not shown). The excitation spectrum of the coumarin substituent does not shift in the position of the maximum, though its excitation intensity was diminished when the coumarin moiety was bound to Pc core. The intensity of the **3a** and **4a** species were more decreased because of restricted conjugation due to the ring-opened molecular structure [26,27]. Fig. 3B shows the fluorescence spectra of Pc derivatives in DMSO at room temperature upon excitation at 380 nm, where the coumarin moiety in Pc absorbs almost all of the light, whereas the Pc core absorbs only several percent [28]. Therefore, the fluorescence emissions around 460 nm occur almost entirely from coumarin derivatives substituted on the Pc core. The fluorescence intensity from the peripherally bonded coumarin derivatives is decreased because of radiative energy transfer resulting from the inner filter effect of the Pc core [29]. Since the core of **4a** gives poorer spectral overlap compare with that of the core of **3a**, the decrease in emission is much more in the case of **3a**. The decrease in emission intensity of the coumarin derivative which was chemically treated is more pronounced, because the increase in the spectral overlap causes the inner filter effect. On the other hand, the emission spectra of **3**, **3a**, **4** and **4a** show 15 nm, 1 nm, 13 nm and 18 nm Stokes shifts, respectively, compared with that of the coumarin moiety itself. These red shifts indicate very little molecular rearrangement in the excited state because of intramolecular interactions [30]. Fig. 4A shows the excitation spectra monitoring the emission at 730 nm of the Pc derivatives. The excitation spectra of **4** and **4a** are nearly identical with their ground-state absorption spectra. This indicates that the energy-transfer process is nearly quantitative, showing the unaggregated forms of the **4** and **4a** species [31,32]. On the other hand, the excitation spectra of **3** and **3a** do not closely match their absorption spectra from 450 to 710 nm, indicating that these three species are essentially aggregated in this medium [33,34]. The steady-state fluorescence spectra of the coumarin substituted Pc derivatives were performed in DMSO, upon excitation at the 620 nm Q-band vibration (Fig. 4B). Emission around 700 nm occurs almost entirely from the phthalocyanine moiety. As seen from the figure, the **3** and **4** species with the same coumarin derivative exhibit higher emission intensity than those of the **3a** and **4a** species. This decrease in emission of the Pc core which has an appended coumarin derivative with a ring-opened structure suggests that the Pc core excited state rapidly decays through radiationless conversion to the ground state. On the other hand, a spectral shift in emission wavelength was not observed. This shows that there is no effect of the different coumarin substituents on the fluorescence emission from the S1 singlet excited state of the Pc core with or without a metal ion [35].

The fluorescence quantum yields (Φ) were determined using the classical formula: $\Phi_x = (\Phi_s x F_x x A_s x n_x^2)/(F_s x A_x x n_s^2)$, where A is the absorbance at the excitation wavelength, F is the area under the fluorescence curve and n is the refraction index. Subscripts s and x refer to the standard and to the sample of unknown quantum yield, respectively. Fluorescence quantum yields in DMSO were determined by a comparative method, using coumarin **1** ($\Phi_s = 0.73$ [36]) in ethanol as the fluorescence standard for the coumarin moiety (390–600 nm region). The excitation wavelength was 380 nm for the coumarin derivative substituted on Pc. The fluorescence quantum yield obtained for the coumarin derivative substituted on ZnPc ($\Phi_f = 0.21$) can be attributed to reduced aggregation on comparison to that of H_2Pc ($\Phi_f = 0.18$). On the other hand, Φ_f values for the ring-opened structure of coumarin derivatives **3a** and **4a** ($\Phi_f = 0.12$ and 0.11, respectively) are substantially decreased compared to compound **3** and **4** and are in

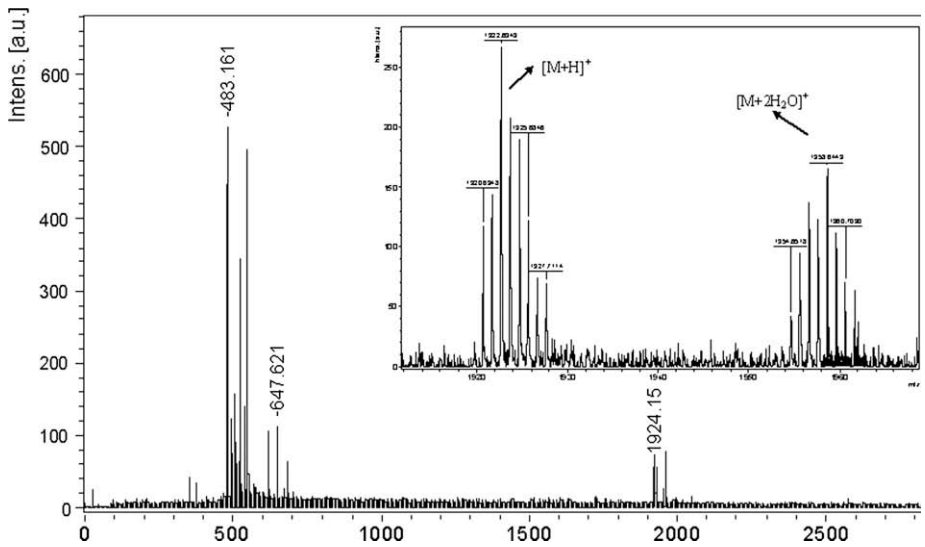


Fig. 2. Positive ion and reflectron mode MALDI-MS spectrum of **4** (in α-cyano-4-hydroxycinnamic acid matrix). Inset spectrum shows the expanded molecular mass region of the **4**.

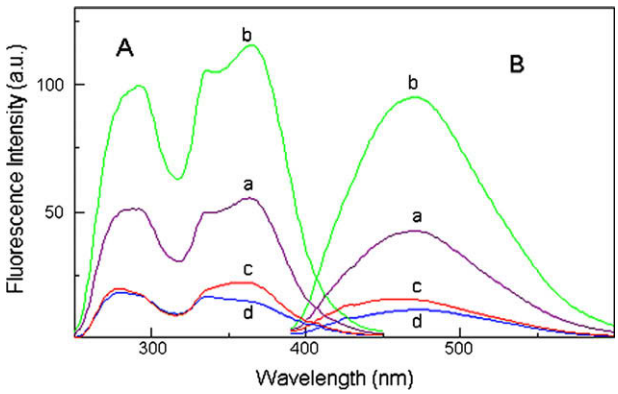


Fig. 3. Excitation (A) and emission (B) spectra of **3** (a), **4** (b), **3a** (c) and **4a** (d) in DMSO (emission excited at 380 nm), Excitation spectra were recorded for an emission peak at 460 nm.

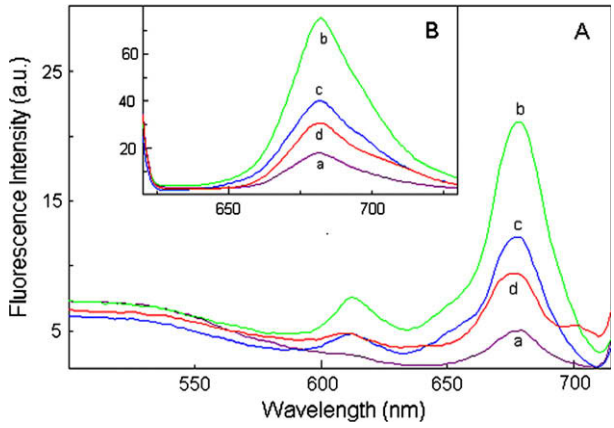


Fig. 4. Excitation (A) and emission (B) spectra of **3** (a), **4** (b), **3a** (c) and **4a** (d) in DMSO. Excitation spectra were recorded for an emission peak at 730 nm. Emission excited at 610 nm.

agreement with cleavage of the lactone ring on the coumarin moiety on the Pc derivatives.

Acknowledgments

We are thankful to the Scientific and Research Council of Turkey (TUBITAK) (107T347 and 108T094), The Research Fund of Marmara University (Commission of Scientific Research Project under Grant FEN-BGS-120707–0149).

References

[1] Y. Lin, H. Skaff, T. Emrick, A.D. Dinsmore, T.P. Russell, Science 299 (2003) 226.
[2] P. Bassoul, T. Toupance, J.J. Simon, Sensor Actuat. B 26 (1995) 150.
[3] M. Kimura, T. Muto, H. Takimoto, K. Wada, K. Ohta, K. Hanabusa, H. Shirai, N. Kobayashi, Langmuir 16 (5) (2000) 2078.
[4] C. Zhong, M. Zhao, C. Stern, A.G.M. Barrett, B.M. Hoffman, Inorg. Chem. 44 (2005) 8272.
[5] Y. Sadaoka, T.A. Jones, W. Göpel, Sensor Actuat. B 1 (1990) 148.
[6] (a) E. Donath, G.B. Sukhorukov, F. Caruso, S.A. Davis, H. Möhwald, Angew. Chem. 110 (1998) 2324;
(b) E. Donath, G.B. Sukhorukov, F. Caruso, S.A. Davis, H. Möhwald, Angew. Chem., Int. Ed. 37 (1998) 2201.
[7] L. Alagna, A. Capobianchi, A.M. Paoletti, G. Pennesi, G. Rossi, M.P. Casaletto, A. Generosi, B. Paci, V.R. Albertini, Thin Solid Films 515 (4) (2006) 2748.
[8] J.P. Viricelle, A. Pauly, L. Mazet, J. Brunet, M. Bouvet, C. Varenne, et al., Mater. Sci. Eng. C 26 (2006) 186.
[9] N.B. McKeown, Phthalocyanine Materials: Synthesis, Structure and Function, Cambridge University Press, Cambridge, 1998.
[10] Z.L. Yang, H.Z. Chen, L. Cao, H.Y. Li, M. Wang, Mater. Sci. Eng. B 106 (2004) 73.
[11] R.J. Li, X.X. Zhang, P.H. Zhu, D.K.P. Ng, N. Kobayashi, J.Z. Jiang, Inorg. Chem. 45 (5) (2006) 2327.
[12] M. Kandaz, S.L.J. Michel, B.M. Hoffman, J. Porphyrins Phthalocyanines 7 (2003) 700.
[13] P. Tau, T. Nyokong, Polyhedron 25 (2006) 1802.
[14] K.P. Mahesh, S.M. Swapnil, M.S. Manikrao, Tetrahedron Lett. 42 (2001) 9285.
[15] S.D. Bose, A.P. Rudradas, M.H. Babu, Tetrahedron Lett. 43 (2002) 9195.
[16] M.C. Laufer, H. Hausmann, W.F. Holderich, J. Catal. 218 (2003) 315.
[17] N.S. Reddy, M.R. Mallireddigari, S. Cosenza, K. Gumireddy, S.C. Bell, E.P. Reddy, et al., Bioorg. Med. Chem. Lett. 14 (2004) 4093.
[18] M. Çamur, M. Bulut, Dyes Pigment 77 (2008) 165.
[19] S.L.J. Michel, A.G.M. Barrett, B.M. Hoffman, Inorg. Chem. 42 (2003) 814.
[20] M.N. Yarasir, M. Kandaz, A. Koca, B. Salih, Polyhedron 26 (2007) 1139.
[21] M. Çamur, A.R. Özkaya, M. Bulut, Polyhedron 26 (2007) 2638.
[22] M. Kandaz, M.N. Yaraşır, A. Koca, Ö. Bekaroğlu, Polyhedron 21 (2002) 255.
[23] N. Sheng, R. Li, C. Choi, W. Su, D.K.P. Ng, X. Cui, K. Yoshida, N. Kobayashi, J. Jiang, Inorg. Chem. 45 (2006) 3794.
[24] J.G. Young, W. Onyebuagu, J. Org. Chem. 55 (1990) 2155.
[25] C.C. Leznoff, A.B.P. Lever, in: C.C. Leznoff, A.B.P. Lever (Eds.), Phthalocyanines: Properties and Applications, vols. 1–4, VCH, Weinheim, 1989–1996.
[26] A. Mallick, B. Haldar, S. Sengupta, N. Chattopadhyay, J. Lumin. 118 (2006) 165.
[27] H. Turki, S. Abid, R.E. Gharbi, S.F. Forgues, C. R. Chimie 9 (2006) 1252.
[28] A.C.H. Ng, X.Y. Li, D.K.P. Ng, Macromolecules 32 (1999) 5292.
[29] B. Valeur, Molecular Fluorescence Principles and Applications, Wiley-VCH, Weinheim, Germany, 2002.
[30] Z. Musil, P. Zimcik, M. Miletin, K. Kopecky, P. Petrik, J. Lenco, J. Photochem. Photobiol. A: Chem. 186 (2007) 316.
[31] C.A. Barker, K.S. Findlay, S. Bettington, A.S. Batsanov, I.F. Perepichka, M.R. Bryce, A. Beeby, Tetrahedron 62 (2006) 9433.
[32] A. Ogunsipe, D. Maree, T. Nyokong, J. Mol. Struct. 650 (2003) 131.
[33] C.A. Barker, X. Zeng, S. Bettington, A.S. Batsanov, M.R. Bryce, A. Bee, Chem. Eur. J. 13 (2007) 6710.
[34] A. Ogunsipe, T. Nyokong, J. Mol. Struct. 689 (2004) 89.
[35] D.K.P. Ng, C. R. Chimie 6 (2003) 903.
[36] S. Nascimento, M.J. Brites, C. Santos, B. Gigante, A. Fedorov, M.N. Berberan-Santos, J. Fluoresc. 16 (2006) 245.

Polyhedron 28 (2009) 239–244

Contents lists available at ScienceDirect

Polyhedron

journal homepage: www.elsevier.com/locate/poly

Synthesis and structural characterization of silver(I) complexes with moon-shaped benzo[1,2-*b*;4,3-*b*′]dithiophene phosphine derivative ligands

M. Helena Garcia [a,*], Pedro Florindo [a], M. Fátima M. Piedade [b], M. Teresa Duarte [b]

[a] Centro de Ciências Moleculares e Materiais, Faculdade de Ciências da Universidade de Lisboa, Ed.C8, Campo Grande, 1749-016 Lisboa, Portugal
[b] Centro de Química Estrutural, Instituto Superior Técnico, Universidade Técnica de Lisboa, Av. Rovisco Pais, 1049-001 Lisboa, Portugal

ARTICLE INFO

Article history:
Received 12 September 2008
Accepted 7 November 2008
Available online 26 December 2008

Keywords:
Silver complexes
Crystal structures
Trifluoromethanesulfonate complexes
Benzo[1,2-*b*;4,3-*b*′]dithiophene

ABSTRACT

New silver complexes of general formula $[Ag(O_3SCF_3)(PPh_2\{bzt\})_n]$ (n = 1–3, bzt = benzo[1,2-*b*;4,3-*b*′]dithiophene) have been synthesized and characterized. Spectroscopic studies shown neutral ligand fluxionallity, typical of silver(I) complexes. The solid state structure of the complexes was determined by X-ray crystallographic studies, showing a decrease in structure complexity with increasing number of neutral ligands in silver coordination sphere: $[Ag(O_3SCF_3)(PPh_2\{bzt\})]$ is a dimer with two bridging triflate anions, further linked into polymeric bidimensional chains along *bc* plane, through Ag···Ph close contacts; $Ag(O_3SCF_3)(PPh_2\{bzt\})_2]$ is also a dimmer with two bridging triflate anions, displaying an interesting packing feature, with *zig-zag* alignment of bzt groups along direction *b*; $[Ag(O_3SCF_3)(PPh_2\{bzt\})_3]$ is a monomer.

© 2008 Elsevier Ltd. All rights reserved.

1. Introduction

The chemistry of poly-nuclear coordination complexes of coinage metals is a field of continuous growing due to the almost unlimited possibilities of chemical designs, ranging from simple molecules to polymeric arrangements [1,2]. Within this area, silver(I) complexes of the type $AgX/(PR_3)_n$, where X is a oxyanion such as NO_3^-, ClO_4^-, NO_2^- and $CF_3SO_3^-$, are known to show interesting structural variations arising from different coordination modes of the anions [3–7]. Despite the intense investigation on the $AgX/(PR_3)_n$ complexes, specially for R = Ph [3–7], complexes of the type $AgX/(PR_2R')_n$ were only sporadically investigated [6,8], nonetheless revealing that the identity of R′ has a large influence both on silver(I) nuclearity and/or solid state packing features. Benzo[1,2-*b*;4,3-*b*′]dithiophen-2-diphenylphosphine is an interesting ligand, in this respect, to study structural features induced by the large volume and moon-shape of the benzo[1,2-*b*;4,3-*b*′]dithiophene (bzt) group and also due to the possibility of this ligand to act as P,S-donor in a bridging bidentate fashion. In this paper we report the synthesis and spectroscopic characterization (^1H, ^{31}P RMN) of novel silver(I) complexes of general formula $[Ag(O_3SCF_3)(PPh_2\{bzt\})_n]$ (n = 1–3), fully supported by single-crystal X-ray studies to understand the relationships between silver(I) nuclearity, $CF_3SO_3^-$ coordinating ability and $PPh_2\{bzt\}$ coordination modes. Also, comparison is made with related compounds to get some insight on the influence of the bzt group on silver nuclearity and solid state packing. Our results show that $PPh_2\{bzt\}$ acts, in this case, only as P-donor and unravel beautiful and unexpected solid state packing features for these complexes.

2. Results and discussion

The ligand benzo[1,2-*b*;4,3-*b*′]dithiophen-2-diphenylphosphine (**L1**) was synthesized based on the procedure reported for the synthesis of the analogue benzo[1,2-*b*;4,3-*b*′]dithiophen-2-carbaldehyde [9], by generation of the benzodithiophene α-anion with *n*-BuLi and subsequent treatment with $(C_6H_5)_2PCl$, affording **L1** in good yield (60%), as a colorless oil.

The silver complexes $[Ag(CF_3SO_3)(PPh_2\{bzt\})_n]$ (**nAg**: n = 1, 2 and 3) were prepared by reaction of $AgCF_3SO_3$ and an adequate molar ratio of **L1** (0.96, 2 and 3, respectively), in dichloromethane. The compounds were obtained as crystalline white solids, stable to air but slightly unstable to light in solution, soluble in dichloromethane, chloroform, acetone, acetonitrile and insoluble in tetrahydrofuran, ethyl ether and hydrocarbons.

The ^1H NMR spectra of the complexes only show the ligand resonances, slightly deshielded upon coordination to the metal center.

For compounds *[Ag(CF$_3$SO$_3$) (PPh$_2$ {bzt})]* **1Ag**, *[Ag(CF$_3$SO$_3$)(PPh$_2${bzt}$)_3$]* **3Ag** and for free **L1**, the resonances of proton H_3 are doublets, with coupling constants ranging from 6.8 to 11.2 Hz, attributed to P(–C–C–)H coupling, while it appears as a singlet in *[Ag(CF$_3$SO$_3$)(PPh$_2${bzt}$)_2$]* **2Ag**.

Although the ^{31}P NMR spectra of **L1** show a resonance at −17.06 as a sharp singlet, the complexes spectra obtained at room temperature revealed no resonances. This behavior is attributed to complexe's fluxionallity, due to the exchanging phenomena involving neutral ligands, typical of silver coordination chemistry [6]. At

* Corresponding author. Tel.: +351 217500972; fax: +351 217500088.
E-mail address: lena.garcia@fc.ul.pt (M.H. Garcia).

0277-5387/$ - see front matter © 2008 Elsevier Ltd. All rights reserved.
doi:10.1016/j.poly.2008.11.013

−60 °C the spectra are resolved, showing the phosphorus resonances as two doblets, with Ag–P coupling constants ranging from 321.0 to 788.5 Hz, although for **1Ag** the second doublet isn't resolved. The large difference between Ag–P coupling constants is attributed both to the different s contribution to the hybridization of the silver centers [10] and to the different phosphorus/oxygen ratio in the silver coordination sphere [11].

2.1. Crystallographic studies

X-ray diffraction studies constitute an unambiguous way to determine both the nuclearity and the geometry of the silver compounds synthesized. In this case, infrared spectra are not useful to distinguish trifluoromethanesulfonate coordination modes, due to ambiguity in the attribution of CF_3, SO_3 and **L1** vibrational modes [12].

Crystals of compounds **1Ag**, **2Ag** and **3Ag** were obtained by slow diffusion of *n*-hexane into dichloromethane solutions. Compound **1Ag** crystallizes in a centrosymmetric spatial group ($P2_1/c$, monoclinic). This compound is a dinuclear derivative of $[Ag_2(CF_3SO_3)_2(PPh_2\{bzt\})_2]$, in which two silver centers are bridged by two equivalent triflate anions using two donor oxygen atoms, O(1) and O(21), forming an eight-atom cycle (Fig. 1). Silver atoms deviate from planarity with the three coordinated atoms.

Table 1 presents selected bond lengths and angles for compound **1Ag**. The Ag(1)–P(1) distance is similar to the Ag-P distances determined for the analogous compounds $[Ag(CF_3SO_3)(PPh_3)]$ (2.3619(10)–2.3736(10) Å) and $[Ag(CF_3SO_3)(PPh_2Me)]$ (2.3628(11)–2.3637(10) Å) [6]; Ag–O distances are also in the interval verified for the referred compounds: 2.250(2)–2.572(3) Å and 2.2792(19)–2.573(2) Å, respectively.

Each silver atom of the dimer $[Ag_2(CF_3SO_3)_2(PPh_2\{bzt\})_2]$ establishes a short contact with a Ph carbon atom (C(125)) of a distinct dimer, the distance between the atoms being of 2.688(2) Å. This contact is not of the usual Ag···(aromatic bond) type, such as in the $AgClO_4$–benzene complex [13] since Ag···C contacts to C neighbor atoms are significantly longer. The Ag(1)···C(125) contact is almost perpendicular to the Ph ring, with angles between this bond and other Ph carbon atoms ranging from 81.97° to 101.97°. A similar Ag···Ph close contact was found for compound $[Ag(CF_3SO_3)(PPh_2Me)]$ (2.721(3)) [6]. The arrangement of **L1** accounts for the establishment of the Ag(1)···C(125) short contact: the large bzt groups are almost perpendicular to the O(1)–Ag(1)–O(21) plane, minimizing the sterical hindrance on the silver center in the opposite side; also, a significant difference (approximately 36°) between angles O–Ag–P is verified, thus allowing the alignment of Ag(1) with C(125). Each dimeric unit interacts with four other units, leading to the formation of a bidimensional polymeric chain along the *bc* plane, packed along the *a* direction. This polymeric arrangement is illustrated in Fig. 2.

Compound **2Ag** is also a dinuclear derivative (Fig. 3) in which the molecule possesses an inversion center, with silver atoms displaying distorted tetrahedral coordination geometry. Each metal center is bonded to two phosphorus atoms of **L1** and two oxygen atoms of distinct, but crystallographically equivalent, triflate anions, forming an eight member cycle similar to the one found for **1Ag**. This structural arrangement is quite common in complexes of general formula $[AgX(PPh_3)_2]$ [6,11]. Table 2 presents selected

Table 1
Selected bond lengths and angles for compound **1Ag**.

Bond lengths (Å)			
Ag1–O1	2.3045(17)	S1–O1	1.4492(17)
Ag1–O3#1	2.5028(17)	S1–O2	1.425(2)
Ag1–P1	2.3738(6)	S1–O3	1.4354(17)
Ag1–C125#2	2.687(2)		
Bond angles (°)			
O1–Ag1–O3#1	83.49(6)	O3–S1–O1	113.83(11)
P1–Ag1–O3#1	110.82(4)	S1–O1–Ag1	120.29(10)
O1–Ag1–P1	147.05(5)	S1–O3–Ag1#1	147.81(11)
O3#1–Ag1–C125#2	77.28(7)	O1–Ag1–C125#2	90.45(7)
P1–Ag1–C125#2	121.09(6)		

Symmetry transformations used to generate equivalent atoms: #1: $-x+1, -y, -z$; #2: $x, -y+1/2, z-1/2$.

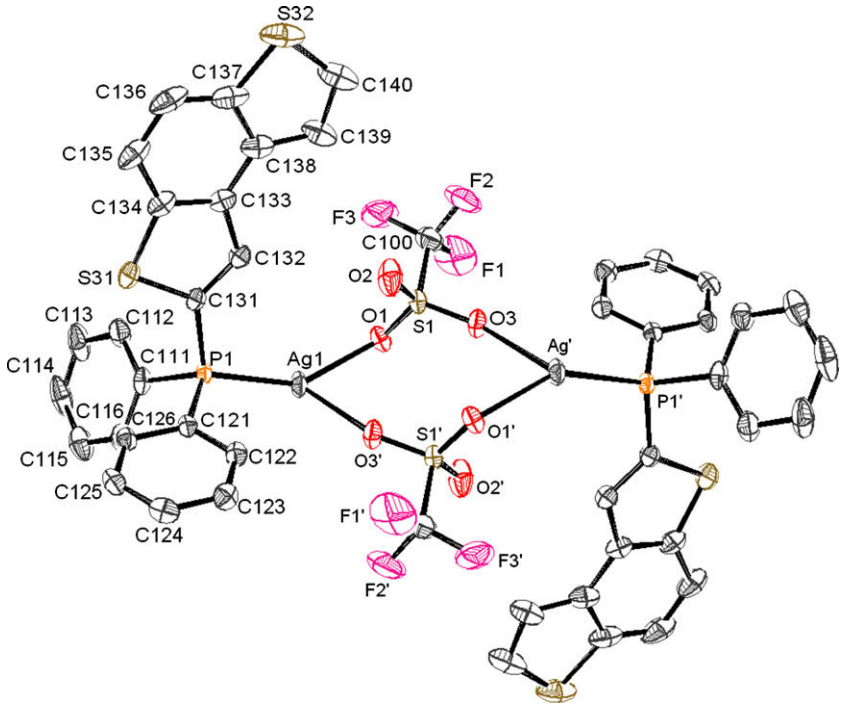


Fig. 1. Molecular diagram of **1Ag** with 50% thermal ellipsoids, showing the labeling scheme. Hydrogen atoms have been omitted for clarity.

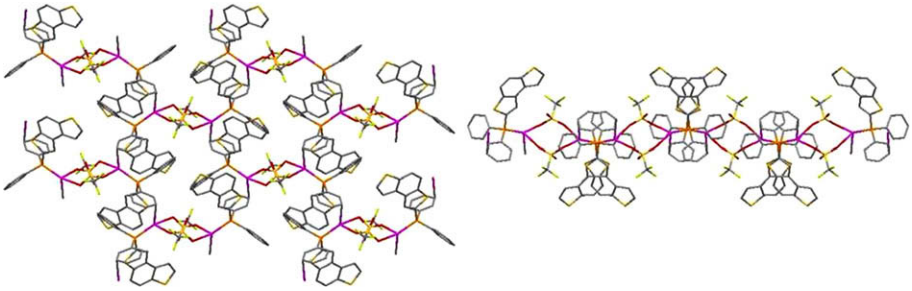


Fig. 2. Perspective of the bidimensional polymeric chain of **1Ag** along *a* (left) and *c* (right).

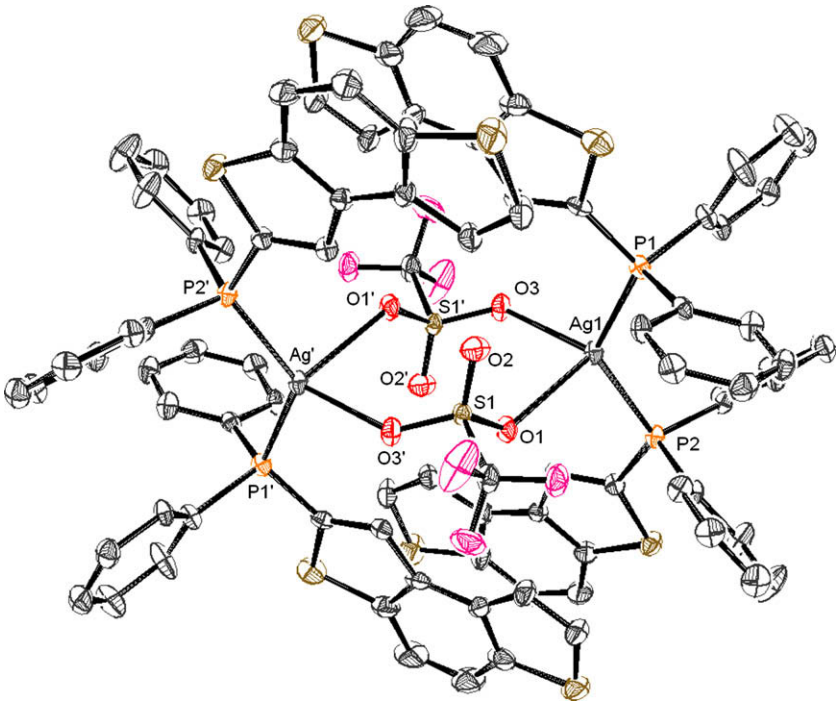


Fig. 3. Molecular diagram of **2Ag** with 40% thermal ellipsoids, showing the labeling scheme. Hydrogen atoms have been omitted for clarity.

bond lengths and angles for compound **2Ag**. Both Ag–P (2.439(2) and 2.434(2) Å) and Ag–O distances are comparable to the ones found for compound $[Ag(O_3SCF_3)(PPh_3)_2]$ (2.409(5) and 2.572(5)) (Ag–P: 2.4321(12) and 2.4339(12); Ag–O: 2.385(13) to 2.578(5) [6]; Ag–O distances resemble the dissimilarity found in compound $[Ag(O_3SCF_3)(PPh_3)_2]$.

Worth noticing the effect of the substitution of one Ph ring by the larger bzt group: compounds $[Ag(O_3SCF_3)(PPh_3)]$ and $[Ag(O_3SCF_3)(PPh_2\{bzt\})]$ (**1Ag**) have totally different solid state arrangements ($[Ag(O_3SCF_3)(PPh_3)]$ is a trinuclear derivative [6,14] while **1Ag** is a bidimensional polymer), compounds $[Ag(O_3SCF_3)(PPh_3)_2]$ and $[Ag(O_3SCF_3)(PPh_2\{bzt\})_2]$ (**2Ag**) have similar arrangements.

Table 2
Selected bond lengths and angles for compound **2Ag**.

Bond distances (Å)			
Ag1–O1	2.572(5)	S1–O1	1.442(5)
Ag1–O3	2.411(5)	S1–O3#1	1.434(5)
Ag1–P1	2.439(2)	S1–O2	1.414(5)
Ag1–P2	2.434(2)		
Bond angles (°)			
O1–Ag1–O3	84.32(15)	P1–Ag1–P2	126.35(7)
O1–Ag1–P1	112.22(12)	S1–O1–Ag1	127.1(3)
O1–Ag1–P2	98.11(12)	S1#1–O3–Ag1	136.8(3)
O3–Ag1–P1	108.65(13)	O3#1–S1–O1	114.9(3)
O3–Ag1–P2	117.78(14)		

Symmetry transformations used to generate equivalent atoms: #1: $-x+1$, $-y$, $-z+1$.

The four bzt groups of each dimer have an almost parallel alignment. This parallel alignment between bzt groups is maintained along direction *a*, through weak hydrogen bonding between the Ph groups and fluorine and oxygen atoms of neighbor dimers (C(225)–H(225)···F2 {2.669(6) Å}, (C(113)–H(113)···O3 {2.657(5) Å} and C(114)–H(114)···F(1) {2.635(6) Å}), forming a columnar packing. The column packing along the *b* direction is made, alternately, between columns symmetrically generated trough an 180° rotation around the *a* axis in relation to the neighbor ones, which results in a *zig-zag* alignment of the bzt groups along *b*, as illustrated in Fig. 4.

Compound **3Ag** · **0.5CH_2Cl_2** crystallizes in the triclinic centrosymmetric space group $P\bar{1}$. The asymmetric unit (Fig. 5) is the monomeric formula unit with the half solvent molecule of CH_2Cl_2. Selected bond lengths and angles are presented in Table 3.

The silver atom is coordinated to three phosphorus atoms of **L1** ligands and to an oxygen atom (O1) of trifluoromethanesulfonate, displaying a distorted tetrahedral coordination. The Ag–P bond distances range from 2.4780(12) to 2.5113(11) Å and are shorter

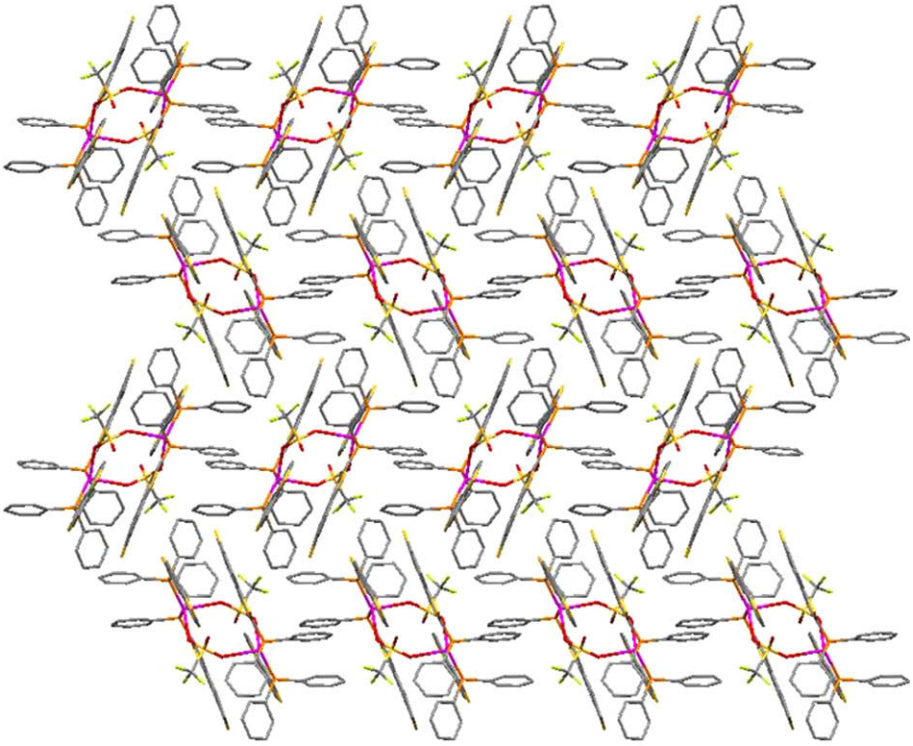


Fig. 4. Perspective of the supramolecular arrangement of **2Ag**, along direction *c*: dimer alignment along direction *a* (horizontal) and *zig-zag* alignment of bzt groups along *b* (vertical).

than the ones found for compounds $[AgX(PPh_3)_3]$ (X = Cl: 2.558(5)–2.582(4); Br: 2.528(3)–2.549(7); I: 2.544(2)–2.780(3) [15]; NO_3: 2.525(1)–2.630(2) [11]; $CO_2C_2F_5$: 2.5432(7)–2.6026(8) Å [16]). P–Ag–P angles range between 111.49(4) and 124.67(4) Å: the angle P(1)–Ag(1)–P(3) is higher (~23 Å) than the other two P–Ag–P angles, minimizing the interaction between **L1** ligands and the anion, and opposite to the longer Ag–P(2) distance, as expected.

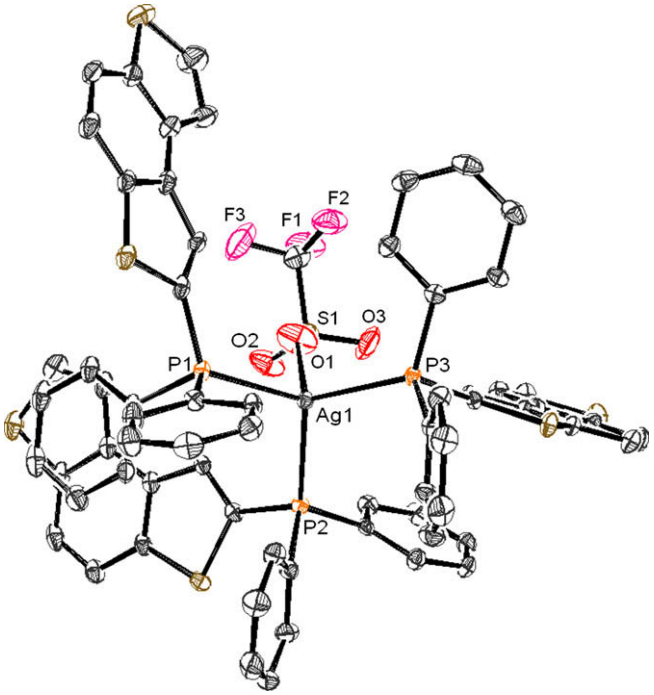


Fig. 5. Molecular diagram of **3Ag** with 40% thermal ellipsoids, showing the labeling scheme. Hydrogen atoms have been omitted for clarity.

Table 3
Selected bond lengths and angles for compound **3Ag** · **0.5CH$_2$Cl$_2$**.

Bond lengths (Å)			
Ag1–O1	2.527(5)	S1–O1	1.414(4)
Ag1–P1	2.4886(12)	S1–O2	1.417(4)
Ag1–P2	2.5113(11)	S1–O3	1.445(5)
Ag1–P3	2.4780(12)		
Bond angles (°)			
P1–Ag1–P2	111.49(4)	O1–Ag1–P3	105.75(12)
P1–Ag1–P3	124.67(4)	S1–O1–Ag1	151.0(3)
P2–Ag1–P3	112.28(4)	O1–S1–O2	119.0(3)
O1–Ag1–P1	100.70(13)	O1–S1–O3	112.1(3)
O1–Ag1–P2	97.04(11)	O2–S1–O3	113.1(3)

3. Experimental

3.1. General procedures

All the experiments were carried out under a dinitrogen atmosphere, using standard Schlenk techniques. All solvents used were dried using standard methods [17]. $AgCF_3SO_3$ and $(C_6H_5)_2PCl$ were purchased from Aldrich and used without further purification. ^1H and ^{31}P NMR spectra were recorded on a Bruker Avance 400 spectrometer at probe temperature, unless stated otherwise. The ^1H NMR (chloroform-*d*) chemical shifts are reported in parts per million (ppm) downfield from internal Me_4Si and the ^{31}P NMR (chloroform-*d*) spectra are reported in ppm downfield from external standard, 85% H_3PO_4. Elemental analyses were obtained at *Laboratório de Análises*, *Instituto Superior Técnico*, using a Fisons

Table 4
Details of data collection and structure refinement for complexes **1Ag**, **2Ag** and **3Ag**.

Compound	**1Ag**	**2Ag**	**3Ag · 0.5CH$_2$Cl$_2$**
Chemical formula	$C_{23}H_{15}AgF_3O_3PS_3$	$C_{45}H_{30}AgF_3O_3P_2S_5$	$C_{67.5}H_{45}AgClF_3O_3P_3S_7$
Formula weight	631.37	1005.80	1421.68
T (K)	150(2)	150(2)	150(2)
Wavelength	0.71073	0.71073	0.71073
Crystal system	monoclinic	monoclinic	triclinic
Space group	$P2_1/c$	$P2_1/n$	$P\bar{1}$
a (Å)	11.2634(9)	12.631(4)	11.2932(7)
b (Å)	18.7654(13)	22.428(7)	12.2422(8)
c (Å)	11.4873(8)	15.754(5)	24.8700(16)
α (°)	90	90	80.429(4)
β (°)	100.619(4)	103.18(2)	86.819(4)
γ (°)	90	90	65.425(4)
V (Å^3)	2386.4(3)	4346(2)	3083.0(3)
Z	4	4	2
Z'	0.5	0.5	1
D_{calc} (g cm^{-3})	1.757	1.537	1.531
Absorption coefficient (mm^{-1})	1.222	0.831	0.743
F(000)	1256	2032	1444
θ Range for data collection (°)	2.82–26.37	1.87–27.70	1.91–27.60
Limiting indices	$-14 \leqslant h \leqslant 14, -23 \leqslant k \leqslant 23, -14 \leqslant l \leqslant 14$	$-15 \leqslant h \leqslant 16, -28 \leqslant k \leqslant 28, -20 \leqslant l \leqslant 20$	$-14 \leqslant h \leqslant 14, -15 \leqslant k \leqslant 15, -32 \leqslant l \leqslant 29$
Reflections collected/unique (R_{int})	70062/4864 (0.0531)	44956/10055 (0.1594)	42714/13939 (0.0693)
Completeness to theta	26.37 (99.8%)	27.70 (98.5%)	27.60 (97.5%)
Refinement method	full-matrix least-squares on F^2	full-matrix least-squares on F^2	full-matrix least-squares on F^2
Data/restraints/parameters	4864/0/307	10055/0/532	13939/0/768
Goodness-of-fit on F^2	1.024	0.994	1.026
Final R indices [$I > 2\sigma(I)$]	$R_1 = 0.0267, wR_2 = 0.0592$	$R_1 = 0.0689, wR_2 = 0.1612$	$R_1 = 0.0575, wR_2 = 0.1295$
Largest difference in peak/hole (e Å^{-3})	0.838/−0.441	0.750/−1.107	1.746/−0.990

Instruments EA1108 system. Data acquisition, integration and handling were performed using a PC with software package EA-GER-200 (Carlo Erba Instruments).

3.2. Synthesis of benzo[1,2-b;4,3-b′]dithiophen-2-diphenylphosphine (*L1*)

To a THF solution (15 mL) of benzo[1,2-*b*;4,3-*b*′]dithiophene (0.19 g, 1 mmol) cooled at −78 °C, was slowly added a 2.0 M *n*-BuLi pentane solution (0.55 mL, 1.1 mmol). The mixture was stirred at −78 °C for 5 min and for 15 min at room temperature. The resulting yellow solution was cooled at −78 °C and treated with Ph_2PCl (0.22 mL, 1.2 mmol). After 1 h under agitation at −78 °C, the solution was warmed to room temperature and quenched with a saturated solution of NH_4Cl (5 mL). The THF was removed under reduced pressure, the crude material was taken up with CH_2Cl_2 (20 mL) and washed with saturated aqueous solution of NH_4Cl (3 × 10 mL) and water (3 × 10 mL). The organic phase was dried over $MgSO_4$, the solvent was removed under reduced pressure and the crude material was purified by means of flash column chromatography (eluent: light petroleum/CH_2Cl_2 4:1). Yield: 60%. Colorless oil. *Anal.* (%): Calc. for $C_{22}H_{15}PS_2$: C, 70.56; H, 4.04; S, 17.13. Found: C, 70.01; H, 3.95; S, 17.35. ^{1}H NMR: 7.30 (m, 6H, Ph), 7.38 (m, 4H, Ph), 7.47 (d, 1H, H_{10}, J_{HH} = 5.2 Hz), 7.59 (d, 1H, H_{11}, J_{HH} = 5.2 Hz), 7.62 (d, 1H, H_7, J_{HH} = 8.4 Hz), 7.71 (d, 1H, H_6, J_{HH} = 8.4 Hz), 8.02 (d, 1H, H_{10}, J_{HP} = 6.8 Hz). ^{31}P NMR: −17.06 (s).

3.3. Synthesis of the complexes [Ag(CF_3SO_3)(PPh_2{bzt})$_n$]

Complexes of general formula [Ag(CF_3SO_3)(PPh_2{bzt})$_n$] were prepared from $AgCF_3SO_3$ (0.128 g, 0.5 mmol) in CH_2Cl_2, in the presence of an adequate quantity of benzo[1,2-*b*;4,3-*b*′]dithiophen-2-diphenylphosphine (n = 1: 0.180 g, 0.49 mmol; n = 2: 0.374 g, 1.00 mmol; n = 3: 0.562 g, 1.5 mmol). The mixtures were stirred overnight at room temperature, protected from light. After filtering and reducing the solvent volume to ≈5 mL), the complexes were recrystallized by slow diffusion of n-hexane, affording white crystalline products.

3.3.1. [Ag(CF_3SO_3)(PPh_2{bzt})] (*1Ag*)

Yield: 94%. White. *Anal.* (%): Calc. for $C_{23}H_{15}S_3O_3PF_3Ag$: C, 43.75; H, 2.39; S, 15.24. Found: C, 44.12; H, 2.39; S, 15.92. ^{1}H NMR: 7.50 (m, 6H, PPh_2), 7.59 (m, 4H, PPh_2), 7.61 (d, 1H, H_{10}, J_{HH} = 4.8 Hz), 7.70 (d, 1H, H_7, J_{HH} = 8.8 Hz), 7.76 (d, 1H, H_{11}, J_{HH} = 5.2 Hz), 7.88 (d, 1H, H_6, J_{HH} = 8.4 Hz), 8.39 (d, 1H, H_3, J_{HP} = 11.2 Hz). ^{31}P NMR (−60 °C): 3.23 (d, J(^{109}Ag–P) = 788.5 Hz).

3.3.2. [Ag(CF_3SO_3)(PPh_2{bzt})$_2$] (*2Ag*)

Yield: 89%. White. *Anal.* (%): Calc. for $C_{45}H_{30}S_5O_3P_2F_3Ag \cdot 0.3CH_2Cl_2$: C, 52.76; H, 2.99; S, 15.54. Found: C, 52.84; H, 3.11; S, 15.60. ^{1}H NMR: 7.38 (m, 4H, PPh_2), 7.48 (m, 2H, PPh_2), 7.53 (d, 1H, H_{10}, J_{HH} = 5.2 Hz), 7.59 (m, 4H, PPh_2), 7.63 (d, 1H, H_{11}, J_{HH} = 4.8 Hz), 7.64 (d, 1H, H_6, J_{HH} = 8.8 Hz), 7.85 (d, 1H, H_6, J_{HH} = 8.8 Hz), 8.46 (s, 1H, H_3). ^{31}P NMR (−60 °C): 0.79 (dd, J(^{109}Ag–P, ^{107}Ag–P) = 553.3, 488.4 Hz).

3.3.3. [Ag(CF_3SO_3)(PPh_2{bzt})$_3$] (*3Ag*)

Yield: 82%. White. *Anal.* (%): Calc. for $C_{67}H_{45}S_7O_3P_3F_3Ag \cdot 0.4CH_2Cl_2$: C, 57.24; H, 3.26; S, 15.87. Found: C, 57.12; H, 3.32; S, 15.88. ^{1}H NMR: 7.08 (m, 4H, PPh_2), 7.23 (m, 2H, PPh_2), 7.38 (d, 1H, H_{10}, J_{HH} = 5.6 Hz), 7.40 (d, 1H, H_{11}, J_{HH} = 5.6 Hz), 7.42 (m, 4H, PPh_2), 7.51 (d, 1H, H_6, J_{HH} = 8.8 Hz), 7.75 (d, 1H, H_6, J_{HH} = 8.8 Hz), 8.34 (d, 1H, H_3, J_{HP} = 7.2 Hz). ^{31}P NMR (−60 °C): 2.90 (dd, J(^{109}Ag–P, ^{107}Ag–P) = 362.5, 321.0 Hz).

3.4. Crystal structure determination

X-ray data for compounds **1Ag**, **2Ag** and **3Ag · 0.5CH$_2$Cl$_2$** were collected on a Bruker AXS APEX CCD area detector diffractometer at 150(2) K using graphite-monochromated Mo Kα (λ = 0.71073 Å) radiation. Intensity data were corrected for Lorentz polarization effects. Empirical absorption correction using SADABS [18] was applied and the data reduction was done with SMART and SAINT programs [19].

All structures were solved by direct methods with SIR97 [20] and SIR2004 [21] and refined by full-matrix least-squares on F^2 with SHELXL97 [22], all included in the package of programs WINGX-Version

1.70.01 [23]. Non-hydrogen atoms were refined with anisotropic thermal parameters whereas H-atoms were placed in idealized positions and allowed to refine riding on the parent C atom. Graphical representations were prepared using ORTEP [24], and MERCURY 1.1.2 [25]. A summary of the crystal data, structure solution and refinement parameters are given in Table 4. In compound **2Ag** a severely disordered solvent molecule was found that could not be modeled so it was removed using SQUEEZE [26]. SQUEEZE calculated an electron count/cell of 143 which matches well with a n-hexane or a dichloromethane molecule per asymmetric unit. Before SQUEEZE $R_1 = 0.0801$, afterwards $R_1 = 0.0764$.

Acknowledgements

The authors thank to Fundação Para a Ciência e Tecnologia (FCT) for financial support (POCTI/QUI/48443/2002). Pedro Florindo thanks FCT for the Ph.D. grant conceded (SFRH/BD/12432/2003).

Appendix A. Supplementary data

CCDC 122345 and 123454 contain the supplementary crystallographic data for **1Ag** and **3Ag**. These data can be obtained free of charge via http://www.ccdc.cam.ac.uk/conts/retrieving.html, or from the Cambridge Crystallographic Data Centre, 12 Union Road, Cambridge CB2 1EZ, UK; fax: (+44) 1223-336-033; or e-mail: deposit@ccdc.cam.ac.uk. Supplementary data associated with this article can be found, in the online version, at doi:10.1016/j.poly.2008.11.013.

References

[1] D. Akrivos, H.J. Katsikis, A. Koumoutsi, Coord. Chem. Rev. 167 (1997) 95.
[2] J.A.S. Howell, Polyhedron 25 (2006) 2993.
[3] R.A. Stein, C. Knobler, Inorg. Chem. 16 (1977) 242.
[4] M. Nardelli, C. Pelizzi, G. Pelizzi, P. Tarasconi, J. Chem. Soc., Dalton Trans. (1985) 321.
[5] G.A. Bowmaker, A. Effendy, B.W. Skelton, A.H. White, J. Chem. Soc., Dalton Trans. (1998) 2123.
[6] M. Bardají, Olga Crespo, A. Laguna, A.K. Fischer, Inorg. Chim. Acta 304 (2000) 7.
[7] A. Cingolani, Effendy, M. Pellei, C. Pettinari, C. Santini, B.W. Skelton, A.H. White, Inorg. Chem. 41 (2002) 6633.
[8] A. Cingolani, Effendy, D. Martini, C. Pettinari, B.W. Skelton, A.H. White, Inorg. Chim. Acta 359 (2006) 2183.
[9] S. Maiorana, A. Papagni, E. Licandro, R. Annunziata, P. Paravidino, D. Perdicchia, C. Giannini, K. Clays, A. Persoons, Tetrahedron 59 (2003) 6481.
[10] (a) E.L. Muetterties, C.W. Alegranti, J. Am. Chem. Soc. 92 (1970) 4114; (b) E.L. Muetterties, C.W. Alegranti, J. Am. Chem. Soc. 94 (1972) 6386.
[11] P.F. Baron, J.C. Dyason, P.C. Healy, L.M. Engelhardt, B.W. Skelton, A.H. White, J. Chem. Soc., Dalton Trans. (1986) 1965.
[12] G.A. Lawrence, Chem. Rev. 86 (1986) 17.
[13] R.K. McMullan, T.F. Koetzle, C.J. Fritchie Jr., Acta Crystallogr., Sect. B 53 (1997) 645.
[14] R. Teroba, M.B. Hursthouse, M. Laguna, A. Mendia, Polyhedron 18 (1999) 807.
[15] L.M. Engelhardt, P.C. Healy, V.A. Patrick, A.H. White, Aust. J. Chem. 40 (1987) 1873.
[16] P. Römbke, A. Schier, H. Schmidbaur, S. Cronje, H. Raubenheimer, Inorg. Chim. Acta 357 (2004) 235.
[17] D.D. Perrin, W.L.F. Amarego, D.R. Perrin, Purification of Laboratory Chemicals, 2nd ed., Pergamon, New York, 1980.
[18] SADABS, Area-Detector Absorption Correction, Bruker AXS Inc., Madison, WI, 2004.
[19] SAINT: Area-Detector Integration Software (Version 7.23), Bruker AXS Inc., Madison, WI, 2004.
[20] A. Altomare, M.C. Burla, M. Camalli, G. Cascarano, G. Giacovazzo, A. Guagliardi, A.G.G. Moliterini, G. Polidoro, R. Spagna, J. Appl. Crystallogr. 32 (1999) 115.
[21] M.C. Burla, M. Camalli, B. Carrozzini, G.L. Cascarano, C. Giacovazzo, G. Polidori, R. Spagna, J. Appl. Crystallogr. 36 (2003) 1103.
[22] G.M. Sheldrick, SHELXL-97: Program for the Refinement of Crystal Structure, University of Gottingen, Germany, 1997.
[23] L.J. Farrugia, J. Appl. Crystallogr. 32 (1999) 837.
[24] L.J. Farrugia, J. Appl. Crystallogr. 30 (1997) 565.
[25] C.F. Macrae, P.R. Edgington, P. McCabe, E. Pidcock, G.P. Shields, R. Taylor, M. Towler, J. Van de Streek, J. Appl. Crystallogr. 39 (2006) 453.
[26] P.v.d. Sluis, A.L. Spek, Acta Crystallogr., Sect. A 46 (1990) 194.

Polyhedron 28 (2009) 245–252

Contents lists available at ScienceDirect

Polyhedron

journal homepage: www.elsevier.com/locate/poly

Single stranded helical supramolecular architecture with a left handed helical water chain in ternary copper(II) tryptophan/diamine complexes

P. Mosae Selvakumar, E. Suresh, P.S. Subramanian *

Analytical Science Division, Central Salt and Marine Chemicals Research Institute (Council of Scientific and Industrial Research), Bhavnagar, 364 002 Gujarat, India

ARTICLE INFO

Article history:
Received 22 September 2008
Accepted 27 October 2008
Available online 27 December 2008

Keywords:
Helicate
Self-assembly
Amino acid
Supramolecular chemistry
Chirality

ABSTRACT

The ternary copper(II) complexes [Cu(L-trp)(bpy)](ClO_4) (**1**) and [Cu(L-trp)(phen)] (ClO_4)·$3H_2O$ (**2**) (where L-trp = L-tryptophan, bpy = bipridyl, phen = phenanthroline) have been synthesized. The single crystal X-ray structures for these complexes revealed that the monocationic Cu^{II}-units are interlinked through Cu–OCO–Cu connectivity and exist as helical coordination polymers. The two different helical strands composed with Cu1 and Cu2 independently, possess a similar pitch distance of 7.713 Å in complex **1**. For complex **2**, existing in the hydrated form, the Cu(II) polymeric strand and the hydrated water molecules have gained a supramolecular helical architecture with a similar pitch distance of 8.133 Å. The two helical strands in complex **1** are associated with right handed (*PP*) supramolecular chirality, while the helical water chain and the Cu^{II}-strand in **2** are self assembled into left handed (*MM*) helicity in the solid state. The solid state CD recorded for **1** and the dehydrated form of **2** exhibit a positive optical sign at their respective d–d band [λ_{max} = 667 nm, **1**; λ_{max} = 630 nm, **2**], the solution state CD for both these complexes are found to be inverted into a negative optical sign, which could be attributed to inversion of their associated supramolecular helicity. The TGA curve illustrates two distinct weight losses at 60 °C and 87 °C, equivalent to one and two water molecules, respectively. The PXRD pattern for the hydrated and dehydrated forms of **2** indicated a change, on comparison with the simulated diffractograph. The fluorescence properties of both these complexes, possessing tryptophan and bipy/phen, were investigated.
© 2008 Elsevier Ltd. All rights reserved.

1. Introduction

Helicity is of paramount importance in nature and in synthetic materials [1–3], and the helical architecture has inspired the syntheses of a variety of helical coordination polymers [4–8], metallohelicates [9], and organohelices [10]. Chiral coordination polymers and helicates composed of chiral building blocks are important supramolecular compounds in view of enantio-selective catalysis [11,12], chiral separation [13–15], and material chemistry [16]. Intensive efforts to investigate the chiroptical properties of supramolecular helices, upon introduction of various chiral residues, such as chiral spacers [17–22], amino acids [23–28], and chiragens [25–28] in the helical skeleton, have been carried out by a number of researchers, including Raymond et al. [29–32], Albrecht et al. [33–35], Kuroda and Telfer [36], and Zelewsky and Ziegler [37]. A number of ternary [Cu(II)(DA)(AA)] [38–51] type complexes composed of optically active D- and L-amino acids (AA) are been known and their optical properties in solution have been studied extensively with intensive focus on structure–reactivity correlation. The rich literature on such complexes indicating the formation of folded and extended conformations, and the present investigation on their supramolecular helical architecture and solid state chiroptical properties are expected to enhance further understanding. In this direction, and in continuation of our recent report [52], we have synthesized and characterized the complexes [Cu(L-trp)(bpy)](ClO_4) (**1**) and [Cu(L-trp)(phen)](ClO_4)·$3H_2O$ (**2**), with a view to investigate the structures and chiroptical properties. The structural analysis of these complexes illustrates that they are single stranded helical coordination polymers. Both these coordination polymers possess the chiral L-tryptophan as a supramolecular building block. The potential chiral sources, *i.e.* the (*P*)/(*M*) sense of supramolecular helicity [53,54], the geometrical chirality (Λ/Δ) [55–58] due to the non-coplanarity at the Cu^{II}-center and conformational chirality λ/δ [59–63] of the chelate rings of the amino acids are analyzed in detail along with CD spectra recorded both in the solid and solution states. These complexes, when composed of the chiral amino acid (L-trp), resulted in single stranded supramolecular helical structures. The solid state optical activity in combination with the solution state CD of these complexes exhibit interesting chiroptical properties. Further, the cooperative self-assembly process of the "helical aqua chain in-between the helical coordination network" observed in **2** signifies that these complexes are parallel with a recent report on water chains. Chakravarty and co-workers [64,65], Vittal and Sreenivasulu [66], and Das and

* Corresponding author. Tel.: +91 278 2567760; fax: +91 278 2566970.
E-mail address: siva140@yahoo.co.in (P.S. Subramanian).

0277-5387/$ - see front matter © 2008 Elsevier Ltd. All rights reserved.
doi:10.1016/j.poly.2008.10.072

co-workers [67] have reported both right and left handed helical water chains. In this direction, the present complex demonstrates the formation of a left handed helical water chain [68–75], similar to the one in the complex $[Cu(sHis)_2] \cdot 4H_2O$ reported by Hong and co-workers [76] The present manuscript, in addition to investigating the structural aspect of the coordination polymers, has further attempted to explore the involvement of the water chain on the supramolecular architecture. Indole is an important fluorophore for monitoring many bio-clinical and catalytic experiments, the fluorescence obtained for these complexes in the present study asserts them as better candidates for photoactive materials.

2. Experimental

2.1. Materials and methods

All reagents and solvents employed were commercially available and were used without further purification. Elemental analysis was performed on a Perkin–Elmer 4100 elemental analyzer. Variable temperature Powder diffraction spectra were recorded using a Philips X-pert MPD Powder X-ray Diffractometer with a 2θ angle ranging from 5° to 40°. Thermogravimetric analysis with heating rate of 5 °C/min was performed using a Mettler Toledo Star SW 7.01. Simulated powder patterns were obtained from the crystallographic software MERCURY version 1.4. The KBr pellets for the CD spectra were prepared with a 1:20 w/w ratio of complex to KBr, and the spectra were measured on a JASCO 815 Spectrometer; fluorescence spectra were recorded on a Perkin Elmer Luminescence Spectrometer LS 50B.

2.1.1. Crystal structure determination

Data collections of **1** and **2** were performed with Mo Kα radiation ($\lambda = 0.71073$ Å) on a Bruker Apex CCD diffractometer at $T = 100(2)$ K. Absorption corrections were applied by using SADABS [77]. The structures were solved by direct methods and all non-hydrogen atoms were refined anisotropically by least-squares on F^2 using the SHELXTL program [78]. Hydrogen atoms of the ligand moiety were geometrically fixed in both complexes, and we could not locate the lattice water hydrogens from the difference Fourier map for O8 and O9.

2.2. Synthesis

2.2.1. [Cu(L-trp)(bpy)](ClO$_4$) (**1**)

A mixture of L-tryptophan (1.02 g, 5 mmol) and NaOH (0.2 g, 5 mmol) dissolved in 10 mL of distilled water was added to an aqueous solution (25 mL) of $CuSO_4 \cdot 5H_2O$ (1.25 g, 5 mmol) with constant stirring for 1 h. The light blue precipitate that formed was dissolved upon addition of a 10 mL ethanol solution of bipyridyl (0.78 g, 5 mmol). To this mixture, $NaClO_4 \cdot H_2O$ (0.7 g) dissolved in distilled water was added gradually. The solution was stirred for another 2 h with heating at 333 K. Slow evaporation of the reaction mixture at 298 K yielded dark blue, needle shaped crystals after a couple of weeks. Yield, 76%. *Anal. Calc.* for $C_{21}H_{19}N_4O_6CuCl$: C, 48.28; H, 3.67; N, 10.72. Found: C, 48.55; H, 3.99; N, 10.80%. IR (ν, cm^{-1}): 3386–2933 (s), 1626, 1595 (ν_{COO}, s), 1445, 1407 (m), 1317 (m), 1110, 1070, 1052 (s, ClO_4), 755, 663 (m).

2.2.2. [Cu(L-trp)(phen)](3H$_2$O)(ClO$_4$) (**2**)

This complex was synthesized following the above procedure, using 1,10-phenanthroline monohydrate (0.94 g, 5 mmol) in place of bipyridyl. Yield 85%. *Anal.* Calc. for $C_{23}H_{25}N_4O_9CuCl$: C, 46.01; H, 4.20; N, 9.33. Found. C, 46.20; H, 4.25; N, 9.50%. IR (ν, cm^{-1}): 3566–2954 (s, br), 1635, 1590 (ν_{COO}, s), 1523, 1433, 1395 (m), 1140, 1112, 1080 (s, ClO_4), 841, 757 (m).

CAUTION! Perchlorate salts of metal complexes are potentially explosive and should be handled with great care.

3. Results and discussion

3.1. Crystal structures and molecular association

Complexes **1** and **2** crystallized in the chiral space groups $P2_1$ and $P2_12_12_1$, respectively. ORTEP diagrams with the atom numbering schemes for **1** and **2** are depicted in Fig. 1 and a summary of the crystallographic data, selected bond distances and bond angles are given in Tables 1 and 2, respectively. The Cu^{II} ion in both these complexes possesses a distorted square pyramidal geometry, the square base around the metal center is occupied by pyridyl nitrogens of the bpy/phen moiety, and NH_2 and COO groups of the amino acid (L-trp). The fifth axial site is occupied by the second oxygen of the carboxylate unit, which bridges the neighboring metal center in a "*syn–anti*" mode and constructs a single stranded one-dimensional helical polymeric network. The *syn–anti* carboxylate coordination of the tryptophan unit in **1** and **2** repeatedly self assembled in screw related 2_1 symmetry, through a spiral coordination polymeric arrangement running through the OCO···Cu^{II}···OCO bridge. The indole moiety of L-tryptophan in the present complexes, possessing some sort of weak intramolecular interaction with the aromatic rings of the diamines and bpy/phen, exists in a folded conformation, as observed in various [Cu$^{(II)}$(DA)(AA)] type complexes.

Complex **1** consists of two independent molecules in the asymmetric unit, with Cu1 and Cu2 as the central metal ions. The carboxylate oxygens O2 and O4 of the tryptophan ligand in **1** [Cu1–O2 = 2.206(3), Cu2–O4 = 2.203(3) Å] interconnect the adjacent Cu^{II} centers and generate two independent helical strands running through Cu1–OCO–Cu1 and Cu2–OCO–Cu2. The Cu^{II} metal ions are placed in the respective polymeric helical strands with intrahelical Cu^{II}–Cu^{II} distances of 5.579 (Cu1–Cu1) and 5.628 Å (Cu2–Cu2). Both these parallel helical strands, possessing a similar pitch distance, exist as screw related right handed (*PP*) helices, as shown in Fig. 2a.

Similar to complex **1**, adjacent Cu^{II} metal ions in **2** are interlinked through the carboxylate oxygen O2 [Cu1–O2 = 2.254(4) Å] and are extended as a one-dimensional helical polymeric strand. Further, complex **2**, crystallizing with three lattice water molecules per Cu(II) unit, exists in the hydrated form. These hydrated water molecules O7, O8, and O9 are entrapped between the Cu^{II}-helical strand and are self assembled into a helical aqua chain. Thus, the molecular packing in **2** is comprised of two different helical assemblies *i.e.* the robust Cu^{II}–OCO–Cu^{II} chiral polymeric strand and the one-dimensional helical water chain. Although these two helical strands differ in their chemical constituents, they possess a similar pitch distance, 8.133 Å, and it is revealed that they are left handed homohelices (*MM*). Unlike complex **1**, the Cu^{II} metal centers in **2** are placed in the helical chain (Cu1–OCO–Cu1) and possess a constant intrahelical Cu^{II}···Cu^{II} distance of 5.946 Å. Adjacent Cu^{II}-helical strands are packed along the *ab* plane, incorporating the infinite helical water chain between them as shown in Fig. 2b.

3.2. Molecular stacking and stereoregular arrangement

Since the π–π stacking interactions [11–16] observed in [Cu(-DA)(AA)] type complexes has been of significant interest, the present complexes, composed of aromatic rings of tryptophan and bpy/phen, and their molecular association mediated through inter and intramolecular interactions like π–π stacking and hydrogen bonding are analyzed in view of their involvement in the construction of the helical arrangement. Accordingly, crystallographically

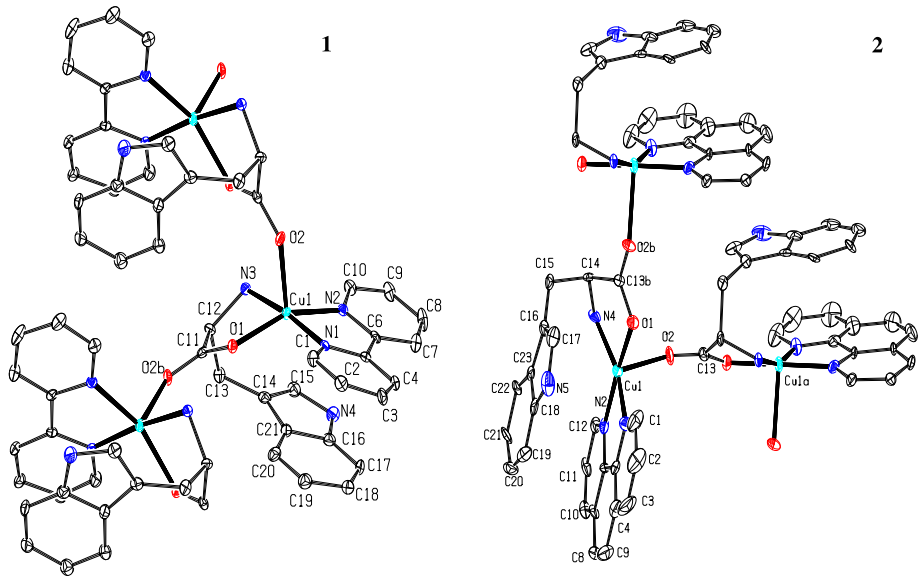


Fig. 1. ORTEP diagram depicting a partial helicationic chain of complexes **1** and **2** with the atom numbering scheme (40% probability factor for the thermal ellipsoids).

Table 1
Summary of crystallographic data for complexes **1** and **2**.

Complex	**1**	**2**
CCDC number	285560	285561
Chemical formula	$C_{42}H_{36}Cl_2Cu_2N_8O_{12}$	$C_{23}H_{21}ClCuN_4O_9$
Formula weight	1042.77	596.43
Radiation used λ (Å)	0.7107	0.7107
Crystal system	monoclinic	orthorhombic
Space group	$P2_1$	$P2_12_12_1$
a (Å)	10.5050(10)	8.1333(19)
b (Å)	7.7135(7)	10.973(3)
c (Å)	25.545(2)	28.154(7)
α (°)	90.0	90.00
β (°)	90.531(2)	90.0
γ (°)	90.0	90.00
Z	2	4
V (Å^3)	2069.9(3)	2512.7(11)
F(000)	1064	1224
Crystal size (mm)	0.38 × 0.28 × 0.24	0.30 × 0.25 × 0.22
$D_{calc.}$ (g cm^{-3})	1.673	1.577
Absorption coefficient, μ (mm^{-1})	1.234	1.036
Temperature (K)	100	100
Reflections measured	12297	14907
Unique reflections used [$I > 2\sigma(I)$]	8090	5748
Parameters (N)	595	343
Goodness-of-fit	1.003	1.148
Final R indices [$I \geqslant 2\sigma(I)$]	R_1 = 0.0419; wR_2 = 0.0874	R_1 = 0.0771; wR_2 = 0.15092
R-indices (All data)	R_1 = 0.0509; wR_2 = 0.0933	R_1 = 0.1032; wR_2 = 0.1663
Maximum/minimum residual (e Å^{-3})	0.623/−0.384	0.810/−0.909
Refinement method	full matrix least-squares on F^2	full matrix least-squares on F^2

Table 2
Selected bond distances (Å) and angles (°) for complexes **1** and **2** with estimated standard deviations in parenthesis.

Bond length (Å)	**1**	**2**	Bond angle (°)	**1**	**2**
Cu(1)–N(1)	1.970(3)	2.012(5)	N(1)–Cu(1)–N(3)	173.67(13)	
Cu(1)–N(2)	2.015(3)	1.996(5)	N(1)–Cu(1)–N(2)	81.23(12)	82.4(2)
Cu(1)–N(3)	1.976(3)		N(3)–Cu(1)–N(2)	100.51(13)	
Cu(1)–O(1)	2.012(3)	1.930(4)	N(3)–Cu(1)–O(1)	82.14(11)	
Cu(1)–N(4)		2.007(5)	N(1)–Cu(1)–O(1)	93.99(11)	92.4(2)
Cu(1)–O(2)		2.254(4)	O(1)–Cu(1)–N(2)	158.02(11)	174.5(2)
			N(1)–Cu(1)–O(2)	89.59(11)	111.83(19)
			N(3)–Cu(1)–O(2)	95.52(11)	
			O(1)–Cu(1)–O(2)	92.02(10)	88.84(17)
			N(2)–Cu(1)–O(2)	109.29(11)	
			N(2)–Cu(1)–N(4)		101.1(2)
			N(4)–Cu(1)–N(1)		161.8(2)
			N(2)–Cu(1)–O(2)		91.54(18)
			O(1)–Cu(1)–N(4)		40(18)
			N(4)–Cu(1)–O(2)		86.03(18)

generated centroids Cg_1 to Cg_5 and Cg_1' to Cg_5' were assigned to the various aromatic rings around the Cu^{II} centers as indicated in Fig. 3.

Cg_1, Cg_2, and Cg_5 represent the centroids of the respective aromatic rings of bpy and phen, and Cg_c represents the centroid of the metal-chelate ring. The centroids for the phenyl and pyrrole rings of the tryptophan moiety in complexes **1** and **2** are assigned as Cg_3 and Cg_4, respectively. The various inter and intramolecular offset π···π stacking interactions between the aromatic rings and the respective distances derived from the crystallographic data are depicted in Table 3. The intramolecular π–π stacking interaction measured between the various aromatic rings of bpy/phen with the phenyl (Cg_3) and pyrrole (Cg_4) rings of the tryptophan moiety are found to be in the range 3.60–3.94 Å, and the corresponding stacked rings are oriented almost parallel to each other. Interestingly, for these complexes existing in the folded conformation, the five membered chelate ring Cg_c (metal-chelate ring of bpy/phen) in **1** and **2** revealed the shortest distance with the phenyl ring of the tryptophan and illustrate the existence of an aryl-metal-chelate ring interaction [43,79–81] (complex **1**, $Cg_c\cdots Cg_4$ = 3.452 Å; $Cg_c\cdots Cg_3$ = 3.37 Å and complex **2**, $Cg_c\cdots Cg_3$ = 3.385 Å; $Cg_c\cdots Cg_4$ = 3.661 Å]. This aryl-metal-chelate interaction between the phenyl ring of the tryptophan and the metal chelate, ring $Cg_c\cdots Cg_3$ = 3.37 Å in **1** and $Cg_c\cdots Cg_3$ = 3.385 Å in **2**, presumably might have helped in stabilizing the folded conformation in both these complexes. Thus, while the inter and intramolecular π–π stacking interactions, along with aryl-metal-chelate interactions, favors the formation of a folded conformation, the carboxylate moiety interconnects the Cu^{II}-units through its Cu–OCO–Cu bridge in a stereoregular manner and gains a helical arrangement.

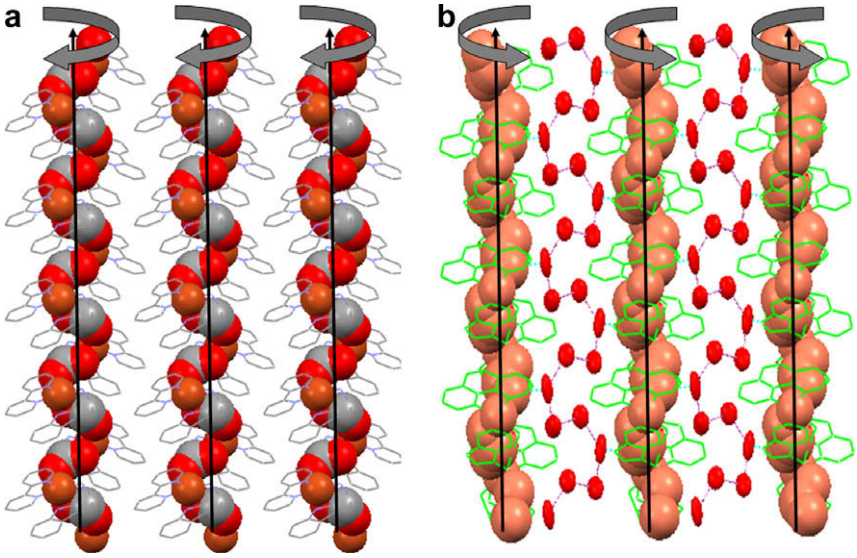


Fig. 2. Helical coordination polymers **1** and **2** along with helical rotation. (a) Complex **1** (*PP*)-helices. (b) Complex **2**. (*MM*)-helices (hydrogen atoms and ClO_4^- anions are removed for clarity; ball and stick model shown in red colour indicates the helical water chain). (For interpretation of the references to colour in this figure legend, the reader is referred to the web version of this article.)

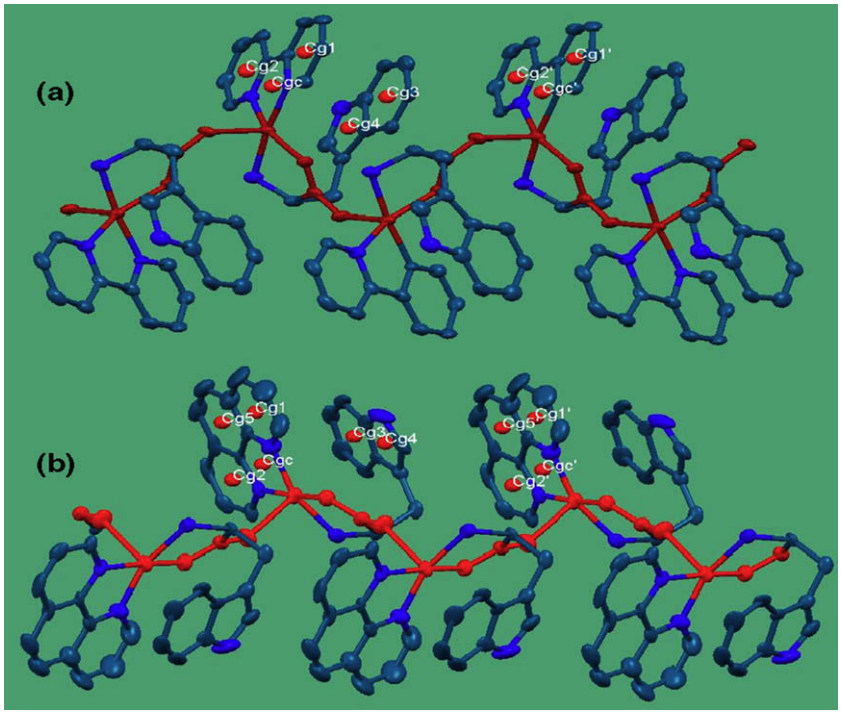


Fig. 3. π···π stacking interaction between the centroids. (a) Complex **1**. (b) Complex **2**.

Table 3
Inter and intramolecular π···π stacking distances in **1** and **2**.

Complex	**1** (Å)	**2** (Å)
Intra π···π	$Cg_1\cdots Cg_4$ = 3.606	$Cg_3\cdots Cg_4$ = 3.940
	$Cg_2\cdots Cg_3$ = 3.715	$Cg_2\cdots Cg_4$ = 3.893
	$Cg_c\cdots Cg_4$ = 3.452	$Cg_c\cdots Cg_3$ = 3.385
	$Cg_c\cdots Cg_3$ = 3.370	$Cg_c\cdots Cg_4$ = 3.661
Inter π···π	$Cg_3\cdots Cg'$ = 3.759	$Cg_4\cdots Cg'_5$ = 3.499

3.3. Helical water chain

The trimeric acyclic water molecules containing O7, O8, and O9 in complex **2** are interconnected themselves through their O–H···O interactions (S1). Selected bond distances and bond angles regarding the helical water chain are depicted in Fig. 4a. Even though the data collection was carried out at liquid nitrogen temperature (100 K), only the hydrogen atoms attached to O7 were located, whereas the hydrogen atoms of O8 and O9 were not obtainable from the difference Fourier map. However, the hydrogen bonding

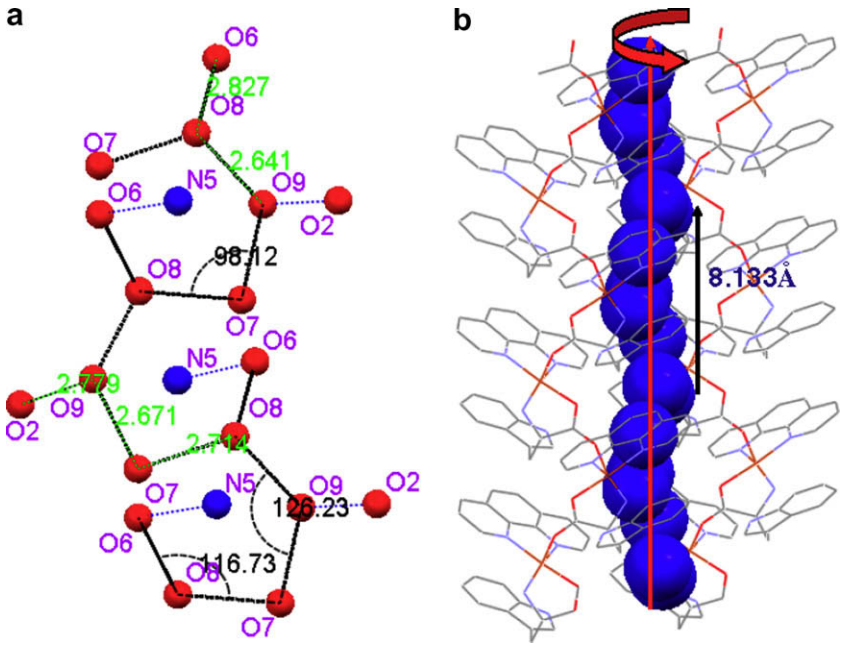
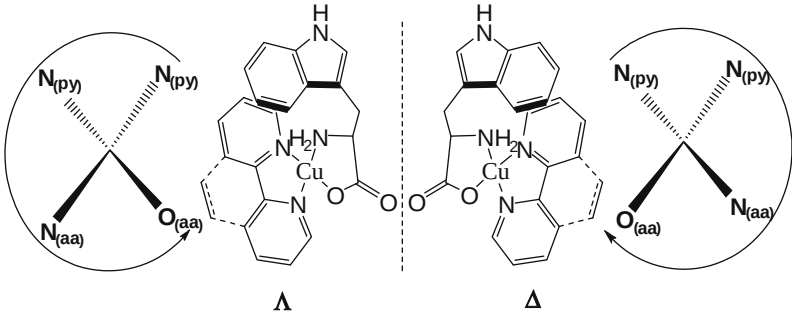


Fig. 4. Lattice helical water chain between the Cu^{II}-helical strands. (a) Water helix with atom numbering, bond distances and bond angles. (b) Pitch distance and left handed helical rotation.

distances and angles (∠O7–H71···O9 = 122°; ∠O7–H72···O8 = 151°) between the 2_1 screw related water oxygens (O7, O8, O9) unequivocally establish the infinite hydrogen bonded helical water chain. The average O···O (2.675 Å) distance and the average angle of 112.30° matches well with reported helical water chains [76,79–82]. The water oxygen O9 further acts as both a donor and an acceptor and makes effective H-bonding with the tryptophan carboxylate oxygen O2 [O9···O2 = 2.779 Å] and phenyl hydrogen H2 [C2···O9 = 3.396 Å; ∠C2–H2···O9 = 146°] of the phenanthroline ring oriented along the periphery of Cu^{II}-strand. O7 water is involved in N–H···O interaction with the tryptophan amino nitrogen N4 [N4···O7 = 3.07 Å; N4–H4···O7 = 151°], whereas O8 water acts as a donor in hydrogen bonding with the perchlorate oxygen O6 [O8···O6 = 2.827 Å]. Thus the adjacent Cu^{II}-helical strands within the interhelical space force the trimeric acyclic water molecules through their contact mediated *via* C–H···O, N–H···O, and O–H···O hydrogen bonds, and stabilize them in the helical arrangement. Interestingly, the helical water chain and the Cu^{II}-strand in complex **2** are associated in a left handed (*MM*) sense of superstructure. In general, the supramolecular helices are usually pack in a racemic fashion [30], comprising of both right and left handed helices. Accordingly, recent literature [22–24] illustrating the packing of both right and left handed helical water chains in schiff base complexes, the present helical water chain, possessing solely left handedness (Figs. 2b and 4b), resembles the water chain similar to the one in $[Cu(sHis)_2]\ 4H_2O$ complex reported by Hong and co-workers [76]. Thus, the observation suggest, that the complex 1 and 2 stabilizes with L-tryptophan in homochiral (*PP*) and (*MM*) helices predominantly is worth mentioning.

3.4. Chiral components and chiroptical properties

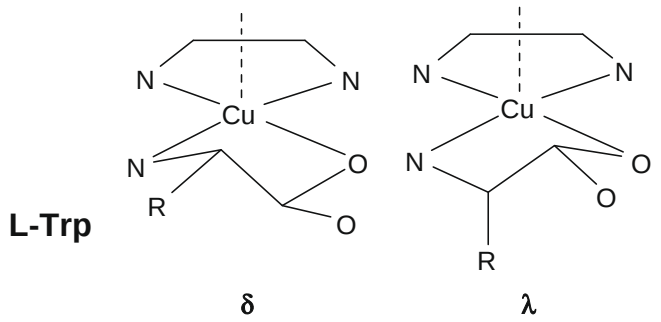
For the complexes **1** and **2** (hydrated), possessing a chiral amino acid, their diastereo-selective crystallization provide homochiral right handed (*PP*) and left handed (*MM*) superstructures in their solid states, respectively. The change in the CD optical sign of these L-tryptophan complexes, in solution and in the solid state, inspired us to investigate their chiroptical properties. Accordingly, the CD spectra for complex **1** and the hydrated and dehydrated forms of complex **2** were recorded both in solution and on ground crystals. An attempt to derive a correlation between the various chiral components in the complexes and their chiroptical properties was carried out. In general, the source of the optical activity could be derived from various chiral sources such as the (*P*)/(*M*) supramolecular helical descriptors, the molecular Δ/Λ descriptors of the chiral metal centers (Scheme 1) and the λ/δ conformational chiral-



Scheme 1. Geometrical descriptors.

ity of the non-planar amino acid chelate ring (Scheme 2). The stereochemical descriptors (*P*) and (*M*) could be assigned to the supramolecular helical assemblies for complexes **1** and **2** depending upon the clockwise and anticlockwise rotation of the helical strand. Further, the existence of molecular chirality can be attributed to the non-coplanar arrangement of the Cu^{II} chromophoric donor atom at the base of the square pyramid or the asymmetric arrangement of the ligand conformation. Accordingly, the molecular descriptors Δ and Λ are assigned for the present complexes depending upon the clockwise (Δ-enantiomer) and anticlockwise (Λ-enantiomer) operation of the ligand coordination around the Cu^{II} center as shown in Scheme 1. The structural analysis for both these complexes denote that the indole ring of the tryptophan and the bipy/phen moieties project outwards and revolved around the helical axis, drawn between the metal centers, with considerable intra and intermolecular π–π stacking interactions, as shown in Fig. 3a and b. The folded isomers in complex **1**, sitting alternatively in a ΔΛΔΛ··· fashion, generate two helical strands *i.e.* Cu1–OCO–Cu1 and Cu2–OCO–Cu2 strands. Thus, the stereoregularly arranged adjacent polymeric Cu1 and Cu2 homohelices are associated with right handed rotation and produce (*PP*) helices as shown in Fig. 2a. Our analysis in complex **1** indicates that this complex preferred the formation of (*PP*) homohelices predominantly.

As stated above, the two helical strands in complex **2** (helical water chain and Cu(II)-strand) are stereospecifically self assembled into left handed (*MM*) helices in the solid state. The supramolecular chiralities associated with complexes **1** and **2**, existing in the folded form, are different and opposite to each other, *i.e.* right handed (*PP*) in **1** and left handed (*MM*) helices in **2** (hydrated). Based on the structural investigation, the molecular chirality at the metal center obviously demonstrates the presence of both Δ and Λ isomers in the helical strand and hence the chirality associated with the molecule is cancelled out. The solid state CD recorded for complex **1** illustrates a broad band centered at ≈660 nm with a positive optical sign, while complex **2**, in its hydrated form, exhibited a negative optical sign at ≈609 nm, as shown in Fig. 5a. As complexes **1** and **2** have very similar chemical compositions, the difference in the stereoregular arrangement observed in their superstructures *i.e.*, right handed (*PP*) in **1** and left handed (*MM*) in **2** (hydrated) must have caused the opposite sign. The bpy rather than phen ring and the helical water chain are the only differences between these complexes, the change observed in their respective helical superstructures is identified as an appropriate candidate for these changes. Hence as a first step, to understand the involvement of the water chain and supramolecular helicity, the water molecules from complex **2** were removed following the thermogravimetric analysis described below. Hence upon dehydrating complex **2** at 110 °C, the corresponding solid state-CD spectra was recorded [Fig 5a (iii)]. Fascinatingly, the CD spectrum obtained for this dehydrated form of complex **2** bears a positive optical sign, which is almost opposite to the respective optical sign obtained for its hydrated counterpart (Fig 5a (ii)). Thus, the hydrated and dehydrated forms of complex **2** produce almost opposite optical signs in their respective solid state-CD spectra, the corresponding structural changes *i.e.* (*MM*) in the hydrated form into (*PP*) in the dehydrated form may tentatively be assigned to the supramolecular helical inversion. This observation indicates that the helical water chain entrapped in between the Cu^{II}-strands, retains the (*MM*) helices, but upon dehydration the left handed Cu^{II}-strand rearranges into right handed (*P*) helices. Thus, the change in the optical sign can be attributed to the hydrated and dehydrated forms. Our attempt to solve the crystal structure for this dehydrated form of complex **2** was unsuccessful.



Scheme 2. Conformations of the amino acid chelate rings.

In general, the five membered amino acid chelate rings can exhibit a dynamic λ ⇌ δ conformational equilibrium [20] in the solution state (Scheme 2). The well documented literature [21] indicates that the position of the equilibrium would be determined by the distortion on the chiral center influenced by various factor such as aromatic rings, bulkiness of the side chain substitution and polarity of the solvent. As mentioned above, phen rather than bpy and the helical water being the only difference between **1** and **2**, they are considered to play a significant role in determining the λ/δ conformation in the solid state. Accordingly, the torsion angles involving the C12C11O1Cu1 and C33C32O3Cu2 motifs measured using the crystal structure of **1** are −6.53° and −3.88°, whilst the respective chelate ring C14C13O1Cu1 in complex **2** shows +10.28°. This observation clearly supports that complex **1** predominantly stabilizes the δ conformation, while **2** favors the λ conformation in the solid state. For complex **2**, possessing a comparatively bulky phenanthroline moiety and the polar water chain in the solid state, the respective λ conformation induces the formation of a (*M*) helix, while complex **1** with a δ conformation induces the (*P*) helix, resembling our earlier reports.

The CD spectra recorded in both the solid state (Fig. 5a) and in solution (Fig. 5b) for complexes **1** and **2** at room temperature give broad signals in the visible region at 450–800 nm. Whilst the solid state-CD spectrum for **1** exhibits a positive sign (λ_{max} = 660 nm), the corresponding solution state CD spectrum gives a negative sign at 598 nm ($\Delta\varepsilon = -1.38\ M^{-1}\ cm^{-1}$). However the respective solid state-CD spectra of the hydrated and dehydrated (λ_{max} = 630 nm) forms of **2** produce opposite optical signs. Interestingly, the solution state CD spectra recorded in methanol solvent for **1** and **2** behave similarly in the visible region, exhibiting a d–d band at 598 nm ($\Delta\varepsilon = -1.38\ M^{-1}\ cm^{-1}$) for **1** and 603 nm ($\Delta\varepsilon = -1.64\ M^{-1}\ cm^{-1}$) for **2**. This shift in the d–d band and the change in the optical sign together suggest that the polymeric helical assembly is destroyed in the solution state and the complexes may exist as monomeric species.

As observed from the single crystal X-ray structures, the supramolecular helical assemblies of complexes **1** and **2**, containing the L-tryptophan ligand, lead to (*PP*) and (*MM*) homohelices. In complex **2**, for the hydrated form, where the metal-chelate ring exists in the λ conformation, the Cu^{II} strand results in (*M*) helices, while the δ conformation is stabilized in (*P*) helices in the dehydrated form. In complex **1**, with a folded conformation, the chelate ring exists in the λ conformation and induces a (*M*) helix, while in complex **2**, due to the incorporation of the left handed helical water chain, the Cu^{II}-strand exists in the (*P*) helix. Astonishingly, upon removing the water molecules the resultant dehydrated form of complex **2** behaves similarly to compound **1** by inverting from the (*P*) into a (*M*) helix, as can be attributed to the changes observed in the CD spectra (Fig. 5).

3.5. Fluorescence property

Cu(II) complexes with phenanthroline and tryptophan [83,84] are extensively used as fluorescent probes to monitor the DNA

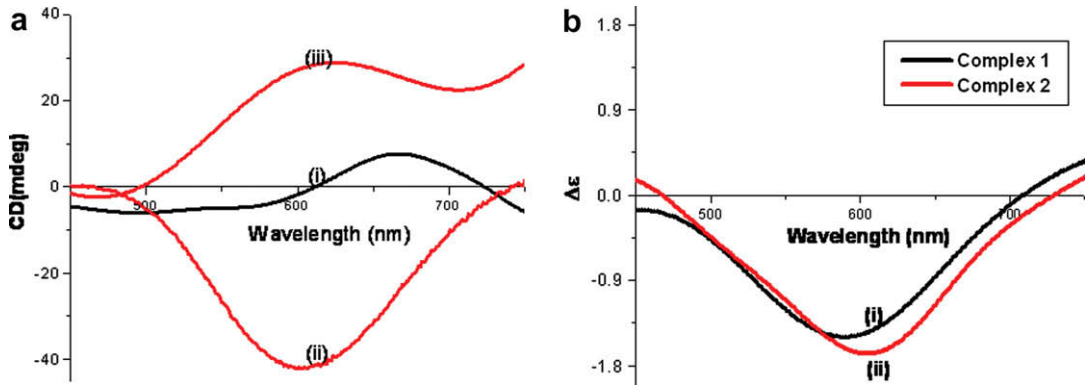


Fig. 5. (a) Solid state-CD spectra for (i) complex **1**, (ii) complex **2**, (iii) complex **2** (dehydrated) in the visible region measured as a KBr discs. (b) Solution state CD spectra for (i) complex **1**, (ii) complex **2** in the visible region measured in methanol.

cleavage. Accordingly, the emission observed both in solution and in the solid state (S2) for **1** and **2** around 350 ± 3 nm (excited at 280 nm) could be attributed to an intra-ligand charge transfer.

3.6. Thermal analysis

To ascertain the thermal stability of the helical water chain, thermogravimetry analysis and powder diffraction studies for the hydrated and dehydrated samples of complex **2** were performed. The TGA curve (S3), indicates two distinct weight losses in the temperature range 40–110 °C. The first endothermic curve showing 2.26% (calc = 2.99) weight loss at 60 °C corresponds to 0.75 water molecule, while the second curve appearing at 87 °C was equivalent to 5.71% (calc = 5.98%), representing 1.9 water molecules. This discrepancy between the observed and theoretical values could be attributable to the evaporation of water molecules and such differences are usual in such hydrated complexes. The two sets of weight loss may be attributable to two distinguishable bindings of trimeric water molecules for "strong" and "weak" H-bonding contacts with the Cu^{II}-helical strand. The water molecules O8, O9, make strong O–H···O interactions with the lattice perchlorate (O6) and carboxylate (O2), whilst the water molecule O7 is involved in weaker N–H···O interactions, making it more labile as observed from the TGA curve.

In addition to the TGA experiment, X-ray powder diffractograms were recorded for complex **2** at different temperatures. Fig. 6 represents the PXRD pattern for simulated, hydrated and dehydrated forms of complex **2**. Evidently, the simulated PXRD pattern from the single crystal X-ray structure, using the crystallographic software package MERCURY 1.4, and the PXRD recorded at room temperature are similar to each other. This similarity in the diffraction pattern confirms that the crystals in the bulk and the single crystal, for which crystal structure was solved, are the same. Diffractogram (ii) and (iii), representing the PXRD recorded at 30 and 110 °C, can be attributed to the hydrated and dehydrated forms of complex **2.** While the diffractogram of the simulated and hydrated forms of complex **2** are similar, the diffraction pattern with respect to the dehydrated form showed some significant changes, which reflects some structural changes upon losing the helical water chain. Structural changes upon loss of water molecules are expected for this complex as the water molecules are an integral part of the supramolecular network. The change in the PXRD pattern recorded for dehydrated form, shown by an arrow compared to the hydrated form at 30 °C, indicates that upon losing all three water molecules the supramolecular crystal system undergoes a major change, which could be attributed to the opposite optical sign observed from the CD spectrum for the dehydrated sample.

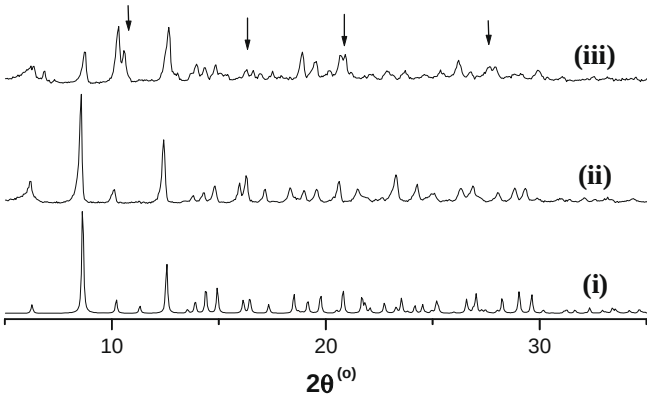


Fig. 6. PXRD of complex **2** (i) simulated, (ii) hydrated form, (iii) dehydrated form.

4. Conclusions

In conclusion, we have shown the formation of two self-assembled single stranded supramolecular Cu^{II} helical coordination polymers. Complexes **1** and **2**, containing L-tryptophan, are found to crystallize in the right handed (*PP*) and left handed (*MM*) sense of helices, respectively. A self-assembled infinite left handed helical water chain entrapped between the Cu^{II} helical strands in complex **2** is meticulously analyzed using various physico-chemical techniques such as TGA and PXRD, and includes a single crystal X-ray structure. The solid state-CD spectra of complex **1** and the dehydrated form of complex **2** exhibit a positive optical sign, whereas the corresponding solution state CD spectra are found to be inverted, with a negative optical sign. The CD activity of complex **2** in its hydrated form, similar to its solution state, infers that the left handed helical water chain entrapped in the lattice inverts its supramolecular chirality. Although the right handed (*PP*) and left handed (*MM*) supramolecular helices are actually observed in the present crystals of **1** and **2**, the formation of the respective (*MM*) and (*PP*) counterpart cannot be ruled out. In this direction, to gain further understanding on the formation of supramolecular helical assemblies, the synthesis of a similar coordination polymer with D-tryptophan is under progress in our laboratory. Both these helical coordination polymers display luminescent properties in solution as well as the solid state and their emission properties signify these compounds as potential fluorescent materials.

Acknowledgments

We are grateful to the Department of Science and Technology New Delhi (India) for financial support vide Project Number SR/

S1/IC-19/2005. We thank Professor Luigi Casella for his valuable suggestions.

Appendix A. Supplementary data

CCDC 285560 and 285561 contain the supplementary crystallographic data for **1** and **2**. These data can be obtained free of charge via http://www.ccdc.cam.ac.uk/conts/retrieving.html, or from the Cambridge Crystallographic Data Centre, 12 Union Road, Cambridge CB2 1EZ, UK; fax: (+44) 1223-336-033; or e-mail: deposit@ccdc.cam.ac.uk. Supplementary data associated with this article can be found, in the online version, at doi:10.1016/j.poly.2008.10.072.

References

[1] J.-M. Lehn, Supramolecular Chemistry. Concepts and Perspectives, VCH, Weinheim, 1995.
[2] N. Giuseppone, J.-L. Schmitt, J.-M. Lehn, J. Am. Chem. Soc. 128 (2006) 16748.
[3] L.J. Prins, J. Huskens, F. De Jong, P. Timmerman, D.N. Reinhoudt, Nature 398 (1999) 498.
[4] K. Biradha, C. Seward, M.J. Zaworotko, Angew. Chem., Int. Ed. 38 (1999) 492.
[5] E.V. Anokhina, A.J. Jacobson, J. Am. Chem. Soc. 126 (2004) 3044.
[6] N. Niklas, F. Hampel, R. Alsfasser, Chem. Commun. (2003) 1586.
[7] Y.T. Wang, M.-L. Tong, H.-H. Fan, H.-Z. Wang, X.-M. Chen, J. Chem. Soc., Dalton Trans. (2005) 424.
[8] U. Siemeling, I. Scheppelmann, B. Neumann, A. Stammler, H.-G. Stammlerand, J. Frelek, Chem. Commun. (2003) 2236.
[9] C. Piguet, G. Bernardinelli, G. Hopfgartner, Chem. Rev. 97 (1997) 2005.
[10] G.D. Pantos, P. Pengo, J.K.M. Sanders, Angew. Chem., Int. Ed. 46 (2007) 194.
[11] D.A. Evans, K.A. Woerpel, M.J. Scott, Angew. Chem., Int. Ed. 31 (1992) 430.
[12] H.-L. Kwong, H.-L. Yeung, W.-S. Lee, W.-T. Wong, Chem. Commun. (2006) 4841.
[13] B. Kesanli, W. Lin, Coord. Chem. Rev. 246 (2003) 305.
[14] D. Bradshaw, T.J. Prior, E.J. Cussen, J.B. Claridge, M.J. Rosseinsky, J. Am. Chem. Soc. 126 (2004) 6106.
[15] R.-G. Xiong, X.-Z. You, B.F. Abrahams, Z. Xue, C.-M. Che, Angew. Chem., Int. Ed. 40 (2001) 4422.
[16] C.S. Purohit, S. Verma, J. Am. Chem. Soc. 129 (2007) 3488.
[17] R. Prabaharan, N.C. Fletcher, M. Nieuwenhuyzen, J. Chem. Soc., Dalton Trans. (2002) 602.
[18] Y. Cui, H.L. Ngo, W. Lin, Chem. Commun. (2003) 1388.
[19] M. Kondo, M. Miyazawa, Y. Irie, R. Shinagawa, T. Horiba, A. Nakamura, T. Naito, K. Maeda, S. Utsuno, F. Uchidac, Chem. Commun. (2002) 2156.
[20] R.-H. Wang, L.-J. Xu, X.-S. Li, Y.-M. Li, Q. Shi, Z.-Y. Zhou, M.-C. Hong, A.S.C. Chan, Eur. J. Inorg. Chem. (2004) 1595.
[21] L.J. Prins, P. Timmerman, D.N. Reinhoudt, J. Am. Chem. Soc. 123 (2001) 10153.
[22] E. Yashima, K. Maeda, T. Nishimura, Chem. Eur. J. 10 (2004) 42.
[23] C.J. Carrano, K.N. Raymond, J. Am. Chem. Soc. 100 (1978) 5371.
[24] A.-K. Duhme, Z. Dauter, R.C. Hider, S. Pohl, Inorg. Chem. 35 (1996) 3059.
[25] M. Duggeli, C. Goujon-Ginglinger, S.R. Ducotterd, D. Mauron, C. Bonte, A.V. Zelewsky, H. Stoeckli-Evans, A. Neels, Org. Biomol. Chem. 1 (2003) 1894.
[26] O. Mamula, A.V. Zelewsky, T. Bark, G. Bernardinelli, Angew. Chem., Int. Ed. 38 (1999) 2945.
[27] O. Mamula, F.J. Monlien, A. Porquet, G. Hopfgartner, A.E. Merbach, A.V. Zelewsky, Chem. Eur. J. 7 (2001) 533.
[28] A.V. Zelewsky, Coord. Chem. Rev. 190–192 (1999) 811.
[29] M. Meyer, B. Kersting, R.E. Powers, K.N. Raymond, Inorg. Chem. 36 (1997) 5179.
[30] B. Kresting, M. Meyer, R.E. Powers, K.N. Raymond, J. Am. Chem. Soc. 118 (1996) 7221.
[31] D. Caulder, K.N. Raymond, J. Chem. Soc., Dalton Trans. (1999) 1185.
[32] J. Xu, T.N. Parac, K.N. Raymond, Angew. Chem., Int. Ed. 38 (1999) 2878.
[33] M. Albrecht, O. Spieβ, M. Schneider, P. Weis, Chem. Commun. (2002) 786.
[34] M. Albrecht, M. Napp, M. Schneider, P. Weis, R. Frohlich, Chem. Eur. J. 7 (2001) 3966.
[35] M. Albrecht, M. Napp, M. Schneider, P. Weis, R. Fröhlich, Chem. Commun. (2001) 409.
[36] S.J. Telfer, R. Kuroda, Chem. Eur. J. 11 (2005) 57.
[37] M. Ziegler, A.V. Zelewsky, Coord. Chem. Rev. 177 (1998) 257.
[38] O. Yamauchi, A. Odani, M. Takani, J. Chem. Soc., Dalton Trans. (2002) 3411.
[39] O. Yamauchi, K. Tsujide, A. Odani, J. Am. Chem. Soc. 107 (1985) 659.
[40] O. Yamauchi, A. Odani, T. Kohzuma, H. Masuda, K. Toriumi, K. Saito, Inorg. Chem. 28 (1989) 4066.
[41] F. Zhang, A. Odani, H. Masuda, O. Yamauchi, Inorg. Chem. 35 (1996) 7148.
[42] S. Suzuki, K. Yamaguchi, N. Nakamura, Y. Tagawa, H. Kuma, T. Kawamoto, Inorg. Chim. Acta 283 (1998) 260.
[43] U. Mukhopadhyay, D. Choquesillo-Lazarte, J. Niclos-Gutierrez, I. Bernal, Cryst. Eng. Commun. 6 (2004) 627.
[44] F. Zhang, T. Yajima, H. Masuda, A. Odani, O. Yamauchi, Inorg. Chem. 36 (1997) 5777.
[45] L.H. Abdel-rahman, L.P. Battaglia, M.R. Mahmoud, Polyhedron 15 (1996) 327.
[46] A. Castineiras, A.G. Sicilia-Zafra, J.M. Gonzalez-Perez, D. Choquesillo-Lazarte, J. Niclos-Gutierrez, Inorg. Chem. 41 (2002) 6956.
[47] N. Nakamura, T. Kohzuma, H. Kuma, S. Suzuki, J. Am. Chem. Soc. 114 (1992) 6550.
[48] J.L. Seymour, F. Turecek, A.V. Malkov, P. Kocovsky, J. Mass. Spectrom. 39 (2004) 1044.
[49] M. Mizutani, S. Tomosue, H. Kinoshita, K. Jitsukawa, H. Masuda, H. Einaga, Bull. Chem. Soc. Jpn. 72 (1999) 981.
[50] T. Sugimori, H. Masuda, N. Ohata, K. Koiwai, A. Odani, O. Yamauchi, Inorg. Chem. 36 (1997) 576.
[51] P.S. Subramanian, E. Suresh, P. Dastidar, S. Waghmode, D. Srinivas, Inorg. Chem. 40 (2001) 4291.
[52] P.S. Subramanian, E. Suresh, L. Casella, Eur. J. Inorg. Chem. 12 (2007) 1654.
[53] V.G. Machado, P.N.W. Baxter, J.-M. Lehn, J. Braz. Chem. Soc. 12 (2001) 431.
[54] M. Albrecht, Chem. Rev. 101 (2001) 3457.
[55] L.-S. Long, J.-W. Cai, Y.-P. Ren, Y.-X. Tong, X.-M. Chen, L.-N. Ji, R.-B. Huang, L.-S. Zheng, J. Chem. Soc., Dalton. Trans. (2001) 845.
[56] S. Khatua, T. Harada, R. Kuroda, M. Battacharjee, Chem. Commun. (2007) 3927.
[57] H. Miyasaka, S. Okamura, T. Nakashima, N. Matsumoto, Inorg. Chem. 36 (1997) 4329.
[58] U. Knof, A.V. Zelewsky, Angew. Chem., Int. Ed. 38 (1999) 302.
[59] L. Casella, M. Gullotti, J. Am. Chem. Soc. 103 (1981) 6338.
[60] L. Casella, M. Gullotti, A. Pasini, A. Rockenbauer, Inorg. Chem. 18 (1979) 2825.
[61] L. Santagostini, M. Gullotti, R. Pagliarin, E. Bianchi, L. Casella, E. Monzani, Tetrahedron Asymmetry 10 (1999) 281.
[62] L. Casella, M. Gullotti, Inorg. Chem. 20 (1981) 1306.
[63] O. Yamauchi, A. Odani, J. Am. Chem. Soc. 107 (1985) 5938.
[64] A. Mukherjee, M.K. Saha, M. Nethaji, A.R. Chakravarty, Chem. Commun. (2004) 716.
[65] A. Mukherjee, M.K. Saha, M. Nethaji, A.R. Chakravarty, New J. Chem. 29 (2005) 596.
[66] B. Sreenivasulu, J.J. Vittal, Angew. Chem., Int. Ed. 43 (2004) 5769.
[67] M. Prabhakar, P.S. Zacharias, S.K. Das, Inorg. Chem. Commun. 9 (2006) 899.
[68] L. Infantes, S. Motherwell, Cryst. Eng. Commun. 4 (2002) 454.
[69] R. Ludwig, Angew. Chem., Int. Ed. 42 (2003) 258.
[70] S. Supriya, S.K. Das, J. Cluster. Sci. 14 (2003) 337.
[71] S. Neogi, P.K. Bharadwaj, Inorg. Chem. 44 (2005) 816.
[72] S. Pal, N.B. Sankaran, A. Samanta, Angew. Chem., Int. Ed. 42 (2003) 1741.
[73] L.E. Cheruzel, M.S. Pometun, M.R. Cecil, M.S. Mashuta, R.J. Wittebort, R.M. Buchanan, Angew. Chem., Int. Ed. 42 (2003) 5452.
[74] S. Manikumari, V. Shivaiah, S.K. Das, Inorg. Chem. 41 (2002) 6953.
[75] B. Sharma, A. Nangia, Cryst. Eng. Commun. 9 (2007) 628.
[76] B. Lou, F. Jiang, D. Yuan, B. Wu, M. Hong, Eur. J. Chem. 16 (2005) 3214.
[77] G.M. Sheldrick, SADABS 2.05, University of Göttingen, Göttingen, Germany.
[78] SHELXTL 6.10, Bruker Analytical Instrumentation, Madison, WI, 2000.
[79] Z.D. Tomic, V.M. Leovac, Z.K. Jacimovic, G. Giester, S.D. Zaric, Inorg. Chem. Commun. 9 (2006) 833.
[80] Z.D. Tomic, S.B. Novakovic, S.D. Zaric, Eur. J. Inorg. Chem. (2004) 2215.
[81] Z.D. Tomic, D. Sredojevic, S.D. Zaric, Cryst. Growth Des. 6 (2006) 29.
[82] J. Breu, H. Domel, A. Stoll, Eur. J. Inorg. Chem. 11 (2000) 2401.
[83] P.R. Reddy, P. Manjula, Verlag Helivitica Chimica Acta, AG. Zurich (Chemical and Biodiversity) 4 (2007) 468.
[84] R.R. Davies, H. Kuang, D. Qi, A. Mazhary, E. Mayaan, M.D. Distefano, Bioorg. Med. Chem. Lett. 9 (1999) 79.

Polyhedron 28 (2009) 253–256

Contents lists available at ScienceDirect

Polyhedron

journal homepage: www.elsevier.com/locate/poly

Hysteretic behavior of diamagnetic molecular assembly: Magnetic field-induced deformation of tubular self-assemblies composed of amphiphilic molecules

Kentaro Suzuki [a,b], Takuya Tomita [a], Taro Toyota [c], Masakazu Iwasaka [d], Tadashi Sugawara [a,b,*]

[a] Department of Basic Science, Graduate School of Arts and Sciences, The University of Tokyo, 3-8-1 Komaba, Meguro, Tokyo 153-8902, Japan
[b] Research Center for Life Sciences as Complex Systems, Graduate School of Arts and Sciences, The University of Tokyo, 3-8-1 Komaba, Meguro, Tokyo 153-8902, Japan
[c] Department of Applied Chemistry and Biotechnology, Graduate School of Engineering, Chiba University, 1-33 Yaoi, Inage, Chiba 263-8522, Japan
[d] Department of Medical System Engineering, Graduate School of Engineering, Chiba University, 1-33 Yaoi, Inage, Chiba 263-8522, Japan

ARTICLE INFO

Article history:
Received 31 October 2008
Accepted 14 November 2008
Available online 27 December 2008

Keywords:
Tubular giant vesicle
Magnetic field effect
Diamagnetic self-assembly
Elasticity
Real-time observation

ABSTRACT

Real-time observation of a morphologies of a multi-component tubular giant vesicle (tGV), which is a self-assembly composed of plural amphiphiles with different packing parameters, was carried out under application of a magnetic field. A tGV, one of the terminals of which was fixed to a bottom of a cell, exhibited the bending deformation under a magnetic field along the perpendicular direction of the long axis. Moreover, the hysteretic behavior in this deformation was observed associated with the increase and decrease of the magnetic fields repeatedly, regardless of the presence or absence of a paramagnetic species. To understand the hysteretic behavior, the molecular cooperative effect, which stabilizes the bending deformation by replacing of the plural kinds of amphiphiles with different packing parameters within a membrane, must be taken into consideration.

© 2008 Elsevier Ltd. All rights reserved.

1. Introduction

Researchers in the field of 'molecular magnetism' are usually interested in para-, ferro- or antiferromagnetic materials composed of organic radicals or transition metal ions [1,2], and they deduce the magnetic properties characteristic to the molecular magnetism from those materials. The contribution of a paramagnetic term of an organic radical with $S = 1/2$ dominates over others at cryogenic temperatures, but the situation becomes different at ambient temperature. The absolute value of a paramagnetic term arisen from a paramagnetic spin and that of a diamagnetic term from a whole molecule are comparable with each at ambient temperature [1]. Hence, one can not ignore the diamagnetic contribution to the entire magnetism of a paramagnetic radical. If the method of magnetic manipulation of diamagnetic materials is explored, it would be utilized in various fields, including medical sciences, because every material is invested with diamagnetism unexceptionally.

Recently, we have studied the non-linear dynamics of giant vesicles [3–6] constructed by amphiphiles through a self-assembling process in water [7]. Our interest, in particular, has been focused on magnetic field response of tubular giant vesicles (tGVs) [8,9] with an anisotropic structure, their lengths and diameters being 10–100 μm and several μm, respectively [10]. A merit of this anisotropic shape of diamagnetic tGV lies in the facile detection of morphological changes under a magnetic field. For instance, tGVs align parallel to the external magnetic field due to a torque exerted by a static magnetic field [11]. Since this magnetic response is merely caused by the magnetic orientation, the scope of its application is rather limited [11–16]. In contrast, the magnetic response of collagen containing tGVs, which we have recently studied [8], can not be explained by the simple magnetic orientation, but their characteristic curved structures exhibited under a magnetic field are recognized as 'elastica' on the basis of dynamical analysis [8]. To note that such curved structures emerge only when the elastic energy of tGV is balanced with the magnetic energy [17].

$$\frac{d^2}{ds^2}\Theta = -A\sin\Theta, \quad A = \frac{\pi r^2 B}{2\mu_B}\cdot\frac{|\Delta\chi|}{K} \tag{1}$$

Here s is a length from the origin, Θ is twice of the degree of inclination of the infinitesimal unit against the applied field, B, r is a radius of the specimen, K is a module of curvature-elasticity of the specimen and $\Delta\chi$ is an anisotropy of the effective diamagnetic susceptibility of the specimen.

In general, the effect of elasticity of tGV is much smaller than that of a magnetic field. This magnetic manipulation of tGV to curved structures is archived by the following trick. When collagen

* Corresponding author. Address: Department of Basic Science, Graduate School of Arts and Sciences, The University of Tokyo, 3-8-1 Komaba, Meguro, Tokyo 153-8902, Japan. Tel.: +81 5454 6742; fax: +81 5454 6997.
E-mail address: suga@pentacle.c.u-tokyo.ac.jp (T. Sugawara).

0277-5387/$ - see front matter © 2008 Elsevier Ltd. All rights reserved.
doi:10.1016/j.poly.2008.11.010

is introduced into tGV, the magnetic response of tGV is suppressed because the diamagnetic anisotropy of collagen fibrils competes with that of tGV and they align perpendicular to the magnetic field [14].

In this study, we carried out real-time observation of a bending deformation of multi-component tGV, one of the terminals of which is fixed on a surface of cover glass, under application of a magnetic field along the perpendicular direction of its long axis. We also notice that the bending deformation exhibits the hysteretic behavior, associated with increase and decrease of the magnetic fields. Incidentally, this non-linear dynamics occurs regardless of the presence or absence of a paramagnetic additive (a spin-probe). Notably, this hysteretic response can not be explained by regarding tGV as an uni-component elastic rod, but by the cooperative effect of plural components of amphiphiles.

2. Experimental

Chemicals were purchased from commercial sources and used without further purification. Oleyl nitronyl nitroxide (ONN) was synthesized from oleylaldehyde by the regular procedure [18]. Thin films, composed of 1,2-dioleoyl-*sn*-glycero-3-phosphocholine (DOPC; 0.5 μmol) and 1-palmitoyl-2-oleoyl-*sn*-glycero-3-[phospho-*rac*-(1-glycerol)] sodium salt (POPG; 0.5 μmol) or of DOPC:POPG:ONN = 5:5:1 (molar ratio) were formed on a glass surface at room temperature, respectively. The films were swelled by 1 mL of phosphate-buffered saline (PBS). The dispersion of tGV was prepared between a pair of glass covers and a spacer with approximately 300 μm thickness and 25 μL volumes (Frame Seal Chamber, MJ Research Inc., Waltham) (Fig. 1). The mount was placed on a 500× objective lens unit (VH-501, KEYENCE, Japan) of a digital microscope camera, and it was inserted in a center of the magnetic field of a perpendicular-type superconducting magnet with a bore radius of 12 cm ($B = \pm 5$ T, sweep time 1 T/min, Microstat BT, Oxford Instruments, Oxon, UK). The direction of the magnetic field was perpendicular to the glass surface of the mount. The morphological change of the specimen during application and removal of the magnetic fields was observed directly under a digital microscope set (VH-5000, KEYENCE, Japan) with a digital video recorder (DDR-TRV50, SONY, Japan).

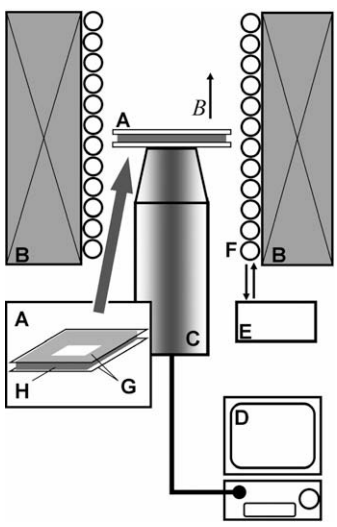


Fig. 1. Illustration of a real-time observation system. (A) a sample mount [volume: *ca.* 25 μL, thickness: *ca.* 300 μm, (G) cover glasses, (H) a spacer], (B) a superconducting magnet, (C) an objective lens of a digital microscope (×500), (D) a digital microscope control unit and a recording system, (E) a circular pump for isothermal water (20 °C), (F) a conduit tube of isothermal water.

3. Results and discussion

3.1. Real-time observation of deformation of a tubular vesicle

A buffered dispersion of tGV with or without ONN were prepared in a mount following a procedure described in the experimental section. As an object of real-time observations, we selected tGV a terminal of which was fixed on the bottom. Magnetic field was applied along the perpendicular direction to the long axis of tGV (Fig. 1).

A series of photo-images recording the deformation dynamics of tGV were shown in Fig. 2. As the magnetic field increased, the length of tGV was shortened and it was recovered to the original length associated with removal of the magnetic field. This shortening and the restoration dynamics of tGV occurred repeatedly more than 10 times. Reproducibility of the geometrical changes was confirmed in many batches, regardless of the presence or absence of a paramagnetic additive (ONN).

3.2. Hysteretic behavior of deformation of tubular vesicle

Magnetic field dependence of the virtual length of tGV was shown in Fig. 3. The length of tGV was kept constant until the magnetic field exceeded a certain threshold value (e.g. *ca.* 3 T), but thereafter it became shortened as the magnetic field increased, and the change was gradually saturated at higher magnetic fields than *ca.* 4.5 T. In the descending process of the magnetic field, the length of tGV remained the same until the magnetic field passed a critical value (e.g. *ca.* 2.5 T), and it started to increase and restored to the original length at null magnetic field, showing the hysteretic behavior: The threshold magnetic field in descending process is lower than that in rising process. This hysteretic behavior is reproducible in other butches, although the absolute value of the critical magnetic field showed sample-dependence.

3.3. Mode of deformation

If tGV is really shortened keeping its volume, the diameter of tGV has to be enlarged. However it is not the case. Hence the shortening of tGV in a microscopic image must come from the observational limitation, that is the depth of field (DOF) of a camera lens. When a magnetic field is applied, tGV deforms as a cantilever beam and the free terminal moves out of DOF of the lens. Such deformation makes the observed length of tGV shorter virtually. The virtual length, L, is determined by a, which is the distance between the center line of tGV at an ambient field ($B = 0$) and the maximum depth of on-focus area (Fig. 4). The maximum value of a is esti-

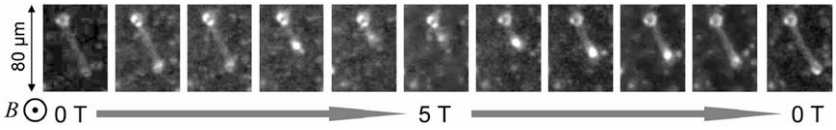


Fig. 2. Real-time observation of geometrically change of tGV composed of phospholipids and ONN association with the application and removal of a magnetic field (0 T → 5 T → 0 T).

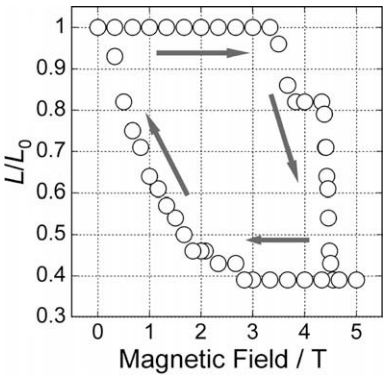


Fig. 3. Magnetic field dependence of virtual length of tGV containing phospholipids and ONN (see Fig. 2). Magnetic field was applied in a sequence of 0 T → 5 T → 0 T.

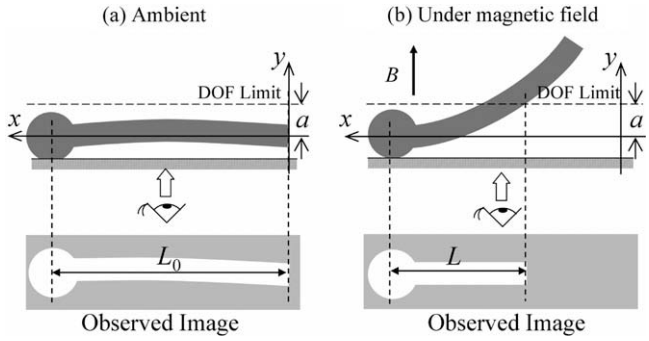


Fig. 4. tGV as a cantilever beam and its objective images.

mated to be 30 μm if the center of tGV is focused. Consequently, the absolute values of the critical magnetic fields are dispersed depending of the accuracy of the focusing positions of each sample, but relative values for the observed lengths of the same tGV is highly reproducible.

3.4. Mechanical analysis of deforming tGV

In order to analyze the virtual length of a tGV upon application or removal of a magnetic field, a mechanical analysis on bending tGV was carried out using a cantilever model. In general, deformation of a cantilever is approximated by the following formula (Eq. (2) and Fig. 4),

$$\frac{d^2}{dx^2}y(x) = -\frac{1}{EI}M(x) \tag{2}$$

where, $M(x)$ is a bending moment, E is a module of elasticity and I is a second moment of area (a product of E and I is defined as a rigidity of tGV). Since a magnetic field is applied uniformly on tGV, this system can be regarded as a uniformly distributed loading system. Hence the bending moment is defined by Eq. (3),

$$M(x) = -\frac{\rho}{2}x^2 \tag{3}$$

where, ρ is a constant, corresponding to an effective magnetic sensitivity. From Eqs. (2) and (3), the displacement y at coordinate x is expressed by Eq. (4), where L_0 is a whole length of tGV.

$$y(x) = \frac{\rho}{2EI}\left(\frac{x^4}{12} - \frac{L_0^3}{3}x + \frac{L_0^4}{4}\right) \tag{4}$$

Since the influence of a magnetic sensitivity, ρ, upon diamagnetism is proportional to the square of the magnetic field, the magnetic field dependence of the virtual length of tGV can be simulated numerically as shown in Fig. 5, considering DOF of a lens. The calculated curves reproduce the observed phenomenon that the virtual length of tGV changes abruptly at the critical magnetic field and it is gradually saturated at higher magnetic fields.

3.5. Origin of hysteretic behavior

According the above analysis, the bending deformation of tGV under a magnetic field can be interpreted in terms of a cantilever model, but the hysteretic behavior, which is another important characteristic of this dynamics, cannot be rationalized by this mechanical model. Then we examine this bending dynamics of tGV using a multi-component tGV model proposed by Stavans and co-workers [19]. When tGV is deformed as an elastic bar, the elastic energy rises. It means a straight tGV is most stable. However, if tGV is made of multi-components with different packing parameters [20], the energy-cost caused by bending can be relaxed by the displacement of individual amphiphiles as schematically depicted by Fig. 6.

Since the current experiments utilize multi-components vesicles made of DOPC:POPG or DOPC:POPG:ONN, optimization of the bending geometry is possible, although apparent shapes of DOPC and POPG do not differ much. In fact, the observed hysteretic behavior indicates that the bent tGV maintains its shape under a

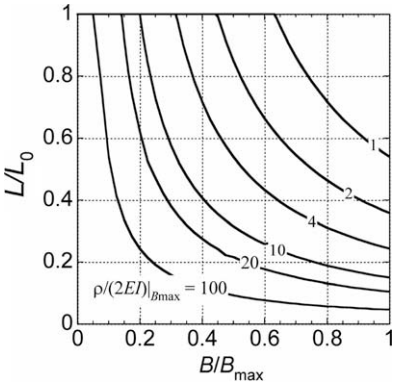


Fig. 5. Numerical-simulation of magnetic filed dependence of observed length of tGV. Parameters, $\rho/(2EI)|_{B=B_{max}} = 1 - 100$, $L_0 = 1$ and $y(x) = a = 0.1$ are used for the calculations.

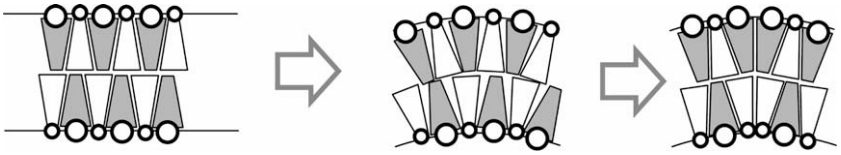


Fig. 6. Stabilization of a curved lipid-bilayer of bent tGV by relocation of membrane molecules with different packing parameters, provided that molecules move freely along the horizontal direction within a single membrane layer. Molecular migration of the vertical direction hardly happens, because the rate of a flip-flop motion is much slower than that of a horizontal diffusion.

lower magnetic field in the field-decreasing processes than that in the increasing processes. The fact that a helical tGV can be formed by egg-yolk lecithin [21], which is a mixture of phospholipids, is indicative of the validity of the multi-components tGV model. We have not examined unicomponent vesicles yet due to the difficulty in preparation of tGVs, there is a possibility to observe a similar behavior because various conformations are conceivable even for a single phospholipid.

In the current study, we have not detected any extra effect caused by the paramagnetic additive, e.g. ONN. This insensibility may be rationalized by the following reasons. (1) Since a spin of nitronyl nitroxide is of a Heisenberg type, the magnetic anisotropy is too small to show the anisotropic magnetic response [22], (2) the diamagnetic susceptibility of ONN (-2.7×10^{-3} emu/mol, estimated by Pascal additive rule) and the paramagnetic one (1.25×10^{-3} emu/mol at 300 K) are comparable with each other. Accordingly, the effect caused by paramagnetic spins is negligibly small, if any.

4. Conclusion

We revealed that tGV deformed toward the perpendicular direction to its long axis under the external magnetic field ($\sim$5 T) due to the diamagnetic anisotropy. Moreover, tGV made of DOPC and POPG exhibited hysteretic response in the bending deformation and its relaxation process with increasing and decreasing magnetic field. Appearance of this hysteretic behavior is derived from the collaborative dynamics of two kinds of membrane molecules (DOPC and POPG) with different packing parameters. If a self-assembly of membrane molecules in which a membrane-affinitive transition metal complex of a large quantum number is buried, the self-assembly, e.g. tubular vesicles, or fibrils, may exhibit more drastic response towards an external magnetic field.

Acknowledgment

This work was partly supported by KAKENHI (Grant-in-Aid for Scientific Research) on Priority Area "Soft Matter Physics" (Area No. 463).

References

[1] O. Karn (Ed.), Molecular Magnetism, VCH Publication Inc., New York, 1993.
[2] K. Ito, M. Kinoshita (Eds.), Molecular Magnetism – New Magnetic Materials, Gordon and Breach Science Publishers, Netherlands, 2000.
[3] K. Takakura, T. Toyota, K. Yamada, M. Ishimaru, K. Yasuda, T. Sugawara, Chem. Lett. (2002) 404.
[4] K. Takakura, T. Totota, T. Sugawara, J. Am. Chem. Soc. 125 (2003) 8134.
[5] K. Takakura, T. Sugawara, Langmuir 20 (2004) 3832.
[6] T. Toyota, H. Tsuha, K. Yamada, K. Takakura, K. Yasuda, T. Sugawara, Langmuir 22 (2006) 1976.
[7] P.L. Luisi, P. Walde, Giant Vesicles, Wiley, New York, 2000.
[8] K. Suzuki, T. Toyota, K. Sato, M. Iwasaka, S. Ueno, T. Sugawara, Chem. Phys. Lett. 440 (2007) 286.
[9] M. Iwasaka, K. Suzuki, T. Sugawara, Sci. Technol. Adv. Mater. 9 (2008) 024216.
[10] I. Sakurai, T. Suzuki, S. Sakurai, Biochim. Biophys. Acta 985 (1989) 101.
[11] I. Sakurai, Y. Kawamura, Biochim. Biophys. Acta 735 (1981) 189.
[12] J. Torbet, J.-M. Freyssinet, G. Hudry-Clergeon, Nature 289 (1981) 91.
[13] J.-M. Freyssinet, J. Torbet, G. Hudry-Clergeon, G. Maret, Proc. Natl. Acad. Sci. USA 80 (1983) 1616.
[14] J. Torbet, M.-C. Ronzière, Biochem. J. 219 (1984) 1057.
[15] A. Yamagishi, T. Takeuchi, T. Higashi, M. Date, Physica B 177 (1992) 523.
[16] W. Bras, G.P. Diakun, J.F. Díaz, G. Maret, H. Kramer, J. Bordas, F.J. Medrano, Biophys. J. 74 (1998) 1509.
[17] C. Truesdell, Bull. Am. Math. Soc. 9 (1983) 293.
[18] E.F. Ullman, J.H. Osiecki, D.G.B. Boocock, R. Darcy, J. Am. Chem. Soc. 94 (1972) 7049.
[19] I. Tsafrir, M.-A. Guedeau-Boudeville, D. Kandel, J. Stavans, Phys. Rev. E 63 (2001) 031603.
[20] J. Israelachvili, D.J. Mitchell, B.W.J. Ninham, J. Chem. Soc., Faraday Trans. 2 72 (1976) 1525.
[21] I. Sakurai, T. Suzuki, S. Sakurai, Biochim. Biophis. Acta 985 (1989) 101.
[22] M. Fujiwara, M. Tamura, M. Hara, K. Suzuki, K. Mukai, J. Phys. Chem. B 111 (2007) 9492.

Polyhedron 28 (2009) 257–262

Contents lists available at ScienceDirect

Polyhedron

journal homepage: www.elsevier.com/locate/poly

Selective metal sensor phthalocyanines bearing non-peripheral functionalities: Synthesis, spectroscopy, electrochemistry and spectroelectrochemistry

Mehmet Kandaz [a,*], Meryem N. Yarasir [a], Atıf Koca [b]

[a] Sakarya University, Department of Chemistry, 54140 Esentepe, Sakarya, Turkey
[b] Marmara University, Department of Chemical Engineering, Faculty of Engineering, 34722 Göztepe, Istanbul, Turkey

ARTICLE INFO

Article history:
Received 12 September 2008
Accepted 11 November 2008
Available online 6 January 2009

Keywords:
Phthalocyanines
Metal sensor
Aggregation
Electrochemistry
Spectroelectrochemistry

ABSTRACT

A novel alcohol-soluble ionophore ligand and its non-peripherally tetrasubstituted functional 1,8,15,22-tetrakis(6-hydroxyhexylsulfanyl) metallophthalocyanines M[Pc(α-$SC_6H_{12}OH)_4$] (M = Cu(II), Zn(II), Co(II); Pc = phthalocyanine) are reported. The aggregation and cation binding behaviors of the phthalocyanine compounds in the presence of soft Ag^{I} and Pd^{II} metal ions were investigated by using UV–Vis spectroscopy. The new compounds have been characterized by elemental analysis, IR, ^{1}H, ^{13}C NMR, UV/Vis spectroscopy, ESI and MALDI–TOF–MS mass spectra. Voltammetric and in-situ spectroelectrochemical studies show that while copper and zinc phthalocyanine complexes give well-defined ring-based reduction and oxidation processes, the cobalt phthalocyanine gives both metal-based and ring-based redox processes which have reversible and diffusion controlled character.

© 2008 Elsevier Ltd. All rights reserved.

1. Introduction

The benefit of phthalocyanines (Pcs) in terms of technological applications is beyond question [1,2]. The family of functional phthalocyanines has been an interesting target for chemists for the development of further chemical reactions on Pc complexes [3,4]. Functional Pcs perturbs the Pcs optical transitions by shifting the absorption from the visible to near-IR or UV-region. Phthalocyanines bearing thia functionalities show optical changes when they bind transition metal ions, while crown-ether substituted ones are well-suited to bind alkaline and alkaline-earth metal ions [5,6]. Although several Pcs bearing different substituents either on the β position or at an axial position have been synthesized and characterized [5,7], papers on the synthesis, electrochemistry and spectroelectrochemistry of non-peripherally functional phthalocyanines are scarce because of the preparation and purification required [8].

In the past few years we have directed our attention to the construction of phthalocyanine-based functional systems [3,9,10]. The introduction of functional groups having rich electron-donor units on the phthalocyanine ring is not only expected to improve its solubility but also to enhance optical or electrochemical properties of the phthalocyanine.

In this study, we therefore report a new ligand and its non-peripherally α-substituted MPcs, M[Pc(α-$SC_6H_{12}OH)_4$] {M = Cu(II) (**2**), Zn(II) (**3**), Co(II) (**4**)}. The cation binding capabilities of the functional substituents on the periphery of MPcs (**2**)–(**4**) as well as voltammetric and in-situ spectroelectrochemical characterization are also reported.

2. Experimental

Chloroform ($CHCl_3$), 4-nitrophthalonitrile, tetrahydrofuran (THF), tetrabutyl ammoniumperchlorate (TBAP), $Zn(OAc)_2$, $CuCl_2$, $CoCl_2$ and all other reagents were purchased from Alfa Aesar and were used as received. The purity of the products was tested in each step by TLC (thin-layer chromatography) (SiO_2, $CHCl_3$, hexane and MeOH). FT-IR (Fourier transform infrared) spectra were recorded on a Perkin–Elmer spectrophotometer with samples were dispersed in KBr discs. Chromatography was performed with silica gel (Merck grade 60 and sephadex) from Aldrich. Elemental analysis (C, H and N) was performed at the instrumental Analysis Laboratory of Marmara University. Time- and applied-resolved UV–Vis spectra were recorded on an Agilent Model 8453 diode array spectrophotometer. ^{1}H NMR, and ^{13}C NMR spectra were recorded on a Bruker 300 spectrometer instrument. The cyclic voltammetry (CV) and differential pulse voltammetry (DPV) measurements were carried out with a Gamry Reference 600 potentiostat/galvanostat controlled by an external PC and utilizing a three-electrode configuration at 25 °C. The working electrode was a Pt disc with a surface area of 0.071 cm^2. The surface of the working electrode was polished with a diamond suspension before each run. A Pt wire served as the counter electrode. A saturated calomel electrode (SCE) was employed as the reference electrode and this was separated from the bulk of the solution by a double bridge. Ferrocene was used as an internal reference. Electrochemical grade

* Corresponding author. Tel.: +90 2642955946; fax: +90 2642955950.
E-mail address: mkandaz@sakarya.edu.tr (M. Kandaz).

0277-5387/$ - see front matter © 2008 Elsevier Ltd. All rights reserved.
doi:10.1016/j.poly.2008.11.035

tetrabutylammonium perchlorate (TBAP) in extra pure dimethylsulfoxide (DMSO) was employed as the supporting electrolyte at a concentration of 0.10 mol dm^{-3}. High purity N_2 was used to remove dissolved O_2 prior to each run and to maintain a nitrogen blanket during the measurements. IR compensation was also applied to the CV scans to minimize the potential control error.

The spectroelectrochemical measurements were carried out with an Ocean-optics QE65000 diode array spectrophotometer equipped with a potentiostat/galvanostat utilizing the three-electrode configuration of a thin-layer quartz spectroelectrochemical cell at 25 °C. The working electrode was Pt tulle. A Pt wire counter electrode separated by a glass bridge and a SCE reference electrode separated from the bulk of the solution by a double bridge were used.

Matrix-assisted laser desorption/ionization-time-of-flight (MALDI–TOF) mass spectra were measured using a Bruker Autoflex III mass spectrometer equipped with a nitrogen UV-Laser operating at 337 nm. Spectra were recorded in the reflectron mode with an average of 50 shots. An α-cyano 4-hydroxycinnamicacid (CHCA) (20 mg/mL in THF) matrix was used. MALDI samples were prepared by mixing the complex (2 mg/mL in THF) with the matrix solution (1:10 v/v) in a 0.5 mL eppendorf® micro tube. Finally, 1 μL of the mixture was deposited on the sample plate, dried and then analyzed.

2.1. Synthesis

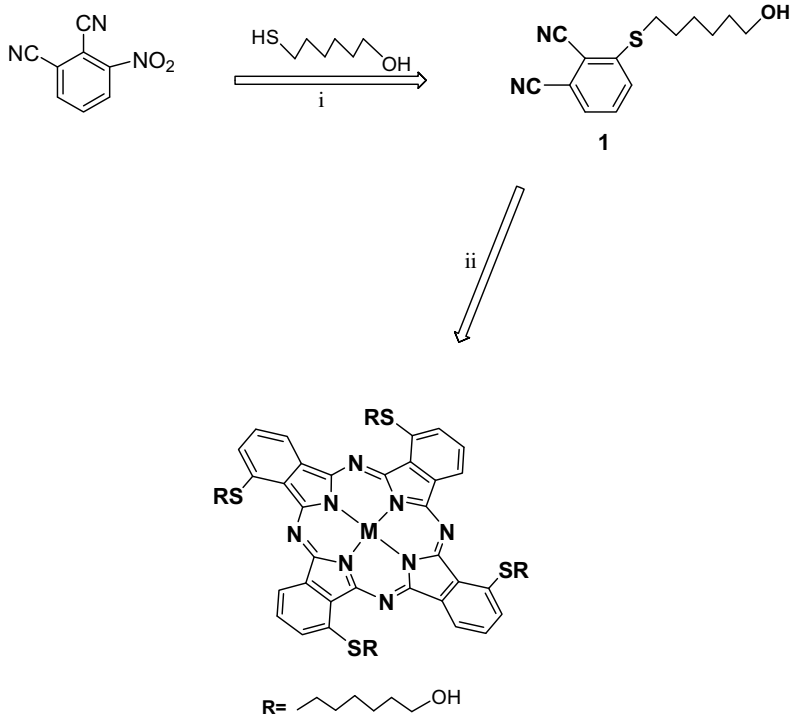
2.1.1. 3′(6-hydroxyhexylthio)-1,2-dicyanobenzene (*1*)

6-Mercapto–1-hexanol (1.55 g, 12.00 mmol, excess) was dissolved in dry DMF and finely ground anhydrous K_2CO_3 (~2.40 g, 17.00 mmol) was added. Then 3-nitrophthalonitrile (2.00 g of 11.56 mmol) was added to this mixture dropwise at 35–40 °C under a N_2 atmosphere. The reaction mixture was stirred efficiently and monitored by TLC ($CHCl_3$) under an inert atmosphere at 40–45 °C for 2 days. After the reaction mixture was cooled to room temperature, it was poured into ca. 300 cm^3 ice-water. The creamy precipitate that formed was filtered and washed with water until the washings became neutral. The crude product was dissolved in $CHCl_3$ and washed with 5% $NaHCO_3$ to remove the unreacted starting thiol compounds. The creamy solution was then dried with anhydrous Na_2SO_4, and filtered. The solvent, $CHCl_3$, was removed under reduced pressure. The final product was chromatographed over a silica gel column using a mixture of $CHCl_3$: MeOH (100/5) as eluent, giving a hydroscopic oily solid. Finally the pure powder was dried in vacuum.

Yield: 0.93 g (61.89 %). M.p.: 77 °C. IR (thin film) /cm^{-1}: 2236 (–CN), 3280 (CH_2–OH), 3080, 3045 (Ar–H), 2933, 2885, 2854 (Aliph-CH_2) 1707 (H–O···H, weak), 1585 (s), 1555, 1476, 1384, 1277, 1145, 1067, 980, 852, 735, 570. ^{1}H NMR ([D6]-DMSO) δ (ppm): 7.85–7.62 (m, 3H, Ar–H, Phenyl Ar–H H3, H4 and H5), 4.19 (t, br, –CH_2–OH, D_2O exchangeable), 3.55 (t, 2H, –CH_2OH), 2.85 (CH_2–CH_2–S–), 1.65 (m, 2H, CH_2–S–Ar), 1.50 (m, 2H, $CH_2CH_2CH_2$–OH), 1.37 (m, 2x$CH_2CH_2CH_2$). ^{13}C NMR (ATP test) (300 MHz, [D6]-DMSO) δ (ppm): 143.23, 135.45, 132.76, 130.09, 116.12, 115.16, 116.95, 116.82, 62.76 (–CH_2 OH), 40.42 (DMSO), 37.16 (S-CH_2), 33.40 (CH_2CH_2OH), 29.12 (SCH_2CH_2), 28.80 ($SCH_2CH_2CH_2$), 25.26 ($CH_2CH_2CH_2CH_2$OH). *Anal.* Calc. for $C_{14}H_{16}N_2OS$ (%): C, 64.62; H, 6.15; N, 10.77. Found (%): C, 64.04; H, 6.05; N, 10.28%. MS (MALDI–TOF): *m*/*z*: 262.3 $[M]^+$, 283.1 $[M+Na]^+$.

2.1.2. 1(4),8(11),15(18),22(25)-(6-Hydroxyhexylthio)-zinc(II)phthalocyanine (*2*)

3′-(6-hydroxyhexylthio)-1,2-dicyanobenzene (**1**) (0.25 g, 0.96 mmol) and anhydrous $ZnCl_2$ (0.022 g), in the presence of quinoline and 1,8-diazabicyclo [5.4.0.] undec–7-ene (DBU, 0.05 ml) as a strong base (Scheme 1), were heated to reflux in a sealed tube



Scheme 1. Synthetic route of the 1,8,15,22-tetrakis{6-hydroxyhexylsulfanyl) metallophthalocyanines M[Pc(α-$SC_6H_{12}OH)_4$] {M = Zn(II) (**2**), Cu(II) (**3**), Co(II) (**4**)}. (i) K_2CO_3, 6-mercapto-1-hexanol, DMF, 40–45 °C, 2 days. (ii) Anhydrous, $Zn(O_2CMe)_2$, $CuCl_2$, $CoCl_2$, DBU.

under a N_2 atmosphere for 6 h. The color of the mixture turned green-blue over this time. After heating for an additional 3 h, the green–blue product was cooled to room temperature. The crude product formed was washed several times, successively with i-PrOH and then cold CH_3CN, to remove impurities. Finally, the product was further purified by silica gel chromatography {$CHCl_3$ and then with $CHCl_3$/MeOH (20:1 v/v)}. After washing the resulting oily product with copious amounts of hexane, diethylether and *i*-PrOH, finally it was dried in vacuum. This product is soluble in MeOH, THF, DMF, DMSO, pyridine and insoluble in diethylether.

Yield of **2**: 0.087 g (32.80%). Anal. Calc. for $C_{56}H_{64}N_8O_4S_4Zn$ (1105.0 g/mol): C, 60.81; H, 5.79; N, 10.14. Found: C, 60.28; H, 5.80%; N, 9.77. IR (KBr) ν/cm^{-1}: 3284 (br, H-bonded), 2926, 2853, 1726 (H–O···H, weak), 1611 (w), 1598, 1484, 1430, 1366, 1223, 1215, 1138, 1066, 1032, 912, 825, 757, 735. ^{1}H NMR ([D6]-DMSO) δ (ppm): 7.88–7.60 (m, 12H, Ar-H, Phenyl Ar-H H3, H4 and H5), 4.21 (t, broad, 4H, –CH_2–OH, D_2O exchangeable), 3.55 (t, 8H, –*CH_2*OH), 2.95 (8H, CH_2–*CH_2*–S–), 1.65 (m, 8H, –*CH_2*CH_2–S–Ar), 1.50 (m, 8H, CH_2*CH_2*CH_2–OH), 1.37 (m, 2x*CH_2*CH_2*CH_2*OH). UV/Vis (THF, λ_{max}/nm: 709 (π–π^*), 668 (agg), 656 (n-π^*), 335 (deeper, π–π^*). MS (MALDI–TOF, α-cyano 4-hydroxycinnamicacid (CHCA) as matrix): *m*/*z* (100 %): 1105 [M+H]$^+$.

2.1.3. 1(4),8(11),15(18),22(25)-(6-Hydroxyhexylthio)-copper(II)phthalocyanine (*3*)

The same procedure as described for the preparation of **2**, starting from **1** (0.150 g, 0.576 mmol) and $CuCl_2$ (0.021 g, 0.170 mmol), was used to prepare compound **3**.

Yield of **3**: 0.06 g (24.16%). Anal. Calc. for $C_{56}H_{64}N_8O_4S_4Cu$ (1103.5 g/mol): C, 60.90; H, 5.80; N, 10.15. Found: C, 60.69; H, 5.77; N, 9.58%. IR (thin film) ν/cm^{-1}: 3250 (H-bonded, OH), 3015, 2975, 2952, 2854, 1727 (H–O···H, weak), 1655 (w), 1598, 1432 (w), 1366 (s), 1360, 1313, 1224, 1218, 1137, 1118, 1034, 910, 887, 873, 811, 742, 687. UV/Vis (THF, λ_{max}/nm: 710 (π–π^*), 662 (agg), 647 (n–π^*), 441 (CT), 333 (deeper, π–π^*). MS (MALDI–TOF, CHCA as matrix): *m*/*z* (100%): 1104 [M+H]$^+$.

2.1.4. 1(4),8(11),15(18),22(25)-(6-Hydroxyhexylthio)-cobalt(II)phthalocyanine (*4*)

The same procedure as described for the preparation of **2**, starting from **1** (0.150 g, 0.576 mmol) and $CoCl_2$ (0.021 g, 0.170 mmol), was used to prepare compound **4**.

Yield of **4**: 0.07 g (27.30%). Anal. Calc. for $C_{56}H_{64}N_8O_4S_4Co$ (1099 g/mol): C, 61.15; H, 5.82; N, 10.19. Found: C, 60.56; H, 5.56; N, 9.59%. IR (KBr thin film) ν/cm^{-1}: 3243 (H-bonded, OH), 3026, 2973, 2928, 2847, 1722 (H–O···H, weak), 1600 (w), 1520, 1431 (w), 1360 (s), 1318, 1233, 1210, 1103, 1044, 933, 873, 781, 750, 694. UV/Vis (THF, λ_{max}/nm: 695 (π–π^*), 654 (agg), 629 (w, n-π^*), 327 (deeper, π–π^*). MS (MALDI–TOF, CHCA as matrix): *m*/*z* (100%):1100 [M+H]$^+$.

3. Results and discussion

3.1. Synthesis and characterization

The introduction of 6-mercapto-1-hexanol groups, having rich electron-donor units, on the Pc ring is not only expected to improve the solubility of phthalocyanines in polar medium such as MeOH, EtOH, THF, DMF, DMSO and *i*-PrOH, but also to enhance the optical or electrochemical properties of the phthalocyanine. In the present work, 3'-(6-hydroxyhexylthio)-1,2-dicyanobenzene (**1**) can be readily synthesized by nucleophilic aromatic substitution reactions of 6-mercapto-1-hexanol on 3-nitrophthalonitrile [11]. MPc complexes (**2**–**4**) were obtained from the reaction of **1** with the appropriate anhydrous metal salts in the presence of quinoline and DBU as a strong base (Scheme 1), followed by chromatographic purification on silica gel columns. The purification steps were tedious because of the peripheral polar functional end-group. The new compounds were characterized by UV–Vis, IR, NMR spectroscopies, MALDI–TOF mass spectra and elemental analysis. All the analytical and spectral data are consistent with the predicted structures.

The sharp peak in the IR spectra for the –C≡N vibrations of **1** at 2230 cm^{-1} disappeared after conversion into the MPcs, indicative of the MPcs formation. A primary aliphatic –OH peak at around 3280 cm^{-1} and the remainder of the spectra for **2**–**4** are closely similar and diagnosed easily. Broad signals in the NMR spectrum of **2** are probably due to chemical exchange associated with aggregation–disaggregation equilibria which occurred at the high concentrations used in the NMR measurements. A broad signal belonging to primary aliphatic exchangeable –OH protons appeared at ca. 4.21 ppm, and this disappeared after addition of D_2O. Splitting of the aromatic protons in the downfield region is less for α-substituted compounds when compared to β-substituted ones [12–15].

The UV/Vis spectra of the MPcs **2**–**4** exhibited characteristic absorptions in the Q-band region at around 695–710 nm, attributed to the π–π^* transition from the HOMO (highest occupied molecular orbital) to the LUMO (lowest unoccupied molecular orbital) of the Pc^{2-} ring, and in the B band region (UV region) at around 300–400 nm, arising from deeper π–π^* transitions [14]. In the UV/Vis absorption spectra of MPcs **2**–**4**, the Q-band absorptions were observed as a single band with high intensity at 709, 710 and 695 nm respectively. There was also a shoulder at the slightly higher energy side of the Q-band at 668, 662 and 654 nm for each phthalocyanine respectively. The Q-band absorptions are shifted to the lower energy side as a result of the electron-donating thioether substituents on periphery of the Pcs compared to those of MPcs bearing oxo substituted moieties, whereas the position of the Soret-like π–π^* bands of all the MPcs are slightly shifted [5,6,9,14,15]. The Q-band of the α (non-peripheral) substituted Pcs is red-shifted by about 20 nm, when compared to the corresponding β (peripheral)-substituted complexes in the same solvent [9,11–13,14]. The observed red spectral shift is typical of Pcs bearing substituents at the α positions and has been explained by the linear combinations of the atomic orbital (LCAO) coefficients at

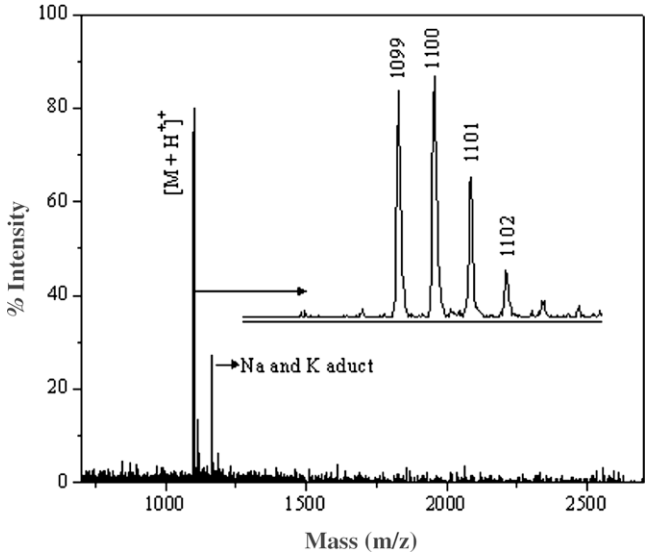


Fig. 1. Positive ion and reflectron mode MALDI–MS spectrum of **4** obtained in α-cyano-4-hydroxycinnamic acid (CHCA) as the MALDI matrix. Inset spectrum shows the expanded molecular mass region of **4**.

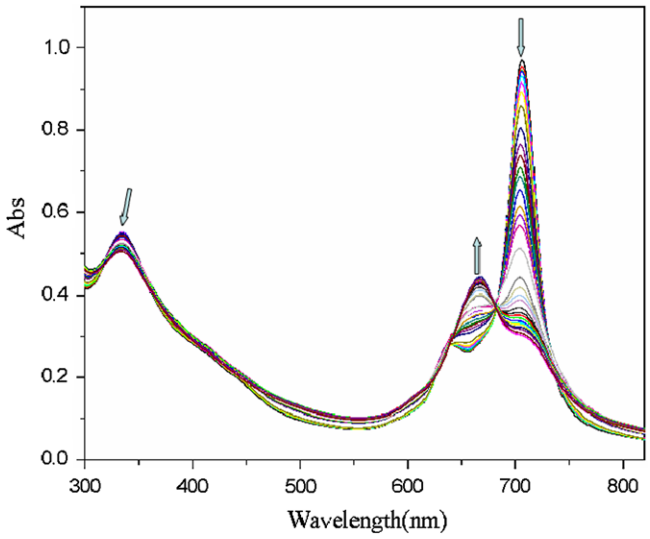


Fig. 2. UV–Vis spectra of **3** in THF/MeOH (90/10 (v/v)) during titration with Ag^{I} (in MeOH).

the α positions for the HOMO [12,13]. As a result, the HOMO level is destabilized more for an α position than a β position. Moreover, the B bands of the complexes in the UV/Vis absorption spectra are broad due to the superimposition of the B1 and B2 bands in the 325–340 nm regions.

The mass spectra of **2**–**4** confirmed the proposed structures. The protonated molecular ion peaks (MALDI matrix; α-cyano-4-hydroxycinnamic acid (CHCA)) were easily identified at *m*/*z*: 1104.20 $[M+H]^+$ for **2**, 1105.78 $[M+H]^+$ for **3** and 1100.30 $[M+H]^+$ for **4** (Fig. 1) and they exactly overlapped with the mass of the complexes calculated theoretically from their elemental compositions [9].

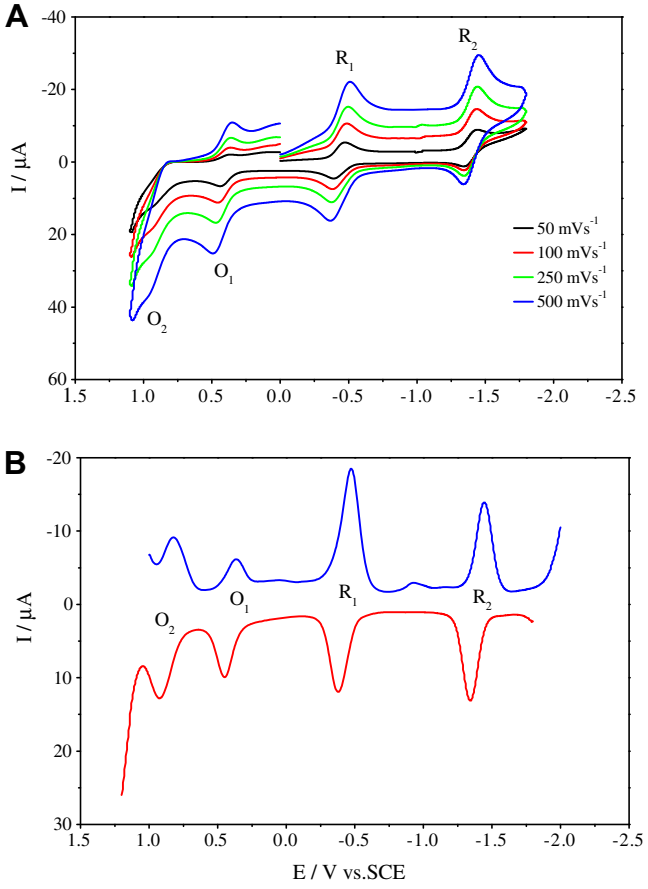


Fig. 3. CVs (A) and DPVs (B) of **4** (5.00×10^{-4} mol dm^{-3}) at various scan rates on Pt working electrode in DMSO/TBAP electrolyte system. DPV parameters: pulse time 50 ms, pulse size 100 mV, step size 5 mV, sample period 100 ms.

Table 1
Voltammetric data of the complexes **2**–**4** with the related metallophthalo cyanines for comparison.

Complex		Ring oxidations		M^{II}/M^{III}	M^{II}/M^{I}	Ring reductions				$^{d}\Delta E_{1/2}$	Ref.
2	$^{a}E_{1/2}$		0.56			−0.91	−1.36			1.47	
	$^{b}\Delta E_p$ (mV)		85			75	80				tw
	$^{c}I_{pa}/I_{pc}$		0.89			0.91	0.88				
3	$^{a}E_{1/2}$	0.34	0.28			−0.96	−1.17			1.24	
	$^{b}\Delta E_p$ (mV)	–	88			80	85				tw
	$^{c}I_{pa}/I_{pc}$	–	0.55			0.85	0.82				
4	$^{a}E_{1/2}$		0.90[e]	0.40	−0.43	−1.39				0.83	
	$^{b}\Delta E_p$ (mV)		71	81	67	93					tw
	$^{c}I_{pa}/I_{pc}$		–	0.75	1.00	0.97					
[g]CoPc	$^{f}E_{1/2}$ (in DMSO)			0.46	−0.36	−1.27				0.82	9
[h]CoPc	$^{f}E_{1/2}$ (in DMSO)		0.99	0.49	−0.36	−1.27		−1.83[e]		0.85	17
[i]ZnPc	$^{f}E_{1/2}$ (in DMSO)		0.77			−0.71		−1.10	−1.43	1.48	[19]
[i]CuPc	$^{f}E_{1/2}$ (in DCM)		0.56			−0.91	−1.27			1.47	[19]
[j]ZnPc	$^{f}E_{1/2}$ (in DCM)		0.85			−0.75		−1.16		1.60	20
[j]CoPc	$^{f}E_{1/2}$ (in DCM)			0.45	−0.42	−1.30				0.87	20

Tw – This work.
[a] $E_{1/2} = (E_{pa} + E_{pc})/2$ at 0.100 Vs^{-1} scan rate.
[b] $\Delta E_p = E_{pa} + E_{pc}$ at 0.100 Vs^{-1} scan rate.
[c] I_{pa}/I_{pc} for reduction, I_{pc}/I_{pa} for oxidation processes at 0.100 Vs^{-1} scan rate.
[d] $\Delta E_{1/2} = E_{1/2}$ (first oxidation) – $E_{1/2}$ (first reduction) = HOMO–LUMO gap for metallophthalocyanines having an electro-inactive metal center (metal to ligand (MLCT) or ligand to metal (LMCT) charge transfer transition gap for MPc having a redox active metal center).
[e] The process is recorded with DPV.
[f] Potentials were given versus SCE.
[g] Substituted with tetrakis(6-hydroxyhexylsulfanyl) moieties.
[h] Substituted with tetrakis-6-(-thiophene-2-carboxylate)-hexylthio moieties.
[i] Substituted with tetra-tricarboethoxyethyl moieties.
[j] Substituted with tetrapentafluorobenzyloxy moieties.

3.2. UV/Vis spectroscopic titrations

We have employed UV/Vis spectroscopic titrations to monitor the capability of our MPcs in sensing/coordinating transition metal ions of different sizes. The room temperature gradual addition (μl) of Ag^{I} and Pd^{II} to solutions of **2** and **3** caused a gradual color change, from blue–green to intractable dark-green, suggesting complex formation of the Mpcs with Ag^{I} and Pd^{II}. Addition of small increments of Ag^{I} to **3** (Fig. 2) leads to the gradual disappearance of monomeric species, which show absorptions at 710 and 708 nm, and simultaneously enhances the intensity of the oligomeric aggregated species at around 662 and 668 nm. Similar spectroscopic changes were observed during the titration of **3** with Pd^{II}, and **2** with Ag^{I} and Pd^{II}. This type of spectroscopic behavior probably results from the complexation of Ag^{I} and Pd^{II} with the Pc complexes. These spectroscopic changes indicate the coordination of Ag^{I} and Pd^{II} with the S donor atoms of the phthalocyanines and the formation of polymer units due to the aggregation of the complexes [2,6,9].

3.3. Electrochemical and spectroelectrochemical measurements

The solution redox properties of the complexes **2–4** were studied using cyclic voltammetry (CV) and differential pulse voltammetry (DPV) in DMSO on a platinum electrode. Table 1 lists the assignments of the redox couples recorded and the estimated electrochemical parameters, which included the half-wave peak potentials ($E_{1/2}$), the ratio of anodic to cathodic peak currents ($I_{p,a}/I_{p,c}$), the peak to peak potential separations (ΔE_p) and the difference between the first oxidation and first reduction processes ($\Delta E_{1/2}$).

When we compare the redox potentials of **2–4** with those of the unsubstituted MPcs [16], MPcs carrying tetrakis-(6-hydroxyhexylsulfanyl) [9] and tetrakis-6-(-thiophene-2-carboxylate)-hexylthio moieties [17], it is clearly shown that the redox potentials of **2–4** shift to negative potentials due to the electron releasing effect of the tetrakis-(6-hydroxyhexylsulfanyl) substituents on the α position of the complexes (Table 1). Within the electrochemical window of TBAP/DMSO, **2** and **3** undergo a one-electron oxidation (two oxidations for **3**) and two one-electron reduction reactions having reversible and diffusion controlled mass transfer processes. Because of the electro-inactive metal center of the complexes, all of these processes are attributed to successive removal of electrons from, or addition of electrons to, the macrocycle orbitals. Fig. 3 shows the CV and DPV of CoPc (**4**) as a representative example of the redox behaviors of the complexes. Within the electrochemical window of TBAP/DMSO, **4** undergo two reversible one-electron oxidation processes and two reversible one-electron reduction processes. The first reduction and first oxidation processes of **4**, recorded at −0.43 and 0.40 V, could be easily assigned to the Co^{II}/Co^{I} and Co^{II}/Co^{III} redox couples respectively and the remaining processes to the phthalocyanine ring. Assignments of the redox couple are confirmed by the spectroelectrochemical measurements given below. For the couples, the ΔE_p values changed from 60 to 120 mV with scan rates from 10 to 500 mVs^{-1} ($\Delta E_{p'}$, 60 to 110 mV, were obtained for the ferrocene reference), supporting reversible electron transfer. Reversibility is illustrated by the similarity in the forward and reverse DPV scans (Fig. 3B) [18]. Unity of the $I_{p,a}/I_{p,c}$ ratio at all scan rates indicated the purely diffusion controlled mass transfer of the complex.

Spectroelectrochemical studies were employed to confirm the assignments in the CVs of the complexes. The complexes **2** and **3** have redox inactive metal centers. Therefore, in-situ UV–Vis spectral changes of **4** are only given as a representative example of the spectral changes of a MPc having a redox active metal center (Fig. 4). Fig. 4A shows the in-situ UV–Vis spectral changes during

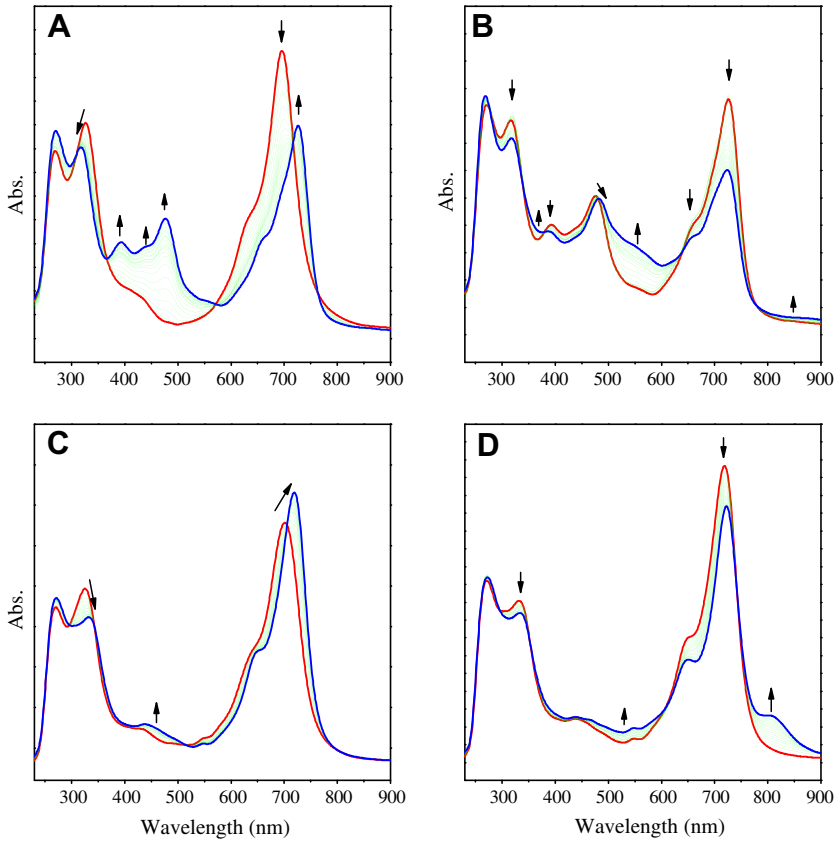


Fig. 4. In-situ UV–Vis spectral changes of **4** (A) E_{app} = −0.50 V. (B) E_{app} = −1.45 V. (C) E_{app} = 0.45 V. (D) E_{app} = 1.00 V.

the controlled potential reduction of **4** at −0.50 V, corresponding to the redox process labelled R_1. The Q-band at 695 nm shifts to 725 nm, while two new bands at 390 and 477 nm appear, as the reduction process continues. At the same time, the B band shifts from 327 to 317 nm with decreasing intensity. The bands at 390 and 477 nm and the red shifting of the Q-band indicate the formation of the $[Co^{I}Pc^{-2}]^{1-}$ species and confirm the CV assignment of the couple R_1 to the $[Co^{II}Pc^{-2}]/[Co^{I}Pc^{-2}]^{1-}$ process [20–25]. Clear isosbestic points at 311, 365, 571, 715 and 764 nm in the spectra and a color change from blue to greenish yellow were observed during this process. Fig. 4B shows the spectral changes during the second reduction process of **4**. During this process, while the Q-band at 725 nm, the band at 390 nm and the B band at 317 nm decrease in intensity, a new band at around 557 nm appears. Clear isosbestic points at 341, 381, 484, 640 and 780 nm in the spectra and a color change from greenish yellow to red were observed during this process. These spectral changes are characteristic of a ring reduction process and are easily assigned to the reduction of the $[Co^{I}Pc^{-2}]^{1-}$ species to $[Co^{I}Pc^{-3}]^{2-}$ at the potential of the couple R_2. Fig. 4C shows the spectral changes observed when the potential corresponding to the process O_1 was applied to the solution of $[Co^{II}Pc^{-2}]$. The Q-band at 695 nm increases in intensity with a red shift to 720 nm, while a new band at 450 nm appears as the oxidation process continues. The intensity of the B band decreases with a red shift from 325 nm to 335 nm. These spectral changes occur with clear isosbestic points at 297, 342, 516 and 706 nm in the spectra. A color change from blue to dark blue was also observed during the process. The band at 443 nm and the increase of the Q-band with a red shift are typical of a metal-based oxidation in cobalt Pc complexes. The final spectrum in Fig. 4C is therefore assigned to the $[Co^{II}Pc^{-2}]/[Co^{III}Pc^{-2}]^{+}$ process, confirming the CV assignments. Fig. 4D shows the further oxidation of the $[Co^{III}Pc^{-2}]^{+}$ species. During this process, the Q-band decreases in intensity without shift and a new band at 809 nm is recorded. The MLCT region between 500 and 600 nm increases slightly in intensity. These spectral changes shows the ring oxidation process and are therefore assigned to the $[Co^{III}Pc^{-2}]^{+}/[Co^{III}Pc^{-1}]^{2+}$ process [20–25].

4. Conclusion

Non-peripheral 6-hydroxyhexylthio substituents of metal (II) phthalocyanines, (M[Pc(α-$SC_6H_{12}OH)_4$](M = Cu(II), Zn(II), Co(II))), exhibited interesting solubility and metal sensing properties. It is important to mention here that the solubility of phthalocyanines is important in terms of high-technological applications. The phthalocyanines synthesized are considerably soluble in polar solvents, such as MeOH, DMSO and DMF. The red shift of the complexes compared to the parent phthalocyanine is due to the electron-donating thioether substituents on the periphery and non-periphery of the Pc. The stronger electron-releasing 6-hydroxy hexylthio substituents on the non-periphery of the Pc also affect the electrochemical behavior of the complexes, shifting to more negative potentials. This redox feature may be useful for the application of the complexes as electro-catalysts for the reduction and/or oxidation of many target species, which will be the subject of our future interest.

Acknowledgements

We thank The Research Fund of Sakarya University and TUBİTAK (Project no: TBAG-108T094).

References

[1] X. Li, L.E. Sinks, B. Rybtchinski, M.R. Wasielewski, J. Am. Chem. Soc. 126 (2004) 10810.
[2] S.J. Lange, J.W. Sibert, A.G.M. Barrett, B.M. Hoffman, Tetrahedron 56 (2000) 7371.
[3] M. Kandaz, S.L.J. Michel, B.M. Hoffman, J. Porphyr. Phthalocya. 7 (2003) 700.
[4] N.B. Mc Keown, Phthalocyanine Materials, Cambridge University Press, 1998.
[5] M. Kandaz, İ. Yılmaz, Ö. Bekaroğlu, Polyhedron 19 (2000) 115.
[6] S.L.J. Michel, A.G.M. Barrett, B.M. Hoffman, Inorg. Chem. 42 (2003) 814.
[7] N. Preethi, H. Shinohara, H. Nishide, React. Funct. Polym. 66 (2006) 851.
[8] S. Lee, A.J.P. White, D.J. Williams, A.G.M. Barrett, B.M. Hoffman, J. Org. Chem. 66 (2001) 461.
[9] M.N. Yarasir, M. Kandaz, B.F. Senkal, A. Koca, B. Salih, Polyhedron 26 (2007) 1139.
[10] Ö.A. Osmanbaş, A. Koca, M. Kandaz, F. Karaca, Int. J. Hydrogen Energy 33 (13) (2008) 3281.
[11] M. Durmuş, T. Nyokong, Inorg. Chem. Commun. 10 (2007) 332.
[12] M. Durmus, T. Nyokong, Spectrochim. Acta 69 (2008) 1170.
[13] C.C. Leznoff, A.B.P. Lever (Eds.), Phthalocyanines: Properties and Applications, vol. 1–4, VCH, Weinheim, 1989.
[14] S. Arslan, İ. Yılmaz, Inorg. Chem. Commun. 10 (2007) 385.
[15] M. Kandaz, H.S. Çetin, A. Koca, A.R. Özkaya, Dyes Pigments 74 (2007) 298.
[16] A.B.P. Lever, E.R. Milaeva, G. Speier, in: C.C. Leznoff, A.B.P. Lever (Eds.), The Redox Chemistry of Metallophthalocyanines in Solution in Phthalocyanines: Properties and Applications, vol. 3, VCH, New York, 1993, pp. 5–27.
[17] M.N. Yarasir, M. Kandaz, B.F. Senkal, A. Koca, B. Salih, Dyes Pigments 77 (2008) 7.
[18] P.T. Kissinger, W.R. Heineman, Laboratory Techniques in Electroanalytical Chemistry, second ed., Marcel Dekker, New York, 1996.
[19] M.K. Şener, A. Koca, A. Gül, M.B. Koçak, Polyhedron 26 (2007) 1070.
[20] A. Koca, A.R. Özkaya, M. Selçukoğlu, E. Hamuryudan, Electrochim. Acta 52 (2007) 2683.
[21] K. Hesse, D. Schlettwein, J. Electroanal. Chem. 476 (1999) 148.
[22] A. Koca, H.A. Dinçer, H. Çerlek, A. Gül, M.B. Koçak, Electrochim. Acta 52 (2006) 1199.
[23] B. Agboola, K.I. Ozoemena, T. Nyokong, Electrochim. Acta 51 (2006) 6470.
[24] A. Koca, E. Gonca, A. Gül, J. Electroanal. Chem. 612 (2008) 231.
[25] A.B.P. Lever, S.R. Pickens, P.C. Minor, S. Licoccia, B.S. Ramaswany, K. Magnell, J. Am. Chem. Soc. 103 (1981) 6800.

Polyhedron 28 (2009) 263–268

Contents lists available at ScienceDirect

Polyhedron

journal homepage: www.elsevier.com/locate/poly

XPS, single crystal X-ray diffraction and cyclic voltammetric studies on 1,10-phenanthroline and 2,2′-bipyridine adducts of bis(piperidinecarbodithioato-*S*,*S*′)cadmium(II) with CdS_4N_2 environment – A stereochemical and electronic distribution investigation

S. Thirumaran [a], K. Ramalingam [a,*], G. Bocelli [b], L. Righi [b]

[a] Annamalai University, Department of Chemistry, Annamalai Nagar, Chidambaram, Tamil Nadu 608 002, India
[b] CNR, IMEM, Parma, Italy

ARTICLE INFO

Article history:
Received 21 March 2008
Accepted 11 November 2008
Available online 31 December 2008

Keywords:
Cadmium
Dithiocarbamate
1,10-Phenanthroline
2,2′-Bipyridine
Crystal structure
Cyclic voltammetry

ABSTRACT

(1,10-Phenanthroline)bis(piperidinecarbodithioato-*S*,*S*′)cadmium(II), [Cd(pipdtc)$_2$(1,10-phen)] (**1**) and (2,2′-bipyridine)bis(piperidinecarbodithioato-*S*,*S*′)cadmium(II), [Cd(pipdtc)$_2$(bipy)] (**2**) adducts were prepared and the crystal structures are reported. Cd–S and Cd–N distances and the angles subtended at cadmium are almost the same in both complexes but the Cd–S distances in the adducts are longer than those in Cd(pipdtc)$_2$ (**3**) complexes due to the presence of an additional neutral ligand. Thioureide C–N distance in **1** and **2** are supported by *ν*C–N bands observed at 1471 and 1470 cm^{-1}, respectively. S2p binding energies for the adducts show a significant reduction in value compared to the parent dithiocarbamate indicating the weakening of the Cd–S bond on adduct formation. The observed reduction in binding energy is due to the increased electron density on the metal in the adducts. The cyclic voltammetric study on the complexes also show an increase of electron density on cadmium in the adducts compared to Cd(pipdtc)$_2$.
© 2008 Elsevier Ltd. All rights reserved.

1. Introduction

Dithiocarbamates of zinc and cadmium have continued to attract attention in recent years on account of their recent industrial application [1,2] and biological profiles [3]. Cadmium dithiocarbamate complexes have been used as a precursor for the synthesis of CdS nanoparticles [4,5]. The dithioacid complexes of CdL_2 (LH_2 X-CS_2H or X_2PS_2H) type are coordinately unsaturated; this leads to the formation of compounds of higher coordination number either by the addition of one or two molecules of a Lewis base or by polymerization of CdL_2 [6,7]. In our efforts to compare electron density on cadmium in CdS_4 and CdS_4N_2 chromophore, in this paper we report the synthesis, XPS and cyclic voltammetric studies on [Cd(pipdtc)$_2$(1,10-phen) (**1**), [Cd(pipdtc)$_2$(bipy)] (**2**) and [Cd(pipdtc)$_2$] (**3**) complexes and single crystal X-ray structures of **1** and **2**.

2. Experimental

All the reagents and solvents employed were commercially available analytical grade materials (BDH) used as supplied without further purification.

2.1. Preparation of the complexes

The simple bis(piperidinecarbodithioato-*S*,*S*′)cadmium(II) was prepared by established procedure [8]. The adducts were prepared by adding a hot solution of 1,10-phenanthroline (2 mmol, 0.4 g) or 2,2′-bipyridine (2 mmol, 0.31 g) in ethanol to a hot solution of [Cd(pipdtc)$_2$] (1 mmol, 0.43 g) in chloroform. The resulting solution was cooled and then added to petroleum ether (boiling range 40–60 °C). Yellow precipitate of the adducts separated out. Single crystals were obtained by recrystallization from a solvent mixture of $CHCl_3$ and CH_3CN.

2.2. Physical measurements

IR spectra were recorded on a JASCO IR-700 spectrophotometer (range 4000–400 cm^{-1}) as KBr pellet. An STA 1500 PL Thermal Sciences instrument was used for thermogravimetric analysis. The heating rate of the furnace was 10 °C per minute.

XPS spectra were recorded on a VG mark II ESCA spectrometer equipped with a twin anode of aluminium and magnesium. Samples were studied by using Mg Kα radiation and the resolution of the instrument was 0.2 eV. The overall minimum peak width is 1.0–1.1 eV. Samples were well powdered and packed tightly in nickel stubs. All measurements were made at room temperature (25 °C) and at 10^{-9} Torr pressure. The peaks were calibrated by

* Corresponding author.
E-mail addresses: sthirumaran@yahoo.com (S. Thirumaran), krauchem@yahoo.com, krchem@rediffmail.com (K. Ramalingam).

0277-5387/$ - see front matter © 2008 Elsevier Ltd. All rights reserved.
doi:10.1016/j.poly.2008.11.019

the methods described earlier for the dithiocarbamato complexes [9].

2.3. Cyclic voltammetric studies

A bioanalytical system 100 electrochemical analyzer was used for all measurements. Working electrodes were of HMDE and platinum; the counter electrode was platinum wire and reference electrode was Ag/AgCl. The solvent used, DMF, was purified by distillation methods [10]. The supporting electrolyte was tetrabutylammonium perchlorate. The experimental solution was thermostated at 28±1 °C and oxygen free atmosphere was provided by bubbling purified nitrogen through the solution.

2.4. X-ray crystal structure analysis

Details of the crystal data, data collection and refinement parameters are summarized in Table 1. The structures were solved by direct methods with SIR97 program [11] and refined by full matrix least squares with SHELX93 [12]. Excepting C3, C6, C7 in **1** and C3, C7 in **2** all other non-hydrogen atoms were refined anisotropically and the hydrogen atoms were refined isotropically. Both the complexes are partially disordered. In complex **1** the C3, C4, C6 and C7 carbon atoms of the piperidine ring were found disordered in two different positions and were anisotropically refined with occupancy factors of 0.64(03) and 0.36(03), respectively. Their hydrogen atoms were put in calculated position. In complex **2** the C3′–C7′ carbon atoms were isotropically refined in two disordered positions with respective occupancy factors of 0.55(04) and 0.45(04). Their hydrogen atoms were not localized. Selected bond distances and angles are given in Table 2.

Table 1
Crystal data, data collection refinement parameters [Cd(pipdtc)$_2$(1,10-phen)] **1** and [Cd(pipdtc)$_2$(bipy)] **2**.

	[Cd(pipdtc)$_2$ (1,10-phen)] **1**	[Cd(pipdtc)$_2$(bipy)] **2**
Formula	$C_{24}H_{28}N_4S_4Cd$	$C_{22}H_{28}N_4S_4Cd$
F_W	613.2	588.1
Crystal system	monoclinic	orthorhombic
Space group	*C*2/*c*	*Pbca*
Cell parameters		
a (Å)	6.786(2)	15.118(3)
b (Å)	18.793(2)	33.474(2)
c (Å)	20.840(3)	10.175(2)
α (°)	90	90
β (°)	98.95(3)	90
γ (°)	90	90
V (Å^3)	2625.4	5149.2
Z	4	8
D_{calc}(g cm^{-3})	1.55	1.52
μ (cm^{-1})	97.9	99.5
F(000)	1248	2400
Crystal dimensions (mm)	0.18 × 0.22 × 0.31	0.17 × 0.23 × 0.31
Diffractometer	Enraf Nonius CAD4	Siemens AED
Radiation, λ (Å)	Cu Kα, 1.5418	Cu Kα, 1.5418
θ range (°)	22.4–36.3	11.3–36.0
Index ranges *h*,*k*,*l*	−1/8, −22/22, −23/25	−16/18, −40/17, −12/9
Collected reflections	5294	5493
Independent reflections	2479	4882
Observed reflections [$F_o > 4\sigma(F_o)$]	2096	2011
Parameters refined	279	393
Final residuals:		
R (for observed reflections)	0.029	0.046
R (for all reflections)	0.040	0.130
R_w	0.090	0.134
Weighting scheme	$W = 1/[\sigma^2F_o^2+(0.065 \cdot P)^2]$ $P = [\max(F_o^2,0)+2F_c^2]/3$	$w = 1/\sigma^2F_o^2+(0.059 \cdot P)^2]$ $P = [\max(F_o^2, 0)+2F_c^2]/3$
Goodness of fit	0.995	0.798
$\Delta\rho_{min/max}$ (e Å^{-3})	−0.51/0.44	−0.56/0.86

Table 2
Bond distances (Å) and angles (°) for [Cd(pipdtc)$_2$(1,10-phen)] **1** and [Cd(pipdtc)$_2$(2,2′-bipy)] **2**.

Bond distances for [Cd(pipdtc)$_2$(1,10-phen)] **1**			
Cd1–S1	2.640 (1)	S1–C1–N2	119.9 (2)
Cd1–S2	2.691 (1)	C1–N2–C7B	122.8 (4)
Cd1–N8	2.415 (3)	C1–N2–C7A	116.9 (6)
S1–C1	1.713 (4)	C1–N2–C3B	121.9 (5)
S2–C1	1.710 (3)	C1–N2–C3A	118.0 (5)
C1–N2	1.329 (5)	Cd1–N8–C13	117.6 (2)
N2–C3A	1.580 (12)	Cd1–N8–C9	124.0 (3)
N2–C3B	1.562 (8)	Bond angles for [Cd(pipdtc)$_2$(2,2′-bipy)] **2**	
N2–C7A	1.600 (17)	S2′–Cd1–N8′	97.7 (2)
N2–C7B	1.519 (11)	S1′–Cd1–N8′	102.8 (2)
Bond distances for [Cd(pipdtc)$_2$(2,2′-bipy)] **2**		S1′–Cd1–S2′	67.9 (1)
Cd1–S1	2.682 (3)	N8–Cd1–N8′	68.2 (3)
Cd1–S2	2.657 (3)	N8–Cd1–S2′	150.8 (2)
Cd1–N8	2.439 (10)	N8–Cd1–S1′	89.8 (2)
Cd1–S1′	2.646 (4)	S2–Cd1–N8′	142.7 (2)
Cd1–S2′	2.635 (4)	S2–Cd1–S2′	110.5 (1)
Cd1–N8′	2.408 (10)	S2–Cd1–S1′	110.1 (1)
S1–C1	1.703 (13)	S2–Cd1–N8	94.3 (2)
S2–C1	1.730 (12)	S1–Cd1–N8′	84.8 (2)
C1–N2	1.335 (16)	S1–Cd1–S2′	98.9 (1)
N2–C3	1.460 (20)	S1–Cd1–S1′	165.3 (1)
N2–C7	1.478 (21)	S1–Cd1–N8	104.7 (2)
S1′–C1′	1.707 (13)	S1–Cd1–S2	67.5 (1)
S2′–C1′	1.738 (13)	Cd1–S1–C1	86.3 (4)
C1′–N2′	1.292 (20)	Cd1–S2–C1	86.6 (4)
N2′–C3′	1.537 (43)	S1–C1–S2	119.5 (7)
N2′–C7′	1.470 (26)	S2–C1–N2	119.9 (8)
N2′–C3″	1.496 (22)	S1–C1–N2	120.5 (8)
N2′–C7″	1.477 (24)	C1–N2–C7	125.1 (11)
Bond angles for [Cd(pipdtc)$_2$(1,10-phen)] **1**		C1–N2–C3	123.0 (12)
S2–Cd1–N8	95.3 (1)	C3–N2–C7	109.9 (12)
S1–Cd1–N8	102.6 (1)	N2–C3–C4	108.5 (13)
S1–Cd1–S2	67.4 (1)	Cd1–S1′–C1′	87.3 (4)
Cd1–S1–C1	87.2 (1)	Cd1–S2′–C1′	87.0 (4)
Cd1–S2–C1	85.7 (1)	S1′–C1′–S2′	117.7 (7)
S1–C1–S2	119.7 (2)	S2′–C1′–N2′	119.6 (10)
S2–C1–N2	120.5 (3)	S1′–C1′–N2′	122.7 (9)

3. Results and discussion

3.1. IR spectral and thermogravimetric studies

The stretching frequencies associated with the ν_{C-N} bond are listed in Table 3. The ν_{C-N} has been used as a measure of the contribution of the thioureide form to the complexes [13]. In the present study complexes **1**, **2** and **3** show the ν_{C-N} bands around 1470 cm^{-1}, indicating the partial double bond character. However, ring frequencies associated with 1,10-phenanthroline and 2,2′-bipyridine are observed in the range of 1600 and 1000 cm^{-1}. In the present study, compound **1** shows bands at 1620 and 1510 cm^{-1} whereas **2** shows a prominent band at 1590 cm^{-1}. Other bands are masked by those due to the dithiocarbamate ligand.

The thermogravimetric studies on the complexes were performed to confirm their stoichiometry. The final product of thermal decomposition was a mixture of CdS and $CdSO_4$ in all complexes. Loss of bipyridine was indicated by a well defined step, whereas the corresponding 1,10-phenanthroline analogue showed a single step decomposition.

Table 3
IR spectral and cyclic voltammetric data.

Compound	IR (cm^{-1})		Cyclic voltammetric data (V)[a]			
	ν_{C-N}	ν_{C-S}	Ep^{red}	Ep^{ox}	Ep^{red}	Ep^{ox}
$Cd(pipdtc)_2$	1479	973	−0.825	−0.675	−0.575	−0.400
$[Cd(pipdtc)_2(1,10\text{-phen})]$	1471	975	−1.750		−0.725	−0.525
$[Cd(pipdtc)_2(2,2'\text{-bipy})]$	1470	988	−1.225		−0.775	−0.550

[a] HMDE was used for determining the given potentials.

Table 4
Binding energies (FWHM)[a] and binding energy shifts[b].

	$Cd(pipdtc)_2$	ΔE	$[Cd(pipdtc)_2$ (1,10 phen)]	ΔE	$[Cd(pipdtc)_2(bipy)]$	ΔE
N1s[c]	400.5(1.7)	−1.1	399.0(2.0)	−2.6	398.8(1.8)	−2.8
S2p[d]	163.0(1.9)	−1.8	162.2(2.4)	−2.8	161.6(2.4)	−3.2
Cd3d	405.5(2.1)	+1.8	404.1(2.1)	+0.4	404.3(2.3)	+0.6
	412.3(1.0)	+1.8	410.8(2.3)	+0.3	411.3(2.3)	+0.8

[a] Full width at half maximum given in parentheses.
[b] Shift in bindings energies (ΔE = observed BE − bare atom BE) with respect to 'bare' atom values quoted in the operation manual for the VG ESCA mark II spectrometer, count rate: 10^3 counts s^{-1}.
[c] Binding energy values for the adducts are unresolved and include those due to 1,10-phenanthroline and bipyridine.
[d] $S2p_{1/2,3/2}$ spin orbit components are not well resolved and the S2p binding energy is the peak maximum of the overall band envelope close to that of the $S2p_{3/2}$ component [27].

3.2. X-ray photoelectron spectroscopy

Binding energy values of core level electrons in different complexes and binding energies (ΔE) of the electrons with respect to the elemental state binding energies are listed in Table 4.

For the adducts, S2p binding energies show a significant reduction in magnitude compared to the parent dithiocarbamate. The observation is a clear indication of the weakening of Cd–S bond on adduct formation. Such a weakening is indicated by the lengthening of Cd–S bond and is observed in the crystal structures of the adducts. The bindings energy values associated with Cd3d electrons in the parent compound are observed at 405.5 and 412.3 eV [14]. On adduct formation, a highly significant reduction in binding energy of 1.5 eV is evident. The observed shift in binding energy very clearly shows the increased electron density on the metal in the adducts.

The metal-dithiocarbamate complexes are known to be highly covalent with effective bonding [15,16]. Unlike the truly planar nickel dithiocarbamate complexes, tetrahedral cadmium dithiocarbamate complexes are dimeric because of less effective charge transfer from the ligands to the metal. On adduct formation, the cadmium dithiocarbamate complexes become hexa-coordinated and the electron density on cadmium increases relatively due to the presence of the nitrogen bases. Weakening of the Cd–S bond on adduct formation is shown by the reduction in Cd3d electron binding energies. Therefore, the present XPS study supports the weakening of the Cd–S bond and the increase of electron density on cadmium as a result of the adduct formation.

3.3. Cyclic voltammetric studies

Representative cyclic voltammograms of $[Cd(pipdtc)_2(bipy)]$ at a HMDE and at a platinum electrodes are given in Fig. 1. In the cyclic voltammogram of $Cd(pipdtc)_2$ at a HMDE electrode, a new redox couple (−0.575 V/−0.400 V) is observed [17]. The magnitude of process 1 depend on the time the electrode is held at the initial potential. This is not observed unless HMDE is used. The process is conspicuously absent when CV is recorded with a platinum working electrode. This suggests that the process 1 (−0.575 V/−0.400 V) might be due to the formation of bimetallic complex such as $[HgCd_2(dtc)_6]$ as follows:

$$Hg(dtc)_2 + 2Cd(dtc)_2 \rightleftharpoons HgCd_2(dtc)_6$$

Synthetically, the formation of bimetallic complexes has been reported earlier [18]. Formation of the bimetallic complexes in all the dithiocarbamate complexes during electrochemical studies is due to the inherent nature of the mercury electrode to undergo exchange reaction with the metal dithiocarbamate complexes to ultimately form $Hg(dtc)_2$ and related complexes [19,20]. This is because of the soft–soft interaction between Hg and S containing ligands.

However, process 2 (−0.825/−0.675 V) in the cyclic voltammogram is for the 2 electron reduction reaction observed before. The process 2 can be written as

$$Cd(dtc)_2 + 2e^- + Hg \rightleftharpoons 2(dtc)^- + Cd(Hg)$$

In the case of the $[Cd(pipdtc)_2(1,10\text{-phen})]$ adduct, the cyclic voltammogram under identical conditions shows two reductive responses *viz.*, −0.725/−0.525 V and −1.750 V. The two reduction processes are identified by process 3 and 4. Process 3 is a redox couple with a large voltage separation (−200 mV). The couple does not appear unless a HMDE electrode is used for the CV studies. The response is totally absent when a platinum electrode is used. Therefore the redox couple identified by process 3 must be due to an electroactive species produced as a result of the interaction of Hg with other species.

Process 4 must be due to the electron addition process such as

$$[Cd(dtc)_2(1,10\text{-phen})] + 2e^- \rightleftharpoons [Cd(dtc)_2(1,10\text{-phen})]^{-2}$$

Controlled potential electrolysis could not be carried out because the response was observed close to the solvent decomposition potential. But, a comparison of the current per unit concentration of the complex with that of the parent dithiocarbamate indicates the nature of the reduction to be a two electron process. The absence of a corresponding oxidative couple for the reduction process is noteworthy. An earlier polarographic study [21] on similar compounds has also indicated the reduction to be a two electron addition process.

Similarly, for $[Cd(pipdtc)_2(bipy)]$ two reductive responses are also observed, indicated by process 5 and 6. Process 5 appears as a redox couple (−0.775/−0.555 V) whereas, the process 6 shows a reduction potential of −1.225 V with the respective oxidative couple missing. Process 5 is not observed if the CV is recorded with

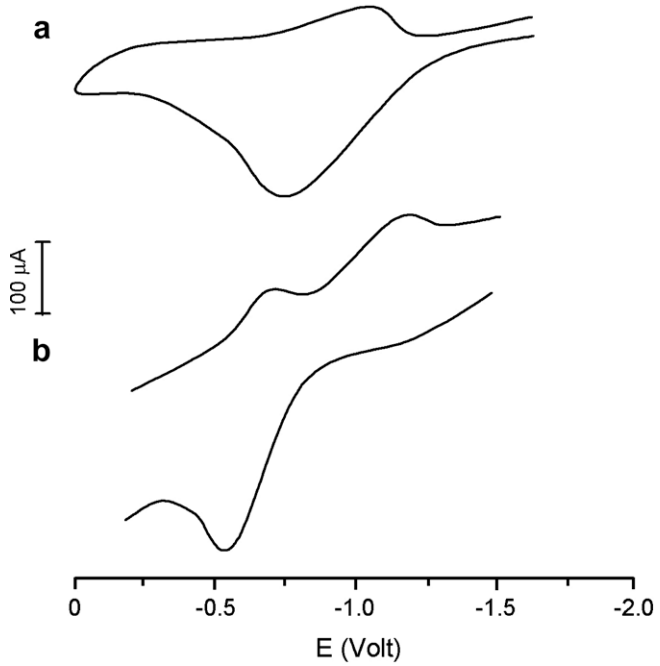


Fig. 1. Cyclic voltammograms of [Cd(pipdtc)$_2$(bipy)] at (a) HMDE and (b) platinum electrode.

a platinum working electrode. Process 6 is similar to the process 4 of the 1,10-phenanthroline analog and hence, must correspond to the two electron addition process.

The most important outcome of the observations is that in both the adducts the electron addition process becomes more difficult compared to the parent bisdithiocarbamate complex. This fact is supported by the very large shift in reduction potentials of the adducts compared to the parent dithiocarbamate (process 4 and 6 versus 2). The observation clearly indicates the presence of excess electron density on cadmium in the adducts compared to the parent dithiocarbamates. As the electron density increases, the electron addition is more difficult and hence a higher negative reduction potential is observed. Of the two adducts, the one involving bipyridine shows a lower reduction potentials than the other indicating less effective electron donation compared to 1,10-phenanthroline [22,23].

The new redox couple observed around −0.700/−0.500 V in both the adducts is not observed when CV are recorded with a platinum electrode. The potential associated with the redox couple is totally different from the values recorded for the corresponding parent complex involving simple dithiocarbamate or the nitrogen bases under identical conditions. This observation clearly also supports the involvement of Hg in the formation of a new electroactive species. In addition, the absence of a reductive response for Hg(dtc)$_2$ (−0.500 V) is an indication of the involvement of the new electroactive species.

3.4. Structure analysis

The ORTEP of [Cd(pipdtc)$_2$(1,10-phen)] and [Cd(pipdtc)$_2$(bipy)] are shown Figs. 2 and 3, respectively. The structures of **1** and **2** contain four and eight discrete monomeric units, respectively per unit cell. In both complexes the cadmium atoms are situated at the centre of a distorted tetragonal bipyramidal arrangement with two sulfur atoms from the chelating dithiocarbamate groups [S2, S2′] and two nitrogen atoms from the chelating neutral ligand [N8, N8′] on the basal plane and the two remaining sulfur atoms as vertices. Selected geometrical parameters for **1–3** are given Table 5.

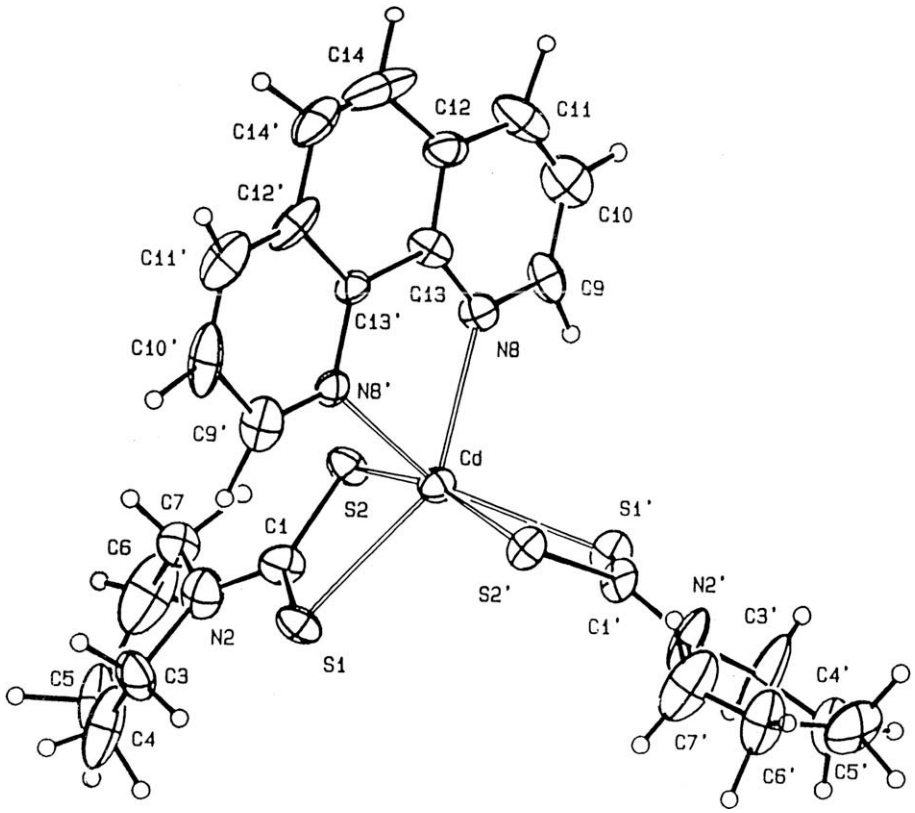


Fig. 2. ORTEP (30% ellipsoids) of [Cd(pipdtc)$_2$(1,10-phen)] **1**.

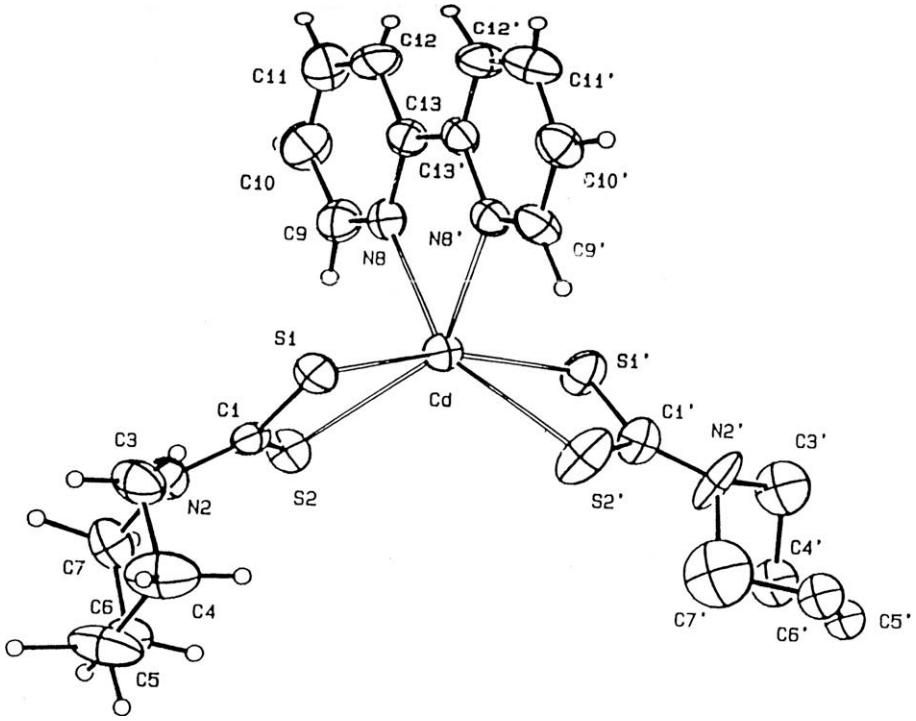


Fig. 3. ORTEP (30% ellipsoids) of [Cd(pipdtc)$_2$(bipy)] **2**.

Table 5
Comparative structural parameters for cadmium compounds.

Compound	Coordination number	S–Cd–S (°)	S–C–S (°)	C–S (Å)	Cd–S (Å)	S_2C–N (Å)	Ref.
Cd(pipdtc)$_2$	4[a]	68.0 (1)	118.7	2.566 (1)	1.734 (3)	1.33 (1)	[6]
[Cd(pipdtc)$_2$ (1,10-Phen)]	6	67.4(1)	119.7(2)	2.666(1)	1.711(2)	1.35(5)	This work
[Cd(pipdtc)$_2$(2,2′-bipy)]	6	67.7(1)	118.6(7)	2.659(4)	1.718(13)	1.32(2)	This work

[a] It has been suggested that the coordination number is essentially five due to the presence of very long Cd–S bond in the dimer.

Table 6
Comparative structural parameters involving the bidentate nitrogen ligands for related cadmium compounds.

Compound	N–Cd–N (°)	Cd–S (Å)	Cd–N (Å)	Ref.
[Cd(S_2COEt$_2$)$_2$(1,10-Phen)]	69.5(3)	2.687(3)	2.386(8)	[25]
[Cd(S_2CSBu)$_2$(2,2′-bipy)]	69.0(1)	2.684(1)	2.363(3)	[26]
[Cd(pipdtc)$_2$(1,10-Phen)]	68.7(5)	2.666(5)	2.415(3)	This work
[Cd(pipdtc)$_2$(2,2′-bipy)]	68.2(3)	2.659(4)	2.424(7)	This work

The bond distances and angles are mean values.

The Cd–S distances observed in **1** and **2** are longer than those observed in **3**. This is attributed to the change in coordination number from 4 to 6 and the steric effect exerted by 1,10-phenanthroline or 2,2′-bipyridine. No significant changes in C–N, C–S bond lengths and in the S–Cd–S and S–C–S angles are observed. In complex **2**, there are considerable differences between the pairs of Cd–S and S–C bonds and it is interesting to note that the shorter Cd–S bonds [2.657(3), 2.635(4) Å compared to 2.682(3), 2.646(4) Å] are associated with the longer S–C distances [1.730(12), 1.738(12) Å versus 1.703(13), 1.707(13) Å]. The fact is that the dithiocarbamate ligand is asymmetrically linked to cadmium and the asymmetric C–S distances are shorter than the typical C–S single bond distance [1.81 Å]. Therefore, all the C–S bonds in the present structure are of partial double bond character as observed in most of the dithiocarbamates [24]. Average C–N distances of **1** and **2** are 1.327(4) and 1.308(17) Å, respectively, which clearly indicates the contribution of the thioureide form to the dithiocarbamate ligand. This contrast well with adjacent typical single bonded N–C distances.

Selected structural parameters involving, 1,10-phenanthroline and 2,2′-bipyridine are also given in Table 6. Cd–N bonds are a symmetric and are longer than those observed in two similar adducts derived from xanthate and thioxanthate complexes [25,26]. The Cd–S distances observed in both the complexes **1** and **2** are the shortest compared to others listed in Table 6. Relatively, as the Cd–S bonds are shorter the Cd–N bonds are long. Therefore, the strength of Cd–S bond is decided at the cost of Cd–N bond and vice versa. The presence of relatively bulky piperidine ring sterically hinders the close approach of the neutral ligands.

Supplementary data

CCDC Nos. 245559 and 245937 contain the supplementary crystallographic data for complexes **1** and **2**, respectively. These data can be obtained free of charge via http://www.ccdc.com.ac.uk/costs/retrieving.html, or from the Cambridge Crystallographic Data Centre, 12 Union Road, Cambridge CB2 1EZ, UK; fax: (+44) 1223-336-033; or e-mail: deposit@ccdc.cam.ac.uk.

References

[1] J. Nieuwenhuizen, A.W. Ellers, J.G. Haashoot, S.R. Janse, J. Reedijk, J. Baernads, J. Am. Chem. Soc. 121 (1999) 163.
[2] J.A. McCleverty, S. Gill, J. Chem. Soc., Dalton Trans. (1982) 493.

[3] E.E. Casa, A. Sanchez, J.B. Vavo, S. Garcia-Fontan, E.E. Castellano, M.M. Jones, Inorg. Chim. Acta 158 (1989) 119.
[4] P. Yan, Y. Xie, Y. Qiam, X. Liu, Chem. Commun. (1999) 1293.
[5] N. Thammakan, E. Somsook, Mater. Lett. 60 (2006) 1161.
[6] A.V. Ivanov, A.V. Gersimenko, A.A. Konzelko, M.A. Ivanov, O.N. Antsutkin, W. Forsling, Inorg. Chim. Acta 359 (2006) 3855.
[7] B. Arulprakasam, K. Ramalingam, G. Bocelli, A. Cantoni, Polyhedron 26 (2007) 4489.
[8] G. Marcotrigiano, G.C. Pellacani, C. Preti, J. Inorg. Nucl. Chem. 36 (1974) 3709.
[9] C. Furlani, G. Polzonetti, C. Preti, G. Tosi, Inorg. Chim. Acta 73 (1983) 105.
[10] A.I. Vogel, A Text Book of Practical Organic Chemistry, 3rd ed., ELBS, 1968.
[11] A. Altomare, G. Cascarano, C. Giacovazzo, A. Guagliardi, A.G.G. Moliterni, M.C. Burla, G. Polidori, M. Camalli, R. Spagna, Private Communication, 1997.
[12] G.M. Sheldrick, SHELX 93, Program for Crystal structure Refinement Univ. of Gottingen, Germany, 1993.
[13] J.O. Hill, R.J. Magee, Rev. Inorg. Chem. 4 (1981) 141.
[14] Operation Manual for the VGESCA Mark II Spectrometer.
[15] D. Coucouvanis, Prog. Inorg. Chem. 11 (1970) 233.
[16] R. Eisenberg, Prog. Inorg. Chem. 12 (1970) 295.
[17] A.M. Bond, R. Colton, M.L. Dillon, A.F. Hollen Kamp, J.E. Moir, Inorg. Chem. 24 (1985) 1591.
[18] R.C. Aggarwall, B. Singh, M.K. Singh, J. Indian Chem. Soc. 59 (1982) 269.
[19] A.M. Bond, J.R. Thackeray, A.T. Casey, Inorg. Chem. 12 (1973) 887.
[20] T.H. Randle, J.J. Cardwell, R.J. Magee, Aust. J. Chem. 28 (1975) 21.
[21] G.K. Budnikov, N.A. Ulakhovich, Zh. Obshich. Khim. 46 (1976) 1129.
[22] L. Nadijo, J.M. Saveant, J. Electroanal. Chem. 33 (1971) 453.
[23] C.P. Andriense, L. Nadjo, J.M. Saveant, J. Electroanal. Chem. 42 (1973) 223.
[24] S. Hugebye, Acta Chem. Scand. 24 (1970) 2198.
[25] C.L. Raston, A.H. White, Aust. J. Chem. 29 (1976) 739.
[26] S.J. Black, F.W.B. Einstein, P.C. Hayes, R. Kurar, D.G. Tuck, Inorg. Chem. 25 (1986) 4181.
[27] R.M. Walton, Coord. Chem. Rev. 31 (1980) 183.

Polyhedron 28 (2009) 269–278

Contents lists available at ScienceDirect

Polyhedron

journal homepage: www.elsevier.com/locate/poly

Investigation of the kinetics of aquation of the 1:2 complex between Cr^{III} and nitrilotriacetic acid

Magdalena E. Mendola [a], Tias Paul [b], Timothy J. Strathmann [b], Richard F. Carbonaro [a,*]

[a] Manhattan College, Department of Civil and Environmental Engineering, Manhattan College Parkway, Riverdale, NY 10471, United States
[b] University of Illinois at Urbana-Champaign, Department of Civil and Environmental Engineering and Center of Advanced Materials for the Purification of Water with Systems, Urbana, IL 61801, United States

ARTICLE INFO

Article history:
Received 16 June 2008
Accepted 14 November 2008
Available online 26 December 2008

Keywords:
Chromium
NTA
Ligand exchange
Aquation
Capillary electrophoresis
ATR-FTIR

ABSTRACT

Aquation of the 1:2 complex between Cr^{III} and nitrilotriacetic acid (NTA) was monitored using a combination of capillary electrophoresis (CE), ultraviolet–visible (UV–vis) spectrophotometry, and attenuated total reflectance-Fourier transform infrared (ATR-FTIR) spectroscopy. To our knowledge, this is the first published report of the use of either CE or ATR-FTIR to monitor the kinetics of ligand exchange reactions of Cr^{III}–aminocarboxylate complexes. The aquation products were identified as the 1:1 Cr^{III} complex with NTA and "free" NTA. The 1:1 complex dimerized to form a 2:2 complex in a slower subsequent reaction step. Rates of disappearance of the 1:2 complex were first-order under all experimental conditions. First-order rate constants for aquation, k_{obs} (h^{-1}), measured using all three techniques were similar at equivalent pH conditions, and with values reported previously in the literature. Measured k_{obs} values exhibited a complicated pH dependence with three distinct regions: (i) at pH < 6.5, k_{obs} values increased with decreasing pH, (ii) between pH 6.5 and 8.0, k_{obs} values were relatively constant, and (iii) at 8.0 < pH < 10.0, k_{obs} increased with increasing pH and then leveled off. A kinetic model incorporating five distinct aquation pathways was successfully employed to model the pH dependence of k_{obs} from 0.0 < pH < 10.0. These results show that CE and ATR-FTIR can be used as tools for better understanding ligand exchange processes occurring in aqueous solution.

© 2008 Elsevier Ltd. All rights reserved.

1. Introduction

Chromium(III) is classically known as a substitution-inert metal ion [1]. This categorization is largely based upon measurements of the rate of water exchange from the first coordination shell of Cr^{III} and other metal aqua ions [2]. The pseudo first-order rate constant for water exchange for $[Cr^{III}(H_2O)_6]^{3+}$ (hexaaquo Cr^{III}) is $2.4 \times 10^{-6}\ s^{-1}$ ($t_{1/2}$ = 3.2 days) [3], one of the smallest in magnitude for all metals. Since replacement of a water molecule from the first coordination shell is an important step in complex formation and many redox processes, many aqueous systems containing hexaaquo Cr^{III} take long periods of time to reach equilibrium [4]. Rate constants for exit of coordinated water/entry of simple inorganic ligands (e.g., Cl^-, Br^-, NO_3^-) vary, but most range between 10^{-6} and $10^{-8}\ M^{-1}\ s^{-1}$ [2].

Replacement of water by hydroxide ion does not involve ligand exchange because it can be achieved via deprotonation of a coordinated water molecule. Consequently, formation of hydroxo species occurs rapidly upon raising the pH of aqueous solutions containing hexaaquo Cr^{III} [5]. This not only alters the speciation of Cr^{III}, but also has been found to increase ligand exchange rates. For example, replacing a coordinated water molecule of hexaaquo Cr^{III} with hydroxide ion to form $[Cr^{III}(H_2O)_5(OH)]^{2+}$ decreases the half-life of water exchange from 3.2 days to approximately 8 h [3]. Rate constants for Cr^{III} oligomerization increase by about a factor of 10^2 with each replacement of a coordinated water molecule by hydroxide ion [6].

Aminocarboxylate chelating agents complex strongly with most metals, thus altering metal bioavailability and mobility in the environment [7]. These compounds are used as laundry detergent builders, boiler scale inhibitors, in metal plating and cleaning operations, in textile manufacture, and in paper and cellulose production. When aminocarboxylate chelating agents occupy two, three, four, or five coordination positions of Cr^{III}, rates of exchange at remaining positions occupied by water can be quite rapid [8–10]. For example, exit of a water molecule and entry of NCS^- (thiocyanate ion) into the inner coordination shell of hexaaquo Cr^{III} has a rate constant of $1.8 \times 10^{-6}\ M^{-1}\ s^{-1}$ [11]. However, replacement of a coordinated water molecule by NCS^- in $[Cr^{III}(edta)(H_2O)]^-$ and $[Cr^{III}(hedta)(H_2O)]^0$ (edta = ethylenediaminetetraacetic acid, hedta = N-(2-hydroxyethyl)-ethylenediaminetriacetic acid) is much more rapid, exhibiting rate constants of 13.7 and $3.32\ M^{-1}\ s^{-1}$, respectively [12].

* Corresponding author. Tel.: +1 718 862 7469.
E-mail address: richard.carbonaro@manhattan.edu (R.F. Carbonaro).

0277-5387/$ - see front matter © 2008 Elsevier Ltd. All rights reserved.
doi:10.1016/j.poly.2008.11.018

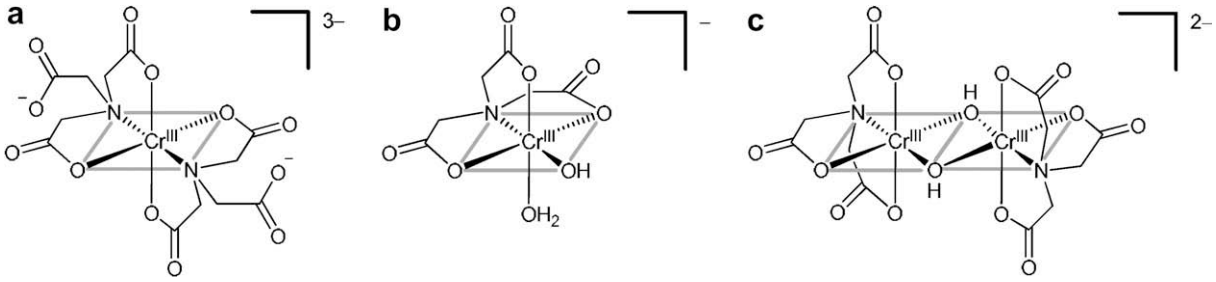


Fig. 1. Structures and stoichiometries and of Cr^{III} complexes with NTA. Identity: (a) *s-fac*-$[Cr^{III}(nta)_2]^{3-}$, b) $[Cr^{III}(H_2O)(OH)(nta)]^{-}$, c) *trans*-$[Cr^{III}_2(\mu\text{-}OH)_2(nta)_2]^{2-}$.

Nitrilotriacetic acid (NTA), a member of the aminocarboxylate family, is of particular interest from a chemical perspective because of the multiple stoichiometries and protonation levels that result when it coordinates metal ions. Cr^{III} complexes with NTA are known to exist in 1:1, 1:2 and 2:2 stoichiometries (Fig. 1). These species interconvert in solution, exhibiting a wide range of reaction rates that are dependent upon pH [13–15]. However, nearly all previous examinations of these complexes have been conducted in acidic media, making it difficult to predict the rates and mechanism of transformation under environmentally-relevant pH conditions.

In our previous work, a capillary electrophoresis (CE) method was developed to speciate various Cr^{III} complexes with aminocarboxylate chelating agents [16]. CE is an effective tool for measuring Cr^{III} speciation because time scales of complex dissociation are longer than the time scale of the CE separation itself. Injections of pure solutions of the 1:1 and 2:2 complexes of Cr^{III} with NTA resulted in distinct, sharp peaks. In this study, we apply this CE method together with complementary ultraviolet–visible (UV–Vis) and attenuated total reflectance-Fourier transform infrared (ATR-FTIR) spectroscopy analyses to study the kinetics and mechanism of the inter-conversion of Cr^{III}–NTA complexes amongst the various forms shown in Fig. 1. ATR-FTIR spectroscopy provides an in situ probe for changes in the molecular properties of metal–organic complexes because many organic functional groups are infrared-active at characteristic vibrational frequencies (e.g., carboxylate, phenolate) [17,18], and spectral features of individual functional groups are sensitive to protonation, metal coordination, and hydrogen bonding [19–22]. Thus, ATR-FTIR spectral changes during Cr^{III}–NTA ligand exchange reactions can be traced to specific changes in metal-binding ligand groups. The ATR sampling technique is particularly suited for probing aqueous solutions because it provides a small highly reproducible spectral pathlength (~few μm), which is necessary because water completely absorbs infrared radiation over longer pathlengths [23]. ATR-FTIR spectroscopy has been used successfully to characterize the structures of carboxylate ligands complexed to aqueous metal ions and adsorbed to mineral surfaces [19–22,24–26].

This contribution examines the kinetics for aquation of the 1:2 complex between Cr^{III} and NTA using the novel combination of techniques described above. The products of the aquation reaction are the 1:1 complex and a "free" NTA molecule. Since ligand exchange rates of Cr^{III}–aminocarboxylate complexes are known to be pH dependent, experiments were conducted over a wide pH range and models that consider changing protonation levels of the reacting complex were developed to quantitatively interpret observed kinetic trends. To our knowledge, this is the first published report of the use of either CE or ATR-FTIR to monitor the kinetics of ligand exchange reactions of Cr^{III}–aminocarboxylate complexes. Additional kinetic experiments were performed using UV–Vis spectrophotometry, the sole method used in earlier studies [13], as a way to verify CE and ATR-FTIR results. Although the experimental system and reaction studied here is very simple in nature, elucidation of the aquation mechanism in this model system has implications for a variety of more complex homogeneous and heterogeneous phenomena involving metal–organic complexes (e.g., metal ion transport, bioavailability, and toxicity).

2. Experimental

All solutions were prepared using distilled, deionized water (DDW) with a resistivity of 18 MΩ cm (Millipore Corp. or Barnstead International). All stock solutions were stored in polypropylene bottles prior to use. All glassware and plasticware were soaked in 5 M HNO_3 or 1 M HCl (Fisher Scientific) and rinsed several times with DDW prior to use.

Nitrilotriacetic acid (NTA) was purchased from Acros Chemicals. N,N′-Diethylpiperazine (DEPP, 4.0 < pH < 5.3), 2-morpholinoethanesulfonic acid (MES, 5.5 < pH < 6.7), 3-(N-morpholino)propanesulfonic acid (MOPS, 6.7 < pH < 7.7), 4-(2-Hydroxyethyl)-1-piperazinepropanesulfonic acid (EPPS, 7.7 < pH < 8.8), and 2-(cyclohexylamino)ethanesulfonic acid (CHES, 8.8 < pH < 10.0) were used as pH buffers. These buffers were selected specifically because they are believed to interact minimally with metal ions in solution [27]. NaCl (sodium chloride), HNO_3 (nitric acid), HCl (hydrochloric acid) and NaOH (sodium hydroxide) were purchased from Fisher Scientific.

Solid *s-fac*-$K_3[Cr^{III}(nta)_2] \cdot 2H_2O$ was synthesized according to the method of Kallen et al. [13]. $K_2[Cr^{III}_2(\mu\text{-}OH)_2(nta)_2] \cdot 2H_2O$ was synthesized according to the method of Koine et al. [28]. Solution standards of $[Cr^{III}(H_2O)_2(nta)]^0$ were prepared by dissolving $K_2[Cr^{III}_2(\mu\text{-}OH)_2(nta)_2] \cdot 2H_2O$ in 0.01 M HCl for 1.0 h as described by Visser et al. [29]. Purity of Cr^{III} salts was ensured by dissolving them in pH buffered solutions and comparison of their UV–Vis spectral features (λ_{max} and ε_{max}) with literature values [15]. Capillary electrophoresis analysis provided a final check since impurities would result in unidentifiable peaks in electropherograms.

2.1. Capillary electrophoresis experiments

Capillary electrophoresis experiments were conducted by adding pre-weighed amounts of solid *s-fac*-$K_3[Cr^{III}(nta)_2] \cdot 2H_2O$ to a 100 mL solution containing 10 mM NaCl and 5.0 mM pH buffer. The resulting initial concentration of *s-fac*-$[Cr^{III}(nta)_2]^{3-}$ was 172 μM. Small amounts of 0.1 M HCl or NaOH were then added to achieve specific pH values. A 500 μL aliquot of this solution was then added to a polypropylene sample tube for analysis by CE. The pH of the solution was measured in the remainder of the solution at the beginning and end of each experiment to ensure that it stayed at a constant value. The samples were maintained at a constant 25 °C via the thermostatted internal sample chamber of the instrument. Repeated injections of the sample were then made at various time intervals. CE experiments were performed over the range $3.72 \leqslant pH \leqslant 10.02$.

A P/ACE MDQ (Beckman Coulter, Fullerton, CA) capillary electrophoresis instrument equipped with a UV–Vis diode array detector was used. Underivatized fused-silica capillaries (75 μm i.d.) were purchased from Polymicro Technologies (Phoenix, AZ). Samples were introduced into the capillary by hydrostatic injection using a pressure of 0.5 psi for 10 s. *s-fac*-$[Cr^{III}(nta)_2]^{3-}$, $[Cr^{III}(H_2O)(OH)(nta)]^-$, and *trans*-$[Cr^{III}_2(\mu\text{-}OH)_2(nta)_2]^{2-}$ were analyzed by CE using methods described in Carbonaro and Stone [16]. Direct detection of these complexes at a wavelength of 214 nm was employed.

2.2. Ultraviolet–visible spectrophotometry experiments

Solutions of *s-fac*-$[Cr^{III}(nta)_2]^{3-}$ used in UV–Vis spectrophotometry experiments were prepared in a similar manner to the CE experiment except the initial concentration was 4.3 mM. Immediately after pH adjustment, a 2.0 mL aliquot of the reaction solution was added to a plastic cuvette (1 cm pathlength) which was then loaded into the UV–Vis spectrophotometer (DU 800, Beckman Coulter). The sample chamber of the spectrophotometer was maintained at 25 °C via a Peltier thermostat system. Repeated measurements of the sample absorbance were then made at selected time intervals at a wavelength of 506 nm. A solution of 10 mM NaCl was used as a blank for background correction. UV–Vis experiments were performed over the range $2.07 \leqslant pH \leqslant 3.48$. An organic pH buffer was not employed in these experiments. Experiments were not performed at higher pH values because of dimerization of the product which occurs at neutral to alkaline pH.

2.3. ATR-FTIR spectroscopy experiments

ATR-FTIR spectra of aqueous samples containing NTA and Cr^{III}–NTA complexes were collected at room temperature (22 ± 2 °C) using a Nicolet Nexus 670 FTIR spectrometer (Thermo Scientific) outfitted with an ATR cell containing a horizontal 45° AMTIR crystal (Pike Technologies), a mid IR source, a KBr beam splitter, and a deuterated triglycine sulfate (DTGS) detector. All reference standard and reaction solutions were prepared in a stirred batch reactor with 10 mM ligand concentration (e.g., 5 mM of the 1:2 complex yields 10 mM ligand) and sufficient NaCl concentration to yield 100 mM total Na^+ in the solution. The pH of the batch reactor was continuously monitored to ensure pH stability during the aquation reaction (no adjustment was necessary). At desired time intervals, a small aliquot of the reactor solution was transferred to the ATR sample cell and an infrared spectrum was obtained by averaging 100 spectral scans acquired at 4 cm^{-1} resolution.

2.4. Data analysis

It was not possible to generate accurate CE or UV–Vis calibration curves for *s-fac*-$[Cr^{III}(nta)_2]^{3-}$ because standard solutions undergo the same transformation reactions we are investigating. Reaction time courses resulting from CE experiments were plotted in terms of corrected peak area instead of concentration. Corrected peak area is defined as the peak area divided by the analyte migration time [30]. Normalizing to migration time has been found to increase reproducibility and lower %RSD of repeated injections of standard solutions [30]. The CE corrected peak area of Cr^{III}–aminocarboxylate complexes is depends linearly upon concentration with a near-zero intercept [16]. Therefore, changes in corrected peak area with time can be used as a surrogate for concentration for determining rate constants [31]. Electropherograms resulting from CE separations are usually reported as absorbance versus electromigration time [30]. However, to correct for run-to-run variability in electroosmotic flow, the electromigration time axis was transformed to effective electrophoretic mobility [30]. Analysis of UV–Vis absorbance data is described after presentation of the experimental results.

ATR-FTIR spectra were analyzed using OMNIC (Version 6.1; Thermo-Nicolet). Spectra of NTA-containing solutions were collected against a deionized water background and spectral contributions from the background electrolyte were manually subtracted using the spectra of 100 mM NaCl solutions that were measured in between measurements of NTA-containing samples; background subtraction factors for individual raw spectra, which varied from 0.1 to 0.98, were selected to minimize spectral noise from water vapor. The resulting spectra were then baseline corrected to remove spectrometer drift. Although care was taken to subtract spectral features of water, contributions from a strong water bending mode ($\delta_{H\text{–}O\text{–}H}$) at ~1630 cm^{-1} cannot be completely eliminated with confidence, so this region of the spectra was used only for qualitative analysis of peak positions and was not considered when conducting quantitative analysis. Spectra of solutions spiked with *s-fac*-$K_3[Cr^{III}(nta)_2] \cdot 2H_2O$ that were collected after different reaction times (0–6 h) were fit with a stoichiometry-constrained linear combination of reference spectra for *s-fac*-$[Cr^{III}(nta)_2]^{3-}$, $[Cr^{III}(H_2O)(OH)(nta)]^-$, and free NTA collected at the same pH condition. Spectral fitting was performed by method of least square residuals using SCIENTIST (Version 3.0; Micromath Scientific).

All observed first-order rate constants for s-fac-$[Cr^{III}(nta)_2]^{3-}$ aquation, k_{obs} (h^{-1}), were determined via linear regression using the slope function of EXCEL (Version 2007; Microsoft). Reaction progress was followed for a minimum of two half-lives. Confidence intervals on rate constants at the 95% confidence level were determined using standard statistical methods facilitated through the use of EXCEL. Model fits of k_{obs} versus pH data were performed using SCIENTIST. Confidence intervals on model parameters (pK_a values and reaction rate constants) were determined at the 95% confidence level using numerical algorithms available in SCIENTIST.

2.5. Notation

The notation used here for Cr^{III} complexes is consistent with that used in the inorganic chemistry literature. When the identity of the metal ion and chelating agent are known, but the protonation level, or overall charge is not established, all of the letters of the abbreviation for a chelating agent are written in upper-case, e.g., Cr^{III}–NTA and Cr^{III}–NTA_2. Lower-case abbreviations for chelating agents correspond to their lowest protonation levels (e.g., nta^{3-}). Protonation of nta^{3-} therefore results in $Hnta^{2-}$, H_2nta^-, and H_3nta. Brackets are used when the chelating agent stoichiometry, protonation level, and overall charge of the metal complex are known, e.g., $[Cr^{III}(nta)_2]^{3-}$ and $[Cr^{III}(H_2O)_2(nta)]^0$. The overall charge of the complex is placed outside the brackets. Since the kinetics of conversion of one complex to another is the focus of study, denotation of the concentration of these complexes requires further delineation and is indicated using a second set of brackets. Thus, $[[Cr^{III}(nta)_2]^{3-}]$ and $[[Cr^{III}(H_2O)_2(nta)]^0]$ represent the concentrations in mol/L of $[Cr^{III}(nta)_2]^{3-}$ and $[Cr^{III}(H_2O)_2(nta)]^0$, respectively.

3. Results and discussion

3.1. Capillary electrophoresis studies

Results from a typical *s-fac*-$[Cr^{III}(nta)_2]^{3-}$ aquation experiment are shown in Fig. 2 for a reaction buffered at pH 6.91. In Fig. 2a, stacked electropherograms are shown at increasing sample injection times. The peak area for *s-fac*-$[Cr^{III}(nta)_2]^{3-}$ (Peak 1) decreased over time from the onset of the reaction. Loss of *s-fac*-$[Cr^{III}(nta)_2]^{3-}$ peak area corresponded with an increase in the areas of Peak 2

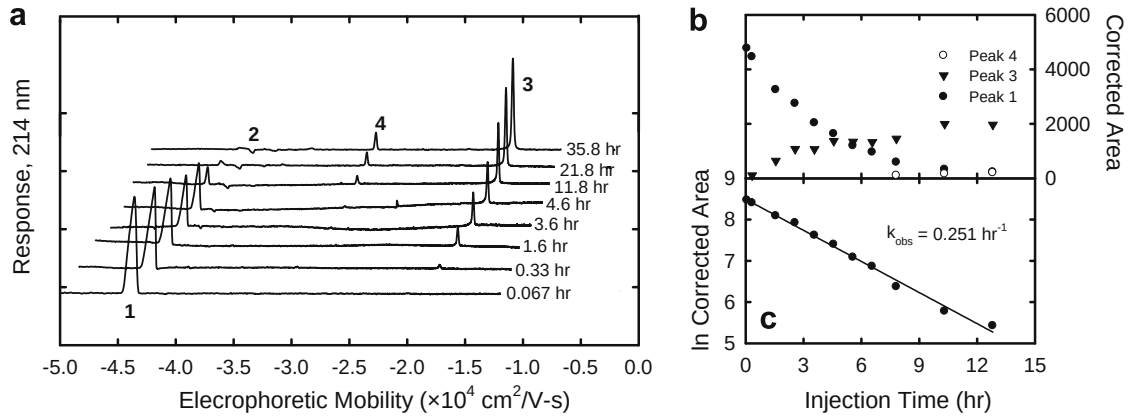


Fig. 2. Aquation of *s-fac*-$[Cr^{III}(nta)_2]^{3-}$ at near-neutral pH monitored using capillary electrophoresis. In (a) electropherograms resulting from successive injection and separation of a pure solution of 172 μM *s-fac*-$[Cr^{III}(nta)_2]^{3-}$ at pH 6.91 (5.0 mM MOPS, 10 mM NaCl). Peak identity: 1. *s-fac*-$[Cr^{III}(nta)_2]^{3-}$, 2. free NTA, 3. $[Cr^{III}(H_2O)(OH)(nta)]^{-}$, 4. $[Cr_2^{III}(\mu\text{-}OH)_2(nta)_2]^{2-}$. In (b) the corrected areas of Peaks 1, 3 and 4 are shown as function of the injection time. In (c), the natural log of the corrected area of Peak 1 is shown vs. the injection time.

(a negative peak) and Peak 3. Peaks 2 and 3 were confirmed to be free NTA and $[Cr^{III}(H_2O)(OH)(nta)]^{-}$, respectively, by spiking samples with known standards of these compounds. A peak corresponding to $[Cr_2^{III}(\mu\text{-}OH)_2(nta)_2]^{2-}$ (Peak 4), typically appeared very slowly after a significant lag period. In Fig. 2b, the corrected peak area of Peaks 1, 3 and 4 are plotted versus time for the same experiment as shown in (a). The corrected peak area for *s-fac*-$[Cr^{III}(nta)_2]^{3-}$ (Peak 1) decreased exponentially with time. Similar results were obtained for all experiments performed using CE.

Based upon the changes in corrected peak area with injection time, the following general "reactions in series" scheme was observed:

$$\textit{s-fac}\text{-}[Cr^{III}(nta)_2]^{3-} \xrightarrow{-NTA} [Cr^{III}(H_2O)(OH)(nta)]^{-} \xrightarrow{(slow)} [Cr_2^{III}(\mu\text{-}OH)_2(nta)_2]^{2-} \quad (1)$$

As *s-fac*-$[Cr^{III}(nta)_2]^{3-}$ aquates to $[Cr^{III}(H_2O)(OH)(nta)]^{-}$, one NTA molecule becomes completely dissociated. A more subtle change occurs in the other NTA molecule still attached to Cr^{III}. As can be seen in the structures shown in Fig. 1, the number of Lewis base groups of the NTA ligand attached to the Cr^{III} center increases from 3 to 4. It is also important to note the nature of the product of the aquation reactions. $[Cr^{III}(H_2O)(OH)(nta)]^{-}$ is the dominant form of the 1:1 Cr^{III} complex with NTA at pH 7.1 (the pH of the CE buffer). However, at moderately-low pH, the coordinated hydroxide ion of $[Cr^{III}(H_2O)(OH)(nta)]^{-}$ protonates to form $[Cr^{III}(H_2O)_2(nta)]^{0}$ [14,32,33]:

$$[Cr^{III}(H_2O)_2(nta)]^{0} \rightleftharpoons [Cr^{III}(H_2O)(OH)(nta)]^{-} + H^{+} \quad pK_{a1} = 5.87 \quad (2)$$

At moderately-high pH, the coordinated water molecule of $[Cr^{III}(H_2O)(OH)(nta)]^{-}$ deprotonates to form $[Cr^{III}(OH)_2(nta)]^{2-}$ [32,33]:

$$[Cr^{III}(H_2O)(OH)(nta)]^{-} \rightleftharpoons [Cr^{III}(OH)_2(nta)]^{2-} + H^{+} \quad pK_{a2} = 8.74 \quad (3)$$

Interconverison of these species occurs typically in sub-millisecond time-scales because Cr^{III} ligand exchange is not involved [5]. Thus, the predominant form of the 1:1 complex depends strongly upon solution pH. For simplicity, Cr^{III}–NTA is used throughout the remainder of this work to denote all protonation levels of the 1:1 complex.

Conversion of Cr^{III}–NTA to $[Cr_2^{III}(\mu\text{-}OH)_2(nta)_2]^{2-}$ (Eq. (1)) is a dimerization reaction which has been investigated in a previous study [34]. Since the concentration of Cr^{III}–NTA is affected by both its formation and dimerization reactions, we chose to determine observed rate constants solely from the loss of *s-fac*-$[Cr^{III}(nta)_2]^{3-}$. Fig. 2c shows that the natural logarithm of the *s-fac*-$[Cr^{III}(nta)_2]^{3-}$

Table 1
Summary of k_{obs} values from *s-fac*-$[Cr^{III}(nta)_2]^{3-}$ aquation experiments.

pH	k_{obs}[a] (h^{-1})
Capillary electrophoresis	
3.72	3.86 ± 0.84
3.77	3.93 ± 0.07
3.95	2.92 ± 0.08
4.23	2.15 ± 0.12
4.27	2.34 ± 0.07
4.38	1.99 ± 0.18
4.40	1.58 ± 0.05
4.54	1.46 ± 0.05
4.65	1.11 ± 0.06
4.79	1.06 ± 0.05
4.82	0.719 ± 0.023
4.84	0.759 ± 0.065
5.17	0.501 ± 0.011
5.23	0.597 ± 0.072
5.45	0.450 ± 0.029
5.91	0.364 ± 0.011
6.17	0.332 ± 0.012
6.79	0.226 ± 0.011
6.91	0.251 ± 0.015
7.25	0.220 ± 0.013
7.72	0.224 ± 0.016
8.20	0.250 ± 0.013
8.91	0.408 ± 0.020
9.40	0.529 ± 0.048
9.75	0.457 ± 0.045
10.05	0.433 ± 0.026
UV–Vis spectrophotometry	
2.07	13.94 ± 0.35
2.14	14.90 ± 0.63
2.35	14.04 ± 0.36
2.40	13.86 ± 0.32
2.82	15.89 ± 0.45
2.96	14.56 ± 0.35
3.27	10.53 ± 0.18
3.40	10.95 ± 0.18
3.48	8.23 ± 0.28
ATR-FTIR spectroscopy	
7.00[b]	0.216 ± 0.090

[a] Reactions conducted at 25 °C unless otherwise indicated. Uncertainty represented at the 95% confidence level.
[b] Experiment conducted at room temperature (22 ± 2 °C).

corrected area versus time is linear, indicating first-order loss of *s-fac*-$[Cr^{III}(nta)_2]^{3-}$. The negative slope of the linear regression line yielded an observed first-order rate constant, k_{obs}, equal to $0.251 \pm 0.015\ h^{-1}$. In general, linear regression provided excellent fits to the data from all experiments performed using CE ($3.6 < pH < 9.4$), yielding k_{obs} values with small confidence intervals (95% confidence level) ranging from 0.220 to $3.93\ h^{-1}$. A summary of all measured k_{obs} values is provided in Table 1.

Attempts at stabilizing *s-fac*-$[Cr^{III}(nta)_2]^{3-}$ by adding "free" NTA (1.0 mM) to solutions buffered at pH 7.0 were unsuccessful. In all cases *s-fac*-$[Cr^{III}(nta)_2]^{3-}$ corrected peak area decreased exponentially as a function of time. Values for k_{obs} were approximately the same as when additional NTA was not added. Thus, back reaction of Cr^{III}–NTA with NTA is kinetically limited and is unimportant under the experimental conditions employed in this study.

3.2. UV–Vis spectrometry studies

At low pH conditions ($pH < 3.6$), rates of *s-fac*-$[Cr^{III}(nta)_2]^{3-}$ aquation were too rapid to be monitored by CE. Instead, UV–Vis spectrophotometry was used in the low-pH experiments to examine reaction progress by measuring the solution absorbance as a function of time. In the experiments where UV–Vis was employed, the absorbance increased as a function of time until it leveled off at a particular value (Fig. 3a for three separate experiments performed at pH 2.35, 2.96, and 3.27).

For an irreversible first-order reaction in a system where the reactant and product(s) have appreciable UV–Vis absorbance, k_{obs} is related by the following equation [31,35]:

$$\ln\left(\frac{D_0 - D_\infty}{D_t - D_\infty}\right) = k_{obs}t \quad (4)$$

where D_0 is the initial sample absorbance, D_∞ is the sample absorbance at infinite time, and D_t is the sample absorbance at time t.

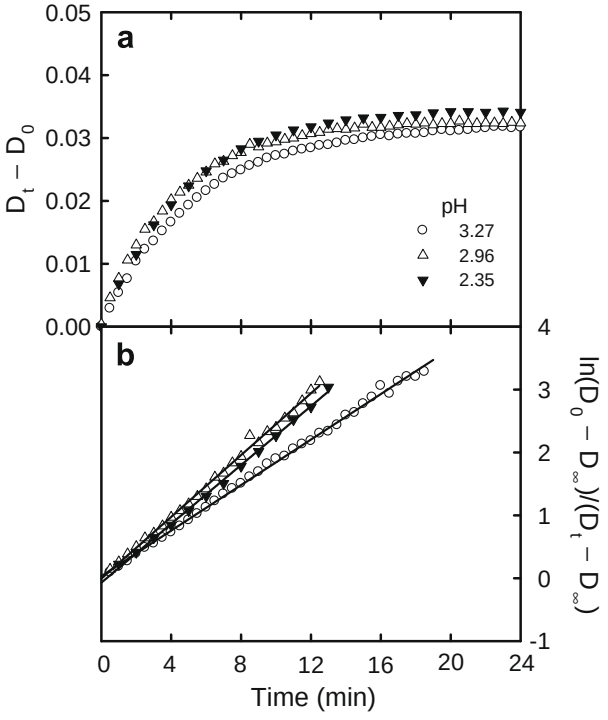


Fig. 3. Aquation of *s-fac*-$[Cr^{III}(nta)_2]^{3-}$ at low pH monitored using UV–Vis spectrophotometry. In (a), the corrected absorbance, $D_t - D_0$, is shown vs. time for three separate solutions of 4.30 mM *s-fac*-$[Cr^{III}(nta)_2]^{3-}$ at pH 2.35, 2.96 and 3.27 (10 mM NaCl). In (b) the data shown in (a) is linearized (see text) to obtain values of k_{obs}.

Although Cr^{III}–NTA dimerizes to form $[Cr_2^{III}(\mu\text{-}OH)_2(nta)_2]^{2-}$ thereby affecting values of D_t and D_∞, previous work has shown that this reaction is relatively unimportant at the low total chromium concentration and pH used in these experiments [15]. Plots of the left-hand side of Eq. (4) versus time were linear (Fig. 3b). The slope resulting from linear regression through data points corresponding to the first 95% of the reaction yielded values of k_{obs} ranging from 8.23 to $15.89\ h^{-1}$ (Table 1).

3.3. ATR-FTIR studies

A kinetic experiment was also performed at pH 7.0 using ATR-FTIR spectroscopy to compare with the results obtained with CE and confirm that the products formed are spectroscopically consistent with expected aquation reaction that generates $[Cr^{III}(H_2O)(OH)(nta)]^-$ and liberates a free NTA molecule. Reference spectra for the reactant and both of the expected products are provided

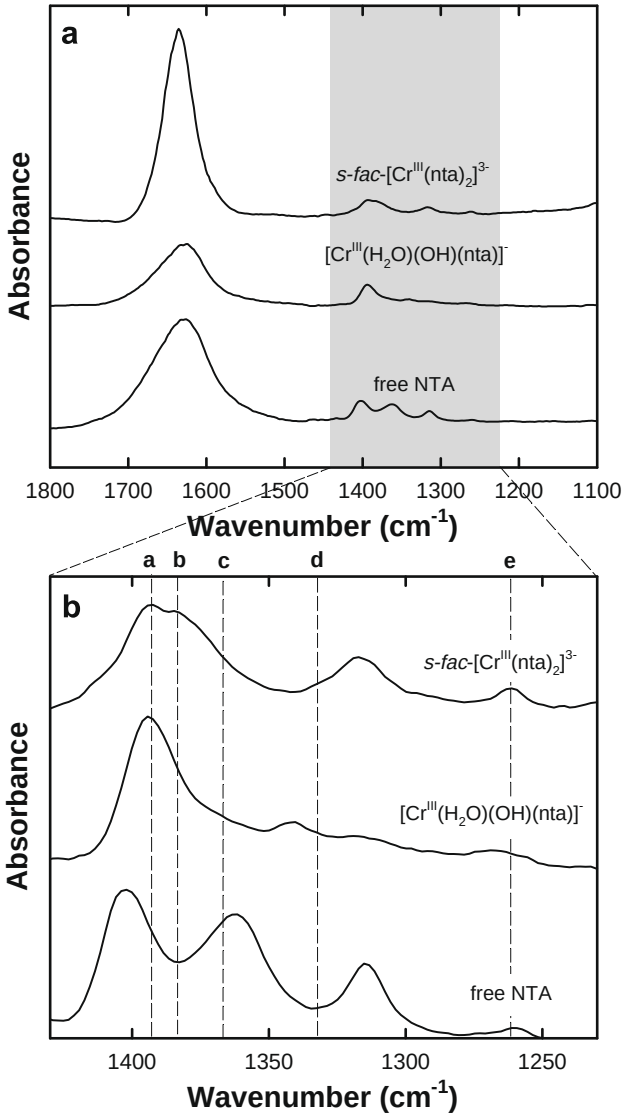


Fig. 4. Reference ATR-FTIR spectra for 10 mM aqueous NTA solutions where the ligand is present predominantly as *s-fac*-$[Cr^{III}(nta)_2]^{3-}$, $[Cr^{III}(H_2O)(OH)(nta)]^-$, and free NTA at pH 7.0 (0.1 M NaCl). Panel A shows the full fingerprint region of the spectra that contains both asymmetric and symmetric carboxylate stretching regions. Panel B shows a close-up of the symmetric carboxylate stretching region used for kinetic analysis. Labels a–e in inset refer to wavenumbers where spectral changes were observed during the aquation of *s-fac*-$[Cr^{III}(nta)_2]^{3-}$ (Fig. 5).

in Fig. 4a. The spectra of NTA species are dominated by contributions from the infrared-active carboxylate groups and are sensitive to protonation, metal coordination, and hydrogen bonding of these groups [36]. The asymmetric stretching mode of the carboxylate group (ν^{as}_{C-O}) occurs near 1600 cm^{-1} and the symmetric modes (ν^{s}_{C-O}) occur in combination with other modes (e.g., C–H stretching modes) in the region between 1300 and 1450 cm^{-1}. Not much difference in the position of ν^{as}_{C-O} is observed for the reference compounds, and variations in the mode's intensity are difficult to interpret here because ν^{as}_{C-O} overlaps with a very strong water bending mode (δ_{H-O-H}) that is difficult to completely subtract out during background correction procedures. Thus, only the spectral region containing ν^{as}_{C-O} was used for quantitative spectral fitting and kinetic analysis.

Fig. 4b shows a close-up on the symmetric stretching region highlighted in Fig. 4a. This region shows several differences between *s-fac*-$[Cr^{III}(nta)_2]^{3-}$ and the two reaction products that reflect changes in the average carboxylate coordination environment. At pH 7.0, free NTA has three deprotonated carboxylate groups and a single protonated bridging nitrogen that can form intramolecular hydrogen bonds with the free carboxylate groups [37]. In the Cr^{III}-coordinated state, the bridging nitrogen is not protonated and intramolecular hydrogen bonding between ligand donor groups is also prevented. Thus, changes in this region of ATR-FTIR spectra can be used to track the progress of the *s-fac*-$[Cr^{III}(nta)_2]^{3-}$ aquation reaction (Fig. 5). A few notable spectral trends are observed during the reaction. The peak at 1393 cm^{-1} (a; letter refers to noted vertical lines in Figs. 4 and 5) blue shifts while a prominent shoulder at 1385 cm^{-1} (b) and peak at 1261 cm^{-1} (e) diminish as the reaction proceeds. At the same time, peak shoulders grow in at both 1367 cm^{-1} (c) and 1336 cm^{-1} (d). Each of these spectral changes are consistent with conversion of *s-fac*-$[Cr^{III}(nta)_2]^{3-}$ into a mixture of $[Cr^{III}(H_2O)(OH)(nta)]^{-}$ and free NTA.

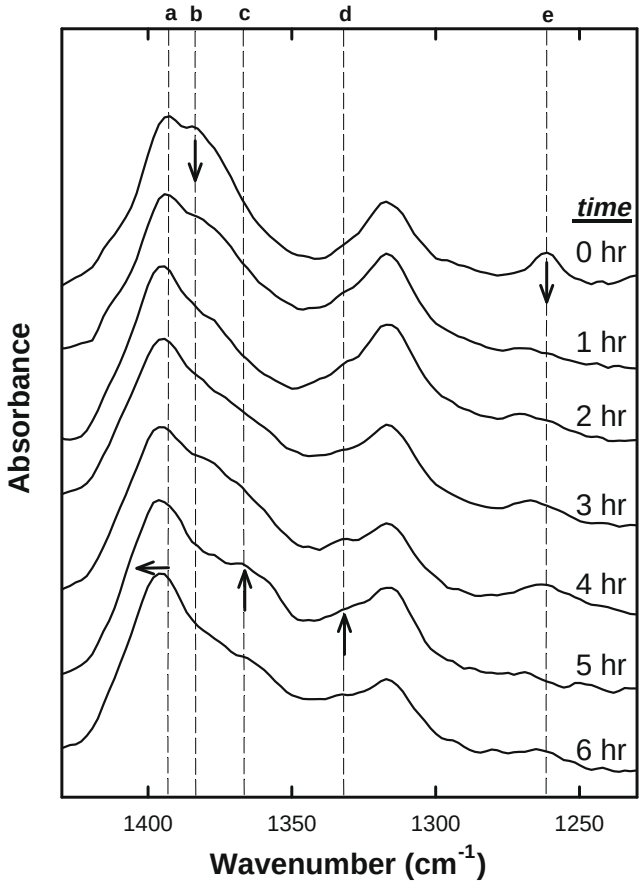


Fig. 5. Time-dependent changes in ATR-FTIR spectra of aqueous solutions initially containing 5.0 mM *s-fac*-$[Cr^{III}(nta)_2]^{3-}$ at pH 7.0 (0.1 M NaCl). Arrows indicate direction of spectral changes during the aquation reaction. Labels a–e indicate wavenumbers at which major spectral shifts were observed and coincide with the same subscripts used in Fig. 4.

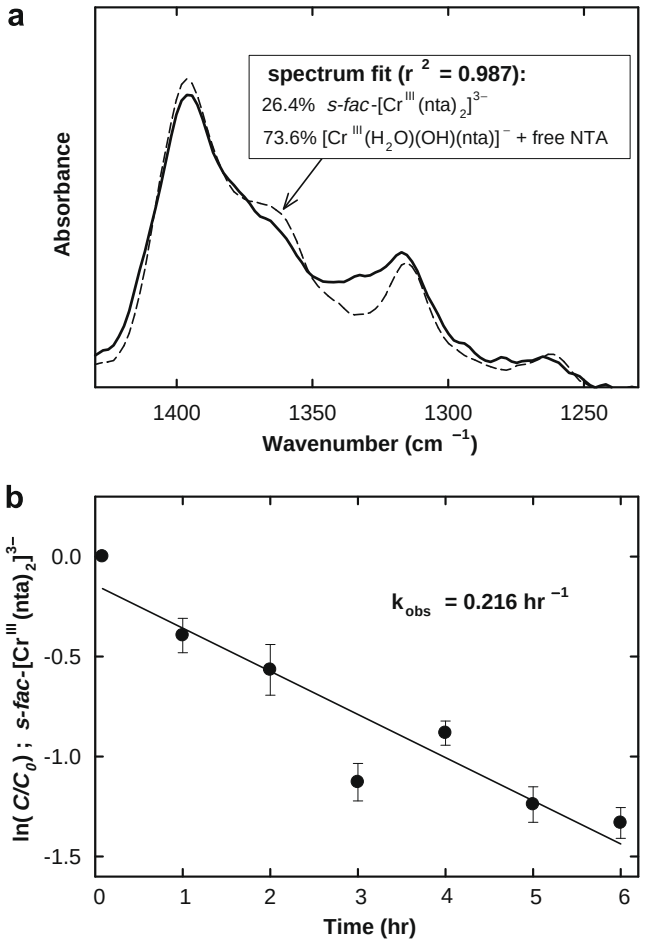


Fig. 6. (a) Comparison of experimental spectrum collected at $t = 6$ h ($C_o = 5$ mM *s-fac*-$[Cr^{III}(nta)_2]^{3-}$, pH 7.0, 0.1 M NaCl) with a model fit-derived spectrum calculated by linear combination of reference spectra for *s-fac*-$[Cr^{III}(nta)_2]^{3-}$, $[Cr^{III}(H_2O)(OH)(nta)]^{-}$, and free NTA shown in Fig. 4. (b) Natural log of the fraction of *s-fac*-$[Cr^{III}(nta)_2]^{3-}$ remaining vs. time and pseudo-first-order kinetic model fit. Error bars represent 95% confidence levels.

The extent of *s-fac*-$[Cr^{III}(nta)_2]^{3-}$ aquation as a function of time was quantified by fitting the observed carboxylate symmetric stretching region spectra in Fig. 5 with a linear combination of the reference spectra shown in Fig. 4b. Similar spectral fitting procedures have previously been used to characterize both homogeneous and heterogeneous kinetic processes [38,39]. Model fits were stoichiometrically constrained by assuming that dissociation of 1 mol of *s-fac*-$[Cr^{III}(nta)_2]^{3-}$ yields 1 mol each of $[Cr^{III}(H_2O)(OH)(nta)]^{-}$ and free NTA. A representative fit of the spectrum collected at $t = 6$ h is provided in Fig. 6a, showing a generally close agreement between the measured and simulated spectrum. The best fit was obtained with 73.6% aquation (that is, a linear combination of 26.4% *s-fac*-$[Cr^{III}(nta)_2]^{3-}$ plus 73.6% $[Cr^{III}(H_2O)(OH)(nta)]^{-}$ and free NTA). It is worth noting that the fit-derived extent of aquation was not found to be significantly different when the stoichiometric constraints were removed during spectral fitting. Fig. 6b shows that decreasing concentrations of *s-fac*-$[Cr^{III}(nta)_2]^{3-}$, determined from spectral fits, followed a first-order rate law, and the k_{obs} value obtained from the slope of

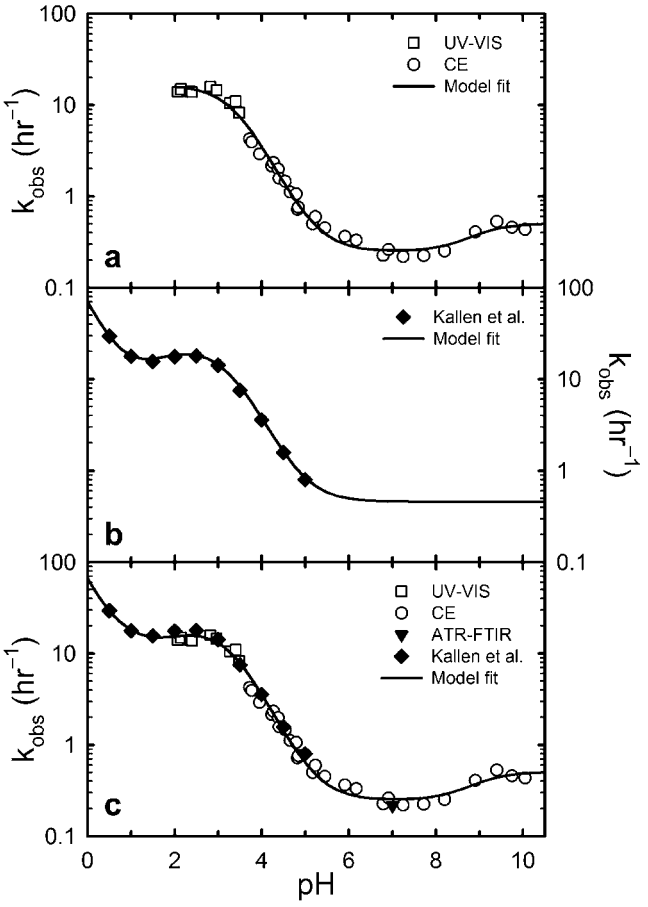


Fig. 7. Observed first-order rate constants, k_{obs}, for aquation of *s-fac*-$[Cr^{III}(nta)_2]^{3-}$ vs. pH. In (a), CE and UV–Vis data from this study is shown with the corresponding model fit according to Eq. (15). In (b), UV–Vis data from Kallen et al. [13] is shown along with the corresponding model fit (conditions: initial [*s-fac*-$[Cr^{III}(nta)_2]^{3-}$] = 172 μM, 25 °C, I = 0.10 M). In (c) CE, UV–Vis, and ATR-FTIR data from this study and UV–Vis data from Kallen et al. is shown with the corresponding model fit according to Eq. (24).

the regression line is equal to 0.216 ± 0.090 h^{-1}. This value agrees closely with the values determined by CE at similar pH conditions (Table 1). The close agreement also indicates that the rate constant for aquation is insensitive to changes in the initial *s-fac*-$[Cr^{III}(nta)_2]^{3-}$ concentration and solution ionic strength since both of these parameters were more than 10-fold higher in the ATR-FTIR experiments than in the CE experiments.

3.4. Modeling the k_{obs} pH dependence from CE and UV–Vis experiments

The k_{obs} values from all CE and UV–Vis experiments are shown as a function of pH in Fig. 7a. The pH dependence is complicated, exhibiting three distinct regions: (i) at pH < 6.5, k_{obs} values increased with decreasing pH, (ii) between pH 6.5 and 8.0, k_{obs} values were relatively constant, and (iii) at 8.0 < pH < 10.0, k_{obs} increased with increasing pH and then leveled off. The solid line in Fig. 7a is a model fit to the k_{obs} data, obtained as described below.

The following three reaction sequences successfully modeled the pH dependence of k_{obs} over the pH range of 2.0–10.0, and are consistent with previously proposed mechanisms for aquation of Cr^{III}–aminocarboxylate complexes [13,40]. Alternate kinetic formulations were explored but did not adequately fit the data (these will be discussed subsequently). Note that *s-fac* has been dropped for simplicity, and the product of the aquation is written as $[Cr^{III}(H_2O)_2(nta)]^0$ in all cases for consistency.

Sequence i:

$$[Cr^{III}(nta)_2]^{3-} + H^+ \underset{(fast)}{\overset{1/K_{a2}}{\rightleftharpoons}} [Cr^{III}(Hnta)(nta)]^{2-} \quad (5)$$

$$[Cr^{III}(Hnta)(nta)]^{2-} + 2H_2O \xrightarrow{k_1} [Cr^{III}(H_2O)_2(nta)]^0 + Hnta^{2-} \quad (6)$$

Sequence ii:

$$[Cr^{III}(nta)_2]^{3-} + 2H_2O \xrightarrow{k_2} [Cr^{III}(H_2O)_2(nta)]^0 + nta^{3-} \quad (7)$$

Sequence iii:

$$[Cr^{III}(nta)_2]^{3-} + H_2O \underset{(fast)}{\overset{K_{a3}}{\rightleftharpoons}} [Cr^{III}(OH)(nta)]^{4-} + H^+ \quad (8)$$

$$[Cr^{III}(OH)(nta)_2]^{4-} + H_2O + 2H^+ \xrightarrow{k_3} [Cr^{III}(H_2O)_2(nta)]^0 + Hnta^{2-} \quad (9)$$

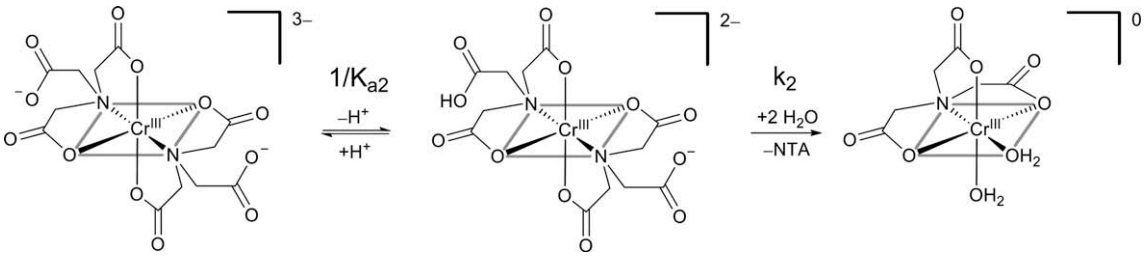
In sequence (i), a reversible protonation reaction is followed by a second reaction where one NTA molecule is replaced by two water molecules. Since *s-fac*-$[Cr^{III}(nta)_2]^{3-}$ has two carboxylate groups that are not coordinated to protons or metal ions (Fig. 1a), one or both of these are expected to protonate in mildly-acidic solution. Equilibrium between $[Cr^{III}(nta)_2]^{3-}$ and $[Cr^{III}(Hnta)(nta)]^{2-}$ is expected to be rapid, and can be described by its law of mass action:

$$K_{a2} = \frac{\left[[Cr^{III}(nta)_2]^{3-}\right][H^+]}{\left[[Cr^{III}(Hnta)(nta)]^{2-}\right]} \quad (10)$$

where K_{a2} is an acidity constant. The second reaction in sequence (i) is an overall reaction which involves exit of NTA and entry of two water molecules into the inner coordination shell of Cr^{III}. Also note that all three carboxylate groups in the complexed ligand become attached to Cr^{III} in the product. Sequence (i) is illustrated below in Scheme 1.

Entry of two water molecules and exit of NTA is expected to be much slower than the preceding protonation step since ligand exchange at the Cr^{III} central ion is involved. Since we do not know whether entry of the first or the second water is the rate limiting step, the k_1 reaction has been written as an overall reaction.

In sequence (ii), an overall reaction is shown where NTA is replaced by two water molecules, thereby forming $[Cr^{III}(H_2O)_2(nta)]^0$ and a "free" NTA molecule. The rate of aquation via sequence (ii) is



Scheme 1.

not dependent upon pH because H^+ or OH^- does not participate prior to or during the rate limiting step. Note however that the nta^{3-} will protonate in a rapid subsequent reaction step.

In sequence (iii), hydroxide ion enters the inner coordination shell of Cr^{III} thereby replacing one Lewis base group of NTA. The equilibrium can be described by its law of mass action:

$$K_{a3} = \frac{\left[[Cr^{III}(OH)(nta)_2]^{4-}\right][H^+]}{\left[[Cr^{III}(nta)_2]^{3-}\right]} \quad (11)$$

where K_{a3} is an acidity constant. The resulting $[Cr^{III}(OH)(nta)_2]^{4-}$ has one NTA molecule coordinated by only 2 Lewis base groups. In the second slower step, the NTA molecule is completely replaced by an incoming water molecule and the last remaining carboxylate group of the other NTA molecule. Sequence (iii) is illustrated below in Scheme 2.

A similar reaction mechanism has been proposed for the aquation of *s-fac*-$[Cr^{III}(ida)_2]^-$ at mildly-alkaline pH [40].

Summing the contributions of these three pathways, the rate of aquation of *s-fac*-$[Cr^{III}(nta)_2]^{3-}$, R (mol L^{-1} h^{-1}), becomes:

$$R = k_1\left[[Cr^{III}(Hnta)(nta)]^{2-}\right] + k_2\left[[Cr^{III}(nta)_2]^{3-}\right] + k_3\left[[Cr^{III}(OH)(nta)_2]^{4-}\right] \quad (12)$$

To simplify this result, $[Cr^{III}–NTA_2]$ was used to represent the sum of the concentrations of $[Cr^{III}(nta)_2]^{3-}$, $[Cr^{III}(Hnta)(nta)]^{2-}$ and $[Cr^{III}(OH)(nta)_2]^{4-}$:

$$\left[Cr^{III}–NTA_2\right] = \left[[Cr^{III}(Hnta)(nta)]^{2-}\right] + \left[[Cr^{III}(nta)_2]^{3-}\right] + \left[[Cr^{III}(OH)(nta)_2]^{4-}\right] \quad (13)$$

Substitution of Eqs. (10), (11), and (13) into Eq. (12) yields the following expression for the rate of aquation of *s-fac*-$[Cr^{III}(nta)_2]^{3-}$:

$$R = -\frac{d[Cr^{III}–NTA_2]}{dt} = \frac{k_1[H^+]^2 + k_2K_{a2}[H^+] + k_3K_{a2}K_{a3}}{[H^+]^2 + K_{a2}[H^+] + K_{a2}K_{a3}}\left[Cr^{III}–NTA_2\right] \quad (14)$$

which produces an expression for k_{obs} which is written in terms of the constants K_{a2}, K_{a3}, k_1, k_2 and k_3:

$$k_{obs} = \frac{k_1[H^+]^2 + k_2K_{a2}[H^+] + k_3K_{a2}K_{a3}}{[H^+]^2 + K_{a2}[H^+] + K_{a2}K_{a3}} \quad (15)$$

Eqs. (14) and (15) assume interconversion between the three protonation levels of Cr^{III}–NTA_2 is much faster than the aquation reactions. Values of k_{obs} therefore represent the loss of Cr^{III}–NTA_2 rather than the loss of any one individual species. Best-fit values for K_{a2}, K_{a3}, k_1, k_2 and k_3 were obtained using a SCIENTIST fit of Eq. (15) to the $\log k_{obs}$ versus pH data obtained from all three experimental methods. The resulting values of K_{a2}, K_{a3}, k_1, k_2 and k_3 are listed in Table 2 as Model 1.

Table 2
Parameters obtained from k_{obs} versus pH model fits.

Parameter	Model fit 1	Kallen et al.[a]	Model fit 2
pK_{a1}		1.87	2.16 ± 1.61
pK_{a2}	3.40 ± 0.10	3.20	3.32 ± 0.14
pK_{a3}	8.94 ± 0.96		8.94 ± 0.88
k_1 (h^{-1})	(1.64 ± 0.24) × 10^1	2.25 × 10^1	(1.91 ± 0.46) × 10^1
k_2 (h^{-1})	(2.48 ± 0.36) × 10^{-1}	4.61 × 10^{-1}	(2.47 ± 0.32) × 10^{-1}
k_3 (h^{-1})	(5.08 ± 0.15) × 10^{-1}		(5.08 ± 0.14) × 10^{-1}
k_4 (h^{-1})		1.10 × 10^1	(1.26 ± 0.74) × 10^1
k_5 (L mol^{-1} h^{-1})		5.98 × 10^1	(5.38 ± 4.49) × 10^1

[a] In Kallen et al. [13], different notation is employed: $K_{a1} = 1/K_1$, $K_{a2} = 1/K_2$, $k_1 = k_4$, $k_2 = k_1$, $k_4 = k_5$, $k_5 = k_H$.

Kinetic schemes where either H^+ or OH^- appear as a reactant often result in a first-order dependence of the reaction rate with respect to these solution constituents. Kinetic models which involve such functional dependences could not reproduce the pH dependence of k_{obs} values in either region (i) or (iii). Since the concentration of H^+ increases by a factor of 10 for every unit decrease in pH, k_{obs} would need to show a similar increase if a reaction sequence was first-order with respect to $[H^+]$. Likewise with OH^-, a unit increase in pH increases $[OH^-]$ by a factor of 10 which would result in a similar increase in k_{obs}. A first-order dependence on $[OH^-]$ is clearly not present in the data as there is a clear leveling out of the value of k_{obs} that occurs at 9.0 < pH < 10.0.

3.5. Modeling the k_{obs} pH dependence using data from Kallen et al.

Observed rate constants for aquation of *s-fac*-$[Cr^{III}(nta)_2]^{3-}$ are available at 25 °C and 1.0 M ionic strength for 0.0 < pH < 5.0 from the UV–Vis kinetic study of Kallen et al. [13]. In their work, observed first-order rate constants showed a unique pH dependence where k_{obs} values increased with decreasing pH, leveled off and then increased again (diamonds, Fig. 7b). The reaction sequence proposed by these authors to explain this pH dependence is compatible with the sequence proposed in this work and is described below.

At low pH, *s-fac*-$[Cr^{III}(nta)_2]^{3-}$ is proposed to undergo two successive protonation steps, whereby each uncoordinated carboxylate group of NTA is protonated [13]:

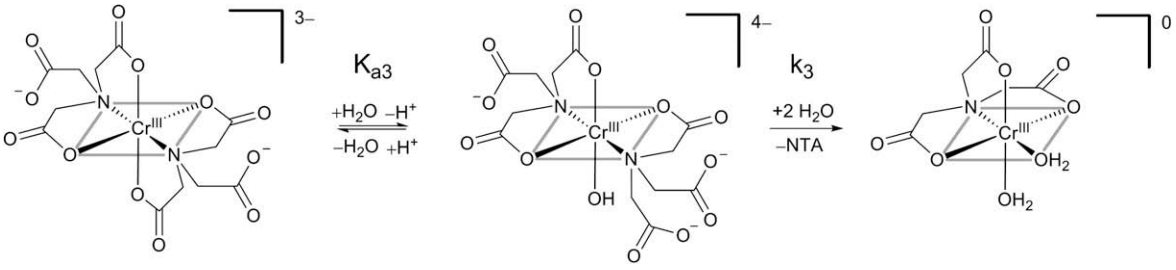
$$[Cr^{III}(nta)_2]^{3-} \overset{1/K_{a2}+H^+}{\underset{-H^+}{\rightleftharpoons}} [Cr^{III}(Hnta)(nta)]^{2-} \overset{1/K_{a1}+H^+}{\underset{-H^+}{\rightleftharpoons}} [Cr^{III}(Hnta)_2]^- \quad (16)$$

The $[Cr^{III}(Hnta)_2]^-$ which results from the second protonation step was proposed to aquate at its own characteristic rate to form Cr^{III}–NTA (Sequence iv):

Sequence iv:

$$[Cr^{III}(nta)_2]^{3-} + 2H^+ \rightleftharpoons [Cr^{III}(Hnta)_2]^- \quad (17)$$

$$[Cr^{III}(Hnta)_2]^- + 2H_2O \overset{k_4}{\rightarrow} [Cr^{III}(H_2O)_2(nta)]^0 + Hnta^{2-} + H^+ \quad (18)$$



Scheme 2.

This sequence alone, however, did not fully explain the pH dependence shown in the k_{obs} data [13]. Therefore, the following acid-catalyzed aquation of $[Cr^{III}(Hnta)_2]^-$ was proposed (Sequence v):

Sequence v:

$$[Cr^{III}(nta)_2]^{3-} + 2H^+ \rightleftharpoons [Cr^{III}(Hnta)_2]^- \quad (19)$$

$$[Cr^{III}(Hnta)_2]^- + H^+ + H_2O \xrightarrow{k_5} [Cr^{III}(H_2O)(Hnta)(H_2nta)]^0 \quad (20)$$

$$[Cr^{III}(H_2O)(Hnta)(H_2nta)]^0 + H_2O \xrightarrow{(fast)} [Cr^{III}(H_2O)_2(nta)]^0 + H_2nta^- + H^+ \quad (21)$$

The reaction shown as Eq. (20) involves exit of a carboxylate group of NTA from the inner coordination shell of Cr^{III}, and entry of a water molecule. This is followed by rapid entry of a second water molecule, exit of one NTA molecule and full attachment of the other NTA molecule. Sequence (v) is illustrated below in Scheme 3:

The solid line shown in Fig. 7b is a SCIENTIST simulation of k_{obs} versus pH using the rate constants and model of Kallen et al. [13] given in Table 2.

Inclusion of Eqs. (17)–(21) into our previously described kinetic model yields five distinct pathways for aquation of Cr^{III}–NTA_2:

$$R = k_1\left[[Cr^{III}(Hnta)(nta)]^{2-}\right] + k_2\left[[Cr^{III}(nta)_2]^{3-}\right] + k_3\left[[Cr^{III}(OH)(nta)_2]^{4-}\right] + k_4\left[[Cr^{III}(Hnta)_2]^-\right] + k_5\left[[Cr^{III}(Hnta)_2]^-\right][H^+] \quad (22)$$

To incorporate the contributions of sequences (iv) and (v) to the rate law, we allow $[Cr^{III}$–$NTA_2]$ to represent the sum of the concentrations of $[Cr^{III}(Hnta)_2]^-$, $[Cr^{III}(Hnta)(nta)]^{2-}$, $[Cr^{III}(nta)_2]^{3-}$, and $[Cr^{III}(OH)(nta)_2]^{4-}$, and substitute the mass action laws corresponding to K_{a1}, K_{a2}, and K_{a3}. The rate of aquation of Cr^{III}–NTA_2 becomes:

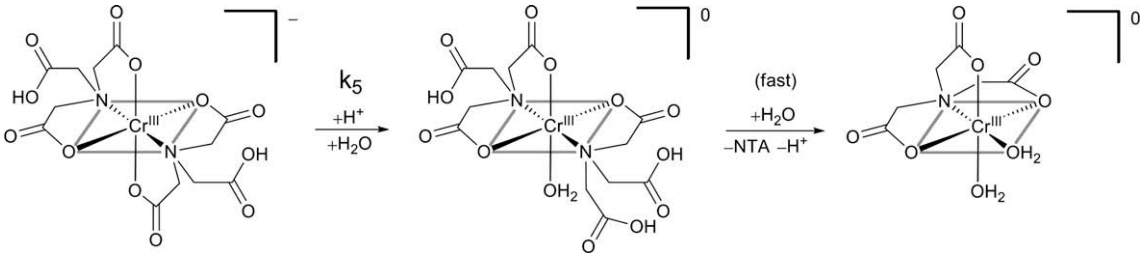
$$R = \frac{k_5[H^+]^4 + k_4[H^+]^3 + k_1K_{a1}[H^+]^2 + k_2K_{a1}K_{a2}[H^+] + k_3K_{a1}K_{a2}K_{a3}}{[H^+]^3 + K_{a1}[H^+]^2 + K_{a1}K_{a2}[H^+] + K_{a1}K_{a2}K_{a3}} \times [Cr^{III}\text{—}NTA_2] \quad (23)$$

which yields an observed first-order rate constant written in terms of K_{a1}, K_{a2} K_{a3}, k_1, k_2, k_3, k_4, and k_5:

$$k_{obs} = \frac{k_5[H^+]^4 + k_4[H^+]^3 + k_1K_{a1}[H^+]^2 + k_2K_{a1}K_{a2}[H^+] + k_3K_{a1}K_{a2}K_{a3}}{[H^+]^3 + K_{a1}[H^+]^2 + K_{a1}K_{a2}[H^+] + K_{a1}K_{a2}K_{a3}} \quad (24)$$

This result is similar to that derived by Kallen et al. [13] with the exception that it includes the contribution of $[Cr^{III}(OH)(nta)]^{4-}$ to the overall rate of aquation. Using the CE, UV–Vis, and ATR-FTIR data generated as part of this study, along with the values measured by Kallen et al. using UV–Vis, a global fit of the k_{obs} versus pH data to Eq. (24) was performed using SCIENTIST. The model fit is shown as the solid line in Fig. 7c. The best-fit values for the three equilibrium constants and five rate constants are shown in Table 2 under Model 2.

Our values for k_{obs} measured with UV–Vis, CE, and ATR-FTIR, supplemented by those of Kallen et al. [13], provide a clear picture



Scheme 3.

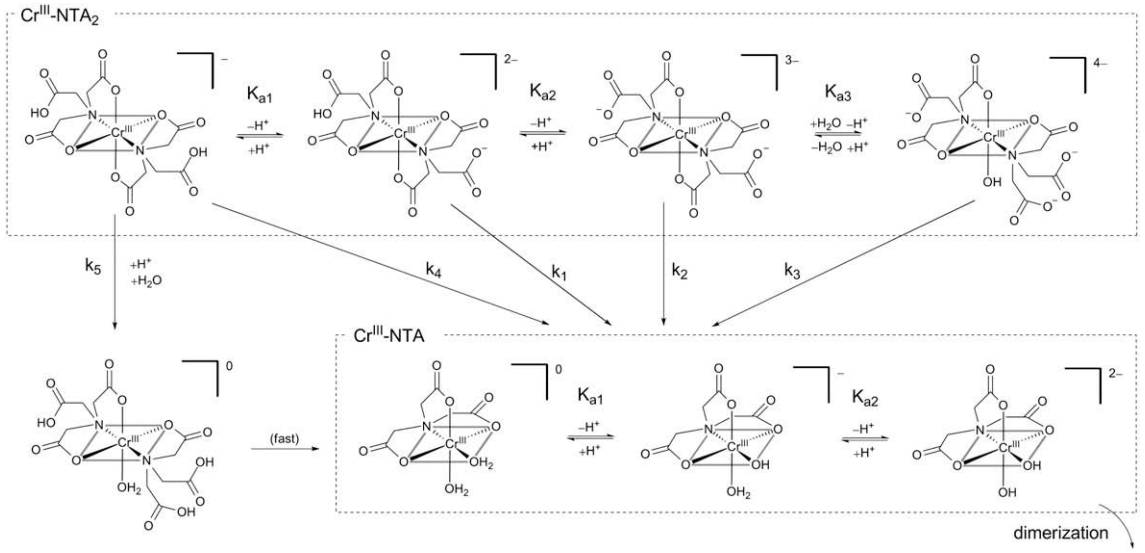


Fig. 8. Proposed kinetic scheme for aquation of *s-fac*-$[Cr^{III}(nta)_2]^{3-}$ for $0.0 \leqslant pH \leqslant 10.0$. Species enclosed in dashed lines are assumed to interconvert rapidly compared to the time scale of aquation.

of the pH dependence of the aquation reaction. These three methods use different initial concentrations of the complex (and different ionic strengths), but k_{obs} values fall nearly on top of one another, and are well replicated by the model line produced from Eq. (24). This fact provides evidence that the observed reaction rate constants are not sensitive to the concentration of the 1:2 complex within the concentration range investigated. This is expected because the reaction is first-order with respect to Cr^{III}–NTA_2. Rate constants obtained by CE are biased low when compared to those reported by Kallen et al. [13] indicating a small ionic strength effect. Model parameters (pK_a values and rate constants) determined from the kinetic models are very similar to one another (Table 2) because of the consistency of the k_{obs} values with those of Kallen et al. [13]. The only large discrepancy is in the value of k_2 (0.461 versus 0.247 h^{-1}). Our k_2 value was fit utilizing k_{obs} values measured by CE at pH values over the entire pH range (Fig. 7c), and therefore provides a better estimate of this parameter.

A visual illustration of the full proposed reaction scheme is shown in Fig. 8. Dashed lines are used to indicate reactions which involve rapid interconversion of either Cr^{III}–NTA_2 or Cr^{III}–NTA. Also indicated on the scheme is an arrow for dimerization of Cr^{III}–NTA to form *trans*-$[Cr_2^{III}(\mu\text{-}OH)_2(nta)_2]^{2-}$. The intermediate product of the acid-catalyzed aquation (Eq. (18)), $[Cr^{III}(H_2O)(Hnta)(H_2nta)]^0$, is indicated with the coordinated water molecule axial to the two nitrogen Lewis base groups. A non-equivalent structure could have been drawn with the coordinated water equatorial to the nitrogen groups. Both of these structures are possible intermediates, but formation of only one was included in the kinetic model for simplicity. Kallen et al. [13] uses the same structure for this intermediate, but does not discuss possibilities for alternate structures.

4. Conclusion

The rate of aquation of *s-fac*-$[Cr^{III}(nta)_2]^{3-}$ and its related forms to produce Cr^{III}–NTA was successfully monitored using a combination of CE and ATR-FTIR. This work is the first published report of the use of either technique to monitor the kinetics of such reactions. Observed first-order rate constants obtained from these techniques were remarkably consistent with those obtained using traditional UV–Vis spectrophotometry. This indicates that CE and ATR-FTIR are viable tools for monitoring Cr^{III} ligand exchange reactions.

As discussed earlier, ligand exchange rates of inorganic Cr^{III} complexes generally increase with increasing pH due to the labilizing effect of coordinated hydroxide ion. For aquation of Cr^{III}–NTA_2, the opposite pH dependence is observed, and the lowest aquation rates occur at circum-neutral pH. This is potentially important for environmental systems (i.e. groundwater, surface water, sediments), which are usually buffered in this same region. In such systems, Cr^{III} speciation in the presence of aminocarboxylate chelating agents may be under kinetic rather than equilibrium control as a result of slow ligand exchange kinetics.

Inorganic chemists have long used substitution-inert metal complexes to gather information about ligand exchange mechanisms and trends in chemical reactivity. In this relatively simple system containing a monomeric Cr-^{III} complex, five rate constants and three equilibrium constants were required to describe the pH dependence of aquation. In natural aquatic environments, there are other ligands (both organic and inorganic) and surfaces present which greatly increases the number of potential ligand exchange reactions that can occur. Which reactions control ligand exchange rates in these more complicated systems? Can we make accurate predictions of ligand exchange rates in natural systems using kinetic models developed from laboratory systems?

We do not have the answers to these questions for many important ligand exchange processes occurring in aqueous solution and at mineral–water interfaces. To begin to answer these questions for processes of environmental interest, it is beneficial to start with well-constrained systems. Knowledge of the acid–base chemistry and structure of the parent complex is required to propose well-supported reaction mechanisms and kinetic models. Metals which exhibit slow ligand exchange kinetics are better suited for study because there are more tools available for observing changes in metal ion speciation during experiments.

Acknowledgements

This research was funded by the National Institute of Environmental Health Sciences through a Superfund Basic Research Program Grant (P42ES10344). Support for Tias Paul was provided by a US Environmental Protection Agency STAR Graduate Fellowship (Agreement No. 91683701-01) and WaterCAMPWS, a Science and Technology Center of Advanced Materials for the Purification of Water with Systems under the National Science Foundation Agreement number CTS-0120978. The authors wish to also thank Christina Manthos, Conor Shea, and Christopher Groth.

References

[1] H.L. Schalfer, G. Gliemann, Basic Principles of Ligand Field Theory, Wiley-Interscience, New York, 1969.
[2] D.T. Richens, The Chemistry of Aqua Ions, John Wiley & Sons, West Sussex, England, 1997.
[3] F.C. Xu, H.R. Krouse, T.W. Swaddle, Inorg. Chem. 24 (1985) 267.
[4] L. Helm, A.E. Merbach, Coord. Chem. Rev. 187 (1999) 151.
[5] L.D. Rich, D.L. Cole, E.M. Eyring, J. Phys. Chem. A 73 (1969) 713.
[6] F.P. Rotzinger, H. Stunzi, W. Marty, Inorg. Chem. 25 (1986) 489.
[7] B. Nowack, Environ. Sci. Technol. 36 (2002) 4009.
[8] Y. Sulfab, R.S. Taylor, A.G. Sykes, Inorg. Chem. 15 (1976) 2388.
[9] H.G. Visser, J.G. Leipoldt, W. Purcell, Polyhedron 13 (1994) 1051.
[10] H. Ogino, I. Watanabe, N. Tanaka, Inorg. Chem. 14 (1975) 2093.
[11] D. Postma, E.L. King, J. Phys. Chem. 59 (1955) 1216.
[12] H. Ogino, M. Shimura, N. Tanaka, Inorg. Chem. 18 (1979) 2497.
[13] T.W. Kallen, M.J. Root, K.A. Schroeder, Inorg. Chem. 18 (1979) 3318.
[14] H.G. Visser, J.G. Leipoldy, W. Purcell, Polyhedron 13 (1994) 1051.
[15] H.G. Visser, W. Purcell, S.S. Basson, Polyhedron 18 (1999) 2. 795–792, 801.
[16] R.F. Carbonaro, A.T. Stone, Anal. Chem. 77 (2005) 155.
[17] L.J. Bellamy, The Infrared Spectra of Complex Molecules, Chapman and Hall, London, 1975.
[18] G.B. Deacon, R.J. Phillips, Coord. Chem. Rev. 33 (1980) 227.
[19] P. Persson, M. Karlsson, L.A. Öhman, Geochim. Cosmochim. Acta 62 (1998) 3657.
[20] T.J. Strathmann, S.C.B. Myneni, Geochim. Cosmochim. Acta 68 (2004) 3441.
[21] J.P. Fitts, P. Persson, G.E. Brown, G.A. Parks, J. Colloid Interface Sci. 220 (1999) 133.
[22] J.S. Loring, M. Karlsson, W.R. Fawcett, W.H. Casey, Spectrochim. Acta, Part A 57 (2001) 1635.
[23] A.J. McQuillan, Adv. Mater. 13 (2001) 1034.
[24] J.S. Loring, M. Karlsson, W.R. Fawcett, W.H. Casey, Polyhedron 20 (2001) 1983.
[25] J.R. Bargar, P. Persson, G.E. Brown, Geochim. Cosmochim. Acta 63 (1999) 2957.
[26] S.J. Hug, D. Bahnemann, J. Electron, Spectrosc. Relat. Phenom. 150 (2006) 208.
[27] Q. Yu, A. Kandegedara, Y. Xu, D.B. Rorabacher, Anal. Biochem. 253 (1997) 50.
[28] N. Koine, R.J. Bianchini, J.I. Legg, Inorg. Chem. 25 (1986) 2835.
[29] H.G. Visser, W. Purcell, S.S. Basson, Polyhedron 18 (1999) 2795.
[30] R. Weinberger, Practical Capillary Electrophoresis, 2nd ed., Academic Press, San Diego, CA, 2000.
[31] F. Wilkinson, Chemical Kinetics and Reaction Mechanisms, Van Nostrand Reinhold, New York, 1980.
[32] H.M.N.H. Irving, R.H. Al-Jarrah, Anal. Chim. Acta 60 (1972) 345.
[33] A.E. Martell, R.M. Smith, R.J. Motekaitis. NIST Critically Selected Stability Constants of Metal Complexes, NIST, 2004.
[34] A. Ricard, P. Souchay, Rev. Chim. Miner. 8 (1971) 859.
[35] R.G. Wilkins, Kinetics and Mechanism of Reactions of Transition Metal Complexes, 2nd Thoroughly Revised ed., VCH, Weinheim, 1991.
[36] K. Nakamoto, Infrared and Raman Spectra of Inorganic and Coordination Compounds, John Wiley & Sons, New York, 1986.
[37] J.P. Fitts, P. Persson, J.G.E. Brown, G.A. Parks, J. Colloid Interf. Sci. 220 (1999) 133.
[38] J.R. Bargar, B.M. Tebo, J.E. Villinski, Geochim. Cosmochim. Acta 64 (2000) 2775.
[39] H. Namli, O. Turhan, Vib. Spectrosc. 43 (2007) 274.
[40] J.A. Weyh, R.E. Hamm, Inorg. Chem. 8 (1969) 2298.

Polyhedron 28 (2009) 279–285

Contents lists available at ScienceDirect

Polyhedron

journal homepage: www.elsevier.com/locate/poly

Synthesis, structure characterization and thermal properties of $[Zr_6(\mu_3\text{-}O)_4(\mu_3\text{-}OH)_4(OOCCH_2{}^tBu)_9(\mu_2\text{-}OH)_3]_2$

P. Piszczek [a,*], A. Radtke [a], A. Wojtczak [a], T. Muzioł [a], J. Chojnacki [b]

[a] Faculty of Chemistry, Nicolaus Copernicus University, ul. Gagarina 7, 87-100 Toruń, Poland
[b] Chemical Faculty, Gdańsk University of Technology, ul. G. Narutowicza 11/12, 80-952 Gdańsk, Poland

ARTICLE INFO

Article history:
Received 10 April 2008
Accepted 19 October 2008
Available online 6 December 2008

Keywords:
Oxo/hydroxo zirconium complexes
Carboxylate ligands
Crystal structure
IR
NMR
Thermal analysis

ABSTRACT

Oxo/hydoxo zirconium(IV) complex of the general formula $[Zr_6(\mu_3\text{-}O)_4(\mu_3\text{-}OH)_4(OOCCH_2{}^tBu)_9(\mu_2\text{-}OH)_3]_2$ has been isolated, when $Zr(O^iPr)_4$ reacted with a 2-fold excess of 3,3-dimethylbutyric acid. Single crystal X-ray diffraction data, collected at 103 and 153 K, showed that the studied compound crystallizes in hexagonal system ($P6_3/m$ (no. 176)). Structure consists of dimers composed of $[Zr_6(\mu_3\text{-}O)_4(\mu_3\text{-}OH)_4(OOCCH_2{}^tBu)_9]$ sub-units, linked by six μ_2-OH bridges. Infrared spectroscopic studies proved the presence of hydroxo groups in the structure of studied clusters and formation of different types of oxo/hydroxo bridges. The application of variable temperature infrared spectroscopy and differential scanning calorimetry revealed that the structure of this complex undergoes the phase transitions at 143–183 and 203–293 K. Comparison of spectral and crystallographic data suggests that these phase transitions might be related to changes in the strength of Zr–O bonds of μ_2-OH bridges linking complex sub-units, and change in symmetry of the crystal lattice (from hexagonal to trigonal). Analysis of thermogravimetric data showed that decomposition of $[Zr_6(\mu_3\text{-}O)_4(\mu_3\text{-}OH)_4(OOCCH_2{}^tBu)_9(\mu_2\text{-}OH)_3]_2$ proceeds with complete conversion to ZrO_2 (monoclinic form) between 603 and 803 K.

© 2008 Elsevier Ltd. All rights reserved.

1. Introduction

Synthesis, structure, and properties of zirconium oxo clusters have been studied extensively in a search of the novel types of hybrid materials having interesting optical, magnetic, and catalytic properties [1–5]. Recently Kickelbick, Schubert et al. have described syntheses and crystal structures of the group of multinuclear Ti(IV) and Zr(IV) oxo acrylate or methacrylate derivatives, which were efficiently used as sol–gel precursors in the fabrication of organic–inorganic materials [6–8]. According to these reports, the reaction of Zr(IV) isopropoxides with corresponding organic acids, using a molar ratio 1:4 and 1:16, respectively, leads to the formation of carboxylate derivatives of general formulas $[Zr_6(OH)_4O_4(OMc)_{12}]$ or $[Zr_4O_2(OMc)_{12}]$ [6–8]. In the structure of $[Zr_6(OH)_4O_4(OMc)_{12}]$, zirconium atoms (coordination number 8) form hexanuclear cores with μ_3-oxo and μ_3-hydroxo bridges, which are stabilized by 12 methacrylate ligands. Three carboxylate ligands form the chelate interactions with Zr(IV) atoms, while other nine participate in *syn–syn* bridges. The reaction of $Zr(O^iPr)_4$ with a 6.5-fold excess of acrylic acid, under the same conditions, proceeds with a formation of approximately 1:3 mixture of an amorphous powder and crystals [8]. The X-ray structural studies revealed the formation of dimers, composed of two $[Zr_6(OH)_4O_4(OAcr)_{12}]$ units linked by four carboxylate bridges. Zr(IV) compounds, also formed by two multinuclear Zr(IV) sub-units linked by alkoxide bridges, were synthesized in the reaction of $Zr(O^nBu)_4$ with 1.6 equiv. of methacrylic acid [9]. The use of ~16-fold excess of the methacrylic acid led to the formation of $[Zr_4O_2(OMc)_{12}]$ [6]. Literature reports concerning oxo zirconate acrylate or methacrylate derivatives, suggest that the type of the formed cluster depends on (a) the $M(OR)_4$/HOOCR′ ratio and (b) the kind of OR groups [9]. The application of sterically diverse carboxylic acids (HOOCR′; R′ = H, CH_3, ^{i}Pr, ^{t}Bu, $CH_2{}^t$Bu) in the reaction with zirconium(IV) isopropoxide ($[Zr(O^iPr)_4 \cdot HO^iPr]_2$, molar ratio 1:1) leads to the formation of the following products: $[Zr_4O_2(O_2CH)_2(O^iPr)_{10}]$, $[Zr_3O(O_2CCH_3)_5(O^iPr)_5]$, $[Zr_2(O^iPr)_6(O_2C^iPr)_2]_2$, $[Zr_2O(O_2C^tBu)(O^iPr)_7](HO^iPr)_2$, $[Zr_2O(O_2CH_2{}^tBu)_2(O^iPr)_6](HO^iPr)$ [10]. The use of the 2-fold excess of organic branched acids (HOOCR′; R′ = ^{t}Bu, $C(CH_3)_2Et$) in the above reaction results in a formation of $[Zr_6(OH)_4O_4(OOCR')_{12}]$ (R′ = ^{t}Bu, $C(CH_3)_2Et$) clusters [11]. Also in this case, the hexanuclear zirconium core was linked by four μ_3-oxo and four μ_3-hydroxo bridges and stabilized by 12 carboxylate *syn–syn* bridges. Simultaneously, spectroscopic studies revealed that the more complicated type of multinuclear Zr(IV) oxo clusters was formed during the 1:2 reaction of $Zr(O^iPr)_4$ with $HOOCCH_2{}^tBu$ [11]. Although the stability of single crystals at room temperature was sufficient, their crystal structure has not been solved. Therefore, the aim of the presented paper is the structural and spectral characterization of the multinuclear Zr(IV) oxo

* Corresponding author. Fax: +48 56 654 24 77.
E-mail address: piszczek@chem.uni.torun.pl (P. Piszczek).

0277-5387/$ - see front matter © 2008 Elsevier Ltd. All rights reserved.
doi:10.1016/j.poly.2008.10.034

carboxylate derivatives, obtained in a reaction of $Zr(O^iPr)_4$ with 2-fold excess of 3,3-dimethylbutyric acid under the inert atmosphere.

2. Results and discussion

2.1. Synthesis and spectral characterization

The studied complex was obtained in the 1:2 reaction of the zirconium isopropoxide ($Zr(O^iPr)_4$, with 3,3-dimethylbutyric acid under Ar atmosphere at room temperature. The colorless crystals were isolated by slow evaporation (glovebox) of the solvent after 1 day. The general formula defined on the basis of the elemental analysis is $Zr_6O_{29}C_{54}H_{103}$, suggesting the possible formation of a similar type of cluster as described for $[Zr_6(\mu_3\text{-}O)_4(\mu_3\text{-}OH)_4(OOCR')_{12}]$ ($R' = {}^t$Bu, $C(CH_3)_2Et$). However, the clear differences between IR spectra of synthesized compound and those reported in [11] indicate the formation of different type of structure (Fig. 1).

The synthesized complex has been characterized by multinuclear NMR spectroscopy in the solid phase and solution ([D_6] benzene) and chemical shifts of the resonance signals are listed in Table 1. The coordination effects were studied mainly as a result of the chemical shift of resonance signals descended from carbon atoms of carboxylate ligands. Three resonance signals attributed to carbon atoms of COO group were found at δ = 174.7, 178.1, and 179.4 ppm (Table 1). Coordination of carboxylate groups caused the shift of resonance signals towards lower fields in comparison to the spectrum of 3,3-dimethylbutyric acid (δ (COO) = 179.9 ppm). Simultaneously, analysis of chemical shifts of carboxylate carbon in spectra of dimeric complex and $[Zr_6(\mu_3\text{-}O)_4(\mu_3\text{-}OH)_4(OOCR')_{12}]$ ($R' = {}^t$Bu, δ = 184.5, 183.9 ppm, $C(CH_3)_2Et$), δ = 184.3, 183.9 ppm [11]) reveals that the shift of the resonance signals of COO group is significantly influenced by the type of the carboxylate ligand. Moreover, splitting of the resonance signals of carboxylate atoms suggests that carboxylate ligands form non-equivalent interactions with zirconium ions of $[Zr_6\text{-}(\mu_3\text{-}O)_4(\mu_3\text{-}OH)_4]$ cores.

Analysis of ^{13}C NMR data, registered in [D_6] benzene solution (Table 1) revealed no significant difference in chemical shifts of resonance signals attributed to the methyl, methylene, and buthyl moiety of the $-CH_2C(CH_3)_3$ group. Simultaneously, only a single peak assigned as the COO group (δ = 179.0 ppm) has been found. This indicates that the stable and highly symmetrical molecules of the synthesized complex exist also in solution.

Table 1
Results of NMR studies of compound synthesized in the reaction $Zr(O^iPr)_4$ with $HOOCCH_2{}^t$Bu, reported in this paper.

Method	δ (ppm)			
	CH_2	CH_3 (^{t}Bu)	C (^{t}Bu)	C (COO)
^{13}C–s.st	50.6	30.3	43.5	179.4 178.1 174.7
$^{13}C\text{–}C_6D_6$	50.7	30.2		179.0
$^{1}H\text{–}C_6D_6$	2.3	1.5		

The XRD patterns, collected one week and one month after crystallization, proved the high stability of crystalline powders stored at room temperature on the air. The obtained compound was insoluble in aliphatic and sparingly soluble in aromatic solvents.

2.2. Description of the structures

Multiple attempts to determine the X-ray crystal structure at room temperature showed that the studied compound crystallized in the trigonal space group *P*3 (no. 143). Although X-ray diffraction measurements at room temperature have been carried out for numerous crystals, their structure has not been solved due to the poor data quality. Therefore, the low temperature measurements at 103 K and 153 K have been carried out. The details of the X-ray analysis are listed in Table 2, selected bond lengths and angles are listed in Table 3.

Low temperature X-ray crystal structure determination revealed that the studied compound crystallizes in the hexagonal system ($P6_3/m$). Its structure consists of dimers composed of $[Zr_6(\mu_3\text{-}O)_4(\mu_3\text{-}OH)_4(OOCR')_9]$ sub-units, linked by six oxygen bridges (Fig. 2). Average distances between Zr–Zr atoms, within the sub-unit are 3.56 Å and between neighboring units are 3.58 Å at 103 K and 3.57 Å at 153 K. Simultaneously, these distances are slightly larger than analogous average distances within

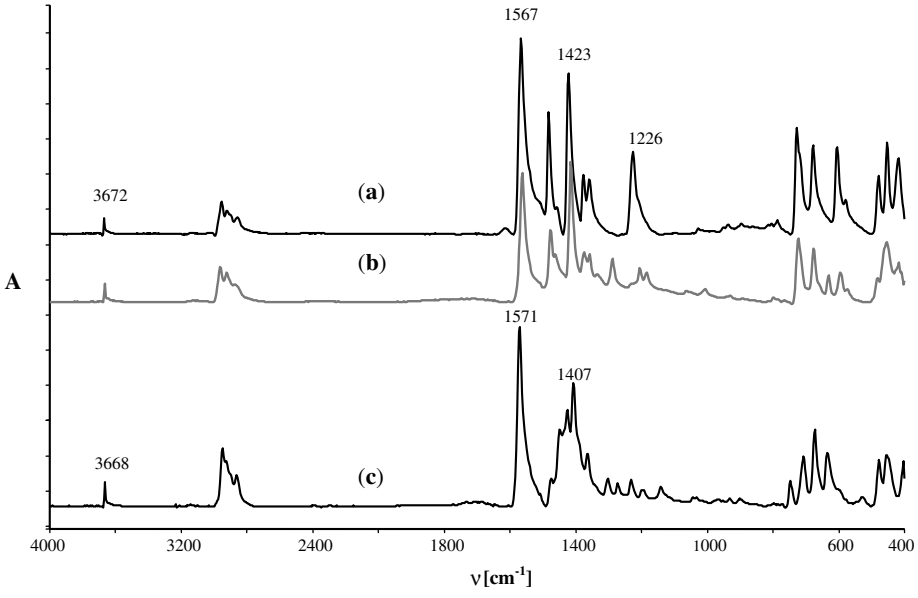


Fig. 1. IR spectra of (a) $[Zr_6O_4(OH)_4(OO{}^tBu)_{12}]$, (b) $[Zr_6O_4(OH)_4(OOCC(CH_3)_2Et)_{12}]$, and (c) compound synthesized in the reaction $Zr(O^iPr)_4$ with $HOOCCH_2{}^t$Bu, reported in this paper.

Table 2
Details of crystallographic data collection and structure refinement.

	103 K	153 K
Formula sum	$Zr_{12}O_{70}C_{144}H_{264}$	$Zr_{12}O_{70}C_{144}H_{264}$
Formula weight	4056	4056
Crystal system	Hexagonal	Hexagonal
Space group	$P6_3/m$ (no. 176)	$P6_3/m$ (no. 176)
Unit cell dimensions		
a (Å)	16.900(2)	16.903(3)
c (Å)	37.160(7)	37.155(9)
V (Å^3)	9191(3)	9194(3)
Z	2	2
D_{calc} (Mg/m^3) (g/cm^3)	1.272	1.289
Absorption coefficient (mm^{-1})	0.716	0.718
$F(000)$	3580	3628
Crystal size (mm)	0.64 × 0.31 × 0.26	0.24 × 0.13 × 0.03
Theta range for data collection (°)	1.77–18.48	2.41–23.99
Index ranges	$-14 < h < 15$ $-12 < k < 12$ $-32 < l < 32$	$-19 < h < 19$ $-19 < k < 19$ $-27 < l < 42$
Reflections collected	41960	44514
Independent reflections	8830	4889
Transmission maximum/minimum	0.8358/0.6573	0.9788/0.8466
Refinement method	Full matrix L.S.	Full matrix L.S.
Data/restraints/parameters	2307/30/281	4889/0/280
Goodness-of-fit on F^2	1.082	1.176
Final R[a] indices [$I > 2\sigma(I)$]	0.0845	0.1133
wR_2[b] indices [$I > 2\sigma(I)$]	0.2538	0.2988
Largest difference in peak and hole (e Å^{-3})	2.719/−0.817	3.922/−1.652

[a] $R = \sum||F_o| - |F_c||/\sum|F_o|$.
[b] $wR_2 = [\sum w(F^2_o - F^2_c)^2/\sum(w|F_o|^2)^2]^{1/2}$.

$[Zr_6(OH)_4O_4]$ core of $[Zr_6(OH)_4O_4(OMc)_{12}]_2$ (3.52 Å [8]). All zirconium atoms in the structure of $[Zr_6O_4(OH)_4(OOCCH_2{}^tBu)_9]$ are eight-coordinate and form two types of surroundings. The $[Zr1O_8]$ polyhedra consist of four oxygen μ_3-O bridges, formed by oxo/hydoxo ligands, and four μ-O of carboxylato ones, whereas $[Zr2O_8]$ are formed by two oxygen atoms of μ_3-O (O/OH), four μ-O (OOC), and two μ_2-O of O/OH bridges (Table 2).

The localization of hydrogen atoms in the zirconium-oxide of dimers core was not possible on the basis of obtained X-ray diffraction data. However, the charge balance requires the presence of hydroxo groups (that problem is also discussed in the next part of this paper, where the IR spectroscopy results are analyzed). Significant differences in Zr–O distances of μ_3-O bridges suggest that oxo and hydroxo bridges can be identified on the basis of this criterion. Analysis of X-ray data, collected at 103 K (Table 2), revealed the formation of four types of μ_3-O bridges per sub-unit (1 × O1, 3 × O2, 1 × O6, and 3 × O3). Short distances between O2 and Zr1, $Zr1^{ii}$, $Zr2^{ii}$ atoms (Zr–O2, 2.044(11)–2.062(12) Å) indicate the formation of μ_3-O bridges [6]. In contrast, O3 is asymmetrically bonded and forms three longer Zr–O bonds, two of them are significantly shorter (2.256(12) and 2.255(11) Å) than the third one (2.327(11) Å). According to previous reports, this type of interactions has been assigned to μ_3-OH bridges [6]. The symmetrical location of oxygen atoms is also observed in bridges formed by O1 (2.242(7)–2.244(7) Å) and O6 (2.189(4) Å). Judged from the length of metal–oxide bonds, bridges formed by O1 can be attributed to μ_3-OH bridges, while the O6 to μ_3-O bridges (Table 2). The electrostatic compensation requires the presence of 14 hydroxo groups in the studied complex. Therefore, bridges formed by O4 and O5 atoms should also correspond to μ_2-OH ligands. Considering these data, the neutral sub-unit cluster should be built with 4:4 systems of oxo/hydroxo bridges, linked by 6 μ_2-OH bridges ($[Zr_6(\mu_3\text{-}O)_4(\mu_3\text{-}OH)_4(OOCCH_2Bu^t)_9(\mu_2\text{-}OH)_3)]_2$). According to data presented in Table 2, carboxylate ligands form two types of bridges. In one of them no significant differences in the length of Zr–O bonds were observed (Zr1–O61, 2.226(13) and $Zr1^{i}$–O62, 2.246(12) Å), while in the second type (asymmetric bridge) the shorter Zr–O bonds Zr1–O72, 2.176(12), $Zr1^{i}$–O82, 2.169(16) Å, and longer bonds Zr2–O81, 2.220(14), Zr2–O71, 2.233(9) Å were observed.

Analysis of data presented in Table 3 revealed that no significant differences were observed in the crystal system and unit cell parameters of $[Zr_6(\mu_3\text{-}O)_4(\mu_3\text{-}OH)_4(OOCCH_2{}^tBu)_9(\mu_2\text{-}OH)_3]_2$ between 103 and 153 K. Moreover, the comparison of the average Zr–Zr distances within $Zr_6(\mu_3\text{-}O)_4(\mu_3\text{-}OH)_4$ cores suggests the lack of significant differences in geometry of clusters at 103 and 153 K. The noticeable differences in the structure of this complex were detected, when the length of Zr–O distances and Zr–O–Zr angles of μ_2-OH bridges were compared at both temperatures. At 103 K, similar values of analogous Zr–O distances (Zr2–O4 = 2.174(6) Å and Zr2–O5 2.173(8) Å) and Zr–O–Zr, O–Zr–O angles (Zr2–O4/5–Zr2 = 110.78(6)° and 110.87(6)°, O4–Zr2–O5 = 66.49(4)°) prove the formation of symmetrical μ_2-OH bridges linking two sub-units. Increase of the temperature up to 153 K causes the clear changes both in the Zr–O bond distances (Zr2–O5 = 2.150(7) Å; Zr2–O4 = 2.169(7) Å) and Zr–O–Zr, O–Zr–O angles (Zr2–O4/5–Zr2 110.7(4)° and 112.2(5)°, O5–Zr2–O4 = 65.2(4)°) of μ_2-OH bridges. These changes influenced also values of dihedral angle between Zr2–O4–Zr2 (x, y, $-z + 1/2$) and Zr2–O5–Zr2 (x, y, $-z + 1/2$) planes being 30.11(0.86)° and 33.57(0.84)° for 103 and 153 K models, respectively. Moreover, the differences in the Zr–O distances of Zr2 coordination sphere were also found (Table 3). Results of these investigations show that the decrease of the strength of metal–oxide bonds in μ_2-OH bridges, linking $[Zr_6O_4(OH)_4(OOCR')_9]$ sub-units is the main effect associated with the temperature increase.

2.3. Analysis of infrared spectra

IR spectroscopy analysis has been carried out in order to detect the hydroxide groups in the structure of the complex, as well as to determine the nature of μ_2-O bridges linking $[Zr_6(\mu_3\text{-}O)_4(\mu_3\text{-}OH)_4(OOCR')_9]$ sub-units. IR spectra were registered between 103 and 293 K to study influence of the temperature increase on the structure of the synthesized complex. Results of spectroscopic investigations are presented in Table 4.

Detection of the band at 3668 cm^{-1}, which was attributed to stretching ν(OH) band, explicitly confirms the presence of hydroxo groups in the structure of the studied complex. According to literature data, the position of the ν(OH) band at higher wavenumbers indicates that OH groups are not involved in hydrogen bonds [11–13]. Only slight changes of ν(OH) motions, which were found in spectra registered at 293 and 103 K, indicate the high stability of hydroxo ligands in the zirconium oxo/hydroxo clusters. Simultaneously analysis of ν(OH) band shape using curve fit method, revealed the slight splitting of this band in the spectrum registered at ~103 K (Fig. 3). This effect can be explained by the presence of nonequivalent hydroxo groups in the complex molecule, resulting in the formation of μ_3-OH and μ_2-OH bridges in the molecule of $[Zr_6(\mu_3\text{-}O)_4(\mu_3\text{-}OH)_4(OOCCH_2{}^tBu)_9(\mu_2\text{-}OH)_3]_2$.

Bands attributed to ν_{as}(COO) and ν_s(COO) vibrations have been detected at 1572 cm^{-1} and 1426 cm^{-1} in spectra registered at 298 K (Table 4). Values of the $\Delta\nu[\nu_{as}(COO) - \nu_s(COO)]$ parameter, being 146 cm^{-1}, is characteristic for bidendate carboxylate groups participating in *syn–syn* bridges [13,17]. Single bands, descended from asymmetric and symmetric vibrations, indicate the lack of significant differences in the strength of carboxylate groups interaction in $[Zr_6(\mu_3\text{-}O)_4(\mu_3\text{-}OH)_4(OOCCH_2{}^tBu)_9]$ sub-unit. Splitting of bands descended from OCO bending and rocking vibrations can result from the asymmetry of carboxylate ligand interactions in *syn–syn* bridges. The slight changes in the way of OOC groups interaction with zirconium atoms with increase of temperature

Table 3
Selected interatomic distances (Å) and angles (°) for $[Zr_6(\mu_3\text{-}O)_4(\mu_3\text{-}OH)_4(OOCCH_2{}^tBu)_9(\mu_2\text{-}OH)_3]_2$ measured at 103 and 153 K.

103 K				153 K			
Distances (Å)		Angles (°)		Distances (Å)		Angles (°)	
Zr1–Zr1^{ii}	3.484(2)	Zr1^{ii}–O1–Zr1	101.87(5)	Zr1–Zr1^{ii}	3.492(2)	Zr1–O1–Zr1^{ii}	101.9(4)
Zr1–Zr1^{i}	3.484(2)	Zr1^{ii}–O1–Zr1^{i}	101.89(2)	Zr1–Zr1^{i}	3.492(2)	Zr1^{i}–O1–Zr1^{ii}	101.9(4)
Zr1–Zr2	3.515(2)	Zr1–O1–Zr1^{i}	101.92(4)	Zr1–Zr2	3.521(2)	Zr1^{i}–O1–Zr1	101.9(4)
Zr1–Zr2^{ii}	3.521(2)	Zr2^{ii}–O2–Zr1^{ii}	118.46(5)	Zr1–Zr2^{ii}	3.527(2)	Zr1^{ii}–O2–Zr2^{ii}	117.6(4)
Zr1–Zr2^{i}	5.020(2)	Zr2^{ii}–O2–Zr1	118.07(5)	Zr1–Zr2^{i}	5.028(2)	Zr1–O2–Zr2^{ii}	118.3(4)
Zr2–Zr1	3.515(2)	Zr1^{ii}–O2–Zr1	115.95(4)	Zr2–Zr1	3.521(2)	Zr1–O2–Zr1^{ii}	116.6(4)
Zr2–Zr2^{ii}	3.681(2)	Zr2–O3–Zr2^{ii}	109.36(5)	Zr2–Zr2^{ii}	3.687(2)	Zr2–O3–Zr2^{ii}	108.9(3)
Zr2–Zr2^{i}	3.681(1)	Zr2–O3–Zr1	100.17(4)	Zr2–Zr2^{i}	3.687(2)	Zr2–O3–Zr1	100.4(3)
Zr2–Zr1^{i}	3.521(2)	Zr2^{ii}–O3–Zr1	100.36(4)	Zr2–Zr1^{i}	3.527(2)	Zr2^{ii}–O3–Zr1	100.5(3)
Zr2–Zr1^{ii}	5.020(2)	Zr2^{iii}–O4–Zr2	110.78(6)	Zr2–Zr1^{ii}	5.028(2)	Zr2–O4–Zr2^{iii}	110.7(5)
Zr2–Zr2^{iii}	3.579(2)	Zr2^{iii}–O5–Zr2	110.87(6)	Zr2–Zr2^{iii}	3.570(2)	Zr2–O5–Zr2^{iii}	112.2(5)
O1–Zr1	2.243(7)	Zr2^{i}–O6–Zr2^{ii}	114.46(3)	O1–Zr1	2.249(6)	Zr2^{ii}–O6–Zr2^{i}	114.6(3)
O1–Zr1^{ii}	2.244(7)	Zr2^{i}–O6–Zr2	114.53(3)	O1–Zr1^{ii}	2.249(6)	Zr2–O6–Zr2^{i}	114.6(3)
O1–Zr1^{i}	2.242(7)	Zr2^{ii}–O6–Zr2	114.50(5)	O1–Zr1^{i}	2.249(6)	Zr2–O6–Zr2^{ii}	114.6(3)
O2–Zr1	2.062(12)	O5–Zr2–O4	66.49(4)	O2–Zr1	2.049(9)	O5–Zr2–O4	65.2(4)
O2–Zr2^{ii}	2.044(11)	O5–Zr2–O81	77.62(3)	O2–Zr2^{ii}	2.059(8)	O5–Zr2–O81	78.4(4)
O2–Zr1^{ii}	2.047(9)	O5–Zr2–O71	116.85(3)	O2–Zr1^{ii}	2.056(8)	O5–Zr2–O71	117.1(4)
O3–Zr2^{ii}	2.256(12)	O5–Zr2–O6^{i}	86.88(6)	O3–Zr2^{ii}	2.265(8)	O5–Zr2–O6	87.3(4)
O3–Zr1	2.327(11)	O4–Zr2–O6^{i}	87.02(5)	O3–Zr1	2.322(8)	O4–Zr2–O6	88.3(4)
O3–Zr2	2.255(11)	O4–Zr2–O81	116.60(3)	O3–Zr2	2.261(8)	O4–Zr2–O81	115.6(4)
O4–Zr2^{iii}	2.174(6)	O4–Zr2–O71	78.27(1)	O4–Zr2^{iii}	2.169(7)	O4–Zr2–O71	77.9(4)
O4–Zr2	2.174(6)	O6^{i}–Zr2–O81	142.25(3)	O4–Zr2	2.169(7)	O6–Zr2–O81	142.5(3)
O5–Zr2^{iii}	2.173(8)			O5–Zr2^{iii}	2.151(7)		
O5–Zr2	2.173(8)			O5–Zr2	2.150(7)		
O6–Zr2^{i}	2.189(4)			O6–Zr2^{i}	2.189(3)		
O6–Zr2^{ii}	2.189(4)			O6–Zr2^{ii}	2.189(3)		
O6–Zr2	2.188(4)			O6–Zr2	2.189(3)		
O61–Zr1	2.226(13)			O61–Zr1	2.225(9)		
O61–C61	1.270(25)			O61–C61	1.254(18)		
O62–Zr1^{i}	2.246(12)			O62^{ii}–Zr1	2.242(9)		
O62–C61	1.272(18)			O62–C61	1.272(18)		
O71–Zr2	2.233(9)			O71–Zr2	2.242(9)		
O71–C71	1.276(20)			O71–C71	1.263(16)		
O72–Zr1	2.176(12)			O72–Zr1	2.186(9)		
O72–C71	1.295(25)			O72–C71	1.253(15)		
O81–Zr2	2.220(14)			O81–Zr2	2.238(9)		
O81–C81	1.305(21)			O81–C81	1.265(16)		
O82–Zr1^{i}	2.169(16)			O82–Zr1^{i}	2.184(9)		
O82–C81	1.257(25)			O82–C81	1.278(16)		

Symmetry codes: For structures determined at 103 K and 153 K – (i) $1-y, 1+x-y, z$; (ii) $-x+y, 1-x, z$; (iii) $x, y, 0.5-z$.

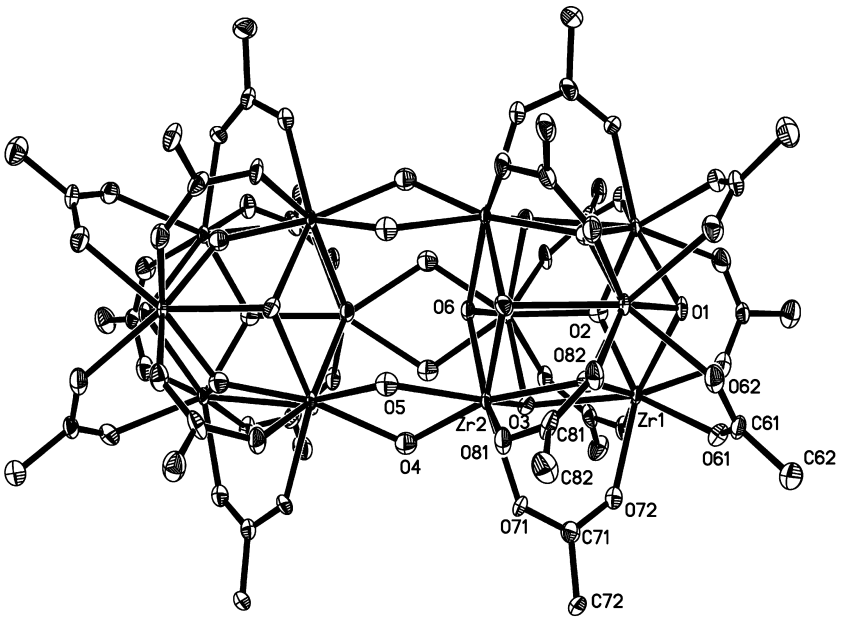


Fig. 2. The zirconium-oxide/hydroxide core of $[Zr_6(\mu_3\text{-}O)_4(\mu_3\text{-}OH)_4(OOCCH_2{}^tBu)_9(\mu_2\text{-}OH)_3]_2$. For clarity, the thermal ellipsoid are plotted at 30% probability, and $CH_2{}^tBu$ groups are omitted. The numbering scheme of the asymmetric unit is identical for both structures reported in the paper. The molecule symmetry includes the 3-fold axis and the center of symmetry. Therefore the alternating OH groups bridging two halves of the complex are labeled O4 and O5.

Table 4
Selected wavenumbers (cm^{-1}) of hydroxo, carboxylato, and oxo/hydroxo bridge vibrations detected in IR spectra of $[Zr_6(\mu_3\text{-}O)_4(\mu_3\text{-}OH)_4(OOCCH_2{}^tBu)_9(\mu_2\text{-}OH)_3]_2$.

Modes	Wavenumber (cm^{-1})		
	293 K	153 K	103 K
ν(OH)			3672 (w)
ν(OH)	3668 (m)	3669 (m)	3669 (m)
ν_{as}(COO)	1572 (s)	1573 (s)	1573 (s)
ν_s(COO)	1426 (s)	1427 (s)	1428 (s)
ν_{as}(–CH_2–)	749 (m)	749 (m)	749 (m)
ν_{as}(Zr–O–Zr)	715 (w)	718 (w)	717 (w)
ν_{as}(Zr–O–Zr)	707 (m)	711 (m)	710 (m)
ν_{as}(Zr–O–Zr)		704 (w)	704 (w)
δ(OCO)	674 (m)	676 (m)	676 (m)
ρ(OCO), out of plane		640 (m)	641(m)
ρ(OCO), out of plane	635 (m)	637 (m)	637 (m)
		550 (vw)	550 (vw)
	530 (w)	532 (w)	532 (w)
		525 (vw)	525 (vw)
ρ(OCO), in plane	480 (m)	481 (m)	481 (m)
ρ(OCO), in plane	456 (m)	458 (m)	458 (m)
ν(CCC)		450 (w)	450 (w)
ν(Zr–O/OH)	404 (m)	407 (m)	407 (m)
ν(Zr–O/OH)		403 (m)	403 (m)

(Table 3) explain the minor differences in spectra registered between 103 and 293 K (Table 4).

The bands corresponding to vibrations of OH groups and Zr–(μ_3-O/OH), Zr–(μ_2-O/OH) bridges were detected between 400 and 1000 cm^{-1} [14–16]. The medium intensity band, which can be assigned to stretching vibrations of metal–oxide/hydroxide bridges (Zr–O/OH–Zr), has been found at 707 cm^{-1} (293 K). In comparison to IR data of $[Zr_6O_4(OH)_4(OOCR')_{12}]$ (R = ^{t}Bu, $C(CH_3)_2Et$), frequency of this band is shifted towards lower wavenumbers (R = $C(CH_3)_2Et$, ν(Zr–O/OH–Zr) = 724 cm^{-1}, R = ^{t}Bu, ν(Zr–O/OH–Zr) = 728 cm^{-1}) [13]. The restrictions of proton migration between oxygen bridges at liquid nitrogen temperature (LNT) and the formation of non-equivalent Zr–(μ_3-O/OH) and Zr–(μ_2-OH) bridges contribute to the splitting of ν(Zr–O–Zr) bands in the spectrum registered at 103 K (Table 4). The splitting of this band decreases at higher temperatures and in the spectrum registered at room temperature the components at 707 and 715 cm^{-1} were observed. The study of the dependencies between integral intensity of ν(OH) and ν_{as}(Zr(O/OH)Zr) bands versus temperature revealed the possible phase transitions in the structure of $[Zr_6(\mu_3\text{-}O)_4(\mu_3\text{-}OH)_4(OOCCH_2{}^tBu)_9(\mu_2\text{-}OH)_3]_2$ at 143–183 K and 203–293 K (Fig. 4) [18]. Considering crystallographic data, the above phase transitions can be coupled to the changes in the strength of Zr–O bonds in μ_2-OH bridges linking $[Zr_6O_4(OH)_4(OOCR')_9]$ sub-units (143–183 K) and the transition of

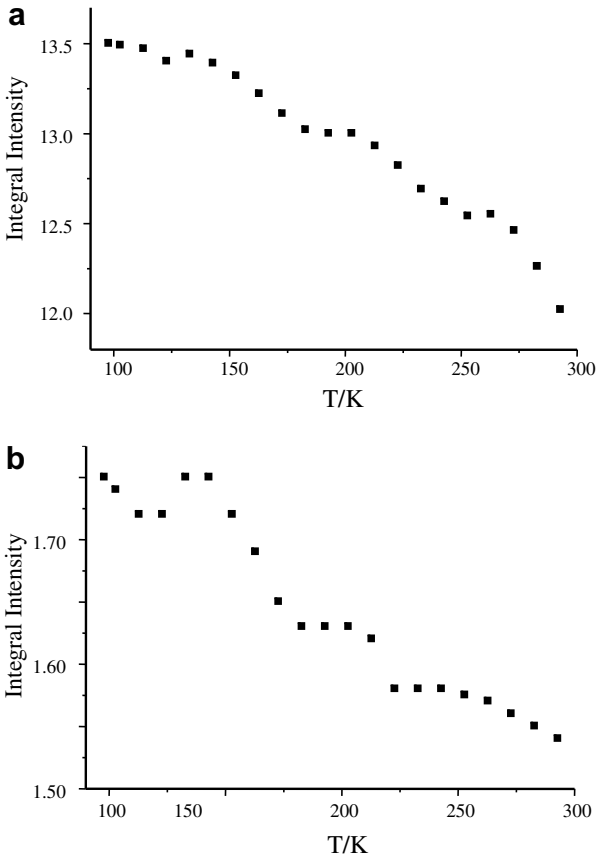


Fig. 4. Variation of the integral intensity of (a) ν(OH) and (b) ν(Zr–O/OH–Zr) bands versus temperature.

crystal system from the hexagonal (stable at 103–203 K) to the trigonal one detected at 293 K. The phase transitions in the structure of $[Zr_6(\mu_3\text{-}O)_4(\mu_3\text{-}OH)_4(OOCCH_2{}^tBu)_9(\mu_2\text{-}OH)_3]_2$ have been also studied using the DSC method (Fig. 5). The obtained results show the phase transition in the structure of this complex at 165 K. However, another phase transition was observed at 189 K, The course of the diagrams presented in Fig. 4 and DSC results indicate the high instability of crystal structure of studied complex between 143 and 293 K. It can be caused by the changes in the strength of Zr–O bonds of μ_2-OH bridges linking $[Zr_6(\mu_3\text{-}O)_4(\mu_3\text{-}OH)_4(OOCCH_2{}^tBu)_9]$ sub-units, as confirmed by the crystal structures reported in this paper.

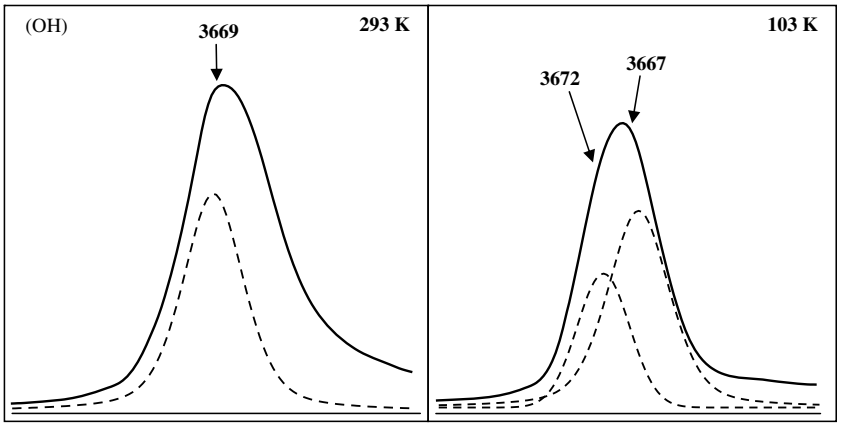


Fig. 3. Curve fit of the band corresponding to the stretching vibrations of OH groups.

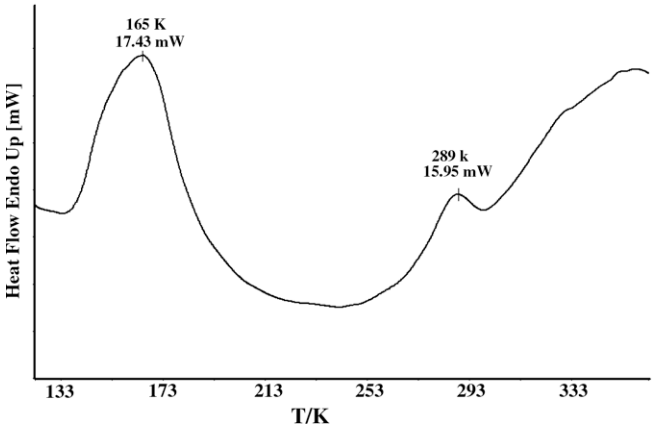


Fig. 5. Results of DSC studies of $[Zr_6(\mu_3\text{-}O)_4(\mu_3\text{-}OH)_4(OOCCH_2Bu^t)_9(OH)_3]_2$.

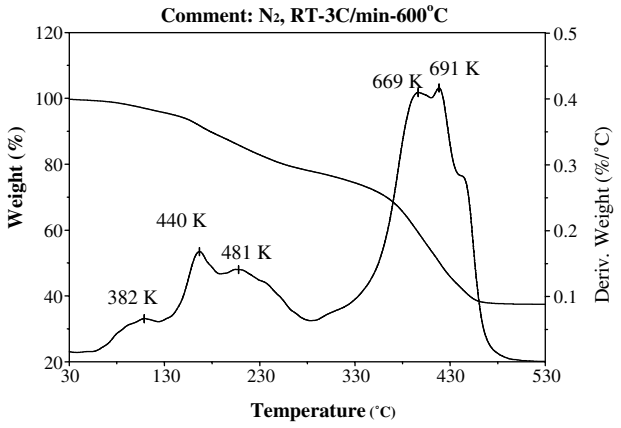


Fig. 6. Thermal analysis of $[Zr_6(\mu_3\text{-}O)_4(\mu_3\text{-}OH)_4(OOCCH_2{}^tBu)_9(OH)_3]_2$.

2.4. Thermogravimetric analysis

Thermal behavior of $[Zr_6(\mu_3\text{-}O)_4(\mu_3\text{-}OH)_4(OOCCH_2{}^tBu)_9(\mu_2\text{-}OH)_3]_2$ was studied using thermogravimetric methods (TGA/DTA) over the temperature range 303–803 K (Fig. 6). Five endothermic steps, with maxima at 382, 440, 481, 669 and 691 K have been detected during the thermolysis of this compound. The weight loss of 63.6% indicates that decomposition of this compound proceeds with complete conversion to ZrO_2 (calculated weight loss 64.1%) in the whole temperature range. It is interesting that the temperature of complete decomposition of dimeric complex is significantly lower than that for $[Zr_6(\mu_3\text{-}O)_4(\mu_3\text{-}OH)_4(OOCR')_{12}]$, which was 742 and 783 K for R′ = ^{t}Bu and C(CH$_3$)$_2$Et, respectively [11]. The formation of ZrO_2 as the main decomposition product of the studied compound has been confirmed using X-ray diffraction (XRD) methods. Analysis of XRD data proved the formation of the monoclinic form of ZrO_2 (literature reports [19]: 28.18 ($\bar{1}11$), 31.47 (111), 34.16 (002), 34.42 (020), 35.31 (200), 49.27 (022), 50.12 (220), found: 28.18 ($\bar{1}11$), 31.46 (111), 34.15 (002), 34.42 (020), 35.30 (200), 49.30 (022), 50.12 (220)).

3. Conclusions

Dimeric hexanuclear zirconium(IV) oxo/hydroxo carboxylato complex, of general formula $[Zr_6(\mu_3\text{-}O)_4(\mu_3\text{-}OH)_4(OOCCH_2{}^tBu)_9(\mu_2\text{-}OH)_3]_2$ has been synthesized in a reaction of Zr(O^{i}Pr)$_4$ with 3,3-dimethylbutyric acid in a molar ratio 1:2. The low temperature crystal structures of this compound were solved with X-ray diffraction data collected at 103 and 153 K. Analysis of X-ray data exhibits that the complex crystallizes in hexagonal system. At the investigated temperature range, the structure of this complex is composed from the $[Zr_6(\mu_3\text{-}O)_4(\mu_3\text{-}OH)_4]_2(\mu_2\text{-}OH)_6$ core, stabilized by 18 *syn–syn* bidendate carboxylate ligand bridges. The cluster geometry does not change significantly with temperature, at which the experiments were conducted. The linkage of $[Zr_6(\mu_3\text{-}O)_4(\mu_3\text{-}OH)_4(OOCCH_2{}^tBu)_9]$ sub-units by six μ_2-OH bridges leads to the formation the dimeric structure of this complex. Comparison of the crystallographic data collected at 103 and 153 K revealed the significant differences in the strength of Zr–O bonds involving μ_2-OH bridges. The phase transitions in the structure of this complex have been detected at 143–183 K and 203–293 K using VT IR spectroscopy and DSC methods. Comparison of spectral and crystallographic data suggests that changes in the strength of Zr–O bonds formed by μ_2-OH bridges and the transformation from hexagonal (103–203 K) to trigonal symmetry (observed at 293 K) are the main factors affecting the structural stability of $[Zr_6(\mu_3\text{-}O)_4(\mu_3\text{-}OH)_4(OOCCH_2{}^tBu)_9(\mu_2\text{-}OH)_3]_2$. TGA/DTA studies have shown that thermal decomposition of this complex proceeds with formation of ZrO_2 monoclinic form between 382 and 703 K.

4. Experimental

4.1. Materials and physical measurement

The employed reagents ($[Zr(O^iPr)_4 \cdot HO^iPr]_2$ and $CH_2{}^tBuCOOH$) were commercially available and used as received without further purification. Studied compounds were synthesized at room temperature under argon atmosphere, using standard Schlenk line and glovebox techniques. The reactions were carried in the 1:1 mixture of *n*-hexane and *i*-propanol used as a solvent. Solvents applied in the synthesis of this complex were freshly distilled and stored over the molecular sieves in the inert gas atmosphere. Infrared (IR) spectra were recorded on Perkin Elmer Spectrum 2000 spectrometer within range 400–4000 cm^{-1} with a medium slit width and peak resolution of 4.0 cm^{-1}. The samples of analyzed compounds were studied as a powder dispersed in a KBr pellet. Variable temperature IR spectra were registered between 98 K and 353 K using the SPECAC variable temperature cell. Solid-state ^{13}C NMR spectra were registered on Bruker AMX 300. The solution ^{1}H and ^{13}C NMR spectra ([D$_6$]-benzene) were recorded using a 5 mm solution probe on Varian Gemini 200. Thermogravimetric analysis (TGA/DTA) was carried out using SDT 2960 TA Instruments, in nitrogen atmosphere between 303 K and 873 K at a ramp rate 3 K^{-1}. Differential scanning calorimetry methods have been used in order to phase transition studies between 103 and 373 K. The measurements were carried out using Diamond DSC PerkinElmer, in Helium atmosphere at the ramp rates 50, 100, and 200 K^{-1}. X-ray powder diffraction (XRD) data were collected with a Philips X'PERT diffractometers; 2Θ ranges 30–50°, Cu Kα radiation and sample spinning (step size – 0.1°, program. res. slit – 0.5, measuring time – 11 s per point).

4.2. Reaction of $Zr(O^iPr)_4$ with $CH_2{}^tBuCOOH$

70% solution of Zr(O^{i}Pr)$_4$ in *i*-propanol (1 g of Zr(O^{i}Pr)$_4$ (2.58 mmol)) was added dropwise to a solution of 3,3-dimethylbutyric acid (0.6 g; 5.16 mmol) in the 3 cm^3 of mixture of *n*-hexane and *i*-propanol (1:1), and stirred for 24 h. Crystals were grown by slow evaporation of the reaction mixture under argon atmosphere (glovebox). The colorless crystals were obtained after 1 day. Yield: 65%. The Zr amount was gravimetrically determined as ZrO_2. *Anal.* Calc. for $C_{108}H_{206}O_{58}Zr_{12}$: C, 36.79; H, 5.84; Zr, 31.05. Found: C, 36.98; H, 5.78, Zr, 31.19%. IR (KBr, cm^{-1}): 724 (ν_s(Zr–O–Zr)),

1478, 1577 (νCOO); 631 δ(OCO) 13C NMR (solid-state, δ, ppm) 30.8 and 30.2 ($CH_3(^tBu)$); 39.5 ($C(^tBu)$); 179.4, 178.1 and 174.7 (COO).

4.3. Single-crystal structure determination

The diffraction data of studied compound were collected at 153 K for the single crystals (0.24 × 0.13 × 0.03 mm) using Oxford Diffraction KM4 CCD diffractometer, Mo Kα radiation λ = 0.71073 Å. The reflections have been measured with ω–2θ method. The numerical absorption correction was applied for studied crystals (RED171 package of programs, Oxford Diffraction, 2000) [20]. At 103 K the diffraction data were collected for the single crystal (0.20 × 0.17 × 0.15 mm) on ID14-1 (EH1) synchrotron beamline (ESRF, Grenoble) at wavelength λ = 0.93400 Å. The data were processed using XDS package [21]. The absorption correction was applied for both studied structures with XDS [21] for 103 K and RED171 package [21] for 153 K structures of $[Zr_6(\mu_3\text{-}O)_4(\mu_3\text{-}OH)_4(OOCCH_2{}^tBu)_9(\mu_2\text{-}O)_3]_2$ were solved by the direct methods and refined with full-matrix least-squares procedure on F^2 using SHELX-97 program package [22,23]. Details of the data collection and structure refinement are presented in Table 2.

Acknowledgment

The authors wish to acknowledge the Polish Committee for Science Research for financial support Grant No. N204 11631/2635.

Appendix A. Supplementary data

CCDC 685574 and 685573 contain the supplementary crystallographic data for $[Zr_6(\mu_3\text{-}O)_4(\mu_3\text{-}OH)_4(OOCCH_2{}^tBu)_9(\mu_2\text{-}O)_3]_2$ at 103 K and 153 K. These data can be obtained free of charge from The Cambridge Crystallographic Data Centre via www.ccdc.cam.ac.uk/data_request/cif. Results of XRD studies of $[Zr_6(\mu_3\text{-}O)_4(\mu_3\text{-}OH)_4(OOCCH_2{}^tBu)_9(\mu_2\text{-}O)_3]_2$ (RT). Supplementary data associated with this article can be found, in the online version, at doi:10.1016/j.poly.2008.10.034.

References

[1] U. Schubert, T. Völkel, N. Moszner, Chem. Mater. 13 (2001) 3811.
[2] U. Schubert, Chem. Mater. 13 (2001) 3487.
[3] Y. Gao, N.R. Choudhury, J. Matisons, U. Schubert, B. Moraru, Chem. Mater. 14 (2002) 4252.
[4] B. Moraru, N. Hüsing, G. Kickelbick, U. Schubert, P. Fratzl, H. Peterlik, Chem. Mater. 14 (2002) 2740.
[5] G. Trimmel, S. Gross, G. Kickelbick, U. Schubert, Appl. Organomet. Chem. 15 (2001) 291.
[6] G. Kickelbick, U. Schubert, Chem. Ber./Recueil 130 (1997) 473.
[7] G. Kickelbick, U. Schubert, J. Chem. Soc., Dalton Trans. (1999) 1301.
[8] G. Kickelbick, P. Wiede, U. Schubert, Inorg. Chim. Acta 284 (1999) 1.
[9] B. Moraru, S. Gross, G. Kickelbick, G. Trimmel, U. Schubert, Monatshefte Chem. 132 (2001) 993.
[10] T.J. Boyle, L.A. Ottley, M.A. Rodriguez, Polyhedron 24 (2005) 1727.
[11] P. Piszczek, A. Radtke, A. Grodzicki, A. Wojtczak, J. Chojnacki, Polyhedron 26 (2007) 679.
[12] H.D. Lutz (Ed.), Structures and Bonding, vol. 82, Springer-Verlag, Berlin, Heidelberg, 1995, p. 85.
[13] K. Nakamoto, Infrared and Raman Spectra of Inorganic and Coordination Compounds, Wiley, New York, part B/V Edition, 1997, p. 58 and 172.
[14] M.A. Hasan, M.I. Zaki, L. Pasupulety, J. Mol. Catal. A: Chem. 178 (2002) 125.
[15] M.A. Diaz-Diaz, A. Macias-Gracia, G. Silvero, R. Gordillo, R. Caruso, Cerams Int. 29 (2003) 471.
[16] G. von Halden, A. Kirilyuk, D. van Heijnsbergen, B. Sartakov, M.A. Duncan, G. Meijer, Chem. Phys. 262 (2000) 31.
[17] V. Koleva, D. Stoilova, J. Mol. Struct. 61 (2002) 1.
[18] A.W. Rakov, Opt. Spectros. 10 (1961) 713.
[19] H. McMurdie, M. Morris, E. Evans, B. Paretzkin, W. Wong-Ng, C. Hubbard, Powder Diffr. 1 (1986) 275.
[20] G.M. Sheldrick, SHELXS97, SHELXL97 and CIFTAB, University of Göttingen, Germany, 1997.
[21] W. Kabsch, J. Appl. Crystallogr. 21 (1988) 916.
[22] Oxford Diffraction, CRYSALIS RED and CRYSALIS CCD, Oxford, Diffraction, Abingdon, Oxfordshire, England, 2000.
[23] B. Bondars, G. Heidemane, J. Grabis, K. Laschke, H. Boysen, J. Schneider, F. Frey, J. Mater. Sci. 30 (1995) 1621.

Polyhedron 28 (2009) 286–290

Contents lists available at ScienceDirect

Polyhedron

journal homepage: www.elsevier.com/locate/poly

Synthesis and characterization of mono and polymeric cyclopalladated compounds: Crystal and molecular structure of $[\{Pd(dmba)(ONO_2)\}_2(\mu\text{-pz})] \cdot H_2O$ (pz = pyrazine)

Sandra R. Ananias [a,b,c], Janaina G. Ferreira [b,c], Antonio E. Mauro [c], Adelino V.G. Netto [c], Stanlei I. Klein [c], Regina H.A. Santos [b,*]

[a] Departamento de Química, Faculdade de Ciências – UNESP, C.P. 1.401, CEP 17033-360, Bauru, SP, Brazil
[b] Departamento de Química e Física Molecular, Instituto de Química de São Carlos – USP, C.P. 780, CEP 13560-970, SP, Brazil
[c] Departamento de Química Geral e Inorgânca, Instituto de Química – UNESP, C.P. 355, CEP 14801-970, Araraquara, SP, Brazil

ARTICLE INFO

Article history:
Received 4 July 2008
Accepted 22 October 2008
Available online 16 December 2008

Keywords:
Cyclometallated
Palladium
Nitro compounds

ABSTRACT

In the treatment of cyclometallated dimer $[Pd(dmba)(\mu\text{-Cl})]_2$ (dmba = N,N-dimethylbenzylamine) with $AgNO_3$ and acetonitrile the result was the monomeric cationic precursor $[Pd(dmba)(NCMe)_2](NO_3)$ (NCMe = acetonitrile) (**1**). Compound **1** reacted with *m*-nitroaniline (*m*-NAN) and pirazine (pz), originating $[Pd(dmba)(ONO_2)(m\text{-NAN})]$ (**2**) and $[\{Pd(dmba)(ONO_2)\}_2(\mu\text{-pz})] \cdot H_2O$ (**3**), respectively. These compounds were characterized by elemental analysis, IR and NMR spectroscopy. The IR spectra of (**2**–**3**) display typical bands of monodentade O-bonded nitrate groups, whereas the NMR data of **3** are consistent with the presence of bridging pyrazine ligands. The structure of compound **3** was determined by X-ray diffraction analysis. This packing consists of a supramolecular chain formed by hydrogen bonding between the water molecule and nitrato ligands of two consecutive $[Pd_2(dmba)_2(ONO_2)_2(\mu\text{-pz})]$ units.
© 2008 Elsevier Ltd. All rights reserved.

1. Introduction

Over the past years the chemistry of cyclopalladated compounds, mainly of those derived from N-donor ligands, has been investigated by numerous research groups [1], due to important applications of these compounds in various fields, such as organic and organometallic synthesis [2], new materials (e.g. metallomesogens) [3], catalysis [4] and medical science (e.g. antitumor drugs) [5].

The relatively low cost and ready availability [6] of $[Pd(dmba)(NCMe)_2](NO_3)$ (**1**), with two of its *cis* coordination sites occupied by quite easily removable ligands, prompted us to try this compound in reactions of the self-assembly type. The general idea had been set forth by Fujita by using traditional transition metal complexes and bidentated nitrogen ligands [7]; moreover, Huck already succeeded in producing dendrimers from cyclopalladated compounds [8], and Spek, van Koten and their group advanced the features of 90° square planar platinum and palladium (II) metallated complexes as corner acceptors units [9]. Therefore, compound **1** seemed suitable for the preparation of tetramers and higher nuclearity compounds, if one could bridge two distinct terminal diamines to the $[Pd(dmba)]^{2+}$ fragments. However, only one terminal amine was allowed to be coordinated to the metal atom in **1**, originating monomers from monoamines and dimer compounds from the addition of diamines to its solutions. The behavior of **1** toward the used nitrogen ligands is discussed below, and the solid state structure of the pyrazine dimer **3** is presented.

2. Experimental

2.1. General comments

The syntheses were performed at room temperature. Commercial reagents and solvents were employed without further purification. The precursor $[Pd(dmba)(NCMe)_2](NO_3)$ (**1**) was prepared according to procedures described in the literature [6].

2.2. Synthesis of $[Pd(dmba)(ONO_2)(m\text{-NAN})]$ (**2**)

0.0720 g (0.0520 mmol) of *m*-nitroaniline (*m*-NAN), dissolved in 10 cm^3 of dichloromethane was added to 15 cm^3 of solution **1** (0.100 g, 0.260 mmol), in the same solvent. The mixture was stirred for 30 min, and the resulting yellow precipitate was isolated by filtration. The product was thoroughly washed with ether and pentane and dried *in vacuo*. The yield was about 90% after recrystallization from dichloromethane and pentane. $PdN_4O_5C_{15}H_{18}$ (**2**) requires: C, 40.87; H, 4.08; N, 12.71. Found: C, 40.3; H, 3,93; N, 12.4%.

2.3. Synthesis of $[\{Pd(dmba)(ONO_2)\}_2(\mu\text{-pz})]$ (**3**)

A solution of 0.389 mmol (0.031 g) of pirazine (pz) in 5 cm^3 of dichloromethane was added to a solution of 0.15 g (0.389 mmol)

* Corresponding author. Tel./fax: +55 16 3373 9975.
E-mail address: reginas@iqsc.usp.br (R.H.A. Santos).

0277-5387/$ - see front matter © 2008 Elsevier Ltd. All rights reserved.
doi:10.1016/j.poly.2008.10.048

of [Pd(dmba)(MeCN)2](NO$_3$) (**1**) in 10 cm^3 of dichloromethane. The mixture was stirred for 1 h. The yellow solid which precipitated was filtered, washed with acetone and pentane and dried *in vacuo*, and re-crystallized. The yield was about 80%. Calc. for $Pd_2N_6O_6C_{22}H_{28}$: C, 38.5; H, 4.08; N, 12.26. Found: C, 39.0; H, 2.95; N, 13.5%.

2.4. Physical measurements

Infrared spectra were recorded as KBr pellets on a Nicolet Impact 400 spectrophotometer (range 4000–400 cm^{-1}). ^{1}H and ^{13}C NMR spectra were obtained as DMSO-d_6 solutions and referred to the high field $SiMe_4$ signal, on a Varian INOVA 500 spectrometer. Molar conductivities were measured in nitromethane solutions ($c \approx 1 \times 10^{-3}$ mol L^{-1}) with a Digimed-DM-31 conductimeter. Elemental analyses were performed by the Central Analítica at IQSC/University of São Paulo.

2.5. X-ray structure determination for compound **3**

A single crystal of the compound [{Pd(dmba)(ONO_2)}$_2$(μ-pz)] (**3**) was mounted on a Enraf-Nonius CAD4 diffractometer at room temperature using graphite monochromated Mo Kα radiation (λ = 0.71073 Å). The data collection was taken in the ω–2θ scan mode. The unit cell parameters were determined using 25 automatically centered reflections. Table 1 shows the data collection and refinement conditions. The intensity data were reduced to F_0 and corrected by absorption factors using the PSISCAN method [10]. The structures were solved by the WINGX system [11], using SIR92 [12] and SHELX97 [13]. The hydrogen atoms belonging to compound **3** were located in their ideal positions. The water H atoms were placed at calculated positions using the HYDROGEN [14]. All non-hydrogen atoms were refined anisotropically. The geometric analysis was performed by the PLATON system [15].

Table 1
Crystal data and details of the structure determination for [{Pd(dmba)(ONO_2)}$_2$(μ-pz)] · H_2O (**3**).

Empirical formula	$C_{22}H_{28}N_6O_6Pd_2 \cdot H_2O$
Formula weight	703.36
Crystal system	monoclinic
Space group	*C*2/*c*
a (Å)	13.402(2)
b (Å)	12.933(2)
c (Å)	14.864(3)
β (°)	95.56(1)
V (Å^3)	2564.2(8)
Z [dimer/cell]	4
D_{calc} (Mg/m^3)	1.822
F(000)	1408
μ(Mo Kα) (mm^{-1})	1.456
Crystal size (mm)	0.25 × 0.25 × 0.40
Temperature (K)	243
Radiation Mo Kα (Å)	0.71073
$\theta_{min.-max.}$ (°)	2.5, 30.0
Dataset	$-18 \le h \le 18$, $0 \le k \le 18$, $-20 \le l \le 0$
Total unique data, R_{int}	3860, 3727, 0.023
Observed data ($I > 2.0(I)$)	3204
N_{ref}, N_{par}	3727, 170
R, *wR*, *S*	0.0470, 0.1440, 1.07
$w = 1/[s^2(F_o^2) + (0.0867P)^2 + 9.5183P]$ where $P = (F_o^2 + 2F_c^2)/3$	
Maximum and average shift/error	0.00, 0.00
Minimum and maximum residual density (e/Å^3)	−1.46, 2.10

3. Results and discussion

3.1. Characteristics of [Pd(dmba)(NCMe)$_2$](NO$_3$) (**1**) and [Pd(dmba)(ONO_2)}(***m***-NAN)] (**2**)

[Pd(dmba)(NCMe)$_2$](NO$_3$), (**1**), can be easily prepared from dichloromethane solutions of [Pd(dmba)Cl$_2$] upon the addition of silver nitrate dissolved in a mixture of dichloromethane and acetonitrile [6]. This precursor is very interesting on its own, due to its exquisite physical properties, which seems to be somewhat dictated by the physical conditions to which it is submitted. For instance, the ionic formulation for **1** seems to be evident from its formulae, and from its solid state IR spectrum, which shows low intensity bands at 2308 and 2249 cm^{-1}, attributed mainly to A_{1g} CN stretches and CCN combination bands of coordinated nitriles [16,17], and quite intense bands for the presence of ionic nitrates [18,19] at 1387 (ν ONO, vs) and 852 cm^{-1} (δ ONO, s). Nevertheless, ready solubility of this compound in solvents such as chloroform is not characteristic of a purely ionic compound. Indeed, molar conductance measurements of **1** made in nitromethane indicated a value of 27.55 μS cm^{-1}, which collocates that species among those considered non-electrolytes [20].

In this context, it is also interesting to research the ^{1}H and ^{13}C NMR spectra of **1**. In spite of the ubiquitous square planar coordination geometry of the [Pd(dmba)(NCMe)$_2$] core, the 125 MHz ^{13}C NMR of **1** in $CDCl_3$ at room temperature seemed to be exceedingly simple, for it did not show the magnetic inequivalence of the ^{13}C nuclei of the acetonitriles. This magnetic inequivalence was expected on the grounds that the acetonitriles must be accommodated, one in the *trans* position to the dmba's nitrogen, and the other, *trans* to the metallated carbon anchor of that ligand. However, in the NMR spectrum there is only one singlet NMR resonance for the two nitriles' CH_3CN at ca. 119, and another singlet resonance CH_3CN carbon at 3 ppm. The other ^{13}C resonances of that spectrum are indicated in Fig. 1.

Upon N-coordination with the palladium metal in cyclopalladated complexes such as **1**, is formed a puckered five-membered ring with a low barrier of inversion. Therefore, fast exchanges from axial to equatorial position are possible, and the benzylic (–N–CH_2–) protons, as well the protons of the [–NMe_2] group of dmba usually appear as singlets in the proton NMR spectrum, and this analysis is valid for complex **1**, where those groups resonate at 3.91 and 2.78 ppm. However, this fast inversion on the NMR time scale does not explain the equivalence of the ^{13}C NMR signals of the coordinated acetonitriles. The 500 MHz ^{1}H spectrum of **1** showed two separated signals for the two distinct acetonitrile groups at 2.78 and 2.36 ppm. The downfield shifted signal at 2.78 ppm was assigned to the methyl group of the acetonitrile in cis position to the metallated aromatic ring since, it is located in the deshielding area generated by the metallated aromatic ring. This signal appeared in the spectrum overlapped by the six-proton singlet of the [–NMe_2] fragment of dmba. A closer examination on other acetonitrile substituted cyclopalladates point to a similar difficulty in a proper assignment of their NMR spectra [21].

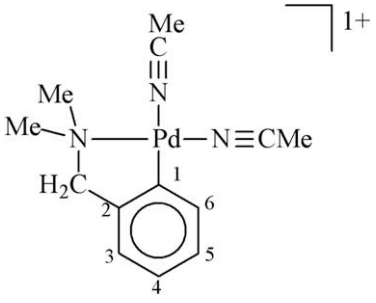


Fig. 1. Additional ^{13}C resonances for the metal containing core of **1**: Me_2N = 51; H_2C = 73; 1 = 147; 2 = 143; 3,6 = 123; 4 = 134; 5 = 123 ppm.

In the first attempt to test the capacity of the precursor compound **1** to react with heterocyclic nitrogen donors, it was chosen the *m*-nitroaniline ligand only as monosubstituted compound; despite the 1:2 stoichiometry of the addition. The IR spectrum of the product suggested the coordination of the *m*-nitroaniline ligand by the disappearance of the bands assigned to *ν*CN of the precursor. However, new bands for a different type of nitrate ligand were also readily assigned in that spectrum, at 1417 and 1305 (*ν*ONO), and at 806 cm^{-1} (*δ*NO), evidencing the presence of a monodentate O-bound nitrate group [18,19].

The ^1H NMR spectrum of **2** showed four multiplets, two at 7.37 and 7.23 ppm assigned to the *m*-nitroaniline, and two at 7.05 and 6.9 ppm, relative to the H-3 to H-5 dmba protons. The upfield shift of dmba's H-6 proton at 5.79 ppm should be the result of the shielding effect of the nearby aromatic ring of the *m*-NAM ligand, a conclusion which allows to allocate the nitrogen ends of *m*-NAM and dmba, *trans* to each other in the complex [22]. Thus, the nitrato ligand, which acts as pseudo-halogen in the structure of compound **2**, is in trans position to the metallated carbon, according to the antisymbiotic effect [x]. The (–N–CH_2–) protons of the dmba ligand resonate at 4.03 ppm, and the [N–$(CH_3)_2$] fragment was indicated by the proton resonance at 2.63 ppm. In the ^{13}C NMR spectrum of **2** there are three important signals: the metallated, the benzylic and the [–NMe_2] carbons, resonating at 148.7, 71.4 and 50.5 ppm, respectively, indicating the presence of dmba in the complex. These evidences and the microanalysis data pointed to the monomeric structure [Pd(dmba)(ONO_2)(*m*-NAN)] for compound **2**.

3.2. Characteristics of cyclopalladated complex [{Pd(dmba)(ONO_2)}$_2$(μ-pz)] (**3**)

The ability of precursor **1** to act as a corner acceptor unit for self-assembled species was tested with the potential bridging ligand pz.

The reactions of **1** with pyrazine were the simplest, in the way that only one type of compound could be detected by the occurrence of only one precipitate, after the mixture of reactants was stirred at room temperature. This compound was determined as μ-pz dinuclear, O-bound NO_3 palladium complex of the type [{Pd(dmba)(ONO_2)}$_2$(μ-pz)], (**3**). For instance, the IR spectrum showed the expected bands at 1621 and 1031 cm^{-1} attributed to the CN stretch and CH deformation of pz, respectively; and the characteristic trio of absorptions for the –ONO_2 coordinated nitrate at 1424, 1296 and 810 cm^{-1} [18,19]. The ^{13}C NMR spectrum of **3** showed the metallated carbon from dmba at 148.1 ppm. The proton NMR spectrum confirms the presence of the pyrazine by signals at 8.84 and 8.74 ppm. Although the signal for symmetrically coordinated pyrazine occurs above 8.6 ppm [23], the presence of two signals for **3** indicated some kind of molecular arrangement as they were the pz protons magnetically non-equivalent. The signals for the diastereotopic protons of the –CH_2– and [–NMe_2] groups of metallated dmba appear in the ^1H NMR spectrum of **3** as slightly broadened resonances at the normal positions of 4.01 and 2.84 ppm, respectively.

3.3. X-ray structure of [{Pd(dmba)(ONO_2)}$_2$(μ-pz)] · H_2O (**3**)

Suitable crystals of [{Pd(dmba)(ONO_2)}$_2$(μ-pz)] · H_2O (**3**) were grown by slow evaporation of a water–acetone solution. The X-ray structure showed that the asymmetric unit consists of a Pd(dmba)(ONO_2) unit linked to half of the pyrazine ring, forming a dimer made by two fold crystallographic axis (Fig. 1). In the asymmetric unit it is also found half water molecule, with the oxygen atom lying in other twofold axis Fig. 2.

The X-ray diffraction study permitted the correct interpretation of the analytical and NMR data, by showing the molecule as a dinuclear compound, with one pz bridging the two metals. The square planar coordination of each palladium atom is composed by the metallated carbon and the nitrogen atom from the dmba, the nitrogen from pz, and the coordinated oxygen of the NO_3 group. This feature could be inferred, but it was not explicit from previous spectroscopic studies. This coordination may reflect the powerful trans-influence of the C–Pd bond, which would labilize a bond between the metal and any incoming σ-donor, neutral L ligand, inducing the coordination to conform to a C–Pd–L *cis* environment in the final compound. In the solid structure, the palladium atom occupies a position slightly below the mean squares plane defined by C_1, N_1, O_1 and N_2 (0.537(1) Å).

Selected interatomic bond lengths and angles are given in Tables 2 and 3. In molecule of **3**, the various bonds and angles involving the metals and directly coordinated atoms agree with previous reports found in the literature for this class of metallated compounds [24–29], but a few particular characteristics of **3** must be discussed. For instance, the short Pd–C_1 bond length of 1.971(4) Å is shorter than a Pd(II)–C sp^3 bond of 2.14 Å [21]. This value may reflect a typical Pd(II)–C sp^2 bond, but there seem to be a consensus that the Pd–C bonds in metallated benzenoid rings must involve some multiple bond character, which would cause a further shortening of this peculiar Pd–C bond [30a]. Also, the trans Pd–O bond

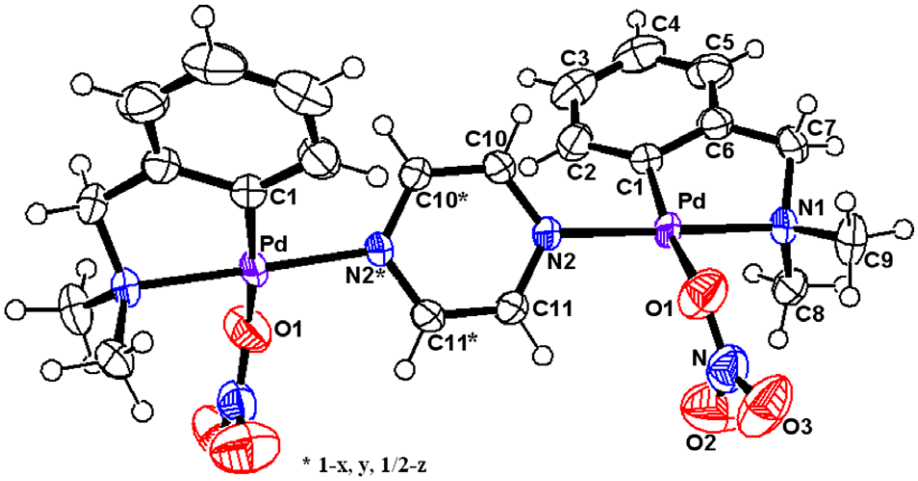


Fig. 2. ORTEP drawing with labeling scheme for [Pd_2(dmba)$_2$(μ-pz)(NO_3)$_2$]. Displacement ellipsoids are drawn at the 50% probability level.

Table 2
Bond distances (Å) for [{Pd(dmba)(ONO_2)}$_2$((−pz)] · H_2O (**3**).

Pd	O1	2.208(4)	Pd	C1	1.971(4)
Pd	N1	2.063(3)	Pd	N2	2.049(3)
O1	N	1.237(5)	O2	N	1.249(7)
O3	N	1.211(6)			
N1	C7	1.497(5)	N1	C8	1.494(5)
N1	C9	1.478(6)	C6	C7	1.493(6)
C1	C2	1.395(6)	C3	C4	1.381(9)
C1	C6	1.417(5)	C4	C5	1.385(8)
C2	C3	1.392(7)	C5	C6	1.380(6)
N2	C10	1.342(5)	C10	C10*	1.383(7)
N2	C11	1.334(5)	C11	C11*	1.383(8)
O1W	H1W	0.930			

* Symmetry code: 1 − *x*, *y*, 1/2 − z.

Table 3
Selected angles (°) for [{Pd(dmba)(ONO_2)}$_2$(μ-pz)] · H_2O (**3**).

O1	Pd	N1	95.8(1)	O1	N	O3	122.3(5)
O1	Pd	N2	87.6(1)	O2	N	O3	119.3(5)
O1	Pd	C1	169.1(2)	O1	N	O2	118.4(5)
N1	Pd	N2	176.4(1)	H1OW	O1W	H1OW**	104.77
N1	Pd	C1	82.0(1)	C1	C2	C3	119.4(5)
N2	Pd	C1	94.9(1)	C2	C3	C4	121.7(5)
Pd	O1	N	119.2(4)	C3	C4	C5	119.3(5)
Pd	N1	C8	110.0(3)	C4	C5	C6	120.2(5)
Pd	N1	C9	113.8(3)	C1	C6	C5	120.9(4)
Pd	N1	C7	106.5(2)	C2	C1	C6	118.4(4)
Pd	N2	C10	125.1(2)	C1	C6	C7	115.3(3)
Pd	N2	C11	118.4(2)	C5	C6	C7	123.7(4)
Pd	C1	C2	128.3(3)	C7	N1	C9	109.0(4)
Pd	C1	C6	113.3(3)	C8	N1	C9	108.6(4)
N2	C10	C10*	121.6(2)	C7	N1	C8	108.8(4)
N2	C11	C11*	121.8(2)	N1	C7	C6	108.5(3)
C10	N2	C11	116.6(3)				

* Symmetry code: 1 − *x*, *y*, 1/2 − *z*.
** Symmetry code: −*x*, *y*, 1/2 − *z*.

Table 4
Hydrogen Bonds (Å, °) for [{Pd(dmba)(ONO_2)}$_2$(μ-pz)] · H_2O (**3**).

D–H···*A*	D–H	H···A	D···A	*D*–H···*A*	Symetry code
O1W–H1W···O3	0.930	2.13	3.043(8)	167.0	*x*, −*y*, −1/2 + *z*
C3–H3···O2	0.940	2.50	3.195(9)	131.1	1 − *x*, −*y*, −*z*
C7–H72···O3	0.980	2.52	3.460(6)	161.8	*x*, −*y*, −1/2 + *z*
C11–H11···Cg3	0.941	2.85	3.804(5)	114	1 − *x*, −*y*, −*z*
C7–H71···Cg3	0.979	3.00	3.492(5)	164	1/2 − *x*, −1/2 − *y*, −*z*

Cg3: benzene ring.

(2.208(4) Å) is in good agreement with a square planar Pd(II) complex structure [29].

The most striking features of the crystal structure of **3** is the tilt (57.6(2)°) of the plane of pz relative to the square plane of the two palladium atoms (C_1, N_1, O_1 and N_2). The pyrazine ring is highly symmetric because it is formed by symmetry operation.

The solid state shows the presence of hydrogen bonds (Table 4). Molecules of **3** self-assemble into a supramolecular chain through intermolecular hydrogen bonds between crystallization water molecules and nitrato ligands of **3**, as can be observed in Fig. 3. As a result of the oxygen atom (from the water molecule) being positioned on the crystallographic twofold axis the polymeric chain is generate by symmetry.

In addition to this hydrogen bond, there are two C–H···O (3.195(9) and 3.460(6) Å) and two C–H···π (3.804(5) and 3.492(5) Å) interactions contributing to the stabilization of the crystal packing, which results in a complex three-dimensional framework.

As mentioned above, the other noteworthy feature of **3** which was disclosed by the X-ray analysis was the severe tilt of the pz plane of 57.6(2)° relative to the square planes defined by the metals and their four immediate bonded atoms. In this geometrical arrangement around a d^8 transition metal, the crystal field theory predicts that the metal's empty $d_{x^2-y^2}$ orbital shall be antibonding, with the other four d orbitals lying close in energy, with the d_{z^2} orbital assuming the role of the HOMO of the ML_4 molecule. In this way, following the σ coordination, there will be essentially two modes through which d–π interactions may develop. The two modes involve the metal and ligand B_{1g} and B_{2g} orbitals. The interaction of the empty B_{1g} $d_{x^2-y^2}$ with the pz HOMO B_{1g} should lower the energy of that otherwise essentially antibonding orbital, and this d←π interaction may thus help in further stabilization of the whole molecular assembly. On the other hand, the full d_{xy} orbital, of B_{2g} symmetry, may interact with the LUMO of pz, which is also B_{2g}, allowing for the development of an effective mechanism for d→π* back donation. The interesting thing is that the d←π and d→π* overlaps can only develop if the plane of pz is severely tilted in relation to the *xy* plane defined by the ML_4 core, a tilting that, in the present case, is 57.6(2)°. These d←π interactions may be found in the half-filled $d_{x^2-y^2}$ of Cu(II) atoms and the B_{1g} HOMO of pz which had been held responsible for magnetic processes in copper dimers and supramolecules [31]. A number of other metal pyrazine compounds which have been analyzed by X-ray crystallography also showed variations in the orientation of the plane of the complexes and the plane of coordinated pz, although the stabilizing effect of such canting has not always been emphasized [32].

4. Conclusions

The nitrate group from the ionic [Pd(dmba)(MeCN)$_2$](NO_3), (**1**), seem to render this compound to be susceptible to a double substitution to yield [Pd(dmba)L_2]$^+$ complexes only with very strong σ donating L such as bipy, in which the interactions enables the detection of polycations from strongly conducting nitromethane solutions [33]. With poorer σ donors such as *m*-NAM or pz only complexes of the type [Pd(dmba)(ONO_2)L] are formed. The biligand nature of pz ensures the formation of the dinuclear compound [Pd(dmba)(ONO_2)]$_2$(μ-pz). This complex showed the square planes defined by the metals ML_4 cores severely tilted in relation to the

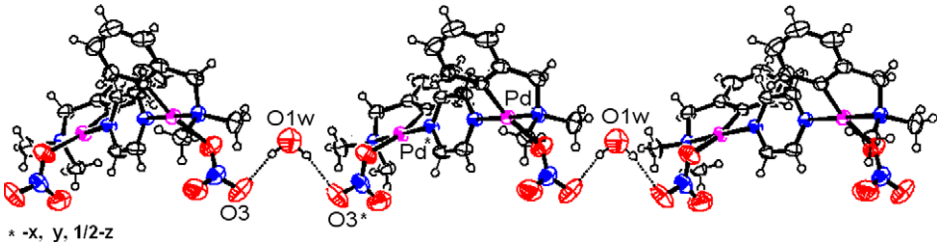


Fig. 3. Supramolecular chain formed by hydrogen bonding in the crystal structure of [{Pd(dmba)(ONO_2)}$_2$(μ-pz)] · H_2O.

plane of pz, suggesting the operation of strong $d\leftarrow\pi$ and $d\rightarrow\pi^*$ interactions between the metals and the pyrazine ring.

Acknowledgements

The authors wish to acknowledge CNPq, FAPESP and CAPES for the financial support.

Appendix A. Supplementary data

CCDC 692054 contains the supplementary crystallographic data for $[\{Pd(dmba)(ONO_2)\}_2(\mu\text{-pz})]\cdot H_2O$. These data can be obtained free of charge via http://www.ccdc.cam.ac.uk/conts/retrieving.html, or from the Cambridge Crystallographic Data Centre, 12 Union Road, Cambridge CB2 1EZ, UK; fax: (+44) 1223-336-033; or e-mail: deposit@ccdc.cam.ac.uk. Supplementary data associated with this article can be found, in the online version, at doi:10.1016/j.poly.2008.10.048.

References

[1] (a) S.R. Ananias, A.E. Mauro, K. Zutin, C.M.C. Picchi, R.H.A. Santos, Transition Met. Chem. 29 (2004) 284;
(b) B.J. O'Keefe, P.J. Steel, Acta Crystallogr., Sect. C 56 (2000) 440;
(c) R. Ares, M. Lópes-Torres, A. Fernández, M.T. Pereira, A. Suárez, R. Mosteiro, J.J. Fernández, J.M. Vila, J. Organomet. Chem. 665 (2003) 87;
(d) J. Vicente, A. Arcas, D. Bautista, M.C.R. de Arellano, J. Organomet. Chem. 663 (2002) 164;
(e) J.W. Slater, J.P. Rouke, J. Organomet. Chem. 688 (2003) 112.
[2] (a) D.L. Davies, O. Al-Duaij, J. Fawcett, K. Singh, J. Organomet. Chem. 693 (2008) 965;
(b) G. Zhao, Q.G. Wang, T.C.W. Mak, J. Organomet. Chem. 574 (1999) 311;
(c) M. Benito, C. López, X. Solans, M. Font-Bardía, Tetrahedron: Asymmetry 9 (1998) 4219;
(d) A.D. Ryabov, R. van Eldik, G. Le Borgne, M. Pfeffer, Organometallics 12 (1993) 1386;
(e) S. Tollari, S. Cenini, C. Tunice, G. Palmisano, Inorg. Chim. Acta 272 (1998) 18;
(f) J. Spencer, M. Pfeffer, Adv. Met.-Org. Chem. 6 (1998) 103.
[3] (a) P. Espinet, J. Perez, M. Marcos, M.B. Ros, J.L. Serrano, J. Barderã, A.M. Levelut, Organometallics 9 (1990) 2028;
(b) J. Buey, P. Espinet, J. Organomet. Chem. 507 (1996) 137;
(c) G.W.V. Cave, D.P. Lydon, J.P. Rourke, J. Organomet. Chem. 555 (1998) 81;
(d) A.M.G. Godquin, Coord. Chem. Rev. 178–180 (1998) 1485;
(e) D.J. Saccomando, C. Black, G.W.V. Cave, D.P. Lydon, J.R. Rourke, J. Organomet. Chem. 601 (2000) 305.
[4] (a) S.A. Kurzeev, G.M. Kazankov, A.D. Ryabov, Inorg. Chim. Acta 305 (2000) 1;
(b) S.M. Islam, A. Bose, B.K. Palit, C.R. Saha, J. Catal. 173 (1998) 268;
(c) A. Bose, C.R. Saha, J. Mol. Catal. 49 (1989) 271.
[5] (a) J.S. Casas, E.E. Castellano, J. Ellena, M.S. Garcıa-Tasende, M.L. Pérez-Parallé, A. Sánchez, A. Sánchez-González, J. Sordo, A. Touceda, J. Inorg. Biochem. 102 (2008) 33;
(b) C. Bincoletto, I.L.S. Tersariol, C.R. Oliveira, S. Dreher, A.C.F. Caíres, Bioinorg. Med. Chem. 13 (2005) 3047;
(c) J.D. Higgins, L. Neely, S. Fricker, J. Inorg. Biochem. 49 (1993) 149;
(d) A.G. Quiroga, C.N. Ranninger, Coord. Chem. Rev. 248 (2004) 119.
[6] S.R. Ananias, A.E. Mauro, V.M. Nogueira, P.S. Haddad, E.T. de Almeida, Eclét. Quím. 26 (2001) 87.
[7] (a) J.M. Lehn, Supramolecular Chemistry, Concepts and Perspectives, VCH, Verlagsgesellschaft, Weinhein, 1995;
(b) Z. Qin, M.C. Jennings, R.J. Puddephartt, Inorg. Chem. 42 (2003) 1956;
(c) M. Fujita, Chem. Soc. Rev. 27 (1998) 417;
(d) S. Leininger, B. Olenyuk, P.J. Stang, Chem. Rev. 100 (2000) 853;
(e) D.S. Cati, J. Ribas, J. Ribas-Ariño, H. Stoeckli-Evans, Inorg. Chem. 43 (2004) 1021.
[8] (a) R.F. Carina, A.F. Williams, G.G. Bernardinelli, J. Organomet. Chem. 548 (1997) 45;
(b) W.T.S. Huck, F.C.J.M. van Veggel, B.L. Kropman, D.H.A. Blank, E.G. Keim, M.M.A. Smithers, D.N. Reinhoudt, J. Am. Chem. Soc. 117 (1996) 8293;
(c) W.T.S. Huck, F.C.J.M. van Veggel, D.N. Reinhoudt, Angew. Chem., Int. Ed. Engl. 32 (1993) 392.
[9] C.H.M. Amijs, A. Berger, F. Soulimani, T. Visser, G.P.M. van Klink, M. Lutz, A.L. Spek, G. van Koten, Inorg. Chem. 44 (2005) 6567.
[10] A.C.T. North, D.C. Phillips, F.S. Mathews, Acta. Crystallogr., Sect. A 24 (1968) 351.
[11] L.J. Farrugia, J. Appl. Crystallogr. 32 (1999) 837.
[12] A. Altomare, G. Cascarano, C. Giacovazzo, A. Guagliardi, J. Appl. Crystallogr. 26 (1993) 343.
[13] G.M. Sheldrick, SHELX97 – Programs for Crystal Structure Analysis (Release 97-2), Institüt für Anorganische Chemie der Universität, Tammanstrasse 4, D-3400 Göttingen, Germany, 1998.
[14] M. Nardelli, J. Appl. Crystallogr. 32 (1999) 563.
[15] A.L. Spek, Acta Crystallogr., Sect. A 46 (1990) C34.
[16] K. Nakamoto, Infrared and Raman Spectra of Inorganic and Coordination Compounds, 3rd., Wiley Interscience Pub., New York, 1978.
[17] G. Socrates, Infrared Characteristic Group Frequencies, 2nd., Wiley, England, 1994.
[18] C.C. Addison, O. Sutton, Complexes containing the nitrate ion, in: F.A. Cotton (Ed.), Progress in Inorganic Chemistry, vol. 8, Wiley Interscience, New York, 1967, p. 195.
[19] N.F. Curtis, Y.M. Curtis, Inorg. Chem. 4 (1965) 804.
[20] W.J. Geary, J. Coord. Chem. Rev. 7 (1971) 81.
[21] J.M. Valke, F. Maassarani, P. van der Sluis, A.L. Spek, J. Boersma, G. van Koten, Organometallics 13 (1994) 2320.
[22] D.St.C. Black, G.B. Deacon, G.L. Edwards, Aust. J. Chem. 47 (1994) 217.
[23] H. Suzuki, N. Tajima, K. Tatsumi, Y. Yamamoto, Chem. Commun. (2000) 1801.
[24] J.M. Vila, M.T. Pereira, J.M. Ortigueira, A. Amoedo, M. Graña, G. Alberdi, M. Lópes-Torres, A. Fernández, J. Organomet. Chem. 663 (2002) 239.
[25] L. Pauling, The Nature of the Chemical Bond, 3rd ed., Cornell University Press, Ithaca, New York, 1960. p. 224.
[26] A.E. Mauro, A.C.F. Caires, R.H.A. Santos, M.T.P. Gambardella, J. Coord. Chem. 48 (1999) 521.
[27] A.M. Santana, A.E. Mauro, E.T. De Almeida, R.H.A. Santos, J.R. Zóia, J. Coord. Chem. 53 (2001) 163.
[28] J.L. Serrano, L. García, J. Pérez, E. Pérez, J. Vives, G. Sánchez, G. López, E. Molins, A.G. Orpen, Polyhedron 21 (2002) 1589.
[29] T. Hudgens, D. Johnson, W. Cordes, T. Barclay, D. Jeter, J. Chem. Crystallogr. 24 (7) (1997) 247.
[30] G.R. Newcome, D.L. Kohl, F.R. Fronkzec, J. Am. Chem. Soc. 104 (1982) 994.
[31] (a) M. Hackmeyer, J.L. Whitten, J. Chem. Phys. 54 (1971) 3739;
(b) H.W. Richardson, W.E. Hatfield, J. Am. Chem. Soc. 98 (1976) 835;
(c) W. Kaim, Angew. Chem., Int. Ed. Engl. 22 (1983) 171;
(d) G. Beobide, O. Castillo, A. Luque, U. Garcia-Couceiro, J.P. Garcia-Terán, P. Román, Inorg. Chem. 45 (2006) 5369.
[32] See, for instance, the interesting iridium tetramer described by H. Suzuki et al., J. Chem. Soc., Chem. Commun. (2000) 1801.
[33] R.D. Sommer, A.L. Rheingold, A.J. Goshe, B. Bosnich, J. Am. Chem. Soc. 123 (2001) 3940.

Polyhedron 28 (2009) 291–299

Contents lists available at ScienceDirect

Polyhedron

journal homepage: www.elsevier.com/locate/poly

Silver nitrate molecular species and coordination polymers with divergent supramolecular morphology constructed from hydrogen-bonding capable dipyridyl ligands

Gregory A. Farnum, Warren R. Knapp, Robert L. LaDuca *

Lyman Briggs College and Department of Chemistry, Michigan State University, E-30 Holmes Hall, East Lansing, MI 48825, USA

ARTICLE INFO

Article history:
Received 14 September 2008
Accepted 22 October 2008
Available online 29 November 2008

Keywords:
Silver
Nitrate
Dipyridine
Coordination polymer
Hydrogen-bonding
Crystal structure
Luminescence

ABSTRACT

Solution phase reaction of silver nitrate with various hydrogen-bonding capable dipyridyl ligands has resulted in three 1-D coordination polymers and one discrete cationic species with diverse silver coordination spheres. $[Ag(NO_3)(4,4'\text{-dpk})]_n$ (**1**, 4,4′-dpk = 4,4′-dipyridylketone), $\{[Ag(4\text{-bpmp})](NO_3)\cdot 6H_2O\}$ (**2**, 4-bpmp = bis(4-pyridylmethyl)piperazine) and $\{[Ag_2(NO_3)(3\text{-bpmp})(H_2O)_2]NO_3\}_n$ (**3**, 3-bpmp = bis(3-pyridylmethyl)piperazine) all display 1-D coordination polymer chain or ribbon motifs. Long-range Ag···O interactions and/or hydrogen-bonding promote the formation of different supramolecular aggregations such as a 2-D double layer slab in **1**, a threefold interpenetrated 3-D diamondoid network in **2**, and a 2-D single layer in **3**. Compound **2** manifests "infinite" 1-D T(5)2 water molecule tapes within its incipient voids. $\{[Ag(2,4'\text{-pmpp})_2](NO_3)\cdot H_2O\}$ (**4**, 2,4′-pmpp = 2-pyridyl(4′-methylpyridyl)piperazine) contains discrete cationic species connected by nitrate-mediated Ag···O interactions into a supramolecular 1-D zig-zag chain. Complexes **1** and **4** undergo weak blue–violet luminescence upon irradiation with ultraviolet light.

© 2008 Elsevier Ltd. All rights reserved.

1. Introduction

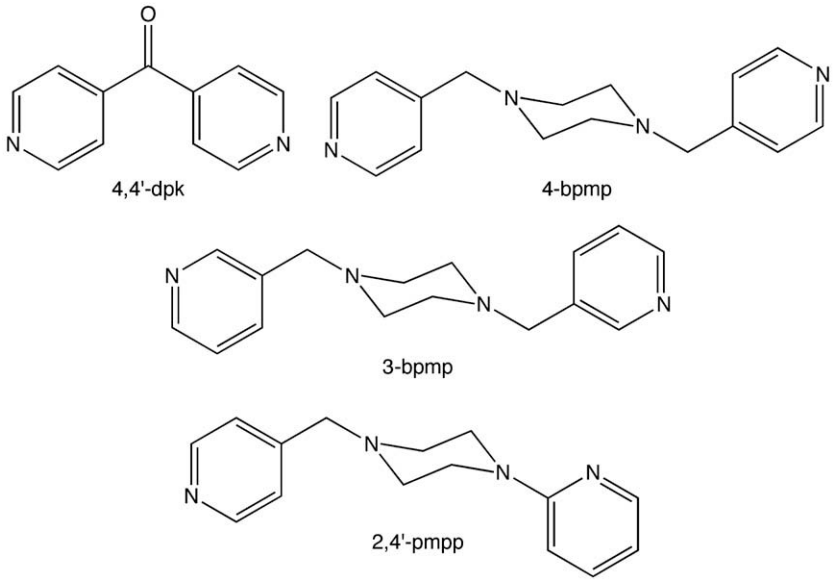
Exploratory synthesis of coordination polymers remains an intensive area of research because of these materials' potential utility in gas storage [1] and luminescence [2], and also as selective absorbents [3], ion-exchange substrates [4] and catalysts [5]. While most of the focus has rested on coordination polymers incorporating divalent transition metal cations, extended inorganic/organic phases based on monovalent silver have also exhibited diverse patterns of covalent and supramolecular connectivity [6–10], in addition to luminescent [11], ion-exchange [7] and even antibacterial properties [12]. The lack of crystal field stabilization at the d^{10} configuration monovalent silver cation allows different coordination environments depending on the particular steric and electronic requirements of the employed tethering ligands, thereby allowing a variety of coordination polymer morphologies [6–10].

A commonly used tethering ligand for the construction of monovalent silver coordination polymers is the rigid-rod spacer 4,4′-bipyridine (4,4′-bpy), giving rise to a variety of structural topologies. While $\{[Ag(4,4'\text{-bpy})(H_2PO_4)]\cdot 2H_2O\}_n$ [6] and $[Ag(4,4'\text{-bpy})(BF_4)]_n$ [7] are simple 1-D coordination polymer chains, $\{[Ag(4,4'\text{-bpy})_{1.5}(CH_3CN)](SbF_6)\}_n$ displays a non-interpenetrated (6,3) honeycomb 2-D grid with large ~17 × ~26 Å rings [8]. Higher dimensionality structures that feature interpenetration are also possible in this system, as $[Ag(4,4'\text{-bpy})(NO_3)]_n$ manifests a triply interpenetrated (10,3) $ThSi_2$ lattice [9] and $\{[Ag(4,4'\text{-bpy})_2](CF_3SO_3)\}_n$ possesses a fourfold 3-D diamondoid network constructed from tetrahedrally coordinated silver cationic connecting nodes [10]. In comparison, there are fewer examples of related silver-based coordination polymers constructed from dipyridyl ligands possessing hydrogen-bonding capable functional groups. In addition to their covalent ligating capabilities, members of this class of ligand can promote structure direction by permitting supramolecular interactions with ligated or unligated counteranions, resulting in structures different from their 4,4′-bpy analogues [13,14]. For instance, $[Ag(2,3'\text{-dpa})(NO_3)]_n$ (2,3′-dpa = 2,3′-dipyridylamine) [13] and $[Ag(4,4'\text{-dpa})(NO_3)]_n$ (4,4′-dpa = 4,4′-dipyridylamine) [14] both exhibit 1-D helical chain structures, although the latter forms a fourfold interpenetrated α-Po primitive cubic-type supramolecular net via long-range Ag···O interactions and hydrogen-bonding mechanisms.

In this study we present three 1-D silver nitrate coordination polymers and one discrete cationic complex containing the potentially ditopic hydrogen-bonding capable pyridyl ligands 4,4′-dipyridylketone (4,4′-dpk), bis(4-pyridylmethyl)piperazine (4-bpmp), bis(3-pyridylmethyl)piperazine (3-bpmp) or 2-pyridyl(4′-methylpyridyl)piperazine (2,4′-pmpp) (Scheme 1). Although our group has recently reported some divalent metal aromatic dicarboxylate coordination polymers including 4-bpmp [15] and 3-bpmp [16],

* Corresponding author. Tel.: +1 5174322268.
E-mail address: laduca@msu.edu (R.L. LaDuca).

0277-5387/$ - see front matter © 2008 Elsevier Ltd. All rights reserved.
doi:10.1016/j.poly.2008.10.028



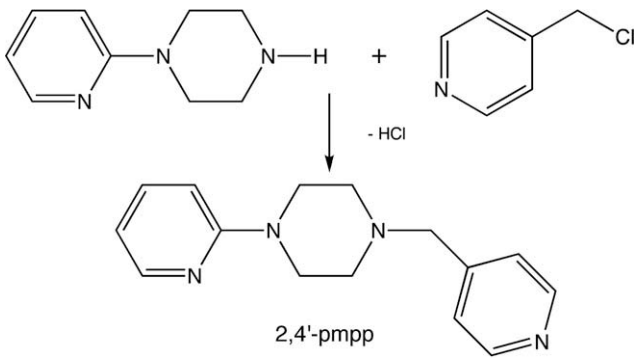
Scheme 1.

the coordination polymer chemistry of 4,4′-dpk and 2,4′-pmpp remains undeveloped. The 0-D discrete cationic species and 1-D coordination polymer chains aggregate into 1-D chain, 2-D layer, 2-D double slab or interpenetrated 3-D supramolecular morphologies via specific long-range Ag···O or hydrogen-bonding interactions, reflecting a degree of structural control exerted by the particular dipyridyl ligand used. Luminescent behavior for two of these phases (**1** and **4**) is also observed.

2. Experimental

2.1. General considerations

Silver nitrate was obtained from Alfa Aesar. The ligands 4,4′-dpk [17], 4-bpmp and 3-bpmp [18] were prepared via published procedures. The ligand 2,4′-pmpp was synthesized by a modification of the procedure for 4-bpmp, through the combination of 2-pyridylpiperazine with 4-chloromethylpyridine (Scheme 2). Water was deionized above 3 MΩ in-house. Elemental analysis was carried out using a Perkin Elmer 2400 Series II CHNS/O Analyzer. IR spectra were recorded on a Perkin Elmer Spectrum One instrument on ground powdered samples. Luminescence spectra were obtained with a Hitachi F-4500 Fluorescence Spectrometer on solid crystalline samples anchored to quartz microscope slides with Rexon Corporation RX-22P ultraviolet-transparent epoxy adhesive.



Scheme 2.

2.2. Preparation of [Ag(NO$_3$)(4,4′-dpk)] (**1**)

Silver nitrate (0.017 g, 0.10 mmol) was dissolved in 1.5 ml H_2O in a glass vial. To this solution was added a 0.75 mL aliquot of 1:1 water–ethanol solution, followed by 1.5 mL of a solution of 4,4′-dpk (0.040 g, 0.22 mmol) in ethanol. Colorless plates of **1** (18 mg, 0.051 mmol, 51% yield based on Ag) formed after standing at 25 °C for two weeks in a dark environment. These were isolated after washing with distilled water, ethanol, acetone and drying in air. *Anal.* Calc. for $C_{11}H_8AgN_3O_4$ (**1**): C, 37.31; H, 2.28; N, 11.87. Found: C, 36.79; H, 2.15; N, 11.76%. IR (cm^{-1}): 3046 (w), 2923 (w), 1745 (w), 1668 (m), 1603 (w), 1554 (w), 1496 (w), 1419 (w), 1392 (m), 1329 (s), 1296 (m), 1280 (s), 1252 (s), 1222 (m), 1155 (m), 1104 (m), 1059 (m), 1040 (m), 1010 (m), 949 (m), 879 (m), 860 (m), 819 (m), 756 (s), 740 (m), 708 (m), 684 (s), 651 (s).

2.3. Preparation of {[Ag(NO$_3$)(4-bpmp)] · 6H$_2$O} (**2**)

A similar procedure as for **1** was followed, with the use of 4,4′-bpmp (0.032 g, 0.12 mmol) as the dipyridyl ligand. Colorless plates of **2** (30 mg, 0.055 mmol, 55% yield based on Ag) formed after standing at 25 °C for two weeks in a dark environment. *Anal.* Calc. for $C_{16}H_{32}AgN_5O_9$ (**2**): C, 35.18; H, 5.90; N, 12.82. Found: C, 34.97; H, 5.60; N, 12.81%. IR (cm^{-1}): 3359 (m, br), 2850 (w), 1650 (w), 1619 (m), 1561 (w), 1468 (w), 1433 (m), 1366 (s, sh), 1330 (vs), 1303 (s, sh), 1268 (m), 1231 (m), 1136 (m), 1118 (m), 1103 (w), 1070 (w), 1032 (w), 993 (m), 972 (w), 939 (m), 857 (m), 835 (m), 804 (s), 684 (s).

2.4. Preparation of {[Ag$_2$(NO$_3$)(3-bpmp)(H$_2$O)$_2$]NO$_3$}$_n$ (**3**)

A similar procedure as for **1** was followed, with the use of 3-bpmp (0.032 g, 0.12 mmol) as the dipyridyl ligand. Colorless plates of **3** (21 mg, 0.032 mmol, 32% yield based on Ag) formed after standing at 25 °C for two weeks in a dark environment. *Anal.* Calc. for $C_{16}H_{24}Ag_2N_6O_8$ (**3**): C, 29.83; H, 3.76; N, 13.05. Found: C, 29.39; H, 3.60; N, 12.91%. IR (cm^{-1}): 3404 (m, br), 2971 (w), 2857 (w), 1628 (w), 1603 (w), 1485 (w), 1463 (w), 1437 (w), 1307 (vs), 1269 (m), 1233 (w), 1216 (w), 1198 (w), 1119 (w), 1104 (m), 1057 (m), 1037 (m), 1002 (w), 981 (m), 947 (w), 937 (w), 836 (w), 824 (w), 804 (s), 708 (s), 668 (w), 659 (w).

2.5. Preparation of {[Ag(2,4′-pmpp)$_2$](NO$_3$) · H$_2$O} (**4**)

A similar procedure as for **1** was followed, with the use of 2,4′-pmpp (0.032 g, 0.13 mmol) as the dipyridyl ligand. Colorless plates of **4** (8.0 mg, 0.011 mmol, 17% yield based on 2,4′-pmpp) formed after standing at 25 °C for two weeks in a dark environment. *Anal.* Calc. for $C_{30}H_{36}AgN_9O_4$ (**4**): C, 51.88; H, 5.22; N, 18.15. Found: C, 50.53; H, 5.26; N, 17.62%. IR (cm^{-1}): 3463 (w, br), 2938 (w), 2810 (w), 1613 (m), 1594 (m), 1560 (w), 1480 (m), 1440 (m), 1428 (m), 1322 (vs), 1313 (s), 1287 (m), 1246 (m), 1231 (m), 1163 (m), 1141 (m), 1105 (m), 1063 (m), 1029 (w), 1009 (m), 977 (m), 946 (m), 930 (w), 839 (w), 825 (m), 801 (w), 781 (s), 739 (m), 722 (w), 667 (w).

3. X-ray crystallography

X-ray diffraction data were collected on single crystals of **1**–**4** at 173 K using either a Bruker-AXS SMART 1k CCD or a Bruker-AXS APEX2 CCD instrument. Reflection data were acquired using graphite-monochromated Mo Kα radiation (λ = 0.71073 Å). Crystals of **2** and **4** were non-merohedrally twinned; the twin laws were found using CELLNOW [19]. The data was integrated via SAINT [20]. Lorentz and polarization effect and absorption corrections were applied with SADABS (**1**, **3**) or TWINABS (**2**, **4**) [21]. The structures were solved using direct methods and refined on F^2 using SHELXTL [22]. For **2** and **4**, reflections from both major twin components were used in the refinements. All non-hydrogen atoms were refined with anisotropic displacement parameters. Hydrogen atoms bound to carbon atoms were placed in calculated positions and refined with isotropic displacement parameters with a riding model. Hydrogen atoms belonging to bound or unbound water molecules were located via Fourier difference map, placed at fixed positions, and refined with isotropic displacement parameters, with the exception of those in **4** which could not be found. Although a structural check indicated the possibility of *I*-centering for **3**, the triclinic space group forbids this. Relevant crystallographic data for **1**–**4** is listed in Table 1.

4. Results and discussion

4.1. Synthesis and spectral characterization

Slow diffusion of aqueous solutions of silver nitrate with ethanolic solutions of the requisite pyridyl ligands cleanly produced single crystals of **1**–**4**. The syntheses were carried out in the dark to avoid photodecomposition. Once formed, the crystalline solids remained insoluble in water and common organic solvents. The infrared spectra of all materials were consistent with their crystal structures. Features corresponding to pyridyl ring puckering mechanisms were observed in the region between 600 cm^{-1} and 820 cm^{-1}. Medium intensity bands in the range of ~1600 cm^{-1} to ~1200 cm^{-1} arise from stretching modes of the pyridyl rings [23]. Bands between 3050 cm^{-1} and 3150 cm^{-1} represent C–H stretching modes. The ketone C=O stretching frequency in **1** was observed at 1668 cm^{-1}. Features corresponding to the N–O stretching frequencies of the nitrate anions are observed in the region of ~1300 cm^{-1} to ~1500 cm^{-1} in all four spectra.

4.2. Structural description of [Ag(NO$_3$)(4,4′-dpk)]$_n$ (**1**)

The asymmetric unit of compound **1** consists of a monovalent silver ion, one monodentate nitrato ion, and one 4,4′-dpk ligand with an inter-ring torsion angle equaling 39.6° (Fig. 1). Despite the use of achiral starting materials, compound **1** crystallizes in the acentric space group $P2_1$. As seen in previous phases incorporating the related amine ligand 4,4′-dpa [14], the locked torsion angle between the aromatic rings of kinked dipyridyl ligands can promote the generation of chiral coordination polymers during

Table 1
Crystal and structure refinement data for **1**–**4**.

Data	**1**	**2**	**3**	**4**
Empirical formula	$C_{11}H_8AgN_3O_4$	$C_{16}H_{32}AgN_5O_9$	$C_{16}H_{24}Ag_2N_6O_8$	$C_{30}H_{38}AgN_9O_4$
Formula weight	354.07	546.34	644.15	696.57
Crystal system	monoclinic	monoclinic	triclinic	monoclinic
Space group	$P2_1$	$P2_1/c$	$P\bar{1}$	$P2_1/c$
a (Å)	7.5367(4)	26.674(11)	7.3783(9)	29.790(6)
b (Å)	8.9196(5)	5.990(2)	10.6172(14)	6.0394(12)
c (Å)	8.8696(5)	14.666(6)	14.5214(19)	17.021(3)
α (°)	90	90	71.145(1)	90
β (°)	101.264(3)	91.974(5)	84.913(1)	96.56(3)
γ (°)	90	90	77.000(1)	90
V (Å^3)	584.77(6)	2341.8(16)	1048.8(2)	3042.2(11)
Z	2	4	2	4
D_{calc} (g cm^{-3})	2.011	1.550	2.040	1.516
μ (mm^{-1})	1.738	0.915	1.925	0.714
Minimum/maximum transmission	0.5447/0.7601	0.5611/0.7456	0.6663/0.7457	0.6449/0.7456
hkl ranges	$-9 \leqslant h \leqslant 9$, $-10 \leqslant k \leqslant 10$, $-10 \leqslant l \leqslant 10$	$-34 \leqslant h \leqslant 34$, $-7 \leqslant k \leqslant 7$, $-19 \leqslant l \leqslant 18$	$-9 \leqslant h \leqslant 9$, $-13 \leqslant k \leqslant 13$, $-19 \leqslant l \leqslant 18$	$-39 \leqslant h \leqslant 38$, $0 \leqslant k \leqslant 7$, $0 \leqslant l \leqslant 21$
Total reflections	11720	23160	10428	11001
Unique reflections	2131	5269	4612	11001
R(int)	0.0208	0.0462	0.0190	0.0624
Parameters/restraints	172/1	319/18	301/6	398/0
R_1[a] (all data)	0.0146	0.1391	0.0235	0.1151
R_1[a] ($I > 2\sigma(I)$)	0.0143	0.0880	0.0195	0.0825
wR_2[b] (all data)	0.0363	0.2065	0.0536	0.2061
wR_2[b] ($I > 2\sigma(I)$)	0.0362	0.1851	0.0512	0.1920
Maximum/minimum residual (e/Å^3)	0.480/−0.424	1.066/−0.786	0.559/−0.400	1.428/−1.746
Goodness-of-fit	1.085	1.060	1.030	1.062

[a] $R_1 = \sum||F_o| - |F_c||/\sum|F_o|$.
[b] $wR_2 = \{\sum[w(F_o^2 - F_c^2)^2]/\sum[wF_o^2]^2\}^{1/2}$.

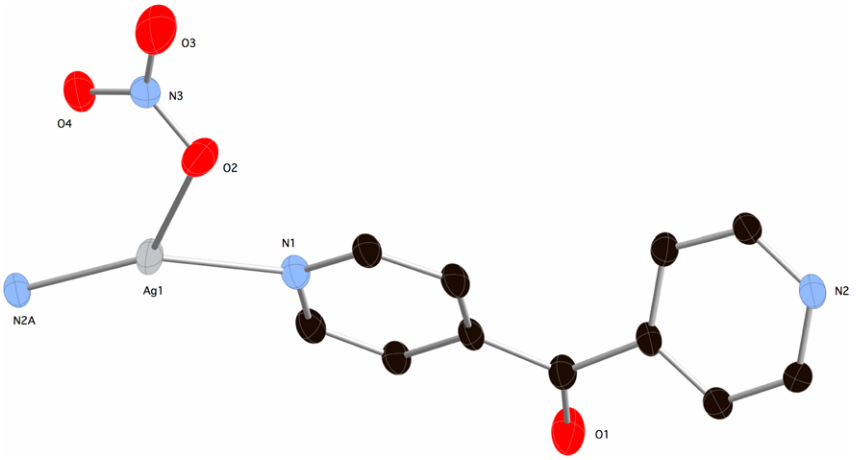


Fig. 1. Coordination environment of **1** with thermal ellipsoids shown at 50% probability. Hydrogen atoms have been omitted for clarity.

their self-assembly. It is thus likely that the kinked nature of 4,4′-dpk allows it to act similarly. Enantiomeric purity within the crystal is indicated by the Flack parameter [24] value of 0.016(19).

The silver ion in **1** adopts a very distorted $\{AgON_2\}$ trigonal planar-type geometry, with bond angles varying between 91.7° and 135.7°. Bond lengths and angles about the silver ion are given in Table 2. Extension of the structure through the 4,4′-dpk ligands generates a 1-D $[Ag(NO_3)(4,4'\text{-dpk})]_n$ coordination polymer chain, in which the nearest neighbor Ag···Ag distance is 11.677 Å (Fig. 2). Adjacent $[Ag(NO_3)(4,4'\text{-dpk})]_n$ chains are connected into a pseudo 2-D slab through long-range Ag···O interactions (2.760 Å) between unligated nitrate oxygen atoms in one chain and silver ions in another (Fig. 3). Within a single slab, the two sets of 1-D chains are arranged parallel to the [1–10] and [−1 −10] directions, respectively. The closest Ag···Ag contact between the sets of chains within the slab is 5.130 Å, well outside of the range of active argentophilic interactions [25]. Neighboring pseudo slabs stack in an *AAA* pattern (Fig. S1) along the *c* crystal direction through non-classical C–H···O hydrogen-bonding (H···O distance = 2.413 Å; C···O distance = 3.319 Å) between the pyridyl rings in one slab and the ketone functional groups of the 4,4′-dpk ligands in another slab.

Table 2
Selected bond distance (Å) and angle (°) data for **1**.

Ag1–N2	2.2072(17)	N2–Ag1–N1	130.60(6)
Ag1–N1	2.2841(18)	N2–Ag1–O2	135.66(6)
Ag1–O2	2.4075(16)	N1–Ag1–O2	91.71(6)

4.3. Structural description of $\{[Ag(NO_3)(4\text{-bpmp})] \cdot 6H_2O\}$ (**2**)

As revealed by single-crystal X-ray diffraction the asymmetric unit of **2** contains one silver ion, one unligated nitrate anion disordered over two positions in a 60/40 ratio, two halves of two crystallographically distinct 4-bpmp molecules ligated via their pyridyl nitrogen atoms, and six water molecules of crystallization (Fig. 4). The centroid of each of the chair conformation piperazinyl rings of the 4-bpmp ligands rests on a crystallographic inversion center. The silver coordination environment is virtually linear (Table 3). Unlike **1**, compound **2** crystallizes in a centrosymmetric space group ($P2_1/c$). Monovalent silver cations are connected through tethering 4-bpmp ligands to construct sets of 1-D $[Ag(4-bpmp)]_n^{n+}$ coordination polymer chains that are oriented parallel to the [−1 3 0] and [1 −3 0] crystal directions (Fig. 5). Within these chains, the Ag···Ag distances through the two crystallographically distinct types of 4-bpmp ligands alternate between 16.062 and 16.148 Å.

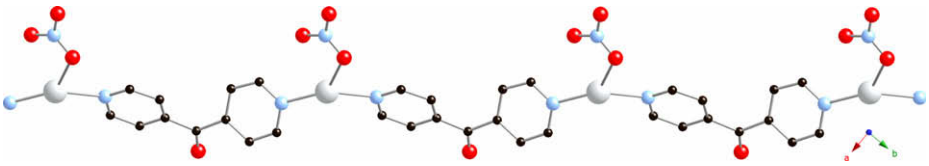


Fig. 2. A single $[Ag(NO_3)(4,4'\text{-dpk})]_n$ coordination polymer chain in **1**.

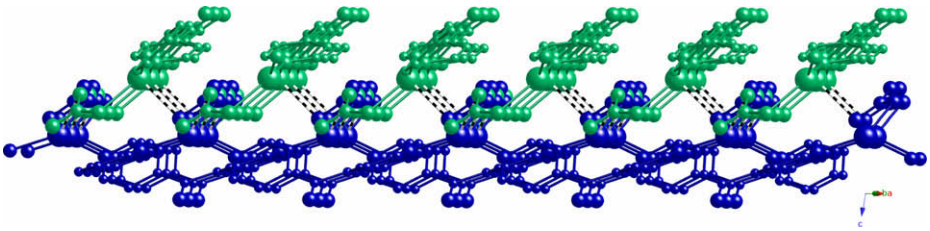


Fig. 3. A pseudo 2-D slab in **1**, illustrating the long-range Ag···O interactions as dashed lines.

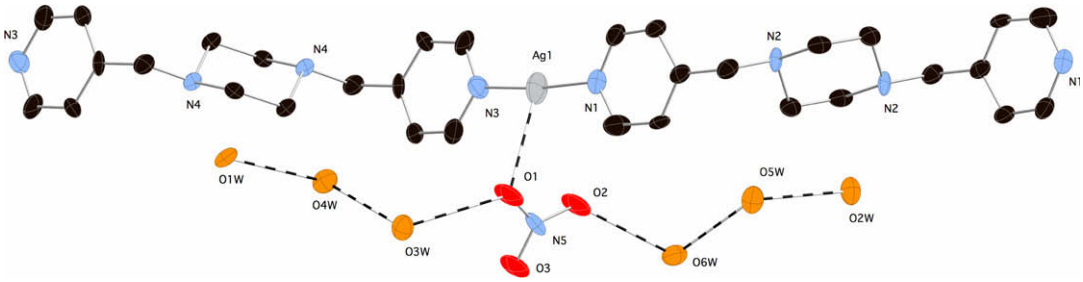


Fig. 4. Coordination environment of **2** with thermal ellipsoids shown at 50% probability. Hydrogen atoms have been omitted for clarity. Hydrogen-bonding and Ag···O long-range interactions are depicted as dashed lines.

Table 3
Selected bond distance (Å) and angle (°) data for **2**.

Ag1–N3	2.127(10)	N3–Ag1–N1	174.6(4)
Ag1–N1	2.129(10)		

The subtle difference between these values is attributed to variances in the conformations of the flexible 4-bpmp bridging ligands, especially in the N–C–C angles (109.8° and 110.8°) defining the connection of the piperazinyl rings to the pyridyl rings.

Neighboring $[Ag(4-bpmp)]_n^{n+}$ chains are linked together through long-range Ag···O interactions (2.918 and 2.927 Å) provided by the charge-balancing nitrate anions. Thus, each silver cation can be considered a 4-connected node, with two connections through 4-bpmp ligands within a $[Ag(4-bpmp)]_n^{n+}$ chain and two others through the long-range supramolecular Ag···O interactions. The 4-connected 3-D supramolecular network thereby formed has a 6^6 topology, corresponding to the diamond lattice. Incipient voids within a single network allows interpenetration of two identical networks, thus resulting in an overall threefold interpenetrated diamondoid net supramolecular topology for **2** (Fig. 6). While many coordination polymers possessing diamondoid networks with odd-numbered interpenetration levels are chiral [26], the presence of the crystallographic inversion centers within the 4-bpmp ligands precludes chirality in this case.

Entrained in the void spaces within the triply interpenetrated supramolecular network, which occupy 27.2% of the unit cell volume according to PLATON [26], are 1-D water tapes belonging to the commonly encountered T(5)2 classification [27] in which cyclic water pentamers share two water molecules between them. The water molecule tapes are conjoined into a supramolecular layer topology via hydrogen-bonding interactions with the unligated nitrate anions (Fig. 7). Geometrical parameters for the hydrogen-bonding interactions in **2** are listed in Table 4. NO void space when all solvent molecules included.



Fig. 5. A single $[Ag(4\text{-bpmp})]_n$ chain motif in **2**.

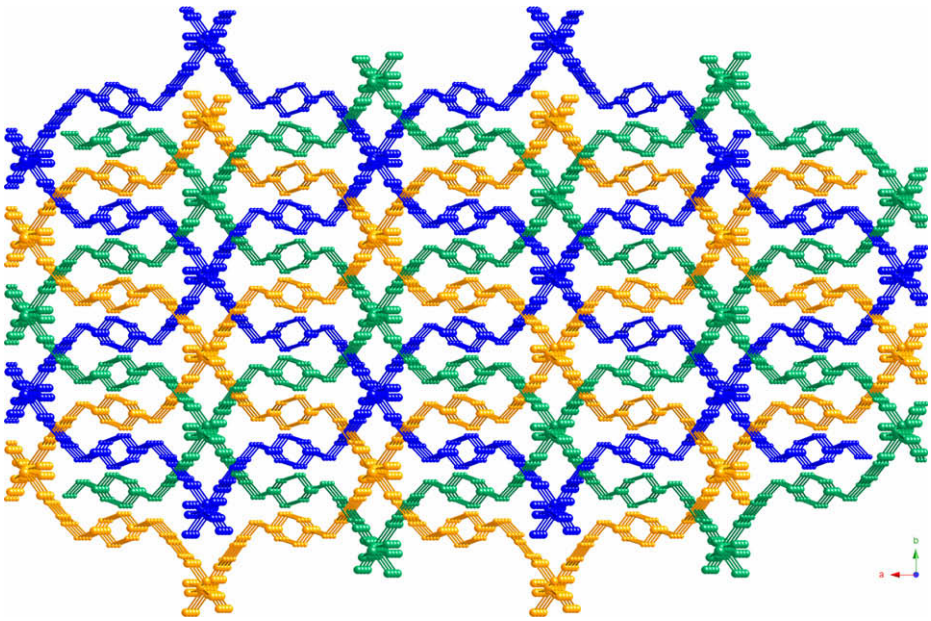


Fig. 6. The threefold interpenetrated diamondoid supramolecular network in **2**.

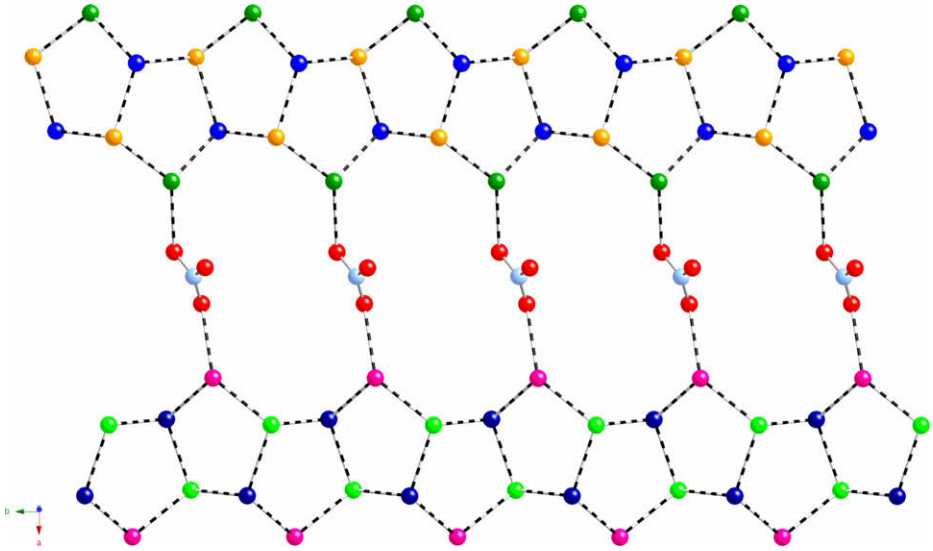


Fig. 7. Two crystallographically distinct T(5)2 classification water tapes within incipient voids in **2**, with hydrogen-bonded nitrate anions situated between them. Hydrogen-bonding interactions are shown as dashed lines.

Table 4
Hydrogen-bonding data for **2** and **3**.

D–H···*A*	*d*(H···*A*)	∠*DHA*	*d*(*D*···*A*)	Symmetry transformation for *A*
Complex ***2***				
O1W–H1WA···N4	2.05(6)	154(10)	2.869(11)	
O1W–H1WB···O4W	1.94(3)	170(10)	2.806(11)	$x, -y-1/2, z+1/2$
O2W–H2WA···O6W	1.92(4)	160(10)	2.776(12)	
O2W–H2WB···O5W	2.13(8)	137(10)	2.848(12)	$x, y-1, z$
O3W–H3WA···O4W	1.88(5)	161(12)	2.739(12)	$x, y-1, z$
O3W–H3WB···O1	2.08(7)	151(11)	2.89(3)	$x, -y-1/2, z-1/2$
O4W–H4WA···O1W	2.27(10)	119(9)	2.806(11)	$x, -y-1/2, z-1/2$
O4W–H4WB···O1W	1.99(3)	167(9)	2.861(12)	$-x, -y, -z+1$
O5W–H5WA···O2W	1.99(4)	162(10)	2.848(12)	$x, y+1, z$
O5W–H5WB···O2W	1.90(3)	169(11)	2.781(12)	$-x+1, y+1/2, -z+3/2$
O6W–H6WA···O5W	2.14(11)	124(11)	2.742(13)	$-x, y-3/2, -z+1/2$
O6W–H6WB···O2	2.13(7)	144(10)	2.90(2)	
Complex ***3***				
O4–H4A···O5	1.970(17)	170(2)	2.826(3)	$x, y-1, z$
O4–H4B···O1	2.017(16)	179(2)	2.878(2)	$x+1, y-1, z$
O8–H8A···O7	2.000(17)	170(2)	2.868(2)	$x+1, y-1, z$
O8–H8B···O3	2.145(17)	168(2)	3.002(3)	$x+1, y, z$

4.4. Structural description of $\{[Ag_2(NO_3)(3\text{-bpmp})(H_2O)_2]NO_3\}_n$ (**3**)

The asymmetric unit of complex **3** contains two monovalent silver cations, one monodentate nitrato ligand, two aqua ligands, two halves of two crystallographically distinct 3-bpmp ligands and one unbound nitrate anion (Fig. 8). Dissimilar to **1** and **2**, there are two crystallographically distinct silver ions in **3**. One (Ag1) is coordinated in an extremely distorted tetrahedral $\{AgN_2O_2\}$ environment, where the two oxygen donors are provided by the two aqua ligands. The nitrogen donors belong to the pyridyl ring of one 3-bpmp ligand and the piperazinyl ring of a second 3-bpmp ligand. The other silver atom (Ag2) adopts a very distorted T-shaped $\{AgN_2O\}$ coordination sphere wherein the nitrogen donor atoms arise from a similar binding pattern as at Ag1; the coordination environment is completed by a nitrato oxygen atom. Pertinent bond lengths and angles for **3** are given in Table 5.

Exotetradentate 3-bpmp ligands connect the silver atoms into a cationic $[Ag_2(NO_3)(3\text{-bpmp})(H_2O)_2]_n^{n+}$ 1-D coordination polymer

Table 5
Selected bond distance (Å) and angle (°) data for **3**.

Ag1–N3	2.2599(16)	N3–Ag1–N2	147.10(5)
Ag1–N2	2.3030(15)	N3–Ag1–O4	87.39(5)
Ag1–O4	2.5777(15)	N2–Ag1–O4	109.99(5)
Ag1–O8	2.6711(16)	N3–Ag1–O8	90.73(5)
Ag2–N1	2.2248(16)	N2–Ag1–O8	97.62(5)
Ag2–N4	2.2677(15)	O4–Ag1–O8	130.64(5)
Ag2–O1	2.5477(14)	N1–Ag2–N4	147.66(5)
		N1–Ag2–O1	97.20(5)
		N4–Ag2–O1	113.94(5)

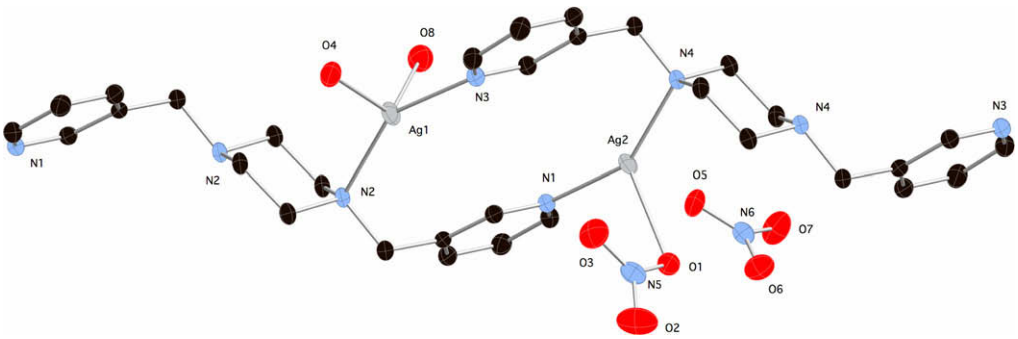


Fig. 8. Coordination environments of **3** with thermal ellipsoids shown at 50% probability. Hydrogen atoms have been omitted for clarity.

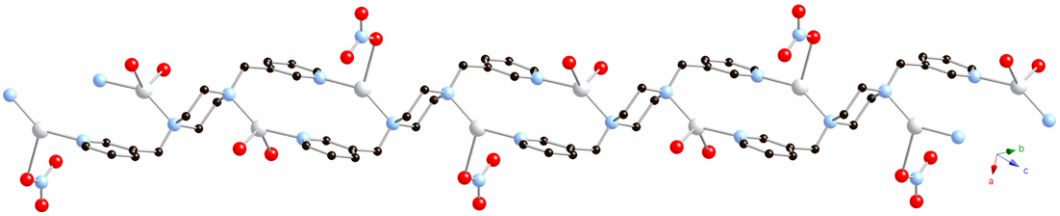


Fig. 9. A single cationic $[Ag_2(3\text{-bpmp})(NO_3)(H_2O)_2]_n$ ribbon in **3**.

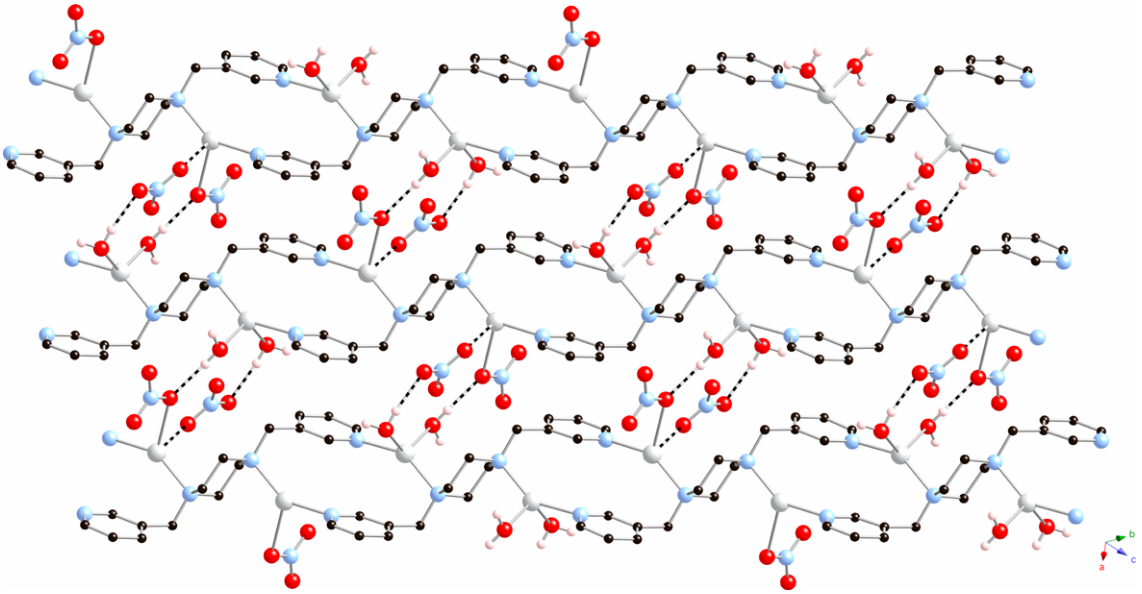


Fig. 10. The supramolecular layer motif in **3**. Hydrogen-bonding interactions are shown as dashed lines.

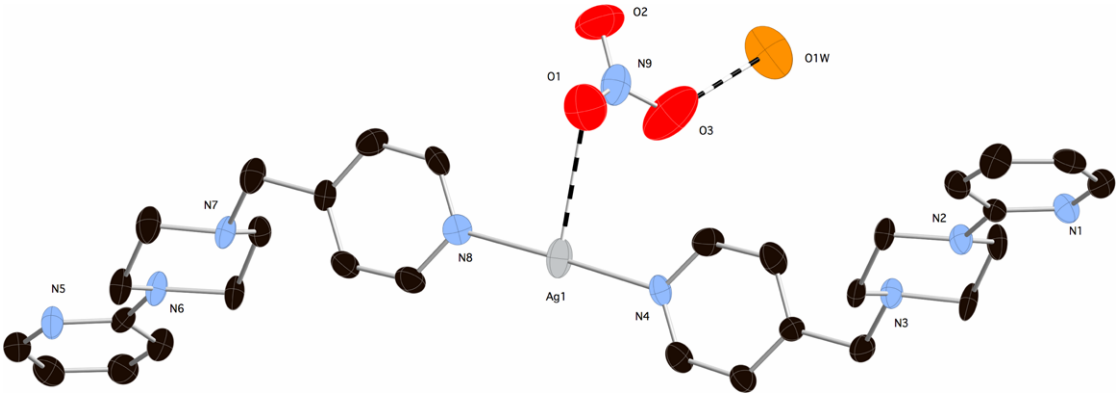


Fig. 11. Asymmetric unit of **4** with thermal ellipsoids shown at 50% probability. Hydrogen atoms have been omitted for clarity. Relevant supramolecular interactions are shown as dashed lines.

ribbon, which can be visualized as being formed from the *spiro* junction of 12-membered $\{AgNCCCN\}_2$ rings with 6-membered {NCCNCC} piperazinyl rings (Fig. 9). The Ag···Ag through-space distance across the 12-membered circuits is 5.362 Å, again beyond the usual range of argentophilic d^{10}–d^{10} interactions. In the very limited coordination polymer chemistry of the 3-bpmp ligand [16], compound **3** appears to be the first instance of metal binding by the piperazinyl nitrogen atoms.

The chain motifs, which are co-linear with the [1 −1 −1] crystal direction, are connected together into a supramolecular pseudo layer pattern (Fig. 10) by means of hydrogen-bonding donation from the aqua ligands to the ligated nitrato anions (Table 4). Supplementary structural stability of the supramolecular layer is provided by long-range Ag···O interactions to the formally unligated nitrates (Ag···O distance = 2.863 Å). Pseudo layers further stack

Table 6
Selected bond distance (Å) and angle (°) data for **4**.

Ag1–N8	2.148(5)	N8–Ag1–N4	178.3(2)
Ag1–N4	2.134(5)		

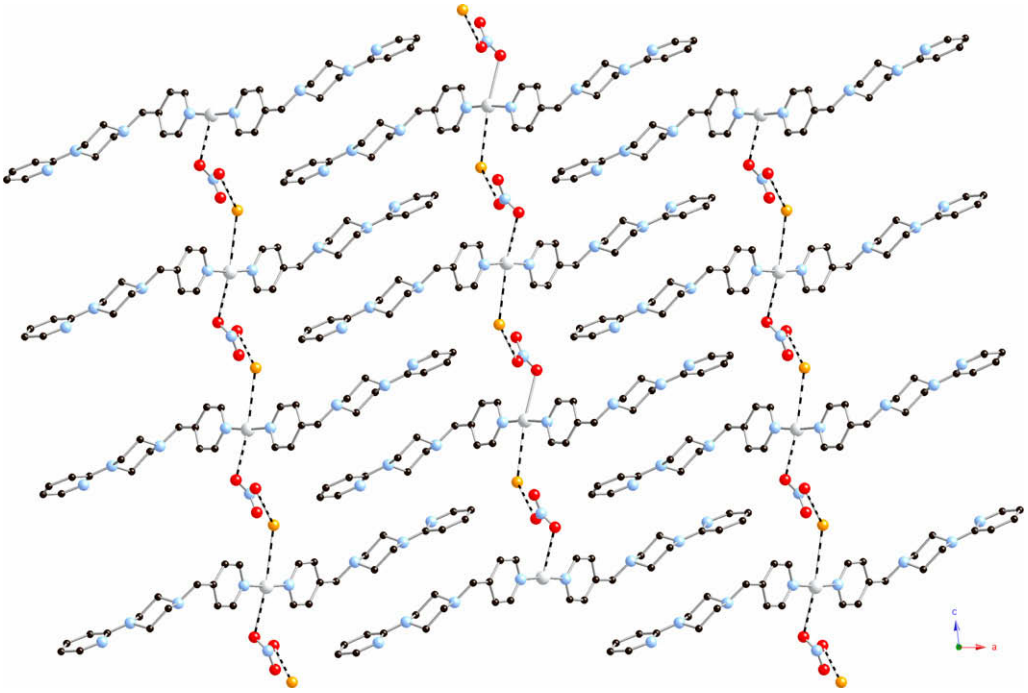


Fig. 12. Interdigitation of pseudo 1-D chain motif in **4** formed via Ag···O and hydrogen-bonding interactions (shown as dashed lines).

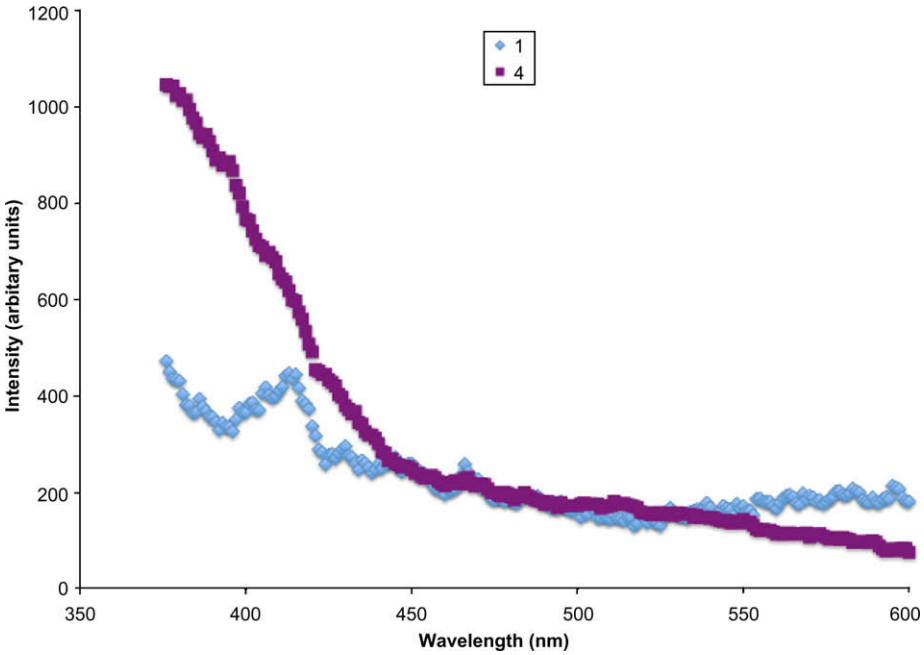


Fig. 13. Emission spectra of **1** and **4** with λ_{ex} = 300 nm.

into 3-D in an *AAA* pattern by hydrogen-bonding donation between aqua ligands and oxygen atoms from ligated nitrato anions (Fig. S2).

4.5. Structural description of {[Ag(2,4′-pmpp)$_2$](NO$_3$) · H$_2$O} (**4**)

The asymmetric unit of compound **4** consists of a monovalent silver cation, two 2,4′-pmpp molecules ligated to silver through their 4′-pyridyl termini, one unligated nitrate anion, and one water molecule of crystallization (Fig. 11). Neither the 2-pyridyl nor piperazinyl nitrogen atoms bind to silver, perhaps due to steric encumbrances failing to permit the orientation of their lone pairs toward a metal center. The silver atom is coordinated in a {AgN$_2$} pseudo-linear fashion as in **2**, with bond length and angle information listed in Table 6.

Individual molecules of **4** are linked into a pseudo 1-D chain through long-range Ag···O interactions (2.908 Å) to nitrate oxygen atoms and hydrogen-bonding pathways between the nitrate anions and the water molecules of crystallization. The chain motifs lie parallel to the *b* crystal direction, wherein the closest Ag···Ag distance of 6.073 Å corresponds to the *b* lattice parameter. Neighboring pseudo chains interdigitate with each other, constructing a pseudo 2-D layer motif parallel with the *ac* crystal plane (Fig. 12).

4.6. Luminescence studies

As numerous silver-based coordination polymers have been found to possess luminescent properties [28], solid samples of **1**–**4** were subjected to ultraviolet irradiation. Although samples of **2** and **3** failed to exhibit any appreciable visible light emission, possibly due to dehydration and loss of crystallinity upon long-term storage, crystals of **1** and **4** showed modest emission of blue–violet light (Fig. 13) upon excitation with ultraviolet light (λ_{ex} = 300 nm). In comparison to previously reported silver-containing coordination polymers, the emissive behavior is ascribed to metal to ligand charge transfer [28c].

5. Conclusion

Employment of long-spanning dipyridyl ligands with hydrogen-bonding capable centers has generated four distinct silver coordination complexes, three of which form 1-D coordination polymer chains. The specific electronic environment enforced by the nitrogen donor disposition and the central amine groups of the ligands during self-assembly results in 1-D, 2-D, or 3-D supramolecular lattices, different from those obtained with the commonly used rigid-rod tether 4,4′-bpy. Although the hydrated species apparently dehydrate over time, compromising crystal quality, the luminescent properties of **1** and **4** reinforce the potential of silver/diimine coordination polymers as substrates in optical devices. Variance of the anionic component in this system is likely to influence and alter molecular-level coordination polymer structure and macroscopic properties. Work in this vein continues in our laboratory and will be reported in due course.

Acknowledgements

The authors gratefully acknowledge Michigan State University and the donors of the American Chemical Society Petroleum Research Fund for financial support of this work. SDG.

Appendix A. Supplementary data

CCDC 699478, 699479, 699480 and 699481 contain the supplementary crystallographic data for **1, 2, 3 and 4**. These data can be obtained free of charge via http://www.ccdc.cam.ac.uk/conts/retrieving.html, or from the Cambridge Crystallographic Data Centre, 12 Union Road, Cambridge CB2 1EZ, UK; fax: (+44) 1223-336-033; or e-mail: deposit@ccdc.cam.ac.uk. Supplementary data associated with this article can be found, in the online version, at doi:10.1016/j.poly.2008.10.028.

References

[1] (a) J.L.C. Roswell, O.M. Yaghi, Angew. Chem., Int. Ed. Engl. 44 (2005) 4670;
(b) M. Kondo, T. Okubo, A. Asami, S.-I. Noro, T. Yoshitomi, S. Kitagawa, T. Ishii, H. Matsuzaka, Angew. Chem., Int. Ed. Engl. 38 (1999) 140;
(c) A.C. Sudik, A.R. Millward, N.W. Ockwig, A.P. Cote, J. Kim, O.M. Yaghi, J. Am. Chem. Soc. 127 (2005) 7110;
(d) A.K. Cheetham, C.N.R. Rao, R.K. Feller, Chem. Commun. (2006) 4780.
[2] (a) S. Zang, Y. Su, Y. Li, Z. Ni, Q. Meng, Inorg. Chem. 45 (2006) 174;
(b) L. Wang, M. Yang, G. Li, Z. Shi, S. Feng, Inorg. Chem. 45 (2006) 2474.
[3] (a) J.S. Seo, D. Whang, H. Lee, S.I. Jun, J. Oh, Y.J. Jeon, K. Kim, Nature 404 (2000) 982;
(b) A. Cingolani, S. Galli, N. Masciocchi, L. Pandolfo, C. Pettinari, A. Sironi, J. Am. Chem. Soc. 127 (2005) 6144.
[4] (a) Q.-R. Fang, G.-S. Zhu, M. Xue, J.-Y. Sun, S.-L. Qiu, Shi-Lun, Dalton Trans. (2006) 2399;
(b) X.-M. Zhang, M.-L. Tong, H.K. Lee, X.-M. Chen, J. Solid State Chem. 170 (2001) 118;
(c) O.M. Yaghi, H. Li, T.L. Groy, Inorg. Chem. 36 (1997) 4292.
[5] (a) S.G. Baca, M.T. Reetz, R. Goddard, I.G. Filippova, Y.A. Simonov, M. Gdaniec, N. Gerbeleu, Polyhedron 25 (2006) 1215;
(b) H. Han, S. Zhang, H. Hou, Y. Fan, Y. Zhu, Eur. J. Inorg. Chem. (2006) 1594;
(c) W. Mori, S. Takamizawa, C.N. Kato, T. Ohmura, T. Sato, Micropor. Mesopor. Mater. 73 (2004) 15.
[6] L.S. Wang, S.P. Yang, J.F. Zhang, Acta Crystallogr., Sect. E 61 (2005) m25.
[7] A.N. Khlobystov, N.R. Champness, C.J. Roberts, S.J.B. Tendler, C. Thompson, M. Schroeder, CrystEngComm 4 (2002) 426.
[8] J.J. Jiang, X.P. Li, X.L. Zhang, B.S. Kang, C.Y. Su, CrystEngComm 7 (2005) 603.
[9] F. Robinson, M.J. Zaworotko, J. Chem. Soc., Chem. Commun. (1995) 2413.
[10] L. Carlucci, G. Ciani, D.M. Proserpio, A. Sironi, J. Chem. Soc., Chem. Commun. (1994) 2755.
[11] (a) Y.N. Chi, K.L. Huang, F.Y. Cui, Y.Q. Xu, C.W. Hu, Inorg. Chem. 45 (2006) 10605;
(b) K.J. Wei, Y.S. Xie, J. Ni, M. Zhang, Q.L. Liu, Inorg. Chem. Commun. 9 (2006) 926.
[12] (a) K. Chenga, H.L. Zhu, Y.G. Li, Z. Anorg. Allgem. Chem. 632 (2006) 2326;
(b) N.C. Kasuga, R. Yamamoto, A. Hara, A. Amano, K. Nomiya, Inorg. Chim. Acta 359 (2006) 4412.
[13] C. Zhou, Y. Wang, D. Li, L. Zhou, P. Liu, Q. Shi, Eur. J. Inorg. Chem. (2006) 2437.
[14] D.B. Cordes, L.R. Hanton, M.D. Spicer, Inorg. Chem. 45 (2006) 7651.
[15] (a) D.P. Martin, R.M. Supkowski, R.L. LaDuca, Cryst. Growth Des. 8 (2008) 3518;
(b) D.P. Martin, R.M. Supkowski, R.L. LaDuca, Polyhedron 27 (2008) 2545.
[16] L. Johnston, D.P. Martin, R.M. Supkowski, R.L. LaDuca, Inorg. Chim. Acta 361 (2008) 2887.
[17] X.D. Chen, T.C.W. Mak, J. Mol. Struct. 743 (2005) 1.
[18] D. Pocic, J.M. Planeix, N. Kyritsakas, A. Jouaiti, H. Abdelaziz, M. Wais, CrystEngComm 7 (2005) 624.
[19] G.M. Sheldrick, CELLNOW, Twin Matrix Determination Program, University of Göttingen, Göttingen, Germany, 2008.
[20] SAINT, Software for Data Extraction and Reduction, Version 6.02, Bruker AXS, Inc., Madison, WI, 2002.
[21] SADABS, Software for Empirical Absorption Correction, Version 2.03, Bruker AXS, Inc., Madison, WI, 2002.
[22] G.M. Sheldrick, SHELXTL, Program for Crystal Structure Refinement, University of Göttingen, Göttingen, Germany, 1997.
[23] M. Kurmoo, C. Estournes, Y. Oka, H. Kumagai, K. Inoue, Inorg. Chem. 44 (2005) 217.
[24] (a) G. Bernardinelli, H.D. Flack, Acta Crystallogr., Sect. A 41 (1985) 500;
(b) H.D. Flack, Acta Crystallogr., Sect. A 29 (1983) 876.
[25] X. Liu, G.C. Guo, M.L. Fu, X.H. Liu, M.S. Wang, J.S. Huang, Inorg. Chem. 45 (2006) 3679.
[26] A.L. Spek, PLATON, A Multipurpose Crystallographic Tool, Utrecht University, Utrecht, The Netherlands, 1998.
[27] (a) L. Infantes, S. Motherwell, CrystEngComm 4 (2002) 454;
(b) L. Infantes, J. Chisholm, S. Motherwell, CrystEngComm 5 (2003) 480.
[28] (a) Y.-B. Dong, H.-Y. Wang, J.-P. Ma, D.-Z. Shen, R.-Q. Huang, Inorg. Chem. 44 (2005) 4679;
(b) G.-G. Luo, R.-B. Huang, J.-H. Chen, L.-R. Lin, L.-S. Zheng, Polyhedron 27 (2008) 2791;
(c) E.D. Genuis, J.A. Kelly, M. Patel, R. McDonald, M.J. Ferguson, Inorg. Chem. 47 (2008) 6184.

Polyhedron 28 (2009) 300–306

Contents lists available at ScienceDirect

Polyhedron

journal homepage: www.elsevier.com/locate/poly

Metal coordination architectures of *N*-acyl-salicylhydrazides: The effect of metal ions and steric repulsion of ligands to their structures of polynuclear metal complexes

Wei Luo [a,*], Xiu-Teng Wang [b], Xiang-Gao Meng [c], Gong-Zhen Cheng [a,*], Zhen-Ping Ji [a]

[a] College of Chemistry and Molecular Sciences, Wuhan University, Wuhan, Hubei 430072, PR China
[b] Beijing National Laboratory for Molecular Sciences, State Key Laboratory of Rare Earth Materials Chemistry and Applications, College of Chemistry and Molecular Engineering, Peking University, Beijing 100871, PR China
[c] Key Laboratory of Pesticide and Chemical Biology Ministry of Education, College of Chemistry, Central China Normal University, Wuhan, Hubei 430079, PR China

ARTICLE INFO

Article history:
Received 10 July 2008
Accepted 22 October 2008
Available online 4 December 2008

Keywords:
Polynuclear Mn and Cu complexes
N-Acyl-salicylhydrazides
Steric effect
Metallacrown
Trinuclear

ABSTRACT

Three polynuclear transition metal complexes $[Mn_8(DMF)_8(L1)_8]\cdot 4DMF$ (**1**), $[Mn_6(DMF)_6(L2)_6]\cdot[Mn_6(DMF)_4(H_2O)_2(L2)_6]\cdot 2DMF$ (**2**), $[Cu_3(L3)_2(py)_2]$ (**3**) of the pentadentate ligands *N*-acyl-salicylhydrazides were synthesized and characterized, their crystal structures were investigated. The oxidation state and properties of the central metal ions are important in crystal structure formation, trivalent Mn(III) ion which easily form stable octahedral coordination metallamacrocycle complexes, metallacrowns **1** and **2** were obtained; while bivalent Cu(II) ion is easier to form square planar, trinuclear complexes **3** was obtained. The steric effect of the *N*-acyl side chains also plays an important role in the structures of these polynuclear complexes. The magnetic property of **1** was also investigated.

© 2008 Elsevier Ltd. All rights reserved.

1. Introduction

Polynuclear transition metal complexes containing nitrogen and phenolic oxygen donor atoms are of considerable interest in inorganic and biomimetic chemistry due to their potential application in catalysis, their biological relevance, and potentially interesting magnetic properties [1]. To prepare such polynuclear complexes with desired structures and properties, it becomes important to understand the delicate factors influencing the formation of those systems [2,3]. The trianionic pentadentate *N*-acyl-salicylhydrazide ligands, a good example of these ligands, have been utilized to construct many interesting polynuclear complexes. Trivalent metal ions such as Ga, Co, Fe and Mn that can generally form stable octahedral coordination are found to yield hexanuclear, octanuclear, decanuclear and dodecanuclear metallamacrocycles with these ligands, known as metallacrowns [4–7], where the ring size and nuclearity of the metallacrowns could be modulated by controlling the steric repulsion of the *N*-acyl side chains. The ligands with flexible linear or β-branched *N*-alkyl groups that have sterically flexible Cα methylene groups tend to yield 18-membered hexanuclear metallacrowns; while for the ligands of α-branched *N*-alkyl groups, metallacrowns with extended nuclearity have been prepared [8]. When the central atoms are bivalent metal ions that can easily form planar square coordination, several trinuclear nickel(II), copper(II) and zinc(II) compounds and one hexanuclear nickel(II) compound with these types of ligands have been reported [9]. Regardless of the ring size, metal ions, nuclearity or stereochemistry of these polynuclear complexes, the binding mode of the ligands around the metal centers are the same, it is the different connectivities of the ligands between the two kinds of metal ions that lead to the formation of metallacrowns and trinuclear complexes.

With the aim of understanding the coordination chemistry of the *N*-acyl-salicylhydrazide with metal ions, and side effect of the *N*-acyl on the formation and structures of these polynuclear complexes, we report three pentadentate ligands *N*-2-methylacryloyl-5-bromosalicylhydrazide (H_3L1), *N*-(phenylacetyl)-5-bromosalicylhydrazide (H_3L2) and *N*-(3-*t*-butylbenzoyl)-5-bromosalicylhydrazide (H_3L3) (Scheme 1) and three polynuclear complexes $[Mn_8(DMF)_8(L1)_8]\cdot 4DMF$ (**1**), $[Mn_6(DMF)_6(L2)_6]\cdot[Mn_6(DMF)_4(H_2O)_2(L2)_6]\cdot 2DMF$ (**2**), $[Cu_3(L3)_2(py)_2]$ (**3**) from these ligands.

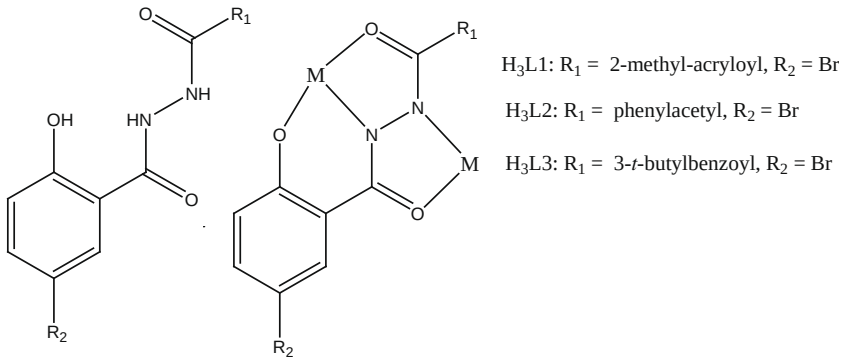
2. Experiment

2.1. General

All reagents for the syntheses were obtained commercially with analytical grade and were used without further purification. ^1H and

* Corresponding authors. Tel.: +86 2787218274 (W. Luo).
E-mail addresses: chemicalluo@163.com (W. Luo), gzcheng@whu.edu.cn (G.-Z. Cheng).

0277-5387/$ - see front matter © 2008 Elsevier Ltd. All rights reserved.
doi:10.1016/j.poly.2008.10.055



Scheme 1. The ligands and their same binding modes.

^{13}C NMR spectra were recorded on a Varian Inova 600 MHz NMR spectrometer at 25 °C. Chemical shifts were referenced to the residual solvent peak. IR spectra were recorded on AVATAR 360 FT-IR spectrophotometer in the range 4000–400 cm^{-1} (KBr pellets). Element analyses were performed on a Perkin–Elmer 2400 CHN elemental analytical instrument. Temperature-dependent magnetic susceptibility measurements were carried out on powdered samples between 2 and 300 K using a Quantum Design (SQUID) magnetometer MPMS-XL-5 in a field of 1 kOe.

2.2. Synthesis of the ligands and metal complexes

2.2.1. N-2-Methyl-acryloyl-5-bromosalicylhydrazide (H_3L1)

2-Methyl-acryloyl chloride (1.9 ml, 19.7 mmol) was added to a solution of chloroform (100 ml) containing water (0.36 ml, 20.0 mmol) and triethylamine (5.7 ml, 40.0 mmol) at 0 °C. The reaction mixture was slowly warmed to ambient temperature. Then a further amount of 2-methyl-acryloyl chloride (1.9 ml, 19.7 mmol) was added to the mixture and stirred for a further 1 h. At the completion of the above reaction, 5-bromosalicylhydrazide (3.7 g, 16.4 mmol) was added to the reaction mixture. The resulting mixture was stirred at ambient temperature for 1 day. The solution was diluted with hexane (90 ml), kept under refrigeration overnight, filtered, and washed with ether (30 ml × 3), dried in vacuo over P_2O_5. Yield: 2.50 g, 83.5%. *Anal.* Calc. for $C_{11}H_{11}N_2O_3Br$: C, 44.17; H, 3.71; N, 9.37. Found: C, 44.06; H, 3.68; N, 9.41%. IR (KBr pellet, cm^{-1}): 3440 (s, broad); 3330 (s); 3130 (s, broad); 2760 (m); 2670 (m); 1670 (s); 1620 (s); 1590 (s); 1530 (m); 1480 (s); 1390 (s). ^{1}H NMR (300 MHz, DMSO-d_6), δ ppm: 12.03 (s, 1H, Ar-OH); 10.52 (s, 1H), 10.27 (s, 1H) (both amide NH's); 8.05 (s, 1H, Ar); 7.59 (s, 1H, Ar); 7.01 (s, 1H, Ar); 5.83 (s, 1H, –C═CH); 5.51 (s, 1H, –C═CH); 1.92 (s, 3H, –CH3). ^{13}C NMR(150.9 MHz, DMSO-d_6), δ ppm: 168.40 (C7); 167.49 (C8); 159.71 (C2); 139.67 (C9); 138.22 (C4); 132.79 (C6); 122.93 (C1); 121.60 (C10); 119.99 (C3); 111.11 (C5); 20.39 (C11).

2.2.2. N-(Phenylacetyl)-5-bromosalicylhydrazide (H_3L2)

The ligand H_3L2 was prepared in a manner analogous to that used for H_3L1, except that phenylacetyl chloride was used instead of 2-methyl-acryloyl chloride. Yield: 4.98 g, 87.4%. *Anal.* Calc. for $C_{15}H_{13}N_2O_3Br$: C, 51.60; H, 3.75; N, 8.02. Found: C, 51.48; H, 3.75; N, 8.09%. IR (KBr pellet, cm^{-1}): 3440 (s); 3170 (s, broad); 2980 (s); 2670 (s); 1640 (s); 1610 (s); 1590 (vs); 1480 (s); 1390 (s); 1220 (s). ^{1}H NMR (300 MHz, DMSO-d_6), δ ppm: 12.02 (s, 1H), 11.80 (s, 1H) (both amide NH's); 10.68 (b, 1H, Ar-OH); 8.02 (s, 1H, Ar); 7.59 (m, 1H, Ar); 7.32 (d, 2H, Bz); 7.25 (dd, 2H, Bz); 7.03 (d, 1H, Ar); 3.57 (s, 2H, –CH2–). ^{13}C NMR(150.9 MHz, DMSO-d_6), δ ppm: 169.15 (C8); 165.15 (C7); 158.24 (C6); 136.85 (C4); 136.27 (C10); 131.74 (C2); 129.77 (C11, C15); 128.95 (C12, C14); 127.23 (C13); 120.32 (C1); 118.08 (C5); 110.78 (C3); 45.97 (C9).

2.2.3. N-(3-t-Butylbenzoyl)-5-bromosalicylhydrazide (H_3L3)

The ligand H_3L3 was prepared in a manner analogous to that used for H_3L1, except that 3-*t*-butylbenzoyl chloride was used instead of 2-methyl-acryloyl chloride. Yield: 4.18 g, 65.2%. *Anal.* Calc. for $C_{18}H_{19}N_2O_3Br$: C, 55.24; H, 4.86; N, 7.16. Found: C, 55.18; H, 4.79; N, 7.21%. IR (KBr pellet, cm^{-1}): 3440 (s); 3190 (s, br); 2970 (s), 2680 (s); 2490 (m); 1750 (s); 1650 (s); 1610 (s); 1480 (s); 1400 (s). ^{1}H NMR (300 MHz, DMSO-d_6), δ ppm: 12.09 (s, Ar-OH); 10.72 (s, 1H), 10.66 (s, 1H) (both amide NH's); 8.04 (m, 1H, Ar); 7.85 (m, 1H, Ar); 7.56(m, 1H, Ar); 7.39 (d, 2H, Bz); 7.04 (d, 2H, Bz); 1.21 (s, 9H, –C(CH$_3$)$_3$. ^{13}C NMR (150.9 MHz, DMSO-d_6), δ ppm: 169.56 (C8); 162.63 (C7); 160.28 (C4); 153.33 (C12); 141.74 (C2); 140.13 (C6); 136.40 (C9); 135.49 (C10, C14); 134.86 (C11, C13); 132.47 (C5); 131.03 (C3); 125.17 (C1); 50.68 (C15); 36.34 (C16, C17, C18).

2.2.4. [$Mn_8(DMF)_8(L1)_8$] · 4DMF (**1**)

H_3L1 (29.9 mg, 0.1 mmol) was dissolved in 30 ml of 2:1 methanol + DMF, and manganese acetate tetrahydrate (24.5 mg, 0.1 mmol) was added to it, stirred for 2 h with the color of the solution changing to dark brown, then the mixture was filtered. After slow evaporation of the mother liquor over several weeks, dark brown block crystals suitable for X-ray diffraction were obtained. Yield: 65.3%. IR (KBr pellet, cm^{-1}): 3430 (s, br); 1650 (s); 1600 (m); 1560 (m); 1510 (s); 1430 (m); 715 (m); 629 (m).

2.2.5. [$Mn_6(DMF)_6(L2)_6$]·[$Mn_6(DMF)_4(H_2O)_2(L2)_6$] · 2DMF (**2**)

Complex **2** was prepared in a manner analogous to that of **1**, use H_3L2 as the ligand. Yield: 72.7%. IR (KBr pellet, cm^{-1}): 3440 (s, br); 1650 (s); 1600 (s); 1550 (s); 1500 (s); 1430 (s); 1380 (s); 729 (m); 633 (m).

2.2.6. [$Cu_3(L3)_2(py)_2$] (3)

H_3L3 (39.0 mg, 0.1 mmol) was dissolved in 30 ml of 1:1 methanol/DMF, and then copper acetate monohydrate (19.9 mg, 0.1 mmol) was added, followed by four drops of pyridine. The mixture was stirred for 1 h, the resulting solution was filtered. After slow evaporation of the mother liquor for several days, blue block crystals suitable for X-ray diffraction were obtained. Yield: 67.5%. *Anal.* Calc. for $C_{46}H_{42}Cu_3N_6O_6Br_2$: C, 49.10; H, 3.76; N, 7.47. Found: C, 49.01; H, 3.71; N, 7.51%. IR (KBr pellet, cm^{-1}): 1610 (m); 1590 (m); 1500 (s); 1410 (s); 634 (w); 559 (w).

2.3. Crystallographic data collection and refinement of the structures

X-ray single-crystal diffraction data for compounds **1**–**3** were collected on a Bruker Smart APEX diffractometer at 293 (2) K with Mo Kα radiation (λ = 0.71073 Å). There was no evidence of crystal decay during data collection of complex **3**. In the data collection of complexes **1** and **2**, suitable crystal was mounted in glass

Table 1
Crystal data and structure refinement parameters for complexes **1**–**3**.

	1	2	3
Formula	$C_{115}H_{131}Br_8Mn_8N_{25}O_{36}$	$C_{222}H_{222}Br_{12}Mn_{12}N_{38}O_{52}$	$C_{46}H_{42}Br_2Cu_3N_6O_6$
F_w	3518.25	5872.58	1125.30
Crystal system	triclinic	triclinic	monoclinic
Space group	$P\bar{1}$	$P\bar{1}$	Cc
a (Å)	18.1638(12)	16.2373(14)	11.0820(10)
b (Å)	19.7532(13)	16.7448(14)	32.210(3)
c (Å)	23.0902(15)	26.53(2)	13.5920(12)
α (°)	75.017(5)	80.082(2)	90
β (°)	69.077(5)	76.886(2)	108.305(2)
γ (°)	79.164(5)	68.216(2)	90
V (Å^{-3})	7433.1(8)	6492(5)	4606.2(7)
Z	2	1	4
D (g cm^{-3})	1.572	1.502	1.623
μ (mm^{-1})	2.885	2.486	3.162
T (K)	294(2)	292(2)	295(2)
R^a/wR^b	0.0953/0.2394	0.0838/0.2019	0.0369/0.0666
Total/unique/R_{int}	71638/25997/0.1594	63076/22736/0.1518	14853/8637/0.0323
$F(000)$	3528	2956	2260

[a] $R = \sum(||F_o| - |F_c||)/\sum|F_o|$.
[b] $wR = [\sum w(|F_o|^2 - |F_c|^2)^2 / \sum w(F_o^2)]^{1/2}$.

capillaries with mother liquor to prevent the loss of the structure solvent molecules. In the complexes **1** and **2**, the crystals diffracted poorly, with a relatively low percentage of observed intensities above the threshold of $2\sigma(I)$ within the 1.73–25.00° (**1**) and 0.97–25.00° (**2**) θ ranges. In complex **2**, the non-coordinated solvent molecules are severely disordered which could not be modeled by discrete atoms in the complexes. Correspondingly, the contribution of the solvent to the diffraction pattern was subtracted using SQUEEZE procedure of the PLATON [10]. These voids consist of about 11.8% of the crystal volume (6492(5) per unit cell). Conventional least-squares refinement of the same solvent-exclude structure model against the original data set converged only at $R_1 = 0.22$. Refinement calculations with the modified data converged at $R_1 = 0.0831$ for 7965 reflections with intensities above the threshold of $2\sigma(I)$. In the three complexes, the structures were solved by direct methods and all non-hydrogen atoms were refined with anisotropic thermal parameters. All hydrogen atoms were located in calculated positions and/or in the position from difference Fourier map. The positions and anisotropy from difference of non-hydrogen atoms were refined on F^2 by full-matrix least-squares techniques with the SHELXTL program package [11,12]. Crystal data of complexes **1**–**3** are listed in Table 1.

3. Results and discussion

3.1. Spectral characterization

In the IR spectra, the ligands H_3L1, H_3L2 and H_3L3 show stretching bands attributed to C=O, PhO–H (phenolic, including intramolecular and intermolecular hydrogen bond) and N–H at 1620, 1670, 2670–3130, 3440 cm^{-1}; 1610, 1640, 2670–3170, 3440 cm^{-1} and 1610, 1650, 2490–3190, 3440 cm^{-1}, respectively [13]. The infrared

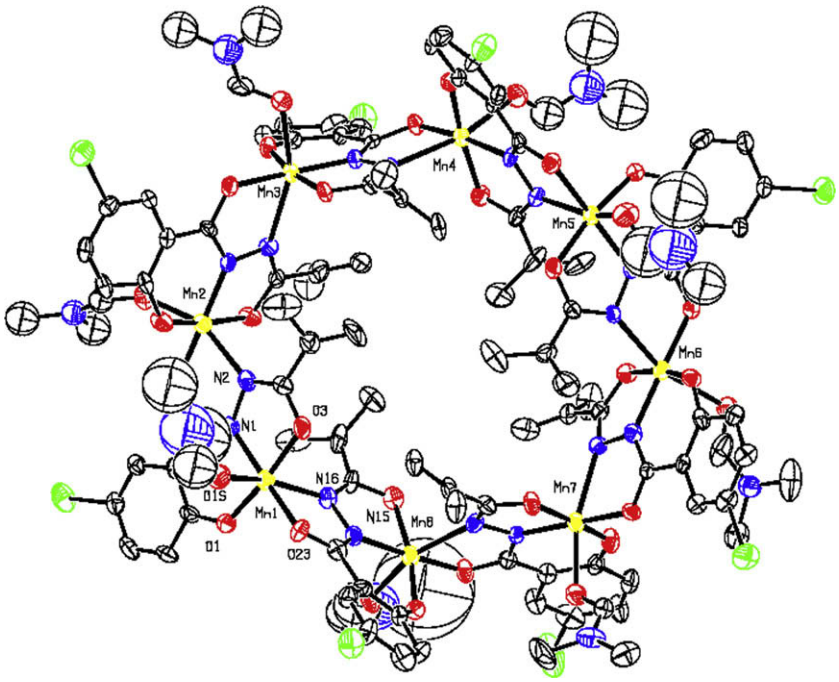


Fig. 1. Ortep plot of complex **1,** H-atoms have been omitted for clarity.

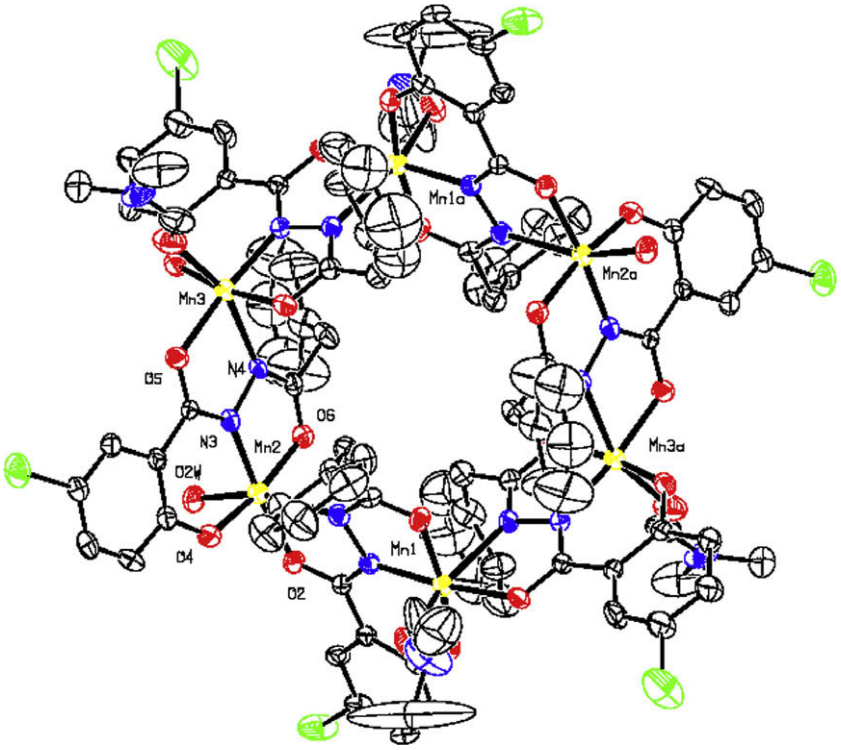


Fig. 2. Ortep plot of complex **2a,** H-atoms have been omitted for clarity.

stretching bands for compounds **1**–**3** are quite similar. The absence of the N–H band and the weakness of the C=O stretching bands are consistent with the deprotonation of the CONH groups and coordination to the Mn(III) and Cu(II) ions, which indicate the same chelating mode of the ligands to metal ions. The deprotonation and coordination are also confirmed in complexes **1**–**3** by the bands at 715, 729 and 634 cm^{-1}, attributed to M–O linkages; bands at 629, 633 and 559 cm^{-1}, attributed to M–N linkages [14]. The C=N–C=N framework bands are found at 1430 and 1410 cm^{-1}, respectively [15].

3.2. Description of the structures of *1*–*3*

The structure of complex **1** is illustrated in Fig. 1. The neighboring Mn···Mn interatomic distance are 4.886–4.935 Å. The Mn···Mn···Mn interatomic angles in the 24-membered core ring are in the range of 124.37–130.96°. These values are very close to the value of the interior angle in an *n*-octagon (135°). The flex-

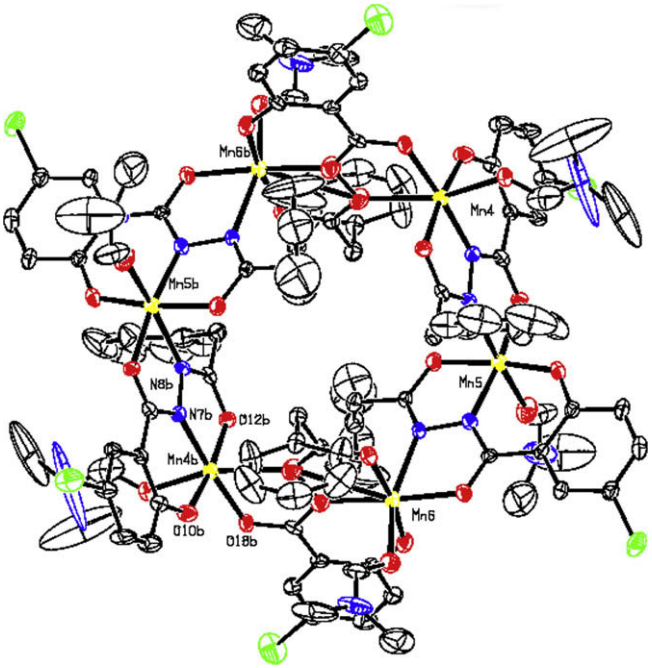


Fig. 3. Ortep plot of complex **2b,** H-atoms have been omitted for clarity.

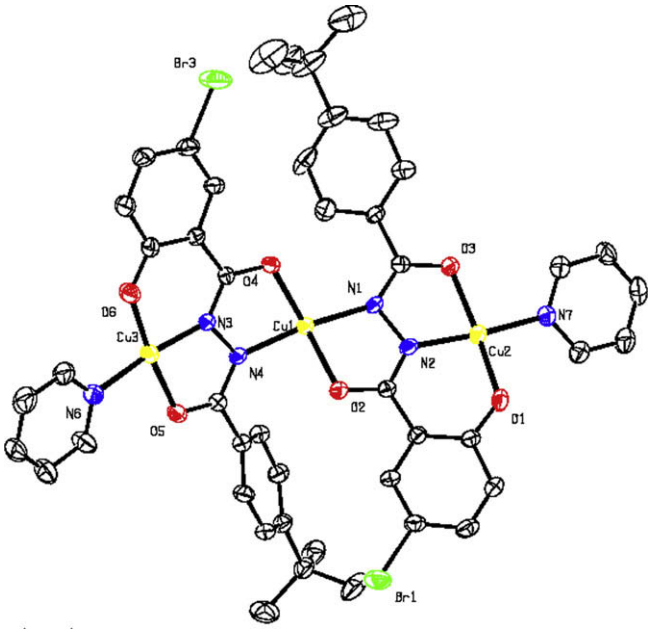
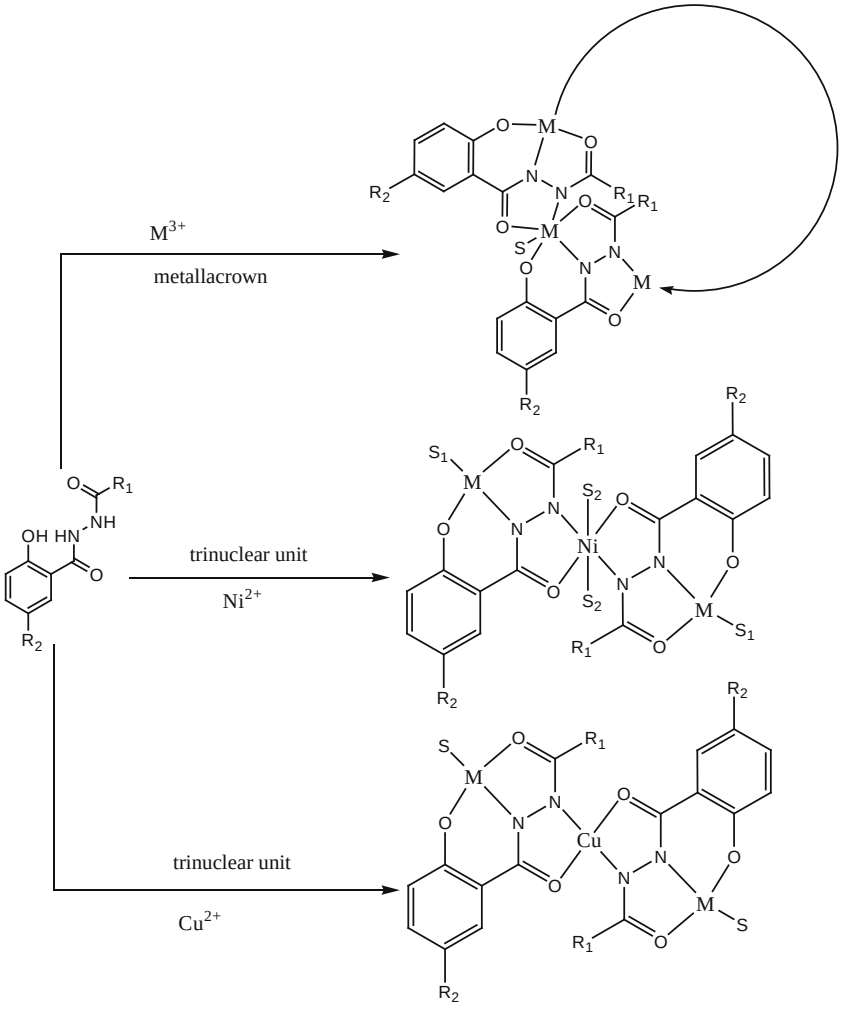


Fig. 4. Ortep plot of complex **3,** H-atoms have been omitted for clarity.



Scheme 2. Connective modes of metallacrown and trinuclear complex.

ibility around the N–N single bond and the conformational adaptability of the deprotonated pentadentate ligand $(L1)^{3-}$ assist the formation of the complex **1** and its propeller configuration of the Mn(III) ions. The chiralities of the manganese ions alternate between the Λ and Δ forms. The four DMF molecules coordinated to Mn centers with Λ configuration are on one face of the metallacrown, while the remaining four DMF molecules coordinated to the other Mn centers with Δ configuration on the other face of the metallacrown. The two faces of each metallacrown molecule have opposite chiralities. All manganese ions in 1 are in a distorted octahedral MnN_2O_4 geometry. In each octahedral environment around Mn(III), the mean axial distance of Mn–O/N is approximately 0.36 Å longer than the mean value of the basal distances due to the Jahn–Teller elongation of the octahedrons.

The X-ray structure analysis results shown in Figs. 2 and 3 reveal that complex **2** is a hexanuclear Mn(III) metallacrown with a $[Mn–N–N]_6$ unit, it has two independent molecules(**2**a and **2**b) in each crystallographic asymmetric unit. All manganese ions of **2** are in an octahedral MnN_2O_4 environment, with the rest axial sites occupied by O atoms from six DMF molecules in **2**b, and four DMF molecules, two H_2O molecules in **2**a. The mean axial distances are about 0.33 Å longer than the average basal bond lengths for each Mn(III) center, which indicates that the elongation of the octahedrons takes place in the axial direction due to the Jahn–Teller distortion of the high-spin d^4 electronic configuration of Mn(III) ion. The pentadentate ligand $(L2)^{3-}$ not only bridge the adjacent manganese ions by –N–N–, but also forces the stereochemistry of the metal ions into a propeller configuration because of the meridional coordination of the neighboring ligands. As a result, the complex **2** exhibits a combination of ΔΛΔΛ chiral configuration. The Mn···Mn distances fall in the range of 4.899–4.938 Å and the Mn···Mn···Mn angles of 112.63–116.02°.

Complex **3** is composed of three Cu(II) ions, two $(L3)^{3-}$ ligands and two pyridine molecules, as shown in Fig. 4. The chelating modes of the ligands to Mn(III) ions and Cu(II) ions are the same, they serve as both bidentate ligand for one metal ions, and at the same time, tridentate ligand for the adjacent metal ions. Central copper ion and two terminal copper ions are connected by two bridging deprotonated $(L3)^{3-}$ ligands, forming a bent trinuclear copper structure unit with a Cu–N–N–Cu–N–N–Cu core. The coordination geometry of the central Cu(1) is distorted square, it is bound to carbonyl oxygen atoms, O(2) and O(4), two hydrazine nitrogen atoms N(1), N(4) from two ligands. For two terminal Cu(II) ions, the square geometry is realized with carbonyl oxygen, hydrazine nitrogen, phenolic oxygen and pyridine nitrogen atoms. The bent angle of Cu(2)···Cu(1)···Cu(3) is 162.7°.

3.3. Coordination architectures

From the structures of complexes **1**–**3** and other trinuclear complexes obtained by us: $[Ni_3(H_2O)_2(DMA)_2(acbshz)_2]\cdot 2DMF$ [9b], $[Cu_3(3,5\text{-dmbzshz})_2(py)_2$, $[Ni_3(pabshz)_2(DMF)_2(py)_2$, $[Ni_3(3\text{-}t$-

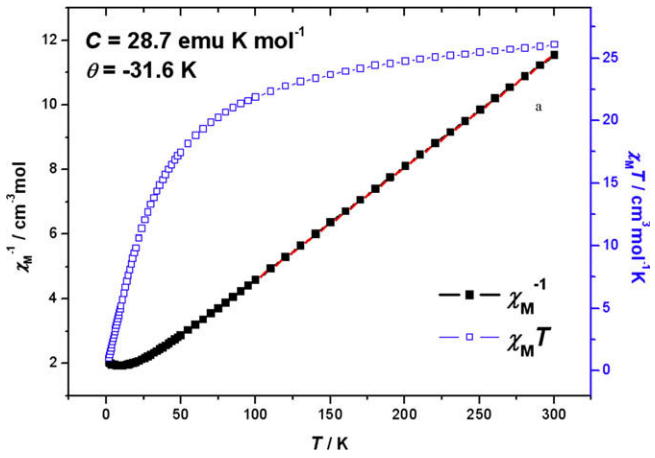


Fig. 5. Temperature dependence of $\chi_M T$ and Ψ_M^{-1} of **1** at $H = 1$ kOe from 2 to 300 K. The line a represents the best fit to the Curie–Weiss law.

bbzshz)$_2$(py)$_4$ · 2H$_2$O [9c], [Ni$_3$(H$_2$O)$_2$(DMA)$_2$(acshz)$_2$] · 2DMF [4i], [Cu$_3$(mashz)$_2$(py)$_2$], [Ni$_3$(mashz)$_2$(py)$_4$] [9e], [Ni$_3$(3,5-dmbzshz)$_2$(py)$_4$] · DMF[1] [9d]. It is obvious that the *N*-acyl-salicylhydrazide ligands act as pentadentate ligands to metal ions, with bidentate to one metal ion centre and tridentate to the adjacent metal ion. The chelating modes of the ligands around the metal centers are the same, but the different connectivities of them lead to the formation of metallacrowns or trinuclear complexes. For trivalent metal ions Mn(III), Fe(III), Co(III) and Ga(III) that can easily form stable octahedral coordination, the two adjacent ligands serve as pentadentate to the central metal ion, and the one-by-one connectivity of these units forms a metallamacrocycle, known as metallacrowns. While for bivalent metal ions such as Cu(II), Ni(II) that are easier to form planar square geometry, the two adjacent ligands serve as tetradentate ligands to the central metal ions, but tridentate ligands to the terminal metal ions forming an isolated unit, so it can only form trinuclear complex (Scheme 2). The steric effect of the *N*-acyl side chains can also effect the formation of these polynuclear complexes. β-branched *N*-alkyl groups that have sterically flexible Cα methylene groups yield 18-membered hexanuclear metallacrown and linear trinuclear Ni(II) complex; while α-branched *N*-alkyl groups yield the 24-membered octanuclear Mn(III) metallacrown and bent trinuclear Ni(II) complex. In the trinuclear Cu(II) complexes, Cu(II) ions all take distorted planar square geometry, while in the trinuclear Ni(II) complexes, two terminal Ni(II) are distorted planar square, the central Ni(II) ions are octahedral. This difference reflects the steric requirement of coordination, and the presence of inter- and intra-molecular interactions. Further research on why the significantly bent molecular conformation is formed is still under way.

3.4. Magnetic properties

The magnetic behavior of complex **1** is illustrated in Fig. 5. The value of $\chi_m T$ decreases slight with decreasing temperature from 26.07 cm^3 mol^{-1} K at 300 K to 18.16 cm^3 mol^{-1} K at 55 K. Below 55 K, $\chi_m T$ decreases rapidly and reaches 0.98 cm^3 mol^{-1} K at 2 K. The $\chi_m T$ value at 300 K is slightly larger than the sum value (24 cm^3 mol^{-1} K) expected for eight spin-only Mn(III) systems with $S = 2$. This behavior is characteristic of antiferromagnetic exchange coupling between the Mn(III) centers. This is further confirmed by a negative Weiss constant $\theta = -31.6$ K, which is calculated from the data within $T > 55$ K. The magnetic data were not fitted based on an eight Mn(III) ring model owing to the computing difficulties of dealing with such a large system. In order to evaluate the exchange interaction values of Mn(III) ions, the data were fitted to a one-dimensional chain model [16] since the ring is large and approximates a one-dimensional chain. The magnetic susceptibility of **1** can be written as [17]:

$$\chi = \frac{NS(S+1)}{3kT} g^2\beta^2 \frac{1-u(K)}{1+u(K)} \times 8 \qquad (1)$$

where $u(K)$ is $1/K - \coth(K)$, $K = 2JS(S+1)/kT$, $S = 2$ for Mn(II) and N, β, K, g and T have their usual meanings. The best fitting was obtained with $g = 2.14(2)$, $J = -1.94(4)$ K. The negative J value indicates the antiferromagnetic couplings between the Mn(III) centers.

4. Conclusion

Three complexes with the ligands derived from *N*-acyl-salicylhydrazides were reported. The 3d Metal coordination architectures of these kinds of ligands were also studied. For trivalent Mn(III), Fe(III), Co(III), Ga(III), which can easily form stable octahedral coordination, metallacrowns were obtained. While for bivalent Cu(II), Ni(II), Zn(II) that are easier to form planar square geometry, trinuclear complexes were obtained. The steric effect of the *N*-acyl side chains can also effect the formation of these polynuclear complexes. Antiferromagnetic couplings were observed between the Mn(III) centers in complex **1**.

Acknowledgment

We greatly thank Prof. Song Gao for his kind help in the magnetic analysis.

Appendix A. Supplementary data

CCDC 678388, 678405 and 665860 contain the supplementary crystallographic data for **1–3**. These data can be obtained free of charge via http://www.ccdc.cam.ac.uk/conts/retrieving.html, or from the Cambridge Crystallographic Data Centre, 12 Union Road, Cambridge CB2 1EZ, UK; fax: (+44) 1223-336-033; or e-mail: deposit@ccdc.cam.ac.uk. Supplementary data associated with this article can be found, in the online version, at doi:10.1016/j.poly.2008.10.055.

References

[1] (a) A. Messerschmidt, A. Rossi, R. Ladenstein, R. Huber, M. Bolognesi, G. Gatti, A. Marchesini, R. Petruzzelli, A. Finazziagro, J. Mol. Biol. 206 (1989) 513;
(b) V. Tangoulis, C.P. Raptopoulou, S. Paschalidou, E.G. Bakalbassis, S.P. Perlepes, A. Terzis, Angew. Chem., Int. Ed. 36 (1997) 1083;
(c) V. Tangoulis, C.P. Raptopoulou, S. Paschalidou, A.E. Tsohos, E.G. Bakalbassis, A. Terzis, S.P. Perlepes, Inorg. Chem. 36 (1997) 5270;
(d) A. Mukherjee, M. Nethaji, A.R. Chakravarty, Angew. Chem., Int. Ed. 43 (2004) 87;
(e) Y. Nishida, S. Kida, J. Chem. Soc., Dalton Trans. (1986) 2633.
[2] (a) S. Leininger, B. Olenyuk, P.J. Stang, Chem. Rev. 100 (2000) 853;
(b) K. Severin, Chem. Commun. (2006) 3859;
(c) J.J. Bodwin, A.D. Cutland, R.G. Malkani, V.L. Pecoraro, Coord. Chem. Rev. 216–217 (2001) 489;
(d) B. Moulton, M.J. Zaworotko, Chem. Rev. 101 (2001) 1629;
(e) B.J. Holliday, C.A. Mirkin, Angew. Chem., Int. Ed. 40 (2001) 2022.
[3] (a) P.J. Stang, B. Olenyuk, Acc. Chem. Res. 30 (1997) 502;
(b) G. Mezei, P. Baran, R.G. Raptis, Angew. Chem., Int. Ed. 43 (2004) 574;
(c) U. Patel, H.B. Singh, G. Wolmershäuser, Angew. Chem., Int. Ed. 44 (2005) 1715;
(d) K.L. Taft, S.J. Lippard, J. Am. Chem. Soc. 112 (1990) 9629;
(e) R. Wang, M. Hong, J. Luo, R. Cao, J. Weng, Chem. Commun. (2003) 1018;
(f) D.T. Puerta, S.M. Cohen, Chem. Commun. (2003) 1278.

[1] H_3acbshz, $H_3$3,5-dmbzshz, H_3pabshz, $H_3$3-*t*-bbzshz, H_3acshz and H_3mashz represent *N*-acyloyl-5-bromosalicylhydrazide, *N*-(3,5-dimethylbenzoyl)salicylhydrazide, *N*-(phenylacetyl)-5-bromosalicylhydrazide, *N*-(3-*t*-butylbenzoyl)salicylhydrazide, *N*-acryloyl-salicylhydrazide and *N*-2-methyl-acryloyl-5-bromosalicylhydrazide, respectively.

[4] (a) B. Kwak, H. Rhee, S. Park, M.S. Lah, Inorg. Chem. 37 (1998) 3599;
(b) G. Mezei, C.M. Zaleshi, V.L. Pecoraro, Chem. Rev. 107 (2007) 4933;
(c) I. Kim, B. Kwak, M.S. Lah, Inorg. Chim. Acta 317 (2001) 12;
(d) S. Lin, S.X. Liu, J.Q. Huang, C.C. Lin, J. Chem. Soc., Dalton Trans. (2002) 1595;
(e) F.P. Xiao, L.F. Jin, W. Luo, G.Z. Cheng, Z.P. Ji, Inorg. Chim. Acta 360 (2007) 3341;
(f) L.F. Jin, F.P. Xiao, G.Z. Cheng, Z.P. Ji, Inorg. Chem. Commun. 9 (2006) 758;
(g) B. Kwak, H. Rhee, M.S. Lah, Polyhedron 19 (2000) 1985;
(h) W. Luo, X.Z. Sun, K. Hu, Z.P. Ji, G.Z. Cheng, X.G. Meng, Transition Met. Chem. 33 (2008) 295;
(i) W. Luo, X.G. Meng, F.P. Xiao, G.Z. Cheng, Z.P. Ji, Polyhedron 27 (2008) 1802.
[5] (a) S. Lin, S.X. Liu, B.Z. Lin, Inorg. Chim. Acta 328 (2002) 69;
(b) B. Li, D.D. Hang, G.Z. Cheng, Z.P. Ji, Inorg. Chem. Commun. 8 (2005) 216;
(c) F.P. Xiao, L.F. Jin, G.Z. Cheng, Z.P. Ji, Polyhedron 26 (2007) 2695;
(d) W. Luo, B. Li, F.P. Xiao, G.Z. Cheng, Z.P. Ji, J. Coord. Chem. 60 (2007) 1037;
(e) D. Moon, J. Song, B.J. Kim, B.J. Suh, M.S. Lah, Inorg. Chem. 43 (2004) 8230;
(f) D. Moon, M.S. Lah, Inorg. Chem. 44 (2005) 1934;
(g) M. Moon, I. Kim, M.S. Lah, Inorg. Chem. 39 (2000) 2710.
[6] (a) S.X. Liu, S. Lin, B.Z. Lin, C.C. Lin, J.Q. Huang, Angew. Chem., Int. Ed. 40 (2001) 1084;
(b) R.P. John, K. Lee, M.S. Lah, Chem. Commun. (2004) 2660;
(c) R.P. John, J. Park, D. Moon, K. Lee, M.S. Lah, Chem. Commun. (2006) 3699;
(d) J.M. Dou, M.L. Liu, D.C. Li, D.Q. Wang, Eur. J. Inorg. Chem. (2006) 4866;
(e) D. Moon, K. Lee, R.P. John, G.H. Kim, B.J. Suh, M.S. Lah, Inorg. Chem. 45 (2006) 7991;
(f) S. Lin, S.X. Liu, Z. Chen, B.Z. Lin, S. Gao, Inorg. Chem. 43 (2004) 2222.
[7] (a) R.P. John, M. Park, D. Moon, K. Lee, S. Hong, Y. Zou, C.S. Hong, M.S. Lah, J. Am. Chem. Soc. 129 (2007) 14142;
(b) K. Lee, R.P. John, M. Park, D. Moon, H.C. Ri, G.H. Kim, M.S. Lah, Dalton Trans. (2008) 131;
(c) M. Park, R.P. John, D. Moon, K. Lee, G.H. Kim, M.S. Lah, Dalton Trans. (2007) 5412.
[8] R.P. John, K. Lee, B.J. Kim, B.J. Suh, H. Rhee, M.S. Lah, Inorg. Chem. 44 (2005) 7109.
[9] (a) S. Lin, M.X. Yang, S.X. Liu, Polyhedron 26 (2007) 4793;
(b) W. Luo, X.G. Meng, X.Z. Sun, F.P. Xiao, J.F. Shen, Y. Zhou, G.Z. Cheng, Z.P. Ji, Inorg. Chem. Commun. 10 (2007) 1351;
(c) W. Luo, X.G. Meng, J.F. Xiang, Y. Duan, G.Z. Cheng, Z.P. Ji, Inorg. Chim. Acta 361 (2008) 2667;
(d) W. Luo, X.T. Wang, X.G. Meng, G.Z. Cheng, Z.P. Ji, Inorg. Chem. Commun. 11 (2008) 1044;
(e) W. Luo, X.G. Meng, G.Z. Cheng, Z.P. Ji, Inorg. Chim. Acta (2008), doi:10.1016/j.ica.2008.05.007;
(f) W. Luo, X.T. Wang, G.Z. Cheng, S. Gao, Z.P. Ji, Inorg. Chem. Commun. 11 (2008) 769.
[10] A.L. Spek, Acta Crystallogr., Sect. A 46 (1990) 194.
[11] G.M. Sheldrick, Acta Crystallogr., Sect. A 46 (1990) 467.
[12] G.M. Sheldrick, SHELXL-97 Program for Crystal Structure Refinement, University of Göttingen, 1997.
[13] S.N. Rao, K.N. Munshi, N.N. Rao, M.M. Bhadbadc, E. Syresh, Polyhedron 18 (1999) 2491.
[14] G.R. Angel, J.F. Juan, B. Ferran, Polyhedron 15 (1996) 4407.
[15] M.A. Ali, A.H. Mirza, R.J. Butcher, M.T.H. Tarafder, Inorg. Chim. Acta 320 (2001) 1.
[16] P. Crewdson, S. Gambarotta, G.P.A. Yap, L.K. Thompson, Inorg. Chem. 42 (2003) 8579.
[17] M.E. Fisher, Am. J. Phys. 32 (1963) 343.

Polyhedron 28 (2009) 307–321

Contents lists available at ScienceDirect

Polyhedron

journal homepage: www.elsevier.com/locate/poly

Structural diversity in phosphoramidate's chemistry: Syntheses, spectroscopic and X-ray crystallography studies

Khodayar Gholivand [a,*], Zahra Shariatinia [b,1], Seyedeh Mahdieh Mashhadi [a], Farzaneh Daeepour [a], Narjes Farshidnasab [a], Hamid Reza Mahzouni [a], Nasrin Taheri [a], Shadi Amiri [a], Sheida Ansar [a]

[a] Department of Chemistry, Tarbiat Modares University, P.O. Box 14115-175, Tehran, Iran
[b] Department of Chemistry, Amirkabir University of Technology, P.O. Box 159163-4311, Tehran, Iran

ARTICLE INFO

Article history:
Received 15 September 2008
Accepted 7 October 2008
Available online 4 December 2008

Keywords:
Bisphosphoramidates
Phosphoramidates
NMR
X-ray crystallography

ABSTRACT

Novel phosphorus compounds of bisphosphoramidate, phosphoramidate and phosphoric triamide derivatives were synthesized using the starting materials PCl_5 and $POCl_3$. The products were then characterized by ^1H, ^{13}C, ^{31}P, ^{19}F NMR, IR spectroscopy and CHN elemental analysis. It is noticeable that the reaction of 4-aminobenzamide with PCl_5 in different molar ratios yields different products, bisphosphoramides and phosphoric triamides. Moreover, we were taken by surprise that the interaction of $POCl_3$ with the first-type aromatic amines gave bisphosphoramidates with P–N–P linkages that exhibited $^2J(P,P) \approx 20.0$ Hz in the ^{31}P NMR spectra. In fact, two simple one-pot pathways are presented here for the synthesis of new bisphosphoramidates, and to the best of our knowledge these are the first instances of bisphosphoramidates that have been obtained up until now. The structures of compounds **I** (4-OCH_3–C_6H_4–CH_2–C_9H_{13}–NH_2Cl), **34** and **44** were further determined by X-ray crystallography. All of these structures produced three dimensional polymeric chains through strong- and weak hydrogen bonds. The presence of chiral aminoacidester moieties in the phosphoric triamides lead to chiral molecules that showed two sets of signals for the two groups. Interestingly, in phosphoric triamides containing cyanoacetamide moieties, the existence of aromatic amine substituents on the P atoms created central chiral phosphorus atoms, i.e. the two aromatic groups revealed two sets of peaks in the ^1H and ^{13}C NMR spectra, while compounds with aliphatic moieties did not display this effect.

© 2008 Elsevier Ltd. All rights reserved.

1. Introduction

Phosphorus chemistry covers a wide area of sciences, including synthesis, coordination, biomedicine and theoretical matters. Phosphoramidates, bisphosphoramidates and phosphoric triamides are some important instances of phosphorus derivatives whose chemistry plays a significant role in various parts of science. Among the phosphoramidates, N-phosphorylated aminoacids have revealed high antitumor, antiviral and anti-HIV activities [1–4]. So far the syntheses and coordination chemistry of many bisphosphoramidates have been reported, containing P–N–P bonds via multi-step reactions [5–9], but here a simple one-pot method is presented to prepare such compounds. These types of compounds are potential bidentate ligands for the coordination to the metal atoms [10,11]. There are some reports on the synthesis of bisphosphoramides containing P(O)–$(CH_2)_n$–P(O) or P(O)–N(CH_3)–(binaphthyl)–N(CH_3)–P(O) moieties [12], as well as the P–$(CH_2)_n$–P group [13,14]. In addition, it is expected that due to the presence of the two phosphorus atoms in their structures, they will show more anticancer, antibacterial and enzyme inhibitory properties than phosphoramidates. Besides, the coordination chemistry of phosphoramidates [15–18], their biological applications [19–22], quantum chemical calculations on their structures [23,24], and their spectroscopic and X-ray crystal structures [25–27] are frequently studied. In the present work, following on from our previous research, we have synthesized and characterized several new phosphorus compounds of phosphoramidates, bisphosphoramidates (including P(O)NHC_6H_4-C(O)NHP(O) and P–N–P linkages), and phosphoric triamides. It is noteworthy that two simple one-pot pathways are presented for the synthesis of the new bisphosphoramidates and, as far as we know, these are the first examples of bisphosphoramidates that have been prepared so far. Furthermore, their NMR, IR and mass spectroscopic features as well as X-ray crystal structures are discussed and compared with our previous data.

2. Experimental

2.1. X-ray measurements

X-ray data of compound **34** were collected on a Bruker APEX II [28] and Siemens P3/PC [29] and those of compounds **I** and **44** on a

* Corresponding author. Tel.: +98 2182884422; fax: +98 2182883455.
E-mail address: gholi_kh@modares.ac.ir (K. Gholivand).
[1] Tel.: +982164543298; fax: +982164543296.

0277-5387/$ - see front matter © 2008 Elsevier Ltd. All rights reserved.
doi:10.1016/j.poly.2008.10.057

Bruker SMART 1000 CCD [30] single crystal diffractometer with graphite monochromated Mo Kα radiation (λ = 0.71073 Å). The structures were refined with SHELXL-97 [31] by full matrix least-squares on F^2. The positions of hydrogen atoms were obtained from the difference Fourier maps. Routine Lorentz and polarization corrections were applied and an absorption correction was performed using the SADABS program for compounds **I** and **44** [32].

2.2. Spectroscopic measurements

^{1}H, ^{13}C and ^{31}P spectra were recorded on a Bruker Avance DRS 500 spectrometer. ^{1}H and ^{13}C chemical shifts were determined relative to internal Me_4Si, ^{31}P and ^{19}F chemical shifts relative to 85% H_3PO_4 and $CFCl_3$ as external standards, respectively. The field strengths for the acquisition of ^{1}H, ^{13}C, ^{31}P and ^{19}F NMR spectra were 500.13, 125.77, 202.46 and 470.54 MHz, respectively. Infrared (IR) spectra were recorded on a Shimadzu model IR-60 spectrometer. Elemental analyses were performed using a Heraeus CHN-O-RAPID apparatus. Melting points were obtained with an electrothermal instrument. The spectroscopic data of the synthesized compounds can be found in the online Supplementary data.

2.3. Syntheses

2.3.1. N,N′-4-Carboxyamidophenyl-bis phosphoramidic tetrachloride (**1**)

A suspension of 16 mmol PCl_5 in 40 mL CCl_4 was prepared and then 4.0 mmol of 4-aminobenzamide was slowly added to the mixture at room temperature. After 24 h stirring, the temperature was raised to 80–90 °C to reflux the flask contents. After 5 h, the yellow solution was cooled to 4 °C and 16.0 mmol of formic acid was added dropwise at −5 °C to oxide the product, releasing CO and HCl. The mixture was stirred for 2 h under these conditions and then the white product was washed with CCl_4 and dried under vacuum. Yield: 76%. m.p. = 115 °C. *Anal.* Calc. for $C_7H_6Cl_4N_2O_3P_2$: C, 22.73; H, 1.64; N, 7.57. Found: C, 22.70; H, 1.64; N, 7.56%. ^{31}P {^{1}H} NMR (CD_3CN): δ 5.44 (s), 6.69 (s). ^{31}P NMR (202.46 MHz; CD_3CN; 85% H_3PO_4): δ 5.44 (m), 6.69 (m). ^{1}H NMR (CD_3CN): δ 7.37 (d, ^3J(H,H) = 8.7 Hz, 2H, Ar–H), 7.93 (d, ^3J(H,H) = 8.7 Hz, 2H, Ar–H), 7.16 (d, ^2J(PNH) = 11.9 Hz, 1H, NH_{amine}), 9.41 (s, 1H, NH_{amide}). ^{13}C NMR (CD_3CN): δ 120.04 (d, ^3J(P,C) = 8.9 Hz), 127.92 (d, ^3J(P,C) = 10.6 Hz), 131.19 (s), 131.45 (s), 134.93 (s), 143.79 (s), 167.25 (d, ^2J(P,C) = 3.5 Hz, C=O). IR (KBr, cm^{-1}): 3405 (s, νNH), 3170 (s, νNH), 3005 (s), 2835 (s, CH), 2595 (s, CH), 2350 (m), 1644 (s, C=O), 1611 (s), 1453 (s), 1272 (s), 1211 (s, νP=O), 1176 (s, νP=O), 1156 (s), 1121 (s), 1098 (s), 1071 (s), 1049 (s), 994 (s, νP–N), 964 (s, νP–N), 750 (m), 537 (m), 478 (s, νP–Cl).

2.3.2. N-(4-Carboxy amidophenyl) phosphoramidic dichloride (**2**)

This compound was prepared in the same way as compound **1**, but the molar ratio of 4-aminobenzamide to PCl_5 was 1:1. Yield: 95%. m.p. = 80 °C. *Anal.* Calc. for $C_7H_7Cl_2N_2O_2P$: C, 33.23; H, 2.79; N, 28.02. Found: C, 33.22; H, 2.78; N, 28.03%. ^{31}P NMR (DMSO-d_6): δ 0.14 (m). ^{1}H NMR (DMSO-d_6): δ 7.38 (d, ^3J(H,H) = 8.2 Hz, 2H, Ar–H), 7.93 (d, ^3J(H,H) = 8.2 Hz, 2H, Ar–H), 9.36 (b, 3H, $NH_{amine,amide}$). ^{13}C NMR (DMSO-d_6): δ 122.05 (s), 128.94 (s), 132.50 (s), 136.29 (s), 167.11 (s, C=O). IR (KBr, cm^{-1}): 3385 (s, νNH), 3185 (s, νNH), 2795 (s, νCH), 2560 (s), 1649 (s, νC=O), 1601 (s), 1577 (s), 1524 (s), 1419 (m), 1293 (m), 1209 (m, νP=O), 1176 (m), 1115 (m), 837 (m, νP–N), 758 (s), 720 (m), 556 (m), 525 (m).

2.3.3. General procedure for the synthesis of compounds **3**–**12**

A solution of 8 mmol of corresponding amines in acetonitrile was added dropwise to a suspension of 1 mmol of compound **1** at −5 °C. After 24 h stirring, the product was filtered and washed with distilled water and recrystallized from a methanol-acetonitrile solution to yield molecules **3–8** and **10**. For the synthesis of diazaphosphole **9**, a solution of 4 mmol diamine plus 4 mmol triethylamine was added to the suspension. Compounds **11**–**13** were synthesized in the same way, but the molar ratio of the corresponding amines to compound **2** was 4:1.

2.3.4. N,N′-4-Carboxyamidophenyl-bis [bis (N″,N‴-isopropyl) phosphoric triamide] (**3**)

Yield: 61%. m.p. = 131.5 °C. *Anal.* Calc. for $C_{19}H_{38}N_6O_3P_2$: C, 49.56; H, 8.32; N, 18.26. Found: C, 49.54; H, 8.31; N, 18.26%. ^{31}P NMR (CD_3OD): δ 9.16 (m), 9.26 (m). ^{1}H NMR (CD_3OD): δ 0.99 (d, ^3J(H,H) = 6.5 Hz, 6H, CH_3), 1.00 (d, ^3J(H,H) = 6.5 Hz, 6H, CH_3), 1.01 (d, ^3J(H,H) = 6.4 Hz, 6H, CH_3), 1.02 (d, ^3J(H,H) = 6.4 Hz, 6H, CH_3), 3.43 (m, 4H CH), 7.17 (d, ^3J(H,H) = 8.7 Hz, 2H, Ar–H), 7.76 (d, ^3J(H,H) = 8.7 Hz, 2H, Ar–H). ^{13}C NMR (CD_3OD): δ 25.41 (d, ^3J(P,C) = 4.7 Hz, CH_3), 25.56 (d, ^3J(P,C) = 5.4 Hz, CH_3), 25.72 (d, ^3J(P,C) = 3.4 Hz, CH_3), 25.77 (d, ^3J(P,C) = 2.1 Hz, CH_3), 44.33 (s, CH), 44.36 (s, CH), 118.05 (d, ^3J(P,C) = 7.0 Hz), 126.20 (d, ^3J(P,C) = 8.0 Hz), 129.48 (s), 130.21 (s), 148.28 (s), 159.98 (s), 170.84 (s, C=O). IR (KBr, cm^{-1}): 3315 (s, νNH), 2950 (s, νCH), 1602 (s, νC=O), 1564 (m), 1449 (s), 1419 (s), 1225 (m, νP=O), 1169 (s, νP=O), 1126 (m), 1020 (m), 927 (m, νP–N), 896 (m, νP–N), 833 (m, νP–N), 762 (m, νP–N), 638 (m), 529 (m).

2.3.5. N,N′-4-Carboxyamidophenyl-bis [bis (N″,N‴-isbutyl) phosphoric triamide] (**4**)

Yield: 58%. m.p. = 193 °C. *Anal.* Calc. for $C_{23}H_{46}N_6O_3P_2$: C, 53.53; H, 8.98; N, 16.27. Found: C, 53.51; H, 8.98; N, 16.26%. ^{31}P NMR (DMSO-d_6): δ 9.35 (m), 10.22 (m). ^{1}H NMR (DMSO-d_6): δ 0.79 (d, ^3J(H,H) = 6.4 Hz, 12H, CH_3), 1.16 (d, ^3J(H,H) = 6.4 Hz, 12H, CH_3), 1.86 (m, 2H, CH), 1.92 (m, 2H, CH), 2.48 (m, 4H CH_2), 2.68 (m, 4H, CH_2), 4.24 (m, 2H, NH), 4.35 (m, 2H, NH), 7.16 (d, ^3J(H,H) = 8.5 Hz, 2H, Ar–H), 7.22 (b, 1H, NH), 7.49 (d, ^3J(H,H) = 8.5 Hz, 2H, Ar–H). ^{13}C NMR (DMSO-d_6): δ 19.96 (s, CH_3), 20.08 (s, CH_3), 28.59 (s, CH_2), 29.35 (d, ^2J(P,C) = 5.6 Hz, CH_2), 45.72 (s, CH), 46.75 (s, CH), 47.73 (s, CH), 48.00 (s, CH), 115.92 (d, ^3J(P,C) = 6.8 Hz), 123.65 (d, ^3J(P,C) = 8.2 Hz), 128.88 (s), 132.72 (s), 147.15 (s), 158.29 (s), 167.83 (s, C=O). IR (KBr, cm^{-1}): 3421 (m, νNH), 3271 (s, νNH), 2959 (s, νCH), 2671 (s, νCH), 1647 (m), 1606 (s, νC=O), 1465 (s), 1252 (m, νP=O), 1190 (s, νP=O), 1090 (s), 922 (m, νP–N), 847 (m, νP–N), 769 (w), 547 (w).

2.3.6. N,N′-4-Carboxyamidophenyl-bis [bis (N″,N‴-diethyl) phosphoric triamide] (**5**)

Yield: 85%. m.p. = 188 °C. *Anal.* Calc. for $C_{13}H_{46}N_6O_3P_2$: C, 39.38; H, 11.69; N, 21.20. Found: C, 39.37; H, 11.68; N, 21.21%. ^{31}P NMR (DMSO-d_6): δ 14.61 (m), 14.96 (m). ^{1}H NMR (DMSO-d_6): δ 0.96–1.06 (m, 24H, CH_3), 2.95–3.07 (m, 16H, CH_2), 7.20 (d, ^3J(H,H) = 8.6 Hz, 2H, Ar–H), 7.31 (d, ^2J(PNH) = 9.1 Hz, 1H, NH_{amine}), 7.77 (d, ^3J(H,H) = 8.6 Hz, 2H, Ar–H), 8.91 (s, 1H, NH_{amide}). ^{13}C NMR (DMSO-d_6): δ 13.82 (d, ^3J(P,C) = 2.3 Hz, CH_3), 14.01 (d, ^3J(P,C) = 2.2 Hz, CH_3), 38.84 (d, ^2J(P,C) = 5.0 Hz, CH_2), 38.92 (d, ^2J(P,C) = 4.6 Hz, CH_2), 116. 43 (d, ^3J(P,C) = 6.7 Hz), 124.61 (d, ^3J(P,C) = 8.7 Hz), 129.13 (s), 131.27 (s), 147.31 (s), 158.95 (s), 167.43 (s,C=O). IR (KBr, cm^{-1}): 3345 (m, νNH), 3153 (s, νNH), 2971 (s, νC–H), 2933 (m, νC–H), 2872 (m, νC–H), 1665 (m), 1607 (s, νC=O), 1523 (m), 1437 (s), 1381 (s), 1268 (s), 1216 (s, νP=O), 1177 (s, νP=O), 1104 (m), 1063 (m), 1026 (s), 941 (m, νP–N), 916 (m, νP–N), 874 (s, νP–N), 843 (s, P–N), 792 (s, P–N), 715 (s), 660 (m), 541(s).

2.3.7. N,N′-4-Carboxyamidophenyl-bis [bis (N″,N‴-cyclohexyl) phosphoric triamide] (**6**)

Yield: 65%. m.p. = 165 °C. *Anal.* Calc. for $C_{31}H_{54}N_6O_3P_2$: C, 59.98; H, 8.77; N, 13.54. Found: C, 59.97, H, 8.77; N, 13.53%. ^{31}P NMR (DMSO-d_6): δ 7.36 (m), 8.08 (m). ^{1}H NMR (DMSO-d_6): δ 1.16 (m,

24H, CH_2), 1.44–1.84 (m, 16H CH_2), 2.83 (m, 4H, CH), 4.07 (m, 2H, NH), 4.17 (m, 2H, NH), 7.10 (d, ^3J(H,H) = 8.7 Hz, 2H, Ar–H), 7.32 (d, ^2J(PNH) = 7.6 Hz, 1H, NH_{amine}), 7.74 (d, ^3J(H,H) = 8.7 Hz, 2H, Ar–H), 9.27 (b, 1H, NH_{amide}). ^{13}C NMR (DMSO-d_6): δ 23.92 (s, CH_2), 24.71 (d, ^3J(P,C) = 2.8 Hz, CH_2), 24.80 (d, ^3J(P,C) = 2.4 Hz, CH_2), 24.93 (d, ^3J(P,C) = 2.6 Hz, CH_2), 25.16 (d, ^3J(P,C) = 3.8 Hz, CH_2), 31.11 (s, CH_2), 35.04 (d, ^2J(P,C) = 6.1 Hz, CH), 35.21 (d, ^2J(P,C) = 6.3 Hz, CH), 35.25 (d, ^2J(P,C) = 7.7 Hz, CH), 35.30(d, ^2J(P,C) = 7.6 Hz, CH), 49.26 (s, CH_2), 49.46 (s, CH_2), 116.03 (d, ^3J(P,C) = 5.8 Hz), 118.12 (s), 123.80 (d, ^3J(P,C) = 7.6 Hz), 124.14 (d, ^3J(P,C) = 7.4 Hz), 128.84 (s), 147.26 (s), 167.71 (s, C=O). IR (KBr, cm^{-1}): 3310 (m, νNH), 2905 (s, νCH), 1618 (m, νC=O), 1598 (m), 1568 (m), 1504 (m), 1438 (m), 1302 (m), 1235 (m, νP=O), 1177 (m, νP=O), 1080 (m), 907 (m, νP–N), 832 (m, νP–N), 635 (m, νP–N), 537 (m), 407 (m).

2.3.8. N,N′-4-Carboxyamidophenyl-bis [bis (N″,N‴-phenyl) phosphoric triamide] (**7**)

Yield: 61%. m.p. = 135 °C. *Anal.* Calc. for $C_{31}H_{30}N_6O_3P_2$: C, 62.41; H, 5.07; N, 14.09. Found: C, 62.40; H, 5.07; N, 14.10%. ^{31}P NMR (DMSO-d_6): δ −3.42 (m), −3.74 (m). ^{1}H NMR (DMSO-d_6): δ 6.9 (m, 4H, Ar–H), 7.11 (m, 4H, Ar–H), 7.14 (m, 14H, Ar–H), 7.20 (m, 4H, NH_{amine}), 7.78 (d, ^3J(H,H) = 9.0 Hz, 2H, Ar–H), 7.84 (d, ^3J(H,H) = 9.0 Hz, 2H, Ar–H), 8.04 (d, ^2J(PNH) = 10.0 Hz, 1H, NH_{amide}). ^{13}C NMR (DMSO-d_6): δ 114.08 (s), 115.94 (s), 117.64 (d, ^3J(P,C) = 6.8 Hz), 117.89 (s), 118.07 (s), 120.18 (s), 120.34 (s), 128.43 (s), 128.59 (s), 128.77 (s), 129.21 (s), 129.74 (s), 147.25 (s), 174.21 (s, C=O). IR (KBr, cm^{-1}): 3160 (m, νNH), 3035 (m, νNH), 2885 (m, νCH), 1644 (s, νC=O), 1486 (s), 1443 (m), 1382 (m), 1275 (s), 1222 (s, νP=O), 1185 (s, νP=O), 926 (s, νP–N), 741 (s, νP–N), 686 (m, νP–N), 488 (m).

2.3.9. N,N′-4-Carboxyamidophenyl-bis (N″-4-chlorophenyl phosphoramidic chloride) (**8**)

Yield: 50%. m.p. = 145 °C. *Anal.* Calc. for $C_{19}H_{16}Cl_4N_4O_3P_2$: C, 41.33; H, 2.92; N, 10.15. Found: C, 41.34; H, 2.92; N, 10.14%. ^{31}P NMR (CD_3OD): δ 2.43 (s), 3.15 (m). ^{1}H NMR (CD_3OD): δ 6.76 (s, 2 H, Ar–$H_{aniline}$), 6.78 (s, 2H, Ar–$H_{aniline}$), 6.99 (d, ^3J(H,H) = 8.5 Hz, 2H, Ar–$H_{4\text{-aminobenzamide}}$), 7.01 (d, ^3J(H,H) = 8.5 Hz, 2H, Ar–$H_{4\text{-aminobenzamide}}$), 7.18 (s, 2H, Ar–$H_{aniline}$), 7.19 (s, 2H, Ar–$H_{aniline}$). ^{13}C NMR ($CD_3OD$): δ 114.09 (s), 115.94 (s), 117.50 (s), 117.64 (d, ^3J(P,C) = 7.2 Hz), 118.07 (s), 120.15 (s), 120.35 (s), 128.50 (s), 128.65 (s), 128.76 (s), 129.29 (s), 129.67 (s), 141.34 (s), 148.68 (s), 169.84 (s, C=O). IR (KBr, cm^{-1}): 3400 (m, νNH), 3305 (m, νNH), 3185 (m, νNH), 2885 (m, νCH), 2570 (m, νCH), 1602 (m, νC=O), 1289 (m), 1260 (m), 1235 (m, νP=O), 1174 (m, νP=O), 1076 (m), 1040 (m), 963 (m, νP–N), 925 (m, νP–N), 842 (m, νP–N), 805 (m, νP–N), 635 (w), 542 (w).

2.3.10. N,N′-4-Carboxyamidophenyl-bis (1,3-dimethyl-1,3,2-diazaphosphole) (**9**)

Yield: 75%. m.p. = 245 °C. *Anal.* Calc. for $C_{15}H_{26}N_6O_3P_2$: C, 45.00; H, 6.55; N, 20.99. Found: C, 45.02; H, 6.55; N, 20.97%. ^{31}P NMR (DMSO-d_6): δ 20.03 (m), 20.16 (m). ^{1}H NMR (DMSO-d_6): δ 2.58 (s, 12H, CH_3), 3.24 (s, 8H, CH_2), 6.15 (s, 1H, NH_{amine}), 6.52 (d, ^3J(H,H) = 5.0 Hz, 1H, Ar–H), 6.61 (d, ^3J(H,H) = 5.0 Hz, 1H, Ar–H), 7.38 (d, ^3J(H,H) = 5.0 Hz, 1H, Ar–H), 7.58 (d, ^3J(H,H) = 5.0 Hz, 1H, Ar–H), 9.37 (b, 1H, NH_{amide}). ^{13}C NMR (DMSO-d_6): δ 30.65 (d, ^2J(P,C) = 5.0 Hz, CH_3), 30.82 (d, ^2J(P,C) = 4.9 Hz, CH_3), 32.44 (s, CH_3), 32.47 (s, CH_3), 44.39 (s, CH_2), 44.42 (s, CH_2), 46.30 (d, ^2J(P,C) = 7.3 Hz, CH_2), 46.41 (d, ^2J(P,C) = 5.7 Hz, CH_2), 116.13 (d, ^3J(P,C) = 6.8 Hz), 126.14 (s), 129.36 (s), 139.16 (s), 146.85 (s), 154.68 (s), 167.45 (s, C=O). IR (KBr, cm^{-1}): 3380 (m, νNH), 3190 (m, νNH), 3010 (m, νNH), 2740 (s, νCH), 2465 (m, νCH), 1656 (s, νC=O), 1626 (s), 1599 (s), 1446 (m), 1223 (m, νP=O), 1164 (m, νP=O), 1119 (m), 1076 (s), 953 (s, νP–N), 843 (m, νP–N), 801 (w), 505 (m).

2.3.11. N,N′-4-Carboxyamidophenyl-[bis (N″,N‴-cyclopentyl) phosphoric triamide] dihydroxy phosphoramidic acid ester (**10**)

Yield: 60%. m.p. = 170 °C. *Anal.* Calc. for $C_{17}H_{28}N_4O_5P_2$: C, 47.44; H, 6.56; N, 13.02. Found: C, 47.45; H, 6.55; N, 13.01%. ^{31}P NMR (D_2O): δ 8.14 (m), 8.81 (m). ^{1}H NMR (D_2O): δ 1.57 (m, 8 H, CH_2), 1.67 (m, 4H CH_2), 1.97 (m, 4H, CH_2), 3.59 (m, 2H, CH), 6.76 (d, ^3J(H,H) = 8.2 Hz, 2H, Ar–H), 7.58 (d, ^3J(H,H) = 8.2 Hz, 2H, Ar–H). ^{13}C NMR (D_2O): δ 23.08 (s, CH_2), 30.16 (s, CH_2), 51.82 (s, CH), 114.58 (s), 120.14 (s), 121.31 (s), 128.22 (s), 129.00 (s), 150.82 (s), 172.11 (s, C=O). IR (KBr, cm^{-1}): 3370 (s, νNH), 3190 (s, νNH), 2895 (s, νCH), 1601 (s, νC=O), 1524 (m), 1415 (m), 1209 (m, νP=O), 1176 (m, νP=O), 1115 (m), 1057 (m), 837 (m, νP–N), 756 (m, νP–N), 720 (m, νP–N), 556 (m), 525 (m), 458 (m).

2.3.12. N-(4-Carboxy amidophenyl)-N′-isobutyl-phosphoramidic chloride (**11**)

Yield: 54%. m.p. = 178 °C. *Anal.* Calc. for $C_{11}H_{17}ClN_3O_2P$: C, 45.61; H, 5.92; N 14.50. Found: C, 45.60; H, 5.90; N, 14.51%. ^{31}P NMR (DMSO-d_6): δ 0.16 (m). ^{1}H NMR (DMSO-d_6): δ 0.87 (d, ^3J(H,H) = 6.5 Hz, 6H, CH_3), 1.85 (m, 1H, CH), 2.58 (m, 2H, Ar CH_2), 4.13 (m, 1H, NH), 6.51 (d, ^3J(H,H) = 8.5 Hz, 2H, Ar–H), 6.80 (b, 1H, NH), 7.57 (d, ^3J(H,H) = 8.5 Hz, 2H, Ar–H), 7.87 (b, 2H, NH_2). ^{13}C NMR (DMSO-d_6): δ 19.77 (s, CH_3), 26.46 (s, CH), 50.80 (s, CH_2), 112.45 (s), 118.21 (s), 120.89 (s), 128.44 (s), 129.07 (s), 151.64 (s), 168.09 (s, C=O). IR (KBr, cm^{-1}): 3466 (s, νNH), 3245 (s, νNH), 2965 (s, νCH), 2805 (s, νCH), 2601 (m), 1608 (s, νC=O), 1619 (s), 1399 (s), 1292 (m), 1183 (m, νP=O), 1095 (m), 850 (m, νP–N), 778 (s, νP–N), 712 (m), 503 (m), 450 (m).

2.3.13. N-(4-Carboxy amidophenyl)-N′,N′-bis (cyclopentyl) phosphoric triamide (**12**)

Yield: 70%. m.p. = 89 °C. *Anal.* Calc. for $C_{17}H_{27}N_4O_2P$: C, 58.27; H, 7.77; N, 15.99. Found: C, 58.25; H, 7.76; N, 15.98%. ^{31}P NMR ($CDCl_3$): δ 3.54 (m). ^{1}H NMR ($CDCl_3$): δ 1.62 (m, 8H, CH_2), 1.85 (m, 4H, CH_2), 2.03 (m, 4H, CH_2), 3.12 (m, 2H, CH), 3.63 (m, 2H, NH), 8.35 (m, 6H, Ar–H), 9.14 (b, 1H, NH). ^{13}C NMR ($CDCl_3$): δ 23.86 (s), 49.05 (s), 53.29 (s), 54.20 (s), 64.36 (s), 117.21 (s), 122.92 (s), 130.07 (s), 144.25 (s), 172.31 (s, C=O). IR (KBr, cm^{-1}): 3445 (m, νNH), 3310 (m, νNH), 3136 (m, νNH), 2940 (s, νCH), 2635 (m, νCH), 1690 (m), 1597 (s, νC=O), 1550 (m), 1506 (m), 1396 (m), 1214 (m), 1176 (m, νP=O), 1089 (m), 840 (m, νP–N), 771 (m, νP–N), 706 (m), 574 (m), 526 (m).

2.3.14. N-(4-Carboxy amidophenyl)-N′,N″-bis (4-bromophenyl) phosphoric triamide (**13**)

Yield: 75%. m.p. = 225 °C. *Anal.* Calc. for $C_{19}H_{17}Br_2N_4O_2P$: C, 43.54; H, 3.27; N, 10.69. Found: C, 43.55; H, 3.27; N, 10.68%. ^{31}P NMR (DMSO-d_6): δ 0.11 (s). ^{1}H NMR (DMSO-d_6): δ 7.20 (d, ^3J(H,H) = 8.5 Hz, 4H, Ar–$H_{bromoaniline}$), 7.29 (d, ^3J(H,H) = 8.6 Hz, 2H, Ar–$H_{4\text{-aminobenzamide}}$), 7.63 (d, ^3J(H,H) = 8.6 Hz, 4H, Ar–$H_{4\text{-aminobenzamide}}$), 7.84 (d, ^3J(H,H) = 8.5 Hz, 4H, Ar–$H_{bromoaniline}$), 8.61–9.52 (m, 5H, NH). ^{13}C NMR (DMSO-d_6): δ 116.44 (s), 118.91 (s), 124.28 (s), 128.89 (s), 129.60 (s), 132.34 (s), 133.43 (s), 140.04 (s), 167.21 (s, C=O). IR (KBr, cm^{-1}): 3402 (s, νNH), 3200 (s, νNH), 2835 (m, νCH), 2569 (s, νCH), 1586 (s, νC8O), 1538 (s), 1514 (s), 1488 (s), 1425 (s), 1405 (s), 1299 (s), 1215 (s, νP=O), 1182 (m), 1106 (m), 1071 (s), 846 (s, νP–N), 818 (s), 767 (s, νP–N), 718 (m), 671 (m), 534 (s), 489 (s), 466 (s).

2.3.15. General procedure for the synthesis of compounds **14**–**21**

A solution of 7 mmol of the corresponding amine in acetonitrile was added dropwise to a solution of 1 mmol *N*-(4-X-phenyl) phosphoramidic dichloride (X = H, F, Cl, and Br) in acetonitrile at −5 °C. The flask contents were stirred for 48 h and then the precipitate was filtered, washed with water and dried in air to yield molecules **14**–**17**. To synthesise compounds **18**–**21**, this procedure was ap-

plied, but a solution of 4 mmol of 4-X-aniline (X = H, F, Cl, and Br) in acetonitrile was added dropwise to a solution of 1 mmol 2-pyridinyl phosphoramidic dichloride in acetonitrile.

*2.3.16. μ^1-(N-Phenyl)-N′-phenyl phosphoramidic chloride-bis [(N″,N‴-phenyl) phosphoric triamide] (**14**)*

Yield: 70%. m.p. = 212 °C. *Anal.* Calc. for $C_{24}H_{23}ClN_4O_2P_2$: C, 58.02; H, 4.67; N, 11.28. Found: C, 58.00; H, 4.67; N, 11.28%. ^{31}P NMR (DMSO-d_6): δ −10.42 (m), −10.28 (d, ^2J(P,P) = 19.7 Hz). ^{31}P NMR (CD_3OD): δ −9.52 (d, ^2J(P,P) = 17.5 Hz), −8.28 (d, ^2J(P,P) = 17.5 Hz). ^1H NMR (DMSO-d_6): δ 6.72–7.20 (m, 20H, Ar–H), 7.54 (b, 1H, NH), 8.17 (d, ^2J(PNH) = 8.8 Hz, 2H, NH). ^{13}C NMR (DMSO-d_6): δ 117.40 (s), 119.31 (s), 120.30 (s), 122.39 (s), 126.78 (s), 128.16 (s), 128.38 (s), 128.65 (s), 129.58 (s), 133.64 (s), 141.03 (s), 142.55 (s). IR (KBr, cm^{-1}): 3375 (m, νNH), 3235 (m, νNH), 3040 (m), 2825 (s, νCH), 2585 (s), 1592 (m), 1486 (s), 1280 (m, νP=O), 1217 (s, νP=O), 1150 (m), 1072 (m), 910 (s, νP–N), 735 (s, νP–N), 685 (s), 466 (m).

*2.3.17. μ^1-(N-4-Fluorophenyl)-N′-4-fluorophenyl phosphoramidic chloride-bis [(N″,N‴-4-fluorophenyl) phosphoric triamide] (**15**)*

Yield: 85%. m.p. = 204 °C. *Anal.* Calc. for $C_{24}H_{19}ClF_4N_4O_2P_2$: C, 50.68; H, 3.37; N, 9.85. Found: C, 50.67; H, 3.37; N, 9.84%. ^{31}P NMR (DMSO-d_6): δ −10.23 (d, ^2J(P,P) 8 19.7 Hz), −9.90 (m). ^{19}F NMR (DMSO-d_6): δ −115.61 (s), −123.71 (s), −124.63 (s). ^1H NMR (DMSO-d_6): δ 6.82–7.06 (m, 16H, Ar–H), 7.54 (b, 1H, NH), 8.15 (d, ^2J(PNH) = 8.6 Hz, 2H, NH). ^{13}C NMR (DMSO-d_6): δ 114.68 (d, ^2J(F,C) 8 22.4 Hz), 115.07 (d, ^2J(F,C) = 22.1 Hz), 115.73 (d, ^2J(F,C) = 20.5 Hz), 118.41 (dd, ^3J[(F,C),(P,C)] = 7.4 Hz), 118.76 (dd, ^3J[(F,C),(P,C)] 8 7.5 Hz), 119.19 (dd, ^3J[(F,C),(P,C)] = 7.6 Hz), 119.48 (d, ^4J(F,C) = 2.3 Hz), 119.54 (d, ^4J(F,C) = 2.5 Hz), 119.72 (d, ^4J(F,C) = 2.6 Hz), 156.69 (d, ^1J(F,C) = 237.3 Hz), 161.68 (d, ^1J(F,C) 8 234.9 Hz), 164.32 (d, ^1J(F,C) = 239.4 Hz). IR (KBr, cm^{-1}): 3398 (m, νNH), 3220 (m, νNH), 2925 (m, νCH), 2785 (m, νCH), 1502 (s), 1383 (m), 1240 (m, νP=O), 1209 (s, νP=O), 1152 (m), 1068 (s), 968 (s, νP–N), 913 (s, νP–N), 821 (s, νP–N), 752 (m), 501 (m), 457 (m).

*2.3.18. μ^1-(N-4-Chlorophenyl)-N′-4-chlorophenyl phosphoramidic chloride-bis [(N″,N‴-4-chlorophenyl) phosphoric triamide] (**16**)*

Yield: 81%. m.p. = 199 °C. *Anal.* Calc. for $C_{24}H_{19}Cl_5N_4O_2P_2$: C, 45.42; H, 3.02; N, 8.83. Found: C, 45.40; H, 3.02; N, 8.84%. ^{31}P NMR (DMSO-d_6): δ −10.75 (d, ^2J(P,P) 8 17.7 Hz), −10.16 (m). ^1H NMR (DMSO-d_6): δ 7.04–7.46 (m, 16H, Ar–H), 8.15 (b, 1H, NH), 8.40 (d, ^2J(PNH) 8 8.6 Hz, 2H, NH). ^{13}C NMR (DMSO-d_6): δ 117.92 (s), 119.00 (d, ^3J(P,C) = 7.4 Hz), 123.35 (s), 123.65 (s), 124.38 (s), 128.19 (s), 128.44 (s), 129.43 (s), 129.92 (s), 134.12 (s), 139.81 (s), 140.56 (s). IR (KBr, cm^{-1}): 3430 (m, νNH), 3210 (m, νNH), 2975 (m, νCH), 2835 (m, νCH), 1587 (m), 1484 (s), 1453 (m), 1382 (m), 1274 (m, νP=O), 1229 (m, νP=O), 1194 (s), 1091 (m), 1037 (s), 941 (s, νP–N), 821 (s, νP–N), 571 (m).

*2.3.19. μ^1-(N-4-Bromophenyl)-N′-4-bromophenyl phosphoramidic chloride-bis [(N″,N‴-4-bromophenyl) phosphoric triamide] (**17**)*

Yield: 67%. m.p. = 196 °C. *Anal.* Calc. for $C_{24}H_{19}Br_4ClN_4O_2P_2$: C, 35.48; H, 2.36; N, 6.90. Found: C, 35.46; H, 2.35; N, 6.91%. ^{31}P NMR (DMSO-d_6): δ −10.92 (d, ^2J(P,P) = 17.7 Hz), −10.61 (m). ^1H NMR (DMSO-d_6): δ 6.76–7.30 (m, 16H, Ar–H), 7.91 (b, 1H, NH), 8.42 (d, ^2J(PNH) = 8.9 Hz, 2H, NH). ^{13}C NMR (DMSO-d_6): δ 111.12 (s), 112.03 (s), 113.12 (s), 118.67 (d, ^3J(P,C) = 7.4 Hz), 119.24 (d, ^3J(P,C) = 7.8 Hz), 119.37 (d, ^3J(P,C) = 6.9 Hz), 131.00 (s), 131.32 (s), 131.69 (s), 140.33 (s), 141.37 (s), 142.35 (s). IR (KBr, cm^{-1}): 3390 (m, νNH), 3190 (m, νNH), 3045 (m, νCH), 2915 (m, νCH), 2585 (m), 1503 (m), 1400 (s), 1296 (m), 1271 (m, $\nu\nu$P=O), 1218 (m, νP8O), 1068 (m), 1004 (m), 964 (m, νP–N), 908 (m, νP–N), 811 (m, νP–N), 532 (m), 405 (m).

*2.3.20. μ^1-(N-2-Pyridinyl)-N′-2-pyridinyl phosphoramidic chloride-bis [(N″,N‴-phenyl) phosphoric triamide] (**18**)*

Yield: 70%. m.p. = 175 °C. *Anal.* Calc. for $C_{22}H_{21}ClN_4O_2P_2$: C, 56.12; H, 4.50; N, 11.90. Found: C, 56.10; H, 4.51; N, 11.90%. ^{31}P NMR (DMSO-d_6): δ −10.30 (m), −10.11 (d, ^2J(P,P) = 20.0 Hz). ^1H NMR (DMSO-d_6): δ 6.69 (t, ^3J(H,H) 8 7.0 Hz, 1H, Ar–H), 6.75 (t, ^3J(H,H) = 7.0 Hz, 2H, Ar–H), 6.86 (d, ^3J(H,H) = 7.9 Hz, 1H, Ar–H), 7.03 (m, 10H, Ar–H), 7.18 (t, ^3J(H,H) = 7.0 Hz, 2H, Ar–H), 7.49 (b, 1H, NH), 8.15 (d, ^2J(PNH) = 8.5 Hz, 2H, NH). ^{13}C NMR (DMSO-d_6): δ 109.81 (s), 117.22 (s), 117.32 (d, ^3J(P,C) = 7.7 Hz), 117.54 (s), 119.24 (s), 120.12 (s), 128.29 (s), 128.57 (s), 129.14 (s), 141.08 (s), 141.90 (s), 142.31 (s), 149.35 (s), 152.60 (s). IR (KBr, cm^{-1}): 3375 (m, νNH), 3235 (s, νNH), 2820 (m, νCH), 1637 (s), 1593 (s), 1487 (s), 1399 (s), 1288 (m, νP=O), 1216 (s, νP=O), 1151 (m), 1063 (s), 955 (s, νP–N), 909 (m, νP–N), 743 (s, νP–N), 688 (s), 506 (m), 476 (m, νP–Cl).

*2.3.21. μ^1-(N-2-Pyridinyl)-N′-2-pyridinyl phosphoramidic chloride-bis [(N″,N‴-4-fluorophenyl) phosphoric triamide] (**19**)*

Yield: 68%. m.p. = 185 °C. *Anal.* Calc. for $C_{22}H_{19}ClF_2N_4O_2P_2$: C, 52.14; H, 3.78; N, 11.06. Found: C, 52.12; H, 3.77; N, 11.06%. ^{31}P NMR (CD_3OD): δ −9.59 (d, ^2J(P,P) = 21.3 Hz), −8.32 (d, ^2J(P,P) = 21.3 Hz); δ_P (202.46 MHz; DMSO-d_6; 85% H_3PO_4) −10.27 (d, ^2J(P,P) = 20.0 Hz), −9.99 (m). ^1H NMR (CD_3OD): δ 6.85–7.05 (m, 16H, Ar–H), 7.49 (b, 1H, NH), 8.13 (d, ^2J(PNH) = 8.4 Hz, 2H, NH). ^{13}C NMR (CD_3OD): δ 114.49 (s), 114.66 (s), 114.98 (d, ^2J(F,C) = 22.1 Hz), 115.43 (d, ^4J(F,C) = 2.5 Hz), 115.63 (s), 116.20 (s), 117.80 (s), 118.02 (s), 118.36 (dd, ^3J[(F,C),(P,C)] = 7.8 Hz), 118.68 (s), 137.33 (s), 143.80 (s), 155.20 (s), 156.62 (d, ^1J(F,C) = 234.8 Hz). IR (KBr, cm^{-1}): 3390 (m, νNH), 3230 (m, νNH), 2940 (m, νCH), 1502 (s), 1463 (m), 1300 (m), 1284 (m, νP=O), 1239 (m, νP=O), 1211 (s), 1153 (m), 1069 (m), 966 (m, νP–N), 913 (s, νP–N), 821 (s, νP–N), 752 (m), 698 (m), 500 (m), 499 (m, νP–Cl).

*2.3.22. μ^1-(N-2-Pyridinyl)-N′-2-pyridinyl phosphoramidic chloride-bis [(N″,N‴-4-chlorophenyl) phosphoric triamide] (**20**)*

Yield: 75%. m.p. = 213 °C. *Anal.* Calc. for $C_{22}H_{19}Cl_3N_4O_2P_2$: C, 48.96; H, 3.55; N, 10.38. Found: C, 48.95; H, 3.55; N, 10.37%. ^{31}P NMR (DMSO-d_6): δ −10.79 (d, ^2J(P,P) = 18.6 Hz), −10.49 (m). ^1H NMR (DMSO-d_6): δ 6.75 (d, ^3J(H,H) = 8.1 Hz, 2H, Ar–H), 7.00–7.14 (m, 4H, Ar–H), 7.87 (b, 1H, NH), 8.38 (d, ^2J(PNH) = 9.0 Hz, 2H, NH). ^{13}C NMR (DMSO-d_6): δ 109.10 (s), 117.68 (s), 118.73 (d, ^3J(P,C) = 7.9 Hz), 118.88 (d, ^3J(P,C) = 7.7 Hz), 121.40 (s), 123.33 (s), 124.21 (s), 128.09 (s), 128.41 (s), 128.76 (s), 135.32 (s), 139.89 (s), 140.93 (s), 147.50 (s). IR (KBr, cm^{-1}): 3370 (m, νNH), 3195 (m, νNH), 2920 (m, νCH), 2808 (m, νCH), 1590 (m), 1485 (s), 1381 (m), 1275 (m, νP=O), 1215 (s, νP=O), 1188 (m), 1006 (m), 965 (m, νP–N), 910 (s, νP–N), 815 (s, νP–N), 650 (m), 539 (m), 480 (m, νP–Cl).

*2.3.23. μ^1-(N-2-Pyridinyl)-N′-2-pyridinyl phosphoramidic chloride-bis [(N″,N‴-4-bromophenyl) phosphoric triamide] (**21**)*

Yield: 75%. m.p. = 230 °C. *Anal.* Calc. for $C_{22}H_{19}Br_2ClN_4O_2P_2$: C, 42.03; H, 3.05; N, 8.91. Found: C, 42.01; H, 3.05; N, 8.90%. ^{31}P NMR (DMSO-d_6): δ −10.82 (d, ^2J(P,P) = 18.4 Hz), −10.66 (m). ^1H NMR (DMSO-d_6): δ 6.63 (d, ^3J(H,H) = 8.6 Hz, 2H, Ar–H), 6.96 (m, 6H, Ar–H), 7.16 (d, ^3J(H,H) = 8.6 Hz, 2H, Ar–H), 7.20 (d, ^2J(PNH) = 7.1 Hz, 2H, Ar–H), 7.23 (d, ^3J(H,H) = 8.7 Hz, 4H, Ar–H), 7.89 (b, 1H, NH), 8.39 (d, ^2J(PNH) = 8.3 Hz, 2H, NH). ^{13}C NMR (DMSO-d_6): δ 112.10 (s), 117.25 (s), 117.35 (s), 119.25 (d, ^3J(P,C) = 7.8 Hz), 130.96 (s), 131.28 (s), 131.47 (s), 133.80 (s), 137.20 (s), 140.27 (s), 146.50 (s), 151.50 (s), 152.10 (s). IR (KBr, cm^{-1}): 3305 (m, νNH), 3190 (m, νNH), 2915 (m, νCH), 1624 (m), 1481 (s), 1379 (m), 1296 (m), 1272 (m, νP=O), 1215 (s, νP=O), 1110 (m), 1068 (m), 962 (s, νP–N), 911 (s, νP–N), 812 (m, νP–N), 639 (m), 570 (m), 485 (m, νP–Cl).

*2.3.24. Phenylalanine benzylester hydrochloride (**22**)*

A solution of 6 mmol DL-phenylalanine was added to a solution of 35 mL of benzyl alcohol and the mixture was refluxed for 5 h. Then the temperature was decreased to −5 °C and 5.8 mL $SOCl_2$ was added dropwise to the mixture to yield the product that was washed with ether. Yield: 95%. m.p. = 200 °C. *Anal.* Calc. for $C_{16}H_{18}ClNO_2$: C, 65.86; H, 6.22; N, 4.80. Found: C, 65.85; H, 6.21; N, 4.81%. ^{1}H NMR (D_2O): δ 3.21 (d, ^3J(H,H) = 6.6 Hz, 2H, CH_2–O), 4.39 (t, ^3J(H,H) = 6.7 Hz, 1H, CH), 5.18 (d, ^2J(H,H) = 11.9 Hz, 1H, CH of CH_2), 5.24 (d, ^2J(H,H) = 11.9 Hz, 1H, CH of CH_2), 7.10 (m, 2H, Ar–H), 7.28–7.40 (m, 8H, Ar–H). ^{13}C NMR (D_2O): δ 35.64 (s), 54.03 (s), 68.66 (s), 127.50 (s), 128.05 (s), 128.90 (s), 131.00 (s), 129.09 (s), 129.21 (s), 129.36 (s), 133.49 (s), 134.39 (s). IR (KBr, cm^{-1}): 3430 (m, νNH), 3135 (m, νNH), 2990 (m, νCH), 2950 (m, νCH), 2860 (m), 1732 (s, νC=O), 1480 (s), 1439 (m), 1367 (m), 1225 (s), 1187 (m), 932 (m), 734 (s), 691 (s), 575 (m).

*2.3.25. General procedure for the synthesis of compounds **23**–**27***

A solution of 2 mmol of the corresponding aminoester plus 2 mmol of triethylamine in acetonitrile was added dropwise to a solution of 1 mmol N-(4-X-phenyl) phosphoramidic dichloride (X = CH_3, Cl, and NO_2) (in the case of compound **24**, 1 mmol of 4-tolyl dichlorophosphate) in acetonitrile at −5 °C. The flask contents were stirred for 48 h and then the precipitate was filtered, washed with water and dried in air to yield the products.

*2.3.26. N,N′-Bis (phenylalanino)-N″-4-methylphenyl phosphoric triamide (**23**)*

Yield: 55%. m.p. = 214 °C. *Anal.* Calc. $C_{25}H_{28}N_3O_5P$: C, 62.36; H, 5.86; N, 8.73. Found: C, 62.35; H, 5.85; N, 8.74%. ^{31}P NMR (DMSO-d_6): δ −0.27 (m). ^{1}H NMR (DMSO-d_6): δ 2.09 (s, 3H, p-CH_3), 3.38 (s, 2H, OH), 3.41 (m, 4H, CH_2), 3.67 (m, 2H, CH), 5.04 (s, 2H, $NH_{a\text{-}mine}$), 6.44–7.32 (m, 15H, Ar–H). ^{13}C NMR (DMSO-d_6): δ 20.06 (s, CH_3), 55.50 (s, CH), 65.62 (s, CH_2), 113.99 (s), 126.32 (s), 126.76 (s), 127.93 (s), 127.96 (s), 128.13 (s), 128.15 (s), 128.18 (s), 128.32 (s), 129.17 (s), 129.20 (s), 129.57 (s), 169.26 (s), 170.14 (s). IR (KBr, cm^{-1}): 3420 (m, νNH), 3275 (s, νNH), 3155 (m, νNH), 3030 (s, νCH), 2855 (m, νCH), 1724 (s, νC=O), 1655 (m), 1602 (m), 1504 (m), 1443 (m), 1284 (m), 1160 (s, νP=O), 1039 (s), 910 (m, νP–N), 744 (m, νP–N), 687 (s, νP–N), 599 (m), 465 (m).

*2.3.27. N,N′-Bis (phenylalanine benzylester)-4-methylphenyl phosphoramidicacid ester (**24**)*

Yield: 50%. m.p. = 220 °C. *Anal.* Calc. for $C_{39}H_{39}N_2O_6P$: C, 70.68; H, 5.93; N, 4.23. Found: C, 70.66; H, 5.93; N, 4.22%. ^{31}P NMR (DMSO-d_6): δ −0.24 (m). ^{1}H NMR (DMSO-d_6): δ 2.19 (s, 3H, p-CH_3), 2.78 (dd, ^3J(PNCH) = 7.9 Hz, ^2J(H,H) = 13.0 Hz, 1H, CH), 2.85 (dd, ^3J(PNCH) = 7.9 Hz, ^2J(H,H) = 13.0 Hz, 1H, CH), 2.98 (dd, ^2J(H,H) = 13.6 Hz, ^3J(H,H) = 8.0 Hz, 1H, CH of CH_2), 3.00 (dd, ^2J(H,H) = 13.6 Hz, ^3J(H,H) = 8.0 Hz, 1H, CH of CH_2), 3.11 (dd, ^2J(H,H) = 13.7 Hz, ^3J(H,H) = 5.6 Hz, 1H, CH of CH_2), 3.14 (dd, ^2J(H,H) = 13.7 Hz, ^3J(H,H) = 5.6 Hz, 1H, CH of CH_2), 4.05 (dd, ^3J(H,H) = 6.5 Hz, ^2J(PNH) = 13.0 Hz, 1H, NH), 4.10 (dd, ^3J(H,H) = 6.4 Hz, ^2J(PNH) = 12.7 Hz, 1H, NH), 4.86 (d, ^2J(H,H) = 12.7 Hz, 2H, CH of CH_2), 5.06 (d, ^2J(H,H) = 12.7 Hz, 2H, CH of CH_2), 6.93–7.32 (m, 24H, Ar–H). ^{13}C NMR (DMSO-d_6): δ 20.19 (s, CH_3), 37.00 (s), 40.35 (d, ^2J(P,C) = 6.3 Hz), 53.73 (s), 56.53 (s), 65.37 (s), 66.61 (s), 119.90 (d, ^3J(P,C) = 4.7 Hz), 126.22 (s), 126.93 (s), 127.81 (s), 128.02 (s), 128.13 (s), 128.19 (s), 128.21 (s), 128.30 (s), 128.32 (s), 128.40 (s), 128.41 (s), 129.05 (s), 129.15 (s), 129.34 (s), 130.25 (s), 135.02 (s), 135.29 (s), 135.78 (s), 137.22 (s), 170.16 (s, C=O), 173.15 (s, C=O). IR (KBr, cm^{-1}): 3390 (m, νNH), 3025 (m, νCH), 2855 (m, νCH), 1732 (s, νC=O), 1598 (m), 1494 (m), 1290 (m), 1205 (s, νP=O), 1150 (s), 1063 (m), 935 (m, νP–N), 907 (m), 734 (m, νP–N), 691 (s, νP–N), 594 (m), 470 (m).

*2.3.28. N,N′-Bis (phenylalanine benzylester)-N″-4-nitrophenyl-phosphoric triamide (**25**)*

Yield: 55%. m.p. = 150 °C. *Anal.* Calc. for $C_{38}H_{37}N_4O_7P$: C, 65.89; H, 5.38; N, 8.09. Found: C, 65.90; H, 5.38; N, 8.10%. ^{31}P NMR (DMSO-d_6): δ 2.04 (m). ^{1}H NMR (DMSO-d_6): δ 2.85 (m, 2H, CH_2), 3.09 (m, 2H, CH_2), 3.21 (m, 1H, CH), 3.92 (m, 1H, NH), 4.31 (m, 1H, NH), 4.85 (m, 2H, OCH_2), 5.12 (m, 2H, OCH_2), 5.31 (m, 1H, CH), 7.07–7.34 (m, 22H, Ar–H), 7.92 (d, ^3J(H,H) = 7.7 Hz, 2H, Ar–H), 8.31 (d, ^2J(PNH) = 6.6 Hz, 1H, NH). ^{13}C NMR (DMSO-d_6): δ 35.58 (s), 39.95 (s), 53.17 (s), 55.87 (s), 65.56 (s), 66.95 (s), 116.19 (d, ^3J(P,C) = 8.1 Hz), 124.81 (s), 126.26 (s), 127.13 (s), 127.76 (s), 127.64 (s), 127.79 (s), 128.02 (s), 128.16 (s), 128.21 (s), 128.26 (s), 128.31 (s), 128.49 (s), 128.99 (s), 129.34 (s), 134.55 (s), 134.76 (s), 135.59 (s), 136.91 (s), 139.03 (s), 168.79 (s, C=O), 172.39 (s, C=O). IR (KBr, cm^{-1}): 3348 (m, νNH), 3255 (s, νNH), 3025 (m, νCH), 2850 (s, νCH), 1732 (s, νC=O), 1590 (s, νNO_2), 1509 (s), 1484 (s), 1446 (s), 1342 (s, νNO_2), 1224 (s), 1290 (m), 1187 (s, νP=O), 1109 (s), 999 (s), 960 (m, νP–N), 846 (m), 735 (m, νP–N), 689 (s, νP–N), 529 (m).

*2.3.29. N-Phenylalanine benzylester-N′-4-chlorophenyl-phosphoramidic chloride (**26**)*

Yield: 65%. m.p. = 146 °C. *Anal.* Calc. for $C_{22}H_{21}Cl_2N_2O_3P$: C, 57.03; H, 4.57; N, 6.05. Found: C, 57.01; H, 4.56; N, 6.05%. ^{31}P NMR (DMSO-d_6): δ 3.75 (m). ^{1}H NMR (DMSO-d_6): δ 2.84 (m, 2H, CH_2), 3.92 (m, 1H, CH), 4.86 (m, 2H, OCH_2), 5.12 (m, 1H, NH), 7.00–7.29 (m, 14H, Ar–H), 7.51 (b, 1H, NH). ^{13}C NMR (DMSO-d_6): δ 39.75 (s), 55.82 (s), 65.57 (s), 118.42 (d, ^3J(P,C) = 6.4 Hz), 122.92 (s), 123.56 (s), 126.37 (s), 127.74 (s), 127.65 (s), 128.13 (s), 128.23 (s), 129.03 (s), 135.64 (s), 136.92 (s), 141.42 (s), 172.41 (s, C=O). IR (KBr, cm^{-1}): 3285 (s, νNH), 3255 (s, νNH), 3025 (m, νCH), 2850 (m, νCH), 1712 (s, νC=O), 1484 (s), 1442 (s), 1381 (s), 1274 (m), 1194 (s, νP=O), 1120 (s), 997 (s), 963 (m, νP–N), 911 (m), 822 (m, νP–N), 746 (m, νP–N), 692 (m, νP–N), 587 (m), 531 (m), 460 (m).

*2.3.30. N,N′-Bis (alaninethylester)-N″-4-methylphenyl-phosphoric triamide (**27**)*

Yield: 85%. m.p. = 76 °C. *Anal.* Calc. for $C_{17}H_{28}N_3O_5P$: C, 52.98; H, 7.32; N, 10.90. Found: C, 52.99; H, 7.31; N, 10.91%. ^{31}P NMR (DMSO-d_6): δ -0.23 (m). ^{1}H NMR (DMSO-d_6): δ 1.20 (t, ^3J(H,H) = 7.0 Hz, 6H, CH_3), 1.40 (d, ^3J(H,H) = 6.5 Hz, 6H, CH_3), 1.41 (s, 3H, p-CH_3), 2.24 (m, 2H, CH), 3.97 (m, 2H, NH), 4.15 (m, 4H, CH_2), 7.19 (s, 4 H, Ar–H). ^{13}C NMR (DMSO-d_6): δ 13.94 (s, CH_3), 15.69 (s, CH_3), 20.49 (s, p-CH_3), 47.86 (s, CH_2), 61.64 (s, CH), 122.16 (s), 129.63 (s), 131.23 (s), 135.83 (s), 169.86 (s, C=O). IR (KBr, cm^{-1}): 3466 (s, νNH), 3245 (s, νNH), 2965 (s, νCH), 2805 (s, νCH), 2601 (m), 1608 (s), 1619 (s, νC=O), 1399 (s), 1292 (m), 1183 (m, νP=O), 1095 (m), 850 (m, νP–N), 778 (s, νP–N), 712 (m), 503 (m), 450 (m).

*2.3.31. N-(2-Pyridinyl) phosphoramidic dichloride (**28**)*

A solution of 6 mmol 2-aminopyridine in acetonitrile was added dropwise to a solution of 3 mmol $POCl_3$ in acetonitrile at −5 °C and the mixture was stirred for 8 h. Then the precipitate was filtered and the solution was evaporated under vacuum to yield the product. Yield: 77%. m.p. = 81 °C. *Anal.* Calc. for $C_5H_5Cl_2NOP$: C, 30.49; H, 2.56; N, 7.11. Found: C, 30.50; H, 2.56; N, 7.12%. ^{31}P NMR (DMSO-d_6): δ −10.69 (s). ^{1}H NMR (DMSO-d_6): δ 6.85 (d, ^3J(H,H) = 6.7 Hz, 1H, Ar–H), 6.97 (d, ^3J(H,H) = 6.7 Hz, 1H, Ar–H), 7.55 (t, ^3J(H,H) = 6.7 Hz, 1H, Ar–H), 8.10 (d, ^3J(H,H) = 6.7 Hz, 1H, Ar–H), 9.12 (s 1H, NH). ^{13}C NMR (DMSO-d_6): δ 111.38 (s), 116.65 (s), 137.96 (s), 147.47 (s), 153.67 (s). IR (KBr, cm^{-1}): 3410 (m, νNH), 3130 (s, νNH), 2935 (m, νCH), 1591 (s), 1468 (s), 1321 (m), 1242 (m), 1214 (s, νP=O), 1149 (m), 985 (s, νP–N), 912 (s), 768 (m), 630 (m), 503 (m), 475 (m).

*2.3.32. N-(2-Pyridinyl)-N′,N″-bis (4-methylphenyl) phosphoric triamide (**29**)*

A solution of 8 mmol *p*-toluidine in acetonitrile was added dropwise to a solution of 2 mmol of compound **28** in acetonitrile at −5 °C and the mixture was stirred for 10 h. Then the precipitate was filtered and washed with water and CH_2Cl_2. Yield: 83%. m.p. = 204 °C. *Anal.* Calc. for $C_{19}H_{21}N_3OP$: C, 67.44; H, 6.26; N, 12.42. Found: C, 67.45; H, 6.25; N, 12.41%. ^{31}P NMR (DMSO-d_6): δ −4.08 (m). ^{1}H NMR (DMSO-d_6): δ 2.13 (s, 6H, CH_3), 6.81 (t, ^3J(H,H) 8 7.0 Hz, 1H, Ar–H), 6.92 (d, ^3J(H,H) = 8.3 Hz, 2H, Ar–$H_{p\text{-toluidine}}$), 7.03 (d, ^3J(H,H) = 8.3 Hz, 2H, Ar–H), 7.54 (t, ^3J(H,H) = 7.0 Hz, 1H, Ar–H), 7.64 (d, ^2J(PNH) = 7.0 Hz, 2H, NH), 8.32 (b, 1H, NH). ^{13}C NMR (DMSO-d_6): δ 20.14 (s, CH_3), 111.17 (d, ^2J(P,C) = 5.5 Hz), 115.94 (s), 117.55 (d, ^3J(P,C) = 7.2 Hz), 128.75 (s), 129.04 (s), 137.63 (s), 139.02 (s), 147.52 (s), 154.64 (s). IR (KBr, cm^{-1}): 3215 (m, νNH), 3025 (m, νNH), 2910 (m, νCH), 1594 (m), 1505 (s), 1461 (m), 1389 (s), 1302 (s), 1288 (s), 1220 (m), 1183 (s, νP═O), 966 (s, νP–N), 804 (s, νP–N), 768 (m), 635 (m), 583 (m), 485 (m). MS (20 eV, EI): *m*/*z* (%): 352 (100) M^+, 259 (7) [(4-CH_3–$C_6H_4NH)_2P(O)]^+$, 246 (73) [(4-CH_3–$C_6H_4NH)P(O)(2$-C_5H_4N–$NH)]^+$, 153 (3) [(4-CH_3–$C_6H_4NH)P(O)]^+$, 140 (7) [(2-C_5H_4N–$NH)P(O)]^+$, 106 (66) [4-CH_3–$C_6H_4NH]^+$, 93 (17) [2-C_5H_4N–$NH]^+$.

*2.3.33. N-[1-(4-methoxybenzyl)-decahydro-isoquinolinyl)] phosphoramidic dichloride (**30**)*

A solution of 3 mmol *N*-[1-(4-methoxybenzyl)-decahydro-isoquinoline)] plus 3 mmol of triethylamine in acetonitrile was added dropwise to a solution of 3 mmol $POCl_3$ in acetonitrile at −5 °C and the mixture was stirred for 12 h. Then the precipitate was filtered and washed with water and diethylether. Yield: 52%. *Anal.* Calc. for $C_{17}H_{22}Cl_2NO_2P$: C, 54.56; H, 5.93; N, 3.74. Found: C, 54.55; H, 5.92; N, 3.75%. ^{31}P NMR (DMSO-d_6): δ 0.26 (m). ^{1}H NMR (DMSO-d_6): δ 1.36 (m, 2H, CH_2), 1.64 (m, 2H, CH_2), 1.78 (m, 1H, CH), 1.93 (s, 3H, CH_3), 2.05 (m, 1H, CH), 2.23 (m, 1H, CH), 2.90 (m, 2H, CH_2), 3.09 (m, 2H, CH_2), 3.77 (s, 4H, CH_2), 6.89 (d, ^3J(H,H) = 8.6 Hz), 7.31 (d, ^3J(H,H) = 8.6 Hz), 7.31 (d, ^3J(H,H) = 8.6 Hz). ^{13}C NMR (DMSO-d_6): δ 21.85 (s), 22.09 (s), 25.85 (s), 26.19 (s), 29.34 (s), 35.37 (s), 38.35 (s), 55.00 (s), 56.30 (s), 113.92 (s), 125.35 (s), 127.95 (s), 128.39 (s), 130.54 (s), 158.19 (s). IR (KBr, cm^{-1}): 3440 (w, νNH), 2925 (s, νCH), 2770 (s, νCH), 2600 (m), 1602 (m), 1503 (s), 1452 (s), 1418 (m), 1297 (m), 1242 (s, νP═O), 1176 (m), 1031 (m), 828 (m, νP–N), 784 (m), 570 (m).

*2.3.34. N-[1-(4-methoxybenzyl)-decahydro-isoquinolinyl)] (phenyl) phosphoramidic chloride (**31**)*

A solution of 3 mmol *N*-[1-(4-methoxybenzyl)-decahydro-isoquinoline)] plus 3 mmol of triethylamine in acetonitrile was added dropwise to a solution of 3 mmol phenyl phosphorodichloridate in acetonitrile at −5 °C and the mixture was stirred for 18 h. Then the precipitate was filtered and washed with water and ethylacetate. Yield: 63%. *Anal.* Calc. for $C_{23}H_{27}ClNO_2P$: C, 66.42; H, 6.54; N, 3.37. Found: C, 66.43; H, 6.54; N, 3.36%. ^{31}P NMR (DMSO-d_6): δ 6.57 (m). ^{1}H NMR (DMSO-d_6): δ 1.42 (m, 2H, CH_2), 1.64 (m, 2H, CH_2), 1.79 (m, 1H, CH), 1.93 (s, 3H, OCH_3), 2.07 (d, ^3J(H,H) = 6.3 Hz, 1H, CH), 2.15 (m, 1H, CH), 2.77 (m, 1H, CH), 2.78 (m, H, CH), 3.09 (m, 2H, CH_2), 4.36 (m, 4H, CH_2), 6.89 (d, ^3J(H,H) = 8.4 Hz, 2H, Ar–H), 7.26 (d, ^3J(H,H) = 8.4 Hz, 2H, Ar–H), 7.36 (dd, ^3J(PCCH) = 13.4 Hz, ^3J(H,H) = 7.4 Hz, 2H, Ar–H), 7.43 (t, ^3J(H,H) = 8.4 Hz, 1H, Ar–H), 7.65 (d, ^3J(H,H) = 7.4 Hz, 2H, Ar–H). ^{13}C NMR (DMSO-d_6): δ 21.81 (s), 22.05 (s), 25.88 (s), 26.18 (s), 29.28 (s), 35.42 (s), 38.23 (s), 54.96 (s), 56.18 (s), 113.90 (s), 125.38 (s), 127.56 (d, ^3J(P,C) = 7.2 Hz), 127.76 (d, ^1J(P,C) = 28.8 Hz), 128.30 (s), 130.33 (s), 130.47 (s), 130.68 (s), 130.73 (d, ^3J(P,C) = 4.9 Hz), 158.16 (s). IR (KBr, cm^{-1}): 3435 (m, νNH), 2910 (s, νCH), 2798 (s, CH), 1503 (s), 1426 (s), 1240 (s, νP═O), 1177 (m), 965 (s, νP–N), 699 (m), 526 (s).

*2.3.35. N-Cyanoacetyl-phosphoramidic dichloride (**32**)*

A solution of 5 mmol of cyanoacetamide in CCl_4 was added slowly to a mixture of 3 mmol PCl_5 in CCl_4 at −5 °C and the mixture was refluxed for 10 h. Then the orange precipitate that formed was filtered and washed with CCl_4 and dried under vacuum. Yield: 55%. *Anal.* Calc. for $C_3H_3Cl_2N_2O_2P$: C, 17.93; H, 1.50; N, 13.94. Found: C, 17.92; H, 1.51; N, 13.95%. ^{31}P NMR (DMSO-d_6): δ −0.56 (d, ^2J(PNH) = 6.1 Hz). ^{1}H NMR (DMSO-d_6): δ 3.77 (s, 2H, CH_2), 9.44 (d, ^2J(PNH) = 6.1 Hz). ^{13}C NMR (DMSO-d_6): δ 26.62 (d, ^3J(P,C) = 10.5 Hz, CH_2), 115.56 (d, ^4J(P,C) = 1.6 Hz, C≡N), 164.04 (s, C═O). IR (KBr, cm^{-1}): 3190 (s, νNH), 2985 (s), 1710 (s, νC═O), 1452 (s, νC≡N), 1265 (s, νP═O), 1153 (m), 982 (m, νP–N), 663 (m), 580 (s), 526 (m).

*2.3.36. N-Cyanoacetyl-N′-benzyl phosphoramidic chloride (**33**)*

A solution of 2 mmol benzylamine in acetonitrile was added dropwise to a solution of 1 mmol of compound **32** in acetonitrile at −5 °C and the mixture was stirred for 15 h. Then the precipitate was filtered and the solvent was evaporated to give the product that was washed with water and *n*-heptane. Yield: 63%. *Anal.* Calc. for $C_{10}H_{11}ClN_3O_2P$: C, 44.22; H, 4.08; N, 15.47. Found: C, 44.21; H, 4.09; N, 15.46%. ^{31}P NMR (DMSO-d_6): δ 1.16 (s). ^{1}H NMR (DMSO-d_6): δ 3.58 (s, 2H, CH_2 of amide), 3.59 (s, Ar–CH_2), 3.98 (m, 1H, NH_{amine}), 7.29–7.474 (m, 5H, Ar–H), 9.46 (b, 2H, NH_{amide}). ^{13}C NMR (DMSO-d_6): δ 25.49 (s, CH_2 of amide), 42.22 (s, Ar–CH_2), 116.31 (s, C≡N), 128.91 (s), 128.54 (s), 128.91 (s), 134.25 (s), 165.93 (s, C═O). IR (KBr, cm^{-1}): 3355 (m, νNH), 3080 (s, νNH), 2980 (s), 1711 (s), 1677 (s, νC═O), 1400 (s, νC≡N), 1212 (s, νP═O), 1101 (s), 980 (s, νP–N), 926 (m, νP–N), 608 (m), 497 (m, νP–Cl).

*2.3.37. General procedure for the synthesis of compounds **34**–**45***

A solution of 8 mmol of the corresponding amine in acetonitrile was added dropwise to a solution of 2 mmol of compound **32** in acetonitrile at −5 °C and the mixture was stirred for 24 h. Then the precipitate tha formed was filtered and washed with water and *n*-hexane. Compound **45** was synthesized in the same way, but 8 mmol of amine was added to 2 mmol of *N*-trifluoroacetyl phosphoramidic dichloride.

*2.3.38. N-Cyanoacetyl-N′,N″-dibenzyl phosphoric triamide (**34**)*

Yield: 56%. *Anal.* Calc. for $C_{17}H_{19}N_4O_2P$: C, 59.64; H, 5.59; N, 16.37. Found: C, 59.65; H, 5.60; N, 16.38%. ^{31}P NMR (DMSO-d_6): δ 7.49 (m). ^{1}H NMR (DMSO-d_6): δ 3.67 (s, 2H, CH_2 of amide), 4.20 (dd, ^3J(PNCH) = 11.5 Hz, ^3J(H,H) = 7.4 Hz, 2H, Ar–CH_2), 5.04 (m, 2H, NH_{amine}), 7.19–7.34 (m, 10H, Ar–H), 9.25 (s, 1H, NH_{amide}). ^{13}C NMR (DMSO-d_6): δ 26.67 (d, ^3J(P,C) = 8.7 Hz, CH_2 of amide), 43.80 (s, Ar–CH_2), 115.58 (s, C≡N), 126.59 (s), 127.25 (s), 128.07 (s), 128.64 (s), 128.82 (s), 140.91 (d, ^3J(P,C) = 5.7 Hz, C_{ipso}), 164.47 (s, C═O). IR (KBr, cm^{-1}): 3305 (m, νNH), 3100 (m, νNH), 2975 (s), 1692 (m, νC═O), 1476 (m, νC≡N), 1446 (m), 1159 (s, νP═O), 932 (m, νP–N), 880 (m, νP–N), 798 (s), 546 (m).

*2.3.39. N-Cyanoacetyl-N′,N″-bis (α-phenylethyl) phosphoric triamide (**35**)*

Yield: 52%. *Anal.* Calc. for $C_{19}H_{23}N_4O_2P$: C, 61.61; H, 6.26; N, 15.13. Found: C, 61.60; H, 6.25; N, 15.13%. ^{31}P NMR (DMSO-d_6): δ 4.02 (m). ^{1}H NMR (DMSO-d_6): δ 1.33 (d, ^3J(H,H) = 7.2 Hz, 3H, CH_3), 1.34 (d, ^3J(H,H) = 7.2 Hz, 3H, CH_3), 3.40 (m, 2H, CH_2 of amide), 4.27 (m, 2H, NH_{amine}), 4.57 (m, 1H, CH), 4.93 (m, 1H, CH), 7.16–7.45 (m, 10H, Ar–H), 8.86 (b, 1H, NH_{amide}). ^{13}C NMR (DMSO-d_6): δ 25.25 (d, ^3J(P,C) 8 5.0 Hz, CH_3), 25.34 (d, ^3J(P,C) = 5.1 Hz, CH_3), 26.51 (d, ^3J(P,C) 8 8.8 Hz, CH_2), 49.77 (s, CH), 50.10 (s, CH), 115.49 (s, C≡N), 125.92 (s), 126.04 (s), 126.34 (s), 126.39 (s), 126.66 (s), 128.00 (s), 128.65 (s), 146.00 (d, ^3J(P,C) = 5.7 Hz, C_{ipso}), 146.15 (d, ^3J(P,C) = 5.4 Hz, C_{ipso}), 164.10 (s, C═O). IR (KBr, cm^{-1}): 3255 (s, νNH), 2250 (m), 1672 (m, νC═O), 1440 (s, νC≡N), 1416 (s), 1328

(m), 1188 (s, *ν*P=O), 1111 (m), 1037 (m), 953 (m, *ν*P–N), 633 (m, *ν*P–N), 503 (m).

*2.3.40. N-Cyanoacetyl-N′,N″-bis (2-chlorobenzyl) phosphoric triamide (**36**)*

Yield: 64%. *Anal.* Calc. for $C_{17}H_{17}Cl_2N_4O_2P$: C, 49.65; H, 4.17; N, 13.62. Found: C, 49.64; H, 4.16; N, 13.61%. ^{31}P NMR (DMSO-d_6): δ 7.38 (m). ^{1}H NMR (DMSO-d_6): δ 3.73 (s, 2H, CH_2 of amide), 4.15 (ddd, ^3J(PNCH) = 11.0 Hz, ^3J(H,H) = 7.2 Hz, ^2J(H,H) = 14.5 Hz, 2H, Ar–CH_2), 5.23 (dd, ^3J(H,H) = 7.2 Hz, ^2J(PNH) 8 10.1 Hz, 2H, NH_{amine}), 7.19–7.62 (m, 10H, Ar–H), 9.26 (s, 1H, NH_{amide}). ^{13}C NMR (DMSO-d_6): δ 26.75 (d, ^3J(P,C) = 8.9 Hz, CH_2 of amide), 41.43 (s, Ar–CH_2), 115.55 (s, C≡N), 126.98 (s), 128.25 (s), 128.86 (s), 129.47 (s), 131.52 (s), 138.00 (s), 164.64 (s, C=O). IR (KBr, cm^{-1}): 3255 (m, *ν*NH), 2915 (m), 1678 (s, *ν*C=O), 1457 (s, *ν*C≡N), 1432 (s), 1184 (s, *ν*P=O), 1082 (m), 1037 (m), 868 (m, *ν*P–N), 741 (m, *ν*P–N), 503 (m), 413 (m).

*2.3.41. N-Cyanoacetyl-N′,N″-bis (cyclopentyl) phosphoric triamide (**37**)*

Yield: 64%. *Anal.* Calc. for $C_{13}H_{23}N_4O_2P$: C, 52.34; H, 7.77; N, 18.78. Found: C, 52.35; H, 7.78; N, 18.77%. ^{31}P NMR (DMSO-d_6): δ 6.13 (m). ^{1}H NMR (DMSO-d_6): δ 1.38 (m, 8H, CH_2), 1.58 (m, 4H, CH_2), 1.71 (m, 4H, CH_2), 3.37 (m, 2H, CH), 3.74 (m, 2H, CH_2 of amide), 4.23 (m, 2H, NH_{amine}), 9.13 (b, 1H, NH_{amide}). ^{13}C NMR (DMSO-d_6): δ 22.76 (s, CH_2), 22.88 (s, CH_2), 26.58 (d, ^3J(P,C) = 8.7 Hz, CH_2 of amide), 33.97 (d, ^3J(P,C) = 5.1 Hz, CH_2), 34.14 (d, ^2J(P,C) = 6.5 Hz, CH), 51.97 (s, CH_2), 115.64 (s, C≡N), 164.16 (s, C=O). IR (KBr, cm^{-1}): 3390 (s, *ν*NH), 3090 (m, *ν*CH), 2920 (s, *ν*CH), 1694 (s, *ν*C=O), 1478 (s, *ν*C≡N), 1155 (s, *ν*P=O), 1105 (m), 977 (m, *ν*P–N), 926 (m, *ν*P–N), 899 (m, *ν*P–N), 565 (m), 461 (m).

*2.3.42. N-Cyanoacetyl-N′,N″-bis (cyclohexyl) phosphoric triamide (**38**)*

Yield: 58%. *Anal.* Calc. for $C_{15}H_{27}N_4O_2P$: C, 55.20; H, 8.34; N, 17.17. Found: C, 55.20; H, 8.33; N, 17.17%. ^{31}P NMR (DMSO-d_6): δ 4.32 (m). ^{1}H NMR (DMSO-d_6): δ 1.09 (m, 10H, CH_2), 1.48 (m, 2H, CH_2), 1.74 (m, 8H, CH_2), 2.85 (m, 2H, CH), 3.73 (m, 2H, CH_2 of amide), 4.14 (m, 2H, NH_{amine}), 8.50 (b, 1H, NH_{amide}). ^{13}C NMR (DMSO-d_6): δ 21.11 (s), 24.55 (d, ^3J(P,C) = 6.6 Hz), 24.73 (d, ^3J(P,C) = 4.0 Hz), 27.36 (s, CH_2 of amide), 31.85 (s), 34.84 (d, ^2J(P,C) = 4.1 Hz, CH), 35.03 (d, ^2J(P,C) = 6.6 Hz, CH), 40.19 (s), 40.22 (s), 115.46 (s, C≡N), 167.26 (s, C=O). IR (KBr, cm^{-1}): 3305 (m, *ν*NH), 2925 (s, *ν*CH), 1692 (m, *ν*C=O), 1476 (m, *ν*C≡N), 1159 (m, *ν*P8O), 1114 (m), 932 (m, *ν*P–N), 868 (m, *ν*P–N), 736 (m, *ν*P–N), 471 (m).

*2.3.43. N-Cyanoacetyl-N′,N″-bis (4-methylpiperidinyl) phosphoric triamide (**39**)*

Yield: 72%. *Anal.* Calc. for $C_{15}H_{27}N_4O_2P$: C, 55.20; H, 8.34; N, 17.17. Found: C, 55.19; H, 8.35; N, 17.16%. ^{31}P NMR (DMSO-d_6): δ 10.12 (m). ^{1}H NMR (DMSO-d_6): δ 0.88 (d, ^3J(H,H) = 6.5 Hz, 6H, CH_3), 1.00 (m, 4H, CH_2), 1.43 (m, 2H, CH), 1.54 (m, 4H, CH_2), 2.55 (m, 4H, CH_2), 3.36 (m, 4H, CH_2), 3.84 (s, 2H, CH_2), 9.12 (s, 1H, NH_{amide}). ^{13}C NMR (DMSO-d_6): δ 21.98 (s), 26.77 (d, ^3J(P,C) 8 8.6 Hz, CH_2 of amide), 130.40 (s), 33.99 (s), 34.06 (d, ^3J(P,C) = 8.6 Hz, CH_2), 34.10 (d, ^3J(P,C) = 5.3 Hz, CH_2), 44.05 (d, ^3J(P,C) = 2.6 Hz, CH_2), 44.32 (d, ^3J(P,C) = 2.8 Hz, CH_2), 115.63 (d, ^4J(P,C) = 1.3 Hz, C≡N), 164.46 (s, C=O). IR (KBr, cm^{-1}): 3430 (w, *ν*NH), 3100 (m, *ν*NH), 2950 (s), 2465 (s), 1639 (s, *ν*C=O), 1631 (m), 1583 (m), 1212 (s, *ν*P=O), 1063 (s), 968 (m, *ν*P–N), 772 (m, *ν*P–N), 538 (m).

*2.3.44. N-Cyanoacetyl-N′,N″-bis (4-fluorophenyl) phosphoric triamide (**40**)*

Yield: 56%. *Anal.* Calc. for $C_{15}H_{13}F_2N_4O_2P$: C, 51.44; H, 3.74; N, 16.00. Found: C, 51.45; H, 3.75; N, 16.00%. ^{31}P NMR (DMSO-d_6): δ -5.92 (s). ^{1}H NMR (DMSO-d_6): δ 3.72 (s, 2H, CH_2 of amide), 6.75 (m, 2H, Ar–H), 6.95 (m, 4H, Ar–H), 7.05 (m, 2H, Ar–H), 7.58 (s, 2H, NH_{amine}), 9.50 (s, 1H, NH_{amide}). ^{13}C NMR (DMSO-d_6): δ 26.41 (s, CH_2 of amide), 115.00 (d, ^2J(F,C) = 22.0 Hz), 115.41 (d, ^2J(F,C) = 22.1 Hz), 115.63 (s, C≡N), 117.23 (dd, ^3J[(F,C), (P,C)] = 7.4 Hz), 118.46 (dd, ^3J[(F,C), (P,C)] = 7.5 Hz), 138.40 (s), 141.08 (s), 155.92 (d, ^1J(F,C) = 232.0 Hz), 156.43 (d, ^1J(F,C) = 235.0 Hz), 163.94 (s, C=O). IR (KBr, cm^{-1}): 3415 (m, *ν*NH), 3285 (m, *ν*CH), 3155 (m, *ν*CH), 2960 (m, *ν*CH), 1671 (s, *ν*C=O), 1500 (s, *ν*C≡N), 1441 (s), 1201 (s, *ν*P=O), 1065 (s), 941 (m, *ν*P–N), 825 (m, *ν*P–N), 500 (m), 481 (m).

*2.3.45. N-Cyanoacetyl-N′,N″-bis (4-chlorophenyl) phosphoric triamide (**41**)*

Yield: 60%. *Anal.* Calc. for $C_{15}H^{13}Cl_2N_4O_2P$: C, 47.02; H, 3.42; N, 14.62. Found: C, 47.00; H, 3.42; N, 14.61%. ^{31}P NMR (DMSO-d_6): δ −5.91 (s). ^{1}H NMR (DMSO-d_6): δ 3.74 (s, 2H, CH_2 of amide), 6.70 (d, ^3J(H,H) = 8.2 Hz, 2H, Ar–H), 7.07 (d, ^3J(H,H) = 9.7 Hz, 2H, Ar–H), 7.09 (d, ^3J(H,H) = 9.7 Hz, 2H, Ar–H), 7.17 (d, ^3J(H,H) = 8.2 Hz, 2H, Ar–H), 7.88 (s, 2H, NH_{amine}), 9.62 (s, 1H, NH_{amide}). ^{13}C NMR (DMSO-d_6): δ 26.52 (d, ^3J(P,C) = 9.8 Hz, CH_2 of amide), 115.53 (s, C≡N), 116.92 (s), 118.70 (d, ^3J(P,C) = 7.5 Hz), 121.13 (s), 123.58 (s), 128.39 (s), 128.67 (s), 140.90 (s), 144.76 (s), 163.99 (s, C=O). IR (KBr, cm^{-1}): 3415 (m, *ν*NH), 3270 (m, *ν*CH), 3125 (m, *ν*CH), 2930 (s, *ν*CH), 1671 (s, *ν*C=O), 1483 (s, *ν*C≡N), 1451 (s), 1389 (m), 1295 (m), 1187 (s, *ν*P=O), 1051 (s), 940 (m, *ν*P–N), 817 (m, *ν*P–N), 532 (m).

*2.3.46. N-Cyanoacetyl-N′,N″-bis (4-bromophenyl) phosphoric triamide (**42**)*

Yield: 63%. *Anal.* Calc. for $C_{15}H_{13}Br_2N_4O_2P$: C, 38.16; H, 2.78; N, 11.87. Found: C, 38.15; H, 2.77; N, 11.88%. ^{31}P NMR (DMSO-d_6): δ −6.01 (s). ^{1}H NMR (DMSO-d_6): δ 3.74 (s, 2H, CH_2 of amide), 6.68 (d, ^3J(H,H) = 8.1 Hz, 2H, Ar–H), 7.01 (d, ^3J(H,H) = 8.1 Hz, 2H, Ar–H), 7.22 (d, ^3J(H,H) = 8.2 Hz, 2H, Ar–H), 7.29 (d, ^3J(H,H) = 8.2 Hz, 2H, Ar–H), 7.90 (s, 2H, NH_{amine}), 9.63 (s, 1H, NH_{amide}). ^{13}C NMR (DMSO-d_6): δ 26.57 (d, ^3J(P,C) = 9.8 Hz, CH_2 of amide), 109.16 (s), 111.38 (s), 115.56 (s, C≡N), 117.83 (s), 119.23 (d, ^3J(P,C) = 7.4 Hz), 131.30 (s), 131.59 (s), 141.36 (s), 144.63 (s), 164.04 (s, C=O). IR (KBr, cm^{-1}): 3345 (m, *ν*NH), 3260 (s, *ν*NH), 3120 (s, *ν*CH), 2835 (s, *ν*CH), 2590 (s), 1670 (s, *ν*C=O), 1478 (s, *ν*C≡N), 1452 (s), 1187 (s, *ν*P=O), 1051 (s), 1005 (m), 938 (m, *ν*P–N), 813 (m, *ν*P–N), 577 (m), 527 (m), 485 (m).

*2.3.47. N-Cyanoacetyl-N′,N″-bis (4-butylphenyl) phosphoric triamide (**43**)*

Yield: 66%. *Anal.* Calc. for $C_{23}H_{23}N_4O_2P$: C, 65.99; H, 5.54; N, 13.39. Found: C, 66.00; H, 5.55; N, 13.40%. ^{31}P NMR (DMSO-d_6): δ −7.09 (m). ^{1}H NMR (DMSO-d_6): δ 0.86 (t, ^3J(H,H) = 7.4 Hz, 6H, CH_3), 1.27 (m, 4H, CH_2), 1.46 (m, 4H, CH_2), 2.43 (m, 2H, CH_2), 2.47 (m, 2H, CH_2), 3.72 (s, 2H, CH_2 of amide), 6.78 (d, ^3J(H,H) = 8.1 Hz, 2H, Ar–H), 6.92 (d, ^3J(H,H) = 8.4 Hz, 2H, Ar–H), 6.95 (d, ^3J(H,H) = 8.4 Hz, 2H, Ar–H), 7.00 (d, ^3J(H,H) = 8.1 Hz, 2H, Ar–H), 7.37 (b, 2H, NH_{amine}), 9.45 (b, 1H, NH_{amide}). ^{13}C NMR (DMSO-d_6): δ 13.68 (s), 13.71 (s), 21.59 (s), 21.64 (s), 26.37 (d, ^3J(P,C) = 9.6 Hz, CH_2 of amide), 33.16 (s), 33.33 (s), 34.02 (s), 34.09 (s), 115.59 (s, C≡N), 117.17 (d, ^3J(P,C) = 6.5 Hz), 119.66 (s), 128.26 (s), 129.03 (s), 133.34 (s), 135.63 (s), 137.44 (s), 139.52 (s), 164.12 (s, C=O). IR (KBr, cm^{-1}): 3354 (m, *ν*NH), 3260 (m, *ν*NH), 3010 (m, *ν*CH), 2840 (s, *ν*CH), 2580 (s), 1669 (s, *ν*C=O), 1504 (s), 1457 (s, *ν*C≡N), 1193 (s, *ν*P=O), 1060 (s), 925 (m, *ν*P–N), 815 (m, *ν*P–N), 535 (m).

*2.3.48. N-Cyanoacetyl-N′,N″-bis (furfuryl) phosphoric triamide (**44**)*

Yield: 60%. *Anal.* Calc. for $C_{13}H_{15}N_4O_2P$: C, 53.79; H, 5.21; N, 19.30. Found: C, 53.80; H, 5.20; N, 19.30%. ^{31}P NMR (DMSO-d_6): δ

7.67 (m). ^{1}H NMR (DMSO-d_6): δ 3.71 (s, 2H, CH_2 of amide), 3.95 (m, 4H, Ar–CH_2), 4.98 (m, 2H, NH_{amine}), 6.22 (d, ^3J(H,H) = 6.5 Hz, 2H, Ar–H), 6.36 (d, ^3J(H,H) = 6.5 Hz, 2H, Ar–H), 7.53 (d, ^3J(H,H) = 6.5 Hz, 2H, Ar–H), 9.30 (s, 1H, NH_{amide}). ^{13}C NMR (DMSO-d_6): δ 26.60 (d, ^3J(P,C) = 8.6 Hz, CH_2 of amide), 37.06 (s, Ar–CH_2), 106.31 (s), 110.34 (s), 115.52 (s, C≡N), 141.82 (s), 153.95 (d, ^3J(P,C) = 6.6 Hz), 164.38 (s, C=O). IR (KBr, cm^{-1}): 3295 (s, νNH), 3095 (m, νCH), 2910 (m, νCH), 1686 (s, νC=O), 1470 (s, νC≡N), 1150 (s, νP=O), 1067 (m), 924 (m, νP–N), 877 (m, νP–N), 748 (m, νP–N), 564 (m).

2.3.49. N-Trifluoroacetyl-N′,N″-bis (4-methyl phenyl) phosphoric triamide (*45*)

Yield: 78%. *Anal.* Calc. for $C_{16}H_{17}F_3N_3O_2P$: C, 51.76; H, 4.62; N, 11.32. Found: C, 51.77; H, 4.62; N, 11.33%. ^{31}P NMR (CD_3CN): δ −5.38 (m). ^{1}H NMR (CD_3CN): δ 2.26 (s, 6H, CH_3), 6.53 (d, ^2J(PNH) = 9.9 Hz, 2H, $NH_{aromatic}$), 7.04 (d, ^3J(H,H) = 8.4 Hz, 2H, Ar–H), 7.07 (d, ^3J(H,H) = 8.4 Hz, 2H, Ar–H), 9.48 (b, 1H, NH_{amide}). ^{13}C NMR (CD_3CN): δ 20.64 (s, CF_3), 119.94 (d, ^3J(P,C) = 6.9 Hz), 130.73 (s), 132.99 (s), 137.89 (s), 167.42 (s, C=O). IR (KBr, cm^{-1}): 3419 (s, νNH), 3279 (s, νNH), 2924 (m, νCH), 1724 (s, νC=O), 1616 (s), 1517 (s), 1459 (s), 1309 (s), 1282 (m), 1208 (s), 1175 (s, νP=O), 966 (m, νP–N), 815 (m, νP–N), 596 (m), 474 (m).

3. Results and discussion

3.1. Spectroscopic study

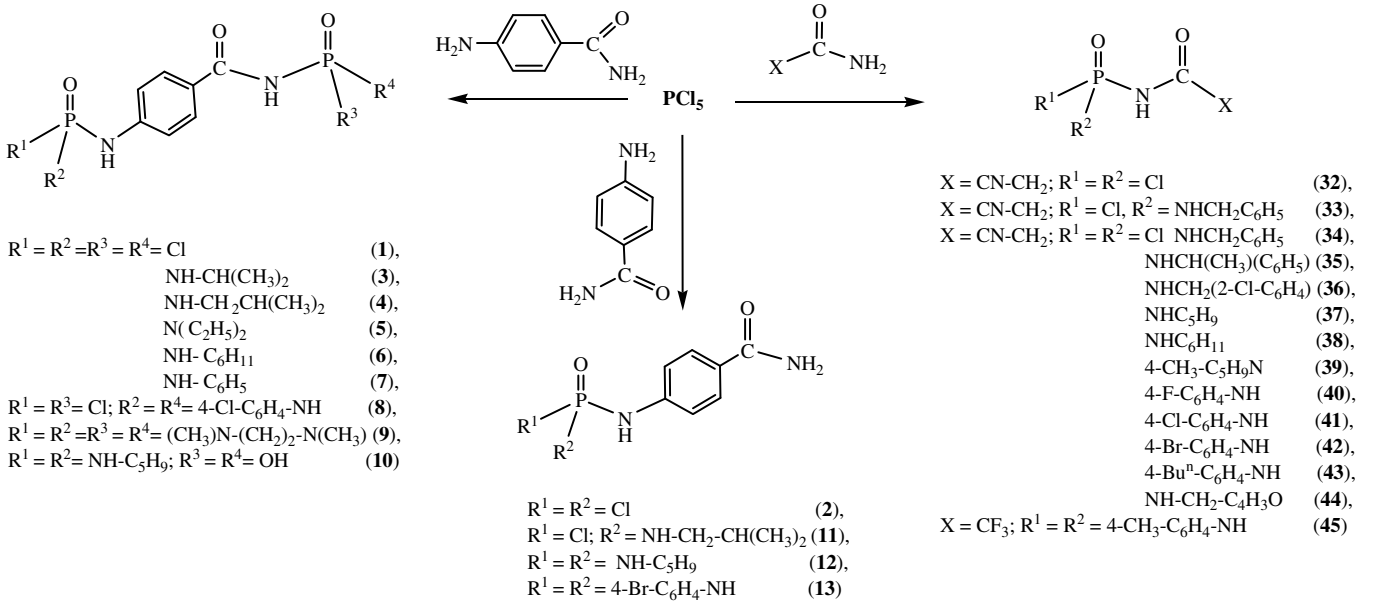
In this work a number of new phosphoramidate derivatives of bisphosphoramidates and phosphoric triamides were synthesized using PCl_5 and $POCl_3$ as starting materials, Schemes 1 and 2. Here, the spectroscopic features of these compounds are studied.

3.1.1. Bisphosphoramidates *1*, *3*–*10*

The syntheses of the bisphosphoramidates **1** and **3–10** (containing the (O)P–NH–C_6H_4–C(O)NH–P(O) linkage) were performed by the reaction of PCl_5 with 4-aminobenzamide in a 1:4 molar ratio to initially yield the bisphosphoramide $Cl_2P(O)NHC_6H_4C(O)NHP(O)Cl_2$ (**1**) that was used as an intermediate to react with different amines to give molecules **3–10**, Scheme 1. As far as we know, these compounds are the first examples of bisphosphoramidates that have been obtained up until now in such a simple one-step reaction.

The ^{31}P{^{1}H} NMR spectrum of compound **1** displays two singlet peaks for the two phosphorus atoms, at 5.44 and 6.69 ppm, and the substitution of different cyclic and acyclic aliphatic amines for the chlorine atoms shifts the δ (^{31}P) downfield, while substitution with phenyl groups leads to upfield shifts. The δ (^{31}P) in this series varies between −3.42 and −3.74 ppm (in **7** containing an aromatic aniline moiety) to 20.03, 20.16 ppm (in **9** containing a heterocyclic aliphatic diazaphosphole ring). The ^{1}H NMR spectrum of **3** displayed four doublet signals for the four types of CH_3 groups of isopropyl moieties due to the fact that the carbon atom of the CH group in the iso-propyl substituent is prochiral, and so the two methyl groups bonded to this group are different and show two signals in both the ^{1}H and ^{13}C NMR spectra. The ^{13}C NMR spectra of compounds **1** and **3–10** displayed six separate signals for the aromatic carbon atoms of the 4-aminobenzamide group and ^2J(P,C=O) = 3.5 Hz for the C=O group in **1**, while this constant was zero for the other compounds.

Compound **6**, with cyclohexyl substituents, displayed 12 peaks in the aliphatic region of the ^{13}C NMR spectrum, with four ^3J(P,C) coupling constants for CH_2 groups, four singlet signals for CH_2 groups and four ^2J(P,C) coupling constants for the CH groups. These results indicate that due to the different spatial orientation of the aliphatic six-membered rings, the four CH groups of the four cyclohexyl groups are different, but other related carbon atoms on one side of the molecule are equal to each other while being unequal to their related carbon atoms on the other side. The ^{13}C NMR spectrum of bis diazaphosphole **9** displayed two ^2J(P,C) = 5.0, 4.9 Hz for the CH_3 groups, two ^2J(P,C) = 7.3, 5.7 Hz for CH_2 moieties, two singlets for CH_3 as well as two singlets for CH_2 groups. A reason for this may be that for the phosphorus and carbon atoms a simple splitting is seen on one side of the molecule, while for the carbon atoms on the other side no coupling is observed. According to the Karplus relationship between the ^3J(P,X), X = H, C coupling constant and the P–N–C–X torsion angle [33], this is due to the P–N–C–H torsion angle values. The ^{13}C NMR spectrum of **10** showed three signals in the aliphatic region for the cyclopentyl moieties and the proton integrals in the ^{1}H NMR spectrum indicate that only two cyclopentyl groups are connected to one of the phosphorus atoms, while for

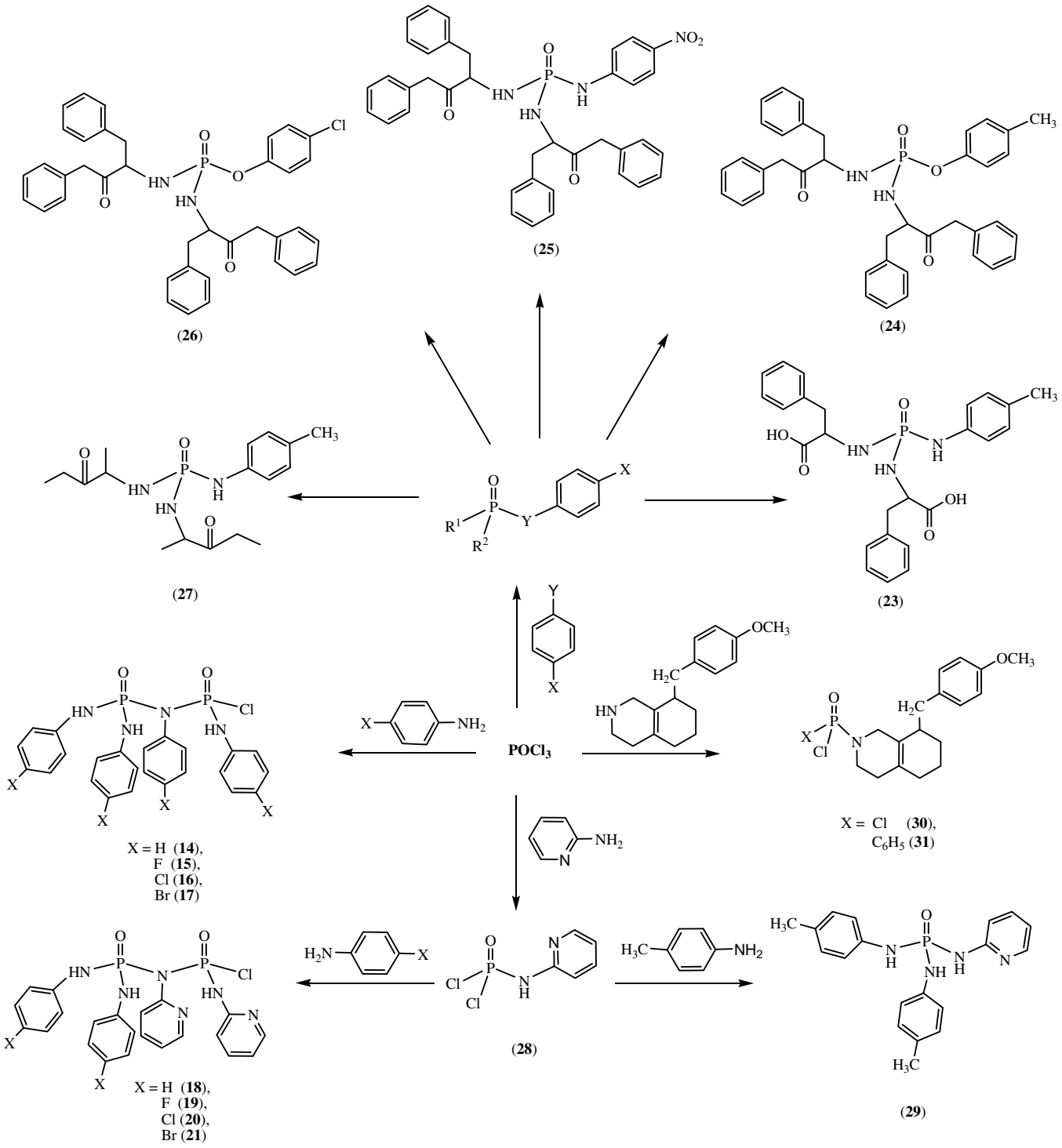


$R^1 = R^2 = R^3 = R^4 =$ Cl (**1**),
NH-CH(CH$_3$)$_2$ (**3**),
NH-CH$_2$CH(CH$_3$)$_2$ (**4**),
N(C$_2$H$_5$)$_2$ (**5**),
NH-C$_6$H$_{11}$ (**6**),
NH-C$_6$H$_5$ (**7**),
$R^1 = R^3$ = Cl; $R^2 = R^4$ = 4-Cl-C$_6$H$_4$-NH (**8**),
$R^1 = R^2 = R^3 = R^4$ = (CH$_3$)N-(CH$_2$)$_2$-N(CH$_3$) (**9**),
$R^1 = R^2$ = NH-C$_5$H$_9$; $R^3 = R^4$ = OH (**10**)

$R^1 = R^2$ = Cl (**2**),
R^1 = Cl; R^2 = NH-CH$_2$-CH(CH$_3$)$_2$ (**11**),
$R^1 = R^2$ = NH-C$_5$H$_9$ (**12**),
$R^1 = R^2$ = 4-Br-C$_6$H$_4$-NH (**13**)

X = CN-CH$_2$; $R^1 = R^2$ = Cl (**32**),
X = CN-CH$_2$; R^1 = Cl, R^2 = NHCH$_2$C$_6$H$_5$ (**33**),
X = CN-CH$_2$; $R^1 = R^2$ = Cl NHCH$_2$C$_6$H$_5$ (**34**),
NHCH(CH$_3$)(C$_6$H$_5$) (**35**),
NHCH$_2$(2-Cl-C$_6$H$_4$) (**36**),
NHC$_5$H$_9$ (**37**),
NHC$_6$H$_{11}$ (**38**),
4-CH$_3$-C$_5$H$_9$N (**39**),
4-F-C$_6$H$_4$-NH (**40**),
4-Cl-C$_6$H$_4$-NH (**41**),
4-Br-C$_6$H$_4$-NH (**42**),
4-Bu^n-C$_6$H$_4$-NH (**43**),
NH-CH$_2$-C$_4$H$_3$O (**44**),
X = CF$_3$; $R^1 = R^2$ = 4-CH$_3$-C$_6$H$_4$-NH (**45**)

Scheme 1. Preparation pathway for compounds using PCl_5 as a starting compound.



Scheme 2. Preparation pathway for compounds using $POCl_3$ as a starting compound.

the other phosphorus atom the two cyclopentyl substituents are replaced by OH groups. This is probably due to the acquisition of the NMR spectra in D_2O solvent, and hence hydrolysis of the molecule occurs. A comparison of δ (^{31}P) in compounds **4** and **11** revealed that in the bisphosphoramide **4** the P atom is far more deshielded than in the phosphoric triamide **11**.

The IR spectra indicated two ν (P=O) for the two P=O bonds and a ν (C=O) in each compound. The $^2J(PNH_{amine})$ coupling constant for compounds **1**, **5** and **6** are 11.9, 9.1 and 7.6 Hz, respectively, and the corresponding $\nu(P–N)$ values are 994, 941 and 907 cm^{-1}. These data reveal that the more the ν(P–N) value increases, i.e., a shorter P–N bond with more s character in the nitrogen hybridization, the more the $^2J(PNH_{amine})$ coupling constant is enhanced.

3.1.2. Bisphosphoramidates *14–21*

The bisphosphoramidates **14–21** (containing the (O)P–N–P(O) linkage) were prepared by the reaction of $POCl_3$ with different first-type aromatic amines, Scheme 2. To our knowledge, this is the first attempt that has been made to obtain these types of

compounds using time-dependent reactions. That is, the synthesis procedure of these molecules is similar to that of phosphoric triamides, but these compounds are obtained after 48 h stirring and if the reaction mixture was allowed to stir for about one or two weeks, the corresponding phosphoric triamides would be yielded. In fact, these compounds are kinetically stable products of the reaction and are not stable with time. Thus after a relatively long time they convert to their related thermodynamically stable phosphoric triamides. The ^2J(P,P) coupling constants observed in the $^{31}P\{^1H\}$ NMR spectra are about 20 Hz. The two phosphorus atoms are not connected directly to each other, because the ^1J(P,P) coupling constants in other similar compounds are reported to be about 200 Hz [34]. The ^2J(P,P) coupling constant in compound **14** was measured as 19.7 Hz in DMSO-d_6 and it decreased to 17.5 Hz in the solvent CD_3OD, probably due to the different hydrogen bonding interactions in this solvent. The ^{31}P NMR spectra of compounds **14** and **18** (containing the anilinium substituent) indicated two signals, the upfield one of them being a multiplet and the other being only a doublet peak. This trend is reverse for compounds **15–17** and **19–21**, including *para*-haloanilinium groups. It is clear that the doublet peak is related to the P^1 atom and the multiplet peak to the P^2 atom (Scheme 3), and the reason for the reduced splitting of P^1 with the NH group of the aromatic amine may be described by the resonance interaction in Scheme 3. The downfield shift of δ (^{31}P) for the P^2 atom in compounds containing *para*-haloanilinium groups is related to the electron withdrawing nature of the electronegative halogen atoms in comparison with the inert H atom.

Comparison of δ (^{31}P) in compounds **14–17** and also in **19–21** revealed that the shielding of the P^1 and P^2 atoms decreases with the decreasing halogen electronegativity from F to Cl to Br (i.e., from **15** to **17** and from **19** to **21**). The shielding of the phosphorus atoms in compounds **14** and **18** containing anilinium moieties are greater than that of compounds containing 4-fluoroanilinium groups, and the shielding order is Br > Cl > H > F. The reason for the greater shielding of the P atoms in compounds with 4-Cl and 4-Br substituents relative to the H substituent can be explained by the electron release of the halogens through resonance. The ^{13}C NMR spectra of **15** and **19** indicate ^{1-4}J(F,C) coupling constants as well as ^3J(P,C) coupling constants. The IR spectra revealed two ν(P=O) frequencies for the two P=O bonds and we can relate the smaller ν(P=O) to the weaker P=O bond and vice versa. In molecules **14** and **18**, the upfield signal is related to P^2 and in compounds **15–17** and **19–21**, it is related to P^1.

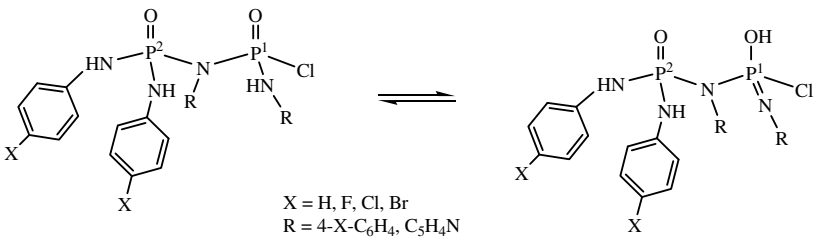
3.1.3. Phosphoramidates and phosphoric triamides

The phosphoramidates **2** and **11–13** were prepared by the reaction of PCl_5 with 4-aminobenzamide in a 1:1 molar ratio and we may judge that the P–N bond is formed from the anilinium NH_2 group not from the amidic $C(O)NH_2$. This is because stronger P–N bonds always have been observed for $P–N_{amine}$ compared to $P–N_{amide}$ in our other synthesized compounds, and also the C(O) group causes weakening of the P–N bond via resonance interactions. A comparison of δ (^{31}P) in these molecules indicated that substitution of aliphatic electron donor amines with the chlorine atoms of **2** leads to a more positive P atom (in **11** and **12**), while the aromatic 4-bromoaniline (in **13**) had the opposite effect. In the ^{13}C NMR spectra of these compounds four singlet signals were observed for the benzamidic ring, while in their related bisphosphoramidates six different signals were obtained for the six carbon atoms of the ring. Replacement of an amine group by a chlorine atom gives a ν(P–N) value indicating a stronger P–N bond and a ν(C=O) value indicating a weaker C=O bond.

For the synthesis of compounds **23–26**, first the hydrochloride salt of the phenylalanine benzylester was obtained for subsequent reaction with an $RP(O)Cl_2$ intermediate, where R = amine or phenol. Phosphoric triamides of this type have shown antitumor, antiviral and anti-HIV properties [1–4] and for this reason we have been interested in studying such molecules. In the case of compound **23**, it is concluded from the ^1H and ^{13}C NMR spectra that the phenylalanine benzylester is hydrolyzed and the phenylalanine is connected to the phosphorus atom. The ^1H and ^{13}C NMR spectra of molecules **23–26** displayed two unequivalent aminoester (or aminoacid) moieties, probably owing to the presence of chiral CH groups as well as the spatial hinderance caused by these two huge substituents. However, this is not observed in the ^1H and ^{13}C NMR spectra of **29** that also contain two chiral aminoester groups. Therefore, the chirality of these moieties is not the reason for the difference between these groups in compounds **23–26**, but it is the various spatial orientations of the aminoester/aminoacid groups (the huge groups are far away from each other due to the repulsion) which result in the creation of a central chiral phosphorus atom.

The ^{31}P NMR spectra exhibited an upfield shift for δ (^{31}P) in compounds including electron donor groups such as *p*-tolyl (**24**), while it is shifted downfield with electronegative 4-nitroanilinium or 4-chloroanilinium groups (**25** and **26**). Both compounds **23** and **27** contain a *p*-toluidinium substituent and their difference is the replacement of the aminoacid groups in **23** with aminoester groups (**27**). The δ (^{31}P) in **23** is upfield, and the P=O bond shows a weaker ν(P=O), whereas the C=O bond has a stronger ν(C=O) relative to those of **27**. The δ (^{31}P) in compound **28** is upfield relative to that of **29**, perhaps due to the greater electron donation of the two chlorine atoms via resonance in comparison to the two *p*-toluidinium groups.

A huge amino group is bonded to the phosphorus atom in molecules **30** and **31**. This kind of amine group has indicated possible clinical applications [35–37] and significant importance in medicine. Our attempts to obtain a single crystal of compound **30** in a methanol/acetonitrile mixture resulted in structure **I**, which is most likely a hydrolyzed product of **30** in the solution (perhaps the P–N bond of this giant amino group is labile due to steric repulsion). The δ (^{31}P) of **30** is at a much higher field relative to that of **31**. Therefore, it could be concluded that the phenyl ring plays an important role as an electron withdrawing group in compound **31**.



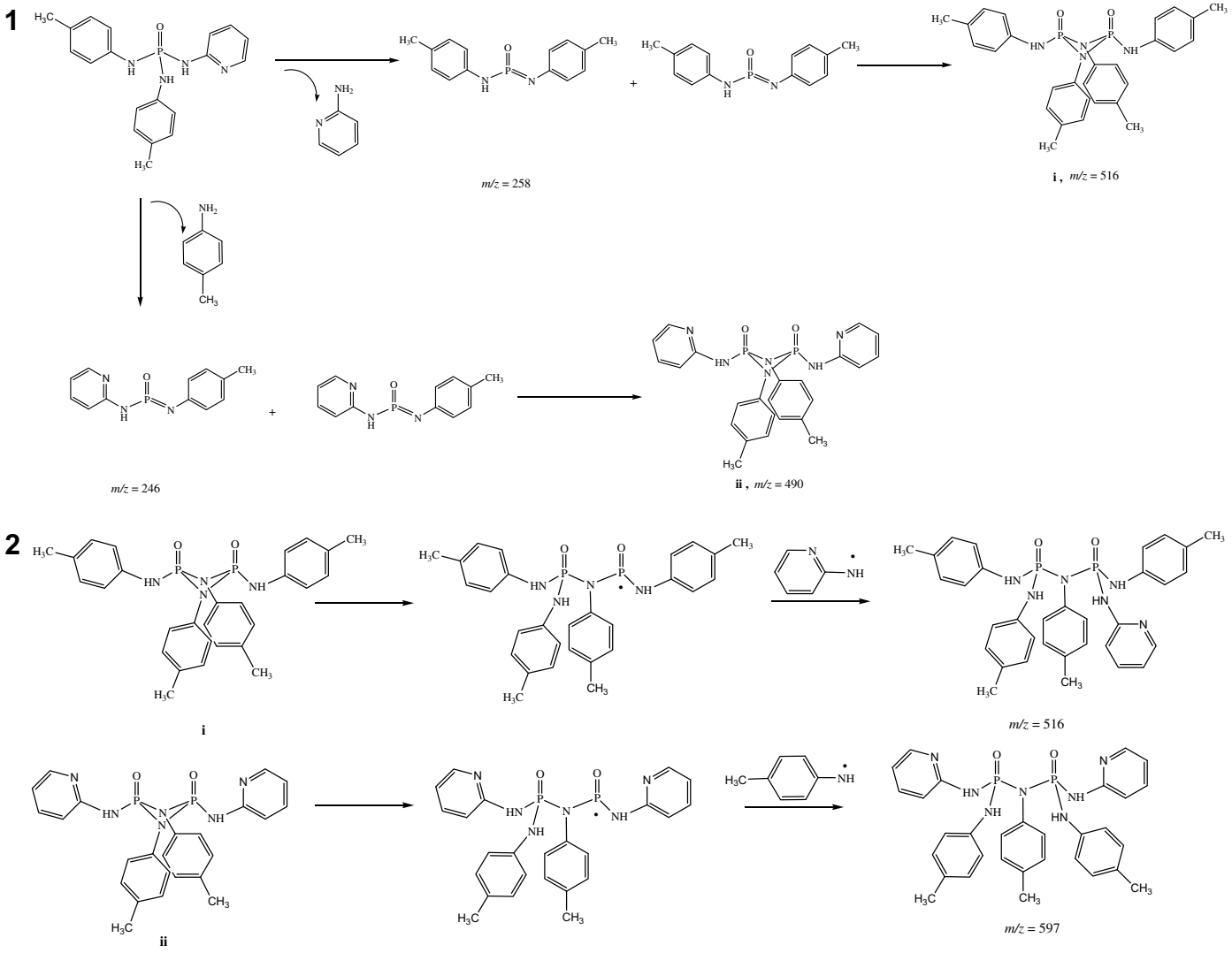
Scheme 3. The resonance interaction in bisphosphoramidates **14–21**.

The ^{31}P NMR spectra of the phosphoramidates **32**–**44**, containing the cyanoacetamide substituent, demonstrated that substitution of the chlorine atoms in compound **32** by aliphatic amino groups result in deshielded phosphorus atoms, while replacing with aromatic amino groups of the formula 4-X–C_6H_4NH, X = F, Cl, Br, $(CH_2)_3CH_3$, leads to much more shielded phosphorus atoms. The connection of *p*-butylaniline to the phosphorus atom causes its shielding, and the δ (^{31}P) is the most upfield in this series. Also, the δ (^{31}P) of the *p*-haloanilinium substituents becomes more positive on decreasing the halogen electronegativity. δ (^{31}P) changed in the order of Br > Cl > F > $(CH_2)_3CH_3$ for compounds **40**–**43**. An interesting feature in the ^{1}H and ^{13}C NMR spectra of compounds **40**–**43**, having *p*-substituted anilinium substituents, is that the two aromatic groups are different and present two sets of signals in the spectra, whereas when aliphatic amino groups are replaced by the two Cl atoms in **32**, they are equal. This characteristic was not seen in the spectra of compound **45**.

The ^{13}C NMR spectra of **32**–**44** revealed that the ^2J(P,C) coupling constant, i.e., the coupling of the amidic CH_2 carbon atom with the P atom, is decreased from 10.5 Hz (in **32**) to about 8.9 Hz (in **33**–**44**). Therefore, replacement of the chlorine atoms by different amino groups reduces the ^2J(P,C) coupling constant. Compound **35** contains α-phenylethyl substituents that have a chiral carbon atom at the CH groups, leading to the appearance of two sets of peaks in its ^{1}H and ^{13}C NMR spectra. The ^{13}C NMR spectrum of compound **37** exhibited five signals for the five carbon atoms of the two aliphatic cyclopentyl moieties owing to the fact that the two aliphatic rings are equal, but the five carbon atoms of the ring are different. The ^{13}C NMR spectra of compounds **38** and **39** display eight separate signals for the aliphatic carbon atoms of the cyclohexyl and 4-methylpiperidinyl groups due to the fact that the two aliphatic groups are not equal. A ^4J(P,C) coupling constant of 1.6 Hz was observed for the splitting of the C≡N carbon atom with the phosphorus atom in **32**, but this coupling did not occur in molecules **33**–**44**.

The mass spectrum of compound **29** indicates ionic fragments corresponding to this molecule as well as a base peak at *m/z* = 352 (100%). There are also some peaks at *m/z* > 352 related to dimerization of the ionic fragments [38]. The following rearrangements are proposed for the mechanism of the dimerizations (Scheme 4(1 and 2)).

(a) The P–N bond of the aminopyridinium group is broken, an aminopyridine group is released and a P=N bond is formed. Then, conjugation of the two similar fragments, i.e. a cycloaddition reaction, will yield the diazadiphosphetidine **i** with *m/z* = 516. (b) If a *p*-toluidine group is separated from the molecule and the resulting



Scheme 4. The proposed fragmentation mechanism of compound **29** in the mass spectrum.

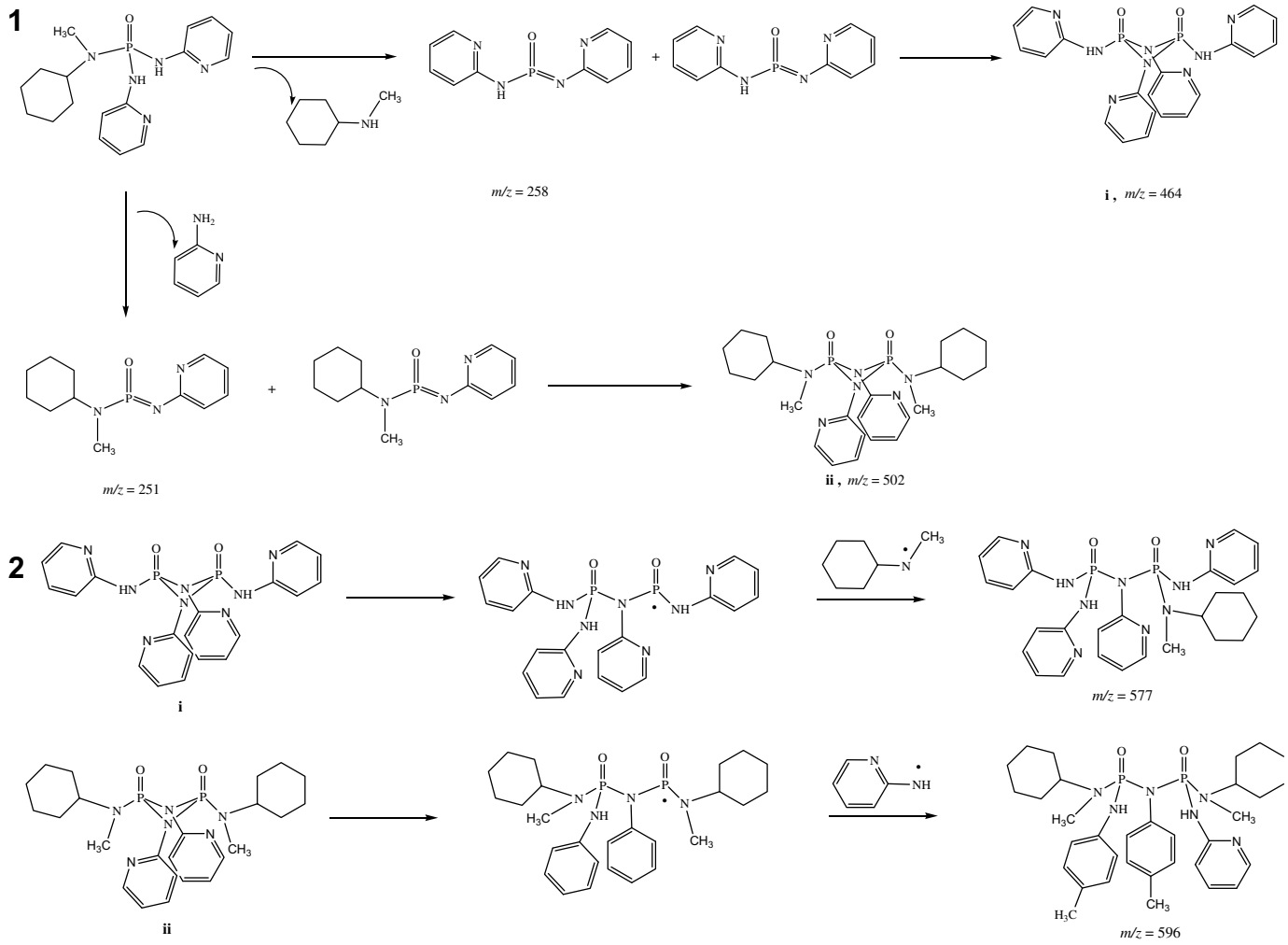
similar fragments are bonded to each other, another diazadiphosphetidine (**ii**) is obtained with $m/z = 490$. (c) If one of the P–N bonds in the cyclic diazadiphosphetidines **i** breaks then an aminopyridinium radical cation is bonded to it, a bisphosphoramidate with $m/z = 516$ could be produced. (d) If one of the P–N bonds in the diazadiphosphetidine **ii** breaks then a *p*-toluidinum radical cation is bonded to it, a bisphosphoramidate with $m/z = 597$ is obtained. This fragmentation pathway is also proposed for the mass spectrum of compound $(C_5H_4N–NH)_2P(O)[N(CH_3)(C_6H_{11})]$ [39] in which there are some molecular ion peaks at m/z greater than the base peak, and a similar mechanism could be considered for its fragmentation (Scheme 5(1 and 2)).

3.2. X-ray crystallography

Single crystals of compounds **I** (4-OCH_3–C_6H_4–CH_2–C_9H_{13}–NH_2Cl), **34** and **44** were obtained from a solution of methanol/chloroform or methanol/acetonitrile/water at room temperature. The crystallographic data and the details of the X-ray analysis of these compounds are represented in Table 1, and selected bond lengths and angles are given in Table 2. Hydrogen bonding data of these structures are presented in Table 3. Molecular structures (ortep views) have been shown in Figs. 1–3.

There are two symmetrically independent molecules in the crystalline lattice of compound **I** due to the differences in the related torsion angles of these two conformers. The torsion angles N(2)–C(1)–C(8A)–C(4A) and N(2′)–C(1′)–C(8′A)–C(4′A) are 6.6(3)° and 8.7(3)° (also, compare the torsion angles N(2)–C(1)–C(9)–C(10), N(2′)–C(1′)–C(9′)–C(10′) and C(14)–C(13)–O(1)–C(16), C(14′)–C(13′)–O(1′)–C(16′) that are −68.0(3)°, −61.0(3)° and −11.4(4)°, −1.8(4)°, respectively). This phenomenon was observed for some of our previously reported structures [17,18,23]. Although there is a C=C double bond between the two unsaturated six-membered rings, they are not planar and show a puckered shape. The C(5)–C(10) and C(5′)–C(10′) carbon atoms of the phenyl ring as well as their corresponding hydrogen atoms in compound **34** revealed disorder in the structure that can be described by free rotation along the C(4)–N(3) bond, causing uncertainty in the determination of the carbon and hydrogen locations of the phenyl ring.

The P=O bond lengths in molecules **34** and **44** are 1.483(16) and 1.491(15) Å, which are larger than the normal P=O bond length (1.450 Å) [40]. The P atoms have slightly distorted tetrahedral configurations, e.g. the surrounding angles around the P atoms of the two symmetrically different molecules in compound **34** are in the range 103.16(10)–117.34(10)°. The P–N_{amide} bond lengths are longer than the P–N_{amine} bond lengths because of the interaction of the N_{amide} atom with the π resonance system of the C=O group, which results in a shorter C–N_{amide} bond length, i.e., 1.687(19) > 1.616(19), 1.620(2) (in **34**), and 1.685(17) > 1.622(18), 1.621(18) Å (in **44**). All of these P–N bonds are shorter than the typical P–N single bond length (1.770 Å) [40]. The nitrogen envi-



Scheme 5. The proposed fragmentation mechanism of compound $(C_5H_4N–NH)_2P(O)[N(CH_3)(C_6H_{11})]$ in the mass spectrum.

Table 1
Crystallographic data for compounds **I**, **34** and **44**.

	I	**34**	**44**
Empirical formula	$C_{17}H_{24}ClNO$	$C_{17}H_{19}N_4O_2P$	$C_{13}H_{15}N_4O_4P$
Formula weight	293.82	342.33	322.26
Temperature (K)	293(2)	293(2)	120(2)
Wavelength (Å)	0.71073	0.71073	0.71073
Crystal system, space group	triclinic, *P 1*	triclinic, $P\bar{1}$	triclinic, $P\bar{1}$
Unit cell dimensions			
a (Å)	8.0732(10)	5.1799(10)	4.9743(5)
b (Å)	9.3318(11)	12.799(3)	10.6382(10)
c (Å)	11.8945(14)	14.177(3)	14.5630(14)
α (°)	88.970(5)	71.44(3)	81.395(2)
β (°)	75.950(5)	84.98(3)	81.346(2)
γ (°)	73.436(5)	85.71(3)	81.013(2)
V (Å^3)	831.95(17)	886.5(4)	746.21(13)
Z, D_{calc} (Mg m^{-3})	2, 1.173	2, 1.282	2, 1.434
Absorption coefficient (mm^{-1})	0.226	0.172	0.208
F(000)	316	360	336
Crystal size (mm)	0.25 × 0.25 × 0.20	0.40 × 0.30 × 0.25	0.43 × 0.08 × 0.07
θ Range for data collection (°)	1.77–26.03	2.60–27.06	1.95–28.03
Limiting indices	$-9 \leqslant h \leqslant 9$; $-11 \leqslant k \leqslant 11$; $-14 \leqslant l \leqslant 14$	$0 \leqslant h \leqslant 6$; $-16 \leqslant k \leqslant 16$; $-18 \leqslant l \leqslant 18$	$-6 \leqslant h \leqslant 6$; $-14 \leqslant k \leqslant 13$; $-19 \leqslant l \leqslant 19$
Reflections collected/unique	6914/6011	4297/3868	7801/3610
R_{int}	0.0134	0.0193	0.0331
Completeness to θ (%)	98.6	99.4	99.7
Absorption correction	semi-empirical from equivalents	none	semi-empirical from equivalents
Maximum and minimum transmission	0.954 and 0.948		0.986 and 0.904
Refinement method	full-matrix least-squares on F^2	full-matrix least-squares on F^2	full-matrix least-squares on F^2
Data/restraints/parameters	6011/3/361	3868/41/199	3610/0/199
Goodness-of-fit on F^2	1.022	1.012	1.040
Final *R* indices	$R_1 = 0.0377$, $wR_2 = 0.0798$	$R_1 = 0.0496$, $wR_2 = 0.1208$	$R_1 = 0.0511$, $wR_2 = 0.1202$
R indices (all data)	$R_1 = 0.0489$, $wR_2 = 0.0842$	$R_1 = 0.0743$, $wR_2 = 0.1265$	$R_1 = 0.0710$, $wR_2 = 0.1334$
Absolute structure parameter	0.02(5)		
Largest difference in peak and hole (e Å^{-3})	0.210 and −0.110	0.364 and −0.474	0.426 and −0.407

Table 2
Selected bond lengths (Å) and angles (°) for compounds **I**, **34** and **44**.

I		**34**		**44**	
C(1)–C(8A)	1.500(3)	P(1)–O(1)	1.483(16)	P(1)–O(1)	1.4914(15)
C(1)–N(2)	1.502(3)	P(1)–N(1)	1.687(19)	P(1)–N(1)	1.6846(17)
C(1)–C(9)	1.554(3)	P(1)–N(2)	1.616(19)	P(1)–N(2)	1.6218(18)
C(1)–H(1A)	0.980	P(1)–N(3)	1.620(2)	P(1)–N(3)	1.6208(18)
C(3)–N(2)	1.483(3)	O(2)–C(1)	1.212(2)	O(2)–C(1)	1.223(2)
N(2)–H(2A)	0.961	N(1)–C(1)	1.355(3)	O(3)–C(5)	1.370(3)
N(2)–H(2B)	0.920	N(1)–H(1N)	0.870	O(3)–C(8)	1.375(3)
C(3)–C(4)	1.514(4)	N(2)–C(11)	1.460(3)	O(4)–C(10)	1.367(3)
C(4)–C(4A)	1.493(4)	N(3)–C(4)	1.477(3)	O(4)–C(13)	1.371(3)
C(1′)–C(8′A)	1.520(4)	N(4)–C(3)	1.133(3)	N(1)–C(1)	1.356(3)
C(1′)–N(2′)	1.501(3)	C(4)–C(5)	1.496	N(1)–H(1A)	0.880
C(1′)–C(9′)	1.537(3)	C(4)–C(5′)	1.460(7)	N(2)–C(4)	1.467(3)
C(1′)–H(1′A)	0.980	C(5)–C(6)	1.3900	N(3)–C(9)	1.465(3)
C(3′)–N(2′)	1.489(3)	C(5′)–C(6′)	1.343(9)	N(4)–C(3)	1.149(3)
N(2′)–H(2′A)	0.996	C(5′)–C(10′)	1.345(10)	C(1)–C(2)	1.525(3)
C(8A)–C(1)–N(2)	112.10(19)	O(1)–P(1)–N(1)	106.00(9)	O(1)–P(1)–N(1)	105.72(9)
C(8A)–C(1)–C(9)	113.44(19)	O(1)–P(1)–N(2)	109.71(10)	O(1)–P(1)–N(2)	108.09(9)
N(2)–C(1)–C(9)	107.56(18)	O(1)–P(1)–N(3)	117.34(10)	O(1)–P(1)–N(3)	119.51(9)
C(8A)–C(1)–H(1A)	107.80	N(2)–P(1)–N(1)	113.04(10)	N(2)–P(1)–N(1)	114.33(9)
N(2)–C(1)–H(1A)	107.80	N(3)–P(1)–N(1)	103.16(10)	N(3)–P(1)–N(1)	102.54(9)
C(9)–C(1)–H(1A)	107.80	N(3)–P(1)–N(2)	107.58(10)	N(3)–P(1)–N(2)	106.89(9)
C(3)–N(2)–C(1)	113.22(18)	C(1)–N(1)–P(1)	125.01(14)	C(1)–N(1)–P(1)	123.40(14)
C(3)–N(2)–H(2A)	107.80	C(1)–N(1)–H(1N)	114.80	C(1)–N(1)–H(1A)	118.30
C(1)–N(2)–H(2A)	110.10	P(1)–N(1)–H(1N)	120.00	P(1)–N(1)–H(1A)	118.30
C(3)–N(2)–H(2B)	111.80	C(11)–N(2)–P(1)	128.27(15)	C(4)–N(2)–P(1)	129.36(15)
C(1)–N(2)–H(2B)	109.10	C(11)–N(2)–H(2N)	115.90	C(4)–N(2)–H(2A)	115.30
C(8′A)–C(1′)–N(2′)	110.93(18)	P(1)–N(2)–H(2N)	115.90	P(1)–N(2)–H(2A)	115.30
C(8′A)–C(1′)–C(9′)	113.20(2)	C(4)–N(3)–P(1)	121.41(15)	N(1)–C(1)–C(2)	115.53(17)
N(2′)–C(1′)–C(9′)	108.70(2)	C(4)–N(3)–H(3N)	114.30	O(2)–C(1)–C(2)	121.63(18)
C(8′A)–C(1′)–H(1′A)	107.90	P(1)–N(3)–H(3N)	123.40	O(2)–C(1)–N(1)	122.84(18)
N(2′)–C(1′)–H(1′A)	107.90	O(2)–C(1)–N(1)	123.70(2)	C(6)–C(5)–O(3)	109.90(2)
C(9′)–C(1′)–H(1′A)	107.90	O(2)–C(1)–C(2)	122.10(2)	C(11)–C(10)–O(4)	109.90(2)

ronment is nearly planar. In compound **34**, the angles C(1)–N(1)–P(1), C(1)–N(1)–H(1N) and P(1)–N(1)–H(1N) are 125.01(14), 114.8° and 120.0°, respectively, with an average of 119.94°. The sum of the surrounding angles around the N(2) and N(3) atoms

Table 3
Hydrogen bonds for compounds **I**, **34** and **44** (Å, °)

Compound	d(H···A)	d(D–H)	d(H···A)	d(D···A)	∠DHA
I	N(2′)–H(2′A)···Cl(1)#1	1.00	2.16	3.160(19)	178
	N(2)–H(2A)···Cl(1)#1	0.96	2.18	3.130(19)	172
	N(2)–H(2B)···Cl(2)#4	0.92	2.15	3.034(2)	160
	N(2′)–H(2′B)···Cl(2)#1	0.90	2.19	3.035(2)	155
34	N(1)–H(1N)···O(1)#5	0.87	1.97	2.833(2)	174
	N(2)–H(2N)···O(2)#3	0.86	2.17	2.946(2)	151
	N(3)–H(3N)···O(1)#2	0.87	2.33	3.178(3)	166
44	N(1)–H(1A)···O(1)#6	0.88	1.89	2.764(2)	174
	N(2)–H(2A)···O(2)#7	0.88	2.11	2.889(2)	147
	N(3)–H(3A)···O(1)#8	0.88	2.08	2.959(2)	177

Symmetry transformations used to generate equivalent atoms: (#1) x, y, z, (#2) $x+1, y, z$, (#3) $x-1, y, z$, (#4) $x+1, y-1, z$, (#5) $-x, -y+1, -z+2$, (#6) $-x, -y+1, -z+1$, (#7) $x-1, y, z$, (#8) $x+1, y, z$.

are 360.07° and 359.11°, respectively. Similar results were obtained for the nitrogen atoms in the structure of **44**, which indicate sp^2 hybridization for the nitrogen atoms, although because of the repulsion and steric effects, some angles were either greater or smaller than 120°. It is noticeable that the P═O and C═O bonds indicate an *anti* configuration with respect to each other in compounds **34** and **44**, which is in agreement with our previously reported results [17,18,25–27].

The two symmetrically independent molecules of **I** are connected to each other through two intermolecular N(2)–H(2A)···Cl(1) and N(2′)–H(2′A)···Cl(1) hydrogen bonds and each of these independent molecules is linked to its symmetrically independent molecules via intermolecular N(2)–H(2B)···Cl(2) and N(2′)–H(2′B)···Cl(2) hydrogen bonds. Considering the weak intermolecular C–H···O and C–H···Cl hydrogen bonds, this creates a three dimensional polymeric chain in the crystalline lattice. Intermolecular N(1)–H(1N)···O(1) hydrogen bonds between the two adjacent molecules in compound **34** create a non-centrosymmetric dimer (because of the disorder in one molecule, the dimer is not centrosymmetric). This dimer is connected to similar dimers by intermolecular N(2)–H(2N)···O(2) and N(3)–H(3N)···O(1) hydrogen bonds. Beside these H-bonds, there are also weak intermolecular hydrogen bonds such as C(16)–H(16A)···O(2), and all of them produce a three dimensional network. The intermolecular N(2)–H(2A)···O(2) and N(3)–H(3A)···O(1) hydrogen bonds in the structure of **44** connect the neighboring molecules to each other to construct a linear chain. The molecules in this polymeric chain are linked to other molecules through intermolecular N(1)–H(1A)···O(1) hydrogen bonds. Repetition of the H-bonds generates a one dimensional polymeric chain. If weak intermolecular C–H···O and C–H···N hydrogen bonds [like C(12)–H(12A)···O(2), C(2)–H(2B)···N(4) and C(13)–H(13A)···N(4)] are taken into account, a 3-D polymeric chain is obtained.

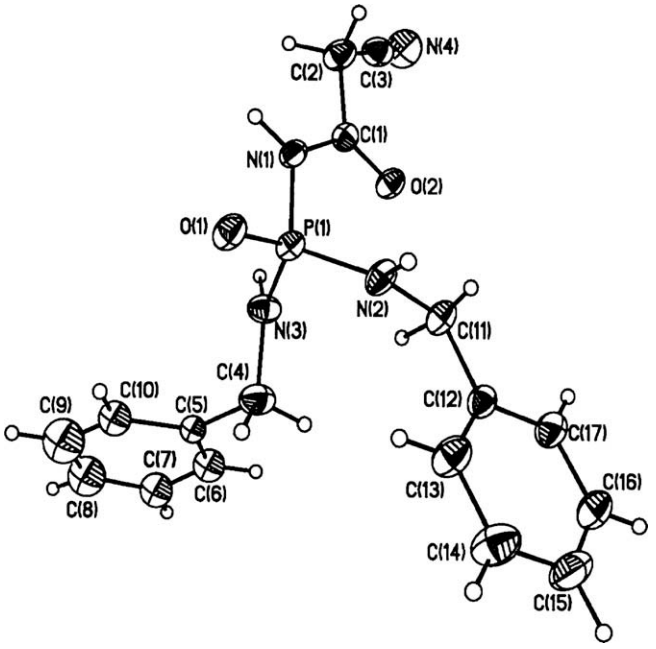


Fig. 2. Molecular structure and atom labelling scheme for C≡N–CH_2C(O)NH-P(O)($NHCH_2C_6H_5$)$_2$, compound **34** (30% probability ellipsoids).

4. Conclusion

Using PCl_5 and $POCl_3$ as starting materials, a number of novel phosphorus derivatives of bisphosphoramidates, phosphoramidates and phosphoric triamides were synthesized. The reaction of 4-aminobenzamide with PCl_5 in different molar ratios yielded different products, bisphosphoramides and phosphoric triamides. Furthermore, the interaction of $POCl_3$ with first-type aromatic

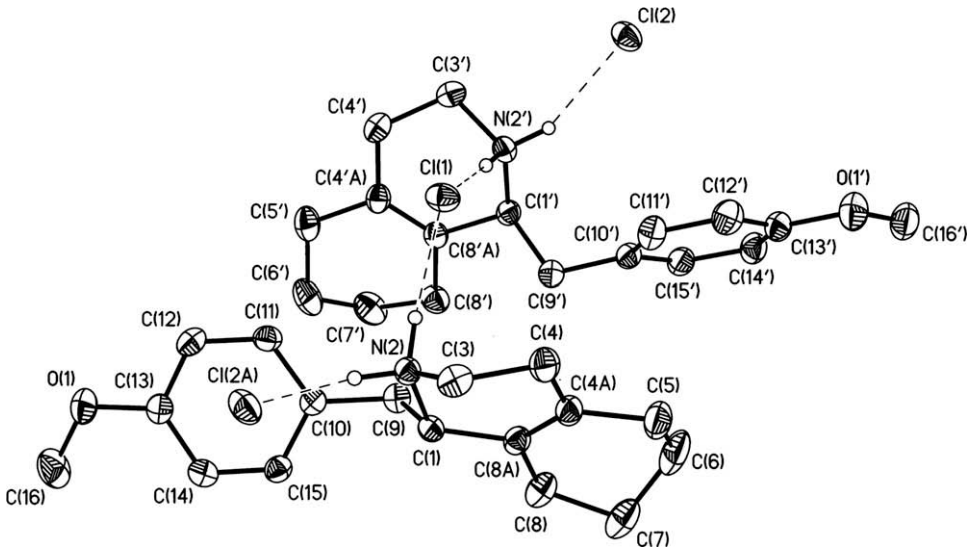


Fig. 1. Molecular structure and atom labelling scheme for 4-OCH_3–C_6H_4–CH_2–C_9H_{13}–NH_2Cl, compound **I** (50% probability ellipsoids).

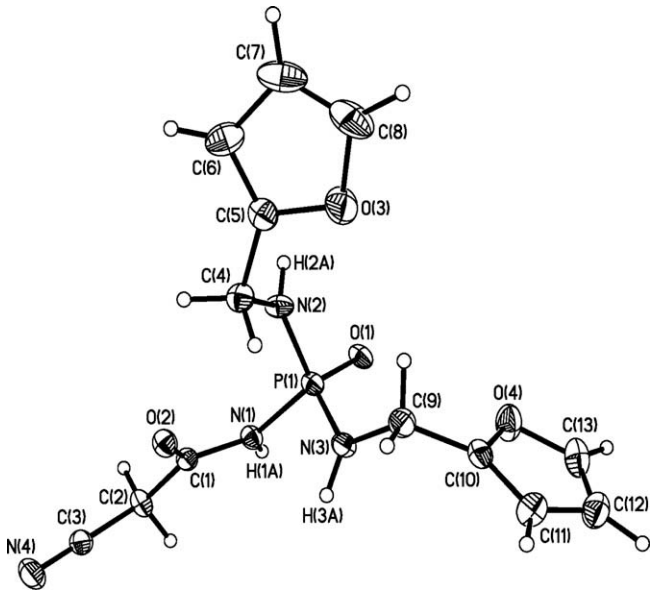


Fig. 3. Molecular structure and atom labelling scheme for C≡N–CH_2C(O)NH-P(O)($NHCH_2C_4H_3O)_2$, compound **44** (50% probability ellipsoids) that shows two conformers in the crystal lattice.

amines gave bisphosphoramidates with a P–N–P linkage that demonstrated $^2J(P,P) \approx 20.0$ Hz in the ^{31}P NMR spectra. Indeed, two simple one-pot pathways are presented here for the synthesis of the new bisphosphoramidates that are, to our knowledge, the first examples of bisphosphoramidates that have been obtained so far. The X-ray crystal structures of compounds **I** (4-OCH_3–C_6H_4–CH_2–C_9H_{13}–NH_2Cl), **34** and **44** were further investigated and all of these structures displayed three dimensional polymeric chains through strong- and weak hydrogen bonds. The presence of chiral amino-acidester moieties in the phosphoric triamides lead to chiral molecules which showed two sets of signals for the two groups.

Acknowledgement

We wish to thank the Research Council of Tarbiat Modares University for the financial support of this work.

Appendix A. Supplementary data

CCDC 604118, 604115 and 678082 contain the supplementary crystallographic data for ($C_{17}H_{24}ClNO$), ($C_{17}H_{19}N_4O_2P$) and ($C_{13}H_{15}N_4O_4P$). These data can be obtained free of charge via http://www.ccdc.cam.ac.uk/conts/retrieving.html, or from the Cambridge Crystallographic Data Centre, 12 Union Road, Cambridge CB2 1EZ, UK; fax: (+44) 1223-336-033; or e-mail: deposit@ccdc.cam.ac.uk. Crystallographic data for the structures of **I**, **34** and **44**. Supplementary data associated with this article can be found, in the online version, at doi:10.1016/j.poly.2008.10.057.

References

[1] N.-H. Nam, Y. Kim, Y.-J. You, D.-H. Hong, H.-M. Kim, B.-Z. Ahn, Bioorg. Med. Chem. 11 (2005) 1021.
[2] T.K. Venkatachalam, P. Samuel, F.M. Ucken, Bioorg. Med. Chem. 13 (2005) 1763.
[3] C. Mc Guigan, J.-C. Thiery, F. Daverio, W.G. Jiang, G. Davis, M. Mason, Bioorg. Med. Chem. 13 (2005) 3219.
[4] A.-L. Villard, G. Coussot, I. Lefebvre, P. Augustijns, A.-M. Aubertin, G. Gosselin, S. Peyrottes, C. Périgaud, Bioorg. Med. Chem. 16 (2008) 7321.
[5] I. Ghesner, A. Soran, C. Silvestru, J.E. Drake, Polyhedron 22 (2003) 3395.
[6] M. Ghesner, A. Silvestru, C. Silvestru, J.E. Drake, M.B. Hursthouse, M.E. Light, Inorg. Chim. Acta 358 (2005) 3724.
[7] C. Silvestru, J.E. Drake, Coord. Chem. Rev. 223 (2001) 117.
[8] K. He, Z. Zhou, L. Wang, K. Li, G. Zhao, Q. Zhao, C. Tang, Tetrahedron 60 (2004) 10505.
[9] M.S. Balakrishna, S.S. Krishnamurthy, H. Manohar, Organometallics 10 (1991) 2522.
[10] O. Bumbu, A. Silvestru, C. Silvestru, J.E. Drake, M.B. Hursthouse, M.E. Light, J. Organomet. Chem. 687 (2003) 118.
[11] I. Ghesner, L. Opris, G. Balazs, H.J. Breunig, J.E. Drake, A. Silvestru, C. Silvestru, J. Organomet. Chem. 642 (2002) 113.
[12] S.E. Denmark, J. Fu, M.J. Lawler, J. Org. Chem. 71 (2006) 1523.
[13] P.K. Baker, M.G.B. Drew, D.S. Moore, J. Organomet. Chem. 664 (2002) 45.
[14] T. Appleby, J.D. Woollins, Coord. Chem. Rev. 235 (2002) 121.
[15] E.A. Trush, V.A. Ovchynnikov, K.V. Domasevitch, J.S. Wiatekkozlowska, V.Y. Zub, V.M. Amirkhanov, Z. Naturforsch. 57b (2002) 746.
[16] V.V. Skopenko, V.M. Amirkhanov, T. Yu. Silva, I.S. Vasilchenko, E.L. Anpilov, A.D. Garnovski, Russ. Chem. Rev. 73 (2004) 737.
[17] K. Gholivand, Z. Shariatinia, M. Pourayoubi, Polyhedron 25 (2006) 711.
[18] K. Gholivand, Z. Shariatinia, J. Organomet. Chem. 691 (2006) 4215.
[19] T.L. Lassiter, R.S. Marshall, L.C. Jackson, D.L. Hunter, J.T. Vu, S. Padilla, Toxicology 186 (2003) 241.
[20] O.I. Guliy, O.V. Ignatov, O.E. Makarov, V.V. Ignatov, Biosens. Bioelectron. 18 (2003) 1005.
[21] K. Kaur, S.A. Adediran, J.K. Lan Martin, R.F. Pratt, Biochemistry 42 (2003) 1529.
[22] K. Gholivand, Z. Shariatinia, K. Khajeh, H. Naderi-Manesh, J. Enzyme Inhib. Med. Chem. 21 (2006) 31.
[23] (a) K. Gholivand, C.O. Della Vedovab, A. Anaraki Firooza, A. Madani Alizadehgana, M.C. Michelinic, R. Pis Diez, J. Mol. Struct. 750 (2005) 64; (b) K. Gholivand, Z. Shariatinia, M. Pourayoubi, Z. Naturforsch. 60b (2005) 67.
[24] M.A.M. Forgeron, M. Gee, R.E. Wasylishen, J. Phys. Chem. A 108 (2004) 4895.
[25] K. Gholivand, M. Pourayoubi, Z. Shariatinia, H. Mostaanzadeh, Polyhedron 24 (2005) 655.
[26] K. Gholivand, Z. Shariatinia, Struct. Chem. 18 (2007) 95.
[27] K. Gholivand, Z. Shariatinia, M. Pourayoubi, Z. Anorg. Allg. Chem. 631 (2005) 961.
[28] Bruker, Programs APEX II, Version 2.0-1; SAINT, Version 7.23A; SADABS, Version 2004/1; XPREP, Version 2005/2; SHELXTL, Version 6.1. Bruker AXS Inc., Madison, WI, USA, 2005.
[29] Siemens P3 and XDISK. Release 4.1. Siemens AXS, Madison, Wisconsin, USA, 1989.
[30] Bruker, SMART. Bruker Molecular Analysis Research Tool, v. 5.059. Bruker AXS, Madison, Wisconsin, USA, 1998.
[31] G.M. Sheldrick, Programs SHELXS97 (crystal structure solution) and SHELXL97 (crystal structure refinement), University of Gottingen, Germany, 1997.
[32] G.M. Sheldrick, SADABS v. 2.01, Bruker/Siemens area detector absorption correction program. Bruker AXS, Madison, WI, USA, 1998.
[33] H.-O. Kalinowski, S. Berger, S. Braun, Carbon-13 NMR Spectroscopy, Wiley, 1991, p. 527.
[34] R.L. Keiter, J.W. Benson, E.A. Keiter, T.A. Harris, M.W. Hayner, L.L. Mosimann, E.E. Karch, C.A. Boecker, D.M. Olson, J. VanderVeen, D.E. Brandt, Organometallics 16 (1997) 2246.
[35] L. Aluisio, B. Lord, A.J. Barbier, I.C. Fraser, S.J. Wilson, J. Boggs, L.K. Dvorak, M.A. Letavic, B.E. Maryanoff, N.I. Carruthers, P. Bonaventure, T.W. Lovenberg, Eur. J. Pharmacol. 587 (2008) 141.
[36] N. Vasdev, F.J. LaRonde, J.R. Woodgett, A. Garcia, E.A. Rubie, J.H. Meyer, S. Houle, A.A. Wilson, Bioorg. Med. Chem. 16 (2008) 5277.
[37] X.-H. Liu, P. Cui, B.-A. Song, P.S. Bhadury, H.-L. Zhu, S.-F. Wang, Bioorg. Med. Chem. 16 (2008) 4075.
[38] E.A.V. Ebsworth, D.W.H. Rankin, S. Cradock, Structural Methods in Inorganic Chemistry, 2nd ed., Blackwell Scientific Publication, 1991.
[39] K. Gholivand, C.O. Della Védova, M.F. Erben, H.R. Mahzouni, Z. Shariatinia, S. Amiri, J. Mol. Struct. 874 (2008) 178.
[40] D.E.C. Corbridge, Phosphorus, an Outline of its Chemistry, Biochemistry and Technology, 5th ed., Elsevier, The Netherlands, 1995, p. 55.

Polyhedron 28 (2009) 322–326

Contents lists available at ScienceDirect

Polyhedron

journal homepage: www.elsevier.com/locate/poly

Heterobimetallic Re–Pd, Re–Au and Re–Cu complexes derived from diphenylphosphino cyrhetrene: Synthesis and X-ray structure

Diego Sierra [a], Andres Muñoz [a], Fernando Godoy [a], A. Hugo Klahn [a,*], Andres Ibañez [b], M. Teresa Garland [b], Mauricio Fuentealba [b]

[a] Instituto de Quimica, Pontificia Universidad Catolica de Valparaíso, Casilla 4059, Valparaíso, Chile
[b] CIMAT, Facultad de Ciencias Físicas y Matemáticas, Universidad de Chile, Casilla 653, Santiago, Chile

ARTICLE INFO

Article history:
Received 3 September 2008
Accepted 27 October 2008
Available online 4 December 2008

Keywords:
Cyrhetrenyldiphenylphosphine ligand
Palladium
Gold
Copper
Complexes

ABSTRACT

Diphenylphosphinecyrhetrene ligand (η^5-$C_5H_4PPh_2$)$Re(CO)_3$ (**1**) reacts with 1 equiv. of $PdCl_2(NCPh)_2$ to form, after workup, the square-planar *trans*-[(η^5-$C_5H_4PPh_2$)$Re(CO)_3$]$PdCl_2$(NCMe) (**2**). Similarly, reaction of **1** with (tetrahydrothiophene)AuCl produces, in excellent yield, the bimetallic complex [(η^5-$C_5H_4PPh_2$)$Re(CO)_3$]AuCl (**3**) with a linear P–Au–Cl moiety. From the reaction of 2 equiv. of **1** with $CuBr(SMe_2)$ the planar-trigonal complex [(η^5-$C_5H_4PPh_2$)$Re(CO)_3$]$_2$CuBr (**4**) was obtained. ^{31}P NMR and X-ray crystallography demonstrate, for the three cases, that (η^5-$C_5H_4PPh_2$)$Re(CO)_3$ acts as a monodentate ligand. The structural parameters of the bimetallic complexes are compared with related diphenylphosphinoferrocene metal complexes, described in the literature.

© 2008 Elsevier Ltd. All rights reserved.

1. Introduction

The diphenylphosphinocyclopentadienyl group η^5-coordinated to metal fragments has proved to be a versatile unsymmetrical mono- or bidentate ligand to form homo- and heterobimetallic complexes [1–3]. Complexes of this type include those which have two metal centers of a very different nature (for example, early and late transition metals) held together through a bridging ligand [4,5] or both a bridging ligand and a metal–metal bond [6–9]. The most common synthetic approach to form simple bridging bimetallic compounds has been to bind first the cyclopentadienyl moiety to one of the transition metals, thus producing a metallo ligand derivative, which may then act as a monodentate phosphorous ligand [4,5]. Several examples of metallo ligands of the type (η^5-$C_5H_4PPh_2$)MLn, M = Fe, Ti, Zr, Co, Mo, Rh, etc. have been used to prepare a large number of bimetallic complexes with interesting chemical, electrochemical and catalytic properties [1,2,10]. Nevertheless, examples of group 7 metallo ligands remain relatively unexplored. (η^5-$C_5H_4PPh_2$)$M(CO)_3$ M = Mn and Re, were first reported by Rausch and Spink in 1989 [11] by reaction of diphenylphosphinocyclopentadienylthallium with $BrM(CO)_5$. Much more recently, Gladysz and co-workers [12] prepared (η^5-$C_5H_4PR_2$)$Re(CO)_3$, R = Ph and *tert*-Bu, by direct reaction of (CpLi)$Re(CO)_3$ with PR_2Cl. Although, the phenyl derivative was used in a palladium-base catalytic system for Suzuki coupling reactions, the bimetallic Re–Pd complex, which is probably involved in the catalytic system, was neither isolated nor characterized *in situ*. The lack of information about the coordination chemistry of (η^5-$C_5H_4PPh_2$)$Re(CO)_3$ (**1**) and the unknown structural data for bimetallic complexes containing this metallo ligand, encouraged us to prepare and fully characterize by spectroscopic and crystallographic techniques the square-planar *trans*-[(η^5-$C_5H_4PPh_2$)$Re(CO)_3$]$PdCl_2$(NCMe) (**2**), linear [(η^5-$C_5H_4PPh_2$)$Re(CO)_3$]AuCl (**3**) and trigonal [(η^5-$C_5H_4PPh_2$)$Re(CO)_3$]$_2$CuBr (**4**) complexes.

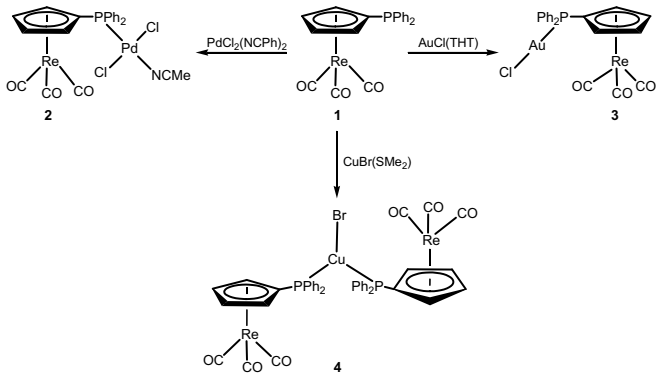
2. Results and discussion

The preparation of diphenylphosphinocyclopentadienyl rhenium tricarbonyl (**1**) was carried out according to the Gladysz procedure [12]. Bimetallic complex (**2**) is formed by the reaction of (η^5-$C_5H_4PPh_2$)$Re(CO)_3$ with commercially available $PdCl_2(NCPh)_2$ (1:1 molar ratio) in $CHCl_3$ under reflux for 4 h. Upon cooling the mixture to room temperature, a red solid is formed which was slightly soluble in chloroform but soluble in MeCN. Crystallization from MeCN–Et_2O yielded orange-red microcrystals of **2** (Scheme 1).

This reaction probably involves in a first step, the formation of the chloro-bridged dimeric complex [$Pd(\mu$-Cl)Cl(η^5-$C_5H_4PPh_2$)-$Re(CO)_3$]$_2$ which then, in the crystallization step, reacts with MeCN to form the observed product. We were unable to characterize the red solid in solution; nevertheless, the elemental analysis is consistent with the proposed formula. Similar palladium chloro-bridged

* Corresponding author. Tel.: +56 32 2273174; fax: +56 32 2273422.
E-mail address: hklahn@ucv.cl (A. Hugo Klahn).

0277-5387/$ - see front matter © 2008 Elsevier Ltd. All rights reserved.
doi:10.1016/j.poly.2008.10.038



Scheme 1.

complexes containing the phosphinoferrocene ligand have been reported [13–15].

Compound **2** is air and moisture stable and moderately soluble in polar organic solvents and insoluble in non polar solvents. The elemental analysis of this compound is in good agreement with the proposed structure. The ^{1}H NMR spectrum (in CD_3CN) of **2** showed in addition to the resonances of the metallo ligand, the presence of coordinated MeCN as a singlet at δ 1.98. The ν(CN) absorption band observed at 2297 cm^{-1} (KBr disc) in the IR spectrum is further evidence for coordinated MeCN. A single resonance in the ^{31}P NMR spectrum indicates a single phosphorous environment due to the presence of the metallo ligand. This resonance is shifted to lower field when compared to the free ligand ($\Delta\delta$ = 38.3). Similar shift have been observed in analogous palladium complexes possessing the diphenylphosphinoferrocene ligand [14].

The Re–Au bimetallic complex (**3**) was formed by reacting the ligand **1** with the recommended gold precursor chloro(tetrahydrothiophene)gold(I) [16] in CH_2Cl_2, at room temperature (Scheme 1). It was isolated as white crystals in 90% yield. The mass spectrum and elemental analysis of this compound agrees well with the presence of a single cyrhetrenylphosphine.

The ^{1}H NMR spectrum of this complex showed, apart from the multiplet from the phenyl protons, the signal of the cyrhetrenyl unit as two multiplets for the cyclopentadienyl protons ring. Like the previous case, the phosphorous resonance (observed at δ 25.7) in the ^{31}P NMR spectrum is shifted to lower field upon coordination to Au(I). $\Delta\delta$ = 42.7, this value is comparable to those observed in diphenylphosphinoferrocenes coordinated to the Au–Cl fragment [17,18].

With regard to the complex (**4**) and considering that the reaction of copper(I) halide, with tertiary organo-phosphines gives a wide range of products of variable stoichiometry and molecular structure [19], we decided to carry out the reaction of $CuBr(SMe_2)$ with an excess of ligand **1** (1:4 molar ratio) (Scheme 1). After overnight stirring (in CH_2Cl_2 at room temperature) followed by solvent evaporation, a white solid was obtained, which showed two resonances in the ^{31}P NMR spectrum (δ −17.0 and δ *−13.5)* due to the presence of uncoordinated **1** and a new compound. Column chromatography allowed the separation of the two compounds; a mixture of CH_2Cl_2/hexane (1:1) moved unreacted **1** whereas the new complex was eluted with acetone. The solid obtained after evaporation of acetone showed the same spectroscopic parameters as the one isolated from the direct reaction of **1** and $CuBr(SMe_2)$ in a 2:1 molar ratio. From the latter procedure, complex **4,** was isolated as white crystals in 81% yield, after crystallization from CH_2Cl_2/hexane. The elemental analysis of **4** is in good agreement with the proposed structure. The ^{31}P NMR spectrum of **4** is consistent with the presence of a single compound in solution (δ −13.5). The small downfield shift from that of the parent ligand ($\Delta\delta$ = 3.5) is comparable to those found in other three-coordinated complexes of copper(I) [20,21].

3. X-ray crystallography

The numbering scheme of the bimetallic Re–Pd complex **2** is presented in Fig. 1. Crystallographic data are presented in Table 1, whereas selected bond lengths and angles are shown in Table 2. In complex **2** the palladium atom exhibits a slightly distorted square-planar geometry which is supported by (i) the displacement of palladium atom by 0.06 Å away from the $PNCl_2$ least-squares plane and (ii) the sum of the four angles around the palladium atom which is 361°. The phosphine and the acetonitrile ligand are found in a *trans* orientation with angles P(1)–Pd–N(1) 175.71°(15), Cl(1)–Pd–Cl(2) 171.25°(9). In the phosphine ligand the phosphorous atom is tetrahedrally surrounded by the two phenyl rings (P–C(14) = 1.808(5) Å and P–C(15) = 1.827(6) Å), and the cyrhetrenyl ligand (P–C(1) = 1.807(5) Å). The latter distance compares well to 1.803(3) Å found in (*trans*-[PdMeCl(PPh_2Fc)$_2$], (PPh_2Fc = ferrocenyldiphenylphosphine) [14]. The bond length Pd–P (2.2217(13) Å) is quite short when compare to the similar distance measured in related phosphinoferrocene complexes (*trans*-[PdMeCl(PPh_2Fc)$_2$], Pd–P = 2.3328(10) Å [14] *trans*-[$PdCl_2$-(PPh_3)$_2$] Pd–P = 2.337(1) Å [22] but it resembles to the one observed in the dimer *trans*-[Pd(μ-Cl)Me(PPh_2Fc)]$_2$ (avg. 2.223(9) Å) [13]. The Pd–N bond length (2.085(5) Å) compares well with those obtained for other square-planar Pd(II) complexes containing coordinated acetonitrile with a *trans* P–Pd–N moiety, such as (MeCN)$PdCl_2$(μ-dpmp)$PdCl_2$ [23].

The C–P–Pd angles are all larger than the ideal 109.5°, and range from 110.48(17)° to 118.25(18)°, while all C–P–C are smaller than expected for normal tetrahedra, i.e. 101.3(2)–104.5(2)°. Similar deviation has been reported for related Pd-complexes and explained in term of the valence shell electron pair repulsion theory [14,24].

The molecular structure of complex **3** is shown in Fig. 2 and selected bond distances and angles are presented in Table 2. Taking into account the gold(I) environment this compound exhibits a very regular linear geometry, with a P–Au–Cl angle of 178.24(4)°

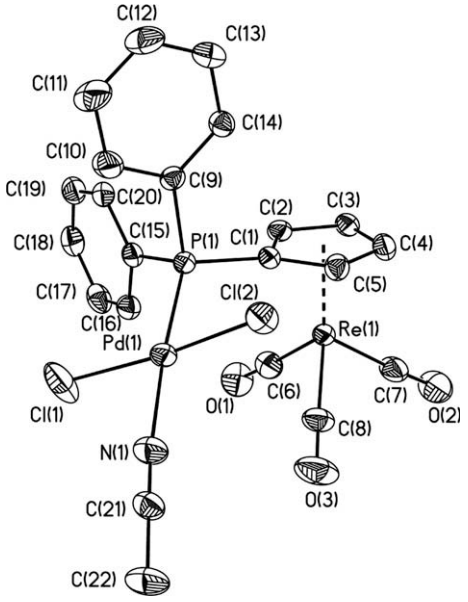


Fig. 1. ORTEP's plots of complex **2** with displacement ellipsoids at the 30% probability level.

Table 1
Summary of crystallographic data and structure refinement for **2**, **3** and **4**.

	2	**3**	**4**
Empirical formula	$C_{22}H_{17}Cl_2NO_3PPdRe$	$C_{20}H_{14}AuClO_3PRe$	$C_{41}H_{30}BrCl_2CuO_6P_2Re2$
Formula mass (g mol^{-1})	737.84	751.90	1267.34
Collection T (K)	298(2)	150(2)	150(2)
Crystal system	monoclinic	monoclinic	monoclinic
Space group	$P2_1/c$	$P2_1/c$	$C2/c$
a (Å)	14.3454(11)	9.414(3)	15.8267(7)
b (Å)	8.9720(7)	22.808(7)	17.8010(7)
c (Å)	18.8294(15)	10.359(3)	14.8485(7)
β (°)	98.0260(10)	117.03	97.1780(10)
V (Å^3)	2399.7(3)	1981.3(10)	4150.5(3)
Z	4	4	4
D_{calc} (g cm^{-3})	2.042	2.521	2.028
Crystal size (mm)	0.29 × 0.152 × 0.13	0.20 × 0.16 × 0.10	0.43 × 0.25 × 0.17
F(000)	1400	1376	2408
Absorption coefficient (mm^{-1})	semi-empirical from equivalents	full-matrix least-squares on F^2	semi-empirical from equivalents
Maximum and minimum transmission	0.452 and 0.305	0.2653 and 0.0155	0.278 and 0.155
θ Range (°)	2.18–28.08	1.79–27.90	1.73–27.81
Range h, k, l	−18/18, −11/11, −23/24	−11/11, −28/29, −13/13	−20/20, −22/23, −19/18
Reflections collected	19649	20673	17275
Independent reflections (R_{int})	5417 (0.0365)	4432 (0.1052)	4730 (0.0369)
Data/restraints/parameters	5417/0/281	4432/0/244	4730/0/250
Final R indices [$I > 2\sigma(I)$]	R_1 = 0.0385, wR_2 = 0.0845	R_1 = 0.0261, wR_2 = 0.0655	R_1 = 0.0319, wR_2 = 0.0849
R indices (all data)	R_1 = 0.0478, wR_2 = 0.0885	R_1 = 0.0284, wR_2 = 0.0667	R_1 = 0.0379, wR_2 = 0.0889
Goodness of fit on F^2	1.084	1.067	1.061
Largest difference in peak and hole (e A^{-3})	1.729 and −0.554	1.657 and −2.174	2.662 and −1.396

Table 2
Select bond lengths (Å) and bond angles (°) for **2**, **3** and **4**.

	2	**3**	**4**
Bond distances			
Re–C(6)	1.909(7)	1.918(5)	1.913(5)
Re–C(7)	1.914(7)	1.941(5)	1.918(5)
Re–C(8)	1.916(6)	1.895(5)	1.923(5)
Re–Cp(centroid)	1.952	1.956	1.961
C(1)–P(1)	1.807(5)	1.791(4)	1.802(4)
M–P(1)	2.2217(13)	2.2214(13)	2.2346(11)
M–X(1)	2.2734(19)	2.2798(13)	2.3416(10)
M–X(2)	2.2952(15)		
M–N	2.086(5)		
Bond angles			
Re–C(6)–O(1)	177.0(6)	177.5(4)	176.8(5)
Re–C(7)–O(2)	177.0(6)	176.6(4)	177.8(5)
Re–C(8)–O(3)	176.5(6)	177.5(4)	178.4(5)
C(1)–P(1)–M	116.56(17)	112.03(16)	114.44(15)
C(9)–P(1)–C(15)	110.40(16)	107.7(2)	103.7(2)
P(1)–M–X(1)	93.56(6)	178.24(4)	119.87(3)
P(1)–M–X(2)	88.36(5)		
P(1)–M–N(1)	175.67(14)		
P(1)–M–P(1)#			120.26(6)

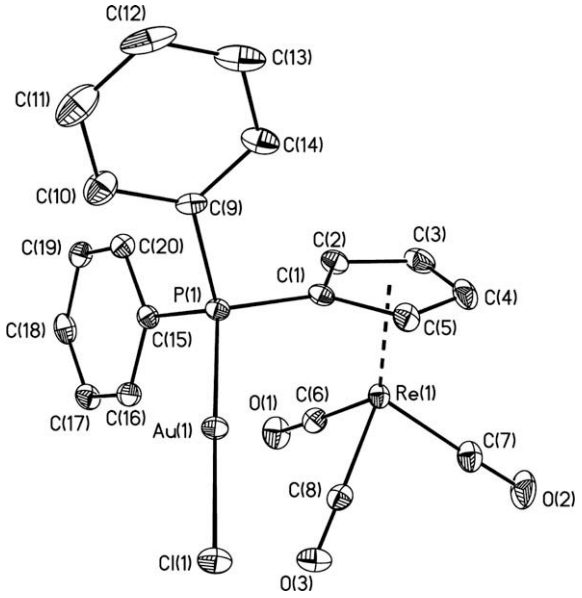


Fig. 2. ORTEP's plots of complex **3** with displacement ellipsoids at the 30% probability level.

which is slightly larger to those found in related ferrocenyl phosphine derivatives, for example, 177.12(10)° in AuCl(PPh$_2$Fc), [17] 176.1(1)° in AuCl(PPhFc$_2$) [25] and 176.01(7)° in AuCl(PPh$_2$CH$_2$Fc) [26]. The Au–Cl and Au–P bond distances of 2.2798(13) Å and 2.2214(13) Å are similar to the ones measured in AuCl(PPh$_2$Fc) and AuCl(PPhFc$_2$) [17,25]. The shortest gold–gold distance in the lattice is 6.640 Å, which excludes the possibility of any bonding interaction between gold atoms.

Crystals of complex **4** were obtained from a of CH$_2$Cl$_2$/hexane mixture (1:5) at room temperature. A view of the molecular structure is presented in Fig. 3 with the relevant interatomic distances and angles summarized in Table 2. The coordination geometry about the copper atom is almost idealized trigonal planar according to (i) the negligible displacement of copper atom away from the P$_2$Br plane and (ii) the sum of the three angles around the copper atom which is 360°. These two last observations are consequences of symmetry operator (C_2 axis) in the Cu–Br bond. The bulky cyrhetrenyl groups adopt an *anti* conformation respect to the trigonal plane. The Cu–Br distance of 2.3416(10) Å is comparable to those observed in other three-coordinated copper(I) compounds [20,21,27]. The Cu–P distance of 2.2346(11) Å is somewhat shorter than that measured previously in copper(I) bromide complexes containing tertiary organo-phosphines [20,21,27]. Within the cyrhetrenyl group the average Re–Cp (centroid) and Re–C(O) distances and Re–C–O angles are comparable to the one observed in complexes **2** and **3**, and are also concordant with the corresponding values reported for other complexes containing the cyrhetrenyl group [28–30].

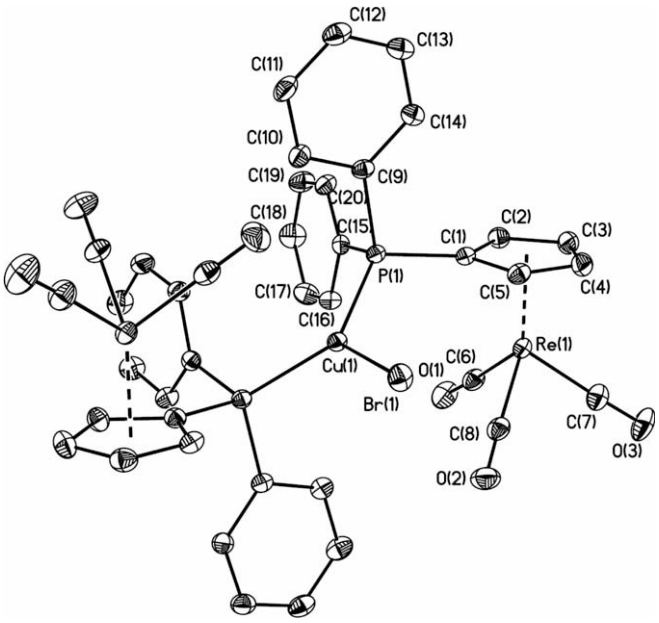


Fig. 3. ORTEP's plots of complex **4** with displacement ellipsoids at the 30% probability level.

4. Experimental

All reactions were carried out under nitrogen atmosphere using standard Schlenk techniques. Solvents were purified as follow: hexane and tetrahydrofuran by distillation from sodium/benzophenone ketyl; dichloromethane, chloroform and acetonitrile by distillation from P_2O_5. $PdCl_2(NCPh)_2$ and $CuBr(SMe_2)$ (Aldrich) were use as received. $(\eta^5\text{-}C_5H_4PPh_2)Re(CO)_3$ (**1**) [12] and (tht)AuCl (tht = tetrahydrothiophene) [16] were prepared following published procedures. Infrared spectra were recorded with a Perkin–Elmer FT-IR Spectrum One spectrophotometer. NMR spectra were recorded with a Bruker Avance 400 spectrometer. ^1H NMR chemical shifts were referenced using the chemicals shifts of residual solvent resonances, and $^{31}P\{^1H\}$NMR chemical shifts were referenced to 85% H_3PO_4 as external standard. The mass spectrum of **3** was obtained on a Thermo-Finnigan MAT 900XP, at the Facultad de Ciencias Químicas y Farmacéuticas, Universidad de Chile.

4.1. trans-[(η^5-$C_5H_4PPh_2$)Re(CO)$_3$]PdCl$_2$(NCMe) (**2**)

To 60 mg (0.116 mmol) of $(\eta^5\text{-}C_5H_4PPh_2)Re(CO)_3$ (**1**) dissolved in 15 mL of chloroform were added 44 mg (0.115 mmol) of solid $PdCl_2(NCPh)_2$ and the mixture was refluxed for 4 h. After cooling at room temperature a red precipitate was formed, this was filtered out and washed with chloroform. The elemental analysis of this material reveals a dimeric nature (*Anal.* Calc. for $[C_{20}H_{14}O_3PCl_2\text{-}RePd]_2 \cdot CHCl_3$: C, 32.52; H, 1.91. Found: C, 32,49; H, 1.89%). Crystallization from acetonitrile/diethylether (1:3) yielded orange-red microcrystals (suitable for analysis of X-ray diffraction) of **2** (62 mg, 0,084 mmol, 73%).

IR (cm^{-1}, CH_3CN) $\nu_{(CO)}$ 2029 (s); 1936 (vs). IR (cm^{-1}, KBr) $\nu_{(CN)}$ 2297 $\nu_{(CO)}$ 2032 (s); 1943 (vs); 1933 (vs). ^1H NMR (CD_3CN) δ: 1.98 (s, 3H, C*H*$_3$CN), 5.60 (m, 2H, C_5H_4), 5.81 (m, 2H, C_5H_4), 7.50–7.74 (m, 10H, C_6H_5). $^{31}P\{^1H\}$ NMR (CD_3CN) δ: 21,3 (s, *P*Ph$_2$). Elemental *Anal.* Calc. for $C_{22}H_{17}O_3NPCl_2RePd$: C, 35.87; H, 2.31. Found: C, 35.79; H, 2.30%.

4.2. [(η^5-$C_5H_4PPh_2$)Re(CO)$_3$]AuCl (**3**)

To a solution of **1** (100 mg, 0.193 mmol) dissolved in 10 mL of CH_2Cl_2 were slowly added 61 mg (0.193 mmol) of (tht)AuCl dissolved in 5 mL of CH_2Cl_2. The transparent mixture was stirred at room temperature for 4 h. Solvent was pumped off and the colorless oil produced was crystallized from CH_2Cl_2/hexane (1.5) to give white crystals of **3** (130 mg, 0.173 mmol, 90%).

IR (cm^{-1}, CH_2Cl_2) $\nu_{(CO)}$ 2032 (s); 1942 (vs). ^1H NMR ($CDCl_3$) δ: 5,56 (m, 2H, C_5H_4), 5,69 (m, 2H, C_5H_4), 7.48–7.62 (m, 10H, C_6H_5). $^{31}P\{^1H\}$ NMR ($CDCl_3$) δ: 25.7 (s, *P*Ph$_2$). Mass spectrum (^{187}Re and ^{35}Cl) *m*/*z*: 752 [M^+], 520 [M^+−AuCl], 492 [M^+−AuCl−CO], 435 [M^+−AuCl−3CO]. Elemental *Anal.* Calc. for $C_{20}H_{14}O_3PClReAu$: C, 31.87; H, 1.86. Found: C, 31.92; H, 1.90%.

4.3. [(η^5-$C_5H_4PPh_2$)Re(CO)$_3$]$_2$CuBr (**4**)

To a solution of ligand **1** (120 mg, 0.231 mmol) in 15 mL of CH_2Cl_2 were added 24 mg (0.115 mmol) of solid $CuBr(Sme_2)$. The pale purple suspension formed was stirred overnight at room temperature. After this time the mixture became a colorless solution. Solvent evaporation to dryness produced a white solid which was crystallized from CH_2Cl_2/hexane (1:5) generating transparent crystals of complex **4** (112 mg, 0.095 mmol, 81%).

IR (cm^{-1}, CH_2Cl_2) $\nu_{(CO)}$ 2028 (s); 1933 (vs). ^1H NMR ($CDCl_3$) δ: 5.36 (broad signal, 2H, C_5H_4), 5.86 (broad signal, 2H, C_5H_4), 7.28–7.40 (m, 10H, C_6H_5). $^{31}P\{^1H\}$ NMR ($CDCl_3$) δ: −13.5 (broad signal, *P*Ph$_2$). Elemental *Anal.* Calc. for $C_{40}H_{28}O_6P_2BrReCu$: C, 40.54; H, 2.36. Found: C, 40.39; H, 2.35.

4.4. X-ray crystal structure determination of complexes **2**, 3 and **4**

Single crystals of complexes **2**, **3** and **4**, obtained as mentioned above, were mounted on the tip of a glass fiber in a random orientation. Intensity data were collected on a Bruker Smart Apex diffractometer equipped with a bidimensional CCD detector using graphite monochromated Mo Kα radiation (λ = 0.71073 Å). Semi-empirical corrections, via ψ-scans, were applied for absorption for complexes **2** and **3,** and face indexing absorption correction was applied to complex **4**. The diffraction frames were integrated using the SAINT package [31] and corrected for absorption with XPREP in SHELXTL-PC [32] and SADABS [33]. The structures were solved using XS in SHELXTL-PC [32] by direct methods and completed (non-H atoms) by difference Fourier techniques. Refinement was performed by the full-matrix least-squares method based on F^2. All non-hydrogen atoms were anisotropically refined. Hydrogen atoms were placed in their calculated positions, assigned fixed isotropic thermal parameters and allowed to ride on their respective parent atoms. A summary of the data collection and structure refinement parameters is given in Table 1. ORTEP plots of complexes **2**, **3** and **4** with displacement ellipsoids at the 30% probability level were generated with XP in SHELXTL-PC [32].

Acknowledgements

A.H.K. acknowledges FONDECYT (Project 1060487) and D.I. Pontificia Universidad Catolica de Valparaiso. D.S. acknowledges MECESUP and FONDECYT for a Doctoral scholarship. We also appreciate the financial support of MECESUP (Project UCH 0116) for a MS instrument. The loan of NH_4ReO_4 from MOLYMET-Chile is also much appreciated.

Appendix A. Supplementary data

CCDC 692241, 692242 and 692243 contain the supplementary crystallographic data for complexes **2, 3** and **4**. These data can be

obtained free of charge via http://www.ccdc.cam.ac.uk/conts/retrieving.html, or from the Cambridge Crystallographic Data Centre, 12 Union Road, Cambridge CB2 1EZ, UK; fax: (+44) 1223-336-033; or e-mail: deposit@ccdc.cam.ac.uk. Supplementary data associated with this article can be found, in the online version, at doi:10.1016/j.poly.2008.10.038.

References

[1] M. Herberhold, Ferrocene Compounds Containing Heteroelements, Ferrocenes: Homogeneous Catalysis-Organic Synthesis-Materials Science, VCH, Weinheim, 1995. p. 22.
[2] R.C.J. Atkinson, N.J. Long, Monodentate Ferrocene Donor Ligands in Ferrocenes: Ligands, Materials and Biomolecules, John Wiley & Sons Ltd., 2008. p. 3.
[3] X.D. He, A. Maisonnat, F. Dahan, R. Poliblanc, Organometallics 8 (1989) 2618.
[4] M.D. Rausch, B.H. Edwards, R.D. Rogers, J.L. Atwood, J. Am. Chem. Soc. 105 (1983) 3882.
[5] M.S. Blais, R.D. Rogers, M.D. Rausch, J. Organomet. Chem. 593 (2000) 142.
[6] R.M. Bullock, C.P. Casey, Acc. Chem. Res. 20 (1987) 167.
[7] C. Corneliben, G. Erker, G. Kehr, R. Fröhlich, Dalton Trans. (2004) 4059.
[8] L.-Ch. Song, G.-A. Yu, Y. Liu, B.-S. Yin, X.-G. Zhang, Q.-M. Hu, Organometallics 26 (2007) 1966.
[9] B. Brumas-Soula, F. Dahan, R. Poilblanc, New J. Chem. (1998) 15.
[10] R.C.J. Atkinson, V.C. Gibson, N.J. Long, Chem. Soc. Rev. 33 (2004) 313.
[11] M.D. Rausch, W.C. Spink, Synth. React. Inorg. Metal–Org. Chem. 19 (1989) 1093.
[12] S. Eichenseher, O. Delacroix, K. Kromm, F. Hampel, J.A. Gladysz, Organometallics 24 (2005) 245.
[13] S. Otto, J. Chem. Crystallogr. 31 (2001) 185.
[14] S. Otto, A. Roodt, J. Smith, Inorg. Chim. Acta 303 (2000) 295.
[15] N.J. Long, A.J.P. White, D.J. Williams, M. Younus, J. Organomet. Chem. 649 (2002) 94.
[16] R. Uson, A. Lagunas, Organomet. Synth. 3 (1986) 322.
[17] K. Robler, T. Ruffer, B. Walfort, R. Packheiser, R. Holze, M. Zharnikov, H. Lang, J. Organomet. Chem. 692 (2007) 1530.
[18] J.E. Aguado, S. Canales, M.C. Gimeno, P.G. Jones, A. Lagunas, D. Villacampa, Dalton Trans. (2005) 3005.
[19] D.J. Fife, W.M. Moore, K.W. Morse, Inorg. Chem. 23 (1984) 1684.
[20] G.A. Bowmaker, L.M. Engelhardt, P.C. Healy, J.D. Kildea, R.I. Papasergio, A.H. White, Inorg. Chem. 26 (1987) 3533.
[21] G.A. Bowmaker, S.E. Boyd, J.V. Hanna, R.D. Hart, P.C. Healy, B.W. Skelton, A.H. White, Dalton Trans. (2002) 2722.
[22] F. Ferguson, R. McCrindle, A.J. McAlees, M. Parvez, Acta Crystallogr., Sect. B 38 (1992) 2679.
[23] R.R. Guimerans, M.M. Olmstead, A.L. Balch, Inorg. Chem. 22 (1983) 2223.
[24] A. Houlton, R.M.G. Roberts, J. Silver, M.G.B. Drew, Dalton Trans. (1990) 1543.
[25] P.C. Jones, C. Freire Erdbrügger, R. Hohbein, E. Schwarzmann, Acta Crystallogr., Sect. C 44 (1988) 1302.
[26] E.M. Barranco, O. Crespo, M. Concepcion Gimeno, A. Lagunas, P.G. Jones, B. Ahrens, Inorg. Chem. 39 (2000) 680.
[27] P.H. Davis, R.L. Belford, I.C. Paul, Inorg. Chem. 12 (1973) 213.
[28] P.J. Fitzpatrick, Y. LePage, I.A. Butler, Acta Crystallogr., Sect. B 37 (1981) 1052.
[29] T. Cautivo, F. Godoy, A.H. Klahn, G.E. Buono-Core, D. Sierra, M. Fuentealba, M.T. Garland, Inorg. Chem. Commun. 10 (2007) 1031.
[30] R. Arancibia, F. Godoy, G.E. Buono-Core, A.H. Klahn, E. Gutierrez-Puebla, A. Monge, Polyhedron 27 (2008) 2421.
[31] SAINT-PLUS (Version 6.02), Bruker Analytical X-ray Systems Inc., Madison, WI, USA, 1999.
[32] SHELXTL Reference Manual (Version 6.14), Bruker Analytical X-ray Systems Inc., Madison, WI, USA, 1998.
[33] G.M. Sheldrick, SADABS (Version 2.05), Bruker Analytical X-ray Systems Inc., Madison, WI, USA, 1999.

Polyhedron 28 (2009) 327–335

Contents lists available at ScienceDirect

Polyhedron

journal homepage: www.elsevier.com/locate/poly

Complexation of 2,6-pyridinedicarboxylic and 2,6-pyridinediacetic acids towards aluminium(III) and iron(III)

G. Giorgio Bombi [a], Reheman Aikebaier [a,b], Annalisa Dean [a], Valerio B. Di Marco [a,*], Daniele Marton [a], Andrea Tapparo [a]

[a] Department of Chemical Sciences, University of Padova, via Marzolo 1, 35131 Padova, Italy
[b] Xinjiang Medical University, Xinyi Road, Urumqi, Xinjiang, PR China

ARTICLE INFO

Article history:
Received 2 October 2008
Accepted 28 October 2008
Available online 4 December 2008

Keywords:
Aluminium
Iron
Carboxylate ligands
Potentiometry
UV–Vis
NMR

ABSTRACT

The complexes formed by 2,6-pyridinedicarboxylic acid (H_3X^+, $pK_{a1} \ll 0.4$, $pK_{a2} = 2.10 \pm 0.01$, $pK_{a3} = 4.383 \pm 0.004$, neutral form H_2X) and 2,6-pyridinediacetic acid (H_3A^+, $pK_{a1} = 2.32 \pm 0.01$, $pK_{a2} = 3.08 \pm 0.01$, $pK_{a3} = 5.92 \pm 0.01$, neutral form H_2A) with Al(III) and Fe(III) were studied by means of potentiometric titrations, UV–Vis, and NMR measurements (for Al(III)), at 25 °C in (Na)Cl 0.6 m aqueous solution. Stoichiometry (and stability constants) of the complexes are the following: AlX^+ (4.72 ± 0.01), $AlXH_{-1}$ (0.37 ± 0.07), AlX_2^-(7.85 ± 0.02), and $AlX_2H_{-1}^{2-}$(2.6 ± 0.3) for Al(III)/H_2X; FeX^+ (8.840 ± 0.003), $FeXH_{-1}$ (6.44 ± 0.05), and FeX_2^- (14.82 ± 0.03) for Fe(III)/H_2X; $AlAH^{2+}$ (8.4 ± 0.1), AlA^+ (5.2 ± 0.1), AlA_2^-(9.1 ± 0.1), and $AlA_2H_{-1}^{2-}$(3.3 ± 0.3) for Al(III)/H_2A; FeA^+ (7.53 ± 0.03), FeA_2H (16.5 ± 0.3), FeA_2^-(13.81 ± 0.04), $FeA_2H_{-1}^{2-}$(10.0 ± 0.1), and FeA_3H^{2-}(22.32 ± 0.08) for Fe(III)/H_2A. An Al(III)/H_2X complex, probably $AlXH_{-1}$, was characterised in the solid state.

H_2X forms stronger complexes towards Al(III) and Fe(III) than does H_2A. The main metal/H_2X complexes can be hypothesised to display a partial tridentate coordination, and the nitrogen of H_2X appears to be involved in the metal chelation. For Al(III)/H_2A, the most probable structure of the complexes AlA^+ and AlA_2^- is a bidentate one involving the two acetate arms.

© 2008 Elsevier Ltd. All rights reserved.

1. Introduction

There is a strong interest in studying the complexes of 2,6-pyridinedicarboxylic acid (dipicolinic acid, H_3X^+, neutral form H_2X, Fig. 1) ([1–11] and references in [6]). Interesting features of H_2X are its biological activity, its ability to stabilize unusual oxidation states, and its usefulness in corrosion inhibition and in decontamination of nuclear reactors [3]. H_2X has been used as reactant for the determination of Al(III), Fe(III), and other biologically and environmentally relevant metal ions, by capillary electrophoresis and ion chromatography ([12,13] and references therein). A vanadium complex with H_2X has been proposed as insulin-mimetic compounds [5,7]. H_2X has been proposed also as proton transfer systems, which can be used in designing of novel layered crystalline materials ([14] and references therein).

Conversely, there is no literature data dealing with the complexing properties of 2,6-pyridinediacetic acid (H_3A^+, neutral form H_2A, Fig. 1). Preliminary metal ion solubility data obtained by Chen et al. [15] indicate that H_2A is a stronger Fe(III) chelator than H_2X. Due to the similar structure, H_2A can in principle display similar properties as H_2X, and it can be proposed for the same applications listed above for H_2X.

Al(III) and Fe(III), as typical hard metal ions, prefer coordination of oxygen donors, especially negatively charged ones, such as carboxylates, phosphates and alcoholates [16]. If a molecule has suitable geometric properties, amine nitrogens can coordinate Al(III) and Fe(III) together with oxygen donors, forming polydentate chelates as, *e.g.* it is the case with ethylenediaminetetraacetic acid (EDTA).

The aim of this paper is to evaluate and to compare the complexing properties of H_2X and H_2A towards hard metal ions like Al(III) and Fe(III). The complexation study has been performed by means of potentiometric titrations, and e.m.f. data have been supported by NMR and UV–Vis measurements. As H_2A is not commercially available, it has been synthesised and characterised.

2. Experimental

2.1. Chemicals

All chemicals were commercially available and of pure grade. Chloroform was purchased by Janssen and absolute Ethanol by Sigma Aldrich (ACS reagent, ⩾99.5%). Magnesium sulphate

* Corresponding author. Tel.: +39 0498275219; fax: +39 0498275175.
E-mail address: valerio.dimarco@unipd.it (V.B. Di Marco).

0277-5387/$ - see front matter © 2008 Elsevier Ltd. All rights reserved.
doi:10.1016/j.poly.2008.10.047

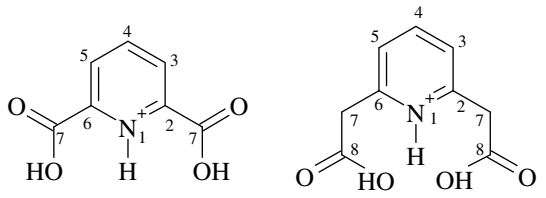


Fig. 1. 2,6-Pyridinedicarboxylic acid (H_3X^+, left) and 2,6-pyridinediacetic acid (H_3A^+, right), shown in the completely protonated form.

anhydrous and HCl (36–38%) were Baker Analyzed Reagent (Holland) products. HBr (ppa ACS reagent 48%), NaCN (ppa ACS reagent) and NaOH (nominal purity 99%+, CO_2 max. 0.5%) were purchased by Fluka. 2,6-Pyridinedicarboxylic acid (H_2X, 99%) was an Acros Organics product. Aluminium wire (Aldrich, nominal purity 99.999%) and iron granules (Aldrich, nominal purity 99.999%) were used to prepare solutions for potentiometric and UV–Vis measurements. For the NMR measurements, D_2O (Sigma, 99.9 atoms% D) $AlCl_3$ (Fluka, 99.5%) KOD (Aldrich, 40% sol. in D_2O, 99.9 at.% D) and DCl (Janssen, 20 wt.% sol. in D_2O, 99+ at.% D) were used.

2.2. Apparatus

IR spectra were registered on a FT-IR Perkin–Elmer spectrophotometer mod. 237 as a nujol suspension. The ^1H and ^{13}C NMR measurements were made at room temperature with a Bruker Avance 300 operating in FT mode using 5 mm tubes. The chemical shifts were given with respect to Me_4Si (TMS) when organic deuterated solvents were employed, and to $Me_3SiCH_2CH_2COONa$ (TSP) when D_2O was used as solvent. HPLC-MS analyses were made with an Agilent instrument mod 1100 equipped with a Luna C-108 column (15 cm × 5 mm i.d.) and an ion-trap quadrupolar mass detector. The eluent was a solution of $HCOONH_4$ 2.1 mM and HCOOH 0.026 mM.

All potentiometric measurements were performed with a Metrohm 765 Dosimat apparatus. UV spectra were recorded with a Perkin–Elmer Lambda 25 spectrophotometer.

2.3. Synthesis of 2,6-pyridinediacetic acid (H_2A)

The synthesis of the H_2A has been performed following a procedure reported in the literature [15], starting from 2,6-pyridinedimethanol (**I**) through the *a–c* steps reported in scheme 1.

2.3.1. Synthesis of 2,6-bis(bromomethyl)pyridine (*II*)

7.0 g (35.9 mmol) of **I** were added with 50 mL of a 48% HBr solution at room temperature in a 250 mL flask, equipped with condenser and magnetic stirrer. The yellow stirred solution was quickly heated and refluxed for 18 h. After cooling, it was reduced to small volume in rotary evaporator under vacuum. A further addition of 20 mL of a 48% HBr solution followed by heating for 18 h was necessary to improve the recovery yield. After solvent removal, 7.6 g of crude product was obtained, containing about 10% of the monobromurated derivative as impurity. The elution of the crude product with $CHCl_3$ on a glass column filled with 20 cm of silica gel (230–400 mesh) yielded 6.0 g (22.6 mmol; 63% yield) of pure **II** · **0.5 HBr** (m.p. 87–89 °C; Lit 84–89 °C [17]).

Anal. Calc. for **II** · **0.5 HBr**: C, 27.13; H, 2.31; N, 4.44. Found: C, 27.52; H, 2.47; N, 4.59%. NMR chemical shifts (ppm) in $CDCl_3$ and TMS as internal standard: ^1H NMR: 7.71 (t, 1H, pyridine), 7.37 (d, 2H, pyridine), 4.54 (s, 4H, methylene); ^{13}C NMR: 156.76, 138.12, 122.80 (pyridine), 33.45 (methylene).

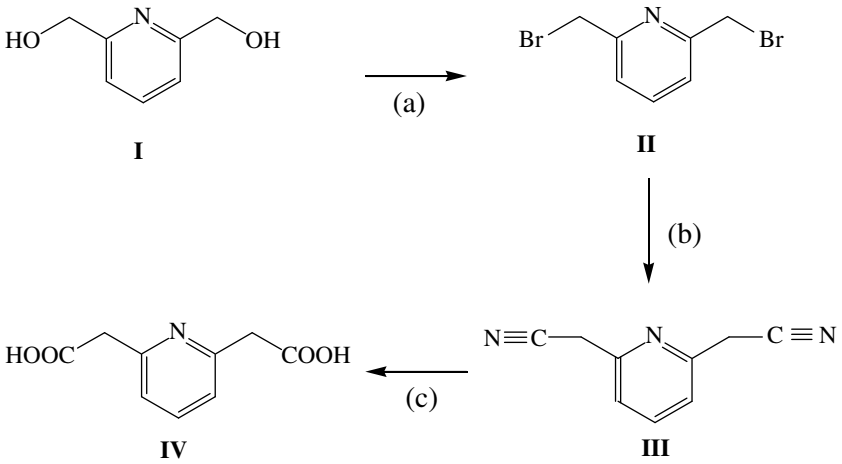
2.3.2. Synthesis of 2,6-pyridinyldiacetonitrile (*III*)

5.0 g (18.9 mmol) of **II** · **0.5 HBr**, 3.5 g (71.4 mmol) of NaCN, and 60 mL of water, were mixed in a 250 mL flask equipped with condenser and magnetic stirrer, and heated (85 °C) for 5 h under stirring. On heating, the colour of the resulting solution changed from yellow to green. After cooling and addition of 30 mL of water, the reaction product was extracted three times, each with 50 mL of $CHCl_3$. The collected organic phases were dried on anhydrous $MgSO_4$ overnight. After filtration and removal of the solvent, a solid green crude product (2.1 g) was obtained (m.p. 85–90 °C), which was crystallized by EtOH to give 1.6 g (10.2 mmol, 53.9% yield) of pure compound **III**, as colourless needles melting at 96–97 °C.

Anal. Calc. for **III**: C, 68.34; H, 4.41; N, 26.56. Found: C, 68.77; H, 4.49; N, 26.74%. NMR chemical shifts (ppm) in $CDCl_3$ and TMS as internal standard: ^1H NMR: 7.8 (t, 1H, pyridine), 7.42 (d, 2H, pyridine), 3.94 (s, 4H, s, 4H, methylene); ^{13}C NMR: 150.98, 138.80, 121.55 (pyridine), 116.61 (–CN group), 26.48 (s, 4H, methylene).

2.3.3. Synthesis of 2,6-pyridinediacetic acid (H_2A, *IV*)

2.7 g (17.2 mmol) of **III** were added with 50 mL of a 37% HCl solution at room temperature in a 250 mL flask, equipped with condenser and magnetic stirrer. The solution was quickly heated at 100 °C for 18 h under stirring. After cooling, the solution was added with 50 mL of water and 1.5 g of activated carbon. After filtration, the clear solution was brought at pH 2 by drop wise addition of a 1 M NaOH solution, then evaporated to about 5 mL under



Scheme 1. Synthesis of 2,6-pyridinediacetic acid (H_2A).

reduced pressure, and held at 4 °C overnight. White needles crystals of pure **IV** were separated from the solution. Yield: 56.4% (1.9 g, 9.7 mmol, m.p.: 211–212 °C).

Anal. Calc. for **IV**: C, 55.75; H, 4.82; N, 7.32. Found: C, 55.39; H, 4.65; N, 7.18%. NMR chemical shifts (ppm) in D_2O and TSP as internal standard: ^{1}H NMR: 8.31 (t, 1H, pyridine), 7.69 (d, 1H pyridine); ^{13}C NMR: 172.97, 150.20, 146.43 (pyridine). The methylenic protons and carbons of the alkyl chain are not observed in D_2O because of a rapid exchange between the protons of the methylenic group and the solvent. The ^{1}H and ^{13}C NMR signals of the methylenic group are detected when the measurements are performed in H_2O using an insert containing D_2O and the solvent presaturation technique: the proton signal resonates at 4.18 ppm, the carbon signal at 39.56 ppm.

2.4. Synthesis of an Al(III)/H_2X complex

Fifty milliliters of a H_2X solution (167.12 mg, 20 mmol/L, pH 3.37) were mixed with 50 mL of an $AlK(SO_4)_2 \cdot 12H_2O$ solution (237.20 mg, 10 mmol/L, pH 1.90). The pH of the resulting solution was 2.40. The solution was slowly basified upon addition of KOH 1 M. A white precipitate (solid A) formed immediately when the pH reached 4.57.

50 mL of another H_2X solution (167.12 mg, 20 mmol/L, pH 3.30) were mixed with 50 mL of an $AlCl_3 \cdot 6\ H_2O$ solution (120.71 mg, 10 mmol/L, pH 1.90). The resulting pH was 1.89. The solution was slowly basified upon addition of NaOH 1 M. A white precipitate (solid B, apparently identical to solid A) formed immediately when the pH reached 5.00. Solids A and B were filtered, washed and dried overnight under vacuum.

Melting points: H_2X 249.6 °C, solid A (decomposition) = 357–359 °C, solid B (decomposition) = 355–357 °C.

IR (nujol mull, KBr): for H_2X: 1690 cm^{-1} (COO asimm. stretching), 1560 cm^{-1} (aromatic CC stretching), 1450 cm^{-1} (COO simm. stretching). For solids A and B: 1640 cm^{-1} (COO asimm. stretching), 1580 cm^{-1} (aromatic CC stretching), and 1375 cm^{-1} (COO simm. stretching).

AAS measurements (26.00 mg solid A + 1 mL HNO_3 conc. in 10 mL, 10.10 mg solid B + 1 mL HNO_3 conc. in 10 mL, both solutions diluted 100 times) verified the absence of K^+ in solid A and of Na^+ in solid B.

Elemental analyses: four different samples of solid A and two of solid B were prepared and elementally analysed. Aluminium content was determined colorimetrically at 535 nm by reaction with eriochromocianine R [18]. Mean values (±standard deviation of the mean) are reported. For solid A, (36.4 ± 0.4)% C, (2.26 ± 0.05)% H, (6.15 ± 0.09)% N, (11.05 ± 0.2)% Al. For solid B, (36.4 ± 0.4)% C, (2.30 ± 0.08)% H, (6.12 ± 0.09)% N, (11.38 ± 0.2)% Al (theoretic values for $AlC_7H_8NO_7$: 34.2% C, 3.26% H, 5.71% N, 11.0% Al). For both solids, the molar ratio Al:C:N is *ca.* 1:7:1.

2.5. Solution equilibria

All analyte concentrations were expressed in the molality scale (mol/kg of water, m). For potentiometric and UV measurements, working solutions of HCl (0.1 m), NaOH (0.1–0.2 m), H_2X (0.008 m), H_2A (0.01 m), $AlCl_3$ (0.04 m, containing HCl 0.3 m) [19] and $FeCl_3$ (0.05 m, containing HCl 0.3 m) [20] were prepared and standardised. The starting solution for each titration and all working solutions contained known amounts of NaCl to assure a constant (Na)Cl 0.6 m (0.594 M) ionic strength during the titrations. Solutions for ^{1}H NMR measurements were prepared by dissolving in D_2O weighed amounts of ligand, $AlCl_3$ and NaCl. The pD was adjusted by the addition of concentrated KOD and/or DCl solutions.

Potentiometric titrations are summarised in Table 1. Temperature was 25.0 ± 0.1 °C. Duplicate potentiometric measurements were executed by using two glass electrodes (VWR 662-1792) and a Ag/AgCl/0.6 m NaCl reference electrode [21,22] with a J-shaped junction. Titrations were discarded if the relative e.m.f. values measured by the two electrodes differed by more than 0.2 mV (*ca.* 0.003 pH units). The acidic liquid junction potential of the reference electrode has been determined previously [20], and it can be represented by the equation [22] $E_j = -S\log(1 + J \cdot [H^+])$, with $J = 3.69 \pm 0.08$ m^{-1}. As a check of the accuracy of the entire experimental system, the pK_w value for water in (Na)Cl 0.6 m was computed from HCl + NaOH titrations. The values obtained from different series of experiments (pK_w = 13.699 ± 0.003 and 13.706 ± 0.001) compare well with the literature value [23] in Na(Cl) 0.6 M at 25 °C (13.727 ± 0.001). All stability constants were calculated using the computer program PITMAP [24]. The following metal-hydroxo species have been considered and the corresponding logβ values kept fixed during the elaboration of the data: AlH_{-1} (logβ = −5.52), AlH_{-2} (−11.3), AlH_{-3} (−17.3), AlH_{-4} (−23.46), Al_3H_{-4} (−13.57), $Al_{13}H_{-32}$ (−109.2) [25], FeH_{-1} (logβ = −2.87), FeH_{-2} (−6.16) [20], FeH_{-3} (−12.2), FeH_{-4} (−22.2), Fe_2H_{-2} (−2.9), Fe_3H_{-4} (−6.3) [26].

Table 1
Potentiometric titrations.

Solution	$C_{metal}/10^{-3}$ m	$C_{ligand}/10^{-3}$ m	C_{ligand}/C_{metal}	pH
1. H_2X		0.41–5.10		2.5–10.0
2. Al(III)/H_2X	0.64–0.91	0.93–2.73	1, 2, 4, 8	2.1–5.2
3. Fe(III)/H_2X	0.45–1.91	1.00–5.05	1, 2, 3, 4, 6, 9	2.1–5.0
4. H_2A		1.98–5.59		2.1–9.0
5. Al(III)/H_2A	0.37–1.70	1.93–5.49	1, 2, 3, 4, 5, 8	1.7–5.5
6. Fe(III)/H_2A	0.36–1.62	1.87–5.61	1, 2, 3, 4, 8	1.8–4.5

Table 2
UV–Vis measurements.

Solution	$C_{metal}/10^{-3}$ m	$C_{ligand}/10^{-3}$ m	pH	λ (nm) for calcul.
1. H_2X		0.94	0.40–2.00	244; 270; 278
2. Al(III)/H_2X	0.99	0.98	2.13–3.49	243; 270; 274
3. Fe(III)/H_2X	0.99	0.99	0.30–1.51	310

UV measurements (Table 2) were carried out for solutions containing the ligand alone, and for solutions containing the ligand and the metal ion, at various pH values (cell path 0.1 cm). When the pH of the solution was below 2.5, it was computed from the stoichiometric concentration of HCl, because the [H$^+$] modifications produced by the other species were negligible under these conditions. In other cases the pH was measured with the same electrodes and procedures as for potentiometric titrations. The logβ values for the metal–ligand complexes were computed by the program PITMAP.

NMR spectra of H_2X and of H_2A were collected at various pD values in D_2O solutions containing only the free ligand, and the ligand together with Al(III). The pD was measured with a Crison 5014 combined glass electrode previously calibrated in buffered solutions at pH 4 and pH 7, and 0.41 pH units were added to the pH-meter readings to correct for isotopic and solvent effects [27].

3. Results and discussion

3.1. Potentiometric results

Both H_2X and H_2A are triprotic acids (see Fig. 1). Table 3 summarises the pK_a values obtained from our potentiometric titrations. The first two deprotonations of H_3X^+ are due to the benzoic groups, and the third one is due to the pyridinium, as the former functional groups are intrinsically much more acidic than the latter. For H_3A^+

Table 3
Acidic properties of H_2X and H_2A at 25 °C, (Na)Cl 0.6 m. Here and in the following tables, values are shown as the mean and standard deviation of the mean[a].

Species	pK_a	Species	pK_a
H_3X+	≪0.4	H_3A^+	2.32 ± 0.01
H_2X	2.10 ± 0.01	H_2A	3.08 ± 0.01
HX^-	4.383 ± 0.004	HA^-	5.92 ± 0.01

[a] The standard deviation of the mean is a measure of the repeatability of our results, not of their accuracy.

Table 5
Log β values for Al(III)/H_2A and Fe(III)/H_2A complexes at 25 °C, (Na)Cl 0.6 m ($pM^{3+} + qA^{2-} + rH^+ = M_pA_qH_r^{3p-2q+r}$).

(*p*, *q*, *r*)	Log β for Al(III)/H_2A	Log β for Fe(III)/H_2A
1, 1, 1	8.4 ± 0.1	
1, 1, 0	5.2 ± 0.1	7.53 ± 0.03
1, 2, 1		16.5 ± 0.3
1, 2, 0	9.1 ± 0.1	13.81 ± 0.04
1, 2, −1	3.3 ± 0.3	10.0 ± 0.1
1, 3, 1		22.32 ± 0.08
1, 3, 0		18.76 ± 0.06

this deprotonation order is less sure as the intrinsic acidity of the acetic arms is comparable to that of pyridinium. The pK_{a2} and pK_{a3} values of H_3X^+ are in reasonable agreement with those reported in the literature (for example, pK_{a2} = 2.09 and pK_{a3} = 4.53 in $NaClO_4$ 0.5 M [2], 2.03 and 4.49 in KCl 0.4 M [5]). Like the cited authors we were not able to determine pK_{a1}: UV–Vis spectra (not shown) at pH values between 0.4 and 2.3 allowed to determine only one pK_a value, 2.02 ± 0.01, which is clearly the pK_{a2}. Thus we can assume that pK_{a1} ≪ 0.4.

The three pK_a values of H_3A^+ are higher than those of H_3X^+ because the resonance effect of the pyridinic ring, which stabilizes the deprotonated form of the carboxylic groups in H_3X^+, is missing in H_3A^+. For this ligand no data is reported in the literature to allow a comparison. We found a data for pyridine-2-acetic acid: here pK_{a1} = 2.73 and pK_{a2} = 5.81 [28]. As expected, pK_{a1} of pyridine-2-acetic acid is higher than pK_{a1} of H_3A^+ due to statistical effects, whereas pK_{a2} of pyridine-2-acetic acid is very similar to pK_{a3} of H_3A^+.

The potentiometric titrations of solutions containing the metal and the ligand allowed the identification of several complexes. The stoichiometry of the complexes and the values of their stability constants are reported in Tables 4 and 5. Typical distribution diagrams drawn from our data are reported in Fig. 2 (2a for Al(III)/H_2X, 2b for Fe(III)/H_2X, 2c for Al(III)/H_2A, 2d for Fe(III)/H_2A).

3.1.1. Al(III)/H_2X

The main Al(III)/H_2X complexes in solution are AlX^+ and $AlXH_{-1}$. AlX_2^- and $AlX_2H_{-1}^{2-}$ are minor species. The acidity of AlX^+ and AlX_2^- (the pK_a value for the reaction $AlX_n^{3-2n} = AlX_nH_{-1}^{2-2n} + H^+$ is 4.35 for AlX^+ and 5.3 for AlX_2^-) is significantly lower than that of $Al(H_2O)_6^{3+}$ (5.52). A similar effect has been observed by Jøns and Johansen [29], who found that the pK_a of the 1:2 Al(III)/picolinate complex (picolinic acid = 2-pyridinecarboxylic acid) is 4.12. The involvement of the pyridinic nitrogen in the metal chelation can represent a possible explanation for these acidity increments, as the Al–N^+ bond can lower the electronic density of the metal center in AlX^+ and in AlX_2^- with respect to $Al(H_2O)_6^{3+}$. It is interesting to observe that the pK_a of the water coordinated to the metal center in Al(III)/pyridine-like complexes is significantly larger than 5.52 when the pyridinic nitrogen is surely not involved in the Al(III) chelation (*e.g.* for the Al(III)/1-methyl-3-hydroxy-4-pyridinecarboxylate and Al(III)/1-methyl-4-hydroxy-3-pyridinecarboxylate complexes [30]).

Al(III)/H_2X titrations had to be stopped at pH ≈ 5–6 due to the precipitation of a white solid. The same observation is reported by Napoli [2], who however did not characterise the precipitate. Our data (see Section 2) demonstrate that the precipitate is not the metal hydroxide $Al(OH)_3$ but a metal/ligand complex in which the metal/ligand ratio is 1:1. This complex is probably the neutral species $AlC_7H_8NO_7$ ($AlXH_{-1}$) with the co-presence of *ca.* 5% of free ligand. The experimental observation of the start of the precipitation at different stoichiometric metal and ligand concentrations can be well modeled considering that the stability constant for the reaction $AlXH_{-1(s)} + H^+ = Al^{3+} + X^{2-}$ is 3.7×10^{-4}. The distribution diagram in Fig. 2a was computed taking into account this data.

Napoli [2] found only two Al(III)/H_2X complexes, AlX^+ and AlX_2^- (Table 4). Data were obtained by potentiometric titrations, and e.m.f. values were elaborated graphically by the Bjerrum method. A paper electrophoretic investigation showed that the Al(III) complexes display opposite charges, mainly positive at pH ⩽ 3 and mainly negative at pH > 4 in the presence of 10^{-2} M H_2X. Unfortunately the Al(III) concentration used for the electrophoretic runs is not reported, but Napoli's data can qualitatively be well interpreted also by our speciation model, according to which the free metal ion and AlX^+ predominate at acidic pH, and the other complexes (neutral or negatively charged) predominate at higher pH values. Also Napoli's UV–Vis results, *i.e.* that at pH 3 only the species AlX^+ exists in solution with a log β value of 4.85 ± 0.03, agree very well with our speciation model and with our UV–Vis results (see below). Nitzsche and Röbisch [10] analysed Al(III)/H_2X solutions at pH 3–5 by means of UV–Vis, and they found the complexes $AlXH^{2+}$ and AlX^+ (Table 4). However, the log β value given for AlX^+ (11.37) is abnormally large, and it implies a not-measurable pK_a value of $AlXH^{2+}$ (7.4 − 11.37 = −4).

3.1.2. Fe(III)/H_2X

The main Fe(III) complexes are FeX^+ and FeX_2^-. FeX^+ already forms at very acidic pH values, and its stability constant can be determined only by UV–Vis measurements at pH values lower than 1 (see below). A water molecule coordinated to the metal center in FeX^+ deprotonates to give $FeXH_{-1}$. The pK_a of FeX^+ (2.40) is lower

Table 4
Log β values for Al(III)/H_2X and Fe(III)/H_2X complexes ($pM^{3+} + qX^{2-} + rH^+ = M_pX_qH_r^{3p-2q+r}$). Literature values are reported for comparison.

(*p*, *q*, *r*)	Log β for Al(III)/H_2X			Log β for Fe(III)/H_2X		
	This work (25 °C, (Na)Cl 0.6 m)	Ref. [2] (25 °C, $NaClO_4$ 0.5 M)	Ref. [10] (25 °C, NaCl 1 M)	This work (25 °C, (Na)Cl 0.6 m)	Ref. [1] (20 °C, ionic strength 0.1 M)	Ref. [11] (25 °C, $NaClO_4$ 1 M)
1, 1, 1			7.4 ± 0.2			
1, 1, 0	4.72 ± 0.01	4.87 ± 0.02	11.37 ± 0.06	8.84 ± 0.01[a]	10.91	8.88
1, 1, −1	0.37 ± 0.07			6.44 ± 0.05		
1, 2, 0	7.85 ± 0.02	8.32 ± 0.02		14.82 ± 0.03	17.13	
1, 2, −1	2.6 ± 0.3					

[a] Determined by UV–Vis, see text.

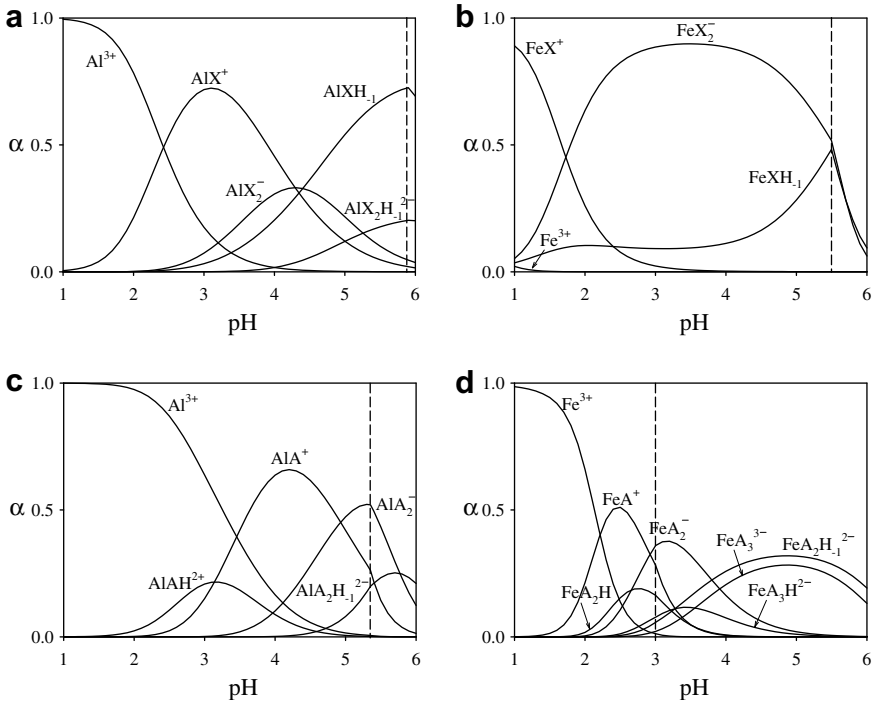


Fig. 2. Distribution diagrams of Al(III)/H_2X (a), Fe(III)/H_2X (b), Al(III)/H_2A (c), and Fe(III)/H_2A (d) complexes in aqueous (Na)Cl 0.6 m, T = 25 °C; $C_{metal} = 10^{-3}$ m, $C_{ligand} = 3 \times 10^{-3}$ m. The dotted line indicates the theoretic start of metal hydroxide (b, c, d) or $AlXH_{-1}$ (a) precipitation.

than that of $FeH_2O_6^{3+}$ (2.87). For the Fe(III) complexes of other pyridine derivatives, when the metal ion is coordinated by carboxylate and hydroxo substituents, we always found pK_a values significantly larger than 2.87 ([31] and references therein). As hypothesised for AlX^+ and AlX_2^-, the high acidity of FeX^+ can be due to the involvement of the nitrogen in the metal chelation.

Fe(III)/H_2X solutions are known to form a mixed FeX^+/FeX_2^- green precipitate if they are allowed to stand for few days at acidic pH values [32]. In our titrations, which we completed within *ca.* 1 h, we did not observe this solid: at pH values larger than *ca.* 5 (depending on metal and ligand concentrations), the precipitation of a brown powder was observed, which we considered to be iron hydroxide.

Bridger et al. [11] studied Fe(III)/H_2X complexes by the Job method at very acidic pH values (between *ca.* 0 and 1.4), and they observed only the species FeX^+ (Table 4). Both the acidic pH speciation (*e.g.* see Fig. 2b) and the log β value of FeX^+ (Table 4) agree very well with our results. Anderegg [1] found the complexes FeX^+ and FeX_2^- (Table 4). The Anderegg's stability constant of FeX^+ appears to be overestimated with respect to our value (Table 4): the absence of $FeXH_{-1}$ in his speciation model likely produced this effect. Anderegg's stepwise stability constant of FeX_2^- (17.13 − 10.91 = 6.22), on the other hand, agrees well with our value (14.82 − 8.84 = 5.98). Napoli [2] showed by paper electrophoresis that the Fe(III) complexes are always negatively charged at pH ⩾ 2. His data can be very well modeled also by our speciation model, according to which FeX_2^- predominates at pH values larger than 2 (Fig. 2b).

3.1.3. Al(III)/H_2A

In Al(III)/H_2A solutions the main species is AlA^+. $AlAH^{2+}$ forms in low amount at acidic pH, AlA_2^- and $AlA_2H_{-1}^{2-}$ become significant at pH close to the start of $Al(OH)_3$ precipitation. The pK_a value of $AlAH^{2+}$ (3.2, it can be calculated from data in Table 5) is almost identical to the pK_{a2} of the free ligand (3.08, Table 3), indicating that in $AlAH^{2+}$ the deprotonating group is a carboxylate. For AlA_2^- the deprotonation can occur only at the coordinated water molecule, so that $AlA_2H_{-1}^{2-}$ is a hydroxospecies. Differently than for AlX_2^-, the pK_a of AlA_2^- (5.8) is larger than that of $Al(H_2O)_6^{3+}$. It is therefore suggested that in the complex AlA_2^- the nitrogen of the ligand is not involved in the metal chelation.

3.1.4. Fe(III)/H_2A

The main Fe(III) complexes are FeA^+, FeA_2H and FeA_2^-. The remaining Fe(III) species can be detected in significant amounts only at large ligand-to-metal ratios and at pH values close to the start of $Fe(OH)_3$ precipitation. The pK_a of the water molecule coordinated to Fe(III) is very similar to that of the unbound carboxylate: for $Fe(H_2O)_6$ pK_a = 2.87 [20], for H_2A pK_a = 3.08 (Table 3). On this basis, for FeA^+, FeA_2^-, and FeA_3^{3-}, two microspecies probably coexist in solution, one having the ligand completely deprotonated, the other one having one protonated carboxylate and one coordinated water molecule deprotonated.

3.1.5. pM calculations

It is useful to compare the complexation strength of the ligands H_2X and H_2A towards Al(III) and Fe(III). The comparison is extended to 2-pyridinecarboxylic acid (picolinic acid), in order to show if the presence of a second carboxylate in H_2X has an effect on the metal complexation. The quantitative comparison can be accomplished by computing pM (=−log[M^{3+}]) *vs.* pH at a given metal and ligand concentration (e.g. $C_{metal} = 10^{-6}$ m and $C_{ligand} = 5 \times 10^{-5}$ m [16]). pM *vs.* pH graphs are reported in Fig. 3. Data for Al(III)/picolinate (25 °C, KNO_3 0.15 M [29]) and Fe(III)/picolinate (35 °C, $NaClO_4$ 1.00 M [33]) are taken from the literature.

A slight difference (0.5 log units) can be observed in the complexation strength of H_2X and H_2A towards Al(III): H_2X is a better Al(III) chelator than H_2A. This difference can be due to the chelation ring size, *i.e.* the 5-membered ring formed by H_2X is more stable than the 6-membered ring formed by H_2A. A similar pAl difference is observed between Al(III)/H_2X and Al(III)/picolinate: this difference can be due to the tridentate coordination mode of

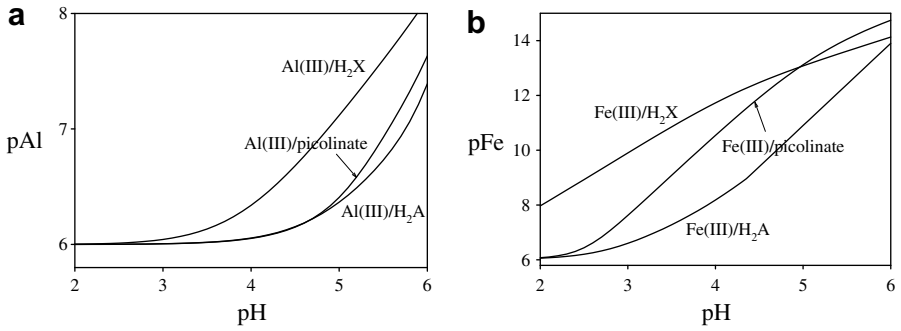


Fig. 3. pM *vs.* pH for various Al(III)/ligands (a) and Fe(III)/ligands (b) ($C_{metal} = 10^{-6}$ m, $C_{ligand} = 5 \times 10^{-5}$ m).

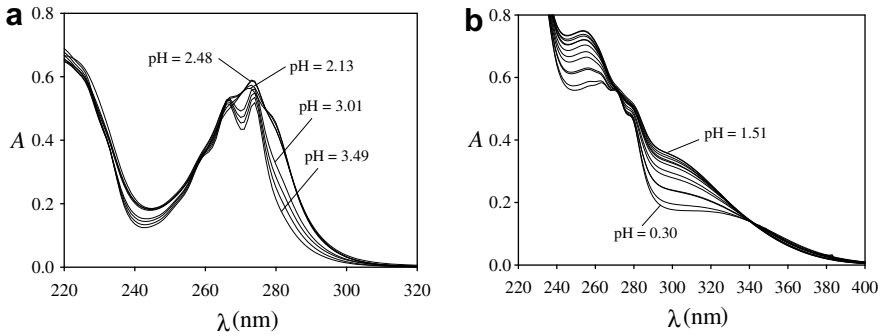


Fig. 4. (a) UV–Vis spectra of Al(III)/H_2X solutions, pH 2.13, 2.30, 2.48, 2.71, 3.01, 3.21, 3.35, 3.49. (b) UV–Vis spectra of Fe(III)/H_2X solutions, pH 0.30, 0.39, 0.59, 0.79, 0.87, 1.02, 1.05, 1.16, 1.22, 1.36, 1.42, 1.51.

AlX^+ and AlX_2^-, which stabilizes Al(III)/H_2X complexes slightly more than Al(III)/picolinate ones. Tridentate coordination is however likely to be only partial, i.e. in equilibrium with a bidentate coordination predominating over the tridentate one, due to the very small pAl difference and to the relative weakness of the Al(III)/H_2X complexes (pAl values are quite low).

As no complexation data of pyridine-2-acetic acid towards Al(III) and Fe(III) is available, it is not possible to verify the role of the second carboxylate of H_2A in the metal complexation. However, due to the weakness of Al(III)/H_2A and Fe(III)/H_2A complexes, we can confidently exclude that these species display a tridentate coordination.

Also Fe(III)/H_2X complexes are more stable than Fe(III)/H_2A ones, the pFe difference is up to 3 log units. The preliminary data of Chen et al. [15], cited above, are therefore not confirmed by our results. Fe(III)/H_2X complexes are also significantly more stable than Fe(III)/picolinate ones at pH values lower than 5: the tridentate coordination of H_2X towards Fe(III) represents the most probable explanation to this data (at pH larger than 5 polynuclear species form in Fe(III)/picolinate solutions [33], so that the pFe increases significantly). It is worth noting that the species FeX_2 was isolated as crystal, and it was showed that the ligand acts as tridentate coordinating through the heterocyclic nitrogen and two carboxyl oxygens [34].

3.2. UV–Vis results

UV–Vis spectra for the Al(III)/H_2X and Fe(III)/H_2X solutions are reported in Fig. 4a and b. In the case of Al(III)/H_2X, the increase of pH causes a general decrease of the absorption coefficients of the aromatic band, especially at around 270 and 280 nm. This effect can be explained by the gradual formation of the metal complex AlX^+, assuming the involvement of the pyridinic ring in the metal complexation and the consequent perturbation of the electronic distribution in the aromatic ring. In the case of Fe(III)/H_2X, the complex formation is revealed by two weak charge-transfer peaks which appear at *ca.* 250 and 310 nm.

The elaboration of the UV–Vis data is complicated by a change of the free ligand ε values with concentration at every wavelength, because of the presence of concentration-dependent ligand–ligand interactions in solution [35]. This problem applies specifically for Al(III)/H_2X spectra, as here the absorption of the complexes overlaps with that of the free ligand. The formation constant of only one Al(III)/H_2X complex, AlX^+, was optimised. For this species, $\log\beta = 4.96 \pm 0.01$. Taking into account the uncertainty of the absorption of the free ligand, this value compares reasonably well with the corresponding potentiometric one ($\log\beta_{1,1,0} = 4.72 \pm 0.01$, Table 4). For Fe(III)/$H_2X$ solutions the problem of the ε change of free ligand can be overcome by elaborating the spectra at a wavelength where the ligand does not absorb (310 nm). From spectra at acidic pH values, the formation constant of FeX^+ was optimised ($\log\beta_{1,1,0} = 8.84 \pm 0.01$, Table 4).

3.3. NMR results

The ^{1}H NMR spectra of H_2X and Al(III)/H_2X solutions are shown in Fig. 5. The ^{13}C NMR spectra of H_2X and Al(III)/H_2X solutions are reported in Fig. 6. The ^{1}H NMR spectra of H_2A and Al(III)/H_2A solutions are shown in Fig. 7.

3.3.1. NMR spectra of H_2X and H_2A

The ^{1}H NMR spectra of the ligands display a typical X_2Y pattern: the doublet is assigned to H_3 and H_5, the triplet to H_4 (refer to Fig. 1 for atom numbering). The methylenic protons of H_2A do not appear in the spectra as they rapidly exchange with the solvent (see Section 2). The H_4 protons of both H_2X and H_2A resonate at very low

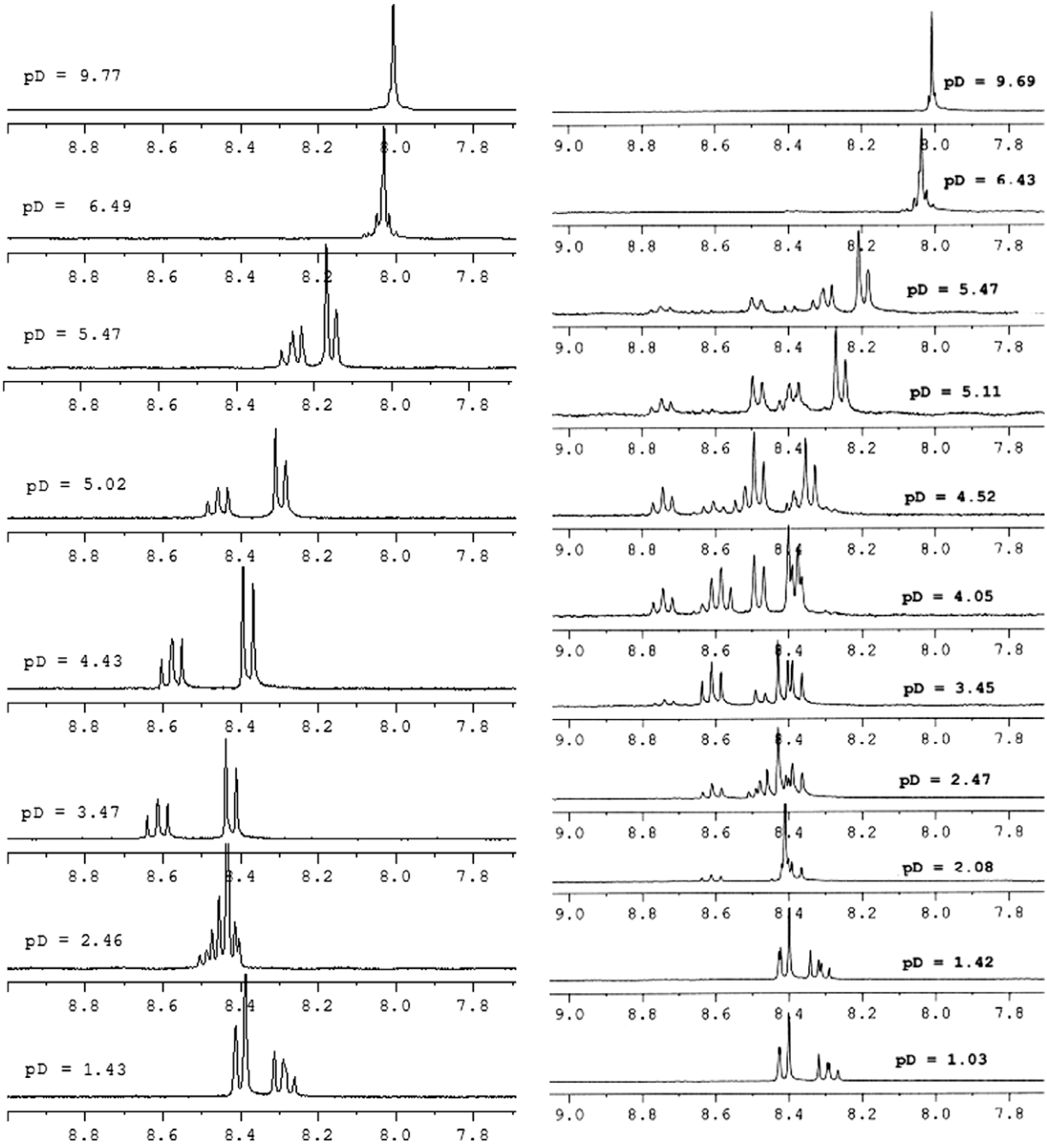


Fig. 5. ^{1}H NMR spectra of D_2O solutions at various pD values containing H_2X 0.0017 m (left), Al(III) 0.0017 m + H_2X 0.0035 m (right).

fields at acidic pH ($\delta > 8.2$) because of the electron-attracting effect of the positively charged pyridinium. The two carboxylic groups in H_2X shift downfield also the signals of H_3 and H_5, whereas the two acetic groups in H_2A do not have a significant electron-attracting effect.

The carboxylate groups have a very strong pD-dependent effect in H_2X (Fig. 5). For this ligand, at pD lower than pK_{a2} (corresponding to the deprotonation of the second carboxylate: pK_{a2} = 2.12 + 0.34 = 2.46 in D_2O according to Rule and La Mer [36]) H_3 and H_5 resonate at lower fields than H_4. At pD ≈ pK_{a2} the two proton signals collapse and the spectrum becomes of the second-order. At pD larger than pK_{a2} and lower than pK_{a3} (pK_{a3} = 4.36 + 0.46 = 4.82 in D_2O [36]) the carboxylate groups are negatively charged and the electron-attracting effect of the positive nitrogen predominates, so that H_3 and H_5 resonate at higher fields than H_4. Finally, when pyridinium deprotonates (pD ≈ pK_{a3}), all signals move upfield and finally collapse again to give a second-order spectrum.

The ^{1}H signals of H_2A do not have any pD-dependent shift (Fig. 7) because the carboxylate can affect only slightly the electronic distribution in the pyridinic ring, and the nitrogen does not deprotonate in the investigated pD range (pK_{a3} = 5.92 + 0.52 = 6.44 in D_2O [36]).

3.3.2. NMR spectra of Al(III)/H_2X 1:2

At pD 2.47 the addition of Al(III) gives rise to two new sets of ^{1}H signals (Fig. 5), a triplet centered at δ 8.6 and a doublet at δ 8.35–8.4. These signals can be attributed to H_4 and to H_3 + H_5 of the com-

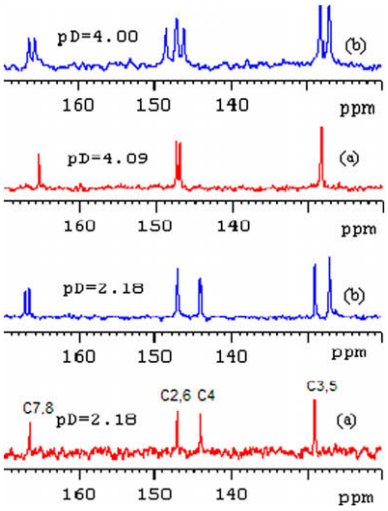


Fig. 6. ^{13}C NMR spectra of D_2O solutions at two pD values containing H_2X 0.15 m (a), Al(III) 0.075 m + H_2X 0.15 m (b).

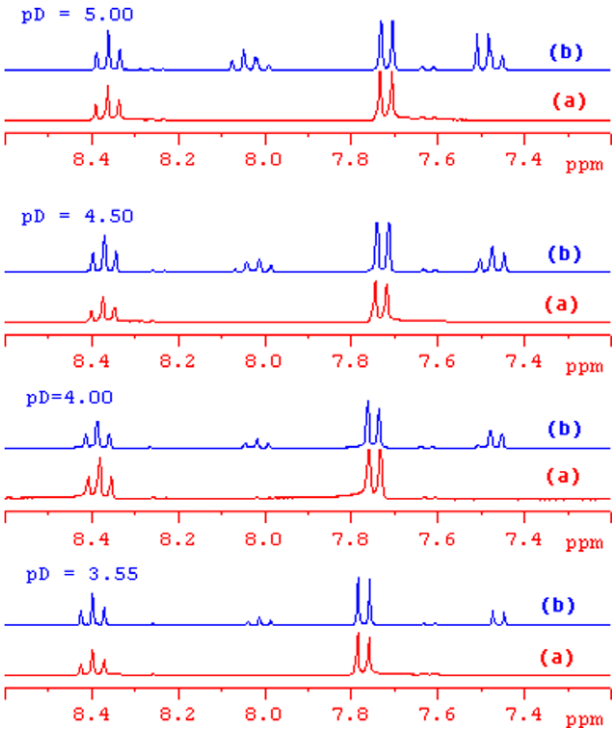


Fig. 7. ^1H NMR spectra of D_2O solutions at various pD values containing H_2A 0.03 m (a), Al(III) 0.01 m + H_2A 0.03 m (b).

plex AlX^+, as according to potentiometric data this species predominates at acidic pD values. Also in the ^{13}C NMR spectrum at pD 2.18 (Fig. 6) three new signals appear in the presence of Al(III), which can be assigned to the same complex.

The signals of AlX^+ are still present in the ^1H NMR spectrum at pD 3.45, even if the triplet is completely overlapped by the triplet of the free ligand (as indicated by the abnormally high intensity of the latter). At this pD a new group of signals appears: a triplet at δ 8.7–8.8, and a doublet at δ 8.45–8.5. According to the potentiometric results, these new sets of signals are assigned to the complex AlX_2^-. Also in the ^{13}C NMR spectrum at pD 4.00 two new signals of $C_{2,4,6}$ appear, suggesting the formation of two complexes (AlX^+ and AlX_2^-).

The same sets of ^1H signals are observed at pD larger than 3.45. Here the change of pD causes a shift of the signals of the free ligand and a change of relative intensities of the peaks of free ligand, AlX^+, and AlX_2^-. Between pD 3.45 and pD 5.47 the ^1H signals of AlX_2^- do not shift, suggesting no deprotonation for this complex in the investigated pD range. The relatively high pK_a value of AlX_2^- expected in D_2O ($pK_a = 5.3 + 0.50 = 5.8$ [36]) is consistent with this data. The signals of AlX^+ ($pK_a = 4.35 + 0.46 = 4.81$ [36]) do not shift with pD, probably because the deprotonation of AlX^+, occurring at a water coordinated to the metal center to produce $AlXH_{-1}$, does not affect significantly the electronic distribution in the aromatic ring.

The signals of the complexes disappear at pD > *ca.* 6–6.5, as expected on the basis of the potentiometric results, due to the precipitation of the metal hydroxide and the formation of $Al(OH)_4^-$.

3.3.3. NMR spectra of Al(III)/H_2A 1:3

Upon addition of Al(III) to a solution containing H_2A at pD 3.55, a new set of signals appears, a doublet at δ 7.45, and a triplet at δ 8.0. These peaks are clearly $H_3 + H_5$ and H_4 of a complex, which according to the potentiometric results is AlA^+. At pD 4.00, pD 4.50 and 5.00, new signals appear, which are partially overlapped with those of AlA^+, and which are attributed to AlA_2^-. The peak intensity of increases with pD, whereas that of AlA^+ and of the free ligand decrease. This behaviour agrees with the potentiometric results.

3.3.4. Structural information

The NMR spectra in the presence of Al(III) show two features which help to understand the structure of the Al(III) complexes. First, in the ^1H spectra H_3 and H_5 resonate as doublets for both ligands, for any complex and at any pD value. Therefore, both ligands bind the metal ion in a symmetric manner (in the NMR time scale), *i.e.*, either the ligand acts as tridentate, or as bidentate with two arms rapidly exchanging with the third one. Second, ^1H spectra show a quite different behaviour for the two ligands. In the case of H_2X, the signal of H_4 in the complexes AlX^+ and AlX_2^- is significantly shifted downfield with respect to the same signal of the free ligand, and the signals of H_3 and H_5 are slightly shifted upfield (at least at acidic pD values). In the case of H_2A, all signals of AlA^+ and AlA_2^- ($H_3 + H_5$ and H_4) are significantly shifted upfield with respect to the same signals of the free ligand. The formation of an Al–N^+ bond (which affects primarily H_4) only in the Al(III)/H_2X complexes, as suggested from thermodynamic data, can explain also this NMR difference.

4. Conclusions

Our results show that the main complexes formed by 2,6-pyridinedicarboxylic acid (H_2X) and by 2,6-pyridinediacetic acid (H_2A) with Al(III) and Fe(III) have a metal:ligand 1:1 and 1:2 stoichiometry. Potentiometric titrations, UV–Vis and NMR measurements gave consistent results. The complexes formed by H_2X with both metal ions are stronger than those formed by H_2A. On the basis of all our data, the main metal/H_2X complexes can be hypothesised to display a partial tridentate coordination, and the nitrogen of H_2X appears to be involved in the metal chelation. For Al(III)/H_2A, the most probable structure of the complexes AlA^+ and AlA_2^- is a bidentate one involving the two acetate arms.

References

[1] G. Anderegg, Helv. Chim. Acta 43 (1960) 1530.
[2] A. Napoli, Talanta 15 (1968) 189.
[3] P. Laine, A. Gourdon, J.P. Launary, Inorg. Chem. 34 (1995) 5129.
[4] P. Laine, A. Gourdon, J.P. Launary, Inorg. Chem. 34 (1995) 5156.
[5] D.C. Crans, L. Yang, T. Jakusch, T. Kiss, Inorg. Chem. 39 (2000) 4409.
[6] M.M. Khalil, A.E. Attia, J. Chem. Eng. Data 45 (2000) 1108.

[7] T. Jakusch, W. Jin, L. Yang, T. Kiss, D.C. Crans, J. Inorg. Biochem. 95 (2003) 1.
[8] V. Lubes, J. Sol. Chem. 34 (2005) 899.
[9] M.L. Lugo, V. Lubes, J. Chem. Eng. Data 52 (2007) 1208.
[10] R. Nitzsche, G. Röbisch, Monatsh. Chem. 124 (1993) 157.
[11] K. Bridger, R.C. Patel, E. Matijević, Polyhedron 1 (1982) 269.
[12] Z. Chen, R. Naidu, J. Chromography A 966 (2002) 245.
[13] Z. Chen, R. Naidu, J. Chromatography A 1023 (2004) 151.
[14] A. Moghimi, A. Shokrollahi, M. Shamsipur, H. Aghabozorg, M. Ranjbar, J. Mol. Struc. 701 (2004) 49.
[15] D. Chen, A.E. Martell, D. McManus, Can. J. Chem. 73 (1995) 264.
[16] T. Kiss, E. Farkas, Perspec. Bioinorg. Chem. 3 (1996) 199.
[17] W. Baker, K.M. Buggle, J.F.W. McOmie, D.A.M. Watkins, J. Chem. Soc. (1958) 3594.
[18] A. Tapparo, L. Soldà, G.G. Bombi, P. Zambenedetti, P.F. Zatta, R. Bertani, B. Corain, Analyst 120 (1995) 2425.
[19] V.B. Di Marco, A. Tapparo, G.G. Bombi, Ann. Chim. (Rome) 89 (1999) 397.
[20] V.B. Di Marco, A. Tapparo, G.G. Bombi, Ann. Chim. (Rome) 91 (2001) 595.
[21] G.J. Janz, Silver - Silver Halide Electrodes, in: D.J.G. Ives, G.J. Janz (Eds.), Reference Electrodes: Theory and Practice, Academic Press, New York, London, 1961.
[22] G. Biedermann, L.G. Sillén, Ark. Kemi 5 (1953) 425.
[23] S. Sjöberg, Y. Hägglund, A. Nordin, N. Ingri, Marine Chem. 13 (1983) 35.
[24] V. B. Di Marco, Ph.D. Thesis, University of Padova, 1998.
[25] L.O. Öhman, Inorg. Chem. 27 (1988) 2565.
[26] C.M. Flynn Jr., Chem. Rev. 84 (1984) 31.
[27] A.K. Covington, M. Paabo, R.A. Robinson, R.G. Bates, Anal. Chem. 40 (1968) 700.
[28] L.O. Öhman, S. Sjöberg, Acta Chem. Scand. A37 (1983) 875.
[29] O. Jøns, E.S. Johansen, Inorg. Chim. Acta 151 (1988) 129.
[30] V.B. Di Marco, A. Dean, M.G. Ferlin, R.A. Yokel, H. Li, A. Venzo, G.G. Bombi, Eur. J. Inorg. Chem. (2006) 1284.
[31] V.B. Di Marco, A. Dean, R.A. Yokel, H. Li, G.G. Bombi, Polyhedron 26 (2007) 3227.
[32] K.A. Abboud, C. Xu, R.S. Drago, Acta Crystallogr. C54 (1998) 1270.
[33] V. Palchevskii, V. Khorounzy, V. Scherbakova, Koord. Khim. 10 (1984) 1076.
[34] G.S. Sanyal, R. Ganguly, P.K. Nath, R.J. Butcher, J. Ind. Chem. Soc. 79 (2002) 489.
[35] F. Peral, E. Gallego, Spectrochim. Acta A 56 (2000) 2149.
[36] C.K. Rule, V.K. La Mer, J. Am. Chem. Soc. 60 (1938) 1974.

Polyhedron 28 (2009) 336–342

Contents lists available at ScienceDirect

Polyhedron

journal homepage: www.elsevier.com/locate/poly

Mono and dinuclear Re(V) complexes with a hydrospirophosphorane HP∼O derived ligand: Synthesis, structural analysis and molecular dynamics

Anna Skarżyńska *, Zbigniew Ciunik

Faculty of Chemistry, University of Wrocław, 14 F. Joliot-Curie Street, 50-383 Wrocław, Poland

ARTICLE INFO

Article history:
Received 8 September 2008
Accepted 15 October 2008
Available online 4 December 2008

Keywords:
Oxo-rhenium(V) complexes
Hydrospirophosphorane ligand
Diaza ligand
Dinuclear compound

ABSTRACT

Two neutral mono and dinuclear rhenium(V) complexes, *cis*-$ReOCl_2(P{\sim}O)(pym)$ (**1**) and *cis*-$[ReOCl_2(P{\sim}O)]_2(\mu$–pym) (**2** · $(CH_3)_2CO$), with the hydrospirophosphorane ligand HP∼O (HP∼O = octamethyl-2,2,3,3,7,7,8,8-tetraoxa-5λ^5 1,4,6,9-phosphaspiro-4,4-nonane) have been prepared. The coordination geometry of the complexes has been determined in solution by NMR and UV–Vis spectroscopy, as well as in the solid state by IR, FIR spectroscopy and single crystal X-ray diffraction. The complexes display distorted octahedral geometries. X-ray structures of **1** and **2** reveal that the $ReCl_2NP$ fragments are equatorially disposed and the oxygens, terminal oxo and alcoholato, lie in axial positions. The pyrimidine coordinates as a monodentate or bridging ligand. Detailed temperature dependent ^1H NMR analysis for both **1** and **2** shows that in solution the diaza moiety exhibits hindered rotation about the Re–N bond. Furthermore two concomitant conformation changes, one in the metallacycle and the second in the phosphorus cycle, are also observed for dimer **2**.

Crown Copyright © 2008 Published by Elsevier Ltd. All rights reserved.

1. Introduction

Attention to the chemistry of bicyclic hydrospirophosphoranes stems not only from their application as convenient reagents providing routes to bolaform- and gemini-type phosphorus acid surfactants, but also as peptide coupling agents as well [1–3]. Tetraoxaspirophosphoranes, represented by 2,2′-spirobi(1,3,2-benzodioxaphosphole), can easily induce the formation of peptide bonds in the process of the construction of dipeptides, polypeptides and proteins with a reduced effect of racemization [4]. Furthermore, it was recently reported that spiro-[10-P-5]-phosphoranes derived from amino acids exhibit a distinct inhibition activity to tyrosinase, a meaningful enzyme in the formation of melanin pigment found in plants and animals [5]. It is worth mentioning that a spirophosphorane compound containing the Ileucine residue reveals a 96% rate of inhibition, better than the whitening reagent Arbutin (88%) used in cosmetology.

A novel application of spirophosphoranes was demonstrated by Gavrilov and coworkers, using P,N and P,O bidentate derivatives of hydrospirophosphoranes as ligands for the synthesis of a range of new systems including Rh, Pd and Pt complexes. Applications of these ligands in metal-promoted homogenous catalyst systems have been described too [6].

In recent years, work in our laboratory has also centred on the coordination chemistry of hydrospirophosphoranes. As a part of the continuing investigations on the spirophosphorane ligand HP∼O [(HP∼O = $HP(OCMe_2CMe_2O)_2$) 2,2,3,3,7,7,8,8-octamethyl-1,4,6,9-tetraoxa-5λ^5 phosphaspiro[4,4]nonane], we were fruitful in our efforts to obtain a class of new rhenium(V) complexes: $ReOX_2(P{\sim}O)L$ (X = Cl, Br, I; L = py, PPh_3, $OPPh_3$) [7,8].

Keeping in mind that metal ions entailment in medicine and biology often needs coordination of planar N-donor ligands such as purines, imidazoles or pyrimidines, we have made an afford to widen the family of oxo-rhenium(V) complexes with the HP∼O ligand. Introducing the diaza molecule along with the bifunctional $P{\sim}O^-$ ligand in the metal complexes should provide stable compounds which might also be considered as biologically non-innocent systems. Spatial orientation of the N-donors with respect to other ligands and their distribution in the molecule is the second reason for incorporation of the diaza molecule into rhenium complexes. This interest has led us to construct new pyrimidine complexes of intermediate oxidation state, mono- and diore oxo-rhenium(V) compounds with the hydrospirophosphorane derived chelate ligand HP∼O. This report includes the description of the synthesis, molecular structure, spectroscopic characterization and fluxionality of two complexes, *cis*-$ReOCl_2(P{\sim}O)pym$ and *cis*-$[ReOCl_2(P{\sim}O)]_2(\mu$-pym).

2. Experimental

2.1. General procedure

Chemicals and deuterated solvents were purchased from Aldrich and Fluka, and were used as received. All preparations were

* Corresponding author. Tel.: +48 71 3757368; fax: +48 71 3282348.
E-mail address: zag@wchuwr.pl (A. Skarżyńska).

0277-5387/$ - see front matter Crown Copyright © 2008 Published by Elsevier Ltd. All rights reserved.
doi:10.1016/j.poly.2008.10.045

performed in an atmosphere of dry, oxygen-free nitrogen, using conventional Schlenk techniques. Solvents were carefully dried and deoxygenated by standard methods [9]. The ligand precursor $HP(OCMe_2CMe_2O)_2$ 2,2,3,3,7,7,8,8-octamethyl-1,4,6,9-tetraoxa-5λ^5 phosphaspiro[4,4]nonane, abbreviated as HP∼O, was prepared according to the literature method [10]. $ReOCl_2(OEt)(pym)_2$ and *trans*-$ReOCl_2(P{\sim}O)(PPh_3)$ were synthesized as previously reported [11,7].

IR and FIR measurements were performed in KBr pellets either with a Nicolet FTIR Impact 400 or in Nujol with a Bruker IFS 113V. ^1H, $^{31}P\{^1H\}$ NMR spectra were obtained on a Bruker AMX and Avance III spectrometers (300 MHz for ^1H NMR). The chemical shifts δ are given in ppm towards TMS (^1H) and H_3PO_4 (^{31}P) using deuterated solvent CD_2Cl_2 as the lock and reference (^1H), respectively. UV–Vis spectra in CH_2Cl_2 solution were obtained on a Carry 500. Elemental analyses were performed on a Vario EL III apparatus.

2.2. Synthesis of the complexes

2.2.1. *cis*-$ReOCl_2(P{\sim}O)(pym)$ (**1**)

Method (a): The hydrospirophosphorane ligand HP∼O (0.24 g, 0.91 mmol) was added to a suspension of *trans*-$ReOCl_2(OEt)(pym)_2$ (0.20 g, 0.42 mmol) in toluene (7 cm^3). The reaction mixture was heated and stirred vigorously for 4 h until the starting compound reacted and a light violet crystalline solid was afforded. The crude product was filtered, washed with diethyl ether and dried *in vacuo* (0.22 g, 85%). Single crystals suitable for X-ray analysis were obtained by re-crystallization from a dichloromethane/ethyl ether solution.

Anal. Calc. for $C_{16}H_{28}Cl_2N_2O_5PRe$: C, 31.17; H, 4.58; Cl, 11.50; N, 4.54. Found: C, 31.29; H, 4.51; Cl, 11.80; N, 4.52%; ν_{max}(KBr)/cm^{-1} 955vs ν(Re═O), 926s and 1018s ν(C–O–P), 1553w and 1558w ν(C═N); ν_{max} (Nujol)/cm^{-1} 149w, 238m, 269m, 289s, 326s (Re–P), (Re–N), (Re–Cl); $\lambda_{max}(CH_2Cl_2)$/nm (ε/$dm^3\,mol^{-1}\,cm^{-1}$) 242 (15040), 344 (4030), 498 (190).

Method (b): A suspension of *trans*-$ReOCl_2(P{\sim}O)(PPh_3)$ (0.20 g, 0.25 mmol) and pyrimidine (0.06 cm^3, 0.76 mmol) in decahydronaphthalene (7 cm^3) was refluxed for 4 h until the starting compound reacted and a light-violet solid was obtained. The product was filtered, washed with diethyl ether and dried *in vacuo* (0.12 g, 78%).

2.2.2. *cis*-$[ReOCl_2(P{\sim}O)]_2(\mu$-pym) ($2\cdot(CH_3)_2CO$)

A toluene suspension (10 cm^3) of *cis*-$ReOCl_2(P{\sim}O)(pym)$ (0.22 g, 0.36 mmol) and *trans*-$ReOCl_2(P{\sim}O)(PPh_3)$ (0.29 g, 0.36 mmol) was refluxed for 3 h, during which time the dark violet suspension turned into a red solution. The solvent was partially removed by evaporation under vacuum. On standing in a fridge for several days, dark red crystals of *cis*-$[ReOCl_2(P{\sim}O)]_2(\mu$-pym) were collected. The product was filtered, washed with diethyl ether and dried (0.25 g, 60%). Crystals appropriate for X-ray analysis were obtained by re-crystallization from acetone/ethyl ether solution.

Anal. Calc. for $C_{28}H_{52}Cl_4N_2O_{10}P_2Re_2$: C, 29.17; H, 4.55; Cl, 12.13; N, 2.43. Found: C, 30.20; H, 4.49; Cl, 12.11; N, 2.14%); ν_{max}(KBr)/cm^{-1} 956vs ν(Re═O), 922s and 1018s ν(C–O–P), 1603w ν(C═N); ν_{max} (Nujol)/cm^{-1} 150w, 231m, 246m, 289m, 310s cm^{-1} (Re–P), (Re–N), (Re–Cl); $\lambda_{max}(CH_2Cl_2)$/nm (ε/$dm^3\,mol^{-1}\,cm^{-1}$) 240sh (15020), 319 (3645), 525 (401);

2.3. Crystal structure determination

The data, collected on KM4CCD diffractometer, were corrected for Lorentz and polarization effects. Data reduction was carried out using the Oxford Diffraction (Poland) programs. The structure was solved by the Patterson method using SHELXS-97 and refined by the full-matrix least-squares method on F^2 using SHELXL-97 software [12]. Non-hydrogen atoms were refined with anisotropic thermal parameters. The hydrogen atoms were set in calculated positions and refined using the riding model with a common fixed isotropic thermal parameter.

3. Results and discussion

3.1. Preparation and spectroscopic characterization

The mononuclear complex *cis*-$ReOCl_2(P{\sim}O)$pym **1** can be prepared according to the method recently published for the analogue *cis*-$ReOCl_2(P{\sim}O)$py [13]. Treatment of the $ReOCl_2(OEt)(pym)_2$ precursor with a two fold excess of the HP∼O ligand, that reacts in its tautomeric deprotonated form as an uninegative bidentate chelate $(OCMe_2CMe_2O)POCMe_2CMe_2O^-$, leads to the replacement of both EtO^- and pym ligands, affording complex **1**. Alternatively **1**

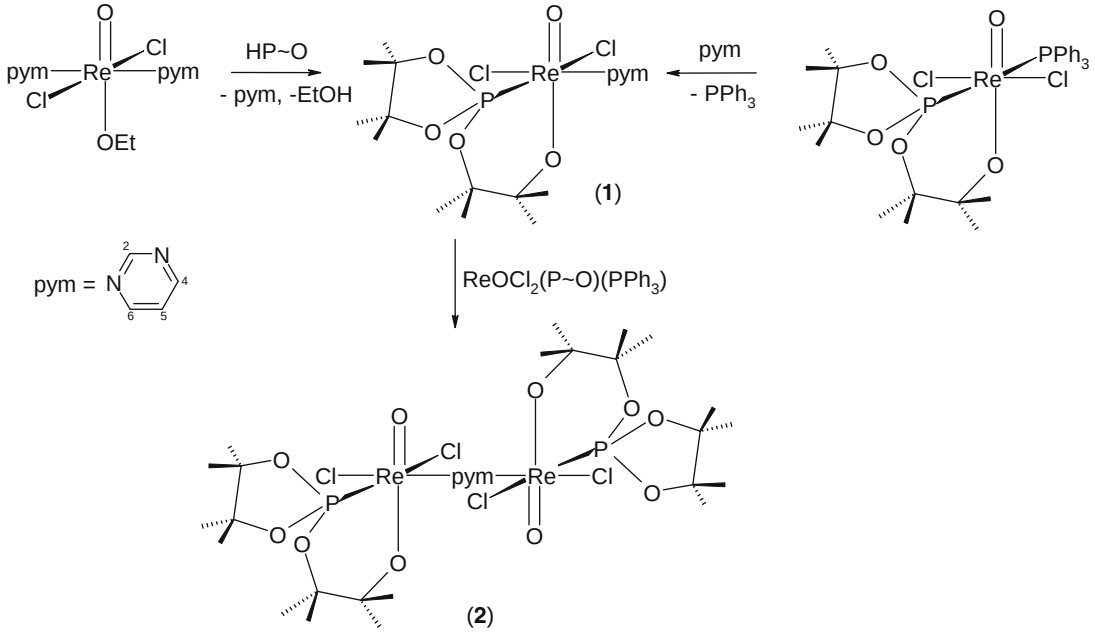


Chart 1.

Table 1
^{1}H NMR and ^{31}P{^{1}H} NMR spectroscopic data of the mononuclear $ReOCl_2(P{\sim}O)(pym)$ **1** and dinuclear $[ReOCl_2(P{\sim}O)]_2(\mu\text{-pym})$ **2** complexes in dichloromethane solution at room temperature.

Complex	^{1}H NMR δ/ppm (int., mult., J/Hz)		^{31}P{^{1}H} NMR δ/ppm
	Methyl groups	Pyrimidine ligand	
$ReOCl_2(P{\sim}O)(pym)$ **1**	0.95, 0.98, 1.20, 1.40, 1.45 1.48, 1.56, 1.58 (24H, s's)	7.66 (1H, tm, 5), 8.86 (1H, m) 9.10 (1H, dm, 2), 9.52 (1H, s)	87.79
$[ReOCl_2(P{\sim}O)]_2(\mu\text{-pym})$ **2**	1.25, 1.42, 1.52, 1.58 (48H, s's)	8.12 (1H, tm, 6), 9.51 (2H, dm, 3) 9.87 (1H, s)	93.44

can be obtained in a substitution reaction of the labile triphenylphosphine ligand for pyrimidine in *trans*-$ReOCl_2(P{\sim}O)(PPh_3)$ (see Chart 1). The synthesis was performed in decahydronaphthalene in order to lower the solubility of the product that precipitates from the reaction mixture. **1** was also employed as the substrate in the preparation of the dinuclear compound *cis*-$[ReOCl_2(P{\sim}O)]_2(\mu\text{-pym})$ **2**. The equimolar reaction of **1** with *trans*-$ReOCl_2(P{\sim}O)(PPh_3)$ in refluxing toluene gave rise to the dimer **2**, which can merely be achieved in a prolonged dimerization process of **1** performed in boiling toluene. Both complexes **1** and **2** were isolated as air-stable, microcrystalline solids, well soluble in dichloromethane, and sparingly in acetone and chloroform.

Compounds **1** and **2** consist of one and two discrete $ReOCl_2(P{\sim}O)N$ units, respectively. Dimer **2** comprises of two subunits of opposite configuration around the stereogenic rhenium centre. The *trans* O═Re–O– entity gives rise to a strong characteristic stretching vibration in the infrared spectra. For mono and dimeric compounds with the $P{\sim}O^-$ ligand, described earlier, the ν(Re═O) stretching vibrations appear at 956 and 975 cm^{-1} [7,14]. The values are roughly the same as reported for other $ReOCl_2(OR)(N\text{-heterocycle})_2$ complexes, usually observed in the 950–975 cm^{-1} region [11,15]. In the FIR area the ambiguity in the assignment of the stretching vibrations ν(Re–P), ν(Re–N) and ν(Re–Cl) can be solved based on the results of our prior experimental and theoretical work [8]. The absorptions of weak and medium intensity (at 149 and 238 or 269 cm^{-1} for **1**; 150 and 231 or 246 cm^{-1} for **2**) might be considered as ν(Re–P) and ν(Re–N) stretching vibrations, respectively. Meanwhile, the higher frequency values at 289 and 326 cm^{-1} (for **1**), and 289 and 310 cm^{-1} (for **2**) can carefully be ascribed as ν_{as}(Re–Cl) and ν_s(Re–Cl) absorptions.

Proton nuclear magnetic resonance (^{1}H NMR) spectroscopy is a powerful method for structural as well as molecular dynamic studies of the mono and dinuclear complexes **1** and **2**. The spectroscopic studies at room temperature reveal two sets of signals relevant to $P{\sim}O^-$ and the pyrimidine ligand. In addition they allow recognition between the monomer and dimer compounds. Eight equal intensity resonance signals for **1**, observed in the aliphatic range (0.6–1.8 ppm), correspond to eight magnetically non-equivalent methyl groups of the spirophosphorane $P{\sim}O^-$ and point to C_1 symmetry around the metal centre (Table 1). Coordination of the pyrimidine ring to the $ReOCl_2(P{\sim}O)$ unit, manifested by four resonances in the aromatic region, both lowers the symmetry of the diaza molecule and shifts the signals downfield.

Variable temperature spectra were recorded at temperatures between ambient and 193 K (Fig. 1). On cooling a solution of **1** to 233 K, all the NMR spectral lines broadened, with the exception of the H4 and H5 signals, due to the *para*- and *meta*-ring protons. Then the resonance lines coalesced at 223 K, and finally sharpened at 203 K. Further reduction of the temperature to 193 K causes widening of some aromatic protons (δ 0.86, 0.935 ppm) and splitting of the *meta*-H5 signal.

In order to obtain more information concerning the capability of the aromatic ring to rotate around the Re–N bond, we measured the variable-temperature ^{1}H NMR spectra of the two isomers *cis*-$ReOCl_2(P{\sim}O)py$ and *trans*-$ReOCl_2(P{\sim}O)py$.[1] A similar splitting of the resonances both in the aliphatic and the aromatic region at lower temperatures was detected for isomer *cis*-$ReOCl_2(P{\sim}O)py$ (Supplementary data, Fig. S1). The resulting pattern of the aliphatic signals for *cis*-$ReOCl_2(P{\sim}O)py$ was roughly the same as for *cis*-$ReOCl_2(P{\sim}O)pym$. Moreover analogous splitting in aromatic range upon freezing to 193 K was noticed for the *ortho*- and *meta*-proton signals of *cis*-$ReOCl_2(P{\sim}O)py$ as well.

The fact that the *o*- and *m*-protons split into non-equal intensity pairs and that there is no temperature changes on the *p*-protons indicates that two different topomers of complex **1** of disparate population may exist in solution (Chart 2). The N-heterocycle occurs in two 'frozen out' environments and the pyrimidine interchanges between these location rapidly at ambient temperature.

While the pyrimidine ligand possesses a pair of nitrogen donor atoms, we also have to take account of the 1,3-metallotropic shift phenomenon, especially as fluxionality of transition metal–azine complexes has been determined previously [16–18]. However ^{1}H NMR spectra performed from room temperature up to 333 K in $CDCl_3$ show no evidence of fluxionality for both **1** and **2**.

The NMR spectra of *cis*-$[ReOCl_2(P{\sim}O)]_2(\mu\text{-pym})$ **2** (Fig. 2) reveal temperature dependant changes too. At the temperature of 298 K four signals (versus eight for **1**) in the aliphatic resonances range, attributed to 16 methyl groups, appear. As the temperature is decreased the signals broaden, and at 223 K they approach coalescence. Eight methyl group resonances of almost equal intensity observed at 213 K split further as the temperature is lowered. At 193 K the structure seems to be frozen and 12 signals (δ 0.96, 1.03, 1.06, 1.11, 1.18, 1.20, 1.29, 1.40, 1.50, 1.59, 1.66, 1.68 ppm) of different intensity were detected. As an inference from this fact we can conclude that in this temperatures range at least two concomitant conformational changes, one in the metallacycle and the second in the phosphorous cycle appear in the system. Our previous studies on *trans*-$ReOCl_2(P{\sim}O)(PPh_3)$ (at rt exist four methyl signals) have shown that low-temperature NMR spectra can detect such dynamic exchange processes, so the proposed conclusion is in accordance with the earlier statement [7].

The aromatic region of the spectrum undergoes changes as well. Three instead of four (for **1**) resonances (at 298 K) for protons H2-pym, H4,6-pym and H5-pym, implying that the pyrimidine ring acts as bridging ligand, were observed. Such a bridging coordination mode of the diaza ligand corroborates the signals integration as well. On freezing, the two resonances at δ 9.51 and 9.87 ppm, assignable to H4,6 and H2 protons, broaden and approximately coalescence at 213 K. Each splits further into two signals of the same intensity, detected at 193 K. The most distant proton H5 of the coordinated ligand experiences the least influence by the rhenium coordination sphere. The changes in the spectra again imply that the pyrimidine H4,6 and H2 protons experience dissimilar chemical environments due to the fixed position of the molecule

[1] Complexes *cis*-ReOCl2(P∼O)(py) and *trans*-ReOCl2(P∼O)(py) were synthesized according to the procedure previously reported elsewhere [8].

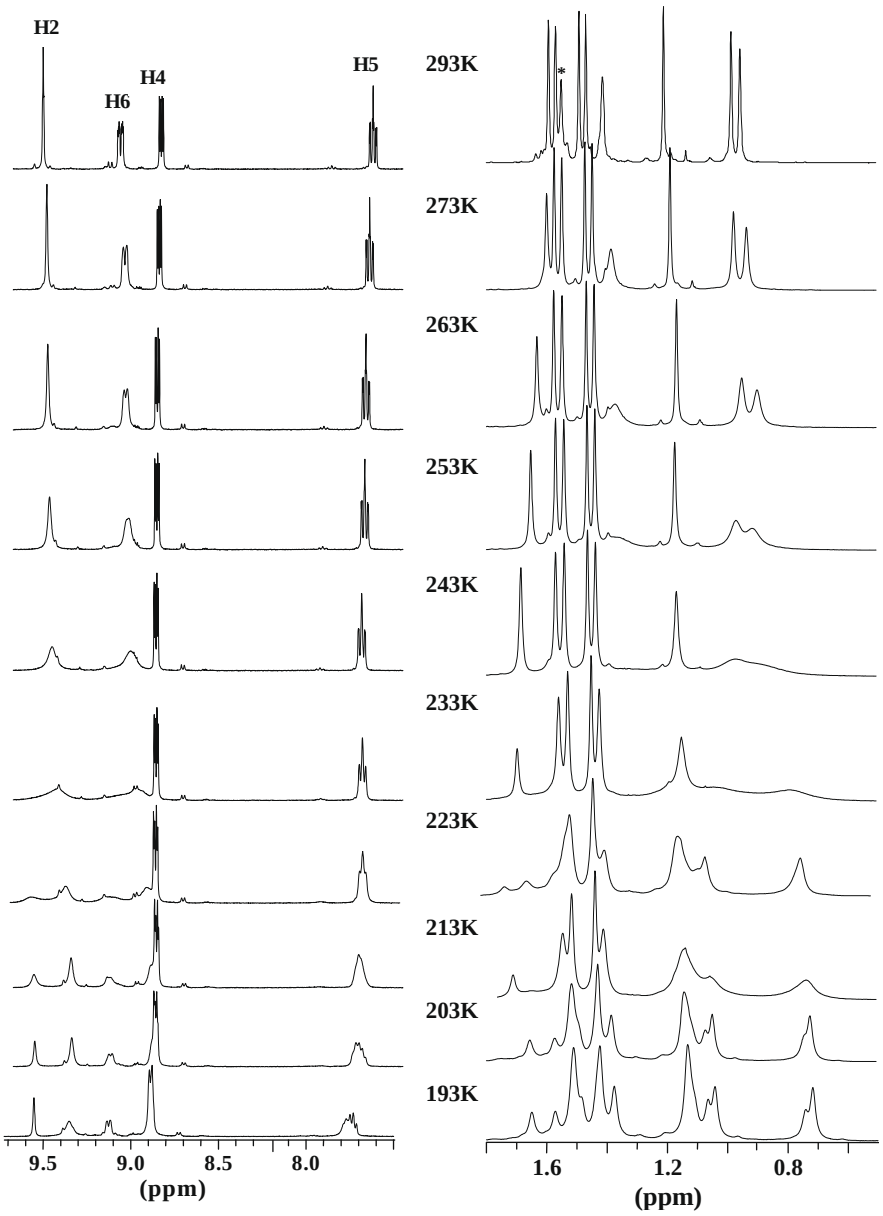


Fig. 1. ^{1}H NMR spectra of **1** run at different temperatures. * denotes H_2O impurity in CD_2Cl_2.

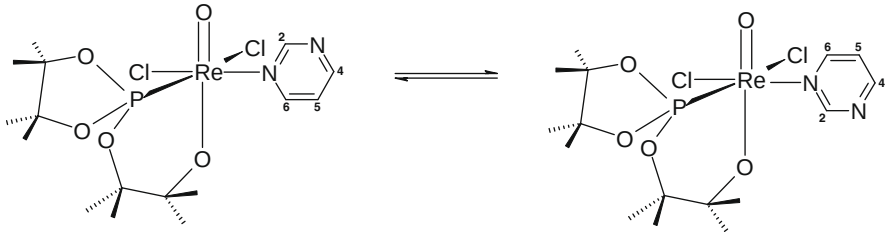


Chart 2. The proposed solution topomers of complex *cis*-$ReOCl_2$(P∼O)(pym) **1**.

upon freezing. The steric hindrance of the rhenium moiety ReOCl2(P∼O) appears to play a determinant role for the pyrimidine rotation.

The electronic spectra of the pink-violet complexes **1** and **2** display relatively weak bands at 525 nm, that are distinct from that reported for *cis*-$ReOCl_2$(P∼O)(py). These transitions are thought to have significant ligand field character d–d (π^*) with a contribution of a metal-to-oxo ligand charge transfer (MLCT). The excitations at about 320 and 340 nm with large absorption coefficients are tentatively assigned to CT bands.

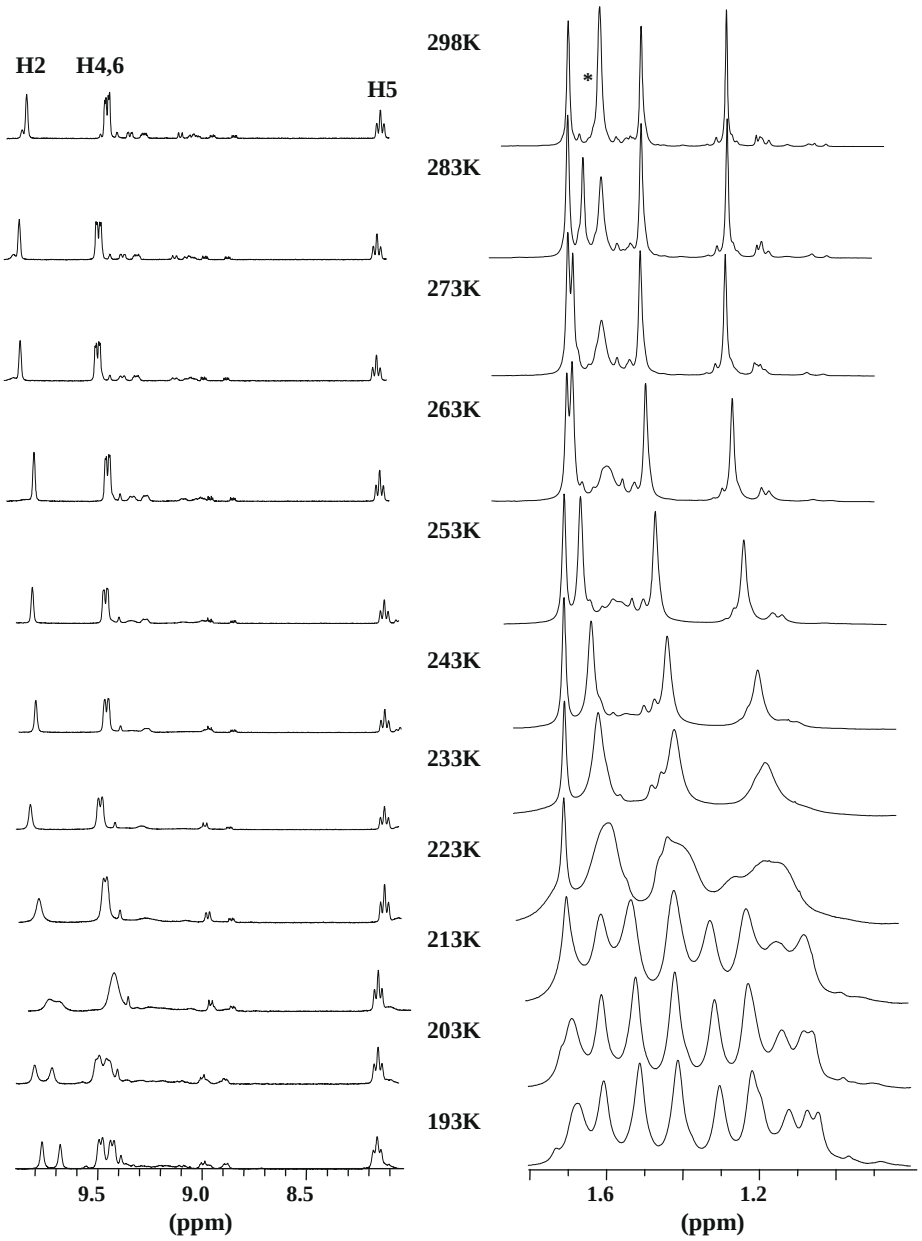


Fig. 2. ^{1}H NMR spectra of **2** run at different temperatures. * denotes overlapped impurity of H_2O in CD_2Cl_2. (The low intensity signals in the aromatic range are due to an impurity of **1**.)

4. X-ray structure analysis of complexes 1 and 2

The crystal structures of the complexes *cis*-$ReOCl_2$(P∼O)(pym) **1** and *cis*-[$ReOCl_2$(P∼O)]$_2$(μ-pym) (**2** · $(CH_3)_2CO$), resolved by X-ray analysis, corroborates that the stereochemistries of the molecules are nearly like those anticipated from the spectroscopic studies in solution for **1** and **2**. The crystallographic data of **1** and **2** are given in Table 2. A perspective drawing of the structures showing the atom numbering are depicted in Figs. 3 and 4, while selected bond lengths and angles are listed in Table 3.

Complex **1** generates enantiomorphic crystals belonging to the orthorhombic space group $P2_12_12_1$, whilst the dinuclear compound **2** crystallizes in the triclinic $P\bar{1}$ space group. The overall geometry about the central rhenium atoms for both complexes **1** and **2** can be best described as a distorted octahedral, with similar $ReOCl_2$(P∼O)N atomic arrangements. The equatorial positions are occupied by two chlorides, one phosphorous and one nitrogen atom in both cases. The apical positions are filled up by oxygens: terminal oxo and alcoholato oxygens. The rhenium atoms are displaced 0.095 and 0.069 Å towards the oxo ligands from the equatorial plane formed by the Cl1Cl2N1P1 atoms for complex **1** and **2**, respectively, and 0.080 Å from the equatorial plane formed by Cl3Cl4N2P2 found for second half of molecule **2**. The short Re–O1 bond lengths of 1.699(5) and 1.700(3) Å, and Re–O2 of 1.703(3) Å are typical for rhenium(V) monooxo complexes and indicate multiple-bond character [19,20]. The Re–$O_{pinacolato}$ bond distances of 1.894–1.898 Å are comparable to that of the alcoholate ligand [21,22] with a *trans* O=Re–O arrangement, in that the total bond order is close to four. The oxygen atoms are not aligned with the metal. The O=Re–O angles are equal to 168.7(3)° for **1** and 166.9(1)° and 164.6(1)° for **2**. Whereas the Re–Cl bond distances appear to be in the normal range (2.35–2.45 Å), the Re–Cl1 and

Table 2
Crystallographic data for $ReOCl_2(P{\sim}O)pym$ **1** and $[ReOCl_2(P{\sim}O)]_2(\mu\text{-pym})$ ($\mathbf{2}\cdot(CH_3)_2CO$).

	$ReOCl_2(P{\sim}O)pym$ **1**	$[ReOCl_2(P{\sim}O)]_2(\mu\text{-pym})$ ($\mathbf{2}\cdot(CH_3)_2CO$)
Empirical formula	$C_{16}H_{28}Cl_2N_2O_5PRe$	$C_{28}H_{52}Cl_4N_2O_{10}P_2Re_2\cdot(CH_3)_2CO$
Formula weight	616.47	1210.93
Temperature (K)	100 (2)	100 (2)
Crystal size (mm)	0.18 × 0.15 × 0.13	0.16 × 0.12 × 0.10
Space group	$P2_12_12_1$	$P\bar{1}$
a (Å)	9.882 (2)	12.6480 (5)
b (Å)	11.792 (2)	12.8420 (4)
c (Å)	18.263 (4)	14.2854 (4)
α (°)	90.00	87.506 (2)
β (°)	90.00	86.193 (3)
γ (°)	90.00	74.261 (3)
V (Å^3)	2128.0 (7)	2227.61 (13)
Z	4	2
ρ_{calc} (Mg m^{-3})	1.924	1.805
λ (Å)	0.71073	0.71073
$F(000)$	1208	1188
θ Range (°)	3.0–27.0	3.2–27.0
Reflection collected	16173	25521
Unique reflection	4643	9696
S	0.928	0.997
R_1/wR_2 indices	0.049/0.073	0.028/0.057

$R_1 = \sum||F_o| - |F_c||/\sum|F_o|$.
$wR_2 = \{\sum[w(F_o^2 - F_c^2)^2]/[w(F_o^2)^2]\}^{1/2}$.
$w = 1/[\sigma^2(F_o^2) + (aP)^2]$ where $P = (F_o^2 + 2F_c^2)/3$, a = 0.0220 (**1**), 0.0331 (**2**).

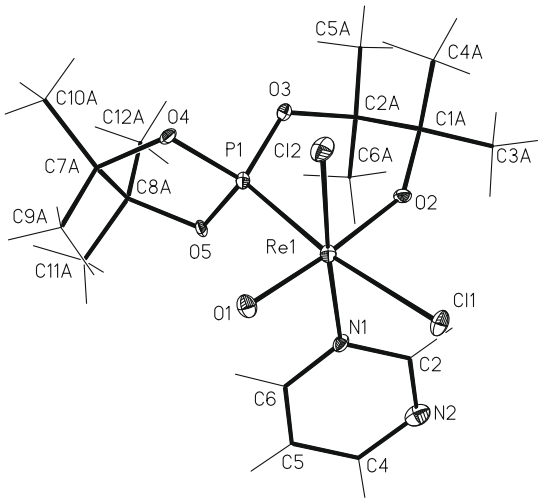


Fig. 3. Molecular structure of *cis*-$ReOCl_2(P{\sim}O)pym$ (**1**).

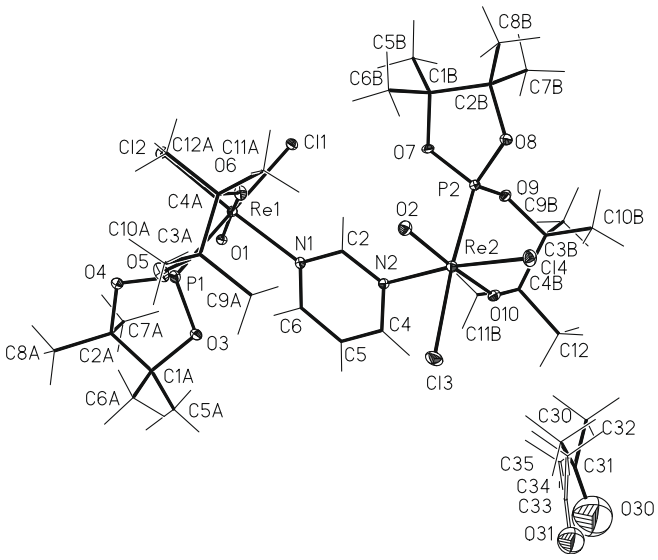


Fig. 4. Molecular structure of *cis*-$[ReOCl_2(P{\sim}O)](\mu\text{-pym})$ ($\mathbf{2}\cdot(CH_3)_2CO$).

Re–Cl3 bonds are moderately elongated by ca. 0.04 Å in comparison with Re–Cl2 and Re–Cl4. One can explain this strengthening as the expense of the steric *trans* effects to the Re–P bond [23], caused by the strong π-acceptor character of the phosphite ligand.

Both the five-membered POCCO and six-membered RePOCCO cycles are puckered. The five-membered rings with tetrahedrally coordinated phosphorous atoms adopt a slightly deformed envelope conformation with a deviation of the C8A atom by 0.52 Å for **1**, C1A and C2B atoms by 0.518 and 0.516 Å from the main planes for **2**. The metallacycles reveal half chair conformations with torsion angles equal to O2Re1P1O3 = −15.08° for **1**, O6Re1P1O5 = 8.16° and O10Re2P2O9 = 5.87° for **2**. As expected, comparison of the bond lengths and bond angles in **1** and **2** with the previously obtained by us congeners *cis*-$ReOCl_2(P{\sim}O)py$ or *trans*-$ReOCl_2(P{\sim}O)py$ shows that the values are in good agreement and the structures do not differ significantly [8,13].

5. Conclusions

The reaction of the oxo starting material $ReOCl_2(OEt)(pym)_2$ with the $HP(OCMe_2CMe_2O)_2$ ligand in toluene has produce *cis*-$ReOCl_2(P{\sim}O)(pym)$ **1**. Attempts to obtain a dinuclear analogue pro-

Table 3
Relevant bond distances (Å) and angles (°) for $ReOCl_2(P{\sim}O)pym$ **1** and $[ReOCl_2(P{\sim}O)]_2(\mu\text{-pym})$ ($\mathbf{2}\cdot(CH_3)_2CO$).

$ReOCl_2(P{\sim}O)pym$ **1**		$[ReOCl_2(P{\sim}O)]_2(\mu\text{-pym})$ ($\mathbf{2}\cdot(CH_3)_2CO$)			
Bond lengths					
Re(1)–O(1)	1.699(5)	Re(1)–O(1)	1.700(3)	Re(2)–O(2)	1.703(3)
Re(1)–O(2)	1.898(5)	Re(1)–O(6)	1.895(3)	Re(2)–O(10)	1.893(3)
Re(1)–N(1)	2.169(7)	Re(1)–N(1)	2.196(3)	Re(2)–N(2)	2.200(3)
Re(1)–P(1)	2.355(2)	Re(1)–P(1)	2.363(1)	Re(2)–P(2)	2.367(1)
Re(1)–Cl(1)	2.423(2)	Re(1)–Cl(1)	2.4271(9)	Re(2)–Cl(3)	2.414(1)
Re(1)–Cl(2)	2.372(2)	Re(1)–Cl(2)	2.3791(9)	Re(2)–Cl(4)	2.356(1)
Bond angles					
O(1)–Re(1)–O(2)	168.7(3)	O(1)–Re(1)–O(6)	166.9(1)	O(2)–Re(2)–O(10)	164.6(1)
O(1)–Re(1)–N(1)	87.1(3)	O(1)–Re(1)–N(1)	86.9(1)	O(2)–Re(2)–N(2)	85.4(1)
O(2)–Re(1)–N(1)	88.0(3)	O(6)–Re(1)–N(1)	88.3(1)	O(10)–Re(2)–N(2)	85.3(1)
O(1)–Re(1)–P(1)	88.2(2)	O(1)–Re(1)–P(1)	85.60(9)	O(2)–Re(2)–P(2)	86.7(1)
O(2)–Re(1)–P(1)	82.0(2)	O(6)–Re(1)–P(1)	82.43(9)	O(10)–Re(2)–P(2)	81.94(8)
N(1)–Re(1)–P(1)	95.0(2)	N(1)–Re(1)–P(1)	91.86(8)	N(2)–Re(2)–P(2)	94.67(9)
O(1)–Re(1)–Cl(2)	94.2(2)	O(1)–Re(1)–Cl(2)	93.18(9)	O(2)–Re(2)–Cl(3)	99.6(1)
N(1)–Re(1)–Cl(2)	175.3(2)	N(1)–Re(1)–Cl(2)	177.06(8)	N(2)–Re(2)–Cl(3)	85.25(9)
P(1)–Re(1)–Cl(2)	89.57(8)	P(1)–Re(1)–Cl(2)	91.07(3)	P(2)–Re(2)–Cl(3)	173.69(4)

vided a dimer with the diastereomeric configuration *cis*-[$ReOCl_2$(P∼O)](μ-pym) **2**. X-ray analysis corroborates a distorted octahedral geometry of the rhenium atoms and the existence of a *trans* O═Re–O– arrangement of the terminal oxygen and pinacolato atoms, determining their high stability. The two complexes, either mono or dinuclear, are new components of the oxo–rhenium(V) complex set, where coordination of hydridospirophosphorane occurs with the breakage of the P–O bond and formation of an opain–chain P(III) derivative. In solution the complexes are fluxional. The low-temperature ^{1}H NMR data for **1** and **2** reveal dynamic exchange process concerning the aza protons. Its resonances are sensitive to the fluxional motion and suggest that interconversion occurs between two topomers. Additionally NMR data show that dimer **2** undergoes two dynamic exchange processes contemporaneously, pertinent for the P∼O^- ligand, one in the metallacycle coupled with the second in the phosphorocycle.

Appendix A. Supplementary data

CCDC 694051 and 694052 contain the supplementary crystallographic data for **1** and **2**. These data can be obtained free of charge via http://www.ccdc.cam.ac.uk/conts/retrieving.html, or from the Cambridge Crystallographic Data Centre, 12 Union Road, Cambridge CB2 1EZ, UK; fax: (+44) 1223-336-033; or e-mail: deposit@ccdc.cam.ac.uk. Supplementary data associated with this article can be found, in the online version, at doi:10.1016/j.poly.2008.10.045.

References

[1] K. Vercruysse-Moreira, C. Dejugnat, G. Etemad-Moghadam, Tetrahedron 58 (2002) 5651.
[2] C. Déjgant, G. Etemad-Moghadam, I. Rico-Lattes, Chem. Commun. (2003) 1858.
[3] J.I.G. Cadogan, I. Gosney, D. Randles, S. Yaslak, R.P. Amblerc, J. Chem. Soc., Chem. Commun. (1982) 298.
[4] J.I.G. Cadogan, I. Gosney, S. Yaslak, United States Patent 4,440,676 1984.
[5] L. Yu, Z. Liu, H. Fang, Q.L. Zeng, Y.F. Zhao, Amino Acids 28 (2005) 369.
[6] K.N. Gavrilov, A.I. Polosukhin, O.G. Bondarev, S.E. Lyubimov, K.A. Lyssenko, P.V. Petrovskii, V.A. Davankov, J. Mol. Catal. A: Chem. 196 (2003) 39.
[7] T. Głowiak, W.K. Rybak, A. Skarżyńska, Polyhedron 19 (2000) 2667.
[8] W.K. Rybak, A. Skarżyńska, L. Szternberg, Z. Ciunik, T. Głowniak, Eur. J. Inorg. Chem. (2005) 4964.
[9] D.D. Perrin, W.L.F. Armarego, Purification of Laboratory Chemicals, 3rd ed., Pergamon Press, Oxford, 1998.
[10] D.L. Haire, E.G. Janzen, I. Hrvoic, Magn. Res. Chem. 37 (1999) 767.
[11] E. Iengo, E. Zangrando, S. Mestroni, G. Fronzoni, M. Stener, E. Alessio, J. Chem. Soc., Dalton Trans. (2001) 1338.
[12] G.M. Sheldrick, SHELXL 97, Program for Crystal Structure Refinement, University of Göttingen, 1997.
[13] W.K. Rybak, A. Skarżyńska, T. Głowniak, Angew. Chem., Int. Ed. 42 (2003) 1725.
[14] A. Skarżyńska, W.K. Rybak, T. Głowiak, Polyhedron 20 (2001) 2667.
[15] S. Fortin, A.L. Beauchamp, Inorg. Chim. Acta 279 (1998) 159.
[16] Y. Chen, R.E. Shepherd, Inorg. Chem. 37 (1998) 1249.
[17] E.W. Abel, P.J. Heard, K.G. Orrell, M.B. Hursthouse, K.M.A. Malik, J. Chem. Soc., Dalton Trans. (1995) 3165.
[18] A. Gelling, K.G. Orrell, A.G. Osborne, V. Šik, J. Chem. Soc., Dalton Trans. (1996) 3371.
[19] W.A. Nugent, J.A. Mayer, Metal–Ligand Multiple Bond, Wiley-Interscience, New York, 1988.
[20] T.R. Cundari, Chem. Rev. 100 (2000) 807.
[21] G.F. Ciani, G.D. Alfonso, P.F. Romiti, A. Sironi, M. Freni, Inorg. Chim. Acta 72 (1983) 29.
[22] R. Chiozzone, R. Gonzales, C. Kremer, G. De Munno, J. Faus, Inorg. Chim. Acta 325 (2001) 203.
[23] B.J. Coe, S.J. Glenwright, Coord. Chem. Rev. 203 (2000) 5.

Polyhedron 28 (2009) 343–348

Contents lists available at ScienceDirect

Polyhedron

journal homepage: www.elsevier.com/locate/poly

A sinapic acid–calix[4]arene hybrid selectively binds Pb^{2+} over Hg^{2+} and Cd^{2+}

Carmelo Sgarlata [a,*], Valeria Zito [b], Giuseppe Arena [a], Grazia Maria Letizia Consoli [c], Eva Galante [c], Corrada Geraci [c,*]

[a] Dipartimento di Scienze Chimiche, Università degli Studi di Catania, Viale A. Doria 6, 95125 Catania, Italy
[b] Istituto di Biostrutture e Bioimmagini, CNR, Sezione di Catania, Viale A. Doria 6, 95125 Catania, Italy
[c] Istituto di Chimica Biomolecolare, CNR, Via del Santuario 110, 95028 Valverde (CT), Italy

ARTICLE INFO

Article history:
Received 31 July 2008
Accepted 20 October 2008
Available online 26 December 2008

Keywords:
Supramolecular chemistry
Calixarenes
Heavy metals
Ion recognition
Selectivity
Stability constants

ABSTRACT

The binding affinity for Pb^{2+}, Cd^{2+} and Hg^{2+} of the sinapic acid–calix[4]arene hybrid **2**, having four sinapyl pendants at the upper rim, has been investigated *via* an UV–Vis study. Compound **2** has better complexing ability than the monomeric *p*-phenetidine derivative **1**. This highlights that the clustering of sinapyl units in a basket-like structure, dictated by the calixarene scaffold, greatly enhances the complexing properties. Ligand **2** forms complexes even with Hg^{2+}, which is not complexed by **1** at all; the complexes formed by **2** with Pb^{2+} and Cd^{2+} are much stronger than the analogous complexes formed by **1**. The UV–Vis investigation shows that the hybrid **2** markedly favors Pb^{2+} over Cd^{2+} and Hg^{2+}. Information on the structural properties of the complex species was obtained by ^{1}H NMR spectroscopy. NMR data show that all three metal ions are placed into the cavity consisting of the calixarene scaffold and the sinapyl pendants, though their binding affects the coordinating regions to a different extent.

© 2008 Elsevier Ltd. All rights reserved.

1. Introduction

The increasing interest in environmental contaminants as Pb^{2+}, Cd^{2+} and Hg^{2+} is documented by the large number of papers appearing about these specific metal ions [1]. These metal ions are largely present in the environment due to fossil fuel combustion, paint, battery and fertilizer industries as well as oil refineries, smelting plants and municipal wastes [2]. Exposure to these non-essential elements remains a serious problem, especially in many developing countries [3]. These highly toxic metals are known to cause health problems such as brain damage [4], nephropathy [5], sluggishness [6], hyperirritability [7], restlessness [8], infertility [9] and a number of diseases in pre-school aged children [4c,10].

Thus, the design and development of efficient ligands that may be used to selectively extract and/or probe these metal ions are turning out to be extremely important. To this end, macrocyclic ligands have been extensively studied [11].

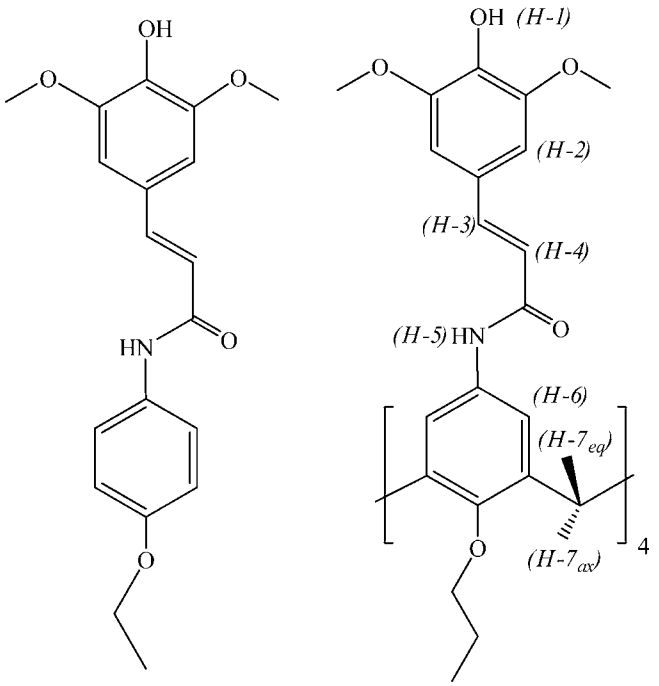
Hydroxycinnamic acids are a class of compounds of biomedical interest widely spread in the plant kingdom [12]. Their biological activity relates not only to their capability to act as antioxidants or enzyme inhibitors but also to their metal chelating properties [13]. Recently, we have reported on the synthesis, the radical scavenging and antioxidant activities of calix[4]arene derivatives bearing hydroxycinnamic acid residues [14].

Calixarene-based macrocycles have been widely used in supramolecular chemistry as platforms to build receptors able to bind ions and molecules of biological and environmental relevance [15]. Among the calix[*n*]arenes, the smallest tetrameric oligomer, calix[4]arene, has attracted significant attention since it may be *ad hoc* tailored to have unique tri-dimensional structures (*cone*, *partial cone*, *1,2-* and *1,3-alternate* conformations) [15a].

Here, we report on the binding ability of the sinapyl–calix[4]arene **2** towards the toxic metals Pb^{2+}, Cd^{2+} and Hg^{2+}. Ligand **2** has the potential to act as a selective binder by virtue of the arrangement of the synapyl units which are anchored onto the calixarene platform in the *all-syn* orientation. In this respect, we compare the chelating ability of **2** to that of the homologous "monomer" *p*-phenetidine derivative **1**.

* Corresponding authors. Tel.: +39 95 738 5071; fax: +39 95 337678 (C. Sgarlata), tel.: +39 95 7212136; fax: +39 95 7212141 (C. Geraci).
E-mail addresses: sgarlata@unict.it (C. Sgarlata), corrada.geraci@icb.cnr.it (C. Geraci).

0277-5387/$ - see front matter © 2008 Elsevier Ltd. All rights reserved.
doi:10.1016/j.poly.2008.10.068



1 **2**

2. Experimental

2.1. General

CH_3CN for spectrophotometry (Merck, Uvasol) was employed throughout. Lead and mercury perchlorates were obtained from Aldrich and were used without any further purification. Cadmium perchlorate solutions were obtained by dissolving a weighed amount of cadmium oxide (Carlo Erba) in CH_3CN, then adding a stoichiometric amount of perchloric acid. Perchlorate solutions were standardized according to the procedures described in the literature [16]. Safer counter ions (*e.g.* tetrafluoroborates) could not be employed owing to their interfering absorption. (**Caution!** *Perchlorates may be explosive and should be handled with caution*). Grade A glassware was used throughout. All reagents for the syntheses and deuterated solvents were purchased from Aldrich and were used without any further purification.

2.2. Synthesis

The *p*-phenetidine derivative **1** was synthesized according to the procedure described by Rajan et al. [17]. Compound **2** was synthesized as described previously [14]; its purity was checked thermogravimetrically as described by Arena et al. [18].

Compound **2**: ^{1}H NMR (400 MHz, CD_3CN/acetone-d_6, 80:20, v/v) δ 1.03 (t, CH_3, J = 7.60 Hz, 12H), 2.32 (CH_2 overlapped CD_3CN), 3.18–4.48 (AX system, $ArCH_2Ar$, J = 13.60 Hz, 8H), 3.74 (s, OCH_3, 24H), 3.87 (t, OCH_2, 8H), 6.49 (d, CH=CH, J = 15.20 Hz, 4H), 6.71 (s, OH, 4H), 6.72 (s, ArH, 8H), 7.04 (s, ArH, 8H), 7.46 (d, CH=CH, J = 15.20 Hz, 4H), 8.31 (s, NH, 4H).

Table 1
$\log\beta$ values[a] for the complex formation of Hg^{2+}, Cd^{2+} and Pb^{2+} with **1** in CH_3CN at 25 °C.

Reaction	$\log\beta$	
	HYPERQUAD	SPECFIT
$Hg^{2+} + \mathbf{1} \leftrightarrows [Hg(\mathbf{1})]^{2+}$	Not detectable	
$Cd^{2+} + \mathbf{1} \leftrightarrows [Cd(\mathbf{1})]^{2+}$	2.62(1)	2.63(1)
$Pb^{2+} + \mathbf{1} \leftrightarrows [Pb(\mathbf{1})]^{2+}$	3.98(3)	3.8(2)

[a] σ in parentheses.

2.3. Spectroscopic measurements

2.3.1. UV–Vis spectra

UV–Vis titrations were carried out as described [19] by using a diode-array spectrophotometer (Agilent 8453) and a precision burette (Hamilton, 1 ml). All measurements were performed in CH_3CN at 25 °C. Addition, equilibration time and data reading were controlled by homemade software. Time intervals for equilibration and reading were systematically changed to avoid artefacts. The titrate concentration ranged from 2.5×10^{-5} to 4.0×10^{-5} mol dm^{-3} and from 1.3×10^{-5} to 1.7×10^{-5} mol dm^{-3} for **1** and **2**, respectively. The titrant (metal ion) concentration was chosen so as to reach the metal/ligand ratio needed to have enough curvature in the molar ratio plot. 55–60 points were recorded for each independent titration run. At least four independent runs were collected for each M–ligand system (M = Hg^{2+}, Pb^{2+} or Cd^{2+}; ligand = **1** or **2**).

Experiments for **1**, carried out with solutions prepared more than 3 h before the titration, showed discrepancies that were time-dependent. For this reason, all **1** solutions had to be freshly prepared and employed immediately. For both ligands the data were collected over the range 215–450 nm for all the cations investigated and were analyzed by using HYPERQUAD [20] and SPECFIT [21]. Both programs allow a multiwavelength treatment of the data. HYPERQUAD follows a procedure that does not imply matrix compression and allows simultaneously refinement of the data from different experimental measurements, whilst SPECFIT combines a chemometric analysis (*Factor Analysis* and Evolving *Factor Analysis*) [22] with a non-linear least squares minimization procedure [23]. Unlike SPECFIT, HYPERQUAD offers the possibility to refine all the titrations simultaneously, which accounts for the smaller standard deviations associated with the values shown in Tables 1 and 2.

2.3.2. NMR spectra

^{1}H NMR (400.13 MHz) spectra were recorded at 25 °C using a Bruker Avance™ 400 spectrometer. Chemical shifts (δ) are expressed in parts per million (ppm) and were referenced to TMS. The complex formation of **2** with Pb^{2+}, Cd^{2+} and Hg^{2+} was studied by adding different aliquots of a stock solution of the metal perchlorate (Pb^{2+} = 2.2×10^{-2} mol dm^{-3}, Hg^{2+} = 0.13 mol dm^{-3} and Cd^{2+} = 0.2 mol dm^{-3} in acetone-d_6) into the NMR tube containing the ligand **2** (5.5×10^{-4} mol dm^{-3}, in CD_3CN/acetone-d_6, 80:20, v/v). NMR spectra were recorded after each addition of metal ion salt (0.5, 1, 1.5 and 3 equiv. for Pb^{2+}; 5, 10, 15 and 25 equiv. for Cd^{2+}, and 3, 6, 9 and 15 equiv. for Hg^{2+}). Changes in the chemical shifts were measured using the free ligand as a reference.

Table 2
$\log\beta$ values[a] for the complex formation of Hg^{2+}, Cd^{2+} and Pb^{2+} with **2** in CH_3CN at 25 °C.

Reaction	$\log\beta$	
	HYPERQUAD	SPECFIT
$Hg^{2+} + \mathbf{2} \leftrightarrows [Hg(\mathbf{2})]^{2+}$	3.84(3)	3.9(2)
$2\,Hg^{2+} + \mathbf{2} \leftrightarrows [Hg_2(\mathbf{2})]^{4+}$	8.14(5)	8.0(1)
$Cd^{2+} + \mathbf{2} \leftrightarrows [Cd(\mathbf{2})]^{2+}$	4.40(9)	4.4(1)
$2\,Cd^{2+} + \mathbf{2} \leftrightarrows [Cd_2(\mathbf{2})]^{4+}$	8.40(8)	8.40(9)
$Pb^{2+} + \mathbf{2} \leftrightarrows [Pb(\mathbf{2})]^{2+}$	7.2(3)	7.2(3)
$2\,Pb^{2+} + \mathbf{2} \leftrightarrows [Pb_2(\mathbf{2})]^{4+}$	11.3(3)	11.3(3)
$Pb^{2+} + 2\,\mathbf{2} \leftrightarrows [Pb(\mathbf{2})_2]^{2+}$	13.3(7)	13.3(7)

[a] σ in parentheses.

3. Results and discussion

3.1. Binding constants

Figs. 1 and 2 show typical titration spectra obtained by titrating a CH_3CN solution of $Cd(ClO_4)_2$ or $Pb(ClO_4)_2$ into a solution of **1** in CH_3CN. Mercury addition does not cause any significant change of the absorption spectrum, indicating that this cation does not form detectable complexes with ligand **1**. The insets of both figures give an immediate perception of how the spectrum changes from the beginning (free ligand) to the end (complex) of the titration.

The spectral changes resulting from the addition of the metal ion were corrected for dilution and analyzed by using two different computer programs (see Section 2). Both programs resort to a multiwavelength treatment of the absorption data; however they use a different refinement strategy. The use of different algorithms and calculation methods minimizes the risk of creation of artefacts [19].

The value of SPECFIT [21] in analysing the data, that is the Evolving Factor Analysis employed by this package, provides a limit to the number of species necessary to explain the changes, *i.e.*, it provides an objective mean of obtaining a chemical model for the system; if the model provided by SPECFIT is also accepted by HYPERQUAD [20], the speciation of the system has to be considered highly reliable. Both packages indicate that the spectrophotometric data may be fitted with a $[M–\mathbf{1}]^{2+}$ ($M = Cd^{2+}$ or Pb^{2+}) species only and that Pb^{2+} binds **1** more efficiently than Cd^{2+}; they also indicate that there are no evidences for the formation of Hg^{2+} complexes (Table 1).

Figs. 3–5 show the UV–Vis titration curves obtained for the hydroxycinnamic acid–calix[4]arene hybrid **2**. It is noteworthy that mercury does not form complexes with the *p*-phenetidine derivative **1**, but it does form complexes with **2**. Furthermore, the shape of molar ratio curves (see insets) show that **2** forms complexes with the three cations having both different stoichiometries and formation constants of different magnitudes. Indeed, this is confirmed by the data analysis that leads to the set of values listed in Table 2.

To obtain molar ratio plots with a curvature suitable for the determination of stability constant values, different metal/ligand ratios had to be reached for the three metal ions, depending upon the magnitude of the stability constants; these ratios were smaller for Pb^{2+} (*i.e.* the metal ion forming the strongest complexes) whereas they were larger for cadmium and mercury. All three cations form species of the type ML and M_2L; Pb^{2+} forms also a species of the type ML_2.

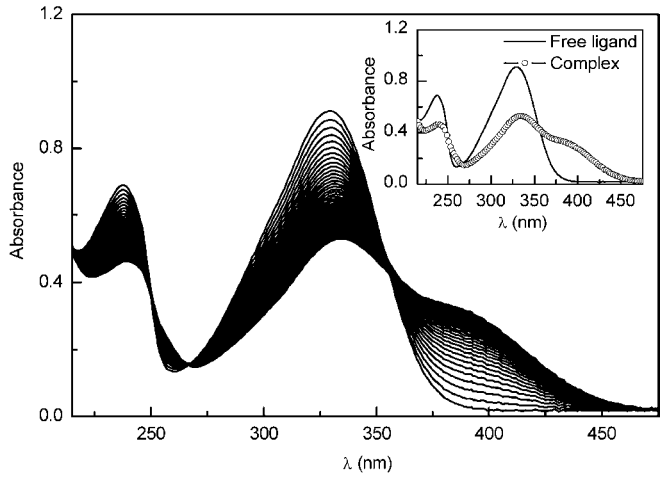


Fig. 1. UV–Vis titration curves for the Cd^{2+}–**1** system in CH_3CN at 25 °C. The inset shows the ligand spectrum before (—) and after (–O–) the metal ion addition.

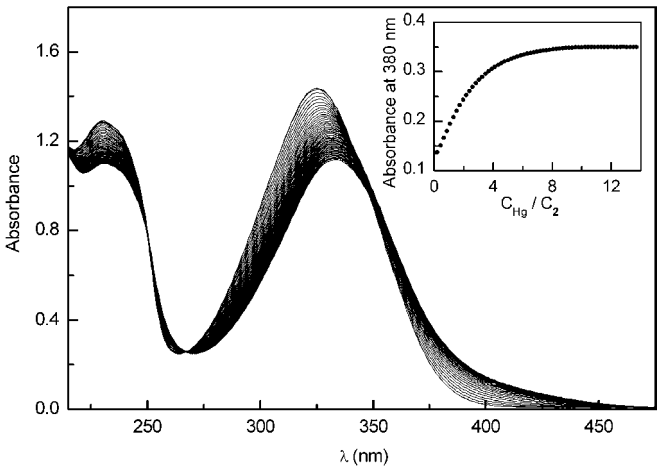


Fig. 3. UV–Vis titration curves and molar ratio curve for the Hg^{2+}–**2** system in CH_3CN at 25 °C.

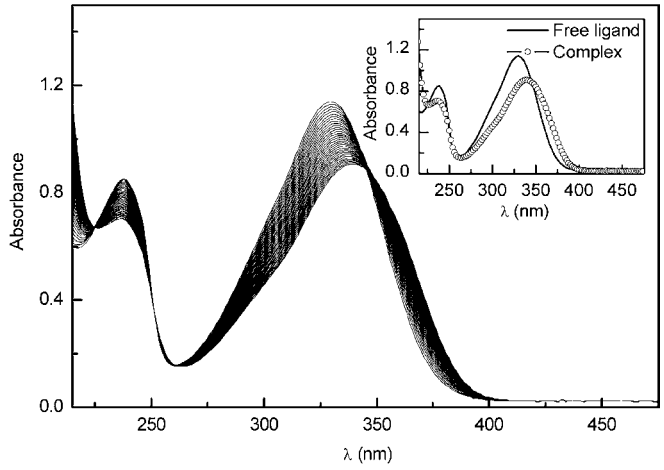


Fig. 2. UV–Vis titration curves for the Pb^{2+}–**1** system in CH_3CN at 25 °C. The inset shows the ligand spectrum before (—) and after (–O–) the metal ion addition.

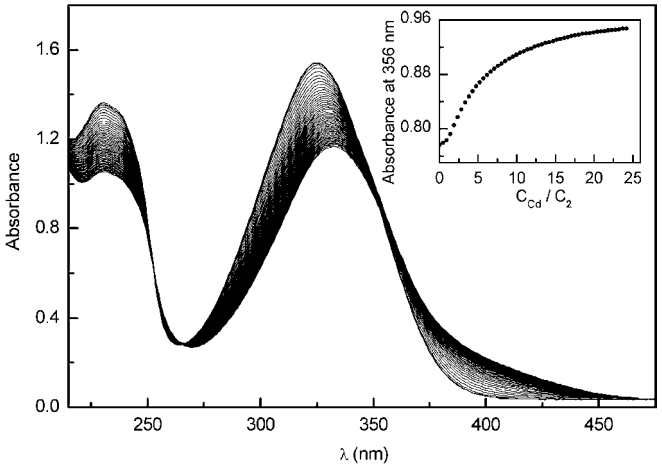


Fig. 4. UV–Vis titration curves and molar ratio curve for the Cd^{2+}–**2** system in CH_3CN at 25 °C.

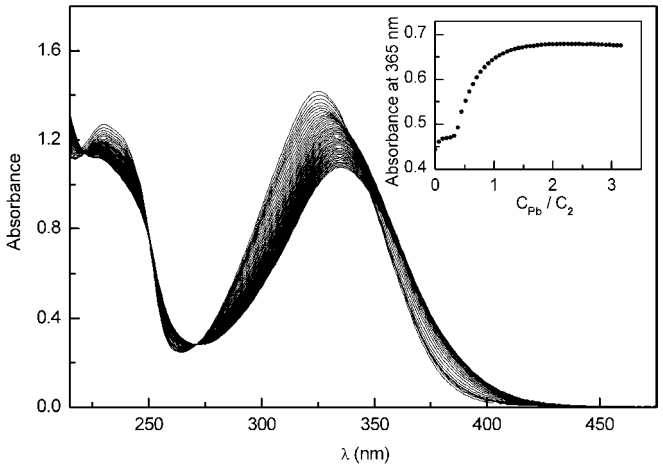


Fig. 5. UV–Vis titration curves and molar ratio curve for the Pb^{2+}–**2** system in CH_3CN at 25 °C.

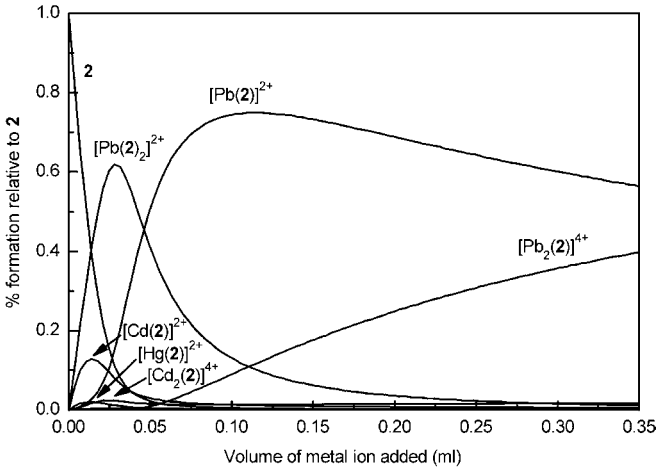


Fig. 6. Species distribution diagram for a M^{2+}–**2** (M = Hg^{2+}, Cd^{2+} and Pb^{2+}) system. $C_{Hg} = 1.10 \times 10^{-3}$ mol dm^{-3}; $C_{Cd} = 2.0 \times 10^{-3}$ mol dm^{-3}; $C_{Pb} = 4.50 \times 10^{-4}$ mol dm^{-3}; $C_2 = 1.50 \times 10^{-5}$ mol dm^{-3}. Initial volume = 1.8 ml.

Among the three cations, Pb^{2+} forms the most stable species. The determination of such values (especially for the ML and ML_2 complexes) required the use of diluted solutions; this likely accounts for the relatively large standard deviation associated with the binding constants of Pb^{2+}, *i.e.* the cation that requires the lowest concentration since it forms the strongest complexes.

Though several calixarene-based ligands have been proposed as sensors [24] or, more in general, as selective ligands [25–27], only a few papers [19b,27] report studies of the stability constants of the proposed ligands with the metal ion(s) of interest, which are the only parameters that really reflect the true binding ability of the receptors. Unlike the 1,3-alternate calix[4]arene derivative reported by us previously [19b], although it forms complexes with large stability constants ($\log\beta > 7$), it is not able to discriminate Pb^{2+} from Hg^{2+}, whereas ligand **2** interacts with Pb^{2+} selectively.

The $\log\beta$ values show that the complexation follows the order $Pb^{2+} > Cd^{2+} > Hg^{2+}$. The same stability order has been found in acetonitrile for a calix[4]arene containing ester and ketone functional groups at the lower rim [27]. However, a straight comparison between the present results and the data reported in Ref. [22] is not possible since the ligands investigated by Danil de Namor et al. are reported to form only 1:1 species. On the other hand, through extraction studies based on a calix[4]arene tetracarboxylic derivative, Ohto et al. [26] have inferred that lead may form a Pb_2L species, which is in line with our results.

The marked selectivity of **2** for Pb^{2+} over Cd^{2+} and Hg^{2+} is clearly shown by the distribution diagram reported in Fig. 6. The figure shows how the three metal ions compete for the ligand in a solution of **2**; even with Pb^{2+} concentrations as low as 1.2×10^{-5} mol dm^{-3} and Hg^{2+} and Cd^{2+} concentrations of 2.7×10^{-5} and 5.4×10^{-5} mol dm^{-3} respectively (*i.e.* at $v = 0.05$ ml, see Fig. 6), the ligand would form almost exclusively species with lead.

There are two more aspects that deserve some comments. Firstly Hg^{2+}, that does not form any species with **1**, does complex **2**, even though to a smaller extent; in addition Pb^{2+} and Cd^{2+} form complexes with **2** that are much more stable than those formed with **1**. This indicates that there is a cooperative effect resulting from the simultaneous presence of four sinapyl units on the calixarene platform. The arrangement of sinapic acid pendants in a bowl-like structure brings the complexing moieties in close proximity and this greatly enhances the complex formation ability of the single monomeric unit. This is supported not only by the magnitude of the binding constant but also by the formation of species other than the simple ML complexes, the only species detected for both Pb^{2+} and Cd^{2+} with **1**.

Secondly, the binding constant values follow the order $Pb^{2+} > Cd^{2+} > Hg^{2+}$, which does not follow the cation size order ($Pb^{2+} > Hg^{2+} > Cd^{2+}$) [28] but parallels the *hard–soft* characteristics of the three metal ions (*hardness* follows the order $Pb^{2+} > Cd^{2+} > Hg^{2+}$) [29]. This leads to the thinking that the donor atoms of the ligand play a different role in the binding of the three metal ions.

Unfortunately, the spectrophotometric experiments do not indicate whether the different coordination modes result from preferences for the phenolic or amide sites. Attempts to monitor (and eventually to model) the extra-proton displacement that would result from the deprotonation at the phenolic or amide sites failed as the ΔpH change measured following the addition of the metal ion was well within the experimental error. On the other hand, the investigation of larger concentrations is hampered by the limited solubility of **2**.

3.2. ^{1}H NMR experiments

To gain insight into the structures of the complexes formed by **2**, we carried out ^{1}H NMR measurements. Unfortunately, the concentrations usually needed to perform NMR experiments could not be reached, due to the scarce solubility of **2** in CD_3CN.

A well resolved spectrum of the ligand was obtained by adding CD_3OD to CD_3CN (30:70, v/v). However, addition of Pb^{2+}, Cd^{2+} or Hg^{2+} perchlorates did not result in significant changes of the chemical shifts of the ligand in this solvent mixture, probably owing to the competitive effect of the protic solvent (CD_3OD). A CD_3CN/acetone-d_6 (80:20 v/v) mixture turned out to be the best solvent for the NMR experiments since it gave both a well resolved ligand spectrum and chemical shifts that changed upon metal ion addition. The amount of metal ion added to ligand **2** reproduced the metal/ligand ratios explored in the UV–Vis experiments. Attempts to explore metal ion concentrations larger than those used in the present NMR study were hampered by the formation of a precipitate and the simultaneous appearance of a yellowish colour.

The chemical shift changes of olefinic (H-3 and H-4), bridging methylene (H-7_{eq} and H-7_{ax}), aromatic (H-2 and H-6), OH (H-1) and NH (H-5) protons were followed to gain information on the sites of **2** involved in the metal binding (see Table 3).

The addition of up to 4–5 equiv. of Cd^{2+} results in significant downfield shifts of the OH, NH, H-3, H-4, H-6, H-7_{eq} and H-7_{ax} proton signals (Fig. 7). At these metal/ligand ratios, the free ligand and ML species predominate while M_2L forms to a lesser extent, as

Table 3
^{1}H NMR chemical shift (δ) and chemical shift changes ($\Delta\delta$) of the ligand protons of **2** by the addition of Pb^{2+}, Cd^{2+} and Hg^{2+} in CD_3CN/acetone-d_6 (80:20, v/v) at 25 °C.

Protons	δ (ppm)	δ (ppm)						
	Free ligand	Pb^{2+}			Cd^{2+}		Hg^{2+}	
		0.5 equiv.	1 equiv.	3 equiv.	5 equiv.	25 equiv.	3 equiv.	15 equiv.
H-1	6.72	0.11	0.25	0.37	0.06	0.21	nd[a]	nd[a]
H-2	6.73	0.00	0.01	0.03	0.00	0.04	0.00	0.00
H-3	6.49	0.03	0.09	0.15	0.01	0.07	0.00	0.08
H-4	7.46	0.09	0.13	0.14	0.01	0.04	0.02	0.13
H-5	8.31	0.26	0.54	0.72	0.13	0.36	0.51	0.91
H-6	7.04	0.04	0.08	0.10	0.05	0.14	0.00	0.00
H-7_{eq}	3.18	0.04	0.10	0.15	0.02	0.06	0.04	0.07
H-7_{ax}	4.48	0.02	0.05	0.08	0.01	0.03	0.02	0.02

[a] not detectable.

shown by the distribution diagram (see Supplementary data). As we increase the metal/ligand ratio, a deshielding of the H-2 proton ($\Delta\delta$ 0.04 ppm) is observed in addition to a more pronounced deshielding of the all above mentioned signals; such deshielding is particularly significant for the OH ($\Delta\delta$ 0.21 ppm) and NH ($\Delta\delta$ 0.36 ppm) protons. These data suggest that, in the presence of larger metal/ligand ratios, two cadmium cations interact with the amide region as well as with the upper part of the sinapyl residue.

The addition of Pb^{2+} to **2** causes shifts of the same protons involved in the cadmium complexation (Fig. 8); remarkably, the OH protons show a pronounced shift ($\Delta\delta$ 0.11 ppm) at a 0.5:1 metal/ligand ratio. This shift may be associated to the formation of a ML_2 structure in which one Pb^{2+} ion holds together two molecules of ligand by binding the external sinapyl OH groups. At the same metal/ligand molar ratio, a small amount of ML species is already present in solution (see distribution diagram in the Supplementary data). The deshielding observed for the NH ($\Delta\delta$ 0.26 ppm) and olefinic ($\Delta\delta$ 0.03 and 0.09 ppm) protons, suggests that the lead ion is positioned in the proximity of the carbonyl region. The affinity of Pb^{2+} for the carbonyl oxygen is in line with the relatively *harder* nature of this metal ion. As the metal/ligand molar ratio is increased to 3:1, the progressive deshielding of the protons, that are diagnostic for the complexation, supports the formation of the M_2L species. The shifts of the calixarene NH, H-6, H-7_{eq}, H-7_{ax} and the sinapyl H-3, H-4, H-2 and OH proton signals ($\Delta\delta$ 0.72, 0.10, 0.15, 0.14, 0.15, 0.14, 0.03 and 0.37 ppm, respectively) show that both the wide rim of the scaffold and the sinapyl pendants are involved in the complexation process. Likely, the first lead ion that is taken up is forced towards the macrocycle wide rim by the coordination of the second lead ion. The tentative structures for the ML_2, ML and M_2L complexes are depicted in Fig. 9.

A different behaviour is shown by Hg^{2+}; the interpretation of the NMR spectrum is somehow difficult due to the coexistence of a significant amount of free ligand in addition to the ML and M_2L species. However, the downfield shifts of H-3, H-4 ($\Delta\delta$ 0.08 and 0.13 ppm, respectively) and NH ($\Delta\delta$ 0.91 ppm) protons show that

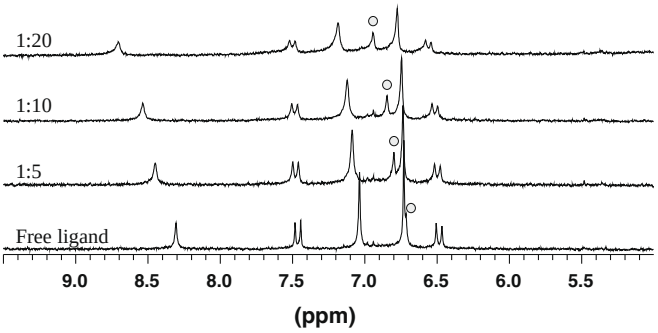


Fig. 7. Changes of the ^{1}H NMR (400 MHz) spectra of **2** in CD_3CN/acetone-d_6 (80:20, v/v) upon addition of Cd^{2+}; the circle labels the OH signals.

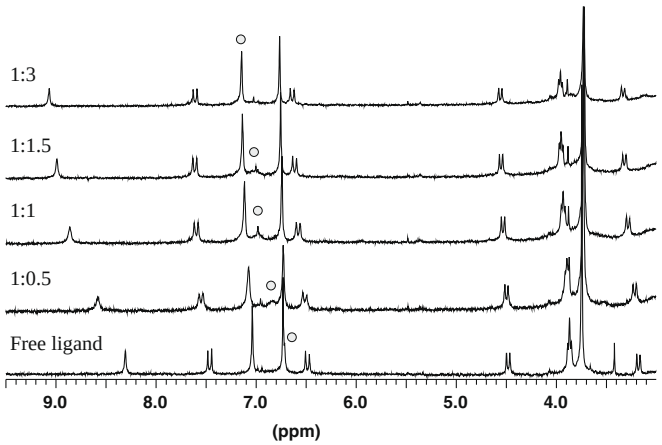


Fig. 8. Changes of the ^{1}H NMR (400 MHz) spectra of **2** in CD_3CN/acetone-d_6 (80:20, v/v) upon addition of Pb^{2+}; the circle labels the OH signals.

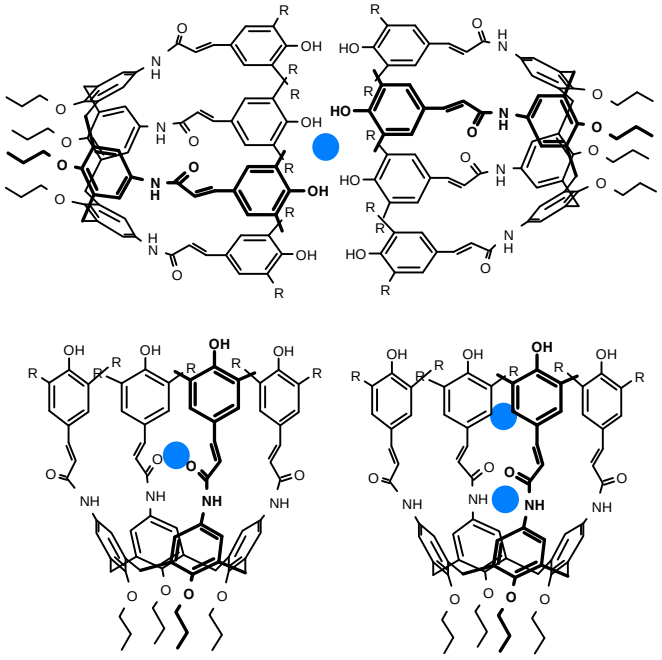


Fig. 9. Tentative structures of the ML_2, ML, and M_2L species for the Pb^{2+}–**2** system.

Hg^{2+}, the *softest* among the three metal ions, has a marked preference for the olefinic *(softer* region) and NH groups of the ligand.

X-ray diffraction analysis is currently underway to obtain more details on the structures of the complexes.

4. Conclusion

This work shows the first example of a sinapic acid–calixarene hybrid capable of forming strong complexes not only with Pb^{2+} and Cd^{2+} but also with Hg^{2+}. The latter metal ion does not form any complex with the monomeric homologous compound **1**. Our results indicate a cooperative effect resulting from the simultaneous presence of multiple sinapyl units arranged on the calix[4]-arene wide rim. The three metal ions show some preference for specific coordination sites of the ligand. Pb^{2+} complexes with ligand **2** are so stable that in principle they are the only ones that would show up in a solution containing a mixture of the three metal ions. The marked preference of ligand **2** for Pb^{2+} may pave the way for new applications of this ligand as an ion-selective sensor.

Appendix A. Supplementary data

Supplementary data associated with this article can be found, in the online version, at doi:10.1016/j.poly.2008.10.068.

References

[1] (a) T.C. Hutchinson, K.M. Meema (Eds.), Lead, Mercury, Cadmium and Arsenic in the Environment, Pergamon Press, Oxford, 1987;
(b) G.M. Gadd, Heavy metal pollutants: environmental and biotechnological aspects, in: Encyclopedia of Microbiology, 2nd ed., vol. 2, 2000, p. 607;
(c) E. Van der Voet, J.B. Guinee, H.A. Udo de Haes (Eds.), Heavy Metals: A Problem Solved Methods and Models to Evaluate Policy Strategies for Heavy Metals, Kluwer, Dordrecht, 2000;
(d) R.K. Sharma, M.J. Agrawal, Environ. Biol. 26 (2005) 301;
(e) S. Mishra, R.S. Dubey, Heavy metal toxicity induced alterations in photosynthetic metabolism in plants, in: Handbook of Photosynthesis, 2nd ed., 2005, p. 845.

[2] (a) M. Hutton, C. Symon, Sci. Total. Environ. 57 (1986) 129;
(b) L.B. Lave, C.T. Hendrickson, F.C. McMichael, Science 268 (1995) 993.

[3] S. Tong, Y.E. von Schirnding, T. Prapamontol, Bull. World Health Organ. 78 (2000) 1068.

[4] (a) M.T. Antonio, M.L. Leret, Life Sci. 67 (2000) 635;
(b) M.T. Antonio, L. Corredor, M.L. Leret, Toxicol. Lett. 143 (2003) 331;
(c) T.I. Lidsky, J.S. Schneider, Brain 126 (2003) 5.

[5] (a) L.M. Fels, Renal Failure 21 (1999) 275;
(b) L. Friberg, C.G. Elinder, T. Kjellstrom, G.F. Nordberg, Cadmium and Health: A Toxicological and Epidemiological Appraisal, CRC Press, Boca Raton, 1986;
(c) S. Satarug, M. Nishijo, P. Ujjn, Y. Vanavanitkun, M.R. Moore, Toxicol. Lett. 157 (2005) 57.

[6] (a) C.D. Klassen, M.D. Amdur, J. Dull, Casarett and Doull's Toxicology, 3rd ed., MacMillan, New York, 1986;
(b) F.J. Vernberg, W.B. Vernberg (Eds.), Pollution and Physiology of Marine Organisms, Academic Press, New York, 1974.

[7] J.E. Fergusson, Heavy Elements: Chemistry Environmental Impact and Health Effects, Pergamon Press, Oxford, 1990.

[8] W. Kaim, B. Schwederski, Bioinorganic Chemistry: Inorganic Elements in the Chemistry of life, an Introduction and Guide, Wiley-Interscience, New York, 1991.

[9] S. Benoff, A. Jacob, I.R. Hurley, Hum. Reprod. Update 6 (2000) 107.

[10] J. Grigg, Arch. Dis. Child. 89 (2004) 244.

[11] (a) V.K. Gupta, A.K. Jain, G. Maheshawari, Int. J. Electrochem. Sci. 2 (2007) 102 and reference therein;
(b) C. Bazzicalupi, A. Bencini, A. Bianchi, L. Borsari, A. Danesi, C. Giorgi, C. Lodeiro, P. Mariani, F. Pina, S. Santarelli, A. Tamayo, B. Valtancoli, J. Chem. Soc., Dalton Trans. (2006) 4000;
(c) L.F. Lindoy, Coord. Chem. Rev. 174 (1998) 327;
(d) R. Hancock, in: A.F. Williams, C. Floriani, A.E. Merbach (Eds.), Perspectives in Coordination Chemistry, VCH, Weinheim, 1992, p. 129;
(e) N.T.K. Dung, R. Ludwig, New J. Chem. 23 (1999) 603;
(f) M.C. Aragoni, M. Arca, A. Bencini, A.J. Blake, C. Caltagirone, G. De Filippo, F.A. Devillanova, A. Garau, T. Gelbrich, M.B. Hursthouse, F. Isaia, V. Lippolis, M. Mameli, P. Mariani, B. Valtancoli, C. Wilson, Inorg. Chem. 46 (2007) 4548.

[12] F. Bailly, F. Cotelle, Curr. Med. Chem. 12 (2005) 1811.

[13] (a) L. Boilet, J.P. Cornard, C. Lapouge, J. Phys. Chem. A 109 (2005) 1952;
(b) J.P. Cornard, C. Lapouge, J. Phys. Chem. A 108 (2004) 4470.

[14] G.M.L. Consoli, E. Galante, C. Daquino, G. Granata, F. Cunsolo, C. Geraci, Tetrahedron Lett. 47 (2006) 6611.

[15] (a) For reviews on calixarenes see: C.D. Gutsche, Calixarenes, in: J.F. Stoddart (Ed.), Monographs in Supramolecular Chemistry, The Royal Society of Chemistry, Cambridge, 1998;
(b) Z. Asfari, V. Böhmer, J. Harrowfield, J. Vicens (Eds.), Calixarenes 2001, Kluwer Academic, Dordrecht, 2001;
(c) V. Böhmer, Angew. Chem., Int. Ed. Engl. 34 (1995) 713;
(d) J. Vicens, J. Harrowfield (Eds.), Calixarenes in the Nanoworld, Springer, Dordrecht, 2007.

[16] (a) I.M. Kolthoff, E.B. Sandell, E.J. Meehan, S. Bruckenstein, Quantitative Chemical Analysis, 4th ed., vol. 2, The Macmillan Company, New York, 1969;
(b) H.A. Flaschka, EDTA Titrations, Pergamon Press, London, 1959.

[17] P. Rajan, I. Vedernikova, P. Cos, D. Van den Berghe, K. Augustyns, A. Haemers, Bioorg. Med. Chem. Lett. 11 (2001) 215.

[18] (a) G. Arena, R. Calì, G.G. Lombardo, E. Rizzarelli, D. Sciotto, R. Ungaro, A. Casnati, Supramol. Chem. 1 (1992) 19;
(b) G. Arena, A. Contino, G.G. Lombardo, D. Sciotto, Thermochim. Acta 264 (1995) 1.

[19] (a) G. Arena, A. Contino, E. Longo, D. Sciotto, C. Sgarlata, G. Spoto, Tetrahedron Lett. 44 (2003) 5415;
(b) G. Arena, A. Contino, E. Longo, D. Sciotto, G. Spoto, J. Chem. Soc., Perkin Trans. 2 (2001) 2287.

[20] P. Gans, A. Sabatini, A. Vacca, Talanta 43 (1996) 1739. http://www.hyperquad.co.uk/hq2000.htm.

[21] Spectrum Software Associates, Chapel Hill, NC, USA.

[22] H. Gampp, M. Maeder, C.J. Meyer, A.D. Zuberbühler, Talanta 32 (1985) 95.

[23] R.M. Dyson, P. Jandanklang, M. Maeder, C.J. Mason, A. Whitson, Polyhedron 18 (1999) 3227.

[24] (a) P.L.H.M. Cobben, R.J.M. Egberink, J.B. Bomer, P. Bergveld, W. Verboom, D.N. Reinhoudt, J. Am. Chem. Soc. 114 (1992) 10573;
(b) E. Malinowska, Z. Brzozka, K. Kasiura, R.J.M. Egberink, D.N. Reinhoudt, Anal. Chim. Acta 298 (1994) 253;
(c) J.K. Choi, S.H. Kim, J. Yoon, K.-H. Lee, R.A. Bartsch, J.S. Kim, J. Org. Chem. 71 (2006) 8011.

[25] (a) E. Lindner, K. Toth, E. Pungor, F. Behm, P. Oggenfuss, D.H. Welti, D. Ammann, W.E. Morf, E. Pretsch, W. Simon, Anal. Chem. 56 (1984) 1127;
(b) F. Arnaud-Neu, G. Barrett, D. Corry, S. Cremin, G. Ferguson, J.F. Gallagher, S.J. Harris, M.A. McKervey, M.J.J. Schwing-Weill, J. Chem. Soc., Perkin Trans. 2 (1997) 575;
(c) M.J. Schwing-Weill, F. Arnaud-Neu, M.A. McKervey, J. Phys. Org. Chem. 5 (1992) 496.

[26] K. Ohto, Y. Fujimoto, K. Inoue, Anal. Chim. Acta 387 (1999) 61.

[27] A.F. Danil de Namor, S. Chahine, D. Kowalska, E.E. Castellano, O.E. Piro, J. Am. Chem. Soc. 124 (2002) 12824.

[28] D.R. Lide (Ed.), Handbook of Chemistry and Physics, 71st ed., CRC Press, Boca Raton, 1990.

[29] (a) R.G. Pearson, J. Am. Chem. Soc. 85 (1963) 3533;
(b) S. Ahrland, J. Chatt, N.R. Davies, Quart. Rev. Chem. Soc. 12 (1958) 265.

Polyhedron 28 (2009) 349–359

Contents lists available at ScienceDirect

Polyhedron

journal homepage: www.elsevier.com/locate/poly

Conversion of novel palladacycles into oxopyrrolo[3,4-b]quinolines

Abdel-Sattar S. Hamad Elgazwy *

Department of Chemistry, Faculty of Science, University of Ain Shams, Abbassia 11566, Cairo, Egypt

ARTICLE INFO

Article history:
Received 3 September 2008
Accepted 8 October 2008
Available online 10 December 2008

Keywords:
Quinoline
Arylpalladium complexes
Oxopyrrolo[3,4-b]quinolines
Isocyanides

ABSTRACT

The quinolinylcyclopalladated complexes **3a–b** were synthesised in good yields (81% and 77%) by the insertion reaction of the prepared dinuclear palladium complexes [Pd(*C,N*-2-C_9H_4N-CHO-3-R-6)Cl(PPh_3)]$_2$ [(R = H (**2a**), R = OMe (**2b**)] with isonitrile XyNC (Xy = 2,6-$Me_2C_6H_3$). The cyclopalladated complexes **3a–b** were also obtained in low yields (39% and 33.5%) via a one pot oxidative addition reaction of quinoline chloride **1a–b** with isonitrile XyNC:Pd(dba)$_2$ (4:1). The reactions of **3a–b** with Tl(TfO) (TfO = triflate, CF_3SO_3) in the presence of H_2O or EtOH causes depalladation reactions of the complexes to provide the corresponding organic compounds **4a–b**, **5a–b** and **6a–b** in yields (41%, 27% and 18–19%). The products were characterized by satisfactory elemental analyses and spectral studies (IR, ^{1}H, ^{13}C and ^{31}P NMR). The crystal structures of **2a**, **3a** and **3b** were determined by X-ray diffraction studies.
© 2008 Elsevier Ltd. All rights reserved.

1. Introduction

The chemistry of arylpalladium complexes is a topic of great interest because such compounds participate in many organic reactions [1–12]. Cyclopalladated complexes (CPCs) are one of the most popular classes of organopalladium derivatives, which are widely applied in organic synthesis, organometallic catalysis and new molecular materials. Among them, the most investigated cyclopalladated complexes are five- or six-membered rings fused with an aromatic ring, and the metallated carbon is usually an aromatic sp^2 carbon [13–17]. However, six-membered palladacycles with iminoyl (C=N–) sp^2 carbon are rather rare [18]. This is probably due to poor stability which brings difficulties of preparation, isolation and characterization of these complexes. The limitation can be overcome by changing the nature of the metallated carbon atom, the type of donor groups and their substituents. Some of these reactions involved *ortho*-functionalized aryl complexes that after insertion of isocyanides gave heterocyclic products in which the ortho group is included [19–21]. Establishing synthetic procedures for these complexes invariably involve the presence of other strongly coordinated ligands, such as PPh_3 [22–24], and these are attracting our interest. There is relatively little known concerning the cyclometallation of aldehyde functionalities [25–34]. The interest of this subject has prompted us to prepare arylpalladium complexes containing *ortho*-–CHO functionalized groups. In this contribution we present the synthesis and characterization of novel mono- and dimeric palladacycles as well as their utility as precursors for the synthesis of valuable organic products. The structure of dimeric [*N*-aryl-Pd-Cl(PPh_3)]$_2$, **2a–b**, with non common '$Pd_2C_2N_2$' central cores formed by oxidative addition of the chloroquinolines **1a–b** to a Pd(0) is supported by X-ray structures. The utility of the cyclopalladated complexes **3a–b** in organic synthesis via their depalladation reactions to provide amidic acid or esters (**4a–b**, **5a–b** and **6a–b**) are the most outstanding points of this manuscript. The sequence of the reactions led eventually to compounds that could potentially possess pharmacological properties [35–53].

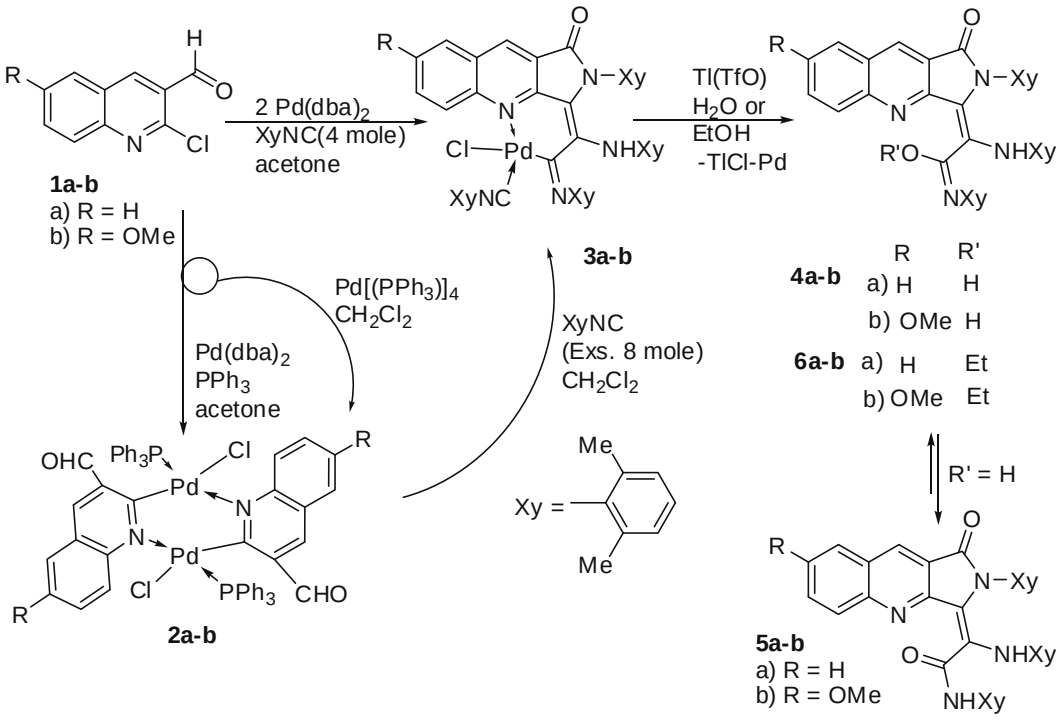
2. Results and discussion

Oxidative addition reactions of 2-chloro-6-R-3-quinolinecraboxaldehydes R = H (**1a**), R = OMe (**1b**) toward a stoichiometric amount of [Pd(dba)$_2$] = ([Pd$_2$(dba)$_3$] · dba; dba = dibenzylideneacetone) [54] in the presence of a neutral ligand such as PPh_3 (1:2:1) under nitrogen in degassed acetone gave the dimeric palladium complexes{Pd[C_9H_5-CHO(3)]Cl(PPh_3)}$_2$ **2a**, {Pd[-6-OCH_3-C_9H_4-CHO(3)]Cl(PPh_3)}$_2$ **2b** in moderate yields (43% and 31%), through the coordination of the quinolinyl nitrogen. Subsequently, the insertion reaction of 2,6-dimethylphenyl isocyanide XyNC (Xy = 2,6-$Me_2C_6H_3$) into the dinuclear complexes in CH_2Cl_2 at room temperature eventually formed the monuclear complexes **3a–b** in high yields (81% and 77%). These palladacycles **3a–b** could also be obtained in low yields (39% and 33.5%) by direct oxidative addition of 2-chloro-6-R-3-quinolinecraboxaldehydes **1a–b** toward Pd(dba)$_2$ in the presence of a stoichiometric amount of isocyanide XyNC in degassed acetone at room temperature, as depicted in Scheme 1.

It was envisaged that the oxidative addition reaction of **1a–b** with Pd(dba)$_2$/PPh_3 could give the expected complex in a *transoid* form (**A**). However, isolation of the *trans* complexes failed, and only a yellow powder solid was isolated in the pure form that

* Tel.: +20 22617 3044; fax: +20 24831 836.
E-mail addresses: hamad@asunet.shams.edu.eg, aselgazwy@yahoo.com

0277-5387/$ - see front matter © 2008 Elsevier Ltd. All rights reserved.
doi:10.1016/j.poly.2008.10.054

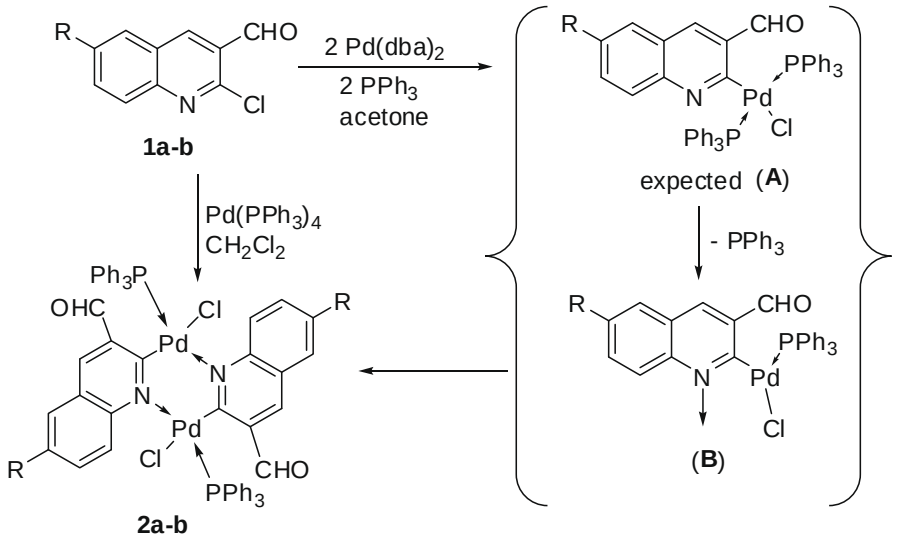


Scheme 1.

corresponded to the dimeric palladium complexes **2a–b**, as outlined in Scheme 2. This is probably due to the result of the interchange between the nitrogen donor of the quinoline ring and the PPh_3 ligand of palladium, which is a very well-known process [55]. One might believe that complexes (**A**) and (**B**) are intermediates for the formation of complexes **2a–b** and also suggest that the presence of PPh_3 as a ligand could be responsible for the interchange of the ligands and existence of complex **2a** or **2b** in solution as a mixture of complexes derived from two *trans* forms. The formation of the dimeric complexes **2a–b** are consistent with the related dimeric palladium complex $[Pd(\mu\text{-pyridine})Cl(PPh_3)]_2$, formed by the oxidative addition of 2-chloropyridine to the complex $Pd(PPh_3)_4$ [56].

These complexes were confirmed by the appearance of one singlet signal in their ^{31}P NMR spectra. The reaction products were identified by comparison of the ^{31}P NMR spectra of the reaction mixture with those of related reported complexes which showed two AB resonance patterns. The ^{31}P NMR spectra recorded in case of R = H (**2a**) and R = OMe (**2b**) showed resonances at δ 20.67 and 21.37 ppm.

The ^{1}H NMR spectra did not show the presence of any impurities for either of the complexes **2a** or **2b**, although the quinoline backbone shows slight variations when complexes **2a** or **2b** are compared. However, we feel that not enough was known about palladium–carbon bonds of these complexes, through four bonds. This promoted us to place emphasis on these data. While this



Scheme 2.

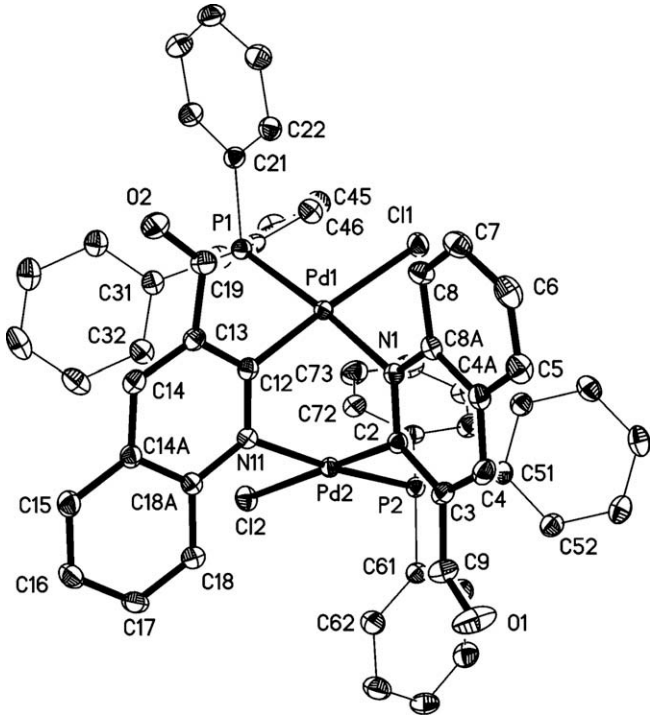


Fig. 1. Thermal ellipsoid plot (50% probability level and solvent omitted CH_2Cl_2) of **2a**. Selected bond lengths (Å) and angles (°): Pd(1)–C(12) = 1.9919(17), Pd(1)–N(1) = 2.0944(14), Pd(1)–P(1) = 2.2906(5), Pd(1)–Cl(1) = 2.3816(6), Pd(1)–Pd(2) = 3.0818.(5), Pd(2)–C(2) = 2.0081(6), Pd(2)–N(11) = 2.1115(14), Pd(2)–P(2) = 2.2661(7), Pd(2)–Cl(2) = 2.3812(5), N(1)–C(2) = 1.330(2), N(11)–C(12) = 1.324(2), C(12)–Pd(1)–N(1) = 82.22(6), C(12)–Pd(1)–P(1) = 92.32(5), N(1)–Pd(1)–P(1) = 174.53(4), C(12)–Pd(1)–Cl(1) = 173.90(5), N(1)–Pd(1)–Cl(1) = 92.30(4), P(1)–Pd(1)–Cl(1) = 93.14(2), C(12)–Pd(1)–Pd(2) = 66.01(5), N(1)–Pd(1)–Pd(2) = 63.12(4), P(1)–Pd(1)–Pd(2) = 114.865(14), Cl(1)–Pd(1)–Pd(2) = 113.865(19), C(2)–Pd(2)–N(11) = 84.88(6), C(2)–Pd(2)–P(2) = 93.24(5), N(11)–Pd(2)–P(2) = 175.12(4), C(2)–Pd(2)–Cl(2) = 174.14(5), N(11)–Pd(2)–Cl(2) = 90.20(4), P(2)–Pd(2)–Cl(2) = 91.91(2), C(2)–Pd(2)–Pd(1) = 66.30(5), N(11)–Pd(2)–Pd(1) = 63.27(4), P(2)–Pd(2)–Pd(1) = 111.854(17), Cl(2)–Pd(2)–Pd(1) = 114.188(16).

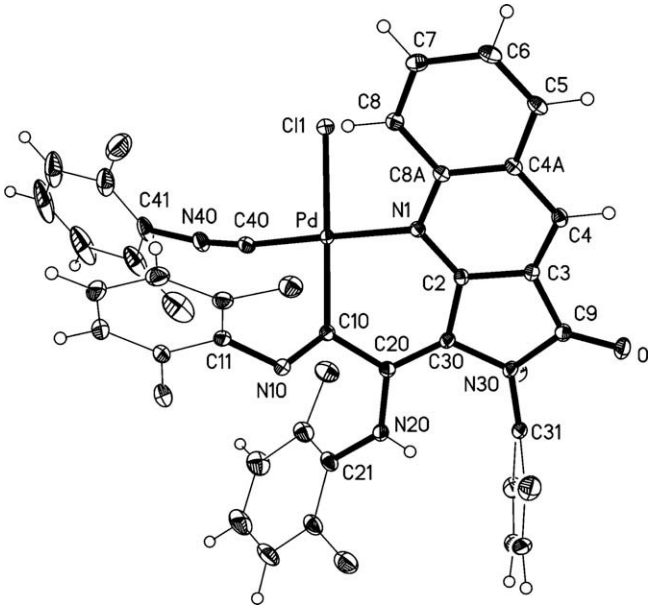


Fig. 2. Thermal ellipsoid plot (50% probability level and solvent omitted) of **3a**. The hydrogen atom attached to N(20) has been displayed for clarity. Selected bond lengths (Å) and angles (°): Pd–C(40) = 1.9425(18), Pd–C(10) = 1.9999(17), Pd–N(1) = 2.0864(14), Pd–Cl(1) = 2.4398(4), N(1)–C(2) = 1.325(2), N(1)–C(8A) = 1.388(2), N(10)–C(10) = 1.270(2), N(10)–C(11) = 1.420(2), N(20)–C(20) = 1.372(2), N(20)–C(21) = 1.418(2), N(30)–C(9) = 1.389(2), N(30)–C(30) = 1.429(2), N(30)–C(31) = 1.434(2), N(40)–C(40) = 1.151(2), N(40)–C(41) = 1.409(2), C(2)–C(30) = 1.452(2), C(3)–C(9) = 1.479(2), C(9)–O = 1.221(2), C(10)–C(20) = 1.505(2), C(20)–C(30) = 1.366(2), C(40)–Pd–C(10) = 91.93(7), C(40)–Pd–N(1) = 178.97(6), C(40)–Pd–Cl(1) = 84.21(5), C(10)–Pd–N(1) = 87.11(6), C(10)–Pd–Cl(1) = 173.33(5), N(1)–Pd–Cl(1) = 96.78(4), C(2)–N(1)–C(8A) = 116.44(14), C(2)–N(1)–Pd = 116.23(11), C(8A)–N(1)–Pd = 126.75(11), C(10)–N(10)–C(11) = 123.11(15), C(20)–N(20)–C(21) = 129.41(17), C(9)–N(30)–C(30) = 112.76(14), C(9)–N(30)–C(31) = 122.82(15), C(30)–N(30)–C(31) = 124.29(14), C(40)–N(40)–C(41) = 171.2(2), N(1)–C(2)–C(3) = 123.94(15), N(1)–C(2)–C(30) = 127.31(15), C(3)–C(2)–C(30) = 108.75(15), C(2)–C(3)–C(9) = 108.26(14), O–C(9)–N(30) = 125.39(17), O–C(9)–C(3) = 129.47(16), N(30)–C(9)–C(3) = 105.12(14), N(10)–C(10)–C(20) = 116.45(15), N(10)–C(10)–Pd = 127.94(13), C(20)–C(10)–Pd = 115.61(11), C(30)–C(20)–N(20) = 122.27(16), C(30)–C(20)–C(10) = 118.02(15), N(20)–C(20)–C(10) = 118.83(15), C(20)–C(30)–N(30) = 127.76(15), C(20)–C(30)–C(2) = 126.11(16), N(30)–C(30)–C(2) = 104.88(13), N(40)–C(40)–Pd = 171.71(16).

observation can be rationalized for **2a–b**, we were surprised that the cyclopalladated product showed almost no change in view of the angular distortion involved in forming the six-membered palladacycles. The IR (Nujol, cm^{-1}) bands assignable to the ν(C=O), ν(C=N) and ν(C=C) modes in **2a–b** indicating the non-coordination of the carbonyl group in these complexes. In complex **2a**, the IR spectrum shows bands at 1688, 1612 and 1582 cm^{-1} and for **2b** these bands appear at slightly lower values at 1678, 1584 and 1546 cm^{-1} respectively. The complexes **2a–b** show in their IR spectra a strong band at ca. 1688 and 1678 cm^{-1} assignable to ν(C=O) of the formyl group. These frequencies are similar to that observed in the starting materials **1a–b**, indicating that there is no coordination of the formyl group to the metal atom.

2.1. Insertion of 2,6-dimethylphenyl isocyanide XyNC (Xy = 2,6-$Me_2C_6H_3$)

Oxidative addition of 2-chloro-6-R-3-quinolinecarboxaldehydes **1a–b** [R = H (**1a**), R = OMe (**1b**)] (1.5) to a mixture of $Pd(dba)_2$ and XyNC (Xy = 2,6-$Me_2C_6H_3$) in 1:4 ratios in acetone at room temperature yields the tri-inserted iminoacyl palladium complexes **3a–b** in low yields (39%, 33.5%). Instead of the required 4:1.5:1 molar ratios of reagents XyNC:**1a–b**:$Pd(dba)_2$ for the formation of **3a–b**, the stoichiometric amounts of this mixtures used were 3:1.5:1, 2:1.5:1, 2:1:1, 1:1.5:1, 1:1:1 (**3a**) and 3:1.5:1, 2:1.5:1, 2:1:1, 1:1.5:1, 1:1:1 (**3b**), unfortunately, it was not possible to isolate the inserted products in this regard.

A mechanistic proposal depicts the formation of the possible intermediates [Pd{C(=NXy)$_3$Ar}Cl(CNXy)] [**I**] which are quickly cyclized to give iminoacyl quinolinylpalladium **3a** and **3b**, and not the expected complex [**II**]. We believe that a nucleophilic attack of the nitrogen of the primarily inserted isocyanide at the formyl carbon could give the isoindole ring [**III–V**]. The intermediate [**IV**] could evolve to [**V**], bearing a carbon–carbon double bond, which could undergo an intermolecular proton migration from the OH group of the intermediate [**V**] to the nitrogen of the second inserted isocyanide. There is no precedent for this type of structure conformation with migration of the proton to the nitrogen atom of the second inserted isocyanide, it was supported by X-ray structures, displaying the nitrogen proton at N(20)–H (**3a**, Fig. 2) and N(5)–H (**3b**, Fig. 3). The favored attack of the quinolinyl nitrogen at the (Pd) metal center in intermediate [**VI**] could turn into iminoacyl quinolinylpalladium **3a** or **3b**. The reported [57–62] synthesis of a highly functionalized ketenimine from di-insertion of XyNC into an (*o*-formylaryl) palladium complex is consistent with the result described here. The formation of such a ketenimine is also the result of the attack of the nitrogen of the primarily inserted isocyanide at the formyl carbon. A mechanistic proposal consistent with literature data [63], is given in Scheme 3.

The reactivity of the dinuclear palladium complexes **2a–b** were examined toward the bulky isocyanide XyNC (Xy = 2,6-$Me_2C_6H_3$),

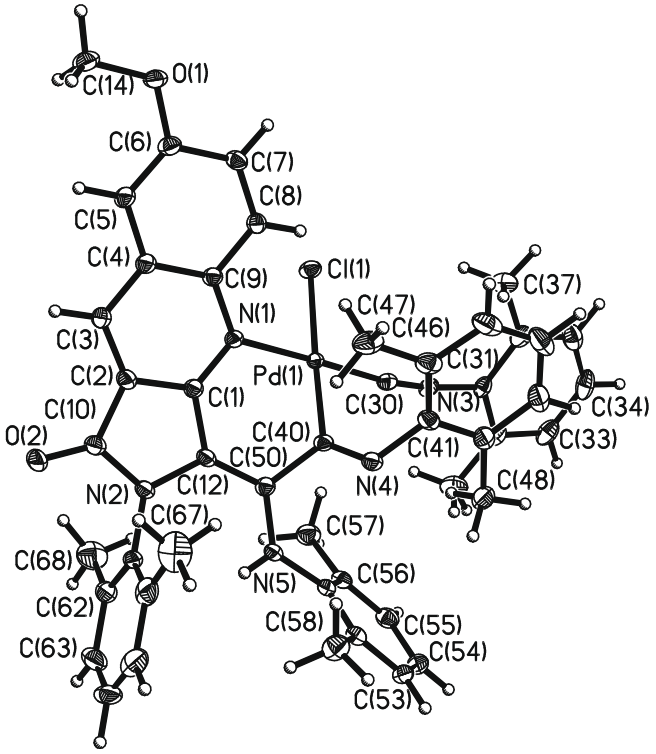


Fig. 3. Thermal ellipsoid plot (50% probability level and solvent omitted) of **3b**. The hydrogen atom attached to N(5) has been displayed for clarity. Selected bond lengths (Å) and angles (°): Pd(1)–C(30) = 1.944(2), Pd(1)–C(40) = 2.002(2), Pd(1)–N(1) = 2.0905(18), Pd(1)–Cl(1) = 2.4283(5), N(1)–C(1) = 1.332(3), N(1)–C(9) = 1.382(3), N(2)–C(10) = 1.383(3), N(2)–C(12) = 1.432(3), N(2)–C(61) = 1.438(3), N(3)–C(30) = 1.153(3), N(3)–C(31) = 1.404(3), N(4)–C(40) = 1.266(3), N(4)–C(41) = 1.429(3), N(5)–C(50) = 1.363(3), C(30)–Pd(1)–C(40) = 91.67(8), C(30)–Pd(1)–N(1) = 178.75(8), C(40)–Pd(1)–N(1) = 87.14(8), C(30)–Pd(1)–Cl(1) = 84.53(6), C(40)–Pd(1)–Cl(1) = 175.94(6), N(1)–Pd(1)–Cl(1) = 96.64(5), C(1)–N(1)–C(9) = 116.68(18), C(1)–N(1)–Pd(1) = 116.25(14), C(9)–N(1)–Pd(1) = 126.45(14), C(10)–N(2)–C(12) = 112.44(18), C(10)–N(2)–C(61) = 119.09(18), C(12)–N(2)–C(61) = 127.39(18), C(30)–N(3)–C(31) = 170.0(2), C(40)–N(4)–C(41) = 120.57(18), C(50)–N(5)–C(51) = 129.11(19), C(6)–O(1)–C(14) = 116.23(18), N(1)–C(1)–C(2) = 122.76(19), N(1)–C(1)–C(12) = 128.49(19).

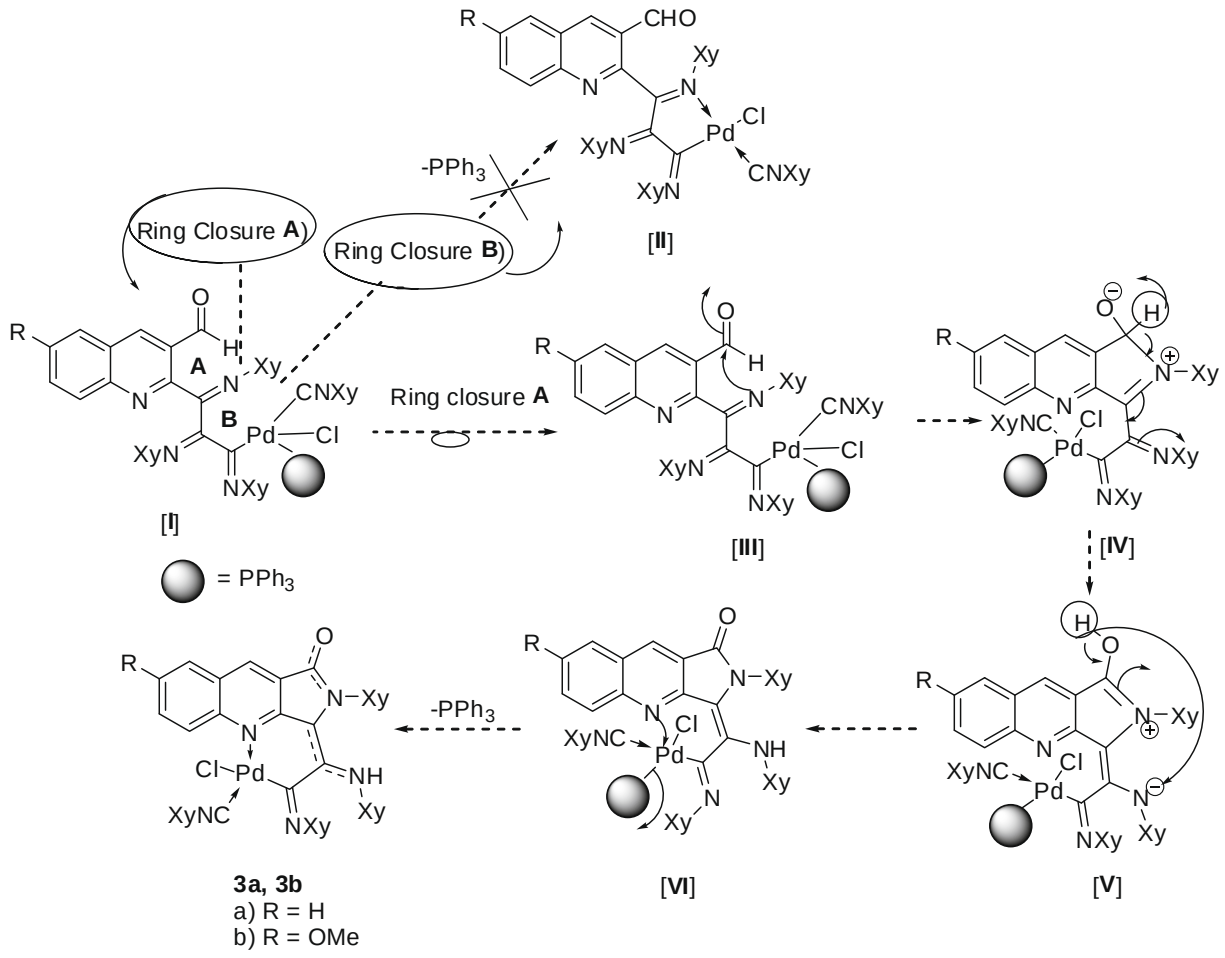
and it depends on nature of the ligands and on the reaction conditions. Thus when the insertion reaction takes place at different molar ratios of XyNC to complex, the inserted products obtained are the result of tri-insertion processes. The mono-insertion and di-insertion of XyNC at 1:1 or 1:2 molar ratios are not being isolated. The reaction of the dinuclear palladium complexes **2a–b** with 8 equiv. of XyNC at room temperature with a longer reaction time (16 h) provided the inserted products of iminoacyl quinolinylpalladium complexes **3a–b**. Instead of the required (8:1) equivalents of XyNC:**2a–b**, the stoichiometric amounts of 3:1, 4:1, 5:1, 6:1 and 7:1 were used, and it was not possible to isolate complexes **3a–b** in case of 3:1, 4:1 and 5:1 molar ratios.

The inserted products were formed from the insertion of 2,6-dimethylphenyl isocyanide (XyNC) into the C–Pd bond and the displacement of PPh_3 by the XyNC ligand. These kinds of complexes are very poorly represented in the iterature, the only example being those recently prepared by Vicente et al. [63] and suggested that the presence of PPh_3 during the insertion of XyNC into the dinuclear palladium complexes **2a–b** could be responsible for the change of reactivity of the intermediate complexes. It is possible that free PPh_3 coordinates in the intermediate complexes, forcing the insertion of the two isocyanide ligands. A mechanistic scheme depicting the formation of the various products, including possible intermediates, consistent with literature data [63] is given in Scheme 4.

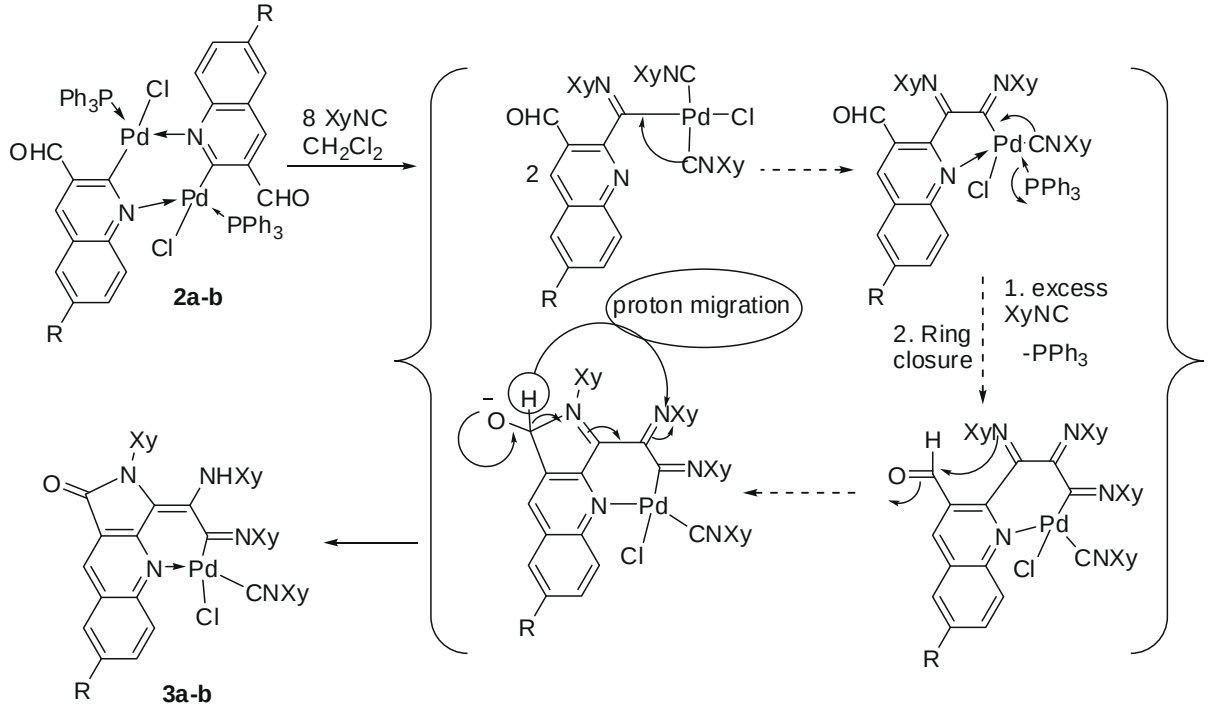
The products were analyzed by IR, ^1H NMR spectroscopy and single-crystal X-ray diffraction studies. IR (Nujol, cm^{-1}) bands were assignable to ν_{NH}, $\nu_{C\equiv N}$, $\nu_{C=O}$ and $\nu_{C=N,}$ for the iminoacyl quinolinylpalladium complexes **3a** and **3b** with no significances differences, indicating the cyclization of the carbonyl group within those complexes. In the case of **3a** the bands appear at ν(NH, broad band) 3338, ν(C≡N) 2361, ν(C=O) 1716 and ν(C=N) 1558 cm^{-1}, and in the case of **3b** the bands appear at ν(NH, broad band) 3360, ν(C≡N) 2182, ν(C=O) 1704 and ν(C=N) 1602 cm^{-1}. This suggests little change in the carbonyl stretching frequency of **3a** or **3b** due to complexation, and the electron releasing methoxyl group could confer special properties to the formyl group, for example, facilitating its coordination to the primarily inserted isocyanide (C=NXy) intermediate and nucleophilic attack of the nitrogen on the formyl carbon could give cyclometallated species of the important isoindolinone. The complexes **3a** and **3b** show a strong band in their IR spectra at 1716 and 1704 cm^{-1} assignable to ν(C=O). This frequency is not similar to that observed in the starting materials **1a–b** or **2a–b** and indicates the coordination of the carbonyl group to the isoindolinone ring. The ^1H NMR spectrum of complex **3a** in $CDCl_3$ was recorded and found to contain seven singlet resonances at different chemical shifts, each corresponding to methyl groups, appearing at δ 2.55 (s, Me, 3H), 2.49 (s, Me, 3H), 2.30 (s, Me, 3H), 2.19 (s, Me, 6H), 2.11 (s, Me, 3H), 1.58 (s, Me, 3H) and 0.62 (s, Me, 3H) ppm. There is one singlet signals integrated for 2 equiv. methyl groups of the coordinated isocyanide (CNXy) which appears at δ 2.19. The ^1H NMR spectrum of complex **3b** in $CDCl_3$ was recorded and found to contain six singlet resonances at different chemical shifts, each corresponding to methyl groups, appearing at δ 2.54 (s, Me, 3H), 2.49 (s, Me, 3H), 2.29 (s, Me, 3H), 2.18 (s, Me, 6H), 2.12 (s, Me, 6H) and 0.62 (s, Me, 3H) ppm. There are two singlet signals for the four methyl groups appearing at δ 2.18 (s, 6H, 2Me(Xy)) and 2.12 (s, 6H, 2Me(Xy)), one of which is for the inserted XyNC, indicating a *cis* geometry and no free rotation of the Xy groups. The other of the two singlet signals integrated to 2 equiv. methyl groups is from the coordinated isocyanide. This suggests steric hindrance that prevents the rotation of three xylyl groups, while the fourth one rotates freely.

2.2. Depalladation via reactions with Tl(TfO)

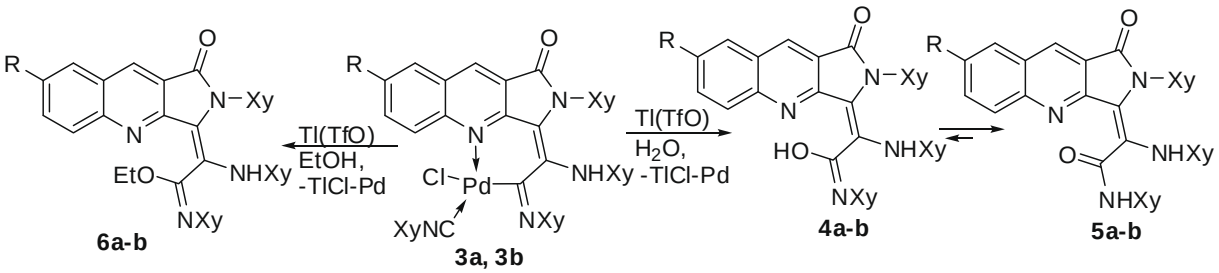
The reaction of complexes **3a–b** with Tl(TfO) was carried out in CH_2Cl_2 to give after 20 h at room temperature a precipitate of TlCl plus metallic palladium and a solution from which the highly functionalized **4a**–**b** and **5a–b** could be isolated (70% total yield, Scheme 5). These tautomers could not be separated by chromatography, but they displayed an exploitable difference in solubility. Thus, when a solution of both products in Et_2O was evaporated to dryness and Et_2O added again, the major tautomer did not redissolve and could be isolated by filtration, while the other tautomer could be similarly separated from the mother liquor. In the solid state **5a–b** and **4a–b** are stable and they do not interconvert. However, if **4a–b** are dissolved in CH_2Cl_2 and refluxed for 16 h, they transform completely into **5a–b**. The latter are stable at room temperature in $CDCl_3$ for several days, while under the same conditions **4a–b** transform partially into **5a–b**. The addition of an acid does not accelerate the interconversion of these products. Several reviews dealing with imidoyl compounds have discussed the question of whether imidic acids can exist in general [64]. They are unstable compounds that may be in equilibrium with the stable amide (**5a–d**) molecules. This is confirmed by theoretical investigations, which demonstrate that the amide form is about 11 kcal/mol more stable than the tautomeric imidic acid (**4a–d**) [65]. When the reaction of **3a–b** with Tl(TfO) was carried out in CH_2Cl_2 plus a drop of EtOH, **6a–b** were obtained and the yields varied from 18% to 40%, depending on the amount of added of EtOH.



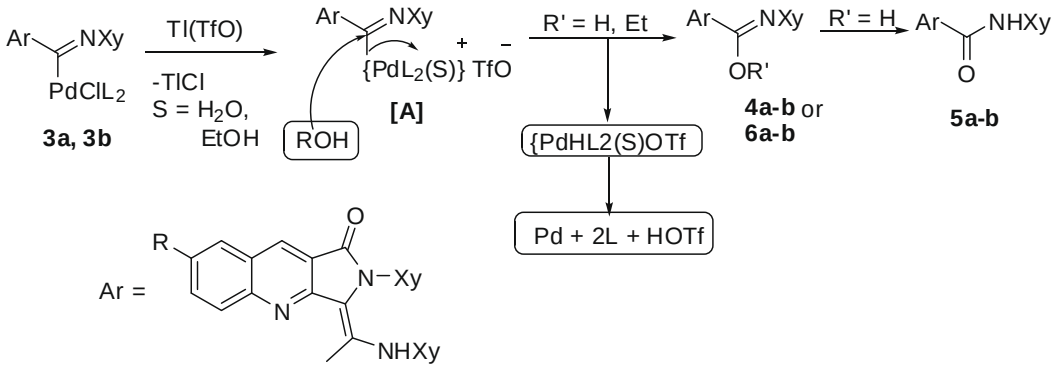
Scheme 3.



Scheme 4.



Scheme 5.



Scheme 6.

Therefore, the depalladation of these inserted complexes represents a stoichiometric synthesis of functionalized arene, *N*-heterocyclic compounds from chloroarenes. As mentioned above, we fruitlessly attempted the synthesis of some of these organic compounds under catalytic conditions. However, catalytic applications of these stoichiometric reactions could still be an objective for future studies. We believe that all depalladation reactions reported here share three common steps, as outlined in Scheme 6

(i) The substitution of the chloro ligand in the iminoacyl quinolinylpalladium complexes **3a–b** by TfO to give the intermediates [**A**], which are formulated as cationic species, assuming that the very labile TfO is substituted by H_2O or EtOH.
(ii) The nucleophilic attack of the iminoacyl carbon (C=NXy)-Pd of intermediate [**A**] by EtOH alcoholysis or H_2O hydrolysis, the latter coming from atmospheric or solvent moisture.
(iii) The decomposition of the resulting adduct (probably through an intermediate) gives the hydrido palladium complex, metallic palladium, neutral ligand L, HOTf and Ar C(=NXy)OR′.

Although the very simple reaction pathways proposed in Scheme 6 allow systematization of the formation of such products, some questions remain unanswered because too many factors can influence the results. Finally, we do not attempt to explain the formation of the enol or ketone form and which of these is more stable, as we cannot account for the influence of the impurities present in the starting material. A mechanistic scheme depicting the formation of various products, including possible intermediates, is outlined in Scheme 6.

2.3. X-ray crystal structures

To further confirm the structures of the products, the molecular structures of yellow crystals of **2a** (Fig. 1), red crystals of **3a** · CH_2Cl_2 (Fig. 2) and reddish crystals of **3b** · CH_2Cl_2 · C_2H_6O (Fig. 3) were determined by X-ray analysis. The Pd–C bond distances of the iminoacyl ligands decrease, in agreement with the decreasing electron delocalization influence of the extended of electron donating group (OMe) located in position (6), as shown in complexes **3a–b** compared with **2a**, or may be decreased due to the *trans* influence of the ligands, thus these values are (in Å): Pd(1)–C(12) 2.0081(16), Pd(2)–C(2) 1.9919(17) (**2a**); Pd–C(40) = 1.9425(18), Pd–C(10) = 1.9999(17) (**3a**); Pd–C(30) = 1.944(2), Pd–C(40) = 2.002(2) (**3b**).

The Pd–Cl distances in (Å) are: Pd(1)–Cl(1) 2.3816(6), Pd(2)–Cl(2) 2.3812(5) **2a**; Pd–Cl 2.4398(4) **3a**, Pd–Cl 2.4283(5) **3b**. Similarly, the Pd–N bond distance in complexes **2a**, **3a** and **3b** were compared: Pd(1)–N(1) 2.0944(14), Pd(2)–N(2) 2.1115(14) **2a**; Pd–N(1) 2.0864(14) **3a** and 2.0905(18) **3b**. Those show the greater *trans* influence of the carbon-donor iminoacyl ligand with respect to the chloro ligand. Looking at these scales, our proposal that the *transphobia* could be directly related to the *trans* influence is reinforced [66] under this assumption; the two ligands with a great *trans* influence will suffer a great *transphobia* [67].

The structure of **2a** (Fig. 1) clearly shows the formation of a palladium atom in a square-planar environment due to the coordination environment consisting of *trans* phosphine, chloro ligands and nitrogen, carbon quinolinyl ligands. The mean deviation of atoms Pd(1), P(1), N(1), Cl(1), C(1) and Pd(2), P(2), N(2), Cl(2), C(2) from the best plane is [Pd(2)–C(2)–Pd(1)–C(12) = 0.0162 Å], [Pd(2)–P(2)–Pd(1)–P(1) = 0.7912 Å], [Pd(2)–Cl(2)–Pd(1)–Cl(1) = 0.004 Å] and [Pd(2)–N(11)–Pd(1)–N(1) = 0.0171 Å]. As expected, for the Pd–C bond distances, Pd(2)–C(2) (2.0081(16) Å) is significantly longer than Pd(1)–C(12) (1.9919(17) Å), the difference being 0.0162 Å. The Pd–N bond distance Pd(2)–N(11) (2.1115(14) Å) is significantly longer than that for Pd(1)–N(1) (2.0944(14) Å), and the difference here is 0.0171 Å, as a result of coordination of the nitrogen atom to Pd(II). However, the Pd–Cl bond distance Pd(2)–Cl(2) (2.3812(5) Å) is just a little bit longer than Pd(1)–Cl(1) (2.3816(6) Å), the difference being 0.004 Å. The Pd–P distance

Pd(2)–P(2) (3.0818(5) Å) is significantly longer than Pd(1)–P(1) (2.2906 Å) and the difference is 0.7912 Å. The reason for the deviation of the Pd(2) compared to Pd(1) in the bond distances for all the ligands around it is due to the greater steric hindrance of PPh_3 and also the trigonal pyramids for the phosphine atom. The angles around Pd(1) and Pd(2) have been compared: C(2)–Pd(2)–N(11) (84.88(6)°) is significantly larger than C(12)–Pd(1)–N(1) (82.22 (6)°) and the difference is 2.66°; C(2)–Pd(2)–P(2) (93.24(5)°) is slightly larger than C(12)–Pd(1)–P(1) (92.32(5)°) and the difference is 0.92°; N(11)–Pd(2)–P(2) (175.12(4)°) is slightly larger than N(1)–Pd(1)–P(1) (174.53(4)°) and the difference is 0.59°; C(2)–Pd(2)–Cl(2) (174.14(5)°) is slightly larger than C(12)–Pd(1)–Cl(1) (173.90(5)°) and the difference is 0.24°; N(11)–Pd(2)–Cl(2) (90.20(4)°) is smaller than N(1)–Pd(1)–Cl(1) (92.30(4)°) by 2.10°; P(2)–Pd(2)–Cl(2) (91.91(2)°) is smaller than P(1)–Pd(1)–Cl(1) (93.14(2)°) by 1.23°; C(2)–Pd(2)–Pd(1) (66.30(5)°) is slightly larger than C(12)–Pd(1)–Pd(2) (66.01(5)°) and the difference is 0.29°; N(11)–Pd(2)–Pd(1) (63.27(4)°) is very slightly larger than N(1)–Pd(1)–Pd(2) (63.12(4)°) and the difference is 0.15°; P(2)–Pd(2)–Pd(1) (111.854(17)°) is smaller than P(1)–Pd(1)–Pd(2) (114.865(14)°) by 3.015°; Cl(2)–Pd(2)–Pd(1) (114.188(16)°) is slightly larger than Cl(1)–Pd(1)–Pd(2) (113.865(19)°) and the difference is 0.323°. These results suggest a delocalization of π electron density around N(1) and P(1) as compared to N(2) and P(2) and distortion of the bond angles around the Pd(1) and Pd(2) due to the greater steric hindrance of PPh_3.

Fig. 2 clearly shows the structure of the red crystalline quinolinepalladium complex **3a**, with the Pd–C distances Pd–C(40) 1.9425(18) Å and Pd–C(10) 1.9999(17) Å. The Pd–Cl(1) distance is 2.4398(4) Å and the Pd–N(1) bond distance is 2.0864(14) Å; these show the greater *trans* influence of the C-donor iminoacyl ligand is with respect to the chloro ligand. The *transphobia* [*T*] is directly related to the *trans* influence of the two ligands and the complex suffers a great *transphobia* effect. The [Pd]C═NXy bond distance of the iminoacyl ligand in complex **3a** is N(10)–C(10) 1.270(2) Å; N(20)–C(20) 1.372(2) Å and N(30)–C(30) 1.429(2) Å are the C═N distances corresponding to the inserted molecule of XyN═C and N(40)–C(40) 1.151(2) Å is the C═N distance corresponding to the inserted molecule of CNXy. All these lengths are as expected for a C═N bond [mean values for the C(aryl)–C═NR distances lie in the range 1.432–1.382 Å] [68–70]. The aryl C═N(Xy)[Pd] distance corresponding to the third inserted molecule of XyNC in **3a** is significantly longer than the other related distances, N(10)–C(10) 1.270(2) Å and N(1)–C(2) 1.325(2) Å, as a result of coordination of the nitrogen atom to Pd(II). This fact, the angles around Pd (C(40)–Pd–C(10) 91.93(7)°, C(40)–Pd–N(1) 178.97(6)°, C(10)–Pd–N(1) 87.11(6)°, C(40)–Pd–Cl(1) 84.21(5)°, C(10)–Pd–Cl(1) 173.33(5)°, N(1)–Pd–Cl(1) 96.78(4)°) and the short C(20)–C(30) bond 1.366(2) Å compared with C(10)–C(20) 1.505(2) Å, suggest a delocalization of π electron density around C(20)–C(30)–N(30) (angle (127.76(15)°) as compared to N(30)–C(30)–C(2) (angle 104.88(13)°), N(20)–C(20)–C(30) (angle 122.27(16)°) and N(20)–C(20)–C(10) (angle 118.83(15)°). The coordination environment of the Pd(II) centre is almost square planar.

Red crystals of **3b**, also suitable for X-ray analysis, were obtained in a similar manner to its analogue **3a**, and the structure of **3b** (Fig. 3) is identical to **3a** except for the different substituents of the OMe group. The Pd–C distances of the iminoacyl quinolinylpalladium complex **3b** are Pd(1)–C(30) 1.944(2) Å and Pd(1)–C(40) 2.002(2) Å. The Pd–Cl distance (Pd(1)–Cl(1) 2.4283(5) Å) and the Pd–N bond distance, Pd(1)–N(1), is 2.0905(18) Å; these again show the greater *trans* influence of the C-donor iminoacyl ligand is with respect to the chloro ligand. Looking at these scales, our proposal that the *transphobia [T]* could be directly related to the *trans* influence is reinforced under this assumption; the two ligands with a great *trans* influence will suffer a great *transphobia [T]* [67]. The [Pd]C═NXy bond distance of the iminoacyl ligand in complex **3b** is N(4)–C(40) 1.266(3) Å; N(5)–C(50) 1.363(3) Å and N(2)–C(12) 1.432(3) Å are the C═N distances corresponding to the inserted molecule of XyN═C and N(3)–C(30) 1.153(3) Å is the C═N distance corresponding to the inserted molecule of CNXy. All these lengths are as expected for a C═N bond [mean values for the C(aryl)–C═NR distances lie in the range 1.432–1.382 Å] [68–70]. The aryl C═N(Xy)[Pd] distance corresponding to the third inserted molecule of XyNC in **3b** is significantly longer than the other related distance, N(4)–C(40) 1.266(3) Å, as a result of coordination of the nitrogen atom to Pd(II). This fact, the angles around Pd (C(30)–Pd(1)–C(40) 91.67(8)°, C(30)–Pd(1)–N(1) 178.75(8)°, C(40)–Pd(1)–N(1) 87.14(8)°, C(30)–Pd(1)–Cl(1) 84.53(6)°, C(40)–Pd(1)–Cl(1) 175.94(6)°, N(1)–Pd(1)–Cl(1) 96.64(5)°) and the short C(12)–C(50) bond 1.365(3) Å compared to C(40)–C(50) 1.507(3) Å, suggest a delocalization of π electron density around the C(50)–C(12)–N(2) (angle 127.34(19)°) as compared to N(2)–C(12)–C(1) (angle 105.08(18)°), N(5)–C(50)–C(12) (angle 123.2(12)°) and N(5)–C(50)–C(40) (angle 119.57(19)°). The coordination environment of the Pd(II) centre is almost square planar.

3. Experimental

Reactions were carried out without precautions to exclude light, atmospheric, oxygen and moisture, unless otherwise stated. Melting points were determined on a Reicher apparatus and are uncorrected. Elemental analyses were carried out with a Carlo Erba 1106 microanalyzer. IR spectra were recorded on a Perkin–Elmer 16F P CFT-IR spectrometer with Nujol mulls between polyethylene sheets or KBr pellets. NMR spectra were recorded in a Bruker AC 200, Avance 300 or a Varian Unity 300 spectrometer at room temperature unless otherwise stated. Chemical shifts were referenced to TMS (^1H and ^{13}C) and H_3PO_4 (^{31}P). The NMR probe temperature was calibrated using ethylene glycol ^1H NMR standard methods. Chromatographic separations were carried out by TLC on silica gel (70–230 mesh). Some of the preparations required the use of highly hazardous Tl(I) salts and they should be handle with caution.

3.1. General method for the synthesis of aryl palladium complexes (*2a–b*)

A mixture of [Pd(dba)$_2$] (432 mg, 0.75 mmol), PPh_3 (393.45 mg, 1.5 mmol) and 2-chloro-6-R-3-quinolinecarboxaldehyde **1a–b** (0.75 mmol) was mixed under N_2 in dry acetone (25 ml). The reaction mixture was stirred for 3–5 h at room temperature, then was concentrated (ca. 2 ml) and CH_2Cl_2 (25 ml) was added. The solution was passed through a pad of silica gel/$MgSO_4$ (3:1) in a fritted funnel, and then evaporated under reduced pressure, and Et_2O (15 ml) was added. The resulting solution was concentrated (ca. 2 ml); a mixture of the complex and dba was precipitated with *n*-hexane. The suspension was stirred for 10 min at RT, filtered off, washed with Et_2O (5 ml), and air-dried to give the yellow solid of **2a–b**.

3.1.1. {Pd[C_9H_5-CHO-(3)]Cl(PPh_3)}$_2$ (*2a*)

Purification via flash column chromatography silica gel (1:1 CH_2Cl_2/acetone) afforded a yellow solid **2a**, Yield: 398 mg, 43%. M.p.: 177–179 °C dec. A diffraction-quality crystal was grown by slow diffusion of Et_2O into a CH_2Cl_2 solution. IR (Nujol, cm^{-1}); *ν*(HC═O) 1688.4, *ν*(C═N and C═C) 1612.0, 1582.0, 1572.0 and 1538.0. ^1H NMR (400 MHz, $CDCl_3$); *δ* 10.39 (s, 2H, CHO), 7.34–7.90 (m, 17H, Ar–H), 7.25–6.91 [(m, 23H, Ar–H and (PPh_3)$_2$], 5.28 [(s, 1H, 1/2 (CH_2Cl_2)] ppm. ^{31}P {^1H} NMR (121 MHz, $CDCl_3$); 20.67 ppm. *Anal.* Calc. for $C_{56}H_{42}N_2O_2Cl_2Pd_2P_2$ (1120.62): C, 60.02; H, 3.78; N, 2.50. Found; C, 60.01; H, 3.75; N, 2.35%.

*3.1.2. [Pd[-6-OCH_3-C_9H_4-CHO-(3)]Cl(PPh_3)}$_2$ (**2b**)*

Purification via flash column chromatography silica gel (1:1 CH_2Cl_2/acetone) afforded a yellow-solid **2b**, Yield: 277 mg, 31.2%. M.p.: 180–182 °C dec. A diffraction-quality crystal was grown by slow diffusion of Et_2O into a CH_2Cl_2 solution of **2b**. IR (Nujol, cm^{-1}); ν(HC=O) 1678.0, ν(C=N and C=C) 1584.0, 1546.0. ^1H NMR (400 MHz, $CDCl_3$); δ 10.43 (s, 2H, CHO), 7.79–7.46 (m, 15H, Ar–H), 7.41–7.05 [(m, 22H, Ar–H and $(PPh_3)_2$], 6.60 (d, 1H, J = 2.6Hz), 3.84 (s, 6H, OMe) ppm. ^{31}P {^1H} NMR (121 MHz, $CDCl_3$); 21.37 ppm. *Anal.* Calc. for $C_{58}H_{46}N_2O_4Cl_2Pd_2P_2$ (1180): C, 59.00; H, 3.93; N, 2.37. Found; C, 59.08; H, 4.04; N, 2.32%.

*3.2. 4-(2,6-Dimethyl-phenyl)-3-(2,6-dimethyl-phenylamino)-2-(2,6-dimethyl-phenylimino)-1-[(2,6-dimethyl-phenylisonitrile)]-2,4-dihydro-1H-4,10b-diaza-acephenanthrylene-5-one-1-palladium(II)chloride complex (**3a**)*

3.2.1. Method (A)

To a suspension of 'Pd(dba)$_2$' (300 mg, 0.52 mmol) and XyNC (274 mg, 2.09 mmol) in acetone (15 ml), 2-chloro-3-quinoline carboxaldehyde **1a** (149.4 mg, 0.78 mmol) was added under nitrogen. The suspension was stirred for 5 h at room temperature, then the solvent was evaporated. The resulting residue was extracted with CH_2Cl_2 (25 ml) and the extract filtrate was filtered over anhydrous $MgSO_4$/silica gel (1:3) in a fritted funnel. The resulting red solution was evaporated and the residue was triturated with Et_2O (15 ml). The precipitate was filtered, washed with Et_2O (2 × 5 ml), and air-dried, giving the red compound **3a**, yield, 254 mg, 39%. Diffraction-quality crystals were grown by slow diffusion of Et_2O into a CH_2Cl_2 solution of **3a**. M.p.: Dec. pt: 255 °C. IR (Nujol, cm^{-1}):): ν(NH, broad band) 3353, ν(C=O) 1716, 1699, ν(C≡N) 2361, 2338, ν(C=N) 1558, 1541. ^1H NMR (200 MHz, $CDCl_3$) δ 8.87 (s, 1H, NH), 8.83–8.78 (d, 1H, *J* = 8.6 Hz), 7.99–7.87 (q, 2H, *J* = 8.6 Hz), 7.63–7.55 (t, 1H, *J* = 7.6 Hz), 7.35–7.22 (m, 3H), 7.19–6.97 (m, 5H), 6.91–6.73 (m, 4H), 6.40–6.37 (d, 1H, *J* = 7.2 Hz), 2.55 (s, Me, 3H), 2.49 (s, Me, 3H), 2.30 (s, Me, 3H), 2.19 (s, Me, 6H), 2.11 (s, Me, 3H), 1.58 (s, Me, 3H) 0.62 (s, Me, 3H) ppm. *Anal.* Calc. for $C_{46}H_{42}N_5OClPd$ (822): C, 67.15; H, 5.15; N, 8.50. Found: C, 67.04; H, 5.09; N, 8.14%.

3.2.2. Method (B)

To a suspension of {Pd[C_9H_5-CHO (3)]Cl(PPh_3)}$_2$ **2a** (268 mg, 0.24 mmol) in CH_2Cl_2 (15 ml), XyNC (248 mg, 1.92 mmol) was added. The suspension was stirred for 24 h at room temperature. The color changed from pale yellow into pale red and then dark red whilst the reaction mixture was monitored. The solvents were filtered over a pad of anhydrous $MgSO_4$/silica gel (1:3) in a fritted funnel. The resulting red solution was evaporated and the residue was triturated with Et_2O (15 ml). The precipitate was filtered, washed with Et_2O (2 × 5 ml), and air-dried, giving the red compound **3a**. Yield: 160 mg, 81%. Diffraction-quality crystals were grown by slow diffusion of Et_2O into a CH_2Cl_2 solution of **3a**.

*3.3. 4-(2,6-Dimethyl-phenyl)-3-(2,6-dimethyl-phenylamino)-2-(2,6-dimethyl-phenylimino)-1-[(2,6-dimethyl-phenylisonitrile)]-8-methoxy-2,4-dihydro-1H-4,10b-diaza-acephenanthrylene-5-one-1-palladium(II) chloride complex (**3b**)*

3.3.1. Method (A)

2-Chloro-6-methoxy-3-quinoline carboxaldehyde **1b** (172.86 mg, 0.78 mmol) was added to a suspension of 'Pd(dba)$_2$' (300 mg, 0.52 mmol) and XyNC (274 mg, 2.09 mmol) in acetone (15 ml) under nitrogen. The suspension was stirred for 5 h at room temperature. The solvents were evaporated, the residue was extracted with CH_2Cl_2, and the extract filtrate was filtered over a pad of anhydrous $MgSO_4$/silica gel (1:3) in a fritted funnel. The resulting red solution was evaporated and the residue was triturated with Et_2O (15 ml). The precipitate was filtered, washed with Et_2O (2 × 5 ml), and air-dried, giving the red solid compound **3b**.Yield: 223 mg, 33.5%. Diffraction-quality crystals were grown by slow diffusion of Et_2O into a CH_2Cl_2 solution of **3b**. M.p.: 238–240 °C. IR (Nujol, cm^{-1}): ν(NH, broad band) 3360, ν(C≡N) 2182.7, ν(C=O) 1704.5, ν(C=N) 1602.4, 1570.1. ^1H NMR (200 MHz, $CDCl_3$) δ 8.75 (s, 1H, NH), 8.71 (d, 1H, $^3J_{HH}$ = 8.6 Hz), 7.67–7.57 (dd, 1H, $^4J_{HH}$ = 2.6, $^3J_{HH}$ = 9.6 Hz, quinoline-H_8), 7.27–7.18 (m, 5H), 7.14–7.11 (s, 1H), 7.07–6.96 (m, 3H), 6.89–6.80 (m, 4H), 6.40–6.36 (d, 1H, $^3J_{HH}$ = 7.6 Hz, quinoline-H), 3.96 (s, 3H, OMe), 2.54 (s, Me, 3H), 2.49 (s, Me, 3H), 2.29 (s, Me, 3H), 2.18 (s, Me, 6H), 2.12 (s, Me, 6H), 0.62 (s, Me, 3H) ppm. *Anal.* Calc. for $C_{47}H_{44}N_5O_2ClPd$ (852) + H_2O = (870.79): C, 64.83: H, 5.32: N, 8.04. Found: C, 64.91: H, 5.12: N, 8.04%.

3.3.2. Method (B)

To a suspension of {Pd[6-OCH_3-C_9H_5-CHO (3)]Cl(PPh_3)}$_2$ (**2b**) (283 mg, 0.24 mmol) in CH_2Cl_2 (15 ml), XyNC (248 mg, 1.92 mmol) was added. The suspension was stirred for 24 h at room temperature and the color changed from pale yellow into pale red and then dark red whilst the reaction mixture was monitored. The solvents were filtered over a pad of anhydrous $MgSO_4$/silica gel (1:3) in a fritted funnel. The resulting red solution was evaporated and the residue was triturated with Et_2O (15 ml). The precipitate was filtered, washed with Et_2O (2 × 5 ml), and air-dried, giving the red compound **3b**. Yield, 158 mg, 77%. Diffraction-quality crystals were grown by slow diffusion of Et_2O into a CH_2Cl_2 solution of **3b**.

4. Depalladation procedure

*4.1. General procedure for the acetamidic acids (**4a**–**b**) and acetamide (**5a**–**b**)*

Tl(TfO) (314 mg, 0.89 mmol) was added to a suspension of **3a–b** (0.89 mmol) in Me_2CO (20 ml). The resulting red suspension was stirred for 20 h. During this time decomposition to metallic palladium was observed and a dark brownish suspension formed. This was filtered over Celite, and the filtrate was concentrated and applied to a preparative TLC plate (eluant: *n*-hexane/Et_2O, 1:2). A yellow band at R_f = 0.25 was collected and extracted with Me_2CO (30 ml). The resulting solution was dried with anhydrous $MgSO_4$ for 1 h and filtered, and the filtrate was evaporated to dryness, giving a 2:3 mixture of both tautomers **5a–b** and **4a–b**. A sample of this mixture (200 mg) was dissolved in Et_2O (30 ml), the solution was evaporated to dryness, and the residue was treated with Et_2O (30 ml), causing the precipitation of a solid, which was filtered and air-dried to give yellow **4a–b** (41%). The same process was repeated with the mother liquor, giving **5a–b** (27%).

*4.2. N-(2,6-Dimethylphenyl)-2-(2,6-dimethylphenylamino)-2-[2-(2,6-dimethylphenyl)-1-oxo-1,2-dihydro-pyrrolo[3,4-b]quinolin-3-ylidene]-acetimidic acid (**4a**)*

M.p.: 206–208 °C. IR (cm^{-1}): ν(OH), ν(NH) 3420, 3232 b, ν(C=O), ν(C=N) 1682, 1668. ^1H NMR (200 MHz, $CDCl_3$) δ 8.77 (d, 1H, quinol-H_4), 8.37 (dd, 1H, $^4J_{HH}$ = 1.6, $^3J_{HH}$ = 8.6 Hz, quinol-H_8), 7.97 (d, 1H, $^3J_{HH}$ = 8.6 Hz, quinol-H_5), 7.73 (dd, 1H, $^3J_{HH}$ = 8.6 and 6.9 Hz, quinol-H_7), 7.43 (dd, 1H, $^3J_{HH}$ = 8.6 and 6.8 Hz, quinol-H_6), 7.30–7.21 (m, 3H), 7.14–6.96 (m, 6H), 6.89 (s, 1H, NH), 5.58 (s, 1H, NH), 2.39 (s, 2Me, 6H), 2.29 (s, 2Me, 6H), 1.63 (s, Me, 6H), 1.54 (s, 1H, OH) ppm. ^{13}C NMR (75 MHz, $CDCl_3$) δ 166.5 (C=O), 164.9 (quaternary C), 156.8 (quaternary C), 151.4 (quaternary C), 148.8 (quaternary C), 147.2 (quaternary C), 139.7 (quaternary C), 137.9 (CH), 131.1 (CH), 130.1 (CH), 129.9 (quaternary C), 129.7

(quaternary C), 128.6 (CH), 127.5 (CH), 127.4 (quaternary C), 127.2 (CH), 127.0 (CH), 126.8 (CH), 126.4 (quaternary C), 124.7 (quaternary C), 124.7 (CH), 124.1 (CH), 123.1 (CH), 122.0 (quaternary C), 105.5 (quaternary C), 18.8 (2 × Me), 18.3 (2 × Me), 18.1 (2 × Me). *Anal.* Calc. for $C_{37}H_{34}N_4O_2$ (566.7): C, 78.42; H, 6.05; N, 9.89. Found: C, 78.36; H, 6.06; N, 9.87%.

4.3. N-(2,6-Dimethylphenyl)-2-(2,6-dimethylphenylamino)-2-[2-(2,6-dimethylphenyl)-7-methoxy-1-oxo-1,2-dihydro-pyrrolo[3,4-b]quinolin-3-ylidene]-acetimidic acid (**4b**)

M.p.: 211–213 °C. IR (cm^{-1}): ν(OH), νNH) 3420, 3232 b, ν(C=O), ν(C=N) 1668. ^{1}H NMR (200 MHz, $CDCl_3$) δ 8.79 (d, 1H, quinol-H_4), 8.42 (dd, 1H, $^4J_{HH}$ = 1.6, $^3J_{HH}$ = 8.7 Hz, quinol-H_8), 7.97 (d, 1H, $^3J_{HH}$ = 8.7 Hz, quinol-H_5), 7.73 (dd, 1H, $^3J_{HH}$ = 8.7 and 6.8 Hz, quinol-H_7), 7.43 (dd, 1H, $^3J_{HH}$ = 8.7 and 6.8 Hz, quinol-H_6), 7.3–7.2 (m, 3H), 7.14–6.95 (m, 6H), 5.58 (s, 1H, NH), 3.96 (s, 3H, OMe), 2.39 (s, 2Me, 6H), 2.29 (s, 2Me, 6H), 1.63 (s, Me, 6H), 1.54 (s, 1H, OH) ppm. ^{13}C NMR (75 MHz, $CDCl_3$) δ 166.5 (C=O), 164.9 (quaternary C), 156.8 (quaternary C), 151.4 (quaternary C), 148.8 (quaternary C), 147.2 (quaternary C), 139.7 (quaternary C), 137.9 (CH), 131.1 (CH), 130.1 (CH), 129.9 (quaternary C), 129.7 (quaternary C), 128.6 (CH), 127.5 (CH), 127.4 (quaternary C), 127.2 (CH), 127.0 (CH), 126.8 (CH), 126.4 (quaternary C), 124.7 (quaternary C), 124.7 (CH), 124.1 (CH), 123.1 (CH), 122.0 (quaternary C), 105.5 (quaternary C), 57.34 (OMe), 18.8 (2 × Me), 18.3 (2 × Me), 18.1 (2 × Me). *Anal.* Calc. for $C_{38}H_{36}N_4O_3$ (596.7): C, 78.49; H,6.06; N, 9.39. Found: C, 78.46; H, 6.04; N, 9.36%.

4.4. N-(2,6-Dimethylphenyl)-2-(2,6-dimethylphenylamino)-2-[2-(2,6-dimethylphenyl)-1-oxo-1,2-dihydro-pyrrolo[3,4-b]quinolin-3-ylidene]-acetamide (**5a**)

M.p.: 146–148 °C. IR (cm^{-1}): ν(NH) 3388, 3366, 3262 broad, ν(C=O) 1698, ν(C=N), 1668. ^{1}H NMR (200 MHz, $CDCl_3$) δ 8.77 (d, 1H, quinol-H_4), 8.37 (dd, 1H, $^4J_{HH}$ = 1.6, $^3J_{HH}$ = 8.6 Hz, quinol-H_8), 7.97 (d, 1H, $^3J_{HH}$ = 8.6 Hz, quinol-H_5), 7.73 (dd, 1H, $^3J_{HH}$ = 8.6 and 6.9 Hz, quinol-H_7), 7.43 (dd, 1H, $^3J_{HH}$ = 8.6 and 6.8 Hz, quinol-H_6), 7.30–7.21 (m, 3H), 7.14–6.96 (m, 6H), 6.89 (s, 1H, NH), 5.07 (s, 1H, NH), 2.44 (s, 2Me, 6H), 2.29 (s, 2Me, 6H), 2.02 (s, Me, 6H) ppm. ^{13}C NMR (75 MHz, $CDCl_3$) δ 165.8 (C=O), 162.6 (C=O), 157.8 (quaternary C), 147.8 (quaternary C), 146.8 (quaternary C), 139.8 (quaternary C), 139.6 (quaternary C), 137.8 (CH), 135.9 (quaternary C), 135.7 (quaternary C), 135.6 (quaternary C), 134.9 (quaternary C), 132.7 (quaternary C), 132.1 (CH), 131.9 (CH), 129.14 (CH), 129.11 (CH), 128.6 (CH), 127.54 (CH), 127.48 (quaternary C), 127.3 (CH), 126.8 (CH), 126.4 (CH), 124.0 (CH), 122.0 (CH), 112.9 (quaternary C), 18.8 (2 × Me), 18.3 (2 × Me), 18.1 (2 × Me). *Anal.* Calc. for $C_{37}H_{34}N_4O_2$ (566.7): C, 78.42; H, 6.05; N, 9.89. Found: C, 78.31; H, 6.12; N, 9.84%.

4.5. N-(2,6-Dimethylphenyl)-2-(2,6-dimethylphenylamino)-2-[2-(2,6-dimethylphenyl)-7-methoxy-1-oxo-1,2-dihydro-pyrrolo[3,4-b]quinolin-3-ylidene]-acetamide (**5b**)

Mp: 146–148 °C. IR (cm^{-1}): ν(NH) 3388, 3366, 3262 broad, ν(C=O) 1698, ν(C=N), 1668. ^{1}H NMR (200 MHz, $CDCl_3$) δ 8.77 (d, 1H, quinol-H_4), 8.37 (dd, 1H, $^4J_{HH}$ = 1.6, $^3J_{HH}$ = 8.6 Hz, quinol-H_8), 7.97 (d, 1H, $^3J_{HH}$ = 8.6 Hz, quinol-H_5), 7.73 (dd, 1H, $^3J_{HH}$ = 8.6 and 6.9 Hz, quinol-H_7), 7.43 (dd, 1H, $^3J_{HH}$ = 8.6 and 6.8 Hz, quinol-H_6),7.30–7.21 (m, 3H), 7.14–6.96 (m, 6H), 6.89 (s, 1H, NH), 5.07 (s, 1H, NH), 3.96 (s, 3H, OMe), 2.44 (s, 2Me, 6H), 2.29 (s, 2Me, 6H), 2.02 (s, Me, 6H), ppm. ^{13}C NMR (75 MHz, $CDCl_3$) δ 165.8 (C=O), 162.6 (C=O), 158.8 (quaternary C), 154.8 (quaternary C), 148.8 (quaternary C), 143.8 (quaternary C), 139.8 (quaternary C), 139.6 (quaternary C), 136.9 (CH), 135.9 (quaternary C), 135.7 (quaternary C), 135.6 (quaternary C), 134.9 (quaternary C), 132.7 (quaternary C), 131.7 (CH), 129.11 (CH), 128.6 (CH), 127.54 (CH), 127.48 (quaternary C), 127.3 (CH), 126.8 (CH), 126.4 (CH), 124.0 (CH), 122.0 (CH), 112.9 (quaternary C), 57.34 (OMe), 18.8 (2 × Me), 18.3 (2 × Me), 18.1 (2 × Me). *Anal.* Calc. for $C_{38}H_{36}N_4O_3$ (596.7): C, 76.49; H, 6.06; N, 9.39. Found: C, 76.41; H, 6.02; N, 9.34%.

4.6. General Procedure of the ethyl esterification of acetamidic acids (**6a**–**b**)

Tl(TfO) (374 mg, 1.06 mmol) and EtOH (one drop) were added to a solution of **3a–b** (1.06 mmol) in CH_2Cl_2 (20 ml). The resulting black suspension was stirred for 20 h and filtered over Celite, and the yellow filtrate was concentrated and applied to a preparative TLC plate (eluant: *n*-hexane/Et_2O, 1:2), where two main yellow bands separated. From the band at R_f = 0.25 a 2:1 mixture of **5a–b** and **4a–b** was obtained in moderate yield. The band at R_f = 0.62 was collected and extracted with Me_2CO (30 ml). The extract was treated with anhydrous $MgSO_4$ for 1 h, filtered and evaporated to dryness, affording the yellow ester **6a–b** in low yields (18–19%).

4.7. N-(2,6-Dimethylphenyl)-2-(2,6-dimethylphenylamino)-2-[2-(2,6-dimethylphenyl)-1-oxo-1,2-dihydro-pyrrolo[3,4-b]quinolin-3-ylidene]acetimidic acid ethyl ester (**6a**)

A suspension solution of **3a** (871.32 mg, 1.06 mmol) in CH_2Cl_2 (20 ml) was used under the reaction conditions to produce **6a** in the yield 122 mg, 19%. M.p.: 210–212 °C. IR (cm^{-1}): ν(NH) 3384, ν(C=O), ν(C=N) 1698, 1694, 1660. ^{1}H NMR (200 MHz, $CDCl_3$) δ 8.86 (d, 1H, quinol-H_4), 8.34 (dd, 1H, $^4J_{HH}$ = 1.6, $^3J_{HH}$ = 8.4 Hz, quinol-H_8), 7.87 (d, 1H, $^3J_{HH}$ = 8.4 Hz, quinol-H_5), 7.73 (dd, 1H, $^3J_{HH}$ = 8.4 and 6.8 Hz, quinol-H_7), 7.45 (dd, 1H, $^3J_{HH}$ = 8.4 and 6.8 Hz, quinol-H_6), 7.10–7.05 (m, 3H), 6.80–6.69 (m, 6H), 4.79 (s, NH, 1H), 4.39 (q, CH_2Me, 2H, $^2J_{HH}$ = 7 Hz), 2.22 (s, 2 × Me, 6H), 1.48 (bs, 4 × Me, 12H), 1.39 (t, CH_2Me, 3H, $^2J_{HH}$ = 7 Hz) ppm. *Anal.* Calc. for $C_{39}H_{38}N_4O_2$ (594.7): C, 78.76; H,6.44; N, 9.42. Found: C, 78.74; H, 6.22; N, 9.35%.

4.8. N-(2,6-Dimethylphenyl)-2-(2,6-dimethylphenylamino)-2-[2-(2,6-dimethylphenyl)-7-methoxy-1-oxo-1,2-dihydro-pyrrolo[3,4-b]quinolin-3-ylidene]acetimidic acid ethyl ester (**6b**)

A suspension solution of **3b** (903.12 mg, 1.06 mmol) in CH_2Cl_2 (20 ml) was used under the reaction conditions to produce **6b** in the yield 120 mg, 18%. M.p.: 206–208 °C. IR (cm^{-1}): ν(NH) 3384, ν(C=O), ν(C=N) 1698, 1694, 1660. ^{1}H NMR (300 MHz, $CDCl_3$) δ 8.86 (d, 1H, quinol-H_4), 8.34 (dd, 1H, $^4J_{HH}$ = 1.6, $^3J_{HH}$ = 8.4 Hz, quinol-H_8), 7.87 (d, 1H, $^3J_{HH}$ = 8.4 Hz, quinol-H_5), 7.73 (dd, 1H, $^3J_{HH}$ = 8.4 and 6.8 Hz, quinol-H_7), 7.45 (dd, 1H, $^3J_{HH}$ = 8.4 and 6.8 Hz, quinol-H_6), 7.10–7.05 (m, 3H), 6.80–6.69 (m, 6H), 4.79 (s, NH, 1H), 4.39 (q, CH_2, 2H, $^2J_{HH}$ = 7 Hz), 2.22 (s, 2 × Me, 6H), 1.48 (bs, 4 × Me, 12H), 1.39 (t, CH_2Me, 3H, $^2J_{HH}$ = 7 Hz) ppm. *Anal.* Calc. for $C_{40}H_{40}N_4O_3$ (624.8): C, 76.90; H, 6.45; N, 8.97. Found: C, 76.83; H, 6.42; N, 9.02%.

4.9. X-ray crystallographic studies

Details of data collection and refinement are given in Table 1. The crystal structures from the single-crystal X-ray diffraction studies for **2a**, **3a** and **3b** were carried out on a Bruker SMART 1000 CCD diffractometer with graphite-monochromated Mo Kα radiation (λ = 0.71073 Å). Cell parameters were obtained by global refinement of the positions of all collected reflections. Intensities were corrected for Lorentz and polarization effects and empirical

Table 1
Details of data collection and structure refinement for the complexes {Pd[C_9H_5-CHO(3)]Cl(PPh_3)}$_2$ **2a**, {PdCl[(C=N-Xy)$_2$-(C-NHXy) (CNXy)C_9H_5N-(3)-CO]} **3a** and {PdCl[(C=N-Xy)$_2$-(C-NHXy) (CNXy) 6-MeO-C_9H_5N-(3)-CO]}**3b**.

	2a · CH_2Cl_2	**3a** · CH_2Cl_2	**3b** · C_2H_6O · CH_2Cl_2
Empirical formula	$C_{56}H_{42}Cl_2N_2O_2P_2Pd_2$	$C_{46}H_{42}ClN_5OPd$	$C_{47}H_{43}ClN_5O_2Pd$
E. F. as X-ray measure	$C_{57}H_{44}C_{l4}N_2O_2P_2Pd_2$	$C_{47}H_{44}Cl_3N_5OPd$	$C_{50}H_{51}Cl_3N_5O_3Pd$
Formula weight	1205.48	907.62	982.71
Temperature (K)	133(2)	133(2)	100(2)
Wavelength (Å)	0.71073	0.71073	0.71073
Crystal habit	yellow rectangular prim	red tablet	red prism
Crystal system	triclinic	monoclinic	monoclinic
Space group	$P\bar{1}$	$P21/c$	$P2(1)/c$
Unit cell dimensions			
a (Å)	11.8384(11)	11.7167(8)	8.3018(3)
b (Å)	13.451(2)	20.1516(14)	19.8319(8)
c (Å)	17.804(3)	18.7484(12)	27.3429(11)
α (°)	106.116(11)	90	90
β (°)	96.793(15)	108.055(4)	95.2830(10)
γ (°)	111.512(12)	90	90
V (Å^3)	2456.0(6)	4208.7(5)	4482.6(3)
Z	2	4	4
D_{calc} (Mg/m^3)	1.630	1.432	1.456
Absorption coefficient (mm^{-1})	1.062	0.674	0.642
F(000)	1212	1864	2028
Crystal size (mm^3)	0.36 × 0.15 × 0.11	0.25 × 0.19 × 0.10	0.25 × 0.15 × 0.14
θ Range for data collection (°)	1.23–30.04	1.53–30.04	1.81–27.10
Index ranges	$-16 \leqslant h \leqslant 16$, $-18 \leqslant k \leqslant 18$, $-25 \leqslant l \leqslant 25$	$-16 \leqslant h \leqslant 16$, $-28 \leqslant k \leqslant 28$, $-26 \leqslant l \leqslant 26$	$-10 \leqslant h \leqslant 10$, $-25 \leqslant k \leqslant 25$, $-35 \leqslant l \leqslant 34$
Reflections collected	46379	66861	50825
Independent reflections (R_{int})	14268 (0.0293)	12314 (0.0476)	9847 (0.0231)
Completeness to θ = 30.00° (%)	99.4	100.0	99.7
Absorption correction	numerical	numerical	semi-empirical from equivalents
Maximum and minimum transmission	0.9069 and 0.7461	0.9387 and 0.8509	0.9155 and 0.8559
Refinement method	full-matrix least-squares on F^2	full-matrix least-squares on F^2	full-matrix least-squares on F^2
Data/restraints/parameters	14268/0/622	12314/0/526	9847/32/571
Goodness-of-fit on F^2	1.029	0.982	1.065
Final R indices [$I > 2\sigma(I)$]	$R1$ = 0.0251, $wR2$ = 0.0630	$R1$ = 0.0306, $wR2$ = 0.0724	$R1$ = 0.0352, $wR2$ = 0.0909
R indices (all data)	$R1$ = 0.0335, wR2 = 0.0664	$R1$ = 0.0478, $wR2$ = 0.0778	$R1$ = 0.0395, $wR2$ = 0.0938
Largest difference in peak and hole (e Å^{-3})	0.997 and −0.960	1.037 and −0.887	1.671 and −0.527

absorption. The structures were solved by direct methods and refined by full-matrix least-squares on F^2. All non-hydrogen atoms were refined anisotropically. All hydrogen atoms placed in calculated positions. Structure solution and refinement were performed by using the SHELXL-97 package. [71] Crystal data and processing parameters for **2a**, **3a** and **3b** are summarized in Table 1.

5. Conclusion

We successfully developed a new type of iminoacyl quinolinyl palladium complexes and palladacycles that allows the preparation of new carbocycles via a depalladation reaction. Overall, this methodology provides an alternative approach to novel quinolinylpalladium complexes and amide **5a–b** or imidic acid **4a–b** from three simple and readily available building blocks via a one-pot, multi-component process. These novel arylpalladium complexes are air- and moisture stable, and further scope of this class of arylpalladium complexes and applications are currently under investigation in our laboratory.

Acknowledgments

This work has been supported by the Ministry of Education and Science Spain and FEDER (EU) during the sabbatical leave of the author as a visiting professor. The author wishes to thank Professor Peter G. Jones' Institut für Anorganische und Analytische Chemie der Technischen Universität, Postfach 3329, 38023 Braunschweig, Germany for the measurement of the single crystal by X-ray analysis.

Appendix A. Supplementary data

CCDC 680962, 680963, 680964 contain the supplementary crystallographic data for **2a**, **3a**, **3b**. These data can be obtained free of charge via http://www.ccdc.cam.ac.uk/conts/retrieving.html, or from the Cambridge Crystallographic Data Centre, 12 Union Road, Cambridge CB2 1EZ, UK; fax: (+44) 1223-336-033; or e-mail: deposit@ccdc.cam.ac.uk. ^{1}H and ^{31}P NMR spectra for compounds **2a**, **3a** and **3b**. Atomic coordinates, bond lengths, bond angles and thermal parameters have been deposited at the Cambridge Crystallographic Data Centre (CCDC). Supplementary data associated with this article can be found, in the online version, at doi:10.1016/j.poly.2008.10.054.

References

[1] R.F. Heck, Palladium Reagents in Organic Synthesis, Academic Press, New York, 1985.
[2] J.F. Hartwig, Angew. Chem., Int. Ed. 37 (1998) 2047.
[3] A.-S.S. Hamad Elgazwy, Appl. Organomet. Chem. 21 (12) (2007) 1041.
[4] A.-S.S. Hamad Elgazwy, Monatshefte Chem. 139 (11) (2008) 1285–1297.
[5] J. Tsuji, Palladium Reagents and Catalysis, Wiley, Chichester, UK, 1995.
[6] J.P. Wolfe, S. Wagaw, J.-F. Marcoux, S.L. Buchwald, Acc. Chem. Res. 31 (12) (1998) 805.
[7] M. Shibasaki, E.M.J. Vogl, Organomet. Chem. 576 (1–2) (1999) 1.
[8] O. Loiseleur, M. Hayashi, M. Keenan, N. Schmees, A.J. Pfaltz, Organomet. Chem. 576 (1–2) (1999) 16.
[9] W.A. Herrmann, V.P.W. Bohm, C.-P.J. Reisinger, Organomet. Chem. 576 (1–2) (1999) 23.
[10] S.J. Cacchi, Organomet. Chem. 576 (1–2) (1999) 42.
[11] R.C. Larock, J. Organomet. Chem. 576 (1–2) (1999) 111.
[12] A. Suzuki, J. Organomet. Chem. 576 (1–2) (1999) 147.
[13] J. Dupont, M. Pfeffer, J. Spencer, Eur. J. Inorg. Chem. 8 (2001). 1917.

[14] A.C. Cope, E.C. Friedrich, J. Am. Chem. Soc. 90 (1968) 909.
[15] H. Alper, J. Organomet. Chem. 61 (1973) C62.
[16] J. Dehand, A. Mauro, H. Ossor, M. Pfeffer, R.H.deA. Santos, J.R. Lechat, J. Organomet. Chem. 250 (1) (1983) 537.
[17] H.M. McPherson, J.L. Wardell, Inorg. Chim. Acta 75 (1983) 37.
[18] Jairton Dupont, Michel Pfeffer (Eds.), Palladacycles: Synthesis, Characterization and Applications, 2008, WILEY-VCH Verlag GmbH & Co. KGaA, Weinheim.
[19] Y. Yamamoto, H. Yamazaki, Synthesis 11 (1976). 750.
[20] K. Gehrig, A.J. Klaus, P. Rys, Helv. Chim. Acta 66 (8) (1983) 2603.
[21] A. Albinati, P.S. Pregosin, R. Rüedi, Helv. Chim. Acta 68 (7) (1985) 2046.
[22] R. Bertani, C.B. Castellani, B. Crociani, J. Organomet. Chem. 269 (1) (1984) C15.
[23] K. Suzuki, H. Yamamoto, Inorg. Chim. Acta 208 (2) (1993) 225.
[24] A.C. Albeniz, N.M. Catalina, P. Espinet, R. Redon, Organometallics 18 (26) (1999) 5571.
[25] E.C. Constable, Polyhedron 3 (9–10) (1984) 1037.
[26] M.I. Bruce, Angew. Chem., Int. Ed. Engl. 16 (2) (1977) 73.
[27] C. Anklin, P.S. Pregosin, F. Bachechi, P. Mura, L. Zambonelli, J. Organomet. Chem. 222 (1) (1981) 175.
[28] H. Motschi, P.S. Pregosin, H. Riiegger, J. Organomet. Chem. 193 (3) (1980) 397.
[29] C.G. Anklin, P.S. Pregosin, J. Organomet. Chem. 243 (1) (1983) 101.
[30] E.F. Landvatter, T.B. Rauchfuss, Organometallics 193 (1982) 506.
[31] A.-S.S. Hamad Elgazwy, Tetrahedron 59 (38) (2003) 7445.
[32] J. Dupont, C.S. Consorti, J. Spencer, Chem. Rev. 105 (6) (2005) 2527.
[33] F.E. Ziegler, L. Chliwner, K.W. Fowler, S.J. Kanfer, S.J. Kuo, N.D. Sinha, J. Am. Chem. Soc. 102 (1980) 790.
[34] K. Tomioka, T. Ishiguro, H. Mizuguchi, N. Komeshima, K. Koga, S. Tsukagoshi, T. Tsuruo, T. Tashiro, S. Tanida, T. Kishi, J. Med. Chem. 34 (1) (1991) 54.
[35] United States Patent 3974165.
[36] United States Patent 4800203.
[37] V. Gein, E. Bezmaternykh, L. Gein, I. Krylova, Chem. Heterocycl. Compd. 40 (10) (2004) 1332.
[38] E. Valencia, A.J. Freyer, M. Shamma, V. Fajardo, Tetrahedron Lett. 25 (6) (1984) 599.
[39] R. Alonso, L. Castedo, D. Domínguez, Tetrahedron Lett. 26 (24) (1985) 2925.
[40] C.J. Moody, G.J. Warellow, Tetrahedron Lett. 28 (48) (1987) 6089.
[41] F. Csende, Z. Szabo, G. Stajer, Heterocycles 36 (8) (1993) 1809.
[42] I. Takahashi, E. Hirano, T. Kawakami, H. Kitajima, Heterocycles 43 (11) (1996) 2343.
[43] J. Epsztajn, R. Grzelak, A. Jozwiak, Synthesis (10) (1996) 1212.
[44] S.M. Allin, C.J. Northfield, M.I. Page, A.M.Z. Slawin, Tetrahedron Lett. 39 (27) (1998) 4905.
[45] Z.-P. Zhuang, M.-P. Kung, M. Mu, H.-F. Kung, J. Med. Chem. 41 (2) (1998) 157.
[46] E. Valencia, V. Fajardo, A.J. Freyer, M. Shamma, Tetrahedron Lett. 26 (8) (1985) 993.
[47] E.C. Taylor, L.D. Jennings, Z. Mao, B. Hu, J.-G. Jun, P. Zhou, J. Org. Chem. 62 (1997) 5392.
[48] J.M. Thompson, R.C. Heck, J. Org. Chem. 40 (1975) 2667.
[49] A. Couture, E. Deniau, P. Grandclaudon, Tetrahedron 53 (30) (1992) 10313.
[50] D.L. Comins, S.P. Joseph, Y.-M. Zhang, Tetrahedron Lett. 37 (6) (1996) 793.
[51] S. Guha, A.K. Mukherjee, M.W. Khan, N.G. Kundu, Acta Crystallogr., Sect. C C55 (5) (1999) 818.
[52] N.G. Kundu, M.W. Khan, R. Mukhopadhyay, Tetrahedron 55 (42) (1999) 12361.
[53] W. Kantlehner, W.W. Mergen, in: A.R. Katritzky, O.C. Meth-Cohn, W. Rees (Eds.), Comprehensive Organic Functional Group Transformations, Pergamon Press, Oxford, 1995, p. 685. vol. 5.
[54] J. Vicente, J.A. Abad, E. Martínez-Viviente, M.C. Ramírez de Arellano, P.G. Jones, Organometallics 19 (2) (2000) 752.
[55] A. Albinati, C.G. Anklin, F. Ganazzoli, H. Rugg, P.S. Pregosin, Inorg. Chem. 26 (1987) 503.
[56] K. Isobe, K. Nanjo, Y. Nakamura, S. Kawaguchi, Bull. Chem. Soc. Jpn. 59 (7) (1986) 2141.
[57] J. Vicente, J.A. Abad, K.F. Shaw, J. Gil-Rubio, M.C. Ramirez de Arellano, P.G. Jones, Organometallics 16 (1997) 4557.
[58] J. Vicente, J.A. Abad, A.D. Frankland, J. Lopez-Serrano, M.C. Ramirez de Arellano, P.G. Jones, Organometallics 21 (2002) 272.
[59] V. Durá-Víla, D.M.P. Mingos, R. Vilar, A.J.P. White, D.J. Williams, J. Organomet. Chem. 600 (1–2) (2000) 198.
[60] S. Otsuka, Y. Tatsuno, K. Ataka, J. Am. Chem. Soc. 93 (1971) 6705.
[61] M.F. Retting, E.A. Kirk, P.M. Maitlis, J. Organomet. Chem. 111 (1) (1976) 113.
[62] J.R. Boehm, A.L. Balch, Inorg. Chem. 16 (4) (1977) 778.
[63] J. Vicente, J.A. Abad, E. Martinez-Viviente, P.G. Jones, Organometallics 21 (2002) 4454.
[64] W. Kantlehner, W.W. Mergen, Comprehensive Organic Functional Group Transformations, in: A.R. Katritzky, O.C. Meth-Cohn, W. Rees (Eds.), Pergamon Press, Oxford, 1995, p. 685. vol. 5.
[65] A. Sygula, J. Chem. Res. (S) 2 (1989) 56.
[66] J. Vicente, M.T. Chicote, C. Rubio, M.C. Ramírezde Arellano, P.G. Jones, Organometallics 18 (1999) 2750.
[67] J. Vicente, A. Arcas, D. Bautista, P.G. Jones, Organometallics 16 (1997) 2127.
[68] R. E Marsh, Acta Crystallogr., Sect. B 53 (1997) 317.
[69] Y. Yamamoto, H. Yamazaki, Bull. Chem. Soc. Jpn. 58 (1985) 1843.
[70] F.H. Allen, O. Kennard, D.G. Watson, L. Brammer, A.G. Orpen, R. Taylor, J. Chem. Soc., Perkin Trans. 2 (1987) S1.
[71] G.M. Sheldrick, SHELXTL-97. Program for the Refinement of Crystal Structures, University of Gottingen, Germany, 1997.

Polyhedron 28 (2009) 360–362

Contents lists available at ScienceDirect

Polyhedron

journal homepage: www.elsevier.com/locate/poly

One-pot metal templated synthesis for the preparation of 2-quinoxalinol salen metal complexes

Xianghong Wu, Hannah K. Hubbard, Brandon K. Tate, Anne E.V. Gorden *

179 Chemistry Building, Department of Chemistry and Biochemistry, College of Science and Mathematics, Auburn University, Auburn, AL 36849-5319, USA

ARTICLE INFO

Article history:
Received 23 September 2008
Accepted 29 October 2008
Available online 10 December 2008

Keywords:
Salen
Quinoxolinol
Copper
Uranyl
Templating

ABSTRACT

Metal complexes of 2-quinoxalinol salen (salqu) ligands can be prepared in a one-pot metal templated synthesis resulting in significantly enhanced yields than if the ligand were prepared and isolated prior to introducing the metal for complexation. Using this method, 12 salqu metal complexes have been prepared and characterized from +2 metal ions.

© 2008 Elsevier Ltd. All rights reserved.

One-pot multicomponent syntheses have received increasing attention of late, because they not only address fundamental principles of synthetic efficiency and reaction design [1–3], but they also expand the possibilities for extending one-pot reactions into combinatorial and solid-phase methods [3,4]. This presents a new way of thinking about "greener" chemistry by allowing for the reduction of synthetic steps, purification solvents, and wastes. A one-pot metal templated strategy for the preparation of metal complexes for use in applications offers the distinct advantages of reduced environmental impacts and easier procedures for workup.

Salen or salph complexes have been used widely in applications for everything from catalysts to molecular recognition. For example, salen Cu, Mn, or Ru complexes have been used as catalysts in the catalytic oxidation of secondary amines [5], as the basis for enantioselective catalysts [6], and as catalysts for ring-opening metathesis [7]. Uranyl (UO_2^{2+}) salophen complexes have been used in molecular recognition studies [8–10]. In addition, salen Mn complexes can act as catalytic scavengers of hydrogen peroxide and have been demonstrated to have a degree of cytoprotectivity [11].

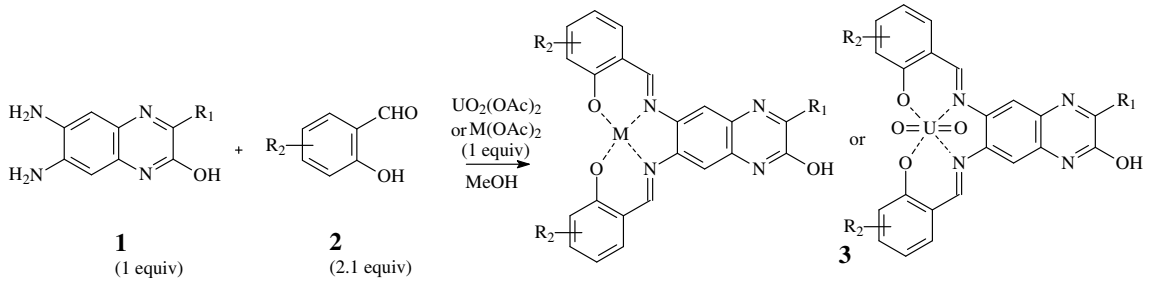
Symmetric and unsymmetric 2-quinoxolinol salen ligands (abbreviated *salqu, e.g.* 3) have been synthesized for use in catalysis using solution phase and combinatorial strategies [12,13]. A disadvantage of this reaction scheme was an extended reaction time required to obtain the optimal yields. Metal complexes of this series of ligands were then prepared by a standard proton transfer procedure [14]. Because applications in solid-phase extraction and catalysts of salqu metal complexes have been developed [15,16], it was thought that it would to be advantageous to find a more efficient, economical method to prepare salqu metal complexes. Here, a one-pot synthetic method based on a metal template synthesis to access salqu metal complexes will be introduced. With this method, 12 salqu metal complexes have been synthesized from diamino-2-quinoxalinol (**1**, Scheme 1) in significantly higher yields in a shorter time than when the ligand is isolated and purified prior to complexation.

Previously, to prepare the salqu metal complexes, two steps were required. The first being the preparation of salqu ligands followed by preparation of the salqu metal complex. In the synthesis of symmetric salqu ligands, the final optimized conditions required that the diamino-2-quinoxalinol intermediate **1** be reacted with 10 equiv. of the desired salicylaldhyde derivatives (**2**) at reflux temperature in methanol for 48 h [12]. The ligand must then be isolated prior to the addition of the metal to prepare the metal complex, resulting in yields around 60.0%. Metal complexes are then prepared from a reaction of the salqu ligand (**3**) with 1.2 equiv. of the desired metal acetate at reflux temperature in either DMF or DCM with MeOH reacted for 2–12 h [14]. The final yields for this step are around 85.0%, resulting in an overall yield for both reactions close to 50%.

Using a metal templating strategy for a one-pot synthetic method, the diamino-2-quinoxalinol intermediate **1** is reacted with 2.1 equiv. of the salicylaldhyde derivative (**2**) and 1.1 equiv. of metal acetate is added directly to the reaction mixture. This also does not require a mixed solvent system, only methanol is used. The mixture was then heated to reflux temperature and allowed to react for 6 h. After the reaction was determined to be complete,

* Corresponding author. Tel.: +1 334 663 3223; fax: +1 334 844 4043.
E-mail address: gordeae@auburn.edu (A.E.V. Gorden).

0277-5387/$ - see front matter © 2008 Elsevier Ltd. All rights reserved.
doi:10.1016/j.poly.2008.10.050



Scheme 1. Method for a one-pot synthesis of salqu metal complexes.

Table 1
Salqu metal complexes synthesized using a one-pot metal templated method.

	$[M]^{2+}$	R_1	R_2	Yield
3a	Cu^{2+}		3,5-di-*tert*-butyl	72.8
3b	Cu^{2+}		H	80.0
3c	Mn^{2+}		3,5-di-*tert*-butyl	76.5
3d	Co^{2+}		3,5-di-*tert*-butyl	69.4
3e	Ni^{2+}		3,5-di-*tert*-butyl	62.7
3f	UO_2^{2+}		3-OH	84.5
3g	UO_2^{2+}		3,5-di-*tert*-butyl	62.0
3h	UO_2^{2+}		H	61.2
3i	UO_2^{2+}		3,5-di-*tert*-butyl	65.3
3j	UO_2^{2+}		H	63.4
3k	UO_2^{2+}		H	67.0
3l	UO_2^{2+}		H	69.8

a large quantity of red or black solid was found to precipitate from solution. The precipitates were filtered and washed with ethanol five times. The solids were dried to obtain salqu metal complexes with purity greater than 95% (purity was identified by NMR and TLC.) Yields were found to range from 60% to 85%. The results are listed in Table 1.

The IR spectral results are indicative of metal complexation. Broad peaks in free ligands seen around 3400 cm^{-1} (3400–3448 cm^{-1}) are indicative of the presence of the hydroxyl groups on the free ligand. These broad signals are seen to be absent in the Cu, Mn, Co, Ni, and UO_2 metal complexes indicating the formation of the metal complex with these oxygens. Coordination through the phenolic hydroxyl unit in the salicylaldehyde coordination site can also be shown a shift in the C–O band for the metal complexes between 1199 and 1213 cm^{-1} as compared to the sharp peak in the free ligands (1263–1276 cm^{-1}) [18]. (**3j** is lower 1146 cm^{-1} although there is not a peak seen as in the range characteristic of the C–O stretch in the starting material.)

The spectra of the free ligands have peaks around 1654–1658 cm^{-1} for the carbon–nitrogen imine stretch. This is seen to shift to 1599–1620 cm^{-1} (**3f–3l**) for the uranyl complexes and is indicative of coordinated imine nitrogens [16,17]. This peak is seen at 1616–1614 cm^{-1} in the Ni^{2+} and Co^{2+} complexes, and in the Cu^{2+} complex (**3b**) but is not as well defined in the Mn^{2+}or in the Cu^{2+} (**3a**) in which the metal may not be strongly coordinating to the imines. Bands around 900 cm^{-1} (897–903 cm^{-1}) seen in the uranyl complexes (**3f–3l**) are due to the asymmetric and symmetric UO_2 stretching characteristic of linear uranyl ion in the complex [17].

In the ^1H NMR spectra of the uranyl (UO_2^{2+}) complexes, a significant shift in the imine CH=N proton is observed in the uranyl metal complexes (9.5–9.8 ppm for **3f–3l**) as compared to the free ligands (8.9–9.3 ppm). This is indicative of the imine nitrogen lone pairs coordinating to the metal center. In a similar fashion, there are three hydroxyl peaks in the ^1H NMR spectra of the free ligands (12.1–13.3 ppm) while in the uranyl (UO_2^{2+}) complexes, only one from the quinoxolinol hydroxyl group remains (12.6–12.7 ppm for **3f**, **3h**, and **3j–3l**, 12.2–12.3 ppm for **3g** and **3i**). (The slight difference seen in the data for **3g** is presumably due to the difference in solvation of the more subsituted and is comparable to **3i**.)

The advantages of the one-pot synthetic method for preparing salqu metal complexes are the shortened reaction time from more than 2 days to 6 h and improved final yields from less than 50.0% to over 60–85%. This also allows us to simplify the procedure and to conserve the amounts of the salicylaldhyde derivatives (2) used while avoiding the use of the more troublesome solvent DMF. This method could be a method for synthesis of these complexes using combinatorial methods because of the simple procedure and high yields.

In conclusion, a one-pot methodology based on a metal templating synthesis using +2 metal ions to more easily and rapidly prepare salqu metal complexes is an efficient method to prepare these metal complexes. With this method, several salqu metal complexes have been synthesized and identified. This will be a more convenient synthetic method in exploring the use of such metal complexes. In the future, a new salqu metal complex library will be prepared in this way.

General procedure and data

All amino acid methyl esters, DFDNB, HCl (37%) and aldehydes were purchased from Acros. Ammonium hydroxide (5.0 N), palladium on carbon (wet, 5%) were purchased from Aldrich. Starting materials were used as received. All organic solvents were purchased from Fisher Scientific and were used directly for synthesis. ^1H and ^{13}C NMR spectra were recorded on Bruker AC 250 spectrometer (operated at 250 and 62.5 MHz, respectively) or Bruker

AV 400 spectrometer (operated at 400 and 100 MHz, respectively). Chemical shifts are reported as δ values (ppm). The solvents used are indicted in the experimental details. Electrospray ionization mass spectrometry was performed on a Micromass QTOF mass spectrometer (Waters Corp, Milford MA). Direct probe samples were on a VG-70S mass spectrometer (Waters Corp, Milford MA). Reaction progress was monitored by thin-layer chromatography (TLC) using 0.25 mm Whatman Aluminum silica gel 60-F254 precoated plates with visualization by irradiation with a Mineralight UVGL-25 lamp. IR spectroscopic data were collected using a SHIM-SDZU Inc. IR, Prestige-21 Fourier Transform Infrared Spectrophotometer and KBr solid samples.

To a 5 ml methanol solution of intermediate **1** (0.05 mmol), 2.1 equiv. of the desired salicylaldehyde derivatives (e.g., **2** 0.105 mmol) and 1.1 equiv. of metal acetate (0.055 mmol) are added. The mixture was heated to reflux temperature with stirring and allowed to react for 6 h. At this time, a dark red or black solid precipitates out, indicating the completion of the reaction. The precipitates were filtered from the reaction solution. They were then washed with ethanol five times. Finally, the solids were dried under high vacuum.

3a: IR: 3067, 2955, 1661, 1586, 1528, 1491, 1416, 1377, 1260, 1209, 1173, 1130 cm^{-1}. MS: 760.0 (M+H); HRMS: found (760.3413); calc. (760.3422).

3b: IR: 3510, 3392, 1655, 1605, 1587, 1560, 1526, 1499, 1442, 1382, 1331, 1200, 1178, 1151 cm^{-1}. MS: 536.1 (M+H); HRMS: found (536.0912); calc. (536.0909).

3c: IR: 3385, 3248, 3208, 2955, 2911, 1670, 1582, 1532, 1462, 1416, 1317, 1248, 1177, 1130 cm^{-1}. MS: 751.3 (M+H); HRMS: found (751.3420); calc. (751.3429).

3d: IR: 3066, 2957, 1665, 1614, 1572, 1524, 1501, 1462, 1410, 1256, 1180, 1128 cm^{-1}. MS: 755.3 (M+H); HRMS: found (755.3369); calc. (755.3372).

3e: IR: 3067, 2955, 2870, 1665, 1616, 1584, 1533, 1598, 1464, 1414, 1379, 1260, 1182, 1130 cm^{-1}. MS: 755.3 (M+H); HRMS: found (755.3461); calc. 755.3471.

3f: ^{1}H NMR (400 MHz DMSO-d^6): δ 4.22 (s, 2H), 6.54–8.67 (m, 13H), 9.55 (s, 1H), 9.71 (s, 1H), 11.77 (bs, 1H), 11.82 (bs, 1H), 12.69 (bs, 1H). ^{13}C NMR: 160.2, 159.4, 155.0, 137.8, 132.8, 132.0, 129.7, 128.9, 126.9, 126.3, 124.1, 124.0, 123.9, 119.5, 117.1, 106.3, 42.0. IR: 3397, 3337, 2965, 1657, 1620, 1582, 1545, 1491, 1445, 1204, 903 cm^{-1}. MS: 816.2 (M+H+CH_3CN); HRMS: found (816.2178); cal (816.2183).

3g: ^{1}H NMR (400 MHz DMSO-d^6): δ 1.19 (s, 18H), 1.64 (s, 18H), 4.11 (s, 2H), 7.09–7.63 (m, 10H), 7.70(s, 1H), 9.19 (s, 1H), 9.32 (s, 1H), 12.18 (bs, 1H). ^{13}C NMR: 173.3, 173.0, 171.2, 165.1, 153.8, 148.8, 144.6, 144.3, 143.5, 142.0, 137.1, 135.9, 134.2, 133.1, 131.3, 128.9, 123.3, 110.6, 42.0, 40.3, 38.6, 36.3, 35.1. IR: 3433, 2957, 1655, 1620, 1383, 1283, 1229, 1153, 937, 760 cm^{-1}. MS: 967.4 (M+H); HRMS: found (967.4514); calc. (967.4524).

3h: ^{1}H NMR (400 MHz DMSO-d^6): δ 4.20 (s, 2H), 6.73–6.77 (t, 2H), 7.00–7.04 (t, 2H), 7.24–7.88 (m, 10H), 8.12(s, 1H), 9.60 (s, 1H), 9.76 (s, 1H), 12.67 (bs, 1H). ^{13}C NMR: 170.8, 170.2, 168.0, 167.3, 161.3, 155.0, 148.9, 143.6, 137.8, 137.3, 136.5, 132.8, 129.7, 128.9, 126.9, 124.8, 121.4, 121.0, 119.5, 117.4, 106.3, 42.3. IR: 3397, 3337, 2965, 1657, 1620, 1582, 1545, 1491, 1445, 1204, 1144, 1040 cm^{-1}. MS: 784.0 (M+H+CH3CN); HRMS: found (784.2280); calc. (784.2285).

3i: ^{1}H NMR (400 MHz DMSO-d^6): δ 1.22 (d, 6H), 1.26 (s, 18H), 1.69 (s, 18H), 3.50 (m, 1H), 7.26–7.80 (m, 6H), 9.30 (s, 1H), 9.46 (s, 1H), 12.28 (bs, 1H). ^{13}C NMR: 173.3, 172.6, 153.4, 148.6, 144.6, 144.4, 143.3, 136.8, 135.7, 134.4, 128.9, 123.3, 110.4, 40.4, 38.6, 36.4, 35.1, 25.1. IR: 3444, 2958, 1710, 1666, 1587, 1423, 1371, 1224, 898 cm^{-1}. MS: 919.2 (M+H); HRMS: found (919.4514); calc. (919.4524).

3j: ^{1}H NMR (400 MHz DMSO-d^6): δ 1.28 (d, 6H), 3.56 (m, 1H), 6.74–8.17 (m, 10H), 9.61 (s, 1H), 9.81 (s, 1H), 12.58 (bs, 1H). ^{13}C NMR: 170.8, 170.2, 170.0, 167.9, 166.6, 154.6, 148.3, 143.5, 137.2, 136.5, 132.5, 131.9, 124.8, 124.6, 121.4, 121.0, 119.4, 117.4, 106.2, 30.5, 20.6. IR: 3406, 2966, 1654, 1602, 1539, 1463, 1400, 1384, 1145, 898 cm^{-1}. MS: 736.2 (M+H); HRMS: found (736.2280); calc. (736.2285).

3k: ^{1}H NMR (400 MHz DMSO-d^6): δ 1.00 (d, 6H), 2.28 (m, 1H), 2.74 (d, 2H), 6.75 (t, 2H), 7.03 (t, 2H), 7.44 (s, 1H), 7.65 (m, 2H), 7.87 (t, 2H), 8.19 (s, 1H), 9.61 (s, 1H), 9.78 (s, 1H), 12.54 (bs, 1H). ^{13}C NMR: 170.8, 170.2, 162.3, 155.2, 148.3, 143.4, 137.2, 136.5, 132.6, 132.0, 124.8, 124.6, 121.4, 121.1, 119.3, 117.4, 106.2, 42.1, 26.8, 23.1. IR: 3395, 2927, 1637, 1606, 1539, 1463, 1435, 1383, 1282, 937 cm^{-1}. MS: 709.2 (M+H); HRMS: found (709.2167); calc. (709.2176).

3l: ^{1}H NMR (400 MHz DMSO-d^6): δ 2.15 (s, 3H), 2.96 (t, 2H), 3.16 (t, 2H), 6.75 (t, 2H), 7.03 (t, 2H), 7.46 (s, 1H), 7.66 (m, 2H), 7.87 (t, 2H), 8.19 (s, 1H), 9.62 (s, 1H), 9.78 (s, 1H), 12.64 (bs, 1H).). ^{13}C NMR: 170.8, 170.2, 168.0, 167.2, 161.1, 155.0, 148.5, 143.5, 137.3, 136.5, 132.7, 131.2, 124.7, 121.4, 121.0, 119.4, 117.5, 106.3, 33.3, 30.5, 15.2. IR: 3395, 2927, 1637, 1606, 1539, 1463, 1435, 1383, 1282, 937 cm^{-1}. IR: 3408, 1655, 1637, 1601, 1583, 1537, 1464, 1440, 1382, 1300, 1199, 1150, 897, 760 cm^{-1}. MS: 768.2 (M+H); HRMS: found (768.2013); calc. (768.2006).

Acknowledgment

We would like to express our appreciation to Dr. Thomas Carrington of Auburn University for his help and helpful discussions.

References

[1] I. Ugi, A. Domling, B. Werner, J. Heterocycl. Chem. 37 (2000) 647.
[2] G.H. Posner, Chem. Rev. 86 (1986) 831.
[3] L. Weber, K. Illgen, M. Almstetter, Synlett (1999) 366.
[4] S. Kobayashi, Chem. Soc. Rev. 28 (1999) 1.
[5] S. Murahashi, T. Naota, H. Taki, J. Chem. Soc., Chem. Commun. (1985) 613.
[6] W. Zhang, J.L. Loebach, S.R. Wilson, E.N. Jacobsen, J. Am. Chem. Soc. 112 (1990) 2801.
[7] M.H. Wu, K.B. Hansen, E.N. Jacobsen, Angew. Chem., Int. Ed. 38 (1999) 2012.
[8] M.M. Reinoso-Garcia, A. Dijkman, W. Verboom, D.N. Reinhoudt, E. Malinowska, D. Wojciechowska, M. Pietrzak, P. Selucky, Eur. J. Org. Chem. (2005) 2131.
[9] Van Axel V. Castelli, A. Dalla Cort, L. Mandolini, V. Pinto, D.N. Reinhoudt, F. Ribaudo, C. Sanna, L. Schiaffino, B.H.M. Snellinkruel, Supramol. Chem. 14 (2002) 211.
[10] D.M. Rudkevich, W.P.R.V. Stauthamer, W. Verboom, J.F.J. Engbersen, S. Harkema, D.N. Reinhoudt, J. Am. Chem. Soc 114 (1992) 9671.
[11] S.R. Doctrow, K. Huffman, C.B. Marcus, G. Tocco, E. Malfroy, C.A. Adinolfi, H. Kruk, K. Baker, N. Lazarowych, J. Mascarenhas, B. Malfroy, J. Med. Chem. 45 (2002) 4549.
[12] X. Wu, A.E.V. Gorden, J. Comb. Chem. 9 (2007) 601.
[13] X. Wu, A.E.V. Gorden, S.A. Tonks, J.Z. Vilseck, J. Org. Chem. 72 (2007) 8691.
[14] X. Wu, T.H. Bray, M. Bharara, B.K. Tate, A.E.V. Gorden, Inorg. Chim. Acta, (2008), in press.
[15] X. Wu, A.E.V. Gorden, Tetrahedron Lett. 49 (2008) 5200.
[16] X. Wu, A.E.V. Gorden, Eur. J. Org. Chem., (2008), in press.
[17] U. Casellato, S. Tamburini, P. Tomasin, P.A. Vigato, Inorg. Chim. Acta 341 (2002) 118.
[18] A.A. Abu-Hussen, J. Coord. Chem. 59 (2006) 157.

Polyhedron 28 (2009) 363–369

Contents lists available at ScienceDirect

Polyhedron

journal homepage: www.elsevier.com/locate/poly

Coordination of bistriflimide and triflate to the uranyl bis(diphenylphosphino)methane dication, $\{UO_2(DPPMO_2)_2\}^{2+}$

Stéphanie M. Cornet [a,*], Iain May [a,1], Michael P. Redmond [a], Andrew J. Selvage [a], Clint A. Sharrad [a], Olivier Rosnel [b]

[a] Centre for Radiochemistry Research, School of Chemistry, The University of Manchester, Oxford Road, Manchester M13 9PL, UK
[b] Ecole Nationale Supérieure de Chimie de Paris, 11 rue Pierre et Marie Curie, 75231 Paris Cedex 05, France

ARTICLE INFO

Article history:
Received 2 March 2008
Accepted 30 October 2008
Available online 16 December 2008

Keywords:
Bistriflimide
Triflate
Bis(diphenylphosphino)methane
Uranyl
^{31}P NMR Spectroscopy

ABSTRACT

The $\{UO_2(DPPMO_2)_2\}^{2+}$ dication (where $DPPMO_2$ = bis(diphenylphosphino)methane) contains the linear uranyl group, $\{UO_2\}^{2+}$, with two bidentate P=O donor ligands. Previously, we have shown that the weakly coordinating oxoanions $[ReO_4]^-$ and $[TcO_4]^-$ (as well as Cl^-) will fill a fifth equatorial coordination site yielding complexes of general formula $[UO_2(DPPMO_2)_2X][X]$ (where X = $[ReO_4]^-$, $[TcO_4]^-$ and Cl^-), with the X^- anion acting in both monodentate coordinated and uncoordinated modes. Seven coordinate pentagonal bipyramidal uranyl complexes with the same general formula have now also been prepared with both the bistriflimide, $((CF_3SO_2)_2N^-, NTf_2^-)$ and triflate ($CF_3SO_3^-$ OTf^-) anions and we report the structural characterisation of both $[UO_2(NTf_2)(DPPMO_2)_2][NTf_2]$ (**1**) and $[UO_2(OTf)(DPPMO_2)_2][OTf]$ (**2**). In the case of **1** the anion is coordinated through a terminal oxygen, representing the first structural characterization of an actinide-bistriflimide complex. Both the solid state uranium-anion bond lengths (for O-donor ligands only) and $^{31}P\{^1H\}$ NMR solution competition studies indicate that the strength of the uranyl-anion bond decreases along the series $Cl^- > [ReO_4]^- > [OTf]^- > [NTf_2]^-$. In addition, $^{31}P\{^1H\}$ NMR competition studies show that both nitrate and excess $DPPMO_2$ will readily displace the weakly coordinating X^- anions.

© 2008 Elsevier Ltd. All rights reserved.

1. Introduction

Interest in uranium coordination chemistry has increased in recent years, with the discovery of novel reagents, reactivity and structural features. This increase in synthetic chemistry is linked with ever improving computational techniques and evolving nuclear fuel processing, waste management and environmental challenges [1]. One area of research that our laboratory have focussed on is the interaction of actinide cations with a range of 'weakly coordinating' anions [2]. In the case of pertechnetate, $[TcO_4]^-$, (and perrhenate, $[ReO_4]^-$) the chemistry has been directed towards improving our understanding of Tc behaviour in the PUREX process (Plutonium and Uranium Recovery by Extraction) [3]. In the case of bis(trifluoromethylsulfonyl)amide (bistriflimide, $(CF_3SO_2)_2N^-$, NTf_2^-) and trifluoromethanesulfonate (triflate, $CF_3SO_3^-$ OTf^-) our initial interest was related to the application of ionic liquids in the electrochemical separation of actinide cations [4].

For many years NTf_2^- was considered to just be a very weak or non-coordinating anion [5], which in turn has led to the extensive use of this anion in ionic liquid research (where NTf_2^- salts with organic cations tend to produce relatively low viscosity ionic liquids) [6]. However, in the absence of more strongly coordinating ligands complexes with *d*-transition metals have been synthesised with a range of bidentate and monodentate coordination modes observed, including η^1-O, η^1-N, η^2-O,O′ and η^2-O,N [7]. This chemistry has also recently been extended to the *f*-elements, although structurally characterised bistriflimide-*f*-element complexes are currently restricted to the lanthanides [8–11], with no reports of structurally characterised actinide bistriflimide complexes. In contrast, there have now been numerous studies into the coordination chemistry of uranium with the triflate anion, with both monodentate and bidentate coordination modes observed [12–17].

We have previously reported the synthesis of a series of isostructural uranyl complexes with the bidentate phosphine oxide ligand $DPPMO_2$ (where $DPPMO_2$ = bis(diphenylphosphino)methane) [18]. These complexes have the general formula $[UO_2(X)(DPPMO_2)_2][X]$, where X = $[TcO_4]^-$, $[ReO_4]^-$ or Cl^-. Perhaps of most interest was the spectroscopic evidence that the cationic species, $[UO_2(TcO_4)(DPPMO_2)_2]^+$ and $[UO_2(ReO_4)(DPPMO_2)_2]^+$ are stable in solution. In the presence of more strongly coordinating anions, F^- and NO_3^-, more than one anion coordinates in the uranyl equatorial plane, forming $[UO_2(\mu\text{-}F)(F)(DPPMO_2)]_2$ and $[UO_2(NO_3)_2(DPPMO_2)]$, respectively [19,20]. In the presence of

* Corresponding author. Tel.: +44 161 275 1405; fax: +44 161 275 4598.
E-mail address: Stephanie.Cornet@manchester.ac.uk (S.M. Cornet).
[1] Present address: Chemistry Division – Inorganic Isotope and Actinide Chemistry (C-IIAC), Los Alamos National Laboratory, Mail Stop J-514, Los Alamos, NM 87545, USA.

0277-5387/$ - see front matter © 2008 Elsevier Ltd. All rights reserved.
doi:10.1016/j.poly.2008.10.070

bidentate bis(β-diketonates) the $DPPMO_2$ ligand is forced into monodentate or bridging coordination modes [20]. Recently, bidentate $DPPMO_2$ coordination has also been observed in the β-diketiminate cationic complex, $[UO_2(Ar_2nacnac)(DPPMO_2)]$, where Ar_2nacnac = (2,6-^{i}Pr$_2$- C_6H_3)*NC*(Me)CHC(Me)*N*(2,6-^{i}Pr$_2C_6H_3$) [21]. It would thus appear that the $\{UO_2(DPPMO_2)_2\}^{2+}$ fragment (two bidentate P=O donor ligands) is only stable in the absence of strongly coordinating anions and can accommodate another monodentate less strongly coordinating anion (*i.e.* 5 coordinate in the $\{UO_2\}^{2+}$ equatorial plane). The chemistry of this $\{UO_2(DPPMO_2)_2\}^{2+}$ dication has been investigated further with the fifth coordination site filled with triphenyl phosphine oxide to form $[UO_2(DPPMO_2)_2(Ph_3PO)]^{2+}$, both as the triflate and BF_4^- salts. The BF_4^- salt can react further to form a mixture of two dimeric uranyl complexes with bridging F^- (abstracted from the anion), with only chelating $DPPMO_2$ observed in one complex and both bridging and chelating $DPPMO_2$ observed in the second complex [22].

In this paper we report the synthesis, structural and spectroscopic characterisation of two more complexes in the $[UO_2(X)(DPPMO_2)_2][X]$ series, where $X = NTf_2^-$ and OTf^-. In addition, a ^{31}P NMR solution spectroscopic study has been undertaken to probe the stability of both $[UO_2(NTf_2)(DPPMO_2)_2]^+$ and $[UO_2(OTf)(DPPMO_2)_2]^+$ in the presence, and absence, of competing anionic ligands.

2. Experimental

Caution: The natural uranium used during the course of this work is a radioactive toxic metal and care should be taken with all manipulations.

2.1. General considerations

All reactions were carried out under an argon atmosphere using standard Schlenk techniques or an inert atmosphere glovebox. All solvents employed were reagent grade and dried by refluxing over appropriate drying agents. $DPPMO_2$, $[UO_2(ReO_4)(DPPMO_2)_2][ReO_4]$ and $[UO_2(Cl)(DPPMO_2)_2][Cl]$ were prepared as described previously, [18] with all other reagents used as received (except for $[Bu_4N][ReO_4]$ – see below). $^{31}P\{^1H\}$, $^{19}F\{^1H\}$ and ^1H NMR spectra were recorded on a Bruker Avance Ultrashield 400 instrument at 161.91, 376.47 and 400 MHz, respectively. Chemical shifts were measured relative to external references H_3PO_4 (85%) (^{31}P), $CFCl_3$ (^{19}F) and TMS (^1H) and. Raman and IR spectroscopy were performed on a Bruker Equinox 55 FTIR/Raman machine. Elemental analysis was performed on a Carlo ERBA Instruments CHNS-O EA1108 elemental analyzer for C, H and N and on a Fisons Horizon Elemental analyser ICP-OED spectrometer for U and P.

2.2. Synthesis of $[Bu_4N][ReO_4]$

$HReO_4$ (0.83 mL, 0.91 mmol) was added dropwise to a solution of $[Bu_4N][Cl] \cdot H_2O$ (0.26 g, 0.91 mmol) in EtOH (15 mL), and the resulting mixture left to stir for 1 h. Evaporation in air afforded colourless plates of the title compound after 10 d which were collected, washed with EtOH (10 mL) and dried *in vacuo* (1.87 g, 93%). IR (solid on ATR cell) (cm^{-1}): 2963 (w), 2876 (w), 1473 (m), 1383 (w), 1165 (w), 1036 (w), 898 (vs), 737 (m). *Anal.* Calc. for $C_{16}H_{36}NO_4Re$: C, 39.02; H, 7.32; N 2.85. Found: C, 38.05; H, 7.52; N, 2.74%.

2.3. Synthesis of $[UO_2(NTf_2)(DPPMO_2)_2][NTf_2]$ (**1**)

UO_3 (0.26 g, 0.91 mmol), $(CF_3SO_2)_2NH$ (0.49 g, 1.80 mmol) and $DPPMO_2$ (0.73 g, 1.80 mmol) were dissolved in MeCN (10 mL), and heated. After stirring at room temperature for 2 days, the resultant yellow solution was filtered to remove trace UO_3 and taken to dryness *in vacuo* yielding a dark yellow powder which was recrystallised from dichloromethane (0.95 g, 63%). ^1H NMR (CD_2Cl_2 – 298 K): δ *4.1–4.3* (t, 4H, CH_2, $^2J_{P-H}$ 12 Hz), 7.2–7.6 and 7.8–8.0 (m, 20H, Ph); $^{31}P\{^1H\}$ NMR (CD_2Cl_2 – 298 K): δ 41.7(s); ^{19}F NMR (CD_2Cl_2 – 298 K): δ −78.6 (s) ppm. Raman (solid in glass capillary) (cm^{-1}): 3068(vs), 2904(s), 1592(m), 1165(w), 1030(m), 1000(s), 854(m), 743(m), 682(w), 617(w). *Anal.* Calc. for $C_{54}H_{44}F_{12}N_2O_{14}P_4S_4U$: C, 38.94; H, 2.64; N, 1.68; P, 7.45; S, 7.69; U, 14.30. Found: C, 38.66; H, 2.67; N, 2.10; P, 7.26; S, 7.52; U, 14.10%.

2.4. Synthesis of $[UO_2(OTf)(DPPMO_2)_2][OTf]$ (**2**)

UO_3 (0.25 g, 0.87 mmol), HSO_3CF_3 (151 μL, 1.74 mmol) and $DPPMO_2$ (0.72 g, 1.74 mmol) were dissolved in acetonitrile (6 mL) and stirred for a week at room temperature. The resulting solution was taken to dryness *in vacuo* yielding a light yellow powder which was purified by recrystallisation from dichloromethane at −15 °C over 5 days (1.18 g, 97%). ^1H NMR (CD_2Cl_2 – 298 K): δ *4.2–4.4* (t, 4H, CH_2, $^2J_{P-H}$ 12 Hz), 7.1–7.5 and 7.8–8.1 (m, 20H, Ph). $^{31}P\{^1H\}$ NMR (CD_2Cl_2 – 298 K) δ 40.6 (dd); ^{19}F NMR (CD_2Cl_2 – 298 K): δ −79.4 (s) ppm. Raman (solid in glass capillary) (cm^{-1}): 3066 (vs), 1592(m), 1031(m), 1000(s), 849(m), 683(w). *Anal . Calc.* for $C_{52}H_{44}F_6P_4S_2U$: C, 44.57; H, 3.14; F, 8.14; P, 8.86; S, 4.57; U, 17.00. Found: C, 44.39; H, 3.21; F, 8.08; P, 8.79; S, 4.16; U, 16.48%.

2.5. Single crystal X-ray diffraction

The crystallographic data for **1** and **2** · $4CH_2Cl_2$ are summarised in Table 1. Diffraction data for 1 were collected on a Bruker Apex CCD diffractometer while those for 2 were measured on an Oxford Diffraction Crysalis CCD diffractometer, both at 100 K using Mo Kα radiation (λ = 0.71073 Å). Both structures were solved by direct methods using SIR-92 and refined using full matrix least squares on F^2 with SHELXL-97 [23,24]. All non-hydrogen atoms were refined anisotropically, while hydrogen atoms were included in calculated positions. Restraints were used motion on the anisotropic thermal of all C-atoms for both structures.

Table 1
Crystal data and structure refinement parameters for **1** and **2** · $4CH_2Cl_2$.

	1	**2**
Empirical formula	$C_{54}H_{44}F_{12}N_2O_{14}P_4S_4U$	$C_{56}H_{52}Cl_8F_6O_{12}P_4S_2U$
Formula weight	1663.06	1740.61
Crystal system	Triclinic	Triclinic
Space group	$P\bar{1}$	$P\bar{1}$
Crystal size (mm)	0.1 × 0.05 × 0.05	0.2 × 0.1 × 0.1
a (Å)	10.6376(17)	13.8469(8)
b (Å)	14.955(2)	15.5793(9)
c (Å)	21.239(3)	18.4841(16)
α (°)	109.517(3)	111.774(7)
β (°)	93.591(4)	105.189(7)
γ (°)	98.993(4)	101.562(5)
Volume (Å)	3121.4(9)	3370.8(4)
Z	2	2
Temperature (K)	100(2)	100(2)
Density (g cm^{-3})	1.769	1.715
μ (mm^{-1})	2.936	2.955
Data/restraints/parameters	10964/384/820	11867/621/802
R indices [>2σ(*I*)]	R_1 = 0.0479	R_1 = 0.0324
	wR_2 = 0.0835	wR_2 = 0.0942
R indices (all data)	R_1 = 0.0893	R_1 = 0.0377
	wR_2 = 0.1206	wR_2 = 0.0995
Goodness of fit (S)	0.709	1.278
Residual electron density	$\Delta\rho_{max}$ = 1.456	$\Delta\rho_{max}$ = 1.843
	$\Delta\rho_{min}$ = −1.433	$\Delta\rho_{min}$ = −1.488

3. Results and discussion

The yellow solids $[UO_2(NTf_2)(DPPMO_2)_2][NTf_2]$ (**1**) and $[UO_2(OTf)(DPPMO_2)_2][OTf]$ (**2**) were prepared by reaction of UO_3 with two equivalents of $DPPMO_2$ and 2 equiv. of the corresponding acid ($HNTf_2$ for **1** and HOTf for **2**) in acetonitrile (MeCN). Both products could be recrystallised from dichloromethane to yield crystals suitable for single crystal X-ray diffraction the latter as a CH_2Cl_2 solvate.

Compounds **1** and **2** both contain monocationic, monomeric uranyl complexes (see Figs. 1 and 2, respectively). The pentagonal bipyramidal geometry around the uranium metal centres are constructed from the two axial uranyl oxygens, two bidentate P=O donor $DPPMO_2$ ligands and either monodentate O-coordinated NTf_2^- (**1**) or monodentate OTf^- (**2**). The charge is balanced by an additional uncoordinated NTf_2^- (**1**) or OTf^- (**2**). Both structures are very similar to the previously structurally characterized perrhenate and chloride complexes, $[UO_2(ReO_4)(DPPMO_2)_2][ReO_4]$ and $[UO_2(Cl)(DPPMO_2)_2][Cl]$ [18]. Selected bond distances and angles given in Table 2.

The uranyl bond lengths for **1** and **2** (range between 1.765(3) Å and 1.771(3) Å) and O_{axial}–U–O_{axial} bond angles (179.7(3)° for **1** and 178.70(13)° for **2**) are as expected for 7-coordinate uranyl complexes, and comparable to those observed in $[UO_2(ReO_4)(DPPMO_2)_2][ReO_4]$ and $[UO_2(Cl)(DPPMO_2)_2][Cl]$ [18]. Turning to the two bidentate coordinated $DPPMO_2$ ligands, the bite angles of both groups (73.52(19)° and 73.0(2)° for **1** and 72.17(10)° and 72.94(10)° for **2**) are slightly more obtuse than those found in the analogous choride complex (70.32(17)° and 71.56(16)°), but similar to the values observed for the perrhenate species (73.1(2)° and 72.9(2)°) [18]. This supports our previous rationale that the larger radius of the fifth equatorial bound anion atom (Cl versus O) leads to the more acute $DPPMO_2$ bite angle.

The U–O bond lengths for coordinated anion is longer for U–$O_{bistriflimide}$ (2.457(6) Å – **1**) versus U–$O_{triflate}$ (2.408(3) Å – **2**) giving some indication that the U–$O_{triflate}$ bond is the stronger of the two. However, uranium–oxygen bond lengths are not always the best measure of comparing bond strength and caution should be taken when making this comparison. The U–$O_{triflate}$ bond length in **2** is significantly longer than the shorter U–$O_{triflate}$ bond length in $UO_2(OTf)_2(thf)_3$ (2.372(6) Å) [17], and also in $UO_2(OTf)_2(py)_3$ (2.372(6) Å) [15], perhaps reflecting the stronger donor properties of the co-ligand in **2**.

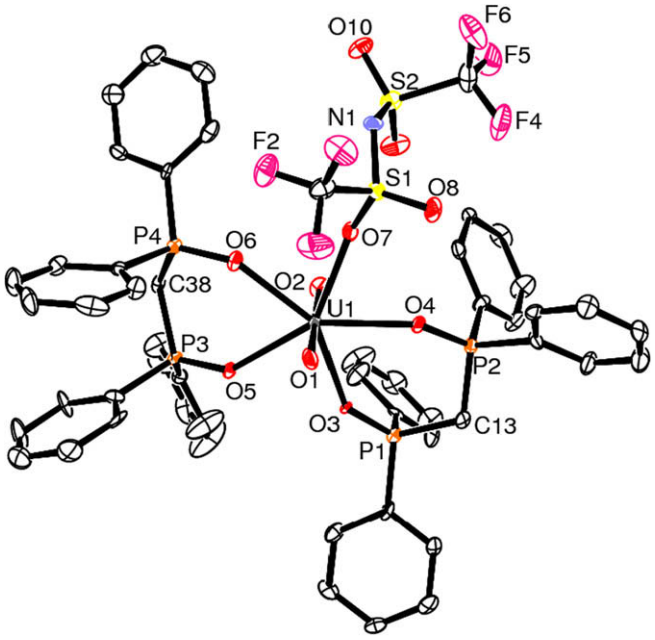


Fig. 1. ORTEP representation of $[UO_2(NTf_2)(DPPMO_2)_2]^+$.

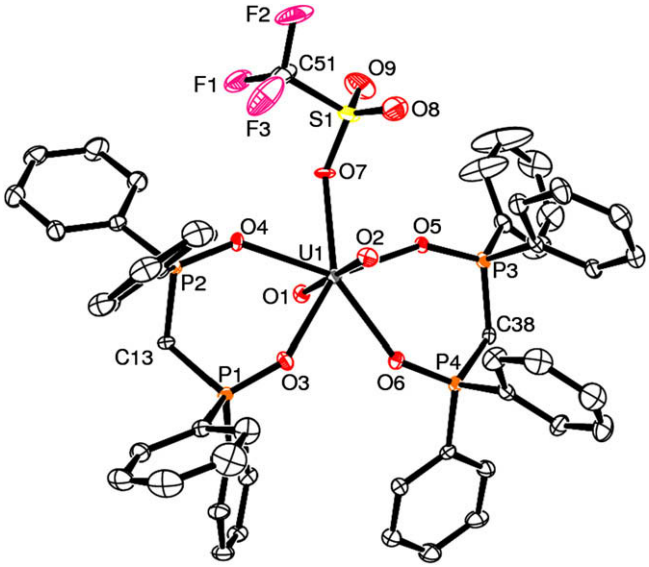


Fig. 2. ORTEP representation of $[UO_2(OTf)(DPPMO_2)_2]^+$.

Table 2
Selected bond distances (Å) and angles (°) for complexes **1** and **2** · $4CH_2Cl_2$.

	1	2
U(1)–O(1)	1.766(6)	1.765(3)
U(1)–O(2)	1.770(6)	1.771(3)
U(1)–O(3)	2.356(6)	2.394(3)
U(1)–O(6)	2.379(6)	2.380(3)
U(1)–O(4)	2.385(6)	2.370(3)
U(1)–O(5)	2.360(6)	2.378(3)
U(1)–O(7)	2.457(6)	2.408(3)
O(1)–U(1)–O(2)	179.7(3)	178.70(13)
O(3)–U(1)–O(4)	73.52(19)	72.17(10)
O(5)–U(1)–O(6)	73.0(2)	72.94(10)

For $[bmpyr]_2[Ln(NTf_2)_5]$ (Ln = Nd or Tb) an increase in S–O bond length for NTf_2^- on coordination to the trivalent lanthanide (mean values of 1.47 Å coordinated versus 1.42 Å uncoordinated) has been observed [11]. For the Pr complex, $[bmpyr]_2[Pr(NTf_2)_5]$, a similar trend is also observed (mean values of coordinated and uncoordinated S–$O_{bistriflimide}$ bond lengths are 1.45 and 1.43 Å) [10]. In addition, significant changes in NTf_2^- bond lengths are observed on N-donor coordination in $[(C_5H_5)Fe(CO_2)(NTf_2)]$ (N–S increases from 1.56–1.57 to 1.630(4)/1.643(4) Å and on O-donor coordination in $(C_5H_5)_2Ti(NTf_2)_2$, where the S–O coordinated bond lengths are quoted as 1.467(4) and 1.468(3) Å) [7a]. However, in our case the S(1)–O(7) (coordinated – 1.450(6) Å) and S(1)–O(8) (uncoordinated – 1.433(7) Å) bond lengths are comparable and we see no systematic change in any of the NTf_2^- bond lengths on coordination, as also previously observed for $La(NTf_2)_3(H_2O)_3$ [8]. In comparison, the S(1)–O(7) bond length (1.455(3) Å) for the triflate oxygen coordinated to uranium in **2** is significantly longer than the S(I)–O(8) and S(I)–O(9) – uncoordinated bond lengths (1.434(4) and 1.435(4) Å, respectively).

The solid state Raman spectra were collected for both **1** and **2** (see Supplementary material). Of most interest was the ν_1 uranyl symmetric stretching frequency, assigned to peaks at 854 and 848 cm^{-1} for **1** and **2**, respectively. These vibrations come at slightly higher frequency than two other structurally similar

uranium $DPPMO_2$ based complexes $([UO_2(ReO_4)(DPPMO_2)_2][ReO_4]$ and $[UO_2(TcO_4)(DPPMO_2)_2][TcO_4]$ (where ν_1 O=U=O = 840, 844 cm^{-1}, respectively), and at a significantly higher value than observed for $[UO_2(Cl)(DPPMO_2)_2][Cl]$ (where ν_1 O=U=O = 824 cm^{-1}) [18]. The higher energy vibration probably reflects a more limited weakening of the O=U=O bond through anion coordination.

Previously we have reported that the room temperature $^{31}P\{^1H\}$ NMR spectra of $[UO_2(ReO_4)(DPPMO_2)_2][ReO_4]$ and $[UO_2(TcO_4)(DPPMO_2)_2][TcO_4]$ both exhibit one single broad peak at 42.2 and 40.8 ppm, respectively in CD_2Cl_2 (shifted from 25.1 ppm for uncomplexed $DPPMO_2$ in the same solvent). As the temperature is lowered the broad peak splits into four bands, with a "roof effect" typical of two doublets when the chemical shift difference between the two different P environments (from the P=O groups distal and adjacent to the perrhenate or pertechnetate anion) is similar to the J_{P-P} coupling constant (an AA′BB′ system). Clearly at higher temperatures there must be an exchange process(es) taking place at a rate comparable to the NMR timescale which could be ring flipping in the 6 membered chelate ring formed from complexed $DPPMO_2$ and/or exchange of coordinated and uncoordinated $[ReO_4]^-$ or $[TcO_4]^-$ anions.

The $^{31}P\{^1H\}$ variable temperature NMR spectra for $[UO_2(OTf)(DPPMO_2)_2][OTf]$ (**2**) in CD_2Cl_2 are shown in Fig. 3a. In contrast with the perrhenate and pertechnetate complexes, the expected AA′BB′ pattern is observed at room temperature. As the temperature is lowered the bands firstly broaden before again sharpening as the temperature is lowered still further. At room temperature the resonances are centred at 40.6 ppm, shifting slightly downfield as the temperature is lowered. We postulate that at room temperature triflate ligand exchange is too rapid to allow the $DPPMO_2$ groups to relax back into the D_{4h} geometry that might be expected for $\{UO_2(DPPMO_2)_2\}^{2+}$ and triflate exchange occurs at the same site in the uranyl equatorial plane (assuming a dissociative mechanism for ligand exchange dominates). As the temperature is lowered there are a range of possible chemical processes with kinetics within the NMR timescale, including flipping between monodentate and bidentate coordination for triflate and coordination of a triflate anion to the uranyl centre *trans* to a leaving triflate group. A minor peak is also observed at *c.a.* 39.1 ppm as the temperature is lowered, with another two minor broad resonances also resolved at −70 °C between 41 and 42 ppm. The variable temperature ^1H NMR spectra of **2** in CD_2Cl_2 simply show a gradual loss of resolution of the phenyl and methylene resonances as a function of temperature, probably a result of decreasing the rate of $P–C_{phenyl}$ bond rotation and $UO_2P_2C_2$ ring flipping. Similar variable temperature ^1H NMR spectra in CD_2Cl_2 are also observed for **1**. The ^{19}F NMR spectrum for **2** at 25 °C reveals just a single resonance at −79.6 ppm (*c.f.* −79.3 ppm for $[UO_2(DPPMO_2)_2(OPPh_3)][OTf]$-[22]) indicating a rapid exchange between coordinated and uncoordinated triflate. At −65 °C, this resonance appears to be splitting into two peaks of comparable intensity, presumably corresponding to coordinated OTf in **2** and uncoordinated OTf (see Fig. 3b).

The $^{31}P\{^1H\}$ variable temperature NMR spectra for $[UO_2(NTf_2)(DPPMO_2)_2][NTf_2]$ (**1**) in CD_2Cl_2 are shown in Fig. 4. As the temperature is lowered a single resonance at 41.7 ppm broadens and then splits into 5 peaks. The major peak is at 41.5 ppm with the four other peaks appearing to form two coupled doublets centred at 42.1 and 42.7 (J_{P-P} = 14.9 Hz). We assign the two doublets to $[UO_2(NTf_2)(DPPMO_2)_2]^+$ and the singlet to the dicationic species $[UO_2(DPPMO_2)_2]^{2+}$. Integration at −70 °C leads to an 1:1.2 ratio of $[UO_2(NTf_2)(DPPMO_2)_2]^+$:$[UO_2(DPPMO_2)_2]^{2+}$. It would thus appear that even in the presence of two molar equivalents of NTf_2^- there is incomplete coordination of NTf_2^- in solution. The ^{19}F NMR of **2** at 25 °C reveals a broad resonance at −78.6 ppm (*c.f.* −80.2 ppm for $XNTf_2$), which is resolved into two peaks at −65 °C. From the incomplete coordination of NTf_2^- in solution observed by $^{31}P\{^1H\}$ NMR we assigned the more intense resonance to uncoordinated NTf_2^- and the less intense resonance to $[UO_2(NTf_2)(DPPMO_2)]^+$.

From the structural and solution $^{31}P\{^1H\}$ NMR studies, it would appear that the order of strength of coordination of weakly

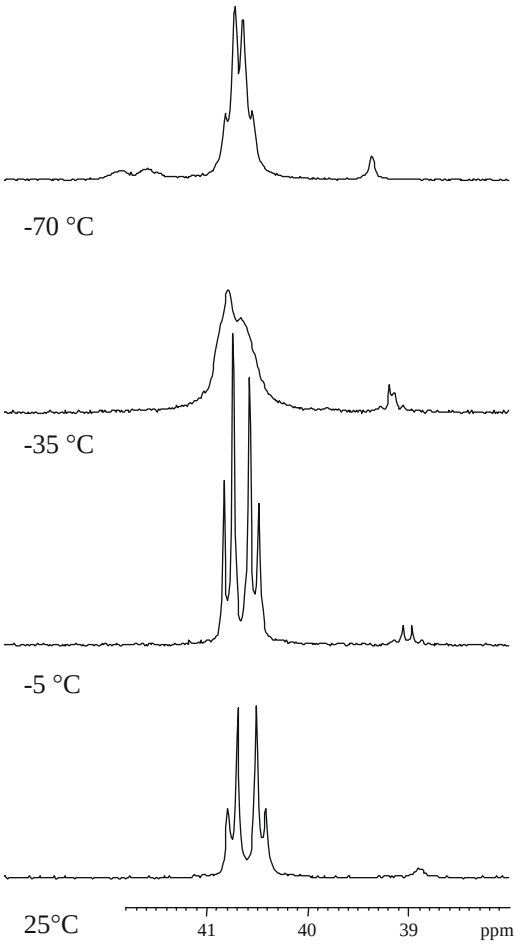


Fig. 3a. Variable Temperature $^{31}P\{^1H\}$ NMR spectra of $[UO_2(OTf)(DPPMO_2)_2][OTf]$ (**2**) in CD_2Cl_2.

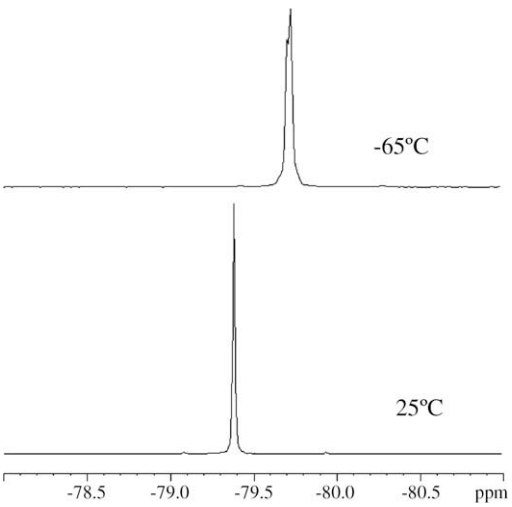


Fig. 3b. Variable Temperature ^{19}F NMR spectra of $[UO_2(OTf)(DPPMO_2)_2][OTf]$ (**2**) in CD_2Cl_2.

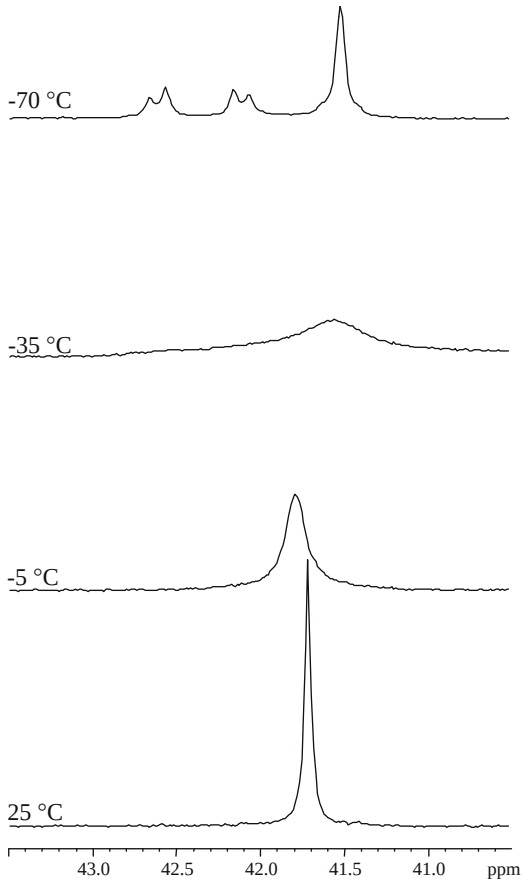


Fig. 4a. Variable temperature $^{31}P\{^1H\}$ NMR spectra of $[UO_2(NTf_2)(DPPMO_2)_2][NTf_2]$ (**1**) in CD_2Cl_2.

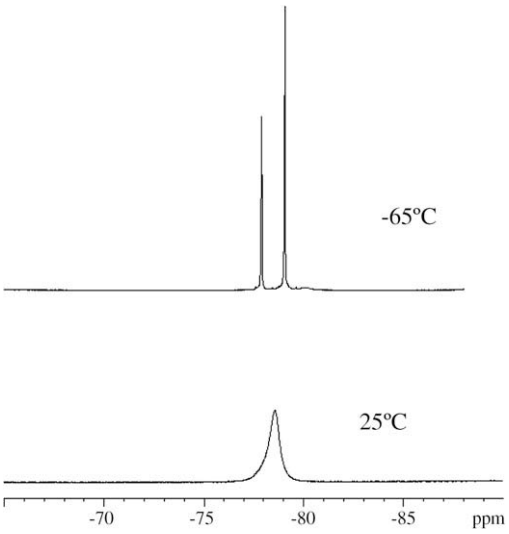


Fig. 4b. Variable temperature ^{19}F NMR spectra of $[UO_2(NTf_2)(DPPMO_2)_2][NTf_2]$ (**1**) in CD_2Cl_2.

coordinating anion to $\{UO_2(DPPMO_2)_2\}^{2+}$ is probably $[ReO_4]^- > OTf_2^- > NTf_2^-$. In addition, chloride, nitrate and excess $DPPMO_2$ should also be able to displace all three of these anions. To prove this hypothesis we undertook competition reactions using $[Bu_4N]^+$ salts of competing anions. The reactions were monitored by ^{31}P NMR spectroscopy in CD_2Cl_2 solution. Firstly, addition of one equivalent of $[Bu_4N][OTf]$ or $[Bu_4N][ReO_4]$ to $[UO_2(NTf_2)(DPPMO_2)_2][NTf_2]$ led to the clean formation of $[UO_2(OTf)(DPPMO_2)_2]^+$ or $[UO_2(ReO_4)(DPPMO_2)_2]^+$ in solution. It took the addition of two molar equivalents of $[Bu_4N][ReO_4]$ to completely displace triflate from the coordination sphere of uranyl when added to a CD_2Cl_2 solution of **2**. It would thus appear that the order of coordinating ability of anion to $\{UO_2(DPPMO_2)_2\}^{2+}$ in solution is $[ReO_4]^- > OTf_2^- >> NTf_2^-$. Example spectra are shown in Fig. 5 where triflate is shown to coordinate to $\{UO_2(DPPMO_2)_2\}^{2+}$ in preference to bistriflimide.

While it was not possible to record the ^{31}P NMR spectrum of $[UO_2(Cl)(DPPMO_2)_2][Cl]$ in CD_2Cl_2 due to solubility issues it was possible to add $[Bu_4N][Cl]$ to CD_2Cl_2 solutions of **1**, **2** and $[UO_2(ReO_4)(DPPMO_2)_2][ReO_4]$. Addition of 1 molar equivalent of $[Bu_4N][Cl]$ to **1** led to spectral changes consistent with almost complete formation of $[UO_2(Cl)(DPPMO_2)_2]^+$. The addition of 2 equiv. of $[Bu_4N][Cl]$ to **2** were required for complete formation of the same product. Finally, addition of two equivalents of $[Bu_4N][Cl]$ to $[UO_2(ReO_4)(DPPMO_2)_2][ReO_4]$ led to the almost complete formation of $[UO_2(Cl)(DPPMO_2)_2]^+$ with $[UO_2(ReO_4)(DPPMO_2)_2]^+$ present as a minor product. In all cases the expected AA'BB' system for $[UO_2(Cl)(DPPMO_2)_2]^+$ was observed at *ca.* 39 ppm. Clearly Cl^- is a more strongly coordinating ligand to $\{UO_2(DPPMO_2)_2\}^+$ than either perrhenate, triflate or bistriflimide. For example spectra see the supporting information.

The addition of one molar equivalent of $[Bu_4N][NO_3]$ to **1**, **2** or $[UO_2(ReO_4)(DPPMO_2)_2][ReO_4]$ in CD_2Cl_2 led to quite distinctive complex spectra. However, the addition of two molar equivalents of $[Bu_4N][NO_3]$ to all three complexes in solution yielded very similar spectra with numerous separate peaks resolvable at low temperature, indicative of complete displacement of weakly coordinating anion by nitrate. As an example, the addition of two equivalents of $[Bu_4N][NO_3]$ to **2** led to a spectrum with 6 peaks (−70 °C) at 44.5, 42.2, 40.6, 40.2, 39.3 and 27.0 ppm (Fig. 6). This system contains 2 NO_3^- and 2 $DPPMO_2$ ligands per $\{UO_2\}^{2+}$. We assign the peak at 39.3 ppm to $[UO_2(NO_3)_2(DPPMO)]$,[20] having recorded a $^{31}P\{^1H\}$ NMR spectrum of this complex in the same solvent. The peaks at 44.5, 42.2 and 27.0 ppm have equivalent intensities and are assigned to a complex containing two monodentate coordinated $DPPMO_2$ ligands and one bidentate coordinated $DPPMO_2$ ligand, $[UO_2(\eta^1\text{-}DPPMO_2)_2(DPPMO_2)]^{2+}$. The peak at 27.0 ppm relates to the uncoordinated P═O groups and the peak at 44.5 ppm relates to the coordinated P═O groups for the two monodentate $DPPMO_2$ ligands. As will be discussed below the two broad peaks for monodentate coordinated $DPPMO_2$ can, in some instances, be resolved into a pair of coupling doublets. The coordinated bidentate $DPPMO_2$ ^{31}P resonance is assigned to a peak at 42.2 ppm. The two peaks at 40.6 and 40.2 ppm are more difficult to assign and our suggested assignments are tentative. One of the two peaks, possibly the broader peak at 40.6 ppm, could well be due to $[UO_2(NO_3)(DPPMO_2)_2]^+$. Alternative, both peaks could relate to complexes with this formula, with both monodentate and bidentate nitrate containing species present in solution.

Finally, the addition of one, and then two molar equivalent of $DPPMO_2$ to **1**, **2** or $UO_2(ReO_4)(DPPMO_2)_2][ReO_4]$ in CD_2Cl_2 led to very similar spectra. Perhaps the best resolved spectrum was recorded at −70 °C on a CD_2Cl_2 solution containing $UO_2(ReO_4)(DPPMO_2)_2][ReO_4]$ and 2 equiv. of $DPPMO_2$ (Fig. 7). As described for the nitrate system, peaks assigned to $[UO_2(\eta^1\text{-}DPPMO_2)_2(DPPMO_2)]^{2+}$ are observed at 45.7 and 28.7 ppm for monodentate coordinated $DPPMO_2$. On this occasion both peaks are clearly split into doublets, as expected for coupling between inequivalent P environments for the same $DPPMO_2$ ligand (J_{P-P} = 14.6 Hz). The peaks for bidentate and uncoordinated $DPPMO_2$ are observed at 43.2 and 27.5 ppm, respectively. These results clearly indicate that monodentate coordinate $DPPMO_2$ P═O donor ligand more strongly coordinates to $\{UO_2\}^{2+}$ than perrhenate, triflate or bistriflimide.

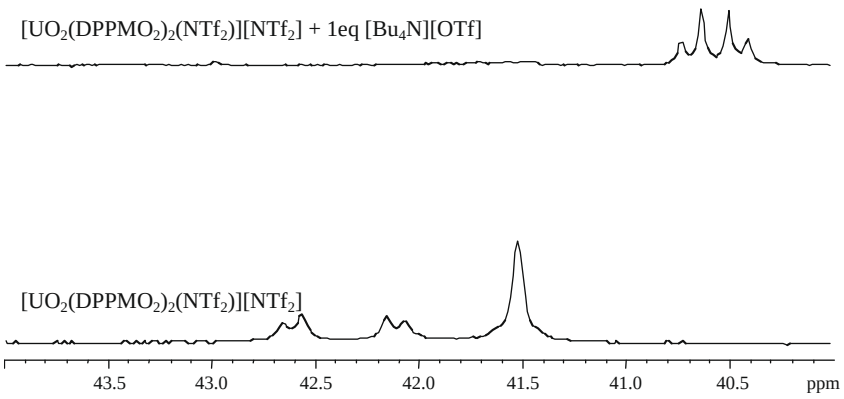


Fig. 5. $^{31}P\{^{1}H\}$ NMR spectra $[UO_2(NTf_2)(DPPMO_2)_2][NTf_2]$ (**1**) before, and after, the addition of one molar equivalent of $[Bu_4N][OTf]$. The spectra were recorded at −70 °C in CD_2Cl_2.

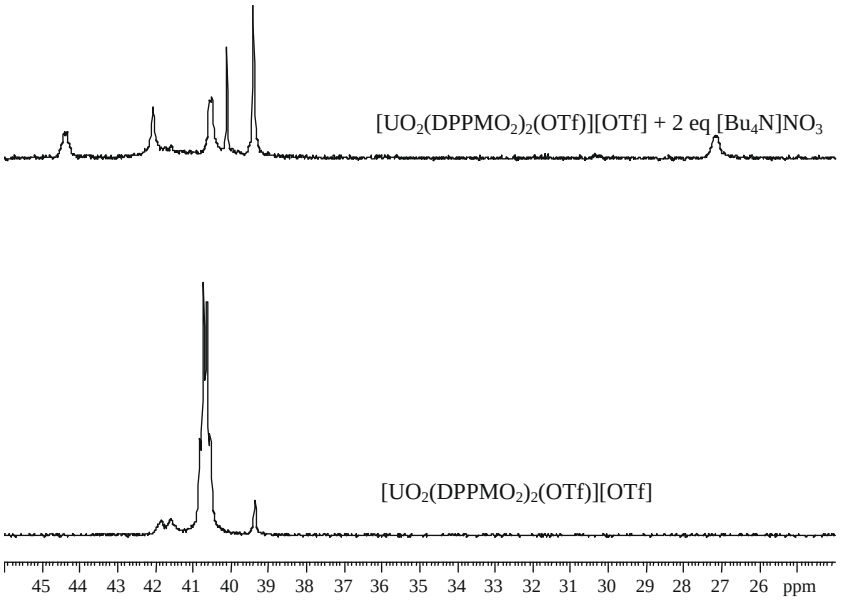


Fig. 6. $^{31}P\{^{1}H\}$ NMR spectra of $[UO_2(OTf)(DPPMO_2)_2][OTf]$ (**2**) before, and after, the addition of two molar equivalents of $[Bu_4N]NO_3$. The spectra were recorded at −70 °C in CD_2Cl_2.

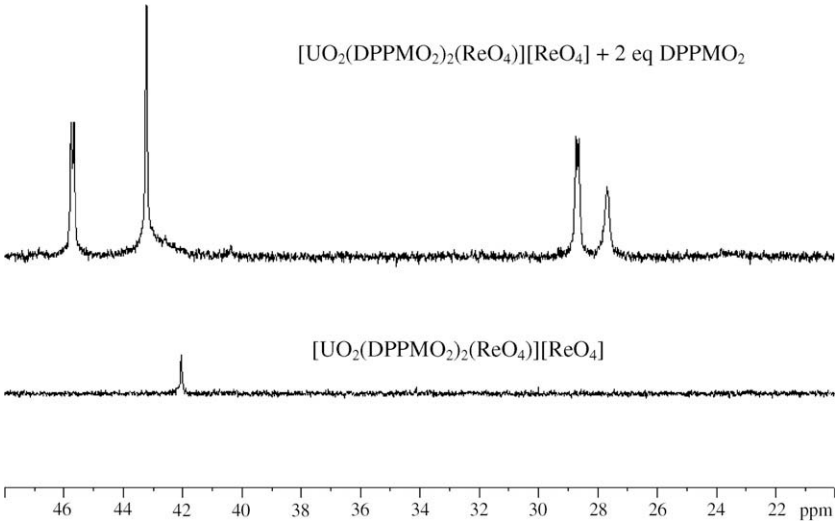


Fig. 7. $^{31}P\{^{1}H\}$ NMR spectra $[UO_2(DPPMO_2)_2(ReO_4)][ReO_4]$ before, and after the addition of two molar equivalents of $DPPMO_2$. The spectra were recorded at −70 °C and −45 °C, respectively in CD_2Cl_2.

4. Conclusions

The $\{UO_2(DPPMO_2)_2\}^{2+}$ dication yields a uranyl equatorial bonding site which can accommodate 'weakly' coordinating anions, as we have now demonstrated by characterising a series of complexes of general formula $[UO_2(DPPMO_2)_2X][X]$ (where $X = [ReO_4]^-$, $[TcO_4]^-$, NTf_2^-, OTf^- and Cl^-). Both $[UO_2(NTf_2)(DPPMO_2)_2][NTf_2]$ (**1**) and $[UO_2(OTf)(DPPMO_2)_2][OTf]$ (**2**) have been prepared in the course of this current study. We have shown this series to be an excellent probe of uranyl – anion bond strength. Solid state structural and solution state ^{31}P NMR studies are in agreement with respect to the order of the strength of the uranyl – anion bonding interaction which decreases along the series $[Cl]^- > [ReO_4]^- > [OTf]^- > [NTf_2^-]^-$. Further ^{31}P NMR competition studies show that both nitrate and excess $DPPMO_2$ will readily displace the weakly coordinating anions that have been investigated, forming complexes in which the $[UO_2(DPPMO_2)_2X][X]$ structural type no longer prevails.

Acknowledgments

We acknowledge the Engineering and Physical Sciences Research Council (EPSRC), Nexia Solutions and School of Chemistry, University of Manchester for funding. In particular, S. M. Cornet was funded from the EPSRC Grant No. GR/S95152/01. We also acknowledge the Heavy Element Chemical Research Program, Chemical Sciences Division of the Office of Basic Energy Sciences, United States Department of Energy and the Los Alamos Laboratory Directed Research and Development Program for current funding (I. May).

Appendix A. Supplementary data

Raman spectra for 1 and 2 and selected 31P {1H} NMR spectra.

CCDC 665999 and 666000 contain the supplementary crystallographic data for 1 and 2. These data can be obtained free of charge via http://www.ccdc.cam.ac.uk/conts/retrieving.html, or from the Cambridge Crystallographic Data Centre, 12 Union Road, Cambridge CB2 1EZ, UK; fax: (+44) 1223-336-033; or e-mail: deposit@ccdc.cam.ac.uk. Supplementary data associated with this article can be found, in the online version, at doi:10.1016/j.poly.2008.10.070.

References

[1] (a) M. Ephritkhine, Dalton Trans. (2006) 2501;
(b) I. Grenthe, J. Drożdżyński, J. Fujino, E.C. Buk, T.E. Albrecht-Schmitt, S.F. Wolf, in: L.R. Morss, N.M. Edelstein, J. Fuger (Eds.), The Chemistry of the Actinide and Transactinide Elements, third ed., vol. 1, Springer, 2006, p. 253;
(c) C.J. Burns, M.P. Neu, H. Boukhalfa, K.E. Gutowski, N.J. Bridges, R.D. Rogers, in: J.A. McCleverty, T.J. Meyer (Eds.), Comprehensive Coordination Chemistry II, vol. 3.3, Elsevier Ltd., 2004, p. 189.
[2] (a) M.R. Rosenthal, J. Chem. Educ. 50 (1973) 331;
(b) S.H. Strauss, Chem. Rev. 93 (1993) 927.
[3] P.D. Wilson (Ed.), The Nuclear Fuel Cycle, Oxford University Press, Oxford, 1996.
[4] (a) A.I. Bhatt, H. Kinoshita, A.L. Koster, I. May, C.A. Sharrad, H.M. Steele, V.A. Volkovich, O.D. Fox, C.J. Jones, B.J. Lewin, J.M. Charnock, C. Hennig, in: G.J. Lumetta, K.L. Nash, S.B. Clark, J.I. Friese (Eds.), Separations for the Nuclear Fuel Cycle in the 21st Century, ACS Symposium series 933, vol. 14, 2006, pp. 219–233;
(b) A.I. Bhatt, N.W. Duffy, D. Collison, I. May, R.G. Lewin, Inorg. Chem. 45 (2006) 1677.
[5] (a) P. Wasserchеid, C.M. Gordon, C. Hilgers, M.J. Mulden, I.R. Dunkin, Chem. Commun. (2001) 1186;
(b) M.A. Klingshirn, G.A. Broker, J.D. Holbrey, K.H. Saughnessy, R.D. Rogers, Chem. Commun. (2002) 1394.
[6] (a) T. Welton, Chem. Rev. 99 (1999) 2071;
(b) P. Wasserscheid, T. Welton, Ionic Liquids in Synthesis, Wiley-VCH, Weinheim, 2002.
[7] (a) D.B. Williams, M.E. Stoll, B.L. Scott, D.A. Costa, W.J. Oldham Jr., Chem. Commun. (2005) 1438;
(b) O.G. Polyakov, S.M. Ivanova, C.M. Gaudinski, S.M. Miller, O.P. Anderson, S.H. Strauss, Organometallics 18 (1999) 3769;
(c) M.J. Earle, U. Hakala, B.J. McAuley, M. Nieuwenhuyzen, A. Ramani, K.R. Seddon, Chem. Commum. 23 (2004) 1368;
(d) W.J. Oldham, D.B. Williams, Electrochem. Ser. Proc. 19 (2002) 983.
[8] A.I. Bhatt, I. May, V.A. Volkovich, D. Collison, M. Helliwell, I.B. Polovov, R.G. Lewin, Inorg. Chem. 44 (2005) 4934.
[9] A.-V. Mudring, A. Babai, S. Arenz, R. Giernoth, Angew. Chem., Int. Ed. 44 (2005) 5485.
[10] A. Babai, A.-V. Mudring, Chem. Mater. 17 (2005) 6230.
[11] A. Babai, A.-V. Mudring, Dalton Trans. (2006) 1828.
[12] J.-C. Berthet, M. Nierlich, M. Ephretikhine, C.R. Chim. 5 (2002) 81.
[13] J.-C. Berthet, M. Lance, M. Nierlich, M. Ephritikhine, Chem. Commun. (1998) 1373.
[14] J.-C. Berthet, M. Lance, M. Nierlich, M. Ephritikhine, Eur. J. Inorg. Chem. (1999) 2005.
[15] J.-C. Berthet, M. Lance, M. Nierlich, M. Ephritikhine, Eur. J. Inorg. Chem. (2000) 1969.
[16] J.-C. Berthet, M. Nierlich, M. Ephritikhine, Dalton Trans. (2004) 2814.
[17] S.M. Oldham, B.L. Scott, W.J. Oldham Jr., J. Appl. Organomet. Chem. 20 (2006) 39.
[18] A.D. Sutton, G.H. John, M.J. Sarsfield, J.C. Renshaw, I. May, L.R. Martin, A.J. Selvage, D. Collison, M. Helliwell, Inorg. Chem. 43 (2004) 5480.
[19] G.H. John, I. May, D. Collison, M. Helliwell, Polyhedron 23 (2004) 3097.
[20] S. Kannan, N. Rajalakshmi, K.V. Chetty, V. Venugopal, M.G.B. Drew, Polyhedron 23 (2004) 1527.
[21] T.W. Hayton, G. Wu, J. Am. Chem. Soc. 130 (2008) 2005.
[22] S. Kannan, M.A. Moody, C.L. Barnes, P.B. Duval, Inorg. Chem. 45 (2006) 9206.
[23] A. Altomare, G. Cascarano, C. Giacovazzo, A. Guagliardi, J. Appl. Crystallogr. 26 (1993) 343.
[24] G.M. Sheldrick, SHELX97. Programs for Crystal Structure Analysis (Release 97-2), University of Gottingen, Germany, 1997.

Polyhedron 28 (2009) 370–380

Contents lists available at ScienceDirect

Polyhedron

journal homepage: www.elsevier.com/locate/poly

Synthesis and characterization of Co(II) and Cu(II) supported complexes of 2-pyrazinecarboxylic acid for cyclohexene oxidation

Pratap Chutia, Shigeru Kato, Toshinori Kojima, Shigeo Satokawa *

Department of Materials and Life Science, Faculty of Science and Technology, Seikei University, Tokyo 180-8633, Japan

ARTICLE INFO

Article history:
Received 15 June 2008
Accepted 22 October 2008
Available online 10 December 2008

Keywords:
Zeolite–Y
Alumina
Organically modified silica
Encapsulation
Immobilization
Cyclohexene oxidation

ABSTRACT

The complexes $[Co(N\hat{}O)_2]$ (**1**) and $[Cu(N\hat{}O)_2]$ (**2**) {N^O = η^2-(N,O) coordinated 2-pyrazinecarboxylic acid} have been synthesized and characterized by elemental (including metal) analyses, FT-IR spectroscopy and powder X-ray diffraction. The molecular structure of complex **2** was determined by single X-ray crystallography. In the molecule, the Cu atom occupies the center of a square planar geometry, which consists of two *trans*-O atoms and two *trans*-N atoms of two 2-pyrazinecarboxylic acid ligands. The complexes **1** and **2** were well encapsulated into zeolite–Y super-cage to yield the corresponding zeolite–Y encapsulated metal complexes, abbreviated herein as $[Co(N\hat{}O)_2]$–Y (**3**) and $[Cu(N\hat{}O)_2]$–Y (**4**). Similarly, the metal complexes **1** and **2** were immobilized on alumina and organically modified silica surfaces to lead to the formation of immobilized metal complexes $[Co(N\hat{}O)_2]$–Al_2O_3 (**5**); $[Cu(N\hat{}O)_2]$–Al_2O_3 (**6**); $[Co(N\hat{}O)_2]$–AMPS (**7**) and $[Cu(N\hat{}O)_2]$–AMPS (**8**) (AMPS = aminopropyl silica). Elemental (including metal) analyses, FT-IR spectroscopy, powder X-ray diffraction and thermal analysis have been used to characterize these materials. The catalytic activity of all the catalysts **1**–**8** towards the oxidation of cyclohexene into different chemically and pharmaceutically important products were evaluated under homogeneous and heterogeneous conditions. In order to obtain a maximum conversion of cyclohexene, the reaction parameters, like reaction temperature and time, were optimized. Under the optimized conditions, a maximum of 90.47% cyclohexene conversion was achieved with $[Cu(N\hat{}O)_2]$–Y (**4**) with a 1:2 molar ratio reaction of cyclohexene and H_2O_2.

© 2008 Elsevier Ltd. All rights reserved.

1. Introduction

Oxidation of olefins to give oxygen containing value added products like alcohols, aldehydes, ketones, acids, epoxides, etc. is an extremely important and useful reaction in both chemical and pharmaceutical industries [1,2]. Amongst the different oxidants used in oxidation catalysis, hydrogen peroxide is ideally suitable due to its low cost. Furthermore, hydrogen peroxide is readily available and creates no hazardous by-products during the reaction [2]. In the last few years, homogeneous catalysts have received great attention in the effective use for oxidation of olefins [3,4]. Despite this interest, such materials suffer from some drawbacks like difficulty in separation from the reaction mixture, catalyst deactivation by dimerization through the formation of oxygen bridges, the high cost of the complex and lack of recycling method, etc., which make them difficult for application on a large scale [1,3]. The search for new oxidation catalysts is one of the most important current topics for both industrial and academic research. The heterogenization of homogeneous catalysts found to exhibit some attractive features like the site isolation effect is a field of continuing interest [5]. To avoid the problems with homogeneous catalysis, various strategies are employed like encapsulation in zeolites, grafting on polymers and MCM-41 silica, and immobilization in polysiloxane membranes, etc., which are offering moderate to excellent results [1,3]. A molecule encapsulated in a zeolite cage is characterized by steric restriction and if the size of the molecule is well fitted within the zeolite cage, the molecule may show interesting properties, which would not be observed under ordinary conditions [6]. Immobilization of transition metal complexes on solid supports such as alumina and organically modified silica has also been studied extensively in order to prepare heterogeneous catalysts with the desired structure and functionality [7]. The supporting tendency of acidic alumina might arise from the presence of oxygen groups on the surfaces, which coordinate easily to metal ion centers [3]. Modified silica is also important due to its chemical and thermal stability and strong ability to bind the metal complexes. Some reported efficient copper containing heterogeneous catalysts for oxidation reactions are Cu(II)-phthalocyanine incorporated inside Y-faujasite and MCM-41 [8], Cu(II)-complexes of 1,2-diaminocyclohexane based ligands encapsulated into zeolite–Y [6], Cu(II)-bis(2-mercaptoanil)benzil complexes supported on alumina [9], Cu(II)-coordination polymers constructed from phthalate–imidazole [2], copper–pyridine complexes encapsulated

* Corresponding author. Tel.: +81 422 37 3749; fax: +81 422 37 3871.
E-mail address: satokawa@st.seikei.ac.jp (S. Satokawa).

0277-5387/$ - see front matter © 2008 Elsevier Ltd. All rights reserved.
doi:10.1016/j.poly.2008.10.063

into a zeolite super-cage [7], (3,10-dialkyl-dibenzo-1,3,5,8,10,12-hexaazacyclotetradecane)Cu(II) encapsulated into zeolite [5], alumina supported Cu(II) *N,N*-bis(salicylidene)-2,2-dimethylpropane-1,3-diamine complexes [3], a copper complex with 8-hydroxyquinoline immobilized on an organically modified silica surface [10], Cu(II)/X and Y zeolite [11], $Cu(OH)_2$/silica [12], etc. Some other supported catalysts of Ni(II), Co(II), Mn(II) and oxovanadium(IV) are also as potentially important as copper complexes in heterogeneous oxidation catalysis [1–3,6,9,13].

The present investigation deals with the encapsulation and immobilization of Co(II) and Cu(II) complexes of 2-pyrazinecarboxylic acid ligand in zeolite–Y, alumina and organically modified silica supports. The neat and supported materials have been screened as catalysts for the oxidation of cyclohexene into different value added products with hydrogen peroxide as the oxygen donor. The effects of different experimental parameters like reaction time and temperature on the catalytic conversion were also investigated in order to optimize the reaction conditions.

2. Experimental

2.1. Materials

Analytical reagent grade cyclohexene, 30% aqueous hydrogen peroxide, copper(II) acetate monohydrate, cobalt(II) acetate tetrahydrate, 3-aminopropyltriethoxysilane, etc. were purchased from Wako Pure Chemical Industries, Ltd., Japan. 2-Pyrazinecarboxylic acid, reference samples of 1,2-epoxycyclohexane, 2-cyclohexen-1-ol, 2-cyclohexen-1-one and 1,2-cyclohexanediol were obtained from Tokyo Kasei Kogyo Co., Ltd. The zeolite–Y, namely HSZ-390HUA ($SiO_2/Al_2O_3 = 750$), was supplied by Tosoh Corporation and alumina and silica supports were supplied by the Catalytic Society of Japan. All other chemicals and solvents used in the present study were of AR grade and were used without further purification.

2.2. Characterization techniques

FT-IR spectra in the range 400–4000 cm^{-1} were recorded using a Jasco 460 plus spectrophotometer in KBr disks. Powder X-ray diffraction patterns were recorded on a Rigaku Miniflex with Cu Kα filtered radiation (30 kV, 15 mA) at a scanning speed of 2°/min. Metal contents were measured by Inductively Coupled Plasma-atomic emission Spectroscopy (ICPS-7500, Shimadzu) after leaching the metal ions with conc. nitric acid and diluting with distilled water. The carbon and nitrogen contents were measured using an Atomic High Sensitive NC analyzer (Sumigraph NC-22A, Sumika Chemical Analysis Service (SCAS)). Thermal analyses of the supported complexes were carried out on a Shimadzu Thermal Analyzer at a heating rate of 10 °C/min. All catalyzed reaction products were analyzed using a Gas Chromatograph (GC-17A, Shimadzu) fitted with a DB-1 capillary column (30 m × 0.25 mm × 0.25 μm) and FID detector. The identities of the products were confirmed by Gas Chromatography Mass Spectroscopy (GCMS-QP5050A, Shimadzu).

2.3. Preparations

2.3.1. Preparation of $[Co(N\hat{}O)_2]$ (**1**) and $[Cu(N\hat{}O)_2]$ (**2**); $N\hat{}O = \eta^2$-(N,O) coordinated 2-pyrazinecarboxylic acid

2-Pyrazinecarboxylic acid (10 mmol, 1.241 g) dissolved in 10 mL warm methanol was added to a solution of $Co(CH_3COO)_2 \cdot 4H_2O$ (5 mmol, 1.245 g) in methanol (10 mL) and reaction mixture was refluxed with stirring on a water bath for 5 h. A light yellow solid of $[Co(N\hat{}O)_2]$ slowly separated out within a few hours on cooling the solution at room temperature. The solid was filtered off, washed repeatedly with methanol and dried at 50 °C in an oven for 10 h. Yield: 79%.

$Cu(CH_3COO)_2 \cdot H_2O$ (5 mmol, 0.998 g) and 2-pyrazinecarboxylic acid (10 mmol, 1.241 g) were treated following the same experimental procedure and conditions as above to obtain a blue solid of $[Cu(N\hat{}O)_2]$. Yield: 88%.

2.3.2. X-ray crystallography

A crystal of complex **2** suitable for X-ray crystallographic analysis was grown from a methanol–water solution. Data collection was performed using a Rigaku Saturn (Rigaku AFC10) diffractometer, full sphere of data with 0.3° slices, −150 °C, Mo Kα radiation and empirical absorption corrections. All non-hydrogen atoms were refined anisotropically with the hydrogen atoms being refined in idealized geometries. The structure refinements were done by full matrix least square on F^2 using the SHELXTL97 computer program [14]. The crystal data and structure refinement for the complex are listed in Table 1.

2.3.3. Preparation of zeolite–Y encapsulated metal complexes

2.3.3.1. Preparation of M–Y (M = Co, Cu). Zeolite powder (H–Y) was activated at 100 °C overnight before use. Three grams of activated zeolite were added to a 100 mL methanolic solution of $Co(CH_3COO)_2 \cdot 4H_2O$ (12.50 mmol, 0.05 M) or $Cu(CH_3COO)_2 \cdot H_2O$ (12.52 mmol, 0.05 M) and suspensions were stirred at ca. 60 °C for about 72 h under dry conditions. The solid compounds of Co–Y and Cu–Y were filtered off and washed repeatedly with warm methanol in order to remove uncomplexed metal ions, and were dried at 100 °C for 24 h.

*2.3.3.2. Preparation of encapsulated $[Co(N\hat{}O)_2]$–Y (**3**) and $[Cu(N\hat{}O)_2]$–Y (**4**).* Co–Y or Cu–Y (2 g) and 2-pyrazinecarboxylic acid (1 g) were transferred to a round bottom flask containing 50 mL of methanol. Then the reaction mixtures were heated at 65 °C under

Table 1
Crystal data and structure refinement of complex **2**.

Empirical formula	$C_{10}H_6N_4O_4Cu$
Formula weight	309.73
Temperature (°C)	−150
Wave length (Å)	0.71070
Crystal system	triclinic
Space group	$P\bar{1}$
a (Å)	5.010(1)
b (Å)	6.994(2)
c (Å)	15.258(4)
α (°)	90.000(3)
β (°)	90.000(3)
γ (°)	105.924(4)
V (Å^3)	514.1(3)
Z value	2
D_{calc} (g cm^{-3})	2.001
Pixel size (mm)	0.137
Detector position (mm)	54.88
$F(000)$	310
Crystal dimensions (mm)	0.40 × 0.20 × 0.08
$2\theta_{max}$ (°)	54.9
Number of reflections measured	4159
Collections	Lorentz-polarization absorption (trans. factors: 0.4204–0.6789)
Refinement method	full-matrix least-squares on F^2
Goodness-of-fit indicator	0.978
Reflection/parameter ratio	9.75
Residuals: R (all reflections)	0.030
Residuals: R_1 ($I > 2.00\sigma(I)$)	0.027
Residuals: wR_2 (all reflections)	0.070
Maximum peak in final difference map (e$^-$ Å^{-3})	0.42
Minimum peak in final difference map (e$^-$ Å^{-3})	−0.61

reflux for 12 h with continuous stirring under dry conditions. The resulting yellow solid of [Co(N^O)$_2$]–Y (**3**) and blue solid of [Cu(N^O)$_2$]–Y (**4**) were filtered off and washed with methanol repeatedly to remove excess ligand and uncomplexed metal ions that may be contained in the cavities as well as in the external surface of the zeolite. The purification process was continued by refluxing the powder samples of **3** and **4** in methanol (50 mL) for 2 h. The unreacted metal ions if any, in the cavity of the zeolite were removed by stirring with aqueous 0.01 M NaCl solution (150 mL) for 10 h. The resulting solids were filtered and washed with distilled water until free from chloride ions. The solids were finally dried at 100 °C for 24 h.

*2.3.4. Preparation of immobilized [Co(N^O)$_2$]–Al$_2$O$_3$ (**5**) and [Cu(N^O)$_2$]–Al$_2$O$_3$ (**6**) complexes*

Alumina was activated at 100 °C overnight before immobilization of the metal complexes. Solutions of [Co(N^O)$_2$] and [Cu(N^O)$_2$] (2.5 g) in 250 mL $CHCl_3$ were added to a 3 g alumina suspension in 25 mL $CHCl_3$. The resulting reaction mixtures were refluxed with stirring for about 12 h. The corresponding yellow solid of complex **5** and blue solid of complex **6** were filtered off and washed with $CHCl_3$. The catalysts [Co(N^O)$_2$]–Al$_2$O$_3$ and [Cu(N^O)$_2$]–Al$_2$O$_3$ were dried at 100 °C for 24 h prior to use.

2.3.5. Preparation of immobilized metal complexes on silica surface

2.3.5.1. Modification of silica by the organic functionality 3-aminopropyltriethoxysilane. Amorphous silica (3 g) was ground and suspended in an ethanolic solution of 3-aminopropyltriethoxysilane $\{(OC_2H_5)_3SiCH_2CH_2CH_2NH_2\}$ such that 2.0 mmol silane/g silica could be obtained. The mixture was refluxed with stirring for 12 h to obtain organically modified silica. The solid was then filtered off and washed with methanol and ether respectively several times. The resulted material is designated as aminopropyl silica (AMPS).

*2.3.5.2. Preparation of immobilized [Co(N^O)$_2$]-AMPS (**7**) and [Cu(N^O)$_2$]-AMPS (**8**).* The AMPS was refluxed with 250 mL aqueous solution of $Co(CH_3COO)_2 \cdot 4H_2O$ (12.50 mmol, 0.05 M) or $Cu(CH_3COO)_2 \cdot H_2O$ (12.52 mmol, 0.05 M) for about 12 h and respective solids of Co–AMPS and Cu–AMPS were filtered and washed thoroughly with water. The Co–AMPS and Cu–AMPS samples were then reacted with 2-pyrazinecarboxylic acid dissolved in methanol to produce the immobilized metal complexes **7** and **8**.

2.3.6. Homogeneous oxidation of cyclohexene

The catalytic oxidation of cyclohexene under homogeneous conditions was carried out using complexes **1** and **2** in a 100 mL flask fitted with a water circulated condenser. In a typical 1:1 molar ratio reaction of substrate to oxidant, neat metal complexes **1** or **2** (0.035 g) in 10 mL acetone and 30% H_2O_2 (1.14 g, 10 mmol) were added to a solution of cyclohexene (0.82 g, 10 mmol). The resulting mixture was then heated at 75 °C for 8 h with continuous stirring in a water bath. The solvent was evaporated under reduced pressure and the crude product analyzed by GC and GC–MS. The corresponding amounts of H_2O_2 for 1:2 and 1:3 molar ratio catalytic reactions were 2.28 g (20 mmol) and 3.42 g (30 mmol). A temperature of 75 °C and reaction period of 8 h were the optimum values for maximum conversion of cyclohexene, and the optimization reactions were carried out separately by changing the temperature and time with a fixed amount of catalyst.

2.3.7. Heterogeneous oxidation of cyclohexene

The reaction conditions as well as the experimental set-up were essentially the same as out lined for the homogeneous catalysis, except for the amount of catalyst used. In all the heterogeneous catalytic reactions, 0.1 g of each catalyst **3**–**8** was used.

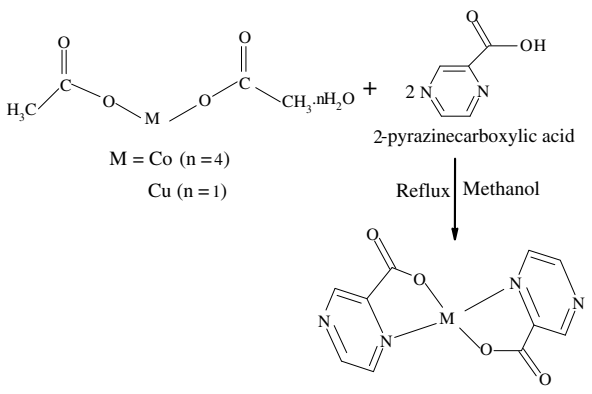
3. Results and discussion

3.1. Synthesis and characterization of catalysts

The reactions of $Co(CH_3COO)_2 \cdot 4H_2O$ or $Cu(CH_3COO)_2 \cdot H_2O$ with 2 M equiv. of 2-pyrazinecarboxylic acid ligand in refluxing methanol yielded the corresponding chelate complexes [Co(N^O)$_2$] (**1**) and [Cu(N^O)$_2$] (**2**); N^O = η^2-(N,O) coordinated 2-pyrazinecarboxylic acid (Scheme 1). The metal as well as C and N contents (Table 2) of the complexes **1** and **2** are in agreement with their general formula, as mentioned above. The preliminary identification of these two complexes was made on the basis of their FT-IR spectra. A sharp band at 1724 cm^{-1} due to the $\nu(COO)_{as}$ stretch of the free ligand shifts to the lower energy region, at 1637 cm^{-1} for **1** and 1645 cm^{-1} for **2**, indicating five membered chelate ring formation through the O- and one of the N-donors of the ligand [15,16]. Some moderately intense bands appeared in the 400–500 cm^{-1} region are assigned to new ν(M–N) and ν(M–O) (M = Co, Cu) bands, which further suggest bond formation between the metal and N- and O-donors of the ligand [17,18]. Powder X-ray diffraction patterns (Fig. 1) of complexes **1** and **2** were recorded over the range 2θ = 5–80°, which infer the well-crystalline nature of each complex.

In order to confirm the structures and to determine the detailed geometries, we tried to grow crystals of the complexes. A good crystal suitable for X-ray structural determination was obtained for complex **2**. The IR and elemental analyses data agree well with the molecular structure of the complex. The arrangements and numbering of the atoms in the crystal are shown in Fig. 2 and important bond lengths and bond angles are summarized in Table 3. In the molecule, the copper atom has a square planar coordination with two *trans*-O atoms and two *trans*-N atoms of two 2-pyrazinecarboxylic acid ligands. One vacant position is occupied by a loosely bonded water molecule, which will not change the coordination environment of the copper atom.

The zeolite–Y encapsulated complexes **3** and **4** (Scheme 2) are the result of the exchange of Co(II) and Cu(II) ions with H^+ ions associated with H–Y, followed by a metal exchange reaction of Co–Y or Cu–Y with the ligand 2-pyrazinecarboxylic acid in solution. Due to flexible nature, the ligand enters into the zeolite–Y nano-cavity and reacts with the previously exchanged metal ions. The purification of the solids by refluxing with a excess of methanol removed excess free ligand that remained uncomplexed in the cavities of the zeolite along with the neat complex formed on the external surface of the zeolite. The excess metal ions that may be present in the cavity were removed by exchange back with aqueous NaCl solution. The metal, C and N contents in each of the catalysts are determined and presented in Table 2, along with their



Scheme 1. Neat Co(II) and Cu(II) complexes.

Table 2
Chemical composition, metal ion loading, physical and analytical data of the catalysts.

Catalysts	Metal ion loading[a] (mmol g^{-1} support)	Colour	% of C (calcd.)	% of N (calcd.)	% of Co (calcd.)	% of Cu (calcd.)	M/N
$[Co(N^O)_2]$ (**1**)		light yellow	35.18 (34.88)	16.21 (16.27)	16.98 (17.13)		1.05
$[Cu(N^O)_2]$ (**2**)		blue	34.30 (34.42)	16.10 (16.03)		18.20 (18.23)	1.13
$[Co(N^O)_2]$–Y (**3**)	2.04	light yellow	7.71	3.54	3.61		1.02
$[Cu(N^O)_2]$–Y (**4**)	2.05	blue	8.63	3.69		3.91	1.06
$[Co(N^O)_2]$–Al_2O_3 (**5**)	1.45	light yellow	5.36	2.59	2.56		0.99
$[Cu(N^O)_2]$–Al_2O_3 (**6**)	2.32	blue	8.92	4.07		4.44	1.09
$[Co(N^O)_2]$–AMPS (**7**)	1.13	light yellow	4.60	1.98	2.00		1.01
$[Cu(N^O)_2]$–AMPS (**8**)	2.84	blue	10.42	4.93		5.42	1.10

[a] $= \frac{\text{Observed metal } \% \times 100}{\text{Atomic weight of metal}}$.

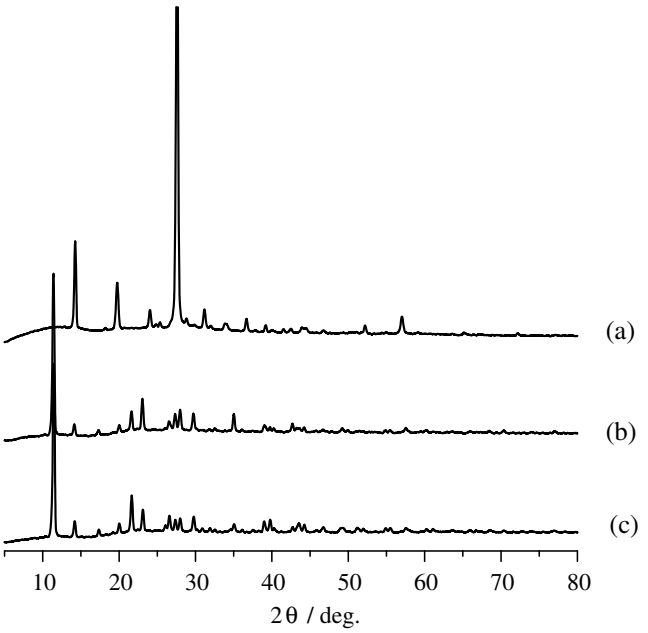


Fig. 1. XRD pattern of (a) 2-pyrazinecarboxylic acid, (b) $[Co(N^O)_2]$ (**1**), (c) $[Cu(N^O)_2]$ (**2**).

expected formula as well as their corresponding colour. As the complexes were purified well, the metal and element contents found after encapsulation are only due to the presence of the metal complexes in the cavity of the zeolite–Y. The chemical analysis of the encapsulated complexes also reveals a metal/N ratio roughly similar to that of the neat complexes **1** and **2** (Table 2), suggesting the same stoichiometry of the neat complexes after encapsulation. The catalysts $[Co(N^O)_2]$–Y (**3**) and $[Cu(N^O)_2]$–Y (**4**) are also well characterized by IR spectroscopy (Fig. 3). These complexes exhibit IR spectral bands essentially similar to their corresponding neat complexes **1** and **2**. The chelating mode of the ligand in these supported complexes is evident from the appearance of $\nu(COO)_{as}$ bands at 1634 and 1641 cm^{-1} for complexes **3** and **4,** respectively, which are shifted to a lower wavenumber (about 83–90 cm^{-1}) compared to the corresponding free ligand band (1724 cm^{-1}). Similar to complexes **1** and **2**, some new moderately intense bands located in the range 400–500 cm^{-1} further corroborate the chelate formation through one of the N- and O-donor sites of the ligand [17,18]. It is worth mentioning that the intensities of all the bands in the encapsulated complexes are weak compared to the corresponding neat complexes, which could be due to the low loading of the complexes into the zeolite matrix [6,19]. The powder X-ray diffraction pattern of H–Y and supported complexes **3** and **4** are presented in Fig. 4. The X-ray patterns are essentially similar, except the intensities of the bands in the encapsulated complexes are slightly lower compared to the parent H–Y, which could be due to the insertion of only a small amount of the metal complexes in the cavity of the zeolite–Y. This is in agreement with the low percentage metal content obtained for the encapsulated complexes **3** and **4** (Table 2). This observation indicates that the framework of the zeolite has not undergone any significant structural change during the encapsulation. This is expected as the ligand, being flexible in nature, enters slowly through the pores of the zeolite and fits nicely in the cavity upon coordination with the metal ions. Similar conclusions were also drawn by previous workers from their XRD patterns of different zeolite–Y encapsulated metal complexes [6,19]. One new but weak peak detected at 2θ values of 12.17° and 12.14° for complexes **3** and **4,** respectively was due to the externally loaded metal complexes. Fig. 5 represents the decomposition

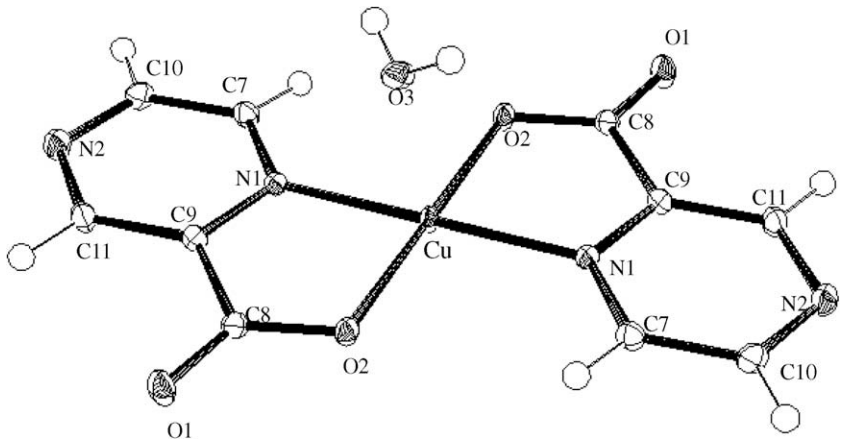
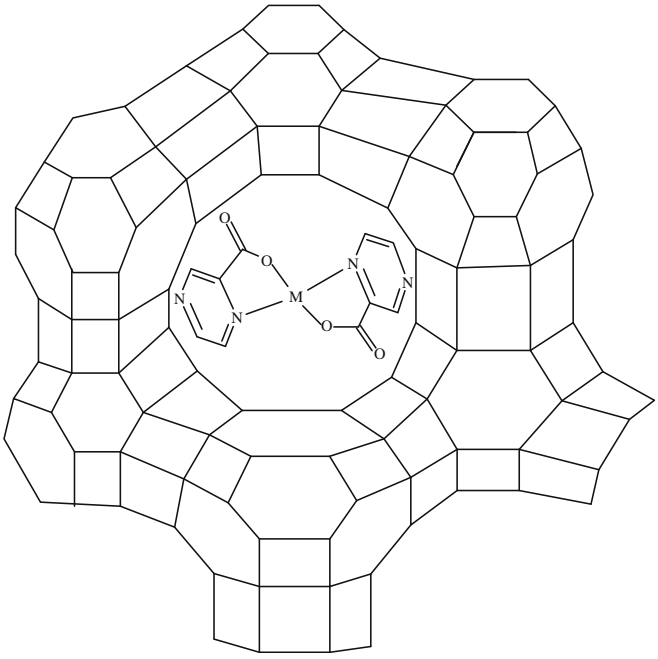


Fig. 2. Molecular structure of $[Cu(N^O)_2]$ (**2**) where N^O = η^2-(N,O) coordinated 2-pyrazinecarboxylic acid.

Table 3
Selected bond lengths and bond angles of complex **2**.

Bond lengths (Å)	
Cu–O2	1.990(1)
Cu–N1	1.991(1)
O2–C8	1.287(2)
O1–C8	1.231(2)
N1–C7	1.339(2)
N1–C9	1.344(2)
N2–C10	1.337(2)
N2–C11	1.344(2)
Bond angles (°)	
O2–Cu–N1	82.62(5)
N1–C9–C8	115.4(1)
Cu–O2–C8	114.9(1)
O2–C8–C9	114.7(1)
Cu–N1–C9	112.2(1)
N1–Cu–N1	180.0(1)
O2–Cu–O2	180.0(1)
Cu–N1–C7	129.4(1)
O1–C8–O2	125.1(1)
O1–C8–C9	120.2(1)



Scheme 2. Metal complexes encapsulated into a zeolite–Y super-cage.

patterns of different groups associated with the complexes on thermogravimetric analysis. Table 4 lists the percent mass loss at different steps and their possible assignments. The decomposition of different groups in the catalysts **3** and **4** occurs in three overlapping steps. The removal of externally trapped water is indicated by endothermic peaks at ca. 60 °C, with a corresponding mass loss of 7.25% (in **3**) and 1.05% (in **4**). The first step is followed by a mass loss of 8.52% and 9.12% for the corresponding complexes **3** and **4**, which could be due to decomposition of water associated with the zeolite framework. The removal of coordinated water molecules from the respective metal ion is also expected to be overlapped in this step [6,19]. The final step is exothermic for both the complexes, and corresponds to the decomposition of the externally loaded metal complexes. The low mass loss percentage (11.73% in **3** and 11.53% in **4**) is consistent with insertion of only a small amount of the metal complexes in the cavity of the zeolite–Y, which is also evident from the metal and elemental analyses results [6,19].

The immobilized catalysts **5** and **6** (Scheme 3) on the alumina surface have been characterized by metal and elemental analyses, FT-IR, XRD and thermal analysis, similar to the encapsulated catalysts **3** and **4**. The chemical composition data (Table 2) confirmed the purity and stoichiometry of these immobilized catalysts. The metal/N ratios in the catalysts are very similar to the corresponding neat complexes, ensuring immobilization of the complexes on the alumina. In the FT-IR spectra, the band corresponding to the $\nu(COO)_{as}$ vibration appears at 1641 and 1644 cm^{-1} for **5** and **6** respectively, suggesting a chelating mode of the ligand. Appearance of moderate intensity bands in the region 400–500 cm^{-1} indicates the coordination of N- and O-donors to the respective metal center. Powder X-ray diffraction patterns (Fig. 6) were also recorded to ensure immobilization. Two new but weak peaks with 2θ values of 11.55° and 14.32° (in **5**) and one weak peak at 11.65° (in **6**) were detected, which could be due to externally loaded metal complexes [3]. These new peaks further ensure the support of $[Co(N\hat{}O)_2]$ and $[Cu(N\hat{}O)_2]$ on the alumina surface. The DTA and TGA curves of the catalysts **5** and **6** have been shown in Fig. 7, and Table 4 presents the percentage of mass loss and possible assignments of different groups that decomposed during pyrolysis. The curves comprise of decomposition in three overlapping steps. First step is due to removal of just trapped water and the subsequent second and third steps indicate the decomposition of coordinated water molecules and metal complex respectively. The percentage of mass loss due to decomposition of the metal complex is low (20.16% in **5**; 18.62% in **6**), suggesting low loading of complexes.

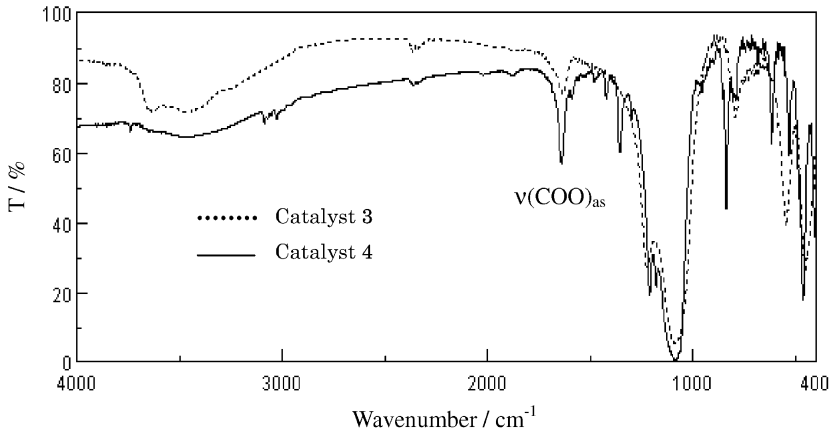


Fig. 3. FT-IR spectral pattern of zeolite–Y encapsulated catalysts $[Co(N\hat{}O)_2]$–Y (**3**) and $[Cu(N\hat{}O)_2]$–Y (**4**).

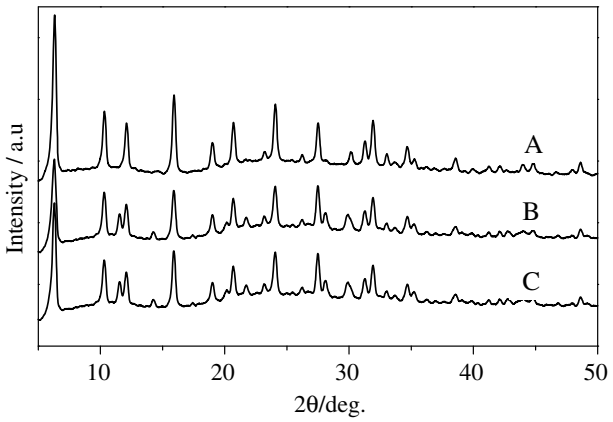


Fig. 4. XRD pattern of (A) H–Y, (B) [Co(N^O)$_2$]–Y (**3**) and (C) [Cu(N^O)$_2$]–Y (**4**).

In order to immobilize metal complexes on a silica surface, it was modified with a common organic functionality 3-aminopropyltriethoxysilane {$(OC_2H_5)_3SiCH_2CH_2CH_2NH_2$}, which gives rise to organically modified silica, designated as aminopropyl silica (AMPS). A preliminary investigation performed by elemental analysis indicates the presence of N (1.22%) and C (3.59%) in AMPS, suggesting the interaction between the organic moiety and the silica surface as pure silica is without C and N. AMPS was further characterized by FT-IR spectroscopy. A comparison of the IR spectra of pure silica as well as AMPS (Fig. 8) reveals that AMPS exhibits all the characteristic bands of 3-aminopropyltriethoxysilane (Table 5), which are not detected in pure silica. These new bands further substantiate the coordination of $(OC_2H_5)_3SiCH_2CH_2CH_2NH_2$ through a Si-bonding site with silica surface [10].

Treatment of AMPS with metal (Co or Cu) followed by 2-pyrazinecarboxylic acid yields the immobilized catalysts **7** and **8** (Scheme 4). The percentages of Co or Cu, N and C are listed in Table 2. The metal/N ratios are comparable with the neat metal complexes, which indicate immobilization of the metal complexes on AMPS. The FT-IR spectra of these catalysts (Fig. 9) exhibit all the characteristic bands of AMPS along with some new bands characteristic for the immobilized metal complexes. The intensities of the characteristic bands of AMPS in the catalysts are relatively weak compared to the parent AMPS. The band due to the $\nu(COO)_{as}$ vibration occurs at 1637 cm^{-1} (in **7**) and 1644 cm^{-1} (in **8**), suggesting a chelating mode of the ligand. These vibrations are almost in same position as that of the corresponding neat complexes **1** and **2** (Fig. 9), which indicates immobilization of the metal complexes on AMPS. The immobilization of the metal complexes on AMPS was further confirmed by a powder X-ray diffraction study (Fig. 10). Similar to the catalysts **3**-**6**, an additional weak peak is detected for both catalysts at 2θ values ~12.04°, indicating immobilization of the metal complexes on the AMPS surface. The DTA and TGA profiles of the catalysts **7** and **8** are presented in Fig 11. Details about the mass loss and possible assignments of the groups lost are illustrated in Table 4. Similar to the catalysts **3**–**6**, a low mass loss percentage corresponding to decomposition of the metal complex is in agreement with the low percentage of metal content obtained for the immobilized complexes.

The actual loading of the metal complex **1** or **2** on the different supports is related to catalytic activity of the supported catalysts

Table 4
Thermogravimetric analyses data of the heterogeneous catalysts **3**–**8**.

Catalysts	Temperature range (°C)	Mass loss (%)	Group lost
[Co(N^O)$_2$]–Y (**3**)	25–110	7.25	trapped H_2O
	110–367	8.52	zeolite H_2O
	367–1000	11.73	metal complex
[Cu(N^O)$_2$]–Y (**4**)	25–103	1.05	trapped H_2O
	103–330	9.12	zeolite H_2O
	330–1000	11.53	metal complex
[Co(N^O)$_2$]–Al_2O_3 (**5**)	25–80	2.00	trapped H_2O
	80–335	5.82	coordinated H_2O
	335–1000	20.16	metal complex
[Cu(N^O)$_2$]–Al_2O_3 (**6**)	25–83	1.12	trapped H_2O
	83–308	12.29	coordinated H_2O
	308–1000	18.62	metal complex
[Co(N^O)$_2$]–AMPS (**7**)	20–110	7.25	trapped H_2O
	110–1000	17.87	metal complex
[Cu(N^O)$_2$]–AMPS (**8**)	20–100	3.07	trapped H_2O
	100–310	15.58	coordinated H_2O
	310–1000	26.02	metal complex

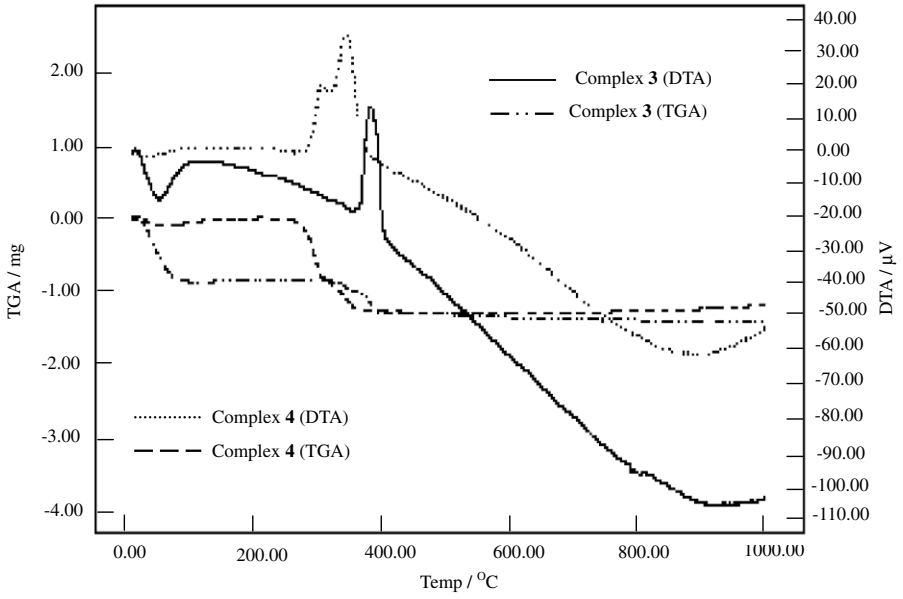
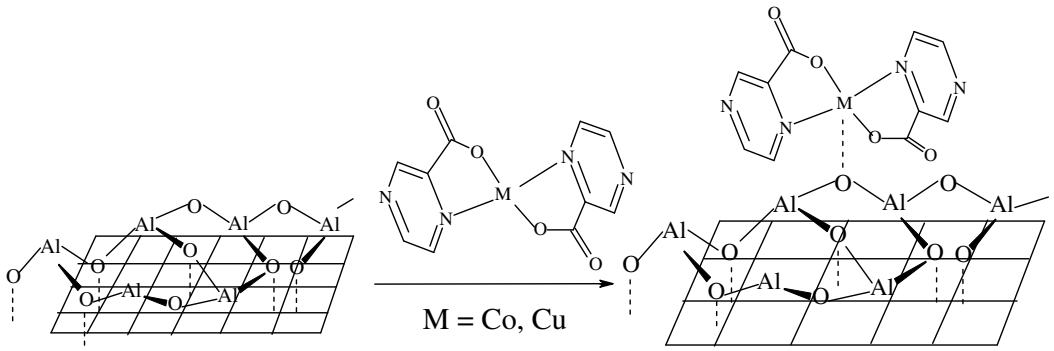


Fig. 5. DTA and TGA profile of [Co(N^O)$_2$]–Y (**3**) and [Cu(N^O)$_2$]–Y (**4**).



Scheme 3. Metal complexes immobilized on an alumina surface.

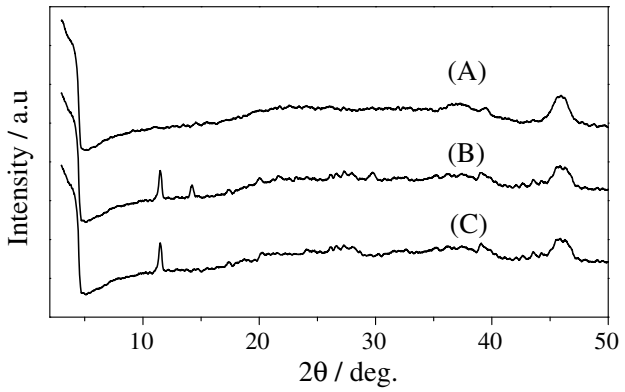


Fig. 6. XRD pattern of (A) parent Al_2O_3, (B) $[Co(N^O)_2]$–Al_2O_3 (**5**) and (C) $[Cu(N^O)_2]$–Al_2O_3 (**6**).

3–**8**. The complex, either **1** or **2**, does not directly interact with the supports. The metal ion loading step was followed by ligand loading. Excess metal ion and also ligand were removed by purification, it is a fact that the metal ion remaining after purification will react with 2 equiv. of the ligands in order to form the metal complex. This indicates that the determination of the metal ion loading on the supported catalysts **3**–**8** is essential, which in turn allows the determination of the catalytic activity in terms of turnover number of the catalysts. The metal ion loading values on the catalysts **3**–**8** are presented in Table 2. The Co loading on the different supports follows the trend zeolite–Y > alumina > silica whereas Cu loading follows the reverse trend under the same experimental conditions. Another important observation is that Cu loading is higher compared to Co loading on each of the supports.

3.2. Catalytic oxidation of cyclohexene using catalysts ***1–8***

Oxidation of cyclohexene to different commercially important products like 1,2-epoxycyclohexane, 2-cyclohexen-1-ol, 2-cyclohexen-1-one and 1,2-cyclohexanediol (Scheme 5) has been investigated by several workers using homogeneous as well as heterogeneous catalysts [1–3,6,9,10,13,20–23]. The catalytic activities of some of these catalysts which are closely related to the investigated ones are presented in Table 6 for a comparison in terms of total conversion of cyclohexene into products. The investigated catalysts **1**–**8** also satisfactorily catalyze the oxidation of cyclohexene in the presence of H_2O_2 as the oxidant. In order to achieve maximum conversion of cyclohexene, the catalytic reactions were carried by varying the reaction temperature and time whilst keeping catalyst amount constant (0.1 g for heterogeneous conditions, 0.035 g for homogeneous conditions). The neat catalyst $[Co(N^O)_2]$ (**1**) and its immobilized catalyst on silica $[Co(N^O)_2]$–AMPS (**7**) were tested as representative catalysts under homogeneous and heterogeneous conditions respectively in order to optimize the conditions. Reaction mixture having cyclohexene

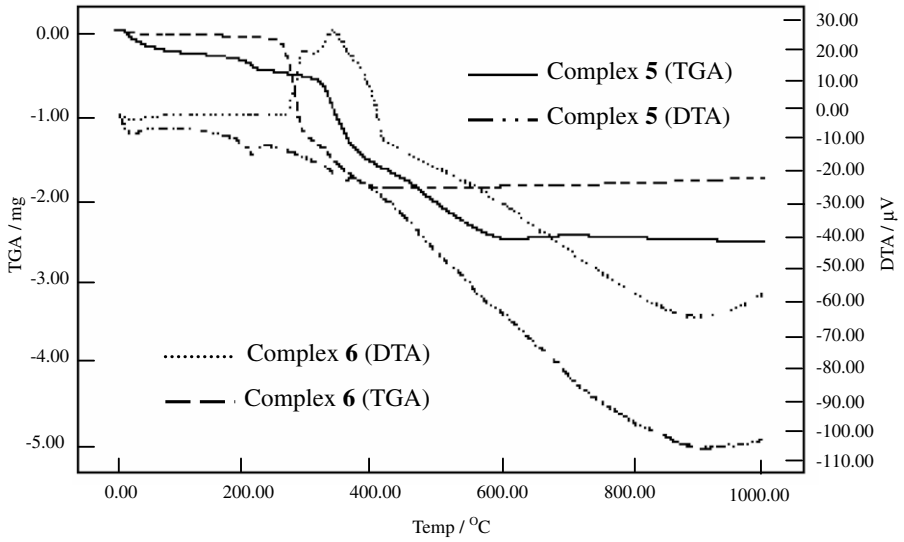


Fig. 7. DTA and TGA profile of $[Co(N^O)_2]$–Al_2O_3 (**5**) and $[Cu(N^O)_2]$–Al_2O_3 (**6**).

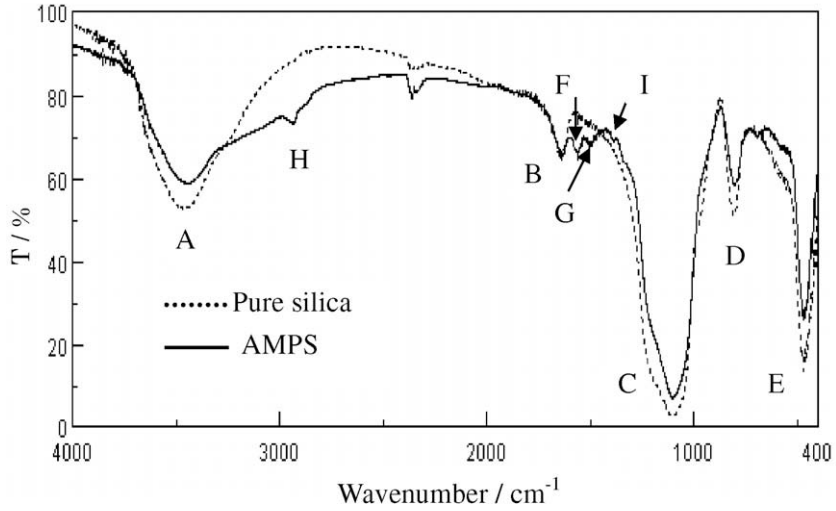
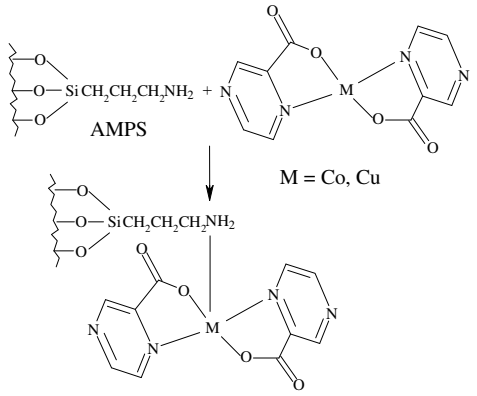


Fig. 8. FT-IR spectra of pure silica and AMPS.

Table 5
Positions (cm^{-1}) and assignments of different bands in pure silica and AMPS.

Common bands for both pure and AMPS		New bands in AMPS	
A	Si–OH stretching: 3475 cm^{-1}	F	N–H bending: 1560 cm^{-1}
B	Si–OH bending: 1644 cm^{-1}	G	C–N vibrational: 1490 cm^{-1}
C	Si–O–Si asymmetric: 1098 cm^{-1}	H	C–H stretching: 2940 cm^{-1}
D	Si–O–Si symmetric: 805 cm^{-1}	I	C–H bending: 1385 cm^{-1}
E	Si–O–Si bending: 460 cm^{-1}		



Scheme 4. Metal complexes immobilized on an organically modified silica surface.

(0.82 g, 10 mmol), catalyst **1** (0.035 g) or catalyst **7** (0.1 g) and 30% H_2O_2 (2.28 g, 20 mmol) in 10 mL acetone were refluxed with stirring at four different temperatures (40, 65, 75 and 80 °C) in order to find a suitable reaction temperature. At 75 °C, the catalysts **1** and **7** show the highest conversion of cyclohexene into products (79.45% by **1** and 90.25% by **7**) with an 8 h reaction time. No further improvement in conversion was obtained at 80 °C. Furthermore, at this reaction temperature, the heterogeneous catalytic mixture became colloidal, making the separation of the catalysts from the reaction mixture difficult. Consequently, 75 °C is considered to be the best suited temperature to carry out the catalytic reactions. Similarly, the representative catalysts exhibit the highest conversion of cyclohexene with a 8 h reaction time, which was selected after carrying out the catalytic reactions for different times, keeping the other conditions as above.

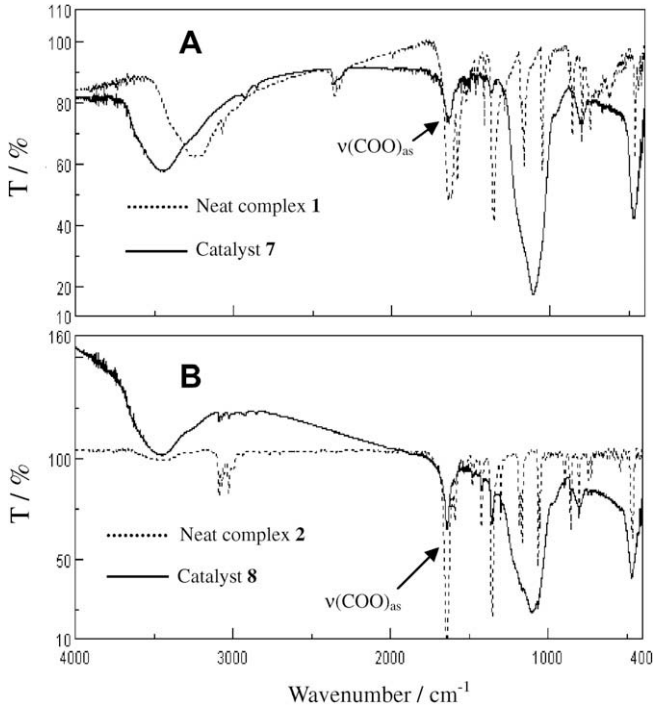


Fig. 9. FT-IR spectra of (A) neat complex **1** and catalyst **7**; (B) neat complex **2** and catalyst **8**.

Applying the optimum reaction conditions (reaction temperature 75 °C, reaction time 8 h, catalyst amount 0.035 g or 0.1 g,

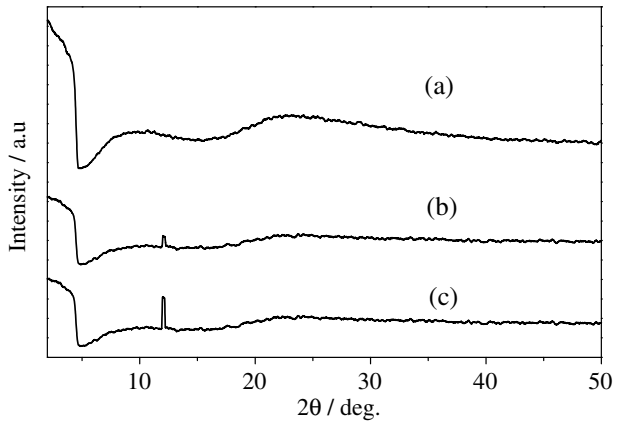


Fig. 10. Powder X-ray diffraction patterns of (a) pure silica, (b) catalyst [Co(N^O)$_2$]-AMPS (**7**) and (c) catalyst [Cu(N^O)$_2$]-AMPS (**8**).

acetone 10 mL), the catalytic potential of all the catalysts were evaluated at three different molar ratios viz. 1:1, 1:2 and 1:3 of cyclohexene to H_2O_2. The catalysts **1** and **2** are homogeneous in nature and dissolved readily in the reaction mixture under the catalytic conditions. The selectivity of various oxidation products and the activity results are presented in Table 7 and Fig. 12. It is clear from the data that for the 1:1 molar ratio reaction between cyclohexene and H_2O_2, a maximum conversion of only 60.14% was shown, by catalyst **8**, which reveals poor catalytic ability of the catalysts. In contrast, all the catalysts exhibit highest efficiency at a 1:2 molar ratio, and a maximum of 90.47% conversion was noted with catalyst **4**. The catalytic ability of the catalysts **1**–**8** at a cyclohexene to H_2O_2 molar ratio of 1:3 is higher than that for the 1:1 molar ratio and the maximum cyclohexene conversion was 84.21% when using catalyst **3**. The most important observation is that compared to the 1:2 molar ratio reaction, the catalytic potential of all the catalysts was reduced remarkably at the 1:3 molar ratio, indicating that a large amount of oxidant is not an essential condition to achieve maximum oxidation. The suppression of conversion for the 1:3 molar ratio reaction may be due to the presence of excess water supplied by H_2O_2 under the catalytic conditions, which blocks the catalysts active sites [6,13,24]. In any molar ratio reaction between cyclohexene and H_2O_2, alumina supported catalysts **5** and **6** exhibit poor catalytic activity compared to the zeolite and silica supported catalysts. Under the optimized reaction conditions, the catalyst [Co(N^O)$_2$]–Al_2O_3 (**5**) shows a maximum of only 37.99% conversion for the 1:2 molar ratio reaction. In general, the selectivity of the products follows the order 2-cyclohexen-1-one > 2-cyclohexen-1-ol > 1,2-cyclohexanediol > 1,2-epoxycyclohexane. The most promising observation is that 2-cyclohexen-1-one is found to be the major product in most of the catalytic reactions. The highest selectivity of 64.16% for 2-cyclohexen-1-one is obtained using the zeolite–Y encapsulated catalyst **4**. Moreover, 1,2-epoxycyclohexane is not a product in some of the catalytic reactions, and it is only formed to a small extent in the remaining catalytic reactions. For the 1:1 molar ratio reaction, a maximum of only 14.46% selectivity of the product 1,2-epoxycyclohexane is obtained using the catalyst [Co(N^O)$_2$]–Al_2O_3 (**5**). Salavati-Niasari [3] reported that epoxidation of cyclohexene by alumina-supported metal complex catalysts occurs effectively in the presence of H_2O_2. It is expected that, under the mentioned reaction conditions, the allylic hydrogen is more reactive than the C=C double bond, irrespective of the supports. Due to this fact the reaction proceeds to yield 2-cyclohexen-1-one as the major product and 1,2-epoxycyclohexane as the minor product in all the catalytic reactions [2,3,9]. For the zeolite–Y supported catalysts **3** and **4**, such allylic oxidation infers that metal complexes **1** or **2** are loaded mainly in the internal pores of the zeolite–Y. The nanospace constraints experienced by complex **1** or **2** located within the pores of the zeolite–Y support suppress the epoxidation pathway and favour allylic oxidation [22]. The heterogeneous catalysts **3**, **4**, 7 and **8** are found to exhibit higher catalytic performance compared to that of the corresponding neat complexes **1** and **2**, mostly due to site isolation of the complexes [1,3]. Another important observation is that performance of the cobalt catalysts towards to cyclohexene oxidation is good compared to the copper catalysts.

Salavati-Niasari et al. reported the highest efficiency by Cu(II), Co(II) and Mn(II) catalysts supported on alumina for oxidation of cyclohexene in dichloromethane solvent [1]. Therefore, in order to investigate the effect of solvent on catalytic performance, the solvent was changed from acetone to dichloromethane whilst keeping the other conditions the same. The catalytic activity of the zeolite encapsulated catalyst **4** in the 1:2 molar ratio reaction of cyclohexene and H_2O_2 is 87. 33%, which is lower than the value of 90.47% obtained using acetone as the solvent. Similarly, the catalytic activity of the alumina supported catalyst **5** reduced from 37.99 to 34.78% when dichloromethane is used as the solvent instead of acetone. The solvent effect has also been investigated

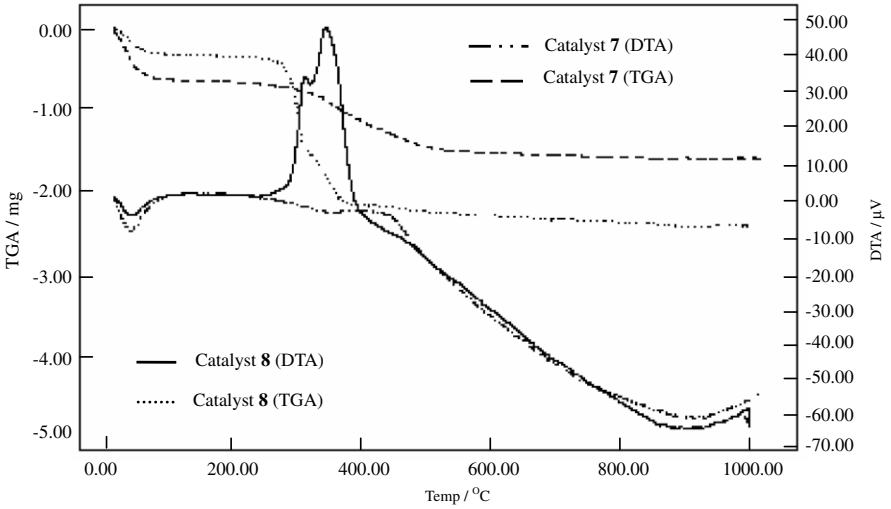
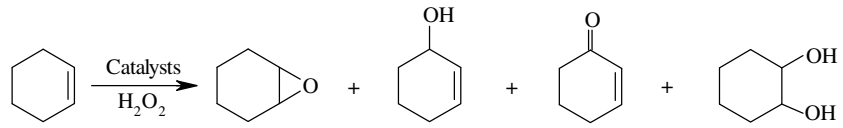


Fig. 11. DTA and TGA profile of [Co(N^O)$_2$]-AMPS (**7**) and [Cu(N^O)$_2$]-AMPS (**8**).



cyclohexene 1,2-epoxycyclohexane 2-cyclohexen-1-ol 2-cyclohexen-1-one 1,2-cyclohexanediol

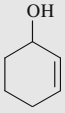
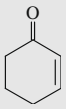
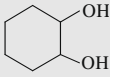
Scheme 5. Various oxidation products of cyclohexene.

Table 6
Catalytic activities towards the cyclohexene oxidation of some previously reported catalysts

Catalysts	Reaction time (h)	Reaction temp. (°C)	Catalysts amount	Oxidant	Conversion (%)	Ref.
VO(sal-dach)]–Y	6	75	0.035 g	H_2O_2	86.60	[6]
CuHq-AMPS	10	50	0.1 g	TBHP	96.00	[8]
[Mn(Me_2salpnMe_2)]–Al_2O_3	8	r.t.	1 g	TBHP	82.80	[1]
[Mn(mabenzil)/Al_2O_3	8	r.t	1.02×10^{-5} mol	TBHP	87.60	[10]
[Mn(salpnMe2)]–Al_2O_3	8	r.t	1 g	TBHP	78.40	[3]
[–CH_2{VO(sal-dach)·DMF}–]$_n$	6	75	0.015 g	TBHP	98.00	[13]

TBHP = *tert*-butylhydroperoxide.

Table 7
Catalytic oxidation of cyclohexene with H_2O_2 using catalysts **1–8**.

Cyclohexene:H_2O_2	Catalysts	Conversion (%)	Product selectivity (%)			
						
1:1	**1**	27.60	3.91	33.50	42.72	19.87
	2	43.50	2.85	25.96	58.13	13.06
	3	42.39 (38.32[a])	8.02	37.91	45.34	8.73
	4	34.65 (29.10[a])	0	26.35	64.16	9.49
	5	28.31(25.12[a])	14.46	28.69	46.47	10.38
	6	11.95 (9.23[a])	4.43	22.65	58.66	14.26
	7	37.89 (35.45[a])	0	41.22	53.74	5.04
	8	60.14 (57.46[a])	13.69	49.55	34.45	2.31
1:2	**1**	79.45	0	29.13	34.29	36.58
	2	70.41	0	17.46	51.42	31.12
	3	88.25 (77.52[a])	0	22.34	38.99	38.67
	4	90.47 (85.23[a])	0	42.36	51.00	6.64
	5	37.99 (34.76[a])	2.15	30.08	51.67	16.10
	6	28.86 (25.69[a])	1.44	31.35	49.12	18.09
	7	90.25 (86.11[a])	0	28.66	54.54	16.80
	8	85.99 (82.33[a])	9.42	49.65	31.87	9.06
1:3	**1**	78.25	0	42.66	46.11	11.23
	2	62.67	0	29.75	51.42	18.83
	3	84.21(76.90[a])	0.11	46.70	35.96	17.23
	4	84.03 (75.14[a])	0	31.39	42.36	26.25
	5	24.69 (21.34[a])	0	27.61	47.57	24.82
	6	17.39 (15.65[a])	0.53	21.51	51.04	26.92
	7	81.49 (79.77[a])	0	25.07	59.80	15.13
	8	81.23 (76.24[a])	0	29.41	49.86	20.73

[a] Activity after first reuse.

using a catalyst on a silica support using a 1:2 molar ratio of substrate and oxidant. The catalytic activity of the silica supported catalyst **7** is 86.34% in dichloromethane while it shows 90.25% activity in acetone. In each case, 2-cyclohexen-1-one and 1,2-epoxycyclohexane are found to be the major and minor products respectively, similar to the catalytic reactions run in acetone.

At the end of the heterogeneous reaction, the catalysts were recovered from the reaction mixture and washed thoroughly with solvent. The FT-IR spectral patterns of the recovered catalysts were quite similar to fresh catalysts, suggesting the purity and also the stoichiometry of the recovered catalysts. Under the similar conditions, the activity of the refreshed catalysts **3–8** after first cycle remains nearly the same as fresh catalysts (Table 7). Thus, high catalytic activities as well as other characteristics like stability, recycling ability and operational flexibility make the supported catalysts superior over neat complexes. A comparison of Tables 6 and 7 will justify the suitability of the investigated catalysts in the cyclohexene oxidation reaction.

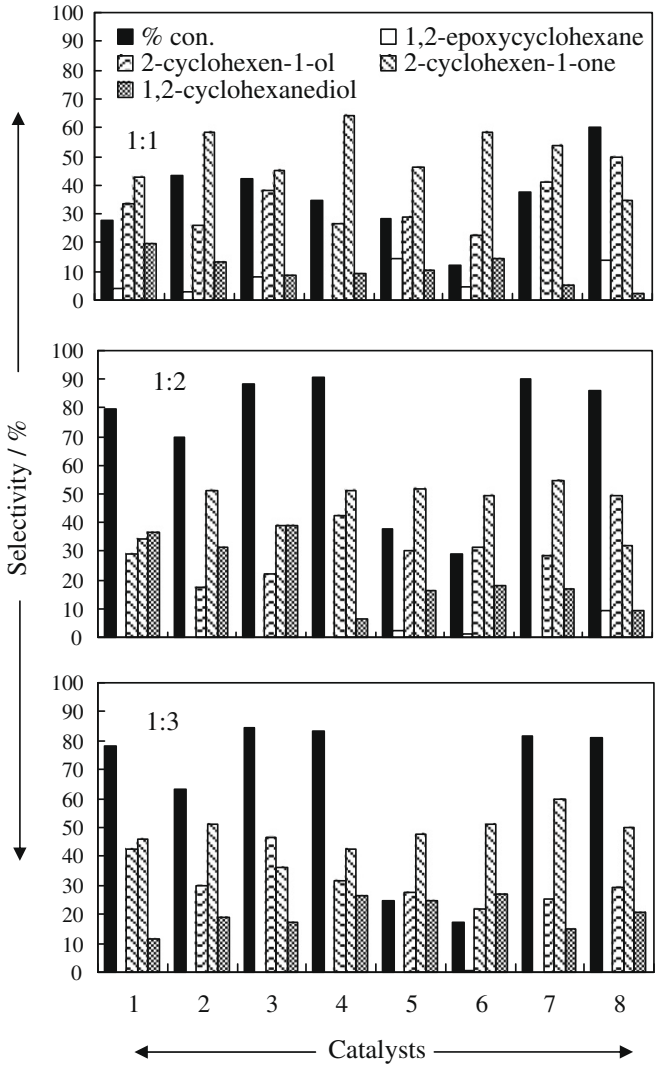


Fig. 12. Oxidation products distribution and total conversion with the catalysts **1–8** in 1:1, 1:2 and 1:3 molar ratio reactions of cyclohexene and H_2O_2.

4. Conclusions

The complexes $[Co(N^O)_2]$ and $[Cu(N^O)_2]$ have been supported on zeolite–Y, alumina and organically modified silica supports and their encapsulation or immobilization have been ensured by different studies. The catalytic activities of the complexes were tested for the oxidation of cyclohexene using H_2O_2 as the oxidant. A maximum of 90.47% cyclohexene conversion with 51.00% selectivity of 2-cyclohexen-1-one has been achieved with the catalyst $[Cu(N^O)_2]$–Y for a 1:2 molar ratio reaction between cyclohexene and H_2O_2. The heterogeneous catalysts $[Co(N^O)_2]$–Y, $[Cu(N^O)_2]$–Y, $[Co(N^O)_2]$–AMPS and $[Cu(N^O)_2]$–AMPS were found to exhibit higher catalytic activity compared to the corresponding neat complexes $[Co(N^O)_2]$ and $[Cu(N^O)_2]$. Oxidation occurs mainly at the allylic site, giving rise to 2-cyclohexen-1-one and 1,2-epoxycyclohexane as the major and minor products, respectively. The high percentage yield of the reactions in the presence of the cobalt complexes compared to the copper complexes seems promising.

Acknowledgements

The authors are thankful to the Tosoh Corporation and Catalytic Society of Japan for supplying zeolite–Y, alumina and silica supports. The authors also wish to record their sincere feelings of appreciation and gratitude to all the reviewers whose comments have helped in publishing this work.

Appendix A. Supplementary data

CCDC 691370 contains the supplementary crystallographic data for this paper. These data can be obtained free of charge via http://www.ccdc.cam.ac.uk/conts/retrieving.html, or from the Cambridge Crystallographic Data Centre, 12 Union Road, Cambridge CB2 1EZ, UK; fax: (+44) 1223-336-033; or e-mail: deposit@ccdc.cam.ac.uk. Supplementary data associated with this article can be found, in the online version, at doi:10.1016/j.poly.2008.10.063.

References

[1] M. Salavati-Niasari, P. Salemi, F. Davar, J. Mol. Catal. A Chem. 238 (2005) 215.
[2] S.G. Baca, M.T. Reetz, R. Goddard, I.G. Filippova, Y.A. Simonov, M. Gdaniec, N. Gerbeleu, Polyhedron 25 (2006) 1215.
[3] M. Salavati-Niasari, M. Hassani-Kabutarkhani, F. Davar, Catal. Commun. 7 (2006) 955.
[4] T. Katsuki, Coord. Chem. Rev. 101 (1995) 189.
[5] M. Salavati-Niasari, F. Davar, Inorg. Chem. Commun. 9 (2006) 304.
[6] M.R. Maurya, A.K. Chandrakar, S. Chand, J. Mol. Catal. A Chem. 270 (2007) 225.
[7] Y. Ukisu, A. Kazusaka, M. Nomura, J. Mol. Catal. 70 (1991) 165.
[8] E. Armengol, A. Corma, V. Fornes, H. Garcia, J. Primo, Appl. Catal. A Gen. 181 (1999) 305.
[9] M. Salavati-Niasari, H. Babazadeh-Arani, J. Mol. Catal. A Chem. 274 (2007) 58.
[10] S. Mukherjee, S. Samanta, A. Bhaumik, B.C. Ray, Appl. Catal. B Environ. 68 (2006) 12.
[11] L. Kevan, J.-S. Yu, Res. Chem. Intermed. 15 (1991) 67.
[12] A.O. Kuzmin, G.L. Elizarova, L.G. Matvienko, E.R. Savinova, V.N. Parmon, Mendeleev Commun. (1998) 211.
[13] M.R. Maurya, A. Kumar, J. Mol. Catal. A Chem. 250 (2006) 190.
[14] G.M. Sheldrick, SHELXTL Program for Refinement of Crystal Structure, University of Gottingen, Gottingen, Germany, 1997.
[15] M.E. de Mesquita, F.R.G. e Silva, R.Q. Albuquerque, R.O. Freire, E.C. da Conceicao, J.E.C. da Silva, N.B.C. Junior, G.F. de Sa, J. Alloy Compd. 366 (2004) 124.
[16] A.L. Magri, A.D. Magri, F. Balestrieri, E. Cardarelli, G. D'Ascenzo, Thermochim. Acta 38 (1980) 225.
[17] N.V. Loginova, T.V. Koval'chuk, R.A. Zhedakova, N.P. Osipovich, V.L. Sorokin, G.I. Polozov, G.A. Ksendzova, G.K. Glushonok, A.A. Chernyavskaya, O.I. Shadyro, Bioorg. Med. Chem. Lett. 16 (2006) 5403.
[18] M.R. Maurya, S. Sikarwar, T. Joseph, S.B. Halligudi, J. Mol. Catal. A Chem. 236 (2005) 132.
[19] M.R. Maurya, A.K. Chandrakar, S. Chand, J. Mol. Catal. A Chem. 274 (2007) 192.
[20] X. Tong, J. Xu, H. Miao, G. Yang, H. Ma, Q. Zhang, Tetrahedron 63 (2007) 7634.
[21] I. Nowak, M. Misiewicz, M. Ziolek, A. Kubacka, V. Cortés Corberán, B. Sulikowski, Appl. Catal. A Gen. 325 (2007) 328.
[22] M. Zimowska, A. Michalik-Zym, J. Połtowicz, M. Bazarnik, K. Bahranowski, E.M. Serwicka, Catal. Today 124 (2007) 55.
[23] Sumita N. Rao, N. Kathale, N.N. Rao, K.N. Munshi, Inorg. Chim. Acta 360 (2007) 4010.
[24] D. Yin, L. Qin, J. Liu, C. Li, Y. Jin, J. Mol. Catal. A Chem. 240 (2005) 40.

Polyhedron 28 (2009) 381–385

Contents lists available at ScienceDirect

Polyhedron

journal homepage: www.elsevier.com/locate/poly

Insertion of tin(II) bromide into Pt–X (X = Cl, Br) bond of dimethylplatinum(IV) complexes: A novel polymorphic form of [$PtBr_2$(bpy)]

Badri Z. Momeni [a,*], Zeinab Moradi [a], Mehdi Rashidi [b], Frank Rominger [c]

[a] Department of Chemistry, K.N. Toosi University of Technology, P.O. Box 16315-1618, Tehran 15418, Iran
[b] Department of Chemistry, College of Sciences, Shiraz University, Shiraz 71454, Iran
[c] Organisch-Chemisches Institut, Universität Heidelberg, D-69120 Heidelberg, Germany

ARTICLE INFO

Article history:
Received 27 September 2008
Accepted 5 November 2008
Available online 16 December 2008

Keywords:
Platinum
Tin
Oxidative addition
Insertion
Stacking

ABSTRACT

The platinum(II) complex [$PtMe_2$(bpy)] (bpy = 2,2′-bipyridine) reacted with a large excess of dihaloalkanes $X(CH_2)_nX$ (n = 1, X = Cl; n = 4, X = Br) to form the platinum(IV) complexes [$PtMe_2X\{(CH_2)_nX\}$(bpy)] (n = 1, X = Cl, **1a**; n = 4, X = Br, **1b**). The reaction of complexes **1a** and **1b** with $SnBr_2$ resulted in insertion of $SnBr_2$ into Pt–X (X = Cl, Br) bond to afford the trihalostannyl complexes [$PtMe_2(SnBr_2X)\{(CH_2)_nX\}$(bpy)] ($n$ = 1, X = Cl, **2a**; n = 4, X = Br, **2b**). The synthesis of such trihalostannylplatinum(IV) complexes is reported for the first time. The complex **2a** was decomposed in CH_2Cl_2 solution and single crystals of [$PtBr_2$(bpy)] (**3a**) were obtained. The X-ray structure determination of **3a** revealed a new polymorphic form of [$PtBr_2$(bpy)]. The molecules undergo a remarkable stacking along the *b*-axis to form a zigzag Pt···Pt···Pt chain containing both short (3.799 Å) and long (5.175 Å) Pt···Pt separations through the crystal. The crystal structure is compared to that of the yellow modification of [$PtBr_2$(bpy)].

© 2008 Elsevier Ltd. All rights reserved.

1. Introduction

Polymetallic complexes of tin and platinum are of particular interest because of their potential use in many catalytic processes such as olefin hydrogenation, isomerization and hydroformylation [1]. In this respect, much attention has been directed to the insertion of $SnCl_2$ into Pt–Cl bond of the dichloroplatinum(II) complexes [1–4]. Many studies on the role of $SnCl_2$ "co-catalyst" were reported, but its role is still uncertain [5]. There is a limited range of reported Pt–Sn complexes containing a mixture of halides at the same time [6,7]. We have recently reported the reaction of *cis* and *trans*-[$PtCl_2(SMe_2)_2$] with $SnBr_2$ to form *cis* and *trans*-[$PtBr_4(SMe_2)_2$] in which $SnBr_2$ acts as both oxidizing and bromination agent [8]. There are already several interesting examples of organoplatinum(IV) complexes containing stannyl group, for example, the reaction of trialkylplatinum(IV) complexes [$PtMe_2Cl$(R)(bpy)] (R = allyl, Me, benzyl) with $SnCl_2$ results in the formation of [$PtMe_2(SnCl_3)$(R)(bpy)] or the oxidative addition of tin(IV) halides to dimethylplatinum(II) complexes which yields [$PtMe_2(SnCl_3)Cl$(NN)], in which NN = bpy or bu_2bpy (bu_2bpy = 4, 4′-di-*tert*-butyl-2,2′-bipyridine) [9–11].

Dimethylplatinum(II) complexes undergo oxidative addition with different reagents, e.g. alkyl halides and dihaloalkanes leading to stable dimethylplatinum(IV) complexes [12–14]. These complexes have been shown to be precursors in the synthesis of new materials with novel properties [12]. There is no report on the reaction of organoplatinum(IV) complexes with $SnBr_2$. In the present study, the insertion of $SnBr_2$ into Pt–X (X = Cl, Br) bond of chloro and bromoalkyl complexes of dimethylplatinum(IV) are investigated.

There is much current interest in the formation of linear chains of square planar diimineplatinum(II) complexes in the solid state. The resulting stacks are often particularly topical due to the remarkable spectroscopic properties. These complexes are polymorphic and can be classified into three categories; monomers with no Pt···Pt interaction and two types of linear chains with platinum centers stacked along an axis to form dimers by predominantly either by Pt···Pt or π···π interaction [15]. It has been known that [$PtCl_2$(bpy)] forms both yellow and red solids. The red color of the latter is due to the very short separations (3.45 Å) while in the former, the molecules are widely separated [16]. We have recently reported the crystal structure of [$PtBr_2$(bpy)] which was isomorphous to the yellow modification of [$PtCl_2$(bpy)] [17]. We now obtained new yellow crystals of [$PtBr_2$(bpy)] adopting a third form, which is different from the red and yellow forms of [$PtCl_2$(bpy)].

2. Experimental

2.1. General remarks

All procedures were performed under an atmosphere of argon. Diethyl ether was distilled from sodium/benzophenone ketyl.

* Corresponding author. Tel.: +98 21 22850266; fax: +98 21 22853650.
E-mail address: momeni@kntu.ac.ir (B.Z. Momeni).

0277-5387/$ - see front matter © 2008 Elsevier Ltd. All rights reserved.
doi:10.1016/j.poly.2008.11.008

Acetone and the other reagents were used without further purification. Elemental analyses were performed by a Heraus CHN or Perkin–Elmer 2400 II elemental analyzer. NMR data were recorded using Bruker Avance DRX 500 or DPX 250 MHz spectrometers. All the chemical shifts and coupling constants are reported in ppm and Hz, respectively, with respect to residual solvent signal. The complex [$PtMe_2$(bpy)] was prepared according to the literature [18].

2.2. Synthesis of cis and trans-[$PtMe_2Cl(CH_2Cl)$(bpy)], **1a**

This complex was synthesized by a modified procedure of Kuyper [19]. A solution of [$PtMe_2$(bpy)] (60 mg, 0.16 mmol) in dichloromethane (15 mL) was stirred at room temperature for 24 h. The red solution turned pale yellow. The solvent was removed under the vacuum and the resulting pale yellow solid was washed with diethyl ether. Yield: 90%; m.p. 216–8 °C. *Anal.* Calc. for $C_{13}H_{16}Cl_2N_2Pt$: C, 33.5; H, 3.5; N, 6.0. Found: C, 33.5; H, 3.4; N, 6.0%. NMR data (500 MHz, $CDCl_3$): δ (^{1}H) (*trans* isomer) 1.36 [s, 6H, ^2J(PtH) = 69.8 Hz, Pt–Me]; 3.60 [s, 2H, ^2J(PtH) = 52.9 Hz, $PtCH_2$] and (*cis* isomer) 0.48 [s, 3H, ^2J(PtH) = 75.3 Hz, Pt–Me, *trans* to Cl]; 1.39 [s, 3H, ^2J(PtH) = 68.6 Hz, Pt–Me, *trans* to N]; 4.40 [d, 1H, ^2J(PtH) = 42.1 Hz, ^2J(HH) = 7.9 Hz, $PtCH_2$]; 4.80 [d, 1H, ^2J(PtH) = 90.3 Hz; ^2J(HH) = 7.9 Hz, $PtCH_2$]; bpy protons of *cis* and *trans* isomers 7.62 (m, H^5, $H^{5'}$); 8.03 (m, H^4, $H^{4'}$); 8.27 (m, H^3, $H^{3'}$); 8.97 (m, H^6); 9.36 (m, $H^{6'}$); δ (^{13}C) (*trans* isomer) −4.7 [s, ^1J(PtC) = 662 Hz, Pt–CH_3]; 23.5 [s, ^1J(PtC) = 867 Hz, $PtCH_2$]; bpy carbons 152.6 (C_2); 121.2 (C_3); 136.9 (C_4); 124.5 (C_5); 144.5 (C_6) and (*cis* isomer) −2.1 [s, ^1J(PtC) = 675 Hz, Pt–CH_3, *trans* to N]; 0.0 [s, ^1J(PtC) = 702 Hz, Pt–CH_3, *trans* to Cl]; 22.0 [s, ^1J(PtC) = 874 Hz, $PtCH_2$], bpy carbons 151.8, 152.8 (C_2, C_2'); 121.3, 121.5 (C_3, C_3'); 136.6, 137.2 (C_4, C_4'); 124.6, 124.7 (C_5, C_5'); 146.7, 144.8 (C_6, C_6', ^2J(PtC) = 16 Hz).

2.3. Synthesis of [$PtMe_2Br\{(CH_2)_4Br\}$(bpy)], **1b**

A solution of [$PtMe_2$(bpy)] (0.06 g, 0.16 mmol) in acetone (40 mL) was treated with an excess of 1,4-dibromobutane (0.5 mL). The reaction mixture was stirred for 8 h after which time a pale yellow solution had developed. The solvent was removed under vacuum and the resulting off white-yellow solid was crystallized from CH_2Cl_2/diethyl ether solution. Yield: 90 %; m.p. 205–7 °C. *Anal.* Calc. for $C_{16}H_{22}Br_2N_2Pt$: C, 32.2; H, 3.7; N, 4.7. Found: C, 32.0; H, 3.6; N, 4.8%. NMR data (250 MHz, $CDCl_3$): δ (^{1}H) (*trans* isomer) 1.38 [s, 6H, ^2J(PtH) = 70.1 Hz, Pt–Me]; 1.50 [t, 2H, ^2J(PtH) = 43.3 Hz, ^3J(HH) = 7.0 Hz, $PtCH_2$]; 0.63 [m, 2H, $PtCH_2CH_2$]; 1.27 [m, 2H, CH_2CH_2Br]; 3.08 [t, 2H, ^3J(HH) = 6.8 Hz, CH_2Br]; bpy protons 7.61 [t, $^4J(H^5H^3)$ = 0.9 Hz, H^5]; 7.97 [t, $^3J(H^4H^5)$ = 7.5 Hz, H^4]; 8.24 [d, $^3J(H^3H^4)$ = 8.1 Hz, H^3]; 8.89 [d, $^3J(H^6H^5)$ = 5.5, ^3J(PtH) = 12.0 Hz, H^6]; (*cis* isomer) 0.49 [s, 3H, ^2J(PtH) = 75.0 Hz, Pt–Me]; 1.41 [s, 3H, ^2J(PtH) not observed, Pt–Me]; 3.55 [t, 2H, ^3J(HH) = 7.0 Hz, CH_2Br]; δ (^{13}C) (*trans* isomer) −3.5 [s, ^1J(PtC) = 644 Hz, Pt–CH_3]; 17.9 [s, ^1J(PtC) = 697 Hz, Pt–CH_2]; 33.4 [s, ^2J(PtC) = 90 Hz, $PtCH_2CH_2$]; 28.7 [s, ^3J(PtC) = 29 Hz, CH_2CH_2Br]; 33.8 [s, ^4J(PtC) = 9 Hz, CH_2Br]; bpy carbons 155.0 (C_2); 123.8 (C_3); 139.1 (C_4); 127.0 (C_5); 147.1 (C_6).

2.4. Synthesis of cis and trans-[$PtMe_2(SnBr_2Cl)(CH_2Cl)$bpy)], **2a**

To a solution of a mixture of *cis* and *trans*-[$PtMe_2\{CH_2Cl\}$(bpy)Cl] (70 mg, 0.15 mmol) in dicholoromethane (10 mL) was added a solution of $SnBr_2$ (47 mg, 0.17 mmol) in THF (1 mL). The reaction mixture was stirred for 2 h under Ar atmosphere. The orange solution turned pale yellow. The solvent was removed at reduced pressure leaving a yellow solid. This was washed with *n*-hexane. Yield: 75 %; m.p. 134 °C. *Anal.* Calc. for $C_{13}H_{16}Br_2Cl_2N_2PtSn$: C, 21.0; H, 2.2; N, 3.8. Found: C, 21.1; H, 2.5; N, 3.5%. NMR data (500 MHz, $CDCl_3$): δ (^{1}H) (*trans* isomer) 1.45 [s, 6H, ^2J(PtH) = 68.9 Hz, ^3J(SnH) = 15.2 Hz, Pt–Me]; 3.56 [s, 2H, ^2J(PtH) = 51.5 Hz, ^3J(SnH) not observed, $PtCH_2$]; bpy protons 7.66 [t, $^3J(H^5H^4)$ = 6.2 Hz, H^5]; 8.08 [t, $^3J(H^4H^5)$ = 7.8 Hz, H^4]; 8.23 [d, $^3J(H^3H^4)$ = 8.0 Hz, H^3]; 8.90 [d, $^3J(H^6H^5)$ = 6.0 Hz, ^2J(PtH) = 20.0, H^6]; (*cis* isomer) 0.82 [s, 3H, ^2J(PtH) = 75.3 Hz, Pt–Me, *trans* to $SnBr_2Cl$]; 1.46 [s, 3H, ^2J(PtH) = 68.6 Hz, Pt–Me, *trans* to N]; 3.38 [s, 2H, ^2J(PtH) = 44.3 Hz, $PtCH_2$]; 9.39 [d, $H^{6'}$]. Single crystals of [$PtBr_2$(bpy)], **3a,** suitable for X-ray crystallographic study were obtained when the complex **2a** was remained in dichloromethane solution for two weeks.

2.5. Synthesis of cis and trans-[$PtMe_2(SnBr_3)\{(CH_2)_4Br\}$(bpy)], **2b**

Following the same procedure as for the preparation of **2a,** this was prepared similarly using [$PtMe_2Br\{(CH_2)_4Br\}$(bpy)] (78 mg, 0.13 mmol) and $SnBr_2$ (40 mg, 0.14 mmol). Yield: 70%; m.p. 139–140 °C. *Anal.* Calc. for $C_{16}H_{22}Br_4N_2PtSn$: C, 21.9; H, 2.5; N, 3.2. Found: C, 21.1; H, 2.5; N, 2.9%. ^{1}H NMR data (500 MHz, $CDCl_3$): δ (^{1}H) (*trans* isomer) 1.41 [s, 6H, ^2J(PtH) = 69.8 Hz, ^3J(SnH) = 23.9 Hz, Pt–Me]; 1.57 [m, 2H, $PtCH_2$]; 0.68 [m, 2H, $PtCH_2CH_2$]; 1.22 [m, 2H, CH_2CH_2Br]; 3.14 [t, 2H, ^3J(HH) = 6.7 Hz, CH_2Br]; bpy protons 7.67 [t, $^3J(H^5H^4)$ = 6.5 Hz, $^4J(H^5H^3)$ = 0.9 Hz, H^5]; 8.08 [t, $^3J(H^4H^5)$ = 8.1 Hz, H^4]; 8.24 [d, $^3J(H^3H^4)$ = 8.1 Hz, H^3]; 8.97 [d, $^3J(H^6H^5)$ = 5.5 Hz, ^3J(PtH) = 15.0 Hz, H^6]; (*cis* isomer) 0.54 [s, 3H, ^2J(PtH) = 74.4 Hz, ^3J(SnH) = 20.4 Hz, Pt–Me]; 1.45 [s, 3H, ^2J(PtH) not observed, Pt–Me]; 3.58 [t, 2H, ^3J(HH) = 7.1 Hz, CH_2Br]; δ (^{119}Sn) in $CH_2Cl_2 \cdot THF \cdot CDCl_3$: −485 [s, $^1J(^{195}Pt–^{119}Sn)$ = 22355 Hz].

2.6. X-ray structure determination

A yellow plate shaped crystal, air stable at room temperature was used for the crystallographic measurements. The measurements on crystals of **3a** were performed on a Bruker APEX CCD area detector using Mo Kα radiation (λ = 0.71073 Å) covering a whole sphere in reciprocal space. Intensities were corrected for Lorentz and polarization effects. An empirical absorption correction was applied using SADABS based on the Laue symmetry of the reciprocal space [20]. The structure was solved by direct methods and refined against F^2 with a Full-matrix least-squares algorithm using the SHELXTL-plus V 6.10 software package [21]. The hydrogen atoms were treated using appropriate riding models. The crystallographic data are listed in Table 1.

3. Results and discussion

3.1. Oxidative addition of dihaloalkanes to [$PtMe_2$(bpy)]

The reaction of [$PtMe_2$(bpy)] with a large excess of dihaloalkanes $X(CH_2)_nX$ (n = 1, X = Cl; n = 4, X = Br), as illustrated in Scheme 1, gave the platinum(IV) products with a general formula [$PtMe_2X\{(CH_2)_nX\}$(bpy)] (n = 1, X = Cl, **1a**; n = 4, X = Br, **1b**) in high yield. Complex [$PtMe_2Cl(CH_2Cl)$(bpy)], **1a**, was characterized as described elsewhere [19,22]. NMR data indicate that the complex **1a** has formed as a mixture of *cis* and *trans* isomers in an approximately 1.2:1 ratio.

The complex [$PtMe_2Br\{(CH_2)_4Br\}$(bpy)], **1b**, was fully characterized by ^{1}H and ^{13}C NMR spectroscopy. NMR data show that complex **1b** is predominately formed as *trans* isomer with a trace amount of the *cis* isomer. The ^{1}H NMR spectrum of complex **1b** in $CDCl_3$ solution contained a signal at δ = 1.38 accompanying with platinum satellites with ^2J(Pt–H) = 70.1 Hz which was assigned to the protons of the methyl groups of the *trans* isomer of complex **1b**, whereas the less symmetrical complex (*cis* isomer) gave two signals at δ = 0.49 with ^2J(Pt–H) = 75.0 Hz and δ = 1.41 which its platinum satellites could not be resolved. The characteristic triplet

Table 1
Experimental details, crystal data and refinement parameters for complex **3a**.

Empirical formula	$C_{10}H_8Br_2N_2Pt$
Formula weight (g/mol)	511.09
Temperature (K)	200(2)
Wavelength (Å)	0.71073
Crystal system	Monoclinic
Space group	$P2_1/n$
Z	4
a (Å)	9.0527(7)
b (Å)	7.3876(6)
c (Å)	17.0156(13)
β (°)	98.068(2)
Volume (Å^3)	1126.70(15)
D_{calc} (g/cm^3)	3.01
Absorption coefficient (mm^{-1})	19.51
Crystal shape	Plate
Crystal size (mm)	0.23 × 0.16 × 0.01
θ range (°)	2.4–28.3
Index ranges	$-12 \leqslant h \leqslant 12$, $-9 \leqslant k \leqslant 9$, $-22 \leqslant l \leqslant 22$
Reflections collected	11 369
Independent reflections [R_{int}]	2797 [0.0543]
Observed reflections	2539 ($I > 2\sigma(I)$)
Absorption correction	Semi-empirical from equivalents
Maximum/minimum transmission	0.83, 0.09
Data/restraints/parameters	2797/0/136
Goodness-of-fit on F^2	1.07
R_1, wR_2 [$I > 2\sigma(I)$]	0.030, 0.075
Largest differences in peak, hole(e Å^{-3})	1.39, −1.21

in the region δ = 3.08 with ^3J(HH) = 6.8 Hz was assigned to the protons of CH_2Br while the $PtCH_2$ protons centered as a triplet at δ = 1.50 with ^2J(Pt–H) = 43.3 Hz. Furthermore, the $PtCH_2CH_2$ and CH_2CH_2Br protons appeared as the multiplets at δ = 0.63 and 1.27, respectively. A small triplet at δ = 3.55 with ^3J(HH) = 7.0 Hz was assigned tentatively to the CH_2Br resonance of the trace of the *cis* isomer. The ^{13}C NMR spectrum of the *trans* isomer of complex **1b** shows a signal at δ = −3.5 with diagnostic ^1J(Pt–C) = 644 Hz in agreement with the symmetry of the product while the carbon atom of Pt–CH_2 group resonated at δ = 17.9 with ^1J(Pt–C) = 697 Hz. The remaining assignments for haloalkyl chain are made on the basis of the magnitude of Pt–C coupling constants, assuming that the coupling decreases the further the carbon is from the platinum. The assignment for bpy ligand was made according to the closely related analogues [13–14]. Full data for **1a**–**1b** are collected in Section 2.

3.2. Insertion of $SnBr_2$ into Pt–X (X = Cl, Br) bond of *1a*–*1b*

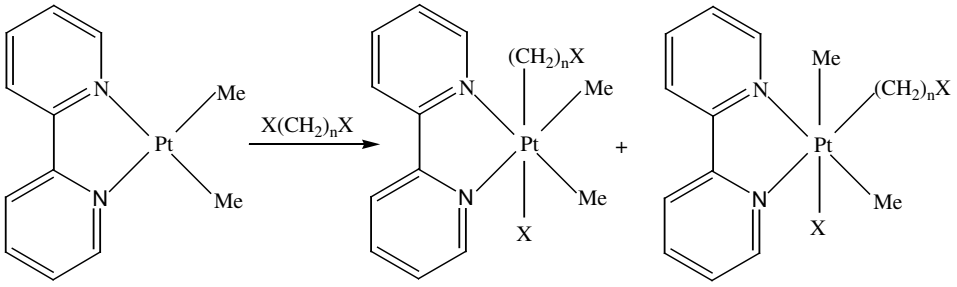
Addition of a tetrahydrofurane solution of $SnBr_2$ to a dichloromethane solution of **1a** or **1b** gave complexes **2a** or **2b**, respectively, as yellow solids (Eq. (1)). NMR data show that complex **2a** exists as a mixture of *cis* and *trans* isomers in an approximately 1:7 ratio while in the case of **2b**, only a trace of the *cis* isomer was observed. It is probable that the steric effects due to the $SnBr_2X$ and $(CH_2)_nX$ ligands do not favor them to be located in *cis* position to each other. Therefore, in the case of **2a**, a mixture of isomers are obtained with the *trans* isomer being formed predominantly while for **2b** having two bigger ligands $SnBr_3$ and $(CH_2)_4Br$, only a trace of the *cis* isomer is formed.

$$\mathbf{1a{-}1b} \xrightarrow{SnBr_2} cis \text{ and } trans - [PtMe_2(SnBr_2X)\{(CH_2)_nX\}(bpy)] \quad \begin{matrix} n = 1, X = Cl & \mathbf{2a} \\ n = 4, X = Br & \mathbf{2b} \end{matrix} \tag{1}$$

The complex **2a** was identified by elemental analysis. The complex **2a** was slowly decomposed in $CDCl_3$ solution. The ^{1}H NMR spectrum of a freshly prepared solution of complex **2a** contained a singlet at δ = 1.45 accompanying with platinum satellites ^2J(Pt–H) = 68.9 with ^3J(SnH) = 15.2 Hz which was assigned to the protons of the methyl groups of *trans*-[$PtMe_2(SnBr_2Cl)(CH_2Cl)$(bpy)], **2a**. The *cis* isomer gave two singlets at δ = 0.82 and 1.46 showing platinum satellites with ^2J(Pt–H) = 75.3 (*trans* to $SnBr_2Cl$) and 68.6 Hz (*trans* to N), respectively. This confirms that the N ligating atoms of bpy ligand has a higher *trans* influence than the $SnBr_2Cl$ group. The CH_2 protons of the *cis* and *trans* isomers of **2a** appeared as singlets at δ = 3.38 and 3.56 ppm with ^2J(Pt–H) = 44.3 and 51.5 Hz, respectively. The complex **2a** was decomposed in CH_2Cl_2 solution and single crystals of [$PtBr_2$(bpy)] (**3a**) were obtained after two weeks.

The complex **2a** has a very low solubility and decomposes in polar solvents, e.g. acetone or nitromethane, and thus no satisfactory ^{119}Sn NMR spectrum could be obtained.

The identity of complex **2b** was established by elemental analysis, ^{1}H and ^{119}Sn NMR spectroscopy. Complex **2b** has very low solubility in different solvents and so its ^{119}Sn NMR spectrum was obtained using an *in situ* solution. The NMR sample was prepared directly in the NMR tube by adding a tetrahydofurane solution of $SnBr_2$ to a dichloromethane solution of **1b** with an approximately 1:1.1 mole ratio of Pt:Sn. The ^{119}Sn NMR spectrum of **2b** reveals a central resonance at δ = −485 flanked by ^{195}Pt satellites with $^1J(^{195}Pt-^{119}Sn)$ = 22 355 Hz which is very close to the reported value for [$PtClMe_2(SnCl_3)(bu_2bpy)$] ($\delta$ = −402 with $^1J(^{195}Pt-^{119}Sn)$ = 25 864 Hz) [11]. The presence of platinum satellites in the ^{119}Sn NMR indicates that the platinum–tin bond is maintained in solution. Moreover, there were several weak signals at δ = −56, −57 and −89 ppm which are tentatively assigned to the halogen scrambling between $SnBr_2$ and chlorinated solvents. This complex



trans isomer *cis* isomer

n = 1, X = Cl **1a**
n = 4, X = Br **1b**

Scheme 1.

represents the first example of tribromostannylplatinum(IV) complex which has been prepared through $SnBr_2$ insertion into the Pt–Br bond.

3.3. Description and discussion of the crystal structure of *3a*

Selected bond lengths and angles are given in Table 2. The crystal structure of complex **3a,** which shows that the platinum center adopts the expected square planar geometry, is given in Fig. 1. The average deviation from the coordination plane is only 0.01 Å. In the crystal structure of complex **3a** (form **A**), two inequivalent Pt–Br distances (2.411 and 2.413 Å) and two inequivalent Pt–N distances (2.017 and 2.021 Å) are noted in contrast to the yellow modification of [$PtBr_2$(bpy)] (form **B**) which has 2 equiv. Pt–Br and 2 equiv. Pt–N bonds (2.414 and 2.017 Å, respectively) [17]. The Pt–N bond lengths are between 2.029 Å in [PtI_2(bpy)] [23] and 2.001 Å in the red form of [$PtCl_2$(bpy)] [24] or 2.006 and 2.011 Å in the yellow form of [$PtCl_2$(bpy)] [16]. This is in accordance with the *trans* influence of halogens which increases in the order of Cl < Br < I [25].

The N–Pt–N and Br–Pt–Br angles are 80.48 and 88.80°, respectively, which are consistent with the previously reported values for form **B** which are 80.54 and 88.93°, respectively [17]. The platinum–platinum vector in the form **A** inclines only by 25.1° with respect to the perpendicular of the coordination plane but it is inclined by 48.6° in the form **B.** This is the major difference of both forms and leads to significantly different Pt–Pt and bpy–bpy distances. Interestingly, in the new polymorph **A**, the flat molecules stack in the *b* direction in a head to tail fashion with two different Pt···Pt distances (see Fig. 2). In this arrangement, the short Pt···Pt distance is 3.80 Å. As mentioned before, the platinum atoms are not placed orthogonal on top of one another. Instead of they are shifted 1.19 Å in the direction towards the bipyridine ligand and 0.58 Å sidewards. Most of the reported values for Pt···Pt interaction is in the range of 3.09–3.40 Å [24]. The Pt···Pt separation is too long to support a significant metal–metal interaction. The corresponding separation between the parallel bipyridine ligand planes is 3.27 Å. However, the bipyridine moieties are anti to each other and they are not overlapping. The second Pt···Pt distance is much longer (5.175 Å). In return for these stacking contacts, there

Table 2
Selected bond lengths (Å) and angles (°) for complex **3a**.

Pt1–N11	2.017(5)
Pt1–N21	2.021(5)
Pt1–Br2	2.4110(7)
Pt1–Br1	2.4131(7)
N11–C16	1.340(8)
N11–C12	1.351(8)
C12–C13	1.396(8)
C12–C22	1.444(8)
C13–C14	1.393(9)
C14–C15	1.352(11)
C15–C16	1.385(10)
N11–Pt1–N21	80.48(19)
N11–Pt1–Br2	95.32(14)
N21–Pt1–Br2	175.74(14)
N11–Pt1–Br1	175.43(14)
N21–Pt1–Br1	95.38(14)
Br2–Pt1–Br1	88.80(3)
C16–N11–C12	119.4(5)
C16–N11–Pt1	126.3(4)
C12–N11–Pt1	114.3(4)
N11–C12–C13	121.1(6)
N11–C12–C22	115.8(5)
C13–C12–C22	123.2(6)
C14–C13–C12	118.7(6)
C15–C14–C13	119.3(6)
C14–C15–C16	120.1(7)
N11–C16–C15	121.5(7)

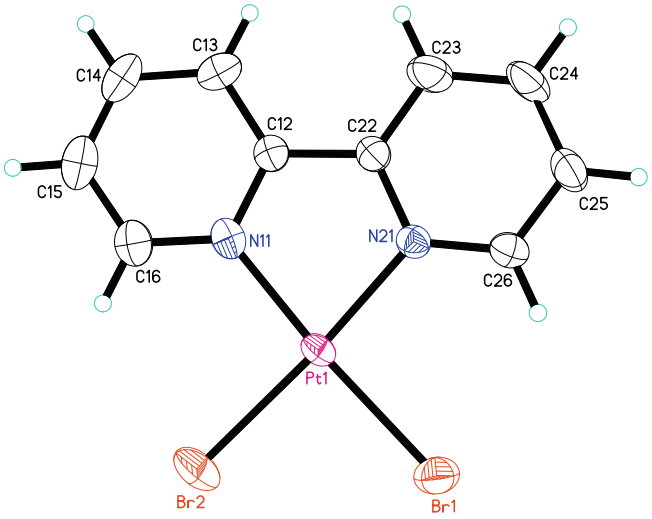


Fig. 1. ORTEP diagram for [$PtBr_2$(bpy)] (**3a**).

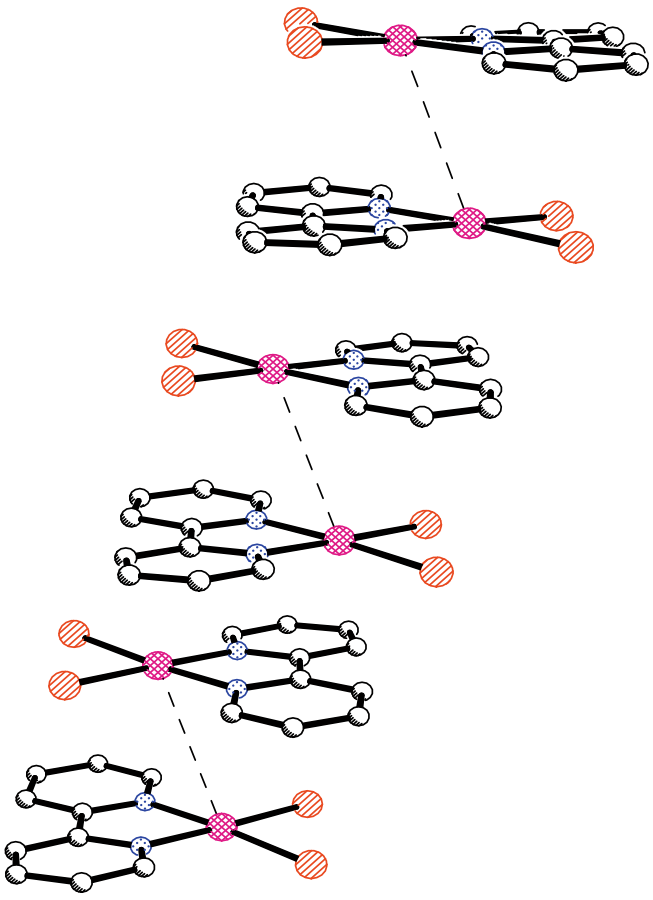


Fig. 2. Crystal packing of [$PtBr_2$(bpy)] (**3a**), the stacking occurs along the *b*-axis.

are partially overlapping bipyridine groups with a distance between the parallel planes of 3.640 Å. In the form **B**, there was a repeat of platinum units with symmetry equivalent contacts, stacking along the crystallographic *c* axis. Moreover, the distances between two planes were 3.400 Å and the Pt centers were 5.164 Å apart [17]. The modification of complex [$PtBr_2$(bpy)], presently investigated, has a crystallographic density (3.01 g/cm^3) which is slightly lower than that of the reported value of form **B** (3.14 g/cm^3) which is consistent with the concept that the form

A has a less efficient mode of packing compared to the form **B**. The red form [$PtCl_2$(bpy)] also has a lower density (D_{calc} = 2.56 g/cm^3) as compared to the yellow form (D_{calc} = 2.65 g/cm^3). It was found that the red form has a lower stability compared to the yellow form and could easily be converted to the latter at room temperature [16,24].

The interaction between bpy ligands is preferred in the yellow form of [$PtCl_2$(bpy)] but in the red form, interaction between platinum atoms is privileged [16,24]. It has been known that the ligand electronics and sterics play the significant roles in Pt···Pt stacking [26]. The formation of a short Pt···Pt distance in form **A** is probably inhibited due to the bromine ligands being rather bulkier than chlorine atoms.

Acknowledgements

We thank the Science Research Council of K.N. Toosi University of Technology for financial support. We also wish to thank Johnson Matthey for a generous loan of platinum salt.

Appendix A. Supplementary data

CCDC 698981 contains the supplementary crystallographic data for this paper. These data can be obtained free of charge via http://www.ccdc.cam.ac.uk/conts/retrieving.html, or from the Cambridge Crystallographic Data Centre, 12 Union Road, Cambridge CB2 1EZ, UK; fax: (+44) 1223-336-033; or e-mail: deposit@ccdc.cam.ac.uk. Supplementary data associated with this article can be found, in the online version, at doi:10.1016/j.poly.2008.11.008.

References

[1] M.S. Holt, W.L. Wilson, J.H. Nelson, Chem. Rev. 89 (1989) 11.
[2] C. Deibele, A.B. Permin, V.S. Petrosyan, J. Bargon, Eur. J. Inorg. Chem. (1998) 1915.
[3] B.Z. Momeni, M.M. Amini, T. Pape, F.E. Hahn, S.W. Ng, J. Mol. Struct. 697 (2004) 97.
[4] B.Z. Momeni, L. Jalili Baleh, S. Hamzeh, F. Rominger, J. Coord. Chem. 60 (2007) 285.
[5] M. Gómez, G. Muller, D. Sainz, J. Sales, X. Solans, Organometallics 10 (1991) 4036.
[6] L. Kollár, T. Kégl, J. Bakos, J. Organomet. Chem. 453 (1993) 155.
[7] E. Farkas, L. Kollár, M. Moret, A. Sironi, Organometallics 15 (1996) 1345.
[8] B.Z. Momeni, Z. Moradi, L. Dianati, K. Shahverdi, J. Coord. Chem. (2008), doi:10.1080/00958970802244950.
[9] S.H.L. Thoonen, M. Lutz, A.L. Spek, B.-J. Deelman, G. van Koten, Organometallics 22 (2003) 1156.
[10] J. Kuyper, Inorg. Chem. 16 (1977) 2171.
[11] M.C. Janzen, M.C. Jennings, R.J. Puddephatt, Organometallics 20 (2001) 4100.
[12] L.M. Rendina, R.J. Puddephatt, Chem. Rev. 97 (1997) 1735.
[13] M. Rashidi, B.Z. Momeni, J. Organomet. Chem. 574 (1999) 286.
[14] S.M. Nabavizadeh, S.J. Hoseini, B.Z. Momeni, N. Shahabadi, M. Rashidi, A.H. Pakiari, K. Eskandari, Dalton Trans. (2008) 2414.
[15] V.H. Houlding, V.M. Miskowski, Coord. Chem. Rev. 111 (1991) 145.
[16] R.H. Herber, M. Croft, M.J. Coyer, B. Bilash, A. Sahiner, Inorg. Chem. 33 (1994) 2422.
[17] B.Z. Momeni, S. Hamzeh, S.S. Hosseini, F. Rominger, Inorg. Chim. Acta 360 (2007) 2661.
[18] P.K. Monagan, R.J. Puddephatt, Organometallics 3 (1984) 444.
[19] J. Kuyper, Inorg. Chem. 17 (1978) 77.
[20] G.M. Sheldrick, SADABS 2008/1, Bruker Analytical X-ray-Division, Madison, Wisconsin, 2008.
[21] G.M. Sheldrick, SHELXTL V 6.10, Acta Crystallogr. A64 (2008) 112.
[22] P.K. Monaghan, R.J. Puddephatt, Organometallics 4 (1985) 1406.
[23] W.B. Connick, H.B. Gray, Acta Crystallogr., Sect. C 50 (1994) 1040.
[24] R.S. Osborn, D. Rogers, J. Chem. Soc., Dalton Trans. (1974) 1002.
[25] T.G. Appleton, H.C. Clark, L.E. Manzer, Coord. Chem. Rev. 10 (1973) 335.
[26] S. Achar, V.J. Catalano, Polyhedron 16 (1997) 1555.

Polyhedron 28 (2009) 393–397

Contents lists available at ScienceDirect

Polyhedron

journal homepage: www.elsevier.com/locate/poly

Copper(II) complexes of a biphenyl-based ligand: Tuning the needs of the metal with those of the ligand

Mitchell R. Malachowski [a,*], Ashraf S. Kasto [a], Mark E. Adams [a], Arnold L. Rheingold [b], Lev N. Zakharov [b], Lawrence D. Margerum [c], Matthew Greaney [c]

[a] Department of Chemistry and Biochemistry, University of San Diego, San Diego, CA 92110, USA
[b] Department of Chemistry and Biochemistry, University of California, San Diego, La Jolla, CA 92093, USA
[c] Department of Chemistry, University of San Francisco, San Francisco, CA 94117, USA

ARTICLE INFO

Article history:
Received 11 August 2008
Accepted 14 November 2008
Available online 2 January 2009

Keywords:
Copper complexes
Biological models
Copper proteins
Pyrazole
Ligand decomposition

ABSTRACT

The novel pyrazole-containing tetradentate ligand 2,2′-bis[[(3,5-dimethylpyrazol-1-yl)methyl]amino]-1,1′-biphenyl (N_4-mpz), **1**, was synthesized and three Cu(II) complexes, **2**–**4**, were prepared from this compound. These complexes were characterized by a combination of elemental analysis, FAB-MS and electrochemistry and were shown to have the structure of [Cu(N_4-mpz)(Pz)]X_2 where X = BF_4 or ClO_4 or [Cu(N_4-mpz)(Cl)]Cl. The X-ray structure of [Cu(N_4-mpz)(Pz)] $(ClO_4)_2 \cdot CH_3OH$, **2**, was determined and it showed the Cu(II) coordinated by the four nitrogen donors from the ligand along with an exogenous pyrazole donor that had been extracted from another molecule of the ligand. Cyclic voltammetry studies indicated that the complexes undergo quasi-reversible one-electron reductions in acetonitrile at potentials between 396 and 422 mV versus Ag/AgCl.

© 2008 Elsevier Ltd. All rights reserved.

1. Introduction

Defining the geometry around a metal ion by using the steric and electronic aspects of ligand sets is a powerful way to generate new and interesting metal complexes. Prudent choice of the electronic and steric features of the donor sets can lead to an immense assortment of metal complexes. We currently are interested in tetradentate ligands as they can be designed from a tremendous variety of motifs and can lead to a vast number of different structures. Using tetradentate ligands, four coordinate metal complexes can be produced that range from tetrahedral to square planar while five-coordinate species cover the spectrum from square pyramidal to trigonal bipyramidal geometries. Much of our inspiration for the preparation of these complexes comes from the variety of structures found in biological systems. As one example, Cu(II) complexes coordinated to multidentate heterocyclic amine donors are found in the type 3 copper proteins hemocyanin and tyrosinase [1–4]. Through the preparation of multidentate ligands, numerous complexes have been prepared and their properties compared to the biological systems [5–7].

We particularly are interested in exploiting the properties of the biphenyl moiety in designing tetradentate ligands as these ligands can be designed to force metal ions into specific geometries in their resultant metal complexes [8]. In the parent biphenyl, the two aromatic rings are not co-planar but rather have a dihedral angle between the rings of 42° [9]. This will force the substituents on the adjacent rings out of plane and any coordinated metal ion will become more tetrahedral-like and less planar-based. Since metals which have Jahn–Teller distortions present (such as Cu(II)) prefer planar-based geometries, complexes formed from these biphenyl-based ligands with metals such as Cu(II) will have to balance the tension between the preferences of the ligand set with those of the metal ion.

We are involved in a systematic study of the impact of structural changes on the physical and chemical properties of synthetic Cu(II) complexes in order to better understand these natural systems [10–13]. We published the results obtained for a biphenyl-based ligand with N_2S_2 donors that spontaneously reduced Cu(II) to Cu(I) upon complexation while a similar N_4 ligand remained in the Cu(II) form [11]. These results confirmed that in order for the spontaneous reduction to occur, the presence of the sulfur donors and the biphenyl rings were essential. We wanted to explore further this premise so we have prepared other tetradentate biphenyl-based ligands with a variety of donor sets. In this work, we report the synthesis of the new ligand, 2,2′-bis[[(3,5-dimethylpyrazol-1-yl)methyl]amino]-1,1′-biphenyl (N_4-mpz). The synthesis and characterization of Cu(II) complexes from this ligand of the type [Cu(N_4-mpz)(Pz)]X_2 where X = BF_4 or ClO_4 and [Cu(N_4-mpz)(Cl)]Cl are presented along with their spectroscopic and electrochemical properties. The molecular structure of [Cu(N_4-mpz)(Pz)]

* Corresponding author.
E-mail address: malachow@sandiego.edu (M.R. Malachowski).

0277-5387/$ - see front matter © 2008 Elsevier Ltd. All rights reserved.
doi:10.1016/j.poly.2008.11.034

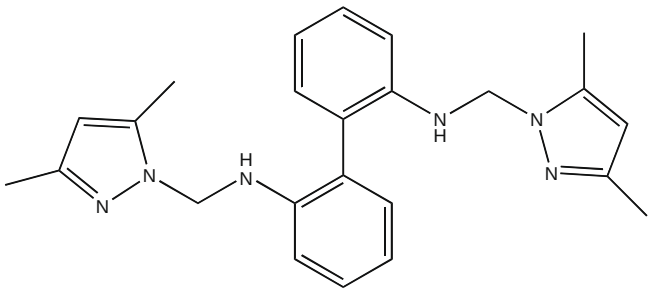


Fig. 1. N_4-mpz ligand.

$(ClO_4)_2 \cdot CH_3OH$ has been determined and comparisons to the pyridine analog explored (Fig. 1).

2. Experimental

Unless otherwise noted, all solvents and reagent grade starting materials were used as received from commercial sources (Aldrich/Sigma). The solvents used for electrochemistry (methanol and acetonitrile) were spectroscopic grade from Aldrich and were dried using activated molecular sieves. Elemental analyses were performed by Oneida Research Services. $^1H/^{13}C$ NMR spectra were recorded on a Varian FT-NMR spectrometer running at 400 MHz. FAB-MS was run at the Midwest Center for Mass Spectrometry in Lincoln, NE.

Cyclic voltammetry (CV) and differential pulse voltammetry (DPV) data were collected using a PAR Model 283 potentiostat and PowerCV electrochemical analysis software. The three-electrode system consisted of a glassy carbon disc electrode, a platinum wire counter electrode and an Ag/AgCl reference electrode (BAS, West Lafayette, IN). The electrodes were polished with alumina on microcloth pads, washed with distilled water, sonicated for five minutes in water and washed with acetone. All solutions were 1–2 mM in **2**–**4** using spectroscopic grade methanol (Aldrich, dried with activated molecular sieves) that contained 100 mM tetrabutylammonium hexafluorophosphate (TBAH, 99%, Aldrich) as the supporting electrolyte. Prior to scanning, all solutions were deoxygenated with methanol-saturated argon for roughly 10 min. All potentials were scaled to the Ag/AgCl electrode (+0.194 V from NHE). Peak currents and peak potentials were estimated with the PowerCV peak analysis software. Using this electrode system, the $E_{1/2}$ of ferrocene was 0.45 V (CH_3CN/0.1 M TBAH).

Caution: Although there were no incidents in our laboratory, transition metal perchlorates may explode violently. They should be prepared in small quantities and handled with care.

2.1. Preparation of 2,2′-bis[[(3,5-dimethylpyrazol-1-yl)-methyl]amino]-1,1′-biphenyl (**1**)

To 2.0 g (15.8 mmol) of 1-hydroxymethyl(3,5-dimethyl)pyrazole in 100 ml of acetonitrile was added 1.396 g (7.92 mmol) of 2,2′-diaminobiphenyl. The solution was stirred at room temperature for 72 h. The solution was reduced under reduced pressure. The resultant oil was crystallized from ethyl acetate/hexanes to give white crystals which were collected by filtration and washed with cold hexanes. Yield, 2.18 g (68.8%), m.p. 106–107 °C. ^1H NMR (400 MHz, $CDCl_3$); δ 2.10 (s, 6H), 2.11 (s, 6H), 4.20 (broad s, 2H), 5.32 (d, 4H), 5.72 (s, 2H), 6.83–7.23 (m, 8H). ^{13}C NMR (400 MHz, $CDCl_3$); δ 149.0, 146.2, 140.3, 128.8, 128.5, 118.2, 117.8, 115.3, 103.2, 50.2, 17.3, 14.3. *Anal.* Calc. for $C_{24}H_{28}N_6$: C, 71.97; H, 7.06; N, 20.97. Found: C, 71.64; H, 6.88; N, 20.68%.

2.2. Preparation of $[Cu(N_4\text{-mpz})(Pz)](ClO_4)_2 \cdot CH_3OH$ (**2**)

To 0.10 g (0.25 mmol) of **1** in 10 ml of MeOH was added a solution of 0.0925 g (0.25 mmol) of $Cu(ClO_4)_2 \cdot (H_2O)_6$ in 10 ml of MeOH. The mixture immediately turned green. The solution was cooled to 0° from which green crystals appeared overnight. The crystals were collected and washed with cold MeOH. Yield, 0.075 g (38.0%). *Anal.* Calc. for $C_{30}H_{39}Cl_2CuN_8O_9$: C, 45.60; H, 4.99; N, 14.17; Cu, 8.04. Found: C, 45.93; H, 5.15; N, 13.88, Cu, 8.22%. FAB-MS (*m*/*z*, %): 562 (26), 463 (68), 367 (100), 317 (15), 271 (66), 209 (10), 159 (24).

2.3. Preparation of $[Cu(N_4\text{-mpz})(Pz)](BF_4)_2 \cdot CH_3OH$ (**3**)

To 0.10 g (0.25 mmol) of the N_4-mpz ligand in 10 ml of MeOH was added a solution of 0.086 g (0.25 mmol) of $Cu(BF_4)_2 \cdot (H_2O)_6$ in 10 ml of MeOH. The mixture immediately turned green. The solution was cooled to 0° from which green crystals appeared over 48 h. The crystals were collected and washed with cold MeOH. Yield, 0.079 g (41.5%). *Anal.* Calc. for $C_{30}H_{39}B_2CuF_8N_8O$: C, 47.10; H, 5.15; N, 14.64; Cu, 8.31. Found: C, 47.50; H, 5.22; N, 14.71; Cu, 8.57%. FAB-MS (*m*/*z*, %): 646 (12), 550 (20), 463 (68), 366 (74), 307 (30), 271 (46), 180 (18), 154 (100).

2.4. Preparation of $[Cu(N_4\text{-mpz})(Cl)]Cl$ (**4**)

To 0.10 g (0.25 mmol) of the N_4-mpz ligand in 10 ml of MeOH was added a solution of 0.043 g (0.25 mmol) of $CuCl_2 \cdot 2H_2O$ in 10 ml of MeOH. The mixture immediately turned pale green. The solution was cooled to 0° from which green crystals appeared over 7 days. The crystals were collected and washed with cold MeOH. Yield, 0.049 g (36.5%). *Anal.* Calc. for $C_{24}H_{28}Cl_2CuN_6$: C, 53.88; H, 5.29; N, 15.70; Cu, 11.88. Found: C, 53.65; H, 5.20; N, 15.53; Cu, 12.03%. FAB-MS (*m*/*z*, %): 498 (38), 463 (45), 367 (62), 271 (23), 154 (100).

2.5. X-ray crystallographic analysis

Single crystals of compound **2** were mounted on quartz capillaries by using paratone oil and were cooled in a nitrogen stream on the diffractometer. Data were collected on a Bruker P4 diffractometer with an APEX area detector. Peak integrations were performed with the Bruker SAINT software package. Absorption corrections were applied using the program SADABS. Space group determinations were performed by the program XPREP. The structure was solved by direct methods and refined with the SHELXTL software package [14]. Hydrogen atoms were fixed at calculated positions or located from difference maps and refined with isotropic thermal parameters, and all non-hydrogen atoms were refined anisotropically unless otherwise noted.

3. Results and discussion

Pyrazole donors have found extensive use in a variety of multidentate ligands coordinated to metal ions [15,16]. The ligand 2,2′-bis[[(3,5-dimethylpyrazol-1-yl)methyl]amino]-1,1′-biphenyl (N_4-mpz) was synthesized using the reaction between a primary amine and 1-hydroxymethyl(3,5-dimethyl)pyrazol-1-ylmethyl. In this case, only one pyrazolylmethylene arm adds to each 1° amine probably as a result of the precipitation of the product as it is formed under the reaction conditions used. Further condensation of the N_4-mpz ligand with 2-picolylchloride or other aromatic amines to give N_6 ligands has been successful and will be reported elsewhere [17]. The ligand has been characterized by ^1H and ^{13}C

NMR and elemental analysis and the data is consistent with the formulated structure.

The copper complexes **2**–**4** were prepared by treating the N_4-mpz ligand with the appropriate copper salt. For complex **4**, elemental and mass spectral analyses data were consistent with the anticipated structure, [Cu(N_4-mpz)(Cl)]Cl. This was not the case for complexes **2** and **3** so single crystals of complex **2** were grown and its X-ray structure solved (vide infra). The elemental analysis and mass spectra were consistent with the formulation of the complexes as [Cu(N_4-mpz)(Pz)]X_2 where X = BF_4 or ClO_4 with an additional pyrazole donor coordinated to the copper in complexes **2** and **3**.

In the FAB-MS, there are many peaks that are diagnostic for the anticipated structures. For complex **2**, the highest mass peak is found at 562*m*/*z* which corresponds to $[Cu(N_4\text{-mpz})^{2+}](ClO_4)^-$. A prominent peak is found at 463*m*/*z* which corresponds to [Cu(N_4-mpz)$^+$]. No evidence for the additional pyrazole donor is found in the mass spectrum of complex **2**. Similar patterns exist for complex **3** where the peak at 550*m*/*z* is consistent with $[Cu(N_4\text{-mpz})^{2+}](BF_4)^-$ and the peak at 463*m*/*z* matches [Cu(N_4-mpz)$^+$]. However, the major difference is that a peak is found at 646*m*/*z* that corresponds with $[Cu(N_4\text{-mpz})(Pz)]^{2+}(BF_4)^-$ showing the presence of the additional pyrazole donor in complex **3**. Although the mass spectral results do not include the exogenous pyrazole donor in complex **2**, the crystallographic results (vide infra) do show its presence. For complex **4**, diagnostic peaks are found at 463*m*/*z* for the [Cu(N_4-mpz)$^+$] and at 498*m*/*z* for the $[Cu(N_4\text{-mpz})^{2+}]Cl^-$ moiety.

The existence of the additional pyrazole in complexes **2** and **3** was unexpected as there was no free pyrazole in the reaction mixture so its presence in the complex must be the result of its extraction by the copper during complexation. There are other examples of this phenomenon [18–23]. We have seen other instances of unusual results for biphenyl-based ligands upon complexation to Cu(II) as the Cu(II) is forced by the biphenyl ligand into a relatively undesirable form with the metal in a non-planar environment. In prior examples of biphenyl-based ligands, the Cu(II) responded to this imposition by spontaneously reducing the Cu(II) to its Cu(I) form in order to relieve the severe steric constraints imposed by the ligand [11]. In the study reported here, the copper in complexes **2** and **3** takes on an additional donor to modify its structure. In this case, the result is a five-coordinate Cu(II) complex with an additional pyrazole nitrogen coordinated. In comparison, complex **4** behaves in a more predictable way by coordinating the ligand and the anion from the copper salt resulting in a five-coordinate complex with the chloride bound.

3.1. Crystallographic analysis of [Cu(N_4-mpz)(Pz)] (ClO_4)$_2$ · CH_3OH (**2**)

Single crystals of [Cu(N_4-mpz)(Pz)] (ClO_4)$_2$ · CH_3OH (**2**) suitable for X-ray diffraction structural determination were grown by vapor diffusion of ether into a solution of the complex in CH_3OH. The molecular structure of complex **2** is shown in Fig. 2. It crystallizes in a triclinic crystal system with space group $P\bar{1}$. The relevant details of the crystals, data collection and structure refinement are found in Table 1. Selected bond distances and bond angles are presented in Table 2. The complete list of bond distances, bond angles, atomic coordinates and anisotropic thermal parameters are presented in supporting information.

Complex **2** is a five-coordinate complex with the copper coordinated by five nitrogen donors. The coordination geometry around the copper is best described as distorted trigonal bipyramidal as revealed by the magnitude of the trigonality index *t* of 0.61. For perfect pyramidal and trigonal bipyramidal geometries, the *t-values* are zero and unity, respectively [24], so this complex only slightly favors the trigonal bipyramidal form. The axial positions are taken up by the pyrazole donors N(6) and N(1) from the pyrazoles of the multidentate ligand while the non-aromatic nitrogens N(4) and N(3) and the exogenous pyrazole N(7) make up the equatorial donors. All bond distances are within expected values with the nitrogen from the exogenous pyrazole at a slightly longer distance (1.99 Å) than the other two pyrazole donors (1.95 Å). In other examples of copper complexes with a pyrazole donor attached to the copper, the Cu–N distance is usually found in the range of 1.99–2.00 Å. The impact on the structure due to the biphenyls is

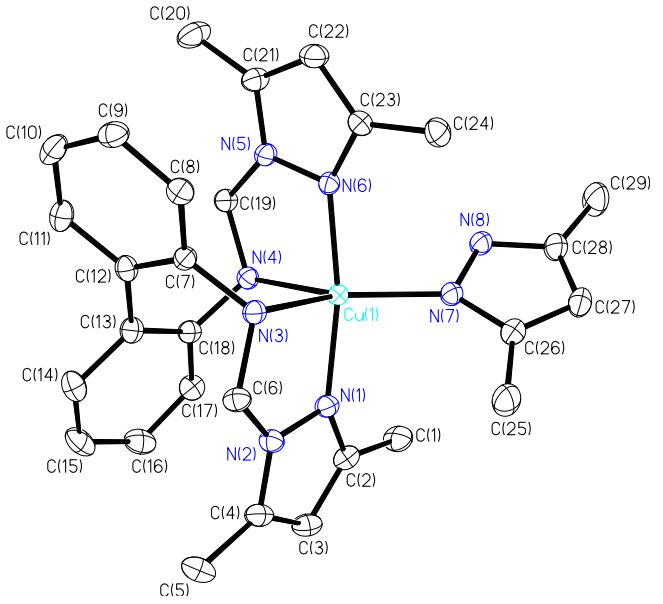


Fig. 2. An ORTEP view of the cation of [Cu(N_4-mpz)(Pz)] (ClO_4)$_2$ · CH_3OH (**2**) (50% probability).

Table 1
Crystal data and structure refinement for [Cu(N_4-mpz)(Pz)] (ClO_4)$_2$ · CH_3OH (**2**).

Empirical formula	$C_{30}H_{40}Cl_2CuN_8O_9$	
Formula weight	791.14	
Temperature	100(2) K	
Wavelength	0.71073 Å	
Crystal system	triclinic	
Space group	$P\bar{1}$	
Unit cell dimensions	a = 10.5321(7) Å	α = 88.0500(10)°
	b = 11.9450(8) Å	β = 74.4410(10)°
	c = 14.3009(10) Å	γ = 86.5600(10)°
Volume	1729.8(2) Å^3	
Z	2	
D_{calc}	1.519 mg/m^3	
Absorption coefficient	0.850 mm^{-1}	
F(000)	822	
Crystal size	0.30 × 0.19 × 0.16 mm^3	
Theta range for data collection	1.48–27.49°	
Index ranges	$-13 \leqslant h \leqslant 13$, $-15 \leqslant k \leqslant 15$, $-18 \leqslant l \leqslant 18$	
Reflections collected	15064	
Independent reflections [R_{int}]	7727 = 0.0154	
Completeness to θ = 27.49°	97.2%	
Absorption correction	semi-empirical from equivalents	
Max. and min. transmission	1.000 and 0.876	
Refinement method	full-matrix least-squares on F^2	
Data/restraints/parameters	7727/0/611	
Goodness-of-fit on F^2	1.054	
Final R indices [$I > 2\sigma(I)$]	R_1 = 0.0358, wR_2 = 0.0891	
R indices (all data)	R_1 = 0.0399, wR_2 = 0.0914	
Largest difference peak and hole	0.764 and −0.457 e Å^{-3}	

Table 2
Bond lengths [Å] and angles [°] for of [Cu(N_4-mpz)(Pz)] $(ClO_4)_2 \cdot CH_3OH$.

Cu(1)–N(6)	1.9453(15)
Cu(1)–N(1)	1.9492(16)
Cu(1)–N(7)	1.9941(16)
Cu(1)–N(4)	2.1886(16)
Cu(1)–N(3)	2.2103(16)
N(6)–Cu(1)–N(1)	169.55(6)
N(6)–Cu(1)–N(7)	94.38(6)
N(1)–Cu(1)–N(7)	96.06(6)
N(6)–Cu(1)–N(4)	80.57(6)
N(1)–Cu(1)–N(4)	92.57(6)
N(7)–Cu(1)–N(4)	132.80(6)
N(6)–Cu(1)–N(3)	91.91(6)
N(1)–Cu(1)–N(3)	80.52(6)
N(7)–Cu(1)–N(3)	134.06(6)
N(4)–Cu(1)–N(3)	93.13(6)

also manifested in the smaller bond angles found for N(6)–Cu(1)–N(4) (80.6°) and for N(1)–Cu(1)–N(3) (80.5°).

It is striking that in other examples where decomposition of pyrazole-based ligands occurs upon reaction with metal salts [18–23], the decomposition typically occurs only with sterically encumbered ligands such as pyrazolylborates or diphenyldipyrazolylmethanes. This also is the case here as the biphenyl ring is forcing the nitrogen donors out of planar type environments when bound to the metal. The mechanism of the decomposition has been hypothesized to involve metal-mediated cleavage of the pyrazole nitrogen–X bond (where X = boron or carbon) [18,19,21]. To determine whether the metal is essential for the decomposition process, we stirred the ligand overnight in the absence of copper and found it to be unperturbed indicating that Cu(II) is required for the pyrazole decomposition [18].

3.2. Electrochemistry

The cyclic voltammogram scans for fresh solutions of complexes **2**–**4** in methanol (Fig. 3) start at positive potentials versus Ag/AgCl and proceed to more negative potentials at a scan rate of 50 mV s^{-1}.

The first cathodic current peaks (E_{pc} in Table 3) are assigned to the reduction of Cu(II) to Cu(I) based on a comparison to our previous studies with the pyridine containing Cu(N_4-mpy) complexes [6]. Reversing the scan direction at a negative potential (−0.1 V) gives the corresponding reoxidation of Cu(I). Table 3 summarizes the electrochemical CV data for all the complexes, along with the peak potentials obtained from DPV (we were not able to get a result for complex **3**). One notes several trends from the electrochemical parameters. First, the $E_{1/2}$ values and ΔE_p values are different for the three complexes, which suggests that the complexes do not have identical coordination spheres around Cu(II) in MeOH. Complexes **2** and **3**, possessing weakly coordinating ClO_4^- or BF_4^-, have similar $E_{1/2}$ values, yet **3** has much larger peak splitting (306 mV) indicating more quasi-reversible redox chemistry and/or more kinetic problems at the electrode compared to complexes **2** and **4**. Complex **4** is slightly harder to reduce than **2** based on the DPV peaks (426 mV versus 456 mV), implying that the electron donating chloride ion has some influence at the metal center. These observations imply that the counterion in **2**–**4** influences the electronics of the metal center. It is not clear from these data that the pyrazole remains in the fifth coordination site during the redox event.

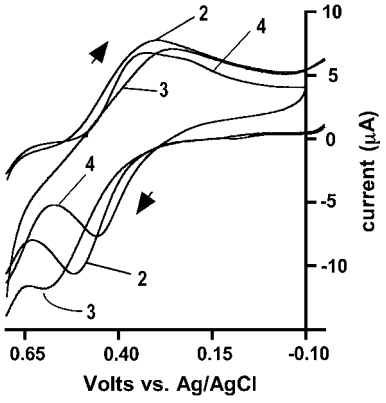


Fig. 3. Cyclic voltammograms at 50 mV s^{-1} using a glassy carbon electrode for complexes **2**, **3**, and **4** dissolved in degassed methanol. All solutions contained 1 mM complex and 0.100 M TBAH.

Table 3
CV and DPV data for complexes **2**–**4**.

Complex	E_{pc}/mV	E_{pa}/mV	ΔE_p/mV	$E_{1/2}$/mV versus Ag/AgCl	$i_{pc}i_{pa}^{-1}$	DPV, E_p/mV
2	318	507	189	422	1.02	456
3	280	586	306	430	1.08	N/A
4	341	451	110	396	1.11	426

CV: methanol containing 0.1 M TBAH, [Cu(II)] = 1–2 mM at a scan rate of 50 mV s^{-1}. DPV: scan rate 5 mV s^{-1}, pulse amplitude/time of 25 mV/50 ms, step height/time of 1 mv/200 ms.

The second point is that all the complexes show quasi-reversible redox behavior that is most likely related to structural changes upon going from Cu(II) to Cu(I) where a tetrahedral geometry is favored. The solvent or a counter ion may slowly exchange into the fifth coordination site as we note the appearance of small shoulder after the DPV reduction peak for complex **4** that increases in intensity after 24 h at room temperature (no change is apparent upon continuous cycles using CV). Finally, the $E_{1/2}$ for complexes **2**–**4** occur at much more positive potentials compared to the pyridine-based [Cu(N_4-mpy)(X)]X complexes studied earlier [11]. For example, [Cu(N_4-mpy)(Cl)]Cl gives an $E_{1/2}$ of +100 mV (ΔE_p = 80 mV) versus Ag/AgCl in methanol compared to +396 mV (ΔE_p = 110 mV) for complex **4**. This result is consistent with the better donor properties of pyridine compared to the dimethylpyrazole-based chelating ligand.

3.3. Conclusions

A new tetradentate pyrazole-containing ligand (N_4-mpz) has been synthesized and three Cu(II) complexes prepared and characterized from it. The crystal structure and spectroscopic data show complexes **2** and **3** to be five-coordinate with the ligand bound along with an additional pyrazole donor. The origin of this pyrazole is due to the abstraction of a pyrazole from an uncomplexed ligand. This is the second example where we have found Cu(II) complexes formed from biphenyl-based ligands behave in unusual ways. We attribute these results to the steric constraints enforced on the metal by the non-planarity of the biphenyl rings and we continue to probe related biphenyl derived ligands and their metal complexes.

Acknowledgements

We are grateful to the Research Corporation and the University of San Diego Faculty Research Grants for financial support of this work.

Appendix A. Supplementary data

CCDC 695515 contains the supplementary crystallographic data for this paper. These data can be obtained free of charge via http://

www.ccdc.cam.ac.uk/conts/retrieving.html, or from the Cambridge Crystallographic Data Centre, 12 Union Road, Cambridge CB2 1EZ, UK; fax: (+44) 1223-336-033; or e-mail: deposit@ccdc.cam.ac.uk. Supplementary data associated with this article can be found, in the online version, at doi:10.1016/j.poly.2008.11.034.

References

[1] E.I. Solomon, U.M. Sundaram, T.E. Machonkin, Chem. Rev. 96 (1996) 2563.
[2] R.L. Lieberman, A.C. Rosenzweig, Nature 434 (2005) 177.
[3] S.T. Prigge, B.A. Eipper, R.E. Mains, L.M. Amzel, Science 304 (2004) 864.
[4] J.P. Klinman, Chem. Rev. 96 (1996) 2541.
[5] E.A. Lewis, W.B. Tolman, Chem. Rev. 104 (2004) 1047.
[6] L.M. Mirica, X. Ottenwaelder, T.D.P. Stack, Chem. Rev. 104 (2004) 1013.
[7] L.Q. Hatcher, K.D. Karlin, J. Biol. Inorg. Chem. 9 (2004) 669.
[8] S. Knapp, T.P. Keenan, X. Zhang, R. Fikar, J.A. Potenza, H.J. Schugar, J. Am. Chem. Soc. 112 (1990) 3452.
[9] V.J. Eaton, D. Steele, J. Chem. Soc., Faraday Trans. 2 (69) (1973) 1601.
[10] J. Chen, R. Russo, W. Chao, L.D. Margerum, M.R. Malachowski, R. White, Z. Thawley, A. Thayer, A.L. Rheingold, L.N. Zakharov, Dalton Trans. (2007) 2571.
[11] M.R. Malachowski, M. Adams, N. Elia, A.L. Rheingold, R.S. Kelly, Dalton Trans. (1999) 2177.
[12] M.R. Malachowski, M.E. Adams, D. Murray, R. White, N. Elia, A. L. Rheingold, L.N. Zakharov, R.S. Kelly, Inorg. Chim. Acta, in press.
[13] M.R. Malachowski, H.B. Huynh, L.J. Tomlinson, R.S. Kelly, Dalton Trans. (1995) 31.
[14] G.M. Sheldrick, in: SHELXTL Version 5.1 Software Reference Manual, Brucker AXS, Madison, WI, 1997.
[15] S. Trofimenko, Chem. Rev. 93 (1993) 943.
[16] N. Kitajima, W.B. Tolman, Prog. Inorg. Chem. 34 (1995) 419.
[17] M.R. Malachowski, M. Adams, unpublished data.
[18] J.L. Schneider, V.G. Young, W.B. Tolman, Inorg. Chem. 40 (2001) 165.
[19] J.L. Shaw, T.B. Cardon, G.A. Lorigan, C.J. Ziegler, Eur. J. Inorg. Chem. (2004) 1073.
[20] S.M. Carrier, C.E. Ruggiero, R.P. Houser, W.B. Tolman, Inorg. Chem. 32 (1993) 4889.
[21] C.H. Dungan, W. Maringgele, A. Meller, K. Niedenzu, H. Noth, J. Serwatowska, Inorg. Chem. 30 (1991) 4799.
[22] E.C.B. Alegria, L.M.D.R.S. Martins, M. Haukka, A.J.L. Pombeiro, Dalton Trans. (2006) 4954.
[23] W. Klaui, M. Berghahn, W. Frank, G.J. Reib, T. Schonherr, G. Rheinwald, H. Lang, Eur. J. Inorg. Chem. (2003) 2059.
[24] A.W. Addison, T. Nageswara, J. Rao, J. Reedijk, J. van Rijn, G.C. Verschoor, Dalton Trans. (1984) 1349.

Polyhedron 28 (2009) 398–406

Contents lists available at ScienceDirect

Polyhedron

journal homepage: www.elsevier.com/locate/poly

Vanadium complexes with thiosemicarbazones: Synthesis, characterization, crystal structures and anti-*Mycobacterium tuberculosis* activity

Pedro I. da S. Maia [a], Fernando R. Pavan [b], Clarice Q.F. Leite [b], Sebastião S. Lemos [c], Gerimário F. de Sousa [c], Alzir A. Batista [d], Otaciro R. Nascimento [e], Javier Ellena [e], Eduardo E. Castellano [e], Elke Niquet [f], Victor M. Deflon [a,*]

[a] *Instituto de Química de São Carlos, Universidade de São Paulo, CP 780, 13560-970 São Carlos, SP, Brazil*
[b] *Faculdade de Ciências Farmacêuticas, Universidade Estadual Paulista, 14801-902 Araraquara, SP, Brazil*
[c] *Instituto de Química, Universidade de Brasília, 70919-970 Brasília, DF, Brazil*
[d] *Departamento de Química, Universidade Federal de São Carlos, 13565-905 São Carlos, SP, Brazil*
[e] *Instituto de Física de São Carlos, Universidade de São Paulo, CP 369, 13560-970 São Carlos, SP, Brazil*
[f] *Institut für Anorganische Chemie, Universität Tübingen, D-72076 Tübingen, Germany*

ARTICLE INFO

Article history:
Received 30 August 2008
Accepted 14 November 2008
Available online 26 December 2008

Keywords:
Oxovanadium(IV)
Dioxovanadium(V)
Thiosemicarbazones
Anti-*Mycobacterium tuberculosis* activity

ABSTRACT

The development of more efficient anti-tuberculosis drugs is of interest. Three oxovanadium(IV) and three *cis*-dioxovanadium(V) complexes with thiosemicarbazone derivatives bearing moieties with different lipophilicity have been prepared and had their inhibitory activity against *Mycobacterium tuberculosis* H_{37}Rv ATCC 27294 evaluated. The analytical methods used by the complexes' characterization included IR, EPR, ^{1}H, ^{13}C and ^{51}V NMR spectroscopies, elemental analysis, cyclic voltammetry, magnetic susceptibility measurement and single crystal X-ray diffractometry. [VO(acac)(aptsc)], [VO(acac)(apmtsc)] and [VO(acac)(apptsc)] (acac = acetylacetonate; Haptsc = 2-acetylpyridinethiosemicarbazone; Hapmtsc = 2-acetylpyridine-N(4)-methyl-thiosemicarbazone and Happtsc = 2-acetylpyridine-N(4)-phenyl-thiosemicarbazone) are paramagnetic and their EPR spectra are consistent with the monoanionic *N,N,S*-tridentate coordination of the thiosemicarbazone ligands, resulting in octahedral structures of rhombic symmetry and with the oxidation state +IV for the vanadium atom. As result of oxidation of the vanadium(IV) complexes above, the diamagnetic *cis*-dioxovanadium(V) complexes [VO_2(aptsc)], [VO_2(apmtsc)] and [VO_2(apptsc)] are formed. Their ^{1}H, ^{13}C and ^{51}V NMR spectra were acquired and support a distorted square pyramidal geometry for them, in accord with the solid state X-ray structures determined for [VO_2(aptsc)] and [VO_2(apmtsc)]. In general, the vanadium compounds show comparable or larger anti-*M. tuberculosis* activities than the free thiosemicarbazone ligands, with MIC values within 62.5–1.56 (μg/mL).

© 2008 Elsevier Ltd. All rights reserved.

1. Introduction

Tuberculosis (TB) is a contagious disease with high mortality worldwide. The statistics indicate that three million people worldwide die annually from complication of tuberculosis and about eight million new cases are estimated to occur every year, 95% of them in developing countries [1]. Therefore, the incidence of tuberculosis is raising at alarming rates, which are coincident with the increase of AIDS cases. In addition, the expanding number of multi drug resistant TB cases does not only create problems for the treatment, but also the costs are ever-increasing. Thus, new drugs are necessary to overcome the current problems of therapy [1,2].

Biological properties of thiosemicarbazones (TSCs) have been studied since 1946, when Domagk et al. [3] reported their activity against *Mycobacterium tuberculosis*. The compound *p*-acetamidobenzaldehyde thiosemicarbazone, commercially available as thiacetazone, has long been employed in the treatment of tuberculosis [4]. Otherwise, its purely bacteriostatic activity *in vivo* and the fast appearance of strains resistant to the thiacetazone during the treatment, besides collateral effects like the induction to the *diabetes mellitus*, limit its utilization [5]. Since then, this and other biological properties of TSCs have been extensively studied owing to their wide variety of biological activities [6]. The mechanism of action of TSCs is closely related to their ability to inhibit the biosynthesis of DNA, possibly by blocking the enzyme ribonucleotide diphosphate reductase; binding to the nitrogen base of DNA, hindering or blocking base replication; creation of lesions in DNA strands by oxidative rupture [7]. Structure–activity relationships evidence not only that the complexation enhances the antimicrobial activity of bioactive ligands against some tested microorganisms but also that the presence of a metal center may

* Corresponding author. Tel.: +55 16 3373 8038.
E-mail address: deflon@iqsc.usp.br (V.M. Deflon).

0277-5387/$ - see front matter © 2008 Elsevier Ltd. All rights reserved.
doi:10.1016/j.poly.2008.11.017

also play a relevant role in the activity of coordination compounds [8,9].

In recent years the medicinal applications of oxovanadium(IV) and dioxovanadium(V) complexes with *N*-, *O*- and *S*-donor chelating ligands have been investigated in special about their potential insulin-mimetic effects [10–15]. Besides these effects, other pharmacological activities of vanadium compounds include tumor growth inhibition and prophylaxis against carcinogenesis [16]. Some vanadium complexes are known to inhibit several enzymes, including phosphatases, ATPases, nucleases, kinases and other enzymes [17].

The antimicrobial activity of vanadium complexes has been explored too little and till this moment we have notices about only two studies on vanadium complexes activities against *M. tuberculosis* [18,19]. Furthermore, once observed that the treatment of the tuberculosis with free thiosemicarbazones ligands may induct *diabetes mellitus* [5], the coordination to vanadium may be advantageous both to the enhancement of the anti-*M. tuberculosis* activity and to the prevention of *diabetes*.

This work describes the preparation, structural characterization, both in solution and in the solid state, of the oxovanadium(IV) complexes [VO(acac)(aptsc)] (**1**), [VO(acac)(apmtsc)] (**2**), and [VO(acac)(apptsc)] (**3**), as well as the *cis*-dioxovanadium(V) complexes [VO_2(aptsc)] (**4**), [VO_2(apmtsc)] (**5**), and [VO_2(apptsc)] (**6**), which involve the thiosemicarbazone derivatives 2-acetylpyridine-thiosemicarbazone (Haptsc), 2-acetylpyridine-N(4)-methyl-thiosemicarbazone (Hapmtsc) and 2-acetylpyridine-N(4)-phenyl-thiosemicarbazone (Happtsc). The activity of complexes, free ligands and common vanadium salts against *M. tuberculosis* H37Rv ATCC 27294 was evaluated. Literature data is available for complex **3**, concerning to its preparation and characterization [20]. A somewhat different preparation route was used here for **3** and the complex characterization was extended by using additional methods.

2. Experimental

2.1. Materials and methods

[$VO(acac)_2$] (ACROS ORGANICS), 2-acetylpyridine, thiosemicarbazide, N(4)-methyl-thiosemicarbazide, N(4)-phenyl-thiosemicarbazide and analytical reagents grade chemicals and solvents were obtained commercially and used without further purification. The ligands were prepared as described by literature methods [21]. FTIR spectra were recorded on a BOMEM FTIR model BM 100 spectrometer. NMR spectra were acquired on a Varian MERCURY plus spectrometer operating at 300.07, 75.46 and 78.92 MHz for ^{1}H, ^{13}C and ^{51}V, respectively. The ^{1}H and ^{13}C{^{1}H} spectra were internally referenced to TMS. The ^{51}V spectrum was externally referenced to $VOCl_3$ ($\delta = 0$), checked against an aqueous $(NH_4)VO_3$ solution containing capillary ($\delta = -541.2$ for VO_4^{3-}). A BAS 100B electrochemical analyzer was used for the cyclic voltammetry studies. Elemental analyses (CHNS) were determined with FISONS EA-1108 analyzer. EPR spectra were collected on an X-band Bruker ER-580 spectrometer equipped with Oxford low temperature system. The spectra were simulated with the EasySpin program [22]. The measurement conditions include microwave frequency of 9.472 GHz, modulation frequency and amplitude of 100 kHz and 0.1 mT, respectively, magnetic field scan range of 248–429 mT, gain of 45 db, microwave power of 8 μW, time constant of 20.48 ms and conversion time of 81.92 ms. Solid samples were measured at room temperature and liquid sample diluted in DMSO solvent were measured at 25 K to prevent microwave power saturation. Magnetic susceptibilities were measured on a JOHNSON MATTHEY MSB balance at 298 K and converted into the corresponding molar susceptibilities in the usual way [23]. Diamagnetic corrections, applied to the molar susceptibilities of the paramagnetic substances, are reported as χ_{diam}. The latter corrections were calculated using the standard Pascal's constants [23]. Enraf-Nonius CAD4 and Nonius Kappa CCD diffractometers equipped with graphite monochromators were used for the X-ray structure analyses, applying standard procedures.

2.2. Preparations

Synthesis of the ligands: The ligands Haptsc, Hapmtsc and Happtsc were prepared by refluxing an equimolar methanolic solution of the desired thiosemicarbazide (10 mmol) and 2-acetylpyridine (10 mmol) for 1 h.

Haptsc: Yellow crystalline solid. Yield 1.50 g (77%). M.p.: 161–162 °C. ^{1}H NMR (DMSO-d_6, δ): 2.39 (s, CH_3), 7.38 (ddd, $J_{2,3}$ = 8 Hz, $J_{2,1}$ = 5 Hz, $J_{2,4}$ = 1 Hz, 1H), 7.79 (ddd, $J_{3,4}$ = $J_{3,2}$ = 8 Hz, $J_{3,1}$ = 2 Hz, 1H), 8.15 (s, NH), 8.42 (s, NH), 8.44 (ddd, $J_{4,3}$ = 8 Hz, $J_{4,2}$ = 1 Hz, 1H), 8.58 (ddd, $J_{1,2}$ = 5 Hz, $J_{1,3}$ = 2 Hz, 1H), 10.33 (s, NH). ^{13}C{^{1}H} NMR (DMSO-d_6, δ): 12.4, 121.1, 124.2, 136.6, 148.4, 148.6 154.9, 179.3.

Hapmtsc: White crystalline solid. Yield 1.52 g (73%). M.p.: 178–179 °C. ^{1}H NMR (DMSO-d_6, δ): 2.38 (s, CH_3), 3.06 (d, $J_{6,5}$ = 5 Hz, N–CH_3), 7.39 (ddd, $J_{2,3}$ = 7, $J_{2,1}$ = 5, $J_{2,4}$ = 1 Hz, 1H), 7.82 (ddd, $J_{3,4}$ = 8, $J_{3,2}$ = 7, $J_{3,1}$ = 1 Hz, 1H), 8.42 (dq, $J_{4,3}$ = 8, $J_{4,2}$ = 1 Hz, 1H), 8.58 (dq, $J_{1,2}$ = 5, $J_{1,3}$ = 1 Hz, 1H), 8.64 (d, $J_{5,6}$ = 5 Hz, 1H), 10.35 (s, 1H). ^{13}C{^{1}H} NMR (DMSO-d_6, δ): 12.0, 31.1, 120.7, 123.8, 136.2, 147.8, 148.4, 154.6, 178.6.

Happtsc: Bright white solid. Yield 2.14 g (79%). M.p.: 171–174 °C. ^{1}H NMR (DMSO-d_6, δ): 2.47 (s, CH_3), 7.24 (ddd, $J_{7,6}$ = 7 Hz, $J_{7,5}$ = 1 Hz, 1H), 7.34–7.44 (m, 3H), 7.55 (dd, $J_{5,6}$ = 9 Hz, $J_{5,7}$ = 1 Hz, 2H), 7.82 (ddd, $J_{3,4}$ = $J_{3,2}$ = 8 Hz, $J_{3,1}$ = 2 Hz, 1H), 8.54 (ddd, $J_{4,3}$ = 8 Hz, $J_{4,2}$ = $J_{4,1}$ = 1 Hz, 1H), 8.61 (ddd, $J_{1,2}$ = 5 Hz, $J_{1,3}$ = 2 Hz, $J_{1,4}$ = 1 Hz, 1H), 10.21 (s, NH), 10.67 (s, NH). ^{13}C{^{1}H} NMR (DMSO-d_6, δ): 12.6, 121.3, 124.2, 125.6, 126.2, 128.2, 136.5, 139.1, 148.5, 149.2, 154.5, 177.3.

Synthesis of the V(IV) complexes: Solutions of 0.133 g (0.5 mmol) [$VO(acac)_2$] and (0.5 mmol) of the desired ligand were prepared separately in minimal amounts of MeCN and then mixed. After stirring for 15 min, the solutions had their volume reduced to half by heating and were then cooled by standing at room temperature. The precipitates formed were filtered off and dried in vacuum.

*[VO(acac)(aptsc)] (**1**):* Dark green precipitate. Yield 0.08 g (46%). M.p. not observed up to 300 °C. (Found: C, 42.90; H, 4.43; N, 15.29; S, 9.02. Calc. for $C_{13}H_{16}N_4O_3SV$: C, 43.46; H, 4.49; N, 15.59; S, 8.92%).

*[VO(acac)(apmtsc)] (**2**):* Dark green precipitate. Yield 0.13 g (72%). M.p. not observed below 300 °C. (Found: C, 44.91; H, 4.98; N, 15.17; S, 8.76. Calc. for $C_{14}H_{18}N_4O_3SV$: C, 45.04; H, 4.86; N, 15.01; S, 8.59%).

*[VO(acac)(apptsc)] (**3**):* Dark brown precipitate. Yield 0.143 g (66%). M.p. not observed below 300 °C. (Found: C, 51.89; H, 4.71; N, 13.02; S, 7.44. Calc. for $C_{19}H_{20}N_4O_3SV$: C, 52.41; H, 4.63; N, 12.87; S, 7.36%).

Synthesis of the V(V) complexes: The compounds were prepared in a similar approach as applied for **1–3**, but preparing more diluted final mixtures (around 100 mL) in MeOH or MeCN, which were stirred during 5 days in order to complete the oxidation process.

*[VO_2(aptsc)] (**4**):* Yellow-brown solid. Yield 0.10 g (70%). M.p. not observed until 300 °C. (Found: C, 34.31; H, 3.34; N, 20.12; S, 11.77. Calc. for $C_8H_9N_4O_2SV$: C, 34.79; H, 3.28; N, 20.29; S, 11.61%). ^{1}H NMR (DMSO-d_6, δ): 2.53 (s, CH_3), 7.62 (dd, $J_{2,3}$ = 8 Hz, $J_{2,1}$ = 5 Hz, 1H), 7.83 (s, NH_2), 8.03 (d, $J_{4,3}$ = 8 Hz, 1H), 8.28 (dd, $J_{3,2}$ = $J_{3,4}$ = 8 Hz, 1H), 8.64 (d, $J_{1,2}$ = 5 Hz, 1H). ^{13}C{^{1}H} NMR (DMSO-d_6, δ): 13.9, 123.7, 125.4, 142.9, 152.9, 154.2, 155.4, 176.0 ppm.

[VO_2(apmtsc)] (**5**): Yellow solid. Yield 0.07 g (50%). M.p. not observed below 300 °C. (Found: C, 36.90; H, 3.72; N, 18.86; S, 10.93. Calc. for $C_9H_{11}N_4O_2SV$: C, 37.25; H, 3.82; N, 19.31; S, 11.05%). ^{1}H NMR (DMSO-d_6, δ): 2.57 (s, CH_3), 2.92 (d, J = 5 Hz, N–CH_3), 7.63 (t, $J_{2,1}$ = 6 Hz, 1H), 8.02–8.14 (m, 2H), 8.29 (t, $J_{3,4}$ = 8 Hz, 1H), 8.65 (d, $J_{1,2}$ = 6 Hz, 1H). ^{13}C{^{1}H} NMR (DMSO-d_6, δ): 13.8, 31.0, 123.9, 125.6, 143.0, 153.1, 154.3, 156.8, 173.3 ppm.

[VO_2(apptsc)] (**6**): Yellow solid. Yield 0.10 g (65%). M.p. not observed below 300 °C. (Found: C, 47.44; H, 3.83; N, 15.59; S, 9.27. Calc. for $C_{14}H_{13}N_4O_2SV$: C, 47.73; H, 3.72; N, 15.90; S, 9.10%). ^{1}H NMR (DMSO-d_6, δ): 2.68 (s, CH_3), 7.07 (t, $J_{7,6}$ = 8 Hz, 1H), 7.37 (dd, $J_{6,5}$ = $J_{6,7}$ = 8 Hz, 2H), 7.71 (dd, $J_{2,3}$ = 7 Hz, $J_{2,1}$ = 5 Hz), 7.76 (d, $J_{5,6}$ = 8 Hz), 8.17 (d, $J_{4,3}$ = 8 Hz, 1H), 8.34 (ddd, $J_{3,4}$ = 8 Hz, $J_{3,2}$ = 7 Hz, $J_{3,1}$ = 2 Hz, 1H), 8.72 (d, $J_{1,2}$ = 5 Hz, 1H), 10.17 (s, NH). ^{13}C{^{1}H} NMR (DMSO-d_6, δ): 14.7, 120.1, 123.0, 124.8, 126.4, 128.7, 140.2, 143.2, 153.2, 153.8, 160.4, 170.3 ppm.

2.3. Crystal structure determinations

Brown crystals of **4** were grown by slow interdiffusion of CH_3CN solutions of [VO(acac)$_2$] and of the corresponding thiosemicarbazone ligand. Light brown crystals of **5** were obtained by slow concentration of an acetonitrile solution of the compound at room temperature. The structures were solved with SHELXS97, by using direct methods [24] and all non-hydrogen atoms were refined with anisotropic displacement parameters with SHELXL97 [25]. Absorption corrections were applied in both cases, as given in Table 1, together with more detailed information about the structure determinations.

Table 1
Crystal data and structure refinement for the complexes [VO_2(aptsc)] (**4**) and [VO_2(apmtsc)] (**5**).

	4	**5**
Empirical formula	$C_8H_9N_4O_2SV$	$C_9H_{11}N_4O_2SV$
Diffractometer	CAD4	Kappa CCD
Formula weight, M	276.19	290.22
Temperature, T (°C)	20(2)	20(2)
Wavelength (pm)/ radiation	71.073/Mo Kα	71.073/Mo Kα
Crystal system	Monoclinic	Orthorhombic
Space group	*C2/c*	*Pbca*
Unit cell dimensions		
a (Å)	15.241(2)	12.2890(4)
b (Å)	7.5891(1)	12.5380(4)
c (Å)	20.499(4)	15.5200(4)
α (°)	90	90
β (°)	109.827(17)	90
γ (°)	90	90
Volume, V (Å^3)	2230.4(6)	2391.31(13)
Z	8	8
μ (mm^{-1})	1.066	0.999
F(000)	1120	1184
Crystal size (mm^3)	0.35 × 0.30 × 0.25	0.100 × 0.060 × 0.029
Method/θ range for data collection (°)	ω scans/3.04 to 27.96	ϕ and ω scans with κ offsets/ 2.62 to 26.02
Limiting indices (h, k, l)	$-20 \rightarrow h \rightarrow 19$, $0 \rightarrow k \rightarrow 10$, $-1 \rightarrow l \rightarrow 26$	$-15 \rightarrow h \rightarrow 15$, $-13 \rightarrow k \rightarrow 15$, $-19 \rightarrow l \rightarrow 19$
Reflections collected	2882	29449
Reflections unique/R_{int}	2671/0.0194	2354/0.0694
Completeness to θ	27.96° (99.7%)	26.02° (99.9%)
Data/restraints/param.	2671/0/181	2354/0/177
Absorption correction	Ψ-scans [26]	Gaussian [27]
Min. and max. transmission	0.91785 and 0.97668	0.968 and 0.927
Refinement method	Full-matrix least-squares on F^2	Full-matrix least-squares on F^2
Hydrogen treatment	Fourier map	Mixed
Final R indices [$I > 2\sigma$(I)]	R_1 = 0.0367, wR_2 = 0.0887	R_1 = 0.0489, wR_2 = 0.1188
R indices (all data)	R_1 = 0.0728, wR_2 = 0.1008	R_1 = 0.0679, wR_2 = 0.1438
Goodness-of-fit, S	1.028	1.153
Extinction coefficient	Not refined	0.026(3)
Largest diff. peak and hole (e Å^{-3})	0.291 and −0.200	1.016 and −0.792

2.4. Determination of MICs

According to the methodology of Franzblau et al. [28], the anti-*M. tuberculosis* activity of the tested compound and standard drug isoniazid (Difco Laboratiories, Detroit, MI, USA) were determined in triplicate by using of the Microplate Alamar Blue Assay (MABA). In this technique, the Minimal Inhibitory Concentration (MIC) of compounds necessary to inhibit in 90% the mycobacterial growth was determined using Alamar Blue as a fluorescent vital dye. The bacterial suspension used was prepared by adjusting its turbidity by the McFarland No. 1 scale, and further dilution (1:25 v/v) in the culture medium 7H9. Concentrations of the complex and isoniazid in DMSO ranged from 1.00 to 100 μg/mL and 0.50 to 0.015 μg/mL, respectively. A negative control was run without bacterial *inoculum* in the medium to confirm that there is no reaction of the complexes themselves with Alamar Blue. The fluorescence of the dye (indicative of bacterial growth) was measured in a SPECTRAfluor Plus microplate reader (Tecan®) in bottom reading mode with excitation at 530 nm and emission at 590 nm.

3. Results and discussion

3.1. Synthesis of the complexes

The oxovanadium(IV) complexes **1**, **2** and **3** form readily in concentrated acetonitrile solutions at room temperature. The compound **3** can be also obtained from a methanol solution, while **1** and **2** suffer oxidation quickly in this solvent. The *cis*-dioxovanadium(V) complexes **4**, **5** and **6**, otherwise, are prepared from more diluted solutions of the corresponding complexing agents and [VO(acac)$_2$] at room temperature, with longer reaction times. In all complexes the thiosemicarbazone derivatives are found to coordinate *N,N,S*-tridentate as monoanionic, deprotonated ligands.

3.2. Magnetic measurements and EPR spectroscopy

The oxidation state of the central vanadium atom in the complexes was confirmed by measurements of the magnetic susceptibility and by EPR spectroscopy. The compounds **1**, **2** and **3** are paramagnetic in the extension of one unpaired electron (d^1) with values of μ_{eff} equal to 1.57 μ_B ($\chi_{diam} = -168.5 \times 10^{-6}$ cm^3 mol^{-1}), 1.60 μ_B ($\chi_{diam} = -180.3 \times 10^{-6}$ cm^3 mol^{-1}) and 1.50 μ_B ($\chi_{diam} = -217.0 \times 10^{-6}$ cm^3 mol^{-1}) at 298 K, respectively, which are typical for vanadium(IV) complexes [29]. The EPR spectra of the paramagnetic samples were measured in powder and diluted samples in DMSO solvent. The anisotropic EPR spectra of powder samples of **1**, **2** and **3** at room temperature are given in Fig. 1. It is possible to see that only one line is observed for each complex, suggesting that the packing in solid state is accompanied by magnetic exchange interaction between neighbour molecules. This phenomenon is very known in Cu(II)-aminoacids, -peptides and other molecules compounds [30–36].

Comparing the line width of the three spectra, it is possible to suggest that the magnetic exchange interaction is greater in **3**, which show the sharper line width, followed by **2** and then by **1**, which shows the broader line width, but it is possible that the line width differences explain differences in relaxation mechanism. To explore better these line width differences, single crystals EPR studies with angular line width variation will be desired. These

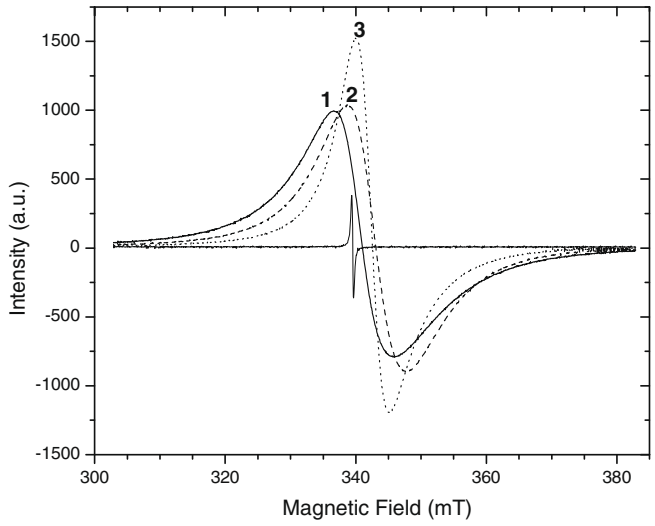


Fig. 1. Experimental EPR spectra of the complexes **1** (solid line), **2** (dashed line) and **3** (dotted line) in solid state. Simulation of these spectra were done using EasySpin program and the EPR parameters are shown in Table 2. The sharp line is a Cr(III) in MgO g-marker (g = 1.9797).

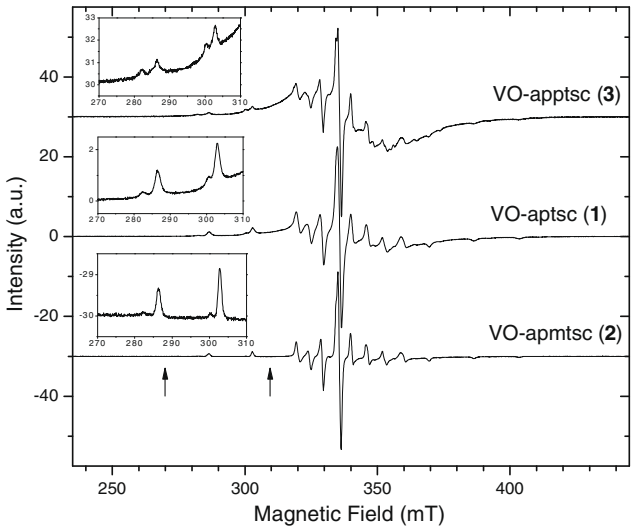


Fig. 2. EPR spectra of **1**, **2** and **3** in DMSO solution at 25 K. The inserts amplifies the magnetic fields region between the arrows, in order to show the two components.

spectra were simulated and the EPR parameters of the best fittings are given in Table 2. Fig. 2 shows the EPR spectra of the DMSO solved paramagnetic samples, collected at 25 K. All spectra are consistent with small rhombic distortion from the axial symmetry structures proposed for **1**, **2** and **3** in Scheme 1. It is important to note that for the compounds **1** and **3** a broaden line, superposed to the diluted compound, is apparent, suggesting that the magnetic exchange interaction are partially persistent for these samples under the experimental conditions or the complete dilutions of these two samples are not achieved. The EPR parameters, specially the g-values, are the same as obtained from the powder samples, but the lines widths (ΔH) are broaden in both cases. For complex **2**, however, a complete dissolution in DMSO solvent is observed.

Additionally, the EPR spectra of the three compounds indicate a second diluted paramagnetic species, also with rhombic distortion, which is present in much lower concentration (see insert in Fig. 2). These more diluted species are supposed to be formed probably by coordination of a DMSO molecule to the vanadium center, displacing one of the oxygen donor atoms from the acac ligand, similarly as observed during the voltammetry studies, described in the next section, which were also conducted by using a coordinating solvent. A component analysis by spectral simulation was done and is shown in Fig. 3, for complex **3**, as an example. The percentage of the components is calculated by numerical double integration of the simulated components with an estimate error of 5%. The complete results showing the EPR parameters and component percentages are shown in Table 2.

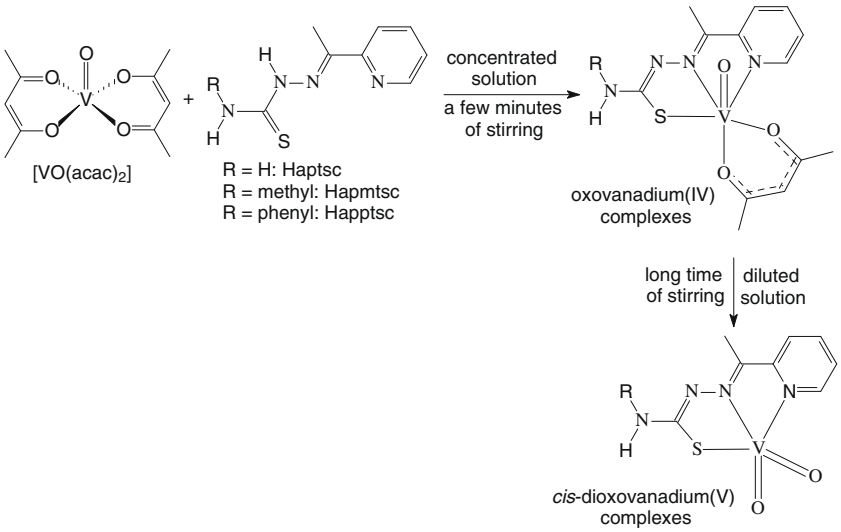
The compounds **4**, **5** and **6** lead to silent EPR signals, which is consistent with the oxidation state +V (d^0) for the vanadium centers.

3.3. Electrochemistry

The cyclic voltammogram (CV) studies for the oxovanadium(IV) complexes **1**, **2** and **3** were realized in DMF solutions. The electrochemical processes are consistent with the oxidative reactions observed for the vanadium(IV) compounds in alcoholic solution, forming the *cis*-dioxovanadium(V) complexes **4**, **5** and **6**, respectively, with loss of the acetylacetonate ligand. As shown in Fig. 4 for the CV curve of complex **1**, the V^{IV}–V^{V} redox processes are irreversible, in accord with the observed behavior for other similar vanadium(IV) complexes [11,12]. Moreover, three oxidation processes are observed for **1**–**3**, which were analyzed applying differential pulse voltammetry (DPV), as depicted in Fig. 5. The anodic peaks for the oxidation processes of the species **1**–**3** are seen with large intensity at 600, 604 and 652 mV, respectively. The two additional oxidation peaks observed for each complex (at 1088 and 1320 mV for **1**; 1080 and 1220 mV for **2**; 1096 and 1284 mV for **3**), with small intensities, are supposed to be originated by species formed upon coordination of one or two DMF molecules in the coordination sites occupied originally by $acac^-$ ligand in **1**–**3**. Under

Table 2
EPR parameters of compounds (**1**), (**2**) and (**3**) obtained by simulation and component analysis.

Compound	Physical state	g-values of the components	A-values (10^{-4} cm^{-1})	ΔH-values (mT)	Percentage of components
(**1**)	Powder	[1.9994 1.9877 1.9727]	–	[6.8 14.1 41.0]	100
	DMSO	[1.9832 1.9884 1.9622]	[51.7 50.7 153.0]	[0.014 1.25]	14
		[1.9793 1.9857 1.9515]	[60.0 52.7 167.5]	[0.014 1.25]	3
		[1.9994 1.9877 1.9727]	–	[22.3 31.7 80.7]	83.0
(**2**)	Powder	[1.9887 1.9732 1.9732]	–	[8.7 12.5 35.0]	100
	DMSO	[1.9832 1.9884 1.9622]	[51.7 50.7 153.0]	[0.014 0.76]	95
		[1.9793 1.9857 1.9515]	[60.0 52.7 167.5]	[0.014 1.25]	5
		–	–	–	0
(**3**)	Powder	[1.9887 1.9827 1.9667]	–	[4.3 7.3 25.1]	100
	DMSO	[1.9832 1.9884 1.9622]	[51.7 50.7 153.0]	[0.014 0.95]	9
		[1.9793 1.9857 1.9515]	[60.0 52.7 167.5]	[0.014 1.25]	2
		[1.9887 1.9827 1.9667]	–	[22.3 31.7 80.7]	89



Scheme 1. Synthesis of the complexes.

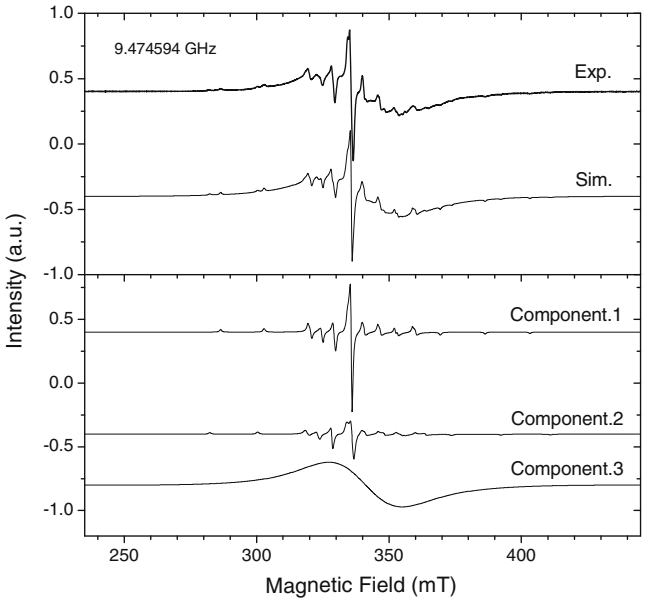


Fig. 3. EPR spectrum of **3** in DMSO solution at 25 K showing the three components. Sim. represents the best fit as a sum of the components in a proper concentrations described in Table 2. The percentage of the components are calculated by numerical double integration of the simulated components.

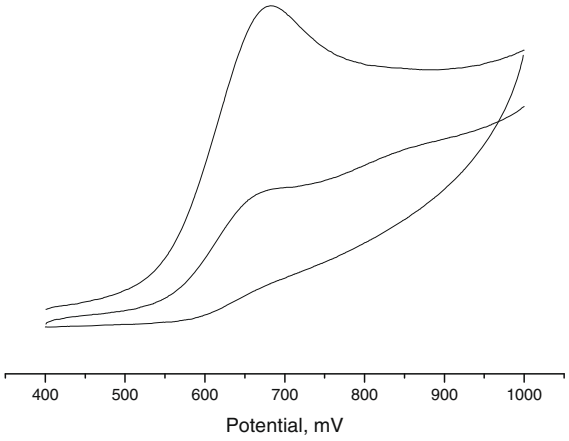


Fig. 4. Cyclic voltammogram of **1** (Ag/AgCl, 0.1 mol/L PTBA, DMF, 100 mV/s). An example of the irreversible redox processes observed for the vanadium(IV).

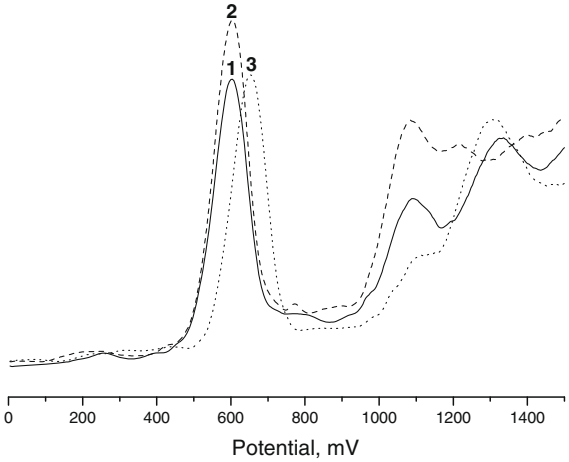


Fig. 5. Differential pulse voltammetry (Ag/AgCl, 0.1 mol/L PTBA, DMF, 20 mV/s) of the complexes **1** (solid line), **2** (dashed line) and **3** (dotted line).

excess of acetylacetone these additional peaks disappear and a new oxidation process is observed at 748 mV, referring to the oxidation of $[VO(acac)_2]$, which is formed in the solution under these circumstances. The formation of $[VO(acac)_2]$ was confirmed by the evaluating the DPV of $[VO(acac)_2]$ lonely under the same experimental conditions. The oxidation of $[VO(acac)_2]$ in equilibrium with the complexes **1**, **2** or **3** in DMF solution under excess of acetylacetone is reported in Fig. 6.

3.4. IR and NMR spectroscopies

Selected IR absorption bands assigned for the free ligands as well as for their vanadium complexes, given in Table 3, evidence *N,N,S*-coordination of the thiosemicarbazone ligands The ν(V=O) absorption band, observed at 998 cm^{-1} for $[VO(acac)_2]$, are observed at 953, 939 and 952 cm^{-1} for **1**, **2** and **3**, respectively. Two ν(O=V=O) absorption bands corresponding to the symmetric and anti-symmetric stretching modes are satisfactorily assigned for the dioxovanadium(V) complexes [15,16].

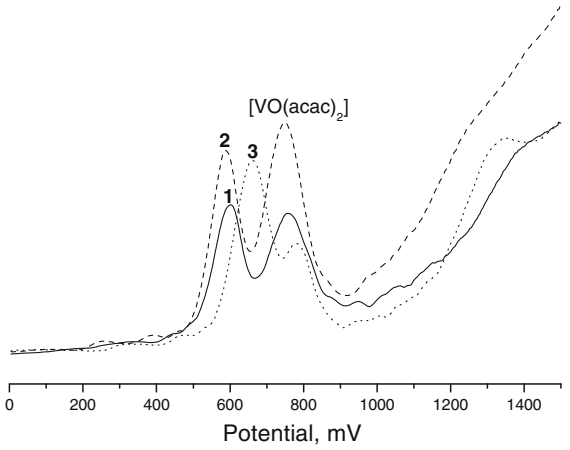


Fig. 6. Differential pulse voltammetry (Ag/AgCl, 0.1 mol/L PTBA, DMF, 20 mV/s) of the complexes **1** (solid line), **2** (dashed line) and **3** (dotted line) and excess of acetylacetone.

The ^{1}H chemical shift values of the free ligands and the diamagnetic complexes **4**, **5** and **6** are given in the experimental section. The Scheme 2 shows the numbered structures of the free ligands. The three new V(V) complexes show similar ^{1}H- and ^{13}C-chemical shift behavior. ^{1}H NMR integrations and signal multiplicities are in agreement with the proposed structures.

In the ^{1}H NMR spectra of the complexes, a down field shift of around ~0.2 ppm for the methyl hydrogens (C–CH_3), compared to the free ligands, evidences the coordination through the azomethine nitrogen atom. In the pyridine ring, the resonance of the hydrogen atoms follows the sequence H1, H4, H3 and H2 for the free ligands, but H1, H3, H4 and H2 for **4**, **5** and **6**, which is consistent with literature data [37]. This up-field shift of proton H4 could be the result of the decreasing of the azomethine anisotropic effect on this proton in the coordinated form of the ligands [38,39]. The values of δ for the azomethine and for the thione/thiolate carbons show clearly the coordination of the thiosemicarbazone ligands in the ^{13}C NMR spectra of the complexes. The δ for the azomethine carbons are found at 148.4, 148.4 and 149.2 ppm for the free ligands Haptsc, Hapmtsc and Happtsc, respectively, and at 154.2, 154.3 and 153.8 ppm for their respective V(V) complexes **4**, **5** and **6**, while the δ for the thione/thiolate carbons are observed at 179.1, 178.6 and 177.3 ppm for the free ligands and at 176.0, 173.3 and 170.3 ppm for the complexes. The ^{51}V NMR spectra of the complexes **4**, **5** and **6** in DMSO-d_6 present single peaks at δ −402.8, −404.2 and at −413.1 ppm, respectively, consistent with the proposed structures of the mononuclear *cis*-dioxovanadium(V) chelate-complexes. The values are in agreement with other penta-coordinated VO_2^+ complexes which involve one sulfur and two nitrogen donor atoms, occupying the three remaining positions at the vanadium coordination sphere [40]. The shielding order $[VO_2(aptsc)] < [VO_2(apmtsc)] < [VO_2(apptsc)]$ is verified for the three complexes, in accordance to the up-shielding effect generally found for semi- and thiosemicarbazone vanadium complexes, which is directly proportional to the volume of the group bound to the N^4 atom [41].

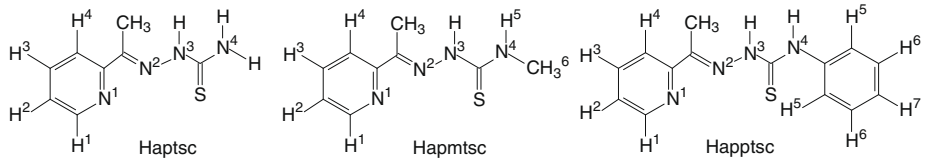
3.5. Crystal structures of the cis-dioxocomplexes $[VO_2(aptsc)]$ (**4**) and $[VO_2(apmtsc)]$ (**5**)

The perspective view of the dioxocomplexes **4** and **5** along with the atom labels is given in Figs. 7 and 8, respectively. The complexes present 5-coordinated vanadium(V) centers bonded to two oxo ligands in a *cis* arrangement, two nitrogen atoms and one sulfur atom from aptsc$^-$, which coordinates monoanionic in the *N,N,S*-tridentate mode, forming two five-membered quelate rings around the vanadium atom. The geometry around the vanadium centers are better defined as distorted square pyramids, as observed by $\tau = 0.23$ for **4** and $\tau = 0.22$ for **5** ($\tau = 1$ for an ideal trigonal bipyramid, $\tau = 0$ for an ideal square pyramid) [6,10]. The basal plane is occupied by the sulfur atom and by the nitrogen atoms N(1) and N(2) from the thiosemicarbazone ligand in both structures, while the fourth corner of the pyramid base is occupied by the oxygen O(1) in **4** and by the oxygen O(2) in **5**. The apical positions are engaged by the oxygen atoms O(2) and O(1) in **4** and **5**, respectively. The bond lengths between the vanadium center and the donor atoms are comparable with the values found in oxovanadium complexes involving structurally similar ligands previously described [42]. Additional information about bond lengths and angles for **4** and **5** can be seen in Table 4.

In the complex **4**, the crystal is stabilized by a net of intermolecular hydrogen bonds, which are shown in Fig. 7. Classic (N–H···O and N–H···N) and non-classic (C–H···O) hydrogen bonds are

Table 3
Selected IR data for the free ligands and their vanadium complexes (cm^{-1}).

Compound	ν(C=C + C=N)	ν(CS)	ν(C=O)	ν(N–H)	ν(V=O)
Haptsc	1602, 1583, 1563	850	–	3374, 3261, 3184	–
1	1615, 1599, 1574	794	1523, 1380	3432, 3306	953
4	1636, 1599, 1552	810	–	3300, 3137	946, 938
Hapmtsc	1578, 1539, 1497	834	–	3289, 3240	–
2	1597, 1559, 1515	770	1515, 1385	3303	939
5	1603, 1579, 1563	776	–	3234	959, 922
Happtsc	1598, 1587, 1527	801	–	3301, 3242	–
3	1597, 1536	781	1518, 1390	3374	952
6	1600, 1550	776	–	3235	959, 916



Scheme 2. Numbering scheme for ^{1}H NMR data.

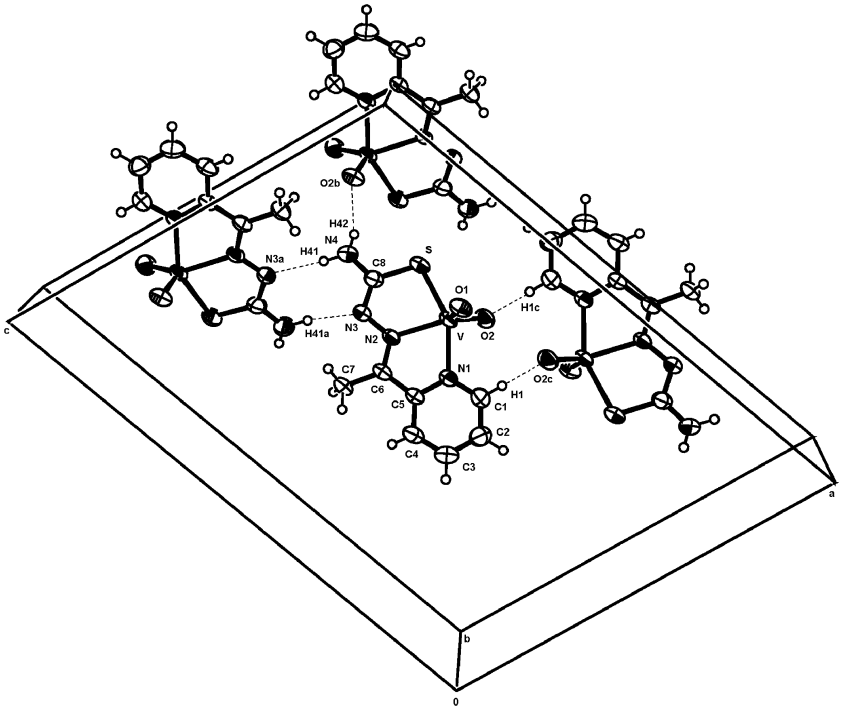


Fig. 7. Crystalline and molecular structure of $[VO_2(aptsc)]$ (**4**) with atom labels. [N(4)···N(3a) = 3.076(4) Å, N(4)–H(41)···N(3a) = 165(3)°], [N(4)···O(2b) = 2.876(3) Å, N(4)–H(42)···O(2b) = 162(3)°] and [C(1)···O(2c) = 3.397(4) Å, C(1)–H(1)···O(2c) = 162(2)°]. Symmetry operations used: (a) $-x, y, -z + 1/2$; (b) $-x + 1/2, y-1/2, -z + 1/2$; (c) $-x + 1/2, -y + 1/2, -z$.

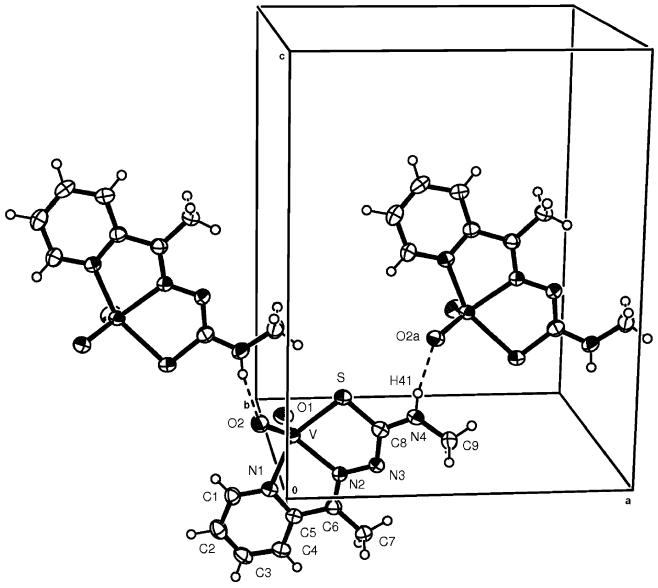


Fig. 8. Hydrogen bonds observed in the crystalline structure of $[VO_2(apmtsc)]$ (**5**), toward the direction [100]. [N(4)···O(2a) = 2.847 Å, N(4)–H(41)···O(2a) = 165.4°]. Symmetry operation used: (a) $x + 1/2, y, -z + 1/2$.

found. The nitrogen atom N(4), of the NH_2 group, is H-bonded through H(41) to the N(3a) atom from a symmetry related molecule, while H(42) interacts with the vanadyl oxygen atom O(2b) of a third complex molecule. Furthermore, the aromatic carbon atom C(1) is H-bonded to the vanadyl oxygen atom O(2c) of a fourth complex molecule.

The crystalline structure of the complex **5** is stabilized by N–H···O hydrogen bonds involving the nitrogen atom N(4) and the oxo ligand O(2a) of a symmetry related molecule, building a zigzag alignment of the complex molecules toward the direction [100], parallel to the *a* axis, as shown in the Fig. 8.

Table 4
Selected bond lengths (Å) and angles (°) refined from X-ray data and calculated for **4** and **5**.

	Complex **4**	Complex **5**
Bond lengths		
V–O(1)	1.6165(2)	1.611(2)
V–O(2)	1.6168(2)	1.631(2)
V–N(1)	2.092(2)	2.093(3)
V–N(2)	2.149(2)	2.155(2)
V–S	2.3658(9)	2.3758(9)
S–C(8)	1.738(3)	1.751(3)
N(1)–C(5)	1.357(3)	1.357(4)
C(5)–C(6)	1.460(3)	1.463(4)
C(6)–N(2)	1.305(3)	1.307(4)
N(2)–N(3)	1.372(3)	1.371(3)
N(3)–C(8)	1.316(3)	1.323(4)
C(8)–N(4)	1.332(4)	1.333(4)
Bond angles		
O(1)–V–O(2)	109.04(10)	109.67(12)
O(1)–V–N(1)	94.44(9)	98.90(10)
O(2)–V–N(1)	99.63(9)	95.55(10)
O(1)–V–N(2)	135.60(9)	113.81(11)
O(2)–V–N(2)	115.08(9)	136.33(11)
N(1)–V–N(2)	73.94(8)	74.15(9)
O(1)–V–S	96.80(7)	101.97(8)
O(2)–V–S	103.49(7)	97.64(8)
N(1)–V–S	149.29(6)	149.83(7)
N(2)–V–S	78.06(6)	77.57(7)
C(8)–S–V	98.56(9)	99.39(10)
C(5)–N(1)–V	118.18(17)	116.9(2)
N(1)–C(5)–C(6)	114.6(2)	114.5(3)
N(2)–C(6)–C(5)	113.8(2)	114.2(3)
C(6)–N(2)–V	118.58(17)	117.07(19)
N(3)–N(2)–V	124.11(14)	125.85(17)
C(8)–N(3)–N(2)	112.4(2)	111.9(2)
N(3)–C(8)–S	125.4(2)	125.0(2)

Table 5
Antibacterial activity against the strains of the *Mycobacterium tuberculosis* $H_{37}Rv$ ATCC 27294 of the free ligands and the derivative complexes.

Compounds	MIC (>90% inhibition)	
	μg/mL	μM
Hacac	50 (no inhibition)	–
$[VO(acac)_2]$	50 (no inhibition)	–
$[VOSO_4]$	50 (no inhibition)	–
NH_4VO_3	50 (no inhibition)	–
Haptsc	31.3	160.9
[VO(acac)(aptsc)] (**1**)	62.5	173.9
$[VO_2(aptsc)]$ (**4**)	31.3	113.1
Hapmtsc	7.8	37.4
[VO(acac)(apmtsc)] (**2**)	3.9	10.4
$[VO_2(apmtsc)]$ (**5**)	3.9	13.4
Happtsc	15.6	57.7
[VO(acac)(apptsc)] (**3**)	1.56	3.6
$[VO_2(apptsc)]$ (**6**)	15.6	44.3
Isoniazid	0.015	0.1

3.6. Anti-*M. tuberculosis* activity

The *in vitro* antimicrobial properties of the three heterocyclic ligands and their vanadium(IV) and (V) complexes were evaluated against the strains of the *M. tuberculosis* $H_{37}Rv$ ATCC 27294 and the results are reported in Table 5.

Analyzing the results obtained for the uncoordinated ligands, it is to note that the substitution of one hydrogen atom linked to N(4) in the thiosemicarbazone moiety for bulky entities (phenyl or methyl group) causes an improvement on their activities. Considering the N(4)-substituted ligands and their complexes studied, it can be seen that the complexes **2**, **5** and **6** have slightly better and similar activities when compared with the free ligands. On the other hand, the vanadium(IV) complex **3** presented a very small value of MIC (1.56 μg/mL), which represents a 10-fold higher activity than its free ligand and is comparable or better than some commonly used anti-*M. tuberculosis* agents like ciprofloxacin (MIC = 2.00 μg/mL), *p*-aminosalicylic acid (MIC = 0.5–>2.0 μg/mL), ethionamide (MIC = 0.63–1.25 μg/mL), cycloserine (MIC = 12.5–50 μg/mL), gentamicin (MIC = 2.0–4.0 μg/mL), ethambutol (MIC = 0.94–1.88 μg/mL), kanamycin (MIC = 1.25–5.0 μg/mL), tobramycin (MIC = 4.0–8.0 μg/mL), clarithromycin (MIC = 8.0–16 μg/mL) and thiacetazone (MIC = 0.125–>2.0 μg/mL) [2,43].

The variation in the oxidation state of the vanadium center between IV and V seems not to play an important role in the activity of the complexes, since no systematic behavior could be observed by varying between V(IV) and V(V), maintaining the thiosemicarbazone ligand, by the studied complexes. Acetylacetone, $[VO(acac)_2]$ and the inorganic vanadium salts $VOSO_4$ and NH_4VO_3 have not shown any inhibition at the concentration of 50 μg/mL, implying that the thiossemicarbazone ligands are the active species and that their activity may be improved upon complexation to vanadium. The reduction of the polarity of a complex as a whole, when compared with the free ions or ligands, by partial sharing of their charges within the coordination compounds, which include the bioactive thiosemicarbazones, may favor their permeation through the lipid layer of the cell membrane, resulting possibly in a better cell uptake of the active species, as suggested former for similar findings [41,44].

4. Conclusions

Neutral oxovanadium(IV) and dioxovanadium(V) complexes having *N,N,S*-donor ligands have been synthesized in satisfactory yields and were characterized by several methods. One of the complexes exhibited *in vitro* antitubercular activity towards *M. tuberculosis* $H_{37}Rv$ better than observed for some medications commonly used in the treatment of tuberculosis. The coordination of thiosemicarbazones to some vanadium (IV) and (V) centers may result in an enhancement of their anti-*M. tuberculosis* activities. The presence of bulky groups (methyl or phenyl units) attached to the N(4) atom of the substituted thiosemicarbazone moiety in the complexes **2**, **3**, **5** and **6** or in the free Hapmtsc and Happtsc ligands increases their inhibitory activity by comparison with the non-substituted Haptsc ligand and its complexes **1** and **4**, which presented the lowest activities in this study. Considering the present results and especially that obtained for the complex **3**, the coordination of a thiosemicarbazone to vanadium may represent a novel strategy to prepare new antitubercular agents. New investigations must be done to know exactly the participation of the vanadium in the bacterial inhibitory effect observed.

Acknowledgments

The Authors thank FAPESP, PRONEX/FAPESP (03/09859-2), FINEP (Infra No. 0970/01), CNPq and CAPES for supporting this work.

Appendix A. Supplementary data

CCDC 669245 and 669246 contain the supplementary crystallographic data for **4** and **5**. These data can be obtained free of charge via http://www.ccdc.cam.ac.uk/conts/retrieving.html, or from the Cambridge Crystallographic Data Centre, 12 Union Road, Cambridge CB2 1EZ, UK; fax: (+44) 1223 336 033; or e-mail: deposit@ccdc.cam.ac.uk. Supplementary data associated with this article can be found, in the online version, at doi:10.1016/j.poly.2008.11.017.

References

[1] M.T. Cocco, C. Congiu, V. Onnis, M.L. Pellerano, A.D. Logu, Bioorg. Med. Chem. 10 (2002) 501.
[2] D. Sriram, P. Yogeeswari, R. Thirumurugan, Bioorg. Med. Chem. Lett. 14 (2004) 3923.
[3] G. Domagk, R. Behnisch, F. Mietzsch, H. Schmidt, Naturwissenchaften 33 (1946) 315.
[4] G.M. Lima, J.L. Neto, H. Beraldo, H.G.L. Siebald, D.J. Duncalf, J. Mol. Struct. 604 (2002) 287.
[5] F.M. Collins, D.L. Klayman, N.E. Morrison, J. Gen. Microbiol. 128 (1982) 1349.
[6] P.I.S. Maia, V.M. Deflon, G.F. de Sousa, S.S. Lemos, A.A. Batista, O.R. Nascimento, E. Niquet, Z. Anorg. Allg. Chem. 633 (2007) 783.
[7] D. Kovala-Demertzi, M.A. Demertzis, J.R. Miller, C. Papadopoulou, C. Dodorou, G. Filousis, J. Inorg. Biochem. 86 (2001) 555.
[8] M.C. Rodríguez-Argüelles, E.C. López-Silva, J. Sanmartín, P. Pelagatti, F. Zani, J. Inorg. Biochem. 99 (2005) 2231.
[9] D.K. Sau, R.J. Butcher, S. Chaudhuri, N. Saha, Mol. Cell. Biochem. 253 (2003) 21.
[10] D. Rehder, Inorg. Chem. Commun. 6 (2003) 604.
[11] P.I.S. Maia, V.M. Deflon, E.J. Souza, E. Garcia, G.F. de Sousa, A.A. Batista, A.T. Figueiredo, E. Niquet, Transit. Met. Chem. 30 (2005) 404.
[12] V.M. Deflon, D.M. Oliveira, G.F. de Sousa, A.A. Batista, L.R. Dinelli, E. Castellano, Z. Anorg. Allg. Chem. 628 (2002) 1140.
[13] K.H. Thompson, C. Orvig, Coord. Chem. Rev. 219 (2001) 1033.
[14] H. Sakurai, Y. Kojima, Y. Yoshikawa, K. Kawabe, H. Yasui, Coord. Chem. Rev. 226 (2002) 187.
[15] A.M.B. Bastos, J.G. da Silva, P.I.S. Maia, V.M. Deflon, A.A. Batista, A.V.M. Ferreira, L.M. Botion, E. Niquet, H. Beraldo, Polyhedron 27 (2008) 1787.
[16] P. Noblía, M. Vieites, B.S. Parajón-Costa, E.J. Baran, H. Cerecetto, P. Draper, M. González, O.E. Piro, E.E. Castellano, A. Azqueta, A.L. Ceráin, A. Monge-Vega, D. Gambino, J. Inorg. Biochem. 99 (2005) 443.
[17] D.C. Crans, J.J. Smee, E. Gaidamauskas, L. Yang, Chem. Rev. 104 (2004) 849.
[18] A. Maiti, S. Ghosh, J. Inorg. Biochem. 36 (1989) 131.
[19] S. David, V. Barros, C. Cruz, R. Delgado, FEMS Microbiol. Lett. 251 (2005) 119.
[20] B.K. Koo, Y.J. Jang, U. Lee, Bull. Korean Chem. Soc. 24 (2003) 1014.
[21] D.L. Klayman, J.F. Bartosevich, T.S. Griffin, C.J. Mason, J.P. Scovill, J. Med. Chem. 22 (1979) 855.
[22] S. Stoll, A. Schweiger, EasySpin, A comprehensive software package for spectral simulation and analysis in EPR, J. Magn. Reson. 178 (2006) 42.
[23] A. Earnshaw, Introduction to Magnetochemistry, Academic Press, New York, 1968;
O. Kahn, Molecular Magnetism, VCH Publishers, New York, 1993.
[24] G.M. Sheldrick, SHELXS97, Program for the Solution of Crystal Structures, University of Göttingen, Germany, 1997.

[25] G.M. Sheldrick, SHELXL97, Program for the Refinement of Crystal Structures, University of Göttingen, Germany, 1997.
[26] A.L. Spek, PLATON, A Multipurpose Crystallographic Tool, University of Utrecht, The Netherlands, 2004.
[27] R. Coppens, L. Leiserowitz, D. Rabinovich, Acta Cryst. 18 (1965) 1035.
[28] S.G. Franzblau, R.S. Witzig, J.C. McLaughlin, P. Torres, G. Madico, A. Hernandez, M.T. Degnan, M.B. Cook, V.K. Quenzer, R.M. Ferguson, R.H. Gilman, J. Clin. Microbiol. 36 (1998) 362.
[29] M. Nakai, M. Obata, F. Sekiguchi, M. Kato, M. Shiro, A. Ichimura, I. Kinoshita, M. Mikuriya, T. Inohara, K. Kawabe, H. Sakurai, C. Orvig, S. Yano, J. Inorg. Biochem. 98 (2004) 105.
[30] P.R. Levstein, R. Calvo, Inorg. Chem. 29 (1990) 1581.
[31] C.D. Brondino, N.M.C. Casado, M.C.G. Passeggi, R. Calvo, Inorg. Chem. 32 (1993) 2078.
[32] D.M. Martino, M.C.G. Passeggi, R. Calvo, O.R. Nascimento, Physica B 225 (1996) 63.
[33] A.J. Costa-Filho, O.R. Nascimento, L. Ghivelder, R. Calvo, J. Phys. Chem. B 105 (2001) 5039.
[34] A.J. Costa-Filho, O.R. Nascimento, R. Calvo, J. Phys. Chem. B 108 (2004) 9549.
[35] E.F. Chagas, R.E. Rapp, D.E. Rodrigues, N.M.C. Casado, R. Calvo, J. Phys. Chem. B 110 (2006) 8052.
[36] R. Calvo, Appl. Magn. Reson. 31 (2007) 271.
[37] M. Carcelli, A. Fochi, P. Pelagatti, G. Pelizzi, U. Russo, J. Organomet. Chem. 626 (2001) 161.
[38] P. Noblia, E.J. Baran, L. Otero, P. Draper, H. Cerecetto, M. González, O.E. Piro, E.E. Castellano, T. Inohara, Y. Adachi, H. Sakurai, D. Gambino, Eur. J. Inorg. Chem. 2 (2004) 322.
[39] M. Hesse, H. Meier, B. Zeeh, In Spectroskopische Methoden in der Organischen Chemie, Georg Thieme Verlag Stuttgart, New York, 1995.
[40] D. Rehder, C. Weidemann, A. Duch, W. Priebsch, Inorg. Chem. 27 (1988) 584.
[41] M.R. Maurya, A. Kumar, M. Abid, A. Azam, Inorg. Chim. Acta 359 (2006) 2439.
[42] M. Sutradhar, G. Mukherjee, G.B. Michael, M.G.B. Drew, S. Ghosh, Inorg. Chem. 45 (2006) 5150.
[43] L.A. Collins, S.G. Franzblau, Antimicrob. Agents Chemother. (1997) 1004.
[44] P.K. Panchal, H.M. Parekh, P.B. Pansuriya, M.N. Patel, J. Enz. Inhib. Med. Chem. 21 (2006) 203.

Polyhedron 28 (2009) 407–415

Contents lists available at ScienceDirect

Polyhedron

journal homepage: www.elsevier.com/locate/poly

An X-ray diffraction study of anion and ratio dependence in the formation of discrete molecules versus polymeric arrays involving silver salts and bipyridine ligands

Fernando Hung-Low, Amanda Renz, Kevin K. Klausmeyer *

Department of Chemistry and Biochemistry, Baylor University, One Bear Place #97348, Waco, TX 76798, United States

ARTICLE INFO

Article history:
Received 20 August 2008
Accepted 14 November 2008
Available online 3 January 2009

Keywords:
Metal–metal interaction
Silver
Coordination modes
Bipy ligands

ABSTRACT

Described are the reaction of the silver(I) salts of trifluoroacetate (tfa^-) and trifluoromethanesulfonate (Otf^-) with the bidentate ligands 4,4′-dimethyl-2,2′-bipyridine (L1), 5,5′-dimethyl-2,2′-bipyridine (L2) and 2,2′-bipyridine (L3), to afford the formation of five structures. A systematic study was conducted to obtain the different coordination moieties possible by changing the ligand to metal ratio and the solvent of crystallization. In total, six discrete molecules (Agtfa)(L1), **1**, (Agtfa)(L2), **2A** and **2B**, $(AgOtf)_2(L2)_3$, **3A** and **3B**, $(AgOtf)_2(L3)_3$, **5,** and one polymeric structure $(AgOtf)(L3)_n$, **4** were obtained. Compounds **2** and **3** form two crystal structures each, where differences in connectivity of the corresponding anion to the metal center are observed, as directed by solvent of crystallization. The varying degree of interaction of the two anions, combined with the functionality of the ligand used in the reaction, gave rise to coordination numbers from 4 to 6, representing capped-trigonal, distorted tetrahedral, trigonal bipyramidal and distorted octahedral environments, which illustrate the range of coordination moieties that can be adopted in silver(I) complexes, and the possibility of systematic control of the coordination framework topology of a compound. This study complements the already reported silver coordinated structures associated with the bipyridine ligands mentioned herein.

© 2008 Elsevier Ltd. All rights reserved.

1. Introduction

Design and construction of self-assembled coordination structures is one of the most active areas of materials research due to their intriguing structural motifs and functional properties such as molecular adsorption, magnetism and luminescence [1–10]. During the past few decades, metal–organic frameworks, coordination polymers and numerous examples of discrete macromolecules have been built based upon the functionality or geometry of the corresponding ligand, ratio of reactants or solvent system [11–14]. Designed coordination architectures can be tuned by predicting supramolecular interactions such as hydrogen bonds, π–π stacking, and host–guest ionic interactions, which are also responsible for unique structural features in multidimensional coordination networks [15–22]. In particular, coordinative structures involving the silver(I) ion have made contributions to this field due to the capability of Ag(I) to vary its geometry and coordination number. This ability has produced an extensive library of silver(I) compounds, and has contributed to the determination of reaction conditions that can deliberately induce structural changes in the topology of the metal complex [23–27]. Accordingly, many self-assembled compounds of silver(I) can be readily obtained with slight variations in ligand and/or anion that directs the formation of both small discrete molecules and polymeric arrays. In this paper several coordinative environments are seen which depend on the solvent of crystallization and the interacting ability of the anion.

The employ of symmetrically methyl-substituted 4,4′-dimethyl-2,2′-bipyridine, L1 and 5,5′-dimethyl-2,2′-bipyridine, L2 and the unsubstituted 2,2′-bipyridine, L3 ligands is determinant in the formation of distinct structural motifs mainly due to the free rotation along the central C–C bond. Therefore, bipy cannot only be regarded as a chelating ligand [28–36], but also as a potential connector between metal centers by acting as a bridging ligand [37–41]. As observed in this series of compounds, the most common mode of binding of these bipy ligands is the chelating fashion by virtue of the proximity of the pyridine rings, forming with the metal center a stable five-member ring. Only with L2 and L3, were both coordination modes observed in a single compound.

Overall, the compounds reported herein illustrate the range of coordination environments that can be adopted in silver(I) complexes, and the possibility of systematic control the coordination framework topology of a compound by aim of the geometry and functionality of the ligand. This report provides an extension of a previous work to encompass silver(I) complexes associated with bipyridine type ligands [28,30,34,35,41]. In conjunction they offer

* Corresponding author. Tel.: +1 254 710 2665; fax: +1 254 710 4272.
E-mail address: Kevin_Klausmeyer@baylor.edu (K.K. Klausmeyer).

0277-5387/$ - see front matter © 2008 Elsevier Ltd. All rights reserved.
doi:10.1016/j.poly.2008.11.040

a compilation of the structural and coordinative factors on which the formation of discrete molecules and polymeric arrays depend.

2. Experimental

2.1. General methods

All experiments were carried out under an argon atmosphere using a Schlenk line and standard Schlenk techniques. Silver(I) trifluoroacetate and silver(I) trifluoromethanesulfonate were purchased from Strem Chemicals Inc. and stored in an inert-atmosphere glovebox; solvents were distilled under nitrogen from the appropriate drying agent immediately before use. 5,5′-dimethyl-2,2′-bipyridine, 4,4′-dimethyl-2,2′-bipyridine, and 2,2′-bipyridine were purchased from Aldrich and used as received. Celite was also purchased from Aldrich and dried at 120 °C prior to use. All flasks were shielded from light with aluminum foil to prevent the photodecomposition of the silver compounds. Percent yields are based upon the amount of silver salt used. ^{1}H NMR spectra were recorded at 202.31 MHz on a Varian 500 MHz NMR spectrometer. Elemental analyses were performed by Atlantic Microlabs Inc., Norcross, GA. High resolution mass spectra (HRMS) were obtained in the Baylor University Mass Spectrometry Core Facility on a Thermo Scientific LTQ Orbitrap Discovery using +ESI.

2.2. Synthesis of Agtfa(L1) (**1**)

The reaction was done in a 1:1 ratio of 4,4′-dimethyl-2,2′-bipyridine (0.073 g, 0.396 mmol) and Agtfa (0.089 g, 0.398 mmol) in CH_3CN. The resulting solution remained clear and colorless, and after stirring for 5 min, the solution was dried in vacuo to obtain a white powder in 69% isolated yield (0.111 g, 0.274 mmol). Colorless blocks were formed by layering hexane over a CH_2Cl_2 solution of **1** at 5 °C. ^{1}H NMR (CD_3CN, 298 K) δ: 2.52 (s, 6H, CH_3), 7.46 (d, 2H, J = 4.5 Hz, aromatic), 8.14 (s, 2H, aromatic), 8.60 (d, 2H, J = 4.9 Hz, aromatic). $C_{14}H_{12}AgF_3N_2O_2$ (405.12): *Anal.* Calc. for C, 41.51; H, 2.99; N, 6.91. Found: C, 41.52; H, 3.02; N, 6.94%. +ESI-HRMS for $[Ag(L1)]^+$ calc. 291.0051 m/z; found: 291.0039 m/z; $[Ag(L1)(CH_3CN)]^+$ calc. 332.0317 m/z; found: 332.0303 m/z; $[Ag(L1)_2]^+$ calc. 475.1052 m/z; found: 475.1034 m/z.

2.3. Synthesis of $[Agtfa(L2)]_2$ (**2A** and **2B**)

This reaction used 1 equiv. of 5,5′-dimethyl-2,2′-bipyridine (0.074 g, 0.404 mmol) in CH_3CN (5 mL) added to a stirred solution of Agtfa (0.089 g, 0.398 mmol) in CH_3CN (5 mL). This was stirred for 5 min and the solvent was removed in vacuo to leave a white powder in 47% isolated yield (0.075 g, 0.093 mmol). Colorless blocks were formed by slow diffusion of hexane into a CH_2Cl_2 solution of the compound at 5 °C, which afforded crystal structure **2A**. A slightly different conformation of the same compound was obtained as colorless blocks formed by slow diffusion of hexane into a THF solution of the resulting product at 5 °C, giving crystal structure **2B**. ^{1}H NMR (CD_3CN, 298 K) δ: 2.45 (s, 6H, CH_3), 7.89 (d, 2H, J = 7.5 Hz, aromatic), 8.14 (d, 2H, J = 7.9 Hz, aromatic), 8.58 (s, 2H, aromatic). $C_{28}H_{24}Ag_2F_6N_4O_4$ (810.25): *Anal.* Calc. for C, 41.51; H, 2.99; N, 6.91. Found: C, 41.64; H, 3.04; N, 6.98. +ESI-HRMS for $[Ag(L2)]^+$ calc. 291.0051 m/z; found: 291.0041 m/z; $[Ag(L2)(CH_3CN)]^+$ calc. 332.0317 m/z; found: 332.0306 m/z; $[Ag(L2)_2]^+$ calc. 475.1052 m/z; found: 475.1040 m/z.

2.4. Synthesis of $(AgOtf)_2(L2)_3$ (**3A**) and $(AgOtf)_2(L2)_3$·MeOH (**3B**)

A solution of 5,5′-dimethyl-2,2′-bipyridine (0.170 g, 0.923 mmol) in CH_3CN (5 mL) was added to AgOtf (0.166 g, 0.602 mmol) in CH_3CN (5 mL) to leave a brownish solid upon evaporation of the solvent. This was then re-dissolved in 10 mL of CH_3CN and filtered through celite to obtain a yellow-white powder in 61% isolated yield (0.195 g, 0.183 mmol). Colorless blocks were formed by layering hexane over a CH_2Cl_2 solution of the compound at 5 °C, which afforded crystal structure **3A**. A slightly different conformation (crystal structure **3B**) of the same compound was obtained as colorless blocks formed by layering ether over a CH_3OH solution of the product at 5 °C, this resulted in the incorporation of a solvent MeOH molecule. ^{1}H NMR (CD_3CN, 298 K) δ: 2.38 (s, 6H, CH_3), 7.90 (d, 2H, J = 7.9 Hz, aromatic), 8.15 (d, 2H, J = 8.5 Hz, aromatic), 8.55 (s, 2H, aromatic). *Anal.* Calc. for $C_{38}H_{36}Ag_2F_6N_6O_6S_2$ (1066.59): C, 39.52; H, 2.56; N, 9.08. Found: C, 40.02; H, 2.49; N, 8.86%. +ESI-HRMS for $[Ag(L2)]^+$ calc. 291.0051 m/z; found: 291.0042 m/z; $[Ag(L2)(CH_3CN)]^+$ calc. 332.0317 m/z; found: 332.0306 m/z; $[Ag(L2)_2]^+$ calc. 475.1052 m/z; found: 475.1041 m/z.

2.5. Synthesis of $[AgOtf(L3)]_n$ (**4**)

To a stirred solution of AgOtf (0.109 g, 0.398 mmol) in CH_3CN (5 mL) was added 2,2′-bipyridine (0.061 g, 0.396 mmol) in CH_3CN (5 mL). The resulting solution was allowed to stir for 5 min and then dried in vacuo to leave a yellow-white solid upon evaporation of the solvent. The resulting product was obtained in 70% isolated yield (0.115 g, 0.278 mmol). Colorless blocks were obtained by slow diffusion of hexane into a CH_2Cl_2 solution of **4** at 5 °C. ^{1}H NMR (CD_3CN, 298 K) δ: 7.63 (t, 2H, J = 5.9 Hz, aromatic), 8.10 (t, 2H, J = 7.9 Hz, aromatic), 8.32 (d, 2H, J = 7.9 Hz, aromatic), 8.70 (d, 2H, J = 4.9 Hz, aromatic). *Anal.* Calc. for $C_{11}H_8AgF_3N_2O_3S$ (413.12): C, 31.98; H, 1.95; N, 6.78; found C, 32.24; H, 2.05; N, 7.05%. +ESI-HRMS for $[Ag(L3)]^+$ calc. 262.9738 m/z; found: 262.9727 m/z; $[Ag(L3)(CH_3CN)]^+$ calc. 304.0004 m/z; found: 303.9993 m/z; $[Ag(L3)_2]^+$ calc. 419.0426 m/z; found: 419.0411 m/z.

2.6. Synthesis of $(AgOtf)_2(L3)_3$ (**5**)

The reaction was done in a 3:2 ratio of 2,2′-bipyridine (0.142 g, 0.923 mmol) and AgOtf (0.164 g, 0.602 mmol) in CH_3CN to leave a off-white solid upon evaporation of the solvent. This was re-dissolved in 10 mL of CH_3CN and filtered through celite. Upon evaporation, the product was obtained in 52% isolated yield (0.153 g, 0.156 mmol). Colorless blocks were formed by layering hexane over a CH_2Cl_2 solution of **5** at 5 °C. ^{1}H NMR (CD_3CN, 298 K) δ: 7.60 (t, 2H, J = 6.9 Hz, aromatic), 8.10 (t, 2H, J = 7.5 Hz, aromatic), 8.33 (d, 2H, J = 7.9 Hz, aromatic), 8.67 (d, 2H, J = 4.9 Hz, aromatic). *Anal.* Calc. for $C_{96}H_{72}Ag_6F_{18}N_{18}O_{18}S_6$ (982.43): C, 39.12; H, 2.46; N, 8.55. Found: C, 39.33; H, 2.31; N, 8.52%. +ESI-HRMS for $[Ag(L3)]^+$ calc. 262.9738 m/z; found: 262.9726 m/z; $[Ag(L3)(CH_3CN)]^+$ calc. 304.0004 m/z; found: 303.9992 m/z; $[Ag(L3)_2]^+$ calc. 419.0426 m/z; found: 419.0411 m/z.

2.7. Crystallographic analyses

Single X-ray diffraction data of compounds **1–5** were collected at 110 K on a Bruker X8 Apex using Mo Kα radiation (λ = 0.71073 Å). All structures were solved by direct methods after correction of the data using SADABS [42,43]. Crystallographic data were collected on crystals with approximate dimensions of 0.285 × 0.245 × 0.084 mm for **1**, 0.120 × 0.290 × 0.364 mm for **2A**, 0.170 × 0.201 × 0.300 mm for **2B**, 0.100 × 0.181 × 0.370 mm for **3A**, 0.130 × 0.190 × 0.390 mm for **3B**, 0.190 × 0.230 × 0.300 mm for **4**, and 0.130 × 0.170 × 0.242 mm for **5**. Details of the crystal parameters, data collection, and refinement are summarized in Table 1. The molecular structure of the compounds is displayed in Figs. 1–6. Summary of selected bond lengths, angles, and interatomic distances are given in Table 2. All data were processed using the Bruker AXS SHELXTL software,

Table 1
Crystallographic data for complexes **1**–**5**.

	1	**2A**	**2B**	**3A**	**3B**	**4**	**5**
Empirical formula	$C_{28}H_{24}Ag_2F_6N_4O_4$	$C_{28}H_{24}Ag_2F_6N_4O_4$	$C_{28}H_{24}Ag_2F_6N_4O_4$	$C_{38}H_{36}Ag_2F_6N_6O_6S_2$	$C_{39}H_{40}Ag_2F_6N_6O_7S_2$	$C_{11}H_8AgF_3N_2O_3S$	$C_{64}H_{48}Ag_4F_{12}N_{12}O_{12}S_4$
Formula mass	810.25	810.25	810.25	1066.59	1098.63	413.12	1964.86
a (Å)	13.1687(17)	12.4897(12)	7.1760(5)	37.5410(6)	8.9694(4)	11.3566(6)	14.0470(7)
b (Å)	10.9361(14)	15.8969(14)	12.9088(8)	8.5243(2)	26.1019(11)	11.3566(6)	43.764(2)
c (Å)	19.218(2)	14.3693(14)	16.8314(11)	13.1995(2)	9.8484(4)	18.0721(19)	16.6627(8)
α (°)	90	90	69.044(2)	90	90	90	90
β (°)	90	92.555(5)	78.3210(10)	105.9150(10)	112.454(2)	90	92.453(2)
γ (°)	90	90	86.9960(10)	90	90	120	90
V (Å^3)	2767.6(6)	2850.2(5)	1425.54(16)	4062.07(13)	2130.89(16)	2018.5(3)	10234.1(9)
Z	4	4	2	4	2	6	6
Crystal system	Orthorhombic	Monoclinic	Triclinic	Monoclinic	Monoclinic	Trigonal	Monoclinic
Space group	*Pcca*	$P2_1/c$	$\bar{P}$	$C2$	$P2_1$	$P3_121$	$P2_1/n$
T (K)	110(2)	110(2)	110(2)	110(2)	110(2)	110(2)	110(2)
$D_{calc.}$ (g cm^{-3})	1.945	1.888	1.888	1.744	1.712	2.039	1.913
μ (mm^{-1})	1.499	1.456	1.456	1.149	1.099	1.699	1.359
$2\theta_{max.}$ (°)	26.70	26.49	26.53	26.39	26.40	30.53	26.45
Reflections measured	49510	67322	44271	12734	17509	16717	103932
Reflections used (R_{int})	2863(0.0631)	5875(0.0354)	5706(0.0311)	7776(0.0298)	7939(0.0322)	4118(0.0412)	20909(0.0451)
Restraints/parameters	0/201	0/401	0/401	20/547	1/570	0/216	57/1460
R_1 [$I > 2\sigma(I)$]	0.0604	0.0205	0.0222	0.0353	0.0268	0.0373	0.0358
wR_2 [$I > 2\sigma(I)$]	0.1287	0.0480	0.0502	0.0799	0.0546	0.0946	0.0747
$R(F_o^2)$ (all data)	0.0647	0.0231	0.0259	0.0390	0.0290	0.0407	0.0465
$R_w(F_o^2)$ (all data)	0.1299	0.0496	0.0545	0.0832	0.0559	0.0980	0.0810
Goodness of fit on F^2	1.449	1.034	1.048	1.028	1.022	1.067	1.035

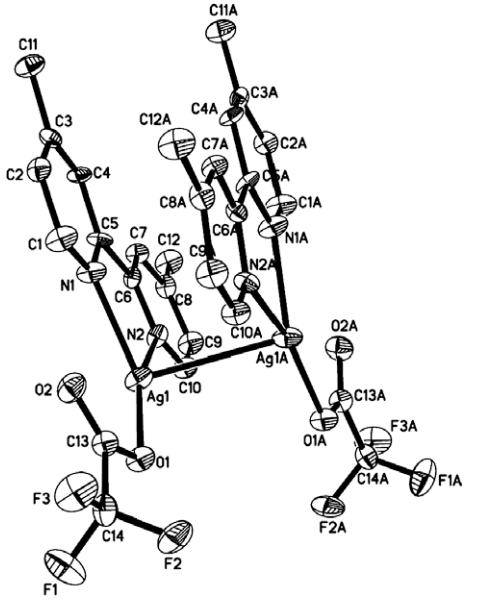


Fig. 1. Thermal ellipsoid plot of **1** with an atomic numbering scheme. Ellipsoids are shown at the 50% level. Hydrogen atoms have been removed for clarity.

version 6.10 [44]. Hydrogen atoms were placed in calculated positions and all non-hydrogen atoms were refined anisotropically, unless specified. The triflate ions for structure **3A** were restrained to have similar bond lengths and angles. The structure of **5** contained one disordered triflate which was modeled over two positions. Corresponding bonds and anisotropic displacement parameters were restrained to be similar.

3. Results and discussion

3.1. Synthesis and NMR spectroscopy

The silver compounds **1–5** were synthesized by reaction of substituted and un-substituted bipy ligands with simple silver salts under ambient conditions. All of the compounds synthesized herein can be isolated as white or off-white powders that appear to be indefinitely stable in solution if kept shielded from light in a sealed container. The powders of each compound have proven themselves to be quite robust, withstanding long exposure to air and room temperatures. Photodecomposition of the white solid is observed to be faster in the Otf compounds when compared to the tfa metal complexes, which result in the formation of a gray-black solid. Purification of the compounds from decomposition products can be achieved by dissolving the solid in CH_3CN and inducing precipitation of the product with ether.

Reaction of Agtfa with each of the bipy ligands only affords metal complexes in a 1:1 ligand to metal ratio; no higher ratios have been isolated for tfa. On the other hand, the use of the moderately interacting triflate yielded compounds that display a 3:2 ligand to metal ratio for 5,5′-dimethyl-2,2′-bipyridine and 4,4′-dimethyl-2,2′-bipyridine. The 3:2 ratio X-ray crystal structure of 4,4′-dimethyl-2,2′-bipyridine to AgOtf was obtained, although it is not reported in this work due to unsatisfactory refinement of the crystallographic data. The unsubstituted L3, which lacks any hindered effects from methyl groups substituted in the pyridine rings, allows the formation of coordinative structures in the different ratios possible, only when the AgOtf salt is used in the reaction. Compounds **2** and **3** each present two different structural conformations from crystals obtained by using distinct crystallization solvent systems. The variations observed in the two conformations for compounds **2A** and **2B** stem solely from slight differences in the interaction of the counterion with the corresponding metal centers, while there is the additional interaction of MeOH in going from **3A** to **3B**. It should be noted that the structural variation that is observed in **2A** and **2B** is repeatable. Several crystal tubes of each were grown and several crystals from each batch were checked by determining the unit cell. In each case the structural motif was preserved by crystallization procedure. Overall, the crystal structures of compounds **1–5** exhibit the silver(I) cation in a variety of settings and coordinative environments which is demonstrative of the effects of two variables: anion and ligand/ratio dependence of structural features. This variability in structure and bonding is enhanced on silver(I) complexes due to the facility with which it varies its coordination sphere to accept the number of donors

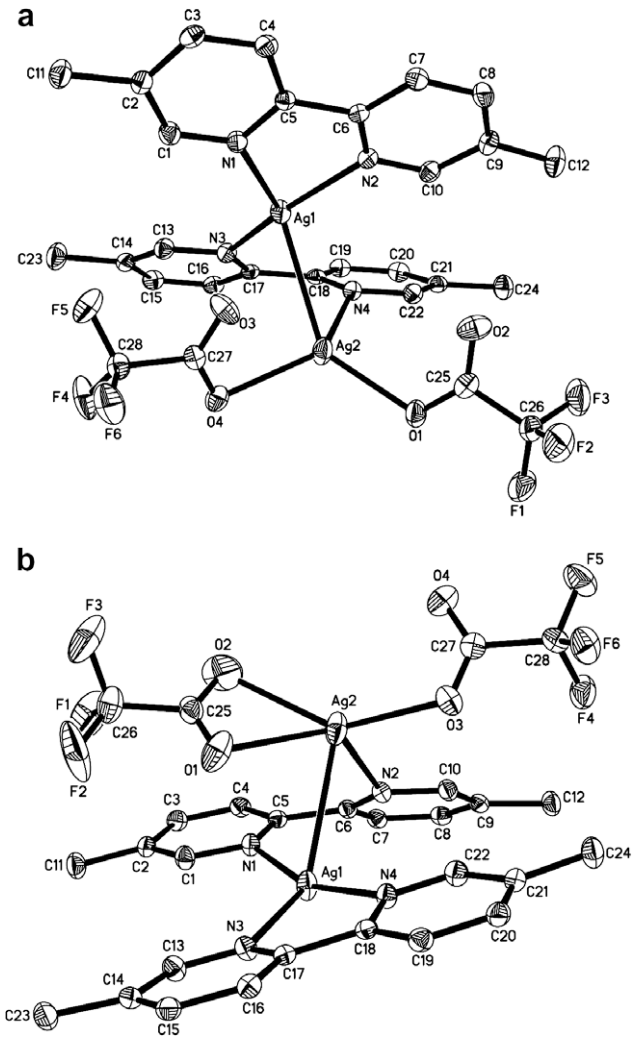


Fig. 2. Molecular structure of **2A** with an atomic numbering scheme. Ellipsoids are shown at the 50% level. Hydrogen atoms have been removed for clarity. Thermal ellipsoid plot of the molecular structure of **2B** with an atomic numbering scheme. Ellipsoids are shown at the 50% level. Hydrogen atoms have been removed for clarity.

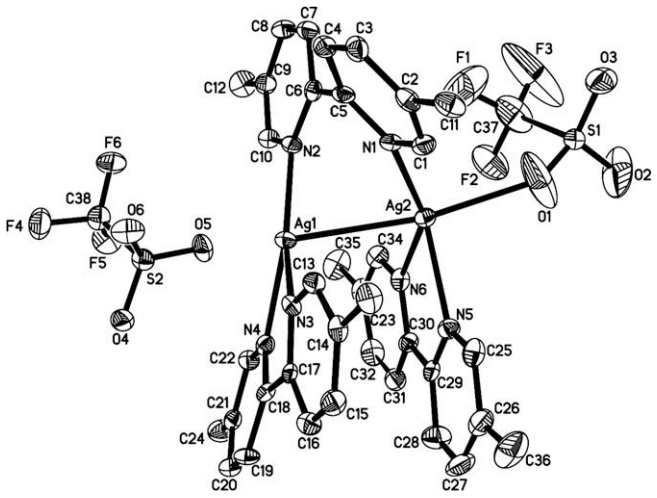


Fig. 3. Thermal ellipsoid of **3A** with an atomic numbering scheme. Ellipsoids are shown at the 50% level. Hydrogen atoms have been removed for clarity.

present, and the functionality of the bipy ligands to either chelate or bridge in the metal complex. A feature that is seen to occur with the noninteracting BF_4^- ion but was not observed here is the temperature dependence of morphology caused by differences in the rate of crystallization. In the present case, interaction of the metal center with the corresponding anion appears to overwhelm any temperature effects that would be had on the structures.

The ^{1}H NMR spectra of compounds **1–5** are, as expected, generally similar, observing the corresponding shifting of the aromatic signals of the bipyridines when compared to the spectra of the free ligands. However, the aromatic protons of a bipy ligand that is terminally bound to a metal center are not distinguishable to those from a bipy that displays a bridging coordination mode in the same compound, thus resulting in equivalent signals as observed in compounds **2**, **3**, and **5**. High Resolution Mass Spectrometry was used in an attempt to determine the nuclearity of the species in solution. The only peaks observed were for $Ag(L)^+$ and $Ag(L)_2^+$ species, confirming that the crystallized compounds dissociate in solution. None of the compounds discussed here exhibited any fluorescence, even at liquid nitrogen temperatures. This agrees with the previous observation that 2,2′-bipy tends to quench luminescence [18,20–22].

3.2. X-ray structure of Agtfa(L1) *1*

The crystal structure of compound **1** consists of two silver atoms, each bonded to a tfa anion and one 4,4′-dimethyl-2,2′-bipyridine ligand displaying a chelating coordination mode (Fig. 1). The center of the Ag–Ag axis is on a crystallographic C2 axis. The metal centers are in capped trigonal planar environments with angles ranging between 72.21(19) and 156.40(18)° (Table 2). The Ag–Ag interaction exhibits a distance of 3.0249(12) Å, and the Ag–N distances fall in the range of reported values. The pyridyl rings of the 4,4′-dimethyl-2,2′-bipyridine ligand are nearly coplanar with a twist angle of 7.7(8)° (Table 3). Adjacent molecules of **1** display π–π interactions between the aromatic rings of the bipy ligands; the distance from a plane drawn through the N2 ring of L1 yields a distance to the facing ring ranging from 3.355 to 3.396 Å (Fig. S1). Addition of another equivalent of 4,4′-dimethyl-2,2′-bipyridine to a 1:1 ligand to metal ratio reaction yielded only compound **1** upon crystallization, likely due to the electronically and sterically crowded silver centers by coordination of the strong interacting tfa anions.

3.3. X-ray structure of [Agtfa(L2)]$_2$ *2A* and *2B*

Due to the same factors that cause the stoichiometric limitations on compound **1**, compound **2** has only been obtainable in a 1:1 ligand/metal ratio. More interesting is the conformation of the bipy ligands in this structure which completely differs from that observed in compound **1**, even though the only difference that exists between the ligands used is the position of the methyl groups on the pyridine rings. Compound **2** is the first example of the series of Ag:bipy structures reported in this work that presents two different conformations arising from the change of the crystallization solvent system. Crystal structure **2A** shown in Fig. 2a was obtained by layering hexane into a solution of the product in CH_2Cl_2 at low temperature, while crystal structure **2B** (Fig. 2b) is formed by using THF/hexane as crystallization solvents. The two structures differ in the bidentate interaction of one of the tfa anions with Ag2 in structure **2B**, while in **2A** both counteranions are bound to silver through a single oxygen. In both structures one 5,5′-dimethyl-2,2′-bipyridine ligand is chelating Ag1, and the other bipy bridges the two silvers, which allows the observed metallophilic interaction. A distinctive characteristic of these poly-

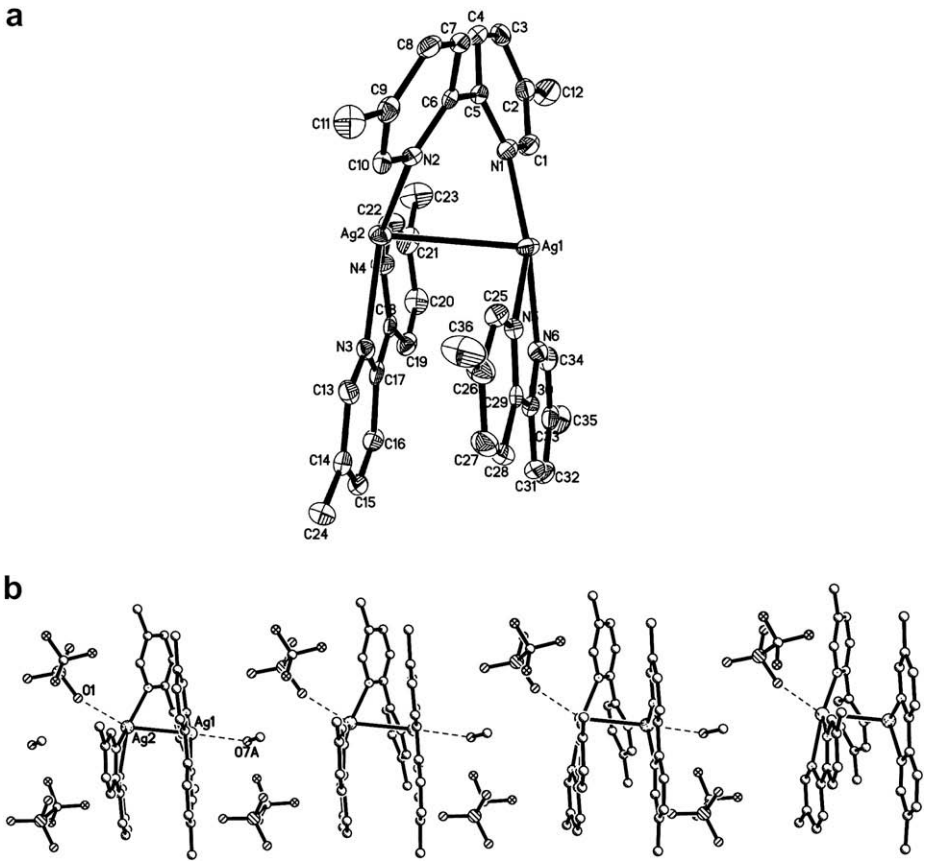


Fig. 4. (a) Thermal ellipsoid plot of **3B** with an atomic numbering scheme. Ellipsoids are shown at the 50% level. Hydrogen atoms, Otf anions and a solvent molecules have been removed for clarity. (b) Ball-and-stick view of the packing structure of **3B**. H atoms have been removed from clarity.

morphs is that both tfa anions are linked to a same silver atom. Relevant literature and CCDC searches reveal this structural feature to be previously unseen. It is then suggested that the functionality of the bipy to chelate and to act as a bridging ligand in the molecule, accounts for Ag1 to be coordinatively saturated, thus aiding the coordination of both tfa anions to Ag2.

The Ag1–Ag2 distance presents values of 2.9833(3) and 2.8921(5) Å for **2A** and **2B** respectively. Despite the similarities between the two structures, the notable difference of about 0.1 Å in the Ag–Ag distances possibly arises from the extra Ag2–O2 interaction in conformation **2B**, that provides extra electron density to the Ag1–Ag2 bond, thus resulting in a contraction of the bond. Angles around the metal centers in **2A** indicate a distorted trigonal pyramidal geometry for both silver atoms, where the sum of the angles of the trigonal base approaches 360° (354.82 and 345.18° for Ag1 and Ag2 respectively). Ag1 also displays a distorted trigonal pyramidal geometry in **2B**, while Ag2 is five coordinate with a wide range of angles between 51.78(6) and 140.02(7)°. The Ag–O distances in **2A** are comparable with values of 2.2953(14) and 2.3733(15) Å for Ag2–O1 and Ag2–O4 respectively. In **2B** the bidentate tfa anion is symmetrically coordinated to Ag2 with equivalent distances of 2.513(2) and 2.518(3) Å for Ag2–O1 and Ag2–O2 respectively. The Ag2–O3 interaction exhibits a shorter contact of 2.3309(16) Å by comparison. The two pyridyl rings of the chelating bipy ligand are nearly coplanar with a twist angle of 7.7(9)° and 6.9(9)° for **2A** and **2B** respectively. As expected, a more pronounced twist is observed for the bridging ligand with angles of 29.1(6)° and 33.6(6)° in **2A** and **2B** respectively. According to Fig. S2, the packing structure of **2B** shows a weak interaction between the only unbound oxygen atom of the monodentate tfa anion and a metal center of the next adjacent molecule (2.662 Å), which consists of a difference of only 0.15 Å when compared to the Ag2–O3 bond distance.

3.4. X-ray structure of $(AgOtf)_2(L3)_3$ **3A** and $(AgOtf)_2(L3)_3 \cdot MeOH$ **3B**

Reaction of AgOtf with 5,5′-dimethyl-2,2′-bipyridine in different ligand to metal ratios (1:1, 2:1, and 3:2), resulted only in the formation of a discrete molecule where two 5,5′-dimethyl-2,2′-bipyridines are chelating two silver atoms, and a third bipy is bridging the metal centers. By using two different crystallization solvent systems, formation of two distinct crystal structures was observed, in which one of the Otf anions is bound to Ag1 in **3A** (layered in CH_2Cl_2/hexane), while in **3B** (layered in CH_3OH/ether) a molecule of Otf^- and CH_3OH exhibit weak interactions of 2.6832(2) and 2.6483(3) Å with Ag2 and Ag1 respectively (Fig. 4). In this case the Ag–Ag distances of both structures are minimally affected by the difference in connectivity, with similar values of 2.8921(5) and 2.9223(4) Å for **3A** and **3B** respectively. Angles around Ag1 in **3A** describe a distorted trigonal bipyramidal geometry in which the axial angle is 170.9(2)° corresponding to the O1–Ag1–Ag2 angle (Fig. 3). Ag2 displays a capped trigonal planar geometry where the angles range between 72.73(14) and 146.02(14)°. In **3B** both silver atoms also present a common capped trigonal planar geometry, regardless of the weak interactions that Ag2 and Ag1 present with a molecule of Otf^- and CH_3OH respectively. The rings of the bridging bipy ligands are twisted from planarity at an angle of 47.0(2)° and 41.8(2)° in **3A** and **3B** respectively.

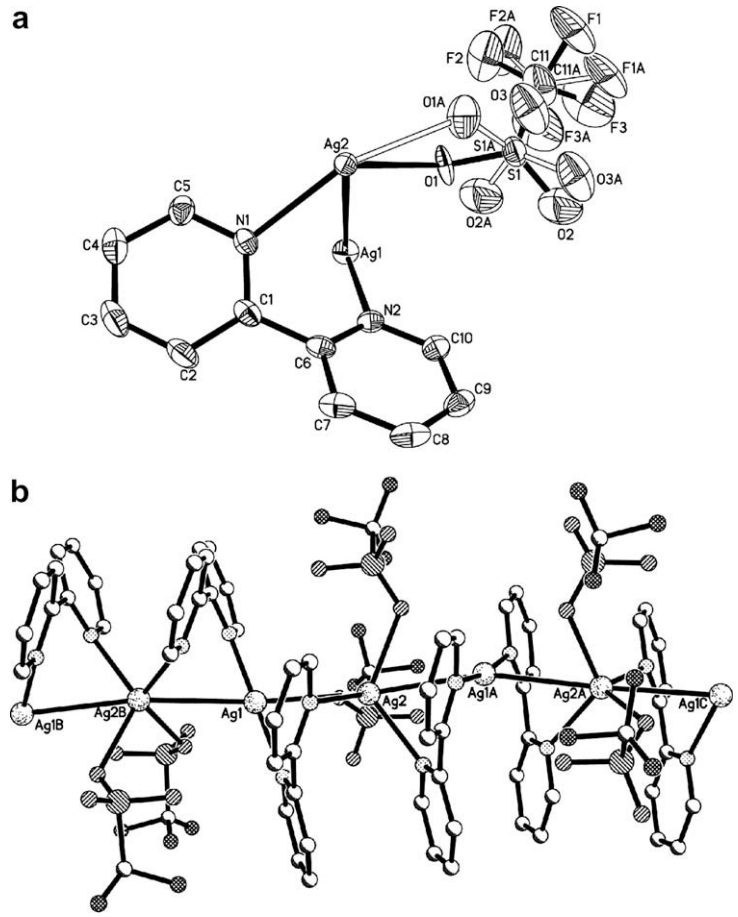


Fig. 5. (a) Molecular structure of **4** with an atomic numbering scheme. Ellipsoids are shown at the 50% level. Hydrogen atoms have been removed for clarity. (b) Ball-and-stick view of the growth molecular structure of 4. Hydrogen atoms have been removed for clarity.

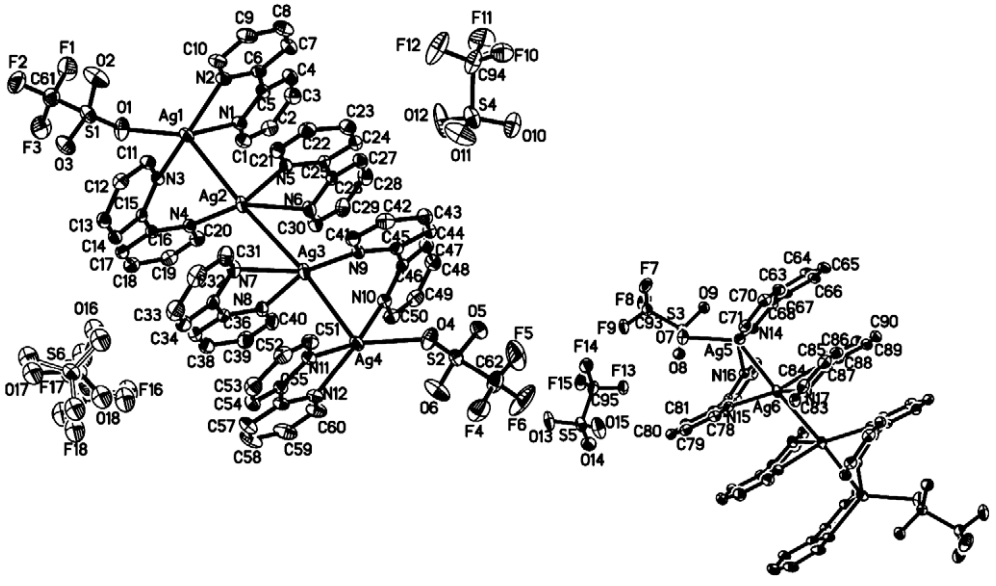


Fig. 6. Thermal ellipsoid of **5** with an atomic numbering scheme. Ellipsoids are shown at the 50% level. Hydrogen atoms have been removed for clarity.

3.5. X-ray structure of [AgOtf(L3)]$_n$ **4**

The 1:1 ratio reaction of 2,2′-bipyridine to AgOtf produces a one-dimensional Ag polymer as shown in Fig. 5. The ball-and-stick view of the molecular growth of **4** is generated by a 3-fold screw axis and a 2-fold rotation as shown in Fig. 5b. The crystal structure of compound **4** reveals the Otf anion playing an integral part in the polymeric chain, and in deciding the geometry of the silver ions. In this molecule the 2,2′-bipyridine is acting solely as a bridging ligand, displaying a twist angle of 35.91(9)°. The Otf is acting as a

Table 2
Selected bond lengths (Å) and bond angles (°) of **1**–**5**.

Compound **1**[a]			
Ag(1)–Ag(1)#1	3.0249(12)	Ag(1)–N(1)	2.294(5)
Ag(1)–N(2)	2.293(5)	Ag(1)–O(1)	2.176(4)
O(1)–Ag(1)–N(2)	156.40(18)	O(1)–Ag(1)–N(1)	131.31(18)
N(2)–Ag(1)–N(1)	72.21(19)	O(1)–Ag(1)–Ag(1)#1	99.71(14)
N(2)–Ag(1)–Ag(1)#1	74.89(15)	N(1)–Ag(1)–Ag(1)#1	98.80(16)
Compound **2A**			
Ag(1)–Ag(2)	2.9833(3)	Ag(1)–N(1)	2.3893(15)
Ag(1)–N(2)	2.2475(15)	Ag(1)–N(3)	2.2053(15)
Ag(2)–N(4)	2.3356(16)	Ag(2)–O(1)	2.2953(14)
Ag(2)–O(4)	2.3733(15)		
N(3)–Ag(1)–N(2)	156.11(6)	N(3)–Ag(1)–N(1)	127.07(5)
N(2)–Ag(1)–N(1)	71.64(5)	N(3)–Ag(1)–Ag(2)	76.44(4)
N(2)–Ag(1)–Ag(2)	103.36(4)	N(1)–Ag(1)–Ag(2)	130.25(4)
O(1)–Ag(2)–N(4)	97.88(5)	O(1)–Ag(2)–O(4)	120.78(5)
N(4)–Ag(2)–O(4)	126.52(5)	O(1)–Ag(2)–Ag(1)	139.45(4)
N(4)–Ag(2)–Ag(1)	67.42(4)	O(4)–Ag(2)–Ag(1)	96.58(4)
Compound **2B**			
Ag(1)–Ag(2)	3.0479(3)	Ag(1)–N(1)	2.2133(18)
Ag(1)–N(3)	2.3940(17)	Ag(1)–N(4)	2.2685(18)
Ag(2)–N(2)	2.3649(18)	Ag(2)–O(1)	2.513(2)
Ag(2)–O(2)	2.518(3)	Ag(2)–O(3)	2.3309(16)
N(1)–Ag(1)–N(4)	161.79(6)	N(1)–Ag(1)–N(3)	121.87(6)
N(4)–Ag(1)–N(3)	71.17(6)	N(1)–Ag(1)–Ag(2)	76.02(5)
N(4)–Ag(1)–Ag(2)	86.27(4)	N(3)–Ag(1)–Ag(2)	121.46(4)
O(3)–Ag(2)–N(2)	92.68(6)	O(3)–Ag(2)–O(1)	131.83(6)
N(2)–Ag(2)–O(1)	125.89(6)	O(3)–Ag(2)–O(2)	140.02(7)
N(2)–Ag(2)–O(2)	115.66(8)	O(1)–Ag(2)–O(2)	51.78(6)
O(3)–Ag(2)–Ag(1)	111.68(4)	N(2)–Ag(2)–Ag(1)	65.61(4)
O(1)–Ag(2)–Ag(1)	69.43(5)	O(2)–Ag(2)–Ag(1)	105.77(5)
Compound **3A**			
Ag(1)–Ag(2)	2.8921(5)	Ag(1)–N(2)	2.175(4)
Ag(1)–N(3)	2.307(4)	Ag(1)–N(4)	2.287(4)
Ag(2)–N(1)	2.234(4)	Ag(2)–N(5)	2.363(4)
Ag(2)–N(6)	2.290(4)	Ag(2)–O(1)	2.480(4)
N(2)–Ag(1)–N(4)	141.22(14)	N(2)–Ag(1)–N(3)	146.02(14)
N(4)–Ag(1)–N(3)	72.73(14)	N(2)–Ag(1)–Ag(2)	77.31(10)
N(4)–Ag(1)–Ag(2)	108.85(10)	N(3)–Ag(1)–Ag(2)	94.25(9)
N(1)–Ag(2)–N(6)	147.96(14)	N(1)–Ag(2)–N(5)	121.69(14)
N(6)–Ag(2)–N(5)	71.89(14)	N(1)–Ag(2)–O(1)	98.4(2)
N(6)–Ag(2)–O(1)	108.8(2)	N(5)–Ag(2)–O(1)	97.38(18)
N(1)–Ag(2)–Ag(1)	74.37(10)	N(6)–Ag(2)–Ag(1)	76.59(10)
N(5)–Ag(2)–Ag(1)	91.26(10)	O(1)–Ag(2)–Ag(1)	170.88(18)
Compound **3B**[a]			
Ag(1)–Ag(2)	2.9223(4)	Ag(1)–N(1)	2.204(3)
Ag(1)–N(5)	2.277(3)	Ag(1)–N(6)	2.342(3)
Ag(1)–O(7)#1	2.6483(3)	Ag(2)–N(2)	2.218(3)
Ag(2)–N(3)	2.299(3)	Ag(2)–N(4)	2.332(3)
Ag(2)–O(1)	2.6832(2)		
N(1)–Ag(1)–N(5)	151.96(10)	N(1)–Ag(1)–N(6)	130.56(10)
N(5)–Ag(1)–N(6)	72.55(10)	N(1)–Ag(1)–Ag(2)	74.01(8)
N(5)–Ag(1)–Ag(2)	88.38(7)	N(6)–Ag(1)–Ag(2)	98.13(7)
N(2)–Ag(2)–N(3)	138.21(10)	N(2)–Ag(2)–N(4)	146.51(10)
N(3)–Ag(2)–N(4)	71.43(10)	N(2)–Ag(2)–Ag(1)	72.77(7)
N(3)–Ag(2)–Ag(1)	93.03(7)	N(4)–Ag(2)–Ag(1)	94.26(7)
Compound **4**[a]			
Ag(1)–Ag(2)#4	3.0437(3)	Ag(1)–N(2)	2.173(3)
Ag(1)–N(2)#3	2.173(3)	Ag(2)–Ag(1)	3.0437(3)
Ag(2)–Ag(1)#2	3.0437(3)	Ag(2)–O(1[a])#1	2.349(8)
Ag(2)–O(1[a])	2.349(8)	Ag(2)–N(1)#1	2.376(3)
Ag(2)–N(1)	2.376(3)	Ag(2)–O(1)	2.407(6)
Ag(2)–O(1)#1	2.407(6)		
N(2)#3–Ag(1)–N(2)	170.62(19)	N(2)#3–Ag(1)–Ag(2)#4	70.92(8)
N(2)–Ag(1)–Ag(2)#4	110.52(8)	N(2)#3–Ag(1)–Ag(2)	110.52(8)
N(2)–Ag(1)–Ag(2)	70.92(8)	Ag(2)#4–Ag(1)–Ag(2)	163.451(18)
Ag(1)#2–Ag(2)–Ag(1)	171.733(16)	O(1A)–Ag(2)–N(1)#1	87.9(3)
O(1A)–Ag(2)–N(1)	160.2(2)	N(1)#1–Ag(2)–N(1)	96.75(16)
N(1)#1–Ag(2)–O(1)	111.44(19)	N(1)–Ag(2)–O(1)	122.18(18)
N(1)#1–Ag(2)–Ag(1)#2	62.19(8)	N(1)–Ag(2)–Ag(1)#2	124.22(8)
O(1)–Ag(2)–Ag(1)#2	113.59(16)	O(1A)–Ag(2)–Ag(1)	99.3(2)
N(1)#1–Ag(2)–Ag(1)	124.22(8)	N(1)–Ag(2)–Ag(1)	62.19(8)
O(1)–Ag(2)–Ag(1)	60.16(16)		
Compound **5**[a]			
Ag(1)–Ag(2)	2.9421(4)	Ag(1)–N(1)	2.326(3)
Ag(1)–N(2)	2.341(3)	Ag(1)–N(3)	2.294(3)
Ag(1)–O(1)	2.469(3)	Ag(2)–Ag(3)	3.0867(4)
Ag(2)–N(4)	2.204(3)	Ag(2)–N(5)	2.227(3)
Ag(2)–N(6)	2.511(3)	Ag(3)–Ag(4)	2.9467(4)
Ag(3)–N(7)	2.507(3)	Ag(3)–N(8)	2.220(3)
Ag(3)–N(9)	2.189(3)	Ag(4)–N(10)	2.308(3)
Ag(4)–N(11)	2.322(3)	Ag(4)–N(12)	2.326(3)
Ag(4)–O(4)	2.563(3)	Ag(5)–Ag(6)	2.9347(4)
Ag(5)–N(13)	2.328(3)	Ag(5)–N(14)	2.320(3)
Ag(5)–N(16)	2.329(3)	Ag(5)–O(7)	2.473(2)
Ag(6)–Ag(6)#1	3.0213(6)	Ag(6)–N(15)	2.228(3)
Ag(6)–N(17)	2.489(3)	Ag(6)–N(18)	2.257(3)
N(3)–Ag(1)–N(1)	147.62(10)	N(3)–Ag(1)–N(2)	117.08(10)
N(1)–Ag(1)–N(2)	71.76(10)	N(3)–Ag(1)–O(1)	91.86(9)
N(1)–Ag(1)–O(1)	109.17(9)	N(2)–Ag(1)–O(1)	123.66(10)
N(3)–Ag(1)–Ag(2)	68.68(7)	N(1)–Ag(1)–Ag(2)	79.02(7)
N(2)–Ag(1)–Ag(2)	102.96(7)	O(1)–Ag(1)–Ag(2)	133.13(7)
N(4)–Ag(2)–N(5)	164.16(11)	N(4)–Ag(2)–N(6)	116.22(10)
N(5)–Ag(2)–N(6)	71.87(10)	N(4)–Ag(2)–Ag(1)	71.42(7)
N(5)–Ag(2)–Ag(1)	92.74(8)	N(6)–Ag(2)–Ag(1)	121.09(8)
N(4)–Ag(2)–Ag(3)	115.00(7)	N(5)–Ag(2)–Ag(3)	80.81(8)
N(6)–Ag(2)–Ag(3)	58.87(8)	Ag(1)–Ag(2)–Ag(3)	173.255(12)
N(9)–Ag(3)–N(8)	161.92(11)	N(9)–Ag(3)–N(7)	118.60(10)
N(8)–Ag(3)–N(7)	71.83(10)	N(9)–Ag(3)–Ag(4)	70.56(7)
N(8)–Ag(3)–Ag(4)	91.62(8)	N(7)–Ag(3)–Ag(4)	117.56(7)
N(9)–Ag(3)–Ag(2)	116.09(8)	N(8)–Ag(3)–Ag(2)	81.82(8)
N(7)–Ag(3)–Ag(2)	58.53(7)	Ag(4)–Ag(3)–Ag(2)	173.148(12)
N(10)–Ag(4)–N(11)	151.71(10)	N(10)–Ag(4)–N(12)	118.64(10)
N(11)–Ag(4)–N(12)	71.72(10)	N(10)–Ag(4)–O(4)	84.36(9)
N(11)–Ag(4)–O(4)	107.26(9)	N(12)–Ag(4)–O(4)	134.44(10)
N(10)–Ag(4)–Ag(3)	68.35(7)	N(11)–Ag(4)–Ag(3)	84.03(7)
N(12)–Ag(4)–Ag(3)	101.88(8)	O(4)–Ag(4)–Ag(3)	123.56(7)
N(14)–Ag(5)–N(13)	72.57(9)	N(14)–Ag(5)–N(16)	143.39(10)
N(13)–Ag(5)–N(16)	112.00(9)	N(14)–Ag(5)–O(7)	120.54(9)
N(13)–Ag(5)–O(7)	123.30(10)	N(16)–Ag(5)–O(7)	88.33(9)
N(14)–Ag(5)–Ag(6)	77.84(7)	N(13)–Ag(5)–Ag(6)	103.91(7)
N(16)–Ag(5)–Ag(6)	65.70(7)	O(7)–Ag(5)–Ag(6)	132.22(6)
N(15)–Ag(6)–N(18)	163.41(10)	N(15)–Ag(6)–N(17)	120.28(9)
N(18)–Ag(6)–N(17)	71.21(10)	N(15)–Ag(6)–Ag(5)	70.47(7)
N(18)–Ag(6)–Ag(5)	93.78(7)	N(17)–Ag(6)–Ag(5)	118.14(7)
N(15)–Ag(6)–Ag(6)#1	113.02(7)	N(18)–Ag(6)–Ag(6)#1	82.75(7)
N(17)–Ag(6)–Ag(6)#1	60.45(7)	Ag(5)–Ag(6)–Ag(6)#1	176.509(15)

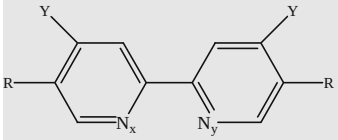
[a] Symmetry transformations used to generate equivalent atoms for **1**: #1 = $-x+1/2, -y, z$. **3B**: #1 = $x-1, y, z-1$. **4**: #1 = $x-1, y+1, -z$; #2 = $-x+y+2, -x+1, z-1/3$; #3 = $-x+2, -x+y+1, -z+1/3$; #4 = $-y+1, x-y-1, z+1/3$. **5**: = #1 $-x+2, -y+2, -z+2$.

coordinating anion, with the characteristic that for every two silver atoms, the two corresponding anions are bound to the same metal center. This structural feature has been reported earlier for compound **2** when the corresponding bipy ligand is also displaying a bridging coordination mode. Therefore, the molecular structure of **4** contains two distinct silver environments which is representative of the coordination extremes mentioned herein. Ag1 is four coordinated to two half of 2,2′-bipyridine ligands and to two silver atoms, which describes a distorted tetrahedral geometry with angles ranging between 70.92(8) and 170.62(19)°. Ag2 exhibits the same bonding as Ag1 in addition to two Otf anions, which makes it a 6 coordinated metal center. The Ag–Ag interactions are typical lengths at 3.0437(3) Å [36,45–48], and are supported by the bridging ligand to form a infinite chain which deviates from linearity with angles of 171.733(16) and 163.451(18)° for Ag(1)#2–Ag(2)–Ag(1) and Ag(2)#4–Ag(1)–Ag(2) respectively. In this molecule the Otf anions are highly disordered about the C–S axis; due to the disorder, they were refined isotropically, and each group was restrained to have the same C–F and S–O bond lengths, angles, and thermal parameters.

3.6. X-ray structure of $(AgOtf)_2(L3)_3$ **5**

Changing the stoichiometry of the reaction between 2,2′-bipyridine and AgOtf to a 3:2 ligand/metal ratio produced compound **5** shown in Fig. 6. It consists of two discrete molecules, each one

Table 3
Intraligand dihedral angle (°).



	1	2A	2B	3A	3B	4	5
	R = H Y = CH_3	R = CH_3 Y = H	R = CH_3 Y = H	R = CH_3 Y = H	R = CH_3 Y = H	R = H Y = H	R = H Y = H
N1/N2	7.8(8)	7.7(9)	6.9(9)	47.0(2)	41.8(2)	35.9(1)	19.8(2)
N3/N4		29.1(6)	33.6(6)	16.2(2)	9.1(2)		36.9(1)
N5/N6				6.4(3)	4.6(2)		29.3(1)
N7/N8							31.7(1)
N9/N10							40.6(1)
N11/N12							17.9(1)
N13/N14							27.1(1)
N15/N16							38.9(1)

containing four silver atoms lying in nearly a straight line, and six 2,2′-bipyridine groups, of which four are chelating and two are bridging. One of these discrete molecules is oriented on an inversion center which gives a Z of 6 for the structure. For each four silver chain, two Otf anions are capping the terminal silver atoms through a single sulfonate oxygen, and the remaining anions show no interaction with the chain. The interacting Otf anions truncate the formation of a polymeric chain as observed in compound **4**. This linear silver chain structure can be described as two molecules of compound **3** linked together through Ag2, to form the same core structure as observed for compound **5**. This observation can be used to suppose possible hindered effects provided by the methyl groups of the 5,5′-dimethyl-2,2′-bipyridine ligand, that encumber the formation of a elongated chain composed of metallophilic interactions. The thermal ellipsoid plot of compound **5** shows distinct silver environments encompassed in one structure, and defined by the functionality of the bipy ligand. The terminal silver atoms (Ag1, Ag4, Ag5, and Ag5#1) display a distorted capped tetrahedral geometry, while the central silver atoms exhibit a distorted trigonal bipyramidal conformation. The Ag–Ag distances fall in the range of reported values, ranging between 2.9347(4) Å for Ag5–Ag6 and 3.0867(4) Å for Ag2–Ag3. The angle between the planes of the π-systems describes a considerable twist of the bipyridine ligands that exhibit either a chelating or a bridging coordination mode. The twist angle for the 2,2′-bipyridines that are chelating range between 19.79(2) and 29.32(1)°, and for the ligands bridging a range between 36.85(1) and 40.58(1)°. It is also noted that the chelating bipy ligands bound to Ag1 and Ag4 respectively, present smaller twist angles when compared to those coordinated to Ag2 and Ag3 where more steric effects can be found in the molecular structure of the compound. One of the noncoordinating Otf anions in the crystal structure is disordered about the position of the sulfur and carbon; therefore it was refined isotropically, and the two sulfur and carbon positions restrained to have the same thermal parameters.

4. Conclusion

Herein we have demonstrated the versatility and functionality of bipy type ligands associated with silver(I) salts of two different anions that exhibit varying degree of interaction. The crystal structures are seen to be highly dependent not only on the coordinating ability of the anion but also on the ratio of ligand/metal. In particular, the simplicity of these ligands made it an appealing candidate for use to study the structural and coordinative factors that produce molecular structures that span from simple discrete molecules to one or two-dimension polymeric conformations. This report complements other studies of coordinative silver structures associated with bipy ligands, where several factors are involved in the construction of such coordinative arrays.

Acknowledgments

This research was supported by funds provided by grant from the Robert A. Welch Foundation (AA-1508). The Bruker X8 APEX diffractometer was purchased with funds received from the national Science Foundation Major Research Instrumentation Program Grant CHE-0321214. Baylor University's Varian 500 MHz NMR was funded by the National Science Foundation's Major Research Instrumentation Program, Award # CHE-0420802. The authors would like to thank Dr. Alejandro Ramirez (Mass Spectrometry Core Facility, Baylor University, Texas) for the HRMS analysis.

Appendix A. Supplementary data

CCDC 698864, 698865, 698862, 698867, 698868, 698863, and 698866 for **1**, **2A**, **2B**, **3A**, **3B**, **4**, and **5** contain the supplementary crystallographic data for this paper. These data can be obtained free of charge from the Cambridge Crystallographic Data Centre via www.ccdc.cam.ac.uk/data_request/cif.

Packing views of compounds **1**, **2A** and **2B**. Supplementary data associated with this article can be found, in the online version, at doi:10.1016/j.poly.2008.11.040.

References

[1] K. Biradha, M. Sarkar, L. Rajput, Chem. Commun. (2006) 4169.
[2] Y.P. Ren, X.J. Kong, L.S. Long, R.B. Huang, L.S. Zheng, Cryst. Growth Des. 6 (2006) 572.
[3] M.J. Zaworotko, Chem. Commun. (2001) 1.
[4] B. Moulton, M.J. Zaworotko, Chem. Rev. 101 (2001) 1629.
[5] M.D. Ward, C.M. White, F. Barigelletti, N. Armaroli, G. Calogero, L. Flamigni, Coord. Chem. Rev. 171 (1998) 4781.
[6] V. Balzani, A. Juris, M. Venturi, Chem. Rev. 1996 (1996) 759.
[7] W.F. Yeung, W.L. Man, W.T. Wong, T.C. Lau, S. Gao, Angew. Chem., Int. Ed. Engl. 40 (2001) 3031.
[8] J. Pang, E.J.P. Marcotte, C.R. Seward, S. Wang, Angew. Chem., Int. Ed. Engl. 40 (2001) 4042.
[9] Q.D. Liu, J.R. Li, S. Gao, B.Q. Ma, H.Z. Kou, L. Ouyang, R.L. Huang, X.X. Zhang, K.B. Yu, Eur. J. Inorg. Chem. (2003) 731.
[10] L. Carlucci, G. Ciani, D.M. Proserpio, Coord. Chem. Rev. 246 (2003) 247.
[11] D. Sun, R. Cao, Y. Sun, W. Bi, X. Li, Y. Wang, Q. Shi, X. Li, Inorg. Chem. 42 (2003) 7512.
[12] S. Kitagawa, R. Kitaura, S. Noro, Angew. Chem., Int. Ed. Engl. 43 (2004) 2334.
[13] I. Goldberg, Chem. Commun. (2005) 1243.
[14] S. Leininger, B. Olenyuk, P.J. Stang, Chem. Rev. 100 (2000) 853.
[15] C. Janiak, Dalton Trans. (2000) 3885.
[16] A.M. Beatty, Coord. Chem. Rev. 246 (2003) 131.

[17] D. Braga, L. Maini, M. Polito, E. Tagliavini, F. Grepioni, Coord. Chem. Rev. 246 (2003) 53.
[18] R.P. Feazell, C.E. Carson, K.K. Klausmeyer, Inorg. Chem. 45 (2006) 935.
[19] R.P. Feazell, C.E. Carson, K.K. Klausmeyer, Inorg. Chem. 44 (2005) 996.
[20] R.P. Feazell, C.E. Carson, K.K. Klausmeyer, Inorg. Chem. 45 (2006) 2627.
[21] R.P. Feazell, C.E. Carson, K.K. Klausmeyer, Inorg. Chem. 45 (2006) 2635.
[22] R.P. Feazell, C.E. Carson, K.K. Klausmeyer, Eur. J. Inorg. Chem. (2005) 3287.
[23] K.K. Klausmeyer, R.P. Feazell, J.H. Reibenspies, Inorg. Chem. 43 (2004) 1130.
[24] C. Di Nicola, Effendy, F. Fazaroh, C. Pettinari, B.W. Skelton, N. Somers, A.H. White, Inorg. Chim. Acta 258 (2005) 720.
[25] P.L. Caradoc-Davies, L.R. Hanton, Chem. Commun. (2001) 1098.
[26] I. Ino, L.P. Wu, M. Munakata, M. Maekawa, Y. Suenaga, T. Kuroda-Sowa, Y. Kitamori, Inorg. Chem. 39 (2000) 2146.
[27] A.N. Khlobystov, A.J. Blake, N.R. Champness, D.A. Lemenovskii, A.G. Majouga, N.V. Zyk, M. Schroder, Coord. Chem. Rev. 222 (2001) 155.
[28] G.A. Bowmaker, Effendy, S. Marfuah, B.W. Skelton, A.H. White, Inorg. Chim. Acta 258 (2005) 4371.
[29] C. Di Nicola, Effendy, F. Marchetti, C. Pettinari, B.W. Skelton, A.H. White, Inorg. Chim. Acta 360 (2007) 1433.
[30] C. Kaes, A. Katz, M.W. Hosseini, Chem. Rev. 100 (2000) 3553.
[31] Effendy, F. Marchetti, C. Pettinari, R. Pettinari, B.W. Skelton, A.H. White, Inorg. Chim. Acta 260 (2007) 1388.
[32] M. Wu, D. Yuan, Y. Huang, W. Wei, Q. Gao, F. Jiang, M. Hong, Cryst. Growth Des. 7 (2007) 1446.
[33] H.L. Zhu, Q. Chen, W.L. Peng, S.J. Qi, A.L. Xu, X.M. Chen, Chin. J. Chem. 19 (2001) 263.
[34] K.K. Klausmeyer, F. Hung-Low, A. Renz, Acta Crystallogr., Sect. E E63 (2007) m2181.
[35] K.K. Klausmeyer, F. Hung-Low, A. Renz, Acta Crystallogr., Sect. E E63 (2007) m2149.
[36] F. Hung-Low, K.K. Klausmeyer, Inorg. Chim. Acta 361 (2008) 1298.
[37] Y. Yu, Y. Wei, R. Broer, K. Wu, Inorg. Chem. Commun. 10 (2007) 1289.
[38] J. Fornies, R. Navarro, V. Sicilia, M. Tomas, Inorg. Chem. 32 (1993) 3675.
[39] A.R. Brown, Z. Guo, F.W.J. Mosselmans, S. Parsons, M. Schroder, L.J. Yellowlees, J. Am. Chem. Soc. 120 (1998) 8805.
[40] R. Uson, J. Fornies, M. Tomas, J.M. Casas, C. Fortuno, Polyhedron 8 (1989) 2209.
[41] A. Bellusci, A. Crispini, D. Pucci, E.I. Szerb, M. Ghedini, Cryst. Growth Des. 8 (2008) 3114.
[42] Bruker, APEX 2 (v.2.0) and SAINTPLUS (V 6.25), Bruker AXS Inc., Madison, Wisconsin, USA, 2003.
[43] G.M. Sheldrick, SHELXS97 and SHELXL97, University of Gottingen, Germany, 1997.
[44] G.M. Sheldrick, SHELXTL (v 6.10), Bruker AXS Inc., Madison, Wisconsin, USA, 2000.
[45] V.J. Catalano, M.A. Malwitz, Inorg. Chem. 42 (2003) 5483.
[46] A.A. Mohamed, L.M. Perez, J.P. Fackler, Inorg. Chim. Acta 358 (2005) 1657.
[47] C.M. Che, M.C. Tse, M.C.W. Chan, K.K. Cheung, D.L. Phillips, K.H. Leung, J. Am. Chem. Soc. 123 (2000) 2464.
[48] Q.M. Wang, T.C.W. Mak, J. Am. Chem. Soc. 123 (2001) 7594.

Polyhedron 28 (2009) 416–424

Contents lists available at ScienceDirect

Polyhedron

journal homepage: www.elsevier.com/locate/poly

Synthesis, photophysical and photochemical studies of water soluble cationic zinc phthalocyanine derivatives

Mopelola Idowu, Tebello Nyokong *

Department of Chemistry, Rhodes University, P.O. Box 94, Eastern Cape, Grahamstown 6140, South Africa

ARTICLE INFO

Article history:
Received 22 June 2008
Accepted 16 November 2008
Available online 26 December 2008

Keywords:
Zinc phthalocyanine
2-Diethylaminoethanethiol
Quaternized
Ionic
Aggregation
Cremophore
Triplet yields
Triplet lifetime

ABSTRACT

Peripherally and non-peripherally 2-diethylaminoethanethiol tetra-substituted zinc phthalocyanine (**5a** and **6a**) and their quaternized derivatives (**5b** and **6b**) have been synthesized and characterized. The quaternized derivatives (**5b** and **6b**) show excellent solubility in aqueous medium. The photophysical and photochemical properties of the 2-diethylaminoethanethiol appended zinc phthalocyanine in dimethylsulfoxide (DMSO) for the non-ionic (**5a** and **6a**) and in both DMSO and aqueous medium (phosphate buffered saline solution PBS, pH 7.4) (in the presence and absence of cremophore EL (CEL)) for the quaternized (**5b** and **6b**) derivatives were studied and compared with that of the peripherally octa-substituted derivatives (**7a** and **7b**). The complexes have intense absorption in the visible/near-IR region though the quaternized forms (**5b**, **6b** and **7b**) were slightly blue shifted and highly aggregate in aqueous solution. The triplet state quantum yields (Φ_T) and the triplet lifetimes (τ_T) were found to be higher in DMSO (Φ_T values ranged from 0.57 to 0.75 while τ_T values ranged from 190 to 220 μs in DMSO for all complexes) compared to aqueous medium (Φ_T values ranged from 0.15 to 0.17 while τ_T values ranged from 20 to 70 μs in pH 7.4 buffer). Addition of cremophore EL in aqueous solution resulted in induced disaggregation leading to increased Φ_T and τ_T.

© 2008 Elsevier Ltd. All rights reserved.

1. Introduction

Metallophthalocyanines (MPcs), a family of aromatic macrocycles based on an extensive delocalized 18π electron system, have been extensively studied due to their unique optical, electronic, catalytic and structural properties [1]. There has been growing interest in the use of phthalocyanines in a variety of new technological fields such as semiconductor devices [2], electrochromic display devices [3], liquid crystals [4], Langmuir–Blodgett films [5], and as photosensitizers in photodynamic therapy of cancer (PDT) [6].

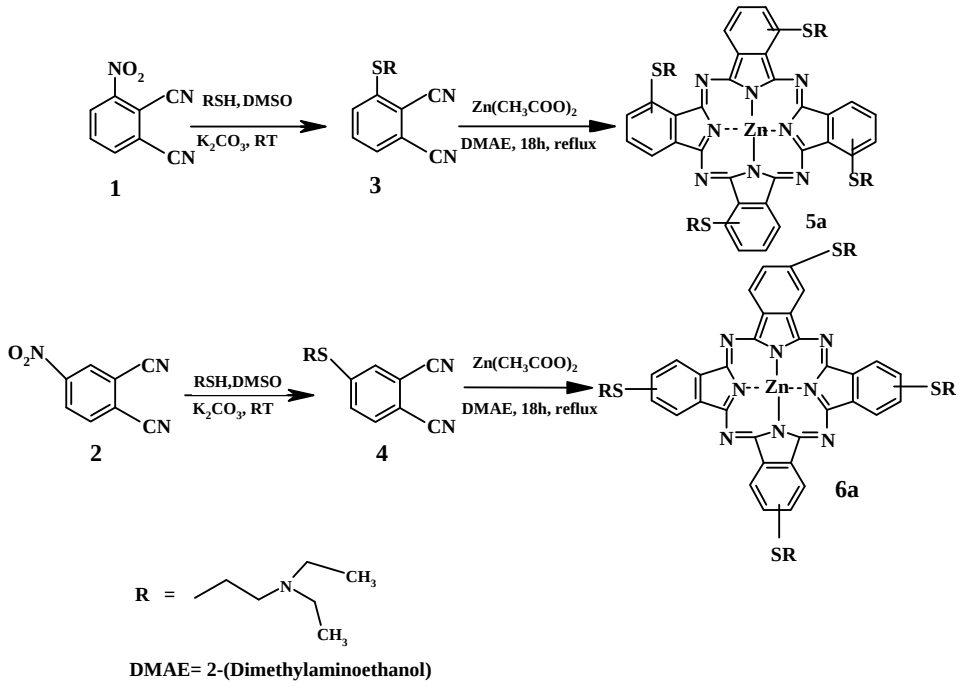
PDT is a prominent application of phthalocyanine derivatives. It is based on a noninvasive treatment of superficial tumors. The concept is that a photosensitizer can be preferentially localized in malignant tissues, followed by activation of the photosensitizer with the light of the appropriate wavelength to generate cytotoxic radical and non-radical species of oxygen that lead to tumor destruction [6–10].

MPcs can be modified in a number of ways by incorporation of substituents in their peripheral (β) and non-peripheral (α) positions. This incorporation increases the π-electron density and makes solvation easier [11]. Tetra-substituted phthalocyanines (Pcs) are usually more soluble than the corresponding octa-substituted Pcs due to the formation of constitutional isomers and the high dipole moment that results from the unsymmetrical arrangement of the substituents at the periphery [12,13]. Incorporation of non-transition metals like zinc in the centre of the phthalocyanine (Pc) ring results in complexes with high triplet state quantum yields and long triplet lifetimes, which are required for efficient photosensitization [14]. MPcs are particularly interesting since anionic or cationic groups such as sulfonic, carboxylic, phosphonic or quaternized amino groups render them water soluble [15–18]. Some cationic phthalocyanines have been reported [19–22] and it has been discovered that they target vulnerable sites in cells [23], showing their importance in tumor necrosis and photoinactivation of bacteria.

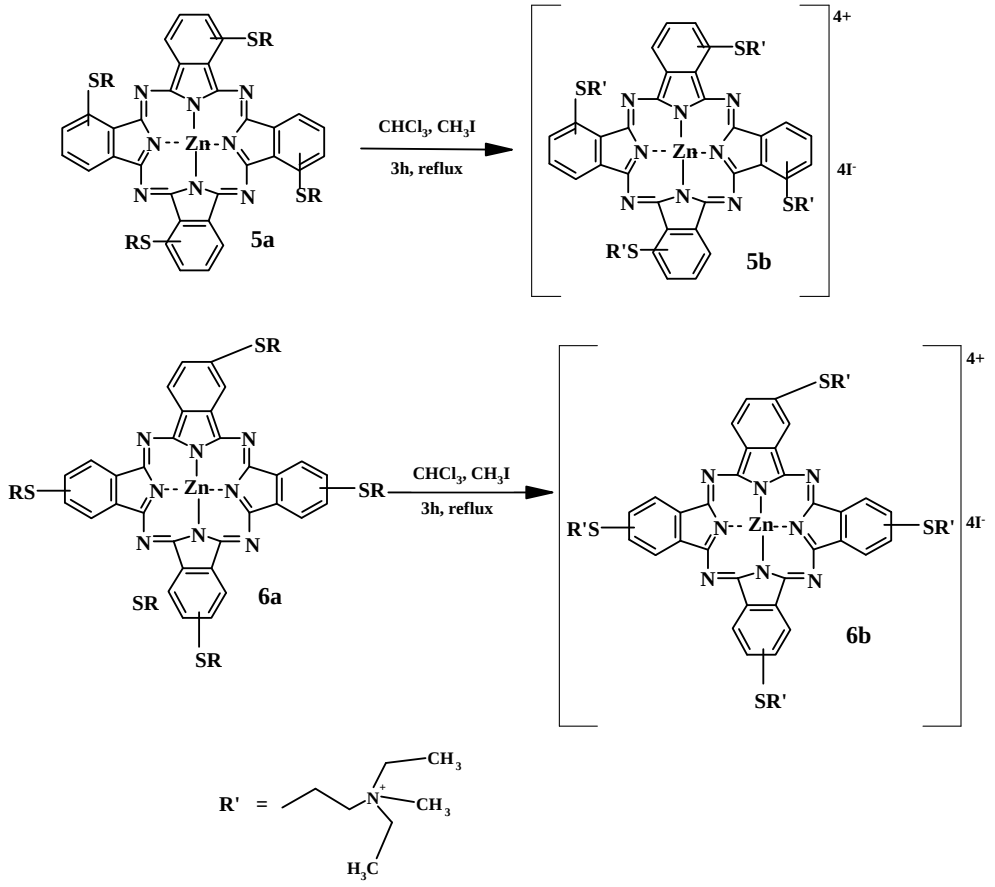
We report herein on the synthesis, of ZnPc tetra-substituted at the (β) peripheral and (α) non-peripheral position with 2-diethylaminoethanethiol (complexes **5a** and **6a**) and their quaternized derivatives (complexes **5b** and **6b**) (Scheme 1). It is expected that substitution at the more sterically crowded α position will result in reduced aggregation tendencies compared to the β position [24]. The spectroscopic, photophysical and photochemical properties of **5a** and **6a** (in DMSO) and **5b** and **6b** (in both DMSO and aqueous medium, phosphate buffered saline solution PBS, pH 7.4) in comparison with the (β) peripherally octa-substituted counterparts (**7a** and **7b**, respectively) has also been investigated to give

* Corresponding author. Tel.: +27 46 6038260; fax: +27 46 6225109.
E-mail address: t.nyokong@ru.ac.za (T. Nyokong).

0277-5387/$ - see front matter © 2008 Elsevier Ltd. All rights reserved.
doi:10.1016/j.poly.2008.11.021



Scheme 1a. Synthesis route of 2-diethylaminoethanethiol substituted zinc(II) phthalocyanine complexes.



Scheme 1b. Synthesis route of quaternized 2-diethylaminoethanethiol substituted zinc(II) phthalocyanine.

an indication of the potential of the complexes as photosensitizers. Peripherally (β) octa-substituted complexes **7a** and **7b** (Fig. 1) have been reported before [22]. As stated above, tetra-substituted MPc complexes are more soluble than octa-substituted ones, hence the are studied in this work. Substitution at the α position results in red shifting of spectra which is useful for PDT applications.

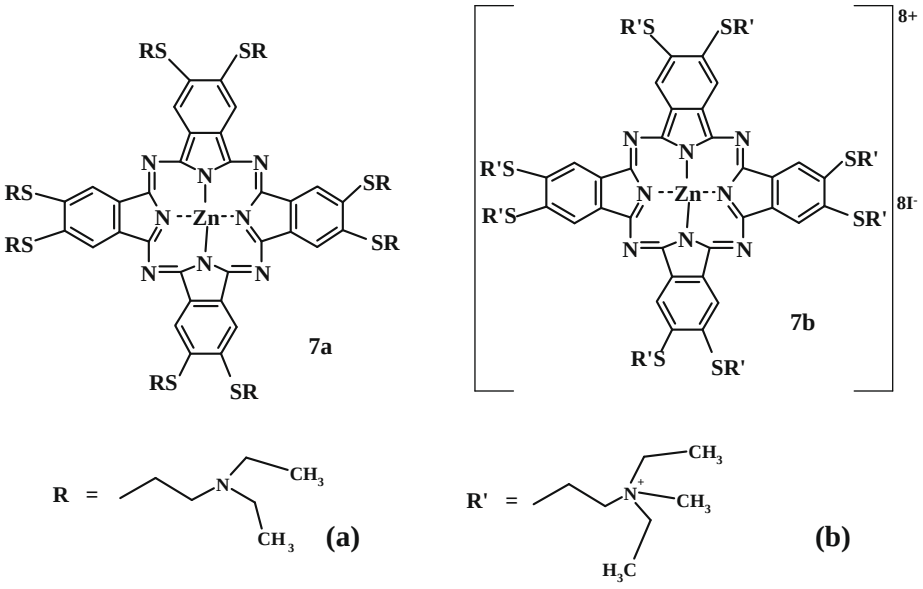


Fig. 1. Molecular structures of complexes **7a** and **7b**.

Lipophilic phthalocyanine derivatives have been reported to have a higher tumor affinity, but they are associated with cutaneous phototoxicity [25], water soluble phthalocyanines are therefore still considered the best targets of photosensitizers [26] since they can be injected directly into the bloodstream, despite their aggregation tendency in aqueous medium [27,28]. However, aggregation can be hindered by addition of surfactants [29,30]. Thus in this work, the quaternized MPcs (**5b**, **6b** and **7b**) are also studied in aqueous medium in the presence of cremophore EL (CEL), a non-ionic surfactant which is an excipient to drugs and can provide a more selective accumulation of the drugs in tissues. The association of the MPc complexes with bovine serum albumin (BSA) has also been investigated since hydrophilic dyes bind preferentially to serum proteins, such as BSA [31] and serum albumin is one of the key components in the body that influences drug delivery [32].

2. Experimental and method

2.1. Materials

Methanol, tetrahydrofuran (THF) and dimethylsulfoxide (DMSO) were dried as described by Perrin and Armarego [33] before use. Deuterated DMSO (d_6-DMSO), 2-diethylaminoethanethiol hydrochloride, cremophore EL (CEL), 3-diphenylisobenzofuran (DPBF), anthracene-9,10-bis-methylmalonate (ADMA), 2-dimethylaminoethanol and zinc acetate were purchased from Sigma–Aldrich. BSA was obtained from Fluka. Chromatography was performed on neutral alumina. Phosphate-buffered saline (PBS) solution (0.01 M, pH 7.4) was prepared using appropriate amounts of Na_2HPO_4, KH_2PO_4 and chloride salts, dissolved in ultra pure water, from a Milli-Q Water System (Millipore Corp., Bedford, MA, USA). Zinc tetrasulfophthalocyanine ($ZnPcS_4$), zinc phthalocyanine (ZnPc) and $ZnPcS_{mix}$ were synthesized, purified and characterized according to literature methods [29,34,35]. 3-Nitrophthalonitrile (**1**), 4-nitrophthalonitrile (**2**), 1,2-dichlorophthalonitrile, [36–38], 3-diethylaminoethylsulfanyl phthalonitrile (**3**), 4-diethylaminoethylsulfanyl phthalonitrile (**4**), and 1,2-bis-(diethylaminoethylsulfanyl)-4,5-dicyanobenzene were all synthesized and purified according to the literature [19,22]. Complexes **7a** and **7b** were synthesized and characterized as reported in literature [22].

2.2. Equipment

UV/Vis spectra were recorded on a Cary 500 UV/Vis/NIR spectrophotometer. IR spectra (KBr pellets) were recorded on a Perkin–Elmer spectrum 2000 FTIR spectrometer. ^{1}H NMR spectra were recorded using a Bruker EMX 400 MHz NMR spectrometer. Low resolution atmospheric pressure chemical ionisation (APCI) mass spectra were recorded on a Finnigan MAT LCQ ion trap mass spectrometer equipped with XCALIBUR software.

Fluorescence excitation and emission spectra were recorded on a Varian Eclipse spectrofluoremeter using a 1 cm pathlength cuvette at room temperature. Laser flash photolysis experiments were performed with light pulses produced by a Quanta-Ray Nd:YAG laser providing 400 mJ, 90 ns pulses of laser light at 10 Hz, pumping a Lambda-Physik FL3002 dye (Pyridin 1 dye in methanol). Single pulse energy was 7 mJ. The analyzing beam source was from a Thermo Oriel xenon arc lamp, and a photomultiplier tube was used as detector. Signals were recorded with a digital real-time oscilloscope (Tektronix TDS 360); the kinetic curves were averaged over 256 laser pulses. The triplet life times were determined by exponential fitting of the kinetic curves using the program ORIGINPRO 7.5. Solutions for triplet yield and lifetime determinations were purged of oxygen (by bubbling with Argon) before laser irradiations. Photo-irradiations for photodegradation or singlet oxygen determination were performed using a General electric Quartz line lamp (300 W). A 600 nm glass cut off filter (Schott) and water were used to filter off ultraviolet and infrared radiations, respectively. An interference filter (Intor, 700 nm with a band width of 40 nm) was additionally placed in the light path before the sample. Light intensity was measured with a POWER MAX5100 (Molelectron detector incorporated) power meter and was found to be 5.14×10^{16} photons s^{-1} cm^{-2} for photobleaching and to be 1.78×10^{16} photons s^{-1} cm^{-2} for singlet oxygen studies.

2.3. Determination of percentage aggregation, equilibrium constant

Percentage aggregation (% Agg) was calculated using Eq. (1) [30,39]

$$\%\ \mathrm{Agg} = \frac{\mathrm{Abs}_{\mathrm{MeOH}} - \mathrm{Abs}}{\mathrm{Abs}_{\mathrm{MeOH}}} \times 100\% \qquad (1)$$

where Abs_{MeOH} and Abs are the absorbances at the *Q-band* monomer maxima in the presence and absence of methanol.

The equilibrium constant of the monomer/dimer equilibrium for $2M \leftrightarrow D$ is defined by Eq. (2)

$$K_D = [D]/[M]^2 \tag{2}$$

where [M] and [D] are the concentrations of the monomer and the dimer, respectively. The total concentration of the MPcs is given by Eq. (3)

$$C = [M] + 2[D] \tag{3}$$

The absorbance of a solution containing both the monomer and the dimer is given by Eq. (4) [40]

$$Abs = \frac{[1 - \sqrt{(1 + 8K_DC)}][\varepsilon_D/2 - \varepsilon_M] + 2\varepsilon_D K_D C]}{4lK_D} \tag{4}$$

where C is the total concentration of the MPcs (monomer and dimer), ε_M and ε_D are the extinction coefficients of the monomer and dimer, respectively, and l the path length.

An estimated value of ε_M obtained from the measurements in aqueous solution within the concentration range at which the Beer–Lambert's law holds for each MPc was substituted in Eq. (4) and the absorbance data were fitted to obtain ε_D and K_D by a non-linear least square procedure using MATLAB 6.1 software.

2.4. Photophysical and photochemical studies

Fluorescence quantum yields (Φ_F) were determined by comparative method using Eq. (5) [41],

$$\Phi_F = \Phi_{F(Std)} \cdot \frac{F \cdot A_{Std} \cdot n^2}{F_{Std} \cdot A \cdot n_{Std}^2} \tag{5}$$

where F and F_{Std} are the areas under the fluorescence curves of the MPc derivatives and the reference, respectively. A and A_{Std} are the absorbances of the sample and reference at the excitation wavelength, and n and n_{Std} are the refractive indices of solvents used for the sample and standard, respectively. ZnPc in DMSO was used as a standard, $\Phi_F = 0.2$ [42]. At least three independent experiments were performed for the quantum yield determinations. Both the sample and the standard were excited at the same relevant wavelength.

Triplet quantum yields were determined using a comparative method based on triplet decay, using Eq. (6)

$$\Phi_T^{Sample} = \Phi_T^{Std} \frac{\Delta A^{Sample} \varepsilon^{Std}}{\Delta A^{Std} \varepsilon^{Sample}} \tag{6}$$

where A_T^{Sample} and A_T^{Std} are the changes in the triplet state absorbance of the sample derivative and the standard, respectively. ε_T^{Sample} and ε_T^{Std} are the triplet state extinction coefficients for the sample and standard, respectively. Φ_T^{Std} is the triplet state quantum yield for the standard. $ZnPcS_4$ in aqueous solution, $\Phi_T^{Std} = 0.56$ [43] and ZnPc ($\Phi_T^{Std} = 0.65$ in DMSO [44]) were used as standards. Quantum yields of internal conversion were obtained from Eq. (7) which assumes that only three processes (fluorescence, intersystem crossing and internal conversion); jointly deactivate the excited singlet states of the complexes.

$$\Phi_{IC} = 1 - (\Phi_F + \Phi_T) \tag{7}$$

The values of photobleaching quantum yields (Φ_P) were determined using Eq. (8)

$$\Phi_{Pd} = \frac{(C_0 - C_t)VN_A}{I_{abs}S \cdot t} \tag{8}$$

where C_t and C_0 are the MPc concentration in mol dm^{-3} after and prior to irradiation, respectively. V is the reaction volume, S is the irradiation area of the cell, t the irradiation time, N_A is the Avogadro's number and I_{abs} the overlap integral of the radiation light source intensity and the absorption of the MPc in the region of the interference filter transmittance [45,46]. Eq. (9) was employed for calculating singlet oxygen quantum yields

$$\Phi_\Delta = \Phi_\Delta^{Std} \cdot \frac{RI_{abs}^{Std}}{R^{Std}I_{abs}} \tag{9}$$

where Φ_Δ^{Std} is the singlet oxygen quantum yield for the standard ($ZnPcS_{mix}$, $\Phi_\Delta^{Std} = 0.45$ in aqueous solution) [47] and ZnPc ($\Phi_\Delta^{Std} = 0.67$ in DMSO [46]). R and R^{Std} are the ADMA or DPBF photobleaching rates in the presence of the respective MPcs under investigation and the standard, respectively. I_{abs} and I_{abs}^{Std} are the rates of light absorption by the MPcs and the standard, respectively. To avoid chain reactions, the concentration of ADMA was kept at $\sim 6 \times 10^{-5}$ mol l^{-1} while that of DPBF was kept at $\sim 3 \times 10^{-5}$ mol l^{-1}.

Solutions of the MPcs with an absorbance of 0.2 at the irradiation wavelength were prepared in the dark and irradiated at the *Q-band* region, monitoring the ADMA and DPBF degradation at 380 nm and 417 nm, respectively. The error was ~10% from several values of Φ_Δ.

2.5. Binding of MPcs to BSA

The binding of the MPcs to BSA was studied by spectrofluorometry at room temperature. An aqueous solution of BSA (fixed concentration) was titrated with varying concentrations of the respective MPc solution. BSA was excited at 280 nm and fluorescence recorded between 290 and 500 nm. The steady decrease in BSA fluorescence with increase in MPc concentration was noted and used in the determination of the binding constants and the number of binding sites on BSA, according to Eq. (10) [40,48,49]

$$\log\left[\frac{(F_0 - F)}{(F - F_\infty)}\right] = \log k_b + n \log[MPc] \tag{10}$$

where F_0 and F are the fluorescence intensities of BSA in the absence and presence of MPc, respectively; F_∞, the fluorescence intensity of BSA saturated with MPc; k_b, the binding constant; n, the number of binding sites on a BSA molecule; and [MPc] the concentration of the different MPc complexes. Plots of $\log\left[\frac{(F_0-F)}{(F-F_\infty)}\right]$ against log [MPc] would provide the values of n (from slope) and k_b (from the intercept). The changes in BSA fluorescence intensity were related to MPc concentrations by the Stern–Volmer relationship, Eqs. (11) and (12) [50]

$$\frac{F_0^{BSA}}{F^{BSA}} = 1 + K_{SV}^{BSA}[MPc] \tag{11}$$

and K_{SV}^{BSA} is given by

$$K_{SV}^{BSA} = k_q \tau_F^{BSA} \tag{12}$$

where F_0^{BSA} and F^{BSA} are the fluorescence intensities of BSA in the absence and presence of MPcs, respectively; K_{SV}^{BSA}, the Stern–Volmer quenching constant; k_q, the bimolecular quenching constant; and τ_F^{BSA}, the fluorescence lifetime of BSA. τ_F^{BSA} is known to be 10 ns, [51–53]. Thus, from the values K_{SV}^{BSA} obtained from the plots of $\frac{F_0^{BSA}}{F^{BSA}}$ versus [MPc], the value of k_q may be determined (Eqs. (11) and (12)).

2.6. Synthesis

2.6.1. 1(4)-Tetra-(2-diethylaminoethylsulfanyl)-phthalocyaninato zinc(II) (**5a**, Scheme 1a) [22]

A mixture of 3-diethylaminoethylsulfanyl phthalonitrile (**3a**) (0.26 g, 1 mmol), 2-(dimethylaminoethanol) (1 ml) and anhydrous

$Zn(CH_3COO)_2$ (0.064 g, 0.35 mmol) was refluxed under N_2 for 18 h. After cooling to room temperature, MeOH:H_2O (1:1) was added to precipitate the product. The dark green product was filtered off and washed with water. It was isolated on a neutral alumina column with THF:MeOH (30:1) as eluent. Yield: 0.11 g (42%). UV–Vis (DMSO): λ_{max} nm (log ε) 339 (4.78), 643 (4.57), 717 (5.30). IR [(KBr) ν_{max}/cm^{-1}]: 3015 (Ar–CH), 2968–2797 (C–H), 1591 (C=C), 737 (C–S–C). ^{1}H NMR (DMSO-d_6) δ = 8.99 (m, 8H, Ar–H), 8.05 (m, 4H, Ar–H), 3.14 (m, 8H, SCH_2), 2.77 (br, 8H, NCH_2), 2.59 (m, 16H, CH_2C), 1.21 (m, 24H, CH_3). LRAPCI-MS *m/z*: Calc. for $C_{56}H_{68}N_{12}S_4Zn$: 1102.85; found $[M+2H]^{2+}$ 1104.4.

2.6.2. 1(4)-Tetra-(2-diethylmethylaminoethylsulfanyl)-phthalocyaninato zinc(II) tetraiodide (**5b**, Scheme 1b)

Compound **5a** (0.03 g, 0.027 mmol) was dissolved in $CHCl_3$ (5 ml), and methyl iodide (0.15 g, 1.059 mmol) was added to this solution. The mixture was refluxed for 3 h. After cooling to room temperature, the green precipitate was filtered off, washed with $CHCl_3$ and dried. Yield: 0.032 g (87%). UV–Vis (DMSO): λ_{max} nm (log ε) 336 (4.81), 636 (4.66), 707 (5.41). IR [(KBr) ν_{max}/cm^{-1}]: 2927 (C–H), 1589–1565 (C=C) ^{1}H NMR (DMSO-d_6) δ = 9.36 (quin, 4H, Ar–H), 8.35 (m, 8H, Ar–H), 4.09 (br, 8H, SCH_2), 3.98 (br, 8H, NCH_2), 3.65 (m, 16H, CH_2C), 3.28 (d, 12H, CH_3), 1.4 (m, 24H, CCH_3). LRAPCI-MS *m/z*: Calc. for $C_{60}H_{80}N_{12}S_4I_4Zn$: 1670.63; found $[M-I+2H]^{2+}$ 1546.

2.6.3. 2(3)-Tetra-(2-diethylaminoethylsulfanyl)-phthalocyaninato zinc(II) (**6a**, Scheme 1a)

Synthesis and purification was as outlined for **5a** except **4a** (0.26 g, 1 mmol) was employed instead of **3a** in the presence of 2-(dimethylaminoethanol) (1 ml) and anhydrous $Zn(CH_3COO)_2$ (0.064 g, 0.35 mmol). Yield: 0.12 g (45%). UV–Vis (DMSO): λ_{max} nm (log ε) 363 (4.83), 627 (4.46), 694 (5.19). IR [(KBr) ν_{max}/cm^{-1}]: 3007 (Ar–CH), 2967–2803 (C–H), 1600 (C=C), 743 (C–S–C). ^{1}H NMR (DMSO-d_6) δ = 8.78 (t, 4H, Ar–H), 8.02 (m, 4H, Ar–H), 7.87 (s, 4H, Ar–H), 3.37 (br, 8H, SCH_2), 3.05 (br, 8H, NCH_2), 2.76 (quin, 16H, CH_2C), 1.16 (t, 24H, CH_3). LRAPCI-MS *m/z*: Calc. for $C_{56}H_{68}N_{12}S_4Zn$: 1102.85; found $[M+3H]^{3+}$ 1106.1.

2.6.4. 2(3)-Tetra-(2-diethylmethylaminoethylsulfanyl)-phthalocyaninato zinc(II) tetraiodine (**6b**, Scheme 1b)

Synthesis and purification was as outlined for **5b** except **6a** (0.03 g, 0.027 mmol) was employed instead of **5a** in the presence of $CHCl_3$ (5 ml) and methyl iodide (0.15 g, 1.059 mmol). Yield: 0.035 g (95%). UV–Vis (DMSO): λ_{max} nm (log ε) 368 (4.85), 621 (4.54), 691 (5.34). IR [(KBr) ν_{max}/cm^{-1}]: 2974 (C–H), 1599 (C=C), 743 (C–S–C). ^{1}H NMR (DMSO-d_6) δ = 9.48 (m, 8H, Ar–H), 8.38 (quin, 4H, Ar–H), 3.95 (br, 8H, SCH_2), 3.74 (br, 8H, NCH_2), 3.56 (t, 16H, CH_2C), 3.15 (d, 12H, CH_3), 1.33 (m, 24H). LRAPCI-MS *m/z*: Calc. for $C_{60}H_{80}N_{12}S_4I_4Zn$: 1670.63; found $[M-I+2H]^{2+}$ 1546.

3. Results and discussion

3.1. Synthesis and characterization

Scheme 1 shows the synthetic pathways for the compounds used in this work. Substituted phthalocyanines are prepared by cyclotetramerization of substituted phthalonitriles. 3-Tetra-substituted phthalocyanines can be synthesized from 3-substituted phthalonitriles while 4-tetra-substituted phthalocyanines are obtained from 4-substituted phthalonitriles [54]. As stated above, the syntheses of complexes **7a** and **7b** (Fig. 1) have been reported before, and gave satisfactory spectroscopic analyses.

The 2-diethylaminoethanethiol substituents on the complex are suitable for conversion into quaternary ammonium groups and this can increase the products' solubility in water. Metal phthalocyanines were obtained in the presence of metal salts and the substituted phthalonitriles. Compounds **5b** and **6b** were obtained by methylation of **5a** or **6a** in $CHCl_3$ in good yield.

The non-ionic complexes (**5a**, **6a** and **7a**) in this study were soluble in organic solvents such as THF, toluene, and DMSO and the ionic complexes (**5b**, **6b** and **7b**) were highly soluble in polar solvents like water, methanol and DMSO. The 2-diethylaminoethanethiol group was tetra-substituted at the α and β positions and octa-substituted at the β position of the ring for comparative purposes.

The complexes were characterized by various spectroscopic methods: IR, UV–Vis, ^{1}H NMR and mass spectra and are consistent with predicted structures. The characteristic nitrile (C≡N) stretch at ~2225 cm^{-1} of **3** and **4** disappears upon formation of the phthalocyanine. The ^{1}H NMR spectra of the complexes showed ring protons between 8.99 and 9.36 ppm with the substituent protons observed between 1.21 and 4.09 ppm for the complexes (see Section 2). Integration of the peaks correctly corresponded to the expected total number of protons for each complex, confirming the relative purity of the complexes, 68 protons for complex **5a** and **6a** and 80 protons for **5b** and **6b**. Although the presence of isomers as well as phthalocyanine aggregation at the concentrations used for the NMR measurements may lead to broadening of the aromatic signals [55], the observed spectra of the complexes were relatively well resolved except for the peaks corresponding to protons attached to the sulfur or nitrogen groups and this is consistent with literature [19].

3.2. Spectrophotometric studies

The ground state electronic absorption spectra of the complexes showed monomeric behaviour evidenced by a single *Q-band,* typical of metallated phthalocyanine complexes (Fig. 2a and b) [56]. The *Q*-bands were observed in the near infrared region between 691 and 717 nm (Table 1) with the B-bands between 340 and 380 nm in DMSO.

The *Q*-bands of the α-tetra-substituted complexes (**5a** and **5b**) are red-shifted by 16 and 21 nm, when compared to the corresponding β-tetra-substituted (**6a** and **6b**) complexes in DMSO. Bathochromic shifts are known to occur into the near infrared region with electron-donating groups with a greater effect when the substitution is at the non-peripheral α positions [57,58] due to a greater destabilization effect of the HOMO level at the α position compared to the β position since linear combinations of the atomic orbitals (LCAO) coefficients at the α positions of the HOMO level are greater than those at the β positions. Therefore, a decreased energy gap between the HOMO and LUMO levels and a subsequent bathochromic shift is observed. Octa β substituted complexes **7a** and **7b**, showed red-shifted spectra compared to the tetra β substituted complexes **6a** and **6b**. The complexes showed monomeric behaviour up to $\sim 1 \times 10^{-5}$ mol dm^{-3} in DMSO.

On quaternization, blue shifts of about 2–10 nm was observed in complexes **5b**, **6b** and **7b** when compared to their corresponding non-ionic forms **5a**, **6a** and **7a** in DMSO (Table 1). This is due to the reduced electron-donating ability of the nitrogen groups when quaternized. The quaternized **5b**, **6b** and **7b** complexes are highly soluble in aqueous medium but were aggregated (Fig. 2c) with the formation of two main bands at ~680–700 nm (not well resolved for the β substituted complexes **6b** and **7b**) due to the monomeric species and ~640–660 nm due to the aggregated species, respectively. Aggregation in MPc complexes is due to a coplanar association of rings, resulting in splitting and broadening of spectra, with a blue shifted peak due to the aggregate. The presence of the bulky quaternized 2-diethylaminoethanethiol substituent at the periphery of the Zn(II)Pc significantly increases its solubility in aqueous medium, but is not so efficient in preventing

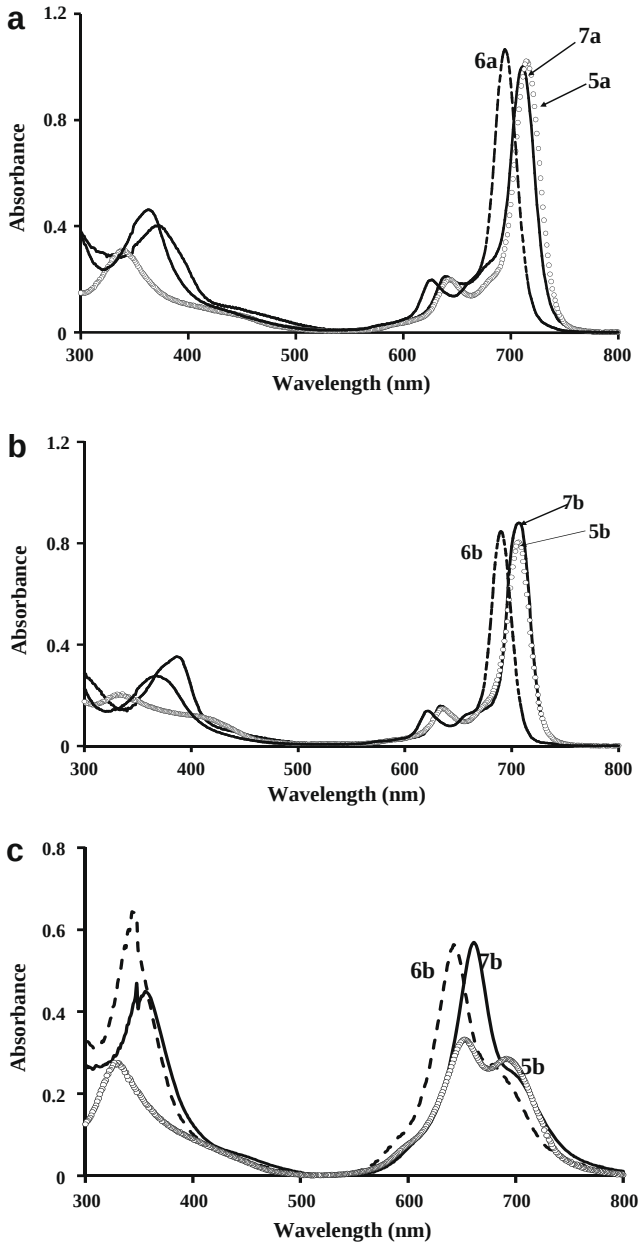


Fig. 2. Ground state electronic absorption spectra of: (a) **5a**, **6a** and **7a**; (b) **5b**, **6b** and **7b** in DMSO (concentration ~5×10^{-6} mol dm^{-3}); (c) **5b**, **6b** and **7b** in aqueous medium (concentration ~4×10^{-6} mol dm^{-3}).

aggregation of the Pc macrocycle. Metal ions like gallium and silicon, containing axial ligands in association with bulky substituents have been found to be more efficient in preventing aggregation of the Pc macrocycles [20,59]; buttressing the fact that aggregation can be dependent on the complexed metal ion. The addition of a surfactant cremophore EL (CEL), to the aqueous solution of **5b**, **6b** or **7b** resulted in a decrease in the intensity of the band due to the aggregates with an increase in the intensity of the band due to the monomeric species as shown for **5b** in Fig. 3, which confirms that the complexes are aggregated in aqueous solution with *Q-band* maxima given in Table 1. The addition of CEL caused ~11 nm red shift for the monomer peak in **5b** due to the disaggregation in water (this shift may have occurred in **6b** and **7b** also but it is not quite evident since their monomer peaks were not well resolved; Table 1). This shift may be due to the difference in media or existence of two or more different types of dimers in solution resulting in different positions and shapes of the absorption bands as has been observed before in sulfonated AlPc complexes [60]. It is also known that the electronic structure of phthalocyanines is perturbed when they are aggregated, therefore leading to an alteration of the ground and excited state properties [24]. The disappearance of the peak due to the aggregates was however not complete for all the complexes as seen in Fig. 3, by the persistent dimeric peak in the ~640–660 nm region. This suggests that strong forces are responsible for the aggregation. Aggregated MPcs are expected to disaggregate and exhibit monomeric behaviour in organic solvents [29], and this was observed in Fig. 2b, with the complexes in dimethylsulfoxide (DMSO).

Percentage aggregation (% Agg) was calculated using (Eq. (1)) for the quaternized complexes, they all exhibit high values as shown in Table 2 with the α substituted complex having the lowest % Agg which may be due to reduced aggregation tendencies when substitution is at the non-peripheral positions [24]. This high % Agg may lead to low photoactivity of the complexes in aqueous solution since aggregation diminishes the photosensitizing ability of MPc complexes. The values of equilibrium constant (K_D) for the monomer/dimer equilibrium are high for the complexes (Table 2) indicating a strong association between the aggregates. These values are within the range for some MPc complexes [30,39]. The values of ε_D (Table 2) and ε_M (Table 1) are within the range reported for some MPc complexes [39,56].

Absorption and fluorescence excitation spectra of MPcs are expected to be similar and mirror images of their emission spectrum. There is however a lack of agreement between these spectra for the complexes (**5b**, **6b** and **7b**) in aqueous medium, as shown in Fig. 4a for complex **6b**. The band around 640 nm, associated with the dimer is not seen in the fluorescence excitation spectra suggesting that only the monomer fluoresces. It has been documented that

Table 1
Spectral, photophysical and photochemical parameters of Zn phthalocyanine derivatives in aqueous and non-aqueous media.

Sample	[a]Solvent	λ_0 (nm) (log ε)	λ_F (nm)	λ_{Exc} (nm)	Φ_F	Φ_T	Φ_{IC}	τ_T (μs)	Φ_Δ	[b]S_Δ	$\Phi_{Pd}/10^4$
5a (αZn)	DMSO	717 (5.30)	725	719	0.07	0.66	0.27	190	0.64	0.97	6.62
5b (αZn)	PBS	653 692 (4.96)	710	703	<0.01	0.15	0.85	20	0.10	0.67	0.93
	PBS + CEL	703 (5.02)	716	710	0.03	0.17	0.80	90	0.12	0.71	1.22
	DMSO	707 (5.41)	716	708	0.09	0.63	0.28	200	0.51	0.81	1.81
6a (βZn)	DMSO	696 (5.19)	707	697	0.13	0.71	0.16	180	0.68	0.96	6.61
6b (βZn)	PBS	643 682 (4.68)	702	699	<0.01	0.28	0.72	70	0.15	0.54	1.09
	PBS + CEL	688 (4.73)	701	694	0.02	0.34	0.64	110	0.26	0.76	1.90
	DMSO	691 (5.34)	701	693	0.18	0.57	0.25	210	0.62	1.09	1.66
7a (βZn)	DMSO	709 (5.13)	721	712	0.05	0.75	0.20	200	0.62	0.83	9.40
7b (βZn)	PBS	661 700 (4.85)	716	709	<0.01	0.17	0.83	40	0.10	0.59	0.51
	PBS + CEL	703 (4.89)	717	710	0.01	0.32	0.67	60	0.24	0.75	0.77
	DMSO	707 (5.37)	716	707	0.08	0.60	0.32	220	0.49	0.82	1.71

[a] CEL, cremophore EL.
[b] $S_\Delta = \Phi_\Delta/\Phi_T$.

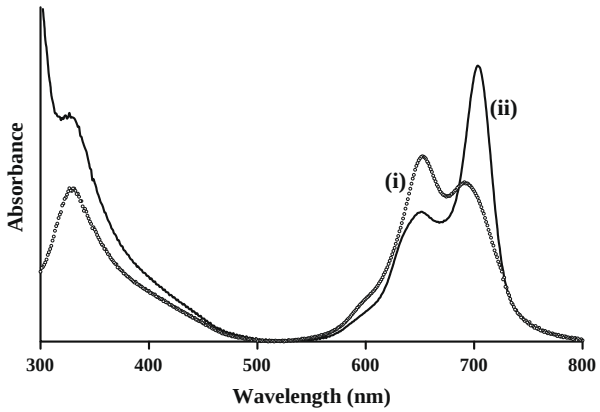


Fig. 3. Absorption spectra of (i) 3.95×10^{-6} mol dm^{-3} **5b** and (ii) **5b** in the presence of 4×10^{-3} mol dm^{-3} CEL.

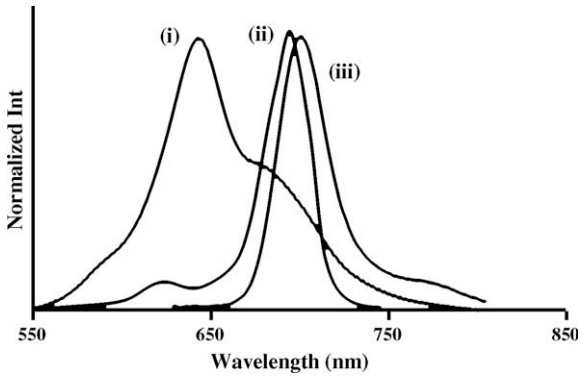


Fig. 4a. Normalized absorption (i), fluorescence excitation (ii) and emission (iii) spectra of **6b** in aqueous medium.

dimers are non-photoactive [43]. In DMSO, the absorption and fluorescence excitation spectra of the complexes (ionic and non-ionic) are similar and are mirror images of their respective emission spectrum (Fig. 4b for complex **7b**). Fig. 4c shows the fluorescence excitation and emission spectra for complex **5b** in aqueous medium in the presence of CEL, they are both mirror images of each other. Stokes' shifts ($\lambda_{ems} - \lambda_{exc}$) were ~10–14 nm, typical of MPc complexes.

In DMSO, excitation spectra were the same as absorption spectra for all the complexes. In PBS in the presence of CEL, the excitation spectra maxima were significantly different from the absorption spectra, suggesting differences in the nuclear configuration of the ground and excited states.

3.3. Photophysical studies

The complexes have relatively low quantum yields of fluorescence (Φ_F) as listed in Table 1. The highest values are exhibited in DMSO for all complexes. It is also interesting to note that the Φ_F values for ionic complexes (**5b**, **6b** and **7b**) were higher than for the non-ionic complexes (**5a**, **6a** and **7a**) in DMSO, where full disaggregation of the complexes has occurred. Aggregation is known to dissipate the electronic energy of the excited singlet state, thereby lowering fluorescence, so the low Φ_F values for (**5b**, **6b** and **7b**) in PBS are expected. Monomerization of aggregates leads to enhanced fluorescence and this is noticed in the Φ_F of (**5b**, **6b** and **7b**) in the presence of CEL in aqueous medium and in DMSO compared to that in aqueous medium alone. The Φ_F values followed the trend PBS 7.4 < PBS 7.4 + CEL < DMSO for complexes **5b**, **6b** and **7b**.

Fig. 5 shows the transient absorption spectrum of **5a** in DMSO. The absorption of the triplet state is at ~540–560 nm. The triplet absorption maxima were also obtained at ~540 nm for all the other complexes. The triplet absorption curve of **5a** in DMSO is shown in Fig. 5 (inset), and it obeyed second order kinetics. This is typical of MPc complexes at high concentrations [61] due to triplet–triplet recombination. The concentrations employed in this work were in this range hence triplet–triplet recombination is expected [61].

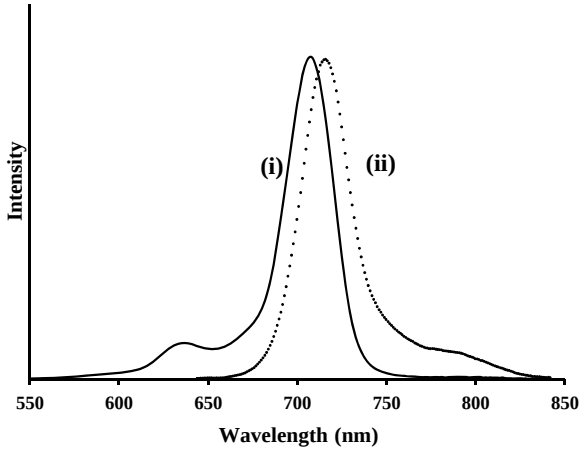


Fig. 4b. Normalized fluorescence excitation (i) and emission (ii) spectra of **7b** in DMSO.

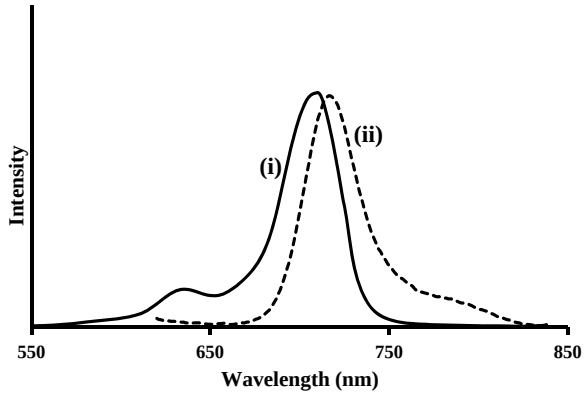


Fig. 4c. Normalized fluorescence excitation (i) and emission (ii) spectra of **5b** in the presence of cremophore EL in aqueous medium.

Table 2
Aggregation parameters and BSA binding data for the quarternized Zn phthalocyanine derivatives in aqueous medium.

Complex	% Agg	log ε_D	K_D (10^{-4} dm^3 mol^{-1})	K_{SV}^{BSA} (10^{-5} M^{-1})	k_q (10^{-13} M^{-1} s^{-1})	k_b (10^{-6} dm^3 mol^{-1})	n
5b (αZn)	54.1	4.26	1.01	1.44	1.44	1.90	1.21
6b (βZn)	65.5	3.99	1.61	2.41	2.41	8.68	1.29
7b (βZn)	73.4	4.14	1.82	3.19	3.19	12.3	1.30

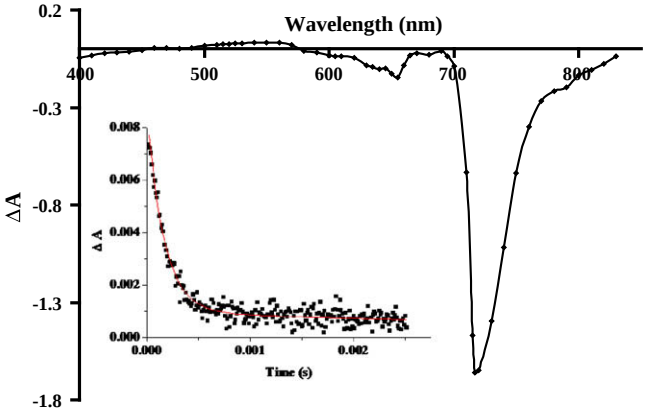


Fig. 5. Transient absorption spectrum for **5a** in DMSO (inset: triplet decay curve of **5a** in DMSO). [**5a**] = ~7.5 × 10^{-6} mol dm^{-3}. λ_{exc} = 717 nm.

Φ_T values were highest for **5a**, **6a** and **7a** in DMSO (Table 1), compared to their quaternized counterparts **5b**, **6b** and **7b**. Φ_T values for the latter were however relatively lower than for the former. The higher Φ_T values of complexes **5a**, **6a** and **7a** correspond to the lower values of Φ_F values for these complexes compared to **5b**, **6b** and **7b** since low values of the later suggest efficient intersystem crossing, hence increased values of the former. As expected, the presence of CEL gave increased Φ_T values for (**5b**, **6b** and **7b**) compared to PBS alone since the MPc complexes experience some disaggregation in this case, monomers have greater tendencies to undergo intersystem crossing because less energy is lost through internal conversion [29].

Φ_{IC} values in DMSO for all the complexes were relatively low, but quite high for (**5b**, **6b** and **7b**) in aqueous medium, due to the dissipation of electronic energy by the aggregates. Φ_{IC} values decreases in the order, PBS 7.4 > PBS 7.4 + CEL > DMSO for (**5b**, **6b** and **7b**) which suggests that molecules are more photoactive in DMSO than in aqueous solution. The decrease in Φ_{IC} values in the presence of CEL is due to its monomerizing effect on the MPc complexes.

An increase in triplet lifetimes (τ_T) in the order, PBS 7.4 < PBS 7.4 + CEL < DMSO is observed with the complexes. The lowest τ_T values exhibited in PBS 7.4 are likely due to the fact that the triplet state of MPcs can be quenched by water [42]. The slight increase in the presence of CEL may be due to less exposure of the phthalocyanine to the aqueous medium.

3.4. Photochemical studies

Energy transfer between the triplet state of photosensitizers and ground state molecular oxygen leads to the production of singlet oxygen, Φ_Δ. Therefore, singlet oxygen quantum yield which is the efficiency of singlet oxygen generation, should depend on the triplet state quantum yield and lifetime, the efficiency of energy transfer, which depends on the energy of the triplet state and the ability of the substituents to quench the triplet state amongst other factors. An efficient production of Φ_Δ in DMSO was observed with values of S_Δ which represents the efficiency of quenching of the triplet excited state by singlet oxygen, near unity for the complexes. The low values of Φ_Δ for **5b**, **6b** and **7b** in PBS (Table 1) are due to low Φ_T values discussed above. There is a slight improvement in Φ_Δ values in CEL.

Oxidative attack on the excited triplet state of MPcs by singlet oxygen brings about photodegradation, since the triplet state is sufficiently long lived to participate in photochemical reactions. Photodegradation quantum yields were highest in DMSO for all the MPc complexes with higher values exhibited in **5a**, **6a** and **7a** compared to their quaternized derivatives **5b**, **6b** and **7b**. The lowest values of photodegradation were exhibited in PBS pH 7.4. Thus, the trend shows that photodegradation is dependent on singlet oxygen. It is believed that singlet oxygen has the ability to react with macrocyclic metal complexes [62].

3.5. Interaction of MPcs (*5b*, *6b* and *7b*) with BSA

3.5.1. Binding constants and fluorescence quenching

Fig. 6a shows quenching of BSA fluorescence by **6b**. This quenching in fluorescence of BSA suggests that the complexes readily bind to BSA. The binding constants (k_b) and binding stoichiometry (n) was therefore estimated using this quenching of fluorescence and Eq. (10). The values of k_b and n shown in Table 2 were estimated from the binding plot (Fig. 6b). The k_b values increased in the order **5b** < **6b** < **7b**. This suggests that the peripherally substituted derivatives **6b** and **7b** bind more strongly to BSA than the non-peripherally substituted derivative, **5b**, probably due to steric hindrance that the substituents of **5b** may be experiencing in binding to BSA. It is also evident that the k_b value for **7b** is the highest in the set, which may be due to the presence of eight substituents on the periphery that are available for binding compared to four in the other derivatives. n values of ~1 are obtained for the complexes suggesting a 1:1 stoichiometry which is characteristic for MPc–BSA interactions in aqueous medium [30,40].

The inset in Fig. 6a shows the Stern–Volmer plot which indicates that within the investigated range of concentrations, Stern–Volmer equation (Eq. (11)) is obeyed. The K_{SV}^{BSA} values were determined from the slopes of plots in Fig. 6a (inset). Table 2 shows that complex **7b** has the highest K_{SV} values, suggesting that the BSA fluorescence quenching is most effective in this complex in this

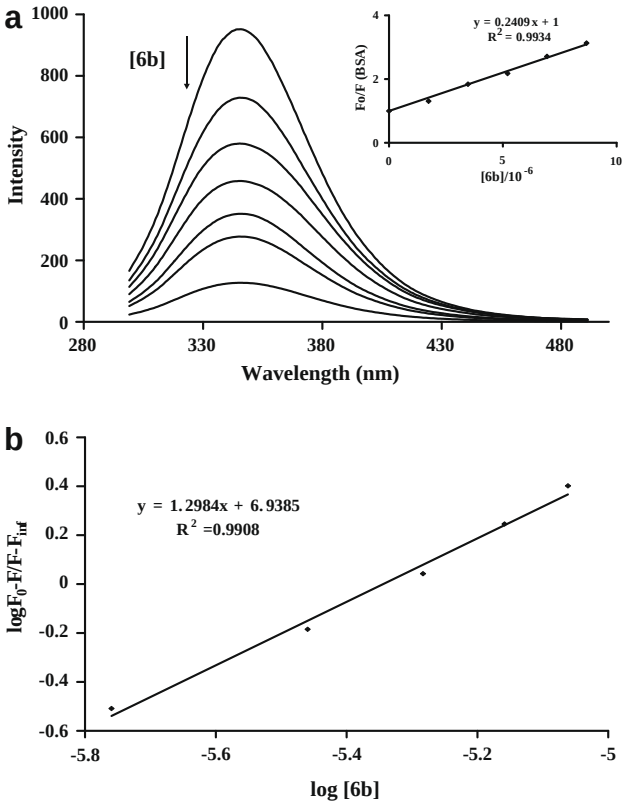


Fig. 6. (a) Spectral changes of BSA (3×10^{-5} mol dm^{-3}) on addition of **6b** (0–8.68×10^{-6} mol dm^{-3}) in aqueous medium. Inset is the Stern–Volmer's plot and (b) binding plot of BSA to **6b**.

particular set. This shows some agreement between k_b and K_{SV} values. The bimolecular quenching constants (k_q) were determined for the individual MPcs using Eq. (12) and the approximate values of fluorescence lifetime of BSA (10 ns) [51–53]. As shown in Table 2, the k_q values are higher (being in the order of 10^{13} dm^3 mol^{-1} s^{-1}) than the proposed value for dynamic quenching (10^{10} dm^3 mol^{-1} s^{-1}) [63] indicating that quenching mechanism in this case is static.

4. Conclusion

Peripherally and non-peripherally 2-diethylaminoethanethiol tetra-substituted zinc phthalocyanine (**5a** and **6a**) and their quaternized derivatives (**5b** and **6b**) have been synthesized and characterized. Their photophysical and photochemical properties and that of their peripherally octa-substituted counterpart have been studied and compared with each other in both aqueous and non-aqueous media. The complexes exhibited similar characteristics dependent on the solvent media. The quaternized complexes were aggregated in aqueous solution, but the addition of cremophore EL hindered aggregation resulting in increased photoactivity and improved photosensitizing ability. Strong binding to BSA occurred in the order **7b** > **6b** > **5b** due to steric effect at the non-peripheral position.

Acknowledgements

This work was supported by the Department of Science and Technology (DST) and National Research Foundation (NRF), South Africa, through DST/NRF South African Research Chairs Initiative for Professor of Medicinal Chemistry and Nanotechnology as well as Rhodes University and Medical Research Council of South Africa. M.I. thanks the Andrew Mellon Foundation and NRF for scholarships.

References

[1] C.C. Leznoff, A.B.P. Lever (Eds.), Phthalocyanines: Properties and Applications, vols. 1–4, VCH Publishers, New York, 1989–1996.
[2] J. Simon, P. Bassoul, Design of Molecular Materials: Supramolecular Engineering, VCH, Weinheim, 2000.
[3] D. Schlettwein, D. Wohrle, N.I. Jaeger, J. Electrochem. Soc. 136 (1989) 2882.
[4] J. Simon, C. Sirlin, Pure Appl. Chem. 61 (1989) 1625.
[5] M.J. Cook, N.B. McKeown, J.M. Simmons, A.J. Thomson, M.F. Daniel, K.J. Harrison, R.M. Richardson, S.J. Roser, J. Mater. Chem. 1 (1991) 121.
[6] J.E. van Lier, in: D. Kessel (Ed.), Photodynamic Therapy of Neoplastic Diseases, vol. 1, CRC Press, Boca Raton, FL, 1990.
[7] R. Bonnett, in: Chemical Aspects of Photodynamic Therapy, Gordon and Breach Science Publishers, Amsterdam, 2000.
[8] R.K. Pandey, J. Porphyr. Phthalocyan. 4 (2000) 368.
[9] I. Rosenthal, Photochem. Photobiol. 53 (1991) 859.
[10] J.D. Spikes, J. Photochem. Photobiol. B: Biol. 6 (1990) 259.
[11] A.C. Tedesco, J.C.G. Rotta, C.N. Lunardi, Curr. Org. Chem. 7 (2003) 187.
[12] W. Eberhardt, M. Hanack, Synthesis (1997) 95.
[13] C.C. Leznoff, S.M. Marcuccio, S. Greenberg, A.B.P. Lever, K.B. Tomer, Can. J. Chem. 63 (1985) 623.
[14] T. Nyokong, Coord. Chem. Rev. 251 (2007) 1707.
[15] Y.C. Yang, J.R. Ward, R.P. Seiders, Inorg. Chem. 24 (1985) 1765.
[16] W. Liu, T.J. Jensen, F.R. Fronczek, R.P. Hammer, K.M. Smith, M.G.H. Vicente, J. Med. Chem. 48 (2005) 1033.
[17] W.M. Sharman, S.V. Kudrevich, J.E. van Lier, Tetrahedron Lett. 37 (1996) 5831.
[18] M.P. de Filippis, D. Dei, L. Fantetti, G. Roncucci, Tetrahedron Lett. 41 (2000) 9143.
[19] L. Zhang, J. Huang, L. Ren, M. Bai, L. Wu, B. Zhai, X. Zhou, Bioorg. Med. Chem. 16 (2008) 303.
[20] M. Durmus, T. Nyokong, Inorg. Chem. Commun. 10 (2007) 332.
[21] M. Durmus, T. Nyokong, Photochem. Photobiol. Sci. 6 (2007) 659.
[22] Z.A. Bayir, Dyes Pig. 65 (2005) 235.
[23] D.J. Ball, S. Mayhew, S.R. Wood, J. Griffiths, D.I. Vernon, S.B. Brown, Photochem. Photobiol. 69 (1999) 390–396.
[24] R.D. George, A.W. Snow, J.S. Shirk, W.R. Barger, J. Porphyr. Phthalocyan. 2 (1998) 1.
[25] G.J. Jori, Photochem. Photobiol. B: Biol. 36 (1996) 87.
[26] D. Jocham, in: J.G. Moser (Ed.), Photodynamic Tumor Therapy. 2° and 3° Generation Photosensitizers, Harwood Academic Publisher, 1998.
[27] A.C.H. Ng, X. Li, D.K.P. Ng, Macromolecules 32 (1999) 5292.
[28] N.A. Kuznetsova, N.S. Gretsova, V.M. Derkacheva, O.L. Kaliya, E.A. Lukyanets, J. Porphyr. Phthalocyan. 7 (2003) 147.
[29] A. Ogunsipe, T. Nyokong, J. Photochem. Photobiol. A: Chem. 173 (2005) 211.
[30] M. Idowu, T. Nyokong, J. Photochem. Photobiol. A: Chem. 197 (2008) 273.
[31] G. Jori, in: B.W. Henderson, T.J. Dougherty (Eds.), Photodynamic Therapy Basic Principles and Clinical Applications, Marcel Dekker, New York, 1992.
[32] A.A. Bhattacharya, S. Curry, N.P. Franks, J. Biol. Chem. 275 (2000) 38731.
[33] D.D. Perrin, W.L.F. Armarego, Purification of Laboratory Chemicals, 2nd ed., Pergamon Press, Oxford, 1989.
[34] J.H. Weber, D.H. Busch, Inorg. Chem. 4 (1965) 469.
[35] H. Tomoda, S. Saito, S. Shiraishi, Chem. Lett. 12 (1983) 313.
[36] R.D. George, A.W. Snow, J. Heterocyclic Chem. 32 (1995) 495.
[37] J.G. Young, W. Onyebuagu, J. Org. Chem. 55 (1990) 2155.
[38] D. Wöhrle, M. Eskes, K. Shigehara, A. Yamada, Synthesis (1993) 194.
[39] S. Khene, A. Ogunsipe, E. Antunes, T. Nyokong, J. Porphyr. Phthalocyan. 11 (2007) 109.
[40] S.M.T. Nunes, F.S. Squilla, A.C. Tedesco, Braz. J. Med. Biol. Res. 37 (2004) 273.
[41] S. Fery-Forgues, D.J. Lavabre, Chem. Ed. 76 (1999) 1260.
[42] A. Ogunsipe, J.Y. Chen, T. Nyokong, New J. Chem. 7 (2004) 822.
[43] A. Harriman, M.C. Richoux, J. Chem. Soc., Faraday Trans. 2 (76) (1980) 1618.
[44] T.H. Tran-Thi, C. Desforge, C. Thies, J. Phys. Chem. 93 (1989) 1226.
[45] I. Seotsanyana-Mokhosi, N. Kuznetsova, T. Nyokong, J. Photochem. Photobiol. A: Chem. 140 (2001) 215.
[46] N. Kuznetsova, N. Gretsova, E. Kalmykova, E. Makarova, S. Dashkevich, V. Negrimovskii, O. Kaliya, E. Lukyanets, Russ. J. Gen. Chem. 70 (2000) 133.
[47] F. Wilkinson, W.P. Helman, A.B. Ross, J. Phys. Chem. Ref. Data 22 (1993) 113.
[48] D.M. Chipman, V. Grisaro, N. Sharon, J. Biol. Chem. 242 (1967) 4388.
[49] S. Lehrer, G.D. Fashman, Biochem. Biophys. Res. Commun. 23 (1966) 133.
[50] J. Rose, Advanced Physico-chemical Experiments, 1st ed., Sir Isaac Pitman and Sons Ltd., London, 1964. p. 257.
[51] M. Guo, J.W. Zou, P.G. Yi, Z.C. Shang, G.X. Hu, Q.S. Yu, Anal. Sci. 20 (2004) 465.
[52] C.Q. Jiang, M.X. Gao, J.X. He, Anal. Chim. Acta 452 (2002) 185.
[53] J.R. Lakowicz, G. Weber, Biochemistry 12 (1973) 4161.
[54] C.C. Leznoff, in: C.C. Leznoff, A.B.P. Lever (Eds.), Phthalocyanines, Properties and Applications, vol. 1, VCH Publishers, New York, 1989 (Chapter 1).
[55] S. Gaspard, P. Maillard, Tetrahedron 43 (1987) 1083.
[56] M.J. Stillman, T. Nyokong, in: C.C. Leznoff, A.B.P. Lever (Eds.), Phthalocyanines: Properties and Applications, vol. 1, VCH Publishers, New York, 1989 (Chapter 3).
[57] G. Chen, X. Peng, G. Hao, V.O. Kennedy, I.N. Ivanov, K. Knappenberger, J.J. Hill, M.A.J. Rodgers, M.E. Kenney, J. Phys. Chem. A 107 (2003) 3503.
[58] J. Mark, M.J. Stillman, J. Am. Chem. Soc. 116 (1994) 1292.
[59] H. Li, T.J. Jensen, F.R. Fronczek, M.G.H. Vicente, J. Med. Chem. 51 (2008) 502.
[60] Z. Petrasek, D. Phillips, Photochem. Photobiol. Sci. 2 (2003) 236.
[61] M.G. Debacker, O. Deleplanque, B. Van Vlierberge, F.X. Sauvage, Laser Chem. 8 (1988) 1.
[62] G. Schnurpfeil, A.K. Sobbi, W. Spiller, H. Kliesch, D. Worhle, J. Porphyr. Phthalocyan. 1 (1997) 159.
[63] S.L. Murov, I. Carmichael, G.L. Hug, Handbook of Photochemistry, 2nd ed., Marcel Decker, New York, 1993. p. 207.

Polyhedron 28 (2009) 425–430

Contents lists available at ScienceDirect

Polyhedron

journal homepage: www.elsevier.com/locate/poly

Effects of chloride ions on electrochemical reactions of manganese(III) complexes

Megumi Kasuno, Masaki Hayano, Manabu Fujiwara, Takayuki Matsushita *

Department of Materials Chemistry, Faculty of Science and Technology, Ryukoku University, 1-5 Yokotani Seta, Otsu, Shiga 520-2194, Japan

ARTICLE INFO

Article history:
Received 4 April 2008
Accepted 3 October 2008
Available online 17 January 2009

Keywords:
Manganese(III) complexes
Schiff base ligand
Oxidation reaction
Chloride ion
Electrochemistry

ABSTRACT

Electrochemical reactions of manganese(III) complexes, $Mn^{III}(L)X$ (L; salen, salpn, 5-NO_2–salen or 5-NO_2–salpn, X; Cl, Br or NO_2) and $Mn^{III}(L')_2X$ (L'; *N*-Bu-sal, *N*-Oct–sal, *N*-Oct–5-Br–sal or *N*-Oct–5-NO_2–sal, X; Cl or Br), were investigated by voltammetry at a glassy carbon electrode in the absence/presence of Cl^- in acetonitrile solution. By the addition of Cl^-, oxidation processes of $Mn^{III}(L)X$ and $Mn^{III}(L')_2X$ have been found to be improved from quasi-reversible to reversible, and their oxidation products, $[Mn^{IV}(L)X]^+$ and $[Mn^{IV}(L')_2X]^+$, were stabilized by the combination with Cl^- resulting in $[Mn^{IV}(L)Cl_2]$ and $[Mn^{IV}(L')_2Cl_2]$, respectively. On the other hand, the reduction processes of $Mn^{III}(L)X$ and $Mn^{III}(L')_2Cl$ were not so significantly affected by Cl^- as those observed for their oxidation. Other types of manganese(III) complexes and iron(III) complex were also investigated. The present study may clarify the role of Cl^- being involved in OEC (oxygen-evolving center) in photosystem II.

© 2008 Elsevier Ltd. All rights reserved.

1. Introduction

Redox reactions of manganese(II), (III) and/or (IV) complex are essential in relation to biological redox systems involving manganese ions, such as oxygen-evolving center (OEC) of photosystem II (PS II) in green plants, manganese-containing catalases and manganese superoxide dismutases. In particular, the reaction center of OEC has been proposed to consist of a cluster $CaMn_4O_4$ and chloride ions in appropriate concentration [1–4]. Moreover, studies of higher oxidation state manganese complexes are of special importance because their potential is employed practically for the oxidation of water to dioxygen in the OEC of PSII. In order to stabilize higher oxidation states of manganese ions, chloride ions have been considered to play an important role as well as preventing to form peroxide, acting to provide charge balance, and helping to shuttle protons to manganese center [5,6]. The role of chloride ions in the OEC, however, is still remained and less well established than that of a calcium ion, and there is no firm evidence that chloride ions are bound to the manganese cluster in OEC [5,6]. The recent study suggests that chloride ions are not absolutely required for the oxidation of water but that reaction rate (possibly at the $S_2 \rightarrow S_3$ step) only slow in the absence of chloride ions [7–9], and therefore it would be considered that chloride ions effect on the oxidation reaction process of manganese cluster in OEC.

There are many reports for syntheses of OEC model complexes binding with Cl^- and electrochemical analyses for redox reactions between Mn(II) and Mn(IV) of the complexes [10–14]. Hureau et al. synthesized the new mononuclear manganese(II) complex and reported that the electrochemical irreversible oxidation process of Mn(II) to Mn(III) complex changed to be reversible by the addition of Cl^- [14]. Chloride-manganese bonds in mononuclear manganese complexes were measured with the chlorine K-edge X-ray absorption spectra by Rompel et al. and then chloride ion in mononuclear compound was found out to bind covalently to manganese ions and the bond strength increased in the order Mn(II) < Mn(III) < Mn(IV) [15]. Previously, we have synthesized a series of dichloromanganese(IV) complexes with bidentate and tetradentate Schiff base ligands and determined their molecular structures, and moreover, pointed out that higher oxidation states of manganese complexes can be stabilized by chloride ions [16–18].

In the present work, effects of chloride ions on redox reactions of manganese(III) complexes have been investigated by voltammetry at a glassy carbon electrode. Manganese(III) complexes used in this work are summarized in Fig. 1. In order to compare an iron(III) complex, Fe^{III}(salen)Cl was also used. Here, H_2salen, H_2salpn, H_2salhexn and Hacac are abbreviation for *N,N′*-disalicylidene-1,2-diaminoethane, *N,N′*-disalicylidene-1,3-diaminopropane, *N,N′*-disalicylidene-1,6-diaminohexane and acetylacetone, respectively.

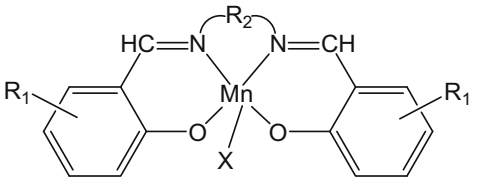
2. Experimental

2.1. Preparation of manganese complexes

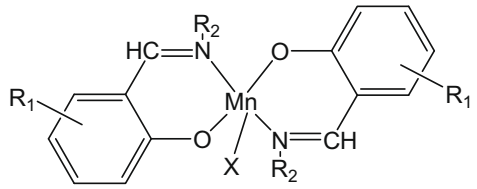
Tetradentate Schiff bases, H_2salen, H_2salpn and H_2salhexn were synthesized by standard methods (Schiff base condensation of 2 mole of the salicylaldehyde with 1 mole of appropriate diamines) [17]. Mn^{III}(salen)Cl, Mn^{III}(salpn)Cl and Mn^{III}(salhexn)Cl complexes were obtained by reacting the respective ligand (1 mmol) with $Mn^{III}(OAc)_3 \cdot H_2O$ (1 mmol) and LiCl (1.5 mmol) in methanol

* Corresponding author. Tel.: +81 77 543 7471; fax: +81 77 543 7483.
E-mail address: matusita@chem.ryukoku.ac.jp (T. Matsushita).

0277-5387/$ - see front matter © 2008 Elsevier Ltd. All rights reserved.
doi:10.1016/j.poly.2008.10.073



R_1	R_2	L	X
H	CH_2CH_2	salen	Cl
H	CH_2CH_2	salen	Br
H	CH_2CH_2	salen	NO_2
H	$CH_2CH_2CH_2$	salpn	Cl
H	C_6H_{12}	salhexn	Cl
5-NO_2	CH_2CH_2	salen	Cl
5-NO_2	$CH_2CH_2CH_2$	salpn	Cl



R_1	R_2	L	X
H	C_4H_9	N-Bu-sal	Cl
H	C_8H_{17}	N-Oct-sal	Cl
5-NO_2	C_8H_{17}	N-Oct-5-NO_2-sal	Cl
5-Br	C_8H_{17}	N-Oct-5-NO_2-sal	Cl

Fig. 1. Manganese(III) Schiff base complexes used in the present work.

solution and the resulting precipitates were collected, washed, and then dried *in vacuo*. They were recrystallized from methanol or dichloromethane [17,19,20]. Although Mn^{III}(salhexn)Cl was also synthesized in a similar manner, of which solubility is very poor in acetonitrile (MeCN) probably due to the formation of a polymeric complex, $[Mn^{III}(salhexn)Cl]_n$, and thus was not adopted in the present work. Mn^{III}(salen)Br or Mn^{III}(salen)NO_2 was prepared in the similar manner with LiBr or $LiNO_2$, respectively, instead of LiCl. Mn^{III}(5-NO_2–salen)Cl and Mn^{III}(5-NO_2–salpn)Cl were obtained in a similar manner as reported previously [19]. Fe^{III}(salen)Cl was also prepared in the similar manner to that of Mn^{III}(salen)Cl but with $FeCl_3$ instead of $Mn(OAc)_3$ and LiCl [21].

Bidentate Schiff base ligands, *N*-alkyl-substituted-salicylideneamine [*N*-R–X–salH where R can be *n*-C_4H_9 (Bu) or *n*-C_8H_{17} (Oct) and X can be H, Br or NO_2] were prepared by a condensation of the salicylaldehydes with butylamine or octylamine [19]. Mn^{III}(*N*-R–X–sal)$_2$Cl or Mn^{III}(*N*-R–X–sal)$_2$Br was synthesized by the reaction of the respective ligand (2 mmol) with $Mn^{III}(OAc)_3 \cdot H_2O$ (1 mmol) and LiCl or LiBr (1.5 mmol) in methanol solution, and the resulting precipitates were collected, washed, and then dried *in vacuo*. They were recrystallized from methanol or dichloromethane [19].

$Mn^{III}(acac)_3$ was prepared by conventional method [22].

2.2. Reagents

MeCN was purified by distillation over P_4O_{10} twice and then distilled further before use. Other solvents were purified by usual methods. Reagent grade tetra-*n*-butylammonium hexafluorophosphate ($TBAPF_6$) and tetraethylammonium chloride (TEACl) were purchased from Wako Pure Chemicals Co., Ltd., and used without further purification.

All other chemicals used were of reagent grade quality.

2.3. Electrochemical measurements

All electrochemical measurements were performed using a single compartment cell containing a three-electrode configuration with ALS 822A Electrochemical Analyzer (CH Instruments, Inc., Austin, TX). The working electrode was a glassy carbon disk with a diameter of 3 mm. Before each measurement, it was polished with 0.05 μm alumina slurry, and then sonicated in a distilled water and dried. An Ag/AgCl (in 3.3 M KCl) electrode (SSE) was used as the reference electrode. All potentials were referred to SSE, which correspond to a potential difference from that of Fc^+/Fc (Fc = ferrocene) couple of 0.43 V in MeCN. The counter electrode was a platinum wire. The solution was deaerated by passing argon gas before measurements, and an atmosphere of argon gas was then maintained over the solution throughout measurements. The supporting electrolyte and the scan rate (v) were $TBAPF_6$ (0.1 M) and 100 mV s^{-1}, respectively. The stock solution of TEACl was adjusted to 0.2 M with MeCN, and the appropriate amount was added to MeCN containing the manganese complex.

The controlled-potential electrolysis was performed at a column electrode [23] by forcing a sample solution deaerated by argon gas to flow through carbon fiber electrodes with the aid of a pump (Cole-Parmer Instrument Co., Model 7518-10) at a flow rate of 0.5 ml min^{-1}. The pretreatment of working electrode was carried out according to the literature [24] by scanning the applying potential between +1.2 and −0.7 V at v of 10 mV s^{-1}. During the pretreatment, 1 M HNO_3 solution was pumped through the carbon fibers.

All the electrochemical measurements were carried out at 25 ± 1 °C.

2.4. Other physicochemical measurements

All complexes used in this study were confirmed by the elemental analysis, IR and UV–Vis spectroscopies and magnetic susceptibilities. Results have been reported previously [17,19–21].

3. Results and discussion

3.1. Redox behavior of Mn^{III}(salen)Cl and Mn^{III}(salpn)Cl in the absence/presence of chloride ion in MeCN

This study has been done to clarify the role of chloride ions (Cl^-) involved in OEC using manganese complexes as models for PSII. We have found that the presence of Cl^- can stabilize the higher oxidation states of manganese ions in terms of electrochemical measurements.

Curve 1 in Fig. 2 is the cyclic voltammogram of 1.0 mM Mn^{III}(salen)Cl in MeCN. Curve 1′ is the background current in the absence of Mn^{III}(salen)Cl. One positive current wave due to the oxidation of Mn^{III}(salen)Cl to $[Mn^{IV}(salen)Cl]^+$ appeared with a half peak potential ($E_{1/2}$) at 0.94 V (versus SSE) in the voltammogram. A peak to peak separation (ΔE_p) is about 0.13 V, which indicates that the electrochemical process for the oxidation of Mn^{III}(salen)Cl is quasi-reversible. The positive peak current (I_{pa}) was proportional to the square root of v in the range between 10 and 200 mV s^{-1} and to the concentration of Mn^{III}(salen)Cl in the range between 0.05 to 1.0 mM, and hence the electrochemical oxidation of Mn^{III}(salen)Cl is considered to be controlled by the diffusion of Mn^{III}(salen)Cl to the surface of the working electrode. One negative current wave due to the reduction of Mn^{III}(salen)Cl to $[Mn^{II}(salen)Cl]^-$ was also obtained with $E_{1/2}$ at −0.20 V as shown in curve 1, which is found to be reversible process and controlled by the diffusion of Mn^{III}(salen)Cl since ΔE_p was about 0.07 V and the negative current peak

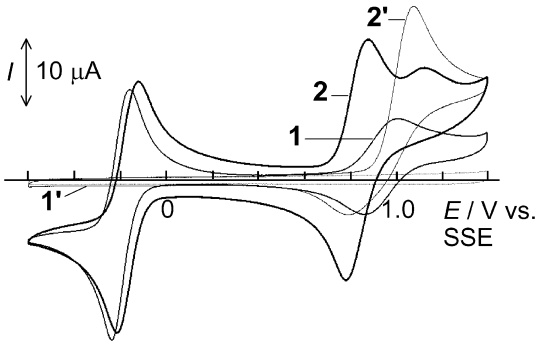


Fig. 2. Cyclic voltammogram of 1.0 mM Mn^{III}(salen)Cl in the absence (curve 1) or presence of 1.0 mM Cl^- (curve 2) in MeCN containing 0.1 M $TBAPF_6$. Curves 1′ and 2′: residual currents of curves 1 and 2 in the absence of Mn^{III}(salen)Cl in MeCN. Scan rate: 0.1 V s^{-1}.

(I_{pc}) was proportional to the v and the concentration of Mn^{III}(salen)Cl. These values are similar to those reported previously [25,26].

The addition of 1.0 equiv. of TEACl per Mn^{III}(salen)Cl dramatically changed its cyclic voltammogram: the $E_{1/2}$ for the redox couple of Mn^{III}(salen)Cl/$[Mn^{IV}$(salen)Cl$]^+$ shifts from 0.94 to 0.83 V as shown in curve 2 in Fig. 2. Curve 2′ is the voltammogram of 1.0 mM TEACl in MeCN. The positive current wave due to the oxidation of Cl^- appeared at the more positive peak potential (E_{pa}) of 1.08 V. Therefore, the voltammogram at $E_{1/2}$ of 0.83 V in curve 2 can be safely assigned to the oxidation of Mn^{III}(salen)Cl and not Cl^-. The I_{pa} at 0.87 V in curve 2 increased upon addition of Cl^- up to maximum of the ratio of Cl^- to Mn^{III}(salen)Cl to be unity, and no significant increase was observed on further addition of Cl^- as shown in Fig. 3. The ΔE_p for the redox potential of Mn^{III}(salen)Cl/$[Mn^{IV}$(salen)Cl$]^+$ changed from 0.13 to 0.09 V upon addition of Cl^- and the ratio of peak heights (I_{pa}/I_{pc}) in curve 2 was almost 1.0, which suggests in the view of uncompensated *IR*-drop that the oxidation of Mn^{III}(salen)Cl become a reversible process rather than quasi-reversible process by the addition of Cl^-. The oxidation product of Mn^{III}(salen)Cl is considered to be stabilized by the combination of the oxidation product of Mn^{III}(salen)Cl with Cl^- resulting in Mn^{IV}(salen)Cl_2 [19]. The reaction stoichiometry is 1.0 equiv. of Cl^- per Mn^{III}(salen)Cl as

$$Mn^{III}(salen)Cl + Cl^- \rightleftarrows [Mn^{IV}(salen)Cl]^+ + e^- + Cl^- \rightleftarrows Mn^{IV}(salen)Cl_2 \quad (1)$$

Here, the irreversible oxidation of Mn^{II} complex was also reported to become reversible upon addition of Cl^- to MeCN by the similar reason [14]. It can therefore be presumed that Cl^- has a role of the stabilization of Mn^{III} and Mn^{IV} complexes in organic solution.

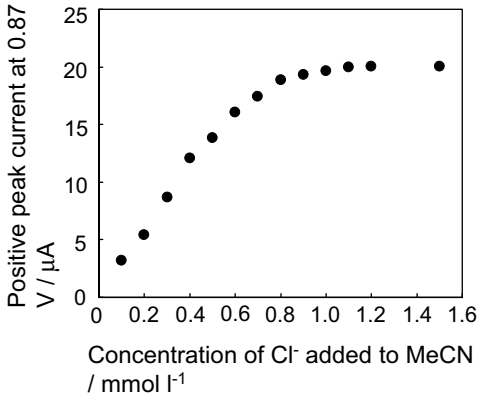


Fig. 3. A plot of positive peak current, I_{pa}, at 0.87 V against the concentration of Cl^- added to MeCN containing 1 mM Mn^{III}(salen)Cl.

The $E_{1/2}$ for the redox couple of $[Mn^{II}$(salen)Cl$]^-$/Mn^{III}(salen)Cl was also shifted from −0.20 to −0.16 V by the addition of Cl^-. It is thought that Cl^- in MeCN prevents the dissociation of $[Mn^{II}$(salen)Cl$]^-$ to Mn^{II}(salen) and Cl^- and makes $[Mn^{II}$(salen)Cl$]^-$ stable

$$Mn^{III}(salen)Cl + e^- \rightleftarrows [Mn^{II}(salen)Cl]^- \quad (2)$$

Similar stabilization of Mn^{III}(salpn)Cl over $[Mn^{IV}$(salpn)Cl$]^+$ by Cl^- in MeCN is also observed, and $E_{1/2}$ and ΔE_p for the redox couples of Mn^{III}(salpn)Cl/$[Mn^{IV}$(salpn)Cl$]^+$ and $[Mn^{II}$(salpn)Cl$]^-$/Mn^{III}(salpn)Cl in the absence/presence of Cl^- are summarized in Tables 1 and 2. The $E_{1/2}$ for the redox couple of Mn^{III}(salpn)Cl/$[Mn^{IV}$(salpn)Cl$]^+$ shifted from 0.95 to 0.85 V by adding Cl^- to MeCN, and ΔE_p decreased from 0.14 to 0.09 V. The I_{pa} at 0.89 V increased upon addition of Cl^- and no longer increased by the addition of Cl^- at the ratio of Cl^- to Mn^{III}(salpn)Cl more than unity as well as the case of those for Mn^{III}(salen)Cl. The $E_{1/2}$ for the redox couple of $[Mn^{II}$(salpn)Cl$]^-$/Mn^{III}(salpn)Cl shifted from −0.08 to 0.05 due to the stabilization of $[Mn^{II}$(salpn)Cl$]^-$ by Cl^-. The ΔE_p, however, increases from 0.07 to 0.10 V, which indicates that the reduction

Table 1
Electrochemical data for the oxidation of complexes.

	Without Cl^-		With Cl^-	
	$E_{1/2}$ (V vs. SSE)[a]	ΔE_p (V)[b]	$E_{1/2}$ (V vs. SSE)[a]	ΔE_p (V)[b]
Mn^{III}(salen)Cl	0.94	0.13	0.83	0.09
Mn^{III}(salpn)Cl	0.95	0.14	0.85	0.09
Mn^{III}(salen)Br	–[c]	–[c]	0.82	0.08
Mn^{III}(salen)NO_2	1.08	0.16	0.83	0.08
Mn^{III}(5-NO_2–salen)Cl	1.09	0.13	0.95	0.10
Mn^{III}(5-NO_2–salpn)Cl	1.14	0.20	0.97	0.09
Mn^{III}(*N*-Bu–sal)$_2$Cl	0.99	0.23	0.86	0.11
Mn^{III}(*N*-Oct–sal)$_2$Cl	1.01	0.26	0.88	0.11
Mn^{III}(*N*-Oct–5-NO_2–sal)$_2$Cl	1.13	0.15	0.96	0.08
Mn^{III}(*N*-Oct–5-Br–sal)$_2$Cl	1.05	0.24	0.90	0.08
Mn^{III}(acac)$_3$	0.99	0.13	–[c]	–[c]
Fe^{III}(salen)Cl[d]	–	–	–	–

(E_{pa} and E_{pc} are anodic and cathodic peak potentials, respectively).
[a] $E_{1/2} = (E_{pa} + E_{pc})/2$.
[b] $\Delta E_p = (E_{pa} - E_{pc})$.
[c] Irreversible oxidation process.
[d] Oxidation current wave was not observed in the voltammogram.

Table 2
Electrochemical data for the reduction of complexes.

	Without Cl^-		With Cl^-	
	$E_{1/2}$ (V vs. SSE)[a]	ΔE_p (V)[b]	$E_{1/2}$ (V vs. SSE)[a]	ΔE_p (V)[b]
Mn^{III}(salen)Cl	−0.20	0.07	−0.16	0.08
Mn^{III}(salpn)Cl	−0.08	0.07	0.05	0.10
Mn^{III}(salen)Br	−0.15	0.08	−0.17	0.08
Mn^{III}(salen)NO_2	−0.18	0.07	−0.15	0.08
Mn^{III}(5-NO_2–salen)Cl	0.16	0.07	0.15	0.07
Mn^{III}(5-NO_2–salbn)Cl	0.27	0.07	0.28	0.08
Mn^{III}(*N*-Bu–sal)$_2$Cl[c]	–	–	–	–
Mn^{III}(*N*-Oct–sal)$_2$Cl[c]	–	–	–	–
Mn^{III}(*N*-Oct–5-NO_2–sal)$_2$Cl[c]	–	–	–	–
Mn^{III}(*N*-Oct–5-Br–sal)$_2$Cl[c]	–	–	–	–
Mn^{III}(acac)$_3$[c]	–	0.39	–	0.47
Fe^{III}(salen)Cl	−0.33	0.10	−0.34	−0.10

(E_{pa} and E_{pc} are anodic and cathodic peak potentials, respectively).
[a] $E_{1/2} = (E_{pa} + E_{pc})/2$.
[b] $\Delta E_p = (E_{pa} - E_{pc})$.
[c] irreversible reduction process.

process of Mn^{III}(salpn)Cl becomes quasi-reversible even under the presence of Cl^-. The reaction mechanisms for the oxidation and reduction of Mn^{III}(salpn)Cl in the presence of Cl^- can be expressed as Eqs. (3) and (4) as well as those of Mn^{III}(salen)Cl

$$Mn^{III}(salpn)Cl + Cl^- \rightleftarrows [Mn^{IV}(salpn)Cl]^+ + e^- + Cl^- \rightleftarrows Mn^{IV}(salpn)Cl_2 \quad (3)$$

$$Mn^{III}(salpn)Cl + e^- \rightleftarrows [Mn^{II}(salpn)Cl]^- \quad (4)$$

Here, it can be seen by comparing the $E_{1/2}$ for the redox couples of $[Mn^{II}(salen)Cl]^-/Mn^{III}(salen)Cl$ and $[Mn^{II}(salpn)Cl]^-/Mn^{III}(salpn)Cl$ in Table 2 that the stabilization of Mn^{III} complex increases with a decrease of chain length in Schiff base ligand. This is probably due to the general argument that a five-membered chelate ring in Mn^{III}(salen)Cl is more stable compared to a six-membered chelate ring for Mn^{III}(salpn)Cl [27]. The similar effect has been found in the case of copper(II) complexes having different ring size [28].

3.2. Redox behavior of Mn^{III}(salen)Br and Mn^{III}(salen)NO_2 in the absence/presence of chloride ion in MeCN

Curve 1 in Fig. 4 is the cyclic voltammogram of 1.0 mM Mn^{III}(salen)Br in MeCN. The voltammogram exhibits the irreversible positive current wave and the reversible negative current wave ($E_{1/2}$ = −0.15, ΔE_p = 0.08 V). This may be caused by the difference in electron density between Br^- and Cl^- [27,29]. Therefore, the $E_{1/2}$ for the couple of $[Mn^{II}(salen)Br]^-/Mn^{III}(salen)Br$ is 0.05 V to more positive than that of $[Mn^{II}(salen)Cl]^-/Mn^{III}(salen)Cl$ (Table 2).

The cyclic voltammogram of curve 2 in Fig. 4 is recorded under the conditions with the same as that for curve 1 but by adding 2.0 mM TEACl. The clear positive current wave appeared in the voltammogram at I_{pa} of 0.86 V in curve 2 increased upon addition of Cl^- up to maximum of the ratio of Cl^- to Mn^{III}(salen)Br to be twice, and no significant increase was observed on further addition of Cl^-. Here, the value of positive current at 0.86 V is about twice as large as that of negative current at −0.22 V, which would be caused by the oxidation reaction of Br^- dissociated from Mn^{III}(salen)Br. The $E_{1/2}$ for the redox couple of $[Mn^{II}(salen)Br]^-/Mn^{III}(salen)Br$ shifted from −0.15 to −0.17 V but the ΔE_p was independent of the Cl^- added to MeCN. The $E_{1/2}$ and ΔE_p of curve 2 in Fig. 4 are almost identical with those of curve 2 in Fig. 2 recorded with Mn^{III}(salen)Cl and Cl^-. Therefore, it can be concluded that Br^- in Mn^{III}(salen)Br is replaced by two Cl^- ions via the oxidation of Mn^{III}(salen)Br as

$$Mn^{III}(salen)Br + 2Cl^- \rightleftarrows [Mn^{IV}(salen)Br]^+ + e^- + 2Cl^- \rightleftarrows Mn^{IV}(salen)Cl_2 + Br^- \quad (5)$$

The reduction of Mn^{III}(salen)Br may be expected to proceed by substitution of Br^- for Cl^- as

$$Mn^{III}(salen)Br + e^- + Cl^- \rightleftarrows [Mn^{II}(salen)Cl]^- + Br^- \quad (6)$$

The effect of Cl^- on the oxidation and reduction of Mn^{III}(salen)-NO_2 was almost identical with that of Mn(salen)Br as summarized in Tables 1 and 2. The NO_2^- in Mn^{III}(salen)NO_2 can be replaced by two Cl^- molecules via the oxidation of Mn^{III}(salen)NO_2, so that the reaction stoichiometry is 2.0 equiv. of Cl^- per Mn^{III}(salen)NO_2 as

$$Mn^{III}(salen)NO_2 + 2Cl^- \rightleftarrows [Mn^{IV}(salen)NO_2]^+ + e^- + 2Cl^- \rightleftarrows Mn^{IV}(salen)Cl_2 + NO_2^- \quad (7)$$

Since the $E_{1/2}$ for the redox couple of $[Mn^{II}(salen)NO_2]^-/Mn^{III}$(-salen)$NO_2$ in the presence of Cl^- exhibits almost the same potential with that of Mn^{III}(salen)Cl, the reduction process of Mn^{III}(salen)-NO_2 in the presence of Cl^- could be also expressed as

$$Mn^{III}(salen)NO_2 + e^- + Cl^- \rightleftarrows [Mn^{II}(salen)Cl]^- + NO_2^- \quad (8)$$

3.3. Redox behavior of Mn^{III}(5-NO_2–salen)Cl and Mn^{III}(5-NO_2–salpn)Cl in the absence/presence of chloride ion in MeCN

Since the solubility of Mn^{III}(5-NO_2–salen)Cl or Mn^{III}(5-NO_2–salpn)Cl was not so good, 0.5 mM Mn^{III}(5-NO_2–salen)Cl or Mn^{III}(5-NO_2–salpn)Cl in MeCN solution was adopted in this section. The cyclic voltammogram of Mn^{III}(5-NO_2–salen)Cl in MeCN is illustrated in curve 1 of Fig. 5. The quasi-reversible positive current wave corresponding to the redox couple of Mn^{III}(5-NO_2–salen)Cl/$[Mn^{IV}$(5-NO_2–salen)Cl$]^+$ and the reversible negative current wave corresponding to the redox couple of $[Mn^{II}$(5-NO_2–salen)Cl$]^-$/Mn^{III}(5-NO_2–salen)Cl appeared in the voltammogram with $E_{1/2}$ at 1.09 and 0.16 V, respectively. When equivalent amounts of TEACl were added to Mn^{III}(5-NO_2-salen)Cl in MeCN, the $E_{1/2}$ for the positive current wave shifted from 1.09 to 0.95 V and the $E_{1/2}$ for the negative current wave, however, was independent of Cl^- as shown in curve 2. The I_{pa} at 1.00 V in curve 2 increased upon addition of Cl^- up to maximum of the ratio of Cl^- to Mn^{III}(5-NO_2–salen)Cl to be unity, and no significant increase was observed on further addition of Cl^-. The ΔE_p for the redox couple of Mn^{III}(5-NO_2–salen)Cl/$[Mn^{IV}$(5-NO_2–salen)Cl$]^+$ decreased from 0.12 to 0.09 V, which indicates that the oxidation of Mn^{III}(5-NO_2–salen)Cl becomes near to the reversible process. ΔE_p and I_{pc} for the negative current wave were not influenced by Cl^- added to MeCN.

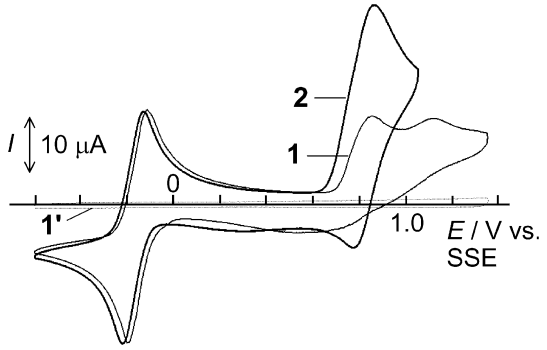


Fig. 4. Cyclic voltammogram of 1.0 mM Mn^{III}(salen)Br in the absence (curve 1) or presence of 2.0 mM Cl^- (curve 2) in MeCN containing 0.1 M $TBAPF_6$. Curve 1′: residual current of curve 1 in the absence of Mn^{III}(salen)Br in MeCN. Scan rate: 0.1 V s^{-1}.

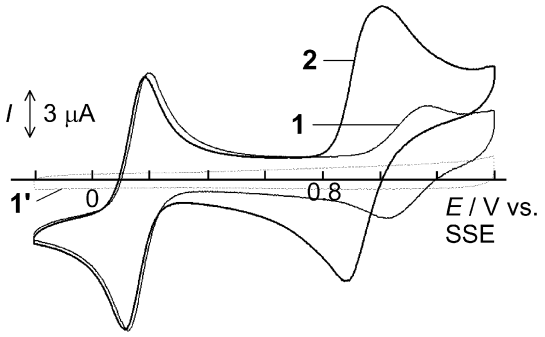


Fig. 5. Cyclic voltammogram of 0.5 mM Mn^{III}(5-NO_2–salen)Cl in the absence (curve 1) or presence of 0.5 mM Cl^- (curve 2) in MeCN containing 0.1 M $TBAPF_6$. Curve 1′: residual current of curve 1 in the absence of Mn^{III}(5-NO_2–salen)Cl in MeCN. Scan rate: 0.1 V s^{-1}.

$E_{1/2}$ and ΔE_p for redox reactions of Mn^{III}(5-NO_2–salpn)Cl in the absence/presence of 0.5 mM Cl^- are summarized in Tables 1 and 2. The effect of Cl^- on the redox reaction of Mn^{III}(5-NO_2–salpn)Cl is similar to that of Mn^{III}(5-NO_2–salen)Cl.

The oxidation reaction stoichiometry for the addition of 1.0 equiv. of Cl^- per Mn^{III}(5-NO_2–salen)Cl or Mn^{III}(5-NO_2–salpn)Cl is shown in Eqs. (9) and (10), respectively

$$Mn^{III}(5\text{-}NO_2\text{-salen})Cl + Cl^- \rightleftarrows [Mn^{III}(5\text{-}NO_2\text{-salen})Cl]^+ + e^- + Cl^- \rightleftarrows Mn^{IV}(5\text{-}NO_2\text{-salen})Cl_2 \quad (9)$$

$$Mn^{III}(5\text{-}NO_2\text{-salpn})Cl + Cl^- \rightleftarrows [Mn^{III}(5\text{-}NO_2\text{-salpn})Cl]^+ + e^- + Cl^- \rightleftarrows Mn^{IV}(5\text{-}NO_2\text{-salpn})Cl_2 \quad (10)$$

The reduction processes of Mn^{III}(5-NO_2–salen)Cl and Mn^{III}(5-NO_2–salpn)Cl are independent of Cl^- as Eqs. (11) and (12)

$$Mn^{III}(5\text{-}NO_2\text{-salen})Cl + e^- \rightleftarrows [Mn^{II}(5\text{-}NO_2\text{-salen})Cl]^- \quad (11)$$

$$Mn^{III}(5\text{-}NO_2\text{-salpn})Cl + e^- \rightleftarrows [Mn^{II}(5\text{-}NO_2\text{-salen})Cl]^- \quad (12)$$

The $E_{1/2}$ potentials for the redox reaction of Mn^{III}(5-NO_2–salen)Cl and Mn^{III}(5-NO_2–salpn)Cl were shifted 0.16 (oxidation) or 0.35 (reduction) V on the average to more positively regardless of the existence of Cl^-. These results can be explained by the introduction of an electron withdrawing substituent of 5-NO_2 group in Mn^{III}(5-NO_2–salen)Cl and Mn^{III}(5-NO_2–salpn)Cl [19,30,31]. This means that Mn–Cl bonds in these cases could not be dissociated after reductions of Mn(III) complexes.

3.4. Redox behavior of Mn^{III}(*N*-Bu–sal)$_2$Cl, Mn^{III}(*N*-Oct–sal)$_2$Cl, Mn^{III}(*N*-Oct–5-NO_2–sal)$_2$Cl and Mn^{III}(*N*-Oct–5-Br–sal)$_2$Cl in the absence/presence of chloride ion in MeCN

Curve 1 in Fig. 6 is the cyclic voltammogram for 1.0 mM Mn^{III}(*N*-Bu–sal)$_2$Cl in MeCN. One quasi-reversible positive current wave and two irreversible negative current waves were observed in the voltammogram. Since two negative current waves due to the reduction of Mn^{III}(*N*-Bu–sal)$_2$Cl appeared in the voltammogram, a part of Cl^- in Mn^{III}(*N*-Bu–sal)$_2$Cl would seem to be dissociated from Mn^{III}(*N*-Bu-sal)$_2$Cl resulting in $[Mn^{III}$(*N*-Bu–sal)$_2]^+$ and Cl^-. The positive current wave at 0.50 V appeared by reverse scan at −0.35 V, and therefore this positive current wave is confirmed to be re-oxidation of the reduction products formed at the potential of the first negative current wave.

When 1.0 mM TEACl was added to MeCN containing 1.0 mM Mn^{III}(*N*-Bu–sal)$_2$Cl, $E_{1/2}$ for the redox couple of Mn^{III}(*N*-Bu–sal)$_2$Cl/$[Mn^{IV}$(*N*-Bu–sal)$_2$Cl$]^+$ shifted from 0.99 to 0.86 V and ΔE_p decreased from 0.23 to 0.11 V (curve 2 in Fig. 6). Therefore, the electrochemical oxidation of Mn^{III}(*N*-Bu–sal)$_2$Cl occurs more easily and attains near to the reversible process in the presence of Cl^-. The I_{pa} at 0.92 V increased with an increase of Cl^- added to MeCN up to maximum of the ratio of Cl^- to Mn^{III}(*N*-Bu–sal)$_2$Cl to be unity, and no significant increase was observed on further addition of Cl^-. The oxidation reaction of Mn^{III}(*N*-Bu–sal)$_2$Cl could be expressed as Eq. (13) as well as Mn^{III}(salen)Cl

$$Mn^{III}(N\text{-Bu-sal})_2Cl + Cl^- \rightleftarrows [Mn^{III}(N\text{-Bu-sal})_2Cl]^+ + e^- + Cl^- \rightleftarrows Mn^{IV}(N\text{-Bu-sal})_2Cl_2 \quad (13)$$

Peak potentials of first and second negative current waves shifted from −0.06 to −0.09 V and from −0.56 to −0.60 V, respectively, and I_{pc} for the second negative current wave increased by the addition of Cl^-. Two negative current waves in curve 1 are thought to be attributable to reductions of Mn^{III}(*N*-Bu–sal)$_2$Cl and $[Mn^{III}$(*N*-Bu–sal)$_2]^+$, but it would be the possibility of the presence of another species, and therefore further discussion about the effect of Cl^- on the reduction reaction is considered to be difficult.

When Mn^{III}(*N*-Oct–sal)$_2$Cl was adopted in MeCN instead of Mn^{III}(*N*-Bu–sal)$_2$Cl, $E_{1/2}$ and ΔE_p for the redox couple of Mn^{III}(*N*-Oct–sal)$_2$Cl/$[Mn^{IV}$(*N*-Oct–sal)$_2$Cl$]^+$ in the absence/presence of 1.0 mM Cl^- are almost identical with those for Mn^{III}(*N*-Bu–sal)$_2$Cl as summarized in Table 1. This result suggests that the redox reactions of Mn^{III}(*N*-Bu–sal)$_2$Cl and Mn^{III}(*N*-Oct–sal)$_2$Cl are not much affected by the alkyl groups of the Schiff base ligands [16]. Mn^{III}(*N*-Oct-5-NO_2–sal)$_2$Cl and Mn^{III}(*N*-Oct–5-Br–sal)$_2$Cl also gave one quasi-reversible positive current wave and two irreversible negative current wave. The coexisting Cl^- in MeCN makes these positive current waves reversible. The $E_{1/2}$ for the redox couple of Mn^{III}(*N*-R–X–sal)$_2$Cl/$[Mn^{IV}$(*N*-R–X–sal)$_2$Cl$]^+$ wave shifted to more positively in the order Mn^{III}(*N*-Oct–sal)$_2$Cl (1.01 V) < Mn^{III}(*N*-Oct–5-Br–sal)$_2$Cl (1.05 V) < Mn^{III}(*N*-Oct–5-NO_2–sal)$_2$Cl (1.13 V) because of electron withdrawing substituent effects such as 5-NO_2 and 5-Br groups in these complexes [19,30,31].

3.5. Redox behavior of Mn^{III}(acac)$_3$ in the absence/presence of chloride ion in MeCN

Curve 1 in Fig. 7 is the cyclic voltammogram of 1.0 mM Mn^{III}(acac)$_3$ in MeCN, which exhibits one quasi-reversible positive current wave corresponding to the redox couple of Mn^{III}(acac)$_3$/$[Mn^{IV}$(acac)$_3]^+$ with $E_{1/2}$ at 0.99 V and one irreversible negative current wave corresponding to the reduction of Mn^{III}(acac)$_3$ to $[Mn^{II}$(acac)$_3]^-$ appeared in the voltammogram with negative current peak potential at −0.25, respectively [32]. When 1.0 mM

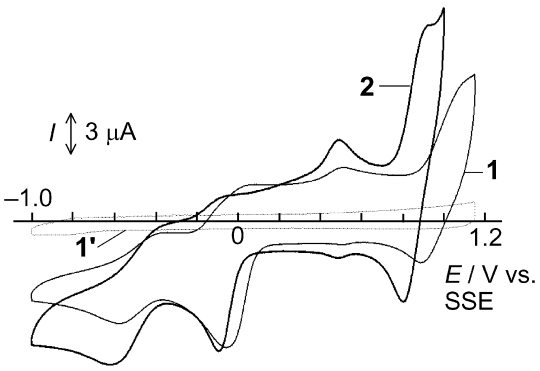


Fig. 6. Cyclic voltammogram of 1.0 mM Mn^{III}(*N*-Bu–sal)$_2$Cl in the absence (curve 1) or presence of 1.0 mM Cl^- (curve 2) in MeCN containing 0.1 M $TBAPF_6$. Curve 1′: residual current of curve 1 in the absence of Mn^{III}(*N*-Bu–sal)$_2$Cl in MeCN. Scan rate: 0.1 V s^{-1}.

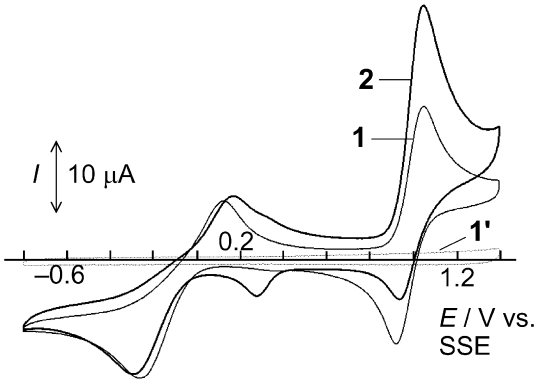


Fig. 7. Cyclic voltammogram of 1.0 mM Mn^{III}(acac)$_3$ in the absence (curve 1) or presence of 1.0 mM Cl^- (curve 2) in MeCN containing 0.1 M $TBAPF_6$. Curve 1′: residual current of curve 1 in the absence of Mn^{III}(acac)$_3$ in MeCN. Scan rate: 0.1 V s^{-1}.

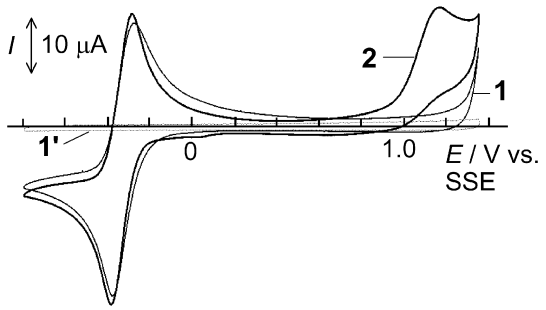


Fig. 8. Cyclic voltammogram of 1.0 mM Fe^{III}(salen)Cl in the absence (curve 1) or presence of 1.0 mM Cl^- (curve 2) in MeCN containing 0.1 M $TBAPF_6$. Curve 1′: residual current of curve 1 in the absence of Fe^{III}(salen)Cl in MeCN. Scan rate: 0.1 V s^{-1}.

TEACl was added to MeCN containing 1.0 mM $Mn^{III}(acac)_3$, the I_{pa} for the oxidation of $Mn^{III}(acac)_3$ increased even though the oxidation process varied to be irreversible. The new negative peak current at 0.28 V appeared by the reverse scan at 1.4 V, which indicates that the new species such as $Mn^{III}(acac)_2Cl$ may be produced by addition of Cl^-. While the negative current peak potential shifted from −0.25 to −0.29, I_{pc} for the reduction of $Mn^{III}(acac)_3$ was independent of Cl^-. $Mn^{III}(acac)_3$ is a six-coordinate complex of which structure is a distorted octahedron, and therefore the oxidation product of $Mn^{III}(acac)_3$ would be hardly stabilized via the combination with Cl^-.

3.6. Redox behavior of Fe^{III}(salen)Cl in the absence/presence of chloride ion in MeCN

Curve 1 in Fig. 8 is the cyclic voltammogram of 1.0 mM Fe^{III}(salen)Cl in MeCN. One negative current wave due to the redox couple of $[Fe^{II}(salen)Cl]^-/Fe^{III}(salen)Cl$ appeared with $E_{1/2}$ at −0.34 V in the voltammogram, and the positive current wave due to the oxidation of $Fe^{III}(salen)Cl$ to $[Fe^{IV}(salen)Cl]^+$ was not observed within the sweep range from −0.80 to 1.40 V. The ΔE_p for the redox couple of $[Fe^{II}(salen)Cl]^-/Fe^{III}(salen)Cl$ is about 0.10 V, which indicates that the electrochemical process for the reduction of $Fe^{III}(salen)Cl$ is almost reversible. The voltammogram of curve 1 was unchanged except for the appearance of the positive current wave at around 1.15 V due to the oxidation of Cl^- even though 1.0 mM TEACl was added to MeCN containing 1.0 mM $Fe^{III}(salen)Cl$ as shown in curve 2 in Fig. 8. This result indicates that the reduction of $Fe^{III}(salen)Cl$ is little affected by the presence of Cl^-, which is strongly contrast to the cases of manganese(III) complexes discussed in the above sections. This is ascribed by the difference in the spin configuration between Mn(III) ($3d^4$ high-spin) and Fe(III) ($3d^5$ high-spin) [25,33]. This means that the oxidation of a half-filled shell of Fe(III) may need more energy compared to the case of Mn(III).

4. Conclusions

Effects of Cl^- on redox reactions of manganese(III) complexes have been ascertained in the present work. The oxidation process of manganese(III) complexes, $Mn^{III}(L)X$ and $Mn^{III}(L')_2X$, became reversible by the addition of Cl^-, and the oxidation products were found to be stabilized by Cl^- resulting in $Mn^{IV}(L)Cl_2$ and $Mn^{IV}(L')_2Cl_2$. The reduction of $Mn^{III}(L)X$ or $Mn^{III}(L')_2Cl$ was affected not so significantly as the oxidation of $Mn^{III}(L)X$ or $Mn^{III}(L')_2Cl$. In OEC, the generation rate of dioxygen from water has reported to be slow when Cl^- is substituted by another anions such as Br^-, F^- and SO_4^{2-} [6]. Results obtained in the present work would support the idea that Cl^- in OEC makes the redox process of manganese cluster reversible and higher valent manganese ions stable.

Acknowledgements

This research was partly supported by Grant-in-Aid for Scientific Research (No. 13650860) from the Ministry of Education, Culture, Sports, Science and Technology, Japan.

References

[1] V.K. Yachandra, K. Sauer, M.P. Klein, Chem. Rev. 96 (1996) 2927.
[2] V.L. Pecoraro, W.Y. Hsieh, Metal Ions in Biological Systems, in: A. Sigel, H. Sigel, (Eds.), vol. 37, Marcel Dekker Inc., New York, 2000 (Chapter 14).
[3] R.D. Britt, in: D.R. Ort, C.F. Yocum (Eds.), Oxygenic Photosynthesis, Kluwer Academic, Dordrecht, 1996, p. 137.
[4] V.L. Pecoraro, Manganese Redox Enzymes, VCH, New York, 1992.
[5] J.P. McEvoy, G.W. Brudvig, Chem. Rev. 106 (2006) 4455.
[6] C.F. Yocum, Coord. Chem. Rev. 252 (2008) 296.
[7] K. Olesen, L.-E. Andréasson, Biochemistry 42 (2003) 2025.
[8] J. Sinclair, Biochim. Biophys. Acta 764 (1984) 247.
[9] H. Wincencjusz, C.F. Yocum, H.J. Gorkom, Biochemistry 38 (1999) 3719.
[10] W. Rüttinger, G.C. Dismukes, Chem. Rev. 97 (1997) 1.
[11] N.A. Law, T.E. Machonkin, J.P. McGorman, E.J. Larson, J.W. Kampf, V.L. Pecoraro, J. Chem. Soc. Chem. Commun. (1995) 2015.
[12] I. Romero, M.N. Collomb, A. Deronzier, A. Liobet, E. Perret, J. Pécaut, L.L. Pape, J.M. Latour, Eur. J. Inorg. Chem. (2001) 69.
[13] M.D. Godbole, E. Grigiotti, P. Zanello, A.M. Mills, A.L. Spek, E. Bouwman, Inorg. Chim. Acta 358 (2005) 233.
[14] C. Hureau, G. Blondin, M.F. Charlot, C. Philouze, M. Nierlich, M. Césario, E. Anxolabéhère-Mallart, Inorg. Chem. 44 (2005) 3669.
[15] A. Rompel, J.C. Andrews, R.M. Cinco, M.W. Wemple, G. Christou, N.A. Law, V.L. Pecoraro, K. Sauer, V.K. Yachandra, M.P. Klein, J. Am. Chem. Soc. 119 (1997) 4465.
[16] T. Matsushita, Y. Hirata, T. Shono, Bull. Chem. Soc. Jpn. 55 (1981) 108.
[17] T. Matsushita, T. Shono, Polyhedron 2 (1983) 613.
[18] H. Asada, M. Fujiwara, T. Matasushita, Polyhedron 19 (2000) 2039.
[19] T. Matsushita, H. Kono, T. Shono, Bull. Chem. Soc. Jpn. 54 (1981) 2646. and the reference cited therein.
[20] S.A. Richert, P.K.S. Tsang, D.T. Sawyer, Inorg. Chem. 27 (1988) 1814.
[21] T. Matsushita, H. Kono, M. Nishino, T. Shono, Bull. Chem. Soc. Jpn. 55 (1982) 2581.
[22] W. Berg, T.J. Truemper, J. Phys. Chem. 64 (1960) 487.
[23] T. Fujinaga, S. Kihara, CRC Critical Rev. Anal. Chem. 6 (1977) 223.
[24] H. Aoyagi, Y. Kitatsuji, Z. Yoshida, S. Kihara, Anal. Chim. Acta 538 (2005) 283.
[25] A. Panja, N. Shaikh, M. Ali, P. Vojtíšek, P. Banerjee, Polyhedron 22 (2003) 1191.
[26] A. Puglisi, G. Tabbì, G. Vecchio, J. Inorg. Biochem. 98 (2004) 969.
[27] K. Mitra, S. Biswas, C.R. Lucas, B. Adhikary, Inorg. Chim. Acta 359 (2006) 1997.
[28] S. Mohanta, S. Baitalik, S.K. Dutta, B. Adhikary, Polyhedron 17 (1998) 2669.
[29] S. Biswas, K. Mitra, C.H. Schwalbe, C.R. Lucas, S.K. Chattopadhyay, B. Adhikary, Inorg. Chim. Acta 358 (2005) 2473.
[30] W.M. Coleman, R.K. Boggess, J.W. Hughes, L.T. Taylor, Inorg. Chem. 20 (1981) 1253.
[31] W.M. Coleman, R.R. Goehring, L.T. Taylor, J.G. Mason, R.K. Boggess, J. Am. Chem. Soc. 101 (1979) 2311.
[32] R. Gorkum, E. Bouwman, J. Reedijk, Inorg. Chem. 43 (2004) 2456.
[33] L.J. Boucher, J. Inorg. Nucl. Chem. 36 (1974) 531.

Polyhedron 28 (2009) 431–436

Contents lists available at ScienceDirect

Polyhedron

journal homepage: www.elsevier.com/locate/poly

Fullerenocene ☆

Roberto Salcedo *

Instituto de Investigaciones en Materiales, Universidad Nacional Autónoma de México, Circuito exterior s/n, Ciudad Universitaria, 04510 Coyoacán, D.F., Mexico

ARTICLE INFO

Article history:
Received 1 July 2008
Accepted 4 November 2008
Available online 26 December 2008

Keywords:
Fullerene
Sandwich compounds
Aromaticity

ABSTRACT

The nature of the molecule $C_{60}CrC_{60}$ was studied from a theoretical point of view. Calculations on this molecule were carried out at the BPW91 level. The results are compared with those from another two molecules, dibenzenechromium that is a known and stable species, and η^6-fullerene chromium(0) η^6-benzene, a nonexisting molecule. This analysis has been carried out in order to study the stability of the target compound and provide useful information for its synthesis. The aromaticity of the rings in the three compounds was analyzed by means of HOMA and NICS methods whereas their intrinsic stability was estimated by means of homodesmotic reactions. The electronic structure of the three molecules was also studied. The results show fullerenocene should be a moderately stable species and should display semiconductor behaviour and some of the interesting properties of fullerene itself.

© 2008 Elsevier Ltd. All rights reserved.

1. Introduction

Dibenzenechromium is a well known organometallic molecule that has been object of several studies [1]. The large symmetry (D_6h) of this species has its origin in the uniform electronic distribution on both decks arising from the aromaticity that gives place to a π bond with perfect hexahapticity [2]. The aromaticity of both benzene fragments does not seem to be affected by the coordination to the metal centre [3]. This system is analogous to ferrocene except that it contains benzene instead of cyclopentadienyl ions.

All the research groups that have studied this structure experimentally as well as theoretically [1,4], are in agreement about the relatively low energy value of the rotational barrier (≈0.9 kcal/mol) between the eclipsed and the staggered isomers, the former being the more stable one. This compound is very interesting because its strong donor capability can lead to a material with one-dimensional conductivity [1d].

Fullerenes [5] are a set of interesting molecules that have been object of many different studies [6]. Their metallic complexes, endohedral as well as exohedral, have also been studied experimentally and theoretically [7]. In this paper, we focused on compounds where the interaction between the fullerene fragment and a phenyl part occurs through a metal centre [8].

The most interesting experimental results are those obtained by Nakamura and co-workers [9]. In these works, Nakamura reported the first ferrocenoid complexes, including a ferrocene fragment molecule. The main characteristics of these complexes are that the π bond on one side of the metal centre is focused on a pentagonal face of the fullerene fragment, the other side forms another π bond with a Cp fragment and in the majority of cases the metal atom has an intrinsic positive charge, as in the case of ferrocene, calculations on this species and analogous have been reported. Additionally, there are some very interesting theoretical reports [8], in which the capability of the fullerene fragments to generate this kind of bonds was studied.

The present study is different because the initial proposition is that the molecules have, in all cases, hexahapto π bonds. This feature was proposed and studied by Jemmis et al. and by Stankevich et al. [8]. The formed complexes should be analogous to the dibenzenechromium. Therefore, the π bond on one side of the metal centre is localised on a six-membered face of the fullerene fragment, whereas on the other side the π bond of the metal atom is associated with a benzene molecule or another hexagonal face of a new fullerene fragment. Furthermore, the metal atom has been considered to have not a formal oxidation state, i.e., in all cases Cr(0). Particularly Stankevich and his group carried out a very interesting work [8d] in which they analysed from a theoretical point of view the same systems considered in the present work. They focused in the capability of the fullerene to generate η^6 bonds and suggested that the large size of the fullerene may be the cause of inhibition of the formation of such molecules, and a perturbation of the symmetry of fullerene by substituents is necessary in order to stabilise the complex.

The aim of this work was to perform theoretical studies of two non existing new molecules. $C_{60}CrC_{60}$ is the fullerene analogue to dibenzenechromium; this molecule has been named fullerenocene, there is only one previous experimental report about the possibility of having a sandwich molecule with fullerene decks. It was isolated as a film and the authors claimed that the structure is possibly a

☆ The author is aware that this name is not correct, but the temptation of the comparison with ferrocene is so strong, that the author decided to introduce this name for the main compound under study in this work.

* Tel.: +52 55 5622 4600; fax: +52 55 5616 1201.
E-mail address: salcedo@servidor.unam.mx

0277-5387/$ - see front matter © 2008 Elsevier Ltd. All rights reserved.
doi:10.1016/j.poly.2008.11.015

polymer with alternate Pd atoms and fullerene units [10a,b]. However, the nature of the bonding in this species is not totally clear. Besides a polymer which contains C_{60}–Co has been studied in a theoretical fashion [10c], the authors suggest these polymers favours ferromagnetic ground states, these results are important for our research because of the emphasis on the electronic mobility in these complexes. Additionally, Stankevich [8d] has studied this molecule ($C_{60}CrC_{60}$) in a theoretical way, analyzing its stability and found moderately stability for fullerenocene although he suggests the substituted derivatives should be more stable.

Dibenzenechromium is a very well known molecule [1]. It has been calculated in the present work in the same conditions that the others in order to validate the method of calculation by comparison with published results [1] and for the internal comparisons with the molecules under study.

Finally, the third molecule is a hybrid molecule similar to that studied by Nakamura [9] and Chystiakov [11] that arose for the interaction among a fullerene fragment, a benzene molecule and a Cr(0) atom. This case has been previously studied by Jemmis and Stankevich [8] by using an energy criterium and semiempirical methods in the first case and DFT methods in the second case.

In this work fullerenocene is studied from a theoretical point of view. The present analysis extended the cited works mainly performed by the comparison of the aromaticity results obtained by means of the ASE factor [12] estimated by homodesmotic reactions, HOMA [13] and NICS [14] routines employing other DFT method. The electronic structure of the three molecules was also studied. Furthermore the most relevant features derived from the study are addressed. The results are analysed on the basis of possible preparation and electronic application of these substances.

2. Methods

All structures were optimised in the gas phase using the JAGUAR 4.0 package [15]. A pure DFT method containing Becke's gradient correction [16] for exchange and Perdew–Wang's for correlation [17] was used for the energy evaluations. All calculations were performed using the 6-31G** basis set. The quality of this combination of method and basis set was validated by comparing the result of total energy of dibenzenechromium (−550.675 au) and the heat of formation of $C_6H_6CrC_{60}$ (947.5 kcal/mol) obtained in this work with the same values obtained by Jemmis (−550.706 au and 977.2 kcal/mol, respectively) [8b]. The frequency calculations were carried out at the same level of theory in order to confirm that the optimised structures were at the minimum of the potential surface. These frequencies were then used to evaluate the zero-point vibrational energy, the thermal vibrational corrections to the enthalpy, and the total enthalpy values. The bond lengths of the optimised structures were used for the HOMA (Harmonic Oscillator Model of Aromaticity) method [13] to study the aromaticity. The NICS (Nucleus Independent Chemical Shifts) [14] is a technique that was proposed by Schleyer as a new aromaticity index. The authors named it 'absolute magnetic shielding' and computed the value at the ring centres, which were determined by the non-weighted mean of the heavy atom coordinates. In this work, NICS calculations were performed following this technique, carried out with GAUSSIAN03 [18] at the BPW91/6-31G** level.

3. Results and discussion

3.1. Energy and aromaticity comparisons

The results of the energy and aromaticity of the molecules under study are shown in this section Fig. 1.

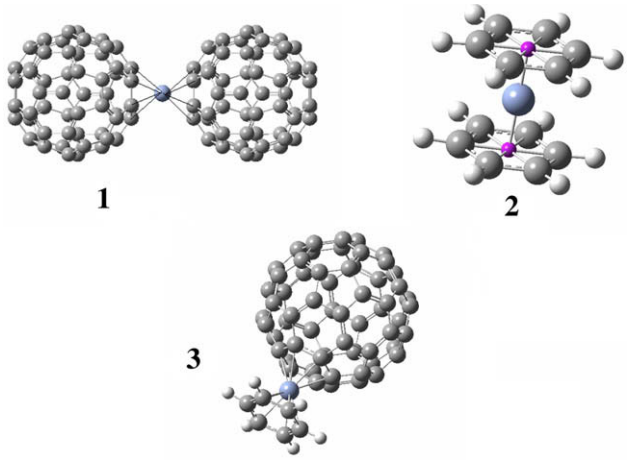


Fig. 1. Molecules under study.

Homodesmotic reactions were developed in order to calculate the ASE (aromatic stabilization energy) [12] in the three cases. In order to develop similar reactions for all cases, a set of two parent molecules were selected for all the species. The first parent molecule is similar to the bis(2,4-dimethylpentadienyl)chromium molecule prepared by Ernst and his group [19], but in our case it is bis(dibutadienyl)chromium. This molecule was chosen because it contains a delocalised electronic system without a clear aromatic scheme, but it has a framework of π bonds and this characteristic makes it suitable for analysing the stabilisation scheme produced by the appearance of aromaticity. The methyl substituents originally found in the compound by Ernst were removed, because these fragments would have been a source of carbon atoms with sp^3 hybridisation, that would be a problem in the definition of homodesmotic reactions. Therefore, the parent molecule is only bis(butadienyl)chromium ($C_8H_{12}Cr$) and its geometry is shown in Fig. 2.

The other parent molecule was 3-ethylene–butadiene (C_6H_8), which is an excellent source of carbon atoms containing only sp^2 hybridization. These species are shown in Fig. 3.

These last two compounds were calculated to find their optimised structures, followed by frequency calculations that were carried out in order to obtain their enthalpy values. In these cases, exactly the same methods and level of theory were used. The developed reactions for each case are shown in the next subsections together with the enthalpy analysis.

3.1.1. Homodesmotic reaction for $C_{60}CrC_{60}$

The homodesmotic reaction for the fullerenocene complexes is:

$$C_8H_{12}Cr + 59\ C_6H_8 \rightarrow C_{120}Cr + 121\ C_2H_2$$

The result is excellent; the ASE value obtained was 7026.698 kJ/mol, which is very large compared with results obtained for fuller-

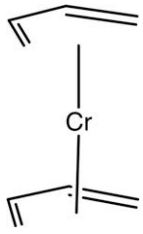


Fig. 2. Bis(butadienyl)chomium.

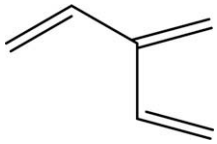


Fig. 3. 3-Ethylene–butadiene (parent molecule).

ene as 2345.88 kJ/mol [20] or 2509 kJ/mol ± 55 kJ/mol (from seven reports) [12]. Indeed the result should be 3521.349 kJ/mol for each fullerene unit with its respective bonds to the metal atom. This feature suggests the extra electronic flux due to the organometallic bonds help to stabilize the complex.

3.1.2. Homodesmotic reaction for dibenzenechromium

In the case of dibenzenechromium ($C_{12}H_{12}Cr$), the reaction was easy and the ASE result was very representative. The corresponding scheme is as follows:

$$C_8H_{12}Cr + 2\ C_6H_8 \rightarrow C_{12}H_{12}Cr + 4\ C_2H_4$$

The homodesmotic reaction yielded a value of ASE of 564.49 kJ/mol. Such a value denotes a highly aromatic behaviour and can be compared with coronene, a known aromatic molecule, with a reported value ~418 kJ/mol [12]. The proposition of Phillips et al. [3] is therefore correct, and hence the coordination on this molecule does not affect the aromaticity of the phenyl ring.

3.1.3. Homodesmotic reaction for $C_6H_6CrC_{60}$

The last homodesmotic reaction is remarkable. The corresponding scheme is

$$C_8H_{12}Cr + 30.5\ C_6H_8 \rightarrow C_{66}H_6Cr + 62.5\ C_2H_4$$

The result is even better than that found for the fullerenocene. The ASE value is 3964.5 kJ/mol.

A direct comparison of these results is not obvious. A valid comparison can be carried out by means of the ASE/π index proposed by Liebman [12]. This index indicates a stabilisation energy per carbon atom that contributes to the resonance framework. The ASE/π is 58.55 kJ/mol for fullerenocene, 47.04 kJ/mol for dibenzencrhomium and 60.07 kJ/mol for $C_6H_6CrC_{60}$. The best value is that for the hybrid molecule $C_6H_6CrC_{60}$ but very near to the fullerenocene. It has been proposed that the fullerene molecule is deficient in electrons [21], and present low polarizability [8c,d]. Indeed the nature of Cp and C_{60} is different since the first one is an electron donor whereas de second one is a weak electron acceptor. This feature changes the behaviour of the bond as it is shown in these results. It is important to note that the ASE is a global criterium of aromaticity, therefore it evaluates the whole system but not a specific zone of the molecules. Therefore, the application of some local criteria is important to reach a conclusion.

4. Aromaticity indices

The global aromaticity of the proposed molecules seems to be large on the basis of the results outlined in the last section; however, an energy criterium is not conclusive because global and local aromaticities can show a different behaviour as outlined by Solà and his co-workers [6g], and Chen and King [21]. Therefore, two popular methods to measure local aromaticity were applied; HOMA [13] and NICS [14].

The HOMA and NICS results for the six-membered face joined to the metal atom and in the centre of the fullerene ligands are shown in Table 1 for the three molecules under study.

The results of HOMA show that the dibenzenechromium is the most aromatic system; however the value is very close to that of fullerenocene and only in the hybrid molecule there is a notable decrease for the fullerene fragment. It is important to note that the large value of aromaticity of the benzene ring joint to the Cr atom is associated with the hybrid molecule. This feature should lead to the full planarity of this ring as compared with the same section in the fullerene fragment, where the phenomenon of pyramidalisation is present. Since HOMA is a geometric criterium, the difference between both kinds of aromatic fragments is emphasised.

Table 1
HOMA and NICS results for the molecules under study.

Molecule	$C_{60}CrC_{60}$	$C_6H_6CrC_6H_6$	$C_6H_6CrC_{60}$
HOMA	0.915	0.918	0.874 (ful) 0.957 (ben)
NICS	−10.08 (centre) −61.99 (η^6-face)	−47.07	−7.95 (ful) −57.90 (ben) −47.08 (η^6-face)

The NICS results follow a slightly different trend but are striking. First, the value of the aromatic rings joined to a metal are very large; this feature has been studied previously and discussed on the basis of paratropic and diatropic σ and π contributions [22]. However, in the present case the results are so high for dibenzenechromium that they indicate a large contribution of C–C(π) orbitals from two decks. The result grows significantly in the case of fullerene. There are two computed values, one for the centre of the sphere and the other for the six-membered face joined to the metal atom. The first one depicts the spherical aromaticity and the value is in the normal gap of NICS. This shows that the fullerene fragments of $C_{60}CrC_{60}$ are more aromatic than the same fragment in the hybrid molecule suggesting a larger current in the first. But the large difference appears for the surface where the trend is the same but the values are much higher, showing that there is a large contribution from the C–C(π) orbitals, which are donating electronic charge to the Cr atom.

The hybrid compound shows a peculiar behaviour similar to that found in the HOMA analysis. The NICS of the benzene ring is almost the same than that of the fullerene six-membered face (although this last one value is in itself very high). This feature means it can be expected a similar behaviour of the bonds from the metal centres with single aromatic fragments as well as for fullerenes, although the nature of this bonding is a little different as it will be discussed in the last section.

A conclusion about aromaticity can be reached with these results: based on the global criterium, the trend can be written as $C_6H_6CrC_{60} \approx C_{60}CrC_{60} > C_6H_6CrC_6H_6$. The HOMA and the NICS results show discrepancies mainly due to the pyramidalisation phenomenon present in the aromatic rings belonging to the fullerene fragments. However, in both cases the fullerenocene exhibited values that suggest a good aromatic behaviour on the faces directly joint to the chromium atom, and this result matches well with the global criterium.

5. Electronic structure

The electronic structure of fullerene has been extensively studied [23]. The scheme of molecular orbitals has been the object of particular attention due the I_h point group symmetry, which is not common in other kinds of molecules. The particular characteristic of this molecule is the nature of the frontier orbitals having a five-fold degenerated set for the HOMO which belongs to the irreducible representation h_u (with a very near HOMO-1 being a four-fold degenerated molecular orbital belonging to the g_g irreducible representation) and a triple degenerated set for the LUMO which belongs to the irreducible representation t_{1u}. Such a richness of electron states leads to a very narrow HOMO–LUMO gap. An

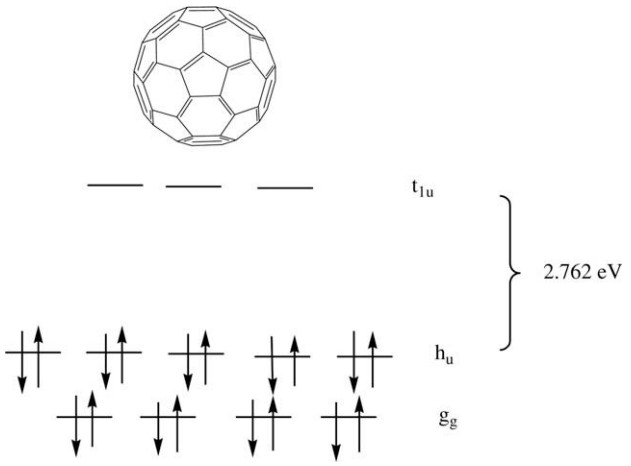


Fig. 4. Frontier molecular orbital scheme for fullerene (results obtained in this work).

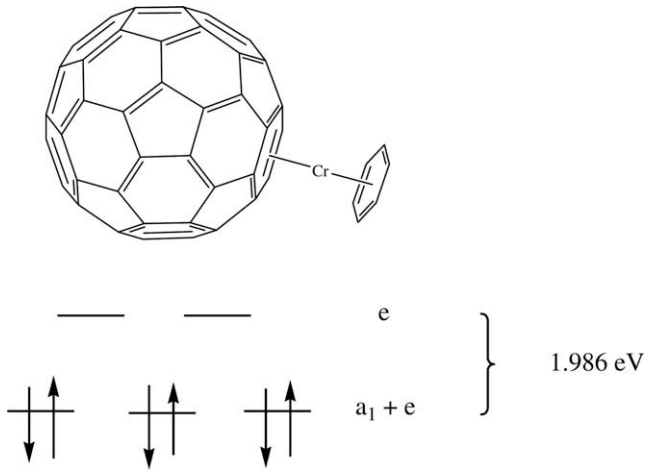


Fig. 6. Frontier molecular orbital for fullerene–benzene–chromium, the HOMO presents accidental degeneracy between irreducible representations a1 and the set e.

anomalous pyramidalisation of the hybridisation of the sp^2 carbon atoms [24] appears as well. The same scheme was used in the present study through the BPW91/6-31G** method in order to compare the energy values on the same scale; the ordering is the same as well as the separation of levels, which yields a gap of 2.762 eV between the Frontier orbitals (see Fig. 4).

The molecular orbital distribution of dibenzenechromium has also been studied [25]. It belongs to the D_6h point group and its main characteristic is a HOMO-1 double degenerated, which belongs to the irreducible representation e_{2g} that is very near the a_{1g} HOMO. The set of frontier orbitals is shown in Fig. 5; again the system was studied at the same level of theory for comparison purposes and in this case the gap between HOMO–LUMO is 3.946 eV.

The hybrid compound presents a peculiar ordering of its molecular orbitals with the molecule belonging to the C_3v point group. It has been seen that in the case of this point group it is possible to find an accidental degeneracy [26], since the C_3v group does not have triple-folded degenerated irreducible representations. However, the molecular orbital scheme for the hybrid molecule shows, at first sight, a triple degenerated set for the HOMO. This set does not correspond to an irreducible representation but to a mixing of a totally symmetric a_1 and a double e irreducible representation. This is a curious example of accidental degeneracy. It is important to note that this set results from the combination of HOMO (a_{1g}) and HOMO-1 (e_{2g}) of the D_6h *dibenzenechromium,* that are two irreducible representations which lie very close together, as pointed out above.

There is no contribution of the fullerene fragment to this last set of molecular orbitals, as the contribution of the fragment is totally concentrated in the LUMO and this feature confirms the weak electron acceptor nature of fullerene. The HOMO–LUMO gap is 1.986 and this result is interesting because such a value suggests that this molecule should have semiconductor behaviour. The large value of aromaticity found by the HOMA and NICS methods for this species

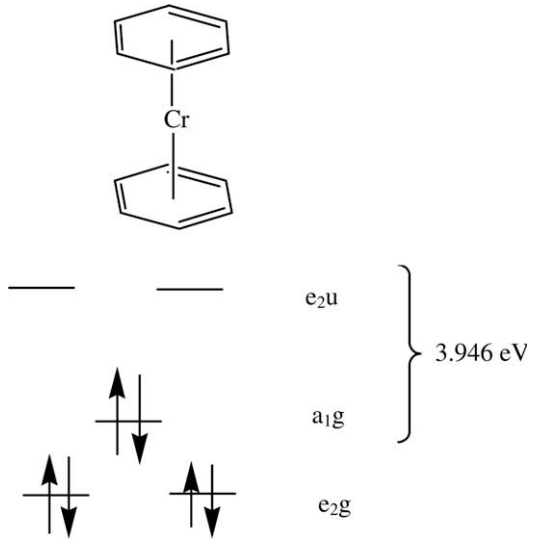


Fig. 5. Frontier orbitals for dibenzenechromium.

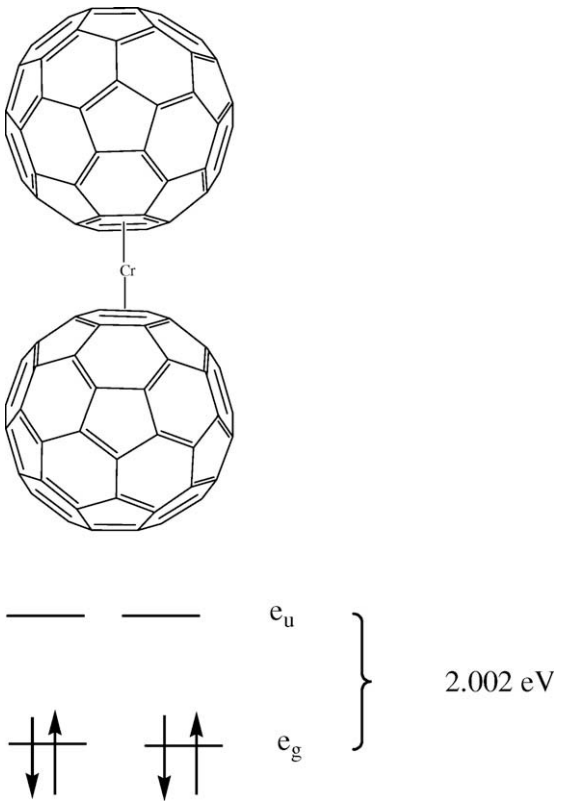


Fig. 7. Frontier molecular orbitals from fullerenocene.

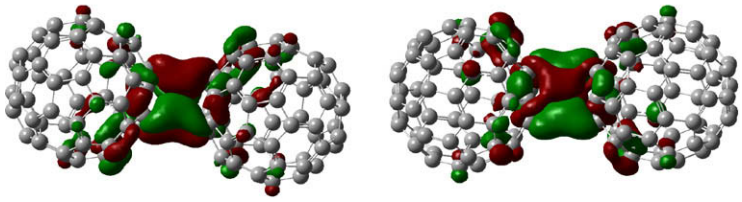


Fig. 8. Degenerated set for the HOMO of fullerenocene 1.

arise from this phenomenon because the *pseudo* triple degenerated set corresponding to the HOMO contributes with six electrons of the same energy to the aromaticity instead of the same six of dibenzenechromium but at different energy levels. The corresponding molecular orbital interaction is shown in Fig. 6.

Concerning the fullerenocene there are also interesting results. The molecule belongs to the D_3d symmetry group and the large symmetry of fullerene changes dramatically. The HOMO, as well as the LUMO are only two-fold degenerated sets. The HOMO belongs to the e_g irreducible representation, whereas the LUMO belongs to the e_u irreducible representation. The interesting point is that the HOMO–LUMO gap is even smaller than that of free fullerene, at 2.002 eV. This again suggests a semiconductor behaviour and all the known electronic characteristics of fullerene [27] must be found in this molecule. The molecular orbital interaction diagram is shown in Fig. 7.

Rayón and Frenking carried out a very interesting analysis by comparing the nature of the bond in ferrocene and that in dibenzenechromium [28]. In this work the authors showed, by means theoretical calculations, that the largest contribution to the orbital interactions in ferrocene comes from the π electronic donation from Cp to Fe. In a different pathway, the main contribution to the orbital interaction in dibenzenechromium is δ back-donation considering the symmetry of the corresponding irreducible representations. A similar analysis in the present case show that the irreducible representations e_g for fullerenocene, corresponding to the degenerated set of the HOMO (into the scheme of D_3d point group) have π symmetry and it contains only the electron donation from fullerene fragments to the d_{xz} and d_{yz} atomic orbitals of the Cr atom (see Fig. 8). On the other hand, the LUMO is again a degenerated set which belongs to the irreducible representation e_u, and this MO has only a contribution from the fullerene fragments without the presence of atomic orbitals coming from the metal atom. The behaviour in this sense is therefore very different than in dibenzenechromium.

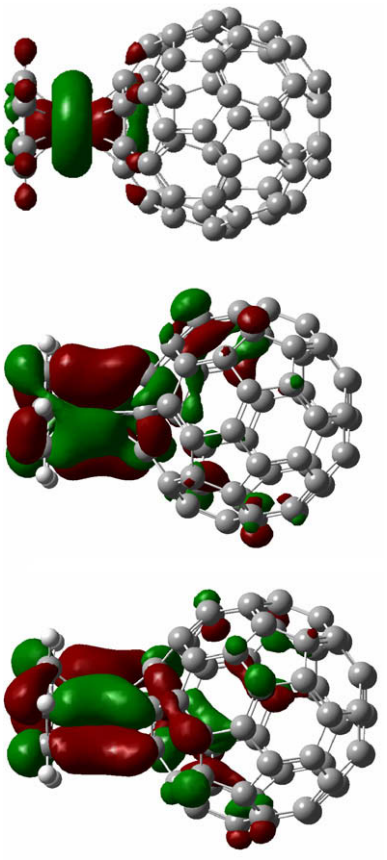


Fig. 9. Degenerated set for the HOMO of molecule 3.

Concerning the hybrid molecule, the behaviour is different but not completely defined. The 'actual' HOMO is a MO which corresponds to the irreducible representation a_1. This orbital has a clear symmetry δ where the main contribution to the d_z^2 atomic orbital arises from the Cr atom. However, the accidental degeneracy produces the pseudo triple-folded set, joining to this single orbital the next degenerated set. This set corresponds to the e irreducible representation with π symmetry (see Fig. 9). Besides, the LUMO that should act as the receptor of the back-donation do not participate in the bonding between the metal atom and the ligands. Therefore, this compound should be again a π-bonded molecule.

It is important to note that the latter results for fullerenocene correspond to an eclipsed isomer, therefore the staggered isomer was also calculated leading to a slightly less stable species. The difference in total energy between both isomers is 3.4132 kJ/mol in favour of the eclipsed structure. The staggered isomer belongs to the D_3 point group and its HOMO as well as its LUMO belong to the a_1 and a_2 irreducible representations respectively. Here again there is a curious phenomenon: the lack of symmetry causes the gap between HOMO and LUMO to be much more open than the corresponding value of the eclipsed one (5.898 eV), therefore this species seems less interesting than its isomer.

6. Conclusions

The aromaticity and relative stability of the fullerene analogue of dibenzenechromium was studied as well as a hybrid species which contains a deck of benzene and a deck of fullerene. The energy study carried out by means of homodesmotic reactions showed that the new structures have both large values of ASE as compared with dibenzenechromium itself, suggesting that these fullerene complexes should be as stable as the classically known π bonded organometallic compounds. Besides, the HOMA and NICS analysis suggested a strong aromatic character in both compounds and a reinforcement of the spherical aromaticity. This last condition is more marked in the case of fullerenocene, which showed a very large value of NICS in the face of the sphere joint to the

metal atom. The analysis of the electronic structure showed that both molecules have narrow HOMO–LUMO gaps suggesting that these molecules might have a semiconductor character. In particular, the molecular orbital analysis results of the hybrid compound were significant because they showed a triple degenerated set corresponding to the HOMO. However, the corresponding point group does not possess an irreducible representation yielding a triplet; therefore, this is a peculiar example of accidental degeneracy. The phenomenon does account for the size of the energy gap which is even narrower than in the free fullerene itself.

Acknowledgements

The author wish to express his gratitude to Prof. Stephen Muhl and Prof. Raul Valenzuela for very useful discussions, Ms. Maria Teresa Vázquez, Ms. Oralia Jimenez, Ms. Sara Jimenez and Mr. Victor Gomez for technical help. The author is also indebted to DGSCA-UNAM and Sun Enterprise for invaluable help in computation work. This research was supported by projects PUNTA-UNAM and CONACYT-57432.

References

[1] (a) I.P. Gloriozov, A.Yu. Vasil'kov, Yu.A. Ustynyuk, Russ. J. Phys. Chem. 80 (2006) 394;
(b) I.P. Gloriozov, A. Yu. Vasil'kov, Yu.A. Ustynyuk, Russ. J. Phys. Chem. 80 (2006) 227;
(c) A. Perrier, D. Gourier, L. Joubert, C. Adamo, Phys. Chem. Chem. Phys. 5 (2003) 1337;
(d) T. Yasuike, S. Yabushita, J. Phys. Chem. A 103 (1999) 4533;
(e) Yu.V. Chizhov, M.M. Timoschenko, L.P. Yur'eva, N.N. Zaitseva, I.A. Uralets, D.N. Kravtsov, N.L. Asfandiarov, J. Organomet. Chem. 361 (1989) 79;
(f) A. Bèrces, T. Ziegler, J. Phys. Chem. 98 (1994) 13233;
(g) R. Shanoun, C. Mijoule, J. Phys. Chem. A 105 (2001) 6176;
(h) R. Pandey, B.K. Rao, P. Jena, M.A. Blanco, J. Am. Chem. Soc. 123 (2001) 3799.
[2] (a) E.O. Fischer, W.Z. Hafner, Z. Naturforsch. B 10B (1955) 665;
(b) R. Davis, L.A.P. Kane-Maguire, in: G. Wilkinson, F.G.A.S. Stone, E.W. Albert (Eds.), Comprehensive Organometallic Chemistry, vol. 3, Pergamon, Oxford, 1982, p. 953.
[3] L. Phillips, F. Separovic, M.J. Aroney, New J. Chem. 27 (2003) 381.
[4] (a) A. Haaland, Acta Chim. Scand. 19 (1965) 41;
(b) E. Keullen, F. Jellineck, J. Organomet. Chem. 5 (1966) 490;
(c) E. Muetterties, J.R. Bleeke, E.J. Wucherer, T.A. Albright, Chem. Rev. 82 (1982) 499;
(d) S.E. Anderson, J. Organomet. Chem. 71 (1974) 263;
(e) J.S. Miller, M. Dermot, M. O'Hare, A. Chakravorty, A.J. Epstein, J. Am. Chem. Soc. 111 (1989) 7853.
[5] H.W. Kroto, J.R. Heath, S.C. O'Brien, R.F. Curl, R.E. Smalley, Nature 318 (1985) 162.
[6] (a) H.W. Kroto, J.E. Fischer, D.E. Cox, The Fullerenes, Pergamon Press, Oxford, 1993;
(b) A. Hirsch, The Chemistry of Fullerenes, Thieme, New York, 1994;
(c) A. Hirsch, Top. Curr. Chem. 199 (1998) 1;
(d) A. Hirsch, B. Nuber, Acc. Chem. Res. 32 (1999) 795;
(e) F. Diederich, R. Kessinger, Acc. Chem. Res. 32 (1999) 537;
(f) F. Diederechi, M. Gómez-López, Chem. Soc. Rev. 28 (1999) 263;
(g) J. Poater, X. Fradera, M. Duran, M. Solà, Chem. Eur. J. 9 (2003) 1113.
[7] (a) Y. Iiduka, T. Wakahara, K. Nakajima, T. Nakahodo, T. Tsuchiya, Y. Maeda, T. Akasaka, K. Yoza, M.T.H. Liu, N. Mizorogi, S. Nagase, Angew. Chem., Int. Ed. 46 (2007) 5562;
(b) J.M. Campanera, J. Muñoz, J. Vázquez, C. Bo, J.M. Poblet, Inorg. Chem. 43 (2004) 6815;
(c) L.-C. Song, P.-C. Liu, J.-T. Liu, F.-H. Su, G.-F. Wang, Q.-M. Hu, P. Zanello, F. Laschi, M. Fontani, Eur. J. Inorg. Chem. (2003) 3201;
(d) P. Zanello, F. Laschi, M. Fontani, L.-C. Song, Y.-H. Zhu, J. Organomet. Chem. 593–594 (2000) 7;
(e) M.M. Olmstead, L. Hao, A.L. Balch, J. Organomet. Chem. 578 (1999) 85.
[8] (a) E.D. Jemmis, P. Parameswaran, A. Anoop, Int. J. Quantum Chem. 95 (2003) 810;
(b) E.D. Jemmis, M. Manoharan, P.K. Sharma, Organometallics 19 (2000) 1879;
(c) E.G. Gal'pern, A.R. Sabirov, I.V. Stankevich, Phys. Solid State 49 (2007) 2330;
(d) N.P. Gambaryan, E.G. Gal'pern, I.V. Stankevich, A.L. Chistyakov, Izv. Akad. Nauk. Ser. Khim. No. 4 (1994) 598.
[9] (a) Y. Matsuo, H. Isobe, T. Tanaka, Y. Murata, M. Murata, K. Komatsu, E. Nakamura, J. Am. Chem. Soc. 127 (2005) 17148;
(b) Y. Kuninoubo, Y. Matsuo, M. Toganoh, M. Sawamura, E. Nakamura, Organometallics 23 (2004) 3259;
(c) E. Nakamura, Pure Appl. Chem. 75 (2003) 427;
(d) Y. Matsuo, K. Matsuo, T. Nanao, R. Marczac, S.S. Gayathri, D.M. Guldi, E. Nakamura, Chem. Asian J. 3 (2008) 841;
(e) H.S. Kang, J. Comp. Chem. 28 (2007) 594.
[10] (a) M.E. Plonska, A. Bettencourt-Dias, A.L. Balch, K. Winkler, Chem. Mater. 15 (2003) 4122;
(b) A.L. Balch, D.A. Costa, K. Winkler, J. Am.Chem. Soc. 120 (1998) 9614;
(c) X. Xu, H.S. Kang, J. Chem. Phys. 128 (2008). Art. No. 074707.
[11] A.L. Chystiakov, I.V. Stankevich, Russ. Chem. Bull. 47 (1998) 2087.
[12] (a) S.W. Slayden, J.F. Liebman, Chem. Rev. 101 (2001) 1541. and references therein;
(b) F. Stahl, P.v.R. Schleyer, H. Jiao, H.F. Schaefer III, K.-H. Chen, N.A. Allinger, J. Org. Chem. 67 (2001) 6599.
[13] (a) T.M. Krygowski, J. Chem. Inf. Comput. Sci. 33 (1993) 70;
(b) T.M. Krygowski, M.K. Cyranski, Chem. Rev. 101 (2001) 1385.
[14] P.V.R. Schleyer, C. Maerker, A. Dransfield, H. Jiao, N.J.R.v.E. Hommes, J. Am. Chem. Soc. 118 (1996) 6317.
[15] JAGUAR 4.0; Schrödinger, Inc.; Portland, OR, 1991–2000.
[16] A.D. Becke, Phys. Rev. A 38 (1988) 3098.
[17] J.P. Perdew, Y. Wang, Phys. Rev. B 45 (1992) 13244.
[18] M.J. Frisch, G.W. Trucks, H.B. Schlegel, G.E. Scuseira, M.A. Robb, J.R. Cheeseman, V.G. Zakrzewski, J.A. Montgomery, Jr., R.E. Stratmann, J.C. Burant, S. Dapprich, J.M. Millarn, A.D. Daniels, K.N. Kudin, M.C. Strain, O. Farkas, J. Tomasi, V. Barone, M. Cossi, R. Cammi, B. Mennucci, C. Pomelli, C. Adamo, S. Clifford, J. Ochterski, G.A. Petersson, P.Y. Ayala, Q. Cui, K. Morokuma, D.K. Malick, A.D. Rabuck, K. Raghavachari, J.B. Foresman, J. Cioslovski, J.V. Ortiz, B.B. Stefanov, G. Liu, A. Liashenko, P. Piskorz, I. Komaromi, R. Gomperts, R.L. Martin, D.J. Fox, T. Keith, M.A. Al-Laham, C.Y. Peng, A. Nanayakkara, C. Gonzalez, M. Challacombe, P.M.W. Gill, B.G. Johnson, W. Chen, M.W. Wong, J.L. Andres, M. Head-Gordon, E.S. Replogle, J.A. Pople, gaussian03, Revision B.04, Gaussian Inc., Pittsburg, PA, 2003.
[19] (a) T.D. Newbound, A.M. Arif, D.R. Wilson, A.L. Rheingold, R.D. Ernst, J. Organomet. Chem. 435 (1992) 73;
(b) T.D. Newbound, J.W. Freeman, D.R. Wilson, M.S. Kralik, A.T. Patton, C.F. Campana, R.D. Ernst, Organometallics 6 (1987) 2432.
[20] R. Salcedo, L. Fomina, Tetrahedron Lett. (2007) 3949.
[21] Z. Chen, R.B. King, Chem. Rev. 105 (2005) 3613. and references therein.
[22] (a) H.Wadepohl&M. Entrialgo-Castaño, Chem. Eur. J. 9 (2003) 5266;
(b) P.v.R. Schleyer, B. Kiran, D.V. Simion, T.S. Sorensen, J. Am. Chem. Soc. 122 (2000) 510.
[23] (a) J. Cioslowski, Electronic Structure Calculations on Fullerene and their Derivatives, Oxford University Press, Oxford, 1995;
(b) P. Fowler, P. Lazzaretti, R. Zanasi, Chem Phys. Lett. 165 (1990) 79;
(c) A.H.H. Chang, W.C. Ermler, R.M. Pitzer, J. Phys. Chem. 95 (1991) 9288.
[24] R.C. Haddon, Science 261 (1993) 1545.
[25] (a) F.A. Cotton, W.A. Dollase & J.S. Wood, J. Am. Chem. Soc. 85 (1963) 1543;
(b) K.F. Purcell, J.C. Kotz, Inorganic Chemistry, W.B. Saunders Company, Philadelhia, 1977.
[26] (a) W.M. Rhee, J. Korean Phys. Soc. 42 (2003) 66;
(b) A. Bauer, G. Tarrago, A. Remy, J. Mol. Spectrosc. 58 (1975) 111.
[27] M. Bendikov, F. Wudl, D.F. Perepichka, Chem. Rev. 104 (2004) 4891. and references therein.
[28] V.M. Rayón, G. Frenking, Organometallics 22 (2003) 3304.

Polyhedron 28 (2009) 437–444

Contents lists available at ScienceDirect

Polyhedron

journal homepage: www.elsevier.com/locate/poly

Novel dinuclear and polynuclear copper(II)-pyrazine-2,3-dicarboxylate supramolecular complexes with 1,3-propanediamine, *N*,*N*,*N*′,*N*′-tetramethylethylenediamine and 2,2′-bipyridine

Okan Zafer Yeşilel [a,*], Aylin Mutlu [a], Orhan Büyükgüngör [b]

[a] Department of Chemistry, Faculty of Arts and Sciences, Eskişehir Osmangazi University, 26480 Eskişehir, Turkey
[b] Department of Physics, Faculty of Arts and Sciences, Ondokuz Mayıs University, 55139 Kurupelit, Samsun, Turkey

ARTICLE INFO

Article history:
Received 20 June 2008
Accepted 14 November 2008
Available online 8 January 2009

Keywords:
Pyrazine-2,3-dicarboxylate Complexes
Coordination polymers
Copper(II) complexes

ABSTRACT

Three novel Cu(II)-pyrazine-2,3-dicarboxylate complexes with 1,3-propanediamine (pen), $[Cu_2(\mu\text{-pzdc})_2(pen)_2]\cdot 2H_2O$ **(1)**, *N*,*N*,*N*′,*N*′-tetramethylethylenediamine (tmen), $\{[Cu(\mu\text{-pzdc})(tmen)]\cdot H_2O\}_n$ **(2)**, and 2,2′-bipyridine (bipy), $\{[Cu(\mu\text{-pzdc})(bipy)]\cdot H_2O\}_n$ **(3)** have been synthesized and characterized by means of elemental and thermal analyses, magnetic susceptibilities, IR and UV/vis spectroscopic studies. The molecular structures of dinuclear **(1)** and polynuclear **(2** and **3)** complexes have been determined by the single crystal X-ray diffraction technique. The pyrazine-2,3-dicarboxylate acts as a bridging ligand through oxygen atom of carboxylate group and N atom of pyrazine ring and one oxygen atom of neighboring carboxylate. It links the Cu(II) ions to generate a distorted square pyramidal geometry forming a one-dimensional (1D) chain. Adjacent chains of 1 and 2 are then mutually linked via hydrogen bonding interactions, which are further assembled to form a two and three-dimensional network, respectively. The chains of complex **3** are further constructed to form three-dimensional framework by hydrogen bonding, C–H···π and ring···ring stacking interactions. In the complexes, Cu(II) ions have distorted square pyramidal geometry. Thermal analyses properties and thermal decomposition mechanism of complexes have been investigated by using thermal analyses techniques (TG, DTG and DTA).

© 2008 Elsevier Ltd. All rights reserved.

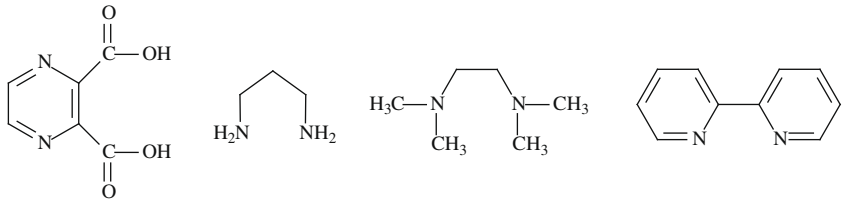
1. Introduction

The rational design and synthesis of metal-directed the supramolecular framework have received much attention in coordination chemistry in recent years owing to their novel and diverse topologies and potential applications in host–guest chemistry, catalysis, electrical conductivity, magnetism, nonlinear optics and gases sensors [1–8]. In crystal engineering the cyclic dicarboxylates [4–36], oxocarbons [37–39] and pyrimidine bases have been used as building blocks [40–42] and many coordination polymers. Pyrazine-2,3-dicarboxylic acid (H_2pzdca, Scheme 1a) generally tends toward react with metal salts to yield insoluble polynuclear materials and it behaves as a polyfunctional ligand in metal complexes and coordinates to metal ions by means of its four carboxylate oxygens and two nitrogen atoms forming monodentate [14], bidentate [15–19], bis(bidentate) bridging [20–23], tridentate bridging [24–29], tetradentate bridging [30–35] and mixed chelating-bridging ligand [36]. The Pyrazine-2,3-dicarboxylate coordinated to the Cu(II) ion for the first time as a monodentate ligand in the $[Cu(pdca)(H_2O)(en)_2]$ and $[Cu(pdca)(H_2O)(dmpen)_2]$ [14], pzdca behaved as a bidentate ligand *via* O atom of carboxylate and N atom of pyrazine ring in the $K_2[Cu(pzdca)_2(H_2O)]\cdot 6H_2O$ [18] complexes, as a bis(bidentate) bridge ligands coordinated to metal ions through two carboxylate oxygen atoms and two nitrogen atoms of pyrazine ring in the [Cu(pzdca)(HCl)] [20] and $\{[Cu(pzdca)(H_2O)_2]\cdot 2H_2O\}_n$ [35]. The pzdca acts as a tridentate and tetradentate bridge between the metal ions forming one-dimensional polymeric chains, its coordination sites being the O atom of carboxylate and N atom of ring and one O atom (for tridentate) or two O atoms (for tetradentate) of neighboring carboxylate group in the $\{[Cu(pzdca)(H_2O)_2]\cdot H_2O\}_n$ [26], $\{[Cu(pzdc)_2]\cdot 3(H_2O)\cdot 2(idzc)\}_n$ [29], $[Cu_2(pzdca)_2(L)]_n$ [35].

In the present study, we describe the syntheses, spectroscopic, thermal studies (TG, DTG and DTA) and crystal structures of novel three supramolecular Cu(II)-pyrazine-2,3-dicarboxylate complexes with 1,3-propanediamine (pen), *N*,*N*,*N*′,*N*′-tetramethylethylenediamine (tmen) and 2,2′-bipyridine (bipy) (Scheme 1b–d); $\{[Cu(\mu\text{-pzdc})(pen)]\cdot H_2O\}_2$ **(1)**, $\{[Cu(\mu\text{-pzdc})(tmen)]\cdot H_2O\}_n$ **(2)** $\{[Cu(\mu\text{-pzdc})(bipy)]\cdot H_2O\}_n$ **(3)**.

* Corresponding author. Tel.: +90 0222 2393750; fax: +90 0222 2393578.
E-mail address: yesilel@ogu.edu.tr (O.Z. Yeşilel).

0277-5387/$ - see front matter © 2008 Elsevier Ltd. All rights reserved.
doi:10.1016/j.poly.2008.11.044



Scheme 1. (a) Pyrazine-2,3-dicarboxylic acid, (b) 1,3-propanediamine, (c) N,N,N′,N′-tetramethylethylenediamine, (d)2,2′-Bipyridine.

2. Experimental

2.1. Preparation of the complexes

2.1.1. Complexes *1* and *3*

A solution of pyrazine-2,3-dicarboxylic acid (0.840 g, 5 mmol) in water (25 mL) was neutralized with NaOH (0.4 g, 10 mmol) and added dropwise with stirring at 50 °C to a solution of $CuCl_2 \cdot 2H_2O$ (0.852 g, 5 mmol) in water (25 mL). The solution immediately became precipitate and was stirred for 4 h at 50 °C. The addition of the pen ligand (0.372 g, 5 mmol) or 2,2'-bipyridine (0.781 g, 5 mmol) in ethanol (10 mL) to the precipitate mixture resulted in a clear solution. The mixture was stirred for 2 h at 50 °C and then cooled to room temperature. The crystals formed were filtered and washed with 10 mL of water and were dried in air. Elemental *Anal.* Calc. (%). Found: C, 34.11; H, 3.88; N, 17.67%. Calc. for $C_{18}H_{28}N_8O_{10}Cu_2$: C, 33.59; H, 4.39; N, 17.41% for **1**. Found: C, 47.99; H, 2.39; N, 14.13%. Calc. for $C_{16}H_{12}N_4O_5Cu$: C, 47.59; H, 3.00; N, 13.87% for **3**.

2.1.2. Complex *2*

A solution of pyrazine-2,3-dicarboxylic acid (0.840 g, 5 mmol) in water (25 mL) was added dropwise with stirring at 50 °C to a solution of $Cu(CH_3COO)_2 \cdot H_2O$ (1 g, 5 mmol) in distilled water (25 mL). The solution immediately became suspension and was stirred for 4 h at 50 °C. Then the tmen ligand (0.581 g, 5 mmol) in water (10 mL) was added dropwise to this suspension. The clear solution was stirred for 2 h at 50 °C and then cooled to room temperature. The crystals formed were filtered and washed with 10 mL of water and were dried in air. Elemental *Anal.* Calc. (%). Found: C, 40.13; H, 5.33; N, 15.68%. Calc. for $C_{12}H_{20}N_4O_5Cu$: C, 39.61; H, 5.54; N, 15.40% for **2**.

2.2. Materials and measurements

All chemicals used were analytical reagent and were commercially purchased. IR spectra were obtained with a Perkin–Elmer 100 FT-IR Spectrometer using KBr pellets in the 4000–400 cm^{-1} range. The UV–Vis. spectra were obtained for the aqueous solution of the complex (10^{-3} M) with a Shimadzu UV-3150 spectrometer in the range 900–190 nm. Magnetic susceptibilities measurements at room temperature were performed using a Sherwood Scientific MXI model Gouy magnetic balance. Elemental analysis for C, H and N were performed using a Carlo Erba 1106 microanalyser. Perkin–Elmer Diamond TG/DTA Thermal Analyser was used to record simultaneous TG, DTG and DTA curves in the static air atmosphere at a heating rate of 10 K min^{-1} in the temperature range 60–550 °C using platinum crucibles.

2.3. Crystallographic analyses

Diffraction experiments were carried out at 296 K on a Stoe IPDS diffractometer. The structures were solved by direct methods and refined using the programs SHELXS97 and SHELXL97 [43]. All non-hydrogen atoms were refined anisotropically by full-matrix least-squares methods [43]. In complex **2**, the tmen ligand shows three-positioned orientational disorder, the final site-occupancy factors for C(7)a–C(7)b/C(8)a–C(8)b/C(9)–C(9)b. The hydrogen atoms were placed in geometrically idealized positions and refined as riding atoms. Data collection: X-Area, cell refinement: X-Area, data reduction: X-RED [44]; program(s) used for molecular graphics: ORTEP-3 for Windows [45]; software used to prepare material for publication: WINGX [46].

3. Results and discussion

3.1. UV–Vis spectra and magnetic properties

The electronic spectra of water solutions of the complexes **1**–**3** display broad absorption bands at 617 (ϵ = 159 L mol^{-1} cm^{-1}), 647

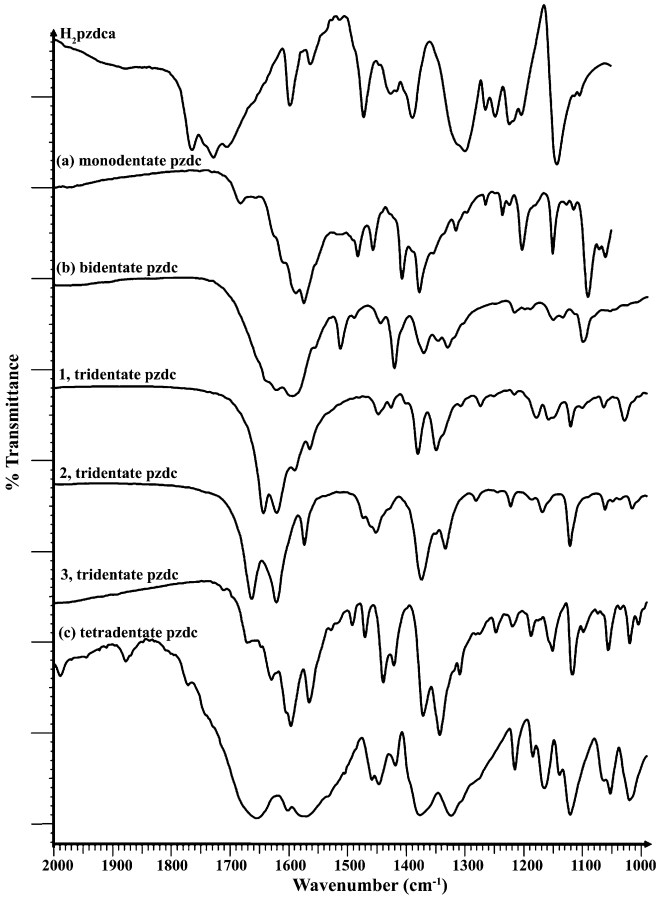


Fig. 1. A comparison of IR spectra of pyrazine-2,3-dicarboxylic acid and Cu(II)-pzdca complexes: (a) $[Cu(pzdca)(H_2O)(en)_2] \cdot H_2O$ [14], (b) $[Cu(pzdca)(phen)_2] \cdot 5.5H_2O$ [15], [Cu(pzdca) (mea)], (mea = monoethanoleamine, in prepare) and complexes 1-3.

(ϵ = 88 L mol^{-1} cm^{-1}) and 700 (ϵ= 127 L mol^{-1} cm^{-1}), respectively, which are assigned to the d_{xz}, $d_{yz} \rightarrow d_{x2-y2}$ ($a_1 \rightarrow b_1$) transition. The strong absorption bands below 300 nm are due to $n \rightarrow \Pi^*$ and $\Pi \rightarrow \Pi^*$ transitions of pen, tmen, bipy and pzdca ligands.

The complexes exhibit magnetic moment value of 1.57 for **2** and 1.58 for **3** which corresponds to one unpaired electron, while the dimeric complex **1** exhibits 2.46 BM, which lower than the spin only value for two unpaired electrons in Cu(II) complexes, indicates to antiferromagnetic effect.

3.2. IR spectra

The most characteristic FT-IR bands of the complexes correspond to the stretching vibrations of carboxyl group in the expected regions. For the coordination modes of carboxylate group, the difference between the asymmetric (ν_{asym}) and symmetric (ν_{sym}) carboxylate stretches ($\Delta = \nu_{asym} - \nu_{sym}$) are often used [47]. The C=N, C=C and OCO stretching band of the free pyrazine-2,3-dicarboxylic acid observed at 1753, 1715 and 1690 cm^{-1} were appear as three strong bands in the frequency range 1667–1568 cm^{-1} in the IR spectra of the complexes. The ν_{asym}(OCO) values were observed at 1568 for **1**, 1576 for **2** and 1569 for **3** and ν_{sym}(OCO) values were also observed at 1355 for **1**, 1339 for **2** and 1349 for **3**. The corresponding $\Delta\nu$ data are 213 for **1**, 237 for **2** and 220 for **3**. The separation between ν_{asym}(OCO) and ν_{sym}(OCO) indicate that the presence of monodentate coordination mode for the pzdca [47]. These conclusions are also supported from the results obtained from X-ray diffraction measurements.

The IR spectra of the complexes shows broad bands at 3507 and 3387 for **1** and 3476 and 3428 cm^{-1} for **2**, 3410 cm^{-1} for **3** the characteristic stretching of crystal water molecule. The bands at 3292 and 3244 cm^{-1} for **1** are attributed to the NH_2 stretching vibration in pen ligand. The weak bands between 3074 and 2893 cm^{-1} are attributed to the ν(CH) and $\nu(CH_2)$ vibrations in the IR spectra of the complexes. The weak bands observed in the 445–553 cm^{-1} region are due to Cu–O and Cu–N stretching vibrations [47]. A comparison between IR spectra of pyrazine-2,3-dicarboxylic acid and the IR spectra of the Cu(II)-pzdca complexes, in which pzdca ligand exhibits monodentate [14], bidentate [15], tridentate bridge and tetradentate bridge coordination modes are shown in Fig. 1.

3.3. Thermal analyses

Thermal decomposition behaviors of the complexes were performed in static atmosphere of air in the temperature range 60–550 °C. Thermoanalytical results (TG, DTG and DTA) on the complexes are summarized in Table 1.

Table 1
Thermoanalytical results (TG, DTG and DTA) on the complexes (1–4).[a]

Complexes	Decomposition		$DTG_{max.}$ (°C)	Remove Group	Mass loss (%)		Total Mass loss(%)		Decomposition product
	Stage	Temp. range			Calc.	Found	Calc.	Found	
$[Cu_2(\mu\text{-pzdc})_2(pen)_2] \cdot 2H_2O$	1	104–134	126(+)	$2H_2O$	5.59	5.57	75.28	77.44	$[Cu_2(\mu\text{-pzdc})_2(pen)_2]$
	2	203–245	–	pzdc-pen	–	–			–
	3	245–518	478(−)	–	–	–			2CuO
$\{[Cu(\mu\text{-pzdc})(tmen)] \cdot H_2O\}_n$	1	89–142	126(+)	H_2O	4.95	4.47	82.49	78.02	[Cu(pzdca)(tmen)]
	2	185–228	228(+)	tmen	31.93	28.67			[Cu(μ-pzdc)]
	3	228–250	232(+)	$2CO_2$	24.18	25.76			Cu(pz)
	4	250–395	344(+)	pz	21.43	19.12			CuO
$\{[Cu(\mu\text{-pzdc})(bipy)] \cdot H_2O\}_n$	1–2	23–81	28(+), 68(+)	H_2O	4.46	5.34	80.24	78.67	[Cu(pzdca)(bipy)]
	3	171–208	208(−)	bipy	38.67	38.44			[Cu(μ-pzdc)]
	4	208–294	294(−)	CO_2 + CO	17.80	16.85			Cu(L)
	5	294–418	417(−)	L	19.31	18.04			CuO

[a] (+) endothermic, (−) exothermic effect.

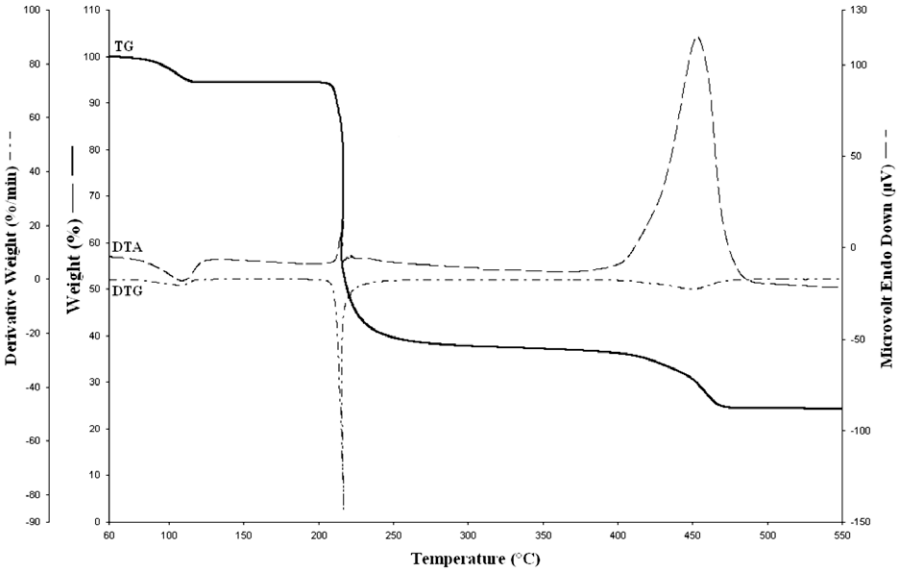


Fig. 2. TG, DTG and DTA curves of 1.

*3.3.1. $[Cu_2(\mu\text{-pzdc})_2(pen)_2] \cdot 2H_2O$ (**1**)*

Complex **1** shows a three stage decomposition process (Fig. 2) and it starts to the lose crystal water molecules between 104 and 134 °C with an experimental mass loss of 5.57% (calc. mass loss 5.59%). Anhydrous complex is stable up to 203 °C and in the second stage, it begins to decompose between 203 and 245 °C and to calculate mass loss value for the release of both pen and pzdca ligands is impossible due to overlapping decomposition processes. In the last exothermic stage, remaining organic part is abruptly burnt (DTA = 478 °C). The total mass loss of all decomposition process is 77.44% (calc. 75.28%) suggest that CuO is the end product at 518 °C.

*3.3.2. $\{[Cu(\mu\text{-pzdc})(tmen)] \cdot H_2O\}_n$ (**2**)*

The complex **2** exhibits four decomposition stages (Fig. 3). In the first stage, endothermic removal of crystal water molecule occurs between 89 and 142 °C (found 4.47, calc. 4.95%, DTA_{max} = 126 °C). In the temperature range of 186–228 °C, the anhydrous Cu(II) complex involves the consecutive decomposition stages of neutral tmen ligand by the endothermic effects (DTA_{max} = 228 °C). The endothermic effects between 228 and 250 °C is likely due to the release of CO_2 from pzdca ligand. The IR spectrum of the complex heated just to the end of this weight loss show no evidence of CO_2 bands. The following stage involves the burning of pyrazine ligand by the exothermic effect (DTG_{max} = 344 °C), leading finally to CuO. The overall mass loss of 78.94% (calc. 78.14%) agrees with the propose structure well.

3.3.3. $\{[Cu(\mu\text{-pzdc})(bipy)] \cdot H_2O\}_n$ (3)

In the stages of range of 28–81 °C, the complex **3** involves endothermic decomposition, corresponding to the loss of crystal water molecule as indicated by TG mass loss (found 5.34, calc. 4.46%). The

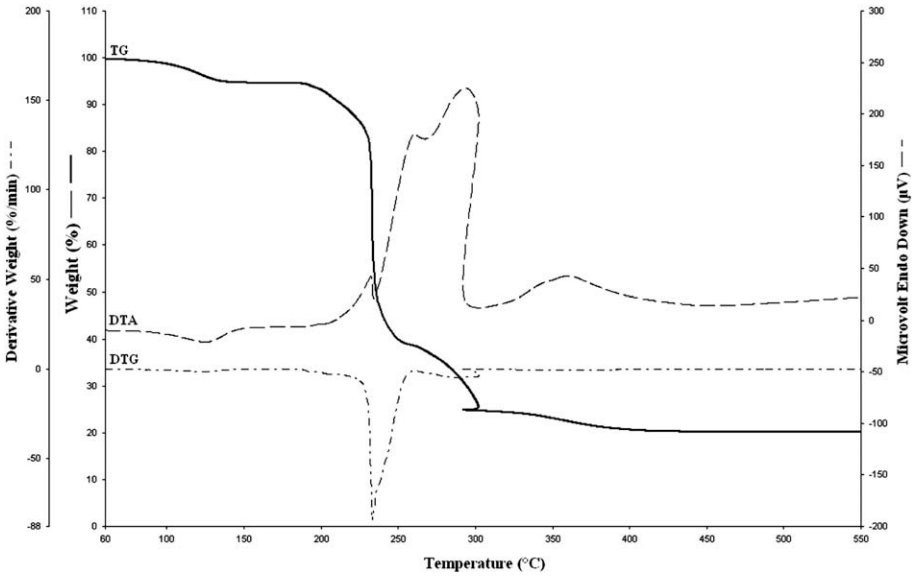


Fig. 3. TG, DTG and DTA curves of 2.

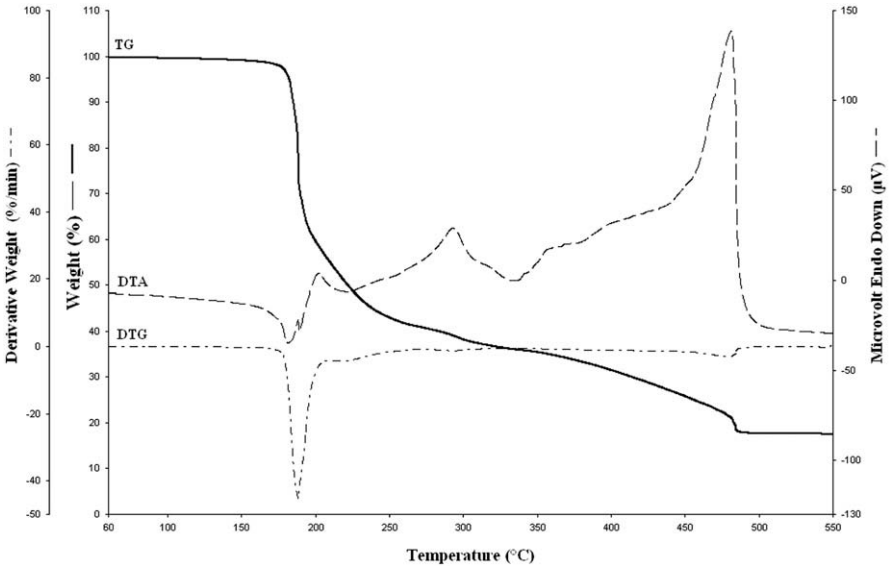


Fig. 4. TG, DTG and DTA curves of 3.

anhydrous complex is thermally stable up to 171 °C. In the third stage between 171 and 208 °C, the complex involves the decomposition of the bipy ligand by giving exothermic effect (found 38.44, cal. 38.67%). The fourth stage is related to the release of CO_2 + CO from the pzdca (found 16.85, calc. 17.80%). The last strong exothermic stage can be assigned to the combustion of the residual organic matter. The final solid product of thermal decomposition was identified as CuO (found 79.90, calc. 80.44%) (Fig. 4).

The final decomposition products were identified by IR spectroscopy and also confirmed by mass loss calculations. On the basis of the first decomposition temperature, the thermal stability of the anhydrous complexes follows the order: **1**, (203 °C) > **2**, (185 °C) > **3**, (171 °C) in static air atmosphere.

3.4. Crystal structures

The relevant crystal data and experimental conditions along with the final parameters are summarized in Table 2. The selected bond lengths and angles together with the hydrogen bonding geometry are given in Tables 3 and 4, respectively. The comparison of the Cu–N_{pzdc}, Cu–O_{pzdc} distances and O_{pzdca}–Cu–N_{pzdca} angle for the similar 2,3-pyrazinedicarboxylic acid complexes are given in Table 5.

3.4.1. $[Cu_2(\mu\text{-pzdc})_2(pen)_2] \cdot 2H_2O$ (1)

The molecular structure of $[Cu_2(\mu\text{-pzdc})_2(pen)_2] \cdot 2H_2O$ with the atom labeling is shown Fig. 5. The selected bond lengths and angles are collected in Table 3. The structure consists of a complex $[Cu_2(\mu\text{-pzdc})_2(pen)_2]$ and two crystal water molecules. Although there are many metal complexes of pzdc forming polymeric structure, dinuclear pzdc complex has been reported only one by our group [15]. In the title dinuclear Cu(II) complex **1**, pzdc dianion acts as a tridentate bridging ligand with the nitrogen atom and oxygen atom of one carboxylate group, chelating the copper atom whereas another oxygen atom of the second carboxylate group binds the symmetry-related Cu atom. Distorted square pyramidal geometry is completed with two nitrogen atoms of bidentate pen ligand. One carboxylate oxygen atom (O1) and three nitrogen atoms (N1, N3, N4) from the pzdc and pen ligands comprise the equatorial plane, while one oxygen atom of carboxylate group ($O3^i$, (i) –x + 1, –y + 1, –z + 1) from the neighboring complex molecule occupy the axial position. The Cu1–N1 and Cu1–O1 bond distances are comparable to those reported for $[Cu_2(pzdc)_2(L)]_n$ [1.99(1) and 1.947(9) Å] [48], $[Cu(pzdc)_2] \cdot 2H_2O$ (1.994(3) and 1.941(3) Å) [49], $[Cu(Hpzdc)_2]_n$ (1.973(3), 1.934(3) Å) and $\{[Cu_4(\mu\text{-pzdc})_4(phen)_2(H_2O)_4] \cdot 10H_2O\}_n$ (1.983(3), 1.998(3) and 1.942(3), 1.947(3) Å) [25]. The Cu–$O3^i$

Table 2
Crystal data and structure refinement parameters for **1**–**3**.

	1	2	3
Empirical formula	$C_{18}H_{28}N_8O_{10}Cu_2$	$C_{12}H_{20}N_4O_5Cu$	$C_{16}H_{12}N_4O_5Cu$
Formula weight	643.56	363.86	403.84
Temperature (K)	293 (2)		
Wavelength (Å)	0.71073 Mo Kα		
Crystal system	monoclinic	orthorhombic	monoclinic
Space group	$P2_1/c$	$P2_12_12_1$	P21/c
a (Å)	7.4592 (11)	8.8942 (5)	11.2781 (4)
b (Å)	7.4487 (10)	12.9013 (7)	11.5931 (4)
c (Å)	21.500 (4)	13.8801 (11)	12.4737 (4)
β (°)	90.777 (14)	90	110.387 (2)
V (Å^3)	1194.5 (3)	1592.70 (18)	1528.75 (9)
Z	2	4	4
Absorption coefficient (mm^{-1})	1.85	1.40	1.47
D_{calc} (Mg m^{-3})	1.789	1.517	1.755
Crystal size (mm)	0.52 × 0.21 × 0.03	0.65 × 0.50 × 0.42	0.75 × 0.49 × 0.16
Theta range for data collection (°)	2.73–27.24	2.16–27.84	1.74–28.58
Measured reflections	4982	10579	37289
Flack parameter [51]	–	0.002(12)	–
Independent reflections	2299	3775	3168
Absorption correction	Integration Stoe X-RED (Stoe and Cie, 2001)		
Final R indices [$I > 2\sigma(I)$]	0.045	0.026	0.076
$R[F^2 > 2\sigma(F^2)]$	0.041	0.052	0.060
$wR(F^2)$	0.077	0.147	0.123
Goodness-of-fit on F^2	1.02	1.03	1.17
Largest difference peak and hole (Å^{-3})	0.36, −0.45	1.33; −0.52	0.51; −0.91

Table 3
The bond distances and angles (Å, °) of the complexes.

Selected atoms			
Complex **1**			
N1–Cu1	2.043(3)	N4–Cu1	1.974(3)
O1–Cu1	1.990(2)	$O3–Cu1^i$	2.212(2)
N3–Cu1	2.011(3)		
$O1–Cu1–O3^i$	106.25 (10)	N1–Cu1–N3	98.96 (12)
$N1–Cu1–O3^i$	88.96 (10)	$N4–Cu1–O3^i$	93.62 (12)
O1–Cu1–N1	80.98 (11)	O1–Cu1–N4	88.97 (11)
$N3–Cu1–O3^i$	101.48 (11)	N1–Cu1–N4	169.95 (11)
O1–Cu1–N3	152.26 (12)	N3–Cu1–N4	90.06 (12)
Complex **2**			
N1–Cu1	2.010 (4)	N4–Cu1	2.255 (5)
O1–Cu1	1.976 (3)	$O3–Cu1^i$	1.969 (3)
N3–Cu1	2.046 (4)		
$O3^{ii}–Cu1–O1$	163.77 (14)	N1–Cu1–N3	172.79 (16)
$O3^{ii}–Cu1–N1$	92.20 (13)	$O3^{ii}–Cu1–N4$	97.51 (19)
O1–Cu1–N1	81.25 (14)	O1–Cu1–N4	98.2 (2)
$O3^{ii}–Cu1–N3$	93.58 (15)	N1–Cu1–N4	98.97 (18)
O1–Cu1–N3	92.05 (15)	N3–Cu1–N4	84.6 (2)
Complex **3**			
N1–Cu1	2.021 (3)	N4–Cu1	2.002 (3)
O1–Cu1	2.151 (3)	O3–Cu1	1.963 (3)
N3–Cu1	2.048 (4)		
O3–Cu1–O1	95.92 (13)	O1–Cu1–N1	79.77 (12)
O3–Cu1–N1	90.25 (13)	O1–Cu1–N4	104.41 (13)
O3–Cu1–N3	172.63 (14)	N1–Cu1–N3	92.59 (13)
O3–Cu1–N4	96.47 (13)	N1–Cu1–N4	171.62 (15)
O1–Cu1–N3	91.27 (14)	N3–Cu1–N4	80.15 (14)

Symmetry codes: (i) –x + 1, –y + 1, –z + 1 for **1**; (i) –x + 1, y + 1/2, –z + 1/2; (ii) –x + 1, y – 1/2, –z + 1/2 for **2**.

Table 4
Hydrogen bonding interactions in the complexes.

D–H···A	d(D–H) (Å)	d(H···A) (Å)	d(D···A) (Å)	<(DHA) (°)
Complex **1**				
$N4–H4A···O5^{ii}$	0.90	2.09	2.892 (5)	148
$N4–H4B···O4^{iii}$	0.90	2.08	2.940 (4)	158
$N3–H3A···O2^{iii}$	0.90	2.47	3.093 (4)	127
$N3–H3B···O2^{iv}$	0.90	2.17	3.030 (4)	160
O5–H5A···O4	0.75 (6)	2.07 (6)	2.798 (5)	164 (6)
$O5–H5B···N2^v$	0.74 (6)	2.28 (7)	2.983 (6)	158 (6)
Complex **2**				
$O5–H5A···O2^i$	0.84 (2)	2.09 (2)	2.922 (5)	173 (6)
$O5–H5B···O4^{ii}$	0.83 (2)	2.01 (2)	2.833 (5)	176 (7)
Complex **3**				
$O5–H5A···O2^{ii}$	0.84 (2)	2.10 (3)	2.910 (5)	164 (6)
$O5–H5B···O4^{iii}$	0.84 (2)	2.10 (2)	2.882 (6)	155 (4)

Symmetry codes: (ii) x, $-y + 3/2$, $z + 1/2$; (iii) $-x$, $-y + 1$, $-z + 1$; (iv) x, $y-1$, z; (v) $-x + 1$, $y + 1/2$, $-z + 1/2$ for **1**; (i) $-x + 1$, $y + 1/2$, $-z + 1/2$; (ii) x, $-y + 3/2$, $z-1/2$ for **2**; (ii) $-x + 1$, $y - 1/2$, $-z + 1/2$; (iii) $x - 1/2$, $-y + 3/2$, $-z$ for **3**.

Table 5
Comparison of the bond distances (Å) and angles (°) of the copper(II)-pyrazine-2,3-dicarboxylic acid complexes.

Complexes	Pzdc mode	Cu–O1/Cu–N1 (Å)	Cu–O3/Cu–O4 (Å)	O_1–Cu–N_1 (°)
$\{[Cu(\mu\text{-pzdc})(pen)]\cdot H_2O\}_2$, **1**	Tridentate, μ_2 (N1,O1,O3)	1.990/2.043	2.212/–	80.98
$\{[Cu(\mu\text{-pzdc})(tmen)]\cdot H_2O\}_n$, **2**	Tridentate, μ_2 (N1,O1,O3)	1.976/2.010	1.969/–	81.25
$\{[Cu(\mu\text{-pzdc})(bipy)]\cdot H_2O\}_n$, **3**	Tridentate, μ_2 (N1,O1,O3)	2.151/2.021	1.963/–	79.77
$[Cu_4(pzdca)_4(phen)_2(H_2O)_4]\cdot 10H_2O$ [25]	Tridentate, μ_2 (N1,O1,O5)	1.947/1.983	–/–	83.4
$\{[Cu(pzdca)_2]\cdot 3(H_2O)\cdot 2(IDZC)\}_n$ [26]	Tridentate, μ_2 (N1,O1,O3)	1.950/1.980	2.420/–	–
$[Cu_2(L)(PDC)_2(H_2O)_2]\cdot 12H_2O$ [28]	Tridentate, μ_2 (N1,O1,O3)	1.932/1.970	2.552/–	83.35
$\{[Cu(pzdca)(H_2O)_2]\cdot H_2O\}_n$ [29]	Tridentate, μ_2 (N1,O1,O3)	1.978/2.061	2.306/–	80.56
$K_2[Cu(pzdca)_2(H_2O\cdot 6H_2O$ [18]	Bidentate, (N1,O1)	1.953/1.994	–/–	–
$Na_2K_2[trans\text{-}Cu(pzdca)_2](SCN)_2\cdot 2H_2O$ [19]	Bidentate, (N1,O1)	1.971/1.970	–/–	82.42
[Cu(pzdca).HCl] [20]	Bis(bidentate) μ_2(N2,O1; N1,O4)	1.990/2.000	−2.190	80.0/114.1
$\{[Cu(pzdca)(H_2O)_2]\cdot 2H_2O\}_n$ [23]	Bis(bidentate) μ_2 (N1,O1)	1.931/1.994	2.479/–	82.9
$\{[Cu_2(pzdca)_2(L)]_n\}$ [35]	Tetradentate, μ_3 (N1,O1,O3,O4)	1.947/1.990	1.973/2.210	81.9

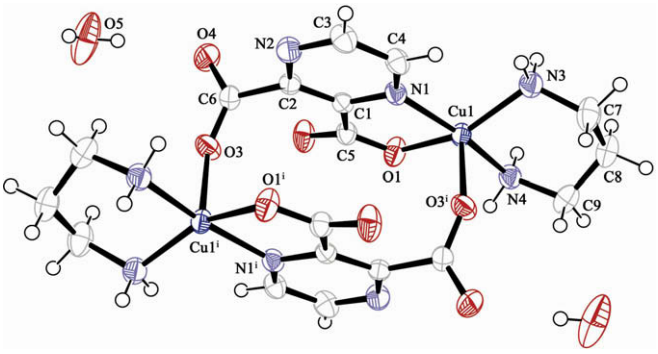


Fig. 5. The molecular structure of 1 showing the atom numbering scheme. The thermal ellipsoids are plotted at the 50% probability level.

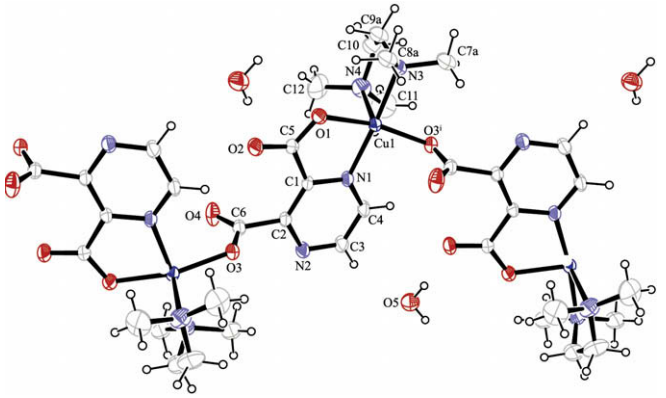


Fig. 7. The molecular structure of 2 showing the atom numbering scheme. The thermal ellipsoids are plotted at the 30% probability level.

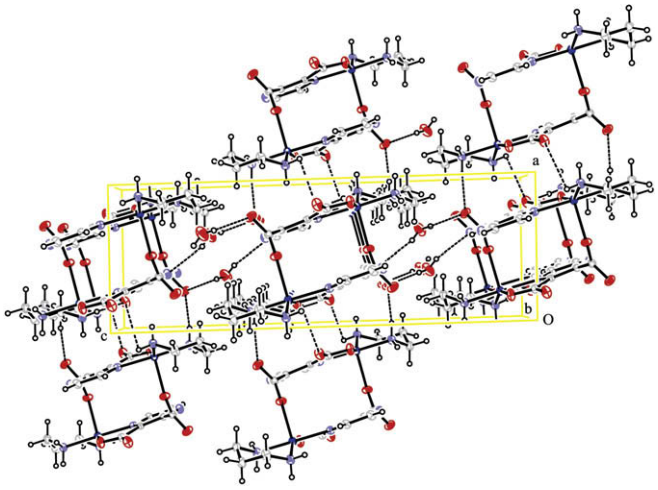


Fig. 6. Packing diagram of 1.

bond distance of 2.212(2) Å are different from the values observed in $\{[Cu_4(\mu\text{-pzdc})_4(phen)_2(H_2O)_4]\cdot 10H_2O\}_n$ (1.937(3) Å) [25], $[Cu_2(pzdc)_2(L)]_n$ [1.973(8) Å] [48] and $[Cu(Hpzdc)_2]_n$ (2.616(3) Å), while the Cu1–$O3^i$ bond distance is in agreement with the corresponding values in $\{(H_2bpe)[Cu(\mu\text{-pzdc})_2]\cdot 2H_2O\}_n$ (2.469(2) Å) [33], $[Cu(pzdc)_2]\cdot 2H_2O$ (2.401(3) Å) [49], $\{[Cu(pzdc)_2]\cdot 3H_2O{\cdot}2idzc\}_n$ (2.420(4) Å) [26], and $\{[Cu(\mu\text{-pzdc})(H_2O)_2]\cdot H_2O\}_n$ (2.306(3) Å) [29].

The complex 1 exhibits a number of intermolecular N–H···O, O–H···O and O–H···N hydrogen bonds as given Table 4. The amine hydrogen atoms of pen participate in hydrogen bonding with the oxygen atoms of pzdc and crystal water molecules. These hydrogen bonding interactions give 3D framework (Fig. 6).

3.4.2. $\{[Cu(\mu\text{-pzdc})(tmen)]\cdot H_2O\}_n$ (2)

The crystal structure of **2** with the atom labeling is shown in Fig. 7. The selected bond lengths and angles and hydrogen bonding geometry are given in Tables 3 and 4, respectively. The Cu(II) ion is bridged by the tridentate pzdc ligand through the oxygen atom of carboxylate group and nitrogen atom of pyrazine ring as a bidentate manner and oxygen atom of carboxylate group of neighboring molecule. Each Cu(II) ion is also coordinated bidentate tmen ligand forming distorted square pyramid geometry. The structure contains of an helicoidal chains devolopping paralel to *b*-axis. The Cu1–O1 and Cu1–N1 bond distances are similar that found in the $\{(H_2bpe)[Cu(\mu\text{-pzdc})_2]\cdot 2H_2O\}_n$ (1.954(1) and 1.978(2) Å) [33], $\{[Cu_4(\mu\text{-pzdc})_4(phen)_2(H_2O)_4]\cdot 10H_2O\}_n$ (1.942(3), 1.947(3) and 1.983(3), 1.998(3) Å) [25] and $\{[Cu(\mu\text{-pzdc})(H_2O)_2]\cdot H_2O\}_n$ (1.978(3) and 2.061(3) Å) [29]. The Cu1–$O3^i$ bond distance is significantly shorter that found in the $\{[Cu(\mu\text{-pzdc})(H_2O)_2]\cdot H_2O\}_n$ (2.306(3)Å) [29] and $\{(H_2bpe)[Cu(\mu\text{-pzdc})_2]\cdot 2H_2O\}_n$ (2.469(2) Å) [33], but is much longer than 1.938(3) Å reported for $\{[Cu_4(\mu\text{-pzdc})_4(phen)_2(H_2O)_4]\cdot 10H_2O\}_n$ [25].

The pzdc ligand is essentially planar with r.m.s. deviation −0.0021 Å and the largest deviation from the mean plane is 0.0080 Å for C4 atom. The carboxylate C–O distances in the pzdc anion also display some variability, depending on their environment. The C–O distances are practically equal in the pzdc anion in pzdca ligand [50].

The crystal water molecule is involved in intermolecular hydrogen bonding with the carboxyl oxygen atoms (O2 and O4) of pzdca ligand. The intermolecular O5–H5A···$O2^{ii}$ and O5–H5B···$O4^{iii}$ hydrogen bonds have the H···O distances of 2.10(3) and 2.10(2) Å,

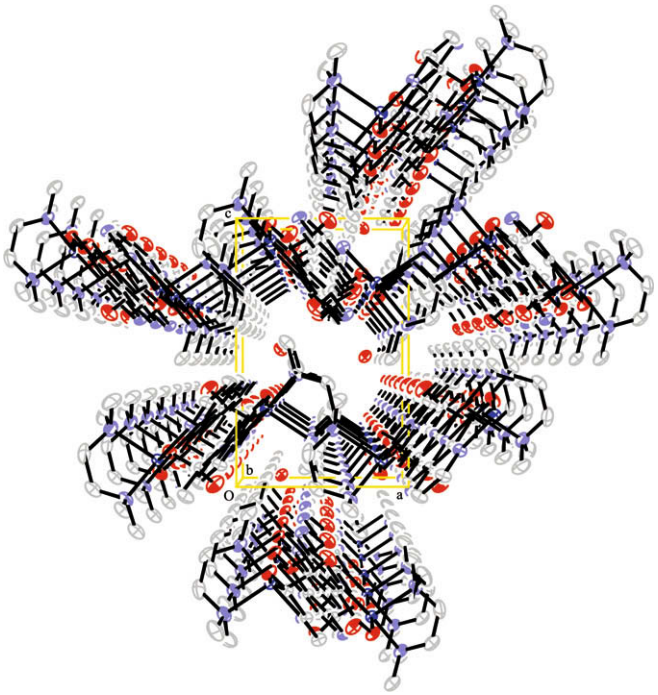


Fig. 8. Packing diagram of 2.

respectively [(ii) −x + 1, y − 1/2, −z + 1/2; (iii) x − 1/2, −y + 3/2, −z]. These hydrogen bonding interactions give three dimensional networks (Fig. 8).

3.4.3. {[Cu(μ-pzdc)(bipy)] · H_2O}$_n$ (**3**)

Crystal structure of polymeric complex **3** with the atom labeling is shown in Fig. 9. Cu(II) ion is coordinated by two N atoms of bipy ligand, O atom of carboxylate group and N atom of pyrazine ring and O atom of symmetry related carboxylate group, forming a distorted square pyramid geometry. Atoms N1, N3, N4 and O3 comprise basal plane, while atom O1 occupy the axial positions. The

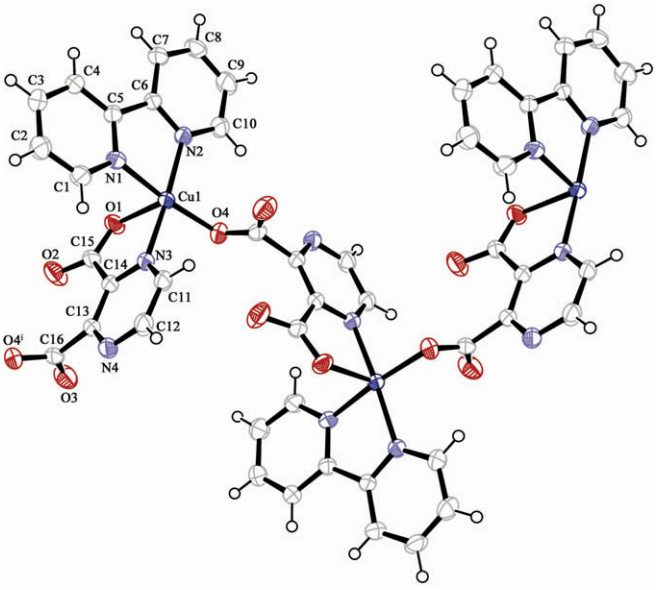


Fig. 9. The molecular structure of 3 showing the atom numbering scheme. The thermal ellipsoids are plotted at the 50% probability level.

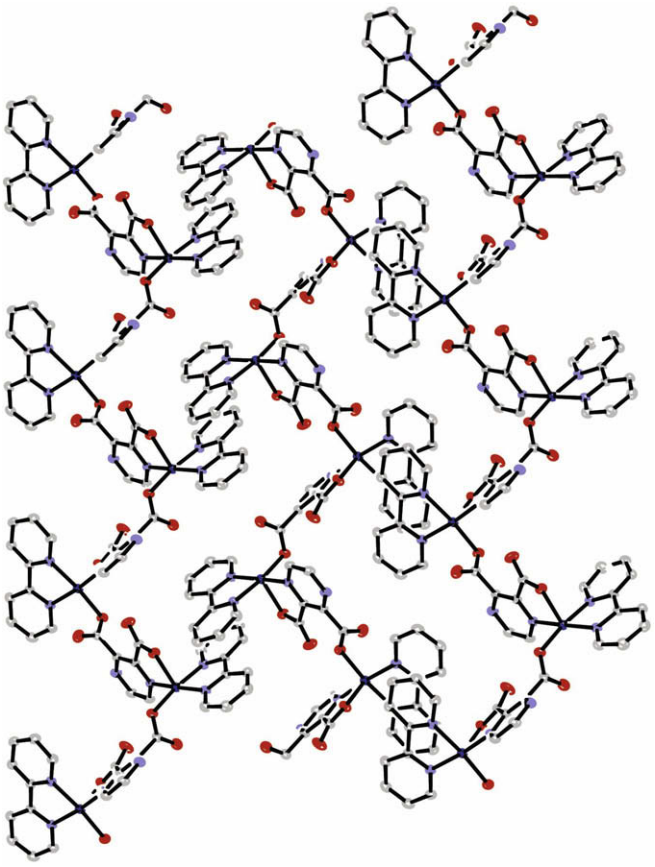


Fig. 10. The two-dimensional structure of 3.

Cu1–O1 and Cu1–N1 bond distances are similar that reported for the related Cu(II) complexes [29]. The Cu1–O3^{i} bond distance is significantly shorter that found Cu(II)-pzdc complexes [29,33]. Pzdc moiety is planar with slightly more rotated carboxylate group in the coordinated one [C1/C5/O1/O2 10.41, C2/C6/O3/O4 71.05°]. The dihedral angle between two carboxylate groups is 72.04°.

The crystal packing of complex is a composite of intermolecular hydrogen bonding, ring···ring and C–H···π interactions. The crystal structure is stabilized through strong intermolecular hydrogen bonding between O atom of crystal water molecule and uncoordinated O atom of carboxylate groups. The distances O5···O2^{i} and O5···O2^{ii} are 2.922(5) and 2.833(5) Å, respectively and the hydrogen bonds are nearly linear (173(6)° and 176(7)°). An intermolecular ring···ring interaction contact occurs between the two symmetry-related bipy ligand [Cg5=N(1), C(1), C(2), N(2), C(3), C(4) and Cg6=N(3), C(7), C(8), C(9), C(10), C(11); Cg5···Cg6^{i} 3.7345 Å, (i): −x,−y,−z], while C–H···π interaction take place between C(2)–H(2) ···Cg(6) [2.91 Å], C(9) –H(9) ···Cg(5) [2.89 Å], C(8) –H(8) ···Cg(7)^{ii} [2.91 Å, (i): −x,−1/2 + y,1/2 − z] and C(15) –H(15) ···Cg(6)^{iii} [2.83 Å, (iii): x,1/2 − y,−1/2 + z] (Fig. 10). From all of these intermolecular interactions give a two-dimensional network results (Fig. 11).

4. Conclusion

We have successfully synthesized and characterized the three novel dimeric and polymeric Cu(II)-pyrazine-2,3-dicarboxylate complexes. The molecular structures of dinuclear **(1)** and polynuclear **(2** and **3)** complexes have also been determined by the single crystal X-ray diffraction technique. The pyrazine-2,3-dicarboxylate behaves as a tridentate bridging ligand.

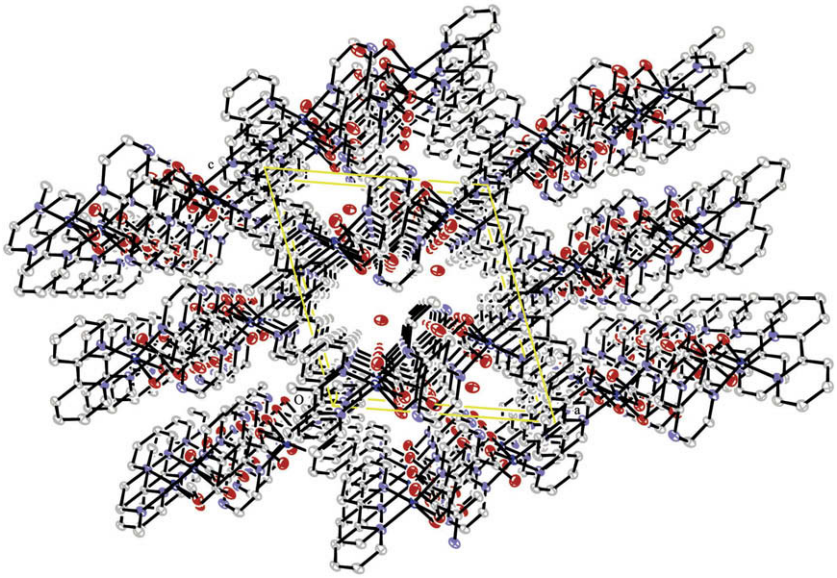


Fig. 11. The packing diagram of 3.

Acknowledgements

This work was supported by the Eskişehir Osmangazi University by project No. 200819042.

Appendix A. Supplementary data

Supplementary CCDC 682132, 675629 and 676221 contain the supplementary crystallographic data for **1**, **2** and **3**. These data can be obtained free of charge via http://www.ccdc.cam.ac.uk/conts/retrieving.html, or from the Cambridge Crystallographic Data Centre, 12 Union Road, Cambridge CB2 1EZ, UK; fax: (+44) 1223 336 033; or e-mail: deposit@ccdc.cam.ac.uk. Supplementary data associated with this article can be found, in the online version, at doi:10.1016/j.poly.2008.11.044.

References

[1] C.W. Yeh, J.D. Chen, J.C. Wang, Polyhedron 27 (2008) 3611.
[2] S.M. Wu, M. Li, J.F. Xiang, L.J. Yuan, J.T. Sun, Acta Crystallogr. E62 (2006) 2951.
[3] H.P. Jia, W. Li, Z.F. Ju, J. Zhang, Eur. J. Inorg. Chem (2006) 4264.
[4] X.Z. Sun, Y.F. Sun, B.H. Ye, X.M. Chen, Inorg. Chem. Commun. 6 (2003) 1412.
[5] A. Demessence, G. Rogez, R. Welter, P. Rabu, Inorg. Chem. 46 (2007) 3423.
[6] X.Z. Sun, Z.L. Huang, H.Z. Wang, B.H. Ye, X.M. Chen, Z. Anorg. Allg. Chem. 631 (2005) 919.
[7] L. Gao, B. Zhao, G. Li, Z. Shi, S. Feng, Inorg. Chem. Commun. 6 (2003) 1249.
[8] Y. Gong, T. Wang, M. Zhang, C.W. Hu, J. Mol. Struc. 833 (2007) 1.
[9] N. Ching, L. Pan, X.Y. Huang, J. Li, Acta Crystallogr. C56 (2000) 1124.
[10] A.L. Chen, K.F. Mok, S.C. Ng, M.G.B. Drew, New J. Chem. 23 (1999) 877.
[11] W.L. Driessen, L. Chang, C. Finazzo, S. Gorter, D. Rehorst, J. Reedijk, M. Lutz, A.L. Spek, Inorg. Chim. Acta 350 (2003) 25.
[12] R. Noguchi, A. Sugie, A. Hara, K. Nomiya, Inorg. Chem. Commun. 9 (2006) 107.
[13] F.Q. Wang, D.F. Weng, X.J. Zheng, J.J. Zhang, H. Ma, L.P. Jin, Inorg. Chim. Acta 360 (2007) 2029.
[14] O.Z. Yeşilel, A. Mutlu, O. Büyükgüngör, Polyhedron 27 (2008) 2471.
[15] O.Z. Yeşilel, A. Mutlu, O. Büyükgüngör, J. Coord. Chem. 61 (2008) 3267.
[16] A.J. O'Connor, E. Sinn, Inorg. Chem. 20 (1981) 545.
[17] M. Wenkin, M. Devillers, B. Tinant, J.P. Declercq, Inorg. Chim. Acta 258 (1997) 113.
[18] O. Castillo, G. Beobide, A. Luque, P. Román, Acta Crystallogr. E59 (2003) m800.
[19] M.S. Wang, L.Z. Cai, G.W. Zhou, G.C. Guo, J.G. Mao, J.S. Huang, Acta Crystallogr. E59 (2003) m212.
[20] A.J. O'Connor, C.L. Klein, R.J. Majeste, L.M. Trefonas, Inorg. Chem. 21 (1982) 64.
[21] H. Xu, H. Ma, M. Xu, W. Zhao and B. GuO, Acta Crystallogr. E64 (2008) m104, 12.
[22] R. Burriel, C.J. O'Conner, R.L. Carlin, Inorg. Chem. 24 (1985) 3706.
[23] T. Okubo, M. Kondo, S. Kitagawa, Synth. Met. 85 (1997) 1661.
[24] H.D. Yin, F.H. Li, C.H. Wang, Inorg. Chim. Acta 360 (2007) 2797.
[25] H. Yin, S.X. Liu, Polyhedron 26 (2007) 3103.
[26] X.H. Li, Q. Shi, M.L. Hu, H.P. Xiao, Inorg. Chem. Commun. 7 (2004) 912.
[27] M. Gryz, W. Starosta, J. Leciejewicz, J. Coord. Chem. 58 (2005) 931.
[28] K.Y. Choi, J. Incl. Phen. Macr. Chem. 43 (2002) 195.
[29] S. Konar, S.C. Manna, E. Zangrando, N.R. Chaudhuri, Inorg. Chim. Acta 357 (2004) 1593.
[30] Z. Bi-Song, Chinese J. Struct. Chem. 24 (2005) 478.
[31] Y. Ma, Y.K. He and Z.B. Han, Acta Crystallogr. E62 (2006) m2528.
[32] J.Z. Zou, Z. Xu, W. Chen, K.L. Lo, X.Z. You, Polyhedron 18 (1999) 1507.
[33] G. Beobide, O. Castillo, A. Luque, U. Garcia-Coucerio, J.P. Garcia-Teran, P. Roman, Inorg. Chem. 45 (2006) 5367.
[34] M.L. Hu, J.X. Yuan, F. Chen, Q. Shi, Acta Crystallogr. C60 (2004) m186.
[35] M. Kondo, T. Okubo, A. Asami, S. Noro, T. Yoshitomi, S. Kitagawa, T. Ishii, H. Matsuzaka, K. Seki, Angew. Chem., Int. Ed. 38 (1999) 1433.
[36] X.J. Zheng, L.P. Jin, S.Z. Lu, Eur. J. Inorg. Chem. (2002) 3356.
[37] S.C. Manna, J. Ribas, E. Zangrando, N.R. Chaudhuri, Inorg. Chim. Acta 360 (2007) 2589.
[38] I. Castro, M.L. Calatayud, J. Sletten, M. Julve, F. Lloret, Comptes Rendus de l'Académie des Sciences - Series IIC - Chemistry 4 (2001) 235.
[39] C.C. Corrêa, R. Diniz, L.H. Chagas, B.L. Rodrigues, M.I. Yoshida, W.M. Teles, F.C. Machado, L.F.C. de Oliveira, Polyhedron 26 (2007) 989.
[40] O.Z. Yeşilel, A. Mutlu, C. Öğretir, O. Büyükgüngör, J. Mol. Struc. 889 (2008) 415.
[41] Li Yanqiu, Ju Yanling, Li Xia, Zhang Tingting, Wang Chunyan and Yu Jingbo, Journal of Rare Earths 25 (2007) 770.
[42] O.Z. Yeşilel and O. Büyükgüngör, Solid State Sciences 9 (2007) 485. 13.
[43] G.M. Sheldrick, SHELXS–97 and SHELXL–97. Program for Refinement of Crystal Structures, University of Göttingen, Germany, 1997.
[44] Stoe and Cie, X-Area (Version 1.18) and X-Red32 (Version 1.04), Stoe and Cie, Darmstadt, Germany, 2001.
[45] L.J. Farrugia, ORTEPIII Program For Molecular Drawing, J. Appl. Crystallogr. 30 (1997) 565.
[46] L.J. Farrugia, WinGX Suite for Single Crystal Small Molecule Crystallography, J. Appl. Crystallogr. 32 (1999) 837.
[47] K. Nakamoto, Infrared and Raman Spectra of Inorganic and Coordination Compounds, fifth ed., Wiley Interscience, New York, 1997, pp. 59–62.
[48] M. Kondo, T. Okubo, A. Asami, S. Noro, S. Kitagawa, T. Ishii, H. Matsuzaka, K. Seki, Angew. Chem. Int., Ed. Engl 38 (1999) 140.
[49] J. Zou, Y. Wu, X. Wei, C. Duan, Y. Liu, Z. Xu, Transition Met. Chem. 23 (1998) 481.
[50] T. Premkumar, S. Govindarajan, W. Starosta, J. Leciejewicz, Acta Crystallogr. E60 (2004) 1305.
[51] H.D. Flack, Acta Crystallogr. A39 (1983) 876.

Polyhedron 28 (2009) 445–452

Contents lists available at ScienceDirect

Polyhedron

journal homepage: www.elsevier.com/locate/poly

Synthesis and structural characterization of copper(II), cadmium(II) and zinc(II) complexes with 4,5-diazaspirobifluorene and bis-9-biphenyl-4,5-diazafluorenyl peroxide

Min Hong [a], Kun Zhang [a], Yi-Zhi Li [b], Jin Zhu [a,*]

[a] Department of Polymer Science and Engineering, School of Chemistry and Chemical Engineering, State Key Laboratory of Coordination Chemistry, Nanjing University, 22 Hankou Road, Nanjing 210093, PR China
[b] Coordination Chemistry Institute, Nanjing University, Nanjing 210093, PR China

ARTICLE INFO

Article history:
Received 17 June 2008
Accepted 14 November 2008
Available online 30 December 2008

Keywords:
Copper
Cadmium
Zinc
4,5-Diazaspirobifluorene
Bis-9-biphenyl-4,5-diazafluorenyl peroxide
Crystal structure

ABSTRACT

The synthesis and structural chemistry of four new divalent transition metal complexes of the fluorene ligands 4,5-diazaspirobifluorene (L1) and bis-9-biphenyl-4,5-diazafluorenyl peroxide (L2), $[Cu_3(L1)_4(NO_3)_6(H_2O)_2]\cdot 2CH_3CN$ (**1**), $[Cu(L1)(CH_3CO_2)_2(H_2O)]\cdot 2H_2O$ (**2**), $[Cd(L1)_2(NO_3)_2]\cdot DMF$ (**3**) (DMF = N,N-dimethylformamide) and $[Zn_2(L2)(\mu\text{-}Cl)_2Cl_2]_\infty$ (**4**) are described. Single-crystal X-ray diffraction analysis reveal that the four complexes exhibit various frameworks due to diverse coordination modes and different conformations of ligands L1 or L2, as well as nitrate, acetate or chloro counterions. L1 in complexes **1**, **2** and **3** present an asymmetric rigid bidentate ligand with two nitrogen atoms as the donor sites. Novel complex **4** was formed through complexation between conformationally bent shaped peroxide ligands and zinc(II) dichlorides that adopt a linear coordination geometry, which can also give rise to extended polymeric chains with a zigzag secondary structure.

© 2008 Elsevier Ltd. All rights reserved.

1. Introduction

Organocopper, cadmium and zinc complexes have been widely explored due to their rich structural chemistry [1] and importance in organic synthesis [2], and in polymerization chemistry [3], e.g., as well-defined catalysts for the copolymerization of CO_2 and epoxides [4]. The applications of these complexes must be based on the fundamental understanding of their components and structure chemistry. Hence it is of interest to study the coordination modes and structural features of the complexes. Several rigid multidentate oxygen-donor ligands have been used to design and synthesize the metal–organic complexes [5,6]. At the same time, many rigid bidentate nitrogen-donor ligands, such as 2,2′-bipyridine and its derivatives have also been used to prepare the metal organic materials [7]. However, the nitrogen-donor ligands with larger volumes are not easy to coordinate with the metal ions because of the large steric hindrance, and larger crystals suitable for single-crystal XRD analysis are difficult to obtain due to the low coordination strength of the nitrogen-donor organic ligands caused by the less negative charge on the nitrogen compared with the oxygen [8]. The coordination chemistry of the rigid ligand 4,5-diazaspirobifluorene has rarely been reported, except for a complex with silver ion [9]. In order to study the structure feature of the transition metal complex with the rigid and bulky ligands and the coordination code of the nitrogen-donor ligands, herein, we report the synthesis, characterization, and crystal structure of copper(II), cadmium(II) and zinc(II) complexes bearing bipyridine-based N,N-chelate fluorene ligands, 4,5-diazaspirobifluorene (L1) and bis-9-biphenyl-4,5-diazafluorenyl peroxide (L2). Remarkably, we have obtained the first zinc complex with peroxide so far, which may have potential applications in catalysis chemistry in the future.

2. Experimental

2.1. General

All of the reagents were commercially available and used as purchased. 9-Biphenyl-4,5-diazafluorenol and 4,5-diazaspirobifluorene was prepared according to the literature [10]. Interestingly, along with the expected 4,5-diazaspirobifluorene, bis-9-biphenyl-4,5-diazafluorenyl peroxide was unexpectedly formed as a by-product by the oxidation of 9-biphenyl-4,5-diazafluorenol with H_2SO_4/HOAc.

The elemental analysis was carried out with a Perkin–Elmer 240C elemental analyzer. ^1H NMR spectra were performed on a Bruker model Advance DRX 500 spectrometer in DMSO-d_6 and were referenced to TMS. The FT-IR spectra were recorded from KBr pellets over the range 4000–400 cm^{-1} with a Vector 22 spectrometer. The emission/excitation spectra were recorded with a

* Corresponding author. Tel.: +86 (25) 8368 6291; fax: +86 (25) 8331 7761.
E-mail address: jinz@nju.edu.cn (J. Zhu).

0277-5387/$ - see front matter © 2008 Elsevier Ltd. All rights reserved.
doi:10.1016/j.poly.2008.11.023

Hitachi 850 fluorescence spectrophotometer by using 1×10^{-4} M CH_3CN solution. Optical absorption spectra were collected on a Shimadzu 3100 spectrophotometer at room temperature. The absorbance was directly proportional to the concentration of complexes in the range from 1×10^{-4} M to 1×10^{-3} M.

2.2. Preparation of $[Cu_3(L)_4(NO_3)_6(H_2O)_2] \cdot 2CH_3CN$ (**1**)

Equimolar amounts of 4,5-diazaspirobifluorene (0.079 g, 0.25 mmol) and $Cu(NO_3)_2 \cdot 3H_2O$ (0.061 g, 0.25 mmol) were stirred together in CH_3CN (30 ml) at room temperature for 2 h. The resulting glaucous solution was filtered and concentrated to 10 ml. Blue block crystals of complex **1** suitable for X-ray diffraction were obtained in 69% yield by slow diffusion of diethyl ether into the filtrate for several days. At room temperature, crystals of complex **1** are unstable and decompose slowly into blue powder over the course of several days. *Anal.* Calc. for $C_{96}H_{62}Cu_3N_{16}O_{20}$ (1950.24): C, 59.12; H, 3.21; N, 11.49. Found: C, 59.36; H, 3.44; N, 11.23%. ^{1}H NMR (DMSO-d_6): δ = 8.09 (s, 4H, $H_{1,7}$), 7.44 (s, 4H, $H_{3,4}$), 7.17 (s, 4H, $H_{5,6}$), 6.68 (s, 2H, H_2), 2.07 (s, 3H, CH_3CN) (see Table 4 for the atom numbering arrangement). IR data (KBr, cm^{-1}): 3447 (s), 3053 (vw), 1578 (w), 1473 (m), 1447 (m), 1406 (s), 1384 (s), 1279 (s), 1169 (w), 1013 (w), 797 (w), 765 (m), 737 (m) cm^{-1}.

2.3. Preparation of $[Cu(L)(CH_3CO_2)_2(H_2O)] \cdot 2H_2O$ (**2**)

Similar procedures were performed to obtain blue crystals of complex **2**, except that $Cu(CH_3CO_2)_2 \cdot 4H_2O$ was used instead of $Cu(NO_3)_2 \cdot 4H_2O$, yield 55%. *Anal.* Calc. for $C_{27}H_{26}CuN_2O_7$ (554.04): C, 58.53; H, 4.73; N, 5.06. Found: C, 58.33; H, 4.77; N, 5.21%. ^{1}H NMR (DMSO-d_6): δ = 8.84 (s, 2H, H_1), 8.07 = (d, 2H, H_7, J = 7.31), 7.46 (t, 2H, H_3, J = 14.11), 7.33 (s, 2H, H_4), 7.18 (s, 4H, $H_{5,6}$), 6.70 (d, 2H, H_2, J = 7.00), 2.45 (s, 6H, CH_3CO_2) (see Table 4 for the atom numbering arrangement). IR data (KBr, cm^{-1}): 3423 (s), 2927 (w), 1606 (s), 1404 (s), 1339 (w), 1163 (w), 807 (w), 762 (m), 737 (m), 676 (w) cm^{-1}.

2.4. Preparation of $[Cd(L)_2(NO_3)_2] \cdot DMF$ (**3**)

A mixture with a stoichiometric 2:1 solution of ligand L1 (0.079 g, 0.50 mmol) and $Cd(NO_3)_2 \cdot 4H_2O$ (0.077 g, 0.25 mmol) in CH_3CN (30 ml) were stirred together for 2 h at room temperature. The clear solution thus obtained was evaporated under vacuum to form a white solid and recrystallized from CH_2Cl_2–DMF to give colorless crystals, yield 70%. *Anal.* Calc. for $C_{52}H_{42}CdN_8O_8$ (1019.34): C, 61.27; H, 4.15; N, 10.99. Found: C, 61.09; H, 3.99; N, 10.46%. ^{1}H NMR (DMSO-d_6): δ = 8.71 (d, 2H, H_1, J = 3.34), 8.07 = (d, 2H, H_7, J = 7.61), 7.96 (s, 1H, DMF–H), 7.45 (d, 2H, H_3, J = 7.49), 7.26 (t, 2H, H_4, J = 6.88), 7.16 (d, 4H, $H_{5,6}$, J = 7.08), 6.70 (d, 2H, H_2, J = 7.64), 2.89, 2.73 (s, 6H, DMF–CH_3) (see Table 4 for the atom numbering arrangement). IR data (KBr, cm^{-1}): 3449 (w), 3074 (w), 2922 (w), 1661 (s), 1582 (m), 1432 (s), 1408 (s), 1383 (s), 1298 (s), 1166 (w), 1089 (w), 1028 (w), 954 (w), 803 (w), 762 (m), 738 (m), 652 (w) cm^{-1}.

2.5. Preparation of $[Zn_2(L2)(\mu\text{-}Cl)_2Cl_2]_\infty$ (**4**)

A solution containing anhydrous zinc dichloride (0.071 g, 0.50 mmol) and bis-9-biphenyl-4,5-diazafluorenyl peroxide (0.168 g, 0.25 mmol) in CH_3CN (30 ml) was stirred for 2 h at room temperature. The resulting light brown solution was filtered, and then it was left open for slow evaporation of the solvent at room temperature. After standing for two weeks, small needle-like crystals of complex **4** were obtained, yield 50%. Because the growing rate of crystal is too fast, the structure quality of complex **4** is not high. Calc. for $C_{23}H_{15}Cl_2N_2OZn$ (471.64): C 58.57, H 3.21, N 5.94. Found: C, 58.44, H, 3.60, N, 5.99%. ^{1}H NMR (DMSO-d_6): δ = 8.35 (d, 2H, H_1, J = 4.00), 8.13 (d, 1H, H_7, J = 8.00), 7.57 (m, 1H, H_{10}, J = 30.00), 7.37 (t, 1H, H_6, J = 14.50), 7.19 (d, 2H, H_3, J = 7.50), 6.97 (t, 1H, H_4, J = 12.00), 6.85 (d, 1H, H_9, J = 7.00), 6.77 (t, 1H, H_8, J = 14.50), 6.54 (t, 2H, H_5, J = 15.00), 5.86 (d, 2H, H_2, J = 7.00) (see Table 4 for the atom numbering arrangement). IR (KBr pellet): ν = 3435 (s), 1600 (m), 1586 (m), 1473 (w), 1438 (w), 1411 (s), 1161 (m), 1008 (m), 814 (w), 769 (m), 707 (m), 557 (w) cm^{-1}.

2.6. Crystal structure determination and refinement

Suitable single crystals were selected for indexing and intensity data were measured with a Bruker Smart Apex CCD diffractometer with graphite-monochromated Mo Kα radiation (λ = 0.71073 Å) at 298 K. The raw data frames were integrated into SHELX-format reflection files and corrected using the SAINT program. Absorption corrections based on multiscans were obtained from the SADABS program. The structures were solved with direct methods and refined with full-matrix least-squares techniques using the SHELXS-97 and SHELXL-97 programs, respectively. Metal atoms in each complex were located from the *E*-maps, and other non-hydrogen atoms were located in successive difference Fourier syntheses, where they were refined with anisotropic thermal parameters on F^2. The hydrogen atoms of the ligands were generated theoretically onto the specific atoms and refined isotropically with fixed thermal factors. The hydrogen atoms of the water molecules were located using the different Fourier method and refined freely. Further details for structural analysis are summarized in Tables 1 and 2.

3. Results and discussion

3.1. Synthesis of metal complexes

Complexes **1**–**4** have been prepared in moderate to good yields (50–70%) by mixing acetonitrile solutions of ligand L1 or L2 with a salt of a divalent metal, M^{II} = Cu, Cd, Zn (Scheme 1). Crystal of **1** or **2** can be obtained through slow diffusion of diethyl ether into the reaction mixture. Otherwise, crystals for cadmium and zinc complex have grown tardily from the solution along with the volatilization of the solvent acetonitrile, respectively. From the crystal structure of complex **1**, we could deduce that ligand L forms a

Table 1
Crystallographic data for complex **1–3**.

	Complex **1**	Complex **2**	Complex **3**
Formula	$C_{96}H_{66}Cu_3N_{16}O_2$	$C_{27}H_{26}CuN_2O_7$	$C_{52}H_{42}CdN_8O_8$
Formula weight	1954.27	554.04	1019.34
Crystal system	triclinic	monoclinic	monoclinic
Space group	$P\bar{1}$	$P2_1/c$	$P2_1/c$
Crystal size (mm)	0.21 × 0.19 × 0.16	0.23 × 0.15 × 0.11	0.30 × 0.24 × 0.22
a (Å)	12.2642(18)	10.0594(13)	12.0376(7)
b (Å)	12.9474(19)	23.117(3)	15.9870(10)
c (Å)	15.649(2)	11.4744(15)	13.0900(8)
α (°)	86.468(2)	90	90
β (°)	75.369(2)	108.732(2)	113.4070(10)
γ (°)	63.026(2)	90	90
V (Å3)	2138.7(5)	2527.0(6)	2311.8(2)
Z	1	4	2
D_{calc} (g cm^{-3})	1.517	1.456	1.464
F(000)	1001	1148	1044
μ (mm^{-1})	0.825	0.914	0.538
Goodness-of-fit on F^2 (S)	1.013	1.049	1.040
Data collected	11693	13716	12500
Unique data (R_{int})	8247 (0.0313)	4947 (0.0532)	4527 (0.0515)
R_1, wR_2 [$I > 2\sigma(I)$]	0.0660, 0.1527	0.0624, 0.1228	0.0622, 0.1263
R_1, wR_2 [all data]	0.0898, 0.1597	0.0891, 0.1286	0.0856, 0.1311

Table 2
Crystallographic data for 9-biphenyl-4,5-diazafluorenol and complex **4**.

	9-Biphenyl-4,5-diazafluorenol	Complex **4**
Formula	$C_{46}H_{32}N_4O_2$	$C_{23}H_{15}ZnCl_2N_2O$
Formula weight	672.76	471.64
Crystal system	orthorhombic	monoclinic
Space group	$P2_12_12_1$	$P2_1/c$
Crystal size (mm)	0.25 × 0.15 × 0.11	0.20 × 0.13 × 0.11
a (Å)	8.0633(6)	8.8988(12)
b (Å)	15.4115(11)	18.567(3)
c (Å)	27.940(2)	12.2080(17)
α (°)	90	90
β (°)	90	94.785(2)
γ (°)	90	90
V (Å3)	3472.1(4)	2010.0(5)
Z	4	4
D_{calc} (g cm^{-3})	1.287	1.559
F(000)	1408	956
μ (mm^{-1})	0.080	1.505
Goodness-of-fit on F^2 (S)	1.000	0.756
Data collected	18394	10863
Unique data (R_{int})	3659 (0.0962)	3940 (0.1107)
R_1, wR_2 [$I > 2\sigma(I)$]	0.0350, 0.0618	0.0504, 0.0604
R_1, wR_2 [all data]	0.0529, 0.0664	0.1502, 0.0721

4:3 complex with copper(II) nitrate (Fig. 1), although the reaction was processed in a 1:1 ratio.

Reactions of ligand L1 with one equivalent of copper(II) acetate yielded complex **2** whose chemical analysis suggested a 1:1 ratio of ligand to metal salt. This result parallels the reaction of substituted 2,2′-bipyridine with copper(II) acetate which forms a simple four-coordinate 1:1 complex [11]. In contrast, crystals from a mixture of ligand L1 and cadmium(II) nitrate with a 2:1 ratio in DMF/CH_2Cl_2 were shown by X-ray crystallography to be a DMF solvate.

The addition of ligand L2 in a 1:2 ratio to a acetonitrile solution of $ZnCl_2$ after two weeks, accompanied with slow evaporation of the solvent at room temperature, results in small needle-like crystals of complex **4**.

3.2. X-ray crystallography

Single crystals suitable for X-ray analysis could be obtained for all five compounds in this study. The solved crystal structures are shown in Figs. 1, 3, 5, 6 and 9, and the selected bond lengths and angles are collected in Table 3.

3.2.1. $[Cu_3(L1)_4(NO_3)_6(H_2O)_2]\cdot 2CH_3CN$ (**1**)

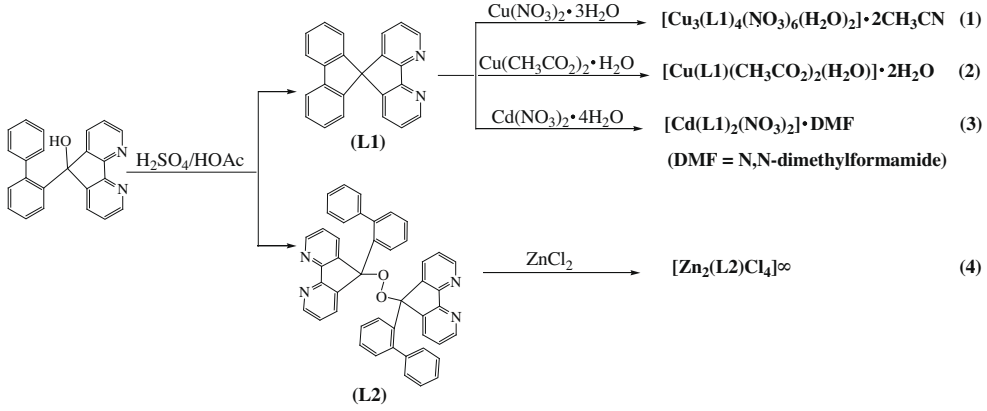
Single-crystal X-ray study reveals that the asymmetric unit of complex **1** consists of three crystallographically independent molecules. Thus, the structure of $[Cu_3(L1)_4(NO_3)_6(H_2O)_2]\cdot 2CH_3CN$ is best represented by the formula $[Cu(L1)_2(H_2O)_2]\cdot[Cu(L1)(NO_3)_3]_2\cdot 2CH_3CN$, and for clarity, of two molecules with identical structures only one is shown in Fig. 1. From crystal structure of complex **1** we can see that the coordination geometry of Cu1 center is unusual in that the elongated Jahn–Teller axis of the molecule lies along the N–Cu–N vector [Cu1–N2 = 2.631(2) Å] and not in the O–Cu–O axis [Cu1–O1 = 2.002(3) Å], which is occupied by water molecules. To our knowledge, this is one of only two examples of $N_2O_2N'_2$ coordination to a Cu(II) center with two water molecules bound *trans* in the equatorial plane and the nitrogen atoms of the chelates directed along the *J–T* axis. [12] This $N_2X_2N'_2$ geometry has been observed in other Cu(II) complexes with the 4,5-diazafluorene template and other anions such as Cl^-, Br^- or NO_3^- [12,13], while complexes with transition metals other than Cu(II) (e.g., Re(I), [14] Co(II) [15]) typically exhibit a more symmetrical coordination.

On the other hand, the environment of Cu2 center is square pyramidal. The basal plane is built by a nitrogen atom from the ligand L1 and three oxygen atoms of three nitrate groups, whereas the apical position is occupied by the other nitrogen atom of the bidentate ligand L1. Main bond distances and angles for non-hydrogen atoms are listed in Table 3. Meanwhile, the structure analysis indicates that biphenyl and 2,2′-bipyridine units in two kinds of coordinated ligand L1 are both perpendicularly cross-linked by a carbon atom. The dihedral angles between the mean planes of the two units are 88.6° (L1 coordinated to Cu1) and 91.5° (L1 coordinated to Cu2), which are very similar to that in the crystal structure of the free ligand L1 we have reported previously [16].

Interestingly, as can be seen from Fig. 2, a one-dimensional supramolecular chain is formed by intermolecular hydrogen bonding involving the water molecules coordinated to the copper center which chelated by two bidentate ligands L1 and the nitrate oxygen atoms coordinated to the other copper center (Table 4). Undoubtedly, these hydrogen bonds contribute to the stability of the whole crystal structure.

3.2.2. $[Cu(L1)(CH_3CO_2)_2(H_2O)]\cdot 2H_2O$ (**2**)

Copper(II) acetate forms a variety of structures with unsubstituted 2,2′-bipyridine. The formation of multinuclear systems containing two or three copper ions [17–19], polymers [20] and a mononuclear cation [21] $[Cu(bipy)_2(acetate)]^+$ are facilitated by the possibility of acetate either acting as a bidentate ligand, or using one oxygen atom to bridge two metal centers. To determine the structure feature of the complex formed by 2,2′-bipyridine-based ligand L1 and copper(II) acetate, complex **2** was synthesized



Scheme 1. Synthetic routes of the ligands L1, L2 and complexes **1**–**4**.

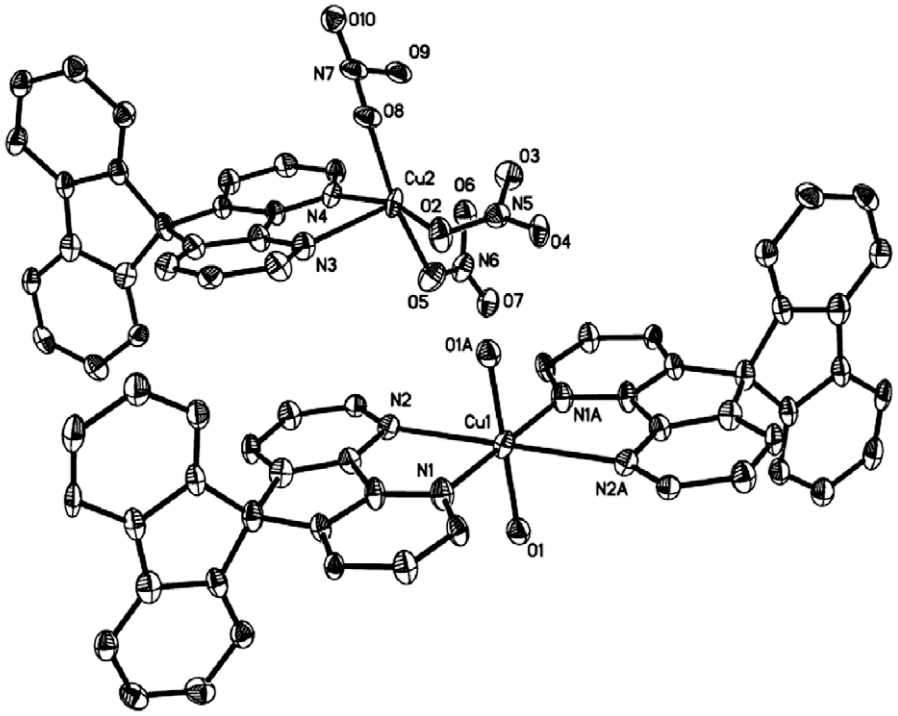


Fig. 1. X-ray single crystal structure of complex **1** (thermal ellipsoids at 30% probability).

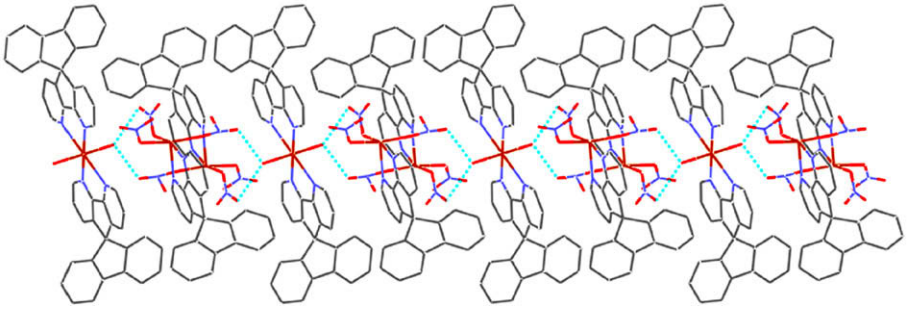


Fig. 2. 1D linear chain of complex **1** via the intermolecular hydrogen bonding, dashed lines indicate the intermolecular hydrogen bonds.

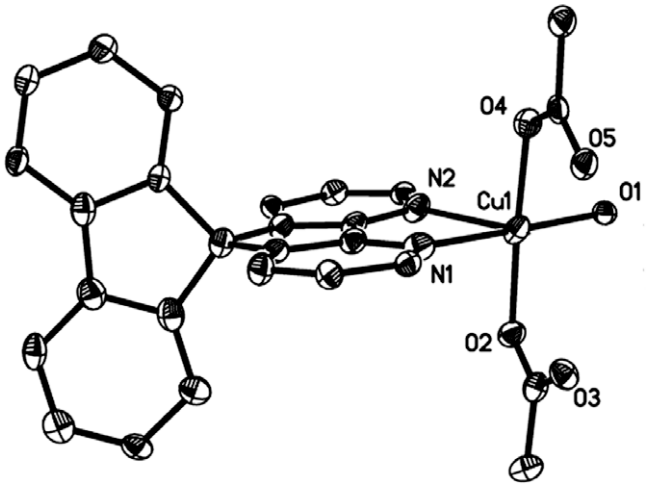


Fig. 3. X-ray single crystal structure of complex **2** (thermal ellipsoids at 30% probability).

in our case, which was characterized by X-ray crystallography. The molecular structure is shown in Fig. 3, which is different from the mononuclear copper(II) complexes mentioned above. The crystal structure of **2** consists of mononuclear units in which the copper(II) center surrounding is square pyramidal. A nitrogen atom (N2) from the bidentate ligand L1 is in the apical position. Two oxygen atoms (O2 and O4) from the monodentate acetate groups, one oxygen atoms (O1) from a water molecule and the other nitrogen atom of ligand L1 (N1) build the basal plane. The Cu–N bond distances are similar to those observed in the foregoing mononuclear five-coordinate molecular structure of complex **1**. However, the Cu–O (water oxygen atom) [1.961(3) Å] is slight shorter than the one [2.002(3) Å] observed in the foregoing another six-coordinate molecular structure of complex **1**. N1, O1, O2, and O4 atoms fall on a plane: the largest deviation from the mean plane is −0.0273 Å for O1. The copper(II) ion is 0.032(3) Å out of this plane. The value of the axial copper-nitrogen distance is 2.489(3) Å, which is much longer than the observed one [2.037(3) Å] in the quadrilateral plane.

In **2** there are no π–π aromatic interactions between the biphenyl or bipyridyl rings, Fig. 4, but there are several sets of intermo-

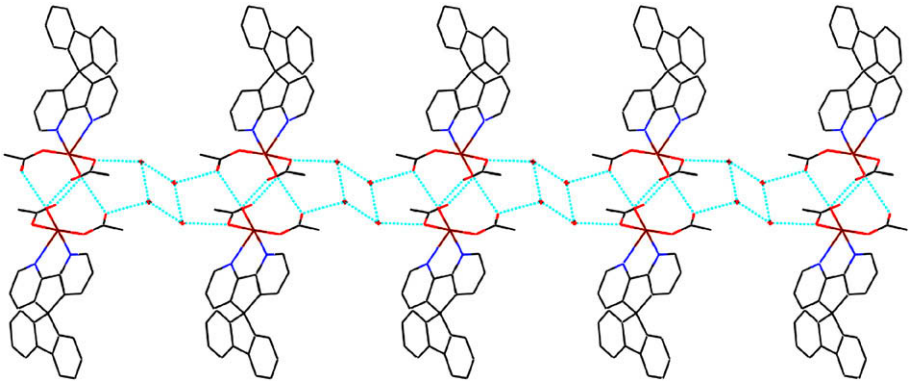


Fig. 4. Perspective view of the one-dimensional chain of complex **2**, dashed lines indicate the weak interaction and the intermolecular hydrogen bonds.

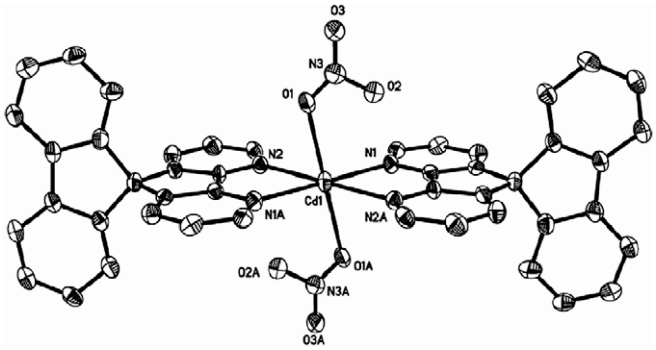


Fig. 5. Molecular structure of complex **3**. Thermal ellipsoids are at the 30% probability level.

lecular hydrogen bonding (see Table 4) between the waters of crystallization and the coordinated acetic groups which link the adjacent molecules into an infinite one-dimensional supramolecular chain (Fig. 4).

3.2.3. $[Cd(L1)_2(NO_3)_2] \cdot DMF$ (**3**)

The crystal structure of complex **3** unambiguously confirms the $[Cd(L1)_2]$ stoichiometry as well as the bidentate nature of the ligand L1 (Fig. 5). The cadmium atom lies on a crystallographic inversion center. N_4O_2 coordination polyhedron around the Cd(II) center is Jahn–Teller distorted octahedron. Four N atoms from the two ligands L1 coordinate to the Cd(II) center in the equatorial plane, wherein, for each ligand moiety, one Cd–N distance is slightly longer than the other [2.447(4) and 2.329(3) Å]. Two nitrate counterions occupy the apical position, d(Cd–O) = 2.411(5) Å. The bite angle of the ligand L1 [77.14°] indicates that there is a certain strain in the six-membered chelate ring. According to the literatures, this is the first example of $N_2O_2N'_2$ coordination to a Cd(II) center with four nitrogens of the chelates bound in the equatorial plane and two *trans* nitrates directed along the *J–T* axis. [22,23] Similar $N_2O_2N'_2$ geometry has been observed in other Cd(II) complex with the 4,5-diazafluorene template and anions NO_3^-, while it typically exhibit a more symmetrical coordination by adopting *cis* structures for two nitrate anions and two bidentate ligands (e.g., 4′,5′-diaza-9′-(4,5-bis(ethylthio)-1,3-dithiole-2-ylidene)-fluorene) [23].

3.2.4. $[Zn_2(L2)(\mu\text{-}Cl)_2Cl_2]_\infty$ (**4**)

A section of the one-dimensional polymer $[Zn_2(L2)(\mu\text{-}Cl)_2Cl_2]_\infty$ is illustrated in Fig. 6; selected intramolecular distances and angles are presented in Table 3. The asymmetric unit contains only one-half of the molecules, the remainder being generated by a center of symmetry located on the O–O bond. The structure features of the peroxide group in **4** are similar to those of ap-9-(*o*-isopropylphenyl)-9-fluorenyl peroxide. [24] They include a C–O–O–C dihedral angle of 180°, and C–O and O–O distances of 1.433(4) and 1.473(5) Å, respectively. One phenyl ring of the biphenyl group is nearly perpendicular to their respective fluorenyl rings [79.7°], and the other is parallel to the fluorenyl ring [21.3°]. Meanwhile, the symmetry requires the two fluorene-ring planes connected by the O–O bond to be anti-parallel, which is also the case for the corresponding four phenyl-ring planes. In the similar fluorene

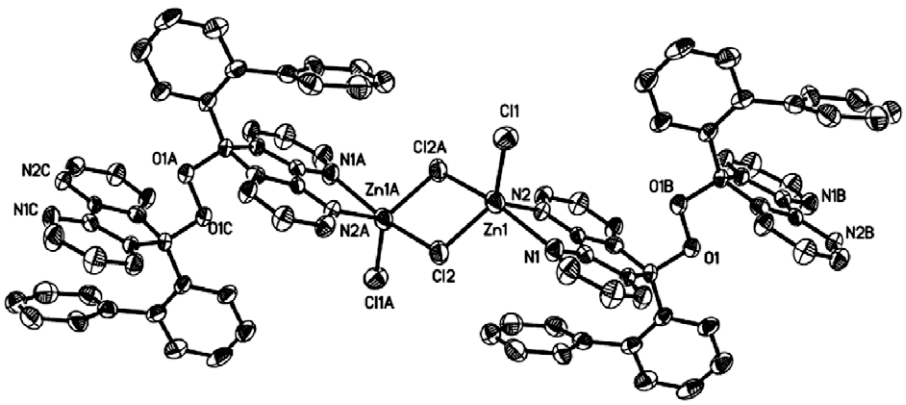


Fig. 6. View of a selected unit of the chain polymer **4** (thermal ellipsoids at 30% probability).

Table 3
Selected bond lengths (Å) and angles for complexes **1**–**4**.

Complex ***1***			
Cu1–O1	2.002(3)	Cu2–O5	1.916(3)
Cu1–N1	1.983(3)	Cu2–O8	2.008(3)
Cu1–N2	2.631(2)	Cu2–N4	2.037(3)
Cu2–O2	2.070(3)	Cu2–N3	2.348(4)
O2–Cu2–N4	161.5(1)	O2–Cu2–O5	82.57(2)
O2–Cu2–N3	80.92(1)	O8–Cu2–N3	86.20(1)
O1–Cu1–N1	88.86(2)	O8–Cu2–N4	91.54(1)
O8–Cu2–O5	171.0(2)		
Complex ***2***			
Cu1–O1	1.962(3)	Cu1–N1	2.037(3)
Cu1–O2	1.948(3)	Cu1–N2	2.489(3)
Cu1–O4	1.936(3)		
O1–Cu1–O2	88.41(1)	O2–Cu1–O4	177.12(1)
O1–Cu1–O4	89.11(1)	O2–Cu1–N1	91.74(1)
O1–Cu1–N1	178.3(1)		
Complex ***3***			
Cd1–N1	2.433(3)	Cd1–O1	2.411(5)
Cd1–N2	2.332(3)		
O1–Cd1–N1	103.4(2)	N1–Cd1–N2	102.7(1)
O1–Cd1–N2	84.10(1)	O1–Cd1–N1^{ii}	76.75(1)
Complex ***4***			
Zn1–N2	2.075(3)	Zn1–N1	2.447(4)
Zn1–Cl1	2.185(1)	Zn1–Cl2^{iii}	2.718(1)
Zn1–Cl2	2.233(1)	O1–O1^{iv}	1.473(5)
N2–Zn1–Cl1	113.9(1)	N2–Zn1–Cl2	124.75(1)
Cl2–Zn1–Cl1	121.2(5)	N2–Zn1–N1	78.78(1)
N1–Zn1–Cl1	96.26(10)	N1–Zn1–Cl2	91.41(1)
N2–Zn1–Cl2^{iii}	88.23(1)	Cl1–Zn1–Cl2^{iii}	99.99(5)
Cl2–Zn1–Cl2^{iii}	86.14(5)	N1–Zn1–Cl2^{iii}	162.3(1)
C11–O1–O1^{iv}	104.7(3)		

Symmetry codes: i, $-x$, $-y+2$, $-z+1$; ii, $-x+1$, $-y+1$, $-z+2$; iii, $-x+1$, $-y$, $-z+2$; iv, $-x$, $-y$, $-z+1$.

Table 4
Hydrogen bonding geometries for complexes **1** and **2** (Å and °).

D–H···A	H···A	D···A	D–H···A
Complexe ***1***			
O(1)-H(1C)···O(4)^{i}	2.10(6)	3.010(5)	157(5)
O(1)-H(1C)···N(5)^{i}	2.62(6)	3.571(5)	171(4)
O(1)-H(1D)···O(10)^{ii}	1.83(6)	2.751(4)	160(5)
Complexe ***2***			
O(1)-H(1A)···O(3)^{iii}	1.69(5)	2.637(4)	173(4)
O(6)-H(6A)···O(7)^{iii}	2.08(6)	2.820(5)	157(5)
O(1)-H(1B)···O(5)^{iii}	1.90(6)	2.689(4)	157(5)
O(7)-H(7A)···O(6)^{iv}	2.15(6)	2.903(5)	175(6)
O(6)-H(6B)···O(2)	2.29(6)	2.959(4)	137(5)

Symmetry codes: i, $-x$, $-y+2$, $-z+1$; ii, $x-1$, y, z; iii, $-x+1$, $-y+1$, $-z+1$; iv, x, y, $z-1$.

peroxide mentioned above [24], there only exists the perpendicular phenyl ring.

In complex **4**, zinc(II) centers are linked by bis-9-biphenyl-4,5-diazafluorenyl peroxide ligands to form an infinite zigzag chain. Terminal and bridged chloro groups complete the distorted trigonal–bipyramidal coordination around each metal ion. The coordination geometry of **4** is novel, in which one nitrogen atoms (N2, from the ligand L2) and two chloride ions (Cl1, Cl2) are in the basal plane, another nitrogen atom of the ligand (N1) and a chloride ion Cl2^{i} from the neighboring molecular unit occupy the axial position [symmetry code i: $1-x$, $2-y$, $-z$]. The distortion of the trigonal-bipyramid is indicated by the fact that the basal donor atoms not planar but deviate by as much as 0.0176 Å from their least-squares plane, and by the angle of N1–Zn1–Cl2^{i} [162.3(1)°]. As usual in the case of zinc(II) compounds, the axial Zn–Cl distance [2.718(1) Å] is much longer than the ones in the basal plane [2.233(1) and 2.185(1) Å].

An additional structural feature of interest is the involvement of four-membered Zn_2Cl_2 ring. The four-membered ring is coplanar completely with four atoms Zn1, Cl2, Zn1^{i} and Cl2^{i}. The Zn–Zn distance in the coordination dimmer is 3.630 Å, which is comparable with the Zn–Zn distance of 3.620 Å in the reported $[ZnCl_2(\mu\text{-bipy})]_\infty$ (bipy = 4,4′-bipyridine) polymer [1a].

Because of the flexibility of the ligand L2, the geometry arrangement between the biphenyl and 2,2′-bipyridine units in complex **4** differentiates markedly from that of the ligand L1. The most interesting characteristic is that one of the phenyl ring is approximately paralleled to the 2,2′-bipyridyl ring.

The role of π–π stacking interaction in the stability of structures in metal–organic coordination compounds has been a topic of much interest. [25,26] In the present complex, π–π interaction involving the 9-biphenyl-4,5-diazafluorenyl peroxide is also observed (Fig. 7). The centroid–centroid distance (d) between the phenyl and the bipyridyl rings is 3.495 Å and their interplanar angle (θ) is 20.9°. It should be noted that the intramolecular π–π interactions play an important role for the structural stability.

All efforts to obtain the crystal structure of the ligand L2 were not successful so far. However, we have determined the structure of the precursor of the ligands L1 and L2, 9-biphenyl-4,5-diazafluorenol. As it is shown from Fig. 8, in each independent fluorenol molecule there is an intramolecular π–π interaction which is extremely identical with the π-π interaction observed in complex **4.** So

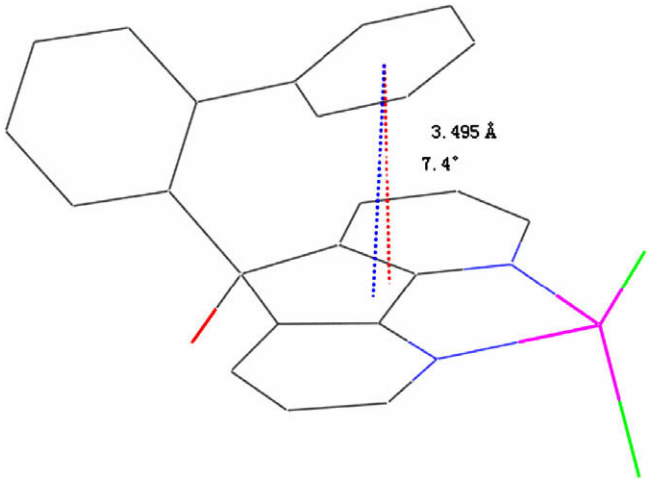


Fig. 8. Intramolecular π–π stacking interaction between the phenyl and fluorenyl rings in the complex **4**.

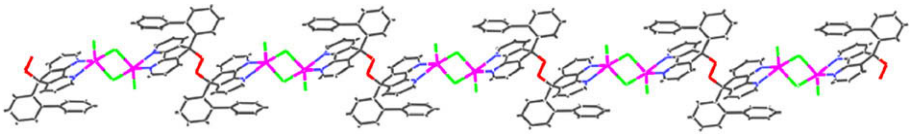


Fig. 7. Perspective view of the one-dimensional polymeric chain of complex **4**.

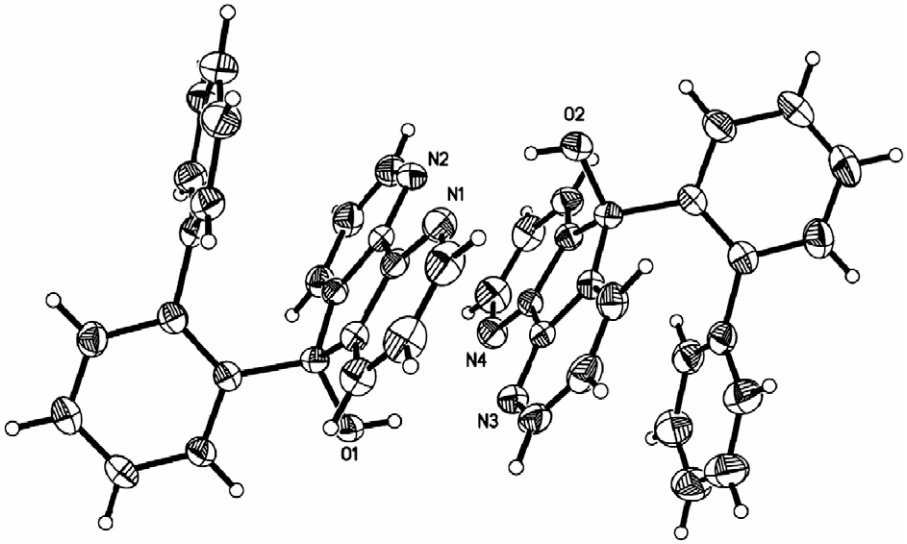
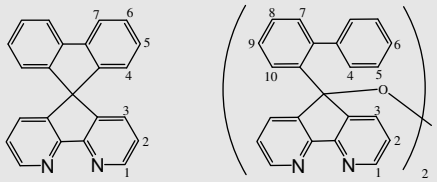


Fig. 9. X-ray single crystal structure of 9-biphenyl-4,5-diazafluorenol (30% probability thermal ellipsoids): showing the parallel stacking of the intermolecular fluorene domains or the intramolecular fluorene and phenyl rings.

Table 5
^{1}H NMR spectroscopic data for complexes containing L1 or L2.



L1 L2

	Hydrogen					
1	8.09 (1,7-H)		7.44 (3,4-H)	7.17 (5,6-H)		6.68 (2-H)
2	8.84 (1-H)	8.07 (7-H)	7.46 (3-H)	7.33 (4-H)	7.18 (5,6-H)	6.70 (2-H)
3	8.71 (1-H)	8.07 (7-H)	7.45 (3-H)	7.26 (4-H)	7.16 (5,6-H)	6.70 (2-H)
4	8.35 (1-H)		8.13 (7-H)	7.57 (10-H)	7.37 (6-H)	7.19 (3-H)
	6.97 (4-H)		6.85 (9-H)	6.77 (8-H)	6.54 (5-H)	5.86 (2-H)

it can be concluded that, when the biphenyl group is not fully fixed to the 9-position carbon atom appeared in the ligand L1, the conformation of one phenyl ring perpendicular to the fluorenyl ring and the other parallel is the most stable. Meanwhile, there also exists intermolecular π–π interaction for the fluorenyl rings between two adjacent 9-biphenyl-4,5-diazafluorenol in the unit cell, which contributes to the stability of the whole crystal structure.

3.3. ^{1}H NMR spectroscopy

All ^{1}H NMR spectra were measured in DMSO-d_6 for consistency. The ^{1}H NMR chemical shifts for complexes **1**–**4** are shown in Table 5.

From the ^{1}H NMR spectra of complexes **1**–**4** we can see that, different metal ions or coordination geometry have less affect on the chemical shift of the ligands in the complex except complex **1**. Both complex **2** and **3** exhibit six sets of aromatic hydrogen between 6.70 and 8.84 ppm. Only obvious difference for the protons at the 1 ortho-position of nitrogen-donor atoms can be found. But for complex **1**, due to the existence of two kinds of coordination geometry between ligand L1 and copper center, and the environment of some aromatic hydrogen have mixed a lot and shown only four

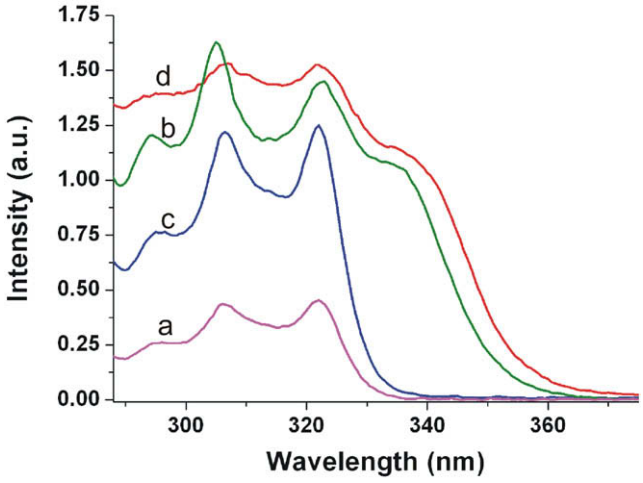


Fig. 10. Absorption spectra of L1 (a) and complex**1** (b), **2** (c), **3** (d) at 298 K in CH_3CN.

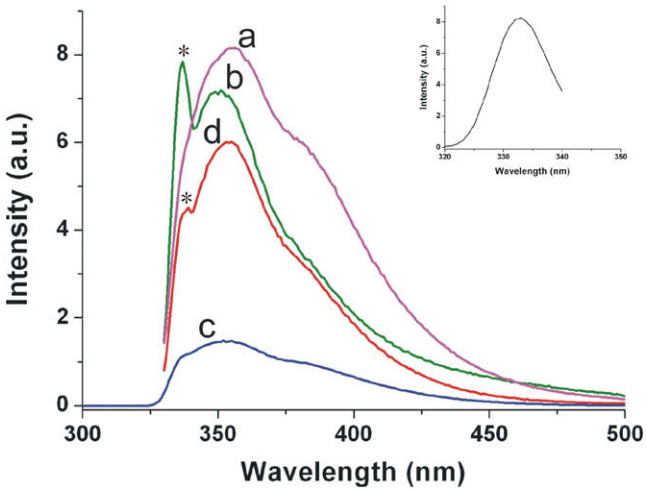


Fig. 11. Emission spectra of the free ligand L1 (a) and complex **1** (b), **2** (c), **3** (d) in CH_3CN solution at room temperature, excited at 333 nm (the peaks with a star are assigned to the scattering of the excitation; *inset:* excitation spectrum of the fluorescent species).

types of chemical shifts in the ^1H NMR spectra. Just like the proton environment of ligand L2 themselves, the ^1H NMR spectra of complex **4** shows ten sets of different types of aromatic hydrogen.

3.4. UV–Vis and fluorescent spectra of complexes *1*–*3*

The UV–Vis spectral data of the ligand L1 and the three complexes in acetonitrile were measured. The dominant vibronic absorption peaks in complexes **1**–**3** at ~294, ~305, and ~322 nm can be ascribed to the ligand-centered (LC) π–π^* transitions. These spectral assignments were made on the basis of their spectral similarities with those of free ligand L1 (see Fig. 10) and a silver(I) complex with L1 [9]. Furthermore, for complex **1** and **3**, the Cu(II) and Cd(II) d–d transitions are observed as a single broad feature centered at 334 nm, consistent with a 6-coordinate mixed N, O coordination environment. [27]

In acetonitrile (CH_3CN), both the ligand L1 and corresponding metal complexes are emissive; fluorescent emission at UV wavelength (354 nm) of the free ligand L1 can be attributed to the ligand-centered π^*–π relaxation (Fig. 11). Ligand-based emission bands (~354 nm) are preserved in the corresponding Cu or Cd complexes, but the Ag complex reported previously is intrinsically nonluminescent throughout 350–800 nm in any organic solvent [9].

Acknowledgements

J.Z. acknowledges support from the National Basic Research Program of China (2007CB925103), the National Natural Science Foundation of China (No. 20604011) and the program for New Century Excellent Talents in University (NCET-06-0451).

Appendix A. Supplementary data

CCDC 671903, 668544, 668545, 668546, and 690767 contain the supplementary crystallographic data for **1**, **2**, **3**, **4** and 9-biphenyl-4,5-diazafluorenol. These data can be obtained free of charge via http://www.ccdc.cam.ac.uk/conts/retrieving.html, or from the Cambridge Crystallographic Data Centre, 12 Union Road, Cambridge CB2 1EZ, UK; fax: (+44) 1223-336-033; or e-mail: deposit@ccdc.cam.ac.uk. Supplementary data associated with this article can be found, in the online version, at doi:10.1016/j.poly.2008.11.023.

References

[1] (a) C.H. Hu, U. Englert, Angew. Chem., Int. Ed. 44 (2005) 2281;
(b) S.N. Wang, J.F. Bai, Y.Z. Li, M. Scheer, X.Z. You, Cryst. Eng. Commun. 9 (2007) 228;
(c) M. Kontturi, E. Laurila, R. Mattsson, S. Peraniemi, J.J. Vepsalainen, M. Ahlgren, Inorg. Chem. 44 (2002) 2400;
(d) K. Hanson, N. Calin, D. Bugaris, M. Scancella, S.C. Sevov, J. Am. Chem. Soc. 126 (2004) 10502;
(e) Z .Y. Du, X.L. Li, Q.Y. Liu, J.G. Mao, Cryst. Growth Des. 7 (2007) 1501.
[2] (a) T. Marino, N. Russo, M. Toscano, J. Am. Chem. Soc. 127 (2005) 4242;
(b) J.S. Casas, E.E. Castellano, M.D. Couce, J. Ellena, A. Sanchez, J. Sordo, C. Taboada, J. Inorg. Biochem. 100 (2006) 124.
[3] Z.Y. Chai, C. Zheng, Z.X. Wang, Organometallics 27 (2008) 1626.
[4] (a) Y.L. Xiao, Z. Wang, K. Ding, Chem. Eur. J. 11 (2005) 3668;
(b) M. Walther, K. Wermann, M. Lutsche, W. Gunther, H. Gorls, E. Anders. J. Org. Chem. 71 (2006) 1399;
(c) I. Kim, S.M. Kim, C.S. Ha, D.W. Park, Macromol. Rapid Commun. 25 (2004) 888.
[5] J. Kim, B. Chen, T.M. Reineke, H. Li, M. Eddaoudi, D.B. Moler, M. O'Keeffe, O.M. Yaghi, J. Am. Chem. Soc. 423 (2003) 705.
[6] O.M. Yaghi, M. O'Keefe, N.W. Ockwig, H.K. Chae, M. Eddaoudi, J. Kim, Nature 423 (2003) 705.
[7] N.C. Fletcher, T.C. Robinson, A. Behrendt, J.C. Jeffery, Z.R. Reeves, M.D. Ward, J. Chem. Soc., Dalton Trans. (1999) 2999.
[8] H.R. Khavasi, A. Abedi, V. Amani, B. Notash, N. Safari, Polyhedron 27 (2008) 1848.
[9] C.C. Wang, C.H. Yang, S.M. Tseng, S.Y. Lin, T.Y. Wu, M.R. Fuh, G.H. Lee, K.T. Wong, R.T. Chen, Y.M. Cheng, P.T. Chou, Inorg. Chem. 43 (2004) 4781.
[10] K.T. Wong, R.T. Chen, FC. Fang, C.C. Wu, Y.T. Lin, Org. Lett. 7 (2005) 1979.
[11] C.R. Rice, S. Onions, N. Vidal, J.D. Wallis, M.C. Senna, M. Pilkington, H. Stoeckli-Evans, Eur. J. Inorg. Chem. (2002) 1985.
[12] S. Menon, M.V. Rajasekharan, Polyhedron 17 (1998) 2463.
[13] B.J. Kraft, H.J. Eppley, J.C. Huffman, J.M. Zaleski, J. Am. Chem. Soc. 124 (2002) 272.
[14] V.W.W. Yam, K.Z. Wang, C.R. Wang, Y. Yang, K.K. Cheung, Organometallics 17 (1998) 2440.
[15] X.H. Shi, X.Z. You, C. Li, R.G. Xiong, K.B. Yu, Transition Met. Chem. 20 (1995) 191.
[16] M. Hong, C. Teng, J. Zhu, Acta Crystallogr., Sect. E 63 (2007) o3304.
[17] G. Christou, S.P. Perlepes, E. Libby, K. Folting, J.C. Huffman, R.J. Webb, D.N. Hendrickson, Inorg. Chem. 29 (1990) 3657.
[18] G. Christou, S.P. Perlepes, K. Folting, J.C. Huffman, R.J. Webb, D.N. Hendrickson, J. Chem. Soc., Chem. Commun. (1990) 746.
[19] S. Meenakumari, S.K. Tiwary, A.R. Chakravarty, Inorg. Chem. 33 (1994) 2085.
[20] S.P. Perlepes, E. Libby, W.E. Streib, K. Folting, G. Christou, Polyhedron 11 (1992) 923.
[21] B.J. Hathaway, N. Ray, D. Kennedy, N.O. Brien, B. Murphy, Acta Crystallogr., Sect. B 36 (1980) 1371.
[22] P.F. Rodesiler, R.W. Turner, N.G. Charles, E.A.H. Griffith, E.L. Amma, Inorg. Chem. 23 (1984) 999.
[23] Q.Y. Zhu, Y. Zhang, J. Dai, X.F. Huan, Chin. J. Inorg. Chem. 22 (2006) 1170.
[24] P.D. Robinson, Y. Hou, C.Y. Meyers, Acta Crystallogr., Sect. C 55 (1999) 9900147.
[25] A. Dutta, S.K. Pati, J. Chem. Phys. 118 (2003) 8420.
[26] Y.B. Dong, P. Wang, J.P. Ma, X.X. Zhao, H.Y. Wang, B. Tang, R.Q. Huang, J. Am. Chem. Soc. 129 (2007) 4872.
[27] A.B.P. Lever, E.S. Dodsworth, in: E.I. Solomon, A.B.P. Lever (Eds.), Electrochemistry, Charge-Transfer Spectroscopy, and Electronic Structure, vol. 2, John Wiley and Sons, New York, 1999, p. 227.

Polyhedron 28 (2009) 453–456

Contents lists available at ScienceDirect

Polyhedron

journal homepage: www.elsevier.com/locate/poly

A mixed anionic lead(II) N-Oxide coordination polymer containing nitrato and benzoate ligands

Rupam Sarma, Jubaraj B. Baruah *

Department of Chemistry, Indian Institute of Technology Guwahati, Guwahati, 781 039 Assam, India

ARTICLE INFO

Article history:
Received 23 September 2008
Accepted 14 November 2008
Available online 26 December 2008

Keywords:
Coordination polymers
Nitrate binding
Lead benzoate
2,2'-Bipyridyl N-oxide
Crystal structure

ABSTRACT

The structures of two forms of a mixed anionic one-dimensional coordination polymers of lead(II) nitrate derived from benzoate and 2,2'-bipyridyl N-oxide are reported. The X-ray crystal structures show subtle differences in the two binding modes of nitrate in the coordination polymers obtained from two independent solvents. The solid state UV–Vis spectra show differences in the absorption pattern of the crystalline solids obtained from different solvents. The solid state UV–Vis spectra as well as the solution spectra are compared.

© 2008 Elsevier Ltd. All rights reserved.

1. Introduction

With the recent advancement in the area of inorganic supramolecular chemistry, there has been increasing interest in the studies on the sub-areas like supramolecular isomerism [1,2], topological isomerism [3], and structural isomerism [4]. Occurrence of such isomerism is dependent on various factors viz. reaction condition, temperature, solvents, etc. [5]. However only few reports are there that exemplify the effect of solvents on the formation of supramolecular isomers [6]. Although, a good number of reports are there regarding coordination polymers of lead [7–12] to our best of knowledge only a limited number of lead complexes show supramolecular isomerism [13]. Recently our group has shown that the nitro group orientation around a binuclear structure of cobalt (II) complex can lead to different supramolecular isomers [14]. With the objective of understanding the effect of different solvents on the orientation of the molecules in a superstructure we have studied the possibility of coordination isomerism in polymeric mixed anionic lead complex containing nitrate group as one of the ligands. Herein, we report the structures of two mixed anionic one-dimensional coordination polymers of lead(II) having composition $[Pb(Ben)(BPNO)(NO_3)]_n$; in which we have observed interesting solid state and solution properties occurring from slightly different orientation of the coordinating nitrate group.

2. Experimental

Solid state UV–Vis spectra were recorded with KBr pellets in a Perkin Elmer Lambda 750 UV–Vis spectrometer (UV–Vis resolution $\leqslant 0.17$ nm). Infrared spectra were recorded with a Perkin–Elmer FT-IR spectrometer in the range 4000–400 cm^{-1} (FT-IR resolution $\leqslant 0.5$ cm^{-1}). The X-ray crystallographic data were collected at 296 K with Mo Kα radiation ($\lambda = 0.71073$ A°) using a Bruker Nonius SMART CCD diffractometer equipped with graphite monochromator. The SMART software was used for data collection and also for indexing the reflections and determining the unit cell parameters; the collected data were integrated using SAINT software. The structures were solved by direct methods and refined by full-matrix least-squares calculations using SHELXTL software. All the non-H atoms were refined in the anisotropic approximation against F^2 of all reflections. The H-atoms, except those attached to N and O were placed at their calculated positions and refined in the isotropic approximation; those attached to heteroatoms (N, O) were located in the difference Fourier maps, and refined with isotropic displacement coefficients. The crystallographic parameters are given in Table 1.

2.1. Synthesis of bidentate-nitrato-$[Pb(Ben)(BPNO)(NO_3)]_n$ (**1**) and monodentate-nitrato-$[Pb(Ben)(BPNO)(NO_3)]_n$ (**2**)

For the synthesis of **1** sodium benzoate (2 mmol, 0.288 g) was dissolved in methanol (10 mL). After stirring for about 30 min lead(II) nitrate (1 mmol, 0.331 g) and 2,2'-bipyridyl N-oxide (1 mmol, 0.188 g) was added and stirred for another 30 min. A white precipitate appeared. The precipitate was dissolved in a methanol:toluene mixture (2:1) (20 mL) by warming. The clear solution was

* Corresponding author. Tel.: +91 361 2582301; fax: +91 361 2690762.
E-mail address: juba@iitg.ernet.in (J.B. Baruah).

0277-5387/$ - see front matter © 2008 Elsevier Ltd. All rights reserved.
doi:10.1016/j.poly.2008.11.020

Table 1
Crystallographic parameters for complexes **1** and **2**.

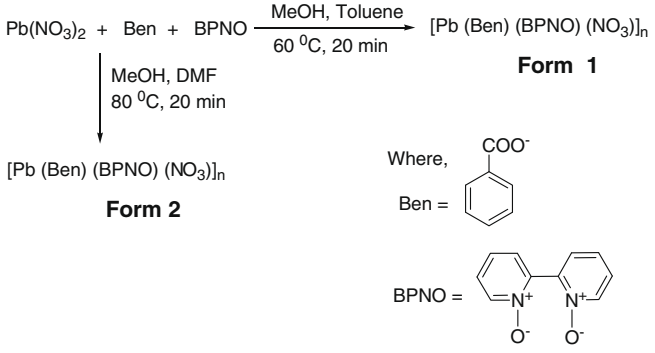
Compound No.	**1** (bidentate nitrato containing lead polymer)	**2** (monodentate nitrato containing lead polymer)
Formulae	$C_{17}H_{13}N_3O_7Pb$	$C_{17}H_{13}N_3O_7Pb$
Formula. wt.	578.49	578.49
Crystal system	monoclinic	monoclinic
Space group	*P2(1)/c*	*P2(1)/c*
a/Å	14.006(5)	14.0260(2)
b/Å	7.436(2)	7.43210(10)
c/Å	22.741(6)	22.7805(3)
α/°	90.00	90.00
β/°	127.870(14)	127.9430(10)
γ/°	90.00	90.00
V/Å^3	1869.7(10)	1872.74(5)
Z	4	4
D_{calc} (Mg m^{-3})	2.055	2.052
Absolute coefficient (mm^{-1})	9.069	9.054
F(000)	1096	1096
Total number of reflections	18138	25226
Reflections, $I > 2\sigma(I)$	4625	4675
Maximum 2θ (°)	28.40	28.39
Ranges (h, k, l)	$-18 \leqslant h \leqslant 18$ $-9 \leqslant k \leqslant 9$ $-30 \leqslant l \leqslant 29$	$-18 \leqslant h \leqslant 18$ $-9 \leqslant k \leqslant 9$ $-30 \leqslant l \leqslant 30$
Complete to 2θ (%)	98.7	99.7
Data/restraints/parameters	4625/0/272	4675/0/271
GOF (F^2)	1.007	1.063
R indices [$I > 2\sigma(I)$]	0.0277	0.0193
R indices (all data)	0.0468	0.0240

then kept for crystallization and good quality colorless crystals of **1** were obtained after 4 days. Isolated yield, 65%. IR (KBr, cm^{-1}): 1591 (m), 1536 (m), 1421 (m), 1384 (s), 1316 (m), 1210 (m), 848 (m). UV (methanol, λ_{max}) 225 nm, 265 nm (sh). *Anal.* Calc. for $C_{17}H_{13}N_3O_7Pb$: C, 35.29; H, 2.26. Found: C, 34.76; H, 2.02%.

From another identical reaction in dimethylformamide (10 mL), the white precipitate formed was dissolved in a mixed solvent of dimethylformamide (10 mL) and methanol (5 mL) followed by warming. Yellow colored crystals of **2** were obtained after a week. Isolated yield, 77%. IR (KBr, cm^{-1}): 1593 (m), 1537 (m), 1424 (m), 1384 (s), 1319 (m), 1208 (m), 847 (m). *Anal.* Calc.: C, 35.29; H, 2.26. Found C, 34.66; H, 2.11%. UV (methanol, λ_{max}) 230 nm, 265 nm (sh).

3. Results and discussion

The reaction between lead(II) nitrate with sodium benzoate in the presence of 2,2′-bipyridyl N-oxide (BPNO) leads to two forms of a mixed anionic coordination polymers (Scheme 1). The two forms of the polymer have differences in their physical properties but they have very closely related structures.



Scheme 1.

The reaction of lead(II) nitrate with sodium benzoate and BPNO in a mixed solvent containing methanol and toluene (2:1) leads to the coordination polymer **1** having composition [Pb(Ben)(BPNO)(-NO_3)]$_n$. Unlike this, the synthesis of **2** was performed using lead(II) nitrate with benzoate and BPNO in dimethylformamide. During both the syntheses the reaction mixtures were refluxed for few minutes, to dissolve the precipitate that appeared after addition of the BPNO ligand. The crystals of **1** were obtained as colorless thin needles whereas **2** crystallize as pale yellow blocks. Good quality crystals of both the forms were obtained within a week or so, which were analyzed by using single crystal X-ray diffraction technique, powder X-ray diffraction technique and also with other spectral analysis viz. UV–Vis spectroscopy and FT-IR spectroscopy.

The X-ray structural analysis of **1** reveals the formation of a mixed anionic one-dimensional coordination polymer. It is a well known fact that the lead complexes can have different co-ordination numbers varying from 2 to 10 [7–10]. Each of the lead(II) centers in coordination polymer **1** is nine coordinated. Four of these coordination are provided by the bridging N-oxide ligands, three by carboxylate and rest two are by a chelating nitrate anion. It crystallizes in the space group *P*2(1)/*c*. In the structure **1** Pb1–O5 distance is 2.721(9) Å and the Pb1–O6 distance is 2.923(4) Å. Some of the important bond angles are Pb1–O5–N3, 101.2(5)°; Pb1–O6–N3, 92.4(3)°; O5–N3–O6, 119.0(6)°. Structure of the coordination polymer is shown in Fig. 1b along with its asymmetric unit in Fig. 1a.

As shown in Fig. 2a, all the lead(II) centers in **2** are eight coordinated. Unlike **1** the nitrate group in **2** coordinates to the lead(II) center in a monodentate fashion. All other coordination remaining identical to **1**, the monodentate nitrate offers the metal node an eight coordinated geometry. However, the bond parameters of the nitrate group in the complexes are so similar that it is difficult to distinguish them with authority. In the coordination polymer 2 the Pb1–O5 distance is 2.683(7) Å and there is no coordinating bond between Pb1 and O6 (distance of separation is 2.935(3) Å) as shown by the software Mercury 1.4.2. The bond angles around the nitrate group of this form are also slightly different from those of **1**: Pb1–O5–N3, 102.7(4)°; Pb1–O6–N3, 92.0(2)°; O5–N3–O6,

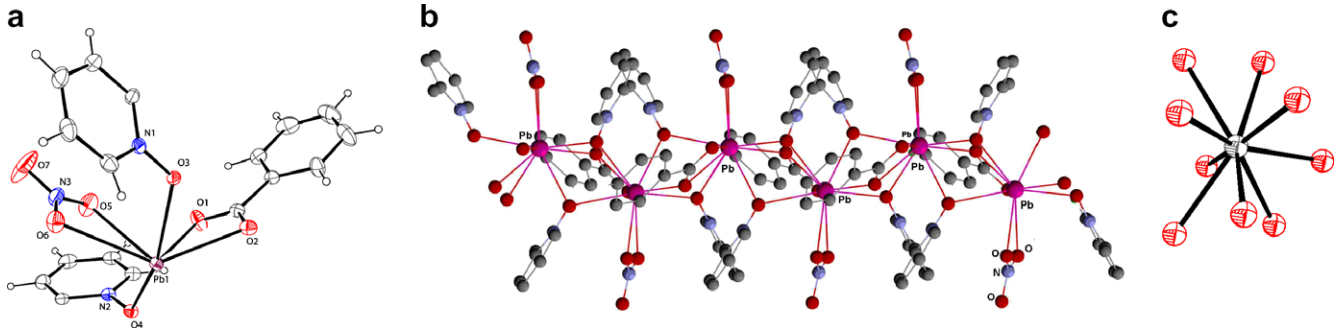


Fig. 1. (a) Smallest building block of **1;** (b) the polymeric structure of **1** showing chelating nitrates; and (c) the nine coordinated environment around lead.

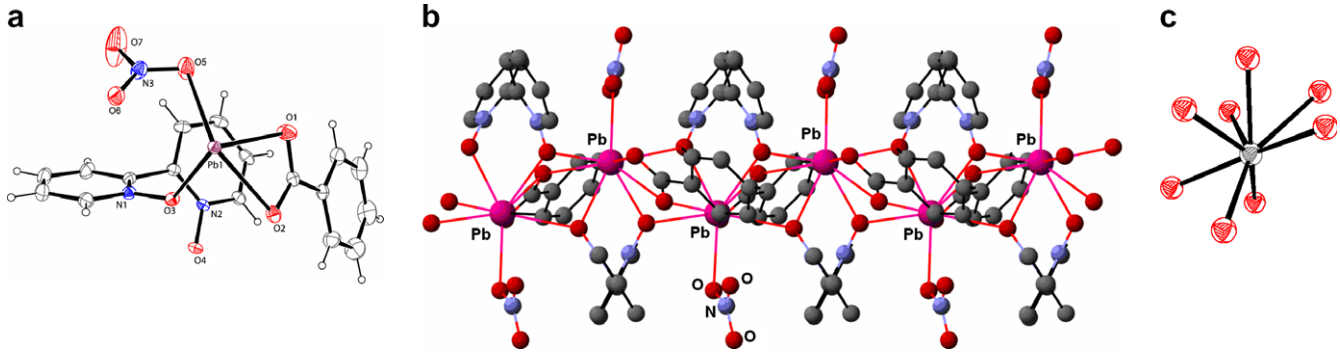


Fig. 2. (a) Smallest building block of **2;** (b) the polymeric structure of **2** showing mono-dentate nitrates; and (c) the eight coordinate geometry around lead.

118.0(4)°. The differences in the bond angles around the nitrate groups of two compounds namely O5–N3–O6 discern the difference in the co-ordination geometry.

To differentiate the coordination environment around the lead various lead-oxygen bond distances in the complexes are listed in Table 2.

The structure of the coordination polymer **2** is shown in Fig. 2b along with its asymmetric unit in Fig. 2a. The compounds have their characteristic IR absorptions at 1421–1424 cm^{-1} and 1316–1319 cm^{-1} due to the metal bound nitrate groups and at 1208–1210 cm^{-1} due to the N-oxide functionality of BPNO. The carbonyl frequency appears at 1591–1593 cm^{-1}. Benzoate ligand can have different binding modes, such as monodentate, bidentate, bridging while binding to lead ions [14,15,11,12,16], however in the present cases, each lead ion is associated with one chelating benzoate, which acts as bridge to anchor another lead ion to make a polymeric chain like structures. The polymeric chains have also two other bipyridine N-oxide bridges. The overall binding mode of benzoates in the complexes can be represented as oxo-bridged chelated carboxylate. Unfortunately, it is very difficult to differentiate the two forms of the polymers **1** and **2** from their FT-IR spectra.

Both the forms are found to crystallize in the same space group *P*2(1)/*c*. The unit cell differs slightly which is obvious as the two complexes differ slightly only in the binding mode of the nitrate ion and have identical composition. To check the bulk property of these forms, we have checked the powder X-ray diffraction pattern, which matches to the simulated one quite well (see Supplementary data). However, the powder X-ray diffraction patterns are also not found to be very informative as it also could not distinguish the two forms.

The colors of the crystals obtained for the two forms differ from one another to a considerable extent. The solid state UV–Vis spectra of both the isomers are shown in Fig. 3. It is clear from the spectra obtained that they are almost identical throughout the region of study except in the range 200–250 nm. Interestingly this region is known to be the region for $\pi \rightarrow \pi^*$ transition of the nitrate group [17]. The compound **1** absorbs at 221 nm while the compound **2** absorbs at 211 nm. This difference in the position of absorbance

Table 2
The lead–oxygen bond distances in the complexes.

Bonds	Bond length for **1** (Å)	Bond length for **2** (Å)
Pb1–O1	2.542(4)	2.545(3)
Pb1–O2	2.622(3)	2.623(2)
Pb1–O3	2.529(3)	2.545(19)
Pb1–O4	2.537(3)	2.534(18)
Pb1–O5	2.721(9)	2.683(7)
Pb1–O6	2.923(4)	2.935(3)

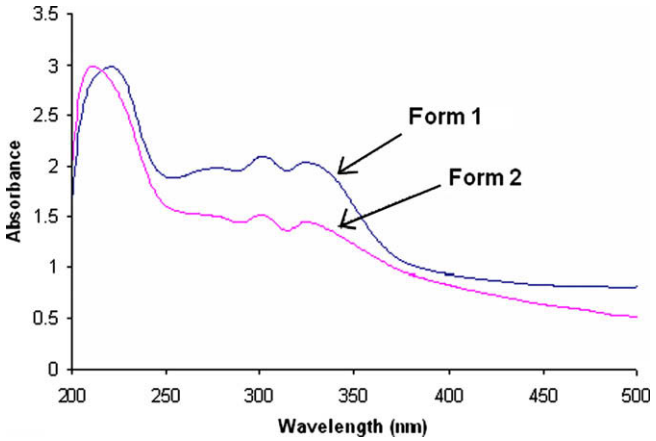


Fig. 3. Solid state UV–Vis spectra (KBr pallet) of **1** and **2**.

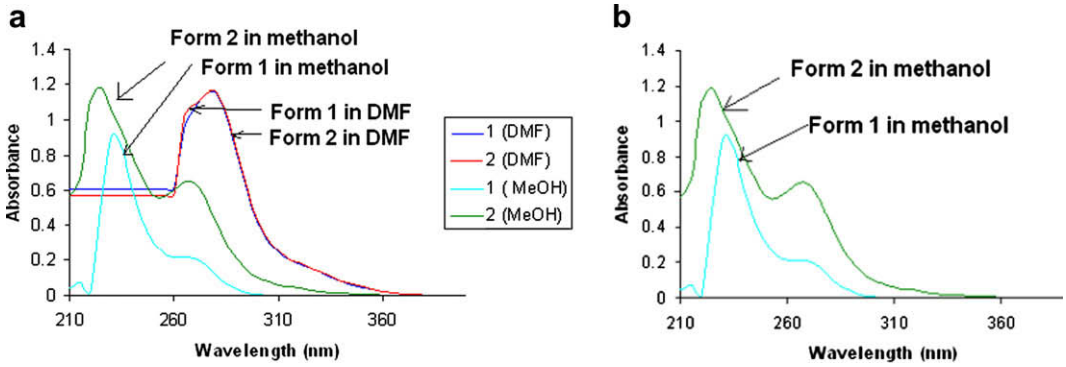


Fig. 4. UV spectra of **1** and **2** in two different solvents: (a) methanol and dimethylformamide and (b) UV–Vis spectra of the **1** and **2** in methanol.

for **1** and **2** in the solid state is significant enough to distinguish them as different forms.

We have also checked the UV–Vis spectral behaviors of the two forms in solution. Interesting solvent dependence of the UV–Vis spectra of the forms is observed as shown in Fig. 4. It is clear from the spectra that the two forms have distinct absorptions in two different solvents. In dimethylformamide both the forms of the compound absorb at 275 nm. However, in methanol the two forms of the compound absorb at different wavelengths, form **1** has absorption at 230 nm with a shoulder at 265 nm and the form **2** has absorption at 225 nm with the shoulder at 265 nm. The bands at 230 nm in the case of **1** and 225 nm in the case of **2** arises due to the $\pi \rightarrow \pi^*$ transition of the nitrate group [18]. The bands at 265 nm are due to the ligand to metal charge transfer transitions, evident from the high values of the molar extinction coefficients (13 000 L mol^{-1} cm^{-1}–19 000 L mol^{-1} cm^{-1}). From these observations, it can be inferred that the two forms adopts two different solvated forms in methanol; whereas in dimethylformamide it preferentially transforms to one state. The spectrum in methanol (Fig. 4b) clearly shows that the two independent solvated intermediates species may be formed from the two forms on solvation with methanol. It is important to note that the two solvents differ in their properties to significant extent as also their H-bonding ability. Methanol being a mono-protic solvent may remain associated to the nitrate ion in solution through only one H-bond, thereby leaving the other two oxygen atoms capable of ligation to the metal node as shown as proposed intermediate species I in Fig. 5. This can stabilize either chelating or monodenate nitrate leading to distinction of the two forms. However in the case of dimethylformamide the possible weak interactions viz. C–H···O interactions along with O–H···O interactions may lead to solvated intermediate having resemblance to a proposed solvated intermediate II shown in Fig. 5. This type of possible interactions of the nitrate ligand with solvent leaves only one oxygen of the ligand capable of ligation to the metal center. So, it can be supposed that the two different solvent imparts different twist to the nitrate ligand that leads to the formation of the two forms. Unfortunately, we are unable to get any pseudo polymorph in this study which could have supported this solvent induced isomerism with a far more logical justification. Recently our group has reported a work on solvent dependence of the conformation of carboxylic acid moieties where the different weak interactions are possible for different solvents and their effect can be seen [19]. From the solution study it is clear that the solvent modifies the structures and the two crystalline forms can thus be obtained from two different solutions which have subtle differences in solid state structures and absorption spectra.

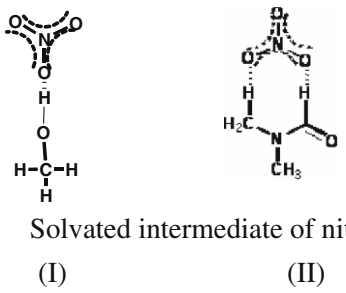


Fig. 5. Two possible ways of interactions of metal bound nitrate ligand with methanol and dimethyl formamide.

4. Conclusions

In conclusion, crystallization of a mixed anionic lead(II) 2,2′-bipyridyl N-oxide coordination polymer from two different solvents showed subtle differences in structures arising from two different nitrate binding modes leading to two different co-ordination numbers. The subtle differences are observed in different response towards UV–Vis spectroscopy in both solid state and solution state arising from mono dentate or bidentate mode of nitrate ligand.

Appendix A. Supplementary data

Supplementary data associated with this article can be found, in the online version, at doi:10.1016/j.poly.2008.11.020.

References

[1] B. Moulton, M.J. Zaworotko, Chem. Rev. 101 (2001) 1629.
[2] A.Y. Robin, K.M. Fromm, Coord. Chem. Rev. 250 (2006) 2127.
[3] A.J. Blake, N.R. Brooks, N.R. Champness, M. Crew, A. Deveson, D. Fenske, D.H. Gregory, L.R. Hanton, P. Hubberstey, M. Schröder, Chem. Commun. (2001) 1432.
[4] S.A. Barnett, A.J. Blake, N.R. Champness, C. Wilson, Chem. Commun. (2002) 1640.
[5] S. Masaoka, D. Tanaka, Y. Nakanishi, S. Kitagawa, Angew. Chem., Int. Ed. Engl. 43 (2004) 2530.
[6] X-C. Huang, J-P. Zheng, Y-Y. Lin, X-M. Chen, Chem. Commun. (2005) 2232.
[7] A. Thirumurgan, R.A. Sanguramath, C.N.R. Rao, Inorg. Chem. 47 (2008) 823.
[8] Y-H. Zhao, Z-M. Su, Y. Wang, Y-M. Fu, S-D. Liu, P. Li, Inorg. Chem. Commun. 10 (2007) 410.
[9] J. Yang, G.D. Li, J-J. Cao, G-H. Li, J-S. Chen, Chem. Eur. J. 13 (2007) 3248.
[10] J-G. Mao, Z. Wang, A. Clearfield, Inorg. Chem. 41 (2002) 6106.
[11] L. Shimoni-Linvny, J.P. Glusker, C.W. Bock, Inorg. Chem. 37 (1998) 1853.
[12] J. Sanchiz, P. Esparza, D. Villagra, S. Domingues, A. Mederos, F. Brito, L. Araujo, A. Sanchez, J.M. Arrieta, Inorg. Chem. 41 (2002) 6048.
[13] L. Chong, J-G. Mao, Y-Q. Sun, J.Solid State Chem. 177 (2004) 2449.
[14] A. Karmakar, R.J. Sarma, J.B. Baruah, Eur. J. Inorg. Chem. 5 (2007) 643.
[15] R. Sarma, J.B. Baruah, Inorg. Chim. Acta (2008), doi:10.1016/j.ica.2008.07.018.
[16] J. Parr, Polyhedron 16 (1997) 551.
[17] M.R.S.J. Foreman, T. Gelbrich, M.B. Hursthouse, M.J. Plater, Inorg. Chem. Commun. 3 (2000) 234.
[18] V. Tomisic, V. Butorac, J. Viher, V. Simeon, J. Sol. Chem. 6 (2005) 613.
[19] J.B. Baruah, A. Karmakar, N. Barooah, CrystEngComm 10 (2008) 151.

Polyhedron 28 (2009) 457–460

Contents lists available at ScienceDirect

Polyhedron

journal homepage: www.elsevier.com/locate/poly

Copper(II) and lanthanoid(III) complexes of a new β-diketonate ligand with an appended non-coordinating phenol group

Stefania Tanase [a,*], Marta Viciano-Chumillas [a], Jan M.M. Smits [b], René de Gelder [b], Jan Reedijk [a]

[a] Leiden Institute of Chemistry, Gorlaeus Laboratories, Leiden University, P.O. Box 9502, 2300 RA, Leiden, The Netherlands
[b] Radboud University Nijmegen, Institute for Molecules and Materials, Heyendaalseweg 135, 6525 AJ, Nijmegen, The Netherlands

ARTICLE INFO

Article history:
Received 10 October 2008
Accepted 16 November 2008
Available online 26 December 2008

Keywords:
Copper(II)
Lanthanoid(III)
β-Diketone
Crystal structure

ABSTRACT

New mononuclear compounds of the ligand 1-(2-hydroxyphenyl)-3-phenylpropane-1,3-dione (H_2L) with Cu(II) and several lanthanoid(III) ions, where Ln(III) = Pr, Nd, Eu, Gd, have been synthesized and characterized by spectroscopic methods and X-ray crystal structure determinations. In all compounds, the ligand coordinates in a bidentate chelating manner, using the diketone function. In the $[Cu(HL)_2]$, the coordination geometry of Cu(II) ion is slightly distorted square-planar; two strong intramolecular (OH···O) hydrogen-bonding interactions are established between the phenolate group and the neighboring ketone function. The lanthanoid(III) compounds have the general formula $[Ln(HL)_3(CH_3OH)_2] \cdot CH_3OH \cdot 2H_2O$; the lanthanoid(III) ion (Ln) is eight-coordinated and the coordination geometry is based on a distorted square-antiprism. In addition to the intramolecular hydrogen bonding (OH···O), intermolecular hydrogen-bonding interactions are also present between the coordinated methanol molecule and the non-coordinated methanol molecule giving rise to a three-dimensional network.

© 2008 Elsevier Ltd. All rights reserved.

1. Introduction

The construction of molecular assemblies through the coordination of a metal ion with polydentate organic ligands has become a fascinating area of interest in inorganic chemistry. Particularly, coordination compounds of β-diketone ligands have attracted considerable attention due to their often supramolecular architectures and their peculiar optical or magnetic properties [1]. Transition-metal complexes based on various analogues of acetylacetone have been largely studied and most of the examples reported so far belong to the category of cluster compounds [1]. Considerably fewer examples of compounds with extended networks have been isolated [1–5]. The coordination ability of β-diketone ligands towards lanthanoid(III) ions has been studied and representative examples of the formation of highly coordinated complexes are the lanthanoid(III) tris-(β-diketonates) containing several nitrogen ligands such as 2,2′-bipyridine, and 1,10-phenanthroline or their derivatives [6–8]. In this work, we report the synthesis, spectroscopic characterization and X-ray crystal structure determination of new Cu(II) and lanthanoid(III) complexes with the ligand 1-(2-hydroxyphenyl)-3-phenylpropane-1,3-dione (H_2L). The ligand was selected because of its potential dual binding modes, namely coordination and hydrogen-bond donor, or bridging coordination.

2. Experimental

2.1. General remarks

Starting materials were purchased from Aldrich and all manipulations were performed using materials as received. The ligand 1-(2-hydroxyphenyl)-3-phenylpropane-1,3-dione (H_2L) was synthesized according to the procedure reported previously for similar ligands [9].

2.2. Synthesis

$[Cu(HL)_2]$ (**1**). A solution of $Cu(NO_3)_3 \cdot 3H_2O$ (0.3 mmol) in 10 ml methanol was added to a solution of the ligand H_2L (0.6 mmol) and triethylamine (0.6 mmol) in 10 ml methanol. Slow evaporation of the resulting solution afforded green single crystals within one day. After filtration, the crystalline material was washed with diethyl ether and dried in air. $C_{30}H_{22}CuO_6$, **1** (M = 542.04 g/mol). Yield: 52% (85 mg). El. Anal. (%): calc. 66.48 C, 4.45 H; exp. 66.98 C, 4.41 H. IR (ν_{max}/cm^{-1}): 2992 (w), 1616 (m), 1584 (m), 1536 (s), 1517 (s), 1481 (s), 1455 (s), 1430 (m), 1389 (s), 1343 (m), 1309 (s), 1243 (m), 1201 (m), 1160 (w), 1137 (m), 1104 (w), 1056 (m), 1020 (m), 941 (m), 845 (m), 806 (w), 787(m), 764 (m), 749 (m), 728 (s), 702 (s), 686 (s), 580 (m), 563 (s), 526 (m) UV–Vis (λ/nm): 270, 365, 415, 620.

2.2.1. Synthesis of the compounds $[Ln(HL)_3(CH_3OH)_2] \cdot CH_3OH \cdot 2H_2O$

A solution of $Ln(NO_3)_3 \cdot 6H_2O$ (0.24 mmol) in 10 ml methanol was added to a solution of the ligand H_2L (0.72 mmol) and trieth-

* Corresponding author.
E-mail address: s.grecea@chem.leidenuniv.nl (S. Tanase).

0277-5387/$ - see front matter © 2008 Elsevier Ltd. All rights reserved.
doi:10.1016/j.poly.2008.11.025

ylamine (0.72 mmol) in 10 ml methanol. Slow evaporation of the resulting solution afforded yellow crystalline material in a few hours. After filtration, the crystalline material was washed with diethyl ether and dried in air.

$C_{48}H_{49}O_{12}Pr$, **2** (M = 990.81 g/mol). Yield: 60% (137 mg). El. Anal. (%): calc. 58.19 C, 4.98 H; exp. 58.71 C, 4.57 H. IR (ν_{max}/cm^{-1}): 3344 (br), 2988 (m), 2858 (m), 1590 (m), 1544 (m), 1509 (s), 1461 (m), 1394 (m), 1343 (m), 1291 (s), 1199 (m), 1138 (m), 1069 (m), 1023 (m), 937 (m), 842 (m), 755 (m), 711 (m), 676 (w), 622 (s), 516 (m). UV–Vis (λ/nm): 270, 345, 410, 485, 608.

$C_{48}H_{49}O_{12}Nd$, **3** (M = 994.32 g/mol). Yield: 61% (145 mg). El. Anal. (%): calc. 57.98 C, 4.97 H; exp. 58.06 C, 4.57 H. IR (ν_{max}/cm^{-1}): 3346 (br), 2988 (m), 2858 (m), 1590 (m), 1544 (m), 1506 (s), 1462 (m), 1397 (m), 1343 (m), 1291 (s), 1199 (m), 1138 (m), 1066 (m), 1023 (m), 937 (m), 842 (m), 754 (m), 711 (m), 676 (w), 623 (s), 516 (m). UV–Vis (λ/nm): 270, 346, 409, 520, 537, 586, 752, 810, 900.

$C_{48}H_{49}O_{12}Eu$, **4** (M = 1001.86 g/mol). Yield: 85% (210 mg). El. Anal. (%): calc. 57.55 C, 4.93 H; exp. 57.25 C, 4.17 H. IR (ν_{max}/cm^{-1}): 3360 (br), 2988 (m), 2858 (m), 1589 (m), 1542 (m), 1508 (s), 1457 (m), 1394 (m), 1339 (m), 1286 (s), 1198 (m), 1137 (m), 1066 (m), 1023 (m), 937 (m), 841 (m), 753 (m), 710 (m), 676 (w), 622 (s), 516 (m). UV–Vis (λ/nm): 270, 348, 408.

$C_{48}H_{49}O_{12}Gd$, **5** (M = 1007.15 g/mol). Yield: 72% (175 mg). El. Anal. (%): calc. 57.24 C, 4.90 H; exp. 57.07 C, 4.51 H. IR (ν_{max}/cm^{-1}): 3360 (br), 2988 (m), 2858 (m), 1590 (m), 1547 (m), 1510 (s), 1461 (m), 1398 (m), 1334 (m), 1286 (s), 1198 (m), 1137 (m), 1066 (m), 1023 (m), 937 (m), 842 (m), 753 (m), 711 (m), 677 (w), 623 (s), 514 (m). UV–Vis (λ/nm): 270, 350, 405.

2.3. Physical measurements

C, H, and N analyses were performed with a Perkin–Elmer 2400 series II analyzer. Infrared spectra (4000–300 cm^{-1}, resol. 4 cm^{-1}) were recorded on a Perkin–Elmer Paragon 1000 FTIR spectrometer equipped with a Golden Gate ATR device, using the reflectance technique. Diffuse reflectance spectra were obtained on a Perkin–Elmer Lambda 900 spectrophotometer using MgO as a reference. X-band powder EPR spectra were obtained on a Bruker-EMX*plus* electron spin resonance spectrometer (Field calibrated with DPPH (g = 2.0036)).

2.4. X-ray crystallography

Intensity data for a single crystal of **1** and **4a** were collected using Mo Kα radiation (λ = 0.71073 Å) on a Nonius Kappa CCD diffractometer. Crystal data for **1** and **4a** are collected in Table 1. The intensity data were corrected for Lorentz and polarization effects, for absorption (multiscan absorption correction) and extinction. The structures were solved by Patterson methods. The programs SABABS [10], DIRDIF96 [11] and SHELXL-97 [12] were used for data reduction, structure solution and structure refinement, respectively. Refinement of F^2 was done against all reflections. The weighted R factor, wR, and goodness of fit S are based on F^2. Conventional R factors are based on F, with F set to zero for negative F^2. All non-hydrogen atoms were refined with anisotropic displacement parameters. All hydrogen atoms were placed at calculated positions and were refined riding on the parent atoms. Geometric calculations and molecular graphics were performed with the PLATON package [13].

3. Results and discussions

3.1. Synthesis and characterization of the complex [Cu(HL)$_2$]

Complex **1** is easily obtained by the reaction of hydrated Cu(II) nitrate with triethylamine and the β-diketone ligand H_2L (1:2:2 ratio) using methanol as solvent. The infrared spectrum of **1** shows the vibration characteristic of the organic ligand; the most important feature that indicates the coordination of the β-diketone ligand to the Cu(II) ion, is the shift of the $\nu_{C=O}$ stretching vibration of the carbonyl group to lower energy, *ca.* 1616 cm^{-1} as compared with the free ligand (at 1657 cm^{-1}). The ligand field spectrum, measured as a solid with the diffuse reflectance technique, shows a broad band at 620 nm which is ascribed to the d-d transitions of the Cu(II) ion and a Cu–O charge transfer band at 415 nm.

The molecular structure of **1** consists of a centrosymmetric mononuclear unit in which the Cu(II) ion is coordinated by two bidentate chelating HL^- ligands that use the diketonate function for coordination to the metal center (Fig. 1). Schematic geometric information is given in Table 2. The coordination geometry of Cu(II) ion is slightly distorted square–planar. The Cu–O bond lengths of 1.889(3) Å and 1.896(4) Å, respectively are normal and comparable with the similar distances in other Cu(II) complexes with β-diketonate ligands [14–18]. The in-plane O–Cu–O angle differs slightly from 90°, being 87.03(15)°. As shown in Fig. 1, the molecular structure is stabilized by two strong intramolecular hydrogen-bonding interactions established between the phenol group and the neighboring coordinating ketonate function (O5···O1 = 2.5038 Å; O5–H5···O1 = 144°). A view of the crystal packing of **1** is shown in Fig. 2; the shortest intermolecular Cu···Cu distance is 5.838 Å.

The X-band spectrum of the complex **1** as a powder, recorded at room temperature (Fig. 3), is slightly anisotropic with a g value of 2.05 and a $g_{||}$ value of 2.25. No hyperfine splitting is resolved. This might be due to some exchange interactions leading to exchange narrowing, in view of the rather short intermolecular Cu···Cu distance indicated by the X-ray crystal structure.

3.2. Synthesis and characterization of the compounds of formula

3.2.1. [Ln(HL)$_3$(CH$_3$OH)$_2$] · CH$_3$OH · 2H$_2$O

The reaction of the hydrated lanthanoid(III) nitrates with the ligand H_2L in the presence of triethylamine as base (1:3:3 molar ratio) and using methanol as solvent afforded yellow crystalline materials. The analytical studies have shown that these compounds have the general formula [Ln(HL)$_3$(CH$_3$OH)$_2$] · CH$_3$OH. An X-ray crystallographic study has been performed for the complex [Ln(HL)$_3$(CH$_3$OH)$_2$] · CH$_3$OH (**4a**) and its crystal structure is described below. The crystallinity of the complexes

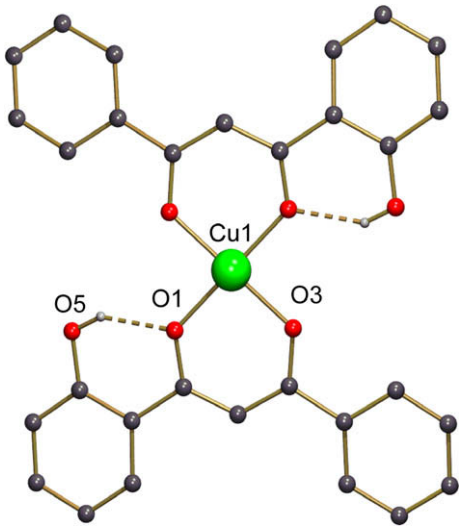


Fig. 1. View of the molecular structure of **1** showing the intramolecular hydrogen bonds. Hydrogen atoms not involved in hydrogen bonding were omitted for clarity.

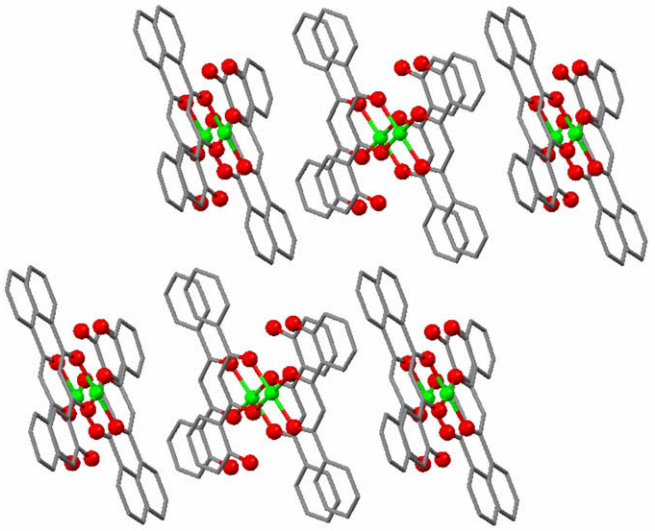


Fig. 2. View of the crystal packing of **1** in the *ac* plane. Hydrogen atoms were omitted for clarity. Cu···Cu contacts are 5.838 Å.

Table 1
Crystallographic data for compounds **1** and **4a**.

	1	**4a**
Formula	$C_{30}H_{22}CuO_6$	$C_{48}H_{45}O_{12}Eu$
Formula weight	542.02	965.80
Crystal system	Monoclinic	Triclinic
Space group	*C*2/*c*	$P\bar{1}$
a (Å)	26.511(3)	12.5036(19)
b (Å)	5.8379(3)	13.9203(15)
c (Å)	16.475(2)	14.406(2)
α (°)	90	67.418(12)
β (°)	114.997(10)	85.335(16)
γ (°)	90	67.022(9)
V (Å^3)	2311.1(4)	2124.5(6)
Z	4	2
D_{calc} (mg m^{-3})	1.564	1.510
μ (Mo-α) (mm^{-1})	0.992	1.541
T (K)	208	208
Data collected	15011	46359
Unique data	2006	9667
R_{int}	0.0317	0.0424
$R(F)$ [$I > 2\sigma(I)$]	0.0686	0.0450
$R_w(F^2)$	0.1877	0.0934
S	1.101	1.120
$\Delta\rho_{min}$, $\Delta\rho_{max}$ (e Å^{-3})	−0.43; 2.33	−0.53, 1.76

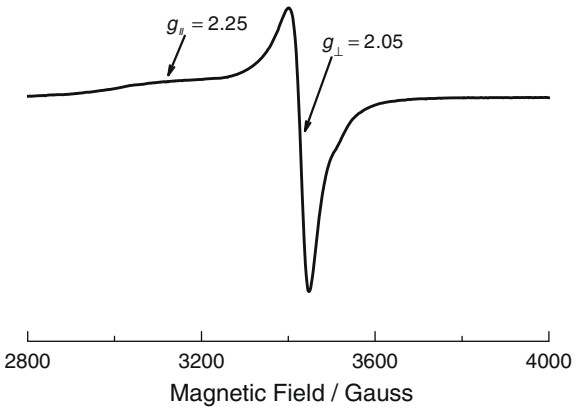


Fig. 3. Room temperature EPR spectrum of complex **1**.

Table 2
Selected bond lengths (Å) and angles (°) for compounds **1** and **4a**.

Complex ***1***			
Cu1–O1	1.889(3)	O1–Cu1–O3	92.97(15)
Cu1–O3	1.896(4)		
Cu···Cu	5.838		
Complex ***4a***			
Eu1–O1a	2.334(3)	O1a–Eu1–O1b	76.17(10)
Eu1–O1b	2.335(3)	O1a–Eu1–O1c	139.98(10)
Eu1–O1c	2.319(3)	O1a–Eu1–O3a	71.90(9)
Eu1–O3a	2.396(3)	O1a–Eu1–O3b	106.77(10)
Eu1–O3b	2.359(3)	O1a–Eu1–O3c	146.77(10)
Eu1–O3c	2.347(3)	O1a-Eu1-O21	76.15(11)
Eu1–O21	2.477(3)	O1a–Eu1–O23	81.96(12)
Eu1–O23	2.447(3)	O1c–Eu1–O1c	143.49(10)
		O1b–Eu1–O3a	138.49(10)
		O1b–Eu1–O3b	70.76(9)
		O1b–Eu1–O3c	76.80(10)
		O1b–Eu1–O21	121.30(9)

$[Ln(HL)_3(CH_3OH)_2] \cdot CH_3OH$ is partly lost upon removing the crystals from the mother liquid and the elemental analysis and spectroscopic studies suggest that these compounds all have the general formula $[Ln(HL)_3(CH_3OH)_2] \cdot CH_3OH \cdot 2H_2O$ (Ln = Pr **2**, Nd **3**, Eu **4**, Gd **5**).

The IR spectra of compounds **2**–**5** are nearly identical, in agreement with the fact that these compounds are isostructural. The binding of the β-diketone ligand to the lanthanoid(III) ions is indicated by the shift of the $\nu_{C=O}$ stretching vibration of the carbonyl group to lower energy, *ca.* 1590 cm^{-1} as compared with the free ligand at 1657 cm^{-1}. The broad band in the range 3200–3400 cm^{-1} is characteristic to the ν_{O-H} stretching vibrations of the lattice water molecules.

The UV–Vis absorption spectrum of the ligand shows characteristic bands at 267, 345 and 425 nm. In the UV range, the spectral features observed for compounds **2**–**5** are similar to those observed for the corresponding ligand. In the visible range, compounds **2** and **3** display the characteristic bands due to the f–f transitions. Room-temperature excitation in the UV absorption bands ($\pi \rightarrow \pi^*$ and $n \rightarrow \pi^*$) of the free ligand does not result in lanthanoid emission in these complexes. This result points to the presence of efficient non-radiative deactivation pathways in all compounds, which is due to the presence of lattice water molecules. Nevertheless, a weak ligand emission was observed at λ_{em} = 545 nm (λ_{exc} = 275 nm).

The crystal structure of **4a** consists of a mononuclear Eu(III)-containing molecule, $[Eu(HL)_3(CH_3OH)_2]$ and a lattice methanol molecule. As shown in Fig. 4, the Eu(III) ion is eight-coordinated by three monodeprotonated ligands (HL^-) and two methanol molecules. The coordination geometry of Eu(III) is based on distorted square-antiprism; the two bases are identical and they are formed by two oxygen atoms of the same bidentate ligand, an oxygen atom of a second HL^- ligand and an oxygen atom from a methanol molecule. Selected bond lengths and angles are listed in Table 2. The Eu–O bond lengths are in the range 2.320(4)–2.479(3) Å, with the Eu–O bond lengths involving the methanol molecules being the longest. The average of the C–O bond length of the β-diketone group is *ca.* 1.269 Å, much shorter than the corresponding bond in other lanthanoid(III) complexes with β-diketone ligands. This short distance suggests a lower π-electron delocalization of the C=O bond [19].

The molecular structure is stabilized by multiple intra- and intermolecular O–H···O hydrogen-bonding interactions (Fig. 5, Table 3). Three intramolecular hydrogen bonds are established between the phenolic group and the neighboring oxygen of the diketonate function. Additionally, the phenolic group of the ligand is also involved in a hydrogen bond with one of the coordinated

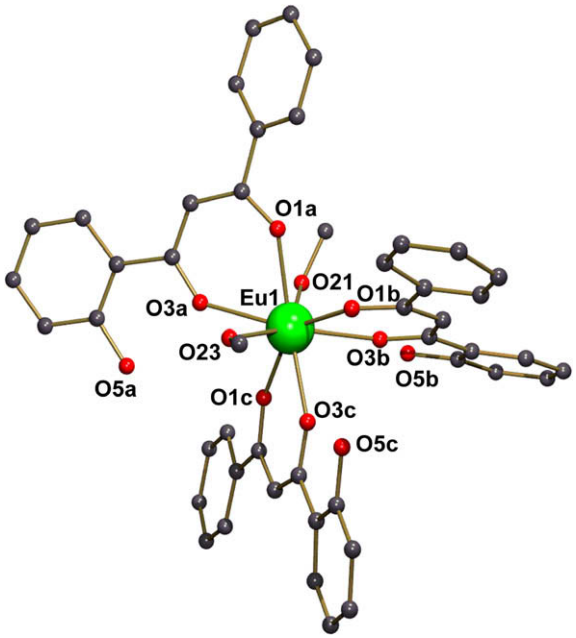


Fig. 4. View of the molecular structure of **2**. The non-coordinated methanol molecule and hydrogen atoms were omitted for clarity.

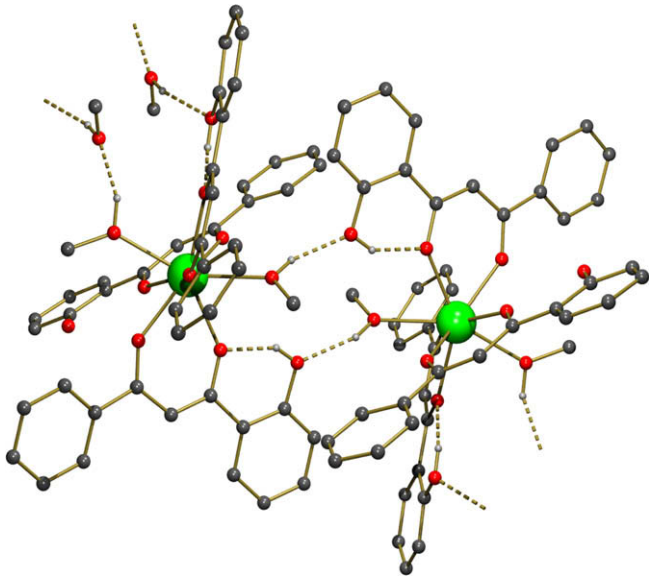


Fig. 5. View of the hydrogen bonding interactions in **2**.

Table 3
Details of the hydrogen bonding interactions in **4a**.

	D–H	H···A	D···A	D–H···A
O5a–H5a···O3a	0.83	1.76	2.489(5)	146.1
O5b–H5b···O3b	0.83	1.75	2.489(4)	146.9
O5c–H5c···O3c	0.83	1.76	2.495(4)	146.5
O21–H21···O5b	0.94	1.89	2.711(4)	144.4
O23–H21···O25	0.94	1.83	2.673(6)	147.3
O25–H25···O5a	0.83	1.98	2.789(6)	163.3

methanol molecule of a neighboring mononuclear unit. The second coordinated methanol molecule establishes a hydrogen bonding interaction with the non-coordinated methanol molecule. All these interactions give rise to a complicated three-dimensional crystal structure. The shortest intermolecular Eu···Eu distance is 13.920 Å along the *b*-axis.

4. Conclusions

The reaction of a new β-diketonate ligand, 1-(2-hydroxyphenyl)-3-phenylpropane-1,3-dione, with Cu(II) and Ln(III) ions does result in the formation of mononuclear complexes. In all compounds, the ligand is coordinated in a bidentate chelating manner, using the diketone function for coordination to the metal center, and stabilization of the chromophore by strong intramolecular hydrogen bonding (OH···O). The preparation of the compounds reported in this paper offers promising prospects in the direction of heterobimetallic polynuclear compounds. We are currently exploring the coordination chemistry of the 1-(2-hydroxyphenyl)-3-phenylpropane-1,3-dione ligand with other metals.

Supplementary data

CCDC 705139 - 705140 contains the supplementary crystallographic data for the compounds **1** and **4a**. These data can be obtained free of charge via http://www.ccdc.cam.ac.uk/conts/retrieving.html, or from the Cambridge Crystallographic Data Centre, 12 Union Road, Cambridge CB2 1EZ, UK; fax: (+44) 1223-336-033; or e-mail: deposit@ccdc.cam.ac.uk.

Acknowledgments

This research was financially supported by a Veni grant from the Netherlands Organization for Scientific Research (NWO) to S. T. and the ECNetwork of Excellence "MAGMANet" (No. 515767-2).

References

[1] G. Aromi, P. Gamez, J. Reedijk, Coord. Chem. Rev. 252 (2008) 964.
[2] J.K. Clegg, K. Gloe, M.J. Hayter, O. Kataeva, L.F. Lindoy, B. Moubaraki, J.C. McMurtrie, K.S. Murray, D. Schilter, Dalton Trans. (2006) 3977.
[3] J.K. Clegg, L.F. Lindoy, J.C. McMurtrie, D. Schilter, Dalton Trans. (2005) 857.
[4] D.V. Soldatov, A.S. Zanina, G.D. Enright, C.I. Ratcliffe, J.A. Ripmeester, Cryst. Growth Des. 3 (2003) 1005.
[5] Y.S. Zhang, S.R. Breeze, S.N. Wang, J.E. Greedan, N.P. Raju, L.J. Li, Can. J. Chem. 77 (1999) 1424.
[6] A. Bellusci, G. Barberio, A. Crispini, M. Ghedini, M. La Deda, D. Pucci, Inorg. Chem. 44 (2005) 1818.
[7] P.N. Remya, S. Biju, M.L.P. Reddy, A.H. Cowley, M. Findlater, Inorg. Chem. 47 (2008) 7396.
[8] A.P. Vigato, V. Peruzzo, T. Tamburini, Coord. Chem. Rev., in press, doi:10.1016/j.ccr.2008.07.013.
[9] T.S. Wheeler, Org. Synth. 32 (1952) 72.
[10] G.M. Sheldrick, SADABS, Program for Empirical Absorption Correction, University of Göttingen, Germany, 1996.
[11] P.T. Beurskens, G. Beurskens, R. de Gelder, S. García-Granda, R.O. Gould, R. Israël, J.M.M. Smits, The DIRDIF Programme, Report on the Crystallography Laboratory, University of Nijmegen, Nijmegen, The Netherlands, 1996.
[12] G.M. Sheldrick, SHELXL97. Program for Crystal Structure Refinement, University of Göttingen, Germany, 1997.
[13] A.L. Spek, PLATON, a Multipurpose Crystallographic Tool, Utrecht University, Utrecht, The Netherlands, 2003.
[14] A.M. Madalan, M. Noltemeyer, M. Neculai, H.W. Roesky, M. Schmidtmann, A. Muller, Y. Journaux, M. Andruh, Inorg. Chim. Acta 359 (2006) 459.
[15] G. Aromi, C. Boldron, P. Gamez, O. Roubeau, H. Kooijman, A.L. Spek, H. Stoeckli-Evans, J. Ribas, J. Reedijk, Dalton Trans. (2004) 3586.
[16] G. Aromi, J. Ribas, P. Gamez, O. Roubeau, H. Kooijman, A.L. Spek, S. Teat, E. MacLean, H. Stoeckli-Evans, J. Reedijk, Chem. Eur. J. 10 (2004) 6476.
[17] A.M. Madalan, V.C. Kravtsov, D. Pajic, K. Zadro, Y.A. Simonov, N. Stanica, L. Ouahab, J. Lipkowski, M. Andruh, Inorg. Chim. Acta 357 (2004) 4151.
[18] G. Aromi, P. Gamez, O. Roubeau, H. Kooijman, A.L. Spek, W.L. Driessen, J. Reedijk, Angew. Chem., Int. Ed. 41 (2002) 1168.
[19] A. Mech, Polyhedron 27 (2008) 393.

Polyhedron 28 (2009) 461–466

Contents lists available at ScienceDirect

Polyhedron

journal homepage: www.elsevier.com/locate/poly

Syntheses and X-ray crystallographic studies of {[Ni(en)$_2$(pot)$_2$]0.5CHCl$_3$} and [Ni(en)$_2$](3-pytol)$_2$

M. Singh [a], A.K. Pandey [c], R.J. Butcher [b], N.K. Singh [a,*]

[a] Department of Chemistry, Banaras Hindu University, Varanasi 221005, India
[b] Department of Chemistry, Howard University, 525 College Street NW, Washington, DC 20059, USA
[c] UP (PG) College, Varanasi 221002, India

ARTICLE INFO

Article history:
Received 19 August 2008
Accepted 18 November 2008
Available online 20 January 2009

Keywords:
Ni(II) 1,3,4-oxadiazole complexes
Mixed-ligand complexes
en complexes

ABSTRACT

Two novel Ni(II) complexes {[Ni(en)$_2$(pot)$_2$]0.5CHCl$_3$} (**3**) {pot = 5-phenyl-1,3,4-oxadiazole-2-thione} (**1**) and [Ni(en)$_2$](3-pytol)$_2$ (**4**) {3-pytol = 5-(3-pyridyl)-1,3,4-oxadiazole-2-thiol} (**2**) have been synthesized using en as coligand. The metal complexes have been characterized by physical and analytical techniques and also by single crystal X-ray studies. The complexes **3** and **4** crystallize in monoclinic system with space group *P*21/*a* and *P*121/*c*, respectively. The complex **3** has a slightly distorted octahedral geometry with *trans* (pot)$^-$ ligands while **4** has a square planar geometry around the centrosymmetric Ni(II) center with ionically linked *trans* (3-pytol)$^-$ ligands. The π···π (face to face) interaction plays an important role along with hydrogen bondings to form supramolecular architecture in both complexes.

© 2008 Elsevier Ltd. All rights reserved.

1. Introduction

The transition metal complexes of dithiocarbazates have attracted considerable attention for their interesting biological applications [1–3]. They behave as versatile ligands and act as monodentate (S or N2), bidentate anionic (via N3–S or S,S) [4–6] and polydentate chelating ligands [7–11]. The conversion of potassium salt of *N*-aroyldithocarbazates and 3-acyldithiocarbazic acid esters to the corresponding 1,3,4-oxadiazoles are reported in the literature [12–16]. A few papers are available on the metal complexes of 5-phenyl-1,3,4-oxadiazole-2-thiol/thione [17–19], 5-(4-pyridyl)-1,3,4-oxadiazole-2-thione [20–25] and 5-(2-pyridyl)-1,3,4-oxadiazole-2-thione [26]. These oxadiazoles have attracted attention in the field of coordination chemistry because of the presence of potential multifunctional donor sites viz. exocyclic sulfur, endocyclic nitrogen and pyridyl nitrogen. The pyridyl containing oxadiazoles are known to show three types of binding modes involving monodentate (N_{oxa}/N_{py}/S)/bidentate (N_{py},N_{oxa}/N_{py},S)/tridentate (N_{py}, N_{oxa}, S) donor sites [21]. Recently, we have reported the X-ray structure of [Ni(en)$_2$(3-pyt)$_2$] {3-pyt = 5-(3-pyridyl)-1,3,4-oxadiazole)-2-thione} where the ligand is covalently bonded through the endocyclic nitrogen [27]. Following our interest in the study of the metal complexes of 1,3,4-oxadiazoles-2-thione/thiol, we report herein the syntheses, spectroscopic and X-ray structural studies of two new Ni(II) complexes viz. {[Ni(en)$_2$(pot)$_2$]0.5CHCl$_3$} (**3**) and [Ni(en)$_2$](3-pytol)$_2$ (**4**).

2. Experimental

2.1. Materials and methods

All starting materials of analytical grade were obtained commercially and used as received. Nicotinamide was purchased from Sigma Aldrich Chemicals (USA) and used as such. Nicotinic acid hydrazide [28], [Ni(en)$_2$(NCS)$_2$] [29], potassium *N*-benzoyldithiocarbazate (**1**) [30] and potassium[pyridine-3-carbonyl)]-hydrazinecarbodithioate (**2**) [21] were synthesized according to the reported methods.

2.2. Synthesis of {[Ni(en)$_2$(pot)$_2$]0.5CHCl$_3$} (3)

A methanol–water (9:1 v/v) solution (20 ml) of [Ni(en)$_2$(NCS)$_2$] (1 mmol) was mixed with the aqueous-methanolic solution (50:50 v/v) (10 ml) of potassium *N*-benzoyldithiocarbazate (**1**) (2 mmol) to which 2 ml of chloroform was added. The resulting solution was filtered off and kept for crystallization. After 12 days, light pink crystals of **3** suitable for an X-ray crystallographic study were obtained.

{[Ni(en)$_2$(pot)$_2$]0.5CHCl$_3$} (**3**): Pink crystals, Yield 67%, *Anal. calc.* (%) for $C_{41}H_{53}Cl_3N_{16}Ni_2O_4S_4$ (1186.00): C, 41.52; H, 4.50; N, 18.90; S, 10.81; Ni, 9.90. Found: C, 40.96; H, 4.30; N, 18.77; S, 10.75; Ni, 9.27%. μ_B = 2.90 BM per Ni(II). M.p. 200 °C (dec.). IR data (*ν*, KBr, cm^{-1}): *ν*(NH of en) 3255m; *ν*(C=N) 1604s; ν_s(C–O–C) 1276w;

* Corresponding author. Tel.: +91 542 6702452; fax: +91 542 2368127.
E-mail addresses: mamatasingh6@gmail.com (M. Singh), singhnk_bhu@yahoo.com (N.K. Singh).

0277-5387/$ - see front matter © 2008 Elsevier Ltd. All rights reserved.
doi:10.1016/j.poly.2008.11.046

ν_{as}(C–O–C) 1182; ν(N–N) 1059s; ν(C=S) 948m; ν(Ni–N) 470. UV–Vis spectrum [λ_{max} in MeOH, cm^{-1}]: 15001, 22345, 32038.

2.3. Synthesis of $[Ni(en)_2](3\text{-pytol})_2$ (**4**)

A methanol solution (10 ml) of $Ni(OAc)_2 \cdot 2H_2O$ (1 mmol) was stirred with the aqueous-methanolic solution (50:50 v/v) (10 ml) of potassium[*N*′-(pyridine-3-carbonyl)-hydrazinecarbodithioate] (**1**) (2 mmol), the precipitated green product was filtered off and washed twice with cold water. The above precipitate was added to a MeOH solution of en and shaken for a few minutes, the resulting solution of **4** was filtered off and kept for crystallization and after 25 days, red-pink crystals of **4** suitable for an X-ray crystallography study were obtained.

$[Ni(en)_2](3\text{-pytol})_2$ (2): Red pink, Yield 58%, Anal. Calc. for $C_{18}H_{24}N_{10}O_2S_2Ni$ (535.30) C, 40.39; H, 4.52; N, 26.17; S; 11.98; Ni, 10.96. Found: C, 39.98; H, 4.86; N, 26.66; S, 11.52; Ni, 10.62%. $\mu_B = 0$, Diamagnetic. M.p. 225 °C (dec.). IR data (ν, KBr, cm^{-1}); ν(NH of en) 3229m; ν(C=N) 1610s; ν_s(C–O–C) 1275; ν_{as}(C–O–C) 1198w ; ν(N–N) 1087s; ν(C–S) 904m; ν(Ni–N) 476; Pyridine ring 699. UV–Vis [λ_{max}, MeOH, cm^{-1}]: 16500, 20350, 31645.

3. Analyses and physical measurements

Carbon, hydrogen, nitrogen and sulfur contents were estimated on a CHN Model CE-440 Analyser and on an Elementar Vario EL III. Magnetic susceptibility measurements were performed at room temperature on a Cahn Faraday balance using $Hg[Co(NCS)_4]$ as the calibrant and the electronic spectra were recorded on an UV-1700 Pharmaspec spectrophotometer. By following standard procedure, the complexes were analyzed for their nickel content, after decomposition with a mixture of conc. HNO_3 and HCl, followed by conc. H_2SO_4 [31]. I.R. spectra were recorded in the 4000–400 cm^{-1} region as KBr pellets on a Varian 3100 FT-IR Excalibur series.

4. Crystal structure determination

Data for the complex **3** was obtained at 173(2) K on a Bruker three-circle diffractometer equipped with a SMART 6000 CCD diffractometer and for **4**, X-ray single crystal refinement, diffraction data collection and data reduction were performed at 200(2) K with a graphite monochromated Mo Kα (λ = 0.71073 Å) radiation source using standard methods [32]. Intensity measurements were performed on a rapidly cooled crystal. The structure was solved by direct methods (SHELX-97) and refined against all data by full-matrix least-squares on F^2 using anisotropic displacement parameters for all non-hydrogen atoms. All hydrogen atoms were included in the refinement at geometrically ideal positions and refined with a riding model [33,34]. MERCURY was used for molecular graphics [35]. Crystal structure diagrams were generated by use of the ORTEP-3 for Windows program [36]. The crystallographic data and structural refinement details of complex **3** and **4** are given in Table 1 whereas the important bond distances and bond angles of complex **3** and **4** are given in Tables 2 and 4. The details of hydrogen bonds are given in Tables 4 and 5.

5. Results and discussion

As a part of our study on metal complexes of 1,3,4-oxadiazole-2-thione/thiol [17,27], we report herein the preparation, spectroscopic and X-ray studies of two new Ni(II) complexes based on 5-phenyl-1,3,4-oxadiazole-2-thione $(pot)^-$ and 5-(3-pyridyl)-1,3,4-oxadiazole-2-thiol $(3\text{-pytol})^-$. The potassium salt of *N*-acyldithiocarbazates lead to ring closure by desulphurization into the corresponding 1,3,4-oxadiazole during complexation [17,27]. Recently, the crystal structure of $[Ni(en)_2(3\text{-pyt})_2]$ based on 5-(3-pyridyl)-1,3,4-oxdiazole-2-thione has been reported [27]. The present work reports the complex $[Ni(en)_2](3\text{-pytol})_2$ of the same ligand in the thiol form. The 5-(3-pyridyl)-1,3,4-oxdiazole-2-thiol can exist in two forms viz. [H(3-pytone)] (thione) and [H(3-pytol)] (thiol). These two forms of the ligand yielded octahedral and square planar complexes, respectively, with Ni(II). It is observed that the reaction of an aqueous-methanol solution of $[K^+(H_2L)^-]$ and methanol solution of $Ni(OAc)_2 \cdot 4H_2O$ formed a green precipitate which dissolved in the methanol solution of en (ethylenediamine) resulting in a red-pink solution which crystallized to give red-pink crystals of $[Ni(en)_2](3\text{-pytol})_2$. However, the reaction of methanol–water solution of $[K^+(H_2L)^-]$ and methanol solution of $[Ni(en)_2(NCS)_2]$ gave a reddish solution which crystallized to form dark red crystals of $[Ni(en)_2(3\text{-pyt})_2]$.

Table 1
Crystal refinement parameters of complexes **3** and **4**.

Parameters	**3**	**4**
Empirical formula	$C_{41}H_{53}Cl_3N_{16}Ni_2O_4S_4$	$C_{18}H_{24}N_{10}O_2S_2Ni$
Formula weight	1186.00	535.30
Space group	*P*21/*a*	*P*121/*c*1
Crystal system	Monoclinic	Monoclinic
T (K)	173(2) K	200(2)
λ, Mo Kα	0.71073	0.71073
a (Å)	12.4655(18)	6.8070(4)
b (Å)	20.993(3)	25.4347(14)
c (Å)	21.540(3)	7.1890(5)
α (°)	90	90
β (°)	90.0010(10)	114.213(7)
γ (°)	90	90
V (Å^3)	5636.6(14)	1135.17(12)
Z	4	2
ρ_{calcd} (Mg/m^3)	1.398	1.566
μ (mm^{-1})	1.011	1.078
F(000)	2456	556
Crystal size (mm^3)	0.50 × 0.25 × 0.18	0.47 × 0.34 × 0.12
Θ range for data collection	0.95–29.59	4.59–34.85
Index ranges	$-17 \leqslant h \leqslant 12$ $-28 \leqslant k \leqslant 28$ $-29 \leqslant l \leqslant 29$	$-10 \leqslant h \leqslant 10$ $-40 \leqslant k \leqslant 36$ $-8 \leqslant l \leqslant 11$
Reflections collected	60761	11926
Independent reflections	15565	4608
Data/restraints/parameters	15565/14/682	4608/0/151
Goodness-of-fit on F^2	0.988	0.925
R_1[a], wR_2[b] [$I > 2\sigma(I)$]	0.0665, 0.2213	0.0413, 0.0761
R_1[a], wR_2[b] (all data)	0.1258, 0.2825	0.0831, 0.0836
Largest difference peak and hole (e Å^{-3})	1.631, −0.690	0.606, −0.392

Table 2
Selected bond lengths and bond angles for complex **3**.

Bond lengths (Å)			
Ni(1)–N(1A)	2.113(4)	Ni(2)–N(2B)	2.118(4)
Ni(1)–N(3A)	2.117(5)	Ni(2)–N(1B)	2.120(4)
Ni(1)–N(2A)	2.125(4)	Ni(2)–N(3B)	2.121(5)
Ni(3)–N(2C)	2.097(4)	Ni(3)–N(3C)	2.104(4)
Ni(3)–N(5C)	2.109(4)	Ni(3)–N(7C)	2.110(4)
Ni(3)–N(1C)	2.111(3)	Ni(3)–N(4C)	2.115(3)
Bond angles (°)			
N(1A)#1–Ni(1)–N(3A)	90.81(18)	N(1B)–Ni(2)–N(3B)	89.23(18)
N(1A)–Ni(1)–N(3A)	89.19(18)	N(3B)#2–Ni(2)–N(3B)	180.00(19)
N(3A)#1–Ni(1)–N(3A)	180.00(19)	N(2C)–Ni(3)–N(3C)	179.29(12)
N(1A)–Ni(1)–N(2A)	82.27(15)	N(3C)–Ni(3)–N(5C)	90.92(16)
N(3A)–Ni(1)–N(2A)	89.21(17)	N(2C)–Ni(3)–N(7C)	89.90(16)
N(2B)–Ni(2)–N(1B)	82.02(15)	N(5C)–Ni(3)–N(7C)	179.63(12)
N(2B)#2–Ni(2)–N(3B)	90.90(17)	N(2C)–Ni(3)–N(1C)	82.83(15)
N(1B)#2–Ni(2)–N(3B)	90.77(18)	N(3C)–Ni(3)–N(1C)	97.31(15)
N(5C)–Ni(3)–N(1C)	91.50(16)	N(7C)–Ni(3)–N(1C)	88.30(15)
N(3C)–Ni(3)–N(4C)	82.64(15)	N(5C)–Ni(3)–N(4C)	88.78(16)
N(1C)–Ni(3)–N(4C)	179.72(13)		

Table 3
Hydrogen bonds for complex **3** [Å and °].

D–H···A	d(D–H)	d(H···A)	d(D···A)	<(DHA)
N(1A)–H(1AC)···S(1A)	0.92	2.70	3.475(5)	141.9
N(1A)–H(1AD)···N(4A)#1	0.92	2.65	3.226(6)	121.6
N(2A)–H(2AC)···S(1A)1#	0.92	2.71	3.487(5)	142.8
N(2A)–H(2AD)···N(4A)	0.92	2.63	3.216(6)	122.4
N(1B)–H(1BC)···N(4B)#2	0.92	2.68	3.252(7)	121.4
N(1B)–H(1BD)···S(1B)	0.92	2.71	3.476(5)	141.3
N(2B)–H(2BC)···N(4B)	0.92	2.63	3.226(6)	123.0
N(2B)–H(2BD)···S(1B)#2	0.92	2.70	3.477(5)	143.1
N(1C)–H(1CC)···S(1C)	0.92	2.75	3.505(4)	140.4
N(1C)–H(1CD)···N(8C)	0.92	2.59	3.174(6)	121.8
N(2C)–H(2CC)···S(2C)	0.92	2.69	3.474(5)	143.3
N(2C)–H(2CD)···N(6C)	0.92	2.57	3.161(6)	122.8
N(3C)–H(3CC)···N(8C)	0.92	2.57	3.160(6)	122.3
N(3C)–H(3CD)···S(1C)	0.92	2.67	3.453(5)	143.4
N(4C)–H(4CC)···N(6C)	0.92	2.65	3.225(6)	120.9
N(4C)–H(4CD)···S(2C)	0.92	2.72	3.477(5)	140.6

Symmetry transformations used to generate equivalent atoms: #1 $-x+1,-y+1,-z+1$ #2 $-x+1,-y+1,-z$.

Table 4
Selected bond lengths and bond angles for complex **4**.

Ni coordination sphere			
Ni–N(11)	2.0235(12)	N(12)–Ni–N(11)#1	95.17(5)
Ni–N(11)#1	2.0235(12)	N(12)#1–Ni–N(11)#1	84.83(5)
Ni–N(12)	2.0138(13)	N(12)#1–Ni–N(11)	95.17(5)
Ni–N(12)#1	2.0138(13)	N(11)–Ni–N(11)#1	180.0
		N(12)–Ni–N(11)	84.83(5)
		N(12)#1–Ni–N(12)	180.00(5)
Ionic distances			
Ni–S#1	2.997	S#1–Ni–S	180.00
Ni–S	2.997		
Ethylenediamine			
N(11)–C(11)	1.483(2)	C(11)–N(11)–Ni	108.23(9)
N(12)–C(12)	1.482(2)	C(12)–N(12)–Ni	107.77(9)
C(11)–C(12)	1.512(2)	N(11)–C(11)–C(12)	107.37(12)
		N(12)–C(12)–C(11)	107.30(13)
Oxadiazole ring			
S–C(1)	1.6915(16)	C(2)–O–C(1)	103.81(11)
O–C(2)	1.3634(18)	C(1)–N(1)–N(2)	107.39(13)
O–C(1)	1.3916(18)	C(2)–N(2)–N(1)	106.72(13)
N(1)–C(1)	1.313(2)	N(1)–C(1)–O	109.79(13)
N(1)–N(2)	1.4047(19)	N(1)–C(1)–S	129.78(13)
N(2)–C(2)	1.290(2)	O–C(1)–S	120.43(11)
N(2)–C(2)–O	112.29(13)	N(2)–C(2)–C(3)	127.65(14)
O–C(2)–C(3)	120.02(13)		

Table 5
Hydrogen bonds for complex **4** [Å and °].

D–H···A	d(D–H)	d(H···A)	d(D···A)	<(DHA)
N(11)–H(11C)···N(1)#1	0.92	2.32	3.1360(18)	147.8
N(11)–H(11D)···N(1)#2	0.92	2.14	3.0302(19)	162.3
N(12)–H(12C)···N(2)	0.92	2.13	3.0456(18)	172.4
N(12)–H(12D)···S#3	0.92	2.86	3.6479(14)	144.1

Symmetry transformations used to generate equivalent atoms: #1 $-x+1,-y+1,-z+1$ #2 $x-1,y,z$ #3 $x-1,y,z-1$

The possible pathways followed for the formation of two types of complexes are shown in scheme 1. The ligand $[K^+(H_2L)^-]$ reacts with $Ni(OAc)_2\cdot 4H_2O$ to give a green precipitate (Scheme 1) in which Ni(II) is bonded through both thiolato sulfur in a square planar form. It is believed that this green product on reaction with a strong chelating ligand en replaced $(H_2L)^-$ and formed $[Ni(en)_2]^{2+}$, maintaining the earlier square planar geometry. During this process $(H_2L)^-$ got cyclized into 5-(3-pyridyl)-1,3,4-oxadizole-2-thiol in the presence of en. The positive charge of the complex cation $[Ni(en)_2]^{2+}$ is balanced by two thiolato (3-pytol)$^-$ ligands resulting in the formation of the complex $[Ni(en)_2](3\text{-pytol})_2$.

The route followed for the formation of $[Ni(en)_2(3\text{-pyt})_2]$ from $[Ni(en)_2(NCS)_2]$ and $[K^+(H_2L)^-]$ is shown in scheme 1(ii) where $[K^+(H_2L)^-]$ is slowly cyclized to 5-(3-pyridyl)-1,3,4-oxadiazole-2-thione in aqueous-methanol which then exchanges N-bonded thiocyanato from $[Ni(en)_2(NCS)_2]$ and finally yields $[Ni(en)_2(3\text{-pyt})_2]$ maintaining the octahedral geometry around Ni(II).

5.1. I.R. spectra

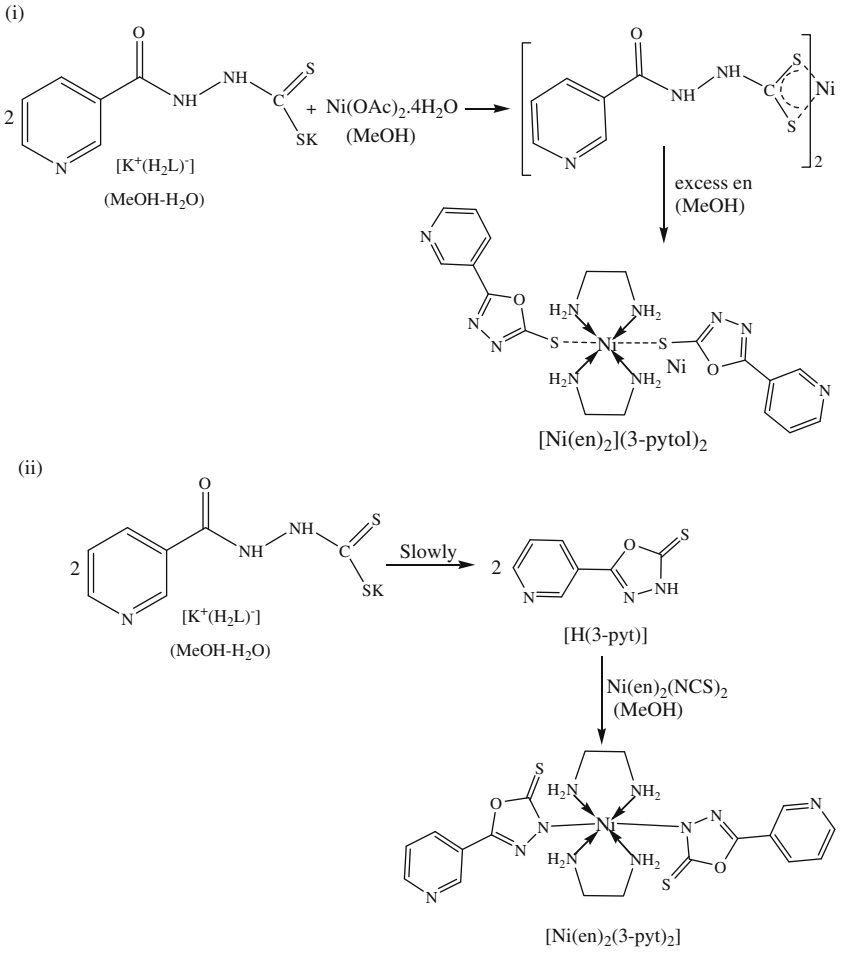
The I.R. spectra of potassium *N*-benzoyldithiocarbazate [17] and potassium[*N*′-(3-pyridine-carbonyl)hydrazinecarbodithioate $[K^+(H_2L)^-]$ [27] are compared with the I.R. spectra of their respective Ni(II) complexes which indicate that bands due to –C(O)NHNHC(S)– moiety i.e. ν(C=O), thioamide I, thioamide II and ν(C=S) are absent [37]. In addition, the I.R. spectra of both complexes are devoid of any peak due to ν(NH) which are present in the ligands **1** and **2**. Appearance of new bands at 1604–1610 cm^{-1} (endocyclic C=N), 1276–1275 [ν_{as}(C–O–C)] and 1182–1198 [ν_s(C–O–C)] cm^{-1}, suggest cyclization of the acyclic dithiocarbazate moiety. The I.R. data are thus consistent with the presence of 1,3,4-oxadiazole moiety [38]. The absorption in the region of 3255–3229 cm^{-1} is due to NH stretching vibrations of en.

5.2. Electronic spectra and magnetic moments

The magnetic moment of 2.90 B.M. for $\{[Ni(en)_2(pot)_2]0.5CHCl_3\}$ and the presence of two d–d bands at 15001 and 22345 cm^{-1} assigned to the $^3A_{2g}(F) \rightarrow {}^3T_{1g}(F)$ and $^3T_{1g}(P)$ transitions, respectively, suggest an octahedral geometry around Ni(II) in the complex **3** [39]. The diamagnetism of $[Ni(en)_2](3\text{-pytol})_2$ and occurrence of two bands at 16500 and 20350 cm^{-1} assigned to the $^1A_{1g} \rightarrow {}^1B_{2g}$ and $^1B_{1g}$ transitions, respectively suggest it to be square planar. Other band at 32035–31645 cm^{-1} in **3** and **4,** respectively, may be due to charge transfer/intraligand transition [39].

6. Crystal structure description of $\{[Ni(en)_2(pot)_2]0.5CHCl_3\}$ (3)

As depicted in Fig. 1, the basic building unit consists of one Ni cation, two (pot)$^-$ ligands and two neutral ethylenediamine (en) molecules resulting in a distorted octahedral geometry with NiN_6 core. One unit of $\{[Ni(en)_2(pot)_2]0.5CHCl_3\}$ possesses the centrosymmetric nickel at inversion center. There are interstitial $CHCl_3$ molecules in the structure of **3** (Fig. 1). The two axial (pot)$^-$ anions around each Ni(II) at *trans* positions are bonded through nitrogen atoms at a distance of Ni1–N(3A), Ni1–N(3A)#1 = 2.117(5) (#1 = $-x+1,-y+1,-z+1$) , Ni2–N(3B), Ni2–N(3B)#1 = 2.121(5) (#1 = $-x+1,-y+1,-z+1$) and Ni3–N(5C) = 2.109(4), Ni3–N(7C) = 2.110(4) Å, respectively and the four equatorial sites are occupied by two bidentate *N,Ń*-ethylenediamine. The bonding of en to Ni(II) through Ni1–N1A = Ni1–N1A#1 and Ni1–N2A = Ni1–N2A#1 with a bond distances of 2.113(4) and 2.125(4) Å form two five membered chelate rings $NiN2AC_2N1A$ and $NiN2BC_2N1B$ with bite angles of 82.28(13)° and 82.03(13)°, respectively. All N1A, N1A#1, N1B and N1B#1 atoms of en involved in bonding with Ni1 lie in the same plane. Similar arrangement of other two units of $[Ni2(en)_2]^{2+}$ and $[Ni3(en)_2]^{2+}$ core are also observed. The geometry and bonding parameters within en molecules are in good agreement with those of related compounds eg $[Ni(en)_2(3\text{-pyt})_2]$ {(3-pyt)$^-$ = 5-(3-pyridyl)-1,3,4-oxadiazole-2-thione [27], [Ni{*trans*-(L)$_2$(en)$_2$]{L = N-(5-chlorouracilato) [40], isothiocyanato [41] and salicylato [42]}. Almost planar (pot)$^-$ ligands in complex **3** bonded to Ni(II) and designated as Ni1–N(3A) = Ni1–N(3A)#1 = 2.117(5), Ni2–N(3B) =



Scheme 1.

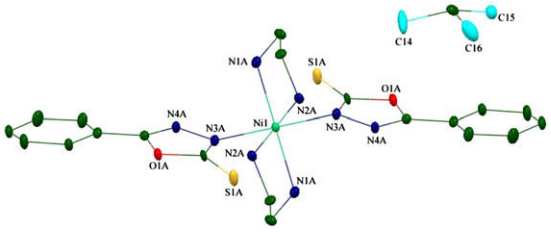


Fig. 1. Molecular structure of {[Ni(en)$_2$(pot)$_2$]0.5CHCl$_3$} with heteroatom labeling scheme. The hydrogen atoms are omitted for clarity.

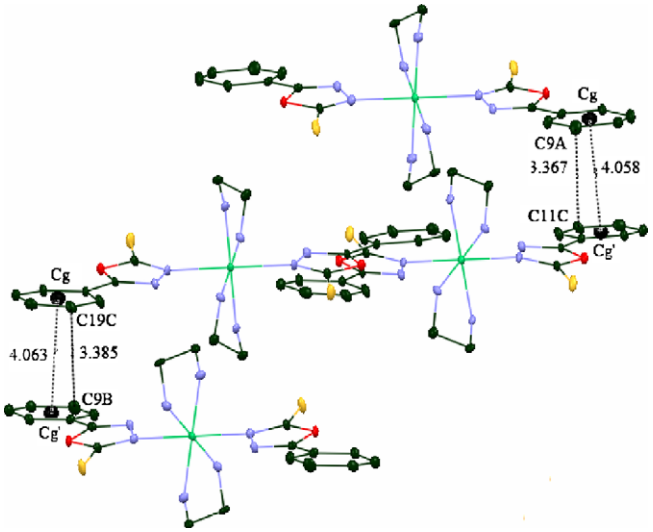


Fig. 2. Mercury view of the crystal packing of {[Ni(en)$_2$(pot)$_2$]0.5CHCl$_3$} showing face to face (π···π) interactions between two phenyl rings.

Ni2–N(3B)#1 = 2.121(5) and Ni3–N(5C) = 2.109(4), Ni3–N(7C) = 2.110(4) Å are almost equal but significantly lengthened in comparison to the corresponding bond lengths of 1.907(3) and 1.895(4) Å reported for [Ni{η^5-(2-dimethylaminoethyl)cyclopentadienyl}(pti)]0.5(C_7H_8) [43], [Ni{η^5-(1-methy-lindene)(pti)(PPh_3)] [44], {pti = phthalimidate} respectively, but comparable to those of ca. 2.1090(14), 2.1150 Å encountered in the related [Ni(en)$_2$(3-pyt)$_2$] {(3-pyt)$^-$ = 5-(3-pyridyl)-1,3,4-oxadiazole-2-thione} [27] and ca. 2.102 Å for *N*-succinimido compound [Ni(succinimido(H_2O)$_4$] · 2H_2O [45]. All hydrogens of NH_2 groups are involved in H-bonding to the thione sulfur and oxadiazole nitrogen of (pot)$^-$, thus providing intramolecuar hydrogen bonding in all three units of the complex **3**. These hydrogen bondings have stabilized **3** in the solid state (Table 3). The shortest intra and interchain Ni···Ni separations are 12.208 and 8.203 Å, respectively. The intermolecular hydrogen bonding between the thione sulfur of one (pot)$^-$ anion of one asymmetric unit with the hydrogen atom of the phenyl ring (S···H = 2.954 Å) extended the chain in one dimension along a axis. Further two π···π interactions between carbon atoms of adjacent phenyl rings have distances of 3.367 (C9A...C11C) and 3.385 (C9B...C19C) Å while centroid (Cg_1)–centroid (Cg_2) separation be-

tween two phenyl rings is 4.058 and 4.063 Å which cause the chain to grow in one dimension (Fig. 2). This one dimensional framework is extended into two dimensional network due to the presence of $[Ni(en)_2]^{2+}$ unit perpendicular to *trans* $(pot)^-$ ligands. The whole arrangement provides one dimensional open channel enclosing the $CHCl_3$ molecules and gives 2D dimensional supramolecular architecture (Fig. 3). The $CHCl_3$ molecules are stable in the open channels due to the presence of weak intermolecular interactions between phenyl ring of $(pot)^-$ and hydrogen atom of the $CHCl_3$.

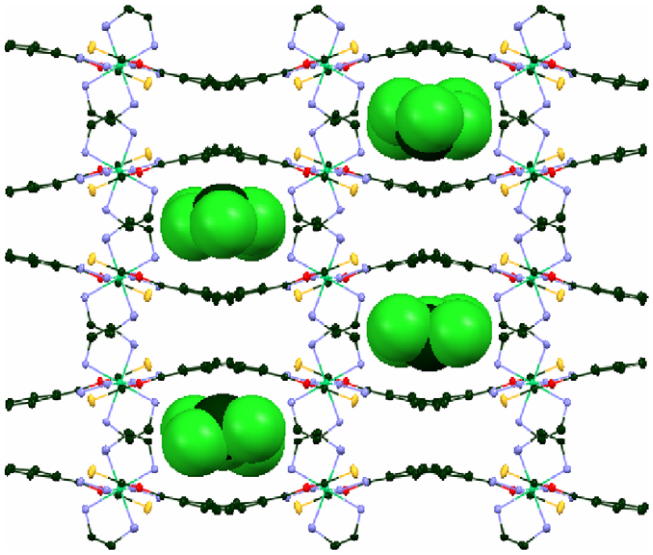


Fig. 3. The molecular packing of $\{[Ni(en)_2(pot)_2]0.5CHCl_3\}$ (**3**), view along *a* axis. The $CHCl_3$ molecules are represented as space filling form.

7. Crystal structure of $[Ni(en)_2](3\text{-pytol})_2$ (4)

The X-ray crystal structure analysis of **4** shows that $[Ni(en)_2]^{2+}$ cation is surrounded by two $(3\text{-pytol})^-$ anions. In the centrosymmetric unit of $[Ni(en)_2](3\text{-pytol})_2$, the metal ion has a square planar geometry where Ni(II) is bonded with four symmetry related N-atoms of two en molecules and is ionically linked with thiolato sulfur of two $(3\text{-pytol})^-$ anions. The two en molecules chelate Ni(II) at equatorial positions and two $(3\text{-pyt})^-$ occupy apical positions in *trans* manner (Fig. 4). The Ni–N distances in complex **4** are in the range of 2.0138(13)–2.0235(12) Å which is almost normal for Ni–N (amine) bonds [21,30]. The bite angle for NiN_4 core is 84.83(5) indicating a substantial distortion in the molecule with two five membered NiC_2N_2 chelate rings around Ni(II). In the $[Ni(en)_2]^{2+}$ the nickel(II) and the donor atoms of ethylenediamine lie in the same plane. Each $[Ni(en)_2]^{2+}$ forms a pair of weak intermolecular Ni···S interactions at a distance of 2.997 Å. The Ni(II) present in a D_{2h} symmetry is bonded to four N atoms of NH_2 group of en which offer interesting hydrogen bonding packing. The elements of the structure are joined to each other in the crystal packing by means of extended system of hydrogen bonding. The π···π interaction is observed between two adjacent pyridine rings as shown in Fig. 5.

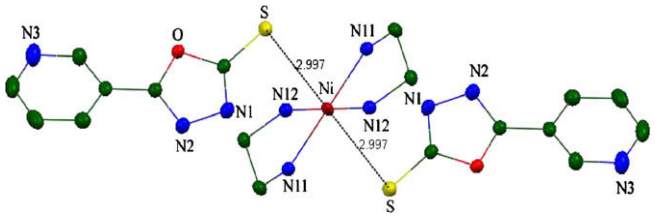


Fig. 4. Molecular structure of $\{[Ni(en)_2](3\text{-pytol})_2$ (**4**) with heteroatom labeling scheme.

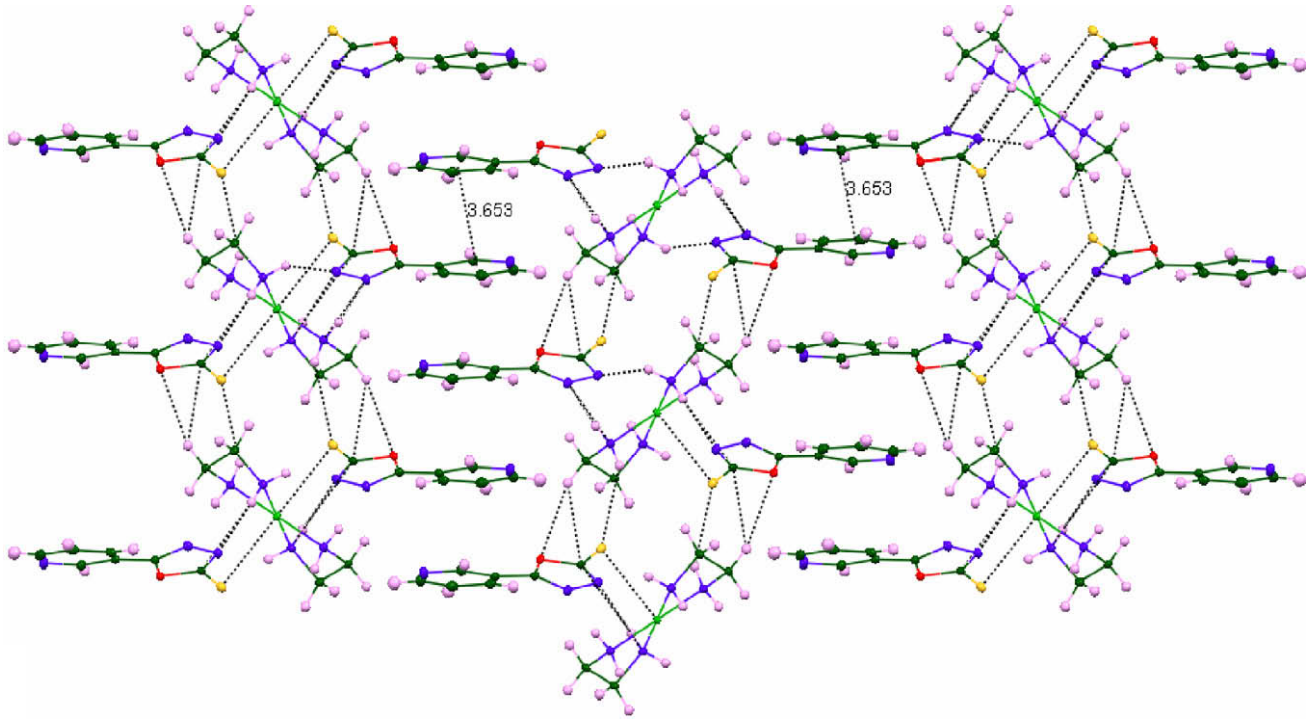


Fig. 5. Mercury view of the crystal packing of $[Ni(en)_2](3\text{-pytol})_2$ showing face to face (π···π) interaction, weak Ni···S and weak C···S interactions along with hydrogen bonding.

The centroid ($C_g$pyridine) to centroid ($C_g$pyridine) separation is of 3.653 Å. The hydrogen bonding parameters are listed in Table 5. The X-ray analysis reveals that in the solid state the molecules are self assembled via. N–H···N, N–H···O and N–H···S intermolecular hydrogen bonding and weak C···S interactions (4.274 Å) between the thioalto sulfur and carbon of phenyl ring. This hydrogen bonding together with π···π interaction form metal organic framework of three dimensional network (Fig. 5).

8. Conclusion

Two new complexes $[Ni(en)_2(pot)_2]0.5CHCl_3$ and $[Ni(en)_2](3\text{-pytol})_2$ containing en and 1,3,4-oxadiazole have been synthesized and fully characterized by X-ray techniques. The desulphurization of the *N*-acylhydrazinecarbodithioate {–C(O)–NHNH–C(S)–} moiety was observed during complexation. The $[Ni(en)_2](3\text{-pytol})_2$ is a rare example of Ni(II) complex containing two en molecules in a square planar geometry.

Acknowledgments

One of the authors (Mamata Singh) is thankful to CSIR, New Delhi, India for the award of SRF in a Project supported by Grant Nos. 01(2152)07/EMR-II and 9/13(160)/2008EMR-I.

Appendix A. Supplementary data

CCDC 656471 and 693644 contain the supplementary crystallographic data for **3** and **4**. These data can be obtained free of charge via http://www.ccdc.cam.ac.uk/conts/retrieving.html, or from the Cambridge Crystallographic Data Centre, 12 Union Road, Cambridge CB2 1EZ, UK; fax: (+44) 1223-336-033; or e-mail: deposit@ccdc.cam.ac.uk. Supplementary data associated with this article can be found, in the online version, at doi:10.1016/j.poly.2008.11.046.

References

[1] M.A. Ali, S.E. Livingston, Coord. Chem. Rev. 13 (1974) 101.
[2] J.P. Scovill, D.L. Klayman, C. Lambros, G.E. Childs, J.D. Notsch, J. Med. Chem. 27 (1984) 87.
[3] J.P. Scovill, D.L. Klayman, C.F. Franchino, J. Med. Chem. 25 (1982) 1261.
[4] M. Das, S.E. Livingston, Inorg. Chim. Acta 19 (1976) 5.
[5] A. Marchi, L. Uccelli, L. Marvelli, R. Rossi, M. Giganti, V. Bertolasi, V. Ferretti, J. Chem. Soc., Dalton Trans. (1996) 3105.
[6] A.I. El-Said, Trans. Met. Chem. 28 (2003) 749.
[7] M.A. Ali, A.H. Mirza, M.H.S.A. Hamid, F.H. Bujang, P.V. Bernhardt, Polyhedron 23 (2004) 2405.
[8] N.R. Pramanik, S. Ghosh, T.K. Raychaudhuri, S. Ray, R.J. Butcher, S.S. Mandal, Polyhedron 23 (2004) 1595.
[9] M.A. Ali, A.H. Mirza, M. Nazimuddin, R. Ahmed, L.H. Gahan, P.V. Bernhardt, Polyhedron 22 (2003) 1471.
[10] M.A. Ali, A.H. Mirza, A.L. Tan, L.K. Wei, P.V. Bernhardt, Polyhedron 23 (2004) 2037.
[11] S. Gou, X. You, Z. Zu, Z. Zhou, K. Yu, Polyhedron 10 (1991) 1363.
[12] A. Hetzheim, K. Möckel, Adv. Heterocycl. Chem. 7 (1966) 183.
[13] B.L. Sharma, S.K. Tandon, Pharmazie 39 (H-12) (1984) 858.
[14] J.R. Reid, N.D. Heindel, J. Heterocycl. Chem. 13 (1976) 925.
[15] H. Foks, J. Mieczkowska, M. Janowiec, Z. Zwolska, Z. Andrzejczyk Chem. Heterocycl. Comp. 38 (2002) 810.
[16] E. Hoggarth, J. Chem. Soc. (1952) 4811.
[17] P. Tripathi, A. Pal, V. Jancik, A.K. Pandey, J. Singh, N.K. Singh, Polyhedron 26 (2007) 2597.
[18] O.H. Amin, L.J. Al-Hayaly, S.A. Al-Jibori, T.A.K. Al-Allaf, Polyhedron 23 (2004) 2013.
[19] C.-L. Ma, G.-R. Tian, R.-F. Zhang, Polyhedron 24 (2005) 1773.
[20] Z.-H. Zhang, Y.-L. Tian, Y.-M. Guo, Inorg. Chim. Acta 360 (2007) 2783.
[21] M. Du, Z.-H. Zhang, X.-J. Zhao, Q. Xu, Inorg. Chem. 45 (2006) 5785.
[22] Z.-H. Zhang, C.-P. Li, Y.-L. Tian, Y.-M. Guo, Inorg. Chem. Commun. 11 (2008) 326.
[23] Y.-T. Wang, G.-M. Tang, W.-Y. Ma, W.-Z. Wan, Polyhedron 26 (2007) 782.
[24] Y.-T. Wang, G.-M. Tang, J. Coord. Chem. 60 (2007) 2139.
[25] Y.-T. Wang, G.-M. Tang, Inorg. Chem. Commun. 10 (2007) 3.
[26] Y.-T. Wang, G.-M. Tang, Z.-W. Qiang, Polyhedron 26 (2007) 4542.
[27] M. Singh, R.J. Butcher, N.K. Singh, Polyhedron 27 (2008) 3151.
[28] T. Curtius, J. Prakt. Chem. 50 (1894) 278.
[29] B.W. Brown, E.C. Lingafelter, Acta Crystallogr. 16 (1963) 753.
[30] M. Busch, M. Starke, J. Prakt. Chem. 93 (1916) 49.
[31] A.I. Vogel, A Text Book of Quantitative Inorganic Analysis, 3rd ed., ELBS, Longman, London, 1969.
[32] Oxford Diffraction (2007). CrysAlis RED and CrysAlis CCD Versions 1.171.31.8. Oxford Diffraction Ltd. Abingdon, Oxafordshire, England.
[33] G.M. Sheldrick, Acta Crystallogr., Sect. A 46 (1990) 467.
[34] G.M. Sheldrick, SHELXL-97, Program for Crystal Structure Refinement, University of Göttingen, Germany, 1997.
[35] I.J. Bruno, J.C. Cole, P.R. Edgington, M. Kessler, C.F. Macrae, P. McCabe, J. Pearson, R. Taylor, Acta Crystallogr. Sect. B 58 (2002) 389.
[36] L.J. Farrugia, J. Appl. Cryst. 30 (1997) 565.
[37] N.K. Singh, M. Singh, A.K. Pandey, M.K. Bharty, R.J. Butcher, Acta Crystallogr. Sect. E 63 (2007) 04327.
[38] P. Gómez-Saiz, J. Garcia-Tojal, M.A. Maestro, F.J. Arnaiz, A. Francisco, T. Roja, Inorg. Chem. 41 (2002) 1345.
[39] A.B.P. Lever, Inorganic Electronic Spectroscopy, 2nd ed., Elsevier, Amsterdam, 1984.
[40] A. Terrón, A. Garcia-Raso, J.J. Fiol, S. Amenqual, M. Barceló-Oliver, R.M. Tótaro, M.C. Apella, E. Molins, I. Mata, J. Inorg. Biochem. 98 (2004) 632.
[41] P.J. Squattrito, T. Iwamoto, S.-I. Nishikiori, Chem. Commun. (1996) 2665.
[42] H. Icbudak, H. Olmez, O.Z. Yesilel, F. Arslan, P. Naumov, G. Jovanovski, A.R. Ibrahim, A. Usman, H.-K. Fun, S. Chantrapromma, S.W. Nq, J. Mol. Struct. 657 (2003) 255.
[43] O. Segnitz, M. Winter, R.A. Fischer, J. Organomet. Chem. 691 (2006) 4733.
[44] I. Dubuc, M.-A. Dubois, F. Bélanger-Gariépy, D. Zargarian, Organometallics 18 (1999) 30.
[45] H.J. Cumming, D. Hall, Acta Crystallogr. Sect. B 32 (1976) 1281.

Polyhedron 28 (2009) 467–472

Contents lists available at ScienceDirect

Polyhedron

journal homepage: www.elsevier.com/locate/poly

Synthesis, characterization and crystal structures of organolead dithiolate compounds displaying transannular interactions D···Pb (D = O, S)

Simplicio González-Montiel [a], Benito Flores-Chávez [a], José G. Alvarado-Rodríguez [a,*], Noemí Andrade-López [a], Juan Antonio Cogordan [b]

[a] Centro de Investigaciones Químicas, Universidad Autónoma del Estado de Hidalgo, Km. 4.5 Carretera Pachuca-Tulancingo, Col. Carboneras, Mineral de la Reforma, Hidalgo, C.P. 42184, Mexico
[b] Instituto de Química, Universidad Nacional Autónoma de México, Circuito Exterior, Ciudad Universitaria, D.F. México. C.P. 04510, Mexico

ARTICLE INFO

Article history:
Received 10 October 2008
Accepted 18 November 2008
Available online 26 December 2008

Keywords:
Organolead compounds
Dithioligands
Hypercoordinated compounds
Non-bonded interactions
Structure elucidation

ABSTRACT

Treatment of Ph_2PbCl_2 with $O(C_6H_4SH)_2$ (**1**a), $S(C_6H_4SH)_2$ (**2**a) and $S(C_6H_3SH)_2O$ (**3**a) afforded the stable organolead compounds [{$O(C_6H_4S)_2$}$PbPh_2$] (**1**b), [{$S(C_6H_4S)_2$}$PbPh_2$] (**2**b) and [{$S(C_6H_3S)_2O$}$PbPh_2$] (**3**b). X-ray structure determinations of dithiolate-diphenyl lead compounds **1**b–**3**b revealed that the trichalcogenated ligands are tridentate in **1**b and **2**b, and bidentate in **3**b. The lead atom acts as an acceptor atom exhibiting weak intramolecular transannular interactions with the donor D atom, with tetrahedral distortions of 48% for **1**b, 51% for **2**b and 45% for **3**b. The local geometry at the lead atom is described as monocapped tetrahedral. The crystal packing of title compounds is stabilized by several non-bonded interactions.

© 2008 Elsevier Ltd. All rights reserved.

1. Introduction

Hypercoordination through non-bonded intramolecular as well as intermolecular interactions is well documented in compounds containing group 14 elements [1,2]. So far lead, the heaviest atom in the group with environmental and toxicological relevance, show the broadest possibilities for coordination numbers and coordination geometries. The higher coordination numbers are usually achieved by intra- or intermolecular bonding with ligands potentially polydentate bearing several soft and/or hard donors [3–7].

On the other hand, we are interested in the synthesis and design of ligands capable to promote the expansion of the coordination number of heavy p-block elements; such ligands are $D(C_6H_4SH)_2$ [D = O, S] and $S(C_6H_4SH)_2O$ and they yield hypercoordinated compounds of type **I** and **II**, respectively [8–12]. In these compounds, hypercoordination is achieved by a transannular D···A interaction (Scheme 1). In general, has been observed that the coordination ability of the ligands can be tuned by the appropriate choice of the exocyclic ligands attached to A, prompting a bidentate or, in most of the cases, tridentate coordination pattern.

Following with the study of hypercoordination in group 14 elements, herein we report the synthesis and characterization of three diphenyl lead organometallic compounds containing a transannular interaction D···Pb, where the flexibility of the ligands is crucial in order to achieve hypercoordination at the lead atom. The choice of the $PbPh_2$ moiety is widely supported due is less toxic than their aliphatic counterparts. The molecular and crystal structures of compounds **1**b, **2**b and **3**b were obtained by X-ray diffraction studies. The detailed description of the synthesis, spectroscopic characterization and crystallographic data are presented and discussed below.

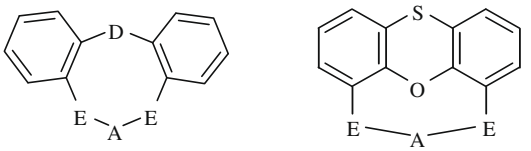
2. Experimental

2.1. Materials and methods

All manipulations were performed under a dry, oxygen-free argon atmosphere using standard Schlenk techniques unless noted otherwise. Solvents were dried by standard methods and distilled prior to use. $S(C_6H_4SH)_2$, [13] $O(C_6H_4SH)_2$ [8] and $S(C_6H_3SH)_2O$ [12] were synthesized according to literature methods. Ph_2PbCl_2 and *n*-BuLi (1.6 M, in hexanes) were purchased from Alfa Aesar and Aldrich respectively and were used as supplied. Melting points were determined with a Mel-Temp II instrument and are uncorrected. Spectra were recorded with the following instruments. Mass spectra: EI, 70 eV, Hewlett Packard MS-598 mass spectrometer. The elemental analyses were recorded with a Perkin–Elmer Series II CHNS/O Analyzer. The IR spectra were recorded in the 4000–400 cm^{-1} range with a Perkin–Elmer System 2000 FT-IR spectrometer, as KBr pellets. The NMR spectra were recorded with a Jeol Eclipse 400 spectrometer at 25 °C, with the residual

* Corresponding author. Tel.: +52 771 7172000.
E-mail address: josegalvarado@yahoo.com (J.G. Alvarado-Rodríguez).

0277-5387/$ - see front matter © 2008 Elsevier Ltd. All rights reserved.
doi:10.1016/j.poly.2008.11.012



I II

Scheme 1.

protio-solvent signal used as referenced for ^{1}H NMR spectra. ^{13}C{^{1}H} NMR spectra were referred through the solvent peaks. Chemical shifts are quoted on the δ scale (downfield shifts are positive) relative to tetramethylsilane (^{1}H, 13C{1H} NMR spectra). Spectra were recorded at 25 °C. ^{1}H NMR spectra; 399.78 MHz, ^{13}C{1H} NMR spectra; 100.53 MHz.

2.2. Synthesis of diphenyl lead organometallic compounds

2.2.1. Synthesis of [{O(C$_6$H$_4$S)$_2$}PbPh$_2$] (**1**b)

n-BuLi in hexanes (1.6 M, 1.6 mL, 2.6 mmol) was added to a solution containing O(C$_6$H$_4$SH)$_2$ (**1**a, 0.27 g, 1.15 mmol) in THF (40 mL) at 0 °C. After the solution was stirred for 30 min, was slowly added a suspension of Ph_2PbCl_2 (0.50 g, 1.15 mmol) in THF (30 mL). The suspension was dissolved, and the yellow solution obtained was stirred for 24 h at room temperature. The white solid formed was filtered out and the solution dried by means of a column of Celite and Na_2SO_4. The solvent was removed in vacuum. The resulting yellow solid was dissolved in chloroform. By slow evaporation **1**b was obtained as yellow crystals. Yield: 66% (0.45 g, 0.76 mmol). Mass spectra (EI-MS, 70 eV) *m*/*z* (rel int) = 594 (5) [M$^+$], 517(3) [M$^+$−Ph], 439(8) [M$^+$−2Ph−H], 397(10) [Ph_2PbSH_2+1], 285(8) [PhPb$^+$], 200(10) [O(C$_6$H$_4$)$_2$S$^+$]. M.p. 115–119 °C. *Anal. Calc.* for $C_{24}H_{18}OPbS_2$ C, 48.55; H, 3.06. Found: C, 48.75; H, 3.12%. ^{1}H NMR ($CDCl_3$): δ = 7.62 [d, 4H, $^3J_H{}^5{-}_H{}^6$ = 7.52 Hz, $^3J(^1H{-}^{207}Pb)$ = 107 Hz, H^5), 7.57 (m, 2H, H^1), 7.40 (t, 4H, $^3J_H{}^6{-}_H{}^5 = {}^3J_H{}^6{-}_H{}^7$ = 7.52 Hz, 4H H^6), 7.29 (m, 2H, H^7), 7.02 (m, 4H, H^2 and H^3), 6.82 (m, 2H, H^4) ppm. NMR ^{13}C{1H} ($CDCl_3$): δ = 157.5 [$^1J(^{13}C{-}^{207}Pb)$ = 535.8 Hz, C^{5a}], 155.3 [$^3J(^{13}C{-}^{207}Pb)$ = 19.2 Hz, C^{4a}], 135.7 [$^2J(^{13}C{-}^{207}Pb)$ = 93.8 Hz, C^5], 135.1 [$^3J(^{13}C{-}^{207}Pb)$ = 20.1 Hz, C^1], 130.2 [$^3J(^{13}C{-}^{207}Pb)$ = 113.8 Hz, C^6], 129.9 [$^4J(^{13}C{-}^{207}Pb)$ = 25.4 Hz, C^7], 127.9 [$^2J(^{13}C{-}^{207}Pb)$ = 26.2 Hz, C^{1a}], 127.2 [C^2], 124.4 [C^3], 119.6 [C^4] ppm. IR (KBr pellet, cm^{-1}): 3063, 1693, 1568, 1461, 1433, 1430, 1260, 11025, 1011, 968, 800, 755, 727, 691.

2.2.2. Synthesis of [{S(C$_6$H$_4$S)$_2$}PbPh$_2$] (**2**b)

This compound was prepared in a similar fashion to compound **1**b, with S(C$_6$H$_4$SH)$_2$ (**2**a, 0.3 g, 1.2 mmol), *n*-BuLi in hexanes (1.6 M, 1.7 mL, 2.7 mmol) and Ph_2PbCl_2 (0.52 g, 1.2 mmol) in THF. By slow evaporation **2**b was obtained as yellow crystals and washed with warm isopropanol. Yield: 68% (0.50 g, 0.82 mmol). Mass spectra (EI-MS, 70 eV) *m*/*z* (rel int) = 610 (5) [M$^+$], 533 (55) [M$^+$−Ph], 456 (5) [M$^+$−Ph−Ph], 439 (20) [Ph_3Pb^+], 397 (5) [Ph_2PbSH_2+1], 285 (20) [PhPb$^+$], 248 (65) [S(C$_6$H$_4$)$_2$S$_2^+$], 216 (100) [S(C$_6$H$_4$)$_2$S$^+$]. M. p. 290–294 °C. *Anal. Calc.* for $C_{24}H_{18}PbS_3$ C, 47.27; H, 2.98. Found: C, 47.10; H, 3.05%. ^{1}H NMR ($CDCl_3$): δ = 7.06 (dd, $^3J_H{}^3{-}_H{}^2 = {}^3J_H{}^3{-}_H{}^4$ = 7.60 Hz, $^4J_H{}^3{-}_H{}^1$ = 1.40 Hz, 2H, H^3), 7.20 (ddd, $^3J_H{}^2{-}_H{}^1 = {}^3J_H{}^2{-}_H{}^3$ = 7.60 Hz, $^4J_H{}^2{-}_H{}^4$ = 1.40 Hz, 2H, H^2), 7.33 (m, 2H, H^7), 7.44 (m, 6H, H^4 y H^6), 7.67 [m, 6H, H^4 and H^5 $^3J(^1H{-}^{207}Pb)$ = 120 Hz] ppm. ^{13}C{1H} NMR ($CDCl_3$): δ = 160.4 [$^1J(^{13}C{-}^{207}Pb)$ = 493.9 Hz, C^{5a}], 141.8 [$^3J(^{13}C{-}^{207}Pb)$ = 34.6 Hz, C^{4a}], 137.0 [$^2J(^{13}C{-}^{207}Pb)$ = 24.6 Hz, C^{1a}], 135.4 [$^2J(^{13}C{-}^{207}Pb)$ = 94.2 Hz, C^5], 134.8 [$^3J(^{13}C{-}^{207}Pb)$ = 22.7 Hz, C^1], 133.6 [C^4], 130.3 [$^3J(^{13}C{-}^{207}Pb)$ = 107.6 Hz, C^6], 129.8 [$^4J(^{13}C{-}^{207}Pb)$ = 25.8 Hz, C^7], 128.2 [C^2], 126.9 [C^3] ppm. IR (KBr pellet, cm^{-1}): 3057, 3040, 1565, 1471, 1438, 1430, 1242, 1099, 1040, 1011, 994, 840, 746, 720, 687 cm^{-1}.

2.2.3. Synthesis of [{S(C$_6$H$_4$S)$_2$O}PbPh$_2$] (**3**b)

Ph_2PbCl_2, (0.13 g, 0.30 mmol) was added to a solution of S(C$_6$H$_3$SH)$_2$O (**3**a, 0.08 g, 0.30 mmol) in 15 mL of dry methanol at room temperature. The solution was refluxed overnight. The yellow solid obtained was filtered and dissolved in chloroform (30 mL). By slow evaporation, **3**b was obtained as yellow crystals. Mass spectra (EI-MS, 70 eV) *m*/*z* (rel int) = 624 (25) [M$^+$], 547(100) [M$^+$−Ph], 470(10) [M$^+$−2Ph−H], 438(50) [M$^+$−2Ph−H], 396(6) [Ph_2PbSH_2], 285(8) [PhPb$^+$], 208(38) [Pb$^+$]. Yield: 54% (0.10 g, 0.16 mmol). M.p. 135–137 °C. *Anal. Calc.* for $C_{24}H_{16}OPbS_3$, C 46.21, H 2.59. Found: C 47.28, H 2.79%. ^{1}H NMR ($CDCl_3$): δ = 7.39 (dd, $^3J_H{}^1{-}_H{}^2$ = 8.00 Hz, $^4J_H{}^1{-}_H{}^3$ = 2.00 Hz, 2H, H^1), 7.26 (m, 6H, H^5, H^6, H^7), 6.93 (dd, $^3J_H{}^2{-}_H{}^1 = {}^3J_H{}^2{-}_H{}^3$ = 8.00 Hz, 2H, H^2), 6.77 (dd, $^3J_H{}^3{-}_H{}^1$ = 8.00 Hz, $^4J_H{}^3{-}_H{}^2$ = 2.00 Hz, 2H, H^3) ppm. ^{13}C{^{1}H} NMR ($CDCl_3$): δ = 155.7 [$^1J(^{13}C{-}^{207}Pb)$ = 560 Hz, C^{5a}], 150.0 [$^3J(^{13}C{-}^{207}Pb)$ = 39.2 Hz, C^{1a}], 135.4 [$^2J(^{13}C{-}^{207}Pb)$ = 90.7 Hz, C^5], 132.9 [$^3J(^{13}C{-}^{207}Pb)$ = 20.0 Hz, C^2], 130.4 [$^3J(^{13}C{-}^{207}Pb)$ = 116.1 Hz, C^6], 130.0 [$^4J(^{13}C{-}^{207}Pb)$ = 26.1 Hz, C^7], 126.3 [$^2J(^{13}C{-}^{207}Pb)$ = 26.1 Hz, C^1], 124.7 [C^3], 124.3 [C^4], 120.7 [C^{4a}] ppm. IR (KBr pellet, cm^{-1}): 3059, 3037, 1566, 1469, 1431, 1401, 1223, 1197, 1055, 1011, 904, 872, 831, 770, 723, 686.

2.3. X-ray crystallography

Suitable single crystals of the compounds **1**b, **2**b (thin plates) and **3**b were grown by slow evaporation from a chloroform solution. X-ray diffraction data were collected at room temperature on a CCD Smart 6000 diffractometer through the use of Mo Kα radiation (λ = 0.71073 Å, graphite monochromator). Data were integrated, scaled, sorted, and averaged using the SMART software package. The primary structure of **2**b was solved by heavy atom method using SHELXS86 [14] and the structures of **1**b and **3**b were

Table 1
Selected crystallographic data for compounds **1**b, **2**b and **3**b.

Compound	**1**b	**2**b	**3**b
Empirical Formula	$C_{24}H_{18}OPbS_2$	$C_{24}H_{18}PbS_3$	$C_{24}H_{16}OPbS_3$
Mr [g/mol]	593.69	609.75	623.74
Crystal size (mm)	0.28 × 0.14 × 0.08	0.27 × 0.10 × 0.04	0.62 × 0.43 × 0.40
Color	Yellow	Yellow	Yellow
Crystal system	Triclinic	Triclinic	Triclinic
Space group	$P\bar{1}$	$P\bar{1}$	$P\bar{1}$
ρ_{calc} (Mg m^{-3})	1.796	1.848	1.844
Z	2	2	2
a (Å)	9.806(1)	9.946(4)	9.115(1)
b (Å)	10.338(1)	10.383(5)	10.716(1)
c (Å)	11.044(1)	11.354(5)	12.460(2)
α (°)	99.098(2)	72.367(1)	76.705(3)
β (°)	96.601(2)	79.010(9)	71.498(3)
γ (°)	90.472(3)	88.678(9)	85.480(2)
V	1097.8(2)	1096.1(8)	1123.1(3)
μ (mm^{-1})	7.886	7.989	7.802
F(000)	568	584	596
θ Range (°)	1.88–26.01	1.92–26.11	1.77–26.09
Goodness-of-fit	1.116	1.003	1.042
Absorption correction	SADABS	SADABS	SADABS
Reflections collected	13245	13633	13624
Unique reflections, R_{int}	4286, 0.0330	4338, 0.0970	4416, 0.0418
R_1, wR_2 [$I > 2\sigma(I)$]	0.0315, 0.0724	0.0523, 0.1045	0.0337, 0.0736
R_1, wR_2 (all data)	0.0440, 0.0860	0.1016, 0.1311	0.0473, 0.0819
Large residuals (e Å^{-3})	0.905, −0.614	1.273, −0.803	0.765, −0.708

solved by direct methods using SHELXTL NT Version 5.10 and refined by full-matrix least squares against F^2 [15]. An empirical absorption correction based on the multiple measurement of equivalent reflections was applied by using the program SADABS [16]. The displacement parameters of non-hydrogen atoms were refined anisotropically. The positions of the hydrogen atoms were kept fixed with a common isotropic displacement parameter. Selected crystallographic data are given in Table 1.

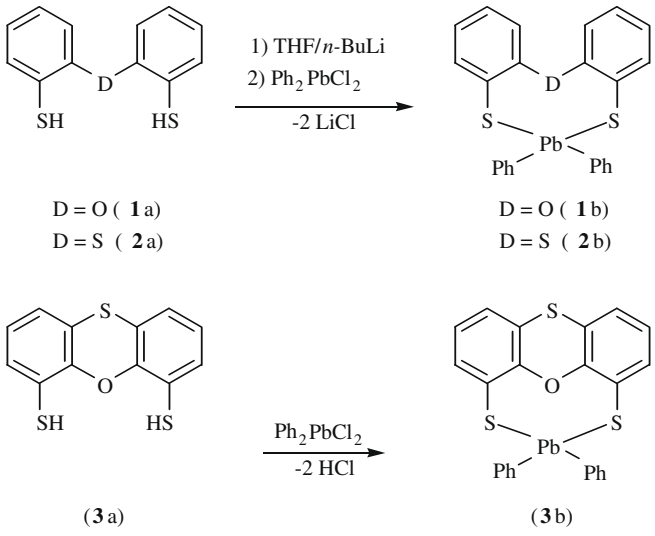
3. Results and discussion

3.1. Synthesis

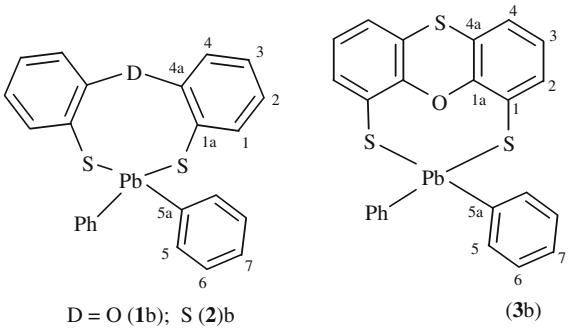
The ligands $O(C_6H_4SH)_2$ (**1**a), $S(C_6H_4SH)_2$ (**2**a) and $S(C_6H_3SH)_2O$ (**3**a) were prepared following the reported method [8,13,12]. The compounds **1**b and **2**b were obtained from the reaction of Ph_2PbCl_2 in THF at 0 °C with the dilithium salt of **1**a and **2**a generated *in situ*, yielding the corresponding Pb(IV) compounds as yellow crystals. **3**b was obtained from the reaction of **3**a with Ph_2PbCl_2 in hot methanol (see Scheme 2). All compounds are air-stable, soluble in chloroform, methylene chloride and benzene, and insoluble in *n*-hexane, pentane, methanol and 2-propanol.

3.2. NMR spectra

NMR spectra of all the complexes were recorded in $CDCl_3$ solutions at room temperature and the chemical shifts are relatives to TMS. The assignments of these compounds were performed by 2D



Scheme 2.



Scheme 3.

experiments (COSY, HETCOR and COLOC). In solution the two DC_6H_4SPbPh [D = O (**1**b); S (**2**b)] and $S(C_6H_3S)OPbPh$ (**3**b) halves are equivalents.

3.2.1. ^1H NMR spectra

In the spectra of title compounds, besides to the disappearance of the signal of the SH protons of the free ligands $O(C_6H_4SH)_2$ (δ = 3.90 ppm), $S(C_6H_4SH)_2$ (δ = 4.10 ppm) and $S(C_6H_3SH)_2O$ (δ = 4.05 ppm), is observed that the $PbPh_2$ moiety deshields the ortho protons to the thiolate sulfurs. Moreover, the protons 5-H in **1**b and **2**b show coupling with the ^{207}Pb isotope [$^3J(^1H-^{207}Pb)$ = 120 and 107 Hz for **1**b and **2**b, respectively]; in **3**b the coupling constant was not observed because the protons of the phenyl groups are displayed as a multiplet.

3.2.2. $^{13}C\{^1H\}$ NMR spectra

In the $^{13}C\{^1H\}$ spectra of title compounds is observed $^{13}C-^{207}Pb$ coupling, with one to four-bond coupling constants. Comparison of ^{13}C data and coupling constants with other related compounds is listed in Table 2, Scheme 3. The $^nJ(^{13}C-^{207}Pb)$ coupling constant diminishes in the order of C5a > C6 > C5 > C7 for the phenyl groups in all compounds. The magnitude of the $^1J(^{13}C-^{207}Pb)$ for the 5a *ipso*-carbon is similar to some thiolate lead compounds with coordination number four [6]. An increase in the coordination number of Pb(IV) is observed when the one-bond $^{13}C-^{207}Pb$ coupling constant and the chemical shift for the 5a *ipso*-carbon are increased; in our compounds we conclude that the O···Pb (**1**b and **3**b) and S···Pb (**2**b) transannular interactions are very weak or completely lacking in solution.

3.3. X-ray crystallographic studies

The crystal structures in crystalline solid state of the title compounds were determined by single crystal X-ray diffraction analy-

Table 2
$^{13}C\{^1H\}$ NMR chemical shift (δ values in ppm), coupling constant [$^nJ(^{13}C-^{207}Pb)$ in Hz] for **1**b, **2**b, **3**b and other related compounds.

Compound	C-1	C-2	C-3	C-4	C-1a	C-4a	C-5	C-5a	C-6	C-7
$O(CH_2CH_2S)_2PbPh_2$							135.6	158.7	129.9	129.2
							^2J = 88.4	[a]	^3J = 109.3	^4J = 19.1
$S(CH_2CH_2S)_2PbPh_2$							135.8	158.7	129.9	129.3
							^2J = 87.5	[a]	^3J = 108.4	^4J = 24.3
1b	135.1	127.2	124.4	119.6	127.9	155.3	135.7	157.5	130.2	129.9
	^3J = 20.1				^2J = 26.2	^3J = 19.2	^2J = 93.8	^1J = 535.8	^2J = 113.8	^4J = 25.4
2b	134.8	128.2	126.9	133.6	137.0	141.8	135.4	160.4	130.3	129.8
	^3J = 22.7				^2J = 24.6	^3J = 34.6	^2J = 94.2	^1J = 493.9	^3J = 107.6	^4J = 25.8
3b	126.3	132.9	124.7	124.3	150.0	120.7	135.4	155.7	130.4	130.0
	^2J = 26.1	^3J = 20.0			^3J = 39.2		^2J = 90.7	^1J = 558.9	^3J = 116.1	^4J = 26.1

[a] The $^1J(^{13}C-^{207}Pb)$ coupling constants are not reported by the authors [17].

ses. The crystals of **2**b were thin plates; this fact influenced the quality of the collected data. The molecular drawings of **1**b, **2**b and **3**b are depicted in Fig. 1 and selected bond lengths, angles and torsion angles are given in Table 3.

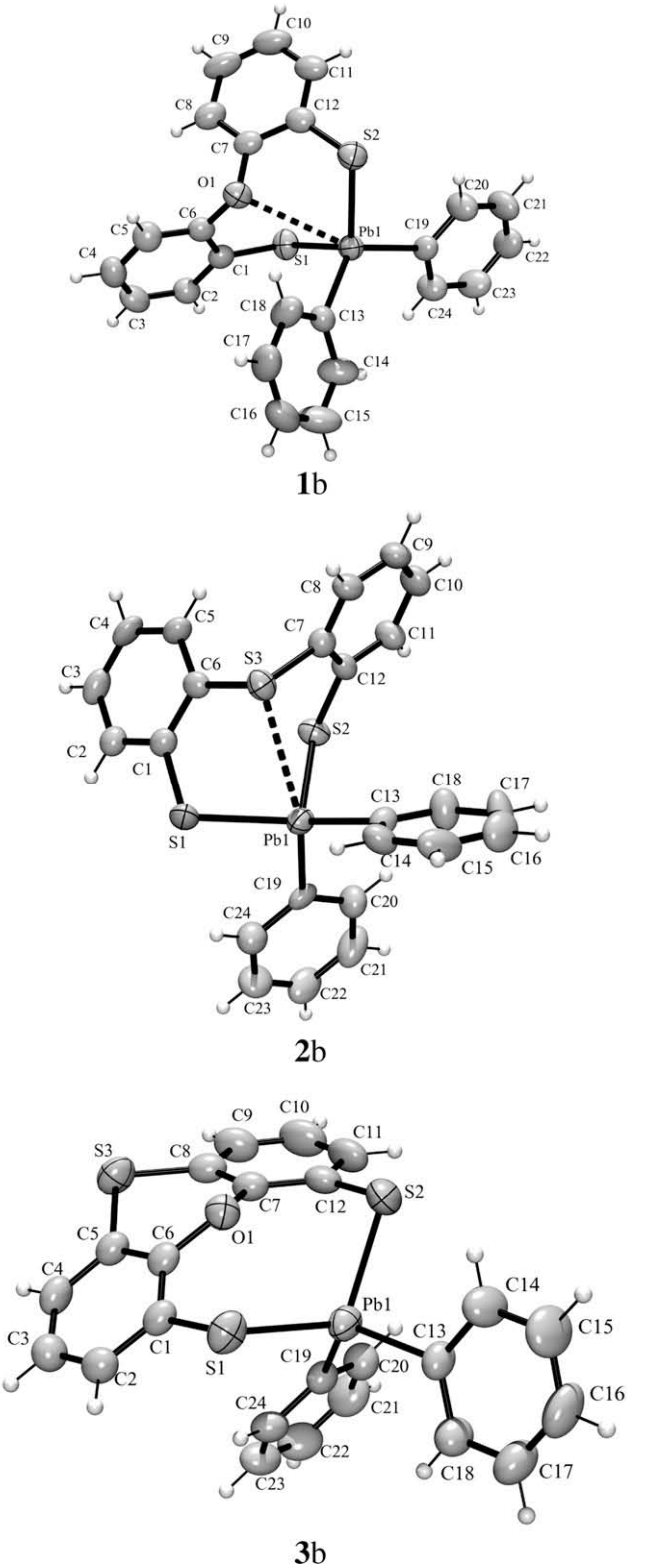


Fig. 1. Molecular structures of $[\{O(C_6H_4S)_2\}PbPh_2]$ (**1**b), $[\{S(C_6H_4S)_2\}PbPh_2]$ (**2**b) and $[\{S(C_6H_3S)_2O\}PbPh_2]$ (**3**b).

Table 3
Selected bond lengths (Å), angles and torsion angles (°) for **1**b, **2**b and **3**b.

Compound	$[\{O(C_6H_4S)_2\}PbPh_2]$ **1**b	$[\{S(C_6H_4S)_2\}PbPh_2]$ **2**b	$[\{S(C_6H_3S)_2O\}PbPh_2]$ **3**b
D	O1	S3	O1
D···Pb1	3.053(4)	3.280(3)	3.113(4)
Pb1–S1	2.531(2)	2.531(3)	2.519(2)
Pb1–S2	2.536(2)	2.521(3)	2.522(2)
Pb1–C13	2.201(6)	2.21(1)	2.198(6)
Pb1–C19	2.211(6)	2.21(1)	2.198(6)
S1–Pb1–S2	112.0(1)	106.5(1)	115.08(6)
C13–Pb1–C19	123.8(2)	114.8(4)	121.2(2)
S1–Pb1–C13	104.9(2)	120.3(3)	104.9(2)
S1–Pb1–C19	97.4(2)	105.4(3)	107.1(2)
S2–Pb1–C13	112.0(2)	108.1(3)	101.8(2)
S2–Pb1–C19	105.9(2)	99.5(3)	107.1(2)
C6–D–C7	118.1(4)	101.9(5)	117.7(4)
D → Pb1–C19	150.0(2)	161.9(3)	90.7(2)
D → Pb1–C13	85.7(2)	82.9(3)	148.0(2)
D → Pb1–S1	65.31(8)	65.73(9)	63.29(8)
C1–C6–D–C7	80.0(7)	132.9(9)	142.8(5)
C12–C7–D–C6	−151.7(5)	−62.8(10)	−141.6(5)
S1–Pb1–S2–C12	1.7(2)	92.9(4)	−78.6(2)
S2–Pb1–S1–C1	−80.2(2)	−7.4(4)	78.7(2)

3.3.1. Molecular structures

All lead–carbon bond distances agree very well with the corresponding covalent radii sum [18]. The lead–sulfur distances also agree with those reported in compounds containing the kernel S_2PbPh_2 into a cyclic system [19–22]. The bond angles around the central lead atom are quite different from the tetrahedral angles. In particular, the S1–Pb1–S2 and C13–Pb1–C19 bond angles in **2**b are the smallest. This difference in angles causes a distortion in the tetrahedron formed by the S1, S2, C13 and C19 vertices enclosing the coordination sphere of the lead atom.

In addition to the four covalent bonds expected for a lead (IV) compound, a relatively short distance involving the transannular D and Pb atoms is observed in the three compounds. The O···Pb lengths in **1**b [3.053(4) Å] and **3**b [3.113(4) Å] are shorter than the van der Waals radii sum [Σr_{vdW}(O,Pb) = 3.54 Å] [23], but 39 and 42% longer than the covalent radii sum [Σr_{cov}(O,Pb) = 2.20 Å] [24]. These distances are longer than those reported for the more flexible plumbocane $[\{O(CH_2CH_2S)_2\}PbPh_2]$ contained in two polymorphs [O···Pb = 2.855(5) and 2.888(6) Å in the orthorhombic system; 2.92(1) and 3.08(1) Å in the triclinic system] [18] and in $Ph_3PbSOCC_6H_4Me$ [2.990(4) Å] [7]. Likewise, the distance S···Pb in **2**b [3.280(3) Å] is also less than the corresponding van der Waals radii sum [Σr_{vdW}(S,Pb) = 4.1 Å] [23] and comparable to distances reported for compounds containing anisobidentate ligands [2.941 and 2.958 Å in $\{(PhCH_2O)_2PS_2\}_2PbPh_2$] [25]; 3.017 Å in $(Ph_2PS_2)_2$-$PbPh_2$ [26]. The magnitude of these intramolecular D···Pb interactions are consistent with a secondary bonding.

The molecular structures of the **1**b and **2**b compounds are similar, despite the presence of different donors atoms (O versus S). On the other hand, there are marked differences between the structures of the **1**b and **3**b compounds with oxygen as a donor atom; in **1**b the eight-membered ring conformation can be described as a twist boat (C_1 symmetry), while in **3**b the ring conformation can be described as boat–chair (*Cs* symmetry), according to the torsion angles listed in the Table 3. In regard to these conformations, it is normally accepted that just the first conformation is consistent with a transannular interaction. These results show the flexibility of the $D(C_6H_4S)_2^{2-}$ [D = S and O] and $S(C_6H_3S)_2O^{2-}$ O potentially tridentate ligands in order to adopt different arrangements.

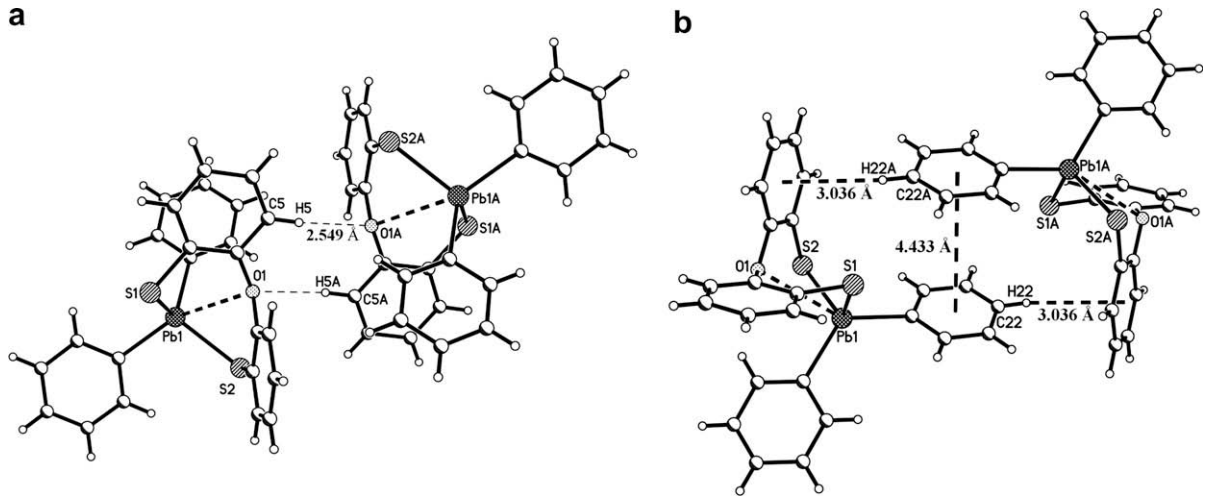


Fig. 2. The crystal packing of compound **1**b. (a) Intermolecular hydrogen bonds (C–H···O) showing the dimeric associations. (b) Arrangement of the π-stacking interactions type offset-stacked and face-tilted-T.

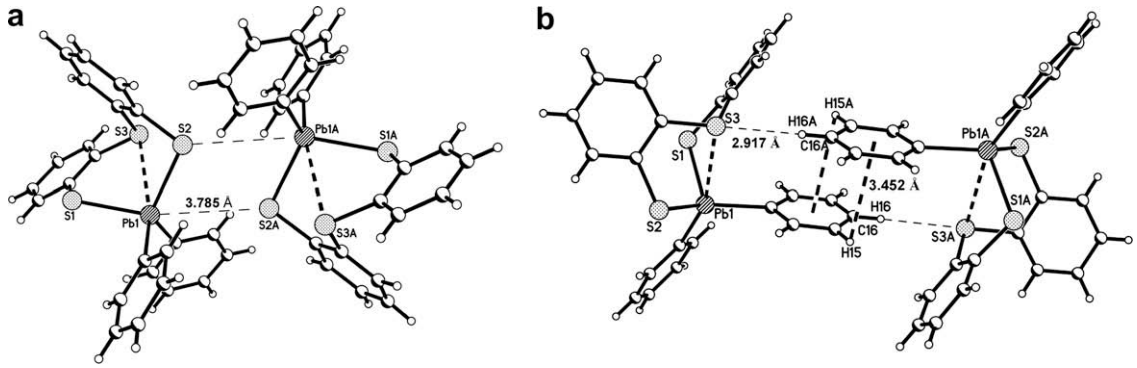


Fig. 3. The crystal packing of compound **2**b. (a) The intra and intermolecular interactions S···Pb, showing the hexacoordinated lead atom. (b) Arrangement of the intermolecular hydrogen bonds in (C–H···S) and the π-stacking interactions.

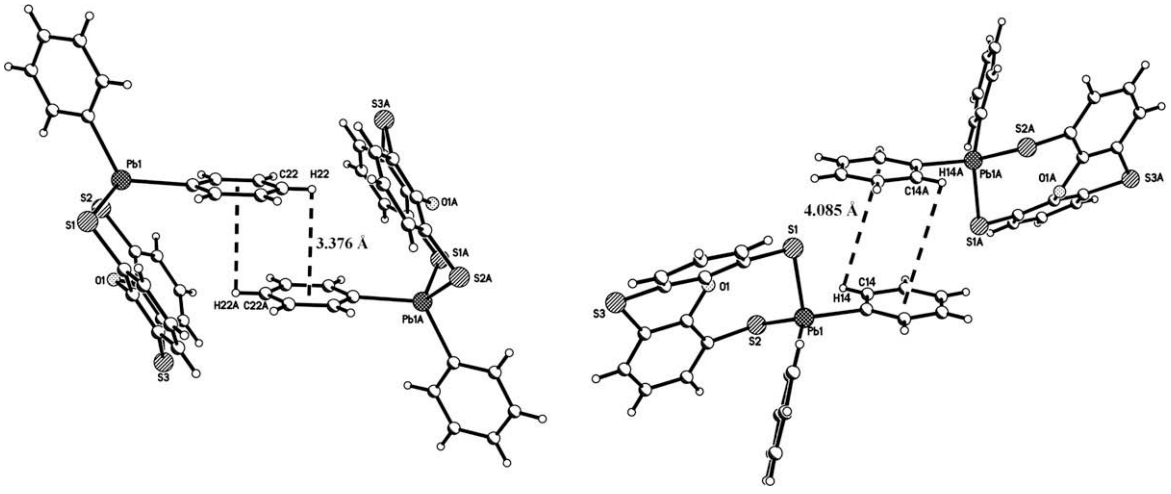


Fig. 4. The crystal packing of compound **3**b. Arrangements of the different π-stacking interactions type offset-stacked.

In order to compare the magnitude of the transannular interaction in all compounds, the Pauling-type bond order (BO) [27,28] has been calculated, according to the formula $BO = 10^{-[1.41(d_{exp}-\sum r_{cov})]}$, where d_{exp} is the D···Pb transannular distance. The BO are 0.063 for **1**b, 0.077 for **2**b and 0.052 for **3**b, respectively. The BO calculated indicates that sulfur is a better donor than the oxygen atom towards lead, however, in all cases the D···Pb transannular interaction is weak.

Considering the four covalent bonds and the secondary interactions D···Pb, the Pb atom in all compounds is penta-coordinated with a coordination sphere geometry described as monocapped tetrahedral, where the D donor atom (O for **1**b and **3**b; S for **2**b) is capping the tetrahedron. This proposal is supported by the short displacement percent from tetrahedral to trigonal bipyramidal geometry calculated for the compounds according to the procedure of Holmes based upon donor-acceptor atom bond length [29–31]. The tetrahedral distortion calculated is 48% for **1**b, 51% for **2**b and 45% for **3**b.

3.3.2. Crystal structures

The crystal packing of title compounds is stabilized by several non-bonded interactions.

In **1**b the molecules are associated by weak hydrogen bonding C–H···O as well as offset-stacked parallel – displaced and face-tilted-T aromatic interactions [32]. In this compound, the lead atom is not involved in intermolecular interactions (Fig. 2).

In the crystal structure of **2**b is observed the presence of molecules associated by S···Pb interactions (3.782 Å, a distance slightly shorter than the corresponding van der Waals radii sum [23]), by weak hydrogen bonding C–H···S and by offset π-stacking interactions (Fig. 3).

If both transannular and intermolecular S···Pb interactions are considered, then the lead atom is hexacoordinated, and its geometry can be described as bicapped tetrahedral.

In the crystal structure of **3**b, only are present dimeric building blocks self-assemble into chains *via* π-stacking interactions between the phenyl groups (see Fig. 4).

4. Conclusions

In order to study the phenomena of hypercoordination in organolead compounds we have synthesized and structurally characterized three new diphenyllead(IV) compounds by employing efficient tridentate ligands. In the solid state, the compounds display a distorted tetrahedral local geometry at Pb(IV) center. In view of the above findings and previous results, we conclude that, for a given $PbPh_2^{2+}$ fragment, the more flexible ligand $D(C_6H_4S)_2^{2-}$ (D = O, S) is able to show a weak interaction, leaving without change the conformation of the eight-membered ring, and displaying a tridentate coordination mode. On the other hand, the more rigid ligand $S(C_6H_3S)_2O^{2-}$ displays a bidentate coordination mode, with a totally different conformation that avoids any transannular interaction.

Acknowledgments

BFC fully acknowledges the scholarship from CONACyT. This research was supported by CONACyT (Project 44009).

Appendix A. Supplementary data

CCDC 704628, 704629 and 704630 contain the supplementary crystallographic data for **1b**, **2b** and **3b**. These data can be obtained free of charge via http://www.ccdc.cam.ac.uk/conts/retrieving.html, or from the Cambridge Crystallographic Data Centre, 12 Union Road, Cambridge CB2 1EZ, UK; fax: (+44) 1223 336 033; or e-mail: deposit@ccdc.cam.ac.uk. Supplementary data associated with this article can be found, in the online version, at doi:10.1016/j.poly.2008.11.012.

References

[1] For an outline see: Y. I. Baukov, S. N. Tandura, Hypervalent compounds of organic germanium, tin and lead derivatives, chapter 16, in: Zvi Rappoport (Ed.), The Chemistry of Organic Germanium, Tin and Lead Compounds Vol. 2, John Wiley & Sons, West Sussex, 2002, 963.
[2] R. Cea Olivares, V. García Montalvo, M.M. Moya Cabrera, Coord. Chem. Rev. 249 (2005) 859.
[3] J.S. Casas, E.E. Castellano, J. Ellena, M.S. García-Tasende, A. Sánchez, J. Sordo, A. Touceda, Polyhedron 27 (2008) 1.
[4] J.S. Casas, E.E. Castellano, J. Ellena, M.S. García-Tasende, A. Sáncheza, J. Sordo, Á. Touceda-Varela, Inorg. Chem. Commun. 7 (2004) 1109.
[5] J.S. Casas, E.E. Castellano, J. Ellena, M.S. García Tasende, A. Sánchez, J. Sordo, M.J. Vidarte, J. Inorg. Chem. 42 (2003) 2584.
[6] A. Esparza-Ruiz, A. Peña-Hueso, I. Ramos-García, A. Flores-Parra, Rosalinda Contreras, J. Organomet. Chem. 693 (2008) 2739.
[7] K. Tani, S. Kato, T. Kanda, S. Inagaki, Org. Lett. 3 (2001) 655.
[8] J.G. Alvarado-Rodríguez, N. Andrade-López, S. González-Montiel, G. Merino, A. Vela, Eur. J. Inorg. Chem. (2003) 3554.
[9] S. González-Montiel, N. Andrade-López, J.G. Alvarado-Rodríguez, Eur. J. Inorg. Chem. (2006) 3762.
[10] S. González-Montiel, N. Andrade-López, V. García-Montalvo, J.A. Cogordan, J.G. Alvarado-Rodríguez, Eur. J. Inorg. Chem. (2006) 4752.
[11] J.G. Alvarado-Rodríguez, S. González-Montiel, N. Andrade-López, L.B. López-Feliciano, Polyhedron 26 (2007) 2929.
[12] B. Flores-Chávez, J. G. Alvarado-Rodríguez, N. Andrade-López, V. García-Montalvo, E. Aquino-Torres, submitted for publication.
[13] D. Sellmann, D. Haussinger, Eur. J. Inorg. Chem. (1999) 1715.
[14] G.M. Sheldrick, SHELXS86, a program for crystal structure determination; University of Göttingen: Göttingen, Federal Republic of Germany, 1986.
[15] SHEXTL 5.10 Bruker AXS, Inc. Madison, WI, USA, 1998.
[16] SADABS: Area-Detector Absorption Correction, Siemens Industrial Automation, Inc. Madison, WI, 1996.
[17] M. Draeger, N. Kleiner, Z. Anorg. Allg. Chem. 522 (1985) 48.
[18] N.W. Alcock Bonding and Structure: Structural principles in inorganic and organic chemistry, Ellis Horwood, West Sussex, 1990, p. 314–315.
[19] M. Drager, N. Kleiner, Z. Anorg. Allg. Chem. 522 (1985) 48.
[20] M. Drager, N. Kleiner, Angew. Chem. Int. Ed. 19 (1980) 923.
[21] B.M. Schmidt, M. Drager, J. Organomet.Chem. 399 (1990) 63.
[22] U. Herzog, G. Rheinwald, J. Organomet.Chem. 648 (2002) 220.
[23] S.S. Batsanov, Inorg. Mater. 37 (2001) 871.
[24] W.W. Porterfield, Inorganic Chemistry: A Unified Approach, second ed., Academic Press Inc, USA, 1993. p. 214.
[25] M.G. Begley, C. Gaffney, P.G. Harrison, A. Steel, J. Organomet. Chem. 289 (1985) 281.
[26] S.N. Olafsson, T.N. Petersen, P. Andersen, Acta Chem. Scand. 50 (1996) 745.
[27] L. Pauling, The Nature of the Chemical Bond, third ed., Cornell University Press, Ithaca, NY, 1960. p. 239.
[28] U. Kolb, M. Beuter, M. Gerner, M. Draeger, Organometallics 13 (1994) 4413–4425.
[29] A. Chandrasekaran, P. Sood, R.O. Day, R.R. Holmes, Inorg. Chem. 38 (1999) 3369.
[30] N.V. Timosheva, A. Chandrasekaran, R.O. Day, R.R. Holmes, Inorg. Chem. 37 (1998) 3862.
[31] D.J. Sherlock, A. Chandrasekaran, R.O. Day, R.R. Holmes, Inorg. Chem. 36 (1997) 5082.
[32] W. Brian Jennings, B.M. Farell, J.F. Malone, Acc. Chem. Res. 34 (2001) 885.

Polyhedron 28 (2009) 473–478

Contents lists available at ScienceDirect

Polyhedron

journal homepage: www.elsevier.com/locate/poly

The modifications of copper work function by layer-by-layer deposition of $[W(CN)_8]^{4-}$ – Co^{2+} bimetallic nanolayers

Tomasz Stawski, Janusz Szklarzewicz *, Andrzej Kotarba, Paweł Stelmachowski

Faculty of Chemistry, Jagiellonian University, R. Ingardena 3, 30-060 Kraków, Poland

ARTICLE INFO

Article history:
Received 4 July 2008
Accepted 19 November 2008
Available online 2 January 2009

Keywords:
Nanolayers
Deposition
Cyano polymers
Tungsten
Cobalt
Work function
Kelvin probe

ABSTRACT

In the reaction of $K_4[W(CN)_8] \cdot 2H_2O$ and $Co^{2+}(aq)$ cations on the polycrystalline or monocrystalline [3 1 1] copper using layer-by-layer deposition, a thin film of the coordination polymer $\{[\{Co(H_2O)_2(\mu\text{-}CN)_4\}_2W] \cdot 4H_2O\}_n$ was formed. The work function of copper and deposited on it bi-layers depended on a number of layers and the concentrations of the deposited precursors. At high complex concentrations work function reached the plateau after several deposition processes, while at low concentrations oscillations in the work function were observed when K^+ or Co^{2+} cations were present in the outside layer. The changes of the work function were also dependent on Co^{2+} salt used ($CoCl_2 \cdot 6H_2O$ or $Co(NO_3)_2 \cdot 6H_2O$). This was interpreted in terms of a layer structure resulting from various coordination of external anions to cobalt cations.

© 2008 Elsevier Ltd. All rights reserved.

1. Introduction

The new class of materials based on cyano-bridged metallic centers (framework materials) is of high interests for the contemporary materials science, due to their vastly unexplored physical properties. The cyano-based bridging (–CN–) provides stable and regular framework connecting metallic centers of different *d*-block elements (possibly at various oxidation levels). For a metallic center of a given coordination number, the certain symmetry of the crystalline network is provided. For a low symmetry coordination surrounding (*e.g.* coordination numbers 5, 7 and 8) an anisotropy in the physical properties can be present. The –CN– network enables interaction of the metallic centers along the $–M_1–CN–M_2–$ chain. Thus, charge transfer, magnetic coupling, colossal positive and negative thermal expansion and other effects may occur, leading to new optical, magnetic or mechanical properties [1].

For the practical applications, positioning of the cyano-bridged network in the form of thin films at the interfaces is essential. The series of interesting experiments in the subject was performed by Culp et al. [2]. The deposition was performed on the air/water interface (in the next stage transferred to a solid polymeric support). A formation of the two dimensional self-assembled square grid was observed in the system of the Langmuir monolayer based on amphiphilic pentacyanoferrate(III) complex and metal ions (Ni^{2+}) in the sub-phase [3,4]. In the further experiments the multilayer was obtained by a step-wise deposition process, in which the monolayer (transferred to a solid support) acted as a substrate, whereas the consequent layers were formed in the iterative process of deposition of Fe^{3+} ions (the first precursor) and hexacyanoferrate(II) complex ion (the second precursor). As a result, a three dimensional network of a Prussian blue was formed. For the Prussian blue Fe^{3+}/Co^{2+} analogs an anisotropic photo-magnetic effect was observed.

The thin layers modify and tailor the electronic properties of the substrate, which is especially important if one is a conductor or a semi-conductor (*e.g.* like the titanium oxide used as a material for the photovoltaic cells). The change of the electronic parameters of the substrate might be associated, among others, with a band gap change or the work function change. Such investigations have not been conducted for the cyanide frameworks. However, a very similar research concerning layer-by-layer deposition involving sequential deposition of polyelectrolytes (alternately, polyanions and polycations) can be found in the literature [5–8]. The properties of the film can be changed in the regime of a single molecular layer. The surface potential is alternately driven by the consequent polyanions or polycations and exhibit oscillations: the reversely varying properties with the surface potential of the terminating layer [9,10].

The formation of a monolayer in a liquid phase (Langmuir) allows the surface morphology adapt to the structure of polymer formed. Thus, the layers deposited have the same structure as of monocrystal of material deposited. Similar problems arise when nanoparticles are precipitated in solution. Other techniques

* Corresponding author. Tel.: +48 12 6632231; fax: +48 12 6340515.
E-mail address: szklarze@chemia.uj.edu.pl (J. Szklarzewicz).

0277-5387/$ - see front matter © 2008 Elsevier Ltd. All rights reserved.
doi:10.1016/j.poly.2008.11.036

involving electrodeposition, CVD methods, etc. can give layers which are much stronger connected with the support, however, the main limit of these methods is the number of substrates available, relative simplicity of layers formed and structures accessible. Recently, it became clear, that less symmetric particles or layers can give rise to more complex and more interesting superstructures. For example it was possible to prepare nanowires of gold isolated along their length, but reactive at their ends [11]. Thus, we decided to develop the method of iterative deposition of the cyanide coordination compounds from aqueous solution, onto the pure metallic substrate, that leads to a layer-by-layer growth of a thin layer of the coordination polymer. The cyano-complexes of transition metals, (for example Fe(II,III), Mo(IV,V), W(IV,V), Mn(II,III,IV), etc.) easily form polymetallic compounds with d-metal cations, insoluble in all solvents studied. This type of reaction is of great importance in contemporary studies of molecular magnets and formation of low dimensional, molecular structures [11,12]. In this study the $K_4[W(CN)_8] \cdot 2H_2O$ salt was used as a starting compound for the monolayer deposition. The tungstate(IV) complex anion is thermally as well as kinetically stable, thus the side reactions (as ligand exchange, metal oxidation or reduction) can be eliminated [13]. High coordination number and the reliability of cyano-ligand to rearrange (from C_s to D_{4d} symmetry) in order to accommodate the structure of the anion to the local surrounding is also important for a high symmetry of the formed polymer [14]. As a cation Co^{2+}(aq) (in the form of $CoCl_2 \cdot 6H_2O$ or $Co(NO_3)_2 \cdot 6H_2O$ solution) was used. The lability of aqua ligands in Co^{2+} cation, enable the formation of insoluble $\{[\{Co(H_2O)_2(\mu\text{-}CN)_4\}_2W] \cdot 4H_2O\}_n$ salt and the possibility of Co^{2+} cation to form up to six cyano-bridges which is essential for desired layer composition [15].

2. Experimental

2.1. Materials and methods

The $K_4[W(CN)_8] \cdot 2H_2O$ was synthesized according to the published procedure [16], whereas $CoCl_2 \cdot 6H_2O$ and $Co(NO_3)_2 \cdot 6H_2O$ were used as received from Aldrich. The elemental analyses were performed using elemental analyzer, Euro EA 3000 (Euro Vector) and the presence of other elements was excluded by the EDXS spectrometry (EDS EDAX Genesis 4000). The thermogravimetric measurements were performed on a TDA/SDTA microanalyser (Mettler Toledo) combined with a Termostar GSD 300T Balzers quadruple mass spectrometer in the 30–1000 °C range, scan speed 5°/min, argon atmosphere. IR spectrum was measured in KBr pallets on a Bruker EQIUNOX 55 spectrometer. The reflectance UV–Vis spectrum was measured on a Shimadzu UV-2101PC spectrophotometer equipped with ISR-260 integrating sphere.

The work function measurements were performed on the vacuum setup equipped with Kelvin probe head (McAllister KP6500). Two plates of copper of required dimensions were cut from polycrystalline and/or monocrystalline copper (the parallel bases were the only requirement; the surface of bases was 1.35 cm^2). The bases (one of each plate) were mechanically polished to the mirror-like surface. The monocrystalline plate was then placed inside the vacuum chamber equipped with sample manipulator and evacuated. The commercial McAllister reference electrode plate, of diameter of 5 mm, was made of stainless steel. The Kelvin probe measurements were carried out at the vacuum level of 5×10^{-2} mbar. The sample was being moved parallel towards the reference electrode (vibrating at 200 Hz) until the contact potential difference (V_{CPD}) values, as well as, the gradient of the electric field values were stable (distance between the electrodes *ca.* 1 mm) at ambient conditions. The accuracy of the measurement was of 2.5 mV. The data were collected by the data acquisition system for further processing. The same parameters of the setup were used in all experiments.

2.2. Synthesis of $\{[\{Co(H_2O)_2(\mu\text{-}CN)_4\}_2W] \cdot 4H_2O\}_n$ (1)

The salt **1** was synthesized using modified method described in literature [15]. The 0.584 g (1 mmol) of $K_4[W(CN)_8] \cdot 2H_2O$ in 10 ml of water and 0.476 g (2 mmol) of $CoCl_2 \cdot 6H_2O$ in 10 ml of water were mixed together under continuous steering. After mixing the steering was continued for 1 h and the resulting precipitate was filtered off on a Büchner funnel, washed with distilled water, ethanol and dried on air at 35 °C for 3 h. Yield: 0.650 g (99%). Calc. for $C_8H_{16}N_8O_8Co_2W$: C, 14.7; N, 17.1; H, 2.47%. Found: C, 14.8; N, 16.7; H, 2.71%. The EDXS analysis of the precipitate excluded presence of potassium and chlorine ions. IR (KBr): 2138 cm^{-1} (ν_{CN}), 1614 cm^{-1} (H_2O), 3416 cm^{-1} (H_2O and hydrogen bonds).

2.3. The layer preparation

(a) The deposition process at high complex concentrations - double deposition manner. Two different aqueous solutions were prepared: 3.42×10^{-3} M $K_4[W(CN)_8] \cdot 2H_2O$ and 6.84×10^{-3} M $CoCl_2 \cdot 6H_2O$ (1:2 molar ratio). The potassium octacyanotungstate(IV) solution had been deposited on the copper monocrystalline plate (of measured V_{CPD}) by dip-coating and left for 60 s, the plate was then rinsed with a distilled water. The cobalt(II) chloride solution was then deposited on the sample in the same manner and left for 60 s. Finally, the plate was rinsed with distilled water again and dried on air. The contact potential difference of the monocrystalline plate, with such a deposited bimetallic bi-layer, was measured by means of Kelvin probe (experimental procedure analogical to the pure copper sample). The procedure was repeated for a number of double deposition processes resulting in a multilayer system (Fig. 1A). The entire procedure was conducted for the polycrystalline copper plate.

(b) The deposition process at high complex concentrations - single deposition manner. The procedure was analogous to (a) but the measurements were taken after each deposition of a monolayer (anionic or cationic) not the bi-layer (Fig. 1 B), (for a polycrystalline copper substrate only).

(c) The deposition process at low complex concentrations - single deposition manner. The procedure was analogous to (b) but 3.42×10^{-6} M $K_4[W(CN)_8] \cdot 2H_2O$ and 6.84×10^{-6} M $CoCl_2 \cdot 6H_2O$ (1:2 molar ratio) were used in each deposition step (Fig. 1 B).

(d) The deposition process at low complex concentrations - single deposition manner. The secondary anion effect. The procedure was analogous to (c) but 3.42×10^{-6} M $K_4[W(CN)_8] \cdot 2H_2O$ and 6.84×10^{-6} M $Co(NO_3)_2 \cdot 6H_2O$ (1:2 molar ratio) were used in each deposition step (Fig. 1 B).

3. Results

3.1. Characterisation of 1

The method of single crystal synthesis of **1** was described earlier in literature [15]. The modified method was used to check if rapid crystallization and formation of a colloidal phase of **1** will give the same product. The synthesized colloidal $Co_2[W(CN)_8] \cdot 8H_2O$ salt is insoluble both in polar and non polar solvents and is stable on air. It is formulated as $[W\{(\mu\text{-}CN)_4Co(H_2O)_2\}_2 \cdot 4H_2O]_n$, but basing on the structure presented it should be rather written as $\{[\{Co(H_2O)_2(\mu\text{-}CN)_4\}_2W] \cdot 4H_2O\}_n$. Both analysis and the IR spectrum of **1** are in agreement with the literature data indicating that

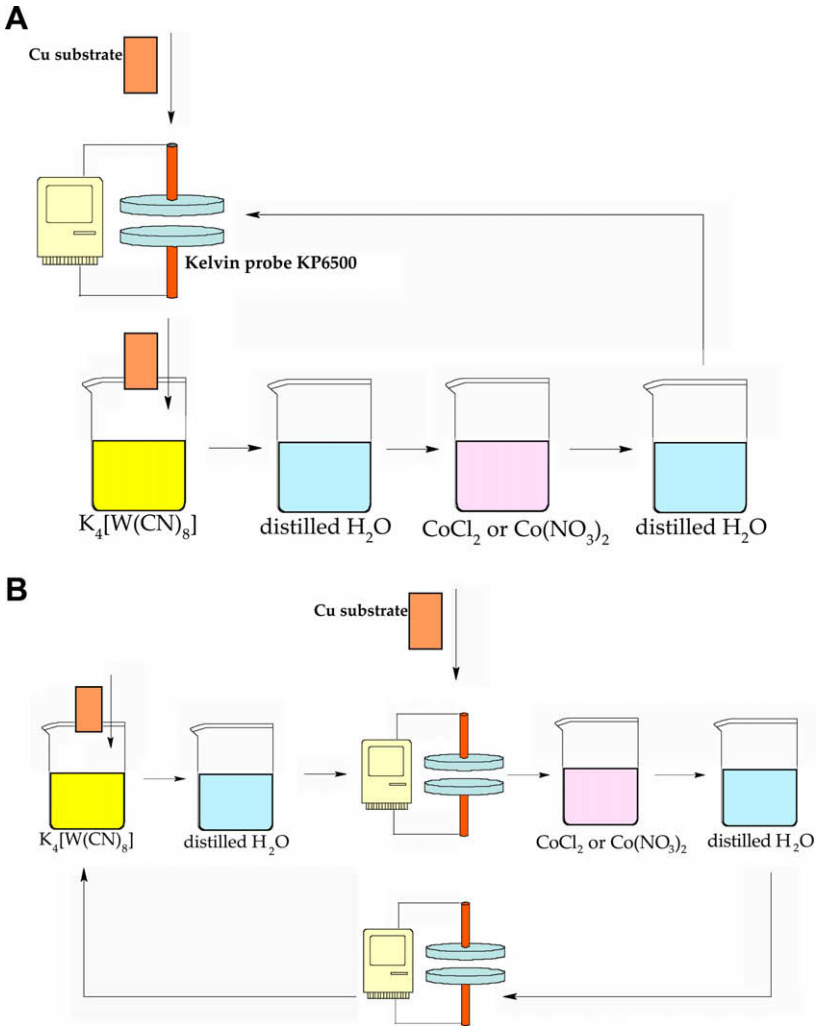


Fig. 1. The double (**A**) and single **(B)** deposition process and work function measurements

the salt composition is independent on the synthetic method used and is identical for single crystals and for colloidal form [15].

The reflectance spectrum of **1** is shown in Fig. 2. The spectrum of **1** differs significantly from that of $K_4[W(CN)_8] \cdot 2H_2O$. The new, low energy transitions at *ca.* 470 and 590 nm, can be observed. The difference can be interpreted as a formation of a low energy band attributed to the ion pair (anion–cation) charge transfer (CT) transition. Similar CT bands were observed for a numerous compounds with $[W(CN)_8]^{4-}$ ion and different cations, including organic ones [17]. According to the literature data, it can be found that formation of Co–NC–W bridges result in close W–Co distance (5.40 Å) and the charge transfer from tungsten to Co^{2+} becomes a relatively low energy process [15]. The formation of cyano-bridges with Co^{2+} is additionally confirmed by the drastic change at the intensity of the band at 240 nm attributed to W–CN CT transition, and shift of that band to lower energy (charge withdrawing effect caused by coordination of Co^{2+} to negatively charged CN^- ligands).

The thermogravimetric analysis of **1** shown in Fig. 3 indicates a complicated decomposition process. Combining with the quadruple mass spectrometer results it can be concluded that in the first step only four water molecules are released. The mass loss after first decomposition process (up to 300 °C) is 10.9% (calculated for four H_2O molecules, 11.0%). The release of four water molecules per tungstate is in agreement with the salt **1** formula and indicates that the net of cyano-bridges bonds remains unaltered at this stage

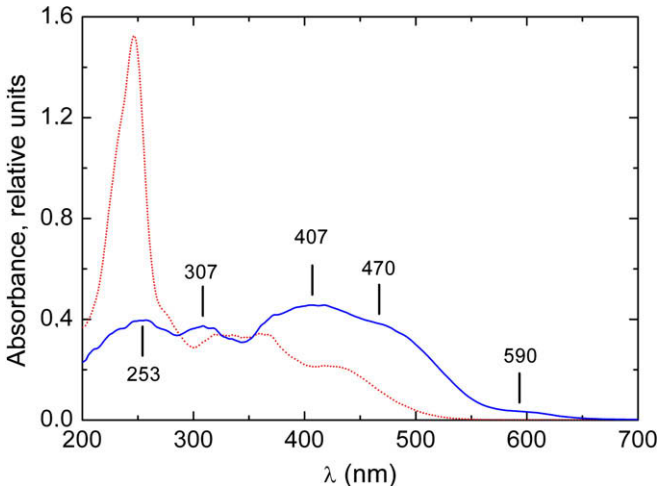


Fig. 2. The reflectance spectrum of **1** (blue line), for comparison spectrum of $K_4[W(CN)_8] \cdot 2H_2O$ is also included (dotted red line). Spectra in absorbance mode, after Kubelka-Munk transformation (For interpretation of the references to colour in this figure legend, the reader is referred to the web version of this article.).

of dehydration. In the next steps total decomposition of **1** with all water molecules and cyano ligands release is observed. The final mass loss is 43.7% (at 650 °C), whereas calculated for eight H_2O

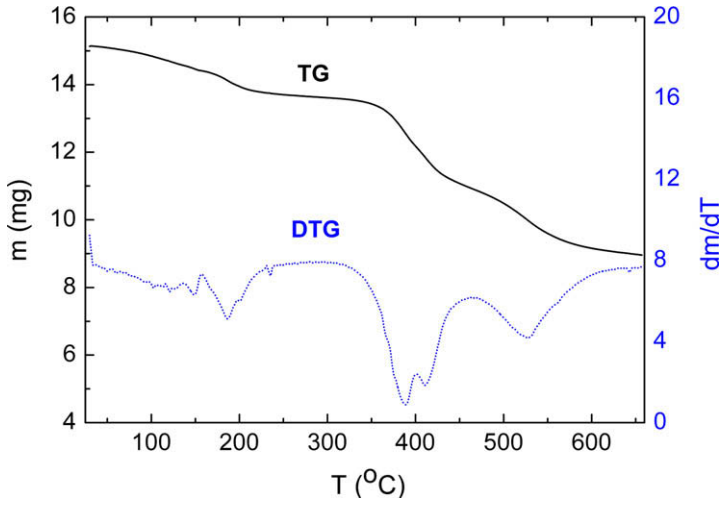


Fig. 3. TG and DTG curves of decomposition of **1**.

and eight CN^- molecules is 46.2%. The observed difference can be caused by still going decomposition at 650 °C (see Fig. 3) and/or presence of small amounts of oxygen in apparatus which can cause formation of oxides of molybdenum and cobalt.

3.2. The deposition process at high complex concentrations

An immersion of the copper substrate in an aqueous $K_4[W(CN)_8] \cdot 2H_2O$ solution for a couple of seconds was the first step of a nanolayer formation, as described in the experimental section. To protect such a formed film on a copper surface, it was necessary to fix it. It is known, that $[W(CN)_8]^{4-}$ ion forms insoluble salts with d-electron metals. We decided to use Co^{2+} cations, as cobalt complexes are one of the best known, with the well-defined coordination number 6 (with aqua ligands) and which form insoluble **1**. Also lability of $[Co(H_2O)_6]^{2+}$ ion was crucial for the fast fixation of tungsten layer [18]. Since copper does not exhibit a well-defined coordination number (4–6) in aqueous solution it cannot be used for this purpose. After $[W(CN)_8]^{4-}$ ions deposition on a copper substrate, it was washed with water (to prevent precipitation of colloidal **1** over the copper surface and its deposition on a solid substrate) and immersed in a solution of Co^{2+} ions (for 60 s) and again washed with water. Such a double deposition process was repeated for a required number of times (up to 50 layers formed) both for monocrystalline [3 1 1] and polycrystalline copper substrate.

The Kelvin probe was used to measure the work function changes of a pure copper substrate and the substrate covered with different numbers of bi-layers. The results are presented in Fig. 4.

As, at the concentration and volume used, number of the $[W(CN)_8]^{4-}$ ions exceeded the number of copper atoms at the surface (*ca.* 8×10^{15} atoms/cm^2) by several orders of magnitude it was assumed that the copper substrate was totally covered with anions in a single deposition process. For the pure metallic substrates, when there was no thin film deposited, the difference between the work functions values of the monocrystalline and polycrystalline copper was of 0.4 eV. As the work function depends on the surface potential, χ which reflects any asymmetric surface charge distribution, therefore oriented monocrystal surfaces and polycrystalline substrates exhibit different work function values [19]. In both cases, the deposition of the first several bi-layers (as low as one for polycrystalline sample but less than five in general; for the monocrystalline copper there was only first and fifth measured) led to the V_{CPD} values reaching the minimum, therefore, the work function of the substrates increased (reaching maximum).

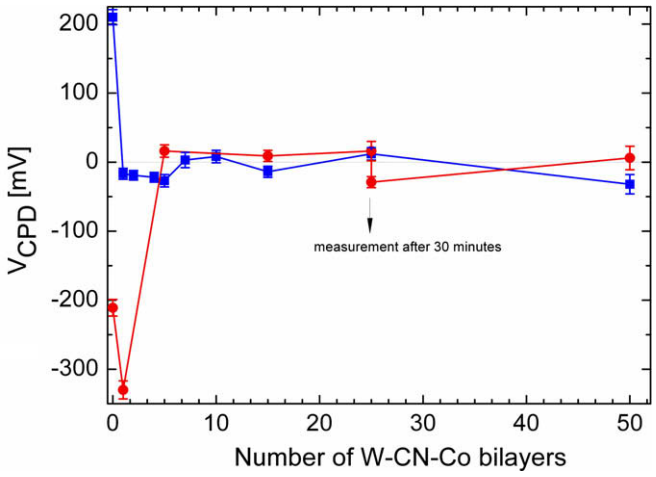


Fig. 4. Contact potential difference values (V_{CPD}) vs. total number of deposited bimetallic W-CN-Co bi-layers for the monocrystalline and polycrystalline copper substrate. High concentrations of the precursors: ■, polycrystalline Cu; ○, monocrystalline [3 1 1] Cu.

For the subsequent bi-layers the work function reached the constant value, equal for both types of copper substrates. The work function changes, for the number of deposition processes larger than five, are practically independent of the number of the bi-layers and/or type of copper substrate. Thus, the formation of the thin film on copper is independent of the crystalline form of the copper. Because after the initial monolayers are deposited and chemically bonded, the work function is permanently changed, reaching the constant value characteristic for the deposited material. The increase in the work function values is caused by the dominant coordination bond formation between octacyanotungstate(IV) anion, charge of which is compensated by the cobalt cations. Two main contributions to the work function value φ come form the band bending part (V) and electron affinity part (X). Thus, the total change of work function is given by the equation:

$$\Delta\varphi = \Delta V + \Delta X$$

The band banding change contribution is connected with strong interaction between the substrate and the absorbed molecule (*e.g.* strong covalent bond formation), whereas the electron affinity change contribution results from weaker interactions with the substrate (*e.g.* charge bindings).

The electron affinity of the deposited complex ion, is larger than the work function of the metal, and the electron density from the substrate is moved towards the ion. In this process a new acceptor level is formed and the band is bent upwards. Both band banding (Fermi level modification) contribution and electron affinity change contribution are taken under the consideration. The extreme in the work function value, observed only for the first several bi-layers, indicates that the dipole layer interacts strongly with the copper substrate. The conclusion is supported by the investigation in which the contact potential difference is measured after each single deposition process, as presented in Fig. 5.

In this case the large change of the work function for the first $[W(CN)_8]^{4-}$ monolayer with a charge compensated by the K^+, indicates that this layer is formed by bonding the complex ion to the Cu by the strong cyano-bridges. The maximum of the work function values is reached for one and a half of the bi-layer as presented in Fig. 5. After the deposition of the first three double layers the constant value of the work function is being reached similarly as in Fig. 4. This result confirms that the initial layer forms Cu–NC–W bridges with the substrate, therefore interacts chemically, not by weak charge bindings (like in the case of polyelectrolyte-based films deposited layer-by-layer, to which the investigated system is in analogy) [20,21].

After the first layer deposition, fixation with Co^{2+} resulted in the potassium cation exchange leading to further work function modification. As it is shown in Fig. 5, after three double deposition processes work function reaches plateau indicating that at this point metal is separated from the surface and only layer properties are important for the work function. Up to this value, work function is not a simple sum of metal and layer properties. It can be seen also, that exchange of K^+ cations into Co^{2+} (points at 1, 2, 3, 4 number of bi-layers) result in decrease of work function (probably as a result of CN bridge formation and easier electron transfer from coppers to the surface).

3.3. The deposition process at low complexes concentrations

In order to study in detail the coverage of the copper surface with the initial first layers of complexes deposited, the method (b) was introduced (see Section 2). The depositions were performed for relatively low concentrations of the precursors, assuming the structure of copper surface. The total number of copper atoms on the surface is of *ca.* 8×10^{15} atom/cm^2. The $[W(CN)_8]^{4-}$ ion radius (*ca.* 7.2 Å) and the Cu–Cu distance in the metal corresponds to less than *ca.* 10^{-8} mol of the anion in solution necessary to bond to each copper available. The applied amount of $[W(CN)_8]^{4-}$ ions in method (b) is close to that minimum, the diffusion of anions from the solution to the surface must be also taken under the consideration, additionally decreasing number of $[W(CN)_8]^{4-}$ ions available for copper atoms. All these factors cause that in method (b) surface of copper was not totally filled with the tungsten complex. The work function measurements were performed after each single deposition process and the results are presented in Fig. 6.

For the low concentrations of the precursors of the order of 10^{-9} mol/cm^3 comparable to the surface concentration of copper, the oscillating pattern of the work function changes is observed. After the first deposition of the complex anion, work function of the substrate increases. The deposition of the charge compensating and cyano-bridge-forming co-cation (one bi-layer deposited, see Fig. 6) resulted in the decrease of work function of copper to the initial value (within the experimental error). Such oscillations repeated on three consecutive deposition processes, after which

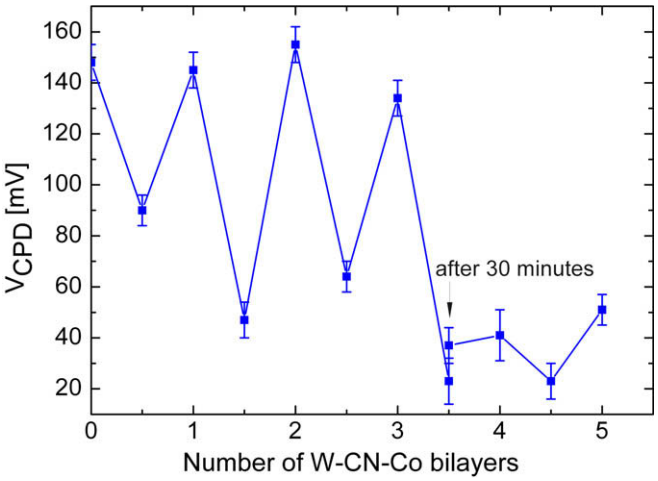


Fig. 6. Contact potential difference values in the function of total number of deposited monolayers ($[W(CN)_8]^{4-}$ or Co^{2+}) for the polycrystalline copper substrate. Low concentrations of the precursors.

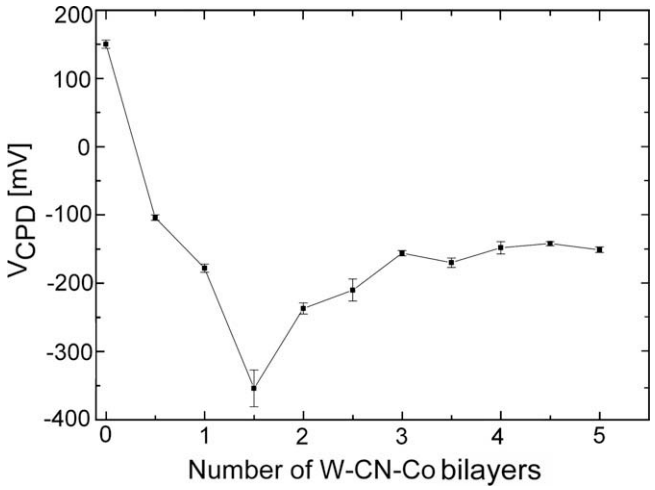


Fig. 5. Contact potential difference values in the function of total number of deposited monolayers ($[W(CN)_8]^{4-}$ or Co^{2+}) for the polycrystalline copper substrate. High concentrations of the precursors.

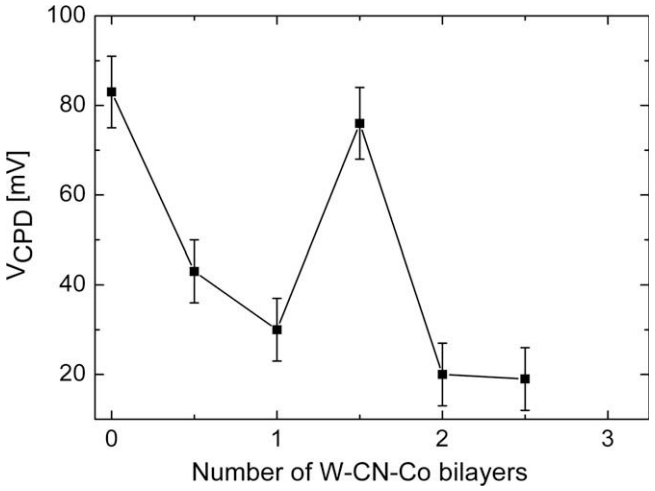


Fig. 7. Contact potential difference values in the function of total number of deposited monolayers ($[W(CN)_8]^{4-}$ or Co^{2+}) for the polycrystalline copper substrate. Low concentration of the precursors, cobalt(II) nitrate(V) instead of cobalt(II) chloride.

the new work function value established, constant for the consequent depositions (in the regime of 30 meV), and higher of 120 meV than the initial work function of copper. If the oscillations had been permanent for a large number of deposited layers their presence would be explained on the basis of the work function modification by the electron affinity part alone (no band banding contribution). Hence, the interaction of the dipole layer with a substrate would be rather weak. In the case investigated in this work, initial several deposition processes leading to the oscillations can be also explained in this way. The deposited precursors, as are of low concentrations, cannot be bonded to all copper atoms. For a Kelvin probe measurements such a deposition can be treated as a formation of a weak interaction between cooper substrate and complex anion from the point of view of the system in general, as the coordination bonds are still formed, but due to the low concentration of $[W(CN)_8]^{4-}$ they have local, not global impact on the work function values. The deposition of the precursors of high concentrations suggest that the layer is interacting with the substrate after the first bi-layer is deposited, as the minimum of the work function is reached after the very first several layers and no oscillations are present (see Fig. 5). Therefore, in the case of low concentrations of ions, the thick layer is obtained after several deposition processes and then the band bending contribution to the work function values starts to be considerable. Such a result is somehow expectable, because the concentration of the precursors is of the surface concentration of copper, the kinetics of the reaction and transport phenomena cause that only a fraction of copper atoms, that can bind the complex anion, actually forms the cyano-bridges (not mentioning that due to the symmetry of the bond and steric interactions this number of bonding places is limited anyway).

The chloride ions are very important in such an interpretation. At high distances between anions cobalt atoms cannot form required numbers of cyano-bridges, the coordination sphere and charge of Co^{2+} cations must be in part compensated by other than $[W(CN)_8]^{4-}$ ions. When (in the third deposition process) anions are again supplied to the system, they can be bonded neither to cobalt cations nor to copper surface. External anions, such as Cl^- are expected to play a role at the very beginning of the deposition process. To study this effect cobalt(II) nitrate(V) was applied instead of $CoCl_2 \cdot 6H_2O$ (method (c), Section 2.3). The results are shown in Fig. 7.

Both secondary anions (Cl^- or NO_3^-) should have the same contribution for the charge compensation, but they differ in sterical interactions. The deposition of the complex anion (0.5 numbers of bi-layers) led to the increase in the work function values, similarly as in Fig. 6, where Cl^- external anions were present. However, the deposition of Co^{2+} precursor with a NO_3^- anion caused further work function increase and also the decrease after the second complex anion deposition process (points at 1 and 2 bi-layers). Then, after 2.5 deposition steps again new constant value of the work function was established. The chaotic, pattern-less behavior of values of work function may be interpreted by the competition between the complex anion forming cyano-bridges with copper and the NO_3^- acting as the ligand to copper. This is possible due to the low concentration of the precursors and, as mentioned before, the kinetics of the reaction and transport phenomena, when the coverage of the substrate by the complex anions is less than 1 ($\Theta < 1$). It is also possible, that bigger NO_3^- ion give additional steric problems for $[W(CN)_8]^{4-}$ ions to reach copper surface, and the separation of metal from deposited layer starts much faster (after 3.5 depositions in case of Cl^- anions, see Fig. 6). Therefore, the appropriate choice of the seemingly unimportant secondary anion is essential for the thin layer deposition process.

4. Conclusion

The bimetallic cobalt–tungsten cyano-bridged layer were interactively deposited in up to 50 double deposition processes from aqueous solutions of potassium octacyanotungstate(IV) and cobalt(II) chloride on the mono and polycrystalline copper surfaces. The work function values were very sensitive to the number of bi-layers deposited as well as to the concentrations of the deposited precursors. When the surface coverage was high (at least one complete monolayer of the deposited precursors was present), then after *ca.* 3 deposited bi-layers the work function was independent of the initial surface work function and was driven only the outer layer properties. As a single bi-layer is *ca.* 0.8 nm thick, then 3 nm complex coating is sufficient to reach the maximum modification of the metallic substrate work function value. When the surface coverage with the first layer is not complete (below one monolayer), the work function values started to oscillate. The characteristic of the oscillations and the number of peaks depended also on a counter anion type, probably due to its coordination to the copper surface. The results presented indicate possibility of an easy fine-tuning of the work function of a metallic substrate (the dependence of its change and the complex anions and cations used is in progress). The strong cyano-bonds between deposited layers and copper substrate can be utilized for the deposition of insulating layer on a metallic substrate providing a precise tool for tuning the work function value which is essential for catalysis on metallic centers.

References

[1] A.L. Goodwin, M. Calleja, M.J. Conterio, M.T. Dove, J.S.O. Evans, D.A. Keen, L. Peters, M.G. Tucker, Science 319 (2008) 794.
[2] J.T. Culp et al., Coord. Chem. Rev. 249 (2005) 2642.
[3] J.T. Culp, J-H. Park, M.W. Meisel, D.R. Talham, Polyhedron 22 (2003) 3059.
[4] J.T. Culp, J-H. Park, I.O. Benitez, M.W. Meisel, D.R. Talham, Polyhedron 22 (2003) 2125.
[5] M. Pyrasch, B. Tieke, Langmuir 17 (2001) 7706.
[6] G. Decher et al., Science 1232 (1997) 277.
[7] L.S. Li, A.D.Q. Li, J. Phys. Chem. B 105 (2001) 10022.
[8] M. Schönhoff, J. Phys.: Condens. Matter 15 (2003) R1781.
[9] M. Schönhoff, Curr. Opin. Colloid Interface Sci. 8 (2003) 86.
[10] B. Schwarz, M. Schönhoff, Langmuir 18 (2002) 2964.
[11] J-S. Yu, J.Y. Kim, S. Lee, J.K.N. Mbindyo, B.R. Martin, T.E. Mallouk, Chem Commun. (2000) 2445;
X. Wang, Y. Li, Inorg. Chem. 45 (2006) 7522.
[12] T.R. Kilne, M. Tian, J. Wang, A. Sen, M.W.H. Chan, T.E. Mallouk, Inorg. Chem. 45 (2006) 7555;
B. Sieklucka, J. Szklarzewicz, T.J. Kemp, W. Errington, Inorg. Chem. 39 (2000) 5156.
[13] W.P. Griffith, Coord. Chem. Rev. 17 (1975) 177;
G. Wilkinson (Ed.), Comprehensive Coordination Chemistry, Pergamon Press, Oxford, 1987;
M.T. Beck, Pure and Apply. Chem. 59 (1987) 1703.
[14] N.W. Alcock, A. Samotus, J. Szklarzewicz, J. Chem Soc. Dalton Trans. (1993) 885;
B. Nowicka, A. Samotus, J. Szklarzewicz, J. Burgess, J. Fawcett, D.R. Russell, Polyhedron 17 (1998) 3167;
J. Szklarzewicz, A. Samotus, B. Nowicka, J. Burgess, J. Fawcett, D.R. Russell, Transition Met. Chem. 24 (1999) 177.
[15] J.M. Herrera, A. Bleuzen, Y. Dromzee, M. Julve, F. Lloret, M. Verdaguer, Inorg. Chem. 42 (2003) 7052.
[16] D. Matoga, J. Szklarzewicz, M. Mikuriya, Inorg. Chem. 45 (2006) 7100.
[17] J. Szklarzewicz, A. Samotus, A. Kanas, Polyhedron 11 (1986) 1733;
N.W. Alcock, A. Samotus, J. Szklarzewicz, J. Chem. Soc. Dalton Trans. (1993) 885;
B. Nowicka, A. Samotus, J. Szklarzewicz, J. Burgess, J. Fawcett, D.R. Russell, Polyhedron 17 (1998) 3167;
J. Szklarzewicz, A. Samotus, B. Nowicka, J. Burgess, J. Fawcett, D.R. Russell, Transition Met. Chem. 24 (1999) 177.
[18] M.L. Tobe, J. Burgess, Inorganic Reaction Mechanisms, Addison-Wesley Longman Ltd., Essex, United Kingdom, 1999. Charter 4, p. 136, Chapter 7, p. 282.
[19] K. Christmann, Introduction to Surface Physical Chemistry, Steinkopff Verlag & Springer-Verlag, Darmstadt & New York, 1991; p. 166.
[20] L.S. Li, Q.X. Jia, A.D.Q. Li, Chem. Mater. 14 (2002) 1159.
[21] L.S. Li et al., Appl. Surf. Sci. 219 (2003) 199.

Polyhedron 28 (2009) 479–484

Contents lists available at ScienceDirect

Polyhedron

journal homepage: www.elsevier.com/locate/poly

Synthesis, photophysical and photochemical properties of octa-substituted antimony phthalocyanines

Desmond Kwena Modibane, Tebello Nyokong *

Department of Chemistry, Rhodes University, P.O. Box 94, Grahamstown 6140, South Africa

ARTICLE INFO

Article history:
Received 25 October 2008
Accepted 25 November 2008
Available online 2 January 2009

Keywords:
Antimony phthalocyanine
Triplet quantum yield
Triplet lifetime
Fluorescence quantum yield
Photodegradation quantum yield

ABSTRACT

This work reports on the synthesis and photophysicochemical parameters of unsubstituted $[Sb^{III}Pc]^{+}I_3^{-}$ and octa-phenoxy ($[Sb^{III}OPPc]^{+}I_3^{-}$) and -4-*t*-butylphenoxy ($[Sb^{III}OTBPPc]^{+}I_3^{-}$) substituted antimony phthalocyanines. Photophysical and photochemical properties were studied for these complexes in dimethylsulfoxide, dimethylformamide and toluene. The excitation spectra of oxidized antimony (Sb(V)Pc) derivates were similar to absorption spectra. Low fluorescence quantum yields, high triplet quantum yields and low triplet lifetimes were observed as the result of heavy atom (antimony ion).

© 2008 Elsevier Ltd. All rights reserved.

1. Introduction

Since their accidental discovery in the early 1900s, metallophthalocyanines (MPcs) have attracted much interest [1] due to their high chemical and thermal stability, high degree of aromaticity, synthetic flexibility and ability to adapt to a wide range of applications, including in non-linear optics [2,3] and photodynamic therapy [4].

MPcs exhibit intense absorption towards the red end of the visible spectrum, and the wavelength varies depending on the central metal and the type, number and position of substituents attached to the phthalocyanine macrocycle [5]. The presence of substituents on the Pc ring increases the solubility and also reduces molecular aggregation. Some central metal ions can allow axial ligation, which increases solubility, reduces molecular aggregation and brings about changes to the electronic structure of the molecule due to the dipole moment of the central metal-axial ligand bond [6]. MPcs containing heavy atoms such as antimony are expected to show enhanced intersystem crossing [7], resulting in improved photophysical and photochemical properties.

There has been less attention paid to MPc derivatives of group-15 elements except for a few reports on antimony and bismuth complexes of phthalocyanine [8–14]. Some properties of SbPc derivatives show distinct differences compared to the majority of MPc complexes. For example, the Sb tetra-*tert*-butyl phthalocyanine $[SbTBPc]I_3$ has shown the formation of J aggregates (red-shifted) in non-aqueous solutions [12]. J aggregates are rare in non-aqueous media for MPc complexes. The $[SbTBPc]I_3$ complex was found to be stable in the dark in chloroform and dichloromethane, but readily demetalated in donor solvents such as dimethylformamide (DMF) and tetrahydrofuran (THF) [15]. Photobleaching of this complex occurred under visible light irradiation in chloroform. Attempts to determine singlet oxygen producing ability of $[SbTBPc]I_3$ using 1,3-diphenylisobenzofuran (DPBF) as a quencher resulted in oxidation of Sb(III) to Sb(V) [15]. It has also been reported that some SbPc complexes do not show fluorescence in the Q-band region [12,15]. However, the behaviour of the triplet state of SbPc complexes has not been explored. Hence, in this work we report on the synthesis of new SbPc complexes: octa-phenoxy ($[Sb^{III}OPPc]^{+}I_3^{-}$) and -4-*t*-butylphenoxy ($[Sb^{III}OTBPPc]^{+}I_3^{-}$) substituted antimony phthalocyanines and on their photophysical and photochemical behaviour.

2. Experimental

2.1. Materials

Acetone, ethanol, chloroform ($CHCl_3$), methanol (MeOH), 1-chloronaphthalene (1-CNP), 1-octanol, tetrahydrofuran (THF), dimethylformamide (DMF), hexane and deuterated chloroform ($CDCl_3$) were obtained commercially and dried before use. Potassium carbonate (K_2CO_3), urea, phenol, 4-*tert*-butylphenol and phthalonitrile were purchased from Aldrich and used as received. Dimethylsulphoxide (DMSO) was purchased from SAARCHEM, and dried in alumina before use. 4,5-Dichlorophthalonitrile (**3**) [16] was synthesized and purified according to literature procedure.

* Corresponding author. Tel.: +27 46 6038260; fax: +27 46 6225109.
E-mail address: t.nyokong@ru.ac.za (T. Nyokong).

0277-5387/$ - see front matter © 2008 Elsevier Ltd. All rights reserved.
doi:10.1016/j.poly.2008.11.052

2.2. Equipment

Ground state electronic absorption spectra were performed on a Varian Cary 500 UV–Vis–NIR spectrophotometer; infrared spectra (KBr pellets) on Perkin–Elmer Spectrum 2000 FT-IR Spectrometer and ^{1}H nuclear magnetic resonance (^{1}H NMR) signals on a Bruker EMX 600 NMR spectrometer. Triplet lifetimes (τ_T) and yields were obtained (at 22 °C) using an Nd-YAG laser providing 400 mJ, 90 ns of laser light at 10 Hz, pumping a Lambda-Physik FL 3002 dye laser. A 300-W xenon arc lamp (Thermo Oriel) provided the analysing light. Kinetic curves were averaged over 256 laser pulses using a Tektronix TDS 360 digital oscilloscope. The τ_T values were obtained by fitting an exponential curve to the kinetic data using ORIGIN Pro 6.0.

Photo-irradiations for photodegradation quantum yield terminations were performed using a General electric Quartz line lamp (300 W), as has been reported before [17]. A 600 nm glass cut off filter (Schott) and water were used to filter off ultraviolet and infrared radiations, respectively. An interference filter (Intor, 700 nm with a band width of 40 nm) was additionally placed in the light path before the sample. Light intensity was measured with a POWER MAX5100 (Molelectron detector incorporated) power meter and was found to be 5.14×10^{16} photons s^{-1} cm^{-2} for photobleaching studies. Elemental analysis was performed at the University of Cape Town, South Africa, using a Thermo Flash EA 1112 series elemental analyzer.

2.3. Photophysical and photochemical properties

Fluorescence quantum yields (Φ_F) were determined by the comparative method, using Eq. (1) [17,18]:

$$\Phi_F = \Phi_F^{std} \frac{F \cdot A_{std} \cdot n^2}{F_{std} \cdot A \cdot n_{std}^2} \quad (1)$$

where F and F_{std} are the areas under the fluorescence curves of the MPc derivatives and the standard, respectively. A and A_{std} are the respective absorbances (which was ~0.05 in all solvents used), of the sample and standard at the excitation wavelengths and n and n_{std} are the refractive indices of the solvents used for sample and standard, respectively. ZnPc was employed as a standard in DMSO (Φ_F = 0.20) [17].

The triplet quantum yields were determined using Eq. (2) [19]:

$$\Phi_T = \Phi_T^{std} \frac{\Delta A_T \cdot \varepsilon_T^{std}}{\Delta A_T^{std} \cdot \varepsilon_T} \quad (2)$$

where ΔA_T and ΔA_T^{std} are the changes in triplet state absorbance of MPc derivatives and the standard, respectively. Φ_T^{std} is the triplet quantum yield for the standard, ZnPc (Φ_T = 0.65 in DMSO [20], 0.58 in DMF [21] and 0.65 in toluene [22]). ε_T and ε_T^{std} are the triplet state molar extinction coefficients for the MPc derivatives and the standard, respectively.

ε_T^{Sample} and ε_T^{std} were determined from the molar extinction coefficients of their respective ground singlet state (ε_S^{Sample} and ε_S^{std}), the changes in absorbances of the ground singlet states (ΔA_S^{Sample} and ΔA_S^{std}) and changes in the triplet state absorptions, (ΔA_T^{Sample} and ΔA_T^{std}) according to Eqs. (2a) and (2b):

$$\varepsilon_T^{Sample} = \varepsilon_T^{Sample} \frac{\Delta A_T^{Sample}}{\Delta A_S^{Sample}} \quad (2a)$$

$$\varepsilon_T^{std} = \varepsilon_T^{std} \frac{\Delta A_T^{std}}{\Delta A_S^{std}} \quad (2b)$$

2.4. Photodegradation quantum yields

To determine the stability of SbPc derivatives, photodegradation quantum yields were calculated using Eq. (3):

$$\Phi_{Pd} = \frac{(c_0 - c_t)VN_A}{I_{abs}St} \quad (3)$$

where C_0 and C_t in mol dm^{-3} are concentrations before and after irradiation, respectively, V the reaction volume, S is the irradiated cell area (2.0 cm^2), t is the irradiation time, N_A is the Avogadro's number and I_{abs} is the overlap integral of the radiation source intensity and the absorption of the Pc (the action spectrum) in the region of the interference filter transmittance.

2.5. Synthesis

4,5-Diphenoxyphthalonitrile (**4a**), and 4,5-bis(4-*t*-butylphenoxy)phthalonitrile (**4b**) were synthesized and characterized according to reported procedures [23–25].

2.5.1. 2,3-Octaphenoxyphthalocyaninatoantimony triiodide ([Sb^{III}OPPc]$^+I_3^-$) (**5a**)

4,5-Diphenoxyphthalonitrile **4a** (0.62 g, 1.99 mmol) was heated to 180 ^{0}C until it completely melted. Then, antimony iodide (0.25 g, 0.50 mmol) was added in small portions to the completely molten solution. The reaction mixture was maintained at 180 ^{0}C for 24 h with constant stirring. The solid product was dissolved in CH_2Cl_2 and precipitated from the solution by addition of methanol. The product was washed with methanol three times, ethanol and then with acetone, respectively, until the washings turned essentially colourless. The solid product was further purified by washing with methanol, ethanol and then with acetone in a Soxhlet apparatus. Yield: 50.0 mg (18%). UV–Vis (DMSO): $\lambda_{max.}$ nm (log ε) 740 (5.03), 667 (4.62), 349 (4.78), 345 (4.78). IR [(KBr) $\nu_{max.}$/cm^{-1}]: 1271 (C–O–C), 1000, 883, 856, 749, 732 (Pc skeletal). ^{1}H NMR (DMSO): δ, ppm 8.72–8.79 (8H, s, Pc–H), 7.35–7.76 (40H, m, phenyl–H). *Anal.* Calc. for $C_{80}H_{48}N_8O_8SbI_3 \cdot 2H_2O$: C, 53.75; H, 2.71; N, 6.27. Found: C, 53.80; H, 3.17; N, 6.60%.

2.5.2. 2,3-[Octakis(4-t-butylphenoxyphthalocyaninato)] antinomy triiodide ([Sb^{III}OTBPPc]$^+I_3^-$) (**5b**)

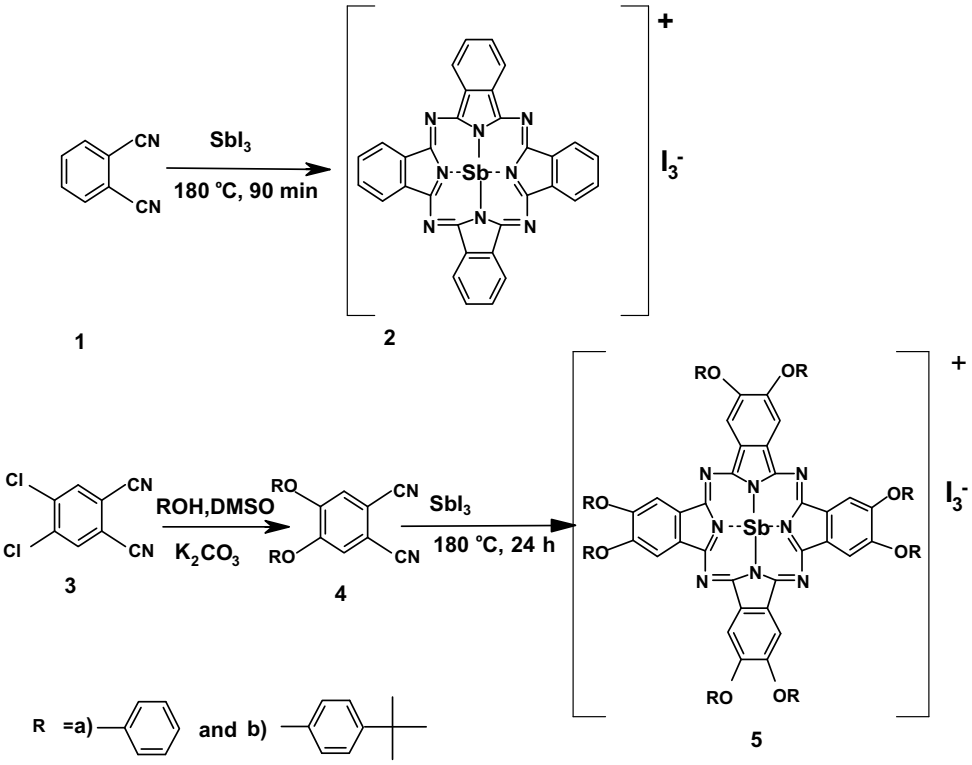
Synthesis and purification of **5b** was as outlined for **5a** except **4b** instead of **4a** was employed. The amounts of the reagents employed were: **4b** (0.84 g, 1.99 mmol) and antimony iodide (0.25g, 0.50 mmol). Yield: 10.0 mg (2.7%). UV–Vis (DMSO): $\lambda_{max.}$ nm (log ε) 740 (5.02), 667 (4.44), 349 (4.73), 345 (4.64). IR [(KBr) $\nu_{max.}$/cm^{-1}]: 1270 (C–O–C), 883, 827, 769, 751,749 (Pc skeletal), 2965 (*t*-butyl-H). ^{1}H NMR (DMSO): δ, ppm 8.70 (8H, s, Pc–H), 7.01–7.40 (32H, m, phenyl–H), 1.11–1.40 (72H, s, ^{t}Bu). *Anal.* Calc. for $C_{112}H_{112}N_8O_8SbI_3 \cdot 2H_2O$: C, 60.15; H, 5.05; N, 5.01. Found: C, 60.57; H, 5.61; N, 5.09%.

The synthesis of phthalocyaninatoantimony triiodide (**2**) has been reported before [26].

3. Results and discussion

3.1. Syntheses and characterization

Scheme 1 gives the synthetic pathways for the SbPc complexes discussed in this work. The general procedure for synthesis of substituted phthalonitrile derivatives has been well documented [27,28] and the preparation of the substituted phenoxy derivatives was carried out as reported before [23–25]. Unsubstituted phthalocyanine (**2**) was prepared according to literature [26] by cyclotetramerization of 1,2-dicyanobenzene in the presence of metal salt. The syntheses of octa-substituted metallophthalocyanine complexes (**5a** and **5b**) were achieved by treatment of 4,5-disubstitutedphthalonitrile with metal salt. Soxhlet extraction was employed to obtain pure products.



Scheme 1. Synthesis of phenoxy ($[Sb^{III}OPPc]^+I_3^-$) and -4-*t*-butylphenoxy ($[Sb^{III}OTBPPc]^+I_3$) octa-substituted and unsubstituted SbPcs.

The MPc derivatives were characterized by UV–Vis, NMR (Fig. S1) and IR (Fig. S2) spectroscopies and elemental analyses. The analyses were consistent with the predicted structures as shown in Section 2. It has been reported before that for large Pc molecules, elemental analyses often gives unsatisfactory results [29]. However, the elemental analyses for complexes **5a** and **5b** gave satisfactory results that were close to calculated values. The sharp peak for the C≡N vibrations in the IR spectra of phthalonitriles **4a** and **4b** at ~2237 and 2224 cm^{-1}, respectively, disappeared after conversion into metallophthalocyanines. All MPc derivatives showed vibrational peaks between 700 and 1000 cm^{-1} which may be assigned to phthalocyanine skeletal vibrations [30]. The characteristic vibrations corresponding to ether groups (C–O–C) at ca. 1265–1275 cm^{-1} and aliphatic CH stretching at ca. 2900–3000 cm^{-1} were observed for the substituted MPc derivatives, Fig. S2.

The antimony phthalocyanines were found to be pure by ^1H NMR with all the substituents and ring protons observed in their respective regions. The phenoxy substituted complex **5a** showed the resonances belonging to ring protons as a singlet at 8.72–8.79 ppm, and a multiplet between 7.35 and 7.76 ppm, integrating for 8 and 40 protons, respectively, Fig. S2. The *tert*-butylphenoxy substituted complex **5b** showed the resonances belonging to ring protons as a singlet at 8.70 ppm and a multiplet between 7.01 and 7.40 ppm for aromatic protons integrating for 8 and 32 protons each, respectively, making a total of 40 protons as expected. The methyl protons appear as multiplets between 1.11 and 1.40 ppm integrating for 72 protons.

The ground state electronic absorption spectra of $[Sb^{III}OPPc]^+I_3^-$ and $[Sb^{III}OTBPPc]^+I_3^-$ show relatively sharp Q-bands typical of unaggregated MPc complexes, as has been reported before for other antimony derivatives [8–14], Fig. 1. It has been reported that the spectra of SbPc complexes are slightly broadened compared to other MPc complexes [12]. Sb(III) is larger than the equilibrium cavity size of the ring and cannot be accommodated without ring expansion; so the metal prutrudes out of the cavity, forming a domed shape. Under this situation, the symmetry of the complex becomes lower than D_{4h} [31]. The symmetry lowering allows some hitherto forbidden transitions; and consequently, spectral splitting and broadening is observed (Figs. 1 and 2). The Q-bands were observed at 730 (log = 5.23), 740 (log = 5.03) and 740 (log = 5.02) nm in DMSO (Fig. 1) for $[Sb^{III}Pc]^+I_3^-$ (**2**), $[Sb^{III}OPPc]^+I_3^-$ (**5a**) and $[Sb^{III}OTBPPc]^+I_3^-$ (**5b**), respectively. The Q-bands are slightly red-shifted in the latter two complexes, suggesting a small electron donating ability of the substituents. As reported before [12], the triiodide ion does not contribute to the Q-band absorption but contributes to the absorption near 360 nm in Fig. 1. Thus, the B band spectra will be affected by absorption from the triiodide ions. A

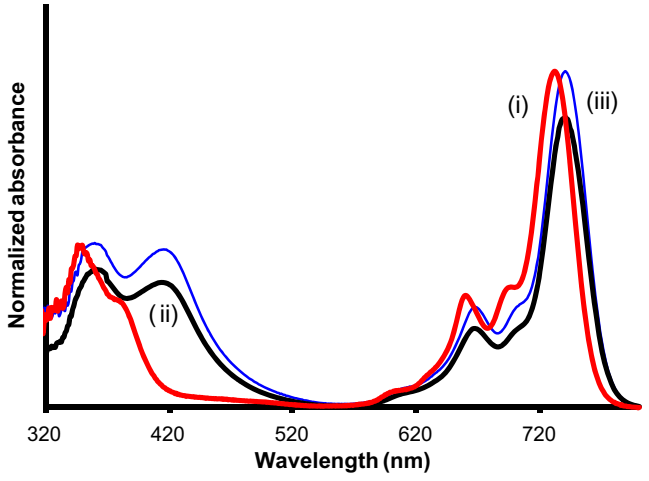


Fig. 1. Absorption spectra of complex (i) **2**, (ii) **5a** and (iii) **5b** in DMSO (~4×10^{-6} M).

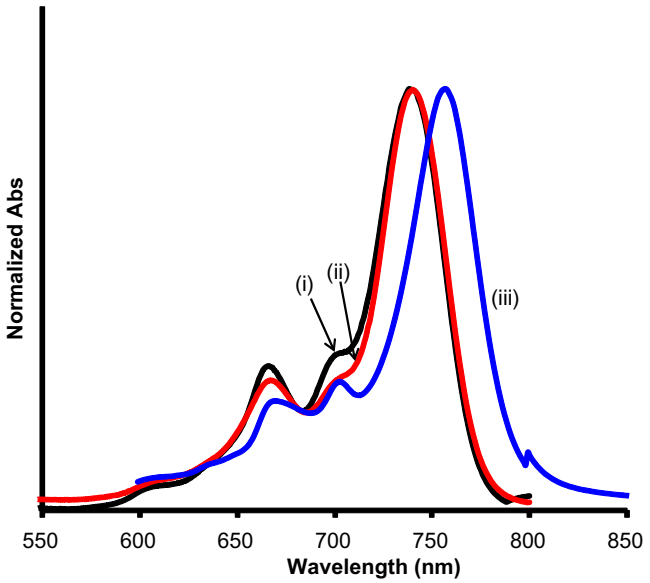


Fig. 2. Absorption spectra of complex **5b** in (i) DMSO, (ii) DMF and (iii) Toluene ($\sim 4 \times 10^{-6}$ M).

large red-shift has been reported in aromatic solvents [32], hence the red-shift of the SbPc derivatives in toluene is not surprising.

Phthalocyanines readily aggregate. The formation of aggregates was explored in this work by recording the spectra on increasing the concentrations of the $[Sb^{III}OPPc]^{+}I_3^{-}$ (**5a**) and $[Sb^{III}OTBPPc]^{+}I_3^{-}$ (**5b**), Fig. 3. At the concentrations employed in Fig. 3 (2×10^{-5}–3×10^{-6} M in DMSO), the intensity of the Q-bands decreased with concentration and no red (or blue) shifting due to aggregated species was observed at high concentration.

Even though some SbPc complexes are known to demetalate in donor solvents such as DMF and THF [15], there was no evidence of demetalation for complexes **2**, **5a** and **5b** in DMSO, DMF and toluene.

Since $Sb^{III}Pc$ derivatives do not fluoresce, we oxidized complexes **2**, **5a** and **5b** to $Sb^{V}Pc$ derivatives in order to study their fluorescence behaviour. The oxidation of antimony complexes has been reported using H_2O_2 as an oxidant [26]. It was found that antimony(III) phthalocyanine complexes can be readily converted to the corresponding antimony(V) derivates through oxidative addition process [26]. Even though H_2O_2 is a readily available oxidant, it is known not to give clean spectra of the resulting $Sb^{V}Pc$

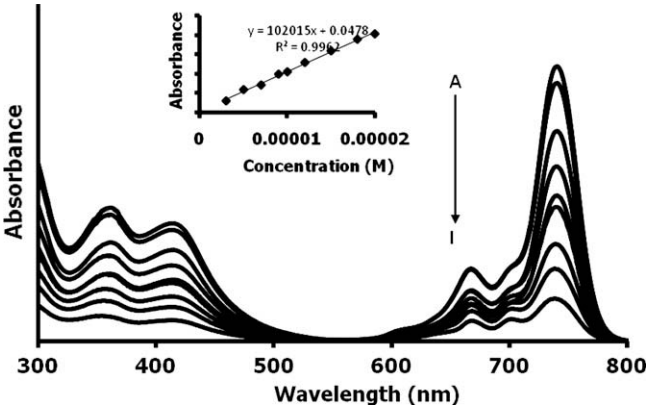


Fig. 3. Absorption spectra of compound **5a** in DMSO at different concentrations: (A) 2×10^{-5}, (B) 1.8×10^{-5}, (C) 1.5×10^{-5}, (D) 1.2×10^{-5}, (E) 1×10^{-5}, (F) 9×10^{-6}, (G) 7×10^{-6}, (H) 5×10^{-6} and (I) 3×10^{-6} M.

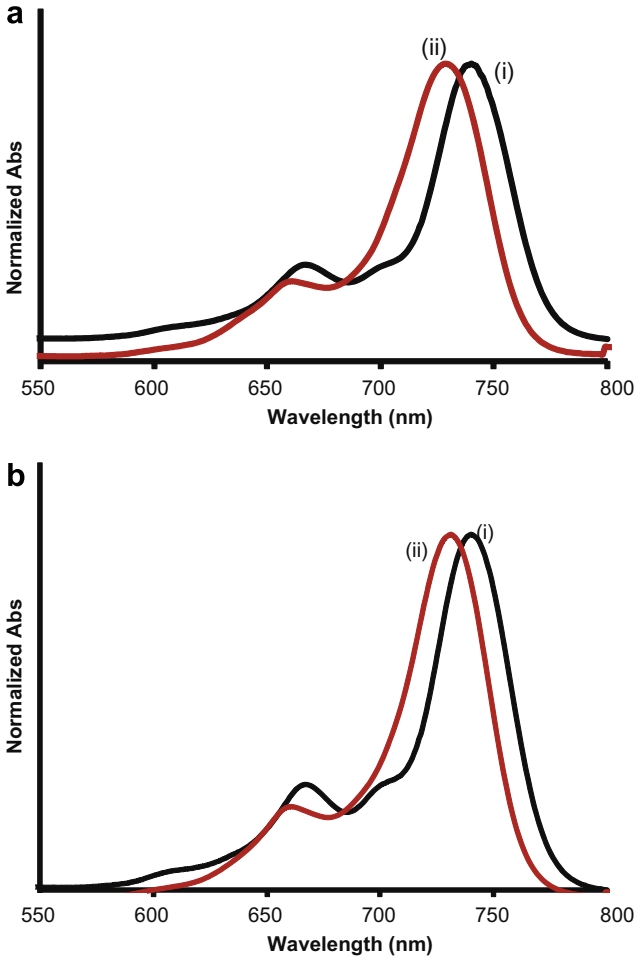


Fig. 4. Absorption spectra before (i) and after (ii) oxidation of complex (a) **5a** and (b) **5b** using TBHP in DMSO as an oxidant. Concentration $\sim 1 \times 10^{-5}$ M.

[33], hence in this work we employed an organic oxidant *t*-butylhydroperoxide (TBHP). The oxidation of $Sb^{III}Pc$ derivatives is known to proceed more cleanly if organic peroxides such as *tert*-butyl perbenzoate are employed as oxidants [33].

After addition of TBHP to $Sb^{III}Pc$ complexes (**2**, **5a** and **5b**), Q-band absorptions were blue-shifted as indicative of oxidized $Sb^{III}Pc$

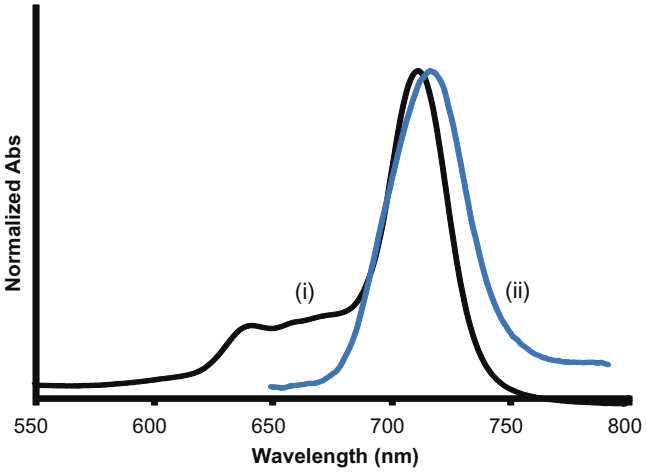


Fig. 5. Absorption (i) and emission (ii) spectra of oxidized compound **2** in DMSO using TBHP as oxidant ($\sim 8 \times 10^{-6}$ M).

Table 1
Spectral, photophysical parameters of $Sb^{III}Pc$ derivatives in DMSO, DMF and toluene.

MPc	Solvent	$\lambda_{max.}$ (nm) absorption	Φ_T	Φ_{Pd} ($\times 10^{-5}$)	τ_T (μs)
[a](I)SbPc (**2**)	DMSO	730	0.75	0.31	30
	DMF	728	0.76	0.52	7
(I)SbOPPc (**5a**)	DMSO	740	0.79	0.42	20
	DMF	735	0.78	0.61	5
	Toluene	758	0.77	0.57	7
(I)SbOTBPPc (**5b**)	DMSO	740	0.80	0.48	30
	DMF	735	0.82	0.53	5
	Toluene	753	0.78	0.81	6

derivates, Fig. 4a and b. The Q-bands were observed at 710, 735 and 731 nm in DMSO for oxidized forms of complexes **2**, **5a** and **5b**, respectively. Sb(V) is smaller than Sb(III) (ionic radii are 0.62 Å and 0.89 Å, respectively), and also more electronegative. The smaller size and higher electronegativity increase the conjugation of the Pc's HOMO with the metal $5p_z$ orbital [34], which results in lower charge density and energy of the Pc's HOMO. The effect of this is the observed blue-shifting of spectral band positions (Fig. 4).

3.2. Photophysical and photochemical properties

3.2.1. Fluorescence spectra and quantum yields

It is known that low valent main group porphyrin and phthalocyanine complexes (such as $Sb^{III}Pc$ derivatives) do not show emission around the Q-band [12]. The $[Sb^{III}Pc]^+I_3^-$ (**2**), $[Sb^{III}OPPc]^+I_3^-$ (**5a**) and $[Sb^{III}OTBPPc]^+I_3^-$ (**5b**) complexes were oxidized to the corresponding $[X_2Sb^{V}Pc]^+I_3$, $[X_2Sb^{V}OPPc]^+I_3^-$ and $[X_2Sb^{V}OTBPPc]^+I_3^-$ (where X represents monoanionic axial ligands containing oxygen donors OR) using TBHP. Fig. 5 shows the absorption and fluorescence spectra of oxidized complex **2** in DMSO. Similar spectra were observed for complexes **5a** and **5b**. The observed emission spectra are red-shifted when compared to their corresponding excitation and absorption spectra. The fluorescence excitation spectral maxima agree very well with absorption of the compounds, Tables 1 and 2, suggesting that there are no differences in the nuclear configuration of the ground and excited states, Fig. 5. The fluorescence emission peaks were observed: 716, 741 and 736 nm for oxidized compound **2**, **5a** and **5b** (in DMSO), respectively.

The fluorescence quantum yield (Φ_F) is the fraction of molecules in the excited state that do return to ground state via fluorescence. It is a parameter that is affected by molecular properties as well as the solvent and environment surrounding the molecule. The Φ_F values for the oxidized **2**, **5a**, **5b** are very low as reported before ($\Phi_F < 0.01$) for Sb(V)Pc complexes [33]. The Φ_F yields were relatively low compared to MPc in general [17] due to the presence of heavy atom effect (antimony ion) which enhances intersystem crossing to populate the triplet state.

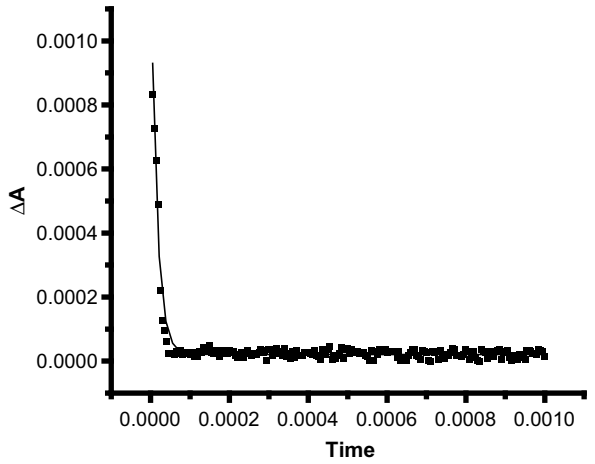


Fig. 6. Triplet decay curve of complex **5a** in DMSO. Excitation wavelength = 510 nm.

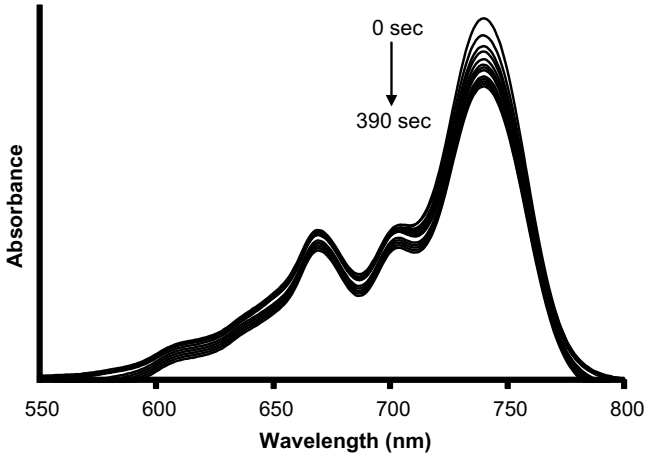


Fig. 7. Photobleaching of complex **5a** in DMSO.

3.2.2. Triplet quantum yields and lifetimes

Both the triplet quantum yields and lifetimes were determined by laser flash photolysis. Fig. 6 shows representative triplet decay curves for the $Sb^{III}Pc$ derivatives, which is similar to those of their oxidized counterparts ($Sb^{V}Pc$). Fig. 6 shows the triplet decay curve for the complexes obeyed second order kinetics. This is typical of MPc complexes at high concentrations (>1×10^{-5} M) [35] due to the triplet–triplet recombination. The concentrations employed in this work were in this range, hence triplet–triplet recombination is expected.

Table 2
Spectral, photophysical parameters of $Sb^{V}Pc$ derivatives in DMSO, DMF and toluene.

MPc	Solvent	$\lambda_{max.}$ (nm)			Φ_T	Φ_{Pd} ($\times 10^{-5}$)	τ_T (μs)
		Absorption	Emission	Excitation			
[a]Oxidized **2**	DMSO	710	716	711	0.71	1.23	70
	DMF	706	710	705	0.72	2.42	8
Oxidized **5a**	DMSO	735	741	736	0.74	1.51	60
	DMF	728	733	727	0.74	2.23	9
	toluene	743	750	742	0.73	3.42	10
Oxidized **5b**	DMSO	731	736	730	0.76	2.01	50
	DMF	730	734	729	0.77	3.22	8
	toluene	742	748	740	0.78	2.42	9

[a] (I)SbPc (**2**) is insoluble in toluene.

Tables 1 and 2 gives the triplet state parameters, Φ_T and τ_T. The triplet quantum yield which are a measure of molecules that undergo intersystem crossing to occupy the triplet state, were calculated using Eq. (2). Table 1 shows high Φ_T values (0.75–0.82, for complexes **2**, **5a** and **5b**) in DMSO, DMF and toluene, due to the presence of antimony. It seems that the introduction of substituents onto the ring had only a small effect on the Φ_T, the values increased from 0.75 for complex **2**, to 0.79 for **5a** and 0.80 for **5b** in DMSO. The Φ_T values (0.71–0.78) for oxidized $Sb^{V}Pc$ complexes were a bit lower than for the $Sb^{III}Pc$ complexes. The values are in general high due to the heavy atom effect of Sb, Table 2.

The triplet lifetime (τ_T) values were found to be low for SbPc complexes compared to ZnPc or AlPc [36] derivatives but are similar to the corresponding InPc [37,38] derivatives, containing a heavy metal. The τ_T values in DMSO (Tables 1 and 2) ranged from 20 to 30 μs for $Sb^{III}Pc$ complexes while in DMF and toluene the τ_T values were less than 10. τ_T Values are lower in DMF than in DMSO because of the greater absorption by DMF (than DMSO) in the region of the complexes' triplet energy [17]. The τ_T values for oxidized complexes $Sb^{V}Pc$ complexes were longer than for corresponding $Sb^{III}Pc$ compounds.

Photodegradation or photobleaching (Φ_{Pd}) is used to determine the photostability of MPc molecules and is identified by a decrease in the intensity of the absorption spectra without the appearance of new peaks. Photodegradation is a function of the nature of the substituents attached to the phthalocyanines periphery, the solvent and the central metal. SbPc derivatives have been shown to photodegrade without transformation to other visible absorbing species [15]. The spectral changes observed during photobleaching were similar for all the complexes (**2**, **5a** and **5b**) during irradiation. The collapse of the absorption spectra without any distortion of the shape confirms clean photodegradation not associated with phototransformation, Fig. 7. All the complexes showed same stability as compared to InPc and GaPc [25,36,37] with Φ_{Pd} of the order of 10^{-5}.

4. Conclusion

In this study, we synthesized and characterized new peripherally (phenoxy and 4-*t*-butylphenoxy) octa-substituted antimony phthalocyanine complexes. For the oxidized $[X_2Sb^{V}Pc]^{+}I_3$, $[X_2Sb^{V}OPPc]^{+}I_3^{-}$ and $[X_2Sb^{V}OTBPPc]^{+}I_3^{-}$ complexes, the excitation spectra were the same as absorption spectra and both are mirror images of the emission spectra. The low fluorescence quantum yields, high triplet quantum yields and low triplet lifetimes were observed as the result of heavy atom (antimony ion).

Acknowledgements

This work was supported by the Department of Science and Technology (DST) and National Research Foundation (NRF), South Africa through DST/NRF South African Research Chairs Initiative for Professor of Medicinal Chemistry and Nanotechnology and Rhodes University. DKM thanks CSIR, for a bursary and also Dr. A. Ogunsipe for useful discussion.

Appendix A. Supplementary data

Supplementary data associated with this article can be found, in the online version, at doi:10.1016/j.poly.2008.11.052.

References

[1] C.C. Leznoff, A.B.P. Lever, (Eds.), Phthalocyanines: Properties and Applications, vols. 1–4, VCH Publications, New York, 1989, 1993, 1996.
[2] G. de la Torre, P. Vasquez, F. Agulló-López, Adv. Mater. 9 (1997) 265.
[3] D. Dini, M. Hanack, The Porphyrin Handbook: Physical Properties of Phthalocyanine-Based Materials, vol. 17, Academic Press, USA, 2003.
[4] R. Bonnett, Chem. Soc. Rev. 24 (1995) 19.
[5] N. Kobayashi, H. Ogata, N. Nonaka, E.A. Luk'yanets, Chem. Eur. J. 9 (2003) 5123.
[6] M. Hanack, T. Schneider, M. Barthel, J.S. Shirk, S.R. Flom, R.G.S. Pong, Coord. Chem. Rev. 219–221 (2001) 235.
[7] E.R. Menzel, K.E. Rieckhoff, E.M. Voigt, J. Chem. Phys. 58 (1973) 5726.
[8] Y. Kagaya, H. Isago, Chem. Lett. (1994) 1957.
[9] H. Isago, Y. Kagaya, Bull. Chem. Soc. Jpn. 67 (1994) 383.
[10] H. Isago, Y. Kagaya, Bull. Chem. Soc. Jpn. 67 (1994) 3212.
[11] H. Isago, Y. Kagaya, Chem. Lett. 35 (2006) 8.
[12] H. Isago, Chem. Commun. (2003) 1864.
[13] H. Isago, Y. Kagaya, S.-I. Nakajima, Chem. Lett. 32 (2003) 112.
[14] Md.H. Zahir, Y. Kagaya, H. Isago, T. Furubayashi, Inorg. Chim. Acta 357 (2004) 2755.
[15] H. Isago, K. Miura, M. Kanesato, J. Photochem. Photobiol. A: Chem. 197 (2008) 313.
[16] D. Wöhrle, M. Eskes, K. Shigehara, A. Yamada, Synthesis (1993) 194.
[17] A. Ogunsipe, J.Y. Chen, T. Nyokong, New J. Chem. 28 (2004) 822.
[18] S. Fery-Forgues, D.j. Lavabre, Chem. Ed. 76 (1999) 1260.
[19] P. Kubát, J. Mosinger, J. Photochem. Photobiol. A: Chem. 96 (1996) 93.
[20] T.H. Tran-Thi, C. Desforge, C. Thiec, J. Phys. Chem. 93 (1989) 1226.
[21] J. Kossanyi, O. Chahraoui, Int. J. Photoenerg. 2 (2000) 9.
[22] S.M. Bishop, A. Beeby, A.W. Parker, M.S.C. Foley, D. Phillips, J. Photochem. Photobiol. A: Chem. 90 (1995) 29.
[23] P. Tau, T. Nyokong, Dalton Trans. (2006) 4482.
[24] P. Tau, T. Nyokong, J. Porphyr. Phthalocya. 10 (2006) 1040.
[25] V. Chauke, A. Ogunsipe, M. Durmas, T. Nyokong, Polyhedron 26 (2007) 2663.
[26] G Knör, Inorg. Chem. 35 (1996) 7916.
[27] T.M. Keller, T.R. Price, J.R. Griffith, Synthesis 74 (1980) 613.
[28] W.M. Sharman, J.E. van Lier, in: K.M. Kadish, K.M. Smith, R. Guilard, (Eds.), The Porphyrin Handbook, vol. 15, Academic Press, New York, 2003 (Chapter 97).
[29] S. Marcuccio, P.I. Svirskaya, S. Greenberg, A.B.P. Lever, Can J. Chem. 63 (1985) 3057.
[30] M.M. El-Nahass, K.F. Abd-El-Rahman, A.A.A. Darwish, Mater. Chem. Phys. 92 (2005) 185.
[31] D.R. Tackley, G. Dent, W.E. Smith, Phys. Chem. Chem. Phys. 3 (2001) 1419.
[32] A. Ogunsipe, T. Nyokong, J. Mol. Struc. 689 (2004) 89.
[33] H. Isago, K. Miura, Y. Oyama, J. Inorg. Biochem. 102 (2008) 380.
[34] J.A. Shelnutt, J. Am. Chem. Soc. 105 (1983) 774.
[35] M.G. Debacker, O. Deleplanque, B. Van Vlierberge, F.X. Sauvage, Laser Chem. 8 (1988) 1.
[36] T. Nyokong, Coord. Chem. Rev. 251 (2007) 1707.
[37] M. Durmus, T. Nyokong, Tetrahedron 63 (2007) 1385.
[38] M. Durmus, T. Nyokong, Polyhedron 26 (2007) 3323.

Polyhedron 28 (2009) 485–492

Contents lists available at ScienceDirect

Polyhedron

journal homepage: www.elsevier.com/locate/poly

Coordination ability of insect kinin analogs

E. Łodyga-Chruścińska [a,*], S. Ołdziej [b], D. Sanna [c], G. Micera [d], L. Chruściński [e], K. Kaczmarek [f], R.J. Nachman [g], J. Zabrocki [f], A. Sykuła [a]

[a] Technical University of Łódź, Institute of General Food Chemistry, ul. Stefanowskiego 4/10, 90-924 Łódź, Poland
[b] Laboratory of Biopolymer Structure, Intercollegiate Faculty of Biotechnology, University of Gdańsk and Medical University of Gdańsk, Kładki 24, 80-822 Gdańsk, Poland
[c] Istituto C.N.R. Chimica Biomolecolare, 07040 Sassari, Italy
[d] Dipartimento di Chimica, University of Sassari, Via Vienna 2, 07100 Sassari, Italy
[e] Faculty of Process and Environmental Engineering, Technical University of Łódź, ul. Wólczańska 213, 90-924 Łódź, Poland
[f] Institute of Organic Chemistry, Technical University of Łódź, ul. Żeromskiego 176, 90-924 Łódź, Poland
[g] Areawide Pest Management Research Unit, Southern Plains Agricultural Research Center, US Department of Agriculture, College Station, TX 77845, USA

ARTICLE INFO

Article history:
Received 14 July 2008
Accepted 25 November 2008
Available online 2 January 2009

Keywords:
Metallopeptides
Complex formation
4-aminopyroglutamate motif

ABSTRACT

Spectroscopic data, including electronic absorption, CD and EPR results, as well as theoretical calculations have shown that the insertion of 4-aminopyroglutamate, a novel *cis*-peptide bond mimic, in the insect kinin peptide leads to an effective ligand towards Cu(II) ions at basic pH ranges. The 4-aminopyroglutamate motif induces a specific peptide conformation which favors the formation of one or two five-membered chelating rings stabilizing a bent structure, with the coordination of 3N-type or 4N-type in the metallopeptide molecule involving in metal bonding C-terminal of modified peptide. It is worth noting that the copper(II) bonding does not undergo hydrolysis even at a very high pH range.

© 2008 Elsevier Ltd. All rights reserved.

1. Introduction

Insect kinins share a highly conserved C-terminal pentapeptide sequence Phe–Xaa–Xbb–Trp–Gly–NH_2, where Xaa can be Tyr, His, Ser or Asn and Xbb can be Ala but is generally Ser or Pro. Insect kinins, and/or analogues, have been reported to inhibit the growth of serious agricultural pests, e.g. the tobacco budworm (*Heliothis virescens*) or corn earworm (*Helicoverpa zea*) [1]. The insect kinins preferentially form a *cis*-Pro, type VI β-turn. An insect kinin analog containing (2S,4S)-4-aminopyroglutamate, a novel *cis*-peptide bond, type VI β-turn motif has demonstrated significant activity in the physiological range in a cricket diuretic assay. This is the first instance of a 4-aminopyroglutamate analog of a peptide with a preference for a type VI β-turn that demonstrates significant bioactivity [2].

Their chelating properties have not been studied yet. Many essential metal ions act as important factors that influence the structure of natural and synthetic oligopeptides and, as a consequence, they may affect their biological activity.

In this work the interaction of copper(II) ions with the peptidomimetic insect kinin analogs, containing 4-aminopyroglutamate (apy or aPy), has been studied. The aim was to identify coordination sites for the metal ion. In peptides and proteins copper ions usually interact with the peptide bond most easily via an amino terminal amine nitrogen anchor then the coordination followed by the sequential deprotonation of neighboring peptide nitrogens. In our case such an anchoring site does not occur because the amine terminal is protected. However, the other anchoring donor atom could be the oxygen of the carbonyl group of the apy/aPy motif. To determine the coordination mode of the metal ion in the formation of the peptide-metal complex, potentiometric, spectroscopic (UV–Vis, CD, EPR) studies, in conjunction with computer modelling optimisation, have been performed on several ligand systems: AcRFapyWG-OH, AcRFFPWG-NH_2 and AcRFaPyWG-NH_2 (Fig. 1). The results reveal that the peptides containing the apy or aPy motif form complexes with 3N or 4N coordination modes above pH 8. One of nitrogen donor atoms is very likely from the pyrrolidine group of the apy/aPy motif. The Cu(II) ion coordination to the AcRFFPWG-NH_2 ligand is not observed until above pH 10.

2. Experimental

2.1. Materials

The insect kinin analogs (AcRF**aPy**WG-NH_2, AcRF**apy**WG-OH) and AcRFFPWG-NH_2 were synthesized according to previously

Abbreviations: apy, (2R,4R)-4-aminopyroglutamate; aPy, (2R,4S)-4-aminopyroglutamate; APy, (2S,4S)-4-aminopyroglutamate.

* Corresponding author. Tel.: +48426313417; fax: +48426362860.
E-mail address: elalodyg@p.lodz.pl (E. Łodyga-Chruścińska).

0277-5387/$ - see front matter © 2008 Elsevier Ltd. All rights reserved.
doi:10.1016/j.poly.2008.11.051

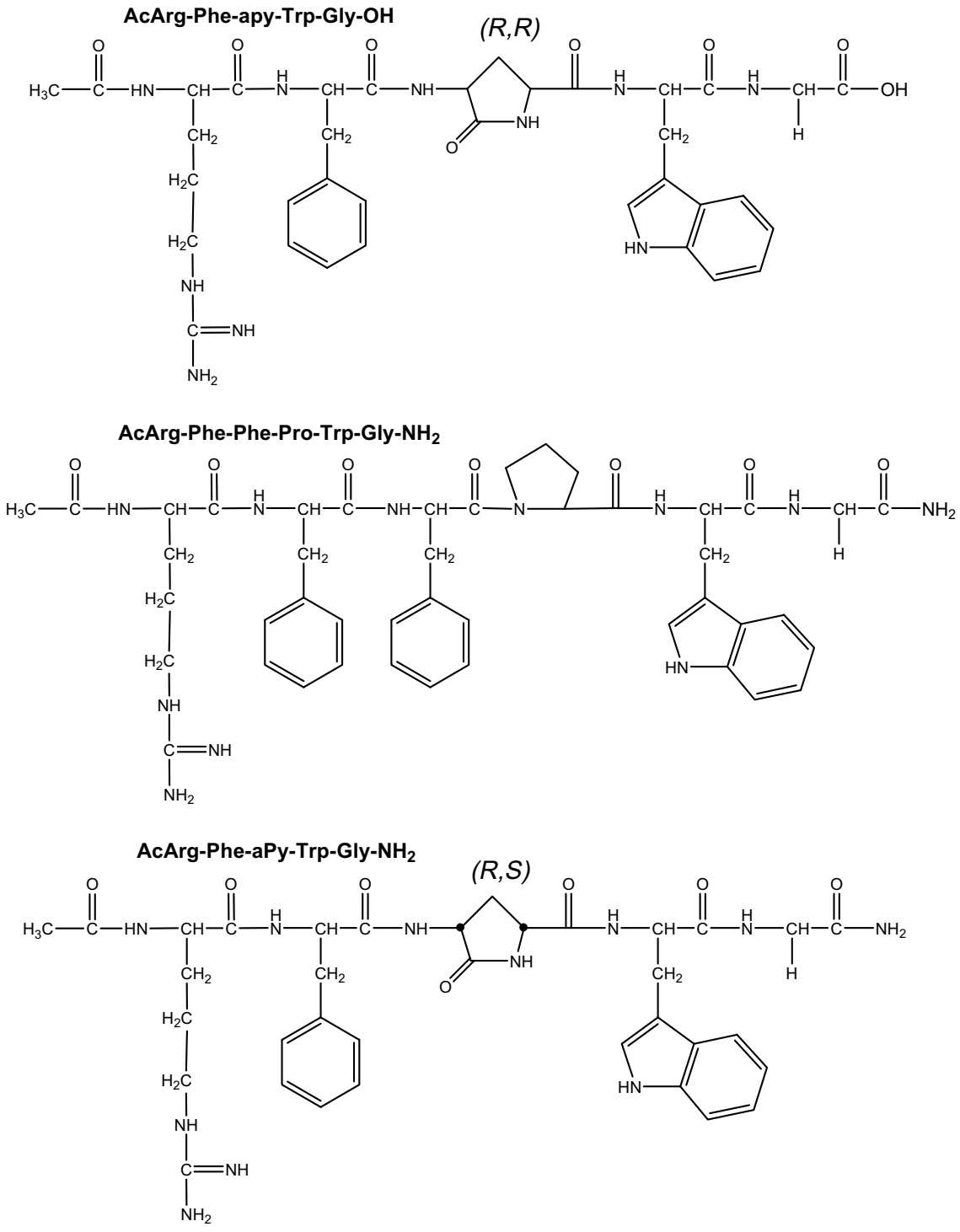


Fig. 1. Chemical structures of studied ligands.

reported procedures [2]. The purity of these ligands was verified by HPLC (high performance liquid chromatography) and mass spectrometry to be >99%. The $Cu(NO_3)_2$, KNO_3, HNO_3 and NaOH were Merck products and used without any further purification.

2.2. Spectroscopic studies

Electronic absorption spectra (UV–Vis) were recorded with a Perkin–Elmer Lambda 11 spectrophotometer. Circular dichroism (CD) spectra were obtained with a Jobin-Yvon CD-6 dichrograph over the range 200–750 nm, using 1 and 0.05 cm cuvettes. The spectra are expressed as $\Delta\varepsilon = \varepsilon_l - \varepsilon_r$, where ε_l and ε_r are the molar absorption coefficients for left and right circularly polarized light, respectively. Electron paramagnetic resonance (EPR) measurements were carried out with a Varian E-9 instrument at the X-band frequency (9.1 GHz) at 120 K; about 10% of ethanediol was added to the samples in order to obtain glasses with the proper viscosity. The EPR parameters were read from the spectra (estimated uncertainties for A_{II} and g_{II} values are 1×10^{-4} cm^{-1} and 0.002, respectively). All measurements were made over the pH 6–11 range, at

a constant ionic strength using 0.1 M KNO_3, a temperature of 298 K, a Cu(II)/L ratio of 1:1, and a metal concentration 1×10^{-3} M. The pH was changed using NaOH.

2.3. Potentiometric studies

The protonation constants (pK_a) of the ligand AcRFapyWG-OH and the stability constants of Cu^{II} complexes (log β) were determined by pH-potentiometric titrations of 2.0 mL samples. The ligand:metal molar ratio was 1,1:1 and the concentration of Cu^{II} was 0.001 M. Measurements were carried out at 298 K and at a constant ionic strength of 0.1 M KNO_3 with a MOLSPIN pH meter (Molspin Ltd., Newcastle-upon-Tyne, UK) equipped with a digitally operated syringe (the Molspin DSI 0.250 mL) controlled by computer. The titrations were performed with a carbonate-free NaOH solution of known concentration (ca. 0.1 M) using a Russel CMAWL/S7 semi-micro combined electrode, calibrated for hydrogen ion concentration by the method of Irving et al. [3]. The number of experimental points was 100–150 for each titration curve. The reproducibility of the titration points included in the evaluation was within 0.005 pH units in the whole pH range examined (2–11). The stability constants of the complexes, reported as the logarithm of the overall formation constants $\beta_{pqr} = [Cu_pL_qH_r]/[Cu]_p[L]_q[H]_r$, where Cu is the copper ion, L is the ligand with the deprotonated carboxylate group of C-terminal, and H is the proton, were calculated with the aid of the SUPERQUAD program [4].

2.4. Computational studies

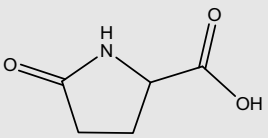
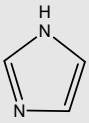
All calculations were carried out using the MOPAC 2007 program [5]. The geometries of ligand and all complexes were fully optimized using the semi-empirical molecular orbital method PM6 [6]. In the case of the copper ion complexes all calculations were carried out using Unrestricted Hartree-Fock (UHF) approximation, assuming the open shell electronic state of the molecule as a doublet, and the solvent (water) environment was simulated by employing the COSMO method [7]. In the first step of our calculations a conformational search of the free ligand was performed to find the lowest energy conformations. The conformational search was performed by random perturbation of torsion angles following by energy minimization. For every investigated ligand about 6000 conformations were energy minimized. The lowest energy conformations of free ligand were used as a starting point for calculations of the copper complexes. For the AcRFapyWG-OH, the copper ion initially bound to the C-terminal carboxyl group. For this complex, a conformational search was performed to determine the most favorable position for the copper ion. To determine the lowest energy conformations we identified structures for which the amide proton is close to the hydration shell of the copper ion. For a given conformation any amide proton closer than 2.5 Å from the copper ion is removed from the system, which corresponds to the deprotonation reaction observed in the potentiometric experiment. Conformational search and deprotonation cycles were repeated until the coordination sphere of the metal ion was occupied by at least four ligand atoms. In the case of the AcRFFPWG-NH_2 and AcRFaPyWG-NH_2 peptides, we do not have a favorable initial coordination site. So in the first step the copper ion was placed close to one of seven oxygen carbonyl atoms. The initial complex conformational search was then performed and structures for which any amide proton is closer than 2.5 Å from the copper ion the proton is removed from the system and the structure is energy minimized. For all ligands the conformational search is terminated if after the generation of a 1000 consecutive new conformations we are not able to find another amide proton close to the central ion.

3. Results and discussion

3.1. The AcRFapyWG-OH peptide

The protonation constant of the studied ligand and several others for comparison are given in Table 1.

Table 1
The protonation constants of AcRFapyWG-OH and several other ligands and the complex formation constants of AcRFapyWG-OH with Cu(II) at 25 °C, I = 0.1 mol dm^{-3} (KNO_3).

Ligand	Species	Logβ	Stepwise protonation constants	Ref.
AcRF**apy**WG-OH	HL	3.47(1)	$pK_{HL} = 3.47$	This work
Copper(II) complexes	$CuH_{-2}L$	−9.35(4)		
	$CuH_{-3}L$	−16.95(3)	$pK_{CuH_{-3}L} = 7.60$	
	$CuH_{-4}L$	−26.05(2)	$pK_{CuH_{-4}L} = 9.10$	
3-Amino-2-Oxopyrrolidine-5-Carboxylic acid (APy) 	HL	~12.39(5)	$\sim pK_{HL} = 12.39$	From [8]
	H_2L	19.54(1)	$pK_{H_2L} = 7.15$	
	H_3L	21.89(2)	$pK_{H_3L} = 2.35$	
Pyroglutamyl-histidyl-prolinamide (TRH)	HL	~13.99	$\sim pK_{HL} = 13.99$	From [9]
	H_2L	20.22	$pK_{H_2L} = 6.23$	
L-Pyroglutamic acid 	HL	3.10	$pK_{HL} = 3.10$	From [9]
Imidazole 	HL	~14.44	$\sim pK_{HL} = 14.44$	From [10,11]
	H_2L	21.56	$pK_{H_2L} = 7.12$	

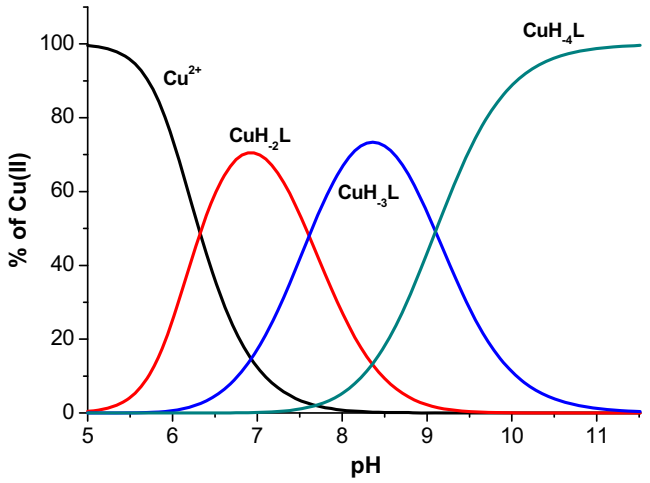


Fig. 2. Species distribution curves for complexes of AcRF**apy**WG at 25 °C and $I = 0.1$ mol dm^{-3} (KNO_3). Metal concentration 1×10^{-3} M. Ligand to metal ion 1, 1:1.

All modified peptides contain an Arg residue (Fig. 1) at the first position of the peptide backbone. The arginine residue contains a very basic terminal nitrogen atom as a result of resonance stabilization of the protonated guanidine group (log $K \approx 12$) [12]. Under the experimental conditions used, the pH is ≈11 and, at this value, the degree of deprotonation of the guanidine group is insignificant. Therefore the proton was considered as unionisable under the conditions used and its protonation constant ignored. Therefore we studied potentiometrically only AcRFapyWG-OH containing a protonation site located on the C-terminus. The pK of the carboxylic group is similar to that of other peptides like tetraGly [13] or tetraAla [14]. The next protonation constant might be assigned to the pyrrolidine nitrogen, but due to its high basicity that determination is problematic. We can only assume that the value could be similar to that found for 3-amino-2-oxopyrrolidine-5-carboxylic acid and the other ligands (see Table 1 and Ref. [8]. The potential electron donor atoms for Cu(II) ion are the oxygen or nitrogen of 4-aminopyroglutamate (apy), the peptide backbone amide groups and the C-terminal carboxyl oxygen. This unusual coordination can be deduced from our previous study of the Pyr–WG–NH_2–Cu(II) system [15]. The best fit of the titration curves indicates the presence of the species $CuH_{-2}L$, $CuH_{-3}L$ and $CuH_{-4}L$ (charges omitted for simplicity, Fig. 2) in pH 5–11 range.

The first detectable complex $CuH_{-2}L$ with the 2N coordination mode, exists around pH 7. It appears as a main species without the coexistence of the 1N complex due to the 2N coordination proceeds in a cooperative manner after Cu(II) ion anchoring at the oxygen of the C-terminal carboxylate. Then coordination follows by sequential deprotonation of NH apy motif group and the neighboring peptide nitrogen $\{N^-_{apy}, N^-_{amide}\}$. The $CuH_{-2}L$ species is supported by spectroscopic data with the d–d transition at 673 nm in absorption and at 640 nm in the CD spectra (Table 2), characteristic for the 2N coordination [16].

Evidence for this species arises from the CD in the 200–240 nm region which is different from that of the "free" ligand (Fig. 3a) and suggests that the chiral chelate conformation prevails over the vicinal contribution of the asymmetric carbon [17]. The EPR parameters with $A_{II} = 176 \times 10^{-4}$ cm^{-1} and $g_{II} = 2.270$ (Table 2) are also in a good agreement with binding of two nitrogen atoms to the Cu(II) ion [18]. The charge transfer band seen in CD spectra at 309 nm, corresponding to a $N^- \rightarrow$ Cu(II) transition, indicates the presence of at least one amide nitrogen donor atom in the copper coordination sphere. The next complex species with the stoichiometry $CuH_{-3}L$ becomes dominant at about pH 8.5 (Fig. 2). Its formation is a result of the CuH_{-2} L deprotonation according to the equilibrium reaction: $CuH_{-2}L \rightleftarrows CuH_{-3}L + H^+$. The deprotonation constant pK = 7.60 (Table 1) indicates the deprotonation and coordination of the second amide nitrogen atom to Cu(II) ion [19,20]. The hypsochromic shift of the d–d absorption maximum to 555 nm in UV–vis and 546 nm in CD spectra and the EPR parameters: $A_{II} = 186 \times 10^{-4}$ cm^{-1}, $g_{II} = 2.207$ support additional amide nitrogen atom binding [16] and a $\{N^-_{apy}, N^-, N^-\}$ coordination (Table 2). The next species $CuH_{-4}L$ was detected by potentiometry above pH 11. The spectrum (Fig. 3a) registered at this pH range indicates

Table 2
Summary of spectroscopic properties of Cu(II) complexes of AcRFapyWG-OH, AcRFFPWG-NH_2 and AcRFaPyWG-NH_2. Metal to ligand ratio = 1:1 $C_{Cu} = 1 \times 10^{-3}$ M.

Coordination mode	Ligand	UV–Vis		CD		EPR	
		λ (nm)	ε (M^{-1} cm^{-1})	λ (nm)	$\Delta\varepsilon$ (M^{-1} cm^{-1})	A_{II}(10^{-4} cm^{-1})	g_{II}
	AcRFapyWG-OH						
2N		673	69	640	0.034	176	2.270
				309	0.047		
				230	1.251		
3N		555	105	546	0.198	186	2.207
				306	0.101		
				226	11.652		
2N	AcRFaPyWG-NH_2	Broad shoulder around 633 nm		604	0.055		
				318	0.068		
				221	13.29		
3N		545	120	576	0.255		
				318	0.068		
				221	51.72		
	AcRFaPyWG-NH_2						
2N				540	−0.022	177	2.270
				310	0.033		
				222	21.016		
3N		550	110	532	−0.094	186	2.209
				307	0.204		
				267	−2.284		
				224	38.716		
4N		518	160	580	0.045	209	2.170
				501	−0.285		
				301	−1.054		
				268	−3.604		
				224	45.828		

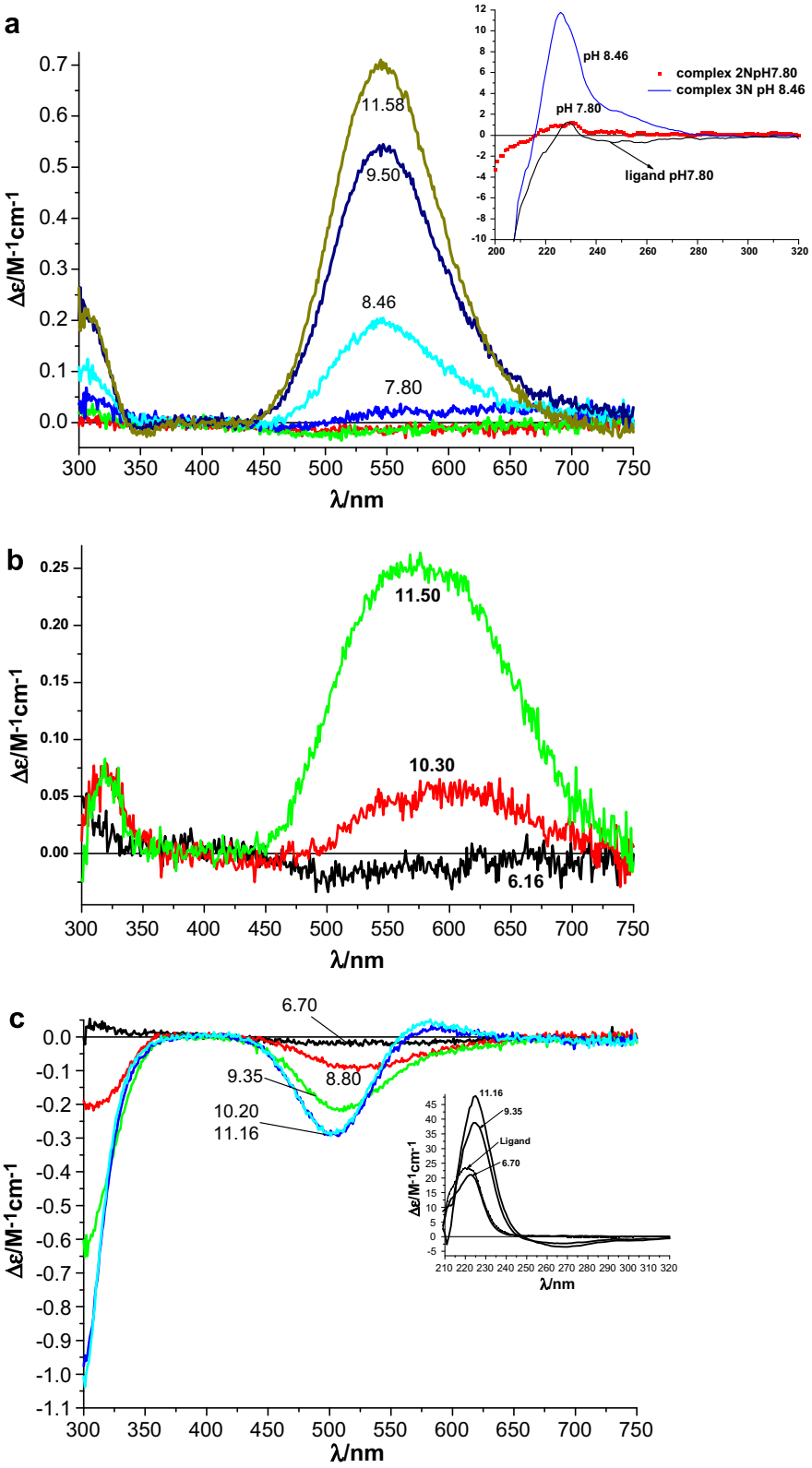


Fig. 3. CD spectra as function of pH for the systems: (a) Cu(II)-AcRF**apy**WG-OH, (b) Cu(II)-AcRF**FP**WG-NH_2 and (c) Cu(II)-AcRF**aPy**WG-NH_2.

that $CuH_{-4}L$ still has the 3N coordination but with very likely deprotonated guanidine group of the Arg residue. This conclusion can be derived from the theoretical calculations. In Fig. 4a the lowest energy conformation of complex of AcRFapyWG-OH with the copper ion deduced from theoretical calculations is presented. The central metal ion is surrounded by three deprotonated amide nitrogens and the C-terminal carboxyl oxygen. Cu–N distances vary from 1.87 to 1.91 Å and the distance Cu–O is 2.01 Å, clearly showing that the typical square planar geometry of coordination is a little bit distorted for this complex. From one side of the

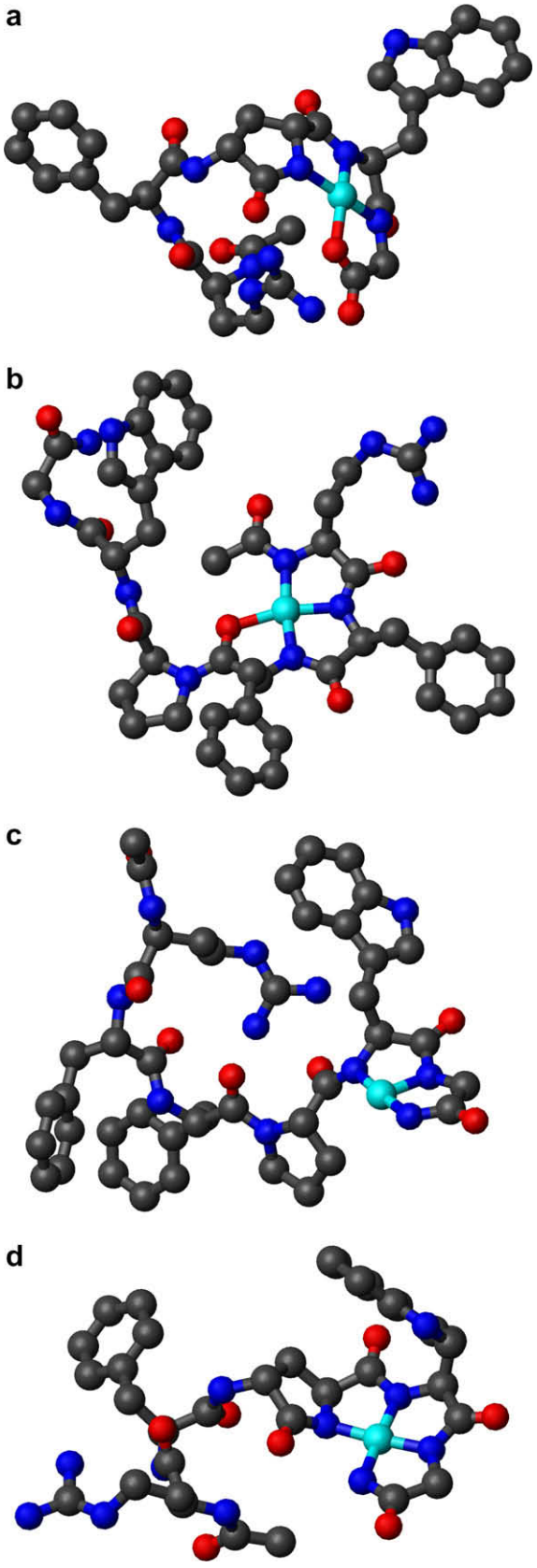


Fig. 4. The structure of complexes obtained from theoretical calculations: (a) *AcRF**apy**WG*; (b) *AcRF**FP**WG-NH*$_2$ N-terminus coordination mode, (c) *AcRF**FP**WG-NH*$_2$ C-terminus coordination mode, (d) *AcRF**aPy**WG-NH*$_2$. All hydrogen atoms are removed for clarity. The copper(II) ion is shown in magenta, oxygen, carbon and nitrogen atoms are shown in red, black and blue respectively.

coordination plane we have located the tryptophane side chain and from another side we have the N-terminus of the peptide. The presence of such large flexible elements can rule out the possibility of the stable location of water molecules to fill the fifth and the sixth coordination sites of the central ion. Interestingly, we find that the protonated guanidine group of the arginine residue is always located very close to the coordination plane and always very close to the C-terminal carboxyl group. The close spatial orientation of both of these groups could suggest an increase in the acidity of the protonated guanidine. This observation could lead to the hypothesis that species $CuH_{-4}L$ is formed due to the deprotonation of guanidine at an unusually low pH ($pK_a = 9.10$) because of favorable electrostatic interactions.

3.2. The AcRFFPWG-NH$_2$ peptide

In the AcRFFPWG-NH$_2$ ligand both N-and C-termini are blocked. The formation of a metallopeptide molecule starts after the anchoring of the copper(II) ion at a carbonyl group. The coordination pattern may continue in a part of any terminus of the peptide, as our calculations suggest. Potential nitrogen donors in this ligand molecule arise from the peptide bonds and from an amidated C-terminus. Following that, the peptide amide bonds undergo deprotonation to form stable fused ring structures. The oxygen donor could be one of the carbonyls, a water or a hydroxide. The Pro residue acts as a breakpoint in the consecutive nitrogen peptide bond coordination because the tertiary amide is a weak donor and not a metal binding site [21]. The detectable CD and electronic absorption spectra are not distinguishable in the Cu(II)-AcRFFPWG-NH$_2$ system before pH 10 (Table 2, Fig. 3b). At this pH the visible absorption spectra exhibit a broad, single absorption band around 630 nm (Table 2) which is in agreement with the presence of two nitrogen donor atoms coordinated to the copper ion [18,19]. The presence in the CD spectra of an $N^- \rightarrow Cu^{2+}$ charge transfer transition at *ca.* 300 nm (Fig. 3b) is consistent with 2N coordination {N^-, N^-} of the peptide to copper(II) ions [22]. At pH 11 the metallopeptide molecule may lose the next amide proton to give a species with three nitrogen donors{N^-, N^-, N^-} or, alternatively, via binding of the Cu(II) ion to a third nitrogen arising from the C-terminal amide without involvement of further deprotonation. The shift of d-d transitions to 545 nm in the electronic absorption and to 576 nm in the CD spectra support the involvement of a third nitrogen donor atom (Table 2). An increase in pH does not affect the band of a $N^- \rightarrow Cu^{2+}$ charge transfer transition (Table 2, Fig. 3b). It may suggest the localization of the third nitrogen at the blocked C-terminus.

In Fig. 4b and c the lowest energy conformations of the complex of AcRFFPWG-NH$_2$ with copper ion from theoretical calculations are presented. Following a conformational search we identified two distinct families of complexes arising from the presence of the proline residue in the middle of the sequence. In both families three deprotonated amide nitrogen atoms are bound to the central metal ion. In Fig. 4b a complex with the metal ion bound to three consecutive amide nitrogens starting from the N-terminus of the peptide is presented. The fourth coordination site is occupied by a carbonyl oxygen from the Phe^3 residue. The geometry of the coordination sphere is square planar with Cu–N distances in the range of 1.88–1.85 Å and a Cu–O distance of 2.02 Å. It is interesting to note that all amino acid side-chains and the C-terminal part of the peptide are located on one side of coordination plane of this complex and thus are not able to isolate the central ion from solvation, which can destabilize the complex. The second complex presented in Fig. 4c is formed with the C-terminal part of the peptide. In this case the coordination plane is composed of three deprotonated amide nitrogens, whereas the fourth coordination site

cannot be filled by any atom from the ligand molecule and is probably occupied by a water molecule. All three nitrogens are located at a distance of 1.84 Å from the central ion and all four atoms (three nitrogens and central ion) are ideally coplanar. We can observe two very interesting interactions, which stabilize the structure of the complex. We can see strong interactions between the protonated arginine side chain and the tryptophane aromatic ring [23]; as well as the formation of a hydrophobic cluster between the aromatic rings of the two phenylalanines. Both of these interactions should decrease the conformational flexibility of the ligand, which usually leads to an increase in complex stability [23]. Based on the computed heat of formation and solvation energies we can conclude that the complex presented in Fig. 4c is more thermodynamically stable and is better solvated. Thus, theoretical calculations support the experimental observation that the C-terminal part of the peptide is involved in coordination with the metal ion. (Table 2, Fig. 3b)

3.3. AcRFaPyWG-NH_2 peptides

The AcRFaPyWG-NH_2 peptide has no protonation constant detectable potentiometrically. Hence, we could not make calculations to find a stoichiometry of complex species. Therefore spectroscopic parameters were only used to support copper coordination. They are, however, good indications of the importance of a particular coordination mode in complex species formation. As deprotonation is a crucial step in the binding of Cu(II) with a peptide, the pH of the solution is expected to significantly affect the formation of a complex. It is evident that three detectable species with different coordination modes are forming in the 7–11 pH range. These complexes have significantly different chiroptical properties (Fig. 3c) and spectral parameters (Table 2). The coordination binding starts very likely after anchoring Cu(II) ion at the oxygen of the aPy motif and then proceeds via the sequential deprotonation of N pyrrolidine and neighboring peptide nitrogens. Evidence for the formation of the first complex is seen at pH 7. The binding mode involves the 2N {N^-_{apy}, N^-} donor set as in other similar peptide analogs [15]. The 2N coordination is clearly confirmed by EPR parameters with $A_{II} = 177 \times 10^{-4}\,cm^{-1}$ and $g_{II} = 2.270$ (Table 2). The charge transfer transition at 310 nm (Fig. 3c) in the CD spectrum corresponds to the involvement of the peptide amide $N^- \rightarrow Cu(II)$. When the pH increases to 8.80 the deprotonation of the next amide nitrogen occurs and the formation of a 3N complex species can be observed. It is accompanied by a change of the Cotton effect in the 300–310 nm range assigned to $N^- \rightarrow Cu(II)$ transition and the band shift of d–d transition observed both in CD and electronic absorption spectra (Fig. 3c, Table 2). Following an increase of the pH to 10–11 the all spectral parameters clearly support the binding of four nitrogen donor atoms to Cu(II) ion in a metallopeptide molecule. The donor set is confirmed by EPR parameters ($A_{II} = 209 \times 10^{-4}\,cm^{-1}$ and $g_{II} = 2.170$). In the electronic absorption spectra, the λ_{max} of the d–d band shifts to 518 nm and its intensity reaches 160 $dm^3\,mol^{-1}\,cm^{-1}$ (Table 2), which is typical for copper(II) oligopeptide complexes [16,18,19]. The amidated C-terminus (NH_2) can deliver the fourth nitrogen donor atom as was reported for Pyr-WG-NH_2 and AcRFapyWG-NH_2 peptides [15]. A modification of the AcRFaPyWG-NH_2 conformation therefore accompanies the formation of a 4N species. It may reflect a specific conformational constraint arising within the peptide backbone as it is induced to wrap around the copper ion. In addition, a negative effect appears at 270 nm (Fig. 3c), which is characteristic of charge transfer (c.t.) transitions due to the nitrogen atom from the amide group [24]. The band is distinctly broad, indicative of the overlap of the NH_2 and N^- c.t. transitions. In the AcRFapyWG-OH and AcRFFPWG-NH_2 spectra this band is not observed (Table 2). It is likely due to a strong tendency of the first amide group in this kinin analogue to undergo deprotonation in a cooperative manner, as a result of a bent structure imposed by the aPy(R,S) motif, leading to the simultaneous coordination of amide nitrogens of the 4N complex that exists at high pH range. The distinct effect of the aPy(R,S) motif is also demonstrated in the visible part of CD spectra. The spectra observed above pH 9 assigned to the 4N species [16,22] exhibits two d-d bands. This splitting is an effect of the (R,S) configuration at the carbons 4 and 2, respectively. The aPy(R,S) motif constrains the conformational freedom of the peptide backbone around the Cu(II) ion. The presence of a split in the d-d bands indicates a deviation from square-planar geometry around the metal ion, as has been observed in other oligopeptides [25,26]. In Fig. 4d the structure of the AcRFaPyWG-NH_2 complex deduced from theoretical calculations is shown. As was the case for the AcRFFPWG-NH_2 peptide, we are not able to identify an initial metal ion binding site. However during a conformational search, we are able to find out that the stereochemistry of the aPy moiety induces the metal ion to bind with the carbonyl oxygen, which immediately brings the amide proton into the coordination sphere and facilitates its dissociation. Such a situation does not exist in the case of regular peptides because peptide bonds are usually present in a *trans* orientation. In a regular peptide, if the metal ion is coordinating to the carbonyl oxygen then the closest amide proton is either located at the opposite side of the peptide chain or at a distance of three of four chemical bonds away. Therefore it is generally kinetically unfavorable to bring the amide proton of a normal peptide into the coordination sphere of a metal ion. Based on this information we can conclude that the initial coordination site is the aPy moiety, which is supported by the likely-low pK_a value associated with this type of molecule [8]. Hence, we assume that the metal ion initially binds to aPy deprotonated moiety for both steric reasons and a low pK_a value. For stereochemical reasons, the metal ion binds simultaneously to the carbonyl oxygen and the amide nitrogen of the aPy motif, which is isolated from the amide bond preceding the motif in the peptide sequence and has an easy access to the peptide bond in the direction of the C-terminus of the peptide. As shown in Fig. 4d, in our complex model structure the metal ion is bound by four deprotonated amide nitrogens from the C-terminal part of the AcRFaPyWG-NH_2 peptide. The central ion and four nitrogen donor atoms form a very regular planar square as would be expected from this type of complex. Cu–N distances demonstrate very little variance in the range from 1.79 to 1.81 Å. Spectroscopy measurements suggest that the square planar coordination geometry can be distorted, although our calculations suggest that the complex is very regular. We presented only one conformation from this family of complexes in which the aPy ring is almost flat. In other structures we observed that the aPy moiety can form a chair conformation (data not shown) and the stability difference between the flat-chair conformation is very small, leading to the conclusion that both of these types of conformations exist in a rapid equilibrium. It is very likely that the fast equilibrium between the two conformations of the aPy ring can lead to the split in the d-d bands observed in CD spectra (Fig. 3c). For the most part, one side of coordination plane is shielded by side chain of tryptophan residue and another side remains open to solvent in low energy structures. The conformationally restricted aPy moiety keeps the N-terminal part of molecule far away from the coordination site.

4. Conclusions

In conclusion, our study has demonstrated the coordination potentiality of oligopeptides containing a novel *cis*-peptide bond.

Incorporation of the apy/aPy motif into the peptide backbone results in the considerable acidification of the neighboring amide hydrogen, making it easier to deprotonate than in an unmodified peptide. This motif does not occur in AcRFFPWG-NH_2 therefore the formation of the first complex cannot be observed before pH 10 (Fig. 3b). One can suppose that the motif could be an anchoring site for copper(II) ion in the pH 7–8 range, providing that the N- or C-terminals are blocked or other possible coordinating anchors, *e.g.* carboxylate or histidine side chains, are not present.

Acknowledgements

Calculations were carried out with the use of computational resources of the Informatics Center of the Metropolitan Academic Network (CI TASK) at the Technical University of Gdańsk. Financial assistance from a grant from the USDA/DOD DWFP Initiative (#0500-32000-001-01R) (RJN,KK,JZ) is gratefully acknowledged.

References

[1] J. Nachman, A. Strey, E. Isaac, N. Pryor, J.D. Lopez, J.G. Deng, G.M. Coast, Peptides 23 (2002) 735–745.
[2] R.J. Nachman, K. Kaczmarek, H.J. Williams, G.M. Coast, J. Zabrocki, Biopolymers 75 (2004) 412.
[3] H. Irving, M.G. Miles, L.D. Pettit, Anal. Chim. Acta 38 (1967) 475.
[4] P. Gans, A. Vacca, A. Sabatini, J. Chem. Soc., Dalton Trans. (1985) 1195.
[5] MOPAC2007 James J.P. Stewart, Stewart Computational Chemistry, Colorado Springs, CO, USA <http://openmopac.net> (2007).
[6] J.J.P. Stewart, J. Mol. Modeling 13 (2007) 1173.
[7] A. Klamt, G. Schüümann, J. Chem. Soc. Perkin Trans. 2 (1993) 799.
[8] E. Łodyga-Chruścińska, S. Ołdziej, D. Sanna, G. Micera, L. Chruściński, K. Kaczmarek, R.F. Nachman, J. Zabrocki, A. Sykuła, Spectroscopic studies of Cu(II) complexes with insect kinin analogs, in: The data presented on 29th European Peptide Symposium, Gdańsk, September 3–8, 2006. Book of Abstracts, M031, p. 112.
[9] Y. Yamada, N. Nakasuka, M. Tanaka, Inorg. Chim. Acta 185 (1991) 49.
[10] P. George, G.I.H. Hanania, D.H. Irvine, I. Abu-Tssa, J. Chem. Soc. (1964) 5689.
[11] A. Chakravorty, F.A. Cotton, J. Phys. Chem. 67 (1963) 2878.
[12] E.R. Clarke, A.E. Martell, J. Inorg. Nucl. Chem. 32 (1970) 911.
[13] I. Sóvágó, in: K. Burger (Ed.), Biocoordination Chemistry: Coordination Equilibria in Biologically Active Systems, Ellis Horwood Limited, 1990, p. 135.
[14] E. Łodyga-Chruścińska, G. Micera, D. Sanna, J. Olczak, J. Zabrocki, Polyhedron 20 (2001) 1915.
[15] E. Łodyga-Chruścińska, S. Ołdziej, D. Sanna, G. Micera, L. Chruściński, K. Kaczmarek, Ronald J. Nachman, J. Zabrocki, A. Sykuła, Pharma Chem. 4 (2006) 10.
[16] H. Kozłowski, G. Micera, in: G. Berthon (Ed.), Handbook of Metal–Ligand Interactions in Biological Fluids, Bioinorganic Chemistry, vol. 1, Marcel Dekker, New York, 1995, p. 566.
[17] N. Gnonlonfoun, S. El Mardi, L. Lambs, G. Berthon, Inorg. Chim. Acta 247 (1996) 175.
[18] D. Pettit, R.A. Robbins, in: G. Berthon (Ed.), Handbook of Metal–Ligand Interactions in Biological Fluids, Bioinorganic Chemistry, vol. 1, Marcel Dekker, New York, 1995, p. 637.
[19] I. Sovago, D. Sanna, A. Dessı, K. Varnagy, G. Micera, J. Inorg. Biochem. 63 (1996) 99.
[20] E. Łodyga-Chruścińska, G. Micera, E. Szajdzińska-Piętek, D. Sanna, J. Agri. Food Chem. 46 (1998) 115.
[21] D.W. Margerum, Pure Appl. Chem. 55 (1983) 23.
[22] L.D. Pettit, J.G. Gregor, H. Kozlowski, in: R.W. Hay, J.R. Dilworth, K.B. Nolan (Eds.), Perspectives on Bioinorganic Chemistry, vol. 1, JAI Press, London, 1990, p. 16.
[23] E. Chruścińska, I. Derdowska, H. Kozłowski, B. Lammek, M. Łuczkowski, S. Ołdziej, J. Świątek-Kozłowska, New J. Chem. 27 (2003) 251.
[24] T. Kowalik-Jankowska, A. Rajewska, W. Szeszel-Fedorowicz, D. Konopinska, Polyhedron 24 (2005) 443.
[25] J.M. Tsangaris, R.B. Martin, J. Am. Chem. Soc. 15 (1970) 4255.
[26] E. Łodyga-Chruścińska, G. Micera, D. Sanna, H. Kozłowski, K. Kaczmarek, J. Olejnik, M.T. Leplawy, J. Inorg. Biochem. 72 (1998) 187.

Polyhedron 28 (2009) 493–500

Contents lists available at ScienceDirect

Polyhedron

journal homepage: www.elsevier.com/locate/poly

Synthesis, spectroscopic characterization, crystal and molecular structure of [ReOBr(hmquin-7-COOH)$_2$] and [ReOCl(hmquin-7-COOH)$_2$] · MeCN complexes. DFT and TD-DFT calculations for [ReOBr(hmquin-7-COOH)$_2$]

B. Machura [a,*], J. Kusz [b], D. Tabak [c], R. Kruszynski [d]

[a] Department of Crystallography, Institute of Chemistry, University of Silesia, 9th Szkolna St., 40-006 Katowice, Poland
[b] Institute of Physics, University of Silesia, 4th Uniwersytecka St., 40-006 Katowice, Poland
[c] Department of Organic Chemistry, Institute of Chemistry, University of Silesia, 9th Szkolna St., 40-006 Katowice, Poland
[d] Department of X-ray Crystallography and Crystal Chemistry, Institute of General and Ecological Chemistry, Lodz University of Technology, 116 Żeromski St., 90-924 Łódź, Poland

ARTICLE INFO

Article history:
Received 21 August 2008
Accepted 26 November 2008
Available online 2 January 2009

Keywords:
Rhenium oxo complexes
Quinoline ligands
X-ray and electronic structure
DFT calculations
NBO analysis

ABSTRACT

Novel [ReOBr(hmquin-7-COOH)$_2$] (**1**) and [ReOCl(hmquin-7-COOH)$_2$] · MeCN (**2** · MeCN) complexes have been prepared by treatment of [ReOX$_3$(AsPh$_3$)$_2$] with an excess of 8-hydroxy-2-methylquinoline-7-carboxylic acid in acetonitrile. The compounds were characterized structurally and spectroscopically. The electronic structure of **1** has been calculated with the density functional theory (DFT) method, and additional information about binding has been obtained by NBO analysis. The UV–Vis spectrum of **1** has been discussed on the basis of TDDFT calculations.

© 2008 Elsevier Ltd. All rights reserved.

1. Introduction

There is considerable interest in the chemistry of inorganic compounds containing an oxygen atom that is multiply bonding to a transition metal in a high oxidation state. These compounds can transfer an oxygen atom to reductants such as phosphines, sulfides, and alkenes. For many years they have been in the centre of interest to those scientists engaged in basic research and to those trying to employ these complexes in catalytic processes. Oxygen atom transfer chemistry has been implicated in various reactions of industrial and biological importance, including olefin epoxidation and catalysis by cytochrome P-450 [1–3].

The chemistry of oxo rhenium complexes arouses particular interest among these compounds. Methyltrioxorhenium and its derivatives are among the most versatile oxidation catalysts known to date [4]. The oxorhenium(V) chelates [ReOCl$_2$(O–N)(PPh$_3$)] with pyridinecarboxylate ligands exhibit a remarkable catalytic activity for the conversion of ethane, under relatively mild conditions, to a mixture of propionic and acetic acids in a single-pot process with various advantages over the industrial ones [5]. The [CH$_3$ReO(pic)$_2$] complex is an active precursor in olefin oxidation and forms epoxides in a two-phase H$_2$O$_2$–H$_2$O/CH$_2$Cl$_2$ system [6].

Furthermore, favourable nuclear properties of ^{186}Re and ^{188}Re nuclides make the compounds with these radioisotopes useful for applications in radioimmunotherapy [7,8].

In this context, the design, synthesis and reactivity of novel rhenium oxocomplexes has become the aim of several laboratories, including ours.

Previously, we investigated structural and spectroscopic properties of [ReOX(hqn)$_2$] and [ReOX(quin-2-c)$_2$] (Hhqn = 8-hydroxyquinoline, quin-2-cH = quinoline-2-carboxylic acid) [9,10]. As an extension of this work, we chose 8-hydroxy-2-methylquinoline-7-carboxylic acid (Hhmquin-7-COOH) as a ligand. Potentially, Hhmquin-7-COOH can act as a bidentate, tridentate or bridging ligand. As a chelate 8-hydroxy-2-methylquinoline-7-carboxylic acid can bind to the metal centre through the pyridine nitrogen and the deprotonated hydroxyl group (N,O-chelation) or through the carboxylate group and the deprotonated hydroxyl group (O,O-chelation).

X-Ray and spectroscopic studies for [ReOBr(hmquin-7-COOH)$_2$] (**1**) and [ReOCl(hmquin-7-COOH)$_2$]·MeCN (**2** · MeCN) confirm N,O-chelation of the hydroxy-2-methylquinoline-7-carboxylic acid. The COOH group of the Hhmquin-7-COOH in the examined complexes is available for further conjugation.

For complex **1** the nature of the frontier orbitals and the electronic transitions involved in the absorption spectrum have been

* Corresponding author.
E-mail addresses: basia@ich.us.edu.pl (B. Machura), rafal.kruszynski@p.lodz.pl (R. Kruszynski).

0277-5387/$ - see front matter © 2008 Elsevier Ltd. All rights reserved.
doi:10.1016/j.poly.2008.11.053

studied by means of density functional and time-dependent density functional calculations. Gancheff and co-workers [11] have performed extended tests of the ability of the B3LYP method in LANL2DZ basis set for rhenium compounds in a geometry optimization and calculation of spectral properties. Although this is not a very extended basis set, its use with DFT has shown to be sufficient for the geometry optimization and calculation of spectral properties. The correctness of B3LYP method with LANL2DZ basis set for rhenium complexes has been also proven in this paper. The experimental geometry of [ReOBr(hmquin-7-COOH)$_2$] is well reproduced and the calculated electronic spectrum is in good accordance with the experimental one.

2. Experimental

2.1. General procedure

The [ReOX$_3$(AsPh$_3$)$_2$] (X = Cl, Br) complexes were synthesised according to the literature methods [12]. 8-hydroxy-2-methylquinoline-7-carboxylic acid was prepared as reported previously [13].

IR spectra were recorded on a Nicolet Magna 560 spectrophotometer in the spectral range 4000–400 cm^{-1} with the samples in the form of KBr pellets. Electronic spectra were measured on a spectrophotometer Lab Alliance UV–Vis 8500 in the range 1000–180 nm in acetonirile solution. Elemental analyses (C H N) were performed on a Perkin–Elmer CHN-2400 analyzer.

2.2. Preparation of [ReOBr(hmquin-7-COOH)$_2$](**1**)

[ReOBr$_3$(AsPh$_3$)$_2$] (0.5 g, 0.47 mmol) was added to 8-hydroxy-2-methylquinoline-7-carboxylic acid (0.28 g, 1.38 mmol) in acetonitrile (50 ml) and the reaction mixture was refluxed for 6 h. The resulting solution was allowed to cool to room temperature and reduced in volume to ~10 ml. A greenish-brown crystalline precipitate of **1** was filtered off and dried in the air. Yield 75%.

Single crystals of **1** were obtained by recrystallization from acetonitrile.

Anal. Calc. for C$_{22}$H$_{16}$N$_2$O$_7$BrRe: C, 38.49; H, 2.35; N, 4.08. Found: C, 38.35; H, 2.43; N, 4.37%.

2.3. Preparation of [ReOCl(hmquin-7-COOH)$_2$] · MeCN (**2** · MeCN)

A procedure similar to that for **1** was used with [ReOCl$_3$(AsPh$_3$)$_2$] (0.5 g, 0.54 mmol) and 8-hydroxy-2-methylquinoline-7-carboxylic acid (0.28 g, 1.38 mmol). Crystalline precipitate of **2** · MeCN was collected in 70% yield.

Anal. Calc. for C$_{24}$H$_{19}$N$_3$O$_7$ClRe: C, 42.20; H, 2.80; N, 6.15. Found: C, 42.98; H, 2.68; N, 6.81%.

2.4. Crystal structures determination and refinement

The X-ray intensity data of **1** and **2** · MeCN were collected on a KM-4-CCD automatic diffractometer equipped with CCD detector and graphite monochromated Mo Kα radiation (λ = 0.71073 Å) at temperature of 293(2) K. Details concerning crystal data and refinement are given in Table 1. Lorentz, polarization and empirical absorption correction using spherical harmonics implemented in SCALE3 ABSPACK scaling algorithm [14] were applied. The structures were solved by the Patterson method and subsequently completed by the difference Fourier recycling. All the non-hydrogen atoms were refined anisotropically using full-matrix, least-squares technique. The hydrogen atoms were treated as 'riding' on their adjacent atoms and assigned isotropic temperature factors equal 1.2 times the value of equivalent temperature factor of the aromatic parent atoms and equal 1.5 times the value of equivalent temperature factor of the methyl parent carbon atom and oxygen atom (OH). SHELXS97 [15], SHELXL97 [16] and SHELXTL [17] programs were used for all the calculations. Atomic scattering factors were those incorporated in the computer programs.

Table 1
Crystal data and structure refinement for **1** and **2** · MeCN complexes.

	1	2 · MeCN
Empirical formula	C$_{22}$H$_{16}$N$_2$O$_7$BrRe	C$_{24}$H$_{19}$N$_3$O$_7$ClRe
Formula weight	686.48	683.07
Temperature	293(2) K	293(2) K
Wavelength	0.71073 Å	0.71073 Å
Crystal system	triclinic	triclinic
Space group	$P\bar{1}$	$P\bar{1}$
Unit cell dimensions	a = 7.5564(5) Å, b = 9.8626(7) Å, c = 15.8327(11) Å, α = 92.417(6)°, β = 102.129(6)°, γ = 106.571(6)°	a = 7.5538(3) Å, b = 10.3044(2) Å, c = 16.3587(2) Å, α = 71.695(4)°, β = 77.391(4)°, γ = 88.826(4)°
Volume	1099.11(13) Å^3	1178.14(5) Å^3
Z	2	2
D_{calc}	2.074 Mg/m^3	1.926 Mg/m^3
Absorption coefficient	7.393 mm^{-1}	5.322 mm^{-1}
F(000)	656	664
Crystal size	0.02 × 0.04 × 0.22 mm	0.03 × 0.15 × 0.48 mm
Θ range for data collection	2.89–25.00°	3.31–25.00°
Index ranges	$-5 \leqslant h \leqslant 8$, $-11 \leqslant k \leqslant 11$, $-18 \leqslant l \leqslant 18$	$-6 \leqslant h \leqslant 8$, $-12 \leqslant k \leqslant 12$, $-19 \leqslant l \leqslant 19$
Reflections collected	6981	7373
Independent reflections (R_{int})	3766 (0.0277)	4012 (0.0214)
Completeness to 2θ = 50°	97.4%	97.1%
Data/restraints/parameters	3766/0/302	4012/0/330
Goodness-of-fit on F^2	1.014	0.986
Final R indices [$I > 2\sigma(I)$]	R_1 = 0.0335, wR_2 = 0.0883	R_1 = 0.0209, wR_2 = 0.0521
R indices (all data)	R_1 = 0.0468, wR_2 = 0.0994	R_1 = 0.0257, wR_2 = 0.0533
Largest difference in peak and hole e Å^{-3}	0.982 and −1.516	1.017 and −0.880

2.5. Computational details

GAUSSIAN 03 program [18] was used in the calculations. The geometry optimization of [ReOBr(hmquin-7-COOH)$_2$] in a singlet state was carried out with the DFT method with the use of B3LYP functional [19,20]. The electronic spectrum of [ReOBr(hmquin-7-COOH)$_2$] was calculated with the TDDFT method [21], and the solvent effect was simulated using the polarizable continuum model with the integral equation formalism (IEF-PCM). The calculations were performed by using ECP basis set on the rhenium atom, the standard 6-31+G** basis for bromine, oxygen and nitrogen, 6-31G* for carbon and 6-31G for hydrogen atoms [22,23]. The Xe core electrons of Re were replaced by an effective core potential and DZ quality Hay and Wadt Los Alamos ECP basis set (LANL2DZ) [24] was used for the valence electrons. Additional d function with exponent α = 0.3811 and f function with exponent α = 2.033 on the rhenium atom were added [25]. The optimized geometry of **1** was verified by performing a frequency calculation. The vibrations in the calculated vibrational spectrum of **1** were real, thus the optimized geometry corresponds to true energy minimum.

Natural bond orbital (NBO) calculations were performed with the NBO code [26] included in GAUSSIAN 03.

3. Results and discussion

3.1. Preparation and infrared data

The [ReOX(hmquin-7-COOH)$_2$] (X = Cl, Br) complexes were prepared in high yields by a route analogous to that used for the

Table 2
Selected IR frequencies [cm^{-1}] values of [ReOBr(hmquin-7-COOH)$_2$] complexes.

Complex	ν(O–H)$_{COOH}$	ν(C=O)$_{COOH}$	ν(N=C)	ν(C–O)$_{COOH}$	ν(C–O)$_{OH}$	ν(Re=O)
[ReOBr(hmquin-7-COOH)$_2$]	3467 3372	1660	1616 1550	1368	1245	976
[ReOCl(hmquin-7-COOH)$_2$]	3467 3358	1716	1620 1549	1378	1235	978

synthesis of the [ReOX(hqn)$_2$] and [ReOX(quin-2-c)$_2$], namely by ligand exchange reactions starting from [ReOX$_3$(AsPh$_3$)$_2$] complexes and 8-hydroxy-2-methylquinoline-7-carboxylic acid in acetonitrile:

$$[ReOX_3(AsPh_3)_2] + 2Hhmquin-7-COOH \rightarrow [ReOX(hmquin-7-COOH)_2] + 2HX + 2AsPh_3$$

Table 3
Hydrogen bonds for **1** and **2** · MeCN complexes.

D	H	A	H···A (Å)	D···A (Å)	D–H···A (°)
1					
O3	H3	O2	0.82	2.589(8)	143.1
O6	H6A	O7#1	0.82	2.629(8)	160.2
C2	H2	O4#2	0.93	3.391(10)	169.8
C10	H10A	O1	0.96	2.882(11)	103.9
C10	H10B	O3#2	0.96	3.460(10)	170.9
C17	H17	O6	0.93	2.729(10)	101.1
2 · MeCN					
O4	H4	O7#3	0.82	2.724(4)	173.4
O6	H6A	O5	0.82	2.552(4)	152.8
C6	H6	O4	0.93	2.716(5)	100.0
C10	H10A	O1	0.96	2.884(5)	101.0
C13	H13	O3#4	0.93	3.263(5)	155.7
C14	H14	O3#5	0.93	3.317(5)	156.8
C98	H98C	O7#6	0.96	3.413(7)	147.8

Symmetry codes: #1 $-x$, $-y+1$, $-z+1$; #2 $x+1$, $y+1$, z; #3 $-x+2$, $-y+1$, $-z+2$; #4 $x-1$, y, z; #5 $-x+1$, $-y+1$, $-z+2$; #6 $x-1$, $y-1$, z.

They were isolated as greenish-brown microcrystalline solids, soluble in common organic solvents.

The selected frequencies observed in the IR spectra of [ReOX(hmquin-7-COOH)$_2$] complexes are collected in Table 2. The assignments are based on those found in the literature for related species [27,28]. Similar to the [ReOX(hqn)$_2$] complexes, the strong ν(Re=O) stretching bands of [ReOX(hmquin-7-COOH)$_2$] appear at ~975 cm^{-1}, in the range typical of six-co-ordinate complexes with a phenolic oxygen *trans* to Re=O [29]. A significant difference between complexes **1** and **2** can be noticed for ν(C=O)$_{COOH}$ stretching frequency. The ν(C=O)$_{COOH}$ stretching vibration of **1** is downshifted in comparison with ν(C=O)$_{COOH}$ for complex **2**. It is a result of delocalisation of CO bonds of the carboxylic group, observed for complex **1** and discussed in detail in crystal structure part (Table 3).

3.2. Crystal structures

The crystallographic data for **1** and **2** · MeCN are given in Table 1. The intermolecular interactions found in the examined structures are shown in the Table 2 [30,31] and Figs. 1 and 2.

The packing of molecules in crystal and in consequence hydrogen bonding scheme of compound **1** distinctly differ from these of compound **2** · MeCN. In compound **1** the medium strength intermolecular O—H···O bond create typical $N_1R_2^2(8)$ motif, but in **2** · MeCN $N_1R_2^2(24)$ motif is created. The intermolecular bonding scheme in both compound is identical (S(6) motif of O—H···O interactions) due to similarity of inner coordination spheres.

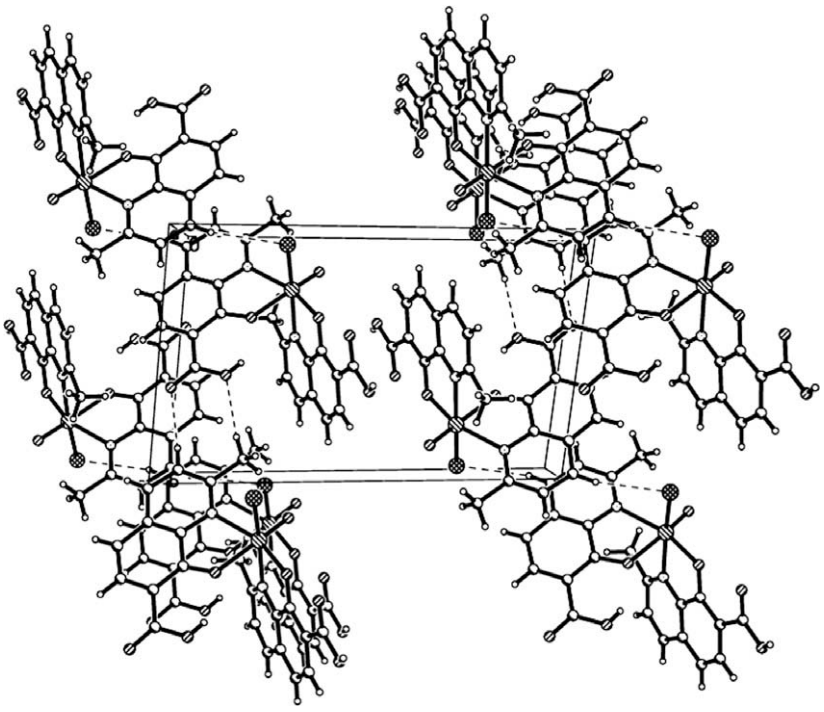


Fig. 1. Packing diagram of **1** showing the shortest intermolecular interactions.

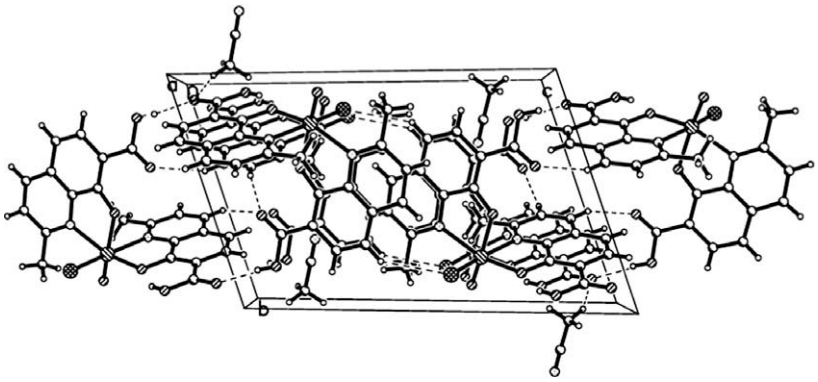


Fig. 2. Packing diagram of **2** · MeCN showing the shortest intermolecular interactions.

The molecular structure of [ReOBr(hmquin-7-COOH)$_2$] is presented in Fig. 3, and the selected bond distances and angles of [ReOX(hmquin-7-COOH)$_2$] complexes are collected in Tables 4 and 5, respectively.

The geometry of [ReOX(hmquin-7-COOH)$_2$] compounds reveals typical features of quasi-octahedral oxorhenium(V)complexes with oxygenated bidentate ligands. For complex **1** the rhenium atom is displaced 0.3240 (28) Å from the equatorial plane formed by the two nitrogens, one oxygen and one bromide atoms (plane A) and 0.0730(30) and 0.0249(25) Å from the axial planes formed respectively by the three oxygen, one nitrogen atoms (plane B) and two oxygens, one bromide and one nitrogen atoms (plane C). Least squares plane A is inclined at 88.90(13)° to the plane B and at 89.81(12)° to the plane C. The planes B and C are inclined at 85.50(14)°. These values for chloride analogue are respectively 0.2916 (13), 0.0773 (13), and 0.0292(12) Å, 89.92(7) 89.25(5) and 83.92(7)°. Clear distortions of the pseudooctahedral environment of Re center in [ReOX(hmquin-7-COOH)$_2$] is induced by the multiple bonding ligand (terminal oxo ligand –O$_t$) and narrow bite angles of the chelating ligands. The last ones are similar to those observed for [ReOX(hqn)$_2$] (75.9(3)° and 80.1(3)°) [9].

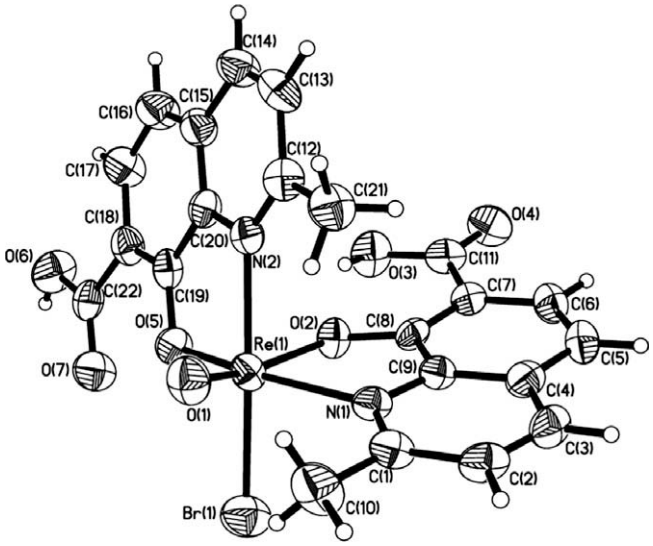


Fig. 3. The molecular structure of [ReOBr(hmquin-7-COOH)$_2$]. Displacement ellipsoids are drawn at 50% probability.

The Re–O$_t$ bond lengths fall in the range typical of mononuclear complexes of rhenium(V) having $[ReO]^{3+}$ core, and indicates the presence of a triple bond Re≡O [32]. The interatomic distance between the rhenium atom and the oxygen atom of hmquin-7-COOH in *trans* position to the terminal oxo ion is somewhat longer than the corresponding Re–O bond in the equatorial plane. This structural *trans* influence is common in mononuclear six-coordinate oxo Re(V) complexes with an monoanionic oxygen *trans* to the oxo group [33]. Noteworthy is fact that CO bonds of indicated by C(22) atom –COOH group of **1** are delocalised and they have can be considered as bonds with multiplicity of 1.5 (all other –COOH groups have localised double C=O and single C–O–H bonds). Such effect should be explained by O–H.O hydrogen bond creating symmetric 8-membered rings ($N_1R_2^2(8)$ motifs).

Table 4
The experimental and optimized bond lengths [Å] and angles [°] for [ReOBr(hmquin-7-COOH)$_2$].

Bond lengths	Experimental	Optimized	Bond angles	Experimental	Optimized
Re(1)–O(1)	1.660(6)	1.687	O(1)–Re(1)–O(2)	163.3(2)	159.22
Re(1)–O(2)	2.068(5)	1.965	O(1)–Re(1)–O(5)	107.7(3)	109.38
Re(1)–O(5)	1.962(5)	1.929	O(2)–Re(1)–O(5)	82.2(2)	85.91
Re(1)–N(1)	2.176(6)	2.202	O(1)–Re(1)–N(1)	95.6(3)	90.44
Re(1)–N(2)	2.166(6)	2.144	O(2)–Re(1)–N(1)	75.5(2)	75.49
Re(1)–Br(1)	2.4773(10)	2.562	O(5)–Re(1)–N(1)	156.6(2)	190.06
O(3)–C(11)	1.335(10)	1.334	O(1)–Re(1)–N(2)	91.1(3)	87.28
O(4)–C(11)	1.201(10)	1.213	O(2)–Re(1)–N(2)	77.1(2)	81.60
O(6)–C(22)	1.269(10)	1.358	O(5)–Re(1)–N(2)	79.8(2)	79.66
O(7)–C(22)	1.264(10)	1.208	N(1)–Re(1)–N(2)	101.7(2)	104.20
			O(1)–Re(1)–Br(1)	101.6(2)	101.46
			O(2)–Re(1)–Br(1)	92.22(15)	92.53
			O(5)–Re(1)–Br(1)	87.03(16)	89.07
			N(1)–Re(1)–Br(1)	86.90(16)	84.70
			N(2)–Re(1)–Br(1)	163.97(17)	167.60

Table 5
The experimental bond lengths [Å] and angles [°] for [ReOCl(hmquin-7-COOH)$_2$].

Bond lengths	Experimental	Bond angles	Experimental
Re(1)–O(1)	1.666(3)	O(1)–Re(1)–O(2)	162.36(12)
Re(1)–O(2)	2.017(2)	O(1)–Re(1)–O(5)	105.96(12)
Re(1)–O(5)	1.993(2)	O(5)–Re(1)–O(2)	83.53(11)
Re(1)–N(1)	2.172(3)	O(1)–Re(1)–N(1)	96.01(13)
Re(1)–N(2)	2.171(3)	O(2)–Re(1)–N(1)	75.80(10)
Re(1)–Cl(1)	2.3345(9)	O(5)–Re(1)–N(1)	157.94(11)
C(11)–O(3)	1.201(5)	O(1)–Re(1)–N(2)	88.42(13)
C(11)–O(4)	1.330(5)	O(2)–Re(1)–N(2)	78.68(11)
O(6)–C(22)	1.323(5)	O(5)–Re(1)–N(2)	79.02(11)
O(7)–C(22)	1.211(5)	N(2)–Re(1)–N(1)	103.98(12)
		O(1)–Re(1)–Cl(1)	102.54(10)
		O(2)–Re(1)–Cl(1)	92.49(7)
		O(5)–Re(1)–Cl(1)	87.85(7)
		N(1)–Re(1)–Cl(1)	85.44(8)
		N(2)–Re(1)–Cl(1)	164.86(9)

3.3. Geometry optimization, charge distribution, electronic structure and NBO analysis

The geometry of **1** was optimized in a singlet state by the DFT method with the B3LYP functional. The optimized geometric parameters of **1** are gathered in Table 4. In general, the predicted bond lengths and angles are in agreement with the values based upon the X-ray crystal structure data, and the general trends observed in the experimental data are well reproduced in the calculations.

Table 6 presents the atomic charges from the Natural Population Analysis (NPA) for **1**. The calculated charge on the rhenium atom is considerable lower than the formal charge +5, corresponding d^2 configuration of the central ion. It results from significant charge donation from the ligands. The charges on the terminal oxo, bromide and oxygen donor atoms of hmquin-7-COOH are significantly smaller than –2, –1 and –1, respectively. The terminal oxo ion is less negative in comparison with the oxygen atom of hmquin-7-COOH ligand. It indicates the higher electron density delocalization from the O_t ligand towards the central ion and corresponds to differences in the Re–$O_{hydroxy}$ and Re–$O_{terminal}$ bond lengths. Similarly, the oxygen atom of hmquin-7-COOH in *trans* position to the bromide ion is less negative in comparison with the corresponding Re–O bond opposite the terminal oxo ligand.

A comparison of the NPA analysis for [ReOBr(hqn)$_2$] and [ReOBr(hmquin-7-COOH)$_2$] allows to notice less efficient ligand-to-metal donation from the bromide ion in the case [ReOBr(hqn)$_2$], resulting in a significantly elongation of the Re–Br bond length in this complex.

The complex [ReOBr(hmquin-7-COOH)$_2$] is a closed-shell structure. Its partial molecular orbital diagram with several highest occupied and lowest unoccupied molecular orbital contours is presented in Fig. 4. In discussion of the orbital character the local symmetry of the rhenium centre has been considered: *z* axis goes along the O–Re–O linkage, and *x* axis – through the N(1)–Re–O(5) bonds.

Table 6
Atomic charges from the natural population analysis (NPA) for [ReOBr(hmquin-7-COOH)$_2$].

Atom	Charge
Re(1)	1.441
O(1)	−0.498
O(2)	−0.722
O(5)	−0.619
N(1)	−0.487
N(2)	−0.486
Br(1)	−0.349

The value of the energy separation between the highest occupied molecular orbital (HOMO) and the lowest unoccupied molecular orbital (LUMO) equals to 2.80 eV. This value is somewhat higher in comparison with the HOMO–LUMO gap calculated for [ReOBr(hqn)$_2$] [9]. The bigger absolute value of the gap energies means better stability of the title complex.

The highest occupied MO of **1** is of d_{xy} type with some contributions from p_π bromide and π-bonding of hmquin-7-COOH. Four lowest virtual orbitals are delocalized among Re, O_t and π-antibonding orbitals of hmquin-7-COOH. As d_{xz} and d_{yz} rhenium orbitals take main part in the LUMO and LUMO+1 orbitals, they are indicated in Table 8 by d_{Re} orbitals, whereas LUMO+1 and LUMO+2 were treated as π-antibonding orbitals of hmquin-7-COOH. The LUMO+6 is of $d_{x^2-y^2}$ character, and d_z^2 rhenium orbital contributes to the LUMO+12.

The nature of rhenium–terminal oxygen interaction in **1** has been studied by NBO analysis. The occupancy and composition of the calculated Re–O_t natural bond orbitals (NBOs) are given in Table 7. Each natural bond orbital (NBO) σ_{AB} can be written in terms of two directed valence hybrids (NHOs) h_A and h_B on atoms A and B:

$$\sigma_{AB} = c_A h_A + c_B h_B$$

where c_A and c_B are polarization coefficients. Each valence bonding NBO must in turn be paired with a corresponding valence *anti*-bonding NBO:

$$\sigma^*_{AB} = c_B h_A - c_A h_B$$

to complete the span of the valence space. The Lewis-type (donor) NBOs are thereby complemented by the non-Lewis-type (acceptor) NBOs that are formally empty in an idealized Lewis picture. The interactions between 'filled' Lewis-type NBOs and 'empty' non-Lewis NBOs lead to loss of occupancy from the localized NBOs of the idealized Lewis structure into the empty non-Lewis orbitals, and they are referred to as 'delocalization' corrections to the zeroth-order natural Lewis structure [26].

The detected natural Re–O_t bond orbitals of **1** are π orbitals – the p_x and p_y oxygen orbitals and d_{xz} and d_{yz} rhenium orbitals are involved in their formation. Not detected σ_{Re-Ot} bond has character of predominant Coulomb-type interactions between the central ion and ligands [34]. The terminal oxo ligand of **1** has two lone pair orbitals, and electron density from one of them is strongly delocalized into non-Lewis rhenium orbital. Accordingly, NBO analysis confirms a triple bond between the rhenium and the terminal oxygen ligand.

3.4. Electronic spectra

The experimental and calculated electronic spectra of **1** are presented in Fig. 5. Each calculated transition is represented by a gaussian function $y = ce^{-bx^2}$ with the height (c) equal to the oscillator strength and b equal to 0.04 nm^{-2}. In order to examine the effect of adding additional basis functions on the heavy atoms, the TDDFT/PCM calculations were performed by using LANL2DZ basis set on the rhenium atom (blue curve) and by using LANL2DZ basis set with additional d function with exponent $\alpha = 0.3811$ and f function with exponent $\alpha = 2.033$ (red curve). As seen in the Fig. 5, the effect of additional d functions for TDDFT calculations is very small. The B3LYP method in LANL2DZ basis set is sufficient for calculation of spectral properties of rhenium compounds.

The spin-allowed singlet–singlet electronic transitions calculated with the TDDFT method for **1** are gathered in Table 8. For the high energy part of the spectrum, only transitions with oscillator strengths larger than 0.030 are listed in Table 8.

The TDDFT/PCM calculations show that the two longest wavelength experimental bands of **1** originate in the HOMO → LUMO

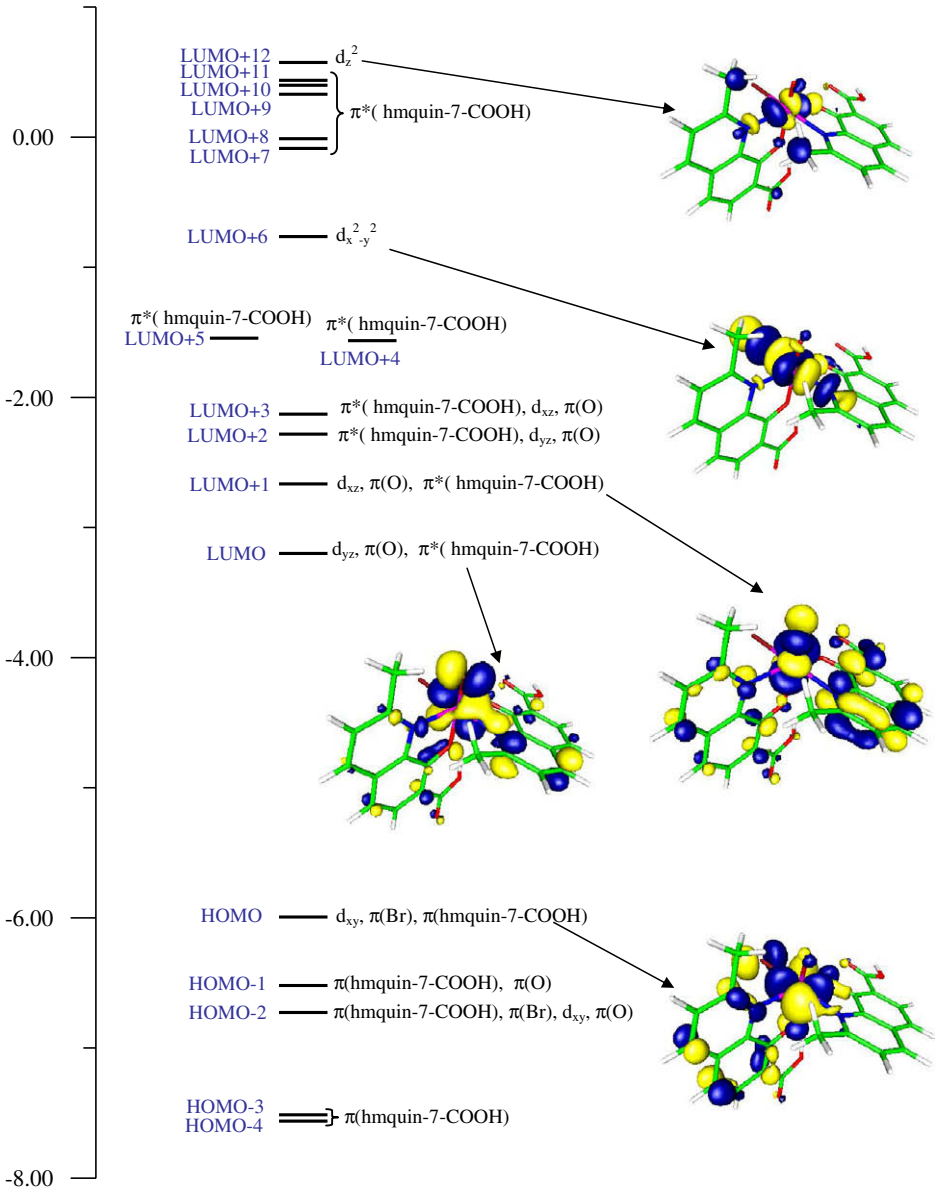


Fig. 4. The energy (eV), character and some contours of the occupied and unoccupied molecular orbitals of [ReOBr(hmquin-7-COOH)$_2$]. Positive values of the orbital contour are represented in blue (0.04 au) and negative values – in yellow (−0.04 au). (For interpretation of the references to colour in this figure legend, the reader is referred to the web version of this article.)

Table 7
The occupancy of the calculated natural bond orbitals (NBOs) between the rhenium and the oxo ligand for [ReOBr(hmquin-7-COOH)$_2$].

BD	Occupancy	Composition of NBO	BD*	Occupancy
Re–O_t	1.993	$0.552(d)_{Re} + 0.834(p)_O$	$0.834(d)_{Re} - 0.552(p)_O$	0.274
Re–O_t	1.983	$0.568(d)_{Re} + 0.823(p)_O$	$0.823(d)_{Re} - 0.568(p)_O$	0.301

BD denotes 2-center bond; * denotes antibond NBO.

and HOMO → LUMO+1 transitions, respectively. As d_{Re} orbitals take main part in the HOMO, LUMO and LUMO+1 orbitals, the HOMO → LUMO and HOMO → LUMO+1 transitions may be attributed to the transitions of d → d character. However, as it can be seen from the Fig. 4, the HOMO, LUMO and LUMO+1 orbitals are delocalized among rhenium ion, bromide, oxo and hmquin-7-COOH ligands so a delocalized *MLLCT* (metal-ligand-to-ligand CT) description can also be used.

The broad absorption band with maximum at 397.8 nm results from the *ligand-metal charge transfer* and *metal-ligand charge transfer* transitions.

The experimental bands below 300 nm nm result mainly from *ligand-ligand charge transfer* and interligand (*IL*) transitions.

The shape of the UV–Vis spectrum of **2** is the same as for the bromo analogue; the absorption bands of the chloro complex were recorded at 802.1, 678.9, 575.9, 398.5, 263.4 and 203.7 nm.

Table 8
The energy and molar absorption coefficients of experimental absorption bands and the electronic transitions calculated with the TDDFT method for [ReOBr(hmquin-7-COOH)$_2$].

The most important orbital excitations	Character	λ (nm)	E(eV)	f	Experimental Λ (nm) (E[eV])ε
H → L	d → d	831.4	1.49	0.0067	807.0 (1.54) 65
H → L+1	d → d	593.2	2.09	0.0037	685.7 (1.81) 170 587.2(2.11)100
H-1 → L	π(hmquin-7-COOH)/π(O_t) → d	473.7	2.62	0.0519	397.8 (3.12) 6380
H → L+3	d → π*(hmquin-7-COOH)	429.4	2.89	0.0491	
H → L+2	d → π*(hmquin-7-COOH)	410.7	3.02	0.1011	
H-1 → L+1	π(hmquin-7-COOH)/π(O) → d	381.3	3.25	0.0950	
H-2 → L+1	π(hmquin-7-COOH)/π(Br)/π(O) → d	371.5	3.34	0.0305	
H → L+5	d → π*(hmquin-7-COOH)	322.7	3.84	0.0540	
H-1 → L+4	π(hmquin-7-COOH) → π*(hmquin-7-COOH)	274.5	4.52	0.2056	263.0 (4.71) 38300
H-4 → L	π(hmquin-7-COOH) → d				
H-10 → L	π(hmquin-7-COOH) → d	264.9	4.68	0.0372	
H-6 → L+2	π(Br)/π(O_t)/π(hmquin-7-COOH) → π*(hmquin-7-COOH)/d	262.7	4.72	0.0385	
H-6 → L+2	π(Br)/π(O_t)/π(hmquin-7-COOH) → π*(hmquin-7-COOH)/d	259.2	4.78	0.0396	
H-8 → L+1	π(hmquin-7-COOH) → d	252.8	4.91	0.0378	
H-11 → L	π(hmquin-7-COOH)/σ(Br)/π(O_t) → d	252.2	4.92	0.2296	
H-3 → L+2	π(hmquin-7-COOH) → π*(hmquin-7-COOH)/d				
H-4 → L+3	π(hmquin-7-COOH) → π*(hmquin-7-COOH)/d	251.6	4.93	0.5531	
H-7 → L+3	π(Br)/π(hmquin-7-COOH) → π*(hmquin-7-COOH)/d	248.8	4.98	0.1090	
H-9 → L+1	π(hmquin-7-COOH)/σ(Br)/π(O_t) → d	244.2	5.08	0.0386	
H-9 → L+2	π(hmquin-7-COOH)/σ(Br)/π(O_t) → π*(hmquin-7-COOH)/d	226.0	5.49	0.0353	206.3 (6.01) 28090
H-3 → L+4	π(hmquin-7-COOH) → π*(hmquin-7-COOH)				
H-3 → L+5	π(hmquin-7-COOH) → π*(hmquin-7-COOH)	224.7	5.52	0.0340	
H-6 → L+4	π(Br)/π(O_t)/π(hmquin-7-COOH) → π*(hmquin-7-COOH)	221.5	5.60	0.0571	
H-4 → L+4	π(hmquin-7-COOH) → π*(hmquin-7-COOH)				
H-6 → L+5	π(Br)/π(O_t)/π(hmquin-7-COOH) → π*(hmquin-7-COOH)	220.8	5.62	0.0419	
H-12 → L+1	π(hmquin-7-COOH) → d	212.0	5.85	0.0603	
H-10 → L+3	π(hmquin-7-COOH) → π*(hmquin-7-COOH)/d	210.7	5.88	0.0422	
H-1 → L+7	π(hmquin-7-COOH)/π(O_t) → π*(hmquin-7-COOH)				
H-1 → L+7	π(hmquin-7-COOH)/π(O_t) → π*(hmquin-7-COOH)	208.7	5.94	0.0420	
H-2 → L+7	π(hmquin-7-COOH)/π(O_t) → π*(hmquin-7-COOH)	205.6	6.03	0.0621	
H-11 → L+3	π(hmquin-7-COOH)/σ(Br)/π(O_t) → π*(hmquin-7-COOH)/d	205.1	6.04	0.0443	

ε – molar absorption coefficient [dm^3 mol^{-1} cm^{-1}]; f – oscillator strength; H – highest occupied molecular orbital; L – lowest unoccupied molecular orbital.

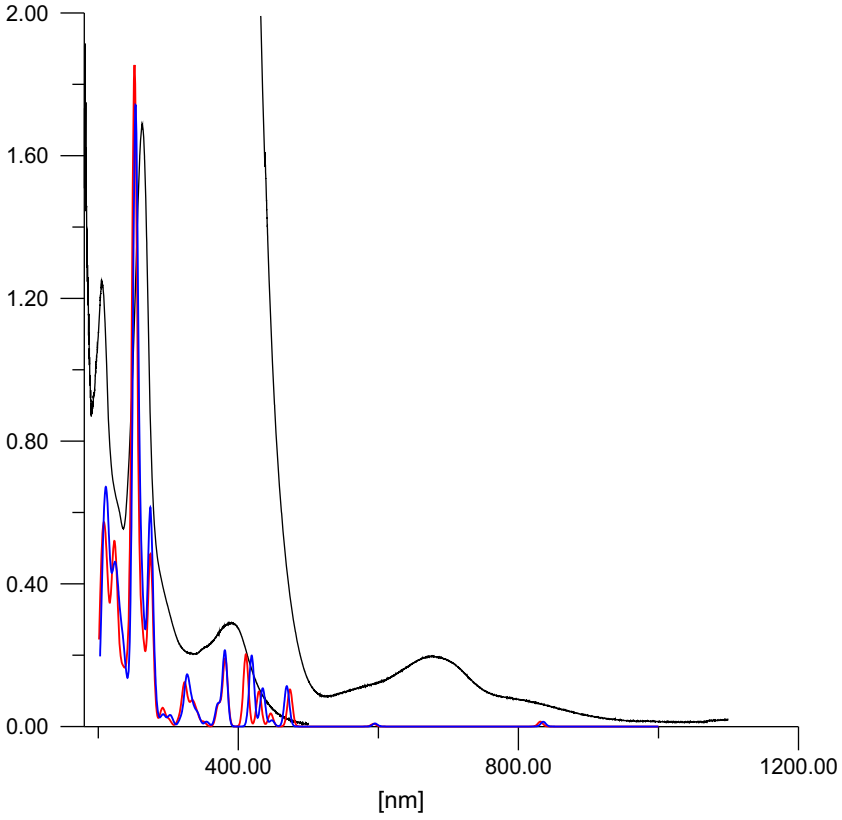


Fig. 5. The experimental (black) and calculated (red and blue) electronic absorption spectra of [ReOBr(hmquin-7-COOH)$_2$]. Red line: spectrum calculated with B3LYP functional and LANL2DZ basis set with additional d and f functions on the rhenium atom. Blue line: spectrum calculated with B3LYP functional and LANL2DZ basis set on the rhenium. (For interpretation of the references to colour in this figure legend, the reader is referred to the web version of this article.)

Supplementary data

CCDC 699353 and 699354 contain the supplementary crystallographic data for $C_{22}H_{16}N_2O_7BrRe$ and $C_{24}H_{19}N_3O_7ClRe$. These data can be obtained free of charge via http://www.ccdc.cam.ac.uk/conts/retrieving.html, or from the Cambridge Crystallographic Data Centre, 12 Union Road, Cambridge CB2 1EZ, UK; fax: (+44) 1223-336-033; or e-mail: deposit@ccdc.cam.ac.uk.

Acknowledgements

The GAUSSIAN 03 calculations were carried out in the Wrocław Centre for Networking and Supercomputing, WCSS, Wrocław, Poland.

References

[1] R.H. Holm, Chem. Rev. 87 (1987) 1401.
[2] C.C. Romão, F.E. Kühn, W.A. Hermann, Chem. Rev. 97 (1997) 3197.
[3] S.B. Seymore, S.N. Brown, Inorg. Chem. 39 (2000) 325.
[4] F.E. Kühn, A. Scherbaum, W.A. Herrmann, J. Organomet. Chem. 689 (2004) 4149.
[5] A.M. Kirillov, M. Haukka, M.V. Kirillova, A.J.L. Pombeiro, Adv. Synth. Catal. 347 (2005) 1435.
[6] A. Deloffre, S. Halut, L. Salles, J.-M. Brégeault, J.R. Gregorio, B. Denise, H. Rudler, J. Chem. Soc., Dalton Trans. (1999) 2897.
[7] W. Volkert, W.F. Goeckeler, G.J. Ehrhardt, A.R. Ketring, J. Nucl. Med. 32 (1991) 174.
[8] E.A. Deutsch, K. Libson, J.L. Vanderheyden, Technetium and Rhenium in Chemistry and Nuclear Medicine, Raven Press, New York, 1990.
[9] B. Machura, R. Kruszynski, Polyhedron 26 (2007) 2957.
[10] B. Machura, J. Kusz, Polyhedron 27 (2008) 187.
[11] J. Gancheff, C. Kremer, E. Kremer, O.N. Ventura, J. Mol. Struct. (Theochem) 580 (2002) 107.
[12] G. Rouschias, G. Wilkinson, J. Chem. Soc. A (1966) 465.
[13] K. Mekouar, J. Med. Chem. 41 (1998) 2846.
[14] CrysAlis RED, Oxford Diffraction Ltd., Version 1.171.29.2.
[15] G.M. Sheldrick, Acta Cryst. A46 (1990) 467.
[16] G.M. Sheldrick, SHELXL97. Program for the Refinement of Crystal Structures, University of Gttingen, Germany, 1997.
[17] G.M. Sheldrick, SHELXTL: release 4.1 for Siemens Crystallographic Research Systems, 1990.
[18] GAUSSIAN 03, Revision B.03, M.J. Frisch, G.W. Trucks, H.B. Schlegel, G.E. Scuseria, M.A. Robb, J.R. Cheeseman, J.A. Montgomery, Jr., T. Vreven, K.N. Kudin, J.C. Burant, J.M. Millam, S.S. Iyengar, J. Tomasi, V. Barone, B. Mennucci, M. Cossi, G. Scalmani, N. Rega, G.A. Petersson, H. Nakatsuji, M. Hada, M. Ehara, K. Toyota, R. Fukuda, J. Hasegawa, M. Ishida, T. Nakajima, Y. Honda, O. Kitao, H. Nakai, M. Klene, X. Li, J.E. Knox, H.P. Hratchian, J.B. Cross, C. Adamo, J. Jaramillo, R. Gomperts, R. E. Stratmann, O. Yazyev, A.J. Austin, R. Cammi, C. Pomelli, J.W. Ochterski, P.Y. Ayala, K. Morokuma, G.A. Voth, P. Salvador, J.J. Dannenberg, V.G. Zakrzewski, S. Dapprich, A.D. Daniels, M.C. Strain, O. Farkas, D.K. Malick, A. D. Rabuck, K. Raghavachari, J.B. Foresman, J.V. Ortiz, Q. Cui, A.G. Baboul, S. Clifford, J. Cioslowski, B.B. Stefanov, G. Liu, A. Liashenko, P. Piskorz, I. Komaromi, R.L. Martin, D.J. Fox, T. Keith, M.A. Al-Laham, C.Y. Peng, A. Nanayakkara, M. Challacombe, P.M. W. Gill, B. Johnson, W. Chen, M.W. Wong, C. Gonzalez, J.A. Pople, Gaussian, Inc., Pittsburgh PA, 2003.
[19] A.D. Becke, J. Chem. Phys. 98 (1993) 5648.
[20] C. Lee, W. Yang, R.G. Parr, Phys. Rev. B 37 (1988) 785.
[21] M.E. Casida, in: J.M. Seminario (Ed.), Recent Developments and Applications in Modern Density Functional Theory Theoretical and Computational Chemistry, vol. 4, Elsevier, Amsterdam, 1996.
[22] P.C. Hariharan, J.A. Pople, Theor. Chim. Acta 28 (1973) 213.
[23] V.A. Rassolov, M.A. Ratner, J.A. Pople, P.C. Redfern, L.A. Curtiss, J. Comput. Chem. 22 (2001) 976.
[24] P.J. Hay, W.R. Wadt, J. Chem. Phys. 82 (1985) 299.
[25] K. Eichkorn, F. Weigend, O. Treutler, R. Ahlrichs, Theor. Chem. Acc. 97 (1997) 119.
[26] E.D. Glendening, A.E. Reed, J.E. Carpenter, F. Weinhold, NBO (version 3.1). E. Reed, L.A. Curtiss, F. Weinhold, Chem. Rev. 88, 1988, 899.
[27] W.P. Griffith, H.I.S. Nogueira, B.C. Parkin, R.N. Sheppard, A.J.P. White, D.J. Williams, J. Chem. Soc., Dalton Trans. (1995) 1775.
[28] S.M.O. Quintal, H.I.S. Nogueira, V. Félix, M.G.B. Drew, New J. Chem. 24 (2000) 511.
[29] U. Mazzi, F. Refosco, F. Tisato, G. Bandoli, M. Nicolini, J. Chem. Soc., Dalton Trans. (1986) 1623.
[30] G.A. Jeffrey, W. Saenger, Hydrogen Bonding in Biological Structures, Springer-Verlag, 1994.
[31] G.R. Desiraju, T. Steiner, The Weak Hydrogen Bond in Structural Chemistry and Biology, Oxford University Press, 1999.
[32] J.M. Mayer, Inorg. Chem. 27 (1988) 3899.
[33] F.H. Allen, Acta Crystallogr., Sect. B 58 (2002) 380.
[34] M.L. Kuznetsov, A.J.L. Pombeiro, J. Chem. Soc., Dalton Trans. (2003) 738.

Polyhedron 28 (2009) 501–504

Contents lists available at ScienceDirect

Polyhedron

journal homepage: www.elsevier.com/locate/poly

The influence of the substituent [PhNHNH– and EtN(NH_2)–] on the *N*-thiophosphorylated thiosemicarbazides RC(S)NHP(S)(O*i*Pr)$_2$ crystal design

Damir A. Safin [a,*], Michael Bolte [b], Elmira R. Shakirova [a], Maria G. Babashkina [a]

[a] *A.M. Butlerov Chemistry Institute, Kazan State University, Kremlevskaya Street 18, 420008 Kazan, Russian Federation*
[b] *Institut für Anorganische Chemie J.-W.-Goethe-Universität, Frankfurt/Main, Germany*

ARTICLE INFO

Article history:
Received 22 October 2008
Accepted 28 November 2008
Available online 13 January 2009

Keywords:
Phenylhydrazine
Ethylhydrazine
Thiosemicarbazide
Crystal structures

ABSTRACT

Two *N*-thiophosphorylated thiosemicarbazides of the common formula RC(S)NHP(S)(O*i*Pr)$_2$ [R = PhNHNH- (**1**); EtN(NH_2)- (**2**)] have been synthesized and characterized by IR, ^{1}H and ^{31}P spectroscopy, and the single crystal X-ray diffraction method. Single crystal X-ray diffraction studies showed the thiosemicarbazides form both intra- and intermolecular hydrogen bonds, which in turn lead to polymeric chain formation. Moreover, according to the X-ray data of the phenylsubstituted thiosemicarbazide, the formation of intermolecular H···η^6-phenyl interactions were established.

© 2008 Elsevier Ltd. All rights reserved.

1. Introduction

N-(Thio)phosphorylated (thio)amides RC(X)NHP(Y)R′$_2$ and (thio)ureas RR′NC(X)NHP(Y)R″$_2$ (X = O, S) have been intensively studied [1,2]. The interest is caused not only from the fact that these compounds show a wide variety of complexes with various metal cations but also from the potential of these amidophosphates as agents for extraction and transporting different cations, anions and organic molecules [3], and as ligands in metal complexes used as single source precursors for thin films, nanocrystals and semiconductors [4].

On the other hand, thiosemicarbazides and their derivatives are very attractive compounds among NS donor compounds because of the large number useful biological properties, particularly their antitumor activity [5,6]. Since 4,4′,4″-phosphinylidynetrisemicarbazide showed the confirmed activity in Walker carcinosarcoma [7] the preparation of additional hydrazine compounds as potential antitumor agents, particularly (thio)phosphorylated derivatives, was encouraged [8–10]. Both compounds reported, herein, are structurally related to agents possessing antimicrobial and anticancer activities [8,10].

Herein, we report two *N*-thiophosphorylated thiosemicarbazides PhNHNHC(S)NHP(S)(O*i*Pr)$_2$ (**1**) and EtN(NH_2)C(S)NHP(S)(O*i*Pr)$_2$ (**2**). Compound **1** was described by us earlier [11] and in this work we present the X-ray structure investigation of it in comparison with **2**.

2. Experimental

2.1. Synthesis

Thiosemicarbazide **1** was synthesized according to the previously described method [9]. Compound **2** was synthesized similarly to **1**: a solution of ethylhydrazine (5 mmol, 0.30 g) in anhydrous CH_2Cl_2 (15 mL) was treated under vigorous stirring with a solution of (*i*PrO)$_2$P(S)NCS (5.5 mmol, 1.31 g) in the same solvent. The mixture was stirred for 2 h. The solvent was removed in a vacuum, and the product was purified by recrystallization from a 1:5 (v/v) mixture of methylene chloride and *n*-hexane.

Compound **1**: ^{1}H NMR ($CDCl_3$): δ = 1.35–1.40 (m, 12H, CH_3), 4.92 (d. sept, $^3J_{POCH}$ = 10.6 Hz, $^3J_{H,H}$ = 6.2 Hz, 2H, OCH), 6.34 (s, 1H, PhNH), 6.84–6.92 (m, 2H, *o*-H, Ph), 6.96–7.05 (m, 1H, *p*-H, Ph), 7.24–7.32 (m, overlapped with the solvent signal, *m*-H, Ph), 8.00 (s, 1H, C(S)NHN), 8.23 (d, 1H, $^2J_{PNH}$ = 13.9 Hz, P(S)NH), 9.44 (d, $^4J_{PNH}$ = 5.6 Hz, C(S)NHN, minor form) ppm. ^{31}P NMR ($CDCl_3$): δ = 53.5 (br t, $^3J_{POCH}$ = 9.8 Hz, 1P), 58.5 (q, $^2J_{PNH}$ = $^3J_{POCH}$ = 12.2 Hz, 1.9P) ppm. IR: ν = 624 (P=S), 1000, 1010 (POC), 1528 (S=C–N), 3224, 3288 (NH) cm^{-1}.

Compound **2**: Yield: 1.27 g (85%). M.p. 97 °C. ^{1}H NMR ($CDCl_3$): δ = 1.25 (t, $^3J_{H,H}$ = 7.2 Hz, 3H, CH_3, Et), 1.37 (d, $^3J_{H,H}$ = 6.2 Hz, 12H, CH_3, O*i*Pr), 3.91 (br s, 2H, NH_2), 4.16 (q, $^3J_{H,H}$ = 7.1 Hz, 2H, CH_2, Et), 4.94 (d. sept, $^3J_{POCH}$ = $^3J_{H,H}$ = 6.2 Hz, 2H, OCH), 8.98 (br s, 1H, P(S)NH) ppm. ^{31}P{^{1}H} NMR ($CDCl_3$): δ = 54.1 (1P), 59.3 (3.5P) ppm. IR: ν = 653 (P=S), 981, 998, 1020 (POC), 1488 (S=C–N), 1627, 3106, 3173, 3208, 3247, 3323 (NH + NH_2) cm^{-1}. *Anal.* Calc. for $C_9H_{22}N_3O_2PS_2$ (299.39): C, 36.11; H, 7.41; N, 14.04. Found: C, 36.18; H, 7.34; N, 14.10%.

* Corresponding author. Tel.: +784 32315397; fax: +784 32543734.
E-mail address: damir.safin@ksu.ru (D.A. Safin).

0277-5387/$ - see front matter © 2008 Elsevier Ltd. All rights reserved.
doi:10.1016/j.poly.2008.11.060

2.2. Physical measurements

Infrared spectra (Nujol) were recorded with a Specord M-80 spectrometer in the range 400–3600 cm^{-1}. NMR spectra were obtained on a Varian Unity-300 NMR spectrometer at 25 °C. ^1H and ^{31}P NMR spectra were recorded at 299.948 and 121.420 MHz, respectively. Chemical shifts are reported with reference to $SiMe_4$ (^1H) and H_3PO_4 (^{31}P). Elemental analyses were performed on a Perkin–Elmer 2400 CHN microanalyser.

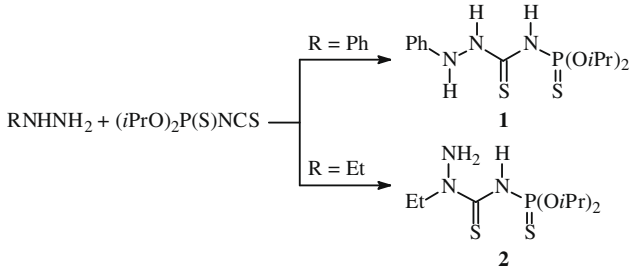
2.3. Crystal structure determination and refinement

The X-ray data were collected on a STOE IPDS-II diffractometer with graphite-monochromatized Mo Kα radiation generated by a fine-focus X-ray tube operated at 50 kV and 40 mA. The images were indexed, integrated and scaled using the X-Area data reduction package [12]. Data were corrected for absorption using the PLATON program [13]. The structure was solved by direct methods using the SHELXS-97 program [14] and refined first isotropically and then anisotropically using SHELXL-97 [14]. Hydrogen atoms were revealed from $\Delta\rho$ maps and those bonded to C were refined using a riding model. H atoms bonded to N were freely refined.

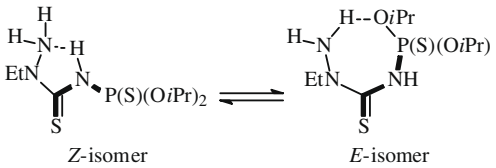
3. Results and discussion

Thiosemicarbazide **1** was synthesized according to the previously described method [9]. Compound **2** was synthesized similar to **1** by treatment of ethylhydrazine isothiocyanate (iPrO)$_2$P(S)NCS (Scheme 1). Their compositions were successfully proved by microanalysis data. Condensations of isocyanates with arylsubstituted hydrazines are reported to yield 1-substituted semicarbazides [15]. The reaction between monoalkylhydrazines and isocyanates, however, gives 2-substituted alkyl semicarbazides [16] due to the greater nucleophilic character of the secondary amine groups.

There are absorption bands for the NH_2 group in the IR spectrum of **2**. This confirms the isothiocyanate addition to the substituted nitrogen atom of the parent hydrazine. The $^{31}P\{^1H\}$ NMR spectrum of **2** contains two signals at 54.1 and 59.3 ppm. The ratio of the integrated intensities at 25 °C is ~1:3.5. When the crystalline material is dissolved in $CDCl_3$ two lines in the $^{31}P\{^1H\}$ NMR spectrum indicate that the equilibrium reaction shown in Scheme 2 is slow on the NMR timescale. We suppose that in a solution of **2** both



Scheme 1. Preparation of **1** and **2**.



Scheme 2.

Table 1
Crystal data, data collection and refinement details for **1** and **2**.

	1	**2**
Empirical formula	$C_{13}H_{22}N_3O_2PS_2$	$C_9H_{22}N_3O_2PS_2$
Formula weight	347.43	299.39
Temperature (K)	173(2)	173(2)
Radiation Mo Kα (Å)	0.71073	0.71073
Crystal system	triclinic	monoclinic
Space group	$P\bar{1}$	$C2/c$
a (Å)	6.1221(6)	22.7946(16)
b (Å)	8.0835(8)	10.1656(5)
c (Å)	17.8130(18)	14.7330(10)
α (°)	99.261(8)	90
β (°)	91.141(8)	113.301(5)
γ (°)	94.760(8)	90
V (Å^3)	866.54(15)	3135.5(3)
Z	2	8
D_{calc} (Mg m^{-3})	1.332	1.268
Absorption correction, μ (cm^{-1})	4.06	4.38
F(000)	368	1280
Crystal size (mm^3)	0.34 × 0.19 × 0.09	0.27 × 0.26 × 0.24
Recording range, θ_{max} (°)	3.34–25.65	2.46–25.93
Number of recorded reflections	10372	17948
Number of recorded independent reflections [R_{int}]	3246 [0.0476]	3049 [0.0377]
Final R indices [$I > 2\sigma(I)$]	R_1 = 0.0308, wR_2 = 0.0779	R_1 = 0.0261, wR_2 = 0.0682
R indices (all data)	R_1 = 0.0373, wR_2 = 0.0802	R_1 = 0.0284, wR_2 = 0.0694
S	1.015	1.026

Table 2
Selected bond lengths (Å), and bond and torsion angles (°) for **1**.

Bond lengths			
P(1)–O(1)	1.5844(12)	S(1)–C(1)	1.6848(16)
P(1)–O(2)	1.5805(12)	N(1)–C(1)	1.369(2)
P(1)–N(1)	1.6917(15)	N(2)–C(1)	1.346(2)
P(1)–S(2)	1.9249(6)	N(2)–N(3)	1.401(2)
Bond angles			
O(2)–P(1)–O(1)	103.80(6)	C(1)–N(1)–P(1)	126.79(12)
O(2)–P(1)–N(1)	106.39(7)	C(1)–N(2)–N(3)	120.84(14)
O(1)–P(1)–N(1)	94.32(7)	N(2)–C(1)–N(1)	115.04(14)
O(2)–P(1)–S(2)	116.17(5)	N(2)–C(1)–S(1)	120.35(12)
O(1)–P(1)–S(2)	116.67(5)	N(1)–C(1)–S(1)	124.58(13)
N(1)–P(1)–S(2)	116.65(6)		
Torsion angles			
O(2)–P(1)–N(1)–C(1)	71.73(15)	N(3)–N(2)–C(1)–S(1)	178.56(12)
O(1)–P(1)–N(1)–C(1)	177.49(14)	P(1)–N(1)–C(1)–N(2)	163.61(12)
S(2)–P(1)–N(1)–C(1)	−59.71(15)	P(1)–N(1)–C(1)–S(1)	−18.3(2)
N(3)–N(2)–C(1)–N(1)	−3.3(2)		

Table 3
Selected bond lengths (Å), and bond and torsion angles (°) for **2**.

Bond lengths			
P(1)–O(1)	1.5754(9)	S(2)–C(1)	1.6750(14)
P(1)–O(2)	1.5772(10)	N(1)–C(1)	1.3694(18)
P(1)–N(1)	1.6716(11)	N(2)–C(1)	1.3512(17)
P(1)–S(1)	1.9329(5)	N(2)–N(3)	1.4187(17)
Bond angles			
O(1)–P(1)–O(2)	105.29(5)	C(1)–N(1)–P(1)	127.86(10)
O(1)–P(1)–N(1)	105.55(6)	C(1)–N(2)–N(3)	117.29(11)
O(2)–P(1)–N(1)	93.85(6)	N(2)–C(1)–N(1)	113.88(12)
O(1)–P(1)–S(1)	115.52(4)	N(2)–C(1)–S(2)	123.83(10)
O(2)–P(1)–S(1)	115.79(4)	N(1)–C(1)–S(2)	122.29(10)
N(1)–P(1)–S(1)	118.08(5)		
Torsion angles			
O(1)–P(1)–N(1)–C(1)	68.99(13)	N(3)–N(2)–C(1)–S(2)	174.79(10)
O(2)–P(1)–N(1)–C(1)	−176.03(12)	P(1)–N(1)–C(1)–N(2)	−172.63(10)
S(1)–P(1)–N(1)–C(1)	61.95(13)	P(1)–N(1)–C(1)–S(2)	7.31(18)
N(3)–N(2)–C(1)–N(1)	−5.27(18)		

Z- and *E*-forms are present, as was previously observed for **1** [9], which are stabilized by intramolecular hydrogen bonds (Scheme 2). The chemical shifts of phosphorus are in the area, which is characteristic for the *Z*- and *E*-isomers of *N*-thiophosphorylthioureas related by structure to the investigated compounds [1]. The ^{1}H NMR spectrum of **2** contains all the characteristic signals.

Crystals of **1** and **2** were obtained by recrystallization from a 1:5 (v/v) mixture of methylene chloride and *n*-hexane (Table 1). The NMR probes and the crystals for the X-ray determination were taken from the same samples. The parameters of the C=S, C–N, P–N and P=S bonds observed for both compounds (Tables 2–4) are in the typical range for *N*-thiophosphorylated thiourea and dithiobiurea derivatives [1,9,17].

Table 4
Hydrogen bond lengths (Å) and angles (°) for **1** and **2**.

	D–H···A*	*d*(D–H)	*d*(H···A)	*d*(D···A)	∠(DHA)
1[a]	N(1)–H(1)···N(3)	0.80(2)	2.23(2)	2.645(2)	112.9(17)
	N(3)–H(3)···S(1)#1	0.81(3)	2.62(3)	3.4295(17)	174(2)
2[b]	N(1)–H(1)···N(3)	0.759(18)	2.142(17)	2.5587(16)	115.2(16)
	N(3)–H(3A)···S(1)#1	0.93(2)	2.75(2)	3.6296(13)	159.1(16)
	N(3)–H(3B)···O(1)#2	0.85(2)	2.40(2)	3.1173(16)	142.4(16)

[a] Symmetry transformations used to generate equivalent atoms: #1 $x-1, y, z$.
[b] Symmetry transformations used to generate equivalent atoms: #1 $-x+1, -y+1, -z+1$; #2 $-x+1, y, -z+3/2$.

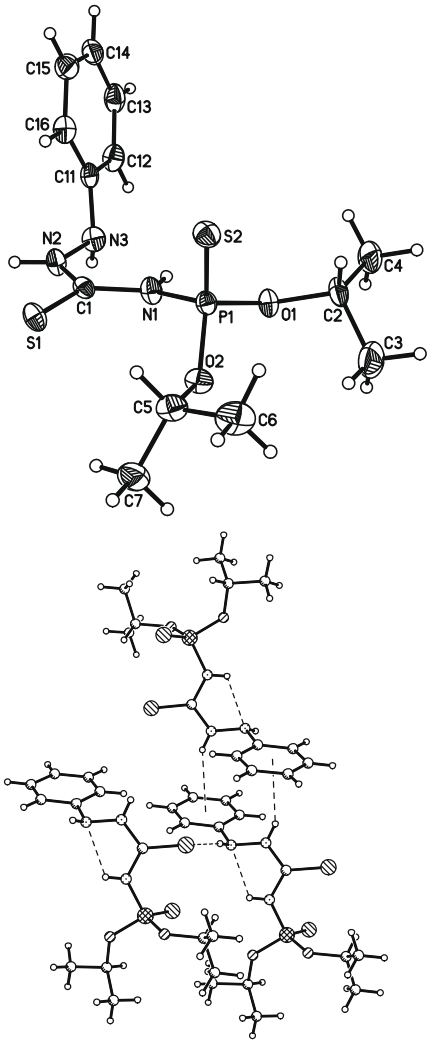


Fig. 1. Molecular structure and crystal packing of **1**.

The molecular conformation of the thiosemicarbazide **1** is shown in Fig. 1, and geometric parameters are given in Table 2. The N1–C1(S1)–N2–N3 moiety is significantly flattened and placed practically orthogonal to the phenyl and P=S groups. The S1–C1–N1–P1 backbone in the crystal phase has a *Z* conformation. The crystal structure of **1** is stabilized by an intramolecular hydrogen bond in the crystal lattice with a N(1)–H(1)···N(3) hydrogen bond. Molecules of **1** in the crystal structure form polymeric chains due to the N(3)–H(3)···S(1)#1 H-bonds (Table 4). Yet another mode of aggregation is found for this thiosemicarbazide. Two neighboring polymeric chains form interactions between the H atoms and the phenyl rings of an adjacent molecule (Fig. 1). For **1** the distance between H and the centroid of the closest phenyl ring measures 2.598 Å.

The molecular conformation of compound **2** in the crystal is shown in Fig. 2, and geometric parameters are given in Table 3. The O2–P1–N1–C1(S2)–N2–N3 moiety is flattened. The S2–C1–N1–P1 backbone, as in **1**, in the crystal phase has a *Z* conformation (Scheme 2). The conformation is supported by an intramolecular N(1)–H(1)···N(3) hydrogen bond in the solid state of **2** (Table 4).

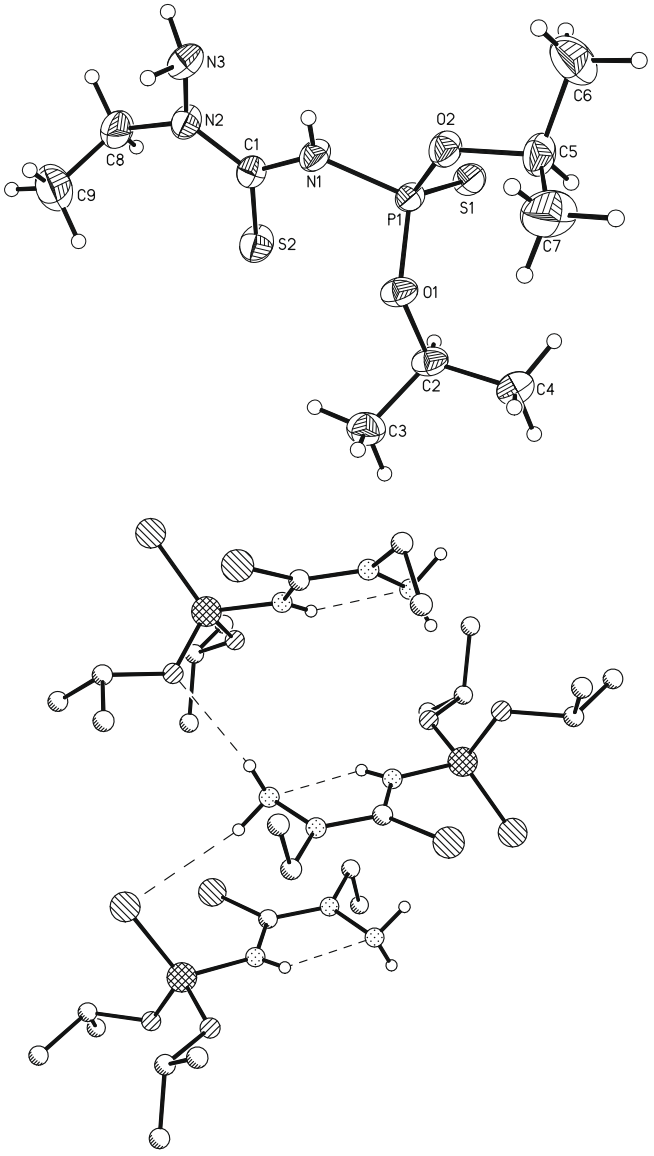


Fig. 2. Molecular structure and crystal packing of **2** (H atoms not involved in hydrogen bonds are omitted for clarity).

Two types of intermolecular H-bonds were found in the structure of the thiosemicarbazide **2**: N(3)–H(3A)···S(1)#1=P(1) and N(3)–H(3B)···O(1)#2–P(1) (Table 4). Due to this, the formation of polymeric chains is also observed for **2** (Fig. 2).

4. Conclusions

In summary, we have demonstrated the syntheses of two *N*-thiophosphorylated thiosemicarbazides by addition of thiophosphorylisothiocyanate to the corresponding phenyl- or ethylhydrazine. It was established that the phenylsubstituted hydrazine yields a 1-substituted thiosemicarbazide, whereas the reaction between ethylhydrazine and isocyanate, under the same conditions, gives a 2-substituted alkyl semicarbazide.

Single crystal X-ray diffraction studies showed the thiosemicarbazides to form both intra- and intermolecular hydrogen bonds which in turn lead to polymeric chain formation. Moreover, according to the X-ray data of the phenylsubstituted thiosemicarbazide, the formation of the intermolecular H···η^6-phenyl interactions were established.

Acknowledgments

This work was supported by the joint program of CRDF and the Russian Ministry of Education and Science (BRHE 2008 Y5-C-07-09); Russian Science Support Foundation.

Appendix A. Supplementary data

CCDC 706169 and 706168 contain the supplementary crystallographic data for **1** and **2**. These data can be obtained free of charge via http://www.ccdc.cam.ac.uk/conts/retrieving.html, or from the Cambridge Crystallographic Data Centre, 12 Union Road, Cambridge CB2 1EZ, UK; fax: (+44) 1223 336 033; or e-mail: deposit@ccdc.cam.ac.uk. Supplementary data associated with this article can be found, in the online version, at doi:10.1016/j.poly.2008.11.060.

References

[1] F.D. Sokolov, V.V. Brusko, N.G. Zabirov, R.A. Cherkasov, Curr. Org. Chem. 10 (2006) 27.
[2] F.D. Sokolov, V.V. Brusko, D.A. Safin, R.A. Cherkasov, N.G. Zabirov, Coordination Diversity of N-Phosphorylated Amides and Ureas Towards VIIIB Group Cations, in: Bence Varga, Levente Kis (Eds.), Transition Metal Chemistry: New Research, in press.
[3] R.C. Luckay, D.A. Safin, M.G. Babashkina, in preparation.
[4] N. Revaprasadu, P. Mdluli, D.A. Safin, E.R. Shakirova, M.G. Babashkina, in preparation.
[5] M.J.M. Campbell, Coord. Chem. Rev. 15 (1975) 279.
[6] I.H. Hall, K.G. Rajendran, D.X. West, A.E. Liberta, Anti-Cancer Drug 4 (1993) 241.
[7] Data from CCNSC, Conformation Defined According to Cancer Chemotherapy Rept. 25 (1962) 1.
[8] L.A. Cates, J. Med. Chem. 10 (1967) 924.
[9] L.A. Cates, J. Med. Chem. 11 (1968) 1075.
[10] L.A. Cates, T.L. Lemke, J. Pharm. Sci. 63 (1974) 1736.
[11] F.D. Sokolov, D.A. Safin, M. Bolte, E.R. Shakirova, M.G. Babashkina, Polyhedron 27 (2008) 3141.
[12] Stoe and Cie, X-Area. Area-Detector Control and Integration Software, Stoe and Cie, Darmstadt, Germany, 2001.
[13] A.L. Spek, J. Appl. Cryst. A36 (2003) 7.
[14] G.M. Sheldrick, Acta Crystallogr., Sect. A 64 (2008) 112.
[15] C. Pacilly, Rec. Trav. Chim. 55 (1936) 101.
[16] I.D. Morton, E. Hoggarth, in: E.H. Rodd (Ed.), Chemistry of Carbon Compounds, 1952, p. 919.
[17] F.D. Sokolov, D.A. Safin, M.G. Babashkina, N.G. Zabirov, V.V. Brusko, N.A. Mironov, D.B. Krivolapov, I.A. Litvinov, R.A. Cherkasov, B.N. Solomonov, Polyhedron 26 (2007) 1550.

Polyhedron 28 (2009) 505–510

Contents lists available at ScienceDirect

Polyhedron

journal homepage: www.elsevier.com/locate/poly

Cobalt(II), silver(I), and lead(II) tetrabromoterephthalates exhibiting the 1-D linear chain, 2-D $CdCl_2$-type layer, and 3-D penta-nodal mixed-connecting coordination frameworks

Cheng-Peng Li, Yi-Ling Tian, Ya-Mei Guo *

Department of Chemistry, Tianjin University, Tianjin 300072, PR China

ARTICLE INFO

Article history:
Received 10 October 2008
Accepted 28 November 2008
Available online 10 January 2009

Keywords:
Metal-directed assembly
Coordination polymer
Metal tetrabromoterephthalate
Network structure

ABSTRACT

Reaction of tetrabromoterephthalic acid (H_2TBTA) with $Co(OAc)_2$, $AgNO_3$, or $Pb(OAc)_2$ under similar conditions affords three new coordination polymers $\{[Co(TBTA)(DMF)_2(H_2O)_2](DMF)_2\}_n$ (**1**), $[Ag(TBTA)_{0.5}]_n$ (**2**), and $[Pb_2(TBTA)_{1.5}(OH)(DMF)]_n$ (**3**). All these complexes have been characterized by elemental analysis, IR, powder X-ray diffraction, and TG-DTA techniques. Single-crystal X-ray diffraction reveals that complex **1** has a 1-D neutral coordination array in which the adjacent Co^{II} centers are bridged by the TBTA spacers, whereas **2** displays a binodal $CdCl_2$-type coordination layer in which the Ag^{I} ions and TBTA ligands function as 3- and 6-connected nodes, respectively. In the structure of **3**, two types of Pb^{II} ions are interconnected via the μ_4- and μ_5-TBTA ligands as well as the μ_3-hydroxyl ions to generate a complicated 3-D penta-nodal coordination framework with (3,4,5)-connectivity. These results clearly suggest that the metal centers with distinct binding tendencies are responsible for the remarkable structural diversity of such crystalline materials.

© 2008 Elsevier Ltd. All rights reserved.

1. Introduction

During the past decade, the design and synthesis of coordination polymers by using crystal engineering strategy has attracted ever-increasing research interests for the sake of inosculating the aesthetic features of intriguing crystalline materials [1–11] with their potential applications in optics, magnetism, adsorption, ion exchange, and catalysis, etc. [12–33]. In principle, the most effective approach for the construction of the coordination framework solids is based upon the sophisticated design and selection of the organic bridging ligand with desired connectivity and the metal ion with certain coordination preference [34,35]. To date, aromatic polycarboxylate compounds have been extensively used to prepare a variety of coordination polymers in virtue of the robust and versatile coordination capability of carboxylate [36–40], especially the rigid dicarboxylate building blocks such as terephthalate and isophthalate [41–49]. However, the related ligands bearing coordination-unfavored substituents on the phenyl group have received less attention at this stage [50]. In this context, tetrabromoterephthalate (TBTA) may serve as a suitable building block to construct novel coordination polymers, which has almost not been explored so far [51]. In this paper, we will present three novel coordination polymers $\{[Co(TBTA)(DMF)_2(H_2O)_2](DMF)_2\}_n$ (**1**), $[Ag(TBTA)_{0.5}]_n$ (**2**), and $[Pb_2(TBTA)_{1.5}(OH)(DMF)]_n$ (**3**) assembled from H_2TBTA with the corresponding metal salts under similar conditions. Interestingly, these complexes display distinct network structures such as the 1-D coordination chain for **1**, 2-D $CdCl_2$-type layer for **2**, and 3-D penta-nodal coordination framework for **3**, revealing the significant metal-directed effect on the structural assembly of such network solids.

2. Experimental

2.1. Materials and general methods

All the reagents were commercially available and used without further purification. Distilled water was used throughout. Fourier transform (FT) IR spectra (KBr pellets) were taken on an AVATAR-370 (Nicolet) spectrometer. Elemental (C, H, and N) analyses were performed on a CE-440 (Leemanlabs) analyzer. Thermal analyses were carried out on a simultaneous TG-DTA system (Rigaku) in the temperature range of 25–600 °C at a heating rate of 10 °C/min under nitrogen atmosphere. An empty Al_2O_3 crucible was used as the reference. Powder X-ray diffraction (PXRD) data were recorded on a Rigaku D/Max-2500 diffractometer at 40 kV and 100 mA for a Cu-target tube. The calculated PXRD patterns were produced from the single-crystal diffraction data using the PLATON software.

* Corresponding author. Tel.: +86 22 27892415; fax: +86 22 27403475.
E-mail address: ymguo@public.tpt.tj.cn (Y.-M. Guo).

0277-5387/$ - see front matter © 2008 Elsevier Ltd. All rights reserved.
doi:10.1016/j.poly.2008.11.055

2.2. Synthesis of complexes **1**–**3**

2.2.1. {[Co(TBTA)(DMF)$_2$(H$_2$O)$_2$](DMF)$_2$}$_n$ (**1**)

The pH value a DMF/H$_2$O solution (5 mL, v/v = 1/4) of H$_2$TBTA (48 mg, 0.1 mmol) was adjusted to *ca.* 6 by dropwise adding a dilute aqueous solution of NaOH, which was placed at the bottom of a straight glass tube. Then, a solution of Co(OAc)$_2 \cdot 4$H$_2$O (25 mg, 0.1 mmol) in methanol (5 mL) was carefully layered onto it. Upon slow evaporation of the solvents, red block single crystals suitable for X-ray diffraction were obtained after 5 days in 67% yield (58 mg). IR (cm^{-1}): 3547s, 3148b, 2935s, 1646vs, 1588s, 1397s, 1324s, 1249w, 1112m, 1075w, 841m, 676m, 608w, 565m, 523w. *Anal.* Calc. for $C_{20}H_{32}CoN_4O_{10}Br_4$: C, 27.71; H, 3.72; N, 6.46. Found: C, 27.72; H, 3.74; N, 6.44%.

2.2.2. [Ag(TBTA)$_{0.5}$]$_n$ (**2**)

The same synthetic procedure as that for **1** was used except that the metal salt was replaced by AgNO$_3$ (17 mg, 0.1 mmol), producing colorless block crystals after a period of one week in 46% yield (16 mg, based on silver nitrate). IR (cm^{-1}): 1618vs, 1563vs, 1401s, 1316s, 1077w, 825m, 574m, 515w. *Anal.* Calc. for $C_4AgO_2Br_2$: C, 13.82. Found: C, 13.87%.

2.2.3. [Pb$_2$(TBTA)$_{1.5}$(OH)(DMF)]$_n$ (**3**)

The same synthetic procedure as that for **1** was used except that the metal salt was replaced by Pb(OAc)$_2 \cdot 3$H$_2$O (38 mg, 0.1 mmol), producing colorless block crystals after a period of one week in 45% yield (28 mg, based on lead acetate). IR (cm^{-1}): 3511s, 1642s, 1585vs, 1404s, 1323s, 1078m, 830m, 726w, 694w, 663w, 565s, 525m. *Anal.* Calc. for $C_{15}H_8Pb_2NO_8Br_6$: C, 14.72; H, 0.66; N, 1.14. Found: C, 14.75; H, 0.62; N, 1.12%.

2.3. X-ray crystallography

Single-crystal X-ray diffraction data for **1**–**3** were collected on a Bruker Apex II CCD diffractometer at room temperature with Mo Kα radiation (λ = 0.71073 Å) by ω scan mode. There was no evidence of crystal decay during data collection. Semi-empirical absorption corrections were applied using SADABS and the program SAINT was used for integration of the diffraction profiles [52]. All structures were solved by direct methods using the SHELXS program of the SHELXTL package and refined with SHELXL [53]. The final refinement was performed by full-matrix least-squares methods on F^2 with anisotropic thermal parameters for all non-H atoms. C-bound hydrogen atoms of the DMF molecules in **1** and **3** were generated geometrically, and the hydrogen atoms of water in **1** and hydroxyl in **3** were first located in difference Fourier syntheses and then treated as riding. Isotropic displacement parameters of the hydrogen atoms were derived from the parent atoms. Further details for crystallographic data of complexes **1**–**3** are listed in Table 1.

Table 1
Crystallographic data and structural refinement summary for complexes **1**–**3**.

Formula	$C_{20}H_{32}CoN_4O_{10}Br_4$	$C_4AgO_2Br_2$	$C_{15}H_8Pb_2NO_8Br_6$
Mr	867.07	347.71	1224.06
Crystal system	triclinic	monoclinic	triclinic
Crystal size (mm)	0.1 × 0.16 × 0.12	0.16 × 0.14 × 0.10	0.14 × 0.10 × 0.06
Space group	$P\bar{1}$	$P2_1/n$	$P\bar{1}$
a (Å)	8.5268(5)	9.679(2)	8.7450(5)
b (Å)	9.4817(5)	5.714(2)	10.8989(7)
c (Å)	10.1833(5)	11.280(3)	13.8371(9)
α (°)	81.201(1)	90	98.746(1)
(°)	74.459(1)	105.810(4)	92.382(1)
γ (°)	88.713(1)	90	107.430(1)
V (Å^3)	783.72(7)	600.3(3)	1238.3(1)
Z	1	4	2
$D_{calc.}$ (g cm^{-3})	1.837	3.847	3.283
μ (mm^{-1})	5.699	16.572	23.299
F(000)	427	628	1086
2 range (°)	2.10–25.02	2.46–25.03	1.99–25.03
Range of h, k, l	−10/10, −11/8, −10/12	−11/11, −6/5, −10/13	−10/9, −12/8, −16/16
Total/independent reflections	2742/2439	1060/9864358/3697	
Parameters	183	82	291
R_{int}	0.0126	0.0501	0.0279
R indices [I > 2σ(I)]	0.0259, 0.0599	0.0280, 0.0663	0.0422, 0.1062
R indices (all data)	0.0305, 0.0623	0.0305, 0.0678	0.0500, 0.1117
Goodness-of-fit	1.037	1.088	1.020

3. Results and discussion

3.1. Preparation and general characterization

All complexes were prepared by layer-separation diffusion of the DMF/H$_2$O solution of ligand and the corresponding CH$_3$OH solution of metal salt at the ambient conditions, which will facilitate the slow crystallization of X-ray quality single crystals of **1**–**3**. In each synthetic case, the equivalent metal/ligand ratio was utilized for the starting materials. However, the resultant complexes are found to have the metal/TBTA stoichiometric compositions of 1:1, 2:1, and 4:3, respectively for complexes **1**–**3**, which were identified by single-crystal X-ray diffraction and elemental analysis. The phase purities of the bulk samples were confirmed by powder X-ray diffraction (PXRD) patterns, which agree well with the calculated ones (see Fig. S1 in Supporting Information).

The IR spectrum of H$_2$TBTA suggests that the characteristic absorption bands of −COOH occur in 1734/1655 and 1344 cm^{-1}, which can be assigned to the antisymmetric and symmetric stretching vibrations, respectively. In the IR spectra of complexes **1**–**3**, the corresponding peaks appear in 1588 and 1324 cm^{-1} for **1**, 1618/1563 and 1316 cm^{-1} for **2**, and 1585 and 1323 cm^{-1} for **3**, respectively, which indicate the complete deprotonation of carboxyl in these complexes [54]. In addition, the observation of strong absorption peaks at 1646 and 1642 cm^{-1} in the IR spectra of **1** and **3** indicates the presence of DMF molecule.

3.2. Structural analysis of **1**–**3**

3.2.1. {[Co(TBTA)(DMF)$_2$(H$_2$O)$_2$](DMF)$_2$}$_n$ (**1**)

As shown in Fig. 1a, the Co^{II} center is located at an inversion center and coordinated by six oxygen atoms coming from a pair of carboxylate groups of different TBTA, two DMF and two aqua ligands. Thus, the local coordination environment around the Co^{II} ion (CoO$_6$) can be properly portrayed as a nearly ideal octahedron, and the Co–O bonds are in range of 2.065(2)–2.130(2) Å (see Fig. 1a caption for details). As for the ligand, the carboxylate groups deviate from the Br$_4$-substituted phenyl ring with a dihedral angle of 85.2° due to the steric effect, which adopt the unidentate coordination modes. Notably, in this series of coordination polymers, the carboxylate groups of TBTA exhibit a variety of binding modes due to the distinct coordination tendencies of the metal ions (see Scheme 1). As a result, the Co^{II} centers are connected by the TBTA dianionic bridges to produce a 1-D linear chain motif along [1 0 $\bar{1}$], as shown in Fig. 1b, in which the adjacent Co···Co separation is 11.396(1) Å. Furthermore, each coordinated aqua molecule forms an intrachain O3–H3B···O2^{i} (i = 2 − x, 1 − y, 1 − z) interaction with the adjacent carboxylate (H···O/O···O distances: 1.914/2.721 Å; O–H···O angle: 158°) as well as an O3–H3A···O5^{ii} (ii = 1 − x, 1 − y, 1 − z) interaction with the lattice DMF (H···O/O···O distances: 1.914/2.763 Å; O–H···mO angle: 176°). These secondary contacts may further stabilize this structure and no significant interchain interaction is found.

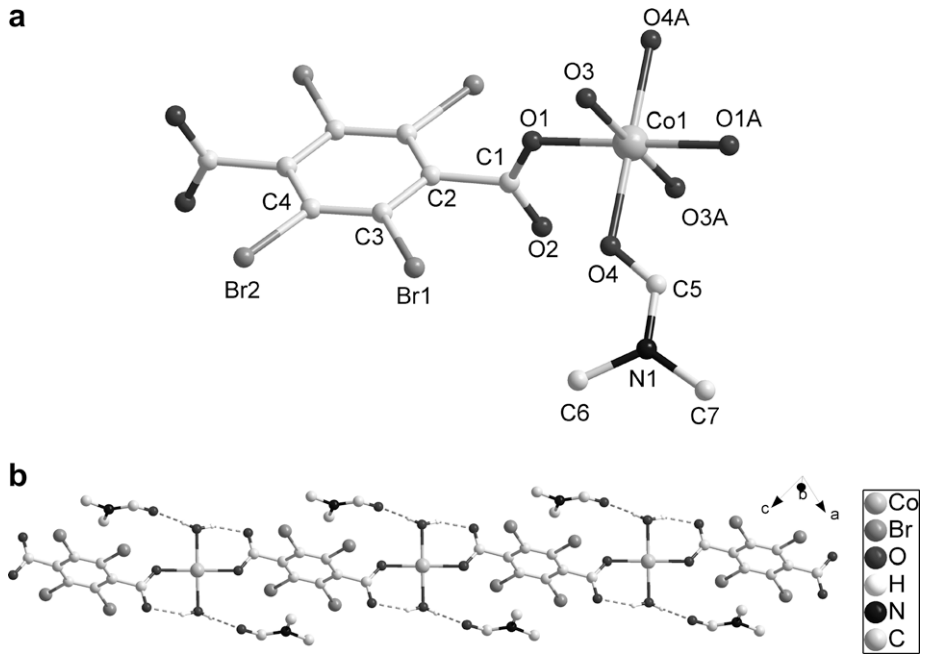
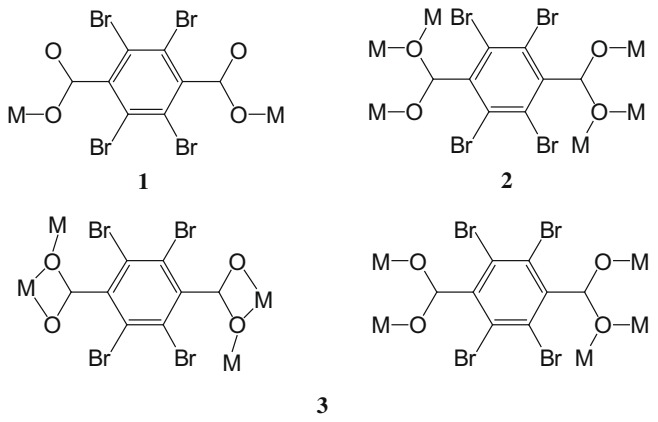


Fig. 1. (a) A portion view of **1** with atom labeling of the asymmetric unit and Co^{II} coordination sphere (symmetry operation A: $-x+2$, $-y+1$, $-z+1$). All H atoms were omitted for clarity. Selected bond parameters: Co1–O1 2.065(2), Co1–O3 2.106(2), Co1–O4 2.130(2) Å; O1–Co1–O3 88.71(7), O1–Co1–O4 90.27(7), O3–Co1–O4 90.39(8)°. (b) 1–D polymeric chain of **1** showing O–H···O hydrogen bonds. Irrelevant H atoms and the terminal DMF ligands were omitted for clarity.



Scheme 1.

3.2.2. $[Ag(TBTA)_{0.5}]_n$ (**2**)

When the close-shell d^{10} Ag^{I} ion with larger radius is applied instead of Co^{II}, a novel 2-D coordination polymer **2** is achieved. Notably, it is of rare occurrence that there exists none H or N atom in this complex. As shown in Fig. 2a, each Ag^{I} center adopts a distorted trigonal coordination geometry (see Fig. 2a caption for detailed bond geometries) which consists of three oxygen atoms from different TBTA ligands. In this case, each carboxylate group of TBTA takes the μ-O, O'_{syn}-μ-O, O coordination fashion (see Scheme 1) and acts as a μ_3-bridge to link three silver ions, which is inclined to the Br_4-substituted phenyl by 72.1°. As a result, each Ag^{I} center is linked to three TBTA ligands and each TBTA is connected to six Ag^{I} ions to afford a 2-D coordination layer along the *ab* plane (see Fig. 2b). This extended structure can be topologically recognized as a binodal (3,6)-connected network (see Fig. 2c) with the Schläfli symbol of $(4^3)_2(4^6.6^6.8^3)$, which is equivalent to that of the $CdCl_2$ lattice [35]. Furthermore, the familiar dimeric $[Ag_2(\mu\text{-}COO)_2]$ subunits are found in this 2-D pattern with the Ag···Ag separation of 2.934(1) Å. This distance is significantly shorter than that of the van der Waals Ag···Ag contact (3.40 Å) and only slightly longer than that in metallic silver (2.89 Å) [55], suggesting the existence of weak argentophilic interaction [7,56–65]. Additionally, these 2-D layers take a parallel stacking mode along [001] in *ABAB* sequence and none significant interlayer interaction is detected.

3.2.3. $[Pb_2(TBTA)_{1.5}(OH)(DMF)]_n$ (**3**)

Divalent lead, as one of the post-transition metal elements, bears larger cation radius with an identifiable void for the disposition of ligands, which can be termed as "inert-pair effect" [66]. Previous study has revealed that the stable and relatively inert outer lone pair of electrons around Pb^{II} causes a nonspherical charge distribution, and thus results in the unusual and rich coordination chemistry with a wide range of coordination numbers and irregular geometries [67]. In the structure of **3**, the fundamental building unit (see Fig 3a) contains two independent Pb^{II} centers, one and a half TBTA ligands, one OH^- ion for the charge-balance requirement, and a DMF molecule. Both Pb^{II} ions adopt the distorted octahedral coordination geometries of $[PbO_6]$ but different surroundings (see Fig. 3a caption for detailed bond geometries). Pb1 is coordinated by five carboxylate oxygen atoms from four TBTA and a hydroxyl ion, whereas the coordination environment around Pb2 is provided by three carboxylate oxygen atoms from different TBTA, two hydroxyl ions and a DMF molecule. Of particular interest is that the coordination geometries of both Pb^{II} ions can be regarded as *hemi-directed*, in which the Pb–O bonds are directed throughout only part of an encompassing globe, implying the presence of a stereochemically active lone pair of electrons [68]. Each carboxylate of the TBTA ligand with centrosymmetry takes the μ-O, O–η–O, O' coordination mode (see Scheme 1) and forms the dihedral angle of 83.5° with the Br_4-substituted phenyl. As for the other TBTA ligand, the two carboxylate groups adopt the μ–O, O'_{syn} and μ–O,

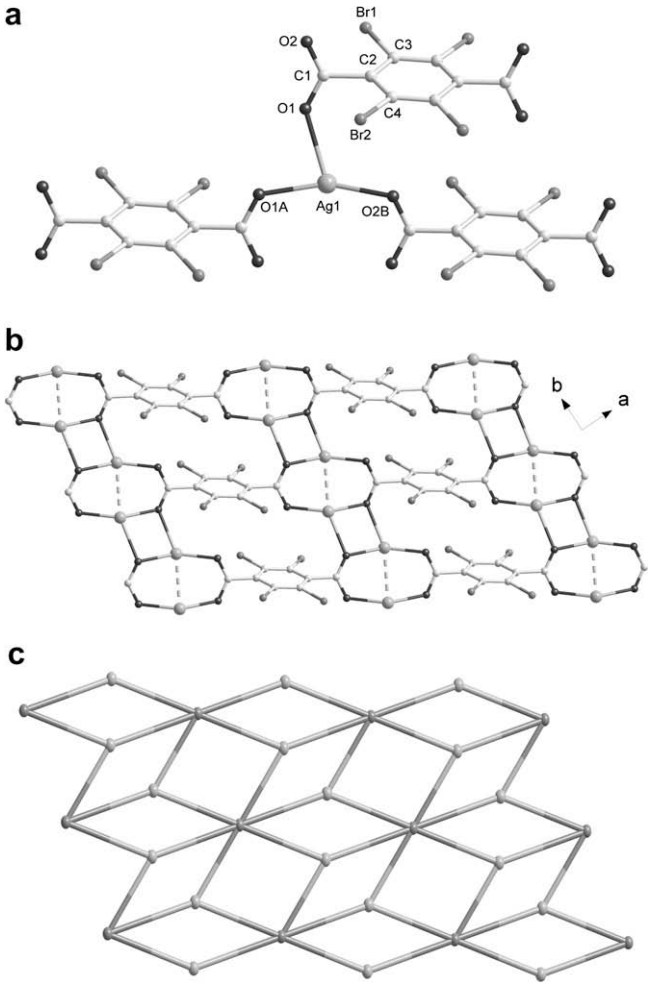


Fig. 2. (a) A portion view of **2** with atom labeling of the asymmetric unit and Ag^{I} coordination sphere (symmetry operations A: $-x, -y+1, -z+1$, B: $x, y-1, z$). Selected bond parameters: Ag1–O1 2.523(3), Ag1–O1A 2.230(3), Ag1–O2B 2.183(3) Å; O1–Ag1–O1A 84.0(1), O1–Ag1–O2B 117.4(1), O1A–Ag1–O2B 153.8(1)°. (b) 2-D coordination layer of **2** showing Ag···Ag interactions as dashed lines. (c) A schematic representation of the layered structure with $(4^3)_2(4^6.6^6.8^3)$ topology.

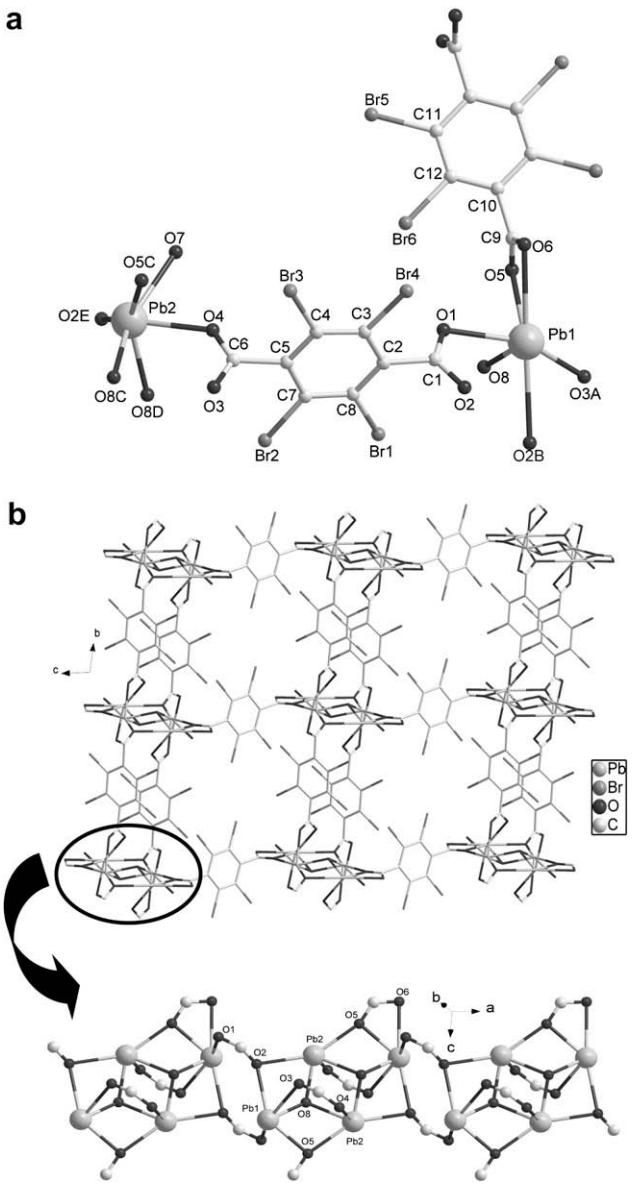


Fig. 3. (a) A portion view of **3** with atom labeling of the asymmetric unit and Pb^{II} coordination spheres (symmetry operations A: $x-1, y-1, z$, B: $-x+1, -y+1, -z+1$, C: $x+1, y+1, z$, D: $-x+1, -y+2, -z+1$, E: $x, y+1, z$). Selected bond parameters: Pb1–O1 2.432(6), Pb1–O2B 2.871(6), Pb1–O3A 2.666(8), Pb1–O5 2.491(7), Pb1–O6 2.833(7), Pb1–O8 2.336(6), Pb2–O2E 2.776(6), Pb2–O4 2.403(6), Pb2–O5C 2.687(8), Pb2–O7 2.67(1), Pb2–O8D 2.354(6), Pb2–O8E 2.545(6) Å; O1–Pb1–O3A 144.4(3), O2B–Pb1–O6 169.1(2), O2E–Pb2–O5C 153.0(2), O7–Pb2–O8C 155.3(3)°. (b) (top) A perspective view of the 3-D coordination framework of **3**. (bottom) 1-D polymeric Pb^{II} chain bridged by carboxylate and hydroxyl. All H atoms were omitted for clarity in Fig. 3.

O'_{syn}–μ–O, O binding modes (see Scheme 1), respectively, which are inclined to the central Br_4-substituted phenyl by 86.83 and 85.6°. With regard to the hydroxyl ion, it plays the trifurcated role to connect two Pb2 and one Pb1 centers. In this way, the Pb^{II} centers are interconnected by the μ_4- and μ_5-bridging TBTA ligands as well as the μ_3-hydroxyl ions to generate a very complicated 3-D coordination framework, in which the 1-D $[Pb_2(COO)_3(OH)]_n$ arrays are shaped along the [100] direction (see Fig. 3b). Examination of this structure with PLATON program [69] reveals that there exists no solvent accessible void.

In order to fully understand this intricate structure, the approach of topological reduction is properly used to simplify the 3-D network by using the TOPOS package [70]. In this instance, both Pb^{II} centers can be viewed as 5-connected nodes ($3\mu_5$-TBTA + μ_4-TBTA + OH^- for Pb1 and $2\mu_5$-TBTA + μ_4-TBTA + $2OH^-$ for Pb2) with the vertex symbols of $(4.4.4.4.4.4.6.6.6_3.8_9)$ for Pb1 and $(4.4.4.4.4.6_2.6_3.6_4.8_{14}.8_{22})$ for Pb2, respectively. In addition, OH^-, μ_4-TBTA, and μ_5-TBTA serve as 3-, 4-, and 5-connected nodes (1Pb1 + 2Pb2 for OH^-, 2Pb1 + 2Pb2 for μ_4-TBTA, and 3Pb1 + 2Pb2 for μ_5-TBTA) with the vertex symbols of $(4.4.4_2)$, $(4_2.4_2.8_4.8_4.8_5.8_5)$, and $(4.4.4.4_2.6.6.6_3.6_4.8_{14}.8_{15})$, respectively. Thus, this 3-D coordination framework can be considered as 5-nodal (3,4,5)-connected network with the Schläfli symbol of $(4^2.8^4)(4^3)_2(4^4.6^4.8^2)_2(4^5.6^3.8^2)_2(4^6.6^3.8)_2$ which represents a new topology type.

3.3. Structural comparison of *1*–*3* with related metal terephthalates

As for Co^{II} terephthalates, four types of 3-D polymeric networks and a 1-D chain motif have been reported hitherto, which were prepared under different conditions [71–77]. In the 3-D coordination complexes $[Co(tp)(H_2O)]_n$ [71,72], $[Co(tp)(DMF)]_n$ [73,74], and $[Co_2(tp)(OH)_2]_n$ [71,75], the secondary co-ligands water, DMF, and hydroxyl thereof play the bridging role, and in $\{[Co_3(tp)_4](NH_2^+(Et)_2)_2(DEF)_3\}_n$ [76], the DEF (diethylformamide) and $NH_2(Et)_2^+$ components are incorporated within the crystalline lattice as templates. Notably, the similar 1-D chain coordination array to that of

1 is observed in complex $\{[Co(tp)(DMF)_2(H_2O)_2](DMF)(H_2O)\}_n$ [77], in the structure of which the dihedral angle between the carboxylate and phenyl is only 20.2°, and the adjacent chains are hydrogen-bonded to the lattice aqua molecules and thus extended to afford a 2-D supramolecular layered structure.

In contrast to **2**, $[Ag_2(tp)]_n$ displays a 3-D polymeric framework [78], in which the similar 2-D coordination layers consisting of dimeric $[Ag_2(\mu\text{-}COO)_2]$ motifs are further interlinked by additional Ag–O bonds. Besides the different coordination modes of carboxylate, other structural difference such as the torsion angle between carboxylate and Ag^I center (154.4° for **2** and 0.3° for $[Ag_2(tp)]_n$) as well as the dihedral angle between carboxylate and phenyl (72.1° for **2** and 23.3° for $[Ag_2(tp)]_n$) is also found for the two structures.

Comparatively, a variety of coordination polymers constructed from Pb^{II} and tp in the presence of different solvents or hydroxyl have been documented [74,79–81]. For instance, complex $[Pb(tp)(H_2O)]_n$ demonstrates a unique binodal (4,7)-connected 3-D network with the Schläfli symbol of $(3^2.4.5^3)(3^4.4^2.5^5.6^9.7)$ [79]. However, in the case of $\{[Pb(tp)(EtOH)](EtOH)\}_n$, each Pb(II) ion is 8-coordinated and bound to the carboxylate groups of four tp connectors to result in a 3-D **sra** framework based on rod-type SBUs [74]. In addition, when dimethylacetamide (DMA) is used instead of the small solvent molecules of H_2O and EtOH, a unique 3-D coordination polymer $[Pb(tp)(DMA)]_n$ is generated, in which the distorted octahedral Pb^{II} centers are linked via μ_2- and μ_4-tp ligands to feature a (3,4)-connected **fsh** network with the topology notation of $(8^3)_2(8^5.10)$ [80]. In a more related example of $[Pb_2(tp)(OH)_2]_n$ [81], the hydroxyl group plays a μ_3-bridging role to interconnect the Pb^{2+} ions into 1-D polymeric chains, which are further linked by the bridging tp ligands to result in a new 3-D (3,6)-connected framework with the Schläfli symbol of $(4^3)_2(4^7.6^7.8)_2(4^8.6^6.8)$.

With regard to the more related halogen-substituted ligand tetrafluoroterephthalate (TFTA), a series of Mn [82], Fe [83], Cu [84,85], Zn [86], Mo [87–91], W [90,91], Rh [92], and Er [93] coordination complexes have been reported, which show diverse discrete or infinite coordination motifs. In the structure of $[Mn(TFTA)_2(C_5H_4N\text{-}2\text{-}CH_2\text{-}OH)_2]_n$ [82], the adjacent Mn^{II} centers are bridged by the TFTA spacers to afford a 1-D polymeric chain that is similar to that in **1**, and the C_5H_4N-2-CH_2-OH co-ligand is chelated to Mn^{II}. Significantly, a mixed-valent iron isoreticular crystalline material $\{Fe_3O[Fe_4(TFTA)_3(H_2O)_3](DMF)_{3.5}\}_n$ [83] is constructed from the trigonal prismatic $[Fe_3(\mu_3\text{-}O)(O_2C\text{–})_6]$ clusters and the TFTA linkers, which has the **acs** network topology and large channels. For the Cu^{II} complexes, $\{[Cu_4(TFTA)_3(ttc)_4](ClO_4)_2(H_2O)_6\}_n$ consists of $[Cu_4(TFTA)_2(ttc)_4]$ tetranuclear units (ttc = 1,4,7-trimethyl-1,4,7-triazacyclononane), which are further bridged by TFTA to feature a 1-D polymeric array [84]. While the 3-D jungle-gym-like microporous framework $[Cu(TFTA)(dacbo)_{0.5}]_n$ can be obtained by a heterogeneous reaction of 1,4-diazabicyclo[2,2,2]octane (dacbo) with the 2-D coordination species $[Cu(TFTA)(CH_3OH)]_n$ based on paddle-wheel-like dinuclear nodes [85], being similar to that of $[Zn_2(TFTA)_2(dabco)]_n$ [86]. Fascinatingly, two structurally related Mo-TFTA coordination polygons, including a molecular square $[cis\text{-}Mo_2(DAniF)_2]_4(TFTA)_4$ and a triangle $[cis\text{-}Mo_2(DAniF)_2]_3(TFTA)_3$ (DAniF = the anion of *N*,*N*′-di-*p*-anisylformamidine), have been found under the dynamic equilibrium in $CDCl_3$ [87]. Similarly, another molecular square $\{[Rh_2(DAniF)_2(CH_3CN)_2]_4(TFTA)_4$ is also obtained [92]. Moreover, in $[Mo_2(DAniF)_3]_2(TFTA)$, two quadruply bonded $Mo_2(DAniF)_3$ units are linked by TFTA, which displays the controllable electrochemical behavior [88,89]. As for $[(^tBuCO_2)_3M_2(TFTA)M_2(O_2C^tBu)_3]_n$ (M = Mo and W) [90,91], the metal ions are interlinked by TFTA to generate a 1-D polymeric chain. Notably, in $\{[Er_2(TFTA)_3(DMF)(H_2O)](DMF)\}_n$ [93], a 3-D rod-packing coordination framework with tiny 1-D pore is observed.

3.4. Thermal stability of *1*–*3*

All complexes are air stable and their thermal stabilities were investigated by thermogravimetric (TG) and differential thermal analysis (DTA) experiments (see *Fig.* S2 Supporting Information for TG curves). The TG curve of **1** shows the first weight loss of 22.37% from 68 to 261 °C, corresponding to the loss of two lattice DMF and two coordinated water molecules (calc.: 21.01%). Accordingly, an endothermic peak is observed at 112 °C in the DTA curve. With that, the residual coordination framework starts to decompose with a sharp weight loss that ends at 448 °C (two exothermic peaks at 360 and 404 °C in the DTA curve). Upon further heating to 600 °C, no weight loss is observed and the final species holds a weight of 20.9% of the total sample. Complex **2** retains intact until heating to 163 °C and then suffers a series of continuous weight loss, which does not end until heating to 600 °C. Only one obvious exothermic peak at 296 °C is observed in the DTA curve. As for **3**, the TG curve indicates that the 3-D coordination framework remains stable upon heating to 204 °C, followed by a series of weight loss that does not end until heating to 600 °C (one endothermic peak at 300 °C and one exothermic peak at 343 °C in the DTA curve).

4. Conclusion

The present work demonstrates that the Br_4-substituted terephthalate ligand TBTA is a reliable and versatile building block to construct novel coordination polymers. The resultant Co^{II}, Ag^I, and Pb^{II} coordination frameworks with TBTA exhibit significant structural diversity from the 1-D chain, 2-D $CdCl_2$-type layer, to 3-D network, which can be ascribed to the metal-directed assembly. In addition, the TBTA ligand displays various coordination modes with these metal ions due to their distinct ion radii, extranuclear electron distributions, and thus coordination preferences. From the results presented in this work and previous research, we can also clearly conclude that the coordination-unfavored –Br substituent attached to the phenyl backbone of terephthalate may display the critical effect on the structural assemblies of coordination architectures. Anyway, these opinions may provide a possible strategy for the rational design and construction of novel metal-organic coordination frameworks, and further useful information for understanding the crystal engineering of such network solids.

Acknowledgement

The authors gratefully acknowledge the financial support by Tianjin University.

Appendix A. Supplementary data

CCDC 697138, 697139 and 697140 contain the supplementary crystallographic data for complexes **1, 2** and **3**. These data can be obtained free of charge via http://www.ccdc.cam.ac.uk/conts/retrieving.html, or from the Cambridge Crystallographic Data Centre, 12 Union Road, Cambridge CB2 1EZ, UK; fax: (+44) 1223 336 033; or e-mail: deposit@ccdc.cam.ac.uk.

Supplementary data associated with this article can be found, in the online version, at doi:10.1016/j.poly.2008.11.055.

References

[1] S.R. Batten, R. Robson, Angew. Chem., Int. Ed. 37 (1998) 1460.
[2] N.W. Ockwig, O. Delgado-Friedrichs, M. O'Keeffe, O.M. Yaghi, Acc. Chem. Res. 38 (2005) 176.
[3] M. Du, X.-J. Jiang, X.-J. Zhao, Chem. Commun. (2005) 5521.

[4] X.-L. Wang, C. Qin, E.-B. Wang, Z.-M. Su, Y.-G. Li, L. Xu, Angew. Chem., Int. Ed. 45 (2006) 7411.
[5] K. Biradha, M. Sarkar, L. Rajput, Chem. Commun. (2006) 4169.
[6] B.-H. Ye, M.-L. Tong, X.-M. Chen, Coor. Chem. Rev. 249 (2005) 545.
[7] C.-L. Chen, B.-S. Kang, C.-Y. Su, Aust. J. Chem. 59 (2006) 3.
[8] J.-P. Zhang, X.-M. Chen, Chem. Commun. (2006) 1689.
[9] L. Carlucci, G. Ciani, D.M. Proserpio, Coord. Chem. Rev. 246 (2003) 247.
[10] V.A. Blatov, L. Carlucci, G. Ciani, D.M. Proserpio, Cryst. Eng. Comm. 6 (2004) 378.
[11] A.Y. Robin, K.M. Fromm, Coord. Chem. Rev. 250 (2006) 2127.
[12] O.R. Evans, W. Lin, Acc. Chem. Res. 35 (2002) 511.
[13] C.L. Cahill, D.T. de Lill, M. Frisch, Cryst. Eng. Comm. 9 (2007) 15.
[14] Y.-F. Zhou, M.-C. Hong, X.-T. Wu, Chem. Commun. (2006) 135.
[15] S.-L. Zheng, X.-M. Chen, Aust. J. Chem. 57 (2004) 703.
[16] D. Maspoch, D. Ruiz-Molina, J. Veciana, Chem. Soc. Rev. 36 (2007) 770.
[17] D. Maspoch, D. Ruiz-Molina, J. Veciana, J. Mater. Chem. 14 (2004) 2713.
[18] S.R. Batten, K.S. Murray, Coord. Chem. Rev. 246 (2003) 103.
[19] G. Férey, Chem. Soc. Rev. 37 (2008) 191.
[20] S. Kitagawa, R. Matsuda, Coord. Chem. Rev. 251 (2007) 2490.
[21] S. Kitagawa, S.-I. Noro, T. Nakamura, Chem. Commun. (2006) 701.
[22] C.J. Kepert, Chem. Commun. (2006) 695.
[23] S. Kitagawa, K. Uemura, Chem. Soc. Rev. 34 (2005) 109.
[24] J.-P. Zhang, X.-M. Chen, J. Am. Chem. Soc. 130 (2008) 6010.
[25] M. Du, X.-J. Zhao, J.-H. Guo, S.R. Batten, Chem. Commun. (2005) 4836.
[26] R.-Q. Zou, H. Sakurai, Q. Xu, Angew. Chem., Int. Ed. 45 (2006) 2542.
[27] C. Janiak, Dalton Trans. (2003) 2781.
[28] S.L. James, Chem. Soc. Rev. 32 (2003) 276.
[29] U. Mueller, M. Schubert, F. Teich, H. Puetter, K. Schierle-Arndt, J. Pastré, J. Mater. Chem. 16 (2006) 626.
[30] N.R. Champness, Dalton Trans. (2006) 877.
[31] X. Lin, J.-H. Jia, P. Hubberstey, M. Schröder, N.R. Champness, CrystEngComm 9 (2007) 438.
[32] C. Janiak, Angew. Chem., Int. Ed. 36 (1997) 1431.
[33] B. Kesanli, W. Lin, Coord. Chem. Rev. 246 (2003) 305.
[34] D. Li, T. Wu, X.-P. Zhou, R. Zhou, X.-C. Huang, Angew. Chem., Int. Ed. 44 (2005) 4175.
[35] M. Du, Z.-H. Zhang, L.-F. Tang, X.-G. Wang, X.-J. Zhao, S.R. Batten, Chem. Eur. J. 13 (2007) 2578.
[36] X.-M. Chen, G.-F. Liu, Chem. Eur. J. 8 (2002) 4811.
[37] A.G. Wong-Foy, A.J. Matzger, O.M. Yaghi, J, Am. Chem. Soc. 128 (2006) 3494.
[38] Z.-Z. Lin, F.-L. Jiang, L. Chen, D.-Q. Yuan, M.-C. Hong, Inorg. Chem. 44 (2005) 73.
[39] J. Tao, Y. Zhang, M.-L. Tong, X.-M. Chen, T. Yuen, C.-L. Lin, X.-Y. Huang, J. Li, Chem. Commun. (2002) 1342.
[40] M. Du, X.-J. Jiang, X.-J. Zhao, Inorg. Chem. 45 (2006) 3998.
[41] S.C. Manna, E. Zangrando, J. Ribas, N.R. Chaudhuri, Dalton Trans. (2007) 1383.
[42] S. Banerjee, P.-G. Lassahn, C. Janiak, A. Ghosh, Polyhedron 24 (2005) 2963.
[43] H.-X. Zhang, B.-S. Kang, A.-W. Xu, Z.-N. Chen, Z.-Y. Zhou, A.S.C. Chan, K.-B. Yu, C. Ren, J. Chem. Soc., Dalton Trans. (2001) 2559.
[44] B.-L. Chen, K.-F. Mok, S.-C. Ng, M.G.B. Drew, New J. Chem. 23 (1999) 877.
[45] H.-K. Fun, S.S.S. Raj, R.-G. Xiong, J.-L. Zuo, Z. Yu, X.-Z. You, J. Chem. Soc., Dalton Trans. (1999) 1915.
[46] J. Cano, G.D. Munno, J.L.Sanz, R. Ruiz, J. Faus, F. Lloret, M. Julves, A. Caneschi, J. Chem. Soc., Dalton Trans. (1997) 1915.
[47] C.S. Hong, Y. Do, Inorg. Chem. 36 (1997) 5684.
[48] T. Loiseau, C. Serre, C. Huguenard, G. Fink, F. Taulelle, M. Henry, T. Bataille, G. Férey, Chem. Eur. J. 10 (2004) 1373.
[49] M. Du, X.-J. Jiang, X.-J. Zhao, Inorg. Chem. 46 (2007) 3984.
[50] S.-C. Chen, Z.-H. Zhang, K.-L. Huang, Q. Chen, M.-Y. He, A.-J. Cui, C. Li, Q. Liu, M. Du, Cryst. Growth Des. 8 (2008) 3437–3445 and references cited therein.
[51] C.-P. Li, Y.-L. Tian, Y.-M. Guo, Inorg. Chem. Commun. 11 (2008) 1405.
[52] AXS Bruker, SAINT Software Reference Manual, Madison, WI, 1998.
[53] G.M. Sheldrick, SHELXTL NT Version 5.1. Program for Solution and Refinement of Crystal Structures, University of Göttingen, Germany, 1997.
[54] K. Nakamoto, Infrared and Raman Spectra of Inorganic and Coordination Compounds, Wiley, New York, 1986.
[55] D. Venkataraman, Y. Du, S.R. Wilson, K.A. Hirsch, P. Zhang, J.S. Moore, J. Chem. Educ. 74 (1997) 915.
[56] C.M. Fitchett, P.J. Steel, Aust. J. Chem. 59 (2006) 19.
[57] T. Dorn, K.M. Fromm, C. Janiak, Aust. J. Chem. 59 (2006) 22.
[58] M.B. Duriska, S.R. Batten, D.J. Price, Aust. J. Chem. 59 (2006) 26.
[59] Y.-B. Xie, J.-R. Li, X.-H. Bu, Aust. J. Chem. 59 (2006) 34.
[60] L. Cunha-Silva, R. Ahmad, M.J. Hardie, Aust. J. Chem. 59 (2006) 40.
[61] S.-L. Zheng, M.-L. Tong, X.-M. Chen, Coord. Chem. Rev. 246 (2003) 185.
[62] N.S. Oxtoby, A.J. Blake, N.R. Champness, C. Wilson, PNAS 99 (2002) 4905.
[63] H.-P. Wu, C. Janiak, G. Rheinwald, H. Lang, J. Chem. Soc., Dalton Trans. (1999) 183.
[64] C. Janiak, L. Uehlin, H.-P. Wu, P. Klüfers, H. Piotrowski, T.G. Scharmann, J. Chem. Soc., Dalton Trans. (1999) 3121.
[65] M. Munakata, L.-P. Wu, T. Kuroda-Sowa, Adv. Inorg. Chem. 46 (1999) 173.
[66] L. Shimoni-Livny, J.P. Glusker, C.W. Bock, Inorg. Chem. 37 (1998) 1853.
[67] A. Pellissier, Y. Bretonnière, N. Chatterton, J. Pécaut, P. Delangle, M. Mazzanti, Inorg. Chem. 46 (2007) 3714.
[68] D.L. Reger, M.F. Huff, A.L. Rheingold, B.S. Haggerty, J. Am. Chem. Soc. 114 (1992) 579.
[69] A.L. Spek, J. Appl. Cryst. 36 (2003) 7.
[70] V.A. Blatov, TOPOS, A Multipurpose Crystallochemical Analysis with the Program Package, Samara State University, Russia, 2004.
[71] M. Kurmoo, H. Kumagai, M.A. Green, B.W. Lovett, S.J. Blundell, A. Ardavan, J. Singleton, J. Solid State Chem. 159 (2001) 343.
[72] J.A. Kaduk, Acta Cryst. B58 (2002) 815.
[73] Y.-L. Fu, J.-L. Ren, S.W. Ng, Acta Cryst. E60 (2004) m1507.
[74] N.L. Rosi, J. Kim, M. Eddaoudi, B. Chen, M. O'Keefee, O.M. Yaghi, J. Am. Chem. Soc. 127 (2005) 1504.
[75] Z.-L. Huang, M. Drillon, N. Masciocchi, A. Sironi, J.-T. Zhao, P. Rabu, P. Panissod, Chem. Mater. 12 (2000) 2805.
[76] R.D. Poulsen, A. Bentien, M. Christensen, B.B. Iversen, Acta Cryst. B62 (2006) 245.
[77] C.-X. Jia, Acta Cryst. E63 (2007) m615.
[78] D.-F. Sun, R. Cao, W.-H. Bi, J.-B. Weng, M.-C. Hong, Y.-C. Liang, Inorg. Chim. Acta 357 (2004) 991.
[79] S.H. Dale, M.R.J. Elsegood, S. Kainth, Acta Cryst. C60 (2004) m67.
[80] J. Yang, G.-D. Li, J.-J. Cao, Q. Yue, G.-H. Li, J.-S. Chen, Chem. Eur. J. 13 (2007) 3248.
[81] A. Schuy, U. Ruschewitz, Z. Anorg. Allg. Chem. 631 (2005) 659.
[82] M. Ito, S. Onaka, Inorg. Chim. Acta 357 (2004) 1039.
[83] J.H. Yoon, S.B. Choi, Y.J. Oh, M.J. Seo, Y.H. Jhon, T.-B. Lee, D. Kim, S.H. Choi, J. Kim, Catal. Today 120 (2007) 324.
[84] K.-S. Bürger, P. Chaudhuri, K. Wieghardt, B. Nuber, Chem. Eur. J. 1 (1995) 583.
[85] R. Kitaura, F. Iwahori, R. Matsuda, S. Kitagawa, Y. Kubota, M. Takata, T.C. Kobayashi, Inorg. Chem. 43 (2004) 6522.
[86] H. Chun, D.N. Dybtsev, H. Kim, K. Kim, Chem. Eur. J. 11 (2005) 3521.
[87] F.A. Cotton, C.A. Murillo, R.-M. Yu, Dalton Trans. (2006) 3900.
[88] F.A. Cotton, C. Lin, C.A. Murillo, J. Chem. Soc., Dalton Trans. (1998) 3151.
[89] F.A. Cotton, J.P. Donahue, C. Lin, C.A. Murillo, Inorg. Chem. 40 (2001) 1234.
[90] B.E. Bursten, M.H. Chisholm, R.J.H. Clark, S. Firth, C.M. Hadad, P.J. Wilson, P.M. Woodward, J.M. Zaleski, J. Am. Chem. Soc. 124 (2002) 12244.
[91] M.H. Chisholm, P.J. Wilson, P.M. Woodward, Chem. Commun. (2002) 566.
[92] F.A. Cotton, L.M. Daniels, C. Lin, C.A. Murillo, S.-Y. Yu, J. Chem. Soc., Dalton Trans. (2001) 502.
[93] B.-L. Chen, Y. Yang, F. Zapata, G.-D. Qian, Y.-S. Luo, J.-H. Zhang, E.B. Lobkovsky, Inorg. Chem. 45 (2006) 8882.

Polyhedron 28 (2009) 511–520

Contents lists available at ScienceDirect

Polyhedron

journal homepage: www.elsevier.com/locate/poly

Designing dicyanamide bridged 1D molecular architecture from a mononuclear copper(II) Schiff base precursor: Syntheses, structural variations and magnetic study

Aurkie Ray [a], Guillaume Pilet [b], Carlos J. Gómez-García [c], Samiran Mitra [a,*]

[a] Department of Chemistry, Jadavpur University, S.C. Mallik Road, Kolkata 700 032, West Bengal, India
[b] Groupe de Cristallographie et Ingénierie Moléculaire Laboratoire des Multimatériaux et Interfaces UMR 5615 CNRS – Université Claude Bernard Lyon 1, Bât. Jules Raulin, 43 bd du 11 Novembre, 1918 69622 Villeurbanne, Cedex, France
[c] Instituto de Ciencia Molecular (ICMol), University of Valencia, Parque Cientifico. 46980 Paterna, Spain

ARTICLE INFO

Article history:
Received 28 August 2008
Accepted 28 November 2008
Available online 8 January 2009

Keywords:
Copper(II) complexes
2-Picolylamine and benzoylacetone
Schiff base
Mononuclear precursor
Dicyanamide bridged polymer
Magnetic properties

ABSTRACT

A new tridentate N_2O donor Schiff base ligand [$(C_6H_5C(OH)$═$CHC(CH_3)$═$NCH_2C_5H_4N)$═**LH**] was obtained by 1:1 condensation of benzoylacetone with 2-picolylamine and has been used to synthesise a mononuclear [CuLCl] (**1**) and an *end-to-end* dicyanamide bridged polynuclear $\{[Cu_2(\mu\text{-}L)_2(\mu_2\text{-}1,5\text{-}(CN)_2N)]ClO_4\}_n$ (**2**) copper(II) complexes. The ligand, **1** and **2** were clearly characterised by elemental analysis, FT-IR, ^{1}H NMR, UV–Vis spectral studies, electrochemical studies and in addition single crystal X-ray diffraction studies were performed for **1** and **2**. The Schiff base ligand [**LH**] shows a significant variation in its coordination behaviour with copper(II) ion in absence and in presence of dicyanamide ion in **1** and **2** respectively. In absence of dicyanamide the deprotonated enolato oxygen of the tridentate Schiff base ligand $[\mathbf{L}]^-$ coordinates the copper(II) ion in a monodentate fashion generating a mononuclear species (**1**) whereas in presence of the dicyanamide ion, the deprotonated enolato oxygen of $[\mathbf{L}]^-$ bridges two adjacent $[CuL(CN)_2N]$ units through μ-OL bridges, forming dimers. The dimeric units are further linked to adjacent dimeric units through μ_2-1,5-dicyanamide bridges to produce 1D polymeric chains in **2**. Variable temperature magnetic susceptibility measurements for **2** in the temperature range 2-300 K reveal the presence of weak antiferromagnetic exchange interactions in the polymeric chain.

© 2008 Elsevier Ltd. All rights reserved.

1. Introduction

Inorganic chemists have shown interest in synthesising coordination complexes derived from a Schiff base ligand since such complexes have wide applicability in catalysis, in designing molecular ferromagnets, in biological modeling as liquid crystals and as heterogeneous catalysts [1–7]. Several authors and our research team have successfully reported a large number of metal complexes derived from Schiff bases containing two, three, four, five and six donor atoms [8–17]. Tridentate Schiff bases with N_2O donor sets have been preferred by authors as such ligands effectively act as a chelate and can block the coordination sites of metal ions leaving the metal ion coordinatively unsaturated. In order to saturate the coordination number of metal ions preferring square planar, square pyramidal and octahedral geometry, different bridging ligands (N_3^-, NCO^-, NCS^-, acetates, carboxylates) have been used, giving rise to dinuclear and multinuclear complexes [11,14,15,18–27]. One such bridging ligand which is gaining interest among many researchers is dicyanamide (dca = $(CN)_2N^-$). Many authors have shown that this ligand may induce a large variety of topologies and magnetic properties due to its versatile coordination modes [28–31]. In comparison to the aforementioned bridging ligands, dca can coordinate metal ions through its eight different kinds of coordination modes (shown in Fig. 1). The *end-to-end* μ_2-1,5 bridging mode of dca with metal ions give rise to a weak antiferromagnetic coupling whereas μ_3-1,3,5 bridging mode is able to produce weak or strong ferromagnetic interactions between the metal centers. Dicyanamide can construct extended architectures by utilising its different bridging modes along with its unusual μ_4-1,1,3,5 and μ_5-1,1,3,5,5 coordination modes [32,33]. Until now our research group has reported four dicyanamide bridged metallo organic polymeric architectures derived from a N_2O donor Schiff base ligand [34–37].

There have been considerable interests for synthesising new N_2O donor tridentate Schiff bases which can effectively coordinate metal ions. To explore the chemistry of the metal complexes derived from N_2O donor tridentate Schiff bases, many authors including our research group have shown that 1:1 condensation of acetylacetone or benzoylacetone and diamines (e.g. 1,2-diaminoethane, 1,2-diaminopropane and 1,3-diaminopropane) under high dilution condition can produce mono-condensed N_2O donor

* Corresponding author. Tel.: +91 033 2414 6666x2505; fax: +91 033 2414 6414.
E-mail address: smitra_2002@yahoo.com (S. Mitra).

0277-5387/$ - see front matter © 2008 Elsevier Ltd. All rights reserved.
doi:10.1016/j.poly.2008.11.054

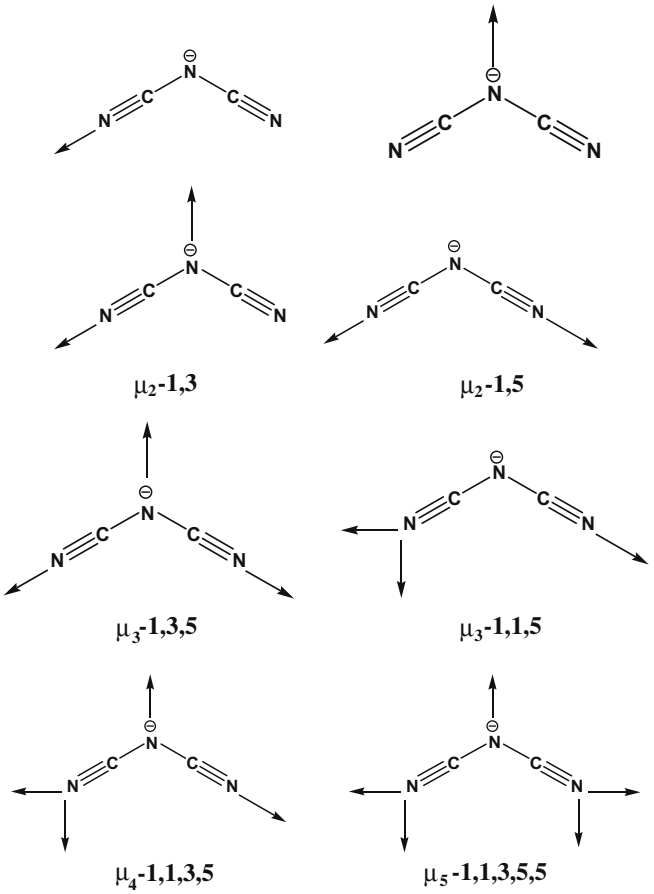


Fig. 1. Bridging modes of dca.

tridentate Schiff bases [32–42]. This group of tridentate ligands have been exhaustively used for the synthesis of mono-, di- and tri-nuclear complexes with first row transition elements [38–49] and are also used as precursor for the synthesis of unsymmetrical tetradentate Schiff bases [38–41,46]. To further explore the coordination behaviour of the N_2O donor tridentate Schiff bases obtained by condensation of benzoylacetone and diamine, some of us have used bridging ligands (N_3^-, NCO^-, SCN^-) and tried to find whether any variation in the coordination behaviour of such tridentate ligand is induced by such bridging ligands. Thus, we have reported mononuclear and polynuclear nickel and copper complexes [50–52] but no significant variation in the coordination behaviour of the N_2O donor ligand was observed in the mononuclear and polynuclear complexes.

As an extension of our earlier work, in this paper we report the synthesis of a new tridentate N_2O donor Schiff base ligand **LH** [(1Z,3E)-3-((pyridin-2-yl)methylimino)-1-phenylbut-1-en-1-ol] obtained by 1:1 condensation of benzoylacetone with 2-picolylamine and we have used it to synthesise a mononuclear and a μ_2-1,5-dicyanamide bridged polynuclear copper(II) complexes, **1** and **2** respectively. From literature survey we found that our group is the first one to characterise the new Schiff base ligand [**LH**] and its metal complexes. Earlier in the year 2002 McNeill with his research group proposed the reaction mechanism to synthesise 3,5-disubstituted and 3,4,5-trisubstituted-2-(2-pyridyl)pyrroles where they showed that **LH** was the precursor of the desired ligand system [53]. The ligand **LH** and the complexes **1** and **2** were clearly characterised by elemental analysis, FT-IR, ^{1}H NMR, UV–Vis spectral studies, and electrochemical studies. Single crystal X-Ray diffraction study of **1** and **2** were performed to investigate the structural aspects of the complexes. It is really interesting to note that unlike the earlier reported complexes derived from benzoylacetone and diamine [11], the ligand **LH** showed significant variation in its coordination behaviour with copper(II) ion in absence and in presence of the dca anion. In absence of dicyanamide the deprotonated enolato oxygen of $[\mathbf{L}]^-$, coordinates the copper(II) ion in its monodentate mode and produces a mononuclear complex (**1**), whereas in presence of dicyanamide the same deprotonated enolato oxygen of $[\mathbf{L}]^-$ bridges two adjacent $[CuL(CN)_2N]$ units through μ-OL bridges forming copper(II) dimers. The dimeric units are further linked to the adjacent dimeric units through μ_2-1,5-dicyanamide bridges to produce a 1D polymeric chain (**2**). The temperature dependence of the magnetic susceptibility has been investigated for **2**.

2. Experimental

2.1. Materials

All solvents were of reagent grade and used without further purification. Benzoylacetone and 2-picolylamine were purchased form Aldrich Chemical Company. Copper chloride dihydrate and sodium dicyanamide were purchased form Fluka and were used as received. Copper perchlorate hexahydrate was prepared by treatment of copper carbonate (E. Merck, India) with 60% perchloric acid (E. Merck, India) followed by the slow evaporation on a steam bath. It was then filtered through a fine glass-frit and preserved in a $CaCl_2$ desiccator for further use.

2.2. Syntheses

Caution! Perchlorate salts are potentially explosive and should be used in small quantity with much care.

2.2.1. Synthesis of the Schiff base ligand

*2.2.1.1. $[C_6H_5C(OH)=CHC(CH_3)=NCH_2C_5H_4N]$ (**LH**).* The Schiff base ligand (**LH**) was prepared by the reflux condensation of a 25 mL methanolic solution of 2-picolylamine (5 mmol, 0.51 mL) with an equivolume methanolic solution of benzoylacetone (5 mmol, 0.18 g). The mixture was refluxed for 2 h until a yellow coloured solution resulted. The colour indicated the formation of the Schiff base (**LH**) which was used without further purification. The scheme of synthesis and the keto-enol tautomerisation of the ligand **LH** is shown in Fig. 2. *Anal.* Calc. for $[C_{16}H_{16}N_2O]$: C, 76.19%; H, 6.35%; N, 11.11%. Found: C, 76.21; H, 6.38; N, 11.14%.

2.2.2. Syntheses of the complexes

*2.2.2.1. [CuLCl] (**1**).* Copper chloride dihydrate (0.170 g, 1 mmol) was dissolved in 5 mL methanol. 20 mL of a yellow methanolic solution of the Schiff base (**LH**) (0.252 g, 1 mmol), was added to the metal solution and stirred. The mixture was allowed to stir for 2 h at 30 °C. The resulting dark green solution was kept in the refrigerator at 16 °C to yield brown needle shaped crystals suitable for X-ray diffraction after a week. Crystals were isolated by filtration and were air-dried. *Anal.* Calc. for $[C_{16}H_{15}Cl_1Cu_1N_2O_1]$: C, 54.81%; H, 4.28%; N, 7.99%. Found: C, 54.85; H, 4.29; N, 8.01%.

*2.2.2.2. $\{[Cu_2(\mu\text{-}L)_2(\mu_2\text{-}1,5\text{-}(CN)_2N)]ClO_4\}_n$ (**2**).* Copper perchlorate hexahydrate (1 mmol, 0.37 g) was added to the brown needle shaped crystals of **1** (2 mmol, 0.70 g) and were dissolved together in 20 mL of methanol with stirring, resulting in a clear green solution. The solution was maintained at 40 °C with continuous stirring and 5 mL methanolic solution of sodium dicyanamide (2 mmol, 0.178 g) was added dropwise, resulting in a dark green solution. The mixture was then further stirred for 3 h at 30–35 °C and then filtered. The dark green solution was kept in the refrigerator at

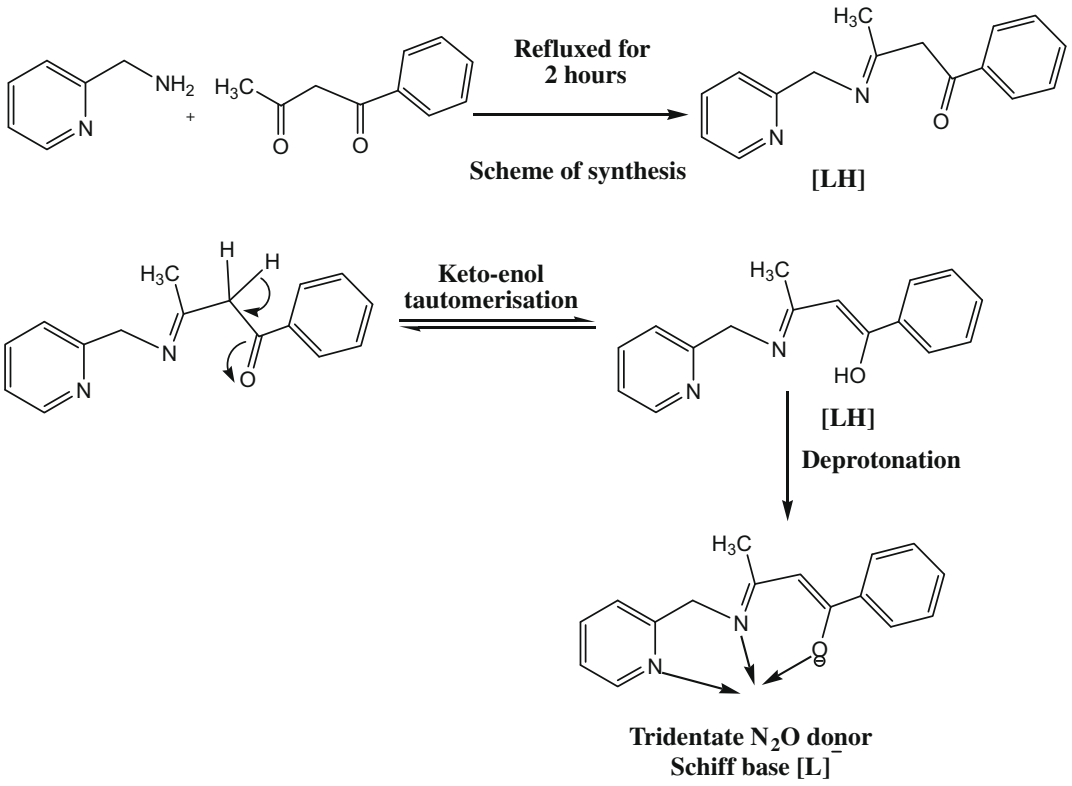


Fig. 2. Scheme of the synthesis and keto-enol tautomerisation of **LH**.

16 °C yielding light brown cubic shaped crystals suitable for X-ray diffraction after two weeks. Crystals were isolated by filtration and were air-dried. *Anal.* Calc. for $[C_{34}H_{30}Cl_1Cu_2N_7O_6]$: C, 51.31%; H, 3.77%; N, 12.32%. Found: C, 51.33; H, 3.78; N, 12.36%.

2.3. Physical measurements

The Fourier transform infrared spectra (4000–300 cm^{-1}) of **LH**, **1** and **2** were recorded on a Perkin–Elmer Spectrum RX I FT-IR system as solid KBr pellets. The electronic spectra of the complexes were recorded at 300 K on a Perkin–Elmer λ-40 UV/Vis-spectrometer using HPLC grade acetonitrile as solvent with a 1 cm quartz cuvette in the range 200–800 nm. C, H, N microanalyses of the ligand and the complexes were carried out with a Perkin–Elmer 2400 II elemental analyser. Electrochemical measurements of the complexes were performed on a VersaStat-PotentioStat II cyclic voltammeter, using HPLC grade acetonitrile as solvent with tetrabutylammonium perchlorate as supporting electrolyte, at a scan rate of 0.05 V/s. Platinum and saturated calomel electrode (SCE) were the working and the reference electrodes in the process, respectively. ^{1}H NMR spectra of the ligand and the complexes were recorded on a BRUKER 300 MHz FT-NMR spectrometer using trimethylsilane as an internal standard in $CDCl_3$. Mass spectra of the ligand (**LH**) was recorded by Qtof Micro YA mass spectrophotometer. Variable temperature susceptibility measurements were carried out in the temperature range 2-300 K with an applied magnetic field of 0.1 T on a polycrystalline sample (40.14 mg) of 2 with a Quantum Design MPMSXL-5 SQUID magnetometer. The isothermal magnetization was performed in the same sample at 2 K with applied magnetic fields of up to 5 T. The susceptibility data were corrected for the sample holder previously measured using the same conditions and for the diamagnetic contributions of the salt as deduced by using Pascal's constant tables ($\chi_{dia} = -454.6 \times 10^{-6}$ emu mol^{-1}).

2.4. X-ray crystallography

Single-crystals X-ray studies of **1** and **2** were carried out using a Nonius Kappa CCD and the related analysis softwares [54]. Crystallographic data and the refinement results are given in Table 1. For **1** absorption correction called *Analytical* [55] (based on the shape of the single crystal used for the X-ray diffraction analyses performed at 150 K) has been applied whereas for **2** a semi-empirical absorption correction MULTISCAN program [56] has been applied to the data sets. Both structures have been solved by direct methods using the SIR97 program [57] combined to Fourier difference syntheses and refined against F using reflections with $[I/\sigma(I) > 3]$ with CRYSTALS program [58]. All atomic displacements parameters for non-hydrogen atoms have been refined with anisotropic terms. The hydrogen atoms were theoretically located on the basis of the conformation of the supporting atom and also found by Fourier Difference. Then they have been refined (positions and isotropic terms) to find their real position keeping some constraints belonging to the supporting atoms.

3. Results and discussion

The formation of the new Schiff base ligand **LH** has been supported by infrared, ^{1}H NMR and mass spectroscopy. IR bands obtained at 1654 cm^{-1} clearly indicate the presence of an imine bond which must have resulted by condensation of 2-picolyl amine with benzoylacetone. IR bands at 3339 and 3302 cm^{-1} for the asymmetric and symmetric $-NH_2$ stretching are not observed which also indicate that the $-NH_2$ functionality of 2-picolyl amine has successfully condensed with one of the carbonyl functionality of benzoylacetone. Moreover, a well defined band due to the enolic O–H stretching frequency at 3406 cm^{-1} is observed in the spectrum of the free ligand which not only support the formation of **LH** but also ensures that the free ligand have undergone tautomerisation

Table 1
Crystallographic and refinement data for **1** and **2**.

Complex	**1**	**2**
Chemical formula	$C_{16}H_{15}Cl_1Cu_1N_2O_1$	$C_{34}H_{30}Cl_1Cu_2N_7O_6$
Formula weight	350.3	795.2
Crystal system	monoclinic	monoclinic
Space group	$P2_1/c$ (No. 14)	$C2/c$ (No. 15)
Z	4	4
a (Å)	7.2843 (3)	21.55 (2)
b (Å)	14.1051 (5)	14.155 (6)
c (Å)	14.0558 (6)	14.21 (2)
α (°)	90	90
β (°)	96.038 (2)	131.07 (3)
γ (°)	90	90
V (Å^3)	1436.2 (1)	3266 (5)
Temperature (K)	150	150
Density (Mg/m^3)	1.620	1.617
Absorption coefficient (mm^{-1})	1.705	1.443
$F(000)$	716	1576
Crystal size (mm)	$0.05 \times 0.07 \times 0.24$	$0.12 \times 0.14 \times 0.14$
θ Range for data collection (°)	2.051–27.876	1.908–28.688
Reflections collected	9790	21473
Independent reflections, (R_{int})	3416, 0.062	4083, 0.092
Number of 'observed' reflections	1742	2059
Goodness-of-fit, S	1.15	1.12
Final R indices [$I > 3\sigma(I)$]	0.0359	0.0351
R indices (all data)	0.0806	0.0753
Largest difference in peak and hole (e Å^{-3})	0.67, −0.39	0.77, −0.38

and exists in the enolic form. In the ^{1}H NMR spectrum of the free ligand **LH** no signal at 5–8 ppm is observed, indicating the absence of free –NH_2 functionality, supporting the formation of the ligand **LH**. The mass spectrum also ensures the formation of the Schiff base ligand **LH**. The mass spectrum of the ligand **LH** shows a peak at m/e 275, which is attributed to the molecular ion peak $[C_{16}H_{16}N_2ONa]^+$. In the mass spectrum the highest intensity peak was obtained at m/e 275 (100%) and may be assigned to the neutral **LH** bound to one sodium ion to generate a molecular ion. Hence, we can state from the mass spectrum that proper condensation of the 2-picolyl amine with benzoylacetone has resulted in the formation of the Schiff base ligand **LH**. The most conclusive evidence which supports the condensation of 2-picolyl amine with benzoylacetone is the single crystal X-ray study of **1** and **2** which clearly indicate the coordination of the deprotonated tridentate ligand $[\mathbf{L}]^-$ to the copper(II) centers.

3.1. Infrared spectra

The IR spectra of **1** and **2** have been analysed in comparison with that of the free ligand **LH** in the region 4000–250 cm^{-1}. The IR spectra of **1** and **2** are very similar to each other except in the regions 2150–2400 cm^{-1} and 1090–1129 cm^{-1}. In **1** none of the three sharp characteristic peaks for the dicyanamide ligand are observed in the region 2290–2170 cm^{-1} clearly indicating the absence of dca. In **2** the three characteristic bands of the free dca ligand [$\nu_{\mathbf{as}} + \nu_{\mathbf{s}}$(C≡N) combination modes (2286 cm^{-1}), $\nu_{\mathbf{as}}$(C≡N) (2232 cm^{-1}) and $\nu_{\mathbf{s}}$(C≡N) (2179 cm^{-1})] are further splitted and are shifted towards higher frequencies: 2292 (m, with shoulder on the high frequency side), 2290 (s) cm^{-1} ($\nu_{\mathbf{as}} + \nu_{\mathbf{s}}$(C≡N)), 2234 (s) cm^{-1} ($\nu_{\mathbf{as}}$(C≡N)) and 2160 (s/m) cm^{-1} ($\nu_{\mathbf{s}}$(C≡N)) (s, strong; m, medium). The splitting of the bands and the displacements observed are consistent with the presence of bridging (bidentate) dca in **2**, as revealed by the X-ray structure determinations [59]. Moreover bands corresponding to the $\nu_{\mathbf{as}}$(C–N) stretching frequencies (1406–1302 cm^{-1} region), and the $\nu_{\mathbf{s}}$(C–N) stretching (930–900 cm^{-1} region), also support the coordination of dca in **2**. The characteristic bifurcated absorbtion band in the region 1059–1121 cm^{-1} for perchlorate anion is observed in **2** but is absent in **1**. A strong sharp absorption band around 1624 cm^{-1} in the spectrum of the Schiff base ligand can be assigned to the C=N group. In **1** and **2** this band is shifted to lower frequencies 1612 and 1611 cm^{-1} upon complexation with the respective metal centers, which can be attributed to the coordination of the nitrogen atom of the imino group to the metal centers [60]. The ligand shows a well defined band at 3412 cm^{-1} due to the enolic O–H stretching frequency which disappears in **1** and **2** and a C–O absorption band that appears at 1056–1095 cm^{-1}, indicating that the deprotonated ligand $[\mathbf{L}]^-$ is coordinated to the copper(II) center. The low energy pyridine ring in-plane and out-of-plane vibrations are observed in the spectrum of the **LH** molecule at 621 and 412 cm^{-1}, respectively, whereas the corresponding bands for **1** and **2** are shifted to higher frequencies at 623, 677 and 419, 422 cm^{-1}, respectively, which are good indications of the coordination of the heterocyclic nitrogen atom to the metal centers [61]. Sharp bands corresponding to ν_{Cu-N} appear in the complexes **1** and **2** at 412 and 408 cm^{-1} respectively indicating the coordination of the nitrogen atom to the metal center.

3.2. NMR spectra

^{1}H NMR spectroscopy has been used to extract information regarding the formation of the Schiff base ligand **LH** and its mode of coordination with the copper(II) centers in **1** and **2**. The NMR spectra of **1** and **2** are almost superimposable but differ significantly from that of the free ligand **LH**. The NMR proton numbering scheme of **LH** along with the NMR spectra of the ligand and the complexes are represented in Fig. 3a and b. The NMR data are summarised in Table 2. In the NMR spectra of the free ligand **LH** a signal at 5–8 ppm is not observed, indicating the absence of free –NH_2 functionality, supporting the formation of the ligand **LH** [62]. In **1** and **2** the signal due to the enolic hydrogen (H8) of the free ligand (11.3 ppm) is absent and the phenyl protons are shifted more downfield (H9 ~0.02 ppm and H10 ~0.02 ppm and H11 ~0.02 ppm) in both the complexes, indicating the coordination of a deprotonated enolic oxygen of $[\mathbf{L}]^-$ in the complexes. The methylene and methyl protons (H5 and H6 respectively) of **LH** attached to the imine nitrogen are shifted downfield (~0.06 ppm and

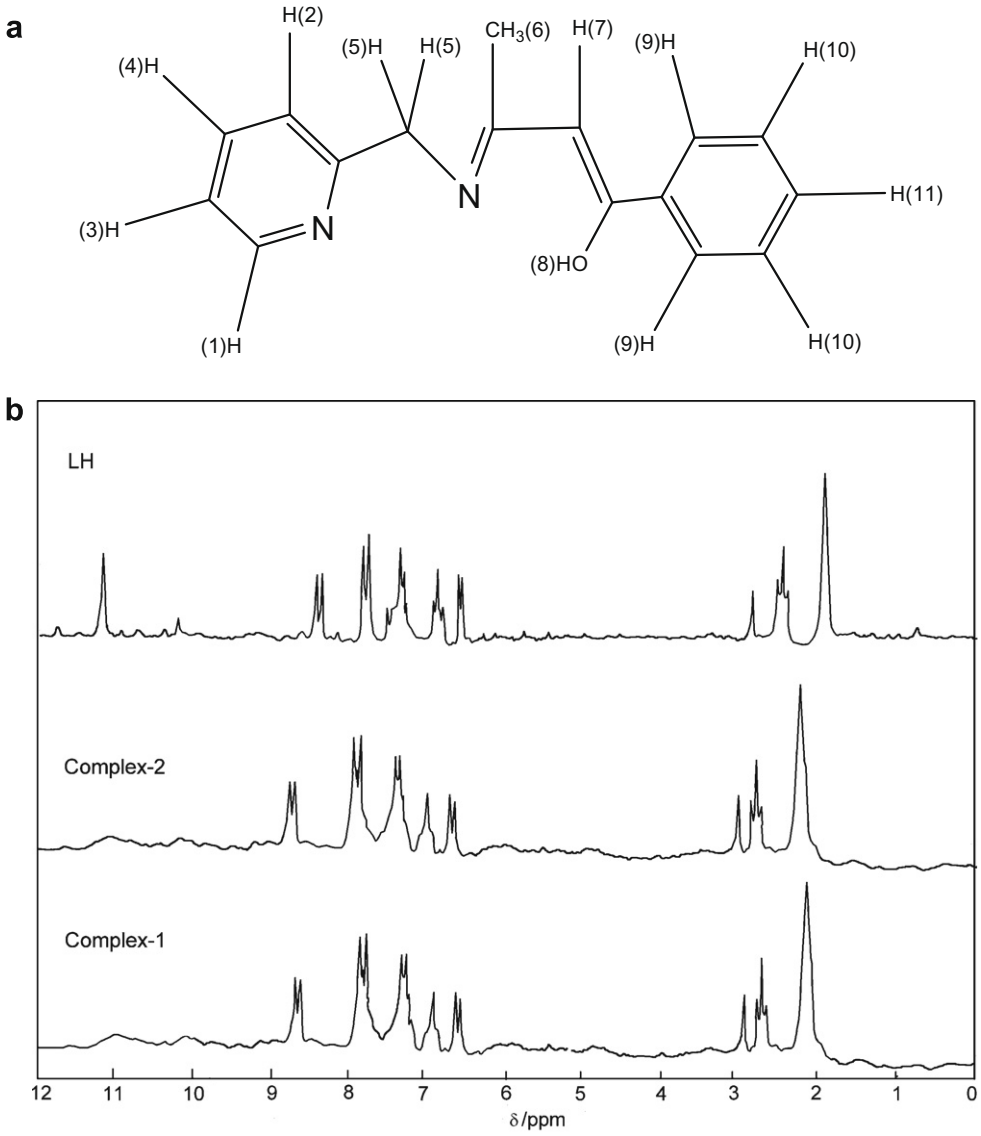


Fig. 3. (a) NMR proton numbering scheme of **LH**. (b) NMR spectra of the Schiff base ligand [**LH**] and the complexes **1**, **2**.

~0.04 ppm, in **1** and **2**, respectively), indicating the coordination of the imine N to the metal center. In the free ligand, the hydrogen atoms of the pyridine ring are deshielded due to the presence of the nitrogen atom in the ring. The ortho and para hydrogen atoms (H1 and H4 respectively) undergo –I and –M effect owing to the nitrogen atom. The –I effect on H1 is greater than that on H4 so H1 is more deshielded than H4 and appears downfield than H4. The meta hydrogen atoms (H2 and H3) undergo only –I effect and –M effect of nitrogen atom is absent hence H2 and H3 appear upfield than H1 and H4. H1 and H4 are shifted significantly downfield (~0.13 ppm and ~0.09 ppm in **1** and **2**, respectively), indicating the coordination of the pyridinium nitrogen to the metal centers [62].

Table 2
NMR data for the ligand **LH** and for complexes **1** and **2**.

Schiff base/ complex	δ (in ppm)
LH	2.0 (3H,s, H6); 2.5 (2H,t, H5); 2.8 (1H,s, H7); 6.85 (1H,d, H2); 7.0 (1H,t, H3); 7.4 (1H,dd, H4); 7.57 (2H,dd, H10); 7.57(1H,t, H11); 7.87 (2H,d, H9); 8.5 (1H,d, H1); 11.3 (1H,s, H8)
1	2.03 (3H,s,H6); 2.54 (2H,t, H5); 2.84 (1H, s, H7); 6.86(1H,d, H2); 7.02 (1H,t, H3); 7.48 (1H,dd, H4); 7.58 (2H,dd, H10); 7.58 (1H,t, H11); 7.88 (2H,d, H9); 8.62 (1H,d, H1)
2	2.04 (3H,s,H6); 2.56 (2H,t, H5); 2.85 (1H, s, H7); 6.87(1H,d, H2); 7.04 (1H,t, H3); 7.49 (1H,dd, H4); 7.59 (2H,dd, H10); 7.59 (1H,t, H11); 7.89 (2H,d, H9); 8.63 (1H,d, H1)

3.3. Electronic spectra

UV–Vis spectra of the ligand and the complexes have been recorded at 300 K in HPLC grade acetonitrile solution. The electronic spectra of the free ligand [**LH**] shows two intraligand charge transfer (CT) bands at 331 nm and 248 nm but for **1** and **2** three different CT bands at 407, 307, 276 nm and 412, 322, 255 nm are observed respectively. In **1** and **2** the bands obtained at 307, 276 nm and 322, 255 nm are assigned to L → L charge transfer transitions but since the spectrum of the free ligand lacks CT bands in the region 407–422 nm hence it can be concluded that in **1** and **2** the CT bands obtained at 407 and 422 nm are associated with the L → M charge transfer transitions. In comparison to the spectrum of the

free ligand, much weaker and less well defined broad bands are found at 602 and 650 nm in the respective complexes and are assigned to d–d transitions. The d–d transition at 602 nm for **1** is attributed to structurally well characterised square planar copper(II) complex, whereas the d–d bands near 650 nm for **2** are more consistent with copper(II) complex with square pyramidal geometry [63].

3.4. Cyclic voltammetry

Electrochemical properties of **1** and **2** have been studied in HPLC grade acetonitrile medium with tetrabutylammonium perchlorate as supporting electrolyte at a scan rate of 50 mVs^{-1}. During the cathodic scan **1** shows a reductive response at −0.283 V versus SCE, which is assigned to the Cu(II) → Cu(I) reduction and during the anodic scan it shows an oxidative response at +0.587 V versus SCE assigned to the Cu(I) → Cu(II) oxidation. These reduction and oxidation are irreversible, characterised by a peak to peak separation (ΔE_p) of 294 mV, which remains unchanged upon changing the scan rate. For **2** two irreversible reductive responses at −0.06 V versus SCE and −0.751 V versus SCE are observed during the cathodic scan which are assigned to the Cu(II) → Cu(I) reductions. The first reductive response at −0.06 V may be assigned to the reduction of one copper(II) center which is followed by a successive reduction (−0.751 V) of the adjacent copper(II) center via the bridging ligands. Similarly during the anodic scan, two metal centered irreversible oxidative responses at +0.21 V and +0.52 V versus SCE are observed which are assigned to the Cu(I) → Cu(II) oxidations of the adjacent copper centers.

3.5. Description of the crystal structure

3.5.1. [CuLCl] (*1*)

The structure of **1** consists of a neutral copper(II) monomer with the metal center residing in a distorted square planar environment surrounded by two nitrogen atoms, one deprotonated oxgyen atom of the tridentate N_2O donor Schiff base ligand and a terminal chloride ion of the precursor metal salt (Fig. 4). In **1** the pyridine nitrogen atom is located in *trans* to the deprotonated enolato oxygen of the Schiff base ligand whereas the imine nitrogen atom of $[\mathbf{L}]^-$ and the chlorine atom occupy the other trans pair. The distortion from the square planar geometry of the copper(II) center is evident from the bond lengths and bond angles (Table 3). The Cu-Cl bond length (2.258(1) Å) is significantly longer than the Cu–N and Cu–O ones (in the range 1.908(3)-2.000(3) Å) and the bond angles

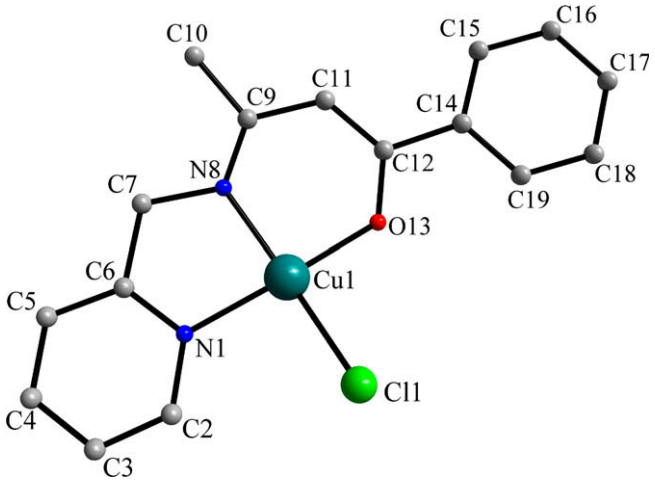


Fig. 4. Mononuclear unit of **1** with the atom labelling scheme.

Table 3
Bond lengths (Å) and angles (°) around the copper centres in **1** and **2**.

1		**2**	
Bond lengths (Å)			
Cu1–Cl1	2.258 (1)	Cu1–O28	2.790 (4)
Cu1–N8	1.943 (3)	Cu1–N11	1.970 (3)
Cu1–O13	1.908 (3)	Cu1–O28	1.912 (2)
Cu1–N1	2.000 (3)	Cu1–N32	1.935 (3)
–	–	Cu1–N39	1.988 (3)
–	–		
Bond angles (°)			
Cl1–Cu1–N1	94.6 (1)	O28–Cu1–N11	82.2 (2)
Cl1–Cu1–N8	166.4 (1)	O28–Cu1–O28	84.4 (1)
N1–Cu1–N8	83.3 (1)	N11–Cu1–O28	87.7 (2)
Cl1–Cu1–O13	90.84 (9)	O28–Cu1–N32	106.5 (1)
N1–Cu1–O13	170.1 (1)	N11–Cu1–N32	171.3 (1)
N8–Cu1–O13	93.3 (1)	O28–Cu1–N32	93.4 (1)
–	–	O28–Cu1–N39	94.9 (1)
–	–	N11–Cu1–N39	95.2 (2)
–	–	O28–Cu1–N39	176.9 (1)
–	–	N32–Cu1–N39	83.8 (1)

deviate from the ideal values (the *trans* angles are in the range 166.4(1)–170.1(1)° and the *cis* angles are in the range 83.3–94.6°). As a consequence of the distortion the copper(II) center, the pyridine nitrogen and the enolato oxygen lie 0.045, 0.195 and 0.192 Å, respectively, below the average plane whereas the imine nitrogen and the terminal chlorine atom lie 0.216 and 0.171 Å above the mean plane. The most significant distortion is associated with the chlorine atom, which is 0.524(1) Å away from the (Cu1, N1, N8, O13) plane. Complex **1** does not show any intramolecular nor intermolecular hydrogen bonding interactions. The chelate bite angles in the five-membered and the six-membered rings formed by the coordination of pyridine-N and the imine-N, and enolato-O and imine-N of the tridentate Schiff base $[\mathbf{L}]^-$ are 83.27° and 93.31° respectively. Both of these five and the six-membered chelate rings formed due to the coordination of the N1, N8 and O13 atoms of the tridentate Schiff base to the copper(II) center lie in the same plane and are almost parallel to the two aromatic rings of $[\mathbf{L}]^-$ with a dihedral angle of 2.76°. The structure packing can be described as monomer columns running along the *a*-axis (Fig. 5). Inside the columns, the monomeric complexes are shifted with an angle of 180° whereas between two neighbour columns, the complexes are shifted with an angle of 43.0(2)° in the *c*-direction (Fig. 6) and are parallel along the *b*-direction.

3.5.2. $\{[Cu_2(\mu\text{-}L)_2(\mu_2\text{-}1,5\text{-}(CN)_2N)]ClO_4\}_n$ (*2*)

The asymmetric unit constructing 1D polymeric architecture of **2** is shown in Fig. 7. The bond lengths and bond angles around the copper (II) centres are given in Table 3. The asymmetric unit of **2** consists of a crystallographic independent copper(II) center, one unit of deprotonated Schiff base ligand $[\mathbf{L}]^-$, one dca $[N(CN)_2]^-$ and one perchlorate counter anion. The asymmetric unit indicates the presence of two different bridging moieties in **2**. Compared to **1**, the deprotonated enolato oxygen of $[\mathbf{L}]^-$ shows a different coordinating behaviour since now it bridges two adjacent asymmetric units in **2** to generate a centrosymmetric dimeric structure. These dimers are further connected to adjacent dimers by *end-to-end* dicyanamide bridges to generate a 1D polymeric chain in **2** (Figs. 8 and 9). The copper(II) centers in the centrosymmetric dimeric units are located in a five-coordinated environment bonded to three coordinating N_2O donor atoms of the tridentate Schiff base ligand $[\mathbf{L}]^-$, one enolato oxygen of the other unit of $[\mathbf{L}]^-$ and a nitrile nitrogen atom of the μ_2-1,5 bridging dicyanamide anion. The charge balance is achieved by the insertion of perchlorate anions in the [(101); *b*] planes, between the cationic chains of **2** (Fig. 10). The chelate bite angles in the five- and six-membered

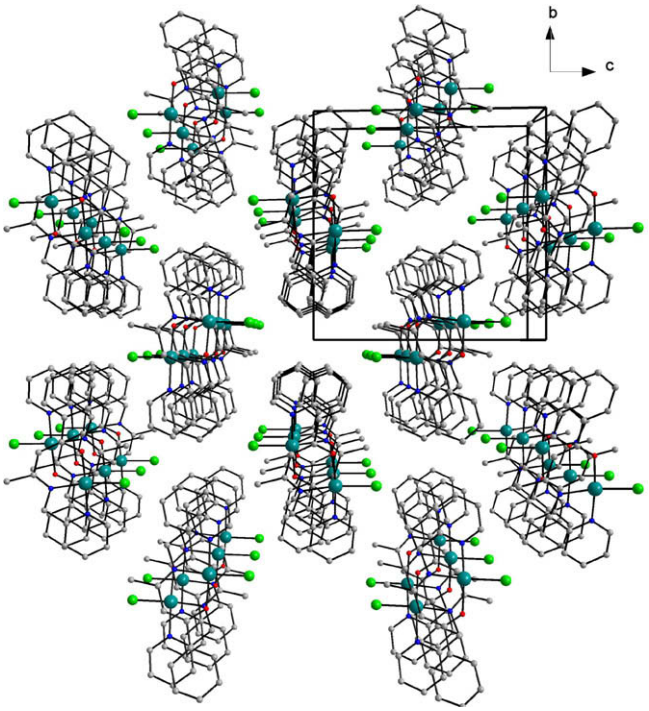


Fig. 5. Packing diagram of **1** showing the monomer columns running along the *a*-axis.

rings formed by the coordination of the pyridine-N and the imine-N, the enolato-O and the imine-N of the tridentate Schiff base $[\mathbf{L}]^-$ are 83.82° and 93.42° respectively and are very close to that of **1**. The geometry of the each copper(II) center is very close to square pyramidal with $\tau = 0.094$, $[\tau = |\beta - \alpha|/60°]$, where β and α are the two largest angles around the central atom; $\tau = 0$ and 1 for the perfect square pyramidal and trigonal bipyramidal geometries, respectively [64]. The square base of each copper(II) center is formed by the pyridyl and imine nitrogen atoms, an enolate oxygen of the tridentate Schiff base ligand $[\mathbf{L}]^-$ and a nitrile nitrogen of the μ_2-1,5 bridging dicyanamide anion. All the equatorial bond lengths are similar (in the range 1.912(2)–1.988(3) Å, Table 3) and much shorter than the axial Cu–O bond distance

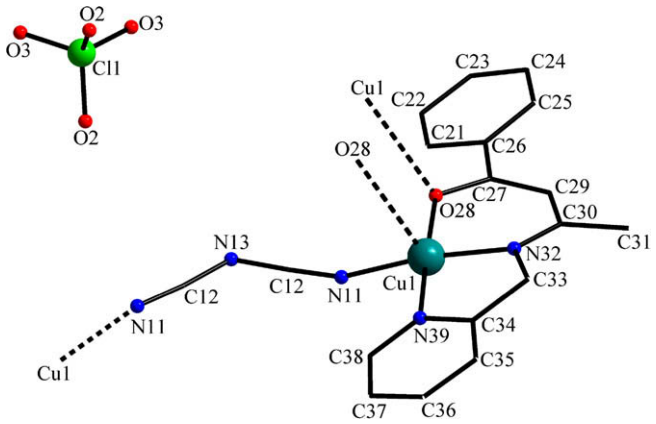


Fig. 7. Asymmetric unit of **2** with the atom labelling scheme.

(2.790(4) Å), in good agreement with those previously reported in the literature. The bridging enolato oxygen atom connects the copper(II) centers of two adjacent $[CuL(CN)_2N]$ independent units in an asymmetric (basal-apical) fashion with two very different bond distances (1.912(2) and 2.790(4) Å, $\Delta d = 0.878$ Å). The Cu1–O28–Cu1 bridging angle in **2** is 95.63° and the Cu1···Cu1 separation inside a dimer is equal to 3.533(3) Å. The other Cu···Cu distances inside the cationic chains are equal to 7.942(9) Å and 8.422(8) Å and are in the same range as those observed between chains (8.374(3) Å and 8.604 (6) Å). The copper(II) atoms in **2** show a displacement of 0.063 Å from the basal plane towards the axially coordinated enolato oxygen constituting the apex of the pyramid. There are no interchain H-bonding interactions in **2**.

3.6. Magnetic study

Room temperature magnetic moment of the mononuclear copper(II) Schiff base precursor complex was recorded for a polycrystalline sample at 30 °C. The $\mu_{effective}$ value was found to be equal to 1.76 BM, which is in excellent agreement with the theoretical value (1.797 BM) for one unpaired electron in magnetically dilute copper(II) complexes. Variable temperature magnetic susceptibility studies of **1** have not been measured as its structural characterisation shows that it is a well isolated copper(II) mononuclear

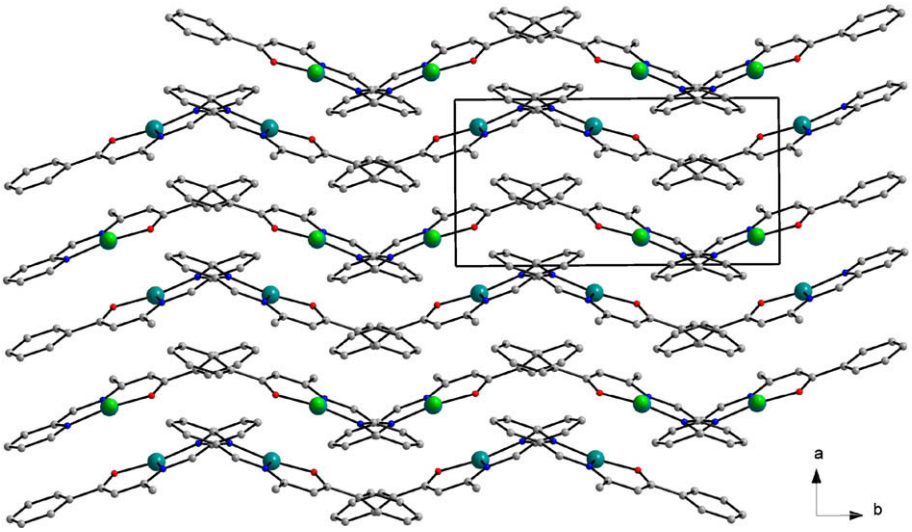


Fig. 6. Packing diagram of **1** showing the orientation of the neighbouring mononuclear units along *c*-axis.

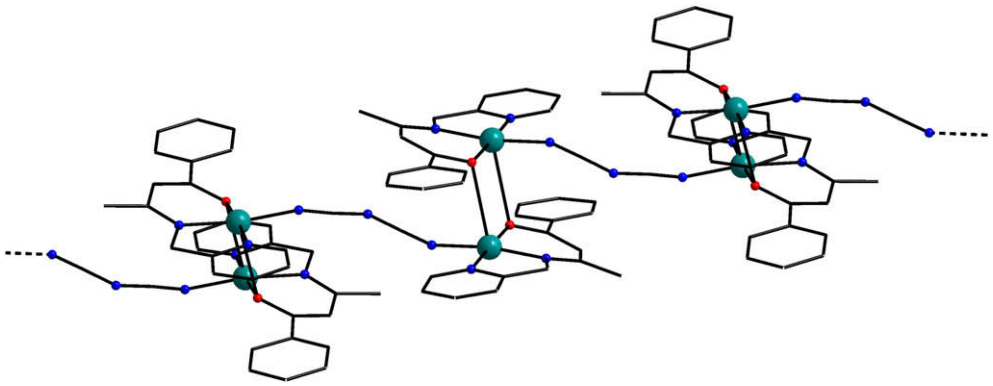


Fig. 8. 1D polymeric chain structure of **2**.

species and therefore, it is expected to show a paramagnetic behavior.

The product of the molar susceptibility times the temperature ($\chi_m T$) for compound **2** shows a room temperature value of ca. 0.80 emu K mol^{-1} (per two copper(II) ions), in agreement with the expected value for two non interacting copper(II) ions ($S = 1/2$). When the temperature is decreased, the $\chi_m T$ product remains constant down to ca. 50 K. Below this temperature the $\chi_m T$ product shows a progressive rounded decrease to reach a value of ca. 0.54 emu K mol^{-1} at 2 K. This behavior indicates that **2** presents a weak, although noticeable, antiferromagnetic coupling.

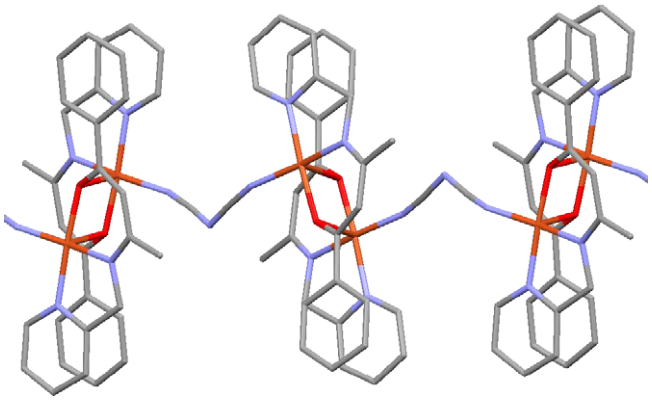


Fig. 9. Projection of the 1D polymeric chain structure of **2** along the *a*-axis.

Since the structure of compound **2** shows the presence of two alternating types of bridges: a dicyanamide bridge and a double (although long) oxo bridge, there are three possible magnetic exchange schemes: (1) A dicyanamide-bridged copper(II) dimmer, if the double long oxo bridges do not contribute to the magnetic exchange, (2) a doubly oxo-bridged copper(II) dimer, if the contribution of the dicyanamide bridge is negligible and (3) an alternating S = 1/2 chain, if both bridges contribute to the magnetic exchange. Accordingly, we have fit the magnetic behavior to the two possible different models: (i) the simple Bleaney–Bowers dimer model for $S = 1/2$ ions (cases 1 and 2) [65] and the alternating $S = 1/2$ chain model of Hatfield et al. (case 3) [66].

The dimer model reproduces quite satisfactorily the magnetic behavior of **2** in the whole temperature range with the following parameters (dotted line in Fig. 11): $g = 2.0532(5)$ and $J = -1.53(1)\,\mathrm{cm}^{-1}$ (the Hamiltonian is written as $H = -JS_1S_2$). Nevertheless, a closer look at the low temperature region (inset in Fig. 11), shows that the low temperature rounded decrease at low temperatures is not perfectly reproduced. The second model used (the alternating $S = 1/2$ chain) reproduces very satisfactorily the magnetic properties of **2** in the whole temperature range (solid line in Fig. 11) with the following parameters: $g = 2.0701(8)$, $J = -1.12(1)\,\mathrm{cm}^{-1}$ and $J' = -1.62(1)\,\mathrm{cm}^{-1}$ ($\alpha = J'/J = 1.43(1)$) (the Hamiltonian is written as $H = -JS_1S_2$). As can be seen in the inset in Fig. 11, this model reproduces much better the rounded decrease at low temperatures, as well as the high temperatures region, sug-

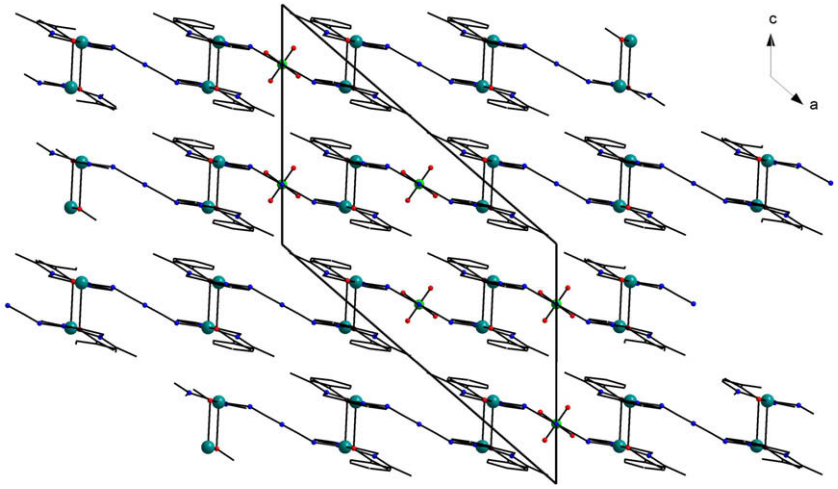


Fig. 10. Projection of **2** along the *b*-axis of the unit-cell showing the 1D parallel cationic chains and the perchlorate counter-ions.

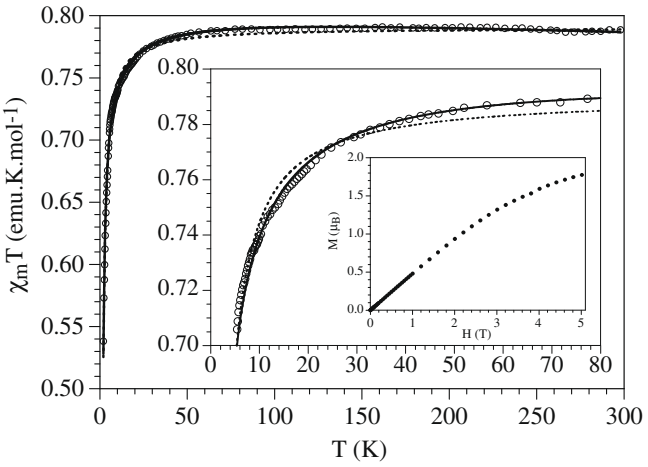


Fig. 11. Thermal variation of the $\chi_m T$ product for 2. Dotted and solid lines are the best fit to the dimer and alternating chain models (see text). Insets show the low temperature region and the isothermal magnetization at 2 K.

gesting that both bridges are operative in the magnetic exchange scheme. Although the assignment of the obtained J values to the two different bridges is not straightforward, the very weak exchanges usually found in dicyanamide bridges (in the range -0.44 to $0.20\ cm^{-1}$ [59,67–73]), suggests that the lower J value ($J = -1.12\ cm^{-1}$) might correspond to the dicyanamide bridge, whereas the higher J value ($J' = -1.62\ cm^{-1}$) would correspond to the double oxo bridge.

Even with this assignment, the dicyanamide exchange coupling found in **2** is slightly higher than those found in other dicyanamide-bridged copper(II) complexes. This fact may be explained from two main structural features: (1) the dicyanamide ligand occupies equatorial positions in both copper(II) ions and (2) the equatorial planes of the copper(II) ions connected through the dicyanamide bridge are almost parallel and also parallel to the dicyanamide plane. Thus, the angles between the dicyanamide plane and the average copper(II) equatorial planes are 16.69 and 16.71°. These two features enable a bigger overlap of the magnetic $d_{x^2-y^2}$ orbitals (that are parallel to the equatorial planes), giving rise to a stronger antiferromagnetic coupling. In fact, the dca-bridged examples with higher magnetic coupling are those where the dca ligand links two equatorial positions [73].

A further confirmation of this weak antiferromagnetic coupling comes from the isothermal magnetization at 2 K which is not saturated at 5 T and shows a value below the expected one (ca. 2 μ_B) (inset in Fig. 11).

4. Conclusions

A novel Schiff base ligand (**LH**) has been prepared by the 1:1 condensation of benzoylacetone with 2-picolylamine. This Schiff base ligand shows a different coordinating behavior towards the copper(II) ions when it is used alone or in presence of dicyanamide ligand. Thus, a mononuclear [CuLCl] (**1**) and an *end-to-end* dicyanamide bridged polynuclear $\{[Cu_2(\mu\text{-}L)_2(\mu_2\text{-}1,5\text{-}(CN)_2N)]ClO_4\}_n$ (**2**) complexes have been prepared and structurally characterised. The magnetic properties of compound **2** have been very well reproduced with an alternating antiferromagnetic $S = 1/2$ chain model that confirm the presence of weak antiferromagnetic exchange interactions in the chain. A comparative study of the dca bridges in **2** and in other dca bridged copper(II) complexes has allowed an assignation of the exchange constants. This assignment shows that the exchange constant in **2** is higher than in other dca bridged copper(II) complexes. This relatively high antiferromagnetic coupling observed in the dca bridges is due to the occupancy of the equatorial positions by the dca ligand in both copper(II) environments and the almost parallel disposition of the equatorial copper(II) and the dca planes.

Acknowledgements

A. Ray is thankful to the Department of Science and Technology, New Delhi, Govt. of India, Council of Scientific and Industrial Research, New Delhi, Govt. of India and All India Council for Technical Education, New Delhi, Govt. of India for financial support. We also thank the European Union for financial support (MAGMANet network of excellence) and the Spanish Ministerio de Educacióny Ciencia (Projects MAT2007-61584 and Consolider-Ingenio 2010 CSD 2007-00010 in Molecular Nanoscience).

Appendix A. Supplementary data

CCDC 664112 and 664109 contain the supplementary crystallographic data for **1** and **2**. These data can be obtained free of charge via http://www.ccdc.cam.ac.uk/conts/retrieving.html, or from the Cambridge Crystallographic Data Centre, 12 Union Road, Cambridge CB2 1EZ, UK; fax: (+44) 1223-336-033; or e-mail: deposit@ccdc.cam.ac.uk. Supplementary data associated with this article can be found, in the online version, at doi:10.1016/j.poly.2008.11.054.

References

[1] C.O. Rodriguez de Barbarin, N.A. Bailey, D.E. Fenton, Q.-Y. He, J. Chem. Soc., Dalton Trans. (1997) 161.
[2] E.J. Larson, V.L. Pecoraro, J. Am. Chem. Soc. 113 (1991) 3810.
[3] M.M. Taqui Khan, D. Srinivas, R.I. Kureshi, N.H. Khan, Inorg. Chem. 29 (1990) 2320 (and references therein).
[4] H. Miyasaka, H. Ieda, N. Mastumoto, R. Crescenzi, C. Floriani, Inorg. Chem. 37 (1998) 255.
[5] I. Ramade, O. Khan, Y. Jennin, F. Robert, Inorg. Chem. 36 (1997) 930.
[6] D. Wohrle, Adv. Polym. Sci. 50 (1983) 45.
[7] N. Hoshino, Coord. Chem. Rev. 174 (1998) 77;
L. Canali, D.C. Sherrington, Chem. Soc. Rev. 28 (1999) 85.
[8] R.H. Holm, G.W. Everett Jr., A. Chakravarty, Prog. Inorg. Chem. 7 (1967) 83.
[9] Y.Y. Chen, D.E. Chu, B.D. McKinney, L.J. Willis, S.E. Cummings, Inorg. Chem. 20 (1981) 1885.
[10] W.M. Coleman, L.T. Taylor, J. Inorg. Nucl. Chem. 42 (1980) 683.
[11] P. Talukder, A. Datta, S. Mitra, G. Rosair, M.S. El Fallah, J. Ribas, Dalton Trans. (2004) 4161.
[12] A. Datta, C.R. Choudhury, P. Talukder, S. Mitra, L. Dahlenburg, T. Matsushita, J. Chem. Res. (2003) 642.
[13] S. Sen, P. Talukder, S.K. Dey, S. Mitra, G. Rosair, D.L. Hughes, G.P.A. Yap, G. Pilet, V. Gramlich, T. Matsushita, Dalton Trans. (2006) 1758.
[14] S.K. Dey, B. Bag, K.M. Abdul Malik, M.S. El Fallah, J. Ribas, S. Mitra, Inorg. Chem. 42 (2003) 4029.
[15] C.R. Choudhury, S.K. Dey, R. Karmakar, C.-D. Wu, C.-Z. Lu, M.S. El Fallah, S. Mitra, New J. Chem. (2003) 1360.
[16] S. Sen, S. Mitra, D.L. Hughes, G. Rosair, C. Desplanches, Polyhedron 26 (2007) 1740.
[17] J. Chakraborty, G. Pilet, M.S.El. Fallah, J. Ribas, Samiran Mitra, Inorg. Chem. Commun. 10 (2007) 489.
[18] E.A. Mauro, I.S. Klein, A.C. Saldana, D. Simone, J. Zukerman-Schpector, E.E. Castellano, Polyhedron 9 (1990) 2937.
[19] R. Vicente, A. Escuer, E. Penalba, X. Solans, M. Font-Badia, J. Chem. Soc., Dalton Trans. (1994) 3005.
[20] A. Ray, S. Banerjee, R.J. Butcher, C. Desplanches, S. Mitra, Polyhedron 27 (2008) 2409.
[21] S. Banerjee, A. Ray, S. Sen, S. Mitra, D.L. Hughes, R.J. Butcher, S.R. Batten, D.R. Turner, Inorg. Chim. Acta 361 (2008) 2692.
[22] J. Ribas, M. Monfort, I. Resino, X. Solans, P. Rabu, F. Maingot, M. Drillan, Angew. Chem., Int. Ed. Engl. 35 (1996) 2520.
[23] G. De Munno, M. Julve, G. Viau, F. Lloret, J. Faus, D. Viterbo, Angew. Chem., Int. Ed. Engl. 35 (1996) 1807.
[24] M. Monfort, J. Ribas, X. Solans, Inorg. Chem. 33 (1994) 4271.
[25] R. Vicente, A. Escuer, J. Ribas, X. Solans, J. Chem. Soc., Dalton Trans. (1994) 259.
[26] J. Ribas, C. Diaz, X. Solans, M. Font-Bardia, J. Chem. Soc., Dalton Trans. (1997) 35.
[27] J. Ribas, C. Diaz, R. Costa, X. Tercero, X. Solans, M. Font-Bardia, Inorg. Chem. 37 (1998) 233.
[28] I. Dasna, S. Golhen, L. Ouahab, N. Daro, J.P. Sutter, New J. Chem. 25 (2001) 1572.

[29] S.R. Batten, P. Jensen, B. Moubaraki, K.S. Murray, R. Robson, Chem. Commun. (1998) 439.
[30] M. Kurmoo, C.J. Kepert, New J. Chem. 22 (1998) 1515.
[31] P. Jensen, S.R. Batten, B. Moubaraki, K.S. Murray, Chem. Commun. (2000) 793.
[32] S.R. Batten, K.S. Murray, Coord. Chem. Rev. 246 (2003) 103.
[33] D. Ghoshal, A.D. Jana, T.K. Maji, G. Mostafa, Inorg. Chim. Acta 359 (2006) 690 (and references therein).
[34] S. Banerjee, S. Sen, S. Basak, S. Mitra, D.L. Hughes, C. Desplanches, Inorg. Chim. Acta 361 (2008) 2707.
[35] S. Sen, S. Mitra, D.L. Hughes, G. Rosair, C. Desplanches, Inorg. Chim. Acta 360 (2007) 4085.
[36] M. Biswas, G. Pilet, M.S. El Fallah, J. Ribas, S. Mitra, Inorg. Chim. Acta 361 (2008) 387.
[37] R. Karmakar, C.R. Choudhury, D.L. Hughes, G.P.A. Yap, M.S. El Fallah, C. Desplanches, J.-P. Sutter, S. Mitra, Inorg. Chim. Acta 359 (2006) 1184.
[38] C.T. Brewer, G. Brewer, J. Chem. Soc. Chem. Commun. (1988) 85.
[39] T. Nagahara, M. Suzuki, K. Kasuga, Inorg. Chim. Acta 149 (1988) 279.
[40] N. Matsumoto, S. Yamashita, A. Ohyoshi, S. Kohata, H. Okawa, J. Chem. Soc., Dalton Trans. (1988) 1943.
[41] M. Kwiatkowski, E. Kwiatkowski, A. Olechnowiez, D.M. Ho, E. Deutsch, J. Chem. Soc., Dalton Trans. (1990) 3063.
[42] B. Sarkar, G. Bocelli, A. Cantoni, A. Ghosh, Polyhedron 27 (2008) 693 (and references therein).
[43] E. Kwiatkowski, M. Kwiatkowski, Inorg. Chim. Acta 82 (1984) 101.
[44] M. Kwiatkowski, E. Kwiatkowski, A. Olechnowiez, D.M. Ho, E. Deutsch, Inorg. Chim. Acta 150 (1988) 65.
[45] N.N. Matsumoto, T. Akui, H. Murakami, J. Kanesaka, A. Ohyoshi, H. Okawa, J. Chem. Soc., Dalton Trans. (1988) 1021.
[46] S. Chattopadhyay, M.S. Ray, S. Chaudhuri, G. Mukhopadhyay, G. Bocelli, A. Cantoni, A. Ghosh, Inorg. Chim. Acta 359 (2006) 1367 (and references therein).
[47] J.P. Costes, F. Dahan, J.P. Laurent, Inorg. Chem. 25 (1986) 413.
[48] J.P. Costes, F. Dahan, J. Ruiz, J.P. Laurent, Inorg. Chim. Acta 239 (1995) 53.
[49] H.-D. Bian, J.-Y. Xu, W. Gu, S.-P. Yan, P. Cheng, D.-Z. Liao, Z.-H. Jiang, Polyhedron 22 (2003) 2927.
[50] P. Talukder, A. Datta, S. Mitra, G. Rosair, Z. Naturforsch 59b (2004) 655.
[51] S. Basak, S. Sen, S. Mitra, C. Marschner, W.S. Sheldrick, Struct. Chem. 19 (2008) 115.
[52] S.K. Dey, C.R. Choudhury, S.P. Dey, D.K. Dey, N. Mondal, S.O.G. Mahalli, K.M.A. Malik, S. Mitra, J. Chem. Res. (S) (2002) 496.
[53] J.J. Klappa, A.E. Rich, K. McNeill, Org. Lett. 4 (2002) 435.
[54] NONIUS, Kappa CCD Program Package: COLLECT, DENZO, SCALEPACK, SORTAV, Nonius B.V., Delft, The Netherlands, 1999.
[55] J. de Meulenaar, H. Tompa, Acta Crystallogr., Sect. A 19 (1965) 1014.
[56] R.H. Blessing, Acta Crystallogr., Sect. A 51 (1995) 33.
[57] G. Cascarano, A. Altomare, C. Giacovazzo, A. Guagliardi, A.G.G. Moliterni, D. Siliqi, M.C. Burla, G. Polidori, M. Camalli, Acta Crystallogr., Sect. A 52 (1996) C-79.
[58] D.J. Watkin, C.K. Prout, J.R. Carruthers, P.W. Betteridge, CRYSTALS, Chemical Crystallography Laboratory, Oxford, UK, 1999, Issue 11.
[59] B. Vangdal, J. Carranza, F. Lloret, M. Julve, J. Sletten, J. Chem. Soc., Dalton Trans. (2002) 566 (and references therein).
[60] M. Dolaz, M. Tümer, M. Diğrak, Transition Met. Chem. 29 (2004) 528.
[61] K. Nakamoto, Infrared and Raman Spectra of Inorganic and Coordination Compounds, fifth ed., vol. 23, Wiley, New York, 1997.
[62] W. Kemp, Organic Spectroscopy, third ed., Palgrave Publishers, 1991.
[63] A.B.P. Lever, Inorganic Electronic Spectroscopy, Elsevier, Amsterdam, 1984. p. 553.
[64] A.W. Addison, T.N. Rao, J. Reedijk, J. van Rijn, G.C. Verschoor, J. Chem. Soc., Dalton Trans. (1984) 1349.
[65] B. Bleaney, K.D. Bowers, Proc. Roy. Soc. London Ser. A 214 (1952) 451.
[66] J.W. Hall, W.E. Marsh, R.R. Weller, W.E. Hatfield, Inorg. Chem. 20 (1981) 1033.
[67] P. Misra, C.-Y. Liao, H.-H. Wei, S. Mohanta, Polyhedron 27 (2008) 1185.
[68] M. Du, X.-J. Zhao, S.R. Batten, J. Ribas, Cryst. Growth Des. 5 (2005) 901 (and references therein).
[69] J.L. Manson, J. Gu, J.A. Schlueter, H.-H. Wang, Inorg. Chem. 42 (2003) 3950.
[70] P. Jensen, D.J. Price, S.R. Batten, B. Moubaraki, K.S. Murray, Chem. Eur. J. 6 (2000) 3186.
[71] H.J. Luo, M.C. Hong, J.B. Weng, J.Y. Zhao, R. Cao, Inorg. Chim. Acta 329 (2002) 59.
[72] W. Gu, H.-D. Bian, J.-Y. Xu, Z.-Q. Liu, P. Cheng, S.-P. Yan, D.-Z. Liao, Z.H. Jiang, Inorg. Chem. Commun. 6 (2003) 966.
[73] J. Carranza, C. Brennan, J. Sletten, F. Lloret, M. Julve, J. Chem. Soc., Dalton Trans. (2002) 3164.

Polyhedron 28 (2009) 521–524

Contents lists available at ScienceDirect

Polyhedron

journal homepage: www.elsevier.com/locate/poly

QTAIM study of transition metal complexes with cyclophosphazene-based multisite ligands I: Zinc(II) and nickel(II) complexes

Marián Gall, Martin Breza *

Department of Physical Chemistry, Slovak Technical University, SK-812 37 Bratislava, Slovakia

ARTICLE INFO

Article history:
Received 7 August 2008
Accepted 28 November 2008
Available online 3 January 2009

Keywords:
Electron structure
Quantum theory of atoms-in-molecule
Phosphazene
Pyridine
Coordination compounds

ABSTRACT

The metal–ligand bonds in $[(ZnCl_2)_2L]$, $[NiLCl]^+$ and two isomers of $[NiLCl_2]$ complexes with multimodal ligand L = hexakis(2-pyridyloxy)cyclotriphosphazene, cyclo-$[NP(NC_5H_4O)_2]_3$, are investigated at DFT level of theory using hybrid B3LYP functional. Electron density is evaluated in terms of QTAIM (quantum theory of atoms-in-molecule) topological analysis of electron density. The bonds of central transition metal atoms with phosphazene nitrogens are shorter, stronger and more polar than with the aromatic pyridine nitrogens. The atomic charges of phosphazene nitrogens are ca twice more negative than at the pyridine ones. The higher mechanical strain in the five-coordinate metal complexes than in the six-coordinate ones may be concluded.

© 2008 Elsevier Ltd. All rights reserved.

1. Introduction

Cyclophosphazenes, cyclo-$(NPX_2)_n$, are an important family of inorganic ring systems. Their heterocyclic rings are particularly well-suited for being used as scaffolds or platforms for the construction of multisite coordination ligands [1]. The phosphazene backbone consists of alternating phosphorus and nitrogen atoms with formally alternating single and double P–N bonds. X-ray crystal structure analysis of cyclic phosphazenes imply that all P–N distances in the cyclophosphazene ring are equal [2–4].

The old "island model" [5,6] describes the bonding between the phosphorus and nitrogen atoms in terms of σ bonding and additional (out-of-plane and in-plane) π bonding arising from the overlap of 3d orbitals of the phosphorus with nitrogen 2p orbitals being combined into sets of three-centre π molecular orbitals ('islands' of electron density over P–N–P units with nodes at the phosphorus centres). Each nitrogen is attached by equally strong π bonds to both neighboring phosphorus atoms. However, the group-theoretical analysis of molecular orbitals in planar cyclophosphazenes of D_{nh} symmetry with odd n [7,8] excludes any d(P)–p(N) bonding and it makes this bonding scheme doubtful in other phosphazenes as well.

More recent bonding models [9–11] are based on prevailingly ionic P–N bonding (involving substantial charge transfer from phosphorus to nitrogen) with negative hyperconjugation contributions resulting from the donor-acceptor interactions of (out-of-plane and in-plane) nitrogen lone pairs into strongly polarized antibonding σ^*_{PN} and σ^*_{PX} orbitals. The extent of this negative hyperconjugation depends significantly on the nature of the X substituents on phosphorus atoms. Unequal negative hyperconjugation contributions provide a previously lacking and compelling explanation for the P–N bond length alternation observed in some linear polyphosphazenes.

The ring nitrogen atoms of cyclophosphazenes have sufficient basicity and can interact with Lewis acids [1]. The Lewis basicity of these ring nitrogen atoms can be modulated by the proper choice of substituents on phosphorus atoms. Relying on the ring nitrogen basicity of cyclophosphazenes as the sole ingredient of ligand design severely restricts the utility of these ring systems as ligands. On the other hand, additional coordination sites may be provided on the cyclophosphazene phosphorus substituents which facilitate binding of the metal ion to the less basic phosphazene ring nitrogen atoms.

Pyridyloxycyclophosphazenes are multisite coordination ligands [1], where the coordinating pyridine ligand is attached to the phosphorus atom of the cyclophosphazene ring by means of a "spacer" oxygen atom. Almost in all cases, the cyclophosphazene ring remains planar. This is in contrast to the situation found for other cyclophosphazene ligands such as pyrazolylcyclophosphazenes, where the ring undergoes puckering upon coordination. The planar cyclophosphazene geometry found in the metal complexes of pyridyloxycyclophosphazenes is probably due to the flexible oxygen spacer that separates the pyridyl group from the cyclophosphazene ring and allows a *strainfree* coordination to the metal ions.

The reactions of hexakis(2-pyridyloxy)cyclotriphosphazene, cyclo-$[NP(NC_5H_4O)_2]_3$, (L) with zinc(II), copper(II), nickel(II) and cobalt(II) halides form a diverse range of five- or six-coordinated

* Corresponding author. Tel.: +421 2 59325 482; fax: +421 2 52493198.
E-mail address: martin.breza@stuba.sk (M. Breza).

0277-5387/$ - see front matter © 2008 Elsevier Ltd. All rights reserved.
doi:10.1016/j.poly.2008.11.043

transition metal complexes which exhibit κ^3N to κ^5N coordination modes where a single cyclophosphazene ring nitrogen atom and two to four pyridyloxy nitrogen atoms are involved [12–15]. Such compounds are very suitable for the comparative studies of the different bonding of these ligands with transition metal ions. The aim of our study is not to describe the bonding in cyclotriphosphazenes which has been published elsewhere [9–11,16]. We will rather focus on the quantum–chemical description of the metal–nitrogen bonding for the nitrogen atoms of aromatic pyridine and non-aromatic phosphazene rings within the same coordination centre. Our results might be important for the utility of cyclophosphazene-based metal complexes in catalytic reactions which remains largely unexplored [1].

2. Method

In the first step, the hydrogen atoms positions in the experimental geometries of the complex compounds under study are optimized by molecular mechanics (MM+ method) [17]. Then, the electronic structure of the complexes is evaluated at DFT level of theory using hybrid B3LYP functional with 6–311G bases for Ni and Zn, 6–31G* bases for P and Cl and 6–31G bases from Gaussian library [18] for the remaining atoms. GAUSSIAN03 software [18] is used for single-point calculations.

The electronic structure of the species under study is investigated using QTAIM (Quantum theory of atoms-in-molecule) topological analysis of electron density [19]. The results are evaluated in terms of atomic volumes V and atomic charges q obtained using the electron density integrated over atomic basins (up to 0.001 e/Bohr^3 level). Bond characteristics are evaluated in terms of electron density ρ, its Laplacian $\nabla^2\rho$

$$\nabla^2\rho = \lambda_1 + \lambda_2 + \lambda_3 \quad (1)$$

and bond ellipticity ε

$$\epsilon = \lambda_1/\lambda_2 - 1 \quad (2)$$

at bond critical points (BCP), where $\lambda_1 < \lambda_2 < 0 < \lambda_3$ are the eigenvalues of the Hessian of the BCP electron density.

d Electron populations on central M atoms, d^x(M), are evaluated in terms of Mulliken population analysis.

AIM200 [20] software packages are utilized for QTAIM analysis of GAUSSIAN03 results. MOLDRAW 2.0 software [21] is used for visualization and geometry manipulation purposes.

3. Results

Using the above mentioned treatment, we have investigated the following transition metal M(II) complexes with hexakis(2-pyridyloxy)cyclotriphosphazene, cyclo-[NP(NC$_5$H$_4$O)$_2$]$_3$, (L) [14]:

(i) The dimetallic neutral complex [(ZnCl$_2$)$_2$L] (model A, see Fig. 1) with five- (κ^3N non-geminal *trans* binding mode of L with the equatorial nitrogen of the phosphazene ring) and four-coordinate (κ^2N geminal binding mode of L without any bond to the phosphazene ring) Zn(II) sites;
(ii) The cationic complex [NiLCl]$^+$ (model B, see Fig. 2) of [NiLCl]PF$_6$ compound with a six-coordinate Ni(II) site (κ^5N tetrapodal binding mode of L);
(iii) The green neutral complex [NiLCl$_2$] (model C, see Fig. 3) with a six-coordinate Ni(II) site (κ^4N tripodal donor binding mode of L);
(iv) The red neutral complex [NiLCl$_2$] (model D, see Fig. 4) with a five-coordinate Ni(II) site (κ^3N non-geminal *trans* binding mode of L with the equatorial nitrogen of the phosphazene ring).

If we denote the metal-bonded nitrogen atoms in cyclotriphosphazene as N' and in pyridine as N, the coordination spheres of individual metal central atoms in the systems under study are summarized in Table 1.

Nickel(II) complexes may be either diamagnetic (singlet spin state) or paramagnetic (triplet spin state). The comparison of total energy data of the systems under study (Table 1) indicate that unlike the expected higher stability of Zn(II) complex A in singlet state (spin multiplicity $M_S = 1$), the triplet state ($M_S = 3$) seems to be more stable for the studied Ni(II) complexes. Due to high sin-

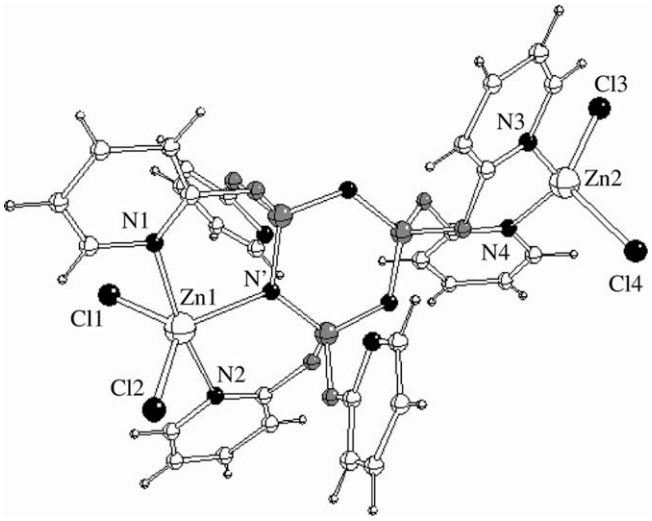


Fig. 1. Structure of [(ZnCl$_2$)$_2$L] complex, L = hexakis(2-pyridyloxy)cyclotriphosphazene cyclo-[NP(NC$_5$H$_4$O)$_2$]$_3$ (model A) [14] with atoms notation (Zn – large white, C – white, H – small white, N – black, Cl – large black, P – large grey and O – grey spheres).

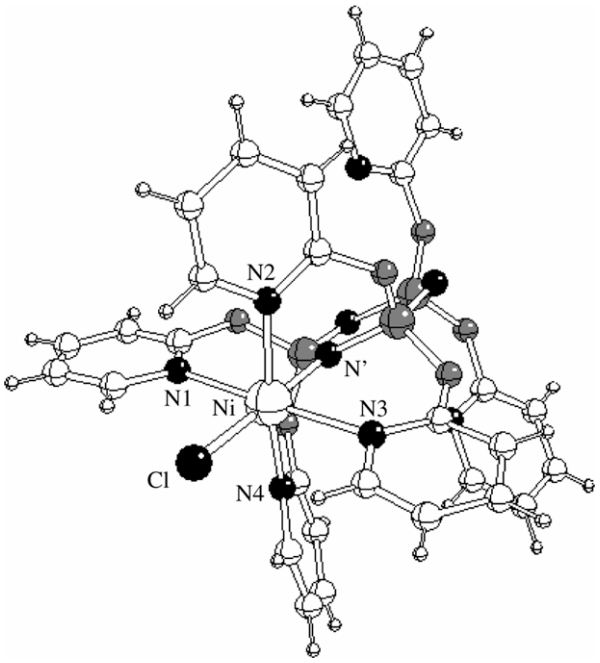


Fig. 2. Structure of [NiLCl]$^+$ complex cation, L = hexakis(2-pyridyloxy) cyclotriphosphazene cyclo-[NP(NC$_5$H$_4$O)$_2$]$_3$ (model B) [14] with atoms notation (Ni – large white, C – white, H – small white, N – black, Cl – large black, P – large grey and O – grey spheres).

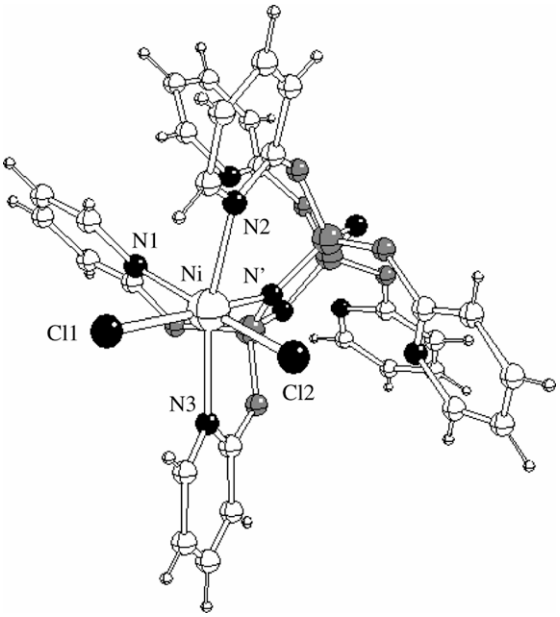


Fig. 3. Structure of green [$NiLCl_2$] complex, L = hexakis(2-pyridyloxy) cyclotriphosphazene cyclo-[$NP(NC_5H_4O)_2]_3$ (model C) [14] with atoms notation (Ni – large white, C – white, H – small white, N – black, Cl – large black, P – large grey and O – grey spheres).

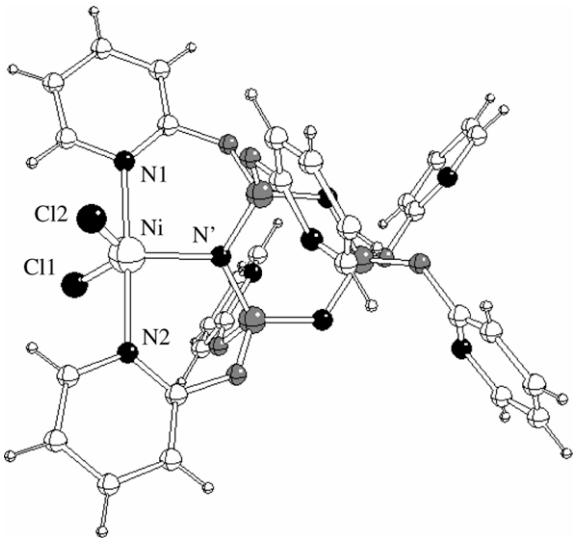


Fig. 4. Structure of red [$NiLCl_2$] complex, L = hexakis(2-pyridyloxy)cyclotriphosphazene cyclo-[$NP(NC_5H_4O)_2]_3$ (model D) [14] with atoms notation (Ni – large white, C – white, H – small white, N – black, Cl – large black, P – large grey and O – grey spheres).

glet–triplet energy separation (over 120 kJ/mol) we will restrict our electronic structure studies to the more stable spin states only.

Our results (Tables 2 and 3) indicate that M–N' bonds with cyclophosphazene nitrogens in all the systems under study are significantly shorter and stronger (higher electron density ρ at BCP) than the M–N ones with pyridine nitrogens at the same M central atom. M–Cl bond strengths decrease much less with bond strengths than the M–N ones. The BCP Laplacians of all metal–ligands bonds are positive as expected, for non-sharing coordination bonding [19]. The higher BCP $\nabla^2\rho$ values of M–N' bonds in comparison with the M–N ones might be explained by their higher polarity (see the atomic charges in Table 3). The shorter metal–nitrogen bonds have higher BCP Laplacians. Except D model, the BCP ellipticity values correspond to σ metal–ligand bonding with small π contribution only. The BCP ε values of M–N' bonds are in most cases higher than the M–N ones and are lower for shorter bonds.

The atomic volumes of central metal atoms decrease with their coordination numbers (Table 3). Phosphazene N' atoms are significantly bigger then the pyridine N atoms. Chlorine atoms taking part in six-coordinate M sites are smaller than in the five-coordinate ones. The phosphazene N' atomic charges are negative and ca twice higher than the pyridine N ones. Chlorine atoms are much less negative. The higher atomic volumes and nearly equal or more positive M charges in five-coordinate A and D complexes than in the six-coordinate B and C ones indicate higher mechanical strain in the five-coordinate systems under study. The bigger phosphazene N' atomic volumes in five-coordinate A and D complexes than in the six-coordinate B and C ones with the nearly equal N' atomic charges imply the same conclusion. Similarly, the higher mechanical strain of more distant N(1) and N(3) atoms (compared to the N(2) and N(4) ones) in model B as well as of the N(2) atom (compared to the N(1) and N(3) ones) in model C may be concluded.

Unfortunately, no data on the magnetic state of the compounds studied are presented in the structural study [14]. Their frontier molecular orbitals are not located at central metal atoms (except D complex with up to 10% location at Ni) which are connected with very small energy differences between the corresponding α and β spinorbitals (maybe except D complex, see Table 4). Any trends in HOMO–LUMO energy separation cannot be extracted because compound A is dinuclear Zn complex and model compound B is a cation. The relation between the color and HOMO–LUMO energy separation in the green C compound (with a hexacoordinated Ni(II)) and in the red D compound (with a pentacoordinated Ni(II)) need not be so straightforward. QTAIM atomic charges of central metal atoms indicate their oxidation states between M(I) and M(II). For this purpose their d electron populations of Mulliken population analysis $d^x(M)$ are more reliable and confirm Zn(II) with $d^x(Zn) = 10.0$ in A compound and Ni(II) with $d^x(Ni) = 8.2$ for the remaining ones (see Table 4).

Our results show that the bonds of central transition metal atoms with phosphazene nitrogens are stronger and more polar than with the aromatic pyridine nitrogens. Increased mechanical strain and thus higher reactivity in five-coordinate metal sites is predicted. Despite the high flexibility of the pyridyloxycyclophos-

Table 1
The model systems under study, their total (E_{tot}) and relative (ΔE) energies in singlet ($M_S = 1$) and triplet ($M_S = 3$) spin states (L = hexakis(2-pyridyloxy) cyclotriphosphazene, cyclo-[$NP(NC_5H_4O)_2]_3$, $\Delta E = E(M_S = 1) - E(M_S = 3)$, the higher stability in bold).

Model	Compound	Coordination sphere	E_{tot} (Hartree)		ΔE (kJ/mol)
			$M_S = 1$	$M_S = 3$	
A	$[(ZnCl_2)_2L]$	$ZnN'N_2Cl_2ZnN_2Cl_2$	**−8524.998799**	−8524.836799	−425.330
B	$[NiLCl]^+$	$NiN'N_4Cl$	−5093.708716	**−5093.772187**	166.643
C	$[NiLCl_2]$ (green)	$NiN'N_3Cl_2$	−5554.082825	**−5554.141134**	153.090
D	$[NiLCl_2]$ (red)	$NiN'N_2Cl_2$	−5554.081409	**−5554.132633**	134.489

Table 2
Bond lengths d, BCP electron densities ρ, their Laplacians $\nabla^2\rho$ and ellipticities ε of metal–ligand bonds in the systems under study (see Figs. 1–4 for atoms notation).

Model	M_S	Bond	d (Å)	ρ (e/Bohr^3)	$\nabla^2\rho$ (e/Bohr^5)	ε
A	1	Zn1–N′	2.089(3)	0.067	0.287	0.067
		Zn1–N1	2.328(3)	0.041	0.147	0.030
		Zn1–N2	2.349(3)	0.039	0.139	0.022
		Zn1–Cl1	2.2447(11)	0.069	0.192	0.016
		Zn1–Cl2	2.2360(11)	0.070	0.197	0.018
		Zn2–N3	2.057(4)	0.074	0.341	0.030
		Zn2–N4	2.057(3)	0.074	0.339	0.031
		Zn2–Cl3	2.2133(13)	0.073	0.210	0.002
		Zn2–Cl4	2.2046(15)	0.074	0.215	0.002
B	3	Ni–N′	2.027(3)	0.076	0.416	0.035
		Ni–N1	2.326(4)	0.039	0.166	0.006
		Ni–N2	2.157(4)	0.057	0.286	0.056
		Ni–N3	2.311(4)	0.040	0.175	0.021
		Ni–N4	2.176(4)	0.055	0.270	0.053
		Ni–Cl	2.3118(10)	0.061	0.186	0.008
C	3	Ni–N′	2.1075(18)	0.112	0.664	0.047
		Ni–N1	2.180(2)	0.041	0.178	0.094
		Ni–N2	2.221(2)	0.031	0.118	0.054
		Ni–N3	2.3652(19)	0.060	0.312	0.006
		Ni–Cl1	2.3860(8)	0.052	0.154	0.059
		Ni–Cl2	2.3358(8)	0.058	0.172	0.023
D	3	Ni–N’	2.023(6)	0.082	0.398	0.297
		Ni–N1	2.160(4)	0.057	0.287	0.037
		Ni–N2	2.160(4)	0.057	0.287	0.037
		Ni–Cl1	2.3136(4)	0.062	0.179	0.145
		Ni–Cl2	2.3136(4)	0.062	0.179	0.145

Table 3
Selected atomic volumes V and charges q in the systems under study (see Figs. 1–4 for atoms notation).

Model	M_S	Atom	V (Bohr^3)	q
A	1	Zn1	72.2	1.25
		N′	98.4	−2.10
		N1	88.1	−1.01
		N2	88.2	−1.02
		Cl1	250.4	−0.65
		Cl2	242.9	−0.65
		Zn2	76.3	1.33
		N3	89.1	−1.02
		N4	89.2	−1.04
		Cl3	254.0	−0.63
		Cl4	251.5	−0.63
B	3	Ni	67.0	1.21
		N′	93.4	−2.11
		N1	88.1	−0.99
		N2	84.2	−0.97
		N3	87.6	−0.97
		N4	85.0	−0.99
		Cl	220.2	−0.62
C	3	Ni	66.2	1.15
		N′	88.8	−2.07
		N1	82.6	−0.90
		N2	87.2	−0.91
		N3	81.8	−0.96
		Cl1	223.3	−0.66
		Cl2	228.3	−0.65
D	3	Ni	73.3	1.15
		N′	99.2	−2.09
		N1	83.1	−0.98
		N2	83.1	−0.98
		Cl1	245.7	−0.64
		Cl2	245.7	−0.64

phazene ligands and the resulting six-membered chelate rings, several strained pyridine nitrogen sites may be deduced. Further, theoretical and experimental studies of cyclophosphazene-based metal complexes are desirable to use these systems in catalytic reactions.

Table 4
Orbital energies of frontier molecular orbitals and d electron populations on central atoms in the model systems under study.

Model	A	B	C	D
M_S	1	3	3	3
Orbital energies (eV)				
HOMO[a] α	−0.21750	−0.32455	−0.17656	−0.19917
β	−0.21750	−0.32609	−0.17845	−0.19160
LUMO[b] α	−0.07236	−0.14917	−0.04924	−0.03814
β	−0.07236	−0.14999	−0.04884	−0.05088
Central atom M	Zn1/Zn2	Ni	Ni	Ni
d^x(M)	9.974/9.974	8.204	8.241	8.219

[a] Highest occupied molecular orbital.
[b] Lowest unoccupied molecular orbital.

Acknowledgements

We thank Slovak Grant Agency (Project No. 1/3566/06) for financial support. This work has benefited from the Center of Excellence Program of the Slovak Academy of Sciences in Bratislava, Slovakia (COMCHEM, Contract No. II/1/2007).

References

[1] V. Chandrasekhar, P. Thilagar, B. Murugesa Pandian, Coord. Chem. Rev. 251 (2007) 1045 and the references therein.
[2] W.M. Daugill, J. Chem. Soc. (1963) 3211.
[3] G.I. Bullen, J. Chem. Soc. A (1971) 1450.
[4] H. Zoer, A.J. Wagner, Acta Crystallogr., B 26 (1970) 1812.
[5] M.J.S. Dewar, E.A.C. Lucken, M.A. Whitehead, J. Chem. Soc. (1960) 2423.
[6] D.P. Craig, N.L. Paddock, J. Chem. Soc. (1962) 4118.
[7] M. Breza, Polyhedron 19 (2000) 389.
[8] M. Breza, J. Mol. Struct. (THEOCHEM) 505 (2000) 161.
[9] V. Luana, A.M. Pendas, A. Costales, G.A. Carriedo, F.J. Garcia-Alonso, J. Phys. Chem. A 105 (2001) 5280.
[10] A.B. Chaplin, J.A. Harrison, P.J. Dyson, Inorg. Chem. 44 (23) (2005) 8407.
[11] L. Kapicka, P. Kubacek, P. Holub, J. Mol. Struct. (THEOCHEM) 820 (2007) 148.
[12] E.W. Ainscough, A.M. Brodie, C.V. Depree, B. Moubaraki, K.S. Murray, C.A. Otter, Dalton Trans. 20 (2005) 3337.
[13] E.W. Ainscough, A.M. Brodie, C.V. Depree, G.B. Jameson, C.A. Otter, Inorg. Chem. 44 (2005) 7325.
[14] E.W. Ainscough, A.M. Brodie, C.V. Depree, C.A. Otter, Polyhedron 25 (2006) 2341.
[15] V. Chandrasekhar, B. Murugesa Pandian, R. Azhakar, Inorg. Chem. 45 (2006) 3510.
[16] (a) M.F. Bobrov, G.V. Popova, V.G. Tsirel'son, Zh. Fiz. Khim. 80 (2006) 682; (b) M.F. Bobrov, G.V. Popova, V.G. Tsirel'son, Rus. J. Phys. Chem. 80 (2006) 584.
[17] HYPERCHEM rel. 7.5 for Windows, Hypercube, Inc., 2003.
[18] M.J. Frisch, G.W. Trucks, H.B. Schlegel, G.E. Scuseria, M.A. Robb, J.R. Cheeseman, J.A. Montgomery Jr., T. Vreven, K.N. Kudin, J.C. Burant, J.M. Millam, S.S. Iyengar, J. Tomasi, V. Barone, B. Mennucci, M. Cossi, G. Scalmani, N. Rega, G.A. Petersson, H. Nakatsuji, M. Hada, M. Ehara, K. Toyota, R. Fukuda, J. Hasegawa, M. Ishida, T. Nakajima, Y. Honda, O. Kitao, H. Nakai, M. Klene, X. Li, J.E. Knox, H.P. Hratchian, J.B. Cross, C. Adamo, J. Jaramillo, R. Gomperts, R.E. Stratmann, O. Yazyev, A.J. Austin, R. Cammi, C. Pomelli, J.W. Ochterski, P.Y. Ayala, K. Morokuma, G.A. Voth, P. Salvador, J.J. Dannenberg, V.G. Zakrzewski, S. Dapprich, A.D. Daniels, M.C. Strain, O. Farkas, D.K. Malick, A.D. Rabuck, K. Raghavachari, J.B. Foresman, J.V. Ortiz, Q. Cui, A.G. Baboul, S. Clifford, J. Cioslowski, B.B. Stefanov, G. Liu, A. Liashenko, P. Piskorz, I. Komaromi, R.L. Martin, D.J. Fox, T. Keith, M.A. Al-Laham, C.Y. Peng, A. Nanayakkara, M. Challacombe, P.M.W. Gill, B. Johnson, W. Chen, M.W. Wong, C. Gonzalez, J.A. Pople, GAUSSIAN 03, Revision C.1, Gaussian Inc., Pittsburgh, PA, 2003.
[19] R.F.W. Bader, Atoms in Molecules: A Quantum Theory, Clarendon Press, Oxford, 1990.
[20] (a) F. Biegler-König, J. Schönbohm, D. Bayles, J. Comp. Chem. 22 (2001) 545; (b) <http://www.aim2000.de/>.
[21] (a) P. Ugliengo, D. Viterbo, G. Chiari, Z. Kristallogr. 207 (1993) 9; (b) P. Ugliengo, MOLDRAW: A Program to Display and Manipulate Molecular and Crystal Structures, Torino, 2006, <http://www.moldraw. unito.it>.

Polyhedron 28 (2009) 525–533

Contents lists available at ScienceDirect

Polyhedron

journal homepage: www.elsevier.com/locate/poly

Tungsten(0)–carbonyl complexes of naphthylazoimidazoles

Papia Datta [a], Ashis Kumar Patra [b], Chittaranjan Sinha [a,*]

[a] Department of Chemistry, Inorganic Chemistry Section, Jadavpur University, Kolkata, West Bengal 700 032, India
[b] Inorganic and Physical Chemistry Department, Indian Institute of Science, Bangalore, India

ARTICLE INFO

Article history:
Received 19 September 2008
Accepted 14 November 2008
Available online 12 January 2009

Keywords:
W(0)–carbonyl
Naphthylazoimidazole
X-ray structure
Electrochemistry
DFT–TD-DFT calculations

ABSTRACT

The reaction of $W(CO)_6$ with 1-alkyl-2-(naphthyl-α-azo)imidazole (α-NaiR) has synthesized $[W(CO)_5$(α-NaiR-N)] (α-NaiR-N refers to the monodentate imidazole-N donor ligand) at room temperature. The structure of $[W(CO)_5$(α-NaiMe-N)] shows a monodentate imidazole-N coordination of 1-methyl-2-(naphthyl-α-azo)imidazole (α-NaiMe). The complexes are characterized by elemental, mass and other spectroscopic data (IR, UV–Vis, NMR). On refluxing in THF at 323 K, $[W(CO)_5$(α-NaiR-N)] undergoes decarbonylation to give $[W(CO)_4$(α-NaiR-N,N′)] (α-NaiR-N,N′ refers to the imidazole-N(N), azo-N(N′) bidentate chelator). Cyclic voltammetry shows metal oxidation (W^0/W^I) and ligand reductions (azo/azo$^-$, azo$^-$/azo$^{=}$). The redox and electronic properties are explained by theoretical calculations using an optimized geometry. DFT computation of $[W(CO)_5$(α-NaiMe-N)] suggests that the major contribution to the HOMO/HOMO − 1 come from W d-orbitals and the orbitals of CO. The LUMOs are occupied by α-NaiMe functions. The back bonding interaction thus originates from the $W(CO)_n$ moiety to the LUMO of α-NaiR. A TD-DFT calculation has ascribed that HOMO/HOMO − 1 → LUMO is a mixture of metal-to-ligand and ligand-to-ligand charge transfer underlying the CO → azoimine contribution. The complexes show emission spectra at room temperature. $[W(CO)_4$(α-NaiR-N,N′)] shows a higher fluorescence quantum yield (ϕ = 0.05–0.07) than $[W(CO)_5$(α-NaiR-N)] (ϕ = 0.01–0.02).

© 2008 Elsevier Ltd. All rights reserved.

1. Introduction

Transition metal–polypyridine complexes are attractive due to their crucial role in catalyses, photophysics and photochemistry, electrochemistry, supramolecular properties, medicinal activity etc. [1–3]. Recent years have witnessed a great deal of interest in the synthesis of new ligands with a diimine group (–N=C–C=N–) [4,5] (in the framework of pyridine derivatives) or the design of isolectronic groups to the diimine function, such as the azoimine function, (–N=N–C=N–) [6–29] (Scheme 1). The azoimine function is capable of stabilizing low valent metal oxidation states [22–25]. Zero valent Group 6 metal carbonyls are also stabilized by the azoimine (–N=N–C=N–) function [30–40]. The *N*-heterocyclic azo molecules belong to the azoimine family and have been used to explore the chemistry of transition [6–25] and non-transition metals [26–29]. We have designed 1-alkyl-2-(naphthylazo)imidazole (**2**) a potential member of the azoimine family [41–43]. The present work is concerned with W(0)–carbonyl complexes of 1-alkyl-2-(naphthyl-α-azo)imidazoles (α-NaiR). The reaction of α-NaiR, with $W(CO)_6$ under ambient conditions (298 K) in the presence of Me_3NO has synthesized the penta-carbonyl complexes, $[W(CO)_5$(α-NaiR-N)] (**3**) (imidazole-N coordinated α-NaiR is abbreviated as α-NaiR-N). Penta-carbonyl Group 6 transition metal complexes are a source of Fischer carbene precursors in the studies of organic transformations [44–46], and are even used as diagnostic probes in the determination of nucleosides by measuring ν_{CO} of the coordinated CO [47].

$[W(CO)_4$(α-NaiR-N,N′)] exhibit high intense fluorescence emissions while $[W(CO)_5$(α-NaiR-N)] are weak emitters. The free ligand is non-fluorescent. The complexes were characterized by different spectroscopic studies (IR, UV–Vis, Mass, NMR, fluorescence), and the electrochemical properties have been studied with cyclic voltammetry. One of the penta-carbonyl complexes, $[W(CO)_5$(α-NaiMe-N)], has been structurally confirmed by a single crystal X-ray diffraction study. Theoretical calculations (DFT and TD-DFT) using an optimized molecular system have been carried out to predict the electronic structure, the spectral, redox and photophysical properties.

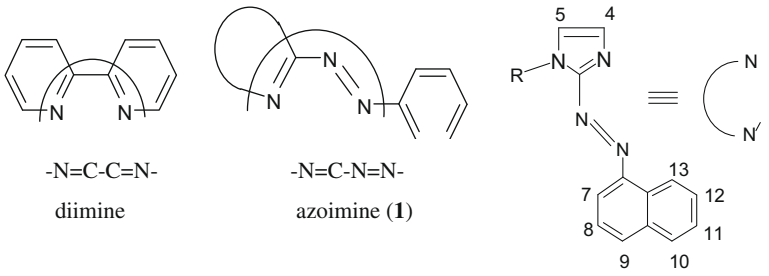
2. Experimental

2.1. Materials and measurements

The 1-alkyl-2-(naphthyl-α-azo)imidazoles (α-NaiR, **2**; R = CH_3 (**a**), CH_2–CH_3 (**b**), CH_2Ph (**c**)) were prepared by the reported procedure [42]. $W(CO)_6$ and $Me_3NO \cdot 2H_2O$ were Sigma–Aldrich reagents. The reactions were carried out under an extremely dry oxygen free atmosphere under atmos bags (Sigma–Aldrich).

* Corresponding author. Fax: +91 033 2413 7121.
E-mail address: c_r_sinha@yahoo.com (C. Sinha).

0277-5387/$ - see front matter © 2008 Elsevier Ltd. All rights reserved.
doi:10.1016/j.poly.2008.11.041



Scheme 1.

$Me_3NO \cdot 2H_2O$ was dehydrated at a controlled temperature under reduced pressure before use. THF and *n*-heptane were dried before use [48]. The solution spectral studies were carried out using spectroscopic grade solvents from Lancester, UK. Microanalyses (C, H and N) were performed using a Perkin Elmer 2400 CHN elemental analyzer. Spectroscopic measurements were carried out using the following instruments: UV–Vis spectra, Lambda 25 Perkin Elmer; IR spectra (KBr disk, 4000–450 cm^{-1}), RX-1 Perkin Elmer; ^1H NMR and ^{13}C NMR spectra in $CDCl_3$, Bruker 300 MHz FT-NMR spectrometers in the presence of TMS as an internal standard. The emission was examined on a LS 55 Perkin Elmer spectrofluorimeter at room temperature (298 K) in benzene under degassed conditions. The FAB-MS was collected from a JEOL-AX 500. Electrochemical measurements were carried out with a computer controlled EG & G PARC VersaStat model 250 Electrochemical instrument using a Pt-disk working electrode, a Pt-wire auxiliary electrode and [*n*-Bu_4N][ClO_4] supporting electrolyte under inert (dry N_2) environment at scan rate of 50 mV S^{-1}. The solution was IR compensated and the results were collected at 298 K. The reported results were referenced to SCE in CH_2Cl_2 and were uncorrected for junction potentials.

The fluorescence quantum yield of the complexes was determined using carbazole as a reference for [$W(CO)_5$(α-NaiR-N)] (**3**) with a known ϕ_R value of 0.42 in C_6H_6 [49] and anthracene (ϕ_R of 0.62 in C_6H_6 [50]) as a reference for [$W(CO)_4$(α-NaiR-N,N′)] (**4**). The complex and the reference dye were excited at the same wavelength, maintaining nearly equal absorbance (~0.1), and the emission spectra were recorded. The areas of the emission spectra were integrated using the software available in the instrument and the quantum yield was calculated according to the following equation:

$$\phi_S/\phi_R = [A_S/A_R] \times [(Abs)_R/(Abs)_S] \times [\eta_S^2/\eta_R^2]$$

here, ϕ_S and ϕ_R are the fluorescence quantum yields of the sample and reference, respectively. A_S and A_R are the areas under the fluorescence spectra of the sample and the reference respectively, $(Abs)_S$ and $(Abs)_R$ are the respective optical densities of the sample and the reference solution at the wavelength of excitation, and η_S and η_R are the values of refractive index for the respective solvents used for the sample and reference.

2.1.1. Preparation of $W(CO)_5$(α-NaiMe-N) (**3a**)

To $W(CO)_6$ (50 mg, 0.142 mmol) dissolved in dry THF (10 ml) was added Me_3NO (11 mg, 0.145 mmol), and the solution was stirred for 1 h. To the resulting yellow solution, α-NaiMe (34 mg, 0.144 mmol) was added and the solution was stirred for 6 h. The color of the solution changed to brown-red. The solvent was evaporated under reduced pressure and the crude product was passed down a neutral Al_2O_3 column. A brown-red solution was eluted with benzene:pet-ether (60–80 °C) (1:1 v/v), followed by a small volume of a violet solution in the same solvent as a tailing band and this was rejected due to the negligibly small amount of the compound. Removal of the solvent of the brown-red solution afforded the analytically pure product (**3a**) in 45% yield.

Microanalytical data are as follows: *Anal.* Calc. for [$W(CO)_5$(α-NaiMe-N)] (**3a**), $C_{19}H_{12}N_4O_5W$: C, 40.71; H, 2.44; N, 10.00. Found: C, 40.66; H, 2.50; N, 10.10%. FAB-MS, M^+ 560, $(M–5CO)^+$ 420; IR (KBr, cm^{-1}) ν_{CO}: 2068, 2015, 1916, 1881; IR in DCM ν_{CO}: 2071, 2023, 1922, 1885; UV (λ_{max}, nm (ε, 10^3 M^{-1} cm^{-1}), benzene): 546 (2.045), 401 (4.696), 343 (3.768) (shoulder). *Anal.* Calc. for [$W(CO)_5$(α-NaiEt-N)] (**3b**), $C_{20}H_{14}N_4O_5W$: C, 41.81; H, 2.44; N, 9.76. Found: C, 42.00; H, 2.50; N, 9.64%. FAB-MS, M^+ 574, $(M–5CO)^+$ 434; IR (KBr, cm^{-1}) ν_{CO}: 2068, 2015, 1907, 1853; IR in DCM ν_{CO}: 2070, 2020, 1925, 1860; UV (λ_{max}, nm (ε, 10^3 M^{-1} cm^{-1}), benzene) 547 (3.822), 403 (15.328), 341 (8.547) (shoulder). *Anal.* Calc. for [$W(CO)_5$(α-NaiBz-N)] (**3c**), $C_{25}H_{16}N_4O_5W$: C, 40.17; H, 2.52; N, 8.81. Found: C, 40.08; H, 2.48; N, 9.00%. FAB-MS, M^+ 636, $(M–5CO)^+$ 496; IR (KBr, cm^{-1}) ν_{CO}: 2068, 2016, 1974, 1918; IR in DCM ν_{CO}: 2075, 2022, 1985, 1924; UV (λ_{max}, nm (ε, 10^3 M^{-1} cm^{-1}), benzene) 548 (4.3), 402 (12.733), 341 (7.342) (shoulder).

2.1.2. Preparation of $W(CO)_4$(α-NaiMe-N,N′) (**4a**)

To $W(CO)_6$ (50 mg, 0.142 mmol) dissolved in dry THF (10 ml) was added Me_3NO (11 mg, 0.145 mmol), and the solution was stirred and refluxed for 0.5 h. To the resulting solution, α-NaiMe (34 mg, 0.144 mmol) was added and the solution was stirred and refluxed for an additional 4 h. The color of the solution changed to brown-violet. Then the solvent was evaporated under reduced pressure and the crude product was passed down a neutral Al_2O_3 column. A small volume of a brown-red band was eluted by benzene:pet ether (60–80 °C) (1:1 v/v), and this was rejected due to the very small amount of the compound. A violet solution was then collected using benzene:pet-ether (60–80 °C) (3:1 v/v) as eluent. Removal of the solvent afforded the analytically pure product (**4a**) in 60% yield.

Microanalytical data are as follows: *Anal.* Calc. for [$W(CO)_4$(α-NaiMe-N,N′)] (**4a**), $C_{18}H_{12}N_4O_4W$: C, 40.60; H, 2.26; N, 10.53. Found: C, 40.54; H, 2.35; N, 10.46%. FAB-MS, M^+ 532, $(M–4CO)^+$ 420; IR (KBr, cm^{-1}) ν_{CO}: 2011, 1913, 1866; IR in DCM ν_{CO}: 2019, 1919, 1872; UV (λ_{max}, nm (ε, 10^3 M^{-1} cm^{-1}), benzene) 551 (7.226), 401 (4.381), 337 (6.121). *Anal.* Calc. for [$W(CO)_4$(α-NaiEt-N,N′)] (**4b**), $C_{19}H_{14}N_4O_4W$: C, 41.76; H, 2.56; N, 10.25. Found: C, 41.68; H, 2.60; N, 10.34%. FAB-MS, M^+ 546, $(M–4CO)^+$ 434; IR (KBr, cm^{-1}) ν_{CO}: 2014, 1915, 1868; IR in DCM ν_{CO}: 2021, 1922, 1871; UV (λ_{max}, nm (ε, 10^3 M^{-1} cm^{-1}), benzene) 552 (4.767), 420 (1.908), 337 (3.808). *Anal.* Calc. for [$W(CO)_4$(α-NaiBz-N,N′)] (**4c**), $C_{24}H_{16}N_4O_4W$: C, 47.37; H, 2.63; N, 9.21. Found: C, 47.43; H,

2.68; N, 9.18%. FAB-MS, M^+ 608, $(M–4CO)^+$ 496; IR (KBr, cm^{-1}) ν_{CO}: 2010, 1907, 1850; IR in DCM ν_{CO}: 2017, 1917, 1861; UV (λ_{max}, nm (ε, 10^3 M^{-1} cm^{-1}), benzene) 552 (8.851), 420 (6.376), 337 (8.289).

2.2. Transformation of [W(CO)$_5$(α-NaiR-N)] (**3**) to [W(CO)$_4$(α-NaiR-N,N′)] (**4**)

Preparation of [W(CO)$_4$(α-NaiMe-N,N′)] (**4a**) from [W(CO)$_5$(α-NaiMe-N)] (**3a**) is detailed below. A THF solution of [W(CO)$_5$(α-NaiMe-N)] (100 mg in 15 ml THF) was heated at 60 °C for 2.5 h, which leads to the preparation of [W(CO)$_4$(α-NaiMe-N,N′)]. The solution is evaporated to dryness and violet crystalline compounds were then isolated by chromatographic purification, as stated before, and dried in a $CaCl_2$ (fused) desiccator. Yield: 73%. Microanalytical data support the chemical formula [W(CO)$_4$(α-NaiR-N,N′)]

2.3. Crystallographic data collection and refinement of [W(CO)$_5$(α-NaiMe-N)] (**3a**)

Crystals were grown by slow evaporation of a benzene solution of [W(CO)$_5$(α-NaiMe-N)] (**3a**). Crystal parameters and refined data are summarized in Table 1. The data of **3a** (0.80 × 0.15 × 0.10 mm) were collected by a fine focus sealed tube at 293(2) K using a fine focus graphite monochromator Bruker Smart CCD Area Detector (Mo Kα radiation, λ = 0.71073 Å). Unit cell parameters were determined from least-squares refinement of setting angles with 2θ in the range $3.86° \le \theta \le 49.42°$. Of 9331 collected data, 3368 with $I > 2\sigma$ (I) were used for the structure solution. The *hkl* range was $-9 \le h \le 9$, $-12 \le k \le 12$, $-14 \le l \le 14$. Reflection data were recorded using the ω-scan technique. Data were corrected for Lorentz polarization effects and for linear decay. Semi-empirical absorption corrections based on ψ-scans were applied. Data reduction was carried out using the Bruker SAINT program. The structure was solved by the direct method using SHELXS-97 [51] and successive difference Fourier syntheses. All non-hydrogen atoms were refined anisotropically. The hydrogen atoms were fixed geometrically and refined using the riding model. In the final difference Fourier map the residual minima and maxima (−0.735, 0.308 e/Å^3) were evaluated using SHELXL-97 [52].

Table 1
Selected crystallographic data for [W(CO)$_5$(α-NaiMe-N)] (**3a**).

	[W(CO)$_5$(α-NaiMe)] (**3a**)
Formula	$C_{19}H_{12}N_4O_5W$
Crystal size (mm^3)	0.80 × 0.15 × 0.10
Formula weight (g M^{-1})	560.18
Crystal system	triclinic
Space group	$P\bar{1}$
a (Å)	7.788(3)
b (Å)	10.656(4)
c (Å)	12.111(5)
α (°)	88.238(6)
β (°)	84.039(6)
γ (°)	82.139(6)
V (Å^3)	990.0(7)
Z	2
T (K)	293(2)
D_{calc} (Mg/m^3)	1.879
λ (Å) (Mo Kα)	0.71073
Absorption coefficient (m M^{-1})	5.872
Data/restraints/parameters	3368/0/262
Goodness-of-fit on F^2	1.086
R (F_o)[a] [$I > 2\sigma$ (I)]	0.0187
wR (F_o)[b] [$I > 2\sigma$ (I)]	0.0438
R [all data] (wR [all data])	0.0206 (0.0445)
Largest difference in peak and hole (e/Å^{-3})	0.308, −0.735

[a] $R = \sum||F_o| - |F_c||/\sum|F_o|$.
[b] $wR = \{\sum[w(F_o^2 - F_c^2)^2]/\sum[w(F_o^2)^2]\}^{1/2}$; $w = [\sigma^2(F_o)^2 + (0.0235P)^2 + 0.1361P]^{-1}$, where $P = (F_o^2 + 2F_c^2)/3$.

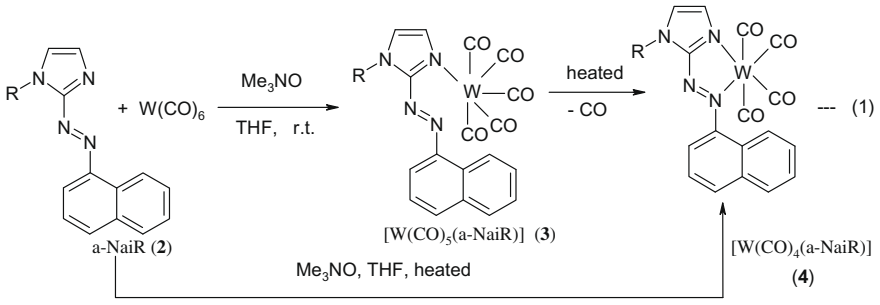
2.4. Computational details

All computations were performed using GAUSSIAN03 (G03) software [53]. The Becke's three-parameter hybrid exchange functional and the Lee–Yang–Parr non-local correlation function [54] (B3LYP) was used throughout the calculations. A LanL2DZ basis set [55] for W, 6–31G(d, p) for C, H, N and O atoms were used for all types of calculations. In all cases, vibrational frequencies were calculated to ensure that the optimized geometries represented local minima. We performed TD-DFT calculations of the low-lying excitation at the singlet optimized geometry. The excitation energies were calculated by the TD-DFT approach.

3. Results and discussion

3.1. Synthesis

1-Alkyl-2-(naphthyl-α-azo)imidazole (Scheme 1: α-NaiR, **2**; R = CH_3 (**a**), CH_2–CH_3 (**b**), CH_2Ph (**c**)), may serve as a monodentate imidazole-N ligand (abbreviated: α-NaiR-N) and as a bidentate chelating agent (abbreviated: α-NaiR-N,N; where N and N′ refer to N(imidazole) and N(azo) donor centers, respectively). The reaction of α-NaiR with W(CO)$_6$ in the presence of Me_3NO resulted in the isolation of the penta-carbonyl [W(CO)$_5$(α-NaiR-N)] (**3**) at room temperature (298 K). The reaction between α-NaiR and W(CO)$_6$ at a higher temperature (323 K) yielded the tetra-carbonyl complex [W(CO)$_4$(α-NaiR-N,N′)] (**4**). The complexes **3** may be converted into **4** by refluxing in a high boiling solvent like acetonitrile, THF and 2-methoxyethanol (Scheme 2). The composition of the complexes is supported by microanalytical and spectroscopic data. The structure of the penta-carbonyl complex has been confirmed by single crystal X-ray structure determination of [W(CO)$_5$(α-



Scheme 2. Preparation of penta-carbonyl and tetra-carbonyl azo-imidazole.

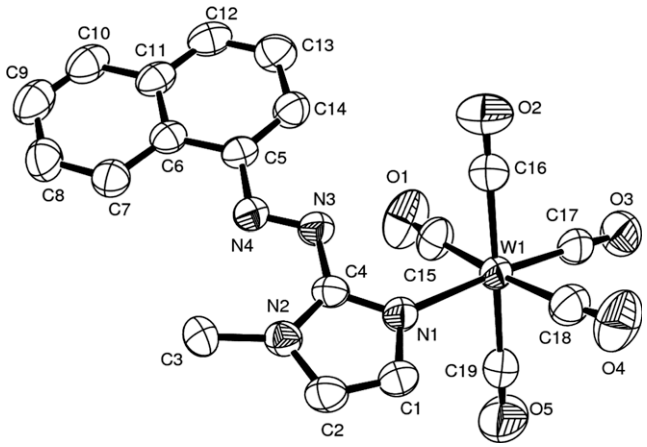


Fig. 1. The ORTEP view of the complex [W(CO)$_5$(α-NaiMe-N)] (**3a**) showing the atom labeling scheme with 50% probability thermal ellipsoids.

NaiMe-N)] (**3a**) (Fig. 1). We have attempted to crystallize [W(CO)$_4$(α-NaiR-N,N′)] (**4**), but failed to get good quality diffracting crystals.

3.2. Molecular structure of [W(CO)$_5$(α-NaiMe-N)] (*3a*)

The X-ray structure of [W(CO)$_5$(α-NaiMe-N)] (**3a**) is shown in Fig. 1 and selected bond parameters are listed in Table 2. The molecule consists of a central W atom surrounded by six coordination centers and the arrangement is distorted octahedral [56–59]. The atomic arrangement involves the coordination of five CO ligands and the imidazole-N of a 1-methyl-2-(naphthyl-α-azo)imidazole ligand. The coordinated imidazole is inclined at an angle of 7.95° to the pendant naphthyl group. The W–N (imidazole) distance is 2.268(3) Å and the W–C(O) distances lie I the range 1.954–2.035 Å. The W–C(17) displays the shortest distance (1.954(4) Å) and this is due to the trans influence of the imidazole-N coordination to the central W atom. The four equatorial W–C(O) distances are within the range 2.028–2.035 Å. The *trans* C–W–C angles are slightly deviated from the ideal value (180°): C(18)–W(1)–C(15), 174.93(14)° and C(19)–W(1)–C(16), 178.63(14)°, while the other C–W–C angles are *cis*-angles and lie in the range 87.8 to 92.5° (see Table 3).

3.3. Spectroscopic characterization

3.3.1. FT-IR and mass spectra

FT-IR spectra were taken in both in solution (CH_2Cl_2) and in the solid phase (solid KBr). The spectra (Fig. 2) show three or four bands [60]. The solution spectra (CH_2Cl_2) show ν(CO) at 5–15 cm^{-1} higher frequency than that of the KBr-phase data. The mean value of the CO frequencies, ν(CO), in these cases is lower ($\Delta\nu$(CO) = 15–25 cm^{-1}) than that of M(CO)$_4$(2-PAP) (2-PAP = 2-(phenylazo)pyridine) [30–37]. This supports weaker π-acidity of the naphthylazoimidazoles than that of phenylazopyridine. On comparing with the spectral pattern and frequency of the CO stretching of [W(CO)$_5$(PQ)] [56–57] (PQ = 2-(2′-pyridyl)quinoxaline) the present complexes are assigned to a penta-carbonyl complex with octahedral coordination where the ligand α-NaiR binds as a monodentate imidazole-N donor agent (α-NaiR-N). The ν(N=N) and ν(C=N) bands appear at 1360–1390 and 1660–1620 cm^{-1}, respectively. The mass fragmentation by FAB-MS of the complexes support the expected fragmentation pattern of M$^+$, (M–CO)$^+$, (M–2CO)$^+$, (M–3CO)$^+$ etc. for both types of complexes.

3.3.2. UV–Vis spectra and emission properties

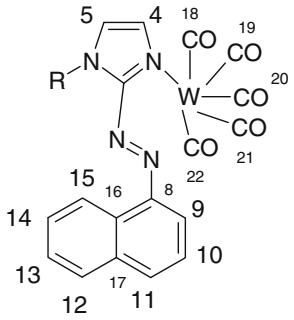
Benzene solutions of [W(CO)$_5$(α-NaiR-N)] (**3**) are brown-red and those of [W(CO)$_4$(α-NaiR-N,N′)] (**4**) are brown-violet. The absorption spectra show three intense ($\varepsilon \sim 10^4$) bands within the region 330–600 nm (Fig. 3). The complexes do not show significant solvatochromism, unlike their Schiff base analogs [43]. In d^6-octahedral complexes of the M(0)-state, the lowest energy electronic transition arises from a filled metal d-orbital to the unoccupied lowest energy π* orbital of the ligand (MLCT). The transition at

Table 2
Selected bond lengths (Å) and angles (°) for the complex [W(CO)$_5$(α-NaiMe-N)] (**3a**) from the X-ray structure and theoretical calculated data by DFT for **3a** and **4a**.

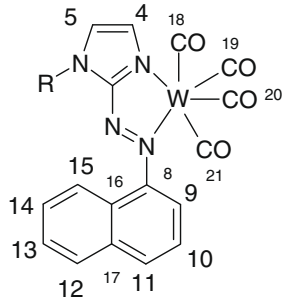
Bond parameters	[W(CO)$_5$(α-NaiMe-N)] (**3a**)		[W(CO)$_4$(α-NaiMe-N,N′)] (**4a**)
	Experimental (e.s.d.)	Theoretical	Theoretical
Bond lengths (Å)			
W(1)–N(1)	2.268(3)	2.258	2.143
W(1)–C(15)	2.035(4)	2.036	[a]
W(1)–C(16)	2.035(5)	2.035	2.049
W(1)–C(17)	1.954(4)	1.989	1.997
W(1)–C(18)	2.028(4)	2.036	2.034
W(1)–C(19)	2.034(4)	2.040	1.968
N(3)-N(4)	1.261(4)	1.301	1.338
W(1)–N(4)	[a]	[a]	2.275
Bond angles (°)			
C(15)–W(1)–N(1)	93.24(12)	89.72	[a]
C(15)–W(1)–C(16)	88.22(16)	90.29	[a]
C(16)–W(1)–N(1)	91.90(13)	89.58	103.12
C(17)–W(1)–C(18)	87.45(15)	89.48	86.38
C(17)–W(1)–C(19)	87.71(16)	90.17	84.44
C(17)–W(1)–C(15)	87.81(15)	89.15	[a]
C(17)–W(1)–C(16)	92.53(16)	89.82	82.23
C(17)–W(1)–N(1)	175.48(11)	178.72	170.32
C(18)–W(1)–C(19)	91.14(16)	89.04	89.77
C(18)–W(1)–C(15)	174.93(14)	178.48	[a]
C(18)– W(1)–C(16)	90.21(16)	90.37	170.23
C(18)–W(1)–N(1)	91.62(13)	91.66	85.91
C(19)–W(1)–C(15)	90.45(17)	90.30	[a]
C(19)–W(1)–C(16)	178.63(14)	179.41	86.61
C(19)–W(1)–N(1)	87.89(13)	90.44	89.66

[a] Because of the monodentate feature of α-NaiMe by the imidazole-N, the azo-N remains free.

Table 3
^{1}H NMR spectral data of the complexes in $CDCl_3$.



[W(CO)$_5$(α-NaiR-N)] (**3**)



[W(CO)$_4$(α-NaiR-N,N′)] (**4**)

Compound	δ (ppm) (J/Hz)							
	4-H[a]	5-H[a]	9-H[c]	10-11H[d]	12-14H[d]	15-H[c]	N–CH_3	N–CH_2
3a	7.50	7.02	8.65 (8.4)	8.12	7.63	7.98 (8.0)	4.10[b]	
3b	7.57	7.17	8.64 (8.1)	8.06	7.70	7.80 (8.0)	1.59[e] (7.5)	4.50[f] (9.0)
3c[g]	7.60	7.21	8.66 (8.0)	8.15	7.74	7.83 (8.0)		5.64[b]
4a	7.66	7.4	8.13 (7.5)	7.91	7.47	7.82 (8.0)	4.01[b]	
4b	7.45	7.20	8.17 (7.5)	7.93	7.50	7.82 (8.0)	1.57[e] (7.5)	4.41[f] (9.0)
4c[g]	7.49	7.23	8.20 (7.5)	7.98	7.54	7.85 (8.0)		5.65

[a] Broad singlet.
[b] Singlet.
[c] Doublet.
[d] Multiplet.
[e] Triplet.
[f] Quartet.
[g] δ[N–(CH_2)]–Ph:7.35–7.45 ppm.

545–555 nm of [W(CO)$_5$(α-NaiR-N)] (**3**) is assigned to a metal-to-ligand charge transfer transition [30–37,61,62]. In [W(CO)$_4$(α-NaiR-N,N′)] (**4**) the bands in the visible region are shifted by ~10 nm to a longer wavelength region, which suggests a decrease in the energy gap between the d π(W)–π*(L) state. Other transitions at ~400 nm and ~340 nm may be attributed to intraligand (n–π*/π–π*) transitions (LLCT or lLCT). DFT and TD-DFT calculations of these complexes have undertaken to verify the electronic structure of the molecules, and they are discussed below.

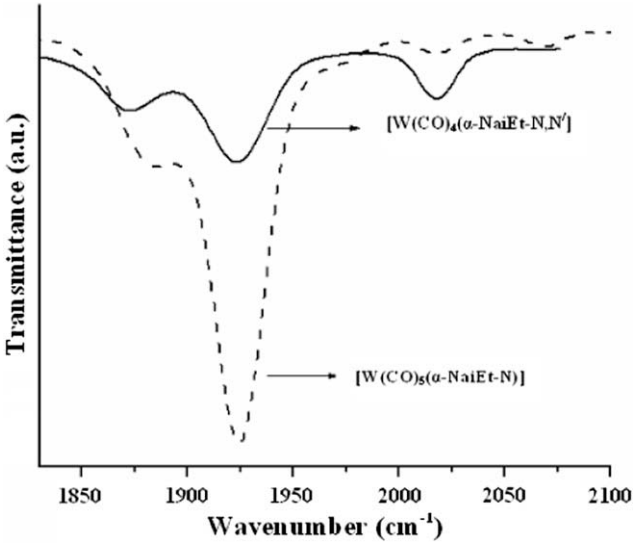


Fig. 2. Solution FT-IR spectra in CH_2Cl_2.

The photoluminescence properties of the complexes (**3** and **4**) were studied at room temperature (298 K) in benzene (Fig. 3). The ligands are photo-inactive. The lowest singlet $S_0 \rightarrow S_1$ transition in the UV region (<400 nm) is in good agreement with the $\pi \cdot \pi^*$ transition. Longer wavelength excitation shows very weak emission. The excitation spectra are perfectly matched with the absorption spectra, which indicate sufficient stability of the excited state upon irradiation and this being structurally rigid against any chemical deformation at least on the spectroscopic timescale. The photophysics of these complexes shows high energy (HE) and low energy (LE) transitions. The low energy emission appears at 615–647 nm and its quantum yield has not been evaluated because of very low intensity. The quantum yields (ϕ) of the excitation at 331–341 nm (Table 4) show a better prospect for [W(CO)$_4$(α-NaiR-N,N′)] (**4**) (ϕ = 0.05–0.07) than [W(CO)$_5$(α-NaiR-N)] (**3**) (ϕ = 0.01–0.02). In the absence of a metal ion, the fluorescence of the ligand is probably deactivated through n–π* states rather than by PET (photoinduced electron transfer) [63].

Lifetime data of the complexes were taken in benzene solution when excited at 370 nm. The fluorescence decay curve was deconvoluted with respect to the lamp profile. The observed florescence decay fits with the bi-exponential nature of the complexes (Fig. 4). We have used the mean fluorescence lifetime ($\tau_f = a_1\tau_1 + a_2\tau_2$ where a_1 and a_2 are the relative amplitudes of the decay process) to compare the excited state (population at S_1 and S_2 states) stability of the complexes. The radiative and non-radiative rate constants (k_r and k_{nr}) are calculated and data show the usual higher k_{nr} value than the k_r value. The excited state is appreciably stable for [W(CO)$_4$(α-NaiR-N,N′)] (**4**). We could not evaluate quantitative

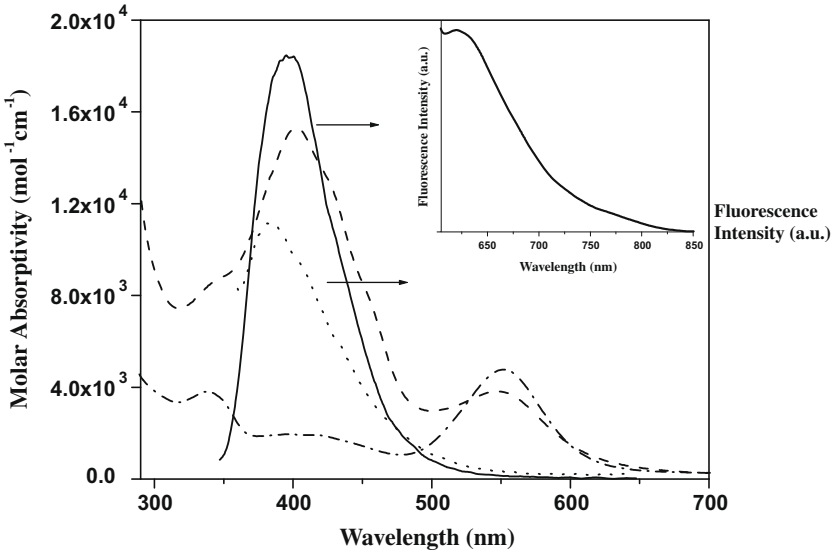


Fig. 3. Absorption spectra of $[W(CO)_5(\alpha\text{-NaiEt-N})]$ (– – –), $[W(CO)_4(\alpha\text{-NaiEt-N,N}')]$ (–·–·–) and fluorescence spectra of $[W(CO)_5(\alpha\text{-NaiEt-N})]$ (. . . . .), $[W(CO)_4(\alpha\text{-NaiEt-N,N}')]$ (—) in benzene. Higher energy emissions are recorded at 341 and 337 nm for **3b** and **4b**, respectively, and the lower energy emission is recorded at 552 nm wavelength for **4b**, shown in the inset figure.

Table 4
Cyclic voltammetry[a], fluorescence spectra[b] and lifetime data.[c]

Compound	Cyclic voltammetric data[a]			λ_{ex} (nm)[b]	λ_{em} (nm)[b]	Quantum yield (ϕ)	τ_f (ns)[d]	χ^2	$k_r \times 10^{-9}$ (s^{-1})	$k_{nr} \times 10^{-9}$ (s^{-1})
	E (ligand), V (ΔE_p, mV)		E (metal), V (ΔE_p, mV)							
	Azo/azo$^-$	Azo$^-$/azo$^{=}$	M^0/M^{+1}							
$[W(CO)_5(\alpha\text{-NaiMe-N})]$ (**3a**)	−0.70 (120)	−1.28 (132)	0.982 (210)	343 (546)	383 (647)	0.0148	[e]	[e]	[e]	[e]
$[W(CO)_5(\alpha\text{-NaiEt-N})]$ (**3b**)	−0.99 (110)	−1.40 (170)	1.04 (230)	341 (550)	385 (622)	0.0154	[e]	[e]	[e]	[e]
$[W(CO)_5(\alpha\text{-NaiBz-N})]$ (**3c**)	−0.78 (120)	−1.33 (160)	1.021 (200)	341 (548)	383 (633)	0.0162	[e]	[e]	[e]	[e]
$[W(CO)_4(\alpha\text{-NaiMe-N,N}')]$ (**4a**)	−0.88 (120)	−1.37 (145)	0.712 (130)	337 (551)	391 (615)	0.0534	4.671	1.16	0.0032	0.2109
$[W(CO)_4(\alpha\text{-NaiEt-N,N}')]$ (**4b**)	−0.65 (120)	−1.14 (140)	0.718 (110)	337 (552)	397 (635)	0.0732	1.457	1.12	0.0503	0.6362
$[W(CO)_4(\alpha\text{-NaiBz-N,N}')]$ (**4c**)	−0.70 (120)	−1.45 (170)	0.814 (125)	337 (550)	393 (634)	0.0601	0.987	1.18	0.0164	0.9965

[a] Solvent, CH_2Cl_2; Pt-working electrode, SCE reference, Pt-auxiliary electrode; $[n\text{-}Bu_4N](ClO_4)$ supporting electrolyte, scan rate 50 mV/s; metal oxidation $E = 0.5\ (E_{pa} + E_{pc})$, V for M^I/M^0 couple, $\Delta E_p = |E_{pa} - E_{pc}|$, mV; where E_{pa} (anodic-peak-potential) and E_{pc} (cathodic-peak-potential).
[b] Solvent C_6H_6, second excitation and emission wavelength are given in brackets.
[c] In C_6H_6 at 298 K.
[d] Excitation at 370 nm.
[e] τ_f, χ^2, k_r and k_{nr} are not determined for these complexes because of very low emissions.

emission parameters of $[W(CO)_5(\alpha\text{-NaiR-N})]$ (**3**). The presence of a dangling non-coordinated naphthylazo motive may be responsible for vibrational relaxation and energy transfer from the excited state that quenches the respective excited state. The emission features of these complexes may arise from the participation of π-acidic, strong field ancillary CO [64,65] with the third-row metal, which also increases the metal–ligand bonding [66–68]. The bi-exponential feature of the fluorescence decay may be due to population of the S_2 state in addition to the usual S_1 population.

3.4. Electrochemistry

The cyclic voltammetry of the compounds show one oxidation and two reductions. By analogy with similar types of α-diimine complexes, $[M(CO)_n(L)]$ (L = diimine or azoimine) [30–40] we advocate that the oxidation is primarily metal-centered. In the case of the tetra-carbonyl complexes (**4**), the oxidation on scan reversal shows a cathodic peak at a potential difference >100 mV to that of the anodic peak and supports quasireversibility (Fig. 5) of the voltammogram, while the penta-carbonyls (**3**) show irreversible oxidation. The results are collected in Table 4. Significantly $[W(CO)_5(\alpha\text{-NaiR-N})]$ shows a higher potential than $[W(CO)_4(\alpha\text{-NaiR-N,N}')]$ by 0.2–0.3 V. This is obviously due to the presence of the strongly π-acidic additional CO group in complexes **3** compared to **4**. The reduction is referred to azo/azo$^-$ and azo$^-$/azo$^{=}$, which appear at a more negative potential than those of the analogous 2-(phenylazo) pyridine complexes [30–37]. This is due to higher π-acidity of pyridine rather than imidazole and the electronic influx of the naphthyl rather than the phenyl group to the azo function.

3.5. DFT and TD-DFT calculations of $[W(CO)_5(\alpha\text{-NaiMe-N})]$ and $[W(CO)_4(\alpha\text{-NaiMe-N,N}')]$

DFT and TD-DFT computations of optimized structures of $[W(CO)_5(\alpha\text{-NaiMe-N})]$ (**3a**) and $[W(CO)_4(\alpha\text{-NaiMe-N,N}')]$ (**4a**) were performed to establish their electronic structure, spectral transitions and redox properties. The calculation has overthrown the earlier concept of MLCT transitions [66–70]. The structural agreement between theory and experiment is satisfactory (Table 2) for $[W(CO)_5(\alpha\text{-NaiMe-N})]$. The theoretical W–N(1) length is 0.01 Å shorter than the observed one, while the W–C(17) bond *trans* to W–N(1) is elongated by ~0.03 Å compared to the experimental results. Other W–C distances are comparable, as are the angles (Table

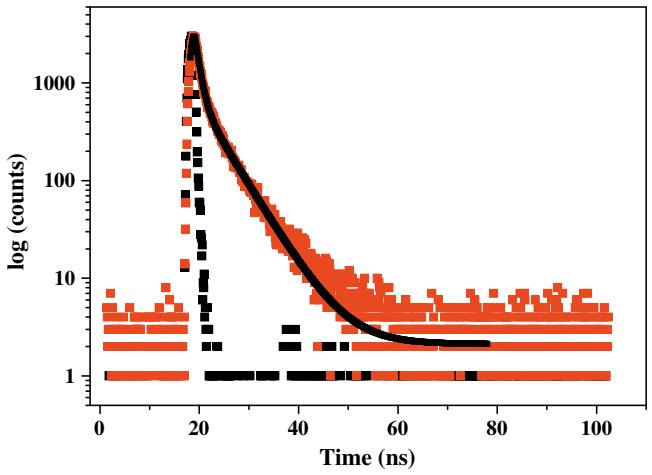


Fig. 4. Bi-exponential decay profile (●) and fitting curve (—) of [W(CO)$_4$(α-NaiBz-N,N′)] (**4c**) in benzene. Excitation is carried out at 370 nm.

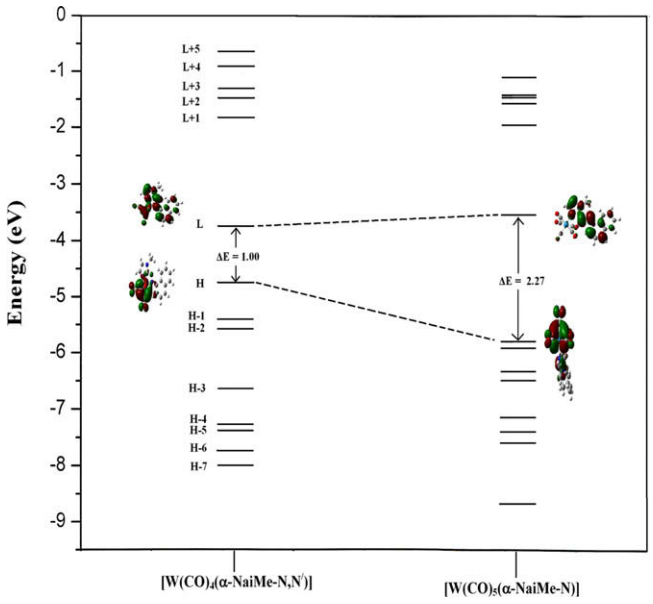


Fig. 6. Energy level correlation diagram in the gas phase.

2). The orbital energies, along with contributions from the ligands and metal, are given in the Supplementary Table. A correlation of MOs is given in Fig. 6. An interesting feature of the valence orbitals in [W(CO)$_5$(α-NaiMe-N)] is that the two highest occupied MOs (HOMO, abbreviated as H; HOMO − 1, abbreviated as H-1) are very close in energy (the difference is only 0.11 eV), with a significant contribution from the metal d-orbitals and the π* orbital of the carbonyls. The contribution from COs is 30–40% while W contributes 50–60%. The two occupied MOs in [W(CO)$_4$(α-NaiMe-N,N′)] (**4a**) H and H-1 are separated by 0.7 eV, while H-1 and H-2 are closely associated (the energy difference is only 0.17 eV). The LUMOs (L + n) are primarily π* of the COs and α-NaiMe. The L (LUMO) and L + 2 (LUMO + 2) are mainly composed of α-NaiMe (L 99% α-NaiMe; L + 2 78% α-NaiMe) while L + 1, L + 3, L + 5 have >70% π* of the COs. Although there is a substantial energy difference (∼ 1.6 eV) between L and L + 1, higher unoccupied MOs (L + 2, L + 3, etc.) are closely spaced. The energy separation between the HOMO and LUMO is lower (ΔE = 1 eV) in [W(CO)$_4$(α-NaiMe-N,N′)] (**4a**) than [W(CO)$_5$(α-NaiMe-N)] (**3a**) (ΔE = 2.27 eV). The bonding scheme has unequivocally suggested the existence of two fragments in the complexes, namely the electron donor group W(CO)$_n$ and the electron acceptor group α-NaiMe.

To gain detailed insight into the electronic transitions, the TD-DFT calculations were performed on two series of complexes, namely [W(CO)$_5$(α-NaiMe-N)] and [W(CO)$_4$(α-NaiMe-N,N′)]. H and H-1 are localized on parts of the metal (55–60%) and CO (30–40%), and L carries 99% ligand character (Supplementary Tables). The transition 545–555 nm may be assigned to H/H-1 → L because of the very small energy difference (0.11 eV) between H and H-1. Thus the transition may be defined as an admixture of MLCT and LLCT transitions, as suggested by Vlcek [70], contradicting the widely accepted MLCT concept. The H-2 → L transition may be responsible for the broadening of the MLCT and LLCT bands. The transitions H/H-1/H-2 → L + 2 may also contribute in part to the MLCT and LLCT transitions. The back-bonding, W → CO transitions may be assigned to H/H-1/H-2 → L + 1/L + 3 transitions, and those may be obstructed by the intraligand π → π* transitions localized on the napthylazoimidazole ligand at 400–420 nm (Table 5). This is indeed observed. The electronic spectra of the complexes ([W(CO)$_5$(α-NaiMe-N)] and [W(CO)$_4$(α-NaiMe-N,N′)]) show three main transition regions: 545–555, 400–420 and 320–345 nm. The intensity of these transitions has been assessed from the oscillator strength (*f*). From the calculations, the longest wavelength band appears at 691.5 (*f*, 0.095) which is assigned to H → L, while other bands around the main transition of low oscillator strength, such as H-1 → L, H-2 → L, and H-4 → L, are a combination of MLCT and LLCT transitions. A second band of high oscillator strength (*f*, 0.321) appears at 460.0 nm, which is also of MLCT origin and the transitions around this band come from H/H-1/H-2 → L + 1, H-2 → L + 4, and are of MLCT and LLCT origin. The third recognized band is located at 334.9 nm (*f*, 0.164) which is a ligand centered

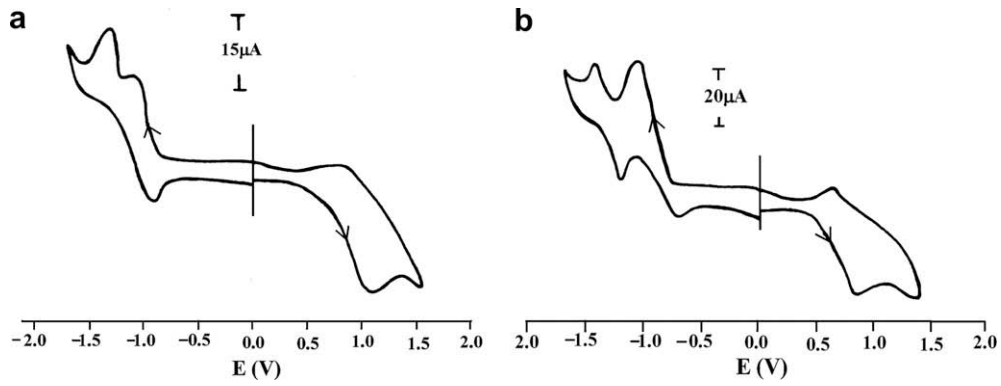


Fig. 5. Cyclic voltammograms of (a) [W(CO)$_5$(α-NaiEt-N)] (**3b**) and (b) [W(CO)$_4$(α-NaiEt-N,N′)] (**4b**) in CH_2Cl_2 using a Pt-disk working electrode, SCE reference and [*n*-Bu_4N][ClO_4] as the supporting electrolyte.

Table 5
Selected list of excitation energies of [W(CO)$_5$(α-NaiMe-N)] (**3a**) and [W(CO)$_4$(α-NaiMe-N,N′)] (**4a**) in the gas phase.

Excited state	λ (nm) ($f \times 10^3$)	Transitions
[W(CO)$_5$(α-NaiMe-N)] (**3a**)		
2	691.5 (0.0952)	(85%) HOMO (H) → LUMO (L) (MLCT)
4	519.7 (0.0082)	(72%) H-4 → L (IL), (12%) H-2 → L (MLCT)
5	460.0 (0.3214)	(75%) H-3 → L (IL)
6	414.4 (0.0113)	(82%) HOMO → L + 1 (MLCT), (11%) H-2 → L + 4 (MLCT)
7	406.3 (0.0094)	(76%) H-1 → L + 1 (MLCT), (10%) H-2 → L + 3 (MLCT)
10	374.2 (0.0463)	(89%) H-5 → L (IL)
13	360.1 (0.0067)	[(38%) H-1 → L + 3, (33%) H-1 → L + 4, (21%) HOMO → L + 4] (MLCT)
14	336.9 (0.0983)	(26%) H-6 → L (IL), [(33%) HOMO → L + 5, (19%) H-2->L + 3, (11%) H → L + 2] (MLCT)
15	334.9 (0.164)	(54%) H-6 → L (IL), (22%) HOMO → L + 5 (MLCT)
17	321.0 (0.0043)	[(73%) HOMO → L + 2, (11%) HOMO → L + 5] (MLCT)
22	283.0 (0.0135)	(88%) HOMO → L + 6 (MLCT)
27	273.4 (0.0582)	[(69%) H-4 → L + 1, (15%) H-3 → L + 3] (IL)
32	261.8 (0.0464)	(47%) H-7 → L (IL)
36	254.8 (0.0662)	(23%) H-3 → L + 5 (IL), [(22%) HOMO → L + 7, (14%) HOMO → L + 8] (MLCT)
39	250 (0.00274)	[(35%) H-1 → L + 7, (21%) H-1 → L + 8] (MLCT)
[W(CO)$_4$(α-NaiMe-N,N′)] (**4a**)		
3	593.3 (0.239)	[(59%) H-2 → L (12%) H-1 → L](MLCT)
4	463.8 (0.255)	(77%) H-3 → LUMO(IL)
5	430.1 (0.0192)	(84%) HOMO → L + 1 (MLCT)
8	387.7 (0.0187)	(54%) H-6 → LUMO, (23%) H-4 → LUMO] (IL)
11	372.6 (0.0084)	(38%) H-2 → L + 3, (25%) H-1 → L + 1, (13%) HOMO → L + 2](MLCT)
13	346.4 (0.0123)	(80%) H-5 → LUMO (IL)
14	334.4 (0.025)	(79%) H-1 → L + 2 (MLCT)
15	318.2 (0.044)	(77%) H-2 → L + 2 (MLCT)
18	292.2 (0.0269)	[(26%) H-1 → L + 6, (13%) HOMO → L + 5, (11%) H-1 → L + 4, (10%) HOMO → L + 8](MLCT)
21	285.6 (0.0163)	[(32%) H-1 → L + 4, (21%) H-1 → L + 6, (18%) HOMO → L + 8](MLCT)
23	278.9 (0.032)	(61%) H-2 → L + 4(MLCT), (10%) H-3 → L + 2(IL)
27	268.4 (0.0249)	[(24%) H-3 → L + 2, (23%) H-7 → LUMO](IL), H-2 → L + 6 (11%) (MLCT)
30	258.0 (0.0142)	[(37%) H-3 → L + 4, (14%) H-4 → L + 2](IL), (13%)H-1 → L + 7 (MLCT)
31	256.7 (0.0237)	(38%) H-1 → L + 5, (23%) H-1 → L + 7, (10%)H-2 → L + 5](MLCT)
32	252.8 (0.0178)	[(28%) H-2 → L + 5, (10%) H-1 → L + 7](MLCT), (24%) H-8 → LUMO (IL)

MLCT: metal-to-ligand charge transfer; LLCT: ligand-to-ligand charge transfer; IL: intraligand charge transfer; H = HOMO; L = LUMO.

transition (H-6 → L), and associated transitions are H → L + 2/L + 5, H-2 → L + 3 which are intra ligand charge transfer and MLCT transitions. High energy transitions appear at 250–280 nm, and those mainly are of intra-ligand charge transfer origin.

4. Conclusion

Tungsten(0)–carbonyl complexes of 1-alkyl-2-(naphthyl-α-azo)imidazoles (α-NaiR) are described. The complexes [W(CO)$_5$(α-NaiR-N)] are obtained at room temperature (298 K), which on heating lose one CO ligand to synthesize [W(CO)$_4$(α-NaiR-N,N′)]. In [W(CO)$_4$(α-NaiR-N,N′)], α-NaiR-N,N′ serve as a bidentate chelating agent and in [W(CO)$_5$(α-NaiR-N)] α-NaiR-N act as a monodentate imidazole-N donor ligand. The structure of [W(CO)$_5$(α-NaiMe-N)] has been confirmed by a single crystal X-ray diffraction study, where α-NaiMe exhibits a monodentate nature. The complexes show emission spectra at room temperature; [W(CO)$_4$(α-NaiR-N,N′)] shows a higher quantum yield (ϕ = 0.05–0.07) than [W(CO)$_5$(α-NaiR-N)] (ϕ = 0.01–0.02). Cyclic voltammetry shows metal oxidation and ligand reductions. DFT calculations of [W(CO)$_5$(α-NaiMe-N)] and [W(CO)$_4$(α-NaiR-N,N′)] explain the origin of the electronic spectra and redox activities. The HOMO/HOMO − 1 → LUMO transition is assigned as a mixture of MLCT and LLCT transitions, underlying the CO → azoimine contribution as calculated by the TD-DFT method.

Acknowledgements

Financial support from the Department of Science and Technology, New Delhi is gratefully acknowledged. PD and AKP give thanks to the Council of Scientific and Industrial Research, New Delhi for fellowships. We thank Dr. S. Chattopadhyay, Kalyani University for his help in recording the cyclic voltammograms.

Appendix A. Supplementary data

CCDC 645195 contains the supplementary crystallographic data for this paper. These data can be obtained free of charge via http://www.ccdc.cam.ac.uk/conts/retrieving.html, or from the Cambridge Crystallographic Data Centre, 12 Union Road, Cambridge CB2 1EZ, UK; fax: (+44) 1223 336 033; or e-mail: deposit@ccdc.cam.ac.uk.

Supplementary data associated with this article can be found, in the online version, at doi:10.1016/j.poly.2008.11.041.

References

[1] J. Reedijk, in: G. Willkinson, J.A. Mccleverty (Eds.), Comprehensive Coordination Chemistry, vol. 2, Pergamon, Oxford, UK, 1987.
[2] G. Wilkinson, F.G.A. Stone, E.W. Abel (Eds.), Comprehensive Organometallic Chemistry, Pergamon Press, New York, 1982.
[3] F.A. Cotton, G. Wilkinson, Advanced Inorganic Chemistry, 5th ed., Wiley, Interscience, New York, 1994.
[4] H.-F. Zhu, L. Li, T. Okamura, W. Zhao, W.-Y. Sun, N. Ueyama, Bull. Chem. Soc. Jpn. 76 (2003) 761.
[5] L.A. Garcia-Escudero, D. Miguel, J.A. Turiel, J. Organomet. Chem. 691 (2006) 3434.
[6] K. Kalyansundaram, Coord. Chem. Rev. 46 (1982) 159.
[7] B.K. Ghosh, A. Chakravorty, Coord. Chem. Rev. 95 (1989) 239.
[8] N. Bag, A. Pramanik, G.K. Lahiri, A. Chakravorty, Inorg. Chem. 31 (1992) 40.
[9] S. Serroni, S. Campagna, F. Puntoriero, C.D. Pietro, N.D. Mcclenaghan, F. Loisean, Chem. Soc. Rev. 30 (2001) 367.
[10] A.C.G. Hotze, H. Kooijman, A.L. Spek, J.G. Haasnoot, J. Reedijk, New J. Chem. 28 (2004) 565.
[11] R.E. Shepherd, Coord. Chem. Rev. 247 (2002) 147.
[12] M.J. Overett, J.R. Moss, Inorg. Chim. Acta 358 (2005) 1715.
[13] C.K. Pal, S. Chattopadhyay, C. Sinha, D. Bandhyopadhyay, A. Chakravorty, Polyhedron 13 (1994) 999.
[14] P.K. Santra, R. Roy, C. Sinha, Proc. Indian Acad. Sci. (Chem. Sci.) 112 (2000) 523.

[15] B.K. Santra, P. Munshi, G. Das, P. Bharadwaj, G.K. Lahiri, Polyhedron 18 (1999) 617.
[16] P.K. Santra, P. Byabratta, S. Chattopadhyay, L.R. Falvello, C. Sinha, Eur. J. Inorg. Chem. 1124 (2002).
[17] M. Panda, S. Das, G. Mostafa, A. Castineiras, S. Goswami, J. Chem. Soc., Dalton Trans. (2005) 1249.
[18] U.S. Ray, Sk. Jasimuddin, B.K. Ghosh, M. Monfort, J. Ribas, G. Mostafa, T.-H. Lu, C. Sinha, Eur. J. Inorg. Chem. (2004) 250.
[19] U.S. Ray, B.G. Chand, G. Mostafa, J. Cheng, T.-H. Lu, C. Sinha, Polyhedron 22 (2003) 2587.
[20] D. Banerjee, U.S. Ray, J.-C. Liou, C.-N. Lin, T.-H. Lu, C. Sinha, Inorg. Chim. Acta 358 (2005) 1019.
[21] U.S. Ray, D. Banerjee, B.G. Chand, J. Cheng, T.-H. Lu, C. Sinha, J. Coord. Chem. 58 (2005) 1105.
[22] T.K. Misra, D. Das, C. Sinha, P. Ghosh, C.K. Pal, Inorg. Chem. 37 (1998) 1672.
[23] T.K. Misra, D. Das, C. Sinha, Polyhedron 16 (1997) 4163.
[24] T.K. Misra, D. Das, C. Sinha, Indian J. Chem. 37A (1998) 741.
[25] S. Pal, T.K. Misra, P. Chattopadhyay, C. Sinha, Proc. Indian Acad. Sci. (Chem. Sci.) 111 (1999) 687.
[26] B.G. Chand, U.S. Ray, J. Cheng, T.-H. Lu, C. Sinha, Polyhedron 22 (2003) 1213.
[27] B.G. Chand, U.S. Ray, G. Mostafa, T.-H. Lu, C. Sinha, Polyhedron 23 (2004) 1669.
[28] B.G. Chand, U.S. Ray, G. Mostafa, T.-H. Lu, C. Sinha, J. Coord. Chem. 57 (2004) 627.
[29] B.G. Chand, U.S. Ray, J. Cheng, T.-H. Lu, C. Sinha, Inorg. Chim. Acta 358 (2005) 1927.
[30] M.N. Ackermann, C.R. Barton, C.J. Deodene, E.M. Specht, S.C. Keill, W.E. Schreiber, Hiodong Kim, Inorg. Chem. 28 (1989) 397.
[31] F. Alper, C. Kayram, S. Ozkar, J. Organomet. Chem. 691 (2006) 2734.
[32] W. Kaim, S. Ernst, S. Kohlmann, Polyhedron 5 (1986) 295.
[33] W. Kaim, S. Kohlmann, Inorg. Chem. 25 (1986) 3442.
[34] W. Kaim, S. Kohlmann, Inorg. Chem. 26 (1987) 68.
[35] M.N. Ackermann, W.G. Fairbrother, N.S. Amin, C.J. Deodene, C.M. Lamborg, P.T. Martin, J. Organomet. Chem. 523 (1996) 145.
[36] M.J. Alder, W.I. Cross, K.R. Flower, R.G. Pritchard, J. Organomet. Chem. 568 (1998) 279.
[37] M.N. Ackermann, S.R. Kiihne, P.A. Saunders, C.E. Barnes, S.C. Stalling, H. Kim, C. Woods, M. Lagunoff, Inorg. Chim. Acta 334 (2002) 193.
[38] M.N. Ackermann, M.P. Robinson, I.A. Maher, E.B. LeBlane, R.V. Raz, J. Organomet. Chem. 682 (2003) 248.
[39] P. Datta, P. Gayen, C. Sinha, Polyhedron 25 (2006) 3435.
[40] B.P. Buffin, P.J. Squattrito, A.O. Ojewole, Inorg. Chem. Commun. 7 (2004) 14.
[41] J. Dinda, D. Das, P.K. Santra, C. Sinha, L.R. Falvello, J. Organomet. Chem. 629 (2001) 28.
[42] S. Pal, D. Das, P. Chattopadhyay, C. Sinha, K. Panneerselvam, T.-H. Lu, Polyhedron 19 (2000) 1263.
[43] P. Datta, C. Sinha, Polyhedron 26 (2007) 2433.
[44] W. Palitzsch, U. Bohme, G. Roewer, Chem. Commun. (1997) 803.
[45] M.M. Abd-Elzahar, T. Froneck, G. Roth, V. Gvozdev, H. Fischer, J. Organomet. Chem. 599 (2000) 288.
[46] H. Fischer, J. Schmidt, J. Mol. Catal. 46 (1988) 277.
[47] J.M.D.R. Toma, D.E. Bergstrom, J. Org. Chem. 59 (1994) 2418.
[48] A.I. Vogel, A Text Book of Practical Organic Chemistry, Longman, London, 1959.
[49] J.N. Deams, G.A. Crosby, J. Phys. Chem. 75 (1971) 991.
[50] W.R. Dawson, M.W. Windsor, J. Phys. Chem. 72 (1968) 3251.
[51] G.M. Sheldrick, SHELXS 97, Program for the Solution of Crystal Structure, University of Gottingen, Germany, 1990.
[52] G.M. Sheldrick, SHELXL 97, Program for the Refinement of Crystal Structure, University of Gottingen, Germany, 1997.
[53] M.J. Frisch, G.W. Trucks, H.B. Schlegel, P.M.W. Gill, B.G. Johnson, M.A. Robb, J.R. Cheeseman, T.A. Keith, G.A. Petersson, J.A. Montgomery, K. Raghavachari, M.A. Al-Laham, V.G. Zakrzewski, J.V. Ortiz, J.B. Foresman, J. Cioslowski, B.B. Stefanov, A. Nanayakkara, M. Challacombe, C.Y. Peng, P.Y. Ayala, W. Chen, M.W. Wong, J.L. Andres, E.S. Replogle, R. Gomperts, R.L. Martin, D.J. Fox, J.S. Binkley, D.J. Defrees, J. Baker, J.P. Stewart, M. Head-Gordon, C. Gonzalez, J.A. Pople, GAUSSIAN98, Gaussian Inc., Pittsburgh, PA, 1998.
[54] C. Lee, W. Yang, R.G. Parr, Phys. Rev. B 37 (1988) 785.
[55] P.J. Hay, W.R. Wadt, J. Chem. Phys. 82 (1985) 270.
[56] I. Veroni, C.A. Mitsopoulou, F.J. Lahoz, J. Organomet. Chem. 691 (2006) 5955.
[57] I. Veroni, C. Makedonas, A. Rontoyianni, C.A. Mitsopoulou, J. Organomet. Chem. 691 (2006) 267.
[58] J. Qin, R.L. Christopher, M.E. Edward, R. van Eldik, J. Phys. Chem. A 101 (1997) 243.
[59] D.-B. Carlos, G. Friedrich-Wilhelm, R. van Eldik, Organometallics 17 (1998) 1669.
[60] L. Rivera-Rivera, F. Colon-Padilla, A. Del Toro-Novales, J.E. Cortes-Figuerca, Synthesis (1998) 1534.
[61] V.N. Nemykin, J.G. Olsen, E. Perera, P. Basu, Inorg. Chem. 45 (2006) 3557.
[62] W.-F. Wu, R.Van. Eldik, Inorg. Chem. 37 (1998) 1044.
[63] B. Valuer, Molecular Fluorescence: Principles and Applications, Wiley-VCH, Weinheim, 2001.
[64] E.Y. Li, Y.-M. Cheng, C.-C. Hsu, P.-T. Chou, G.-H. Lee, I.-H. Lin, Y. Chi, C.-S. Liu, Inorg. Chem. 45 (2006) 8041.
[65] P.A. Anderson, F.R. Keene, T.J. Meyer, J.A. Moss, G.F. Stouse, J.A. Treadway, J. Chem. Soc., Dalton Trans. (2002) 3820.
[66] C.-L. Lee, R.R. Das, J.-J. Kim, Chem. Mater. 16 (2004) 4642.
[67] M.K. Nazeemuddin, R. Humphry-Baker, D. Bermer, S. River, L. Zuppiroli, M. Graetzel, J. Am. Chem. Soc. 125 (2003) 8790.
[68] A. Vlcek Jr., Coord. Chem. Rev. 230 (2002) 225.
[69] S. Zalis, M. Burby, T. Kotrba, P. Maouses, M. Towrie, A. Vleck Jr., Inorg. Chem. 43 (2004) 1723.
[70] I.R. Farrell, A. Vlcek, Coord. Chem. 208 (2000) 87.

Polyhedron 28 (2009) 534–540

Contents lists available at ScienceDirect

Polyhedron

journal homepage: www.elsevier.com/locate/poly

Solid state synthesis and characterization of a triple chain calcium(II) coordination polymer showing two different bridging 4-nitrobenzoate coordination modes

Bikshandarkoil R. Srinivasan [a,*], Santosh Y. Shetgaonkar [a], Christian Näther [b], Wolfgang Bensch [b]

[a] Department of Chemistry, Goa University, Goa 403 206, India
[b] Institut für Anorganische Chemie, Christian-Albrechts Universität Kiel, D-24098 Kiel, Germany

ARTICLE INFO

Article history:
Received 8 October 2008
Accepted 17 November 2008
Available online 27 December 2008

Keywords:
4-Nitrobenzoate
2-Methylimidazole
Coordination polymer
Pentagonal bipyramid
Monoatomic bridging
Triple chain

ABSTRACT

The solid state reaction of $[Ca(H_2O)_4(\eta^1\text{-4-nba})(\eta^2\text{-4-nba})]$ **1** (4-nba = 4-nitrobenzoate) with 2-methylimidazole (L^2) at 100 °C results in the formation of a Ca(II) coordination polymer $[Ca(H_2O)(L^2)(4\text{-nba})_2]_n$ **2**. Compound **2** was characterized by elemental analysis, spectral and thermal methods, and its structure determined. The coordination polymer **2** crystallizes in the centrosymmetric monoclinic space group $P2_1/n$ with all atoms situated in general positions and its structure consists of a central Ca(II), a monodentate 2-methylimidazole, a bridging water ligand (μ_2-H_2O), a bidentate bridging (μ_2-η^1:η^1) 4-nba ligand and a monoatomic bridging (μ_2-η^2) 4-nba ligand. Each seven-fold coordinated Ca(II) in the title compound is bonded to a nitrogen atom of a terminal 2-methylimidazole (L^2) ligand, two symmetry related water molecules and four symmetry related 4-nba ligands, resulting in a distorted pentagonal bipyramidal $\{CaO_6N\}$ polyhedron. Due to the bridging nature of the aqua and 4-nba ligands [(2-methylimidazole)calcium(II)] units in **2** are linked into a one-dimensional coordination polymer consisting of three chains, all of which propagate along *b*-axis. In the triple chain coordination polymer a Ca···Ca separation of 3.8432(3) Å is observed between neighbouring Ca(II) ions. The oxygen atoms of the carboxylate and nitro functionalities of the 4-nba ligand and the coordinated water are involved in O–H···O, N–H···O and C–H···O interactions. A comparative study of nine alkaline-earth 4-nitrobenzoate compounds is described.

© 2008 Elsevier Ltd. All rights reserved.

1. Introduction

In recent years metal-organic frameworks (MOFs) or coordination polymers have attracted much attention because of their topology and potential applications in catalysis, adsorption (gas storage), separation, luminescence, magnetism, drug delivery etc [1–9]. Ligands containing carboxylic acid functional groups are attractive candidates for the construction of coordination polymers as metals can be linked into an extended chain with the aid of bridging binding modes of the carboxylate ligand [10,11]. Depending on the electronic and steric requirements of the central metal, the flexibility, binding modes and hydrogen bonding characteristics of the carboxylate ligand, the presence of additional bridging or terminal ligands, coordination polymers of differing dimensionalities (D) namely one (1D)-, two (2D)- and three (3D)-dimensional can be constructed.

Compared to the extensive chemistry of coordination polymers based on transition metals, the coordination chemistry of group 1 and 2 metal compounds with organic ligands is a relatively less explored area. Recently there is a growing interest in the chemistry of the coordination compounds of s-block elements as alkali and/or alkaline-earth metal cations are preferred to transition or lanthanide metal ions because most of the s-block cations have the advantage of being non-toxic, cheap and soluble in aqueous media. The recent work of Fromm [12] provides an overview on different ligand and polymer types of the s-block compounds. In the past decade several MOFs of alkaline earth metals have been synthesized, structurally characterized and their properties investigated [13–48].

For the preparation of coordination polymers different synthetic methodologies have been reported. These include the aqueous reaction of basic metal sources like metal carbonate or hydroxide with the carboxylic acid under ambient conditions [13–26], reaction of aqueous metal chloride or nitrate with the carboxylic acid in the presence of a mild base [27–41], the hydrothermal reaction of metal sources with carboxylic acids in autoclaves under autogeneous pressures [42–48]. Based on a review of the synthetic methods of s-block coordination compounds, it has been noted that microwave and solid state synthesis are scarce for the preparation of alkaline-earth metal-organic frameworks unlike the solution or hydrothermal methods of synthesis, which have been more widely used [12].

* Corresponding author. Tel.: +91 832 6519316; fax: +91 832 2451184.
E-mail addresses: srini@unigoa.ac.in, brsrinivasan@gmail.com (B.R. Srinivasan).

0277-5387/$ - see front matter © 2008 Elsevier Ltd. All rights reserved.
doi:10.1016/j.poly.2008.11.022

Recently we reported [49] that the zero-dimensional compound $[Ca(H_2O)_4(\eta^1\text{-4-nba})(\eta^2\text{-4-nba})]$ (4-nba = 4-nitrobenzoate) **1** can be readily transformed into a one-dimensional Ca(II) coordination polymer $[Ca(L^1)(4\text{-nba})_2]_n$ by heating it in the presence of *N*-methylimidazole (L^1) (Scheme 1) demonstrating that thermal reactions can be employed as an useful alternative method for the preparation of new coordination polymers. The loss of coordinated water molecules during the thermal reaction leads to a reorganization of the coordination sphere around Ca(II) resulting in the formation of a polymeric chain compound. In the present work, we have investigated the solid state reaction of compound **1** with 2-methylimidazole (L^2) which is an isomer of L^1 (Scheme 1). It is interesting to note that the reaction of **1** with L^2 at 100 °C results in the formation of a new mixed ligand one-dimensional Ca(II) coordination polymer **2** consisting of three chains.

2. Experimental

2.1. Materials and methods

All the chemicals used in this study were of reagent grade and were used as received. The starting materials and reaction products are air stable and hence were prepared under normal laboratory conditions. The compounds $[Ca(H_2O)_4(\eta^1\text{-4-nba})(\eta^2\text{-4-nba})]$ **1** [50] and $[Ca(H_2O)(4\text{-nba})_2]$ **1a** [49] were prepared as described earlier. Infrared (IR) spectra were recorded on a Shimadzu (IR Prestige-21) FT-IR spectrometer in the range 4000–400 cm^{-1}. The samples for the IR spectra were diluted with KBr in the solid state and the signals referenced to polystyrene bands. UV–Vis diffuse-reflectance spectra were obtained using a Shimadzu UV-2450 double beam spectrophotometer. $BaSO_4$ powder was used as reference (100% reflectance). Absorption data were calculated from the reflectance data using the Kubelka–Munk function $(a/S = (1-R)^2/2R$ where a is the absorption coefficient, R the reflectance and S the scattering coefficient). ^{1}H NMR spectrum was recorded in DMSO-d_6 on a Bruker 400 MHz FT-NMR spectrometer. Luminescence spectra were recorded at RT using a Perkin–Elmer LS 55 Luminescence spectrophotometer. TG-DSC measurements were performed in flowing air, in Al_2O_3 crucibles on a STA-409PC simultaneous thermal analyzer from Netzsch. A heating rate of 10 K min^{-1} was employed for all measurements. The insoluble 4-nbaH obtained on acid treatment of the complexes was weighed as described earlier [51] and metal analysis was performed titrimetrically following a standard procedure. Isothermal weight loss studies were performed in an electric furnace.

2.2. Preparation of $[Ca(H_2O)(L^2)(4\text{-nba})_2]_n$ **2**

A powdered sample of compound **1** (0.444 g, 1 mmol) was mixed well with 2-methylimidazole (L^2) (0.082 g, 1 mmol) and the solid mixture was heated on a steam bath for ~30 min. The hot reaction mixture was cooled, washed well with ether and dried in air to obtain compound **2** as a yellow powder in quantitative yield. Crystals suitable for structure determination were prepared by recrystallizing the powdered sample from hot water (~10 ml) containing L^2 (0.246 g, 3 mmol). The crystalline needles of **2** were washed with cold water followed by alcohol and then dried in air. The infrared spectrum and the DSC thermogram of the crystalline product are identical with that of the yellow powder. **2** can also be prepared by first heating a powdered sample of **1** on a steam bath for ~20 min to obtain the monohydrate $[Ca(H_2O)(4\text{-nba})_2]$. The N-donor ligand ($L^2$) was mixed with this freshly prepared monohydrate and left at 100 °C for 15 min to obtain **2**.

Anal. Calc. for $CaC_{18}H_{16}N_4O_9$ (**2**): Ca 8.48; 4-nbaH 70.75; CaO 11.87; C 45.76; H 3.41; N 11.86. Found: Ca, 8.45; 4-nbaH, 70.30, CaO, 11.81; C, 45.73; H, 3.63; N, 11.8%.

IR data: 3536 (υ_{O-H}), 3264 (υ_{N-H}), 3117, 2204, 1944, 1622, 1591, 1570, 1514, 1487, 1412, 1346, 1323, 1280, 1169, 1148, 1103, 1011, 997, 876, 854, 827, 795, 787, 752, 721, 673, 600, 517, 440 cm^{-1}.

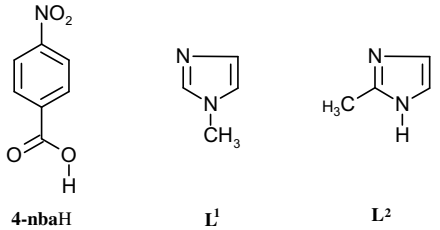
^{1}H NMR (DMSO-d_6) δ (in ppm): 2.25 (s, 3H); 6.83 (d, 2H); 7.14 (d, 2H); 8.14 (q, 2H); 11.52 (s, H).

DSC data (in °C): 172 (*endo*) 410 (*exo*) 559 (*exo*).

UV–Vis (diffuse reflectance): 251, 330 nm.

2.3. X-ray crystal structure determination

Intensity data for **2** was collected on a STOE Image Plate Diffraction System using graphite-monochromated Mo Kα radiation. The structure was solved with direct methods using SHELXS-97 [52] and refinement was done against F2 using SHELXL-97 [52]. All non-hydrogen atoms were refined anisotropically. Aromatic hydrogens were introduced at their calculated positions and included in the refinement riding on their respective parent atoms. The H atoms of the coordinated water molecule were located in the difference Fourier map and refined with fixed isotropic displacement parameters. The technical details of data acquisition and some selected refinement results are summarized in Table 1.



4-nbaH **L**^{1} **L**^{2}

Scheme 1.

Table 1
Crystal data and structure refinement for $[Ca(H_2O)(L^2)(4\text{-nba})_2]_n$ **2**.

Empirical formula	$C_{18}H_{16}CaN_4O_9$
Formula weight	472.43 g mol^{-1}
Temperature	220(2) K
Wavelength	0.71073 Å
Crystal system	Monoclinic
Space group	$P2_1/n$
Unit cell dimensions	a = 15.5486(13) Å
	b = 7.0358(4) Å
	c = 18.4282(15) Å
	α = 90°
	β = 98.789(10)°
	γ = 90°
Volume	1992.3(3) Å^3
Z	4
D_{calc}	1.575 mg/m^3
Absorption coefficient	0.377 mm^{-1}
$F(000)$	976
Crystal size	0.4 × 0.3 × 0.2 mm^3
Θ range for data collection	2.65–28.09°
Index ranges	$-20 \leqslant h \leqslant 20$, $-8 \leqslant k \leqslant 9$, $-24 \leqslant l \leqslant 24$
Reflections collected	18549
Independent reflections	4768 [R_{int} = 0.0334]
Completeness to theta = 28.09°	98.0%
Refinement method	Full-matrix least-squares on F^2
Data/restraints/parameters	4768/0/291
Goodness-of-fit on F^2	1.055
Final R indices [$I > 2\sigma(I)$]	R_1 = 0.0399, wR_2 = 0.1069
R indices (all data)	R_1 = 0.0484, wR_2 = 0.1123
Extinction coefficient	0.027(3)
Largest differences in peak and hole	0.337 and −0.386 e Å^{-3}

3. Results and discussion

3.1. Synthesis and spectroscopy

The solid state reaction of an intimate mixture of the tetraaqua compound $[Ca(H_2O)_4(4\text{-nba})_2]$ **1** and 2-methylimidazole (L^2) at 100 °C resulted in the formation of the mixed ligand Ca(II) compound $[Ca(L^2)(H_2O)(4\text{-nba})_2]$ **2** in quantitative yield (Scheme 2). Compound **2** was formulated based on the elemental analysis and the mass loss leading to the formation of CaO on pyrolysis. The use of excess L^2 in the thermal reaction did not result in the formation of new products containing additional N-donor ligands. The mixed ligand compound **2** can also be synthesized in a two step process. The first step involves the synthesis of a monohydrate compound $[Ca(H_2O)(4\text{-nba})_2]$ **1a** by heating **1** at 100 °C. The reaction of L^2 with **1a** at 100 °C afforded the new compound **2**, which is insoluble in all common solvents like water, CH_3CN, CH_2Cl_2, DMF etc. The solid is partially soluble in DMSO and this property was used to study its NMR spectrum, which exhibits the characteristic signals of the organic moieties 4-nba and L^2.

The thermal reaction of **1** was investigated with other N-donor ligands like pyridine (pKa 5.1), benzimidazole (pKa 5.4) and 4-picoline (pKa 6.02). However from these reactions no new product containing N-donor ligand could be obtained. In all these cases the product obtained consisted of a mixture of $[Ca(H_2O)(4\text{-nba})_2]$ and unreacted N-donor ligand. The unreacted ligand could be quantitatively recovered by washing the mixture with ether. The non-incorporation of N-donor ligand can be attributed to the less basic nature of benzimidazole and the pyridine ligands as compared to L^1 (pKa 7.1) or L^2 (pKa 7.75). The N-donor ligands L^1 and L^2 are isomers and differ in terms of the positioning of the methyl substituent. The ligand L^2 employed in this work resulted in the formation of a final product containing a mole of water for each mole of Ca, unlike imidazole or N-methylimidazole (L^1) which yielded anhydrous compounds having molar composition of Ca:4-nba:L^1 1:2:1 [49]. Crystals of **2** suitable for structure determination were prepared by recrystallising compound **1** from an aqueous solution containing L^2. The crystalline nature of **2** (Fig. 1) can be evidenced from the sharp signals in its powder diffractogram. A comparison of the powder pattern of the bulk sample with that of the theoretically calculated pattern from the single crystal data (*vide infra*) reveals the phase purity of the mixed ligand product **2**. The presence of water in **2** is inferred from the strong signal in its infrared spectrum at 3536 cm^{-1}. The signal at 3264 cm^{-1} can be assigned to the υ_{N-H} (L^2) vibration (Supplementary Fig. 1) of the N-donor ligand. It is to be noted that the profile of the infrared spectra in the region 3500–2800 cm^{-1} of compound **2** is quite different as compared to that of the tetraaqua compound **1** or the monohydrate $[Ca(H_2O)(4\text{-nba})_2]$ **1a**. Compound **2** exhibits several signals in the mid IR region indicating the presence of the organic moieties. The strong signals at 1514 and 1346 cm^{-1} can be assigned to the asymmetric and symmetric stretching vibrations of the $-NO_2$ group of 4-nba while the bands at 1591 and 1570 cm^{-1} are assignable to the asymmetric vibration of the carboxylate group. The signal at 1411 cm^{-1} is assigned for the symmetric vibration of the –COO group. However based only on the infrared data, the exact nature of the binding of the 4-nba ligand cannot be unambiguously determined. In view of the insolubility of **2** in all common solvents the diffuse reflectance spectrum was recorded in the UV–Vis region. The observed signals at 251 and 330 nm in the spectrum can be attributed to the intraligand charge transfer bands of the 4-nba ligand based on a comparison of the reflectance spectra of compounds **2** and **1** (Fig. 2). The luminescence studies of alkaline-earth metal complexes are of considerable importance since the divalent cations Mg and Ca are the most abundant in living cells and play vital roles in many cellular processes [1]. Two emission maxima are observed at around 450 and 490 nm for compound **2**. Interestingly both 4-nbaH and L^2 exhibit emission signals around 450 nm. A scrutiny of the emission spectra reveals that the emission of the Ca(II) compound **2** is reduced as compared to that of the free ligands (Fig. 3). A reduction in the emission intensity has

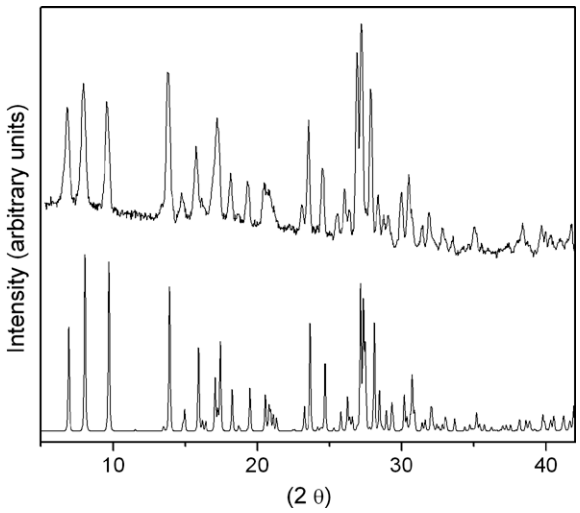
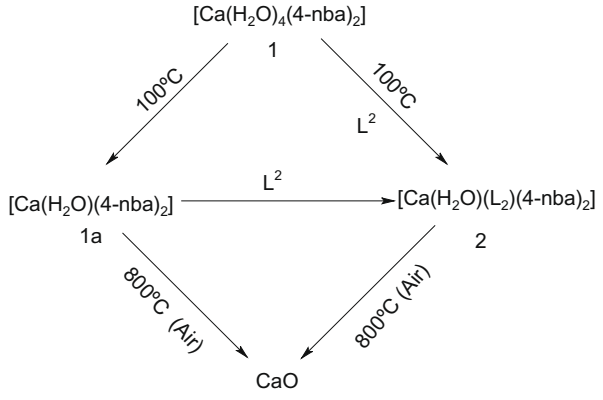


Fig. 1. X-ray powder pattern of a bulk sample of $[Ca(H_2O)(L^2)(4\text{-nba})_2]_n$ **2** (top); theoretical pattern calculated from single crystal data (bottom).



Scheme 2.

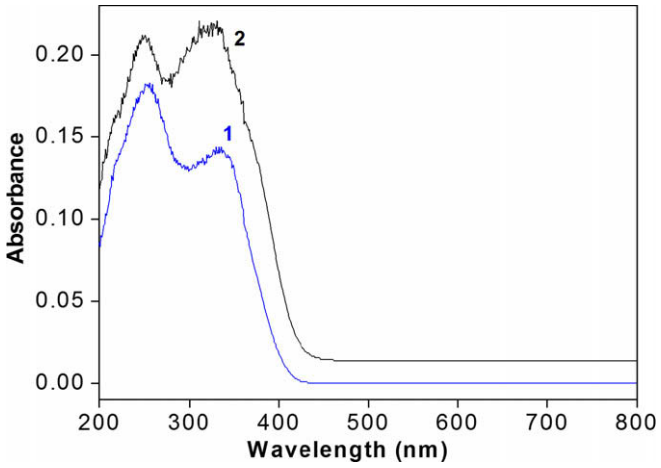


Fig. 2. Diffuse reflectance spectra of **1** and **2**.

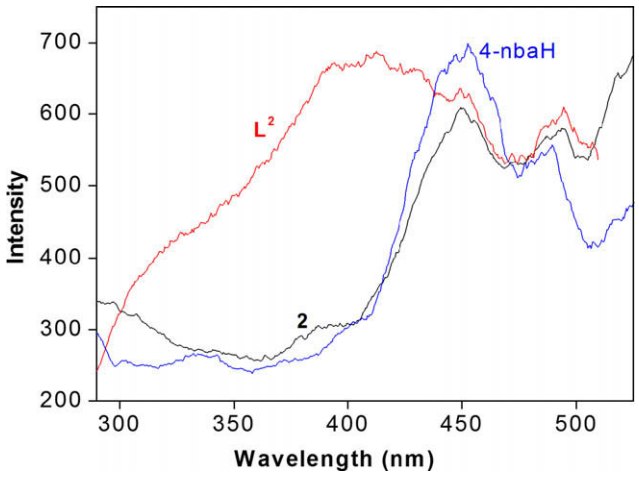


Fig. 3. Luminescence spectra of **2** and free the ligands.

been recently reported for the 1D coordination polymer $[Ca(SA)_2(phen)]_n$ (SA = salicylate; phen = 1,10-phenanthroline) [53].

3.2. Crystal structure description of **2**

Compound **2** crystallizes in the centrosymmetric monoclinic space group $P2_1/n$ with all atoms situated in general positions. The structure reveals that **2** is a coordination polymer and can be formulated as $[Ca(H_2O)(L^2)(4\text{-nba})_2]_n$. The structure of *catena*-poly[[(2-methylimidazole)calcium(II)](μ_2-aqua)(μ_2-η^1:η^1-4-nitrobenzoato)(μ_2-η^2-4-nitrobenzoato)] **2** consists of a central Ca(II) ion, a terminal 2-MeIm ligand, a bridging aqua ligand and two crystallographically independent bridging 4-nba ligands

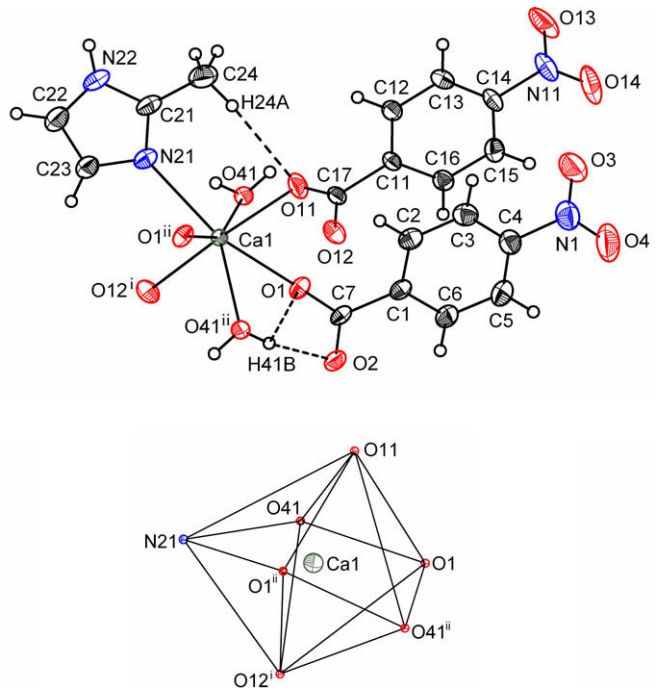


Fig. 4. A view of the coordination sphere of Ca(II) in $[Ca(H_2O)(L^2)(4\text{-nba})_2]_n$ **2**, showing the atom-labeling scheme. Displacement ellipsoids are drawn at the 50% probability level excepting for the H atoms, which are shown as circles of arbitrary radius (top). Intramolecular H-bonding is shown by the broken lines. The distorted pentagonal bipyramidal coordination polyhedron around Ca(II) in **2** (bottom). Symmetry code: (i) $-x+1/2, y-1/2, -z+3/2$; (ii) $-x+1/2, y+1/2, -z+3/2$.

(Fig. 4). In the crystal structure, each Ca(II) is bonded to a nitrogen atom of a terminal 2-methylimidazole ligand, two oxygen atoms from two symmetry related aqua ligands and four oxygen atoms from four symmetry related 4-nba ligands resulting in a distorted $\{CaO_6N\}$ pentagonal bipyramidal polyhedron around Ca (Fig. 4). The geometric parameters of the 4-nba anions and 2-MeIm are in the normal range. The O–Ca–O and O–Ca–N angles range from 65.73(3) to 172.63(5)°, The Ca–O distances in **2** range from 2.3100(11)–2.5654(11) Å (Table 2) and are in agreement with literature values [49,50,53]. A Ca–N bond distance of 2.5024(13) Å is observed. The oxidation state of the central metal in compound **2** based on the bond valence sum was found to be 2.139 [54]. The bond valence sum for the precursor calcium compound $[Ca(H_2O)_4(4\text{-nba})_2]$ **1**, the mixed ligand compound $[Ca(H_2O)_3(Im)(4\text{-nba})_2]\cdot Im$ and the 1-D ladder polymer $[Ca(L^1)(4\text{-nba})_2]_n$ are 2.187, 2.27 and 2.177, respectively. It is interesting to note that the bond valence sums are very close to the expected value of 2 for the bivalent metal and the estimated bond valence sums for the coordination polymers **2** and $[Ca(L^1)(4\text{-nba})_2]_n$ are slightly less than those observed for the zero-dimensional calcium compounds.

The coordinated water (O41) functions as a μ_2-bridging ligand with the O41 atom linked to two symmetry related Ca(II) ions resulting in the formation of an infinite chain extending along *b*-axis (Supplementary Fig. 2). It is interesting to note that both 4-nitrobenzoates in each formula unit are coordinated to the central Ca(II) in different bridging modes. One of the two unique 4-nba anions in each formula unit is coordinated to two different Ca(II) ions through one of the carboxylate oxygen atoms (O1), which functions as a monoatomic bridge (μ_2-η^2) resulting in an extended chain along *b*-axis (Supplementary Fig. 3). The second independent 4-nba ligand functions as a bridging bidentate ligand (μ_2-η^1:η^1) and is linked to two symmetry related Ca(II) ions via O11 and O12 oxygen atoms. An infinite chain extending along *b*-axis is formed due to this binding mode of 4-nba. Due to the bridging nature of the aqua and 4-nba ligands, [(2-methylimidazole)calcium(II)] units in **2** are linked into a one-dimensional coordination polymer consisting of three chains, all of which propagate along *b*-axis (Fig. 5). In the triple chain coordination polymer a Ca···Ca separation of 3.8432(3) Å is observed between neighbouring Ca(II) ions. This value is comparable with the Ca···Ca distance of 3.8585(7) Å reported for the related compound $[Ca(L^1)(4\text{-nba})_2]_n$ [49] and in several other Ca(II) coordination polymers.

A scrutiny of the structure reveals that the oxygen atoms of the carboxylate and nitro functionalities of the 4-nba ligand and the coordinated water are involved in O–H···O, N–H···O and C–H···O interactions. A total of six H-bonding interactions with H···O dis-

Table 2
Selected bond lengths and bond angle (Å, °) for $[Ca(H_2O)(L^2)(4\text{-nba})_2]_n$ **2**.

Ca(1)–O(11)	2.3100(11)	Ca(1)–O(41)	2.4978(11)
Ca(1)–O(12)^{i}	2.3119(11)	Ca(1)–N(21)	2.5024(13)
Ca(1)–O(1)^{ii}	2.4205(11)	Ca(1)–O(41)^{ii}	2.5654(11)
Ca(1)–O(1)	2.4912(11)	Ca(1)–Ca(1)^{ii}	3.8432(3)
O(11)–Ca(1)–O(12)^{i}	172.63(5)	O(12)^{i}–Ca(1)–N(21)	83.69(5)
O(11)–Ca(1)–O(12)^{ii}	87.00(4)	O(1)^{ii}–Ca(1)–N(21)	77.74(4)
O(12)–Ca(1)–O(1)^{ii}	100.11(4)	O(1)–Ca(1)–N(21)	146.38(4)
O(11)–Ca(1)–O(1)	79.52(4)	O(41)–Ca(1)–N(21)	80.64(4)
O(12)^{i}–Ca(1)–O(1)	93.94(4)	O(11)–Ca(1)–O(41)^{ii}	95.97(4)
O(1)^{ii}–Ca(1)–O(1)	135.28(3)	O(12)^{i}–Ca(1)–O(41)^{ii}	85.31(4)
O(11)–Ca(1)–O(41)	85.80(4)	O(1)^{ii}–Ca(1)–O(41)^{ii}	65.73(3)
O(12)^{i}–Ca(1)–O(41)	88.42(4)	O(1)–Ca(1)–O(41)^{ii}	73.50(4)
O(1)^{ii}–Ca(1)–O(41)	155.67(4)	O(41)–Ca(1)–O(41)^{ii}	138.19(3)
O(1)–Ca(1)–O(41)	65.76(3)	N(21)–Ca(1)–O(41)^{ii}	139.17(4)
O(11)–Ca(1)–N(21)	99.84(5)		

Symmetry transformations used to generate equivalent atoms: $-x+1/2, y-1/2, -z+3/2$; (ii) $-x+1/2, y+1/2, -z+3/2$.

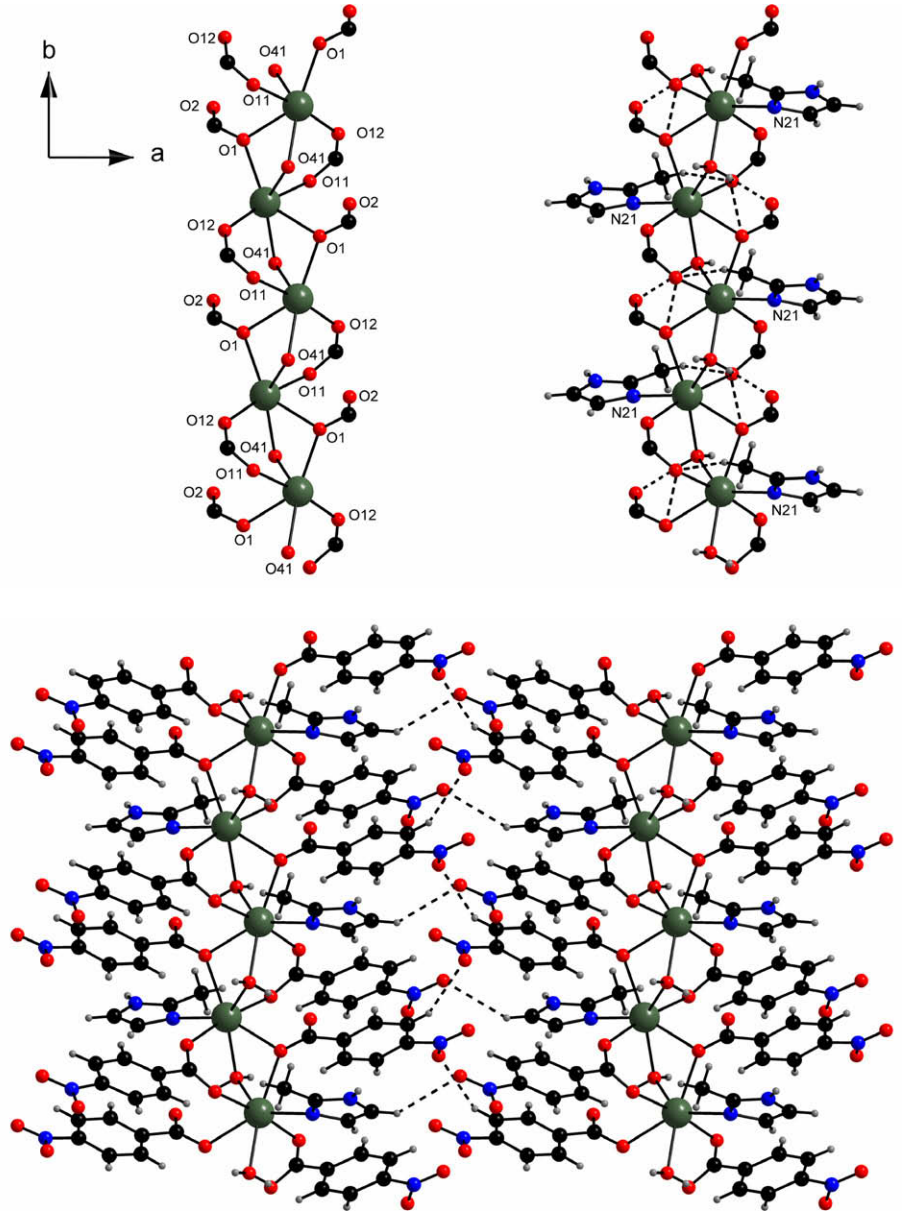


Fig. 5. A part of the triple chain extending along *b*-axis due to the bridging binding modes of the aqua (O41) and the crystallographicaly independent μ_2-η^2 (O1) and μ_2-η^1:η^1 (O11, O12) 4-nba ligands in **2**. For clarity, only the –COO groups of 4-nba and the O atom of water are shown (top right). The H-atoms of the bridging water and the terminal L^2 ligand (N21) are included in the triple chain to show the intrachain H-bonding interactions in broken lines (top left). A view along *c* axis is shown for the crystallographic packing of **2**. Two adjacent polymeric chains of **2** in the *ab* crystallographic plane are linked by weak C–H···O bonds shown in broken lines (bottom).

Table 3
Hydrogen-bonding geometry (Å, °) for $[Ca(H_2O)(L^2)(4\text{-nba})_2]_n$ **2.**

D–H···A	*d*(D–H)	*d*(H···A)	*D*(D···A)	<DHA	Symmetry code
Intrachain interactions					
C24–H24A···O11	0.971	2.411	3.347	162	
O41–H41B···O2	0.820	1.831	2.642	170	[−*x* + 1/2, *y* − 1/2, −*z* + 3/2]
O41–H41B···O1	0.820	2.600	3.026	114	[−*x* + 1/2, *y* − 1/2, −*z* + 3/2]
Interchain interactions					
N22–H22···O2	0.870	2.012	2.873	170	[*x* − 1/2, −*y* + 3/2, *z* − 1/2]
O41–H41A···O13	0.820	2.160	2.972	171	[−*x* + 1, −*y* + 1, −*z* + 1]
C5–H5···O3	0.940	2.532	3.398	153	[−*x* + 3/2, *y* + 1/2, −*z* + 3/2]

tances ranging from 1.831 to 2.600 Å (Table 3) are observed. These can be classified as intra- and interchain interactions. The C24–H24A···O11, O41–H41B···O2 and O41–H41B···O1 interactions occur within the triple chain 1-D polymer, while the N22–H22···O2, O41–H41A···O13 and C5–H5···O3 interactions serve to link adjacent polymeric chains (Fig. 5).

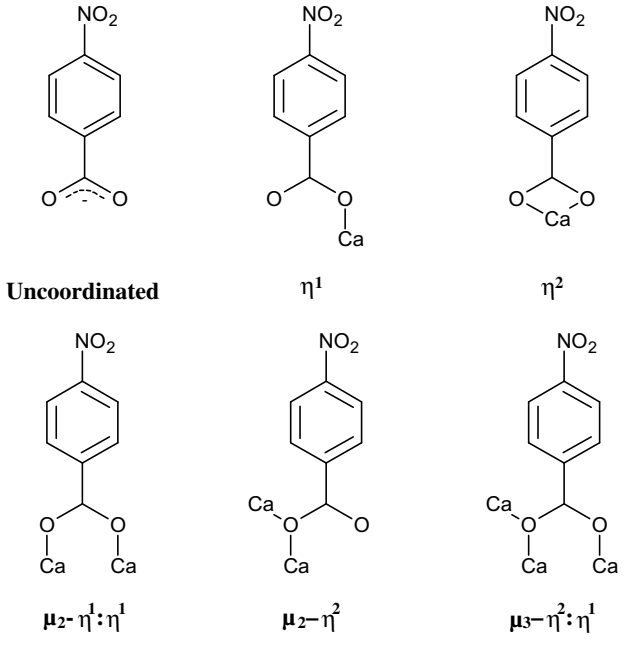
Table 4
Structural features of 4-nitrobenzoates of alkaline-earth metals.

Compound	C.N.	Space group	Nuclearity	Binding mode of 4-nba	H-bonding	Reference
$[Mg(H_2O)_6](4\text{-nba})_2 \cdot 2H_2O$	6	$P\bar{1}$	Monomer	Uncoordinated	O–H···O	[56]
$[Mg(H_2O)_2(Im)_2(4\text{-nba})_2]$	6	$P\bar{1}$	Monomer	η^1	O–H···O, N–H···O	[55]
$[Mg(H_2O)(L^1)_2(4\text{-nba})_2]_2$	6	$P\bar{1}$	Dimer	η^1, μ_2-η^1:η^1	O–H···O	[56]
$[Ca(H_2O)_4(4\text{-nba})_2]_n$	7	$P2_1/c$	Monomer	η^1, η^2	O–H···O, C–H···O	[50]
$[Ca(H_2O)_3(Im)(4\text{-nba})_2] \cdot Im$	6	$P2_1/c$	Monomer	η^1	O–H···O, N–H···O, O–H···N	[55]
$[Ca(L^1)(4\text{-nba})_2]_n$	6	$P\bar{1}$	Polymer	μ_2-η^1:η^1, μ_3-η^2:η^1	C–H···O	[49]
$[Ca(H_2O)(L^2)(4\text{-nba})_2]_n$	7	$P2_1/n$	Polymer	μ_2-η^1:η^1, μ_2-η^2	O–H···O, C–H···O, N–H···O	This work
$[Sr(H_2O)_7(4\text{-nba})](4\text{-nba}) \cdot 2H_2O$	9	$P2_1/c$	Monomer	η^2, uncoordinated	O–H···O, C–H···O	[57]
$[Ba(H_2O)_5(4\text{-nba})_2]_n$	9	$P2_1/c$	Polymer	η^2, μ_2-η^1:η^1	O–H···O, C–H···O	[58]

Abbreviations: C.N. = coordination number; 4-nba = 4-nitrobenzoate; Im = imidazole; L^1 = *N*-methylimidazole; L^2 = 2-methylimidazole.

3.3. Comparative study of alkaline-earth 4-nitrobenzoates

The coordination polymer $[Ca(H_2O)(L^2)(4\text{-nba})_2]_n$ **2** described in this work and the reported compounds $[Ca(H_2O)_4(\eta^1\text{-4-nba})(\eta^2\text{-4-nba})]$ **1** [50], $[Ca(H_2O)_3(Im)(\eta^1\text{-4-nba})_2] \cdot Im$ [55], and $[Ca(L^1)(4\text{-nba})_2]_n$ [49] constitute a group of Ca(II) compounds with a 1:2 mol ratio of Ca:4-nba and exhibit different binding modes of the 4-nba ligand. In addition to these 4-nitrobenzoates of Ca(II), five other 4-nba compounds containing Mg, Sr and Ba have been structurally characterized [55–58]. The availability of structural features of several compounds (Table 4) permits a comparative study of the structural chemistry of alkaline-earth 4-nitrobenzoates, the details of which are described below. All the structurally characterized alkaline-earth 4-nitrobenzoates listed in Table 4, exhibit a metal:4-nba ratio of 1:2 and crystallize in centrosymmetric space groups. The nuclearity of the compounds ranges from monomer (five compounds) to dimer (one compound) and polymer (three compounds). The coordination number of the central metal varies from 6 to 9, with the Mg(II) compounds showing hexacoordination. The Sr and Ba compounds exhibit nine coordination while both hexa and hepta coordination are observed in the Ca(II) compounds. In addition to functioning as charge balancing anions for the bivalent metal in all the compounds, 4-nba is bonded to the central metal as a monodentate (η^1) or bidentate or (η^2) or as a bridging (μ-) ligand (Scheme 3). In $[Mg(H_2O)_6](4\text{-nba})_2 \cdot 2H_2O$ the 4-nba anions are not coordinated to the central metal, while in $[Sr(H_2O)_7(4\text{-nba})](4\text{-nba}) \cdot 2H_2O$ one unique 4-nba remains uncoordinated with the other 4-nba functioning as a chelating bidentate ligand. The bridging bidentate binding mode (μ_2-η^1:η^1) is observed in the mixed ligand dimeric Mg(II) compound as well as in the three coordination polymers. The monoatomic bridging binding mode (μ_2-η^2) and the tridentate bridging coordination modes (μ_3-η^2:η^1) are observed in the Ca(II) coordination polymers. Interestingly in the four different Ca(II)-4-nitrobenzoates a total of five different coordination modes of the 4-nba ligand are observed. All the compounds exhibit several H-bonding interactions resulting in different H-bonded networks.



Scheme 3. Structurally characterized binding modes of 4-nba ligand in alkaline-earth 4-nitrobenzoates.

3.4. Thermal studies

The TG–DSC thermogram of compound **2** is depicted in Fig. 6. The DSC curve of compound **2** exhibits three thermal events. The first endothermic process at 172 °C can be assigned to the loss of a neutral water ligand. The observed mass loss of 10.52% is much more than the loss expected for the loss of a mole of water. The drop in the TG curve indicates that the loss of water results in the loss of the neutral N-donor ligand. The isothermal weight loss studies at this temperature showed a mass loss of 13% which is much more than the loss expected for a mole of water and much less than loss due to either L^2 or a combination of two neutral ligands in **2**. The exothermic events at 410 and 559 °C correspond to the degradation of the 4-nba ligand as evidenced by the rapid drop in the TG curve. The assignment of the endothermic signal at 410 °C for the decomposition of 4-nba gains more credence as a similar behaviour has been observed for the related Ca(II) com-

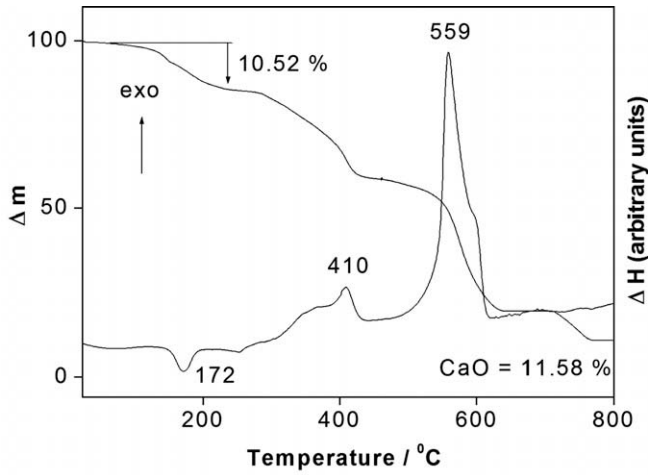


Fig. 6. TG–DSC thermogram of compound **2**.

pounds **1** and **1a** [49]. The TG curve above 750 °C is parallel to the temperature axis and observed residue of 11.58% is in very good agreement with the expected value of 11.87% for the formation of CaO. The formation of CaO as the final residue has been confirmed based on the X-ray powder pattern of the residue (Supplementary Fig. 4) as well as isothermal weight loss studies.

4. Conclusions

In summary, we have shown that the zero-dimensional mononuclear tetraaqua Ca(II) compound **1** can be transformed into a phase pure Ca(II) coordination polymer $[Ca(H_2O)(L^2)(4\text{-nba})_2]_n$ **2** by heating it in the presence of 2-methylimidazole (L^2). The key step in this solid state transformation is the formation of an intermediate monohydrate compound followed by incorporation of the N-donor ligand into the coordination sphere of Ca(II) resulting in the formation of a triple stranded coordination polymer. A comparative study of the structural features of nine 4-nitrobenzoate compounds of alkaline-earth metals reveals five different binding modes of the 4-nba ligand all of which are observed in the structurally characterized compounds $[Ca(H_2O)_4(4\text{-nba})_2]_n$ **1** $[Ca(H_2O)_3(Im)(4\text{-nba})_2]\cdot Im$, $[Ca(L^1)(4\text{-nba})_2]_n$ and $[Ca(H_2O)(L^2)(4\text{-nba})_2]_n$ **2**.

Acknowledgements

BRS thanks Miss J.V. Sawant for helpful discussions and Prof. R. Murugavel, Department of Chemistry, IIT-Mumbai for the luminescence spectral data. This work is supported by the Department of Science and Technology, New Delhi under Grant No. SR/S1/IC-41/2003.

Appendix A. Supplementary data

CCDC 688701 contains the supplementary crystallographic data for compound **2**. These data can be obtained free of charge via http://www.ccdc.cam.ac.uk/conts/retrieving.html, or from the Cambridge Crystallographic Data Centre, 12 Union Road, Cambridge CB2 1EZ, UK; fax: (+44) 1223 336 033; or e-mail: deposit@ccdc.cam.ac.uk. Supplementary data associated with this article can be found, in the online version, at doi:10.1016/j.poly.2008.11.022.

References

[1] C. Janiak, J. Chem. Soc. Dalton Trans. 2781 (2003).
[2] M. Eddaoudi, D.B. Moler, H. Li, B. Chen, T.M. Reineke, M. O'Keeffe, O.M. Yaghi, Acc. Chem. Res. 34 (2001) 319.
[3] J. Kim, B. Chen, T.M. Reineke, H. Li, M. Eddaoudi, D.B. Moler, M. O'Keeffe, O.M. Yaghi, J. Am. Chem. Soc. 123 (2001) 8239.
[4] S. Surblé, F. Millange, C. Serre, T. Düren, M. Latroche, S. Bourrelly, P.L. Llewellyn, G. Férey, J. Am. Chem. Soc. 128 (2006) 14889.
[5] H. Dathe, E. Peringer, V. Roberts, A. Jentys, J.A. Lercher, C.R. Chimie 8 (2005) 753.
[6] S.S. Han, W.-Q. Deng, W.A. Goddard, Angew. Chem. Int. Ed. 46 (2007) 6289.
[7] P. Horcajada, C. Serre, M. Vallet-Regi, M. Sebban, F. Taulelle, G. Ferey, Angew. Chem. Int. Ed 45 (2006) 5974.
[8] M. Dinca, J.R. Long, J. Am, Chem. Soc. 127 (2005) 9376.
[9] J.A. Rood, B.C. Noll, K.W. Henderson, Inorg. Chem. 45 (2006) 5521.
[10] R.C. Mehrotra, A. Singh, Prog. Inorg. Chem. 46 (1997) 239.
[11] F.A. Cotton, G. Wilkinson, C.A. Murillo, M. Bochmann, Advanced Inorganic Chemistry, sixth ed., John Wiley & Sons, Inc, Chichester, 1999. p. 487.
[12] K.M. Fromm, Coord. Chem. Rev. 252 (2008) 856. and references therein.
[13] H.-F. Zhu, Z.-H. Zhang, W.-Y. Sun, T. Okamura, N. Ueyama, Crystal Growth Design 5 (2005) 177.
[14] M. Dan, A.K. Cheetham, C.N.R. Rao, Inorg. Chem. 45 (2006) 8227.
[15] Z. Fei, T.J. Geldbach, D. Zhao, R. Scopelliti, P.J. Dyson, Inorg. Chem. 44 (2005) 5200.
[16] B.R. Srinivasan, S.Y. Shetgaonkar, P. Raghavaiah, J. Chem. Sci. 120 (2008) 249.
[17] S.H. Dale, M.R.J. Elsegood, Acta Crystallogr. C 59 (2003) m540.
[18] M. Odabaşoğlu, O. Büyükgüngör, Acta Crystallogr. E 63 (2007) m712.
[19] Z. Fei, T.J. Geldbach, R. Scopelliti, P.J. Dyson, Inorg. Chem. 45 (2006) 6331.
[20] R.K.B. Nielsen, K.O. Kongshaug, H. Fjellvåg, Solid State Sci. 8 (2006) 1237.
[21] K. Aliouane, N. Rahahlia, A.-G. Laidoudi, S. Dahaoui, C. Lecomte, Acta Crystallogr. E63 (2007) m1834.
[22] S. Wörl, I.O. Fritsky, D. Hellwinkel, H. Pritzkow, R. Krämer, Eur. J. Inorg. Chem. (2005) 759.
[23] R. Murugavel, P. Kumar, M.G. Walawalkar, R. Mathialagan, Inorg. Chem. 46 (2007) 6828.
[24] R. Murugavel, S. Banerjee, Inorg. Chem. Commun. 6 (2003) 810.
[25] A. Bacchi, M. Carcelli, C. Pelizzi, G. Pelizzi, P. Pelagatti, D. Rogolino, M. Tegoni, C. Viappiani, Inorg. Chem. 42 (2003) 5871.
[26] S. Fox, I. Büsching, W. Barklage, H. Strasdeit, Inorg. Chem. 46 (2007) 818.
[27] Q. Shuai, S. Chen, S. Gao, Inorg. Chim. Acta. 360 (2007) 1381.
[28] A. Grirrane, A. Pastor, E. Álvarez, R. Moyano, A. Galindo, Inorg. Chem. Commun. 10 (2007) 1125.
[29] R. Murugavel, V.V. Karambelkar, G. Anantharaman, M.G. Walawalkar, Inorg. Chem. 39 (2000) 1381.
[30] J.-G. Zhao, S. Gao, Z.-Y. Zhang, L.-H. Huo, H. Zhao, Acta Crystallogr. E 62 (2006) m278.
[31] R. Murugavel, V.V. Karambelkar, G. Anantharaman, Indian J. Chem. 39A (2000) 843.
[32] R. Murugavel, K. Baheti, G. Anantharaman, Inorg. Chem. 40 (2001) 6870.
[33] Y. Yang, G. Jiang, Y.-Z. Li, J. Bai, Y. Pan, X.-Z. You, Inorg. Chim. Acta 359 (2006) 3257.
[34] L.B. Cole, E.M. Holt, Inorg. Chim. Acta 108 (1985) 159.
[35] D.A. Lenev, K.A. Lyssenko, R.G. Kostyanovsky, Euro. J. Inorg. Chem. (2003) 2979.
[36] I. Senkovska, U. Thewalt, Acta Crystallogr. C61 (2005) m448.
[37] R.H. Groeneman, J.L. Atwood, Crystal Eng. 2 (1999) 241.
[38] W.-D. Song, X.-X. Guo, C.-H. Zhang, Acta Crystallogr. E 63 (2007) m399.
[39] S. Yano, M. Numata, M. Kato, S. Motoo, T. Nishimura, Acta Crystallogr. E 57 (2001) m488.
[40] M.L.G. Salido, P.A. Mascaros, R.L. Garzon, M.D.G. Valero, J.N. Low, J.F. Gallagher, C. Glidewell, Acta Crystallogr. B 60 (2004) 46.
[41] I. Senkovska, Z. Naturforsch. 61b (2006) 1383.
[42] L. Pan, T. Frydel, M.B. Sander, X. Huang, J. Li, Inorg. Chem. 40 (2001) 1271.
[43] C.A. Williams, A.J. Blake, C. Wilson, P. Hubberstey, M. Schroder, Crystal Growth Design 8 (2008) 911.
[44] C. Volkringer, T. Loiseau, G. Férey, J.E. Warren, D.S. Wragg, R.E. Morris, Solid State Sci. 9 (2007) 455.
[45] L.-C. Yu, Z.-F. Chen, H. Liang, C.-S. Zhou, Y. Li, J. Mol. Struct. 750 (2005) 35.
[46] R.-X. Yuan, R.-G. Xiong, Z.-F. Chen, X.-Z. You, S.-M. Peng, G.-H. Lee, Inorg. Chem. Commun. 4 (2001) 430.
[47] I. Senkovska, S. Kaskel, Eur. J. Inorg. Chem. (2006) 4564.
[48] M.J. Plater, A.J. Roberts, J. Marr, E.E. Lachowski, R.A. Howie, J. Chem. Soc. Dalton Trans. (1998) 797.
[49] B.R. Srinivasan, S.Y. Shetgaonkar, J.V. Sawant, P. Raghavaiah, Polyhedron 27 (2008) 3299.
[50] B.R. Srinivasan, J.V. Sawant, P. Raghavaiah, Indian J. Chem. 45A (2006) 2392.
[51] B.R. Srinivasan, S.C. Sawant, Thermochim. Acta 402 (2003) 45.
[52] G.M. Sheldrick, Acta Crystallogr. A64 (2008) 112.
[53] R. Murugavel, R. Korah, Inorg. Chem. 46 (2007) 11048.
[54] Bond valence sums were determined using the software VaList. A.S. Wills, VaList, Program available from www.ccp14.ac.uk.
[55] B.R. Srinivasan, J.V. Sawant, P. Raghavaiah, J. Chem. Sci. 119 (2007) 11.
[56] B.R. Srinivasan, J.V. Sawant, C. Näther, W. Bensch, J. Chem. Sci. 119 (2007) 243.
[57] B.R. Srinivasan, P. Raghavaiah, J.V. Sawant, Acta Crystallogr. E63 (2007) m2251.
[58] B.R. Srinivasan, J.V. Sawant, S.C. Sawant, P. Raghavaiah, J. Chem. Sci. 119 (2007) 593.

Polyhedron 28 (2009) 541–547

Contents lists available at ScienceDirect

Polyhedron

journal homepage: www.elsevier.com/locate/poly

Synthesis, spectroscopy, computational study and prospective biological activity of two novel 1,3,2-diazaphospholidine-2,4,5-triones

Khodayar Gholivand [a,*], Nasrin Oroujzadeh [a], Mauricio F. Erben [b], Carlos O. Della Védova [b,c,*]

[a] Department of Chemistry, Tarbiat Modarres University, P.O. Box 14115 – 175, Tehran, Iran
[b] CEQUINOR (UNLP-CONICET, CCT-La Plata), Departamento de Química, Facultad de Ciencias Exactas, Universidad Nacional de La Plata, CC 962, 47 esq. 115, 1900 La Plata, Argentina
[c] Laboratorio de Servicios a la Industria y al Sistema Científico UNLP-CIC-CONICET), Departamento de Química, Facultad de Ciencias Exactas, Universidad Nacional de La Plata, La Plata, Argentina

ARTICLE INFO

Article history:
Received 26 August 2008
Accepted 18 November 2008
Available online 29 December 2008

Keywords:
Phospholidine
Phosphoramidate
Dynamic NMR
Free energy of activation
Ab initio calculation
Biological activity prediction

ABSTRACT

The preparation of two new 1,3,2-diazaphospholidine-2,4,5-triones is reported. Thus, 2-chloro-1,3,2-diazaphospholidine-2,4,5-trione [ClP(O)(NHC(O)C(O)NH) (**I**)] and 2-benzylamino-1,3,2-diazaphospholidine-2,4,5-trione [$C_6H_5CH_2NHP(O)(NHC(O)C(O)NH)$ (**II**)] have been synthesized by the reaction of $POCl_3$ with the corresponding carboxylic diamide salts. The characterization of the compound **I** was performed by multinuclear (^1H, ^{13}C, ^{31}P) NMR and FTIR spectroscopies, elemental analysis and also mass spectrometry. Both compounds show two signals at room temperature in the low field region of the ^1H NMR spectrum, which collapsed to a single peak when the temperature is increased. Dynamic NMR (^1H DNMR) and quantum chemical studies were performed to gain insight from this conversion process. The free activation energies, calculated at the coalescence temperatures are 18.51 and 17.45 kcal/mol for compounds (**I**) and (**II**), respectively, which are associated with a tautomeric interconversion process, most likely between the lactam and lactim forms. The relative energy, molecular geometry and vibrational properties of several plausible tautomers were analyzed by using quantum chemical calculations at the HF/6-311G** and B3LYP/6-311++G** levels of the theory. The nuclear magnetic shielding tensors have been calculated for both tautomeric forms using the gauge independent atomic orbital (GIAO) method at the B3LYP/6-311++G(3df,2p) level of approximation. A biological activity prediction using the PASS software shows that compound (**I**) can be characterized by a superb anti-HIV activity whereas compound (**II**) is a very good antineoplastic.

© 2008 Elsevier Ltd. All rights reserved.

1. Introduction

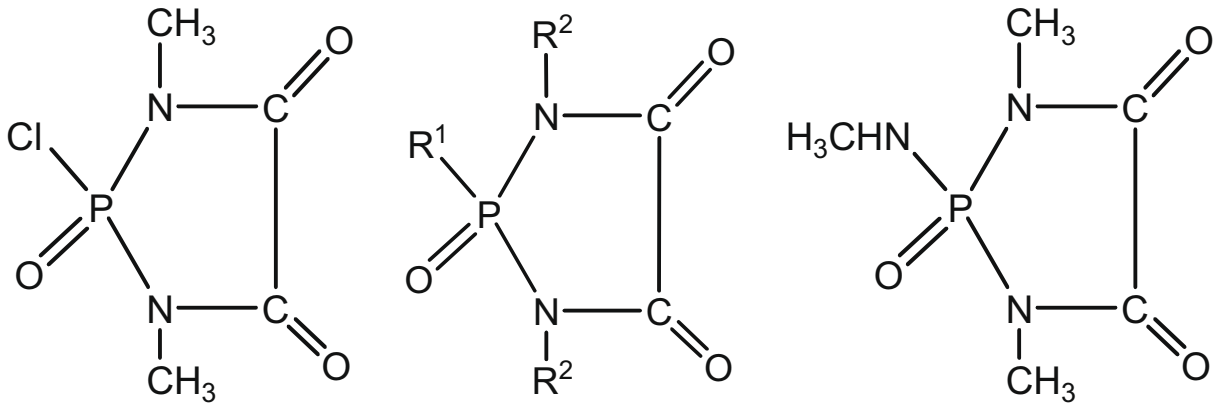
N-heterocycles formed by oxo group(s) constitute a family of polar ligands with peculiar properties since they may change either their hydrogen-bond donating or accepting sites through the protonation/deprotonation process or by a tautomeric transformation. Pyrimidine and purine derivatives are the best-known examples for such oxo-hydroxy (lactam-lactim) tautomerism [1,2]. 3-OH and 5-OH isooxazoles also show this proton relocation mechanism [3–5]. Another important class of molecules with this versatility consists of five-membered heterocycles with at least two more N atoms in the ring. In the neutral form, N-atom is bounded to a mobile H-atom (pyrrolic N–H) whereas the remaining N-atoms posses a basic character being their lone pairs formally situated in the ring plane. Imidazole is the most well-known representative of this family [6–8].

The syntheses of heterocycles containing N- and pentavalent P-atoms (phospholidines) as well as carbonyl groups (Scheme 1) were conducted by Becke-Goehring and Wolf [9] reacting oxamide with PCl_5. In such a five-membered ring heterocycles, the reactivity of the heteroatom towards nucleophiles is greatly enhanced in comparison with the acyclic analogues. The reactivity of phospholidines towards amines and alcohols, as well as the mechanism and the influence of steric hindrance have been reported [10]. Moreover, the molecular structure for the 1,3-dimethyl-2-methylamino-1,3,2-diazaphospholidine-2,4,5-trione (Scheme 1) has been studied from an X-ray diffraction analysis [11].

Carbacylamidophosphate compounds with general formula $R'C(O)NHP(O)R_2$ have a decisive role in catalytic and metabolism processes [12–14], and many applications in agricultural and pharmacological industries [15–19]. Their rich biological activity is related with the presence of a peptide group in these compounds. Some *N*-ethyleneimine derivatives at the phosphoryl group have been proposed as anti-cancer drugs [20–22]. Furthermore, carbacylamidophosphate compounds are also potential O,O′-donor

* Corresponding authors. Address: CEQUINOR (UNLP-CONICET, CCT-La Plata), Departamento de Química, Facultad de Ciencias Exactas, Universidad Nacional de La Plata, CC 962, 47 esq. 115, 1900 La Plata, Argentina. Tel.: +54 221 4259485 (C.O. Della Védova); tel.: +98 21 8011001x3443 (K. Gholivand).
E-mail addresses: gholi_kh@modares.ac.ir (K. Gholivand), carlosdv@quimica.unlp.edu.ar (C.O. Della Védova).

0277-5387/$ - see front matter © 2008 Elsevier Ltd. All rights reserved.
doi:10.1016/j.poly.2008.11.024



Scheme 1. Five membered heterocycles (phospholidines) related with the species studied in this work. *Left:* 1,3-Dimethyl-2-chloro-1,3,2-diazaphospholidine-2,4,5-trione [9]. *Centre:* 1,3-(R^2)-2-R^1-1,3,2-diazaphospholidine-2,4,5-trione, with (R_1 = Alk, OAlk, OAr, R_2 = Me, CH_2Ph) [10]. *Right:* 1,3-dimethyl-2-methylamino-1,3,2-diazaphospholidine-2,4,5-trione [11].

ligands for metal ions and play a dominant role as ligands in the development of transition metal-catalyzed asymmetric synthesis specially as powerful chelating systems, closely related to β-diketonates [23–25]. Carboxylamides have a very low nucleophilic reactivity on their nitrogen moieties due to the interaction between N-atom and the C=O π-system [26,27]. In addition, reactions of phosphorus halides with amides lead to products in which the contribution of the P–O linkage is more evident than the corresponding P–N linkages [12,26,27]. This wide range of applications has stimulated a great research effort involving preparations and characterizations of compounds possessing the –C(O)NHP(O)– moiety [22,23,28–36].

In the present study, two new cyclic diazaphospholidine species have been synthesized by the reaction of $POCl_3$ with the carboxylic diamide (oxamide) salt. The characterization of the products was carried out by IR, ^1H, ^{13}C, ^{31}P NMR spectroscopy, elemental analysis and also mass spectrometry for compound (**I**). Both compounds show two signals at room temperature in the low field region of the ^1H NMR spectrum, which collapsed to a single peak when the temperature is increased. Dynamic NMR (DNMR) and quantum chemical studies were performed to clarify this process. Moreover, a prediction of the biological activity for these compounds was performed using the PASS (prediction of activity spectra for substances) software [37–43].

2. Results

2.1. Synthesis

The synthesis of the compound **I** was carried out according to Eq. (1)

$$Na_2(H_2N_2C_2O_2) + POCl_3 \rightarrow ClP(O)(NHC(O)C(O)NH) + 2NaCl \quad (1)$$

A mixture of oxamide ($H_2NC(O)C(O)NH_2$) and NaH dissolved in toluene was stirred at ca. 110 °C. After 3.5 h, the mixture was filtered and the solvent was distilled off in vacuum. To the formed oxamide natrium salt in benzene was added a large excess of $POCl_3$ under stirring. After 6 h refluxing, the mixture was filtered and **I** was obtained in a yield of 83 %. All reactions were done under inert (dry gas N_2) atmosphere.

Compound **II** was subsequently prepared by reaction of **I** with benzyl amine according to Eq. (2)

$$ClP(O)(NHC(O)C(O)NH) + C_6H_5CH_2NH_2 \rightarrow C_6H_5CH_2NHP(O)(NHC(O)C(O)NH) + HCl \quad (2)$$

Compound **I** and benzyl amine were dissolved in chloroform at 0 °C and stirred for 5 h. The mixture was then filtered and the remaining solid was purified by washing with DMF and Et_2O. Compound **II** was obtained in a yield of 90%.

2.2. Mass spectrometry

Mass spectrum of **I** reveals the presence of the molecular ion at *m*/*z* 168. Its fragmentation shows two peaks at *m*/*z* 133 and 105, corresponding to the loss of Cl and ClC=O groups and three intense peaks at *m*/*z* 89, 59, 42 due to the P(O)NC=O, NPN and NC=O fragments, respectively.

2.3. NMR spectroscopy

^1H NMR spectra of the products show two signals corresponding to amidic H-atom at 7.68 ppm and 7.97 ppm for **I** and at 7.66 ppm and 7.92 ppm for **II**. In addition **II** shows typical signals corresponding to the aromatic ring and to the methylene group. As expected for compound **I**, the ^{13}C NMR spectrum shows only one single peak in the carbonylic region at 163.4 ppm assigned to the C=O group. For compound **II**, the ^{13}C NMR shows in addition peaks from the aromatic ring and the methylene moiety. In the ^{31}P NMR spectra both compounds present a signal near −0.8 ppm.

The peaks near 7.8 ppm in the ^1H NMR spectra disappear when compounds **I** and **II** are dissolved in D_2O. Whereas no changes are observed by decreasing the temperature of the aqueous solutions, both peaks collapse at higher temperatures. The coalescence temperatures (T_c) are 90 °C for (**I**), and 70 °C for (**II**) (Fig. 1).

2.4. Vibrational spectra

To our knowledge, no vibrational spectra for phospholidinones have been reported. The analysis of calculated harmonic vibrational frequencies can be useful in the present circumstances for both purposes, the assignment of the experimental vibrational data and the search for the occurrence of tautomeric forms (See Fig. 2). A tentative assignment of the observed bands was carried out by comparison with theoretical wavenumbers, as well as with relevant data reported in the literature for related molecules [45–47]. The main features in the vibrational spectra can be satisfactorily interpreted on the basis of the presence of one most stable oxo tautomer. Characteristic fundamental modes assigned to the vibrations of cyclic N-carbonyl phosphordiamidates moiety in compounds **I** and **II** are shown on Table 1.

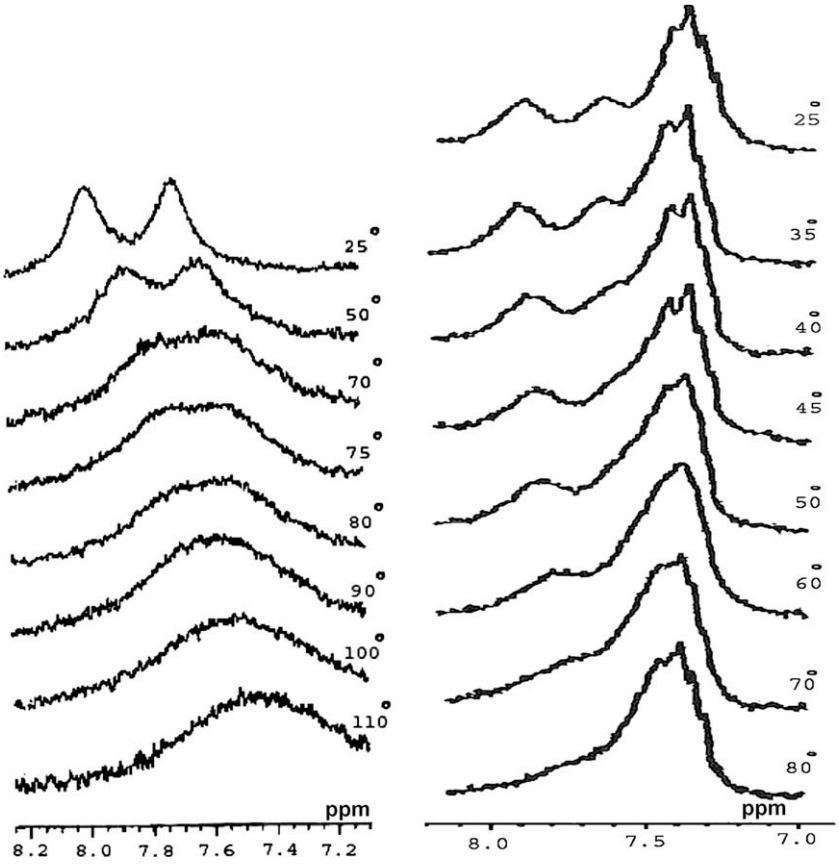


Fig. 1. Dynamic ^{1}H NMR spectra in the 7-8.2 ppm region of compounds **I** (left) and **II** (right).

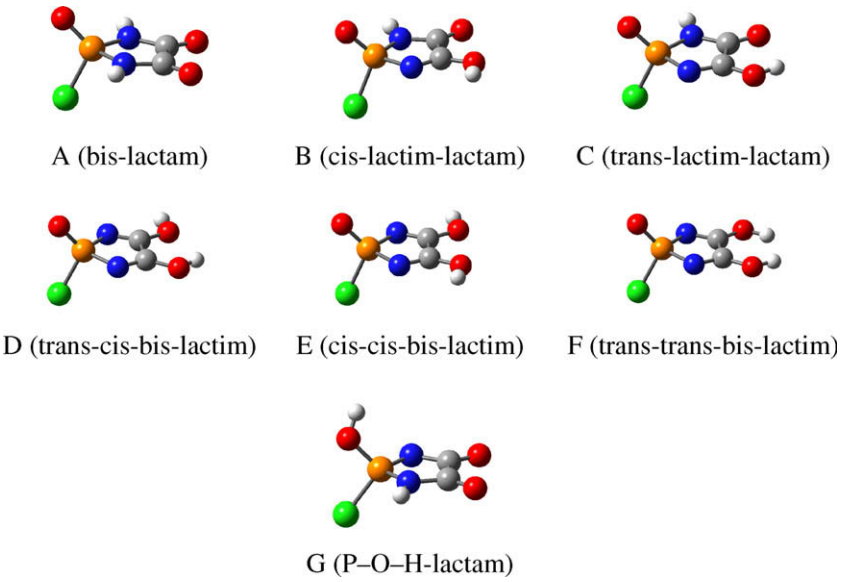


Fig. 2. Molecular models for tauromeric forms (A–G) of compound **I**.

The infrared spectra for the title compounds are dominated by strong absorptions in the high frequency range near 3360 cm^{-1} and 3150 cm^{-1}. These bands are assigned to the antisymmetric and symmetric N–H stretching mode, respectively. A third ν(N–H) mode is expected for compound **II**, due to the $-CH_2-NH-$ moiety, which was observed as an intense band in the infrared spectrum at 2975 cm^{-1}. The strong integrated intensity displayed for these bands, as well as the difference in the frequency values observed between these modes, can serve as an evidence of the presence of hydrogen bond interactions in the solid state. These interactions are obviously absent in the free molecule. Therefore, the theoretical calculations predict quite similar values for the antisymmetric and symmetric N–H stretching mode. The strong intensity band near 1650 cm^{-1} for compounds **I** and **II** can be as-

Table 1
Experimental and calculated vibrational data (cm^{-1}) for compounds **I** and **II**.

Experimental[a]		Calculated[b]		Tentative assignment[b]
I	**II**	**I**	**II**	
3365 s	3365 s	3596 (28) A″	3603 (14)	ν_{as}(N–H)
3125 s	3165s	3595 (2) A′	3601 (8)	ν_{sym}(N–H)
–	2975 vs	–	3574 (6)	ν(CH_2N–H)
1653 vs	1654 vs	1854 (20) A″	1836 (41)	ν_s(C=O)
		1849 (100) A′	1831 (100)	ν_{as}(C=O)
1339 m	1330 m	1371 (34) A′	1356 (17)	δ_{sym}(N–H)
1278 m	1280 m	1287 (80) A′	1281 (94)	ν(P=O)
		1265 (27) A′	1257 (12)	ν_{sym}(C–N)
1090 m	1106 m	1161 (8) A″	1176 (9)	ν_{as}(C–N)
965 w	965 m	912 (13) A″	892 (2)	ν_{as}(P–N)
882 w	876 m	892 (11) A′	879 (12)	ν_{sym}(P–N)
791 w	787 w	728 (5) A	718 (4)	Breath ring
681 w	691 m	624 (3) A″	632 (1)	δ_{as}(C=O)
528 w	571 m	578 (12) A′	526 (6)	ρ_s(N–H)
489 w	493 w	491 (2) A″	488 (2)	ρ_s(N–H)

[a] Solid in KBr pellets.
[b] B3LYP/6-311++G** method without factor scale correction, in parentheses relative band strength; 100 % 636.7 and 649.2 Km/mol for compounds **I** and **II**, respectively. Symmetry modes for compound **I** based on calculated Cs molecular symmetry.

signed to the C=O stretching vibrations. This relatively low frequency value could be related again with the presence of hydrogen bond interaction in the solid phase. Calculated values for the υ(C=O) mode are 1849 and 1831 cm^{-1} for compounds **I** and **II**, respectively. The bands observed near 1280 cm^{-1} in the infrared spectra of both compounds **I** and **II**, can be assigned with confidence to the P=O stretching mode. The computed values are in good agreement with this assignment (1287 and 1281 cm^{-1}, respectively). Other characteristic fundamental modes of vibration for these molecules are the N–C and N–P symmetric and antisymmetric stretching modes, observed in the 1100–800 cm^{-1} region as bands of medium intensity.

2.5. Ab initio calculations

The species studied in the present work can exist as different lactam-lactim tautomers [19]. Moreover different conformations are plausible for each lactim tautomer, depending on the relative mutual orientation of the C=N double bond and the O–H single bond. The P–O–H-lactam tautomer has been also considered. Accordingly, seven structures of **I**, whose molecular models are shown in Fig. 2, have been taken into consideration. Full geometry optimizations and frequency calculations were performed for each of these structures by using quantum chemical calculations at the HF and B3LYP methods with the 6-311G** and 6-311++G** basis sets, respectively. Relative ΔE° energy values (corrected by zero point energy) are listed in Table 2.

All computational methods predict the bis-lactam structure (form A in Fig. 2) as the most stable form of compound **I** and a molecular structure with C_S symmetry. The second and third stable forms correspond to the lactim-lactam tautomers represented as structures B and C in Fig. 2, respectively. HF and B3LYP approximations predict a slightly different order for the energy difference of these conformers. The HF/6-311G** level of the theory computes the structure B and C 9.67 and 10.10 kcal mol^{-1} higher in energy than the lactam form, respectively. Similar values are computed with the B3LYP/6-311++G** (9.74 and 9.00 kcal mol^{-1}, respectively). The bis-lactim tautomers (forms D–F in Fig. 2) result also in minima of the potential hypersurface. They are located ca. 20 kcal mol^{-1} higher in energy than the global minimum. The P–O–H-lactam tautomer (form G) also results to be a high energy minimum (ΔE^0 > 24 kcal/mol).

Table 2
Calculated relative energies (corrected by zero-point energy) in kcal mol^{-1} for the different tautomers and conformers of compound **I**.

Tautomer	HF/6-311G**	B3LYP/6-311++G**	PCM/B3LYP /6-311++G**[a]
A	0.00	0.00	0.00
B	9.67	9.74	9.32
C	10.10	9.00	11.50
D	27.98	26.13	24.38
E	24.19	23.49	20.82
F	–[b]	37.46	30.92
G	26.04	24.65	21.08

[a] DMSO dielectric constant was used in the PCM calculations.
[b] Converges to structure D.

The influence of the solvent on the tautomeric equilibrium is well known. Changes in the difference of polarity among tautomers can induce significant variations of their relative energies in solution. As the very first approximation, we decided the use of the PCM/B3LYP approximation to compute the influence of solvent effects on tautomerism. Because DMSO is the solvent used in our NMR experiments, its dielectric constant was used for these calculations. It is important to mention, however, that the PCM model does not consider the presence of explicit solvent molecules; hence specific solute–solvent interactions are not described and the calculated solvation effects arise only from mutual solute–solvent electrostatic polarization. Results obtained at the PCM/B3LYP/6-311++G** level of approximation are also given in Table 2. It is observed that the inclusion of electrostatic polarization has minor influence on the calculated relative energy values. Thus, the order of stability for DMSO solvated (ε = 46.7) molecules of **I** affords the following trend: A > B > C > E > G > D > F.

The optimized geometrical parameters for the gas phase and DMSO-solvated species for the main tautomers are summarized in Table SM1 given as Supplementary data. For comparison, the geometrical parameters determined from X-ray diffraction analysis for the closely related 1,3-dimethyl-2-methylamino-1,3,2-diazaphospholidine-2,4,5-trione [11] (see Scheme 1) are also listed in Table SM1.

The similarity between the computed and experimental [11] structural parameters for molecule **I** is remarkable. The 1,3,2-diazaphospholidine ring together with the C=O groups tend to adopt a planar system. The planarity of the ring promotes further stereoelectronic interactions of the P- and the N-atoms of the ring. The P–N distance in the compound **I** **(ca.** 1.68 Å) is significantly shorter than that reported for single P–N bond (1.78 Å). A similar range (1.60–1.66 Å) was observed for this bond length for a variety of carbacylamidophosphates [22,23,28–31]. By comparison of the acyclic moiety, dramatic changes in the geometry of the oxamide skeleton result from its incorporation into a five-membered phospholidine ring. The formation of a ring from the acyclic moiety constrains the N–C–C angles to near 108°, which represents an unusually low value for a sp^2 hybridized C-atom. As suggested previously, the trigonal geometry around the N-atoms and the small N–P–N angle caused by the cyclic structure (91°) enable stabilizing interactions between the vacant d orbitals on phosphorus and the two 2p non-bonding orbitals of the ring nitrogen atoms, suggesting the presence of a delocalized π system, which could play a important role in the chemical properties of this species [10].

As expected, the main differences in the geometrical structure of lactam/lactim tautomers are related with the N–C and C=O bonds. In the most stable oxo form, the N–C and C=O bond length values are 1.688 and 1.196 Å (B3LYP/6-311++G**), which can be considered as typical values for N-carbonyl phosphoramidate compounds. These values are 0.12 Å shorter and longer in the tautomeric hidroxo structure, respectively, denoting a strengthening of the N=C bond order and the concomitant diminution of the C–

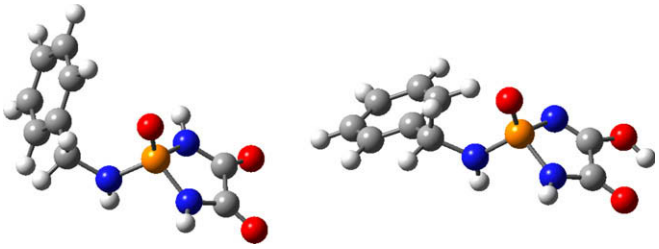


Fig. 3. Molecular models for the most stable tautomeric forms of compound **II**.

O(H) bond order. The influence of solvent effects on the geometrical parameters can be clearly seen through the changes of bond lengths and bond angles, as shown in Table SM1 given as Supplementary data. In general, the changes are more significant in the oxo- than in the hydroxy-form tautomer. The N–C bond parameter is mostly affected by the solvation. In the oxo tautomer, both bonds become shorter in solution than in the gas phase by 0.018 Å. In the hydroxy-form, the most affected parameters correspond to the C–O(H) and N=C bond lengths, which increase their lengths by ca. 0.011 and 0.014 Å, respectively, when the structure B (Fig. 2) is formally transferred from the gas phase to DMSO solution. As expected, the oxo form tautomers have slightly larger dipole moments than their hydroxy-form counterparts. In DMSO, this difference is 0.66 D.

Taking into consideration the results obtained for compound **I**, the two main tautomers were calculated for compound **II**. Molecular models for these forms are shown in Fig. 3. At the HF/6-311G** level of calculations, the lactam tautomer is more stable than the lactim form by 11.9 kcal/mol. The gas phase optimized geometrical parameters for these structures are summarized in Table SM2 in the Supplementary data section.

2.6. PASS results (biological activity prediction)

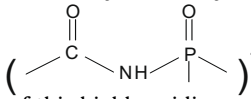
The title compounds were considered by the software PASS (prediction of activity spectra for substances) [37–43]. The current version of PASS predicts simultaneously 900 biological activity types for 45 000 compounds with a mean accuracy of 85% [48,49]. The results of the PASS for a certain compound are presented to be either active (Pa) or inactive (Pi). The total PASS list is reported on the web-site [45]. The Pa values should be considered in the following way. In the case that Pa > 0.7 the expectation of activity is high. By the contrary, if Pa < 0.7 the activity should be considered less probable. Selected biological activity spectra for compound (**I**) and (**II**) are given in Table 3 (The whole spectra are given as Supplementary data). According to this table, the prediction of the activity as HIV-1 protease inhibitor and antiviral (HIV) activities in compound (**I**) and antineoplastic activity in compound (**II**) are remarkably high.

Table 3
Biological activity spectra for compound (**I**) and (**II**) evaluated by the PASS 1.913 program.

Compound **I**			Compound **II**		
Biological activity	Pa	Pi	Biological activity	Pa	Pi
HIV-1 protease inhibitor	0.997	0.000	Antineoplastic	0.957	0.006
Antiviral	0.995	0.002	Cytostatic	0.835	0.005
Antiviral (HIV)	0.995	0.001	Leukopoiesis inhibitor	0.838	0.003
Carcinogenic, group 1	0.923	0.005	Carcinogenic, group 1	0.836	0.007
CYP2C19 human substrate	0.889	0.003	CYP2C19 human substrate	0.777	0.006
Leukopoiesis inhibitor	0.819	0.004	Toxic	0.726	0.018
Antiviral (Poxvirus)	0.786	0.007	Alkylator	0.671	0.006
Cardiotoxic	0.736	0.027	Cardiotoxic	0.664	0.048
Immunomodulator	0.654	0.035	Teratogen	0.619	0.022
Antiviral (Herpes)	0.646	0.016	Immunosuppressant	0.620	0.021
Nucleotide metabolism regulator	0.548	0.054	Embryotoxic	0.614	0.021
Cytostatic	0.528	0.015	Hematopoietic inhibitor	0.604	0.008

Pa = predictive activity, Pi = predictive inactivity.

3. Discussion

Intramolecular interactions of the N–H group could occur either with the P=O or with the C=O moiety in carbacylamidophosphate compounds with structure  . Therefore, the spectroscopic consequence of this highly acidic proton is a shift to low field in the ^{1}H NMR spectra. Moreover, carbacylamidophosphates generally show values of $^2J_{PNH}$ coupling constants between the phosphorus and the amino proton [23,29,50,51]. Unexpectedly, no evidence of coupling between the phosphorus and the amidic protons ($^2J_{PNH}$) was observed in the ^{1}H NMR spectra for both synthesized molecules. ^{1}H NMR spectra of compounds **I** and **II** show two singlet peaks with roughly equal intensities at 7.97 and 7.68 ppm for compound (**I**) and 7.92 and 7.66 ppm for compound (**II**), respectively.

Dynamic NMR study of both compounds **I** and **II** shows that by increasing the temperature, the two amine proton single peaks collapse into one single resonance with a coalescence temperature of ca. 90 °C for **I**, and 70 °C for **II**. The rate constant and the activation free energy for this process calculated *via Eyring* equation [44] for compounds **I** and **II** are 18.5 and 17.5 kcal/mol, respectively.

To understand the exchange process, the following points should be considered:

(a) Since the P–N amidic bonds in **I** and **II** are restricted, there are no rotations around these bonds and the calculated energies could not be considered as rotational barrier.
(b) According to the quantum chemical calculations both molecules present planar N-atoms with sp^2 hybridization in their ground states. The planarity of the N-atoms was also determined by X-ray crystallography for phospholidines [11] and similar carbacylamidophosphates [22,23,29,30]. Thus, the calculated activation free energies ($\Delta G^{\#}$) could not be due to an inversion barrier.
(c) The tautomeric equilibrium of hydroxypyridines has been studied theoretically owing to their relevance in the oxoamino ↔ hydroxyamino tautomerism of nucleic acids [52]. The 2-pyridone/2-hydroxypyridine system has also been subject of several studies [53–55], the estimated activation energies for the tautomeric conversion has been recently determined by IR spectroscopy [56]. On the other hand, the lactam/lactim equilibrium in parabanic acid has been studied by NMR techniques. No lactim form has been found at room temperature, the activation energy for the formation of the lactim form appear to be extremely high for this compound [57].

The activation free energy values $\Delta G^{\#}$ derived from D NMR for compounds **I** and **II** in DMSO solution can be associated with a tautomeric interconversion process, most likely between the main bis-lactam (A) and the *cis*-lactim-lactam (B) forms. Molecular orbital calculations at the B3LYP/6-311++G** level of approximation for compound **I** in vacuum and DMSO-solvated show that A is more stable than B by 9.74 and 9.32 kcal mol^{-1}, respectively.

Further calculations of the NMR properties of compounds **I** and **II** support this assumption. For compound **I**, the computed B3LYP/6-311++G(3df,2p) magnetic isotropic shielding tensors for both N–H protons in the main form (A) is 6.45 ppm (referred to TMS). The calculated values for the N–H and O–H protons in the cis-lactam-lactim (B) tautomer are 5.48 and 5.40 ppm, respectively. These results are in a qualitative agreement with the ^{1}H-NMR spectrum (Fig. 1), and allow tentatively assigning the corresponding N–H and O–H shift to the signals at 7.97 and 7.68 ppm, respectively.

The chemical shifts for N–H and O–H protons present in the lactam and lactim tautomers of compound **II** were also computed. Due to the C_1 molecular symmetry, both N–H protons in the most stable form of compound **II** are expected to occur at slightly different values. Calculated [B3LYP/6-311++G(3df,2p)] chemical shifts are 5.73 and 5.42 ppm. In the lactim tautomers the N–H proton suffers a little shift to 5.82 ppm and the O–H proton is predicted to appear at lower fields (8.21 ppm). These features are in qualitative good agreement with the experimental spectra taken below the coalescence temperature, where two signals appear at 7.92 and 7.66 ppm.

Thus, quantum chemical calculations suggest that both species exists in DMSO solution in the dynamic equilibrium of the lactam and lactim forms. The extreme low solubility showed by compounds **I** and **II** precludes the study of the solvent effect for these equilibria.

4. Experimental

4.1. Materials and methods

^{1}H, ^{13}C, ^{31}P NMR spectra were recorded on a Bruker (Avance 500, DRY) spectrometer. ^{1}H NMR spectra at high temperatures were recorded on a Jeol–Ex90A spectometer. ^{1}H-, ^{13}C-, ^{31}P-chemical shifts were determined relative to TMS and 85% H_3PO_4, respectively.

Infrared (IR) spectra were recorded on a Shimadzu IR 460 spectrometer. The elemental analysis was performed using a Foss Heraeus model CHN–O-Rapid chemical analysis.

Mass spectroscopy was performed with an 8430 magnetic sector Finnigan-Mat mass spectrometer using 70 eV as ionization energy.

Benzene and chloroform were distilled, other chemicals were used without any further purification and were purchased from the following companies: phosphoryl chloride supra pure (Merck), Toluene 99% (Fluka), Diethylether >9% (Merck), *N*,*N*-dimethylformamide 99% (Merck), phosphorylchloride >99% (Merck), Oxamid 99% (Merck), Benzylamine 99% (Merck), sodium hydride 85% (Merck).

4.2. Synthesis

4.2.1. 2–Chloro–1,3,2.–diazaphospholidine–2,4,5–trione (*I*)

A mixture of 1.1 g (12.5 mmol) oxamide, 0.9 g (37.5 mmol) NaH in 40 ml toluene was stirred at reflux temperature. After 3.5 h, the mixture was filtered and the solvent was distilled off in the vacuum and a salt of oxamide was obtained. Then, 7.67 g (50 mmol) $POCl_3$ was gradually added to a stirred mixture of 25 ml benzene and 0.66 g (5 mmol) salt of oxamide ($Na^+H^-NC(O)C(O)NH^-Na^+$). After 6 h refluxing, the mixture was filtered. The compound (**I**) was obtained in 83 % yield.

Anal. Calc. for (NHC(O)C(O)NH)P(O)Cl: C , 14.2 ; H , 1.2 ; N , 16.6 . Found: C, 14.1; H, 1.3; N, 16.8%; IR Spectrum (KBr, cm^{-1}) : 3365 (s), 3125 (s), 1653 (vs), 1339 (ms), 1278 (m), 1090 (m), 965 (w), 882 (w), 791 (m), 681 (w), 528 (w), 489 (w); ^{1}H NMR (DMSO):$\delta_{(ppm)}$ = 7.68 (s), 7.97 (s); ^{13}C-NMR (DMSO) $\delta_{(ppm)}$ = 163.4 (s); ^{31}P NMR (DMSO): $\delta_{(ppm)} = -0.89$ (s); MS: m/e 168: [(NHC(O)C(O)NH)-P(O)Cl]$^+$ (molecular ion), 133: [(NHC(O)C(O)NH)P(O)]$^+$, 105: [(NHC(O) NH)P(O)]$^+$, 89: [P(O)NC(O)]$^+$, 59: [NPN]$^+$ and 42: [NC(O)]$^+$.

4.2.2. 2-Benzylamino–1,3,2–diazaphospholidine–2,4,5–trione (*II*)

0.428 g (4 mmol) of benzyl amine was added to a stirred mixture of 0.337 g (2 mmol) of compound (**I**) and 25 ml chloroform at 0 °C. After 5 h, the mixture was filtered, the remaining residue was purified by washing with *N*,*N*-dimetyl formamide and diethyl ether, respectively. Then, compound (**II**) was obtained with a yield of 90%.

Anal. Calc. for (NHC(O)C(O)NH)P(O)($NHCH_2Ph$): C, 45.2; H, 4.2, N, 17.6. Found: C, 45.0; H, 4.4; N, 17.9%. IR spectrum (KBr, cm^{-1}): 3365 (s), 3165 (ms), 2975 (vs), 1654 (vs), 1372 (m), 1330 (m), 1280 (m), 1106 (m), 965 (m), 876 (m), 787 (w), 691 (m), 571 (m), 493 (w); ^{1}H NMR (DMSO): $\delta_{(ppm)}$ = 2.07 (s), 3.98 (s), 7.33–7.50 (m), 7.66 (s), 7.92 (s); ^{13}C NMR (DMSO) : $\delta_{(ppm)}$ = 161.1 (s), 40.7 (s), 132.8 (s), 127.6 (s), 127.2 (s), 126.8 (s); ^{31}P NMR (DMSO): $\delta_{(ppm)} = -0.87$ (s).

4.3. Computational methods

All quantum chemical calculations were performed with the GAUSSIAN 98 program package [58]. HF and B3LYP methods were employed with standard basis sets up to the extended valence triple-ζ basis sets augmented with polarization and diffuse functions for both hydrogen and non-hydrogen atoms (6-311++G** basis sets). Gradient techniques were used for the geometry optimizations and vibrational calculations. The stationary structures are confirmed by ascertaining that all ground states have only real frequencies. The tautomeric forms were also optimized in solvents according to the polarisable continuum method, which exploits the generating polyhedra procedure to build the cavity in the polarisable continuum medium, where the solute is accommodated [59–61]. The magnetic isotropic shielding tensors were calculated within the gauge independent atomic orbital (GIAO) method [62] at the B3LYP method with the extended 6-311++G(3df,2p) basis set, using the lowest energy optimized structures calculated at the B3LYP/6-31G(d) level of approximation. Chemical shifts were derived with respect to the NMR isotropic magnetic shielding tensors (in ppm) from the corresponding standard tensor (TMS = 31.62 ppm for ^{1}H [B3LYP/6-311++G(3df,2p)]).

Appendix A. Supplementary data

Supporting material for this article is available from the web or from the authors. Computed (B3LYP/6-311++G**) geometrical parameters for the most stable lactam and lactim-lactam tautomers for **I** and **II** in the gas as well as in solution phases are given in Tables SM1 and SM2, respectively. The whole biological activity spectra for compound **I** and **II** evaluated by the PASS program are given in Table SM3. Supplementary data associated with this article can be found, in the online version, at doi:10.1016/j.poly.2008.11.024.

References

[1] T. Eicher, S. Hauptmann, The Chemistry of Heterocycles, Wiley-VCH, Weinheim, Germany, 2003.
[2] G. Rauhut, in: A.R. Katritzky (Ed.), Advances in Heterocyclic Chemistry, vol. 81, Academic Press, San Diego, 2001, p. 1.
[3] S. Woodcock, D.V.S. Green, M.A. Vincent, I.H. Hillier, M.F. Guest, P. Sherwood, J. Chem. Soc. Perkin Trans. 2 (1992) 2151.
[4] I.R. Gould, I.H. Hillier, J. Chem. Soc. Perkin Trans. 2 (1993) 1771.
[5] C.J. Cramer, D.G. Truhlar, J. Am. Chem. Soc. 115 (1993) 8810.
[6] J.-M. Arrang, M. Garbarg, J.-C. Lancelot, J.-M. Lecomte, H. Pollard, M. Robbs, W. Schunack, J.-C. Schwartz, Nature (London) 327 (1987) 117.

[7] R. Lipp, J.-M. Arrang, M. Garbarg, P. Luger, J.-C. Schwartz, W. Schunack, J. Med. Chem. 35 (1992) 4434.
[8] P.I. Nagy, F.R. Tejada, W.S. Messer, J. Phys. Chem. B 109 (2005) 22588.
[9] M. Becke-Goehring, M.R. Wolf, Z. Anorg. Allg. Chem. 373 (1970) 245.
[10] J.-M. Grévy, M. Mulliez, J. Chem. Soc. Perkin Trans. 2 (1995) 1809.
[11] A.T. Hutton, T.A. Modro, M.L. Niven, S. Scaillet, J. Chem. Soc. Perkin Trans. 2 (1986) 17.
[12] C. Schultz, Bioorg. Med. Chem. 11 (2003) 885.
[13] L.Y. Wu, J.C. Do, M. Kazak, H. Page, Y. Toriyabe, M.O. Anderson, C.E. Berkman, Bioorg. Med. Chem. Lett. 18 (2008) 281.
[14] T.K. Venkatachalam, M. Sarquis, S. Qazi, F.M. Uckun, Bioorg. Med. Chem. 14 (2006) 6420.
[15] D.E.C. Corbridge, Phosphorus: An Outline of its Chemistry, fifth ed., Biochemistry and Technology, Elsevier, Amsterdam, 1995.
[16] C.-B. Xue, Y.-W. Yin, J. Chem. Soc. Perkin Trans. 2 (1990) 431.
[17] A.L. Rozvukhin, G.N. Dolenko, S.A. Krupoder, Magn. Reson. Chem. 23 (1985) 221.
[18] Kh. Gholivand, C.O. Della Védova, M.F. Erben, F. Mojahed, A.M. Alizadehgan, J. Mol. Struct. 840 (2007) 66.
[19] L.I. Katzin, G.W. Mason, D. Peppard, Spectrochim. Acta 34A (1978) 57.
[20] K.E. Gubina, J.A. Shatrava, V.A. Ovchynikov, V.M. Amirkhanov, Polyhedron 19 (2000) 2203.
[21] V.A. Ovchynicov, V.M. Amirkhanov, A.A. Kapshuk, T.Y. Sliva, T. Glowiak, H. Kozlowski, Z. Naturforsch. 53B (1998) 836.
[22] K.E. Gubina, V.A. Ovchynikov, V.M. Amirkhanov, T.Y.U. Silvia, V.V. Skopenko, T. Glowiak, H. Kozowski, Z. Naturforsch. 54B (1999) 1357.
[23] Kh. Gholivand, M. Pourayoubi, Z. Shariatinia, H. Mostaanzadeh, Polyhedron 24 (2005) 655.
[24] V.V. Skopenko, V.M. Amirkhanov, Zh. Neorg. Khim. (Russ) 41 (1996) 611.
[25] L.J. Caudle, E.N. Duesler, R.T. Pain, Inorg. Chem. 24 (1985) 4441.
[26] M. Sterll, K. Rast, Chem. Ber. 90 (1957) 1905.
[27] I. Ugi, R. Meyr, Angew. Chem. 70 (1958) 702.
[28] B.C. Challis, J.N. Iley, J. Chem. Soc. Perkin Trans. II (1987) 1489.
[29] K.E. Gubina, V.M. Amirkhanov, Z. Naturforsch. 55B (2000) 1015.
[30] K.E. Gubina, V.A. Ovchinicov, V.M. Amirkhanov, V.V. Spenko, O.V. Shishkin, Z. Naturforsch. 55B (2000) 495.
[31] P.M. Narula, C.S. Day, B.A. Powers, M.A. Odian, A. Lachgar, W.T. Pennington, R.E. Noftle, Polyhedron 18 (1999) 1751.
[32] T. Chivers, M. Krahn, G. Schatte, M. Parvez, Inorg. Chem. 42 (2003) 3994.
[33] M.P. Duplessis, T.A. Modro, L.R. Nassimbeni, Acta Crystallogr. B 38 (1982) 1504.
[34] S. Bauermister, A.M. Modro, T.A. Modro, A. Zwierzak, Can. J. Chem. 69 (1991) 811.
[35] H. Wan, T.A. Modro, Synthesis (1996) 1227.
[36] A.B. Ouryupin, M.I. Kadyko, P.V. Petrovskii, E.I. Fedin, Tetrahedron Assym. 6 (1995) 1813.
[37] A.V. Stepanchikova, A.A. Lagunin, D.A. Filimonov, V.V. Poroikov, Curr. Med. Chem. 10 (2003) 225.
[38] S. Anzali, G. Barnickel, B. Cezanne, M. Krug, D.A. Filimonov, V.V. Poroikov, J. Med. Chem. 44 (2001) 2432.
[39] A.A. Geronikaki, J.C. Dearden, D.A. Filiminov, L. Galaeva, J. Med. Chem. 47 (2004) 2870.
[40] V.V. Poroikov, D.A. Filimonov, Yu.V. Borodina, A. Kosa, J. Chem. Inf. Comput. Sci. 40 (2000) 1349.
[41] T.A. Gloriozova, D.A. Filiminov, A.A. Lagunin, V.V. Poroikov, Pharm. Chem. J. 32 (1998) 658.
[42] A. Sadym, A.A. Lagunin, D.A. Filiminov, V.V. Poroikov, SAR and QSAR Environ. Res. 14 (2003) 339.
[43] D.A. Filiminov, V.V. Poroikov, Y.V. Borodina, T.A. Gloriozova, J. Chem. Inf. Comput. Sci. 39 (1999) 666.
[44] Horst Friebolin, Basic One- and Two-dimensional NMR Spectroscopy, second ed., VCH, Weiheim, New York, NY, 1993.
[45] Kh. Gholivand, S. Dehghanpour, G. Gerivani, Phosph. Sulfur Silicon 11 (2000) 157.
[46] Kh. Gholivand, C.O. Della Védova, M.F. Erben, H.R. Mahzouni, Z. Shariatinia, S. Amiri, J. Mol. Struct. 874 (2008) 178.
[47] A.G. Iriarte, M.F. Erben, Kh. Gholivand, J.L. Jios, S.E. Ulic, C.O. Della Védova, J. Mol. Struct. 886 (2008) 66.
[48] V.V. Poroikov, D.A. Filiminov, A.V. Stepanchkova, A.P. Budunova, E.V. Shilova, Pharm. Chem. J. 30 (1996) 570.
[49] Web-Site: http://www.Ibmh.msk.Su/PASS.
[50] Kh. Gholivand, S. Ghadimi, H. Naderimanesh, A. Forouzanfar, Magn. Reson. Chem. 39 (2001) 1.
[51] E.A. Robinson, D.S. Lavery, Spectrochim. Acta. 28A (1971) 1099.
[52] P. Cieplak, P. Bash, U.C. Singh, P.A. Kollman, J. Am. Chem Soc. 109 (1987) 6283.
[53] C.J. Cramer, D.G. Truhlar, J. Am. Chem. Soc. 113 (1991) 8552.
[54] M. Szafran, M.M. Karelson, A.R. Katritzky, J. Koput, M.C. Zerner, J. Comput. Chem. 14 (1993) 371.
[55] P. Beak, Acc. Chem. Res. 10 (1977) 186.
[56] H.I. Abdulla, M.F. El-Bermani, Spectrochim. Acta 57A (2001) 2659.
[57] J.A. Glasel, Org. Magn. Reson. 1 (1969) 481.
[58] M. J. Frisch, G. W. Trucks, H. B. Schlegel, G. E. Scuseria, M. A. Robb, U. R. Cheeseman, V. G. Znkrzewski, G. A. Montgomery Jr., R. E. Startman, J. C. Burant, S. Dapprich, J. M. Millam, A. D. Daniels, K. N. Kudin, M. C. Strain, O. Farkas, J. Tomasi, V. Barone, M. Cossi, R. Cammi, B. Mennucci, C. Pamelli, G. Adamo, S. Clifford, J. Ochterski, G. A. Petersson, P. Y. Ayala, Q. Cui, K. Raghavachari, K. Morokoma, D. K. Malick, A. D. Rubuck, K. Raghavachari, J. B. Foresman, J. Cioslawski, J. V. Oritz, B. B. Stlefanov, G. Liu, A. Liashenko, P. Piskorz, I. Komaromi, R. Comper, R. L. Martin, P. J. Fox, T. Keith, M. A. Al-Laham, C. Y. Peng, A. Nanay akkara, C. G. Gonzales, M. Challa Combe, P. M. W. Gill, B. Johnson, W. Chem, M. W. Wong, J. L. Andres, C. Gonzales, M. Head-Gordon and E. S. Replogle, GASSIAN98, Revision A.6, Gaussian Inc., Pittsburgh PA,1998.
[59] V. Barone, M. Cossi, J. Tomasi, J. Comp. Chem. 19 (1998) 404.
[60] V. Barone, M. Cossi, J. Phys. Chem. A 102 (1998) 1995.
[61] M. Cossi, V. Barone, B. Mennucci, J. Tomasi, Chem. Phys. Lett. 286 (1998) 253.
[62] J.R. Cheeseman, G.W. Trucks, T.A. Keith, M.J. Frisch, J. Chem. Phys. 104 (1996) 5497.

Polyhedron 28 (2009) 548–552

Contents lists available at ScienceDirect

Polyhedron

journal homepage: www.elsevier.com/locate/poly

Structural studies on Ph_3MSMPh_3 (M = Sn, Pb): Quest for a metal–metal bond

Neetu Singh, Rajendra Prasad, Subrato Bhattacharya *

Department of Chemistry, Banaras Hindu University, Varanasi 221 005, India

ARTICLE INFO

Article history:
Received 17 October 2008
Accepted 19 November 2008
Available online 2 January 2009

Keywords:
Organotin
Organolead
Metal sulfide
Weak interaction
Metal–metal bonding

ABSTRACT

The title compounds $Ph_3PbSPbPh_3$ (**1**) and $Ph_3SnSSnPh_3$ (**2**) were prepared in high yields by a reaction of Na_2S, respectively, with $Ph_3Pb(SOCMe)$ and $Ph_3Sn(SOCMe)$. X-ray crystallographic and density functional studies were made to understand the structure and bonding in these molecules. Though the Pb–Pb distance in **1** is only marginally shorter than the sum of the corresponding van der Waals' radii, a smaller Pb–S–Pb angle suggests for a Pb···Pb interaction. DFT calculations were performed to analyse the nature of M···M interaction in **1** and **2**. Strong intramolecular π–π interactions subsist between the different phenyl rings of the molecules.

© 2008 Elsevier Ltd. All rights reserved.

1. Introduction

The synthesis of compounds with bonds between heavier main group elements have attracted attention of chemists over the last decade due to their structures, bonding and in some cases, unusual properties [1]. A large number of bi/polynuclear compounds of group 14 metals have been prepared and many of them contain M–M bonds. Though distannane [2] and diplumbane [3] with M–M covalent bonds are known for a long time, a large number of compounds containing various types of tin–tin [4] and lead–lead bonds [5] have been synthesized during past few years. On the other hand, compounds with Sn–Sn or Pb–Pb weak interactions in bi/polynuclear M(II) or M(IV) complexes are rare. Recently, Magyar et al. [6] have reexamined the structures of some Pb(II) compounds and have found the existence of a weak intramolecular interaction in tetraphenylarsonium Pb(II) *iso*-maleonitriledithiolate, $[AsPh_4]_4[Pb_2(i\text{-mnt})_4]$. Importance of such interactions though unrevealed yet, should be viewed in light of enzyme binding with the heavy metal (poisoning). Here, we report a new route of synthesis of Ph_3MSMPh_3 [M = Pb(**1**), Sn(**2**)] and their X-ray structures along with the results of quantum chemical studies to critically analyse the possibility of a weak metal–metal interaction of significance.

2. Experimental

2.1. Starting materials

All solvents were of reagent grade quality and purchased commercially. These were purified by standard methods [7]. Anhydrous sodium sulfide (E. Merck), triphenyltin chloride (Aldrich) and triphenyllead chloride were used as received. Thioacetic acid (96%, Aldrich) was distilled before its use.

2.2. Instrumentation

Elemental analyses were performed using an Exter Model E-440 CHN analyser. NMR spectra were obtained using a JEOL AL 300 FTNMR spectrometer.

2.3. X-ray crystal structure determination

Single-crystal X-ray data on **1** and **2** were collected on a Bruker SMART APEX CCD diffractometer using graphite monochromated Mo Kα radiation (λ = 0.71073 Å). The data integration and reduction were processed with SAINT+ [8] software. The structures were solved by the direct method and then refined on F^2 by the full-matrix least-squares technique with the SHELXL-97 software [9] using the WinGX (version 1.70.01) program package [10]. All non-hydrogen atoms were refined anisotropically. All hydrogen atoms were treated as riding atoms using SHELX default parameters. Other crystallographic data are summarized in Table 1. Since the data collections were done at room temperature the thermal ellipsoids on the carbon atoms are large leading to large esds on the C–C distances.

2.4. Theoretical calculations

All theoretical calculations were performed with the GAUSSIAN 03W set of programs [11]. The effective core potential (ECP) standard basis set LanL2DZ [12] was utilized for all the atoms. Polarization functions (*d,p*) were included in the basis set for calculation of

* Corresponding author. Tel.: +91 542 6702451/2307321x107; fax: +91 542 2368127.
E-mail address: s_bhatt@bhu.ac.in (S. Bhattacharya).

0277-5387/$ - see front matter © 2008 Elsevier Ltd. All rights reserved.
doi:10.1016/j.poly.2008.11.033

Table 1
Crystallographic data of compounds **1** and **2**.

Compound	**1**	**2**
Empirical formula	$C_{36}H_{30}Pb_2S$	$C_{36}H_{30}Sn_2S$
Crystal color and habit	yellow needles	colorless rods
Crystal system	orthorhombic	orthorhombic
Space group	$P2(1)2(1)2(1)$	$P2(1)2(1)2(1)$
a (Å)	9.9124(11)	17.616(4)
b (Å)	17.741(2)	9.835(2)
c (Å)	18.481(2)	18.456(4)
α (°)	90	90
β (°)	90	90.099(4)
γ (°)	90	90
Volume (Å^3)	3250.0(6)	3197.6(11)
Z	4	4
Density (calculated) (Mg Å^{-3})	1.858	1.521
$F(000)$	1704	1448
Index ranges	$-13 \leqslant h \leqslant 8$, $-23 \leqslant k \leqslant 23$, $-24 \leqslant l \leqslant 24$	$-23 \leqslant h \leqslant 22$, $-13 \leqslant k \leqslant 12$, $-24 \leqslant l \leqslant 20$
Temperature (K)	293(2)	293(2)
θ range (°) for data collection	2.30–28.36	2.21–28.42
Reflections collected/unique	21497/7933	20981/7833
R_{int}	0.0724	0.048
R_1 $[I > 2\sigma(I)]$[a]	0.0459	0.0400
wR_2 $[I > 2\sigma(I)]$[b]	0.0963	0.0909
S (all data)	0.96	1.11
Largest difference between peak and hole (e Å^{-3})	0.848 and −0.699	0.56 and −0.74

[a] $R_1 = \Sigma(||F_0| - |F_c||)/\Sigma|F_0|$.
[b] $wR_2 = \{\sum[w(F_0^2 - F_c^2)]/\sum[w(F_0^2)^2]\}^{1/2}$.

bond order. Attempts to use LanL2DZ for Sn/Pb and 6–31V + G** [13] for all other atoms were unsuccessful as convergence criteria [14] could not be met in single point energy calculations using X-ray atomic coordinates.

2.5. Synthesis

2.5.1. Improved preparation of complexes

In a typical synthesis of **1**, THF solutions of triethylamine (0.025 g, 0.25 mmol) (10 ml) and thioacetic acid (0.019 g, 0.25 mmol) were mixed and added to a stirred solution of triphenyllead chloride (0.120 g, 0.25 mmol) in the same solvent (25 ml). After stirring for 4 h the solvent was removed under reduced pressure and the residue was extracted in benzene (25 ml). The filtered solution was then added to a stirred suspension of anhydrous sodium sulfide (0.019 g, 0.25 mmol). After stirring for 3 h the precipitate was filtered off and the solvent was evaporated from the filtrate. The residue was recrystallized from its benzene solution by slow evaporation of the solvent. Yield (0.183 g) 80%. *Anal.* Calc. for $C_{36}H_{30}Pb_2S$: C, 47.56; H, 3.33. Found: C, 47.05; H, 3.30%. **2** was also prepared following a similar procedure. Yield (85%), *Anal.* Calc. for $C_{36}H_{30}S$: C, 59.06; H, 4.13. Found: C, 58.71; H, 4.19%.

3. Results and discussion

3.1. Syntheses

Bahr and Boudjouk have reported the synthesis of **1** in 58% yields by a reaction of Ph_3PbCl with Na_2S (generated in situ by a reaction of elemental sulfur and sodium metal in presence of a catalytic amount of naphthalene) [15]. In a similar reaction, when triphenyllead chloride was treated with thioacetic acid in presence of triethylamine followed by a reaction with anhydrous sodium sulfide **1** was isolated in more than 80% yields. In an analogous reaction when Ph_3PbCl was replaced with its tin analogue **2** was obtained:

$$Ph_3MCl + MeCOSH + Et_3N \xrightarrow{M=Pb,\,Sn} Ph_3M(SOCMe) + Et_3NHCl$$

$$2Ph_3M(SOCMe) + Na_2S \rightarrow (Ph_3M)S + 2Na(OSCMe)$$

3.2. X-ray crystallography

Single crystals suitable for X-ray diffraction analyses were grown from its benzene solution. **1** crystallizes in orthorhombic crystal system ($P2_12_12_1$). Molecular structure and numbering scheme are given in Fig. 1 and important bond dimensions are given in Table 2. The discrete molecular unit contains two Ph_3Pb groups bonded to the sulfur asymmetrically. The two S–Pb distances are different and so are the alignments of the two Ph_3Pb groups with respect to each other. As can be seen in Fig. 1 there are two phenyl rings bonded to Pb1 atom which are sufficiently close to other two phenyl rings bonded to Pb2 to allow π–π interactions. Both the phenyl ring pairs are arranged in a displaced T-shape with centroid–centroid distances of 4.86 and 5.24 Å.

An interesting feature in the molecular structure is the Pb···Pb distance of 3.989 Å which is little shorter than the sum of their van der Waals' radii (4.04 Å) [16]. On the other hand the Pb–Pb distance in $[AsPh_4]_4[Pb_2(i\text{-mnt})_4]$ is much shorter being 3.70 Å. Similarly, in a binary intermetallic compound $Ti_6Pb_{4.8}$ the Pb–Pb distance is 3.74 Å [17]. In these compounds the existence of a Pb···Pb bond though weak is unquestionable. Structures of a few β-diketonates of lead have been reported recently. The Pb···Pb distance in these dimeric compounds varies from 3.80 to 4.14 Å [18–20] and existence of any Pb···Pb bonding is ambiguous in these complexes.

It is sometimes vexing to interpret the nature of Pb–Pb bonding based on just bond distance measurements [21–22] The PbPb double bond is known to be longer than the single bond [23]. Similar inconsistencies are apparent in weak interactions too. Although the sum of van der Waals' radii is 4.04 Å [16], Pb–Pb distances in $Pb_6O(OH)_6^{4+}$ ranges between 3.44 and 4.09 Å.[24]. The chains and layers in both α- and β-PbO are held together by real Pb–Pb bonds (not just van der Waals' forces) but the Pb–Pb distances are quite long (up to 3.97 Å) [25].

To gain further insight in the bonding we have reexamined the molecular structure of the analogous tin compound **2**. An ORTEP drawing of the molecular structure of **2** is given in Fig. 2. Results of our study are not much different from the earlier report [26]. However, we could refine the structure much better. The Sn–Sn

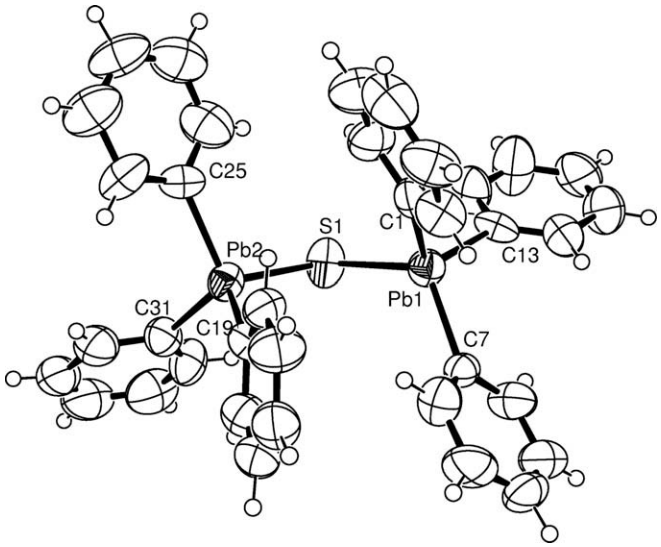


Fig. 1. ORTEP drawing of **1**.

Table 2
Selected geometric parameters of **1** and **2**.

Distances (Å)	M = Pb	M = Sn
M–M	3.989	3.879
S–M1	2.491	2.402
S–M2	2.484	2.397
C1–M1	2.214	2.120
C7–M1	2.200	2.148
C13–M1	2.202	2.142
C19–M2	2.179	2.126
C25–M2	2.196	2.138
C31–M3	2.199	2.145
Angles (°)		
M_1–S–M_2	106.61	107.86
Dihedral angles (°)		
M1–S–M2–C19	−24.8	−27.7
M1–S–M2–C25	97.7	94.76
M1–S–M2–C31	145.1	−147.0
M2–S–M1–C13	−166.9	−46.97
M2–S–M1–C7	76.4	−163.92
M2–S–M1–C1	−49.7	78.8

distance in this molecule being 3.879 Å (Table 2) is quite shorter than the sum of their van der Waals' radii (4.34 Å) which is indicative of a weak Sn···Sn bonding.

The M–S–M angle in **1** is smaller than that in **2** which may apparently be attributed to the higher electronegativity of **1** (VSEPR theory). Glidewell and Liles have rationalized the geometrical properties of $(R_3M)_2S$ molecules on the basis of second order Jahn–Teller effect. They have concluded that the angular geometry of S will be anomalous in the context of the VSEPR [26]. Since the electronegativity decreases from Ge to Sn (2.01 and 1.96, respectively) the M–S–M angle also decrease in the same fashion (Ge–S–Ge = 111.0°; Sn–S–Sn = 107.86°). Since electronegativity of Pb is higher (2.33) than both Sn and Ge the Pb–S–Pb angle should be still larger. Thus a smaller Pb–S–Pb angle in **1** indicates the existence of a Pb–Pb bond.

3.3. Theoretical studies

Since in the present case the Pb–Pb distance is almost at the edge we performed theoretical calculations using density functional theory (DFT) method [27] to understand the electronic structure of the compound and nature of the Pb···Pb bond. The atomic coordinates for the calculations were obtained from the X-ray data. Single point energy calculation and bond order calculations were performed using LanL2DZ (*d*,*p*) basis set at B3LYP level. Pb···Pb bond order (Wiberg) is only 0.0085 which is too small to be of any significance.

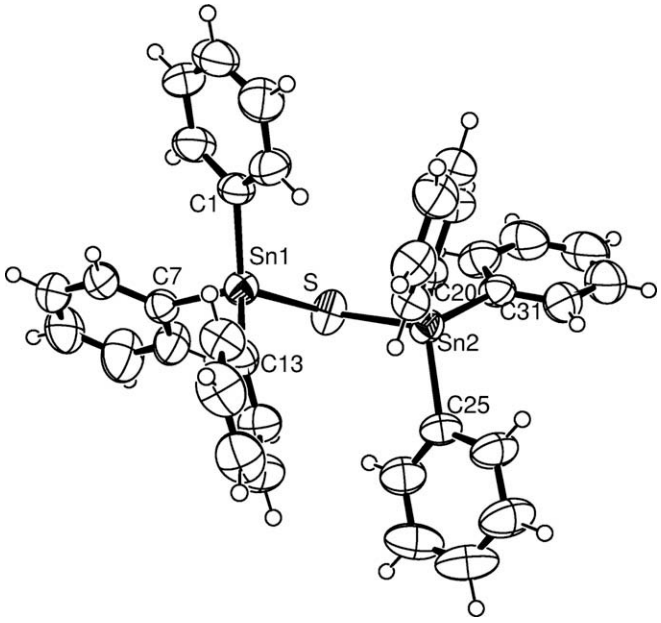


Fig. 2. ORTEP drawing of **2**.

Recently, Inagaki and co-workers have reported the structures of $RC(O)SMR'_3$ (M = Ge, Sn, Pb) [28]. On the basis of NBO analyses they have concluded intramolecular $n_O \rightarrow \sigma_{MS}$ interactions to be responsible for short M–O distances in these molecules. Results of second order perturbation theory analysis of Fock matrix (NBO) using LanL2DZ basis set reveal that similar bonding interactions are present both in **1** and **2** due to electron transfers from σ_{SM} to $\sigma^*_{M'C}$ orbitals. The contour diagram showing the overlap of

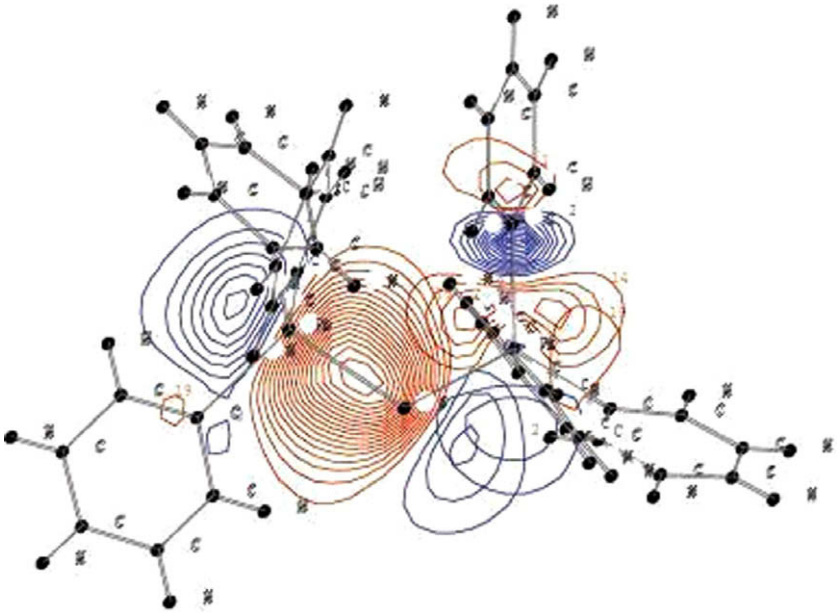


Fig. 3. Contour diagram showing natural bond orbital overlap.

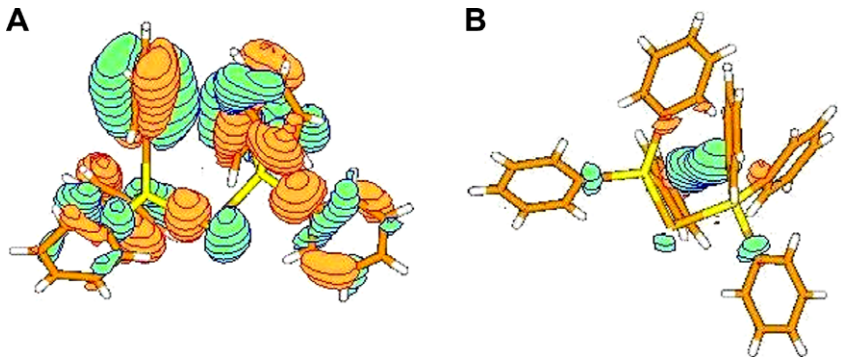


Fig. 4. π–π interactions in **1**.

orbitals is given in Fig. 3. It is clear from the figure that the extent of overlap is small and the nature of bond is essentially very weak. The stabilization energies associated with the delocalization are only 1.62 and 1.24 kcal/mol for **1** and **2**, respectively. The stabilization energies reported for $RC(O)SMR'_3$ molecules are also of the same order (0.64–2.25 kcal/mol). Similar weak bonding by overlap of molecular orbitals has also been reported in case of some thioacylsulfanylarsines [29]. However, to our understanding it is not logical to draw any conclusion on the basis of such small stabilization energies. Moreover, the lowering in energy does not corroborate to the M–M distance shortening: Sn···Sn distance is shorter than Pb···Pb distance but the stabilization energy is greater in the later case. It should be kept in mind that the crystal packing and even π-stacking energies [30,31] are often higher than the above mentioned delocalization energies. As described already, π–π interactions exist among the phenyl rings in both **1** and **2** (Fig. 4). To evaluate the extent of π–π interactions calculations on benzene dimers have been performed. Single point energies of the benzene dimers have been calculated after constructing them using the atomic coordinates of the carbon atoms of phenyl ring pairs from the X-ray data of **1** while the positions of the hydrogen atoms were optimized. The energies of same benzene dimers without any π–π interactions were then calculated by replacing the C and H atoms of one ring in each turn by ghost atoms. All the calculations were carried out at B3LYP level using 6–31 + G* basis set. Interaction energies were found to be −0.44 and −0.83 kcal/mol for the benzene pairs with centroid–centroid distances of 4.86 and 5.24 Å, respectively.

4. Conclusion

Ph_3MSMPh_3 (M = Sn, Pb) have been prepared using $Ph_3M(SOCMe)$ in high yields. X-ray structures of the compounds showed short M–M distances (compared to the sum of the corresponding van der Waals' radii) which are indicative of weak M···M interactions. DFT studies though revealed electron transfers from σ_{SM} to $\sigma^*_{M'C}$ orbitals but the corresponding stabilizations are too small to contribute to the structure of the molecules. The short MM distances are due to crystal packing effects and π–π interactions.

Acknowledgements

The authors are grateful to the coordinator DSA program, Department of Chemistry, Banaras Hindu University and the coordinator, X-ray crystallographic facility, Indian Institute of Technology, Kanpur, respectively, for providing computational facility and X-ray data collection of the compounds. Financial assistance to one of us (S.B.) from the Council of Scientific and Industrial Research and University Grants Commission, New Delhi, is gratefully acknowledged.

Appendix A. Supplementary data

CCDC 691835 and 691836 contain the supplementary crystallographic data for $(Ph_3Sn)_2S$ and $(Ph_3Pb)_2S$, respectively. These data can be obtained free of charge via http://www.ccdc.cam.ac.uk/conts/retrieving.html, or from the Cambridge Crystallographic Data Centre, 12 Union Road, Cambridge CB2 1EZ, UK; fax: (+44) 1223-336-033; or e-mail: deposit@ccdc.cam.ac.uk. Supplementary data associated with this article can be found, in the online version, at doi:10.1016/j.poly.2008.11.033.

References

[1] F.G.A. Stone, R. West (Eds.), Adv. Organomet. Chem. (1996) 39.
[2] A.G. Davies, Organotin Chemistry, Wiley-VCH Verlag GmbH, Weinheim, 2003.
[3] H. Preut, F. Huber, Anorg. Allg. Chem. 419 (1976) 92.
[4] L. Pu, A.D. Phillips, A.F. Richards, M. Stender, R.S. Simons, M.M. Olmstead, P.P. Power, J. Am. Chem. Soc. 125 (2003) 11626. and references therein.
[5] A. Schnepf, Chem. Soc. Rev. 36 (2007) 745.
[6] J.S. Magyar, T.-C. Weng, C.M. Stern, D.F. Dye, Brian W. Rous, John C. Payne, B.M. Bridgewater, A. Mijovilovich, G. Parkin, J.M. Zaleski, J.E. Penner-Hahn, H.A. Godwin, J. Am. Chem. Soc. 127 (2005) 9495.
[7] B.S. Furniss, A.J. Hannaford, P.W.G. Smith, A.R. Tatchell, Vogel's Textbook of Practical Organic Chemistry, 5th ed., Dorling Kindersley, India, 2006.
[8] SAINT+, 6.02 ed., Bruker AXS, Madison, WI, 1999.
[9] G.M. Sheldrick, SHELXL-97: Program for Crystal Structure Refinement, University of Göttingen, Göttingen, 1997.
[10] L.J. Farrugia, J. Appl. Cryst. 32 (1999) 837.
[11] M.J. Frisch, G.W. Trucks, H.B. Schlegel, G.E. Scuseria, M.A. Robb, J.R. Cheeseman, J.A. Montgomery Jr., T. Vreven, K.N. Kudin, J.C. Burant, J.M. Millam, S.S. Iyengar, J. Tomasi, V. Barone, B. Mennucci, M. Cossi, G. Scalmani, N. Rega, G.A. Petersson, H. Nakatsuji, M. Hada, M. Ehara, K. Toyota, R. Fukuda, J. Hasegawa, M. Ishida, T. Nakajima, Y. Honda, O. Kitao, H. Nakai, M. Klene, X. Li, J.E. Knox, H.P. Hratchian, J.B. Cross, V. Bakken, C. Adamo, J. Jaramillo, R. Gomperts, R.E. Stratmann, O. Yazyev, A.J. Austin, R. Cammi, C. Pomelli, J.W. Ochterski, P.Y. Ayala, K. Morokuma, G.A. Voth, P. Salvador, J.J. Dannenberg, V.G. Zakrzewski, S. Dapprich, A.D. Daniels, M.C. Strain, O. Farkas, D.K. Malick, A.D. Rabuck, K. Raghavachari, J.B. Foresman, J.V. Ortiz, Q. Cui, A.G. Baboul, S. Clifford, J. Cioslowski, B.B. Stefanov, G. Liu, A. Liashenko, P. Piskorz, I. Komaromi, R.L. Martin, D.J. Fox, T. Keith, M.A. Al-Laham, C.Y. Peng, A. Nanayakkara, M. Challacombe, P.M.W. Gill, B. Johnson, W. Chen, M.W. Wong, C. Gonzalez, J.A. Pople, GAUSSIAN 03, Revision D.01, Gaussian Inc., Wallingford, CT, 2004.
[12] P.J. Hay, W.R. Wadt, J. Chem. Phys. 82 (1985) 299.
[13] K.D. Dobbs, W.J. Hehre, J. Comp. Chem. 8 (1987) 880.
[14] J.B. Foresman, A. Frisch, Exploring Chemistry with Electronic Structure Methods, 2nd ed., Gaussian Inc., Pittsburgh, 1995, p. 41.
[15] S.R. Bahr, P. Boudjouk, Inorg. Chem. 31 (1992) 415.
[16] A. Bordi, J. Phys. Chem. 68 (1964) 441.
[17] M. Kleinke, J. Solid State Chem. 159 (2001) 134.
[18] M.A. Malik, P. O'Brien, M. Motealli, A.C. Jones, T. Leedham, Polyhedron 18 (1999) 1641.
[19] K. Lyezko, J. Narbutt, B. Paluchowska, J.K. Maurin, I. Pearson, J. Chem. Soc., Dalton Trans. (2006) 3972.
[20] J.M. Harrowfield, S. Maghaminia, A.A. Soudi, Inorg. Chem. 43 (2004) 1810.
[21] Y. Wang, B. Quillians, P. Wei, X.J. Yang, G.H. Robinson, Chem. Commun. (2004) 2224.
[22] L. Pu, B. Twamley, P.P. Power, J. Am. Chem. Soc. 122 (2000) 3524.
[23] M. Sturmann, W. Saak, H. Marsmann, M. Weidenbruch, Angew. Chem., Int. Ed. 38 (1999) 187.
[24] T.G. Spiro, D.H. Templeton, A. Zalkin, Inorg. Chem. 8 (1969) 856.
[25] G. Triniquier, R. Hoffmann, J. Phys. Chem. 88 (1984) 6696.

[26] C. Glidewell, D.C. Liles, J. Organomet. Chem. 224 (1981) 237.
[27] R.G. Parr, W. Yang, Density-functional Theory of Atoms and Molecules, Oxford University Press, Oxford, 1989.
[28] K. Tani, S. Kato, T. Kanda, S. Inagaki, Org. Lett. 3 (2001) 655.
[29] K. Tani, S.-i. Hanabusa, S. Kato, S.-y. Mutoh, S.-i. Suzuki, M. Ishida, J. Chem. Soc., Dalton Trans. (2001) 518.
[30] P. Hobza, H.L. Selzle, E.W. Schlag, J. Am Chem. Soc. 116 (1994) 3500.
[31] J. Huang, S. Kingsbury, M. Kertesz, Phys. Chem. Chem. Phys. 10 (2008) 2626.

Polyhedron 28 (2009) 553–561

Contents lists available at ScienceDirect

Polyhedron

journal homepage: www.elsevier.com/locate/poly

Controlling self-assembly of zinc(II)-benzoate coordination complexes with 1,4-bis(4-pyridyl)ethane by varying solvent and ligand-to-metal ratio: Their catalytic activities

Han Kwak [a], Sun Hwa Lee [a], Soo Hyun Kim [a], Young Min Lee [a], Byeong Kwon Park [a], Yu Jin Lee [a], Je Yeol Jun [a], Cheal Kim [a,*], Sung-Jin Kim [b,*], Youngmee Kim [b]

[a] Department of Fine Chemistry, Eco-Product and Materials Education Center, Seoul National University of Technology, 172 Kongnung 2-Dong Nowon-Gu, Seoul 139-743, Republic of Korea
[b] Department of Chemistry and Nano Science, Ewha Womans University, Seoul 120-750, Republic of Korea

ARTICLE INFO

Article history:
Received 1 October 2008
Accepted 19 November 2008
Available online 2 January 2009

Keywords:
Zinc-benzoate
Coordination polymers
Transesterification
Catalytic activity

ABSTRACT

Four new coordination polymers formed by zinc-benzoate with the 1,2-bis(4-pyridyl)ethane (bpe) bridging ligand have been prepared and characterized. Zinc-benzoates can be rationally tuned to form four different structures with a bridging bpe ligand by controlling ligand-to-zinc-benzoate molar ratios and by using different solvent systems, and reveal three coordination polymers having similar one-dimensional characteristics but having different mono-, di-, trinuclear nodes (**1**–**3**), and a dinuclear ring type molecule (**4**). This work reveals that the ligand-to-metal ratio and solvent play very important roles in the formation of different coordination structures. We have also shown that the compounds **1**–**4** catalyzed efficiently the transesterification of a variety of esters. The complex **3** showed the most efficient reactivity and is the best among the catalytic efficiencies reported previously with zinc-containing coordination and polymeric compounds. The substrates with the electron-withdrawing substituents have undergone faster transesterification than those with the electron-donating ones. In addition, the scope of the application of **1**–**4** as transesterification catalysts has been expanded to now include ethanol and propanol, suggesting that this catalytic system can be potentially useful for preparing various esters by transesterification. Moreover, the transesterification reaction mechanism was discussed by ^{1}H NMR study.
© 2008 Elsevier Ltd. All rights reserved.

1. Introduction

The design and construction of metal-organic coordination polymers has recently attracted much attention not only due to their structural and topological novelty [1–8], but also for their potential applications as functional materials such as gas storage [9–15], ion-exchange [16,17], catalysis [18–27], magnetism [28–30], and molecular sensing [31]. The rational design of these coordination polymers is highly affected by several factors such as the coordination geometry of metal ions [32,33], the structure of organic ligands [34–36], the solvent system [37,38], pH value [39–41], temperature [42,43], the counteranion [44,45], and the ligand-to-metal ratio [46,47]. Therefore, an investigation for understanding the relationships between the structures of complexes and those factors is at the center of controlling coordination network assembly.

Though numerous coordination polymers and macrocycles have been generated from transition metal nodes with a variety of organic spacers over the past few years, there is still little understanding of how ligand-to-metal stoichiometry and solvent system among several factors can be used to control the type of polymeric structures. While these two factors are relatively notable in copper- and silver-containing coordination polymers [48–53], their influence on the formation of coordination polymers, especially, with zinc ion is much less well understood and systematic studies of their role are very scarce [54–56].

Quite recently, we have reacted zinc-benzoate with pyrazine and its derivatives, 2,3-dimethylpyrazine, 2,5-dimethylpyrazine, 2,6-dimethylpyrazine, and quinoxaline, and characterized five new Zn(II)-benzoate coordination architectures, from dinuclear, trinuclear and pentanuclear complexes to one-dimensional and two-dimensional coordination polymers [57]. These results have shown that the substituents of pyrazine are very important roles for construction of various zinc-benzoate complexes. Interestingly, the compounds catalyzed efficiently the transesterification of a variety of esters.

As an extension of our previous work, in this study, we have investigated the complex formation of zinc-benzoate with another bridging ligand 1,2-bis(4-pyridyl)ethane (bpe) in order to further

* Corresponding authors. Tel.: +82 2 970 6693; fax: +82 2 973 9149 (C. Kim), tel.: +82 2 3277 3589; fax: +82 2 3277 3419 (S.-J. Kim).
E-mail addresses: chealkim@snut.ac.kr (C. Kim), sjkim@ewha.ac.kr (S.-J. Kim).

0277-5387/$ - see front matter © 2008 Elsevier Ltd. All rights reserved.
doi:10.1016/j.poly.2008.11.048

prepare functional supramolecular complexes with intriguing structures and potential applications especially in catalysis and to systematically investigate the influence of the concentration and solvent effects less studied on the assembly processes of the structure of zinc-carboxylate containing coordination polymers. Here, we report the syntheses, characterization and crystal structures of four zinc coordination complexes $[Zn_2(O_2CPh)_4(H_2O)_2][Zn(O_2CPh)_2\text{-}(bpe)]_n$ (**1**), $[Zn_3(O_2CPh)_6(bpe)]_n$ (**2**), $[(Zn_3(O_2CPh)_6)(\mu\text{-}bpe)(Zn_2(O_2CPh)_4)]_n$ (**3**), and $[Zn_2(O_2CPh)_4(bpe)_2]$ (**4**) from the reaction of zinc-benzoate and bpe which were obtained by tuning solvent mixtures and ligand-to-zinc-benzoate ratios. These complexes contain mononuclear nodes **1**, trinuclear nodes **2**, and trinuclear alternating with dinuclear nodes **3** and a discrete dinuclear complex **4**, respectively. These results illustrate how both stoichiometry and solvent play a vital role in affecting the product formation, their structures and topology. We have also reported that the compounds **1**–**4** catalyzed efficiently the transesterification of a variety of esters with different alcohols, and discussed about the reaction mechanism of the transesterification reaction based on ^{1}H NMR study.

2. Experimental

Materials: Acetone, methanol, ethanol, methylene chloride, propanol, 2-propanol, *para*-substituted phenyl acetate, *para*-substituted phenyl benzoate, methylacetate, methylbenzoate, 1,2-bis(4-pyridyl)ethane (bpe), ammonium benzoate, and zinc nitrate hexahydrate were purchased from Aldrich and were used as received. 4-Fluorophenyl acetate and 4-nitrophenyl benzoate were obtained from Lancaster.

Instrumentation: Elemental analysis for carbon, nitrogen, and hydrogen was carried out by using an EA1108 (Carlo Erba Instrument, Italy) in the Organic Chemistry Research Center of Sogang University, Korea. IR spectra were measured on a BIO RAD FTS 135 spectrometer as KBr pellets. Product analysis for the transesterification reaction was performed on either a Hewlett–Packard 5890 II Plus gas chromatograph interfaced with Hewlett–Packard Model 5989B mass spectrometer or a Donam Systems 6200 gas chromatograph equipped with a FID detector using 30-m capillary column (Hewlett–Packard, HP-1, HP-5, and Ultra 2). ^{1}H NMR spectra were recorded on a Varian Mercury 400 spectrometer. Chemical shifts (δ) are reported in ppm, relative to TMS (0.00).

*Synthesis of $[Zn_2(O_2CPh)_4(H_2O)_2][Zn(O_2CPh)_2(bpe)]_n$ (**1**):* 38.0 mg (0.125 mmol) of $Zn(NO_3)_2 \cdot 6H_2O$ and 36.0 mg (0.25 mmol) of $C_6H_5COONH_4$ were dissolved in 4 ml water and carefully layered by 4 ml acetone solution of 1,2-bis(4-pyridyl)ethane (11.6 mg, 0.0625 mmol). The yield was 34.5 mg (21.2%) for compound **1**. Suitable crystals of compound **1** for X-ray analysis were obtained in a week. The structure **1** was also obtained with the same ratio of bpe to zinc-benzoate in methylene chloride (4 ml) /methanol (4 ml) system. *Anal.* Calc. for $C_{66}H_{56}N_4O_{13}Zn_3$ (1309.26), **1**: C, 60.54; H, 4.32; N, 4.28. Found: C, 60.45; H, 4.30; N, 4.55%. IR (KBr): ν (cm^{-1}) = 3422(br), 3064(w), 2362(m), 1619(s), 1572(m), 1364(s), 1229(w), 1070(w), 1030(w), 940(w), 720(s), 684(w), 550(m).

*Synthesis of $[Zn_3(O_2CPh)_6(bpe)]_n$ (**2**):* 38.0 mg (0.125 mmol) of $Zn(NO_3)_2 \cdot 6H_2O$ and 36.0 mg (0.25 mmol) of $C_6H_5COONH_4$ were dissolved in 4 ml methanol and carefully layered by 4 ml methylene chloride solution of 1,2-bis(4-pyridyl)ethane (23.3 mg, 0.125 mmol). The yield was 53.7 mg (38.9%) for compound **2**. Suitable crystals of compound **2** for X-ray analysis were obtained in 5 days. The structure **2** was also obtained with the ratio of bpe to zinc-benzoate (0.5:1) in ethanol/water system. *Anal.* Calc. for $C_{54}H_{42}N_2O_{12}Zn_3$ (1107.01), **2**: C, 58.58; H, 3.83; N, 2.53. Found: C, 58.64; H, 3.93; N, 2.65%. IR (KBr): ν (cm^{-1}) = 3078(w), 2958(w), 2362(w), 1613(s), 1572(m), 1445(m), 1367(s), 1227(m), 1066(m), 1032(m), 939(w), 842(w), 812(m), 715(s), 683(m), 558(w), 524(m), 431(w).

*Synthesis of $[(Zn_3(O_2CPh)_6)(\mu\text{-}bpe)(Zn_2(O_2CPh)_4)]_n$ (**3**):* 38.0 mg (0.125 mmol) of $Zn(NO_3)_2 \cdot 6H_2O$ and 36.0 mg (0.25 mmol) of $C_6H_5COONH_4$ were dissolved in 4 ml water and carefully layered by 4 ml acetone solution of 1,2-bis(4-pyridyl)ethane (26.6 mg, 0.25 mmol). The yield was 58.3 mg (24.5%) for compound **3**. Suitable crystals of compound **3** for X-ray analysis were obtained in a week. *Anal.* Calc. for $C_{94}H_{74}N_4O_{20}Zn_5$ (1906.42), **3**: C, 59.22; H, 3.92; N, 2.94. Found: C, 59.51; H, 3.81; N, 2.72%. IR (KBr): ν (cm^{-1}) = 3077(brm), 1619(s), 1573(s), 1438(m), 1364(s), 1229(m), 1173(m), 1069(m), 1032(m), 940(w), 841(m), 811(m), 719(s), 684(m), 558(w), 524(m), 439(w).

*Synthesis of $[Zn_2(O_2CPh)_4(bpe)_2]$ (**4**):* 38.0 mg (0.125 mmol) of $Zn(NO_3)_2 \cdot 6H_2O$ and 36.0 mg (0.25 mmol) of $C_6H_5COONH_4$ were dissolved in 4 ml water and carefully layered by 4 ml methanol solution of 1,2-bis(4-pyridyl)ethane (23.3 mg, 0.125 mmol). The yield was 78.0 mg (63.4%) for compound **4**. Suitable crystals of compound **4** for X-ray analysis were obtained in five days. The structure **4** was also obtained with the ratios of bpe to zinc-benzoate (2:1 and 4:1) in methanol/water and (3:1 and 4:1) in ethanol/water system, respectively. *Anal.* Calc. for $C_{52}H_{44}N_4O_8Zn_2$ (983.65), **4**: C, 63.49; H, 4.52; N, 5.70. Found: C, 63.70; H, 4.49; N, 5.47%. IR(KBr): ν (cm^{-1}) = 3078(m), 2958(w), 1612(s), 1572(s), 1429(m), 1367(s), 1227(m), 1171(w), 1066(m), 1032(m), 939(w), 842(m), 812(m), 715(s), 683(m), 558(m), 524(m), 431(m).

*Catalytic activity of compounds **1**–**4**:* Catalytic homogeneous reaction conditions: Ester (0.05 mmol) was dissolved in an appropriate solvent (1 ml), methanol or propanol, and the catalyst (1.3 mg, 1.10×10^{-3} mmol for **1**, 1.9 mg, 1.01×10^{-3} mmol for **2**, 1.0 mg, 1.00×10^{-3} mmol for **3**, and 0.986 mg, 1.00×10^{-3} mmol for **4**, respectively) were added and shaken in an incubator at 50 °C (450 rpm). Reaction conversion was monitored by GC/Mass analysis of 20 μl aliquots withdrawn periodically from the reaction mixture. All reactions were run at least three times and the average conversion yields are presented.

*NMR experiments for the structural determination of the complex **4** before and after the transesterification reaction:* ^{1}H NMR spectra of ammonium benzoate and bpe were obtained in CD_3OD at room temperature. For ammonium benzoate, ^{1}H NMR (CD_3OD, 400 MHz): δ 7.91–7.94 (m, 2H, aromatic-*ortho*-H), *δ 7.30–7.44* (m, 3H, aromatic-*meta*-H and aromatic-*para*-H). For bpe, ^{1}H NMR (CD_3OD, 400 MHz): δ 8.38–8.40 (d, 2H, aromatic-*meta*-H), *δ 7.27–7.29* (d, 2H, aromatic-*ortho*-H), *δ* 3.032 (s, 4H, CH_2). ^{1}H NMR spectrum of the complex **4** was obtained in CD_3OD; ^{1}H NMR (CD_3OD, 400 MHz): δ 8.02–8.05 (m, 2H, aromatic-*ortho*-H for benzoate), *δ 7.45–7.50* (q, 1H, aromatic-*para*-H for benzoate), *δ 7.37–7.42* (q, 2H, aromatic-*meta*-H for benzoate), *δ 8.40–8.43* (d, 2H, aromatic-*meta*-H for bpe), *δ 7.29–7.32* (d, 2H, aromatic-*ortho*-H for bpe), *δ* 3.045 (s, 4H, CH_2 for bpe). ^{1}H NMR spectrum of the complex **4** was again obtained after the reaction mixture of **4** and phenyl acetate in CD_3OD was incubated for 1 day at 50 °C. The transesterification reaction of phenyl acetate was found to be complete by GC and ^{1}H NMR. ^{1}H NMR (CD_3OD, 400 MHz): 8.02–8.05 (m, 2H, aromatic-*ortho*-H for benzoate), *δ 7.45–7.50* (q, 1H, aromatic-*para*-H for benzoate), *δ 7.37–7.41* (q, 2H, aromatic-*meta*-H for benzoate), *δ 8.41–8.43* (d, 2H, aromatic-*meta*-H for bpe), *δ 7.29–7.31* (d, 2H, aromatic-*ortho*-H for bpe), *δ* 3.045 (s, 4H, CH_2 for bpe).

X-ray crystallography: The X-ray diffraction data for all four compounds were collected on a Bruker SMART AXS diffractometer equipped with a monochromater n the Mo Kα (λ = 0.71073 Å) incident beam. Each crystal was mounted on a glass iber. The CCD data were integrated and scaled using the Bruker-SAINT software package, and the structure was solved and refined using SHEXTL V6.12 [58]. All hydrogen atoms were placed in the calculated positions. The crystallographic data for compounds **1**–**4** are listed in Table 1.

Table 1
Crystallographic data for compounds **1**, **2**, **3**, and **4**.

	1	**2**	**3**	**4**
Empirical formula	$C_{66}H_{56}N_4O_{13}Zn_3$	$C_{54}H_{42}N_2O_{12}Zn_3$	$C_{94}H_{74}N_4O_{20}Zn_5$	$C_{52}H_{44}N_4O_8Zn_2$
Formula weight	1309.26	1107.01	1906.42	983.65
Temperature (K)	293(2)	293(2)	293(2)	293(2)
Wavelength (Å)	0.71073	0.71073	0.71073	0.71073
Space group	$P\bar{1}$	$P\bar{1}$	$P\bar{1}$	$C2/c$
a (Å)	11.9043(14)	10.2901(8)	10.1724(6)	19.617(5)
b (Å)	14.5166(17)	11.0667(8)	10.8612(7)	12.185(3)
c (Å)	19.116(2)	13.1179(10)	22.0757(14)	21.739(6)
α (°)	77.967(2)	76.1630(10)	81.6880(10)	90.000
β (°)	73.248(2)	67.4350(10)	83.8290(10)	115.665(4)
γ (°)	79.207(2)	64.9150(10)	66.2990(10)	90.000
Volume (Å^3)	3065.0(6)	1244.13(16)	2206.6(2)	4684(2)
Z	2	1	1	4
$D_{calc.}$ (Mg/m^3)	1.419	1.478	1.435	1.395
Absorption coefficient (mm^{-1})	1.232	1.500	1.412	1.083
Crystal size (mm^3)	0.30 × 0.25 × 0.20	0.15 × 0.05 × 0.05	0.10 × 0.05 × 0.05	0.15 × 0.10 × 0.08
Reflections collected	19307	6994	12504	12342
Independent reflections [R_{int}]	13650 (0.0482)	4776 (0.0179)	8479 (0.0204)	4597 (0.0469)
Data/restraints/parameters	13650/0/781	4776/0/322	8479/0/556	4597/0/298
Goodness-of-fit on F^2	0.935	1.044	0.972	1.012
Final R indices [$I > 2\sigma(I)$]	R_1 = 0.0423, wR_2 = 0.1112	R_1 = 0.0312, wR_2 = 0.0823	R_1 = 0.0371, wR_2 = 0.0865	R_1 = 0.0566, wR_2 = 0.1451
R indices (all data)	R_1 = 0.0661, wR_2 = 0.1157	R_1 = 0.0400, wR_2 = 0.0852	R_1 = 0.0556, wR_2 = 0.0920	R_1 = 0.0809, wR_2 = 0.1629
Largest difference between peak and hole (e Å^{-3})	1.930 and −0.546	0.307 and −0.430	0.367 and −0.375	1.603 and −0.744

3. Results and discussion

To investigate the effect of solvent and ligand-to-metal ratio on the structures of zinc-containing coordination polymers, we have reacted Zn(II)-benzoate with 1,2-bis(4-pyridyl)ethane (bpe) by changing the solvent systems and ligand-to-zinc-benzoate ratios. The coordination complexes **1**–**4** were prepared cleanly as single phase crystalline products, respectively. The infrared spectra of **1**–**4** were fully consistent with their formulations. Asymmetric and symmetric C=O stretching modes of the ligated benzoate moieties were evidenced by very strong, slightly broadened bands at ~1600 cm^{-1} and ~1400 cm^{-1} [59–61]. The absence of any bands in the area of ~1710 cm^{-1} indicates full deprotonation of all carboxylate groups in **1**–**4** [59–61].

The reaction of zinc-benzoate with the bpe ligand revealed four different structures as a function of ligand concentration in the different solvent systems. The relationship between the molar ratio of bpe-to-zinc-benzoate and the solvent system is shown in Table 2. Compound **1** was obtained with the molar ratio of bpe-to-zinc-benzoate of 0.5:1 both in the acetone/H_2O system and in the methylene chloride/methanol system. Compound **2** was obtained with the molar ratios of bpe-to-zinc-benzoate of 0.5:1 in the ethanol/H_2O system and of 1:1 in the methylene chloride/methanol system, respectively, and compound **3** was obtained with the molar ratio of 2:1 in the acetone/H_2O system. When we use the methanol/H_2O system, only compound **4** was obtained with any molar ratios of bpe-to-zinc-benzoate (1:1, 2:1, and 4:1). **4** was also obtained with the molar ratios of both 3:1 and 4:1 in the ethanol/H_2O system, and **4** could not be obtained from the acetone/H_2O system. These results indicate that the formation of compounds **1**–**4** depends primarily on both the bpe ligand-to-zinc-benzoate ratios and the solvent systems.

*The structure of compound (**1**):* An X-ray structural analysis revealed that compound **1** consists of mononuclear $Zn(O_2CC_6H_5)_2$ units bridged by bpe (bpe = 1,2-bis(4-pyridyl)ethane) ligand to form a one-dimensional zigzag chain (Fig. 1a). Zn(II) ion is coordinated by two monodentate benzoate ligands, two bridging bpe ligands with a tetrahedral geometry. The Zn–$O_{benzoate}$ bond distances are 1.932(2) and 1.964(1) Å that are similar to those found in $[Zn(O_2CCH_3)_2(\mu\text{-bpe})]\cdot 2H_2O$ (1.922(3) and 1.949(3) Å) [62] and $[Zn(O_2CCH_3)_2(py)_2]$ (1.941(4) and 1.945(2) Å, py = pyridine)[63] and the Zn–N_{bpe} bond distances range from 2.036(2) to 2.075(2) Å which are typical in Zn complexes (ranging from 2.010(3) to 2.044(3) Å) [62,63]. The packing diagram of the one-

Table 2
Relationship between bpe-to-zinc-benzoate molar ratios and solvent systems.

bpe: zinc-benzoate	Acetone/H_2O[a]	Ethanol/H_2O[b]	Methanol/H_2O[c]	Methylene chloride/methanol[d]
0.5:1	**1**[e]	**2**[f]	–[i]	**1**
1:1	–	–	**4**[h]	**2**
2:1	**3**[g]	**–**	**4**	**–**
3:1	–	**4**	–	–
4:1	–	**4**	**4**	**–**

[a] Zinc-benzoate ($Zn(NO_3)_2\cdot 6H_2O + C_6H_5COONH_4$) was dissolved in water and layered by an acetone solution of bpe.
[b] Zinc-benzoate ($Zn(NO_3)_2\cdot 6H_2O + C_6H_5COONH_4$) was dissolved in water and layered by an ethanol solution of bpe.
[c] Zinc-benzoate ($Zn(NO_3)_2\cdot 6H_2O + C_6H_5COONH_4$) was dissolved in water and layered by a methanol solution of bpe.
[d] Zinc-benzoate ($Zn(NO_3)_2\cdot 6H_2O + C_6H_5COONH_4$) was dissolved in methanol and layered by a methylene chloride solution of bpe.
[e] A one-dimensional zigzag chain containing $Zn(O_2CPh)_2$ units bridged by bpe ligands with dinuclear paddle-wheel $Zn_2(O_2CPh)_4(H_2O)_2$, $[Zn_2(O_2CPh)_4(H_2O)_2]$-$[Zn(O_2CPh)_2(bpe)]_n$.
[f] A one-dimensional chain containing trinuclear $Zn_3(O_2CPh)_6$ units bridged by bpe ligands, $[Zn_3(O_2CPh)_6(bpe)]_n$.
[g] A one-dimensional chain containing trinuclear $Zn_3(O_2CPh)_6$ units and dinuclear $Zn_2(O_2CPh)_4$ units bridged by bpe ligands alternatively, $[(Zn_3(O_2CPh)_6)(\mu\text{-bpe})(Zn_2(O_2CPh)_4)]_n$.
[h] A dinuclear ring molecule containing two $Zn(O_2CPh)_2$ bridged by two bpe ligands, $[Zn_2(O_2CPh)_4(bpe)_2]$.
[i] We could not obtain any crystals suitable for X-ray analysis under these conditions.

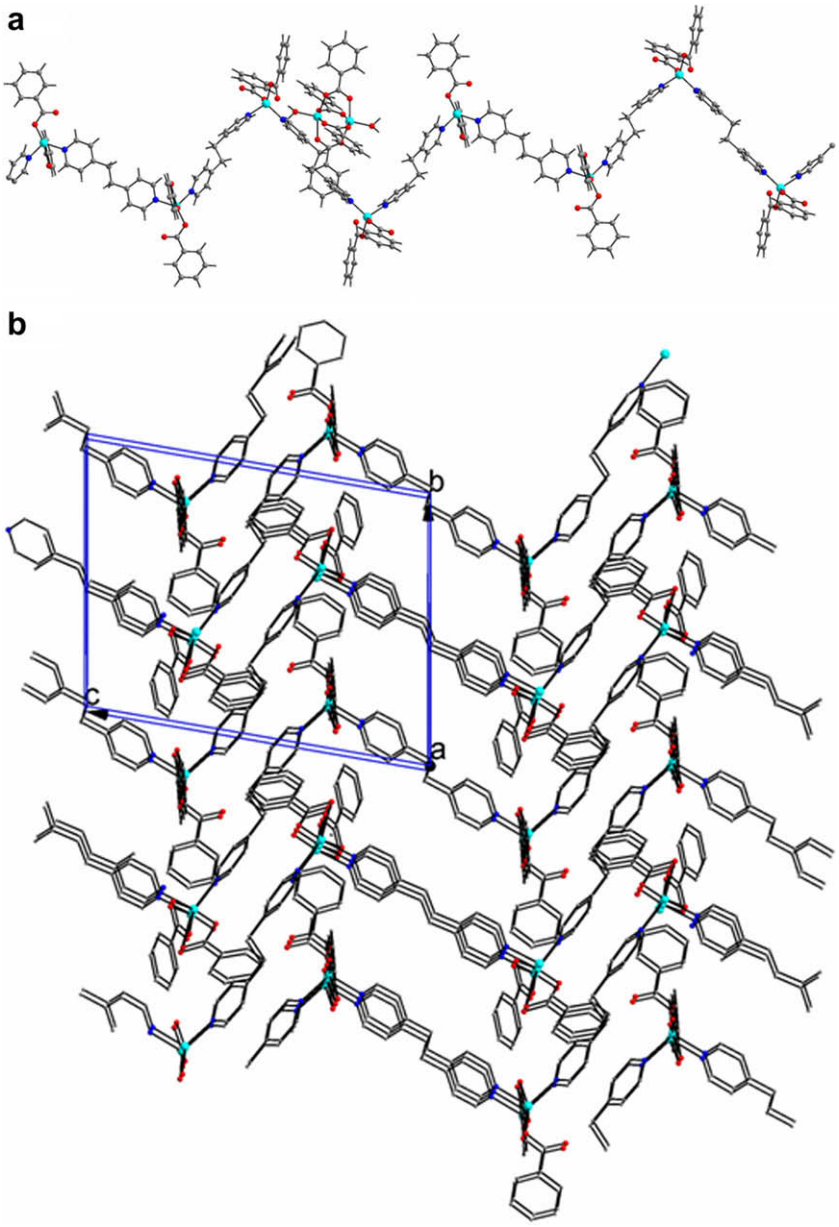


Fig. 1. (a) Structure of one-dimensional zigzag chain coexisting with dinuclear paddle-wheel Zn complex, **1**. (b) The packing diagram of the one-dimensional zigzag chains along an axis. All hydrogen atoms were omitted for clarity.

dimensional zigzag chains is shown in Fig 1b. There coexist dinuclear paddle-wheel type $Zn_2(O_2CC_6H_5)_4$ molecules with water axial ligands (Fig. 1a). Each Zn atom in this unit has distorted square-pyramidal environment, with four oxygen atoms from benzoates, which form the equatorial plane, and one water oxygen atom. The $Zn–O_{benzoate}$ bond distances range from 2.042(2) to 2.062(2) Å longer than those of the 1-D zigzag chain, but similar to those of the paddle-wheel type complexes [64–67], and the $Zn–O_{water}$ bond distance is 1.986(1) Å (Table 3). The Zn···Zn distance is 2.983(2) Å similar to those found in $Zn_2(MeCH{=}CHCO_2)_4(quinoline)_2]$ (2.976 Å) [64], $[Zn_2(O_2CPh)_4(py)_2]$ (2.927(4) Å) [65], [Zn(bdc)·(DMF)(H_2O)] (2.940(3) Å) [66], and $[Zn_2(bdc)_2(dabco)]$ (2.909(1) Å, bdc = 1,4-benzenedicaboxylate and dabco = 1,4-diazabicyclo[2.2.2]octane) [67]. There is a hydrogen bond interaction between oxygen atom of a benzoate ligand in a zigzag chain and the axial water hydrogen atom of a dinuclear unit ($O22_{benzoate}$···$H15A–O15_{water}$ 1.657(2) Å). Importantly, this is the first example of coexistence of 1-D and Zn dinuclear paddle-wheel type, to our best knowledge.

*The structure of compound (**2**):* An X-ray structural analysis revealed that compound **2** consists of trinuclear $Zn_3(O_2CC_6H_5)_6$ units bridged by bpe ligand to form a one-dimensional chain (Fig. 2a). A trinuclear Zn(II)-benzoate unit is constructed by six bridging benzoate ligands and similar to the previously described trinuclear zinc-carboxylate with axial N- or O-donor ligands [57,65,68–70]. There is an inversion center on the central Zn atom. Out of three Zn centers the central Zn is all O-donor hexa-coordinated from six benzoate groups to form a distorted octahedral geometry. The other two Zn centers are symmetric to each other, and each has a bridging bpe ligand and four oxygen atoms from benzoate ligands. Thus each Zn1 center has NO4 coordination environment with distorted trigonal bipyramid geometry. The coordination modes of benzoate ligands show two kinds of bridging modes [71–73]: one mode is a typical bridging mode, and the other is

Table 3
Selected bond distances for compounds **1**, **2**, **3**, and **4**.

	1	2	3	4
Zn–O (Å)	1.932(2)–2.062(2)	1.9628(16)–2.2640(19)	1.9607(19)–2.373(2)	1.950(3), 1.951(3)
Zn–N (Å)	2.036(2)–2.075(2)	2.0384(18)	2.035(2)	2.039(3), 2.064(3)
Zn–Zn (Å)	2.9827(7) (paddle-wheel type unit)	3.370(2)	2.9541(5) (paddle-wheel type unit), 3.347(2) (trinuclear unit)	8.502(14)

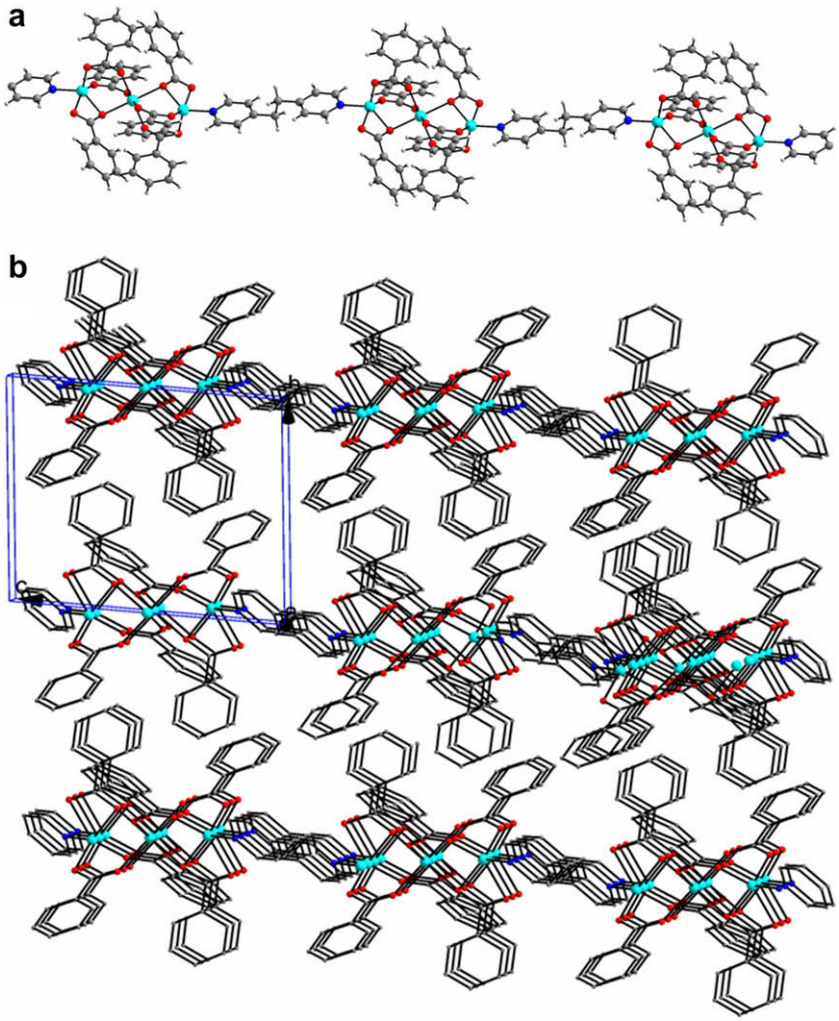


Fig. 2. (a) Structure of one-dimensional chain **2** containing trinuclear Zn units bridged by bpe ligands. (b) The packing diagram of the one-dimensional zigzag chains along an axis. All hydrogen atoms were omitted for clarity.

the unusual coordination mode, a monatomic coordination mode, that chelates to one Zn2 atom and, at the same time, bridges the other Zn1 atom as shown in Fig. 2a. This unusual coordination mode of carboxylate group provides a big distortion around Zn1. The packing diagram is shown in Fig. 2b. In the typical bridging carboxylate coordination mode, Zn1–$O_{bridging}$ distances are 1.963(1) and 1.968(1) Å, and Zn2–$O_{bridging}$ distances are 2.014(1) and 2.098(1) Å. In the unusual coordination mode, Zn2–$O_{bridging}$ distance is 2.207(2) Å which is a little longer than typical one, and Zn1–$O_{chelating}$ distances are 2.103(1) and 2.264(1) Å. Zn–N bond distance is 2.038(1) Å which is typical in Zn complexes (Table 3) [68–70]. The Zn···Zn distance is 3.370(2) Å that is much longer than that of dinuclear one in the compound **1**, and that can be comparable to those found in $[Zn_3(MeCH{=}CHCO_2)_6(quinoline)_2]$ (3.26 Å) [68], $[Zn_3(O_2CPh)_6(2,3\text{-diMepz})_2]$ (3.362(4) Å, 2,3-diMepz = 2,3-dimethylpyrazine) [57], $\{[Zn_3(1,4\text{-BDC})_3(DEF)_2]\cdot DEF\}_\infty$ (3.228(4) and 3.528(4) Å, 1,4-BDC = 1,4-benzene dicarboxylate and DEF = diethylformamide) [70].

*The structure of compound (**3**):* An X-ray structural analysis revealed that compound **3** consists of dinuclear paddle-wheel type $Zn_2(O_2CC_6H_5)_4$ units and trinuclear $Zn_3(O_2CC_6H_5)_6$ units bridged by bpe ligands alternatively to form a one-dimensional chain (Fig. 3a). Trinuclear $Zn_3(O_2CC_6H_5)_6$ units are similar to that of compound **2**, and dinuclear paddle-wheel type $Zn_2(O_2CC_6H_5)_4$ units are similar to that of the dinuclear one in compound **1**. While the trinuclear zinc-carboxylate units and the dinuclear paddle-wheel zinc-carboxylate units of structures from zinc-carboxylates have been often reported in literature [63,64–70], this arrangement in which bipyridyl ligands bridge dinuclear units and trinuclear units alternatively is unprecedented, to our best knowledge. On the other hand, it is worthwhile to mention that in $Cu_2(maa)_4$/bpp systems (Hmaa = 2-methylacrylic acid, bpp = 1,3-bis(4-pyridyl)pro-

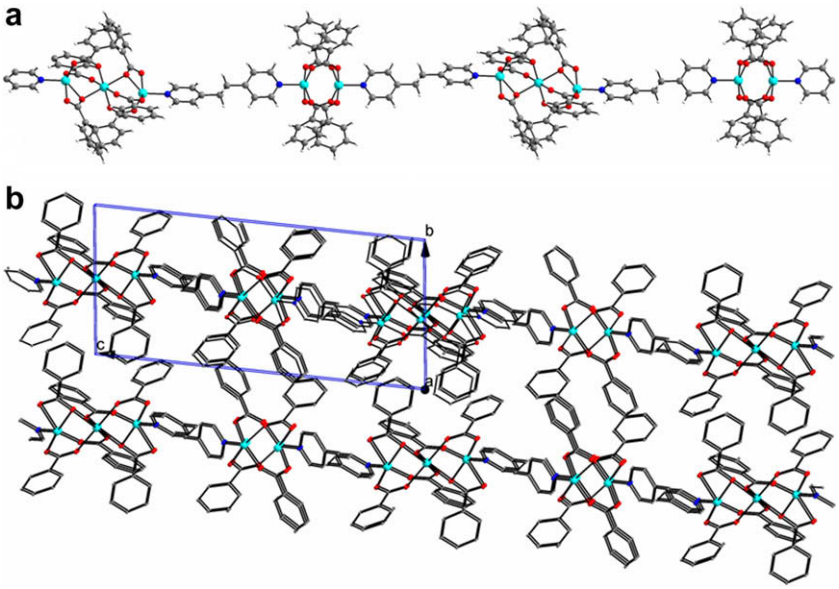


Fig. 3. (a) Structure of one-dimensional chain **3** containing dinuclear and trinuclear units bridged by bpe ligands alternatively. (b) The packing diagram of the one-dimensional zigzag chains along an axis. All hydrogen atoms were omitted for clarity.

pane), dinuclear and mononuclear alternating paddle-wheel 1-D instead of trinuclear and dinuclear alternating 1-D has been observed [48]. However, we could not obtain the dinuclear and mononuclear alternating polymer systems in our Zn systems. The packing diagram is shown in Fig. 3b. In the dinuclear unit, the Zn–$O_{bridging}$ bond distances range from 2.0240(19) to 2.054(2) Å similar to those of the dinuclear unit in the compound **1**, and the Zn–N bond distance is 2.035(2) Å which is typical in Zn complexes [64–67]. In the trinucelar unit, the Zn–$O_{bridging}$ bond distances of the typical bridging mode range from 1.9607(19) to 2.0903(19) Å, the Zn2–$O_{chelating}$ bond distances of the unusual coordination mode are 2.0491(17) and 2.373(2) Å, and the Zn1–$O_{bridging}$ bond distance of the unusual mode is 2.2428(17) Å which is a little longer than that of compound **2**. The Zn–N bond distance of the unusual mode is 2.035(2) Å which is typical in Zn complexes (Table 3) [68–70]. The Zn···Zn distances of dinuclear and trinuclear units are 2.9541(5) and 3.347(2) Å, respectively, which are shortened from dinuclear unit of **1** and trinuclear unit of **2**.

*The structure of compound (**4**):* An X-ray structural analysis revealed that compound **4** consists of two $Zn(O_2CC_6H_5)_2$ bridged by two bpe ligands to form a dinuclear molecule (Fig. 4). The Zn(II) ion has a distorted tetrahedral environment with two monodentate benzoate ligands and two bridging bpe ligands. The bpe ligand adopts a gauche conformation to form a ring type molecule. The Zn–O bond distances are 1.950(1) and 1.951(1) Å which are a little shorter than those of compounds **1**, **2**, and **3**, and the Zn–N bond distances are 2.039(2) and 2.064(6) Å which are typical in Zn complexes (Table 3). The Zn···Zn distance is 8.502(14) Å.

Structural diversity of zinc polymeric compounds by tuning ligand-to-metal ratio and solvent system: Zinc-benzoates can be rationally tuned to form four different structures with a bridging bpe ligand by controlling ligand-to-zinc-benzoate molar ratios and by using different solvent systems, and reveal three coordination polymers having similar one-dimensional characteristics but having different mono-, di-, trinuclear nodes, and a dinuclear ring type molecule. In case of the low concentration of the bpe ligand such as the bpe-to-zinc-benzoate molar ratio of 0.5:1 in both acetone/H_2O and CH_2Cl_2/MeOH solvent systems, compound **1** was obtained and revealed unprecedented one-dimensional zigzag chains coexisting with the paddle-wheel type dinuclear Zn_2 units which would not participate to form an one-dimensional chain. If the concentration of bpe ligand increases such as 1:1 molar ratio in acetone/MeOH solvent system, compound **2** was obtained and revealed trinuclear units connected by bpe ligands to form one-dimensional chains without the paddle-wheel type Zn_2 units. In ethanol/H_2O solvent system, **2** was also obtained in 0.5:1 bpe-to-zinc-benzoate molar ratio. If the concentration of bpe ligands increases more such as 2:1 molar ratio in acetone/H_2O system, compound **3** was obtained and revealed trinuclear and dinuclear units connected by bpe ligands alternatively, that is the first example in zinc-carboxylate systems. If the concentration of bpe ligands increases much more such as 4:1 molar ratio in EtOH/H_2O system, compound **4** was obtained and revealed the dinuclear ring type molecule which is a totally different structure from the previous structures. In MeOH/H_2O solvent system, importantly, only **4** was obtained without respect to the molar ratio of bpe-to-zinc-benzoate.

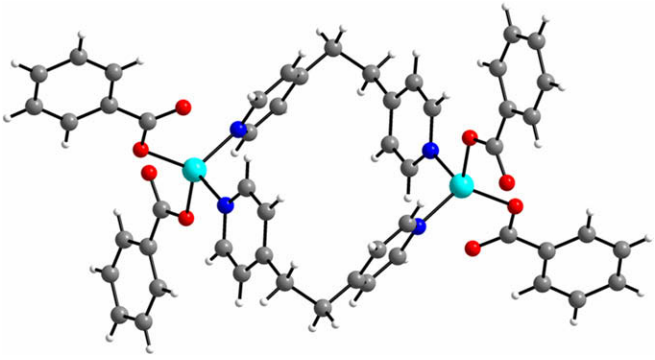


Fig. 4. Structure of dinuclear molecule **4**.

This result indicates that the solvent and the ligand-to-metal ratio are simultaneously playing a controlling role over the structure. Further, solvent seems to have more effect than the ligand-to-metal ratio, because in a certain case only one class of complexes was obtained (e.g., only **4** in MeOH/H_2O system), although the ratios of bpe-to-zinc-benzoate increase from 1 to 2 to 4. Interestingly, the solvents used in this work were not involved in the structures of

Table 4
Transesterification of esters by methanol and propanol in the presence of compounds **1**, **2**, **3**, and **4** at 50 °C.[a]

Entry	Substrate	**1**		**2**		**3**		**4**	
		MeOH[c]	PrOH[d]	MeOH[c]	PrOH[d]	MeOH[c]	PrOH[d]	MeOH[c]	PrOH[d]
		(time/days)[b]	(time/days)[b]	(time/days)[b]	(time/days)[b]	(time/days)[b]	(time/days)[b]	(time/days)[b]	(time/days)[b]
1	4-Nitrophenyl acetate	0.7	2.5	0.9	1.5	0.3	0.5	0.6	1
2	4-Fluorophenyl acetate	2.5	11	4.5	9	2	11	3	15
3	Phenyl acetate	1.5	5	1.5	7	0.5	2	1	4
4	4-Methylphenyl acetate	5.5	18	4.5	18	4	14	3	17
5	4-Nitrophenyl benzoate [e]	2.5	6	3.5	10	0.3	9	0.7	18
6	4-Chlorophenyl benzoate	2	17	2.5	17	0.5	5	2	10
7	Phenyl benzoate	5	24	5	33	2	7	2	17
8	4-Methylphenyl benzoate	5	24	5	12	2	17	4	35
9	Vinyl acetate	1.5	2.5	0.9	3.5	0.3	0.5	0.7	1

[a] All esters were completely converted to the corresponding products, methyl acetate and methyl benzoate. Reaction conditions: esters; 0.05 mmol, catalyst; 1.10×10^{-3} mmol for **1**, 1.01×10^{-3} mmol for **2**, 1.00×10^{-3} mmol for **3**, 1.00×10^{-3} mmol for **4**, solvent; methanol or propanol (1 ml). See Section 2 for the detailed reaction conditions.
[b] Time necessary for the complete conversion of substrate to product.
[c] Transesterification of esters was carried out in methanol (MeOH).
[d] Transesterification of esters was carried out in propanol (PrOH).
[e] The solvent was a mixture of $MeOH/CH_2Cl_2$ or $PrOH/CH_2Cl_2$ (1/1) because of low solubility of substrate in MeOH or PrOH.

1–4 which means that the coordinating solvents such as H_2O, methanol, and ethanol, act as the "templating" role rather than the "coordination" one [38]. Therefore, the solvent used in this preparation should be considered as an innocent one instead of a potential participant in any coordination polymer formation.

In addition, the structural diversity of compounds **1–4** shows that the dinuclear paddle-wheel Zn(II) units can be rationally controlled and can serve as mono-, di-, and trinuclear nodes towards a dipyridyl ligand, respectively, and that four classes of mixed-ligand complexes can be obtained simply by manipulating the ligand-to-zinc-benzoate molar ratio and the solvent. This result led us to suggest that the ligand concentration as well as the solvent system can tune topology in the system of zinc-benzoate with a variety of bipyridyl bridging ligands.

*Catalytic transesterification reactions by the compounds **1–4**:* Transesterifications are important transformations in organic synthesis in industrial as well as in academic laboratories [74–76]. As part of our efforts to design transesterification catalysts based on metal ions that are not redox active, therefore, we have recently synthesized several discrete complexes and coordination polymers and reported that some of them could carry out efficiently the catalytic transesterification of a range of esters with methanol under the mild conditions [77–79]. While these catalyst systems constitute a promising class of catalysts that appears to be an efficient, mild, and easily recyclable method for the alcoholysis of esters, there is still more demand to develop new types of catalysts that show better efficiency. With our previous experience, therefore, compounds **1–4** have been also employed as a catalyst for transesterification reaction in methanol under a homogeneous condition. The ester, *p*-nitrophenyl acetate, was initially used as a substrate (Eq. (1)):

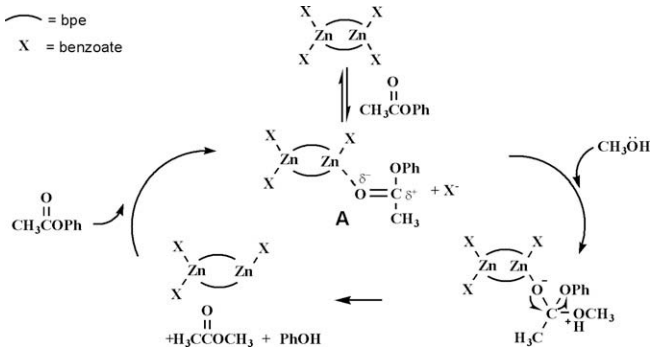


(1)

We observed that compounds **1–4** catalyzed the reaction of *p*-nitrophenyl acetate with methanol, with quantitative conversion to methyl acetate in 0.3–0.9 day (see the entry 1 of Table 4) at 50 °C under the neutral conditions. Among them, the complex **3** shows the most efficient reactivity. Importantly, this result is the second best among the catalytic efficiencies reported previously with zinc-containing coordination and polymeric compounds, to our best knowledge [77–84]. Since we have established that **1–4** represent excellent catalysts for the tansesterification reaction of *p*-nitrophenyl acetate with methanol, we have investigated the transesterification of various *p*-substituted phenyl acetates and benzoates. As shown in Table 4, the substrates with the electron-withdrawing substituents have undergone faster transesterification (entries 1 and 5) than those with the electron-donating ones (entries 4 and 8). In addition, vinyl acetate as a precursor widely used for ester synthesis [85–87] was converted efficiently to the product methyl acetate by **1–4** within 0.3–1.5 day (entry 9). This result suggests that this catalytic system can be useful for preparing various esters by transesterification. Moreover, it is worthwhile that 4-nitrophenyl acetate and 4-nitrophenyl benzoate with nitro substituents at the *para*-position, which are known to be problematic substrates for the transesterification reaction due to undesirable side reactions such as isomerization or polymerization [88], were also converted quantitatively to the corresponding products.

Furthermore, this promising result led us to test the transesterification with more challenging nucloephiles such as ethanol, 2-propanol, and propanol, in the presence of the catalysts **1–4**. Phenyl acetate reacted very slowly with either ethanol (70 days) or 2-propanol (90 days), respectively, whereas with propanol the transesterification reaction was complete within 2–7 days in the presence of **1–4**, respectively (entry 3). The complex **3** again shows the most efficient reactivity. This result is the best among the catalytic efficiencies reported previously with zinc-containing coordination and polymeric compounds, to our best knowledge [77–84]. Various esters were also examined with propanol as a nucleophile in the presence of **1–4**. The substrates with the electron-withdrawing substituents have undergone faster conversion to the corresponding products (entries 1 and 5), while those with the electron-donating ones have shown slow transesterification reaction (entries 4 and 8).

Though we do not know, at this moment, about the exact reactive species and the reaction mechanism for the transesterification reaction by the catalysts, it has been proposed that the mechanism of metal ion catalyzed transesterification probably involves electrophilic activation of the carbon center of the carbonyl moiety by binding of the metal to the carbonyl oxygen [89–93]. Therefore, Lewis acidity of the metal center may be important in catalytic transesterification. Based on this idea and our previous proposal on the transesterification reactions [79,94,95], a possible transesterification mechanism in these catalyst systems can be proposed with the catalyst **4** as shown in Scheme 1. The complex **4** could



Scheme 1. Plausable transesterification mechanism.

possibly be a catalytic species because only **4** has been obtained in methanol/H_2O without respect to the ligand-to-metal ratios and because the transesterification reactions were carried out in methanol. At the first step, the substrate phenyl acetate substitutes a labile ligand benzoate to give the adduct **A** (Scheme 1). Then, the nucleophile methanol would attack the carbon atom of carbonyl moiety of the adduct to produce the product methyl acetate. After the catalytic reaction, the structure of **4** was proved to be kept, based on ^{1}H NMR experiments. ^{1}H NMR data of benzoate and bpe of **4** appear at different positions from those of free benzoate and free bpe (see Section 2). ^{1}H NMR data of benzoate and bpe of the complex **4** taken after the transesterification reaction were exactly identical to those of benzoate and bpe of the starting complex **4** and we were not able to observe any free benzoate and bpe separated from **4** (see Section 2). This result indicates that there is no structural change of **4** after the transesterification reaction. This investigation was consistent with the proposed transesterification mechanism. Further detailed mechanistic studies are currently under investigation.

4. Conclusion

We have shown here how the structures of the coordination compounds of the bpe ligand with zinc-benzoate are able to be varied not only by the traditional method such as solvent control but also by changes in the ratio of ligand-to-zinc-benzoate. This work reveals that both the ligand-to-metal ratio and the solvent play very important roles in the formation of different coordination structures, and this offers the possibility to control the formation of such structures by varying those factors. Furthermore, these results led us to suggest that many of zinc-containing coordination polymers previously reported on specific solvents and ligand-to-metal ratios may be converted to yet unknown new structures according to the change of the reaction conditions such as solvent and ligand-to-metal ratio.

We have also shown that the compounds **1**–**4** catalyzed efficiently the transesterification of a variety of esters. Importantly, the overall transesterification reactivity shown by the catalyst **3** is the best among the catalytic efficiencies reported previously with zinc-containing coordination and polymeric compounds, to our best knowledge. In addition, the scope of the application of **1**–**4** as transesterification catalysts has been expanded to now include ethanol and propanol. Further explorations into the uses of this catalyst family in organic transformations as well as mechanistic investigations are ongoing.

Taken all together, this observation is very significant since it encourages us to construct new polymeric compounds that might be efficiently used as homogeneous or heterogeneous catalysts friendly to the environment simply by altering the ratio of ligand-to-metal and solvent system in the reaction mixtures.

Acknowledgements

Financial support from the Korea Research Foundation (2007-314-C00159), The SEOUL R&BD Program, Environmental Korea Ministry Environment "ET-Human resource development Project", the Korean Science and Engineering Foundation (R01-2008-000-20704-0), and the SRC program of the Korea Science and Engineering Foundation (KOSEF) through the Center for Intelligent Nano-Bio Materials at Ewha Womans University (Grant R11-2005-008-00000-0) is gratefully acknowledged.

Appendix A. Supplementary data

CCDC 687836, 687837, 687838, and 687839 contain the supplementary crystallographic data for **1**, **2**, **3**, and **4**, respectively. These data can be obtained free of charge via http://www.ccdc.cam.ac.uk/conts/retrieving.html, or from the Cambridge Crystallographic Data Centre, 12 Union Road, Cambridge CB2 1EZ, UK; fax: (+44) 1223-336-033; or e-mail: deposit@ccdc.cam.ac.uk. Supplementary data associated with this article can be found, in the online version, at doi:10.1016/j.poly.2008.11.048.

References

[1] S.R. Batten, R. Robson, Angew. Chem., Int. Ed. 37 (1998) 1460.
[2] D.B. Moler, H. Li, B. Chen, T.M. Reineke, M. O'Keeffe, O.M. Yaghi, Acc. Chem. Res. 34 (2001) 319.
[3] B. Moulton, M. Zaworotko, J. Chem. Rev. 101 (2001) 1629.
[4] K. Kim, Chem. Soc. Rev. 31 (2002) 96.
[5] (a) O.R. Evans, W. Lin, Acc. Chem. Res. 35 (2002) 511; (b) C. Janiak, Dalton Trans. (2003) 2781.
[6] P.J. Hagrman, D. Hagrman, J. Zubieta, Angew. Chem., Int. Ed. 38 (1999) 2638.
[7] S. Noro, R. Kitaura, M. Komdo, S. Kitagawa, T. Ishii, H. Matsuzaka, M. Yamashita, J. Am. Chem. Soc. 124 (2002) 2568. and references therein.
[8] S.L. James, Chem. Soc. Rev. 32 (2003) 276.
[9] A.J. Fletcher, E.J. Cussen, D. Bradshaw, M.J. Rosseinsky, K.M. Thomas, J. Am. Chem. Soc. 126 (2004) 9750.
[10] D.N. Dybtsev, H. Chun, K. Kim, Angew. Chem., Int. Ed. 43 (2004) 5033.
[11] E.-Y. Choi, K. Park, C.-M. Yang, H. Kim, J.-H. Son, S.W. Lee, Y.H. Lee, D. Min, Y.-U. Kwan, Chem. Eur. J. 10 (2004) 5535.
[12] J.L.C. Rowsell, O.M. Yaghi, Angew. Chem., Int. Ed. 44 (2005) 4670.
[13] B. Kesanli, Y. Cui, M.R. Smith, E.W. Bittner, B.C. Bockrath, W. Lin, Angew. Chem., Int. Ed. 44 (2005) 72.
[14] H. Chun, D.N. Dybtsev, H. Kim, K. Kim, Chem. Eur. J. 11 (2005) 3521.
[15] K.L. Mulfort, J.T. Hupp, J. Am. Chem. Soc. 129 (2007) 9604.
[16] K.S. Min, M.P. Suh, J. Am. Chem. Soc. 122 (2000) 6834.
[17] J. Fan, L. Gan, H. Kawaguchi, W.-Y. Sun, K.-B. Yu, W.-X. Tang, Chem. Eur. J. 9 (2003) 3965.
[18] S.K. Yoo, J.Y. Ryu, J.Y. Lee, C. Kim, S.-J. Kim, Y. Kim, Dalton Trans. (2003) 1454.
[19] S. Takizawa, H. Somei, D. Jayaprakash, H. Sasai, Angew. Chem., Int. Ed. 42 (2003) 5711.
[20] S.J. Hong, J.Y. Ryu, J.Y. Lee, C. Kim, S.-J. Kim, Y. Kim, Dalton Trans. (2004) 2697.
[21] S. Kitagawa, R. Kitaura, S.-I. Noro, Angew. Chem., Int. Ed. 43 (2004) 2334.
[22] S.J. Hong, J.S. Seo, J.Y. Ryu, J.H. Lee, C. Kim, S.-J. Kim, Y. Kim, A.J. Lough, J. Mol. Struct. 751 (2005) 22.
[23] C.-D. Wu, A. Hu, L. Zhang, W. Lin, J. Am. Chem. Soc. 127 (2005) 8940.
[24] X. Wang, X. Wang, H. Guo, Z. Wang, K. Ding, Chem. Eur. J. 11 (2005) 4078.
[25] H. Han, S. Zhang, H. Hou, Y. Fan, Y. Zhu, Eur. J. Inorg. Chem. (2006) 1594.
[26] D.N. Dybtsev, A.L. Nuzhdin, H. Chun, K.P. Bryliakov, E.P. Talsi, V.P. Fedin, K. Kim, Angew. Chem., Int. Ed. 45 (2006) 916.
[27] S. Hasegawa, S. Horike, R. Matsuda, S. Furukawa, K. Mochizuki, Y. Kinoshita, S. Kitagawa, J. Am. Chem. Soc. 129 (2007) 2607.
[28] J.I. Kim, H.S. Yoo, E.K. Koh, H.C. Kim, C.S. Hong, Inorg. Chem. 46 (2007) 8481.
[29] J. Zhang, A. Lachgar, J. Am. Chem. Soc. 129 (2007) 250.
[30] L.M. Toma, R. Lescouezec, J. Pasan, C. Ruiz-Perez, J. Vaissermann, J. Cano, R. Carrasco, W. Wernsdorfer, F. Lloret, M. Julve, J. Am. Chem. Soc. 128 (2006) 4842.
[31] G.A. Mines, B.C. Tzeng, K.J. Stevenson, J. Li, J.T. Hupp, Angew. Chem., Int. Ed. 41 (2002) 154.
[32] M.C. Hong, Y.J. Zhao, W.P. Su, R. Cao, M. Fujita, Z.Y. Zhou, A.S.C. Chan, J. Am. Chem. Soc. 122 (2000) 4819.
[33] J.F. Ma, J.F. Liu, X. Yan, H.Q. Jia, Y.H. Lin, J. Chem. Soc., Dalton Trans. (2000) 2403.
[34] D.M. Shin, I.S. Lee, Y.-A. Lee, Y.K. Chung, Inorg. Chem. 42 (2003) 2977.
[35] C. Richardson, P.J. Steel, D.M. D'Alessandro, P.C. Junk, F.R. Keene, J. Chem. Soc., Dalton Trans. (2002) 2775.
[36] K. Biradha, M. Fujita, J. Chem. Soc., Dalton Trans. (2000) 3805.
[37] O.-S. Jung, S.H. Park, K.M. Kim, H.G. Jang, Inorg. Chem. 37 (1998) 5781.

[38] M.A. Withersby, A.J. Blake, N.R. Champness, P.A. Cooke, P. Hubberstey, W.-S. Li, M. Schroder, Inorg. Chem. 38 (1999) 2259.
[39] W.-X. Chen, S.-T. Wu, L.-S. Long, R.-B. Huang, L.-S. Zheng, Crystal Growth Design 7 (2007) 1171.
[40] R.-Q. Fang, X.-M. Zhang, Inorg. Chem. 45 (2006) 4801.
[41] Y.B. Go, X. Wang, E.V. Anokhina, A. Jacobson, J. Inorg. Chem. 44 (2005) 8265.
[42] Y.-B. Dong, Y.-Y. Jiang, J. Li, J.-P. Ma, F.-L. Liu, B. Tang, R.-Q. Huang, S.R. Batten, J. Am. Chem. Soc. 129 (2007) 4520.
[43] C.-M. Liu, S. Gao, D.-Q. Zhang, D.-B. Zhu, Crystal Growth Design 7 (2007) 1312.
[44] L. Carlucci, G. Ciani, D.M. Proserpio, S. Rizzato, Chem. Eur. J. 5 (1999) 237.
[45] H.-P. Wu, C. Janiak, G. Rheinwald, H. Lang, J. Chem. Soc., Dalton Trans. (1999) 183.
[46] A.J. Blake, N.R. Brooks, N.R. Champness, P.A. Cooke, A.M. Deveson, D. Fenske, P. Hubberstey, M. Schroder, J. Chem. Soc., Dalton Trans. (1999) 2103.
[47] R.W. Saalfrank, I. Bernt, M.M. Chowdhry, F. Hampel, G.B.M. Vaughan, Chem. Eur. J. 7 (2001) 2765.
[48] X.-J. Luan, X.-H. Cai, Y.-Y. Wang, D.-S. Li, C.-J. Wang, P. Liu, H.-M. Hu, Q.-Z. Shi, S.-M. Peng, Chem. Eur. J. 12 (2006) 6281.
[49] Z.-M. Hao, X.-M. Zhang, Crystal Growth Design 7 (2007) 64.
[50] R.P. Feazell, C.E. Carson, K.K. Klausmeyer, Inorg. Chem. 45 (2006) 935.
[51] M. Oh, C.L. Stern, C.A. Mirkin, Inorg. Chem. 44 (2005) 2647.
[52] Y.-B. Dong, H.-Y. Wang, J.-P. Ma, D.-Z. Shen, R.-Q. Haung, Inorg. Chem. 44 (2005) 4679.
[53] S. Sailaja, M.V. Rajasekharan, Inorg. Chem. 42 (2003) 5675.
[54] M.A. Withersby, A.J. Blake, N.R. Champness, P.A. Cooke, P. Hubberstery, W.-S. Li, M. Schroder, Inorg. Chem. 38 (1999) 2259.
[55] S. Subramanian, M.J. Zaworotko, Angew. Chem., Int. Ed. 34 (1995) 2127.
[56] R.W. Gable, B.F. Hoskins, R. Robson, J. Chem. Soc., Chem. Commun. (1990) 1677.
[57] H. Kwak, S.H. Lee, S.H. Kim, Y.M. Lee, B.K. Park, E.Y. Lee, Y.J. Lee, C. Kim, S.-J, Kim, Y. Kim, Polyhedron 27 (2008) 3484.
[58] Bruker, SHELXTL/PC. Version 6.12 for Windows XP, Bruker AXS Inc., Madison, Wisconsin, USA, 2001.
[59] K. Nakamoto, Infrared and Raman Spectra of Inorganic and Coordination Compounds, John Wiley and Sons, New York, 1986.
[60] J. Tao, M.-L. Tong, X.-M. Chen, J. Chem. Soc., Dalton Trans. (2000) 3669.
[61] W. Chen, J.-Y. Wang, C. Chen, Q. Yue, H.-M. Yuan, J.-S. Chen, S.-N. Wang, Inorg. Chem. 42 (2003) 944.
[62] M.T. Ng, T.C. Deivaraj, W.T. Kloosret, G.J. McIntyre, J.J. Vittal, Chem. Eur. J. 10 (2004) 5853.
[63] B. Singh, J.R. Long, F.F. de Biani, D. Gattesch, P. Stavropoulos, J. Am. Chem. Soc. 119 (1997) 7030.
[64] W. Clegg, I.R. Little, B.P. Straughan, J. Chem. Soc., Dalton Trans. (1986) 1283.
[65] A. Karmaker, R.J. Sarma, J.B. Baruah, Inorg. Chem. Commun. 9 (2006) 1169.
[66] H. Li, M. Eddaoudi, T.L. Groy, O.M. Yaghi, J. Am. Chem. Soc. 120 (1998) 8571.
[67] H. Chun, J. Moon, Inorg. Chem. 46 (2007) 4371.
[68] W. Clegg, I.R. Little, B.P. Straughan, J. Chem. Soc., Chem. Commun. (1985) 73.
[69] W. Clegg, I.R. Little, B.P. Straughan, Inorg. Chem. 27 (1988) 1916.
[70] C.A. Williams, A.J. Blake, P. Hubberstey, M. Schroder, Chem. Commun. (2005) 5435.
[71] M. Casarin, C. Corvaja, C.D. Nicola, D. Falcomer, L. Franco, M. Monari, L. Pandolfo, C. Pettinari, F. Piccinelli, Inorg. Chem. 44 (2005) 6265.
[72] B.-H. Ye, M.-L. Tong, X.-M. Chen, Coord. Chem. Rev. 249 (2005) 545.
[73] F. Li, T. Li, X. Li, X. Li, Y. Wang, R. Cao, Crystal Growth Design 6 (2006) 1458.
[74] M.-H. Lin, T.V. RajanBabu, Org. Lett. 2 (2000) 997.
[75] G.A. Grasa, R.M. Kissling, S.P. Nolan, Org. Lett. 4 (2002) 3583.
[76] G.A. Grasa, T. Guveli, R. Singh, S.P. Nolan, J. Org. Chem. 68 (2003) 2812.
[77] J.Y. Lee, S.J. Hong, C. Kim, S.-J. Kim, Y. Kim, Inorg. Chem. Commun. 8 (2005) 692.
[78] Y.M. Lee, S.J. Hong, H.J. Kim, S.H. Lee, H. Kwak, C. Kim, S.-J. Kim, Y. Kim, Inorg. Chem. Commun. 10 (2007) 287.
[79] H. Kwak, S.H. Lee, S.H. Kim, Y.M. Lee, E.Y. Lee, B.K. Park, E.Y. Kim, C. Kim, S.-J. Kim, Y. Kim, Eur. J. Inorg. Chem. (2008) 408.
[80] J.S. Seo, D. Whang, H. Lee, S.I. Jun, J. Oh, Y.J. Jeon, K. Kim, Nature 404 (2000) 982.
[81] J.Y. Ryu, J.H. Han, J.Y. Lee, S.J. Hong, S.H. Choi, C. Kim, S.-J. Kim, Y. Kim, Inorg. Chim. Acta 358 (2005) 3659.
[82] Y. Kim, S.-J. Kim, S.H. Choi, J.H. Han, S.H. Nam, J.H. Lee, H.J. Kim, C. Kim, D.W. Kim, H.G. Jang, Inorg. Chim. Acta 359 (2006) 2534.
[83] J.Y. Kwon, Y. Kim, S.-J. Kim, S.H. Lee, H. Kwak, C. Kim, Inorg. Chim. Acta 361 (2008) 1885.
[84] L. Xu, Y. Kim, S.-J. Kim, H.J. Kim, C. Kim, Inrog. Chem. Commun. 10 (2007) 586.
[85] G.W. Nyce, J.A. Lamboy, E.F. Connor, R.M. Waymouth, J.L. Hedrick, Org. Lett. 4 (2002) 3587.
[86] D. Tashiro, Y. Kawasaki, S. Sakaguchi, Y. Ishii, J. Org. Chem. 62 (1997) 8141.
[87] Y. Ishii, M. Takeno, Y. Kawasaki, Y. Muromachi, Y. Nishiyama, S. Sakaguchi, J. Org. Chem. 61 (1996) 3088.
[88] V.K. Aggarwal, A. Mereu, Chem. Commun. (1999) 2311.
[89] F.E. Jacobsen, J.A. Lewis, S.M. Cohen, J. Am. Chem. Soc. 128 (2006) 3156.
[90] J. Weston, Chem. Rev. 105 (2005) 2151.
[91] G. Parkin, Chem. Rev. 104 (2004) 699.
[92] W.D. Horrocks Jr., J.N. Ishley, R.R. Whittle, Inorg. Chem. 21 (1982) 3265.
[93] W.D. Horrocks Jr., J.N. Ishley, R.R. Whittle, Inorg. Chem. 21 (1982) 3270.
[94] D.-W. Yoo, J.-H. Han, S.H. Nam, H.J. Kim, C. Kim, J.-K. Lee, Inorg. Chem. Commun. 9 (2006) 654.
[95] B.K. Park, S.H. Lee, E.Y. Lee, H. Kwak, Y.M. Lee, Y.J. Lee, J.Y. Jun, C. Kim, S.-J. Kim, Y. Kim, J. Mol. Struct. 890 (2008) 123.

Polyhedron 28 (2009) 562–568

Contents lists available at ScienceDirect

Polyhedron

journal homepage: www.elsevier.com/locate/poly

Synthesis and characterization of three novel molybdenum(VI) complexes: Mononuclear $[MoO_2(C_6H_4(O)CH{=}NCH(COO)CH_2C{=}(O)NH_2)]$, $[MoO_2(C_{19}H_{19}N_2O_5)(CH_3OH)]Cl \cdot CH_3OH$ and dinuclear $[Mo_2O_4(C_6H_4(O)CH{=}NCH(COO)CH_2C{=}(O)NH_2)_2]$

Marina Cindrić [a,*], Gordana Galin [a], Dubravka Matković-Čalogović [a], Predrag Novak [a], Tomica Hrenar [a], Ivan Ljubić [b], Tanja Kajfež Novak [a]

[a] Department of Chemistry, Faculty of Science, University of Zagreb, Horvatovac 102 a, 10001 Zagreb, Croatia
[b] Department of Physical Chemistry, Ruđer Bošković Institute, Bijenička Cesta 54, 10002 Zagreb, Croatia

ARTICLE INFO

Article history:
Received 16 June 2008
Accepted 20 November 2008
Available online 23 January 2009

Keywords:
Molybdenum chelates
N, O ligands
X-ray diffraction
NMR spectroscopy

ABSTRACT

The molybdenum(VI) complexes $[Mo_2O_4(C_6H_4(O)CH{=}NCH(COO)CH_2C{=}ONH_2)_2]$ (**1**), $[MoO_2(C_6H_4(O)CH{=}NCH(COO)CH_2C{=}(O)NH_2)]$ (**3**) and $[MoO_2(C_{19}H_{19}N_2O_5)(CH_3OH)]Cl \cdot CH_3OH$ (**4**), of salicylaldehyde amino acid derivatives (DL-asparagine or L-ornithine hydrochloride) have been synthesized and characterized. The Schiff base containing a saturated heterocyclic ring (in complex **4**) is the first example of such a molecule derived from salicylaldehyde and the amino acid, L-ornithine hydrochloride. We proposed that the formation of a molybdenum(VI) complex coordinated by a Schiff base containing a saturated heterocyclic ring depends upon the nature of the solvent and upon the presence of molybdenum(VI). In the absence of molybdenum(VI), the condensation product obtained from the reaction of L-ornithine hydrochloride and salicylaldehyde was the Schiff base *N*-salicylidene-L-ornithine (**5**). In the dinuclear complex **1** and the mononuclear complexes **3** and **4**, the molybdenum atoms are octahedrally coordinated with two *cis* oxo-oxygen atoms (in **3** and **4**), oxo-bridging atoms (in **1**) and the Schiff base ligand. In **3** the *N*-salicylidene-DL-asparaginato ligand coordinates molybdenum tetradentately while in **1** and **4** the Schiff base ligand acts as a tridentate ligand.

© 2008 Elsevier Ltd. All rights reserved.

1. Introduction

During the last decade, intensive studies have been carried out on the biochemical, pharmacological and physicochemical functions of molybdenum. In particular, many kinds of dioxomolybdenum(VI) compounds have been synthesized as models of molybdoenzymes in order to study and elucidate catalytic oxygen atom transfer reactions [1–7]. For example, dioxomolybdenum(VI) complexes have been studied as models for oxidized forms of molybdoenzymes, e.g. aldehyde oxidase and sulfite oxidase which are supposed to contain *cis*-$MoOX_2$ units (X = O, S) coordinated to sulfur, nitrogen and oxygen donor atoms in the protein structure [4–7]. During the enzymatic turnover, the mononuclear molybdenum center is proposed to cycle between the IV and VI oxidation states, with the paramagnetic V state being the obligatory catalytic intermediate in the oxidative half-reaction of the enzyme. In the context of model systems for this type of reaction, a few studies have been concerned with the preparation and reactivity of molybdenum(VI) complexes of *N*-salicylidene-L-amino acids and their derivatives [8].

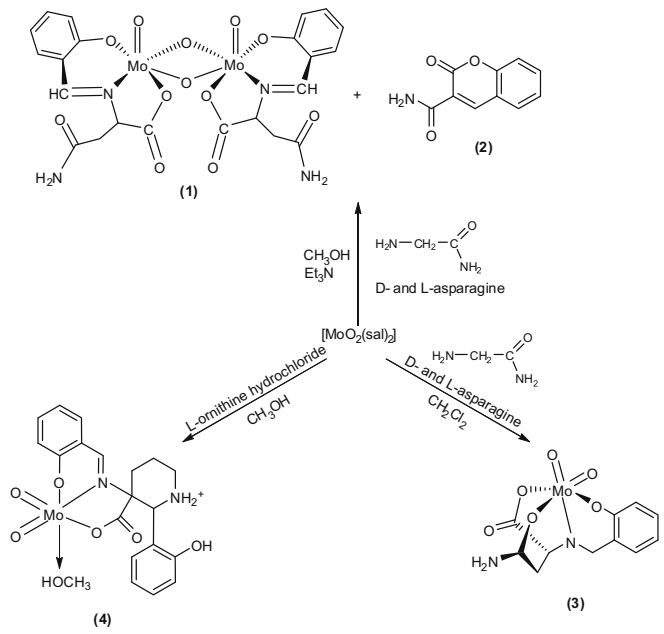
In the present work we describe products of the template synthesis of potentially tridentate and tetradentate Schiff base ligands, derived from salicylaldehyde (salH) and the amino acids DL-asparagine and L-ornithine hydrochloride, with the dioxomolybdenum(VI) core (Scheme 1).

Complex formation of $[MoO_2(sal)_2]$ with DL-asparagine and L-ornithine hydrochloride was studied in methanolic and dichloromethane solutions. The presence of mononuclear dioxomolybdenum(VI) centers in the complexes $[MoO_2(C_6H_4(O)CH{=}NCH(COO)CH_2C{=}(O)NH_2)]$ (**3**) and $[MoO_2(C_{19}H_{19}N_2O_4)(CH_3OH)]Cl \cdot CH_3OH$ (**4**) was confirmed by the crystal structure determinations, while the chemical structure of the complex $[Mo_2O_4(C_6H_4(O)CH{=}NCH(COO)CH_2C{=}(O)NH_2)_2]$ (**1**) was determined by NMR spectroscopy.

Computational studies were proved and were concerned with the role of the molybdenum atom in the cyclization of the Schiff base derived from L-ornithine hydrochloride and salicylaldehyde.

* Corresponding author. Tel.: +385 1 460 6351; fax: +385 1 460 6340.
E-mail address: marina@chem.pmf.hr (M. Cindrić).

0277-5387/$ - see front matter © 2008 Elsevier Ltd. All rights reserved.
doi:10.1016/j.poly.2008.11.058



Scheme 1. Reactions of $[MoO_2(sal)_2]$ with D- and L-asparagine and L-ornithine hydrochloride.

2. Experimental

Materials and methods: L-Ornithine hydrochloride, DL-asparagine and triethylamine were of reagent grade and were used as purchased. Methanol was dried using magnesium turnings and iodine, and then distilled. Dichloromethane was dried over P_2O_5. The starting complex $[MoO_2(sal)_2]$ was prepared as described in the literature [9].

IR spectra: Infrared spectra were recorded in KBr with a Spectrum RX I spectrophotometer in the 4500–450 cm^{-1} region.

Elemental analyses: The Analytical Services Laboratory of the Rudjer Bošković Institute provided C, H and N analyses. Molybdenum was determined according to the method described in the literature [10].

2.1. Syntheses of the molybdenum(VI) complexes

2.1.1. Synthesis of di-μ-oxo-di(N-salicylidene-DL-asparaginato) dioxodimolybdenum(VI), $[Mo_2O_4(C_6H_4(O)CH{=}NCH(COO)CH_2C{=}(O)NH_2)_2]$ (**1**)

$[MoO_2(sal)_2]$ (0.63 g, 1.7 mmol) was dissolved in dry methanol (35 ml) and the solution was refluxed under an argon atmosphere for 15 min before addition of DL-asparagine (0.45 g, 3.4 mmol) and a few drops of triethylamine. The reaction mixture was refluxed under an argon atmosphere for 7 h. The color of the solution changed from pale yellow to red. The yellow crystalline product, (**1**), that formed after 7 h was filtered off, washed with cold methanol and dried in vacuo. Yield: 0.08 g (13%). After six weeks needle-like transparent crystals of coumarin-3-carboxamide (**2**) were obtained from the mother liquor at room temperature. Yield: 0.06 g (10%).

(**1**) *Anal.* Calc. for $C_{22}H_{20}Mo_2N_4O_{13}$: C, 35.69; H, 2.72; N, 7.57; Mo, 25.91. Found: C, 35.30; H, 2.75; N, 7.62; Mo, 26.30%. IR (KBr) ν/cm^{-1}: 3382, 1716, 1680, 1610, 1556, 1472, 1414, 908, 944, 820, 762, 638.

(**2**) *Anal.* Calc. for $C_{10}H_7NO_3$: C, 63.53; H, 3.73; N, 7.41. Found: C, 63.55; H, 3.40; N, 7.39%. IR (KBr) ν/cm^{-1}: 3390, 3146, 1714, 1564, 1388, 1162, 1008, 770, 618.

2.1.2. Synthesis of cis-dioxo(N-salicylidene-DL-asparaginato) molybdenum(VI), $[MoO_2(C_6H_4(O)CH{=}NCH(COO)CH_2C{=}(O)NH_2)]$ (3)

$[MoO_2(sal)_2]$ (0.63 g, 1.7 mmol) was dissolved in dry dichloromethane (35 ml) and the solution was refluxed under an argon atmosphere for 15 min before addition of DL-asparagine (0.45 g, 3.4 mmol). The reaction mixture was refluxed under an argon atmosphere for 5 h. The color of the solution changed to yellow. The yellow crystalline product, (**3**), that formed after 5 h was filtered off, washed with cold dichloromethane and dried *in vacuo*. Yield: 0.1 g (16%).

Anal. Calc. for $C_{11}H_{10}MoN_2O_6$: C, 36.48; H, 2.78; N, 7.74; Mo, 26.49. Found: C, 36.59; H, 2.75; N, 7.52; Mo, 26.30%. IR (KBr) ν/cm^{-1}: 3372, 1730, 1665, 1600, 1576, 1422, 1410, 928, 944.

2.1.3. Synthesis of 3-[(2,5-salicylideneiminato)-2-(2-hydroxyphenyl) (piperidinum)-3-carboxylato)methanol dioxomolybdenum(VI)] chloride methanol, (1/1) $[MoO_2(C_{19}H_{19}N_2O_4)(CH_3OH)]Cl \cdot CH_3OH$ (**4**)

$[MoO_2(sal)_2]$ (0.15 g, 0.41 mmol) and L-ornithine hydrochloride (0.14 g, 0.83 mmol) were dissolved in dry methanol (35 ml). The mixture was refluxed for 5 h under an argon atmosphere. After a few days an unstable yellow-green crystalline product (**4**) was obtained. The product was filtered off, washed with cold methanol and dried *in vacuo* under an argon atmosphere. Yield: 0.1 g (42%).

Anal. Calc. for $C_{21}H_{27}ClMoN_2O_8$: C, 44.49; H, 4.80; N, 4.94; Cl, 6.25; Mo, 16.92. Found: C, 43.96; H, 4.56; N, 5.01; Cl, 6.20; Mo, 16.63%. IR (KBr) ν/cm^{-1}: 3172, 3028, 2938, 1668, 1624, 1600, 1454, 1428, 934, 909.

2.1.4. Synthesis of N-salicylidene-L-ornithine hydrochloride, $C_6H_4(OH)CH_2NHCH(COOH)(CH_2)_3NH_2{\cdot}HCl$ (**5**)

L-Ornithine hydrochloride (0.84 g, 5 mmol) was dissolved in potassium hydroxide solution (0.289 g KOH in 10 ml water) and added to salicylaldehyde (1.22 g, 10 mmol in 10 ml EtOH). The mixture was stirred under reflux for 1 h with the almost immediate appearance of a yellow product. It was filtered off, washed with cold ethanol and dried in vacuo. Yield: 0.84 g (61.83%).

(**5**) *Anal.* Calc. for $C_{12}H_{17}ClN_2O_3$: C, 52.85; H, 6.28; N, 10.27; Cl, 13.00. Found: C, 53.01; H, 6.10; N, 9.87; Cl, 12.65%. IR (KBr) ν/cm^{-1}: 3050, 2948, 1638, 1582, 1514, 1410, 1338, 1284, 846, 750.

2.2. X-ray crystallography

Crystal parameters, data collection details and refinement results for compounds **3** and **4** are summarized in Table 1. Diffraction data for **3** were collected on an Oxford Diffraction Xcalibur 3 CCD diffractometer at 295 K, and those for **4** on an Enraf-Nonius Mach 2000 diffractometer at 110 K. Graphite-monochromated Mo Kα radiation ($\lambda = 0.71073$ Å) was used for both data collections. The data were corrected for Lorentz and polarization effects by CRYSALIS [11] and DENZO programs [12] for **3** and **4**, respectively. Both structures were solved by direct and Fourier methods using SHELXS-97 [13] and SHELXL-97 [14], respectively. They were refined by the full-matrix least-squares method based on F^2 values against all reflections assuming anisotropic temperature factors for all non-H atoms using the SHELXL-97 program integrated in the WINGX package [15]. All hydrogen atoms were found, however due to the somewhat poor geometry, those on carbon atoms were generated and left to ride on their parent atoms. The two amino-hydrogen atoms in **3** were refined isotropically. The positional parameters of the hydrogen atoms attached to the nitrogen and oxygen atoms in **4** were left as found in the difference Fourier map and only their isotropic thermal parameter was refined. Figures were made with the programs ORTEP [16] and PLATON [17].

Table 1
General and crystal data, summary of intensity data collection and structure refinement for compounds **3** and **4**.

	3	**4**
Formula	$C_{11}H_{10}MoN_2O_6$	$C_{21}H_{27}ClMoN_2O_8$
Formula weight	362.15	566.84
Color	yellow	yellow-green
Temperature (K)	293(2)	110(2)
Wavelength (Å)	0.71073	0.71073
Crystal system	monoclinic	triclinic
Space group	$P2_1/a$	$P\bar{1}$
Unit cell parameters		
a (Å)	12.059(2)	9.6417(19)
b (Å)	7.364(3)	10.134(2)
c (Å)	15.329(3)	12.701(3)
α (°)	90	79.83(3)
β (°)	111.730(19)	78.28(3)
γ (°)	90	78.09(3)
V (Å^3)	1264.5(6)	1177.2(5)
Z	4	2
ρ_{calc} (g cm^{-3})	1.902	1.599
$F(000)$	720	580
Crystal size (mm^3)	0.31 × 0.11 × 0.07	0.25 × 0.20 × 0.17
θ range for data collection (°)	4.3–29.5	3.5–28.3
No. of measured reflections	14209	10712
No. of independent reflections [R_{int}]	3484 [0.0495]	5812 [0.0133]
No. of observed reflections, $I \geq 2\sigma(I)$	2390	5296
No. parameters	189	306
Absorption correction	integration	integration
μ (mm^{-1})	1.065	0.720
Range of transmission factors	0.825, 0.913	0.822, 0.863
R[a], wR[b] [$I \geq 2\sigma(I)$]	0.0508, 0.1419	0.0243, 0.0579
R, wR (all data)	0.0708, 0.1572	0.0281, 0.0595
g_1, g_2 in w[c]	0.0921, 0	0.0186, 0.7504
Goodness-of-fit on F^2, S[d]	1.110	1.075
Minimum and maximum electron density (e Å^{-3})	−0.981, 1.724	−0.486, 0.399

[a] $R = \sum||F_o| - |F_c||/\sum|F_o|$.
[b] $wR = [\sum(F_o^2 - F_c^2)^2/\sum w(F_o^2)^2]^{1/2}$.
[c] $w = 1/[\sigma^2(F_o^2) + [g_1P + g_2P]$ where $P = (F_o^2 + 2F_c^2)/3$.
[d] $S = \sum[w(F_o^2 - F_c^2)^2/(N_{obs} - N_{param})]^{1/2}$.

2.3. NMR measurements

One and two-dimensional NMR spectra were recorded on Bruker Avance DRX500 and Bruker Avance DPX 300 spectrometers equipped with a 5 mm diameter inverse detection probe and a 5 mm $^1H/^{13}C$ dual probe, respectively, and z-gradient accessory. TMS was used as the internal standard. Standard spectral conditions were used for the ^1H and ^{13}C (PENDANT) NMR experiments. The sample concentration was 20 mg ml^{-1} in [D_6]DMSO solutions. The digital resolution was 0.1 and 0.3 Hz per point for ^1H and ^{13}C spectra, respectively. COSY spectra were recorded with spectral width of 4000 Hz in each domain and with 1024 points in the f2 dimension. A 2s relaxation delay was used to acquire 512 increments for each data set. Free induction decays were processed using a 2K × 1K matrix with appropriate zero filling and sine weighting. The digital resolution was 3.9 and 15.6 Hz per point in the f2 and f1 dimensions, respectively. The HSQC and HMBC spectra were recorded with a relaxation delay of 1.5 s and 32 scans per increment. The spectral width was 31 000 Hz in acquisition domain f2 and 4000 Hz in time domain f1. Data were collected into a 2048 × 512 acquisition matrix and processed using a 2K × 1K transformed matrix with zero filling in the f1 domain. Sine multiplication was performed before Fourier transformations. In HMBC spectra the delay for long-range couplings was set to 60 ms.

2.4. Computational details

In all calculations we consistently used the same generalized gradient (GGA) corrections in determining the self-consistent charge density and the exchange-correlation (XC) part of the energy corresponding to the charge density. The used functional was the recently proposed OPBE [18], which combines the OPTX exchange devised by Handy and Cohen [19] with the correlation term proposed by Perdew et al. [20]. The local density approximation (LDA) part was based upon the Vosko–Wilk–Nusair (VWN) [21] parameterization of electron gas. The relativistic effects were accounted for via the scalar zeroth order regular approximation (ZORA) formalism [22], which was employed throughout. We made use of a basis set built from Slater type functions (STOs) and tailored especially for the ZORA approach, as reflected by the use of much steeper functions in the core region. The basis set consisted of a TZP quality set on the Mo atom with all the orbitals up to, and including 3d treated as a frozen core, DZP sets on the C, N and O atoms with the 1s orbital frozen, and a DZP set on the H atoms. In [$MoO_2(C_{19}H_{19}N_2O_4)$] (the complex cation of **4** without coordinated and solvated methanol molecules) there thus resulted a total of 473 symmetrized fragment orbitals. The recommended sets of auxiliary fit functions to facilitate computations of the Coulomb potential were employed unchanged. All the DFT calculations were performed using the ADF program system [23].

3. Results and discussion

3.1. Synthesis of the complexes

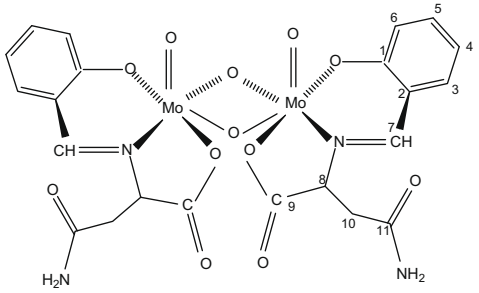
The yellow dinuclear molybdenum(VI) complex [Mo_2O_4-(C_6H_4(O)CH=NCH(COO)CH_2C=(O)NH_2)$_2$] (**1**) and coumarin-3-carboxamide $C_{10}H_7NO_3$ (**2**) were obtained by the reaction of [MoO_2(sal)$_2$] and DL-asparagine in dry methanol under an argon atmosphere. Cavaco et al. isolated coumarin 3-carboxamide and the vanadium(IV) complex [VO(sal-L-asn)(py)(H_2O)] in the reaction of $VOSO_4$, salicylaldehyde and L-asparagine, and they proposed a mechanism of oxidative decarboxylation of L-asparagine [24]. These reactions of biochemical and chemical decarboxylation of α-amino acids activated by metal ions are well documented [25–27].

The compounds **1** and **2** were characterized by IR spectra and the chemical structure of compound **1** was determined by the combined use of one- and two-dimensional NMR spectroscopy. The NMR results for compound **2** were in accordance with the literature data [24]. The proton and carbon chemical shifts of **1** are displayed in Table 2.

The two amide protons in **1** were readily assigned in the proton spectrum since their signals disappeared after the addition of D_2O owing to a rapid proton/deuterium exchange. Also the HMBC spectrum revealed connectivities from these protons to the C(11) carbonyl carbon. The HMBC correlation peak between one of the amide protons and C(10) was further established. In addition, the imino proton H(7) showed connectivities to C(2), C(3) and C(1) in the aromatic ring and to C(8) which was further correlated to

Table 2
^1H and ^{13}C chemical shifts (ppm) of **1**.

Atom (compound **1**)	^1H	^{13}C
1		159.74
2		121.53
3	7.67	134.79
4	7.11	121.34
5	7.61	135.99
6	6.99	118.55
7	8.76	164.89
8	4.92	65.91
9	–	174.67
10	2.93	39.21
11		170.79
NH_2	7.34, 7.31	



Scheme 2. $[Mo_2O_4(C_6H_4(O)CH{=}NCH(COO)CH_2C{=}(O)NH_2)_2]$ (**1**).

H(10). HMBC correlation peaks between H(8) and C(9) and C(11) were also observed corroborating the structure depicted in Scheme 2.

In the IR spectrum of compound **1**, the strong absorption bands at 820 cm^{-1} and in the region 908–944 cm^{-1} were assigned to the bridging and terminal Mo–O groups of the $Mo_2O_4^{4+}$ core and are in accordance to the literature data for the same type of complexes [28].

The mononuclear molybdenum(VI) complex, $[MoO_2(C_6H_4(O)CH{=}NCH(COO)CH_2C{=}(O)NH_2)]$ (**3**) was obtained by the reaction of $[MoO_2(sal)_2]$ and DL-asparagine in dry dichloromethane under an argon atmosphere. In the dinuclear **1** and mononuclear **3** complexes, molybdenum is coordinated by the deprotonated tridentate ONO (in **1**) and tetradentate OONO (in **3**) *N*-salicylidene-DL-asparaginato ligand. The coordination sphere in **1** is completed by one oxo-oxygen and two oxo-bridging atoms, and in **3** by two *cis* oxo-oxygen atoms.

The mononuclear molybdenum(VI) complex $[MoO_2(C_6H_4(O)CH{=}NC_5H_7(COO)NH_2C_6H_4(O)(CH_3OH)]Cl \cdot CH_3OH$ (**4**) was obtained in the reaction of $[MoO_2(sal)_2]$ and L-ornithine hydrochloride in dry methanol under an argon atmosphere (Scheme 3). We were able to isolate complex **4** from the methanolic solution, however the same reaction in dichloromethane (with or without addition of triethylamine) was unsuccessful.

Since L-ornithine contains an additional side-chain amino group we expected the formation of a molybdenum(VI) complex coordinated by a *bis*-Schiff base such as $[MoO_2C_6H_4(O)CH{=}NCH(COOH)(CH_2)_3N{=}CH(O)C_6H_4]$. However, X-ray investigations showed that in the obtained molybdenum(VI) complex, the molybdenum atom is coordinated by a Schiff base containing a saturated heterocyclic ring. According to the literature data [29] such Schiff base ligands are formed from the condensation reaction of 2-pyridinecarboxaldehyde derivatives with certain polyamines. Different metal salts (e.g. Fe(II), Ni(II), Zn(II)) have been reported to yield complexes of the corresponding Schiff base obtained in the condensation reaction of 2-pyridinecarboxaldehyde and α,ω-triamines [30].

In absence of molybdenum(VI) the condensation product obtained from the reaction of L-ornithine hydrochloride and salicylaldehyde in a 1:2 molar ratio was the Schiff base *N*-salicylidene-L-ornithine hydrochloride, $C_6H_4(OH)CH_2NHCH(COOH)(CH_2)_3NH_2 \cdot HCl$.

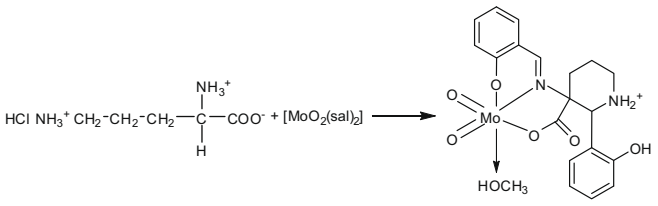
The IR spectra of all the described molybdenum(VI) complexes showed characteristic vibrations for this type of compound and the data are in accordance with that in the literature [28]. Complexes **3** and **4** underwent a rapid decomposition when dissolved in DMSO–d_6 and they were found to be insoluble in other solvents.

3.2. Structural studies

3.2.1. Structures of $[MoO_2(C_6H_4(O)CH{=}NCH(COO)CH_2C{=}(O)NH_2)]$ (3) and $[MoO_2(C_{19}H_{19}N_2O_5)(CH_3OH)]Cl \cdot CH_3OH$ (4)

In both structures the main feature is the mononuclear, octahedrally coordinated molybdenum atom with two *cis* oxo-oxygen atoms and a bound Schiff base ligand. In **3** the *N*-salicylidene-DL-asparaginato ligand coordinates molybdenum tetradentately (Fig. 1), while in **4** (2,5-salicylideneiminato)-2-(2-hydroxophenyl)(piperidinum)-3-carboxylate acts as a tridentate ligand. The coordination sphere in **4** is completed by a methanol molecule (Fig. 2). Selected bond distances and angles are presented in Table 3 for both structures.

Distortion from an ideal octahedral geometry is more pronounced in **3** with the acute angle N(1)–Mo–O(6) of 70.40(8)°, obtuse angle O(1)–Mo–O(2) of 105.96(15)° closed by two *cis* oxo-oxygen atoms, and the *trans* chelating angle O(2)–Mo–N(1) of 150.92(11)°. This is caused by more strain imposed by the rigid geometry of the tetradentate Schiff base ligand in **3**. The greatest distortion from the octahedral geometry in **4** is that of the *trans* chelating angle O(3)–Mo–O(4) of 151.07(5)°. An analysis was carried out on structures deposited with the Cambridge Structural Database [31] by defining an octahedrally coordinated mononuclear molybdenum atom, a Schiff base *N*-donor, three single bonded oxygen atoms and two *cis* oxo-oxygen atoms. The search gave 55 hits. The Mo=O bond is the shortest, with a mean value of 1.701(1) Å. The mean Mo–O bond that is *trans* to the Mo–O single bond is 1.945(4) Å (Mo–O range 1.887–2.025 Å, O–Mo–O range 147.4–158°), whereas the one *trans* to the oxo-oxygen atom is lengthened due to the *trans*-influence and amounts to 2.334(6) Å (Mo–O range 2.171–2.416 Å, O=Mo–O range 160.7–175.6°). The lengths of the Mo–O(1) and Mo–O(2) bonds in both structures are within the normal range for typical *cis*-MoO_2 structures. The coordinating oxygen atoms O(3) and O(5) of the Schiff base ligand are *trans* to each other and their distance to Mo is close to the mean value from the CSD. The Mo–O(6) bond in **3** exhibits a *trans*-influence and is significantly longer than the two unaffected bonds mentioned above. This bond length is comparable to those found in the complexes $[MoO_2L(ROH)]$ (L = tridentate Schiff bases derived



Scheme 3. Molybdenum(VI) coordinated by a Schiff base containing a saturated heterocyclic ring.

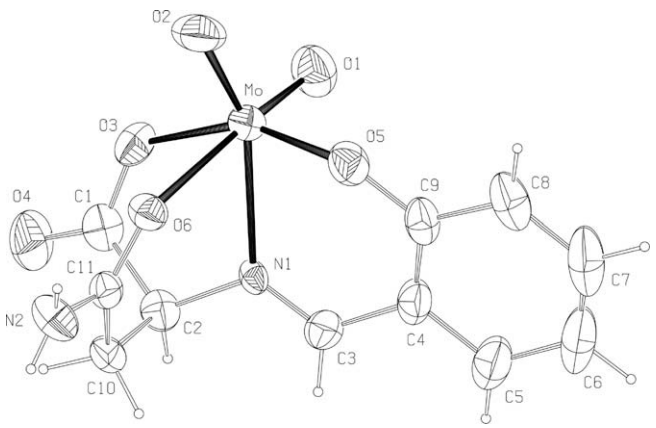


Fig. 1. ORTEP projection of **3** with ellipsoids at the 50% probability level.

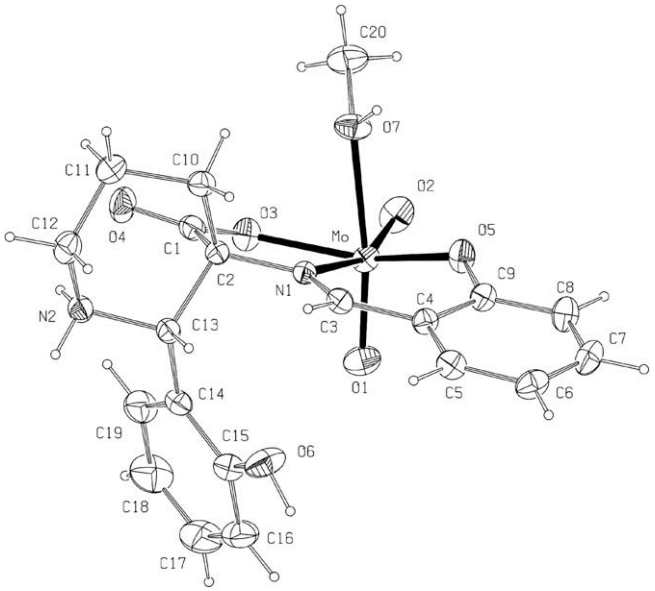


Fig. 2. ORTEP projection of **4** with ellipsoids at the 50% probability level.

Table 3
Selected bond distances (Å) and angles (°) for compounds **3** and **4**.

Distances (Å)	3	4	Angles (°)	3	4
Mo–O(1)	1.679(3)	1.6985(14)	O(1)–Mo–O(2)	105.96(15)	104.99(7)
Mo–O(2)	1.701(3)	1.6964(13)	O(1)–Mo–O(3)	94.52(13)	97.51(6)
Mo–O(3)	2.023(3)	2.0243(14)	O(1)–Mo–O(5	97.61(14)	99.63(7)
Mo–O(5)	1.937(3)	1.9140(13)	O(1)–Mo–O(6)	171.91(13)	169.71(6)
Mo–O(6)[a]	2.351(2)	2.2925(14)	O(1)–Mo–N(1)	102.52(13)	93.62(6)
Mo–N(1)	2.253(3)	2.2510(14)	O(2)–Mo–O(3)	97.34(14)	94.75(6)
C(1)–O(3)	1.297(5)	1.295(2)	O(2)–Mo–O(5)	101.10(15)	103.05(6)
C(1)–O(4)	1.210(4)	1.222(2)	O(2)–Mo–O(6)[a]	80.77(12)	84.12(6)
C(1)–C(2)	1.524(5)	1.535(2)	O(2)–Mo–N(1)	150.92(11)	159.28(6)
C(2)–N(1)	1.465(4)	1.479(2)	O(3)–Mo–O(5)	154.16(14)	151.07(5)
C(3)–N(1)	1.243(4)	1.288(2)	O(3)–Mo–O(6)[a]	79.97(11)	76.64(5)
C(3)–C(4)	1.458(5)	1.445(2)	O(3)–Mo–N(1)	74.50(10)	73.48(5)
C(9)–O(5)	1.347(5)	1.3502(19)	O(5)–Mo–N(1)	80.62(11)	82.31(5)
			O(5)–Mo–O(6)[a]	85.27(11)	82.63(6)
			N(1)–Mo–O(6)[a]	70.40(8)	76.67(5)

[a] Symmetry transformation used to generate equivalent atoms: $-x$, $-y$, $-z$.

from salicylaldehyde or 2-hydroxy-1-naphthaldehyde and 2-(hydroxymethyl)aniline or 2-aminoethanol; R = CH_3 or C_2H_5) [32] and [MoO_2LD] (L = tridentate Schiff bases derived from 2-hydroxy-1-naphthaldehyde or 2-hydroxy-3-methoxybenzaldehyde and 2-amino-*p*-cresol; D = methanol, ethanol, DMSO, imidazole or 4,4′-bipyridine) [33]. A CSD search similar to the one described above was carried out, this time defining that the single bonded oxygen atom in the *trans* position to the oxo-oxygen is from methanol. This search gave 20 hits with a Mo–O mean distance of 2.357(7) Å (range 2.311–2.414 Å, O=Mo–O range 165.8–173.2°). The methanol oxygen atom O(7) is *trans* to the terminal oxo-group in **4** and is at 2.2925(14) Å from Mo. It is the shortest bond of that kind found so far. Only one Mo–OCH_3 bond is shorter but it is from a binuclear complex in which the methoxo group bridges two molybdenum atoms [34]. In the 55 structures from the CSD, the imine nitrogen is always *trans* to the terminal oxo-oxygen with a mean value of the Mo–N distance of 2.272(5) Å (range 2.202–2.413 Å, N–Mo=O 156.1–168.6°). The Mo–N(1) distance is similar in **3** and **4** (2.253(3) and 2.2510(14) Å, respectively) and slightly shorter than the mean value. It is similar to that in [MoO_2(L)(D)] (L = tridentate Schiff baze, D = azole ligand) [35]. The C(3)–N(1) bond distance is close to the usual C=N bond length [33,36]. The

Table 4
Hydrogen bond geometry (distances (Å), angles (°)) in **3**.

D–H···A	D–H	H···A	D···A	D–H···A
N(2)–H(21)···O(3)[i]	0.79(5)	2.31(5)	3.043(5)	153(5)
N(2)–H(22)···O(6)[ii]	0.75(6)	2.23(6)	2.932(5)	158(5)
C(10)–H(10A)···O(2)[iii]	0.97	2.53	3.336(5)	141
C(10)–H(10B)···O(6)[ii]	0.97	2.53	3.451(2)	159
C(3)–H(3)···O(2)[iii]	0.93	2.51	3.396(2)	159

Symmetry transformations used to generate equivalent atoms: (i) $-1/2-x$, $1/2+y$, $-z$; (ii) $-x$, $1-y$, $-z$; (iii) x, $1+y$, z.

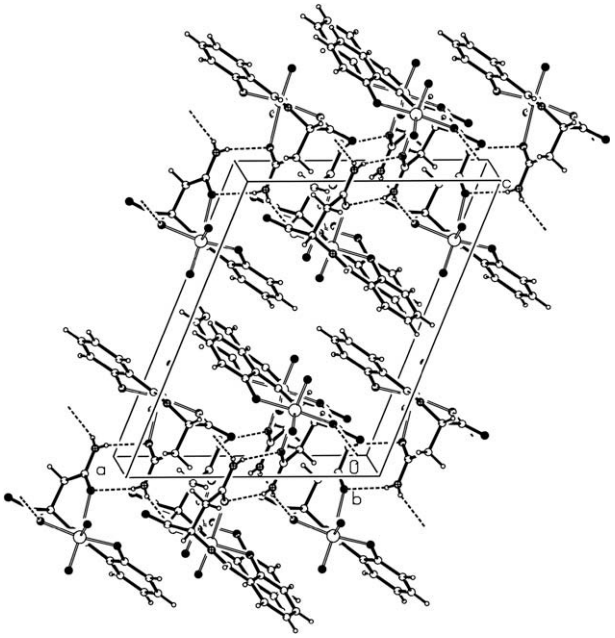


Fig. 3. Packing of **3** in the unit cell. Hydrogen bonds are shown by dashed lines.

angle between the planes of the two chelate rings Mo–O(3)–C(1)–C(2)–N(1) and Mo–O(5)–C(9)–C(4)–C(3)–N(1) is 11.28(6) and 17.72(14)° in **3** and **4**, respectively. Two centrosymmetrical hydrogen bonds of the type N–H···O (Table 4, Fig. 3) interconnect each molecule of **3** to two neighboring ones, thus forming infinite chains along [1 0 0].

In **4** a network of hydrogen bonds interconnects the complex cation, chloride anion and the methanol solvent molecule (Fig. 4, Table 5). One hydrogen atom of the non-coordinating N(2) atom in the piperidinium ring is linked by intra- and intermolecular hydrogen bonds to the carboxylic oxygen atom O(6) at 2.880(2) and 2.871(2) Å, respectively, while the other hydrogen atom forms an intermolecular hydrogen bond to the chloride ion at 3.0389(17) Å. The oxygen atom of the methanol molecule O(8) is linked by two hydrogen bonds, as an acceptor from the hydroxo group of the 2-hydroxophenolic ring O(5) at 2.647(2) Å, and as a donor toward the oxo-oxygen atom O(1) at 2.858(2) Å. The coordinating methanol ligand forms a hydrogen bond with the chloride ion. The crystal structure is additionally stabilized by weak C–H···O hydrogen bonds in the range 3.288(2)–3.670(2) Å.

3.3. Computational studies

Computational studies were primarily concerned with the role of the molybdenum atom in the cyclization step, which connects the reactant **R** with product **P** (Figs. 2 and 5). The latter is essentially equivalent to complex **4**, apart from the omission of the solvent CH_3OH molecule from the Mo coordination sphere. As the

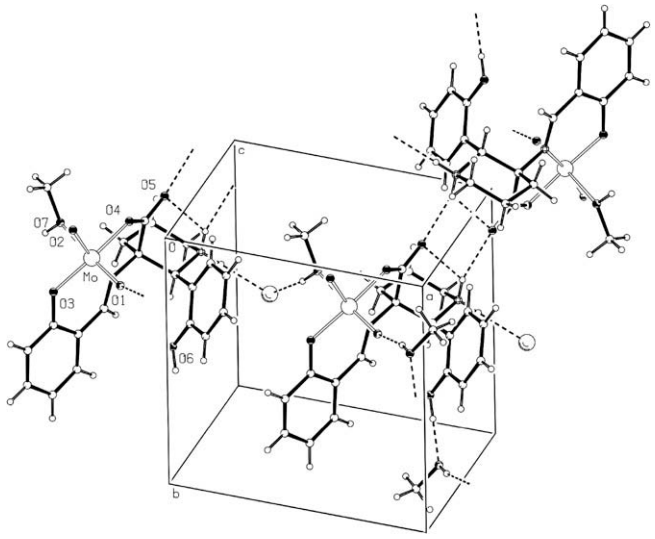


Fig. 4. Complex cation, chloride anion and methanol molecule of **4** interconnected by hydrogen bonds (shown by dashed lines).

Table 5
Hydrogen bond geometry (distances (Å), angles (°)) in **4**.

D–H···A	D–H	H···A	D···A	D–H···A
N(2)–H(2[a])···O(4)	0.85	2.29	2.880(2)	127
N(2)–H(2[a])···O(4)[i]	0.85	2.12	2.871(2)	146
N(2)–H(2B)···Cl[ii]	0.88	2.17	3.0389(17)	169
O(6)–H(6[a])···O(8)[iii]	0.92	1.74	2.647(2)	171
O(7)–H(71)···Cl	0.91	2.05	2.9527(15)	168
O(8)–H(8[a])···O(1)[iv]	0.88	1.99	2.858(2)	169
C(3)–H(3)···Cl[iii]	0.93	2.63	3.5436(19)	167
C(10)–H(10[a])···Cl[iii]	0.97	2.83	3.670(2)	146
C(6)–H(6)···O(2)[v]	0.93	2.51	3.396(2)	159
C(7)–H(7)···O(2)[vi]	0.93	2.57	3.288(2)	135

[a] Symmetry transformations used to generate equivalent atoms: (i) $2-x, -y, 1-z$; (ii) $1+x, y, z$; (iii) $1-x, 1-y, 1-z$; (iv) $-1+x, y, 1+z$; (v) $x, 1+y, z$; (vi) $1-x, 1-y, -z$.

most demanding test of accuracy of the current theoretical approach, the calculated distances of the Mo–ligand bonds in **P**, as well as the torsional angles within the MoO_2 containing ring, are compared to the experimental ones in Table 6.

The **P** complex is 2.8 kcal mol^{-1} less stable than **R**, which is not much considering the unfavorable steric interactions arising in **P**, where the 6-membered heterocyclic ring has to accommodate the two very large substituents in a vicinal position (Fig. 5).

To get a better understanding of the role of the Mo atom in the cyclization process, reference test compounds were devised by substituting MoO_2 with a CH_2 group. These are labelled as P(CH_2) and R(CH_2) in analogy with the parent compounds. The energy difference between P(CH_2) and R(CH_2) now increases to 6.7 kcal mol^{-1}. More importantly, substantial differences are observed between the MoO_2 and CH_2 containing rings. The former is much less puckered owing to the additional Mo binding to the imine N(1), which makes the ring more rigid, thus restricting its conformational mobility. As a result, the steric repulsions are less pronounced in P than in P(CH_2). Still, it seems that the reaction involving the CH_2 substituted compounds would proceed as well, albeit with much more difficulty.

The basic assumptions about the mechanism include the activation of C(2) as a nucleophile, which is achievable either *via* abstraction of the attached H atom by a base (whereby a carbanion is formed), or via a keto-enol tautomerism. With regards to the tautomerism, the energy difference between the keto and enol form in R is 16.3 kcal mol^{-1}, being in favor of the former form. This however is much less than that for R(CH_2), where the difference equals 26.4 kcal mol^{-1}. The calculated Hirshfeld charges [37] concerned the trends in the charge re-distribution on going from the keto to the enol tautomeric form in R and R(CH_2). The main differences may be summarized in the O(4) atom, which upon enolization passes considerably more (by ca. 0.05e) of its negative charge in R than in R(CH_2). One small part of it (ca. 0.01e) is received by the Mo atom, however, most importantly the C(3) atom (Fig. 2) receives a major part (0.06e) of the charge in R, whereas in R(CH_2) the equivalent atom receives effectively none. In the enol forms, C(1) of R(CH_2) gets notably richer (by ca. 0.05e) than in R, while negligible differences between R and R(CH_2) upon the charge redistribution are found only for the C(2) and N(1) atoms. The near flatness of the MoO_2 containing ring (Table 6) brings about a much more effective delocalization of the charge via resonance effects, all the way to C(3). Thus, R is much better adapted to the emergence of the double C(1)=C(2) bond of the enol form than R(CH_2). An alternative route of activating the C(2) atom via H transfer to the vicinal imine N(1) is highly unlikely. In this case, upon protonation, N(1) rapidly escapes the Mo coordination sphere, which severely distorts the MoO_2 containing ring and destabilizes the structure by several 10s of kcal mol^{-1}. Similarly, the N(2) Schiff base is itself far too weak to directly deprotonate the C(2) atom. Indicative of this are the very high energies (around 60 kcal mol^{-1} above **R**) when the proton is moved away from C(2) toward N(2). According to our calculations, yet another prerequisite for the cyclization to occur involves H transfer from O(6) to the imine N(2), whereby the electrophilicity of the vicinal C(13) is enhanced, making it much more prone to attack by the nucleophilic C(2), which completes the cyclization. The structures with the H atom on O(6) and N(2) are effectively isoenergetic, the energy difference being only 2.9 kcal mol^{-1} in favor of the structure with the protonated O(6). The corresponding H bond is a very strong one, around 15 kcal mol^{-1}. Similar activation steps involving H transfer from

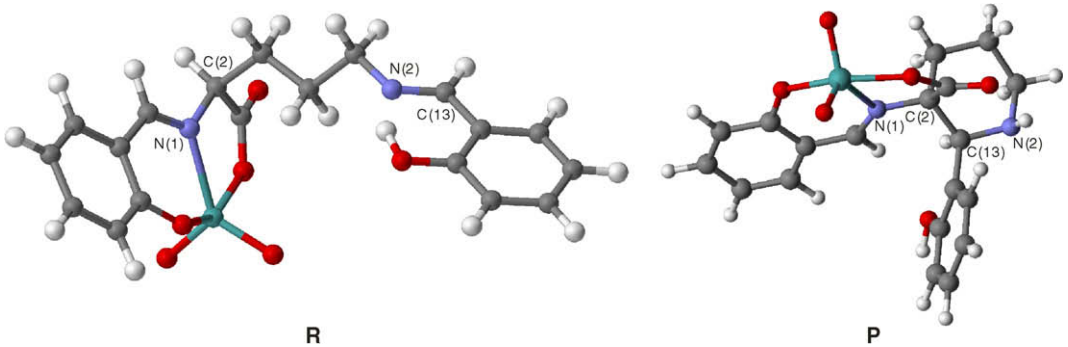


Fig. 5. Optimized structures of reactant **R** and product **P**.

Table 6
Selected structural parameters for complex **4** (product **P**) (distances in Å and torsional angles in °).

Geometrical parameter	OPBE/TZ2P(DZP)	Experimental
r[Mo–N(1)]	2.237	2.251(1)
r[Mo–O(1)]	1.699	1.699(1)
r[Mo–O(2)]	1.698	1.696(1)
r[Mo–O(3)]	1.994	2.024(1)
r[Mo–O(5)]	1.984	1.914(1)
τ[C(4)–C(9)–O(5)–Mo]	−27.9	−32.8(2)
τ[C(9)–C(4)–C(3)–N(1)]	10.7	13.5(3)
τ[C(4)–C(3)–N(1)–C(2)]	−175.2	−178.4(2)
τ[C(3)–N(1)–C(2)–C(1)]	−157.4	−175.5(1)
τ[C(2)–C(1)–O(3)–Mo]	3.8	−9.6(2)

an OH group to a nearby Schiff base have been discovered several times in the past [38].

Finally, the mutual approach of the C(2) and C(13) reaction centers is easily achieved owing to the mobility of the aliphatic $–(CH_2)_3–$ chain, e.g. the conformations of **R** likely to precede the cyclization are less than 10 kcal mol^{-1} above the most stable conformer of **R**. In the Supplementary movie it is seen that the reaction proceeds without a barrier once the C(2) and C(13) are separated by ca. 2.5 Å, and the enol and N(2) protonated forms are realized. Simultaneously as the C(2)–C(13) bond is formed, the proton attached to O(4) is smoothly abstracted by the N(2) atom, thus restoring the carbonyl bond. At the end a zwitterionic species is formed with the positive ammonium and negative phenolate parts. Additional calculations confirmed this zwitterionic form as unstable, with the proton eventually returning from N(2) to the O(6) atom. In conclusion, the formation of the tautomeric enol form (nucleophilic activation of C(2)) accompanied by the H transfer from O(6) to N(2) (electrophilic activation of C(13)) are the most probable initiation steps under the experimental conditions (CH_3OH as the solvent). By far the largest barrier is expected for the keto-enol tautomerism, which is therefore the most likely candidate for the rate-determining step.

4. Conclusions

In this study it was shown that the *N*-salicylidene-DL-asparaginato anion coordinates to molybdenum(VI) as a tridentate OON (in **1**) or a tetradentate OONO (in **4**) ligand, depending on the reaction conditions (solvent). The coumarine-3-carboxamide (**2**) was obtained as a product of decarboxylation of DL-asparagine in methanolic solution and in the presence of molybdenum(VI). The reaction of L-ornithine hydrochloride and the salicylaldehydato molybdenum(VI) complex in methanol resulted in a mononuclear molybdenum(VI) complex (**4**) coordinated by a Schiff base containing a saturated heterocyclic ring. The presence of molybdenum(VI) and methanol as the solvent were important for obtaining this type of complex.

Acknowledgments

We thank Prof. Boris Kamenar and Dr. sc. Višnja Vrdoljak, Assist. Prof., for useful discussions. Financial support for this research was provided by the Ministry of Science and Technology of the Republic of Croatia (Grant Nos. 119-1101342-1082, 119-1191342-1083, 119-1193079-1084, 119-1191342-2959, 098-0982915-2944).

Appendix A. Supplementary data

CCDC 652690 and 652691 contain the supplementary crystallographic data for complexes **3** and **4**, respectively. These data can be obtained free of charge via http://www.ccdc.cam.ac.uk/conts/retrieving.html, or from the Cambridge Crystallographic Data Centre, 12 Union Road, Cambridge CB2 1EZ, UK; fax: (+44) 1223-336-033; or e-mail: deposit@ccdc.cam.ac.uk. Supplementary data associated with this article can be found, in the online version, at doi:10.1016/j.poly.2008.11.058.

References

[1] C.G. Young, A.G. Wedd, Chem. Commun. (1997) 1251.
[2] L.F. Veiros, A. Prazers, P.J. Costa, C.C. Romao, F.E. Kuhn, M.J. Calhorda, J. Chem. Soc., Dalton Trans. (2006) 1383.
[3] R.R. Mendel, J. Chem., Dalton Trans. (2005) 3404.
[4] R. Hill, Chem. Rev. 96 (7) (1996) 2757.
[5] B.E. Schultz, S.F. Gheller, M.C. Muetterties, M.J. Scott, R.H. Holm, J. Am. Chem. Soc. 115 (1993) 2714.
[6] F.E. Inscore, S.Z. Knottenbelt, N.D. Rubie, H.K. Joshi, M.L. Kirk, J.H. Enemark, Inorg. Chem. 45 (2006) 967.
[7] R.J. Greenwood, G.L. Wilson, J.R. Pilbrow, A.G. Wedd, J. Am. Chem. Soc. 115 (1993) 5385.
[8] L. Casella, M. Gullotti, A. Pintar, Inorg. Chim. Acta 144 (1988) 89.
[9] K. Yamanuochi, S. Yamada, Inorg. Chim. Acta 9 (1974) 83.
[10] G.A. Parker, Analytical Chemistry of Molybdenum, Springer-Verlag, New York, 1983, p. 29.
[11] CRYSALIS Software system, Version 1.170, Xcalibur CCD system, Oxford Diffraction Ltd., 2003.
[12] Z. Otwinowski, W. Minor, DENZO-SCALEPACK, processing of X-ray diffraction data collected in oscillation mode, in: C.W. Carter Jr., R.M. Sweet (Eds.), Methods in Enzymology, Vol. 276: Macromolecular Crystallography, Part A, Academic Press, 1997, p. 307.
[13] G.M., Sheldrick, SHELXS-97, Program for Crystal Structure Solution, University of Göttingen, Germany, 1997.
[14] G.M. Sheldrick, SHELXL-97, Program for the Refinement of Crystal Structures, University of Göttingen, Germany, 1997.
[15] L.J. Farrugia, J. Appl. Crystallogr. 32 (1999) 837.
[16] L.J. Farrugia, ORTEP3 for windows, J. Appl. Crystallogr. 30 (1997) 565.
[17] (a) A.L. Spek, PLATON, A Multipurpose Crystallographic Tool, Utrecht University: Utrecht, The Netherlands, 1998;
(b) A.L. Spek, Acta Crystallogr., Sect A 46 (1990) C34.
[18] M. Swart, A.W. Ehlers, K. Lammertsma, Mol. Phys. 102 (2004) 2467.
[19] N.C. Handy, A. Cohen, J. Mol. Phys. 99 (2001) 403.
[20] J.P. Perdew, K. Burke, M. Ernzerhof, Phys. Rev. Lett. 77 (1996) 3865.
[21] S.H. Vosko, L. Wilk, M. Nusair, Can. J. Phys. 58 (1980) 1200.
[22] (a) E. van Lenthe, J.G. Snijders, E.J. Baerends, J. Chem. Phys. 105 (1996) 6505;
(b) E. van Lenthe, A.E. Ehlers, E.J. Baerends, J. Chem. Phys. 110 (1999) 8943.
[23] (a) E.J. Baerends, J. Autschbach, A. Bérces, C. Bo, P.M. Boerrigter, L. Cavallo, D.P. Chong, L. Deng, R.M. Dickson, D.E. Ellis, L. Fan, T.H. Fischer, C.F. Guerra, S.J.A. van Gisbergen, J.A. Groeneveld, O.V. mGritsenko, M. Grüning, F.E. Harris, P. van den Hoek, H. Jacobsen, G. van Kessel, F. Kootstra, E. van Lenthe, D.A. McCormack, V.P. Osinga, S. Patchkovskii, P.H.T. Philipsen, D. Post, C.C. Pye, W. Ravenek, P. Ros, P.R.T. Schipper, G. Schreckenbach, J.G. Snijders, M. Sola, M. Swart, D. Swerhone, G. te Velde, P. Vernooijs, L. Versluis, O. Visser, E. van Wezenbeek, G. Wiesenekker, S.K. Wolff, T.K. Woo, T. Ziegler, ADF 2005.01 Release, SCM, Theoretical Chemistry, Vrije Universiteit, Amsterdam, <http://www.scm.com>; (b) G. te Velde, F.M. Bickelhaupt, S.J.A. van Gisbergen, C.F. Guerra, E.J. Baerends, J.G. Snijders, T. Ziegler, J. Comput. Chem. 22 (2001) 931
[24] I. Cavaco, J.C. Pessoa, M.T. Duarte, R.D. Gillard, P. Matias, Chem. Commun. (1996) 1365.
[25] M.C. Pirrung, J. Cao, J. Chen, Chem. Biol. 5 (1998) 49.
[26] S. Goldstein, G. Czapski, H. Choen, D. Meyerstein, R. van Eldik, Inorg. Chem. 33 (1994) 3255.
[27] W. Bal, M.I. Djuran, D.W. Margerum, E.T. Gray Jr., M.A. Mazid, R.T. Tom, E. Nieboer, P.J. Sadler, J. Chem. Soc., Chem. Commun. (1994) 1889.
[28] A. Syamal, M.R. Maurya, Synth. React. Inorg. Met.-Org. Chem. 16 (1986) 857.
[29] M. Boča, D. Valigura, W. Linert, Tetrahedron 56 (2000) 441.
[30] N. Brefuel, C. Lepetit, S. Shova, F. Dahan, J.-P. Tuchagues, Inorg. Chem. 44 (2005) 8916.
[31] (a) Cambridge Structural Database, V5.28, Cambridge Crystallographic Data Centre, 12 Union Road, Cambridge, England, 2006; (b) F.H. Allen, The Cambridge structural database: a quarter of a million crystal structures and rising, Acta Crystallogr. B58 (2002) 380.
[32] M. Cindrić, N. Strukan, V. Vrdoljak, T. Kajfež, B. Kamenar, Z. Anorg. Allg. Chem. 628 (2002) 2113.
[33] M. Cindrić, N. Strukan, V. Vrdoljak, B. Kamenar, Z. Anorg. Allg. Chem. 630 (2004) 585.
[34] X. Xu, X. Wang, H. Liu, X. You, J. Chem. Soc., Dalton Trans. (1993) 1377.
[35] C. Zhang, G. Rheinwald, V. Lozan, B. Wu, P.-G. Lassahn, H. Lang, C. Janiak, Z. Anorg. Allg. Chem. 628 (2002) 1259.
[36] A. Rana, R. Dindo, P. Sengupta, S. Ghosh, L.R. Falvello, Polyhedron 21 (2002) 1023.
[37] F.L. Hirshfeld, Theor. Chim. Acta 44 (1977) 129.
[38] (a) H. Merz, G. Zundel, Biochem. Biophys. Res. Commun. 138 (1986) 819;
(b) C. Ögretir, D. Hakan, H. Berber, F.F. Taktak, J. Chem. Eng. Data 51 (2006) 46.

Polyhedron 28 (2009) 569–573

Contents lists available at ScienceDirect

Polyhedron

journal homepage: www.elsevier.com/locate/poly

Synthesis and structure of new cationic methallyl molybdenum(II) complexes supported by α-diimine ligands

Thouraya Turki [a], Taha Guerfel [b], Faouzi Bouachir [a,*]

[a] Faculté des Sciences de Monastir, Laboratoire de Chimie de Coordination, Monastir 5000, Tunisia
[b] Laboratoire de Chimie de Solide, Faculté des Sciences de Monastir, 5000 Monastir, Tunisia

ARTICLE INFO

Article history:
Received 21 May 2008
Accepted 21 November 2008
Available online 20 January 2009

Keywords:
Molybdenum
α-Diimine
Molybdenum(II) allylic complexes
Solid-state structure

ABSTRACT

Cationic complexes $[Mo(\eta^3\text{–}C_3H_4\text{–}Me\text{–}2)(N\text{–}N)(CO)_3]^+PF_6^-$, {N–N = bipy **(2)**; DAD (Ar–N=C(Me)–C(Me)=N–Ar: Ar = o-Me–C_6H_4 **(3)**, 2,6-Me_2–C_6H_3 **(4)**; Ar–BIAN (Ar = o-Me–C_6H_4 **(5)**, Ar = iPr_2–C_6H_3 **(6)**}; were synthesized by treating the compound $Mo(CO)_3$(p-xylene) with the allyloxyphosphonium salt in situ in presence of diimine ligand. Complex **4** was characterized by single crystal X-ray diffraction. The solid state structure of the complexes revealed a preference for the more unsymmetrical axial isomer.
© 2008 Elsevier Ltd. All rights reserved.

1. Introduction

Molybdenum(II) complexes of the type $[Mo(\eta^3\text{-}C_3H_4)(CO)_2(NCMe)_2X]$ (X = halide or pseudohalide) have been used extensively over several decades as synthetic precursors for a wide variety of Mo(II)-allyl derivatives containing the 12e-$[Mo(CO)_2\text{-}(\eta^3\text{-allyl})]^+$ fragment which are formed by substitution of the labile nitrile ligands and/or the anion X [1]. It has been recently found that the pseudooctahedral $[MoX(CO)_2(\eta^3\text{-allyl})(N\text{–}N)]$ (N–N = 2,2′-bipyridine, bipy; 1,10-phenanthroline, phen) complexes react with organolithium or organomagnesium reagents and with sodium alkoxides to afford new alkyl [2], alkynyl [3] and alkoxo [4] complexes by selective halide substitution. The same reaction with NaCN has provided access to the complexes $[Mo(CN)(\eta^3\text{-allyl})(CO)_2(N\text{–}N)]$ [5].

The well known allyl complex $[Mo(\eta^3\text{-}C_3H_4)(CO)_2(NCMe)_2X]$ has been shown as a useful precursor to prepare mononuclear derivatives, used both as catalysts for polymerisation of certain dienes [6] and in organic synthesis for allylic alkylations [7]. Their cationic anologues, having the two nitriles replaced by a L–L ligand, for instance, always show a fac arrangement of the $\eta^3\text{-}C_3H_4$ and the two CO ligands and exhibit two isomers, B (equatorial) with C_s symmetry and A (axial) without symmetry (Scheme 1).

An increased interest in the chemistry of α-diimine ligands and their complexes [8–12] was stimulated by the recent discovery by Brookhart and co-workers of Ni(II) and Pd(II) α-olefin polymerization catalyst containing bulky α-diimine ligands [13–16].

In the last few years, several new cationic allyl complexes of palladium and nickel with α-diimine ligands have been synthesized by our group [17]. We wish therefore to report new cationic Mo(II) allyl complexes of general formula $[Mo(\eta^3\text{-}C_3H_4\text{–}Me\text{-}2)(CO)_3(N\text{–}N)]^+PF_6^-$ with N–N as an α-diimine ligands. The solid state structure of the cation **4** (N–N = 2,6-Me_2–C_6H_3–N=C(Me)–C(Me)=N–C_6H_3–2,6-Me_2) was determined at room temperature, allowing the observation of the allyl geometry in great detail.

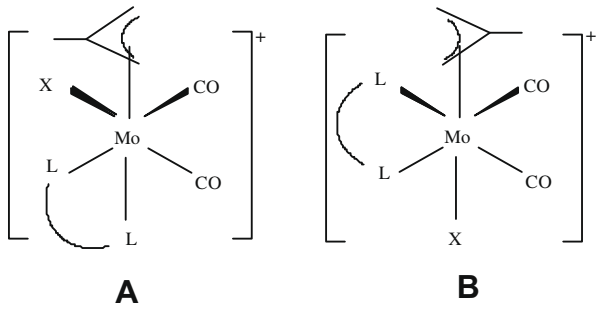
2. Results and discussion

Allyl complexes of the type $[Mo(\eta^3\text{-}C_3H_4\text{–}Me\text{-}2)(CO)_3(N\text{–}N)]^+PF_6^-$ **(2–6)** (N–N = bipy, Ar-BIAN [18], DAD [19]) can be obtained successfully in high yields by an oxidative addition of methallyloxyphosphonium [20] to the zerovalent compound $Mo(CO)_3$(p-xylene) in tetrahydrofuran to produce the axial isomer $[Mo(\eta^3\text{-}C_3H_4\text{–}Me\text{-}2)(CO)_3(THF)_2]^+PF_6^-$ **(1)** whereas "equatorial" isomers are found for halide analogues [21]. The reaction in situ of compound **1** with the α-diimine ligand in methylene chloride at room temperature offered the cationic η^3-methallyl molybdenum complexes **(2–6)** supported by the α-diimine ligands (Scheme 2).

Compounds **2–6**, crystallized as red crystals for complex **2**, blue-purple for complexes **3–4** and green for complexes **5–6** from CH_2Cl_2/n-hexane, and are soluble in methylene chloride, chloroform and acetonitrile but only sparingly soluble in diethylether. They are stable at room temperature under an inert atmosphere; however, significant decomposition can be observed at high temperature. These compounds have been characterized by various techniques including ^1H, ^{13}C, IR spectroscopy and the single crystal X-ray structure determinations of the complex **4**.

* Corresponding author. Tel.: +216 98503997; fax: +216 71 704 329.
E-mail address: bouachirf@yahoo.de (F. Bouachir).

0277-5387/$ - see front matter © 2008 Elsevier Ltd. All rights reserved.
doi:10.1016/j.poly.2008.11.050



Scheme 1.

The variation of the steric and electronic proprieties of α-diimine ligands is possible by changing the aromatic substituent on the imine N atom. The new complexes exhibit spectroscopic data in accord with the proposed structures. The formation of the allyl complexes **2–6** is clear from the observed syn and anti allylic proton signals in the ^{1}H NMR. These signals were attributed considering that in allyl complexes, the syn protons resonate at higher frequencies than the anti protons [21,22]. Thus, the two resonances are located, respectively, at 1.07, 1.72 and 1.97, 0.92 and 1.43 ppm for H_{anti} and 1.23, 2.98, 2.58, 2.19 and 3.22 ppm for H_{syn} for complexes **2–6**. In ^{13}C NMR spectroscopy, the two terminal allylic carbons C1 and C3 appear at 61.6, 67.0, 69.0, 63.2 and 70.6 ppm, respectively, for complexes **2–6**. The C=N functions are shifted to high frequency when compared to free ligands and appear at 172.1, 171.0, 176.0 and 168.6, for complexes **3–6**, respectively. Two carbonyl carbon signals are shown in the ^{13}C NMR spectra.

The IR spectra are also instructive. The complexes **2–6** show in IR spectroscopy a C=N stretching frequency in the region 1606–1690 cm^{-1}, which is in agreement with those reported for other α-diimine complexes coordinated as an s-cis conformation [18,23]. Moreover, complexes **2–6** exhibit the frequency of the corresponding counteranion. The $\nu(PF_6^-)$ value is evident (843 cm^{-1}). The IR data for **2–6** show two strong carbonyl bands of equal intensity, consistent with cis-carbonyl groups in the [Mo(CO)$_2$(η^3-allyl] moiety.

A single crystal X-ray diffraction study confirms the identity of complex **4.** The molecular structure of **4** with the adopted numbering Scheme is shown in Fig. 1 with details of the structure determination, including unit-cell data, summarized in Table 1 and relevant bond distances and angles in Table 2. The coordination environment of the molybdenum center is pseudooctahedral with two carbon atoms from the carbonyl groups and the centroid of the allyl ligand determining a fac stereochemistry. The structure of complex **4** consists of loosely associated [(η^3-C$_3$H$_4$–Me-2)Mo(CO)$_3$(N–N)]$^+$ cation and octahedral PF_6^- counteranion without direct interactions as appears from the large distance between the metal and the nearest fluorine atom (Mo–F4 = 4.369 Å) which is close to other cationic allyl complexes [17].

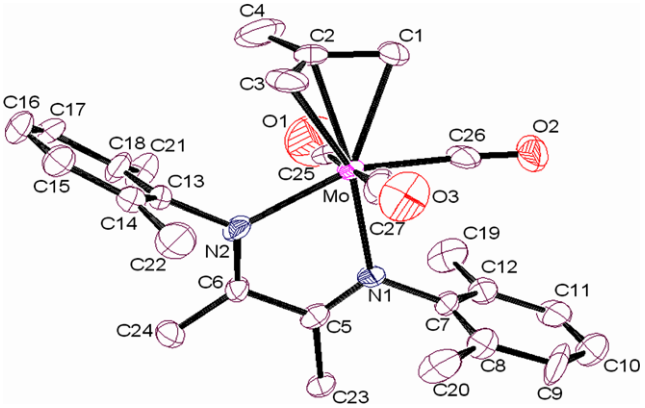
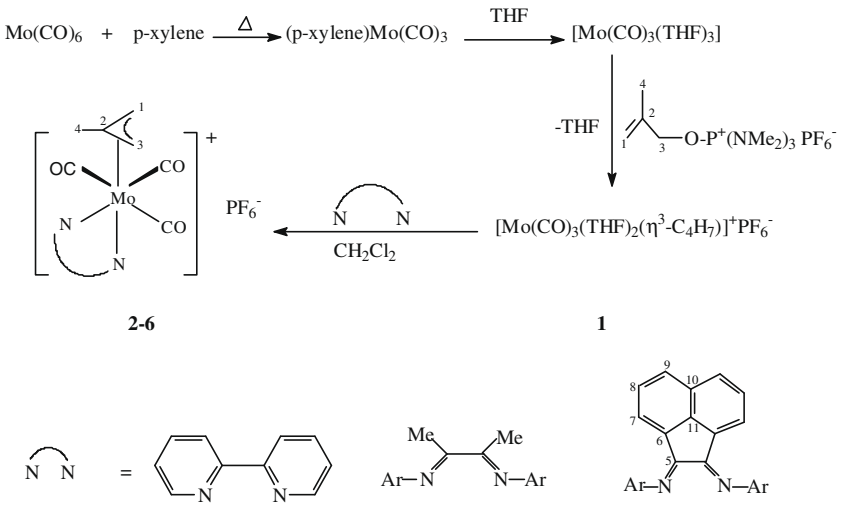


Fig. 1. ORTEP diagram of **4**.Thermal ellipsoids are drawn at the 50% probability level. PF_6^- anion and hydrogen atoms have been omitted for the sake of clarity.

In complex **4** structure, the allyl ligand adopts the usual endo conformation in the solid or in the solution state, with the open side eclipsing the two carbonyls C26O2 and C27O3. The two nitrogen donors from the (N–N) fragment occupy an equatorial and an axial coordination position (B in Scheme 2) which is in agreement with those reported for other diimine complexes [21,22].

In all complexes, the remaining equatorial position is taken by a carbonyl ligand. The α-diimine ligand is coordinated in a symmetric fashion as seen in Fig. 1, with Mo–N bond lengths of 2.213(7) and 2.267(9) Å which are very close to those reported for other related complexes [21,22]. The N1–Mo–N2 angle of 70.8(3)° reflects a



Scheme 2.

Table 1
Summary of crystallographic data and X-ray experimental details for **4**.

Empirical formula	C27H31F6MoN2O3P
Formula weight	672.45
Crystal system	monoclinic
Space group	$P2_1/c$
Z	4
a (Å)	9.459(3)
b (Å)	19.113(5)
c (Å)	16.234(7)
α (°)	90
β (°)	92.98(3)
γ (°)	90
V (Å^3)	2931.0(17)
ρ_{calc} (g cm^{-3})	1.524
Crystal dimension (mm)	0.12 × 0.19×0.33
Temperature (K)	293(2)
Radiation, λ (Å)	Mo, 0.71073
$F(000)$	1368
2θ range (°)	1.65–27.13
Limiting indices	$-12 \leqslant h \leqslant 12$, $-2 \leqslant k \leqslant 24$, $-20 \leqslant l \leqslant 2$
No. of scanned reflections	8879
No. of independent reflections	6422
No. of observed reflections	6422
No. of parameters varied	354
Absorption correction	empirical (DIFABS)
Data reductions programs	XCAD4
Programs used	SHELX-97
$R_1(F_0)$, $wR_2(F_0^2)$ ($I > 2\sigma(I)$) (%)	8.80, 21.75
Goodness-of-fit on F^2	0.960

Table 2
Bond lengths (Å) and angles (°) for **4**.

Mo–N1	2.213(7)	Mo–N2	2.267(9)
Mo–C1	2.344(10)	Mo–C2	2.302(11)
Mo–C3	2.37(10)	N2–C6	1.289(11)
N1–C5	1.289(13)	N2–C13	1.468(11)
N1–C7	1.448(12)	Mo–C25	2.227(9)
Mo–C26	1.960(13)	Mo–C27	1.857(16)
N1–Mo–N2	70.8(13)		
N1–Mo–C1	147.1(4)	N2–Mo–C3	87.3(4)
N1–Mo–C3	152.2(4)	N2–Mo–C1	137.9(3)
N1–Mo–C2	165.6(4)	N2–Mo–C2	102.4(4)
C2–Mo–C3	34.0(5)	C1–Mo–C2	35.9(4)
C1–Mo–C3	60.1(4)		
C5–N1–C7	117.8(8)	C6–N2–C13	117.1(9)
C5–N1–Mo	119.9(6)	C6–N2–Mo	118.6(6)
C7–N1–Mo	122.2(6)	C13–N2–Mo	124.1(6)

slightly distorted pseudo-octahedral coordination sphere which is identical to known values in the literature for other molybdenum allyl complexes [21,22]. The metal chelate ring (Mo–N1–C5–C6–N2) in complex **4** is almost flat as indicated by the torsion angles of −2.7(16), 7.0(13) and −3.0(13)° for N1–C5–C6–N2, Mo–N2–C6–C5 and Mo–N1–C5–C6, respectively. The allyl ligand is bonded symmetrically to the molybdenum center (Mo–C1 = 2.344(10) Å and Mo–C3 = 2.369(10) Å). We note that the Mo–C(allyl) distances are reasonable for an allyl trans to a ligand of moderate trans influences. The methyl on the allyl group is in the same plane of the allyl ligand as indicated by the torsion angle of 178.1° for C4–C2–C3–C1. The geometric arrangement found for the studied complex can be easily characterized by ϕ, which is the angle between the Mo–C25 with the line defined by the centroid of the allyl moiety and the molybdenum with Mo–C25. This ϕ parameter gives the orientation of the allyl fragment relative to the monodentate ligand and determines unequivocally the position of the bidentate ligand in the metal coordination sphere. Thus, in complex **4**, the ϕ angle takes an approximate value of 90° and the chelating of the α-diimine ligand occur via equatorial and axial sites.

The N1–C5, N2–C6 and C5–C6 bond distances of 1.289(13), 1.289(11) and 1.502(13) Å, respectively, confirm the conjugated nature of this ligand [24]. The o,o′-dimethylphenyl groups make an angle of approximately 90° to the plane of the C=N bonds, due to the presence of the o-methyl substituents, as appears from the torsion angles of −82.5(13), 98.5(11), 100.2(12) and −80.4(13) for C6–N2–C13–C18, C6–N2–C13–C14, C5–N1–C7–C12 and C5–N1–C7–C8, respectively.

3. Conclusion

π-Allyldicarbonyl complexes of molybdenum and tungsten formulated as [M(η^3-allyl)X(CO)$_2$L$_2$] (M = Mo, W; X = halogen; L = 2-electron donating molecule) have been extensively explored [25], since [M(η^3-allyl)(CO)$_2$] fragment often plays a role of the key in the catalytic organic transformations [26]. From this point of view, much effort has been made on the synthesis and reaction of these compounds bearing various monodendate (2-electron donor) and bidentate (4-electron donor) ligands [27].The nitrile complexes [Mo(η^3-C$_3$H$_5$)X(CO)$_2$(NCMe)$_2$] (X = halide) have been shown to act as precursors in the ring-opening metathesis polymerization of norbornene [28] and polymerization of terminal acetylenes as well as catalyze the oligomerization of *n*Ph(CC)*n*Ph, (*n* = 1, 2) [29]. Following these results, we prepared and characterized new complexes of the type [Mo(η^3-C$_3$H$_4$–Me-2)-(N–N)(CO)$_3$]$^+$PF$_6^-$ (N–N = α-diimine).

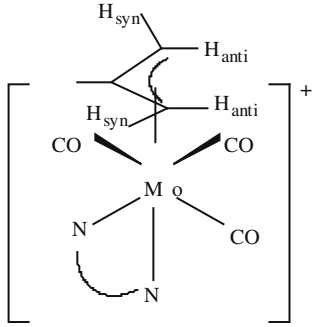
The X-ray structure of the complexes studied showed the presence of the equatorial-axial isomer, B in Scheme 1.

The synthetic procedure for preparing **2–6** complexes offers great versatility for the generation of other α-diimine allyl complexes of possible catalytic interest. The application of these compounds in catalytic reaction such as polymerisation of alkenes (ethylene, styrene, etc.), functional alkenes (methyl acrylate) and ring opening metathesis polymerisation of norbornene is currently under study.

4. Experimental

4.1. General

All manipulations were carried out under an atmosphere of dry argon using standard schlenk techniques. Diethyl ether was distilled from sodium benzopheneone; methylene chloride and hexane was distilled over P_2O_5. 2-Methylaniline, 2,6-diisopropylaniline were distilled from potassium hydroxide prior to use. Bipyridine (Bipy) and acenaphtenquinone were used as received from commercial sources. p-xylene was purified via column on alumna. α-diimine ligands were prepared according to literature methods [18,19]. NMR spectra were recorded on a Bruker AMX 300 spectrometer. H and C chemical shifts were given in ppm and referenced to the residual solvent resonance relative to TMS; H_{syn} and H_{anti} designate the syn- and the anti-H atoms, respectively, of the allyl ligand. The atom labelling scheme for the allyl complexes was shown below.



4.2. General procedure for the preparation of [(α-diimine)Mo(CO)$_3$ (η^3-C_3H_4–Me-2)]$^+PF_6^-$ complexes

In an inert atmosphere, $Mo(CO)_6$ compound (1 equiv.) was dissolved in small amount of p-xylene and refluxed for 2 h. Methallyloxyphosphonium [$C_4H_7OP^+(NMe_2)_3PF_6^-$] was added to the cold solution previously prepared in tetrahydrofuran. The yellow solution was stirred at room temperature for 24 h. The solvent was removed under vacuum to afford an oil compound which was dissolved in anhydrous CH_2Cl_2 and a α-diimine ligand was added. The solution was stirred at room temperature for 24 h. The supernatant was separated by filtration through a Celite filter, and the solvent was removed under vacuum to afford the oil complex. This was washed with n-hexane (3 × 15 ml) and dried in vacuum. The solid was crystallized from methylene chloride/ n-hexane solution at room temperature. Yields ranged from 83% to 94%.

4.2.1. Synthesis of [(Bipy)Mo(CO)$_3$(η^3-C_3H_4–Me-2)]$^+PF_6^-$ (**2**)

Following the general procedure, from $Mo(CO)_6$ (0.080 g, 0.3 mmol), p-xylene (5 ml), THF (15 ml), 2-methylallyloxyphosphonium (0.1 g, 0.26 mmol) and Bipy. (0.049 mg, 0.31 mmol) was obtained 0.188 g of **2** as a red solid after crystallization from a mixture (n-hexane/CH_2Cl_2: 9/1).

Yield 91%: IR [ν cm^{-1}] (KBr): 1606 (C=N); 1937, 1840 (CO); 848 (PF_6^-).

^{1}H NMR (300 MHz, $CDCl_3$, 25 °C, δ [ppm]): 1.02 (s, 3H, H_4); 1.05–1.07 (d, 2H, H_{anti}, J_{HH} = 6 Hz), 1,23 (s, 2H, H_{syn}); 7.50–8.80 (m, 8H, bipy).

^{13}C NMR (75.5 MHz, $CDCl_3$, 25 °C, δ [ppm]): 19.7 (C_4); 61.6 ($C_{1,3}$), 81.9 (C_2); 124.7, 126.9, 141.4, 151.3, 154.3 (bipy); 205, 208 (CO).

4.2.2. Synthesis of [(o-CH_3–C_6H_4N=C(Me)–C(Me)=N–C_6H_4–o-CH_3) Mo(CO)$_3$ (η^3-C_3H_4–Me-2)]$^+PF_6^-$ (**3**)

Following the general procedure, from $Mo(CO)_6$ (0.080 g, 0.3 mmol), p-xylene (5 ml), THF (15 ml), 2-methylallyloxyphosphonium (0.1 g, 0.26 mmol) and (*o-CH_3–C_6H_4N=C(Me)–C(Me)=N–C_6H_4–o-CH_3*) (0.079 mg, 0.3 mmol) was obtained 0.180 g of **3** as a blue-purple solid after crystallization from a mixture (n-hexane/CH_2Cl_2: 8/2).

Yield 93%. IR [ν cm^{-1}] (KBr): 1608 (C=N); 1949, 1860 (CO); 846 (PF_6^-).

^{1}H NMR (300 MHz, $CDCl_3$, 25 °C, δ [ppm]): 1.18 (s, 6H, o-CH_3); 1.57 (s, 3H, H_4); 1.72 (s, 2H, H_{anti}); 2.14 (s, 3H, CH_3–C=N); 2.31 (s, 3H, CH_3–C=N); 2.98 (s, 2H, H_{syn}); 7.01–7.38 (m, 8H, H_{ar}).

^{13}C NMR (75.5 MHz, $CDCl_3$, 25 °C, δ [ppm]): 18.1 (o,o-CH_3), 20.4 (o′,o′-CH_3); 21.5, 26.9 (CH_3–C=N); 30.1 (C_4); 67.0 ($C_{1,3}$); 71.0 (C_2); 104 ($C_{ortho'}$); 121.1 (C_{para}); 127.9 (C_{ortho}); 128.1 ($C_{meta'}$); 131.8 (C_{meta}); 149.8 (C_{ipso}); 172.1 (C=N); 204, 205 (CO).

4.2.3. Synthesis of [(2,6-(CH_3)$_2$–C_6H_3N=C(Me)–C(Me)=N–C_6H_3–2,6-(CH_3)$_2$)Mo(CO)$_3$ (η^3-C_3H_4–Me-2)]$^+PF_6^-$ (**4**)

Following the general procedure, from $Mo(CO)_6$ (0.080 g, 0.3 mmol), p-xylene (5 ml), THF (15 ml), 2-methylallyloxyphosphonium (0.1 g, 0.26 mmol) and (*2,6-(CH_3)$_2$–C_6H_3N=C(Me)–C(Me)=N–C_6H_3–2,6-(CH_3)$_2$*) (0.087 mg, 0.3 mmol) was obtained 0.190 g of **4** as a blue-purple solid after crystallization from a mixture (n-hexane/CH_2Cl_2: 8/2).

Yield 94%. IR [ν cm^{-1}] (KBr): 1622 (C=N); 1940, 1857 (CO); 843 (PF_6^-).

^{1}H NMR (300 MHz, $CDCl_3$, 25 °C, δ [ppm]): 1.25 (s, 6H, o,o′-CH_3); 1.73 (s, 3H, H_4); 1.97 (s, 2H, H_{anti}); 2.18 (s, 6H, o,o′-CH_3); 2.24 (s, 6H, CH_3–C=N); 2.58 (s, 2H, H_{syn}); 7.00–7.26 (m, 6H, H_{ar}).

^{13}C NMR (75.5 MHz, $CDCl_3$, 25 °C, δ [ppm]): 17.5 (o,o-CH_3), 18.6 (o′,o′-CH_3); 20.2, 23.4 (CH_3–C=N); 24.1 (C_4); 69.0 ($C_{1,3}$); 86.0 (C_2); 127.2 ($C_{ortho,ortho'}$); 128.7 (C_{para}); 129.0 (C_{meta}); 149.8 (C_{ipso}); 171 (C=N); 200, 207 (CO).

4.2.4. Synthesis of [(o-CH_3–C_6H_4–BIAN)Mo(CO)$_3$ (η^3-C_3H_4–Me-2)]$^+PF_6^-$ (**5**)

Following the general procedure, from $Mo(CO)_6$ (0.080 g, 0.3 mmol), p-xylene (5 ml), THF (15 ml), 2-methylallyloxyphosphonium (0.1 g, 0.26 mmol) and (*o-CH_3–C_6H_4–BIAN*) (0.108 g, 0.3 mmol) was obtained 0.185 g of **5** as a green solid after crystallization from a mixture (n-hexane/CH_2Cl_2: 8/2).

Yield 91%. IR [ν cm^{-1}] (KBr): 1638, 1690 (C=N); 1948, 1854 (CO); 840 (PF_6^-).

^{1}H NMR (300 MHz, MeOD, 25 °C, δ [ppm]): 0.92 (s, 2H, H_{anti}); 1.29 (s, 3H, H_4); 2.19 (s, 2H, H_{syn}); 2.39(s, 3H, o,o′-CH_3); 2.69 (s, 3H, o,o′-CH_3); 7.15–7.29 (m, 14H, 8H_{ar} + 6 $H_{7,8,9}$).

^{13}C NMR (75.5 MHz, MeOD, 25 °C, δ [ppm]): 14.2 (o,o′-CH_3); 22.7 (C_4); 63.2 ($C_{1,3}$); 71.6 (C_2); 113.1 ($C_{ortho'}$); 123.6 (C_7); 127.1 (C_{para}); 127.2 (C_{ortho}); 127.6 ($C_{meta'}$); 128.9 (C_8); 129.7(C_9); 129.9 (C_{10}); 130.3 (C_{meta}); 131.5 (C_6); 139.2 (C_{11}); 148.1 (C_{ipso}); 176 (C=N); 203, 205 (CO).

4.2.5. Synthesis of [(2,6-(iPr)$_2$–C_6H_3–BIAN)Mo(CO)$_3$ (η^3-C_3H_4–Me-2)]$^+PF_6^-$ (**6**)

Following the general procedure, from $Mo(CO)_6$ (0.080 g, 0.3 mmol), p-xylene (5 ml), THF (15 ml), 2-methylallyloxyphosphonium (0.1 g, 0.26 mmol) and (*2,6-(iPr)$_2$–C_6H_3–BIAN*) (0.142 g, 0.3 mmol) was obtained 0.226 g of **6** as a green solid after crystallization from a mixture (n-hexane/CH_2Cl_2:8/2).

Yield 88%. ^{1}H NMR (300 MHz, $CDCl_3$, 25 °C, δ [ppm]): 0.77–0.79 (d, 12 H, J_{HH} = 6.6 Hz, CH_3–iPr); 1.05–1.03 (d, 12H, J_{HH} = 6.9 Hz, CH_3–iPr); 1.25 (s, 3H, H_4); 1.43 (s, 2H, H_{anti}); 2.81–2.86 (sept, 4H, J_{HH} = 6,6 Hz, CH–iPr); 3.22 (s, 2H, H_{syn}); 6.43–6.45 (d, 2H, J_{HH} = 7.2 Hz, H_7); 7.07–7.37 (m, 6H, H_{ar}), 7.67–7.70 (d, 2H, H_9, J = 8.1 Hz).

^{13}C NMR (75.5 MHz, $CDCl_3$, 25 °C, δ [ppm]): 14.1 (C_4); 23.7, 24.3, 25.0, 25.3, 25.7, 26.5 (CH_3–iPr); 28.0, 28.5, 29.4, 29.7 (CH–iPr); 70.6 ($C_{1,3}$); 75.1 (C2); 125.0 (C_7); 125.3 (C_{meta}); 125.7 (C_{para}); 127.5 (C_8); 128.1(C_9); 128.6 (C_6); 130.3 (C_{10}); 139.5 (C_{ortho}); 141.0(C_{11}); 147.7 (C_{ipso}); 168.6 (C=N); 203, 205 (CO).

4.3. X-ray crystallographic study

The X-ray crystallographic study of complex **4** is carried out on a MACH3 Enraf Nonius diffractometer using monochromated Mo Kα radiation (λ = 0.71073 Å) at 293 K. Accurate unit cell parameters and orientation matrix are determined from 25 reflections in the range 13–15°. Intensity data are collected by using the ω–2θ scan mode with a range of 2 < θ < 27°. All the intensity data are corrected for Lorentz and polarization effects. The crystal structure solution carried out with direct methods from the SHELXS-97 permitted the location of all non-hydrogen atoms. After anisotropic least-squares refinement, hydrogen atoms are placed at their geometrically calculated positions and refined riding on the corresponding atoms with isotropic thermal parameters. Final refinement based on the reflections [$I > 2\sigma(I)$] converged at R_1 = 0.0880, wR_2 = 0.2175 and GoF = 0.960. The experimental conditions of data collection, strategy followed for the structure determination, and final results are given in Table 1.

Appendix A. Supplementary data

CCDC 276931 contains the supplementary crystallographic data for this article. These data can be obtained free of charge via http://www.ccdc.cam.ac.uk/conts/retrieving.html, or from the Cambridge Crystallographic Data Centre, 12 Union Road, Cambridge CB2 1EZ,

UK; fax: (+44) 1223-336-033; or e-mail: deposit@ccdc.cam.ac.uk. Supplementary data associated with this article can be found, in the online version, at doi:10.1016/j.poly.2008.11.050.

References

[1] S.K. Chowdhury, V.S. Joshi, A.G. Samuel, V.G. Puranik, S.S. Tavale, S. Sarkar, Organometallics 13 (1994) 4092.
[2] J. Pérez, L. Riera, V. Riera, S. Garcia-Granda, E. Garcia-Rodriguez, J. Am. Chem. Soc. 123 (2001) 7469.
[3] J. Pérez, L. Riera, V. Riera, S. Garcia-Granda, E. Garcia-Rodriguez, D. Miguel, Organometallics 21 (2002) 1622.
[4] E. Hevia, J. Pérez, L. Riera, V. Riera, D. Miguel, Organometallics 21 (2002) 1750.
[5] J. Pérez, E. Hevia, L. Riera, V. Riera, S. Garcia-Granda, E. Garcia-Rodriguez, D. Miguel, Eur. J. Inorg. Chem. (2003) 1113.
[6] (a) F. Dawans, J. Dewailly, J. Meunier-Piret, P. Piret, J. Organomet. Chem. 76 (1974) 53;
(b) F. Dawans, E. Goldenberg, Brevet d'Invention, Inst. Int. Prop. Indust. 2. 120 (1972) 573.
[7] (a) B.M. Trost, M.J. Lautens, Organometallics 2 (1983) 1687;
(b) B.M. Trost, M.J. Lautens, J. Am. Chem. Soc. 104 (1982) 5543;
(c) B.M. Trost, M.J. Lautens, J. Am. Chem. Soc. 105 (1982) 3343;
(d) B.M. Trost, M.H. Hung, J. Am. Chem. Soc. 105 (1983) 7757.
[8] R.A. Klein, F. Hartl, C.J. Elsevier, Organometallics 16 (1997) 1284.
[9] R. Van Asselet, C.J. Elsevier, C. Amatore, A. Jutand, Organometallics 16 (1997) 317.
[10] R. Van Asselt, K. Vrieze, J.C. Elsevier, J. Organomet.Chem. 27 (1994) 480.
[11] J.H. Groen, J.G.P. Delis, W.N.M. Van Leeuwen, K. Vreize, Organometallics 16 (1997) 68.
[12] J.H. Groen, C.J. Elsevier, K. Vreize, W.J.J. Smeets, A.L. Spek, Organometallics 15 (1996) 3445.
[13] M. Brookhart, E. Hauptman, D. Lincoln, J. Am. Chem. Soc. 114 (1992) 10394.
[14] F.C. Rix, M. Brookhart, J. Am. Chem. Soc. 117 (1995) 1137.
[15] F.C. Rix, M. Brookhart, P.S. White, J. Am. Chem. Soc. 118 (1996) 4746.
[16] F.C. Rix, M. Brookhart, P.S. White, J. Am. Chem. Soc. 118 (1996) 2436.
[17] (a) A. Mechria, M. Rzaigui, F. Bouachir, Tetrahedron Lett. 41 (2000) 7199;
(b) A. Mechria, C. Bavoux, F. Bouachir, J. Organomet. Chem. 677 (2003) 53;
(c) A. Mechria, M. Rzaigui, F. Bouachir, Tetrahedron Lett. 44 (2003) 6773.
[18] R. Van Asselt, C.J. Elsevier, W.J.J. Smeets, A.L. Spek, R. Benedix, Recl. Trav. Chim. Pay-Bas 113 (1994) 88.
[19] H. tom Dieck, I.W. Renk, Chem. Ber. 104 (1971) 92.
[20] D. Neibecker, These, Universite de Nancy I, 1975.
[21] J.R. Ascenso, C.G. de Azevedo, M.J. Calhorda, M.A.A.F. de C.T. Carrondo, P. Costa, A.R. Dias, M.G.B. Drew, V. Felix, A.M. Galvao, C.C. Romao, J. Organomet. Chem. 632 (2001) 197.
[22] B.E. Mann, B.L. Shaw, G.J. Shaw, J. Chem. Soc. A (1971) 3536.
[23] M. Svoboda, H. tom Dieck, J. Organomet. Chem. 191 (1980) 321.
[24] F. W-Grevels, K. Kerpen, W.E. Klotzbücher, K. Schaffner, R. Goddard, B. Weimann, C. Keyran, S. Özkar, Organometallics 20 (2001) 4775.
[25] P.K. Baker, Adv. Organomet. Chem. 40 (1996) 45.
[26] (a) B.M. Trost, I. Hachiya, J. Am. Chem. Soc. 120 (1998) 1104;
(b) S.W. Krska, D.L. Hughes, R.A. Reamer, D.J. Mathre, Y. Sun, B.M. Trost, J. Am. Chem. Soc. 124 (2002) 12656.
[27] (a) B.J. Brisdon, D.A. Edwards, J.W. White, J. Organomet. Chem. 156 (1978) 427;
(b) J. Pérez, V. Riera, A. Rodriguez, S.G. Granda, Angew. Chem., Int. Ed. 41 (2002) 1427.
[28] Y. Yamaguchi, A. Fujita, N. Suzuki, T. Ito, J. Mol. Catal.: Chem. 240 (2005) 226.
[29] J.W. Goodyear, C.W. Hemingway, R.W. Harrington, M.R. Wiseman, B.J. Brisdon, J. Organomet. Chem. 664 (2002) 176.

Polyhedron 28 (2009) 574–578

Contents lists available at ScienceDirect

Polyhedron

journal homepage: www.elsevier.com/locate/poly

Synthesis, reactivity and structural characterization of lanthanide hydroxides stabilized by a carbon-bridged bis(phenolate) ligand

Xiao-Ping Xu, Rui-Peng Qi, Bin Xu, Ying-Ming Yao *, Kun Nie, Yong Zhang, Qi Shen

Key Laboratory of Organic Synthesis of Jiangsu Province, College of Chemistry, Chemical Engineering and Materials Science, Dushu Lake Campus, Soochow University, Suzhou 215123, PR China

ARTICLE INFO

Article history:
Received 9 October 2008
Accepted 21 November 2008
Available online 26 December 2008

Keywords:
Lanthanide
Bis(phenolate)
Hydroxide
Isocyanate
Reactivity
Crystal structure

ABSTRACT

The synthesis of lanthanide hydroxo complexes stabilized by a carbon-bridged bis(phenolate) ligand 2,2'-methylene-bis(6-*tert*-butyl-4-methylphenoxo) ($MBMP^{2-}$) was described, and their reactivity toward phenyl isocyanate was explored. Reactions of $(MBMP)Ln(C_5H_5)(THF)_2$ with a molar equiv. of water in THF at −78 °C afforded the bis(phenolate) lanthanide hydroxides as dimers $[\{(MBMP)Ln(\mu\text{-}OH)(THF)_2\}_2]$ [Ln = Nd (**1**), Yb (**2**)] in high yields. Complexes **1** and **2** reacted with phenyl isocyanate in THF, after workup, to give the desired O−H addition products, $[(MBMP)Ln(\mu\text{-}\eta^1\text{:}\eta^2\text{-}O_2CNHPh)(THF)_2]_2$ [Ln = Nd (**3**), Yb (**4**)] in excellent isolated yields. These complexes were well characterized, and the molecular structures of complexes **2** to **4** were determined by X-ray crystallography. The ytterbium atom in complex **2** is coordinated to six oxygen atoms to form a distorted octahedral geometry, whereas each metal center in complexes **3** and **4** is seven-coordinated, and the coordination geometry can be best described as a distorted pentagonal bipyramid.

© 2008 Elsevier Ltd. All rights reserved.

1. Introduction

Carbon-bridged bis(phenol)s, such as 2,2'-methylene-bis(6-*tert*-butyl-4-methylphenol) ($MBMPH_2$) and 2,2'-ethylidene-bis(4,6-di-*tert*-butylphenol) ($EDBPH_2$), have been used in transition and main group metal coordination chemistry for a long time. These ligands have been found to be able to act as dianionic ligands, which have the advantage of providing a stereochemically rigid framework for the metal center that could affect stereospecific transformations. Meanwhile, some of these transition and main group metal complexes have shown great potential application in homogeneous catalysis [1–13]. In contrast, the synthesis and reactivity of lanthanide complexes stabilized by carbon-bridged bis(phenolate) groups has seldom been studied.

Our recent studies have demonstrated that the carbon-bridged bis(phenolate) lanthanide complexes also have interesting reactivity [14–19]. For example, the neutral trivalent lanthanide alkoxo complexes based on these ligand systems can initiate efficiently the ring-opening polymerization of ε-caprolactone in a controlled manner [15,17]; the neutral and anionic lanthanide amides stabilized by the $MBMP^{2-}$ group can be synthesized in a controlled manner using $[(MBMP)Ln(\mu\text{-}Cl)(THF)_2]_2$ as the precursors by tuning of the molar ratio of the reagents, and the neutral bis(phenolate) lanthanide amides $[(MBMP)Ln\{N(SiMe_3)_2\}(THF)_2]$ cannot only initiate efficiently ε-caprolactone polymerization, but also activate carbodiimide to give lanthanide guanidinate complexes [18]. During our further study of the reactivity of $[(MBMP)Nd\{N(SiMe_3)_2\}(THF)_2]$ with phenyl isocyanate, an unexpected by-product $[\{(MBMP)Nd(\mu\text{-}\eta^1\text{:}\eta^2\text{-}O_2CNHPh)(THF)_2\}_2]$ was isolated. The proposed formation mechanism of this complex is that the partial hydrolysis of bis(phenolate) neodymium amide forms the corresponding neodymium hydroxide first, and then phenyl isocyanate inserts to the O−H bond to form the final product as shown in Scheme 1. Although the lanthanide hydroxides have been known for a long time, to our best knowledge, there is only one paper which reported the regioselective transformation of the hydroxo group of the organolanthanide hydroxides. Zhou et al. recently reported the reactivity of the lanthanocene hydroxides toward some small molecules [20]. This promoted us to study the synthesis and reactivity of bis(phenolate) lanthanide hydroxides. Here we report the results.

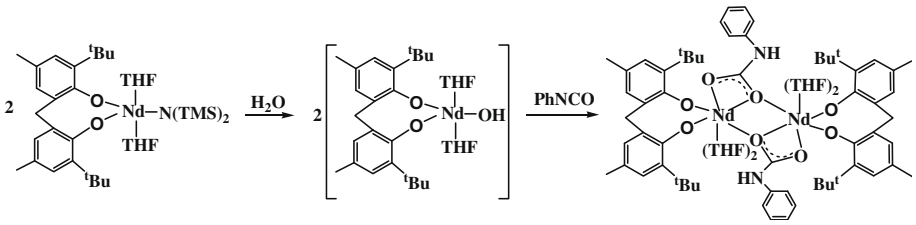
2. Results and discussion

2.1. Synthesis and characterization of bis(phenolate) lanthanide hydroxides

In order to confirm the above postulation, we intend to synthesize the bis(phenolate) lanthanide hydroxides and explore their reactivity toward phenyl isocyanate. Our previous work has demonstrated that carbon-bridged bis(phenolate) lanthanide

* Corresponding author. Tel.: +86 512 65882806; fax: +86 512 65880305.
E-mail address: yaoym@suda.edu.cn (Y.-M. Yao).

0277-5387/$ - see front matter © 2008 Elsevier Ltd. All rights reserved.
doi:10.1016/j.poly.2008.11.031

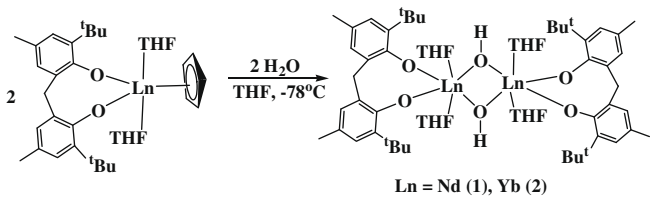


Scheme 1.

cyclopentadienyl complexes, $[(MBMP)Ln(C_5H_5)(THF)_n]$, are good precursors for the synthesis of the corresponding lanthanide derivatives via protic exchange reactions and a partial hydrolysis product was isolated [15,19]. Thus, $[(MBMP)Ln(C_5H_5)(THF)_n]$ were used as starting materials to synthesize the bis(phenolate) lanthanide hydroxides by controlled hydrolysis reaction. $[(MBMP)Ln(C_5H_5)(THF)_2]$ (Ln = Nd, Yb) reacted with distilled water in THF in a 1:1 molar ratio at −78 °C, the color of the solution changed gradually from blue to pale blue (for neodymium) or yellow to pale yellow (for ytterbium). After workup, pale blue (complex **1**) or pale yellow (complex **2**) microcrystals were obtained in good isolated yields. Elemental analysis results revealed that these complexes consist of one dianionic bis(phenolate) group ($MBMP^{2-}$), one hydroxide, and two coordinated THF molecules at the metal center. Their IR spectra show the characteristic absorption bands of hydroxo group at about 3605 cm^{-1}, and aromatic rings in the region 1400–1600 cm^{-1} (skeletal vibrations). Further molecular structure determination of complex **2** confirmed that they have solvated dimeric structures $[\{(MBMP)Ln(\mu\text{-}OH)(THF)_2\}_2]$ [Ln = Nd (**1**), Yb (**2**)] as shown in Scheme 2.

The molecular structure of complex **2** is shown in Fig. 1, and its selected bond lengths and angles are listed in Table 1. Complex **1** has a dimeric structure, and two molecules are connected together by two bridged hydroxo groups. The molecule has approximate C_2 symmetry. Each ytterbium atom is six-coordinated with two oxygen atoms from one bridged bis(phenolate) group, two oxygen atoms from two bridged hydroxo groups and two oxygen atoms from two THF molecules. The coordination geometry at ytterbium atom can be described as a distorted octahedron, in which O(1), O(2), O(5) and O(6) can be considered to occupy the equatorial positions, and O(7) and O(8) to occupy the apical positions, and the angle of O(7)–Yb–O(8) is distorted away from the idealized 180° to 171.9(2)°.

The average Yb–O(Ar) bond length of 2.085(6) Å falls in the range of Yb–O(Ar) bond lengths in other carbon-bridged bis(phenolate) ytterbium complexes, such as $[\{(MBMP)_2Yb(\mu\text{-}OPr^i)(THF)_2\}_2]$ [15], $[Li(THF)_4][(MBMP)Yb\{N(SiMe_3)_2\}_2]$, and $[\{(MBMP)Yb(\mu\text{-}Cl)(THF)_2\}_2]$ [18] [2.059(2)–2.120(3) Å]. The Yb–O(H) bond lengths range from 2.211(4) to 2.241(4) Å, giving the average of 2.227(5) Å, which is comparable well with the corresponding bond lengths in $[\{(MBMP)_2Yb(THF)_2\}_2(\mu\text{-}OCH_2Ph)(\mu\text{-}OH)]$ [2.211(4) Å] [15], $[\{Yb(OC_6H_3\text{-}2,4,6\text{-}Bu^t_3)_2(\mu\text{-}OH)(THF)\}_2]$ [2.208(6) Å] [21], $[\{Yb(OC_6H_3\text{-}2,6\text{-}Bu^t_2)_2(\mu\text{-}OH)(THF)\}_2]$ [2.217(7) Å] [22] and $[(Me_3SiC_5H_4)_2Yb(\mu\text{-}OH)_2]$ [2.29(2) Å] [23]. The most remarkable feature of the structure of complex **2** is that there is remote O–H···Yb interaction involving the hydroxide hydrogen atom. The Yb(2)–H(5A) bond length of 2.75(4) Å is significantly longer than the Ln–H bond lengths in most of the organolanthanide hydrides [24,25], but it accords with the Lu(1)–H(2) of 2.70(5) Å in $[\{(C_5Me_4SiMe_3)LuH_2\}_4]$ [25], and Y(1)–H(16e) of 2.935(6) Å in $[(C_5Me_5)Y(OC_6H_3{}^tBu_2)CH(SiMe_3)_2]$ [26].



Scheme 2.

2.2. Reactivity with phenyl isocyanate

Reactions of complexes **1** and **2** with phenyl isocyanate in THF, after workup, gave the desired O–H addition products, $[\{(MBMP)Ln(\mu\text{-}\eta^1\text{:}\eta^2\text{-}O_2CNHPh)(THF)_2\}_2]$ [Ln = Nd (**3**), Yb (**4**)] in excellent isolated yields as shown in Scheme 3. Complexes **3** and **4** were characterized by elemental analysis and IR spectroscopy, and their definitive molecular structures were provided by single-crystal X-ray diffraction. These reactions are quite different from those of lanthanocene hydroxides with phenyl isocyanate reported by Zhou et al. and complexes **3** and **4** can be considered as the proposed intermediate species (II) in the latter [20]. Attempts to eliminate the N–H proton with $[(C_5H_5)_3Ln(THF)]$ as that reported by Zhou were unsuccessful, and the isolated compound is the starting material. These results revealed that the ancillary ligands have a profound effect on the reactivity of the corresponding lanthanide complexes.

Complexes **3** and **4** are isostructural, and only the molecular structure of complex **3** is shown in Fig. 2, and their selected bond lengths and angles are provided in Table 2. Both complexes have solvated C_2 symmetric dimeric structures. Two molecules are connected together by two bridged oxygen atoms from carbaminate groups $PhNHCO_2$, and the eight atoms Nd(1), O(3), C(24), O(4), Nd(1A), O(3A), C(24A), and O(4A) form an interlinked tricyclic structure via the two bridged Nd–O bonds [Nd(1)–O(3A) and Nd(1A)–O(3)]. The corn structure is similar to those of $[\{(CH_3C_5H_4)_2Y(\mu\text{-}\eta^1\text{:}\eta^2\text{-}S_2CNPh_2)\}_2]$ [27], and $[\{Cp_2Ln(\mu\text{-}\eta^1\text{:}\eta^2\text{-}O_2CCHEtPh)\}_2]$ (Ln = Yb, Er, Y) [20], but different from that of $[\{(C_5Me_5)_2Sm(\mu\text{-}O_2CEPh)\}_2]$ [28]. Each central metal atom is seven-coordinated by two oxygen atoms from one bridged bis(phenolate) ligand, and one oxygen atom from a $PhNHCO_2$ group, and two oxygen atoms from another $PhNHCO_2$ group, and two oxygen atoms from two THF molecules. The coordination geometry around the central metal atom can be described as a distorted pentagonal bipyramid, in which O(1), O(5), O(4A), O(3A) and O(3) can be considered to occupy the equatorial positions with the sum of the bond angles of 360.2° in complex **3**, and 359.7° in complex **4**, respectively, and O(2) and O(6) to occupy the axis positions. The bond angles of O(2)–Ln–O(6) are slightly distorted away from the ideal value of 180° to 164.6(1)° in complex **3**, and 162.8(1)° in complex **4**, respectively.

The Nd–O(Ar) bond distances are 2.267(3) and 2.154(4) Å, giving the average of 2.210(4) Å, which is very close to those observed in related neodymium complexes $[\{(MBMP)_2Nd(\mu\text{-}OPr^i)(THF)_2\}_2]$ [2.215(6) Å] [15], $[\{(EDBP)Nd(\mu\text{-}O^iPr)(THF)\}_2]$ [2.225(5) Å] [17], $[(MBMP)Nd\{N(TMS)_2\}(THF)_2]$ [2.200(2) Å], and $[Li(THF)_4][(MBMP)Nd\{N(TMS)_2\}_2]$ [2.195(3) Å] [18]. The carbaminate group is asymmetrically coordinated to the neodymium atom with the var-

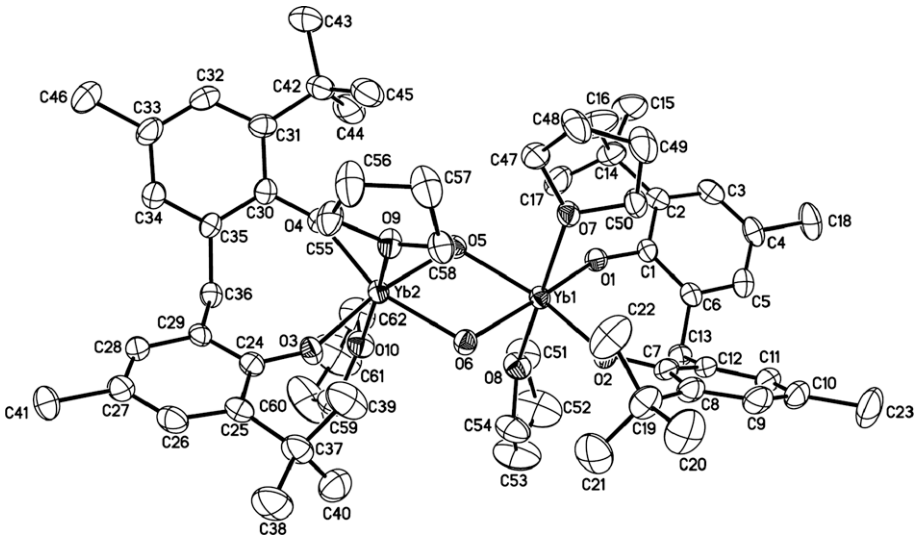


Fig. 1. ORTEP diagram of complex **2** showing atom-numbering scheme. Thermal ellipsoids are drawn at the 30% probability level. Hydrogen atoms are omitted for clarity.

Table 1
Selected bond distances (Å) and angles (°) for complex **2**.

Bond distance			
Yb(1)–O(1)	2.085(4)	Yb(2)–O(3)	2.078(4)
Yb(1)–O(2)	2.088(4)	Yb(2)–O(4)	2.090(4)
Yb(1)–O(5)	2.221(4)	Yb(2)–O(5)	2.241(4)
Yb(1)–O(6)	2.237(4)	Yb(2)–O(6)	2.211(4)
O(1)–C(1)	1.344(6)	O(3)–C(24)	1.338(6)
O(2)–C(7)	1.351(6)	O(4)–C(30)	1.340(6)
Bond angle			
O(1)–Yb(1)–O(2)	97.4(2)	O(3)–Yb(2)–O(4)	97.8(2)
O(2)–Yb(1)–O(6)	88.8(2)	O(4)–Yb(2)–O(5)	90.6(2)
O(5)–Yb(1)–O(6)	71.7(1)	O(5)–Yb(2)–O(6)	71.9(1)
O(1)–Yb(1)–O(5)	102.9(1)	O(6)–Yb(2)–O(3)	100.8(2)
O(8)–Yb(1)–O(7)	171.9 (2)	O(9)–Yb(2)–O(10)	172.7(1)

iation in Nd–O bond lengths of about 0.07 Å [2.493(3) and 2.563(3) Å, respectively], which is similar to those found in [{$Cp_2Ln(\mu\text{-}\eta^1{:}\eta^2\text{-}O_2CCHEtPh)$}$_2$] (Ln = Yb, Er, Y) [20]. The Nd–O(3) bond length of 2.395(3) Å is comparable with the averaged bridged Nd–O(Ar) bond length in neodymium bis(phenolate) guanidinate complex [{(μ-O-MBMP)Nd[(^{i}PrN)$_2$CN(TMS)$_2$]}$_2$] (2.401 Å) [18], but is apparently smaller than the bond lengths of Nd–O(3A) [2.493(3) Å] and Nd–O(4A) [2.563(3) Å]. The latter compare well with the bond lengths of Nd–O(THF) [2.458(3) and 2.567(4) Å], which revealed that these bonds are donating bond of neutral oxygen-donor ligands. It is worthy to note that the bridged Nd–O(3A) bond is shorter than the terminal Nd–O(4A) bond, which is quite different from those in [{$Cp_2Ln(\mu\text{-}\eta^1{:}\eta^2\text{-}O_2CCHEtPh)$}$_2$] (Ln = Yb, Er, Y) [20]. Generally, the bridged bond is longer than the terminal one. The shorter bridged Nd–O bond length in our case might be attributed to the relatively weak electron delocalization within the carbaminate group. Because the C(24)–O(4) bond length of 1.249(6) Å falls in the range

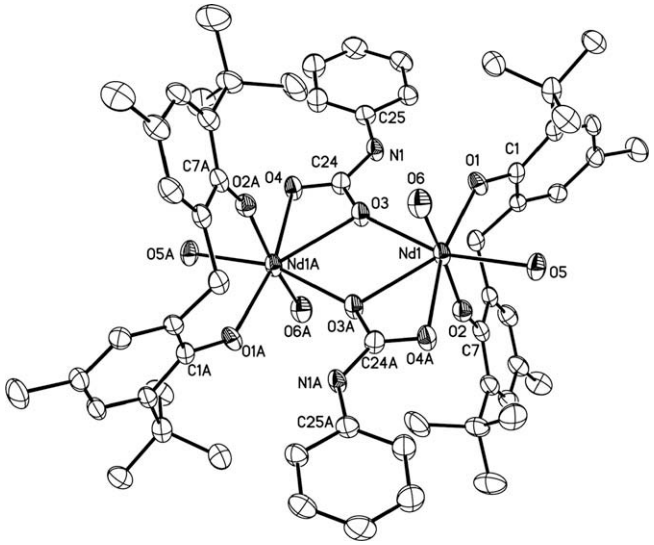
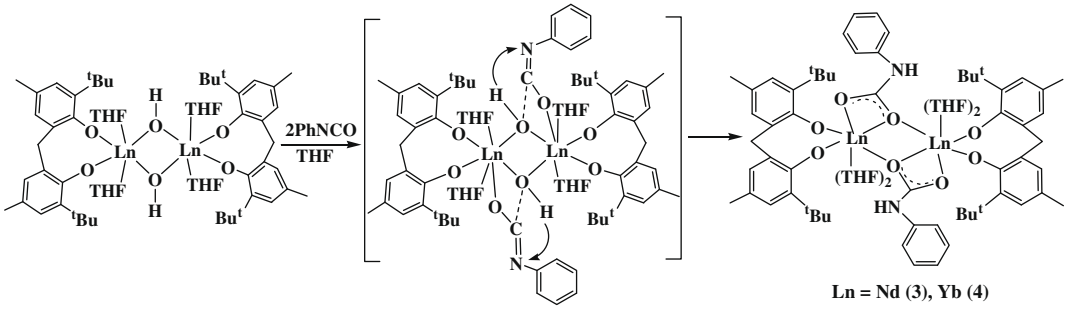


Fig. 2. ORTEP diagram of complex **3** showing atom-numbering scheme. Thermal ellipsoids are drawn at the 30% probability level. Hydrogen atoms and carbon atoms of THF molecules are omitted for clarity. Complex **4** is isostructural with complex **3**.



Scheme 3.

Table 2
Selected bond distances (Å) and angles (°) for complexes **3** and **4**.

	3	4		3	4
Bond length					
Ln(1)–O(1)	2.267(3)	2.157(3)	Ln(1)–O(2)	2.154(4)	2.068(3)
Ln(1)–O(3)	2.395(3)	2.285(3)	Ln(1)–O(3A)	2.493(3)	2.368(3)
Ln(1)–O(4A)	2.565(3)	2.421(3)	Ln(1)–O(5)	2.458(3)	2.326(3)
Ln(1)–O(6)	2.567(4)	2.407(4)	Ln(1)–C(24A)	2.924(5)	2.780(5)
O(3)–C(24)	1.307(5)	1.308(6)	O(4)–C(24)	1.249(6)	1.240(6)
Bond angle					
O(2)–Ln(1)–O(6)	164.6(1)	162.8(1)	O(1)–Ln(1)–O(5)	87.7(1)	84.9(1)
O(5)–Ln(1)–O(4A)	76.1(1)	76.3(1)	O(4A)–Ln(1)–O(3A)	51.7(1)	54.4(1)
O(3A)–Ln(1)–O(3)	64.9(1)	64.5(1)	O(3)–Ln(1)–O(1)	79.8(1)	79.6(1)
Ln(1)–O(3)–Ln(1A)	115.2(1)	115.6(1)			

of C=O double bond and the C(24)–O(3) bond length of 1.307(5) Å falls in the range of C–O single bond, and the deviation of their bond distances is apparently larger than the corresponding values found in [{$Cp_2Ln(\mu\text{-}\eta^1{:}\eta^2\text{-}O_2CCHEtPh)$}$_2$] (Ln = Yb, Er, Y) [20]. There is a strong π interaction of the carbon atom of the carbaminate group with the neodymium atom. The Nd–C(24A) bond length of 2.924(5) Å is apparently lower than the Nd–C contact observed in [{(MBMP)Nd(μ-O^{i}Pr)(THF)$_2$}$_2$] [3.101(7) Å] [15] and compares well with those observed in the neutral arene neodymium complexes [Nd(η^6-C_6H_6)($AlCl_4$)$_3$] [2.933(18) Å] [29], [Nd(η^6-C_6H_5Me)($AlCl_4$)$_3$] [2.926(5) Å] [30], and [Nd(η^6-1,3,5-$C_6H_3Me_3$)($AlCl_4$)$_3$] [2.916(9) Å] [31], in which the Nd–C π interaction was considered to exist unambiguously.

In complex **4**, the average Yb–O(Ar) bond length is 2.112(3) Å, which accords with those found in the carbon-bridged bis(phenolate) lanthanide complexes mentioned above when the difference in ionic radii is considered. The Yb–O(3) bond distance of 2.285(3) Å is also apparently smaller than the Yb–O(3A) and Yb–O(4A) bond distances, which revealed the Yb–O(3A) and Yb–O(4A) bond are donating bond. The Yb–C(24A) bond length of 2.780(5) Å compares well with that in complex **3**, when the difference in ionic radii is considered, but apparently lower than that found in the neutral arene ytterbium complex [Yb(η^6-1,3,5-C_6Me_6)($AlCl_4$)$_3$] [2.87(4) Å] [32], which indicating the presence of strong π interaction. Similar to that in complex **3**, the terminal Yb–O(4A) bond is longer than the bridged Yb–O(3A) bond.

Table 3
Details of the crystallographic data and refinements for complexes **2**–**4**.

Compound	**2** · 3.5THF	**3** · $2C_7H_8$	**4** · $2C_7H_8$
Formula	$C_{76}H_{122}O_{13.50}Yb_2$	$C_{90}H_{120}N_2Nd_2O_{12}$	$C_{90}H_{120}N_2O_{12}Yb_2$
Formula weight	1597.81	1710.36	1767.96
T (K)	293(2)	193(2)	193(2)
Crystal system	Triclinic	Monoclinic	Monoclinic
Space group	$P\bar{1}$	$P2_1/n$	$P2_1/n$
a (Å)	13.081(1)	14.398(2)	14.064(2)
b (Å)	15.570(1)	17.475(2)	17.228(3)
c (Å)	19.844(2)	17.148(2)	17.453(3)
α (°)	85.319(5)		
β (°)	87.009(5)	102.362(3)	99.842(3)
γ (°)	80.354(4)		
V (Å^3)	3968.0(6)	4214.4(8)	4166.7(11)
Z	2	2	2
D_{calc} (g/cm^{-3})	1.336	1.348	1.409
μ (mm^{-1})	2.399	1.278	2.291
F(000)	1650	1780	1820
Crystal size (mm)	0.80 × 0.48 × 0.39	0.50 × 0.40 × 0.20	0.60 × 0.48 × 0.20
2θ range (°)	50.7	50.7	50.7
Reflections collected	37676	40212	39220
Independent reflections	14415	7698	7611
Reflections with $I \geqslant 2.0\sigma(I)$	11882	6591	6685
Parameters refined	829	512	488
GOF	1.109	1.185	1.145
R	0.0471	0.0546	0.0456
wR	0.1033	0.1103	0.0968

3. Conclusion

In summary, the lanthanide hydroxides stabilized by a carbon-bridged bis(phenolate) ligand were prepared, and their reactivity toward phenyl isocyanate was explored. The structural properties of some of these complexes were provided by X-ray diffraction. Controlled hydrolysis of bis(phenolate) lanthanide cyclopentadienyl complexes in THF at low temperature gave the corresponding lanthanide hydroxides as dimers. These lanthanide hydroxo complexes reacted with phenyl isocyanate in THF to give the desired O–H addition products, which provided an alternative route to synthesize lanthanide carbaminate complexes. In comparison with the final products of the reactions of lanthanocene hydroxides with phenyl isocyanate, theses results revealed that the ancillary ligands have a profound effect on the reactivity of the corresponding lanthanide complexes.

4. Experimental

4.1. Materials and methods

All of the manipulations described below were performed under an argon atmosphere, using the standard Schlenk techniques. Solvents were dried and freed of oxygen by refluxing over sodium or sodium benzophenone ketyl and distilled under argon prior to use. [(MBMP)Ln(C_5H_5)(THF)$_2$] were prepared according to the literature methods [15,19]. The other reagents were purchased from Acros and used as received without further purification. Metal analyses were carried out using complexometric titration. Carbon, hydrogen, and nitrogen analyses were performed by direct combustion on a Carlo Erba-1110 instrument; Quoted data are the average of at least two independent determinations. IR spectra were recorded on a Nicolet-550 FTIR spectrometer as KBr pellets. The uncorrected melting points of crystalline samples in sealed capillaries (under argon) are reported as ranges.

4.2. Synthesis of [{(MBMP)Nd(μ-OH)(THF)$_2$}$_2$] (**1**)

A solution of [(MBMP)Nd(C_5H_5)(THF)$_2$] (1.47 g, 2.13 mmol) in THF (30 mL) was cooled to −78 °C. The solution was stirred half an hour, and then a THF solution (30 mL) containing distilled water (38 mg, 2.13 mmol) was added dropwise. The color of the solution was changed gradually from blue to pale blue. The mixture was stirred for 2 h, and then warmed to room temperature and stirred overnight. Little precipitate was separated by centrifugation, and the resulting pale blue solution was concentrated to about

18 mL. Pale blue microcrystals were obtained at room temperature in a few days (0.97 g, 71%), m.p.: 176–178 °C (dec). *Anal. Calc.* for $C_{62}H_{94}Nd_2O_{10}$: C, 57.82; H, 7.36; Nd, 22.40. Found: C, 57.58; H, 7.81; Nd, 22.66%. IR (KBr pellet, cm^{-1}): 3607(m), 3385(m), 2955(s), 2913(m), 1605(m), 1461(s), 1433(s), 1350(m), 1212(s), 1158(s), 867(w), 729(w).

4.3. Synthesis of [{(MBMP)Yb(μ-OH)(THF)$_2$}$_2$] (**2**)

The synthesis of complex **2** was carried out in the same way as that described for complex **1**, but [(MBMP)Yb(C_5H_5)(THF)$_2$] (1.34 g, 1.86 mmol) was used instead of [(MBMP)Nd(C_5H_5)(THF)$_2$]. Pale yellow microcrystals were obtained at room temperature in a few days (0.75 g, 60%), m.p.: 180–182 °C (dec). *Anal. Calc.* for $C_{62}H_{94}O_{10}Yb_2$: C, 55.35; H, 7.04; Yb, 25.72. Found: C, 55.60; H, 7.10; Yb, 25.42%. IR (KBr, cm^{-1}): 3605(m), 3389(m), 2956(s), 2916(m), 1605(m), 1464(s), 1434(s), 1353(m), 1213(s), 1156(s), 864(w), 728(w). The crystals suitable for an X-ray crystal structure determination were obtained in THF solution at room temperature.

4.4. Synthesis of [{(MBMP)Nd(μ-η^1:η^2-O$_2$CNHPh)(THF)$_2$}$_2$] (**3**)

A Schlenk flask was charged with complex **1** (0.77 g, 0.60 mmol) and THF (30 mL). Phenyl isocyanate (PhNCO) (0.65 mL, 1.20 mmol) was added by syringe. The reaction mixture was stirred overnight at room temperature. After removed the volatiles under reduced pressure, the pale blue residue was washed with cooled THF twice. The pale blue powder was dried at room temperature (0.77 g, 84%), m.p.: 218–220 °C (dec). *Anal. Calc.* for $C_{76}H_{104}N_2Nd_2O_{12}$: C, 59.81; H, 6.87; N, 1.83; Nd, 18.90. Found: C, 59.41; H, 6.42; N, 1.95; Nd, 19.11%. IR (KBr, cm^{-1}): 3346(w), 2953(m), 2904(m), 1616(s), 1590(s), 1538(vs), 1445(s), 1337(m), 1298(s), 1239(m), 1024(m), 864(m), 779(m). The crystals suitable for an X-ray crystal structure determination were obtained by recrystallization from THF-toluene solution at room temperature.

4.5. Synthesis of [{(MBMP)Yb(μ-η^1:η^2-O$_2$CNHPh)(THF)$_2$}$_2$] (**4**)

The synthesis of complex **4** was carried out in the same way as that described for complex **3**, but complex **2** (0.67 g, 0.50 mmol) was used instead of complex **1**. Pale yellow powder was obtained at room temperature (0.64 g, 81%), m.p.: 198–200 °C (dec). *Anal.* Calc. for $C_{76}H_{104}N_2O_{12}Yb_2$: C, 57.64; H, 6.62; N, 1.77; Yb, 21.85. Found: C, 57.39; H, 6.50; N, 1.91; Yb, 21.54%. IR (KBr, cm^{-1}): 3347(w), 2953(m), 2905(m), 1617(s), 1591(s), 1538(vs), 1446(s), 1338(m), 1298(s), 1239(m), 1025(m), 864(m), 780(m). The crystals suitable for an X-ray crystal structure determination were obtained by recrystallization from THF-toluene solution at room temperature.

4.6. X-ray structures determination

Suitable single-crystals of complexes **2**–**4** were sealed in a thin-walled glass capillary for determination the single-crystal structure. Intensity data were collected with a Rigaku Mercury CCD area detector in ω scan mode using Mo Kα radiation (λ = 0.71070 Å). The diffracted intensities were corrected for Lorentz polarization effects and empirical absorption corrections. Details of the intensity data collection and crystal data are given in Table 3.

The structures were solved by direct methods and refined by full-matrix least-squares procedures based on $|F|^2$. All of the non-hydrogen atoms were refined anisotropically. All of the hydrogen atoms were held stationary and included in the structure factor calculation in the final stage of full-matrix least-squares refinement. The structures were solved and refined using SHELXL-97 programs.

Acknowledgement

Financial support from the National Natural Science Foundation of China (Grants 20632040 and 20771078), the Natural Science Foundation of Jiangsu province (BK2007505), the Major Basic Research Project of the Natural Science Foundation of the Jiangsu Higher Education Institutions (07KJA15014), and Key Laboratory of Organic Synthesis of Jiangsu Province is gratefully acknowledged.

Appendix A. Supplementary data

CCDC 700053, 700054 and 700055 contain the supplementary crystallographic data for complexes **2**–**4**. These data can be obtained free of charge via http://www.ccdc.cam.ac.uk/conts/retrieving.html, or from the Cambridge Crystallographic Data Centre, 12 Union Road, Cambridge CB2 1EZ, UK; fax: (+44) 1223 336 033; or e-mail: deposit@ccdc.cam.ac.uk. Supplementary data associated with this article can be found, in the online version, at doi:10.1016/j.poly.2008.11.031.

References

[1] T.J. Boyle, L.A.M. Ottley, Chem. Rev. 108 (2008) 1896.
[2] J.C. Wu, T.L. Yu, C.T. Chen, C.C. Lin, Coord. Chem. Rev. 250 (2006) 602. and references herein.
[3] D.C. Bradley, R.C. Mehrotra, I.P. Rothwell, A. Singh, Alkoxo and Aryloxo Derivatives of Metals, Academic Press, New York, 2001.
[4] B.T. Ko, C.C. Wu, C.C. Lin, Organometallics 19 (2000) 1864.
[5] W. Braune, J. Okuda, Angew. Chem. Int. Ed. 42 (2003) 64.
[6] M.L. Hsueh, B.H. Huang, J.C. Wu, C.C. Lin, Macromolecules 38 (2005) 9482.
[7] B.H. Huang, B.T. Ko, T. Athar, C.C. Lin, Inorg. Chem. 45 (2006) 7348.
[8] A. van der Linden, C.J. Schaverien, N. Meijboom, C. Granter, A.G. Orpen, J. Am. Chem. Soc. 117 (1995) 3008.
[9] F.G. Sernetz, R. Mulhaupt, S. Fokken, J. Okuda, Macromolecules 30 (1997) 1562.
[10] M.H. Chisholm, K. Folting, W.E. Sterib, D.D. Wu, Inorg. Chem. 37 (1998) 50.
[11] D. Takeuchi, T. Nakamura, T. Aida, Macromolecules 33 (2000) 725.
[12] M. Gonzalez-Maupoey, T. Cuenca, L.M. Frutos, O. Castaño, E. Herdtweck, Organometallics 22 (2003) 2694.
[13] D. Zhang, Organometallics 26 (2007) 4072.
[14] M.Y. Deng, Y.M. Yao, Q. Shen, Y. Zhang, J. Sun, Dalton Trans. (2004) 944.
[15] Y.M. Yao, X.P. Xu, B. Liu, Y. Zhang, Q. Shen, Inorg. Chem. 44 (2005) 5133.
[16] X.P. Xu, M.T. Ma, Y.M. Yao, Y. Zhang, Q. Shen, Eur. J. Inorg. Chem. (2005) 676.
[17] X.P. Xu, Y.M. Yao, M.Y. Hu, Y. Zhang, Q. Shen, J, Polym. Sci.: Part A: Polym. Chem. 44 (2006) 4409.
[18] X.P. Xu, Z.J. Zhang, Y.M. Yao, Y. Zhang, Q. Shen, Inorg. Chem. 46 (2007) 9379.
[19] R.P. Qi, B. Liu, X.P. Xu, Z.J. Yang, Y.M. Yao, Y. Zhang, Q. Shen, Dalton Trans. (2008) 5016.
[20] C.M. Zhang, R.T. Liu, J. Zhang, Z.X. Chen, X.G. Zhou, Inorg. Chem. 45 (2006) 5867.
[21] G.B. Deacon, T. Feng, S. Nickel, M.I. Ogden, A.H. White, Aust. J. Chem. 45 (1992) 671.
[22] G.B. Deacon, G. Meyer, D. Stellfeldt, G. Zelesny, B.W. Skelton, A.H. White, Z. Anorg. Allg. Chem. 627 (2001) 1652.
[23] P.B. Hitchcock, M.F. Lappert, S. Prashar, J. Organomet. Chem. 413 (1991) 79.
[24] W.J. Evans, J.H. Meadows, A.L. Wayda, W.E. Hunter, J.L. Atwood, J. Am. Chem. Soc. 104 (1982) 2008.
[25] O. Tardif, M. Nishiura, Z.M. Hou, Organometallics 22 (2003) 1171.
[26] W.T. Klooster, L. Brammer, C.J. Schaverien, P.H.M. Budzelaar, J. Am. Chem. Soc. 121 (1999) 1381.
[27] H.R. Li, Y.M. Yao, Q. Shen, L.H. Weng, Organometallics 21 (2002) 2529.
[28] W.J. Evans, K.A. Miller, J.W. Ziller, Inorg. Chem. 45 (2006) 424.
[29] B. Fan, Q. Shen, Y.H. Lin, Chin. J. Org. Chem. 9 (1989) 414.
[30] Q.C. Liu, Q. Shen, Y.H. Lin, Acta Crystallogr., Sect. C 53 (1997) 1579.
[31] Y.M. Yao, Y. Zhang, Q. Shen, Q.C. Liu, Q.J. Meng, Y.H. Lin, Chin. J. Chem. 19 (2001) 588.
[32] H.Z. Liang, Q. Shen, Y.H. Lin, J. Organomet. Chem. 474 (1994) 113.

Polyhedron 28 (2009) 579–585

Contents lists available at ScienceDirect

Polyhedron

journal homepage: www.elsevier.com/locate/poly

Synthesis and characterization of titanates of the formula $MTiO_3$ (M = Mn, Fe, Co, Ni and Cd) by co-precipitation of mixed metal oxalates

Yogesh Kumar Sharma, Mamta Kharkwal, S. Uma, R. Nagarajan *

Materials Chemistry Group, Department of Chemistry, University of Delhi, Delhi 110 007, India

ARTICLE INFO

Article history:
Received 7 October 2008
Accepted 25 November 2008
Available online 23 January 2009

Keywords:
Inorganic compounds
Oxides
Diffraction
Infrared spectroscopy
Raman spectroscopy
Stoichiometry and homogeneity

ABSTRACT

When divalent metal chloride solutions of Mn, Fe, Co, Ni and Cd were mixed with potassium titanyl oxalate solution, mixed metal oxalates were obtained in the case of Fe, Co and Ni at room temperature in the pH range 1.5–3. In the case of manganese, heating was found to be necessary to induce precipitation and complete precipitation occurred at 80 °C. Mixed cadmium and titanyl oxalate precipitation was complete at a pH of 3 at room temperature. Various physico-chemical techniques were employed to characterize the as-dried oxalate precursors and the final $MTiO_3$ oxide powders (M = Mn, Fe, Co, Ni and Cd) obtained on thermal decomposition. All these experimental results relating to the synthesis and characterizations of $MTiO_3$ oxides are presented in this paper. The results suggest that the reaction of potassium titanyl oxalate and metal chloride solutions may not lead to the formation of a single molecular precursor by direct salt elimination reaction in the pH range 1.5–3.

© 2008 Elsevier Ltd. All rights reserved.

1. Introduction

The chemical synthesis of solid inorganic materials is making an increasingly important contribution to the development and manufacture of ceramic materials [1,2]. It also plays a vital role in the development of fabrication techniques for the successful exploitation of various useful properties of ceramics [3]. There is a growing realization that a single source precursor with different metals assembled in one molecule in the desired metal ratios can lead to nanometer level defined morphology and interesting physical properties [4,5]. The metal titanates of the general formula $MTiO_3$ (M = Ba, Pb, Cd, Mn, Fe, Co, Ni, Cu and Zn), possessing perovskite or ilmenite structures, have been studied extensively as inorganic functional materials [6–9]. Of these, $BaTiO_3$, a well-known component of high dielectric constant ceramics for manufacturing capacitors, has been the subject of intense investigation by various research groups ([6] and the references cited therein). The microstructure and consequently the dielectric properties of $BaTiO_3$ are very much dependent on the stoichiometry with regard to the Ba/Ti ratio. The single source or molecular precursor, such as barium titanyl oxalate which is isostructural to potassium titanyl oxalate, has been used to control the final stoichiometry of $BaTiO_3$ [10].

The titanates of other divalent cations, such as Pb, Cd or transition metals Mn, Fe, Co, Ni, Cu and Zn, have wide applications ranging from solid oxide gas sensors to fuel cells [11–16]. In general, a solid state reaction of the respective oxides and/or carbonates of the respective metals is usually employed in industrial processes because of cost effectiveness. However, the ceramic method suffers from several disadvantages such as non-uniform distribution of grains, longer schedule of heating cycles etc. There have been many chemical methods such as co-precipitation, polymerized complexes and sol–gel that have been reported as alternate strategies to synthesize these titanates [17–36]. The sol–gel method of synthesis is not an ideal alternative route since it is not very cost effective. Among the other wet chemical methods, co-precipitation is a simple and convenient method of obtaining solids containing two or more metals.

Balyaev et al. [37] reported the preparation and thermal decomposition of cobalt titanyl oxalate, a molecular precursor for $CoTiO_3$. The authors have claimed that a molecular precursor was obtained when $CoCl_2 \cdot H_2O$ was reacted with potassium titanyl oxalate solution; however there was no clear structural characterization of the precursor and the final product. The authors have also reported that crystallization of $CoTiO_3$ occurred at temperatures as low as 650 °C. Prasad Rao and Suresh [32] studied the pH dependence of the formation of a stoichiometric precursor of the type $M[TiO(C_2O_4)_2] \cdot xH_2O$ (M = Ca, Cd and Pb), but it did not yield conclusive results. Dhage et al. [38] carried out a detailed work on the preparation of $PbTiO_3$ using potassium titanyl oxalate and concluded that the anionic species $TiO(C_2O_4)_2^{2-}$, obtained by dissolving potassium titanyl oxalate in water, is stable over a narrow range of pH and is destabilized by the addition of $PbCl_2$ solution to

* Corresponding author. Tel.: +91 11 2766 2650; fax: +91 11 2766 6605.
E-mail address: rnagarajan@chemistry.du.ac.in (R. Nagarajan).

0277-5387/$ - see front matter © 2008 Elsevier Ltd. All rights reserved.
doi:10.1016/j.poly.2008.11.056

produce the mixed metal oxalates, PbC_2O_4 and $TiO(C_2O_4)$. Lopes et al. [28] prepared $NiTiO_3$ and $CoTiO_3$ by a modified Pechini method in which they proposed the formation of ilmenite phases from $MTi(C_6H_5O_7)_2$ through an intermediate of the type $MTiO(C_2O_4)_2$ (M = Ni and Co).

With this background, the present investigation was carried out to examine whether a single source precursor of the type $MTiO(C_2O_4)_2$ can be obtained by a simple salt elimination reaction between divalent transition metal chlorides and potassium titanyl oxalate in an aqueous medium. This study has clearly shown that the stability of $TiO(C_2O_4)_2^{2-}$ could not be retained in aqueous solutions by the addition of divalent transition metal chlorides to yield a molecular precursor; instead a very fine mixture of transition metal oxalate and titanyl oxalate was obtained. The potassium titanyl oxalate played the dual role of the precipitating agent as well as the titanium source. The thermal decomposition of these mixed metal oxalates yielded a pure ilmenite structure in case of $MnTiO_3$ at significantly lower temperatures as compared to the standard ceramic method [19]. However, in the cases of Fe, Co, Ni and Cd, few impurities were present along with the ilmenite phase after decomposition. In all these cases, the ilmenite phase appeared after an initial firing at low temperatures.

2. Experimental

2.1. Synthesis

A solution of $MCl_2 \cdot xH_2O$ (M = Mn, Fe, Co, Ni and Cd) was prepared in 100 ml (0.2 M) of double distilled water. The starting metal salts were AnalaR Grade from CDH, India. Potassium titanyl oxalate (A.R. Grade, Specpure, India) solution was also prepared in double distilled water (0.1 M in 100 ml). To 100 ml of the potassium titanyl oxalate solution in a 500 ml beaker, 50 ml of $MCl_2 \cdot xH_2O$ solution was added dropwise under constant stirring. After complete addition, the pH of the mixture was measured. A pale pink colored precipitate was obtained by mixing the cobalt(II) chloride solution and potassium titanyl oxalate solution at room temperature. The pH of the solution containing the precipitate was found to be between 2 and 2.5. A sky blue colored precipitate was the product when the nickel(II) chloride solution was added. The pH of the solution containing the precipitate was found to be 1.5–2.0. A yellow colored precursor was obtained by the addition of iron(II) chloride solution to potassium titanyl oxalate solution. The pH of the solution containing the precipitate was between 2 and 3. In the case of $MnCl_2$, a precipitate did not appear at room temperature even though the pH of the mixed solution was in the range between 2 and 2.5. However, on heating to around 80 °C for nearly an hour, a white colored solid separated out. Also the addition of $CdCl_2$ solution to the potassium titanyl oxalate solution did not yield any solid product. However, when the pH of the solution was adjusted from 2 to 3, by the addition of ammonia solution, a white colored precipitate was obtained. The precipitates obtained in all the above cases were digested and filtered. The air dried powders were then subjected to various analyses.

2.2. Characterization

The thermal analysis studies in air and flowing nitrogen were carried out on a combined TG/DTA instrument Shimadzu model DTG-60 employing a heating rate of 10 °C/min. The FT-IR spectra were recorded in KBr medium using a Perkin–Elmer 2000 spectrometer. The powder X-ray diffraction patterns were recorded using a Philips X'Pert diffractometer as well as a Bruker D8 high resolution diffractometer employing Cu Kα radiation at a scan rate of 1°/min. The FT-Raman spectra of the samples were recorded on a Ranishaw spectrometer equipped with a CCD camera detector and an Ar ion laser operating at 514.5 nm at a power level of 10 mW. The Brunauer, Emmett and Teller (BET) method has been used to determine the specific surface area by means of a nitrogen adsorption isotherm on a Micromeritics, ASAP 2000. The SEM micrograph of the sample was recorded on a JEOL 200 keV instrument and a Zeiss EVO 50 machine. The EDX analysis of the samples was carried out using a Cambridge scanning electron microscope with an EDX attachment.

3. Results and discussion

Since there is a report on the formation of a molecular precursor in the case of cobalt in the literature by Balyaev et al. [37], the very first reaction that we carried out was between cobalt(II) chloride and potassium titanyl oxalate solutions. The EDX spectrum of the pale pink precipitate, obtained from this reaction, showed the ratio between Co and Ti to be 1:1 (Fig. 1a). The thermal analysis of the precursor in air showed that the mass loss took place in two major steps. This behavior is typical of metal oxalates and the total mass loss of 61% might correspond to $CoTiO_3$ or a physical mixture of

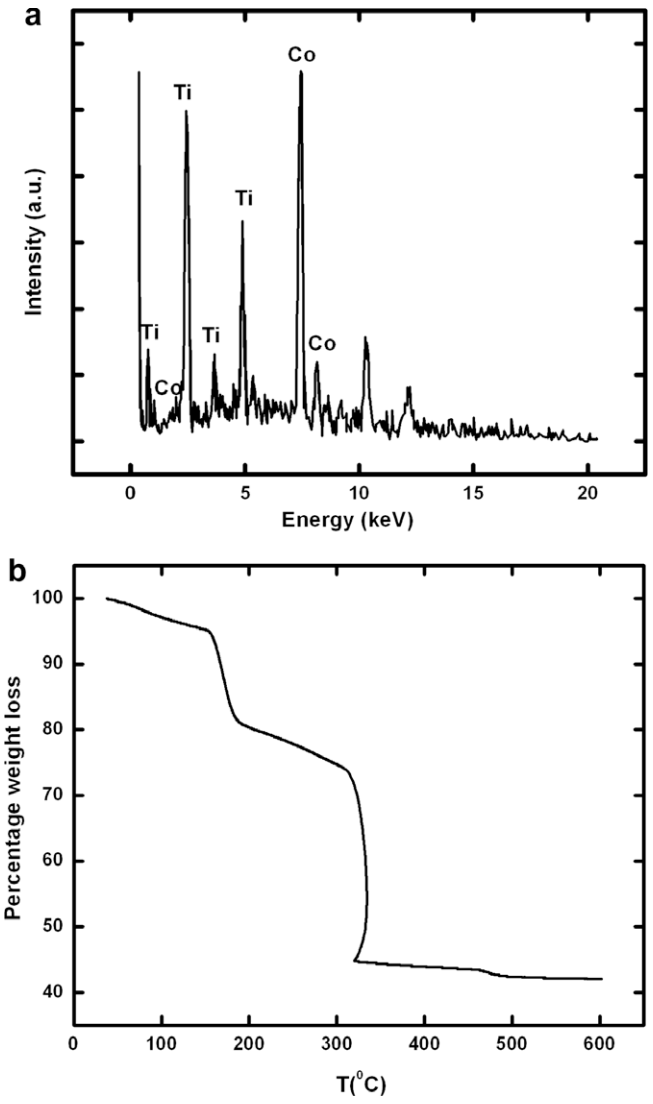


Fig. 1. (a) EDX spectrum of the precursor containing cobalt and titanium oxalates. (b) Thermogravimetric analysis of the precursor obtained from the reaction between solutions of $CoCl_2 \cdot 2H_2O$ and potassium titanyl oxalate in air.

CoO and TiO_2 as decomposition products (Fig. 1b). Two thermal events, one endothermic and one exothermic, were observed accompanying the mass loss in the DTA experiments. However, Balyaev et al. [37] reported three thermal events, two endotherms and one exotherm, during the thermal decomposition in air. The small exotherm around 650 °C, which the authors ascribed to the crystallization of $CoTiO_3$, was not observed in our preparation.

The powder X-ray diffraction pattern of the precursor showed that the product was poorly crystalline, while the major reflections corresponded to cobalt(II) oxalate as per the JCPDS File No. 48-1069 (Fig. 2a). The precursor was decomposed in air as well as in nitrogen at different temperatures. Peaks due to Co_3O_4 and TiO_2 (anatase) were observed in the powder X-ray diffraction pattern of the product decomposed at 500 °C in nitrogen (Fig. 2b). $CoTiO_3$ was the major phase formed along with the Co_2TiO_4 phase when the precursor was decomposed at 1100 °C in air over 12 h (Fig. 2c) (JCPDS File No. 15-0866). The spinel structured Co_2TiO_4

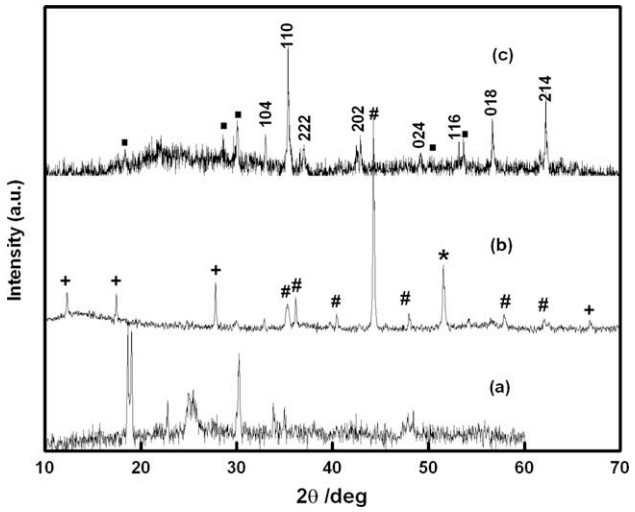


Fig. 2. Powder X-ray diffraction pattern of the Co precursor (a) at room temperature, or decomposed on (b) heating at 500 °C in N_2, (c) heating at 1100 °C in air. The peaks marked with + are due to TiO_2, peaks, peaks with ∗ are due to Co_3O_4, peaks marked with # are due to $CoTiO_3$ and peaks marked with ■ are due to Co_2TiO_4.

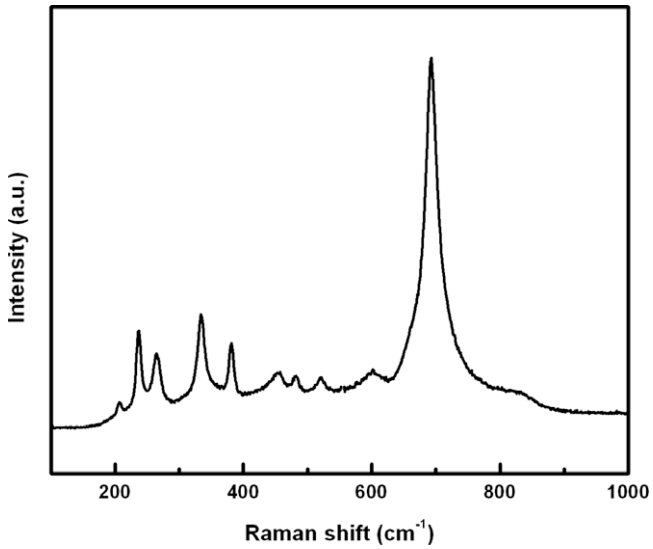


Fig. 3. Raman spectrum of $CoTiO_3$.

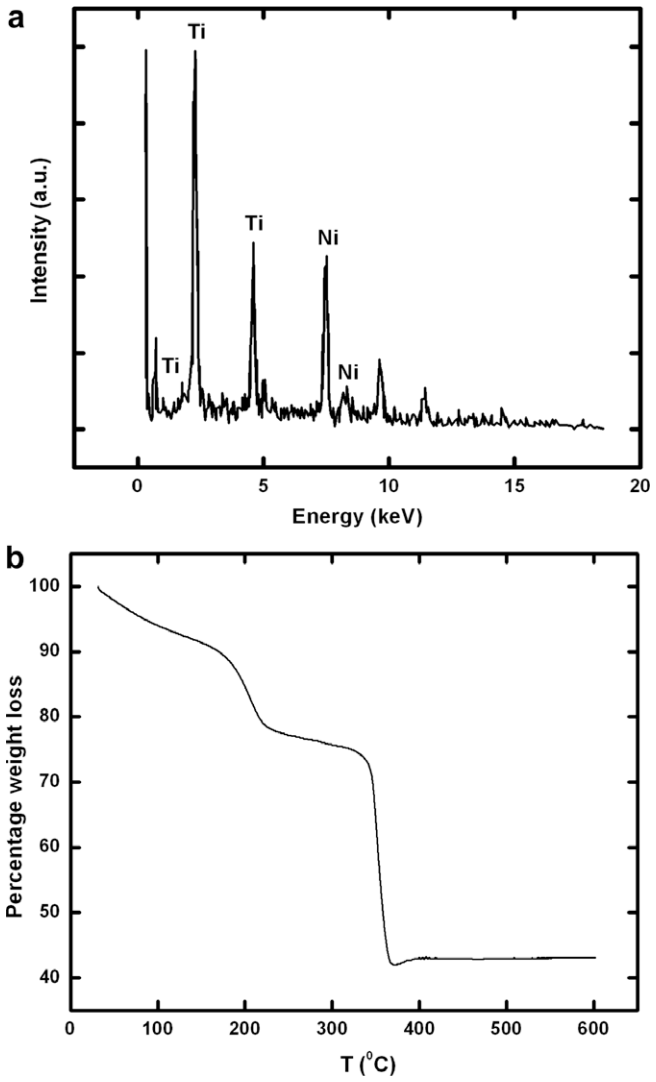


Fig. 4. (a) EDX spectrum of the precursor containing nickel and titanium oxalates. (b) Thermogravimetric analysis of the precursor obtained from the reaction between solutions of $NiCl_2 \cdot 2H_2O$ and potassium titanyl oxalate in air.

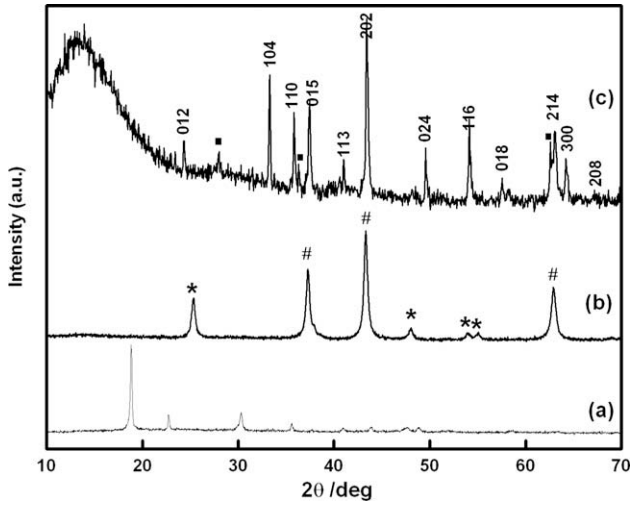


Fig. 5. Powder X-ray diffraction pattern of (a) the precursor containing nickel and titanium oxalates (b) heated at 500 °C (c) heated at 1100 °C The peaks marked with ∗ are due to TiO_2 anatase, the peaks marked with # are due to $NiTiO_3$ and peaks marked with ■ are due to Ni_2TiO_4.

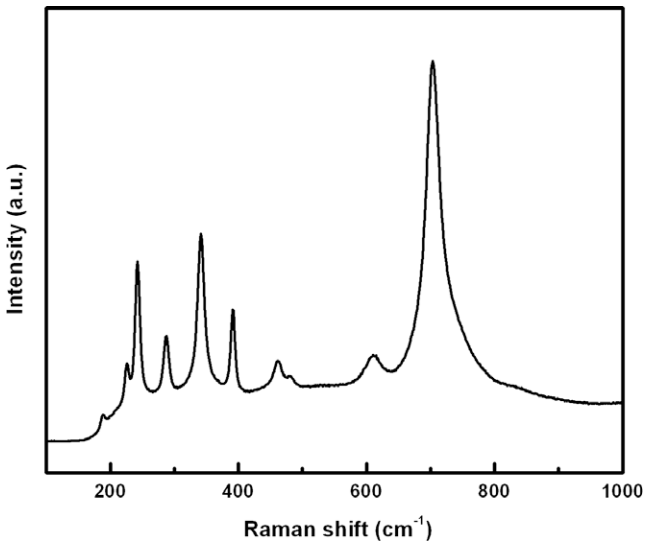


Fig. 6. Raman spectrum of $NiTiO_3$.

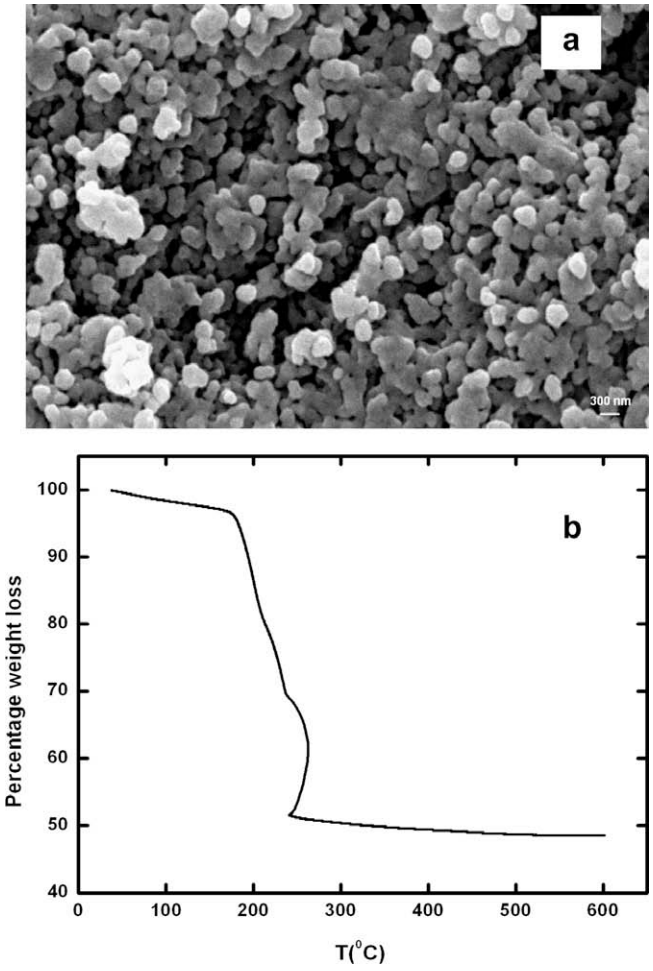


Fig. 7. (a) Thermogravimetric analysis of the product obtained from the reaction between solutions of $FeCl_2 \cdot 2H_2O$ and potassium titanyl oxalate in air. (b) SEM micrograph of precursor containing iron and titanium oxalates.

was reported to be a highly competitive phase with the ilmenite structured $CoTiO_3$ in the solid state reaction leading to $CoTiO_3$ [39]. Also, it was reported that repeated grinding and heating at 1200 °C between Co_3O_4 with TiO_2 was necessary to obtain pure $CoTiO_3$ [40]. However, in the present study, the precursor contained oxalates of cobalt and titanium, and therefore the in situ generation of the respective oxides might have taken place during the decomposition, leading to a diffusion controlled solid state reaction [38].

The FT-IR and FT-Raman spectra confirmed the formation of the ilmenite structure of $CoTiO_3$. The FT-IR spectrum exhibited two bands at 640 and 450 cm^{-1} due to O–Ti–O and Co–Ti–O bond formation, and showed the absence of metal carbonates. The Raman spectrum showed nine bands at 693, 603, 521, 480, 459, 383, 335, 267 and 246 cm^{-1} (Fig. 3). As per the theoretical analysis, 10 Raman modes ($5A_g + 5E_g$) were expected for the ilmenite structure of $CoTiO_3$ [41].

The surface morphology and surface area of the precursor, from mixing nickel(II) chloride and potassium titanyl oxalate solutions, were examined by the SEM and BET methods, respectively. An agglomeration of the particles was observed in the SEM and the observed BET surface area value of 4 m^2/g also suggested agglomeration. The EDX analysis of the precursor showed the ratio between Ni and Ti to be 1:1 (Fig. 4a). The thermal analysis of the product in air is shown in Fig. 4b. The total mass loss of 56% at 600 °C suggested that $NiTiO_3$ or a mixture of NiO and TiO_2 might be the decomposition products. The powder X-ray diffraction pattern of the precursor was highly crystalline as shown in Fig. 5a. The precursor contained peaks from nickel(II) oxalate (JCPDS File No. 47-0798) showing no indication of the presence of titanyl oxalate. This may be due to the higher scattering power of nickel (26) compared with titanium (18) [42]. The powder X-ray diffraction pattern of the precursor decomposed at 500 °C showed peaks due to NiO and the anatase form of TiO_2 (Fig. 5b). When this product was heated at 950 °C for 12 h in air, evolution of ilmenite $NiTiO_3$ was observed. The major peaks matched with JCPDS File No. 89-7131. Further heat treatment at 1100 °C for 12 h in air resulted in yellow colored $NiTiO_3$ (JCPDS File No. 33-0960) with a few peaks from Ni_2TiO_4 and one unidentified impurity (Fig. 5c).

The strong bands at 643 and 473 cm^{-1} in the FT-IR spectrum could be assigned to O–Ti–O and Ni–O–Ti bond formation. Ilmenite $NiTiO_3$ exhibited ten sharp bands in FT-Raman spectrum at 187, 224, 242, 289, 340, 391, 456, 498, 610 and 703 cm^{-1}, as reported earlier (Fig. 6) [41]. In our preparation, the anatase form of TiO_2 was generated in situ and the phase pure product was obtained at 1100 °C. In the standard ceramic method for the preparation

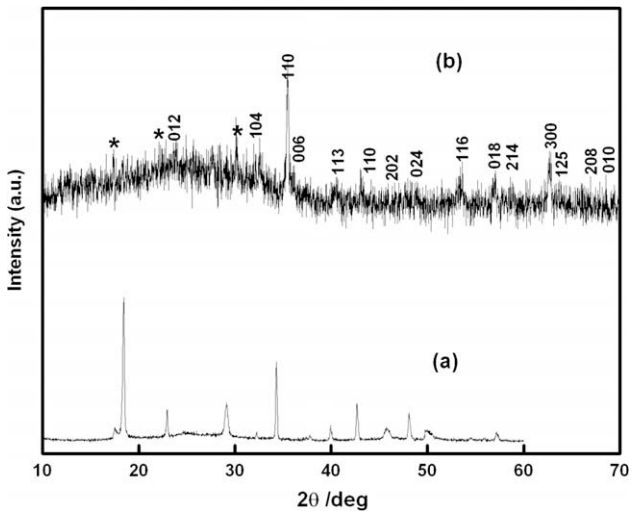


Fig. 8. Powder X-ray diffraction pattern of (a) the precursor containing the (Fe + Ti) oxalates, (b) heated at 600 °C. The peaks marked with * are due to Fe_3O_4.

of $NiTiO_3$, repeated heating at a high temperature of 1475 °C was required [40]. In the present method, the pure product can be obtained at 1100 °C.

The SEM micrograph of the yellow colored solid, obtained from the reaction of iron(II) chloride and potassium titanyl oxalate solution, showed agglomeration of particles (Fig. 7a). The thermal analysis was performed in nitrogen atmosphere to prevent the oxidation of Fe^{2+} during decomposition. The decomposition showed a total weight loss of 48.6% in two steps in nitrogen as shown in Fig. 7b. The decomposition was complete before 400 °C. The powder X-ray diffraction pattern of the precursor corresponded to iron(II) oxalate (Fig. 8a) (JCPDS File No. 14-0762). A brown black colored solid was obtained when the precursor was heated at 600 °C in flowing nitrogen for 12 h. The powder X-ray diffraction showed that the major phase was ilmenite $FeTiO_3$ (JCPDS File No. 29-0733) with a few peaks due to Fe_3O_4 (Fig. 8b).

Evidence for the presence of Fe–O–Ti and O–Ti–O bonds was obtained from the FT-IR spectrum of $FeTiO_3$ which showed strong bands at 480 and 570 cm^{-1}. The FT-Raman spectrum of $FeTiO_3$ showed nine bands at 233, 260, 301, 356, 404, 453, 480, 624 and 719 cm^{-1}, as shown in Fig. 9. Among the co-precipitation methods used for preparing $FeTiO_3$, hydroxide precipitation was found to be very sensitive to the amount of precipitant, and carbonate co-precipitation required higher decomposition temperatures to yield the final oxide [22]. However, in the present method the amount of precipitant did not pose a problem because no extra precipitating agent was used. In addition to this, the formation of ilmenite $FeTiO_3$ was observed at temperatures as low as 600 °C.

The thermal analysis of the white solid, obtained in case of manganese, was carried out in flowing nitrogen to prevent oxidation similar to iron containing titanates. The thermal decomposition of the precursor exhibited a total mass loss of 46% in two steps (Fig. 10). The powder X-ray diffraction pattern of the precursor matched that of manganese(II) oxalate (Fig. 11a) (JCPDS File No. 14-0713). Decomposing the precursor at 500 °C in nitrogen for 10 h resulted in the ilmenite form of $MnTiO_3$ (Fig. 11b), the peaks matching well with JCPDS File No. 29-0902 with a broad hump around $2\theta \sim 25°$. When the precursor was decomposed at 600 °C for 10 h this resulted in the muddy brown colored ilmenite $MnTiO_3$ with the removal of the hump (Fig. 11c).

In the FT-IR spectrum strong bands at 533 and 620 cm^{-1} were present, which can be assigned to Mn–O–Ti and O–Ti–O vibrational modes, respectively. The FT-Raman spectrum showed seven bands at 234, 273, 335, 452, 527 and 695 cm^{-1}, with the most intense one at 695 cm^{-1} (Fig. 12) as observed by others [18]. The synthesis of $MnTiO_3$ by the ceramic method required temperatures as high as 1200 °C [19]. Therefore the present mode of synthesis has significant advantages over the ceramic method.

The white colored solid, obtained from the reaction between cadmium(II) chloride and potassium titanyl oxalate solutions, was subjected to thermal analysis in air. The plot of the percentage mass loss with temperature is shown in Fig. 13. The mass loss took place in three steps, the first one was attributed to the removal of water molecules followed by the release of gaseous products such as CO and CO_2. The total mass loss of 48% suggested $CdTiO_3$ might be the end product. The powder X-ray diffraction of the precursor was highly crystalline, showing the presence of cadmium(II) oxalate (JCPDS File No. 14-0712) (Fig. 14a). When the precursor was decomposed at 600 °C in air for 6 h, it resulted in ilmenite $CdTiO_3$, which was dirty white in color (Fig. 14b) (JCPDS File No. 29-0277), along with peaks of CdO. Further heating at 750 °C for 12 h in air improved the reduction in the intensity of the CdO peaks (Fig. 14c).

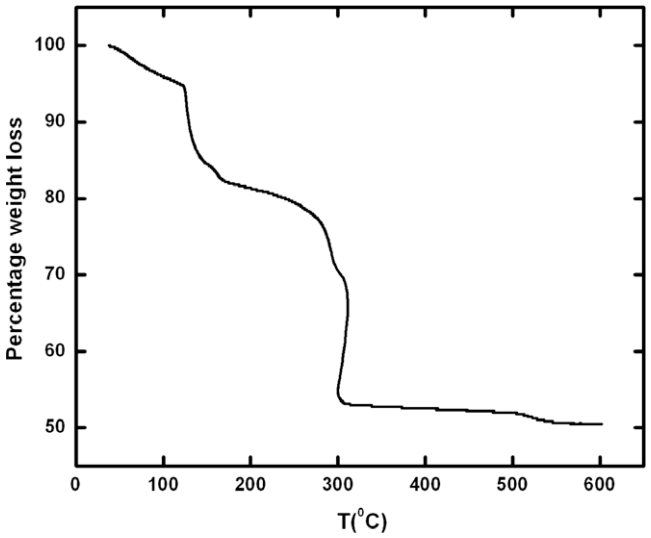


Fig. 10. Thermogravimetric analysis of the product obtained from the reaction between solutions of $MnCl_2 \cdot 2H_2O$ and potassium titanyl oxalate in air.

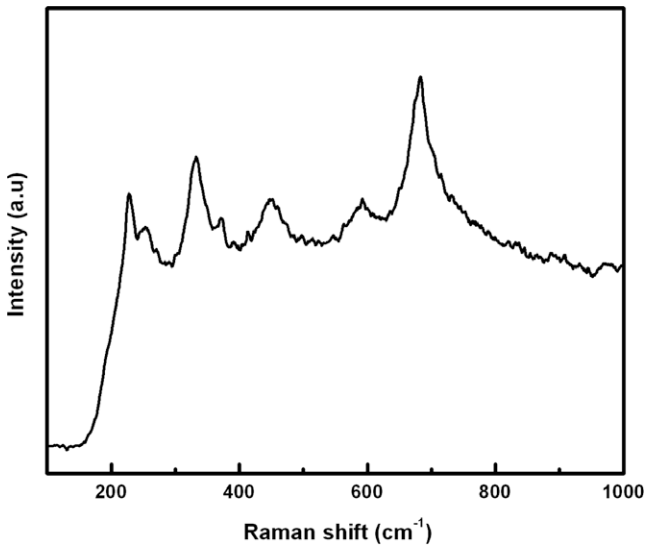


Fig. 9. Raman spectrum of $FeTiO_3$.

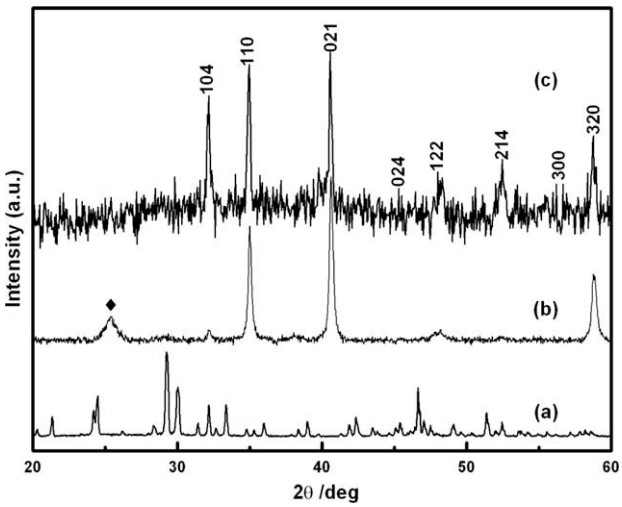


Fig. 11. Powder X-ray diffraction pattern of (a) the precursor containing the (Mn + Ti) oxalates (b) heated at 500 °C, the peak marked with was an unidentified impurity, (c) heated at 600 °C.

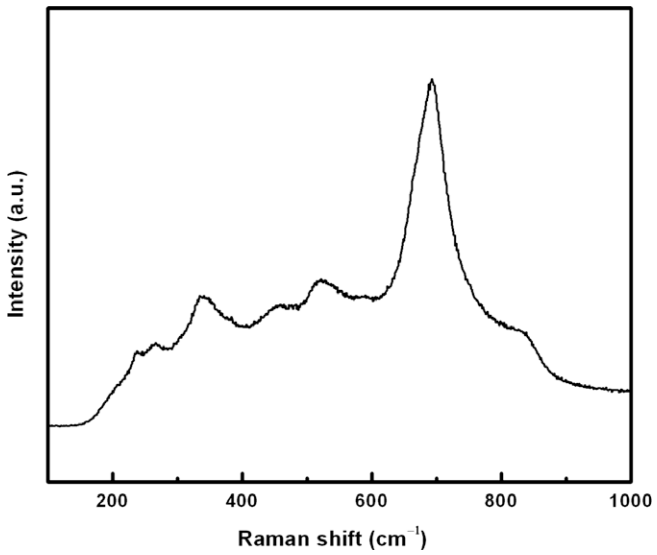


Fig. 12. Raman spectrum of $MnTiO_3$.

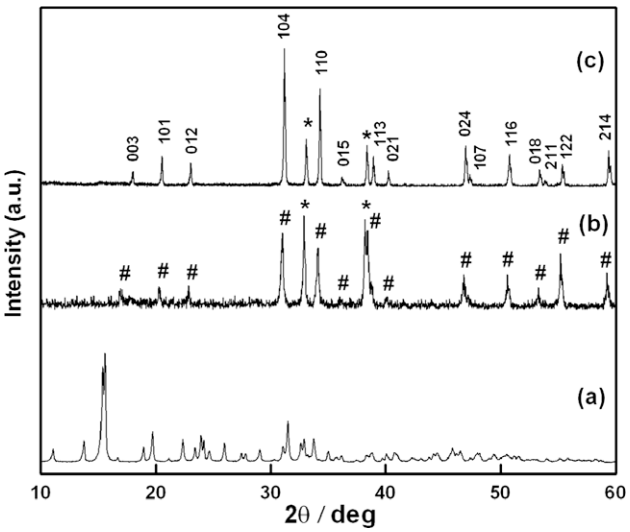


Fig. 14. Powder X-ray diffraction pattern of (a) the precursor containing the (Cd + Ti) oxalates (b) heated at 600 °C (c) heated at 750 °C. The peaks marked with # are due to $CdTiO_3$ and the peaks marked with ∗ are due to CdO.

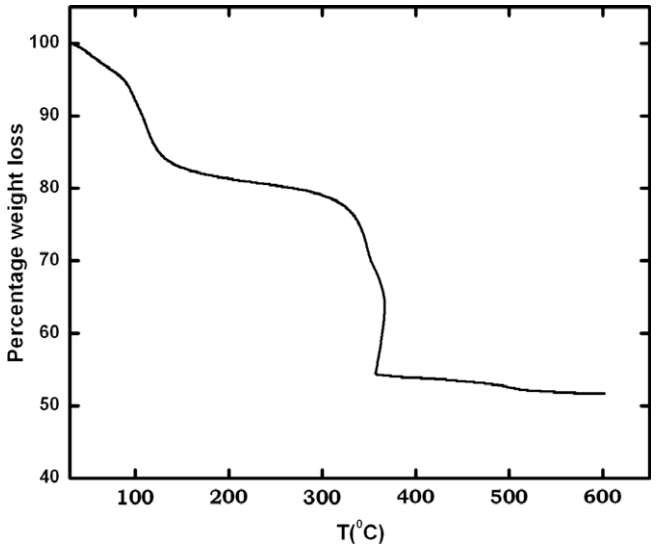


Fig. 13. Thermogravimetric analysis of the product obtained from the reaction between solutions of $CdCl_2 \cdot 2H_2O$ and potassium titanyl oxalate in air.

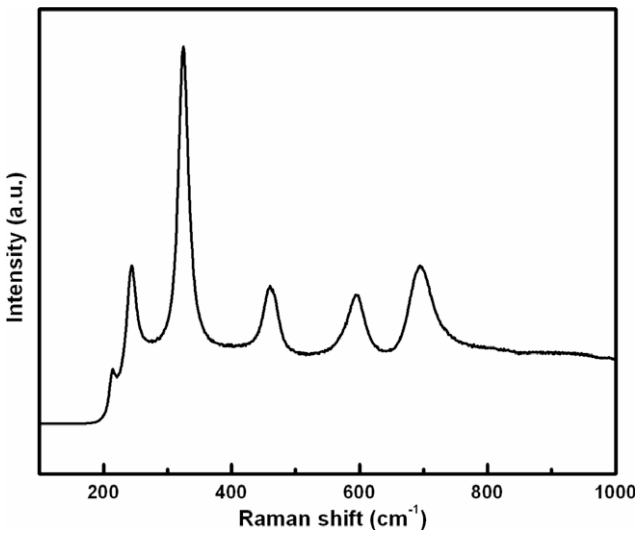


Fig. 15. Raman spectrum of $CdTiO_3$.

The FT-IR spectrum of the decomposed powder residue showed bands at 436 and 586 cm^{-1} and the FT-Raman spectrum exhibited seven bands at 213, 242, 324, 460, 593 and 694 cm^{-1}, as shown in Fig. 15. These bands were assigned to the ilmenite structure of $CdTiO_3$ [33]. The synthesis of the phase pure bulk $CdTiO_3$ possessing the ilmenite structure was reported to be difficult [32,33]. The volatile and toxic natures of CdO as well as the phase transition from the ilmenite to perovskite structure were cited to be some of the reasons for the difficulty. Bersani et al. [33] synthesized $CdTiO_3$, both in the ilmenite and perovskite forms, employing the sol–gel method in nitric acid. However, they observed the presence of rutile TiO_2 as an impurity together with the ilmenite phase even after heating at the higher temperature of 800 °C [33]. A modified sol–gel method using ethylene glycol and a hydrothermal method were found to be very effective in obtaining phase pure ilmenite $CdTiO_3$ [34,35]. In the present study, $CdTiO_3$ possessing the ilmenite structure was obtained from the very fine mixture of oxalates of cadmium and titanium by adjusting the pH to 3. Earlier, Prasad Rao and Suresh [32] attempted to prepare $CdTiO_3$ by oxalate co-precipitation by adjusting the pH to 7, which yielded a mixture of $CdTiO_3$, CdO and TiO_2.

4. Conclusions

The present study suggests that a molecular precursor of the formula M $[TiO(C_2O_4)] \cdot xH_2O$ may not be possible for M = Mn, Fe, Co, Ni and Cd by the reaction of their chlorides with potassium titanyl oxalate solution in the pH range 2–3. The addition of transition metal chlorides solution did not facilitate to stabilize the $TiO(C_2O_4)_2^{2-}$ species so as to result in the molecular precursor. The narrow pH range of the stability of the titanyl species may be one of the reasons for the unsuccessful attempt towards the molecular precursor preparation, but this may also arise from structural considerations. In the reported single crystal structure of $BaTiO(C_2O_4)$, the Ba^{2+} ion is both nine and ten coordinated by oxygen. The ionic radius of Ba^{2+} (1.50 Å) is comparable to the potassium ion under similar coordination environments. However, the ionic radii of the metal ions, Co^{2+}, Ni^{2+}, Fe^{2+}, Mn^{2+} and Cd^{2+} are

much smaller compared with either the Ba^{2+} or K^{+} ion. The smaller size of these ions might be destabilizing the molecules and consequently might prevent the molecular precursor formation. This chemical co-precipitation as oxalates has many advantages in synthesizing transition metal containing titanates. They can be obtained in the pure form at relatively low temperatures with very few heating cycles. The dual role of potassium titanyl oxalate as a precipitating agent as well as the titanium source avoids excess precipitant, thereby improving the purity of the final oxides as compared to the standard ceramic method.

Acknowledgements

The authors would like to thank UGC-DAE Consortium, Indore and Dr.C.Shivakumara, SSCU, IISC, Bangalore for their help in recording powder X-ray diffraction spectra and the University of Delhi for financial assistance under the "Scheme to strengthen R&D Doctoral program in Universities". Also thanks are due to Mr. Raman Malhotra of USIC, University of Delhi for recording the Raman spectra.

References

[1] C.N.R. Rao, J. Gopalakrishnan, New Directions in Solid State Chemistry, 2nd Ed., Cambridge University Press, UK, 1997.
[2] David Segal, J. Mater. Chem. 7 (1997) 1297.
[3] Masahiro Yoshimura, Jacques Livage (Guest Eds.), MRS Bulletin, September, 2000.
[4] Liliane G. Hubert-Pfalzgraf, J. Mater. Chem. 14 (2004) 3113.
[5] V.G. Kesler, Chem Commun. (2003) 1213.
[6] R. Roy, Solid State Ionics 32/33 (1989) 3.
[7] A.R. Phani, S. Santucci, Mater. Lett. 21 (2001) 1.
[8] D.J. Taylor, P.F. Fleig, R.A. Page, Thin Solid Films 408 (2002) 104.
[9] N. Dharamraj, H.C. Park, C.K. Kim, H.Y. Kim, D.R. Lee, Mater. Chem. Phys. 87 (2004) 5.
[10] Wendell E. Rhine, Robert B. Hallock, Chem. Mater. 4 (1992) 1208.
[11] D.S. Ginley, M.A. Butter, J. Appl. Phys. 48 (1997) 2019.
[12] T. Fujii, M. Kayano, Y. Takada, M. Nakanishi, J. Takada, Solid State Ionics 172 (2004) 289.
[13] Y. Zu, Y.Y. Lei, Chem. World 2 (1992) 49.
[14] O. Yamamoto, Y. Takeda, R. Kanno, M. Noda, Solid State Ionics 22 (1987) 241.
[15] T. Bein, K. Brown, G.C. Fye, C.J. Briler, J. Am. Ceram. Soc. 111 (1989) 7640.
[16] C.D. Chandler, C. Roger, M.J. Hampden-Smith, Chem. Rev. 93 (1993) 1205.
[17] G.W. Zhou, Y.S. Kang, Mater. Sci. Eng. C 24 (2004) 71.
[18] Z.Q. Song, S.B. Wang, W. Yang, M. Li, H. Wang, H. Yan, Mater. Sci. Eng. B 113 (2004) 121.
[19] J.J. Stickler, S. Kern, A. Wold, G.S. Heller, Phys. Rev. 164 (1967) 765.
[20] Hai-Yan He, Jian-Feng Huang, Li-Yun Cao, Jian-Peng Wu, Sensors Actuators B 132 (2008) 5.
[21] Y. Syono, S. Iti Akimoto, Y. Ishikawa, Y. Endoh, J. Phys. Chem. Solids 30 (1969) 1665.
[22] J. Mona, S.N. Kale, A.B. Gaikwad, A.V. Murugan, V. Ravi, Mater. Lett. 60 (2006) 1425.
[23] K. Iwauchi, M. Kiyama, T. Nakamura, Phys. Stat. Sol. (a) 127 (1991) 567.
[24] F. Pacheco, M. Gonzalez, A. Medina, S. Velumani, J.A. Ascencio, Appl. Phys. A. 78 (2004) 531.
[25] Lan Zhou, Shu-yi Zhang, Jian-chun Cheng, Li-de Zhang, Zhi Zeng, Mater. Sci. Eng. B 49 (1997) 117.
[26] Vadivel Murugan, Violet Samuel, S.C. Navale, V. Ravi, Mater. Lett. 60 (2006) 1791.
[27] Y.-J. Lin, Y.H. Chang, W.D. Yang, B.S. Tsai, J. Non-Cryst. Sol. 352 (2006) 789.
[28] K.P. Lopes, L.S. Cavalcante, A.Z. Simões, J.A. Varela, E. Longo, E.R. Leite, J. Alloys Comp, 2008, doi:10.1016/j.jallcom.2007.12.085.
[29] H. Taguchi, D. Matsuda, M. Nagao, K. Tanihara, Y. Miyamato, J. Am. Ceram. Soc. 75 (1992) 201.
[30] Xioxue Zhang, Hao Wang, Anaping Huang, Haiyan Xu, Yongcai Zhang, Dunbo Yu, Bo Wang, Hui Yan, J. Mater. Sci. 38 (2003) 2353.
[31] B.E. Watts, H. Dabkowska, B.M. Wanklyn, J. Cryst. Growth. 94 (1989) 125.
[32] A.V. Prasada Rao, M. Suresh, Ferroelectrics 229 (1999) 141.
[33] D. Bersani, P.P. Lottici, M. Canali, A. Montenero, G. Gnappi, J. Sol–Gel Sci. Technol. 8 (1997) 337.
[34] Hao Wang, XiaoXue Zhang, AnPing Huang, HaiYan Xu, ManKang Zhu, Bo Wang, Hui Yan, Masahiro Yoshimura, J. Cryst. Growth. 246 (2002) 150.
[35] A.R. Phani, M. Passacantando, S. Santucci, J. Mater. Sci. 35 (2000) 5295.
[36] P. Duran, F. Capel, J. Tattaj, D. Gutierrez, C. Moure, Solid State Ionics 141–142 (2001) 529.
[37] I.N. Balyaev, S.V. Bandareva, N.D. Skibina, Russ. J. Inorg. Chem. 13 (1968) 9.
[38] S.R. Dhage, Y.B. Khollam, H.S. Potdar, S.B. Deshpande, B.D. Sarwade, S.K. Date, Mater. Lett. 56 (2002) 564.
[39] A. Yankin, O. Vikhreva, V. Balakirev, J. Phys, Chem. Solids 60 (1999) 139.
[40] Prabhakaran Sreekumari Anjana, Mailadil Thomas Sebastian, J. Am. Ceram. Soc. 89 (2006) 2114.
[41] M.I. Baraton, G. Busca, M.C. Prieto, G. Ricchiardi, J. Solid State Chem. 112 (1994) 9–14.
[42] B.D. Cullity, Elements of X-ray diffraction, 2nd Ed., Addison-Wesley Publishing Company Inc., 1977.

Polyhedron 28 (2009) 586–592

Contents lists available at ScienceDirect

Polyhedron

journal homepage: www.elsevier.com/locate/poly

Synthesis, crystal structures, DNA binding and oxidative cleavage studies of copper(II) complexes of N_2S_2 tetradentate ligands

Si-Ping Tang [a,b], Lei Hou [a], Zong-Wan Mao [a,*], Liang-Nian Ji [a]

[a] MOE Key Laboratory of Bioinorganic and Synthetic Chemistry, School of Chemistry and Chemical Engineering, Sun Yat-Sen University, Guangzhou 510275, China
[b] Department of Chemistry and Material Science Hengyang Normal University, Hengyang Hunan 421008, China

ARTICLE INFO

Article history:
Received 17 September 2008
Accepted 25 November 2008
Available online 8 January 2009

Keywords:
Copper(II) complex
Aminothioether ligand
Crystal structure
DNA binding
Nuclease activity

ABSTRACT

Two new copper(II) complexes with aminothioether ligands, $[Cu(L^1)(ClO_4)](ClO_4)\cdot 0.5H_2O$ (**1**) and $[Cu(L^2)(H_2O)](ClO_4)_2\cdot H_2O$ (**2**) (L^1 = 2-benzyl-1,3-bis(aminoethylthio)propane and L^2 = 2-(4-butylbenzyl)-1,3-bis(aminoethylthio)propane), have been synthesized and characterized. The single crystal X-ray diffraction analysis reveals that both **1** and **2** adopt distorted square pyramidal geometries. The binding modes of both complexes with calf thymus DNA were investigated by UV–Vis and CD spectroscopies. The results show that both complexes mainly adopt an electrostatic attraction binding mode with DNA and the binding constants are $(1.62 \pm 0.02) \times 10^3$ and $(2.02 \pm 0.02) \times 10^3$ M^{-1}, respectively. Both complexes are able to cleave pBR322 plasmid DNA efficiently in the presence of ascorbic acid and the activity of **2** is higher than that of **1**. The DNA cleavage by **1** and **2** were inhibited strongly in the presence of DMSO and tert-butyl alcohol, which suggests that hydroxyl radicals are the reactive oxygen species for the cleavage.

© 2008 Elsevier Ltd. All rights reserved.

1. Introduction

DNA cleavage can occur by hydrolytic or oxidative pathways. Hydrolytic cleavage directly breaks the phosphodiester bond, but does not result in sugar damage [1,2]. Oxidative cleavage involves either oxidation of the deoxyribose moiety by abstraction of sugar hydrogen or oxidation of nucleobases [3]. Copper complexes have been widely used as nuclease mimics. Since $[Cu(OP)_2]^{2+}$ was reported to break the DNA chain in the presence of H_2O_2 (OP = 1,10-phenanthroline) [4–6], many mononuclear [7–18] and multi-nuclear copper(II) complexes [19–22] have been widely synthesized and some of them show efficient oxidative cleavage activities. Especially, many mononuclear copper(II) complexes of N_3 tridentate [23–25] and N_4 tetradentate ligands [26] have been recently investigated and are revealed to show efficient DNA cleavage activities in the presence of reducing agents.

However, studies involving aminothioether tetradentate ligand complexes are very limited [27]. Further, no investigations of DNA cleavage involving aminothioether S_2N_2 complexes with different hydrophobic groups on the backbone of the ligands have been reported. We have designed two new aminothioether ligands: 2-benzyl-1,3-bis(aminoethylthio)propane (L^1) and 2-(4-tert-butylbenzyl)-1,3-bis(aminoethylthio)propane (L^2), and have successfully synthesized two copper(II) complexes with these ligands, $[Cu(L^1)(ClO_4)](ClO_4)\cdot 0.5H_2O$ (**1**) and $[Cu(L^2)(H_2O)](ClO_4)_2\cdot H_2O$ (**2**). Because of the different hydrophobicity of the ligands, different DNA binding abilities and 'chemical nuclease' activities in the presence of ascorbic acid are expected for these two complexes.

2. Experimental

2.1. Materials and general information

2-Aminoethanethiol hydrochloride and ascorbic acid were purchased from Alfa Aesar Co. Ltd. $LiAlH_4$, distamycin and SOD were purchased from Sigma–Aldrich Chemical Co., pBR 322 DNA was purchased from MBI, tris(hydroxymethyl)aminomethane (Tris) and catalase were purchased from BBI, CT-DNA and ethidium bromide were purchased from Sino-American Biotechnology, 2,2,6,6-tetramethyl-4-piperidone monohydrate (TEMP) was purchased from Acros organic. Other reagents of analytical grades were obtained from domestic chemical corporations and were used without further purification except that thionyl chloride was purified by distillation. Milli-Q water was used in all physical measurement experiments.

Microanalyses (C, H and N) were carried out on an Elementar Vario EL elemental analyzer. ESI-mass spectra were recorded using a LCMS-2010A Liquid Chromatograph Mass Spectrometer. ^{1}HNMR spectra were collected on a Varian Mercury-plus 300 NMR spectrometer.

* Corresponding author. Tel.: +86 20 84113788; fax: +86 20 84112245.
E-mail address: cesmzw@mail.sysu.edu.cn (Z.-W. Mao).

0277-5387/$ - see front matter © 2008 Elsevier Ltd. All rights reserved.
doi:10.1016/j.poly.2008.11.057

2.2. Synthesis

2.2.1. 2-Benzyl-1,3-propanediol

$LiAlH_4$ (2.26 g, 59.6 mmol) was suspended in dry THF (150 mL) under N_2 at 0 °C. 2-Benzyldiethylmalonate [28] (5.37 g, 21.5 mmol) in dry THF (40 mL) was carefully added dropwise during constant stirring. The reaction was allowed to warm to room temperature and stirred for 12 h. Quenching was performed at 0 °C with constant stirring by careful dropwise addition of 2.26 mL H_2O, 2.26 mL 15% NaOH and 6.78 mL H_2O in sequence. The resulting precipitate was filtered off and washed with ethyl acetate (150 mL). The filtrate was dried with anhydrous Na_2SO_4, filtered and evaporated to afford a solid crude product, which was crystallized from petroleum/hexane (1:1) to give 2.84 g (79.8%) of 2-benzyl-1,3-propanediol as a white solid mp 66.9–67.5 °C (Ref. [29]. Mp 66–68 °C); ^1H NMR ($CDCl_3$, 300 MHz): δ 2.01–2.11 (m, 1H), 2.14 (brs, 2H), 2.64 (d, J = 7.5 Hz, 2H), 3.65–3.71 (m, 2H), 3.79–3.84 (m, 2H), 7.25 (m, 5H).

2.2.2. 2-(4-Tert-butylbenzyl)-1,3-propanediol

2-(4-Tert-butylbenzyl)-1,3-propanediol was synthesized from 2-(4-butylbenzyl)diethylmalonate [30], as described for 2-benzyl-1,3-propanediol, in 75.7% yield. ^1H NMR ($CDCl_3$, 300 MHz) δ 1.32 (s, 9H), 1.97 (brs, 2H), 2.03–2.14 (m, 1H), 2.60 (d, J = 7.5 Hz, 2H), 3.70–3.72 (m, 2H), 3.80–3.81 (m, 2H), 7.11 (d, J = 8.1 Hz, 2H), 7.30 (d, J = 8.4 Hz, 2H).

2.2.3. 2-Benzyl-1,3-dichloropropane

$SOCl_2$ (10 mL) was carefully added to a mixture of 2-benzyl-1,3-propanediol (2.00 g, 12.1 mmol) and pyridine (0.1 mL) at 0 °C in an ice-water bath with constant stirring. After the addition, the mixture was permitted to warm to room temperature and then refluxed at 70 °C for 12 h. The reaction mixture was then cooled to room temperature and the excess $SOCl_2$ was evaporated. The residue was treated with 40 mL H_2O and the mixture was extracted with ethyl acetate (50 mL × 3). The ethyl acetate extracts were combined, washed with 100 mL saturated $NaHCO_3$ solution and H_2O (100 mL × 2), then dried over anhydrous Na_2SO_4. The ethyl acetate was removed on a rotary evaporator to give 2-benzyl-1,3-dichloropropane as a pale yellow oil, yield 2.29 g (93.8%). ^1H NMR ($CDCl_3$, 300 MHz) δ 2.29–2.41 (m, 1H), 2.79 (d, J = 7.2 Hz, 2H), 3.54–3.60 (m, 2H), 3.66–3.71 (m, 2H), 7.19–7.34 (m, 5H).

2.2.4. 2-(4-Tert-butylbenzyl)-1,3-dichloropropane

2-(4-Tert-butylbenzyl)-1,3-dichloropropane was prepared from 2-(4-tert-butylbenzyl)-1,3-propanediol in 95.0% yield. The synthetic method was similar to that of 2-benzyl-1,3-dichloropropane. ^1H NMR ($CDCl_3$, 300 MHz) δ 1.32 (s, 9H), 2.31–2.35 (m, 1H), 2.75 (d, J = 7.2 Hz, 2H), 3.56–3.71 (m, 4H), 7.13 (d, J = 7.8 Hz, 2 H), 7.33 (d, J = 6.9 Hz, 2H).

2.2.5. 2-Benzyl-1,3-bis(aminoethylthio)propane (L^1)

L^1 was prepared by a modified procedure [31,32]. 2-Aminoethanethiol hydrochloride (4.42 g, 38.9 mmol) was added to a solution of sodium (1.79 g, 77.80 mmol) in absolute ethanol (25 mL) with stirring under N_2. The mixture was refluxed at 70 °C for 1 h and cooled to room temperature, and then KI (2.66 g, 16.00 mmol) was added. A solution of 2-benzyl-1,3-dichloropropane (1.63 g, 8.01 mmol) in 12 mL of absolute ethanol was added dropwise to the above mixture at 0 °C in an ice-water bath with constant stirring. After the addition, the mixture was again refluxed with stirring at 70 °C for 20 h under N_2, cooled and filtrated to remove the precipitate of sodium and potassium salts. The filtrate was concentrated to remove almost all of the solvent and H_2O (100 mL) was added to the residue. The strongly basic solution was extracted three times with 300 mL dichloromethane. The dichloromethane extracts were combined, washed three times with 300 mL H_2O, dried over anhydrous Na_2SO_4 and then the dichloromethane was removed on a rotary evaporator to give 2-benzyl-1,3-bis(aminoethylthio)propane (L^1) as a pale yellow oil, yield 2.15 g (94.3%). ESI-MS, m/z: 285.4 ($[M+H]^+$). This crude material was quite satisfactory for the preparation of the copper(II) complex.

2.2.6. 2-(4-Tert-butylbenzyl)-1,3-bis(aminoethylthio)propane (L^2)

L^2 was prepared in a similar procedure to that of L^1 from 2-(4-tert-butylbenzyl)-1,3-dichloropropane and 2-aminoethanethiol hydrochloride, in 96.1% yield. ESI-MS, m/z: 341.3 ($[M+H]^+$), 379.3 ($[M+K]^+$). This crude material was quite satisfactory for the preparation of the copper(II) complex.

Table 1
Crystallographic data and structural refinements for complexes **1** and **2**.

Complex	**1**	**2**
Formula	$C_{14}H_{25}Cl_2CuN_2O_{8.5}S_2$	$C_{18}H_{36}Cl_2CuN_2O_{10}S_2$
Formula weight (g/mol)	555.92	639.05
T (K)	293(2)	293(2)
Wavelength (Å)	0.71073	0.71073
Crystal system	monoclinic	monoclinic
Space group	$P2_1/c$	$P2_1/c$
a (Å)	11.758(2)	22.411(2)
b (Å)	10.231(1)	12.1513(9)
c (Å)	36.527(5)	10.3904(7)
β (°)	94.112(2)	95.259(1)
V (Å^3)	4383.0(1)	2817.6(3)
Z	8	4
D_{calc} (g cm^{-3})	1.685	1.506
μ (mm^{-1})	1.477	1.163
$F(000)$	2288	1332
Crystal size (mm)	0.49 × 0.43 × 0.10	0.46 × 0.28 × 0.10
2θ range for data collection (°)	4.48–54.18	1.82–52.00
Limiting indices	$-14 < h < 15$, $-13 < k < 10$, $-46 < l < 46$	$-27 < h < 27$, $-14 < k < 14$, $-12 < l < 12$
Reflections collected/unique [R_{int}]	13389/4765 = 0.0375	21358/5531 = 0.0311
Data/restraints/parameters	4765/0/267	5531/0/316
Goodness-of-fit on F^2	1.039	1.066
Final R_1[a], wR_2[b] indices [$I > 2\sigma(I)$]	R_1 = 0.0498, wR_2 = 0.1220	R_1 = 0.0501, wR_2 = 0.1435
R_1[a], wR_2[b] indices (all data)	R_1 = 0.0842, wR_2 = 0.1401	R_1 = 0.0621, wR_2 = 0.1569

[a] $R_1 = \sum||F_o| - |F_c||/\sum|F_o|$.
[b] $wR_2 = [\sum w(F_o^2 - F_c^2)^2/\sum w(F_o^2)^2]^{1/2}$.

Table 2
Selected bond lengths (Å) and bond angles (°) for complexes **1** and **2**.

Complex **1**		Complex **2**	
Cu1–N1	1.993(3)	Cu1–N1	2.021(3)
Cu1–N2	2.004(3)	Cu1–N2	2.013(3)
Cu1–S1	2.314(1)	Cu1–S1	2.309(1)
Cu1–S2	2.303(1)	Cu1–S2	2.3289(9)
Cu1–O1	2.428(3)	Cu1–O1W	2.243(3)
N1–Cu1–N2	96.6 (1)	N2–Cu1–N1	97.7 (1)
N1–Cu1–S2	171.2(1)	N2–Cu1–O1W	96.9(1)
N2–Cu1–S2	87.3(1)	N1–Cu1–O1W	94.9(1)
N1–Cu1–S1	86.9 (1)	N2–Cu1–S1	164.6(1)
N2–Cu1–S1	174.2(1)	N1–Cu1–S1	87.0 (1)
S2–Cu1–S1	88.59(4)	O1W–Cu1–S1	97.34(9)
N1–Cu1–O1	92.4 (1)	N2–Cu1–S2	87.37(9)
N2–Cu1–O1	86.2(1)	N1–Cu1–S2	168.2 (1)
S2–Cu1–O1	95.76(8)	O1W–Cu1–S2	95.05(9)
S1–Cu1–O1	98.33(8)	S1–Cu1–S2	85.45(4)

2.2.7. $[Cu(L^1)(ClO_4)](ClO_4) \cdot 0.5H_2O$ (**1**)

L^1 (0.29 g, 1.02 mmol), dissolved in 2 mL ethanol, was added to 2 mL ethanol solution of $Cu(ClO_4)_2 \cdot 6H_2O$ (0.51 g, 1.37 mmol) with stirring. A purple precipitate appeared immediately, which was filtrated and washed with ethanol several times, and a purple powder was obtained. The powder was recrystallized from MeOH, filtrated and dried in a vacuum desiccator, and 0.20 g purple microcrystals were obtained (34.9%). *Anal.* Calc. for $C_{14}H_{25}Cl_2CuN_2O_{8.5}S_2$: C, 30.25; H, 4.53; N, 5.04. Found: C, 30.69; H, 3.92; N, 5.17%. Single crystals suitable for X-ray analysis were obtained by slow evaporation of a methanol solution of complex **1**.

2.2.8. $[Cu(L^2)(H_2O)](ClO_4)_2 \cdot H_2O$ (**2**)

Complex **2** was prepared in a similar way to that of **1**, 0.34 g (1.0 mmol) L^2 gave 0.15 g complex **2** as purple microcrystals (23.5%). *Anal.* Calc. for $C_{18}H_{36}Cl_2CuN_2O_{10}S_2$: C, 33.83; H, 5.68; N, 4.38. Found: C, 34.18; H, 5.60; N, 4.49%. Evaporating a methanol solution of **2** gave single crystals for X-ray analysis.

Caution: Copper(II) perchlorates are potentially explosive chemicals, and they should be prepared in small quantities and handled with care.

2.3. X-ray crystallography

Single crystals, sized $0.49 \times 0.43 \times 0.10$ mm and $0.46 \times 0.28 \times 0.10$ mm for **1** and **2**, respectively, were used for X-ray diffraction analyses. Data collections of **1** and **2** were performed with Mo Kα ($\lambda = 0.71073$ Å) radiation on a Bruker AXS SMART CCD area detector diffractometer at 293(2) K. An absorption correction by multi-scan was applied to the intensity data. The structures were solved by direct methods and the heavy atoms were located from the E-map. The remaining non-hydrogen atoms were determined from the successive difference Fourier syntheses. The non-hydrogen atoms were refined anisotropically, whereas the hydrogen atoms were generated geometrically with isotropic thermal parameters. The structures were refined on F^2 by full-matrix least-squares methods using the SHELXTL-97 program package [33]. Crystallographic details, and selected bond lengths and angels for **1** and **2** are given in Tables 1 and 2, respectively.

2.4. CD spectroscopy

CD spectra of CT-DNA were recorded on a Jasco J-810 spectropolarimeter at room temperature in the absence or the presence of 20 μM and 40 μM complexes **1** or **2** ($r = 0.2$, 0.4. r = [complex]/[DNA]). The concentration of DNA was 100 μM and 5 mM Tris–50 mM NaCl solution (pH 7.5) was the buffer solution. Each test solution was scanned at a speed of 50 nm min^{-1} for four repetitions and the average spectra were used. The buffer background was subtracted automatically.

2.5. UV–Vis spectroscopy

UV–Vis spectra were recorded on a Varian Cary 300 UV–Vis spectrophotometer attached to a Cary Peltier temperature controller. The concentration of the complexes was 60 μM and the buffer solution was the same as that of CD spectroscopy.

2.6. DNA cleavage

The cleavage of pBR322 plasmid DNA (38 μM bp) was performed in 20 mM Tris buffer (pH 7.2) by treating DNA with a certain concentration of the complex in the presence of 20-fold ascorbic acid. The total volume of 10 μL sample solution was incubated in a sealed plastic vessel and the cleavage was carried out at 37 °C for 1 h, then 4 μL loading buffer (0.05% bromophenol blue, 50% glycerol and 2 mM EDTA) was added. The sample was stored at −20 °C for preservation, and then it was loaded onto a 0.9% agarose gel and electrophoresed at a constant voltage of 120 V for 100 min in TBE buffer (100 mM Tris–2 mM EDTA–HBO_3, pH 8.3). DNA bands were visualized in an electrophoresis documentation and analysis system 120.

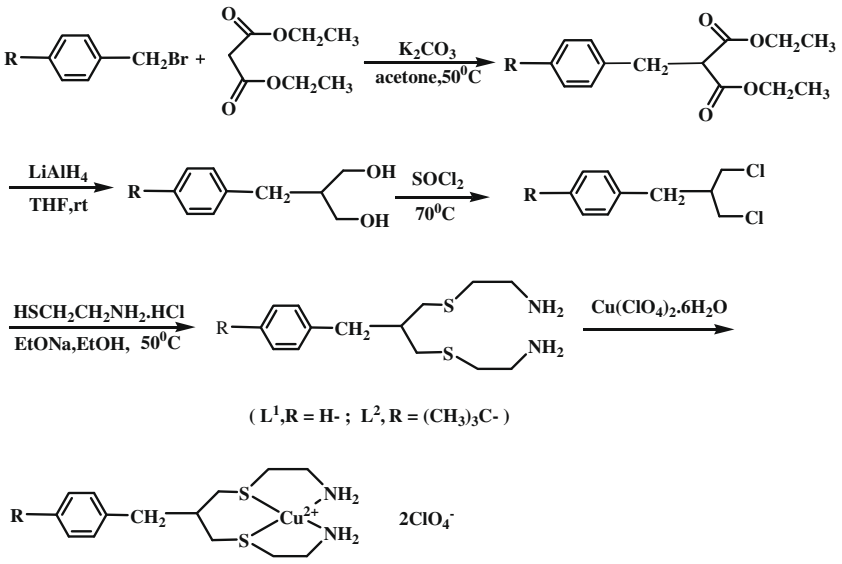
3. Results and discussion

3.1. Preparation of the Cu(II) complexes

The synthesis route for ligands L^1 and L^2, and their complexes **1** and **2**, is shown in Scheme 1. **1** and **2** are stable in air and are soluble in water and common polar organic solvents. The electronic absorption of **1** is similar to that of **2** (Fig. S2 in the Supporting data). Both complexes display an absorption band at 244 nm (**1** ε 4950 M^{-1} cm^{-1}, **2** ε 5290 M^{-1} cm^{-1}) which was assigned as the π-π^* transition of benzene of the ligands. The strong absorption peaks of 322 nm (**1** ε 9230 M^{-1} cm^{-1}) and 323 nm (**2** ε 9620 M^{-1} cm^{-1}) were assigned as metal-to-thioether transfer transitions. At 567 nm, both **1** and **2** showed a weak electronic absorption band (**1**, ε 674 M^{-1} cm^{-1}; **2**, ε 723 M^{-1} cm^{-1}), typical for d–d transitions of Cu(II) [34,35].

3.2. Crystal structure of complexes *1* and *2*

The molecular structure of complex **1** consists of one $[CuL^1(ClO_4)]^+$ unit, one free ClO_4^- anion and half of one water molecule, as shown in Fig. 1. In **1**, the Cu(II) ion has a geometric parameter of $\tau = 0.05$ and suggests a distorted square pyramidal geometry [36], with two N and two S atoms of L^1 located in the basal plane and one O atom from one of ClO_4^- anions in the apical position with a Cu–O distance of 2.428(3) Å (Table 2). The Cu–S and Cu–N distances are within the range 2.303(1)–2.314(1) Å and 1.993(3)–2.004(3) Å, respectively, comparable with the distances in complexes containing 14-member S_4^- [2.303(1) Å] [37] or N_4-donor [1.976(1) Å] ligands [38]. Each L^1 ligates one metal ion with two N and two S atoms to form a 12-member macrometallocycle, moreover, L^1 in **1** is significantly non-planar with the terminal phenyl ring pointing to the C3 atom [C4–C8–C9 113.4(4)°] due to intramolecular C–H···π interactions between them (H···π 2.608 Å), which also leads to the obvious slant between the terminal phenyl ring and the CuN_2S_2 plane with a dihedral angle of 48.5°. In the solid state, the molecules of **1** are stabilized by intermolecular hydrogen bond interactions (Fig. S3 in the Supporting data). Each water O1w atom acts as hydrogen acceptors to bond two –NH groups



Scheme 1. Synthetic route for the ligands and their copper(II) complexes.

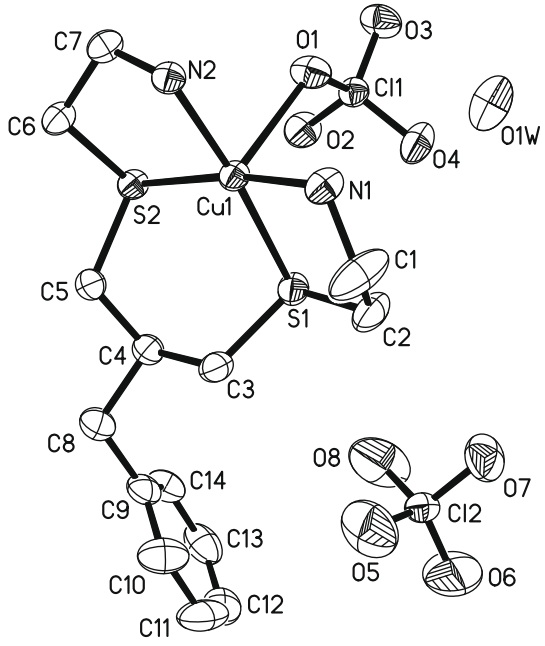


Fig. 1. View of the molecular structure of **1** with displacement ellipsoids drawn at the 30% probability level. The H atoms are omitted for clarity.

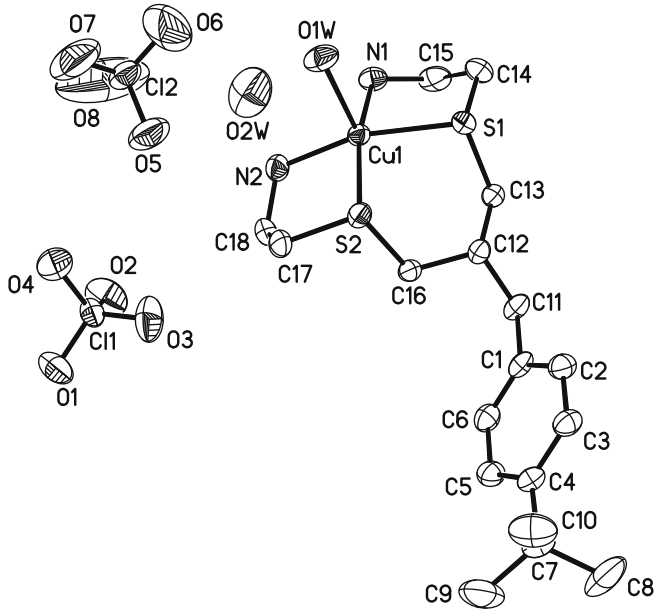


Fig. 2. View of the molecular structure of **2** with displacement ellipsoids drawn at the 30% probability level. The H atoms are omitted for clarity.

[N1···O1w 2.933 Å] from two different L^1 ligands. Meanwhile, O1w also serves as a donor to hydrogen bond to two coordinated ClO_4^- anions, and thus each water molecule can be viewed as a four-connected node to connect four $[CuL^1(ClO_4)]^+$ units to generate a two-dimensional supramolecular structure [O1w···O2 2.832 Å].

The crystal structure of complex **2** is similar to that of **1**, as shown in Fig. 2, it contains one $[CuL^2(H_2O)]^{2+}$ cation, two ClO_4^- anions and one water solvate. The Cu(II) ion in **2** also has a distorted square pyramidal geometry ($\tau = 0.06$) with two N and two S atoms of L^2 forming the basal plane, however the apical position is occupied by one water ligand with a Cu–O distance of 2.243(3) Å (Table 2). The Cu–S and Cu–N distances are in the regions 2.309(1)–2.329(9) and 2.013(3)–2.021(3) Å, respectively, similar to those of **1**. Just as for L^1 in **1**, L^2 is also non-planar in **2** owing to intramolecular C–H···π interactions (H···π 2.673 Å) between the terminal phenyl ring and the H16A atom of the –CH group [C1–C11–C12 113.9(3)°]. The terminal phenyl ring is tilted about the CuN_2S_2 plane with a dihedral angle of 33.4°, smaller than that of L^1 in **1**. In the crystal packing of **2**, a strong hydrogen bond is formed between the coordinated water O1w as a hydrogen donor and a solvent water molecule [O1w···O2w 2.652 Å] to give a $(H_2O)_2$ dimer, which is further hydrogen-bonded to two different ClO_4^- anions [O1w···O8 3.008 Å and O2w···O2 2.794 Å]. Additionally, the ClO_4^- anions are involved in intermolecular hydrogen bonding interactions with two –NH groups (N1···O4 3.049 Å and N1···O7 3.029 Å)

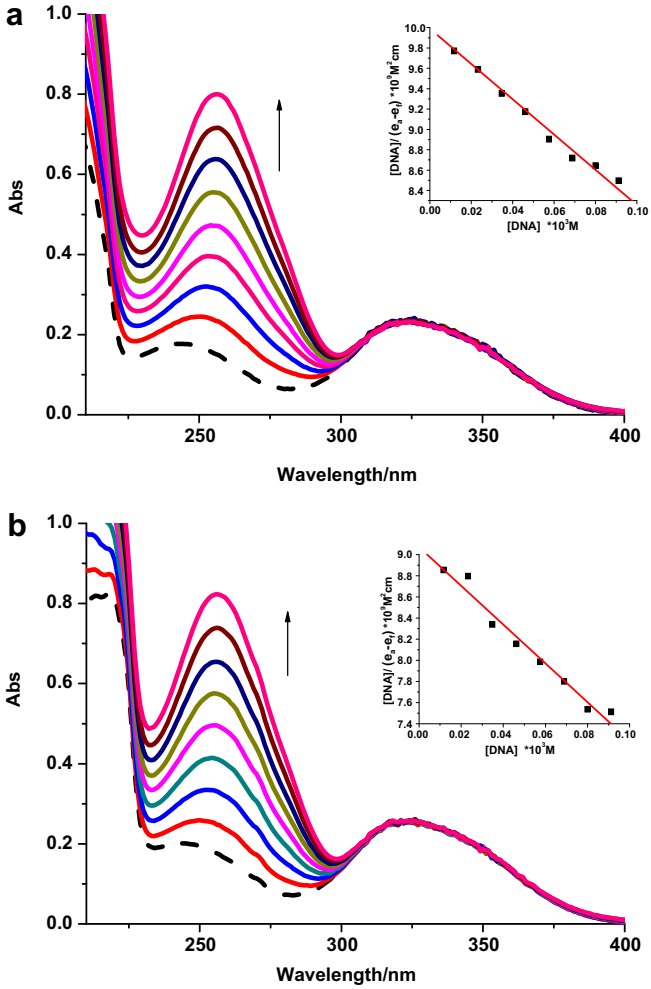


Fig. 3. Absorption spectra of 6.0×10^{-5} M **1** (a) and **2** (b) in the absence (dot line) and the presence (solid line) of increasing amounts of CT-DNA ($0–8 \times 10^{-5}$ M) in 5 mM Tris–50 mM NaCl aqueous buffer solution (pH 7.5) at 25 ± 0.1 °C.

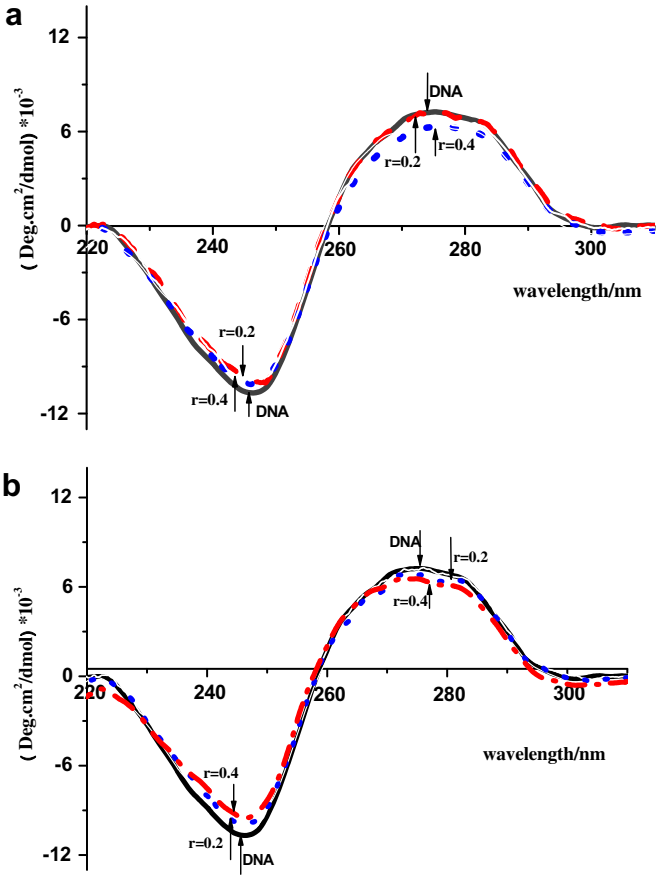


Fig. 4. CD spectra of CT-DNA (1.0×10^{-4} M) in the absence and the presence of **1** (a) and **2** (b) at ratio [complex]/[DNA] = 0.2, 0.4 in 5 mM Tris–50 mM NaCl aqueous buffer solution (pH 7.5).

of L^2 from a neighboring $[CuL^2(H_2O)]^{2+}$ unit to generate a one-dimensional zig-zag chain (Fig. S4 in the Supporting data).

3.3. Interaction with CT-DNA

The interactions between both complexes and CT-DNA were evaluated by UV–Vis spectroscopy titration and CD spectroscopy. The UV–Vis spectra are shown in Fig. 3. In both spectra of complexes **1** and **2**, hyperchromicity was observed on the addition of CT-DNA ($0–8 \times 10^{-5}$ M). The hyperchromicity argued that the binding mode of these two complexes as 6.0×10^{-5} M solutions towards CT-DNA should not be intercalation, since intercalation would bring on hypochromicity as a result of the stacking effect of π electrons [39], which leads to a decrease of the transition probability of π electrons, and ultimately results in a decrease of absorption. The intrinsic binding constants (K_b) of **1** and **2** were calculated as $(1.62 \pm 0.02) \times 10^3$ and $(2.02 \pm 0.02) \times 10^3$ M^{-1}, respectively, which are much smaller than those reported for typical intercalators (e.g. EB-DNA, $\sim 10^6$ M^{-1}) [40,41], but are comparable with some reported non-intercalators [22,42]. The quite low K_b values do not favor intercalation binding. Furthermore, the higher K_b value of **2** indicates the interaction of **2** with DNA is stronger than that of **1**.

The interaction between the two complexes and CT-DNA was further studied by CD spectroscopy (Fig. 4). The CD spectrum of CT-DNA consists of a positive band at 277 nm due to base stacking and a negative band at 245 nm because of helicity, which is characteristic of DNA in the right-handed B form [26]. Intercalation of small molecules with DNA enhances the intensities of both bands, while groove binding and electrostatic interactions show little or no perturbations to the base stacking and helicity bands. With increasing concentrations of **1** and **2**, both positive and negative bands show little change, which implies a non-intercalative mode between DNA and complexes again. The cationic core of **1** and **2** could exert a strong electrostatic attraction to the anionic phosphate backbone of DNA, thus, the electrostatic binding mode is highly possible. This inference was further demonstrated in the following section.

3.4. DNA cleavage studies

The oxidative DNA cleavage activities of complexes **1** and **2** were studied in the presence of ascorbic acid. Fig. 5 exhibits the concentration dependence of the cleavage reactions after 60 min incubation (pH 7.2, 37 °C). Comparing the ligands with **1** and **2**, both ligands L^1 and L^2 showed very low nuclease activity even at a concentration of 100 μM. For complex **1**, the amount of form II DNA increased with the increase of complex concentration, form I DNA disappeared completely and form III started to appear when the complex concentration reached 50 μM. Complex **2** behaved similarly to **1** except that the appearance of form III DNA occurred at a lower concentration (40 μM), and at 40 μM form I DNA was converted to form II and form III completely. This suggests that **2** exhibits slightly higher nuclease activity than **1**. The difference of

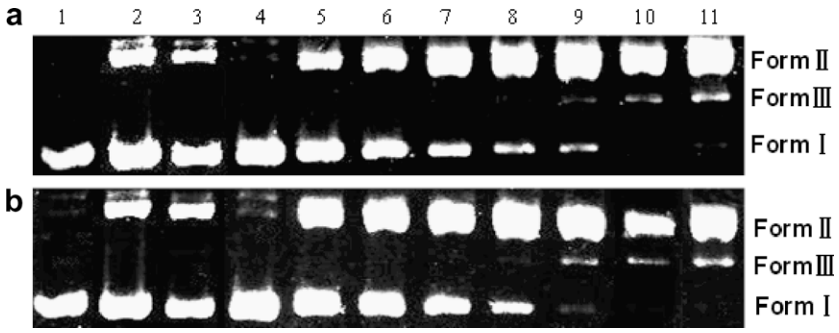


Fig. 5. Cleavage of pBR322 DNA by **1** (a) and **2** (b) in the presence of ascorbic acid. DNA (38 μM bp) was incubated with **1**, **2** for 60 min in 20 mM Tris–$HClO_4$/0.1 M $NaClO_4$ aqueous buffer solution (pH 7.2) at 37 °C. Lane 1, DNA control; lane 2, DNA + ascorbic acid (2 mM); lane 3, DNA + 100 μM ligand + ascorbic acid (2 mM); lane 4, DNA + complex (100 μM); lane 5–11, DNA + complex (5, 10, 20, 30, 40, 50 and 70 μM) + ascorbic acid (20-fold of complex).

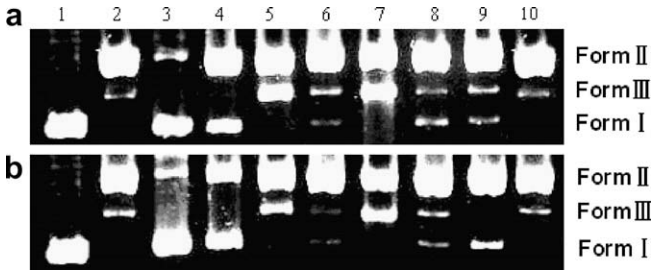


Fig. 6. Cleavage of pBR322 DNA by 50 μM **1** (a) and **2** (b) in the presence of different inhibitors with a 20-fold excess of ascorbic acid. DNA (38 μM bp) was incubated with **1** and **2** for 60 min in 20 mM Tris–$HClO_4$/0.1 M $NaClO_4$ aqueous buffer solution (pH 7.2) at 37 °C. Lane 1, DNA control; lane 2, no inhibitor; lane 3, 0.5 M DMSO; lane 4, 0.5 M t-BuOH; lane 5, 1.2 mM His; lane 6, 0.5 mM TEMP; lane 7, 500 U/mL catalase; lane 8, 500 U/mL SOD; lane 9, 10 μM distamycin; lane 10, 10 μM methyl green.

the nuclease activities of both complexes may be ascribed to the influence of the substituted groups in L^1 and L^2. Compared with the structure of **1**, complex **2** has a hydrophobic t-butyl group on the backbone of L^2, which makes **2** interact with DNA more effectively. This suggestion has been supported by their K_b values.

The reactive oxygen species were also investigated, as shown in Fig. 6. The strong inhibitions of DNA cleavage to complexes **1** and **2** were observed in the presence of the hydroxyl radical scavengers DMSO and tert-butyl alcohol, indicating that hydroxyl radicals are responsible for the cleavage. The singlet oxygen scavengers histidine and 2,2,6,6-tetramethyl-4-piperidone monohydrate, and the hydrogen peroxide scavenger catalase failed to inhibit cleavage, suggesting that singlet oxygen and hydrogen peroxide are not likely to be the reactive oxygen species. A weak inhibition was observed by the addition of the superoxide anion radical scavenger SOD, arguing that the superoxide anion radical may play a role in the cleavage, but is not a major active species.

The minor groove binding agent distamycin and major groove binding agent methyl green were used to probe the potential interacting site of the small molecular complexes **1** and **2** with DNA, which are shown in Fig. 6. The major groove binding agent methyl green did not affect the cleavage activity of **1** and **2** at all (lane 10), and the minor groove binder distamycin displayed different degrees of inhibition in the DNA cleavage (lane 9): for **1**, form I appeared but form III was not changed at all. However, for **2**, form III disappeared completely, and form I was present to a much greater extent than for **1**, which suggests that distamycin shows a certain cleavage but not complete inhibition for both complexes and displays a stronger inhibition ability for **2**. The conclusion can then be drawn that the groove binding mode exists but it is not the major binding mode for both complexes. So, together with the results of the UV–Vis and CD spectroscopies, electrostatic attraction should be the major binding mode.

4. Conclusion

The present work describes the synthesis, characterization and DNA binding studies of two new CuS_2N_2 complexes. Both complexes have similar structures and adopt distorted square pyramidal geometries, having plentiful N–H···Ow, Ow–H···O (**1**) and Ow–H···Ow, Ow–H···O and Ow–H···N (**2**) intermolecular hydrogen bonds linking the mononuclear molecules into stable supramolecular structures. The complexes interacted with CT-DNA mainly by electrostatic attraction. Both **1** and **2** exhibit efficient nuclease activities in the presence of ascorbic acid, especially, complex **2** whose higher nuclease activity was attributed to the hydrophobic t-butyl group on the backbone of the ligand L^2. Hydroxyl radicals are mainly the reactive oxygen species.

Acknowledgements

This work was supported by the National Natural Science Foundation of China (Nos. 20529101, 20671098, 20725103 and 20770494), the Guangdong Provincial Natural Science Foundation (No. 07117637), National Basic Research Program of China (973 Program No. 2007CB815306) and the Foundation of Hunan Province Education Office (No. 08C178).

Appendix A. Supplementary data

CCDC 691654 and 691655 contain the supplementary crystallographic data for complexes **1** and **2**. These data can be obtained free of charge via http://www.ccdc.cam.ac.uk/conts/retrieving.html, or from the Cambridge Crystallographic Data Centre, 12 Union Road, Cambridge CB2 1EZ, UK; fax: (+44) 1223-336-033; or e-mail: deposit@ccdc.cam.ac.uk. Supplementary data associated with this article can be found, in the online version, at doi:10.1016/j.poly.2008.11.057.

References

[1] F. Mancin, P. Scrimin, P. Tecillab, U. Tonellato, Chem. Commun. (2005) 2540.
[2] C. Liu, M. Wang, T. Zhang, H. Sun, Coord. Chem. Rev. 248 (2004) 147.
[3] (a) W.K. Pogozelski, T.D. Tullius, Chem. Rev. 98 (1998) 1089;
(b) Q. Jiang, N. Xiao, P.-F. Shi, Y.-G. Zhu, Z.-J. Guo, Coord. Chem. Rev. 251 (2007) 1951.
[4] D.S. Sigman, D.R. Graham, V.D. Aurora, A.M. Stern, J. Biol. Chem. 254 (1979) 12269.
[5] D.S. Sigman, Acc. Chem. Res. 19 (1986) 180.
[6] D.S. Sigman, A. Mazumder, D.M. Perrin, Chem. Rev. 93 (1993) 2295.

[7] D.R. Graham, L.E. Marshall, K.A. Reich, D.S. Sigman, J. Am. Chem. Soc. 102 (1980) 5419.
[8] S. Goldstein, G. Czapski, J. Am. Chem. Soc. 108 (1986) 2244.
[9] B.K. Santra, P.A.N. Reddy, G. Neelkanta, S. Mahadevan, M. Nethaji, A.R. Chakravarty, J. Inorg. Biochem. 89 (2002) 191.
[10] A.M. Thomas, G. Neelkanta, S. Mahadevan, M. Nethaji, A.R. Chakravarty, Eur. J. Inorg. Chem. (2002) 2720.
[11] A.M. Thomas, M. Nethaji, S. Mahadevan, A.R. Chakravarty, J. Inorg. Biochem. 94 (2003) 171.
[12] P.A.N. Reddy, M. Nethaji, A.R. Chakravarty, Eur. J. Inorg. Chem. (2004) 1440.
[13] S. Dhar, P.A.N. Reddy, M. Nethaji, S. Mahadevan, M.K. Saha, A.R. Chakravarty, Inorg. Chem. 41 (2002) 3469.
[14] R. Pradhan, A.M. Thomas, A. Mukherjee, S. Dhar, M. Nethaji, A.R. Chakravarty, Indian J. Chem. 44A (2005) 18.
[15] R. Rao, A.K. Patra, P.R. Chetana, Polyhedron 26 (2007) 5331.
[16] M. Chikira, Y. Tomizawa, D. Fukita, T. Sugizaki, N. Sugawara, T. Yamazaki, A. Sasano, H. Shindo, M. Palaniandavar, W.E. Antholine, J. Inorg. Biochem. 89 (2002) 163.
[17] X. Wang, H. Chao, H. Li, X. Hong, L. Ji, X. Li, J. Inorg. Biochem. 98 (2004) 423.
[18] A.M. Thomas, M. Nethaji, A.R. Chakravarty, J. Inorg. Biochem. 98 (2004) 1087.
[19] S.T. Frey, H.H.J. Sun, N.N. Murthy, K.D. Karlin, Inorg. Chim. Acta 242 (1996) 329.
[20] K.J. Humphreys, K.D. Karlin, S.E. Rokita, J. Am. Chem. Soc. 124 (2002) 8055.
[21] Y. Zhao, J. Zhu, W. He, Z. Yang, Y. Zhu, Y. Li, J. Zhang, Z. Guo, Chem. Eur. J. 12 (2006) 6621.
[22] J.-W. Chen, X.-Y. Wang, Y. Shao, J.-H. Zhu, Y.-G. Zhu, Y.-Z. Li, Q. Xu, Z.-J. Guo, Inorg. Chem. 46 (2007) 3306.
[23] V.G. Vaidyanathan, B.U. Nair, J. Inorg. Biochem. 93 (2003) 271.
[24] V. Uma, V.G. Vaidyanathan, B.U. Nair, Bull. Chem. Soc. Jpn. 78 (2005) 845.
[25] V. Uma, M. Kanthimathi, T. Weyhermuller, B.U. Nair, J. Inorg. Biochem. 99 (2005) 2299.
[26] V. Uma, A. Castineiras, B.U. Nair, Polyhedron 26 (2007) 3008.
[27] G.N. De Iuliis, G.A. Lawrance, S. Fieuw-Makaroff, Inorg. Chem. Commun. 3 (2000) 307.
[28] O. Rotthaus, S. LeRoy, A. Tomas, K.M. Barkigia, I. Artaud, Eur. J. Inorg. Chem. (2004) 1545.
[29] P.L. Anelli, F. Montanari, S. Quici, J. Org. Chem. 53 (1988) 5292.
[30] A. Avdagic, M. Gelo-Pujic, V. Sunjic, Synthesis (1995) 1427.
[31] E. Altona, A.N. Wilson, F.W. Holly, K. Folkers, J. Am. Chem. Soc. 76 (1954) 1146.
[32] R.W. Hay, P.M. Gidney, G.A. Lawrance, J. Chem. Soc., Dalton Trans. (1975) 779.
[33] G.M. Sheldrick, Acta Crystallogr., Sect. A 64 (2008) 112.
[34] A.J. Elliott, G.A. Lawrance, G. Wei, Polyhedron 12 (1993) 851.
[35] P. Comba, G.A. Lawrance, M. Rossignoli, B.W. Skelton, A.H. White, Aust. J. Chem. 41 (1988) 773.
[36] A.W. Addison, T.N. Rao, J. Reedijk, J.V. Rijn, G.C. Verschoor, J. Chem. Soc., Dalton Trans. (1984) 1349.
[37] M.D. Glick, D.P. Gavel, L.L. Diaddario, D.B. Rorabacher, Inorg. Chem. 15 (1976) 1190.
[38] P. Comba, T.W. Hambley, G.A. Lawrance, Helv. Chim. Acta. 68 (1985) 2332.
[39] E.C. Long, J.K. Barton, Acc. Chem. Res. 23 (1990) 271.
[40] M. Baldini, M. Belicchi-Ferrari, F. Bisceglie, P.P. Dall'Aglio, G. Pelosi, S. Pinelli, P. Tarasconi, Inorg. Chem. 43 (2004) 7170.
[41] J.B. Le Pecq, C. Paoletti, J. Mol. Biol. 27 (1967) 87.
[42] J.-H. Li, J.-T. Wang, Z.-W. Mao, L.-N. Ji, Inorg. Chem. Commun. 11 (2008) 865.

Polyhedron 28 (2009) 593–599

Contents lists available at ScienceDirect

Polyhedron

journal homepage: www.elsevier.com/locate/poly

Mechanism of complex formation between $[AuCl_4]^-$ and L-methionine

A.V. Vujačić [a], J.Z. Savić [a], S.P. Sovilj [b], K. Mészáros Szécsényi [c], N. Todorović [d], M.Ž. Petković [a], V.M. Vasić [a,*]

[a] Department of Physical Chemistry, Vinča Institute of Nuclear Sciences, P.O. Box 522, 11001 Belgrade, Serbia
[b] University of Belgrade, Faculty of Chemistry, P.O. Box 158, 11000 Belgrade, Serbia
[c] University of Novi Sad, Faculty of Sciences and Mathematics, Department of Chemistry, 21000 Novi Sad, Trg D. Obradovića 3, Serbia
[d] Institute for Chemistry, Technology and Metallurgy, Studentski trg 12-16, 11000 Belgrade, Serbia

ARTICLE INFO

Article history:
Received 30 September 2008
Accepted 25 November 2008
Available online 3 January 2009

Keywords:
Gold(III)
L-Methionine
Complex formation
Kinetics

ABSTRACT

The kinetics of the reaction between the tetrachloroaurate(III) ion and L-methionine (L-Met) (0.1 M $HClO_4$, pH 1.0–2.5) have been studied spectrophotometrically using a stopped-flow technique at different temperatures. Initially, the fast substitution reaction was ascribed to the formation of the short-lived square-planar Au(III)–(L-Met) that was followed by the replacement of a Cl^- ligand and a subsequent, slower reduction to Au(I)–(L-Met). This is an intermolecular process, involving attack on the $[AuCl_4]^-$ complex by an outer-sphere L-methionine. The activation parameters ($\Delta H^{\neq}$ and $\Delta S^{\neq}$) for substitution and reduction were determined. IR spectroscopy indicates that L-methionine acts as a bidentate ligand, most likely coordinating *via* the S and N atoms, while ^1H and ^{13}C NMR data indicate methionine sulfoxide as the final product. Finally, the components of the reaction were treated thermally in order to investigate the solid phase synthesis of the resulting complex.

© 2008 Elsevier Ltd. All rights reserved.

1. Introduction

Interest in Au(III) reactions with amino acids, peptides and proteins arises from the proposal that these compounds may be involved in the reactions of potential antitumor agents [1,2]. However, the clinical application of gold complexes is limited since they are extremely unstable under physiological conditions [3]. Similar to Pt(II) compounds, Au(III) species are capable of binding DNA, and this is the reason for their cytotoxicity. The molecular basis of these toxic effects are still poorly understood, but the coordination of a thioether group to gold(III) by sulfur-donor ligands in the side-chains of amino acids, peptides and proteins, accompanied by the reduction of Au(III) to Au(I), could be responsible for the observed cytotoxicity [3,4]. It has been suggested that the reduction of Au(III) could take place by interactions with basic amino acids from the cell wall, since Au(III) compounds are able to oxidize several biomolecules such as L-methionine, L-cysteine, histidine and glycine [5–9]. Surprisingly, there are only a few reports of reactions of Au(III) with sulfur containing amino acids, and these have focused on stereo-specific oxidation, where the identity of the intermediates was not clarified [10,11].

The naturally occurring L-methionine amino acid, containing a thioether group, is an important molecule in living organisms that provides the metal binding sites in many enzymes. It forms chelates with metal ions mostly by coordinative binding to amino and carboxyl groups of α-amino acid residues [12]. Kinetic studies of the reduction of Au(III) by L-methionine and dialkyl sulfides have been reported [10,11], but there is a lack of data concerning the ligand substitution steps in the overall reaction mechanism. The interest in the speciation of Au(III) and L-methionine complexes arises from their relevance to the fundamental aspects of environmental and medical science, since the coordinated Au(III) ion may serve as an electron acceptor in biochemical processes within the cell [13–16]. Reactions between L-methionine derivatives and Au(III) have shown that the oxido-reduction process that occurs induces the production of sulfoxide and a Au(I)–L-methionine species [12,13]. The Au(III)-induced oxidation of L-methionine and related amino acids may be important in relation to the severe toxicity of gold-based drugs [17]. To our knowledge, a stable complex between Au(III) and L-methionine has not been isolated, but recently, Au(III) mononuclear complexes with some L-methionine containing peptides were synthesized and structurally characterized [18]. Au(III) was coordinated through the S atom from a L-methionine fragment and a N atom from an amino group residue, forming a macrochelate ring.

The elucidation of a stepwise Au(III) reduction mechanism, including the ligand substitution, provides the basis for obtaining further insights into the mechanism of drug toxicity. In this view, it is necessary to understand the chemistry of gold–biomolecule interactions. In this paper, special attention was paid to the detailed investigation of the equilibrium and kinetics of the reaction between $[AuCl_4]^-$ and L-methionine, as it may have a significant impact on the further exploration of Au(III) reactions with similar nucleophiles.

* Corresponding author. Tel.: +381 11 2453 967; fax: +381 11 244 72 07.
E-mail address: evasic@vinca.rs (V.M. Vasić).

0277-5387/$ - see front matter © 2008 Elsevier Ltd. All rights reserved.
doi:10.1016/j.poly.2008.11.045

2. Experimental

2.1. Chemicals

Tetrachloroaurate(III) acid ($HAuCl_4 \cdot 3H_2O$, Merck), L-methionine, potassium hydroxide (Zorka, Šabac) and potassium chloride (Merck) and all other reagents were commercial products of the highest purity available. Stock solutions of 1×10^{-2} M $HAuCl_4 \cdot 3H_2O$ and L-methionine were prepared directly before use in 0.1 M $HClO_4$ to suppress formation of the aqua and hydroxo complexes. More dilute solutions were obtained by appropriate dilution with double distilled water. The acidities were obtained by addition of HCl or NaOH. To control the Cl^- concentration, KCl was used.

2.2. Physical methods

Absorption spectra were recorded using a Perkin–Elmer Lambda 35 UV–Vis spectrophotometer. For the stopped-flow experiments, the universal rapid kinetic accessory HI-TECH model SFA 12, with a dead time of 20 ms, was fitted to the spectrophotometer. The pH of the solutions was measured by a Beckman Expandometric pH meter.

NMR spectra were obtained on a Bruker ADVANCE III 500 spectrometer (500.26 MHz for ^1H, 125.8 MHz for ^{13}C) at 298 K, using a BBO multinuclear probehead and 5 mm tubes. The solvent was D_2O, pD 1 adjusted by D_2SO_4. The chemical shift reference was sodium 3-(trimethylsilyl)-propanesulfonate. The ^1H NMR spectra of L-methionine and $HAuCl_4 \cdot 3H_2O$ equimolar mixtures (66 mM) were measured 12, 25 and 50 min after mixing. The ^{13}C NMR spectra were obtained 1 h after mixing. The chemical shifts are reported in ppm, and the coupling constants (J) in Hz.

Thermal analysis was carried out using an SDT Q600 thermal analyzer from TA Instruments in a flowing nitrogen gas carrier with heating rates of 20, 5 and 2 °C min^{-1}. The pans were made of aluminium with an empty pan as a reference cell.

IR spectra were recorded at room temperature using KBr pellets in the range of 4000–400 cm^{-1} on a ThermoNicolett NEXUS 670 FT-IR spectrometer. The spectra were obtained with a resolution of 4 cm^{-1} after 32 scans.

FT-IR spectra were recorded with a ZnSe crystal on the Excalibur™ FT-IR Spectrometer (Varian, Darmstadt, Germany). All spectra were analyzed with Digilab Resolutions Pro Software. The solution of L-methionine was applied on the crystal as a thin film to cover the entire surface. After drying in the nitrogen stream, a solution of $HAuCl_4$ was applied on the L-methionine film and spectra were recorded 5 and 30 min after beginning the reaction.

2.3. Kinetic measurements

The kinetic experiments were performed by mixing equal volumes of $[AuCl_4]^-$ and L-methionine solutions. The temperature was controlled to ±0.1 °C in the interval from 282 to 303 K. The kinetic curves were monitored at 225 and 280 nm. The experimental points in the pseudo first-order experiments were fitted by a single exponential function. All kinetic measurements were reproducible within limits of error of ±5%. The values reported are averages of at least five runs under identical experimental conditions.

3. Results and discussion

3.1. Complex formation between $[AuCl_4]^-$ and L-methionine

The absorption spectra of solution containing 2.5×10^{-5} M $[AuCl_4]^-$ and L-methionine in 0.1 M $HClO_4$ in the presence of 0.1 M KCl were recorded on the dependence of time and are presented in Fig. 1. Two reaction steps can be deduced from the change of the absorbance vs. time at 280 and 225 nm. The faster one, accompanied by the absorbance increase at 280 nm, followed by two well-defined isosbestic points at 245 and 295 nm, indicated the short-lived complex formation between $AuCl_4^-$ and L-methionine. The slower reaction step, accompanied by the decrease in absorbance, can be ascribed to the reduction of Au(III). The second-order complex formation (fast) and first-order (slow) Au(III) reduction (Fig. 2, inset) are confirmed by analyzing the kinetic curves at 225 and 280 nm (Fig. 2) for two equimolar solutions containing 2.5×10^{-5} M or 5×10^{-5} M $[AuCl_4]^-$ and L-methionine in 0.1 M $HClO_4$. The 1:1 stoichiometry of the complex formed in the fast reaction step was determined from the absorbance vs. time curves at 280 nm by using Jobb's and molar ratio methods at 280 nm. It is of note, that the maximum of the kinetic traces was independent of L-methionine concentration. The molar absorptivity of the complex ($a = 3.64 \times 10^3$ M^{-1} dm^3) was determined as the average value on the plateau of the kinetic traces at 280 nm.

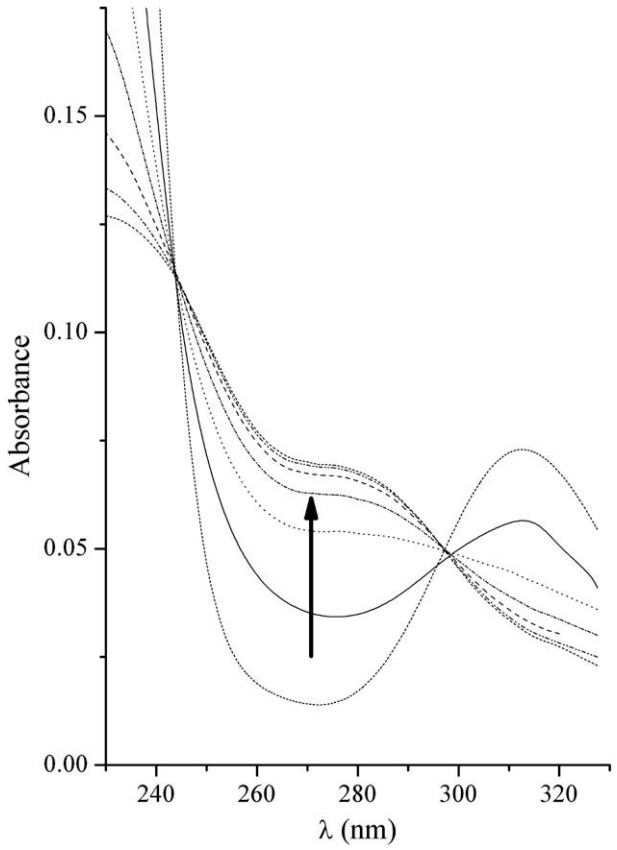


Fig. 1. Time dependence of UV–Vis spectra of solution containing 2.5×10^{-5} M $[AuCl_4]^-$ and L-methionine in 0.1 M $HClO_4$ at 10 °C. The time interval between two consecutive spectra was 2 s.

In the ^1H NMR spectrum measured 12 min after mixing the components, one could observe traces of some intermediary species, with approximately 10% of the product probably originating from the Au(III)–(L-methionine) complex (data not shown). The ^1H NMR spectrum measured 25 min after mixing, and the ^{13}C NMR data, show only the presence of methionine sulfoxide as a diastereomeric mixture (Table 1) [19,19a].

Regarding the NMR data, free ligand and complex mostly differ in the chemical shifts of the nuclei adjacent to the S atom (Table 1). In both the ^1H and ^{13}C NMR spectra of the complex, the signals of the γCH_2 and CH_3 groups are significantly shifted downfield, while the ^1H NMR signal of the γCH_2 showed a typical, diastereotopic

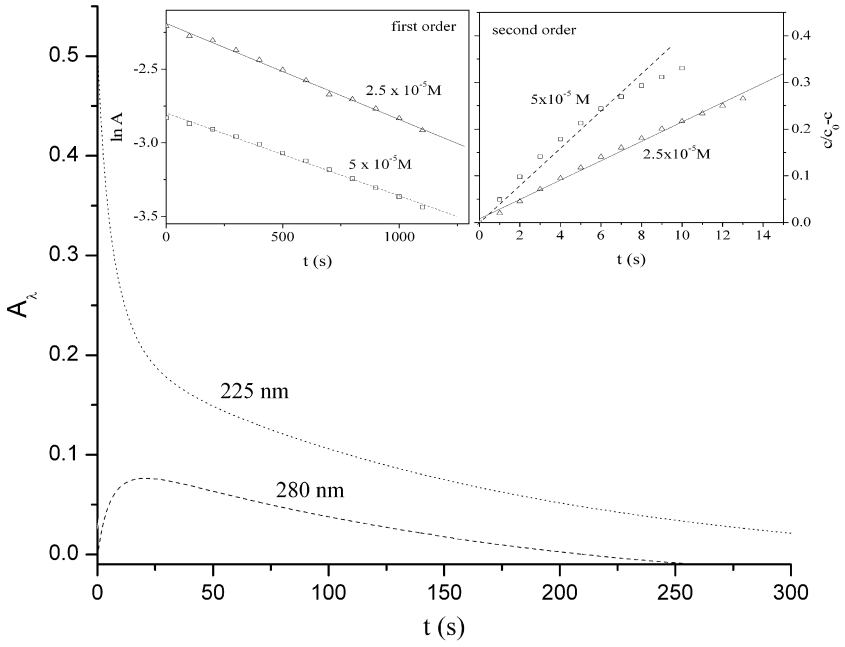


Fig. 2. Kinetic curves of solution containing 2.5×10^{-5} M $[AuCl_4]^-$ and L-methionine in 0.1 M $HClO_4$ at 280 nm and 225 nm at 20 °C. *Inset:* The kinetic analysis of the ascending (second-order) and descending (first-order) branch of the kinetic curve at 280 nm for 2.5×10^{-5} M and 5×10^{-5} M equimolar solutions.

Table 1
The ^1H and ^{13}C NMR chemical shifts (ppm) of L-methionine and methionine sulfoxide at pD 1.

	Position	L-Methionine δ (multiplicity, J)	Methionine sulfoxide [a] δ (multiplicity, J)
^1H	α	4.22 (1H, dd, 6, 6.8)	4.29, 4.28 (1H, 2xdd, 6.1, 6.9; 6.4, 6.7)[b]
	β	2.16–2.35 (2H, m)	2.34–2.52 (2H, m)[c]
	γ	2.7 (2H, t, 7.4)	2.96–3.26 (2H, m)[c]
	CH_3	2.13 (3H, s)	2.75, 2.76 (3H, 2xs)[d]
^{13}C [e]	α	54.49	54.18, 54.32[f]
	β	31.57	25.76, 26.01[f]
	γ	31.19	50.50, 50.64[f]
	CH_3	16.54	39.19, 39.27[f]
	C=O	174.49	173.40

[a] The 1H δ values are from the spectrum measured after 25 min.
[b] The signals are overlapped, but distinguishable.
[c] Signals overlapped.
[d] Signals are not fully overlapped, enabling separate integration major/minor = 2/1.
[e] The assignation of ^{13}C signals was proven by H–C correlations in HSQC spectra of both, ligand and its sulfoxide (data not shown).
[f] First and second value are for the major and minor diastereoisomer, respectively; the same is valid for αH and CH_3 in ^1H NMR spectrum.

pattern. This clearly indicates S-coordination in the Au(I)–(L-methionine) complex.

The NMR findings were further confirmed with FT-IR analysis of 1×10^{-1} M L-methionine (lines are indicated in Fig. 3) and a solution containing 1×10^{-1} M Au(III) and L-methionine (Fig. 3). These results also imply S,N-coordination. The spectrum recorded 5 min after starting the reaction represents the spectrum of the Au(III)–(L-methionine) complex in solution. After 30 min of the reaction the band located approximately at 1650 cm^{-1} disappeared.

Shifts of the NH_2 scissoring vibrations in the IR spectrum of L-methionine (shifted from 1650 to 1700 cm^{-1}) and the suppression of the –C–S stretching vibration in the region of 790–830 cm^{-1} after the addition of $HAuCl_4$ indicate that both N- and S-atoms from the L-Met are involved in the formation of coordinative bonds in the complex.

In order to check if there was a complex formation between the components and to isolate the final product, the reaction was carried out as a solid-state thermal reaction. TA measurements of a solution containing 2.5×10^{-5} M $AuCl_4^-$ and 1.0×10^{-3} M L-methionine in an inert (N_2) atmosphere did not suggest the reduction of Au(III). In order to follow the complex formation in the solid-state, the components were mixed in a mortar. However, the reduction of Au(III) to Au(0) was observed when mixing $HAuCl_4 \cdot 3H_2O$ and L-methionine. To avoid the reduction of Au(III), the components were put directly into the crucible without mechanical mixing in a molar ratio of about 1:1, with L-methionine being in excess (~10 m/m%). The mixture was equilibrated at 50 °C and then heated at a heating rate of 5 °C min^{-1} up to 140 °C. At about 90 °C, almost all of the water content of the mixture was removed. However, before the evaporation of water had finished, another processes began. The extruded gases were bubbled through a $AgNO_3$ solution. In the temperature range of 90–130 °C, a white precipitate indicated HCl evaporation, which was most likely followed by organic fragments of the uncoordinated L-methionine.

Additionally, a stepwise (SWI), or quasi-isothermal method [20], was applied to a similar mixture of $HAuCl_4 \cdot 3H_2O$ and L-methionine. In this experiment, an intermediate with low stability was isolated at 118 °C (Fig. 4). The mass loss of 24.4% was much higher compared to dehydration (66 °C) and a loss of HCl (calcd. 10.71%). It might be a consequence of the sublimation of L-methionine. However, its sublimation temperature, according to literature data [21], should be higher by about 50 °C. It is more likely that the higher mass loss is a consequence of the reduction of Au(III) to Au(I) and the departure of the corresponding oxidation product – sulfoxide.

The IR spectrum of the intermediate was compared to the spectrum of L-methionine. There is a change in the position and intensity of the νCS bands [22,23] in the range of about 800–600 cm^{-1} (data not shown). The most significant shift of the corresponding bands is in the range of 1730–1500 cm^{-1}. Namely, bands at 1612 and 1511 cm^{-1} assigned to $\nu_{as}NH_3^+$ and $\nu_{as}COO^-$, respectively [22,23], suffered a blue shift to 1723 and 1687 cm^{-1}. The spectrum of the intermediate may support complex formation of Au(III) with

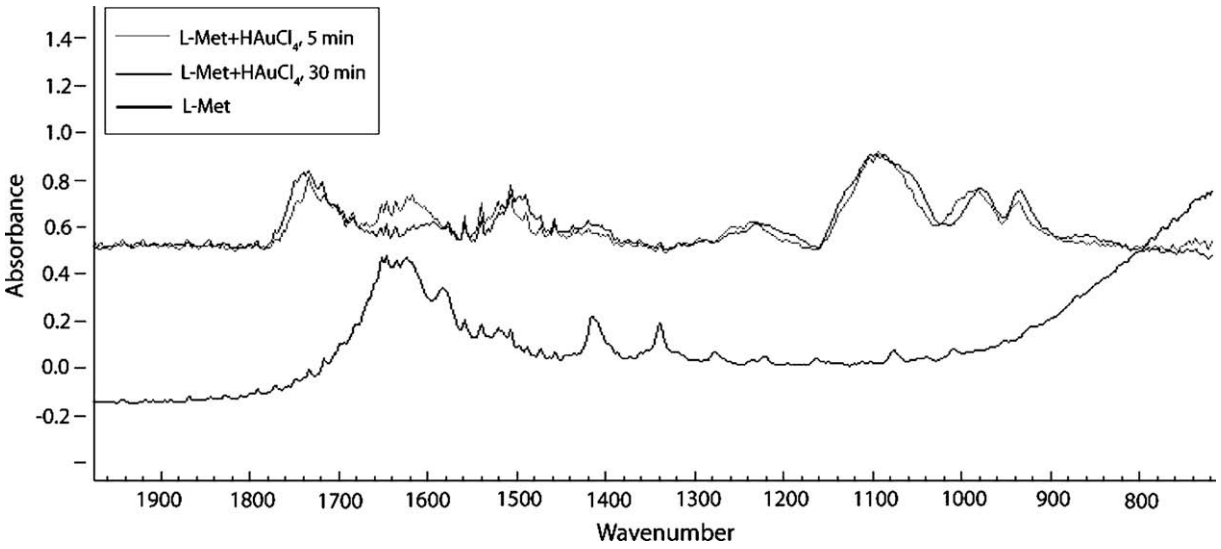


Fig. 3. FT-IR spectra of solution containing 1×10^{-1} M L-methionine and $[AuCl_4]^-$ in 0.1 M $HClO_4$ after 5 and 30 min after starting the reaction.

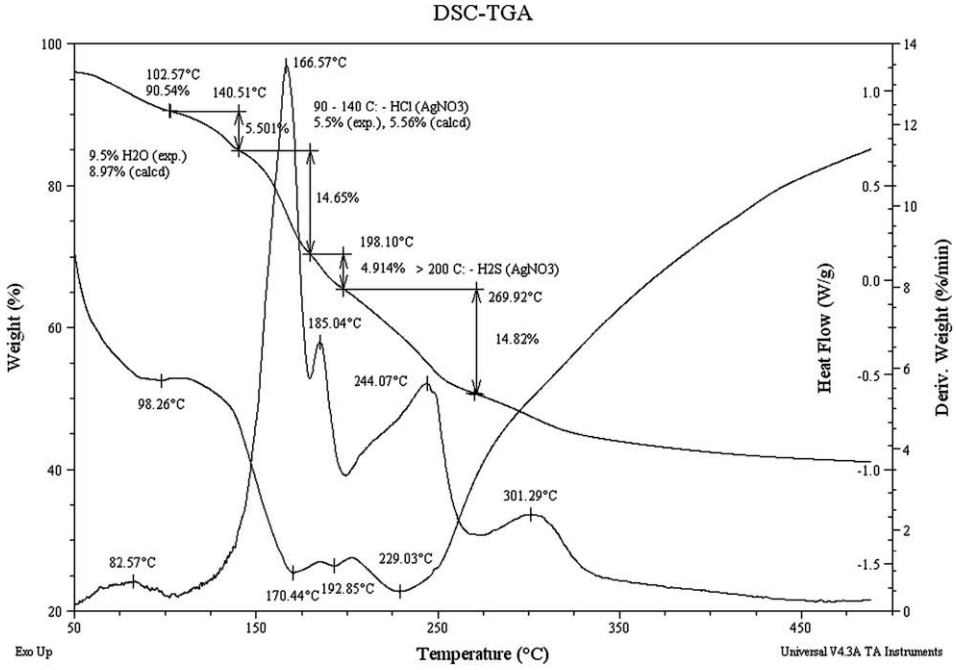


Fig. 4. Thermal curves of the mixture of $HAuCl_4 \cdot 3H_2O$ and L-methionine solids.

L-methionine as a bidentate ligand with S,N-coordination. Also, the lower intensity of the bands in the 800–600 cm^{-1} range of the intermediate may support the partial oxidation of the ligand into the corresponding sulfoxide. The bands of the uncoordinated ligand did not change position.

An additional solid-state reaction was carried out by heating the reaction mixture up to 70 °C at a heating rate of 2 °C min^{-1} in cycles. At the third cycle, the mass loss was less than 0.4%. The complete mass loss of 11.0% compared to the calculated one (12.73%) corresponds most likely to the loss of three H_2O molecules and one HCl molecule (Fig. 4). The solid-state reaction is endothermic up to 300 °C, suggesting an endothermic reduction of the central atom, which means that the increase in entropy is the determining stabilizing factor in the complex formation.

The IR spectrum of the end product of this reaction shows the unchanged bands of the uncoordinated ligand, similar to the spectrum of the intermediate obtained using the SWI method.

3.2. Kinetics of ligand substitution and oxido-reduction

The kinetics were investigated at pH 1.0 in the presence 0.1 M KCl under pseudo first-order conditions, keeping the concentration of $[AuCl_4^-]$ constant (2.5×10^{-5} M) and varying [L-methionine] from 2×10^{-4} M to 1×10^{-3} M. The rise and fall of the absorbance at 280 nm as a function of time is characteristic for a reaction that involves an intermediate B in the overall process during which A is transformed into P, as shown in Eq. (1), and the time dependence for B is given by Eq. (2):

$$A \overset{k_{obs1}}{\rightarrow} B \overset{k_{obs2}}{\rightarrow} P \quad (1)$$

$$[B] = \frac{k_{obs1}}{k_{obs2} - k_{obs1}} [B]_{\infty} (e^{-k_{obs1}t} - e^{-k_{obs2}t}) \quad (2)$$

In Eq. (1) B represents the 1:1 complex resulting from nucleophilic attack of the sulfur donor of the thioether group in L-methionine and Cl^- substitution. In Eq. (2), [B] and $[B]_\infty$ are the concentrations of the complex at t and when equilibrium is reached, and k_{obs1} and k_{obs2} are pseudo first-order rate constants for the reactions (1). Fig. 5 represents the change of complex concentration as a function of time obtained from the kinetic curve (A_{280} *versus* t, Fig. 5, inset) for the solution containing 2.5×10^{-5} M $[AuCl_4]^-$ and 1×10^{-4} M L-methionine. The first-order rate constants $k_{obs1} = (0.46 \pm 0.03)\ s^{-1}$ and $k_{obs2} = (1.08 \pm 0.02) \times 10^{-2}\ s^{-1}$ were determined from the separate treatment of the ascending and descending branch of the kinetic curve and were used to recalculate the dependence of [B] *versus* t. The results are presented in Fig. 5 as a solid line, since the points represent the experimentally obtained data. As can be seen, the calculated results are in good agreement with the experimental results.

The rising parts of the kinetic curves were single exponentials in all cases. The observed rate constant (k_{obs1}) as a function of the total concentration of L-methionine can be described by the well known two-term rate law common for substitution reactions of square-planar complexes [23]:

$$k_{obs1} = k_I + k_{II}\ [\text{L-methionine}] \quad (3)$$

where k_I is the solvent-dependent rate constant and k_{II} is the second-order rate constant, which is characteristic for direct nucleophilic attack and formation of a Au(III)–L-methionine complex. The rate constants k_I and k_{II} were determined from the intercept and the slope of the linear plots of k_{obs1} *versus* [L-methionine].

The slow reaction path leads to the reduction of gold by forming a linear two-coordinated Au(I)–(L-methionine) complex [10,11]. It is apparent that a second L-methionine is required in order to promote the reduction of Au(III)–(L-methionine) since the pseudo first-order rate constants for the reduction are a function of the L-methionine concentration and obey the relationship:

$$k_{obs2} = k_2\ [\text{L-methionine}] \quad (4)$$

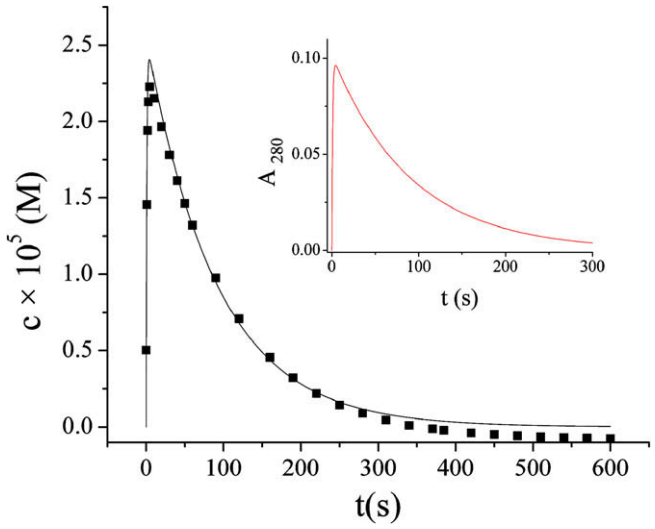


Fig. 5. Dependence of complex concentration on time for the reaction between 2.5×10^{-5} M $[AuCl_4]^-$ and 1×10^{-4} M L-methionine at pH 1.0 and 0.1 M KCl. Solid curve represents Eq. (2) fitted to the experimental values (points). Inset: dependence of absorbance at 280 nm on time.

In this reaction step, the L-methionine was oxidized in the presence of water to the corresponding sulfoxide [11,14]:

$$[Au^{III}Cl_3(HMet)]^+ \overset{k}{\rightarrow} Au^{I}Cl(HMet)^+ + 2Cl^- + 2H^+ \quad (5)$$

$$[Au^{III}Cl_3(HMet)]^+ + HMet^+ + H_2O \rightarrow [Au^{I}Cl(HMet)]^+ + SOCH_3CH_2CH_2CH(-COOH)(-H_2N) + H^+ \quad (6)$$

The rate constants k_{obs1} and k_{obs2}, as a function of ligand concentration at various temperatures and pH 1.0 are summarized in Tables 2 and 3, along with the determined values for k_I, k_{II} and k_2.

3.3. Reaction mechanism

The pH dependence of the pseudo first-order rate constants (pH profile) for solutions containing 2.5×10^{-5} M $[AuCl_4]^-$, 10-fold excess L-methionine and 0.1 M KCl, obtained by analysis of the ascending branch of the kinetic curves at 280 nm, is presented in Fig. 6. The results show the significant increase of k_{obs1} with the decrease of acidity in the pH range of 1–2.5. This behavior indicates that different reacting species of Au(III) ($AuCl_4^-$, $AuCl_3OH^-$) are involved in the forward reaction [24]. Also, two acid–base forms of the ligand are present ($pK_{COOH} = 2.28$) [25]. The appearance of species containing OH^- groups may be interpreted using the HSAB principle [26]: a hard OH^- base has a preferences for hard Au(III) acids, even in an acidic solutions, which is also promoted by steric hindrance. A reaction scheme for ligand substitution compatible with the pH dependence of k_{obs} is given by reactions (7)–(10). However, it is more probable that reactions (9) and (10) are faster compared to (7) and (8) [27]. The assumption was made that the protolytic equilibria (reactions (12) and (13)) are faster compared to substitution of the ligand, and consequently that the equilibrium between Au(III) species was maintained throughout the kinetic run [24]. This is in accordance with the observations at low temperature, and the solid-state reactions up to 70 °C. In addition,

Table 2
The observed pseudo first-order rate constants (k_{obs}) for Cl^- substitution as a function of L-methionine concentration and temperature. $[AuCl_4^-] = 2.5 \times 10^{-5}$ M.

	$10^2 k_{obs}$ (s^{-1})		
T (K)	282	294	303
$C_{L\text{-methionine}}$ (M)			
2.5×10^{-4}	24.60 ± 0.7	47.45 ± 0.7	54.20 ± 0.3
3.75×10^{-4}	34.45 ± 0.5	61.44 ± 0.9	65.37 ± 2.5
5×10^{-4}	38.12 ± 0.6	81.25 ± 0.6	85.40 ± 0.5
7.5×10^{-4}	66.82 ± 1	101.79 ± 1.5	107.80 ± 0.8
1×10^{-3}	77.47 ± 1.2	141.14 ± 2.1	158.60 ± 3.2
1.25×10^{-3}	98.8 ± 0.5	138.04 ± 2.1	195.40 ± 4
$10^2 k_I$ (s^{-1})	5.5 ± 0.1	27.6 ± 0.1	12.9 ± 0.1
$10^{-2} k_{II}$ ($M^{-1}\ s^{-1}$)	7.45 ± 0.03	9.83 ± 0.02	14.29 ± 0.06

Table 3
The observed pseudo first-order rate constants (k_{obs}) for Au(III) reduction as a function of L-methionine concentration and temperature. $[AuCl_4^-] = 2.5 \times 10^{-5}$ M.

	$10^3 k_{obs}$ (s^{-1})		
T (K)	282	294	303
$C_{L\text{-methionine}}$			
2.5×10^{-4}	0.49 ± 0.02	1.76 ± 0.05	2.8 ± 0.1
3.75×10^{-4}	1.71 ± 0.3	3.72 ± 0.6	5.17 ± 0.6
5×10^{-4}	2.52 ± 0.6	6.44 ± 0.3	8.09 ± 0.4
7.5×10^{-4}	4.04 ± 0.4	7.74 ± 0.8	13.07 ± 0.5
1×10^{-3}	4.81 ± 0.6	11.46 ± 0.4	17.43 ± 0.2
1.25×10^{-3}	7.32 ± 0.4	15.02 ± 0.4	19.59 ± 0.6
k_2 ($M^{-1}\ s^{-1}$)	5.3 ± 0.2	11.5 ± 0.6	16.3 ± 0.9

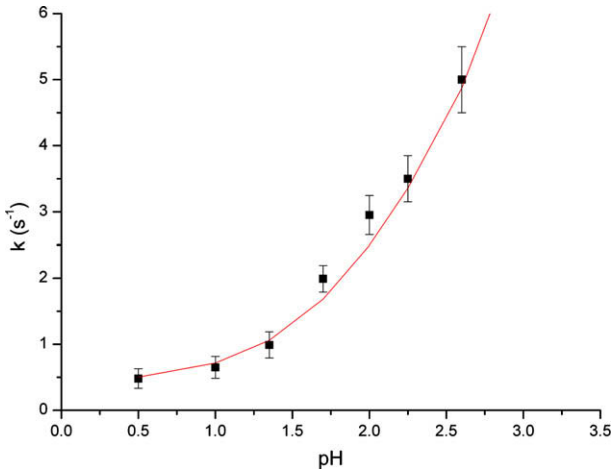


Fig. 6. Dependence of k_{obs1} on pH in solution containing 2.5×10^{-5} M $[AuCl_4]^-$, 2.5×10^{-4} M L-methionine and 0.1 m KCl at 20 °C.

both Au(III)–(H^+L-methionine) and Au(III)–(L-methionine) are formed under these experimental conditions, as found previously in reactions between Pd(II) and –SH containing amino acids and peptides [28–31]:

$$AuCl_4^- + HMet^+ \underset{k_1'}{\overset{k_1}{\rightleftharpoons}} AuCl_3(HMet)^+ + Cl^- \quad (7)$$

$$AuCl_4^- + Met \underset{k_2'}{\overset{k_2}{\rightleftharpoons}} AuCl_3Met + Cl^- \quad (8)$$

$$AuCl_3OH^- + HMet^+ \underset{k_3'}{\overset{k_3}{\rightleftharpoons}} AuCl_3(HMet)^+ + OH^- \quad (9)$$

$$AuCl_3OH^- + Met \underset{k_4'}{\overset{k_4}{\rightleftharpoons}} AuCl_3Met + OH^- \quad (10)$$

$AuCl_3(HMet)^+$ + Cl^- → (fast) → $[AuCl_2HMet]^{+2}$ ⇌ $[AuCl_2Met]^{+1}$

$HMet^+$ and Met represent L-methionine with and without a protonated $-NH_2$ group, respectively. It can be easily shown that under the above mentioned experimental conditions, a pH dependence of k_{obs} can be described as follows:

$$k_{obs} = \frac{k_I[H^+]^2 + k_{II}[H^+] + k_{III}}{\alpha \cdot \beta} \quad (11)$$

where $\alpha = [H^+] \cdot [Cl^-] + K_1$, $\beta = [H^+] + K_a$, $k_I = k_1 \cdot [Cl^-]$, $k_{II} = k_2 \cdot K_a \cdot [Cl^-] + k_3 \cdot K_1$ and $k_{III} = k_4 \cdot K_1 \cdot K_a$.

In addition, the following equilibrium must be taken into account:

$$HMet^+ \overset{K_a}{\rightleftharpoons} H^+ + Met \quad (12)$$

$$AuCl_4^- + H_2O \overset{K_1}{\rightleftharpoons} AuCl_3OH^- + H^+ + Cl^- \quad (13)$$

The experimentally determined pH dependence of k_{obs} is shown by the points in Fig. 6. The best fit to Eq. (11) was obtained using $k_{I–III}$ as variable parameters. The agreement between the experimentally determined and calculated values of k_{obs} was obtained for the following set of $k_{I–III}$:$k_I = 3.98 \times 10^{-2}$ M^{-1} s^{-1}, $k_{II} = 3.68 \times 10^{-3}$ s^{-1} and $k_{III} = 2.68 \times 10^{-6}$ M^{-1} s^{-1}.

The individual rate constants $k_{1–4}$ were easily determined knowing values of $k_{I–III}$, and are presented in Table 4. The parameter k_{II} gives the sum of the contributions of paths 2 and 3 (Eqs. (8) and (9)). The individual rate constants k_2 and k_3 were estimated

Table 4
Individual rate constants for different reaction paths in the system Au(III)–L-methionine.

Reaction path	Metal ion	Ligand	$k_{1–4}$ (M^{-1} s^{-1})
1	$AuCl_4^-$	$HMet^+$	0.39 ± 0.05
2	$AuCl_4^-$	Met	4.97 ± 0.09
3	$AuCl_3OH^-$	$HMet^+$	5.25×10^4
4	$AuCl_3OH^-$	Met	$(5.18 \pm 0.20) \times 10^2$

assuming that one of the two rate constants is equal to zero, and vice versa. The obtained values are the upper limits of the individual rate constants. Taking into account the experimental conditions (Cl^- concentration and pH range), the contribution of path 3 could be considered negligible, since the concentration of protonated L-methionine significantly decreased with a pH > 2.

3.4. Activation parameters

The temperature dependencies of the rate constants (k_{II} and k_2, Table 2) obtained for complex formation between $AuCl_4^-$ and L-methionine allowed the calculation of the enthalpies and entropies of activation by using Eyring's equation [26]:

$$\text{Rate constant} = kT/h \exp(\Delta S^{\neq}/R) \exp(-\Delta H^{\neq}/RT) \quad (14)$$

It is important to point out that under the stated experimental conditions (pH 1, 0.1 M KCl), the ligand was protonated and Au(III) was in the form of $AuCl_4^-$, so the reaction pathways described by reactions (8)–(10) can be neglected. The same equation was applied for the reduction process under the same experimental conditions. The values of enthalpy ($\Delta H^{\neq}$ = 19.19 kJ mol^{-1}) and entropy ($\Delta S^{\neq}$ = −121.66 J mol^{-1} K^{-1}) for the forward reaction in ligand replace-

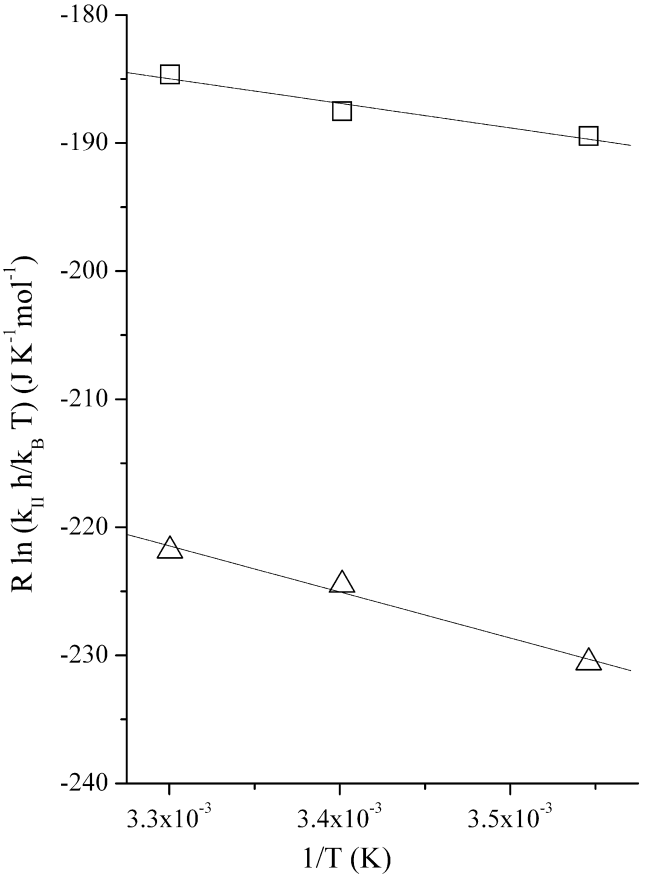


Fig. 7. Dependence of $R \ln(k_f h/k_b T)$ (J K^{-1} mol^{-1}) on $1/T$ for ligand substitution and reduction.

ment were obtained from the intercept and the slope of the plot (Fig. 7). Values of $\Delta H^{\neq} = 35.97$ kJ mol^{-1} and $\Delta S^{\neq} = -102.75$ J mol^{-1} K^{-1} for Au(III) reduction were also obtained.

4. Conclusion

Based on the experimental results presented in this work and other literature data concerning the reaction between $[AuCl_4]^-$ and some amino acids and dialkyl sulfides, which were obtained using multi-instrumental techniques [5,6,14], the conclusion was made that the reaction mechanism takes place in a few steps. The first one is the second-order coordination of the ligand with chloroaurate(III), displacing the chloride anion.

In addition, our point of interest was to investigate how L-methionine acts towards gold under the conditions of the experiment. The hypothesis that L-methionine acts as bidentate S- and N-donor ligand forming $[Au^{III}Cl_2(HMet)]^{+2}$ was confirmed in the solid-state as well in solution, since the ring-closing process is favored by the large chelate effect, even though the amino group is almost totally protonated due to the acidity of the reaction medium [23]. This is also supported by the pH profile. By keeping the Cl^- concentration at 0.1 M, Au(III) is predominantly in the $AuCl_4^-$ form [24]. Above pH 2, the dissociation of the –COOH group occurs, and consequently L-methionine is in its zwitterionic form. However, the –COOH group is not responsible for complex formation, but these results indicate that in a less acidic medium, the zwitterionic ligand enhanced the participation of the unprotonated amino group of L-methionine in the reaction process.

The inequality in enthalpic contribution appears to reflect a variance in structural transformations to break old bonds and form new ones in the transition state, depending on the type of processes (substitution/reduction reaction), thus producing the corresponding difference in the nature of the bonds between metal ions and their respective ligand. It should be noted that the negative value of the entropy term, exhibiting the change in the order of the system, is indeed expected for the substitution reaction followed by reduction [23]. However, a large negative value of the entropy of activation is compatible with an associative mode of activation (Ia or A mechanism) in the first reaction step. This finding indicates that bond-making with the entering ligand is important in the activation processes, and that the leaving ligand is still tightly bound to the metal center in the transition state.

Acknowledgements

This work was supported by the Serbian Ministry of Science, Grant No. 142051. Authors are grateful to Dr. Irina Estrela-Lopis, Institute of Medical Physics and Biophysics, Faculty of Medicine, University of Leipzig, Germany, for her assistance in FT-IR spectroscopy.

References

[1] C.F. Shaw III, Chem. Rev. 99 (1999) 2589–2600.
[2] C. Gabbiani, A. Casini, L. Messori, Gold Bull. 40 (2007) 73–81.
[3] S. Carotti, A. Guerri, T. Mazzei, L. Messori, E. Mini, P. Orioli, Inorg. Chim. Acta 281 (1998) 90–94.
[4] B.P. Esposito, R. Najjar, Coord. Chem. Rev. 232 (2002) 137–149.
[5] J. Zou, Z. Guo, J.A. Parkinson, Yu Chen, P.J. Sadler, Chem. Commun. (1999) 1359–1360.
[6] J.A. Cuadrado, W. Zhang, W. Hang, V. Majidi, J. Environ. Monit. (2000) 355–359.
[7] T. Kolev, B.B. Koleva, S.Y. Zareva, M. Spiteller, Inorg. Chim. Acta 359 (2006) 4367–4376.
[8] P.L. Witkiewicz, C.F. Shaw, J.C.S. Chem. Commun. (1981) 1111–1114.
[9] A.A. Isab, P.J. Sadler, Biochim. Biophys. Acta 492 (1977) 322–330.
[10] G. Natile, E. Bordignon, L. Cattalini, Inorg. Chem. 15 (1976) 246–248.
[11] E. Bordingnon, L. Catalini, G. Natile, A. Scatturin, J.C.S. Chem. Commun. (1973) 878–879.
[12] E. Raux, H.K. Leech, R. Beck, H.L. Schubert, P.J. Santander, C.A. Roessner, A.I. Scott, J.H. Martens, D. Jahn, C. Thermes, A. Rambach, M.J. Warren, Biochem. J. 370 (2003) 505–516.
[13] S. Saito, M. Kuraski, Res. Commun. Mol. Pathol. Pharmacol. 1 (1996) 101–107.
[14] G. Annibale, L. Canovese, L. Cattalini, G. Natile, J.C.S. Dalton Trans. (1980) 1017–1022.
[15] J.A. Cowan, Inorganic Biochemistry, An Introduction, VCH, New York, 1993.
[16] P.J. Sadler, R.E. Sue, Metal Based Drugs 1 (1994) 107–144.
[17] S.L. Best, T.K. Chattopadhyay, M.I. Djuran, R.A. Palmer, P.J. Sadler, I. Sóvágó, K.J. Varagy, J.C.S. Dalton Trans. (1997) 2587–2596.
[18] B.B. Ivanova, M. Mitewa, J. Coord. Chem. 57 (2004) 217–221.
[19] M. Kalic, J. Lauterwein, G. Busselmann, G. Kamp, Biochem. Biophys. Res. Commun. 269 (2000) 76–80.
[19a] Z.-Y. Wang, M. Shimonaga, Y. Muraoka, M. Kobayashi, T. Nozawa, Eur. J. Biochem. 268 (2001) 3375–3382.
[20] J. Paulik, F. Paulik, in: G. Svehla (Ed.), Comprehensive Analytical Chemistry, vol. XII, Elsevier, 1981, pp. 47–71.
[21] <http://webbook.nist.gov/chemistry> (accessed 04.06.08).
[22] X. Cao, G. Fischer, J. Phys. Chem. A 106 (2002) 41–50.
[23] J.D. Atwood, Inorganic and Organometallic Reaction Mechanisms, Wiley-VCH Inc., 1997. p. 46.
[24] V. Vasić, S. Premović, M. Čakar, B. Radak, G. Milovanović, J. Serb. Chem. Soc. 65 (2000) 345–352.
[25] C.R. Cantor, P.R. Schimmel, Biophysical Chemistry, Part I, W.H. Freeman, San Francisco, 1980. p. 49.
[26] R.G. Pearson, J. Am. Chem. Soc. 85 (1963) 3533–3539.
[27] R.G. Wilkins, Kinetics and Mechanism of Reactions of Transition Metal Complexes, Verlag, Berlin, 1991. p. 300 (Chapter 4).
[28] V.M. Vasić, M.A. Živanović, M.M. Čakar, J.Z. Savić, J.M. Nedeljković, Ž.D. Bugarčić, J. Phys. Org. Chem. 18 (2005) 441–447.
[29] V. Vasić, M. Čakar, J. Savić, B. Petrović, J. Nedeljković, Z. Bugarčić, Polyhedron 22 (2003) 279–286.
[30] M.S. Tošić, V.M. Vasić, J.M. Nedeljković, Lj. Ilić, Polyhedron 16 (1997) 1157–1160.
[31] V.M. Vasić, M.S. Tošić, T. Jovanović, Lj. Vujisić, J.M. Nedeljković, Polyhedron 17 (1998) 399–403.

Polyhedron 28 (2009) 600–608

Contents lists available at ScienceDirect

Polyhedron

journal homepage: www.elsevier.com/locate/poly

Metal–organic frameworks (MOFs) constructed from Zn^{II}/Cd^{II}-2,2′-bipyridines and polycarboxylic acids: Synthesis, characterization and microstructural studies ☆

Rishikesh Prajapati [a], Lallan Mishra [a,*], Keisaku Kimura [b], Pallepogu Raghavaiah [c]

[a] Department of Chemistry, Faculty of Science, Banaras Hindu University, Varanasi 221 005, India
[b] Graduate School of Material Science, University of Hyogo, Hyogo 678-1297, Japan
[c] National Single Crystal X-ray Diffractometer Facility, School of Chemistry, University of Hyderabad, Hyderabad 500 046, India

ARTICLE INFO

Article history:
Received 15 August 2008
Accepted 26 November 2008
Available online 8 January 2009

Keywords:
2,2′-Bipyridyl metal complexes
Polycarboxylate ligands
Metal–organic framework
Photoluminescence
Microstructures

ABSTRACT

Metal–organic frameworks with the compositions $[Zn(bpy)(bdc)(H_2O)]_n$ **1**, $[Zn(bpy)(btec)_{1/2}(H_2O)]_n$ **2**, $[Cd(bpy)(bdc)(H_2O)]_n$ **3** and $Cd(bpy)(btec)_{1/2}(H_2O)]_n$ **4** (H_2bdc = 1,4-benzenedicarboxylic acid = terephthalic acid, H_4btec = 1,2,4,5-benzenetetracarboxylic acid and bpy = 2,2′-bipyridine) have been synthesized and characterized using spectroscopic and single-crystal X-ray diffraction techniques. In these complexes, Zn^{II}/Cd^{II}-2,2′-bipyridine units and carboxylate anions exists as nodes and spacers respectively. An infinite 1D zig-zag chain structure is observed for both complexes **1** and **3**, whereas complexes **2** and **4** display a 3D supramolecular architecture. The complexes are found to be photoluminescent, porous and show significant thermal stability.

© 2008 Elsevier Ltd. All rights reserved.

1. Introduction

Recent years have witnessed rapid progress made in the construction of metal–organic frameworks (MOFs) owing to their intriguing molecular topologies [1–7] and potential applications in porosity [8–10], catalysis [11–15], ion exchange [16], chirality [17–21], luminescence [22–26], non-linear optics (NLO) [27–31], conductivity [32–35], optoelectronics [36,37], magnetism [38–42], spin-transition behavior [43–46], gas storage [47–49] and selective binding of molecules through absorption [13,50]. Most of the current studies in this area involve d^{10} transition metal ions with functional ligands. However, it is still considered a challenge to explore successful synthetic routes for the preparation of MOFs that could be exploited for targeted applications.

In this context, polycarboxylates are widely used in the development of supramolecular networks organized through coordination bonds, hydrogen bonds and π–π stacking interactions. Among these anionic polycarboxylates, 1,4-benzenedicarboxylic (H_2bdc) acid and 1,2,4,5-benzenetetracarboxylic acid (H_4btec) are extensively exploited as ligands in the construction of supramolecular architectures through their self-assembly [51–53].

In recent years, functional coordination polymers caught the attention of researchers owing to their potential applications in technology. Di-anionic dicarboxylate ligands are commonly used as molecular tethers for this work. These ligands can link metal cations into coordination polymer chains, layers or networks, in the process providing the charge balance necessary to avoid the inclusion of porosity-inhibiting smaller anions. The disposition of the donor groups within the dicarboxylate moieties, the coordination geometry preferences at the metal ions and the array of accessible carboxylate binding modes have been shown to act synergistically in the structure directed self-assembly of coordination polymers in solution. On the other hand, auxiliary ligands like 2,2′-bipyridine also impact on the conformations of the flexible carboxylic ligand (*trans*- or *cis*-), and play an important role in the formation of the final structure of the complex [54]. The terminal ligand 2,2′-bpy tends to construct low-dimension structures which can be extended into high-dimensional supramolecular networks through hydrogen bonds and π–π stacking interactions.

Thus, the present article is thought to be of worth as it deals with the synthesis and characterization of the structures obtained on the skeleton of d^{10} divalent metal (Zn^{II},Cd^{II})2,2′-bipyridines together with 1,2-benzenedicarboxylic acid and 1,2,4,5-tetracarboxylic acid. Since such types of metal–organic frameworks show the formation of porous structures [5], micro structural studies have also been carried out on these synthesized complexes.

2. Experimental

2.1. Materials and methods

Reagents of A.R. purity were purchased from standard commercial sources (Sigma–Aldrich, Merck) and were used without further

☆ A Part of the manuscript has been presented in RSC-CRSI Joint symposium NSC-10 held during January 31–February 03, 2008 at IISc Bangalore, India.

* Corresponding author. Tel.: +91 542 6702449; fax: +91 542 2368174.
E-mail address: lmishrabhu@yahoo.co.in (L. Mishra).

0277-5387/$ - see front matter © 2008 Elsevier Ltd. All rights reserved.
doi:10.1016/j.poly.2008.11.059

purification. Elemental analyses have been carried on a Carbo-Erba elemental analyzer 1108, and IR spectra were recorded as KBr pellets on a Varian 3100 FT-IR spectrometer. TGA measurements were performed on a Perkin Elmer Pyris diamond TG-DTA instrument at a heating rate of 5 °C/min in a nitrogen atmosphere with a flow rate of 200 ml/min in the temperature range 50–800 °C. Photoluminescence (PL) was measured using a Hitachi F-4500 spectrofluorometer. $M(bpy)(NO_3)_2 \cdot H_2O$ ($M = Zn^{II}/Cd^{II}$) were prepared using the procedure as reported by Sen et al. [55] for analogous complexes.

2.2. X-ray crystallographic studies

Suitable X-ray quality crystals of the complexes were grown directly from their corresponding reaction mixtures in DMF/EtOH/H_2O (6:2:0.4 by volume) at room temperature and X-ray crystallographic data were collected by mounting a single-crystal of the sample on a glass fiber. An Oxford diffraction XCALIBUR-S and Bruker SMART CCD area detector diffractometer equipped with an LN-2 low-temperature attachment was used for the determination of cell parameters and intensity data collection. Appropriate empirical absorption corrections using the programs multi-scan were applied. Monochromated Mo Kα radiation (λ = 0.71073 Å) was used for the measurements. The crystal structures were solved by direct methods [56] and refined by full matrix least squares SHELXL-97 [57]. Drawings were carried out using MERCURY [58] and DIAMOND [59], and special computations were carried out with PLATON [60].

2.3. Synthesis of the complexes

The complexes were synthesised by general procedures as reported by Guo et al. [61]. In a typical synthetic procedure, Zn^{II}(2,2′-bipyridyl)$(NO_3)_2 \cdot H_2O$ (0.363 g, 1 mmol) and Cd^{II}(2,2′-bipyridyl)$(NO_3)_2 \cdot H_2O$ (0.410 g, 1 mmol) were added separately to the corresponding solutions of H_2bdc (0.166 g, 1.0 mmol) and H_4btec (0.127 g, 0.5 mmol) dissolved in DMF (6 ml) and ethanol (2 ml) at room temperature, containing an equimolar amount of triethylamine. Few drops of 5N-HNO_3 (pH 4–5) was added until the mixture become clear. The mixture was heated at 120 °C for 6–8 h to give the corresponding complexes in 65–90% yield. The complexes thus isolated were found to be insoluble in water and common organic solvents.

2.3.1. Synthesis of [Zn(2,2′-bpy)(bdc)(H_2O)] **1**

Using the above procedure, after heating the components together at 120 °C for 6 h then cooling to room temperature, tiny round shaped crystals were obtained after two weeks, which were washed several times with diethylether. Yield: ~77%. *Anal.* Calc. for $C_{18}H_{14}N_2O_5Zn$ (**1**): C, 53.55; H, 3.50; N, 6.94. Found: C, 53.99; H, 3.68; N, 7.52%. IR (KBr, cm^{-1}): 3207 (w), 1590 (vs), 1474 (m), 1439 (s), 1376 (vs), 1313 (s) 1152 (w), 1020 (w), 840 (w), 753 (vs), 658 (m), 549 (m).

2.3.2. Synthesis of [Zn(2,2′-bpy)(btec)$_{1/2}$(H_2O)] **2**

Complex **2** was also synthesized using a similar method as used for the synthesis of complex **1** except that H_4btec was used instead of H_2bdc. After heating at 120 °C for 8 h and then cooling to room temperature colorless block shaped crystals were obtained after 10 days, which were washed with diethylether and dried. Yield: ~93%. *Anal.* Calc. for $C_{15}H_{11}N_2O_5Zn$ (**2**): C, 49.41; H, 3.04; N, 7.68. Found: C, 49.72; H, 3.38; N, 7.79%. IR (KBr, cm^{-1}): 3409 (w), 3071 (m), 1634 (vs), 1580 (s), 1483 (m), 1381 (vs), 1129 (vs), 1020 (s), 817 (m), 763 (vs), 654 (m), 540 (m), 458 (m).

2.3.3. Synthesis of [Cd(2,2′-bpy)(bdc)(H_2O)] **3**

Complex **3** was also synthesized using a similar procedure as used for the synthesis of complex **1** but $Cd(bpy)(NO_3)_2 \cdot H_2O$ was used instead of $Zn(bpy)(NO_3)_2 \cdot H_2O$. Colorless block shaped crystals of **3** were recovered after one week, which were washed several times with methanol followed by diethylether. Yield: ~66%. *Anal.* Calc. for $C_{18}H_{14}N_2O_5Cd$ (**3**): C, 47.97; H, 3.13; N, 6.22. Found: C, 48.22; H, 3.34; N, 5.92%. IR (KBr, cm^{-1}): 3368 (w), 3199 (w), 1571 (vs), 1434 (m), 1380 (vs), 1310 (m) 1153 (s), 1014 (s), 820 (s), 74 (vs), 651 (m), 534 (m).

2.3.4. Synthesis of [Cd(2,2′-bpy)(btec)$_{1/2}$(H_2O)] **4**

Using the above procedure, complex **4** resulted in colorless tiny round shaped crystals after three weeks, which were washed with methanol followed by diethylether. Yield: ~69%. *Anal.* Calc. for

Table 1
Summary of crystallographic data for complexes **1–4**.

Parameters	1	2	3	4
Formula	$C_{18}H_{14}N_2O_5Zn$	$C_{15}H_{11}N_2O_5Zn$	$C_{18}H_{14}N_2O_5Cd$	$C_{15}H_{11}N_2O_5Cd$
M	403.68	364.63	450.73	411.66
Crystal system	Triclinic	Triclinic	Monoclinic	Monoclinic
Temperature/K	150(2)	150(2)	133 (2)	298(2)
Space group	$P\bar{1}$	$P\bar{1}$	$P2_1/c$	$C2/c$
a (Å)	9.0826(11)	7.7085(3)	9.961(2)	18.991(4)
b (Å)	10.1697(12)	8.8712(5)	16.251(3)	7.6220(17)
c (Å)	10.5345(15)	10.7317(6)	11.901(2)	19.921(4)
α (°)	103.392(11)	80.690(5)	90	90
β (°)	113.643(12)	69.966(5)	117.41(1)	95.695(3)
γ (°)	100.673(10)	78.027(4)	90	90
V (Å)^3	823.83(18)	671.17(6)	1710.21	2869.3(11)
Z	2	2	4	8
D_c (Mg m^{-3})	1.627	1.804	1.750	1.906
Reflections collected	7670	6574	16866	14148
Reflections unique	2895	2360	3893	2821
R_{int}	0.0177	0.0280	0.0251	0.0271
Index ranges	$-10 \leqslant h \leqslant 10$	$-9 \leqslant h \leqslant 9$	$-12 \leqslant h \leqslant 12$	$-23 \leqslant h \leqslant 23$
	$-12 \leqslant k \leqslant 12$	$-10 \leqslant k \leqslant 10$	$-21 \leqslant k \leqslant 21$	$-9 \leqslant k \leqslant 9$
	$-12 \leqslant l \leqslant 12$	$-12 \leqslant l \leqslant 12$	$-15 \leqslant l \leqslant 15$	$-24 \leqslant h \leqslant 24$
Refinement method		Full-matrix, least squares on F^2		
wR_2	0.0568	0.0549	0.0689	0.0582
R_1	0.0212	0.0231	0.0283	0.0251
Goodness-of-fit (GoF)	1.059	1.047	0.975	1.058

Table 2
Selected bond lengths (Å) and angles (°) for complexes **1**–**4**.

*Compound **1***			
Zn(1)–O(4)	2.0240(12)	O(4)–Zn(1)–O(1)	128.65(5)
Zn(1)–O(1)	2.0346(13)	O(1)–Zn(1)–N(2)	128.24(6)
Zn(1)–O(2)	2.0423(12)	O(4)–Zn(1)–N(2)	103.05(5)
Zn(1)–N(2)	2.0946(15)	O(2)–Zn(1)–N(1)	164.17(6)
Zn(1)–N(1)	2.1650(15)	N(2)–Zn(1)–N(1)	76.88(6)
O(1)–H(102)	0.83(3)	O(4)–Zn(1)–N(1)	97.33(5)
O(1)–H(101)	0.91(3)	O(4)–Zn(1)–O(2)	94.87(5)
O(5)–C(15)	1.246(2)	H(102)–O(1)–H(101)	104(2)
*Compound **2***			
Zn(1)–O(2)	1.9843(14)	O(2)–Zn(1)–N(2)	125.10(6)
Zn(1)–O(1)	2.0356(17)	O(1)–Zn(1)–N(2)	134.33(7)
Zn(1)–O(5)#1	2.0580(14)	O(2)–Zn(1)–O(1)	100.04(7)
Zn(1)–N(2)	2.0818(19)	O(5)#1–Zn(1)–N(1)	162.03(6)
Zn(1)–N(1)	2.1649(18)	O(2)–Zn(1)–N(1)	103.70(6)
O(1)–H(101)	0.91(3)	O(2)–Zn(1)–O(5)#1	94.24(6)
O(1)–H(102)	0.76(3)	N(2)–Zn(1)–N(1)	76.85(7)
O(3)–C(11)	1.215(3)	H(101)–O(1)–H(102)	111(3)
*Compound **3***			
Cd(1)–O(1)	2.213(10)	O(3)–Cd(1)–N(1)	88.10(5)
Cd(1)–O(3)	2.395(11)	O(3)–Cd(1)–O(4)	55.18(7)
Cd(1)–O(4)	2.371(13)	O(4)–Cd(1)–N(2)	95.51(7)
Cd(1)–O(5)	2.265(12)	N(1)–Cd(1)–N(2)	71.35(5)
Cd(1)–N(1)	2.314(12)	O(1)–Cd(1)–N(1)	157.63(6)
Cd(1)–N(2)	2.336(13)	O(5)–Cd(1)–N(1)	126.31(6)
O(5)–H(13)	0.943(4)	O(5)–Cd(1)–N(2)	97.41(4)
O(5)–H(14)	0.902(3)	O(1)–Cd(1)–O(4)	106.65(7)
C(11)–O(2)	1.249(4)	H(13)–O(5)–H(14)	112.18(5)
*Compound **4***			
Cd(1)–O(4)	2.2286(18)	O(1)–Cd(1)–N(2)	88.07(9)
Cd(1)–O(2)	2.2753(18)	O(2)–Cd(1)–O(1)	77.03(9)
Cd(1)–O(1)	2.309(2)	O(2)–Cd(1)–O(7)#3	53.18(6)
Cd(1)–N(1)	2.312(2)	O(1)–Cd(1)–N(1)	142.71(9)
Cd(1)–N(2)	2.332(2)	N(1)–Cd(1)–N(2)	70.83(7)
Cd(1)–O(7)#3	2.589(2)	O(4)–Cd(1)–N(2)	157.23(8)
O(1)–H(1A)	0.79(4)	N(2)–Cd(1)–O(7)#3	106.24(7)
O(1)–H(2B)	0.82(5)	O(4)–Cd(1)–O(7)#3	86.34(7)
C(11)–O(5)	1.241(3)	H(1A)–O(1)–H(2B)	108(4)

$C_{15}H_{11}N_2O_5Cd$ (4): C, 43.76; H, 2.69; N, 6.80. Found: C, 44.23; H, 2.61; N, 7.02%. IR (KBr, cm^{-1}): 3405 (w), 3065 (m), 1560 (vs), 1491 (m), 1379 (vs), 1319 (w) 1135 (m), 1014 (s), 869 (s), 769 (vs), 651 (m), 532 (m).

3. Result and discussion

3.1. IR spectra

Major peaks observed between ~1600 and ~1200 cm^{-1} are assigned to υ(bpy) and υ(phenyl) of the benzenecarboxylate ligands. The $\upsilon_{as}(COO^-)$ and $\upsilon_s(COO^-)$ bands are observed at ~1570 and ~1380 cm^{-1} respectively [62]. The peaks lying in the region ~3400 to ~3200 cm^{-1} are assigned to υH_2O(coordinated) whereas $\rho r H_2O$(coordinated) and $\rho w H_2O$(coordinated) appear at ~655 and ~540 cm^{-1} respectively.

3.2. Structural description of the complexes

Crystallographic data and refinement details for the structural analyses of all the complexes are summarized in Table 1. Selected bond lengths and bond angles with their estimated standard deviations are presented in Table 2 while selected parameters for weak interactions are listed in Table 3. Molecular structures (ORTEP diagrams) of the complexes **1**–**4** are shown in Fig. 1.

3.2.1. Complex *1* and *2*

The X-ray single-crystal structure determination reveals that complex **1** exists as a neutral one-dimensional infinite zig-zag coordination chain. Each Zn^{II} center is surrounded by two N donors from the 2,2′-bipyridine ring, two oxygen atoms from two carboxylate groups of two different terephthalic acid molecules together with one water molecule, in a distorted pentacoordinated geometry, as depicted in Fig. 1a. The neighboring Zn^{II} centers are connected by a terephthalate dianionic moiety which acts as a bridge through its benzene ring, as shown in Fig. 2a. The two terephthalate units are almost orthogonal to each other with a dihedral angle of 88.87° and the two Zn^{II} centres are separated at a distance of 11.10 Å. In this structure, the 2,2′-bipyridine molecule acts as a

Table 3
Selected parameters for weak interactions in complexes **1**–**4**.

D–H···A	D–H (Å)	H···A (Å)	D···A (Å)	DHA (°)	Symmetry code
1					
O(1)–H(101) ···O(3)	0.91	1.74	2.6056	158	–
O(1)–H(102)···O(5)	0.83	1.86	2.6895	177	1 − *x*, 1 − *y*, 1 − *z*
C(1)–H(1)···O(5)	0.93	2.54	3.3322	143	1 − *x*, 1 − *y*, 1 − *z*
C(7)–H(7)···O(4)	0.93	2.49	3.3072	146	−*x*, −*y*, −*z*
C(10)–H(10)···O(2)	0.93	2.45	3.0188	119	–
C(18)–H(18)···O(1)	0.93	2.54	3.4108	156	1 − *x*, 1 − *y*, 1 − *z*
2					
O(1)–H(101)···O(2)	0.91	1.75	2.656	176	1 − *x*, 1 − *y*, −*z*
O(1)–H(102)···O(4)	0.76	2.11	2.7422	141	–
O(1)–H(102)···O(4)	0.76	2.59	3.0607	122	−*x*, 1 − *y*, −*z*
C(3)–H(3)···O(3)	0.93	2.55	3.1815	125	1 − *x*, 1 − *y*,1 − *z*
C(7)–H(7)···O(4)	0.93	2.42	3.325	164	−*x*, 1 − *y*, 1 − *z*
C(10)–H(10)···O(5)	0.93	2.52	3.716	118	–
3					
O(5)–H(13)···O(2)	0.94	1.75	2.662	162	–
O(5)–H(14)···O(4)	0.90	1.79	2.688	178	1 − *x*, −*y*, −*z*
C(4)–H(4)···O(3)	0.95	2.35	3.275	165	*x*, 1 − *y*, 1 − *z*
C(7)–H(5)···O(3)	0.95	2.59	3.498	160	−*x*, −*y*, −*z*
C(16)–H(11)···O(3)	0.95	2.49	2.805	131	–
C(14)–H(10)···O(4)	0.95	2.56	2.853	112	*x*, ½ − *y*, ½ + *z*
4					
O(1)–H(1A)···O(5)	0.79	2.07	2.7904	152	½ − *x*, ½ + *y*, ½ − *z*
O(1)–H(2B)···O(2)	0.82	1.89	2.6867	162	½ − *x*, −½ + *y*, ½ − *z*
C(2)–H(2)···O(7)	0.93	2.44	3.3543	166	−*x*, 2 − *y*, −*z*
C(3)–H(3)···O(2)	0.93	2.59	3.5000	165	*x*, 2 − *y*, −½ + z
C(4)–H(4)···O(5)	0.93	2.49	3.3802	162	½ − *x*, $3/_2$ − *y*, -*z*
C(8)–H(8)···O(7)	0.93	2.58	3.1141	117	½ − *x*, $^5/_2$ − *y*, −*z*

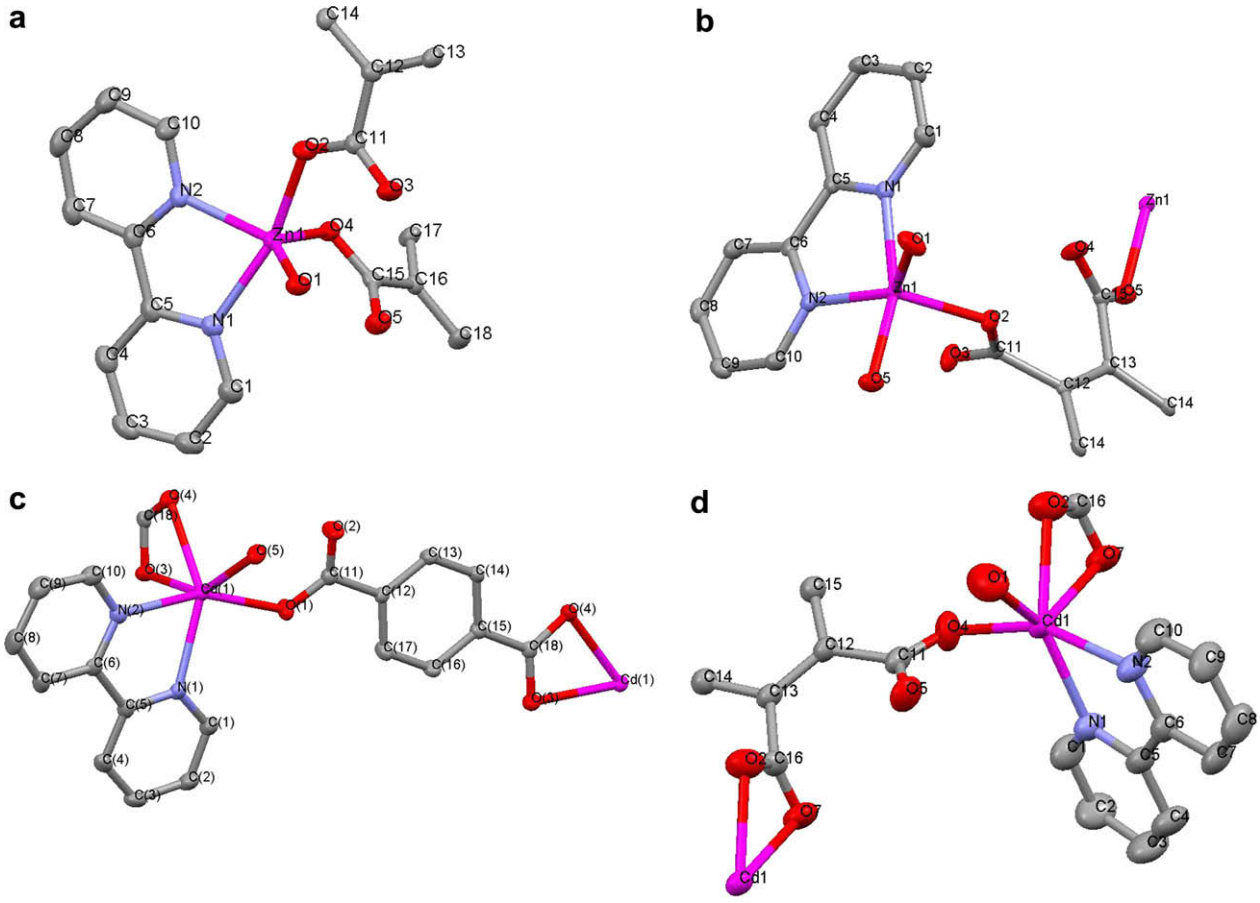


Fig. 1. Molecular structures of complexes **1**(a), **2**(b), **3**(c) and **4**(d).

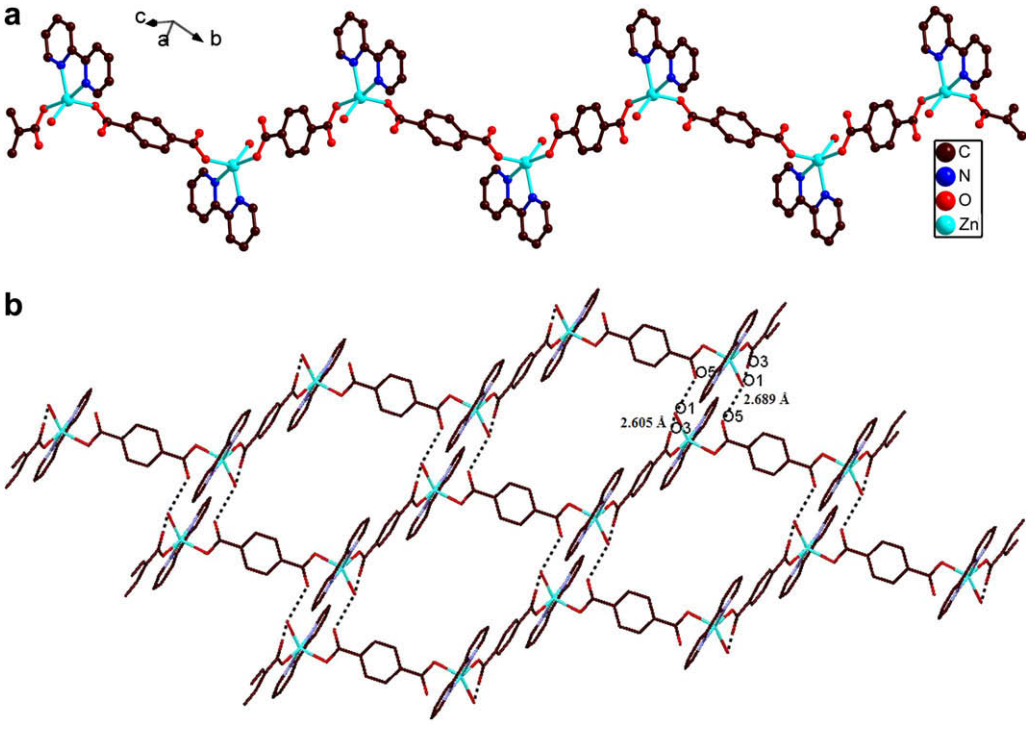


Fig. 2. ID zig-zag chain (a) and supramolecular 2D sheet network of complex **1** containing hydrogen bonds and π–π stacking (b).

peripheral ligand. It prevents the chain growth in a straight forward direction; hence a zigzag chain is formed.

It is very interesting to note that two independent chains are linked through hydrogen bonds formed between coordinated

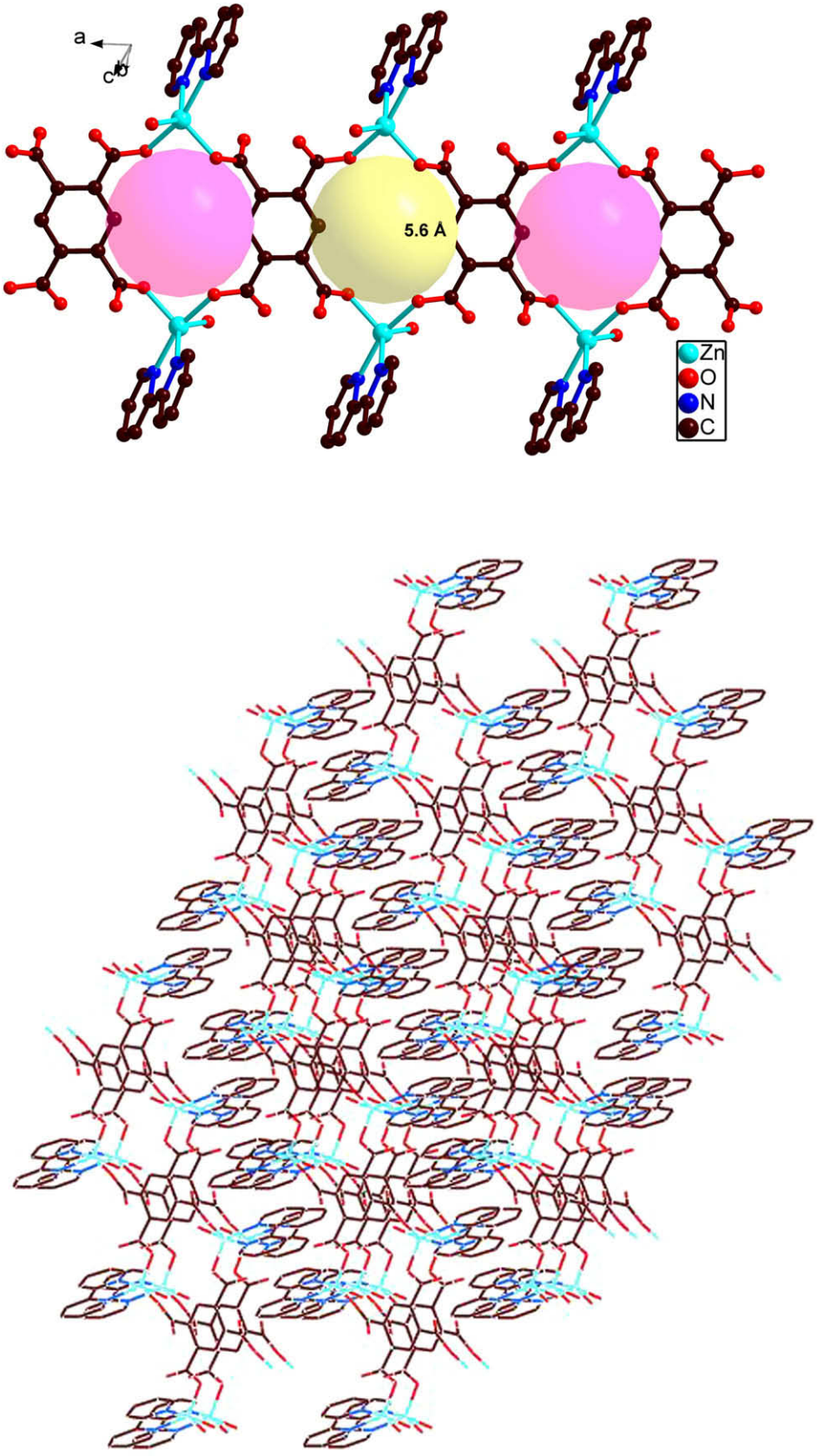


Fig. 3. 1D linear chain with the continuous cavity of diameter ~5.6 Å (a), crystal packing in complex **2** through inter- and intra-molecular H-bonding and π–π stacking (b).

water molecules and the carbonyl oxygen atoms of theterephthalate dianion, in addition to π–π stacking interactions between the 2,2′-bpy rings at a distance of 3.80 Å. It results in the formation of a 2D sheet-like supramolecular structure (Fig. 2c).

Crystal packing analysis of complex **1** shows the formation of independent intra-chain (O–H···O) as well as inter-chain (O–H···O) hydrogen bonds (Table 3). The intra-chain hydrogen bond is formed between the O–H group of the coordinated water molecule and an uncoordinated carboxylate oxygen at a D···A distance of 2.6056 Å and an O–H–O angle of 158°. However, in the formation of the inter-chain O–H···O hydrogen bonds, the O–H group of the coordinated water molecule of one chain is linked through the uncoordinated oxygen atoms of the terephthalate dianion of the adjacent chain at a D···A distance of 2.6895 Å and an O–H–O angle of 177°. The KPI for this complex, found to be 71.8%, indicates compact packing in its crystal lattice.

The molecular structure of the Zn^{II} complex with benzenetetracarboxylic acid (H_4btec), **2**, is depicted in Fig. 1b. This complex is also pentacoordinated, but the two carboxylate oxygen atoms (O2 and O5) come from two different carboxylate groups, acting in a monodentate fashion, together with one oxygen atom (O1W) of the coordinating water molecule and in addition to two nitrogen atoms (N1 and N2) from the 2,2′-bipyridine ring. As shown in Table 2, one Zn–O (carboxylate) distance, Zn(1)–O(2) 1.9843(14) Å, is found to be shorter than the Zn–O (carboxylate) distance Zn(1)–O(2) = 2.0423(12) Å as found in complex **1**. Other distances in this complex are comparable with the bond distances observed in complex **1**.

It is quite interesting to observe from Fig. 3a, that each carboxylate group is acting as a linker between four Zn(bpy) units, out of these four units, two units are common in the formation of a 16-membered macrocyclic ring of diameter ~5.6 Å. This 16-membered macrocyclic ring extends along the molecular axis in a linear fashion and provides a chain structure. The distance between two Zn^{II} centres across the cavity is found to be 8.144 Å, whereas adjacent Zn^{II} centres are separated by a distance of 7.709 Å (Fig. 3b).

Weak force studies reveal that six hydrogen bonds are formed in the molecular packing of complex **2**. Three hydrogen bonds are conventional hydrogen bonds whereas the remaining three

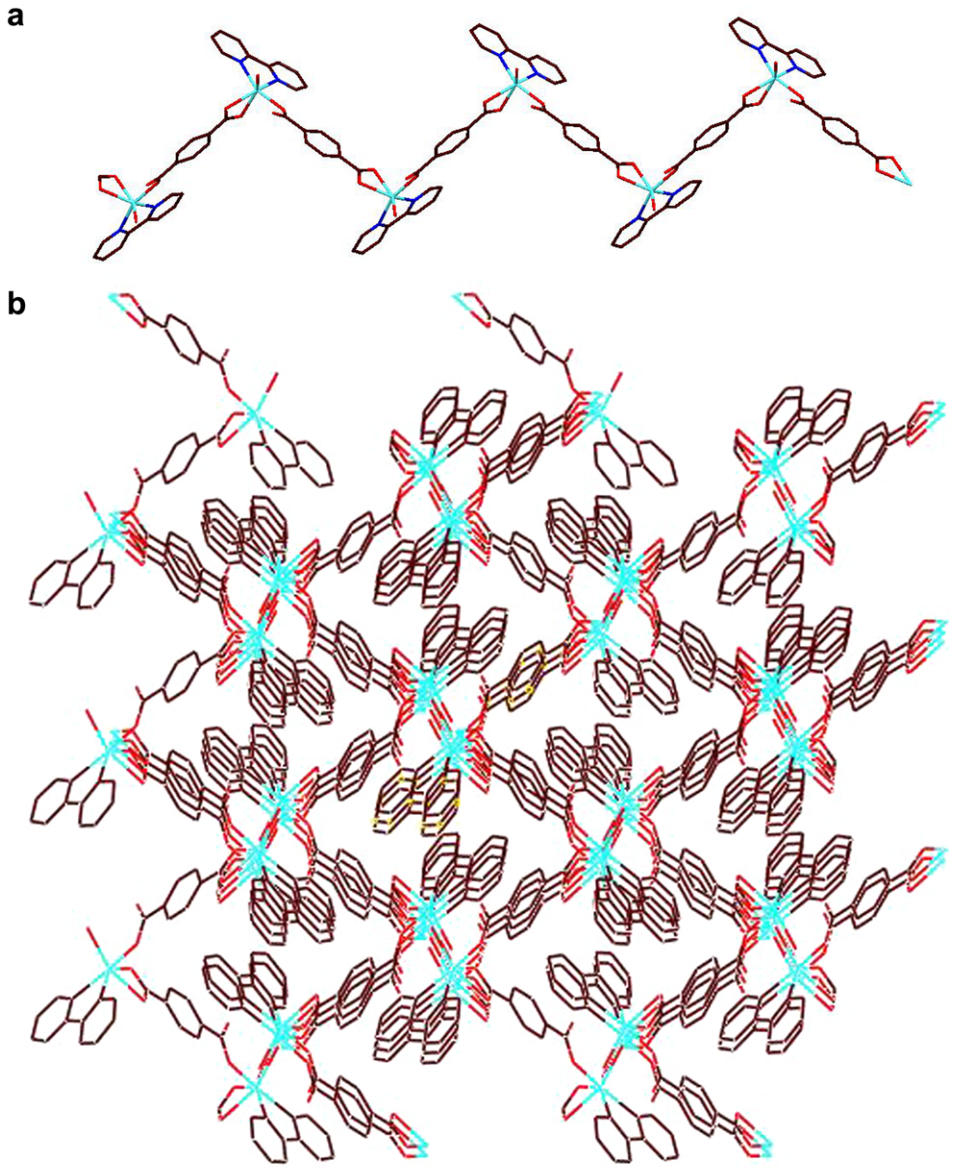


Fig. 4. 1D zig-zag chain (a), view of the crystal packing along the *a*-axis, the packing is stabilized through π–π stacking between bipyridyl rings and H-bonding in complex **3**.

bonds are non-conventional hydrogen bonds. The non-conventional hydrogen bonds involve C–H units as donor groups, whereas the acceptors are oxygen atoms in each case (Table 3). This complex has a Kitagorodskii Packing Index (KPI) of 76.6%, indicating a compact packing with no solvent accessible voids. In complex **1** the KPI value is found to be 71.8%. Thus the Zn(bpy)-benzenetetracarboxylate complex **2** possess more compact packing as compared to the Zn(bpy)-dicarboxylate complex **1**.

Both inter and intra molecular hydrogen bonds, in addition to π–π stacking interactions, provide a 3D supramolecular architecture (Fig. 3b) in complex **2**.

3.2.2. Complex *3* and *4*

Complex **3** is a Cd^{II} analogue of complex **1**. It also possesses an infinite zig-zag one-dimensional chain structure, but each Cd^{II} ion is hexa-coordinated in a highly distorted octahedral geometry (Fig. 4a). The formation of a seven coordinated CdN_2O_5 core has been reported [63] for a complex of Cd^{II} with the terephthalate dianion, but it contains 1,10-phenanthroline as one of the components instead of 2,2′-bipyridine as used in the present complex.

In the present complex **3**, the CdN_2O_4 coordinated core consists of two nitrogen atoms (N1 and N2) from 2,2′-bpy, one oxygen atom [O(5)] from a water molecule together with one oxygen atom (O1) from one terephthalate dianion and other two oxygen donors atoms [O(3) and O(4)] from another terephthalate unit which lies nearly orthogonal to the first terephthalate unit (dihedral angle: 80.16 °). It is interesting to note that each terephthalate unit serves as a bridging ligand between two cadmium atoms, forming a one-dimensional zig-zag polymeric chain (Fig. 4a). However, the bridging terephthalate dianion linked to two Cd^{II} ion, acts as monodentate at one coordination end and bidentate to another coordination end. Thus, one bridging terephthalate unit overall acts as a tridentate ligand and links two Cd^{II} ions at a distance of 11.341 Å. This distance is a little larger than the distance of 11.10 Å observed between the two Zn^{II} ions in complex **1**. This difference may be explained by the larger size and higher coordination mode of the Cd^{II} ion as compared to the Zn^{II} ion.

The cell packing analysis, as depicted in Fig. 4b, shows that both coordinated planes, as well as the bridging ligand plane, are more tilted from the crystallographic plane as compared to that

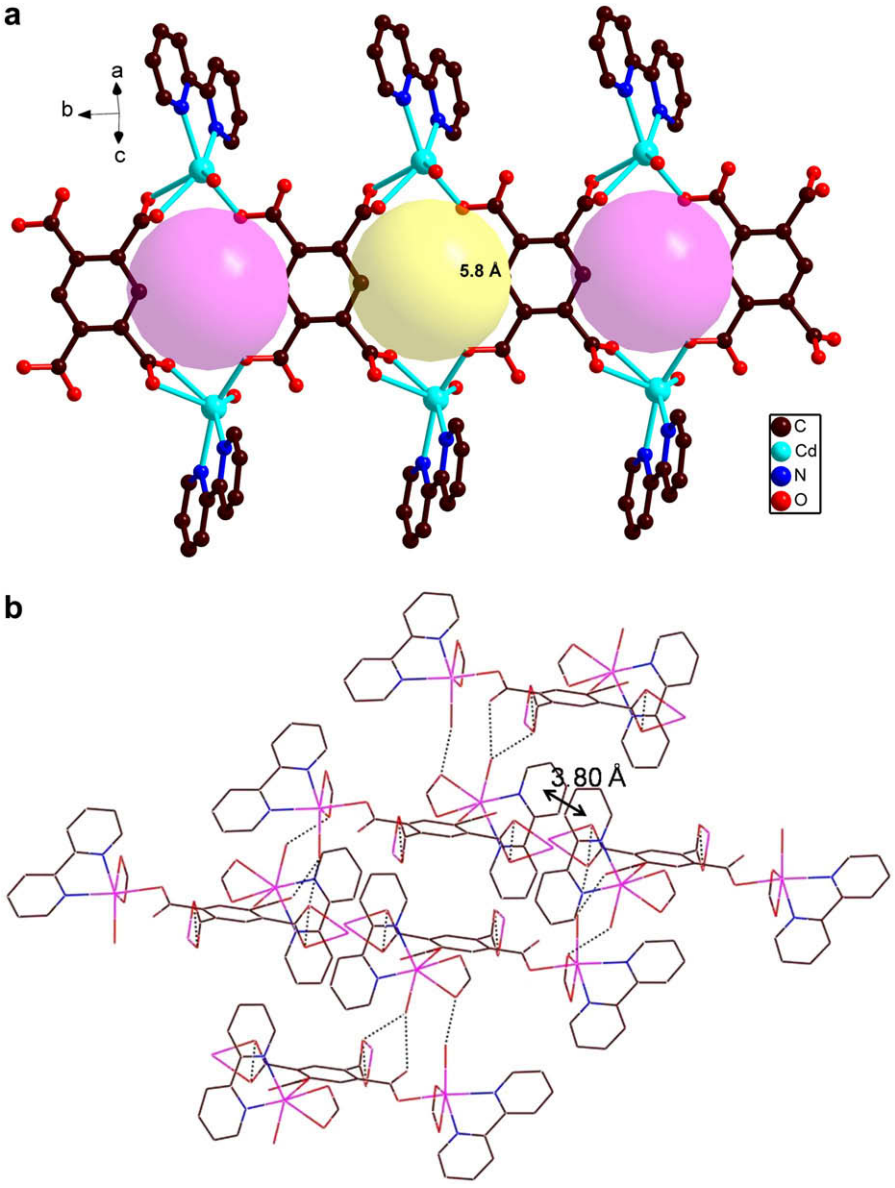


Fig. 5. 1D linear chain containing the continuous cavity of diameter of ~5.8 Å (a), packing of molecules in the crystal lattice; H-bonding and π–π stacking in complex **4**.

observed in the analogous Zn^{II} complex **1**. This may be understood due to the different modes of coordination (monodentate and bidentate) of the same ligand.

The crystal packing of complex **3** consists of two conventional and four non-conventional hydrogen bonds. In all cases, oxygen atoms acts as the acceptor atoms. The intra-molecular hydrogen bonding is formed between O(5)–H(13) and O(2) at a H···A distance of 1.75 Å with an O–H–O angle of 162°, whereas inter-molecular hydrogen bonding between O(5)–H(14) is formed at a H···A distance of 1.79 Å with an O–H–O angle of 178°. It indicates that two structural units are attached closely through hydrogen bonding. Out of the four non-conventional hydrogen bonds, two intra-molecular hydrogen bonds are formed at H···A distances of 2.35 (C4–H4···O3) and 2.59 Å (C7–H5···O3), whereas inter-molecular non-conventional hydrogen bonds are formed at the larger distances of 2.49 and 2.56 Å.

Complex **4** also possesses a distorted octahedral coordination geometry with a CdN_2O_4 coordination core around the Cd^{II} ion. In the construction of this structure, btec acts as hexadentate ligand, bis (bidentate + monodentate). However, again in a recently reported Cd^{II} complex containing 1,10-phenanthroline as a terminal ligand, btec acted in a tetrakis(bidentate) fashion [63]. Thus, the presence of the 2,2′-bipyridine ring as a terminal ligand alters the mode of coordination of the btec ligand. Additionally, one btec ligand links four Cd^{II} ions in the present complex **4** whereas the same btec ligand linked six Cd^{II} ions in the earlier reported complex [63]. Thus, the effect of the terminal ligand on the coordinating mode of the tetradentate ligand is quite evident.

The unit cell packing mode of complex **4**, depicted in Fig. 5a, again shows the formation of a 16-membered ring, but a little change in the ring size is observed (5.8 Å diameter in complex **4** as compared to 5.6 Å in complex **2**). Six hydrogen bonds (two conventional and four non-conventional) are found in the weak force studies of complex **4**.

3.3. Photoluminescent properties

The photoluminescent properties of complexes **1–4** are examined at room temperature and the corresponding spectral features are shown in Fig. 6. Upon excitation at λex = 340 nm, complex **1** emits at 365 nm with a shoulder at 430 nm, while in complex **2** the corresponding peaks are red shifted and appear at 370 and 435(sh) nm. Since solid-state emissions from the free 2,2′-bpy group are also observed in a similar region at λem = 360 and 385 nm due to the π–π^* transition, the strong emissions arising from complexes **1** and **2** are assigned to intra-ligand fluorescence of the coordinated 2,2′-bpy ligand. However, weak emissions from complexes **1** and **2** observed at 430 (sh) and 435 (sh) nm respectively are considered to arise from a charge-transfer transition, consistent with earlier reports [64–66]. Additionally, multiple emissions arising at 400, 462(sh) and 520(sh) nm for complex **3**, and 401, 465(sh) and 523(sh) nm for complex **4** are assigned to a combination of strong π–π^* transitions of the coordinated 2,2′-bpy ligand along with weak π–π^* transition from both bdc and btec ligands.

3.4. Thermogravimetric (TG) analysis

Thermogravimetric analyses (TGA) performed on crystalline samples under a nitrogen atmosphere are depicted in S1. In complex **1**, a weight loss of 4.40% at 100–220 °C is assigned to the loss of coordinated water molecules (calculated per formula unit weight loss = 4.45%). This loss is further followed by a second weight loss of 38.60% in the temperature range 241–270 °C, corresponding to the loss of the terminal 2,2′-bpy group. The final decomposition starts at 280 °C and continues up to 800 °C, at which only 45% residue remains, which may be due to carbon residues as well as metal oxides. Complex **2** shows a weight loss (47.9%) only after 230 °C, corresponding to the removal of the coordinated water molecule together with the 2,2′-bpy ligand (calculated 47.71%) from the structural framework. At 800 °C complex **2** also shows 41.25% residue remains. Multiple steps of weight loss occur upon heating complexes **3** and **4**.

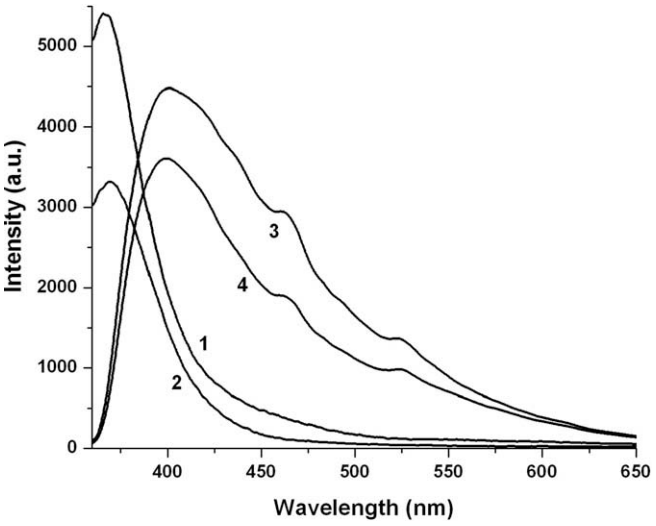


Fig. 6. Photoluminescence spectra of complexes **1**–**4** in the solid-state at room temperature.

3.5. Microstructural studies

Since such structural frameworks of complexes are constructed from hetero components, the formation of porosity in their bulk structure may be looked upon. Therefore, their SEM images were recorded. The SEM images of the complexes show the formation of micro-sized grains varying from 10–30 μm in complex **1** to 15–70 μm in complex **2**. In between these grains, pores can be seen which are dispersed throughout the structure (marked as 'P') (S2). The SEM micrograph of complex **3** shows the presence of parallelepipeds crystals with an average size of $25 \times 5 \times 4\ \mu m^3$ whereas in complex **4**, the grain size varies in the 15–30 μm range.

4. Conclusion

In summary, the reactions of Zn^{II}/Cd^{II}-2,2′-bipyridine with di and tetra carboxylates under mild conditions (pH 4–5) provide a series of photoluminescent polymeric complexes with diverse architectures from zig-zag chains (complexes **1** and **3**) to straight chains (complexes **2** and **4**). The weak forces of inter-molecular and intra-molecular hydrogen bonding interactions together with π–π aromatic stacking interactions provide a two-dimensional layer for complex **1**, whereas for complexes **2**, **3** and **4**, three-dimensional supramolecular networks result as a secondary structure. The complexes with the tetracarboxylate ligand provide a 16-membered metallomacrocyclic cavity of diameter 5.6 Å in **2** and 5.8 Å in **4**. Additionally, the presence of 2,2′-bipyridine rings is found to alter the coordination behavior of the carboxylates.

Acknowledgements

Authors thank the authorities of SAIF, CDRI, Lucknow and IIC, IIT Roorkee, India for providing analytical data. Help rendered by Prof. T. Shinmyozu, Kyushu University, Japan for X-ray analysis is grate-

fully acknowledged. Financial assistances received from UGC, CSIR New Delhi and BRNS, Mumbai, India are gratefully acknowledged.

Appendix A. Supplementary data

CCDC 646994, 650284, 685998 and 696004 contain the supplementary crystallographic data for **1–4**. These data can be obtained free of charge via http://www.ccdc.cam.ac.uk/conts/retrieving.html, or from the Cambridge Crystallographic Data Centre, 12 Union Road, Cambridge CB2 1EZ, UK; fax: (+44) 1223-336-033; or e-mail: deposit@ccdc.cam.ac.uk. Supplementary data associated with this article can be found, in the online version, at doi:10.1016/j.poly.2008.11.059.

References

[1] B. Moulton, M.J. Zaworotko, Chem. Rev. 101 (2001) 1629.
[2] Q.R. Fang, G.S. Zhu, M. Xue, J.Y. Sun, Y. Wei, S.L. Qiu, R.R. Xu, Angew. Chem., Int. Ed. 44 (2005) 3845.
[3] M. Eddaoudi, D.B. Moler, H. Li, B. Chen, T.M. Reineke, M. O'Keefee, O.M. Yaghi, Acc. Chem. Res. 34 (2001) 319.
[4] X. Zhao, B. Xiao, A.J. Fletcher, K.M. Thomas, D. Bradshaw, M.J. Rosseinsky, Science 306 (2004) 1012.
[5] S. Kitagawa, R. Kitaura, S. Noro, Angew. Chem., Int. Ed. 43 (2004) 2334.
[6] C. Janiak, J. Chem. Soc., Dalton Trans. (2003) 2781.
[7] S.R. Batten, R. Robson, Angew. Chem., Int. Ed. 37 (1998) 1460.
[8] A.C. Sudik, A.R. Millward, N.W. Ockwig, A.P. Côté, J. Kim, O.M. Yaghi, J. Am. Chem. Soc. 127 (2005) 7110.
[9] B.L. Chen, C.D. Liang, J. Yang, D.S. Contreras, Y.L. Clancy, E.B. Lobkovsky, O.M. Yaghi, S. Dai, Angew. Chem., Int. Ed. 45 (2006) 1390.
[10] L. Pan, H.M. Liu, X.G. Lei, X.Y. Huang, D.H. Olson, N.J. Turro, J. Li, Angew. Chem., Int. Ed. 42 (2003) 542.
[11] M. Fujita, Y.K. Kwon, S. Washizu, K. Ogura, J. Am. Chem. Soc. 116 (1994) 1151.
[12] U. Mueller, M. Hesse, L. Lobree, M. Hoelzle, J.D. Arndt, P. Rudolf, WO 2002/070526, 2002, BASF Aktiengesellschaft.
[13] J.S. Seo, D. Whang, H. Lee, S.I. Jun, J. Oh, Y.J. Jeon, K. Kim, Nature 404 (2000) 982.
[14] T. Sawaki, T. Dewa, Y. Aoyama, J. Am. Chem. Soc. 120 (1998) 8539.
[15] T. Sawaki, Y. Aoyama, J. Am. Chem. Soc. 121 (1999) 4793.
[16] S.L. James, Chem. Soc. Rev. 32 (2003) 276.
[17] C. Janiak, Angew. Chem., Int. Ed. Engl. 36 (1997) 1431.
[18] M.A. Withersby, A.J. Blake, N.R. Champness, P. Hubberstey, W.-S. Li, M. Schröder, Angew. Chem., Int. Ed. Engl. 36 (1997) 2327.
[19] X. Shi, G.S. Zhu, S.L. Qiu, K.L. Huang, J.H. Yu, R.R. Xu, Angew. Chem., Int. Ed. 43 (2004) 6482.
[20] R. Xiong, X. You, B.F. Abrahams, Z. Xue, C. Che, Angew. Chem., Int. Ed. 40 (2001) 4422.
[21] A.J. Blake, N.R. Champness, A.N. Khlobystov, S. Parsons, M. Schröder, Angew. Chem., Int. Ed. Engl. 39 (2000) 2317.
[22] T.M. Reineke, M. Eddaoudi, M. Fehr, D. Kelley, O.M. Yaghi, J. Am. Chem. Soc. 121 (1999) 1651.
[23] M.C. Brandys, R.J. Puddephatt, J. Am. Chem. Soc. 123 (2001) 4839.
[24] Q.R. Fang, G.S. Zhu, X. Shi, G. Wu, G. Tian, R.W. Wang, S.L. Qiu, J. Solid State Chem. 177 (2004) 1060.
[25] J.-C. Dai, X.-T. Wu, Z.-Y. Fu, C.-P. Cui, S.-M. Hu, W.-X. Du, L.-M. Wu, H.-H. Zhang, R.-Q. Sun, Inorg. Chem. 41 (2002) 1391.
[26] H.-K. Fun, S.S.S. Raj, R.-G. Xiong, J.-L. Zuo, Z. Yu, X.-Z. You, J. Chem. Soc., Dalton Trans. (1999) 1915.
[27] O.R. Evans, R.-G. Xiong, Z.Y. Wang, G.K. Wong, W. Lin, Angew. Chem., Int. Ed. 38 (1999) 536.
[28] H. Hou, X. Meng, Y. Song, Y. Fan, Y. Zhu, H. Lu, C. Du, W. Shao, Inorg. Chem. 41 (2002) 4068.
[29] H. Hou, Y. Wei, Y. Song, Y. Zhu, L. Li, Y. Fan, J. Mater. Chem. 12 (2002) 838.
[30] H. Hou, Y. Song, Y. Fan, L. Zhang, C. Du, Y. Zhu, Inorg. Chim. Acta 316 (2001) 140.
[31] H. Hou, Y. Wei, Y. Fan, C. Du, Y. Zhu, Y. Song, Y. Niu, X. Xin, Inorg. Chim. Acta 319 (2001) 212.
[32] C.N.R. Rao, A. Ranganathan, V.R. Pedireddi, A.R. Raju, Chem. Commun. (2000) 39.
[33] Y. Zhao, M. Hong, Y. Liang, R. Cao, W. Li, J. Weng, S. Lu, Chem. Commun. (2001) 1020.
[34] S. Wang, D.B. Mitzi, C.A. Field, A.M. Guloy, J. Am. Chem. Soc. 117 (1995) 5297.
[35] D.B. Mitzi, S. Wang, C.A. Field, C.A. Chess, A.M. Guloy, Science 267 (1995) 1473.
[36] W. Chen, H.M. Yuan, J.Y. Wang, Z.Y. Liu, J.J. Xu, M. Yang, J.S. Chen, J. Am. Chem. Soc. 125 (2003) 9266.
[37] Q.R. Fang, G.S. Zhu, M. Xue, Q.L. Zhang, J.Y. Sun, X.D. Guo, S.L. Qiu, S.T. Xu, P. Wang, D.J. Wang, Y. Wei, Chem. J. Eur. 12 (2006) 3754.
[38] S.R. Batten, P. Jensen, B. Moubaraki, K.S. Murray, R. Robson, Chem. Commun. (1998) 439.
[39] J.L. Manson, C.R. Kmety, Q. Huang, J.W. Lynn, G.M. Bendele, S. Pagola, P.W. Stephens, L.M. Liable-Sands, A.L. Rheingold, A.J. Epstein, J.S. Miller, Chem. Mater. 10 (1998) 2552.
[40] P. Jensen, S.R. Batten, G.D. Fallon, B. Moubaraki, K.S. Murray, D.J. Price, Chem. Commun. (1999) 177.
[41] A.M. Kutasi, S.R. Batten, Chem. Commun. (2002) 1050.
[42] B. Moubaraki, K.S. Murray, J. Chem. Soc., Dalton Trans. (2002) 819.
[43] P.J. van Koningsbruggen, Y. Garcia, E. Codjovi, R. Lapouyade, O. Kahn, L. Fournès, L. Rabardel, J. Mater. Chem. 7 (1997) 2069.
[44] E. Codjovi, L. Sommier, O. Kahn, C. Jay, New J. Chem. 20 (1996) 503.
[45] J. Kröber, J.-P. Audière, R. Claude, E. Codjovi, O. Kahn, J.G. Haasnoot, F. Grolière, C. Jay, A. Bousseksou, J. Linarès, F. Varret, A. Gonthier-Vassal, Chem. Mater. 6 (1994) 1404.
[46] O. Kahn, C.J. Martinez, Science 279 (1998) 44.
[47] J.L.C. Roswell, O.M. Yaghi, Angew. Chem., Int. Ed. Engl. 44 (2005) 4670.
[48] A.C. Sudik, A.R. Millward, N.W. Ockwig, A.P. Cote, J. Kim, O.M. Yaghi, J. Am. Chem. Soc. 127 (2005) 7110.
[49] M. Kondo, T. Okubo, A. Asami, S.-I. Noro, T. Yoshitomi, S. Kitagawa, T. Ishii, H. Matsuzaka, Angew. Chem., Int. Ed. Engl. 38 (1999) 140.
[50] A. Cingolani, S. Galli, N. Masciocchi, L. Pandolfo, C. Pettinari, A. Sironi, J. Am. Chem. Soc. 127 (2005) 6144.
[51] L.-Y. Zhang, G.-F. Liu, S.-L. Zheng, B.-H. Ye, X.-M. Zhang, X.-M. Chen, Eur. J. Inorg. Chem. (2003) 2965, and references therein.
[52] X.-M. Lu, P.-Z. Li, X.-T. Wang, S. Gao, X.-J. Wang, S. Wang, Y.-H. Deng, Y.-J. Zhang, L. Zhou, Polyhedron 27 (2008) 2402.
[53] W. Chen, J.-Y. Wang, C. Chen, Q. Yue, H.-M. Yuan, J.-S. Chen, S.-N. Wang, Inorg. Chem. 42 (2003) 944, and references therein.
[54] H.-P. Jia, W. Li, Z.-F. Ju, J. Zhang, Eur. J. Inorg. Chem. (2006) 4264.
[55] S. Sen, S. Mitra, P. Kundu, M.K. Saha, C. Kruga, J. Bruckmann, Polyhedron 16 (1997) 2475.
[56] G.M. Sheldrick, SHELXS-97 Program for the Solution of Crystal Structures, University of Gottingen, Gottingen, Germany, 1997.
[57] G.M. Sheldrick, Acta Crystallogr., Sect. A 46 (1990) 467.
[58] MERCURY, New software for searching the Cambridge structural database and visualizing crystal structures I.J. Bruno, J.C. Cole, P.R. Edgington, M.K. Kessler, C.F. Macrae, P. McCabe, J. Pearson, R. Taylor, Acta Crystallogr., Sect. B 58 (2002) 389.
[59] K. Brandenburg, H. Putz, DIAMOND Version 3.0, Crystal Impact, GbR, Postfach 1251, D-53002 Bonn, Germany, 2004.
[60] Platon, A.L. Spek, J. Appl. Cryst. 36 (2003) 7.
[61] X. Guo, G. Zhu, Z. Li, F. Sun, Z. Yang, S. Qiu, Chem. Commun. (2006) 3174.
[62] K. Nakamoto, Infrared and Raman Spectra of Inorganic and Coordination Compounds, 3rd ed., John Wiley & Sons, New York, 1978.
[63] J.-Y. Wu, C.-H. Chang, T.-W. Tseng, K.-L. Lu, J. Mol. Struc. 796 (2006) 69.
[64] W. Chen, J.-Y. Wang, C. Chen, Q. Yue, H.-M. Yuan, J.-S. Chen, S.-N. Wang, Inorg. Chem. 42 (2003) 944.
[65] J. Tao, M.-L. Tong, J.-X. Shi, X.-M. Chen, S.W. Ng, Chem. Commun. (2000) 2043.
[66] J. Tao, J.-X. Shi, M.-L. Tong, X.-X. Zhang, X.-M. Chen, Inorg. Chem. 40 (2001) 6328.

Polyhedron 28 (2009) 609–613

Contents lists available at ScienceDirect

Polyhedron

journal homepage: www.elsevier.com/locate/poly

Kinetics of complex formation between palladium(II) acetate and bis(diphenylphosphino)ferrocene

Mahbubeh Pourshahbaz, Mohsen Irandoust, Ezzat Rafiee, Mohammad Joshaghani *

Chemistry Department, Razi University, Kermanshah 67149, Iran
Kermanshah Oil Refining Company, Kermanshah, Iran

ARTICLE INFO

Article history:
Received 27 October 2008
Accepted 27 November 2008
Available online 31 December 2008

Keywords:
Phosphine
Palladium
Kinetics
Ferrocene
dppf
NMR

ABSTRACT

The kinetics of complex formation between palladium(II) acetate, and 1,1'-bis(diphenylphosphino)ferrocene, dppf, in two different deuterated solvents $CDCl_3$ and DMSO-d_6 were investigated using ^{31}P NMR spectroscopy. The mole ratio and the ^{31}P-chemical shifts in DMSO-d_6 solution revealed the formation of an intermediate, which is gradually converted into the more stable [Pd(dppf)$OAc)_2$] species with a dppf acting as a chelate ligand. In the chloroform solution however, the interaction of metal ion and the ligand resulted directly in the formation of [Pd(dppf)$OAc)_2$] species with a chelating dppf. The rate constant for the complexation reaction was evaluated from computer fitting of the corresponding integration-time data.

© 2008 Elsevier Ltd. All rights reserved.

1. Introduction

Since the time of the synthesis of 1,1'-bis(diphenylphosphino) ferrocene [1], dppf, this ligand is probably the most intensively studied ferrocenyl phosphines compounds to date and a variety of transition-metal complexes stabilized by dppf have been characterized [2–12]. Among them, the Pd-dppf complexes have richer chemistry and have been widely used as catalysts especially for carbon-carbon bond forming reactions [13–27]. It is well known that the bidentate dppf shows a versatile coordination ability adapting its steric bite angle as well as electronic properties to the geometric and electronic requirements of the metal through the appropriate coordination [28–30]. Although the chelating coordination mode is the predominant character of dppf, multinuclear complexes containing bridging dppf are also known [31–60].

While very high efficiency of Pd-dppf catalysts is due to a combination of electronic and steric parameters of these precursors, no comprehensive study on the rate of the formation of dppf complexes has been carried out, albeit to the best of our knowledge. We have recently reported the application of Pd-phosphine catalysts in the Suzuki cross coupling reactions [61]. Our interest in the physicochemical properties of the dppf [62], encouraged us to determine the rate constants for formation of the Pd-dppf complexes and to gain some useful information about the mechanism of complex formation.

2. Experimental

$CDCl_3$ and DMSO-d_6 were commercially available from the Aldrich and used as received. The ligand dppf was prepared as previously described [62]. An authentic sample of Pd(dppf)$(OAc)_2$ was synthesized by the reaction of equimolar amounts of palladium(II) acetate and dppf according to literature procedure for preparation of Pd(dppf)Cl_2 [63] and characterized by multi-nuclear NMR spectroscopy as well as ICP elemental analysis. *Anal. calc.* for $C_{38}H_{34}FeO_4P_2Pd$, C, 58.29%, H, 4.92%, Fe, 7.13%, P, 7.91%, Pd, 13.59%. Found C, 58.87, H, 4.65, Fe, 7.52, P, 7.75, Pd, 13.91%. ^1H NMR (200 MHz, $CDCl_3$): δ 2.15 (s, 6, CH_3 of acetate ions), 4.00–4.45 (m, 8), 7.15–7.90 (m, 20); $^{31}P\{^1H\}$ NMR (81.014 MHz, $CDCl_3$): δ 28.05 (s). $^{31}P\{^1H\}$ NMR (81.014 MHz, DMSO-d_6): δ 24.58 (s).

All NMR measurements were made on a Bruker Avance (DPX) 200FT- NMR spectrometer with a field strength of 4.7 T (47 KG) equipped with a temperature controller, (±0.1 °C). At this field, ^{31}P resonates at 81.014 MHz. In ^{31}P NMR experiments, the standard was %85 H_3PO_4. All chemical shift measurements were carried out at a temperature of 25.0 ± 0.1 °C.

One milliliter of stock solution of the ligand (0.0554 g in 1 mL, 0.1 M) in each solvent was placed in a NMR tube and then, 50 μL of the stock metal solution of Pd$(OAc)_2$ dissolved in the same solvent (0.0673 g in 0.3 mL, 1 M, calculated for monomeric form)

* Corresponding author. Fax: +98 831 4274559.
E-mail addresses: MJoshaghani@razi.ac.ir, joshaghanim@yahoo.com (M. Joshaghani).

0277-5387/$ - see front matter © 2008 Elsevier Ltd. All rights reserved.
doi:10.1016/j.poly.2008.11.038

was added. The ^{31}P NMR spectrum of the resulting solution was measured at different times.

3. Results and discussion

In the solid state, palladium(II) acetate exists as a trimer and has a maximum at 370–450 nm in its UV–Vis spectrum [64,65]. In contrast, the UV–Vis spectra of this salt in both solvents $CDCl_3$ and DMSO-d_6 do not have such typical signal (Fig. 1). In addition, the trimer–monomer equilibrium strongly depends on the addition of ligand; led to formation of monomeric form of palladium(II) acetate in solution. Therefore, it could be possible to consider it as monomer in kinetic calculations.

NMR spectroscopy has been widely used for the investigation of the kinetics and mechanisms of inorganic reactions. The chemical shifts, line broadening, and the integral of the signals are quantitative factors used for this purposes. In the cases where the changes in the chemical shifts and line broadening are negligible, the integral of the signals could be used as a very sensitive measure of the concentration of a particular species. This tool has been particularly used for consecutive reactions.

The kinetics of the complexation between palladium(II) acetate and dppf were sufficiently slow to lead us monitor all species formed during the complexation.

Initial investigation of reaction rates was carried out using different metal to ligand mole ratio. It was observed that the concentration of the product as a measure of the rate of reaction, increases with increasing the concentration of palladium(II) acetate linearly. This evidence led us to conclude that the reaction is first-order with respect to the palladium source (Fig. 2).

The best intensity changes in the ^{31}P NMR lines were observed at 0.5 metals to ligand mole ratio. In addition, many reports have been published in where, the catalytic reactions were carried out using this mole ratio [66]. Therefore, the kinetic studies were investigated using this mole ratio.

3.1. Investigation of the species involved in the $CDCl_3$ solution

In $CDCl_3$ solution, 1,1'-bis(diphenylphosphino)ferrocene, dppf, has two chemically and magnetically equivalent phosphorus atoms, which appear as a singlet at −18.90 ppm, with respectto an internal standard solution of H_3PO_4 (Fig. 3). During the complexation at 25 °C, the intensity of this signal is gradually decreased and simultaneously, a signal at 28.05 ppm downfield-shifted from the ligand appears which corresponds to $[Pd(dppf)(OAc)_2]$ [67].

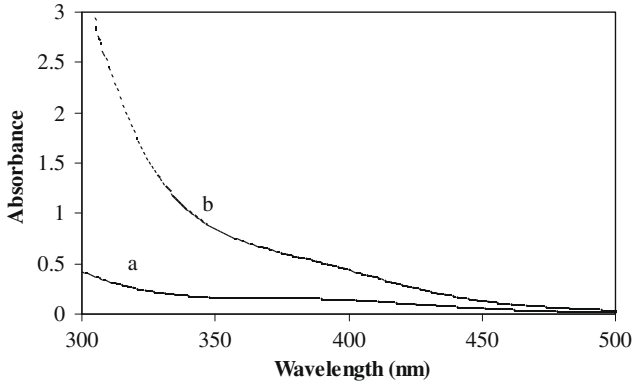


Fig. 1. Spectra of Pd(II) acetate (4.5×10^{-4} M, calculated for the monomeric form) at 25 °C in $CDCl_3$ (a) and DMSO-d_6 (b).

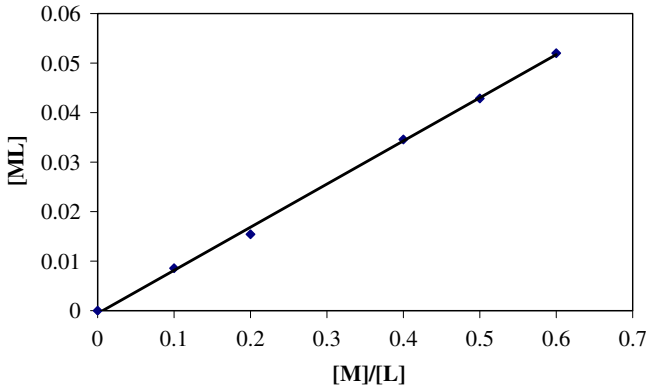


Fig. 2. The product formation as a measure of the rate of reaction vs. the metal to ligand mole ratio. All concentrations were determined by the integration of their ^{31}P NMR signals at the same times.

The ICP elemental analysis confirms the formation of $[Pd(OAc)_2(dppf)]$ (Scheme 1).

Therefore, the reaction may be considered as a simple second-order reaction either reversible Eq. (1) or irreversible reactions Eq. (2)

$$[Pd] + dppf \underset{k_{-1}}{\overset{k_1}{\rightleftharpoons}} [Pd(dppf)] \quad (1)$$

$$[Pd] + dppf \xrightarrow{k_1} [Pd(dppf)] \quad (2)$$

where [Pd] represents the starting palladium(II) acetate.

3.2. Kinetic studies in chloroform solution

The concentration of the free dppf and its Pd complex are determined by the integration of their ^{31}P NMR signals. The stack diagram for the ^{31}P NMR spectra is shown in Fig. 4.

At the first stage, calculations were carried out using the second-order reversible Eq. (1). The resulted rate constants show that the forward rate constant is much greater than the backward rate constant (Table 1). In addition, careful monitoring of the ^{31}P NMR spectra rules out any dissociation of dppf and reaction reversibility. Therefore, the overall reaction may be considered as irreversible Eq. (2) which involves the following rate law Eq. (3):

$$\frac{1}{[dppf]_0 - [Pd]_0} \mathrm{Ln} \frac{[Pd]_0[dppf]_t}{[dppf]_0[Pd]_t} = k_1 t \quad (3)$$

with subscripts t and 0 representing time t and 0, respectively. A plot of the left term of Eq. (3) versus time should be a straight line with a positive slope equal to k (Fig. 5). The overall rate constant of the reaction is listed in Table 1.

It is reported that even if one reagent (here [Pd]) be maintained in only a two-fold excess over another reagent (here [dppf]), the error in the computed second-order rate constant is $\leqslant$2% for 60% conversion and as the reaction proceeds toward the end of the reaction, pseudo first-order conditions certain hold [68,69]. Similar re-computation of our kinetics data for pseudo first-order irreversible reaction was carried out and the resulted rate constant confirmed this hypothesis (Table 1, entry 3). Other re-computations of the kinetic data for other kinetic models such as third-order resulted poor regressions.

3.3. Investigation of the species involved in the DMSO-d_6 solution

In the DMSO-d_6 solution, the free ligand appears at −19.27 ppm. This signal is gradually decreased during the complexation and a

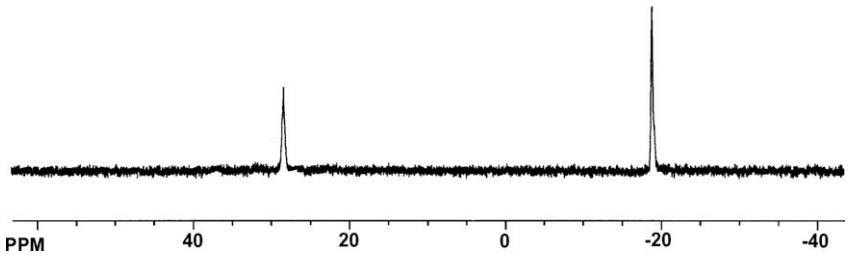
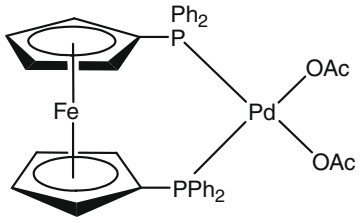


Fig. 3. ^{31}P NMR spectrum of reaction mixture of Pd(II) acetate/dppf in $CDCl_3$ at 25 °C.



Scheme 1. Structure of $[Pd(dppf)(OAc)_2]$ complex.

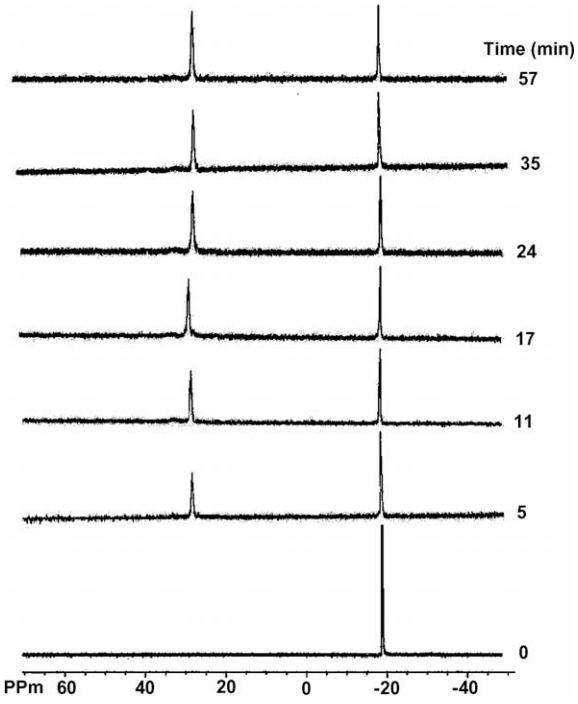


Fig. 4. The change in the ^{31}P NMR spectra vs. time in $CDCl_3$ at 25 °C.

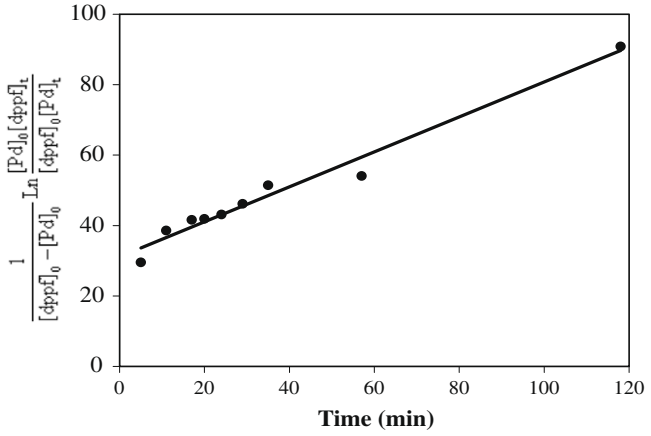


Fig. 5. Second-order irreversible plot for reaction of Pd(II) acetate:dppf in $CDCl_3$ at 25 °C.

Table 1
Rate and stability constants of reaction of Pd(II) acetate:dppf in $CDCl_3$ at 25 °C.

Entry	Type of reaction	k_1 (s^{-1} M^{-1})	k_{-1}(s^{-1}) × 10^4	K_e (M^{-1})
1	Reversible second-order	0.52 ± 0.03	5.2× ± 0.2	1000 ± 90
2	Irreversible second-order	0.50 ± 0.02		
3	Pseudo first-order	0.53 ± 0.03		

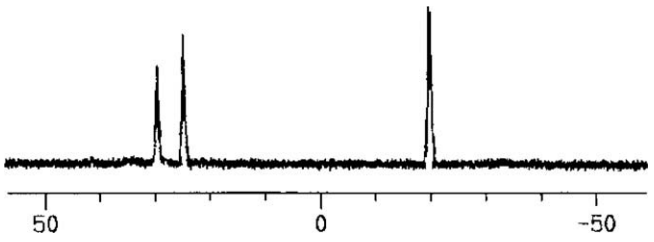


Fig. 6. ^{31}P NMR spectrum of Pd(II) acetate/dppf in DMSO-d_6 and at 25 °C.

signal appears at 29.70 ppm, which may be due to the formation of a M_2L_2 di-palladium intermediate (Fig. 6) [70–72]. The observation of this intermediate is probably due to the coordinating ability of DMSO, which probably makes the coordination of dppf slower and allows the formation of the intermediate.

The relative intensities of both signals are decreased on going to continue the reaction and an additional signal appears at 24.58 ppm corresponding to the ML species involved chelating dppf [67]. The ICP elemental analysis confirms the formation of $[Pd(OAc)_2(dppf)]$. The pattern of relative intensity changes indicates that the ML is produced possibly from two paths; directly from the starting reactants via a consecutive reaction as a main path [73,74] together with a simple second-order reaction Eq. (4)

$$\begin{cases} Pd + dppf \xrightarrow{k_1} \frac{1}{2}[Pd_2(\mu - dppf)_2] \xrightarrow{k_2} [Pd(dppf)] \\ Pd + dppf \xrightarrow{k_3} [Pd(dppf)] \end{cases} \quad (4)$$

3.4. Kinetic studies in DMSO-d_6 solution

The concentration of the free dppf and its Pd complexes are determined by the integration of their characteristic ^{31}P NMR signals. Distribution of all species versus time is shown in Fig. 7. It should be noticed that the concentration of the free ligand could not exponentially decay to zero since it is used in two-fold excess.

Initial calculation based on Eq. (5) was carried out by simultaneously solving of three equations for the change of concentration

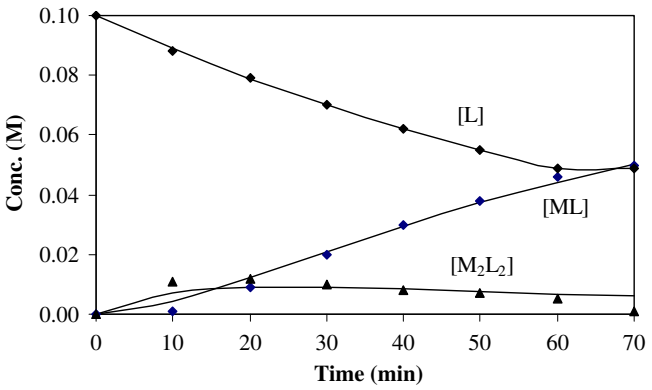


Fig. 7. Distribution diagram for involving species in the reaction of Pd(II) acetate and dppf in DMSO-d_6 at 25 °C. The solid lines are the best trendlines obtained by Excel program.

Table 2
Rate constants of the reaction of Pd(II) acetate:dppf (1:2) in DMSO-d_6 at 25 °C.

Entry	Type of reaction	k_{obs} $(s^{-1}\,M^{-1}) \times 10^2$	k_2 $(s^{-1}) \times 10$
	Parallel consecutive and irreversible reactions	1.0 ± 0.1	1.0 ± 0.1

of the ligand, [L]; the intermediate, $[M_2L_2]$; and the final chelating complex; [ML], with time Eq. (5)

$$\begin{cases} [L] = [L_0]e^{-k_{obs}t} \\ [M_2L_2] = \frac{k_{obs}[L]}{k_2 - k_{obs}}\{e^{-k_{obs}t} - e^{-k_2 t}\} \\ [ML] = [L]\left\{1 - \frac{1}{k_2 - k_{obs}}(k_2 e^{-k_{obs}t} - k_{obs}e^{-k_2 t}\right\} \end{cases} \quad (5)$$

The corresponding rate constants are calculated by Excel-fitting of the experimental points (Fig. 7) and are given in Table 2.

As Eq. (5) shows, determination of individual amounts of k_1 and k_3 is impossible and a summation of them as k_{obs} could be obtained in this way. An approximate value for these rate constants could be easily calculated by considering two extremes of Eq. (5)

$$\begin{cases} a) k_1 >> k_3 \Rightarrow\ k_{obs} \approx k_1 \\ b) k_1 << k_3 \Rightarrow k_{obs} \approx\ k_3 \end{cases}$$

The first extreme was arisen if the consecutive reaction is the major contributor of the overall rate constant while the second extreme could be obtained if the second-order path is the major contributor.

The relative magnitude of the k_{obs} [Pd] (s^{-1}) and k_2 (s^{-1}) rate constants shows that the consecutive reaction is the major contributor of the overall reaction rate. Therefore, the first extreme is more logic.

Interestingly, the intermediate was observed only in metal to ligand mole ratios near 0.5. This may be because both rate of formation (k_1) and consumption (k_2) of the intermediate depend on the concentrations of metal and ligand as a same way (steady state approximation).

4. Conclusion

In comparison, the complex formation is faster in $CDCl_3$ than DMSO, which may be due to the coordinating ability of DMSO. This coordination probably makes the coordination of dppf slower and allows the formation of the intermediate. It also decreases the electrophilicity of metal as well as the steric crowding at the metal center [75]. The better solubility of the reactants in $CDCl_3$ also plays an important role. The difference in the reaction rates make such kinetic studies very important in the catalytic reactions in where, a mixture of metal and ligand are used as catalyst. For example, it is reported that using methanol as solvent, no methoxycarbonylation of 2-bromoaniline was observed. Changing to a solvent mixture of toluene-methanol increased remarkable the conversion [76]. This feature is of greater importance particularly whenever the complex formation between metal and ligand is the rate determining step and/or one of previous catalytic cycle.

Another noteworthy of such kinetics studies outcome on comparing the rate of catalytic reactions using a ML catalyst with *in situ* prepared catalyst by addition of metal and ligand. The similarity between the rates of both reactions may be an excellent evidence for the presence of a similar mechanism.

Acknowledgments

The authors thank the Razi University Research Council and Kermanshah Oil Refining Company for support of this work.

References

[1] J.J. Bishop, A. Davison, M.L. Katcher, D.W. Lichtenberg, R.E. Merrill, J.C. Smart, J. Organomet. Chem. 27 (1971) 241.
[2] K.-S. Gan, T.S.A. Hor, in: A. Togni, T. Hayashi (Eds.), Ferrocenes-Homogeneous Catalysis Organic Synthesis Materials Science, VCH, Weinheim, Germany, 1995.
[3] A.W. Rudie, D.W. Lichtenberg, M.L. Katcher, A. Davison, Inorg. Chem. 17 (1978) 2859.
[4] W.R. Cullen, J.D. Woollins, Coord. Chem. Rev. 39 (1981) 1.
[5] T. Hayashi, M. Kumada, Acc. Chem. Res. 15 (1982) 395.
[6] D.A. Clemente, G. Pilloni, B. Corain, B. Longato, M. Tiripicchino- Camellini, Inorg. Chim. Acta 115 (1986) L9.
[7] L.-T. Phang, S.C.F. Au-Yeung, T.S.A. Hor, S.B. Khoo, Z.-Y. Zhou, T.C.W. Mak, J. Chem, Soc. Dalton Trans. 1 (1993) 165.
[8] G.M. deLima, C.A.L. Filgueiras, M.T.S. Giotto, Y.P. Mascarenhas, Transition Met. Chem. 20 (1995) 380.
[9] S. Otto, A. Roodt, Acta Crystallogr. Sect. C c53 (1997) 1414.
[10] S.A. Bodolosky, S. Schreiner, Synthesis, characterization and reactivity of platinum -bis(diphenylphosphino) ferrocene complexes: Book of Abstracts, in: 213th ACS National Meeting, San Francisco, 1997, p. 13.
[11] T.A. Peganova, N.V. Vologdin, P.V. Petrovskii, I.D. Nesterov, K.A. Lyssenko, O.V. Gusev, Russ. Chem. Bull. 55 (2006) 683.
[12] X.L. Lu, S.Y. Ng, J.J. Vittal, G.K. Tan, L.Y. Goh, T.S.A. Hor, J. Organomet. Chem. 688 (2003) 100.
[13] T.J. Colacot, Platinum Met. Rev. 45 (2001) 22.
[14] T. Hayashi, M. Konishi, Y. Kobori, M. Kumada, T. Higuchi, K. Hirotsu, J. Am. Chem. Soc. 106 (1984) 158.
[15] B.E. Bosch, I. Brümmer, K. Kunz, G. Erker, R. Frölich, S. Kotila, Organometallics 19 (2000) 1255.
[16] M. Ogasawara, K. Yoshida, T. Hayashi, Organometallics 19 (2000) 1567.
[17] A.L. Boyes, I.R. Butler, S.C. Quayle, Tetrahedron Lett. 39 (1998) 7763.
[18] W. Mägerlein, A.F. Indolese, M. Beller, Angew. Chem. Int. Ed. Engl. 40 (2001) 2856.
[19] M.S. Driver, J.F. Hartwig, J. Am. Chem. Soc. 118 (1996) 7217.
[20] T.E. Müller, M. Berger, M. Grosche, E. Herdtweck, F.P. Schmidtchen, Organometallics 20 (2001) 4384.
[21] K. Mikami, K. Aikawa, Org. Lett. 4 (2002) 99.
[22] V. Cadierno, P. Crochet, J. Diez, S.E. Garcia-Garrido, J. Gimeno, S. Garcia-Garrido, Organometallics 22 (2003) 5226.
[23] V. Cadierno, P. Crochet, J. Diez, S.E. Garcia-Garrido, J. Gimeno, Organometallics 23 (2004) 4836.
[24] T. Ohe, N. Miyaura, A. Suzuki, J. Org. Chem. 58 (1993) 2201.
[25] M. Sato, A. Miyaura, A. Suzuki, Chem. Lett. (1989) 1408.
[26] W.J. Thompson, J. Gaudino, J. Org. Chem. 49 (1984) 5237.
[27] O.R. Hughes, J.D. Unruh, J. Mol. Catal. 12 (1981) 71.
[28] B. Therrien, L. Vieille-Petit, J. Jeanneret-Gris, P. Stepnicka, G. Suess-Fink, J. Organomet. Chem. 689 (2004) 2456.
[29] T. Sixt, J. Fiedler, W. Kaim, Inorg. Chem. Commun. 3 (2000) 80.
[30] P.J. Stang, B. Olenyuk, J. Fan, A.M. Arif, Organometallics 15 (1996) 904.
[31] T.S.A. Hor, S.P. Neo, C.S. Tan, T.C.W. Mak, K.W.P. Leung, R.J. Wang, Inorg. Chem. 31 (1992) 4510.
[32] S.P. Neo, T.S.A. Hor, J. Organomet. Chem. 464 (1994) 113.
[33] S.P. Neo, Z.-Y. Zhou, T.C.W. Mak, T.S.A. Hor, J. Chem. Soc., Dalton Trans. (1994) 3458.
[34] S.G. Bott, K. Yang, M.G. Richmond, J. Chem. Cryst. 25 (1995) 263.
[35] L.T. Phang, T.S.A. Hor, Z.Y. Zhou, T.C.W. Mak, J. Organomet. Chem. 469 (1994) 253.

[36] I.D. Salter, V. Sik, S.A. William, T. Adatia, J. Chem. Soc., Dalton Trans. (1996) 652.
[37] V.W.-W. Yam, S.W.-K. Choi, K.-K. Cheung, J. Chem. Soc., Dalton Trans. (1996) 3415.
[38] P.M.N. Low, A.L. Tan, T.S.A. Hor, Y.-S. Wen, L.-K. Liu, Organometallics 15 (1996) 2595.
[39] F. Canales, M.C. Gimeno, A. Laguna, P.G. Jones, Organometallics 15 (1996) 3412.
[40] G. Pilloni, R. Graziani, B. Longato, B. Corain, Inorg. Chim. Acta 190 (1991) 165.
[41] U. Caselato, R. Graziani, G. Pilloni, J. Crystallogr. Spectrosc. Res. 23 (1993) 571.
[42] B.H. Aw, K.K. Looh, H.S.O. Chan, K.L. Tan, T.S.A. Hor, J. Chem. Soc., Dalton Trans. (1994) 3182.
[43] I.D. Salater, S.A. Williams, T. Adatia, Polyhedron 14 (1995) 2803.
[44] S. Onaka, T. Moriya, S. Takagi, A. Mizuno, H. Furuta, Bull. Chem. Soc. Jpn. 65 (1992) 1415.
[45] S. Onaka, A. Mizuno, S. Takagi, Chem. Lett. (1989) 2040.
[46] W.H. Watson, A. Nelg, S. Hwang, M.G. Richmond, J. Organomet. Chem. 445 (1993) 170.
[47] S. Onaka, M. Otsuka, A. Mizuno, S. Takagi, K. Sako, M. Otomo, Chem. Lett. (1994) 48.
[48] S.T. Chacon, W.R. Cullen, M.I. Bruce, O.B. Shawkataly, F.W.B. Einstein, R.H. Jones, A.C. Willis, Can. J. Chem. 68 (1990) 2001.
[49] M.I. Bruce, P.A. Humphrey, O.B. Shawkataly, M.R. Snow, E.R.T. Tiekink, W.R. Cullen, Organometallics 9 (1990) 2910.
[50] G. Rheinwald, H. Stoeckli-Evans, G. Suess-Fink, J. Organomet. Chem. 512 (1996) 27.
[51] A.J. Blake, A. Harrison, B.F.G. Johnson, E.J.L. McInnes, S. Parsons, D.S. Shephard, L.J. Yellowless, Organometallics 14 (1995) 3160.
[52] L.K. Liu, Y.S. Wen, T.S.A. Hor, H.S.O. Chan, K.-L. Tan, L-T. Phang, Y.K. Yan, Polyhedron 10 (1991) 2437.
[53] Y.K. Yan, H.S.O. Chan, T.S.A. Hor, K.-L. Tan, L.-K. Liu, Y.-S. Wen, J. Chem. Soc., Dalton Trans. (1992) 426.
[54] Y.K. Yan, T.S.A. Hor, S.-L. Lam, Y.-X. Cui, C.C.F. Au-Yeung, Inorg. Chem. 33 (1994) 2407.
[55] C. Jiang, Y.-S. Wen, L.-K. Liu, T.S.A. Hor, Y.K. Yan, Organometallics 17 (1998) 173.
[56] T.J. Kim, S.C. Kwon, Y.H. Kim, N.H. Heo, M.M. Teeter, A. Yamano, J. Organomet. Chem. 426 (1992) 71.
[57] Z.-G. Fang, Y.-S. Wen, R.K.L. Wong, S.-C. Ng, L.-K. Liu, T.S.A. Hor, J. Cluster Sci. 5 (1994) 327.
[58] S.M. Draper, C.E. Housecroft, A.L. Rheingold, J. Organomet. Chem. 435 (1992) 9.
[59] T.S.A. Hor, L.T. Phang, L.-K. Liu, Y.-S. Wen, J. Organomet. Chem. 397 (1990) 29.
[60] W.-Y. Yeh, S.-B. Chen, S.-M. Peng, G.-H. Lee, J. Organomet. Chem. 481 (1994) 183.
[61] M. Joshaghani, M. Daryanavard, E. Rafiee, J. Xiao, C. Baillie, Tetrahedron Lett. 48 (2007) 2025.
[62] M.B. Gholivand, A. Babakhanian, M. Joshaghani, Anal. Chim. Acta 584 (2007) 302.
[63] T. Hayashi, M. Konishi, Y. Kobori, M. Kumada, T. Higuchi, K. Hirotsuf, J. Am. Chem. Soc. 106 (1984) 158.
[64] A.C. Skapski, M.L. Smart, J. Chem. Soc. D, Chem. Commun. (1970) 659.
[65] J. Evans, L. O'Neill, V.L. Kambhampati, G. Rayner, S. Turin, A. Genge, A.J. Dent, T. Neisius, J. Chem. Soc., Dalton Trans. (2002) 2212.
[66] For example B. Wei, T.S.A. Hor, J. Mol. Catal. A 132 (1998) 229.
[67] B. Corain, B. Longato, G. Favero, D. Ajò, G. Pilloni, U. Russo, F.R. Kreissl, Inorg. Chim. Acta 157 (1989) 266.
[68] J. Rawlings, S. Wherland, H.B. Gray, J. Am. Chem. Soc. 99 (1977) 1968.
[69] J.L. Jensen, R.C. Kanner, G.R. Shaw, Int. J. Chem. Kinetics 22 (1990) 1211.
[70] M. López-Torres, A. Fernández, J.J. Fernández, A. Suárez, S. Castro-Juíz, J.M. Vila, M.T. Pereira, Organometallics 20 (2001) 1350.
[71] A. Fernández, D. Vázquez-Garcıá, J.J. Fernández, M. López- Torres, A. Suárez, S. Castro-Juíz, J.M. Vila, New J. Chem. 26 (2002) 404.
[72] S.R. Ananias, A.E. Mauro, V.A. De Lucca Neto, Trans. Met. Chem. 26 (2001) 570.
[73] P. Hendry, A.M. Sargeson, Inorg. Chem. 25 (1986) 865.
[74] E.T. Gray Jr., R.W. Taylor, D.W. Margerum, Inorg. Chem. 16 (1977) 3047.
[75] B.A. Steinhoff, S.R. Fix, S.S. Stahl, J. Am. Chem. Soc. 124 (2002) 766.
[76] I.J.S. Fairlamb, S. Grant, P. McCormack, J. Whittall, J. Chem. Soc., Dalton Trans. (2007) 865.

Polyhedron 28 (2009) 614–620

Contents lists available at ScienceDirect

Polyhedron

journal homepage: www.elsevier.com/locate/poly

Linking patterns of ligands containing pyridyl–amine or two pyridyl terminals and their cadmium compounds: $[CdL^1_2(NO_3)_2]$, $[CdL^2_2(NO_3)_2]$ and $[Cd_2L^3_2(NO_3)_4(H_2O)_4]\cdot(C_4H_8O)_2$

L^1 = (3-py)–CH=N–C_6H_4–O–C_6H_4–NH_2;
L^2 = (4-py)–CH=N–C_6H_4–O–C_6H_4–NH_2;
L^3 = (3-py)–CH=N–C_6H_4–O–C_6H_4–N=CH–(3-py)]

Hye Jung Yun, Sook-Hyun Lim, Soon W. Lee *

Department of Chemistry (BK21), Sungkyunkwan University, Natural Science Campus, Suwon 440-746, Republic of Korea

ARTICLE INFO

Article history:
Received 10 November 2008
Accepted 1 December 2008
Available online 20 January 2009

Keywords:
Linking ligands
An intervening oxydianiline
Coordination polymer
A discrete dinuclear macrocycle

ABSTRACT

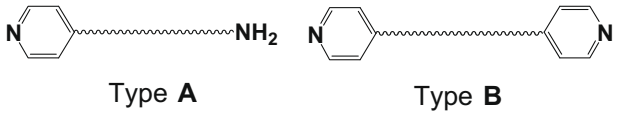
We have prepared four potential linking ligands, [(3-py)–CH=N–C_6H_4–O–C_6H_4–NH_2, **L^1**], [(4-py)–CH=N–C_6H_4–O–C_6H_4–NH_2, **L^2**], [(3-py)–CH=N–C_6H_4–O–C_6H_4–N=CH–(3-py), **L^3**] and [(4-py)–CH=N–C_6H_4–O–C_6H_4–N=CH–(4-py), **L^4**], all of which contain an intervening oxydianiline fragment. Whereas ligands **L^1** and **L^2** have two types of terminal groups (pyridyl and amine groups), ligands **L^3** and **L^4** have a single type of terminal group (pyridyl groups at both terminals). Ligands **L^1**–**L^3** reacted with cadmium nitrate ($Cd(NO_3)_2\cdot 6H_2O$) to produce $[CdL^1_2(NO_3)_2]$ (**1**), $[CdL^2_2(NO_3)_2]$ (**2**) and $[Cd_2L^3_2(NO_3)_4(H_2O)_4]\cdot(C_4H_8O)_2$ (**3**), respectively. Compound **1** is a 2-D brick-wall coordination polymer and compound **2** is a 1-D double-strand-chain polymer. On the other hand, compound **3** is a discrete dinuclear macrocycle (molecule) with a double-helical structure, which contains THF (C_4H_8O) guest molecules.

© 2008 Elsevier Ltd. All rights reserved.

1. Introduction

Much attention has been continually paid to the design and synthesis of coordination polymers, due to their useful zeolite-like properties applicable to various fields such as size-selective sorption, gas storage, host–guest recognition and catalysis [1–13]. In preparing these polymers, experimental parameters such as a metal ion with a proper coordination sphere, a proper linking ligand set, reaction temperature, pH, concentration and synthetic methods (hydrothermal, solvothermal, hydro(solvo)thermal, and layer methods) are crucial in determining the ultimate structures of the resulting polymers.

Relatively long linking ligands containing terminal pyridyls were recently employed for the preparation of coordination polymers with various topologies [14–21]. We also reported several long bis-pyridine-type ligands **L1**–**L8** (Chart 1) and their coordination polymers [22–28]. All these ligands commonly contain pyridyls at their ends. During our ongoing research, we have become interested in the comparison of the linking patterns between ligands containing two types of terminal groups (pyridyl and amine groups) and those containing a single type of terminal groups (pyridyl groups at both terminals). In this context, we have prepared four potential linking ligands possessing an intervening 4,4′-oxydianiline fragment (a flexible spacer group), two of which contain pyridyl–amine terminals (Type **A**) and another two of which contain two pyridyl terminals (Type **B**): 4-(4-aminophenoxy)-*N*-(pyridin-3-ylmethylene)aniline (**L^1**), 4-(4-aminophenoxy)-*N*-(pyridin-4-ylmethylene)aniline (**L^2**), *N*,*N*′-4,4′-oxybis(*N*-(pyridin-3-ylmethylene)aniline) (**L^3**) and *N*,*N*′-4,4′-oxybis(*N*-(pyridin-4-ylmethylene)aniline) (**L^4**). Herein, we report the preparation of these ligands and their cadmium compounds, $[CdL^1_2(NO_3)_2]$ (**1**), $[CdL^2_2(NO_3)_2]$ (**2**) and $[CdL^3(NO_3)_2(H_2O)_2]\cdot(C_4H_8O)_2$ (**3**).



Type **A** Type **B**

2. Experimental

All the solid chemicals were purified by recrystallization, and all solvents were distilled and stored over molecular sieves. ^1H and

* Corresponding author. Tel.: +82 31 290 7066; fax: +82 31 290 7075.
E-mail address: soonwlee@skku.edu (S.W. Lee).

0277-5387/$ - see front matter © 2008 Elsevier Ltd. All rights reserved.
doi:10.1016/j.poly.2008.12.020

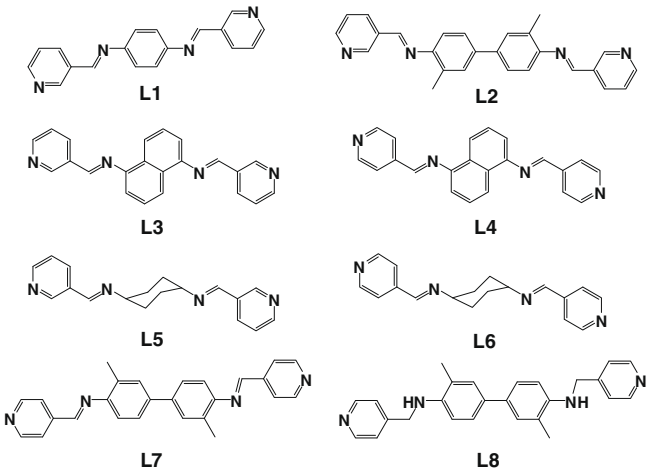


Chart 1.

$^{13}C\{^1H\}$ NMR data were collected on a 500 MHz Varian Inova spectrometer at the Cooperative Center for Research Facilities (CCRF), Sungkyunkwan University. Infrared (IR) samples were prepared as KBr pellets, and their spectra were obtained in the range 400–4000 cm^{-1} on a Nicolet 320 FTIR spectrophotometer. Elemental analyses were performed with an EA1110 (CE instrument, Italy) at the Korea Basic Science Institute. Thermogravimetric analysis (TGA) was conducted on a TA4000/SDT 2960 instrument (CCRF). X-ray powder diffraction (XRPD) spectra were obtained with a Rigaku D/Max-RC diffractometer.

2.1. Preparation of the ligands

All the ligands were prepared in the same way. To 3-pyridinecarboxaldehyde (0.53 g, 4.9 mmol) in ethanol (50 ml) was added 4,4-oxydianiline (1.00 g, 4.9 mmol) at room temperature. After the addition of dichloromethane (30 ml) and then two drops of formic acid, the mixture was stirred at room temperature for 24 h and filtered. The resulting yellow crystalline solid was washed with ethanol (3 × 10 ml) and hexane (3 × 10 ml), and crystallized from CH_2Cl_2–hexane to give ligand **L**^{1}.

Data for ligand **L**^{1}: Yield 85%. ^1H NMR (500 MHz, $CDCl_3$) δ: 9.01 (m, 1H), 8.71 (m, 1H), 8.53 (d, 1H), 8.29 (m, 1H), 7.42–6.63 (9 H), 3.58 (br, NH_2). $^{13}C\{^1H\}$ NMR (125 MHz, $CDCl_3$) δ: 158.2, 156.4, 152.0, 151.0, 148.7, 147.0, 145.7, 143.2, 142.0, 135.0, 132.1, 124.0, 122.7, 122.5, 121.3, 119.8, 118.1, 116.4. Anal. *Calc.* for $C_{18}H_{15}N_3O$ (M_r = 289.33): C, 74.72; H, 5.23; N, 14.52. Found: C, 74.11; H, 5.69; N, 14.47%. Mp: 96–98 °C (decomp.). IR (KBr, cm^{-1}): 3300 (m), 3204 (m), 1627 (m), 1498 (s), 1417 (m), 1251 (m), 1099 (m), 837 (s), 697 (s), 543 (m).

Data for ligand **L**^{2}: Yield 84%. ^1H NMR ($CDCl_3$) δ: 8.76 (m, 2H), 8.48 (d, 1H), 7.74 (d, 2H), 7.30–6.63 (8 H), 3.59 (br, NH_2). $^{13}C\{^1H\}$ NMR ($CDCl_3$) δ: 158.7, 157.1, 156.6, 156.2, 150.7, 148.5, 146.5, 145.1, 143.2, 122.8, 121.4, 119.8, 118.0, 116.4. Anal. *Calc.* for $C_{18}H_{15}N_3O$ (M_r = 289.33): C, 74.72; H, 5.23; N, 14.52. Found: C, 74.33; H, 5.52; N, 14.42%. Mp: 112–114 °C (decomp.). IR (KBr, cm^{-1}): 3308 (m), 3202 (m), 1627 (m), 1498 (s), 1410 (s), 1325 (s), 1254 (s), 1102 (m), 981 (m), 838 (s), 546 (m).

Data for ligand **L**^{3}: Yield 88%. ^1H NMR ($CDCl_3$) δ: 9.06 (m, 2H), 8.71 (d, 2H), 8.55 (d, 2H), 8.39 (br, 2H), 7.51–7.06 (10 H). $^{13}C\{^1H\}$ NMR ($CDCl_3$) δ: 156.4, 152.2, 151.1, 147.0, 135.0, 132.1, 124.0, 122.7, 119.7. Anal. *Calc.* for $C_{24}H_{18}N_4O$ (M_r = 378.43): C, 76.17; H, 4.79; N, 14.81. Found: C, 75.66; H, 5.02; N, 14.77%. Mp: 152–154 °C (decomp.). IR (KBr, cm^{-1}): 1624 (s), 1578(s), 1493 (s), 1416 (m), 1278 (s), 1188 (s), 1100 (s), 1021 (s), 848 (s), 703 (s), 538 (s).

Data for ligand **L**^{4}: Yield 86%. ^1H NMR ($CDCl_3$) δ: 8.77 (m, 4 H), 8.49 (s, 2H), 7.75 (m, 4 H), 7.30 (m, 4 H), 7.09 (m, 4 H). $^{13}C\{^1H\}$ NMR ($CDCl_3$) δ: 157.1, 156.6, 150.8, 146.5, 143.1, 122.9, 122.4, 119.8. Anal. *Calc.* for $C_{24}H_{18}N_4O$ (M_r = 378.43): C, 76.17; H, 4.79; N, 14.81. Found: C, 75.58; H, 5.42; N, 14.64%. Mp: 174–176 °C (decomp.). IR (KBr, cm^{-1}): 1623 (s), 1581 (m), 1493 (s), 1408 (s), 1277 (s), 1099 (m), 972 (s), 843 (s), 544 (m).

2.2. Preparation of the polymers $[Cd\mathbf{L}^1{}_2(NO_3)_2]$ (**1**) and $[Cd_2\mathbf{L}^2{}_4(NO_3)_4]$ (**2**)

Polymers **1** and **2** were prepared in the same way. At room temperature, a methanol (2 ml) solution containing $Cd(NO_3)_2 \cdot 6H_2O$ (30 mg, 0.097 mmol) was layered onto the top of a dichloromethane solution (2 ml) containing ligand **L**^{1} (57 mg, 0.195 mmol). After 5 days, the resulting crystals were filtered, washed with ethanol (3 × 5 ml), and air-dried to give $[Cd\mathbf{L}^1{}_2(NO_3)_2]_\infty$ (78 mg, 0.096 mmol, 98%). Anal. *Calc.* for $C_{36}H_{30}N_8O_8Cd_1$ (M_r = 815.08): C, 53.05; H, 3.71; N, 13.75. Found: C, 53.38; H, 3.89; N, 13.59%. Mp: 258–260 °C (decomp.). IR (KBr, cm^{-1}): 3315 (m), 1630 (m), 1499 (s), 1421 (m), 1229 (m), 1037 (m), 832 (m), 698 (s), 520 (m).

Data for polymer **2**. Yield 99%. Anal. *Calc.* for $C_{36}H_{30}CdN_8O_8$ (M_r = 815.08): C, 53.05; H, 3.71; N, 13.75. Found: C, 53.24; H, 3.97; N, 13.71%. Mp: 208–210 °C (decomp.). IR (KBr, cm^{-1}): 3378 (w), 1685 (m), 1577 (s), 1528 (s), 1503 (s), 1412 (s) 838 (m), 770 (m).

2.3. Preparation of $[Cd_2\mathbf{L}^3{}_2(NO_3)_4(H_2O)_4] \cdot (C_4H_8O)_2$ (**3**)

At room temperature, a methanol (2 ml) solution containing $Cd(NO_3)_2 \cdot 6H_2O$ (30 mg, 0.097 mmol) was layered onto the top of a tetrahydrofuran solution (2 ml) containing ligand **L**^{3} (37 mg, 0.097 mmol). After 5 days, the resulting crystals were filtered, washed with ethanol (3 × 5 ml), and air-dried to give compound **3** $\cdot (C_4H_8O)_2$ (68 mg, 0.094 mmol, 97%). Anal. *Calc.* for $C_{56}H_{60}Cd_2N_{12}O_{20}$ (M_r = 1445.96): C, 46.52; H, 4.18; N, 11.62. Found: C, 45.98; H, 4.02; N, 11.50%. Mp: 266–268 °C (decomp.). IR (KBr, cm^{-1}): 1630 (m), 1500(s), 1392 (m), 1244 (m), 1044 (m), 834 (m), 696 (m), 535 (m).

2.4. X-ray structure determination

All X-ray data were collected on a Bruker Smart APEX2 diffractometer (CCRF) equipped with a Mo X-ray tube. Absorption corrections were made by SADABS based upon the Laue symmetry of equivalent reflections [29]. All calculations were carried out with SHELXTL programs [30]. All structures were solved by direct methods. All non-hydrogen atoms were refined anisotropically.

A colorless crystal of polymer **1**, shaped as a block of approximate dimensions 0.22 × 0.18 × 0.06 mm, was used for crystal and intensity data collection. The NH_2 hydrogen atoms were located and refined isotropically, and the remaining hydrogen atoms were generated in ideal positions and refined in a riding mode. A yellow crystal of polymer **2** (a block, 0.14 × 0.10 × 0.08 mm) was used, and the NH_2 hydrogen atoms were located and refined isotropically. A colorless crystal of compound **3** (a block, 0.24 × 0.20 × 0.04 mm) was used, and the hydrogen atoms in the aqua ligands were located. The nitrato ligands in polymer **1** and compound **3** are slightly disordered, but the disorder was not resolved and anisotropic refinements applying several possible site occupation factors were unstable. Site occupancy refinements of the nitrato atoms all yielded values close to unity. Details of the crystal data, intensity collection and refinement are given in Table 1. Selected bond lengths and angles for compounds **1**–**3** are given in Tables 2–4, respectively.

3. Results and discussion

3.1. Preparation of the ligands

Four potential linking ligands **L¹**–**L⁴**, all of which contain an intervening 4,4′-oxydianiline fragment, were prepared in high yields by a simple and straightforward Schiff-base condensation. At room temperature, 4,4′-oxydianiline reacted with 1 equiv. of 3-pyridine-carboxaldehyde and 1 equiv. of 4-pyridine-carboxaldehyde to give pyridyl–amine-type ligands **L¹** and **L²**, respectively. In the same way, bis-pyridine-type ligands **L³** and **L⁴** were obtained by treating 4,4′-oxydianiline with 2 equiv. of pyridine-carboxaldehyde (Scheme 1). Ligands **L¹** and **L²** are structural isomers due to the difference in the nitrogen positions in the terminal pyridyl groups. Ligands **L³** and **L⁴** are also structural isomers.

The IR spectra of all the ligands display a common absorption band at 1623–1627 cm^{-1}, assignable to the C=N bond, consistent with the fact that C=N stretching frequencies of Schiff bases appear in the range 1680–1603 cm^{-1} [31–33]. In particular, the IR spectra of ligands **L¹** and **L²** display two characteristic N–H absorption bands (3300 and 3204 cm^{-1} for ligand **L¹**; 3308 and 3202 cm^{-1} for ligand **L²**), which strongly support the presence of the terminal NH_2 group in both ligands.

Table 1
X-ray data collection and structure refinement details.

	1	2	3
Empirical formula	$C_{36}H_{30}CdN_8O_8$	$C_{36}H_{30}CdN_8O_8$	$C_{56}H_{60}Cd_2N_{12}O_{20}$
Formula weight	815.08	815.08	1445.96
Temperature (K)	296(2)	296(2)	296(2)
Crystal system	monoclinic	monoclinic	triclinic
Space group	*C*2/*c*	*C*2/*c*	$P\bar{1}$
a (Å)	30.4223(16)	28.919(2)	7.6197(2)
b (Å)	9.1824(5)	14.000(1)	9.2639(2)
c (Å)	12.7442(7)	21.257(2)	23.3894(5)
α (°)	80.532(1)		
β (°)	107.144(3)	108.411(1)	87.953(1)
γ (°)			69.013(1)
V (Å³)	3401.9(3)	8166(1)	1520.0(6)
Z	4	8	1
D_{calc} (g cm^{-3})	1.591	1.326	1.580
μ (mm^{-1})	0.709	0.591	0.785
F(000)	1656	3312	736
T_{min}	0.8596	0.9219	0.8340
T_{max}	0.9587	0.9543	0.9693
No. of reflections measured	14288	35999	39479
No. of reflections unique	4142	9870	7494
No. of reflections with $I > 2\sigma(I)$	2601	2601	5351
No. of parameters refined	248	494	422
θ range (°)	2.74–28.38	4.56–28.33	2.39–28.43
Max., in Δρ (e $Å^{-3}$)	1.176	0.574	0.632
Min., in Δρ (e $Å^{-3}$)	−0.361	−0.391	−0.448
Goodness-of-fit on F^2	0.925	0.950	0.916
R_1[a]	0.0541	0.0600	0.0366
wR_2[b]	0.1371	0.1423	0.0721

[a] $R_1 = \sum[|F_o| - |F_c|]/\sum|F_o|$.
[b] $wR_2 = \sum[w(F_o^2 - F_c^2)^2]/\sum[w(F_o^2)^2]^{1/2}$.

Table 2
Selected bond lengths (Å) and angles (°) in polymer **1**.

Cd1–N1	2.331(4)	Cd1–O2	2.3814	Cd1–N3#2	2.394(4)
N3–HN3A	0.93(6)	N3–HN3B	0.89(7)	N3–C16	1.426(5)
N1#1–Cd1–N1	86.4(2)	N1–Cd1–O2	81.8(1)	N1#1–Cd1–N3#3	175.9(1)

Symmetry transformations used to generate equivalent atoms: #1 = −*x*, *y*, −*z* + 1/2; #2 = *x* + 1/2, *y* + 1/2, *z* + 1; #3 = −*x* − 1/2, *y* + 1/2, −*z* − 1/2.

Table 3
Selected bond lengths (Å) and angles (°) in polymer **2**.

Cd1–N4	2.340(4)	Cd1–N1	2.342(4)	Cd1–N3#1	2.375(5)
Cd1–O3	2.394(4)	Cd1–N6#2	2.391(4)	Cd1–N3	16.709(5)
N3–HN3A	0.94(8)	N3–HN3B	0.74(9)	N6–HN6A	0.80(6)
N6–HN6B	1.09(6)				
N1–Cd1–N4	89.6(2)	C10–O1–C13	119.6(4)	C28–O2–C31	117.1(4)

Symmetry transformations used to generate equivalent atoms: #1 = −*x*, *y* − 1, −*z* + 1/2; #2 = −*x*, *y* + 1, −*z* + 1/2.

Table 4
Selected bond lengths (Å) and angles (°) in compound **3**.

Cd1–O9	2.296(2)	Cd1–N1	2.314(2)	Cd1–N4#1	2.321(2)
Cd1–O8	2.326(2)	Cd1–O2	2.417(2)	Cd1–O6	2.620(3)
Cd1–O5	2.641(4)	Cd1–O3	2.868(3)		
O9–Cd1–N1	89.32(8)	O9–Cd1–O8	172.06(10)	N1–Cd1–N4#1	171.08(7)

Symmetry transformations used to generate equivalent atoms: #1 = −*x*, −*y* + 1, −*z*.

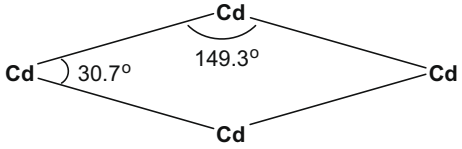
3.2. Coordination polymers *1* and *2*

Two coordination polymers $[CdL^1_2(NO_3)_2]$ (**1**) and $[CdL^2_2(NO_3)_2]$ (**2**) were prepared by layering a methanol solution containing $Cd(NO_3)_2 \cdot 6H_2O$ onto the top of a dichloromethane solution containing the corresponding ligand (Eqs. (1) and (2)). Reactions involving benzene or tetrahydrofuran in place of dichloromethane produced very poor crystalline products:

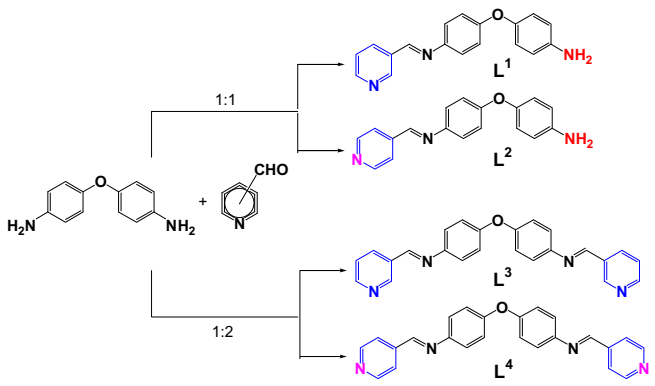
$$Cd(NO_3)_2 + \mathbf{L^1} \xrightarrow{MeOH/CH_2Cl_2} [CdL^1_2(NO_3)_2] \quad (1)$$

$$Cd(NO_3)_2 + \mathbf{L^2} \xrightarrow{MeOH/CH_2Cl_2} [CdL^2_2(NO_3)_2] \quad (2)$$

A monomer unit of polymer **1** with the atom-numbering scheme is presented in Fig. 1, which shows an asymmetric unit consisting of one half Cd metal, one **L¹** ligand and one nitrato ligand. The Cd metal is six-coordinate with a $[CdN_4O_2]$ core and is coordinated by two pyridyl N atoms and two amine N atoms from four ligands as well as two O atoms from two η^1-NO_3 ligands (Table 2). The Cd metal is located on a crystallographic twofold axis. The NH_2 hydrogen atoms participate in N–H···O (O4) hydrogen bonds. The N(pyridyl)···N(amino) separation N1···N3 is 14.161(5) Å. Fig. 2 shows a packing diagram of polymer **1**, which displays a 2-D brick-wall structure extending approximately in the [1 0 1] direction. This structure consists of quasi-parallelogram units, each of which contain four Cd metals and four **L¹** ligands to form a large 64-membered (60 ligand atoms and four Cd metals) ring with a Cd···Cd separation of 17.337(1) Å. However, the Cd···Cd···Cd angles are far from 90°, and therefore the size of the quasi-parallelogram is rather small. Fig. 3 shows small channels approximately along the *b*-axis.



An asymmetric monomer unit of polymer **2** is given in Fig. 4, which is composed of one Cd metal, two **L²** ligands and two nitrato ligands. As is the case for polymer **1**, the pseudo-octahedral Cd metal in polymer **2** is coordinated by two pyridyl N, two amino N and two O atoms (Table 3). The NH_2 hydrogen atoms participate in N–H···O (O5, O7, O8) hydrogen bonds. The two N(pyridyl)···N(amino) separations are practically the same: N1···N3 = 14.628(7) Å and N4···N6 = 14.599(6) Å, and are somewhat longer than that



Scheme 1.

(14.161(5) Å) in polymer **1**, consistent with the expectation based on the different nitrogen positions in the terminal pyridyl rings. A packing diagram of polymer **2** is given in Fig. 5, which illustrates a 1-D wave-like chain structure. The ligands link the $Cd(NO_3)_2$ fragments approximately along the *b*-axis, and the overall structure can be described as a chain of double strands. The Cd···Cd separation is 16.732(1) Å and the Cd···Cd···Cd angle is 113.59(1)°.

Several coordination polymers with interesting topologies, $[M(NCS)_2(4,4'\text{-oda})_2]$ (M = Ni, Co), $[M(N)_3(4,4'\text{-oda})_2](NO_3)$ (M = Cd, Co) and $[Cd(SCN)_2(4,4'\text{-oda})_2]$, which are related to polymers **1** and **2**, were prepared previously by employing 4,4′-oxydianiline (4,4′-oda) as a linking ligand [34,35]. For example, in the local coordination of Co in the polymer $[Co(NCS)_2(4,4'\text{-oda})_2]$, four amine (aniline) N atoms form an equatorial plane and two thiocyanate N atoms occupy axial positions. This polymer has a two-dimesional sheet structure, which resembles the brick-wall structure found for polymer **1**, and has a 48-memebered ring unit (44 ligand atoms and four Co atoms) [34].

To examine the thermal behavior of polymers **1** and **2**, thermogravimetric analyses (TGA) were performed by heating them up to 800 °C. The framework of polymer **1** is stable up to 250 °C, above which an abrupt weight loss occurs at 280–310 °C, corresponding to the loss one NO_3 and the pyridine aldehyde fragment of the ligand $\mathbf{L^1}$ (calculated: 20%; observed: 18%). Above this temperature range a gradual weight loss continues. Polymer **2** is stable up to 200 °C, and a steady weight follows from 200 to 540 °C. These data indicate that the thermal stability of the framework of polymer **1** is somewhat higher than that of polymer **2**.

3.3. Molecular compound *3*

A macrocyclic dinuclear cadmium compound $[Cd_2\mathbf{L^3}_2(NO_3)_4(H_2O)_4]\cdot(C_4H_8O)_2$ (**3**) was obtained by layering a methanol solution containing $Cd(NO_3)_2\cdot 6H_2O$ onto the top of a tetrahydrofuran solution containing ligand $\mathbf{L^3}$ (Eq. (3)). Unlike compounds **1** and **2**, compound **3** is a molecular species with a double-helical structure, not a coordination polymer:

$$2Cd(NO_3)_2 + 2\mathbf{L^3} \xrightarrow{MeOH/THF} [Cd_2\mathbf{L^3_2}(NO_3)_4(H_2O)_4](THF)_2 \quad (3)$$

The molecular structure of compound **3** is presented in Fig. 6, which shows an asymmetric unit consisting of one Cd metal, one $\mathbf{L^3}$ ligand, two nitrato ligands, two aqua ligands and one C_4H_8O (THF) guest molecule. The Cd metal is eight-coordinated by two pyridyl N atoms, two aqua O atoms and four nitrate (η^2-NO_3) O atoms (Table 4). All the aqua H atoms are involved in O–H···O hydrogen bonds. In paricular, the THF guest molecule interacts with the aqua ligands by a hydrogen bond (O9–H = 0.955 Å; H···O10 = 1.778 Å; O9···O10 = 2.730 Å; O9–H···O10 = 174°). The N1···N4 and Cd···Cd separations are 17.0801(3) and 17.1837(5) Å, respectively, and the Cd···O1···Cd angle is 101.61(1)°. A space filling model of compound **3** (Fig. 7) demonstrates its double-helical structure.

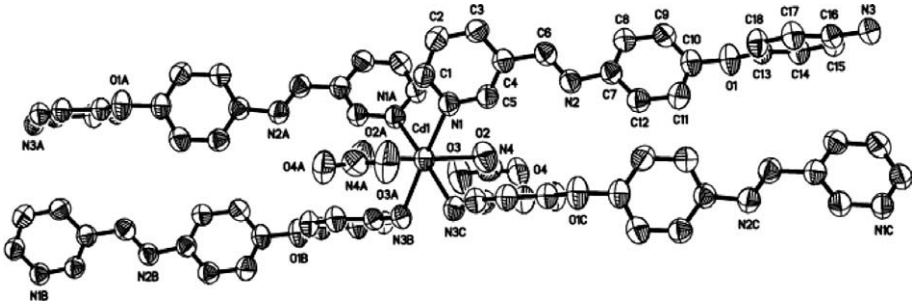


Fig. 1. Local coordination environment of cadmium in compound **1**.

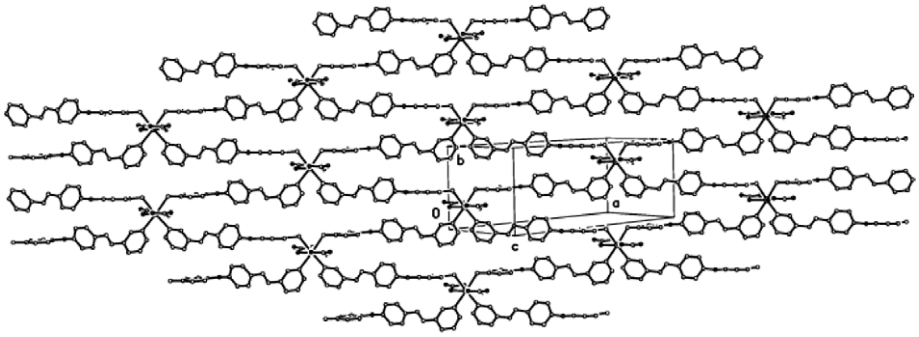


Fig. 2. Packing diagram of polymer **1**, showing a 2-D brick-wall structure.

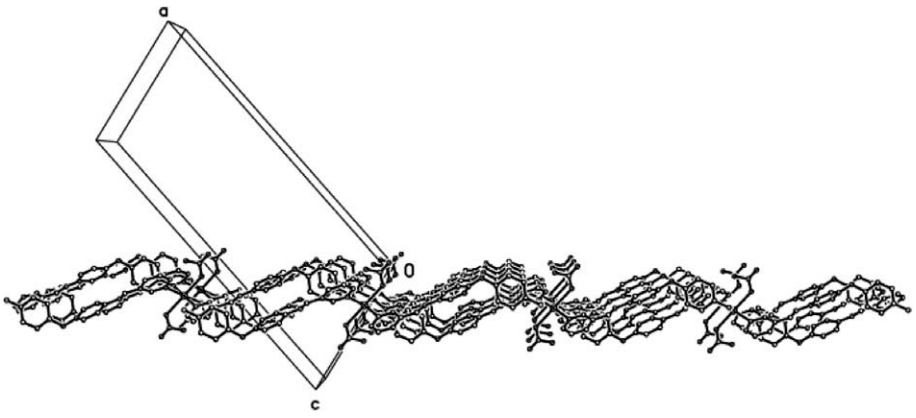


Fig. 3. Projection of compound **1**, showing a channel approximately along the *b*-axis.

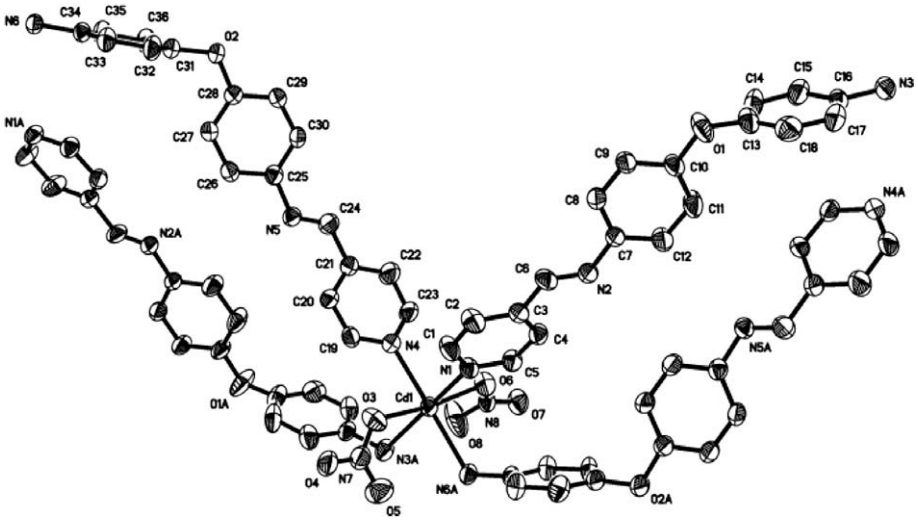


Fig. 4. Local coordination environment of cadmium in compound **2**.

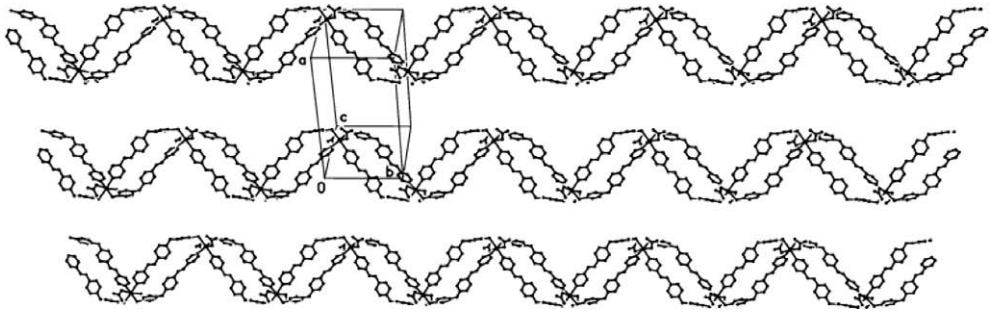


Fig. 5. Packing diagram of compound **2**, showing a 1-D wave-like chain of double strands.

Several flexible Schiff-base-type ligands, **L9**–**L11** (Chart 2), have been prepared recently and have been employed to prepare intriguing compounds. Examples are the cage-like $[Ag_2(\mathbf{L9})_2][BF_4]_4$, the triple-helical $[Co_2(\mathbf{L9})_3](BF_4)_4$, the triple-helical $[Ni_2(\mathbf{L9})_3](BF_4)_4$ [36], the triple-helical $[Ni_2(\mathbf{L10})_3](BF_4)_4$-$(MeOH)_2$ [37], the triple-helical $[Zn_2(\mathbf{L10})_3](ClO_4)_4(DMF)(CH_3CN)_2$ [38], the double-helical $[Cu_2(\mathbf{L10})_2](BF_4)_2$ [39], the triple-helical $[Fe_2(\mathbf{L10})_3]Cl_4$ [40] and the double-helical $[Ag_2(\mathbf{L11})_2](PF_6)_2$ complexes [41]. In these compounds the central imine N atoms (–CH=N–) as well as the 2-pyridyl N atoms in ligands **L9**–**L11** are bound to the metal, indicating that these ligands act as typical Schiff-base-type ligands. Furthermore, all the compounds containing these ligands are molecular species rather than polymeric species (coordination polymers). It is worth noting that ligands $\mathbf{L^3}$ and $\mathbf{L^4}$ have 3-pyridyl and 4-pyridyl terminal groups, respectively, and the imine nitrogen of $\mathbf{L^3}$ in polymer **3** does not coordinate to the Cd metal (Fig. 6). The difference in the binding pattern between the ligands **L9**–**L11** and ligand $\mathbf{L^3}$ is presumably due to the different nitrogen positions in the terminal pyridyl groups (2,2′ versus 3,3′). Although we failed to prepare a compound containing ligand $\mathbf{L^4}$, we speculate the resulting complex to be a molecular species.

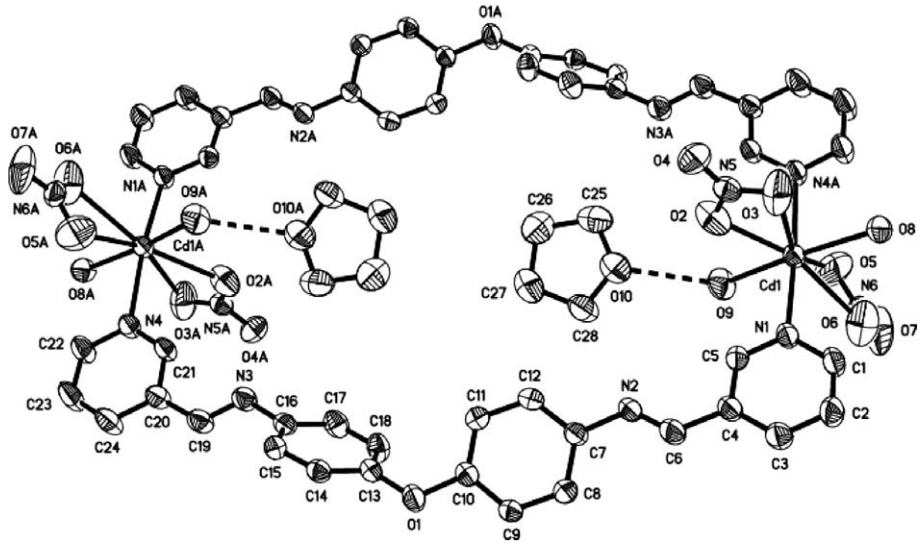


Fig. 6. ORTEP drawing of compound 3.

TGA of compound **3** shows that the first weight loss occurs at 120–150 °C, which corresponds to the loss of the THF guest (calculated: 10%; observed: 10%). Between 150 and 270 °C, the compound framework appears to be stable. Above this temperature range, the second weight loss occurs abruptly and then continues steadily up to 480 °C. At the second phase, ligand $\mathbf{L^3}$, one NO_3 ligand and two aqua ligands seem to be lost (calculated: 64%; observed: 64%), and the framework breaks down.

On the basis of the TGA analysis, the guest-free form of compound **3** was obtained by heating it at 150 °C for 24 h. The XRPD patterns of the original compound (Fig. 8a) and its guest-free form (Fig. 8b) show some discrepancies in the *d*-spacing and peak shape (the peaks with asterisks in Fig. 8a and b). To examine the reversibility of the desorption–resorption of the THF guest molecules, we took the XRPD spectrum of a sample that was prepared by immersing the guest-free form in THF in a capped vial at 50 °C for 24 h. The XRPD spectrum of this sample (Fig. 8c) clearly shows that compound **3** is restored. These XRPD data indicate a roughly reversible desorption–resorption behavior of the guest THF molecules. By contrast, the sorption of benzene, dichloromethane, acetone or 1,4-dioxane for the guest-free form is not observed. Moreover, pyridine and DMSO dissolve compound **3**.

In summary, we have prepared four ligands, [(3-py)–CH=N–C_6H_4–O–C_6H_4–NH_2, $\mathbf{L^1}$], [(4-py)–CH=N–C_6H_4–O–C_6H_4–NH_2, $\mathbf{L^2}$],

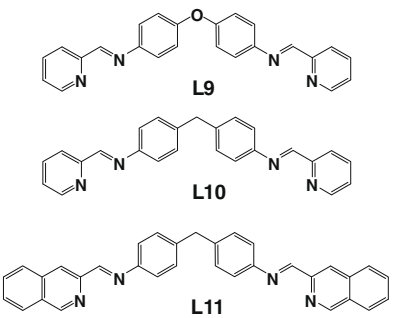


Chart 2.

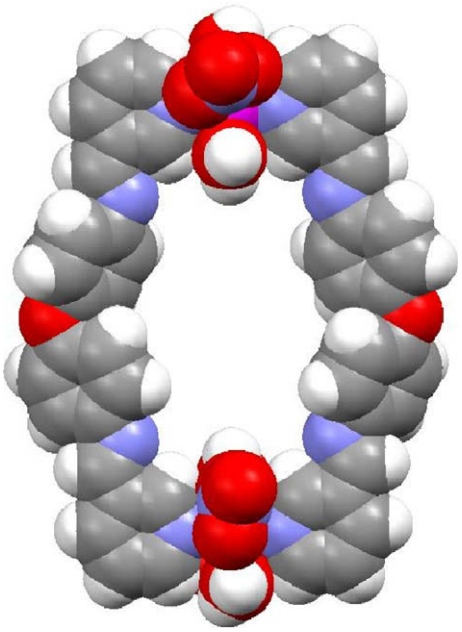


Fig. 7. A space filling model of compound 3 showing its double-helical structure: purple, Cd; red, O; blue, N; grey, C; white, H. (For interpretation of the references to color in this figure legend, the reader is referred to the web version of this article.)

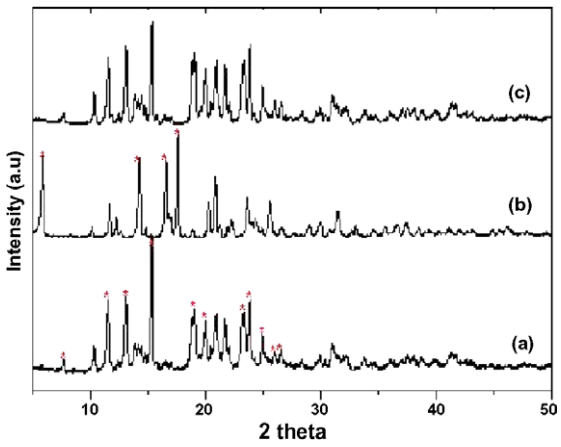


Fig. 8. XRD patterns of compound **3**: (a) original form; (b) guest-free form and (c) THF-resorbed form.

[(3-py)–CH=N–C_6H_4–O–C_6H_4–N=CH–(3-py), $\mathbf{L^3}$] and [(4-py)–CH=N–C_6H_4–O–C_6H_4–N=CH–(4-py), $\mathbf{L^4}$], all of which contain an intervening oxydianiline fragment. Whereas ligands $\mathbf{L^1}$ and $\mathbf{L^2}$ have two types of terminal groups (pyridyl and amine groups), ligands $\mathbf{L^3}$ and $\mathbf{L^4}$ have a single type of terminal group (pyridyl groups at both terminals). Ligands $\mathbf{L^1}$–$\mathbf{L^3}$ reacted with $Cd(NO_3)_2 \cdot 6H_2O$ to produce [Cd$\mathbf{L^1}_2(NO_3)_2$] (**1**), [Cd$\mathbf{L^2}_2(NO_3)_2$] (**2**) and [Cd$\mathbf{L^3}_1(NO_3)_2$-$(H_2O)_2$] $\cdot (C_4H_8O)_2$ (**3**), respectively. Compounds **1**–**3** were structurally characterized by X-ray diffraction. Compound **1** is a 2-D brick-wall coordination polymer and compound **2** is a 1-D double-strand-chain polymer. On the other hand, compound **3** is a discrete dinuclear molecule with a double-helical structure, which contains THF (C_4H_8O) guest molecules. Compound **3** exhibited a roughly reversible desorption–sorption behavior toward THF. The above results revealed that the ligands containing one pyridyl and one amine terminal group created coordination polymers, whereas those containing only the terminal pyridyl groups gave a molecular species.

Supplementary data

CCDC 705524–705526 contain the supplementary crystallographic data for compounds **1**–**3**, respectively. These data can be obtained free of charge via http://www.ccdc.cam.ac.uk/conts/retrieving.html, or from the Cambridge Crystallographic Data Centre, 12 Union Road, Cambridge CB2 1EZ, UK; fax: (+44) 1223-336-033; or e-mail: deposit@ccdc.cam.ac.uk.

Acknowledgement

This paper was supported by Samsung Research Fund, Sungkyunkwan University, 2008.

References

[1] G.F. Swiergers, T.J. Malefetse, Chem. Rev. 100 (2000) 3483.
[2] M.J. Zaworotko, B. Moulton, Chem. Rev. 101 (2001) 1629.
[3] M. Eddaoudi, D.B. Moler, H. Li, B. Chen, T.M. Reineke, M.O. Keeffe, O.M. Yaghi, Acc. Chem. Res. 34 (2001) 319.
[4] M. Eddaoudi, J. Kim, N. Rosi, D. Vodak, J. Wachter, M. O'Keeffe, O.M. Yaghi, Science 295 (2002) 469.
[5] C. Janiak, J. Chem. Soc., Dalton Trans. (2003) 2781.
[6] B. Kesanli, W. Lin, Coord. Chem. Rev. 246 (2003) 305.
[7] S.A. Barnett, N.R. Champness, Coord. Chem. Rev. 246 (2003) 145.
[8] J.L.C. Rowsell, O.M. Yaghi, Micropor. Mesopor. Mater. 73 (2004) 3.
[9] B.-H. Ye, M.-L. Tong, H.-M. Chen, Coord. Chem. Rev. 249 (2005) 545.
[10] N.W. Ockwig, O.D. Friedrichs, M. O'Keeffe, O.M. Yaghi, Acc. Chem. Res. 38 (2005) 176.
[11] A.Y. Robin, K.M. Fromm, Coord. Chem. Rev. 250 (2006) 2127.
[12] S. Kitagawa, R. Matsuda, Coord. Chem. Rev. 251 (2007) 2490.
[13] K. Li, D.H. Olson, J.Y. Lee, W. Bi, K. Wu, T. Yuen, J. Li, Adv. Funct. Mater. 18 (2008) 2205.
[14] H.-F. Zhu, L.-Y. Kong, T.-A. Okamura, J. Fan, W.-Y. Sun, N. Ueyama, Eur. J. Inorg. Chem. (2004) 1465.
[15] X.-M. Quyang, B.-L. Fei, T.-A. Okamura, H.-W. Bu, W.-Y. Sun, W.-X. Tang, N. Ueyama, Eur. J. Inorg. Chem. (2003) 618.
[16] M.B. Zaman, M.D. Smith, D.M. Curtin, H.-C. zur Loye, Inorg. Chem. 41 (2002) 4895.
[17] E. Bosch, C.L. Barnes, New J. Chem. 25 (2001) 1376.
[18] Y.-B. Dong, M.D. Smith, R.C. Layland, H.-C. zur Loye, Chem. Mater. 12 (2000) 1156.
[19] Y.-B. Dong, M.D. Smith, H.-C. zur Loye, Inorg. Chem. 39 (2000) 4927.
[20] Y.-B. Dong, M.D. Smith, H.-C. zur Loye, J. Solid State Chem. 155 (2000) 143.
[21] M.A. Withersby, A.L. Blake, N.R. Champness, P.A. Cooke, P. Hubberstey, W.-S. Li, M. Schröder, Inorg. Chem. 38 (1999) 2259.
[22] H.N. Kim, H.K. Lee, S.W. Lee, Bull. Korean Chem. Soc. 26 (2005) 6.
[23] D. Min, Y.-B. Cho, H.K. Lee, S.W. Lee, Inorg. Chim. Acta 359 (2006) 577.
[24] Y.-B. Cho, D. Min, H.K. Lee, S.W. Lee, Cryst. Growth Des. 6 (2006) 342.
[25] S.H. Kim, H.S. Huh, S.W. Lee, J. Mol. Struct. 841 (2007) 78.
[26] H.S. Huh, S.W. Lee, Inorg. Chem. Commun. 10 (2007) 1244.
[27] H.S. Huh, H.J. Yun, S.W. Lee, Inorg. Chim. Acta 361 (2008) 2101.
[28] D. Min, H.S. Huh, S.W. Lee, Polyhedron 27 (2008) 2083.
[29] G.M. Sheldrick, SADABS, Program for Absorption Correction, University of Göttingen, 1996.
[30] Bruker, SHELXTL, Structure Determination Software Programs, Bruker Analytical X-ray Instruments Inc., Madison, Wisconsin, USA, 1997.
[31] M. Calligaris, L. Randaccio, in: G. Wilkinson, R.D. Gillard, J.A. McCleverty (Eds.), Comprehensive Coordination Chemistry, vol. 2, Pergamon Press, New York, 1987, pp. 715–738.
[32] P.A. Vigato, S. Tanburini, Coord. Chem. Rev. 248 (2004) 1717.
[33] R. Hernanddez-Molina, in: J.A. McCleverty, T.J. Meyer (Eds.), A. Acyclic and Macrocyclic Schiff Base Ligands in Comprehensive Coordination Chemistry II, vol. 2, Pergamon Press, New York, 2004, pp. 411–446.
[34] H.-J. Chen, X.-M. Chen, D.-Y. Zhou, Y.-C. Zhou, Supramol. Chem. 14 (2002) 21.
[35] H.-J. Chen, W.-J. Yu, X.-M. Chen, W.-J. Zheng, Acta Crystallogr. C57 (2001) 1285.
[36] H. Cheng, C.-Y. Duan, C-J. Fang, Q-J. Meng, J. Chem. Soc., Dalton Trans. (2000) 2419.
[37] M.J. Hannon, C.L. Painting, A. Jackson, J. Hamblin, W. Errington, Chem. Commun. (1997) 1807.
[38] N. Yoshida, K. Ichikawa, M. Shiro, J. Chem. Soc., Perkin Trans. 2 (2000) 17.
[39] L.J. Childs, N.W. Alcock, M.J. Hannon, Angew. Chem., Int. Ed. 40 (2001) 1079.
[40] J.M.C.A. Kerckhoffs, J.C. Peberdy, I. Meistermann, L.J. Childs, C.J. Isaac, C.R. Pearmund, V. Reudegger, S. Khalid, N.W. Alcock, M.J. Hannon, A. Rodger, J. Chem. Soc., Dalton Trans. (2007) 734.
[41] M.J. Hannon, C.L. Painting, N.W. Alcock, Chem. Commun. (1999) 2023.

Polyhedron 28 (2009) 621–629

Contents lists available at ScienceDirect

Polyhedron

journal homepage: www.elsevier.com/locate/poly

New organometallic Ru(II) and Fe(II) complexes with tetrathia-[7]-helicene derivative ligands

Maria Helena Garcia [a,*], Pedro Florindo [a], Maria de Fátima M. Piedade [b], Stefano Maiorana [c], Emanuela Licandro [c]

[a] Centro de Ciências Moleculares e Materiais, Faculdade de Ciências da Universidade de Lisboa, Ed.C8, Campo Grande, 1749-016 Lisboa, Portugal
[b] Centro de Química Estrutural, Instituto Superior Técnico, Universidade Técnica de Lisboa, Av. Rovisco Pais, 1049-001 Lisboa, Portugal
[c] Dipartimento di Chimica Organica e Industriale, Università degli Studi di Milano, Via C. Golgi, 19, I-20133 Milano, Italy

ARTICLE INFO

Article history:
Received 9 July 2008
Accepted 2 December 2008

Keywords:
Heterohelicenes
Tetrathia-[7]-helicene
Ruthenium(II)
Iron(II)
Monocyclopentadienyl

ABSTRACT

A series of organometallic complexes possessing new tetrathia-[7]-helicene nitrile derivative ligands [**TH-7**] as chromophores, of general formula [MCp(P–P)(NC{TH-[7]-Y}Z)][PF_6] (M = Ru, Fe, P–P = DPPE, Y = H, NO_2, Z = H, C≡N; M = Ru, L–L = $2PPh_3$, Y = H, Z = H) has been synthesized and fully characterized. ^{1}H NMR, FT-IR and UV–Vis. spectroscopic data were analyzed with in order to evaluate the existence of electronic delocalization from the metal centre to the coordinated ligand to have some insight on the potentialities of these new compounds as non-linear optical molecular materials. Slow crystallization of compound [$RuCp(PPh_3)_2$(NC{TH-[7]-H}H)][PF_6] **2Ru** revealed an interesting isomerization of the helical ligand with formation of two carbon-carbon bonds between the two terminal thiophenes, leading to the total closure of the helix (**2**∗**Ru**).

© 2008 Elsevier Ltd. All rights reserved.

1. Introduction

The search for new organic and organometallic materials with significant non-linear optical (NLO) properties has been an area of considerable interest due to their relevance to optical device technology [1–6]. Nevertheless, the observation of even-order non-linearity is limited to the asymmetric crystallization of the bulk materials. Thus, chiral structures appear as ideal systems to investigate second-order NLO effects due to their intrinsic non-centrosymmetry, which allows these effects to be observed even in symmetric media such as chiral isotropic liquids [7]. Large chiral effects have been demonstrated in surface NLO responses of films of chiral molecules adsorbed at the air/water interface [8] and of Langmuir–Blodgett films of chiral polymers [9].

In this context, the intrinsically chiral structures of helicenes [10] make these compounds very attractive to be investigated, leading to several theoretical and experimental studies of carbohelicenes [11] and heterohelicenes [12]. The easier functionalization of thiaheterohelicenes, compared to carbohelicenes, allows the introduction of several different functional groups, either in the terminal thiophene rings (formyl, alkoxycarbonyl, trifluoromethyl, amide, trialkylsilyl, cyanoacrylic and acrylates) or in the central benzene rings (alkyl and electron-withdrawing groups such as alkoxycarbonyl and trifluoromethyl) [13]. The reported optimized synthesis of tetrathia-[7]-helicene (TH[7]) and the convenient preparation of the formyl derivative 2-CHO-TH[7] [13a] paved the way for the synthesis of a variety of substituted heterohelicenes.

The present work reports the synthesis of three new TH[7] derivatives, through the functionalization of one terminal thiophene ring with a nitrile group (**L1**), two terminal thiophene rings with two nitrile groups (**L2**) and one terminal thiophene group with one nitrile group followed by nitration in the benzene rings (**L3**). These new TH[7] derivatives were used as ligands for the synthesis of a new family of η^5-monocyclopentadienyl ruthenium(II) and iron(II) organometallic complexes represented by the general formulation [MCp(PP)(NC{TH-[7]-Y} Z)] [PF_6] (M = Ru(II), Fe(II), P–P = DPPE, Y = H, NO_2, Z = H, C≡N; M = Ru(II), L–L = $2PPh_3$, Y = H, Z = H).

The new compounds have been characterized by the usual FT-IR, UV–Vis, ^{1}H and ^{31}P NMR spectroscopic techniques. Nevertheless, the poor solubility of the compounds in common deuterated solvents did not allow the characterization by ^{13}C NMR. The crystallization of compound [$RuCp(PPh_3)_2$(NC{TH-[7]-H}H)] [PF_6] **2Ru**, by slow diffusion of *n*-hexane into an acetone solution of the compound, afforded single crystals suitable for X-ray diffraction studies. This revealed isomerization of the helical ligand, due to the formation of two new carbon–carbon bonds between the terminal thiophene rings, giving the new complex **2**∗**Ru**.

* Corresponding author. Tel.: +351 21 750 00 75/6; fax: +351 21 750 00 88.
E-mail address: lena.garcia@fc.ul.pt (M.H. Garcia).

0277-5387/$ - see front matter © 2008 Elsevier Ltd. All rights reserved.
doi:10.1016/j.poly.2008.12.036

2. Results and discussion

2.1. Synthesis of the tetrathia-[7]-helicene ligands *L1*, *L2* and *L3*

The synthesis of the TH[7] derived nitrile ligands, tetrathia-[7]-helicene-2-carbonitrile (**L1**), tetrathia-[7]-helicene-2,13-dicarbonitrile (**L2**) and tetrathia-[7]-helicene-2-carbonitrile (**L3**), bearing the nitro group in an unidentified position of the helix, is summarized in Scheme 1.

Tetrathia-[7]-helicene-2-carbaldehyde (**2**) was synthesized in good yield by electrophilic formylation of the α-anion of tetrathia-[7]-helicene, generated with *n*-BuLi at −78 °C in DMF, following Ref. [13a]. The ligand tetrathia-[7]-helicene-2-carbonitrile (**L1**) was synthesized from compound **2** and hydroxyl ammonium chloride in pyridine, with *in situ* dehydration by acetic anhydride.

The reaction of **L1** with nitric acid in acetic anhydride was carried out with the purpose of synthesizing tetrathia-[7]-helicene-13-nitro-2-carbonitrile, nitrated at the opposite end of the helix relatively to the nitrile group, as would be expected following our previous experience with benzo[1,2-b;4,3-b′]dithiophene derivative complexes [14]. However the analysis of the ^{1}H NMR spectrum of the obtained compound showed the presence of two doublets at 6.65 and 7.57 ppm (J_{HH} = 5.6 Hz), attributed to the thiophene ring protons, revealing that the nitration had occurred in one of the benzene rings. Nevertheless, substitution of the H on the two terminal thiophene rings was possible with two nitrile groups (**L2**), whilst the introduction of NO_2 in position 13 through an electrophilic substitution failed, thus demonstrating that the only way to functionalize the helical system in a regioselective manner is through the generation of anions in the positions 2 and 13 and the reaction with electrophilic reagents. ^{13}C NMR studies were not carried out due to the low solubility of the organic ligands in common deuterated solvents (acetone-d_6, chloroform-*d*, acetonitrile-d_3 and DMSO-d_6) even at high temperatures and, consequently, further characterization by *HMQC* and *HMBC* NMR techniques could not be applied to identify the position of the NO_2 group; therefore, the structure proposed for **L3** in Scheme 1 is simply one out of six possible structures.

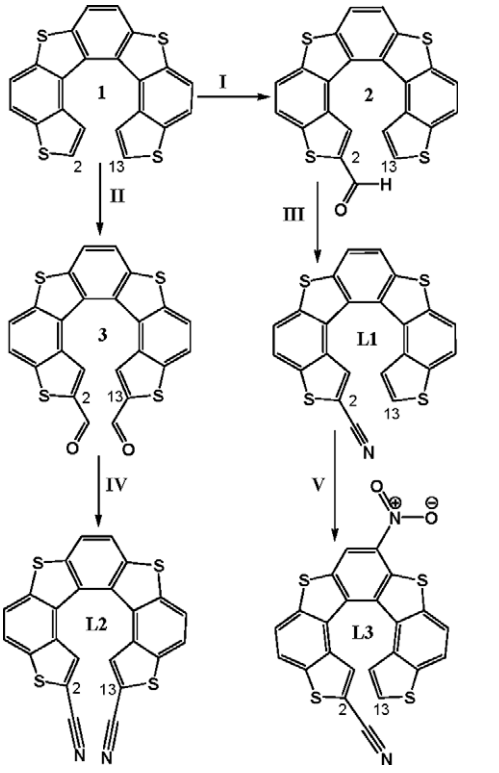
Tetrathia-[7]-helicene-2,13-dicarbonitrile (**L2**) was synthesized by the reaction of tetrathia-[7]-helicene (**1**) with two equivalents of *n*-BuLi at −78 °C in DMF, affording tetrathia-[7]-helicene-2,13-dicarbaldehyde (**3**), which was used, without purification, in the reaction with hydroxylammonium chloride in pyridine, and dehydration *in situ* with acetic anhydride.

2.2. Synthesis of complexes [M(η^5-C$_5$H$_5$)(PP)(L)][PF$_6$]

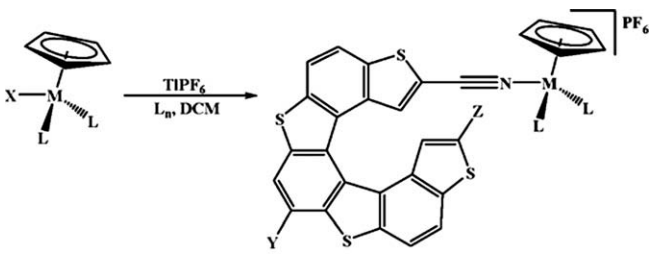
Complexes of the general formula [M(η^5-C$_5$H$_5$)(PP)(L)][PF$_6$] (M = Ru and Fe, PP = DPPE, L = **L1**, **L2** and **L3**; M = Ru(II), (PP) = 2PPh$_3$, L = **L1**) were prepared by halide abstraction with TlPF$_6$ from the parent neutral complexes [M(η^5-C$_5$H$_5$)(PP)X] (M = Fe, X = I; M = Ru, X = Cl) in dichloromethane, in the presence of an adequate excess of the corresponding nitrile (Scheme 2).

The reactions were carried out at reflux, stirring overnight under inert atmosphere. The compounds were recrystallized by slow diffusion of n-hexane in acetone or dichloromethane, affording microcrystalline products with colours ranging from orange to dark red. The compounds were fairly stable in air and moisture, both in the solid state and in solution, and were obtained in fair yields of 27–56%. The formulation of the new compounds is supported by analytical data, FT-IR and ^{1}H, ^{31}P NMR spectroscopic data, with the exception of compounds **L3** and **2Ru**, for which the elemental analysis always gave a significant error. Nevertheless, the elemental percentages for **L3** containing complexes are in good agreement with the proposed formulations. An effort is currently being made at our laboratory to obtain suitable crystals for X-ray diffraction studies of any of the compounds **L3**, **4Ru** and **4Fe**, so that the structure of **L3** can be unequivocally determined.

The solid state FT-IR spectra (KBr pellets) of the complexes presented the characteristic bands of the cyclopentadienyl ligand (≈ 3060 cm^{-1}), the PF_6^- anion (840 and 560 cm^{-1}) and the coordinated nitrile (ν_{CN} from 2214 to 2191 cm^{-1}) in all of the studied complexes. As observed for other ruthenium and iron related compounds,[14,15] negative shifts were found for ν_{CN}, compared to the corresponding values of the uncoordinated nitrile, in particular for the iron compound containing the coordinated TH-[7] functionalized with the strong acceptor NO_2 group (**L3**), where a shift of −24 cm^{-1} was found. Negative shifts in the nitrile and acetylide



Scheme 1. Synthesis of ligands **L1**, **L2** and **L3**. **I** –THF, −78 °C, (i) *n*-BuLi, (ii) DMF [13a]; **II** – THF, −78 °C, (i) *n*-BuLi, (ii) DMF; **III** – (i) $HONH_2 \cdot HCl$, (ii) Ac_2O; **IV** – (i) $HONH_2 \cdot HCl$, (ii) Ac_2O; **V** – HNO_3/Ac_2O.



1Ru	M=Ru; (LL) = DPPE; L1 (Z=H ; Y=H)
1Fe	M=Fe; (LL) = DPPE; L1 (Z=H ; Y=H)
2Ru	M=Ru; (LL) = 2PPh$_3$; L1 (Z=H ; Y=H)
3Ru	M=Ru; (LL) =DPPE; L2 (Z=C≡N; Y=H)
3Fe	M=Fe; (LL) = DPPE; L2 (Z=C≡N; Y=H)
4Ru	M=Ru; (LL) = DPPE; L3 (Z=H; Y=NO$_2$)
4Fe	M=Fe; (LL) = DPPE; L3 (Z=H; Y=NO$_2$)

Scheme 2. Reaction scheme for the synthesis and numbering of the tetrathia-[7]-helicene Ru/Fe derived complexes.

coordinated ligands have been attributed to π-back donation, due to π bonding between the d orbitals of the metal and the π^* orbital of the nitrile group, leading to a decreased C≡N bond order [14,15]. The magnitude of the ν_{CN} negative shift has been clearly related to the electron-donor capacity of the organometallic fragment $[MCp(P–P)]^+$ and the electron-attractor capacity of the substituent group on the chromophore.

^{1}H NMR resonances of the cyclopentadienyl ring are in the characteristic range of monocationic ruthenium(II) and iron(II) complexes. The coordination of TH-[7] derived nitriles leads to a shielding of most of the protons, especially the one in the thiophene ring adjacent to the nitrile group coordinated to the metal. The upfield shift of this proton was more significant for compounds with DPPE as a coligand, up to −1.57 ppm for compound **3Fe**. The unexpected higher shielding (∼0.2 ppm) found for compounds **3Ru** and **3Fe** (with **L2**) than for the analogues **4Ru** and **4Fe** with the better acceptor **L3** might be explained by the spatial effect of the neighbouring uncoordinated C≡N group of **L2**.

^{31}P NMR spectra of the complexes showed a resonance at −144.1 ppm, characteristic of PF_6^-, and resonances of the coordinated phosphines. For compounds **2Ru**, **4Ru** and **4Fe**, the phosphine resonance signals are singlets, but for compounds **1Ru**, **1Fe**, **3Ru** and **3Fe**, the phosphine resonances appear as two doublets with coupling constants ranging from 23.1 to 33.5 Hz, characteristic of phosphorus–phosphorus coupling. This effect may be due to interactions of the phosphines with the opposite end of the helical ligand, causing the unequivalency of the phosphorus atoms. For compounds **4Ru** and **4Fe**, the higher planarity predicted for the helical ligand **L3**, due to the resonant structures originating from the donor (organometallic moiety)-acceptor (NO_2) conjugation, should minimize the referred interactions, while for compound **2Ru**, the less rigid PPh_3 coligands, relatively to DPPE, must allow the phosphorus equivalency.

Table 1
Optical spectral data for the complexes $[M(\eta^5\text{-}C_5H_5)(PP)(L_n)][PF_6]$ and for the free TH[7] derived ligands **L1**, **L2** and **L3**, in CH_2Cl_2 and MeOH (ca. 10^{-4} M) solutions.

Compound	λ_{max}/nm (ε, $M^{-1}\,cm^{-1}$)	
	CH_2Cl_2	MeOH
(L1)	243(27000) 255(sh) 289(16900) 324(13000) 365(sh) 384(13100) 400(13200)	
$[Ru(\eta^5\text{-}C_5H_5)(DPPE)(L1)][PF_6]$ (1Ru)	287(sh) 327(13900) 360(sh) 382(sh) 398(13300) 418(sh)	285(sh) 327(22400) 379(sh) 394(21600) 420(sh)
$[Fe(\eta^5\text{-}C_5H_5)(DPPE)(L1)][PF_6]$ (1Fe)	286(sh) 330(15900) 400(13900) 415(13800) 465(sh)	287(sh) 329(20600) 395(17900) 407(17900) 457(sh)
$[Ru(\eta^5\text{-}C_5H_5)(PPh_3)_2(L1)][PF_6]$ (2Ru)	289(sh) 334(17400) 360(sh) 381(sh) 400(16600) 417(14800)	288(sh) 331(22300) 361(sh) 377(sh) 396(21400) 414(sh)
L2	260(27600) 291(20300) 326(16400) 339(24200) 391(19200) 411(20900)	
$[Ru(\eta^5\text{-}C_5H_5)(DPPE)(L2)][PF_6]$ (3Ru)	290(26300) 325(sh) 339(25300) 391(sh) 409(22300)	288(23500) 301(sh) 323(sh) 338(22300) 390(sh) 407(20600)
$[Fe(\eta^5\text{-}C_5H_5)(DPPE)(L2)][PF_6]$ (3Fe)	291(24300) 341(19000) 398(sh) 414(17500) 471(sh)	326(sh) 340(24900) 396(22700) 412(22900) 460(sh)
L3	254(26000) 276(sh) 349(7000) 430(10700)	
$[Ru(\eta^5\text{-}C_5H_5)(DPPE)(L3)][PF_6]$ (4Ru)	339(sh) 355(19300) 366(sh) 432(20000)	343(sh) 362(17100) 428(16700)
$[Fe(\eta^5\text{-}C_5H_5)(DPPE)(L3)][PF_6]$ (4Fe)	353(11900) 368(sh) 430(16700)	350(sh) 364(15300) 426(19800) 511(sh)

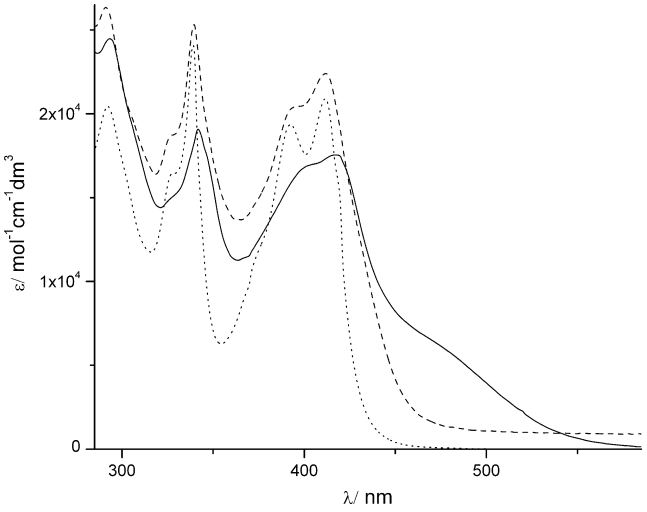


Fig. 1. Electronic spectra of compounds **3Ru**(– – –), **3Fe**(—) and of the ligand **L2**(· · ·) in CH_2Cl_2.

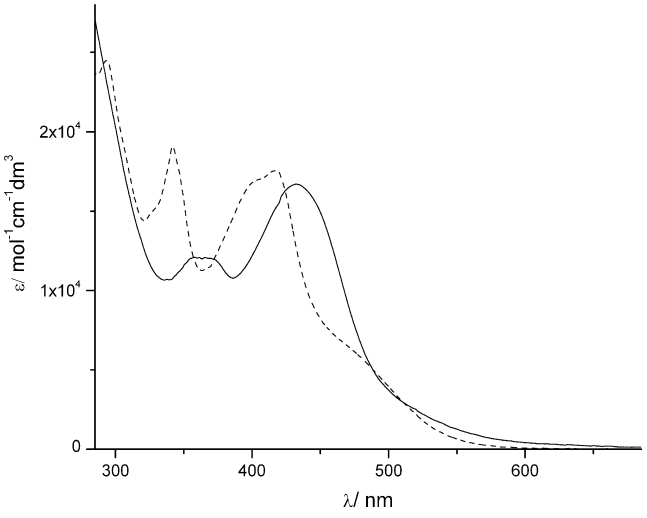


Fig. 2. Electronic spectra of compounds **3Fe**(– – –) and **4Fe**(—) in CH_2Cl_2.

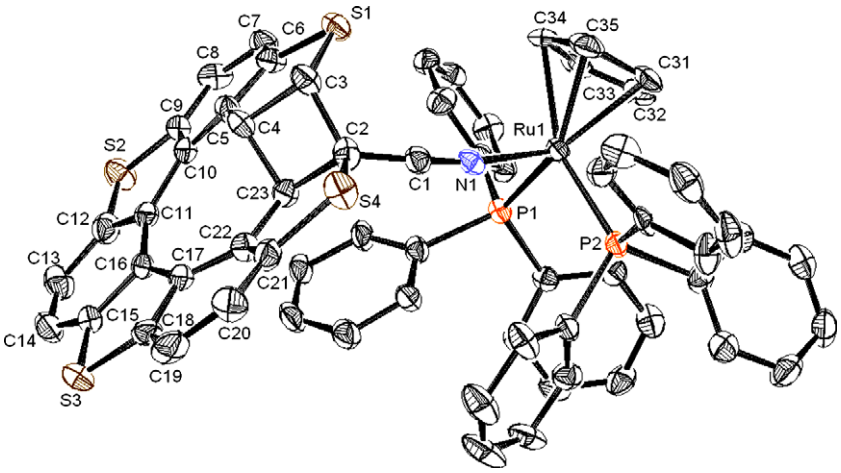


Fig. 3. ORTEP of the cation of compound **2∗Ru**.

2.3. Electronic spectra

Optical absorption spectra of all the complexes $[M(\eta^5\text{-}C_5H_5)(P\text{–}P)(L)][PF_6]$ were recorded in 10^{-4} M dichloromethane and methanol solutions (Table 1), in order to identify the M → L charge transfer and $\pi\text{–}\pi^*$ absorption bands expected for these complexes.

The electronic spectra of the helical ligands show several bands in the UV region due to their extensive π conjugated systems. As would be expected, the introduction of acceptor groups, either CN or NO_2, leads to a bathochromic shift of these bands.

The electronic spectra of the organometallic compounds are characterized by an intense absorption in the range 230–280 nm, attributed to the organometallic fragments $[MCp(P\text{–}P)]^+$, and in the range 280–430 nm, attributed to internal transitions in the TH-[7] derived ligands, by comparison to the free ligand spectra. For compounds **1Fe** and **3Fe**, an additional band is found, as a shoulder, in the ligands lower energy band, attributed to a metal to ligand charge transfer, $d(M^{II}) \rightarrow \pi^*(L)$. For compound **4Fe** no additional band was verified, although enlargement of the lower energy band of the ligand can obscure the existence of any superimposed MLCT band, as was observed before for other compounds with NO_2 substituted nitrile ligands [15e].

In the ruthenium compounds there is no evidence for any MLCT band, although it might be superimposed with the lower energy ligand internal transitions bands. Fig. 1 shows the electronic spectra of compounds $[MCp(DPPE)(NC\{TH\text{-}[7]\}CN)][PF_6]$, **3Ru** and **3Fe**, and of the free ligand **L2**. The existence of a CT band at lower energy is very obvious in compound **3Fe**, in accordance with the spectroscopic data discussed above.

Superimposition of the electronic spectra of compounds **3Fe** and **4Fe**, pictured in Fig. 2, shows that the ~500 nm CT band found in **3Fe** seems also occur in **4Fe**, although in this case it might be obscured by the enlargement of the band at a lower energy.

Table 2
Selected bond distances and bond and torsion angles for compound **2∗Ru**.

Bond distances (Å)			
Ru(1)–N(1)	2.030(5)	P(2)–C(221)	1.850(7)
Ru(1)–Cp[a]	1.8595(6)	P(2)–C(231)	1.829(6)
Ru(1)–P(1)	2.350(2)	N(1)–C(1)	1.147(8)
Ru(1)–P(2)	2.353(2)	C(1)–C(2)	1.433(9)
P(1)–C(111)	1.843(6)	C(2)–C(3)	1.598(9)
P(1)–C(121)	1.831(7)	C(3)–C(4)	1.535(9)
P(1)–C(131)	1.817(7)	C(4)–C(23)	1.519(9)
P(2)–C(211)	1.846(7)	C(23)–C(2)	1.565(9)
Bond angles (°)			
N(1)–Ru(1)–Cp[a]	121.79(14)	C(1)–C(2)–C(3)	115.3(6)
N(1)–Ru(1)–P(1)	87.93(14)	C(2)–C(3)–C(4)	88.8(5)
N(1)–Ru(1)–P(2)	90.83(15)	C(2)–C(23)–C(4)	90.6(5)
P(1)–Ru(1)–P(2)	99.84(6)	C(3)–C(4)–C(23)	91.2(5)
P(1)–Ru(1)–Cp[a]	124.15(5)	C(3)–C(2)–C(23)	87.2(5)
P(2)–Ru(1)–Cp[a]	122.98(5)	C(5)–C(4)–C(23)	106.9(6)
Ru(1)–N(1)–C(1)	169.9(5)	C(4)–C(23)–C(22)	107.7(5)
N(1)–C(1)–C(2)	175.7(7)	C(2)–C(3)–S(1)	119.3(5)
C(1)–C(2)–C(23)	116.4(6)	C(3)–C(2)–S(4)	116.5(5)
Torsion angles (°)			
Ru(1)–N(1)–C(1)–C(2)	29(11)	N(1)-C(1)–C(2)–C(23)	62(9)
N(1)–C(1)–C(2)–C(3)	−38(9)	C(2)–C(3)–C(4)–C(23)	-11.0(5)
N(1)–C(1)–C(2)–S(4)	−175(9)		

[a] Cp ring centroid.

In the ruthenium compounds there is no evidence for any MLCT band, although it might be superimposed with the lower energy ligand internal transitions bands. Fig. 1 shows the electronic spectra of compounds $[MCp(DPPE)(NC\{TH\text{-}[7]\}CN)][PF_6]$, **3Ru** and **3Fe**, and of the free ligand **L2**. The existence of a CT band at lower energy is very obvious in compound **3Fe**, in accordance with the spectroscopic data discussed above.

Superimposition of the electronic spectra of compounds **3Fe** and **4Fe**, pictured in Fig. 2, shows that the ~500 nm CT band found in **3Fe** seems also occur in **4Fe**, although in this case it might be obscured by the enlargement of the band at a lower energy.

2.4. X-ray crystallographic studies

Crystals of compound $[RuCp(PPH_3)_2(NC\{TH\text{-}[7]\})][PF_6] \cdot (CH_3)_2CO$ were obtained by slow diffusion of *n*-hexane in an acetone solution. The results obtained by X-ray diffraction studies showed that the molecular structure of the cation does not correspond to the one expected and confirmed by ^{1}H NMR spectroscopy, due to isomerization of the coordinated ligand **L1**. As can be seen in Fig. 3, the opposite ends of the helical structure of **L1** are bonded (C(2)–C(3) and C(4)–C(23)) in a four-member ring arrangement, with a change in the hybridization of the carbon atoms involved in these bonds from sp^2 to sp^3. A similar phenomenon was reported for another TH[7] derivative [13a], although only one new bond is formed between the helix end rings in that case. Selected bond distances and angles are presented in Table 2. For isomer distinction, the isomer identified by X-ray diffraction is designated as **2∗Ru**.

The referred isomerization was only detected when X-ray diffraction studies were performed, since the initial ^{1}H NMR spectrum of compound **2Ru** is consistent with the predicted structure, with the chemical shifts of the thiophene rings protons and the coupling constant J_{3-4} (5.6 Hz) in the normal ranges for these structures. The isomerization must happen during the slow recrystallization and the **2∗Ru** isomer crystallized preferentially to **2Ru**. The ^{1}H NMR spectrum of **2∗Ru**, described in Section 4, is in accordance with the structure determined by X-ray, showing a significant shielding of protons H(4), H(23) and H(3), compared with **2Ru**, due to the hybridization change in the correspondent carbon atoms. Moreover, H(4) appears as a double doublet, due to coupling with H(3) and H(23), with coupling constants of 6.3 and 8.6 Hz, respectively. The chemical shifts of H(23) and H(3) were attributed based on the coupling constant magnitudes, since J_{23-4} is expected to be higher than J_{3-4} due to the larger H–C–C–H dihedral angle.

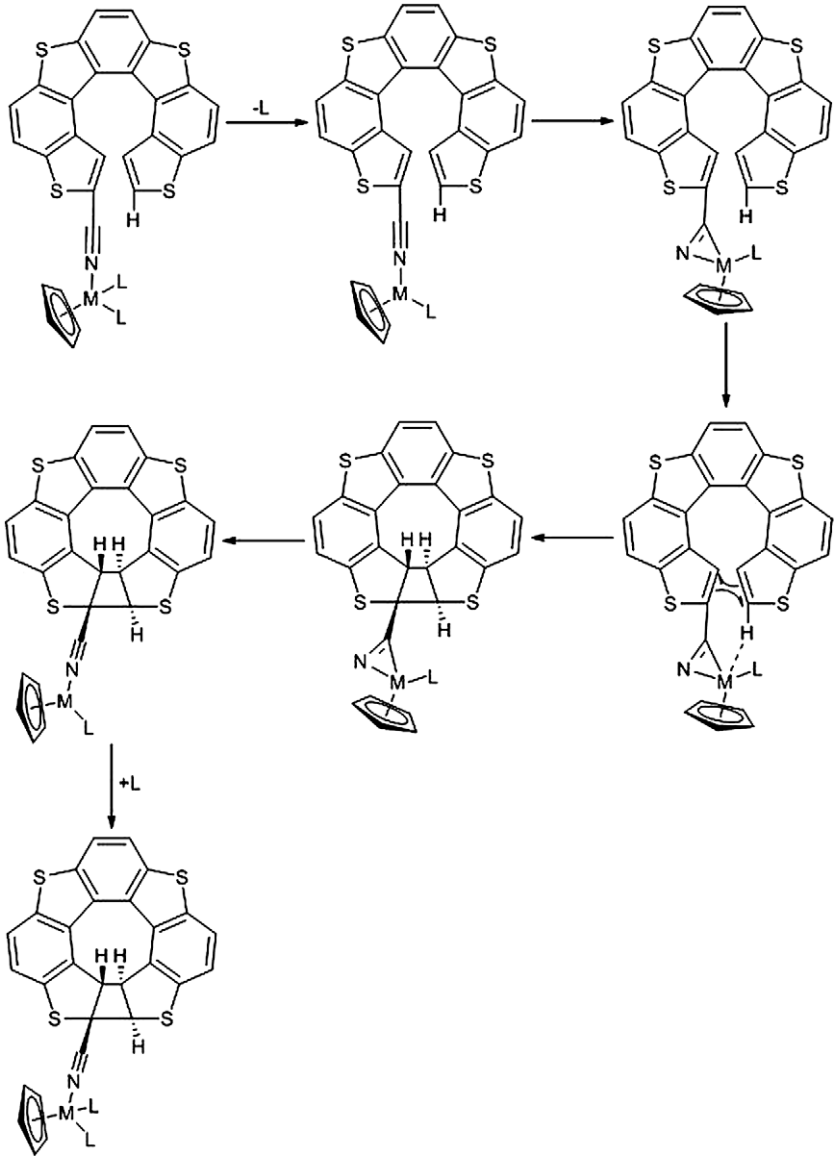
Compound **2∗Ru** crystallizes in the centrosymmetric space group $P\bar{1}$. The coordination geometry around the metal centre shows the typical structure of cyclopentadienyl complexes in pseudo-octahedral three-legged piano stool geometry, on the assumption that the cyclopentadienyl ring takes up three coordination sites, with the two PPh_3 phosphorus atoms and the nitrile nitrogen atom occupying the other three sites. The angles P–Ru–P and (C≡)N–Ru–P, close to 90°, and the angles Cp(centroid)–Ru–N(≡C) and Cp(centroide)–Ru–P (121.79(14)–124.15(5)°), along with the distances of the coordinated ligands to the metal centre, are within the range found for η^5-monocyclopentadienylruthenium nitrile derivatives with coordinated phosphines [14,15c,16]. The bond lengths of the cycle formed by atoms C(2), C(3), C(4) and C(23) are in the range 1.519(9)–1.598(9) Å, with bond lengths C(3)–C(4) (1.535(9) Å) and C(2)–C(23) (1.565(9) Å) clearly superior to the analogous ones verified in compounds [MCp(L-L)(NC{BDT}Z)][Y] [14], showing loss of the double bond character. Angles C(5)–C(4)–C(23) (106.9(6) Å) and C(4)–C(23)–C(22) (107.7(5) Å) show the almost superposition of the helix ends.

A possible mechanism to explain the isomerization of **2Ru** to **2∗Ru** is depicted in Scheme 3. It can be assumed that the metal center is involved in the isomerization of the helical ligand. The decoordination of a PPh_3 ligand, followed by the sliding of the nitrile to side-on (four-electron-donor) coordination allow the interaction of the metal centre with H(3). Nucleophilic attack at C(3)

Table 3
Interplanar angles, θ, between adjacent rings and the terminal rings of the thiophene rings (°) and the mean-square atom deviations, Δ, from ring least-squares planes, for compound **2∗Ru**.

θ		Δ	
Ring(1)–ring(2)	6.33	ring(1)	0.0063
Ring(2)–ring(3)	6.64	ring(2)	0.0590
Ring(3)–ring(4)	4.57	ring(3)	0.0250
Ring(4)–ring(5)	4.86	ring(4)	0.0279
Ring(5)–ring(6)	8.01	ring(5)	0.0295
Ring(6)–ring(7)	6.80	ring(6)	0.0489
Ring(1)–ring(7)	4.43	ring(7)	0.0235

Ring(1): (C(3), C(4), C(5), C(6), S(1)); ring(2): (C(5), C(6), C(7), C(8), C(9), C(10)); ring(3): (C(9), C(10), C(11), S(2)); ring(4): (C(11), C(12), C(13), C(14), C(15), C(16)); ring(5): (C(15), C(16), C(17), C(18), S(3)); ring(6): (C(17), C(18), C(19), C(20), C(21), C(22)); ring(7): (C(21), C(22), C(23), C(24), S(4)).



Scheme 3. Proposed mechanism for formation of **2∗Ru**.

Table 4
Intermolecular contacts for compound **2∗Ru**.

2∗Ru	
C(35)–H(35)···F(1)	2.568
C(124)–H(124)···F(4)	2.647
C(3)–H(3)···F(4)	2.619
C(13)–H(13)···O(100)	2.491

and subsequent rearrangement results in bonding between the helix ends. Return of the nitrile to end-on coordination and coordination of PPh_3 affords **2∗Ru**. This mechanism is supported by the fact that isomerization was only detected in one complex, and not in the free ligand, and this being the complex with coordinated monodentate phosphines.

The dihedral angles between adjacent rings and terminal rings of the helicene ligand of compound **2∗Ru,** as well as the mean-square atom deviations Δ from the ring least-squares planes, are listed in Table 3. The planarity of the aromatic rings in the molecules is apparent from the mean deviations of the atoms from the least-squares plane of the ring (Table 3). The terminal rings 1 and 7 have an almost flat configuration, but the planarity is poorer towards the middle thiophene rings and is poorest in the benzene rings. Also, a decrease of the dihedral angle towards the middle part of the helix can be noticed, although the deformation of the rings from planarity does not follow the same correlation. This behavior is opposite to that observed in free TH[7] [17]. A possible explanation for this different structural arrangement is the isomerization of the helical ligand that forces a smaller aperture in the two terminal thiophene rings, as reflected by the dihedral angle between the rings 1 and 7 (4.43° vs. 45.9° for free TH[7]).

The pitch of the helix in **2∗Ru** compound is very similar to the free TH[7] ligand (14.30 Å vs. 14.03 Å), since the two thiahelicenes have the same number of rings [18].

The evaluation of the crystal packing of **2∗Ru** revealed the formation of pseudo dimeric units, with parallel alignment of the chromophores of distinct cations, via intermolecular interactions with the PF_6 anion and one acetone molecule (Table 4), reinforced through π–π interactions of the helical ligand.

This pseudo dimeric arrangement is illustrated in Fig. 4, where it can also be seen that these units are constituted by two enantiomers, (+) and (−), relative to the helix orientation.

Analysis of the crystal packing disclosed an interesting supramolecular array for this compound, which displays holes in the *c* direction, as illustrated in Fig. 5, suggesting that this network can possibly be used for selectively storing guests material [19]. These holes, that have an almost square shape, have the smaller dimensions between two fluorine atoms of the counter-ion PF_6, 4.851 Å, and two of the carbons of the acetone solvent molecule, 4.750 Å. The holes are created by two of the parallel lines produced via intermolecular interactions involving the helicene–PF_6–acetone. A similar array with a significant degree of porosity was verified for the compound $[RuCp(PPh_3)_2(NC(BDT))][PF_6]$ (BDT = benzo[1,2-b;4,3-b′]dithiophene) [14], although the holes aperture is larger in this compound.

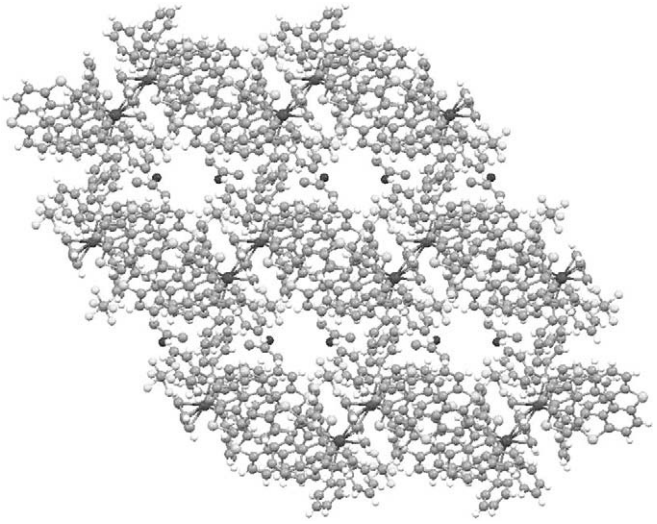


Fig. 5. Supramolecular arrangement of the compound **2∗Ru**, displaying holes along direction *c*.

3. Conclusion

We have described here the synthesis of the new organometallic complexes $[MCp(P–P)(NC\{TH\text{-}[7]\text{-}Y\}Z)][PF_6]$ (M = Ru, Fe, P–P = DPPE, Y = H, NO_2, Z = H, C≡N; M = Ru, L-L = $2PPh_3$, Y = H, Z = H), with coordinated helical ligands derived from tetrathia-[7]-helicene. Spectroscopic data revealed the electron-donor effect of the organometallic fragments $[MCp(P–P)]^+$. The magnitude of this effect depends on the metal and on the presence and/or position of the acceptor group (C≡N, NO_2), showing a good conjugation between the metal centre and the acceptor group on the chromophore.

The three new substituted tetrathia-[7]-helicene derivatives, synthesized in this work and used as ligands in the presented organometallic complexes, may also be interesting as organic materials for NLO purposes, according to the significant β values predicted by theoretical studies for other tetrathia-[7]-helicene derivatives [20].

The major interest in this family of compounds is the intrinsic chirality for NLO purposes, which has not yet been exploited, since the TH[7] ligands were prepared as a racemic mixture. Nevertheless, the synthetic procedure developed in the present work is valid for the synthesis of the pure isomers complexes, starting from the respective isomerically pure TH[7], bearing in mind that isomer inter-conversion is not possible.

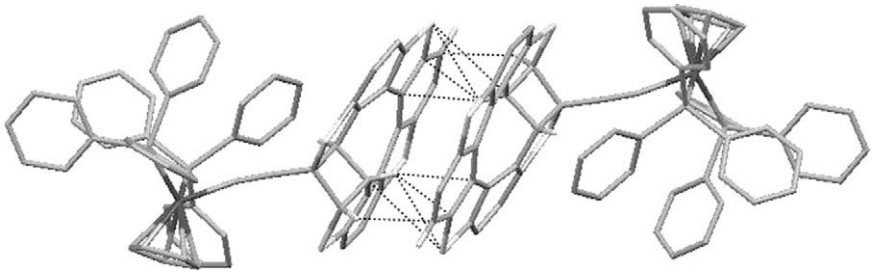


Fig. 4. Dimeric units of compound **2∗Ru**, showing intermolecular π–π interactions of the helical ligand.

4. Experimental

4.1. General procedures

All experiments were carried out under nitrogen atmosphere using standard Schlenk techniques. All of the solvents used were dried using standard methods [21]. The starting materials were prepared following the methods described in the literature: [Ru(η^5-C_5H_5)(DPPE)Cl] and [Ru(η^5-C_5H_5)(PPh_3)$_2$Cl] [22]; [Fe(η^5-C_5H_5)(DPPE)I] [15c]; tetrathia-[7]-helicene and tetrathia-[7]-helicene-2-carbox aldehyde [16a]. FT-IR spectra were recorded in a Mattson Satelite FTIR spectrophotometer with KBr; only significant bands are quoted in the text. ^{1}H and ^{31}P NMR spectra were recorded on a Brüker Avance 400 spectrometer at the probe temperature. ^{1}H (DMSO-d_6) chemical shifts are reported in parts per million (ppm) downfield from internal Me_4Si and coupling constants are reported in Hertz; ^{31}P (DMSO-d_6) NMR spectra are reported in ppm downfield from the external standard, 85% H_3PO_4. Elemental analyses were obtained at the Laboratório de Análises, Instituto Superior Técnico, using a Fisons Instruments EA1108 system. Data acquisition, integration and handling were performed using a PC with software package EAGER-200 (Carlo Erba Instruments). Electronic spectra were recorded at room temperature on a Jasco V-560 spectrometer in the range 200–900 nm.

4.2. Synthesis of the organic ligands

4.2.1. Tetrathia-[7]-helicene-2-carbonitrile (**L1**)

An $H_2NOH \cdot HCl$ (0.14 g, 2 mmol) solution in pyridine (4 mL) was added to a stirred solution of tetrathia-[7]-helicene-2-carbaldehyde (0.22 g, 0.5 mmol) in pyridine (5 mL), cooled to 5 °C. After stirring for 1 h at 5 °C, acetic anhydride (1 mL) was added, and the mixture was refluxed for 2 h. After cooling, the mixture was poured onto ice and the resulting precipitate was dissolved in CH_2Cl_2 (30 mL), washed with a saturated solution of $NaHCO_3$ and water, and dried over $MgSO_4$. The solvent was removed under reduced pressure and the product was purified by flash column chromatography (eluent:*n*-hexane/CH_2Cl_2 1:1), affording 0.10 g (47%) of pure tetrathia-[7]-helicene-2-carbonitrile as a yellow solid. *Anal.* (%) Calc. for $C_{23}H_9NS_4 \cdot 0.1C_6H_{14}$: C, 64.99; H, 2.40; N, 3.21. Found: C, 65.72; H, 2.13; N, 3.23. IR (KBr, cm^{-1}): ν(CN) 2206. ^{1}H NMR (DMSO-d_6): 6.49 (d, 1H, J_{HH} = 5.6), 7.23 (s, 1H) 7.40 (d, 1H, J_{HH} = 5.6), 8.28 (d, 1H, J_{HH} = 8.4), 8.29 (m, 4H), 8.51 (d, 1H, 8.8).

4.2.2. Tetrathia-[7]-helicene-2,13-dicarbonitrile (**L2**)

A *n*-BuLi 2.0 M pentane solution (0.55 mL, 1.1 mmol) was added dropwise to a stirred solution of tetrathia-[7]-helicene (0.20 g, 0.5 mmol) in dry THF (20 mL) at −78 °C. The solution was stirred for 40 min at −78 °C, and the resulting dark orange solution was treated with dry DMF (0.11 mL, 1.2 mmol). After 4 h at −78 °C, the solution was warmed up to room temperature and quenched with a saturated aqueous solution of NH_4Cl (5 mL). The THF was removed under reduced pressure, and the crude was taken up with CH_2Cl_2 (20 mL) and washed with water and a saturated solution of NH_4Cl. The solvent was removed under reduced pressure, affording tetrathia-[7]-heliceno-2,2′-dicarbaldehyde, as a dark oil, used without further purification. The product was dissolved in pyridine, cooled to 5 °C, and an $H_2NOH \cdot HCl$ (0.14 g, 2.0 mmol) solution in pyridine (4 mL) was added. After stirring for 5 min at 5 °C, acetic anhydride (1 mL) was added and the mixture was refluxed for 2 h. After cooling, the mixture was poured onto ice and the resulting precipitate was dissolved in CH_2Cl_2 (20 mL), washed with water and dried over $MgSO_4$. The product was purified by flash column chromatography (eluent:*n*-hexane/CH_2Cl_2 2:3), affording 0.05 g (25%) of pure tetrathia-[7]-helicene-2,13-dicarbonitrile as a yellow solid. *Anal.* (%) Calc. for $C_{24}H_8N_2S_4$: C, 63.69; H, 1.78; N, 6.19. Found: C, 64.02; H, 1.86; N, 5.99. IR (KBr, cm^{-1}): ν(CN) 2209. ^{1}H NMR (DMSO-d_6): 7.21 (s, 2H), 8.46 (s, 2H), 8.49 (d, 2H, J_{HH} = 8.8), 8.58 (d, 2H, J_{HH} = 8.8).

4.2.3. Tetrathia-[7]-helicene-?-nitro-2-carbonitrile (**L3**)

Nitric acid (0.02 mL, 0.35 mmol) was added to a stirred solution of tetrathia-[7]-helicene-2-carbonitrile (0.11 g, 0.26 mmol) in acetic anhydride (8 mL), cooled to 5 °C. After 1 h, the solution was poured onto ice and the resultant precipitate was dissolved in CH_2Cl_2 (15 mL). The solution was washed with a saturated solution of $NaHCO_3$, water, dried over $MgSO_4$ and the solvent removed under reduced pressure. The product was purified by flash column chromatography (eluent:*n*-hexane/CH_2Cl_2 2:3), affording 0.05 g (41%) of tetrathia-[7]-helicene-?-nitro-2-carbonitrile as an orange solid. IR (KBr, cm^{-1}): ν(CN) 2215, ν(NO_2) 1507 and 1316, δ (NO_2) 731. ^{1}H NMR (DMSO-d_6): 6.65 (d, 1H, J_{HH} = 5.6), 7.29 (s, 1H), 7.57 (d, 1H, J_{HH} = 5.6), 8.45 (d, 1H, J_{HH} = 8.8), 8.54 (m, 3H), 9.60 (s, 1H).

4.3. Synthesis of the complexes [M(η^5-C_5H_5)(P–P)(NC{TH-[7]-Y}Z)][PF_6]

Complexes of the general formula [M(η^5-C_5H_5)(P–P)(NC{TH-[7]-Y}Z)][PF_6] were prepared by halide abstraction from the parent neutral complexes [M(η^5-C_5H_5)(LL)X] (1 mmol) with $TlPF_6$ (1 mmol) in dichloromethane, in the presence of a slight excess (1.1 mmol) of the ligands tetrathia-[7]-helicene-2-carbonitrile (**L1**), tetrathia-[7]-helicene-2,2′-carbonitrile (**L2**) or tetrathia-[7]-helicene-?-nitro-2-carbonitrile (**L3**), at reflux for 48 h under an inert atmosphere. After cooling to room temperature, filtering and removing the solvent, the complexes were washed with *n*-hexane (3 × 15 mL) and recrystallized from dichloromethane/*n*-hexane or acetone/*n*-hexane, giving crystalline products.

4.3.1. [Ru(η^5-C_5H_5)(DPPE)(NC{TH-[7]})][PF_6] (**1Ru**)

Orange. Yield: 48%. Recrystallized from dichloromethane/*n*-hexane. *Anal.* (%) Calc. for: $C_{54}H_{38}NS_4P_3F_6Ru$: C, 57.04; H, 3.37; N, 1.23. Found: C, 57.30; H, 3.56; N, 1.60. IR (KBr, cm^{-1}): ν(C–H, η^5-C_5H_5) 3051, ν(CN) 2210, ν(PF_6^-) 839; ^{1}H NMR ($(CD_3)_2SO$): 2.65 (m, 4H, –CH_2–), 4.91 (s, 5H, η^5-C_5H_5), 6.06 (s, 1H), 6.22 (d, 1H, J_{HH} = 5.6), 7.04 (d, 1H, J_{HH} = 5.6), 7.24 (m, 4H, C_6H_5, DPPE), 7.36 (m, 6H, C_6H_5, DPPE), 7.51 (m, 6H, C_6H_5, DPPE), 7.78 (m, 4H, C_6H_5, DPPE), 8.28 (d, 1H, J_{HH} = 8.8), 8.41 (d, 1H, J_{HH} = 8.4), 8.47 (m, 4H). ^{31}P NMR ($(CD_3)_2SO$): −144.1 (qt, PF_6^-, J_{PF} = 711.0), 78.3 (d, DPPE, J_{PP} = 24.5), 79.5 (d, DPPE, J_{PP} = 24.5).

4.3.2. [Fe(η^5-C_5H_5)(DPPE)(NC{TH-[7]})][PF_6] (**1Fe**)

Red. Yield: 46%. Recrystallized from dichloromethane/*n*-hexane. *Anal.* (%) Calc. for $C_{54}H_{38}NS_4P_3F_6Fe \cdot 0.3CH_2Cl_2$: C, 58.54; H, 3.48; N, 1.25. Found: C, 58.29; H, 3.78; N, 1.26. IR (KBr, cm^{-1}): ν(C–H, η^5-C_5H_5) 3052, ν(CN) 2193, ν(PF_6^-) 840. ^{1}H NMR ($(CD_3)_2SO$): 2.46 (m, 2H, –CH_2–), 2.62 (m, 2H, –CH_2–), 4.53 (s, 5H, η^5-C_5H_5), 5.97 (s, 1H), 6.22 (d, 1H, J_{HH} = 5.6), 7.04 (d, 1H, J_{HH} = 5.6), 7.06 (m, 4H, C_6H_5, DPPE), 7.56 (m, 12H, C_6H_5, DPPE), 7.81 (m, 4H, C_6H_5, DPPE), 8.25 (d, 1H, J_{HH} = 8.8), 8.43 (m, 5H). ^{31}P NMR ($(CD_3)_2SO$): −144.1 (qt, PF_6^-, J_{PF} = 710.2), 96.4 (d, DPPE, J_{PP} = 33.2), 96.8 (d, DPPE, J_{PP} = 33.5).

4.3.3. [Ru(η^5-C_5H_5)(PPh_3)$_2$(NC{TH-[7]})][PF_6] (**2Ru**)

Orange. Yield: 27%. Recrystallized from acetone/*n*-hexane. IR (KBr, cm^{-1}): ν(C–H, η^5-C_5H_5) 3053, ν(CN) 2210, ν(PF_6^-) 840. ^{1}H NMR ($(CD_3)_2SO$): 4.61 (s, 5H, η^5-C_5H_5), 6.45 (d, 1H, J_{HH} = 5.6), 6.90 (s, 1H), 7.21 (m, 12H, C_6H_5, PPh_3), 7.31 (m, 12H, C_6H_5, PPh_3), 7.40 (d, 1H, J_{HH} = 5.6), 7.44 (m, 6H, C_6H_5, PPh_3), 8.14 (d, 1H, J_{HH} = 8.8), 8.24 (d, 1H, J_{HH} = 8.8), 8.40 (d, 1H, J_{HH} = 8.8), 8.43 (d,

1H, J_{HH} = 8.4), 8.47 (d, 1H, J_{HH} = 8.4), 8.55 (d, 1H, J_{HH} = 8.8). ^{31}P NMR ($(CD_3)_2SO$): −144.1 (qt, PF_6^-, J_{PF} = 711.1), 41.31 (s, PPh_3).

(***2*Ru***): Orange. ^{1}H NMR ($(CD_3)_2SO$): 3.29 (d, 1H, H(3), J_{3-4} = 6.4), 4.41 (dd, 1H, H(4), J_{4-3} = 6.3, J_{4-23} = 8.6), 5.27 (d, 1H, H(23), J_{23-4} = 8.8), 6.76 (m, 5H, C_6H_5, PPh_3), 6.96 (m, 6H, C_6H_5, PPh_3), 7.07 (m, 6H, C_6H_5, PPh_3), 7.17 (m, 5H, C_6H_5, PPh_3), 7.26 (m, 3H, C_6H_5, PPh_3), 7.35 (m, 3H, C_6H_5, PPh_3), 7.48 (m, 2H, C_6H_5, PPh_3), 7.62 (d, 1H, J_{HH} = 8.3), 7.69 (d, 1H, J_{HH} = 8.4), 7.99 (d, 1H, J_{HH} = 8.3), 8.07 (d, 1H, J_{HH} = 8.3), 8.39 (d, 1H, J_{HH} = 8.6), 8.42 (d, 1H, J_{HH} = 8.4).

4.3.4. [Ru(η^5-C_5H_5)(DPPE)(NC{TH-[7]}CN)][PF_6] (***3Ru***)

Dark red. Yield: 56%. Recrystallized from dichloromethane/*n*-hexane. *Anal.* (%) Calc. for $C_{55}H_{37}N_2S_4P_3F_6Ru$: C, 56.84; H, 3.21; N, 2.41. Found: C, 56.40; H, 3.38; N, 2.41. IR (KBr, cm^{-1}): ν(C–H, η^5-C_5H_5) 3051, ν(CN) 2212, $\nu(PF_6^-)$ 839. ^{1}H NMR ($(CD_3)_2SO$): 2.20 (m, 2H, –CH_2–), 2.79 (m, 2H, –CH_2–), 4.89 (s, 5H, η^5-C_5H_5), 5.70 (s, 1H), 6.88 (s, 1H), 7.22 (m, 4H, C_6H_5, DPPE), 7.50 (m, 12H, C_6H_5, DPPE), 7.91 (m, 4H, C_6H_5, DPPE), 8.37 (d, 2H, J_{HH} = 8.8), 8.51 (m, 4H), 8.71 (d, 2H, H_6, J_{HH} = 8.8). ^{31}P NMR ($(CD_3)_2SO$): −144.1 (qt, PF_6^-, J_{PF} = 711.4), 78.3 (d, DPPE, J_{PP} = 25.1), 79.7 (d, DPPE, J_{PP} = 23.1).

4.3.5. [Fe(η^5-C_5H_5)(DPPE)(NC{TH-[7]}CN)][PF_6] (***3Fe***)

Dark red. Yield: 59%. Recrystallized from dichloromethane/*n*-hexane. *Anal.* (%) Calc. for $C_{55}H_{37}N_2S_4P_3F_6Fe$: C, 59.15; H, 3.34; N, 2.51. Found: C, 59.01; H, 3.70; N, 2.14. IR (KBr, cm^{-1}): ν(C–H, η^5-C_5H_5) 3052, ν(CN) 2191, $\nu(PF_6^-)$ 839. ^{1}H NMR ($(CD_3)_2SO$): 2.37 (m, 2H, –CH_2–), 2.70 (m, 2H, –CH_2–), 4.52 (s, 5H, η^5-C_5H_5), 5.64 (s, 1H), 6.85 (s, 1H), 7.26 (m, 4H, C_6H_5, DPPE), 7.56 (m, 12H, C_6H_5, DPPE), 7.93 (m, 4H, C_6H_5, DPPE), 8.35 (d, 2H, J_{HH} = 8.8), 8.67 (d, 2H, H_6, J_{HH} = 8.8). ^{31}P NMR ($(CD_3)_2SO$): −144.1 (qt, PF_6^-, J_{PF} = 710.6), 96.8 (d, DPPE, J_{PP} = 33.4), 97.4 (d, DPPE, J_{PP} = 32.7).

4.3.6. [Ru(η^5-C_5H_5)(DPPE)(NC{TH-[7]-NO_2})][PF_6] (***4Ru***)

Dark red. Yield 40%. Recrystallized from dichloromethane/*n*-hexane. *Anal.* (%) Calc. for $C_{54}H_{37}N_2O_2S_4P_3F_6Ru$: C, 54.87; H, 3.15; N, 2.37. Found: C, 54.52; H, 3.56; N, 2.63. IR (KBr, cm^{-1}): ν(C–H, η^5-C_5H_5) 3054, ν(CN) 2214, $\nu(NO_2)$ 1507 and 1314, $\delta(NO_2)$ 730, $\nu(PF_6^-)$ 839. ^{1}H NMR ($(CD_3)_2SO$): 2.34 (m, 2H, –CH_2–), 2.67 (m, 2H, –CH_2–), 4.84 (s, 5H, η^5-C_5H_5), 5.98 (s, 1H), 6.40 (d, 1H, J_{HH} = 5.6), 7.29 (d, 1H, J_{HH} = 5.6), 7.35 (m, 6H, C_6H_5, DPPE), 7.51 (m, 6H, C_6H_5, DPPE), 7.72 (m, 8H, C_6H_5, DPPE), 8.33 (d, 1H, J_{HH} = 8.8), 8.52 (d, 1H, J_{HH} = 8.8), 8.59 (s, 2H), 9.75 (s, 1H). ^{31}P NMR ($(CD_3)_2SO$): −144.1 (qt, PF_6^-, J_{PF} = 712.7), 78.7 (s, DPPE).

4.3.7. [Fe(η^5-C_5H_5)(DPPE)(NC{TH-[7]-NO_2})][PF_6] (***4Fe***)

Dark red. Yield 44%. Recrystallized from dichloromethane/*n*-hexane. *Anal.* (%) Calc. for $C_{54}H_{37}N_2O_2S_4P_3F_6Fe \cdot 0.3CH_2Cl_2$: C, 56.11; H, 3.26; N, 2.41. Found: C, 55.91; H, 3.39; N, 3.08. IR (KBr, cm^{-1}): ν(C–H, η^5-C_5H_5) 3052, ν(CN) 2191, $\nu(NO_2)$ 1507 and 1313, $\nu(PF_6^-)$ 839. ^{1}H NMR ($(CD_3)_2SO$): 2.12 (m, 2H, –CH_2–), 2.35 (m, 2H, –CH_2–), 4.57 (s, 5H, η^5-C_5H_5), 5.90 (s, 1H), 6.39 (d, 1H, J_{HH} = 5.6), 7.32 (d, 1H, J_{HH} = 5.6), 7.35 (m, 8H, C_6H_5, DPPE), 7.55 (m, 8H, C_6H_5, DPPE), 7.74 (m, 4H, C_6H_5, DPPE), 8.30 (d, 1H, J_{HH} = 8.8), 8.49 (d, 1H, J_{HH} = 8.8), 8.57 (s, 2H), 9.72 (s, 1H). ^{31}P NMR ($(CD_3)_2SO$): −144.1 (qt, PF_6^-, J_{PF} = 710.2), 97.0 (s, DPPE).

4.4. X-ray crystallography

X-ray data for compound **2*Ru** was collected on a Bruker AXS APEX CCD area detector diffractometer at 293(2) K using graphite-monochromated Mo Kα (λ = 0.71073 Å) radiation. Intensity data were corrected for Lorentz polarization effects. Empirical absorption corrections, using SADABS [23], were applied and the data reduction was done with SMART and SAINT programs [24]. All structures were solved by direct methods with SIR97 [25] and refined by full-matrix least-squares on F^2 with SHELXL97 [26], both included in the package of programs WINGX-Version 1.70.01 [27].[7] Non-hydrogen atoms were refined with anisotropic thermal parameters, whereas H-atoms were placed in idealised positions and allowed to refine riding on the parent C atom. Graphical representations were prepared using ORTEP [28] and Mercury 1.1.2 [29]. Crystallographic data: crystal colour orange, crystal habit plate, crystal dimensions 0.10 × 0.09 × 0.02 mm, empirical formula $C_{67}H_{44}F_6NO_3P_3S_3Ru$, M = 1315.25, crystal system triclinic, space group $\bar{P}$, a = 14.038(3), b = 14.992(3), c = 16.937(3) Å, α = 110.185(7), β = 103.719(6), γ = 102.132(6)°, V = 3079.0(10) Å^3, Z = 2, $D_{calc.}$ = 1.765 g cm^{-3}, T = 150(2) K, reflections collected/unique 23 172/13 568, parameters 748, final R indices [$I > 2\sigma(I)$]: R_1 = 0.0687; wR_2 = 0.1422.

Supplementary data

CCDC 688367 contains the supplementary crystallographic data for **2*Ru**. These data can be obtained free of charge via http://www.ccdc.cam.ac.uk/conts/retrieving.html, or from the Cambridge Crystallographic Data Centre, 12 Union Road, Cambridge CB2 1EZ, UK; fax: (+44) 1223-336-033; or e-mail: deposit@ccdc.cam.ac.uk.

Acknowledgements

The authors thank Fundação Para a Ciência e Tecnologia (FCT) for financial support of Project POCTI/QUI/48443/2002. Pedro Florindo thanks FCT for his Ph.D. Grant (SFRH/BD/12432/2003).

E. Licandro and S. Maiorana acknowledge joint financial support from the Ministero dell'Istruzione, dell'Università e della Ricerca Scientifica (MUR), Rome, and the University of Milan (FIRB project, Bando 2003, Progetto RBNE033KMA, title of the project: "Molecular compounds and hybrid nanostructured materials with resonant and non resonant optical properties for photonic devices" and the University of Milan for the PRIN 2005 project: "Nuovi sistemi catalitici stereoselettivi e sintesi stereoselettiva di molecole funzionali". Centro di Eccellenza CIMAINA and the C.N.R. of Rome is also acknowledged.

References

[1] H.S. Nalwa, Appl. Organomet. Chem. 5 (1991) 349.
[2] N.J. Long, Angew. Chem., Int. Ed. Engl. 34 (1995) 21.
[3] S.R. Marder, in: D.W. Bruce, D. O'Hare (Eds.), Inorganic Materials, 2nd ed., Wiley, Chichester, 1996, p. 121.
[4] I.R. Whittall, A.M. McDonagh, M.G. Humphrey, M. Samoc, Adv. Organomet. Chem. 42 (1998) 291.
[5] E. Goovaerts, W.E. Wenseleers, M.H. Garcia, G.H. Cross,in: H.S. Nalwa (Ed.), Handbook of Advanced Electronic and Photonic Materials, vol. 9, 2001, p. 127 (Chapter 3).
[6] S. Di Bella, Chem. Soc. Rev. 30 (2001) 355.
[7] M. Kauranen, T. Verbiest, A. Persoons, J. Nonlinear Opt. Phys. Mater. 8 (1999) 171.
[8] T. Petralli-Mallow, T.M. Wong, J.D. Byers, H.I. Yee, J.M. Hicks, J. Phys. Chem. 97 (1993) 1383.
[9] M. Kauranen, T. Verbiest, E.W. Meijer, E.E. Havinga, M.N. Teerenstra, A.J. Schouten, R.J.M. Nolte, A. Persoons, Adv. Mater. (Weinheim, Germany) 7 (1995) 641.
[10] R.H. Martin, Angew. Chem., Int. Ed. 13 (1974) 649.
[11] (a) T. Verbiest, S. Vanelshocht, M. Kauranen, L. Hellemans, J. Snauwaert, C. Nuckolls, T.J. Katz, A. Persoons, Science 282 (1998) 913;
(b) S. Sioncke, S. Van Elshocht, T. Verbiest, A. Persoons, M. Kauranen, K.E.S. Phillips, T.J. Katz, J. Chem. Phys. 113 (2000) 7578;
(c) D. Belijonne, Z. Shuai, J.L. Brédas, M. Kauranen, T. Verbiest, A. Persoons, J. Chem. Phys. 104 (1998) 1301;
(d) L. Minuti, A. Taticchi, A. Marrocchi, E. Gacs-Baitz, R. Galeazzi, Eur. J. Org. Chem. (1999) 3155;
(e) H. Soon Choi, K.S. Kim, J. Phys. Chem. B 104 (2000) 11006.
[12] H. Ashitaka, H. Sasabe, Non-linear Opt. 14 (1995) 81.
[13] (a) S. Maiorana, A. Papagni, E. Licandro, R. Annunziata, P. Paravidino, D. Perdicchia, C. Giannini, K. Clays, A. Persoons, Tetrahedron 59 (2003) 6481;
(b) C. Baldoli, A. Bossi, C. Giannini, E. Licandro, S. Maiorana, D. Perdichia, Synlett (2005) 1137;

(c) A. Bossi, S. Maiorana, C. Graiff, A. Tiripicchio, E. Licandro, Eur. J. Org. Chem. 27 (2007) 4499;
(d) C. Baldoli, C. Giannini, E. Licandro, S. Maiorana, M. Monteforte, C. Rigamonti, M.T. Ticozzelli, Synthesis 21 (2006) 3670;
(e) T. Kawasaki, K. Suzuki, E. Licandro, A. Bossi, S. Maiorana, K. Soai, Tetrahedron: Asymmetry 17 (14) (2006) 2050.
[14] M.H. Garcia, P. Florindo, M.F.M. Piedade, M.T. Duarte, M.P. Robalo, J. Heck, C. Wittenburg, J. Holtmann, E. Licandro, J. Organomet. Chem., doi: 10.1016/j.jorganchem.2008.05.035.
[15] (a) A.R. Dias, M.H. Garcia, M.P. Robalo, M.L.H. Green, K.K. Lai, A.J. Pulham, S.M. Klueber, G. Balavoine, J. Organomet. Chem. 453 (1993) 241;
(b) A.R. Dias, M.H. Garcia, J.C. Rodrigues, M.L.H. Green, S.M. Kuebler, J. Organomet. Chem. 475 (1994) 241;
(c) M.H. Garcia, M.P. Robalo, A.R. Dias, M.F.M. Piedade, A. Galvão, M.T. Duarte, W. Wenseleers, E. Goovaerts, J. Organomet. Chem. 619 (2001) 252;
(d) W. Wenseleers, A.W. Gerbrandij, E. Goovaerts, M.H. Garcia, M. Paula Robalo, Paulo J. Mendes, João C. Rodrigues, A.R. Dias, J. Mater. Chem. 8 (1998) 925;
(e) M.H. Garcia, P.J. Mendes, M.P. Robalo, A.R. Dias, J. Campo, W. Wenseleers, E. Goovaerts, J. Organomet. Chem. 692 (2007) 3027.
[16] (a) R.L. Cordiner, D. Albesa-Jové, R.L. Roberts, J.D. Farmer, H. Puschmann, D. Corcoran, A.E. Goeta, J.A.K. Howard, P.J. Low, J. Organomet. Chem. 690 (2005) 4908;
(b) R.L. Cordiner, D. Corcoran, D.S. Yufit, A.E. Goeta, J.A.K. Howard, P.J. Low, J. Chem. Soc., Dalton Trans. (2003) 3541.
[17] H. Nakagawa, A. Obata, K. Yamada, H. Kawazura, M. Konno, H. Miyamae, J. Chem. Soc., Perkin Trans. II (II) (1985) 1899.
[18] T. Caronna, M. Catellani, S. Luzzati, L. Malpezzi, S.V. Meille, A. Mele, C. Richter, R. Sinfisi, Chem. Mater. 13 (2001) 3906.
[19] (a) K.E. Maly, E. Gagnon, T. Maris, J.D. Wuest, J. Am. Chem. Soc. 129 (2007) 4306;
(b) X. Lin, J. Jia, X. Zhao, K.M. Thomas, A.J. Blake, G.S. Walker, N.R. Champness, P. Hubberstey, M. Schröder, Angew. Chem., Int. Ed. 45 (2006) 7358.
[20] (a) C.A. Daul, I. Ciofini, V. Weber, Int. J. Quantum Chem. 91 (2003) 297;
(b) A. Bossi, E. Licandro, S. Maiorana, C. Rigamonti, S. Righetto, G.R. Stephenson, M. Spassova, E. Botek, B. Champagne, J. Phys. Chem. ACS ASAP (2008);
(c) B. Campagne, J.-M. André, E. Botek, E. Licandro, S. Maiorana, A. Bossi, K. Clays, A. Persoons, ChemPhysChem 5 (2004) 1438.
[21] D.D. Perrin, W.L.F. Amarego, D.R. Perrin, Purification of Laboratory Chemicals, 2nd ed., Pergamon, New York, 1980.
[22] G.S. Ashby, M.I. Bruce, I.B. Tomkins, R.C. Walli, Aust. J. Chem. 32 (1979) 1003.
[23] SADABS: Area-Detector Absorption Correction, Bruker AXS Inc., Madison, WI, 2004.
[24] SAINT: Area-Detector Integration Software, Version 7.23, Bruker AXS Inc., Madison, WI, 2004.
[25] A. Altomare, M.C. Burla, M. Camalli, G. Cascarano, G. Giacovazzo, A. Guagliardi, A.G.G. Moliterini, G. Polidoro, R. Spagna, J. Appl. Crystallogr. 32 (1999) 115.
[26] G.M. Sheldrick, SHELXL-97: Program for the Refinement of Crystal Structure, University of Gottingen, Germany, 1997.
[27] L.J. Farrugia, J. Appl. Crystallogr. 32 (1999) 837.
[28] L.J. Farrugia, J. Appl. Crystallogr. 30 (1997) 565.
[29] C.F. Macrae, P.R. Edgington, P. McCabe, E. Pidcock, G.P. Shields, R. Taylor, M. Towler, J. Van de Streek, J. Appl. Crystallogr. 39 (2006) 453.

Polyhedron 28 (2009) 630–636

Contents lists available at ScienceDirect

Polyhedron

journal homepage: www.elsevier.com/locate/poly

Chiral supramolecular metal-organic architectures from dinuclear copper complexes

Chullikkattil P. Pradeep, Samar K. Das *

School of Chemistry, University of Hyderabad, Hyderabad, Andhra Pradesh 500 046, India

ARTICLE INFO

Article history:
Received 3 November 2008
Accepted 4 December 2008
Available online 18 January 2009

Keywords:
Chiral complexes
Copper
Chiral amino alcohols
Hydrogen bonding
Supramolecular chemistry

ABSTRACT

Two new chiral dinuclear Cu(II) complexes $[Cu_2(\mu\text{-}Cl)_2(HL^1)_2]\cdot C_2H_5OH$ (**1**) and $[Cu_2(\mu\text{-}Cl)_2(HL^2)_2]\cdot CH_3OH$ (**2**), have been synthesized and structurally characterized, where the chiral ligands H_2L^1 and H_2L^2 are derived from the chiral amino alcohols (S)-(−)-2-amino-3-phenyl-1-propanol and (S)-(+)-2-phenylglycinol. Single-crystal X-ray crystallographic analyses revealed that in these complexes, the dominant hydrogen bonding property of metal bound chloride anion directs the self assembly of complex molecules through C–H···Cl hydrogen bonding interactions leading to the formation of intriguing hydrogen bonded metallo-supramolecular architectures in their respective crystal lattices. The supramolecular systems described here belong to the rare class of metal-organic architectures that are formed as a result of metal directed hydrogen bonding interactions among chiral complex molecules. Complexes **1** and **2** are further characterized by IR, ESR, UV–Vis and CD spectroscopy.

© 2009 Elsevier Ltd. All rights reserved.

1. Introduction

The influence of transition metals on hydrogen bonding (H-bonding) is a current topic of fundamental relevance [1]. Transition metals and their primary coordination sphere can exert considerable control over H-bonds, affecting the nature of intermolecular interactions in synthetic as well as natural systems [2–4]. In nature, the active sites of metalloenzymes exhibit many H-bonding interactions which are influential in deciding their properties [5]. Many interesting synthetic supramolecular systems are being developed in recent years having relevance to host–guest [6–8], bio-inorganic [9], medicinal [10,11], organometallic [12,13] and solid state [14,15] chemistry, by strategically combining the properties of transition metals with that of H-bonding ligands. Nevertheless, the design and synthesis of metallo-supramolecular systems is still a daunting task, as it involves a number of variables such as properties of ligands, metal ions, solvents and counterions. Incorporation of a powerful H-bonding functionality into the molecular building unit, capable of directing its supramolecular self-assembly is vital in the design of such systems [16–20]. In this respect, metal bound chlorine (M–Cl) is recognized as a strong H-bond functionality in metallo-supramolecular chemistry [21–27].

Meanwhile, chiral metallo-supramolecular systems are in demand for specific applications such as non-linear optics, chiral catalysis, sensing and enantioselective inclusion studies [28–31]. One strategy to ensure the chirality of supramolecular architectures is to employ chiral building units [32–36]. Chiral amino alcohols are a promising class of chiral sources employed for the synthesis of chiral coordination compounds [37–42]. Eventhough chiral amino alcohol based coordination compounds are well known for their applications in asymmetric catalysis [43–46], the number of structurally characterized coordination complexes derived from chiral amino alcohol based ligands are limited in the literature [37–42]. Structural studies of such complexes will help to design new systems with improved functionalities.

Herein we report the synthesis, structural characterization and properties of two chiral dinuclear copper complexes containing Cu–Cl as the dominant H-bond acceptor, which self assemble through C–H···Cl–Cu, C–H···O, etc. interactions leading to the formation of fascinating H-bonded metal-organic architectures in the solid state.

2. Experimental

2.1. Materials and measurements

Microanalytical (C, H, N) data were obtained with a FLASH EA 1112 Series CHNS Analyzer. A Shimadzu 3101-PC UV–Vis–NIR spectrophotometer was used to record the electronic spectra. Infrared spectra were recorded by using KBr pellets on a Jasco-5300 FT-IR spectrophotometer. ^1H NMR spectra in $CDCl_3$ solutions were recorded with a Bruker DRX-400 spectrometer, using $Si(CH_3)_4$ as an internal standard. Room temperature solid state magnetic susceptibilities were measured by using a Sherwood Scientific

* Corresponding author. Tel.: +91 40 2301 1007; fax: +91 40 2301 2460.
E-mail address: skdsc@uohyd.ernet.in (S.K. Das).

0277-5387/$ - see front matter © 2009 Elsevier Ltd. All rights reserved.
doi:10.1016/j.poly.2008.12.012

magnetic susceptibility balance. The CD spectra were measured in solution phase with a JASCO J-810 spectropolarimeter. EPR spectra were recorded on a Jeol JES-FA200 spectrometer. Solvents used for UV and CD analyses were of HPLC grade and procured from E. Merck (India). The metal salts used were of analytical grade and purchased from S.D. Fine Chem. Ltd. (India). All other chemicals used were of analytical grade.

2.2. Synthesis of chiral ligands H_2L^1 and H_2L^2

The chiral ligands employed in this study are prepared by the Schiff base condensation reactions of 5-H- and 5-Br-substituted salicylaldehydes with (S)-(+)-2-phenylglycinol and/or (S)-(−)-2-amino-3-phenyl-1-propanol. A schematic representation of ligand synthesis is given in Scheme 1. Synthesis and characterization data for the chiral ligand $C_{16}H_{17}NO_2$ (H_2L^1) are reported elsewhere [47].

2.2.1. Synthesis of H_2L^2

(S)-(+)-2-phenylglycinol (0.137 g, 1 mmol) and 5-bromosalicylaldehyde [5-bromo-2-hydroxybenzaldehyde] (0.201 g, 1 mmol) were stirred together in methanol (15 ml) for 1 h at room temperature. The resulting yellow solution was filtered and the filtrate was kept for 2 days in an open beaker for slow evaporation. Yellow solid of H_2L^2 thus obtained was washed with hexane and dried at room temperature.

MF: $C_{15}H_{14}BrNO_2$, MW: 320.18 Yield: 0.278 g, 87%. *Anal.* Calc. for $C_{15}H_{14}BrNO_2$: C, 56.27; H, 4.41; N, 4.37. Found: C, 56.33; H, 4.35; N, 4.44%. IR (KBr, cm^{-1}): 3414, 3026, 2920, 1630, 1568, 1475, 1452, 1371, 1278, 1205, 1182, 1128, 1057, 1028, 914, 893, 852, 823, 761, 698, 638, 625, 559, 530, 459. ^1H NMR (400 MHz, $CDCl_3$): δ 3.95 (d, 2H, J = 6.54 Hz, CH_2-OH), 4.5 (t, 1H, J = 6.55 Hz, CH), 7.28–7.44 (m, 7H, Ar), 6.89 (d, 1H, Ar, *ortho* to OH), 8.43 (s, 1H, HC=N). UV–Vis (CH_3CN); λ_{max}/nm ($\varepsilon/M^{-1}\,cm^{-1}$): 327 (4685), 255 (12801). CD (CH_3CN, 10^{-4} M); λ_{max}/nm (mdeg): 327 (−5.08), 255 (−20.02).

2.3. Synthesis of chiral copper complexes **1** and **2**

2.3.1. Synthesis of $[Cu_2(\mu\text{-}Cl)_2(HL^1)_2]\cdot C_2H_5OH$ (**1**)

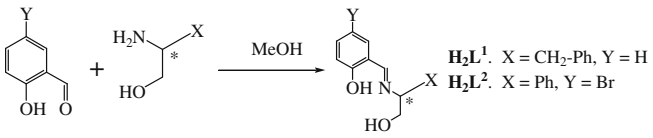
To a methanolic solution of the ligand H_2L^1 (0.25 g, 1 mmol) was added $CuCl_2\cdot 2H_2O$ (0.179 g, 1 mmol). The mixture was allowed to stir at room temperature in air overnight. The resultant green solution was evaporated to dryness using rotavapor and vacuum pump. The green solid, thus obtained, was recrystallized from ethanol.

MF: $[Cu_2(\mu\text{-}Cl)_2(HL^1)_2]\cdot C_2H_5OH$, MW: 752.67, Yield: 0.210 g, 56%. *Anal.* Calc. for $C_{34}H_{38}N_2O_5Cl_2Cu_2$: C, 54.26; H, 5.09; N, 3.72. Found: C, 53.94; H, 5.11; N, 3.66%. IR (KBr, cm^{-1}): 3749, 3026, 1635, 1601, 1541, 1446, 1394, 1288, 1197, 1151, 1082, 1028, 904, 790, 748, 700, 584, 516, 445. UV–Vis (MeOH); λ_{max}/nm ($\varepsilon/M^{-1}\,cm^{-1}$): 680 (190), 372 (9816), 270 (24011). CD (CH_3CN, 10^{-4} M); λ_{max}/nm (mdeg): 380 (−5.92), 290 (−1.8).

2.3.2. Synthesis of $[Cu_2(\mu\text{-}Cl)_2(HL^2)_2]\cdot CH_3OH$ (**2**)

To a methanolic solution of the ligand H_2L^2 (0.32 g, 1 mmol) was added $CuCl_2\cdot 2H_2O$ (0.179 g, 1 mmol). The mixture was allowed to stir at room temperature in air overnight. The resultant green solution was evaporated to dryness using rotavapor and vacuum pump. The green solid thus obtained was recrystallized from methanol.

MF: $[Cu_2(\mu\text{-}Cl)_2(HL^2)_2]\cdot CH_3OH$. MW: 868.39, Yield: 0.273 g, 63%. *Anal.* Calc. for $C_{31}H_{30}Br_2N_2O_5Cu_2Cl_2$: C, 42.88; H, 3.48; N, 3.23. Found: C, 42.60; H, 3.49; N, 3.30%. IR (KBr, cm^{-1}): 3468, 1633, 1577, 1521, 1456, 1294, 1172, 1132, 1055, 833, 761, 698, 644, 528, 457. UV–Vis (MeOH); λ_{max}/nm ($\varepsilon/M^{-1}\,cm^{-1}$): 706 (166), 383 (5011), 271 (13476). CD (MeOH, 10^{-4} M); λ_{max}/nm (mdeg): 388 (−4.1), 274 (−0.97).



Scheme 1. Synthesis scheme for chiral ligands H_2L^1 and H_2L^2.

2.4. Single-crystal structure determination of $[Cu_2(\mu\text{-}Cl)_2(HL^1)_2]\cdot C_2H_5OH$ (**1**) and $[Cu_2(\mu\text{-}Cl)_2(HL^2)_2]\cdot CH_3OH$ (**2**)

A summary of the crystallographic data for complexes **1** and **2** is given in Table 1. Suitable green crystals of **1** and **2** were grown from ethanol and methanol solutions, respectively, by slow evaporation method. The X-ray data were collected at room temperature with a Bruker–Nonius SMART APEX CCD single-crystal diffractometer using graphite monochromated Mo Kα radiation (0.71073 Å). The SMART software [48] was used for intensity data acquisition and the SAINTPLUS software [48] was used for data extraction. In each case, absorption correction was performed with the help of SADABS program [48]. The structures were solved by direct methods and refined on F^2 by full-matrix least-squares procedures using programs of SHELX-97 [49]. All the non-hydrogen atoms were refined anisotropically. The hydrogen atoms were included in the structure factor calculation by using a riding model. The absolute configurations for the enantiopure complex molecules were successfully determined by refining the Flack parameters [50].

For complex **1**, hydrogen atoms were not located in association with alcoholic oxygens of the ligands. The highest residual electron density of 1.99 (e/Å^3) is observed near Cu3 atom at a distance of 1.156 Å for this complex.

3. Results and discussion

3.1. Syntheses and characterization of complexes **1** and **2**

Complexes **1** and **2** were synthesized in moderate yields by 1:1 molar reactions of the respective chiral ligand (H_2L^1 or H_2L^2) with $CuCl_2\cdot 2H_2O$ in methanol at room temperature. The reaction mix-

Table 1
Crystallographic data and refinement parameters for complexes **1** and **2**.

Complex	**1**	**2**
Empirical formula	$C_{34}H_{38}N_2O_5Cu_2Cl_2$	$C_{31}H_{30}Br_2Cl_2Cu_2N_2O_5$
Formula weight	752.64	868.37
Crystal system	Triclinic	Tetragonal
Space group	*P*1	*P*43
a (Å)	14.3436(7)	16.0266(3)
b (Å)	16.4026(8)	16.0266(3)
c (Å)	17.5196(8)	13.2426(5)
α (°)	62.3290(10)	
β (°)	84.7990(10)	
γ (°)	73.1370(10)	
V (Å^3)	3488.8(3)	3401.39(16)
Z	4	4
μ (mm^{-1})	1.414	3.798
ρ_{calc} ($g\,cm^{-3}$)	1.433	1.696
Independent reflections	40729 (R_{int} = 0.0365)	39729 (R_{int} = 0.0516)
Observed reflections	30824	7740
Parameters	1621	407
R_1, wR_2 [$(I > 2\sigma(I))$]	0.0888 and 0.1870	0.0427 and 0.0826
Goodness-of-fit	0.972	1.007
Flack parameter	−0.008(15)	0.000(8)
Largest peak and hole (e/Å^3)	1.992 and −0.416	0.578 and −0.214

tures on evaporation gave green solids which on recrystallization from ethanol/methanol provide analytically pure crystalline samples of dinuclear copper complexes **1** and **2**. Elemental analyses revealed 1:1 ligand to metal ratio in these complexes.

The IR peaks observed for these complexes in the range of 2800–3000 cm^{-1} are most likely due to the aliphatic and aromatic C–H stretches.These complexes show a strong peak around 1635 cm^{-1} due to υ(C=N). The strong peak observed around 1550 cm^{-1} is characteristic of the phenolic C–O stretch acquiring partial double bond character through conjugation with the imine system in the chelate ring. The peaks observed in the range 1570–1600 cm^{-1} can be assigned to C=C stretch. Alcoholic C–O stretch for these complexes appears in the range 1055–1082 cm^{-1}.

The electronic spectra for the complexes **1** and **2** were recorded in methanol solutions. The absorption spectra of these complexes show a weak d–d band in the visible region around 700 nm. The strong band observed around 380 nm is assigned to phenolate to copper charge transfer transition (LMCT). The sharp peaks in the 200–290 nm range of the electronic spectrum are due to intra-ligand charge transfer (ILCT) transitions, judging from their molar extinction coefficient values. The optical activity of the complexes **1** and **2** is induced by the enantiopure ligands. The circular dichroism (CD) spectra of the complexes recorded in methanol solutions show bands corresponding to their d–d, LMCT and ILCT transitions. The d–d bands of these complexes are observed as a negative Cotton effect at high concentrations.

The X-band EPR measurements for the complexes **1** and **2** were performed at liquid nitrogen temperature in methanol solutions. The EPR spectra of the complexes **1** and **2** are similar and typical of a mononuclear square planar/square-pyramidal Cu(II) complex with a $d_{x^2-y^2}$ ground-state doublet, see Fig. 1. The data suggest that the bis(μ-halo)-bridged structures [(HL)Cu(μ-Cl)$_2$Cu(HL)] get dissociated in solution presumably due to interaction with the solvent molecules. This observation is also consistent with the fact that the chloride bridges in the dinuclear complexes **1** and **2** are rather weak as shown by the large Cu–Cl distances (2.8802(16), 2.6872(15) Å, etc., *vide infra*) in their crystal structures. Similar behavior has also been observed for some analogous chlorobridged dimeric copper complexes [51,52]. The *g*-values observed for complexes ($g_{||}$ = 2.28–2.29, $g_{\perp}$ = 2.06–2.07, $A_{||}$ = 160–168 G) are comparable to those of other similar dinuclear Cu(II) complexes [51,52]. The detailed EPR parameters as well as the room temperature magnetic susceptibility data for the powdered samples of the complexes **1** and **2** are given in Table 2. The magnetic moments for dinuclear complexes **1** and **2** are in the range 2.63–2.90μ_B which are less than the spin only values expected for two non-interacting Cu(II) centers.

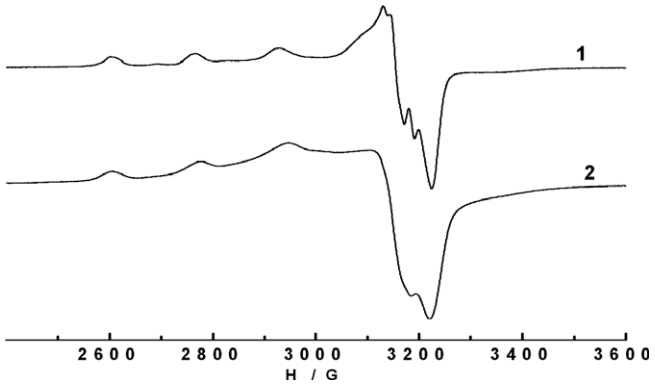


Fig. 1. X-band EPR spectra of complexes **1** and **2** in methanol at liquid nitrogen temperature.

Table 2
EPR data and magnetic moments for complexes **1** and **2**.

Complex	$g_{||}$	$g_{\perp}$	$A_{||}$	μ_{eff}/μ_B
1	2.29	2.06	160	2.63
2	2.28	2.07	168	2.90

*3.2. Crystal structure and supramolecular chemistry of the complex $[Cu_2(\mu\text{-}Cl)_2(HL^1)_2]\cdot C_2H_5OH$ (**1**)*

The complex **1** crystallizes in the non-centrosymmetric space group triclinic *P*1. Interestingly, the asymmetric unit contains four molecules of complex **1** (i.e., $Z' = 4$). Such complexes having $Z' > 1$ are of interest crystallographically [53] and are less common in the literature. In each of these four dichlorobridged dinulcear copper complexes present in the asymmetric unit, the copper centers are penta-coordinated with the Schiff base ligand coordinating to the metal ion *via* the phenolate oxygen, alcohol oxygen and imine nitrogen. The fourth and fifth coordination sites of these copper centers are satisfied by bridging chloro ligands. The thermal ellipsoid plot of a representative dinuclear complex of **1** is presented in Fig. 2.

For convenience, the four dinuclear complexes present in the asymmetric unit of complex **1** are labeled as CuA (containing copper centers Cu1 and Cu2), CuB (containing Cu3 and Cu4), CuC (containing Cu5 and Cu6) and CuD (containing Cu7 and Cu8). These four dinuclear complexes show slight variations in their respective bond lengths and angles. The asymmetric bridging of two copper centers through two chloro ligands leads to the formation of a central non-planar Cu_2Cl_2 ring in all of these complex structures. The dihedral angle between the planes defined by Cu1, Cl1, Cl2 and Cu2, Cl1, Cl2 for the representative dinuclear complex given in Fig. 2 (CuA) is 28.69°. The corresponding dihedral angles for other three dinuclear complexes are 23.11° (CuB), 23.46° (CuC) and 22.57° (CuD). Selected bond lengths and angles for a representative dinuclear complex (CuA) are listed in Table 3. Analysis of the shape-determining angles of the copper centers present in the asymmetric unit of complex **1,** using the approach of Reedijk and co-workers [54], yielded τ values in the range 0.05–0.38 (ideally, $\tau = 0$ for a square pyramidal and $\tau = 1$ for a trigonal bipyramidal

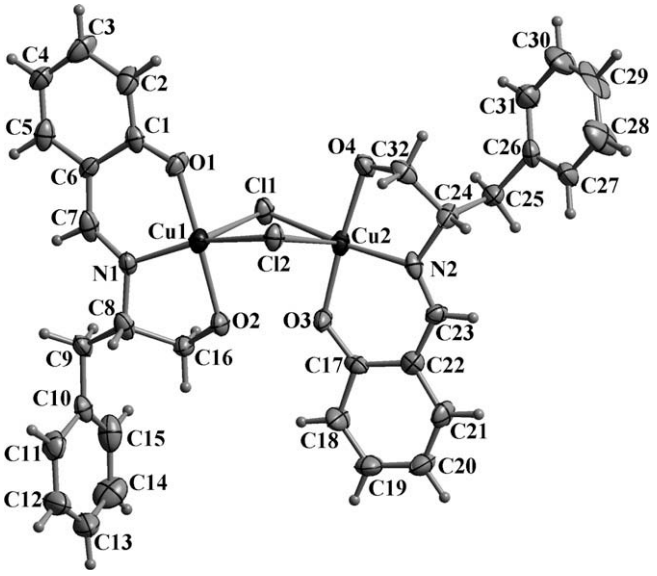


Fig. 2. Thermal ellipsoid plot (20%) of complex **1** showing atom labeling scheme. The solvent molecule is omitted.

Table 3
Selected bond distances (Å) and angles (°) for complex **1**.

Cu1–O1	1.895(8)	Cu2–O3	1.883(9)
Cu1–O2	2.033(8)	Cu2–O4	1.988(8)
Cu1–N1	1.944(9)	Cu2–N2	1.959(10)
Cu1–Cl1	2.256(3)	Cu2–Cl1	2.901(3)
Cu1–Cl2	2.748(3)	Cu2–Cl2	2.252(3)
Cu1–Cu2	3.492(2)		
O1–Cu1–N1	95.2(4)	O3–Cu2–N2	91.2(4)
O1–Cu1–O2	177.6(3)	O3–Cu2–O4	174.4(4)
N1–Cu1–O2	82.7(4)	N2–Cu2–O4	83.4(4)
O1–Cu1–Cl1	94.8(3)	O3–Cu2–Cl2	92.1(3)
N1–Cu1–Cl1	162.2(3)	N2–Cu2–Cl2	171.4(3)
O2–Cu1–Cl1	87.5(2)	O4–Cu2–Cl2	93.4(3)
O1–Cu1–Cl2	91.5(3)	O3–Cu2––Cl1	95.7(3)
N1–Cu1–Cl2	102.1(3)	N2–Cu2–Cl1	99.1(3)
O2–Cu1–Cl2	87.8(3)	O4–Cu2–Cl1	83.4(3)
Cl1–Cu1–Cl2	92.37(11)	Cl2–Cu2–Cl1	88.54(10)
O1–Cu1–Cu2	108.4(3)	O3–Cu2–Cu1	82.1(2)
N1–Cu1–Cu2	133.5(3)	N2–Cu2–Cu1	136.6(3)
O2–Cu1–Cu2	72.4(2)	O4–Cu2–Cu1	100.5(2)
Cl1–Cu1–Cu2	55.75(9)	Cl2–Cu2–Cu1	51.85(8)
Cl2–Cu1–Cu2	40.12(6)	Cl1–Cu2–Cu1	40.01(6)
Cu1–Cl1–Cu2	84.25(10)	Cu2–Cl2–Cu1	88.03(10)

complex). Hence the structural distortions of the copper centers in complex **1** are more towards square pyramidal rather than trigonal bipyramidal geometry.

The geometry of the copper centers present in complex **1** is therefore distorted square pyramidal with four short bonds in the basal plane formed by two trans oxygen atoms and one nitrogen atom of the tridentate ligand and a bridge chloride ion. The fifth axial long bond is formed by a chloride ion which is in the basal plane of the neighbouring copper center. As expected, the basal Cu–Cl bonds are found to be considerably shorter than the axial Cu–Cl bonds for each copper center [for the four dinuclear complexes present in the asymmetric unit of **1**, the average basal Cu–Cl bond length = 2.257(4) Å and average axial Cu–Cl bond length = 2.808(4) Å]. The average Cu–Cl–Cu bond angle and Cu···Cu distance for these complexes are 86.10(10)° and 3.605(2) Å, respectively. These observed geometrical features of Cu centers in **1** are quite comparable to those of the similar dinuclear complexes reported in the literature [55–62].

Supramolecular analysis of the crystal structure of complex **1** revealed the presence of dominant intermolecular C–H···Cl H-bonding interactions among the four dinuclear complexes present in the asymmetric unit. In the crystal lattice, the dinuclear units CuA and CuB are interconnected through two intermolecular C–H···Cl interactions [C23–H23···Cl4 and C55–H55···Cl2] resulting in the formation of an infinite one-dimensional chain (1-D chain) structure as shown in Fig. 3a. At the same time, the dinuclear complexes CuC and CuD are interconnected through another C–H···Cl interaction [C119–H119···Cl5] forming a discrete H-bonded dimer (Fig. 3b). Interestingly, these discrete dimers are 'hooked' to the 1-D chains formed by CuA and CuB through yet another C–H···Cl interaction [C69–H69···Cl2]. The final supramolecular structure of complex **1** appears, as if, the discrete H-bonded dimers are 'hanging' from the infinite 1-D chain as shown in Fig. 3c. The relevant H-bonding parameters are given in Table 4, which are comparable to those of the previously reported similar systems [21–27]. This kind of supramolecular structures are not known in metal complexes, and it can be assumed that the dominant H-bonding nature of Cu–Cl moiety plays an important role in forming such an intriguing metal-organic architecture. Also these extensive H-bonding interactions might be having a stabilizing effect in the formation of such a large asymmetric unit containing four dinuclear copper complexes.

In addition to these C–H···Cl interactions, there are also some intra- and intermolecular O–H···O H-bonding interaction, present in the crystal structure of complex **1**. These interactions involve the intramolecular H-bonding between one pair of metal bound alcoholic and a phenolic oxygens in each dinuclear complexes. Although the relevant hydrogen atoms are not located, it appears that, in these interactions, the protonated alcoholic oxygens act as donors while the deprotonated phenolic oxygens act as acceptors. The relevant parameters are O2···O3 2.638(12) Å (CuA), O8···O5 2.588(13) Å (CuB), O10···O11 2.612(11) Å (CuC) and O16···O13 2.688(12) Å. The other pair of metal bound alcoholic and phenolic oxygens, present in each complex molecule, is H-bonded to one solvent ethanol molecule through intermolecular O–H···O (in CuA, CuB and CuD) and C–H···O (in CuC) interactions. The relevant parameters are O19···O1 2.887(14) Å and O19···O4 2.552(14) Å for CuA, O6···O17 2.576(12) Å and O17···O7 2.866(12) Å for CuB and O14···O20 2.601(12) Å and O20···O15 2.794(12) Å for CuD. The relevant C–H···O H-bonding parameters for CuC are presented in Table 4. These intra- and intermolecular O–H···O and C–H···O interactions do not affect the Cu–Cl directed supramolecular assembly of complex **1**, nevertheless, these interactions help to stabilize the overall crystal packing.

3.3. Crystal structure and supramolecular chemistry of $[Cu_2(\mu\text{-}Cl)_2(HL^2)_2] \cdot CH_3OH$ (**2**)

Single crystals of complex **2**, suitable for X-ray analysis, were grown from methanol solutions by slow evaporation method. The complex crystallizes in chiral tetragonal space group $P4_3$. The asymmetric unit contains one molecule of complex **2** and one solvent methanol molecule. Complex **2** has a dichlorobridged dinuclear geometry containing two penta-coordinate copper(II) centers bridged by two chloro ligands, similar to the structure of complex **1**, see Fig. 4. Each Cu center has a distorted square pyramidal geometry as ascertained by Reedijk and co-workers' τ factor [54] of 0.1588 for Cu2 and 0.255 for Cu1. The central Cu_2Cl_2 ring is non-planar with a dihedral angle of 25.59° between the planes de-

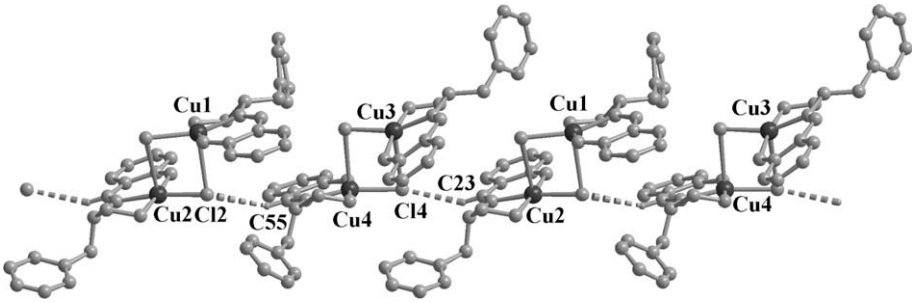


Fig. 3a. 1-D chain structure formed by C–H···Cl–Cu interaction in the crystal lattice of complex **1**. H-bonding interactions are represented by dotted lines.

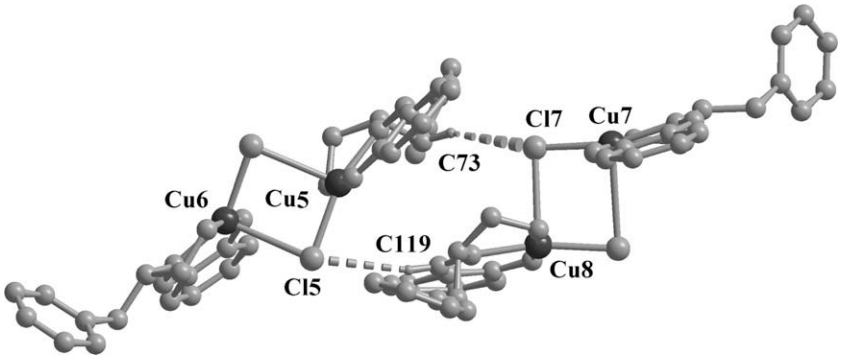


Fig. 3b. Discrete dimer formed by C–H···Cl–Cu interaction in the crystal lattice of complex **1**. H-bonding interactions are represented by dotted lines.

fined by Cu1, Cl1, Cl2 and Cu2, Cl1, Cl2. Selected bond distances and angles for complex **2** are tabulated in Table 5.

The geometry of the copper centers present in complex **2** are quite similar to that of complex **1**, viz. distorted square pyramidal with four short bonds in the basal plane formed by two trans oxygen atoms and one nitrogen atom of the tridentate ligand and a bridge chloride ion. The fifth axial long bond is formed by a chloride ion which is in the basal plane of the neighbouring copper center. The basal Cu–Cl bond lengths are 2.2600(14) and 2.2753(14) Å while the axial Cu–Cl bond lengths are 2.7327(15) and 2.7263(15) Å. The average Cu–Cl–Cu bond angle and Cu···Cu distance for this complex are 84.44(5)° and 3.3752(8) Å, respectively. These geometrical features are comparable to those reported in the literature for similar dinuclear copper complexes [55–62].

This complex also exhibits dominant C–H···Cl interactions through which adjacent molecules are interconnected leading to the formation of 1-D homochiral helices in the crystal lattice. In these interactions, the metal bound chlorine Cl1 acts as the H-bond acceptor while the aromatic carbon C29 of the ligand acts as the H-bond donor. The C–H···Cl H-bonding parameters are quite comparable to those of the reported C–H···Cl systems [21–27], see Table 6 for details. The helix propagates through crystallographic *c* axis. One full turn of the helix has a pitch distance of 13.24 Å and contains four molecules of the dinuclear copper complex. The path of the helix can be traced by following the H-bonds counter-clockwise around the fourfold screw axis of the helix. Here, the local chirality of the enantiopure ligand H_2L^2 ensures the supramolecular chirality, leading to the formation of only left handed helices at the supramolecular level (Fig. 5).

The solvent methanol molecule is H-bonded to the complex through two intermolecular O–H···O interactions. In addition, there is also an intramolecular H-bonding between the metal coordinated alcoholic and phenolic oxygens of the complex. The details of these H-bonding interactions are summarized in Table 6.

Table 4
H-bonding parameters (Å, °) for complex **1**.

Donor–H···acceptor	D–H	H···A	D···A	∠D–H···A
C69–H69···Cl2	0.93	2.88	3.578(14)	132.5
C55–H55···Cl2#1[a]	0.93	2.84	3.687(12)	152.1
C23–H23···Cl4	0.93	2.75	3.598(12)	152.1
C119–H119···Cl5#1	0.93	2.81	3.711(14)	164.2
C132–H13A···O9#2[b]	0.96	1.87	2.815(15)	168
C132–H13B···O12#2	0.96	1.72	2.631(15)	158

[a] #1 *x*, 1 + *y*, *z*.
[b] #2 1 + *x*, *y*, *z*.

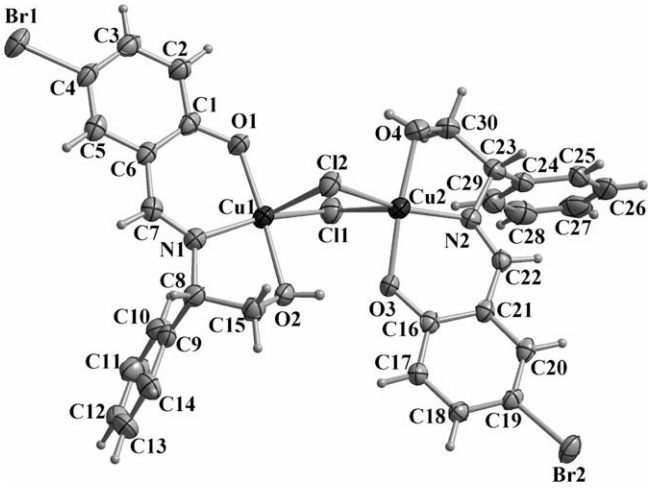


Fig. 4. Thermal ellipsoid plot (30%) of complex **2** with atom labeling scheme. The solvent molecule is omitted.

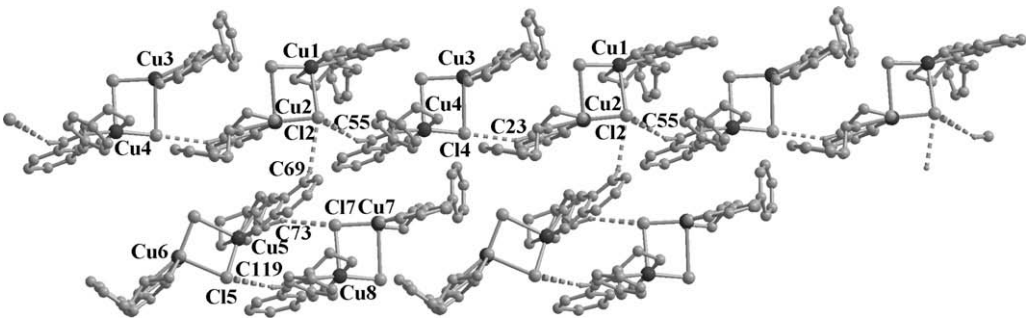


Fig. 3c. Discrete dimers 'hooked' on to the 1-D chain through C–H···Cl–Cu interactions. H-bonding interactions are represented by dotted lines.

Table 5
Selected bond distances (Å) and angles (°) for complex **2**.

Cu1–O1	1.906(3)	Cu2–O3	1.912(3)
Cu1–O2	2.028(3)	Cu2–O4	1.996(4)
Cu1–N1	1.937(4)	Cu2–N2	1.937(4)
Cu1–Cl1	2.2600(14)	Cu2–Cl2	2.2753(14)
Cu1–Cl2	2.7327(15)	Cu2–Cl1	2.7263(15)
Cu2–Cu1	3.3752(8)		
O1–Cu1–N1	94.35(16)	O3–Cu2–N2	92.43(14)
O1–Cu1–O2	175.28(16)	O3–Cu2–O4	173.25(16)
N1–Cu1–O2	81.24(16)	N2–Cu2–O4	80.97(16)
O1–Cu1–Cl1	91.64(11)	O3–Cu2–Cl2	94.44(10)
N1–Cu1–Cl1	159.97(13)	N2–Cu2–Cl2	163.72(12)
O2–Cu1–Cl1	93.07(12)	O4–Cu2–Cl2	92.30(13)
O1–Cu1–Cl2	93.93(12)	O3–Cu2–Cl1	90.78(11)
N1–Cu1–Cl2	105.59(13)	N2–Cu2–Cl1	101.81(12)
O2–Cu1–Cl2	85.68(11)	O4–Cu2–Cl1	89.18(14)
Cl1–Cu1–Cl2	93.02(5)	Cl2–Cu2–Cl1	92.85(5)
O1–Cu1–Cu2	106.78(10)	O3–Cu2–Cu1	80.97(9)
N1–Cu1–Cu2	141.05(12)	N2–Cu2–Cu1	142.29(12)
O2–Cu1–Cu2	76.02(10)	O4–Cu2–Cu1	103.36(13)
Cl1–Cu1–Cu2	53.54(4)	Cl2–Cu2–Cu1	53.66(4)
Cl2–Cu1–Cu2	42.12(3)	Cl1–Cu2–Cu1	41.81(3)
Cu1–Cl1–Cu2	84.65(5)	Cu2–Cl2–Cu1	84.22(5)

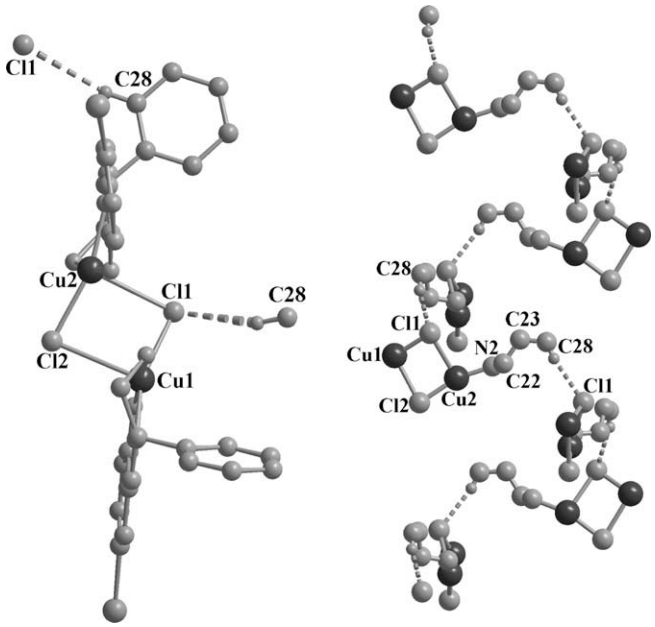


Fig. 5. Left: C–H···Cl–Cu H-bonding pattern of a single molecule of complex **2**. Right: homochiral helical structure formed as a result of C–H···Cl–Cu H-bonding interactions in the crystal lattice of complex **2**. H-bonding interactions are represented by dotted lines.

Table 6
H-bonding parameters (Å, °) for complex **2**.

Donor–H···acceptor	D–H	H···A	D···A	∠D–H···A
O2–H2A···O3	0.87(6)	1.73(6)	2.588(4)	170(6)
O4–H4A···O5	0.79(6)	1.83(7)	2.617(6)	173(9)
O5–H5A···O1	0.82	1.98	2.792(6)	171
C29–H29···Cl1#1[a]	0.93	2.76	3.657(6)	161

[a] #1 1 − *x*, *y*, 0.25 + *z*.

4. Concluding remarks

The synthesis, structural characterization and supramolecular chemistry of two new chiral dinuclear copper complexes containing Cu–Cl as the main H-bond acceptor has been discussed in this paper. The basic coordination sites of the ligands in these complexes are kept the same, minor structural changes have been introduced onto the ligand periphery. These small structural changes are found to have pronounced role in determining the supramolecular outcome of these dinuclear complexes. The chirality of the starting complexes ensures supramolecular chirality of the resulting metal-organic architectures, especially in the case of complexes **2**, which gave homochiral helices in its crystal lattice.

In the complexes described here, the metal bound chloride is found to act as strong H-bond acceptor and is pivotal in directing the supramolecular assembly. It was found that these complexes exhibit C–H···Cl–Cu, C–H···O and O–H···O H-bonding interactions in their crystal lattices resulting in quite different supramolecular architectures. It is interesting to note here that the main supramolecular structures in complexes **1** and **2** are formed solely through the interactions between the complex molecules, and no solvent molecules are involved in their formation. Such molecular building blocks are very important in terms of supramolecular chemistry, since they can be reliably employed in the synthesis of predictable supramolecular systems [2]. Finally, it has been shown that the tridentate chiral Schiff bases H_2L^1 and H_2L^2 derived from substituted salicylaldehydes and chiral amino alcohols are versatile ligands forming interesting H-bonded metallo-supramolecular architectures with copper.

Supplementary data

CCDC 681491 and 681492 contain the supplementary crystallographic data for compounds **1** and **2**, respectively. These data can be obtained free of charge via http://www.ccdc.cam.ac.uk/conts/retrieving.html, or from the Cambridge Crystallographic Data Center, 12 Union Road, Cambridge CB2 1EZ, UK; fax: (+44) 1223-336-033; or e-mail: deposit@ccdc.cam.ac.uk.

Acknowledgments

We thank the Department of Science and Technology, Government of India, for financial support (Project No. SR/SI/IC-23/2007). The National X-ray Diffractometer facility at the University of Hyderabad by the Department of Science and Technology, Government of India, is gratefully acknowledged. We are grateful to University Grants Commission (UGC), New Delhi, for providing the infrastructure facility at the University of Hyderabad under University with Potential for Excellence (UPE) Grant. C.P.P. thanks University Grants Commission (UGC), New Delhi, for a fellowship.

References

[1] D. Natale, J.C. Mareque-Rivas, Chem. Commun. (2008) 425.
[2] L. Brammer, Chem. Soc. Rev. 8 (2004) 476.
[3] L. Brammer, Dalton Trans. (2003) 3145.
[4] A.M. Beatty, CrystEngComm 3 (2001) 243.
[5] A.S. Borovik, Acc. Chem. Res. 38 (2005) 54. and references therein.
[6] P.D. Beer, F. Szemes, V. Balzani, C.M. Salá, M.G.B. Drew, S.W. Dent, M. Maestri, J. Am. Chem. Soc. 119 (1997) 11864.
[7] S.G. Galbraith, P.G. Plieger, P.A. Tasker, Chem. Commun. (2002) 2662.
[8] D. Astruc, M.-C. Daniel, J. Ruiz, Chem. Commun. (2004) 2637.
[9] S. Das, C.D. Incarvito, R.H. Crabtree, G.W. Brudwig, Science 312 (2006) 1941.
[10] S. Aime, A. Barge, A.S. Batsanov, M. Botta, D.D. Castelli, F. Fedeli, A. Mortillaro, D. Parker, H. Puschmann, Chem. Commun. (2002) 1120.
[11] X. Liang, J.A. Parkinson, M. Weishäupl, R.O. Gould, S.J. Paisey, H.-S. Park, T.H. Hunter, C.A. Blindauer, S. Parsons, P.J. Sadler, J. Am. Chem. Soc. 124 (2002) 9105.
[12] M. Yamakawa, I. Yamada, R. Noyori, Angew. Chem., Int. Ed. 40 (2001) 2818.
[13] L.N. Appelhans, D. Zuccaccia, A. Kovacevic, A.R. Chianese, J.R. Miecznikowski, A. Macchioni, E. Clot, O. Eisenstein, R.H. Crabtree, J. Am. Chem. Soc. 127 (2005) 16299.
[14] M. Albrecht, M. Lutz, A.L. Spek, G. Van Koten, Nature 406 (2000) 970.
[15] C.J. Adams, H.M. Colquhoun, P.C. Crawford, M. Lusi, A.G. Orpen, Angew. Chem., Int. Ed. 46 (2007) 1124.

[16] M.W. Hosseini, Acc. Chem. Res. 38 (2005) 313.
[17] D. Braga, F. Grepioni, Acc. Chem. Res. 33 (2000) 601.
[18] S.B. Copp, S. Subramanian, M.J. Zaworotko, J. Am. Chem. Soc. 114 (1992) 8719.
[19] S. Kitagawa, S. Kawata, Y. Nozaka, M. Munakata, J. Chem. Soc., Dalton Trans. (1993) 1399.
[20] C.B. Aakeröy, A.M. Beatty, D.S. Leinen, CrystEngComm 55 (2002) 310.
[21] G. Aullón, D. Bellamy, L. Brammer, E.A. Bruton, A.G. Orpen, Chem. Commun. (1998) 653.
[22] P.J. Davies, N. Veldman, D.M. Grove, A.L. Spek, B.T.G. Lutz, G. van Koten, Angew. Chem., Int. Ed. Engl. 35 (1996) 1959.
[23] A.L. Gillon, A.G. Orpen, J. Starbuck, X.-M. Wang, Y. Rodríguez-Martín, C. Ruiz-Péres, Chem. Commun. (1999) 2287.
[24] A. Angeloni, A.G. Orpen, Chem. Commun. (2001) 343.
[25] D.K. Kumar, A. Das, P. Dastidar, CrystEngComm 8 (2006) 805.
[26] L. Carlucci, G. Ciani, D.M. Proserpio, F. Porta, CrystEngComm 8 (2006) 696.
[27] V. Balamurugan, M.S. Hundal, R. Mukherjee, Chem.-Eur. J. 10 (2004) 1683.
[28] S.J. Lee, W. Lin, Acc. Chem. Res. 41 (2008) 521.
[29] R.N. Patel (Ed.), Stereoselective Biocatalysis, Marcel Dekker, New York, 1999.
[30] J.-M. Lehn, Supramolecular Chemistry, Concepts and Perspectives, VCH, Weinheim, 1995.
[31] B. Paul, C. Näther, K.M. Fromm, C. Janiak, CrystEngComm 7 (2005) 309.
[32] G. Baum, E.C. Constable, D. Fenske, C.E. Housecroft, T. Kulke, Chem.-Eur. J. 5 (1999) 1862. and references therein.
[33] S.G. Telfer, R. Kuroda, Coord. Chem. Rev. 242 (2003) 33.
[34] V. Balzani, L. De Cola (Eds.), Supramolecular Chemistry, NATO ASI Series, Kluwer Academic Publishers, Dordrecht, 1992.
[35] U. Knof, A. Von Zelewsky, Angew. Chem., Int. Ed. 38 (1999) 302.
[36] C. Piguet, G. Bernardinelli, G. Hopfgartner, Chem. Rev. 97 (1997) 2005.
[37] C.P. Pradeep, P.S. Zacharias, S.K. Das, Eur. J. Inorg. Chem. (2007) 5377.
[38] C.P. Pradeep, T. Htwe, P.S. Zacharias, S.K. Das, New. J. Chem. 28 (2004) 735.
[39] C.P. Pradeep, P.S. Zacharias, S.K. Das, Eur. J. Inorg. Chem. (2005) 3405.
[40] S.G. Telfer, T. Sato, R. Kuroda, J. Lefebvre, D.B. Leznoff, Inorg. Chem. 43 (2004) 421.
[41] R. Fleischer, H. Wunderlich, M. Braun, Eur. J. Org. Chem. (1998) 1063.
[42] J. Hartung, S. Drees, M. Greb, P. Schmidt, I. Svoboda, H. Fuess, A. Murso, D. Stalke, Eur. J. Org. Chem. (2003) 2388.
[43] J.L. Vicario, D. Badía, L. Carrillo, E. Reyes, J. Etxebarria, Curr. Org. Chem. 9 (2005) 219.
[44] G. Lu, Y.–M. Li, X.–S. Li, A.S.C. Chan, Coord. Chem. Rev. 249 (2005) 1736.
[45] L. Pu, H.–B. Yu, Chem. Rev. 101 (2001) 757.
[46] D.J. Ager, I. Prakash, D.R. Schaad, Chem. Rev. 96 (1996) 835.
[47] C.P. Pradeep, P.S. Zacharias, S.K. Das, Polyhedron 24 (2005) 1410.
[48] Bruker, SADABS, SMART, SAINTPLUS and SHELXTL, Bruker AXS Inc., Madison, WI, USA, 2000.
[49] G.M. Sheldrick, Acta Crystallogr. A64 (2008) 112.
[50] H.D. Flack, Acta Crystallogr., Sect. A: Found. Crystallogr. 39 (1983) 876.
[51] S.J. Brown, X. Tao, T.A. Wark, D.W. Stephan, P.K. Mascharak, Inorg. Chem. 27 (1988) 1581.
[52] S.J. Brown, X. Tao, D.W. Stephan, P.K. Mascharak, Inorg. Chem. 25 (1986) 3377.
[53] J.W. Steed, CrystEngComm 5 (2003) 169.
[54] A.W. Addison, T.N. Rao, J. Reedijk, J.V. Rijn, G.C. Verschoor, J. Chem. Soc., Dalton Trans. (1984) 1349.
[55] M. Rodríguez, A. Llobet, M. Corbella, A.E. Martell, J. Reibenspies, Inorg. Chem. 38 (1999) 2328.
[56] M. Rodríguez, A. Llobet, M. Corbella, Polyhedron 19 (2000) 2483. and references therein.
[57] F. Nepveu, F.-J. Bormuth, L. Walz, J. Chem. Soc., Dalton Trans. (1986) 1213.
[58] W. Maniukiewicz, M. Bukowska-Strzyżewska, Acta Crystallogr. C56 (2000) 562.
[59] W. Maniukiewicz, M. Bukowska-Strzyżewska, J. Chem. Crystallogr. 24 (1994) 133.
[60] W. Maniukiewicz, M. Bukowska-Strzyżewska, J. Chem. Crystallogr. 25 (1995) 505.
[61] W. Maniukiewicz, M. Bukowska-Strzyżewska, J. Chem. Crystallogr. 26 (1996) 43.
[62] C.P. Pradeep, P.S. Zacharias, S.K. Das, J. Chem. Sci. 117 (2005) 133.

Polyhedron 28 (2009) 637–645

Contents lists available at ScienceDirect

Polyhedron

journal homepage: www.elsevier.com/locate/poly

Synthesis and X-ray structure of platinum(II), palladium(II) and copper(II) complexes with pyridine–pyrazole ligands: Influence of ligands' structure on cytotoxic activity

Elzbieta Budzisz [a,*], Magdalena Miernicka [a], Ingo-Peter Lorenz [b], Peter Mayer [b], Urszula Krajewska [c], Marek Rozalski [c]

[a] Department of Cosmetic Raw Materials Chemistry, Faculty of Pharmacy, Medical University of Lodz, Muszynskiego 1, 90-151 Lodz, Poland
[b] Department of Chemistry and Biochemistry, Ludwig Maximilians University, Butenandtstr. 5-13 (D), D-81377 Munich, Germany
[c] Department of Pharmaceutical Biochemistry, Faculty of Pharmacy, Medical University of Lodz, Muszynskiego 1, 90-151 Lodz, Poland

ARTICLE INFO

Article history:
Received 14 August 2008
Accepted 5 December 2008
Available online 8 January 2009

Keywords:
Synthesis
X-ray structure
Cytotoxic effect
Pyrazole ligands
Platinum(II), Palladium(II), Copper(II) complexes
9-Methylguanine

ABSTRACT

The new pyrazole ligand 5-(2-hydroxyphenyl)-3-methyl-1-(2-pyridylo)-1*H*-pyrazole-4-phosphonic acid dimethyl ester (**2a**) has been used to obtain a series of platinum(II), palladium(II) and copper(II) complexes (**3a**–**7a**) as potential anticancer compounds. The molecular structures of the platinum(II) and copper(II) complexes **3a** and **6a** have been determined by X-ray crystallography. The cytotoxicity of the phosphonic ligand **2a** and its carboxylic analog **2b** as well as their complexes has been evaluated on leukemia and melanoma cell lines. Copper(II) complexes were found to be more efficient in the induction of melanoma cell death than the platinum(II) or palladium(II) complexes. Cytotoxic effectiveness of compound **7b** against melanoma WM-115 cells was two times better than that of cisplatin. The reaction of compound **5b** with 9-methylguanine has been studied.

© 2008 Elsevier Ltd. All rights reserved.

1. Introduction

New, efficient therapy for cancer is the challenge for medicine of the XXI century. The clinical success of cisplatin and carboplatin as antitumor agents constitutes the most impressive contribution to the use of metals in medicine [1]. The severe problems associated with these anticancer metal-based drugs include serious toxicity and side-effects, and major difficulties concerning tumor cells resistance. New potent and selective antitumor drugs are urgently needed.

A new series of antitumor *cis*- and *trans*-platinum(II) complexes that have nonplanar heterocyclic amine ligands such as piperidine, piperazine and 4-picoline have been described [2,3]. Some of these complexes, especially the *trans* analogs, could overcome multifactorial cisplatin resistance in human ovarian cell lines. The possibility to overcome cisplatin resistance could be related to the ability of these compounds to form DNA lesions that are different from those formed by cisplatin. While cisplatin interacts with double-helical DNA forming preferentially 1,2-GG or AG intrastrand cross-links, the trans complexes cannot form in double-helical DNA intrastrand cross-links between adjacent purines. Trans complexes can cross-link two bases on the same strand only if they are separated by at least one intervening base, forming mostly 1,3-GNG cross-links, where N is adenine, cytosine or thymine. Importantly, these cross-links are stable in single-stranded DNA, while in double-stranded DNA some of these cross-links readily isomerize to the interstrand cross-links [4–7].

Novel metal-based complexes containing metal such as palladium, copper, ruthenium, gold and rhodium have been reported with promising chemotherapeutic potential and different mechanisms of action in comparison with the platinum based drugs [8–10].

Synthesis and structures of palladium(II) complexes containing pyrazole and thiocyanate ligands have been documented in the literature [11]. Thiocyanate complexes of palladium(II) have been applied in analytical determinations [12] and in chemotherapy [13].

Copper(II) plays an important biological role in all living systems as an essential trace element [14]. The copper(II) complexes with organic ligands have been used as analgesic, antipyretic, antiinflammatory and platelet antiaggregating agents. Recently, several reports have appeared in the literature describing the anticancer activity of copper(II) derivatives of many classes of nitrogen donors including thiosemicarbazone and imidazole [15]. There are also examples of copper complexes of ligands containing

* Corresponding author. Tel.: +48 42 677 91 25; fax: +48 42 678 83 98.
E-mail address: elora@ich.pharm.am.lodz.pl (E. Budzisz).

0277-5387/$ - see front matter © 2008 Elsevier Ltd. All rights reserved.
doi:10.1016/j.poly.2008.12.013

α-diimino (N=C–C=N) moiety such as phenanthroline that can induce apoptosis [16] and 2-(4′-thiazolyl)benzimidazole that have antimicrobial activity [17]. Various anticancer copper(II) complexes occurred to alter the cell cycle and decrease the telomerase activity [18–21]. A wide variety of biological activities of copper(II) complexes can also be exemplified by recent finding of their antiamoebic activity against *Entamoeba histolytica* [22].

The interest in dinuclear copper(II) complexes with nitrogen-containing ligands is caused by their resemblance to the active sites of several copper-containing proteins. Besides that, the investigation of the magnetic properties of such complexes provides more insight into the relationship between their structural features and the strength of magnetic exchange interactions between the metal ions [23–29].

The introduction of the aromatic *N*-containing ligands as pyrazole, pyridine, imidazole and 1,10-phenanthroline and their derivatives whose donor properties are similar to the purine and pyrimidine bases to antitumor agents is drawing attention [30]. Complexes of pyrazole-type ligands have been used in catalysis [31,32], chemotherapy [33,34], electrochemical reduction of carbon dioxide [35], as metallomesogens [36,37] and as models of active sites in metalloenzymes [38].

In our previous papers we described the synthesis of 5-(2-hydroxybenzoyl)-3-methyl-1-(2-pyridinyl)pyrazol-4-carboxylic acid methyl ester **2b** and its complexes with platinum(II) (**3b**), palladium(II) (**4b**) and copper(II) (**5b** and **6b**) [39,40]. The cytotoxicity assay of the ligand **2b** and its complexes **3b**–**5b** were performed on L1210 and K562 leukemia cell lines. The complexes showed lower cytotoxicity than cisplatin and the platinum(II) (**3b**) and copper(II) (**5b**) complexes were found to be more efficient in the induction of leukemia cell death than the palladium(II) complex **4b**. Our investigation indicated that the antiproliferating activity of the platinum(II) (**3b**) and copper(II) (**5b**) complexes was partly due to the modulation of cellular differentiation. However, all these complexes **3b**–**5b** were not strong cellular differentiation inducers in comparison to cisplatin [40].

Here, we present the synthesis of new chelating ligand 5-(2-hydroxybenzoyl)-3-methyl-1-(2-pyridinyl)pyrazol-4-phosphonic acid dimethyl ester **2a** and its solid complexes with platinum(II), palladium (II) and copper(II) (**3a**–**7a**), the new copper(II) complex **7b** with carboxylic ligand **2b** as well as X-ray structures of the phosphonic platinum(II) and copper(II) complexes **3a** and **6a**, cytotoxic studies of both ligands **2a** and **2b** and their complexes performed on leukemia and melanoma cell lines and the reaction of copper(II) complex **5b** with 9-methylguanine (9MeG).

Synthesis of dimethyl 2-methyl-4-oxo-4*H*-chromen-3-yl-phosphonate (**1a**) [41], 2-methyl-4-oxo-4*H*-chromene-3-carboxylic acid methyl ester (**1b**) [42], 5-(2-hydroxyphenyl)-3-methyl-1-(2-pyridylo)-1*H*-pyrazole-4-carboxylic acid methyl ester (**2b**) [39] and its platinum(II) (**3b**), palladium(II) (**4b**) [40] and copper(II) (**5b** and **6b**) [39,40] complexes were described elsewhere.

2. Experimental

2.1. Materials

All substances were used without further purification. Potassium tetrachloridoplatinate(II), potassium tetrachloridopalladate(II), copper(II) chloride dihydrate and copper(II) perchlorate hexahydrate were purchased from Aldrich. Chloroform-d and DMSO–d_6 solvents for NMR spectroscopy were obtained from Dr. Glaser AG, Basel. Solvents for synthesis (acetone, diethyl ether, dimethylformamide, ethanol, ethyl acetate and methanol) were reagent grade or better and were dried according to standard protocols [43]. The melting points were determined using an Electrothermal 1A9100 apparatus and they are uncorrected. The IR spectra were recorded on a Pye-Unicam 200G Spectrophotometer in KBr and CsI. The ^{1}H NMR spectra were registered at 300 MHz on a Varian Mercury spectrometer. The MS data were obtained on a LKB 2091 mass spectrometer (70 eV ionisation energy). The MS-FAB data were determined on Finnigan Matt 95 mass spectrometer (NBA, Cs^+ gun operating at 13 keV). For the new compounds satisfactory elemental analyses were obtained using a Perkin–Elmer PE 2400 CHNS analyser.

Dimethyl 2-methyl-4-oxo-4*H*-chromen-3-yl-phosphonate (**1a**) [41], 2-methyl-4-oxo-4*H*-chromene-3-carboxylic acid methyl ester (**1b**) [42], 5-(2-hydroxyphenyl)-3-methyl-1-(2-pyridylo)-1*H*-pyrazole-4-carboxylic acid methyl ester (**2b**) [39] and its platinum(II) (**3b**), palladium(II) (**4b**) [40] and copper(II) (**5b** and **6b**) [39,40] complexes were prepared as described elsewhere.

2.2. Synthesis of the ligand

2.2.1. 5-(2-Hydroxybenzoyl)-3-methyl-1-(2-pyridinyl)-1H-pyrazol-4-phosphonic acid dimethyl ester (*2a*)

2-Hydrazinopyridin (109.1 mg, 1 mmol) in EtOH (5 ml) was added at room temperature to a solution of dimethyl 2-methyl-4-oxo-4*H*-chromen-3-yl-phosphonate **1a** (268.0 mg, 1 mmol) in EtOH (5 ml). The mixture was stirred for 24 h in room temperature. EtOH was evaporated under reduced pressure. Ethyl acetate was added to the oil product and it was left in 4 °C for 24 h. The solid white product was filtered off and dried. Yield: 179.0 mg (49.72%), mp: 101–105 °C. IR: ν_{max}/cm^{-1} 3170 (OH); 2940 (C–CH_3); 1607 (C=C, phenyl); 1228 (P=O); 1031 (O–CH_3); 807 (P–O) cm^{-1}. ^{1}H NMR ($CDCl_3$): δ = 6.88–7.53 (m, 8H, aromat.); 2.56 (s, 3H, CH_3); 3.52–3.63 (dd, 6H, O–CH_3). ^{13}C NMR ($CDCl_3$): δ = 14 (C–CH_3); 52.5 (O–CH_3); 107.3 (C–P); 154 (C–CH_3); 146 (C=C, pyrazole); 147.5 (C=N, pyridin); 151 (C–N); 155.5 (C–OH). ^{31}P NMR ($CDCl_3$): δ = 17.0. MS *m/z*: 358.0. *Anal.* Calc. for $C_{17}H_{18}N_3O_4P$ (359.322): C, 56.82; H, 5.05; N, 11.69. Found: C, 56.59; H, 4.95; N, 11.32%.

2.3. Synthesis of the complexes

2.3.1. Pt complex *3a*

The aqueous solution of $K_2[PtCl_4]$ (41.5 mg, 0.1 mmol, in 1 ml) was slowly added drop-wise to the methanolic solution of the ligand **2a** (36 mg, 0.1 mmol, in 5 ml). The mixture was stirred at room temperature for 1 h. The yellow solid that precipitated after 24 h was filtered off, washed with water and diethyl ether and dried to yield complex **3a**. Yield: 24.0 mg (38.4%), td: 120 °C. IR: ν_{max}/cm^{-1} 3401 (OH); 2955 (C–CH_3); 1612 (C=C, phenyl); 1226 (P=O); 808 (P–O); 1028 (O–CH_3); 493 (Pt–N) cm^{-1}. ^{1}H NMR (DMSO–d_6): δ = 6.67–7.53 (m, 8H, aromat.); 2.56 (s, 3H, CH_3); 3.38–3.50 (dd, 6H, O–CH_3). ESI MS(−): 624.1. *Anal.* Calc. for $C_{17}H_{18}N_3O_4PPtCl_2$ (625.306): C, 32.65; H, 2.90; N, 6.72. Found: C, 32.01; H, 2.43; N, 6.48%.

2.3.2. Pd complex *4a*

An aqueous solution of $K_2[PdCl_4]$ (33.0 mg, 0.1 mmol, in 1 ml) was slowly added drop-wise to a methanolic solution of ligand **2a** (36.0 mg, 0.1 mmol, in 5 ml). The mixture was left with stirring at room temperature for 1 h. After 24 h the resulting yellow crystals were filtered off, washed with water, diethyl ether and dried. Yield: 41.0 mg (77.6%), td: 345 °C. IR: ν_{max}/cm^{-1} 3399 (OH); 2955 (C–CH_3); 1611 (C=C, phenyl); 1226 (P=O); 1028 (O–CH_3); 811 (P–O); 495 (Pd–N) cm^{-1}. ^{1}H NMR (DMSO–d_6): δ = 6.60–7.60 (m, 8H, aromat.); 2.82 (s, 3H, CH_3); 3.44–3.53 (dd, 6H, O–CH_3). ESI MS(−): 535.9. *Anal.* Calc. for $C_{17}H_{18}N_3O_4PPdCl_2$ (536.648): C, 38.05; H, 3.38; N, 7.83. Found: C, 37.39; H, 3.57; N, 7.56%.

*2.3.3. Cu complex **5a***

A methanolic solution of $CuCl_2 \times 2H_2O$ (18.0 mg, 0.1 mmol, in 1 ml) was slowly added drop-wise to a solution of ligand **2a** in ethyl acetate (36.0 mg, 0.1 mmol, in 5 ml). The mixture was left with stirring at room temperature for 0.5 h. After 24 h the resulting green crystals were filtered off, washed with diethyl ether and dried. Yield: 39.0 mg (79.6%), td: 163.8 °C. IR: ν_{max}/cm^{-1} 3482 (OH); 2959 (C–CH_3); 1605 (C=C, phenyl); 1546 (C=N); 1239 (P=O); 1038 (O–CH_3); 799 (P–O); 508 (Cu–N) cm^{-1}. ESI MS(+): 457.0. *Anal.* Calc. for $C_{17}H_{18}N_3O_4PCuCl_2$ (493.774): C, 37.14; H, 3.42; N, 7.50; Cl, 15.99. Found: C, 40.75; H, 3.59; N, 8.09; Cl, 14.36%.

*2.3.4. Cu complex **6a***

Recrystallization done by the diffusion of diethyl ether (5 ml) into a DMF solution of **5a** (20.0 mg, 0.04 mmol, in 1 ml) gave a complex **6a**. Yield: 21.0 mg (91.3%), mp: 185 °C. IR: ν_{max}/cm^{-1} 3410, 3061 (OH); 2953 (C–CH_3); 1644 (C=O); 1600 (C=C, phenyl); 1233 (P=O); 1045 (O–CH_3); 797 (P–O); 419 (Cu–N) cm^{-1}. *Anal.* Calc. for $C_{20}H_{25}N_4O_5PCuCl_2$ (566.869): C, 42.38; H, 4.95; N, 9.88. Found: C, 41.59; H, 4.61; N, 9.74%.

*2.3.5. Cu complex **7a***

A methanolic solution of $Cu(ClO_4)_2 \times 6H_2O$ (26.5 mg, 0.07 mmol, in 2 ml) was slowly added drop-wise to a solution of ligand **2a** in ethyl acetate (51.3 mg, 0.14 mmol, in 5 ml). The mixture was refluxed 24 h. The resulting green crystals were filtered off, washed with diethyl ether and dried. Yield: 59.4 mg (84.9%), td: 285.4 °C. IR: ν_{max}/cm^{-1} 3371 (OH); 2956 (C–CH_3); 1614 (C=C, phenyl); 1230 (P=O); 1102 (ClO_4^-); 1033 (O–CH_3); 800 (P–O); 622 (ClO_4^-); 569 (Cu–N) cm^{-1}. ESI MS(+): 781.2. *Anal.* Calc. for $C_{34}H_{36}N_6O_{16}P_2CuCl_2$ (981.088): C, 41.62; H, 3.70; N, 8.57; P, 6.31; Cl, 7.23. Found: C, 41.32; H, 3.48; N, 8.24; P, 6.19; Cl, 7.21%.

*2.3.6. Cu complex **7b***

A methanolic solution of $Cu(ClO_4)_2 \times 6H_2O$ (30.9 mg, 0.08 mmol, in 2 ml) was slowly added drop-wise to a solution of ligand **2a** in ethyl acetate (51.5 mg, 0.16 mmol, in 5 ml). The mixture was refluxed 24 h. The resulting green crystals were filtered off, washed with diethyl ether and dried. Yield: 41.2 mg (56.1%), td: 268.8 °C. IR: ν_{max}/cm^{-1} 3383 (OH); 2951 (C–CH_3); 1723 (C=O); 1617 (C=C, phenyl); 1109 (ClO_4^-); 1048 (O–CH_3); 622 (ClO_4^-); 569 (Cu–N) cm^{-1}. ESI MS(+): 681.2. *Anal.* Calc. for $C_{34}H_{30}N_6O_{14}CuCl_2$ (881.094): C, 46.34; H, 3.43; N, 9.54; Cl, 8.05. Found: C, 46.01; H, 3.32; N, 8.88; Cl, 6.65%.

*2.3.7. Cu complex **8b***

A methanolic solution of 9-methylguanine (11.6 mg, 0.07 mmol, in 10 ml) was added to a methanolic solution of **5b** (31.0 mg, 0.07 mmol, in 5 ml). The mixture was refluxed 24 h. The resulting green solid was filtered off, washed with diethyl ether and dried. Yield: 19.9 mg (46.1%), mp: 202.9–203.4 °C. IR: ν_{max}/cm^{-1} 3493 (C–NH_2); 3125 (OH); 2924 (C–CH_3); 2849 (N–CH_3); 1713 (C=O); 1601 (C=C, phenyl); 1547 (C=N); 1011 (O–CH_3); 695 (Cu–N) cm^{-1}. UV–Vis: λ_{max} = 285.5 nm. MS-FAB (*m*/*z*): 686 (20%), $[LCu9MeGCl_2+DMSO+H]^+$; 681 (100%), $[LCu9MeGCl_2+4H_2O]$; 644 (10%) $[LCu9MeGCl_2+2H_2O]$; 623 (5%), $[LCu9MeGCl_2+H_2O]$; 537 (10%), $[LCu9MeG]^{2+}$; 443 (10%), $[LCuCl_2]$; 408 (10%), $[LCuCl]^+$; 372 (40%), $[LCu]^{2+}$. *Anal.* Calc. for $C_{23}H_{22}N_8O_4CuCl_2 \times H_2O$ (626.93): C, 44.06; H, 3.53; N, 17.87. Found: C, 44.29; H, 3.84; N, 17.36%.

2.4. Cell and cytotoxicity assay

2.4.1. Cell cultures

Human skin melanoma WM-115 cells as well as human leukemia promyelocytic HL-60 and lymphoblastic NALM-6 cell lines were used. Leukemia cells were cultured in RPMI 1640 medium supplemented with 10% fetal bovine serum and antibiotics (100 μg/ml streptomycin and 100 U/ml penicillin). For melanoma WM-115 cells Dulbecco's minimal essential medium (DMEM) instead of RPMI 1640 was used. Cells were grown in 37 °C in a humidified atmosphere of 5% CO_2 in air.

2.4.2. Cytotoxicity assay by MTT

Cytotoxicity of ligands **2a**, **b**, their complexes **3a**, **b**–**7a**, **b**, carboplatin and cisplatin was determined by the MTT [3-(4,5-dimethylthiazol-2-yl)-2,5-diphenyltetrazolium bromide, Sigma, St. Louis, MO] assay as described [44]. Briefly, after 46 h of incubation with drugs, the cells were treated with the MTT reagent and incubation was continued for 2 h. MTT-formazan crystals were dissolved in 20% SDS and 50% DMF at pH 4.7 and absorbance was read at 562 and 630 nm on an ELISA-plate reader (ELX 800, Bio-Tek, USA). The values of IC_{50} (the concentration of test compound required to reduce the cells survival fraction to 50% of the control) were calculated from concentration–response curves and used as a measure of cellular sensitivity to a given treatment. Ligands, complexes, carboplatin and cisplatin were tested for their cytotoxicity in a final concentration 10^{-7}–10^{-3} M. As a control, cultured cells were grown in the absence of drugs. Data points represent means of at least 12 repeats ± S.D.

2.5. X-ray measurements

A crystal of **3a** suitable for X-ray crystallography was selected by means of a polarization microscope, mounted on the tip of a glass fiber, and investigated on a Nonius KappaCCD diffractometer (Mo Kα radiation, λ = 0.71073 Å). A multi-scan absorption correction of the reflection intensities was performed with SADABS [45]. The structure was solved by direct methods with SHELXS-97 [46] and refined by full-matrix least-squares calculations based on F^2 (SHELXL-97) [47]. All non-hydrogen atoms are refined anisotropically. The C-bound hydrogen atoms are riding on their parent atoms while the O-bound hydrogen atoms were located from the electron density map.

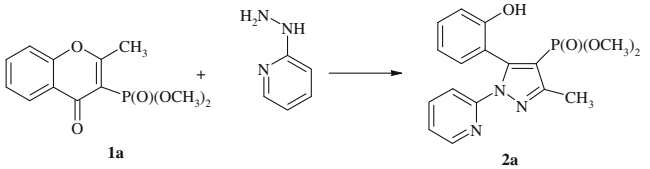
A crystal of **6a** suitable for X-ray crystallography was selected by means of a polarization microscope, mounted on the tip of a glass fiber, and investigated on a Nonius KappaCCD diffractometer (Mo Kα radiation, λ = 0.71073 Å). The structure was solved by direct methods with SIR-97 [48] and refined by full-matrix least-squares calculations based on F^2 (SHELXL-97) [47]. All non-hydrogen atoms are refined anisotropically. The hydrogen atoms are riding on their parent atoms.

3. Results and discussion

3.1. Preparation of the ligands and their complexes

In the reaction of dimethyl 2-methyl-4-oxo-4*H*-chromen-3-ylphosphonate [41] with 2-hydrazinopyridine in methanolic solution we have obtained the new ligand **2a** (Scheme 1).

First we have investigated this reaction with the phosphonic derivative **1a** in an NMR tube. The progress of the conversion of **1a** to **2a** was monitored by ^{31}P NMR spectroscopy and by thin layer



Scheme 1. The synthesis of new highly substituted pyrazole ligand **2a**.

chromatography. In the ^{31}P NMR spectrum (Fig. 1) obtained within one hour after starting the reaction, the signal of one new product at 17.20 ppm was observed, in addition to the signal of the substrate **1a** at 17.91 ppm. The intensity of this signal at 17.20 ppm gradually increased until only traces of substrate were left and we observed only one signal in the reaction mixture, what corresponds to only one product formed during this reaction. According to literature data hydrazinopyridine has only one dissociation constant $K_1 = 7.24$ for N2 and this nitrogen atom is responsible for nucleophilic attack [49]. The N1 does not have nucleophilic activity. Therefore, the first step of reaction is nucleophilic attack of hydrazinopyridine N2 atom at the chromone derivative **1a** C2 atom. The second step of the reaction is the opening of the γ-pyrone ring and cyclization to pyrazole derivative (Scheme 2). This reaction proceeds according to the general mechanism described for the reaction of chromones with nitrogen nucleophiles [50,51] such as hydrazines [52–54]. A multimilligram reaction of **1a** and **1b** with one equivalent of 2-hydrazinopyridine gave the same products as in the NMR tube.

The substituted pyrazoles **2a** and **2b** (Fig. 2) were used as the ligands L in the formation of the $MLCl_2$ complexes with platinum(II), palladium(II) and copper(II) ions (M) (Scheme 3 and 4). Complexes **3b**, **4b** and **5b** were obtained to compare the influence of the functional group on cytotoxic activity. The synthesis of the carboxylic ligand **2b** and its complexes **3b**, **4b**, **5b** and **6b** are described elsewhere [39,40].

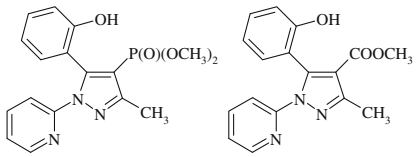


Fig. 2. Structures of ligands **2a** and **2b**.

Complexes **3a** and **4a** were obtained by adding aqueous solution of K_2PtCl_4 or K_2PdCl_4, respectively, to the methanolic solution of the ligand **2a** (Scheme 3). The copper(II) complexes were obtained in molar ratio L:Cu 1:1 (**5a** and **5b**) by adding methanolic solution of $CuCl_2 \times 2H_2O$ or 2:1 (**7a** and **7b**) by adding methanolic solution of $Cu(ClO_4)_2 \times 6H_2O$ to the solution of ligands **2a** or **2b** in

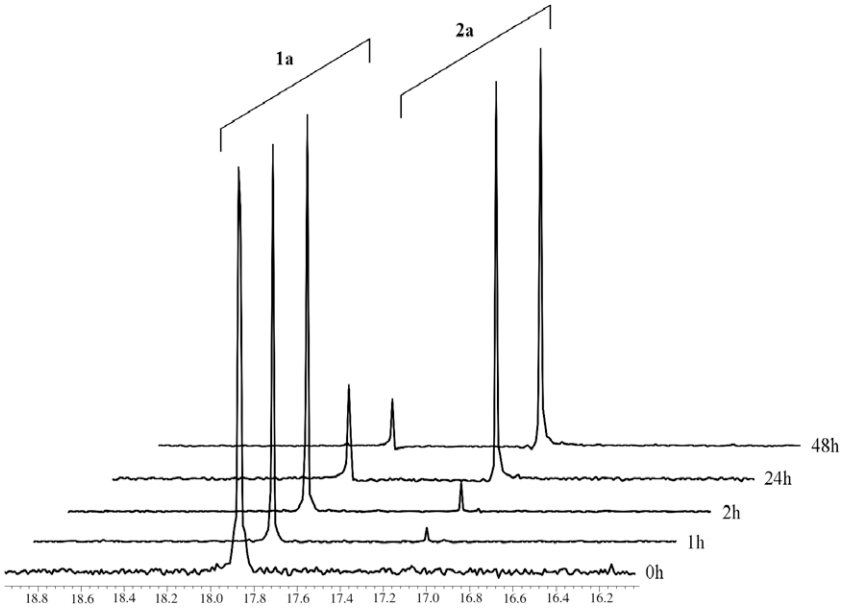
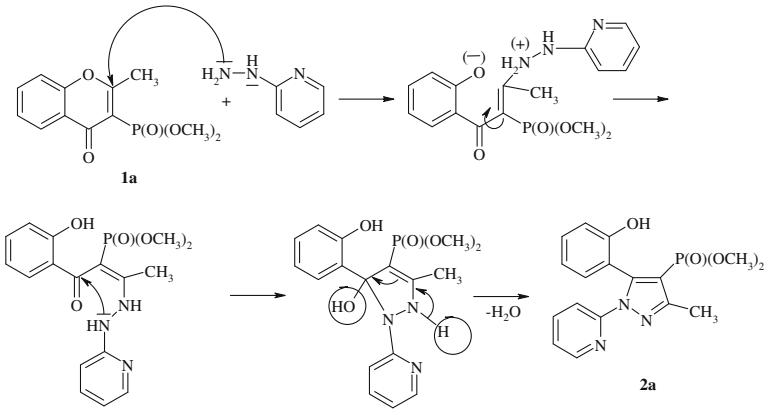
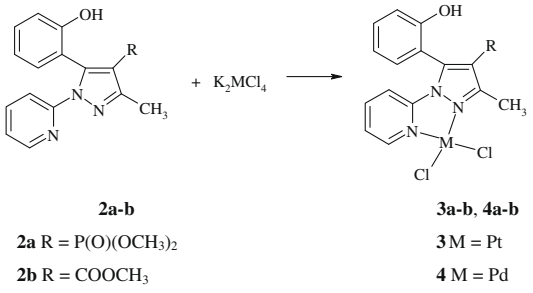


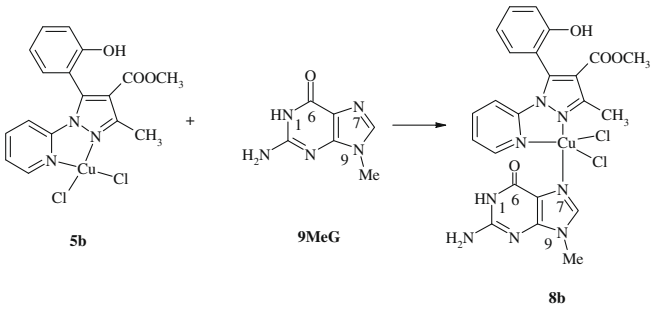
Fig. 1. ^{31}P NMR spectra of the reaction of transformation **1a** to **2a**.



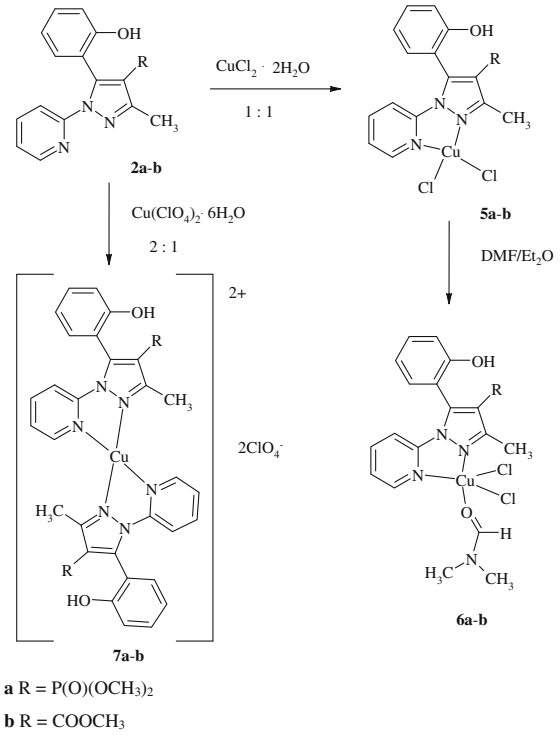
Scheme 2. Mechanism of formation of the ligand **2a**.



Scheme 3. Synthesis of the Pt(II) and Pd(II) complexes.



Scheme 5. Synthesis and proposed structure of complex **8b**.



Scheme 4. Synthesis of copper(II) complexes.

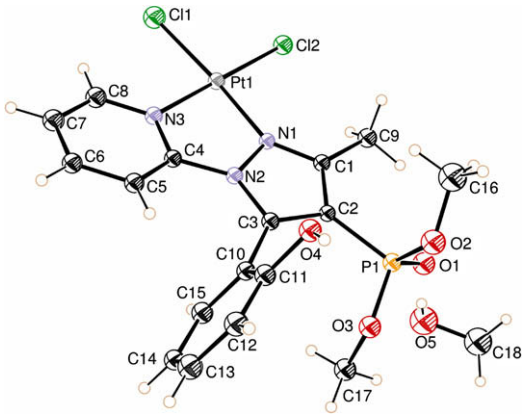


Fig. 3. The molecular structure of platinum(II) complex **3a**.

ethyl acetate (for complex **5a**) or methanol (for complexes **5b**, **7a** and **7b**). In one of our earlier works [39] we postulated that the interaction of ligand **2b** with copper(II) ions in solution might be related to interaction of the phenol 2-hydroxy group with metal ion. The ionisation of this group introduces an additional negative charge and enhances the donor properties of the potential nitrogen functions. As a result copper(II) complexes in two different L:Cu molar ratios, 1:1 or 2:1, could be formed (Scheme 4). Complexes **5a** and **5b** (L:Cu molar ratio: 1:1) occured to be neutral and complexes **7a** and **7b** (L:Cu molar ratio: 2:1) occured to be ionic.

Recrystallization of compounds **5a** and **5b** by dissolving in DMF and the diffusion of diethyl ether into the solution gave complexes **6a** and **6b**, respectively. All complexes were recrystallized but, unfortunately only compound **3a**, **6a** and **6b** yielded crystals suitable for X-ray diffraction. **6b** structure was described in our recent paper [40]. The structures **3a** and **6a** are presented here.

Knowledge of the type of interactions and the structural environment of metal complexes in relation to potential targets and other biomolecules has helped to establish binding patterns and can assist in the rational design of drugs. In this respect, interactions with DNA bases in particular have been investigated in detail resulting in a growing body of structural data on metal-nucleobase adducts [55]. Here, we have studied the reaction of complex **5b** with 9-methylguanine model DNA bases and we have obtained a complex **8b**. The compound **5b** was chosen basing on the fact that it was one of the most active among studied compounds. In this reaction we have observed the change of colors from yellow (complex **5b**) to green (complex **8b**), what can suggest occurring the pentacoordinated compound. Scheme 5 shows a probable structure of complex **8b** that has been proposed on the basis of complex **6a** structure (Fig. 4). It is possible that 9-methylguanine could coordinate to complex **5b** similar to DMF molecule.

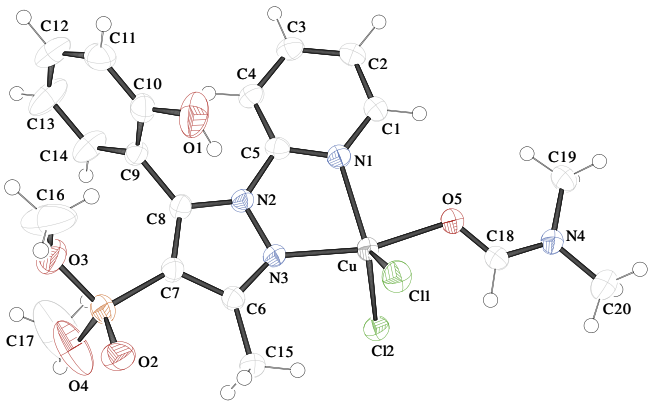


Fig. 4. Molecular structure of Cu(II)–complex **6a**.

Table 1
IR data (ν, cm^{-1}) for ligand **2a**, its complexes **3a–7a** and complex **7b**.

ν (cm^{-1})	C–OH	C=C, phenyl	P=O	C=O	P–O	O–CH_3	C–CH_3	M–N
2a	3170	1607	1228		807	1031	2940	
3a	3401	1612	1226		808	1028	2955	493
4a	3399	1611	1226		811	1028	2955	495
5a	3482	1605	1239		799	1038	2959	508
6a	3410	1600	1233	1644	797	1045	2953	419
	3061 DMF			DMF				
7a	3371	1614	1230		800	1033	2956	569
7b	3383	1617		1723		1048	2951	569

3.2. Structural studies. Spectroscopic characterization of ligands **2a** and **2b** and their complexes

Spectroscopic characterization of ligand **2b** and its complexes with platinum(II) (**3b**), palladium(II) (**4b**) and copper(II) (**5b** and **6b**) have been described in our previous papers [39,40].

The assignments of the most important bands in the IR spectra for ligand **2a** and the platinum(II), palladium(II) and copper(II) complexes **3a–7a** and **7b** are listed in Table 1.

The IR-band at 3170 cm^{-1} of the free ligand is assigned to hydroxy group of the phenyl ring. Shift of this band to lower energy may indicate the presence of hydrogen bond OH···O in the ligand's structure. This band shifts to higher energy for the complexes. The IR spectra of ligand **2a** and complexes show a large number of absorptions in the 797–1723 cm^{-1} range, which can be assigned to the different vibration modes of phosphonic and carboxylate function. The characteristic band at 2940 cm^{-1} of the methyl group of the free ligand which is assigned to the C–H vibration shifts to higher energy for the complexes. The new bands at about 493–569 cm^{-1} in complexes may correspond to the metal–nitrogen vibrations involving the N-atoms of the pyrazole ring [56]. The new bands at 3061 and 1644 cm^{-1} in **6a** complex may correspond to the C–OH and C=O vibration, respectively, involving the atoms of DMF. The bands observed at 1102 and 622 cm^{-1} in the spectrum of **7a** and 1109 and 622 cm^{-1} in the spectrum of **7b** are characteristic for non-coordinated perchlorate ions [57].

The selected chemical shifts assigned in the ^1H NMR spectra of the ligand **2a** and its platinum(II) and palladium(II) complexes **3a** and **4a** are shown in Table 2. The spectra are quite similar.

The ligand **2a** and its complexes **3a** and **4a** show signals in the range δ 2.56–2.82 ppm for the methyl groups of pyrazole ring, 3.38–3.63 for O–CH_3 of phosphonic groups and 6.60–7.60 for phenyl groups. The ^1H NMR spectra of copper(II) complexes could not be measured due to their paramagnetism.

The main peaks in ESI MS spectra of copper(II) complexes were observed for cations without chlorido or perchlorido ligands.

Occurring of the complex **8b** has been confirmed by IR, UV–Vis, FAB-MS and elemental analysis. Some characteristic IR vibrations for the complex **8b** are given in experimental section. Significant differences in the IR spectra of complex **8b** have been observed in comparison with that of complex **5b**. The latter shows a strong band at 1717 cm^{-1} due to ν(C=O). This band is shifted by 4 cm^{-1} to lower frequencies in the spectra of complex **8b** [57]. Beside this we have observed the new bands characteristic for 9-methylguanine. In UV–Vis spectrum we have observed the change of λ_{max} from 287 nm for complex **5b** to 285.5 for complex **8b**.

The FAB mass spectrum of **8b** recorded in positive ion mode contains a peak at m/z 686 due to $[LCu9MeGCl_2+DMSO+H]^+$ ion and a strong peak at m/z 681(100%) attributed to $[LCu9MeGCl_2+4H_2O]$. The peaks at m/z 537 and 443, have been assigned to $[LCu9MeG]^{2+}$ and $[LCuCl_2]$, correspondingly. The purity of complex **8b** has been confirmed by elemental analysis.

Table 2
^1H NMR spectra of ligand **2a** and the corresponding complexes with platinum(II) (**3a**) and palladium(II) (**4a**) metal ions (chemical shifts are given in ppm).

	C–CH_3	O–CH_3	Aromaticity
2a	2.56	3.52–3.63	6.88–7.53
3a	2.56	3.38–3.50	6.67–7.53
4a	2.82	3.44–3.53	6.60–7.60

3.2.1. X-ray structure of platinum(II) complex **3a**

The molecular structure of complex **3a** is shown in Fig. 3, and selected bond lengths and angles are given in Table 1S. The monomeric complex **3a** contains the bidentate pyridine–pyrazole ligand and two chlorido ligands in *cis*-position. **3a** exhibits a distorted tetragonal planar configuration at the Pt(II) centre; the sum of the angles around Pt1 is exactly 360.00°. While the two Pt–Cl bonds are equal (Pt1–Cl1 2.2875(12), Pt1–Cl2 2.2871(13) Å), both Pt–N bond lengths differ slightly (Pt1–N1 2.020(3), Pt1–N3 2.030(4) Å). The angle N1–Pt1–N3 (80.11(13)°) of the chelate ligand is the smallest, then follows the angle Cl1–Pt1–Cl2 (86.38(5)°), whereas the two angles Cl1–Pt1–N3 = 94.00(9)° and Cl2–Pt–N1 = 99.51(11)° are significantly larger than 90°, because of the small angle of the *N*,*N*′-chelate system.

The five- and six-membered rings of pyridine–pyrazole lie in the same plane together with the substituents (C9, C10 and P1) at the pyrazole.

The phenolic substituent at atom C3 is bent out from this molecular plane, because of steric hindrance and the OH group at C11, which forms the hydrogen bridge O4–H4–O5′ (2.603(6) Å and 174°) with the O atom of a CH_3OH molecule associated with **3a**.

The phosphite substituent at C2 shows a distorted tetrahedral configuration at the P(III) centre with two similar P–O distances (P1–O2 1.571(4), P1–O3 1.557(4) Å) but a short P1–O1 distance (1.459(4) Å) indicating the P=O double bond of the P(III) ester function.

3.2.2. X-ray structure of copper(II) complex **6a**

The molecular structure of complex **6a** is shown in Fig. 4, and selected bond lengths and angles are given in Table 2S. The monomeric Cu(II) complex **6a** with the coordination number 5 for the central Cu(II) contains the bidentate pyrazole ligand, two chlorido ligands and an O-coordinated DMF solvent molecule. **6a** exhibits a distorted trigonal bipyramidal configuration at the Cu centre, whereby the two chlorido ligands Cl1 and Cl2 as well as the N1 atom of the chelate system form the equatorial plane, whereas the second N atom N3 together with the O5 atom of the DMF molecule lie in the axial positions. The Cu–Cl bonds differ more (Cu–Cl1 2.3677(9), Cu–Cl2 2.2982(9) Å) than in a similar complex published earlier by us [40], and the equatorial Cu–N bond (Cu–N1 2.101(2) Å) is surprisingly longer than the axial Cu–N3 bond (2.006(2) Å).

The Cu–O5 bond length (1.962(2) Å) is the shortest observed in **6a** around Cu, but is similar with those found in related Cu(II) complexes. The distortion of the trigonal bipyramide results from the three different angles within the trigonal plane (Cl1–Cu–Cl2 113.98(3), Cl1–Cu–N1 114.15(7), Cl2–Cu–N1 131.87(7)° and from the non-linear angle N3–Cu–O5 164.91(9)°).

The angle N1–Cu–N3 of 77.85(8)° is the smallest one observed in the trigonal bipyramide, and the other are larger than 90°C (Cl1–Cu–N3 96.83(7), Cl2–Cu–N3 96.02(6), Cl1–Cu–O5 92.38(7), Cl2–Cu–O5 91.09(6)°) with the only exception of N1–Cu–O5 angle (87.49(9)°).

The phosphite substituent at C7 shows a distorted tetrahedral configuration at the P(III) centre with two similar P–O distances (P–O3 1.551(3), P–O4 1.545(4) Å) but a short P–O2 distance (1.464(3) Å) indicating the P═O double bond of the P(III) ester function.

The bidentate heterocycle together with the connected atoms C9 and P of the substituents is nearly planar, with a maximum deviation from planarity of 1° (at C4).

The only exception is the phenyl substituent which shows the distortion angle N2–C8–C9–C10 of 70.2(4)°.

A view to the crystal packing of **3a** shows that the associated MeOH molecule forms two short and almost linear O–H–O bridges (O4–H4–O5′ 2.603(6) Å/173(7)°; O5–H5–O1′ 2.689(6) Å/174(6)° resulting in a polymeric chain shown in Fig. 5. Compound **6a**, however, forms a dimmer because of the hydrogen bonds (O1–H1–O2′ 3.009(2) Å/137.5(2)°) which are longer and significantly bent (Table 3).

Table 3
Crystallographic data of Pt(II) complex **3a** and Cu(II) complex **6a**.

Net formula	$C_{18}H_{22}Cl_2N_3O_5PPt$	$C_{20}H_{25}Cl_2CuN_4O_5P$
M_r (g mol^{-1})	657.342	566.862
Crystal size (mm)	0.20 × 0.12 × 0.02	0.13 × 0.10 × 0.08
T (K)	200(2)	200(2)
Crystal system	Triclinic	Triclinic
Space group	$P\bar{1}$	$P\bar{1}$
a (Å)	8.5306(3)	9.6019(3)
b (Å)	9.1983(3)	10.3758(3)
c (Å)	15.4352(5)	12.8774(3)
α (°)	73.1170(19)	74.7244(17)
β (°)	82.9815(19)	77.1466(16)
γ (°)	69.927(2)	87.7010(17)
V (Å^3)	1088.21(6)	1206.37(6)
Z	2	2
Calculated density (g cm^{-3})	2.00615(11)	1.56056(8)
μ (mm^{-1})	6.802	1.232
Transmission factor range	0.448–0.873	–
Reflections measured	20466	10477
R_{int}	0.0441	0.0316
Mean $\sigma(I)/I$	0.0371	0.0539
θ range	3.16–27.20	3.36–27.48
Observed reflections	4348	4144
x, y (weighting scheme)	0.0346, 1.4247	0.0584, 0.7208
Reflections in refinement	4792	5518
Parameters	283	303
Restraints	2	0
$R(F_{obs})$	0.0293	0.0446
$R_w(F^2)$	0.0700	0.1240
S	1.069	1.051
Shift/error$_{max}$	0.001	0.001
Minimum/maximum electron density (e Å^{-3})	−1.056, 2.142	−0.767, 1.112
CCDC	679540	679541

3.3. Biological activity

In our recent publication [40] we presented the cytotoxicity assays of the ligand **2b** and its complexes **3b**–**5b** performed on L1210 and K562 leukemia cell lines. Here we present biological studies of these compounds as well as newly synthesized ligand **2a** and its complexes on human acute leukemia HL-60 and NALM-6 and melanoma WM-115 cell lines in order to compare the influence of the functional group on cytotoxic activity (Table 4). Compounds **6a** and **6b** were not tested for biological activity, as they were obtained only to establish X-ray structures. It can be supposed that their cytotoxicity would be strictly related to the presence of DMF molecule in their structure and DMF is highly cytotoxic by itself. That is why the test of biological activity of the clear complexes **5a** and **5b** without DMF molecule was only provided. Cisplatin and carboplatin were used as the reference compounds. Ligands **2a** and **2b** have very low cytotoxic activity. Most phosphonic compounds exhibited lower cytotoxicity than carboxylic analogs. The cytotoxic effect of platinum(II) and palladium(II) complexes are rather low. All copper(II) complexes exhibited relatively high cytotoxic activity with the IC_{50} values in micromolar range against leukemia cell

Table 4
IC_{50} values (in μM) of the ligands **2a** and **2b** and their complexes.

Compound	HL-60	NALM-6 IC_{50}[a]	WM-115
2a	716.5 ± 28.9	875.1 ± 119.9	>1000
2b	649.4 ± 74.4	>1000	>1000
3a	613.1 ± 22.2	766 ± 40.4	549.0 ± 68.5
3b	58.1 ± 2.2	55.1 ± 3.8	76.7 ± 13.4
4a	610.2 ± 40.8	804.2 ± 57.2	591.3 ± 51.9
4b	133.9 ± 28.8	413.7 ± 40.4	483.6 ± 22.3
5a	56.96 ± 4.97	49.88 ± 2.23	90.5 ± 11.69
5b	48.9 ± 1.7	54.1 ± 2.4	93.4 ± 5.0
7a	43.9 ± 3.6	47.6 ± ± 4.6	81.7 ± 3.2
7b	6.5 ± ± 0.3	40.7 ± 5.5	8.0 ± 0.3
Cisplatin	0.8 ± 0.1	0.7 ± 0.3	18.2 ± 4.3
Carboplatin	4.3 ± 1.3	0.7 ± 0.2	422.2 ± 50.2

[a] IC_{50} – concentration of a tested compound required to reduce the fraction of surviving cells to 50% of that observed in the control, non-treated cells. Mean values of IC_{50} (in μM) ± S.D. from four experiments are presented.

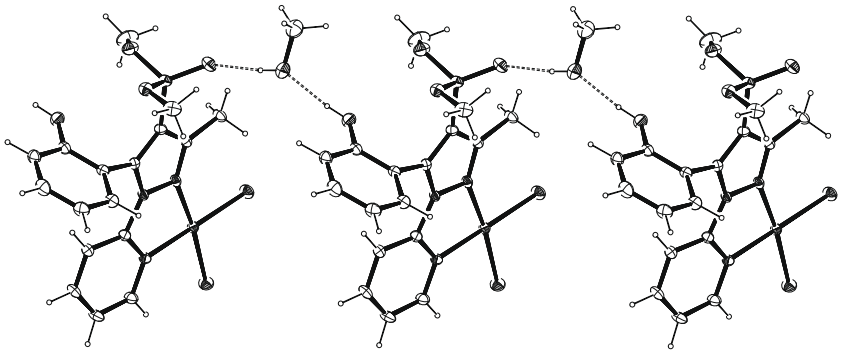


Fig. 5. Part of the crystal packing of **3a** with the intermolecular hydrogen bridges with MeOH.

lines although their cytotoxic effectiveness was lower in comparison to cisplatin and carboplatin. The copper(II) complex **7b** exhibited the highest cytotoxic activity with IC_{50} values in the range of 6.5 μM for HL-60 and 8.0 μM for WM-115 cell lines. So, cytotoxic effectiveness of compound **7b** against melanoma WM-115 cells was two times better than that of cisplatin. The result strongly support the view that the observed cytotoxicity can be confidently attributed to the presence of the metal centres.

4. Conclusions

In this paper, we presented the synthesis and investigation of highly substituted phosphonic pyrazole ligand and its complexes with platinum(II), palladium(II) and copper(II). Cytotoxic activity of these new compounds was compared with activity of their carboxylic analogs in order to assess the influence of chemical groups on cytotoxic activity of the compounds.

The new phosphonic ligand **2a** was obtained in the reaction of dimethyl 2-methyl-4-oxo-4*H*-chromen-3-yl-phosphonate with 2-hydrazinopyridine in methanolic solution.

By monitoring the reaction by ^{31}P NMR spectroscopy we observed only one product after the opening of the γ-pyrone ring and cyclization to pyrazole derivative. This is in accordance to the fact that 2-hydrazinopyridine has only one dissociation constant for N2 and this nitrogen atom is responsible for nucleophilic attack at the chromone derivative C2 atom.

The highly substituted phosphonic pyrazole **2a** was used as ligand for the synthesis of novel neutral platinum(II), palladium(II) and copper(II) complexes **3a–7a**. Phosphonic compounds were compared with previously synthesized carboxylic analogs **2b**–**7b**, whose cytotoxic assay had been performed on L1210 and K562 leukemia cell lines. Copper(II) complexes with both phosphonic and carboxylic ligands were synthesized in 1:1 and 2:1 molar ratio. The structure of the ligands and their metal complexes was confirmed by spectral and elemental analyses. The molecular structures of phosphonic complexes of platinum(II) **3a** and copper(II) **6a** were confirmed by X-ray analysis. The complexes exhibit distorted tetragonal planar configuration and trigonal bipyramidal configuration at the platinum(II) and copper(II) centres, respectively.

Studies on the cytotoxicity evaluated on leukemia and melanoma cell lines showed that in most cases carboxylic compounds have higher activity than that of phosphonic analogs. Cytotoxic effectiveness of compound **7b** against melanoma WM-115 cells was two times better than that of cisplatin. Copper(II) complexes were more active in the induction of melanoma cell death than the platinum(II) and palladium(II) complexes. Higher cytotoxic activity of investigated copper(II) complexes suggests that the mechanism of actions of these compounds may differ from the mechanism of action of platinum(II) or palladium(II) complexes. The reaction of complex **5b** with 9-methylguanine has been investigated and we have obtained a new compound **8b** of the formula $LCu9MeGCl_2$.

Acknowledgements

Financial support from Medical University of Lodz (Grant No. 502-13-629) and the DAAD for fellowship No. A/07/01244 and Grant No. 503-3015-2 to Department of Pharmaceutical Biochemistry at Medical University of Lodz are gratefully acknowledged.

Appendix A. Supplementary data

CCDC 679540 and 679541 contains the supplementary crystallographic data for **3a** and **6a**. These data can be obtained free of charge via http://www.ccdc.cam.ac.uk/conts/retrieving.html, or from the Cambridge Crystallographic Data Centre, 12 Union Road, Cambridge CB2 1EZ, UK; fax: (+44) 1223-336-033; or e-mail: deposit@ccdc.cam.ac.uk. Supplementary data associated with this article can be found, in the online version, at doi:10.1016/j.poly.2008.12.013.

References

[1] L.R. Kelland, N.P. Farrell, S. Spinelli, in: N.P. Farell (Ed.), Uses of Inorganic Chemistry in Medicine, The Royal Society of Chemistry, 1999. pp. 109–144.
[2] Y. Najajreh, J.M. Perez, C. Navarro-Ranninger, D. Gibson, J. Med. Chem. 45 (2002) 5189.
[3] E. Khazanov, Y. Barenholtz, D. Gibson, Y. Najajreh, J. Med. Chem. 45 (2002) 5196–5204.
[4] V. Brabec, Prog. Nucleic Acid Res. Mol. Biol. 71 (2002) 1.
[5] M. Kartalou, J.M. Essigman, Mut. Res. 478 (2001) 23.
[6] V. Brabec, J. Kasparkova, Drug Resist. Updates 51 (2002) 47.
[7] J. Kasparkova, V. Marini, Y. Najajreh, D. Gibson, V. Brabec, Biochemistry 42 (2003) 6321.
[8] M. Gielen, E.R.T. Tiekink (Eds.), Metallotherapeutic Drugs and Metal – based Diagnostic agents, The Use of Metals in Medicine, Wiley, 2005, p. 359.
[9] M. Devereux, D. O'Shea, A. Kellett, M. McCarn, M. Walsh, D. Egan, C. Deegan, K. Kedziora, G. Rosair, H. Mueller-Bunz, J. Inorg. Biochem. 101 (2007) 881.
[10] E. Budzisz, Pol. J. Cosm. 9 (2006) 212.
[11] A.V. Godoy Netto, R.C.G. Frem, A.E. Mauro, Transition Met. Chem. 27 (2002) 279.
[12] J. Hamacek, J. Havel, J. Chromatogr. A 834 (1999) 321.
[13] A.R. Amundsen, W.E. Stern, Chem. Abstr. 100 (1984) 161.
[14] M.C. Linder, M. Hazeqh-Azam, Am. J. Clin. Nutr. 63 (1996) 797S.
[15] R. Huang, A. Wallquist, D.G. Covell, Biochem. Pharmacol. 100 (2006) 1389.
[16] B. Coyle, P. Kiusella, M. McCann, D. Devereux, R. O'Connor, M. Clynes, K. Kavanagh, Toxicol. In Vitro 18 (2004) 63.
[17] M. Devereux, M. McCann, D. O'Shea, R. Kelly, D. Egan, C. Deegan, K. Kavanagh, V. McKee, G. Finn, J. Inorg. Biochem. 98 (2004) 1023.
[18] J. Easmon, G. Purstinger, G. Heinish, T. Roth, H.H. Fiebig, W. Holzer, W. Jager, M. Jenny, J. Hofmann, J. Med. Chem. 44 (2001) 2164.
[19] F. Liang, C. Wu, H. Lin, T. Li, D. Gao, Z. Li, J. Wei, C. Zheng, M. Sun, Bioorg. Med. Chem Lett. 13 (2003) 2469.
[20] M.C. Rodriguez-Arguelles, M.B. Ferrari, F. Bisceglie, C. Pelizzi, G. Pelosi, S. Pinelli, M. Sassi, J. Inorg. Biochem. 98 (2004) 313.
[21] M.B. Ferrari, F. Bisceglie, G. Pelosi, P. Tarasconi, R. Albertini, P.P. Dall'Aglio, S. Pinelli, A. Bergamo, G. Sava, J. Inorg. Biochem. 98 (2004) 301.
[22] S. Sharma, F. Athar, M.R. Maurya, F. Naqui, A. Azam, Eur. J. Med. Chem. 40 (2005) 557.
[23] S. Torelli, C. Belle, I. Gautier-Luneau, J.L. Pierre, E. Saint-Aman, J.M. Latour, L. Le Pape, D. Luneau, Inorg. Chem. 39 (2000) 3526.
[24] S. Torelli, C. Belle, S. Hamman, J.L. Pierre, E. Saint-Aman, Inorg. Chem. 41 (2002) 3983.
[25] K. Selmeczi, M. Reglier, M. Giorgi, G. Speier, Coord. Chem. Rev. 24 (2003) 5191.
[26] M. Thirumavalavan, P. Akilan, M. Kandaswamy, Kandaswamy Chinnakali, G. Senthil Kumar, H.K. Fun, Inorg. Chem. 42 (2003) 3308.
[27] H. Borzel, P. Comba, H. Pritzkow, Chem. Commun. (2001) 97.
[28] E. Monzani, G. Battaini, A. Perotti, L. Casella, M. Gullotti, L. Santagostini, G. Nardin, L. Randaccio, S. Geremia, P. Zanello, G. Opromolla, Inorg. Chem. 38 (1999) 5359.
[29] I.A. Koval, K. van der Schilden, A.M. Schuitema, P. Gamez, C. Belle, J.-L. Pierre, M. Luken, B. Krebs, O. Roubeau, J. Reedijk, Inorg. Chem. 44 (2005) 4372.
[30] G. Zhao, H. Lin, Curr. Med. Chem. Anti-Cancer Agents 5 (2005) 137.
[31] A. Orejon, C. Claver, L.A. Oro, A. Elduque, M.T. Pinillos, J. Mol. Catal. A Chem. 136 (1998) 279.
[32] C. Claver, P. Kalck, M. Ridmy, A. Thorez, L.A. Oro, M.T. Pinillos, M. Carmen-Apreda, F.H. Cano, C. Foces-Foces, J. Chem. Soc., Dalton Trans. 6 (1988) 1523.
[33] N. Saha, A. Saha, A. Misra, Polyhedron 13 (1994) 2025.
[34] K. Sakai, Y. Tomita, T. Ue, K. Goshima, M. Ohminato, T. Tsubomura, K. Matsumoto, K. Ohmura, K. Kawakami, Inorg. Chim. Acta 297 (2000) 64.
[35] A.G.M.M. Hossain, T. Nagaoka, K. Ogura, Electrochim. Acta 41 (1996) 2773.
[36] S.J. Kim, S.H. Kang, K.-M. Park, H. Kim, W.-C. Zin, M.-G. Choi, K. Kim, Chem. Mater. 10 (1998) 1889.
[37] J. Barbera, A. Elduque, R. Gimenez, L.A. Oro, J.L. Serrano, Angew. Chem., Int. Ed. Engl. 35 (1996) 2832.
[38] A. Looney, G. Parkin, R. Alsfasser, M. Ruf, H. Vahrenkamp, Angew. Chem., Int. Ed. Engl. 31 (1992) 92.
[39] A. Kufelnicki, M. Wozniczka, L. Checinska, M. Miernicka, B. Budzisz, Polyhedron 26 (2007) 2589.
[40] M. Miernicka, A. Szulawska, M. Czyz, I.-P. Lorenz, P. Mayer, B. Karwowski, E. Budzisz, J. Inorg. Biochem. 102 (2008) 157.
[41] K. Kostka, S. Pastuszko, M. Porada, Phosphorus Sulfur Silicon Related Elements 71 (1992) 67.
[42] G.M. Coppola, R.W. Dodsworth, Synthesis 7 (1981) 523.
[43] C.G. Van Kralingen, J.K. De Ridder, J. Reedijk, Inorg. Chim. Acta 36 (1979) 69.
[44] E. Budzisz, U. Krajewska, M. Rozalski, Pol. J. Pharmacol. 56 (2004) 473.

[45] G.M. Sheldrick, SADABS, Version 2, Multi-Scan Absorption Correction Program, University of Gottingen, Germany, 2001.
[46] G.M. Sheldrick, SHELXS-97, University of Göttingen, Germany, 1997.
[47] G. M. Sheldrick, SHELXL-97, University of Göttingen, 97-2 Version, 1997.
[48] A. Altomare, M.C. Burla, M. Camalli, G.L. Cascarano, C. Giacovazzo, A. Guagliardi, A.G.G. Moliterni, G. Polidori, R. Spagna, J. Appl. Crystallogr. 32 (1999) 115.
[49] G. Anderegg, Helv. Chim. Acta 54 (1971) 509.
[50] K. Kostka, Chem. Anal. 14 (1969) 1145.
[51] K. Kostka, Rocz. Chem. 47 (1973) 305.
[52] V.P. Chila, A. Aitmanbetov, U. Usmailov, L.G. Grishko, Khim. Prirodnych Soedin. (1993) 629.
[53] D.C.G.A. Pinto, A.M.S. Silva, J.A.S. Cavaleiro, C. Foces-Foces, A.L. Llamas-Saiz, N. Jagerovic, J. Elguero, Tetrahedron 55 (1999) 10187.
[54] S. Kerrison, P.J. Sadler, Chem. Commun. 23 (1977) 861.
[55] B. Lippert, Coord. Chem. Rev. 182 (1999) 263.
[56] J.T. Wrobel, Preparatyka i elementy syntezy organicznej, PWN, Warszawa, 1983, pp. 9–52.
[57] V.C. da Silveira, J.S. Luz, C.C. Oliveira, I. Graziani, M.R. Ciriolo, A.M. da Costa Ferreira, J. Inorg. Biochem. 102 (2008) 1090.

Polyhedron 28 (2009) 647–652

Contents lists available at ScienceDirect

Polyhedron

journal homepage: www.elsevier.com/locate/poly

Syntheses, characterization and luminescent properties of two lead(II) fumarate metal-organic frameworks

Kou-Lin Zhang [a,*], Wei Liang [a], Yan Chang [a], Li-Min Yuan [b], Seik Weng Ng [c]

[a] College of Chemistry and Chemical Engineering, Yangzhou University, Yangzhou 225002, PR China
[b] Test and Analysis Center, Yangzhou University, Yangzhou 225002, PR China
[c] Department of Chemistry, University of Malaya, 50603 Kuala Lumpur, Malaysia

ARTICLE INFO

Article history:
Received 14 March 2008
Accepted 30 October 2008
Available online 5 February 2009

Keywords:
Lead(II) complexes
Characterization
MOFs
Coordination gap
Photoluminescence

ABSTRACT

It is of interest that the hydrous 3D metal-organic framework (MOF) $\{[Pb_2(fum)_2(H_2O)_4]\cdot 2H_2O\}_n$ (**1**) has been synthesized by the reaction of the fum dianion with the lead(II) ion (fum = fumarate) in the presence of pyrazole, while the anhydrous 3D MOF $[Pb(fum)]_n$ (**2**) is obtained by the reaction of the fum dianion with the lead(II) ion in the presence of pyrazine. These complexes were further characterized by FT-IR spectroscopy, thermogravimetric analysis (TG), X-ray analysis and solid state photoluminescence spectra. The arrangement of the ligands displays a coordination gap around the Pb atom, occupied possibly by a stereoactive lone pair of electrons on lead(II), with the coordination around both the eight-coordinated lead atom in **1** and six-coordinated lead atom in **2** exhibiting a hemidirected geometry. The fum ligand shows different ligation behavior toward the lead(II) ions in these complexes. These compounds exhibit photoluminescence with the maximum emission located in the UV region.

© 2008 Published by Elsevier Ltd.

1. Introduction

Recently, the design and syntheses of metal-organic frameworks (MOFs) has been an impetus for supramolecular chemistry and property-oriented crystal engineering. Yaghi, Williams, Kitagawa, Férey, Chen and co-workers have worked in the area of coordination polymers and considered diverse problems restricting the development of porous MOFs, and successfully developed a strategy to design porous materials [1–3]. However, most of the work so far has been focused on d-block transition metal-organic frameworks; main group metal-organic frameworks remain less developed. In contrast to transition metal ions, the Pb(II) ion also has a tendency to form polynuclear complexes and the potential to provide a stable framework structure [4]. In particular, the Pb(II) ion possesses evidence of coordination sphere distortions as a consequence of the presence of a $6s^2$ lone-pair. The intrinsic features of Pb(II), the presence of a $6s^2$ electron configuration, cause chemists' intense interest in coordination chemistry, photophysics and photochemistry [5]. So, the coordination chemistry of lead(II) has recently been investigated and frequently discussed with regard to the coordination and stereoactivity of the valence shell lone electron pair, in addition to its great potential use to extract this harmful metal from the environment [6–11]. There have been some well-defined cluster-type lead(II) polymers reported, such as $Pb_4(OH)_4$, $Pb_6O(OH)_6$, $Pb_6(OH)_4O_4$, Pb_8O_8 [4]. Few lead(II) carboxylate-bridged complexes with layered or 3D network structures have been reported [12–16]. The rigid fum ligand is a suitable candidate for assembling complexes with novel structures and functional properties [17]. The rigid fum ligand is expected to more likely form novel hybrid materials with porous 3D network architectures through the self-assembly with the lead(II) ion. To the best of our knowledge, there are no lead(II) coordination polymers based on the rigid fum ligand reported as yet.

In the present paper, we report the syntheses and characterization of two lead(II) MOFs, $\{[Pb_2(fum)_2(H_2O)_4]\cdot 2H_2O\}_n$ (**1**) and $[Pb(fum)]_n$ (**2**), based on the fum ligand. This is a case that reveals some N-containing compounds, such as pyrazine and pyrazole, may have an influence on the structure of some MOFs in this system. Photoluminescence properties of the two complexes have been examined in the solid state at room temperature.

2. Experimental

2.1. Materials and characterization

All the reagents were used as purchased. Elemental analyses (C, H and N) were carried out on a 240 °C Elemental analyzer. Infrared spectra (400–4000 cm^{-1}) were recorded from KBr pellets in a Magna 750 FT-IR spectrophotometer. The solid state emission spectra of the compounds were recorded using a 48000DSCF fluorescence spectrometer.

* Corresponding author. Tel./fax: +86 514 87695171.
E-mail addresses: klzhang@yzu.edu.cn, koulinzhang2002@yahoo.com (K.-L. Zhang).

0277-5387/$ - see front matter © 2008 Published by Elsevier Ltd.
doi:10.1016/j.poly.2008.10.074

2.2. Synthesis of $[Pb_2(fum)_2(H_2O)_4] \cdot 2H_2O_n$ (**1**)

Pyrazole (0.0136 g, 0.2 mmol) was dissolved in water (8 ml) and then a solution of $Pb(NO_3)_2 \cdot 4H_2O$ (0.0333 g, 0.1 mmol) in water (6 ml) was added. To this solution a mixture of H_2fum (0.0116 g, 0.1 mmol) and NaOH (0.5000 mol/l, 0.40 ml) in water (20 ml) was added and then filtered. The filtrate (pH 4.1) was kept at ambient temperature for several days and colorless block crystals were formed. They were filtered and washed with methanol and dried in vacuum (yield: 42.1% based on H_2fum). *Anal.* Calc. for: $C_8H_{16}O_{14}Pb_2$: C, 12.80; H, 2.15. Found: C, 12.68; H, 2.11%.

2.3. Synthesis of $[Pb(fum)]_n$ (**2**)

Pyrazine (0.0160 g, 0.2 mmol) was dissolved in water (8 ml) and then a solution of $Pb(NO_3)_2 \cdot 4H_2O$ (0.0330 g, 0.2 mmol) in water (6 ml) was added whilst stirring. To this solution a mixture of H_2fum (0.0116 g, 0.1 mmol) and NaOH (0.5000 mol/l, 0.40 ml) in water (20 ml) was added. The filtrate (pH 6.1) was kept at ambient temperature for several days and white crystals were formed (47.3% based on H_2fum). *Anal.* Calc. for $C_4H_2O_4Pb$: C, 14.95; H, 0.63. Found: C, 14.77; H, 0.59%.

2.4. X-ray single-crystal structure determination

Crystallographic data for the two compounds were collected at 293(2) K with a Siemens SMART CCD diffractometer using graphite-monochromated (Mo Kα) radiation ($\lambda = 0.71073$ Å), with ψ and ω scans mode. The structures were solved by direct methods and refined by the full-matrix least-squares on F^2 method using the SHELXL-97 program [18]. Intensity data were corrected for Lorenz and polarization effects and an empirical absorption correction was performed. All non-hydrogen atoms were refined anisotropically. All the hydrogen atoms were added geometrically and allowed to ride on their respective parent atoms. The contribution of these hydrogen atoms was included in the structure factor calculations. Details of the crystal data, collection and refinement are listed in Table 1.

Table 1
Crystallographic data and structure refinement for the complexes.

Compounds	**1**	**2**
Empirical formula	$C_8H_{16}O_{14}Pb_2$	$C_4H_2O_4Pb$
Formula weight	750.59	321.25
Temperature (K)	295(2)	295(2)
Wavelength (Å)	0.71073	0.71073
Crystal system	Triclinic	Monoclinic
Space group	$P\bar{1}$	$P2_1/c$
a (Å)	7.0909(6)	8.4508(7)
b (Å)	7.6603(7)	6.7670(6)
c (Å)	8.0389(7)	9.1214(8)
α (°)	80.2140(10)	90
β (°)	77.9730(10)	93.1170(10)
γ (°)	71.0220(10)	90
Volume (Å^3)	401.39(6)	520.85(8)
Z	1	4
D_{calc} (Mg/m^3)	3.105	4.097
Absorption coefficient (mm^{-1})	10.45	32.314
F(000)	340	560
Crystal size (mm)	0.12 × 0.10 × 0.08	0.10 × 0.08 × 0.06
Θ range for data collection	2.61–27.49	2.41–27.49°
Index ranges	$-7 \leqslant h \leqslant 9$, $-9 \leqslant k \leqslant 9$, $-10 \leqslant l \leqslant 10$	$-10 \leqslant h \leqslant 10$ $-8 \leqslant k \leqslant 8$ $-11 \leqslant l \leqslant 11$
Reflections collected	3425	4212
Independent reflections [R_{int}]	1783 (0.0233)	1172 (0.0348)
Completeness to θ_{max}	97.0%	98.3%
Max. and min. transmission	0.2842 and 0.1870	0.2473 and 0.1405
Data/restraints/parameters	1783/0/112	1172/0/83
Goodness-of-fit on F^2	1.076	1.022
Final R indices [$I > 2\sigma(I)$]	$R_1 = 0.0280$ $wR_2 = 0.0742$	0.0280 0.0733
R indices (all data)	$R_1 = 0.0292$ $wR_2 = 0.0752$	0.0293 0.0745
Largest difference peak and hole (e Å^{-3})	2.541 and −1.906	3.837 and −2.441

3. Results and discussion

3.1. Preparation

It is of great interest that the hydrous lead(II) fumarate **1** was obtained in the presence of pyrazole, while the anhydrous lead(II) fumarate **2** was obtained in the presence of the pyrazine. It should be noted that the hydrous compound **1** was also obtained when the lead(II) ion reacts only with the fum ligand without the presence of pyrazole, but the anhydrous complex 2 cannot be obtained without the presence of pyrazine. These facts indicate that some N-containing compounds, such as pyrazine and pyrazole, may have great influence on the structures of some MOFs in this system, which may be attributed to the different initial pH values of the mixed reaction solution (4.1 for **1** and 6.1 for 2).

3.2. Structural description of **1**

The hydrous lead(II) fumarate $\{[Pb_2(fum)_2(H_2O)_4] \cdot 2H_2O\}_n$, **1**, has a 3D porous structure with an asymmetric unit of 24 non-hydrogen atoms. There are two crystallographically equivalent hemidirected Pb^{2+} ions, two fum anions, four coordinated water molecules and two lattice water molecules in the asymmetric unit (Figs. 1 and 3). From a chemical point of view, the coordinated water in this formula cannot be replaced by oxygen or hydroxyl groups. The fum anion acts as a tetradentate ligand and exhibits

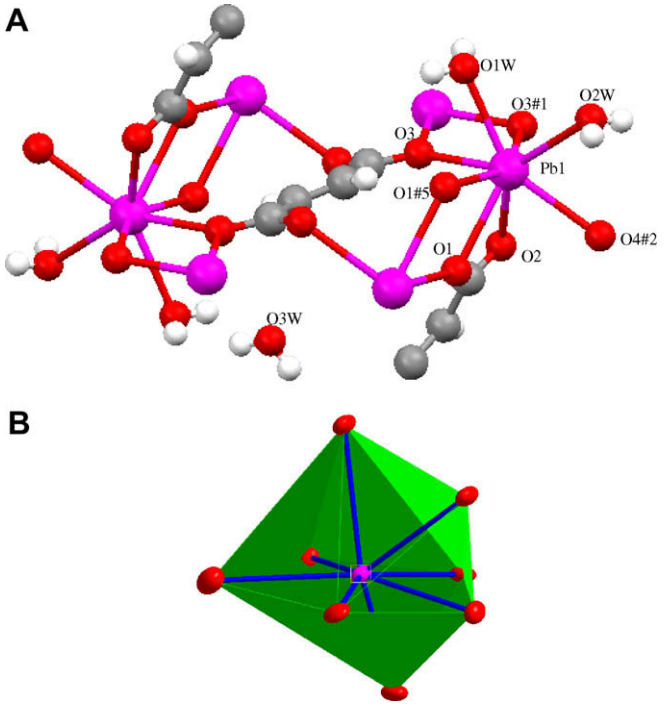


Fig. 1. (A) Octacoordination of Pb(II) by the fumarate ligands in **1**. Symmetry transformations: #1 $-x+1, -y+1, -z+1$; #2 $x+1, y, z$; #5 $-x, -y+2, -z+1$. (B) Polyhedral representation of PbO_8 in **1**.

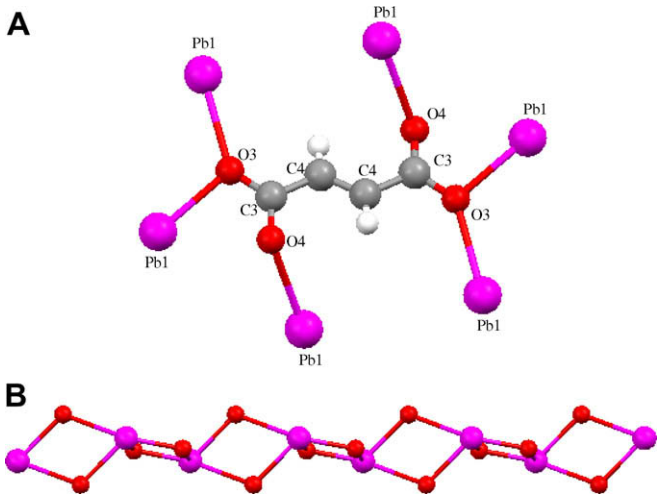


Fig. 2. (A) Tetradentate fumarate ligand in **1**. (B) Pb–O chain formed by Pb atoms and μ-O atoms running along the *b*-axis in **1**, showing the preferences of the $[Pb_2O_2]$ units.

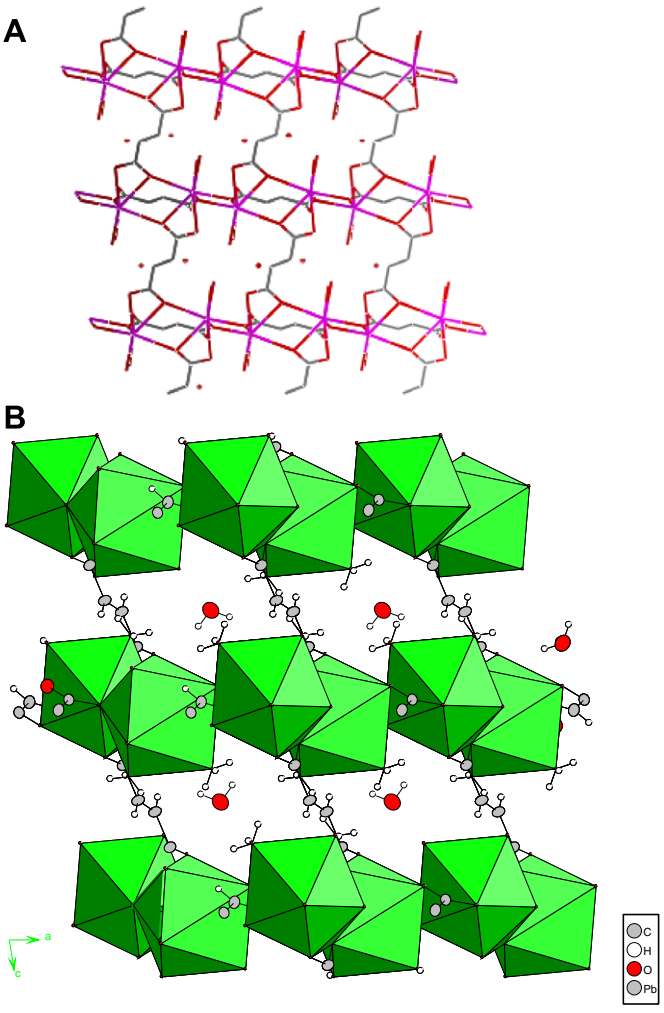
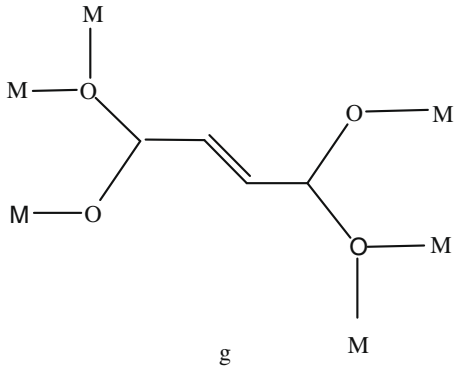
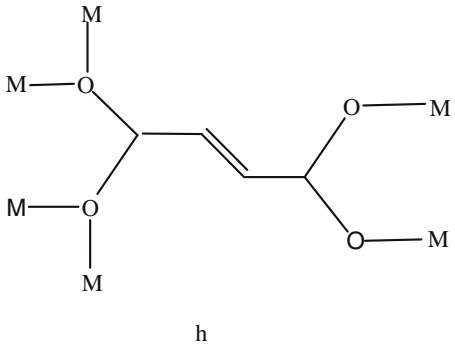


Fig. 3. (A) 3D MOF with 1D channel along the a direction. The red dots represent the lattice water molecules. (B) The 1D channel structure along the b direction. (For interpretation of the references to colour in this figure legend, the reader is referred to the web version of this article.)





Scheme 1. Coordination modes of the complexes. g: **1**; h: **2**.

only one coordination mode (Scheme g; Fig. 2A). The lead ion is eight-coordinated (PbO_8), two oxygens are from the coordinated water molecules and six are from four different fum anions. Four of these oxygens (two O1 and two O2) have μ_2 connections, linking one Pb(1) with two different Pb(1) atoms. Two Pb atoms are linked by two μ-O atoms of fum ligands, forming two planar four-membered rings Pb1–O1–Pb1A–O1A and Pb1–O3–Pb1A-O3A. The two four-membered rings link each other to form a 1D Pb–O chain through a corner-sharing Pb polyhedron along the *a*-axis (Fig. 2B), where the angle between the two neighboring planes is 74.99°. The Pb_2O_2 units are bridged by two fum ligands along the *a*-axis and by two other fum ligands along the *c*-axis, yielding a 3D framework with 1D channels running parallel to the *a* and *b*-axes as shown in Fig. 3A and B, respectively. The guest water molecules, (O3W), which do not show any covalent interactions, fill in the channel. Thus, the $Pb(1)O_8$ polyhedral share edges with each other forming a dimeric $Pb(1)_2O_{14}$ unit. The Pb–O bond lengths are in the range 2.542(4)–2.893(6) Å (Table 2). The dimers are connected to each other by one of the two fum ligands into a 2D Pb–O–Pb layer. The layers are further connected by the other fum ligand, forming a 3D porous structure (Fig. 3). Hydrogen bonds exist extensively in **1**, which further stabilize the 3D metal-organic framework structure. The details of the hydrogen bonds are listed in Table 3.

3.3. Structural analysis of **2**

The anhydrous complex Pb(fum) adopts a 3D structure wherein 1D channels are arranged along the *c* direction (Fig. 6), while the reported complex lead(II) maleate (PbMAL) exhibits a quite different 2D layered structure [19]. This fact indicates that the rigid fum ligand is more likely to form a 3D porous structure with the lead(II) ion than the flexible maleate ligand. The single independent lead atom is bonded to six oxygen atoms [with distances ranging from 2.399(5) to 2.811(4) Å] (Table 2), belonging to five symmetry-equivalent deprotonated fumarate ligands, as seen in Fig. 4. The

Table 2
Selected bond lengths [Å] and angles [°] for **1** and **2**.

Compound **1**			
Pb(1)–O(2)	2.517(5)	Pb(1)–O(3)#1	2.542(4)
Pb(1)–O(3)	2.649(5)	Pb(1)–O(1W)	2.720(5)
Pb(1)–O(4)#2	2.740(5)	Pb(1)–O(2W)	2.893(6)
Pb(1)–O(1)#5	2.858(5)	Pb(1)–O(1)	2.770(4)
O(2)–Pb(1)–O(3)#1	72.82(16)	O(2)–Pb(1)–O(3)	71.12(15)
O(3)#1–Pb(1)–O(3)	62.92(17)	O(2)–Pb(1)–O(1W)	138.54(15)
O(3)#1–Pb(1)–O(1W)	80.52(16)	O(3)–Pb(1)–O(1W)	68.60(16)
O(2)–Pb(1)–O(4)#2	70.00(15)	O(3)#1–Pb(1)–O(4)#2	100.49(14)
O(3)–Pb(1)–O(4)#2	140.80(15)	O(1W)–Pb(1)–O(4)#2	147.54(16)
O(2)–Pb(1)–O(2W)	139.39(16)	O(3)#1–Pb(1)–O(2W)	105.84(16)
O(3)–Pb(1)–O(2W)	145.91(18)	O(1W)–Pb(1)–O(2W)	78.00(17)
O(4)#2–Pb(1)–O(2W)	70.49(17)		
Compound **2**			
Pb(1)–O(1)	2.399(5)	Pb(1)–O(2)#1	2.420(4)
Pb(1)–O(3)#2	2.493(5)	Pb(1)–O(4)#3	2.656(4)
Pb(1)–O(3)	2.811(5)	Pb(1)–O(4)	2.783(4)
O(1)–Pb(1)–O(2)#1	82.80(16)	O(1)–Pb(1)–O(3)#2	83.70(14)
O(2)#1–Pb(1)–O(3)#2	76.84(16)	O(1)–Pb(1)–O(4)#3	82.74(14)
O(2)#1–Pb(1)–O(4)#3	84.95(14)	O(3)#2–Pb(1)–O(4)#3	158.50(12)

Symmetry transformations: **1**: #1: $-x+1,-y+1,-z+1$; #2: $x+1,y,z$; #3: $x-1,y,z$; #4: $-x+1,-y+2,-z$; #5: $-x,-y+2,-z+1$; **2**: #1: $x,-y+3/2,z+1/2$; #2: $-x+2,-y+2,-z+1$; #3: $-x+2,-y+1,-z+1$; #4: $x,-y+3/2,z-1/2$.

Table 3
Details of the hydrogen bonds for the compounds.

D–HA	d(D–H)	d(HA)	d(DA)	<DHA	Symmetry of A
Compound **1**					
O1W–H11 ... O3W	0.8200	2.0600	2.796(9)	150.00	
O1W–H12 ... O2	0.8200	1.9600	2.730(8)	156.00	$1-x,1-y,1-z$
O2W–H21 ... O2	0.8200	2.1700	2.975(8)	168.00	$2-x,1-y,1-z$
O2W–H22 ... O3	W 0.8200	2.3000	2.935 (9)	134.00	$1+x,y,z$
O3W–H31 ... O2	0.8200	2.4600	3.206(9)	152.00	$-1+x,y,1+z$
O3W–H31 ... O4	0.8200	2.4800	3.025(9)	125.00	$x,y,1+z$
O3W–H32 ... O1W	0.8200	2.5200	2.796(9)	101.00	
Compound **2**					
C3–H3 ... O1	0.9300	2.4800	2.789(10)	100.00	

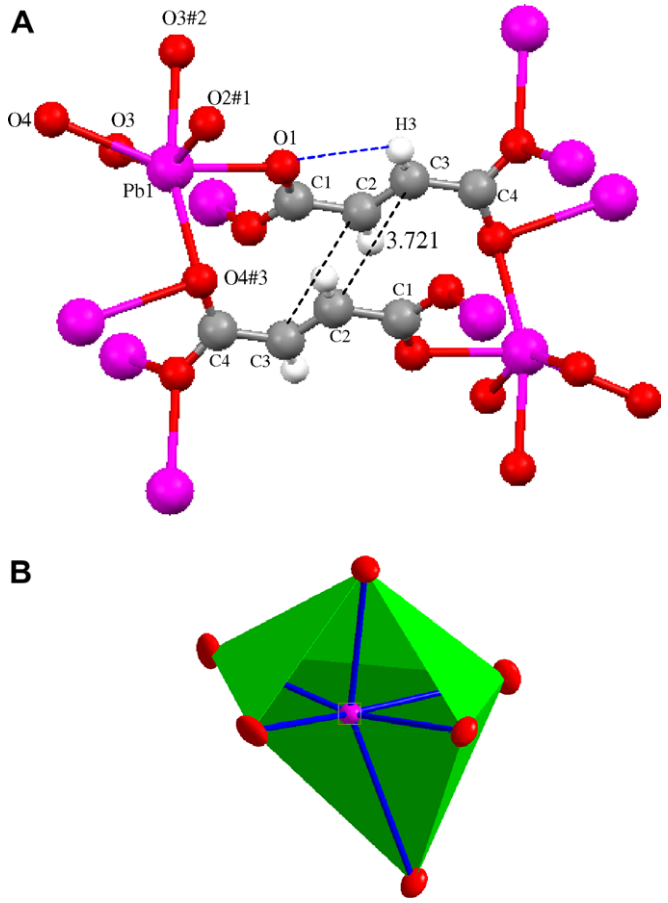


Fig. 4. (A) Hexacoordination environment of Pb(II) by the fumarate ligand in **2**, showing the 14-membered macrometallocycle in **2**. The blue dashed line represents the C-HO interaction, while the black dashed lines represent the ππ stacking interactions Symmetry transformations: #1: $x,-y+3/2,z+1/2$; #2: $-x+2,-y+2,-z+1$; #3: $-x+2,-y+1,-z+1$. Polyhedral representation of PbO_6 in **2**. (For interpretation of the references to colour in this figure legend, the reader is referred to the web version of this article.)

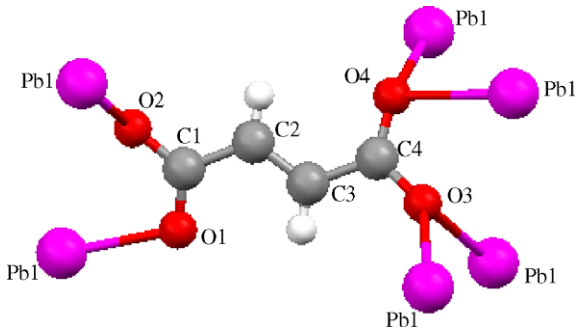


Fig. 5. Coordination mode of the tetradentate fum ligand in **2**.

coordination sphere around the Pb^{2+} is asymmetric and hemidirected. It is of interest that the fumarate units in this structure lie parallel, with a nearest C2C3 distance of 3.721 Å, which indicates that there are ππ stacking interactions between the nearest fumarate dianions. Intramolecular hydrogen bonds exist between the C3 and O1 atoms, with a C3–H3O1 distance of 2.789(10) Å. Each fum ligand is bonded to six lead atoms: O1 and O2 are each bonded to one lead atom; whereas O3 and O4 are each bonded to two lead atoms (Scheme h, Fig. 5). This coordination mode is observed for the first time for the fum ligand. Thus, a 14-membered macrometallocycle is formed as depicted in Fig. 4.

3.4. Coordination geometry of lead(II)

Researchers have found that the coordination geometry of the PbO_n polyhedral in Pb(II) compounds is hemidirected for low coordination numbers (2–5) and holodirected for high coordination numbers (9, 10), and either a hemidirected or holodirected stereochemistry is found for intermediate coordination numbers (6–8) [20–21]. It has been found through *ab* initial molecular orbital studies of Pb(II) complexes in the gas-phase that a hemidirected geometry occurs if the ligands are hard, the ligand coordination number is low and attractive interactions exist between the ligands [22–23]. For the PbO_8 polyhedra in **1**, a hemidirected geometry is exhibited (Fig. 1B). The six-coordinated Pb(II) cations in **2** also exhibit a hemidirected geometry (Fig. 4B).

3.5. FT-IR spectra

The FT-IR spectrum of compound **1** shows broad peaks in the range of 3600–3200 cm^{-1} due to the existence of water molecules. In the middle of the stretching vibrations, IR results are commonly employed to distinguish the coordination modes of carboxylate

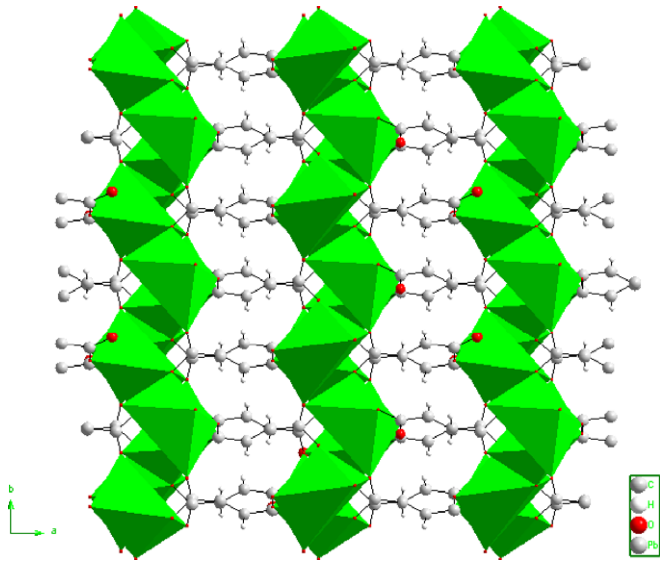


Fig. 6. 3D MOF viewed along the c direction.

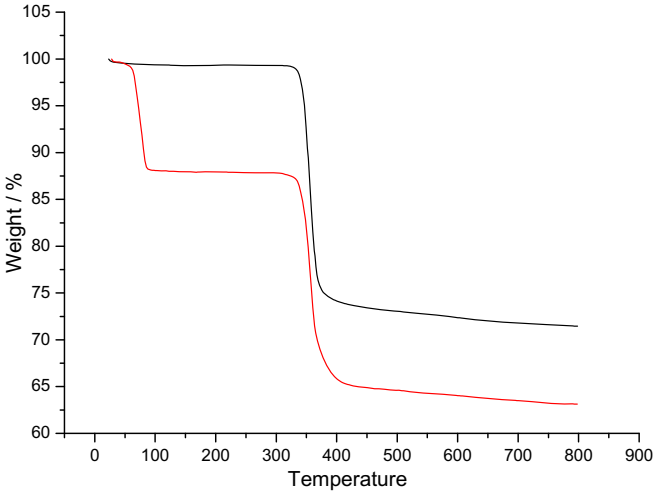


Fig. 7. TG curves of the complexes (**1**: red; **2**: black). (For interpretation of the references to colour in this figure legend, the reader is referred to the web version of this article.)

groups. A correlation of the carboxylate coordination mode to metal ions is usually made by examining the difference $\Delta\nu(\mathrm{COO}) = \nu_{as}(\mathrm{COO}) - \nu_{s}(\mathrm{COO})$ of the compound [24]. The vibrations of $\nu_{as}(\mathrm{COO})$ and $\nu_{s}(\mathrm{COO})$ are at 1523 and 1377 cm^{-1} for **1**, and at 1554, 1532 and 1378 cm^{-1} for **2**, respectively. These facts indicate that the carboxylate groups of the fum ligand exhibit different coordination modes in these two complexes. In all these cases, the results of the X-ray analysis allowed us to assign unambiguously the binding modes of the carboxylate groups.

3.6. Thermogravimetric analysis

To study the thermal stability of the compounds, thermogravimetric analysis (TG) was performed on polycrystalline samples under a nitrogen atmosphere in flowing N_2 with a heating rate of 10 °C min^{-1} (Fig. 7).

The thermogravimetric analysis (TGA) of **1** revealed two distinct thermal events. The first step is ascribed to the gradual loss of both

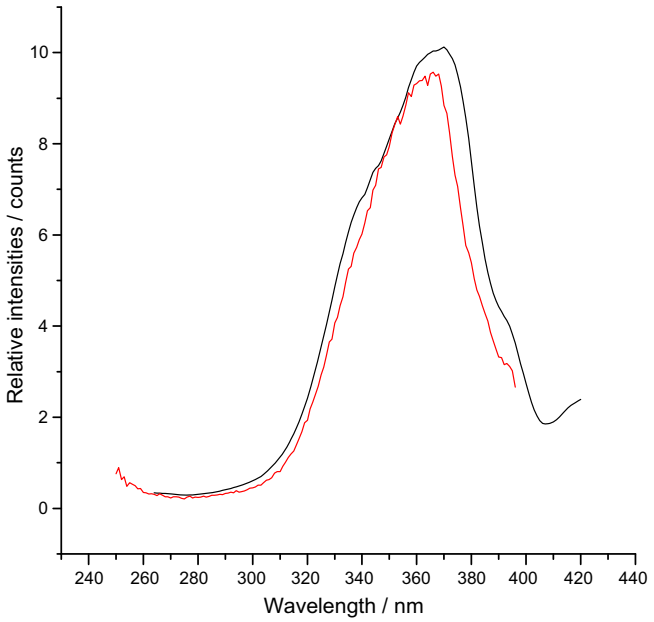


Fig. 8. Solid-state emission spectra of the complexes at room temperature (red: **1**, λ_{ex} = 208 nm; black: **2**, λ_{ex} = 213 nm). (For interpretation of the references to colour in this figure legend, the reader is referred to the web version of this article.)

the coordinated and lattice water molecules, starting at around 50 °C, and leading to a corresponding weight loss of 12.62% (calculated 14.38%). This dehydration step is followed by decomposition of the compound. The decomposition is achieved at about 425 °C, and no further thermal events are observed. One main weight loss event was noted in the TGA of **2**, corresponding to the decomposition of the compound with an onset temperature of 330 °C. No weight loss is observed below 250 °C, confirming the absence of lattice water in the phase.

3.7. Photoluminescence properties

The solid-state photoluminescence spectra of the title complexes at room temperature are depicted in Fig. 8. Fumaric acid exhibits a broad fluorescent emission centered on 323 nm with an excitation maximum at 302 nm. In the case of the MOFs **1** and **2**, a large red-shifted photoluminescence with the main emission at 368 nm (λ_{ex} = 208 nm) and 374 nm (λ_{ex} = 213 nm), respectively, is observed, which is red-shifted about 45 nm and 51 nm, respectively compared to that of free H_2fum acid. Apparently, these strong fluorescence emissions may arise from the Pb^{2+} lone pair to ligand charge transfer [25], and the red-shifted effect may be due to both the coordination or an excited metal-perturbed intraligand state and the fact that the ΔE value [ΔE = E(LUMO)-E(HOMO)] of the fumarate dianion (0.18181 a.u) is smaller than that of fumarate acid (0.19165 a.u), which was obtained through DFT calculations using the b3lyp/lan12mb method [26]. The fluorescent intensity of complex **1** is weaker than that of the complex **2**, which may be due to the existence of both the coordinated and lattice water molecules in complex **1**.

4. Conclusion

In summary, two new lead(II) fumarate MOFs with 1D channels, **1** and **2**, have been successfully synthesized. Both the eight-coordinated lead atom in **1** and the six-coordinated lead atom in **2** show hemidirected geometries. The fum ligands in these complexes exhibit different coordination modes. The fact that complex **1** is hy-

drous while complex **2** is anhydrous shows that some N-containing compounds, such as pyrazine and pyrazole, may have great influence on the structure and composition of some MOFs in this system, which may partially result from the different intial pH values of the reaction solutions. A new strategy to design anhydrous MOFs may be found through further thoroughly investigation on how anhydrous complex **2** was formed. In addition, the solid state photoluminescence properties of the coordination polymers **1** and **2** have been studied.

Acknowledgments

We gratefully acknowledge the Foundation of Jiangsu Provincial Key Program of Physical Chemistry in Yangzhou University for the financial support of this work.

Appendix A. Supplementary data

Supplementary CCDC 674007 and 674006 contain the supplementary crystallographic data for **1** and **2**. These data can be obtained free of charge via http://www.ccdc.cam.ac.uk/conts/retrieving.html, or from the Cambridge Crystallographic Data Centre, 12 Union Road, Cambridge CB2 1EZ, UK; fax: (+44) 1223-336-033; or e-mail: deposit@ccdc.cam.ac.uk. Supplementary data associated with this article can be found, in the online version, at doi:10.1016/j.poly.2008.10.074.

References

[1] (a) H.K. Chae, D.Y. Siberio-Perez, J. Kim, Y. Go, M. Eddaoudi, A.J. Matzger, M. O'Keeffe, O.M. Yaghi, Nature 427 (2004) 523;
(b) M. Eddaoudi, J. Kim, N. Rosi, D. Vodak, J. Wachter, M. O'Keeffe, O.M. Yaghi, Science 295 (2002) 469.
[2] (a) B. Chen, N.W. Ockwig, F.R. Fronczek, D.S. Contreras, O.M. Yaghi, Inorg. Chem. 44 (2005) 181;
(b) M. Eddaoudi, D.B. Moler, H. Li, B. Chen, T.M. Reineke, M. O'Keeffe, O.M. Yaghi, Acc. Chem. Res. 34 (2001) 319;
(c) N.W. Ockwig, O. Delgado-Friedrichs, M. O'Keefee, O.M. Yaghi, Acc. Chem. Res. 38 (2005) 176;
(d) A.C. Sudik, A.R. Millward, N.W. Ockwig, A.P. Cote, J. Kim, O.M. Yaghi, J. Am. Chem. Soc. 127 (2005) 7110;
(e) C. Livage, N. Guillou, J. Chaigneau, P. Rabu, M. Drillon, G. Férey, Angew. Chem., Int. Ed. 44 (2005) 6488;
(f) S.S.-Y. Chui, S.M.-F. Lo, J.P.H. Charmant, A.G. Orpen, I.D. Williams, Science 283 (1999) 1148;
(g) T. Devic, C. Serre, N. Audebrand, J. Marrot, G. Férey, J. Am. Chem. Soc. 127 (2005) 12788;
(h) J.P. Zhang, Y.Y. Lin, W.X. Zhang, X.M. Chen, J. Am. Chem. Soc. 127 (2005) 14162;
(i) G. Férey, C. Mellot-Draznieks, C. Serre, F. Millange, Acc. Chem. Res. 38 (2005) 217.
[3] S. Kitagawa, R. Kitaura, S. Noro, Angew. Chem., Int. Ed. 43 (2004) 2334.
[4] (a) S.M. Grimes, S.R. Jonston, I. Abrahams, J. Chem. Soc., Dalton Trans. (1995) 2081;
(b) F. Frostemark, L.A. Bengtsson, B. Holmberg, J. Chem. Soc., Faraday Trans. 90 (1994) 2531;
(c) Y.H. Yeom, Y. Kim, K. Seff, Micropor. Mesopor. Mater. 28 (1999) 103;
(d) Y.H. Yeom, Y. Kim, K. Seff, J. Phys. Chem. B 101 (1997) 5314.
[5] (a) A. Strasser, A. Vogler, J. Photochem. Photobiol. A 165 (2004) 115;
(b) A. Vogler, H. Nikol, Pure Appl. Chem. 64 (1992) 1311.
[6] M.A.R. Dakers, M.N.S. Hill, J.C. Lockhart, D.J. Rushton, J. Chem. Soc., Dalton Trans. (1994) 209.
[7] P. Schwerdtheger, G.A. Heath, M. Dolg, M.A. Bennett, J. Am. Chem. Soc. 114 (1992) 7518.
[8] K. Byriel, K.R. Dunster, L.R. Gahan, C.H.L. Kennard, J.L. Latten, I.L. Swann, P.A. Duckworth, Polyhedron 11 (1992) 1205.
[9] P. Pyykko, Chem. Rev. 88 (1988) 563.
[10] A. Bashall, M. Mcpartlin, B.P. Murphy, D.E. Fenton, S.J. Kitchen, P.A. Tasker, J. Chem. Soc., Dalton Trans. (1990) 505.
[11] A.K. Cheetham, G. Ferey, T. Loiseau, Angew. Chem., Int. Ed. 38 (1999) 3268.
[12] A.K. Hall, J.M. Harrowfield, A. Morsali, A.A. Soudi, A. Yanovsky, CrystEngComm. 2 (2000) 82.
[13] A.A. Soudi, F. Marandi, A. Ramazani, E. Ahmadi, A. Morsali, C. R. Chimie 8 (2005) 157.
[14] J.M. Harrowfield, N. Lugan, F. Marandi, G.H. Shahverdizadeh, A.A. Soudi, Aust. J. Chem. 59 (2006) 400.
[15] (a) M.R.St.J. Foreman, T. Gelbrich, M.B. Hursthouse, M.J. Plater, Inorg. Chem. Commun. 3 (2000) 234;
(b) M. Du, H. Cai, X.J. Zhao, Inorg. Chim. Acta 358 (2005) 4034.
[16] M. Du, H. Cai, X.-J. Zhao, Inorg. Chim. Acta 359 (2006) 673.
[17] B. Chen, S. Ma, F. Zapata, F.R. Fronczek, E.B. Lobkovsky, H.-C. Zhou, Inorg. Chem. 46 (2007) 1233.
[18] G.M. Sheldrick, SHELXL 97 Programs for Crystal Structure Analysis (Release 97-2), University of Götinggen, Germany, 1997
[19] F. Bonhomme, T.M. Alam, A.J. Celestian, D.R. Tallant, T.J. Boyle, B.R. Cherry, R.G. Tissot, M.A. Rodriguez, J.B. Parise, M. Nyman, Inorg. Chem. 44 (2005) 394.
[20] S. Ayyappan, G. Diaz de Delgado, A.K. Cheetham, G. Férey, C.N.R. Rao, J. Chem. Soc., Dalton Trans. (1999) 2905.
[21] T. Glowiak, H. Kozlowski, L.S. Erre, G. Micera, B. Gulinati, Inorg. Chim. Acta 202 (1992) 43.
[22] L. S-Livny, J.P. Glusker, C.W. Bock, Inorg. Chem. 37 (1998) 1853.
[23] C.W. Watson, S.C. Parker, J. Phys. Chem. B 103 (1999) 1258.
[24] K. Nakamoto, Infrared and Raman Spectra of Inorganic and Coordination Compounds, 4th ed., Wiley, New York, 1986.
[25] H.G. Zhu, Y. Xu, Z. Yu, Q.J. Wu, H.K. Fun, X.Z. You, Polyhedron 18 (1999) 3491.
[26] S.-R. Fan, L.-G. Zhu, Inorg. Chem. 45 (2006) 7935.

Polyhedron 28 (2009) 653–660

Contents lists available at ScienceDirect

Polyhedron

journal homepage: www.elsevier.com/locate/poly

Segregated self-assembly and pillaring action of aliphatic dicarboxylic acids in the super structure of Cu–picolinate complexes

Chaitali Biswas [a,b], Atish Dipankar Jana [c], Michael G.B. Drew [d], Golam Mostafa [c,*], Ashutosh Ghosh [a,*]

[a] Department of Chemistry, University College of Science, University of Calcutta, 92, A.P.C. Road, Kolkata 700 009, India
[b] Sarojini Naidu College for Women, 30, Jessore Road, Kolkata 700 028, India
[c] Department of Physics, Jadavpur University, Kolkata 700 032, India
[d] School of Chemistry, The University of Reading, P.O. Box 224, Whiteknights, Reading RG6 6AD, UK

ARTICLE INFO

Article history:
Received 29 October 2008
Accepted 26 November 2008
Available online 4 February 2009

Keywords:
Copper(II)
Co-crystal
Cu(picolinate)$_2$
Malonic acid
Succinic acid
Hydrogen bonding
Crystal structure

ABSTRACT

Three new supramolecular assemblies of co-crystallized metal complexes and aliphatic dicarboxylic acids, $\{[Cu(pic)_2(H_2O)_2](H_2mal)\}_n$ (**1**), $\{[Cu(pic)_2(H_2O)_2](H_2mal)_2(H_2O)_2\}_n$ (**2**) and $\{[Cu(pic)_2(MeOH)](H_2succ)\}_n$ (**3**) {Hpic = 2-picolinic acid, H_2mal = malonic acid and H_2succ = succinic acid} have been synthesized and characterized by X-ray single-crystal structure determination. The crystal packings of the complexes reveal that supramolecular associations of the monomeric complex units lead to the formation of layers through hydrogen bonding. In all the complexes, the dicarboxylic acid units connect the 2-D layers to act as pillars. The interaction between water molecules and the dicarboxylic acid plays an important role in the overall supramolecular assembly.

© 2008 Elsevier Ltd. All rights reserved.

1. Introduction

Self-assembly of molecular components give rise to composite molecular aggregates with specific structures and activities, and is at the heart of various biological processes which are very sophisticated and complex. The first step in understanding these complicated processes is to unravel the interplay of non-covalent interactions [1–3] (such as hydrogen bonding, π–π, C–H···π, C–H···O, metal–π interactions, etc.) that are responsible for crystal or solid formation.

The dicarboxylic acids [HOOC–$(CH_2)_n$–COOH] represent supramolecular connectors that can generate infinite high-dimensional networks through complementary hydrogen bonds involving a variety of basic building blocks such as amines, dipyridines and pyrazins, and their analogues have been documented recently [4–6]. However, there are only a very few examples where dicarboxylic acid molecules and metal complexes are used as supramolecular building blocks [7,8].

Cu–picolinate complexes are simple systems [9], but the reported self-assembled structures of this system are diverse [10–13], and the controlling factors pertaining to the robust features of the self-assembly can be only explored through a systematic study. In the present study we have adopted the principle of co-crystallization [14–16] by choosing aliphatic dicarboxylic acids in the Cu–picolinate system bearing a complementarity relationship. Co-crystallization is an emerging area of research, despite appearing in the literature for a considerable time under various guises, and has provided a venue for the practical application of crystal engineering. A co-crystal is a crystalline material made up of two or more components [17–20], usually in a stoichiometric ratio, each component being an atom, ionic compound or molecule. Numerous authors have investigated the co-crystallization of carboxylic acid-functionalized molecules with organic derivatives [21–26], but examples utilizing inorganic derivatives are scant [7,8]. Generally, these studies focus on the isolation of organic co-crystals, giving less emphasis to metal-containing co-crystal systems. Here, we are concerned with co-crystals of dicarboxylic acids with the [Cu(picolinate)$_2$(H_2O)$_2$] moiety to understand the role of non-covalent interactions occurring in the solid-state structure.

We are reporting in this paper three co-crystal supramolecular assemblies, $\{[Cu(pic)_2(H_2O)_2](H_2mal)\}_n$, $\{[Cu(pic)_2(H_2O)_2](H_2mal)_2(H_2O)_2\}_n$ and $\{[Cu(pic)_2(MeOH)](H_2succ)\}_n$, of Cu(pic)$_2$ (Hpic = 2-picolinic acid) with malonic acid (H_2mal) or succinic acid (H_2succ = succinic acid). The effect of the short malonic acid and relatively longer and flexible succinic acid in the self-assembled structures is investigated. We also report the effect of the increased concentration of dibasic acids and discuss the effect of the solvent on the self-assembly.

* Corresponding authors.
E-mail addresses: mostafa@phys.jdvu.ac.in (G. Mostafa), ghosh_59@yahoo.com (A. Ghosh).

0277-5387/$ - see front matter © 2008 Elsevier Ltd. All rights reserved.
doi:10.1016/j.poly.2008.11.061

2. Experimental

2.1. Reagents

All chemicals were commercial products of reagent grade and were used without further purification.

2.2. Preparations

2.2.1. Synthesis of $\{[Cu(pic)_2(H_2O)_2](H_2mal)\}_n$ (**1**)

A methanol solution (30 ml) of copper(II) malonate (1.859 g, 5 mmol) was mixed with a methanol solution (10 ml) of 2-picolinic acid (0.615 g, 5 mmol) followed by the addition of a methanol solution (5 ml) of malonic acid (0.520 g, 5 mmol). The resultant mixture was refluxed for ca. 2 h and then allowed to cool to ambient temperature. The resulting solution was filtered to remove a small amount of $Cu(pic)_2$ that separated out immediately, and the filtrate was kept at room temperature. Blue colored single crystals suitable for X-ray analysis were obtained from the filtrate after several days.

Yield: 1.30 g (58%) based on Cu. *Anal.* Calc. for $C_{15}H_{16}CuN_2O_{10}$: C, 40.23; H, 3.60; N, 6.26. Found: C, 40.45; H, 3.47; N, 6.58%. μ_{eff} = 1.75 BM (per copper ion); IR (KBr, cm^{-1}): 3391 for υ(O–H), 2927 for υ(C–H), 1708 for υ(C–O of COOH), 1628 and 1601 for υ(C–O and C–C), 1568 for υ(C–N) and 1400 for υ(C–H). λ_{max} (solid, reflectance): 675 nm.

2.2.2. Synthesis of $\{[Cu(pic)_2(H_2O)_2](H_2mal)_2(H_2O)_2\}_n$ (**2**)

Complex **2** was obtained by following a similar procedure to that of **1**, but 10 mmol of malonic acid were added in place of 5 mmol. Dark blue colored single crystals suitable for X-ray analysis were obtained from the filtrate after two weeks.

Yield: 1.62 g (55%) based on Cu. *Anal.* Calc. for $C_{18}H_{24}CuN_2O_{16}$: C, 36.77; H, 4.11; N, 4.76. Found: C, 36.96; H, 4.23; N, 4.59%. μ_{eff} = 1.77 BM (per copper ion); IR (KBr, cm^{-1}): 3385 for υ(O–H), 2960 for υ(C–H), 1714 for υ(C–O of COOH), 1628 and 1603 for υ(C–O and C–C), 1571 for υ(C–N), 1477 for υ(C–H). λ_{max} (solid, reflectance): 680 nm.

2.2.3. Synthesis of $\{[Cu(pic)_2(MeOH)](H_2succ)\}_n$ (**3**)

This was synthesized by following a similar procedure to that adopted for **1**, but using a methanol solution of succinic acid (5 mmol, 0.590 g) instead of a methanol solution of malonic acid. Overnight, light-blue single crystals of **3**, suitable for X-ray diffraction, were obtained.

Yield: 1.24 g (54%) based on Cu. *Anal.* Calc. for $C_{17}H_{18}CuN_2O_9$: C, 44.59; H, 3.96; N, 6.12. Found: C, 44.45; H, 3.07; N, 6.15%. μ_{eff} = 1.71 BM (per copper ion); IR (KBr, cm^{-1}): 3441 for υ(O–H), 2931 for υ(C–H), 1699 for υ(C–O of COOH), 1642 and 1600 for υ (C–O and C–C), 1475 for υ(C–H). λ_{max} (solid, reflectance): 688 nm.

2.3. Physical measurements

Elemental analyses (carbon, hydrogen and nitrogen) were performed using a Perkin–Elmer 240 C elemental analyzer. IR spectra in KBr (4500–500 cm^{-1}) were recorded using a Perkin–Elmer RXI FT-IR spectrophotometer. Electronic spectra in acetonitrile (1200–350 nm) were recorded in a Hitachi U-3501 spectrophotometer. The magnetic susceptibility measurements were done with an EG&PAR vibrating sample magnetometer, model 155 at room temperature and diamagnetic corrections were made using Pascal's constants. Thermal analyses (TG-DTA) were carried out on a Mettler Toledo TGA/SDTA 851 thermal analyzer in a dynamic atmosphere of dinitrogen (flow rate = 30 cm^3 min^{-1}). The samples were heated in an alumina crucible at a rate of 10 °C min^{-1}.

2.4. X-ray crystallography

Data were measured with Mo Kα radiation at 150 K using an X-Calibur CCD diffractometer from Oxford Instruments. The crystals were positioned at 50 mm from the CCD and 330 frames were measured with a counting time of 10 s. Data analysis was carried out with the Crysalis program [27] to provide 2626, 6071 and 5048 independent reflections, respectively. The structures were solved using direct methods with the SHELX97 program [28]. Non-hydrogen atoms were refined with anisotropic thermal parameters. The hydrogen atoms bonded to carbon were included in geometric positions and given thermal parameters equivalent to 1.2 times those of the atom to which they were attached. All the hydrogen atoms bonded to oxygen were located in difference Fourier maps and refined with distance constraints. The structures were refined on F^2 using SHELX97 [28]. Crystal data for the three crystals are given in Table 1.

3. Results and discussion

3.1. Synthesis of the complexes

To construct the hydrogen-bonded molecular self-assemblies of $Cu(pic)_2$ with aliphatic dicarboxylic acids we dissolved the individual components, copper salts (malonate or succinate), picolinic acid and the corresponding dicarboxylic acid (H_2mal or H_2succ) in methanol in 1:2:1 ratios. The complex compound $Cu(pic)_2$, which is formed immediately by the reaction of the Cu(II) salts and picolinic acid, remains in solution in the acidic pH of the resulting solution and the desired supramolecular H-bonded assemblies **1** and **3** were separated out on slow evaporation of methanol. In order to investigate the possibility to obtain any other assembly, we increased the proportion of the respective dicarboxylic acid in solution and got crystals of compound **2** when the H_2mal:$Cu(pic)_2$ ratio was 2:1 or higher. For H_2succ we did not get any compound other than **3**, even on increasing the H_2succ:-$Cu(pic)_2$ ratio up to 5:1.

3.2. Crystal structures of complexes

X-ray crystallographic analysis reveals that all three structures consist of a copper complex containing two bidentate 2-picolinate ligands in an equatorial plane, together with 1 or 2 solvent molecules weakly bound in axial positions. In addition, in each case a dicarboxylic acid co-crystallises with the complex but is not bonded to the metal, instead it forms a hydrogen-bonded network

Table 1
Summary of crystallographic data for the complexes.

	1	**2**	**3**
Formula	$C_{15}H_{16}CuN_2O_{10}$	$C_{18}H_{24}CuN_2O_{16}$	$C_{17}H_{18}CuN_2O_9$
Formula weight	447.84	587.93	457.87
Crystal system	monoclinic	triclinic	triclinic
Space group	$C2/c$	$P\bar{1}$	$P\bar{1}$
a (Å)	6.1202(9)	7.3145(9)	6.822(6)
b (Å)	12.941(2)	11.0404(14)	10.7410(10)
c (Å)	22.727(4)	15.5565(19)	14.0073(14)
α (°)	90	87.772(10)	69.877(9)
β (°)	90.76(1)	82.276(10)	78.855(8)
γ (°)	90	72.054(11)	72.183(9)
V (Å^3)	1799.9(5)	1184.3(3)	918.43
Z	4	2	2
D_{calc} (g cm^{-3})	1.653	1.649	1.656
μ (mm^{-1})	1.273	1.007	1.245
R [$I > 2\sigma(I)$]	0.0480	0.0643	0.0432
Temperature (K)	150	150	150

Table 2
Selected bond lengths (Å) and angles (°) for the complexes.

	1	2	3
Cu(1)–O(100)	2.497(2)	2.538(2)	2.312(9)
Cu(1)–N(11)	1.987(2)	1.966(3)	1.969(10)
Cu(1)–O(18)	1.944(2)	1.943(2)	1.953(8)
Cu(1)–O(200)	–	2.574(2)	–
Cu(1)–N(21)	–	1.955(3)	1.968(10)
Cu(1)–O(28)	–	1.963(2)	1.948(8)
O(18)–Cu(1)–N(11)	83.6(1)	83.6(1)	83.4(4)
O(18)–Cu(1)–O(100)	91.3(1)	92.1(1)	98.9(4)
O(18)–Cu(1)–O(28)	–	177.3(1)	169.5(4)
O(18)–Cu(1)–N(21)	–	94.2(1)	95.8(4)
O(18)–Cu(1)–O(200)	–	88.7(1)	–
N(11)–Cu(1)–O(100)	90.1(1)	89.0(1)	91.9(4)
N(11)–Cu(1)–O(28)	–	98.9(1)	97.0(4)
N(11)–Cu(1)–N(21)	–	177.7(1)	177.2(4)
N(11)–Cu(1)–O(200)	–	92.2(1)	–
O(100)–Cu(1)–O(28)	–	89.1(1)	91.6(4)
O(100)–Cu(1)–N(21)	–	90.3(1)	90.9(4)
O(100)–Cu(1)–O(200)	–	178.6(1)	–
O(28)–Cu(1)–N(21)	–	83.3(1)	83.3(4)
O(28)–Cu(1)–O(200)	–	90.1(1)	–
N(21)–Cu(1)–O(200)	–	88.5(1)	–

Table 3
Hydrogen bonding interactions (Å, °) for complexes **1**–**3**.

Complex	D–H···A	D–H	H···A	D···A	<D–H···A
1	O100–H1···O19[a]	0.89	1.82	2.702(3)	173(3)
	O100–H2···O19[b]	0.86	1.90	2.709(3)	158(3)
	O91–H91···O100	0.84	1.73	2.567(3)	172(2)
2	O100–H1···O19[c]	0.85	1.93	2.741(3)	160(3)
	O100–H2···O18[d]	0.85	2.49	3.253(3)	151(3)
	O100–H2···O19[d]	0.85	2.01	2.771(3)	150(3)
	O200–H3···O29[e]	0.84	1.92	2.756(3)	176(3)
	O200–H4···O28[f]	0.86	1.93	2.787(3)	176(3)
	O300–H5···O59[d]	0.85	2.05	2.824(5)	153(4)
	O300–H6···O44	0.86	1.91	2.756(4)	168(3)
	O400–H8···O54	0.85	1.91	2.739(4)	165(3)
	O43–H43···O200	0.86	1.73	2.576(4)	165(4)
	O48–H48···O300[g]	0.72	1.89	2.589(4)	162(6)
	O53–H53···O100	0.85	1.75	2.592(4)	172(5)
	O58–H58···O400[h]	0.72	1.91	2.611(4)	166(5)
3	O73–H73···O29	0.83	1.77	2.585(2)	166(3)
	O78–H78···O77[i]	0.84	1.84	2.678(3)	180(6)
	O81–H81···O19[j]	0.82	1.88	2.682(2)	165(3)
	C15–H15···O29[k]	0.93	2.49	3.345(5)	153
	C25–H25···O19[l]	0.93	2.44	3.314(3)	157

Symmetry elements: [a] = 1 + *x*, *y*, *z*; [b] = 1 − x, −*y*, 2 − *z*; [c] = 1 + *x*, *y*, *z*; [d] = 1 − *x*, 2 − *y*, 1 − *z*; [e] = −1 + *x*, *y*, *z*; [f] = 2 − *x*, 1 − *y*, 1 − *z*; [g] = 1 − *x*, 1−*y*, 2 − *z*; [h] = 2 − *x*, 2 − *y*, −*z*; [i] = 1 − *x*, 1 − *y*, −1 − *y*; [j] = 1 − *x*, 1 − *y*, −*z*; [k] = *x*, 1 + *y*, *z*; and [l] = *x*, −1 + *y*, *z*.

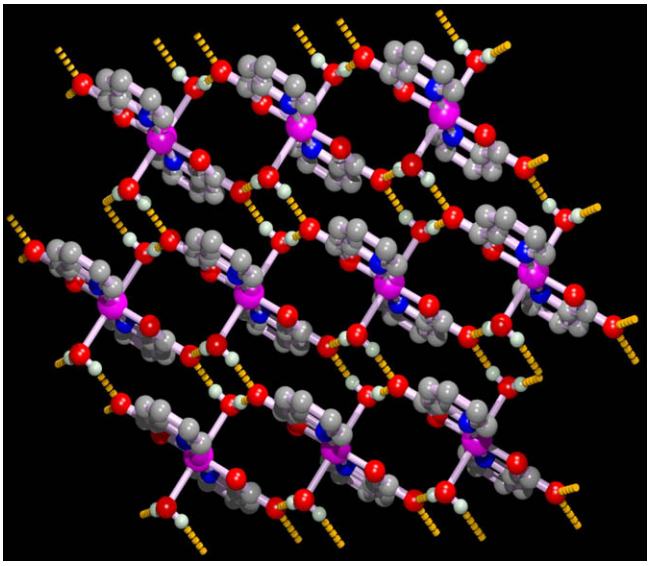


Fig. 2. The supramolecular layer of $[CuL_2(H_2O)_2]$ units through the formation of $R_4^2(8)$ synthons.

with the complex. Dimensions in the metal coordination spheres are given in Table 2, with details of the hydrogen bond networks in Table 3.

3.2.1. Structure of $\{[Cu(pic)_2(H_2O)_2](H_2mal)\}_n$ (**1**)

The ORTEP diagram (Fig. 1) reveals that the asymmetric unit of **1** consists of a half of a Cu atom, a 2-picolinate molecule and half of the malonic acid molecule. The metal complex $[Cu(pic)_2(H_2O)_2]$ is situated on a centre of symmetry. The two bidentate 2-picolinate ligands occupy the equatorial plane, coordinated by the pyridine N atoms (N11) and the carboxylate O atoms (O18) with Cu–N and Cu–O bond lengths as expected, being 1.987(2) and 1.944(2) Å, respectively. There are water molecules (O100) in axial positions at 2.497(2) Å. One of the carboxylate oxygen atoms (O19) remains uncoordinated and acts as hydrogen bond acceptor site for the uncoordinated malonic acid donor molecule, which has a crystallographic twofold axis through the central carbon atom.

The supramolecular association of the monomeric units through hydrogen bonding leads to layers (*ab* plane) of $[Cu(pic)_2(H_2O)_2]$ monomeric units, in which the adjacent monomers are united through coordinated water mediated hydrogen bonding. Water molecules in association with the uncoordinated picolinate carboxylate oxygen atoms (O19) form a $R_4^2(8)$ hydrogen bonding synthon [29–32]. Diagonally opposite corners of this rectangular

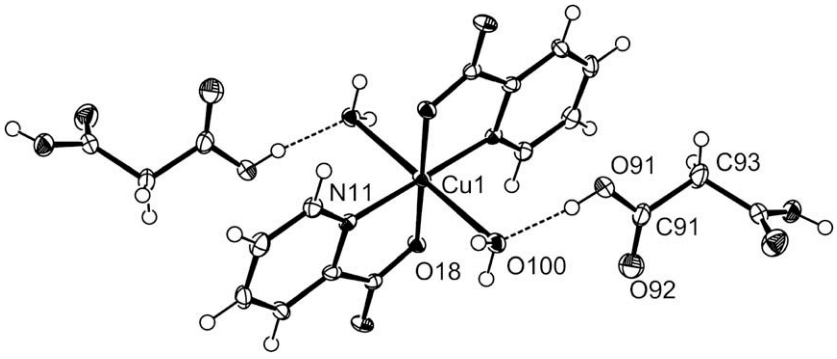


Fig. 1. The structure of **1** with ellipsoids at 50% probability. Hydrogen bonds shown as dotted lines.

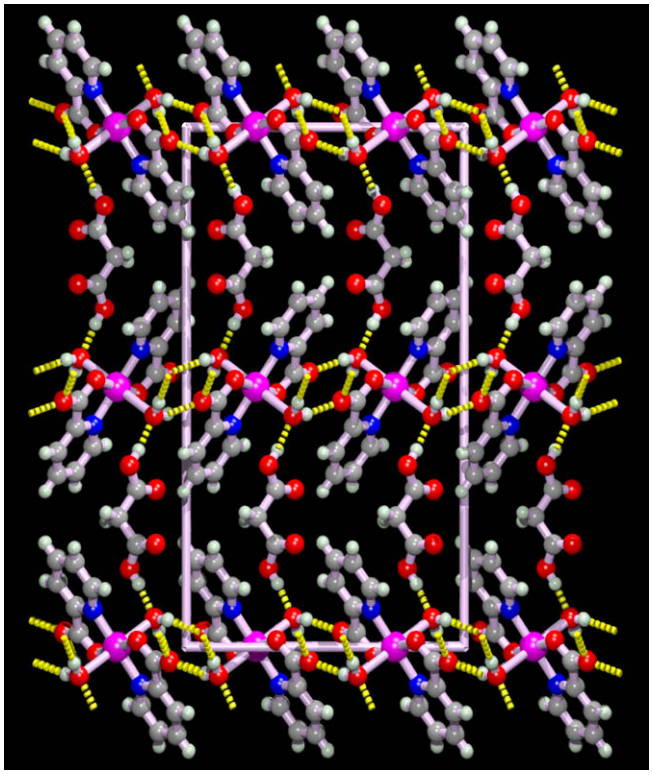


Fig. 3. Pacing of successive $[CuL_2(H_2O)_2]_n$ layers. Malonic acid molecules act as pillars separating the layers.

motif are occupied by water molecules (O100) and picolinate carboxylate O19 atoms, respectively (Table 3), and these form an infinite two-dimensional four-connected sublayer 4^4-net along the [1 1 0] direction (Fig. 2). The copper–copper distances within this 4^4-net are 11.23 and 6.12 Å. In this supramolecular assembly the malonic acid molecule is attached directly to the coordinated water molecule O(1 0 0) of the Cu–picolinate moiety, through an O–H···O H-bond, exhibiting the recognition phenomenon of the dicarboxylic acid by the neutral coordination complex.

Successive $[Cu(pic)_2(H_2O)_2]_n$ layers are stacked (along the *c*-axis) in such a way that malonic acid units connect them in a one to one fashion by acting as hydrogen bond donors to coordinated water molecules on adjacent layers. The malonic acid molecules thus act as pillars between the layers (Fig. 3, Table 3). A characteristic of this structure is that all the available hydrogen bond donors and acceptors are engaged in a fully supramolecular assembly.

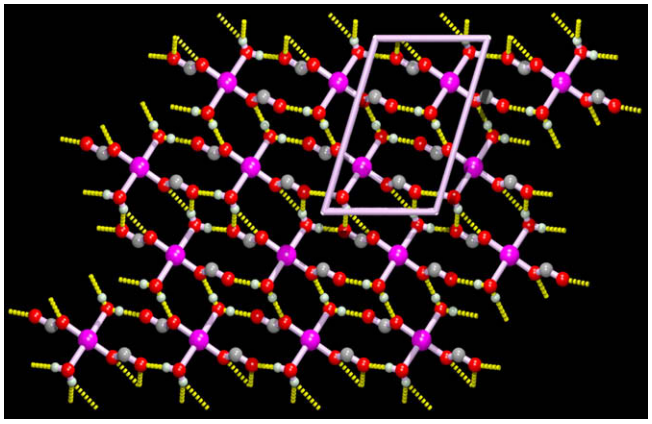


Fig. 5. The supramolecular layer of $[CuL_2(H_2O)_2]$ units in **2** (picolinate pyridine rings have been omitted for clarity).

3.2.2. Structure of $\{[Cu(pic)_2(H_2O)_2](H_2mal)_2(H_2O)_2\}_n$ (**2**)

The crystal structure determinations reveal that complex **2** is a pseudo-polymorph of complex **1**. The ORTEP diagram (Fig. 4) reveals that the asymmetric unit of **2** consists of a Cu atom, two 2-picolinate ligands, two malonic acid molecules and four water molecules (two coordinated and two lattice). Analyses of crystal packing of **2** shows that the $[Cu(pic)_2(H_2O)_2]$ complex is in a general position, although the structure is equivalent to that found in **1**. There are two acid groups per complex, unlike **1** where the ratio is 1 to 1. The bond lengths to the pyridine nitrogen atoms (N11 and N21) are 1.955(3) and 1.966(3) Å, to the acid oxygen atoms (O18 and O28) 1.943(2) and 1.963(2) Å and the bonds to the water molecules (O100 and O200) in the axial positions 2.538(2) and 2.574(2) Å. Two lattice water molecules (O300 and O400) and two malonic acid molecules remain as independent units and take part only in hydrogen bonding.

The supramolecular assembly of the monomeric units of **2** is also in the form of hydrogen-bonded layers of $[Cu(pic)_2(H_2O)_2]$ (Fig. 5). The layers are the (1 1 0) planes. The mode of hydrogen bonding association in this layer is slightly different from that in **1**. While the similar $R_4^2(8)$ hydrogen-bonded rectangular motifs be-

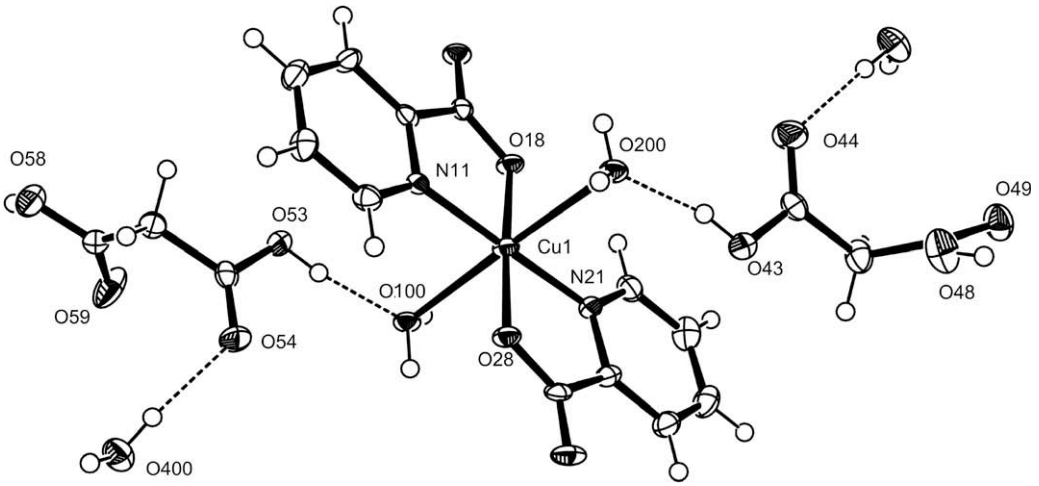


Fig. 4. The structure of **2** with ellipsoids at 50% probability. Hydrogen bonds shown as dotted lines.

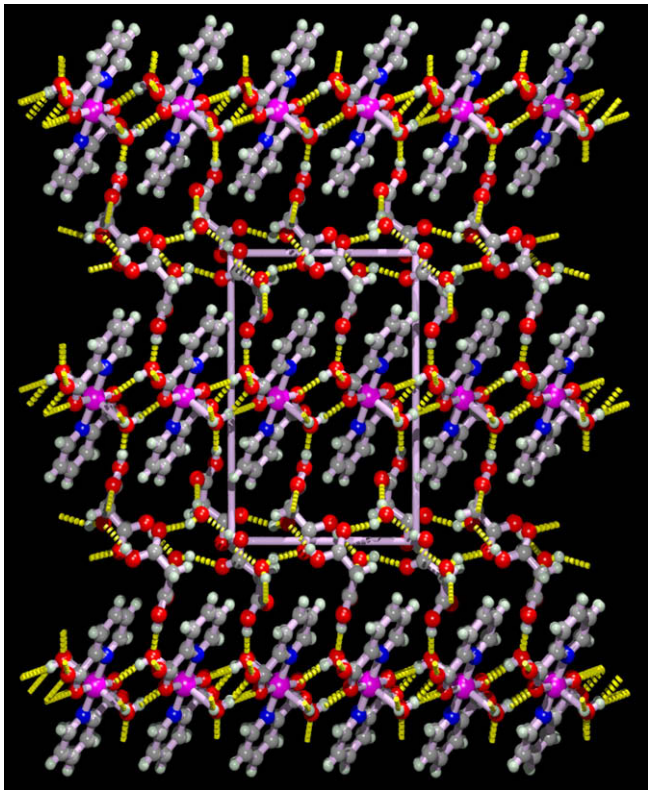


Fig. 6. Packing of successive layers in **2**.

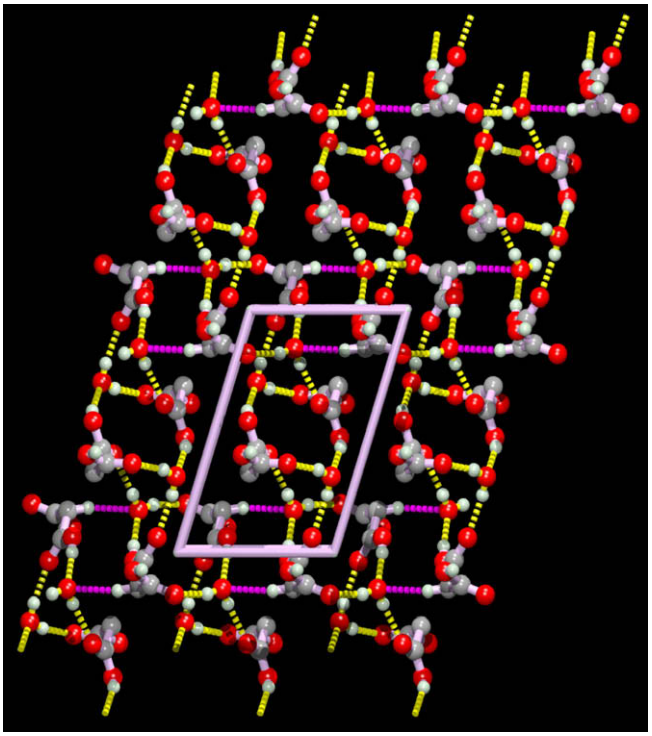


Fig. 7. The malonic acid water hydrogen-bonded supramolecular layer in **2**. Dotted lines represent H–bond.

tween the coordinated O100 water molecules and the uncoordinated carboxylate O19 atoms of picolinate still persists in **2**, due to perturbation another elongated ring motif $R_4^4(12)$ arises which is the result of hydrogen bonding between coordinated water molecules (O200) and both coordinated (O28) and uncoordinated (O29) carboxylate oxygen atoms of the 2-picolinate moiety (Table 3). These two ring motifs co-exist and the $R_4^2(8)$ motif slightly adjusts itself so that in this motif the hydrogen bond is bifurcated and the water oxygen atom (O100) donate its proton (H2) simultaneously to both the coordinated (O18) and uncoordinated carboxylate (O19) atoms of picolinate.

Successive $[Cu(pic)_2(H_2O)_2]_n$ layers are stacked along the *c*-axis (Fig. 6), but unlike **1**, the single malonic acid molecules do not act as pillars in **2**. Two sets of malonic acid molecules and lattice water molecules O300 and O400 self-assemble into hydrogen-bonded (Table 3) centro-symmetric layers (Fig. 7) in **2**, on both sides of which carboxylate terminals of malonic acid molecules protrude out and act as hydrogen bond donors for the coordinated water molecules that are part of the $[Cu(pic)_2(H_2O)_2]_n$ layers on either side. The O300 water molecule forms two donor hydrogen bonds to malonic acid carboxylate O59 atoms at 2.824(5) Å and with O44 atoms at 2.756(4) Å, and also acts as an acceptor of a hydrogen

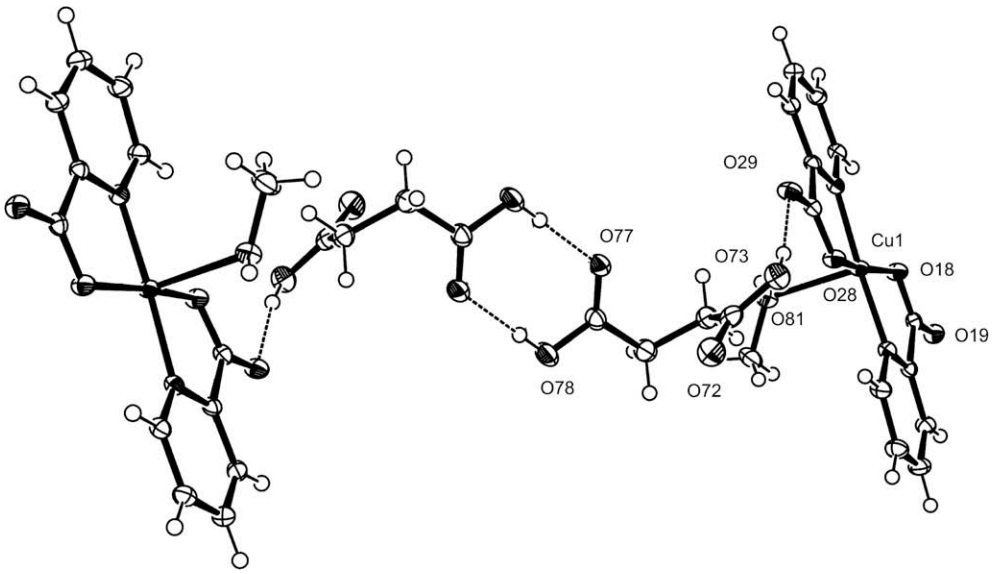


Fig. 8. The structure of **3** with ellipsoids at 50% probability. Hydrogen bonds shown as dotted lines.

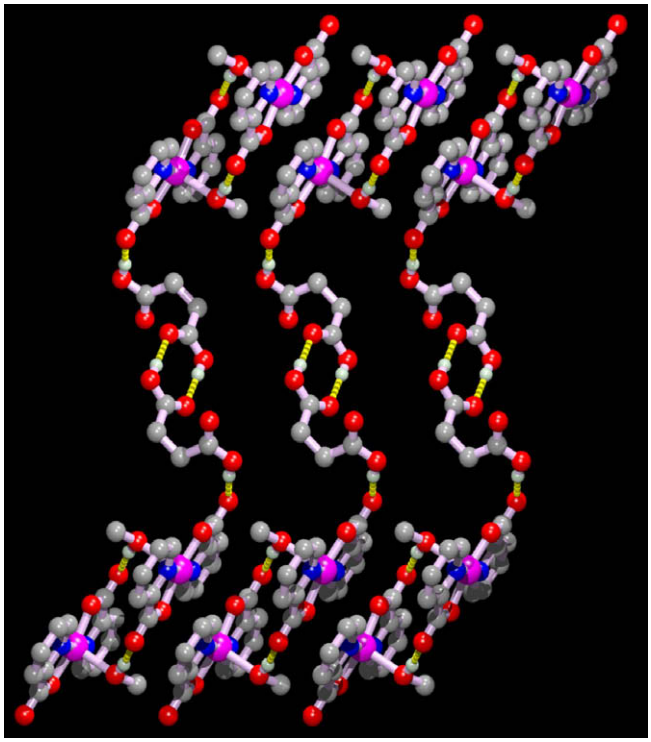


Fig. 9. The mode of binding of dimeric succinic acid pillars in complex **3**.

bond to O48 at 2.589(4) Å. On the other hand, the lattice water O400 molecule forms only one donor hydrogen bond with O54 at 2.739(4) Å and one accepter hydrogen bond with O58 at 2.611(4) Å, (Table 3), which leads to one dimensional hydrogen-bonded ribbons of malonic acid and water molecules along the [0 1 0] direction (Fig. 7). The supramolecular entity of two malonic acid molecules and two lattice water molecules here act as pillars between $[Cu(pic)_2(H_2O)_2]_n$ layers, and this entity is part of the water–malonic acid supramolecular layer.

3.2.3. Structure of $\{[Cu(pic)_2(MeOH)](H_2succ)\}_n$ (**3**)

The ORTEP diagram (Fig. 8) reveals that the asymmetric unit of **3** consists of a Cu atom, two 2-picolinate ligands, one succinic acid molecule and one coordinated methanol molecule. The crystal packing analyses of **3** shows that the copper complex $[Cu(pic)_2(MeOH)]$ is five coordinate with a square pyramidal environment in which the methanol occupies an axial position with a Cu–O(81) distance of 2.312(9) Å. In the equatorial plane, the Cu–O distances are 1.953(8) and 1.948(8) Å, and the Cu–N distances are 1.968(10) and 1.969(10) Å. This complex is unique in that the dicarboxylic acid forms a hydrogen bond to O(29) of the 2-picolinate ligand rather than to the solvent methanol.

Like the previous complexes, the $[Cu(pic)_2(MeOH)]$ units in **3** are also self-assembled into supramolecular layers which are pillared by dimeric units of succinic acid molecules (Fig. 9). The $[Cu(pic)_2(MeOH)]_n$ supramolecular layers have been depicted in Fig. 10. The basic supramolecular unit in this layer is the centrosymmetric dimer of $[Cu(pic)_2(MeOH)]$ monomers, which is the result of hydrogen bonding between coordinated methanol (O81) and the uncoordinated picolinate carboxylate oxygen O19 atoms of complementary monomers (Table 3). These dimeric units are arranged in the form of a 1D supramolecular chain as a result of C–H···O hydrogen bonding, shown in Fig. 10 (Table 3). These 1D chains are aligned side by side due to π···π interactions (Table 4) between the pyridine rings of adjacent chains, resulting in the supramolecular layer which is the (0 0 1) plane. Two succinic acid molecules form an end to end dimeric unit through the formation a $R_2^2(8)$ hydrogen bonding synthon (Table 3) and through the other terminals form hydrogen bond with the picolinate carboxylate O29 oxygen atoms (Fig. 9), and thus act as pillars between the layers.

3.3. Discussion

To facilitate an easy comparison, the structural features have been summarized in Table 5. Pseudo-polymorphs **1** and **2** have identical building blocks, but whereas for **1** $Z = 4$, for **2** $Z = 2$. Complex **1** possesses higher symmetry than **2**. The environmental parameter that is responsible for this is the increased concentration of malonic acid in **2**. The structural features discussed in the previous section reveals that the robust feature of the self-assembly in all three complexes is that the 2-picolinate ligands and the Cu(II) ions form monomeric complexes which are self-organized into distinct layers and the organic acid molecules also organize themselves in a separate region in between the Cu–picolinate layers and act as pillars for these layers. In the self-organization of the metal picolinate layers, in the case of complexes **1** and **2** coordinated water molecules play a very important role to steer successive monomeric units through the formation of a $R_4^2(8)$ hydrogen-

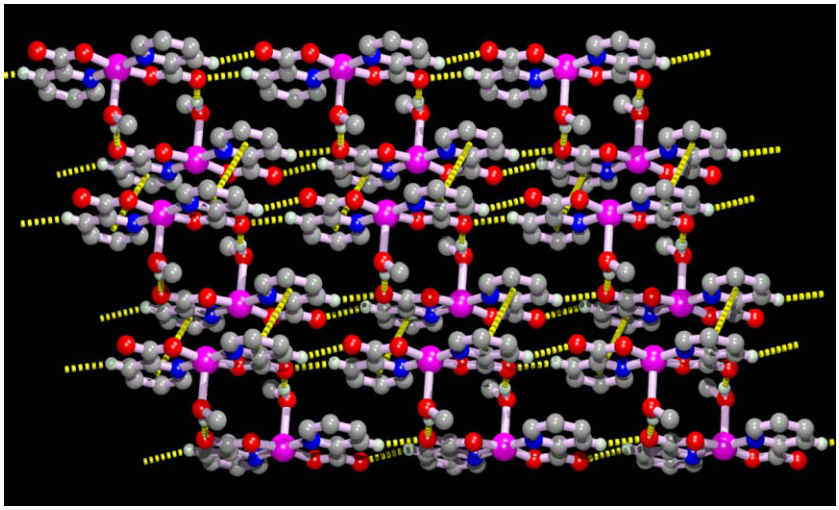


Fig. 10. Formation of $[CuL_2(MeOH)]_n$ supramolecular layers through hydrogen bonding and π–π interactions.

Table 4
Data for the π–π interactions in complex **3**.

Ring(i) → ring(j)	Dihedral angle (i,j) (°)	Slip angle (i,j) (°)	Distance of centroid (i) from ring (j) (Å)	Distance between the (i,j) ringcentroids (Å)
R(3) → R(4)[i]	6.33	31.66	3.389	3.8455
R(4) → R(4)[ii]	0.00	31.09	3.377	3.9440

Symmetry elements: [i] = $-x$, $1-y$, $-z$, [ii] = $1-x$, $-y$, $-z$.

Table 5
Comparison of salient features of complexes **1**–**3**.

	1	**2**	**3**
Coligand	malonic acid	malonic acid	succinic acid
Crystal system	monoclinic	triclinic	triclinic
Space group	$C2/c$	$P\bar{1}$	$P\bar{1}$
Asymmetric unit	Cu(II) at the symmetry position	Cu(II) not at the symmetry position	One Cu(II) center
Coordination environment	octahedral	octahedral	square pyramidal
Axial sites occupied by	water molecules	water molecules	methanol
Supramolecular architecture	pillared layered	pillared layer	pillared bilayer
Supramolecular interaction	H-bonding $R_4^2(8)$ synthon, water tetramer analogue and only O–H···O	H-bonding $R_4^4(8)$ and $R_2^2(12)$ synthon, water tetramer analogue and both O–H···O and C–H···O	H-bonding $R_2^2(8)$ synthon and π–π

bonded synthon [29,31,32] with the uncoordinated carboxylate oxygen atom of picolinate. In **2** the organization has accommodated an additional synthon $R_4^4(12)$ and as a result the original synthon is distorted. This indicates the labile but robust nature of the $R_4^2(8)$ synthon, and it should be noted that this kind of organization has been observed in many other cases. This motif can be assumed to be the analogous motif of the planar water tetramer in which two water molecules have been replaced by picolinate oxygen atoms. In complex **2**, in between the Cu–picolinate layers malonic acid water supramolecular layers position themselves, but the basic pillaring action of malonic acid remains unchanged. In complex **3** though, instead of water, a methanol molecule is coordinated to Cu which has a square pyramidal coordination environment, yet the same Cu–picolinate layer structure is achieved through the formation of supramolecular dimeric complexes that organize themselves through hydrogen bonding and π···π interactions. The succinic acid molecules in this case act as pillars between the layers; in this process it forms a dimeric unit.

3.4. Thermal studies

To examine the thermal stabilities of the co-crystalline complexes, thermal gravimetric (TG) analyses were carried out in air on powdered samples of **1**–**3**. In **1**, the first endothermic weight loss of 7.92%, corresponding to the departure of two water molecules (Calc. 8.04%), was observed between 50 and 100 °C, the second endothermic weight loss of 22.92% was observed between 120 and 200 °C due to the removal of one malonic acid molecule (Calc. 22.99%). On further heating the $Cu(pic)_2$ complex start to decompose endothermally at 240 °C. Similarly the TG curve of **2** exhibits three endothermic weight loss in the temperature ranges 50–100 °C, 130–190 °C and 290–340 °C, corresponding to the release of four water molecules (Found 12.3%, Calc. 12.25%), two malonic acid molecules (Found 34.5%, Calc. 35.03%) and decomposition of $Cu(pic)_2$, respectively. Complex **3** also shows weight loss stages in the temperature ranges 80–120 °C, 130–190 °C and 270–360 °C corresponding to the release of one methanol molecule (Found 6.83%, Calc. 6.99%), one succinic acid molecule (Found 27.5%, Calc. 25.55%) and decomposition of $Cu(pic)_2$, respectively.

4. Conclusions

The viability of a crystal engineering approach to the identification of stable co-crystals has been demonstrated through the rational synthesis of metal-containing co-crystals of picolinate with malonic and succinic acids. In all three cases the organic acid was found to interact through hydrogen bonds act as a pillar to the $R_4^2(8)$ synthon assisted Cu–picoinate layer. Research with other neutral carboxylic acids is in progress to explore the metal-containing co-crystals.

Acknowledgments

This work was supported by the University Grants Commission (UGC), India (Fellowship for C. Biswas, Sanction No. UGC/29/Jr. Fellow (Sc). 2005/2006). We thank EPSRC and the University of Reading for funds for the X-Calibur system. G.M. thanks the UGC for JU research grant under the UGC Scheme of University with potential for excellence.

Appendix A. Supplementary data

CCDC 695481, 695482 and 695483 contain the supplementary crystallographic data for **1**, **2** and **3**, respectively. These data can be obtained free of charge via http://www.ccdc.cam.ac.uk/conts/retrieving.html, or from the Cambridge Crystallographic Data Centre, 12 Union Road, Cambridge CB2 1EZ, UK; fax: (+44) 1223-336-033; or e-mail: deposit@ccdc.cam.ac.uk. Supplementary data associated with this article can be found, in the online version, at doi:10.1016/j.poly.2008.11.061.

References

[1] G.R. Desiraju, Nature 412 (2001) 397.
[2] G.R. Desiraju, Acc. Chem. Res. 35 (2002) 565.
[3] E.A. Meyer, R.K. Castellano, F. Diederich, Angew. Chem., Int. Ed. 42 (2003) 1210.
[4] B.R. Bhogala, S. Basavoju, A. Nangia, CrystEngCommun. 7 (2005) 551.
[5] W.-H. Wang, P.-H. Xi, X.-Y. Su, J.-B. Lan, Z.-H. Mao, J.-S. You, R.-G. Xie, Crystallogr. Growth Des. 7 (2007) 741.
[6] J.F. Remenar, S.L. Morissette, M.L. Peterson, B. Moulton, J.M. MacPhee, H.R. Guzman, O. Almarsson, J. Am. Chem. Soc. 125 (2003) 8456.
[7] D.M. Shin, Y.K. Chung, I.S. Lee, Crystallogr. Growth Des. 2 (2002) 493.
[8] R. Horikoshi, C. Nambu, T. Mochida, New J. Chem. 28 (2004) 26.
[9] C.-X. Zhang, Y.-Y. Zhang, J. Sheng, J. Coord. Chem. 58 (2005) 189.
[10] C. Biswas, P. Mukherjee, M.G.B. Drew, C.J. Gomez-Garcia, J.M.C. Juan, A. Ghosh, Inorg. Chem. 46 (2007) 10771.
[11] B. Zurowska, J. Ochocki, J. Mrozinski, Z. Ciunik, J. Reedijk, Inorg. Chim. Acta 357 (2004) 755.
[12] M. Mikuriya, H. Azuma, R. Nukada, Y. Sayama, K. Tanaka, J.-W. Lim, M. Handa, Bull. Chem. Soc. Jpn. 73 (2000) 2493.
[13] J.H. Luo, M.C. Hong, Q. Shi, Y.C. Liang, Y.J. Zhao, R.H. Wang, R. Cao, J.B. Weng, Transition Met. Chem. 27 (2002) 311.
[14] M.J. Zaworotko, Crystallogr. Growth Des. 7 (2007) 4.
[15] A.N. Sokolov, T. Frii, L.R. MacGillivray, J. Am. Chem. Soc. 128 (2006) 2806.
[16] G.R. Desiraju, CrystEngCommun. 5 (2003) 466.
[17] C.B. Aakeröy, N. Schultheiss, J. Desper, C. Moore, New J. Chem. 30 (2006) 1452.
[18] C.B. Aakeröy, J. Desper, M.E. Fasulo, CrystEngCommun. 8 (2006) 586.
[19] C.B. Aakeröy, A.M. Beatty, B.A. Helfrich, J. Am. Chem. Soc. 124 (2002) 14425.
[20] C.B. Aakeröy, A.M. Beatty, B.A. Helfrich, Angew. Chem., Int. Ed. 113 (2001) 3340.
[21] P. Vishweshwar, J.A. McMahon, J.A. Bis, M.J. Zaworotko, J. Pharm. Sci. 95 (2006) 499.
[22] W. Jones, W.D.S. Motherwell, A.V. Trask, MRS Bull. 31 (2006) 875.
[23] A.V. Trask, W.D.S. Motherwell, W. Jones, Crystallogr. Growth Des. 5 (2005) 1013.
[24] Ö. Almarsson, M.J. Zaworotko, Chem. Commun. (2004) 1889.
[25] T. Frii, L.R. MacGillivray, Chem. Commun. (2005) 5748.
[26] X. Gao, T. Frii, L.R. MacGillivray, Angew. Chem., Int. Ed. 115 (2003) 234.
[27] Crystalis Program, Version 1, Oxford Instruments, 2005.

[28] G.M. Sheldrick, SHELXL97, Program for Crystal Structure Refinement, University of Gottingen, 1997.
[29] M.C. Etter, Acc. Chem. Res. 23 (1990) 120.
[30] M.C. Etter, J. Phys. Chem. 95 (1991) 4601.
[31] J. Bernstein, R.E. Davis, L. Shimoni, N.-L. Chang, Angew. Chem., Int. Ed. Engl. 34 (1995) 1555.
[32] M.C. Etter, J.C. MacDonald, J. Acta Crystallogr., Sect. B B46 (1990) 256.

Polyhedron 28 (2009) 661–664

Contents lists available at ScienceDirect

Polyhedron

journal homepage: www.elsevier.com/locate/poly

Synthesis and physical properties of ruthenium bipyridine complexes with TCNQ and TCNE ligands

Maria do Socorro de P. Silva, Izaura C.N. Diógenes, Luis Gonzaga de F. Lopes, Ícaro de Sousa Moreira [1], Idalina M.M. de Carvalho *

Departamento de Química Orgânica e Inorgânica, Universidade Federal do Ceará, Cx. Postal 12200, Campus do Pici s/n, 60455-760 Fortaleza-CE, Brazil

ARTICLE INFO

Article history:
Received 29 August 2008
Accepted 5 December 2008
Available online 8 January 2009

Keywords:
TCNQ
TCNE
Ruthenium complexes
Electron transfer

ABSTRACT

[Ru(bpy)($dcbH_2$)(TCNQ)Cl] · (Ru–TCNQ) and [Ru(bpy)($dcbH_2$)(TCNE)Cl] · (Ru–TCNE) complexes, where bpy = 2,2'-bipyridine, $dcbH_2$ = 4,4'-dicarboxy-2,2'-bipyridine, TCNQ = 7,7,8,8-tetracyano-*p*-quinodimethane, and TCNE = tetracyanoethylene, were synthesized and characterized by spectroscopic and electrochemical techniques. Comparatively to the TCNX ligands (TCNQ and TCNE) free of coordination, the infrared vibrational spectra of the complexes indicate that the coordination to the ruthenium atom occurs through only one nitrile group. Also, the downshift of these bands is indicative of the TCNX reduced form ($TCNX^{\cdot-}$). This conclusion is reinforced by EPR spectra with $g = 2.005$ and 2.010 for the Ru–TCNQ and Ru–TCNE complexes, respectively. In addition, the structured absorption spectra observed for both complexes indicate that the TCNX moieties are coordinated as anion radicals, ($TCNX^{\cdot-}$). Preliminaries luminescence studies indicate that the Ru–TCNX complexes present emission properties with reasonable lifetimes. The degree of charge transfer for the Ru–TCNQ and Ru–TCNE compounds was evaluated as 0.66 and 0.78, respectively. The $Ru^{III/II}$ redox potentials (E_{ox}) for the Ru–TCNQ and Ru–TCNE complexes are observed, respectively, at 0.70 V and 1.30 V versus NHE. The data, all together, suggest that the TCNE species presents a higher charge uptake capability than TCNQ ligand.

© 2008 Elsevier Ltd. All rights reserved.

1. Introduction

Photophysical and photochemical properties of ruthenium polypyridyl complexes have been extensively studied for many years mainly due to their potential applications in energy conversion processes [1–6]. An extensive literature [7] coverage of spectroscopic properties and performance in solar cells has been limited for a series of ruthenium(II) complexes of bis(dicarboxylic acid bipyridine), *cis*-[Ru($dcbH_2$]LL′], in which $dcbH_2$ is 4,4'-$(CO_2H)_2$-2,2'-bipyridine and L and/or L' are ancillary ligands, and for ruthenium complexes with polypyridine ligands having non-carboxylic acid anchoring groups. The field of donor–acceptor compounds involving metallic fragments and organic acceptor molecules challenges synthetic work to design interesting supramolecular systems [8] which, depending on the electronic properties and relative arrangement, present different physical properties. Conjugated TCNX polynitrile ligands such as tetracyanoethylene (TCNE) and 7,7,8,8-tetracyano-*p*-quinodimethane (TCNQ) are very unusual because of their variable coordination behaviour, proven ability to bridge up to four metal centers, tendency to form aggregates via π–π interaction, and "non-innocence", i.e. their very facile reduction to anion radicals and further to dianionic forms [9–13]. The design of dπ–pπ molecular systems with efficient electronic communication is a long-standing goal in the field of inorganic chemistry. The first organic magnet [14] was $[Fe(C_5Me_5)_2]^{\cdot+}[TCNQ^{\cdot-}]$. Several related compounds were studied to identify a structure–function relationship that could be used to aid in preparing new magnets [15]. Recently, studies have been developed on Ru_2–CNX type complexes in order to prepare new magnets with higher critical temperatures [16–18]. Indeed, several papers have been reported on the dependence of the electronic characteristics of Ru–TCNX compounds and on the nature of the metallic fragment [11–13].

The aim of this work is to investigate physical properties such as charge uptake, absorption, emission, and oxidation state of the TCNX ligands in the [Ru(bpy)($dcbH_2$)(TCNQ)Cl] and [Ru(bpy)($dcbH_2$)(TCNE)Cl] complexes, hereafter named Ru–TCNQ and Ru–TCNE, respectively, where bpy = 2,2'-bipyridine and $dcbH_2$ = 4,4'-dicarboxy-2,2'-bipyridine. The planar representations of the complexes are illustrated in Fig. 1.

* Corresponding author.
E-mail address: idalina@dqoi.ufc.br (I.M.M. de Carvalho).
[1] In memoriam.

0277-5387/$ - see front matter © 2008 Elsevier Ltd. All rights reserved.
doi:10.1016/j.poly.2008.12.008

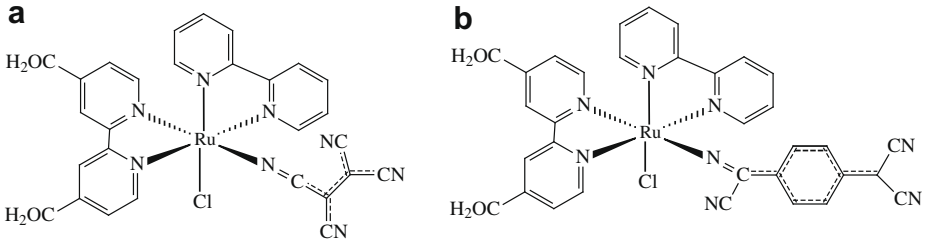


Fig. 1. Planar representation of the Ru–TCNE (a) and Ru–TCNQ (b) complexes.

2. Experimental

2.1. Materials and methods

Equipments: UV–Vis absorption spectra were measured with a Hewlett-Packard 8453 diode array spectrophotometer. IR spectra were recorded on an ABB Bomem FTLA 2000-102 FTIR instrument. EPR spectra were recorded in the X band on a Bruker System ESP 300. Electrochemical experiments were performed on a BAS 100 W electrochemical analyzer (Bioanalytical Systems – BAS, West Lafayette, IN) at 25 ± 0.2 °C. A three-electrode glass cell was used with used as working and auxiliary electrodes in the characterization of the complexes. An Ag/AgCl electrode, for which the ferrocene/ferrocenium ($Fc^{+/0}$) redox process was observed at 0.51 V in *N*,*N*-dimethilformamide (DMF) containing 0.1 mol L^{-1} tetrabutylammonium perchlorate (TBAP) was prepared 1 h prior to the beginning of the experiments and used as reference electrode.

Materials: $RuCl_3$ (Aldrich), dimethylformamide (DMF, Merck), acetone, methanol were all used as received. Tetracyanoquinodimethane (TCNQ) and tetracyanoethylene (TCNE) were purchased from Aldrich and used upon recrystallization. All manipulations had to be carried out in rigorously dried solvents under an argon atmosphere.

2.2. Synthesis

2.2.1. cis-[Ru(bpy)(dcbpy)Cl_2]

This compound was prepared by following the method described by Meyer and co-workers [19].

2.2.2. cis-[Ru(bpy)(dcbpy) · (TCNQ)Cl]

A solution of *cis*-[Ru(bpy)(dcbpy)Cl_2] (50 mg, 0.086 mmol) in water (5 mL) was added slowly to TCNQ (21 mg, 0.103 mmol) dissolved in acetone (5 mL). After stirring for 24 h, a brown precipitate was collected and dried under vacuum. Yield: 80%. *Anal.* Calc. for $C_{33}H_{20}N_8O_4ClRu$ (728.57): C, 55.13; H, 2.70; N, 15.13. Found: C, 55.08; H, 2.80, N, 15.90%. UV–Vis (DMF) λ_{max} in nm (ε in mol L^{-1} cm^{-1}): 295 (2.6×10^4), 315 (1.8×10^4), 403 (2.5×10^4), 489 (3.2×10^3), 750 (3.3×10^3), 850 (5.0×10^3).

2.2.3. cis-[Ru(bpy) · (dcbpy)(TCNE)Cl] · H_2O

A solution of *cis*-[Ru(bpy)(dcbpy)Cl_2] · (50 mg, 0.086 mmol) and TCNE (13.2 mg, 0.103 mmol) in water/methanol solution (10 mL) was kept under stirring and reflux for 8 h. The brown precipitate was collected and dried under vacuum. Yield: 85%. *Anal.* Calc. for $C_{27}H_{18}N_8O_5ClRu$ (670.57): C, 49.22; H, 2.63; N, 16.40. Found: C, 49.15; H, 2.72, N, 16.00%. UV–Vis (DMF) λ_{max} in nm (ε in mol L^{-1} cm^{-1}): 295 (2.4×10^4), 398 (1.1×10^4), 420 (1.2×10^4), 461 (1.0×10^4).

3. Results and discussion

TCNQ and TCNE ligands react with one molar equivalent of Ru(bpy)(dcbpy)Cl_2 to yield Ru–TCNX complexes. The electronic spectra in the ultraviolet and visible regions (UV–Vis) of the Ru–TCNE and Ru–TCNQ complexes (Fig. 2) present, besides the intraligand transitions of the bpy and $dcbH_2$ ligands [20], lower energy absorptions which, based on the solvent dependence, are assigned as charge transfer (CT) transitions. The maximum of these transitions are observed at 489 and 461 nm in DMF medium for the Ru–TCNQ and Ru–TCNE complexes, respectively. The electronic spectrum of the Ru-TCNQ complex in DMF exhibits the typical long-wavelength absorptions of the TCNQ radical anion ($TCNQ^{\cdot-}$) at 850, 750 and 403 nm. Absorptions at 295 and 489 nm are also observed and assigned to the bpy ($\pi^* \leftarrow \pi$) and charge transfer transition, $\pi^*(bpy) \leftarrow d\pi(Ru^{II})$, respectively. For the Ru–TCNE complex, the bands assigned to the TCNE ligand are observed at 398 and 420 nm. The very distinct, partially structured absorption spectra observed for both complexes indicate that the TCNX moieties are coordinated as anion radicals, $TCNQ^{\cdot-}$.

The luminescence spectra, with excitation at 500 nm in DMF, exhibited emission with maximum of intensity at 605 and 570 nm for the Ru–TCNE and Ru–TCNQ complexes, respectively. The luminescence decay of the complexes with excitation at 500 nm follows a biexponential behaviour. For the Ru–TCNQ complex, the lifetimes are 11 and 503 ns whereas for the Ru–TCNE complex are 15 and 563 ns. The short lifetime is related to the singlet–singlet energy transfer of the TCNX ligands while the long lifetime component is suggested to be due to an energy transfer between the close lying triplet states of the TCNX moieties and the ruthenium metal center.

The infrared (IR) vibrational spectra of the Ru–TCNE and Ru–TCNQ complexes, illustrated in Fig. 3, are dominated by the vibrational modes of the bipyridine ligands.

The bands assigned to the OH and C=O bonds of the $dcbH_2$ ligand [21] are observed at *c.a.* 3120 and 1721 cm^{-1}, respectively.

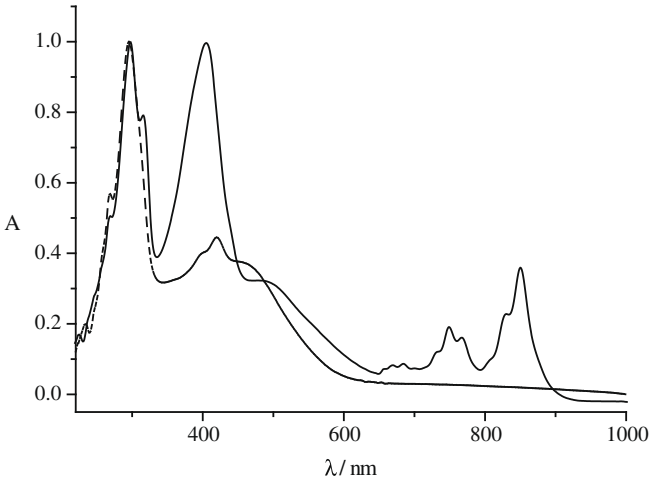


Fig. 2. Electronic spectra of the complexes: (a) Ru–TCNQ and (b) Ru–TCNE, in DMF (10^{-5} M) at 293 K.

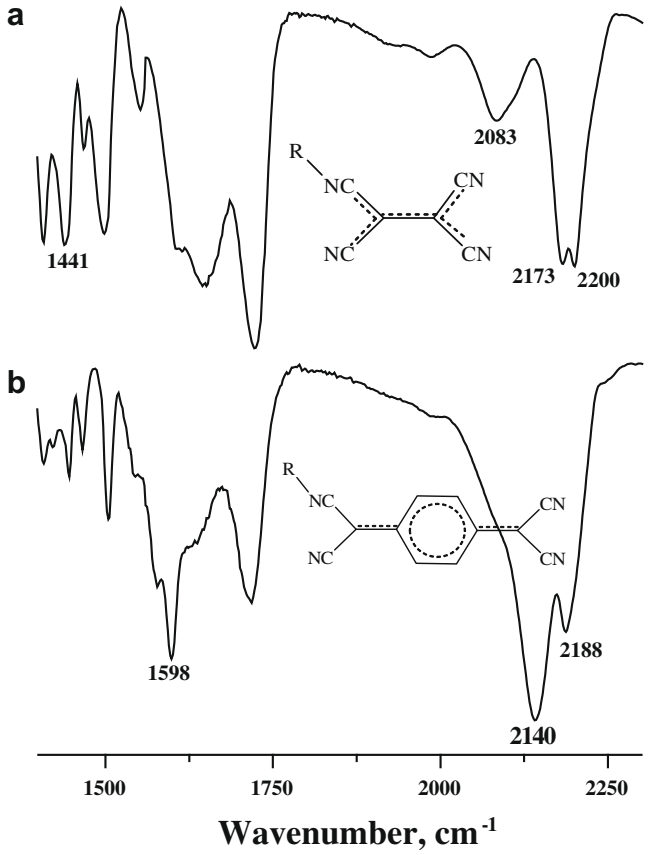


Fig. 3. Infrared spectra of (a) Ru–TCNE and (b) Ru–TCNQ complexes dispersed in KBr.

Concerning the TCNX ligands, as expected for single nitrile-N coordinated ($TCNQ^{n-}$ ligands [9,22–24], multiple bands are observed in the cyanide vibrational region (from 2050 to 2300 cm^{-1}). For the Ru–TCNQ complex these bands are observed at 2188 and 2140 cm^{-1}. For the Ru–TCNE complex, three bands relative to the nitrile group are observed at 2200, 2173 and 2083 cm^{-1}. Compared to the free non-reduced ligands (2224 cm^{-1} for TCNQ [25] and 2262 cm^{-1}, and 2230 cm^{-1} for TCNE [26] ligands), the absorption of the νCN modes of the complexes are more intense and shifted to lower frequency values. This result is assigned to an electronic density enhancement on the TCNX ligands which populates antibonding orbitals of the nitrile moiety thus decreasing the CN bond order and, as consequence, the frequency value of the respective vibrational mode. Also, the bands observed at 1441 and 1598 cm^{-1}, assigned to the C=C stretching mode, νCC, of the TCNE [27,28] and TCNQ [22,23] ligands, respectively, reinforce the assignment of the reduced form for the TCNX ligands. In fact, whereas isolated $([TCNQ]^{\cdot-}$ exhibits two νCN absorptions at 2183 and 2144 cm^{-1} and a νCC peak at 1421 cm^{-1}, deviations from these values suggest that $([TCNQ]^{\cdot-}$ is bonded to a metal ion [29]. In addition, according to Miller [29], the lower symmetry $([TCNQ]^{\cdot-}$ motif frequently exhibits more than two bands as it is the case for the Ru–TCNE complex. These observations indicate the reduced form for the TCNE moiety, indeed.

By accounting for the fact that the absorption of radiation by CT complexes involves electron transfer between appropriate energy levels of donor and acceptor species, the CT degree can be estimated based on energy displacements, $\Delta\nu$, of certain vibrational modes observed in a vibrational spectra [30]. If the observed shifts are small, then the relation between $\Delta\nu$ and the degree of CT, Z, is described in a first approximation [31,32] by Eq. (1)

$$Z = 2\left(\frac{\Delta\upsilon}{\upsilon_0}\right)\cdot\left[1-\left(\frac{\upsilon_1^2}{\upsilon_0^2}\right)\right]^{-1} \quad (1)$$

where υ_0 e υ_1 are the frequency values of the investigated bands in the spectra of the "free" component and its radical ion, respectively. Table 1 shows Z values for the Ru–TCNE and Ru–TCNQ complexes by considering the displacements of the νCN b_{2u} active mode of the related TCNX ligand in the oxidized form, $TCNX^0$, upon coordination to the ruthenium metal center.

The calculated values show a characteristic distribution over the range of Z between zero and one. It is well known that CT-complexes with values in the range of $0.35 < Z < 0.75$ are electronic conductors with even metallic conductivity [33].

The Ru–TCNE and Ru–TCNQ complexes were also electrochemically characterized by means of cyclic voltammetry in non-aqueous medium. Table 2 displays electrochemical data obtained for the for TCNX free and coordinated ligands (E_{red}) as well as for the ruthenium metal atom (E_{ox}).

For the Ru–TCNQ complex, the half-wave potentials observed at 0.51 and 0.1 V vs NHE are assigned to the $(TCNQ^{\cdot-}/TCNQ^0$ and $(TCNQ^{2-}/TCNQ^{-}$ redox processes, respectively. A third process at 0.70 V is observed and assigned to the $Ru^{III/II}$ process, thus indicating a stabilization of the ruthenium metal atom in the reduced state, Ru^{II}, since this process is observed at 0.61 V in the starting complex. For the Ru-TCNE complex, the $(TCNE^{\cdot-}/TCNE^0$ and $(TCNE^{2-}/(TCNE^{\cdot-}$ redox processes are observed 0.78 and 0.10 V while that of the ruthenium metal atom is observed at 1.30 V.

For both complexes, the decrease in the potential difference between the two redox processes of the TCNX ligands, comparatively to the free ligand, is indicative of the coordination [11]. Also, this potential difference ($\Delta E = E_{red1} - E_{red2}$) changes indicates the charge uptake by the coordinated TCNX ligands in the complexes [34]. The comproportionation constants (K_c) calculated based on Eq. (2) and displayed in Table 2 reinforce this conclusion

$$RT.\ln K_c = nF.\Delta E,$$
$$K_{=}10^{\Delta E/0.059V}\ (T = 298\ K) \quad (2)$$

The difference between the K_c values calculated for the TCNX ligands before and after coordination (ΔK_c) indicates the overlapping level between the ligand π^* and Rudπ orbitals. Accounting for the fact that the value calculated for the TCNE ligand ($\Delta K_c = 10^{16.6} - 10^{11.5} = 10^{5.1}$) is higher than that calculated for the TCNQ ligand

Table 1
νCN and $\nu_1 - \nu_0$ frequency values (cm^{-1}), and Z values for $TCNX^-$ and Ru–TCNX species.

Compound	ν_1[a] (cm^{-1})	$\nu_1 - \nu_0$[b] (cm^{-1})	Z
$(TCNQ^{\cdot-}$	2183	41	1
Ru–TCNQ	2197	27	0.66
$(TCNQ^{\cdot-}$	2183	79	1
Ru–TCNE	2200	62	0.78

[a] ν_1 = values of νCN b_{2u} mode of the $TCNX^-$ ligands.
[b] ν_0 = 2224 and 2262 cm^{-1} for $TCNQ^0$ and $TCNE^0$ species, respectively.

Table 2
Electrochemical data (in V vs. NHE) of the ligands and complexes in 0.1 mol L^{-1} TBAP solution at 100 mV s^{-1}.

Compound	Solvent	E_{ox}	E_{red1}	E_{red2}	K_c^*
TCNQ	DMF	–	0.65	0.05	$10^{10.1}$
Ru–TCNQ	DMF	0.70	0.51	0.10	$10^{6.9}$
TCNE	CH_3CN	–	0.50	−0.48	$10^{16.6}$
Ru–TCNE	DMF	1.30	0.78	0.10	$10^{11.5}$

$Fc^{+/0}$: 0.23 V in DMF; 0.37 V in CH_3CN.
* Comproportionation constant for monoanion from Eq. (2).

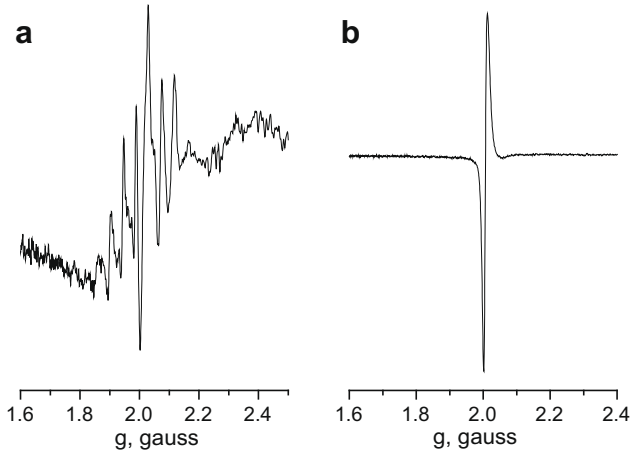


Fig. 4. EPR spectra of the solid (a) Ru–TCNE and (b) Ru–TCNQ complexes at 77 K.

($\Delta K_c = 10^{10.1}-10^{6.9} = 10^{3.2}$) there is a stronger mixing of TCNE ligand π^* and Rudπ orbitals.

In order to confirm the oxidation states of the Ru–TCNX complexes, EPR measurements of the species were carried out. The X-band EPR spectra were acquired at 77 K and are shown in Fig. 4. The Ru–TCNQ complex showed one single signal at $g = 2.005$ while, for the Ru–TCNE complex, hyperfine lines centered at $g = 2.010$ are observed. Based on the literature [12,35,36], the observation of these lines are assigned to the interaction of an unpaired electron and a magnetic nucleus. The occurrence of these g tensors values is consistent with the assignment of the anion radical form for the TCNX ligands upon coordination. This conclusion is reinforced by the partially structured absorption spectra observed for both complexes.

The spectra are showing that the electrons are centered on the ligands and that the interactions of the metal with the TCNE species are stronger than with the TCNQ ligand. The electrochemical experiments reinforce this conclusion since the half-wave potential for the $Ru^{III/II}$ redox couple is observed at 1.30 and 0.70 V for the Ru–TCNE and Ru–TCNQ complexes, respectively. The different EPR spectral profiles observed for both the complexes are explained based on the assumption that, for the Ru–TCNE complex, the unpaired electron is probably closer to the ruthenium which, as consequence, results in the observation of the hyperfine lines.

4. Conclusions

The results presented in this work show that the TCNQ and TCNE ligands are coordinated to the ruthenium metal center through only one nitrile group. The UV–Vis and EPR spectra acquired for the Ru–TCNX complexes strongly suggest the anion radical form, $(TCNQ^{\cdot-}$, for the TCNX ligands upon coordination. Preliminaries luminescence studies indicate that the Ru–TCNX complexes present emission properties with reasonable lifetimes. Photophysical measurements are currently under investigation in order to establish the decay mechanism. The electrochemical and vibrational data indicate that the charge transfer process of the TCNX ligands is enhanced upon coordination. Therefore, these η^1-coordinated $(TCNQ^{\cdot-}$ containing complexes may be suitable as components with special magnetic, optical, or conductive properties.

Acknowledgment

The authors acknowledge CNPq, FUNCAP and CAPES, the Brazilian financial agencies.

References

[1] T.J. Meyer, Pure Appl. Chem. 50 (1986) 1293.
[2] D.M. Roundhill, Photochemistry and Photophysics of Metal Complexes, Plenum, New York, 1994.
[3] M. Grätzel, Platinum Met. Rev. 38 (1994) 151.
[4] K. Kalyanasundaram, M. Grätzel, Photosensitization and Photocatalysis Using Inorganic and Organometallic Compounds, Kluwer, Dordrecht, The Netherlands, 1993.
[5] M. Alebbi, C.A. Bignozzi, T.A. Heimer, G.M. Hasselmann, G.J.J. Meyer, Phys. Chem. B 102 (1998) 7577.
[6] Md.K. Nazeeruddin, A. Kay, I. Rodicio, R. Humphry-Baker, E. Müller, N. Vlachopoulos, M. Grätzel, J. Am. Chem. Soc. 115 (1993) 6382.
[7] O. Kohle, S. Ruile, M. Graetzel, Inorg. Chem. 35 (1996) 4779.
[8] C. Chen, K.S. Suslick, Coord. Chem. Rev. 128 (1993) 293.
[9] W. Kaim, M. Mosherosch, Coord. Chem. Rev. 129 (1994) 157.
[10] H. Hartmann, W. Kaim, M. Wanner, A. Klein, S. Frantz, C. Duboc-Toia, J. Fiedler, S. Zális, Inorg. Chem. 42 (2003) 7018.
[11] M. Moscherosch, E. Waldhör, H. Binder, W. Kaim, J. Fiedler, Inorg. Chem. 34 (1995) 4326.
[12] S.E. Bell, J.S. Field, R.J. Haines, M. Moscherosch, W. Matheis, W. Kaim, Inorg. Chem. 31 (1992) 3269.
[13] L. Ballester, M.C. Barral, R. Jiménes-Aparicio, B. Olombrada, Polyhedron 15 (2) (1996) 211.
[14] J.S. Miller, J.C. Calabrase, H. Rommelmann, S. Chittapeddi, J.H. Zhang, W.M. Reiff, A.J. Epstein, J. Am. Chem. Soc. 109 (1987) 769.
[15] J.S. Miller, A.J. Epstein, Coord. Chem. Rev. 206–207 (2000) 651.
[16] N. Motokawa, H. Miyasaka, M. Yamashita, K.R. Dunbar, Angew. Chem., Int. Ed. 47 (2008) 7760.
[17] H. Miyasaka, T. Izawa, N. Takahashi, M. Yamashita, K.R. Dunbar, J. Am. Chem. Soc. 128 (2006) 11358.
[18] W.W. Shum, J.N. Schaller, J.S. Miller, J. Phys. Chem. C 112 (2008) 7936.
[19] B. Durham, J.L. Walsh, C.L. Carter, T.J. Meyer, Inorg. Chem. 19 (1980) 860.
[20] P. Liska, N. Vlachopoulos, M.K. Nazeeruddin, P. Comte, M. Gratzel, J. Am. Chem. Soc. 110 (1998) 3686.
[21] S.M. Zakereruddin, Md.K. Nazeeruddin, R. Humphry-Baker, M. Grätzel, Inorg. Chem. 37 (1998) 5251.
[22] M.F. Rettig, R.M. Wing, Inorg. Chem. 8 (1969) 2685.
[23] H. Hartmann, B. Sarkar, W. Kaim, J. Fiedler, J. Organomet. Chem. 687 (2003) 100.
[24] A.J. Epstein, S. Etemad, A.F. Garito, A.J. Heeger, Phys. Rev. B 5 (1972) 952.
[25] R. Gross-Lannert, W. Kaim, B. Olbrich-Deussner, Inorg. Chem. 29 (1990) 5046.
[26] S.B. Khoo, J.F. Foley, C. Korzeniewski, S. Pons, C. Marcott, J. Electroanal. Chem. 233 (1987) 223.
[27] J. Stanley, D. Smith, B. Latimer, J.P. Devlin, J. Phys. Chem. 70 (1966) 2011.
[28] M.S. Khatkale, J.P. Devlin, J. Phys. Chem. 83 (1979) 1636.
[29] J.S. Miller, Angew. Chem. 45 (2006) 2508.
[30] A. Zehe, J.G.R. Martinez, J. Mol. Struct. (Theochem) 709 (2004) 215.
[31] J.S. Chapell, A.N. Bloch, W.A. Bryden, M. Maxfield, T.O. Poehler, D.O. Cowan, J. Am. Chem. Soc. 103 (1981) 2442.
[32] R.S. Mulliken, W.B. Pearson, Molecular Complexes, Academic Press, New York, 1969.
[33] E. Kampar, O. Neilands, Russ. Chem. Rev 55 (1996) 334.
[34] H. Hartmann, W. Kaim, M. Wanner, A. Klein, S. Frantz, C. Duboc-Toia, J. Fiedler, S. Zalis, Inorg. Chem. 42 (2003) 7018.
[35] J.E. Wertz, J.R. Bolton, Electron Spin Resonance Elementary Theory and Practical Applications, Chapman and Hall, New York, 1986.
[36] A.N. Maity, B. Schwederski, W. Kaim, Inorg. Chem. Commun. 8 (2005) 600.

Polyhedron 28 (2009) 665–672

Contents lists available at ScienceDirect

Polyhedron

journal homepage: www.elsevier.com/locate/poly

Concomitant polymorphism of an antiferromagnetically coupled dicopper(II,II) complex with single strand helical assembly: Synthesis, structure, DSC, magnetic and heterogeneous catalytic studies

Md. Mijanuddin [a], Atish Dipankar Jana [b], Michael G.B. Drew [c], Chang Seop Hong [d], Basab Chattopadhyay [e], Monika Mukherjee [e], Mahasweta Nandi [f], Asim Bhaumik [f], Madeline Helliwell [g], Golam Mostafa [h], Mahammad Ali [a,*]

[a] Department of Chemistry, Jadavpur University, Kolkata 700 032, India
[b] Department of Physics, Sripat Singh College, Jiaganj, Murshidabad, WB 742 123, India
[c] Department of Chemistry, University of Reading, Whiteknights, Reading, RG6 6AD, UK
[d] Department of Chemistry and Center for Electro- and Photo-Responsive Molecules, Korea University, Seoul 136-701, Republic of Korea
[e] Solid State Physics Department, Indian Association for the Cultivation of Science, Jadavpur, Kolkata 700 032, India
[f] Department of Materials Science and Centre for Advanced Materials, Indian Association for the Cultivation of Science, Jadavpur, Kolkata 700 032, India
[g] Department of Chemistry, University of Manchester, Manchester M13 9PL, UK
[h] Department of Physics, Jadavpur University, Kolkata 700 032, India

ARTICLE INFO

Article history:
Received 3 July 2008
Accepted 9 December 2008
Available online 11 February 2009

Keywords:
Cu^{II}-complexes
Concomitant polymorphism
Antiferromagnetically coupled
Immobilization
Hexagonal mesoporous silica
Heterogeneous catalysis
Epoxidation

ABSTRACT

Two concomitant polymorphic coordination complexes (dark blue – **I** and black – **II**) with the formula ($Cu_2C_{44}H_{60}N_4O_4$) have been synthesized and characterized crystallographically. Magnetic measurements show the presence of a strong antiferromagnetic interaction and the 2*J* value corresponds extremely well to the theoretically calculated one, indicating the fact that it follows nicely the magneto-structural relationship. Immobilization of the copper(II) complex **1** on a 2D-hexagonal mesoporous silica showed good catalytic efficiency in the liquid phase partial oxidation of olefins in the presence of TBHP as an oxidant.
© 2009 Elsevier Ltd. All rights reserved.

1. Introduction

The designed synthesis of coordination complexes towards functional materials has become an active area of research during the last decade. Judicious choice of organic ligands and suitable transition metals has led to the controlled synthesis of transition metal complexes of different nuclearities with desired functionalities, such as catalytic activity, magnetism, non-linear optical properties, which have found promising industrial applications. Dinuclear copper complexes, in many cases, have shown interesting functional properties and the rational syntheses of these complexes have received current interest. Bulky Schiff-base ligands with O-donor atoms in many cases have been successfully used to control the synthesis of dinuclear copper complexes and phenolate/bis-phenolate ligands, in particular, have shown great promise towards this end [1–7].

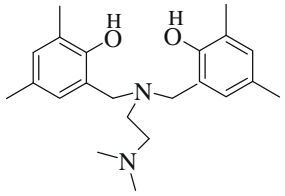
Copper(II)–bisphenolate complexes are also important for their catalytic activity and during recent times they have been used as functional models of various biomolecules [1–6]; as a functional model of galactose oxidase (GO) [7], copper amine oxidases, etc. Immobilization of copper complexes over silica supports can be an effective methodology for the synthesis of active heterogeneous catalysts in the liquid phase partial oxidation of alkenes using peroxides as the oxidant [8,9]. The channels of hexagonal mesoporous silica (**HMS**) materials provide a confined space (2–50 nm) for stabilization and enhancement of the catalytic performance by influencing the chemo-, regio- and shape-selectivity of the reaction, and offer further opportunity to study "single molecular chemistry", which could take place in nano-restricted environments. Detailed studies of chemical reactions in a confined space would allow us to gain a fundamental understanding of the effects of local environment on the control of reaction pathways and the increase of product yield. A transition metal present at the surface of a mesoporous material with a very high surface area particularly showed excellent catalytic activity in liquid phase partial oxidation

* Corresponding author.
E-mail address: mali@chemistry.jdvu.ac.in (M. Ali).

0277-5387/$ - see front matter © 2009 Elsevier Ltd. All rights reserved.
doi:10.1016/j.poly.2008.12.047

reactions in the presence of *tert*-butyl hydroperoxide (TBHP) as an oxidant [10]. In the present contribution, we report the syntheses and crystal structures of two binuclear copper(II) complexes (**I** and **II**) of a tetra-coordinated amine-bisphenol ligand (H_2L), which are interestingly concomitant polymorphs. We have also shown that the immobilization of the soluble copper(II) complex **I** over highly ordered mesoporous silica resulted in a heterogeneous catalyst, which showed very good catalytic activity and epoxide selectivity in the oxidation of cyclohexene and styrene in the presence of TBHP as an oxidant. A low temperature magnetic study on complex **I** shows strong antiferromagnetic coupling between the two phenoxo-bridged Cu(II) centers.

H_2L



2. Experimental

2.1. Materials and methods

Starting materials for the synthesis of the ligand *N*,*N*-amine-bis(4,6-dimethylphenol)-*N*,*N*-dimethylethylenediamine(H_2L) viz 2,4-dimethylphenol (Lancaster), *N*,*N*-dimethylethylenediamine (Lancaster) and formaldehyde (E-Merck, Germany) were of reagent grade and were used without further purification. Solvents including acetone, methanol, dichloromethane (Merck, India) and triethylamine (SRL, India) were of reagent grade and were dried by standard methods before use. The hydrated salt of copper(II) acetate (A.R. Loba, India) was used as received.

2.1.1. Synthesis of the ligand (H_2L)

The ligand *N*,*N*-amine-bis(4,6-dimethylphenol)-*N*,*N*-dimethylethylenediamine (H_2L) was prepared by the reported method [11].

2.1.2. Synthesis of the complex [$Cu_2(L)_2$]

H_2L (0.356 gm, 1 mmol) dissolved in dry methanol/dichloromethane mixture (1:1, v/v) (20 ml) was refluxed with triethylamine (0.20 gm, 2 mmol) for 15 min to yield a yellow solution. To this solution was added $[Cu(OAc)_2] \cdot 2H_2O$ (0.20 gm, 1 mmol), and the solution was refluxed for another 5 h and filtered to remove the slight brown precipitate. Single-crystals were grown by slow evaporation at room temperature (~27 °C). The dark blue needle shape crystals (**I**) appeared within 2 days at the upper part of the vessel, while black block shape crystals (**II**) were obtained after 5 days (Fig. 1). Yield, black needles ~30%, dark blue blocks ~40%.

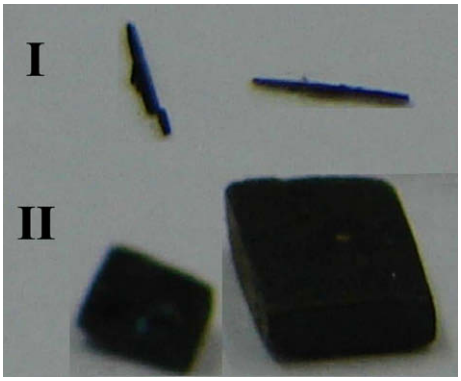


Fig. 1. Photograph of the two forms of $[Cu_2(L)_2]$ growing in $MeOH/CH_2Cl_2$ (1:1 v/v). Complex **I** gives needle-like crystals growing at the upper part of the beaker, while **II** is the block like crystals that grow at the lower part of the beaker.

Attempts to grow single-crystals at relatively low temperature (~5 °C) resulted in only **II** in 5–7 days, with no trace of **I**. *Anal.* Calc. for $C_{44}H_{60}Cu_2N_4O_4$ (836.06 g mol^{-1}): C, 63.21; H, 7.23; N, 6.70 Found: C, 62.94; H, 7.11; N, 6.41%. IR (cm^{-1}): 3423(br), 2993–2831(s), 1610(s), 1475(s), 1319(s), 1251(s), 858, 800.

2.2. Immobilization of complex **1** on 2D-hexagonal mesoporous silica

Highly ordered 2D-hexagonal mesoporous silica has been synthesized by using a mixture of cationic (cetyltrimethylammonium bromide, CTAB) and non-ionic (Brij-35, $C_{12}H_{25}$–$(OC_2H_4)_{23}$–OH, a polyether and aliphatic hydrocarbon chain) surfactant system as the supramolecular structure directing agent, by the method reported elsewhere [12]. This ordered mesoporous material was used as the catalyst support in this study. Immobilization of the metal complexes was carried out by dispersing 0.5 g of the mesoporous silica in a solution containing 120 mg of the metal complex dissolved in 25 ml dry acetonitrile. The resultant slurry was vigorously stirred at room temperature for 4 h. Then the solid was filtered, washed with acetonitrile and dried under vacuum. Hexagonal mesoporous silica and its corresponding immobilized analogs of **I** are designated as **HMS** and **HMS-Cu-I**, respectively. Both the host and the immobilized catalysts were characterized by powder XRD, electron microscopy and spectroscopic techniques.

2.3. Physical measurements

Elemental analyses were carried out using a Perkin–Elmer 240 elemental analyzer. The infrared spectrum (400–4000 cm^{-1}) was recorded from KBr pellets on a Nickolet Magna IR 750 series-II FTIR spectrophotometer. The variable-temperature magnetic susceptibility of complex **I** was performed using a SQUID magnetometer on a crystalline sample in the temperature range 300–2 K with an applied field of 0.5*T*. DSC thermograms were recorded on a Perkin–Elmer Pyris Diamond TGA/DTA thermal analyzer under a dynamic nitrogen environment.

2.4. X-ray crystallography

For complex **1**, data were measured at 293(2) K on a Bruker SMART APEX CCD area detector system [λ(Mo K_α) = 0.71073 Å], graphite monochromator with an ω-scan, crystal-detector distance 60 mm, collimator 0.5 mm. Data reduction by SAINTPLUS [13], absorption correction using an empirical method (SADABS) [14], structure solution using SHELXS-97 [15] and refined using SHELXL-97 [16]. All non-H atoms were refined anisotropically. Hydrogen atoms on the ligand were introduced in calculated positions and included in the refinement, riding on their respective parent atoms. For complex **II**, data were collected at 293(2) K with Mo K_α radiation using the MAR research image plate system positioning the crystals at 70 mm away from the image plate. One hundred frames were measured at 2° intervals with a counting time of 2 min. Data analysis was carried out with the XDS program [17]. The structure of **II** was solved by the direct method, and refined by full-matrix least-squares techniques on F^2 using SHELXS-97 [15] and SHELXL-97 [16]. The thermal parameters of all non-H-atoms were treated anisotropically. H-atoms were located from the difference Fourier map and refined isotropically. Crystal data for **I** and **II** are provided in Table 1.

Table 1
Crystal data and structure refinement for polymorphs **I** and **II**.

Parameters	Polymorph-**I**	Polymorph-**II**
Empirical formula	$C_{44}H_{60}Cu_2N_4O_4$	$C_{44}H_{60}Cu_2N_4O_4$
Formula weight	836.04	836.04
Temperature (K)	293	293
Wavelength (Å)	0.71073	0.71073
Crystal system	orthorhombic	orthorhombic
Space group	$P2_12_12_1$	*Pnna*
a (Å)	12.0097(16)	12.6479(6)
b (Å)	15.334(2)	14.1640(7)
c (Å)	23.780(3)	23.194(1)
V (Å^3)	4379.3(10)	4155.2(4)
Z, calculated density (Mg/m^3)	4, 1.268	4, 1.337
Absorption coefficient (mm^{-1})	1.048	1.070
F(000)	1768	1768
Crystal size (mm)	0.12 * 0.20 * 0.50	0.11 * 0.17 * 0.19
Crystal color	dark-blue	black
Crystal shape	needle	block
θ range for data collection (°)	1.6–25.0	1.76–26.40
Limiting indices	$-14 \leqslant h \leqslant 14$ $-18 \leqslant k \leqslant 18$ $-28 \leqslant l \leqslant 28$	$-15 \leqslant h \leqslant 15$ $-17 \leqslant k \leqslant 17$ $-29 \leqslant l \leqslant 28$
Reflections collected/unique [R_{int}]	42 266/7719 [0.049]	31 413/4264 [0.0244]
Data/restraints/parameters	6162/0/499	4264/0/364
Goodness-of-fit-on F^2	1.02	1.042
Final *R* indices [$I > 2\sigma(I)$]	$R_1 = 0.0384$, $wR_2 = 0.0956$	$R_1 = 0.0243$, $wR_2 = 0.0690$
Largest difference peak and hole (e Å^{-3})	0.38 and −0.17	0.334 and −0.222

Samples (**HMS** and **HMS-Cu-I**) were identified by powder XRD (PXRD) using a Seifert 3000P X-ray diffractometer on which small and wide-angle goniometers were mounted. The X-ray source was Cu K_α radiation (α = 0.15406 nm) with an applied voltage and current of 40 kV and 20 mA, respectively. Mesophases of different samples were analyzed using a JEOL, JEM 2010 TEM at an accelerating voltage of 200 kV. N_2 adsorption measurements were carried out using a Quantachrome Autosorb-1C-TCD at 77 K. Pre-treatment of the sample was done at 423 K for 3 h under high vacuum. For the Fourier transform infrared (FT-IR) measurement a Nicolet Magna IR 750 Series II was used. A Shimadzu AA-6300 double beam atomic absorption spectrophotometer was used for studying the loading of Cu through wet chemical analysis. UV–visible diffuse reflectance spectra for the immobilized catalysts were recorded on a Shimadzu 2401PC UV–visible spectrophotometer with an integrating sphere attachment using $BaSO_4$ as a background standard.

The oxidation reactions were carried out using 0.5 g of substrate and 0.10 g of loaded catalyst in 6 ml of CH_3CN under stirring in a two-neck round-bottom flask fitted with a water condenser and placed in an oil bath at 333 K. *tert*-Butylhydroperoxide (TBHP, 70 wt% aqueous, equimolar with respect to the substrate) was added immediately before the start of the reaction. Aliquots of the reaction mixture were withdrawn at various time intervals to study the progress of the reaction. In a typical operation, 0.5 cm^3 solution was taken out with the help of a micro-pipette and the solution was subjected to multiple ether extraction and the extract was concentrated. From this, 1 μl solution was withdrawn with the help of a gas tight syringe and injected to the GC port (Agilent 6890A, FID). For the identification of the products the GC retention times of different reaction products were compared with those of commercial standards.

3. Results and discussion

3.1. Structure of I and II

Both polymorphic forms, (**I**) and (**II**) (Figs. 2 and 3), of the title complex crystallize in the orthorhombic system with almost similar lattice constants (Table 1). The similarity of the unit cell dimensions of the two polymorphs suggests that the crystal structures of **I** and **II** are also related, although the space group for polymorph **I** is non-centrosymmetric, $P2_12_12_1$, with $Z = 4$, while that of polymorph **II** is a centric one, Pbnn, with $Z = 4$. Consequently, the asymmetric unit of **I** consists of a dinuclear Cu_2L_2 molecule with two phenolate O atoms acting as a $(\mu\text{-O})_2$ bridge between the metal centers. In **II**, however, only half of the complex molecule, i.e. a mononuclear CuL moiety, forms the asymmetric unit.

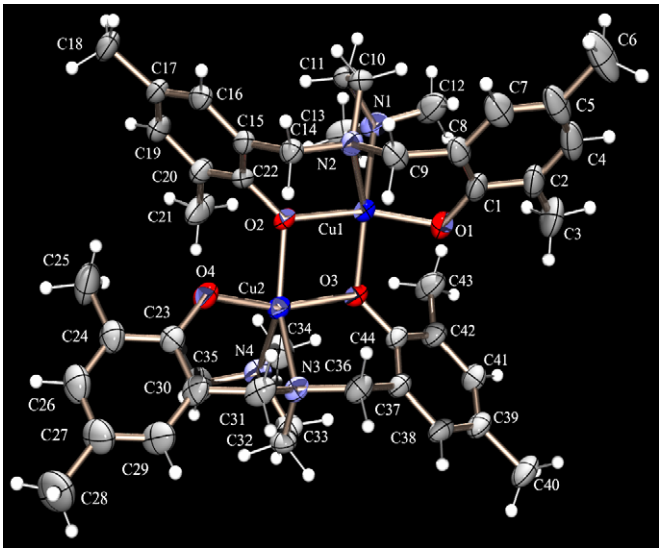


Fig. 2. ORTEP diagram (30% probability) of **I** with the atom numbering scheme.

The coordination geometry about the Cu-centers in both polymorphs can be best described as distorted square pyramidal with one phenolate oxygen, one amine nitrogen and two bridging oxygen atoms [N2, O1, O2, O3 around Cu1 and O4, N3,O3,O2 around Cu2 in **I**; O1, N2, O2, O2* (* = $x, 3/2-y, -z$) around Cu1 in **II**] defining the basal plane; the remaining amine N atoms N1, N4 in **I** and N1 in **II** occupy the apical sites. The displacement of the metal center towards the axial N atom from the least-squares plane through the basal atoms are 0.322(1) and 0.314(1) Å for Cu1 and Cu2 in **I** and 0.3146(2) Å for Cu1 in **II**. The dihedral angle of 63.74(12)°

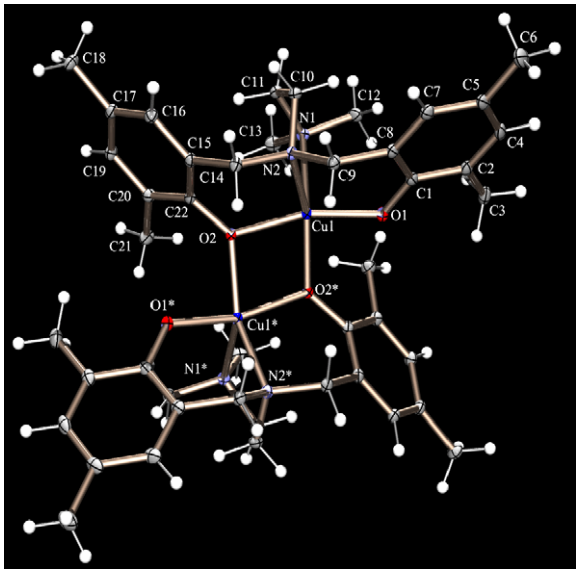


Fig. 3. ORTEP diagram (30% probability) of **II** with the atom numbering scheme.

between the two basal planes in **I** indicates a *syn-clinial* arrangement. The trigonality index parameter τ [$=(\phi_1-\phi_2)/60$, where ϕ_1 and ϕ_2 are the two largest L-M-L angles of the coordination sphere] has been calculated for the pentadentate copper sites [18,19]. The τ values of 0.25 and 0.13 for Cu1 and Cu2, respectively, in **I** indicate a different degree of distortion of the two metal sites (for a perfect square pyramid $\tau = 0$ and for a perfect trigonal bipyramid $\tau = 1$). In **II** the τ parameter for Cu1 is 0.24.

The Cu–O bond distances in the two polymorphs, lying in the range 1.866(3)–2.016(3) Å, are in agreement with that reported for analogous copper(II) systems [20–22]. The Cu–N (equatorial) bond lengths in **I** and **II**, ranging between 2.059(1) and 2.072(3) Å, are consistent with the corresponding values for similar Cu^{II}-diamine complexes [20–22]. The shortening of the Cu–N (equatorial) bond lengths [2.072(3)–2.078(3) Å in **I**, and 2.059(1) Å in **II**] in comparison to the Cu–N (axial) distances [2.352(3)–2.377(3) Å] is typical for a d^9 configuration of the Cu^{II} ion. The intramolecular Cu···Cu separations in the two polymers [2.950(1) and 3.007(1) Å] fall within the range of known Cu···Cu distances in double-bridged copper polynuclear systems [20–22]. The Cu1··O2··Cu2 angle is 96.76° and Cu1··O3··Cu2 is 96.24° for **I** and the Cu1··O2···Cu1 angle is 99.33° for **II**.

Both polymorphs exhibit a similar type of intramolecular C–H··· (arene) hydrogen bond (Table 2) involving the ethylene H- atoms and terminal phenyl rings, which influence the overall molecular conformations. In **I**, besides the intramolecular C–H··· interactions, there exists an additional intermolecular C–H··· interaction (Table 3), through which the individual dinuclear entities self assemble in the form of helices along the crystallographic *b*-axis (Fig. 4). The inherently curved nature of the dinuclear entities facilitates this helical assembly in which successive units of opposite curvature are united by CH···π interactions. The pitch of the helix is 15.33 Å. Adjacent helices are arranged in such a way that a central helix is surrounded by six other helices (Fig. 5).

The packing of the dinuclear units in **II** is also in the form of a helix, but now there are no intermolecular CH···π interactions, instead only weak van der Waals interactions leading to the association of successive units. The axis of the helix now is the crystallographic *a*-axis (Fig. 6). Inherently, the curved nature of the dinuclear entities facilitates this helical assembly in which successive units of opposite curvature stand up around a common axis. The pitch of the helix is 12.65 Å. Three-dimensional packing of these helices again is in the form of a hexagon, in which a central helix is flanked by six other helices (Fig. 7).

3.2. Heterogeneous catalysis

From the small angle powder diffraction patterns of **HMS** and **HMS-Cu-I** (SUP Fig. 1) it is clear that all four planes (100, 110, 200 and 210) of the 2D-hexagonal mesophase of **HMS** have been retained in **HMS-Cu-I**. BET surface areas and mesopore volumes for **HMS** and **HMS-Cu-I** are 1438 m^2g^{-1} and 0.93 ccg^{-1}; 976 m^2g^{-1} and 0.65 ccg^{-1}, respectively. The peak pore diameters for these two samples employing BJH pore size distribution are 2.8 and 2.1 nm, respectively. The decrease in surface area, pore diameter and pore volume of HMS after the loading of the Cu complex suggests that the metal complex has occupied the internal channel of the mesopores and is distributed uniformly inside the mesoporous channels, which is essential for utilizing the high surface area of the mesoporous host in liquid phase partial oxidation reactions.

In Table 4, the results of the catalytic activity of complex **I** immobilized over silica surfaces, **HMS-Cu-I,** are shown. Acetonitrile has been used as the solvent in all these liquid phase reactions. The major products for the partial oxidation of both styrene and cyclohexene were their respective epoxides. In Fig. 8, the time-on-stream for the conversion and epoxide selectivities in these reactions are plotted. It is clear from the figure that the selectivity of the epoxide for both substrates was high at the initial stage of the reaction. However, with time as the conversions reach

Table 2
Selected intramolecular contacts (Å, °) for polymorphs **I** and **II**.

D–H···A	D–H	H···A	D···A	D–H···A
I				
C11–H11A···Cg9	0.970	2.84	3.645(4)	149
C33–H33A···Cg11	0.970	2.86	3.730(5)	150
II				
C11–H11A···Cg6	0.955	2.69(2)	3.556(2)	150

Table 3
The intermolecular C–H···π contacts (Å, °) in polymorph **I**.

D–H···A	D–H	H···A	D···A	D–H···A
I				
C10–H10B···Cg10	0.969	2.90	3.645(5)	135

In polymorph **I**: Cg9 = C15–C16–C17–C19–C20–C22, Cg10 = C23–C24–C26–C27–C29–C30, Cg11 = C37–C38–C39–C41–C42–C44
In polymorph **II**: Cg6 = C15–C16–C17–C19–C20–C22

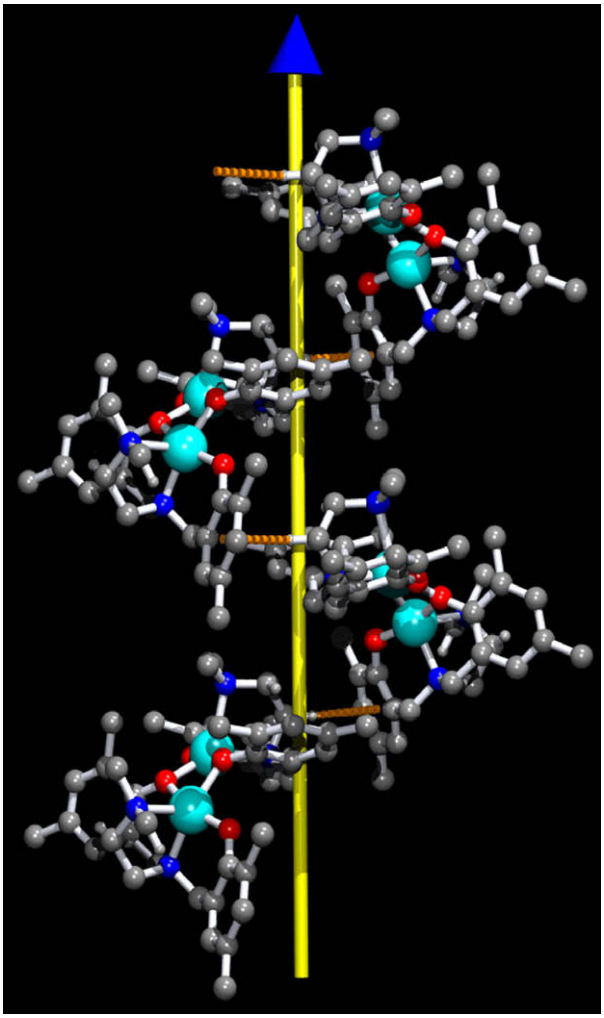


Fig. 4. Helical arrangement of the dinuclear units through C–H···π interactions in **I**.

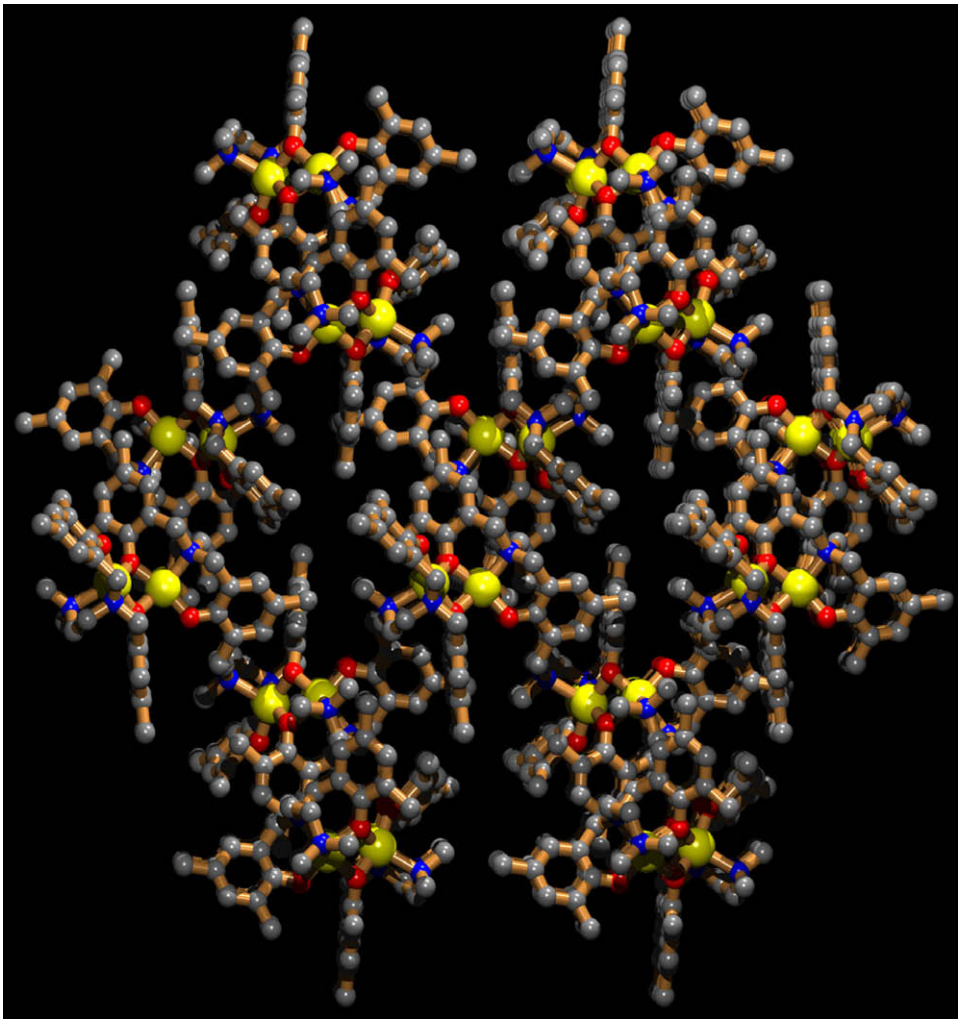


Fig. 5. Molecular packing in **I** viewed along the *a*-axis, revealing the hexagonal array of helices.

the respective maximums, the epoxide selectivities go down to some extent. This could be attributed to the hydrolysis of the epoxides to the respective diols, which is quite common for the liquid phase partial oxidation of olefins over a heterogeneous catalyst [10], as water coming from the oxidant in the reaction mixture promotes the epoxide ring opening. In Table 4, the TOF (turn over frequency) for different catalytic runs are also given. The TOF for cyclohexene conversion was relatively more than that for styrene. The immobilized catalyst shows moderately high TOFs for both the substrates. In order to show the superiority of the heterogeneous catalysts over the homogeneous ones, these reactions were carried out under homogeneous conditions and it was observed that the TOFs were found to be very poor (Table 4). These results suggest that the immobilization of complex **1** in the mesoporous matrix drastically enhances the catalytic activity. Nevertheless, the relatively high TOFs for the oxidation of styrene and cyclohexene suggest high catalytic efficiency for the Cu-hydroperoxo species that could form at the active sites in the presence of the TBHP oxidant [10]. For both the substrates the corresponding diols are the other major products. Hydrophobic aromatic ligands attached to the Cu-centers in the immobilized catalyst could provide the affinity towards the olefinic substrates. This may facilitate the adsorption of the substrates near the vicinity of the active sites and their subsequent oxidations. This could be responsible for high TOFs in these partial oxidation reactions.

3.3. Low temperature magnetic studies

The magnetic susceptibility of complex **I** was measured at 0.5*T* in the temperature range 2–300 K, and this is shown in Fig. 9. At 300 K, the $_{m}T$ value of 0.412 $cm^3\,Kmol^{-1}$ is significantly smaller than the expected value for two uncoupled Cu(II) ions. On lowering the temperature $_{m}T$ undergoes a monotonic decrease down to 80 K, suggestive of strong antiferromagnetic interactions operating. Below this temperature the $_{m}T$ value shows a constant non-zero value which may be due unaccounted background noise, as due to the strong antiferromagnetic nature we expect a zero $_{m}T$ value in this region. The magnetic data were properly fitted using the Bleaney–Bowers Eq. (1), derived from an isotropic exchange Hamiltonian $H = -JS_1 \cdot S_2$, and considering a small amount of non-coupled Cu(II) species (ρ).

$$\chi_m = (1-\rho)(2Ng^2\beta^2/kT)/[3+\exp(-J/kT)] + \rho(Ng^2\beta^2/2kT) \quad (1)$$

A best fit gives magnetic parameters of $g = 2.07$, $J = -341\ cm^{-1}$ and $\rho = 0.06$. The large negative J value indicates that the strong antiferromagnetic interactions are transmitted between Cu spins via the phenoxide linkage. The magnitude of the magnetic exchange coupling constant falls into the usual range of hydroxo-bridged Cu(II) dimers [23–25]. As depicted in SUP Fig. 2, the field dependence of the magnetization shows that the experimental magnetization value of 0.093 Nβ at 7 T is significantly lower that

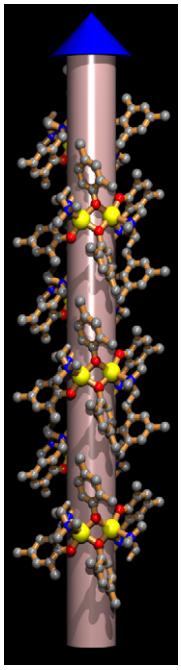


Fig. 6. Helical arrangement of dinuclear units through van der Waals interactions in **II**.

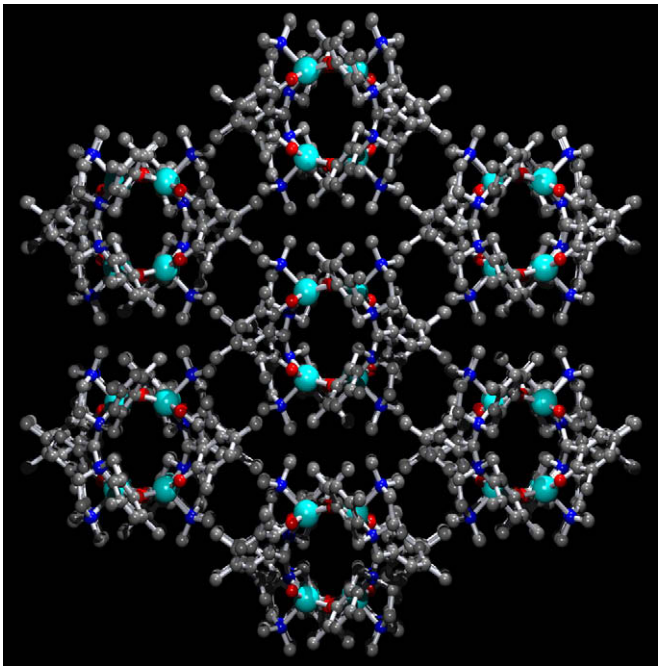


Fig. 7. Packing of helical units in **II** viewed along the *b*-axis.

the theoretical value (2.04 Nβ per Cu_2), confirming the presence of strong antiferromagnetic coupling between the Cu(II) ions through the phenoxide bridges.

3.4. Magneto-structural correlation

It is well known that the magnetic behavior of divalent copper complexes bridged equatorially by a pair of hydroxide [23–25], alkoxide [26,27] or phenoxide [28–38] oxygen atoms is highly dependent on the Cu–O–Cu bridge angle. Also it can be influenced

Table 4
Catalytic activity of **HMS-Cu-I** in the partial oxidation of olefins.[a]

Substrate	Time (h)	Conversion (%)	Epoxide (%)	Diol (%)	Others (%)	Turn over frequency (TOF)[b]
Styrene	12	89.4	63.2	16.9	19.9	48.0
Styrene[c]	12	4.2	15.5	81.4	3.1	
Styrene[d]	12	13.14	80.6	16.2	3.2	0.88
Cyclohexene	10	82.6	48.0	44.2	7.8	67.7
Cyclohexene[c]	12	1.6	4.8	84.5	10.7	
Cyclohexene[d]	12	34.81	22.6	72.1	5.3	2.96

[a] Reaction conditions: substrate 0.5 g; catalyst: **HMS-Cu-I**: 0.1 g, substrate: TBHP = 1:1; solvent: acetonitrile - 6 ml.
[b] TOF = moles of substrate converted per mole of Cu per h, Cu loading was estimated by AAS.
[c] Pure HMS was used as the catalyst.
[d] Pure Cu complex **I** (homogeneous) was used as catalyst.

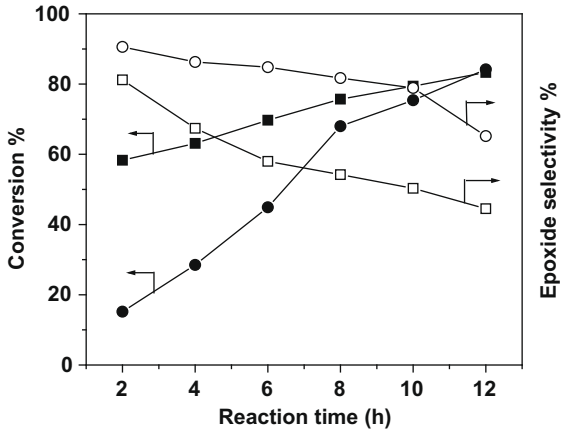


Fig. 8. Conversions of styrene (filled circle) and cyclohexene (filled square) for different reaction times in the liquid phase partial oxidation over **HMS-Cu-I**. Corresponding selectivities of styrene oxide (open circle) and cyclohexene oxide (open square) are at the right hand axis.

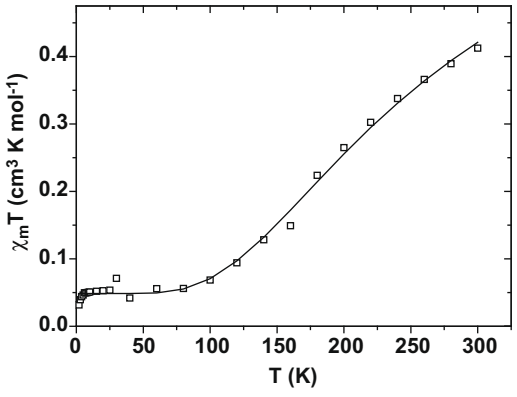


Fig. 9. Plot of $_{m}T$ versus T at 0.5T for **I**. The solid line gives a best fit with the modified Bleaney–Bowers equation.

to a smaller measure by the Cu–O (bridge) distance, the Cu···Cu separation, the geometry around the copper(II) centers and the geometry around the bridging oxygen atom. The magneto structural correlations in bis(μ-phenoxide)-bridged macrocyclic copper(II) complexes with flat dinuclear centers and no electronic perturbations have been studied [30], and a linear relationship between the exchange integral (J) and the phenoxide bridging angle (ϕ) of the form: $2J = -31.95\phi + 2462$ has been proposed. Using this

relationship a bridging angle of 96.76° for **I** leads to an expected 2*J* value of $-629.5\ cm^{-1}$, contrary to the experimental 2*J* value of $-341\ cm^{-1}$. This is probably due to the many other factors affecting the 2*J* values, especially the non-flat nature of the dinuclear unit in the present case.

3.5. Study of polymorphism

The gross composition of the complexes has been determined via elemental analysis, which is consistent with the single-crystal X-ray study. Qualitatively, the physical differences of the two polymorphs are revealed in their color, shape and melting points. The synthetic method was both reliable and predictable as under repeated crystallization experiment two polymorphs could concurrently be obtained. It is interesting that though the polymorphs are concomitant in nature due to kinetic factors, complex **I** appeared more quickly (within 2 days), on the upper part of the vessel when there was no trace of the complex **II**, and could be collected easily. With the gradual evaporation of the reaction mixture and increasing concentration of the solution, growth of complex **I** was inhibited and complex **II** was favored, and this complex appeared in the lower part of the vessel. This provided an easy way of isolating the two polymorphs. It is to be noted that when the crystallization experiment was conducted at relatively low temperature only complex **II** was favored, indicating the temperature sensitivity of the nucleation processes.

As mentioned earlier, complexes **I** and **II** are concomitant polymorphs of each other. Concomitant polymorphs arise when a material crystallizes in two or more forms out of the same reaction mixture [39]. It is also the subtlest and most challenging type of polymorphism, as screening out different crystal forms is often difficult. We were lucky that the two polymorphic forms could easily be separated as the crystals of polymorph **II** have been obtained at the later stage of the crystallization. The densities of complexes **I** and **II** are 1.268 and 1.337 g/cm^3, respectively, and according to the well known 'density rule', [39] the polymorph **II** with the higher density is most likely to be more stable and should appear latter. This is consistent with the fact that crystals of polymorph **II** have been obtained at the later stage of crystallization. Melting point determination provides a convenient means of assessing the relative stabilities of the different polymorphic forms of a substance [40–44]. Accordingly, attempts have taken to carry out DSC measurements to investigate melting behavior of complexes **I** and **II** (SUP. Fig. 3). The solid-state reaction corresponds to the large endothermic peak in the regions of 253 and 258 °C for **I** and **II,** respectively, which shows sharp mass loss in the TGA curves, indicating that the melting points of the two polymorphs are slightly different. In the case of **I**, an additional small endothermic peak at temperature 197 °C is observed, indicating the fact that it is stable up to 197 °C and after this temperature a phase transition occurs [45].

4. Conclusions

Using established crystal engineering methodologies we have been able to synthesize two dinuclear Cu(II)-bisphenolate complexes having interesting functional properties. The complexes are concomitant polymorphs and the X-ray crystal structure determination reveals the versatility of the self-assembly phenomena in which the weak interactions such as C–H···π and van der Waals forces crucially determine the molecular packing within the crystal, giving rise to two different modes of self-assembly and consequently two concomitant polymorphs. The strong antiferromagnetic property of the polymorph **I** strongly correlates with the crystal structure. The efficient heterogeneous catalytic activity of the copper(II) complex **1**, due to immobilization on a 2D-hexagonal mesoporous silica, in the liquid phase partial oxidation of olefins to epoxide in the presence of TBHP as an oxidant is noteworthy. We have confined our studies to complex **I**, as the complexes **I** and **II** differ from each other only by weak non-covanent interactions, and they are expected to behave identically, particularly in solution.

Acknowledgements

M.A. gratefully acknowledges the financial assistances from the DST (Ref. No. SR/S1/IC-35/2006), and CSIR (Ref. No. 01(7329)/07/EMR-II), New Delhi, India. M.A. also thanks to Dr. S. Das, School of Chemistry, University of Hyderabad, Hyderabad 500 046, India for X-ray data collection on complex **I**. M.N. thanks CSIR, New Delhi for a Senior Research Fellowship. A.B. wishes to thank DST, New Delhi for a Ramanna Fellowship Grant.

Appendix A. Supplementary data

CCDC 612752 and 612753 contain the supplementary crystallographic data for this article. These data can be obtained free of charge via http://www.ccdc.cam.ac.uk/conts/retrieving.html, or from the Cambridge Crystallographic Data Centre, 12 Union Road, Cambridge CB2 1EZ, UK; fax: (+44) 1223 336 033; or e-mail: deposit@ccdc.cam.ac.uk. Supplementary data associated with this article can be found, in the online version, at doi:10.1016/j.poly.2008.12.047.

References

[1] P. Chaudhuri, M. Hess, U. Flörke, K. Wieghardt, Angew. Chem., Int. Ed. Engl. 37 (1998) 2217.
[2] P. Chaudhuri, M. Hess, T. Weyhermüller, K. Wieghardt, Angew. Chem., Int. Ed. Engl. 38 (1999) 1095.
[3] P. Chaudhuri, M. Hess, J. Müller, K. Hildenbrand, E. Bill, T. Weyhermüller, K. Wieghardt, J. Am. Chem. Soc. 121 (1999) 9599.
[4] Y. Wang, J.L. DuBois, K.O. Hodgson, T.D.P. Stack, Science 279 (1998) 537.
[5] S. Itoh, M. Taki, S. Takayama, S. Nagatomo, T. Kitagawa, N. Sakurada, R. Arakawa, S. Fukuzumi, Angew. Chem., Int. Ed. Engl. 38 (1999) 2774.
[6] F. Thomas, G. Gelbon, I.G. Luneau, E.S. Aman, J.-L. Pierre, Angew. Chem., Int. Ed. Engl. 41 (2002) 3047.
[7] T.K. Paine, T. Weyhermüller, K. Wieghardt, P. Chaudhuri, J. Chem. Soc., Dalton Trans. (2004) 2092.
[8] A.R. Silva, K. Wilson, A.C. Whitwood, J.H. Clark, C. Freire, Eur. J. Inorg. Chem. (2006) 1275.
[9] S. Mukherjee, S. Samanta, A. Bhaumik, B.C. Roy, Appl. Catal. B Environ. 68 (2006) 12.
[10] S. Samanta, N.K. Mal, A. Bhaumik, J. Mol. Catal. A Chem. 236 (2005) 7.
[11] M. Hirotsu, M. Kojima, Y. Yoshikawa, Bull. Chem. Soc. Jpn. 70 (1997) 649.
[12] D. Chandra, N.K. Mal, M. Mukherjee, A. Bhaumik, J. Solid State Chem. 179 (2006) 1802.
[13] Software for the CCD Detector System, Bruker Analytical X-ray Systems Inc., Madison, WI, 1998.
[14] G.M. Sheldrick, SADABS, A Program for Absorption Correction with the Siemens SMART.
[15] G.M. Sheldrick, SHELXS-97, A Program for Solution of Crystal Structures, University of Göttingen, Germany, 1997.
[16] G.M. Sheldrick, SHELXL-97, A Program for Refinement of Crystal Structures, University of Göttingen, Germany, 1997.
[17] K. Kabsch, J. Appl. Crystallogr. 21 (1988) 916.
[18] M. Ali, A. Ray, W.S. Sheldrick, H. Mayer-Figge, S. Gao, A.I. Sahmes, New J. Chem. 28 (2004) 412.
[19] A.W. Addision, T.N. Rao, J. Reedijk, J. van Rijn, G.C. Verschoor, J. Chem. Soc., Dalton Trans. (1984) 1349.
[20] H. Saimiya, Y. Sunatsuki, M. Kojima, S. Kashino, T. Kambe, M. Hirotsu, H. Akashi, K. Nakajima, T. Tokii, J. Chem. Soc., Dalton Trans. (2002) 3737.
[21] D.G. Lonnon, S.B. Colbran, D.C. Craig, Eur. J. Inorg. Chem. (2006) 1190.
[22] S. Wang, Z. Pang, K.D.L. Smith, Inorg. Chem. 32 (1993) 4992.
[23] V.H. Crawford, H.W. Richardson, J.R. Wasson, D.J. Hodgson, W.E. Hatfield, Inorg. Chem. 15 (1976) 2107.
[24] D.J. Hodgson, Prog. Inorg. Chem. 19 (1975) 173;
A. Asokan, B. Varghese, P.T. Manoharan, Inorg. Chem. 38 (1999) 4393.
[25] M.F. Charlot, S. Jeannin, O. Kahn, J. Licrece-Abaul, J. Martin-Freere, Inorg. Chem. 18 (1979) 1675.

[26] M. Handa, N. Koga, S. Kida, Bull. Chem. Soc. Jpn. 61 (1988) 3853.
[27] M. Kodera, N. Terasako, T. Kita, Y. Tachi, K. Kano, M. Yamazaki, M. Koikawa, T. Tokii, Inorg. Chem. 36 (1997) 3861.
[28] R. Gupta, S. Mukherjee, R. Mukherjee, J. Chem. Soc., Dalton Trans. (1999) 4025.
[29] S.K. Dutta, U. Flörke, S. Mohanta, K. Nag, Inorg. Chem. 37 (1998) 5029.
[30] L.K. Thompson, S.K. Mandal, S.S. Tandon, J.N. Bridson, M.K. Park, Inorg. Chem. 35 (1996) 3117.
[31] H. Adams, N.A. Bailey, I.K. Campbell, D.E. Fenton, Q.-Y. He, J. Chem. Soc., Dalton Trans. (1996) 2233.
[32] D. Block, A.J. Blake, K.P. Dancey, A. Harrison, M. McPatlin, S. Parsons, P.A. Tasker, G. Whitlaker, M. Schröder, J. Chem. Soc., Dalton Trans. (1998) 3953.
[33] Y. Sunatsuki, M. Nakamura, N. Matsumoto, F. Kai, Bull. Chem. Soc. Jpn. 70 (1997) 1851.
[34] M. Vaidyatham, R. Viswanathan, M. Palaniandavar, T. Balasubramanian, P. Prabhaharan, T.P. Muthiah, Inorg. Chem. 37 (1998) 6418.
[35] N.R. Sangeetha, K. Baradi, R. Gupta, C.K. Pal, V. Manivannan, S. Pal, Polyhedron 18 (1999) 1425.
[36] J. Galy, J. Jaud, O. Kahn, P. Tola, Inorg. Chim. Acta 36 (1979) 229.
[37] S.S. Tandon, L.K. Thompson, J.N. Bridson, Inorg. Chem. 32 (1993) 32.
[38] Y. Xie, H. Jiang, A.S.C. Chan, Q. Liu, X. Xu, C. Du, Y. Zhu, Inorg. Chim. Acta 333 (2002) 138.
[39] J. Bernstein, R.J. Davey, J.-O. Henck, Angew. Chem., Int. Ed. 38 (1999) 3441.
[40] J. Bernstein, Polymorphism in Molecular Crystals, Oxford University Press, Oxford, 2002.
[41] A. Burger, R. Ramberger, Mikrochim. Acta 2 (1979) 259.
[42] A. Burger, R. Ramberger, Mikrochim. Acta 2 (1979) 273.
[43] D. Giron, Thermochim. Acta 248 (1995) 1.
[44] L. Yu, J. Huang, K.J. Jones, J. Phys. Chem. B 109 (2005) 19915.
[45] D.V. Soldatov, A.T. Henegouwen, G.D. Enright, C.I. Ratcliffe, J.A. Ripmeester, Inorg. Chem. 40 (2001) 1626.

Polyhedron 28 (2009) 673–678

Contents lists available at ScienceDirect

Polyhedron

journal homepage: www.elsevier.com/locate/poly

Neutral nickel complexes chelating monoamidinate ligands: Syntheses, characterizations and catalytic properties toward ethylene oligomerization and norbornene polymerization

Feng-Shou Liu [a,b], Hai-Yang Gao [a,*], Ke-Ming Song [a], Ye Zhao [a], Jie-Ming Long [a], Ling Zhang [a], Fang-Ming Zhu [a,b], Qing Wu [a,b,*]

[a] Institute of Polymer Science, School of Chemistry and Chemical Engineering, Sun Yat-Sen University, Guangzhou 510275, China
[b] PCFM Lab, OFCM Institute, Sun Yat-Sen (zhongshan) University, Guangzhou 510275, China

ARTICLE INFO

Article history:
Received 21 October 2008
Accepted 10 December 2008
Available online 15 January 2009

Keywords:
Monoamidinate nickel complex
Ethylene
Oligomerization
Norbornene
Polymerization

ABSTRACT

Three new neutral monoamidinate nickel complexes [(2,6-^{i}Pr–C_6H_3)N=C(Ar^1)–N(Ar^2)]Ni(Ph)(PPh_3) (**1**, Ar^1 = phenyl, Ar^2 = 2,6-diispropyphenyl; **2**, Ar^1 = *p*-tolyl, Ar^2 = 2,6-dimethylphenyl; **3**, Ar^1 = *p*-tolyl, Ar^2 = pentafluorophenyl) have been synthesized and characterized. The molecular structure of **3** has been determined by X-ray diffraction analysis. The nickel complexes activated with MAO were found to exhibit very high activity, up to 1.94×10^7 g PNBE/(mol Ni h), for vinyl-addition polymerization of norbornene and oligomerize ethylene producing a mixture of dimers and trimers with a moderate turnover frequency.

© 2008 Elsevier Ltd. All rights reserved.

1. Introduction

Amidinates of the type [$R^1C(NR^2)(NR^3)$] (R^1, R^2, R^3 = H, alkyl, aryl or $SiMe_3$) have been widely used in recent years to form a multitude of complexes with main group and transition metals [1–3]. Due to the fact that they can be modified by tuning the substituents R^1, R^2, and R^3, different steric and electronic properties are achieved easily. Amidinates are considered as a steric equivalent of the cyclopentadienyl (Cp) moiety, and its anionic ligand $[R^1C(NR^2)(NR^3)]^-$ can provide four electrons, which promote higher electrophilicity at the metal center compared to six-electron of $[Cp]^-$. Therefore, various group IV and rare earth metal complexes bearing amidinate ligands have been developed as non-Cp olefin polymerization catalysts [4–20].

Besides, it has been found that the amidinate ligands are very useful in the preparation of new late transition metal complexes [2]. This type of ligands are extremely flexible in bonding mode (shown in Scheme 1), thus various well-characterized complexes, such as iron, cobalt, nickel, palladium, platinum and so on, have been reported [21–25]. In comparison with early transition complexes, late transition metal complexes bearing chelating amidinate ligands were less applied in olefin polymerization field due to their instability and small bite angle (62–69°). Eisen and co-workers synthesized nickel complexes with chelating monobenzamidinate or bisbenzamidinate ligands, and found that the reaction of nickel metal compounds with amidinate ligands is complicated [26–28]. In the presence of methylaluminoxane (MAO), these nickel complexes showed high activity for the addition polymerization of norbornene and also efficiently oligomerized ethylene and propylene.

Recently, much attention has been focused on neutral nickel catalysts such as salicylaldiminato Ni(II) complexes because they are less oxophilic and therefore able to tolerate polar functional-containing monomers [29–32]. In an effort to develop bulky neutral monoamindinate nickel complexes as olefins polymerization catalysts, we synthesized and characterized a series of bulky monoamindinate nickel complexes with triphenylphosphine ancillary ligand. Furthermore, ethylene oligomerization and norbornene polymerization catalyzed by neutral monoamindinate nickel complexes after activation with MAO were also investigated.

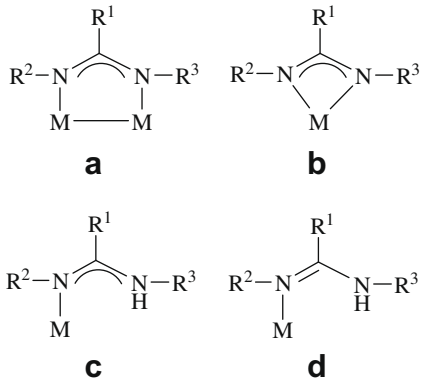
2. Experimental

2.1. General procedures

All manipulations were performed under nitrogen atmosphere using glove box and Schlenk techniques. Polymerization-grade ethylene and extra-pure-grade nitrogen were further purified

* Corresponding authors. Address: Institute of Polymer Science, School of Chemistry and Chemical Engineering, Sun Yat-Sen University, Guangzhou 510275, China (Q. Wu).
E-mail address: ceswuq@mail.sysu.edu.cn (Q. Wu).

0277-5387/$ - see front matter © 2008 Elsevier Ltd. All rights reserved.
doi:10.1016/j.poly.2008.12.019



Scheme 1.

before feeding into the reactor by passing through a DC-IB gas purification instrument. Norbornene was purified by distillation over potassium and used as a solution (0.4 g/ml) in toluene. Toluene and hexane were refluxed over metallic sodium for 24 h before use. Dichloromethane was dried over phosphorus pentoxide for 8 h, and distilled under nitrogen atmosphere. 2,6-Diisopropylaniline and 2,6-dimethylaniline were purchased from Aldrich Chemical Co. and distilled under reduced pressure before use. Pentafluoroaniline, *p*-toluoyl chloride and *n*-butyllithium (2.6 M) in hexane were purchased from Aldrich Chemical Co. and used as received. Benzoyl chloride was purchased from Guangzhou Chemical Reagent Co. and used without further purification. *Trans*-chloro(phenyl)bis(triphenylphosphine) nickel(II) was synthesized according to the procedure in the literature [33]. Methylaluminoxane (MAO) was prepared by partial hydrolysis of trimethylaluminum (TMA) in toluene at 0–60 °C with $Al_2(SO_4)_3 \cdot 18H_2O$ as the water source. The initial $[H_2O]/[Al]$ in molar ratio was 1.3.

2.2. Characterization

NMR spectra were recorded on a Varian Mercury-Plus 300 MHz NMR spectrometer and referenced versus TMS as standard. Elemental analyses were determined with a Vario EL series elemental analyzer from Elementar. MS-FAB spectra were obtained with a VG ZAB-HS scan instrument, using *m*-nitrobenzylalcohol as matrix. The GC–MS data were recorded with a Finnigan Voyager GC-8000 Top series GC–MS system with DB-5MS GC column. Gel permeation chromatography (GPC) analyses of the molecular weight and molecular weight distribution of the polymers were performed on a Waters Alliance GPC-2000 instrument using standard polystyrene as the reference and with 1,2,4-trichlorobenzene as the eluent at 135 °C. The polymer samples were processed into KBr thin films for IR measurements. Fourier transform infrared (FTIR) spectra were recorded on a Nicolet NEXUS–670 FTIR spectrometer. The X-ray diffraction data of single crystal of complex **2** was obtained with the $\omega-2\theta$ scan mode on a Bruker SMART 1000 CCD diffractiometer with graphite-monochromated Mo Kα radiation (λ = 0.71073 Å) at 173 K. The structure was solved using direct methods, and further refinement with full-matrix least squares on F^2 was obtained with the SHELXTL program package. All non-hydrogen atoms were refined anisotropically. Hydrogen atoms were introduced in calculated positions with the displacement factors of the host carbon atoms except disordered hexane molecule.

2.3. Ethylene oligomerization

Ethylene oligomerization reactions were performed in a 50 ml glass flask equipped with magnetic stirrer, oil control of temperature, and continuous feed of ethylene was used. A typical reaction was performed by adding proper amount of MAO solid and introducing toluene (19 ml) into the reactor under ethylene atmosphere. The toluene catalyst solution (1 ml, [Ni] = 5 μmol) was injected into the reactor *via* syringe. Ethylene was continuously fed in order to maintain the ethylene pressure at 0.5 atm. After 30 min, the reaction was stopped by cooling the system to 0 °C, and terminated by addition of cold acidic ethanol (ethanol–HCl, 95:5). The organic layer was analyzed quickly by gas chromatography (GC) for determining the composition and mass distribution of oligomers.

2.4. Norbornene polymerization

Norbornene polymerization reactions were performed in a 50 ml glass flask equipped with magnetic stirrer, oil control of temperature. A typical reaction was performed by adding proper amount of MAO solid and introducing toluene (14 ml) into the reactor under nitrogen atmosphere. Toluene solution of norbornene (10 ml, 0.4 g/ml) and the toluene catalyst solution (1 ml, [Ni] = 1 μmol) was injected into the reactor *via* syringe. After 10 min, the reaction was terminated by adding 200 ml of the acidic ethanol (ethanol–HCl, 95:5). The precipitated polymer was collected and treated by filtering, washing with ethanol several times, and then drying in vacuum at 60 °C to a constant weight.

2.5. Synthesis of bis(2,6-diisopropylphenyl)benzamidine (*L1*)

Benzoyl chloride (1.1 ml, 10 mmol) and triethylamine (1.6 ml, 11 mmol) were added to a vigorously stirred solution of 2,6-diisopropylaniline (1.9 ml, 10 mmol) in CH_2Cl_2 (45 ml). After 3 h, the precipitate of $(C_2H_5)_3N \cdot HCl$ was filtrated, and white solid benzamide was obtained by evaporating the solvent. Then, an excess of thionyl chloride (2.0 ml, 28 mmol) was added to the benzamide, and the reaction mixtures were stirred for 2 h at 80 °C. The remainder thionyl chloride was distilled off under reduced pressure, to obtain the imidoyl chloride as yellow, slowly solidifying oil. Successively, toluene (50 ml), triethylamine (1.6 ml, 11 mmol) and 2,6-diisopropylaniline (1.9 ml, 10 mmol) were added to the reaction system. The mixtures were heated to reflux for 12 h under the protection of nitrogen atmosphere. $(C_2H_5)_3N \cdot HCl$ was removed by filtration, and toluene was evaporated from the filtrate. After recrystallization of the product from ethanol/water, bis(2,6-diisopropylphenyl)benzamidine (**L1**) as a colorless crystal was obtained in 60% yield (2.65 g, 6.02 mmol). EI-MS (*m*/*z*): 441 $[M]^+$. ^1H NMR (300 MHz, $CDCl_3$), δ (ppm): 7.35–6.85 (m, 11H, Ar–*H*), 5.65 (s, 1H, N*H*), 3.25 (m, 4H, C*H*$(CH_3)_2$), 1.31 (d, 12H, CH(C*H*$_3)_2$), 0.94 (d, 12H, CH(C*H*$_3)_2$). ^{13}C NMR (300 MHz, $CDCl_3$), δ (ppm): 153.43 (*C*=N), 145.19, 143.81, 139.27, 135.05, 134.02, 129.11, 128.78, 127.66, 127.47, 123.61, 123.42, 123.22, 28.57, 25.15 (*C*H$(CH_3)_2$), 22.45, 22.30 (CH(*C*H$_3)_2$). Anal. *Calc*. for $C_{31}H_{40}N_2$: C, 84.49; H, 9.15; N, 6.36. Found: C, 84.07; H, 9.20; N, 6.28%.

2.6. Synthesis of 2,6-diisopropylphenyl-4-methyl-N-(2,6-dimethylphenyl) benzamidine (*L2*)

L2 was prepared according to the method described above in 72% yield. EI-MS (*m*/*z*): 400 $[M]^+$. ^1H NMR (300 MHz, $CDCl_3$), δ (ppm): 7.36–6.90 (m, 10H, Ar–*H*), 5.73 (s, 1H, N*H*), 3.24 (m, 2H, C*H*$(CH_3)_2$), 2.38 (s, 3H, 4-C*H*$_3C_6H_2$), 1.38 (s, 6H, C*H*$_3$), 1.04 (d, 12H, CH(C*H*$_3)_2$). ^{13}C NMR (300 MHz, $CDCl_3$), δ (ppm): 154.20 (*C*=N), 145.18, 143.68, 139.44, 134.77, 131.75, 129.10, 128.40, 128.05, 127.48, 126.33, 123.55, 122.89, 28.53 (*C*H$(CH_3)_2$), 24.52 (CH_3–Ph), 22.08 (*C*H$_3$–Ph), 18.98 (CH(*C*H$_3)_2$). Anal. *Calc*. for $C_{28}H_{34}N_2$: C, 84.37; H, 8.60; N, 7.03. Found: C, 84.18; H, 8.51; N, 6.92%.

2.7. Synthesis of 2,6-diisopropylphenyl-4-methyl-N-(pentafluorophenyl)benzamidine (**L3**)

L3 was prepared according to the method described above. The resulting product was purified by column chromatography on silica gel using petroleum ether/ethyl acetate (10/1) as eluent, and then recrystallized from ethanol in 49% yield. EI-MS (*m*/*z*): 461 $[M]^+$. ^1H NMR (300 MHz, $CDCl_3$), δ (ppm): 7.35–7.17 (m, 7H, Ar–*H*), 6.16 (s, 1H, N*H*), 3.43 (m, 2H, C*H*$(CH_3)_2$), 2.35 (s, 3H, 4-C*H*$_3C_6H_2$), 1.37 (d, 12H, CH(C*H*$_3)_2$). ^{13}C NMR (300 MHz, $CDCl_3$), δ (ppm): 162.26 (C=N), 146.80, 140.73, 138.73, 138.63, 136.33, 132.00, 131.71, 129.59, 128.79, 127.17, 126.58, 123.69, 28.93 (*C*H$(CH_3)_2$), 24.21 (*C*H$_3$–Ph), 21.36 (CH(*C*H$_3)_2$). Anal. *Calc.* for $C_{26}H_{25}F_5N_2$: C, 67.82; H, 5.47; N, 6.08. Found: C, 67.93; H, 5.32; N, 6.02%.

2.8. Synthesis of [(2,6-^{i}PrC$_6$H$_3$)N=C(ph)-N(2,6-^{i}PrC$_6$H$_3$)]Ni(PPh$_3$)(Ph) (**1**)

n-BuLi (0.43 ml, 2.6 M, 1.1 mmol) in hexane was added dropwise to a solution of **L1** (0.44 g, 1 mmol) in toluene (20 ml) at −78 °C. The mixtures were warmed up to room temperature and stirred overnight. *Trans*-chloro(phenyl)bis(triphenylphosphine) nickel(II) (0.69 g, 1.0 mmol) in toluene (20 ml) was added and continuously stirred overnight at room temperature. After filtration, the filtrate was concentrated to a volume of *ca.* 5 ml under reduced pressure, and then *n*-hexane (20 ml) was added. Solvent was removed from the precipitate via cannula filtration, and the residual orange powder was washed with *n*-hexane (3 × 5 ml). Drying in vacuo produces the desired nickel complex in 45% yield. FAB$^+$-MS: *m*/*z*: 836, 837, 838, $[M]^+$; 574, 575, 576, 577, $[M-PPh_3]^+$; 497, 498, $[M-PPh_3-Ph]^+$; 440, 441, 442, $[L1]^+$; 262, 263, 264, $[PPh_3]^+$. Anal. *Calc.* for $C_{55}H_{59}N_2NiP$: C, 78.85; H, 7.10; N, 3.34. Found: C, 78.32; H, 7.00; N, 3.15%.

2.9. Synthesis of [(2,6-^{i}PrC$_6$H$_3$)N=C(4-CH$_3$C$_6$H$_4$)-N(2,6-MeC$_6$H$_3$)]Ni(PPh$_3$)(Ph) (**2**)

Complex **2** was prepared according to the same method described for **1**. Because of the good solubility in hexane, **2** was obtained in 26% yield. FAB$^+$-MS: *m*/*z*: 794, 795, 796, $[M]^+$; 532, 533, 534, $[M-PPh_3]^+$; 455, 456, 457, $[M-PPh_3-Ph]^+$; 398, 399, 400, $[L2]^+$; 262, 263, 264, $[PPh_3]^+$. Anal. *Calc.* for $C_{52}H_{53}N_2NiP$: C, 78.50; H, 6.71; N, 3.52. Found: C, 78.39; H, 6.70; N, 3.25%.

2.10. Synthesis of [(2,6-^{i}PrC$_6$H$_3$)N=C(4-CH$_3$C$_6$H$_4$)-N(pentafluorophenyl)]Ni(PPh$_3$)(Ph) (**3**)

Complex **3** was prepared according to the same method described for **1** in 52% yield. FAB$^+$-MS: *m*/*z*: 836, 837, 838, $[M]^+$; 556, 557, 558, 559, 860, $[M-PPh_3]^+$; 594, 595, 596, 597, $[M-PPh_3-Ph]^+$; 460, 461, 462, $[L3]^+$; 262, 263, 264, $[PPh_3]^+$. Anal. *Calc.* for $C_{50}H_{44}F_5N_2NiP$: C, 70.03; H, 5.17; N, 3.27. Found: C, 70.55; H, 5.05; N, 3.04%.

3. Results and discussion

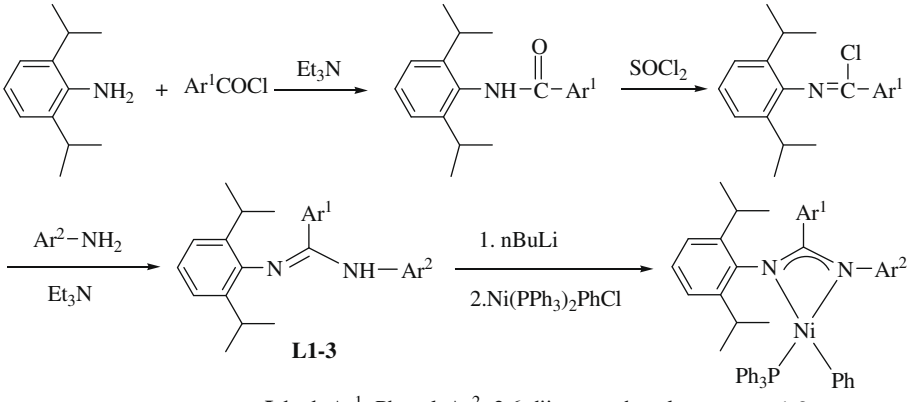
3.1. Synthesis and characterizations of complexes

As shown in Scheme 2, the ligands were prepared according to a modified literature procedure in high yield [16]. Among these ligands, **L1** has been reported [17,34]. Benzamides were easily available from 2,6-diisopropylaniline and benzoyl chloride. Imidoyl chloride could be produced by the dehydration reaction between benzamide and the excess of thionyl chloride. After distilling the residue of thionyl chloride off, the crude products were obtained by the reaction between the quantitative anilines and imidoyl chlorides in refluxing toluene. Pure ligands **L1** and **L2** were recrystallized from ethanol/water solution, while **L3** was purified using silica chromatography and then recrystallized from ethanol. All of these ligands had been characterized by EI-MS, NMR and elemental analysis.

After the amidinate ligands were treated with *n*-butyllithium in toluene, an equimolar amount of *trans*-chloro(phenyl)bis(triphenylphosphine) nickel(II) was added to the solution and nickel complexes **1**–**3** were obtained as orange solids in a moderate yield.

Single crystal of complex **3** suitable for X-ray diffraction was grown from toluene/hexane solution under nitrogen atmosphere at ambient temperature. The diagram of the single-crystal structure is presented in Fig. 1 along with selected bond lengths and bond angles. Besides, the data collection and structure refinement parameters are summarized in Table 1.

Complex **3** in the solid state cocrystallizes with half a hexane molecule, which does not interact with the metal center and is omitted for clarity. As seen in Fig. 1, complex **3** contains one chelating amidinate, one phenyl, and one triphenylphosphine ancillary ligand around the nickel metal center, adopting a slightly distorted square planar coordination geometry (the sum of the angles around the nickel atom is near 360°). The aryl rings in aniline



L1, **1**: Ar^1=Phenyl, Ar^2=2,6-diispropyphenyl;
L2, **2**: Ar^1= *p*-tolyl, Ar^2=2,6-dimethylphenyl;
L3, **3**: Ar^1= *p*-tolyl, Ar^2= pentafluorophenyl;

Scheme 2. Synthesis route of nickel complexes **1**–**3**.

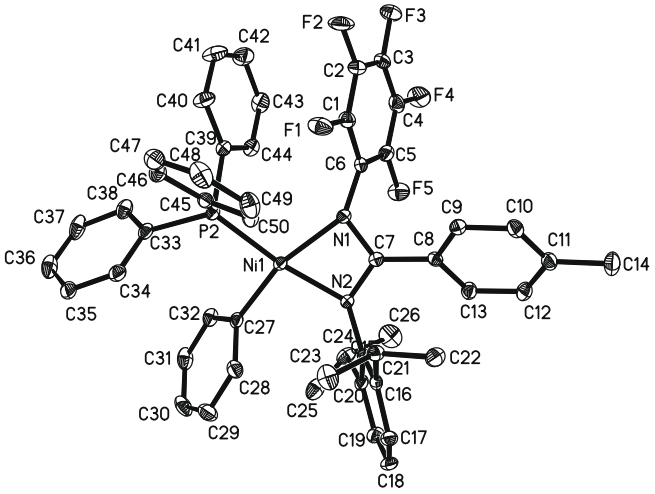


Fig. 1. Molecular structure of complex **3** depicted with 30% thermal ellipsoids. Hydrogen atoms and the uncoordinated hexane molecule have been omitted for clarity. Selected bond distances (Å) and angles (°): C(7)–N(1) 1.350(4), C(7)–N(2) 1.317(4), Ni(1)–C(27) 1.883(3), Ni(1)–N(1) 2.012(3), Ni(1)–N(2) 1.936(2), Ni(1)–P(1) 2.139 (1), C(27)–Ni(1)–N(2) 97.5(1), C(27)–Ni(1)–N(1) 164.2(1), N(1)–Ni(1)–N(2) 66.9(1), C(27)–Ni(1)–P(1) 92.6(1), N(2)–Ni(1)–P(1) 166.8(1), N(1)–Ni(1)–P(1) 103.2(1).

Table 1
Crystallographic data for complexes **3** **1**/**2** hexane.

	3 **1/2** hexane
Formula	$C_{53}H_{51}F_5N_2PNi$
Formula weight	900.64
Crystal color, form	red block
Crystal size (mm)	0.48 × 0.28 × 0.26
Crystal system	triclinic
Space group	$P\bar{1}$
T (K)	173(2)
a (Å)	11.6755(12)
b (Å)	11.7115(12)
c (Å)	19.168(2)
α (°)	96.642(2)
β (°)	98.991(2)
γ (°)	115.716(2)
V (Å^3)	2282.3(4)
D_{calc} (g cm^{-3})	1.300
$F(000)$	928
Z	2
μ (mm^{-1})	0.518
Reflections collected	17993
R_{int}	0.0286
Data/parameters	8852/554
Goodness-of-fit	1.054
R_1/wR_2 $[I > 2\sigma(I)]$*	0.0503/0.1319
R_1/wR_2 (all data)	0.0783/0.1521
Largest difference peak and hole (e Å^{-3})	1.363/−0.508

* $R_1 = \sum||F_o| - |F_c||/\sum|F_o|$, $wR_2 = [\sum w(F_o^2 - F_c^2)^2/\sum w(F_o^2)^2]^{1/2}$.

moieties are tilted to the chelate ring, the dihedral angles being 65° for the ring bonded to N(1), and 75° for the ring bonded to N(2), respectively. The C(7)–N(1) and C(7)–N(2) bond length are 1.350(4) and 1.317(4) Å, respectively. It is similar to typical C(sp^2)–N(sp^2) single and double bonds length, which indicate rather significant delocalization in the amidinate complex. The C_{ph}–Ni bond length (1.883(3) Å) in **3** is similar to that of neutral salicylaldiminato Ni(II), while P–Ni bond length (2.139(1) Å) in **3** is slightly shorter than that of neutral salicylaldiminato Ni(II) (2.172(2) Å) [29], suggesting there is a stronger interaction between nickel metal center and the triphenylphosphine. The N(1)–Ni–N(2) bite angle in **3** is 66.9(1)°, smaller than that of Ni(II) monoamidinate acetylacetonate complexes (69.7(1)°) and bisamidinate nickel complex (68.6(1)°) [28,35].

3.2. Ethylene oligomerization

As reported in the literature, for neutral salicylaldiminato Ni(II) complexes, Ni(COD)$_2$ usually was used as phosphine scavenger in ethylene polymerization [29–32]. The phosphine scavenger bound PPh_3 more strongly than the nickel(II) center, effectively removing phosphine from the salicylaldiminato nickel catalysts. However, in attempts to polymerize ethylene with **1** or **3** combined with two or 20-fold Ni(COD)$_2$, neither polymers nor oligomers of ethylene were obtained. The similar phenomenon was also found in neutral iminophosphonamide (PN_2) nickel complex [36,37]. In contrast, these neutral nickel complexes could be activated for ethylene oligomerization upon the addition of MAO. **1**–**3**/MAO showed moderate turnover frequency (TOF) of *ca.* 5×10^3 mol ethylene/(mol Ni h) for ethylene oligomerization at 0.5 atm of ethylene pressure (see Table 2).

The structure of the nickel complexes slightly influences their catalytic activities. Bulky nickel complex **1** showed a higher TOF than **2**, while **3** with an electron-withdrawing pentafluorophenyl group exhibited the highest TOF for ethylene oligomerization. A reasonable explanation for the TOF enhancement is that the introducing of an electron-withdrawing group would generate a more electrophilic nickel center, thus reducing activation energy for ethylene insertion, and favoring the olefin coordination and insertion [38,39].

GC–MS analysis (Fig. 2) confirmed that the oligomer obtained at 20 °C mainly contained dimers (*ca.* 65%) and trimers (*ca.* 35%) of ethylene. In addition, with an increase in the reaction temperature from 20 to 40 °C, the TOF and selectivity of products were also enhanced. At 40 °C, **3** showed a high selectivity of dimerization of ethylene, up to 94%.

Even though **1** has two bulky 2,6-diisopropylphenyl substituents, only low-molecular-weight oligomers were obtained from the catalysis reaction. Obviously, the results can be attributed to the unique structure of the complex. Recent DFT-based stochastic simulation on amidinate nickel complexes in ethylene polymerization indicated that the insertion barrier versus chain transfer is lower than 0.8 kcal/mol, suggesting there is a relatively rapid rate of chain transfer in ethylene oligomerization [37]. Moreover, as shown in X-ray single-crystal structure of **3**, the coordinated bite angle of four-membered ring complex is 66.9(1)°, resulting in the steric substituents in axial location being far away from the nickel center. The unshielded metal center easily leads to rapid β-H elimination or chain transfer in the process of polymerization. Therefore, low-molecular-weight oligomers rather than high-molecular-weight polymers were obtained.

Table 2
The results of ethylene oligomerzation with **1**–**3**/MAO.

Entry	Complex	T (°C)	Oligomers (mol%)			TOF[c]
			C_4	C_6	C_8–C_{12}	
1[a]	**1** or **3**	20	–	–	–	inactive
2	**1**	20	63.4	36.0	0.6	4.6
3	**2**	20	68.5	31.5	–	4.3
4	**3**	20	63.9	36.1	–	5.7
5[b]	**3**	40	94.3	5.7	–	7.5

Reaction conditions: Ni complex, 15 μmol; Al/Ni = 600; t_p, 0.5 h; toluene, 20 ml; ethylene pressure, 0.5 atm.
[a] Two or 20-fold Ni(COD)$_2$ instead of MAO.
[b] Ni, 5 μmol.
[c] 10^3 mol ethylene/(mol Ni h).

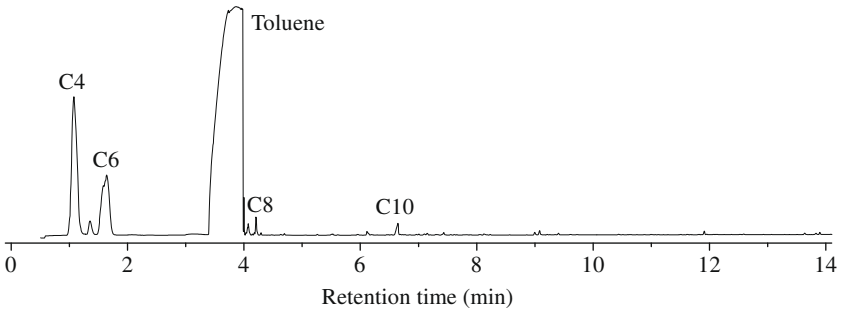


Fig. 2. GC spectrum of oligomer obtained by **1**/MAO at 20 °C (entry 2 in Table 2).

3.3. Norbornene polymerization

The monoamidinate nickel complexes were also tested for norbornene (NBE) polymerization with MAO as cocatalyst and the polymerization results are summarized in Table 3. These three complexes showed very high activities (*ca.* 10^7 g PNBE/mol Ni h) for norbornene polymerization. As shown in Table 3, the reaction temperature strongly affected the catalytic activities. With an increase in reaction temperature, the catalytic activity for norbornene polymerizations increased and then decreased. All of the complexes showed the highest activities for norbornene polymerization at 60 °C. Polymerization temperature also affected the molecular weights of the polymers. The M_n values of the obtained polymers decreased with an increase in polymerization temperature, suggesting that chain transfer or termination began to accelerate at a high temperature. The molecular weight distributions (MWDs) were close to 2 and appeared as a single modal in GPC chromatograms, which indicated that the polymerizations occur at the single active site.

Table 3
The results of norbornene polymerization with **1**–**3**/MAO.

Entry	Complex	T (°C)	Yield (g)	Activity[a]	M_n (kg/mol)	MWD
1	**1**	0	0.96	0.58	375.8	2.31
2	**1**	40	1.59	0.95	335.0	2.55
3	**1**	60	2.47	1.48	304.0	2.44
4	**1**	80	2.38	1.43	265.3	2.63
5	**2**	0	1.08	0.65	311.1	2.70
6	**2**	40	1.62	0.97	284.3	2.52
7	**2**	60	2.34	1.40	209.4	2.47
8	**2**	80	1.76	1.06	146.2	2.58
9	**3**	0	2.01	1.21	282.8	2.67
10	**3**	40	2.58	1.55	195.8	2.66
11	**3**	60	3.24	1.94	123.6	2.71
12	**3**	80	2.94	1.76	82.5	2.46

Reaction conditions: Ni complex, 1 μmol; norbornene, 4 g; Al/Ni = 600; t_p, 10 min; total solution volume, 25 ml toluene.
[a] In unit of 10^7 g PNBE/(mol Ni h).

Moreover, a comparison between the polymerization results of three catalytic systems at 60 °C showed that the structure of the nickel complex played effects on the polymerization. Through the comparison between **1** and **2**, it is found that the steric hindrance of complex did not clearly affect the catalytic activity, but obviously affected the molecular weight of the polymer. The M_n values of the obtained polynorbornenes by different catalysts were in the order of **1** > **2** > **3**, which is well consistent with the steric bulk of these complexes. Additionally, complex **3** with an electron-withdrawing pentafluorophenyl group exhibited the highest catalytic activity for norbornene polymerization, which might result from a more electrophilic nickel center allowing the rapid olefin insertion.

All of the obtained polynorbornenes are soluble in chlorobenzene, *o*-dichlorobenzene and cyclohexane at room temperature, and show similar IR and ^{1}H NMR spectra. The IR spectrum revealed no traces of double bond which often appeared at 1620–1680, 966 and 735 cm^{-1}, while the existence of vibration bands of bicyclics of norbornene units was at 941 cm^{-1}. The ^{1}H NMR spectrum (0.86–2.38 ppm) (Fig. 3) also proved no traces of any double bond, ensuring the occurrence of vinyl-type polymerization rather than ring-opening metathesis polymerization [40–43]. TGA curves of the obtained polynorbornenes showed that the polymer samples were stable up to 450 °C. Attempts to measure glass transition temperature (T_g) of the polynorbornenes by DSC were unsuccessful

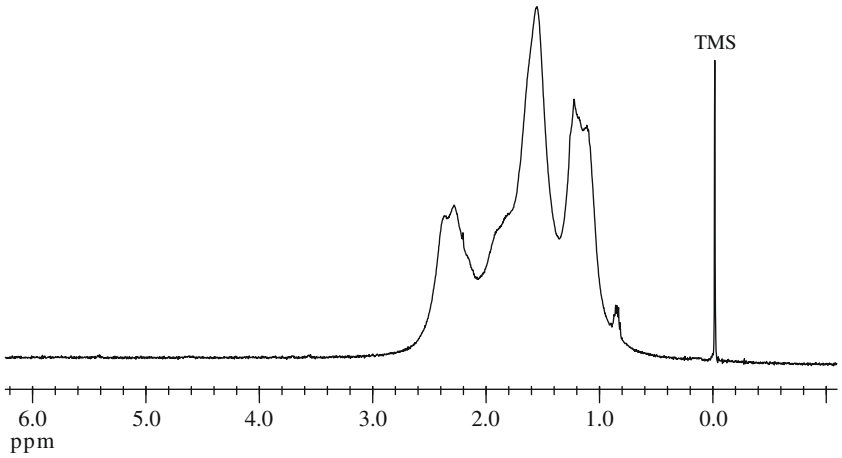


Fig. 3. ^{1}H NMR spectrum of polynorbornene prepared by **1**/MAO at 60 °C.

because T_g was close to the decomposition temperature [44]. The wide-angle X-ray diffraction analysis of the obtained polynorbornene showed two major broad peaks ($2\theta = 9–11^\circ$ and $17–19^\circ$), which indicated that the obtained polymer was non-crystalline and had low stereoregularity [45,46].

4. Conclusion

Three monoamidinate nickel complexes have been synthesized and characterized. The solid-state structure of complex **3** reveals four-coordination and a rough planar geometry with nickel center. Though monoamidinate nickel complexes had bulky steric hindrance, the small bite angle of four-membered ring complex led to ethylene oligomerization in the presence of MAO, and the obtained products were mainly dimers and trimers. However, complexes **1**–**3** activated with MAO showed very high catalytic activities for vinyl-addition polymerization of norbornene. Complex **1** with the most steric hindrance groups produced the highest molecular-weight polynorbornene, while complex **3** with an electron-withdrawing group exhibited the highest catalytic activity for norbornene polymerization.

Acknowledgments

The financial Supports by NSFC (Projects 20734004, 20674097 and 20604034), the Science Foundation of Guangdong Province (Projects 8251027501000018 and 06300069) and the Ministry of Education of China (Foundation for Ph.D. Training) are gratefully acknowledged. We thank Dr. Wei-Xiong Zhang for single-crystal X-ray technical assistance.

Appendix A. Supplementary data

CCDC 700699 contains the supplementary crystallographic data for complex **1**. These data can be obtained free of charge via http://www.ccdc.cam.ac.uk/conts/retrieving.html, or from the Cambridge Crystallographic Data Centre, 12 Union Road, Cambridge CB2 1EZ, UK; fax: (+44) 1223-336-033; or e-mail: deposit@ccdc.cam.ac.uk. Supplementary data associated with this article can be found, in the online version, at doi:10.1016/j.poly.2008.12.019.

References

[1] F.T. Edelmann, Coord. Chem. Rev. 137 (1994) 403.
[2] J. Barker, M. Kilner, Coord. Chem. Rev. 133 (1994) 219.
[3] M.P. Coles, J. Chem. Soc., Dalton Trans. (2006) 985.
[4] D. Liguori, F. Grisi, I. Sessa, A. Zambelli, Macromol. Chem. Phys. 204 (2003) 164.
[5] D. Liguori, R. Centore, A. Tuzi, F. Grisi, I. Sessa, A. Zambelli, Macromolecules 36 (2003) 5451.
[6] E. Otten, P. Dijkstra, C. Visser, A. Meetsma, B. Hessen, Organometallics 24 (2005) 4374.
[7] A. Lisovskii, M.S. Eisen, Topics. Organomet. Chem. (2005) 63.
[8] V. Volkis, M. Rodensky, A. Lisovskii, Y. Balazs, M.S. Eisen, Organometallics 25 (2006) 4934.
[9] P.B. Hitchcock, M.F. Lappert, P.G. Merle, J. Chem. Soc., Dalton Trans. (2007) 585.
[10] K.C. Jayaratne, L.R. Sita, J. Am. Chem. Soc. 122 (2000) 958.
[11] Y. Zhang, L.R. Sita, Chem. Commun. (2003) 2358.
[12] Y. Zhang, R.J. Keaton, L.R. Sita, J. Am. Chem. Soc. 125 (2003) 9062.
[13] Y. Zhang, L.R. Sita, J. Am. Chem. Soc. 126 (2004) 7776.
[14] M.B. Harney, Y. Zhang, L.R. Sita, Angew. Chem., Int. Ed. Engl. 45 (2006) 2400.
[15] M.B. Harney, Y. Zhang, L.R. Sita, Angew. Chem., Int. Ed. Engl. 45 (2006) 6140.
[16] S. Bambirra, D.V. Leusen, A. Meetsma, B. Hessen, J.H. Teuben, Chem. Commun. (2003) 522.
[17] B. Thomas, M. Vince, V.B. Johannes, A.M. PCT, Int. Appl., 1999, WO 9905154.
[18] S. Bambirra, M.W. Bouwkamp, A. Meetsma, B. Hessen, J. Am. Chem. Soc. 126 (2004) 9182.
[19] S. Bambirra, A. Meetsma, B. Hessen, Organometallics 25 (2006) 3454.
[20] A.A. Trifonov, G.G. Skvortsov, D.M. Lyubov, N.A. Skorodumova, G.K. Fukin, E.V. Baranov, V.N. Glushakova, Chem. Eur. J. 12 (2006) 5320.
[21] J. Barker, N. Cameron, M. Kilner, M.M. Mahoud, S.C. Wallwork, J. Chem. Soc., Dalton Trans. (1986) 1359.
[22] J. Barker, M. Kilner, R.O. Gould, J. Chem. Soc., Dalton Trans. (1987) 2687.
[23] C.L. Yao, L.P. He, J.D. Korp, J.L. Bear, Inorg. Chem. 27 (1988) 4389.
[24] D.I. Arnold, F.A. Cotton, D.J. Maloney, J.H. Matonic, Polyhedron 16 (1997) 133.
[25] J.F. Berry, F.A. Cotton, S.A. Ibragimov, C.A. Murillo, X. Wang, Inorg. Chem. 44 (2005) 6129.
[26] E. Nelkenbaum, M. Kapon, M.S. Eisen, J. Organomet. Chem. 690 (2005) 2297.
[27] E. Nelkenbaum, M. Kapon, M.S. Eisen, J. Organomet. Chem. 690 (2005) 3154.
[28] E. Nelkenbaum, M. Kapon, M.S. Eisen, Organometallics 24 (2005) 2645.
[29] C. Wang, S. Friedrich, T.R. Younkin, R.T. Li, R.H. Grubbs, D.A. Bansleben, M.W. Day, Organometallics 17 (1998) 3149.
[30] T.R. Younkin, E.F. Conner, J.I. Henderson, S.K. Friedrich, R.H. Grubbs, D.A. Bansleben, Science 287 (2000) 460.
[31] S.D. Ittel, L.K. Johnson, M. Brookhart, Chem. Rev. 100 (2000) 1169.
[32] V.C. Gibson, S.K. Spitzmesser, Chem. Rev. 103 (2003) 283.
[33] A. Zeller, E. Herdtweck, T. Strassner, Eur. J. Inorg. Chem. (2003) 1802.
[34] R.T. Boeré, V. Klassen, G. Wolmershäuser, J. Chem. Soc., Dalton Trans. (1998) 4147.
[35] C.A. Nijhuis, E. Jellema, T.J.J. Sciarone, A. Meetsma, P.H.M. Budzelaar, B. Hessen, Eur. J. Inorg. Chem. (2005) 2089.
[36] R.L. Stapleton, J. Chai, N.J. Taylor, S. Collins, Organometallics 25 (2006) 2514.
[37] S. Collins, T. Ziegler, Organometallics 26 (2007) 6612.
[38] D.P. Gates, S.A. Svejda, E. Onate, C.M. Killian, L.K. Johnson, P.S. White, M. Brookhart, Macromolecules 33 (2000) 2320.
[39] C. Carlini, A. Macinai, F. Masi, A.M.R. Galletti, R. Santi, G. Sbrana, A. Sommazzi, J. Polym. Sci., Part A: Polym. Chem. 42 (2004) 2534.
[40] T.F.A. Haselwander, W. Heitz, Macromol. Rapid Commun. 18 (1997) 689.
[41] H.-Y. Gao, W.-J. Guo, F. Bao, G.-Q. Gui, J.-K. Zhang, F.-M. Zhu, Q. Wu, Organometallcs 23 (2004) 6273.
[42] H.-Y. Gao, J.-K. Zhang, Y. Chen, F.-M. Zhu, Q. Wu, J. Mol. Catal. A: Chem. 240 (2005) 178.
[43] H.-Y. Gao, L.-X. Pei, Y.-F. Li, J.-K. Zhang, Q. Wu, J. Mol. Catal. A: Chem. 280 (2008) 81.
[44] P.G. Lassahn, C. Janiak, J.S. Oh, Macromol. Rapid Commun. 23 (2002) 16.
[45] T.F.A. Haselwander, W. Heitz, S.A. Krugel, J.H. Wendorff, Macromol. Chem. Phys. 197 (1996) 3435.
[46] C. Zhao, M.R. Ribeiro, M.N. Pinho, V.S. Subrahmanyam, C.L. Gil, A.P. Lima, Polymer 42 (2001) 2455.

Polyhedron 28 (2009) 679–688

Contents lists available at ScienceDirect

Polyhedron

journal homepage: www.elsevier.com/locate/poly

Construction of metal–organic frameworks with transitional metals based on the 3,5-bis(4-pyridyl)-1*H*-1,2,4-triazole ligand

Xiao-Feng Xie, San-Ping Chen, Zheng-Qiang Xia, Sheng-Li Gao *

Key Laboratory of Synthetic and Natural Functional Molecule Chemistry of Ministry of Education, Department of Chemistry, Northwest University, Xi'an, Shaanxi 710069, China

ARTICLE INFO

Article history:
Received 10 October 2008
Accepted 12 December 2008
Available online 3 February 2009

Keywords:
3,5-Bis(4-pyridyl)-1*H*-1,2,4-triazole (Hbpt)
In situ metal/ligand reaction
Coordination complex
Benzenedicarboxylate ligand
X-ray diffraction

ABSTRACT

Based on the versatile ligand 3,5-bis(4-pyridyl)-1*H*-1,2,4-triazole (Hbpt) derived from an in situ metal/ligand reaction, a series of coordination compounds $CoCl_4(H_3bpt)(H_2O)$ (**1**), $Cu(H_2bpt)_2(SO_4)_2(H_2O)_6$ (**2**), $[Ag(bpt)]_n$ (**3**), $[Co(Hbpt)(pa)]_n$ (**4**), $[Co(Hbpt)(pda)]_n$ (**5**) and $[Cu(Hbpt)(pda)(H_2O)]_n$ (**6**) have been constructed (pa = phthalate, pda = 1,3-phenylenediacetate). The structures of these targeted complexes have been characterized by X-ray single-crystal diffraction techniques. Structural analysis reveals that Hbpt adopts versatile coordination modes to arrange the metal ions in 0-D point, simple (4,4) layers and dinuclear core chains in **1**–**3**, which are further extended via the benzenedicarboxylate connectors to give rise to a variety of coordination networks such as (4,4), $(4^{12}\cdot 6^3)$, $(6^4\cdot 8^2)$ topologies in **4**–**6**. The supramolecular organization through hydrogen bonds is analyzed for these complexes and thermal stability of these crystalline materials has been explored by TG-DTG.

© 2009 Elsevier Ltd. All rights reserved.

1. Introduction

In coordination and supramolecular chemical fields, metal–organic frameworks (MOFs) have intrigued great interest for their potential application in catalysis, gas absorption, non-linear optics, ion-exchange, luminescence, magnetism and many other fields [1–7]. In principle, the design and syntheses of metal–organic networks via the self-assembly of metal ions and multifunctional ligands greatly depend on the organic ligands (spacers) and metal ions (nodes). Linear 4,4′-bipyridine(4,4′-bpy) and 4,4′-bipyridine-like N,N′-donor ligands are often used as spacers to form open metal–organic frameworks [8–11]. Through introducing moieties between the two 4-pyridyl groups, several couples of bent N,N′-donor ligands, such as 2,5-bis(4-pyridylethynyl) thiophene and 4-amino-3,5-bis(4-pyridyl)-1,2,4-triazole, have been used as building blocks to extend metal–organic frameworks [12–17]. Here we introduce the 1*H*-1,2,4-triazole moiety between the two 4-pyridyl groups due to the following considerations. First, it can act as a bridge between metal centers, thus mediating exchange coupling, and represents a hybrid of pyrazole and imidazole with regard to the arrangement of its three heteroatoms thus promising a rich and versatile coordination chemistry. Second, the prototropy and conjugation between the 1*H*-1,2,4-triazole and 4-pyridyl groups not only alter the electron density in different parts of the molecule, but also make the ligand more flexible, in addition, the wide application in spin-crossover materials and pharmacologically active compounds also makes this moiety more attractive [18–20]. Benzenedicarboxylate species such as phthalate (pa), isophthalate (ip), 1,3-phenylenediacetate (pda) and terephthalate (tp) are widely used in the construction of MOFs, because of their abilities to form non-covalent cooperative forces such as hydrogen bonding and/or aromatic stacking, and to compensate the charge for the neutral ligand [21–24].

Nowadays in situ metal/ligand reactions show great merit in both coordination chemistry and organic synthesis [25,26]. Herein, by using a coordination compound as an intermediate, 3,5-bis(4-pyridyl)-1*H*-1,2,4-triazole has been synthesized via an in situ metal/ligand reaction.

With this understanding, one crucial aim of this work is to explore the introduction effect of 1*H*-1,2,4-triazole for tuning the structural assembly, which may provide further insights in designing new hybrid crystalline materials. In the present work, we report the synthesis of Hbpt and six new coordination polymers, namely $CoCl_4(H_3bpt)(H_2O)$ (**1**), $Cu(H_2bpt)_2(SO_4)_2(H_2O)_6$ (**2**), $[Ag(bpt)]_n$ (**3**), $[Co(Hbpt)(pa)]_n$ (**4**), $[Co(Hbpt)(pda)]_n$ (**5**) and $[Cu(Hbpt)(pda)(H_2O)]_n$ (**6**). The compounds have been structurally determined by single-crystal X-ray diffraction, and characterized by IR and TG-DTG.

2. Experimental

2.1. Materials and analytical methods

All of the reagents were commercially available without further purification. C, H, N contents were determined on a Vario EL III

* Corresponding author.
E-mail address: gaoshli@nwu.edu.cn (S.-L. Gao).

0277-5387/$ - see front matter © 2009 Elsevier Ltd. All rights reserved.
doi:10.1016/j.poly.2008.12.046

analyzer. IR spectra were recorded on a Tensor 27 spectrometer (Bruker Optics, Ettlingen, Germany). All NMR spectra were measured on a Varian INOVA 400 MHz spectrometer. Thermogravimetric analysis was performed on a Netzsch STA 449C simultaneous TGA with a heating rate of 10 °C min^{-1} under nitrogen.

2.2. Syntheses and characterization

2.2.1. 3,5-Bis(4-pyridyl)-1H-1,2,4-triazole (Hbpt)

The Hbpt ligand was synthesized via an in situ metal/ligand reaction and demetallation as followed (Scheme 1): a mixture of 4-cyanopyridine (1.04 g, 10.0 mmol), aqueous ammonium (2.0 mL), $CuSO_4 \cdot 5H_2O$ (0.249 g, 1.0 mmol) and water (5 mL) in a 20-mL Teflon-lined autoclave was treated at 140 °C for 72 h. The resulting mixture was filtered to give crystalline $[Cu_2(bpt)_2]$ in 40% yield based on 4-cyanopyridine.

The product then underwent a process of demetallation: the powder was placed in a 200 mL flask containing 100 mL water, into which 2 mL ammonium sulfide was dropped with stirring. After 0.5 h the solution became dark, and then was boiled to make CuS crystallize out completely. It was then filtered to give a colorless solution and concentrated to afford 3,5-bis(4-pyridyl)-1*H*-1,2,4-triazole (Hbpt) (390 mg, 35% based on 4-cyanopyridine) as a white powder.

Mp 296–297 °C; IR (cm^{-1}, KBr): 3408(w), 3088(m), 2623(m), 1606(s), 1580(s), 1447(m), 1423(m), 1378(m), 1362(m), 1152(s), 1015(m), 987(m), 832(s), 720(m), 709(m), 528(s); ^1H NMR (400 MHz, DMSO-d_6, δ ppm): 8.010–8.025 (4H, d, J = 4.4 Hz), 8.768–8.779 (4H, d, J = 4.4 Hz), 15.232 (1H, s, Triazole-H); *Anal.* Calc. for $C_{12}H_9N_5$: C, 64.56; H, 4.06; N, 31.37. Found:C, 64.63; H, 4.19; N, 32.00%.

2.2.2. $CoCl_4(H_3bpt)(H_2O)$ (**1**)

$CoCl_2 \cdot 6H_2O$ (0.047 g, 0.2 mmol) was added to a methanol solution (10 mL) of Hbpt (44.6 mg, 0.2 mmol) with stirring. The resulting solution was filtered and kept at room temperature for crystallization. After 10 days, light blue crystals of **1** suitable for an X-ray crystallographic study were obtained in a yield of 27% (based on Co). *Anal.* Calc. for **1** ($C_{12}H_{13}Cl_4CoN_5O$): C, 32.46; H, 2.95; N, 15.77. Found: C, 32.41; H, 2.87; N, 15.76%. IR (cm^{-1}, KBr): 3404(w), 3085(m), 2617(m), 1636(m), 1606(w), 1570(s), 1445(s), 1374(m), 1366(m), 1154(s), 1045(m), 967(m), 812(s), 710(m), 521(s).

2.2.3. $Cu(H_2bpt)_2(SO_4)_2(H_2O)_6$ (**2**)

The same synthetic procedure as that for **1** was used except that $CoCl_2 \cdot 6H_2O$ was replaced by $CuSO_4 \cdot 5H_2O$, and blue block X-ray-quality crystals were obtained in a yield of 27% (based on Cu). *Anal.* Calc. for **2** ($C_{24}H_{32}CuN_{10}O_{14}S_2$): C, 35.49; H, 3.97; N, 17.24. Found: C, 35.57; H, 3.88; N, 16.98%. IR (cm^{-1}, KBr): 3409(w), 3085(m), 3019(w), 2617(m), 1626(w), 1570(s), 1426(s), 1374(m), 1366(m), 1154(s), 1017(m), 967(m), 840(s), 736(m), 521(s).

2.2.4. $[Ag(bpt)]_n$ (**3**)

A solution of Hbpt (4.46 mg, 0.020 mmol) in MeOH (10 mL) was carefully layered onto a solution of $AgNO_3$ (3.40 mg, 0.020 mmol) in H_2O (10 mL). The solution was left for 6 days at room temperature, and colorless crystals were obtained in a yield of 78% (based on Ag). *Anal.* Calc. for **3** ($C_{12}H_8AgN_5$): C, 43.66; H, 2.44; N, 21.22. Found: C, 43.54; H, 2.60; N, 21.34%. IR (cm^{-1}, KBr): 3502(w), 3321 (w), 1635(s), 1375(vs), 1532(w), 1482(w), 1307(s), 1215(m), 1037(w), 834(s), 735(w).

2.2.5. $[Co(Hbpt)(pa)]_n$ (**4**)

A mixture containing $Co(OAc)_2 \cdot 4H_2O$ (24.9 mg, 0.10 mmol), Hbpt (22.3 mg, 0.10 mmol), H_2pa (16.6 mg, 0.10 mmol) and water (6 mL) was sealed in a 20 mL Teflon-lined stainless steel vessel, which was heated at 140 °C for 3 days and then cooled to room temperature at a rate of 5 °C/h. Red prism crystals of **4** were collected in a yield of 55% (based on Co). *Anal.* Calc. for **4** ($C_{20}H_{15}CoN_5O_5$): C, 51.74; H, 3.26; N, 15.08. Found: C, 51.65; H, 3.31; N, 15.15%. IR (cm^{-1}, KBr): 3345(s), 3260(s), 1643(w), 1604(s), 1550(s), 1485(s), 1461(s), 1403(s), 1378(s), 1225(m), 1038(w), 1060(w), 1020(s), 995(m), 952(w), 839(m), 771(m), 731(m), 704(s), 604(s), 508(m).

2.2.6. $[Co(Hbpt)(pda)]_n$ (**5**)

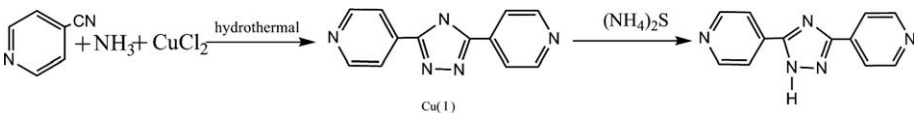
The same synthetic procedure as that for **4** was used except that H_2pa was replaced by H_2pda, and red prismatic crystals of **5** were collected in a yield of 50% (based on Co). *Anal.* Calc. for **5** ($C_{22}H_{17}CoN_5O_4$): C, 55.71; H, 3.61; N, 14.76. Found: C, 55.65; H, 3.58; N, 14.85%. IR (cm^{-1}, KBr): 3332(s), 1635(s), 1615(s), 1581(m), 1544(s), 1456(s), 1399(s), 1220(m), 1036(w), 917(w), 836(s),740(s), 720(s), 615(m), 521(m), 433(m).

2.2.7. $[Cu(Hbpt)(pda)(H_2O)]_n$ (**6**)

The same synthetic procedure as that for **5** was used except that $Co(OAc)_2 \cdot 4H_2O$ was replaced by $Cu(OAc)_2 \cdot 4H_2O$, and blue prismatic crystals of **6** were collected in a yield of 57% (based on Cu). *Anal.* Calc. for **6** ($C_{22}H_{19}CuN_5O_5$): C, 53.17; H, 3.85; N, 14.09. Found: C, 53.22; H, 3.88; N, 14.14%. IR (cm^{-1}, KBr): 3410(w), 1635(s), 1605(s), 1575(m), 1537(s), 1404(s), 1378(s), 1235(m), 1112(w), 1032(w), 910(w), 854(s),735(s), 700(s), 613(m), 523(m), 444(m).

2.3. Crystal structure determination and structure refinement

All diffraction data for complexes **1–6** were collected on a Bruker/Siemens Smart Apex II CCD diffractometer with graphite monochromated Mo Kα radiation (λ = 0.71073 Å) at 293(2) K. Cell parameters were retrieved using SMART [27] software and refined using SAINTPLUS [28] for all observed reflections. Data reduction and correction for Lp and decay were performed using the SAINTPLUS software. Absorption corrections were applied using SADABS [29]. All structures were solved by the direct methods using the SHELXS program of the SHELXTL-97 [30] package and refined with SHELXL. Metal atoms in all the complexes were located from the E-maps and other non-hydrogen atoms were located in successive difference Fourier syntheses. The final refinements were performed by full-matrix least squares methods with anisotropic thermal parameters for non-hydrogen atoms on F^2. The H atoms of triazole and pyridyl(N) in Hbpt were located from difference Fourier maps, all other hydrogen atoms were included in calculated positions and refined with isotropic thermal parameters riding on those of the parent atoms. The oxygen atoms (O(1), O(2)) of pda anions in **6** are disordered and an occupancy ratio of 0.6:0.4 was found. Details of the data collection and refinement are given



Scheme 1. In situ synthesis of the Hbpt ligand.

Table 1
Crystal data for **1–6**.

	1	2	3	4	5	6
Formula	$C_{12}H_{13}Cl_4CoN_5O$	$C_{24}H_{32}CuN_{10}O_{14}S_2$	$C_{12}H_8AgN_5$	$C_{20}H_{15}CoN_5O_5$	$C_{22}H_{17}CoN_5O_4$	$C_{22}H_{19}CuN_5O_5$
Formula weight	444.00	812.26	330.10	464.30	474.34	496.46
Crystal system	monoclinic	triclinic	monoclinic	triclinic	monoclinic	monoclinic
Space group	*Cc*	$P\bar{1}$	$P2_1/c$	$P\bar{1}$	C_2/c	C_2/c
a (Å)	11.951(3)	7.108(2)	7.609(2)	8.006(4)	24.347(7)	17.779(4)
b (Å)	18.004(3)	8.365(2)	11.332(3)	10.491(5)	10.291(3)	11.958(3)
c (Å)	8.303(2)	14.786(3)	12.944(4)	12.987(6)	16.337(5)	20.137(4)
α (°)	90	73.586(4)	90	66.922(9)	90	90
β (°)	94.423	88.270(4)	104.414(6)	80.276(9)	90.854(6)	97.473(5)
γ (°)	90	67.658(3)	90	68.379(9)	90	90
V (Å^3)	1781.2(7)	777.1(3)	1081.0(6)	932.5(8)	4093(2)	4245(2)
Z	4	1	4	2	8	8
D_{calc} (g cm^{-3})	1.656	1.736	2.028	1.654	1.540	1.554
F(000)	892	419	648	474	1944	2036
R_{int}	0.0425	0.0235	0.0489	0.0844	0.0948	0.0657
Goodness-of-fit on F^2	0.958	0.841	0.997	1.171	0.916	1.130
R_1[a], wR_2[b] [$I > 2\sigma(I)$]	0.0356, 0.0515	0.0449, 0.1268	0.0379, 0.1128	0.1130, 0.2433	0.0473, 0.0536	0.0579, 0.1223
R_1[a], wR_2[b] [all data]	0.0605, 0.0566	0.0660, 0.1558	0.0717, 0.1224	0.2043, 0.2656	0.1275, 0.0617	0.1221, 0.1347
Largest difference in peak/hole (e Å^{-3})	0.264 and −0.304	0.725 and −0.838	0.454 and −0.660	1.146 and −1.599	0.398 and −0.343	0.767 and −0.551

[a] $R_1 = \sum(|F_O| - |F_C|)/\sum|F_O|$.
[b] $R_2 = \{\sum[w(F^2_O - F^2_C)^2]/\sum w(F^2_O)^2]\}^{1/2}$.

in Table 1, selected bond lengths and angles are tabulated in Table S1 and selected hydrogen-bonding geometries for **1**, **2**, **4**, **5** and **6** are listed in Table S2. Further details are provided in the Supplementary data.

3. Results and discussion

3.1. Syntheses of the compounds and IR spectroscopy

3,5-Bis(4-pyridyl)-1*H*-1,2,4-triazole (Hbpt) can be considered as a new member of the group of five-membered heterocyclic ring bridging organic ligands. Compared with other widely investigated N,N′-bipyridine-type ligands, Hbpt is endowed with more structural information, especially for the diverse configurations of the protons on the N atoms. The nitrogen atoms of Hbpt are potential acceptors and donors for hydrogen bonds to expand polymeric frameworks. Interestingly, in the MOFs **1–6**, the ligand exhibits four different states: bpt^-, Hbpt, H_2bpt^+ and H_3bpt^{2+}, which results in the formation of abundant hydrogen bonds (Scheme 2). It is worth noting that ammonium sulfide is an excellent agent for the demetallation of the copper complex. The current approach provides a novel facile route to synthesize this kind of compound.

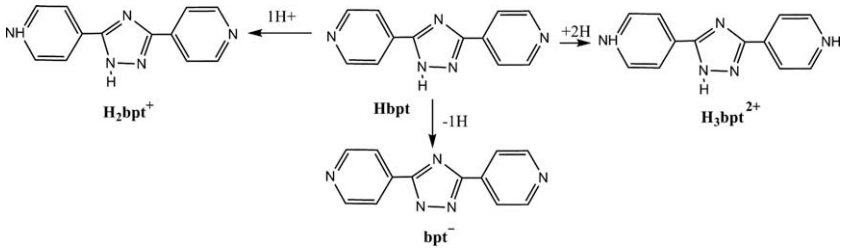
Three synthetic approaches were applied to construct these coordination polymers. With regard to MOFs **4–6**, they were prepared under hydrothermal conditions, whereas assemblies of the others were carried out under aqueous conditions or using diffusion. In each synthetic case, an approximate metal/ligand composition of 1:1:1/1:1 was utilized for the starting materials. Coordination polymers **1–6** are air stable with the maintenance of their crystallinity for at least several weeks.

In the IR spectra of complexes **1**, **2** and **6**, the broad band centered at 3400 cm^{-1} indicates the O–H stretching of the aqua molecules. The absorption band resulting from the skeletal vibrations of the aromatic rings for all three complexes appears in the 1400–1600 cm^{-1} region. In complexes **4–6**, the characteristic bands of the dicarboxylate groups unit are found at 1610 and 1490 cm^{-1} for asymmetric stretching and 1380 cm^{-1} for symmetric stretching. The strong bands between 1640 and 1630 cm^{-1} and near 1037 cm^{-1} are assignable to the characteristic bands of 1,2,4-triazole. All these spectral features are consistent with the crystal structures as described below.

3.2. Descriptions of crystal structures

3.2.1. Structure of $CoCl_4(H_3bpt)(H_2O)$ (**1**)

As shown in Fig. 1 **1** contains one H_3bpt^{2+} ion, one $[CoCl_4]^{2-}$ ion and one lattice water (Fig. 1). The cobalt cation is coordinated by four chloride anions, which forms a tetrahedral structure. The average Co–Cl bond length is 2.28 Å and the Cl–Co–Cl bond angles are in the range 104.75(6)–112.45(6)°, which are close to the ideal tetrahedral value and are in good agreement with the previously reported bond lengths and angles of a tetrahedral cobalt compound [31]. The Hbpt ligand is protonated by two protons which are attached to the two terminal N atoms (N4, N5). All the three N–H groups (include triazole-H) interact with the chlorides and the water molecule, forming many hydrogen bonds, with O···Cl distances of 3.203(5), 3.106(5), N···Cl distances of 3.222(4), 3.257(5) and N···O distances of 2.700(6), 3.173(3) Å (Fig. 2, Table S2). As is well-known, a water molecule has two hydrogen atoms and two lone-electron pairs, which enables it to participate in four



Scheme 2. Different forms of the Hbpt ligand in **1–6**.

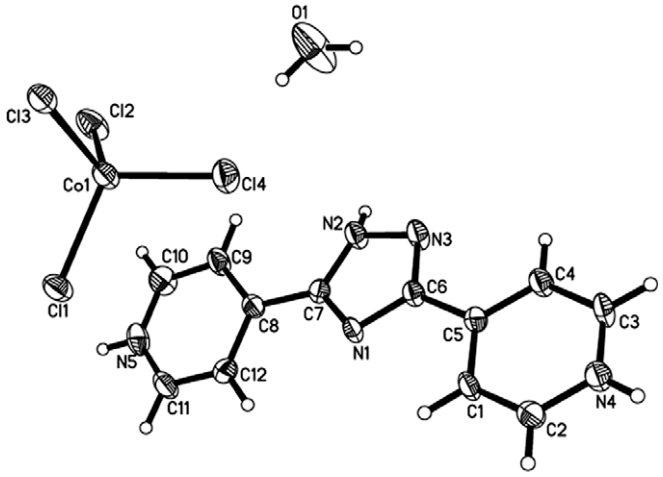


Fig. 1. Thermal displacement diagrams (30%) for **1**.

hydrogen bonds in a tetrahedral configuration, but it also frequently shows a 3-coordinate configuration [32]. In **1**, the lattice water O1 also shows a 3-coordinate mode. Through these hydrogen bonds, the molecule is assembled into a three-dimensional structure (Fig. 2).

3.2.2. Structure of $Cu(H_2bpt)_2(SO_4)_2(H_2O)_6$ (**2**)

Compound **2** consists of a discrete centrosymmetrical $[Cu(H_2bpt)_2(H_2O)_4]^{4+}$ cation, two $[SO_4]^{2-}$ anions and two lattice water molecules, it is more accurate to describe the complex as $[Cu_{0.5}(H_2bpt)(H_2O)_2](SO_4)(H_2O)$. The crystal structure of the cationic mononuclear unit is depicted in Fig. 3. The Cu^{II} ion is located at a crystallographic inversion center, and six coordinated to four aqua ligands in the equatorial plane, as well as two H_2bpt^+ ligands in axial positions. To the two N atoms in the terminal pyridyl (N1, N5) of Hbpt ligand, N5 is coordinated to Cu, while the other is saturated with a proton, forming a +1 cation. The coordination geometry of the metal center can be described as a slightly distorted octahedron with O–Cu–N and O–Cu–O angles in the range

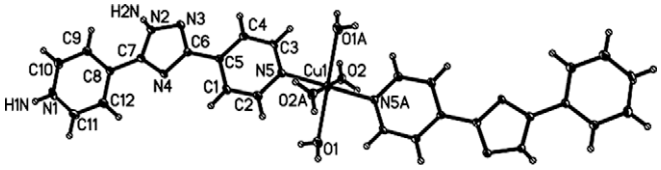


Fig. 3. Thermal displacement diagrams (30%) for **2** ($[Cu(H_2bpt)_2(H_2O)_4]^{4+}$ cation).

86.41(6)–93.59(6)°. The two pyridine rings within each ligand form dihedral angles of 10.03 and 3.42°, respectively, with the central triazole plane, and a dihedral angle of 8.59° with each other.

Herein the Hbpt ligand uses only one of the pyridyl nitrogen atoms to bind the metal center. The other uncoordinated pyridyl nitrogen serves as the hydrogen bond donor to the sulfate anions with a O···N distance of 2.696(4) Å. In the S_4 tetramer of the coordinated aqua molecules (the tetramer of water can be defined as having S_4 symmetry), every monomer acts as a donor for the oxygen atoms from the sulfate ion. The lattice water O7 also serves as a hydrogen bond donor to form two hydrogen bonds with N4 from Hbpt and O4 from the sulfate ions, resulting in a $R_2^2(8)$ ring [33]. All the water molecules show a 2-coordinate configuration hydrogen bond. It is noteworthy that the four oxygen atoms of the sulfate ion form seven different hydrogen bonds with the Hbpt, coordinated water and lattice water. A $R_4^4(12)$ hydrogen bond ring is formed by the two adjacent sulfate anions and two coordinated water molecules (Fig. 4b) [33]. In **2**, the sulfate anions act as a binder extending the block $Cu(H_2bpt)_2(SO_4)_2(H_2O)_6$ into a three-dimensional network by mass hydrogen bonds (Fig. 4a).

3.2.3. Structure of $[Ag(bpt)]_n$ (**3**)

Single-crystal analysis of **3** reveals (Fig. 5) that the Ag^I lies in a trigonal planar (sum of N–Ag–N angles = 359.97°) coordination environment, which consists of two $N_{triazole}$ donors (N(3)–Ag(1) = 2.303(5) and Ag(1)–N(2) = 2.214(5) Å) from two $Hbpt^-$ ligands (the Hbpt ligand loses $H_{triazole}$ forming the bpt^- ion) and one $N_{pyridyl}$ donor (Ag(1)–N(1) = 2.254(5) Å) from the third Hbpt ligand. The Ag–$N_{triazole}$ bond length is considerably longer than those of the Ag–$N_{pyridyl}$ bonds, but all the Ag–N bond distances in

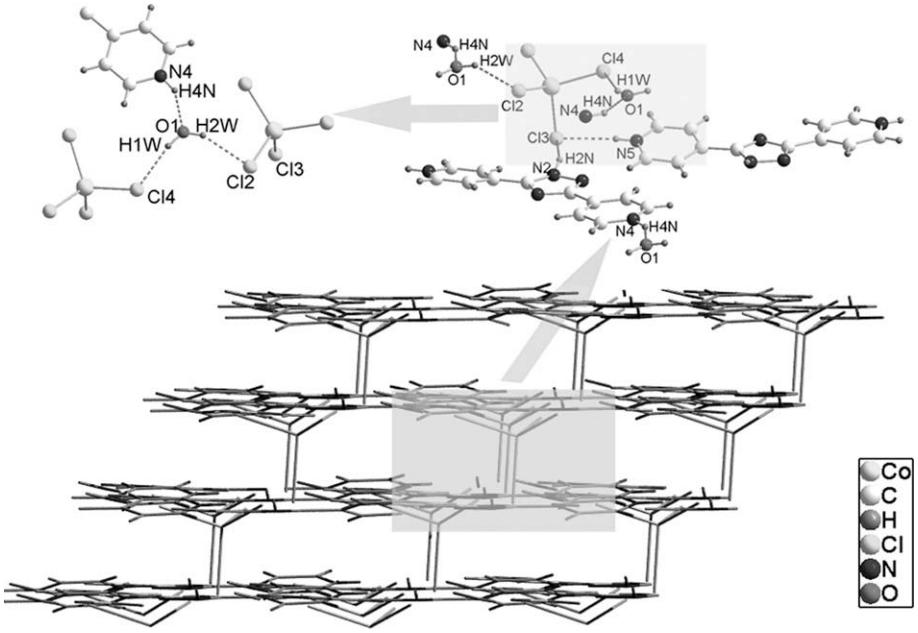


Fig. 2. The supramolecular structure formed by hydrogen bonds (H-bonds: dashed lines) for **1**.

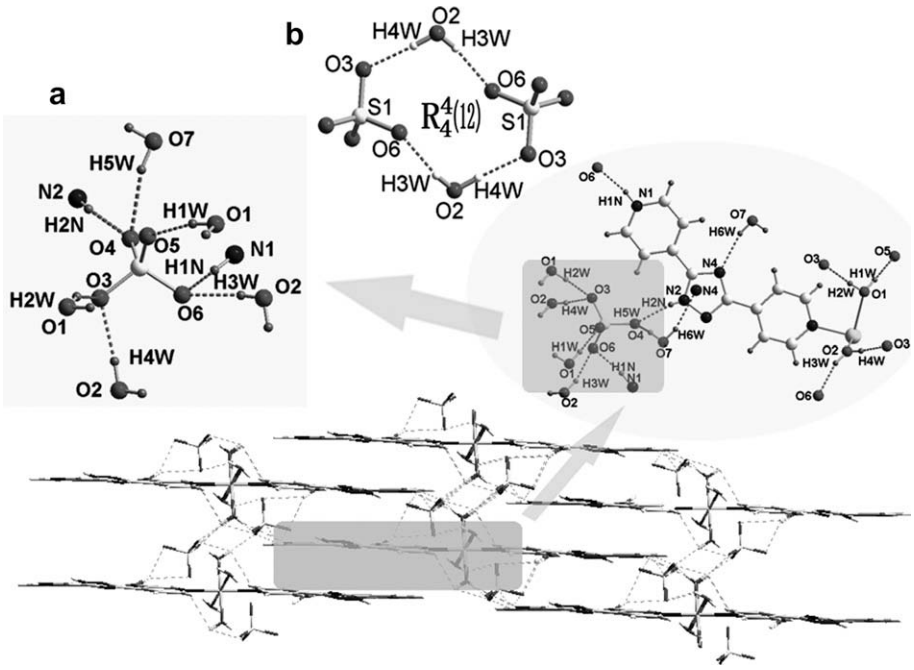


Fig. 4. (a) The supramolecular structure formed by hydrogen bonds (H-bonds: dashed lines) for **2**. (b) The R_4^4 (12) ring.

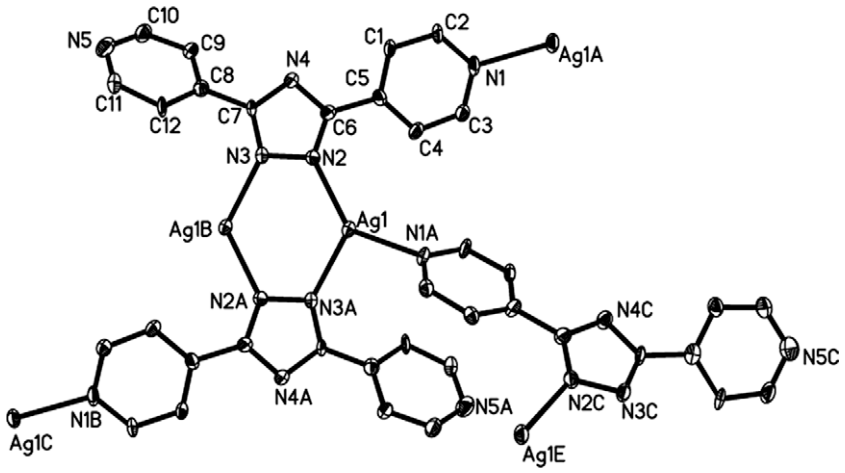


Fig. 5. Thermal displacement diagrams (30%) for **3**.

3 are within the normal range for N-containing heterocyclic Ag(I) complexes [17,34,35]. Each ligand is bonded to three Ag(I) centers (N1–Ag1A, N2–Ag1, N3–Ag1B). Interestingly, the two similar $N_{pyridyl}$ atoms of the Hbpt ligand have very different coordination behavior: N1 coordinates to one Ag atom while the N5 does not. Two Ag(1) atoms are bridged by four $N_{triazole}$ atoms into a dinuclear core with a short Ag···Ag contact of 3.492 Å (Fig. 6), which reveals the existence of an attractive metallophilic interaction [36,37]. The ligand itself is not planar, the corresponding dihedral angles between the three rings are [N(1)···C(5)]–[N(2)···N(3)] = 14.11°, [N(1)···C(5)]–[N(5)···C(12)] = 45.95° and [N(2)···N(3)]–[N(5)···C(12)] = 33.54°.

In the solid state, the Ag(I) centers and bpt^- ligands are linked together into a novel two-dimensional sheet, which is parallel to the [1 1 0] plane. As shown in Fig. 7, the single net mainly consists of a large ring. The large ring comprises a tetrameric unit, in which four Ag(I) centers are linked together by bpt^- ligands into an elliptical 32-membered macrocycle. While the two uncoordinated

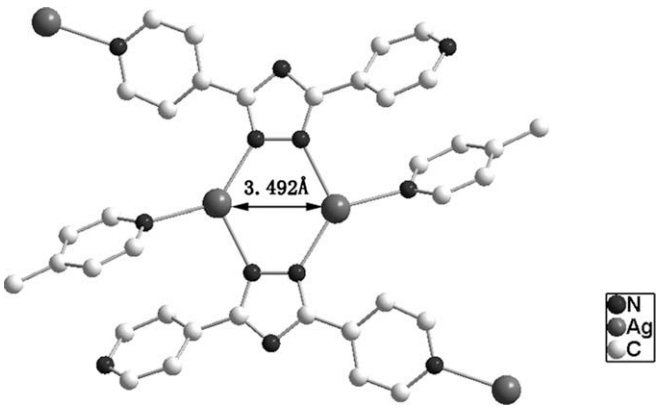


Fig. 6. Short Ag···Ag contacts in compound **3**.

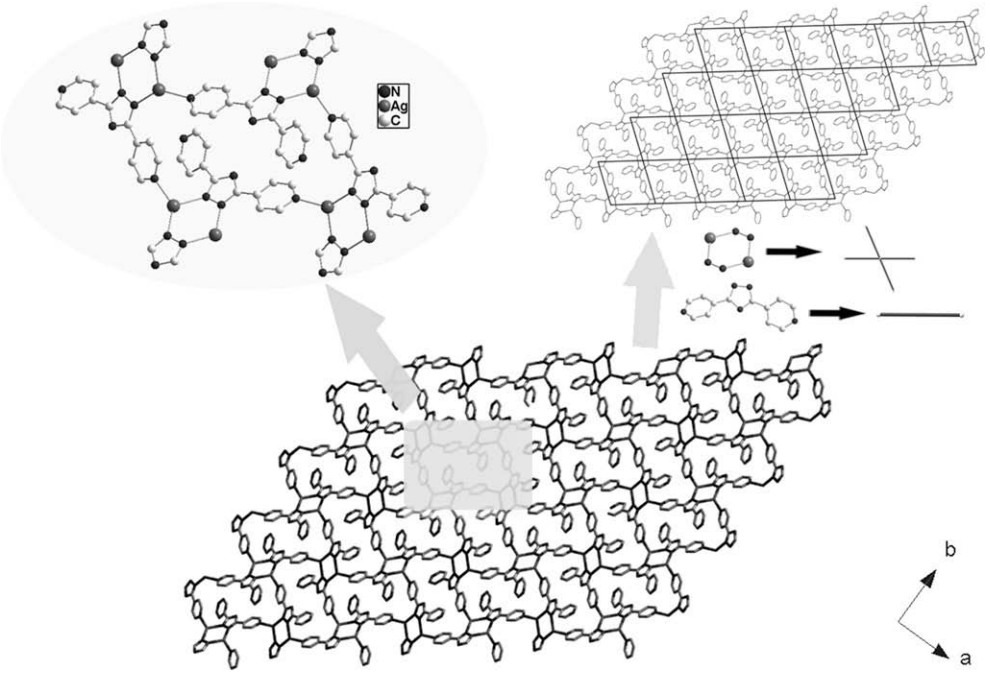


Fig. 7. The two-dimensional (4,4) sheet of compound **4**.

pyridyls of the bpt$^-$ ligands are embedded in this macrocycle. A schematic presentation for the construction of the two-dimensional (4,4) sheet is shown in Fig. 7.

3.2.4. Structure of $[Co(Hbpt)(pa)]_n$ (**4**)

The asymmetric coordination unit of **4** (see Fig. 8a) consists of a pair of Co^{II} ions, one Hbpt, one pa dianion and one aqua ligand. Both crystallographically independent Co^{II} ions lie on inversion centers and display a similar octahedral environment, which are provided by two pyridyl N donors and four carboxylate/water O atoms. As illustrated in Fig. 8b, one carboxylate is monodentate whereas the other adopts a *syn–anti* bridging mode. As a consequence, each Co^{II} ion forms a 7-membered chelated ring with pa, and the adjacent Co^{II} centers are connected by pa components with a separation of 5.245 Å to furnish a polymeric chain along the [0 1 0] direction, with phenyl decorating both sides alternatively. These 1-D arrays are further interlinked through Hbpt spacers to generate a 2-D (4,4) coordination layer along the *bc* plane with a Co···Co separation of 14.237 Å.

Further investigation of the crystal packing reveals that these parallel 2-D arrays are extended via interlayer N2–H2N···O5 interactions (see Table S2 for details) along [1 0 1] to build a 3-D architecture (see Fig. 8c). These hydrogen bonds show a pattern of R_2^2 (18) rings and a large R_2^2 (44) ring [33].

3.2.5. Structure of $[Co(Hbpt)(pda)]_n$ (**5**) and $[Cu(Hbpt)(pda)(H_2O)]_n$ (**6**)

Compounds **5** and **6** display a similar coordination environment as depicted in Fig. 9. Each distorted octahedral Co^{II}/Cu^{II} center is defined by four equatorial oxygen donors and two axial nitrogen atoms from three pda and a pair of Hbpt ligands (see Table S1 for detailed bond parameters). The carboxylate groups in each pda ligand function as a chelated bidentate and in a *syn–syn* bridging mode.

In **5** and **6**, the flexible carboxylate groups ($-CH_2COO^{2-}$) exhibit a *trans* configuration, which has a lesser steric hindrance effect and favors crystal growth [38]. However, the two terminal carboxylates ($-COO^{2-}$) of H_2pda are placed with two different patterns as shown

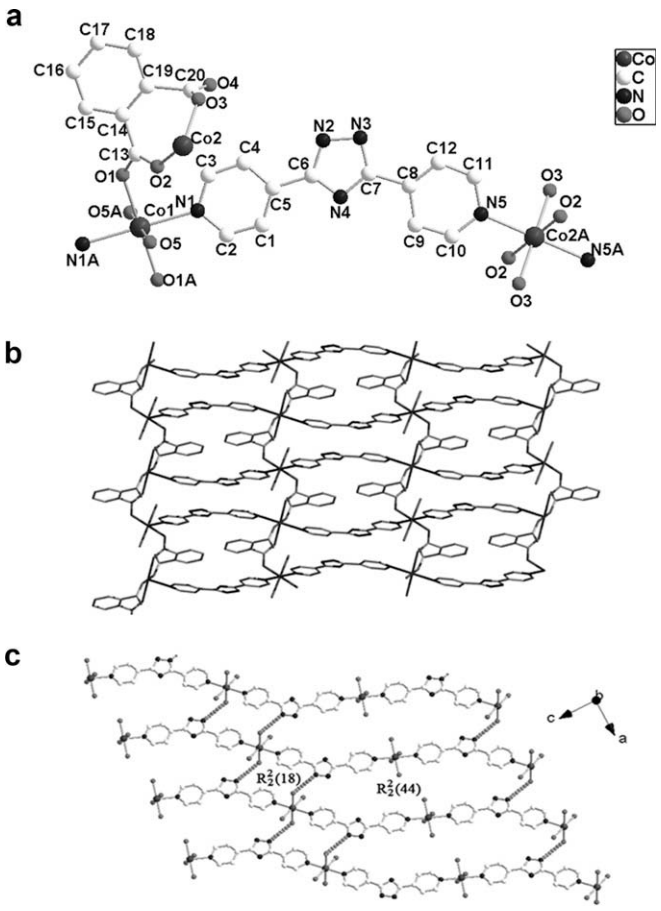


Fig. 8. (a) A portion view of **4** with the atom labelling of the asymmetric unit and Co^{II} coordination. The symmetry code is listed in Table S1. (b) 2-D (4,4) layered coordination framework of **4**. All hydrogen atoms are omitted for clarity. (c) The interlayer hydrogen-bonding interactions construct the 2-D layers into a 3-D network (H-bonds: dashed lines, the phenyl group of the pa ligand was omitted).

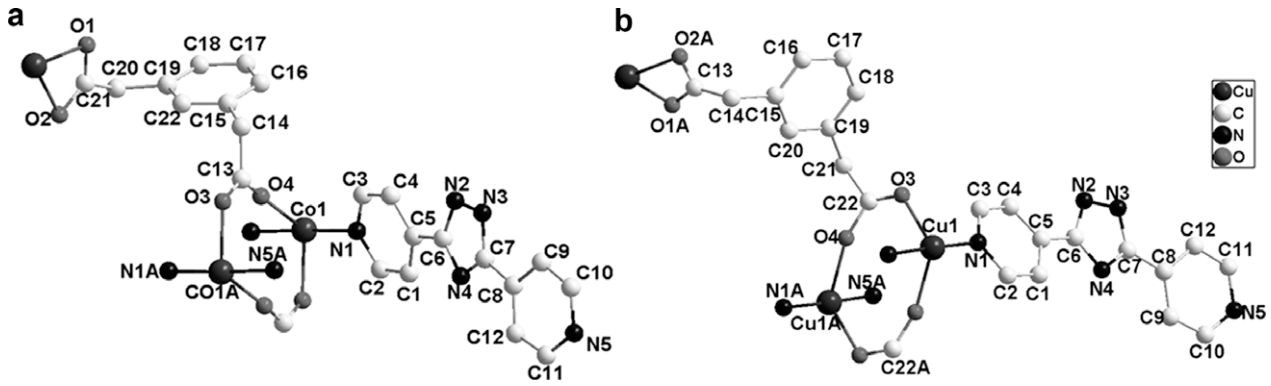


Fig. 9. A portion view of **4** with the atom labelling of the asymmetric unit and Co^{II} coordination. The symmetry code is listed in Table S1: (a) complex **5**; (b) complex **6**.

in Fig. 10, which significantly influences the final 3-D structure of these two similar complexes.

For **5**, as illustrated in Fig. 11a, the carboxylate adopts a chelated bidentate and *syn–syn* mode to bridge the adjacent Co^{II} centers together into a novel two-dimensional sheet parallel to the [1 0 0] plane. The 2-D sheet is composed of two different individual rings. A small dinuclear 7-membered-ring consists of two Co^{II} with two carboxylate groups of pda (Co···Co = 4.118 Å). The larger one comprises a tetrameric unit, in which four dinuclear core Co^{II} centers are linked by pda ligands into an elliptical 40-membered macrocycle. The two-dimensional macrocycle-containing nets can also be represented as a (4,4) net as Fig. 11b. From the *b* axes, the 2-D sheet can further assemble into a 3-D network through Hbpt ligands (Fig. 11c and d). A schematic presentation for the construction of the 3-D network is shown as Fig. 11b and e, the 3-D structure can be simplified as a $(4^{12}\cdot 6^3)$ or α-Po topology.

In **6**, a similar carboxylate group bridges the adjacent Cu^{II} centers together into a novel infinite chain rather than a plane view along the *c* axis; another similar chain is also formed in a different direction, and the pattern of these two similar chains is depicted in Fig. 12c. As shown in Fig. 12b, two Hbpt spacers bridge two adjacent dinuclear cores into a double-strand chain. The chains show an interconnected style as shown in Fig. 12d, the angle between the former two chains and the latter chain is 53.631(1)°. A schematic presentation for the construction of the 3-D network is shown in Fig. 12e, which is very different from **5** and can be simplified as $(6^4\cdot 8^2)$ or $CdSO_4$ topology.

It is also noteworthy that the hydrogen bond of $N_{triazole}$–$H_{triazole}$–O_{pda} links the adjacent Hbpt chains, which further stabilizes the 3-D network. A $R_2^2(18)$ hydrogen bond ring is also found in **6** as depicted in Fig. 13 [33].

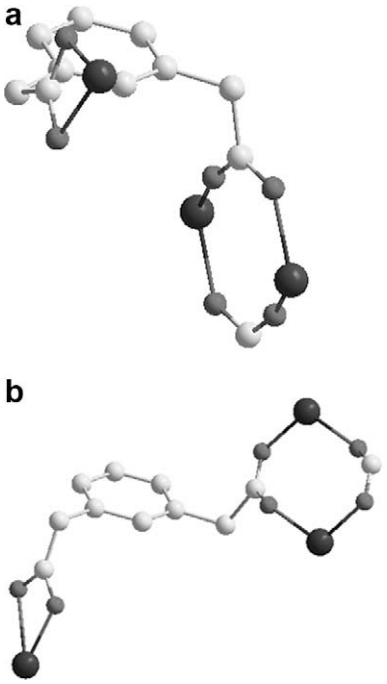


Fig. 10. The two patterns of Hpda in complex **5** (a) and **6** (b).

3.2.6. The coordination modes for the 3,5-bis(4-pyridyl)-1H-1,2,4-triazole ligand

It is noteworthy that Hbpt displays versatile valance states and abundant coordination modes in these metal–organic frameworks. In MOFs **1–6**, the ligand exhibits +2, +1, 0, −1 valance states and several coordination patterns, as illustrated in Schemes 2 and 3, respectively. When Hbpt acts as a neutral ligand, it behaves as a uniform bidentate connector in the 2-D, 3-D coordination networks in **4**, **5** and **6**. While Hbpt present in the form of H_2bpt^+ adopts a monodentate mode in **2**. No coordination action is found in **1** when all the two pyridyls are saturated by protons. An interesting tridentate mode is found in **3** where Hbpt loses the triazole proton.

It is obvious that the introduction of auxiliary dicarboxylate ligands greatly influences the coordination modes of Hbpt as well as the final supramolecular structures. In MOFs **1–3**, Hbpt exhibits abundant coordination modes, whereas it mostly behaves as a uniform bidentate connector in the mixed-ligand complexes **4–6**. In **4–6**, the carboxylate groups adopt the unidentate, chelating and bridging modes, which would be mostly responsible for the structural diversity. In MOFs **4** and **5**, with the variation of the phenyl dicarboxylate building blocks (from pa to pda), their network arrays are changed from 2-D isolated layer (4,4 topology) to 3-D network ($(4^{12}\cdot 6^3)$ topology). On the other hand, the choice of metal center plays a significant role in the resultant networks of MOFs, as shown in **5** and **6**.

The formation of many hydrogen bonds also accompanies the change of Hbpt ligand. In the complexes, except the deprotoned form of **3**, all the hydrogen atoms of the $N_{triazole}$ atoms serve as a donor forming strong hydrogen bonds with oxygen from water or the benzenedicarboxylate ligand with N···O distances ranging from 2.47(2) to 3.23(1) Å [39,40]. The protoned $N_{pyridyl}$ in **1** and **2** also serves as a donor, while the others serve as acceptors in the hydrogen bonds.

3.3. Thermal gravimetric analyses

All the compounds are air stable and can retain their crystallinity at room temperature for at least several weeks. Hence, TGA

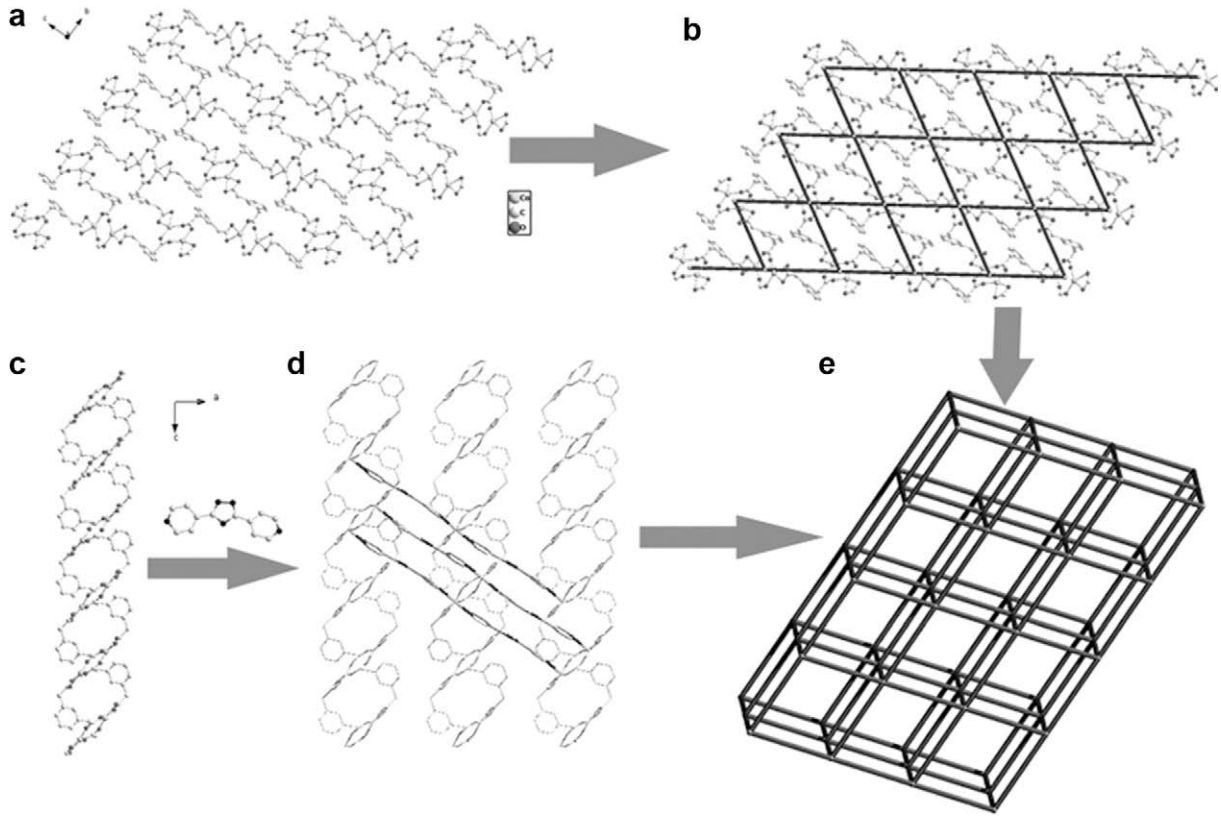


Fig. 11. Construction of the 3-D network for compound **5**: (a) 2-D sheet; (b) simplified 2-D sheet; (c) the 2-D sheet view from the *b* axis; (d) bridge the 2-D to 3-D network; (e) schematic presentation of the $(4^{12} \cdot 6^3)$ network.

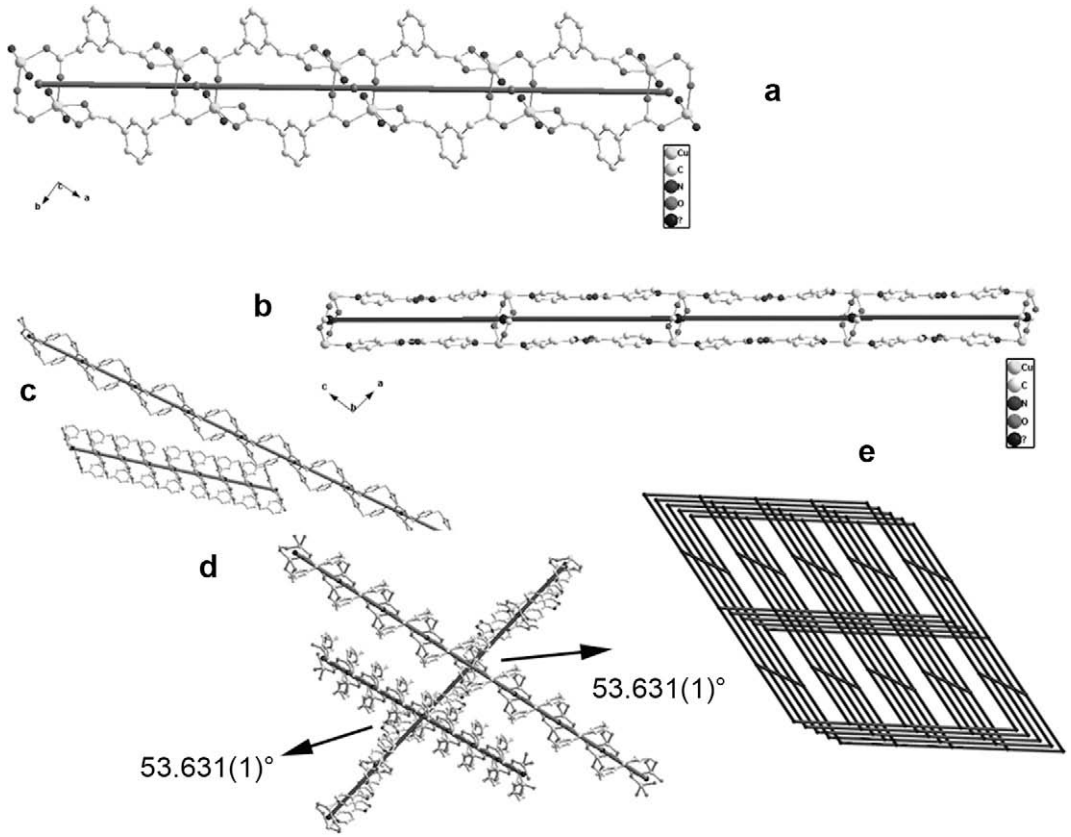


Fig. 12. Construction of the 3-D network for compound **6**: (a) the chain linked by the ip ligand; (b) the double-strand chain linked by bpt; (c) the pattern of the two ip-linked chain; (d) the interconnected style of three chain; (e) schematic presentation of the $(6^4 \cdot 8^2)$ network.

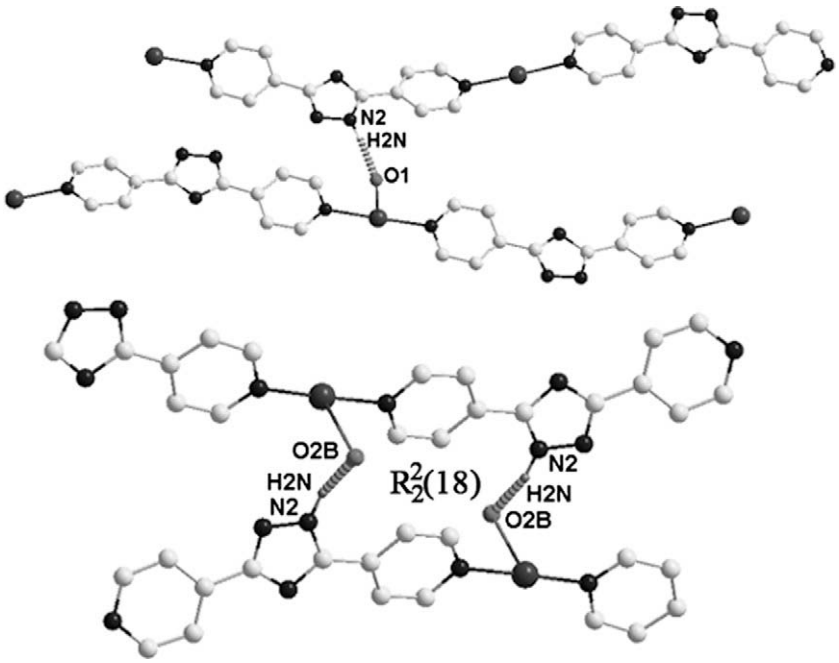
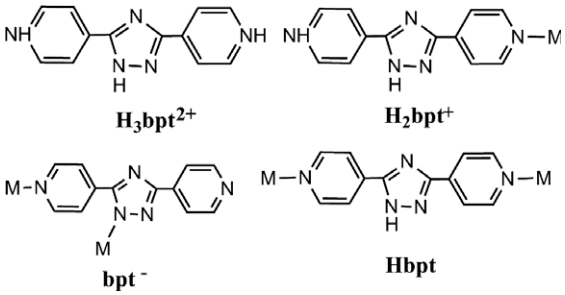


Fig. 13. The hydrogen-bonding interactions for compounds **5** (a) and **6** (b) (H-bonds: dashed lines).



Scheme 3. Coordination modes of the Hbpt ligand in **1**–**6**.

experiments were carried out to explore their thermal stability (see Figs. S1–S5 for TGA curves), which is an important parameter for coordination polymers. **1** quickly loses the free Hbpt ligand and lattice water and is completely converted to the corresponding oxide. In the TGA curve of **2**, the first weight loss of 4.40% in the range 177–243 °C (peak: 227 °C) corresponds to the expulsion of lattice water. The remaining substance is thermally stable up to 310 °C, following that, a series of weight losses occur, which do not end until 810 °C. **3** undergoes consecutive steps of weight loss (peaks: 372.5 and 393.1 °C) from 330.1 °C, which do not stop until 850 °C. For **4**, it remains stable up to 295.5 °C, and then undergoes two step weight losses, corresponding to the loss of the pa and Hbpt ligands, respectively before 675 °C. In **5**, we cannot see two such steps as in **4**, instead a total weight loss from 440 to 750 °C is present. **6** firstly loses the lattice water around 150 °C, and then is stable until 230.5 °C, after that a series of weight losses up to 750 °C are found. In this study, the lattice water molecules in **6** can be facilely excluded upon heating, the residuals have moderate thermal stability. Compound **5** shows the best thermal stability and is stable up to 375 °C, which could be ascribed to the stable 3-D network without lattice guests.

4. Conclusion

In summary, by using the new ligand 3,5-bis(4-pyridyl)-1*H*-1,2,4-triazole (Hbpt), six coordination compounds have been synthesized and characterized. Among them Hbpt exhibits various conformations and adopts different coordinate modes, which may be ascribed to the interactions between the 4-pyridyl and 1*H*-1,2,4-triazole groups. The introduction of dicarboxylate ligands greatly influences the coordination modes of Hbpt as well as the final supramolecular structures. Many hydrogen bonds are formed by the protonated and deprotonated forms of the Hbpt ligand. The results of this study not only illustrate the coordinated behavior of the versatile ligand, but also represent a new inorganic-assisted organic synthesis method. It is anticipated that more metal complexes containing this interesting ligand, as well as more ligands based on this method, will be synthesized.

Acknowledgements

We are grateful to financial support from the National Science Foundation of China (Nos. 20771089, 20873100) and the Natural Science Foundation of Shaanxi Province (Nos. 2007B02, SJ08B09).

Appendix A. Supplementary data

CCDC 697542, 697543, 697544, 697545, 697546 and 697547 contain the supplementary crystallographic data for **1**, **2**, **3**, **4**, **5** and **6**. These data can be obtained free of charge via http://www.ccdc.cam.ac.uk/conts/retrieving.html, or from the Cambridge Crystallographic Data Centre, 12 Union Road, Cambridge CB2 1EZ, UK; fax: (+44) 1223-336-033; or e-mail: deposit@ccdc.cam.ac.uk. Supplementary data associated with this article can be found, in the online version, at doi:10.1016/j.poly.2008.12.046.

References

[1] M. Eddaoudi, D.B. Moler, H.L. Li, B.L. Chen, T.M. Reineke, M. O'Keeffe, O.M. Yaghi, Acc. Chem. Res. 34 (2001) 319.
[2] B. Moulton, M.J. Zaworotko, Chem. Rev. 101 (2001) 1629.
[3] J.S. Seo, D. Whang, H. Lee, S.I. Jun, J. Oh, Y.J. Jeon, K. Kim, Nature 404 (2000) 982.
[4] O.M. Yaghi, M. O'Keeffe, N.W. Ockwig, H.K. Chae, M. Eddaoudi, J. Kim, Nature 423 (2003) 705.
[5] S. Kitagawa, R. Kitaura, S. Noro, Angew. Chem., Int. Ed. 43 (2004) 2334.
[6] H.L. Li, C.E. Davis, T.L. Groy, D.G. Kelley, O.M. Yaghi, J. Am. Chem. Soc. 120 (1998) 2186.

[7] J.P. Zhang, Y.Y. Lin, X.C. Huang, X.M. Chen, Chem. Commun. (2005) 1258.
[8] L.Y. Zhang, J.P. Zhang, Y.Y. Lin, X.M. Chen, Cryst. Growth Des. 6 (2006) 1684.
[9] X.M. Zhang, Z.M. Hao, H.S. Wu, Inorg. Chem. 44 (2005) 7301.
[10] M. Yaghi, H.L. Li, J. Am. Chem. Soc. 118 (1996) 295.
[11] B.H. Ye, M.L. Tong, X.M. Chen, Coord. Chem. Rev. 249 (2005) 545.
[12] Z. Huang, M. Du, H.B. Song, X.H. Bu, Cryst. Growth Des. 4 (2004) 71.
[13] H. Hou, L. Xie, G. Li, T. Ge, Y. Fan, Y. Zhu, New J. Chem. 28 (2004) 191.
[14] X.M. Zhang, R.Q. Fang, H.S. Wu, CrystEngCommun (2005) 96.
[15] M. Du, X.J. Jiang, X.J. Zhao, Inorg. Chem. 45 (2006) 3998.
[16] M. Du, X.J. Jiang, X.J. Zhao, Inorg. Chem. 46 (2007) 3984.
[17] Y.B. Dong, H.Y. Wang, J.P. Ma, R.Q. Huang, M.D. Smith, Cryst. Growth Des. 5 (2005) 789.
[18] A.R. Katritzky, C.W. Rees (Eds.), Comprehensive Heterocyclic Chemistry, vol. 2, Pergamon Press, Oxford, 1997, p. 734.
[19] J.A. McCleverty, T.J. Meyer (Eds.), Comprehensive Coordination Chemistry II, vol. 2, Pergamon Press, Oxford, 1997, p. 425.
[20] M.H. Klingele, S. Brooker, Coord. Chem. Rev. 241 (2003) 119.
[21] S. Horike, S. Bureekaew, S. Kitagawa, Chem. Commun. (2008) 471.
[22] J. Tao, Y. Zhang, M.L. Tong, X.M. Chen, T. Yuen, C.L. Lin, X.Y. Huang, J. Li, Chem. Commun. (2002) 1342.
[23] Y.F. Zhou, R.H. Wang, B.L. Wu, R. Cao, M.C. Hong, J. Mol. Struct. 697 (2004) 73.
[24] K. Uemura, K. Saito, S. Kitagawa, H. Kita, J. Am. Chem. Soc. 128 (2006) 16122.
[25] X.M. Chen, M.L. Tong, Acc. Chem. Res. 40 (2007) 162.
[26] J.P. Zhang, Y.Y. Lin, X.C. Huang, X.M. Chen, J. Am. Chem. Soc. 127 (2005) 5495.
[27] Bruker AXS, SMART, Version 5.0, Bruker AXS, Madison, WI, USA, 1998.
[28] Bruker AXS, SAINT-plus, Version 6.0, Bruker AXS, Madison, WI, USA, 1999.
[29] R.H. Blessing, Acta Crystallogr., Sect. A 51 (1995) 33.
[30] G.M. Sheldrick, Acta Crystallogr., Sect. A 64 (2008) 112.
[31] A.L. Gillon, G.R. Lewis, A.G. Orpen, S. Rotter, J. Starbuck, X.M. Wang, Y. Rodriguez-Martin, C. Ruiz-Perez, J. Chem. Soc., Dalton. Trans. (2000) 3897.
[32] G.A. Jeffrey, H. Maluszynska, Acta Crystallogr., Sect. B 46 (1990) 546.
[33] R.E. Joel Bernstein, D. Liat Shimoni, Ning-Leh Chang, Angew. Chem., Int. Ed. 34 (1995) 1555.
[34] M. Bertelli, L. Carlucci, G. Ciani, D. Proserpio, A. Sironi, J. Mater. Chem. 7 (1997) 1271.
[35] Kaes Christian, M.W.H. Clifton, E.F. Rickard, B.W. Skelton, A.H. White, Angew. Chem., Int. Ed. 37 (1998) 920.
[36] J.P. Zhang, Y.Y. Lin, X.C. Huang, X.M. Chen, Eur. J. Inorg. Chem. (2006) 3407.
[37] J.P. Zhang, Y.Y. Lin, X.C. Huang, X.M. Chen, Inorg. Chem. 44 (2005) 3146.
[38] A.N. Khlobystov, A.J. Blake, N.R. Champness, D.A. Lemenovskii, A.G. Majouga, N.V. Zyk, M. Schroder, Coord. Chem. Rev. 222 (2001) 155.
[39] L. Spek. PLATON, University of Utrecht: Utrecht, the Netherlands, 1998.
[40] A.L. Spek, J. Appl. Crystallogr. 36 (2003) 7.

Polyhedron 28 (2009) 689–694

Contents lists available at ScienceDirect

Polyhedron

journal homepage: www.elsevier.com/locate/poly

Synthesis and spectroscopic characterization of tris(*O*,*O*′-ditolyl dithiophosphato) arsenic/antimony/bismuth(III) compounds: Crystal structures of $[As\{S_2P(OC_6H_4Me\text{-}m)_2\}_3]\cdot 0.5C_6H_{14}$, $[Sb\{S_2P(OC_6H_4Me\text{-}m)_2\}_3]$ and $[Bi\{S_2P(OC_6H_4Me\text{-}m)_2\}_3]$

Seema Maheshwari [a], John E. Drake [b], Kavita Kori [a], Mark E. Light [c], Raju Ratnani [a,*]

[a] Department of Pure and Applied Chemistry, M.D.S. University, Ajmer 305 009, India
[b] Department of Chemistry and Biochemistry, University of Windsor, Windsor, Ont., Canada N9B 3P4
[c] Department of Chemistry, University of Southampton, Highfield, Southampton SO17 1BJ, UK

ARTICLE INFO

Article history:
Received 18 October 2008
Accepted 12 December 2008
Available online 27 January 2009

Keywords:
Arsenic(III)
Antimony(III)
Bismuth(III) compounds
O,*O*′-Ditolyl dithiophosphates
Crystal structures

ABSTRACT

Arsenic(III), antimony(III) and bismuth(III) compounds of the type, $[M\{S_2P(OR)_2\}_3]$ (where M = As, Sb and Bi; R = *o*-, *m*-, *p*-C_6H_4Me) were obtained by reactions of MCl_3 with ammonium salts of the corresponding *O*,*O*′-ditolyl dithiophosphate on refluxing in benzene. These compounds were characterized by elemental analysis, IR, ^1H NMR and ^{31}P NMR spectroscopy. The single crystal X-ray structures of three representative compounds were determined. $[As\{S_2P(OC_6H_4Me\text{-}m)_2\}_3]\cdot 0.5C_6H_{14}$ crystallizes as triclinic in the space group $P\bar{1}$ with $a = 10.9396(1)$, $b = 14.1891(2)$, $c = 17.5359(2)$ Å, $\alpha = 70.731(1)$, $\beta = 84.734(1)$, $\gamma = 74.205(1)^\circ$, $Z = 4$, $V = 2472.37(5)$ Å^3. $[Sb\{S_2P(OC_6H_4Me\text{-}m)_2\}_3]$ and $[Bi\{S_2P(OC_6H_4Me\text{-}m)_2\}_3]$ both crystallize as monoclinic in the space group $P2_1$ with $a = 12.4520(3)$, $b = 22.8760(5)$, $c = 16.2165(4)$ Å, $\beta = 93.022(1)^\circ$, $Z = 4$, $V = 4612.9(2)$ Å^3 and with $a = 12.4903(2)$, $b = 22.9554(4)$, $c = 16.1032(3)$ Å, $\beta = 92.4300(10)^\circ$, $Z = 4$, $V = 4612.96(14)$ Å^3, respectively. In all three molecules, the central metal atom is surrounded by all six sulfur atoms of the three chelating anisobidentate *O*,*O*′-ditolyl dithiophosphate groups in a pseudo trigonally distorted octahedron with a lone pair positioned on one of the triangular octahedral faces. The three metal sulfur bonds adjacent to the lone pair (capped face) are longer than the three furthest from the lone pair (uncapped face). Inter-ligand angles between the longer bonds are greater than those between the shorter bonds.

© 2008 Elsevier Ltd. All rights reserved.

1. Introduction

Ligands containing the $-S_2P$ grouping are known to exhibit a remarkable diversity in their coordination patterns towards metals which can be classified as monodentate [1,2], bidentate [3,4] and bridging [5]. The most interesting results are obtained when the dithiophosphate ligand is attached to a non-transition metal atom. The presence of a stereochemically active lone pair of electrons on the group 15 elements, arsenic, antimony and bismuth, combined with small ligand bites and molecular associations, adds to the interest in structural variations. Over the past several decades, various dithio ligating systems in, arsenic, antimony and bismuth complexes have been studied with *O*,*O*′-dialkyl [1–10], alkylene [11,12] and mixed ligand [13–15] dithiophosphates. Although only one X-ray structure of an arsenic compound, $[As\{S_2P(OMe)_2\}_3]$ [16], has been reported, there have been several of antimony and bismuth including $[Sb\{S_2P(OMe)_2\}_3]$ [17], $[Sb\{S_2P(OEt)_2\}_3]$ [18], $[Sb\{S_2P\{O(i\text{-}Pr)\}_2\}_3]$ [17], $[Bi\{S_2P(OMe)_2\}_3]$ [6], $[Bi\{S_2P(OEt)_2\}_3]$ [7], $[Bi\{S_2P\{O(i\text{-}Pr)\}_2\}_3]$ [2], $[Bi\{S_2POCHMeCHMeO\}_3]$ [12] and $[Bi\{S_2POCH_2CEt_2CH_2O\}_3]$ [12].

O,*O*′-Dialkyl dithiophosphate derivatives of arsenic, antimony and bismuth are used in industry as analytic reagents [19,20], lubricant additives [21] and show tribological activity to improve anti-friction and antiwear properties [22]. The anticancer activity of $[Ph_2Sb\{S_2P\{O(i\text{-}Pr)\}_2]$ has been investigated [23,24] and the use of $[Sb\{S_2P(OEt)_2\}_3]$ [18] and $[Bi\{S_2P(OEt)_2\}_3]$ [7] as passivation agents for decontaminant metals in the catalytic cracking of petroleum has been reported.

The literature contains substantial amount of work on arsenic, antimony and bismuth derivatives of *O*,*O*′-dialkyl and alkylene dithiophosphates but much less information on their bulky analogous derivatives of *O*,*O*′-(*o*-, *m*-, *p*-ditolyl) dithiophosphate ligands. However, some metal complexes with the *O*,*O*′-ditolyl dithiophosphate ligands have been synthesized and characterized by us [25–27] and, chlorobis(ditolyl dithiophosphate)arsenic(III) compounds were reported recently [28]. $[NMe_4][Zn\{S_2P(OC_6H_4Me\text{-}p)_2\}_3]$ [29] and some derivatives of antimony [30] and cobalt [31,32] ditolyl

* Corresponding author. Tel.: +91 11 145 2640059.
E-mail address: ratnaniraju@yahoo.co.uk (R. Ratnani).

0277-5387/$ - see front matter © 2008 Elsevier Ltd. All rights reserved.
doi:10.1016/j.poly.2008.12.017

dithiophosphates have industrial applications and tributyltin(IV)*O*,*O*′-diaryl dithiophosphates are useful in agriculture [33,34].

In this paper, we report the synthesis, characterization and comparative study of *O*,*O*′-ditolyl dithiophosphate complexes of $[As\{S_2P(OR)_2\}_3]$, $[Sb\{S_2P(OR)_2\}_3]$ and $[Bi\{S_2P(OR)_2\}_3]$ (R = *o*-, *m*-, *p*-C_6H_4Me), along with the single crystal X-ray diffraction of $[As\{S_2P(OC_6H_4Me\text{-}m)_2\}_3]\cdot 0.5C_6H_{14}$, $[Sb\{S_2P(OC_6H_4Me\text{-}m)_2\}_3]$ and $[Bi\{S_2P(OC_6H_4Me\text{-}m)_2\}_3]$.

2. Results and discussion

Tris(*O*,*O*′-ditolyl dithiophosphato)arsenic(III)/antimony(III)/bismuth(III) have been synthesized by the reactions of the corresponding metal chloride with the ammonium salts of *O*,*O*′-ditolyl dithiophosphoric acid in 1:3 molar ratio. These reactions are quite facile but to ensure completion reaction solutions were refluxed with stirring for 4–5 h in anhydrous benzene.

$$MCl_3 + 3NH_4S_2P(OR)_2 \xrightarrow{4-5\ h\ refluxing} [M\{S_2P(OR)_2\}_3] + 3NH_4Cl$$
$$(M = As, Sb, Bi, R = o\text{-}, m\text{-}, p\text{-}C_6H_4Me)$$

These newly synthesized novel derivatives are pale yellow crystalline solids, with the exception of viscous $[As\{S_2P(OC_6H_4Me\text{-}p)_2\}_3]$, $[Sb\{S_2P(OC_6H_4Me\text{-}o)_2\}_3]$, $[Sb\{S_2P(OC_6H_4Me\text{-}p)_2\}_3]$ and $[Bi\{S_2P(OC_6H_4Me\text{-}p)_2\}_3]$. All of these compounds are soluble in common organic solvents such as benzene, chloroform, toluene and acetone, and also in coordinating solvents such as DMSO and DMF and conversely are insoluble in non-polar organic solvents such as carbon tetrachloride and n-hexane. The complexes are moisture sensitive but are stable when kept moisture free in an inert atmosphere. The products were characterized by elemental analysis and IR, ^1H and ^{31}P NMR spectroscopy.

2.1. IR spectra

The relevant assignments of the IR bands have been made on the basis of comparisons with the spectra of ammonium salts of *O*,*O*′-(*o*-, *m*-, *p*-ditolyl) dithiophosphoric acids [35–37] and the analogous tris(*O*,*O*′-dialkyl dithiophosphato)-arsenic(III)/antimony(III)/bismuth(III) compounds [38]. The two strong intensity bands present in the regions 1114-1173 and 900–952 cm^{-1} are assigned to ν[(P)–O–C] and ν[P–O–(C)] stretching vibrations, respectively, in the complexes **1**–**9**. Two strong bands due to ν(P=S) or $\nu(P\text{–}S)_{asym}$ that are observed in the regions 680–690 and 596–598 cm^{-1} in the parent ammonium salts are shifted to lower wave-number in the corresponding tris(*O*,*O*′-ditolyl dithiophosphato)-arsenic(III)/antimony(III)/bismuth(III) compounds consistent with coordination to metal atom. Bands of strong to medium intensities present in the region 510–563 cm^{-1} are due to ν(P–S) or $\nu(P\text{–}S)_{sym}$ stretching vibrations.

2.2. ^1H NMR spectra

The ^1H NMR spectra for complexes **1**–**9** were recorded in $CDCl_3$ solutions at room temperature. The spectral data for tris(*O*,*O*′-ditolyl dithiophosphato)-arsenic(III)/antimony(III)/bismuth(III) compounds are remarkably similar to those of the corresponding ammonium salts of *O*,*O*′-ditolyl dithiophosphoric acids probably due to the large separation between metal and protons. In complexes **1**–**9**, the methyl protons, observed as singlets in the region 2.19–2.31 ppm, display negligible shifts compared to those in the corresponding salts. Similarly, the phenyl protons, which appear in the range 6.61–7.41 ppm, only undergo a negligible downfield shift compared to their positions in the free ligand as a consequence of coordination of the ligand.

2.3. ^{31}P NMR spectra

The proton decoupled ^{31}P NMR spectra of complexes **1**–**9** recorded in $CDCl_3$ all exhibit a sharp singlet, which, is in the region 83.95–85.58 ppm for the compounds of arsenic (**1**–**3**), 87.45–88.70 ppm for those of antimony (**4**–**6**) and 94.23–95.27 ppm for those of bismuth (**7**–**9**). On examining the proton decoupled ^{31}P NMR chemical shifts of a number of metal dialkyldithiophosphates, Glidewell [39] concluded that complexes containing bidentate ligands had signals in the range 82–101 ppm while those with signals less than 82 ppm had monodentate ligands. This suggests that in solution any bidentate coordination of the dithiophosphate groups is relatively strong for bismuth and becomes progressively weaker for antimony and arsenic. The observation of only one sharp singlet for all compounds **1**–**9** reflects the equivalent nature of phosphorous nuclei and the purity of the compound.

2.4. Molecular structures of $[As\{S_2P(OC_6H_4Me\text{-}m)_2\}_3]\cdot 0.5C_6H_{14}$, $[Sb\{S_2P(OC_6H_4Me\text{-}m)_2\}_3]$ and $[Bi\{S_2P(OC_6H_4Me\text{-}m)_2\}_3]$

$[As\{S_2P(OC_6H_4Me\text{-}m)_2\}_3]\cdot 0.5C_6H_{14}$ (**2**) crystallizes as triclinic in space group $P\bar{1}$ whereas, $[Sb\{S_2P(OC_6H_4Me\text{-}m)_2\}_3]$ (**5**) and $[Bi\{S_2P(OC_6H_4Me\text{-}m)_2\}_3]$ (**8**) both crystallize as monoclinic in space group $P2_1$. There are two molecules in the asymmetric units of **5** and **8** and in both cases one of the molecules is disordered so for clarity only the molecules that are not disordered are shown in Figs. 2 and 3, respectively. Similarly, for purposes of comparison, the component of n-hexane in the asymmetric unit of **2** is not included in Fig. 1.

$[Sb\{S_2P(OC_6H_4Me\text{-}m)_2\}_3]$ (**5**) and $[Bi\{S_2P(OC_6H_4Me\text{-}m)_2\}_3]$ (**8**) are isostructural, as are the corresponding analogues $[Sb\{S_2P(OEt)_2\}_3]$ [18] and $[Bi\{S_2P(OEt)_2\}_3]$ [7]. However, $[Sb\{S_2P\{O(i\text{-}Pr)\}_2\}_3]$ [17] and $[Bi\{S_2P\{O(i\text{-}Pr)\}_2\}_3]$ [2] are not isostructural nor are $[As\{S_2P(OMe)_2\}_3]$ [16], $[Sb\{S_2P(OMe)_2\}_3]$ [17] and $[Bi\{S_2P(OMe)_2\}_3]$ [6], but all of these structures consist of similar discrete

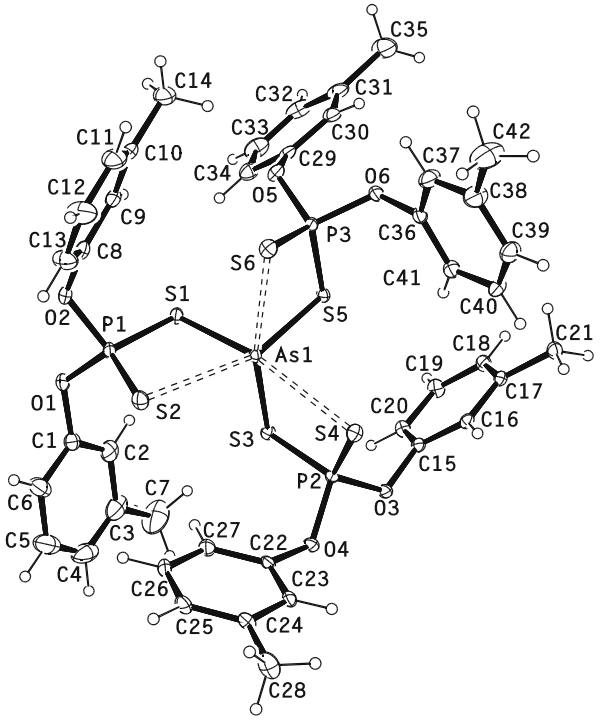


Fig. 1. ORTEP plot of the molecule of $[As\{S_2P(OC_6H_4Me\text{-}m)_2\}_3]\cdot 0.5C_6H_{14}$. The fraction of the C_6H_{14} molecule in the asymmetric unit is omitted for clarity. The non-hydrogen atoms are drawn with 30% probability ellipsoids.

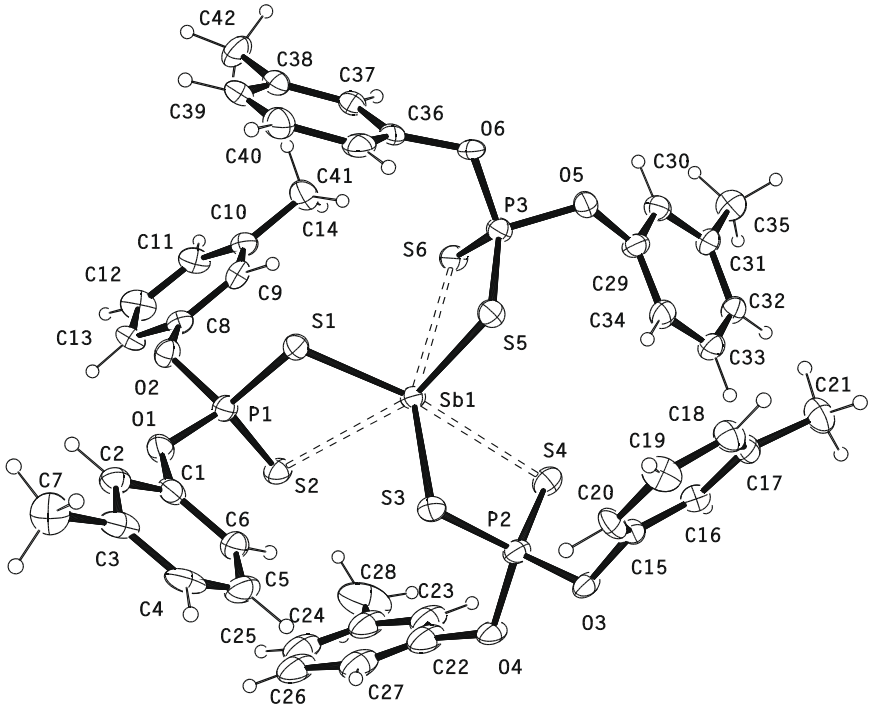


Fig. 2. ORTEP plot of the molecule of $[Sb\{S_2P(OC_6H_4Me\text{-}m)_2\}_3]$ in the asymmetric unit that is not disordered. The non-hydrogen atoms are drawn with 30% probability ellipsoids.

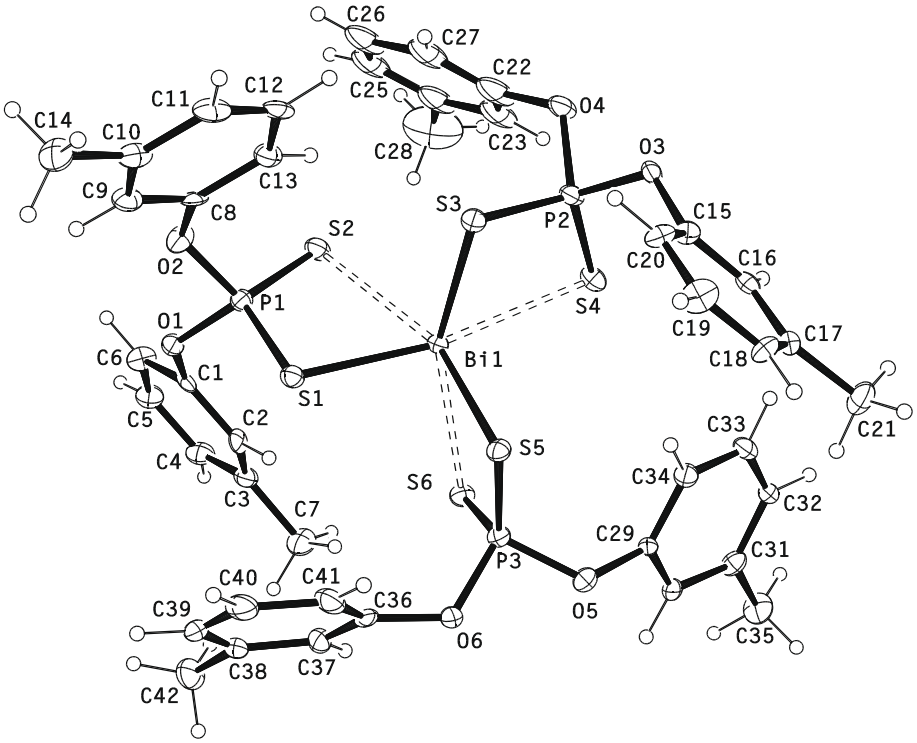


Fig. 3. ORTEP plot of the molecule of $[Bi\{S_2P(OC_6H_4\text{-}Me\text{-}m)_2\}_3]$ in the asymmetric unit that is not disordered. The non-hydrogen atoms are drawn with 30% probability ellipsoids.

$[M\{S_2P(OR)_2\}_3]$ units with a distorted octahedral arrangement of sulfur atoms. This can be seen in the ORTEP diagrams of **2**, **5** and **8** in Figs. 1–3. These demonstrate the anisobidentate coordination of the phosphorodithioate ligands in **2**, **5** and **8** with the longer (secondary) bonds identified by dashed lines and that there are no inter-molecular associations. The coordination polyhedron on the metal atom can be described as a distorted capped octahedron with a stereochemically active lone pair of electrons in the capping position and approximately on a molecular pseudo triad axis, which passes through the metal atom. The vertices of the distorted octahedron are occupied by the six sulfur atoms of the three anisobidentate phosphorodithioate ligands.

It is assumed that lone pair-bond pair repulsions in the metal coordination sphere [2,7,17,18] result in longer M–S bonds (2.9345(6)–3.0284(6) Å in **2**, 2.980(2)–3.031(2) Å in **5** and 2.926(2)–2.953(2) Å in **8**) for those bonds adjacent to the lone pair and shorter M–S bonds (2.3242(6)–2.3415(6) Å in **2**, 2.543(2)–2.549(2) in **5** and 2.678(2)–2.705(2) Å in **8**) for those more remote. These ranges are consistent with typical values reported for the short and long ligand bonds in $[As\{S_2P(OMe)_2\}_3]$ (2.320(1) and 3.029(1) Å) [16], $[Sb\{S_2P(OMe)_2\}_3]$ (2.535(2) and 3.006(2) Å) [17], $[Sb\{S_2P(OEt)_2\}_3]$ (2.583(1) and 2.86(1) Å) [18], $[Sb\{S_2P\{O(i\text{-}Pr)\}_2\}_3]$ (2.519(4) and 3.000(5) Å) [17], $[Bi\{S_2P(OEt)_2\}_3]$ (2.747(14) and 2.795(12) Å) [7] and $[Bi\{S_2P\{O(i\text{-}Pr)\}_2\}_3]$ (2.702(6) and 2.8784(6) Å) [2]. The overall difference between long and short M–S distances decreases in the order As (0.65) > Sb (0.47) > Bi (0.25 Å) emphasizing that for **2**, **5** and **8** and other related $[M\{S_2P(OR)_2\}_3]$ derivatives, the As compounds are clearly anisobidentate, and possibly close to monodentate. The longest As–S bond for $[As\{S_2P(OC_6H_4Me\text{-}m)_2\}_3]$ is 3.0284(6) Å comparable to 3.025(1) Å for $[As\{S_2P(OMe)_2\}_3]$ [16] so regardless of whether R is the smallest alkyl group or a relatively large aryl group, the longer As–S distance is essentially unchanged. By contrast, the shorter and longer bonds are relatively similar in length in **8** as well as in $[Bi\{S_2P(OEt)_2\}_3]$ [7] and $[Bi\{S_2P\{O(i\text{-}Pr)\}_2\}_3]$ [2].

The small S–M–S bite angles (75.51(2)–77.47(2)° for **2**), (72.52(7)–72.98(7)° for **5**) and (72.10(6)–72.45(6)° for **8**), which are also similar in the related compounds, might be expected to inevitably result in considerable distortion of the remaining angles from 90.00°. However, this is not the case for the angles involving the three stronger M–S bonds from each ligand in **2** (S(1)–M(1)–S(5), S(3)–M(1)–S(5) and S(1)–M(1)–S(5) which have angles of 91.26(2)°, 91.90(2)° and 92.05(2)°, respectively. This is consistent with the ligands in **2** being close to monodentate. By contrast, the corresponding S–M–S bite angles in **5** and **8** cover a wider range of 84.87(7)–91.81(8)° and 84.45(6)–93.06(7)°, respectively. The interligand angles involving the longer M-S bonds are all considerably larger ranging from 91.74(2)° to 102.46(2)° (for **2**), 94.90(7)–112.29(7)° (for **5**), and 95.27(6)–111.46(6)° (for **8**), with once again values for **5** and **8** being similar and differing from those of **2**.

Finally, unsymmetrical chelation is also reflected in the P–S bond distances which fall into two classes; the shorter distances (ave. 1.927(2) in **2**, 1.940(5) in **5** and 1.961(2) Å in **8**) are associated with S atoms forming the longer M–S interactions while the longer P–S bonds (ave. 2.060(4) in **2**, 2.032(3) in **5** and 2.010(4) Å in **8**) are allied with S atoms forming the shorter bonds to the metal, as is plausible to maintain bond order conservation around sulfur. Notably the largest difference in these bond lengths is for **2** where the difference in the longer and shorter M–S bonds is greatest. Thus the crystal structures provide confirmation of the structural conclusions reached on the basis of the ^{31}P NMR spectra of **2**, **5** and **8** as discussed earlier.

3. Experimental

As_2O_3, $BiCl_3$ and P_2S_5 were purchased from E. Merck and used as such. $SbCl_3$, $SOCl_2$, *o*-, *m*-, *p*-cresols (E. Merck) were distilled prior to use. Solvents (benzene, n-hexane and petroleum ether) were dried and distilled before use. Because the starting materials and newly synthesized compounds readily undergo hydrolysis, stringent precautions were taken to exclude atmospheric moisture throughout all experimental manipulations. Literature methods were used for the preparation of *O*,*O*′-ditolyl dithiophosphoric acids [35–37]. Ammonium salts of the dithiophosphoric acids were prepared by reaction of the parent acid with ammonia in benzene. $AsCl_3$ was prepared by the reaction of arsenic trioxide and thionyl chloride [40].

Table 1
Crystal data and structure refinement for $[As\{S_2P(OC_6H_4Me\text{-}m)_2\}_3]\cdot 0.5C_6H_{14}$(**2**), $[Sb\{S_2P(OC_6H_4Me\text{-}m)_2\}_3]$ (**5**) and $[Bi\{S_2P(OC_6H_4Me\text{-}m)_2\}]_3$ (**8**).

Compound	**2**	**5**	**8**
Empirical formula	$C_{45}H_{49}O_6P_3S_6As$	$C_{42}H_{42}O_6P_3S_6Sb$	$C_{42}H_{42}O_6P_3S_6Bi$
Formula weight	1046.03	1049.78	1137.01
Temperature (K)	120(2)	120(2)	120(2)
Wavelength (Å)	0.71073	0.71073	0.71073
Crystal system	triclinic	monoclinic	monoclinic
Space group	$P\bar{1}$	$P2_1$	$P2_1$
a (Å)	10.9396(1)	12.4520(3)	12.4903(2)
b (Å)	14.1891(2)	22.8760(5)	22.9554(4)
c (Å)	17.5359(2)	16.2165(4)	16.1032(3)
α (°)	70.731(1)		
β (°)	84.374(1)	93.022(1)	92.430(1)
γ (°)	74.2050(1)		
Volume (Å^3)	2472.37(5)	4612.9(2)	4613.0(1)
Z	2	4	4
D_{calc} (g/cm^3)	1.405	1.512	1.637
Absorption coefficient (mm^{-1})	1.083	1.019	4.243
F(000)	1082	2136	2264
Crystal size (mm^3)	0.60 × 0.20 × 0.20	0.24 × 0.12 × 0.08	0.08 × 0.04 × 0.03
θ range for data collection (°)	3.09–25.03	2.93–25.03	2.95–25.03
Index ranges	$-13 \leqslant h \leqslant 13$, $-16 \leqslant k \leqslant 16$, $-20 \leqslant l \leqslant 20$	$-14 \leqslant h \leqslant 14$, $-27 \leqslant k \leqslant 27$, $-19 \leqslant l \leqslant 18$	$-14 \leqslant h \leqslant 14$, $-27 \leqslant k \leqslant 25$, $-18 \leqslant l \leqslant 19$
Reflections collected	49266	50766	38021
Independent reflections [R_{int}]	8694 [0.0438]	16232 [0.1175]	13992 [0.0397]
Max. and min. transmission	0.8126 and 0.5627	0.9230 and 0.7921	0.8833 and 0.7277
Refinement method	Full-matrix least-squares on F^2	Full-matrix least- squares on F^2	Full-matrix least-squares on F^2
Data/restraints/parameters	8694/0/557	16232/2/1017	13992/2/1008
Goodness-of-fit on F^2	1.031	1.024	1.105
Final R indices [$F^2 > 2\sigma(F^2)$]	$R_1 = 0.0304$, $wR_2 = 0.0729$	$R_1 = 0.0618$, $wR_2 = 0.1242$	$R_1 = 0.0408$, $wR_2 = 0.0853$
R indices (all data)	$R_1 = 0.0377$, $wR_2 = 0.0767$	$R_1 = 0.1104$, $wR_2 = 0.1457$	$R_1 = 0.0489$, $wR_2 = 0.0901$
Absolute structure parameter		−0.06(2)	0.089(5)
Extinction coefficient	0.0016(3)	0.0044(2)	
Largest difference in peak and hole (e Å^{-3})	0.582 and −0.428	0.783 and −0.724	1.063 and −0.716

Sulfur was estimated gravimetrically as barium sulfate (Messenger's method). Arsenic and antimony were estimated iodometrically and bismuth by titration against standard EDTA solution using xylenol-orange as indicator. IR spectra were recorded on an ABB Bomem FTLA 2000-100 FT-IR spectrometer in KBr pellets in the range (4000–350) cm^{-1}. ^1H and ^{31}P NMR spectra were recorded on a Bruker DRX-300 spectrometer in $CDCl_3$ solutions using tetramethylsilane as an internal standard and H_3PO_4 as an external standard, respectively.

3.1. Preparations

3.1.1. [As{$S_2P(OC_6H_4Me$-o)$_2$}$_3$] (**1**)

Typically, a suspension of $NH_4S_2P(OC_6H_4Me$-o$)_2$ (1.13 g, 3.47 mmol) in benzene (10 ml) was added to a benzene solution of arsenic trichloride (0.21 g, 1.15 mmol) in 3:1 molar ratio with constant stirring followed by refluxing for 5 h at room temperature. The precipitate of ammonium chloride was removed by filtration under anhydrous conditions and excess solvent was removed from the filtrate in vacuo resulting in a pale yellow viscous oily liquid, which was crystallized by adding n-hexane and keeping the solution refrigerated for 2–3 days to obtain yellow crystals. Yield: 1.10 g, 94%; m.p. 60 °C. *Anal.* Calc. for $C_{42}H_{42}O_6S_6P_3As$: As, 7.47; S, 19.18. Found: As, 7.60; S, 19.17%. ^1H NMR ($CDCl_3$): δ 2.19 (s, CH_3, 18H), 6.91–7.10 (m, 24H, OC_6H_4); ^{31}P NMR ($CDCl_3$): δ 83.95 ppm; IR (KBr) (cm^{-1}): 1114s, ν\{(P)–O–C\}; 934s, ν\{P–O–(C)\}; 710s, 664s, ν(P═S); 529m, ν(P–S).

3.1.2. [As{$S_2P(OC_6H_4Me$-m$)_2$}$_3$] (**2**)

Method as above gave yellow needle shaped crystals. Yield: 1.10 g, 90%; m.p. 46 °C. *Anal.* Calc. for $C_{42}H_{42}O_6S_6P_3As$: As, 7.47; S, 19.18. Found: As, 7.58; S, 19.23%.^1H NMR ($CDCl_3$): δ 2.30 (s, CH_3, 18H), 7.00–7.26 (m, 24H, OC_6H_4), ^{31}P NMR ($CDCl_3$): δ 84.64 ppm; IR (KBr) (cm^{-1}): 1140s, ν\{(P)–O–C\}; 952s, ν\{P–O–(C)\}; 691s, 662s, ν(P═S); 545m, ν(P–S).

3.1.3. [As{$S_2P(OC_6H_4Me$-p$)_2$}$_3$] (**3**)

Method as above gave a yellow oily viscous liquid. Yield: 1.05 g, 86%; *Anal.* Calc. for $C_{42}H_{42}O_6S_6P_3As$: As, 7.47; S, 19.18. Found: As, 7.52; S, 19.27%. ^1H NMR ($CDCl_3$): δ 2.21 (s, CH_3, 18H), 6.61–7.08 (m, 24H, OC_6H_4), ^{31}P NMR ($CDCl_3$): δ 85.58 ppm; IR (KBr) (cm^{-1}): 1170s, ν\{(P)–O–C\}; 940s, ν\{P–O–(C)\}; 690s, 631s, ν(P═S); 563m, ν(P–S).

3.1.4. [Sb{$S_2P(OC_6H_4Me$-o$)_2$}$_3$] (**4**)

Method as above gave a yellow viscous liquid. Yield: 1.179 g, 99.06%; *Anal.* Calc. for $C_{42}H_{42}O_6S_6P_3Sb$: Sb, 11.60; S, 18.33. Found: Sb, 11.80; S, 18.32%. ^1H NMR ($CDCl_3$): δ 2.26 (s, CH_3, 18H), 7.04–7.24 (m, 24H, OC_6H_4), ^{31}P NMR ($CDCl_3$): δ 87.45 ppm; IR (KBr) (cm^{-1}): 1170s, ν\{(P)–O–C\}; 934s, ν\{P–O–(C)\}; 709s, 656s, ν(P═S); 533m, ν(P–S).

3.1.5. [Sb{$S_2P(OC_6H_4Me$-m$)_2$}$_3$] (**5**)

Method as above gave a yellow crystalline solid. Yield: 1.2807 g, 88.23%; m.p. 50 °C. *Anal.* Calc. for $C_{42}H_{42}O_6S_6P_3Sb$: Sb, 11.60; S, 18.33. Found: Sb, 11.20; S, 18.30%. ^1H NMR ($CDCl_3$): δ 2.31 (s, CH_3, 18H), 7.04–7.24 (m, 24H, OC_6H_4), ^{31}P NMR ($CDCl_3$): δ 88.70 ppm; IR (KBr) (cm^{-1}): 1142s, ν\{(P)–O–C\}; 948s, ν\{P–O–(C)\}; 690s, 649s, ν(P═S); 522m, ν(P–S).

3.1.6. [Sb{$S_2P(OC_6H_4Me$-p$)_2$}$_3$] (**6**)

Method as above gave a yellow viscous liquid. Yield: 1.006 g, 90.81%; *Anal.* Calc. for $C_{42}H_{42}O_6S_6P_3Sb$: Sb, 11.60; S, 18.33. Found: Sb, 11.40; S, 18.35%. ^1H NMR ($CDCl_3$): δ 2.31 (s, CH_3, 18H), 7.00–7.10 (m, 24H, OC_6H_4), ^{31}P NMR ($CDCl_3$): δ 87.65 ppm; IR (KBr) (cm^{-1}): 1165s, ν\{(P)–O–C\}; 936s, ν\{P–O–(C)\}; 700s, 643s, ν(P═S); 510m, ν(P–S).

3.1.7. [Bi{$S_2P(OC_6H_4Me$-o$)_2$}$_3$] (**7**)

Method as above gave a yellow crystalline solid. Yield: 1.12 g, 76%; m.p. 110 °C. *Anal.* Calc. for $C_{42}H_{42}O_6S_6P_3Bi$: Bi, 18.38; S, 16.92. Found: Bi, 13.80; S, 16.32%. ^1H NMR ($CDCl_3$): δ 2.30 (s, CH_3, 18H), 6.95–7.21 (m, 24H, OC_6H_4), ^{31}P NMR ($CDCl_3$): δ 94.82 ppm; IR (KBr) (cm^{-1}): 1173s, ν\{(P)–O–C\}; 900s, ν\{P–O–(C)\}; 679s, 641m, ν(P═S); 546m, ν(P–S).

Table 2
Selected bond lengths (Å) and angles (°) for [As{$S_2P(OC_6H_4Me$-m$)_2$}$_3$]·0.5C_6H_{14} (**2**), [Sb{$S_2P(OC_6H_4Me$-m$)_2$}$_3$] (**5**) and [Bi{$S_2P(OC_6H_4Me$-m$)_2$}$_3$] (**8**).[a]

Compound	2	5	8
M(1)–S(1)	2.3242(6)	2.544(2)	2.678(2)
M(1)–S(2)	3.0284(6)	3.031(2)	2.953(2)
M(1)–S(3)	2.3415(6)	2.549(2)	2.705(2)
M(1)–S(4)	2.9861(6)	2.980(2)	2.926(2)
M(1)–S(5)	2.3278(6)	2.543(2)	2.681(2)
M(1)–S(6)	2.9345(6)	3.025(2)	2.937(2)
S(1)–P(1)	2.0619(8)	2.033(3)	2.010(3)
S(2)–P(1)	1.9270(8)	1.945(3)	1.962(3)
S(3)–P(2)	2.0556(8)	2.031(3)	2.006(3)
S(4)–P(2)	1.9294(8)	1.935(4)	1.962(3)
S(5)–P(3)	2.0615(8)	2.032(3)	2.013(3)
S(6)–P(3)	1.9255(8)	1.940(3)	1.960(3)
P(1)–O(1)	1.594(2)	1.600(6)	1.604(5)
P(1)–O(2)	1.591(2)	1.584(5)	1.597(6)
P(2)–O(3)	1.594(2)	1.589(6)	1.592(6)
P(2)–O(4)	1.594(2)	1.585(6)	1.596(6)
P(3)–O(5)	1.584(2)	1.593(6)	1.590(6)
P(3)–O(6)	1.596(2)	1.595(6)	1.599(6)
S(1)–M(1)–S(2)	75.51(2)	72.69(7)	72.40(6)
S(3)–M(1)–S(4)	76.10(2)	72.98(7)	72.10(6)
S(5)–M(1)–S(6)	77.47(2)	72.52(7)	72.45(6)
S(1)–M(1)–S(3)	91.90(2)	91.81(8)	93.06(7)
S(1)–M(1)–S(5)	91.26(2)	84.87(7)	84.45(6)
S(3)–M(1)–S(5)	92.05(2)	86.90(7)	86.93(6)
S(1)–M(1)–S(4)	167.38(2)	164.67(8)	165.16(7)
S(3)–M(1)–S(6)	167.13(2)	155.87(7)	155.14(6)
S(5)–M(1)–S(2)	162.13(2)	157.46(7)	156.82(6)
S(1)–M(1)–S(6)	95.73(2)	98.56(8)	98.45(7)
S(3)–M(1)–S(2)	100.21(2)	91.56(7)	92.99(6)
S(5)–M(1)–S(4)	93.03(2)	92.25(7)	94.39(6)
S(2)–M(1)–S(4)	102.46(2)	108.80(7)	107.66(6)
S(2)–M(1)–S(6)	91.74(2)	112.29(6)	111.46(6)
S(4)–M(1)–S(6)	96.79(2)	94.90(7)	95.27(6)
P(1)–S(1)–M(1)	94.14(3)	92.8(1)	90.08(8)
P(1)–S(2)–M(1)	77.44(3)	80.9(1)	83.37(9)
P(2)–S(3)–M(1)	93.00(3)	91.5(1)	89.2(1)
P(2)–S(4)–M(1)	77.84(3)	81.3(1)	83.87(9)
P(3)–S(5)–M(1)	90.73(3)	92.9(1)	89.97(9)
P(3)–S(6)–M(1)	77.07(3)	81.3(1)	83.86(9)
O(1)–P(1)–O(2)	94.76(9)	93.7(3)	94.3(3)
O(1)–P(1)–S(1)	107.12(7)	107.6(3)	110.3(2)
O(1)–P(1)–S(2)	116.14(7)	116.9(3)	112.2(2)
O(2)–P(1)–S(1)	106.56(7)	109.4(3)	109.5(2)
O(2)–P(1)–S(2)	117.54(7)	113.8(2)	114.6(3)
S(1)–P(1)–S(2)	112.85(4)	113.5(1)	114.1(1)
O(3)–P(2)–O(4)	94.56(8)	93.9(3)	95.3(3)
O(3)–P(2)–S(3)	107.00(6)	109.7(3)	110.7(3)
O(3)–P(2)–S(4)	116.33(7)	114.2(3)	112.5(3)
O(4)–P(2)–S(3)	107.47(7)	108.4(3)	109.7(3)
O(4)–P(2)–S(4)	106.71(7)	116.1(3)	113.7(3)
S(3)–P(2)–S(4)	112.94(3)	112.9(1)	113.5(1)
O(5)–P(3)–O(6)	100.89(9)	94.2(3)	94.5(3)
O(5)–P(3)–S(5)	108.47(7)	108.2(2)	109.9(2)
O(5)–P(3)–S(6)	111.04(7)	115.0(3)	113.6(2)
O(6)–P(3)–S(5)	106.36(7)	109.3(2)	109.9(2)
O(6)–P(3)–S(6)	116.14(7)	115.2(2)	113.6(2)
S(5)–P(3)–S(6)	113.04(4)	113.2(1)	113.7(1)

[a] Data are not included in **2** for C_6H_{14} and in **5** and **8** for the molecules that are disordered.

*3.1.8. [Bi{$S_2P(OC_6H_4Me\text{-}m)_2$}$_3$] (**8**)*

Method as above gave a yellow crystalline solid. Yield: 0.95 g, 95%; m.p. 40 °C. *Anal.* Calc. for $C_{42}H_{42}O_6S_6P_3Bi$: Bi, 18.38; S, 16.92. Found: Bi, 14.20; S, 16.94%. ^{1}H NMR ($CDCl_3$): δ 2.23 (s, CH_3, 18H), 6.65–7.41 (m, 24H, OC_6H_4), ^{31}P NMR ($CDCl_3$): δ 94.23 ppm; IR (KBr) (cm^{-1}): 1139s, ν\{(P)–O–C\}; 950s, ν\{P–O–(C)\}; 691s, 634s, ν(P═S); 556m, ν(P–S).

*3.1.9. [Bi{$S_2P(OC_6H_4Me\text{-}p)_2$}$_3$] (**9**)*

Method as above gave a yellow viscous liquid. Yield: 1.10 g, 93%. *Anal.* Calc. for $C_{42}H_{42}O_6S_6P_3Bi$: Bi, 18.38; S, 16.92. Found: Bi, 14.20; S, 16.93%. ^{1}H NMR ($CDCl_3$): δ 2.30 (s, CH_3, 18H), 6.69–7.12 (m, 24H, OC_6H_4), ^{31}P NMR ($CDCl_3$): δ 95.27 ppm; IR (KBr) (cm^{-1}): 1167s, ν\{(P)–O–C\}; 934s, ν\{P–O–(C)\}; 697s, 639s, ν(P═S); 524s, ν(P–S).

3.2. Crystallography

A colorless block crystal of [As{$S_2P(OC_6H_4Me\text{-}m)_2$}$_3$]·0.5$C_6H_{14}$ (**2**), a colorless fragment of [Sb{$S_2P(OC_6H_4Me\text{-}m)_2$}$_3$] (**5**) and a yellow block crystal of [Bi{$S_2P(OC_6H_4Me\text{-}m)_2$}$_3$] (**8**) were mounted on glass fibres. Data were collected on a Bruker–Nonius CCD area detector diffractometers, with φ and ω scans chosen to give a complete asymmetric unit. Cell refinement [41] gave cell constants corresponding to a triclinic cell for **2** and monoclinic cells for **5** and **8** whose dimensions are given in Table 1 along with other experimental parameters. An absorption correction was applied [42].

The structures were solved by direct methods [43] and were refined using the WINGX version [44] of SHELX-97 [45]. All of the non-hydrogen atoms were treated anisotropically. All of the hydrogen atoms were included in idealized positions, with isotropic thermal parameters set at 1.2 times that of the carbon atom to which they were attached. The 58/42 (for **5**) and 77/23 (for **8**) disorder in one of the two molecules of the asymmetric unit was successfully modelled by placing restraints on distances and thermal parameters within the groups. The final cycle of full-matrix least-squares refinement was based on 8694 for **2**, 16232 for **5** and 13992 for **8** observed reflections (7602 for **2**, 10886 for **5** and 12758 for **8** for $F^2 > 4\sigma(F^2)$) and 557 for **2**, 1017 for **5** and 1008 for **8** variable parameters and converged (largest parameter shift was 0.001 times its esd).

Selected bond distances and angles are given in Table 2 and the molecules are displayed as ORTEP diagrams in Figs. 1–3. Additional material available from the Cambridge Crystallographic Data Centre comprises the final atomic coordinates and thermal parameters for all atoms and a complete listing of bond distances and angles.

4. Concluding comments

We have prepared and characterized the following compounds of the type, [M{$S_2P(OR)_2$}$_3$] (where M = As, Sb and Bi; R = *o*-, *m*-, *p*-C_6H_4Me). The IR, ^{1}H and ^{31}P NMR spectral data of these compounds are consistent with the presence of complexes containing bidentate ligands and hence a distorted octahedral structure. The molecular structures of [As{$S_2P(OC_6H_4Me\text{-}m)_2$}$_3$]·0.5$C_6H_{14}$, [Sb{$S_2P(OC_6H_4Me\text{-}m)_2$}$_3$] and [Bi{$S_2P(OC_6H_4Me\text{-}m)_2$}$_3$] confirm this to be the case and that in the solid state the ligands are more accurately described as anisobidentate.

Acknowledgements

M.E.L. thanks the UK Engineering and Physical Sciences Council for support of the X-ray facilities at Southampton University. We are also thankful to RSIC, CDRI, Lucknow for the spectral analyses.

Appendix A. Supplementary data

CCDC 703657–703659 contain the supplementary crystallographic data for [As{$S_2P(OC_6H_4Me\text{-}m)_2$}$_3$]·0.5$C_6H_{14}$, [Sb{$S_2P(OC_6H_4Me\text{-}m)_2$}$_3$] and [Bi{$S_2P(OC_6H_4Me\text{-}m)_2$}$_3$], respectively. These data can be obtained free of charge via http://www.ccdc.cam. ac.uk/conts/retrieving.html, or from the Cambridge Crystallographic Data Centre, 12 Union Road, Cambridge CB2 1EZ, UK; fax: (+44) 1223-336-033; or e-mail: deposit@ccdc.cam.ac.uk. Supplementary data associated with this article can be found, in the online version, at doi:10.1016/j.poly.2008.12.017.

References

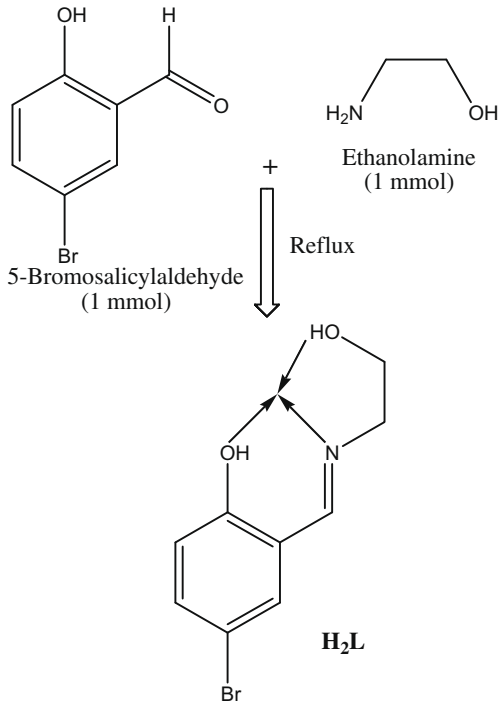
[1] H.P.S. Chauhan, G. Srivastava, R.C. Mehrotra, Phosphorus Sulfur Silicon 17 (1983) 161.
[2] S.L. Lawton, C.J. Fuhrmeister, R.G. Hass, C.S. Jarman, F.G. Lohmeyer, Inorg. Chem. 13 (1974) 135.
[3] B.P. Singh, G. Srivastava, R.C. Mehrotra, J. Organomet. Chem. 35 (1979) 171.
[4] J.C. Lefferts, K.C. Molloy, J.J. Zuckerman, I. Haiduc, C. Guta, D. Ruse, Inorg. Chem. 19 (1980) 1662.
[5] I. Haiduc, D.B. Sowerby, S.F. Lu, Polyhedron 14 (1995) 3389.
[6] M. Weiber, M. Shrocef, Phosphorus Sulfur Silicon 102 (1995) 265.
[7] M. Iglesias, C.D. Pino, S.M. Carrera, Polyhedron 8 (1989) 483.
[8] A. Muller, V.V.K. Rao, G. Klinksiek, Chem. Ber. 104 (1971) 1892.
[9] H.P.S. Chauhan, N.M. Shaik, K. Kori, Main Group Met. Chem. 26 (2003) 213.
[10] P.N. Nagar, G. Srivastava, R.C. Mehrotra, Synth. React. Inorg. Met. – Org. Chem. 12 (1982) 749.
[11] H.P.S. Chauhan, G. Srivastava, R.C. Mehrotra, Polyhedron 3 (1984) 1337.
[12] R. Bohra, H.P.S. Chauhan, G. Srivastava, R.C. Mehrotra, Phosphorus Sulfur Silicon 60 (1991) 167.
[13] H.P.S. Chauhan, G. Srivastava, R.C. Mehrotra, Polyhedron 2 (1983) 359.
[14] H.P.S. Chauhan, R.K. Singh, K. Kori, Main Group Met. Chem. 25 (2002) 511.
[15] H.P.S. Chauhan, N.M. Shaik, U.P. Singh, Appl. Organomet. Chem. 19 (2005) 1132.
[16] T. Ito, Acta Crystallogr., Sect. E (60) (2004) 783.
[17] D.B. Sowerby, I. Haiduc, A.B. Rusu, M. Salajan, Inorg. Chim. Acta 68 (1983) 87.
[18] R.O. Day, M.M. Chauvin, W.E. McEwen, Phosphorus Sulfur Silicon 8 (1980) 121.
[19] I.S. Levin, V.V. Sergeeva, I.A. Vorsina, Ser. Khim. Nauk 2 (1975) 107.
[20] I.S. Levin, V.V. Sergeeva, I.A. Vorsina, Chem. Abstr. 83 (1975) 66255.
[21] H.H. Farmer, B.W. Malone, H.F. Tompkis, Lubrication Eng. 23 (1967) 57.
[22] L. Chen, J. Dong, G. Chen, Lubrication Sci. 11 (2006) 1.
[23] C. Silvestru, C. Socacia, A. Bara, I. Haiduc, Anticancer Res. 10 (1990) 803.
[24] C. Socaciu, I. Pasca, C. Silvestru, I. Haiduc, A. Bara, Metal Based Drugs 1 (1994) 291.
[25] L. Awwal, J.E. Drake, M.B. Hursthouse, R. Kumar, M.E. Light, R. Ratnani, K. Saraswat, Polyhedron 26 (2007) 3973.
[26] J.E. Drake, C. Gurnani, M.B. Hursthouse, M.E. Light, M. Nirwan, R. Ratnani, Appl. Organomet. Chem. 21 (2007) 539.
[27] A.L. Bingham, J.E. Drake, M.E. Light, M. Nirwan, R. Ratnani, Polyhedron 25 (2006) 945.
[28] A. Kumar, D. Kumar, S.K. Pandey, Synth, React. Inorg. Met. – Org. Nano-Met. Chem. 37 (2007) 697.
[29] J.A. McCleverty, R.S.Z. Kowalski, N.A. Bailey, R. Mulvaney, D.A. O'Cleirigh, J. Chem. Soc., Dalton Trans. 4 (1983) 627.
[30] W.E. McEwen, V.C. Si, B.J. Kalbacher, Phosphorus Sulfur Silicon Relat. Elem. 11 (1981) 191.
[31] N.N. Glebova, O.K. Sharaev, E.I. Tienyakova, B.A. Dolgoplosk, Vysokomolekul. Soedin. Seriya 37 (1995) 1145.
[32] N.N. Glebova, O.K. Sharaev, E.I. Tienyakova, B.A. Dolgoplosk, Chem. Abstr. 125 (1996) 14337g.
[33] Q. Xie, N. Luo, J. Li, X. Jing, Youji Huaxue 12 (1992) 159.
[34] Q. Xie, N. Luo, J. Li, X. Jing, Chem. Abstr. 117 (1992) 26650w.
[35] R. Ratnani, J.E. Drake, C.L.B. Macdonald, A. Kumar, S.K. Pandey, J. Chem. Crystallogr. 35 (2005) 447.
[36] A.L. Bingham, J.E. Drake, C. Gurnani, M.B. Hursthouse, M.E. Light, M. Nirwan, R. Ratnani, J. Chem. Crystallogr. 36 (2006) 627.
[37] A. Kumar, K.R. Sharma, S.K. Pandey, Phosphorus Sulfur Silicon Relat. Elem. 182 (2007) 1023.
[38] H.P.S. Chauhan, Coord. Chem. Rev. 173 (1998) 1.
[39] C. Glidewell, Inorg. Chim. Acta 25 (1977) 159.
[40] K. Kori, Ph.D. Thesis, Devi Ahilya University, Indore, India, 2005.
[41] A.J.M. Duisenberg, J. Appl. Crystallogr. 25 (1992) 92.
[42] G.M. Sheldrick, SADABS, Version 2007/2, Bruker AXS Inc., Madison, Wisconsin, USA, 2007.
[43] G.M. Sheldrick, Acta Crystallogr. A46 (1990) 467.
[44] L.J. Farrugia, J. Appl. Crystallogr. 32 (1999) 837.
[45] G.M. Sheldrick, SHELXL97, University of Göttingen, Germany, 1997.

condensation of 5-bromosalicyldehyde and ethanolamine (Scheme 1). The salicylidene-2-ethanolamine (H_2sae) type of ligands can act with both bridging and chelating coordination modes and they have a strong tendency to participate in different kinds of phenoxide or alkoxide bridges, exploiting the property of terminal oxygens as good bridging groups. Previously H_2sae and its derivatives have been incorporated into a number of alkoxo- or phenoxo-bridged tetranuclear Cu^{II}, Ni^{II} and Fe^{II} clusters with cubane structures [25–28]. However, in our case, the chelating ability of this ONO donor ligand has been utilized selectively to achieve the desired chloro-bridged complex. Complex **1** has been completely characterized with elemental analysis, FT-IR, UV–Vis, EPR spectra, and single crystal X-ray diffraction analysis. In this paper, we report a combined structural and magnetic study of complex **1**. Magnetic susceptibility measurements (2–300 K) show a prominent ferromagnetic interaction in the dimer with J = +43.2(5) cm^{-1}, and a weak interdimer antiferromagnetic interaction of J' = –0.276(8) cm^{-1}. To the best of our knowledge, complex **1** presents the highest ferromagnetic coupling reported till date in any doubly chloro-bridged Cu^{II} dimer. Additionally, the catalytic activity of the complex towards the oxidation of hydrocarbons using H_2O_2 as terminal oxidant has also been investigated. The results of this study reveal that complex **1** behaves as active catalyst for oxygenation of cyclohexane and cycloheptane to their corresponding hydroxylated and oxygenated products affording good yield and turnover number (TON).

2. Experimental

2.1. Materials

$CuCl_2 \cdot 2H_2O$ was purchased from Merck India Ltd. and 5-bromosalicylaldehyde and ethanolamine from Sigma–Aldrich, USA. All the chemicals and solvents employed for the syntheses were of analytical grade and used as received without further purification. Cyclohexane, cycloheptane, cyclohexanone, cyclohexanol, cycloheptanone, cycloheptanol, cyclopentanone were purchased from Sigma–Aldrich, USA, and used as received. Solvents used for spectroscopic studies were purified and dried by standard procedures before use [29].



Scheme 1.

2.2. Syntheses

2.2.1. Synthesis of the Schiff base ligand [2-((E)-(2-hydroxyethylimino)methyl)-4-bromophenol] (***H_2L***)

Ethanolamine (0.12 ml, 2 mmol) was added to a solution of 5-bromosalicylaldehyde (0.402 g, 2 mmol) in 20 ml methanol and the mixture was refluxed for 1 h at 65 °C. A yellow solid was formed which was filtered, washed with methanol and vacuum dried. Yield: 0.141 g (85%). *Anal.* Calc. for $C_9H_{10}BrNO_2$: C, 44.29; H, 4.13; N, 5.74. Found: C, 44.32; H, 4.10; N, 5.81%. FT-IR (KBr, cm^{-1}): ν(C=N) 1640. UV–Vis (λ, nm): 261, 393.

2.2.2. Synthesis of the complex $[Cu(HL)Cl]_2 \cdot H_2O$ (***1***)

The appropriate quantity of solid Schiff base ligand **H_2L** (0.165 g, 1 mmol) was dissolved in 20 ml of methanol. This ligand solution was added dropwise to a 10 ml methanolic solution of $CuCl_2 \cdot 2H_2O$ (0.160 g, 1 mmol) with constant stirring. The mixture was refluxed for 45 min at 65 °C. The resulting deep green solution was then left undisturbed. After 7 days blue block-shaped X-ray diffraction quality single crystals appeared. Yield: 82%. *Anal.* Calc. for $C_{18}H_{20}Br_2Cl_2Cu_2N_2O_5$: C, 30.79; H, 2.87; N, 3.99. Found: C, 30.72; H, 2.89; N, 3.94%.

2.2.3. Experimental procedure for oxidation of cyclohexane and cycloheptane

The catalytic hydrocarbon oxidation reactions by complex **1** involving cyclohexane and cycloheptane as substrates were carried out with the following procedure: 2.5–10 mmol of hydrogen peroxide (30% in H_2O) was added to the metal complex (0.025 mmol) in 3 ml of acetonitrile in a two-neck round bottom flask fitted with a condenser. To this solution, HNO_3 (0.25 mmol) was added followed by the addition of 0.927 mmol of substrate. The reaction was initiated by stirring the above mixture for 48 h at room temperature under atmospheric pressure. Aliquots were collected after regular time intervals and 90 μl of cyclopentanone was added as internal standard. The substrate and products from the reaction mixture were extracted with 10 ml of diethyl ether and they were analyzed by gas chromatography. The identification was achieved by comparison with known standards.

2.3. Physical measurements

The Fourier transform infrared spectra of the ligand and the complex were recorded on a Perkin–Elmer Spectrum RX I FT-IR spectrophotometer with a KBr pressed pellet in the range 4000–200 cm^{-1}. The electronic spectra were recorded on a Perkin–Elmer Lambda 40 (UV–Vis) spectrometer using HPLC grade acetonitrile as solvent in the range 800–200 nm. Elemental analyses were carried out on a Perkin–Elmer 2400 II Elemental Analyser. Electron paramagnetic resonance (EPR) spectrum of **1** was recorded on a polycrystalline sample or in CH_3CN and *N*,*N*-dimethylformamide (DMF) solutions with an X-band Bruker EMX spectrometer at 298 and 120 K. The spectra were simulated with the computer program Bruker WinEPR SimFonia. The magnetic susceptibility measurements were carried out in the temperature range 2–300 K with an applied magnetic field of 0.1 T on a polycrystalline sample of complex **1** (mass = 45.00 mg) with a Quantum Design MPMS-XL-5 SQUID magnetometer. The isothermal magnetization was performed on the same sample at 2 K with magnetic fields up to 5 T. The susceptibility data were corrected for the sample holders previously measured using the same conditions and for the diamagnetic contributions of the salt as deduced by using Pascal's

constant tables ($\chi_{dia} = -332.3 \times 10^{-6}$ emu mol^{-1}). Gas chromatography analysis was performed with an Agilent Technologies 6890N network GC system equipped with a fused silica capillary column (30 m × 0.32 mm) and a FID detector.

2.4. Crystallographic data collection and structure refinements

A diffraction quality single crystal of **1** was mounted on a Bruker X8 Apex 2 CCD diffractometer equipped with a graphite monochromator and Mo Kα radiation ($\lambda = 0.71073$ Å). Data collection was carried out using the Bruker APEX2 software [30]. Multiscan absorption correction was applied using SADABS [31]. The structure of the complex was solved by direct methods with SHELXS, and refined by full-matrix least squares based on F^2 with SHELXL [32]. All non-hydrogen atoms were refined anisotropically. The C-bound H atoms were constrained to ideal geometry and were included in the refinement in the riding model approximation while those of the water molecules were located in difference Fourier maps. Further crystallographic analysis and figure production were carried out using PLATON99 [33] and ORTEP [34] programs. Details of the data collection parameters and crystallographic information for the complex are summarized in the Table 1.

3. Results and discussion

3.1. Infrared and electronic spectra

In the IR spectrum of complex **1**, the strong absorption band at 1603 cm^{-1} can be assigned to the imine stretching frequency of the coordinated ligand, whereas for the free ligand molecule the same band is observed at 1640 cm^{-1}. The shift of this band towards lower frequency on complexation with the metal suggests coordination to the metal ion through imine nitrogen atom [35,36]. The ν(C–O) mode is present as a very strong band at about 1195 cm^{-1}. Ligand coordination to the metal center is substantiated by prominent bands appearing at 445 and 370 cm^{-1} which can be attributed to ν(Cu–N) and ν(Cu–O), respectively. The two bands observed at 310 and 297 cm^{-1} are characteristic of Cu–Cl vibrations [37]. The broad band at 3440–3255 cm^{-1} is attributable to O–H stretching vibrations of lattice water molecule.

The electronic spectral data for the complex in HPLC grade acetonitrile solvent are in good agreement with its geometry. The two strong absorption bands in the region 350–385 nm are clearly charge transfer in origin [38] attributed to the transition from the coordinated unsaturated ligand to the metal ion (LMCT). Again, the intense high energy bands at about 245 and 380 nm may be assigned to the intraligand $\pi \rightarrow \pi^*$ and $n \rightarrow \pi^*$ transitions, respectively. The broad low-intensity absorption band centered at 605 nm is a typical *d*–*d* band for the copper(II) ion [38,39].

3.2. Crystal structure description of complex *1*

A perspective ORTEP view with the atom-labeling scheme of complex **1** is presented in Fig. 1. Selected bond lengths and angles for the complex are given in Table 2. The asymmetric unit of **1** consists of a $[Cu(HL)Cl]_2$ dimeric unit with a lattice water molecule. In the complex, the Schiff base 2-((*E*)-(2-hydroxyethylimino)methyl)-4-bromophenol (**H_2L**) behaves as a monoanionic, tridentate ligand which coordinates to the metal center through its imine nitrogen, alkoxy oxygen and deprotonated phenolic oxygen atoms. The crystal structure determination reveals that complex **1** is a double chloro-bridged dimer in which the copper ions are pentacoordinated, being bonded to three coordinating donor sites of the Schiff base ligand and two bridging chloride anions as shown in Fig. 1. The coordination number 5 for Cu^{II} is very common and usually presents either a square-pyramidal (SP) or a trigonal–bipyramidal (TBP) geometry (or any of the distorted intermediate geometries). For a pentacoordinated metal center, the distortion of the coordination environment from TBP to SP can be evaluated by the Addison distortion index, τ defined as $\tau = [|\theta - \Phi|/60]$, where θ and Φ are the two largest coordination angles and $\tau = 0$ for perfect SP and 1 for ideal TBP [40,41]. In complex **1**, the calculated τ values for Cu1 and Cu2 are 0.147 and 0.200, respectively, clearly suggesting a distorted SP geometry for each copper ion. The square base of each of the two structurally similar copper atoms is constructed by

Table 1
Summary of crystal data and refinement details for **1**.

Empirical formula	$C_{18}H_{20}Br_2Cl_2Cu_2N_2O_5$
Formula weight	702.16
Crystal dimension (mm)	0.40 × 0.20 × 0.16
Crystal system	monoclinic
Space group	$P2_1/n$
a (Å)	14.1643(19)
b (Å)	7.6871(11)
c (Å)	21.515(3)
β (°)	92.241(3)
V (Å^3)	2340.9(6)
Z	4
Temperature (K)	100(2)
D_{calc} (g cm^{-3})	1.992
μ (mm^{-1})	5.492
F(000)	1376
θ (°)	1.75–23.90
Total data	17644
Unique data	3412
Observed data [$I > 2\sigma(I)$]	2539
R^a	0.0354
$R_w{}^b$	0.0803
Goodness-of-fit on F^2, *S*	1.06
R_{int}	0.060
$\Delta\rho_{max}$ (e Å^{-3})	1.32
$\Delta\rho_{min}$ (e Å^{-3})	−0.78

[a] $R = \Sigma(|F_o - F_c|)/\Sigma|F_o|$.
[b] $R^w = \{\Sigma[w(|F_o - F_c|)^2]/\Sigma[w|F_o|^2]\}^{1/2}$.

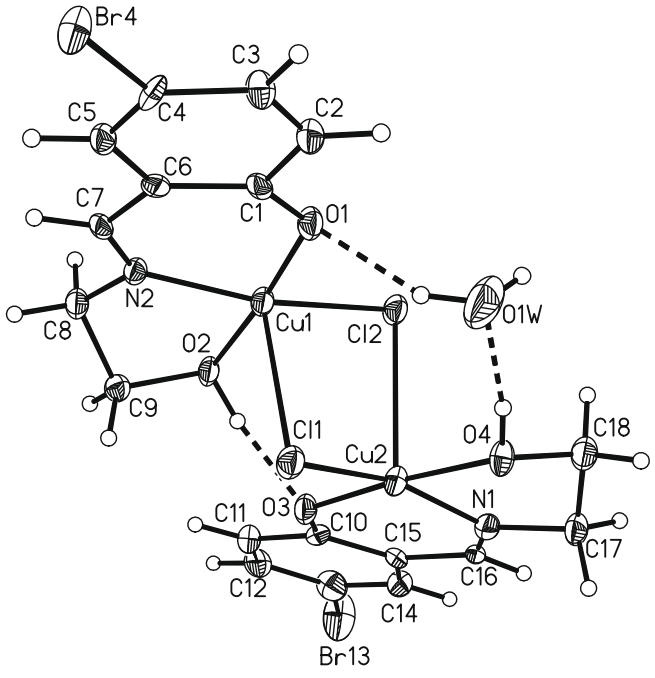


Fig. 1. ORTEP representation of complex **1**. Thermal ellipsoids have been drawn at 40% probability level. Dashed lines indicate hydrogen bonds.

Table 2
Selected bond lengths and bond angles for **1**.

Bond lengths (Å)			
Cu1–O1	1.913(4)	Cu2–O3	1.915(4)
Cu1–N2	1.937(4)	Cu2–N1	1.939(5)
Cu1–O2	2.012(4)	Cu2–O4	1.985(4)
Cu1–Cl2	2.2672(15)	Cu2–Cl1	2.2680(15)
Cu1–Cl1	2.6853(16)	Cu2–Cl2	2.6685(16)
Bond angles (°)			
O1–Cu1–N2	94.24(18)	O3–Cu2–N1	93.26(18)
O1–Cu1–O2	175.70(16)	O3–Cu2–O4	175.11(15)
N2–Cu1–O2	82.16(17)	N1–Cu2–O4	82.24(18)
O1–Cu1–Cl2	92.93(12)	O3–Cu2–Cl1	91.75(12)
N2–Cu1–Cl2	160.88(15)	N1–Cu2–Cl1	163.11(15)
O2–Cu1–Cl2	89.79(11)	O4–Cu2–Cl1	92.04(12)
O1–Cu1–Cl1	94.47(12)	O3–Cu2–Cl2	93.87(12)
N2–Cu1–Cl1	104.31(14)	N1–Cu2–Cl2	102.54(14)
O2–Cu1–Cl1	88.73(12)	O4–Cu2–Cl2	88.99(12)
Cl2–Cu1–Cl1	92.76(5)	Cl1–Cu2–Cl2	93.19(5)
Cu1–Cl2–Cu2	84.66(5)	Cu2–Cl1–Cu1	84.25(5)

the imine nitrogen atom, the alkoxy and phenoxy oxygen atoms from the Schiff base ligand and a bridging chlorine atom, while the apical position of the pyramid is occupied by the other bridging chlorine atom. The Cu–N_{imine} and Cu–$O_{phenolic}$ bond distances are in the ranges observed for similar systems [24]. The Cu–O(phenolic) distances are slightly shorter than those of the Cu-O(alkoxy). The substantial elongation of the axial Cu–Cl bonds [2.685(2) and 2.668(2) Å for Cu1 and Cu2, respectively] compared to the equatorial Cu–Cl bonds [2.267(2) and 2.268(2) Å for Cu1 and Cu2, respectively] is caused by the active Jahn–Teller distortion of the copper(II) ion. Interestingly, for the Cu1 center, Cl2 occupies the basal position of the pyramid and Cl1 is apical, whereas in case of the other copper center (Cu2), Cl1 is in the basal plane and Cl2 is in the apical position. As a result, the geometry of the complex consists of two square pyramids sharing one base-to-apex edge but with nearly parallel basal planes [13,21,42]. The axial–equatorial configuration of the two chloro bridges is depicted clearly in Fig. 2. Both Cu1 and Cu2 are displaced from the mean equatorial plane towards the corresponding axial chloro bridging atoms, Cl1 and Cl2, by 0.183 and 0.167 Å, respectively.

Within the Cu(μ-Cl)$_2$Cu core, the Cu–Cu distance of 3.3371(10) Å is much shorter than the average value for chloro-bridged copper(II) dimers (3.499 Å) in CSD [43]. The Cu_2Cl_2 core is considerably distorted from an ideal square as reflected from the average Cl–Cu–Cl and Cu–Cl–Cu bond angles of 92.97° and 84.45°, respectively, both deviating from the ideal angle of 90°. Moreover, these small Cu–Cl–Cu angles play an important role in determining the magnetic coupling within the dimer. The asymmetric nature of the double bridge is also evident from the different Cu–Cl bond lengths. Both basal (ca. 2.27 Å) and axial (ca. 2.67 Å) Cu–Cl distances are comparable with the average literature values of 2.309 Å for short and 2.554 Å for long Cu–$Cl_{bridging}$ distances, respectively.

On one side of the dimer, the two Schiff base ligands are intramolecularly connected through a hydrogen bond between atoms H2H on alkoxy O2 and phenolic O3 (Fig. 1). As a consequence, the two ligands are moved away from each other on the opposite side to maintain the structural integrity of the complex. This segregation generates a hole where a H_2O solvent molecule is inserted, optimizing the interactions at this site by creating a double hydrogen bond. Thus the interaction between phenolic oxygen O1 and alkoxy oxygen O4 is mediated through the intermolecular hydrogen bonds O1W–H12W···O1 and O4–H4H···O1W (Table S1, Supplementary data). Finally, there are two very short Br···Br contacts between adjacent dimers of only 3.6906(11) and 4.0550(2) Å connecting the dimers in the *ac* plane and a longer Br···Br contact of 4.99 Å connecting the dimers in the *b* direction (Fig. S2, Supplementary data).

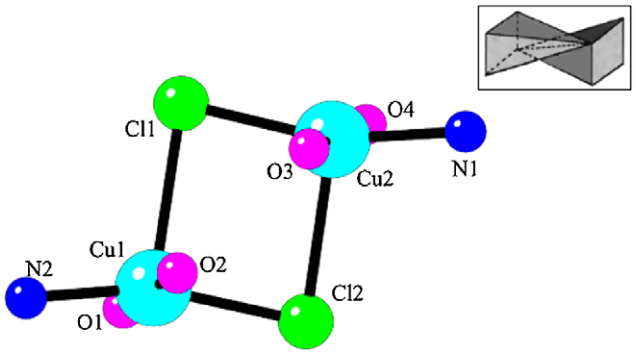


Fig. 2. Coordination environment of the two Cu^{II} ions in complex **1** showing the axial–equatorial configuration of the two Cl bridges (*inset:* arrangement of the two square pyramids).

3.3. EPR spectra

EPR spectra recorded at 298 and 120 K on polycrystalline complex **1** are characterized by two *g* values ($g_{||}$ = 2.222 and $g_{\perp}$ = 2.094), which follow the trend $g_{||} > g_{\perp} > g_e$ (Fig. 3). The forbidden singlet-triplet transition ($\Delta Ms = \pm 2$), often detected at half-field for dimeric copper(II) complexes, is observable only with high instrumental gains. The EPR spectral features can be associated to an axial symmetry having $d_{x^2-y^2}$ as ground state [44,45], where the geometry can correspond to an elongated octahedral, a square-pyramidal or a square planar. The observed *g* values confirm that the geometry of the binuclear species is close to the square pyramid with the deprotonated phenolic and alkoxy oxygens, the imine nitrogen and the bridging Cl^- ion in the equatorial plane and a second Cl^- in the axial position.

The double chloro bridge is destroyed when complex **1** is dissolved in a coordinating solvent like DMF or CH_3CN and the mononuclear unit is formed. This happens because the solvent molecules can easily replace the labile chloride ligands in the coordination sphere of copper ion as found in many other similar complexes [46,47]. EPR spectrum of **1** dissolved in DMF or CH_3CN shows an axial symmetry (Fig. 4). The spectral parameters: $g_{||}$ = 2.270 and $A_{||} = 169.0 \times 10^{-4}\ cm^{-1}$ in DMF and $g_{||}$ = 2.275 and $A_{||} = 176.5 \times 10^{-4}\ cm^{-1}$ in CH_3CN, can be explained postulating a five-coordinated structure with phenolic-O^-, imine-N, alkoxo-O and a Cl^- in

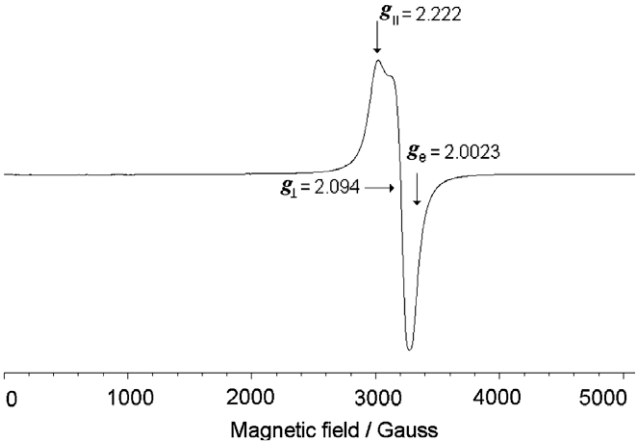


Fig. 3. X-band EPR spectrum of polycrystalline complex **1** at 120 K.

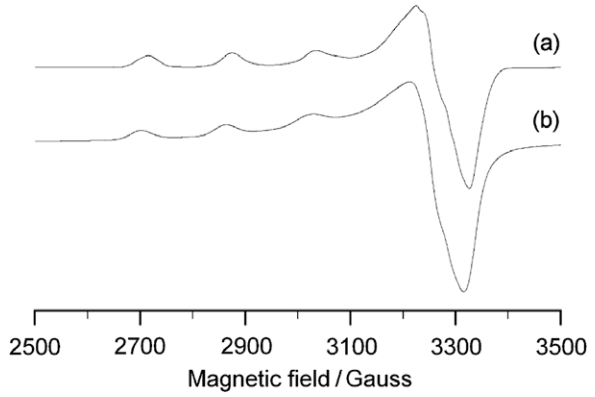


Fig. 4. X-band EPR anisotropic spectra of complex **1** recorded at 120 K in: (a) DMF and (b) CH_3CN.

the equatorial plane and one molecule of solvent weakly bound in the axial position.

3.4. Magnetic studies

The thermal variation of the molar magnetic susceptibility times the temperature ($\chi_m T$) for complex **1** is shown in Fig. 5. At room temperature, the value for $\chi_m T$ is ca. 0.92 emu K mol^{-1} which is slightly higher than the expected one for two non interacting copper(II) $S = 1/2$ ions (0.75 emu K mol^{-1} for $g = 2.0$). When cooling down the sample, the $\chi_m T$ product remains constant down to 180 K and below this temperature it shows a continuous increase to reach a maximum of ca. 1.14 emu K mol^{-1} at 12 K. Below 12 K, $\chi_m T$ decreases to reach a value of ca. 1.07 emu K mol^{-1} at 2 K. This behavior indicates that complex **1** presents predominant ferromagnetic interactions, as suggested by the increase in $\chi_m T$ observed at low temperatures. The $\chi_m T$ value of the maximum (1.14 emu K mol^{-1}) is close to the expected value for the $S = 1$ spin ground state arising from the ferromagnetic coupling of two $S = 1/2$ spins. The decrease observed at low temperatures can be attributed to the presence of antiferromagnetic interactions between the $S = 1$ dimers at low temperatures and/or to a zero field splitting (ZFS) of the $S = 1$ ground spin state. Since the structure of this complex shows the existence of Cu^{II} dimer connected by double chloride bridges, we have fitted the magnetic properties of complex **1** to a simple ferromagnetic $S = 1/2$ dimer with an interdimer exchange interaction (J') to account for the decrease of $\chi_m T$ at low temperatures (the Hamiltonian is written as $H = -JS_iS_{i+1}$) [48]:

$$\chi = 2Ng^2\beta^2[kT - \frac{2J'}{3 + e^{-x}}]^{-1}[3 + e^{-x}]^{-1},$$

where $x = J/kT$.

This model reproduces very satisfactorily the magnetic data of complex **1** in the whole temperature range with the following set of parameters: $g = 2.156(1)$, $J = 43.2(5)$ $K = 30.0(4)$ cm^{-1} and $J' = -0.276(8)$ $K = -0.192(6)$ cm^{-1} (solid line in Fig. 5). As expected (see below), the intradimer magnetic coupling is ferromagnetic and the interdimer one is much weaker and antiferromagnetic.

An additional proof of the ferromagnetic nature of the coupling in complex **1** comes from the isothermal magnetization measurements at low temperature (Fig. 6). This measurement shows a saturation value of ca. 2.2μ_B, very close to the expected value for an $S = 1$ spin state, resulting from the ferromagnetic coupling of the two $S = 1/2$ Cu^{II} ions. Furthermore, the magnetization can be reproduced well with a Brillouin function for an $S = 1$ with a g value of 2.131(4) (solid line in Fig. 6).

As already mentioned in the introduction, there have been several attempts to establish magneto-structural correlations in dinuclear dichloro-bridged Cu^{II} complexes, from the pioneering work of Willett and co-workers [49] and Hatfield and co-workers [9,15] that related the magnetic coupling with the Cu–Cl–Cu angle (α) and with the α/R ratio, respectively (where R is the Cu–Cl_{bridge} distance), to the more recent works of Rodríguez et al. [50], Mrozinski and co-workers [51] and Julve and co-workers [8]. All these correlations indicate that the exchange coupling constant J depends on the value of the Cu–Cl–Cu bridging angle, α, as well as on the bond length of the axial (longer) Cu–Cl bond, R in SP geometry. However, these parameters are not the only factors playing an important role in determining the magnetic coupling. The different types of arrangement of the two copper(II) polyhedra have a great influence on the magnetic behavior of such complexes. The global arrangement of the two square pyramids gives rise to three types of geometries: (a) square pyramids sharing one base-to-apex edge but with parallel basal planes (Type-I), (b) square pyramids sharing one base-to-apex edge with the two bases nearly perpendicular to one another (Type-II) and (c) square pyramids sharing a basal edge with coplanar basal planes (Type-III). Complex **1** belongs to the Type-I class of compounds, as evident from its structural features (Fig. 2). Thus, for the parallel bases arrangement (Type-I as in the case of the title complex), extended Hückel calculations [50] show that the magnetic interaction occurs through a π^* type interaction

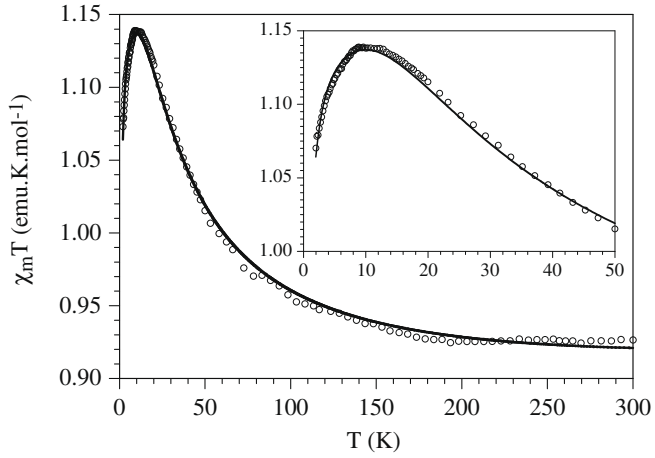


Fig. 5. Thermal variation of the $\chi_m T$ product for complex **1**. Solid line represents the best fit to the model (see text). Inset shows the low temperature region.

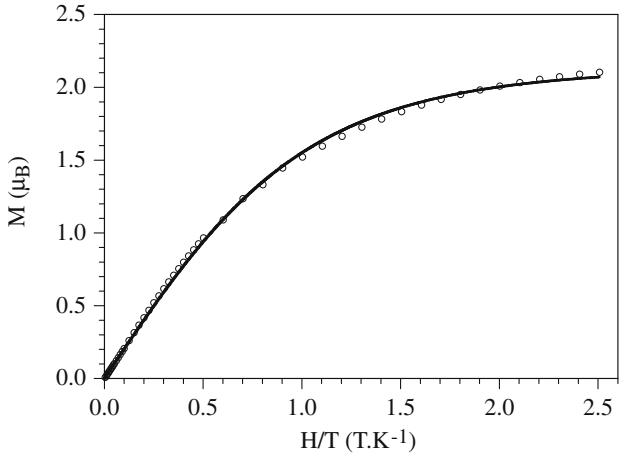


Fig. 6. Isothermal magnetization at 2 K of complex **1**. Solid line represents the best fit to the Brillouin function for an $S = 1$ spin state (see text).

between the $d_{x^2-y^2}$ Cu orbital and the p orbital of the chlorine atoms. The extent of this magnetic coupling is decided by the small structural deviations from the ideal square Cu_2Cl_2 core. Recently, Mrozinski and co-workers [51] established a theoretical correlation between the magnetic coupling and both parameters (α and R) showing that for small α values and short Cu–Cl distances the magnetic coupling is ferromagnetic. When the α and R values of complex **1** [α = 84.66(5)° and 84.25(5)° and R = 2.6853(16) and 2.6685(16) Å] are reported to this relationship, a moderately strong ferromagnetic coupling is predicted, which is in agreement with the experimental results. Furthermore, these α and R values are expected to produce the strongest ferromagnetic coupling of all the known Cu^{II} dimers involving a similar dichloro bridge. Interestingly, corroborating with the theoretical predictions, complex **1** is found to present the highest ferromagnetic coupling [J = +43.2(5) cm^{-1}] reported so far for any bis(μ-chloro) copper(II) dimers. An analysis of the α and R values of the other known dichloro-bridged Cu^{II} complexes [8,15,50,51] shows that the main reason explaining this particular situation are the small α values of complex **1**, which are about 5° smaller than the average value of 89.40(5)° [14]. Previously, the smallest α value reported was 82.9° for the complex $[Cu_2(baamo)_2Cl_2]$ (baamo = 8-amino-5-aza-4-methyl-3-octene-2-onate), where a ferromagnetic coupling of 12 cm^{-1} had been found even when the Cu–Cl distance was as high as 2.81 Å [52]. In the present complex the small α values are accompanied by much shorter R values (ca. 2.67 Å) compared to the above complex, giving rise to the unusually strong ferromagnetic coupling. A detailed look at the structure of complex **1** reveals that the presence of the intradimer hydrogen bonds (Fig. 1) may be responsible for the unusually small Cu–Cl–Cu angles since both intra- and intermolecular hydrogen bonds force the copper(II) ions to be closer, decreasing the Cu–Cl–Cu bond angle.

Finally, the antiferromagnetic weak interdimer exchange can be attributed to the presence of some short interdimer Br···Br contacts (Fig. S2, Supplementary data).

3.5. Catalytic oxidation of cyclohexane and cycloheptane

The study of the oxidation of various hydrocarbons catalyzed by a metal complex has now become an important research topic since it involves conversion of crude oil and natural gas constituents into oxygenated derivatives of immense industrial importance, such as alcohols or carbonyl compounds.

Here, we have examined the catalytic activity of the complex towards cyclohexane and cycloheptane oxidation using hydrogen peroxide as oxidant under the same experimental conditions for both the substrates. It is found that complex **1** behaves as active catalyst for the liquid biphasic (acetonitrile/water) oxidation of cyclohexane and cycloheptane by H_2O_2 in a slightly acidic medium at room temperature and atmospheric pressure. The corresponding products are cycloalkanol and cycloalkanone. Optimization has been achieved by varying the relative proportions of nitric acid, hydrogen peroxide as well as time period of the reactions. In the literature [53,54], it has been clearly pointed out that the presence of nitric acid has a positive role. The catalyst activation is created by the increase of unsaturation at the metal center with simultaneous increase in oxidation properties. As a result decomposition of peroxide is retarded and the peroxo intermediate gets stabilized.

During the present study, we have verified that the addition of nitric acid is mandatory in the hydrogen peroxide oxidation of cyclohexane and cycloheptane in presence of complex **1** as the catalyst. The amount of oxidized products remains almost unchanged in the 10–50 range of $n(HNO_3)/n$(catalyst), whereas further increase of such ratio decreases the yield. When the oxidation of the substrate was carried out in absence of nitric acid, the reaction did not proceed at all. The highest conversion of the substrate is achieved when $n(HNO_3)/n$(catalyst) is 10. The geometry around the Cu center in the catalyst is pentacoordinated having labile sites like Cu–Cl. These would require nitric acid so as to increase unsaturation at the metal site as a result of ligand protonation. Such observations evoked us to maintain a ratio of $n(HNO_3)/n$(catalyst) = 10 in the rest of the studies.

The results of cyclohexane oxidation are shown in Table 3a. It is clearly seen from the table that the maximum conversions of cyclohexane to the corresponding cyclohexanol and cyclohexanone are 31.4% and 20.9%, respectively, when $n(H_2O_2)/n$(catalyst) ratio is 300 with the reaction time 48 h. Table 3b contains the details of the conversion of cycloheptane influenced by the relative amounts of hydrogen peroxide, amount of nitric acid and the reaction period. The maximum conversions of cycloheptane to the corresponding cycloheptanol and cycloheptanone achieved are 24.0% and 15.0%, respectively. The results of these oxidation reactions are comparable with those obtained for other copper complexes reported earlier [53,55,56]. In contrast, simple copper salt like, $Cu(NO_3)_2$ under the same reaction conditions exhibits a much lower activity towards oxidation of the substrates with 3.9–5.4% yield, under the same peroxide-to-catalyst molar ratio. Thus it is evident that the presence of N,O donor ligands are quite relevant.

In the case of complex **1**, the coordination environment around the copper(II) ion is easily accessible for an external ligand, as a result copper(II) can bind the peroxo-group on treatment with peroxides. This *in situ* generated intermediated peroxo-type species seems to be capable of transferring the oxo functionality to the organic substrates to give the corresponding oxidized products. In order to find out the probable mechanisms, we have carried out the catalytic reaction of cyclohexane with complex **1** maintaining $n(HNO_3)/n$(catalyst) ratio of 10 and $n(H_2O_2)/n$(catalyst) ratio of 300 in presence of TEMPO (2,2,6,6-tetramethylpiperidin-1-oxyl) and diphenylamine. The yield of the reaction is greatly suppressed in presence of these compounds. TEMPO and diphenylamine are

Table 3a
Oxidation of cyclohexane by complex **1**.

Entry	Catalyst	$n(H_2O_2)/n$(catalyst)	Time (h)	Yield (%)			TON[a]
				Cyclohexanol	Cyclohexanone	Total	
1	Complex **1**	150	6	20.1	15.4	35.5	13.2
2			48	26.3	20.1	46.4	17.2
3		300	6	24.5	14.1	38.6	14.3
4			48	31.4	20.9	52.3	19.4
5		750	6	20.5	16.9	37.4	13.9
6			48	26.0	19.1	45.1	16.7
7	$Cu(NO_3)_2$	150	48	1.8	1.1	2.9	–
8		300	48	3.4	1.7	5.1	–
9		750	48	3.6	1.8	5.4	–

[a] Turnover number.

Table 3b
Oxidation of cycloheptane by complex **1**.

Entry	Catalyst	$n(H_2O_2)/n$(catalyst)	Time (h)	Yield (%)			TON
				Cycloheptanol	Cycloheptanone	Total	
1	Complex **1**	150	6	19.1	14.3	33.4	12.4
2			48	22.2	15.2	37.4	13.9
3		300	6	17.9	11.7	29.6	11.0
4			48	24.0	15.0	39.0	14.5
5		750	6	19.3	11.1	31.4	11.6
6			48	23.5	13.6	37.1	13.8
7	$Cu(NO_3)_2$	150	48	2.1	1.0	3.1	–
8		300	48	3.5	1.7	5.2	–
9		750	48	3.3	2.1	5.4	–

well known as carbon-radical and oxygen-radical traps respectively [57]. This indirectly indicates that oxidation reactions occur mainly by mechanisms involving the formation of both carbon-centered and oxygen-centered radicals. An electrophilic attack of an oxidized metal-peroxo, metal-superoxo or metal-oxo center to a C–H bond of the substrate with heterolytic cleavage of this bond to form an organocopper intermediate can be proposed which has been noted for other metals [58].

4. Conclusion

The present complex shows the feasibility of the ONO donor Schiff bases to form dinuclear dichloro-bridged Cu^{II} complexes with an unusually strong ferromagnetic coupling. In fact, complex **1** presents the strongest ferromagnetic coupling observed till date in any doubly (μ-chloro)-bridged Cu^{II} complex. The previously established magneto-structural correlations attribute this strong ferromagnetic coupling to the unusually small Cu–Cl–Cu bond angles. A detailed structural analysis reveals that the intradimer hydrogen bonds of both intra- and intermolecular types are responsible for bringing the two copper centers closer, thereby decreasing the bridging angle. Besides this, the complex is also found to possess efficient catalytic properties in the oxidation of cyclohexane and cycloheptane by H_2O_2 to their corresponding alcoholic and carbonyl derivatives.

Acknowledgements

Santarupa Thakurta gratefully acknowledges the Council of Scientific and Industrial Research, New Delhi, India, for the award of Research Fellowship to her (CSIR Sanction No. 09/096(0519)/2007-EMR-I) and thanks are extended to Prof. P. Banerjee of Department of Inorganic Chemistry, Indian Association for the Cultivation of Science, Kolkata 32, for providing valuable supports. Carlos J. Gómez-García acknowledges the European Union for financial support (MAGMANet network of excellence) and the Spanish Ministerio de Educación y Ciencia (Projects MAT2007-61584 and Consolider-Ingenio 2010 CSD 2007-00010 in Molecular Nanoscience).

Appendix A. Supplementary data

CCDC 703082 contains the supplementary crystallographic data for complex **1**. These data can be obtained free of charge via http://www.ccdc.cam.ac.uk/conts/retrieving.html, or from the Cambridge Crystallographic Data Centre, 12 Union Road, Cambridge CB2 1EZ, UK; fax: (+44) 1223-336-033; or e-mail: deposit@ccdc.cam.ac.uk. Supplementary data associated with this article can be found, in the online version, at doi:10.1016/j.poly.2008.12.016.

References

[1] K.D. Karlin, Z. Tyeklar, Bioinorganic Chemistry of Copper, Chapman and Hall, New York, 1993.
[2] R.H. Holm, P. Kennepohl, E.I. Solomon, Chem. Rev. 96 (1996) 2239.
[3] R.L. Lieberman, A.C. Rosenzweig, Nature 434 (2005) 177.
[4] J. Yoon, E.I. Solomon, Inorg. Chem. 44 (2005) 8076.
[5] J.R. Friedman, M.P. Sarachik, J. Tejada, R. Ziolo, Phys. Rev. Lett. 76 (1996) 3830.
[6] L. Thomas, L. Lionti, R. Ballou, D. Gatteschi, R. Sessoli, B. Barbara, Nature 383 (1996) 145.
[7] P.J. Hay, J.C. Thibeault, R. Hoffmann, J. Am. Chem. Soc. 97 (1977) 4884.
[8] M. Grove, J. Sletten, M. Julve, F. Lloret, J. Chem. Soc., Dalton Trans. (2001) 2487.
[9] W.E. Marsh, W.E. Hatfield, D.J. Hodgson, Inorg. Chem. 21 (1982) 2679.
[10] M. Rodríguez, A. Llobet, M. Corbella, A.E. Martell, J. Reibenspies, Inorg. Chem. 38 (1999) 2328.
[11] S.S. Roberts, D.R. Bloomquist, R.D. Willett, H.W. Dodgen, J. Am. Chem. Soc. 103 (1981) 2603.
[12] S.K. Hoffmann, D.J. Hodgson, W.E. Hatfield, Inorg. Chem. 24 (1985) 1194.
[13] X.-H. Bu, M. Du, Z.-L. Shang, L. Zhang, Q.-H. Zhao, R.-H. Zhang, M. Shionoya, Eur. J. Inorg. Chem. (2001) 1551.
[14] A. Bernalte-García, A.M. Lozano-Vila, F. Luna-Giles, R. Pedrero-Marín, Polyhedron 25 (2006) 1399.
[15] W.E. Marsh, K.C. Patel, W.E. Hatfield, D.J. Hodgson, Inorg. Chem. 22 (1983) 511.
[16] D.J. Hodgson, E. Pedersen, Acta Chem. Scand., Ser. A 36 (1982) 281.
[17] R.F. Drake, V.H. Crawford, N.W. Laney, W.E. Hatfield, Inorg. Chem. 13 (1974) 1246.
[18] J.A. Carrabirie, M. Sundaralingarn, J. Am. Chem. Soc. 92 (1970) 369.
[19] X.-H. Bu, M. Du, L. Zhang, Z.-L. Shang, R.-H. Zhang, M. Shionoya, J. Chem. Soc., Dalton Trans. (2001) 729.
[20] M. Mégnamisi-Bélombé, M.A. Novotny, Inorg. Chem. 19 (1980) 2470.
[21] F. Tuna, L. Patron, Y. Journaux, M. Andruh, W. Plass, J.-C. Trombe, J. Chem. Soc., Dalton Trans. (1999) 539.
[22] W.A. Alves, S.A. Almeida-Filho, R.H.A. Santos, A.M.D.C. Ferreira, Inorg. Chem. Commun. 6 (2003) 294.
[23] Y.-B. Jiang, H.-Z. Kou, R.-J. Wang, A.-L. Cui, Eur. J. Inorg. Chem. (2004) 4608.
[24] S.-L. Ma, X.-X. Sun, S. Gao, C.-M. Qi, H.-B. Huang, W.-X. Zhu, Eur. J. Inorg. Chem. (2007) 846.
[25] A. Sieber, C. Boskovic, R. Bircher, O. Waldmann, S.T. Ochsenbein, G. Chaboussant, H.U. Gudel, N. Kirchner, J. Van Slageren, W. Wernsdorfer, A. Neels, H. Stoeckli-Evans, S. Janssen, F. Juranyi, H. Mutka, Inorg. Chem. 44 (2005) 4315.
[26] H. Oshio, N. Hoshino, T. Ito, M. Nakano, J. Am. Chem. Soc. 126 (2004) 8805.
[27] N. Hoshino, T. Ito, M. Nihei, H. Oshio, Chem. Lett. (2002) 844.
[28] M. Dey, C.P. Rao, P.K. Saarenketo, K. Rissanen, Inorg. Chem. Commun. 5 (2002) 380.
[29] D.D. Perrin, W.L.F. Armarego, D.R. Perrin, Purification of Laboratory Chemicals, 2nd Ed., Pergamon Press, Oxford, UK, 1980.
[30] APEX 2, version 2.2. Bruker AXS Inc., Madison, WI, 2006.
[31] G.M. Sheldrick, SADABS, Programs for Area Detector Adsorption Correction, Institute for Inorganic Chemistry, University of Göttingen, Germany, 1996.
[32] G.M. Sheldrick, SHELXTL, version 5.1, Program for the Solution and Refinement of Crystal Structures, Bruker AXS Inc., Madison, WI, 1999.
[33] A.L. Spek, PLATON, Molecular Geometry Program, University of Utrecht, The Netherlands, 1999.
[34] L.J. Farrugia, ORTEP3 for Windows, J. Appl. Crystallogr. 30 (1997) 565.
[35] S. Thakurta, J. Chakraborty, G. Rosair, J. Tercero, M. Salah El Fallah, E. Garribba, S. Mitra, Inorg. Chem. 47 (2008) 6227.
[36] K. Nakamoto, Infrared and Raman Spectra of Inorganic and Coordination Compounds, Parts A and B, 5th Ed., John Wiley, New York, 1997.
[37] B. Crociani, R. Boschi, R. Pietropaolo, U. Belluco, J. Chem. Soc. A (1970) 531.
[38] A.B.P. Lever, Inorganic Electronic Spectroscopy, 2nd Ed., Elsevier, New York, 1984.
[39] S. Shit, P. Talukder, J. Chakraborty, M. Salah El Fallah, J. Ribas, S. Mitra, Polyhedron 26 (2007) 1357.
[40] B.J. Hathaway, G. Wilkinson, R.D. Gillard, J.A. McCleverty (Eds.), Comprehensive Coordination Chemistry, vol. 5, Pergamon Press, Oxford, UK, 1987.

[41] A.W. Addison, T.N. Rao, J. Reedijk, J. Van Rijn, G.C. Verschoor, J. Chem. Soc., Dalton Trans. (1984) 1349.
[42] S.C. Lee, R.H. Holm, Inorg. Chem. 32 (1993) 4745.
[43] F.H. Allen, O. Kennard, Chem. Des. Autom. News 8 (1993) 31.
[44] B.J. Hathaway, D.E. Billing, Coord. Chem. Rev. 5 (1970) 143.
[45] B.J. Hathaway, Struct. Bond. 57 (1984) 55.
[46] J.C. Jeffery, J.P. Maher, C.A. Otter, P. Thornton, M.D. Ward, J. Chem. Soc., Dalton Trans. (1995) 819.
[47] E. Garribba, G. Micera, D. Sanna, L. Strinna Erre, Inorg. Chim. Acta 299 (2000) 253.
[48] O. Kahn, Molecular Magnetism, VCH Publishers, 1993.
[49] S.G.N. Roundhill, D.M. Roundhill, D.R. Bloomquist, C. Landee, R.D. Willett, D.M. Dooley, H.B. Gray, Inorg. Chem. 18 (1979) 831.
[50] M. Rodríguez, A. Llobet, M. Corbella, Polyhedron 19 (2000) 2483.
[51] K. Skorda, T.C. Stamatatos, A.P. Vafiadis, A.T. Lithoxoidou, A. Terzis, S.P. Perlepes, J. Mrozinski, C.P. Raptopoulou, J.C. Plakatouras, E.G. Bakalbassis, Inorg. Chim. Acta 358 (2005) 565.
[52] E. Kwiatkowski, M. Kwiatkowski, A. Olechnowicz, J. Mrozinski, D.M. Ho, E. Deutsch, Inorg. Chim. Acta 158 (1989) 37.
[53] A.M. Kirillov, M.N. Kopylovich, M.V. Kirillova, M. Haukka, M.F.C. Guedes da Silva, A.J.L. Pombeiro, Angew. Chem., Int. Ed. 44 (2005) 4345.
[54] P. Roy, K. Dhar, M. Manassero, P. Banerjee, Eur. J. Inorg. Chem. (2008) 4404.
[55] A.M. Kirillov, M.N. Kopylovich, M.V. Kirillova, E.Yu. Karabach, M. Haukka, M.F.C. Guedes da Silva, A.J.L. Pombeiro, Adv. Synth. Catal. 348 (2006) 159.
[56] C.D. Nicola, E.Yu. Karabach, A.M. Kirillov, M. Monari, L. Pandolfo, C. Pettinari, A.J.L. Pombeiro, Inorg. Chem. 46 (2007) 221.
[57] L.M. Slaughter, J.P. Collman, T.A. Eberspacher, J.I. Brauman, Inorg. Chem. 43 (2004) 5198.
[58] C. Jia, T. Kitamura, Y. Fujiwara, Acc. Chem. Res. 34 (2001) 633.

$[Bi_2(4\text{-bpdh})Br_9]\cdot 3(4\text{-Hbpdh})$ (**3**) {3-bpdb = 1,4-bis(3-pyridyl)-2,3-diaza-1,3-butadiene, 3-bpdh = 2,5-bis(3-pyridyl)-3,4-diaza-2,4-hexadiene and 4-bpdh = 2,5-bis(4-pyridyl)-3,4-diaza-2,4-hexadiene} (Fig. 1)}.

The three nitrogen donor-based ligands 3-bpdb, 3-bpdh and 4-bpdh that were used have been selected, amongst other reasons, as they are capable to act as bridging ligands and thus may be able to form polymeric structures. Recent investigations have addressed the use of these three ligands for the preparation of coordination polymers with other metal ions [45–54]. These studies have demonstrated that the long conjugated rigid ligands are capable of coordinating transition metal centers via both the terminal pyridyl and the diaza nitrogen donors and that they are able to generate novel coordination polymers. We will show that subtle changes in the use of these conformationally flexible ligands as spacers in the design and construction of coordination polymers may lead to new polymeric networks with different structural motifs and topologies. As the counter-ion in these Bi(III) coordination polymers we decided to use bromide anions, which may be able to act as additional bridges between the metal centers.

2. Experimental

With the exception of the ligands 3-bpdb, 3-bpdh and 4-bpdh, which were prepared according to the literature procedures [55,56], all reagents and solvents for the synthesis and analysis were commercially available and were used as received. IR spectra were recorded using Perkin–Elmer 597 and Nicolet 510P spectrophotometers. Microanalyses were carried out using a Heraeus CHN-O-Rapid analyzer. Melting points were measured on an Electrothermal 9100 apparatus and are uncorrected. The thermal behavior was measured with a PL-STA 1500 apparatus. Single crystal diffraction measurements were made at 100(2) K using a Bruker AXS SMART APEX CCD diffractometer. The intensity data were collected using graphite monochromated Mo Kα radiation. The structures were solved by direct methods and refined by full-matrix least-squares techniques on F^2. All hydrogen atoms were placed in calculated positions and were refined with an isotropic displacement parameter 1.2 times that of the adjacent carbon atom. The molecular structure plots were prepared using Mercury [57] and ORTEPIII [58] (see Tables 1 and 2).

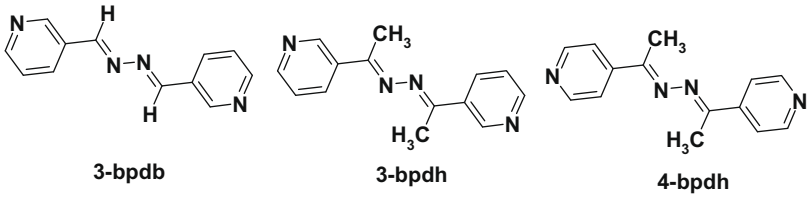


Fig. 1. Organic nitrogen donor-based ligands used in the construction of bismuth(III) bromide coordination polymers.

Table 1
Crystal data and structure refinement for $[Bi_2(3\text{-bpdb})_2Br_8]\cdot(3\text{-}H_2bpdb)$ (**1**), $[Bi_2(3\text{-Hbpdh})_2Br_8]$ (**2**) and $[Bi_2(4\text{-bpdh})Br_9]\cdot 3(4\text{-Hbpdh})$ (**3**).

Identification code	**1**	**2**	**3**
Empirical formula	$C_{36}H_{32}Bi_2Br_8N_{12}$	$C_{28}H_{28.55}Bi_2Br_{6.55}N_8$	$C_{56}H_{59}Bi_2Br_9N_{16}$
Formula weight	1689.90	1418.44	2093.34
Temperature (K)	100(2)	100(2)	100(2)
Wavelength (Å)	0.71073	0.71073	0.71073
Crystal system	monoclinic	monoclinic	triclinic
Space group	$P2_1/n$	$P2_1/c$	$P\bar{1}$
Unit cell dimensions			
a (Å)	12.4124(17)	7.203(2)	12.2439(16)
b (Å)	11.6316(16)	13.913(4)	13.8364(18)
c (Å)	16.273(2)	18.845(5)	20.524(3)
α (°)	90	90	80.935(2)
β (°)	93.664	92.734(5)	77.734(2)
γ (°)	90	90	85.863(2)
Volume (Å^3)	2344.6(6)	1886.3(10)	3352.5(8)
Z	2	2	2
D_{calc} (Mg/m^3)	2.394	2.497	2.074
Absorption coefficient (mm^{-1})	14.354	16.285	10.654
Crystal size (mm)	0.22 × 0.19 × 0.13	0.17 × 0.14 × 0.11	0.35 × 0.24 × 0.1
Theta range for data collection (°)	2.40–29.73	2.61–29.63	2.16–24.76
Index ranges	$-16 \leqslant h \leqslant 16$	$-9 \leqslant h \leqslant 9$	$-16 \leqslant h \leqslant 16$
	$-15 \leqslant k \leqslant 15$	$-18 \leqslant k \leqslant 18$	$-18 \leqslant k \leqslant 18$
	$-21 \leqslant l \leqslant 21$	$-20 \leqslant l \leqslant 25$	$-27 \leqslant l \leqslant 27$
Reflections collected	5820	4666	16476
Independent reflections	4711	3695	10558
Absorption correction	multi-scan	multi-scan	multi-scan
Maximum and minimum transmission	0.071 and 0.155	0.093 and 0.167	0.084 and 0.345
Refinement method	full-matrix least-squares on F^2	full-matrix least-squares on F^2	full-matrix least-squares on F^2
Data/restraints/parameters	5820/0/262	4666/1/215	16476/0/774
Goodness-of-fit on F^2	1.063	1.012	1.016
Final R indices [$I > 2\sigma(I)$]	$R_1 = 0.0503$	$R_1 = 0.0338$	$R_1 = 0.0625$
	$wR_2 = 0.1427$	$wR_2 = 0.0597$	$wR_2 = 0.1577$
R indices (all data)	$R_1 = 0.0636$	$R_1 = 0.0508$	$R_1 = 0.1088$
	$wR_2 = 0.1514$	$wR_2 = 0.0657$	$wR_2 = 0.1832$
Largest difference in peak, hole (e Å^{-3})	3.141 and −5.990	1.469 and −1.425	2.714 and −3.658

Table 2
Bond lengths (Å) and angles (°) for $[Bi_2(3\text{-bpdb})_2Br_8]\cdot(3\text{-}H_2bpdb)$ (**1**), $[Bi_2(3\text{-Hbpdh})_2Br_8]$ (**2**) and $[Bi_2(4\text{-bpdh})Br_9]\cdot 3(4\text{-Hbpdh})$ (**3**).

1		2		3	
Bi(1)–N(1)	2.605(8)	Bi(1)–N(1)	2.600(4)	Bi(1)–Br(4)	2.7865(16)
Bi(1)–Br(1)	2.6398(15)	Bi(1)–Br(3)	2.6586(10)	Bi(1)–N(1)	2.431(8)
Bi(1)–Br(4)	2.6881(13)	Bi(1)–Br(2)	2.6761(8)	Bi(1)–Br(1)	2.7756(13)
Bi(1)–Br(2)	2.7840(11)	Bi(1)–Br(1)	2.7769(9)	Bi(1)–Br(3)	2.8030(13)
Bi(1)–Br(3)	3.0388(11)	Bi(1)–Br(4)	2.9905(12)	Bi(1)–Br(2)	2.8100(12)
Bi(1)–Br(3)	3.0491(11)	Bi(1)–Br(4)	3.0320(12)	Bi(1)–Br(5)	2.867(7)
N(1)–Bi(1)–Br(1)	86.60(18)	N(1)–Bi(1)–Br(3)	81.74(10)	Bi(1)–Br(5)	2.937(7)
N(1)–Bi(1)–Br(4)	85.22(17)	N(1)–Bi(1)–Br(2)	85.98(10)	Bi(2)–N(3)	2.432(10)
Br(1)–Bi(1)–Br(4)	91.43(4)	Br(3)–Bi(1)–Br(2)	94.73(3)	Bi(2)–Br(7)	2.7559(14)
N(1)–Bi(1)–Br(2)	176.22(18)	N(1)–Bi(1)–Br(1)	175.50(10)	Bi(2)–Br(8)	2.7565(15)
Br(1)–Bi(1)–Br(2)	89.91(4)	Br(3)–Bi(1)–Br(1)	94.32(2)	Bi(2)–Br(9)B	2.765(3)
Br(4)–Bi(1)–Br(2)	93.44(3)	Br(2)–Bi(1)–Br(1)	92.23(3)	Bi(2)–Br(6)	2.8376(14)
N(1)–Bi(1)–Br(3)	82.59(17)	N(1)–Bi(1)–Br(4)	86.85(10)	Bi(2)–Br(9)A	2.861(3)
Br(1)–Bi(1)–Br(3)	89.91(4)	Br(3)–Bi(1)–Br(4)	86.50(3)	Bi(2)–Br(10)	2.864(3)
Br(4)–Bi(1)–Br(3)	167.63(3)	Br(2)-Bi(1)–Br(4)	172.46(3)	Bi(2)–Br(10)	3.026(3)
Br(2)–Bi(1)–Br(3)	98.86(3)	Br(1)–Bi(1)–Br(4)	95.09(3)	N(1)–Bi(1)–Br(1)	81.8(2)
N(1)–Bi(1)–Br(3)	88.07(18)	N(1)–Bi(1)–Br(4)	84.88(10)	N(1)–Bi(1)–Br(4)	88.8(2)
Br(1)–Bi(1)–Br(3)	174.26(4)	Br(3)–Bi(1)–Br(4)	157.01(3)	Br(1)–Bi(1)–Br(4)	95.54(5)
Br(4)–Bi(1)–Br(3)	90.26(3)	Br(2)–Bi(1)–Br(4)	102.90(3)	N(1)–Bi(1)–Br(3)	83.7(2)
Br(2)–Bi(1)–Br(3)	95.47(3)	Br(1)–Bi(1)–Br(4)	99.55(3)	Br(1)–Bi(1)–Br(3)	165.48(4)
Br(3)–Bi(1)–Br(3)	87.28(3)	Br(4)–Bi(1)–Br(4)	74.14(3)	Br(4)–Bi(1)–Br(3)	85.45(5)
Bi(1)–Br(3)–Bi(1)	92.72(3)	Bi(1)–Br(4)–Bi(1)	105.86(3)	N(1)–Bi(1)–Br(2)	87.0(2)
				Br(1)–Bi(1)–Br(2)	87.06(4)
				Br(4)–Bi(1)–Br(2)	174.74(6)
				Br(3)–Bi(1)–Br(2)	90.88(4)
				N(1)–Bi(1)–Br(5)	165.7(3)
				Br(1)–Bi(1)–Br(5)	94.00(15)
				Br(4)–Bi(1)–Br(5)	77.91(14)
				Br(3)–Bi(1)–Br(5)	100.36(14)
				Br(2)–Bi(1)-Br(5)	106.51(13)
				N(1)–Bi(1)–Br(5)	166.9(2)
				Br(1)–Bi(1)–Br(5)	86.18(14)
				Br(4)–Bi(1)–Br(5)	97.63(14)
				Br(3)–Bi(1)–Br(5)	108.08(14)
				Br(2)–Bi(1)–Br(5)	87.09(13)
				Br(5)–Bi(1)–Br(5)	20.6(2)
				N(3)–Bi(2)–Br(7)	85.4(2)
				N(3)–Bi(2)–Br(8)	83.1(3)
				Br(7)–Bi(2)–Br(8)	88.42(5)
				N(3)–Bi(2)–Br(9)B	102.1(3)
				Br(7)–Bi(2)–Br(9)B	172.46(9)
				Br(8)–Bi(2)–Br(9)B	93.31(7)
				N(3)–Bi(2)–Br(6)	84.6(3)
				Br(7)–Bi(2)–Br(6)	89.95(4)
				Br(8)–Bi(2)–Br(6)	167.68(5)
				Br(9)B–Bi(2)–Br(6)	89.89(7)
				N(3)–Bi(2)–Br(9)A	75.3(3)
				Br(7)–Bi(2)–Br(9)A	160.08(10)
				Br(8)–Bi(2)–Br(9)A	94.08(8)
				Br(9)B–Bi(2)–Br(9)A	27.08(11)
				Br(6)–Bi(2)–Br(9)A	83.40(8)
				N(3)–Bi(2)–Br(10)	160.3(3)
				Br(7)–Bi(2)–Br(10)	114.21(10)
				Br(8)–Bi(2)–Br(10)	98.45(8)
				Br(9)B–Bi(2)–Br(10)	58.28(12)
				Br(6)–Bi(2)–Br(10)	93.36(8)
				Br(9)A–Bi(2)–Br(10)	85.00(13)
				N(3)–Bi(2)–Br(10)	164.8(2)
				Br(7)–Bi(2)–Br(10)	82.40(9)
				Br(8)–Bi(2)–Br(10)	87.55(8)
				Br(9)B–Bi(2)–Br(10)	90.34(12)
				Br(6)–Bi(2)–Br(10)	104.34(8)
				Br(9)A–Bi(2) –Br(1)	117.43(13)
				Br(10)–Bi(2)–Br(10)	33.52(16)

To isolate single crystals of $[Bi_2(3\text{-bpdb})_2Br_8]\cdot(3\text{-}H_2bpdb)$ (**1**), $[Bi_2(3\text{-Hbpdh})_2Br_8]$ (**2**) and $[Bi_2(4\text{-bpdh})Br_9]\cdot 3(4\text{-Hbpdh})$ (**3**), one mmol of each of the ligands 3-bpdb, 3-bpdh and 4-bpdh and one mmol of bismuth(III) bromide were placed in the main arm of a branched tube. Methanol was carefully added to fill both arms. The tube was sealed and the ligand-containing arm immersed in an oil bath at 60 °C while the other arm was kept at ambient temperature. After 7–10 days, yellow, yellow and red crystals of compounds **1–3**, respectively, that deposited in the cooler arm were isolated. The single crystals were filtered off, washed with acetone and ether, and air dried.

Product **1**: m.p. = 290 °C. *Anal*. Calc. for $C_{36}H_{32}Bi_2Br_8N_{12}$: C, 25.56; H, 1.89; N, 9.94. Found: C, 25.40; H, 1.70; N, 9.80%. IR (cm^{-1}, KBr): 493w, 678m, 801m, 858w, 1039w, 1299m, 1407w, 1615s.

Product **2***:* m.p. = 274 °C. *Anal.* Calc. for $C_{28}H_{28.55}Bi_2Br_{6.55}N_8$: C, 23.68; H, 2.01; N, 7.89. Found: C, 23.50; H, 2.10; N, 7.50%. IR (cm^{-1}, KBr): 406m, 566w, 642w, 817s, 1006m, 1050w, 1363w, 1596s.

Product **3***:* m.p. = 270 °C. *Anal.* Calc. for $C_{56}H_{59}Bi_2Br_9N_{16}$: C, 32.10; H, 2.81; N, 10.70. Found: C, 32.20; H, 2.70; N, 10.55%. IR (cm^{-1}, KBr): 631w, 659m, 778s, 847w, 1032w, 1287w, 1370m, 1526m, 1600m, 1939w, 3045vs.

3. Results and discussion

The reaction between 3-bpdb, 3-bpdh and 4-bpdh with bismuth(III) bromide provided crystalline materials of the general formulae $[Bi_2(3\text{-bpdb})_2Br_8]\cdot(3\text{-}H_2bpdb)$ (**1**), $[Bi_2(3\text{-Hbpdh})_2Br_8]$ (**2**) and $[Bi_2(4\text{-bpdh})Br_9]\cdot 3(4\text{-Hbpdh})$ (**3**), respectively. The IR spectra of these compounds show characteristic absorption bands for the 3-bpdb, 3-bpdh and 4-bpdh ligands, such as the typical pyridyl vibrations in the frequency range 1400–1580 cm^{-1}, and the elemental analysis data agree well with the numbers expected for the respective formulae given above.

Detailed solid state structures of all three complexes were determined by single crystal X-ray diffraction analysis (Figs. 2–7). For compound **2**, the occupancies were refined for all bromine atoms and the sum of these occupancies was set to the sum of the positive charges from the bismuth ions and the occupancy of the pyridinium hydrogen atoms. In compound **3**, the bromine atom Br10 is disordered across an inversion center. This induces a 1:1 disorder of the neighboring bromine atom Br9. Complex **1** is a salt in the solid state and consists of a $[Bi_2(3\text{-bpdb})_2Br_8]^{2-}$ anion and a $3\text{-}H_2bpdb^{2+}$ cation. The complex anion is dinuclear in nature and the bismuth atoms are coordinated to the nitrogen atoms of the 3-bpdb ligand and also to the five bromide atoms, two of which are bridging between the two different Bi atoms. The metal coordination number in this complex is six and the coordination around Bi is distorted octahedral. An interesting point is that the $3\text{-}H_2bpdb^{2+}$ cations must have been created by proton transfer between the molecular species in solution. The $3\text{-}H_2bpdb^{2+}$ cations are linked by hydrogen bonding (Fig. 5) via their protonated pyridyl nitrogen atoms as N–H hydrogen bond donors. Hydrogen bond acceptors are the uncoordinated and unprotonated pyridyl N

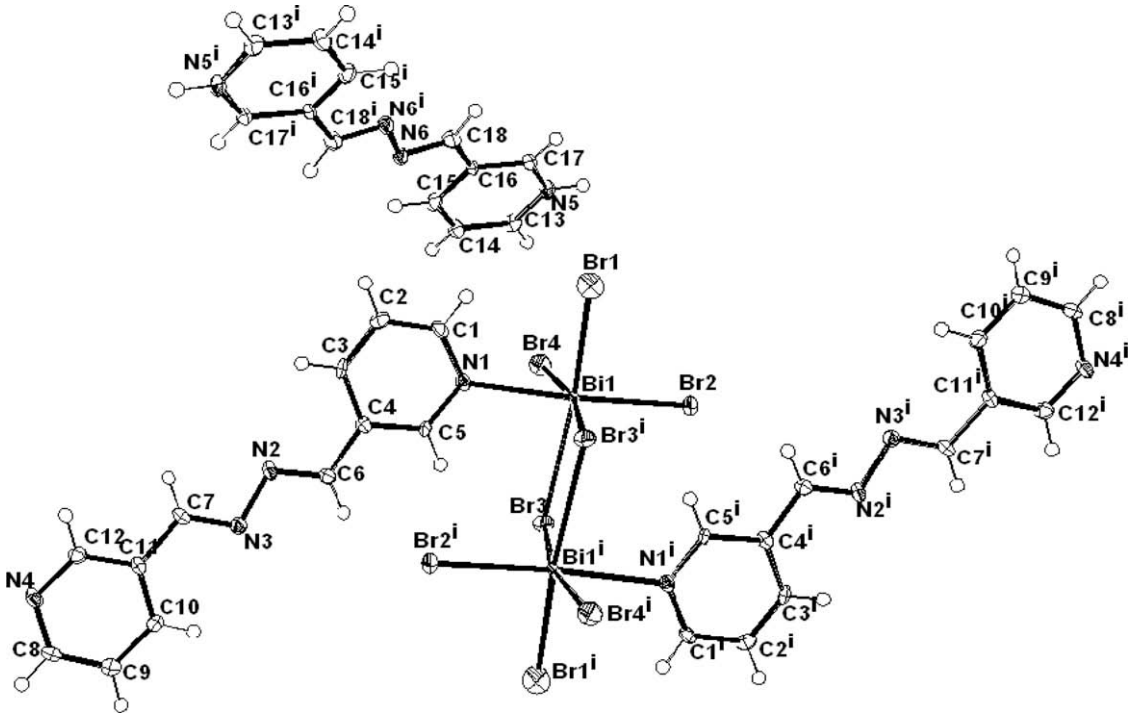


Fig. 2. X-ray crystal structure showing the linking and non-coordination of the ligands 3-bpdb and 3-Hbpdb in $[Bi_2(3\text{-bpdb})_2Br_8]\cdot(3\text{-}H_2bpdb)$ (**1**), respectively, (30% thermal displacement ellipsoids).

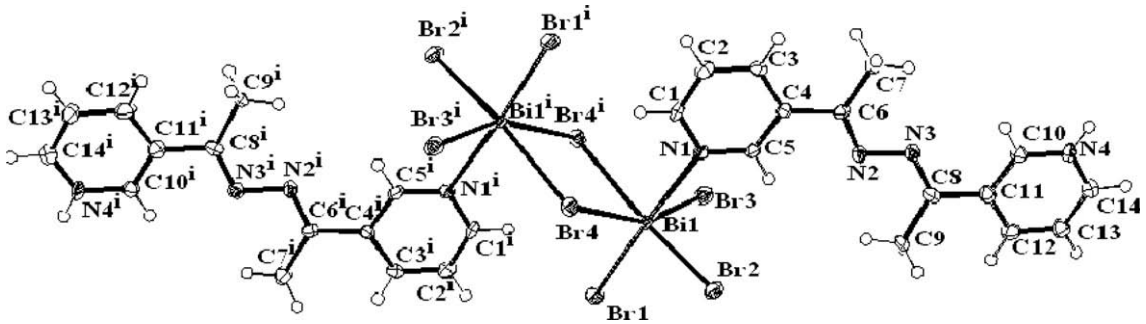


Fig. 3. X-ray crystal structure of $[Bi_2(3\text{-Hbpdh})_2Br_8]$ (**2**), (50% thermal displacement ellipsoids).

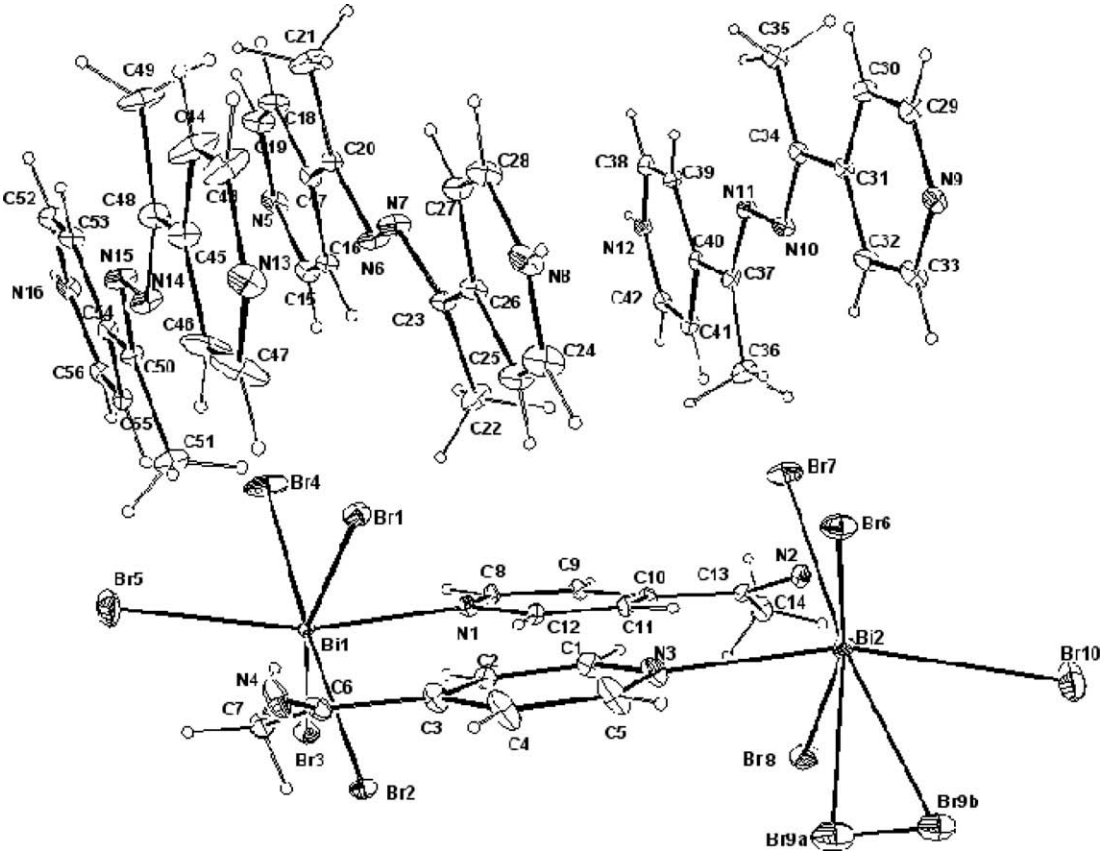


Fig. 4. X-ray crystal structure showing the linking and non-coordination of the ligands 4-bpdh and 3-Hbpdh in $[Bi_2(4\text{-bpdh})Br_9]\cdot 3(4\text{-Hbpdh})$ (**3**), respectively, (30% thermal displacement ellipsoids).

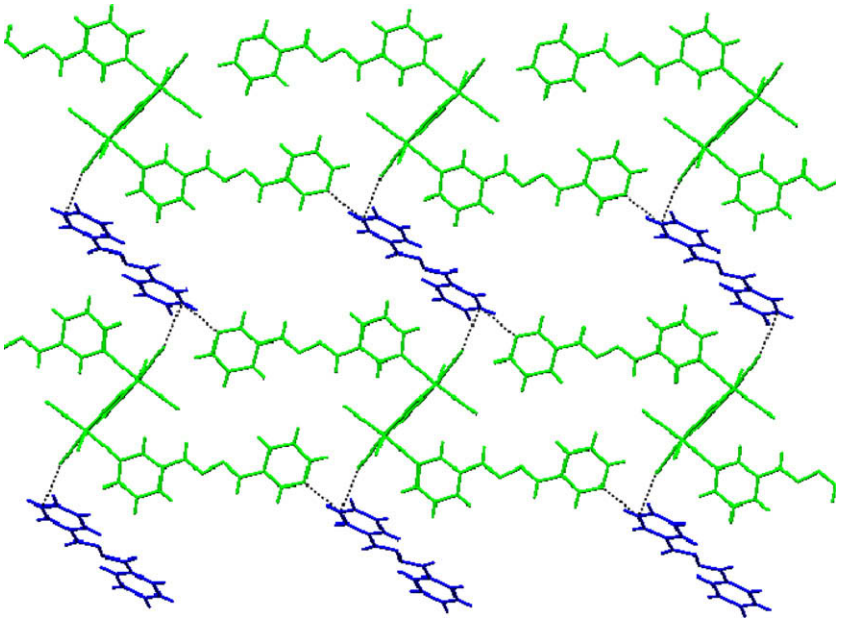


Fig. 5. The 2D supramolecular structure generated via the N-H···N and N-H···Br interactions in $[Bi_2(3\text{-bpdb})_2Br_8]\cdot(3\text{-}H_2bpdb)$ (**1**).

atoms of the $[Bi_2(3\text{-bpdb})_2Br_8]^{2-}$ anions. Hydrogen bond distances d(D–H), d(H···A), d(D···A), and angles <(DHA)} for N5–H5A···N4 are 0.86, 1.87, 2.681(12) Å, and 157.7°, respectively, and for N7–H7A···N6^{i} they are 0.88, 1.83, 2.694(9) Å, and 167.7°, respectively [symmetry operator $i = -1 + x, 1 + y, z$]. Another interesting feature of this complex is that there is a short Br···H–N interaction (Fig. 5) with a distance of 3.348(9) Å. Consequently, the dimeric structure is grown by the hydrogen bonds and Br···H–N interactions into a

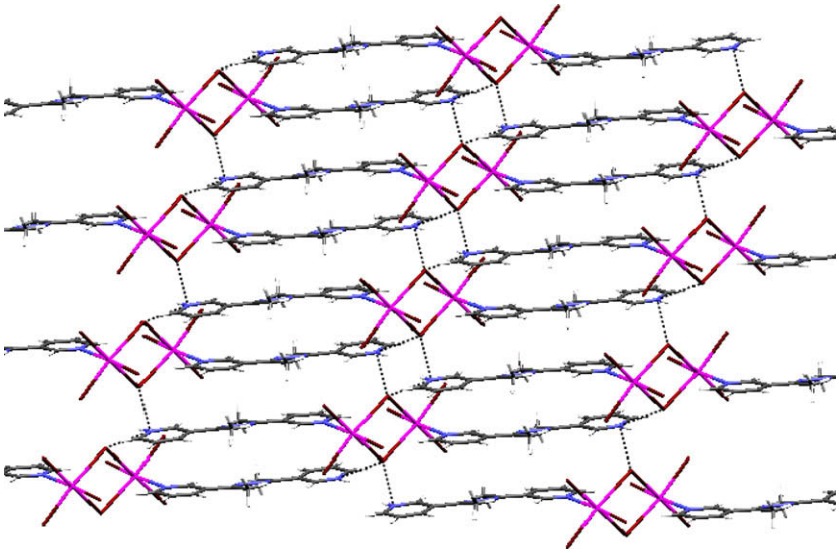


Fig. 6. The 2D supramolecular structure generated via the N-H···Br interactions in $[Bi_2(3\text{-Hbpdh})_2Br_8]$ (**2**).

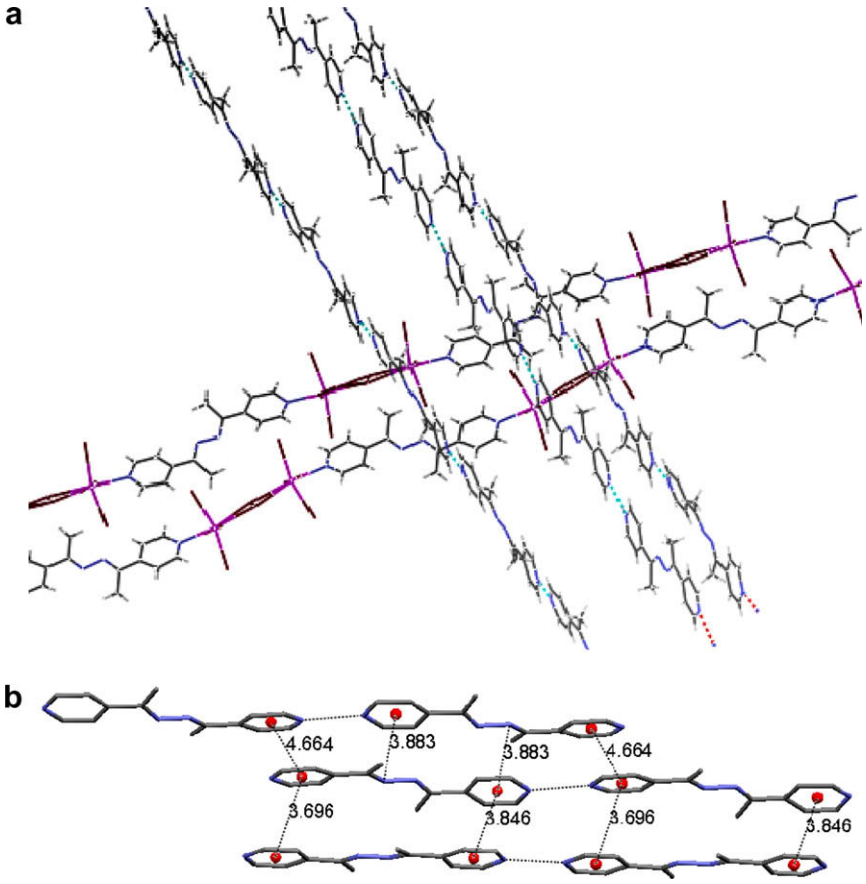


Fig. 7. a) The two perpendicular 1D chains and **b**) the π-π stacking in $[Bi_2(4\text{-bpdh})Br_9]\cdot 3(4\text{-Hbpdh})$ (**3**).

two-dimensional network (Fig. 5). Supramolecular compounds generated from hydrogen bonding between protonated ligands have been reported before [30,54,59,60].

Determination of the structure of compound **2** by X-ray crystallography showed the complex in the solid state to consist of dimeric units (Fig. 3). The bismuth atoms are linked by one nitrogen atom of the 3-Hbpdh ligand and by five bromide atoms, and can be considered to be six-coordinate with a Br_5N array of donor atoms. The coordination environment around Bi is distorted octahedral. One pyridyl nitrogen atom of the 3-bpdh ligand is not coordinated to Bi atoms (Fig. 3) and is instead protonated. The aromatic rings of the coordinated 3-Hbpdh ligand are coplanar with a dihedral angle between the two pyridyl rings of only 1.27(17)°. The hydrogen atoms of the protontated and uncoordi-

Table 3
H-bonds (Å and °) in the structures of $[Bi_2(3\text{-bpdb})_2Br_8]\cdot(3\text{-}H_2bpdb)$ (**1**), $[Bi_2(3\text{-Hbpdh})_2Br_8]$ (**2**) and $[Bi_2(4\text{-bpdh})Br_9]\cdot 3(4\text{-Hbpdh})$ (**3**).

D–H···A	*d*(D–H)	*d*(H···A)	*d*(D···A)	<(DHA)
For $[Bi_2(3\text{-bpdb})_2Br_8]\cdot(3\text{-}H_2bpdb)$ (**1**)				
N5–H5···N4	0.86	1.87	2.681(12)	157.7
For $[Bi_2(3\text{-Hbpdh})_2Br_8]$ (**2**)				
N4–H4···Br4	0.88	2.67	3.239(5)	123.5
For $[Bi_2(4\text{-bpdh})Br_9]\cdot 3(4\text{-Hbpdh})$ (**3**)				
N8–H8A···N5	0.86	1.86	2.717(13)	175.4
N12–H12A···N9	0.86	1.84	2.704(12)	178.2
N16–H16A···N13	0.86	1.83	2.7694(12)	178.1

nated nitrogen atoms are involved in N–H···Br interactions, thus acting as weak hydrogen-bond donors towards the Br atoms. Consequently, the dimeric structure is grown by the weak hydrogen bonds into a two-dimensional network (Fig. 6).

The molecular structure of complex **3** consists of one $[Bi_2(4\text{-bpdh})Br_9]^{3-}$ anionic unit and three 4-Hbpdh$^+$ cationic entities (Fig. 4). The anions form infinite one dimensional polynuclear $[Bi_2(4\text{-bpdh})Br_9]_n^{3n-}$ chains in which the bismuth atoms are bridged by both the 4-bpdh ligands and the bromide ions. The Bi coordination number in these chains is six and the coordination around Bi is distorted octahedral. Similar to compounds **1** and **2** the 4-Hbpdh$^+$ cations in **3** seem to result from a proton transfer between molecular species in solution. The 4-Hbpdh$^+$ cations are linked to each other by hydrogen bonding (Fig. 7 and Table 3). As shown in Fig. 7, the hydrogen bonding yields infinite chains of 4-Hbpdh$^+$ relatively perpendicular to the one-dimensional chains of $[Bi_2(4\text{-bpdh})Br_9]_n^{3n-}$. Consequently, the two perpendicular 1D chain systems, produced by the covalent coordination polymer of $[Bi_2(4\text{-bpdh})Br_9]_n^{3n-}$ and the non-covalent hydrogen-bonding polymer of $[4\text{-Hbpdh}]_n^{n+}$, forms into a hybrid three-dimensional network. There are π–π stacking and $\pi_{centroid}$–N interactions between the pyridine groups of the 4-Hbpdh$^+$ cations with centroid to centroid and $\pi_{centroid}$–N distances of 4.664(4) and 3.696(5) Å, respectively (Fig. 7). However, the hydrogen bonding, π–π stacking and N···π interactions may control the packing of complex **3**.

4. Thermogravimetric analysis

To examine the thermal stability of the compounds $[Bi_2(3\text{-bpdb})_2Br_8]\cdot(3\text{-}H_2bpdb)$ (**1**), $[Bi_2(3\text{-Hbpdh})_2Br_8]$ (**2**) and $[Bi_2(4\text{-bpdh})Br_9]\cdot 3(4\text{-Hbpdh})$ (**3**), thermal gravimetric (TG) and differential thermal analyses (DTA) were carried out between 30 and 700 °C in a static atmosphere of nitrogen. Compound **1** is stable and does not decompose up to 174 °C. At this temperature the decomposition of compound **1** starts and the final decomposition

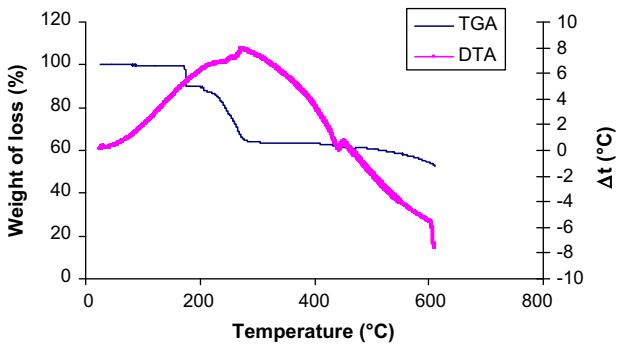


Fig. 8. Thermal behavior of compound **1**.

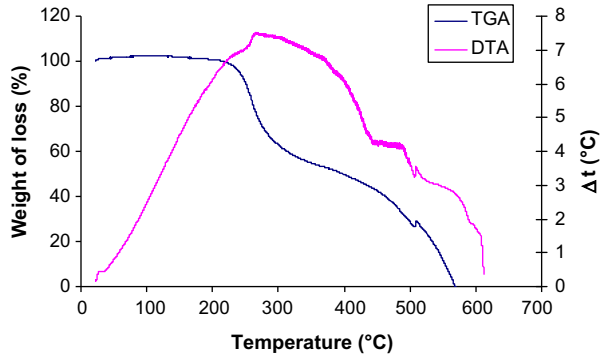


Fig. 9. Thermal behavior of compound **2**.

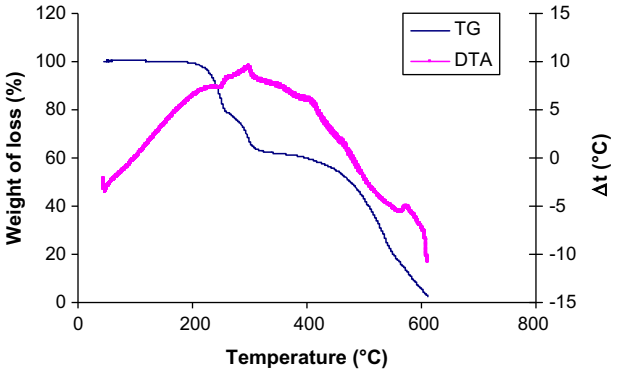


Fig. 10. Thermal behavior of compound **3**.

product is suggested to be $BiBr_3$ (mass loss of 46.80%, calc. 45.80%). The DTA curve displays an exothermic peak at 280 °C and an endothermic peak at 445 °C (Fig. 8). The TG curve of compound **2** indicates that this compound does not melt and is stable up to 220 °C at which temperature it begins to decompose. Decomposition is finished at 500 °C with an exothermic peak at 270 °C and an endothermic peak at 515 °C (Fig. 9). Compound **3** is stable and does not decompose up to 200 °C. At this temperature decomposition of compound **3** starts. Removal of three 4-Hbpdh units occurs between 200 and 315 °C with a mass loss of 63.5% (calc. 65%) and decomposition is continued up to 610 °C with no residue, indicating complete sublimation of $BiBr_3$. The DTA curve displays two endothermic peaks at 255 and 570 °C and an exothermic peak at 302 °C (Fig. 10).

5. Conclusions

Three new bismuth(III) coordination polymers with 1,4-bis (3-pyridyl)-2,3-diaza-1,3-butadiene (3-bpdb), 2,5-bis(3-pyridyl)-3,4-diaza-2,4-hexadiene (3-bpdh) and 2,5-bis(4-pyridyl)-3,4-diaza-2,4-hexadiene (4-bpdh), namely $[Bi_2(3\text{-bpdb})_2Br_8]\cdot(3\text{-}H_2bpdb)$ (**1**), $[Bi_2(3\text{-Hbpdh})_2Br_8]$ (**2**) and $[Bi_2(4\text{-bpdh})Br_9]\cdot 3(4\text{-Hbpdh})$ (**3**), have been synthesized using a thermal gradient approach, the branched tube method. In the assembly processes of compounds **1–3**, all factors such as the metal, inorganic anions, solvent medium and metal/ligand ratio are kept constant and the only variable parameter is the nature of the ligand, 3-bpdb, 3-bpdh and 4-bpdh. The compounds are structurally diverse, showing dimeric and polymeric structures. The coordination polymers obtained from $BiBr_3$ with the ligands 3-bpdb and 3-bpdh are dimeric in nature and in these compounds the $BiBr_3$ units are connected to each other via the Br^- anions and the ligands 3-bpdb and 3-bpdh

coordinating to the Bi atoms through each of the pyridyl nitrogen atoms. The 3-bpdh ligand in compound **3** acts as a bridging ligand via two pyridyl nitrogen atoms. Interestingly in all three compounds the ligands 3-bpdb, 3-bpdh and 4-bpdh were protonated – similar to that observed in $[4,4'\text{-bipyH}]_n^{n-}[\text{Bi}(4,4\text{-bipy})\text{Br}_4]_n^{n-}$ [30]–to yield the cations H_2bpdb^{2+}, 3-$Hbpdh^+$ and 4-$Hbpdh^+$, an observation only rarely seen for the other metal ion coordination polymers with this type of ligand [47–57]. This shows that the Bi^{+3} ion may be the ion of choice when one wants to prepare supramolecular compounds that contain protonated pyridyl ligands. Thus this research not only shows the significant influences of the coordination modes and flexibilities of the ligands 3-bpdb, 3-bpdh and 4-bpdh on the structural topology, but also illustrates the effect of the metal ion, here Bi^{+3} ions, on the polymeric components, which provides valuable information for the rational design of coordination polymers with specific molecular architectures.

Acknowledgements

This work was supported by the Iran National Science Foundation.

Appendix A. Supplementary data

CCDC 686962, 686963 and 686964 contains the supplementary crystallographic data for **3**, 2 and **1**. These data can be obtained free of charge via http://www.ccdc.cam.ac.uk/conts/retrieving.html, or from the Cambridge Crystallographic Data Centre, 12 Union Road, Cambridge CB2 1EZ, UK; fax: (+44) 1223-336-033; or e-mail: deposit@ccdc.cam.ac.uk. Supplementary data associated with this article can be found, in the online version, at doi:10.1016/j.poly.2008.12.048.

References

[1] H.K. Chae, D.Y. Siberio-Perez, J. Kim, Y. Go, M. Eddaoudi, A.J. Matzger, M.O. Keeffe, O.M. Yaghi, Nature 427 (2004) 523.
[2] Y. Kim, M. Suh, D.Y. Jung, Inorg. Chem. 43 (2004) 245.
[3] Z. Huang, H.-B. Song, M. Du, S.-T. Chen, X.-H. Bu, J. Ribas, Inorg. Chem. 43 (2004) 931.
[4] A.P. Carvalho, C. Castanheira, B. Cardoso, J. Pires, A.R. Silva, C. Freire, B. de Castro, M.B. de Carvalho, J. Mater. Chem. 14 (2004) 374.
[5] J.Y. Lu, A.M. Babb, Chem. Commun. (2003) 1346.
[6] Y.-G. Li, N. Hao, Y. Lu, E.-B. Wang, Z.-H. Kang, C.-W. Hu, Inorg. Chem. 42 (2003) 3119.
[7] R. Kitaura, S. Kitagawa, Y. Kubota, T.C. Kobayashi, K. Kindo, Y. Mita, A. Matsuo, M. Kobayashi, H.-C. Chang, T.C. Ozawa, M. Suzuki, M. Sakata, M. Takata, Science 298 (2002) 2358.
[8] B. Moulton, M.J. Zaworotko, Chem. Rev. 101 (2001) 1629.
[9] C. Janiak, J. Chem. Soc., Dalton Trans. (2003) 2781.
[10] S.L. James, Chem. Soc. Rev. 32 (2003) 276.
[11] S.-L. Zheng, X.-M. Chen, Aust. J. Chem. 57 (2004) 703.
[12] D. Maspoch, D. Ruiz-Molina, J. Veciana, J. Mater. Chem. (2004) 2713.
[13] S.R. Batten, K.S. Murray, Coord. Chem. Rev. 243 (2003) 103.
[14] Y. Zhou, M. Hong, X. Wu, Chem. Commun. (2006) 135.
[15] S. Kitagawa, R. Kitaura, S. Noro, Angew. Chem., Int. Ed. 116 (2004) 2388.
[16] P.J. Hagrman, D. Hagrman, J. Zubieta, Angew. Chem., Int. Ed. 38 (1999) 2638.
[17] M. Eddaoudi, J. Kim, D. Vodak, A. Sudik, J. Wachter, M. O'Keeffe, O.M. Yaghi, PNAS 99 (2002) 4900.
[18] L. Carlucci, G. Ciani, D. Proserpio, Coord. Chem. Rev. 246 (2003) 247.
[19] M.J. Plater, M.R. St, J. Foreman, T. Gelbrich, S.J. Coles, M.B. Hursthouse, J. Chem. Soc., Dalton Trans. (2000) 3065.
[20] Y.H. Liu, Y.L. Liu, H.C. Wu, J.C. Wang, K.L. Lu, Inorg. Chem. 43 (2002) 2592.
[21] S.M. Kuznicki, V.A. Bell, S. Nair, H.W. Hillhouse, R.M. Jacubinas, C.M. Braunbarth, B.H. Toby, M. Tsapatsis, Nature 412 (2001) 720.
[22] S.A. Bourne, J. Lu, A. Mondal, B. Moulton, M.J. Zaworotko, Angew. Chem., Int. Ed. 40 (2001) 2111.
[23] J. Lu, A. Mondal, B. Moulton, M.J. Zaworotko, Angew. Chem., Int. Ed. 40 (2001) 2113.
[24] M. Aoyagi, K. Biradha, M. Fujita, J. Am. Chem. Soc. 121 (1999) 7457.
[25] C.V.K. Sharma, S.T. Griffin, R.D. Rogers, Chem. Commun. (1998) 215.
[26] S.R. Batten, B.F. Hoskins, R. Robson, J. Am. Chem. Soc. 117 (1995) 5385.
[27] A. Askarinejad, A. Morsali, Helv. Chim. Acta 89 (2006) 265.
[28] A. Askarinejad, A. Morsali, Inorg. Chem. Commun. 9 (2006) 143.
[29] A. Morsali, L.G. Zhu, Helv. Chim. Acta 89 (2006) 81.
[30] A. Morsali, Solid State Sci. 8 (2006) 82.
[31] A. Morsali, R. Kempe, Helv. Chim. Acta 88 (2005) 2267.
[32] A. Morsali, V.T. Yilmaz, C. Kazak, Z. Anorg. Allg. Chem. 631 (2005) 11577.
[33] A. Morsali, J. Abedini, Inorg. Chem. Commun. 8 (2005) 460.
[34] A. Morsali, A.R. Mahjoub, Polyhedron 23 (2004) 2427.
[35] A. Morsali, L.G. Zhu, Inorg. Chem. Commun. 7 (2004) 1184.
[36] A. Lezzi, S. Cobianco, A. Roggero, J. Polym. Sci. A 32 (1994) 877.
[37] N.N. Greenwood, A. Earnshaw, Chemistry of the Elements, Pergamon press, Oxford, 1984.
[38] G. Wilkinson, R.D. Gillard, J.A. McCleverty (Eds.), Comprehensive Coordination Chemistry, vols 1–7, Pergamon, London, 1987.
[39] A. Bondi, J. Chem. Phys. 68 (1964) 441.
[40] R.D. Rogers, A.H. Bond, S. Aguinaga, J. Am. Chem. Soc. 114 (1992) 2960.
[41] R.D. Rogers, A.H. Bond, S. Aguinaga, J. Am. Chem. Soc. 114 (1992) 1967.
[42] J.P.H. Charmant, N.C. Norman, A.G. Orpen, J. Starbuck, Acta Crystallogr., Sect. E 59 (2003) m1000.
[43] J.P.H. Charmant, A.H.M.M. Jahan, N.C. Norman, A.G. Orpen, T.J. Podesta, CrystEngCommun 6 (2004) 29.
[44] S.C. James, N.C. Norman, A.G. Orpen, J. Starbuck, CrystEngCommun 4 (2000) 67.
[45] M. Cattaneo, F. Fagalde, E.N. KatzM, Inorg. Chem. 45 (2006) 127.
[46] A.E. Dennis, M.H. Grace, F.M. Mary, C.M. Kieran, R.G.R. Guy, Polyhedron 17 (1998) 2321.
[47] Y.-J. Shi, L.-H. Li, Y.-Z. Li, Y. Xu, X.-Tai Chen, Z. Xue, X.-Z. You, Inorg. Chem. Commun. 5 (2002) 1090.
[48] Y.-B. Dong, J.-Y. Cheng, J.-P. Ma, H.-Y. Wang, R.-Q. Huang, D.-S. Guo, M.D. Smith, Solid State Sci. 5 (2003) 1177.
[49] Y.-B. Dong, M.D. Smith, R.C. Layland, H.-C. zur Loye, Inorg. Chem. 39 (2000) 4927.
[50] Y.-B. Dong, J.-P. Ma, R.-Q. Huang, F.-Z. Liang, M.D. Smith, J. Chem. Soc., Dalton Trans. (2003) 1472.
[51] Y.-B. Dong, L. Wang, J.-P. Ma, D.-Y. Zhao, D.-Y. Shen, R. Huang, Cryst. Growth Des. 6 (2006) 2475.
[52] D.M. Ciurtin, Y.-B. Dong, M.D. Smith, T. Barclay, H.-C. Zur Loye, Inorg. Chem. 40 (2001) 2825.
[53] G. Mahmoudi, A. Morsali, A.D. Hunter, M. Zeller, CrystEngCommun 9 (2007) 704.
[54] G. Mahmoudi, A. Morsali, Polyhedron 27 (2008) 1070.
[55] Y.-B. Dong, M.D. Smith, R.C. Layland, H.-C. Zur Loye, Chem. Mater. 12 (2000) 1156.
[56] E.C. Kesslen, W.B. Euler, Tetrahedron Lett. 36 (1995) 4725.
[57] Mercury 1.4.1, Copyright Cambridge Crystallographic Data Centre, 12 Union Road, Cambridge, CB2 1EZ, UK, 2001–2005.
[58] L.J. Farrugia, Appl. Cryst. 30 (1997) 565.
[59] R.-S. Zhou, X.-B. Cui, J.-F. Song, X.-Y. Xu, J.-Q. Xu, T.-G. Wang, J. Solid State Chem. 181 (2008) 2099.
[60] Z.-P. Qi, Z.-S. Bai, Q. Yuan, T.-A. Okamura, K. Cai, Z. Su, W.-Y. Sun, N. Ueyama, Polyhedron 27 (2008) 2672.

when another pyrimidine derived hydrazone ligand ($H_2L'_1$) was employed for complexation with $MoO_2(acac)_2$, a similar ligand transformation occurred and the complex $[MoO_2(L_4)Cl]$ (**4**) was produced. These ligand transformations are probably initiated by a Mo mediated C=N bond cleavage of the used ligands in the reaction medium.

2. Experimental

2.1. Materials and physical measurements

$MoO_2(acac)_2$ was prepared as described in the literature [25]. Reagent grade solvents were used as received. 4,6-Dimethyl 2-hydrazino pyrimidine and 2,4-dihydrazino pyrimidine were prepared as described in the literature [26]. Salicylaldehyde, *o*-hydroxy acetophenone and tetraethyl ammonium perchlorate (TEAP) used for electrochemical work were purchased from Aldrich Chemical Company, USA and were used as received. Elemental analyses (C, H and N), IR spectra (KBr disks, 4000–200 cm^{-1}), ^1H NMR spectra (d_6-DMSO)/$CDCl_3$ of the ligands and the complexes and UV–Vis spectra (DMF) of the complexes were recorded with a Perkin–Elmer Model 240 C CHN analyzer, a Jasco FTIR model 420 spectrophotometer, Bruker AM300L (300 MHz) superconducting FT-NMR and a Hitachi U-3501 spectrophotometer, respectively. Cyclic voltammetry (CV) experiments were carried out using Sycopel Model 77 AEW2 1820F/S instrument. The measurements were performed at 300 K in a DMF solution containing 0.2 M TEAP and 10^{-3}–10^{-4} M Mo(VI) complexes **1–4** deoxygenated by bubbling with nitrogen. A platinum wire, a platinum coil and a SCE were used as working, counter and reference electrodes, respectively.

2.2. Crystallographic measurements

The crystals were measured on an Enraf-Nonius CAD-4 diffractometer using Mo Kα radiation ($\lambda = 0.71073$ Å) and a graphite monochromator at −80 °C. The unit cell dimensions were obtained from a least squares fit to the setting angles of 25 accurately determined reflections. The data were collected using the $\omega-2\theta$ scan technique with a 2θ range of 4−55° and were corrected by an empirical method for absorption, Lorentz and polarization effects. Calculations were carried out using XCAD-49 (data reduction) and SHELXTL (absorption corrections, structure solution refinements and molecular graphics). The structures were solved using direct methods and refined on F^2 using full matrix least squares techniques with anisotropic displacement factors for all non-hydrogen atoms. Positions of the hydrogen atoms were calculated from the geometry of the molecular skeleton and their thermal displacement parameters were refined isotropically on a groupwise basis.

2.3. Synthesis of the ligands HL_1 and HL_2

The ligands HL_1 and HL_2 were synthesized in a similar way by refluxing an ethanolic solution (20 mL) of 4,6-dimethyl 2-hydrazino pyrimidine (10 mmol, 1.38 g) as a common reagent with salicylaldehyde (10 mmol,1.22 g for HL_1) and *o*-hydroxy acetophenone (10 mmol, 1.36 g for HL_2), respectively, also taken in ethanol solution (20 mL). Refluxing was continued for ca. 2 h at water bath temperature. The mother liquor was cooled and left for slow evaporation for the final separation of a solid compound. It was filtered, washed with ethanol and dried over fused $CaCl_2$. The crude product was recrystallized from an ethanol–water mixture (4:1 v/v). The ligand HL_1 has been prepared and used in one of our previous works [27].

HL_1: M.p.: 165 °C. Yield: 1.936 g (80%). Elemental *Anal.* Calc. for $C_{13}H_{14}N_4O$: C, 64.4; H, 5.78; N, 23.14. Found: C, 64.2; H, 5.66; N, 23.05%. IR (KBr pellet) ν/cm^{-1}: 3283 (N–H), 3175 (O–H), 1546.9 (C=N), 1609 (C=C). ^1H NMR (300 MHz, $CDCl_3$, 25 °C, TMS) δ/ppm: 6.68 (s, 1H, C_5–H Pyrimidine), 6.8–7.3 (m, 4H, $-C_6H_4$), 8.2 (s, 1H, –CH=N–), 12.8 (s, 1H, aromatic-OH), 2.28 (s, 1H, N–H of hydrazone), 2.46–2.53 (m, 6H, CH_3, t).

HL_2: M.p.: 169 °C. Yield: 1.98 g (80%). Elemental *Anal.* Calc. for $C_{14}H_{16}N_4O$: C, 65.88; H, 6.27; N, 21.96. Found: C, 65.62; H, 6.11; N, 21.46%. IR (KBr pellet) ν/cm^{-1}: 3274 (N–H), 3180 (O–H), 1537 (C=N), 1609 (C=C). ^1H NMR (300 MHz, $CDCl_3$, 25 °C, TMS) δ/ppm: 6.62 (s, 1H, $-C_5$–H Pyrimidine), 6.8–7.5 (m, 4H, $-C_6H_4$), 2.57 (s, 3H, $-C(CH_3)$ =N–), 12.8 (s, 1H, aromatic-OH), 2.28 (s,1H, N–H of hydrazone), 2.46–2.53 (m, 6H, CH_3) 2.4.

2.4. Synthesis of the ligand $H_2L'_1$

The ligand $H_2L'_1$ was synthesized by refluxing an aqueous solution (10 mL) of 2,4-dihydrazino pyrimidine (10 mmol, 1.40 g) with salicylaldehyde (10 mmol,1.22 g), taken in ethanol (20 mL). Refluxing was continued for ca. 2 h at water bath temperature, during which time the solid ligand started to precipitate. The reaction mixture was cooled and the ligand was filtered, washed with ethanol and dried over fused $CaCl_2$. The crude product was recrystallized from an ethanol–water mixture (4:1 v/v).

$H_2L'_1$: M.p. above 200 °C. Yield: 2.20 g (63%). Elemental *Anal.* Calc. for $C_{18}H_{16}N_6O_2$: C, 62.06; H, 4.59; N, 24.13. Found: C, 61.67; H, 4.23; N, 23.79%. IR (KBr pellet) ν/cm^{-1}: 3303 (N–H), 3159 (O–H), 1533.9 (C–N), 1616 (C=C). ^1H NMR (300 MHz, d_6-DMSO, 25 °C, TMS) δ/ppm: 7.6 (d, ^2J(H,H) = 6,1H, $-C_5$–H Pyrimidine), 8.1 (d, ^2J(H,H) = 6,1H, $-C_4$–H Pyrimidine), 6.5–7.3 (m, 8H, $-C_6H_4$), 8.2, 8.4 (s, 2H, –CH=N–), 11.2, 11.8 (s, 2H, aromatic-OH), 2.46, 3.2 (s, 2H, N–H of hydrazone).

2.5. Synthesis of complex **1**

The complex $[MoO_2(L_1)Cl]$ (**1**) was prepared by mixing an ethanolic solution (10 mL) of $MoO_2(acac)_2$ (0.5 mmol, 0.163 g), acidified with 5–6 drops of concentrated HCl, (or an ethanolic solution of $(NH_4)_2MoO_4$ dissolved by adding 5–6 drops of HCl) with an ethanolic solution of HL_1 (0.5 mmol, 0.122 g). On mixing the two components an orange color was immediately observed. The mixed solution was refluxed and the complex was separated as orange crystals within 5 min. These were filtered, washed with ethanol and dried over fused $CaCl_2$. It was observed that due to poor solubility, complex **1** separated from the reaction mixture even at room temperature within 5 min.

$[MoO_2(L_1)Cl]$ (**1**): Yield: 0.120 g (60%). Elemental *Anal.* Calc. for $C_{13}N_4O_3H_{13}MoCl$ (403.5): C, 38.6; H, 3.22; N, 13.87. Found: C, 37.75; H, 3.55; N, 13.46%.

2.6. Synthesis of complex **2**

When an ethanolic solution (10 mL) of $MoO_2(acac)_2$ (0.5 mmol, 0.163 g), acidified with 5–6 drops of concentrated HCl, was mixed with an ethanolic solution of HL_2 (0.5 mmol, 0.128 g), an orange yellow color was immediately observed. On keeping the solution for slow evaporation after filtration, X-ray quality crystals of **2** appeared within 48 h, with the gradual disappearance of the solution color. The crystals were filtered, washed with ethanol and dried over fused $CaCl_2$.

$[MoO_2(L_3)Cl_2]$ (**2**): Yield: 0.050 g (25%). Elemental *Anal.* Calc. for $C_{11}N_4O_2H_{14}MoCl_2$ (400): C, 33.0; H, 3.5; N, 14.0. Found: C, 32.91; H, 3.65; N, 13.30%.

2.7. Synthesis of complex **3**

When an ethanolic solution (10 mL) of $MoO_2(acac)_2$ (0.5 mmol, 0.163 g), acidified with 5–6 drops of concentrated HCl, was added

to an ethanolic solution of HL_2 (0.5 mmol, 0.128 g), an orange color was immediately observed. This orange solution was refluxed for several hours, during which time its color changed to light pink. The solution was then cooled and filtered. On keeping the solution for slow evaporation after filtration, light pink crystals of **3** appeared within 48 h. These were filtered, washed with ethanol and dried over fused $CaCl_2$.

$[Mo_2O_5(L_3)_2Cl_2]$(**3**): Yield: 0.093 g (25%). Elemental *Anal.* Calc. for $C_{22}N_8O_5H_{28}Mo_2Cl_2$ (745): C, 35.43; H, 3.75; N, 15.03. Found: C, 34.91; H, 3.65; N, 13.80%.

2.8. Synthesis of the complex 4

Complex $[MoO_2(L_4)Cl]$ (**4**) was prepared by adding an acidified (by a few drops of conc. HCl) ethanolic solution (10 mL) of $MoO_2(acac)_2$ (0.5 mmol, 0.163 g) to an ethanolic solution of H_2L_1' (0.25 mmol, 0.087 g). On mixing the two components, the solution immediately turned orange yellow. The complex separated as dark red crystals on slow evaporation of the filtered reaction mixture. The crystals were filtered, washed with ethanol and dried over fused $CaCl_2$.

$[MoO_2(L_4)Cl]$ (**4**): Yield: 0.058 g (50%). Elemental *Anal.* Calc. for $C_{16}N_6O_3H_{16}MoCl$ (454.5): C, 40.80; H, 3.40; N, 17.85. Found: C, 40.18; H, 3.51; N, 17.15%. Relevant IR, UV–Vis, NMR and electrochemical characterization data for the complexes are summarized in Table 1.

3. Results and discussion

3.1. Synthesis

The ligands HL_1 and HL_2 were isolated as 1:1 condensation products of 4,6-dimethyl 2-hydrazino pyrimidine with salicylaldehyde (for HL_1) and *o*-hydroxy acetophenone (for HL_2). The complexes **1–3** were prepared by simply mixing $MoO_2(acac)_2$ and the respective ligands in a dehydrated ethanol medium at room temperature or at reflux under acidic conditions maintained by adding conc. HCl. Complex **4** was prepared using the same method with the ligand H_2L_1'. As the ligands can act, at best, as a tridentate monoanionic ligands, a few drops of HCl were added to furnish the Cl^- ion to satisfy the sixth coordination position as well as for the requirement of charge balance of the MoO_2^{2+} core.

An ethanolic solution of the ligand HL_1, when added to an acidified ethanolic solution of $MoO_2(acac)_2$, either at room temperature or under refluxing conditions, yielded $[MoO_2(L_1)Cl]$ (**1**) which separated in the crystalline form within 5 min. No other products were obtained on keeping the mother liquor for several days for slow evaporation. When $(NH_4)_2MoO_4$ was used instead of $MoO_2(acac)_2$ the same observations were recorded. With HL_2 and $MoO_2(acac)_2$ complex **2** was isolated at room temperature as the exclusive product over a period of 48 h. Contrary to this observation, under refluxing conditions, the same reaction mixture yields complex **3** as the only product. The conditions which favor the formation of **2**, the mononuclear complex of the transformed ligand L_3, or **3**, its oxo bridged binuclear analog, could not be ascertained. However, from the reaction conditions it is implied that **3** demands a higher temperature for its formation as it is the thermodynamically controlled product. It should be mentioned that using $(NH_4)_2MoO_4$ as the metal precursor with HL_2 only a green residue could be found, which could not be characterized. In order to explain these results we suggest that for the formation of complexes **2** and **3** from HL_2, an in situ ligand transformation takes place. This is triggered by Mo(VI) mediated C=N bond cleavage of the used ligand. The C=N bond cleavage of the hydrazone part of ligand sets the 2-hydrazino 4,6-dimethyl pyrimidine free, which on subsequent condensation cum cyclization with the acetyl acetonate anion obtained from $MoO_2(acac)_2$ produces the substituted pyrimidyl pyrazole ligand (L_3). This L_3 ligand, in turn, partially encapsulates the MoO_2^{2+} core to give complexes **2** and **3**. The role of the metal was ascertained by the fact that the ligands, when subjected to similar acid media in the same solvents, did not undergo any C=N cleavage. Complex **1** was found to have a completely different absorption behavior from the complexes of the transformed ligand L_3, i.e. **2** and **3**. When HL_2 was used as a ligand towards the $MoO_2(acac)_2$ target, initially the reaction mixture showed an absorption pattern similar in nature to complex **1**. Gradually, this peak diminished and peaks characteristic of **2** appeared. This implies that after the formation of the expected complex in solution, HL_2 slowly converts to the pyrimidyl pyrazole derivative via metal catalyzed C=N bond cleavage with the concomitant chelation of the original metal center by the newly formed ligand (L_3). This also explains the non-responsive behavior of the ligand HL_1 towards the ligand transformation reaction. It was found that on mixing $MoO_2(acac)_2$ and the ligand in ethanolic solution acidified by HCl, complex **1** precipitated within 5 min. The metal mediated ligand transformation could not take place as complex **1** did not remain soluble long enough in the reaction mixture to allow it. This view was reinforced by employing another salicyl hydrazone ligand,

Table 1
Characterization of complexes **1**–**4**.

Complex	IR (ν/cm^{-1}) (Mo=O), (Mo–O–Mo)	NMR (^{1}H/δ TMS)	UV–Vis (λ_{max}/nm)	DRS	CV(E/V) E_{pc} Mo(VI)/Mo(V), Mo(V)/Mo(IV)
1	907, 936	8.4 (–CH=N) 2.28 (–NH–N=) 6.68 (C_{Pym}–H) 6.8–7.3(C_6H_4) 2.46–2.53 (C_{pym}–CH_3)	334 (3349) 304 (3064) 295 (3016)	372 355	−0.69, −1.33
2	911, 944	6.68 (C_{Pym}–H) 2.46–2.53 (C_{pym}–CH_3) (C_{pyz}–CH_3) 6.2 ($C3_{Pyz}$–H)	261.5 (60400) 254 (6474)	285	−0.83, −1.38
3	910, 942 754	6.68 (C_{Pym}–H) 2.46–2.53 (C_{pym}–CH3) (C_{pyz}–CH_3) 6.2 ($C3_{Pyz}$–H)	264 (51500) 257 (5200) 253 (28600)	285 479	–0.86, −1.24
4	904, 935	2.4, 3.2(2) (–NH–N=) 8.0, 8.2(2) (–CH=N) 6.3(1) (Pz–C_4H) 6.5–7.3 (C_6H_4)(4H) 7.6 (C_5–H Pyrimidine) 8.1 (C_4–H Pyrimidine)	319 (3323) 305 (3750)	371 355	−0.9, −1.2

$H_2L'_1$ (the bis salicyl hydrazone of 2,4-dihydrazino pyrimidine) for complexation with $MoO_2(acac)_2$ under similar conditions as with the ligands HL_1 and HL_2.The formation of complex **4**, where the used ligand was found to have transformed into L_4 (the deprotonated form of the salicyl hydrazone of 2-hydrazino-4-(3,5-dimethyl-1-pyrazolyl) pyrimidine) via a partial Mo mediated reaction showed that such ligand transformation can also take place with salicyl hydrazones if the resulting complex remains soluble in the reaction medium. All these synthetic observations are summarized in Scheme 1.

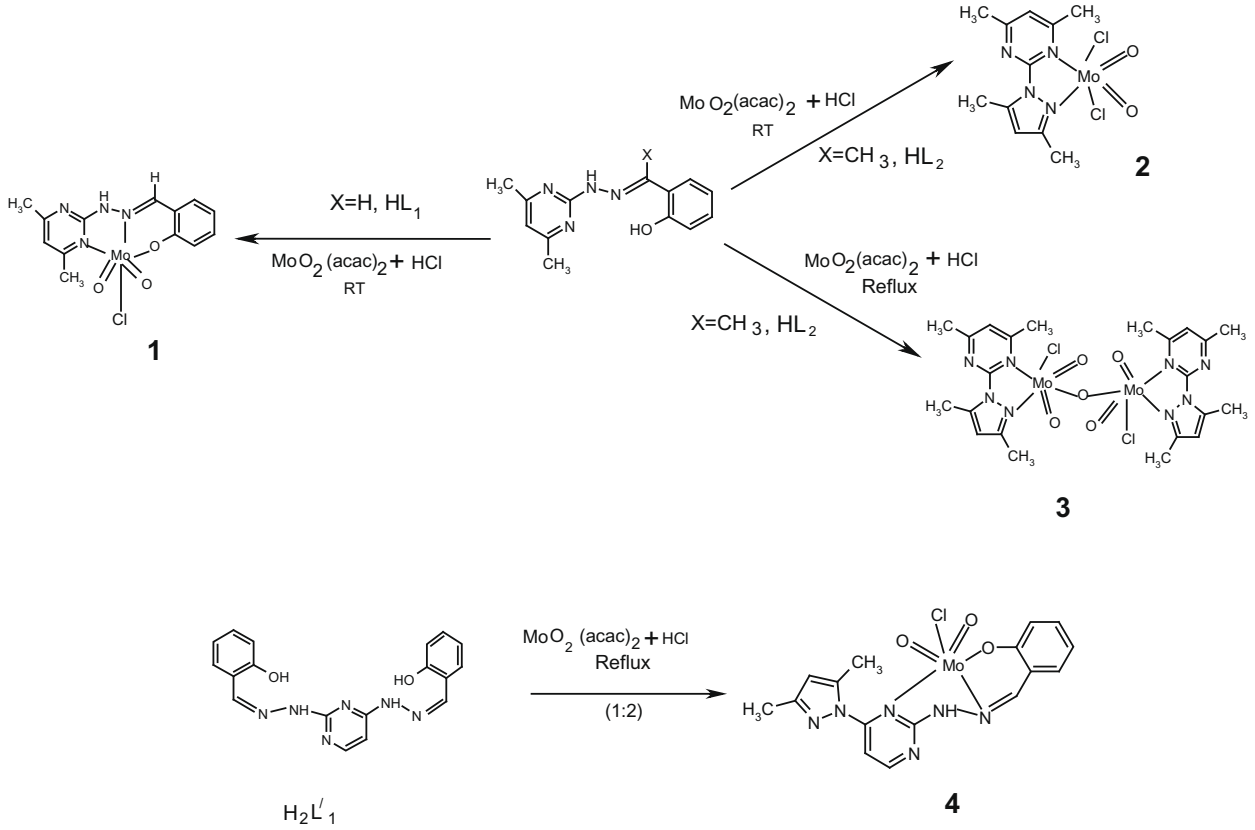
3.2. Spectroscopic characterization

1D proton NMR spectra of the Mo(VI) complexes as well as the ligands were recorded. The aromatic OH signal at δ 11.2–12.8 [28,29], which is found in the ligands HL_1, HL_2 and $H_2L'_1$ is absent in the spectra of the complexes. This may be attributed to the complexation by the ligand in a mononegative fashion and/or ligand transformation during complex formation. The azomethine (CH=N) signal, which is found at δ *8.2–8.25* [30] in the spectra of the ligands [HL_1, and $H_2L'_1$], shifts downfield in the complexes **1** and **4** due to a shift of electron density from the C=N bond as a result of complexation. Appearance of a signal at δ *6.2–6.3* [31], corresponding to the pyrazole C–H in the spectra of complexes **2**, **3** and **4**, provides the evidence for the ligand transformation that takes place while forming these complexes.

IR spectra of the ligands HL_1, HL_2 and $H_2L'_1$ shows bands at 3159–3191 cm^{-1} for H-bonded O–H stretching and at 3274–3322 cm^{-1} for N–H stretching vibrations [32,33]. In complex **1** the O–H peak of HL_1 is absent as the ligand gets deprotonated prior to complexation. Absence of both the signals for O–H and N–H stretching vibrations of HL_2 in complexes **2** and **3** indicates that ligand transformation has taken place in these cases. However, in complex **4**, the N–H peak of $H_2L'_1$ is retained and the O–H peak of $H_2L'_1$ disappears because formation of complex **4** results from only a partial transformation of $H_2L'_1$. The signals of C=N and C=C stretching [34] vibrations appear up to 30 cm^{-1} lower in energy in the complexes as compared to the free ligands. The Mo=O asymmetric and symmetric stretching frequencies in the dioxomolybdenum(VI) complexes **1–4** appear at 904–911 cm^{-1} and 935–944 cm^{-1} [35,36]. In the μ-oxo Molybdenum(VI) complex **3**, ν(Mo–O–Mo) exhibits a strong peak at 754 cm^{-1} [37].

The electronic spectrum of complex **1** in DMF displays two strong absorption bands at 334 and 304 nm. These peaks may be assigned as charge transfer transitions of the type N(pπ)–Mo(dπ) LMCT and O(pπ)–Mo(dπ) LMCT, respectively [38,39], as the ligand based orbitals are either N or O donor types. The ligand HL_2 yields only complexes **2** and **3**, which are the outcome of a ligand transformation process. Both complexes **2** and **3** show no peaks in the visible range in their electronic spectra recorded in DMF solution. However, charge transfer bands at 261–264 nm, assigned to N(pπ)–Mo(dπ) transitions, are observed in both complexes. As the coordination sphere in **2** is approximately similar to that of **3**, barring the substitution of a chloride donor in **2** by a bridging oxo group in **3**, the peaks obtained are very similar in both complexes. An additional peak appearing at 257 nm [37] in **3** is assigned as a characteristic [μ-oxo → Mo(VI)] LMCT band.

Complex **2** or **3** is obtained as the exclusive product with the ligand HL_2 under different reaction temperatures. On mixing HL_2 and $MoO_2(acac)_2$ in EtOH solution, acidified by adding conc. HCl, first an orange color develops with an absorption maxima at 327 nm, but gradually over a period of 36 h this peak disappears and a peak at 261 nm appears. This shows that catalysis by MoO_2^{2+} in the C=N bond cleavage of the hydrazone portion takes place slowly following complexation by the ligand HL_2.



Scheme 1. Reaction schemes showing the syntheses of **1–4**.

The diffuse reflectance spectra (DRS) of complex **1** show an absorption band at lower energy compared to those in solution. This may be attributed to a greater destabilization of the metal LUMO than the ligand HOMO in DMF solution. Interestingly, complex **3**, which shows no absorption peaks in DMF solution in the visible region, exhibits a peak at 479 nm in its DRS indicating that solvation with DMF brings out an appreciable change in the coordination sphere in this complex. Complex **4** has a coordination sphere which is very similar to that in complex **1** and shows LMCT transition bands at 319 and 305 nm.

3.3. Electrochemistry

The electrochemical behavior of all the complexes **1–4** were examined in DMF solution using cyclic voltammetry at a platinum electrode with 0.1 M TEAP as a supporting electrolyte. The corresponding data are supplied in Table 1. In the potential range −1.0–1.5 V the complexes show two reductive responses during a cathodic scan for Mo(VI)/Mo(V) and Mo(V)/Mo(IV) [21]. Each one is assigned to a one electron process established by comparison of current heights with an authentic one electron process. Complexes **2** and **3** show two reductive responses on a cathodic scan, which are again of an irreversible type. However, in both complexes the peak corresponding to Mo(VI)/Mo(V) tends to disappear and a single two electron reductive response appears for Mo(VI)/Mo(IV) when the scan rate is increased. Comparing the reductive responses of **2** and **3** with those of **1**, it was observed that the Mo(VI)/Mo(V) peak appears at greater negative potentials for complexes **2** and **3**. Complex **4** shows two irreversible reductive responses at −0.9 and −1.2 V. Despite the similar environment, a slight change in the geometry of the coordination sphere (as has been found from the X-ray structure) from **1** may be responsible for the slight deviation of the redox behavior of **4**.

3.4. EPR and magnetic properties

All the complexes **1–4** were found to be diamagnetic and epr silent.

3.5. Description of the structures

Crystal data and details of the data collection are listed in Table 2. Selected bond angles and bond lengths are supplied in Table 3.

3.5.1. Structure of the ligand HL_2

The crystal structure of the ligand HL_2 has been investigated as a representative of the hydrazone ligands. The ligand crystallizes in the $P2(1)/a$ space group with 8 molecules per unit cell. The crystal is centrosymmetric with a dihedral angle of ca. 60° between the mean planes of the two molecules in the asymmetric unit. There is one strong intramolecular H-bonding interaction among O1–H1–N1 and another comparatively weaker intermolecular interaction among N2–H2–N3 (between the two asymmetric units, atoms labeled using A and B suffixes in Fig. 1). Comparable bond lengths

Table 2
Crystal data and structure refinement for complexes **1–4** and the ligand HL_2.

Identification code	Complex **1**	Complex **2**	Complex **3**	Complex **4**	Ligand HL_2
Empirical formula	$C_{13}H_{13}ClMoN_4O_3$	$C_{11}H_{14}Cl_2MoN_4O_2$	$C_{22}H_{28}Cl_2Mo_2N_8O_5$	$C_{16}H_{15}ClMoN_6O_3$	$C_{14}H_{16}N_4O$
Formula weight	404.66	401.10	747.30	470.73	256.31
T (K)	293(2)	173(2)	173(2)	296(2)	173(2)
λ (Å)	1.54178	0.71073	0.71073	0.71073	0.71073
Crystal system	monoclinic	monoclinic	monoclinic	triclinic	monoclinic
Space group	$P2(1)/n$	$P2(1)/n$	$C2/c$	$P1$	$P2(1)/a$
Unit cell dimensions					
a (Å)	7.582(3)	8.105(4)	12.3062(11)	7.0928(7)	13.8237(12)
b (Å)	14.284(5)	13.167(7)	16.0731(14)	11.3186(17)	11.3817(10)
c (Å)	13.813(5)	14.885(8)	15.7423(14)	11.959(4)	16.8897(14)
α (°)	90	90	90	75.06(2)	90
β (°)	92.17(4)	102.500(7)	104.0390(10)	78.313(17)	95.7790(10)
γ (°)	90	90	90	87.862(10)	90
V (Å^3)	1494.9(10)	1550.9(15)	3020.8(5)	908.3(4)	2643.9(4)
Z	4	4	4	2	8
Absorption Coefficient (mm^{-1})	8.996	1.195	1.052	0.900	0.085
$F(000)$	808	800	1496	472	1088
Crystal size (mm^3)	0.12 × 0.36 × 0.18	0.590 × 0.320 × 0.120	0.61 × 0.52 × 0.28	0.47 × 0.41 × 0.35	0.85 × 0.64 × 0.315
θ Range for data collection (°)	6.20–68.02	2.09–30.13	2.53–30.78	4.47–32.47	2.16–29.67
Index ranges	$-9 \leqslant h \leqslant 0$, $0 \leqslant k \leqslant 17$, $-16 \leqslant l \leqslant 16$	$-11 \leqslant h \leqslant 10$, $-18 \leqslant k \leqslant 16$, $-20 \leqslant l \leqslant 20$	$-16 \leqslant h \leqslant 17$, $-22 \leqslant k \leqslant 22$, $-22 \leqslant l \leqslant 17$	$-9 \leqslant h \leqslant 10$, $-16 \leqslant k \leqslant 17$, $-17 \leqslant l \leqslant 17$	$-19 \leqslant h \leqslant 19$ $-13 \leqslant k \leqslant 15$ $-23 \leqslant l \leqslant 23$
Reflections collected	2943	9969	16980	13352	28970
Independent reflections (R_{int})	2716 (0.0994)	3890 (0.0505)	4407 (0.0206)	5948 (0.0472)	7388 (0.0234)
Completeness to θ	99.8% (68.02)	94.2% (25.00°)	99.0%(25.00°)	99.3%	99.5% (25.00°)
Absorption correction	empirical	semi-empirical from equivalents	semi-empirical from equivalents	semi-empirical from equivalents	semi-empirical from equivalents
Maximum and minimum transmission	0.6742 and 0.0816	1.000 and 0.323	1.000 and 0.732	1.00000 and 0.66157	0.865 and 0.784
Refinement method	full-matrix least-squares on F^2	full-matrix least-squares on F^2	full-matrix least-squares on F^2	full-matrix least-squares on F^2	full-matrix least-squares on F^2
Data/restraints/parameters	2716/0/204	3890/0/185	4407/0/283	5948/4/258	7388/0/365
Goodness-of-fit on F^2	1.056	1.053	1.120	0.929	1.067
Final R indices	R_1 = 0.0667, wR_2 = 0.1720	R_1 = 0.0700, wR_2 = 0.1751	R_1 = 0.0336, wR_2 = 0.0832	R_1 = 0.0566, wR_2 = 0.1334	R_1 = 0.0455, wR_2 = 0.1242
[$I > 2\sigma(I)$] R indices (all data)	R_1 = 0.0928, wR_2 = 0.1984	R_1 = 0.0839, wR_2 = 0.1896	R_1 = 0.0397, wR_2 = 0.0860	R_1 = 0.1205, wR_2 = 0.1486	R_1 = 0.0564, wR_2 = 0.1316
Largest difference in peak and hole (e Å^{-3})	1.150 and −1.220	3.510 and −2.665	0.999 and −0.563	0.875 and −0.758	0.352 and −0.278

Table 3
Selected bond lengths and bond angles of complexes **1**, **2**, **3**, **4** and the ligand HL_2.

Selected bonds	Values (Å)	Selected angles	(°)
*Complex **1***			
Mo–O1	1.686(6)	O(1)–Mo–O(2)	104.6(3)
Mo–O(2)	1.715(6)	O(2)–Mo–O(3)	100.0(3)
Mo–O(3)	1.914(6)	O(1)–Mo–N(2)	100.7(3)
Mo–N(2)	1.914(6)	O(2)–Mo–N(2)	89.7(3)
Mo–N(1)	2.227(6)	O(3)–Mo–N(2)	151.2(3)
Mo–Cl	2.282(7)	O(1)–Mo–N(1)	163.9(3)
N(1)–N(3)	2.577(2)	O(2)–Mo–N(1)	89.6(3)
N(2)–C(8)	1.374(8)	O(3)–Mo–N(1)	81.4(2)
N(3)–C(8)	1.333(10)	N(2)–Mo–N(1)	71.5(2)
C(8)–N(4)	1.383(10)	O(1)–Mo–Cl	87.2(2)
	1.329(9)	O(2)–Mo–Cl	164.3(3)
		O(3)–Mo–Cl	87.1(2)
		N(2)–Mo–Cl	77.73(18)
		N(1)–Mo–Cl	77.48(18)
*Complex **2***			
Mo–O(2)	1.698(4)	O(2)–Mo–O(1)	105.0(2)
Mo–O(1)	1.713(4)	O(2)–Mo–N(1)	91.2(2)
Mo–N(1)	2.317(5)	O(1)–Mo–N(1)	163.4(2)
Mo–Cl(1)	2.3697(16)	O(2)–Mo–Cl(1)	98.33(17)
Mo–N(2)	2.394(5)	O(1)–Mo–Cl(1)	96.83(14)
Mo–Cl(2)	2.4075(17)	N(1)–Mo–Cl(1)	84.06(12)
N(1)–C(2)	1.351(7)	O(2)–Mo–N(2)	159.31(19)
N(1)–N(3)	1.368(7)	O(1)–Mo–N(2)	95.48(18)
N(3)–C(6)	1.416(7)	N(1)–Mo–N(2)	68.16(16)
		Cl(1)–Mo–N(2)	81.49(11)
		O(2)–Mo–Cl(2)	95.47(16)
		O(1)–Mo–Cl(2)	94.08(14)
		N(1)–Mo–Cl(2)	80.60(12)
		Cl(1)–Mo–Cl(2)	159.52(6)
		N(2)–Mo–Cl(2)	80.26(11)
		N(2)–C(6)–N(3)	115.1(4)
		N(1)–N(3)–C(6)	117.8(4)
*Complex **3***			
Mo–O(3)	1.694(2)	O(3)–Mo–O(1)	104.88(9)
Mo–O(1)	1.6965(17)	O(3)–Mo–O(2)	99.67(10)
Mo–O(2)	1.8874(7)	O(1)–Mo–O(2)	99.39(10)
Mo–N(1B)	2.312(4)	O(3)–Mo–N(1B)	163.36(17)
Mo–N(1)	2.343(4)	O(1)–Mo–N(1B)	91.46(16)
Mo–Cl	2.3846(8)	O(2)–Mo–N(1B)	80.33(18)
Mo–N(2B)	2.435(6)	O(3)–Mo–N(1)	89.26(13)
Mo–N(2)	2.451(3)	O(1)–Mo–N(1)	165.84(13)
O(2)–Mo#1	1.8875(7)	O(2)–Mo–N(1)	78.49(18)
N(3)–C(6)	1.297(4)	N(1B)–Mo–N(1)	74.38(17)
N(3)–N(1)	1.371(2)	O(3)–Mo–Cl	96.10(10)
C(2)–N(1)	1.371(2)	O(1)–Mo–Cl	95.09(7)
N(3B)–N(1B)	1.379(3)	O(2)–Mo–Cl	155.02(5)
N(3B)–C(6B)	1.273(5)	N(1B)–Mo–Cl	79.05(19)
C(2B)–N(1B)	1.331(3)	N(1)–Mo–Cl	82.48(17)
		O(3)–Mo–N(2B)	97.78(16)
		O(1)–Mo–N(2B)	157.32(15)
		O(2)–Mo–N(2B)	75.4(2)
		N(1B)–Mo–N(2B)	66.0(2)
		N(1)–Mo–N(2B)	8.7(2)
		Cl–Mo–N(2B)	83.3(2)
		O(3)–Mo–N(2)	155.46(12)
		O(1)–Mo–N(2)	99.64(11)
		O(2)–Mo–N(2)	75.12(12)
		N(1B)–Mo–N(2)	9.14(19)
		N(1)–Mo–N(2)	66.23(15)
		Cl–Mo–N(2)	82.49(13)
		N(2B)–Mo–N(2)	57.69(16)
		Mo–O(2)–Mo#1	148.87(14)
*Complex **4***			
MoA–Cl1A	2.6406(12)	O3B–MoB–N2	90.43(15)
MoA–O1	1.9111(19)	Cl1B–MoB–O3B	165.4(2)
MoA–O2	1.719(2)	Cl1A–MoA–O1	81.46(6)
MoA–O3A	1.5774(18)	Cl1A–MoA–O2	83.58(8)
MoA–N1	2.267(2)	Cl1A–MoA–O3A	164.36(8)
MoA–N2	2.186(2)	Cl1A–MoA–N1	77.75(6)
MoB–O1	1.932(2)	Cl1A–MoA–N2	78.61(6)
MoB–O2	1.718(2)	O1–MoA–O2	106.38(10)
MoB–N1	2.287(3)	O1–MoA–O3A	102.89(9)
MoB–N2	2.182(2)	O1–MoA–N1	82.48(8)
MoB–Cl1B	2.636(3)	O1–MoA–N2	149.98(8)
MoB–O3B	1.578(4)	O2–MoA–O3A	109.06(10)
N1–N3	1.379(3)	O2–MoA–N1	157.95(9)
		O2–MoA–N2	93.48(9)
		O3A–MoA–N1	87.86(9)
		O3A–MoA–N2	91.16(8)
		N1–MoA–N2	71.54(8)
		O1–MoB–O2	105.50(11)
		O1–MoB–N1	81.52(9)
		O1–MoB–N2	148.28(10)
		Cl1B–MoB–O1	82.95(8)
		O1–MoB–O3B	106.00(16)
		O2–MoB–N1	155.18(10)
		O2–MoB–N2	93.62(10)
		Cl1B–MoB–O2	77.93(10)
		O2–MoB–O3B	109.8(3)
		N1–MoB–N2	71.22(8)
		Cl1B–MoB–N1	79.41(9)

of the free ligand have been found to have altered somewhat in complexes **2** and **3** both as a result of ligand transformation as well as complexation.

3.5.2. Structure of complexes *1* and *4*

A perspective view of complexes **1** and **4** along with the atom numbering scheme is shown in Figs. 2 and 3. In both these complexes, the coordination environment of the Mo atoms are roughly similar. All of them bear a distorted octahedral geometry where the ligand HL_1 (for **1**) or HL_4 (for **4**) occupies three equatorial positions in their deprotonated form. Two oxo atoms and one chloride complete the coordination sphere. The ligand binds through the enolate oxygen, pyrimidine nitrogen and the azomethine nitrogen, and forms a five membered and a six membered chelate ring at the metal center in the equatorial XY plane [40]. One oxo group is present in the same plane, *trans* to the azomethine nitrogen. The other oxo group is in the axial position, *trans* to a chloride donor. In complex **4** the two axial bonds are disordered over two positions. Between the two structures the deviation of the Mo atoms from the mean plane containing the equatorial donors is higher in complex **4** (0.3 Å). Also the ligand assumes a more planar arrangement in **4** than in **1**. This ensures a better electron delocalization in complex **4** and probably explains its better redox stability as compared to **1**. The bond distances in the coordination sphere are unexceptional [41]. Among the Mo–N bonds the one *trans* to the equatorial oxo group is longer in each case due to the *trans* effect of the Mo=O bond [28]. In the coordination sphere of complexes **1** and **4** the axial angle bears the highest value (164°). None of the bond angles in the coordination sphere in the three complexes corroborate to an ideal octahedral geometry. Weak H-bond interactions are found in the superstructures of each complex. In complex **1**, there is an intermolecular H-bond interaction between N3–H3B–Cl, while in complex **4** it is between Cl1–H3B–N3.

3.5.3. Structure of complex *2*

The structure of complex **2** is again best described as a distorted octahedral one. Here, the ligand is 2-(3,5-dimethyl-1-pyrazolyl)4,6-dimethyl pyrimidine (L_3). This ligand is typically a bidentate neutral NN donor and occupies two coordination positions in the equatorial plane. Two other positions in the equatorial plane are occupied by the two oxo groups [42] (Fig. 4). This is unlike complex **1** where the oxo groups occupy one axial and one equatorial position. The two chloride donors are present in the axial plane. The two heterocyclic rings of the ligand are essentially coplanar with the maximum deviation of any atom from the mean plane containing the ring atoms not exceeding 0.174 Å. The metal is situated in the same plane as the equatorial donors (N1, N2, O1 and O2) but

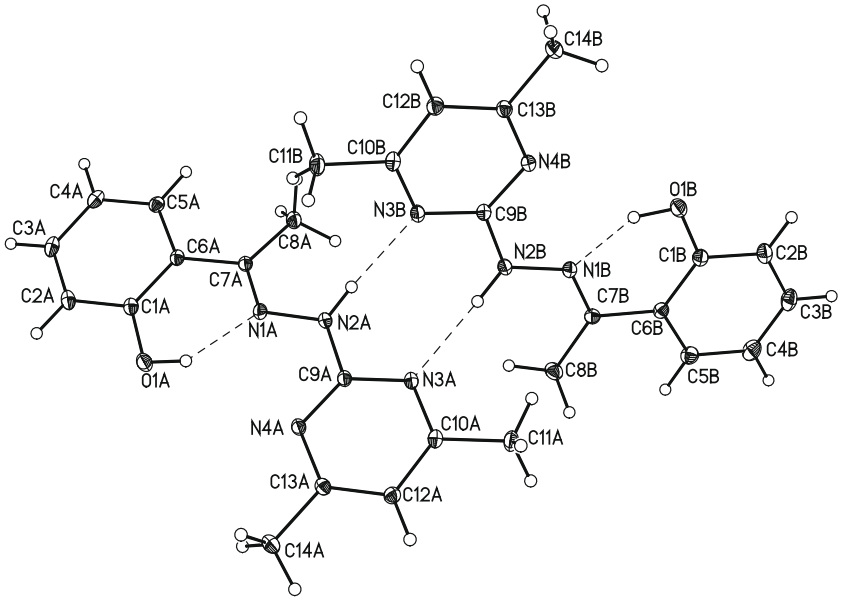


Fig. 1. Structural representation of HL_2.

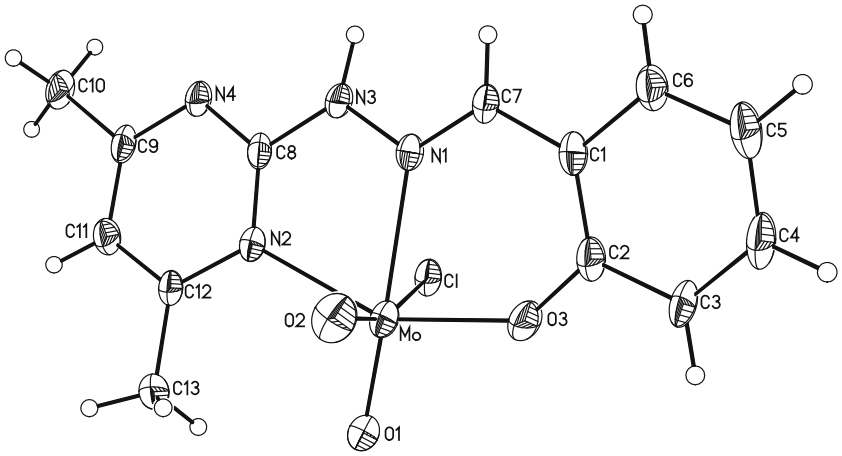


Fig. 2. Structural representation of **1**.

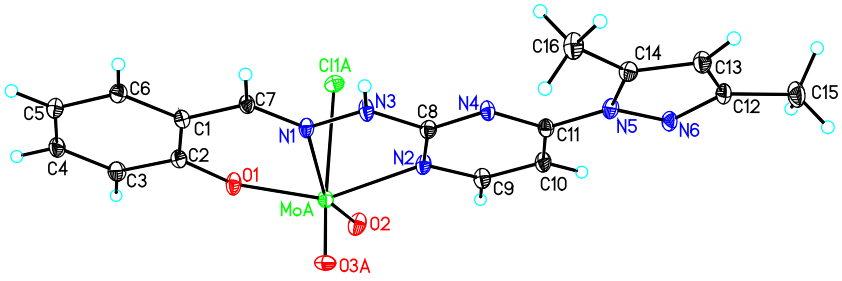


Fig. 3. Structural representation of **4** (disordered positions of the Mo and Cl atoms are omitted for clarity).

the five membered chelate ring formed at the metal center assumes an envelope conformation with Mo at the tip of the envelope. The bond distances in the coordination sphere are found to be similar to other reported complexes of the general formula MoO_2X_2L (where L is a neutral bidentate ligand) [43]. Interestingly, there is a notable difference between the Mo–N1 and Mo–N2 bond distances. This may be rationalized considering the better donor capacity of the pyrazole nitrogen over the pyrimidine nitrogen. Both Mo–N1 and Mo–N2 bonds are slightly elongated due to the *trans* effect of the oxo groups. The two axial Mo–Cl bonds are very similar. The Mo–$N_{(pym)}$ bond is found to be slightly longer in complex **2** than in complex **1**, indicating that the extent of binding of the pyrimidine N is affected by the ligand geometry. When comparable bond lengths of L_3 (in **2**) and the parent ligand HL_2 are studied, only slight deviations are observed. Bond angles in the equatorial plane of complex **2** closely obey the VSEPR theory's con-

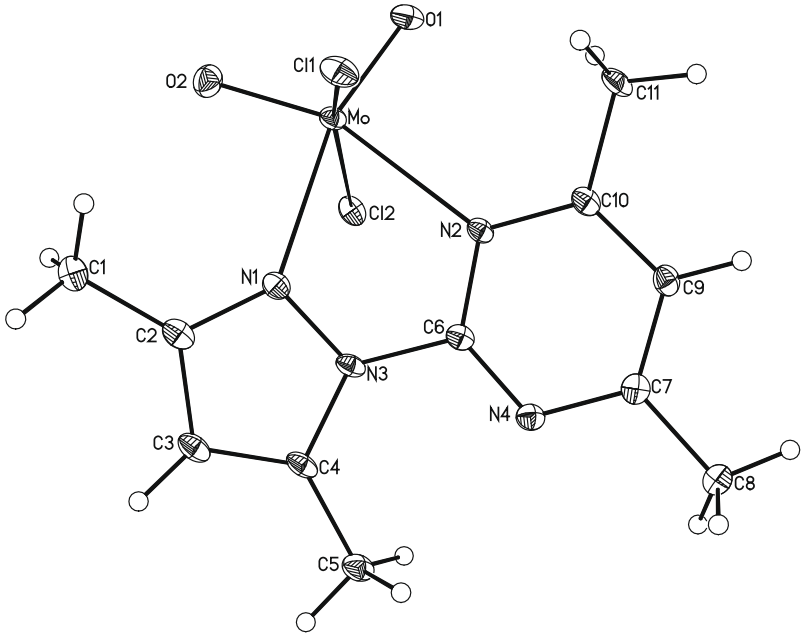


Fig. 4. Structural representation of complex **2**.

sideration that repulsion between adjacent bonds follows the order:

- double bond–double bond > double bond–single bond > single bond–single bond.

Thus, the observed order of values for the angles O2–Mo–O1 > N1–Mo–O2 ~ N2–Mo–O1 > N1–Mo–N2 can be easily explained. Similarly the axial angles Cl2–Mo–N1 and Cl2–Mo–N2 are found to be smaller than the angles Cl2–Mo–O1 and Cl2–Mo–O2 [44]. No appreciable H-bonding interactions, either intra- or intermolecular, could be ascertained.

*3.5.4. Structure of complex **3***

Complex **3** is an oxo bridged dimer of complex **2**. Here, the geometry around each molybdenum is approximately the same as in complex **2**. The only difference is that the Mo atom in complex **2** is ligated by two chloride ions from the axial end whereas in complex **3** an oxo group bridges the two monomeric units by substituting one chloride from each unit and occupying the common axial position of the two octahedral moieties (Fig. 5). The non bridging oxo groups share equatorial positions with the ligand donor atoms. As in complex **2**, here also the ligand plane and the mean equatorial plane at the metal center are not coplanar. The deviation is found to be slightly greater (dihedral angle 20.69° as

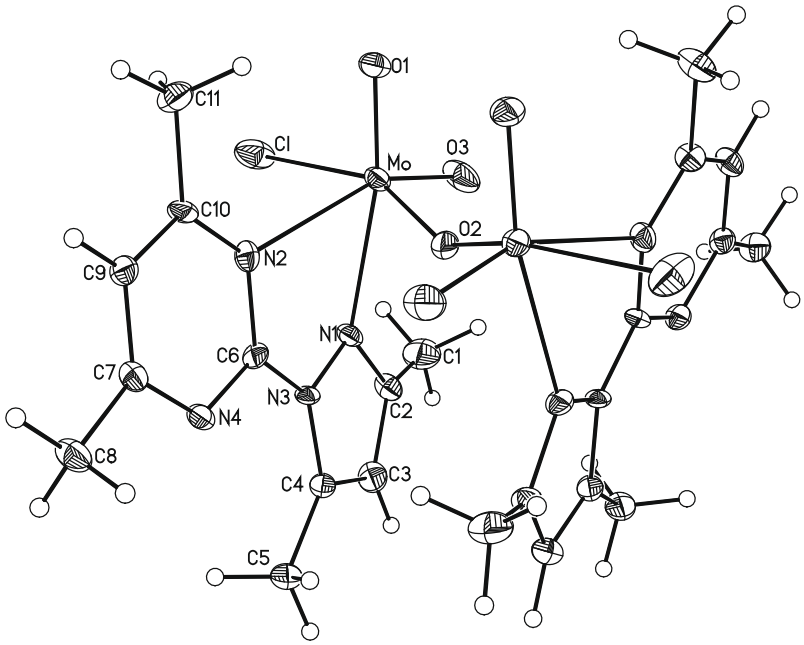


Fig. 5. Structural representation of complex **3** (the disordered nature of the ligand is omitted for clarity).

compared to 18° in **2**). The mean equatorial planes at the two Mo centers make a dihedral angle of 12.24° between themselves. No remarkable deviation of the bond lengths are observed in **3** as compared to **2** and other oxo bridged dimeric Mo complexes [45,46]. Both the Mo–O2 bond lengths are same indicating equivalence of the Mo centers. The bridging oxo groups are further away from each Mo center (1.887 Å) than the terminal oxo groups (1.664–1.697 Å). The Mo–Mo distance of 3.363 Å indicates that no me-

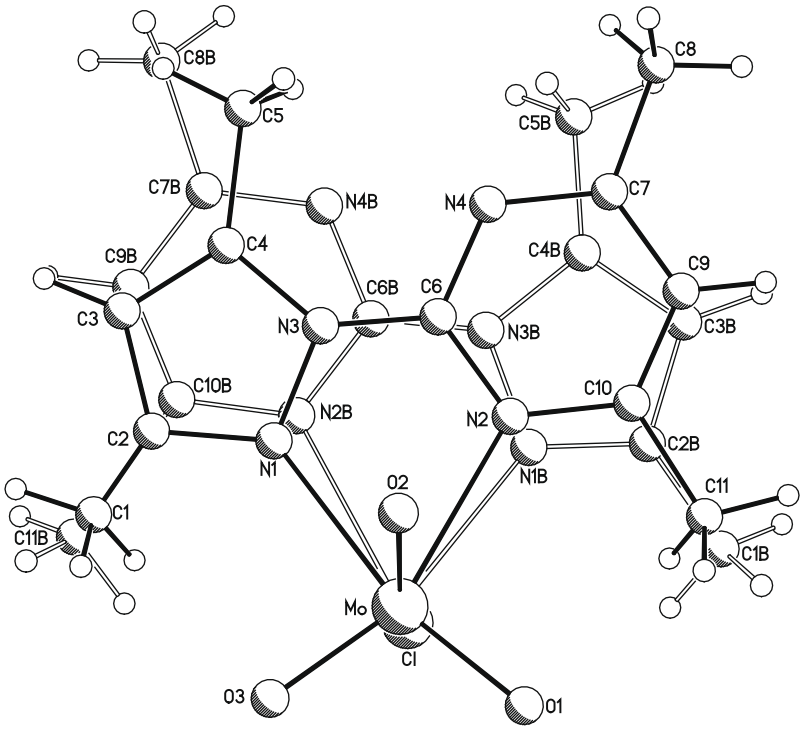


Fig. 6. Disordered nature of the ligand in complex **3** (shown at one Mo center).

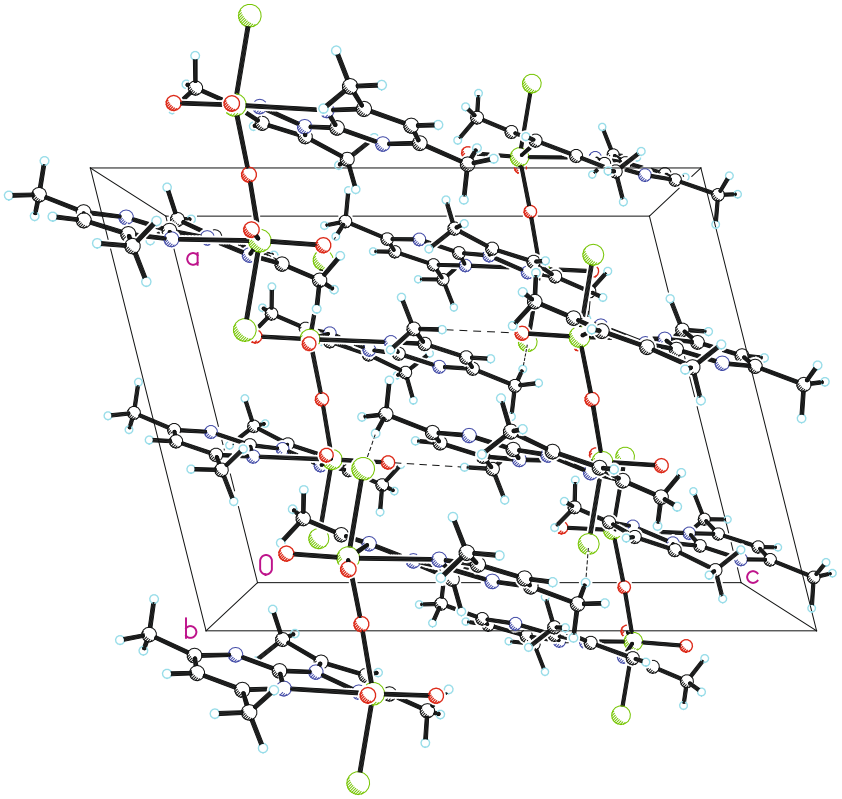


Fig. 7. Packing diagram of **3**.

tal–metal bonding is present [45–47]. The angles surrounding the metal centers are comparable to those in complex **2**. The Mo–O2–Mo bridge angle has a value of 148.87 Å, which is to the lower side of the range observed for singly oxo bridged binuclear Mo complexes (values may range up to 180°) [37].

An interesting feature of the structure is that the ligand has two disordered configurations, with the Mo–N1 and Mo–N2 bonds almost interchanging positions as a result of flipping of the ligand moieties (Fig. 6). When the structure of the complex is viewed along the Mo–O2–Mo bond, it is found that while one of the oxo groups (O1) is *syn* to the one another, the axial chloro groups are anti to one another, and the other oxo group (O3) and the chelate ring bear a mutually skewed configuration. The skewed configuration of the ligands at the two Mo centers ensures that the π-clouds of the pyrazole rings (pyrazole and pyrimidine rings, if the disordered position is considered) are close enough to allow a considerable π–π interaction. The centroid to centroid distance between the heterocyclic rings is calculated to be within the range 3.69–3.73 Å. The angle of inclination (dihedral angle) of 18° between the two ligand planes and the smaller value of the Mo–O2–Mo angle also facilitate the closing in of the π-clouds for an appreciable interaction. A packing mode for **3** is shown in Fig. 7.

4. Conclusion

The syntheses, spectroscopic, electrochemical studies and structural characterization of four molybdenum(VI) complexes have been described here. The complexes are not exceptional with regard to their structural features, however the notable observation in this work is the ligand based chemistry which leads to the transformation of the used ligands (HL_2 and $H_2L'_1$) in the reaction media. Molybdenum catalyzed oxidative cleavage of C=N in a tosyl hydrazone was reported long ago [48]. Numerous hydrazone based ligands have been reported for complexation with Mo(VI) ions. However, the novelty of this work lies in the fact that the ligands reported here are the only examples in which the metal center cleaves the C=N bond intrinsically. Perhaps some speciality in the ligand structure or environment plays the key role for such unusual behavior. Again, the previous example of Mo catalyzed C=N cleavage using the Mo(VI) species MoF_6 or the Mo(V) species $MoOCl_3$ resulted in reduction of the metal center. In this work formation of the complexes **2**, **3** and **4** has occurred with no change in the oxidation state of the Mo(VI) precursor. A closer look at the used ligands vis-a-vis the ligands L_3 and HL_4 (the transformed ligand in **2, 3** and **4,** respectively) reveals that one C=N bond cleavage has taken place at the cost of the formation of two other C=N bonds with acetylacetone in order to gain stability through the formation of an aromatic pyrazole ring. However, in the absence of acetyl acetone (i.e. when $(NH_4)_2MoO_4$ is used as the metal precursor), the ligands generated by the initial C=N cleavage process cannot stabilize the MoO_2^{2+} core.

Acknowledgments

Financial support [01(1916)/04/EMR-II] from the Council of Scientific and the Industrial Research (CSIR), New Delhi, India is gratefully acknowledged. Acknowledgement is also made to the University Grants Commission, New Delhi, India, for awarding a major research project in science [F. 30-65/2004(SR)] to S.K. Kar.

Appendix A. Supplementary data

CCDC 678937, 678940, 678938, 678942 and 678939 contain the supplementary crystallographic data for **1**, **2**, **3**, **4** and HL_2. These data can be obtained free of charge via http://www.ccdc.cam.ac.uk/conts/retrieving.html, or from the Cambridge Crystallographic Data Centre, 12 Union Road, Cambridge CB2 1EZ, UK; fax: (+44) 1223 336 033; or e-mail: deposit@ccdc.cam.ac.uk. Supplementary data associated with this article can be found, in the online version, at doi:10.1016/j.poly.2008.12.057.

References

[1] E.I. Stiefel, in: M.P. Coughlan (Ed.), Molybdenum and Molybdenum Containing Enzymes, Pergamon Press, Oxford, England, 1979, p. 43.
[2] E.I. Stiefel, Science 272 (1996) 1599.
[3] R.J.P. Williams, J.J.R.F. Da Silva, Biophys. Biochem. Res. Commun. 292 (2002) 293.
[4] E.I. Stiefel, Prog. Inorg. Chem. 22 (1977) 1.
[5] G.D. Lawrence, J.T. Spence, Biochemistry 14 (1975) 3626.
[6] G.D. Lawrence, J.T. Spence, Biochemistry 16 (1977) 3087.
[7] R.A.D. Wentworth, Coord. Chem. Rev. 18 (1976) 1.
[8] R. Hille, Chem. Rev. 96 (1996) 2757.
[9] J.H. Enemark, J.J.A. Cooney, J.-J. Wang, R.H. Holm, Chem. Rev. 104 (2004) 1175.
[10] D. Sellman, Angew. Chem., Int. Ed. Engl. 32 (1993) 64.
[11] J. Kim, D. Wood, D.C. Ress, Biochemistry 32 (1993) 7104.
[12] R.C. Bray, Enzymes 12 (1975) 299.
[13] R.H. Holm, P. Kennepohl, E.I. Solomon, Chem. Rev. 96 (1996) 2239. and references cited therein.
[14] A.C. Fernandes, C.C. Romão, Tetrahedron Lett. 48 (2007) 9176.
[15] D. Eierhoff, W. Chau Tung, A. Hammerschmidt, B. Krebs, Inorg. Chim. Acta 362 (2009) 915.
[16] J.T. Spence, Coord. Chem. Rev. 48 (1983) 59.
[17] E.W. Harlan, J.M. Berg, R.H. Holm, J. Am. Chem. Soc. 108 (1986) 6992. and references cited therein.
[18] S. Purohit, A.P. Koley, L.S. Prasad, P.T. Manoharan, Inorg. Chem. 28 (1989) 3735.
[19] J.U. Mondal, J.G. Zamora, M.D. Kinon, F.A. Schultz, Inorg. Chim. Acta 309 (2000) 147.
[20] R. Dinda, P. Sengupta, S.P. Ghosh, H. Mayer-Figge, W.S. Sheldrick, J. Chem. Soc., Dalton Trans. (2002) 4434.
[21] S. Gupta, A.K. Barik, S. Pal, A. Hazra, S. Roy, R.J. Butcher, S.K. Kar, Polyhedron 26 (2007) 133.
[22] E.B. Seena, M.R.P. Kurup, Polyhedron 26 (2007) 3595.
[23] M. Mancka, W. Plass, Inorg. Chem. Commun. 10 (2007) 677.
[24] A. Hroch, G. Gemmecker, W.R. Thiel, Eur. J. Inorg. Chem. (2000) 1107.
[25] G.J.J. Chen, J.W. McDonald, W.E. Newton, Inorg. Chem. 15 (1976) 2612.
[26] B. Chiswell, F. Lions, Aust. J. Chem. 22 (1961) 71.
[27] S. Gupta, S. Pal, A.K. Barik, A. Hazra, S. Roy, T.N. Mandal, S.-M. Peng, G.-H. Lee, M.S.E. Fallah, J. Tercero, S.K. Kar, Polyhedron 27 (2008) 2519.
[28] N.R. Pramanik, S.P. Ghosh, T.K. Roychowdhury, S. Ray, R.J. Butcher, S.S. Mandal, Polyhedron 23 (2004) 1595.
[29] T. Glowiak, L. Jerzykiewicz, J.M. Sobczak, J.J. Ziolkowski, Inorg. Chim. Acta 356 (2003) 387.
[30] C. Bustos, O. Burckhardt, R. Schrebler, D. Carrillo, A.M. Arif, A.H. Cowley, C.M. Nunn, Inorg. Chem. 29 (1990) 3996.
[31] E.D.P. Carreiro, G. Yong-En, A.J. Burke, Inorg. Chim. Acta 359 (2006) 1519.
[32] W. Kemp, Organic Spectroscopy, Macmillan, Hamshire, 1987, p. 565.
[33] K. Nakamoto, Infrared and Raman Spectra of Inorganic and Coordination Compounds, Wiley, New York, 1986, p. 241.
[34] N.S. Biradar, B.R. Havinale, Inorg. Chim. Acta 17 (1976) 157.
[35] S.A. Attia, S.F. El-Mashtoly, M.F. El-Shahat, Polyhedron 22 (2003) 894.
[36] M. Kato, K. Nakajima, Y. Yoshikawa, M. Hirotsu, M. Kojima, Inorg. Chim. Acta 311 (2000) 69.
[37] M. Cindrić, N. Strukan, V. Vrdoljak, M. Devčić, Z. Veksli, B. Kamenar, Inorg. Chim. Acta 304 (2000) 260.
[38] S. Purohit, S.P. Ghosh, J. Chem. Res. (s) (1988) 158.
[39] R. Hahn, U. Kusthardt, W. Scherer, Inorg. Chim. Acta 210 (1993) 177.
[40] J.A. Craig, E.W. Harlan, B.S. Snyder, M.A. Whitener, R.H. Holm, Inorg. Chem. 28 (1989) 2082.
[41] J.M. Berg, R.H. Holm, J. Am. Chem. Soc. 106 (1984) 3035.
[42] F.E. Kühn, E. Herdtweck, J.J. Haider, W.A. Herrmann, I.S. Goncalves, A.D. Lopes C.C. Rom~ao, J. Organomet. Chem. 583 (1999) 3.
[43] F.E. Kühn, M. Groarke, E.- Bencze, E. Herdtweck, A. Prazeres, A.M. Santos, M.J. Calhorda, C.C. Rom~ao, I.S. Gonc¸alves, A.D. Lopes, M. Pillinger, Chem. Eur. J. 8 (2002) 2370.
[44] Z. Petrovski, M. Pillinger, A.A. Valente, I.S. Goncalves, A. Hazell, C.C. Rom~ao, J. Mol. Catal. A: Chem. 227 (2005) 67.
[45] W. Yang, C. Lu, X. Lin, C. Wu, D. Wu, H. Zhuang, Inorg. Chem. Commun. 4 (2001) 285.
[46] L. Stelzig, S. Kötte, B. Krebs, J. Chem. Soc., Dalton. Trans. (1998) 2921.
[47] E. Kahrović, K. Molcanov, L. Tusek-Bozić, B. Kojić-Prodić, Polyhedron 25 (2006) 2459.
[48] G.A. Olah, J. Welch, G.K. Suryaprakash, T.-L. Ho, Syn. Commun. (1976) 808.

with vinylsilanes, which should exhibit better thermal stability and volatility than the β-diketonate derivatives. Moreover, Cu(I) carboxylate complexes with vinylsilanes can form dimeric or oligomeric structures, with difficult to predict modes of ligand arrangements around the central ions. Besides that, carboxylates of Cu(I) are much more air and moisture sensitive than their Cu(II) analogs and their thermal decomposition processes have not been studied. Literature data on the perfluorinated carboxylate complexes of the copper triad metals give no direct dependences between the thermal stability of the M–O bond and the perfluorinated chain length [4]. To the best of our knowledge, there is a lack of reports on Cu(I) organometallics with hard σ donor ligands such as perfluorocarboxylates and π acceptor vinylsilanes.

In the present paper, variable temperature spectroscopic and thermal studies of $[Cu(L)(\mu\text{-}O_2CR)]_n$, where $L = CH_2{=}C(H)SiMe_3$ (VTMS), $CH_2{=}C(H)SiEt_3$ (VTES), $CH_2{=}C(H)Si(OMe)_3$ (VTMOS); $R = CF_3$, C_2F_5; $n = 2$ or 3, are described. It is known that perfluorinated carboxylates improve the volatility of complexes and organometallic compounds [1], but the Cu(I)–O bond is not stable, hence in this paper vinylsilanes as secondary, stabilizing ligands are applied. The results of EI-MS and variable temperature IR studies are used for elucidation of the thermal decomposition mechanisms and selection of compounds suitable for CVD experiments.

2. Experimental

2.1. Materials

Vinyltrimethylsilane (VTMS) (97%), vinyltriethylsilane (VTES) (97%), vinyltrimethoxysilane (VTMOS) (98%), copper powder (99%) and CF_3COOH (99%) and C_2F_5COOH (97%) were purchased from Aldrich, whereas $CuCO_3 \cdot Cu(OH)_2$, was purchased from Riedel–Han, and all were used as received. $[Cu(O_2CC_2F_5)_2]$, $[Cu(O_2CCF_3)_2]$ and the sodium salts were prepared as reported [21]. Acetonitrile (Aldrich; 99.93%), was dried and deoxygenated by standard methods.

2.2. Instrumentation

Mass spectra were detected with a Finnigan MAT 95 mass spectrometer, using the EI ionization method in the temperature range 303–573 K. IR spectra were measured with a Perkin–Elmer Spectrum-2000 FT-IR spectrometer, using KBr (400–4000 cm^{-1}) and polyethylene disks or plates (100–400 cm^{-1}). Variable temperature IR (VT IR) spectra of solid samples, deposited on a KBr disk, were measured with a SPECAC cell over the temperature range 303–523 K, at dynamic vacuum $p = 100$ Pa using the same instrument. The complete inertness of the studied compounds in contact with KBr was tested at different temperatures before the registration of the VT IR spectra. VT IR spectra of vapors, transported in Ar (carrier gas) were registered in a specially constructed reactor, described previously [22]. The glass vessel with the precursor sample (~100 mg) was placed in the reactor tube and heated ($T = 303$–623 K), under dynamic vacuum ($p = 100$ Pa). The content of Cu was determined with a Carl–Zeiss Jena AAS spectrophotometer. Thermal studies (TGA/DTA) were performed on a SDT 2960 TA analyzer (dry N_2; heating rate – 2.5° min^{-1}, for (**1**) – 1° min^{-1}; sample mass 12–18 mg). Gaseous products of the thermal decomposition (TGA/DTA) of (**1**) were detected by a FT-IR BioRad Excalibur spectrometer equipped with a thermal connector ($T_L = 343$ K in the range 285–463 K and $T_L = 413$ K over 463 K) for gases. Powder X-ray diffraction data of the residues from the thermal analysis were collected with a Philips X'PERT diffractometer using a Cu Kα line.

Deposition experiments were carried out using a horizontal *hot-wall* CVD reactor as described in the literature [23–25]. Copper films were deposited on the following substrates: Si(1 1 1), stainless steel, ITO (In_2O_3/SnO_2) and quartz, under 100 Pa, at the vaporization temperature 483 K for (**1**) and 503 K for (**2**), whereas the substrate temperatures were between 693 and 793 K. Morphology studies were carried out using scanning electron microscopy (SEM – LEO 1460 V, operating voltage 28 kV). XPS spectra were obtained with monochromatized Al Kα radiation (1486.6 eV) at room temperature using a PHI 5700/660 ESCA spectrometer, after 30 min Ar^+ ion sputtering.

2.3. Synthesis

The syntheses were carried out using Schlenk glassware under an argon atmosphere, according to a slightly modified method [21,26–30]. In the general procedure, copper(II) carboxylate (0.5×10^{-3} mol) was dissolved in 20 cm^3 of dried and deoxygenated acetonitrile, and copper powder (2.5×10^{-3} mol) was added. The obtained reaction mixture was stirred until the acetonitrile solution turned pale yellow. Next vinylsilane was added (1.1×10^{-3} mol), the suspension was stirred for 12 h at ambient temperature and filtered. The final product was isolated at 273 K by solvent evaporation under reduced pressure. The yields were 70–85%. No crystals suitable for an X-ray structure determination were obtained. The results of elementary analyses and spectroscopic data are given below:

$[Cu(VTMS)(\mu\text{-}O_2CC_2F_5)]_n$ **(1)**: Cu (calc./found) % 19.3/18.7. EI-MS $T = 489$ K (m/z, RI %) $[VTMS]^+$ 100, 19; $[Cu_2(O_2CC_2F_5)]^+$ 289, 100; $[Cu_2(O_2CC_2F_5)_2]^{+\cdot}$ 452, 57; $[Cu_3(O_2CC_2F_5)_2]^+$ 517, 2. IR (KBr, cm^{-1}): 1682, 1413, 1216, 1166, 1028, 933, 833 [25]; PE 541, 289, 243.

$[Cu(VTES)(\mu\text{-}O_2CC_2F_5)]_n$ **(2)**: Cu (calc./found) % 17.2/17.4. EI-MS $T = 441$ K (m/z, RI %) $[Cu_2(O_2CC_2F_5)]^+$ 289, 11; $[Cu_2(O_2CC_2F_5)_2]^{+\cdot}$ 452, 8; $[Cu_3(O_2CC_2F_5)_2]^+$ 517, 3; $[Cu_2(VTES)(O_2CC_2F_5)]^+$ 431, <1; $[Cu_2(VTES)(O_2CC_2F_5)_2]^{+\cdot}$ 736, 2. IR (KBr, cm^{-1}): 1687, 1416, 1215, 1164, 1031, 931, 820 [25]; PE 540, 279, 253 cm^{-1}.

$[Cu(VTMS)(\mu\text{-}O_2CCF_3)]_2$ **(3)**: Cu (calc./found) % 22.9/23.4. EI-MS $T = 540$ K (m/z, RI %) $[VTMS]^+$ 100, 26; $[Cu_2(O_2CCF_3)]^+$ 239, 98; $[Cu_2(O_2CCF_3)_2]^{+\cdot}$ 352, 46; $[Cu_2(VTMS)(O_2CCF_3)_2]^{+\cdot}$ 452, 2. IR (KBr, cm^{-1}): 1684, 1438, 1328, 1215, 1160, 1031, 942, 819; PE 523, 280, 247 cm^{-1}.

$[Cu(VTES)(\mu\text{-}O_2CCF_3)]_2$ **(4)**: Cu (calc./found) % 19.9/18.7. EI-MS $T = 508$ K (m/z, RI %) $[Cu_2(O_2CCF_3)]^+$ 239, 98; $[Cu_2(O_2CCF_3)_2]^{+\cdot}$ 352, 46. IR (KBr, cm^{-1}): 1681, 1433, 1374, 1203, 1138, 1035, 840, 797, 725, 594; PE 524, 279, 247.

$[Cu(VTMOS)(\mu\text{-}O_2CC_2F_5)]_2$ **(5)**: Cu (calc./found) % 16.9/15.5. EI-MS $T = 452$ K (m/z, RI %) $[Cu_2(O_2CC_2F_5)]^+$ 289, 100; $[Cu_2(O_2CC_2F_5)_2]^{+\cdot}$ 452, 34; $[Cu_2(C_2F_5)(VTMOS)(O_2CC_2F_5)]^{+\cdot}$ 553, ~1. IR (KBr, cm^{-1}): 1688, 1411, 1327, 1251, 1168, 1032, 973, 817; PE 543, 299, 227.

3. Results and discussion

The obtained compounds **1–4** were dark brown, fine-crystalline powders, stable under an inert atmosphere for few months, while **5** was isolated as a brown oil, highly air and moisture sensitive.

The absorption bands of the carboxylic group asymmetric and symmetric stretching vibrations were detected at: $\nu_{as}(COO) = 1681$–1690 cm^{-1} and $\nu_s(COO) = 1410$–1438 cm^{-1}. The calculated $\Delta\nu = \nu_{as}(COO) - \nu_s(COO)$ parameter for the compounds $[Cu(L)(\mu\text{-}O_2CC_2F_5)]_n$ (**1**, **2**, **5**) was $\Delta\nu = 269$–278 cm^{-1}, whereas in the case of $[Cu(L)(\mu\text{-}O_2CCF_3)]_2$ (**3**, **4**) the values of Δ were 247 and 246 cm^{-1}. These values are close to the same parameter found for the appropriate sodium salts: $\Delta\nu(C_2F_5COONa) = 268$ cm^{-1} and $\Delta\nu(CF_3COONa) = 223$ cm^{-1}, which suggests a bridging coordination mode of the carboxylate groups [21,31]. The bridging mode

of the carboxylates is in favor of dimeric or trimeric structures of the complexes in the solid state. The vinylsilane absorption band of the C=C stretching vibrations were detected as a shoulder at 1632 cm^{-1}, whereas Cu–|| was in the range 523–543 cm^{-1} [31], which confirms the coordination of the vinylsilane. Assuming the bridging coordination of the carboxylates and dihapto coordination of the vinylsilane, a C_{2v} microsymmetry for the coordination sphere of Cu(I) appears in the studied complexes. The calculated irreducible representations of the metal–ligand bond vibrations are: Cu–O stretching ($A_1 + B_1$) and O–Cu–O deformation (A_1). Spectra in the range of the metal–ligand vibrations (400–50 cm^{-1}) revealed bands which can be assigned to Cu–O stretching vibrations (A_1 = 227–253 cm^{-1} symmetric and B_1 = 279–299 cm^{-1} asymmetric).

Thermal analysis of **1**–**4** indicates multistage, endothermic decomposition processes followed by metallic copper formation in the range 537–548 K (Supplementary data Fig. S1). In the case of **5**, besides the endothermic processes, one exotherm was detected in the range 593–643 K, whereas the reaction completed at a significantly higher temperature (823 K). TGA analysis suggests mainly vinylsilane detachment for the first stage of the thermal decomposition. The band at 2357 cm^{-1}, characteristic for CO_2, was detected in the studied temperature range. X-ray powder diffractograms of the final products revealed lines at 43.50°, 50.59° and 74.26° 2θ, which correspond to those reported for Cu: 43.47°, 50.37° and 73.99° 2θ by the JCPDS International Center for Diffraction Data [32].

3.1. Mass spectra analysis

Mass spectra (MS-EI) of studied compounds were measured between 303 and 573 K and used for structural characterization and identification of metallated fragments, which can be transported in the CVD process.

In the case of $[Cu(VTMS)(\mu\text{-}O_2CC_2F_5)]_n$ (**1**) (Table 1) and $[Cu(VTMS)(\mu\text{-}O_2CCF_3)]_2$ (**3**) the following silicon atoms binding fragments, characteristic for vinyltrimethylsilane, were detected: $[CH_2{=}C(H)SiMe_3]^+$ (m/z = 100), $[SiCH_3]^+$ (43 m/z), $[SiCH]^+$ (41 m/z) and $[SiC]^+$ (40 m/z), among which the $[SiCH]^+$ ion exhibits RI = 100% for **1** over 309–471 K, whereas for **3** RI was 90% over 377–551 K. The MS specta of $[Cu(VTES)(\mu\text{-}O_2CC_2F_5)]_n$ (Supplementary data Table S1) exhibited the following fragments: $[SiCH_2]^+$ (42 m/z), $[SiCH_3]^+$ (43 m/z), $[SiC_2H_5]^+$ (57 m/z), $[SiC_2H_6]^+$ (58 m/z), indicative for VTES fragmentation. Among the latter fragments the most abundant silicon embodying ion $[SiCH_3]^+$, (RI = 100%) was observed in the range 309–573 K. Simultaneously the intensity of $[SiC_2H_6]^+$ changed from 95%, (below 445 K), to 35% in the range 473–549 K. Moreover, for $[Cu(VTMOS)(\mu\text{-}O_2CC_2F_5)]_2$ (**5**) the VTMOS ligand fragments: $[SiCH]^+$ (41 m/z, RI 100–2%, 334–485 K), $[Si(OMe)_3]^+$ (121 m/z, RI 7–4%, 334–374 K) and $[CSi(OMe)_3]^+$ (133 m/z, RI 2%, 334 K) were detected. Analysis of these data indicates a low thermal stability of the metal–alkene bond in the studied Cu(I) complexes and detachment of the vinylsilane ligands in the first step of the thermal decomposition.

The following di- and trimetallic ions: $[Cu_3(O_2CR)_2]^+$, $[Cu_3(O_2CR)_3]^{+\cdot}$, $[Cu_3(O_2CR)_5]^+$, $[Cu_2(CO_2)(O_2CR)]^+$, $[Cu_2(O_2CR)_2]^{+\cdot}$, $[Cu_2(O_2CR)]^+$, $[Cu_2(L')(O_2CR)_2]^{+\cdot}$ and $[Cu_2(L')(O_2CR)]^+$ (L′ = vinylsilane or its parts), $[Cu_2CF_3]^+$, $[Cu_2F]^+$, $[Cu_2]^{+\cdot}$ were noted in the gas phase of the complexes studied (Table 1, Fig. 1). These stable fragments suggest the presence of di- or trimeric structures of the studied compounds in the solid phase (Supplementary data Fig. S2), which are retained during vaporization. The dimeric or trimeric forms give further support for the carboxylates bridging coordination mode in the synthesized complexes that have been postulated from IR spectral analysis. The ions $[Cu_2(O_2CR)]^+$ and $[Cu_2(O_2CR)_2]^{+\cdot}$ (for **1**–**5**) revealed the highest signal intensity among the metallated fragments. In the case of **1**, the ion $[Cu_2(O_2CC_2F_5)]^+$ showed the highest intensity (RI = 100%) over the temperature range 489–507 K (Table 1), whereas for **5** the same ion exhibited RI = 100% above 452 K. However, for complex **2**, the $[Cu_2(O_2CR)]^+$ and $[Cu_2(O_2CR)_2]^{+\cdot}$ ions exhibited much lower RI values (8–12%) over 433–445 K (Supplementary data Table S1). Moreover, the vaporization temperature onset was lower for the pentafluoropropionate complexes $[Cu(L)(\mu\text{-}O_2CC_2F_5)]_n$ (443–463 K) than for the trifluoroacetate complexes $[Cu(L)(\mu\text{-}O_2CCF_3)]_2$ (511–553 K) [33], which suggests that precursors with the pentafluoropropionate ligand can be more promising for CVD purposes than those with the trifluoroacetate ligand. The ion $[Cu_2F]^+$ is also important because its intensity reached 20–30% depending of the compound and temperature. Moreover, $[Cu_2]^{+\cdot}$ (126 m/z, RI < 4%) and $[Cu]^+$ (63 m/z, RI < 24%) ions were noted for the studied complexes as the terminal products of the fragmentation.

The low population of the $[Cu_2(L')(O_2CR)_2]^{+\cdot}$ and $[Cu_2(L')(O_2CR)]^+$ ions (L′ = vinylsilane or its parts) and the lack of copper–vinylsilane fragments confirm the TGA results that vinylsilanes are detached at the first stage of the thermal decomposition.

To the best of our knowledge there is a lack of data on the mass spectra of Cu(I) pentafluoropropionate complexes, however, MS studies of copper(I) carboxylates $[Cu(O_2CR)]$ (R = H, Me, Bu^t, CF_3) [34,35] revealed that these carboxylates are thermally stable and sublime without decomposition, forming in the gas phase copper

Table 1
MS data of $[Cu(VTMS)(\mu\text{-}O_2CC_2F_5)]_n$ (**1**).

Fragments	m/z	I (%)								
		309 K	386 K	430 K	471 K	489 K	507 K	531 K	556 K	573 K
$[SiCH]^+$	41	100	100	100	100	6	8	2	1	1
$[CO_2H]^+$	45		3	6	41	27	56	100	100	100
$[CF_3]^+$	69	5	2	4	28	18	57	89	87	84
$[C_2F_5]^+$	119	1<	3	4	36	37	45	99		85
$[VTMS]^+/[C_2F_4]^+$	100	6	3	5	40	19	52	89	88	83
$[Cu]^+$	63				7	15	22	8	7	10
$[Cu_2]^{+\cdot}$	126				1	4	4	2	2	3
$[Cu_2F]^+$	145				8	13	21	8	10	12
$[Cu_2CF_3]^+$	195					1	2			
$[Cu_2(O_2CC_2F_5)]^+$	289	1	2	2	57	100	99	33	11	51
$[Cu_2(O_2CC_2F_5)_2]^{+\cdot}$	452	1<	1<	1<	38	57	68	12	17	21
$[Cu_3(O_2CC_2F_5)_2]^+$	517				2	2	2			
$[Cu_2(O_2CC_2F_5)_3]^+$	615				1	2	2			
$[Cu_3(O_2CC_2F_5)_3]^{+\cdot}$	680				1	1	1			
$[Cu_3(O_2CC_2F_5)_5]^+$	1006				11	11	8			

bonded fragments: $[Cu_2(O_2CR)]^+$, $[Cu_2(O_2CR)_2]^{+\cdot}$ and $[Cu_2(CO_2)(O_2CR)]^+$. On the other hand, MS spectra of Cu(I) salts with unsaturated carboxylates $[Cu(O_2CR)]$ (R = C_2H_3, C_3H_5, Ph) demonstrate, besides the $[Cu_2(O_2CR)]^+$ and $[Cu_2(O_2CR)_2]^+$ ions, the organometallic fragments $[Cu_2(O_2CR)(R)]^{+\cdot}$ are also observed. The latter salts appeared to be thermally unstable and decompose during sublimation.

In the case of the trifluoroacetate complexes **3** and **4** MS spectra exhibit the $[Cu_2(CO_2)(O_2CCF_3)]^+$ ion over 455–551 K (RI 4–18%), which correlates with the simultaneous high intensity of the $[CF_3]^+$ ion (RI 100%). On the other hand, the $[Cu_2(CO_2)(O_2CC_2F_5)]^+$ ion was not observed in the MS of **1**, **2** and **5**. The latter can be related to properties of the CF_3COO^- ion (Lewis base), which is a harder ligand than $C_2F_5COO^-$ and thus can decrease the stability of the $[Cu_2(O_2CCF_3)_2]^{+\cdot}$ ion in relation to $[Cu_2(O_2CC_2F_5)_2]^{+\cdot}$.

The presence of the tricopper ion $[Cu_3(O_2CR)_5]^+$ (RI = 11–8%) over 471–507 K for **1** and the dicopper ion $[Cu_2(O_2CR)_3]^+$ for **2** suggests for these complexes different than the dimeric structure or formation of tricopper derivatives during thermolysis. The tricopper ion formation can be related to the following reactions:

$$3[Cu(L)(\mu\text{-}O_2CR)]_2 \xrightarrow{-6L} 3[Cu_2(O_2CR)_2] \rightarrow 3Cu^0 + [Cu_3(O_2CR)_6]$$

$$[Cu_3(O_2CR)_6] \xrightarrow{-RCOO^-} [Cu_3(O_2CR)_5]^+.$$

For the studied organometallic compounds the fragmentation pattern is presented at Fig. 1. One can conclude that the availability of copper for CVD comes from stable dimeric Cu(I) carboxylate binding species such as $[Cu_2(O_2CR)_2]$.

The complex **5** was isolated as an oil and the MS demonstrate intensive dicopper ions signals over 452–573 K, which is in favor of CVD applications. However, the compound exhibits low air and moisture resistance along with a high final temperature of the thermal decomposition.

The above discussed results (MS, TGA) and the physicochemical properties prompted us to carry out CVD studies of **1** and **2** as copper precursors. However, the proper determination of CVD parameters demands further characterization of precursor's stability and transport mechanism in the gas phase.

3.2. Variable temperature IR studies of *1* and *2*

Variable temperature IR (VT IR) spectra of solid samples were registered in order to study the thermal stability of the complexes and to characterize the structural changes caused by the thermolysis processes (Figs. 2, and 3, Supplementary data Fig. S3). The previous experiments confirm the completely inertness of the samples in contact with KBr plates. Moreover, absorption spectra of vapors, formed during the decomposition process of **1** and **2** were examined by the VT IR method and the results for **1** are presented in Fig. 4.

The most important changes in the spectra of **1** and **2** over 303–523 K were noted in the range 1360–1750 cm^{-1}, where absorption bands of coordinated carboxylate (ν_{as}(COO), ν_s(COO)) and VTMS/VTES ligands (ν(C=C), $\delta(CH_2,CH_3)$) were detected (Fig. 2). In order to assign the COO and C=C vibrations properly, the second derivative spectra were calculated and the frequencies are listed in Table 2. The stretching vibrations of the COO group were noted at: ν_{as}(COO) = 1657–1720 cm^{-1} and ν_s(COO) = 1389–1415 cm^{-1}, whereas ν(C=C) = 1631–1633 cm^{-1} and $\delta(CH_2,CH_3)$ = 1436–1439 cm^{-1}. The following spectral effects caused by the heating of **1** and **2** were detected: (a) intensity decrease of ν(C=C) and $\delta(CH_2,CH_3)$ bands between 303 and 433 K, (b) reduction of the ν_{as}(COO) and ν_s(COO) band numbers in the range 303–523 K.

The above mentioned effects can be correlated with the integral intensity changes of the ν_{as}(COO) and $\nu(CF_2,CF_3)$ bands presented at Fig. 3 (Supplementary data Fig. S3). On the other hand, the stretching bands of $\nu(CH,CH_2,CH_3)$ = 2800–3100 cm^{-1} and ν(Si–C) at 823 cm^{-1} revealed an intensity reduction (Fig. 2). Simultaneously in the spectra of vapors, collected over 373–413 K, the vibrations bands of CH, CH_2, CH_3 and $Si(CH_3)_n$ (2800–3100, 1042, 934, 906, 728 and 701 cm^{-1}) exhibit higher intensity (Fig. 4a), which suggests the detachment of the VTMS/VTES ligands during the thermolysis of **1** and **2**. Therefore, the following decomposition reaction for **1** and **2** can be proposed (Eq. (1)):

$$2[Cu(VTAS)(\mu\text{-}O_2CC_2F_5)]_n(s) \xrightarrow{350-433\ K} [Cu_2(O_2CC_2F_5)_2]_n(s) + 2n\ VTAS(g), \quad (1)$$

where VTAS = VTMS, VTES.

The integral intensities of the ν_{as}(COO) and $\nu(CF_2,CF_3)$ bands (over 413–433 K) were only slightly changed in the spectra of the solid samples, which can be related to the formation of stable copper carboxylate derivatives, Fig. 3 (Supplementary data Fig. S3). At temperatures above 433 K, the reduction of the $\nu(CF_2,CF_3)$ integral intensity bands was noted in the solid state, along with the simultaneous appearance of these bands in the spectra of the vapors (Supplementary data Fig. S3). Therefore, the latter can be re-

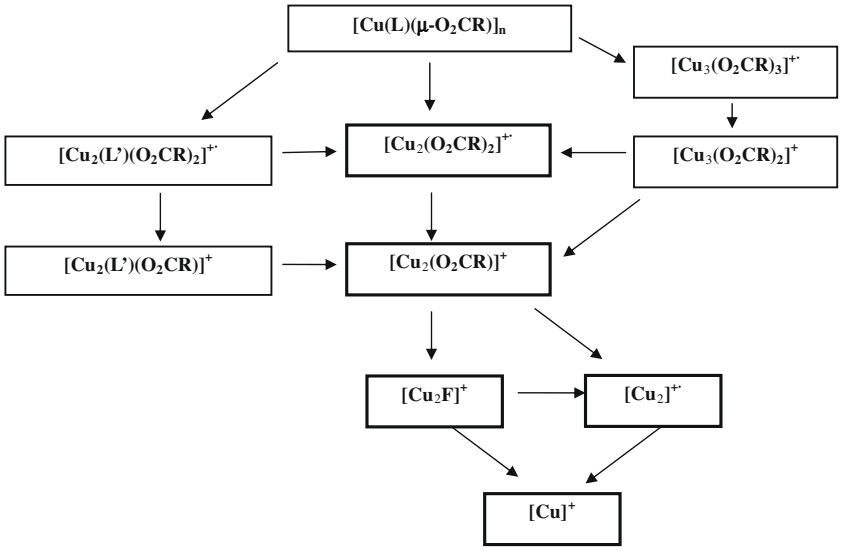


Fig. 1. Fragmentation scheme for the metallated fragments of $[Cu(L)(\mu\text{-}O_2CR)]_n$.

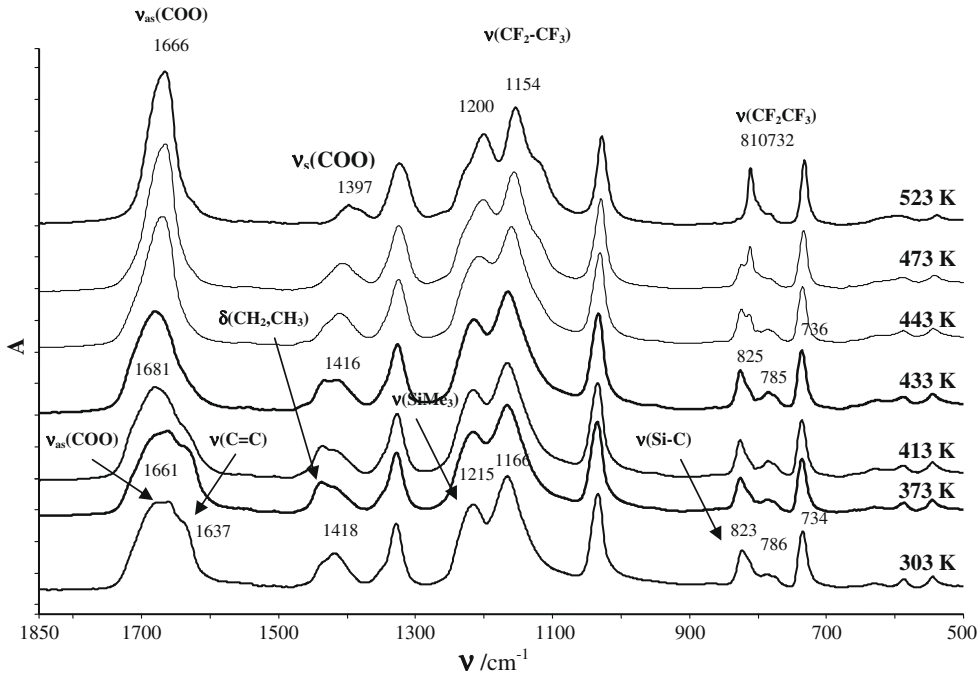


Fig. 2. Variable temperature spectra of $[Cu(VTMS)(\mu\text{-}O_2CC_2F_5)]_n$ (**1**) in the solid state (303–523 K).

lated to the decomposition processes of the studied precursors with the formation of the volatile C_xF_{2x+2}, $[Cu_2(CF_3)_n]$ and $[Cu_2(O_2CC_2F_5)_2]$ species above 433 K.

Moreover, the spectra of the vapors evolved from **1** (413 K) exhibit absorption bands at 1776, 1228, 1193 and 1158 cm^{-1}, from the species containing –C═O, $-CF_2$ and $-CF_3$ groups. In the spectra of **1**, registered at 433 K, new components in the vapors were noted. Among them acid anhydride bands at 1819 and 1776 cm^{-1}, Cu(I) carboxylate species (weak bands $\nu_{as}(COO) = 1649$ and $\nu_s(COO) = 1419$ cm^{-1}) and fluorocarbon species (strong C–F, C–C stretching bands at 1337, 1223, 1172, 1140 and 1031 cm^{-1}) (Fig. 4a) were observed. Moreover, the intensity of the latter bands was stronger in the range 453–493 K (Fig. 4b and S3). The highest concentration of the volatile Cu–O_2CR derivatives was achieved at 493 K. Two $\nu_{as}(COO)$ bands, which appear at 1706 and 1645 cm^{-1} (Fig. 4b), suggest that two types of volatile Cu–carboxylate species are transported in the vapors. The latter conclusion is further supported by the two values of the $\Delta\nu$ parameter (262 and 201 cm^{-1}), which comes from the carboxylate groups bound to Cu(I) in different ways. The geometry of the dicopper species in the gas phase is presented at Fig. 5. Simultaneously, the absorption bands, which can be assigned to Cu–carboxylate fragments, were not detected in the spectra registered at higher temperatures. According to the above, this stage of thermolysis for **1** and **2** can be exemplified by Eq. (2)

$$[Cu_2(O_2CC_2F_5)_2]_n(s) \overset{433-493K}{\rightarrow} n[Cu_2(O_2CC_2F_5)_2](g) \quad (2)$$

The intensity of VT IR absorption bands collected for **2** at 513 K exhibits the highest concentration of the volatile Cu–O_2CR derivatives ($\nu_{as}(COO) = 1699$ cm^{-1}; $\nu_s(COO) = 1436$ cm^{-1}; $\Delta\nu = 263$ cm^{-1}), although the intensity of these bands decreases at higher temperatures, similarly as for **1**.

The structural features of the Cu–carboxylate species transported in the vapors are important for the elaboration of the deposition parameters for CVD and the precursor selection. MS studies of copper carboxylates revealed that thermal decomposition proceeds with the formation of volatile dimeric species [34,35]. Ogura and Fernando postulated the formation of four types of Cu(I) carboxylate dimers in the vapors [35], similar to that presented in Fig. 5. In the spectrum of **1** (at 493 K) the band at 1706 cm^{-1} can be attributed to $\nu_{as}(COO)$ in dimeric Cu(I) carboxylates linked by bidentate O_2CR bridges ($\Delta\nu = 262$ cm^{-1} Fig. 5a). Simultaneously, the band at 1645 cm^{-1} ($\Delta\nu = 201$ cm^{-1}) can be assigned to asymmetric stretching vibrations of carboxylate groups, which form a chelate with an additional monoatomic bridge in the $[Cu_2(O_2CC_2F_5)_2]$ dimers (Fig. 5b). The spectrum of **2** exhibits a broad band for $\nu_{as}(COO)$ at 1699 cm^{-1}, which suggests the presence of different dimeric species in the vapors. The above proposed decomposition mechanism of **1** and **2** indicates the formation of volatile dimers $[Cu_2(O_2CC_2F_5)_2]$ between 433 and 493 K. The preliminary CVD experiments revealed that metallic copper films can be manufactured between 693 and 793 K using **1** and **2** as precursors [25]. Considering the proposed thermolysis

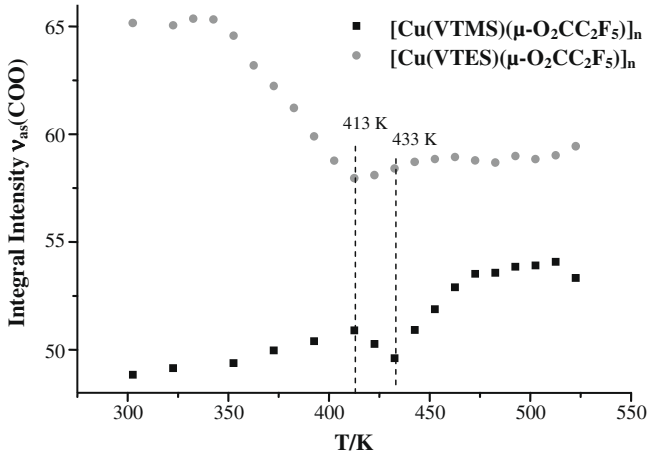


Fig. 3. Integral intensity of $\nu_{as}(COO)$ bands for **1** and **2** (solid samples deposited on KBr disk) as a function of temperature.

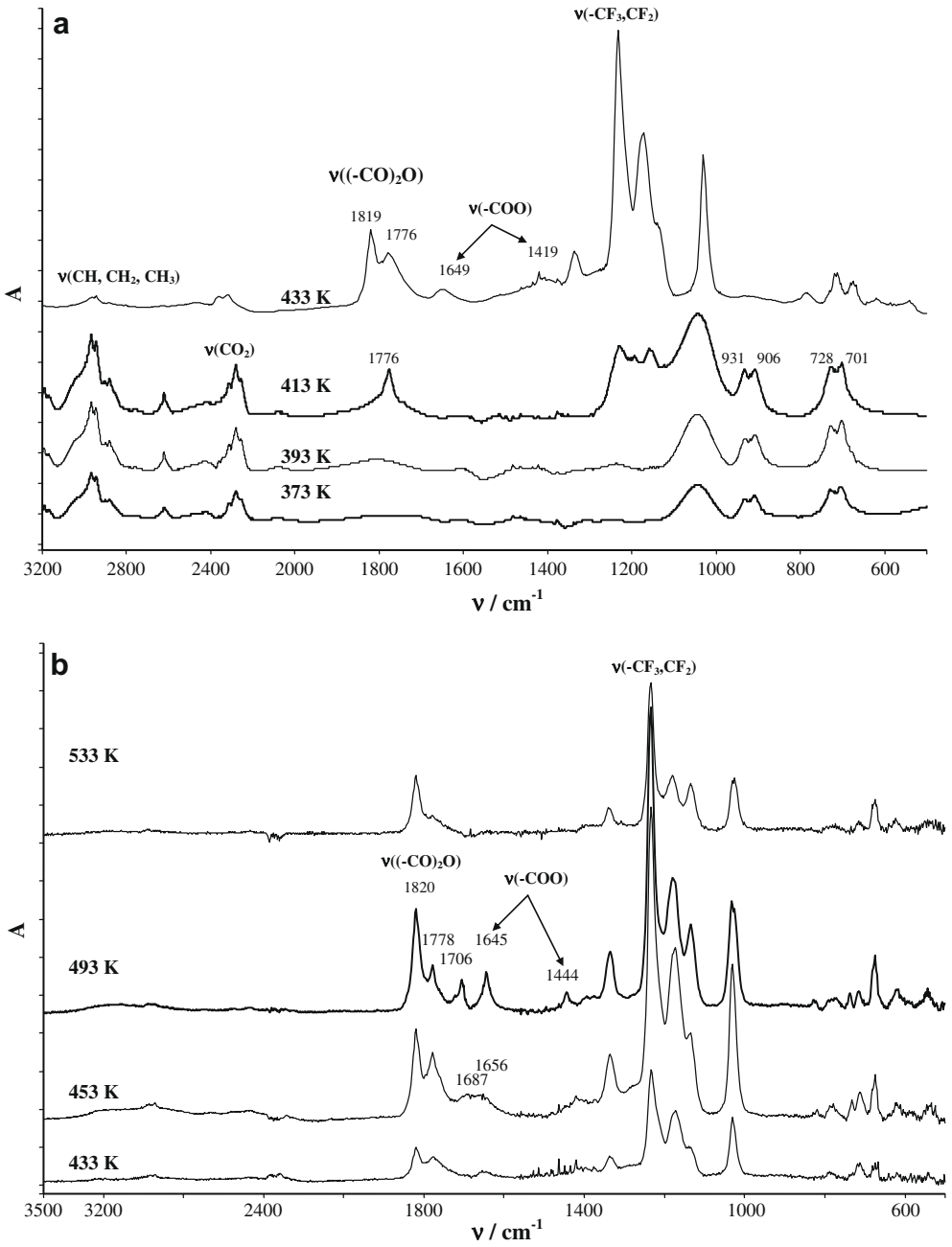


Fig. 4. IR spectra of vapors formed during the thermolysis of **1**: (a) 373–433 K and (b) 433–533 K.

Table 2
Selected IR absorption bands of **1** and **2** (calculated as the second derivative) over 303–523 K (cm^{-1}).

	1			**2**		
	303 K	433 K	523 K	303 K	433 K	523 K
ν_s(COO)	1394		1399	1389		1400
	1415	1411		1415	1411	1407
δ(CH_2,CH_3)	1439	1437		1438	1436	
ν(C=C)	1632	1633		1631		
ν_{as}(COO)	1658	1662	1657	1663	1662	1657
		1678				
	1699	1697	1690	1689	1688	1690
	1713	1715		1708	1720	

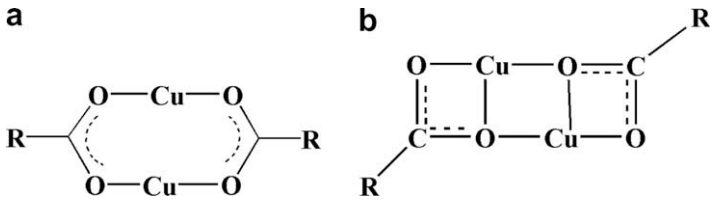


Fig. 5. Postulated structural forms for the dimer $[Cu_2(O_2CR)_2]$: (a) bridging mode and (b) chelating mode with an additional monoatomic bridge.

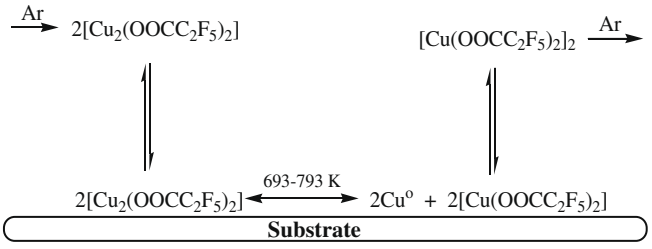


Fig. 6. Proposed mechanism of copper layers formation for precursors **1** and **2**.

pathway, one can conclude that the formation of copper layers is affected by the decomposition of $[Cu_2(O_2CC_2F_5)_2]$ on the substrate surface upon heating (Fig. 6).

The decomposition pathway assumes precursor adsorption on the substrate, followed by disproportionation to Cu^0 and $[Cu(O_2CC_2F_5)_2]_2$, and desorption of the copper(II) derivatives. The proposed mechanism of deposition assumes that in the first step the VTMS, VTES ligands are detached and Cu(I) carboxylate derivatives are formed (Eq. (2)). This is followed by a disproportionation

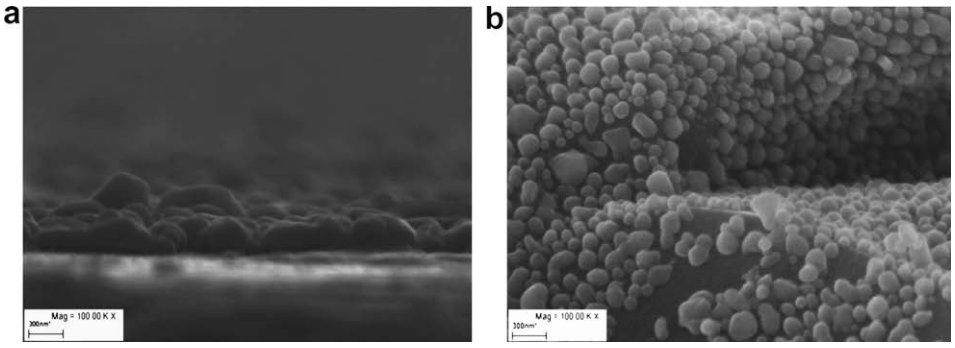


Fig. 7. SEM images of copper films cross section, deposited from **1**, on: (a) flat surface and (b) surface of the shaped composite (T_V = 493 K, T_D = 693 K, p = 100 Pa, Ar, Si(1 1 1), r_D = 2.0 μg min^{-1}).

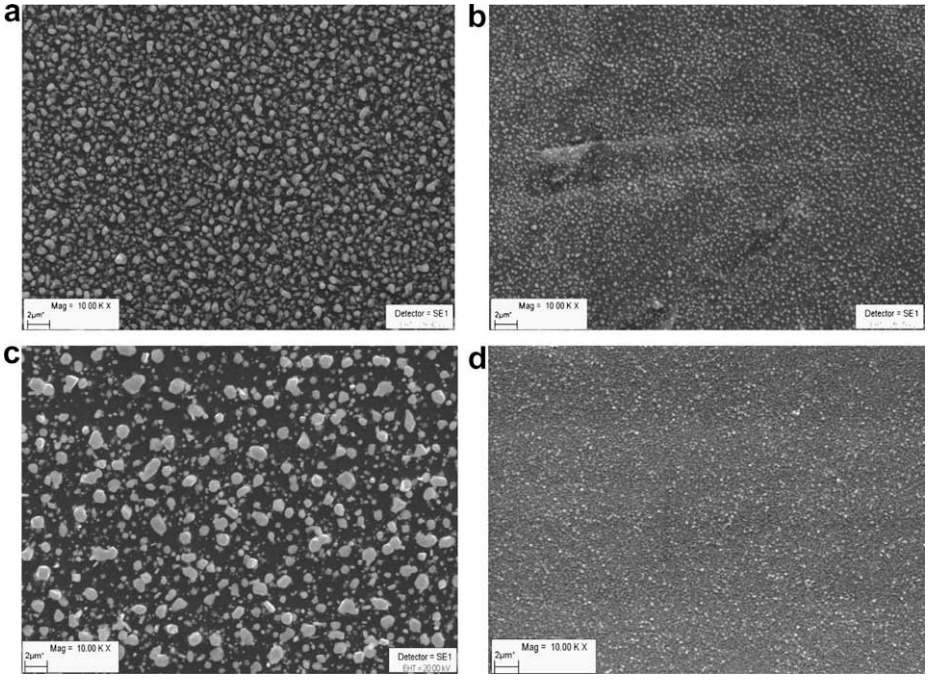


Fig. 8. SEM images of copper films deposited from **1** on different substrates: (a) Si(1 1 1), (b) steel, (c) ITO and (d) quartz (precursor **1**, T_V = 493 K, T_D = 713 K, p = 100 Pa, Ar, t = 60 min).

reaction (Fig. 6), which results in deposition of a metallic copper film.

3.3. CVD of copper layers using **1** and **2** as precursors

Detected in the vapors of **1** and **2** (by MS-EI and VTIR) are volatile and stable metal containing species, which prompted us to use these complexes as precursors for *hot-wall* CVD. According to the proposed decomposition mechanism, copper films were deposited between 693 and 793 K. The SEM images (Fig. 7) demonstrate that Cu monolayers, obtained at 693 K, are composed of loosely packed grains, the diameter of which changes from 50 to 300 nm. The average film thickness, deposited under these conditions, was between 100 and 300 nm.

The morphology studies (SEM) proved that the copper films prepared from the selected precursors uniformly coated not only the flat substrate surfaces (Figs. 7a and 8a), but also the three-dimensional trench-like structure (Fig. 7b). The conformal Cu^0 films growth is important for applications in microelectronic technologies. Variations in the morphology of copper films deposited at 713 K on different substrates are presented at Fig. 8. On smooth surfaces of Si(1 1 1), the metallic film revealed dense compacted grains (diameter 100–800 nm) (Fig. 8a) and XRD patterns demonstrate strong peaks, which correspond to cubic copper [25]. In the case of the steel substrate, uniform layers composed of metallic grains (200–400 nm) were noted (Fig. 8b), whereas for the ITO substrate layers of loosely packed Cu monocrystals (300–2000 nm) were detected (Fig. 8c). Simultaneously amorphic smooth copper films composed of densely packed grains were obtained on the surface of quartz plates (Fig. 8d). This leads to the conclusion that the morphology of the copper layers depends on the properties of the substrate, such as the smoothness and structure of the surface.

XPS studies revealed that the copper films obtained from **1** and **2** are slightly contaminated by carbon (<9%) and oxygen (<5%) [25] and there is a lack of fluorine and silicone impurities. The low content of carbon impurities and the lack of silicone ones can be related to the detachment of the VTMS/VTES ligands below the precursor vaporization temperature (>433 K). However, the possible adsorption of $[Cu_2(O_2CC_2F_5)_2]$ and dissociation of C_2F_5COO species on the substrate surface and their further decomposition can cause inclusion of carbon and oxygen impurities (C, CO) to the copper layers (Fig. 6).

4. Conclusions

The coordination sphere of Cu(I) in compounds $[Cu(L)(\mu\text{-}O_2CR)]_n$ (R = CF_3, C_2F_5; L = VTMS, VTES, VTMOS) consists of dihapto bonded vinylsilanes and bridging carboxylates. The results of MS (MS-EI) suggest that the solid structures of $[Cu(L)(\mu\text{-}O_2CCF_3)]_2$ (L = VTMS, VTES) and $[Cu(VTMOS)(\mu\text{-}O_2CC_2F_5)]_2$ are dimeric, however, in the case of $[Cu(L)(\mu\text{-}O_2CC_2F_5)]_2$ (L = VTMS, VTES,) the structure is more complicated than dimeric, or copper(II) carboxylates are the products of a disproportionation reaction in the source of the spectrometer. Moreover, results of MS (MS-EI) and variable temperature IR studies proved that dimeric carboxylate species are the main source of copper for CVD processes. The thermal decomposition pathway, qualitative and quantitative composition of vapors for **1** and **2** indicate that these complexes are more promising CVD precursors than **3** and **4**. Therefore, only **1** and **2** have been applied as precursors in CVD experiments and the obtained copper layer confirmed their usefulness at a deposition temperature above 573 K. The formation of copper layers is affected by the decomposition of $[Cu_2(O_2CC_2F_5)_2]$ on the heated substrate. The decomposition pathway is based on the adsorption of the precursor on the substrate material and disproportionation to Cu^0 and $[Cu(O_2CC_2F_5)_2]_2$, followed by desorption of the Cu(II) compound.

The presented results of VT IR and MS studies suggest the usefulness of the proposed methodology for CVD precursor selection and allowed a preliminary determination of CVD experimental parameters.

Acknowledgement

The authors wish to acknowledge MNiSzW for financial support Grant No. PBZ-KBN-118/T09/11.

Appendix A. Supplementary data

Supplementary data associated with this article can be found, in the online version, at doi:10.1016/j.poly.2008.12.052.

References

[1] T.T. Kodas, M.J. Hampden-Smith, in: The Chemistry of Metal CVD, VCH, Weinheim 1994, pp. 20–30, 175, 239, 242.
[2] M. Hoshino, K. Kasai, J. Komeno, Jpn. J. Appl. Phys. 31 (1992) 4403.
[3] S.P. Murarka, Mater. Sci. Eng. 19 (1997) 76.
[4] A. Grodzicki, I. Łakomska, P. Piszczek, I. Szymańska, E. Szłyk, Coord. Chem. Rev. 249 (2005) 2232.
[5] R. Kalyanaraman, S. Oktyabrsky, J. Narayan, J. Appl. Phys. 85 (1999) 6636.
[6] P. Doppelt, Coord. Chem. Rev. 178–180 (1998) 1785.
[7] J.A.T. Norman, B.A. Muratore, P.N. Dyer, D.A. Roberts, A.K. Hochberg, L.H. Dubois, Mater. Sci. Eng. B 17 (1993) 87.
[8] M.J. Hampden-Smith, T.T. Kodas, M.F. Paffett, J.D. Farr, H.K. Shin, Chem. Mater. 2 (1990) 636.
[9] C.G. Dupy, D.B. Beach, Jr. J.E. Hurst, J.M. Jasinski, Chem. Mater. 1 (1989) 16.
[10] D. Blessmann, A. Grafe, R. Heinen, F. Jansen, Th. Kruck, C. Terfloth, Mater. Sci. Eng. B 17 (1993) 104.
[11] H.K. Shin, K.M. Chi, M.J. Hampden-Smith, T.T. Kodas, J.D. Farr, M.F. Paffett, Chem. Mater. 4 (1992) 788.
[12] M.J. Hampden-Smith, T.T. Kodas, Chem. Vapor. Depos. 1 (1995) 8.
[13] K.-M. Chi, Y.-H. Lu, Chem. Vapor. Depos. 7 (2001) 117.
[14] L.H. Maarten, M.L.H. ter Heerdt, P.J. van der Put, J. Schoonaman, Chem. Vapor. Depos. 7 (2001) 199.
[15] L.-S. Hong, M.-G. Jeng, Appl. Surf. Sci. 161 (2000) 149.
[16] V.V. Krisuik, A.E. Turgambaeva, S.W. Rhee, Polyhedron 23 (2004) 809.
[17] J.A.T. Norman, B.A. Muratore, P.N. Dyer, D.A. Roberts, A.K. Hochberg, J. Phys. IV 1 (1991) C2–271.
[18] M.L.H. ter Heerdt, J.J. Overdijk, P.J. van der Put, J. Schoonman, Chem. Mater. 11 (1999) 3470.
[19] A. Jain, T.T. Kodas, R. Jairath, M.J. Hampden-Smith, J. Vac. Sci. Technol. 11 (1993) 2107.
[20] Apel. Friese, A. Abdul-Hak, B. Schwierzi, U. Höhne, Microelectron. Eng. 37/38 (1997) 157.
[21] E. Szłyk, I. Szymańska, Polyhedron 18 (1999) 2941.
[22] P. Piszczek, A. Grodzicki, M. Richert, A. Radtke, Mater. Sci.-Poland 23 (2005) 663.
[23] E. Szłyk, P. Piszczek, I. Łakomska, A. Grodzicki, J. Szatkowski, T. Błaszczyk, Chem. Vapor. Depos. 6 (2000) 105.
[24] I.B. Szymańska, P. Piszczek, W. Bała, K. Bartkiewicz, E. Szłyk, Surf. Coat. Technol. 201 (2007) 9015.
[25] P. Piszczek, I. Szymańska, W. Bała, K. Bartkiewicz, E. Talik, J. Heiman, Thin Solid Films 516 (2008) 3924.
[26] E. Szłyk, R. Kucharek, I. Szymańska, J. Coord. Chem. 53 (2001) 55.
[27] E. Szłyk, R. Kucharek, I. Szymańska, Pol. J. Chem. 75 (2001) 337.
[28] E. Szłyk, R. Kucharek, I. Szymańska, L. Pazderski, Polyhedron 22 (2003) 3389.
[29] I. Szymańska, L. Pazderski, R. Kucharek, E. Szłyk, Pol. J. Chem. 79 (2005) 1705.
[30] E. Szłyk, R. Kucharek, I. Szymańska, Mater. Sci.-Poland 21 (2003) 245.
[31] K. Nakamoto, in: Infrared and Raman Spectra of Inorganic and Coordination Compounds, part B, John Wiley and Sons, New York, 1997, pp. 59–62, 276–282.
[32] Powder Diffraction File, Sets 4-836, Joint Committee on Diffraction Standards, 1977.
[33] I.B. Szymańska, Ann. Pol. Chem. Soc. (2007) 585.
[34] D.C.K. Lin, J.B. Westmore, Can. J. Chem. 51 (1973) 2999.
[35] T. Ogura, Q. Fernando, Inorg. Chem. 12 (1973) 2611.

The product was filtered by aspiration and was washed thrice, alternating methanol and acetone. Water was also used as a wash only if preliminary XRD analysis indicated a water-soluble phase. The product was dried for at least 20 min by aspiration and placed in a 120 °C oven overnight. Cadmium containing compounds were dried in a Drierite-filled desiccator.

2.2. Analysis

Constituent ions were analyzed qualitatively by first dissolving the compound in 3 M nitric acid. Phosphate was identified qualitatively using 0.5 M ammonium molybdate reagent. Chloride, bromide, and iodide were identified qualitatively with 0.1 M silver nitrate. The cations were identified qualitatively by standard methods.

The identities of the products were determined by XRD using a Philips 3520 XRD system with a monochrometer and a copper X-ray tube. Phase identity was established using figure of merit (FOM) values as well as careful visual matching of peaks with those in the International Center for Diffraction Data (ICDD) PDF-2 Sets 1–44 Inorganics (includes zeolites and minerals) (1994) database. The presence of fluoride was confirmed by dissolving the sample in 3 M HNO_3, followed by a search for an ^{19}F resonance on a Varian INOVA 500 MHz NMR spectrometer at 470.12 MHz.

3. Results and discussion

3.1. Nonaqueous syntheses

Apatites of barium, calcium, cadmium, lead, and strontium were successfully prepared by the reaction routes shown below, where M and X are the cation and anion incorporated into $M_5(PO_4)_3X$ (MApX):

(A) $5MX_2 + 3Na_3PO_4 \rightarrow M_5(PO_4)_3X + 9NaX$
(B) $5MX_2 + 3Na_3PO_4 \cdot 12H_2O \rightarrow M_5(PO_4)_3X + 9NaX + 12H_2O$
(C) $5MX_2 + 3K_3PO_4 \rightarrow M_5(PO_4)_3X + 9KX$
(D) $5MX_2 + 3(NH_4)_2HPO_4 \rightarrow M_5(PO_4)_3X + 6NH_4X$
(E) $5M(NO_3)_2 + 3Na_3PO_4 + NaX \rightarrow M_5(PO_4)_3X + 10NaNO_3$
(F) $5M(NO_3)_2 + 3Na_3PO_4 + NH_4X \rightarrow M_5(PO_4)_3X + 9NaNO_3 + NH_4NO_3$
(G) $5MX_2 + 3(CH_3O)_3PO \rightarrow M_5(PO_4)_3X + 9CH_3X.$

The solvents differed depending on M and X and no single route was found to be superior for the preparation of all apatite products. In addition, product formation could not be predicted solely from the solubility of the starting materials. Most reactions were run at 80–120 °C for at least 1 day to increase the dissolution of the starting materials and the yield of product. Yields ranged from 50% to 70% with no apparent relationship to route or solvent. As evidenced in a PbApCl synthesis in DMSO, increased temperature seemed to improve the purity as indicated by a decrease in the XRD figure of merit values. In many cases, the powder diffraction pattern contained sharper lines than are routinely obtained using aqueous methods. The routes and conditions for successful preparations are summarized in Table 1. The xrd line patterns for PbApF, prepared using TMP in DMSO, and for BaApCl, prepared in anisole, are shown in Figs. 1 and 2.

3.2. Barium apatites

The syntheses of barium apatites in DMSO generally require the absence of sodium ion because of preferential formation of $NaBaPO_4$. For example, attempted preparation of BaApF in anisole and 18-crown-6 using route B produced a precipitate identified as $NaBaPO_4$. The insolubility of BaF_2 in all solvents probably contributed to the difficulty in obtaining the apatite.

Barium chloroapatite was obtained in anisole using routes B and C, and in anisole with 18-crown-6 by routes B and C.

The attempted preparation of BaApCl in DMSO, routes A, B, C, and D yielded Na_3PO_4, $NaBaPO_4$, an amorphous product, and $BaHPO_4$, respectively. In phenol, route C produced $BaHPO_4$. The formation of barium hydrogen phosphate may be due to the protic nature of phenol and ammonium hydrogen phosphate. Barium bromoapatite was not prepared successfully in anisole with 18-crown-6 using routes B and C which yielded barium phosphate. The preparation of barium hydroxyapatite was unsuccessful in anisole with 18-crown-6 by route B and in pyridine by route D.

3.3. Cadmium apatites

Cadmium fluoroapatite was obtained using route F in anisole with 2 mL of glacial acetic acid presumably because cadmium nitrate tetrahydrate and sodium phosphate were soluble in anisole and ammonium fluoride was moderately soluble in glacial acetic acid. It was identified by ^{19}F NMR and XRD. Cadmium chloroapatite was successfully prepared by route A in a 1:1 anisole and ethanol mixture. The purity of the product improved with repeated washings with distilled water due primarily to the removal of the NaCl byproduct. The reactions were done in mixed solvents because sodium phosphate showed the highest solubility in anisole while cadmium chloride was most soluble in DMSO or ethanol.

The synthesis of cadmium fluoroapatite was attempted in DMSO using route A, but resulted in CdF_2. Attempts to prepare CdApCl using route B in anisole with 18-crown-6 ether produced a mixture of NaCl and Na_3PO_4. An attempt using route A in DMSO produced sodium phosphate. Although $CdBr_2$ is soluble in DMSO, CdApBr could not be obtained by route A in a 1:1 DMSO and anisole mixture (sodium phosphate was obtained). An attempt at cadmium hydroxyapatite by route E in anisole produced sodium nitrate and $Cd(OH)NO_3$.

3.4. Calcium apatites

Calcium fluoroapatite was obtained using route F with anisole and 2 mL glacial acetic acid). Although the XRD of the product indicated a mixture of CaF_2 and either the fluoro or hydroxy apatite (the patterns for the hydroxy- and fluoroapatites are very similar), the acidic reaction mixture confirms the presence of the fluoroapatite. Calcium hydroxyapatite was produced with route E in anisole. Route E, using NaOH, was preferred to the use of calcium hydroxide for solubility reasons.

Attempts to prepare CaApF using route B in ethanol and route A in a 1:1 DMSO and anisole mixture resulted in calcium fluoride. Calcium chloroapatite could not be obtained using route A or B in ethanol, route A in 1:1 ethanol and anisole mixture, route A in 1:1 ethanol–anisole containing 15-crown-5 ether, and when a solution of calcium chloride in ethanol was titrated into anisole with sodium phosphate. In DMSO, route A resulted in sodium phosphate, route B produced sodium phosphate and sodium chloride, route D produced NH_4HPO_4, route A with 2:1 anisole and DMSO mixture and 18-crown-6 ether resulted in sodium phosphate. Route A with methanol and 15-crown-5 ether was attempted because of the solubility of starting materials in this mixture, but resulted in Na_2HPO_4. Attempts to prepare CaApOH using route B in anisole with 18-crown-6 ether and in ethanol produced calcium hydroxide, as did route A in TMP and DMSO.

Table 1
Summary of solvents and conditions for successful preparations of apatites.

Compound	Route	Solvent(s)	Reaction time (days)	Temperature (°C)
BaApCl	B	anisole	1	110
	C	anisole	1	123
	A	anisole + 18-crown-6	6	125
	B	anisole + 18-crown-6	2	125
	C	anisole + 18-crown-6	2	110
CaApF	F	anisole + glacial acetic acid	2	115
CaApOH	E	anisole	2	130
CdApF	F	anisole + glacial acetic acid	3	120
CdApCl	A	anisole + EtOH	2	81
PbApBr	D	DMSO	4	21
PbApCl	C	anisole + 18-crown-6	4	125
	D	DMSO	1	115
	C	phenol	4	110
	G	DMSO	2	150
PbApF	D	DMSO	2	114
	G	DMSO	4	150
PbApOH	D	pyridine	3	85
SrApCl	G	DMSO	3	130
SrApOH	A	anisole + 18-crown-6	4	115

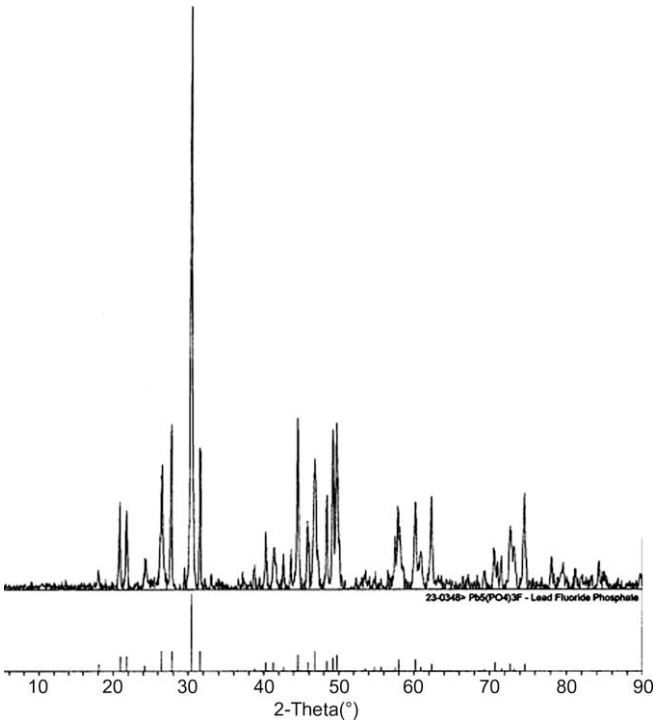


Fig. 1. The XRD line pattern, and its database comparison, for PbApF synthesized with TMP in DMSO.

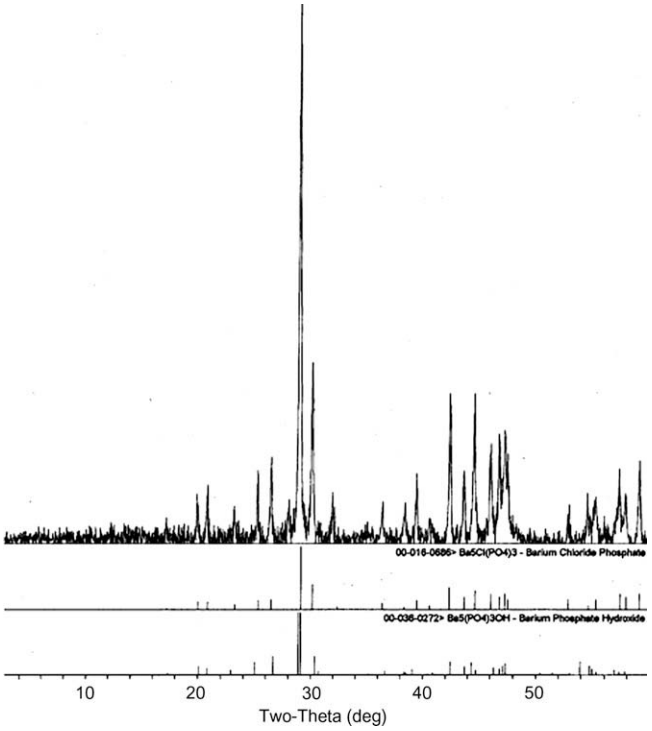


Fig. 2. The XRD line pattern, along with the database comparison, for BaApCl, prepared in anisole.

3.5. Lead apatites

In most of the solvents used, the formation of sodium lead phosphate double salts $NaPb_4(PO_4)_3$ or $NaPbPO_4$ were obtained as the main product. The presence of potassium ion (route C) resulted in the formation of $KPb_4(PO_4)_3$ in DMSO and the apatite in anisole with 18-crown-6 ether as well as in phenol. Most successful lead apatite syntheses utilized route D.

Lead fluoroapatite was successfully prepared by route D in DMSO. It was identified by both XRD and ^{19}F NMR spectroscopy. Lead chloroapatite was obtained with route C in anisole with 18-crown-6 for 4 days (heating for 2 days produced lead chloride) and in phenol. It was also successfully prepared by route D in DMSO at room temperature or with heating. The purity of the product increased with heating as indicated by XRD figure of merit values. Lead bromoapatite was obtained with route D in DMSO at room temperature. The preparation of lead hydroxyapatite was successful using route D in pyridine (chosen because of the solubility of lead hydroxide and NH_4HPO_4 and its basicity), as well as with a 1:1 mixture of pyridine and DMSO.

Attempts to prepare PbApF using route B in anisole with 18-crown-6 ether produced $NaPb_4(PO_4)_3$. The chloroapatite could not be obtained with anisole and DMSO; all attempts using route B in DMSO or anisole with 18-crown-6 gave $NaPb_4(PO_4)_3$. Due to its insolubility only the starting lead chloride was isolated in route A in anisole with 18-crown-6 ether. Attempts to prepare PbApOH using route E with 1:1 anisole and DMSO resulted in $NaPb_4(PO_4)_3$.

Table 2
Comparison of aqueous and nonaqueous syntheses [1,2][a].

Compound	Synthesis in aqueous solution	Synthesis in nonaqueous solvent
BaApBr	no	no
BaApCl	yes	yes
BaApF	yes	no
BaApOH	yes	no
CaApBr	no	no
CaApCl	no	no
CaApF	yes	yes
CaApOH	yes	yes
CdApBr	no	no
CdApCl	yes	yes
CdApF	yes	yes
CdApOH	yes	no
PbApBr	yes	yes
PbApCl	yes	yes
PbApF	yes	yes
PbApOH	yes	yes
SrApBr	no	no
SrApCl	yes	yes
SrApF	yes	no
SrApOH	yes	yes

[a] Including syntheses with TMP.

3.6. Strontium apatites

Even under anhydrous conditions, strontium hydroxyl apatite forms preferentially to all other strontium apatites: SrApOH was formed in routes B and C in anisole with 18-crown-6 ether in syntheses for hydroxy-, chloro-, and bromoapatites.

Syntheses of SrApF were attempted by route D in DMSO, but only the starting material SrF_2 was isolated. Attempts to prepare SrApF produced the hydroxyapatite. Sodium phosphate was formed when preparations were attempted in DMSO by routes A and B and in anisole by route A.

3.7. Trimethylphosphate as a phosphate source and solvent

Trimethylphosphate (TMP) was used as a phosphate source in the reaction with the following metal salts: $BaCl_2$, BaF_2, $SrCl_2$, SrF_2, $SrBr_2$, $CaCl_2$, $Ca(OH)_2$, CaF_2, $CdCl_2$, $PbCl_2$, $Pb(OH)_2$, and PbF_2. Lead fluoroapatite, lead chloroapatite, and strontium chloroapatite were formed with TMP in DMSO.

4. Conclusions

Of the 20 apatites listed in Table 2, 15 have been prepared in aqueous solution and 10 have now been prepared in nonaqueous solvents. In general, the solubilities of the starting materials in the solvents studied were very limited and the reactions required heating from 1 to 6 days. Because some hydrated salts are more soluble in these solvents, the hydrates were utilized in some reactions. The formation of hydrogen phosphates of the divalent cation, which hinders formation of CaApCl, CaApBr, and PbApOH in aqueous solution [1], was alleviated in routes A through F. The formation of nonapatitic double salts, such as $NaPb_4(PO_4)_3$, $NaPbPO_4$, $KPb_4(PO_4)_3$, $Cd(OH)NO_3$, and $NaBaPO_4$ occurred with some regularity due to the limited solubility of these salts in the solvents used. Although the use of the crown ether did improve the solubility of some salts, it was not helpful in all solvents. It was used with anisole because of its effect on the solubility of the hydrated sodium phosphate and barium salts, and with methanol to dissolve anhydrous sodium phosphate and calcium chloride.

Understandably, there was no single route or solvent that could be employed for all preparations. Moreover, the solubilities of the starting materials was not always an indication of the success of the synthesis. It was often the case that the complete dissolution of the simple salts was not necessary. For example, the starting materials in the preparation of CdApCl using route A in EtOH and anisole formed a white slurry but the reaction successfully produced the chloroapatite. However, anisole was used more frequently than the other solvents in the successful preparations (Table 1).

The reaction of metal salts with trimethyl phosphate was of interest because of the easy formation of the lead apatites in the reaction:

$$3(CH_3)_3PO_4 + 5PbX_2 \rightarrow Pb_5(PO_4)_3X + 9CH_3X.$$

This method produced PbApCl, PbApF, and SrApCl in TMP/DMSO mixtures. However, numerous attempts to prepare other apatites, including BaApF, BaApCl, CaApCl, CaApBr, SrApF, and SrApBr, using this method were unsuccessful. The reaction as written above for the formation of PbApCl, for example, is thermodynamically favorable and is easily accomplished with due caution for the toxicity of TMP. Reaction with TMP produces SrApCl, which could not be obtained using inorganic phosphates in nonaqueous solvents.

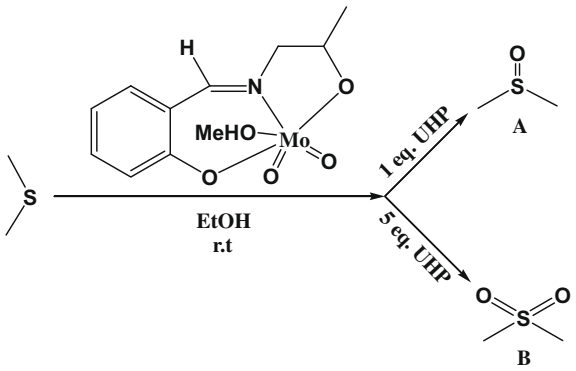
A combination of nonaqueous and TMP methods, therefore, can be used to prepare most apatites that have previously been prepared in aqueous solution. The nonaqueous conditions also produce double salts that may be of interest for other reasons. These include $NaPb_4(PO_4)_3$, $NaPbPO_4$, $KPb_4(PO_4)_3$, $Cd(OH)NO_3$, and $NaBaPO_4$.

Acknowledgments

The authors are indebted to Franklin and Marshall College, Elizabethtown College, and the Petroleum Research Fund, administered by the American Chemical Society for support of their work.

References

[1] Y.M. Pan, M.E. Fleet, in: M.J. Kohn, J. Rakovan, J.M. Hughes (Eds.), Phosphates: Geochemical, Geobiological, and Materials Importance, Mineralogical Society of America, Chantilly, VA, 2002, pp. 13–49.
[2] N.J. Flora, K.W. Hamilton, R.W. Schaeffer, C.H. Yoder, Synth. React. Inorg. Met-Org. Chem. 34 (2004) 503.
[3] A. Yasukawa, H. Yakase, K. Kandori, T. Ishikawa, Polyhedron 13 (1994) 3071.
[4] A. Yasukawa, T. Matsuura, M. Nakajima, K. Kandori, T. Ishikawa, Mater. Res. Bull. 34 (1999) 589.
[5] H. Tanaka, A. Yasukawa, K. Kandori, T. Ishikawa, Langmuir 13 (1997) 821.
[6] K. Kandori, A. Fujiwara, A. Yasukawa, t. Ishikawa, Colloid Surface A 150 (1999) 161.
[7] T. Ishikawa, H. Tanaka, A. Yasukawa, K.J. Kandori, Mater. Chem. 5 (1995) 1963.
[8] A. Yasukawa, T. Yokoyama, T. Ishikawa, Mater. Res. Bull. 36 (2001) 775.
[9] A. Yasukawa, T. Kunimoto, K. Kamiuchi, K. Kandori, T.J. Ishikawa, Mater. Chem. 9 (1999) 1825.



Scheme 1.

accomplished by GC on a Shimadzu GC-16A instrument using a 25 m CBP1-S25 (0.32 mm ID, 0.5 μm coating) capillary column. IR spectra were recorded on a Perkin–Elmer 780 instrument. UV–Vis spectra were recorded on a 160 Shimadzu spectrophotometer. NMR spectra were recorded on a Brucker Avance DPX 300 and 500 MHz instrument. Mass spectra were recorded on a Shimadzu GC–MS-QP5050A.

2.3. General oxidation procedure

To a solution of sulfides (1 mmol), $[MoO_2(L)(CH_3OH)]$ (0.05 mmol) in 5 ml ethanol was added urea hydrogen peroxide (1 mmol for sulfoxide formation and 5 mmol for sulfones formation) and the reaction mixture was stirred under air at room temperature for required time. The reaction progress was monitored by TLC and the yield of products was determined by GC analysis.

Table 1
Crystal data and structure refinement for $[MoO_2(L)(CH_3OH)]$ complex.

Entry	Compound	$[MoO_2(L)(CH_3OH)]$
1	empirical formula	$C_{11}H_{15}MoNO_5$
2	formula weight	337.18
3	temperature (K)	100(2)
4	wavelength (Å)	0.71073
5	crystal system	monoclinic
6	space group	$P2_1/c$
7	unit cell dimensions	
	a (Å)	10.3301(17)
	b (Å)	9.3971(15)
	c (Å)	13.695(2)
	α (°)	90
	β (°)	109.643(3)
	γ (°)	90
8	V (Å^3)	1252.1(3)
9	Z	4
10	D_{calc} (Mg/m^3)	1.789
11	absorption coefficient (mm^{-1})	1.060
12	$F(000)$	680
13	crystal size (mm^3)	0.5 × 0.4 × 0.2
14	θ range for data collection	2.68–30.04°
15	index ranges	$-14 \leqslant h \leqslant 14$ $-13 \leqslant k \leqslant 13$ $-19 \leqslant l \leqslant 19$
16	reflections collected	13329
17	independent reflections [R_{int}]	3627 [0.0306]
18	completeness to θ = 30.04° (%)	98.8
19	absorption correction	semi-empirical from equivalents
20	max. and min. transmission	0.811 and 0.610
21	refinement method	full-matrix least-squares on F_2
22	data/restraints/parameters	3627/0/165
23	goodness-of-fit on F^2	1.013
24	final R indices [$I > 2\sigma(I)$]	R_1 = 0.0226, wR_2 = 0.0632
25	R indices (all data)	R_1 = 0.0242, wR_2 = 0.0642
26	largest difference in peak and hole	0.815 and −0.954 (e Å^{-3})

Higher purification of products was achieved by chromatography over silica gel (Eluent: n-hexane/ethyl acetate 70:30 for solfoxides isolation and 90:10 for sulfones isolation). Assignments of products were made by comparison with authentic samples or were identified by their IR, ^{1}H NMR, and MS spectral data.

2.4. X-ray crystallography

The yellow single crystals of complex $[MoO_2(L)(CH_3OH)]$ obtained by slow evaporation of solvent from acetonitrile solution of $[MoO_2(L)CH_3OH)]$ at room temperature. All the measurements were performed using graphite-monochromatized Mo Kα radiation at 100 K: $C_{11}H_{15}MoNO_5$, M_r 337.18, monoclinic, space group $P2_1/c$, a = 10.3301(17) Å, b = 9.3971(15) Å, c = 13.695(2) Å, V = 1252.1(3) Å^3, Z = 4, D_{calc} = 1.789 g cm^{-3}, μ = 1.060 mm^{-1}. A total of 13329 reflections were collected (θ_{max} = 30.04°), from which 680 were unique (R_{int} = 0.0226), with 1605 having $I > 2\sigma(I)$. The structure was solved by direct methods (SHELXS-97) [25] and refined by full-matrix least-squares techniques against F^2 (SHELXL-97) [26]. Final R indices of R_1 = 0.0226 and wR_2 = 0.0632 (Goodness-of-fit = 1.013) were obtained. The data collection and refinement processes are summarized in Table 1. Fig. 1 shows the stereoscopic ORTEP [27] plot of $[MoO_2(L)(CH_3OH)]$ complex at 50% probability level with atomic numbering along with selected bond lengths (Å) and angles (°). The stereo view of the unit cell of $[MoO_2(L)(CH_3OH)]$ compound and showing the atomic numbering scheme is shown in Fig. 2.

3. Results and discussion

3.1. Structural discussion of $[MoO_2(L)(CH_3OH)]$

Dioxo-molybdenum complex $[MoO_2(L)(CH_3OH)]$ was prepared by the reaction of 2-[(2-hydroxypropylimino)methyl]phenol and dioxo-molybdenum(VI) acetylacetonate which was characterized

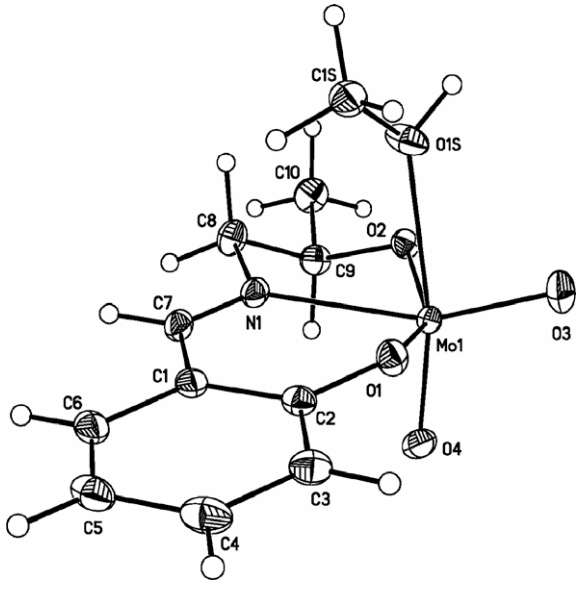


Fig. 1. ORTEP of complex $[MoO_2(L)(CH_3OH)]$ at 50% probability level with atomic numbering. Selected bond lengths (Å) and angles (°): Mo(1)–O(4) 1.7038(12), Mo(1)–O(3) 1.7094(11), Mo(1)–O(2) 1.9529(10), Mo(1)–O(1) 1.9603(11), Mo(1)–N(1) 2.2747(12), Mo(1)–O(1S) 2.3556(12), N(1)–C(7) 1.283(2), N(1)–C(8) 1.4679(19), O(1)–C(2) 1.3426(18), O(4)–Mo(1)–O(3) 107.05(6), O(4)–Mo(1)–O(2) 98.01(5), O(3)–Mo(1)–O(2) 97.34(5), O(4)–Mo(1)–O(1) 97.80(5), O(3)–Mo(1)–O(1) 101.00(5), O(2)–Mo(1)–O(1) 151.04(4), O(4)–Mo(1)–N(1) 93.07(5), O(4)–Mo(1)–N(1)–C(7) 79.85(13), O(3)–Mo(1)–N(1)–C(7)–112.65(17), O(2)–Mo(1)–N(1)–C(7) 177.32(13), O(1)–Mo(1)–N(1)–C(7)–17.54(12), O(1S)–Mo(1)–N(1)–C(7) 99.98(13).

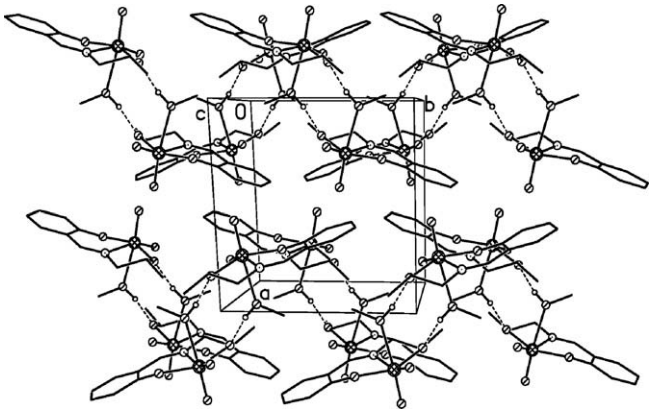


Fig. 2. The unit cell of $[MoO_2(L)(CH_3OH)]$ (Fragment of crystal packing along *c* crystal axes. Hydrogen atoms that do not take part in hydrogen bonding are not depicted for clarity. H-bonds are shown with dashed lines).

by elemental analysis, IR, NMR, and UV–Vis spectral data. The Schiff base ligand is bonded to the MoO_2^{+2} ion through two phenolic oxygen atoms and an imine nitrogen atom, which is trans to an oxo group. The IR spectra of $[MoO_2(L)(CH_3OH)]$ in KBr matrix confirm the presence of imine bond (C=N) mode at 1638 cm^{-1} and the C=C vibration band of the aromatic ring at 1584 cm^{-1} and the Mo–O vibration band at 900 and 924 cm^{-1}. All crystal data for $[MoO_2(L)(CH_3OH)]$ complex is shown in Table 1, and the relevant bond distances and angles collected in Fig. 1. The O=Mo=O angle is 107.05° and Mo=O distances are 1.7038 and 1.7094 Å.

3.2. The catalytic activity of $[MoO_2(L)(CH_3OH)]$ in the oxidation of sulfides using UHP

The oxidation of thioanisole using UHP which did not proceed in the absence of catalyst under mild conditions was used as a model reaction. To find optimum reaction conditions, the influence of different factors affecting the conversion and selectivity of the oxidation reaction such as catalyst concentration, solvent nature and the molar ratio of UHP/sulfide, were investigated in this study. Performing the oxidation reaction of thioanisole in the presence of 1 mol% of molybdenum catalyst and equimolar ratio of UHP and sulfide in methanol improved markedly the conversion of substrate (67%), however, the same yields of the related sulfoxide and sulfone were obtained (Table 2, entry 2). It was observed that the highest yield and selectivity to sulfoxide were achieved in the presence of 5 mol% of the catalyst within 30 min. Also an increase in the catalyst/sulfide molar ratio up to 10 mol% does not affect the reaction rate and yield of sulfoxide product in this catalytic system (Table 2).

The influence of solvent nature on the selectivity and reaction rate in this reaction system was also studied. From the examination of five reaction solvents such as dichloromethane, acetone, acetonitrile, methanol and ethanol in this catalytic reaction, it was observed that two protic solvents, methanol and especially ethanol, significantly enhanced the yield and the selectivity of sulfoxide product (Fig. 3). The eco-friendly property of ethanol strongly induced us to employ it as the reaction solvent in this oxidation system. In this green solvent we obtained 92% yield of sulfoxide without any overoxidation to sulfone. It should be mention that the use of dried ethanol as the reaction media decreases the selectivity of sulfoxide (90%) and no affect on the conversion rate was observed.

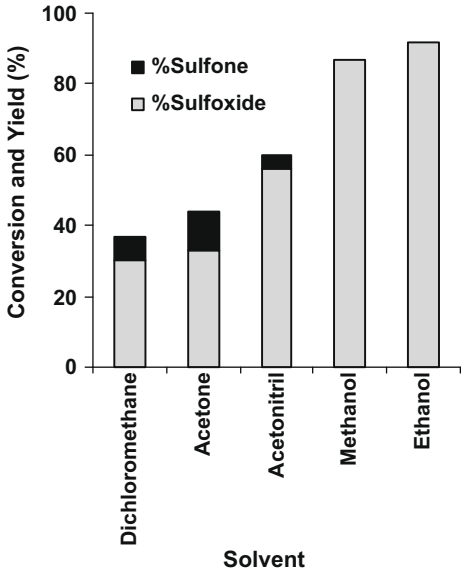


Fig. 3. The solvent effect on the conversion rate and selectivity of thioanisole oxidation using UHP catalyzed by $[MoO_2(L)(CH_3OH)]$.

To improve the conversion rate and yield of sulfoxide, the various molar ratios of UHP/sulfide in the catalytic oxidation of thioanisole were performed in ethanol (Fig. 4). As outlined in Fig. 4 while, the conversion of thioanisole oxidation improved from 92% to 100% as the molar ratio increase from 1 to 1.5, the selectivity of sulfoxide dropped remarkably from 100% to 70%. Thus, the reaction gave optimal yields and selectivities of sulfoxide at an equimolar ratio of UHP/sulfide. Moreover, according to Fig. 4 the employment of an excess amount of UHP (up to five equivalents) promoted considerably the overoxidation of sulfoxide in the reaction and sulfone was achieved in excellent yield and selectivity (98% for oxidation of thioanisole after 30 min). Thus, the method worked well for oxidation of sulfide to both sulfoxide and sulfone selectively.

Table 2
The influence of Mo-catalyst concentration on the oxidation of thioanisole using UHP in methanol.[a]

Entry	mol% catalyst	Conversion (%)	Sulfoxide yield (%)[b]	Selectivity (%)
1	0	0	0	0
2	1	67	34	50
3	3	72	63	87
4	5	87	87	100
5	7	88	88	100
6	10	85	85	100

[a] The reactions were run for 30 min under air at rt in methanol and the molar ratio of thioanisole/UHP was 1:1.
[b] GC yields based on the starting sulfide.

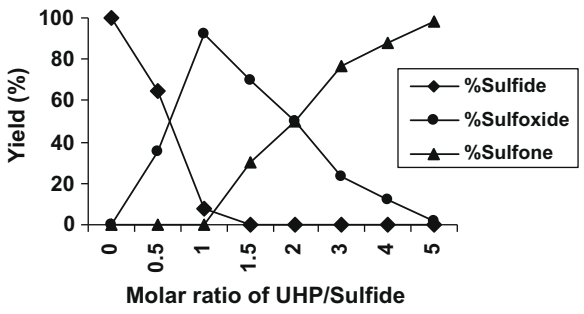
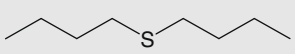
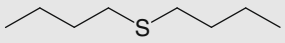
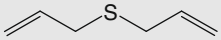
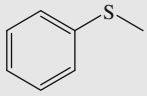
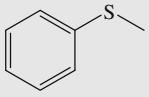
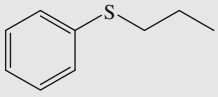
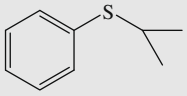
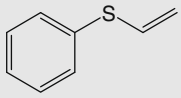
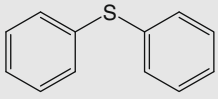
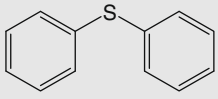
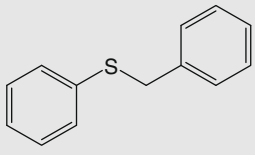
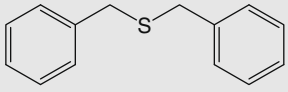


Fig. 4. Reaction profile for the oxidation of thioanisole using various molar ratios of UHP/sulfide.

Table 3
Oxidation of various sulfides by UHP catalyzed by $[MoO_2(L)(CH_3OH)]$ in ethanol.[a]

Entry	Sulfide	UHP/sulfide	Conversion (%)[b]	Selectivity (%)[b,c]	
				Sulfoxide	Sulfone
1		1	100	100	0
2		5	100	0	100
3		1	100	100	0
4		1	92	100	0
5		5	100	2	98
6		1	90	97	3
7		1	87	>98	<2
8		1	93	>99	<1
9		1	75	93	7
10		5	95	<3	>97
11		1	95	>98	<2
12		1	93	100	0

[a] The reactions were run under air at room temperature and in the present of 5 mol% of $[MoO_2(L)(CH_3OH)]$.
[b] The conversion and yield % were measured by GC based on the starting sulfides after 10 min for entries 1 and 3, and 30 min for others.
[c] All products were identified by their IR, ^1H NMR, and MS spectral data in comparison with literature [29,30].

The influence of axial nitrogenous bases having dramatic effects on the rate and selectivity in the oxidation reaction catalyzed by various transition metal complexes such as porphyrin and salen catalysts [28] has also been studied. In the present oxidation meth-

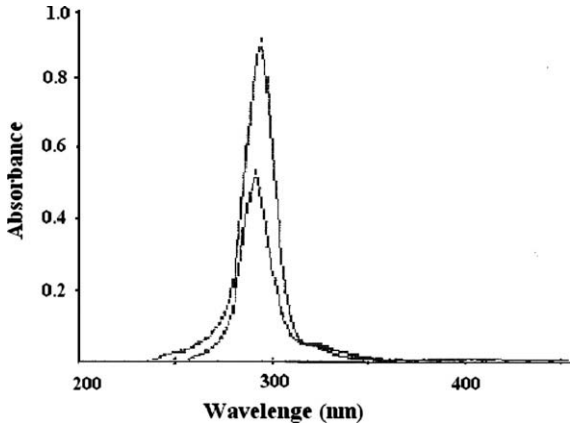


Fig. 5. UV–Vis spectral changes of $[MoO_2(L)(CH_3OH)]$ complex (λ_{max} = 290 nm) during the oxidation of diphenyl sulfide (30 min) using UHP in ethanol.

od, however, the same yields and selectivity were obtained for thioanisole oxidation in the presence or in the absence of various nitrogen donors such as imidazole and pyridine.

Encouraged by the excellent catalytic performance for the thioanisole oxidation to sulfoxide, different sulfides were subjected to the reaction system in the presence of UHP, and the results are listed in Table 3. All substrates could be smoothly converted to sulfoxides with good to high conversion rates, and excellent selectivities were obtained under mild conditions. The highest yields were obtained for dialkyl and diallylsulfide (98–100%) after 10 min. The replacement of one or both alkyl or aryl groups with phenyl or benzyl group enhanced the reaction times (30 versus 10 min); however, no regular trends in electronic and steric requirements have been observed. It should be mentioned that the present catalytic system was highly selective. Sulfoxides could be nearly stoichiometrically produced and the generation of the corresponding sulfones was well controlled, which makes this process a good alternative for sulfoxide production.

However, the increasing of molar ratio of UHP/sulfide up to five readily conduct a new procedure for easy access to sulfone products with high/excellent yields under the influence of the same concentration of catalyst (Table 3, entries 2, 5 and 10).

Another salient feature of the present sulfoxidation system is its excellent chemo-selectivity. A sulfide also having a carbon–carbon double bond (Table 3, entries 3 and 8), was cleanly transformed into the corresponding sulfoxide in excellent yield. In addition, benzyl phenyl and dibenzyl sulfides (Table 3, entries 11 and 12) were selectively oxidized to their corresponding sulfoxide without formation of any benzylic oxidation by-products.

The high yields of oxidation products (70–100%) obtained by this catalytic system in desired times (10–30 min) indicate the high efficiency of Mo–Schiff base catalyst. More evidences for this important feature of the present catalyst have been obtained by determining of the turnover frequency (TON/*h* = TOF) and total turnover numbers of Mo-catalyst, indicating the activity and stability of catalyst during the oxidation reaction, respectively (TON = mol product/mol catalyst). We performed the oxidation of thioanisole under mild conditions using 2000:2000:1 molar ratio for sulfide:UHP: catalyst. The relative high TOF (300) and TON (940/24 h) obtained in the oxidation of thioanisole, confirmed clearly the high activity and also relative stability of Mo-catalyst towards oxidative degradation in the oxidation of thioanisole. While, the lower TOF (20) and TON (80/24 h) observed in the oxidation of less reactive diphenyl sulfide can be related to competing destruction of the catalyst, as shown by UV–Vis spectral changes of Schiff base complex (λ_{max} = 290 nm) during the oxidation reaction (Fig. 5). However, by comparing of the absorbance (at λ_{max}) at the end of the reaction (*A* = 0.57 at 30 min) with that observed before the addition of UHP (*A* = 0.89) we found that 64% of the catalyst remained intact, which is a promising result for stability of a Schiff base complex.

4. Conclusion

In summary, the synthesis of a new Mo complex $[MoO_2(L)(CH_3OH)]$ with 2-[(2-hydroxypropylimino)methyl]phenol ligand (H_2L), has been developed by reaction between 2-[(2-hydroxypropylimino)methyl]phenol and dioxo-molybdenum(VI) acetylacetonate. The crystal structure of $[MoO_2(L)(CH_3OH)]$ showed a monoclinic space group $P2_1/c$.

Oxidation of sulfides using UHP was efficiently enhanced under the influence of $[MoO_2(L)(CH_3OH)]$ catalyst in ethanol under mild conditions. The high/excellent selectivity of this oxidation method combined with the use of UHP and ethanol as green oxygen source and solvent respectively, makes it more attractive for oxidation of sulfides to both sulfoxides and sulfones. The promising results for stability of this Mo–Schiff base complex and high turnover rates obtained in the oxidation reactions highlight the novelty of this new Mo-catalyst.

Acknowledgments

Support for this work by Research Councils of Shahid Bahonar University of Kerman and the University of Birjand are highly appreciated.

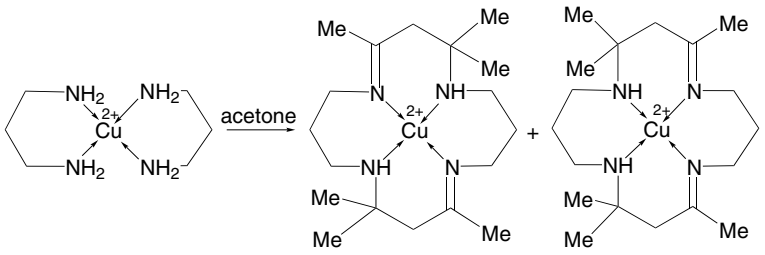
Appendix A. Supplementary data

CCDC 688077 contains the supplementary crystallographic data for this article. These data can be obtained free of charge via http://www.ccdc.cam.ac.uk/conts/retrieving.html, or from the Cambridge Crystallographic Data Centre, 12 Union Road, Cambridge CB2 1EZ, UK; fax: (+44) 1223-336-033; or e-mail: deposit@ccdc.cam.ac.uk. Supplementary data associated with this article can be found, in the online version, at doi:10.1016/j.poly.2008.12.044.

References

[1] O.A. Rajan, A. Chakravorty, Inorg. Chem. 20 (1981) 660.
[2] M.M. Abu-omar, A. Loaiza, N. Hontzeas, Chem. Rev. 105 (2005) 2227.
[3] J. Topich, Inorg. Chem. 20 (1981) 3704.
[4] E.I. Stiefel, Science 272 (1996) 1599.
[5] R.H. Holm, Coord. Chem. Rev. 100 (1990) 183.
[6] J.T. Spence, Coord. Chem. Rev. 48 (1983) 59.
[7] J. Liimatainen, A. Lehtonen, R. Sillanpaa, Polyhedron 19 (2000) 1133.
[8] C.P. Rao, A. Sreedhara, S. Venkateswara, P.V. Rao, N.K. Lokanath, M.A. Sridhar, J.S. Prasad, K. Rissanen, Polyhedron 18 (1999) 289.
[9] M. Cindric, N. Strukan, V. Vrdoljak, B. Kamenar, Z. Anorg. Allg. Chemie 628 (2002) 2113.
[10] H. Arzoumanian, G. Agrifoglio, H. Krentzien, M. Capparelli, J. Chem. Soc., Chem. Commun. (1995) 655.
[11] H. Arzoumanian, L. Maurino, G. Agrifoglio, J. Mol. Catal. A: Chem. 117 (1997) 471.
[12] M.M. Farahani, F. Farzaneh, M. Ghandi, Catal. Commun. 8 (2007) 6.
[13] M.M. Farahani, F. Farzaneh, M. Ghandi, J. Mol. Catal. A: Chem. 248 (2006) 53.
[14] K. Ambroziak, R. Pelech, E. Milchert, T. Dziembowska, Z. Rozwadowski, J. Mol. Catal. A: Chem. 211 (2004) 9.
[15] S.N. Rao, N. Kathale, N.N. Rao, K.N. Munshi, Inorg. Chim. Acta 360 (2007) 4010.
[16] K.C. Gupta, A.K. Sutar, Coord. Chem. Rev. 252 (2008) 1420.
[17] E. Clark, in: J.I. Kroschwitz, M. Howe-Grant (Eds.), Encyclopedia of Chemical Technology, 4th Ed., vol. 23, Wiley, Kirk-Othmer, New York, 1997, pp. 134–146.
[18] P.C.B. Page, Organosulfur Chemistry I and II, Springer, Berlin, 1999.
[19] I. Fernandez, N. Khiar, Chem. Rev. 103 (2003) 3651.
[20] A.M. Khenkin, R. Neumann, J. Am. Chem. Soc. 124 (2002) 4198.
[21] L.A. Paquette, Synlett. (2001) 1.
[22] C. Najera, J.M. Sansano, Recent Res. Dev. Org. Chem. 2 (1998) 637.
[23] R. Chinchila, C. Najera, Recent Res. Dev. Org. Chem. 1 (1997) 437.
[24] G.J.J. Chen, J.W. McDonald, W.E. Newton, Inorg. Chem. 15 (1976) 2612.

[25] G.M. Sheldrik, SHELXL97 and SHELXS97, University of Gottingen, Germany, 1997.
[26] Stoe and Cie, X-AREA (version 1.31) and X-SHAPE (version 2.05), Stoe and Cie, Darmstadt, Germany, 2005.
[27] C.K. Johnson, ORTEP Report ORNL-3794, Oak Ridge National Laboratory, Tennessee, USA, 1965.
[28] S.-E. Park, W.J. Song, Y.O. Ryu, M.H. Lim, R. Song, K.M. Kim, W. Nam, J. Inorg. Biochem. 99 (2005) 424 and references therein.
[29] M.H. Ali, D.R. Leach, C.E. Schmitz, Synth. Commun. 28 (1998) 2969.
[30] M.H. Ali, G.J. Bohnert, Synth. Commun. 28 (1998) 2983.



Scheme 1. Showing the products of the bis(propane-1,3-diamine)copper(II) perchlorate acetone reaction.

N-rac-[Cu(*cis*-Me_6[15]diene)]$_2Cl(ClO_4)_3$ (*cis*-Me_6[15]diene = 6,8,8,13,13,15-hexamethyl-1,5,9,12-tetraazacyclopentadec-5,15(1)-diene) [12], *N-meso*-[Cu(*cis*-Me_6[18]diene)]$(ClO_4)_2$ and *N-rac*[Cu-(*trans*-Me_6[18]diene)]$(ClO_4)_2$ [10]. Structures have been reported for the nickel(II) analogues *N-rac*- [17,18] and *N-meso*-[Ni(*trans*-Me_6[14]diene)]$(ClO_4)_2$ [17], *N-meso*-[Ni(*cis*-Me_6[14]diene)]$(ClO_4)_2$ [19] and *N-rac*-[Ni(*trans*-Me_6[15]diene)]$(ClO_4)_2$ (*trans*-Me_6[15]-diene = 5,7,7,13,15,15-hexamethyl-1,4,8,12-tetraazacyclopentadec-4,12-diene) [20].

Compound [Cu([16]ane)]$(ClO_4)_2$ ([16]ane = 1,5,9,13-tetraazacyclohexadecane) has a centrosymmetrical (configuration III) cation with alternating chair and boat conformation chelate rings [21]. Compounds [Cu(*trans*-Me_6[16]ane)][$ZnCl_4$] and –$(ClO_4)_2$ both have *R,R,R,R* nitrogen configurations with NH groups alternating on opposite sides of the molecular 'plane' around the ring [6]. They have saddle shaped conformations of the macrocycle; with the substituted chelate rings in similar chair conformations with both axial methyl substituents on the same side of the CuN_4 group. For the perchlorate salt both unsubstituted chelate rings have twist-boat conformations while for the tetrachlorozincate salt one has a chair and the other a twist-boat conformation. Compound [Cu($Me(NO_2)$[16]ane)]$(ClO_4)_2$ ($Me(NO_2)$[16]ane = 3-methyl-3-nitro-1,5,9,13-tetraazacyclohexadecane) has the *RRSR* configuration, with the (N1)–H and (N5)–H groups of the substituted chelate ring on the same side and the (N9)–H and (N13)–H groups of the "opposite" chelate ring on opposing sides of the plane, with both chelate rings in boat conformations [22]. Both "side" chelate rings have "somewhat twisted" chair conformations with (N5)–H and (N9)–H on the same side, (N13)–H and (N1)–H on opposing sides of the plane.

Significant dimensions for these compounds are shown in Table 1.

2. Structural studies

Diffraction data was collected for a crystal of the perchlorate salt of the condensation product of bis-(propane-1,3-diamine)copper(II) perchlorate with acetone, [Cu($C_{18}H_{36}N_4$)]$(ClO_4)_2$ [1,2], grown from water, of a tetrachlorozincate salt [Cu($C_{18}H_{36}N_4$)]-[$ZnCl_4$] which crystallized from a solution of this perchlorate salt in methanol containing zinc chloride, of a thiocyanato compound, [Cu($C_{18}H_{36}N_4$)(NCS)]ClO_4, which similarly crystallised from an aqueous solution containing sodium thiocyanate and of a very sparingly soluble tetracyanonickelate(II) compound, [Cu($C_{18}H_{36}N_4$)Ni(CN_4)]·H_2O, also crystallised from water. See Section 4.2 for crystallographic details.

2.1. The structure of N-rac-(6,8,8,14,16,16-hexamethyl-1,5,9,13-tetraazacyclohexadeca-5,13-diene)copper(II) · N-meso-(6,8,8,14,14,16-hexamethyl-1,5,9,13-tetraazacyclohexadeca-5,16(1)-diene)copper(II) perchlorate

The solution of this structure presented problems with space group selection. Solutions were attempted in space groups *C2/m*, *P*$\bar{1}$ and *P*1 in attempts to resolve this, with solutions with R_1 = 0.063, 0.063 and 0.055, respectively. In all three solutions the presence of 16-membered (1,5,9,13-tetraazacyclohexadecadiene)copper(II) cations of two types, both with equatorially oriented methyl substituents at ring positions 6, 8, 14 and 16 is unambiguous.

Table 1
Dimensions (Å/°) for compounds related to the [Cu(Me_6-[16]diene)]$^{2+}$ compounds, with means of chemically equivalent values indicated by *.

Equivalent values are marked as ∗.Compound	Cu–N_{imine}, C=N distances	Cu–N_{amine}, C–N distances	*trans*-N–Cu–N angles	Cu-axial atom, distance	Ref.
N-rac-[Cu(*cis*-Me_6[14]diene)]$(ClO_4)_2$ twofold symmetrical	1.927(6), 1.284(2)	1.891(6), 1.501(2)	planar	O, 3.018(1)	[16]
N-meso-[Cu(*trans*-Me_6[14]diene)]$(ClO_4)_2$ centrosymmetrical	1.974(5), 1.273(9)	2.027(7), 1.492(8)	planar	O	[15]
N-rac-[Cu(*trans*-Me_6[14]diene)]$(ClO_4)_2$ twofold symmetrical	1.97, 1.31	2.00, 1.51	179, 174	O, 2.49	[14]
N-meso-[Cu(*trans*-Me_8[14]diene)]$(ClO_4)_2$ · centro-symmetrical	1.985(3), 1.277(4)	2.010(2), 1.497(4)	planar	O, 2.779(3)	[23]
[Cu(*cis*-Me_6[15]diene)]$_2$ · Cl · $(ClO_4)_3$	1.986(7)∗, 1.28(1)∗	2.013(7)∗, 1.49(1)∗	158.0(3), 168.3(3)	Cl, 2.83(1); O, 2.94(1)	[17]
N-meso-[Cu(*cis*-Me_6[18]diene)]$(ClO_4)_2$	1.987(6)∗, 1.26(1)∗	2.017(6)∗, 1.49(1)∗	152.7(2), 154.6(2)	O, 4.11	[11]
N-rac-[Cu(*trans*-Me_6[18]diene)]$(ClO_4)_2$ · $2H_2O$	1.977(8)∗, 1.29(1)∗	2.053(8)∗, 1.52(1)∗	170.5(5), 174.4(6)	O, 4.08	[11]
N-rac-[Ni(*trans*-Me_6[16]diene)][$Zn(NCS)_{2.1}Cl_{1.9}$]	1.890(6)∗, 1.29(1)∗	1.950(6)∗, 1.51(1)∗	172∗, 170∗		[3]
N-rac-[Cu(*trans*-Me_6[16]ane)][$ZnCl_4$]		2.00(1)∗	135.0(2), 146.6(2)	Cl, 4.23(1)	[6]
N-rac-[Cu(*trans*-Me_6[16]ane)]$(ClO_4)_2$		1.99(2)∗	143.8(7), 155.0(6)	O, 4.33(1)	[6]
[Cu($Me(NO_2)$[16]ane)]$(ClO_4)_2$		2.02(1)∗	149.7(3), 161.2(3)	O, 2.58(1); O, 2.70(1)	[22]
[Cu([16]ane)$(OClO_3)_2$] · centro-symmetrical		2.036∗	planar	O, 2.603	[21]
		2.036∗	planar	O, 2.603	[21]

One cation type has the Cu atom on a crystallographic ($C2/m$) or approximate ($P1$ and $P\bar{1}$) twofold axis, normal to the CuN_4 group, which is compatible with the *N-rac*-[Cu(*trans*-Me_6[16]diene)]$^{2+}$ cation. These cations have the CuN_4 group appreciably folded, with ca. 2.4 Å Cu–O axial interactions with perchlorate ion oxygen atoms. The other type of cation site has atoms C3, Cu and C11 on a crystallographic ($C2/m$) or approximate ($P1$ and $P\bar{1}$) mirror plane, normal to the CuN_4 group, which is compatible with the *N-meso*-[Cu(*cis*-Me_6[16]diene)]$^{2+}$ cation. These cations have coplanar (or near coplanar) CuN_4 groups and the Cu atoms have no close axial interactions.

For both cation types disorder is associated with the location of the imine functions and associated axial components of the *gem*-dimethyl groups present. The perchlorate ions also exhibit severe disorder of the oxygen atoms and final *R*-factors are largely determined by treatment of this, although the perchlorate treatment has little impact on the dimensions of the cations. The solutions in space groups $C2(m)$ and $P\bar{1}$ are discussed below.

2.1.1. Solution in space group P1 (R_1 = 0.055)

The solution in space group $P1$ has as asymmetric unit four independent [Cu(azamacrocycle)]$^{2+}$ cations, labelled {Cu1}–{Cu4}, with ring atoms labelled N1–C16, N21–C36, etc., and eight perchlorate ions with chlorine atoms labelled Cl1–Cl8, with poorly ordered oxygen atoms labelled O11, O12, etc. There is no imposed symmetry.

The four (tetraazamacrocycle)copper(II) cations have saddle shaped conformations with the secondary amine NH groups and both unsubstituted 1,3-diamine chelate rings tilted towards one side of the CuN_4 "plane" and both trimethyl-substituted 1,3-amine-imine chelate rings tilted towards the other side of this plane.

The cations {Cu1} and {Cu2} have approximate twofold symmetry, with the axis through the Cu, normal to the CuN_4 group, with appreciable folding of the CuN_4 group, each with a ca. 2.4 Å Cu–O axial interaction with a perchlorate ion oxygen atom on one side of the CuN_4 "plane" and with two longer off-axial interactions with oxygen atoms from different perchlorate ions on the other side of the plane. The tetrahedral twisting of the N_4 group and displacement of the Cu atom from this plane are ±0.10(1) and 0.16(1) Å for {Cu1} and ±0.09(1) and 0.19(1) Å for {Cu2}.

The cations {Cu3} and {Cu4} have approximate mirror symmetry, with the plane through C3, Cu and C11, normal to the CuN_4 group, with the CuN_4 group near coplanar and with no close axial interactions by the Cu atom. The tetrahedral twisting of the N_4 group and displacement of the Cu atom from this plane are ±0.02(1) and 0.07(1) Å for {Cu3} and ±0.02(1) and 0.04(1) Å for {Cu4}.

For all cations equatorially oriented methyl substituents are present at ring sites C6, C8, C14 and C16, labelled C61, C81, etc.

For the cation {Cu1} two axially oriented methyl substituent sites were resolved on ring atoms C8 and C16 (labelled C82 and C162), oriented to the same side of the plane, with the NH groups oriented to the other side, i.e. compatible with the *N-rac*-[Cu(*trans*-Me_6[16]diene)]$^{2+}$ cation. The Cu–N and C–N distances and associated bond angles are in agreement with the assigned imine character for the nitrogen atoms N5 and N13 and secondary amine character for atoms N1 and N9, see Fig. 1 and Table 2.

The cation {Cu2} has similar overall geometry, but with appreciable electron density peaks in the axial substitution sites associated with atoms C26, C28, C34 and C36. These were assigned as partial occupancy axially oriented methyl groups (labelled C262, C282, etc.) all oriented towards the side of the CuN_4 "plane" towards which the unsubstituted chelate rings are tilted, with partial occupancy H(N) atoms on the opposite side. Site occupancy factors (sof) were refined, linking the sof for the axial methyl substituent group atoms and the adjacent H(N) atom, which indicates the fractional secondary amine/imine character of the nitrogen atom. Refinement with complementary sof for the methyl substituents on each chelate ring resulted in similar sof for the pairs (C262 and C342), (C282 and C362), suggesting the presence of the *trans*-diene macrocycle. Refinement with common sof for these pairs gave sof of 0.52(2) for (C282 and C362), 0.48(2) for (C262 and C342), indicating equal occupancies of all axial methyl sites within the relevant uncertainties. For the final refinement the sof of all axial groups were fixed at 0.5 with, no change in *R*-values, which are insensitive to these ratios.

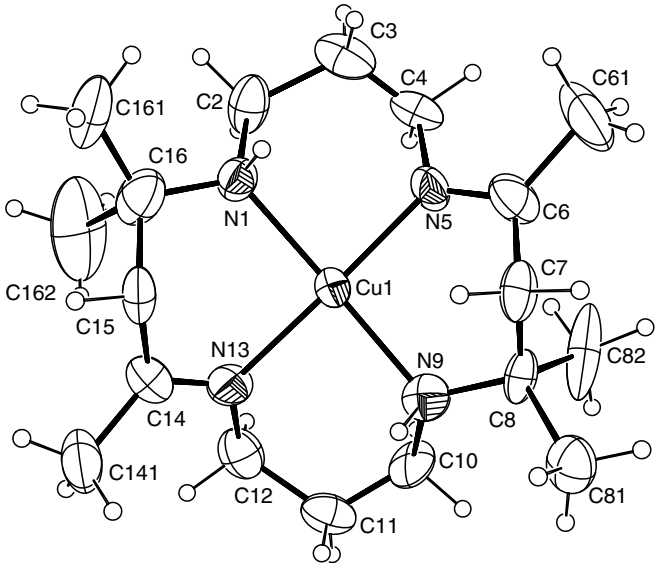


Fig. 1. The cation {Cu1} of *N-rac*-(6,8,8,14,16,16-hexamethyl-1,5,9,13-tetraazacyclohexadeca-5,13-diene)copper(II) *N-meso*-(6,8,8,14,14,16-hexamethyl-1,5,9,13-tetraazacyclohexadeca-5,16(1)-diene)copper(II) perchlorate, with probability ellipsoids drawn [28] at the 30% confidence level. Hydrogen atoms are represented by circles of arbitrary radii. The cation {Cu2} is similar, but with half-occupancy axially oriented methyl substituents at C6, C8, C14 and C16.

A similar pattern was observed for cations {Cu3} and {Cu4}. Cation {Cu3} has the dimensions expected for *N-meso*-[Cu(*cis*-Me_6[16]diene)]$^{2+}$, with near mirror symmetry, with dimensions supporting assignment with imine functions at N41 and N45, secondary amine functions at N49 and N53 and with axial methyl substituents (C482)H_3 and (C542)H_3, oriented to the same side of the plane, with the NH groups oriented to the other side, see Fig. 2 and Table 2.

Cation {Cu4} also has near mirror symmetry, with broad regions of electron density in the axial substituent regions C66–C68 and C74–C76. This was resolved as partial occupancy axial methyl substituents at sites C662, C682, C742 and C762. Refinement of sof as for {Cu2} gave sof for {(C682)H_3 + H69} of 0.67(2) and for {(C742)H_3 + H73} of 0.60(2), with complementary values for the C662 and C762 groups, indicating the presence of the *cis*-diene isomer. Refinement as for cation {Cu3}, i.e. with common sof for the (C662 and C762), (C682 and C742) groups, gave sof of 0.67(2) for C682 and C742, with complementary values for the C662 and C762 groups, though the *R*-values are insensitive to this ratio. Final refinement used fixed sof of 0.667 and 0.333 for these disorder components without change in the *R*-values.

The presence of these partial occupancy axial methyl sites for cations {Cu2} and {Cu4} can be explained if these sites are occupied by cations with reversed orientations of the amine-imine chelate rings N25–N29 and N33–N21 for {Cu2}, N65–N69 and N73–N61 for {Cu4}. The saddle-like macrocycle conformations for all cations require that both NH groups of each cation lie on the same side of

Table 2
Dimensions (Å/°) of $[Cu(Me_6[16]diene)]^{2+}$ compounds (space group *P*1 solution for perchlorate salt).

Compound/cation	N1	N5	N9	N13	*trans*-N–Cu–N[a]	Cu-axial[b]
Perchlorate salt, N-rac-[Cu(trans-Me$_6$[16]diene)]$^{2+}$						
{Cu1}					165.4(5) 175.7(6)	O11, 2.38(2)
Cu1–N[c]	2.05(1)	1.98(1)	2.07(1)	2.01(1)		
C–N/C=N[d]	1.45(2)	1.33(2)	1.44(2)	1.26(2)		
{Cu2}					163.6(6), 174.9(6)	O52, 2.42(1)
Cu2–N[c]	2.02(1)	2.05(1)	2.00(1)	2.02(1)		
C–N/C=N[d]	1.41(2)	1.33(2)	1.41(2)	1.41(2)		
Perchlorate salt, N-meso-[Cu(cis-Me$_6$[16]diene)]$^{2+}$						
{Cu3}					178.2(6), 176.2(6)	O61, 3.64(2); O21, 3.93(2)
Cu3–N[c]	1.97(1)	2.00(2)	2.06(1)	2.02(1)		
C–N/C=N[d]	1.34(2)	1.30(2)	1.35(2)	1.37(2)		
{Cu4}					176.5(6), 177.9(6)	O72, 3.62(2); O61, 4.00(2)
Cu4–N[c]	2.05(1)	1.98(1)	2.03(1)	2.03(1)		
C–N/C=N[d]	1.31(2)	1.41(2)	1.46(2)	1.46(2)		
N-rac-[Cu(cis-Me$_6$[16]diene)][ZnCl$_4$]					139.3(1), 155.9(1)	Cl2, 3.3404(7)
Cu–N[c]	2.031(2)	1.980(2)	2.037(2)	2.008(2)		
C–N/C=N[d]	1.290(3)	1.285(3)	1.511(3)	1.522(3)		
[Cu(Me$_6$[16]diene)(NCS)] $ClO_4 \cdot H_2O$					planar	N30, 2.199(7)
Cu–N[c]		2.041(5)	2.0291(5)			
C–N/C=N[d]		1.376(8)	1.316(8)			
[Cu(Me$_6$[16]diene)-(NC)Ni(CN)$_3$] H$_2$O						
{Cu1}					161.4(7), 162.7(8)	N17, 2.11(2)
Cu1–N[c]	1.96(2)	1.97(2)	2.01(2)	1.96(2)		
C–N/C=N[d]	1.35(3)	1.34(3)	1.37(3)	1.34(2)		
{Cu2}					165.4(6), 159.2(6)	N37, 2.16(2)
Cu2–N[c]	1.95(2)	1.98(2)	2.06(2)	2.02(2)		
C–N/C=N[d]	1.26(3)	1.21(3)	1.35(2)	1.38(2)		

[a] Angles N1–Cu–N9 and N5–Cu–N13.
[b] Closest axial atom(s), distance Cu-axial atom.
[c] Distances Cu–N1, Cu–N5, Cu–N9, Cu–N13.
[d] Distances N5–C6, C8–N9, N13–C14, C16–N1.

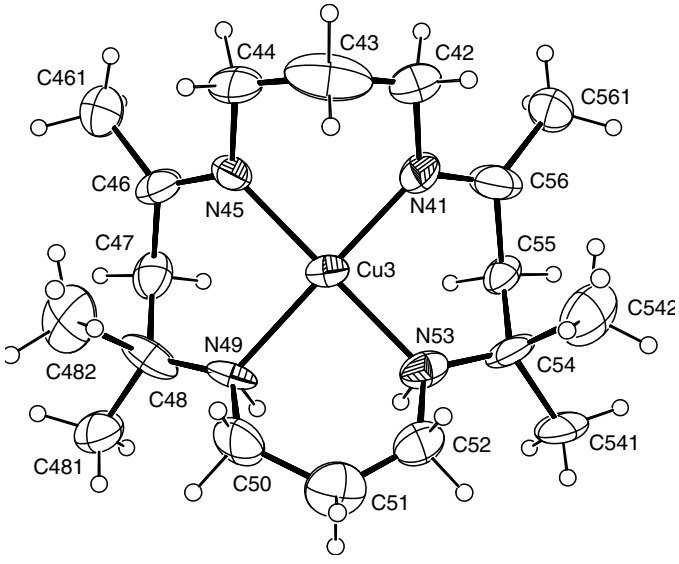


Fig. 2. The cation {Cu3}, represented similarly to Fig. 1. The cation {Cu4} is similar, but with partial-occupancy axially oriented methyl substituents at C6, C16 (sof = 0.333) and C8 and C14 (sof = 0.667).

the macrocycle 'plane', permitting the presence of only the *N-rac*-isomer for the [Cu(*trans*-Me$_6$[16]diene)]$^{2+}$ cation for {Cu1} and of only the *N-meso*-isomer for the [Cu(*cis*-Me$_6$[16]diene)]$^{2+}$ cation for {Cu3}. In principle, for cation site {Cu2} with sof = 0.5 for all axial substituents and hence equal occupancies for the two chelate ring orientations, either *cis* or *trans* diimine arrangements could be present in equal proportions. However, site {Cu2} has overall near-twofold symmetry, with the cation overall geometry very similar to that of cation {Cu1}. The superimposed forms are most probably the *RR*- and *SS*-enantiomorphs of the *N-rac*-[Cu(*trans*-Me$_6$[16]diene)]$^{2+}$ cation. Since the {Cu1} site has the *RR* configuration (the Flack parameter [23] is reported by SHELXL as 0.00, with no s.u.) the asymmetric unit contains the enantiomers in 3:1 ratio. Cation {Cu4} has overall near-mirror symmetry and overall geometry similar to that of cation {Cu3}, so the disorder components are most probably the same *N-meso*-isomer of the [Cu(*cis*-Me$_6$[16]-diene)]$^{2+}$ cation, rotated by 180° about an axis through Cu4, present in 2:1 proportions. Structural features supporting these assignments include the unsubstituted chelate ring conformations, the locations of the axial methyl groups, and the CuN_4 group geometry and axial interactions, which are all similar for the pair of cations {Cu1} and {Cu2} and the pair {Cu3} and {Cu4}.

The Cu–N and C–N distances and associated bond angles for cations {Cu1} and {Cu3} are in agreement with the assigned amine or imine character of the nitrogen atoms, though the differences are smaller than observed for [Cu(*cis*-Me$_6$[16]diene)][$ZnCl_4$], below, or [Ni(*trans*-Me$_6$[16]diene][Zn(NCS/Cl)$_4$] [3]. For the cations {Cu2} and {Cu4} these dimensions have intermediate values, see Table 2.

The substituted six-membered amine-imine chelate rings of the disordered macrocycle cations {Cu2} and {Cu4} have superimposed arrangements with a chelate ring with one planar trigonal coordinated imine nitrogen atom and one tetrahedral coordinated secondary amine nitrogen atom. The two disorder components of the macrocycle occupying these cation sites would have these chelate ring arrangements reversed. The reversed chelate ring components would not conform well, leading to anomalous calculated bond lengths and angles and larger adp values for the chelate ring atoms and the methyl substituents, particularly the axial substituents. This disorder would be expected to extend to the nitrogen atoms and also to the adjacent atoms of the linking chelate rings, and be manifest largely as anomalous adp values.

For all the cations the trimethyl-substituted amine-imine chelate rings have asymmetric boat conformations. For the [Cu(*trans*-Me_6[16]diene)]$^{2+}$ cations {Cu1} and {Cu2} the unsubstituted 1,3-diamine chelate rings have chair conformations, the overall conformation being similar to that of the analogous nickel(II) cation [3]. For the [Cu(*cis*-Me_6[16]diene)]$^{2+}$ cation {Cu3} the diimine chelate ring N31–N35 has a boat conformation and the diamine chelate ring N39–N43 has a chair conformation. For the mixed occupancy [Cu(*cis*-Me_6[16]diene)]$^{2+}$ cation site {Cu4}, the conformation of the chelate ring N69–N73 is a chair and that of N61–N65 has N61, C62, C63, C64 and N65 close to coplanar, though both show indications of positional disorder for the central methylene group, as would be expected for superimposed components with the {Cu3} structure reversed. The chair–chair conformations of these chelate rings observed for {Cu1} and {Cu2} are most compatible with the *trans*-diimine macrocycle, while the chair–boat conformation observed for {Cu3} is more compatible with the *cis*-diimine macrocycle. For comparison, for *N-rac*-[Cu(*cis*-Me_6-[16]diene)][$ZnCl_4$] (below) the N9–N13 (diamine) chelate ring has a chair conformation, and the N1–N5 (diimine) chelate ring has a twist conformation. Displacements of atoms from selected mean planes for the chelate rings are listed in the Supplementary data.

Each of the cations is associated with three perchlorate anions, one approximately axially located on the less crowded side of the CuN_4 'plane' and two off-axis on the more crowded side with the axial substituents and N–H groups. The perchlorate oxygen atom sites are generally poorly defined, but there is a significant axial interaction on the less crowded side for {Cu1} and {Cu2} and probable hydrogen bonds formed by all cations on the other side toward which the NH groups are directed. The treatment of the perchlorate ion disorder and hydrogen bonding is described in the Supplementary data.

The closest approaches of perchlorate ions to copper(II) ions (less crowded side first) are: Cu1···Cl1, 3.69(2); Cu1···Cl3 and Cl7, ca. 4.72; Cu2···Cl5, 3.69(2); Cu2···Cl3 and Cl7, ca. 4.7; Cu3···Cl3, 4.63(2); Cu3···Cl2, 4.48(2); Cu3···Cl6, 4.78(2); Cu4···Cl4, 4.63(2); Cu4···Cl6, 4.48(2) and Cu4···Cl2, 4.80(2) Å. Cations {Cu1} and {Cu2} are approximately inversion related, with Cu1···Cu2 = 7.27(2) Å, linked by perchlorate ions Cl2 and Cl3. Similarly, cations {Cu3} and {Cu4} are approximately inversion related, with Cu3···Cu4 = 6.79(2) Å and linked by perchlorate ions Cl6 and Cl7. Perchlorate ions Cl4 and Cl8 have no close association with cations. See Fig. 3 for a representation of the contents of the unit cell. The rotational disorder of the perchlorate ions probably arises because these ions are only weakly restrained by hydrogen bonding and the closest neighbours of many perchlorate oxygen atoms are hydrogen atoms of partial occupancy axial methyl groups.

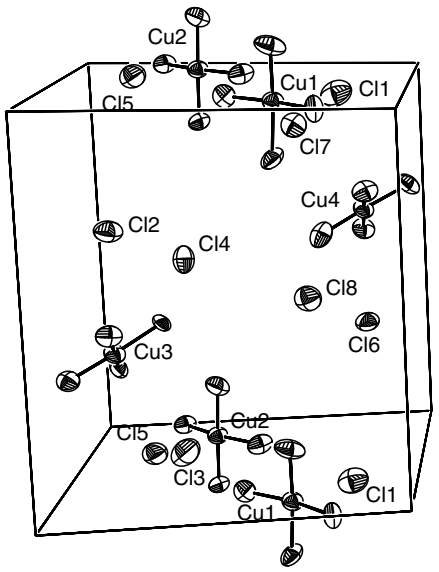


Fig. 3. The unit cell contents for *N-rac*-(6,8,8,14,16,16-hexamethyl-1,5,9,13-tetraazacyclohexadeca-5,13-diene)copper(II) *N-meso*-(6,8,8,14,14,16-hexamethyl-1,5,9,13-tetraazacyclohexadeca-5,16(1)-diene)copper(II) perchlorate, projected normal to the 100 plane, showing only the Cu, N and Cl atoms.

2.1.2. Solution in space group C2/m (cell: a, 14.740(4); b, 23.452(4); c, 14.364(3) Å; , 96.54(3)°; R_1 = 0.063)

The asymmetric unit consists of the halves of two (tetraazacycohexadecadiene)copper(II) cations, {Cu1} and {Cu2}, with the CuN_4 groups of {Cu1} and {Cu2} approximately normal. Cation {Cu1} has atom Cu1 on a twofold axis, normal to the CuN_4 group, compatible with the *N-rac-trans*-[16]diene macrocycle. Cation {Cu2} has atoms Cu2, C23 and C31 on a mirror plane, compatible with the *N-meso-cis*-[16]diene macrocycle. The chlorine atoms Cl1–Cl4 of four "half" perchlorate ions and a number of the perchlorate oxygen atoms are also in special positions, with Cl1 on the same twofold axis as Cu1 and with Cl3 and Cl4 (and O32, O33, O41, O42 and O43) on the same plane as Cu2, C23 and C31.

Both cations have saddle conformations with the substituted and the unsubstituted chelate rings tilted to opposite sides of the CuN_4 group, requiring the two NH groups to lie on the same side of this group, determining the *N-rac-trans*-configuration for {Cu1} and the *N-meso-cis*-configuration for {Cu2}. The two-fold symmetry {Cu1} cation has appreciable folding of the N_4 group, with *trans*-N–Cu–N angles of 176.0(3)° and 163.7(2)°, while for cation {Cu2} the CuN_4 group is inherently planar. For both cations the unsubstituted chelate rings have chair conformations and the substituted chelate rings have boat conformations.

For both cations equatorially oriented methyl substituents are present for C6 and C8 and hence also for the symmetry related atoms C14 and C16. Significant electron density peaks are present at axial substituent sites near the same ring atoms, all lying on the same side of the CuN_4 "plane" towards which the unsubstituted chelate rings are tilted. Assigning these as partial occupancy methyl groups and refinement of site occupancy factors, (linking the sof for the axial methyl substituent group and adjacent NH group, with complementary sof for the methyl substituents on each chelate ring, as discussed above), resulted in values for sof of the C62 group of 0.61(2) for {Cu1} and of 0.63(2) for {Cu2}. The *R*-values were unchanged when these sof were fixed at 0.667, indicating a 2:1 ratio of the *trans*-enantiomers for {Cu1} and of the rotated forms of the *cis*-isomer for {Cu2}, within the relevant uncertainties. The disorder components have the N5–N9 amine-imine chelate ring reversed and the two arrangements of the chelate ring would not conform well, so the dimensions observed are likely to be anomalous, as discussed above. The C–N distances within the amine-imine chelate ring are intermediate to the usual C–N and C=N distances.

2.1.3. Solution in space group $P\bar{1}$ (R_1 = 0.063)

For the solution in space group $P\bar{1}$, there are two full [Cu(azamacrocycle)]$^{2+}$ cations and four perchlorate ions in the asymmetrical unit, with no imposed symmetry. The cation {Cu1} has approximate twofold symmetry (axis through Cu1, normal to the CuN_4 "plane"), with appreciable folding of the N_4 group and a ca. 2.4 Å Cu–O axial interaction with a perchlorate ion oxygen atom. The cation {Cu2} has approximate mirror symmetry (plane through C23, Cu2 and C31), a planar CuN_4 group, and no close axial interaction.

The ring conformations and axial substituent patterns are similar to those in the *P*1 and *C*2/*m* solutions, with partial occupancy

axial methyl sites present for both cations. For each chelate ring the site occupation factors for the axial methyl groups and adjacent H(N) atoms were refined with complementary values, as for the *P*1 solution. For cation {Cu1} the values of the sof for the pairs C62 and C142, C82 and C162 and for cation {Cu2} the values for the pairs C62, C162 and C82, C142 were similar and the structure was refined with common sof for the pairs. The resulting value for cation {Cu1} for the sof for C62 and C142 was 0.65(1) and for cation {Cu2} the sof for C62 and C162 was 0.66(1), both approximating to 0.667 within the relevant uncertainties. The sof values were fixed at 0.667 for the final refinement cycles, with no change in the *R*-values. These results are compatible with sites {Cu1} having *N-rac*-[Cu(*trans*-Me_6[16]diene)]$^{2+}$ cations with enantiomers present in 2:1 proportions and with sites {Cu2} having *N-meso*-[Cu(*cis*-Me_6[16]diene)]$^{2+}$ cations, with rotated arrangements also present in 2:1 proportions. The C-N distances within the amine–imine chelate ring are intermediate to the usual C–N and C=N distances.

The closest interactions between Cu and oxygen atoms for Cu1 are half occupancy O47 at 2.48(1)} and O48 at 2.50(1) Å, with the closest axial approach for Cu2 with O11 at 3.61(1) Å. The cation {Cu1} of the $P\bar{1}$ solution becomes approximately inversion related pairs of cations, {Cu1} and {Cu2} in the *P*1 solution and likewise {Cu2} of $P\bar{1}$ become the pairs {Cu3} and {Cu4} in *P*1. Similarly the perchlorate ions including Cl1, Cl2, Cl3 and Cl4 in $P\bar{1}$ become approximately inversion related pairs Cl1 and Cl5, Cl2 and Cl6, Cl3 and Cl7, Cl4 and Cl8 in *P*1.

The closest axial interactions between copper and oxygen atoms for Cu1 is with O11 at 2.50(1) Å, while the closest axial approach for Cu2 is with O41 at 3.61(1) Å. The four full perchlorate ions present show individualistic rotational disorder, treated similarly to the *P*1 solution.

2.2. The structure of N-rac-(5,8,8,14,14,16-hexamethyl-1,5,9,13-tetraazacyclohexadeca-5,16(1)-diene)copper(II) tetrachlorozincate N-rac-[Cu(cis-Me_6[16]diene)][$ZnCl_4$]

The structure was determined for the blue product which crystallized when a solution of the perchlorate salt in methanol containing zinc chloride was allowed to evaporate.

The structure of this compound shows no disorder and unequivocally confirms the presence of *N-rac*-(5,8,8,14,14,16-hexamethyl-1,5,9,13-tetraazacyclohexadeca-5,16(1)-diene)copper(II) cations, *N-rac*-[Cu(*cis*-Me_6[16]diene)]$^{2+}$, shown in Fig. 4, with the *cis* locations of the imine functions supported by N1–C16 and N5–C6 distances, see Table 2, and the trigonal angles about these atoms. The group N9–H9 and axial methyl substituent (C142)H_3 are oriented to one side of the CuN_4 "plane" and groups N13–H13 and axial methyl group (C82)H_3 are oriented to the other side, confirming the *N-rac* configuration. The asymmetric unit contains the *RR* enantiomer (Flack parameter [23] = 0.007(7)).

The Cu–N distances are similar to values for related [Cu(tetraazamacrocycle)]$^{2+}$ cations with ring sizes ranging from 14- to 18-members, see Table 1. The mean Cu–N_{imine} distance {2.006(3) Å} is slightly shorter than the mean Cu–N_{amine} distance {2.023(3) Å}, though this difference is less than the ca. 0.03 Å observed for related compounds.

The CuN_4 group has irregular geometry, approximately midway between square-planar and tetrahedral. The diamine chelate rings have conformations Cu, N1, N5, twist; Cu, N9, N13, chair {dihedral angle between CuN_2 planes 46.7(1)°}; amine-imine chelate rings Cu, N5, N9 and Cu, N13, N1, twist-boat {dihedral angle between planes 45.7(1)°}. Displacements of atoms from the relevant least squares planes are listed in the Supplementary data.

The cation and tetrachlorozincate anion are linked by hydrogen bonds [D–H···A, distances D–H, H···A, D···A (Å); angle D–H···A (°): N9–H9···Cl3 [0.90, 2.55, 3.370(2); 152]; N13–H13···Cl2: [0.84, 2.86, 3.465(2); 130°] and N13–H13···Cl4 [0.84, 2.89, 3.649(2); 151], with the closest axial interaction Cu1···Cl2 = 3.340(2) Å.

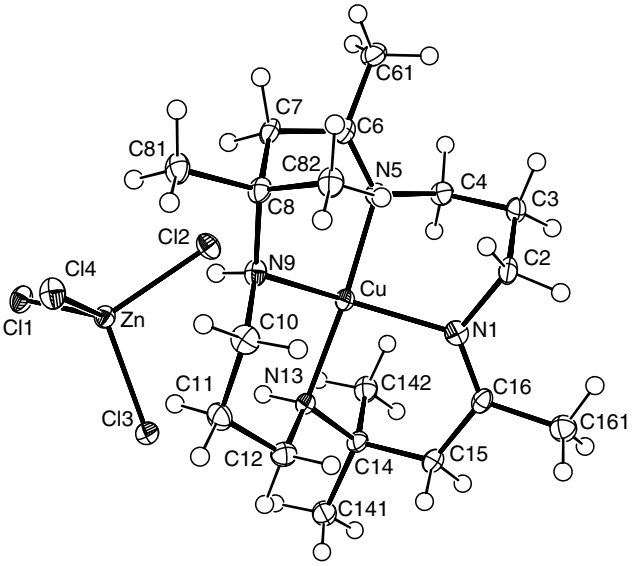


Fig. 4. The asymmetric unit of *N-rac*-(5,8,8,14,14,16-hexamethyl-1,5,9,13-tetraazacyclohexadeca-5,16(1)-diene)copper(II) tetrachlorozincate drawn as for Fig. 1, but with probability ellipsoids drawn at the 50% confidence level.

2.3. The structure of (hexamethyl-1,5,9,13-tetraazacyclothexadecadiene)(isothiocyanato)copper(II) perchlorate, [Cu(Me_6[16]diene)(NCS)]ClO_4

The structure was determined for the blue product which crystallized when a solution of the perchlorate salt in water containing sodium thiocyanate evaporated. Poor data and disorder precluded a fully satisfactory refinement; though the main structural features are clear.

The asymmetric unit has a square pyramidal hexamethyl-1,5,9,13-tetraazacyclohexadecadiene)(isothiocyanato)copper(II) cation, see Fig. 5, and a perchlorate anion. The cation has the Cu

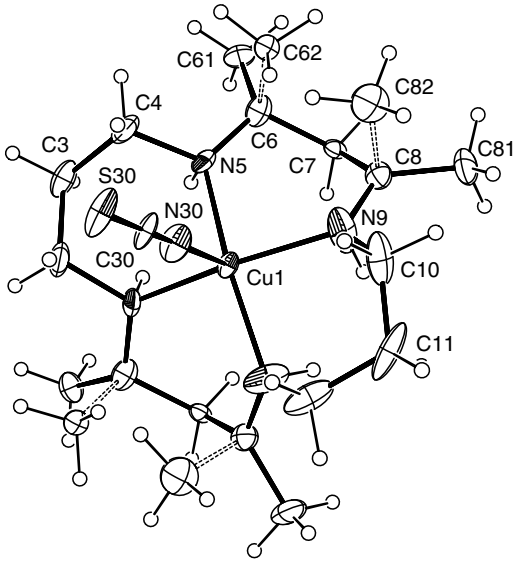


Fig. 5. The cation of (hexamethyl-1,5,9,13-tetraazacyclothexadeca-diene)(isothiocyanato)copper(II) perchlorate, drawn as for Fig. 1, with atoms of the asymmetric unit labelled. Methyl sites C62 and C82 have complementary sof.

atom and the C30, N30 and S30 atoms of the coordinated thiocyanate ion on a twofold axis. The Cu atom is displaced by 0.329(4) Å from the coplanar CuN_4 group, towards the N-atom of the linear thiocyanate group, which has dimensions N30–C30 = 1.16(1) and C30–N30 = 1.64(1) Å. The azamacrocycle has an overall saddle conformation; with the unsubstituted (1,3-diamine) chelate ring tilted towards the same side of the N_4 plane as the *N*-thiocyanato ligand with a chair conformation (which distances the central methylene group $(C3)H_2$ from the thiocyanato ligand atoms). The trimethyl-substituted 1-amine-3-imine chelate ring is tilted to the opposite side of the N_4 plane from the thiocyanate ligand with a boat conformation, which places the axial groups on the opposite side of the N_4 plane. Displacements of atoms from the relevant CuN_2 chelate planes are listed in the Supplementary data.

Significant electron density is present in the axial substitution sites near both C6 and C8 (and symmetry related sites near C14 and C16). This was assigned as partial occupancy methyl groups $(C62)H_3$ and $(C82)H_3$ (with associated partial occupancy H5 and H9) as discussed above. Refinement with complementary sof for $\{(C62)H_3 + H5\}$ and $\{(C82)H_3 + H9\}$ gave values of sof of 0.59(1) and 0.41(1), respectively.

The twofold symmetry of the cation is most compatible with the *N-rac*-[Cu(*trans*-Me_6[16]diene)]$^{2+}$ cation, with the cation site occupied by the enantiomers in approximately equal proportions. The N5–C6 and C8–N9 distances are similar, intermediate to the values usual for secondary amine and imine functions, see Table 2. As discussed above, the differing conformations of the superimposed reversed forms of the amine–imine chelate ring would be expected to result in non-standard dimensions, particularly of distances to axial substituents (see Table 2).

The saddle conformation of the cation is also compatible with the *N-meso*-[Cu(*cis*-Me_6[16]diene)]$^{2+}$ cation, with the observed twofold symmetry requiring the presence of equal proportions of the rotated arrangements, which would result in equal half-occupancies for the $(C62)H_3$ and $(C82)H_3$ methyl sites. However, R_1 increased from 0.064 to 0.065 when the sof of these groups were fixed at 0.5.

It is concluded that the structure determination supports the assignment as *N-rac*-[Cu(*trans*-Me_6[16]diene)]$^{2+}$, but does not permit unambiguous assignment of configuration.

The rotationally disordered perchlorate ion has the chlorine atom Cl1 and oxygen atom O1 on a mirror plane. The remaining oxygen atoms are effectively in free rotation about the Cl1–O1 axis, modelled with six equally half-occupied oxygen atom sites.

The unit cell contains interlinked columns of cations, with alternating orientations of the axial thiocyanate group, with Cu···Cu ($x, -y, -z$) = 7.416 Å and S30···S30 ($x, -y, -z$) = 4.591 Å. The S-atoms from an intersecting cation column, normal to the first, lie between the cations (on the side remote from the thiocyanate ion) on the same plane and interacting equally with N5–H and N9–H, with Cu1···S30 ($-x, -y + ½, z + ½$) and Cu1···S30 ($-x, y + ½, -z + ½$) = 4.356 Å. The perchlorate ions form columns between the cation columns; with oxygen O1 located midway between the pairs of S···S atoms of adjacent columns (O1···S30 = 6.818 Å), with all O-atoms remote from NH groups. Hydrogen bonds [D–H···A, distances D–H, H···A, D···A (Å); angle D–H···A (°)]: N5–H5···S30 ($-x + 1, -y + 3/2, z - ½$) [0.93, 2.81, 3.705(6); 160.9]; N9–9···S30 ($x, y - ½, -z + 3/2$) [2.91, 3.789(7); 158.6] are present.

Table 3
Crystallographic details.

Formula	$[Cu(C_{18}H_{36}N_4)](ClO_4)_2$[a]	$[Cu(C_{18}H_{36}N_4)][ZnCl_4]$[b]	$[Cu(C_{18}H_{36}N_4)(NCS)]ClO_4 \cdot H_2O$[c]	$[Cu(C_{18}H_{36}N_4)Ni(CN)_4] \cdot H_2O$[d]
Formula weight	570.95	553.2	529.58	552.85
Crystal system	triclinic	orthorhombic	orthorhombic	monoclinic
Space group	$P\bar{1}$	*Pna*2(1)	*Cmca*	*P*2(1)/*c*
a (Å)	13.9276(3)	12.679(1)	20.548(8)	11.252(4)
b (Å)	13.9443(2)	14.828(1)	15.531(5)	14.120(5)
c (Å)	14.5950(3)	14.828(1)	15.581(6)	33.45(1)
α (°)	93.565(1)	90	90	90
β (°)	93.564(1)	90	90	94.516(7)
γ (°)	115.276(1)	90	90	90
V (Å^3)	2545.78(8)	2423.0(4)	4973(3)	5298(4)
Z	4	4	8	8
Cell determination (reflection, θ_{min}, θ_{max} (°))	[e]	16181, 2.09, 26.39,	1371, 2.62, 24.69,	5573, 2.26, 25.33,
Temperature (K)	153(2)	93(2)	93(2)	153(2)
θ Range (°)	[e]	2.09, 26.39	1371, 2.62, 24.68	20381, 2.11, 18.85
ρ_{calc} (g/cm^3)	1.490	1.572	1.415	1.386
Crystal size (mm)	[e]	0.15 × 0.30 × 0.30	0.02 × 0.15 × 0.30	[e]
T_{max}, T_{min}	0.8905, 0.6032	1.000, 0.749	1.000, 0.831	1.00, 0.39
F(000)	1196	1156	2232	2328
μ (mm^{-1})	1.116	2.317	1.103	1.543
Index range *h*	−18, 18	−15, 15	−23, 25	−10, 10
Index range *k*	−17, 18	−16, 18	−19, 19	−12, 12
Index range *l*	−18, 19	−16, 15	−17, 16	−30, 30
θ Range/°	1.40, 28.26	2.09, 26.39	1.98, 26.41	2.11, 18.85
Reflections number (average *R* equivalent)	21728 (0.0343)	20464 (0.0322)	9043 (0.115)	20381 (0.092)
Reflections total	16437	4868	1416	4111
Reflections [$I > 2\sigma(I)$]	9408	4441	1416	2741
Parameters (restraints)	1375 (115)	262 (1)	165 (9)	584 (9)
Goodness-of-fit on F^2 [all data]	0.961	0.926	1.11	1.133
Final *R* indexes [$I > 2\sigma(I)$]	R_1, 0.055; *wR*, 0.126	R_1, 0.021; *wR*, 0.048	R_1, 0.064; *wR*, 0.116	R_1, 0.086; *wR*, 0.202
Final *R* indexes [all data]	R_1, 0.104, *wR*, 0.151	R_1, 0.025, *wR*, 0.049	R_1, 0.118, *wR*, 0.130	R_1, 0.129, *wR*, 0.238

[a] *N-rac*-(6,8,8,14,16,16-hexamethyl-1,5,9,13-tetraazacyclohexadeca-5,13-diene)copper(II) *N-meso*-(6,8,8,14,14,16-hexamethyl-1,5,9,13-tetraazacyclohexadeca-5,16(1)-diene) copper(II) perchlorate.
[b] *N-rac*-(5,8,8,14,14,16-hexamethyl-1,5,9,13-tetraazacyclohexadeca-5,16(1)-diene)copper(II) tetrachlorozincate *rac*-[Cu(*cis*-Me_6[16]diene)][$ZnCl_4$].
[c] (Hexamethyl-1,5,9,13-tetraazacyclothexadecadiene)(isothiocyanato)copper(II) perchlorate, $[Cu(Me_6[16]diene)(NCS)]ClO_4$.
[d] {(Hexamethyl-1,5,9,13-tetraazacyclothexadeca-5,16(1)-diene)copper(II)}-μ-cyano-{tetracyanonickelate(II)} hydrate, $[Cu(Me_6[16]diene)(\mu\text{-}NC)Ni(CN)_3] \cdot H_2O$.
[e] Information lost.

2.4. The structure of {Hexamethyl-1,5,9,13-tetraazacyclothexadecadiene)copper(II)}–cyano-{tetracyanonickelate(II)} hydrate, $[Cu(Me_6[16]diene)(\mu\text{-}NC)Ni(CN)_3] \cdot H_2O$

The structure was determined for this very sparingly water-soluble blue compound, which precipitated as very fine crystals when a solution of $Na_2[Ni(CN)_4] \cdot 3H_2O$ was added to an aqueous solution of the perchlorate salt. The compound was recrystallised from water, with repeated thermal cycling, but the crystals remained tiny and generally poorly formed. Disorder and poor data precluded a fully satisfactory analysis, but the essential structural features are clear.

The asymmetric unit contains two similar "molecules", each with copper(II) ions in square-pyramidal coordination by the four nitrogen atoms of a hexamethyl-1,5,9,13-tetraazacycloretradecadiene azamacrocycle, each with one cyanide nitrogen atom of a tetracyanonickelate(II) ion coordinated axially, and two independent water molecules. The geometries of the (azamacrocycle)copper(II) cations, labelled {Cu1} and {Cu2}, are similar and generally similar to that of the thiocyanate compound, 2.3 above, but with no imposed symmetry.

For both cations the N_4 groups are near-coplanar, with the Cu displaced towards the axial cyanide nitrogen [tetrahedral twisting of N_4 group, displacement of Cu from N_4 plane/Å: {Cu1}, ±0.013(8), 0.308(1); {Cu2}: ±0.053(8), 0.307(8)]. The macrocycles have saddle-shaped conformations. The unsubstituted diamine chelate rings have chair conformations; tilted to the same side of the azamacrocycle as the *N*-coordinated cyano group while the substituted amine–imine chelate ring have boat conformations tilted to the other side, see Fig. 6. Displacements of atoms from relevant mean planes for chelate rings are listed in the Supplementary data.

For both cations there is appreciable electron density in the axial sites associated with C6, C8, C14 and C16 for {Cu1} and C26, C28, C34 and C36 for {Cu2}. This was assigned as axially oriented methyl substituents, refined with complementary sof for the methyl groups and associated H(N) atoms for each chelate ring as for the previous compounds. For cation {Cu1} the sof values for C62 and C142 are 0.45(2) and 0.54(2), respectively, in agreement with approximately equal occupancy of the axial sites, which could occur for equal proportions of either the *trans*- or the *cis*-cation. For cation {Cu2} the values are 0.39(2) and 0.62(2), respectively, in best agreement for the *cis*-cation in ca. 2:1 ratio of 180° rotated arrangements. The *R*-values obtained were insensitive to the sof ratios for the axial substituents so do not permit unambiguous assignment of configuration but it seems probable that this compound has equal proportions of the *N-rac*-[Cu(*trans*-Me_6[16]-diene)]$^{2+}$ and *N-meso*-[Cu(*cis*-Me_6[16]diene)]$^{2+}$ cations.

The tetracyanonickelate(II) moities are close to square-planar, with mean distances Ni1–C = 1.81(4); C–N = 1.11(4) and Ni2–C 1.87(2); C–N = 1.17(4) Å and angles Cu1–N17–C17 = 172.2(2) and Cu2–N37–C37 = 164.9(1)°.

The "molecules" are arranged in stacks with parallel azamacrocyles, aligned with the *X* axis. Cations {Cu1} and {Cu2} form separate columns, with alternating columns reversed, with Cu-atom separation in the columns of 11.252(4) Å (the *a* cell dimension). A $Ni(CN)_4$ group lies between adjacent Cu(azamacrocyle) groups, with cyanide groups N-coordinated to copper(II) on one side, and with the *trans*-cyanide group hydrogen bonded to NH groups of the next azamacrocyle on the other side. Columns of water molecules lie between the azamacrocyle columns, with O18 hydrogen bonded to cyanide N40 ($-x$, $y + ½$, $-z + ½$) and O38 to N38 ($-x$, $-y$, $-z$), and also to N–H groups. These cyanide-N and water-O atoms are approximately symmetrically positioned off the tetragonal axis with respect to the Cu atoms, with Cu1···N19 = 3.85(4), Cu1···O38 ($-x$, $-y$, $-z$) = 3.68(4) and Cu2···N39 = 3.85(4), Cu2···O18 ($-x$, $y + ½$, $-z + ½$) = 3.65(4) Å.

Hydrogen bonds [D–H···A, distances H···A, D···A (Å); angle D–H···A (°), N–H = 0.91 Å] are: N1–H1···O38^{i} [2.22, 3.06(4); 154.4]; N5–H5···O38^{i} [2.38, 3.25(2); 159.5]; N9–H9···N19^{ii} [2.32, 3.19(2); 160.3]; N13–H13···N19^{ii} [2.36, 3.249(2); 161.5]; N21–H21···O18^{iii} [2.42, 3.24(2); 151.8]; N25–H25···O18^{iii} [2.32, 3.15(2);, 153.0]; N29–H29···N39^{iv} [2.40, 3.27(2); 158.3]; N33–H33···N39^{iv} [2.32, 3.21(2); 165.9]; symmetry operators: i = $-x + 1$, $-y + 1$, $-z + 1$; ii = $x - 1$, y, z; iii = $-x + 2$, $y - ½$, $-z + ½$; iv = $x + 1$, y, z. Hydrogen atoms of the water molecules were not located.

The structure of a μ-cyano-bridged tetracyanonickelate(II) compound of (13-ethyl-5,7,7-trimethyl-13-nitro-1,4,8,11-tetraazacyclotetradeca-4-ene)copper(II), with a tetracyanonickelate ion similarly axially coordinated to copper(II) has been reported [24].

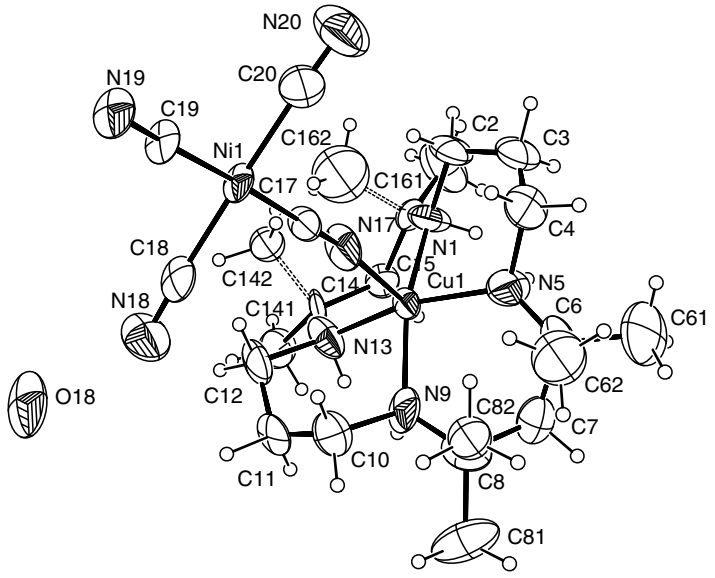


Fig. 6. The molecule containing {Cu1} and associated water molecule O18 of {(hexamethyl-1,5,9,13-tetraazacyclothexadecadiene)copper(II)}-μ-cyano-{tetracyanonickelate(II)} hydrate, drawn as for Fig. 1. Methyl sites C62, C82, C142 and C162 have sof of 0.5. The molecule including {Cu2} and associated water molecule O28 is similar.

The structures of compounds with two [Cu(*cis*-[14]diene)]$^{2+}$ cations linked by a [Ni(CN)$_4$]$^{2-}$ bridging group [16] and of chain polymeric [–Ni(*trans*-Me$_6$[14]diene)-NC–Ni(CN)$_2$–CN–]$_n$ [20] have been reported.

3. Discussion

The only azamacrocycle cations likely to be formed from the reaction of bis(propane-1,3-diamine)copper(II) perchlorate with acetone are [(5,8,8,14,16,16-hexamethyl-1,5,9,13-tetraazacyclohexadeca-5,13-diene)copper(II)]$^{2+}$, [Cu(*trans*-Me$_6$[16]diene)]$^{2+}$ and [(5,8,8,14,14,16-hexamethyl-1,5,9,13-tetraazacyclohexadeca-5,16(1)-diene)copper(II)]$^{2+}$, [Cu(*cis*-Me$_6$[16]diene)]$^{2+}$. The structural determination for crystals of a tetrachlorozincate salt, crystallised in low yield from the original perchlorate salt, unambiguously confirms the presence of the *N-rac*-[Cu(*cis*-Me$_6$[16]diene)]$^{2+}$ cation, so that the condensation reaction produces *at least some* of the [Cu(*cis*-Me$_6$-[16]diene)]$^{2+}$ cation. Thus, the original perchlorate salt must either have only the [Cu(*cis*-Me$_6$-[16]diene)]$^{2+}$ cation, or contain both the [Cu(*cis*-Me$_6$[16]diene)]$^{2+}$ and [Cu(*trans*-Me$_6$-[16]diene)]$^{2+}$ cations, as a mixture, or in some co-crystallised form.

The structural solutions for the perchlorate salt in space groups *P*1, $P\bar{1}$, and *C*2/*m* all indicate the presence of cations of two types, with increasing levels of averaging over sites. One type has twofold or approximate two-fold symmetry, appreciably bent CuN$_4$ group and a relatively short Cu-O interaction; properties which fit best for the *N-rac*-[Cu(*trans*-Me$_6$[16]diene)]$^{2+}$ cation. The other type has mirror, or approximate mirror symmetry, near planar CuN$_4$ group, and no close axial interaction, properties which fit best for the *N-meso*-[Cu(*cis*-Me$_6$[16]diene)]$^{2+}$ cation.

For both cation types in all three space group solutions there is disorder in the location of the imine functions and axial methyl substituents. For the *P*1 solution there are four cation sites; the cation {Cu1} unambiguously has the 5,13-diene *trans*-diimine structure as a single *RR*-enantiomer and the site {Cu2} most probably has the 5,13-diene *trans*-diimine structure, with equal proportions of the *RR* and *SS*-enantiomers. The {Cu3} site unambiguously has the 9,16(1)-diene *cis*-diimine cation and the {Cu4} site has the *cis*-diimine cation, with two disorder components, with rotated arrangements of the cation present in 2:1 proportions.

The solutions in space groups *C*2/*m* and $P\bar{1}$ also support the conclusion that both geometric isomers of the cation are present in the crystal, both with disorder in the location of the imine function and axial methyl substituents. In the $P\bar{1}$ solution for the [Cu(*trans*-Me$_6$[16]diene)]$^{2+}$ cation {Cu1} this is described by the presence of the *N-rac* stereo-isomers in 2:1 ratio. For the [Cu(*cis*-Me$_6$[16]-diene)]$^{2+}$ cation it is described by the presence of rotated arrangements, also in 2:1 ratio.

The solutions in the three space groups thus all indicate the presence of both *N-rac*-[Cu(*trans*-Me$_6$[16]diene)]$^{2+}$ and *N-meso*-[Cu(*cis*-Me$_6$[16]diene)]$^{2+}$ cations. All agree that the *N-meso*-[Cu(*cis*-Me$_6$[16]diene)]$^{2+}$ cation is present with disorder in the locations of the imine functions and axial methyl substituents, with the disorder components present in 2:1 ratio. All agree that the *N-rac*-[Cu(*trans*-Me$_6$[16]diene)]$^{2+}$ cation is present as the *RR* and *SS* enantiomorphs, present in 3:1 proportions for the P1 solution but in 2:1 proportions for the $P\bar{1}$ and *C*2/*m* solutions. These ratios are determined by the sof for the axial substituents, which are determined by the separation of a broad volume of electron density in the axial substituent region into distinct methyl groups, with these carbon atom sites having large adp's and separated by ca 1.7–1.9 Å. The ratios are also influenced by the treatment of the perchlorate ion disorder as partial occupancy oxygen atoms are in the vicinity of the axial methyl substituents.

From a chemical perspective the structures in all space groups indicate that the synthesis yields both the *cis*- and *trans*-diimine isomers of the azamacrocycle cation. The perchlorate salt contains the *N-rac-trans*-cation and the *N-meso-cis*-cation. The latter is present with a preponderance of the *RR*-enantiomer, so the crystal must be chiral.

The thiocyanato perchlorate and tetracyanonickelate(II) compounds both have appreciable disorder which precluded unambiguous assignment of configuration. The thiocyanato compound has the cation on a twofold axis, which is most compatible with the presence of the *N-rac*-[Cu(*trans*-Me$_6$[16]diene)]$^{2+}$ cation.

The tetracyanonickelate(II) compound is very sparingly soluble in water, so the product initially precipitated in high yield from a solution of the perchlorate salt which contains both isomers. The recrystallisation from water also gave the product in high yield so the recrystallised product probably contains both isomers. The structural study shows the presence of two independent cations, with somewhat different geometries, both with disorder of the imine functions and axial substituents. The sof values indicate that cation {Cu2} most probably has the *cis*-structure, while the cation {Cu1} could have either structure. The occupancy values are similar to those of cations {Cu2} and {Cu4}, respectively, of the perchlorate salt, which were assigned with *trans*- and *cis*-structures, respectively, so it seems likely that the two "molecules" of the tetracyanonickelate compound with the {Cu1} and {Cu2} cations have *N-rac-trans*- and *N-meso-cis*- arrangements, respectively.

It is concluded that the reaction of bis-(propane-1,3-diamine)copper(II) with acetone produces both the *cis*- and *trans*-diene macrocyclic cations, as observed for the analogous reactions with ethane-1,2-diamine and butane-1,4-diamine complexes. These isomers co-crystallize as the perchlorate salt, but the *cis*-macrocycle cation crystallises preferentially for the tetrachlorozincate salt.

The [Cu(*cis*-Me$_6$[16]diene)]$^{2+}$ cation present for the tetrachlorozincate salt has the *N-rac* configuration and for the perchlorate salt the *N-meso* configuration. For the perchlorate salt, with co-crystallised *cis* and *trans*-isomeric cations, the *N-meso-cis*-cation is approximately mirror symmetrical, with the CuN$_4$ group near coplanar, with no significant axial interactions. In contrast, the *N-rac-cis*-cation of the tetrachlorozincate salt has an asymmetric, highly twisted CuN$_4$ group, with one diamine chelate ring in a twist conformation, again with no significant axial interactions. The nearest comparisons are with *N-meso*-[Cu(*cis*-Me$_6$[18]-diene)](ClO$_4$)$_2$ and *N-rac*-[Cu(*trans*-Me$_6$[18]diene)](ClO$_4$)$_2$ where the CuN$_4$ group for the *cis*-cation is highly twisted and that for the *trans*-cation is closer to planar, but with a more puckered macrocycle [10].

The Cu–N bond lengths for the compounds are similar to those reported for tetraaza-amine-imine macrocycle compounds with 14–18 ring members, see Table 1. Strain energy calculations indicate the optimal ring-sized tetraaza macrocycle for Cu(II) has a 14-membered ring, with strain energy increasing for larger rings. This strain for larger rings is accommodated by increased ring puckering and/or distortion of the coordination geometry, rather than by increasing the Cu-N distances, as also observed for the analogous nickel(II) compounds [16].

Several of the compounds described show a form of disorder associated with reversal of 2,4,4-trimethyl-1-imine-5-amine chelate rings. The phenomenon has been reported for compounds of 5,7,7,13-tetramethyl-13-nitro-1,4,8,11-tetraazacyclotetradeca-4-ene (and the 13-ethyl homologue) with copper(II) [24,25] and nickel(II) [26] and also occurs for compounds of these macrocycle with the imine and/or nitro groups reduced [27]. In some cases (as for [Cu(*trans*-[16]diene]$^{2+}$) the disorder can be described as co-crystallisation of enantiomorphs, in others (as for [Cu(*cis*-[16]diene]$^{2+}$) as orientational disorder.

4. Experimental

4.1. Preparation of compounds

4.1.1. Perchlorate salt

This was prepared by reaction of bis(propane-1,3-diamine)copper(II) perchlorate with acetone as reported [1,2] and recrystallised from water.

4.1.2. Tetrachlorozincate salt

The perchlorate salt was dissolved in methanol, zinc chloride added and the solution evaporated. Blue crystals which separated in low yield were filtered off and washed with methanol.

4.1.3. Thiocyanato perchlorate compound

This was prepared as for the tetrachlorozincate salt, by evaporation of an aqueous solution of the perchlorate salt containing sodium thiocyanate. IR, band maxima/cm^{-1}: ν(NH) 3169; ν(C≡N) 2082; ν(C=N) 1657.

4.1.4. Tetracyanonickelate(II) compound

This very sparingly soluble compound precipitated when an aqueous solution of $Na_2[Ni(CN)_4] \cdot 3H_2O$ was added to an aqueous solution of the perchlorate salt. This was filtered off and recrystallised from water, using repeated thermal cycling, which still resulted in a mass of tiny, poorly formed crystals. IR, band maxima/cm^{-1}: ν(OH), 3549, 3468, 3461; ν(NH) 3214, 3166; ν(C≡N) 2154, 2122(str); ν(C=N) 1661.

4.2. Crystallography

See Table 3 for details. Diffraction data was collected [29] by using Bruker CCD diffractometers with Mo Kα radiation (0.71073 Å) from fine-focus sealed tubes with graphite monochromators, using phi and omega scans. Multi-scan absorption corrections were applied [29]. The structures were solved by direct methods and full-matrix refined [30], with anisotropic parameters for all non-H atoms (except where specified). Axially oriented methyl substituents were located from difference maps and their sof refined as separate SHELXL parts, as discussed in the text. Hydrogen atoms are in calculated positions and refined using a riding model with SHELXL defaults.

The perchlorate ions exhibit severe rotational disorder. For $[Cu(Me_6[16]diene)](ClO_4)_2$, the model used is reported in the Supplementary data. The details of the treatment had little impact on the dimensions of the cations, but did influence the sof of the axial substituents. For $[Cu(Me_6[16]diene)(NCS)]ClO_4$ the Cl and one O of the perchlorate ion lie on a mirror plane, with the ion effectively in free rotation about this Cl–O direction. This was modeled with six other oxygen sites with sof = 0.5, with default SADI restraints [30] for the Cl–O distances.

Appendix A. Supplementary data

CCDC 6985234, 698522, 698524, 698525 contain the supplementary crystallographic data for $[Cu(Me_6[16]diene)](ClO_4)_2$, *N-rac*-$[Cu(cis\text{-}Me_6[16]diene)][ZnCl_4]$, $[Cu(Me_6[16]diene)(NCS)]ClO_4$, $[Cu(Me_6[16]diene)(\mu\text{-}NC)Ni(CN)_3] \cdot H_2O$. These data can be obtained free of charge via http://www.ccdc.cam.ac.uk/conts/retrieving.html, or from the Cambridge Crystallographic Data Centre, 12 Union Road, Cambridge CB2 1EZ, UK; fax: (+44) 1223-336-033; or e-mail: deposit@ccdc.cam.ac.uk. Supplementary data associated with this article can be found, in the online version, at doi:10.1016/j.poly.2008.12.029.

References

[1] D.A. House, N.F. Curtis, J. Am. Chem. Soc. 86 (1964) 223.
[2] D.F. Cook, N.F. Curtis, J. Chem. Soc., Dalton Trans. (1973) 1076.
[3] N.F. Curtis, R. Pawley, W.T. Robinson, Polyhedron 26 (2007) 3003.
[4] E.K. Barefield, D.H. Busch, Inorg. Chem. 10 (1971) 108.
[5] E.K. Barefield, D.H. Busch, Inorg. Chem. 10 (1971) 1216.
[6] N.F. Curtis, O.P. Gladkikh, Aust. J. Chem. 53 (2000) 727.
[7] N.F. Curtis, Coord. Chem. Rev. 3 (1968) 3.
[8] N.F. Curtis, Y.M. Curtis, H.K.J. Powell, J. Chem. Soc., Sect. A (1966) 1015.
[9] N.F. Curtis, J. Chem. Soc., Dalton Trans. (1972) 1357.
[10] J.H. Timmons, P. Rudolf, A.E. Martell, J.W.L. Martin, A. Clearfield, Inorg. Chem. 19 (1980) 2331.
[11] J.W.L. Martin, J.H. Timmons, A.E. Martell, C.J. Willis, Inorg. Chem. 19 (1980) 2328.
[12] O.P. Gladkikh, N.F. Curtis, Acta Crystallogr., Sect. C 52 (1996) 1418.
[13] N.F. Curtis, G.J. Gainsford, Aust. J. Chem. 39 (1986) 1509–1523.
[14] T.J. Lee, T.H. Lu, C.S. Chung, T.Y. Lee, Acta Crystallogr., Sect. C 40 (1984) 70.
[15] T.H. Lu, T.J. Lee, B.F. Liang, C.S. Chung, J. Inorg. Nucl. Chem. 43 (1981) 2333.
[16] N.F. Curtis, K. Flood, W.T. Robinson, Polyhedron 25 (2006) 1579.
[17] D.J. Szalda, E. Fujita, Acta Crystallogr., Sect. C 48 (1992) 1767.
[18] M.F. Bailey, I.E. Maxwell, J. Chem. Soc., Dalton Trans. (1972) 938.
[19] B.T. Kilbourn, R.R. Ryan, J.D. Dunitz, J. Chem. Soc., Sect. A (1969) 2407.
[20] G.J. Gainsford, N.F. Curtis, Aust. J. Chem. 37 (1984) 1799.
[21] K. Panneerselvam, T.-H. Lu, T.-Y. Chi, F.-L. Liao, C.-S. Chung, Anal. Sci. 15 (1999) 201.
[22] P. Comba, N.F. Curtis, G.A. Lawrance, M.A. O'Leary, B.W. Skelton, A.H. White, J. Chem. Soc., Dalton Trans. (1988) 2145.
[23] H.D. Flack, Acta Crystallogr., Sect. A 39 (1983) 876.
[24] N.F. Curtis, H. Puschmann, Acta Crystallogr., Sect. C 60 (2004) m410.
[25] N.F. Curtis, H. Puschmann, Polyhedron 25 (2006) 1204.
[26] N.F. Curtis, K. Flood, W.T. Robinson, Polyhedron 25 (2006) 1313.
[27] N.F. Curtis, K. Flood, W.T. Robinson, J.M. Waters, Polyhedron, submitted for publication.
[28] L.J. Farrugia, J. Appl. Crystallogr. 30 (1997) 565.
[29] Bruker SMART (Version 5.054), SADABS (Version 2.03) and SAINT (Version 6.02A), Bruker AXS Inc., Madison, Wisconsin, USA, 1997.
[30] G.M. Sheldrick, SHELXTL (Version 5.10). Programs for the Solution and Refinement of Crystal Structures, 1997.

demonstrated that the initial precipitate was not in most cases the thermodynamically stable phase [17]. Consequently, the evolution with time of a carbonate-containing suspension of $Fe(OH)_2$, stored at room temperature in anoxic conditions, was also studied. The results presented in this paper rely mainly on the use of Attenuated Total Reflectance Fourier Transform Infrared Spectroscopy (ATR/FT-IR) as characterisation method. A specific analytical procedure under controlled atmosphere was developed to protect from air the synthetic Fe(II) hydroxides and hydroxysalts that are very sensitive to the oxidising action of O_2. Infrared micro-spectroscopy was also used to characterise chukanovite in corrosion layers of an archaeological sample. Finally, the vibration bands of the infrared spectrum of chukanovite were interpreted by comparison with the spectra of malachite $Cu_2(OH)_2CO_3$, rosasite $(Cu,Zn)_2(OH)_2CO_3$ and pokrovskite $Mg_2(OH)_2CO_3$ [14,18–22].

2. Materials and methods

2.1. Archaeological sample: description and characterisation methods

An iron nail coming from the archaeological site of Glinet (France, Seine Maritime) was analysed. The site corresponds to an ancient forge and is dated from the 16th century. The nail was excavated in July 2004 and stored in ethanol, without having been cleaned, until its sampling for analysis. It corresponds to a set of nails, analysed previously by other techniques [3,23–25] and presenting a large amount of $Fe_2(OH)_2CO_3$ as certified by micro X-ray diffraction [9,10].

The archaeological nail was embedded in epoxy resin and cut with a diamond wire saw in order to work on cross sections. Nujol was used as lubricant to provide an oily protective film for the surface exposed to air during the cutting. To avoid any use of water, the section was polished in hexane with silicium carbide to grade 4000 (grain size of 5 μm). The analyses were performed using a Continuum microscope coupled with a Nexus spectrometer (Thermo-Nicolet). The microscope is equipped with a 15× objective, 10× oculars and a MCT-A detector. The background was acquired using a gold mirror as a sample. Spectra were obtained with the Omnic acquisition software at a resolution of 8 cm^{-1} and by averaging at least 128 scans. After acquisition, the specular reflectance spectra were treated by Kramers-Krönig transform. Previous experiments proved that natural Fe(II) hydroxysalts could remain unaffected by an exposure to air during several hours [26]. The analysis time being short enough, experiments were carried out without specific protection to avoid exposure of the sample to the atmosphere. Note that the MCT-A detector of the microscope limits the spectral window to 650–4000 cm^{-1}.

When necessary, the infrared spectroscopy study was completed with a Raman spectroscopy analysis. Raman measurements were carried out at room temperature on a Jobin Yvon High Resolution Raman spectrometer (LabRAM HR) equipped with a microscope (Olympus BX 41) and a Peltier-based cooled charge coupled device detector. Excitation was provided by a He–Ne laser at a wavelength of 632.8 nm. The laser power was reduced by filters to avoid any transformation of the matter by heating. Spectra were recorded with the Labspec acquisition software at a resolution of 2 cm^{-1}.

2.2. Synthesis of iron(II) precipitate in carbonate-containing media

Solutions prepared with $FeCl_2 \cdot 4H_2O$ (Fluka, 99%), NaOH (Riedel de Haën, concentrated 32% solution) and $Na_2CO_3 \cdot 10H_2O$ (Fluka, 99%) dissolved in water deaerated with an argon flow, were mixed together. Three concentrations of Fe^{2+} ions were considered: 0.12, 0.16 and 0.22 mol L^{-1} for a concentration of OH^- ions kept constant at 0.2 mol L^{-1}. The experimental conditions will be given using the concentration ratio of the reactants $R = [FeCl_2 \cdot 4H_2O]/[NaOH]$, that is equal to 0.6, 0.8 and 1.1. For each value of R, the $Na_2CO_3 \cdot 10H_2O$ concentration was varied. It is expressed similarly via the concentration ratio $R' = [Na_2CO_3 \cdot 10H_2O]/[NaOH]$. Five values of R′ were considered: 0.1, 0.3, 0.5, 0.7 and 0.9. This range of R and R′ values correspond to the domain of pH and carbonate concentration that extends from $Fe(OH)_2$ (smallest R and R′ values) to $Fe_2(OH)_2CO_3$ (largest R and R′ values). The mixing of the solutions led immediately to the formation of a precipitate. Each suspension was then poured in a flask filled up to the brim, closed hermetically to avoid dissolution of oxygen in the liquid and aged 24 h at room temperature before analysis. The resulting solid products were analysed by ATR/FT-IR spectroscopy.

A previous similar study devoted to the Fe(II) hydroxychloride β-$Fe_2(OH)_3Cl$ showed that the thermodynamically stable compound could be sometimes obtained after long times of ageing [17]. It was more precisely observed that $Fe(OH)_2$ could be obtained in conditions where β-$Fe_2(OH)_3Cl$ was the stable phase, and that the complete transformation of $Fe(OH)_2$ into β-$Fe_2(OH)_3Cl$ required months. In order to show if a similar phenomenon could occur in carbonate-containing media, a specific experiment was carried out. First, $Fe(OH)_2$ was synthesised by mixing a solution of $FeCl_2 \cdot 4H_2O$ and a solution of NaOH, prepared in deaerated water. The concentration ratio $R = [FeCl_2 \cdot 4H_2O]/[NaOH]$ was equal to 0.6, and the NaOH concentration to 0.2 mol L^{-1}. According to [17], these conditions are adequate for the formation of $Fe(OH)_2$ and β-$Fe_2(OH)_3Cl$ should not form. The suspension was aged 24 h at room temperature. Then, a deaerated solution of $NaHCO_3$ (Fluka, 99%) was added to the suspension so that the ratio $R'' = [NaHCO_3]/[NaOH]$ became equal to 0.9. The resulting precipitate was analysed 24 h and 2 months after the addition of carbonate species in the medium. The pH of the suspension was measured at the same times.

2.3. FT-IR analysis of synthetic Fe(II) hydroxides and hydroxysalts

Synthetic Fe(II) hydroxides and hydroxysalts are very sensitive to the oxidising action of O_2 and a specific procedure had to be developed [17]. The measurements were performed with the Thermo-Nicolet Nexus spectrometer equipped with a KBr beamsplitter and a DTGS detector by use of a Smart MIRacle ATR accessory with a diamond crystal. The precipitate was filtered under vacuum and rinsed with ethanol while being sheltered from air. The paste was then rapidly set on the crystal and covered by a cell insulating the sample holder and allowing a nitrogen flow to pass through. After a complete evaporation of the ethanol remaining in the filtered product, verified by the spectrum pre-visualisation option of the Omnic acquisition software, spectra were recorded with a resolution of 8 cm^{-1} and at least 128 scans. The background was also acquired under the nitrogen flow.

3. Results

3.1. Characterisation of $Fe_2(OH)_2CO_3$ on an archaeological sample

Fig. 1 shows the infrared spectra of two carbonated Fe(II) compounds detected in the inner corrosion layer of the nail of Glinet. The first spectrum (Fig. 1a) corresponds to siderite $FeCO_3$. It is characterised by a large and intense band at 1415 cm^{-1} and sharp peaks at 864 and 737 cm^{-1}. This mineral was already identified in the rust layers of archaeological artefacts [2]. The other spectrum (Fig. 1b) is similar to that of chukanovite reported by [14]. Note that the same spectrum has been reported earlier, and attributed to a "basic ferrous carbonate", that is a hydroxycarbonate [11].

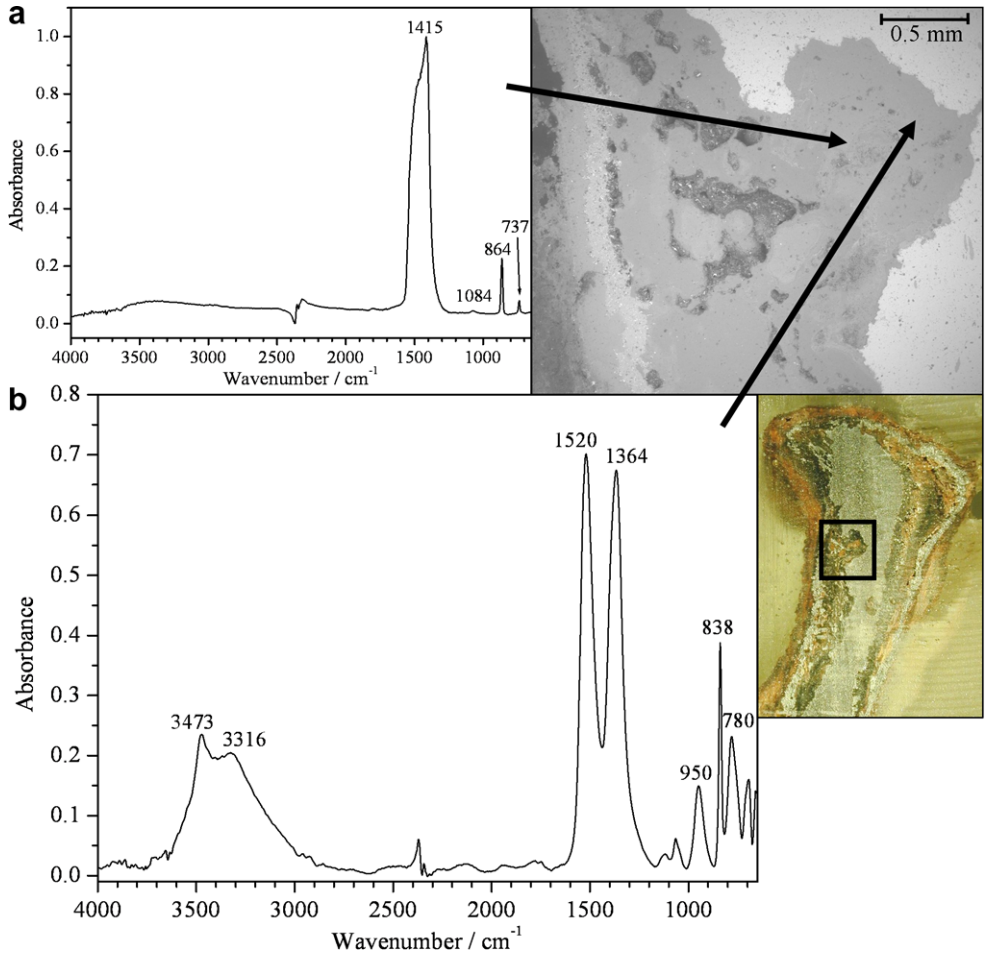


Fig. 1. Photography, micrography and micro-FT-IR spectra of carbonated phases identified on an archeaological iron nail. (a) Siderite, (b) chukanovite.

So, siderite and chukanovite were the only carbonated iron compounds identified in the whole corrosion layer of this sample. Chukanovite was detected on large zones since the surface lightened by the infrared beam during the acquisition could vary between 400 and 2500 μm^2. It was rather localised at the metal/rust layer interface. The products present in the outer parts of the rust layer were mainly magnetite and goethite. These observations are in agreement with previous analyses of similar archaeological nails, achieved using various other techniques [9,10].

3.2. Synthesis of chukanovite

Precipitates obtained with R = 0.6, 0.8 and 1.1 and R′ = 0.1, 0.3, 0.5, 0.7 and 0.9 were analysed. The influence of the concentration of dissolved carbonate species on the nature of the Fe(II) precipitate is studied through the parameter R′. Each precipitate was analysed 24 h after its preparation (Figs. 2–4). An evolution of the composition of the precipitates with R′ can be observed for each R value. Two compounds are clearly identified: Fe(II) hydroxide $Fe(OH)_2$ and chukanovite $Fe_2(OH)_2CO_3$. $Fe(OH)_2$ is identified via the characteristic band at 3624 cm^{-1} [27]. The spectrum of synthetic chukanovite is the same as the spectrum of the corrosion product formed on the archaeological nail. A typical example is the spectrum obtained for R = 1.1 and R′ = 0.9 (Fig. 4).

For the smallest ratio R considered in this study, R = 0.6 (Fig. 2), $Fe(OH)_2$ is present whatever the amount of carbonate species in the medium, as testified by the sharp typical peak of $Fe(OH)_2$ at 3624 cm^{-1}. The spectrum obtained for R′ = 0.1 does not show the

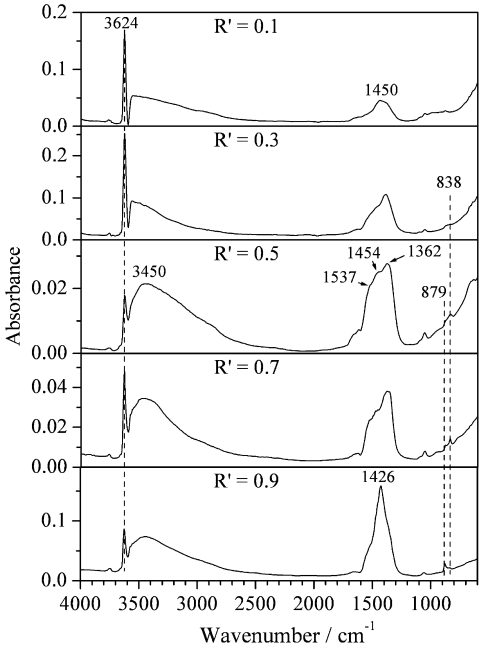


Fig. 2. FT-IR spectra of the Fe(II) precipitates obtained by mixing $FeCl_2 \cdot 4H_2O$, NaOH (0.2 mol L^{-1}) and $Na_2CO_3 \cdot 10H_2O$ solutions with R = $[FeCl_2 \cdot 4H_2O]$/[NaOH] = 0.6 for various R′ = $[Na_2CO_3 \cdot 10H_2O]$/[NaOH] concentration ratios. The precipitates were aged 24 h at room temperature.

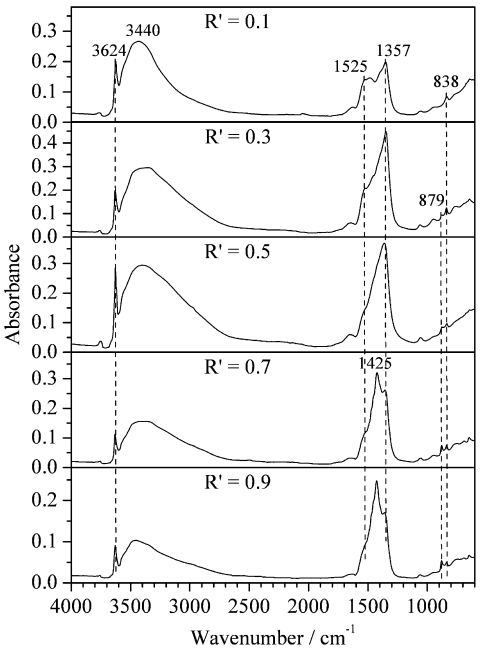


Fig. 3. FT-IR spectra of the Fe(II) precipitates obtained by mixing $FeCl_2 \cdot 4H_2O$, NaOH (0.2 mol L^{-1}) and $Na_2CO_3 \cdot 10H_2O$ solutions with R = $[FeCl_2 \cdot 4H_2O]/[NaOH]$= 0.8 for various R′ = $[Na_2CO_3 \cdot 10H_2O]/[NaOH]$ concentration ratios. The precipitates were aged 24 h at room temperature.

characteristic peaks of chukanovite. However, it presents a large vibration band at 3450 cm^{-1}. This OH stretching mode is more likely due to adsorbed water molecules. This spectrum also shows a weak band at ~1450 cm^{-1}. This band becomes more and more intense as R′ increases which indicates that it relates to carbonate species. As a matter of fact, it is located in the wavenumber region characteristic of the antisymmetric-stretching mode of CO_3^{2-} ions. It does neither correspond to siderite nor to chukanovite (see Fig. 1 for instance) and may correspond to carbonate ions adsorbed on the surface of the $Fe(OH)_2$ crystals or to a hydroxycarbonate with an intermediate composition between $Fe(OH)_2$ and $Fe_2(OH)_2CO_3$, that is $Fe_2(OH)_{4-2x}(CO_3)_x$ with $0 < x < 1$. On the spectra obtained for R′ = 0.5–0.9, a small peak at 838 cm^{-1} is visible. It may also be present for R′ = 0.3. For these R′ values, the band located in the wavenumber region of the antisymmetric-stretching mode of CO_3^{2-} is broad and seems to be constituted of many overlapping peaks. It may result from the superimposition of the doublet of chukanovite at 1537 and 1362 cm^{-1} with the band at ~1425–1455 cm^{-1}. This indicates that a small amount of chukanovite is present.

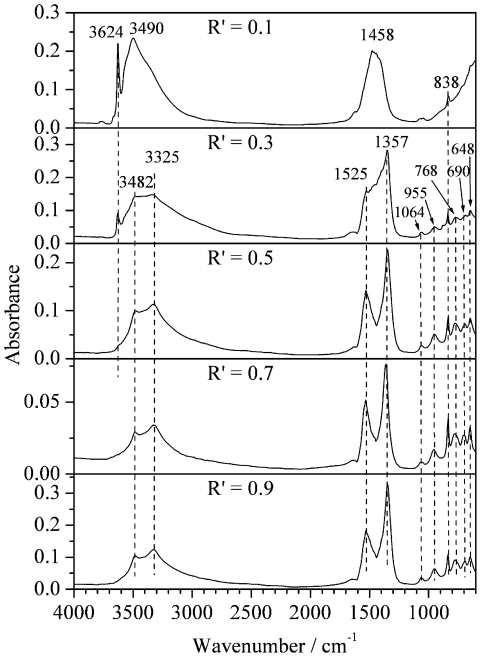


Fig. 4. FT-IR spectra of the Fe(II) precipitates obtained by mixing $FeCl_2 \cdot 4H_2O$, NaOH (0.2 mol L^{-1}) and $Na_2CO_3 \cdot 10H_2O$ solutions with R = $[FeCl_2 \cdot 4H_2O]/[NaOH]$ = 1.1 for various R′ = $[Na_2CO_3 \cdot 10H_2O]/[NaOH]$ concentration ratios. The precipitates were aged 24 h at room temperature.

For the largest value of R considered in this study, that is R = 1.1, $Fe(OH)_2$ is precipitated only for the weakest values of R′, 0.1 and 0.3 (Fig. 4). A small shoulder near 3620 cm^{-1} suggests that it is still present for R′ = 0.5. Chukanovite is present whatever the R′ value, as testified by the presence of its characteristic peak at 838 cm^{-1}. For the largest ratios R′ = 0.7 and 0.9, chukanovite is the only product to precipitate.

For the intermediate ratio R = 0.8, an intermediate situation is observed (Fig. 3). $Fe(OH)_2$ and chukanovite are formed together for every values of R′. The band at ~1425–1455 cm^{-1} already observed for R = 0.6 increases with the value of R′, so that it overlaps with the doublet of chukanovite at 1525 and 1357 cm^{-1}. The increase of a small peak at 879 cm^{-1} with increasing values of R′ is also noticed and this trend is observed for R = 0.6 as well. So the band at ~1425–1455 cm^{-1} and the peak at 879 cm^{-1} are associated and could correspond to the same carbonated species.

3.3. Transformation of $Fe(OH)_2$ into $Fe_2(OH)_2CO_3$

$Fe(OH)_2$ was prepared by mixing deaerated $FeCl_2 \cdot 4H_2O$ and NaOH solutions. The ratio R was chosen equal to R = 0.6, a value sufficiently low to avoid the formation of β-$Fe_2(OH)_3Cl$, i.e. to insure that ferrous hydroxide is the only compound to precipitate. The suspension was aged 24 h in a flask and the solid was analysed by ATR/FT-IR spectroscopy. The spectrum presented in Fig. 5a shows a single sharp peak at 3624 cm^{-1}, which confirms that the only solid phase present at that time was $Fe(OH)_2$. A deaerated solution of $NaHCO_3$ was then added to the suspension, so that the resulting R″ = $[NaHCO_3]/[NaOH]$ ratio was equal to 0.9. The system was then aged at room temperature.

The pH of the suspension was measured 24 h and 2 months after the addition of carbonate species. It increased from

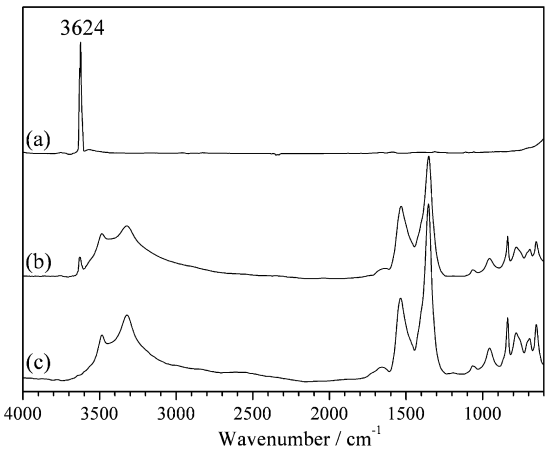


Fig. 5. FT-IR spectra of the Fe(II) precipitate obtained by mixing $FeCl_2 \cdot 4H_2O$ and NaOH solutions with R = $[FeCl_2 \cdot 4H_2O]/[NaOH]$ = 0.6 after 24 h of ageing (a) and after addition of a $NaHCO_3$ solution so that R″ = $[NaHCO_3]/[NaOH]$ = 0.9 and 24 h of ageing (b) or 2 months of ageing (c).

9.06 ± 0.01 to 9.43 ± 0.01. The ATR/FT-IR spectra of the precipitate obtained after the same ageing times are presented in Fig. 5b and c, respectively. It can be seen that after 24 h, the precipitate was already mainly composed of chukanovite. The characteristic peak of $Fe(OH)_2$ at 3624 cm^{-1} was still present, indicating that the transformation was not complete. After 2 months, only chukanovite was obtained.

3.4. Spectral interpretation

The initial precipitate corresponding to R = 1.1 and R′ = 0.9 was analysed after two months of ageing. The spectrum proved to be made of sharper lines as ageing led to an increase of particle size and crystallinity. The spectrum recorded was thus considered as a reference suitable for spectral interpretation. Baseline adjustment and smoothing were performed with the Origin® software. The fitting procedure was performed by use of the Fityk® fitting peaks software with a Voigt function for each peak (Fig. 6).

Chukanovite is related to the minerals of the rosasite group. Comparison was made on the one hand with assignments proposed by [11] and on the other hand with bands of malachite [$Cu_2(OH)_2CO_3$], rosasite [$(Cu,Zn)_2(OH)_2CO_3$] and pokrovskite [$Mg_2(OH)_2CO_3$] between 4000 and 600 cm^{-1} (Table 1). First of all, two main bands are observed at 3481 and 3326 cm^{-1}, that is in the region corresponding to OH stretching vibrations. The fitting of this spectral region revealed four other bands (Fig. 6a). According to the interpretation for rosasite [19,21], the bands at 3538 and 3426 cm^{-1} could be assigned to OH stretching vibrations while the bands at 3222 and 2992 cm^{-1} could be attributed to water adsorbed on the surface of the crystals.

The carbonate C–O stretching region (Fig. 6b) shows two intense bands centred on 1357 and 1525 cm^{-1} corresponding to the ν_3 antisymmetric mode. [11] mentioned three bands at 1530, 1400 and 1355 cm^{-1}. But in fact these are resolved into four bands at 1535, 1500, 1392 and 1358 cm^{-1}. The presence of four bands is interpreted by a lifting of degeneracy due to the site symmetry C_1 of the CO_3^{2-} ions in minerals of the rosasite group [19]. For the same reason, the bands assigned to the ν_4 in-plane bending mode of carbonate ions, centred on 775, 700 and 650 cm^{-1} are splitted in two (Fig. 6c). The band at 1070 cm^{-1} was assigned to the ν_1 symmetric CO_3^{2-} stretching mode because the Raman spectrum collected on the archaeological sample showed the same characteristic peak (Fig. 6d). On the infrared spectrum, it overlaps with a small band at 1053 cm^{-1} that was assigned to a δ OH bending mode. [20] mentioned that in theory the band corresponding to the ν_1 symmetric CO_3^{2-} stretching mode should not be active in infrared but explained its presence by symmetry reduction of the carbonate anion. The band at 955 cm^{-1} can correspond to the one at 880 cm^{-1} for malachite and the one at 870 cm^{-1} of rosasite. For malachite it is assigned to δ OH deformation mode [18,19] since for rosasite the band was mentioned as due to the ν_2 out-of-plane bending mode of carbonate ions [20,21]. Frost et al. [21] indeed mentioned a lifting of degeneracy of this mode characterised by two associated bands at 870 and 818 cm^{-1}. In the case of chukanovite, the sharp band at 836 cm^{-1} is in fact accompanied by a small one at 840 cm^{-1}. It is not quite clear on the considered spectrum. But on the spectrum of natural chukanovite showed by [14] the two peaks are clearly distinguished. They can be assigned to the ν_2 out-of-plane (CO_3^{2-}) bending mode. The band at 955 cm^{-1} can thus be assigned to δ OH bending mode. Bellow 600 cm^{-1}, bands

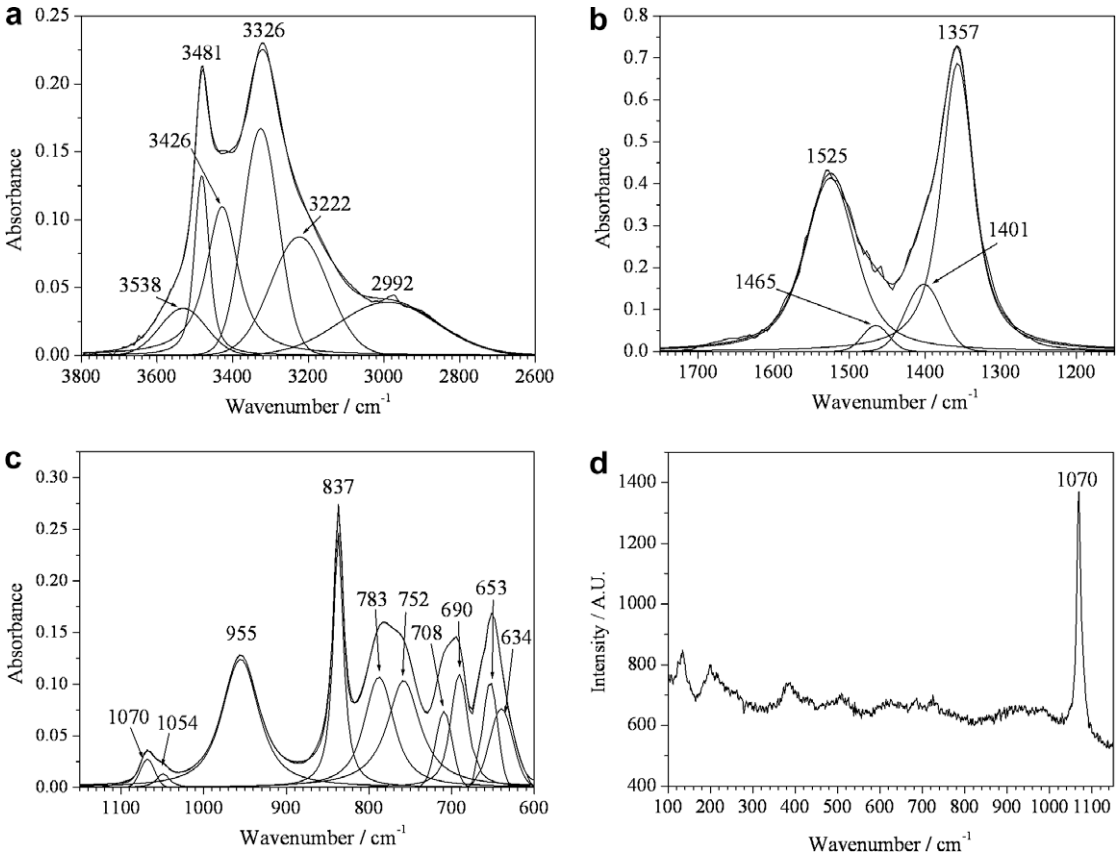


Fig. 6. Curve fitting of the infrared spectrum of a synthetic chukanovite aged during 2 months (a, b, c) and Raman spectrum of chukanovite identified in the corrosion layers of an archaeological iron nail (d).

Table 1
Vibration bands observed by IRTF in chukanovite $Fe_2(OH)_2CO_3$ compared with those of malachite $Cu_2(OH)_2CO_3$, rosasite $(Cu,Zn)_2(OH)_2CO_3$ and pokrovskite $Mg_2(OH)_2CO_3$.

Chukanovite		Malachite		Rosasite	Pokrovskite	Assignments
Present paper	[11]	[18]	[19]	[20–21]	[22]	
3538				3486		OH stretching
3481	3450	3415	3412	3401	3587	OH stretching
3426				3370		OH stretching
3326	3310	3327	3317	3311	3550	OH stretching
3222				3228		adsorbed water
2992				3139		adsorbed water
1525	1530	1511	1517	1522	1556	ν_3 antisym. CO_3^{2-} stretching
1465			1500	1488		ν_3 antisym. CO_3^{2-} stretching
1401	1400	1429	1421	1425		ν_3 antisym. CO_3^{2-} stretching
1357	1355	1393	1393	1388	1392	ν_3 antisym. CO_3^{2-} stretching
		1100	1096			δ OH deformation
1070	1066		1085	1096	1080	ν_1 sym. CO_3^{2-} stretching
1053		1055	1048	1046		δ OH deformation
955	955	908	920	1023	939	δ OH deformation
		880	883			δ OH deformation
				889		impurities
840			832	870		ν_2 CO_3^{2-} bending or δ OH deformation
836	840	820	821	818	846	ν_2 CO_3^{2-} bending
788	780	772	783	781	763	ν_4 CO_3^{2-} bending
755	760	752	751	748	733	ν_4 CO_3^{2-} bending
708	715		734		707	ν_4 CO_3^{2-} bending
690	690	714	714	710	683	ν_4 CO_3^{2-} bending
654					641	ν_4 CO_3^{2-} bending
642						ν_4 CO_3^{2-} bending

corresponding to Fe–O interactions can be expected but the ATR SmartMIRacle accessory did not allow to observe them.

4. Discussion

Chukanovite could be obtained alone, that is without $Fe(OH)_2$ or $FeCO_3$, for R = 1.1 and with R′ between 0.5 and 0.7. In other cases, $Fe(OH)_2$ was present together with chukanovite after 24 h of ageing, except for the smallest values of R and R′ where it was obtained alone.

The precipitation reaction of $Fe_2(OH)_2CO_3$ from $FeCl_2$, NaOH and Na_2CO_3 can be written as followed:

$$RFe^{2+} + OH^- + R'CO_3^{2-} + 2RCl^- + (2R'+1)Na^+ \rightarrow 1/2Fe_2(OH)_2CO_3 + (R'-1/2)CO_3^{2-} + (R-1)Fe^{2+} + 2RCl^- + (2R'+1)Na^+ \quad (1)$$

So R = 1 and R′ = 0.5 correspond to the stoichiometric conditions of the formation of chukanovite. For $R \geqslant 1$ and $R' \geqslant 0.5$, Fe^{2+} and CO_3^{2-} ions would remain in excess in the solution while all the OH^- ions are consumed. In agreement, chukanovite was observed as the unique compound forming when R = 1.1 and $R' \geqslant 0.5$ (Fig. 4).

In contrast, $Fe(OH)_2$ was obtained for R = 0.6 and R = 0.8, whatever the R′ value (Figs. 2 and 3), and for R′ = 1.1 with R′ = 0.1 and 0.3 (Fig. 4). This means that, when at least one of the conditions $R \geqslant 1$ or $R' \geqslant 0.5$ is not verified, $Fe(OH)_2$ precipitates. The reaction leading to the formation of $Fe(OH)_2$ is

$$RFe^{2+} + OH^- + R'CO_3^{2-} + 2RCl^- + (2R'+1)Na^+ \rightarrow 1/2Fe(OH)_2 + R'CO_3^{2-} + (R-1/2)Fe^{2+} + 2RCl^- + (2R'+1)Na^+ \quad (2)$$

The stoichiometric conditions are R′ = 0 and R = ½. For R′ > 0 and R > ½, conditions considered in this study, an excess of carbonate species and dissolved Fe(II) species remains in solution.

However, $Fe(OH)_2$ and $Fe_2(OH)_2CO_3$ may precipitate together in proportions related to the values of R and R′. Omitting Cl^- and Na^+ ions that are not involved in the process, the reaction could be written as

$$RFe^{2+} + OH^- + R'CO_3^{2-} \rightarrow \alpha/2Fe(OH)_2 + \beta/2Fe_2(OH)_2CO_3 + (R'-\beta/2)CO_3^{2-} + (R-\alpha/2-\beta)Fe^{2+} \quad (3)$$

with

$$\alpha + \beta = 1 \quad (4)$$

The proportions α and β of $Fe(OH)_2$ and $Fe_2(OH)_2CO_3$ would then be governed by the amount of (i) Fe(II) or (ii) carbonate species available. In the first case, the concentration of Fe(II) dissolved species is negligible after precipitation and the proportions α and β are such that

$$\alpha/2 + \beta = R \quad (5)$$

Eqs. (4) and (5) lead to $\alpha = 2(1-R)$ and $\beta = 2R-1$, with $\beta/2 \leqslant R'$, according to Eq. (3).

If the proportions α and β are governed by the amount of carbonate species available then

$$\beta = 2R' \quad (6)$$

This leads to $\alpha = 1 - 2R'$, with $\beta \leqslant 2R - 1$ according to Eq. (3).

The values of α and β computed for all the experimental conditions considered in the study are listed in Table 2. For R = 0.6, the smallest $[Fe^{2+}]/[OH^-]$ concentration ratio, the proportion of chukanovite is limited to $\beta = 0.2$ whatever R′ by the lack of Fe(II) species. For the value R′ = 0.1, its is simultaneously limited by the lack of Fe(II) and carbonate species. For R = 0.8, the proportion of chukanovite is limited at R′ = 0.1 to $\beta = 0.2$ by the lack of carbonate species and, for larger R′ values, to $\beta = 0.4$ by the lack of Fe(II). This explained why the increase of R′ did not favour the formation of chukanovite. Finally, for R′ = 1.1, the condition $R' \geqslant 1.0$ is verified and the amount of Fe(II) is sufficient to form chukanovite. So, the formation of the hydroxycarbonate is limited by the lack of carbonate species when R′ < 0.5, and chukanovite is the only phase obtained when $R' \geqslant 0.5$.

The pH of the suspensions, measured after 24 h of ageing, is also clearly linked to the species that controlled the formation of chukanovite. Where the amount of chukanovite obtained is limited by the amount of carbonate species, the pH is slightly acidic, since al-

Table 2
Proportions α and β of $Fe(OH)_2$ and $Fe_2(OH)_2CO_3$ computed using Eqs. (5), (6) and pH of the corresponding suspensions. Italic: cases where the precipitation is controlled by the amount of Fe(II) species – Eq. (5). Bold: cases where the precipitation is controlled by the amount of carbonate species – Eq. (6). Italic + bold: cases where the precipitation leads to the integration of the whole amount of both carbonate and Fe(II) species into the precipitate – Eqs. (5) and (6) both applied.

	R = 0.6		R = 0.8		R = 1.1	
R′ = 0.1	***α = 0.8***	***pH = 10.38***	**α = 0.8**	**pH = 6.17**	**α = 0.8**	**pH = 6.01**
	β = 0.2		**β = 0.2**		**β = 0.2**	
R′ = 0.3	*α = 0.8*	*pH = 10.70*	***α = 0.4***	***pH = 9.05***	**α = 0.4**	**pH = 6.10**
	β = 0.2		***β = 0.6***		**β = 0.6**	
R′ = 0.5	*α = 0.8*	*pH = 11.42*	*α = 0.4*	*pH = 10.23*	**α = 0**	**pH = 6.52**
	β = 0.2		*β = 0.6*		**β = 1.0**	
R′ = 0.7	*α = 0.8*	*pH = 11.07*	*α = 0.4*	*pH = 10.38*		pH = 6.63
	β = 0.2		*β = 0.6*			
R′ = 0.9	*α = 0.8*	*pH = 10.98*	*α = 0.4*	*pH = 10.58*		pH = 9.34
	β = 0.2		*β = 0.6*			

most all the carbonate species are incorporated inside the solid phase and Fe(II) dissolved species are left in excess in the solution. Where the amount of chukanovite is limited by the amount of Fe(II) species, the pH is larger than 10, as CO_3^{2-} anions are in excess in the solution while the Fe(II) species are incorporated inside the solid phase.

Some discrepancies between the computations listed in Table 2 and the experimental results presented in Figs. 2–4 are observed. For instance, at R = 0.6, chukanovite was clearly observed only for $R' \geqslant 0.5$, whereas the same proportion of chukanovite could have been obtained for R′ = 0.1 and 0.3. Three explanations can be given

1. Carbonate species are not only present in chukanovite, as testified by the vibration bands detected on most of the IRTF spectra at 1426 and 879 cm^{-1}.
2. $Fe(OH)_2$ may have formed in some cases as a metastable compound that would transform into chukanovite after a long period of ageing. In the pH range where HCO_3^- predominates (6.4 < pH < 10.3), the corresponding reaction is

$$2Fe(OH)_2 + HCO_3^- \leftrightarrow Fe_2(OH)_2CO_3 + H_2O + OH^- \quad (7)$$

The addition of a $NaHCO_3$ solution to a suspension of $Fe(OH)_2$ led to the formation of chukanovite and to a complete transformation after two months. In agreement with Eq. (1), the pH increased as the transformation proceeded. This experiment was achieved in conditions where R = 0.6 and $R'' = [NaHCO_3]/[NaOH] = 0.9$. It indicates that in similar conditions, that is with small R values and large R′ values, a long period of ageing should lead to the transformation of the initially precipitated $Fe(OH)_2$ into chukanovite.

3. In contrast with the previous explanation, $Fe(OH)_2$ may be stable with respect to chukanovite in the conditions corresponding to the smallest carbonate concentration and the largest pH values. This corresponds to the smallest R and R′ values, i.e. R = 0.6 and R′ = 0.1 or 0.3.

In the absence of any thermodynamic data about chukanovite, it is not possible to argue for one of these explanations. The thermodynamic study of chukanovite, the equilibrium conditions between $Fe(OH)_2$, $FeCO_3$ and $Fe_2(OH)_2CO_3$, and the oxidation process of chukanovite will be the object of another study.

Finally note that in spite of the presence of Cl^- ions in the solutions, brought by the Fe(II) salt $FeCl_2 \cdot 4H_2O$, up to a concentration of 0.44 mol L^{-1} for R = 1.1, no chlorinated compounds were detected. The Fe(II) hydroxychloride β-$Fe_2(OH)_3Cl$ could have been expected in precipitates corresponding to R = 0.8 and R = 1.1, because in these cases, the ratio $[Cl^-]/[OH^-]$ equal respectively to 1.6 and 2.2 is consistent with its formation [17]. This proves that the hydroxycarbonate $Fe_2(OH)_2CO_3$ has formed preferentially to β-$Fe_2(OH)_3Cl$. This is also observed in the case of Fe(II–III) hydroxysalts of the green rust type: Carbonated green rust forms preferentially to chlorinated green rust when both CO_3^{2-} and Cl^- anions are present in the environment [28].

5. Conclusion

Chukanovite $Fe_2(OH)_2CO_3$ could be prepared by precipitation from $FeCl_2 \cdot 4H_2O$, NaOH and $Na_2CO_3 \cdot 10H_2O$ solutions at room temperature. It was characterised by FTIR spectroscopy and each vibration band could be interpreted. In the experimental conditions considered here, that is $[NaOH] = 0.2$ mol L^{-1}, $[FeCl_2 \cdot 4H_2O] = R\,[NaOH]$ and $[Na_2CO_3] = R'\,[NaOH]$, the formation of chukanovite is mainly controlled by the amount of Fe(II) and carbonate species available. $Fe(OH)_2$ is obtained together with chukanovite when the concentration of one of these reactants is not sufficient. The absence of chukanovite for the smallest Fe(II) and carbonate concentrations (R = 0.6 and R′ = 0.1 or 0.3) could not be completely elucidated.

Chukanovite was also identified as one of the main corrosion products of ferrous archaeological artefacts. So, $Fe_2(OH)_2CO_3$ is one of the Fe(II) compounds, with siderite, that has been observed as the result of long term corrosion of iron, while $Fe(OH)_2$ has never been detected in the corrosion layers of the analysed objects reported in literature. Since it was demonstrated that $Fe(OH)_2$ could gradually transform into $Fe_2(OH)_2CO_3$ after long periods of ageing, more likely via a dissolution/reprecipitation mechanisms, it can be suggested that $Fe(OH)_2$ was observed in some of our experiments as a metastable phase that will transform with time into chukanovite. To give ruling on this question, it is necessary to determine the standard Gibbs free energy of formation of chukanovite, which will constitute the next study.

Acknowledgements

This work was supported by the French research national agency (ANR) as part of the "ARCOR" (ANR-06-BLAN-0313-04) project. We also thank Delphine Neff from the Pierre Süe Laboratory for providing the archaeological nails.

References

[1] M. Reffass, R. Sabot, C. Savall, M. Jeannin, J. Creus, Ph. Refait, Corros. Sci. 48 (2006) 709.
[2] H. Matthiesen, L.R. Hilbert, D.J. Gregory, Stud. Conserv. 48 (2003) 183.
[3] D. Neff, P. Dillmann, L. Bellot-Gurlet, G. Beranger, Corros. Sci. 47 (2005) 515.
[4] Z. Tang, S. Hong, W. Xiao, J. Taylor, Corros. Sci. 48 (2006) 322.
[5] G. Palombarini, M. Carbucicchio, Hyperfine Interact. 167 (2006) 791.
[6] S.H. Drissi, Ph. Refait, M. Abdelmoula, J.-M.R. Génin, Corros. Sci. 37 (1995) 2025.
[7] Ph. Refait, M. Abdelmoula, J.-M.R. Génin, R. Sabot, C.R. Geosci. 338 (2006) 476.
[8] L. Legrand, L. Mazerolles, A. Chaussé, Geochim. Cosmochim. Acta 68 (2004) 3497.
[9] M. Saheb, D. Neff, Ph. Dillmann, H. Matthiesen, E. Foy, J. Nucl. Mater. (2008) 118.
[10] M. Saheb, D. Neff, Ph. Dillmann, H. Matthiesen, in: Metal07, Proceedings of the Interim Meeting of the ICOM-CC Metal WG, Amsterdam, September 2007, vol. 2, p. 69.
[11] E. Erdös, H. Altorfer, Werkstoffe und Korrosion 27 (1976) 304.
[12] R.K. Kukkadapu, J.M. Zachara, J.K. Fredrickson, D.W. Kennedy, A.C. Dohnalkova, D.E. Maccready, Am. Mineral. 90 (2005) 510.
[13] E.A.J. Burke, G. Ferraris, New minerals approved in 2005 nomenclature modifications approved in 2005 by the commission on new minerals and mineral names International Mineralogical Association. http://www.geo.vu.nl/ima-cnmmn/minerals2005.
[14] I.V. Pekov, N. Perchiazzi, S. Merlino, V.N. Kalachev, M. Merlini, A.E. Zadov, Eur. J. Mineral. 19 (2007) 891.
[15] R.T. Wilkin, R.W. Pulls, Capstone Report on the Application, Monitoring, and Performance of Permeable Reactive Barriers for Ground-Water Remediation, Reports to the United States Environmental Protection Agency, EPA/600/R-03/045a and EPA/600/R-03/045b.

[16] N. Perchiazzi, S. Merlino, Eur. J. Mineral. 18 (2006) 787.
[17] C. Rémazeilles, Ph. Refait, Corros. Sci. 50 (2008) 856.
[18] M. Schmidt, H.D. Lutz, Physics Chem. Miner. 20 (1993) 27.
[19] D. Stoilova, V. Koleva, V. Vassileva, Spectrochim. Acta Part A 58 (2002) 2051.
[20] R.L. Frost, D.L. Wain, W.N. Martens, B.J. Reddy, Polyhedron 26 (2007) 275.
[21] R.L. Frost, D.L. Wain, W.N. Martens, B.J. Reddy, Spectrochim. Acta Part A 66 (2007) 1068.
[22] R.L. Frost, J. Raman Spectrosc. 39 (2006) 910.
[23] D. Neff, S. Reguer, L. Bellot-Gurlet, P. Dillmann, R. Bertholon, J. Raman Spectrosc. 35 (2004) 739.
[24] S. Reguer, P. Dillmann, F. Mirambet, L. Bellot-Gurlet, Nucl. Instrum. Meth. B 240 (2005) 500.
[25] S. Reguer, P. Dillmann, F. Mirambet, Corros. Sci. 49 (2007) 2726.
[26] S. Reguer, D. Neff, C. Rémazeilles, E. Guilminot, F. Nicot, C. Pelé, M. Meguelati, F. Mirambet, P. Dillmann, P. Refait, N. Huet, F. Mielcarek, J. Rebière, L. Bertrand, in: Metal07, Proceedings of the Interim Meeting of the ICOM-CC Metal WG, Amsterdam, September 2007, vol. 2, p. 60.
[27] H.D. Lutz, H. Möller, M. Schmidt, J. Mol. Struct. 328 (1994) 121.
[28] Ph. Refait, S.H. Drissi, J. Pytkiewicz, J.-M.R. Génin, Corros. Sci. 39 (1997) 1699.

band of the semiconductor, and the ground state potential match the redox level of the redox couple in the electrolyte, thus avoiding energetic losses during the processes of electron transfer and regeneration. Desirably, the dye should contain ligands, most often carboxylate or phosphonate groups, which may firmly attach to the surface of the nanostructured semiconductor [9].

Titanium dioxide electrodes have been successfully sensitized with different polypyridyl–ruthenium complexes. The nc-DSCs sensitized with a *cis*-dithiocyanatobis(4,4′-dicarboxyl-2,2′-bipyridine-)ruthenium(II) complex, dye N3, have shown a high incident photon-to-current conversion efficiency (IPCE) and provided an overall light-to-electricity conversion efficiency of about 10–11% (AM 1.5, 100 mW cm^{-2}). The amphiphilic dyes N-719 and Z-907 both contain two thiocyanates, but have different electron donating ligands attached to their bipyridyl groups. In Z-907 one of the 4,4′-dicarboxyl-2,2′-bipyridine has been replaced with 4,4′-dinonyl-2,2′-bipyridine, thus increasing the hydrophobic character of the dye. The purpose is to improve the stability of the solar cell performance, emerging from the water insolubility of the dye. In previous studies, nc-DSCs sensitized with Z-907 have reached IPCE of 74% (at 540 nm) yielding an overall conversion efficiency of 5.3% (AM 1.5, 100 mW cm^{-2}) [10]. In conjunction with a quasi-solid-state polymer gel electrolyte, an efficiency of more than 6% was reached, and the device sustained heating and showed excellent stability under long-term soaking at 55 °C in full sunlight [11].

As co-adsorbent, the amphiphile hexadecylmalonic acid, HDMA, has been added to sensitizers [12]. Like the dyes N-719 and Z-907, HDMA contains two carboxylate groups by which it is anchored on the TiO_2 surface. By co-grafting, the amphiphiles all together formed an insolating hydrophobic barrier (spacer) for the unwanted back transfer of electrons from the semiconductor to oxidizing species in the electrolyte. nc-DSCs with Z-907 as light harvester and HDMA as co-adsorbent generated improved results as compared to the Z-907 cells lacking the additive, resulting in an overall conversion efficiency of 7.8% under simulated full sunlight (AM 1.5) [12].

A series of polypyridyl–ruthenium complexes with strongly electron donating β-diketonatos replacing the two thiocyanates as an ancillary ligand, have shown good light absorption over the whole visible spectrum extending into the near IR region, resulting in high performances in photoelectrochemical solar cells [13]. The one-electron oxidation of the bidentate diketonato complexes proved to be reversible, contrarily to the irreversible process occurring in monodentate dithiocyanate compounds, a certainly desirable feature for dye molecules, thus offering an improved electrochemical stability of the solar cells. The chelating structure of the β-diketonato ligand is assumed to prevent possible ligand loss processes and nc-DSCs sensitized with the dye $[(dcbpy)_2$-Ru(acetylacetonate)$]Cl^-$ reached a conversion efficiency of 6% (AM 1.5). Long-chain hydrocarbon substituents have been introduced on the β-diketonato ligands in order to suppress unwanted aggregation of dye molecules on the TiO_2 surface [14].

In this work, the performance of nc-DSCs sensitized with a dye composed of N-719, Z-907 or a β-diketonato Ru-complex, and containing room-temperature ionic liquids or a standard organic-liquid-based electrolyte, has been studied. The effect from adding a co-adsorbent of HDMA to the dye or TiO_2 nanoparticles (P25) to the electrolyte was also investigated.

2. Experiments

2.1. Preparation of dye-sensitized nanocrystalline solar cells (nc-DSCs)

Photoelectrodes (also called working electrodes, WE) consisting of a transparent, nanocrystalline, mesoporous titanium dioxide film (12 μm thickness, average particle size 12 nm) on a conducting glass substrate, were prepared from a solution of 36.6 wt% TiO_2 (Degussa P25) in MQ-water. TiO_2 was applied to the fluorine-doped tin oxide glass (Hartford Glass Company Inc.), fixed by Scotch tape, by using the doctor blading technique, and then compressed (600 kg cm^{-2}) [15]. The photoelectrodes were sintered for 30 min at 450 °C in a hot airflow, cooled to 80 °C before transferred into a dye solution and left for at least 4 h. The typical area of the photoelectrode was around 1 cm^2.

The counter electrodes (CE) were platinized by putting a few droplets (0.2 ml) of 5 mM H_2PtCl_6 (Aldrich) in 2-propanol on conducting glass substrates and then heated for 30 min at 380 °C.

The sandwich-structured solar cell was constructed by placing a transparent CE on top of a WE. All solar cells studied were sealed and the electrodes separated by using a thermoplastic thin film, consisting of a 60 μm thick Surlyn frame, as a spacer. The sandwich complex was heated to 120 °C in vaccum for 2 min. An electrolyte was applied to the CE through prefabricated, drilled holes. After being covered by Surlyn and a microscope cover plate, the holes were laminated and a sealed solar cell thus prepared. Finally, silver paint was applied (“Leitsilber”, Hans Wolbring GbmH) on the conducting side of each electrode.

2.2. Photosensitizers

polypyridyl–ruthenium complexes with different electron donating ligands were studied while used as photosensitizers in nc-DSCs. The amphiphilic dyes N-719 and Z-907 have two thiocyanate ligands, but different substituents attached to their bipyridyl groups, see Fig. 1. The chemical formulas of N-719 and Z-907 are $[cis\text{-}Ru(II)(H_2dcbpy)_2(NCS)_2(TBA)_2]$ and $[cis\text{-}Ru(II)(H_2dcbpy)(dnbpy)(NCS)_2]$, respectively, where dcbpy is 4,4′-dicarboxyl-2,2′-bipyridine, dnbpy is 4,4′-dinonyl-2,2′-bipyridine, NCS is thiocyanate and TBA is tetra-n-butylammonium. The sensitizers were both purchased from Solaronix S.A. A batch of Z-907 was also provided as a gift from Dr. M. Zakeeruddin at the Swiss Federal Institute of Technology (EPFL), Switzerland, synthesized as previously described in literature [11].

A polypyridyl–ruthenium complex with a strongly electron donating β-diketonato ligand, $[(dcbpy)_2Ru(acetylacetonate)]Cl^-$, was synthesized according to the procedure described in literature [13]. The dye solutions containing N-719 or the β-diketonato complex were prepared by using 99.9% ethanol as solvent and for Z-907, a mixture of acetonitrile and *tert*-butanol in a volume ratio (1:1) was used, see Table 1.

As co-adsorbent, the amphiphile hexadecylmalonic acid, HDMA (Solaronix S.A.) was added to the sensitizers (Fig. 1).

2.3. Electrolytes

A selection of ionic liquids and one organic-liquid-based standard was prepared to be used as electrolytes in nc-DSCs, see Table 2. The standard electrolyte was prepared by grinding the chemicals into fine particles, before dissolving in an appropriate solvent at room temperature. The iodine-doped, molten-salt electrolytes were prepared by mixing organic sulfonium or imidazolium iodides with elemental iodine, in an iodide-to-iodine-molar proportion 100:1. The organic sulfonium and imidazolium iodides were prepared according to methods that have previously been described, see Refs. [2,8].

The effect of dispersed nanoparticles of titanium dioxide (Degussa P25) in the electrolyte was also studied for solar cells sensitized by the dye N-719. A suspension of typically 1 wt% of P25 TiO_2 in the electrolyte was grinded in an agate mortar, thus forming a gel phase.

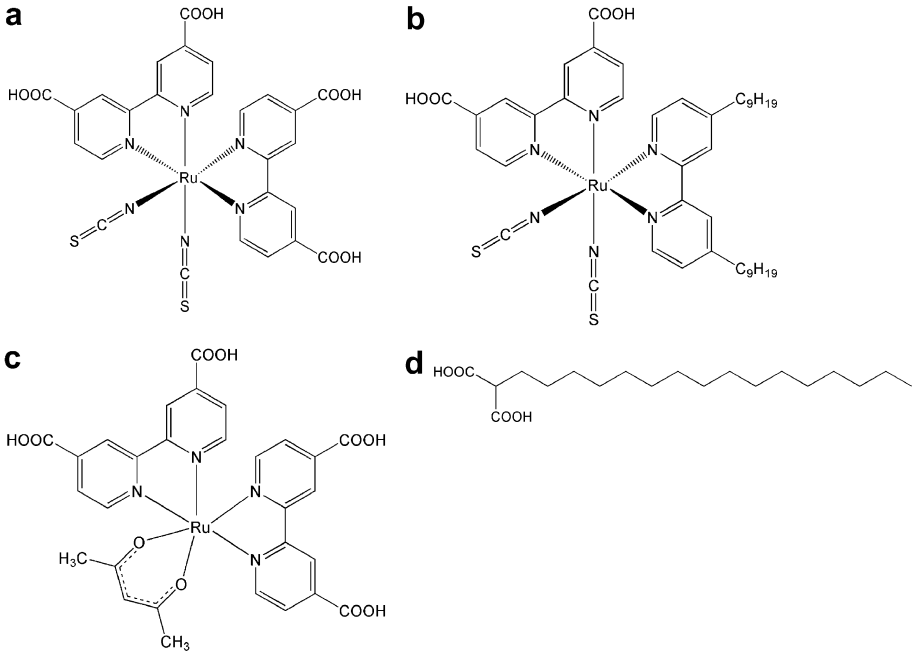


Fig. 1. The molecular structures of the dyes (a) N-719 (b) Z-907 and (c) β-diketonato complex (monopositively charged), and the co-adsorbent (d) HDMA.

Table 1
The dyes used as photosensitizers in nanocrystalline solar cells of Grätzel type.

Dye	Chemical formula	Dye-solution
N-719	[*cis*-Ru(II)(H_2dcbpy)$_2$(NCS)$_2$(TBA)$_2$]	500 μM dye in EtOH
N-719 + HDMA[a]		500 μM dye, 125 μM HDMA in EtOH
Z-907 Sol	[*cis*-Ru(II)(H_2dcbpy)(dnbpy)(NCS)$_2$]	300 μM dye in AcN/*t*-BuOH[b]
Z-907 Sol + HDMA[a]		300 μM dye, 75 μM HDMA in AcN/*t*-BuOH[b]
Z-907 Zak	[*cis*-Ru(II)(H_2dcbpy)(dnbpy)(NCS)$_2$]	300 μM dye in AcN/*t*-BuOH[b]
Diketonato	[(dcbpy)$_2$Ru(acetylacetonate)]Cl^-	500 μM dye in EtOH
Diketonato + HDMA[a]		500 μM dye, 125 μM HDMA in EtOH

[a] HDMA, hexadecyl malonic acid.
[b] AcN, acetonitrile, volume ratio of solvents (1:1).

2.4. Photoelectrochemical measurements

2.4.1. Photocurrent density-photovoltage measurements

The photocurrent density-photovoltage (*J*–*V*) characteristics of a solar cell represents its electrical output, which depends on the collaborative efficiencies of the cell processes, such as excitation by light, separation and migration of mobile charge carriers, injection, transfer and collection of charges. In *J*–*V* diagrams the short-circuit photocurrent density (J_{sc}) and the open-circuit voltage (V_{oc}) are displayed. The fill factor (FF) and overall light-to-electric energy conversion efficiency (η) may be determined using the defined equations:

$$F = (JV)_{MAX}/(J_{sc}V_{oc}) \quad (1)$$

$$\eta = J_{sc}V_{oc}FF/P_s \quad (2)$$

P_s represents the intensity of the incident light (W m^{-2}). The *J*–*V* diagrams were monitored and recorded using a computerized Keithley Model 2400 source/meter. As solar simulator a microwave–powered sulfur plasma lamp, Light drive™ 1000 was used. The obtained electrical power is calibrated versus solar light making the presented efficiencies (η) to correspond to the use of an AM 1.5 simulated solar light spectrum with the light intensity 100–1000 W m^{-2}).

2.4.2. IPCE measurements

The incident monochromatic photon-to-current conversion efficiency, IPCE, or external quantum efficiency, is the product of the quantum absorptivity, the injection efficiency and the current collection quantum efficiency. It expresses the ratio of the number of electrons that reaches the external circuit of the solar cell to the number of incident photons absorbed. It can be described as:

$$\mathrm{IPCE} = hcJ_{ph}/(e\lambda P_s) = 1240J_{ph}/(\lambda P_s) \quad (3)$$

where J_{ph} is the photocurrent density (A m^{-2}), λ the wavelength of monochromatic light (nm) and P_s the input light power density (W m^{-2}), 1240 is the product of the constants *h*, *c* and *e* being the

Table 2
The electrolytes used in dye-sensitized, nanocrystalline solar cells.

Electrolyte	
Standard	0.5 M LiI, 50 mM I_2, 0.5 M 1-MBI in 3-MPN[a]
(Et_2MeS)I:I_2 (100:1)[b]	(Et_2MeS)I = diethylmethylsulfonium iodide
(Bu_2MeS)I:I_2 (100:1)[b]	(Bu_2MeS)I = dibutylmethylsulfonium iodide
(HxMeIm)I:I_2 (100:1)[b]	(HxMeIm)I = 3-hexyl-1-methylimidazolium iodide

[a] MBI, methyl-benzimidazole; MPN, methoxypropionitrile.
[b] Iodide-to-iodine-molar proportion.

Planck's constant, the speed of light in vacuum and the elementary charge, respectively. IPCE was recorded as a function of illumination wavelength for a two-electrode solar cell using a computer-controlled potentiostat. IPCE-action spectra were recorded using a computerized set-up consisting of a 300 W arc lamp, a high-intensity monochromator, a Keithley Model 2400 source/meter and appropriate filters and lenses. A Newport 1830-C power-meter with 818-UV detector-head was used for calibration.

3. Results and discussion

3.1. Comparison of the dyes N-719 and Z-907

Photoelectrochemical measurements of nc-DSCs with the dye N-719 showed higher overall light-to-electricity conversion efficiencies than solar cells sensitized with the more hydrophobic dye Z-907, see Table 3. It should be noted, that the results reported represents the calculated average data achieved from measuring two identical solar cells, sensitized with the same dye and containing the same electrolyte. The deviation of the efficiency results was typically ±0.3. The trend, showing the N-719 cells being superior to the Z-907 cells, was applicable to all electrolytes studied and basically due to the higher short-circuit photocurrent densities and open-circuit voltages achieved by the N-719 cells. This was an unexpected result, since the dye Z-907 is more hydrophobic than N-719, based on the long-chain nonyl substituent attached to the bipyridyl ligand. The nonyl group is assumed to form an insolating hydrophobic barrier (spacer) for the unwanted back transfer of electrons from the semiconductor to oxidizing species in the electrolyte, thus expected to result in higher current densities due to reduced dark currents. Also the IPCE results were higher for the N-719-sensitized cells, for all electrolytes studied. However, in 100 W m^{-2} illumination, higher fill factors were achieved by the Z-907 cells, which was most apparent for those containing the most viscous electrolyte, the iodine-doped (HxMeIm)I.

The results achieved by nc-DSCs sensitized with either the dye Z-907 Sol (from Solaronix) or Z-907 Zak (from M. Zakeeruddin, EPFL), were almost identical or within experimental errors, for all electrolytes studied in this work (Table 3).

3.2. Comparison of the dyes N-719 and β-diketonato complex

Nc-DSCs sensitized with the β-diketonato complex $[(dcbpy)_2$-Ru(acetylacetonate)]Cl^- showed lower photoelectrochemical results in comparison to the N-719 cells, see Table 3. However, good overall conversion efficiencies were achieved, especially for those solar cells containing the standard, organic-liquid-based electrolyte, reaching at most 2.1% (100 W m^{-2}, AM 1.5). The β-diketonato sensitized solar cells containing ionic liquid electrolytes obtained open-circuit potentials and fill factors that were comparable to the values produced by the organic-liquid-based cells. However, the short-circuit current densities were poorer, thus resulting in lower conversion efficiencies.

3.3. Addition of co-adsorbent HDMA to the dye

The amphiphile hexadecylmalonic acid, HDMA, was added as a co-adsorbent, to dye solutions of N-719, Z-907 or the β-diketonato complex. Like the dyes, HDMA contains two carboxylate groups by which it may be anchored to the TiO_2 surface, in order to form a

Table 3
Results from *J–V* measurements of solar cells sensitized with different dyes, using a solar simulator with light intensity of 100 or 1000 W m^{-2} (AM 1.5 illumination). The results reported here are calculated average data achieved by two identically sensitized solar cells, containing the same electrolyte.

Electrolyte	Dye	100 W m^{-2}				1000 W m^{-2}			
		η (%)	J_{sc} (mA cm^{-2})	V_{oc} (V)	FF	η (%)	J_{sc} (mA cm^{-2})	V_{oc} (V)	FF
Standard	N-719	4.1	1.00	0.62	0.67	2.5	8.6	0.69	0.41
	N-719 + HDMA	2.9	0.66	0.61	0.72	2.5	6.2	0.70	0.57
	N-719 El + P25	4.6	0.95	0.68	0.71	3.3	9.3	0.72	0.49
	Z-907 Sol	3.7	0.94	0.57	0.69	2.2	7.2	0.63	0.47
	Z-907 Zak	3.6	0.81	0.64	0.69	2.5	7.2	0.71	0.50
	Z-907 Sol + HDMA	4.0	1.07	0.59	0.64	2.3	8.0	0.66	0.45
	Diketonato	2.0	0.59	0.53	0.66	1.7	5.4	0.61	0.50
	Diketonato + HDMA	2.0	0.59	0.48	0.69	1.7	6.5	0.57	0.46
$(Et_2MeS)I:I_2$	N-719	1.7	0.65	0.46	0.58	1.8	2.2	0.58	0.71
	N-719 + HDMA	1.6	0.53	0.46	0.67	0.9	2.3	0.56	0.70
	N-719 El + P25	1.7	0.63	0.45	0.61	1.1	2.7	0.55	0.74
	Z-907 Sol	1.4	0.56	0.42	0.60	0.8	2.3	0.51	0.69
	Z-907 Zak	1.2	0.47	0.43	0.60	0.8	2.5	0.54	0.63
	Z-907 Sol + HDMA	1.4	0.52	0.43	0.62	1.1	3.0	0.52	0.68
	Diketonato	0.3	0.14	0.35	0.52	0.4	1.6	0.49	0.52
	Diketonato + HDMA	0.4	0.15	0.40	0.69	0.5	2.0	0.50	0.51
$(Bu_2MeS)I:I_2$	N-719	2.3	0.80	0.55	0.52	0.5	1.2	0.63	0.69
	N-719 + HDMA	2.0	0.72	0.50	0.55	0.3	0.8	0.58	0.70
	N-719 El + P25	2.3	0.79	0.50	0.58	0.4	0.9	0.59	0.73
	Z-907 Sol	2.0	0.73	0.49	0.56	0.5	1.3	0.57	0.71
	Z-907 Zak	2.2	0.73	0.53	0.56	0.5	1.1	0.62	0.70
	Z-907 Sol + HDMA	2.0	0.74	0.48	0.57	0.5	1.2	0.56	0.69
	Diketonato	0.7	0.24	0.46	0.62	0.3	0.7	0.53	0.70
	Diketonato + HDMA	1.1	0.34	0.48	0.65	0.3	0.9	0.56	0.66
$(HxMeIm)I:I_2$	N-719	1.4	0.59	0.51	0.45	0.3	0.9	0.63	0.57
	N-719 + HDMA	1.3	0.43	0.53	0.59	0.3	0.9	0.64	0.62
	N-719 El + P25	1.7	0.66	0.49	0.53	0.3	0.8	0.58	0.69
	Z-907 Sol	1.2	0.46	0.49	0.55	0.2	0.6	0.57	0.68
	Z-907 Zak	1.3	0.46	0.52	0.55	0.2	0.6	0.33	0.63
	Z-907 Sol + HDMA	1.3	0.44	0.49	0.59	0.2	0.5	0.56	0.70
	Diketonato	0.5	0.18	0.45	0.58	0.3	0.5	0.53	0.61
	Diketonato + HDMA	0.5	0.19	0.45	0.59	0.2	0.6	0.54	0.64

hydrophobic spacer for unwanted electron transfer to species in the electrolyte. This effect was assumed to be most apparent for solar cells sensitized with Z-907, incorporating the most hydrophobic character of the dyes, due to the long-chain nonyl groups. By co-grafting on the TiO_2 layer the two amphiphiles, Z-907 and HDMA that may form a mixed monolayer, more tightly packed than when the dye is adsorbed alone, the aim was to produce a more efficient insulating barrier to reduce so-called dark currents.

From the photocurrent density-photovoltage measurements, the nc-DSCs containing the standard organic-liquid-based electrolyte, using Z-907 as light harvester and HDMA as co-adsorbent, generated improved overall conversion efficiencies and short-circuit currents, as compared to Z-907 cells without the additive, see Table 3. For the Z-907-sensitized solar cells, an addition of HDMA entailed increased results of η (from 3.7% to 4.0%) and J_{sc} (from 0.94 to 1.07 mA cm^{-2}), thus attaining the highest short-circuit current density achieved in 100 W m^{-2} illumination of all dyes studied in this work (see Table 3). The Z-907 + HDMA-sensitized solar cells containing electrolytes of sulfonium or imidazolium iodide-based ionic liquids gave essentially the same almost similar results, concerning η, J_{sc}, V_{oc} and FF, as those Z-907 cells without the co-adsorbent.

However, for the β-diketonato-sensitized solar cells containing ionic liquid electrolytes, the addition of HDMA to the dye generally gave improved results concerning the short-circuit current densities, the open-circuit voltages, the fill factors as well as the conversion efficiencies. For the solar cells sensitized with the dye N-719, the overall conversion efficiencies were in fact reduced by the addition of HDMA, basically due to decreased short-circuit current densities, observed for all electrolytes studied.

3.4. Addition of TiO_2 nanoparticles to the electrolyte

Titanium dioxide nanoparticles (P25), spherical with a diameter of about 25 nm, were dispersed in the electrolytes, resulting in ionic, nanocomposite, gel electrolytes. Photoelectrochemical measurements of nc-DSCs sensitized with dye N-719 showed that the overall light-to-electricity conversion efficiencies were improved only for those cells containing the standard, organic-liquid-based electrolyte, from 4.1% to 4.6%, and the iodine-doped (HxMeIm)I, from 1.4% to 1.7%, see Table 3. Concerning the organic-liquid-containing cells, the improved η was due to increased V_{oc} and fill factors, and for the (HxMeIm)I cells due to increased J_{sc} and fill factors. For solar cells containing the organic sulfonium iodide-based electrolytes, the results were unaffected by the addition of TiO_2 nanoparticles.

3.5. Variation of the light intensity

For nc-DSCs containing the standard organic-liquid-based electrolyte, the short-circuit photocurrent densities were almost proportionally increased upon changing the light intensity of the solar simulator from 100 to 1000 W m^{-2}, for all sensitizers studied, see Fig. 2. The solar cells sensitized with the dyes N-719 or Z-907 generally showed higher J_{sc} values as compared to the β-diketonato cells, within the light intensity interval studied. However, for each electrolyte the best J_{sc} results were obtained for solar cells of different dye compositions. For the organic sulfonium iodides, solar cells using sensitizers based on Z-907 were most efficient, meanwhile the N-719 based dyes were superior using the imidazolium iodide electrolyte.

In 1000 W m^{-2} illumination (AM 1.5), the highest short-circuit current density, 9.3 mA cm^{-2}, was achieved by the N-719-sensitized cells containing the TiO_2 nanocomposite electrolyte (Table 3). The dye-sensitized solar cells containing the standard, organic-liquid electrolyte achieved short-circuit current densities

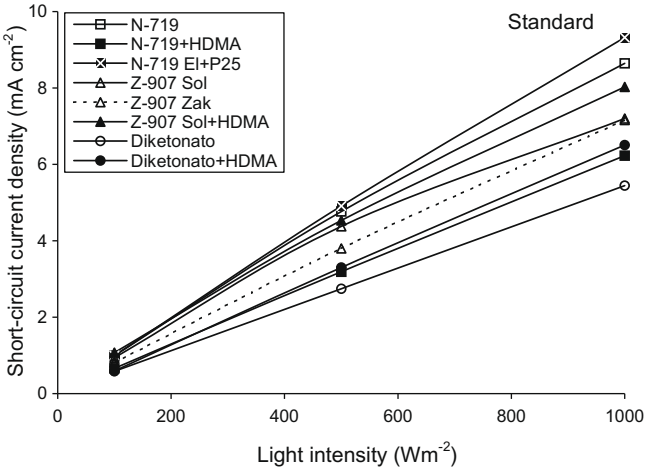


Fig. 2. The short-circuit current density measured at different light intensities for solar cells containing a standard organic-liquid-based electrolyte sensitized with different dyes.

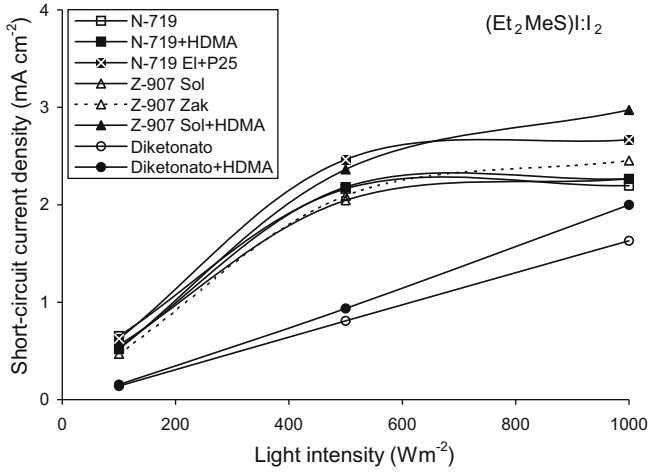


Fig. 3. The short-circuit current density measured at different light intensities for solar cells containing an iodine-doped (Et_2MeS)I electrolyte sensitized with different dyes.

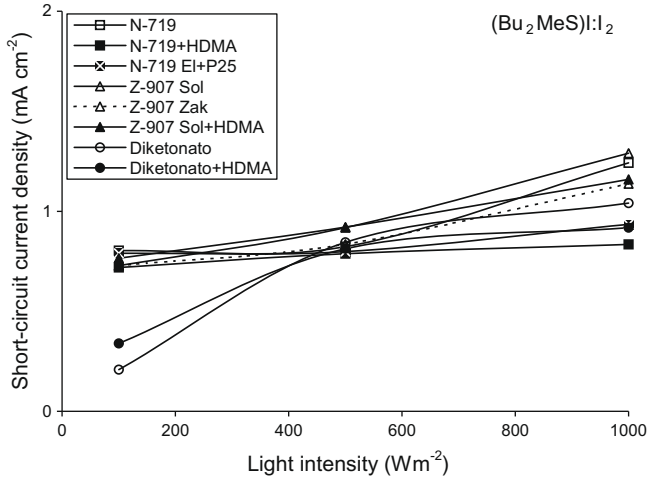


Fig. 4. The short-circuit current density measured at different light intensities for solar cells containing an iodine-doped (Bu_2MeS)I electrolyte sensitized with different dyes.

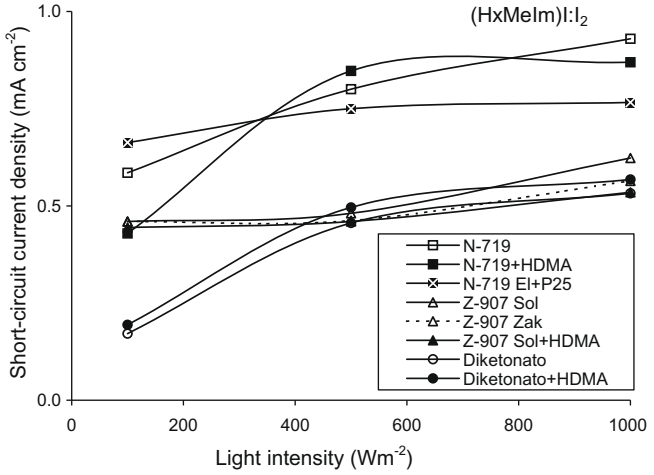


Fig. 5. The short-circuit current density measured at different light intensities for solar cells containing an iodine-doped (HxMeIm)I electrolyte sensitized with different dyes.

ranging from 5.4 to 9.3 mA cm^{-2}, meanwhile the ionic liquid-based cells showed J_{sc} values of 1.6–2.7 mA cm^{-2} for $(Et_2MeS)I:I_2$ (Fig. 3), 0.7–1.2 mA cm^{-2} for $(Bu_2MeS)I:I_2$ (Fig. 4) and 0.5–0.9 mA cm^{-2} for $(HxMeIm)I:I_2$ (Fig. 5).

For most nc-DSCs containing ionic liquid electrolytes, there seem to exist a limited short-circuit current density, a J_{lim} value, which emerges at different light intensities going from 100 to 1000 W m^{-2}. For some sensitizers this saturation phenomenon was observed already at 100 W m^{-2}. A short-circuit current density limitation has formerly been reported for N-719-sensitized solar cells using sulfonium or imidazolium iodide-containing ionic liquids [16].

However, for the solar cells sensitized with the β-diketonato complex containing the $(Et_2MeS)I:I_2$ electrolyte, no short-circuit current density limitation was observed within the intensity interval studied, see Fig. 3. The material transport and the diffusion of triiodides are not limited in these systems because of the low short-circuit current densities.

4. Conclusions

The solar cells sensitized with the dye N-719 showed higher overall light-to-electricity conversion efficiencies than the Z-907 cells, for all electrolytes studied. This is caused by the higher short-circuit photocurrent densities and open-circuit voltages. Since the dye Z-907 is more hydrophobic, expected because of the long-chain nonyl group, it is assumed to form an insulating barrier for the unwanted back transfer of electrons to oxidizing species in the electrolyte, thus resulting in higher current densities due to reduced dark currents.

The addition of an amphiphilic co-adsorbent, the hexadecylmalonic acid (HDMA), resulted in increased overall light-to-electricity conversion efficiencies only for the Z-907 solar cells with an organic-liquid electrolyte. The efficiencies of cells containing sulfonium or imidazolium iodide-based ionic liquids were almost unaffected. The improvement may be explained by co-grafting, as the amphiphilic dye and HDMA together form an insolating hydrophobic barrier.

The presence of TiO_2 (P25) nanoparticles is assumed to support electron transfer reactions in the electrolyte. The dispersion of TiO_2 nanoparticles resulted in improved overall conversion efficiencies only for the N-719 solar cells containing the standard, organic-liquid electrolyte, caused by increased open-circuit voltages and fill factors. The N-719-sensitized solar cells with the nanocomposite-containing, organic-liquid electrolyte achieved the highest short-circuit current density of all cells studied in this work. For solar cells containing the organic sulfonium iodide-based electrolytes, the results were essentially unaffected by the addition of TiO_2 nanoparticles.

In summary, for solar cells sensitized with N-719, Z-907 or the β-diketonato complex and containing electrolytes of sulfonium or imidazolium iodide ionic liquids, no striking improvement concerning the overall conversion efficiency could be noticed by an addition of HDMA to the dye or nanoparticles to the electrolyte.

Acknowledgements

The Swedish National Research Council is acknowledged for financial support. We thank Anna Holmberg, Erik Pettersson and William Kylberg at the Department of Physical Chemistry, Uppsala University, for their help in preparing the solar cells. Henriette Wolpher at the Department of Organic Chemistry, Stockholm University, is acknowledged for the help in the synthesis of the β-diketonato complex. We are grateful to M. Zakeeruddin at Swiss Federal Institute of Technology (EPFL), Switzerland, for his kindness to provide us with a sample of dye Z-907.

References

[1] B. O'Regan, M. Grätzel, Nature 353 (1991) 737.
[2] N. Papageorgiou, Y. Athanassov, M. Armand, P. Bonhote, H. Pettersson, A. Azam, M. Grätzel, J. Electrochem. Soc. 143 (1996) 3099.
[3] W. Kubo, S. Kambe, S. Nakade, T. Kitamura, K. Hanabusa, Y. Wada, S. Yanagida, J. Phys. Chem. B 107 (2003) 4374.
[4] P. Wang, S.M. Zakeeruddin, J.E. Moser, R. Humphry-Baker, M. Grätzel, J. Am. Chem. Soc. 126 (2004) 7164.
[5] P. Wang, S.M. Zakeeruddin, M. Gratzel, W. Kantlehner, J. Mezger, E.V. Stoyanov, O. Scherr, Appl. Phys. A 79 (2004) 73.
[6] P. Wang, S.M. Zakeeruddin, J.E. Moser, M. Grätzel, J. Phys. Chem. B 107 (2003) 13280.
[7] H. Usui, H. Matsui, N. Tanabe, S. Yanagida, J. Photochem. Photobiol. A: Chem. 164 (2004) 97.
[8] H. Paulsson, A. Hagfeldt, L. Kloo, J. Phys. Chem. B 107 (2003) 13665–13670.
[9] M. Grätzel, J. Photochem. Photobiol. A: Chem. 164 (2004) 3.
[10] P. Wang, S. Zakeeruddin, I. Exnar, M. Grätzel, Chem. Commun. (2002) 2972.
[11] P. Wang, S.M. Zakeeruddin, J.E. Moser, M.K. Nazeeruddin, T. Sekiguchi, M. Grätzel, Nature Mater. 2 (2003) 402.
[12] P. Wang, S. Zakeeruddin, P. Comte, R. Charvet, R. Humphry-Baker, M. Grätzel, J. Phys. Chem. B 107 (2003) 14336.
[13] Y. Takahashi, H. Arakawa, H. Sugihara, K. Hara, A. Islam, R. Katoh, Y. Tachibana, M. Yanagida, Inorg. Chim. Acta 310 (2000) 169.
[14] A. Islam, H. Sugihara, M. Yanagida, K. Hara, G. Fujihashi, Y. Tachibana, R. Katoh, S. Murata, H. Arakawa, New J. Chem. 26 (2002) 966.
[15] H. Lindström, E. Magnusson, A. Holmberg, S. Södergren, S.-E. Lindquist, A. Hagfeldt, Sol. Energy Mater. Sol. Cells 73 (2002) 91.
[16] H. Paulsson, L. Kloo, A. Hagfeldt, G. Boschloo, J. Electroanal. Chem. 586 (2006) 56.

co-workers [13]. This protonation constant, which is lower because of the structural difference due to the second nitrogen atom in the ring and to the aliphatic substituents, led us to study the aspergillic acid–Fe(III) system. In fact, in a recent paper [14], we pointed out how a decrease in the basicity of coordinating groups, which induces a decrease of both protonation and complex formation constants, can be accompanied by an increase of pFe, i.e. of the real chelating ability of the ligand. The major problem we encountered was the commercial unavailability of aspergillic acid, which lead us to prepare it via a biosynthetic method starting from *Aspergillus flavus*.

2. Experimental

2.1. Reagents

NaOH, HCl, $HClO_4$, $NaClO_4$, NaCl, KCl, $CHCl_3$, $CDCl_3$, CH_3OH and $FeCl_3$ were purchased from Aldrich. Tryptone was purchased from Microbiol S.n.c.

2.2. Synthesis of aspergillic acid

2.2.1. Growth of Aspergillus flavus

The *A. flavus* strain ATCC 46283 was used in all the experiments (Fig. 1). Spores were grown for 7 days on LB Petri dishes at 25 °C in the dark. An inoculum of 10^5–10^6 spores was grown in 1 L of 2% Tryptone, 5% NaCl at 25 °C for 5 days in the dark without shaking. Heavy, white and wrinkled pellicle was formed 48 h after inoculation. After 5 days the pH of the liquid under the pellicle was 7.5–8. The aspergillic acid yield from a litre of culture was 5–10 mg. The Aspergillic acid production did not change significantly with the use of a yeast extract medium and longer growth time.

2.2.2. Isolation of pure aspergillic acid

The growth medium after 5 days was filtered to separate the spores from the medium solution. One litre of medium was concentrated by low pressure evaporation to a 100–200 mL final volume. The concentrated medium was then extracted with $CHCl_3$. After chloroform evaporation, the crude aspergillic acid was sublimated at low pressure at 75–80 °C. The isolation of pure product from the culture filtrate performed according to the MacDonald procedure [15] did not allow a significantly higher amount of pure product.

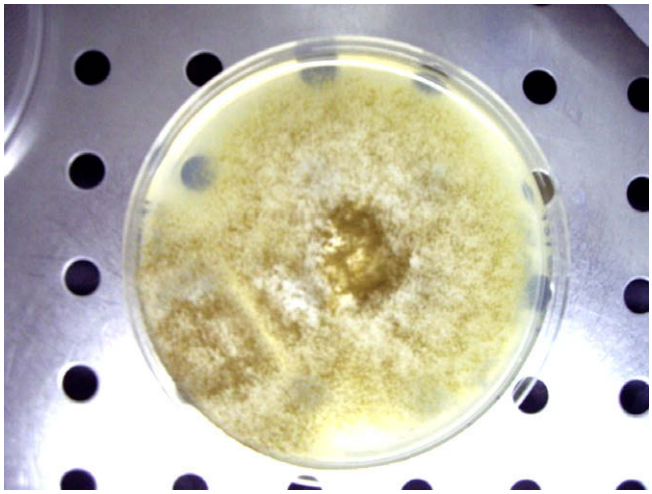


Fig. 1. The *Aspergillus flavus* ATCC 46283 on the LB Petri dish.

2.3. Purity check

The MS experiment was carried out with an Agilent 1200 Series mass spectrometer. Spectra were acquired in the positive ion mode and the solutions were injected into the MS source with a solvent flow rate of 3 μL/min. The temperature of the spray chamber was 200 °C. A capillary 4000 V voltage was applied. Data were obtained in 50–1000 *m/z* range. Purity was also checked by ^{1}H NMR spectra in $CDCl_3$.

2.4. Potentiometric measurements

Potentiometric titrations were performed on CH_3OH:H_2O 80:20 w/w solutions (1.5 mL total volume) using a MOLSPIN automatic titrator with a Russel CMAW 711 microcombined glass electrode (KCl aqueous solution was replaced with 0.1 M NaCl in CH_3OH:H_2O 80:20 w/w) at constant temperature (25 °C) and ionic strength (0.1 M $NaClO_4$) under argon flow using NaOH as the titrant. The pH-meter was calibrated daily in terms of hydrogen ion concentration using $HClO_4$ and a pK_w 14.42 was established. The purity of the ligand and its exact concentration were determined by the Gran method [16]. NaOH was added using a 0.250 mL micrometer syringe calibrated both by weight titration and by standard material titration. The ligand concentration was 4.7×10^{-4} M and the metal:ligand ratios were 1:1 and 1:3. Protonation constants and Fe(III) complex formation constants were calculated using SUPERQUAD [17] and HYPERQUAD [18] programs. The standard deviations computed by SUPERQUAD and HYPERQUAD refer to random errors only; they are, however, good indicators of the importance of a particular species at equilibrium [19].

2.5. UV–Vis absorption spectroscopy

Absorption spectra were recorded on a Cary 300 Bio spectrophotometer. The spectra were obtained in the 2–10.5 pH range on solutions containing metal:ligand molar ratios 1:1 and 1:3 at constant ligand concentration 2.4×10^{-3} M. The molar absorptivities were calculated at the maximum concentration of each species obtained from the potentiometric results.

2.6. NMR measurements

^{1}H NMR spectra were determined on a Varian Inova-400 spectrometer at 399.94 MHz, with a 5 mm diameter sample tube at 25 °C. ^{1}H NMR spectra were recorded in $CDCl_3$, and chemical shifts were referenced to TMS.

2.7. Quantum chemical calculations

Theoretical calculations were performed with the SPARTAN'06 program [20]. The geometries were optimised using semi-empirical [21] methods, with the AM1 [22] and AM1/SM2 [23,24] for ligands and PM3 [25] basis sets for metal complexes.

3. Results and discussion

3.1. Pure ligand

The purity of aspergillic acid obtained with the procedure described in the Section 2 was checked using MS and ^{1}H NMR spectra. The MS spectrum of pure aspergillic acid ($C_{12}H_{20}N_2O_2$), showing an ion at 225.1585 *m/z* and isotope forms at 226.1618 and 227.1562 *m/z*, is shown in Fig. 2. The aspergillic acid exists also in the minor oxidised form at 223.1439 *m/z*. The signal due to the isotope form of the oxidised species at 225.1505 *m/z* is masked

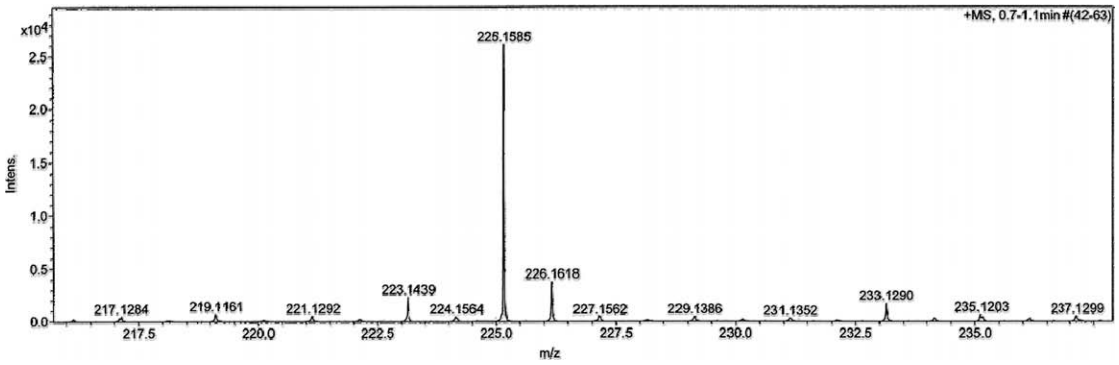


Fig. 2. MS spectrum of aspergillic acid.

Table 1
Experimental and calculated MS data for aspergillic acid.

Molecular formula	Experimental *m/z*	Calculated *m/z*
$C_{12}H_{20}N_2O_2$	225.1585	225.1602
	226.1618	226.1633
	227.1562	227.1661
$C_{12}H_{19}N_2O_2$	223.1439	223.1446
	224.1564	224.1477
		225.1505

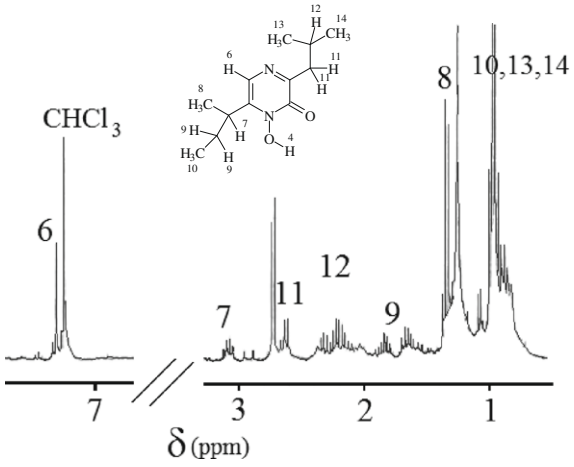


Fig. 3. ^{1}H NMR spectrum of aspergillic acid at 400 MHz.

Table 2
Experimental and literature-based chemical shifts of ^{1}H NMR spectra of aspergillic acid.

Proton number	δ^a (ppm)$_{\text{experimental data}}$	δ^a (ppm)$_{\text{literature data}}$ [26]
6	7.284	7.26
7	3.085	3.06
8	1.315	1.29
9	1.747	1.67
10	0.967	0.87
11	2.691	2.66
12	2.226	2.16
13,14	0.867	0.86

Proton numbers according to Fig. 3.
[a] The ^{1}H NMR shifts are referred to TMS.

by the signal at 225.1585 *m/z* of aspergillic acid. All the obtained results are in good agreement with the freeware ISOPRO 2.1 computer calculations (Table 1) and confirm that the synthesized product was aspergillic acid. The ^{1}H NMR spectrum of aspergillic acid (Fig. 3) also confirms the purity of product. The δ (ppm) values of the signals agree with those reported by Brotzu et al. [26], even though a different appearance of the 400 MHz spectrum with respect to that at 100 MHz presented in the cited paper. In Table 2 ^{1}H NMR data with their relative assignments are reported. As can be observed in Fig. 3, the signals of the different protons are split in two distinct parts that can be attributed to two different isomers of aspergillic acid. Impurities of the same magnitude order of the main molecule can in fact be ruled out on the basis of the mass spectrum in Fig. 2. We can then hypothesize, in agreement with Brotzu et al. [26], that there exist two isomers in which the two

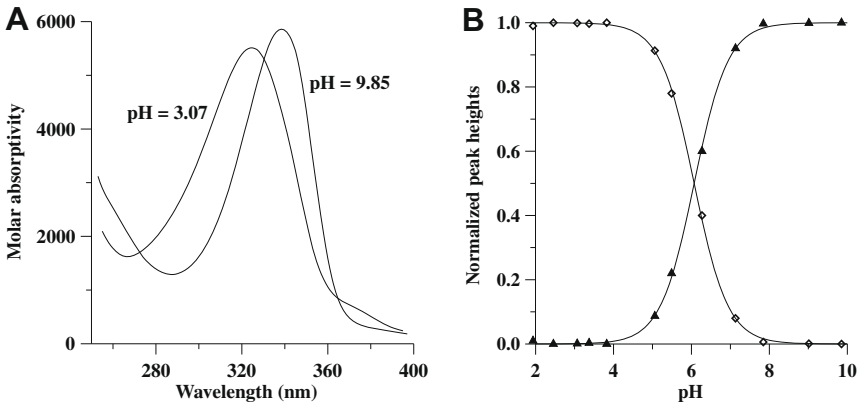


Fig. 4. (A) Absorptivity spectra of aspergillic acid in the acidic and basic forms. (B) Distribution plots of aspergillic acid calculated with log$K$ = 6.07 potentiometrically determined (continuous lines), and normalized heights (symbols) of the peaks at 308 nm (acidic form HL) and 344 nm (basic form L^-).

alkylic groups are interchanged. This is supported by the findings of MacDonald [27] who, working with radioactive ^{14}C leucine and isoleucine, demonstrated that these compounds were incorporated in the formed aspergillic acid. It would be thus equivalent to obtain one or the other of the two isomers, since the aspergillic acid biosynthesis occurs from these two amino acids. Aspergillic acid is a monoprotic acid (HL) characterized by a hydroxamic acid proton. The potentiometric titration in methanol:water 80:20 w/w solution shows one protonation with log$K$ 6.07, which seemingly differs from the log$K$ 5.3 reported by Dutcher [9], or from the log$K$ 5.5 reported in the Merck Index [28]. It should be noted that the medium is reported neither by Dutcher nor by the Merck Index. The log$K$ value of 6.07 obtained by potentiometric titrations is supported by the results of spectrophotometric measurements. Twelve spectra were collected in the pH interval 2–10, of which those at pH 3.07 and 9.85 are reported in Fig. 4A as an example. The 12 spectra were decomposed into the component Gaussian peaks with the SPECPEAK program [29]. The normalized heights of the band centred at 308 nm (attributable to the acidic form HL) and of the band at 344 nm (attributable to the basic form L^-) are reported as symbols in Fig. 4B. On the same figure, the distribution plots are also reported as continuous lines, calculated with the log$K$ = 6.07 obtained from potentiometric measurements; a perfect agreement can be observed.

3.2. Iron complexes

The complex formation equilibria between aspergillic acid and Fe(III) were studied both potentiometrically and spectrophotometrically. In fact, since iron was almost completely complexed at the starting of the potentiometric titration, the first complex formation constant of ML species had to be determined only spectrophotometrically. A set of 12 solutions in the ~1–2.5 pH range was prepared by additions of HCl, then spectra were collected. In all the work pH represents –log[H^+] at constant ionic strength 0.1 M; in strongly acidic solutions the ionic strength 0.1 M was reached by proper amount of HCl and NaCl. The spectra show a band centred at ~470 nm of increasing intensity, whose appearance changes when the pH further increases (Fig. 5). The visible bands in the molar ratio 1:3 solutions progressively disappear after pH ~6 with an increase of the baseline, indicating the breaking of iron complexes with the formation of iron hydroxides and free ligand. In solutions with a 1:1 molar ratio, the precipitation of iron takes place at pH 4. The analysis of the spectrophotometric data in the pH range ~1–2.5 with the SPECFIT program [30–32] allowed the evaluation of

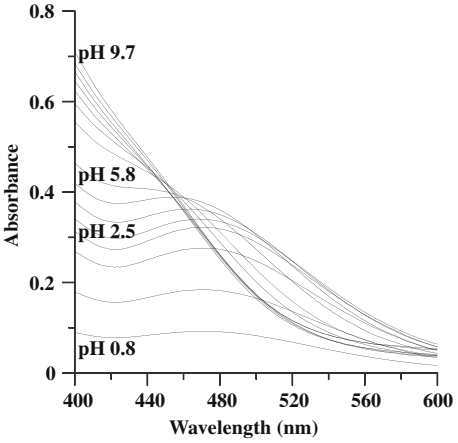


Fig. 5. Visible spectra of the system Fe(III)–aspergillic acid with a total iron concentration of 8×10^{-4} M and a total ligand concentration of 2.4×10^{-3}, optical path 0.5 cm.

Table 3
Complex formation constants estimated from potentiometric and spectrophotometric measurements for the Fe(III)–aspergillic acid system*. Wavelengths of maxima and absorptivities for ligand and all complex species.

Species	Logβ	λ (nm)	ε (cm^{-1} mol^{-1} L)
HL	6.07(4)	324 (HL)	5400
		339 (L^-)	5900
FeL	7.92(2)	310	6000
		464	772
$FeH_{-1}L$	3.69(5)	310	6255
$FeH_{-2}L$	−0.13(5)	311	6872

* Hydroxide formation constants were FeH_{-1} −2.56, FeH_{-2} −6.20, FeH_{-3} −11.41, FeH_{-4} −21.88, Fe_2H_{-2} −2.84 and Fe_3H_{-4} −6.05 [34].

the formation constant 7.92 for FeL^{2+} complex. The potentiometric data relative to the titrations at different molar ratios were then processed with the HYPERQUAD program [18] keeping fixed the value 7.92 for FeL^{2+} formation. The complex formation model reported in Table 3 with the relative stability constants was obtained, and the distribution curves are illustrated in Fig. 6. The chelating behaviour of aspergillic acid can be compared with those of 1-hydroxy-2-pyridinone and 1,4-dihydroxy-2-pyridinone (Table 4 and Fig. 7), both of which are characterized by a hydroxamic group inserted into an aromatic ring. The distribution curves together with the numerical values enable a direct comparison of the formation constants, taking into account the proton competition and the different stoichiometries. As far as the 1-hydroxy-2-pyridinone is

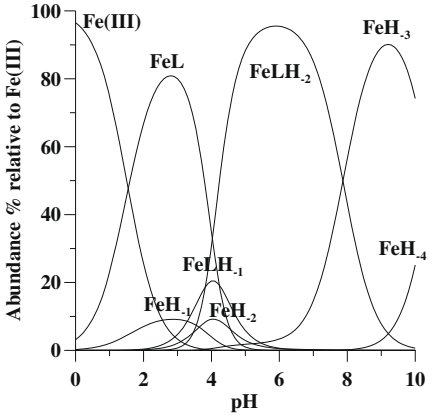


Fig. 6. Distribution plot of the Fe(III)–aspergillic acid system at 1:3 metal/ligand ratio, with a total iron concentration of 1.5×10^{-4} M, and a total ligand concentration of 4.7×10^{-4}.

Table 4
Literature protonation and iron(III) complex formation constants for 1-hydroxy-2-pyridinone and 1,4-dihydroxy-2-pyridinone.

Species*	1-Hydroxy-2-pyridinone		1,4-Dihydroxy-2-pyridinone [11]
	[12]	[13]	
LH	5.86	5.78	8.28
LH_2	7.06	4.88	14.42
LH_3			14.54
MLH			18.5
ML	10.61	10.3	
ML_2H_2			34.26
ML_2H			25.62
ML_2	20.11	19.3	21.31
ML_3H_2			41.35
ML_3H			35.02
ML_3	27.21	26.9	28.18

* Charges were omitted for clarity.

concerned, we remark the significative difference between the second protonation constants of Li and Martell [12] and Scarrow et al. [13], $\log K_2$ 1.2 and −0.9, respectively, that at acidic pH values greatly affects the distribution plots for the pure ligand and for iron complexes. The found differences are to be ascribed to the fact that potentiometric and/or spectrophotometric measurements were used to determine the protonation constant β_{H2L} and the complex formation constant β_{FeL}. In the actual cases in which the equilibria lie outside the range of potentiometric measurements, the use of spectrophotometric measurements allows to obtain more reliable results. At any rate, the formation of the FeL^{2+}, FeL_2^{+} and FeL_3 complexes is unquestionable, as for most hydroxypiridinones, with the last complex completely formed at pH 4. More interesting is the case of 1,4-dihydroxy-2-pyridinone that results in the formation of $FeLH^{2+}$, $FeL_2H_2^{+}$ and $FeL_3H_2^{-}$ (similar to the previous FeL^{2+}, FeL_2^{+} and FeL_3 complexes with the phenolic group in the protonated form). These occur at pH values higher than those observed in the case of 1-hydroxy-2-pyridinone complexes. In our opinion, this is to be ascribed to the fact that the two protonation constants are in reality macroconstants, and that the protonation of the hydroxamic group takes place at a pH higher than in the case of 1-hydroxy-2-pyridinone. The proton competition with iron for the hydroxamic group is consequently higher and the complex formation is delayed. The binding modes of aspergillic acid are completely different from those of the other cyclic hydroxamates; in fact, it does not form complexes of 1:2 and 1:3 stoichiometries, but the FeL^{2+} complex stabilizes with the loss of two protons from the coordinated water molecules, with p*K* values of 3.8 and 4.2. This is in strong contrast with the behaviour of the two hydroxypyridinones, especially taking into account the medium used. In order to find an explanation for this different behaviour of aspergillic acid, we performed a quantum mechanical study of the most stable isomer of the complexes with different stoichiometries, i.e. FeL_2^{+} and FeL_3 on one side, and $FeLOH^{+}$ and $FeL(OH)_2$ on the other. Apart from the energetic results, which are not directly comparable, the analysis of the structures presented in Fig. 8 allows us to obtain some significant insight: the FeL_2^{+} and above all the FeL_3 structures show that hydrophobic cages around the central metal ion are formed when aspergillic acid coordinates FeL^{2+}, at the same time neutralizing the charge of the complex. This fact, also observed

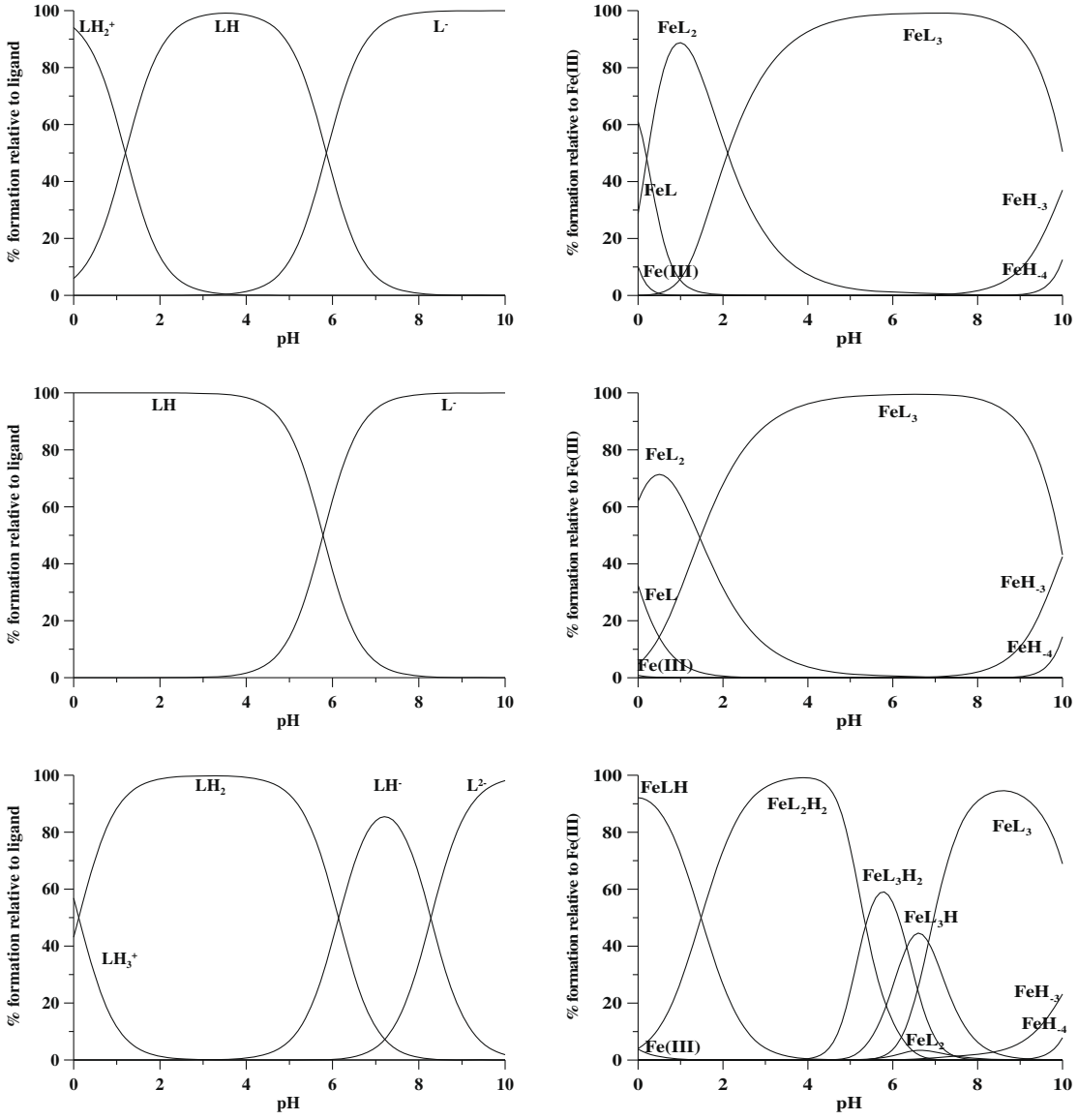


Fig. 7. Protonation and Fe(III) complex distribution plots for system at a total metal concentration of 1×10^{-3} M and a total ligand concentration of 3×10^{-3} M; in the upper plots the ligand is 1-hydroxy-2-pyridinone, stability constants from Ref. [12]; in the medium plots the ligand is 1-hydroxy-2-pyridinone, stability constants from Ref. [13] and in the lower plots the ligand is 1,4-dihydroxy-2-pyridinone, stability constants from Ref. [11].

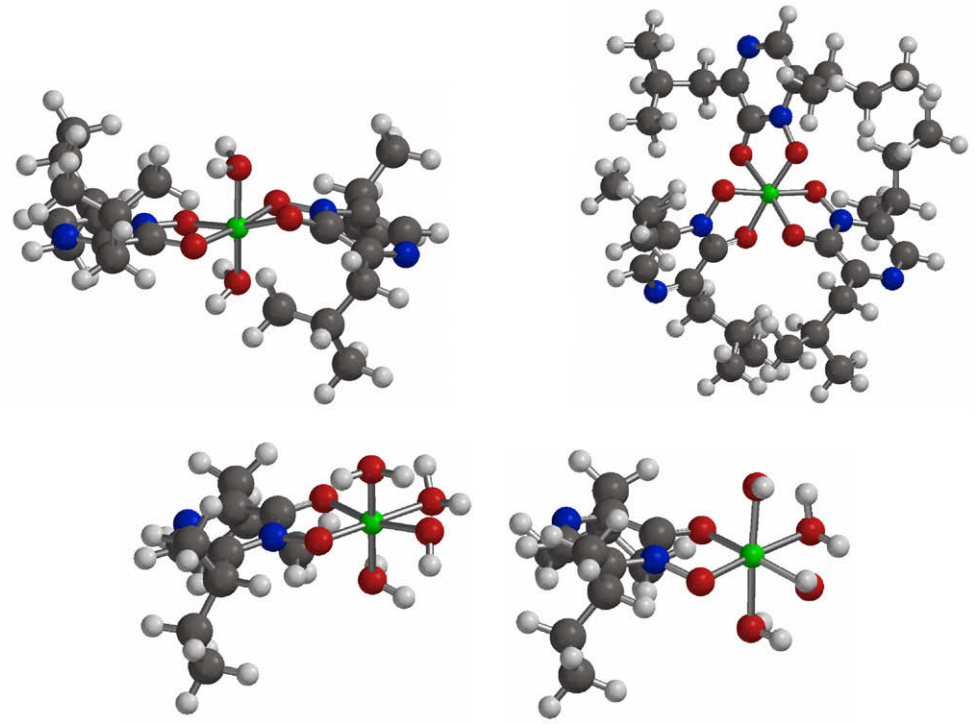


Fig. 8. SPARTAN'06 calculated structures of the most stable isomer of the FeL_2^+ (upper left), FeL_3 (upper right), $FeLOH^+$ (lower left), and $FeL(OH)_2$ (lower right) complexes.

in the low water medium used in our study, prevents a positive interaction of the FeL_2^+ and FeL_3 complexes with the solvent, and therefore, creates unfavourable conditions for the formation of such complexes. On the other hand, the formation of the hydroxo complexes $FeLOH^+$ and $FeL(OH)_2$ stabilizes the already hydrophobic 1:1 complex FeL^{2+} by creating positive interactions of the coordinated OH^- groups via hydrogen bonds with the solvent. Summing up, even though aspergillic acid cannot be classified as an iron chelator and taken into account for the treatment of iron overload, its characteristic coordination model is useful to clearly demonstrate the effect of a hydrophobic side chain in determining the coordination modes of the ligand.

Acknowledgements

V.M.N. thanks Fondazione Banco di Sardegna for the financial support. J.I.L. is in-debt with Prof. H. Kozlowski for the availability of the Molspin titrator and for the helpful discussions and with N. Zinnarosu for NMR spectra collection. All the authors express gratitude to Prof. S. Cosentino and Dr. B. Pisano for their useful advice and assistance in biological procedures.

References

[1] G. Faa, G. Crisponi, Coord. Chem. Rev. 184 (1999) 291.
[2] G. Crisponi, V.M. Nurchi, R. Silvagni, G. Faa, Polyhedron 18 (1999) 3219.
[3] E. Gumienna-Kontecka, R. Silvagni, R. Lipinski, M. Lecouvey, F. Cesare Marincola, G. Crisponi, V.M. Nurchi, Y. Leroux, H. Kozlowski, Inorg. Chim. Acta 339 (2002) 111.
[4] G. Crisponi, V.M. Nurchi, T. Pivetta, J. Inorg. Biochem. 102 (2) (2008) 209.
[5] V.M. Nurchi, G. Crisponi, T. Pivetta, M. Donatoni, M. Remelli, J. Inorg. Biochem. 102 (4) (2008) 684.
[6] G. Crisponi, V.M. Nurchi, T. Pivetta, J. Gałęzowska, E. Gumienna-Kontecka, T. Bailly, R. Burgada, H. Kozłowski, J. Inorg. Biochem. 102 (7) (2008) 1486.
[7] G. Crisponi, M. Remelli, Coord. Chem. Rev. 252 (2008) 1225.
[8] E.C. White, J.H. Hill, J. Bacteriol. 45 (1943) 433.
[9] J.B. Dutcher, J. Biol. Chem. 171 (1947) 321.
[10] G.J. Kontoghiorghes, A. Kolnagou, Curr. Med. Chem. 12 (2005) 2695.
[11] E.T. Clarke, A.E. Martell, Inorg. Chim. Acta 196 (1992) 185.
[12] Y.J. Li, A.E. Martell, Inorg. Chim. Acta 214 (1993) 103.
[13] R.C. Scarrow, P.E. Riley, K. Abu-Dari, D.L. White, K.N. Raymond, Inorg. Chem. 24 (1985) 954.
[14] V.M. Nurchi, G. Crisponi, T. Pivetta, J.I. Lachowicz, J. Inorg. Biochem., doi:10.1016/j.jinorgbio.2008.10.011.
[15] J.C. MacDonald, Can. J. Biochem. 31 (1973) 1311.
[16] G. Gran, Analyst 77 (1952) 661.
[17] P. Gans, A. Sabatini, A. Vacca, J. Chem. Soc., Dalton Trans. (1985) 1195.
[18] P. Gans, A. Sabatini, A. Vacca, Talanta 43 (1996) 1739.
[19] D. Valensin, M. Luczkowski, F.M. Mancini, A. Legowska, E. Gaggelli, G. Valensin, K. Rolka, H. Kozlowski, J. Chem. Soc., Dalton Trans. (2004) 1284.
[20] SPARTAN'06, Wavefunction, Inc.
[21] J.A. Pople, D.A. Beveridge, Approximate Molecular Orbital Theory, McGraw-Hill, New York, 1970.
[22] M.J.S. Dewar, E.G. Zoebisch, E.F. Healy, J.J.P. Stewart, J. Am. Chem. Soc. 107 (1985) 3902.
[23] C.C. Chambers, G.D. Hawkins, C.J. Cramer, D.G. Truhlar, J. Chem. Phys. 100 (1996) 16385.
[24] C.J. Cramer, D.G. Truhlar, Structure and Reactivity in Aqueous Solution, in: ACS Symposium Series, 568, American Chemical Society, Washington D.C., 1994.
[25] J.J.P. Stewart, J. Comput. Chem. 10 (1989) 209.
[26] G. Brotzu, G. Crisponi, R. Garzia, A. Lai, G. Paschina, Z.L. Rossetti, G. Saba, Rendiconti Seminario Facoltà Scienze, Cagliari University, XLV (1975) 225.
[27] J.C. MacDonald, J. Biol. Chem. 236 (1961) 512.
[28] The Merck Index, 11th ed., Rahway, 1990.
[29] M.C. Aragoni, M. Arca, G. Crisponi, V.M. Nurchi, Anal. Chim. Acta 316 (1995) 195.
[30] H. Gampp, M. Maeder, Ch.J. Meyer, A.D. Zuberbuhler, Talanta 32 (1985) 1133.
[31] H. Gampp, M. Maeder, Ch.J. Meyer, A.D. Zuberbuhler, Talanta 33 (1986) 943.
[32] H. Gampp, M. Maeder, Ch.J. Meyer, A.D. Zuberbuhler, Anal. Chim. Acta 193 (1987) 287.
[34] C.F. Baes, R.E. Mesmer, The Hydrolysis of Cations, John Wiley and Sons, Inc., New York, 1976.

water and dried in vacuum. Yield 0.060 g, 57%. *Anal.* Calc. for $C_8H_{26}ClN_8O_3Rh_2$: C, 18.35; H, 5.00; N, 21.40; Cl, 6.77; Rh, 39.31. Found: C, 17.95; H, 4.70; N, 21.15; Cl, 6.55; Rh, 38.7%. **IR** (KBr pellets, cm^{-1}), 3540s ν(OH), 3442s ν(OH), 3335vs ν(NH), 3263s ν(NH), 2975vw ν(CH), 2958vw ν(CH), 2915w ν(CH), 2848vw ν(CH), 1633m δ(OH), 1503vs ν^{as}(C(=NH)NH), 1426m, 1373vw, 1296vs ν^{s}(C(=NH)NH), 1204m, 1040vw, 735m, 683s, 640m, 580m. **EPR** (solid, 77 K), $g_\perp = 2.0679$, $g_\parallel = 1.9622$ and $A_\parallel = 2.5$ mT. **EPR** (DMSO, 77 K), $g_\perp = 2.0683$, $g_\parallel = 1.9621$ and $A_\parallel = 2.5$ mT.

2.2. Preparation of $[Rh_2\{HN(HN{=})CCH_3\}_4\{OS(CH_3)_2\}_2]Cl$, **2**

Compound **1** (0.05 g) was dissolved in hot DMSO (1 mL). The compound **2** was precipitated from this solution by adding tetrahydrofurane (20 mL). The violet product was washed with THF and dried in air. Yield 0.0514 g, 86%.

Table 1
Crystal data and structure refinement for complex $[Rh_2\{HN(HN{=})CCH_3\}_4\{OS(CH_3)_2\}_2]Cl$, **2**.

Empirical formula	$C_{12}H_{32}ClN_8O_2Rh_2S_2$
Formula weight	625.83
T (K)	100
λ (Å^3)	0.71073
Crystal system	triclinic
Space group	$P\bar{1}$
a (Å^3)	9.0592(12)
b (Å^3)	11.2684(12)
c (Å^3)	11.8841(12)
α (°)	86.01(1)
β (°)	73.21(1)
γ (°)	82.27(1)
V (Å^3)	1150.3(2)
Z	2
D_{calc} (Mg m^{-3})	1.807
μ (mm^{-1})	1.756
F(000)	630
Crystal size (mm)	0.05·0.05·0.03
θ range (°)	3.16–28.36
Ranges of h,k,l	−12/11; −13/15; −14/15
Reflections collected	8069
Ind. reflect. (R_{int})	5069 (0.0705)
Data/parameters	5069/252
Goodness-of-fit (F^2)	0.978
Final R_1/wR_2 indices ($I > 2\sigma_I$)	0.0633/0.1061
Largest difference in peak/hole (e·Å^{-3})	1.225/−1.174

The crystalline complex **2** can be obtained by layering of solution of **1** in DMSO with tetrahydrofurane. Violet crystals were slowly formed, collected by filtration and washed with THF and dried in air. *Anal.* Calc. for $C_{12}H_{32}ClN_8O_2Rh_2S_2$: C, 23.03; H, 5.15; N, 17.90; Cl, 5.66. Found: C, 22.82; H, 4.90; N, 17.58; Cl, 5.85%. **IR** (KBr pellets, cm^{-1}), 3530sh ν(OH), 3434vs 3395s ν(OH), 3335vs ν(NH), 3250vs ν(NH), 2992m ν(CH), 2980m ν(CH), 2970m ν(CH), 2915m ν(CH), 2840w sh ν(CH), 1631m δ(OH), 1503vs ν^{as}(C(=NH)NH), 1426s, 1370w, 1344 m, 1295vs ν^{s}(C(=NH)NH), 1060s ν^{as}(S=O), 1022s ν^{s}(S=O), 968w, 955w, 942w, 763m, 745m, 715m, 683s, 640m, 586s, 545w. **EPR** (DMSO, 77 K), $g_\perp = 2.0670$, $g_\parallel = 1.9627$ and $A_\parallel = 2.5$ mT.

Complex **2** can be also prepared in reaction of $Na_4[Rh_2(CO_3)_4] \cdot 2.5H_2O$ with ethanimidamide hydrochloride ($CH_3C(=NH)NH_2 \cdot HCl$) in water containing 20% of DMSO, however, the yield of reaction is low.

Single crystals of $[Rh_2\{HN(HN{=})CCH_3\}_4\{OS(CH_3)_2\}_2]Cl$, **2**, for X-ray measurements were obtained in tubes (diameter 5 mm) by slow diffusion of THF into the solution of complex **1** in DMSO.

2.3. X-ray crystallographic measurements

X-ray data were collected at low temperature using an Oxford Cryosystem device on a Kuma KM4CCD κ-axis diffractometer with graphite-monochromated MoKα radiation ($\lambda = 0.71073$ Å). Accurate cell parameters were determined and refined by least-squares fit of the strongest reflections. The data were corrected for Lorentz and polarization effects as well as for analytical absorption correction. Data reduction and analysis were carried out with the Oxford Diffraction (Poland) Sp. z o.o. programs. The structure was solved by direct methods (program SHELXS97 [17]) and refined by the full-matrix least-squares method on all F^2 data using the SHELXL97 [18] programs. Non-hydrogen atoms were refined with anisotropic displacement parameters; hydrogen atoms were included from geometry of molecules and $\Delta\rho$ maps. They were fixed or treated as riding groups during refinement of the structure.

2.4. Computational details

The molecular and electronic structure UV–Vis and IR spectra of the complex **2** of C_i symmetry have been studied with the GAUSSIAN

Table 2
Bond lengths (Å) and angles (°) for complex **2**.

Bonds	Bond lengths X-ray	Bond lengths calc.	Bonds angles	X-ray	Calc.
Rh(1)–N(3)	2.018(7)	2.031	N(3)–Rh(1)–N(1)	173.4(3)	175.1
Rh(1)–N(1)	2.018(6)	2.068	N(3)–Rh(1)–N(2)	90.7(3)	89.8
Rh(1)–N(2)	2.027(7)	2.061	N(1)–Rh(1)–N(2)	87.8(3)	89.5
Rh(1)–N(4)	2.037(6)	2.061	N(3)–Rh(1)–N(4)	91.0(3)	90.2
Rh(1)–S(1)	2.451(2)	2.557	N(1)–Rh(1)–N(4)	89.8(3)	90.1
Rh(1)–Rh(1)#1	2.5108(14)	2.480	N(2)–Rh(1)–N(4)	173.5(3)	175.2
Rh(2)–N(13)	1.995(7)		N(3)–Rh(1)–S(1)	96.2(2)	101.2
Rh(2)–N(12)	2.021(7)		N(1)–Rh(1)–S(1)	90.3(2)	83,7
Rh(2)–N(11)	2.034(7)		N(2)–Rh(1)–S(1)	92.1(2)	92.1
Rh(2)–N(14)	2.052(8)		N(4)–Rh(1)–S(1)	93.9(2)	92.6
Rh(2)–S(2)	2.438(2)		N(3)–Rh(1)-Rh(1)#1	86.30(19)	87.6
Rh(2)–Rh(2)#2	2.5104(15)		N(1)–Rh(1)–Rh(1)#1	87.19(19)	87.5
N(1)–C(1)	1.323(10)	1.324	N(2)–Rh(1)–Rh(1)#1	87.8(2)	87.6
C(1)–N(3)#1	1.322(10)	1.338	N(4)–Rh(1)–Rh(1)#1	86.12(19)	87.6
C(1)–C(2)	1.518(11)	1.523	S(1)–Rh(1)–Rh(1)#1	177.48(7)	171.2
N(4)–C(3)	1.314(10)	1.330	N(3)#1–C(1)–N(1)	119.2(7)	120.0
C(3)–N(2)#1	1.314(10)	1.331	N(3)#1–C(1)–C(2)	121.7(7)	119.7
N(3)–C(1)#1	1.322(10)	1.338	N(1)–C(1)–C(2)	119.1(8)	120.3
S(1)–O(1)	1.499(6)	1.516	N(4)–C(3)–N(2)#1	121.7(8)	120.3
S(1)–C(6)	1.760(9)	1.819	N(4)–C(3)–C(4)	119.7(7)	119.7
S(1)–C(5)	1.788(8)	1.820	N(2)#1–C(3)–C(4)	118.6(8)	12.1

Symmetry transformations used to generate equivalent atoms: #1: $-x+1, -y, -z$; #2: $-x+1, -y-1, -z+1$.

03 package of programs [19] using the DFT B3LYP and MPW1PW91 methods with the 3-21G* basis set.

3. Results and discussion

Complex $[Rh_2\{\mu\text{-}HN(HN{=})CCH_3\}_4(H_2O)_2]Cl \cdot H_2O$, **1**, can be easily obtained in reaction of the $Na_4[Rh_2(CO_3)_4] \cdot 2.5H_2O$ with ethanimidamide hydrochloride ($CH_3C(=NH)NH_2 \cdot HCl$) what allows to decompose sodium tetracarbonatorodate with evolving of CO_2. During reaction in air rhodium(II) is easily oxidized by oxygen: $2Na_4[Rh_2(CO_3)_4] + 10CH_3C(=NH)NH_2 \cdot HCl + 0.5O_2 \rightarrow 2Rh_2\{HN(HN{=})CCH_3\}_4(H_2O)_2]Cl + CH_3C(=NH)NH_2 + 8CO_2 + 8NaCl + 7H_2O$

The complexes **1** and **2** are soluble in water, dimethyl sulfoxide, *N*,*N*-dimethylformamide and similar solvents. They are stable in air both in solutions and solid state. Ligands coordinated in axial positions are easily substituted by solvent molecules giving $[Rh_2\{HN(HN{=})CCH_3\}_4(solv)_2]^+$ cations (*c.f.* UV–Vis spectra). An X-ray crystallography revealed that complex **2** crystallizes in the $P\bar{1}$ space group crystallographic data are given in Table 1 and selected bond lengths and angles in Table 2. The ORTEP view of the complex **2** is depicted in Fig. 1. There are two independent molecules in the crystal. Each of rhodium atoms has distorted octahedral coordination. The equatorial positions are occupied by four nitrogen atoms of bridging ethanimidamidato ligands. The remaining axial coordination sites are occupied by the sulfur atom of dimethyl sulfoxide ligand and rhodium atom. The Rh1–Rh#1 and Rh2–Rh#2 distances differ only sightly and are equal to 2.5108(14) Å and 2.5104(15) Å, respectively. Thus the Rh–Rh bonds in compound **2** are longer for *c.a.* 0.05–0.06 Å than those in other amidine Rh_2^{5+} complexes (Table 3) [1,9–11], however, the Rh–N distances are similar to those in other $[Rh_2(RC(=NR')NR'')_4]^+$ compounds. The elongation of Rh–Rh bond is caused by coordination of dimethyl sulfoxide ligands via S atoms, which are considerably more soft Lewis bases than O or N ligands and show relatively strong trans influence. Both molecules have eclipsed conformation. Torsion angles are very small: N2–Rh1–Rh#1–N#4 = 2.1°, N3–Rh1–Rh#1–N#1 = 1.3°, N12–Rh2–Rh#2–N#14 = 0.2°, N11–Rh2–Rh#2–N#13 = 0.0°. The O atoms are in transoidal positions, the torsion angle O1–S1–S#1–O#1 = 180°.

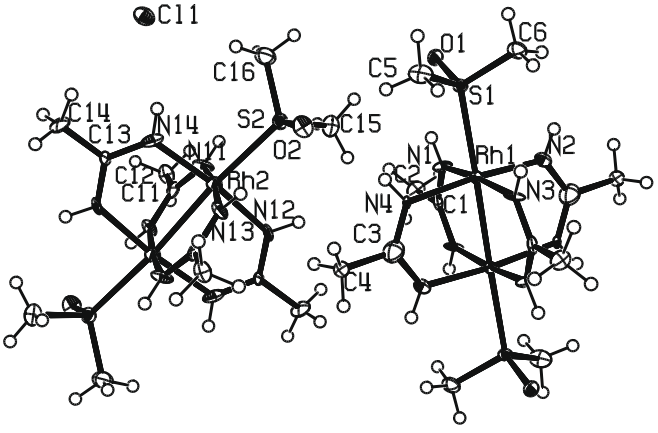


Fig. 1. Ortep drawing of $[Rh_2\{HN(HN{=})CCH_3\}_4\{OS(CH_3)_2\}_2]^+$ independent units in $[Rh_2\{HN(HN{=})CCH_3\}_4\{OS(CH_3)_2\}_2]Cl$, **2**, showing the atomic numbering scheme.

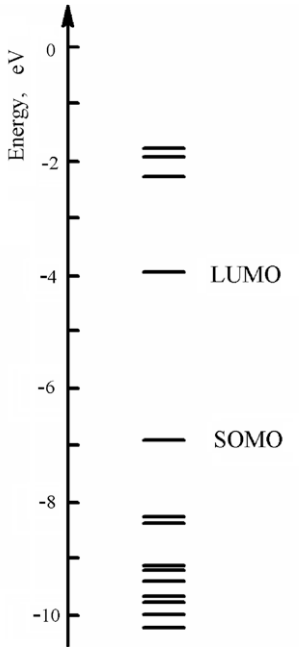


Fig. 2. Scheme of MO for $[Rh_2\{HN(HN{=})CCH_3\}_4\{OS(CH_3)_2\}_2]^+$.

To explain the properties of compound **2** and to compare the structure of the isolated $[Rh_2(CH_3(=NH)NH)_4(DMSO)_2]^+$ cation

Table 4
Energy of molecular orbitals of $Rh_2\{HN(HN{=})CCH_3\}_4\{OS(CH_3)_2\}_2]^+$.

Orbital	Energy (eV)
140 $\sigma_{RhRh}\sigma_{RhS}$	−10,323
141 $\sigma_{RhS}\sigma^*_{RhRh}$	−9984
142 π^*_{NCN}	−9754
143 $\pi_{RhRh}\pi_{RhS}$	−9631
144 $\pi_{RhRh}\pi_{RhS}$	−9315
145 $\delta_{RhRh}\pi^*_{NCN}$	−9089
146 $\sigma_{RhRh}\sigma^*_{RhS}$	−9026
147 $\pi_{RhS}\pi^*_{RhRh}$	−8412
148 $\pi_{RhS}\pi^*_{RhRh}$	−8229
149 $\delta^*_{RhRh}\pi^*_{NCN}$	−6817
150 π^*_{NCN}	−3986
151 π^*_{NCN}	−2294
152 π^*_{NCN}	−1977
153 $\sigma^*_{RhRh}\sigma^*_{RhS}$	−1854

Table 3
The Rh–Rh and Rh–ligand distances in amidinato complexes with Rh_2^{5+} core [1,9–11].

Compound	*d* (Rh–Rh) (Å)	*d* (Rh–L_{ax}) (Å)	Axial atom (s)
$[Rh_2\{CH_3C(NH)NH\}_4(DMSO)_2]Cl$	2.5108(14) 2.5104(15)	2.451(2) 2.438(2)	S
$[Rh_2(DPhF)_4(NCCH_3)]ClO_4$	2.466(1)	2.074(6)	N
$[Rh_2(DTolF)_4]ClO_4$	2.447(1)		
$[Rh_2(DTolF)_4(H_2O)]O_2CCF_3$	2.452(2)	2.165(2)	O
$[Rh_2(DTolF)_4][C(CN)_3]$	2.463(4)	2.07(3)	C
$Rh_2(DTolF)_3(\mu\text{-}NO_3)_2$	2.485(1)	2.09(1) 2.38(1)	O
cis-$[Rh_2(DTolF)_2(\mu\text{-}O_2CCF_3)_2(OOCCF_3)(AgO)CCF_3)_2]_2$	2.448(2) 2	2.20(1) 2.24(2)	O
$[Rh_2(DAniF)_4Cl]\cdot CHCl_3$	2.467(1)	2.400(2)	Cl

DPhF = $HC(=NC_6H_5)NHC_6H_5$; DtolF = $HC(=NC_6H_4Me\text{-}4)NHC_6H_4Me\text{-}4$; DaniF = $HC(=NC_6H_4OMe\text{-}4)NHC_6H_4OMe\text{-}4$.

with that in the crystal in complex **2**, the molecular and electronic structures of this cation have been studied with unrestricted DFT methods. The B3LYP functional with 3-21G* basis set was applied for geometry optimization and IR spectra calculations. The excitation energies were calculated with MPW1PW91 TD method with a 3-21G* basis set. The optimized interatomic distances and angles agree well with the crystallographic data (Table 2). The greater differences were observed for Rh–Rh bond, shorter by 0.03 Å, and Rh–S bond, longer by 0.1 Å, than those in solid state. This suggests strong mutual trans influence of Rh–Rh and Rh–S bonds, the shorter Rh–Rh distance the longer Rh–S bond. The energy of molecular orbitals increase in the series: $\sigma_{RhRh}\sigma_{RhS} < \sigma^*_{RhRh}\sigma_{RhS} < \pi_{HNCNH} < \pi_{RhRh}\pi_{RhS} < \delta_{RhRh} < \sigma_{RhRh}\sigma^*_{RhS} < \pi^*_{RhRh}\pi_{RhS} < \delta^*_{RhRh}$(SOMO) $< \pi^*_{NCN} < \sigma^*_{RhRh}\sigma^*_{RhS}$ (Fig. 2, Table 4). The rhodium d orbitals are relatively delocalized, the σ_{RhRh} and π_{RhRh} orbitals are at the same time bonding or antibonding rhodium–ligand orbitals (Fig. 3). The δ^*_{RhRh} (SOMO) orbital is also, to some extent, delocalized onto the bridging HN–C–NH groups with the $\pi^*_{RhndashHNCNH}$ character. The calculated excitation energies agree very well with electronic spectrum of complex **2** (Table 5). The most intense band in the visible region observed at 16500 cm^{-1} in the spectrum of $[Rh_2\{HN(HN{=})CCH_3\}_4\{OS(CH_3)_2\}_2]Cl$, **2**, in DMSO should be mainly assigned to the $(\sigma_{RhRh}\sigma^*_{RhS}) \rightarrow (\delta^*_{RhRh}\pi^*_{NCN})$ (SOMO), $(\pi_{RhRh}\pi_{RhS}) \rightarrow (\delta^*_{RhRh}\pi^*_{NCN})$ (SOMO) and $(\delta_{RhRh}\pi^*_{NCN}) \rightarrow (\delta^*_{RhRh}\pi^*_{NCN})$ (SOMO) transitions. The participation of other transitions is much lower. The participations of δ^*_{RhL} and π_{RhL} orbitals to the Rh–Rh orbitals explain the dependence of energy of this band on the ligands L coordinated along the Rh–Rh axis. Thus transitions in the spectra in the region 12000–19500 cm^{-1} should be assigned to the transition between orbital with prevailing participation of d orbitals of rhodium and bands of energy above 25000 cm^{-1} to the MLCT from d orbitals to π^*_{HNCNH} antibonding orbitals. The most intensive band in the visible region in the spectrum of **2** is shifted to higher energy when hard ligands are coordinated in the axial coordination sites and to lower energy in the case of soft ligands (Table 6). Thus this band for compound **1** in water solution is observed at 18500 cm^{-1}, in $H_2O + 3Br^-$ at 17700 cm^{-1}, in $H_2O + 3I^-$ at 17500 cm^{-1} and in DMSO at 16500 cm^{-1}.

The EPR spectrum of complex **2** in DMSO solution shows an axial signal with $g_\perp = 2.0670$ and $g_\parallel = 1.9627$ at 78 K, the latter of which is split into a 1:2:1 triplet ($A_\parallel = 2.5$ mT) by the two equivalent rhodium nuclei. The $g_\parallel < g_e < g_\perp$ is consistent with the main occupation of δ^*_{RhRh} SOMO orbital and confirms the results of calculations. Very similar spectra were observed for *N,N′*-diarylamidine Rh_2^{5+} complexes [9,10]. The EPR spectra of complex **2** in DMSO in the presence of $[NEt_4]CN$ revealed that CN^- anions are coordinated along Rh–Rh axis (Fig. 4). At the **2**:CN = 1:1 EPR spectrum shows

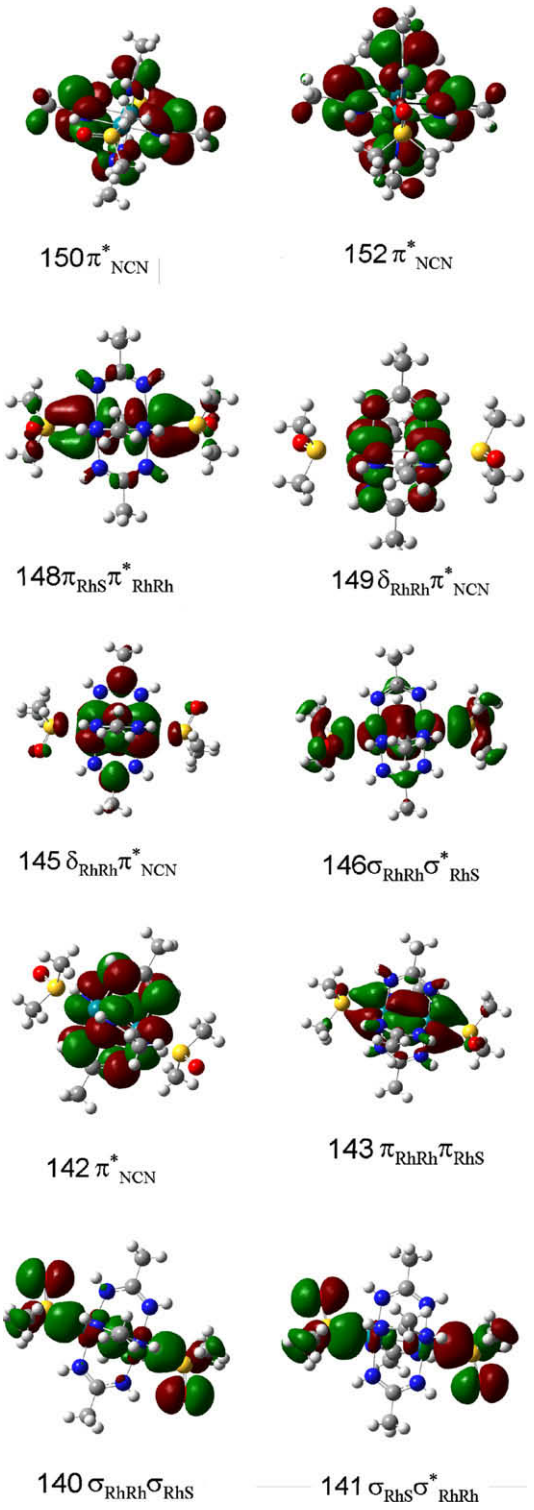


Fig. 3. Molecular orbitals of $[Rh_2\{HN(HN{=})CCH_3\}_4\{OS(CH_3)_2\}_2]^+$ (Rh – blue, N – deep-blue, O – red, S – yellow). (For interpretation of the references to colour in this figure legend, the reader is referred to the web version of this article.)

Table 5
Experimental electronic spectrum and calculated excitation energies for complex **2**.

Spectrum of **2** in DMSO $\nu(\varepsilon)$, cm^{-1} ($M^{-1}cm^{-1}$)	Calculated excitation energies, ν, cm^{-1}	Transition
35500(16300),	33000	$141\sigma^*_{RhRh}\sigma_{RhS} \rightarrow 150\pi^*_{NCN}$ $148\pi_{RhRh}\pi_{RhS} \rightarrow 150\pi^*_{NCN}$ $146\sigma_{RhRh}\sigma^*_{RhS} \rightarrow 150\pi^*_{NCN}$
	32450	$142\pi_{NCN} \rightarrow 150\pi^*_{NCN}$ $144\pi_{RhRh}\pi_{RhS} \rightarrow 150\pi^*_{NCN}$ $148\pi_{RhRh}\pi_{RhS} \rightarrow 150\pi^*_{NCN}$ $146\sigma_{RhRh}\sigma^*_{RhS} \rightarrow 150\pi^*_{NCN}$
32400(18300),	31550	$148\pi^*_{RhRh}\pi_{RhS} \rightarrow 150\pi^*_{NCN}$ $146\sigma_{RhRh}\sigma^*_{RhS} \rightarrow 150\pi^*_{NCN}$ $143\pi_{RhRh}\pi_{RhS} \rightarrow 150\pi^*_{NCN}$
26500sh(1520),	26800	$143\pi_{RhRh}\pi_{RhS} \rightarrow 150\pi^*_{NCN}$
21000(1070),	22300	$145\delta_{RhRh}\pi^*_{NCN} \rightarrow 150\pi^*_{NCN}$ $146\sigma_{RhRh}\sigma^*_{RhS} \rightarrow 150\pi^*_{NCN}$ $144\pi_{RhRh}\pi_{RhS} \rightarrow 150\pi^*_{NCN}$ $\sigma^*_{RhRh}\sigma_{RhS} \rightarrow 150\pi^*_{NCN}$
16500(4700),	16050	$144\pi_{RhRh}\pi_{RhS} \rightarrow 149\delta^*_{RhRh}\pi^*_{NCN}$ SOMO $141\sigma_{RhRh}\sigma^*_{RhS} \rightarrow 149\delta^*_{RhRh}\pi^*_{NCN}$ SOMO $145\delta_{RhRh}\pi^*_{NCN} \rightarrow 149\delta^*_{RhRh}\pi^*_{NCN}$ SOMO
13100sh(880)	13300	$143\pi_{RhRh}\pi_{RhS} \rightarrow 149\delta^*_{RhRh}\pi^*_{NCN}$ SOMO $142\pi_{NCN} \rightarrow 149\delta^*_{RhRh}\pi^*_{NCN}$ SOMO $146\sigma_{RhRh}\sigma^*_{RhS} \rightarrow 149\delta^*_{RhRh}\pi^*_{NCN}$ SOMO

Table 6
Electronic spectra of adducts of [Rh2($H_2N_2CCH_3$)$_4$L$_2$]Cl.

L	ν (cm^{-1}) (ε, M^{-1} cm^{-1})
H_2O, reflectance spectrum	44600, 35700, 26500, 19300, *17900*[*], 16300, 14300,12700
H_2O	44600 sh(9700), 40500 sh (6080), 26600 (590), 19200 (2900), *18500* (2950), 17000 sh (2800), 14300 sh (1550)
H_2O + 3Br^-	44600 sh(13900), 40800 sh (9500), 36200 (4400), 26600 (870), 19100 sh (2750), *17700* (2900), 16700 sh (2650), 14300 sh (1900)
H_2O + 3I^-	36400 sh (7300), 32700 sh (6400), 29100(6200) 26500 sh (3600), 18800 sh (2650), *17500* (3050), 16400 sh (2650), 14300 sh (1800)
H_2O + $EtNH_2$	44600 sh(10400), 40500 sh (7100), 26600 (600),*19300* (2950), 17700 sh (2700), 14300 sh (1000)
H_2O + 3tpa[*]	36600 (9200), 33100 (8800), 23400 (1220), 20200 sh (1750), *17700* (2500), 14300 sh (550)
DMSO	35500 (16300), 32400 (18300), 26500 sh (1520), 21000 (1070), *16500* (4700), 13100 sh (880)
DMSO + 3[Et_4N]CN	36400 (9900), 31500 (3900) sh, 26600 (810) sh, 19600 (1400) sh, *17400* (2000), 13900 (300)

[*] tpa = 1,3,5-triaza-7-phosphatricyclo[3.3.1.1^{3,7}]decane.

the presence of two compounds: [Rh_2(μ-HN(HN=)CCH_3)$_4$($DMSO)_2$]$^+$ ($g_\perp$ = 2.0670 and $g_\parallel$ = 1.9635) and [Rh_2(μ-HN(HN=)CCH_3)$_4$(CN)(DMSO)]$^+$ ($g_\perp$ = 2.0892, $g_\parallel$ = 2.0206 and $g_\parallel$ = 2.0072) of similar concentration. The latter complex shows two $g_\parallel$ values because rhodium atoms are not equivalent. At the **2**:CN = 1:2 only small amount of complex [Rh_2(μ-HN(HN=)CCH_3)$_4$(CN)(DMSO)] is observed, the prevailing form is [Rh_2(μ-HN(HN=)CCH_3)$_4$$(CN)_2$]$^-$ ($g_\perp$ = 2.0884 and $g_\parallel$ = 1.9470). The spectrum of complex **2** in DMSO:H_2O = 1:1.5 at **2**:NaCN = 1:3 revealed that in solution was present only dicyano complex [Rh_2(μ-HN(HN=)CCH_3)$_4$$(CN)_2$]$^-$ ($g_\perp$ = 2.0813 and $g_\parallel$ = 1.9552).

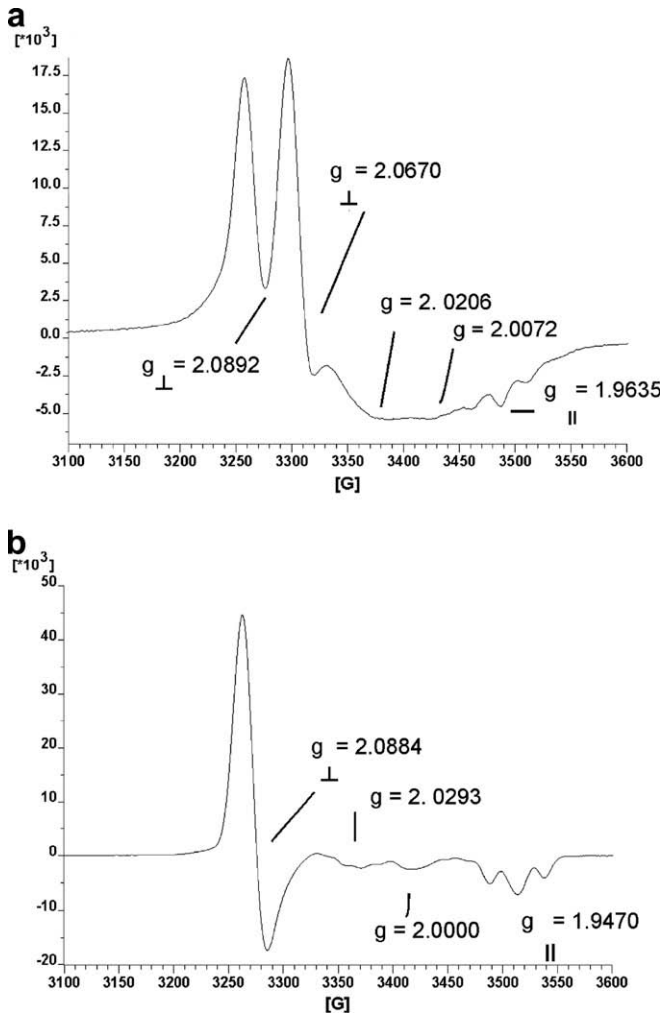


Fig. 4. EPR spectra (77 K) of frozen DMSO solutions of [Rh_2{HN(HN=)CCH_3}$_4$-{$OS(CH_3)_2$}$_2$]Cl + [NEt_4]CN at molar ratios: a – 1:1, b – 1:2.

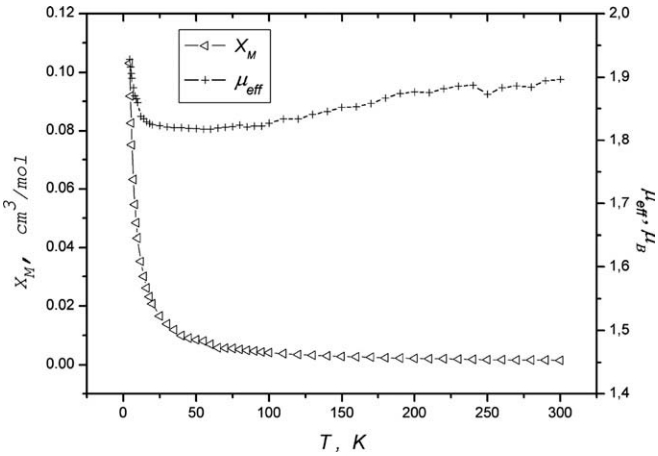


Fig. 5. Temperature dependences of molar magnetic susceptibility and effective magnetic moment for [Rh_2{HN(HN=)CCH_3}$_4${$OS(CH_3)_2$}$_2$]Cl, **2**.

The IR spectrum of complexes **1** and **2** shows very intense ν(OH) and ν(NH) vibrations in the region 3550–3250 cm^{-1}. The strong bands assigned to the ν^{as}(CNN) and ν^{s}(CNN) stretching vibrations are observed at 1503 and 1295 cm^{-1}, respectively. They have also δ(NH) character. The band at 1060 cm^{-1} in the spectrum of **2** should be assigned to the ν^{as}(S=O) vibration with some participation of $\delta(CH_3)$ of ethanimidamidato and DMSO ligands and band at 1022 cm^{-1} to the ν^{s}(S=O) with participation of $\delta(CH_3)$ of DMSO. These bands were not observed in the spectrum of compound **1**. The energy of these vibrations is relatively low as compared with mononuclear DMSO complexes with M–S bond [20].

The dependences of the magnetic susceptibility and magnetic moment for the complex **2** on temperature are shown in Fig. 5. The magnetic moment at 300 K is equal to 1.986 μ_B and is slightly greater than the spin only moment. This suggests slight orbital contribution to the magnetic moment. The magnetic moment slightly diminishes with decreasing of temperature to about 50 K and at lower temperatures again increases to the 1.928 μ_B.

4. Conclusion

Dinuclear Rh(II)Rh(III) complex [[Rh_2(μ-HN(HN=)CCH_3)$_4$($H_2O)_2$]Cl · H_2O (**1**) containing Rh_2^{5+} core can be easily prepared in the reaction of $Na_4[Rh_2(CO_3)_4] \cdot 2.5H_2O$ with ethanimidamide hydrochloride (CH_3C(=NH)NH2 · HCl) at molar ratio of 1:10. Aqua ligands can be easily substituted by DMSO giving complex [Rh_2(μ-HN(HN=)CCH_3)$_4$$(DMSO)_2$]Cl (**2**) The EPR spectra of complexes **1** and **2** and calculations accomplished for [Rh_2{μ-HN(HN=)CCH_3}$_4$$(DMSO)_2$]$^+$ cation using DFT B3LYP and MPW1PW91 methods with 3-21G* basis set indicate that δ^*_{RhRh} is SOMO orbital. The rhodium atoms are equivalent, both in solid state in complex **2**

and in solutions in $[Rh_2\{\mu\text{-}HN(HN{=})CCH_3\}_4L_2]^+$ cations and non-equivalent in complexes containing two different axial ligands $[Rh_2\{\mu\text{-}HN(HN{=})CCH_3\}_4LL']^+$. The intense bands in the electronic spectra in the range 13 000–19 000 cm^{-1} are caused by transitions with prevailing d–d character and should be assigned to the $(\sigma_{RhRh}\sigma^*_{RhS}) \rightarrow (\delta^*_{RhRh}\pi^*_{NCN})$ (SOMO), $(\pi_{RhRh}\pi_{RhS}) \rightarrow (\delta^*_{RhRh}\pi^*_{NCN})$ (SOMO) and $\delta_{RhRh} \rightarrow (\delta^*_{RhRh}\pi^*_{NCN})$ (SOMO) transitions. The very intense bands above 25 000 cm^{-1} are MLCT transition from Rh d orbitals to π^*_{HNCNH} antibonding orbitals. The participations of δ^*_{RhL} and π_{RhL} orbitals to the Rh–Rh orbitals explain the dependence of energy of the bands in the visible region on the ligands L coordinated along the Rh–Rh axis. The UV–Vis and EPR spectra proof fast exchange of axial ligands. Effective magnetic moment (1.986 μ_B at 300 K), suggests slight orbital contribution to the magnetic moment.

Supplementary data

CCDC 702638 contains the supplementary crystallographic data for compound **2**. These data can be obtained free of charge via http://www.ccdc.cam.ac.uk/conts/retrieving.html, or from the Cambridge Crystallographic Data Centre, 12 Union Road, Cambridge CB2 1EZ, UK; fax: (+44) 1223-336-033; or e-mail: deposit@ccdc.cam.ac.uk.

Acknowledgment

The authors are grateful to the Ministry of Science and Higher Education for support of this work (Grant PBZ-KBN-118/T09/09).

References

[1] H.T. Chifotides, K.R. Dunbar, in: F.A. Cotton, C.A. Murillo, R.A. Walton (Eds.), Multiple Bonds Between Metal Atoms, Springer Science and Business Media, Inc., New York, 2005, p. 465.
[2] F.P. Pruchnik, in: E.R.T. Tiekink, M. Gielen (Eds.), Metallotherapeutic Drugs and Metal-Based Diagnostic Agents. The Use of Metals in Medicine, J. Wiley, Chichester, 2005, p. 379.
[3] D.J. Timmons, M.P. Doyle, in: F.A. Cotton, C.A. Murillo, R.A. Walton (Eds.), Multiple Bonds Between Metal Atoms, Springer Science and Business Media Inc., New York, 2005, p. 591.
[4] M.P. Coles, Dalton Trans. (2006) 985.
[5] K.A. Schug, W. Lindner, Chem. Rev. 105 (2005) 67.
[6] V.Y. Kukushkin, A.J.L. Pombeiro, Chem. Rev. 102 (2002) 1771.
[7] T. Ren, C. Lin, E.J. Valente, J.D. Zubkowski, Inorg. Chim. Acta 297 (2000) 283.
[8] C.T. Chifitides, K.V. Catalan, K.R. Dunbar, Inorg. Chem. 42 (2003) 8739.
[9] S. Lo Schiavo, G. Bruno, P. Zanello, F. Laschi, P. Piraino, Inorg. Chem. 36 (1997) 1004.
[10] J.L. Bear, C.-L. Yao, R.S. Lifsey, J.D. Korp, K.M. Kadish, Inorg. Chem. 30 (1991) 336.
[11] T. Kawamura, M. Maeda, M. Miyamoto, H. Usami, K. Imaeda, M. Ebihara, J. Am. Chem. Soc. 120 (1998) 8136.
[12] G.A. Rizzi, M. Casarin, E. Tondello, P. Piraino, G. Granozzi, Inorg. Chem. 26 (1987) 3406.
[13] F. Lafolet, S. Chardon-Noblat, C. Duboc, A. Deronzier, F.P. Pruchnik, M. Rak, Dalton Trans. (2008) 2149.
[14] G.L. Rempel, P. Legzdins, H. Smith, G. Wilkinson, Inorg. Synth. 13 (1972) 90.
[15] C.R. Wilson, H. Taube, Inorg. Chem. 14 (1975) 405.
[16] O. Kahn, Molecular Magnetism, VCH Publishers, New York, 1993.
[17] G.M. Sheldrick, SHELXS 97 Program for Solution of Crystal Structures, University of Göttingen, 1997.
[18] G.M. Sheldrick, SHELXL 97, Program for Crystal Structure Refinement, University of Göttingen, 1997.
[19] M.J. Frisch, G.W. Trucks, H.B. Schlegel, G.E. Scuseria, M.A. Robb, J.R. Cheeseman, J.A. Montgomery Jr., T. Vreven, K.N. Kudin, J.C. Burant, J.M. Millam, S.S. Iyengar, J. Tomasi, V. Barone, B. Mennucci, M. Cossi, G. Scalmani, N. Rega, G.A. Petersson, H. Nakatsuji, M. Hada, M. Ehara, K. Toyota, R. Fukuda, J. Hasegawa, M. Ishida, T. Nakajima, Y. Honda, O. Kitao, H. Nakai, M. Klene, X. Li, J.E. Knox, H.P. Hratchian, J.B. Cross, C. Adamo, J. Jaramillo, R. Gomperts, R.E. Stratmann, O. Yazyev, A.J. Austin, R. Cammi, C. Pomelli, J.W. Ochterski, P.Y. Ayala, K. Morokuma, G.A. Voth, P. Salvador, J.J. Dannenberg, V.G. Zakrzewski, S. Dapprich, A.D. Daniels, M.C. Strain, O. Farkas, D.K. Malick, A.D. Rabuck, K. Raghavachari, J.B. Foresman, J.V. Ortiz, Q. Cui, A.G. Baboul, S. Clifford, J. Cioslowski, B.B. Stefanov, G. Liu, A. Liashenko, P. Piskorz, I. Komaromi, R.L. Martin, D.J. Fox, T. Keith, M.A. Al-Laham, C.Y. Peng, A. Nanayakkara, M. Challacombe, P.M.W. Gill, B. Johnson, W. Chen, M.W. Wong, C.Gonzalez, J.A. Pople, GAUSSIAN 03, Revision B.04, Gaussian Inc., Pittsburgh, PA, 2003.
[20] U. Śliwińska, F.P. Pruchnik, I. Pelińska, S. Ułaszewski, A. Wilczok, A. Zajdel, J. Inorg. Biochem. 102 (2008) 1947.

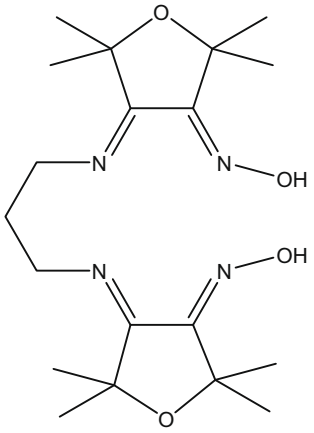


Chart 1. TMFPreH ligand.

dianionic when complexed to a metal, this new ligand is monoanionic on coordination to Cu(II) thereby producing a monocationic copper complex.

The synthesis of the ligand proceeded as expected, and when the Cu(II) and Ni(II) complex were prepared in ethanol, the crystal structures were similar to those of other diiminedioxime complexes. However, when the Cu(II) complex was prepared from $Cu(OAc)_2$ in warmed mixture of acetonitrile and acetone, the crystal structure revealed an unusual example of the acetone bound to the carbon atom of what had formerly been one of the imine double bonds.

2. Experimental

All manipulations were performed in aerobic conditions using reagents as received except for ethanol, which was distilled from sodium under argon immediately before use. FTIR spectra were obtained using a Bruker Vector 22 (Billerica, MA) equipped with a Pike MIRacle single-bounce ATR accessory (Madison, WI). Elemental analyses were performed by Atlantic Microlab, Inc. (Atlanta, GA). ^{1}H NMR spectra were obtained using a Varian Gemini 200 or 500 MHz spectrometer (Palo Alto, CA), and chemical shifts are reported relative to the TMS. Proton shifts are annotated as follows: assignment, integration, multiplicity, coupling constant.

Caution: Although no problems were observed with these complexes, perchlorate salts are potentially explosive and should be handled with care and only in small quantities.

2.1. 2,2,5,5-Tetramethyl-furan-3,4-dione monooxime (TMF oxime)

The oxime was prepared by treating 2,2,5,5-tetramethyldihydrofurane-3(2*H*)-one (TMF, Aldrich) with MeONO as described by Finke [10]. Briefly, a solution of TMF (50 mmol, 8.53 g) in ether (25 mL) and concentrated HCl (0.75 mL) was treated with methyl nitrite, which was bubbled directly into the reaction mixture over a period of approximately 2 h. The reaction mixture was then opened to the atmosphere, the excess methyl nitrite allowed to dissipate, and the HCl was neutralized with 5 mL 5% (w/v) $NaHCO_3$. The solution was extracted with ether (4×7 mL), dried over $MgSO_4$, filtered (Whatman #1), and the ether removed by rotary evaporation. The resulting oil was placed in the refrigerator overnight to give the product as a white crystalline solid. The product was collected on a sintered glass filter, washed with hexane, and allowed to air dry. The yield was 50%. m.p. (uncorrected) 118–119 °C. *Anal.* Calc. for $C_8H_{13}NO_3$: C, 56.13; H, 7.65; N, 8.18; O, 28.04. Found: C, 56.42; H, 7.67; N, 7.91; O, 28.02%. Selected IR data (cm^{-1}): 1635 cm^{-1}, 1743 cm^{-1}; $\nu_{C=N}$. ^{1}H NMR (200 MHz, DMSO-d_6): δ 1.61 (–CH_3, 6H, s), 1.36 (–CH_3, 6H, s).

2.2. 4-[3-(4-Hydroxyimino-2,2,5,5-dimethyl-dihydro-furan-3-ylideneamino)-propylimino]-2,2,5,5-tetramethyl-dihydro-furan-3-one oxime) (**LH$_2$**)

The diiminedioxime ligand was prepared by Schiff base condensation of TMF oxime and 1,3-diaminopropane in ethanol [11]. Briefly, a solution of 1,3-diaminopropane (346 mg, 4.67 mmol) in ethanol (10 mL) was added dropwise (1.5–2 h) to a solution of the oxime (1.6 g, 9.35 mmol) in 10 mL warm ethanol (35–40 °C) under argon, and the reaction mixture was stirred for 18 h. On cooling, a white precipitate formed which was collected on a sintered glass frit, washed with cold ethanol and acetone, and dried in a vacuum desiccator. Yield – 30%. *Anal.* Calc. for $C_{19}H_{32}N_4O_4$: C, 59.98; H, 8.48; N, 14.73; O, 16.82. Found: C, 59.73; H, 8.54; N, 14.76; O, 17.14%. Selected IR data (cm^{-1}): $\nu_{C=N}$ 1599, 1664 cm^{-1}. ^{1}H NMR (200 MHz, DMSO-d_6) 1.226 (–CH_3, 12H, s), 1.439 (–CH_3, 12H, s), 1.959 ($CH_2CH_2CH_2$, 2H, t, 0.035), 3.825 ($CH_2CH_2CH_2$, 4H, t, 0.032), 12.082 (NO*H*, 1H, s).

2.3. {Cu[Cu(**LH**)]$_2$}(ClO$_4$)$_2$ (**1**)

Solid $Cu(ClO_4)_2 \cdot 6H_2O$ (82.5 mg, 0.221 mmol), suspended in 5 mL absolute ethanol, was added dropwise to a suspension of **LH$_2$** (100 mg, 0.262 mmol) in warm (30–35 °C) absolute ethanol (15 mL), and the reaction mixture was stirred for 2 h without further heating. The solvent was removed under vacuum, the product was suspended in water, collected on a medium frit, and washed with cold water. A crystalline red–brown product was obtained by addition of ether to a methanolic solution of the complex. Crystals suitable for X-ray diffraction were grown by slow diffusion of ether into a solution of the complex in methanol. Yield – 30–35% *Anal.* Calc. for $C_{38}H_{60}Cl_2Cu_3N_8O_{16}$: C, 39.81; H, 5.28; Cl, 6.18; Cu, 16.63; N, 9.77; O, 22.33. Found: C, 39.96; H, 5.29; N, 9.77%. Selected IR data (cm^{-1}): $\nu_{C=N}$ 1560 cm^{-1}.

2.4. [Cu(**L'H**)]ClO$_4$ (**2**)

Solid $Cu(OAc)_2 \cdot H_2O$ (23 mg, 0.12 mmol) dissolved in 1 mL acetonitrile was added to the suspension of **LH$_2$** (70 mg, 0.18 mmol) in 3 mL acetone. The reaction mixture was refluxed for 1.5 h. and the solvent was allowed to evaporate slowly to produce a reddish-brown semi-solid to which water was added. Red crystals of **1** suitable for X-ray diffraction precipitated from this solution. Because of its instability, no elemental analysis or IR spectra were obtained for this product.

2.5. [Ni(**LH**)]ClO$_4$ (**3**)

The nickel(II) complex was prepared similarly to **1**. $Ni(NO_3)_2 \cdot 6H_2O$ (38.21 mg, 0.131 mmol) was dissolved in 5 mL of absolute ethanol, and this solution was added dropwise to a suspension of **LH$_2$** (50 mg, 0.131 mmol) in ethanol (5 mL). The color of the reaction mixture became reddish-brown as the Ni^{II} solution was added. The deep orange product was isolated as the perchlorate salt by addition of a saturated aqueous solution of $NaClO_4$. The solution was cooled in the refrigerator, the product collected on a sintered-glass frit, and washed with cold H_2O. Yield – 30 mg (42%). Crystals suitable for X-ray diffraction were obtained by slow diffusion of saturated aqueous $NaClO_4$ into an ethanolic solution of the product. Yield – 40% *Anal.* Calc. for $C_{19}H_{31}ClN_4NiO_{16}$: C, 42.45; H, 5.81; Cl, 6.59; N, 10.42; Ni, 10.92; O, 23.81. Found: C, 42.55; H, 5.84; N, 10.37%. Selected IR data (cm^{-1}): $\nu_{C=N}$ 1561 cm^{-1}.

Table 1
Crystallographic data.

Compound	1	2	3
Formula	$C_{38}H_{60}Cl_2Cu_3N_8O_{16}$	$C_{22}H_{37}ClCuN_4O_9$	$C_{38}H_{62}Cl_2N_8Ni_2O_{16}$
Formula weight, (g mol^{-1})	1146.46	600.55	537.64
Color of crystal, habit	Red, needle	red, needle	red, needle
Space group	$P2_1/c$	$P2_1/c$	$P2_1/c$
a (Å)	12.765(2)	13.6145(17)	27.472(3)
b (Å)	14.147(2)	8.0878(9)	7.9667(9)
c (Å)	13.954(2)	24.249(3)	25.588(3)
β (°)	102.485(3)	97.105(2)	114.988(2)
V (Å^3)	2460.3(7)	2649.5(6)	4877.6(9)
Z	2	4	8
T (K)	213(2)	213(2)	213(2)
Radiation	Mo Kα	Mo Kα	Mo Kα
ρ_{calc} (g cm^{-1})	1.548	1.506	1.464
μ (mm^{-1})	1.467	0.982	0.955
θ Range	2.08–28.28°	1.51–28.03°	1.66–25.00°
Reflections collected	15735	16676	25019
Independent reflections	5868	5782	8597
Data/restraints/parameters	5868/0/312	5782/0/334	8597/0/619
Goodness-of-fit (GOF) F^2	1.154	0.921	1.122
R_1[a] $[I > 2\sigma(I)]$	0.0460	0.0536	0.0651
wR_2[b] $[I > 2\sigma(I)]$	0.1271	0.1133	0.1297
R_1 (all data)	0.0600	0.1446	0.0955
wR_2 (all data)	0.1359	0.1345	0.1409

[a] $R_1 = \Sigma||F_o|-|F_c||/\Sigma|F_o|$.
[b] $wR_2 = [|\Sigma w(|F_o|^2-|F_c|^2)|/\Sigma|w(F_o)^2|]^{1/2}$, $w = 1/[(F_o^2)^2 + (0.01103P)^2$, where $P = (F_o^2 + 2F_c^2)/3$.

2.6. X-ray data collection and refinement

Data were collected using a Bruker SMART CCD (charge coupled device) diffractometer equipped with an LT-3 low-temperature apparatus operating at 213 K. Suitable crystals were chosen and mounted on glass fibers using grease. Data collection parameters are summarized in Table 1. All non-hydrogen atoms were refined anisotropically. Except as noted, hydrogens were calculated by geometrical methods and refined as a riding model. Data were measured using omega scans of 0.3° per frame for 30 s, such that a hemisphere of data was collected. The first 50 frames were recollected at the end of data collection to monitor for decay. None of the crystals used for the diffraction study showed any decomposition during data collection. Cell parameters were retrieved using SMART software [12] and refined using SAINT [13] on all observed reflections. Data reduction was performed using the SAINT software, which corrects for Lp and decay. The structures were solved by the direct method using the SHELXS-97 program and refined by least squares method on F^2 using SHELXL-97 [14], incorporated in SHELXTL-PC V 5.10 [15]. Crystal structure drawings were prepared using ORTEP-3 for Windows [16]. Least-squares planes were calculated using Platon for Windows [17].

For complex **3**, the disorder in C10 was refined to ratio of C10/C10B = 0.77. The hydrogen between O1 and O2 was modeled 50% on O1 and 50% on O2.

3. Results and discussion

A new furanone-containing diiminedioxime ligand and its Cu(II) and Ni(II) complexes were prepared and characterized. The ligand itself is unusual in that there are very few examples of ligands in which furanone is incorporated into the ligand backbone. One example of this is the Tc-Q12 complexes referred to previously [9]. In the Q12 case, the furanone replaces the benzene ring in the Schiffs base salen, and the ligand has a −2 charge when complexed to a metal. Another example is found in the work of Gottschaldt, et al in which furanone replaces the ethylenediamine backbone of a salen-type ligand and the ligand again has a −2 charge when complexed to the metal [18]. For Cu(II), these ligands would produce neutral complexes that would not be expected either to accumulate in the myocardium or be substrates for Pgp. The diiminedioxime derivative is, we believe, the first example of a monoanionic furanone-functionalized ligand.

3.1. Synthesis

The tetramethyl furanone ligand, $\mathbf{LH_2}$, was prepared using a method analogous to that used previously to prepare linear alkyl derivatives of the diiminedioxime ligand system [6]. In contrast to previous derivatives of the diiminedioxime system, the TMF derivative contains a cyclic ether moiety, which is expected to improve the rate at which the ^{64}Cu complex is cleared from the blood and liver. It may also be the case that the increased ligand rigidity imposed by the TMF system increases the in vivo stability of the ^{64}Cu complex. This possibility will be evaluated when the ^{64}Cu complex is prepared.

The syntheses of the Cu(II) and Ni(II) complexes were readily accomplished when the reactions were carried out in ethanol. However, an unexpected result was encountered when the copper complex was prepared from $Cu(OAc)_2$ with acetone in the solvent mixture. In this case, there was significant decomposition of the reaction mixture and a product was isolated that contained an acetone adduct of the ligand. This is an unusual, but not unprecedented, result. There are several examples of acetone adducts of imine ligands in the literature [19–21] including one Cu(II) complex [19]. This is, however, apparently the first example of this being observed in a ligand of this type.

3.2. Descriptions of the structures

3.2.1. {Cu[Cu(**LH**)]$_2$}(ClO$_4$)$_2$ (**1**)

An ORTEP drawing of **1** is shown in Fig. 1. Selected bond lengths and angles are summarized in Table 2. The complex crystallizes as a Cu(II)-bridged dimer with the central Cu(II) atom bonded to four oxime oxygens. The two halves of the dimer are related by a center of symmetry at Cu1, and the molecules are linked in infinite chains along the c axis by weak interactions between Cu2 and the per-

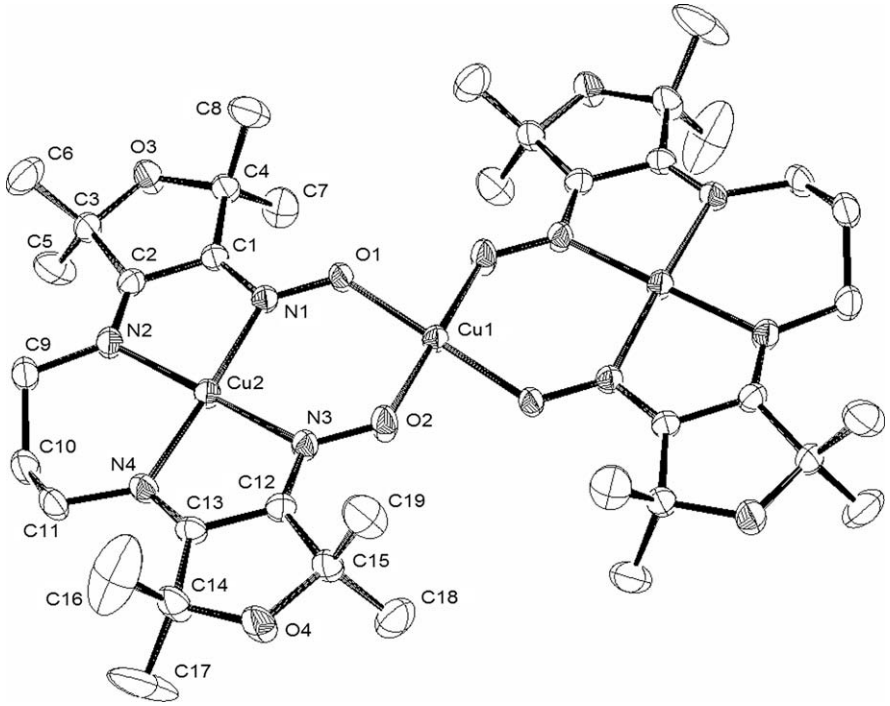


Fig. 1. Molecular structure of $\{Cu[Cu(\mathbf{LH})]_2\}^{2+}$ dimer (**1**) showing atom labeling scheme.

chlorate counter-ions (Cu2–O5, 2.532(3) Å, Cu2–O8 2.577(3) Å) (Fig. 1).

The bridging Cu(II) atom is coplanar with the four oxime oxygen atoms, while the second Cu(II) atom sits slightly (0.0400(4) Å) above the plane defined by the four nitrogen atoms. The four Cu–N bonds are very similar in length (range 1.990(2) Å to 1.994(2) Å) and are somewhat longer than the Cu–N values observed in the prototypical complex of this series, $[Cu(PreH)]^+$ ($PreH_2$ = 3,3'-(trimethylenedinitrilo)bis(2-butanone oxime)), where they range between 1.945(7) Å and 1.972(7) Å [22]. The difference in bond lengths is apparently due to spreading of the ligand by the bridging copper atom. This spreading can be seen in the greater distance between the oxime oxygen atoms in **1** versus $[Cu(PreH)]^+$, 3.021 Å for **1** compared to 2.492 Å for $[Cu(PreH)]^+$, and in the smaller displacement of the Cu(II) atom from the basal plane (0.0400 Å versus 0.097 Å).

Table 2
Selected bond lengths (Å) and angles (°) for $\{Cu[Cu(LH)]_2\}(ClO_4)_2$ (**1**).

Bond lengths (Å)	
Cu(1)–O(2)	1.936(2)
Cu(1)–O(1)	1.955(2)
Cu(2)–N(1)	1.990(2)
Cu(2)–N(2)	1.992(3)
Cu(2)–N(3)	1.991(3)
Cu(2)–N(4)	1.994(2)
Cu(2)–O(5)	2.532(3)
Bond angles (°)	
O(1)–Cu(1)–O(1)[a]	180.0
O(1)–Cu(1)–O(2)	101.86(9)
O(1)–Cu(1)–O(2)[a]	78.14(9)
O(1)[a]–Cu(1)–O(2)	78.14(9)
O(1)[a]–Cu(1)–O(2)[a]	101.86(9)
O(2)–Cu(1)–O(2)[a]	180.0(1)
N(1)–Cu(2)–N(2)	83.9(1)
N(1)–Cu(2)–N(3)	97.9(1)
N(1)–Cu(2)–N(4)	177.6(1)
N(1)–Cu(2)–O(5)	93.7(1)
N(2)–Cu(2)–N(3)	176.4(1)
N(2)–Cu(2)–N(4)	94.1(1)
N(2)–Cu(2)–O(5)	85.6(1)
N(3)–Cu(2)–N(4)	84.0(1)
N(3)–Cu(2)–O(5)	97.4(1)
N(4)–Cu(2)–O(5)	87.5(1)

[a] Symmetry transformations used to generate equivalent atoms: #1 $-x+1,-y,-z+1$.

There are relatively few examples of oxime-bridged Cu(II)-dimers. One example is $[Cu(Cu(PreH))_2][ClO_4]_2$ [23], the Cu(II)-bridged dimer of $[Cu(PreH)H_2O]^+$. The structures of the two dimers are, however, strikingly different. Complex **1** is almost planar with O2–Cu1–O2 and O1–Cu1–O1 angles of 180° and the Cu atom located in the plane defined by the four oxime oxygen atoms. The coordination environment about the central Cu atom in $[Cu(Cu(PreH))_2][ClO_4]_2$ is, in contrast, distorted tetrahedral with O–Cu–O angles of 152.26(7)° and 158.47(7)°. And while **1** is essentially planar, in $[Cu(Cu(PreH))_2][ClO_4]_2$ the two sides of the dimer are bent upwards at almost 60° relative to the CuO_4 core, and the two CuN_4 centers are loosely connected through the ClO_4^- counter-ion (Cu–O 2.838(2) Å). In contrast to this intramolecular ClO_4^- bridge, in complex **1** the dimers are linked in infinite chains along *b* by the perchlorate counter-ion (Fig. 2). One possible reason for the difference in conformations between the two complexes is the steric effect of the methyl groups on the furanone rings. Examination of space-filling models suggests that these groups will interact with those on the opposite side of the dimer if the two sides are folded towards each other, as they are in $[Cu(Cu(PreH))_2][ClO_4]_2$.

3.2.2. $[Cu(\mathbf{L'H})]ClO_4$ (**2**)

Selected interatomic distances and angles for **2** are summarized in Tables 3 and 4, and an ORTEP drawing of the complex is shown in Fig. 2. The coordination geometry around the Cu(II) atom approximately square planar with the Cu(II) atom 0.0268(6) Å above the plane defined by the four nitrogen atoms.

The most distinctive feature of this complex is the reduction of the N2–C3 double bond by addition of acetone across the imine bond with concomitant acetone adduct formation at C3 and addition of a hydrogen atom to N2. The C3 atom is clearly sp3, in con-

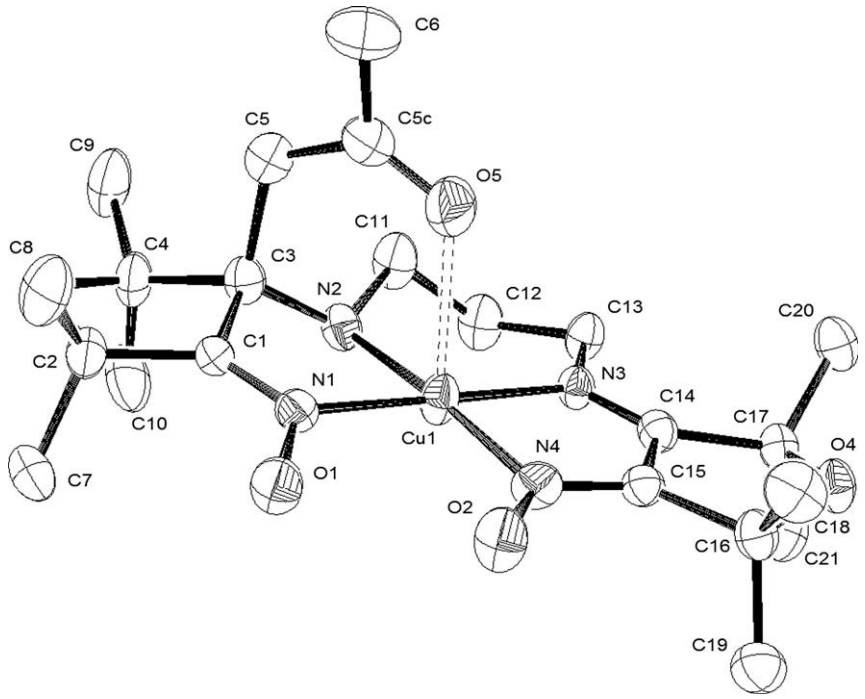


Fig. 2. Molecular structure of $[Cu(\mathbf{L'H})]^+$ cation (acetone adduct) (**2**) showing atom labeling scheme.

trast to C14, the corresponding atom in the second furanone ring in the complex, which is sp2. The difference between the two carbon atoms can be clearly seen in the differences in the bond lengths and angles as well as the differences between the amine and imine nitrogen atoms, N2 and N3 (Tables 3 and 4). The parameters for the imine nitrogen are similar to those observed in the *diimine*dioxime complex $[Cu(PreH)H_2O]^+$ [22], while the parameters for the amine nitrogen are similar to those observed in the *diamine*dioxime complexes $[Cu(ReO_4)(PnAO)]$ (HPnAO = 2,2′-(1,3-diaminopropane)bis(2-methyl-3-butanone oxime)) [24] and [Cu(CN)(PnAO)] [25]. This pattern is also observed when N2- and N3-Cu bonds are compared. The remainder of the ligand is structurally similar to **1** and to $[Cu(PreH)H_2O]^+$ [22].

In contrast to the other examples of acetone adducts [19–21] in which the oxygen atom is oriented away from the metal, in this case the oxygen atom occupies an axial position in the complex; Cu–O 2.399(4) Å. This compares to the 2.294(6) Å Cu–O distance for an acetone oxygen in a Cu-dien complex [26]. The somewhat greater distance in this case is perhaps a consequence of geometric constraints imposed by the ligand which displaces the oxygen away from an ideal apical location (N2–Cu–O5 = 82.3(1)°).

Table 3
Selected bond lengths (Å) $[Cu(L'H)]ClO_4$ (**2**).

Cu(2)–N(1)	1.965(4)
Cu(2)–N(2)	1.995(3)
Cu(2)–N(3)	1.965(3)
Cu(2)–N(4)	1.964(4)
Cu(2)–O(5)	2.399(4)
N(2)–C(3)	1.486(5)
N(2)–C(11)	1.484(5)
N(3)–C(13)	1.460(5)
N(3)–C(14)	1.273(5)
C(3)–C(4)	1.567(6)
C(3)–C(5)	1.573(6)
C(5)–C(5c)	1.526(7)
C(5c)–C(6)	1.491(7)
C(5c)–O(5)	1.226(6)

Other than O8 of the perchlorate counter-ion (Cu–O8, 2.649(5) Å), there are no significant intermolecular interactions.

3.2.3. Structure [Ni(**LH**)]ClO_4 (**3**)

An ORTEP drawing of this complex is shown in Fig. 3, and selected bond lengths and angles are summarized in Table 5. The complex crystallizes with two independent molecules in the asymmetric unit. In molecule A, the Ni(II) atom is 0.1435(6) Å above the plane defined by the four N atoms, and in molecule B, the Ni(II) atom is 0.1108(6) Å above the plane. When viewed edge

Table 4
Selected bond angles (°) for $[Cu(L'H)]ClO_4$ (**2**).

N(1)–Cu(1)–N(2)	83.5(2)
N(1)–Cu(1)–N(3)	178.7(2)
N(1)–Cu(1)–N(4)	95.01(2)
N(2)–Cu(1)–N(3)	97.7(1)
N(2)–Cu(1)–N(4)	175.6(2)
N(3)–Cu(1)–N(4)	83.9(2)
N(1)–Cu(1)–O(5)	84.9(1)
N(2)–Cu(1)–O(5)	82.3(1)
N(3)–Cu(1)–O(5)	94.5(1)
N(4)–Cu(1)–O(5)	101.7(2)
Cu(1)–N(2)–C(3)	106.8(3)
Cu(1)–N(2)–C(11)	117.0(3)
C(3)–N(2)–C(11)	118.4(3)
Cu(1)–N(3)–C(13)	126.4(3)
Cu(1)–N(3)–C(14)	109.5(3)
C(13)–N(3)–C(14)	124.0(4)
N(2)–C(3)–C(1)	108.0(3)
N(2)–C(3)–C(4)	118.6(4)
N(2)–C(3)–C(5)	111.0(4)
C(1)–C(3)–C(4)	100.7(4)
C(1)–C(3)–C(5)	109.0(4)
C(4)–C(3)–C(5)	108.8(4)
N(3)–C(14)–C(15)	120.1(4)
N(3)–C(14)–C(17)	133.0(4)
C(15)–C(14)–C(17)	106.9(4)
Cu(1)–O(5)–C(5c)	123.3(3)

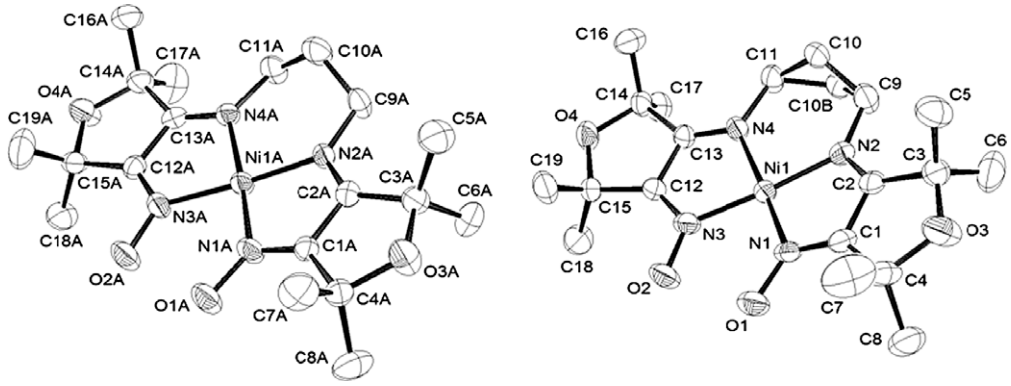


Fig. 3. Molecular structure of [Ni(**LH**)]$^+$ cations (**3**) showing atom labeling scheme.

on, molecule A is slightly more distorted from planarity than molecule B as evidenced by the larger displacements of the ether oxygen atoms in the furanone ring from the N_4 plane. In molecule A, the O3 and O4 atoms are −0.385(4) Å and −0.623(4) Å below the plane versus −0.271(4) Å and −0.202(4) Å for molecule B.

The coordination environment around the two independent Ni(II) atoms is unremarkable. The Ni–N bond lengths range from 1.884(4) to 1.921(4) Å, slightly longer than those observed for [Ni(PreH)]ClO_4, which range from 1.869(5) to 1.892(5) Å [27] and Ni–Me_2PreH, which range from 1.866(5) to 1.887(3) Å [28]. The lengthening of the Ni–N bonds is presumably due to the greater displacement of the Ni atom from the plane in this complex than in the two previous examples (0.018 Å for Ni–PreH [27] and 0.056 Å for Ni–Me_2PreH [28]) and shorter Ni–O(perchlorate) distance (2.504(5) Å and 2.512(4) Å) in this complex compared to the two Ni–PreH complexes (2.84 Å and 2.902(5) Å). The structure of the ligand itself is similar to that seen in **1** and **2** except that in this case the central carbon atom of the trimethylene bridge is disordered in molecule B. There are no significant intermolecular interactions.

Table 5
Selected bond lengths (Å) and angles (°) [Ni(LH)]ClO_4 (**3**).

Bond lengths (Å)	
Ni(1)–N(1)	1.891(4)
Ni(1)–N(2)	1.911(4)
Ni(1)–N(3)	1.890(4)
Ni(1)–N(4)	1.905(4)
Ni(1)–O(5)	2.504(5)
Ni(1A)–N(1A)	1.885(4)
Ni(1A)–N(2A)	1.910(4)
Ni(1A)–N(3A)	1.884(4)
Ni(1A)–N(4A)	1.921(4)
Ni(1A)–O(5A)	2.512(4)
Bond angles (°)	
N(1)–Ni(1)–N(2)	83.8(2)
N(1)–Ni(1)–N(3)	94.2(2)
N(1)–Ni(1)–N(4)	171.1(2)
N(1)–Ni(1)–O(5)	99.0(2)
N(2)–Ni(1)–N(3)	171.4(2)
N(2)–Ni(1)–N(4)	96.3(2)
N(2)–Ni(1)–O(5)	97.3(2)
N(3)–Ni(1)–N(4)	84.4(2)
N(3)–Ni(1)–O(5)	91.2(2)
N(4)–Ni(1)–O(5)	89.8(2)
N(1A)–Ni(1A)–N(2A)	84.6(2)
N(1A)–Ni(1A)–N(3A)	93.6(2)
N(1A)–Ni(1A)–N(4A)	173.2(2)
N(1A)–Ni(1A)–O(5A)	97.7(2)
N(2A)–Ni(1A)–N(3A)	173.1(2)
N(2A)–Ni(1A)–N(4A)	96.5(2)
N(2A)–Ni(1A)–O(5A)	84.0(2)
N(3A)–Ni(1A)–N(4A)	84.4(2)
N(3A)–Ni(1A)–O(5A)	102.9(2)
N(4A)–Ni(1A)–O(5A)	89.1(2)

4. Conclusions

The tetramethylfuranone diiminedioxime ligand 4-[3-(4-Hydroxyimino-2,2,5,5-dimethyl-dihydro-furan-3-ylideneamino)-propylimino]-2,2,5,5-tetramethyl-dihydro-furan-3-one oxime) (**LH_2**) was successfully synthesized as were its Cu(II) and Ni(II) complexes. However, when the synthesis of the Cu(II) complex was attempted in a mixture of acetonitrile and acetone, an unusual example of an acetone adduct of the ligand was observed. This observation suggests that caution should be observed when using acetone as a solvent to prepare copper–imine complexes.

Efforts are currently underway to prepare the corresponding ^{64}Cu complex so that the effect of the tetramethylfuranone moiety on the biodistribution of the complex can be determined.

Acknowledgements

This work was supported by NIH grant CA-81084 (ABP) and US Army BCRP grant DAMD17-99-1-9125 (ABP). The CCD-based X-ray diffractometer at Harvard University was purchased through NIH grant 1S10RR11937-01.

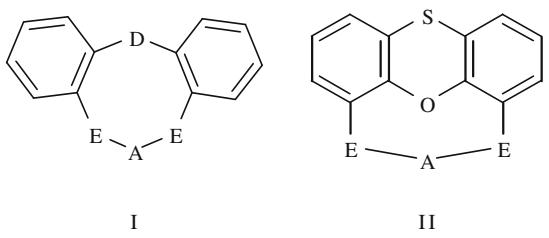
Appendix A. Supplementary data

CCDC 211872, 211871 and 211873 contain the supplementary crystallographic data for **1**, **2** and **3**, respectfully. These data can be obtained free of charge via www.ccdc.cam.ac.uk/conts/retrieving.html or from the CCDC, 12 Union Road, Cambridge CB2 1EZ, UK; fax: (+44) 1223-336-033; or e-mail: deposit@ccdc.cam.ac.uk. Supplementary data associated with this article can be found, in the online version, at doi:10.1016/j.poly.2008.12.006.

References

[1] M.M. Gottesman, I. Pastan, Ann. Rev. Biochem. 62 (1993) 385.
[2] D. Piwnica-Worms, M.L. Chiu, M. Budding, J.F. Kronauge, R.A. Kramer, J.M. Croop, Cancer Res. 53 (1993) 977.
[3] C.L. Crankshaw, M. Marmion, G.D. Luker, V. Rao, J. Dahlheimer, B.D. Burleigh, E. Webb, K.F. Deutsch, D. Piwnica-Worms, J. Nucl. Med. 39 (1998) 77.
[4] J.R. Ballinger, J. Bannerman, I. Boxen, P. Firby, N.G. Hartman, M.J. Moore, J. Nucl. Med. 37 (1996) 1578.
[5] R.D. Neirinckx, J.F. Kronauge, M.D. Loberg, Int. J. Appl. Radiat. Isot. 34 (1983) 721.
[6] A.B. Packard, J.F. Kronauge, E. Barbarics, S. Kiani, S.T. Treves, Nucl. Med. Biol. 29 (2002) 289.
[7] B.L. Holman, A.G. Jones, J. Lister-James, A. Davison, M.J. Abrams, J.M. Kirshenbaum, S.S. Tumeh, R.J. English, J. Nucl. Med. 25 (1984) 1350.

[8] F.J. Wackers, D.S. Berman, J. Maddahi, D.D. Watson, G.A. Beller, H.W. Strauss, C.A. Boucher, M. Picard, B.L. Holman, R. Fridrich, J. Nucl. Med. 30 (1989) 301.
[9] C. Rossetti, G. Vanoli, G. Paganelli, M. Kwiatkowski, F. Zito, F. Colombo, C. Bonino, A. Carpinelli, R. Casati, K. Deutsch, M. Marmion, S.R. Woulfe, F. Lunghi, E. Deutsch, F. Fazio, J. Nucl. Med. 35 (1994) 1571.
[10] R.G. Finke, B.L. Smith, W.A. McKenna, P.A. Christian, Inorg. Chem. 20 (1981) 687.
[11] R.R. Gagne', J.L. Allison, R.S. Gall, C.A. Koval, J. Am. Chem. Soc. 99 (1977) 7170.
[12] SMART V 5.054 (NT), Software for the CCD Detector System, Bruker Analytical X-ray Systems, Madison, WI, 1998.
[13] SAINT V 6.01 (NT), Software for the CCD Detector System, Bruker Analytical X-ray Systems, Madison, WI, 1999.
[14] G. Sheldrick, Acta Crystallogr., Sect. A 64 (2008) 112.
[15] SHELXTL 5.10 (PC/NT-Version), Program library for Structure Solution and Molecular Graphics, Bruker Analytical X-ray Systems, Madison, WI, 1998.
[16] L. Farrugia, J. Appl. Crystallogr. 30 (1997) 565.
[17] L.J. Farrugia, PLATON for Windows, 1.14, University Of Glasgow, Glasgow, 2008.
[18] M. Gottschaldt, D. Koth, H. Gorls, Org. Biomol. Chem. 3 (2005) 1170.
[19] M.J. MacLachlan, M.K. Park, L.K. Thompson, Inorg. Chem. 35 (1996) 5492.
[20] B. Kamenar, B. Kaitner, V. Katovic, D.H. Busch, Inorg. Chem. 18 (1979) 815.
[21] W.K. Seok, K. Karaghiosoff, T.M. Klapotke, P. Mayer, Z. Naturforsch 58b (2003) 1087.
[22] O.P. Anderson, A.B. Packard, Inorg. Chem. 18 (1979) 1940.
[23] D. Luneau, H. Oshio, H. Okawa, S. Kida, J. Chem. Soc., Dalton Trans. (1990) 2283.
[24] I.B. Liss, E.O. Schlemper, Inorg. Chem. 14 (1975) 3035.
[25] E.O. Schlemper, M.S. Hussain, R.K. Murmann, Acta Crystallogr., Sect. B 37 (1981) 234.
[26] M.J. Scott, R.H. Holm, J. Am. Chem. Soc. 116 (1994) 11357.
[27] Y.M. Wang, C.S. Chung, C.Y. Cheng, S.L. Wang, Acta Crystallogr., Sect. C 46 (1990) 1429.
[28] T.H. Lu, F. Tseng, H. Luh, C.S. Chung, Acta Crystallogr., Sec. C 49 (1993) 666.



Scheme 1.

differences were observed between the diorganyl- and halogen-containing compounds in both solution and solid state. The detailed description of the synthesis, spectroscopic characterization and crystallographic data are presented and discussed below.

According to our results, the acidity of the $GeRHal^{2+}$ fragment in **4**–**6** enhances the transannular O···Ge interaction, prompting a boat–boat eight-membered ring conformation and a trigonal bipyramidal germanium local geometry; the GeR_2^{2+} less acid fragment present in **2** and **3** has an opposite effect.

2. Experimental

2.1. Materials and methods

All manipulations were performed under a dry, oxygen-free nitrogen atmosphere using standard Schlenk techniques. Solvents were dried by standard methods and distilled prior to use. All organogermanium chlorides, $GeCl_4$ and phenoxathiin were obtained commercially (Aldrich). Melting points were determined with a Mel-Temp II instrument and are uncorrected. Spectra were recorded with the following instruments. Mass spectra for EI, a Hewlett–Packard 5989A mass spectrometer was used. Elemental analyses were recorded with a Perkin–Elmer Series II CHNS/O Analyzer. The IR spectra were recorded in the 4000–400 cm^{-1} range with a Perkin–Elmer System 2000 FT-IR spectrometer, as KBr pellets. NMR: Jeol Eclipse 400 spectrometer at 25 °C; with the residual protio-solvent signal used as referenced for ^1H NMR (399.78 MHz) spectra. $^{13}C\{^1H\}$ NMR (100.53 MHz) spectra were referred through the solvent peaks. Chemical shifts are quoted on the δ scale (downfield shifts are positive) relative to tetramethylsilane (^1H, $^{13}C\{^1H\}$ NMR spectra).

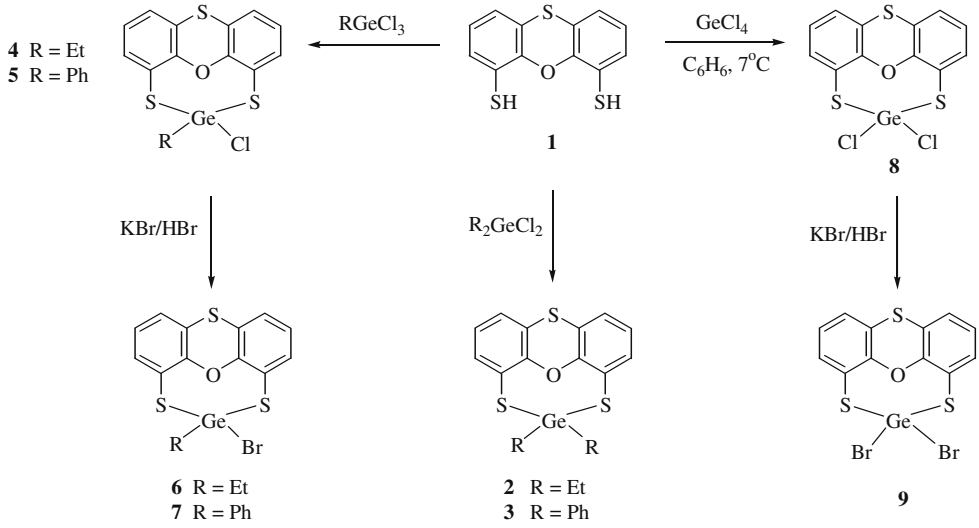
2.2. Synthesis of the ligand $S(C_6H_3SH)_2O$ (**1**)

Phenoxathiin (7.00 g, 34.95 mmol) and TMEDA (15.20 mL, 101.36 mmol) were dissolved in THF (80 mL). The mixture was immersed in an ice-bath and a solution of *n*BuLi in hexanes (0.5 M, 160.80 mL, 80.39 mmol) was added dropwise. The solution was stirred for 24 h keeping the ice-bath. Elemental sulfur (3.36 g, 104.86 mmol) was added with vigorous stirring, and the resulting yellow suspension was stirred for 36 h. Then, $LiAlH_4$ (1.99 g, 185.25 mmol) was added in small portions. ***Caution: A vigorous reaction takes place and the reaction suspension starts to foam.*** Subsequently, the suspension was stirred by 4 h and the resulting mixture was cautiously added in small portions to a mixture of crushed ice (60 g) and concentrated hydrochloric acid (25 mL) immersed in an ice-bath. ***Caution: Vigorous evolution of H_2S occurs, and this reaction must be carried out in a well ventilated fumehood.*** After the ending of the vigorous reaction, further concentrated hydrochloric acid (15 mL) was added. The resulting suspension was extracted with $CHCl_3$ (3 × 50 mL). The combined organic phases were passed through a column of celite and anhydrous sodium sulphate, and evaporation of the solvent yielded a yellow solid. The compound is recrystallized with a mixture of toluene–hexane at −30 °C. Yield: 5.54 g (60%) p.f. 64–67 °C, ^1H NMR ($CDCl_3$): δ = 7.12 (m, 2H, H3) 6.91 (m, 4H, H2, H1), 4.10 (s, 2H, SH), ppm, $^{13}C\{^1H\}$ NMR ($CDCl_3$): δ = 148.2, 128.7, 125.0, 124.1, 121.9, 121.4 ppm.

2.3. Synthesis of the phenoxathiin-4,6-dithiolate germanium compounds $[\{S(C_6H_3S)_2O\}GeR_nHal_{2-n}]$

2.3.1. Synthesis of $[\{S(C_6H_3S)_2O\}GeEt_2]$ (**2**)

$S(C_6H_3SH)_2O$, (0.27 g 1.01 mmol) was added to a solution containing 15 mL of dry methanol at room temperature. After the solution was stirred for 30 min, a white suspension resulted, and Et_2GeCl_2, (0.15 mL, 1.02 mmol) was added via a syringe. The solution was refluxed overnight; during this time the mixture acquired homogenous clear brown coloration. It was filtered while hot; an oily compound was separated from the methanolic mother liquor, and dissolved when chloroform was added. The mother liquor and chloroform solution were slowly evaporated, yielding colourless crystals. Yield: 0.11 g (28%) Mass spectrum (EI-MS, $CHCl_3$, 30 eV) *m*/*z* (rel. int.) = 394(30) $[M]^{+\cdot}$, 365 (base peak) $[M-Et]^+$, 336(12)



Scheme 2.

$[M-2Et]^{+\cdot}$ 304(6) $[C_{12}H_6S_2OGe]^{+\cdot}$, 246(40) $[C_{12}H_6S_3]^{+\cdot}$, 214(13) $[C_{12}H_6S_2]^{+\cdot}$. M.p. 64–67 °C. *Anal.* Calc. for $S(C_6H_3S)_2OGeEt_2$: C, 48.89; H, 4.10. Found: C, 49.61; H, 4.21%. ^1H NMR ($CDCl_3$): δ = 7.33 (dd $^3J_{H3-H2}$ = 7.68 Hz $^4J_{H3-H1}$ = 1.12 Hz, 2H, H3), 7.09 (dd $^3J_{H1-H2}$ = 7.68 Hz, $^4J_{H1-H3}$ = 1.32 Hz, 2H, H1), 7.00 (dd $^3J_{H2-H1}$ = $^3J_{H2-H3}$ = 7.68 Hz, 2H, H2), 1.08 (m, 4H, H5), 1.02 (m, 6H, H6) ppm. $^{13}C\{^1H\}$ NMR ($CDCl_3$): δ = 151.5, 131.8, 125.3, 125.3, 125.2, 123.7, 12.4, 8.7 ppm.

Compounds **3**, **4** and **5** were prepared in a similar fashion to compound **2**.

2.3.2. Synthesis of [{S(C6H3S)2O}GePh2] (3)

$S(C_6H_3SH)_2O$ (0.20 g, 0.76 mmol) and Ph_2GeCl_2 (0.16 mL 0.76 mmol). Colourless crystals. Yield: 0.16 g (42%) Mass spectrum (EI-MS, $CHCl_3$, 30 eV) *m/z* (rel. int.) = 490(95) $[M]^{+\cdot}$, 413 (base peak) $[M-Ph]^+$, 336(3) $[M-2Ph]^{+\cdot}$, 246(35) $[C_{12}H_6S_3]^{+\cdot}$, 214(13) $[C_{12}H_6S_2]^{+\cdot}$. M.p. 204–205 °C. *Anal.* Calc. for $S(C_6H_3S)_2OGePh_2$: C, 58.93; H, 3.30. Found: C, 59.00; H, 3.63%. ^1H NMR ($CDCl_3$): δ = 7.44 (m, 6H, H5, H7), 7.27 (m, 6H, H3, H6), 6.98 (dd $^3J_{H2-H1}$ = $^3J_{H2-H3}$ = 7.69 Hz, 2H, H2), 6.95 (dd $^3J_{H1-H2}$ = 7.67 Hz, $^4J_{H1-H3}$ = 1.83 Hz, 2 H, H1) ppm. $^{13}C\{^1H\}$ NMR ($CDCl_3$): δ = 150.4, 133.4, 130.9, 130.5, 128.6, 125.2, 125.1, 124.9, 123.5 ppm.

2.3.3. Synthesis of [{S(C6H3S)2O}GeEtCl] (4)

$S(C_6H_3SH)_2O$ (0.33 g. 1.26 mmol) and $EtGeCl_3$, (0.17 mL, 1.32 mmol). Colourless crystals. Yield: 0.17 g (34%). Mass spectrum (EI-MS, $CHCl_3$, 30 eV) *m/z* (rel. int.) = 400 (70) $[M]^{+\cdot}$, 371 (base peak) $[M-Et]^+$, 336(8) $[M-Cl]^{+\cdot}$, 246(38) $[C_{12}H_6S_3]^{+\cdot}$, 214(13) $[C_{12}H_6S_2]^{+\cdot}$. M.p. 139–142 °C. *Anal.* Calc. for $S(C_6H_3S)_2OGeClEt$: C, 42.09; H, 2.78. Found: C, 43.07; H, 3.05%. ^1H NMR ($CDCl_3$): δ = 7.27 (dd$^3J_{H3-H2}$ = 7.68 Hz $^4J_{H3-H1}$ = 2.56 Hz, 2H, H3), 7.07 (dd $^3J_{H2-H1}$ = $^3J_{H2-H3}$ = 7.68 Hz, 2H, H2), 7.05 (dd $^3J_{H1-H2}$ = 7.68 Hz, $^4J_{H1-H3}$ = 1.32 Hz, 2H, H1), 2.02 (q $^3J_{H5-H6}$ = 7.88 Hz, 2H, H5), 1.28 (t $^3J_{H6-H5}$ = 7.88 Hz, 3H, H6) ppm. $^{13}C\{^1H\}$ NMR ($CDCl_3$): δ = 147.6, 127.7, 126.4, 125.4, 124.2, 123.7, 28.6, 8.4 ppm.

2.3.4. Synthesis of [{S(C6H3S)2O}GePhCl] (5)

$S(C_6H_3SH)_2O$ (1.01 g, 3.83 mmol) and $PhGeCl_3$ (1.00 g, 3.91 mmol). Yellow crystals. Yield: 0.65 g (37%). Mass spectrum (EI-MS, $CHCl_3$, 30 eV) *m/z* (rel. int.) = 448 (base peak) $[M]^{+\cdot}$, 371 $[M-Et]^+$, 336(8) $[M-Cl]^{+\cdot}$, 246(38) $[C_{12}H_6S_3]^{+\cdot}$, 214(13) $[C_{12}H_6S_2]^{+\cdot}$. M.p. 128 °C. *Anal.* Calc. for $S(C_6H_3S)_2OGePhCl$: C, 48.31; H, 2.48. Found: C, 48.88; H, 2.71%. ^1H NMR ($CDCl_3$): δ = 7.59 (dd $^3J_{H5-H6}$ = 7.68 Hz $^4J_{H5-H7}$ = 1.68 Hz, 2H, H5) 7.27 (m, 3H, H6, H7), 7.19 (dd $^3J_{H3-H2}$ = 7.69 Hz $^4J_{H3-H1}$ = 1.46 Hz, 2H, H3), 6.93 (dd $^3J_{H2-H1}$ = $^3J_{H2-H3}$ = 7.69 Hz, 2H, H2), 6.87 (dd $^3J_{H1-H2}$ = 7.69 Hz, $^4J_{H1-H3}$ = 1.46 Hz, 2H, H1) ppm. $^{13}C\{^1H\}$ NMR ($CDCl_3$): δ = 147.1, 140.5, 131.3, 131.2, 129.0, 127.4, 126.3, 124.4, 123.3 ppm.

2.3.5. Synthesis of [{S(C6H3S)2O}GeEtBr] (6)

[{$S(C_6H_3S)_2O$}GeClEt] (0.06 g, 0.15 mmol), KBr (0.18 g, 1.50 mmol) and HBr 48% (1 mL, 18.41 mmol) were suspended in benzene (60 mL) and refluxed for 24 h. The water was removed from the resulting colourless solution with a Dean–Stark trap. The yellow solution was dried using a column of anhydrous sodium sulphate and celite. The solution was left under a nitrogen flow to afford colourless crystals of (**5**), Yield: 0.03 g (40%). Mass spectrum (EI-MS, $CHCl_3$, 30 eV) *m/z* (rel. int.) = 444 (78) $[M]^{+\cdot}$, 415(95) $[M-Et]^+$, 365(28) $[M-Br]^+$, 336(22) $[M-Et, -Br]^{+\cdot}$, 246 (base peak) $[C_{12}H_6S_3]^{+\cdot}$, 214(28) $[C_{12}H_6S_2]^{+\cdot}$. M.p. 146–148°C. *Anal.* Calc for $S(C_6H_3S)_2OGeEtBr$ 0.25THF: C, 39.00; H, 2.84. Found: C, 39.40; H, 2.64%. ^1H NMR ($CDCl_3$): δ = 7.26 (m, 2H, H3), 7.06 (m, 4H, H1, H2), 2.08 (q $^3J_{H5-H6}$ = 7.88 Hz, 2H, H5), 1.26 (t $^3J_{H6-H5}$ = 7.88 Hz, 3H, H6) ppm $^{13}C\{^1H\}$ NMR ($CDCl_3$): δ = 147.8, 127.6, 126.3, 125.6, 124.4, 123.7, 29.2, 8.9 ppm.

2.3.6. Synthesis of [{S(C6H3S)2O}GePhBr] (7)

The compound **7** was prepared in a similar fashion to compound **6**. [{$S(C_6H_3S)_2O$}GePhCl] (0.10 g (0.22 mmol), KBr (0.27 g, 2.24 mmol) and HBr 48% (1.5 mL (27.61 mmol). Yellow solid. Yield: 0.05 g (43%); Mass spectrum (EI-MS, $CHCl_3$, 30 eV) *m/z* (rel. int.) = 492 (75) $[M]^{+\cdot}$,415 (6) $[M-Ph]^+$, 413 (base peak) $[M-Br]^+$, 336(5) [M, –Ph, –Br]$^{+\cdot}$, 246(38) $[C_{12}H_6S_3]^{+\cdot}$, 214(13) $[C_{12}H_6S_2]^{+\cdot}$. M.p. 167.7–168.5 °C. *Anal.* Calc. for $S(C_6H_3S)_2OGePhBr$: C, 43.94; H, 2.25. Found: C, 44.46; H, 2.25. ^1H NMR ($CDCl_3$): δ = 7.74 (m, 2H, H5) 6.86 (m, 5H, H3, H6, H7) 6.42 (m, 4H, H1, H2) ppm. $^{13}C\{^1H\}$ NMR ($CDCl_3$): δ = 147.6, 141.0, 131.1, 129.0, 127.4, 126.0, 125.1, 124.3, 123.3 ppm.

2.3.7. Synthesis of [{S(C6H3S)2O}GeCl2] (8)

$GeCl_4$ (0.4 mL, 3.51 mmol) was dissolved in dry benzene (20 mL) at 7 °C and added via a syringe to a solution of $S(C_6H_3SH)_2O$ (0.90 g, 3.40 mmol) in dry benzene (20 mL). The solution was kept at 7 °C overnight. It was filtered and the benzene was slowly evaporated. A yellow solid was obtained. Yield: 0.88 g (60%); Mass spectrum (EI-MS, $CHCl_3$, 30 eV) *m/z* (rel. int.) = 406(20) $[M]^{+\cdot}$, 371(5) $[M-Cl]^+$. M.p. 132–133 °C. *Anal.* Calc. for S $(C_6H_3S)_2OGeCl_2$ 0.5 C_6H_6: C, 40.49; H, 2.04. Found: C, 40.07; H, 2.99%. ^1H NMR ($CDCl_3$): δ = 7.28 (m, 2H, H3), 7.11 (m, 4H, H1, H2) ppm $^{13}C\{^1H\}$ NMR($CDCl_3$): δ = 146.1, 128.2, 126.5, 125.6, 123.0, 122.0 ppm.

2.3.8. Synthesis of [{S(C6H3S)2O}GeBr2] (9)

This compound was prepared in a similar fashion to compound **6**. [{$S(C_6H_3S)_2O$}$GeCl_2$] (0.100 g, 0.25 mmol), KBr (0.59 g, 4.93 mmol) and HBr 48% (3 mL, 55.23 mmol). Yellow solid. Yield: 0.05 g (40%); Mass spectrum (EI-MS, $CHCl_3$, 30 eV) *m/z* (rel. int.) = 496 (base peak) $[M]^{+\cdot}$, 415(95) $[M-Br]^+$, 336 (15) $[M-2Br]^{+\cdot}$, 246 (50) $[C_{12}H_6S_3]^{+\cdot}$, 214 (15) $[C_{12}H_6S_2]^{+\cdot}$. M.p. 198.1–201.6 °C. ^1H NMR ($CDCl_3$): δ = 7.32 (m, 2H, H3) 7.14 (m, 4H, H1, H2) ppm $^{13}C\{^1H\}$ NMR ($CDCl_3$): δ = 147.6, 129.4, 126.3, 126.2, 124.5, 121.9 ppm.

2.4. X-ray crystallography

Suitable single crystals of the compounds **2–6** were grown by slow evaporation from a chloroform solution. X-ray diffraction data on **2–6** were collected at room temperature on a CCD Smart 6000 diffractometer through the use of Mo Kα radiation (λ = 0.71073 Å, graphite monochromator). Data were integrated, scaled, sorted, and averaged using the SMART software package. The structures were solved by direct methods, using SHELXTL NT Version 5.10 and refined by full-matrix least squares against F^2 [18]. An empirical absorption correction based on the multiple measurement of equivalent reflections was applied by using the program SADABS [19]. The displacement parameters of non-hydrogen atoms were refined anisotropically. The positions of the hydrogen atoms were kept fixed with a common isotropic displacement parameter. Selected crystallographic data are given in Table 1.

3. Results and discussion

3.1. Synthesis

The 4,6-dimercaptophenoxathiin ligand (OS_2–H_2 **1**) was prepared via a four-step reaction from phenoxathiin by modification of a reported method [10] (See Section 2 for details). The reaction of **1** with the corresponding organylgermanium(IV) chloride in dry methanol yielded the corresponding Ge(IV) compounds **2–5**. Treatment of **1** with $GeCl_4$ in benzene at 7 °C afforded the dichlorogermanium compound **8**. A subsequent treatment of **4**, **5** and **8** with

Table 1
Selected crystallographic data for compounds **2**–**6**.

Compound	**2**	**3**	**4**	**5**	**6**
Empirical formula	$C_{16}H_{16}GeOS_3$	$C_{24}H_{16}GeOS_3$	$C_{14}H_{11}ClGeOS_3$	$C_{18}H_{11}ClGeOS_3$	$C_{14}H_{11}BrGeOS_3$
Mr (g/mol)	393.06	489.14	399.45	447.49	443.91
Crystal size (mm)	0.48 × 0.36 × 0.25	0.55 × 0.37 × 0.25	0.18 × 0.11 × 0.09	0.50 × 0.37 × 0.10	0.58 × 0.30 × 0.28
Crystal system	triclinic	triclinic	orthorhombic	monoclinic	orthorhombic
Space group	$P\bar{1}$	$P\bar{1}$	*Pnma*	*P*2(1)/*c*	*Pnma*
$\rho_{Calc.}$ (Mg m^{-3})	1.577	1.513	1.659	1.619	1.811
Z	2	2	4	8	4
a (Å)	7.8988(17)	9.1414(10)	7.694(3)	12.5005(14)	7.7002(10)
b (Å)	8.3653(17)	10.2519(11)	13.797(6)	10.3635(11)	14.0401(18)
c (Å)	14.172(3)	12.3095(13)	15.062(6)	28.864(3)	15.056(2)
α (°)	99.270(4)	78.196(2)	90	90	90
β (°)	90.241(4)	72.008(2)	90	100.843(3)	90
γ (°)	115.965(4)	86.348(2)	90	90	90
V (Å^3)	828.0(3)	1074.0(2)	1598.8(11)	3672.6(7)	1627.7(4)
μ (mm^{-1})	2.223	1.731	2.465	2.157	4.713
F(000)	400	496	800	1792	872
Goodness-of-fitness (GoF)	1.091	0.495	0.997	0.947	1.122
Absorption correction	SADABS	SADABS	SADABS	SADABS	SADABS
Reflections collected	9351	7672	18743	25922	9927
Unique reflections, R_{int}	2905; 0.0297	4631; 0.0265	1654; 0.1300	8012; 0.0814	1674; 0.0415
R_1, wR_2 [I > 2σ(I)]	0.0306; 0.0767	0.0425; 0.0967	0.0469; 0.0970	0.0568; 0.1092	0.0392; 0.0984
R_1, wR_2 (all data)	0.0388; 0.0906	0.0668; 0.1140	0.1107; 0.1193	0.1304; 0.1341	0.0640; 0.1277
Largest residuals (e Å^{-3})	0.475/−0.279	0.480/−0.343	0.700/−0.268	0.676/−0.307	0.314/−0.464

Table 2
^{1}H NMR chemical shifts (δ-values [ppm]) for **1**–**9** in $CDCl_3$ at 25 °C.

Compound	R^1	R^2	H-1	H-2	H-3	H-5	H-6	H-7
OS_2–H_2 (**1**)	–	–	6.91	6.91	7.12	–	–	–
2	Et	Et	7.09	7.00	7.33	1.08	1.02	–
3	Ph	Ph	6.95	6.98	7.27	7.44	7.27	7.44
4	Cl	Et	7.05	7.07	7.27	2.02	1.28	–
5	Cl	Ph	6.87	6.93	7.19	7.59	7.27	7.27
6	Br	Et	7.06	7.06	7.26	2.08	1.26	–
7[a]	Br	Ph	6.42	6.42	6.86	7.74	6.86	6.86
8	Cl	Cl	7.11	7.11	7.28	–	–	–
9	Br	Br	7.14	7.14	7.32	–	–	–

[a] C_6D_6.

a mixture of KBr/HBr in benzene yielded the corresponding bromo compounds **6**, **7** and **9** (Scheme 2). All germanium compounds are air-stable, soluble in chloroform and benzene.

3.2. Mass spectra

Electron impact mass spectra for all compounds [{$S(C_6H_3S)_2O$}-GeR^1R^2] exhibit a variable intensity ion with the appropriate isotopic ratio representing the molecular ion ($M^{\cdot+}$). In all cases the M–R^1, M–R^2 and M–R^1–R^2 fragments were observed with variable intensity confirming the binding of germanium to the sulfur thiolate-like atoms [R^1 = Et (**2**), Ph (**3**), Cl (**4**), Cl (**5**), Br (**6**), Br (**7**), Cl (**8**), Br (**9**); R^2 = Et (**2**), Ph (**3**), Et (**4**), Ph (**5**), Et (**6**), Ph (**7**), Cl (**8**), Br (**9**)]. In compounds **5** and **9** the base peak corresponds to the molecular ion, whereas in **2**, **3**, **4** and **6** corresponds to the M–R^2 fragment. More assigned peaks are listed in Section 2.

3.3. NMR spectroscopy

NMR spectra were recorded in $CDCl_3$ solutions at 25 °C. ^{1}H and ^{13}C{^{1}H} spectroscopic data for the free OS_2–H_2 ligand and germanium compounds **2**–**9** are given in Tables 2 and 3, Scheme 3. The assignments were carried out by heteronuclear and homonuclear correlation two-dimension experiments (HETCOR, COLOC and COSY).

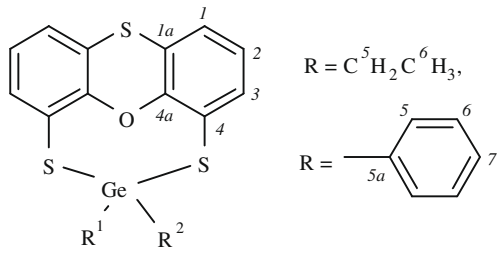
In solution both $S(C_6H_3S)O$ halves are equivalent. The ^{1}H spectrum of free OS_2–H_2 ligand displayed the –SH group at 4.10 ppm as a singlet. The formation of compounds **2**–**5** and **8** was confirmed by the vanishing of the –SH signal. All germanium compounds and free ligand spectra showed three signals in the aromatic region for the $\{S(C_6H_3S)_2O\}$ moiety as an ABC pattern. Because of the electron withdrawing effect of the halogen substituents on the germanium atom, the protons of the ethyl groups in **4** and **6** are more shifted to high frequencies than those of **2**.

^{13}C{^{1}H} NMR spectrum for the free ligand showed six signals at 121.4–148.2 ppm. The comparison of the chemical shift values of the C1a and C4 carbons for the ligand OS_2–H_2 respect to those of the compounds **2**–**9** showed a deshielding effect attributable to

Table 3
^{13}C{^{1}H} NMR chemical shifts (δ-values [ppm]) for **1**–**9** in $CDCl_3$ at 25°C.

	R^1	R^2	C-1	C-1a	C-2	C-3	C-4	C-4a	C-5	C-5a	C-6	C-7
OS_2–H_2 (**1**)	–	–	124.1	121.4	125.0	128.7	121.9	148.2	–	–	–	–
2	Et	Et	125.3	123.7	125.3	131.8	125.2	151.5	12.4	–	8.7	–
3	Ph	Ph	125.1	123.5	125.2	130.5	124.9	150.4	133.4	[b]	128.6	130.9
4	Cl	Et	124.2	123.7	126.4	127.7	125.4	147.6	28.6	–	8.4	–
5	Cl	Ph	124.4	123.3	126.3	127.4	[b]	147.1	131.2	140.5	129.0	131.3
6	Br	Et	124.4	123.7	126.3	127.6	125.6	147.8	29.2	–	8.9	–
7[a]	Br	Ph	124.3	123.3	126.0	127.4	125.1	147.6	131.1	141.0	129.0	131.1
8	Cl	Cl	125.6	122.0	126.5	128.2	123.0	146.1	–	–	–	–
9	Br	Br	126.2	121.9	126.3	129.4	124.5	147.6	–	–	–	–

[a] C_6D_6.
[b] Not observed signal at room temperature.



Scheme 3.

the formation of the S–Ge bond, see Table 2. In the mono- and dihalogenate germanium compounds **4**–**9**, the C4a carbon is shifted to lower frequencies respect to OS_2–H_2, whereas it is shifted to higher frequencies in the diorganyl-germanium complexes **2** and **3**. The observed shielding may be attributed to a change in the chemical environment of the oxygen atom, which could be accounted for either by the existence of different conformational isomers – involving the eight-membered ring with a more or less constrained oxygen atom – or by means of electron density transference from the oxygen to the germanium acceptor atom. This later proposal supports an increase of the germanium coordination number in complexes **4**–**9**.

3.4. X-ray structures of compounds 2–6

The molecular structures in crystalline solid state of **2**–**6** were determined by single crystal X-ray diffraction analyses. The unit cell of **5** has two crystallographic independent molecules (**5a** and **5b**). The molecular ORTEP drawings are depicted in Fig. 1 and selected bond lengths, angles and torsion angles are given in Table 4.

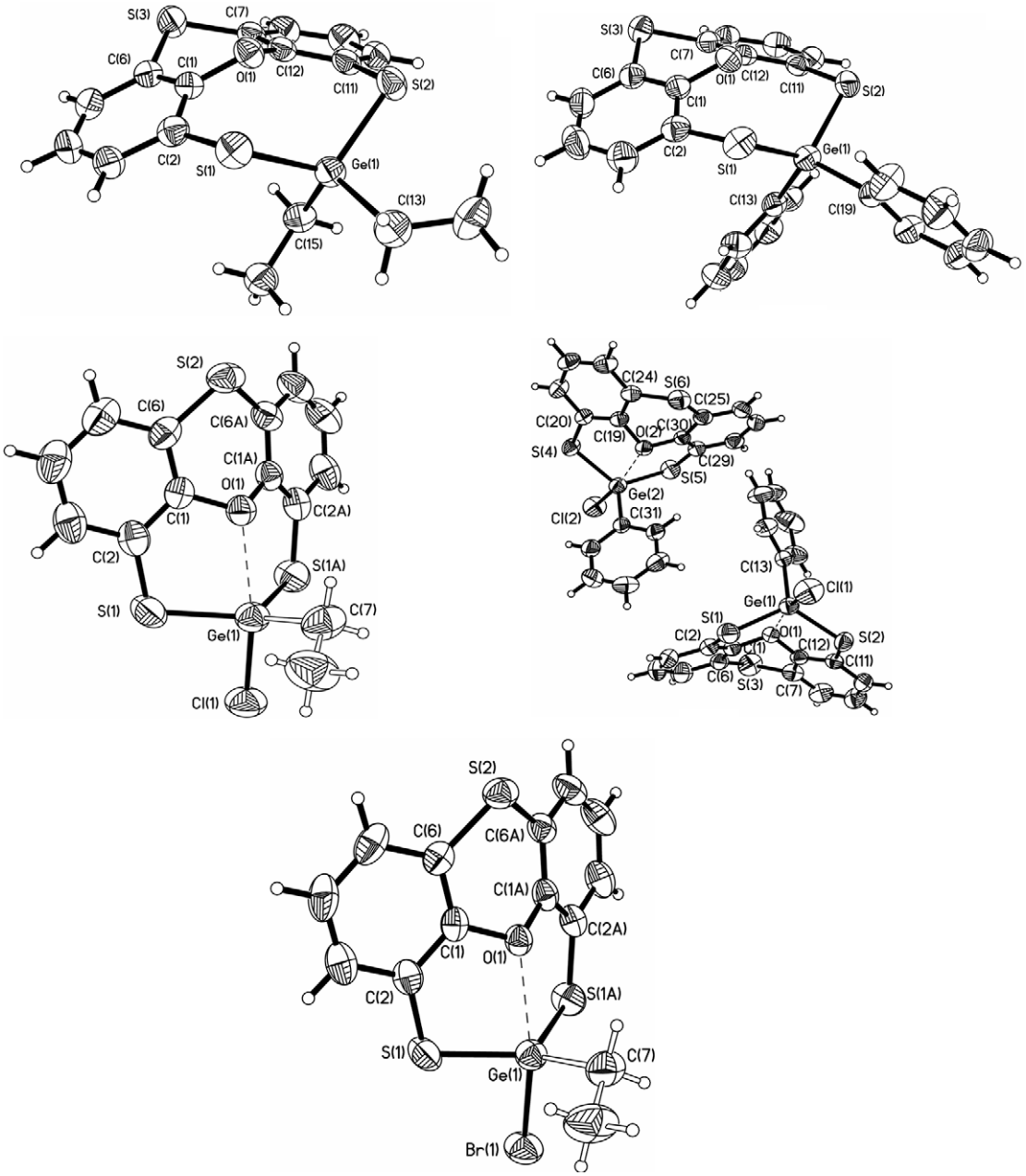


Fig. 1. Molecular structures of [{S(C6H3S)2O}GeEt2] (**2**), [{S(C6H3S)2O}GePh2] (**3**), [{S(C6H3S)2O}GeEtCl] (**4**), [{S(C6H3S)2O}GePhCl] (**5**) and [{S(C6H3S)2O}GeEtBr] (**6**). (In **4** and **6** only one disordered ethyl group is shown).

Table 4
Selected bond lengths (Å) and bond angles (°) of [{S(C$_6$H$_3$S)$_2$O}GeR^{1}R^2].

Compound[a]	2	3	4[b]	5a	5b	6[b]
R^1	Et	Ph	Cl	Cl	Cl	Br
R^2	Et	Ph	Et	Ph	Ph	Et
O···Ge	3.019(2)	3.043(2)	2.482(4)	2.440(3)	2.464(3)	2.488(4)
Ge–S1	2.2591(10)	2.2547(10)	2.2252(17)	2.2296(17)	2.2284(15)	2.2327(14)
Ge–S2	2.2471(10)	2.2519(10)	2.2252(17)	2.2256(15)	2.2181(17)	2.2327(14)
Ge–R^1	1.951(3)	1.942(3)	2.201(2)	2.1897(17)	2.1875(16)	2.3612(10)
Ge–R^2	1.939(3)	1.943(3)	1.969(10)	1.926(5)	1.924(6)	1.966(10)
C–S(thioether)	1.772(3)[c]	1.781(4)[c]	1.765(5)	1.742(20)[c]	1.765(11)[c]	1.767(5)
C–S(thiolate)	1.776(2)[c]	1.776(4)[c]	1.763(6)	1.758(5)[c]	1.769(3)[c]	1.763(5)
C–O	1.387(5)[c]	1.393(4)[c]	1.400(5)	1.408(2)[c]	1.404(4)[c]	1.407(5)
O···Ge–R^1	90.21(10)	95.54(10)	165.32(11)	167.43(9)	167.91(10)	165.09(10)
O···Ge–R^2	155.76(13)	149.62(12)	87.6(3)	86.48(18)	86.39(17)	88.1(3)
S1–Ge–S2	117.12(4)	118.84(4)	122.37(9)	121.14(6)	120.60(7)	122.89(8)
R^1–Ge–R^2	113.89(16)	114.83(14)	106.8(3)	106.04(17)	105.56(16)	106.6(3)
S1–Ge–R^1	102.50(12)	102.18(11)	94.47(6)	96.12(7)	93.35(6)	94.43(4)
S1–Ge–R^2	108.03(10)	108.79(11)	125.5(4)	113.95(16)	118.31(16)	107.0(5)
S2–Ge–R^1	105.88(11)	102.12(11)	94.47(6)	94.40(7)	96.59(7)	94.43(4)
S2–Ge–R^2	109.45(10)	109.98(10)	125.5(4)	118.09(17)	114.76(16)	107.0(5)
C–O–C	116.0(2)	115.8(3)	116.4(5)	115.6(4)	114.8(4)	116.0(5)
C–S–C	98.13(14)	97.86(16)	98.4(3)	99.5(3)	97.6(3)	98.4(3)

[a] R^1 and R^2 mean an atom directly attached to the central germanium atom (v.gr. carbon in the ethyl group).
[b] Molecules with mirror symmetry.
[c] Average distances; their e.s.d. values were calculated from the sample standard deviation formula.

In all compounds there are not intermolecular interactions between no hydrogen atoms shorter than the van der Waals radii sum, being essentially monomeric molecules. Compounds **4** and **6** crystallized with mirror symmetry in space group *Pnma*; the two S(C$_6$H$_3$S)OGe halves are related by a mirror plane containing the S–O–Ge atoms; in both compounds the ethyl groups are mirror disordered over two sites. The unit cell of **5** has two crystallographically independent molecules (**5a** and **5b**).

All the germanium–sulfur, germanium–carbon and germanium–halogen bond distances agree very well with the corresponding covalent radii sum [20]. In the diorganylgermanium compounds **2** and **3**, the S–Ge–S bond angles [117.12(4)° and 118.84(4)°] are significantly shorter than those found in compounds **4**, **5** and **6** [ranging from 120.60(7)° to 122.89(8)°], though they are larger than the ideal tetrahedral angles. Since the presence of the two organyl groups attached to the central germanium in **2** and **3** can not be the only reason for this shortening, it is convenient to carry out a more detailed examination of the molecular structure of the compounds in order to explain these subtle structural differences. Firstly, the germanium compounds display two different conformations on the eight-membered central ring. The conformation of the central ring in **2** and **3** is described as boat–chair-shaped whereas in **4**, **5** and **6** is boat–boat-shaped (Fig. 2). This later conformation has been found in nearly every dibenzometallocine complex known to date (type I, Scheme 1), certainly exhibiting different distortion degrees. The boat–chair conformation has only been observed in some phosphorus and silicon similar compounds [12–14].

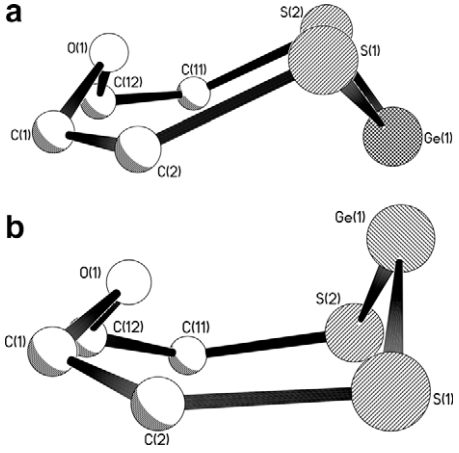


Fig. 2. Eight-membered central ring conformation observed in compounds [{S(C$_6$H$_3$S)$_2$O}GeR^{1}R^2]: (a) boat–chair; (b) boat–boat.

Secondly, in the monohalogenate compounds **4**–**6** was observed a relatively short transannular distance between the O and Ge atoms. The O···Ge bond distances in **4**, **5** and **6** are 2.482(4), 2.452(3) and 2.488(4) Å, respectively, which are 32%, 30% and 32% longer than the covalent radii sum of Ge and O (1.88 Å) but significantly shorter than the van der Waals radii sum (3.47 Å) [20], and are considered as secondary bonds [21]. These O···Ge bond distances are slightly longer than those reported for O(CH$_2$CH$_2$S)$_2$GeCl$_2$ [2.36(1) and 2.39(1) Å], a flexible germocane with a GeCl$_2^{2+}$ acid fragment [22]. On the other hand, in compounds **2** and **3** with two organyl exocyclic ligands, the O···Ge distances are 3.019(2) and 3.043(2) Å, respectively, which are 60% and 62% longer than covalent radii sum. This weakening of the transannular interaction is also reflected on the R^1–Ge–R^2 bond angles, which are the shortest angles observed in our systems.

In order to assign the local geometry of the germanium atom and compare the title compounds with other dibenzogermocines, were determined the degree of geometrical displacement [23–25] at Ge from tetrahedral to trigonal bipyramidal (TBP), and the Pauling-type bond order [26,27] for the transannular interaction. The results are reported in Table 5.

Table 5
Comparison of O···Ge–R^1 geometrical bond parameters in compounds **2**–**6**; bond lengths (Å), bond angles (°), % TBP and Pauling bond order (BO).

	R^1	Central ring conformation	O···Ge	O···Ge–R^1	% TBP	Δd[a]	BO[b]
2	Et	boat–chair	3.019(2)	90.21(10)	28	1.139	0.0248
3	Ph	boat–chair	3.043(2)	95.54(10)	27	1.163	0.0229
4	Cl	boat–boat	2.482(4)	165.32(11)	62	0.602	0.1416
5[a]	Cl	boat–boat	2.440(3)	167.43(9)	65	0.560	0.1623
5b	Cl	boat–boat	2.464(3)	167.91(10)	63	0.584	0.1502
6	Br	boat–boat	2.488(4)	165.09(10)	62	0.608	0.1389

[a] Bond widening, $\Delta d = [d_{exp} - \Sigma r_{cov}(Ge,O)]$, according to standard bond distances (O···Ge) 1.88 Å.
[b] Mode of calculation of bond order for the O···Ge interaction: $BO = 10^{-(1.41\ \Delta d)}$.

It is clear that the TBP% and the bond order for the diorganylgermanium compounds **2** and **3** displaying a boat–chair conformation are the shortest in the series, whereas the corresponding values for the monohalogenate compounds **4**–**6** displaying a boat–boat conformation are the largest. In this respect, it is also noteworthy to note that these values are indeed the largest know to date for related dibenzogermocine complexes.[11] Therefore, the local geometry of the germanium atom in **2** and **3** is best described as tetrahedral, whereas in **4**–**6**, the geometry is best described as TPB, considering the O···Ge interaction. From these data it is reasonable to conclude that there exist a very close connection between the strength of the transannular interaction, the ring conformation as well as the coordination geometry, and the nature of the atoms in *trans* position to the secondary bonding.

4. Conclusion

In order to study the phenomena of hypervalence in germanium heterocyclic compounds we have synthesized and structurally characterized eight new $[\{S(C_6H_3S)_2O\}GeR_nHal_{2-n}]$ compounds (R = Et, Ph; Hal = Cl, Br; n = 2–0) by employing an efficient $\{S(C_6H_3S)_2O\}^{2-}$ ligand. In the solid state, the compounds with two organyl exocyclic ligands display a distorted tetrahedral local geometry at Ge(IV) center. On the other hand, the compounds with halogen pendant ligands exhibit a trigonal bipyramidal coordination geometry, and considerable strong O···Ge intramolecular interactions, due to an increase of the Lewis acidity on the germanium atom. In addition, the conformation is significantly influenced by the intramolecular interaction being boat–boat if the secondary bonding is strong enough and boat–chair if it may be neglected.

Acknowledgment

BFC fully acknowledges the scholarship from CONACyT. This research was supported by CONACyT (Project 44009).

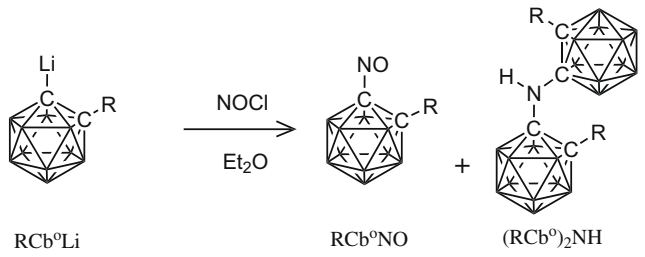
Appendix A. Supplementary data

CCDC 674108, 674109, 674110**,** 674111 and 674112 contain the supplementary crystallographic data for **2**, **3**, **4**, **5** and **6**. These data can be obtained free of charge via http://www.ccdc.cam.ac.uk/conts/retrieving.html, or from the Cambridge Crystallographic Data Centre, 12 Union Road, Cambridge CB2 1EZ, UK; fax: +44 1223 336 033; or e-mail: deposit@ccdc.cam.ac.uk.

Supplementary data associated with this article can be found, in the online version, at doi:10.1016/j.poly.2008.12.007.

References

[1] P. De la Cruz Burelo, V. Montiel Palma, M.A. Muñoz Hernández, Main Group Chem. 5 (2006) 61.
[2] Z. Janas, L.B. Jerzykiewicz, P. Sobota, K. Szczegot, D. Wioeniewska, Organometallics 24 (2005) 3987.
[3] Y. Takashima, Y. Nakayama, T. Hirao, H. Yasuda, A. Harada, J. Organomet. Chem. 869 (2004) 612.
[4] H. Hanaoka, Y. Imamoto, T. Hino, Y. Oda, J. Organomet. Chem. 691 (2006) 4968.
[5] Y. Takashima, Y. Nakayama, H. Yasuda, A. Nakamura, A. Harada, J. Organomet. Chem. 664 (2006) 234.
[6] R.R. Holmes, Acc. Chem. Res. 37 (2004) 746.
[7] D. Sellmann, F. Geipel, F. Lauderbach, F.W. Heinemann, Angew. Chem., Int. Ed. 41 (2002) 632.
[8] R.R. Holmes, Acc. Chem. Res. 31 (1998) 535 and references therein cited.
[9] Y.I. Baukov, S.N. Tandura, Hypervalent compounds of organic germanium, tin and lead derivatives, Chapter 16, in: Zvi Rappoport (Ed.), The Chemistry of Organic Germanium, Tin and Lead Compounds, vol. 2, John Wiley and Sons, West Sussex, 2002, p. 963.
[10] J.G. Alvarado-Rodríguez, N. Andrade-López, S. González Montiel, G. Merino, A. Vela, Eur. J. Inorg. Chem. (2003) 3554.
[11] S. González Montiel, N. Andrade López, V. García Montalvo, J.A. Cogordan, J.G. Alvarado-Rodríguez, Eur. J. Inorg. Chem. 1 (2006) 4752.
[12] A. Chandrasekaran, N.V. Timosheva, R.R. Holmes, Phosphorus, Sulfur, Silicon, Relat. Elem. 181 (2006) 1493.
[13] N.V. Timosheva, A. Chandrasekaran, R.R. Holmes, Inorg. Chem. 45 (2006) 10836.
[14] N.V. Timosheva, T.K. Prakasha, A. Chandrasekaran, R.O. Day, R.R. Holmes, Inorg. Chem. 35 (1996) 3614.
[15] L.A. van der Veen, P.H. Keeven, G.C. Shoemaker, J.N.H. Reek, P.C.J. Kamer, P.N.M. van Leeuween, M. Lutz, A.L. Spek, Organometallics 19 (2000) 872.
[16] P. Dierkes, S. Ramdeehul, L. Barloy, A. De Cian, J. Fisher, P.C.J. Kamer, P.W.N.M. van Leeuwen, J.A. Osborn, Angew. Chem., Int. Ed. 37 (1998) 3116.
[17] M.A. Zuideveld, B.H.G. Swennenhuis, M.D.K. Boele, Y. Guari, G.P.F. van Strijdocnk, J.N.H. Reek, P.C.J. Kamer, K. Goubitz, J. Fraanje, M. Lutz, A.L. Spek, P.W.N.M. van Leeuwen, J. Chem. Soc., Dalton Trans. 1 (2002) 2308.
[18] SHEXTL 5.10, Bruker AXS, Inc., Madison, WI, USA, 1998.
[19] SADABS: Area-Detector Absorption Correction, Siemens Industrial Automation, Inc., Madison, WI, 1996.
[20] N.W. Alcock, Bonding and Structure: Structural principles in Inorganic and Organic Chemistry, Ellis Horwood, West Sussex, 1990. p. 314.
[21] N.W. Alcock, Adv. Inorg. Chem. Radiochem. 15 (1972) 1.
[22] M. Draeger, Z. Anorg. Allg. Chem. 423 (1976) 53.
[23] A. Chandrasekaran, P. Sood, R.O. Day, R.R. Holmes, Inorg. Chem. 38 (1999) 3369.
[24] N.V. Timosheva, A. Chandrasekaran, R.O. Day, R.R. Holmes, Inorg. Chem. 37 (1998) 3862.
[25] D.J. Sherlock, A. Chandrasekaran, R.O. Day, R.R. Holmes, Inorg. Chem. 36 (1997) 5082.
[26] L. Pauling, The Nature of the Chemical Bond, third ed., Cornell University Press, Ithaca, New York, 1960. p. 239.
[27] U. Kolb, M. Beuter, M. Gerner, M. Draeger, Organometallics 13 (1994) 4413.



R = Me	Pentane	-40°C	69%	11%
	Pentane	-117°C	77%	22%
	DME	-40°C	0%	63%
	DME	-78°C	10%	55%
R = Ph	Pentane	-40°C	61%	10%
	Pentane	-117°C	42%	0%
	DME	-40°C	0%	55%
	DME	-78°C	5%	56%

Scheme 1.

[13], and di-isocyanates OCNCb^{m}NCO (Cb^{m} = 1,7-$C_2B_{10}H_{10}$) have been converted into diamines $H_2NCb^{m}NH_2$ for use in polymers [14]. The nitrosyl chloride–lithio-carborane reaction by contrast appears to have been studied by only two research groups, and not at all during the past thirty years, despite the range of C–N carborane derivatives in principle accessible *via* nitroso-carboranes [1,3]. Unfortunately the early reports by Kauffman et al. and Zakharkin et al. gave conflicting yields of nitroso derivatives (25–80%) and limited experimental details.

2. Results and discussion

2.1. Synthetic aspects

In our studies of low-temperature reactions between the lithio-carboranes, MeCb°Li or PhCb°Li, and nitrosyl chloride in equivalent amounts (Scheme 1), we used 1:1 mixtures of diethyl ether and pentane, or of diethyl ether and dimethoxyethane (DME), as solvent. The products obtained were broadly in line with those reported by Zakharkin et al. [2,3]. In diethyl ether and pentane, the nitroso-carboranes RCb°NO were the main product (42–77%), though some dicarboranylamine $(RCb^{\circ})_2NH$ could normally also be isolated (0–22%). However, when diethyl ether and DME were used as a solvent mix, the secondary amines $(RCb^{\circ})_2NH$ were the main products (55–63%), yields of nitroso-carboranes being 10% or less. Although overall yields varied with the temperature at which the reaction was carried out, the product balance did not. Our work-up procedure involved treatment with aqueous potassium hydrogen carbonate followed by sublimation to obtain the blue nitroso compounds RCb°NO. The strong NO stretching absorptions at *ca.* 1565 cm^{-1} in the IR spectra of these compounds show that their CNO units are bent at nitrogen [15], with the nitrosyl groups acting as one-electron ligands to the carborane cages. The colourless secondary amines $(RCb^{\circ})_2NH$ were recovered after treatment of the unsublimed material with methanol (for details, see Section 4).

We infer that the nitroso-carboranes are formed in the first stage of the reaction (Eq. (1)) and that the secondary amines result from the reaction of the nitroso-carborane with a second mole of lithio-carborane, despite competition from excess nitrosyl chloride (Eq. (2));

$$RCb^{\circ}Li + NOCl \rightarrow RCb^{\circ}NO + LiCl \quad (1)$$

$$RCb^{\circ}NO + RCb^{\circ}Li \rightarrow (RCb^{\circ})_2NOLi \quad (2)$$

It is not clear, however, how the lithio-hydroxylamine $(RCb^{\circ})_2NOLi$ is then reduced to the amine, $(RCb^{\circ})_2NH$. It may be significant that the bidentate coordinating solvent, 1,2-dimethoxyethane, $MeOCH_2CH_2OMe$, favours reaction (2). There are parallels here with aromatic ring chemistry, in that both aryl nitroso compounds ArNO and diarylamines Ar_2NH are accessible from ArLi or ArMgX and NOCl [16].

Our early preparations of anionic species $[RCb^{\circ}X]^{-}$ from neutral parent species used proton sponge, PS, $C_{10}H_6(NMe_2)_2$, to deprotonate the hydroxycarborane PhCb°OH and the thiol PhCb°SH [6,7]. We therefore attempted to deprotonate the amine $(PhCb^{\circ})_2NH$ in toluene by proton sponge. This failed; the amine crystallised unchanged from these solutions. However, addition of a solution of potassium *t*-butoxide and an equimolar proportion of 18-crown-6 deposited pale yellow crystals, with 77% yield of the salt $[K(18\text{-crown-6})]^{+}[(PhCb^{\circ})_2N]^{-}$. This pale yellow salt is, surprisingly, stable to air and moisture, though the parent amine, $(PhCb^{\circ})_2NH$ is regenerated by ethanoic acid. In previous studies we were unable to obtain the amide $PhCb^{\circ}NH^{-}$ by deprotonation of the amine $PhCb^{\circ}NH_2$; cage degradation occurred instead [9]. Although the yellow salt appears to crystallise well from 1,2-dichlorobenzene, single crystals suitable for X-ray diffraction were grown from a solution in diethyleneglycol dimethyl ether, $(MeOC_2H_4)_2O$, into which cyclohexane diffused slowly from an upper layer. The colourless salt $[K(18\text{-crown-6})]^{+}[(MeCb^{\circ})_2N]^{-}$ was similarly formed in 86% yield from a solution of potassium *t*-butoxide and an equimolar proportion of 18-crown-6 with amine $(MeCb^{\circ})_2NH$. The contrast in the formation and stability between the anions $PhCb^{\circ}NH^{-}$ and $(RCb^{\circ})_2N^{-}$ suggests that the $PhCb^{\circ}NH^{-}$ anion is capable of a nucleophilic attack on a second carborane molecule leading to cage degradation, whereas the two bulky cages in the anion $(RCb^{\circ})_2N^{-}$ inhibit the capacity of this amide to attack a second carborane molecule.

2.2. Structural aspects

In crystalline PhCb°NO (Fig. 2), the N=O bond (length 1.182(2) Å) lies roughly in the C(2)–C(1)–N(1) plane. The phenyl ring is perpendicular to this plane. The C(1)–N(1) bond length of 1.490(2) Å is consistent with negligible *exo*-C–N π-bonding, as is the C(1)–C(2) cluster bond length of 1.677(2) Å, virtually identical to that in the computed geometry of PhCb°F (1.674 Å), and slightly different from that in the computed geometry of PhCb°H (1.659 Å) with a similarly orientated phenyl group [9]. Reported X-ray-derived geometries of PhCb°H with the orientation of the phenyl group roughly coplanar with the H(1)–C(1)–C(2) plane reveal shorter C(1)–C(2) bond distances of 1.643(2) and 1.649(2) Å [5,17–19]. The C(1)–N=O bond angle of 113.0(2)° is midway between typical trigonal planar and tetrahedral bond angles. As a comparison nitrosobenzene, PhNO, has N=O and C–N bond lengths of 1.241(7) and 1.421(7) Å, respectively, and its C–N=O bond angle is 114.8(5)° [20]. All of these features imply that the NO substitu-

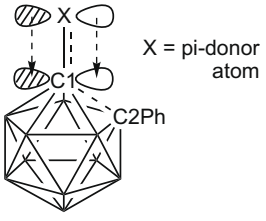


Fig. 1. Orbitals involved in the lengthening of the C1–C2 distance of PhCb°X.

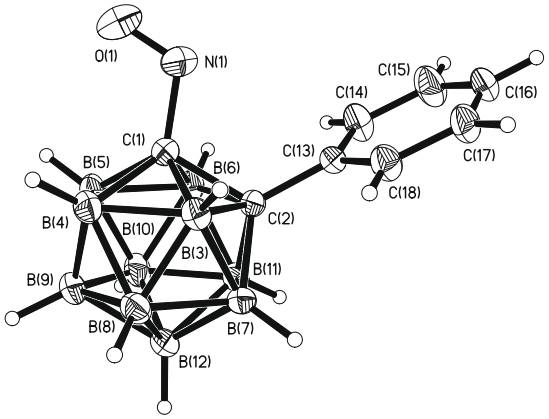


Fig. 2. Molecular structure of PhCb°NO (**1**). Selected bond lengths (Å) and angles (°), N(1)–O(1) 1.182(2), C(2)–C(13) 1.510(2), C(2)–C(1)–N(1) 112.1(2), C(13)–C(2)–C(1) 120.3(2). Displacement ellipsoids are drawn at the 50% probability level.

ent is acting as a one-electron ligand to the cage even though its orientation aligns the nitrogen lone pair sp^2 AO in the same plane as (though divergent from) the C1 *p*–AO involved in C1–C2 σ-bonding.

Table 1
Selected bond lengths (Å) and angles (°) for $(MeCb^{\circ})_2NH$, $(PhCb^{\circ})_2NH$ and $[(PhCb^{\circ})_2N]^-$ (averages for equivalent bonds).

	$(MeCb^{\circ})_2NH$ (**2**)	$(PhCb^{\circ})_2NH$ (**3**)	$(PhCb^{\circ})_2N^-$ (**4**)
C(1)–N(1)	1.410(4)	1.405(2)	1.350(4)
C(1)–C(2)	1.750(4)	1.798(3)	1.987(3)
C(2)–C(13)	1.512(4)	1.504(3)	1.491(4)
C(1)–N(1)–C(1′)	131.1(2)	132.0(2)	127.0(2)
N(14)–C(1)–C(2)	117.2(2)	117.09(14)	118.8(2)
C(13)–C(2)–C(1)	117.0(2)	117.94(14)	116.7(2)

The molecular structures of the secondary amines, $(MeCb^{\circ})_2NH$ and $(PhCb^{\circ})_2NH$, and of the anion $(PhCb^{\circ})_2N^-$ of the salt $[K(18\text{-crown-}6)]^+[(PhCb^{\circ})_2N]^- \cdot 0.5(MeOC_2H_4)_2O$, are shown in Fig. 3. Selected bond distances and angles are given in Table 1. There are small differences between the lengths of corresponding bonds in the two cages in each compound that are not regarded as significant; average values for equivalent bonds are used in the discussion where appropriate. The conformations of the two amines and amide anion in their respective crystal structures are very similar, and the trigonal nitrogen atoms of the two amines have a planar configuration. Fig. 4 shows the environment surrounding the amide anion in the salt, including the cation and diglyme molecule.

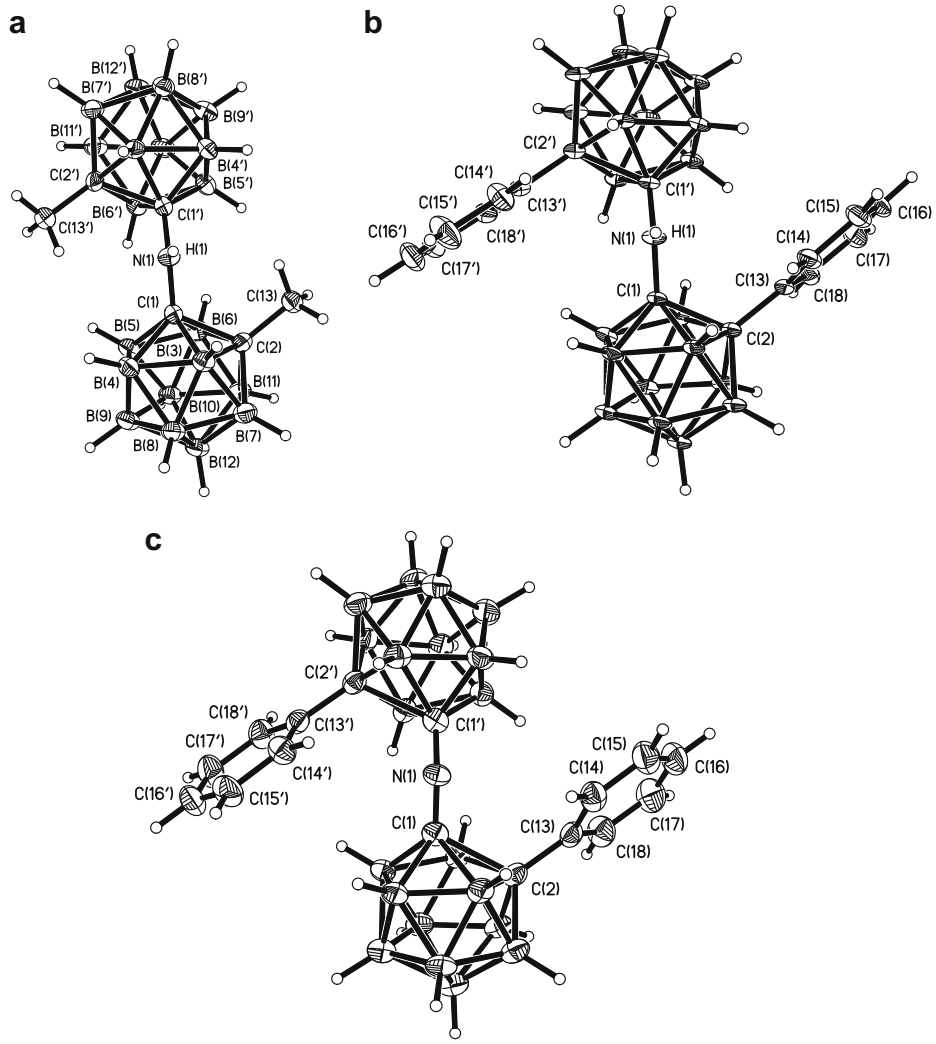


Fig. 3. Molecular structures of the dicarboranyl amines, (a) $(MeCb^{\circ})_2NH$ (**2**) and (b) $(PhCb^{\circ})_2NH$ (**3**), and (c) the $(PhCb^{\circ})_2N^-$ anion of the salt $[K(18\text{-crown-}6)][(PhCb^{\circ})_2N] \cdot 0.5(MeOC_2H_4)_2O$ (**4**).

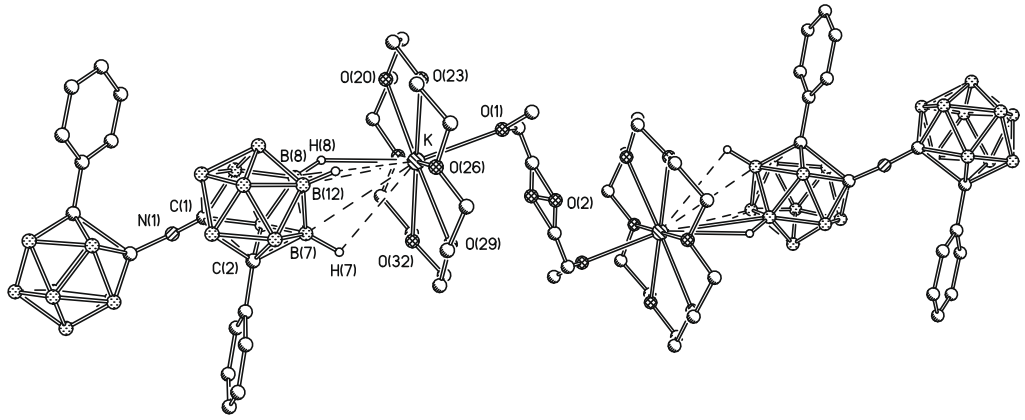


Fig. 4. Crystal structure of the salt $[K(18\text{-crown-6})][(PhCb^{\circ})_2N]\cdot 0.5(MeOC_2H_4)_2O$ (**4**) showing interactions between the cation and anion and between cation and solvent. Selected distances in Å, B(8)...K 3.53, B(7)...K 3.85, B(12)...K 3.74, O(1)...K 2.756(4). Both disorder components are shown for the solvent molecule. H atoms have been omitted except for those involved in the cation-anion interactions.

The potassium cation effectively caps a triangular face of one of the two cages (a face remote from the two cage carbon atoms) in a manner common in potassium-18-crown-6 salts of carborane anions [21]. The diglyme molecule, with its central oxygen atom O(2) disordered over two sites in the crystal structure, is coordinated through its outer oxygen atoms to two cations.

The structures of the amines and amide anion differ from that of the nitroso derivative PhCb°NO in showing clear evidence, in their conformations, bond distances and angles, of significant *exo*-N=C dative π-bonding from one nitrogen *p*-AO to both cages, which show concomitant distortion (C(1)–C(2) bond lengthening). The features that lead us to this conclusion are as follows (see Table 1).

The CNC angle in the phenyl amine $(PhCb^{\circ})_2NH$ is 132° and falls to 127° in the amide anion $[(PhCb^{\circ})_2N]^-$, showing that the nitrogen atom remains sp^2 hybridised on deprotonation, the 'lone pair' having greater repulsive effect than the NH bond which it replaces. The CNC angles are perhaps slightly affected by the repulsion between the two cages since the closest H···H separation between the cages is *ca.* 2.47 Å, longer than corresponding distances of 2.27 and 2.25 found in the related biscarboranyl sulfide, $(PhCb^{\circ})_2S$, and sulfoxide, $(PhCb^{\circ})_2SO$, respectively [8]. The CNC angle in diphenylamine Ph_2NH is 129° and falls to 121° in the Ph_2N^- anion [22,23].

In all three compounds the radial planes of the C–C bonds of both cages, *i.e.* their CCN planes, are roughly perpendicular to the trigonal nitrogen CNC plane so that the nitrogen *p*-orbital containing an electron pair is aligned with the cage C–C bonds. The closely similar conformation of the three compounds effectively precludes the possibility that this conformation is the fortuitous result of crystal packing forces, since these are unlikely to have the same effect in the crystal structures of the amines, still less in that of the ionic amide with large counter-ions.

We conclude that both carborane cages in each amine $(RCb^{\circ})_2NH$, and in the anion $(PhCb^{\circ})_2N^-$, are oriented to allow dative π-bonding from the *p*-orbital perpendicular to the C–N–C plane into the *p*-orbital on C1 that is aligned for cage C1–C2 σ-bonding (Fig. 1). Evidence for that *exo*-C=N π-bonding is provided by the C–N distances in these systems (Table 1), which at 1.404(2)–1.410(4) Å in the amines $(RCb^{\circ})_2NH$ and 1.354(4)–1.355(4) Å in the amide $(PhCb^{\circ})_2N^-$ are far shorter than would be appropriate for single C–N bonds between three- or even two-coordinate nitrogen and six-coordinate carbon atoms. The shorter C=N bond in the amide $(PhCb^{\circ})_2N^-$ is intelligible in that deprotonation of the amine $(PhCb^{\circ})_2NH$ increases the π-donor capacity of the nitrogen atom. The average C–N distances in diphenylamine Ph_2NH and in the diphenylamide Ph_2N^- anion are 1.400(4) and 1.370(5) Å, respectively [22,23].

Involvement of the tangentially orientated *p*-AO at C1 in the X–C1–C2 plane as the acceptor orbital for dative *exo*-π-bonding from nitrogen reduces the C1–C2 σ-bonding contribution to the cage bonding orbital, and so lengthens the cage C–C bond (Fig. 1). The effect is most marked in the amide anion $(PhCb^{\circ})_2N^-$, which has C–C bonds of length 1.980(3) and 1.995(3) Å, effectively the same length as in the anion $[PhCb^{\circ}O]^-$ (2.001(3) and 2.065(7) Å) [6,9], even though one nitrogen lone pair is shared between two cages. In the amines $(RCb^{\circ})_2NH$, the cage C–C bonds, 1.748(4) and 1.752(4) Å when R = Me and 1.794(3) and 1.799(3) Å when R = Ph, are understandably shorter than those in the amide. The difference of 0.05 Å between the two amines can be attributed to a π-bonding contribution from the phenyl group [5].

3. Conclusions

This paper reports improved low-temperature procedures by which reactions between lithio-carboranes and nitrosyl chloride can be used as preparative routes to two important categories of carborane derivatives, *viz.* nitroso derivatives $RCb^{\circ}NO$, and dicarboranylamines $(RCb^{\circ})_2NH$, the former using mixtures of diethyl ether and pentane as solvent and the latter using 1,2-dimethoxyethane instead of pentane in the solvent mix. Deprotonation of the amines $(RCb^{\circ})_2NH$ in toluene by potassium *t*-butoxide in the presence of the macrocyclic ether 18-crown-6 afforded the air- and moisture-stable salts $[K(18\text{-crown-6})]^+[(RCb^{\circ})_2N]^-$.

The crystal structures of $PhCb^{\circ}NO$, $(PhCb^{\circ})_2NH$, $(MeCb^{\circ})_2NH$ and $[K(18\text{-crown-6})]^+[(PhCb^{\circ})_2N]^-\cdot 0.5(MeOC_2H_4)_2O$ have been determined, and shown to shed further useful light on the capacity of the *ortho*-carborane cage to function as a sensitive probe of the π-donor characteristics of cage C-attached ligands. The cage C1–C2 and the *exo*-C–N bond lengths and the ligand orientations in these compounds reinforce the generalisation that π-donor ligands attached to an *ortho*-carborane carbon atom adopt an orientation that involves in *exo*-π-bonding the *p*-orbital on carbon that otherwise participates in cage C1–C2 σ-bonding.

4. Experimental

All air-sensitive manipulations were carried out under dry, oxygen-free N_2. Stirring refers to use of a magnetic stirrer. Pentane was distilled over sodium. 1,2-Dimethoxyethane was dried by reflux and distillation over potassium; ether refers to diethyl ether dried, where appropriate, over sodium. Ether solutions were dried over magnesium sulfate and evaporated near room temperature. 1-

Methyl-*ortho*-carborane [24] and 1-phenyl-*ortho*-carborane [25] were prepared by literature methods and dried by sublimation at 0.01 mm Hg. Commercial nitrosyl chloride (BDH Chemicals Ltd.) was used as received.

Melting points were measured in capillary tubes with an Electrothermal 9200 heating block. Infrared spectra were recorded from KBr discs on Perkin–Elmer 1600 series FTIR or Perkin–Elmer 1720× FTIR spectrometers and ultraviolet spectra with a Shimadzu UV 1201. Elemental carbon, hydrogen and nitrogen analyses were performed using Exeter Analytical CE-440 or Carlo Erba Strumentazione EA Model 1106 instruments. Mass spectra (MS) were recorded on a VG Micromass 7070E instrument under E.I conditions (EI) at 70 eV. Values of *M* show the isotope range $^{10}B_n$ to $^{11}B_n$ including a ^{13}C contribution if observed. NMR spectra were measured using Varian Unity-300 (^1H, ^{11}B, ^{13}C), Bruker AM250 (^1H, ^{13}C), Bruker Avance 400 (^1H, ^{11}B, ^{13}C) and/or Varian Inova 500 (^1H, ^{11}B) instruments. All chemical shifts are reported in δ (ppm) and coupling constants in Hz. ^1H NMR spectra were referenced to residual protio impurity in the solvent ($CDCl_3$, 7.26 ppm; CD_3CN, 1.85 ppm). ^{13}C NMR spectra were referenced to the solvent resonance ($CDCl_3$, 77.0 ppm; CD_3CN, 118.3 ppm). ^{11}B NMR spectra were referenced externally to $Et_2O \cdot BF_3$, $\delta = 0.0$ ppm. Peak assignments of cage boron and hydrogen atoms were determined where possible with the aid of 2D $^{11}B\{^1H\}$–$^{11}B\{^1H\}$ COSY, selective $^1H\{^{11}B\}$ and $^1H\{^{11}B\}$–$^{11}B\{^1H\}$ correlation spectra.

5. Reaction of 1-methyl- and 1-phenyl-*ortho*-carboranes with nitrosyl chloride

Nitrosyl chloride (5 ml) was condensed into a calibrated tube cooled to *ca.* −25 °C, transferred under reduced pressure into the co-solvent, ether or pentane (20 ml), at *ca.* −40 °C and the flask was brought to atmospheric pressure with dinitrogen. A solution of the lithio-carborane, prepared by slowly adding butyllithium (6.6 ml, 1.6 M in hexane; 10.5 mmol) to the substituted *ortho*-carborane (10.0 mmol) in 1,2-dimethoxyethane or pentane, (20 ml), was added dropwise with stirring at −40 °C (acetone/CO_2), −78 °C (acetone/CO_2) or −117 °C (ethanol/N_2) during *ca.* 35 min and the mixture was allowed to warm to room temperature during *ca.* 3 h. The solution was added in small portions to potassium hydrogen carbonate (40 g) in water (110 ml), the organic layer was diluted with ether, washed with water, dried and evaporated. The blue nitroso-compounds were separated from the resulting semi-solid by sublimation at *ca.* 70 °C/0.01 mm Hg and the residue was triturated with methanol (12 ml; the nitroso-carboranes are unstable to this solvent) to give the amines as white crystalline powders. The yields of nitroso-compounds and amines obtained using various bath temperatures and co-solvents are summarised in Scheme 1.

1-Methyl-2-nitroso-*ortho*-carborane formed volatile blue crystals identical with a sample prepared under the literature conditions; attempts to measure the melting point of this compound in open capillary tubes caused evaporation of the sample, leaving a colourless residue which melted sharply at the temperature, 208–210 °C, given in the literature [3] for the nitroso-derivative. A DSC scan showed a broad exotherm at 230 °C and the residue was shown by IR to consist of boric acid and *closo*-carborane products. 1-Phenyl-2-nitroso-*ortho*-carborane gave blue crystals m.p. 43–44 °C (literature [2] 54–55 °C).

1-Methyl-2-nitroso-*ortho*-carborane: Found: C, 19.2, H, 8.0, N, 7.0 $C_3H_{15}B_{10}NO$ requires C, 19.2, H, 8.0, N, 7.4; MS (EI^+, *m*/*z*)$[M]^+$ 186–190; 188 (100); IR (KBr disc, cm^{-1}) 3106w, 3063w, 2948w (methyl CH); 2599s, br (BH); 1567s (NO); 1445; 1389; 1111; 1046; 1022; 948; 921; 892; 721m (carborane skeleton); 697w, 640w, 540w; $^1H\{^{11}B\}$ NMR ($CDCl_3$) δ: 2.74 (s, 3H, C*H*$_3$), δ: 2.53 (s, 2H, H7, 11), 2.50 (s, 1H, H12), 2.41 (s, 2H, H3,6), 2.19 (s, 3H, H8,9,10), 1.88 (s, 2H, H4,5); $^{11}B\{^1H\}$ NMR ($CDCl_3$) δ: −2.4 (s, 1B, B12), −6.6 (s, 1B, B9), −10.2 (s, 4B, B7,8,10,11), −11.0 (s, 2B, B3,6), −12.6 (s, 2B, B4,5); $^{13}C\{^1H\}$ NMR ($CDCl_3$) δ: 111.4 (s, carborane C1), 73.3 (s, carborane C2), 23.0 (s, *C*H$_3$).

1-Phenyl-2-nitroso-*ortho*-carborane (**1**) (crystals for X-ray diffraction were obtained by slow vacuum sublimation 40°C/0.01 mm Hg): Found: C, 38.9; H, 6.0; N, 5.2; $C_8H_{15}B_{10}NO$ requires: C, 38.5; H, 6.1; N, 5.6%; MS (EI^+, *m*/*z*) $[M]^+$ 245–253; 249 (100); IR (KBr disc, cm^{-1}) 3098, 3072 (Ar CH); 2577br (BH); 1560s (NO), 1493m, 1446m; 1340w; 1270w, 1059s; 897; 867m; 753s; 724w (carborane skeleton), 688.8s; $^1H\{^{11}B\}$ NMR ($CDCl_3$) δ: 7.83 (d, $^3J_{HH}$ 8 Hz, 2H, *ortho*-phenyl), 7.49 (t, $^3J_{HH}$ 7.4 Hz, 1H, *para*-phenyl), 7.42 (t, $^3J_{HH}$ 7.8 Hz, 2H, *meta*-phenyl), 2.99 (s, 2H, H4,5), 2.67 (s, 3H, H7,11,12), 2.33 (s, 3H, H8,9,10), 2.09 (s, 2H, H3,6). $^{11}B\{^1H\}$ NMR ($CDCl_3$) δ: −2.0 (s, 1B, B12), −4.4 (s, 1B, B9), −9.8 (s, 2B, B7, 11), −10.4 (s, 2B, B8, 10), −12.6 (s, 2B, B3, 4, 5, 6); ^{13}C NMR ($CDCl_3$) δ: 131.1 (d of t, $^1J_{CH}$ 159 Hz, $^2J_{CH}$ 7 Hz, *m*-C phenyl), 130.1 (d of t, $^1J_{CH}$ 161 Hz, $^2J_{CH}$ 7 Hz, *m*-C phenyl), 128.9 (d of d, $^1J_{CH}$ 162 Hz, $^2J_{CH}$ 8 Hz, *o*-C phenyl), 114.1 (carborane C1), 81.3 (carborane C2).

Bis(2-methyl-1-*ortho*-carboranyl)amine (**2**) gave colourless crystals from hexane, m.p. 205.5–207 °C. Found: C, 21.4; H, 8.3; N, 4.0. $C_6H_{27}B_{20}N$ requires: C, 21.9; H, 8.2; N, 4.3. MS (EI^+, *m*/*z*) $[M]^+$ 245–253; 249(100); IR ν_{max} (KBr) [cm^{-1}]: 3389 (NH); 2963, 2943 (methyl CH); 2680w, 2670w, 2606, 2573, 2541 (BH); 1496; 1443, 1383 (methyl CH); 1297 (CN); 1261; 1084; 1029; 800; 727 (carborane skeleton); 475; 416; $^1H\{^{11}B\}$ NMR ($CDCl_3$), δ: 4.84 (br.s, 1H, NH), 2.51 (s, 4H, H4,5), 2.41 (s, 4H, H3,6), 2.30 (s, 4H, H7,11), 2.28 (s, 2H, H9), 2.22 (s, 2H, H12), 2.10 (s, 6H, CH_3), 2.09 (s, 4H, H8,10); $^{11}B\{^1H\}$ NMR ($CDCl_3$), δ: −5.2 (2B, B9), −6.4 (2B, B12), −10.3 (12B), −11.7 (4B, B8,10); $^{13}C\{^1H\}$ NMR ($CDCl_3$), δ: 90.9 (C1), 81.8 (C2), 22.1 (CH_3). $^1H\{^{11}B\}$ NMR (CD_3CN), δ: 6.76 (br.s, 1H, NH), 2.58 (s, 4H, BH), 2.38 (s, 4H, BH), 2.35 (s, 6H, CH_3), 2.29 (s, 4H, BH), 2.16 (s, 4H), 2.02 (s, 4H); $^{11}B\{^1H\}$ NMR (CD_3CN), δ: −6.1, −7.0 (4B, B9,12), −10.8 (12B), −12.3 (4B); $^{13}C\{^1H\}$ NMR (CD_3CN), δ: 93.3 (C1), 83.7 (C2), 22.2 (CH_3).

Bis(2-phenyl-1-*ortho*-carboranyl) amine (**3**) formed colourless rhombic crystals from xylene m.p. 242–244.5 °C, literature [2] 239–241 °C. Found: C, 41.8; H, 7.0; N, 2.9; $C_{16}H_{31}B_{20}N$ requires: C, 42.4; H, 6.9; N, 3.1%. MS (EI^+, *m*/*z*) 440–458; 454(100), IR (KBr disc, cm^{-1}) : 3391 (NH); 3062w, 2989w (Aryl CH); 2654, 2633, 2602s, 2584 (BH); 1508 (NH); 1495, 1447 (Ar. skeleton); 1306s (CN); 1069; 1039; 1004; 798; 755, 689 (C_6H_5); 729 (carborane skeleton). $^1H\{^{11}B\}$ NMR ($CDCl_3$), δ: 7.57 (d, 4H, *ortho* phenyl CH), 7.52 (t, 2H, *para* phenyl CH), 7.52 (t, 4H, *meta* phenyl CH); 4.46 (m, 1H, NH); 2.71 (s, 4H, H3,6), 2.30 (s, 4H, H4,5), 2.28 (s, 2H, H12), 2.21 (s, 2H, H9), 2.03 (s, 8H, H7,8,10,11); $^{11}B\{^1H\}$ NMR ($CDCl_3$), δ: −3.6 (s, 2B, B9), −5.8 (s, 2B, B12), −10.4 (8B, B3,4,5,6), −12.2 (8B, B7,8,10,11); ^{13}C NMR ($CDCl_3$), δ: 131.3 (C_6H_5 *para*), 129.6 (C_6H_5 *ipso*); 131.7, 128.9 (C_6H_5 *ortho* and *meta*), 94.4 (C2 or C1), 90.3 (C1 or C2). $^1H\{^{11}B\}$ NMR (CD_3CN), δ: 7.73 (d, 4H, *ortho* phenyl CH), 7.59 (t, 2H, *para* phenyl CH), 7.47 (t, 4H, *meta* phenyl CH); 6.55 (m, 1H, NH); 3.00 (s, 4H, H3,6), 2.20 (s, 8H, BH), 1.90 (s, 4H, BH), 1.77 (s, 4H, BH); $^{11}B\{^1H\}$ NMR (CD_3CN), δ: −4.2 (s, 2B, B9), −6.7 (s, 2B, B12), −10.7 (8B), −12.1 (4B), −13.1 (4B).

6. Potassium-18-crown-6 salt of bis(2-phenyl-1-*ortho*-carboranyl)amide

Bis(2-phenyl-1-*ortho*-carboranyl)amine (255 mg, 5.6 mmol) in warm (*ca.* 55 °C) toluene (10 ml) was added under nitrogen to a solution of potassium *t*-butoxide (160 mg, 13.4 mmol) and 18-crown-6 (390 mg, 14.5 mmol) in toluene (5 ml). The mixture was heated briefly (*ca.* 90 °C, 1 min) and the blue–green oil which separated initially formed a pale yellow granular solid within a few

seconds. After standing overnight at room temperature the solid was washed with toluene to give the amide salt as a pale yellow powder (325 mg, 77%). Found: C, 44.2; H, 7.3; N, 1.7. $C_{28}H_{54}B_{20}KO_6N$ requires: C, 44.5; H, 7.2; N, 1.9%. Recrystallisation from 1,2-dichlorobenzene furnished yellow rectangular prisms, m.p. 254–257 °C, whose colour deepens reversibly on warming and which gave the same analysis as before. The crystalline amide is unchanged by exposure to air or contact with water but rapidly forms the parent amine in contact with ethanoic acid. Single crystals of the hemisolvate (**4**) suitable for X-ray diffraction were grown from a solution in diethyleneglycol dimethyl ether into which cyclohexane was diffused slowly from an upper layer.

M.p. 254–257 °C; MS (EI$^+$, *m*/*z*) 440–457; 453(100, M$^+$), MS (CI$^+$, NH_3, m/z) 282 (18-C-6+NH_4^+); IR (KBr disc, cm^{-1}): 3062w (Ar. CH); 2899, 1472, 1351, 1108s, 966, 838 (18-crown-6); 2575s, 2555s (BH); 1495, 1447 (Ar. skeleton); 1395s, br (CN); 1284; 1248; 1072; 1039, 1004w; 775, 883w, 806w, 775w; 745, 691 (C_6H_5 o.o.p.); 732w (carborane skeleton); 643w; 570w; 525. $^1H\{^{11}B\}$ NMR (CD_3CN), δ: 7.36 (d, 4H, *ortho* phenyl CH), 7.23 (t, 2H, *para* phenyl CH), 7.17 (t, 4H, *meta* phenyl CH); 3.47 (s, 24H, 18-C-6); 2.68 (s, 4H, H4,5), 2.13 (s, 10H, H3,6,7,9,11), 1.72 (s, 2H, H12), 1.58 (s, 4H, H8,10). $^{11}B\{^1H\}$ NMR (CD_3CN), δ: −4.4 (1B, B9), −8.3 (2B, B3,6); −10.5 (2B, B7,11); −12.6 (3B, B4,5,12); −16.3 (2B, B8,10). $^{13}C\{^1H\}$ NMR (CD_3CN), δ: 137.7 (C_6H_5 *ipso*); 129.3 (C_6H_5 *para*); 131.1, 128.8 (C_6H_5 *ortho* and *meta*); 129.5 (C1), 89.8 (C2); 70.9 (18-C-6). λ_{max} (THF, 20 °C): 317 nm (log ε, 3.92).

7. Potassium-18-crown-6 salt of bis(2-methyl-1-*ortho*-carboranyl)amide

By a similar procedure as above with bis(2-methyl-1-*ortho*-carboranyl)amine as the starting carborane, colourless crystals of the desired salt (86% yield) were obtained from toluene solution. M.p. 209–210 °C; Found: C, 34.3; H, 8.1; N, 1.8. $C_{18}H_{50}B_{20}KO_6N$ requires: C, 34.2; H, 8.0; N, 2.2%. MS (ES$^-$, *m*/*z*) 323–332; 328 (100, M$^-$), MS (ES$^+$, m/z) 303 (K18-C-6$^+$); IR (KBr disc, cm^{-1}): 2914, 1471, 1350, 1110s, 967, 839 (18-crown-6); 2560s (BH); 1413s, br (CN); 1369; 1283; 1246; 1072; 1034, 730w (carborane skeleton); 695w; 419. $^1H\{^{11}B\}$ NMR (CD_3CN), δ: 3.47 (s, 24H, 18-C-6); 2.30 (s, 4H, H4,5), 2.15 (s, 4H, H3,6), 1.98 (s, 4H, H7,11), 1.85 (s, 6H, CH_3), 1.82 (s, 2H, H9), 1.59 (s, 4H, H8,10), 1.53 (s, 1H, H12). $^{11}B\{^1H\}$ NMR (CD_3CN), δ: −7.5 (1B, B9), −8.8 (2B, B3,6); −11.3 (2B, B7,11); −12.3 (2B, B4,5); −13.7 (1B, B12), −15.4 (2B, B8,10). $^{13}C\{^1H\}$ NMR (CD_3CN), δ: 120.0 (C1), 87.0 (C2), 70.9 (18-C-6), 22.2 (CH_3).

Table 2
Crystal data and refinement information for compounds **1**–**4**.

Compound	**1**	**2**	**3**	**4**
Formula	$C_8H_{15}B_{10}NO$	$C_6H_{27}B_{20}N$	$C_{16}H_{31}B_{20}N$	$C_{31}H_{61}B_{20}KNO_{7.5}$
M	249.3	329.5	453.6	823.1
Crystal system	monoclinic	monoclinic	monoclinic	triclinic
Space group	$P2_1/c$	$P2_1/n$	$P2_1/n$	$P\bar{1}$
a (Å)	10.942(2)	11.302(6)	10.560(3)	10.370(3)
b (Å)	8.4999(12)	12.705(7)	13.135(4)	14.629(4)
c (Å)	15.068(2)	14.167(7)	18.695(6)	15.790(4)
α (°)				101.80(3)
β (°)	102.986(4)	107.03(2)	97.48(3)	92.53(2)
γ (°)				102.81(2)
V (Å^3)	1365.6(3)	1945(2)	2571.0(14)	2276.3(11)
Z	4	4	4	2
Data collected	6842	7511	4420	5825
Unique data	2392	2784	4356	5825
R_{int}	0.038	0.055	0.030	
Refined parameters	182	251	339	551
R (on *F*, $F^2 > 2\sigma$)	0.049	0.076	0.059	0.063
R_w (on F^2, all data)	0.143	0.168	0.165	0.196
Min., max. electron density (e Å^{-3})	0.25, −0.23	0.22, −0.20	0.30, −0.28	0.76, −0.35

8. Crystal structure determinations

Crystals of the compounds **1**–**4** were examined on Bruker SMART (**1**, **2**) and Stoe STADI4 (**3**, **4**) diffractometers with Mo Kα radiation (λ = 0.71069 Å; Cu Kα with λ = 1.54184 Å for **3**) at 160 K (180 K for **4**). Crystal data and other information are given in Table 2. Standard methods and software were employed, including refinement on all F^2 values [26]; no absorption corrections were applied, and no structural disorder was found.

Acknowledgements

We thank EPSRC for funding (WC, MAF, JAHM, RJP).

Appendix A. Supplementary data

CCDC 690385, 690386, 690387 and 690388 contain the supplementary crystallographic data for **1**, **2**, **3** and **4**. These data can be obtained free of charge via http://www.ccdc.cam.ac.uk/conts/retrieving.html, or from the Cambridge Crystallographic Data Centre, 12 Union Road, Cambridge CB2 1EZ, UK; fax: (+44) 1223 336 033; or e-mail: deposit@ccdc.cam.ac.uk.

Supplementary data associated with this article can be found, in the online version, at doi:10.1016/j.poly.2008.12.014.

References

[1] J.M. Kauffman, J. Green, M.S. Cohen, M.M. Fein, E.L. Cottrill, J. Am. Chem. Soc. 86 (1964) 4210;
L.I. Zakharkin, V.N. Kalinin, G.G. Zhigareva, Izv. Akad. Nauk. SSSR Ser. Khim. (1970) 912.
[2] L.I. Zakharkin, V.N. Kalinin, Doklady Akad. Nauk. SSSR 164 (1965) 577.
[3] L.I. Zakharkin, G.G. Zhigareva, Zh. Obshch. Khim. 45 (1975) 1293.
[4] W. Clegg, H.M. Colquhoun, R. Coult, M.A. Fox, W.R. Gill, P.L. Herbertson, J.A.H. MacBride, K. Wade, Spec. Publ. R. Soc. Chem. 143 (1994) 232;
K. Wade, M.G. Davidson, M.A. Fox, W.R. Gill, T.G. Hibbert, J.A.H. MacBride, Phosphorus, Sulfur and Silicon 125 (1997) 73;
L.A. Boyd, H.M. Colquhoun, M.G. Davidson, M.A. Fox, W.R. Gill, P.L. Herbertson, T.G. Hibbert, J.A.H. MacBride, R.J. Peace, G.P. Rivers, K. Wade, Spec. Publ. R. Soc. Chem. 201 (1997) 289;
M.A. Fox, R.J. Peace, J.A.H. MacBride, K. Wade, J. Chem. Soc., Dalton Trans. (1998) 401;
W. Clegg, R. Coult, M.A. Fox, W.R. Gill, J.A.H. MacBride, K. Wade, Polyhedron 12 (1993) 2711.
[5] E.S. Alekseyeva, M.A. Fox, J.A.K. Howard, J.A.H. MacBride, K. Wade, Appl. Organomet. Chem. 17 (2003) 499.
[6] D.A. Brown, W. Clegg, H.M. Colquhoun, J.A. Daniels, I.R. Stephenson, K. Wade, J. Chem. Soc., Chem. Commun. (1987) 889.
[7] R. Coult, M.A. Fox, W.R. Gill, K. Wade, W. Clegg, Polyhedron 11 (1992) 2717.
[8] A.S. Batsanov, W. Clegg, R.C.B. Copley, M.A. Fox, W.R. Gill, R.S. Grimditch, T.G. Hibbert, J.A.K. Howard, J.A.H. MacBride, K. Wade, Polyhedron 25 (2006) 300.
[9] L.A. Boyd, W. Clegg, R.C.B. Copley, M.G. Davidson, M.A. Fox, T.G. Hibbert, J.A.K. Howard, A. Mackinnon, R.J. Peace, K. Wade, Dalton Trans. (2004) 2786.
[10] J.M. Oliva, N.L. Allan, P.v.R. Schleyer, C. Viñas, F. Teixidor, J. Am. Chem. Soc. 127 (2005) 13547.
[11] R. Kivekäs, R. Sillanpää, F. Teixidor, C. Viñas, R. Nuñez, Acta Crystallogr., Sect. C 50 (1994) 2027;
R. Kivekäs, R. Sillanpää, F. Teixidor, C. Viñas, R. Nuñez, Acta Crystallogr., Sect. C 51 (1995) 1864;
R. Kivekäs, F. Teixidor, C. Viñas, R. Nuñez, Acta Crystallogr., Sect. C 51 (1995) 1868;
J.M. Oliva, C. Viñas, J. Mol. Struct. 55 (2000) 33;
J. Llop, C. Viñas, J.M. Oliva, F. Teixidor, M.A. Flores, R. Kivekäs, R. Sillanpää, J. Organomet. Chem. 657 (2002) 232.
[12] T.L. Heying, J.W. Ager Jr., S.L. Clark, R.P. Alexander, S. Papetti, J.A. Reid, S.I. Trotz, Inorg. Chem. 2 (1963) 1097;
L.I. Zakharkin, V.N. Kalinin, Zh. Obshch. Khim. 35 (1965) 1882.
[13] S.B. Kahl, R.A. Kasar, J. Am. Chem. Soc. 118 (1996) 1223;
Y. Endo, T. Iijima, Y. Yamakoshi, M. Yamaguchi, H. Fukasawa, K. Shudo, J. Med. Chem. 42 (1999) 1501;
R.A. Kasar, G.M. Knudsen, S.B. Kahl, Inorg. Chem. 38 (1999) 2936;
M. Scobie, M.D. Threadgill, J. Chem. Soc., Perkin Trans. I (1994) 2059;
T. Totani, K. Aono, K. Yamamoto, K. Tawara, J. Med. Chem. 24 (1981) 1492.

[14] V.V. Korshak, N.I. Bekasova, N.G. Komarova, L.G. Komarova, V.V. Vagin, Acta Polym. 40 (1989) 439;
A. Rusanov, L. Komarova, G. Kats, M. Prigozhina, Int. J. Polym. Mater. 25 (1994) 117.
[15] C.E. Housecroft, A.G. Sharpe, Inorganic Chemistry, 3rd Ed. Pearson, 2008, p. 653–654.
[16] W.L. Waters, P.G. Marsh, J. Org. Chem. 40 (1975) 3344;
P. Buck, G. Kobrich, Tetrahedron Lett. (1967) 1563;
H. Gilman, J. Am. Chem. Soc. 49 (1927) 1052;
E. Muller, H. Metzer, Chem. Ber. 89 (1956) 396;
W.L. Waters, P.G. Marsh, J. Org. Chem. 40 (1975) 3349.
[17] R.L. Thomas, G.M. Rosair, A.J. Welch, Acta Crystallogr., Sect. C 52 (1996) 1024.
[18] I.V. Glukhov, K.A. Lyssenko, A.A. Korlyukov, M.Y. Antipin, Russ. Chem. Bull. 54 (2005) 547.
[19] M. Tsuji, J. Org. Chem. 69 (2004) 4063;
I.V. Glukhov, K.A. Lyssenko, A.A. Korlyukov, M.Y. Antipin, Faraday Discuss. 135 (2007) 203;
I.V. Glukhov, M.Y. Antipin, K.A. Lyssenko, Eur. J. Inorg. Chem. 7 (2004) 1379.
[20] M. Gdaniec, T. Bytner, M. Szyrszyng, T. Połonski, J. Inclusion Phenom. Macrocyclic Chem. 40 (2001) 243.
[21] K. Chui, H.-W. Li, Z. Xie, Organometallics 19 (2000) 5447;
G. Zi, H.-W. Li, Z. Xie, Organometallics 21 (2002) 5415;
T. Marx, B. Mosel, I. Pantenburg, S. Hagen, H. Schulze, L. Wesemann, Chem. Eur. J. 9 (2003) 4472;
M.A. Fox, A.E. Goeta, A.K. Hughes, A.L. Johnson, J. Chem. Soc., Dalton Trans. (2002) 2132;
R. Littger, U. Englich, J.T. Spencer, Inorg. Chem. 36 (1997) 6434;
M.-S. Cheung, H.-S. Chen, Z. Xie, Organometallics 23 (2004) 517.
[22] M.A. Rodriguez, S.D. Bunge, Acta Crystallogr., Sect. E 59 (2003) o1123.
[23] M.G. Davidson, S. Lamb, Polyhedron 16 (1997) 4393;
P.B. Hitchcock, A.V. Khvostov, M.F. Lappert, A.V. Protchenko, J. Organomet. Chem. 647 (2002) 198.
[24] M.F. Hawthorne, T.D. Andrews, P.M. Garrett, E.P. Olsen, M. Reintjes, F.N. Tebbe, L.F. Warren, P.A. Wegner, D.C. Young, Inorg. Synth. 10 (1967) 91.
[25] P.T. Brain, J. Cowie, D.J. Donohoe, D. Hnyk, D.W.H. Rankin, D. Reed, B.D. Reid, H.E. Robertson, A.J. Welch, M. Hofmann, P.v.R. Schleyer, Inorg. Chem. 35 (1996) 1701.
[26] G.M. Sheldrick, Acta Crystallogr., Sect. A 64 (2008) 112.

[43–49] gave sterically hindered salen analogues which resulted in oligo- and polynuclear cobalt species with varied coordination geometry and oxidation states.

Our research group has been working on Schiff base cobalt complexes derived from different donor set ligands since the last decade and has successfully reported a few of them [52–54], though mixed valence cobalt Schiff base complexes are few. In this paper we report three new cobalt complexes of which two are mixed valence complexes and one is a dinuclear cobalt(III) species. The three different Schiff base ligands used to synthesise **1**, **2** and **3** were obtained by the selective and non-selective condensation of 1,3-diaminopropane and 1,3-diaminopentane with 2-hydroxyacetophenone (Fig. 1) and the chelating behaviour of the ligands with the cobalt ion has been investigated. Pseudohalides (NCO^- and N_3^-) have been used to increase the nuclearity of the complexes. To synthesise **1** we selectively condensed one of the two primary amines in 1,3-diaminopropane with 2-hydroxyacetophenone and obtained the N_2O donor Schiff base ligand $\mathbf{HL^1}$. Although similar N_2O donor Schiff bases complexes were obtained earlier with copper and nickel, the corresponding cobalt species were not obtained [55,56]. For **2** the N_2O donor Schiff base ligand $\mathbf{HL^2}$ was synthesised by condensing the less hindered $-NH_2$ functionality of 1,3-diaminopentane with 2-hydroxyacetophenone in order assess any structural variations arising from ethyl substitution at the uncondensed $-NH_2$ end of $\mathbf{HL^2}$. Single crystal X-ray diffraction studies on **1** and **2** confirmed this structural variation. In **1** the asymmetric unit comprises five mixed valence mononuclear cobalt centers, whereas **2** is a dinuclear cobalt(III) species with *end-on* azido bridges. In order to synthesise **3**, both 1,3-diaminopropane primary amine functionalities were non-selectively condensed with 2-hydroxyacetophenone to obtain the symmetric N_2O_2 donor Schiff base ligand $\mathbf{H_2L^3}$, which in the presence of the azide ion formed an *end-on* azido and μ_2-phenoxo bridged trinuclear Co^{III}–Co^{II}–Co^{III} core where the central cobalt(II) center is on a center of inversion. Earlier Mitra et al. reported a trinuclear copper complex with $\mathbf{H_2L^3}$ [57], but **3** is the first azido bridged cobalt complex with $\mathbf{H_2L^3}$. The complexes were characterized by physical techniques and their structures were confirmed from single crystal X-ray studies. EPR analyses were carried out for the mixed valence cobalt complexes **1** and **3**, and DNA binding studies were performed for all three complexes.

2. Experimental

2.1. Materials

All chemicals and solvents used for the syntheses were of analytical grade. 1,3-Diaminopropane, 1,3-diaminopentane, 2-hydroxyacetophenone, cobalt nitrate hexahydrate, sodium cyanate and sodium azide were purchased form Aldrich Chemical Co. and were used without further purification. The CT-DNA was purchased from Bangalore Genie, the Tris buffer, sodium chloride and hydrochloric acid (AR) were purchased from Merck.

2.2. Syntheses

2.2.1. Synthesis of the Schiff base ligands

2.2.1.1. HL^1. To a vigorously stirred cool dilute ethanolic solution (50 ml, $T = 5$–10 °C) of 1,3-diaminopropane (0.833 ml, 10 mmol), an absolute ethanolic solution (40 ml) of 2-hydroxyacetophenone (0.96 ml, 8 mmol) was added dropwise. After the addition was complete, the mixture was stirred for 15–30 min and then refluxed for 15–60 min. The resulting solution was evaporated under vacuum to remove the solvent and the excess diamine was extracted by benzene. The product was collected by filtration, washed with diethyl ether and dried in air. *Anal.* Calc. for $[C_{11}H_{16}N_2O]$: C, 68.72; H, 8.39; N, 14.57. Found: C, 68.67; H, 8.34; N, 14.45%.

2.2.1.2. HL^2. The same above method was adopted to synthesise $\mathbf{HL^2}$. 1,3-Diaminopentane (1.19 ml, 10 mmol) and 2-hydroxyaceto-

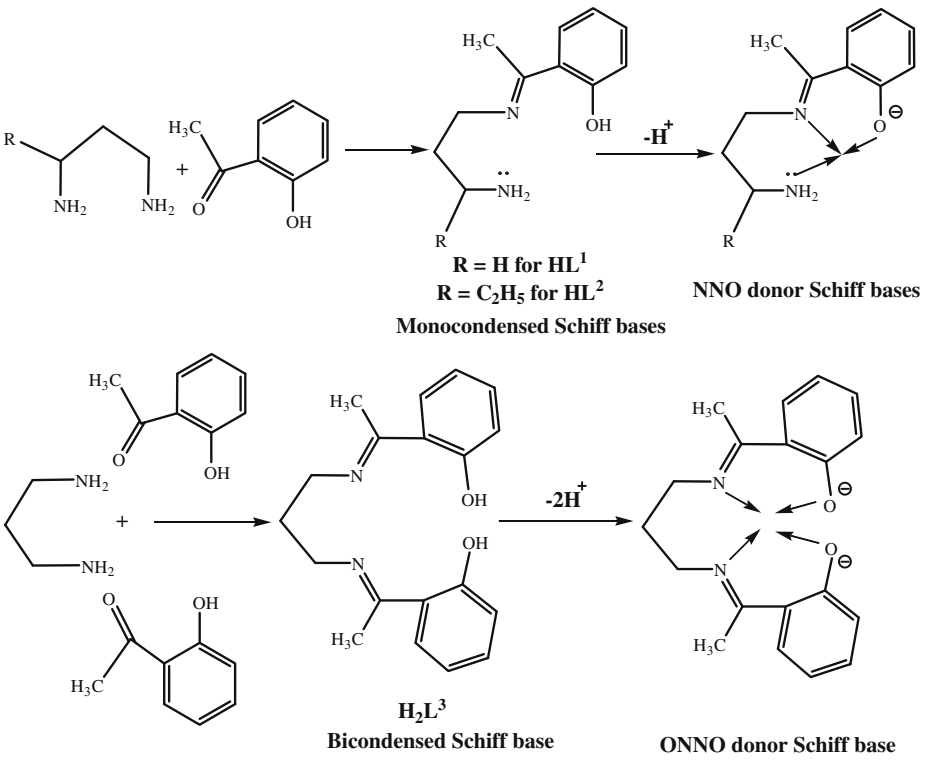


Fig. 1. Scheme of synthesis for the selectively and non-selectively condensed Schiff bases.

phenone (0.96 ml, 8 mmol) were used to obtain **HL²**. The resulting solution was evaporated under vacuum to remove the solvent, and the excess diamine was extracted by benzene. The product was collected by filtration, washed with diethyl ether and dried in air. *Anal.* Calc. for $[C_{13}H_{20}N_2O]$: C, 70.87; H, 9.15; N, 12.72. Found: C, 70.76; H, 9.09; N, 12.69%.

2.2.1.3. H_2L^3. The symmetrical **H_2L^3** was prepared following the literature method [57]. On refluxing a methanolic solution (100 ml) of 1,3-diaminopropane (0.83 ml, 10 mmol) with 2-hydroxyacetophenone (2.4 ml, 20 mmol) for 40 min an orange yellow Schiff base resulted. It was then cooled and the yellow crystalline product was collected by filtration, washed with diethyl ether and dried in air. *Anal.* Calc. for $[C_{19}H_{22}N_2O_2]$: C, 73.52; H, 7.14; N, 9.03. Found: C, 73.49; H, 7.06; N, 9.01%.

2.2.2. Syntheses of the complexes

*2.2.2.1. $[Co(L^1)_2]_2$ $[Co(NCO)_4]$ (**1**).* To a (20 ml) methanolic solution of cobalt nitrate hexahydrate (0.291 g, 1 mmol), a methanolic solution (30 ml) of **HL¹** (0.384 g, 2 mmol) was added dropwise and the mixture was stirred to produce a dark red solution. Sodium cyanate (0.0.65 g, 1 mmol) in a minimum volume of water–methanol mixture was added to the stirring solution to give a dark green colour and the resulting solution was further stirred for 3 h at 40 °C. The dark green solution was kept at 16 °C, yielding red needle shaped crystals suitable for X-ray diffraction after a week. The crystals were isolated by filtration and air-dried. *Anal.* Calc. for $[Co(L^1)_2]_2$ $[Co(NCO)_4]$: C, 51.89; H, 5.40; N, 15.14. Found: C, 51.86; H, 5.11; N, 15.12%.

*2.2.2.2. $[Co_2(\mu\text{–}N_3)_2(L^2)_2(N_3)_2]$ (**2**).* **HL²** (0.22 g, 1 mmol) was dissolved in (30 ml) methanol, and was added dropwise to a methanolic solution (20 ml) of cobalt nitrate hexahydrate (0.291 g, 1 mmol) to give an orange red solution. The solution was stirred for 20 min then sodium azide (0.130 g, 2 mmol) in a minimum volume of a water–methanol mixture was carefully added to produce a dark brown solution. The resulting solution was further stirred for 2 h at room temperature. The dark brown solution was kept at 20 °C yielding red needle shaped crystals suitable for X-ray diffraction after a week. The crystals were isolated by filtration and air-dried. *Anal.* Calc. for $[C_{26}H_{38}Co_2N_{16}O_2]$: C, 43.05; H, 5.24; N, 30.91. Found: C, 43.0; H, 5.21; N, 30.89%.

*2.2.2.3. $[(H_2O)_2Co(\mu\text{–}N_3)_2(\mu\text{–}L^3)_2Co_2(N_3)_{1.25}(CH_3O)_{0.75}]H_2O$ (**3**).* To a methanolic solution (20 ml) of cobalt nitrate hexahydrate (0.291 g, 3 mmol), a methanolic solution (30 ml) of **H_2L^3** (0.64 g, 2 mmol) was added dropwise to produce a dark red solution which was refluxed for 20 min and then cooled at room temperature. Sodium azide (0.130 g, 2 mmol) in a minimum volume of water–methanol mixture was added to the dark red solution to give a dark brown colour which was then stirred for 4 h at 40 °C. The dark brown solution was kept at 20 °C, yielding brown needle shaped crystals suitable for X-ray diffraction after ten days. The crystals were isolated by filtration and air-dried. *Anal.* Calc. for $[C_{38.75}H_{48.25}Co_3N_{13.75}O_{7.75}]$: C, 46.16; H, 4.79; N, 19.12. Found: C, 46.12; H, 4.75; N, 19.09%.

2.3. Procedure for DNA binding

Using the electronic absorption spectral method, the relative binding of the two complexes to calf thymus (CT)-DNA was studied in 5 mM Tris–HCl/NaCl buffer (pH 7.2). The solution of CT-DNA gave a ratio of UV absorbance at 260 nm and 280 nm, A_{260}/A_{280}, of 1.8–1.9, indicating that the DNA was sufficiently free of protein. The stock solution of CT-DNA was prepared in 50 mM Tris–HCl/NaCl buffer, pH 7.2 (stored at 4 °C). The concentration of CT-DNA was determined from its absorption intensity at 260 nm with a molar extinction coefficient of 6600 M^{-1} cm^{-1} with respect to base [58]. The binding constant was determined using the following equation [59]:

$$1/\Delta A = 1/\Delta A_{max} + 1/K_{app}\Delta A_{max} \times 1/(C_D - C_0) \quad (1)$$

where ΔA is the decrease in absorbance at 367 nm for **1** and 292 nm for **2**. ΔA_{max} indicates the same parameter where the complex is totally bound to DNA (saturation). C_D and C_0 denote the concentration of CT-DNA and initial concentration of the complexes, respectively. K_{app} is the apparent binding constant of the complexes to CT-DNA and is the reciprocal of K_d, where K_d is the dissociation constant of the complex DNA interaction.

2.4. Physical measurements

The Fourier Transform Infrared spectra of the complexes were recorded on a Perkin–Elmer Spectrum RX I FT-IR in the range 4000–300 cm^{-1} as a solid KBr disc. The electronic spectra were recorded at 300 K on a Perkin–Elmer λ-40 UV–Vis-spectrometer using HPLC grade acetonitrile as the solvent with 1 cm quartz cuvettes in the range 200–800 nm. C, H, N microanalyses were carried out with a Perkin–Elmer 2400 II elemental analyzer. Electrochemical measurements were performed on a VersaStat–PotentioStat II cyclic voltammeter using HPLC grade acetonitrile solution as the solvent, and tetrabutylammonium perchlorate was used as the supporting electrolyte at a scan rate 0.05 V/s. Platinum and a saturated calomel electrode (SCE) were the working and the reference electrodes in the process, respectively. The X band EPR spectra of polycrystalline samples were taken with Bruker ESP-300 spectrometer using a rectangular cavity equipped with 100 kHz field modulation. The EPR spectra were recorded at room temperature and at liquid nitrogen temperature using a liquid nitrogen dewar. DPPH was used for the calibration of g values. The g values were estimated by comparing the experimental spectrum with those obtained by the computer simulation program (WIN EPR SYMPHONIA) working at the second order of perturbation theory.

2.5. X-ray crystallography

The X-ray diffraction experiments were carried out at 100 K on a Bruker X8 Apex 2 diffractometer Single crystals were coated in Paratone-N heavy oil and mounted in a Cryoloop before being transferred to the cold stream on the diffractometer. Intensity data were collected using graphite monochromatised Mo Kα radiation (λ = 0.71073 Å). Data collection, reduction and absorption corrections were done with the APEX2 suite of programs [60]. All non-hydrogen atoms were refined anisotropically by full-matrix least-squares based on F^2 using SHELXTL. All non-hydrogen atoms were refined with anisotropic displacement parameters. Hydrogen atom isotropic displacement parameters were all treated as riding on the bound atom (1.2 Ueq C/N for all except methyl H atoms). All carbon bound H atoms were generated geometrically and were included in the refinement in the riding model approximation. In **1** all H atoms were constrained to idealised geometries, in **2** the coordinates of H atoms bound to amine N9 were freely refined, and there was disorder in the methylene portion of chelate ring, 60:40% occupancy ratio for C10A, C11A and C10B, C11B, respectively. In **3** all the water H atoms were found in the difference map and initially restrained to O–H 0.90(4) Å, H···H 1.50(2) Å before being fixed for the final cycles, as refinement of their positions was unstable. Selected crystallographic data are summarised in the Table 1.

Table 1
Crystal data and structure refinement for **1**, **2** and **3**.

	1	2	3
Empirical formula	$2(C_{22}H_{30}CoN_4O_2)$, $C_4CoN_4O_4$	$C_{26}H_{38}Co_2N_{16}O_2$	$C_{38.75}H_{48.25}Co_3N_{13.75}O_{7.75}$
Formula weight	1109.87	724.58	1007.45
Temperature (K)	100(2)	100(2)	100(2)
Wavelength (Å)	0.71073	0.71073	0.71073
Crystal system	triclinic	triclinic	orthorhombic
Space group	$P\bar{1}$	$P\bar{1}$	*Pna*2(1)
a (Å)	11.0511(12)	8.0287(5)	14.4748(9)
b (Å)	12.1454(14)	10.1587(7)	28.5012(16)
c (Å)	18.597(2)	10.5387(7)	11.2272(7)
α (°)	83.539(4)	105.500(4)	90
β (°)	74.746(4)	106.617(3)	90
γ (°)	85.742(4)	95.320(3)	90
Volume (Å^3)	2390.2(5)	780.27(9)	4631.8(5)
D_{calc} (g cm^{-3})	1.542	1.542	1.445
Absorption coefficient (mm^{-1})	1.097	1.118	1.125
F(000)	1154	376	2080
Crystal size (mm)	0.42 × 0.18 × 0.10	0.42 × 0.18 × 0.04	0.64 × 0.28 × 0.24
θ Range for data collection (°)	2.45–26.04	2.69–33.63	1.43–24.47
Reflections collected	24028	25562	54803
Independent reflections (R_{int})	8851 (0.0653)	6034 (0.0358)	7597 (0.0519)
Data/restraints/parameters	8851/0/650	6034/0/234	7597/51/597
Goodness-of-fit on F^2	1.059	0.905	0.983
Final *R* indices [$I > 2\sigma(I)$]	$R_1 = 0.0763$, $wR_2 = 0.1628$	$R_1 = 0.0397$, $wR_2 = 0.0920$	$R_1 = 0.0541$, $wR_2 = 0.1517$
R indices (all data)	$R_1 = 0.1301$, $wR_2 = 0.1847$	$R_1 = 0.0722$, $wR_2 = 0.1079$	$R_1 = 0.0630$, $wR_2 = 0.1595$

3. Results and discussion

3.1. Infrared spectra

The IR spectra of **1**, **2** and **3** were analysed in comparison with that of their free ligands **HL^1** **HL^2** and **H$_2$L^3** in the region 4000–250 cm^{-1}. The strong sharp absorption band around 1627, 1617 and 1620 cm^{-1} in the spectra of the free ligands **HL^1**, **HL^2** and **H$_2$L^3** can be assigned to the C=N stretching, but in the complexes these bands are shifted to lower frequencies, which can be attributed to the coordination of the imine nitrogen to the metal center. The bands at 1598, 1596 and 1595 cm^{-1} are assigned to the imine stretching frequencies in the complexes **1**, **2** and **3**, respectively [35]. The three Schiff ligands show a well defined band at 3460, 3447 and 3449 cm^{-1} due to O–H stretching, which disappears in the respective complexes indicating the deprotonation of the respective Schiff base ligands upon complexation. The strong phenolic C–O stretching obtained at 1222, 1218 and 1206 cm^{-1} for **HL^1**, **HL^2** and **H$_2$L^3** shifts to a lower frequency in the respective complexes, at 1181, 1163 and 1159 cm^{-1}, supporting the coordination of the deprotonated phenolato oxygen atoms to the metal centers [61]. Two sharp bands obtained at 3472 and 3525 cm^{-1} for **1** and 3311 and 3368 cm^{-1} for **2** are assigned to the asymmetric and symmetric N–H stretching modes of the primary amine [62], indicating the coordination of the selectively condensed Schiff bases [**L^1**]$^-$ and [**L^2**]$^-$ to the respective metal centers, whereas no such bands are obtained for **3**. Complex **1** shows one strong band at 2208 cm^{-1}, which indicates the presence of NCO as terminal ligands [63]. In the spectra of **2** and **3** strong, well resolved sharp bands with a bifurcated peak at 2066, 2016 and 2060, 2015 cm^{-1} were obtained, respectively, which are assigned to $\upsilon_{N=N}$ of the azide moiety coordinated to two different metal centers simultaneously. The ligand coordination to the metal centre is substantiated by a υ_{M-N} band appearing at 420, 406 and 412 cm^{-1} for **1**, **2** and **3**, respectively.

3.2. Electronic spectra

The UV–Vis spectrum of **1** shows a d–d transition band at 586 nm and several CT bands are observed in the region 442–382 nm. The d–d band at 586 nm is due to the $^1A_{1g} \rightarrow {}^1T_{1g}$ transition for the distorted octahedral cobalt(III) ion in the complex [64]. The higher energy band, $^1A_{1g} \rightarrow {}^1T_{2g}$, is obscured by ligand to metal charge transfer bands. The bands for the tetrahedral cobalt(II) center in $[Co(NCO)_4]^{2-}$, corresponding to the spin allowed transition $^4A_2 \rightarrow {}^4T_1(P)$, should be located on the higher energy side of the overlapping charge transfer bands. Similarly for **2**, a d–d transition band at 570 nm is obtained which again supports the presence of distorted octahedral cobalt(III) centers in the complex. The higher energy band $^1A_{1g} \rightarrow {}^1T_{2g}$ is obscured by ligand to metal charge transfer bands, obtained in the broad range 410–375 nm. The UV–Vis spectrum of **3** shows two very broad d–d transition bands at 542 and 625 nm, supporting the presence of both octahedral cobalt(II) as well as octahedral cobalt(III) ions in the complex. The band at 542 nm is due to the $^4T_{1g}(F) \rightarrow {}^4T_{1g}(P)$ transition and the weak shoulder at 656 nm is probably due to the $^4T_{1g}(F) \rightarrow {}^4A_{2g}$ transition for the octahedral cobalt(II) unit [64]. The band at 625 nm is due to a $^1A_{1g} \rightarrow {}^1T_{1g}$ transition for the distorted octahedral cobalt(III) ion in the complex. Apart from d–d bands, several charge transfer bands can be observed in the region 442–382 nm for **3** (see Fig. 1).

3.3. Cyclic voltammetry

The cyclic voltammetry experiments for **1**, **2** and **3** were performed in acetonitrile solution at ambient temperature (300 K) within the potential range ±2 V using platinum as the working electrode and a saturated calomel electrode (SCE) as the reference electrode in the process. In order to compare the cyclic voltammograms of **1**, **2** and **3** they have been represented in Fig. 2. The voltammograms of **1** and **3** are quite alike, but differ significantly from that of **2**. During the cathodic scan, **1** and **3** display two different irreversible reductive responses at −0.121, −0.946 and −0.392, −0.987 V, respectively, whereas a single irreversible reductive response at −0.18 V was obtained for **2**. Similarly during the anodic scan **1** and **3** exhibit two irreversible oxidative responses at +0.604, +1.132 and +0.801, +1.276 V, respectively, whereas a single irreversible oxidative peak at +0.36 V was observed for **2**. For **2** the peak at −0.18 V is attributed to the reduction of the $Co^{III} \rightarrow Co^{II}$ centers, whereas the oxidation of the $Co^{II} \rightarrow Co^{III}$ centers in the

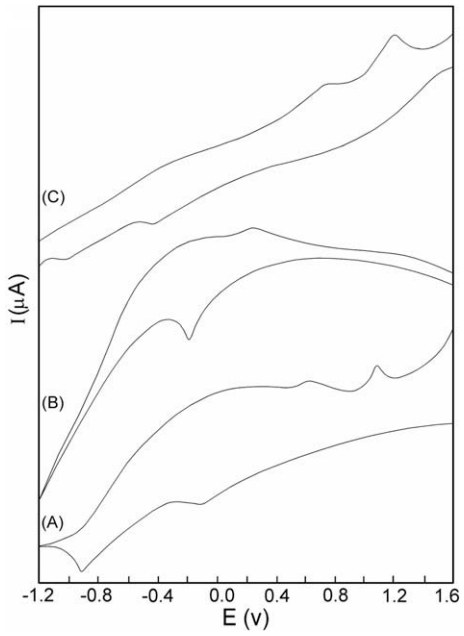


Fig. 2. A, **B** and **C** are the representative cyclic voltammograms of **1**, **2** and **3**, respectively, at room temperature in acetonitrile solvent.

complex is associated with the peak at +0.36 V. Such oxidations and reductions are similar to those of the earlier reported cobalt-(III) dinuclear species with cobalt(III) ions residing in a similar coordination environment [65]. Unlike **2**, for **1** and **3** the two different irreversible reductive responses obtained at −0.121, −0.946 (**1**) and −0.392, −0.987 V (**3**) are attributed to two different $Co^{III} \rightarrow Co^{II}$ reductions, and two irreversible oxidative responses at +0.604, +1.132 (**1**) and +0.801, +1.276 V (**3**) are associated with two different $Co^{II} \rightarrow Co^{III}$ oxidations. Such reductions are indicative of the presence of two types of structurally different cobalt(III) centers residing in non-identical coordination environments for **1** and **3**. Similarly the two different oxidative responses suggest the oxidations of two structurally dissimilar cobalt(II) centers in the respective complexes. Thus from the cyclic voltammograms of **1**, **2** and **3** we can propose that unlike **2**, **1** and **3** are mixed valence cobalt species containing cobalt(II) as well as cobalt(III) centers whereas **2** is a solely cobalt(III) species. The cyclic voltommograms of **1** and **3** are compared to that of the earlier reported mixed valence Co^{III}–Co^{II}–Co^{III} trinuclear species [34]. In contrast to that of **1** and **3**, for the earlier reported mixed valence trinuclear cobalt species only a single irreversible oxidative response at +1.72 V was followed by an irreversible reductive response at −1.44 V using a Ag–AgCl electrode with a three electrode configuration. From the structural studies of the trinuclear complex [34] it is found that the two cobalt(III) centers reside in similar coordination environments as a result of which only a single irreversible reductive response is observed, whereas for **1** and **3** the two irreversible reductive responses indicate that the cobalt(III) centers are expected to reside in two different coordination environments. A similar argument is applicable for the Co^{II} centers in the respective complexes.

3.4. EPR spectra

The X band EPR spectra of polycrystalline samples **1** and **3** are shown in Fig. 3. The EPR spectra were recorded both at room temperature and at liquid nitrogen temperatures. The EPR spectra were recorded to distinguish the valence and spin state of cobalt ion (S = ½ and 3/2) and also to get information about the coordination and symmetry around the transition metal ion. The cobalt ion exhibits two oxidation states (II and III), where cobalt(III) with a t_{2g}^6 configuration is diamagnetic in nature and hence EPR silent, whereas cobalt(II) exist in both low spin (S = 1/2) and high spin (S = 3/2) states and is paramagnetic, and so can be investigated by EPR spectroscopy. The EPR parameters observed for low spin hexacoordinated cobalt complexes with axial elongation along the z axis and a $^2A_1(d_{z2})$ ground state showed the trend $g_\perp$ ($\sim$2} < $g_{||}$ (2.02–2.01), $A_\perp^{Co} < A_{||}^{Co}$ and exhibit relatively small anisotropy in the g value [66–68]. In addition to this, the EPR of low spin cobalt complexes is observable at room temperature as its spin lattice relaxation time is sufficiently long. The ^4F ground state of isolated cobalt(II) (S = 3/2) in a purely octahedral crystal field splits into a $^4A_2$ (singlet) ground state and two $^4T_1$ and $^4T_2$ excited states (triplets). The combined effect of spin orbit coupling and lower crystal fields further splits the $^4A_2$ ground state into two Kramer's doublets, $E_{1/2}$ and $E_{3/2}$, with a zero field splitting equal to 2D. However if there is a very large zero field splitting, the EPR spectra can be described with an effective spin S = 1/2. If the energy gap between the two Kramer doublets is high enough ($\wedge E \geqslant kT$), only the ground state is expected to be sufficiently populated. Furthermore, the presence of low lying excited states above the orbital singlet state contribute towards fast electronic relaxation, hence the EPR spectrum is observed at low temperature.

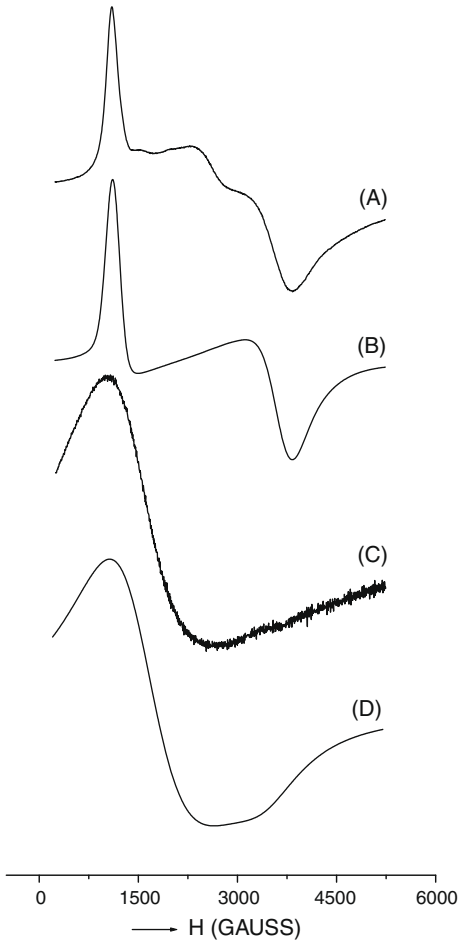


Fig. 3. EPR spectra of (A) Co complex **1** at 77 K. (B) Simulated spectrum with $g_{||}$ = 6.15 Δ_{pp} = 200 G, $g_\perp$ = 1.85, Δ_{pp} = 1200 G. (C) Co complex **3**. (D) simulated spectrum with $g_{||}$ = 2.00 Δ_{pp} = 1200 G, $g_\perp$ = 4.55, Δ_{pp} = 800 G.

The X band EPR spectra of polycrystalline samples of mixed valence cobalt complexes **1** and **3** were recorded in the temperature range 80–300 K. The EPR measurements were not recorded for **2** as

it is a Co(III)–Co(III) diamagnetic dinuclear species. Low temperature EPR spectra containing very broad and featureless signals (signals without any hyperfine structure, ^{57}Co, 100% abundance, $I = 7/2$) appeared for both the complexes. Increasing the temperature up to room temperature caused further broadening of the signals and the signals were broadened so much that the bands were not detected at room temperature. This behaviour is attributed to the short spin lattice relaxation time of high spin cobalt complexes in octahedral fields at room temperature. Fig. 3 shows the EPR spectra of polycrystalline samples of **1** and **3** at liquid nitrogen temperature. The EPR signal of complex **1** consists an intense signal with $g_{||} = 6.15$ ($\Delta_{pp} = 200$ G) and $g_{\perp} = 1.85$ ($\Delta_{pp} = 1200$ G) which is attributed to the $[Co(II)NCO_4]^{2-}$ anion having a tetrahedral arrangement of NCO [69,70]. The EPR spectrum of **3** could be interpreted in terms of an axial spectrum with $g_{\perp} = 4.550$ ($\Delta_{pp} = 1200$ G) and $g_{||} = 2.000$ ($\Delta_{pp} = 800$ G). The EPR spectrum is typical of distorted six coordinated cobalt(II) ions in a high spin configuration ($S = 3/2$) with the ground state being $S = 1/2$ [71,72]. In **3**, the cobalt ions are of mixed valence (II and III) and have a tendency to form trinuclear species viz, Co(III)–Co(II)–Co(III) [35]. The central cobalt(II) center is EPR active and has a highly distorted octahedral geometry (the equatorial sites are occupied by water of hydration and oxygen atoms of the bridging phenoxo group, whereas the axial sites are occupied by nitrogen atoms of two *end-on* bridging azido groups).

3.5. Description of the crystal structures

3.5.1. $[Co(L^1)_2]_2$ $[Co(NCO)_4]$ (**1**)

An ORTEP diagram of **1** is presented in Fig. 4 and relevant bond length and bond angle data are listed in Table 2. The structure consists of four $[Co^{III}\mathbf{L}^1{}_2]^+$ monocations, where the cobalt ions are on centres of inversion, and one $[Co^{II}(NCO)_4]^{2-}$ anionic unit [52]. Therefore the $[Co^{III}\mathbf{L}^1{}_2]^+$ ions are in a 2:1 ratio to $[Co(NCO)_4]^{2-}$. Structurally, there is no significant difference between the four $[Co\mathbf{L}^1{}_2]$ units, they are all six coordinate with distorted octahedral geometries with the Co–N bonds slightly longer than the Co–O bonds. The interligand bite angles for all four six coordinate cobalt centers differ slightly. Co(3) has the largest interligand bite angle of 96.20° whereas Co(2) has the shortest interligand bite angle of 93.56°. The Co(1) and Co(4) centres have similar interligand bite angles of 95.28° and 95.17°, respectively. The $[Co^{II}(NCO)_4]^{2-}$ anion has a cobalt(II) center with a tetrahedral arrangement of NCO^- ligands where all four NCO^- ligands are almost linear with N–C–O bond angles to within a degree of 179°. Several hydrogen bonding interactions are found in the structure (Table 3). The hydrogen atoms [H(10A), H(10G)] of the free amine fragment participate in hydrogen bonding with the deprotonated phenoxo oxygens [O(1D) and O(1A) respectively] and thereby connect the two adjacent mononuclear Co(1) and Co(4) units, as shown in Fig. 5. The Co(1) and Co(4) centres are connected to the tetrahedral Co(5) unit by hydrogen bonding interactions involving the remaining two hydrogen atoms [H(10B), H(10H)] of the other free amine functionality with oxygen atom O(21) of $[Co(II)NCO_4]^{2-}$. Similarly the H atoms of the free amine fragment of the Schiff bases coordinated to Co(2) and Co(3) participate in NH···O hydrogen bonding with oxygen atom O(24) of $[Co(II)NCO_4]^{2-}$. In **1** all five mononuclear

Table 2
Selected bond lengths (Å) and bond angles (°) for **1.**

Bond lengths (Å)		Bond lengths (Å)	
Co(1)–O(1A)	1.892(5)	Co(3)–N(8C)	1.960(6)
Co(1)–N(8A)	1.947(5)	Co(4)–O(1D)	1.873(5)
Co(1)–N(10A)	1.990(5)	Co(4)–N(8D)	1.945(6)
Co(2)–O(1B)	1.884(5)	Co(4)–N(10D)	1.975(5)
Co(2)–N(8B)	1.964(6)	Co(5)–N(23)	1.951(7)
Co(2)–N(10B)	1.973(5)	Co(5)–N(22)	1.961(7)
Co(3)–O(1C)	1.892(4)	Co(5)–N(24)	1.963(7)
Co(3)–N(10C)	1.946(5)	Co(5)–N(21)	1.981(7)
Bond angles (°)		Bond angles (°)	
O(1A)#1–Co(1)–O(1A)	180.0(3)	O(1C)–Co(3)–N(8C)	89.2(2)
O(1A)#1–Co(1)–N(8A)	90.8(2)	N(10C)–Co(3)–N(8C)	86.1(2)
O(1A)–Co(1)–N(10A)	84.8(2)	N(8A)–Co(1)–N(10A)	87.5(2)
O(1D)–Co(4)–N(8D)	89.9(2)	O(1D)#4–Co(4)–N(10D)	95.2(2)
O(1B)–Co(2)–N(8B)	88.5(2)	N(8D)–Co(4)–N(10D)	85.7(2)
O(1B)#2–Co(2)–N(10B)	93.6(2)	N(23)–Co(5)–N(22)	114.8(3)
N(8B)–Co(2)–N(10B)	87.6(2)	N(23)–Co(5)–N(24)	104.1(3)
N(22)–Co(5)–N(24)	109.0(3)	N(23)–Co(5)–N(21)	109.3(3)
O(1C)–Co(3)–N(10C)#3	96.2(2)	N(22)–Co(5)–N(21)	109.0(3)
N(24)–Co(5)–N(21)	110.5(3)	–	–

Symmetry transformations used to generate equivalent atoms: #1, $-x+1$, $-y+1$, $-z+1$; #2, $-x+2$, $-y$, $-z+2$; #3, $-x$, $-y+1$, $-z$; #4, $-x+2$, $-y+1$, $-z+1$.

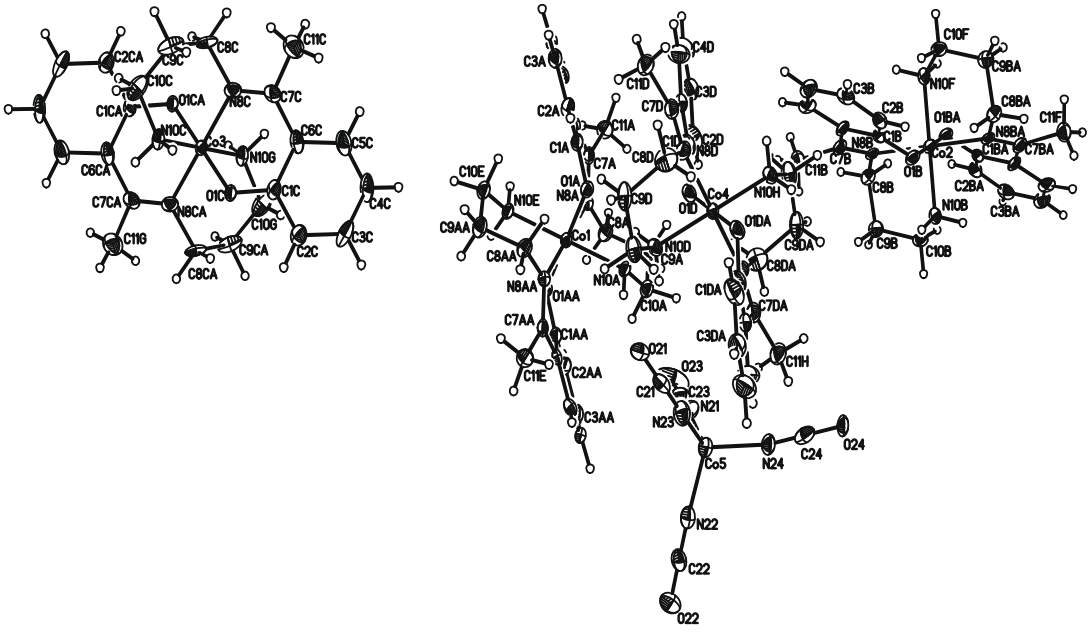


Fig. 4. ORTEP view drawn with 30% probability ellipsoids showing five mononuclear units of **1**.

Table 3
Hydrogen bond parameters of **1**.

D–H···A	d(D–H) Å	d(H···A) Å	d(D···A) Å	<(DHA) (°)
N(10A)–H(10A)···O(1D)	0.92	2.21	3.126(7)	172.7
N(10A)–H(10B)···O(21)	0.92	2.35	3.241(8)	163.1
N(10B)–H(10E)···O(24)#5	0.92	2.12	2.974(8)	153.4
N(10B)–(10F)···O(1C)#1	0.92	2.45	3.281(7)	150.6
N(10C)–(10M)···O(24)#6	0.92	2.08	2.963(8)	159.3
N(10C)–(10N)···O(23)#7	0.92	2.23	3.029(9)	144.8
N(10D)–H(10G)···O(1A)	0.92	2.48	3.401(7)	176.1
N(10D)–H(10G)···N(10A)	0.92	2.84	3.415(8)	121.4
N(10D)–H(10H)···O(21)	0.92	2.01	2.878(8)	155.7

Symmetry transformations used to generate equivalent atoms: #1, $-x+1$, $-y+1$, $-z+1$; #2, $-x+2$, $-y$, $-z+2$; #3, $-x$, $-y+1$, $-z$; #4, $-x+2$, $-y+1$, $-z+1$; #5, $-x+2$, $-y+1$, $-z+2$; #6, $x-1$, y, $z-1$; #7, x, y, $z-1$.

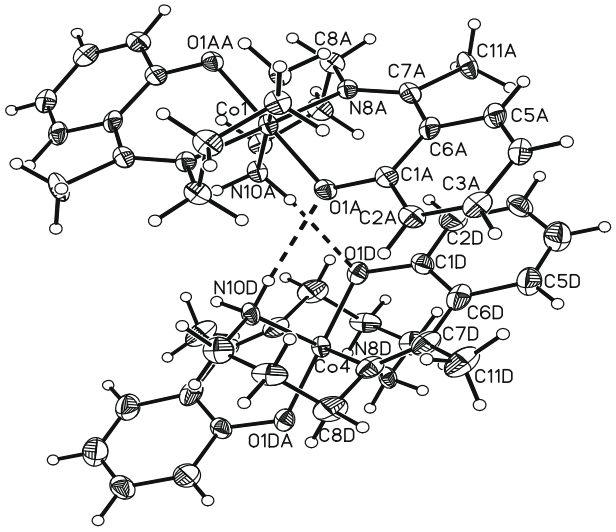


Fig. 5. H-bonding interactions connecting Co(1) and Co(4) mononuclear units of **1**.

cobalt centres are interconnected to each other by H-bonding, forming a 3D network as shown in Fig. 6.

3.5.2. $[Co_2(\mu\text{–}N_3)_2(L^2)_2(N_3)_2]$ (**2**)

An ORTEP diagram of **2** with the atom numbering scheme is given in Fig. 7 and bond lengths and angles are listed in Table 4. It is a centrosymmetric dinuclear unit. The two cobalt(III) centers in **2** are six coordinate with a relatively shorter metal–metal separation of 3.0555(5) Å. Both cobalt(III) centers have slightly distorted octahedral coordination geometries, a consequence of the coordination of

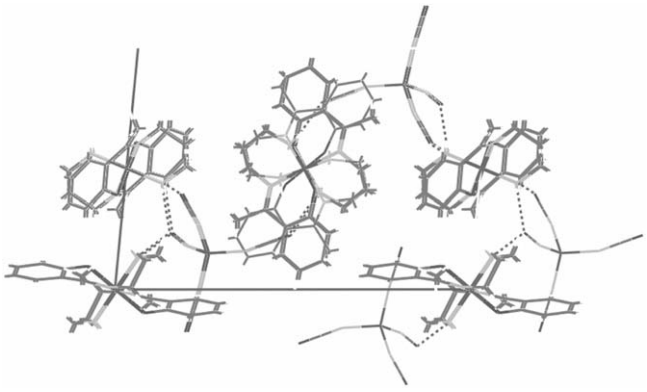


Fig. 6. Packing diagram of **1**, viewed down the *a*-axis.

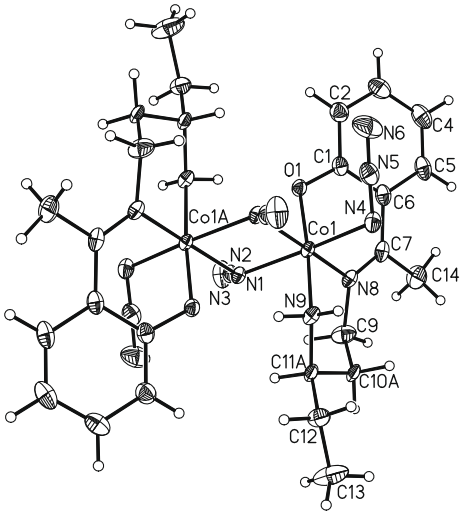


Fig. 7. ORTEP view of **2** drawn with 50% probability ellipsoids.

Table 4
Selected bond lengths (Å) and bond angles (°) for **2**.

Bond lengths (Å)		Bond lengths (Å)	
Co(1)–O(1)	1.8832(12)	Co(1)–N(9)	1.9757(16)
Co(1)–N(8)	1.9206(14)	Co(1)–N(1)	1.9893(14)
Co(1)–N(4)	1.9371(16)	Co(1)–N(1)#1	1.9952(14)
Bond angles (°)		Bond angles (°)	
N(8)–Co(1)–N(1)	96.44(6)	O(1)–Co(1)–N(8)	89.60(6)
N(4)–Co(1)–N(1)	171.51(6)	O(1)–Co(1)–N(4)	94.05(6)
N(9)–Co(1)–N(1)	88.75(7)	N(8)–Co(1)–N(4)	91.53(7)
O(1)–Co(1)–N(1)#1	87.02(6)	O(1)–Co(1)–N(9)	174.91(6)
N(8)–Co(1)–N(1)#1	175.02(6)	N(8)–Co(1)–N(9)	95.17(6)
N(4)–Co(1)–N(1)#1	92.35(6)	N(4)–Co(1)–N(9)	87.61(7)
N(9)–Co(1)–N(1)#1	88.10(6)	–	–

the tridentate N_2O donor ligand $(\mathbf{L^2})^-$ and three azide ions. The equatorial sites of both cobalt(III) centers are occupied by four nitrogen atoms: one imine nitrogen atom of the deprotonated Schiff base, two azido nitrogen atoms coordinating in an *end-on* fashion and another terminally coordinated azido nitrogen atom. The two axial sites of each distorted octahedral cobalt(III) center are occupied by one deprotonated phenoxo oxygen atom and the nitrogen atom of the uncondensed amine of $(\mathbf{L^2})^-$. In the dinuclear unit, the imine nitrogen, the *end-on* and the two terminally coordinating azide ions are displaced by 0.052(1), 0.054(1) and 0.056(1), 0.057(1) Å, respectively, from the N_4 equatorial plane. The two $\mu_{1,1}$-bridging azide ions and the two terminally coordinated azide ions are almost linear, with N–N–N angles ranging from 177.22° to 177.7°. The 3+ oxidation state assigned to both cobalt ions is attributed to the coordination of the two terminal azide ions to each cobalt center. Both intramolecular and intermolecular hydrogen bonding interactions are found in **2** (Table 5). All four hydrogen atoms of the two uncondensed Schiff base $-NH_2$ functionalities participate in hydrogen bonding. Two hydrogen atoms participate

Table 5
Hydrogen bond parameters for **2**.

D–H···A	d(D–H) Å	d(H···A) Å	d(D···A) Å	<(DHA) (°)
N(9)–H(9N)···N(2)	0.87(2)	2.61(2)	2.954(2)	105(2)
N(9)–H(9N)···O(1)#1	0.87(2)	2.08(2)	2.901(2)	156(2)
N(9)–H(9M)···N(3)#2	0.86(2)	2.54(2)	3.356(2)	159(2)

Symmetry transformations used to generate equivalent atoms: #1, $-x$, $-y$, $-z+1$; #2, $x+1$, y, z.

in intermolecular H-bonding interactions with the nitrogen atoms of the *end-on* bridging azide ions on two adjacent molecules whilst the other two hydrogen atoms form intramolecular hydrogen bonds with the deprotonated phenoxo oxygen atoms. Thus the dinuclear units are interconnected to each other by intermolecular H-bonding interactions to form a 1D chain (Fig. 8).

3.5.3. $[(H_2O)_2Co(\mu\text{-}N_3)_2(\mu\text{-}L^3)_2Co_2(N_3)_{1.25}(CH_3O)_{0.75}]H_2O$ (**3**)

An ORTEP view of **3** with the atom labelling scheme is shown in Fig. 9, and relevant bond distances and angles are listed in Table 6. In this trinuclear complex the bond distances around the Co(1) and Co(3) centers are considerably shorter than those around the Co(2) centre, which is attributed to the differing oxidation states where Co(1) and Co(3) are 3+ whilst Co(2) is 2+ thus generating a mixed valence cobalt complex of the (Co^{III}–Co^{II}–Co^{III}) type. Unlike the similar previously reported trinuclear cobalt Schiff base complexes [34,35], the coordination modes of the deprotonated phenoxo oxygen atoms differ despite the ligand $\mathbf{H_2L^3}$ being symmetrical. Two phenoxo oxygen atoms [O(2), O(4)] of the two units of doubly deprotonated Schiff base ligands $(\mathbf{L^3})^{2-}$ are terminally coordinated whereas the immediate neighbours on the other end [O(1), O(3)] bridge two cobalt centers simultaneously, which is rarely observed

Table 6
Selected bond lengths (Å) and bond angles (°) for **3**.

Bond lengths (Å)		Bond lengths (Å)	
Co(1)–O(2)	1.910(5)	Co(2)–O(10)	2.095(6)
Co(1)–O(1)	1.929(4)	Co(2)–N(12)	2.168(6)
Co(1)–N(7)	1.947(6)	Co(2)–N(1)	2.184(6)
Co(1)–N(8)	1.934(6)	Co(3)–O(4)	1.899(6)
Co(1)–N(4)	1.947(6)	Co(3)–O(3)	1.919(5)
Co(1)–N(1)	1.995(6)	Co(3)–N(30)	1.930(6)
Co(2)–O(1)	2.054(4)	Co(3)–N(29)	1.954(7)
Co(2)–O(3)	2.072(5)	Co(3)–N(12)	1.994(6)
Co(2)–O(5)	2.083(6)	Co(3)–O(9)	1.959(8)
Bond angles (°)		Bond angles (°)	
O(2)–Co(1)–N(7)	174.9(2)	O(4)–Co(3)–N(30)	89.3(3)
O(1)–Co(1)–N(7)	86.0(2)	O(3)–Co(3)–N(30)	175.4(2)
O(2)–Co(1)–N(8)	88.7(2)	O(4)–Co(3)–N(29)	174.5(2)
O(1)–Co(1)–N(8)	175.9(2)	O(3)–Co(3)–N(29)	85.8(2)
N(7)–Co(1)–N(8)	96.4(3)	N(30)–Co(3)–N(29)	95.6(3)
O(2)–Co(1)–N(1)	86.7(2)	O(4)–Co(3)–N(12)	85.1(3)
O(1)–Co(1)–N(1)	81.3(2)	O(3)–Co(3)–N(12)	80.2(2)
N(4)–Co(1)–N(1)	172.5(2)	N(30)–Co(3)–O(9)	91.2(3)
O(1)–Co(2)–O(3)	101.59(19)	N(29)–Co(3)–O(9)	89.5(3)
O(1)–Co(2)–O(10)	169.9(2)	N(12)–Co(3)–O(9)	170.5(4)
O(5)–Co(2)–O(10)	89.7(2)	Co(1)–O(1)–Co(2)	104.9(2)
O(3)–Co(2)–N(12)	72.9(2)	Co(3)–O(3)–Co(2)	105.6(2)
O(10)–Co(2)–N(12)	92.1(2)	Co(1)–N(1)–Co(2)	98.1(2)
O(1)–Co(2)–N(1)	74.2(2)	Co(3)–N(12)–Co(2)	99.6(3)
O(5)–Co(2)–N(1)	92.4(2)	N(5)–N(4)–Co(1)	117.4(5)
N(12)–Co(2)–N(1)	168.7(2)	C(100)–O(9)–Co(3)	117.2(8)

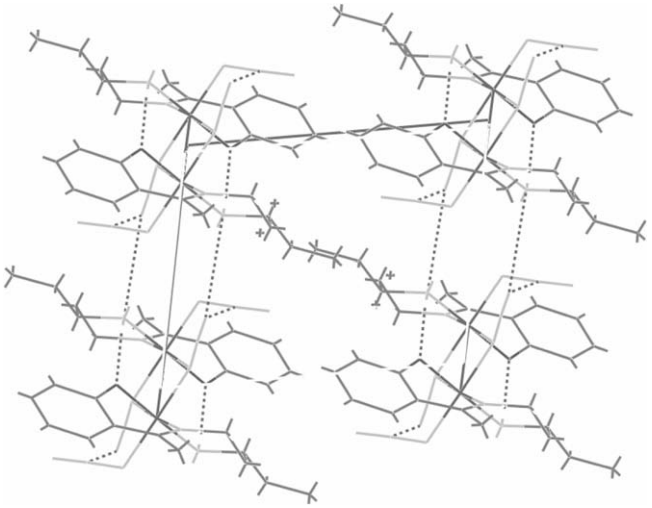


Fig. 8. Hydrogen bonding in **2** resulting in a 1D polymeric chain structure (H-bonding shown as dotted lines down the *c*-axis).

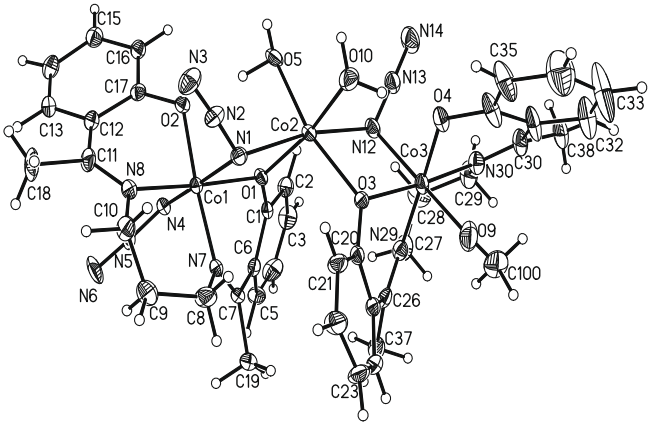


Fig. 9. ORTEP view of **3** drawn with 30% probability ellipsoids. The sites occupied by O9 and C100 are 75% MeO and 25% N_3. The minor azide is not shown and there is one molecule of water disordered over three sites.

in such salen-type Schiff base complexes [34,35,57]. Thus there are actually two different kinds of phenolato oxygen atoms present in the ligand: one of them is terminally coordinated to the individual cobalt centers and the other is in a μ-bridging mode which helps to interconnect the two adjacent cobalt centers. Co(1) has a six coordinated distorted geometry in which N(8), bridging O(1) of another unit of $(\mathbf{L^3})^{2-}$ and N(1), N(4) of the *end-on* and terminally coordinated azide ions constitute the equatorial plane. The axial sites of Co(1) are occupied by N(7) and the terminally coordinated O(2) atom of $(\mathbf{L^3})^{2-}$. Similarly Co(3) also resides in a six coordinated distorted octahedral geometry, but the equatorial sites are occupied by N(30), bridging O(3) of $(\mathbf{L^3})^{2-}$, *end-on* bridging N(12) atom of

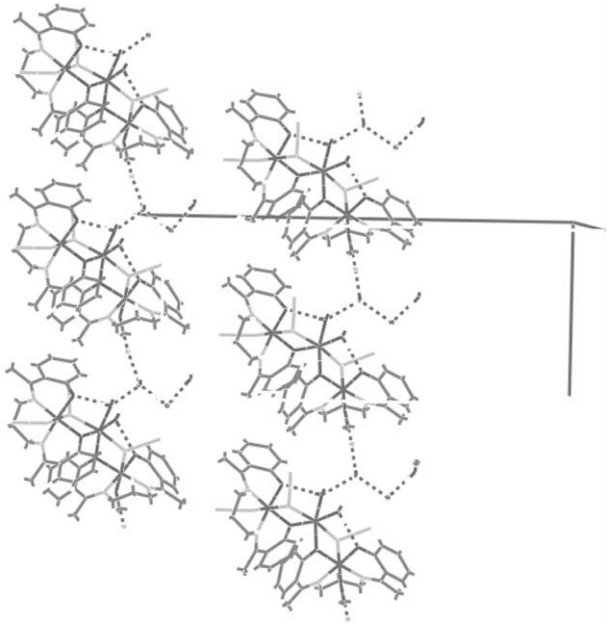


Fig. 10. Hydrogen bonded 1D polymeric chain structure of **3** (H-bonding shown as dotted lines down the *a*-axis).

the azido ligand and a terminally coordinated O(9) atom of the deprotonated methanol molecule. The two axial sites of Co(3) are occupied by N(29) and the terminally coordinated O(4) of $(\mathbf{L^3})^{2-}$. The central Co(2) center, being a d^7 species, is subjected to a *z*-out Jahn–Teller distortion and resides in a highly distorted octahedral geometry. The equatorial sites are occupied by O(5) and O(10) atoms of two water molecules and O(1) and O(3) atoms of the two μ-bridging phenoxo oxygens. The relatively longer axial sites are occupied by the N(1) and N(12) atoms of the two *end-on* bridging azido ligands connecting Co(2) with the adjacent Co(1) and Co(3) centers. The two imine nitrogen and the two deprotonated phenoxo oxygens of the Schiff base coordinated to Co(1) ion lie in the same plane, but the two aromatic rings of 2-hydroxyacetophenone and the three carbon atoms of the 1,3-diamino propane constituting the ligand $(\mathbf{L^3})^{2-}$ lie in three different planes. The dihedral angle between the planes containing the two aromatic rings with the almost planar N(7)N(8)O(1)O(2)Co(1) are 46.33° and 54.68° and the dihedral angle between the planes containing the two aromatic rings is 79.78°. Similarly for the other unit of the deprotonated $(\mathbf{L^3})^{2-}$ coordinated to Co(3) it is found that the dihedral angle between the planes containing the two aromatic rings with the almost planar N(29)N(30)O(3)O(4)Co(3) are 40.7° and 52.88° and the dihedral angle between the planes containing the two aromatic rings is 86.56°. Such dihedral angles suggest the coexistence of two saddle shaped moieties in **3** generated by the two Schiff base ligands coordinated to the Co(1) and Co(3) centers. Another interesting conformational vanity in the complex is that of the two six-membered rings, the one containing Co(1), the azomethine nitrogens and the three carbon atoms of the connecting 1,3-diamino propane is in a chair conformation whereas the other six-membered ring containing Co(3), the azomethine nitrogens and the three carbon atoms of the connecting 1,3-diamino propane is in a boat conformation. The hydrogen atoms of the two water molecules coordinated to Co(2) participate in intramolecular H-bonding with the nitrogen atoms of the *end-on* bridging azide ions and with the singly coordinated deprotonated oxygen atom of the Schiff base ligand. One of the hydrogen atoms of a water molecule coordinated to Co(2) participates in intermolecular hydrogen bonding with the oxygen atom of the disordered water molecule residing in the lattice. The oxygen atom of the lattice water molecule is further interconnected by hydrogen bonding to one of the hydrogen atoms of the deprotonated methanol molecule of the adjacent trinuclear unit. Thus the adjacent trinuclear units are interconnected by H-bonding interactions to generate a 1D polymeric chain (Fig. 10). The H-bonding parameters of **3** are listed in Table 7.

3.6. DNA binding

The DNA binding abilities of **1**, **2** and **3** were examined by UV–Vis absorption spectroscopy using calf-thymus DNA (CT-DNA) at biological pH. The stability of all three complexes in 50 mM Tris–HCl/NaCl buffer (pH 7.2) at room temperature was monitored by UV–Vis spectroscopy for 24 h and liberation of the ligand was not observed under these conditions. These suggest that the complexes are stable under the conditions studied and can be titrated with CT-DNA. Before titrating the complexes with CT-DNA, control experiments with the cobalt ion and the respective Schiff bases ($\mathbf{HL^1}$, $\mathbf{HL^2}$ and $\mathbf{H_2L^3}$) were performed with CT-DNA. The DNA absorption peak obtained for a particular concentration of CT-DNA was found to remain unaffected by increasing the cobalt ion concentration. Moreover no significant changes were observed at the three different regions (366–368, 292–295 and 256–260 nm) where the characteristic charge transfer bands appear in the spectra of **1**, **2** and **3**. Similar titration methods were adopted for $\mathbf{HL^1}$, $\mathbf{HL^2}$ and $\mathbf{H_2L^3}$ with CT-DNA in order to investigate whether certain changes appeared within the regions 366–368, 292–295 and 256–260 nm for the respective free Schiff bases. On varying the CT-DNA concentration with a constant amount of $\mathbf{HL^1}$, $\mathbf{HL^2}$ and $\mathbf{H_2L^3}$ it was found that although the 260 nm peak of the CT-DNA increased with increasing DNA concentration, no charge transfer bands at 366–368, 292–295 and 256–260 nm were detected for the respective Schiff bases. This clearly indicates that the characteristic charge transfer bands for **1**, **2** and **3** appearing at 366–368, 292–295 and 256–260 nm are of LMCT origin. The control studies ensure that the results obtained for **1**, **2** and **3** with CT-DNA are not due to the interaction of the cobalt ion with CT-DNA nor that of the free Schiff bases with CT-DNA.

The potential CT-DNA binding ability of **1**, **2** and **3** was studied by UV spectroscopy by following the intensity changes of the LMCT bands at 366–368, 292–295 and 256–260 nm for the respective complexes. All the complexes were kept in buffer solution of the order of 5 μM and it was found that on increasing the concentration of CT-DNA from 10 to 120 μM **1** shows an appreciable hypochromism whereas for **2** only a small degree of hypochromism was observed (shown in Fig. 11). The trinuclear complex **3** shows a reluctance to DNA binding as neither hyperchromism nor hypochromism were detected. From the observed spectral changes the value of the apparent binding constant K_{app} ($4.096 \times 10^4\ l\ mol^{-1}$ for **1** and $1.54 \times 10^4\ l\ mol^{-1}$ for **2**) was determined by regression analysis using Eq. (1) (under Section 2.3). As we know that the extent of hypochromism is commonly consistent with the strength of the DNA binding interaction [73], we can rationalise the DNA binding affinity of the three complexes by studying the rate of hypochromism as shown in the UV–Vis spectra of the complexes. It is very clear from the DNA binding constants of **1** and **2** that on increasing the nuclearity of the cobalt complexes from mononuclear to dinuclear there is a significant drop in the DNA binding ability, which can be attributed to the aspect of charge neutrality in **2**. Complex **1** comprises of relatively smaller mononuclear cationic units, and this is the reason why it shows a high affinity for the electron rich DNA double helix and therefore undergoes easy binding with the DNA strands, but **2**, being a neutral dinuclear unit, shows a lesser degree of DNA binding compared to **1**. On moving to the trinuclear complex **3**, we found that it is inactive toward DNA binding which can be explained by the non-planarity of the crystal structure of **3** which prevents the molecule from interacting with the strands of DNA.

Table 7
Hydrogen bond parameters of **3**.

D–H···A	d(D–H) Å	d(H···A) Å	d(D···A) Å	<(DHA) (°)
O(1W)–H(11W)···O(10)	0.77	2.55	3.080(14)	127.8
O(10)–H(10X)···O(4)	0.86(4)	1.79(5)	2.606(9)	158(10)
O(10)–H(10X)···N(12)	0.86(4)	2.88(10)	3.070(9)	95(7)
O(10)–H(10X)···N(13)	0.86(4)	3.08(10)	3.303(10)	97(7)
O(10)–H(10Y)···O(1W)	0.92(4)	2.26(6)	3.080(14)	149(8)
O(10)–H(10Y)···O(2X)#1	0.92(4)	2.85(8)	3.43(2)	122(7)
O(5)–H(51)···O(1W)	0.88(4)	2.02(6)	2.668(14)	130(7)
O(5)–H(52)···O(2)	0.95(4)	1.73(5)	2.622(7)	155(8)

Symmetry transformations used to generate equivalent atoms: #1, $-x+1/2$, $y-1/2$, $z-1/2$.

4. Conclusions

In this paper the authors have skillfully increased the nuclearity of **1**, **2** and **3** by complexing cobalt(II) ions with three different Schiff bases obtained by selective and non-selective condensation of 1,3-diamines with 2-hydroxyacetophenone. By localising the two amine functionality at the 1,3-position in all the three Schiff bases we observed significant structural variations for **1**, **2** and **3** which have been elaborately described in this paper. This work

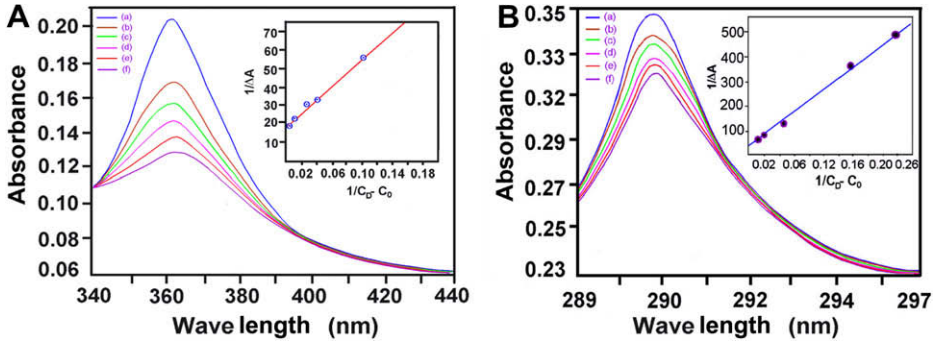


Fig. 11. (**A**) Absorption spectra of **1** (5.4 μM) in the absence (a) and in presence of increasing amounts of CT-DNA (0–120 μM; b–f) at room temperature in 5 mM Tris–HCl/NaCl buffer (pH 7.2). Inset: double reciprocal plot of $1/\Delta A$ against $1/(C_D - C_O)$; K_{app}: 4.096×10^4 l mol^{-1} for **1**. (**B**) Absorption spectra of **2** (5 μM) in the absence (a) and in presence of increasing amounts of CT-DNA (0–100 μM; b–f) at room temperature in 5 mM Tris–HCl/NaCl buffer (pH 7.2). Inset: double reciprocal plot of $1/\Delta A$ against $1/(C_D - C_O)$; K_{app}: 1.54×10^4 l mol^{-1} for **2**.

adds two new contributions to the rare class of mixed valence cobalt complexes and is supported by EPR analysis. From the DNA binding constants of the complexes it can be concluded that **1** shows greater affinity to DNA binding than that of **2**, whereas **3** was found to be inactive for DNA binding.

Acknowledgements

A. Ray is thankful to the Council of Scientific and Industrial Research New Delhi, Govt. of India, for financial support. The authors also acknowledge the financial help obtained from the All India Council for Technical Education, New Delhi, Govt. of India. A. Ray conveys her special thanks to Prof. Saurabh Das of Jadavpur University for enriching her with his valuable suggestions.

Appendix A. Supplementary data

CCDC 636957, 678480 and 664110 contain the supplementary crystallographic data for complexes **1**, **2** and **3**. These data can be obtained free of charge via http://www.ccdc.cam.ac.uk/conts/retrieving.html, or from the Cambridge Crystallographic Data Centre, 12 Union Road, Cambridge CB2 1EZ, UK; fax: (+44) 1223-336-033; or e-mail: deposit@ccdc.cam.ac.uk. Supplementary data associated with this article can be found, in the online version, at doi:10.1016/j.poly.2008.12.040.

References

[1] F.A. Cotton, G. Willkinson, C.A. Murrilo, M. Bochmann, Advanced Inorganic Chemistry, 6th ed., Wiley, New York, 1999. p. 598.
[2] V.G. Makhankova, O.Y. Vassilyeva, V.N. Kokozay, J. Reedijk, G.A. Vanalbada, J. Jezierska, B.W. Skelton, Eur. J. Inorg. Chem. (2002) 2163.
[3] C. Demunno, F. Cipriani, D. Armentano, M. Julve, J.A. Real, New J. Chem. 25 (2001) 1031.
[4] D.M. Ciurtin, Y.B. Dong, M.D. Smith, T. Barclay, H.C. Zurloye, Inorg. Chem. 40 (2001) 2825.
[5] C.J. Matthews, L.K. Thompson, S.R. Parsons, Z. Xu, D.O. Miller, S.L. Heath, Inorg. Chem. 40 (2001) 4448.
[6] A. Sreekanth, U.L. Kala, C.R. Nayar, M.R.P. Kurup, Polyhedron 23 (2004) 41.
[7] T. Shiga, H. Oshio, Polyhedron 26 (2007) 1881.
[8] S. Taşcıoğlu, B. Yalçın, T.M. Nasrullayeva, Ö. Andaç, O. Büyükgüngör, A. Aydın, A. Akber Medjidov, Polyhedron 25 (2006) 1279.
[9] C.P. Pradeep, P.S. Zacharias, S.K. Das, Eur. J. Inorg. Chem. (2007) 5377.
[10] O.R. Evans, W. Lin, Acc. Chem. Res. 35 (2002) 511.
[11] L. Sacconi, M. Ciampolini, G.P. Speroni, Inorg. Chem. 4 (1965) 1116.
[12] R. Dreos, G. Nardin, L. Randaccio, P. Siega, G. Tauzher, V. Vrdoljak, Inorg. Chim. Acta 349 (2003) 239.
[13] R. Lescouezec, J. Vaissermann, C. Ruiz-Perez, F. Lloret, R. Carrasco, M. Julve, M. Verdager, Y. Dromzee, D. Gatteschi, W. Wernsdorfer, Angew. Chem., Int. Ed. 42 (2003) 1483.
[14] L.M. Toma, R. Lescouezec, F. Lloret, M. Julve, J. Vaissermann, M. Verdager, Chem. Commun. (2003) 1850.
[15] F.B. Hulsbergen, R.W.M. Ten Hoedt, G.C. Verschoor, J. Reedijk, A.L. Spek, J. Chem. Soc., Dalton Trans. (1983) 539.
[16] K. Sakai, Y. Yamada, T. Tsubomura, M. Yabuki, M. Yamaguchi, Inorg. Chem. 35 (1996) 542.
[17] T. Nakamoto, Q. Wang, Y. Miyazaki, M. Sorai, Polyhedron 21 (2002) 1299.
[18] J.K. Beattie, J.A. Klepetko, A.F. Masters, P. Turner, Polyhedron 22 (2003) 947.
[19] T.S. Billson, J.D. Crane, O.D. Fox, S.L. Heath, Inorg. Chem. Commun. 13 (2000) 718.
[20] A.A. Gridnev, Ya.D. Lampeka, B.R. Smirnov, K.B. Yatsimirskii, Theor. Exp. Chem. 23 (2004) 293.
[21] Q.L. Li, J. Huang, Q. Wang, N. Jiang, C.Q. Xia, H.H. Lin, J. Wu, X.Q. Yu, Bioorg. Med. Chem. 14 (2006) 4151.
[22] C.S. Gail, C.T. William, J. Am. Chem. Soc. 117 (1995) 3983.
[23] Q. Huang, Z.Q. Pan, P. Wang, Z.P. Chen, X.L. Zhang, H.S. Xu, Bioorg. Med. Chem. Lett. 16 (2006) 3030.
[24] M.C.B. Oliveira, M.S.R. Couto, P.C. Severino, T. Foppa, G.T.S. Martins, B. Szpoganicz, R.A. Peralta, A. Neves, H. Terenzi, Polyhedron 24 (2005) 495.
[25] R. Hettich, H.J. Schneider, J. Am. Chem. Soc. 119 (1997) 5638.
[26] N.E. Dixon, R.J. Geue, J.N. Lambert, S. Moghaddas, D.A. Pearce, A.L. Sargeson, Chem. Commun. (1996) 1287.
[27] B. Peng, H. Chao, B. Sun, F. Gao, L.-N. Ji, Transit. Met. Chem. 32 (2007) 271.
[28] R.L. De, K. Samanta, K. Maiti, E. Keller, Inorg. Chim. Acta 316 (2001) 113.
[29] Sk.H. Rehaman, H. Chowdhury, D. Bose, R. Ghosh, C.-H. Hung, B.K. Ghosh, Polyhedron 24 (2005) 1755.
[30] H.-J. Kim, W. Kim, A.J. Lough, B.M. Kim, J. Chin, J. Am. Chem. Soc. 127 (2005) 16776.
[31] A.A. Khander, B. Shaabani, F. Belaj, A. Bakhtiari, Polyhedron 25 (2006) 1893. and references therein.
[32] M. Fondo, N. Ocampo, A.M. Garcia-Deibe, M. Corbella, M.S. El Fallah, J. Cano, J. Sanmartin, M.R. Bermejo, J. Chem. Soc., Dalton Trans. (2006) 4905.
[33] C. Fukuhara, E. Asato, T. Simoji, K. Kastura, M. Mori, K. Matsumoto, S. Ooi, J. Chem. Soc., Dalton Trans. (1987) 1305.
[34] S. Chattopadhyay, G. Bocelli, A. Musatti, A. Ghosh, Inorg. Chem. Commun. 9 (2006) 1053.
[35] S. Banerjee, J.-T. Chen, C.-Z. Lu, Polyhedron 26 (2007) 686.
[36] H. Kawasaki, G. Sakane, T. Shibahara, Inorg. Chem. Commun. 8 (2005) 777.
[37] T.S. Billson, J.D. Crane, O.D. Fox, S.L. Heath, Inorg. Chem. Commun. 3 (2000) 718.
[38] B. Ballet, A. Bino, S. Cohen, H. Rubin, T. Zor, Inorg. Chim. Acta 188 (1991) 91.
[39] D.A. Pantazis, J.E. McGrady, J. Am. Chem. Soc. 128 (2006) 4128.
[40] M. Calligaris, G. Nardin, L. Randaccio, J. Chem. Soc., Dalton Trans. (1973) 419.
[41] N. Bresciani, M. Calligaris, G. Nardin, L. Randaccio, J. Chem. Soc., Dalton Trans. (1974) 498.
[42] A. Pasini, M. Gullotti, R. Ugo, J. Chem. Soc., Dalton Trans. (1977) 346.
[43] C.-W. Ho, W.-C. Cheng, M.-C. Cheng, S.-M. Peng, K.-F. Cheng, C.-M. Che, J. Chem. Soc., Dalton Trans. (1996) 405.
[44] P. Woodman, P.B. Hitchcock, P. Scott, Chem. Commun. (1996) 2735.
[45] K. Bernardo, S. Leppard, A. Robert, G. Commenges, F. Dahan, B. Meunier, Inorg. Chem. 35 (1996) 387.
[46] P.R. Woodman, I.J. Munslow, P.B. Hitchcock, P. Scott, J. Chem. Soc., Dalton Trans. (1999) 4069.
[47] P.R. Woodman, N.W. Alcock, I.J. Munslow, C.J. Sanders, P. Scott, J. Chem. Soc., Dalton Trans. (2000) 3340.
[48] W.A. Herrmann, M.U. Rauch, G.R.J. Artus, Inorg. Chem. 35 (1996) 1988.
[49] K.J.C. van Bommel, W. Verboom, H. Kooijman, A.L. Spek, D.N. Reinhoudt, Inorg. Chem. 37 (1998) 4197.
[50] M. Calligaris, G. Nardin, L. Randaccio, Coord. Chem. Rev. 7 (1972) 385.
[51] S. Yamada, Coord. Chem. Rev. 1 (1966) 415.
[52] S. Sen, P. Talukder, S.K. Dey, S. Mitra, G. Rosair, D.L. Hughes, G.P.A. Yap, G. Pilet, V. Gramlich, T. Matsushita, J. Chem. Soc., Dalton Trans. (2006) 1758.
[53] N. Mondal, D.K. Dey, S. Mitra, K.M. Abdul Malik, Polyhedron 19 (2000) 2707.

[54] B. Samanta, J. Chakraborty, S. Shit, S.R. Batten, P. Jensen, J.D. Masuda, S. Mitra, Inorg. Chim. Acta 360 (2007) 2471.
[55] S. Banerjee, M.G.B. Drew, C.-Z. Lu, J. Tercero, C. Diaz, A. Ghosh, Eur. J. Inorg. Chem. (2005) 2376.
[56] P. Mukherjee, C. Biswas, M.G.B. Drew, A. Ghosh, Polyhedron 26 (2007) 3121.
[57] A. Datta, C.R. Choudhury, P. Talukder, S. Mitra, L. Dahlenburg, T. Matsushita, J. Chem. Res. (S) (2003) 642.
[58] M.E. Reichmann, S.A. Rice, C.A. Thomas, P. Doty, J. Am. Chem. Soc. 76 (1954) 3047.
[59] S. Roy, R. Banerjee, M. Sarkar, J. Inorg. Biochem. 100 (2006) 1320.
[60] APEX2, Version 2.1, SMART, SAINT, SADABS, XPREP, XS, XL, XP, Bruker AXS Inc., Madison, Wisconsin, USA, 2004–2006.
[61] Z.-L. You, H.-L. Zhu, Z. Anorg. Allg. Chem. 630 (2004) 2754.
[62] K. Nakamoto, Infrared and Raman Spectra of Inorganic and Coordination Compounds: Theory and Applications in Inorganic Chemistry, Part-A, 5th ed., John Willey and Sons Inc., New York, 1997. p. 11.
[63] P. Talukder, A. Datta, S. Mitra, G. Rosair, M.S. El Fallah, J. Ribas, J. Chem. Soc., Dalton Trans. (2004) 4161.
[64] A.B.P. Lever, Inorganic Electronic Spectroscopy, 2nd ed., Elsevier, Amsterdam, 1984. p. 473.
[65] A. Ray, S. Banerjee, R.J. Butcher, C. Desplanches, S. Mitra, Polyhedron 27 (2008) 2409.
[66] S.A. Carabineiro, P.T. Gomes, L.F. Veiros, C. Freire, L.C.J. Pereira, R.T. Henriques, J.E. Warren, S.I. Paseu, J. Chem. Soc., Dalton Trans. (2007) 5460.
[67] V. Suni, M.R. Prathapachandra Kurup, M. Nethaji, Polyhedron 26 (2007) 5203.
[68] M.A. Hitchman, Inorg. Chem. 16 (1977) 1985.
[69] M.T. Werth, S.-F. Tang, G. Formicka, M. Zeppezauer, M.K. Johnson, Inorg. Chem. 34 (1998) 218.
[70] R. March, W. Clegg, R.A. Coxall, L. Cucurull-S'anchez, L. Lezama, T. Rojo, P. Gonzalez-Duarte, Inorg. Chim. Acta 353 (2003) 129.
[71] C. Bresson, R. Spezia, S. Esnouf, P.L. Solari, S. Coantic, C.D. Auwer, New J. Chem. 31 (2007) 1789.
[72] A. Tamayo, J. Casabo, L. Esriche, P. Gonzalez, C. Lodeiro, A.C. Rizzi, C.D. Brondino, M.C.G. Passeggi, R. Kivekas, R. Sillanpaa, Inorg. Chem. 46 (2007) 5665.
[73] S.A. Tysoe, R.J. Morgan, A.D. Baker, T.C. Strekas, J. Phys. Chem. 97 (1993) 1707.

2. Experimental

All manipulations were carried out under an atmosphere of dry argon using Schlenk and glovebox techniques. Solvents were rigorously dried with sodium benzophenoate. *N*,*N*-Dimethylaminoethanol (dmaeH) was purchased from Aldrich and purified by refluxing over K_2CO_3 for 10 h and distilled immediately before use, while $Ba(dmae)_2$ was prepared by the literature procedure [19]. All other reagents were also purchased from Aldrich.

Elemental analyses were performed using a CHN analyzer LECO model CHNS-932. The melting point was determined in a capillary tube using an electrothermal melting point apparatus, model MP.D Mitamura Riken Kogyo (Japan) and is uncorrected. The FT-IR spectrum was recorded on a single reflectance ATR instrument (4000–400 cm^{-1}, resolution 4 cm^{-1}). TGA measurements were carried out by using a Seiko SSC/S200 model at a heating rate of 10 °C/min under N_2 flow. The mass spectrum was recorded on a Kratos concept IS instrument. XRPD studies were carried out by means of a Bruker AXS D8 diffractometer using monochromatic Cu Kα radiation. The morphology of the films was characterized by a FEG-SEM Philips XL30. Samples were carbon coated before observation and EDAX-DX_4 was used to calculate the composition (metallic ratio) of the films. The thickness of the films was measured with a Dektak 8 Stylus profilometer. The voltage–current characteristics of the thin films were measured with a Jandel Voltmeter, Model RM3, by the four-probe method.

2.1. Synthesis of $Ba_2(\mu\text{-}OAc)_4(OAc)_2Cu_4(\mu\text{-}dmae)_4(OH)_2$ (**1**)

To 0.5 g (2.5 mmol) of copper(II) acetate monohydrate [$Cu(OAc)_2 \cdot H_2O$] suspended in 20 ml of toluene in a 50 ml Schlenk tube fitted with a magnetic stirrer and a nitrogen line, was added drop by drop a solution of 0.35 g (1.12 mmol) of $Ba(dmae)_2$ in toluene. The mixture was stirred for 2 h at room temperature and then heated to 60 °C on oil bath for another 2 h. The excess of $Cu(OAc)_2 \cdot H_2O$ was separated by cannula filtration. The filtrate was evaporated to dryness under vacuum and the solid was redissolved in 5 ml of tetrahydrofuran to give a 70% yield of blue crystals after several days at room temperature, m.p.: 95 °C. The analysis of the resulting product resembled that for $Ba_2(\mu\text{-}OAc)_4(OAc)_2Cu_4(\mu\text{-}dmae)_4(OH)_2$, as determined by X-ray crystallography. *Anal.* Calc. for $C_{28}H_{60}Ba_2Cu_4N_4O_{18}$: C, 26.49; H, 4.76; N, 4.41. Found: C, 26.39; H, 4.56; N, 3.52%. FT-IR (KBr, cm^{-1}): 3421br, 2905w, 1654vs, 1554m, 1406s, 1340m, 1067m, 1020m, 595m, 528w, 503w, 480w. APCI-MS: *m*/*z* calcd. (found) 1252.64 (1251.7), $[Ba_2Cu_4(dmae)_4(OAc)_6(OH)]^+$; 977.98 (978.1), $[Cu_4(dmae)_4(OAc)_6(OH)]^+$; 775.23 (777.1), $[Ba_2(dmae)_3(OAc)_4]^+$; 620.46 (620.8), $[Ba_2Cu(dmae)(OAc)_3(OH)]^+$; 585.61 (586.5), $[Cu_2(dmae)_3(OAc)_3(OH)]^+$; 548.53 (547.4), $[Cu_4(dmae)_2(OAc)_2]^+$; 544.03 (545.2), $[Cu_3(dmae)_2(OAc)_3]^+$; 494.76 (494.8), $[Ba(dmae)_3(OAc)(OH)_2]^+$; 448.68 (448.3), $[Ba(dmae)_2(OAc)_2(OH)]^+$; 424.09 (423.7), $[BaCu(dmae)(OAc)_2(OH)]^+$; 421.43 (422.7), $[Cu_2(dmae)_2(OAc)_2]^+$; 350.3 (351.2), $[Cu_2(dmae)(OAc)_2(OH)]^+$; 320.35 (319.1), $[Cu_2(dmae)_2(OH)]^+$; 279.18 (279.6), $[Cu_2(OAc)_2(OH)_2]^+$; 220.13 (219.5), $[Cu_2(OAc)(OH)_2]^+$; 139.59 (139.7), $[Cu(OAc)(OH)]^+$. TGA: 90–130 °C (3.13 wt% loss), 130–210 °C (21.76 wt% loss), 210–367 °C (residue 48.96%).

2.2. X-ray crystallography

Single crystal X-ray data were collected on a Bruker Smart Apex CCD diffractometer using Mo radiation. Crystallographic and structure refinement data for complex (**1**): Empirical formula; $C_{28}H_{60}Ba_2Cu_4N_4O_{18}$, formula wt. 1269.64, temp. = 100(2) K, λ = 0.71073 Å, triclinic, space group $P\bar{1}$, a = 8.9330(11), *b* = 9.8500(12), *c* = 13.4880(17) Å, α = 101.705(2), β = 94.685(2), γ = 106.671(2)°, *V* = 1100.8(2) $Å^3$, *Z* = 1, ρ_{calc} = 1.915 Mg m^{-3}, μ = 3.728 mm^{-1}, 9204 reflections collected, 4906 unique (R_{int} = 0.0234), Refinement was by full-matrix least-squares on F^2; goodness-of-fit on F^2 was 1.114. Final *R* indices where $I > 2\sigma(I)$ are R_1 = 0.0759 and wR_2 = 0.2112. The *R* indices (all data)[a] are R_1 = 0.0838 and wR_2 = 0.2160 [a] $R_1 = \sum ||F_o| - |F_c|| / \sum |F_o|$ [b] $wR_2 = [\sum w(F_o^2 - F_c^2)^2 / \sum w(F_o^2)^2]^{1/2}$. The largest difference peak and hole are 4.016 and −3.689 e $Å^{-3}$, respectively.

2.3. Deposition of thin films

Thin film deposition was performed via aerosol-assisted chemical vapour deposition (AACVD) by dissolving 0.07 g of the precursor in 10 ml toluene in a two neck round bottomed flask. On one side, the flask was connected via tubing to a quartz reactor loaded with 2.5 × 1 cm glass substrates inside a carbolite tube furnace and a flow of argon gas was regulated using a Platon flow gauge on the other. The flask was set in an ultrasonic humidifier (Pifco) (Fig. 1) equipped with a piezoelectric modulator that generated droplets of the precursor solution which were then transferred by the carrier gas into the reactor chamber. Glass substrates were washed in concentrated nitric acid, subsequently washed with deionized water several times and then oven dried.

The deposition was carried out at 400 °C with a flow rate of 130 ml/min on glass substrates for 2.5 h.

3. Results and discussion

3.1. Synthesis and characterization

The synthetic procedure used for the heterobimetallic complex (**1**) is simple and involves the mixing of the reactants in the appropriate stoichiometric ratios. Dissolution of $Cu(OAc)_2 \cdot H_2O$ in the reaction mixture indicates completion of the reaction as given in Eq. (1).

$$4Cu(OAc)_2 \cdot H_2O + 2Ba(dmae)_2 \rightarrow Ba_2(dmae)_4Cu_4(OAc)_6(OH)_2 + 2HOAc + 2H_2O \quad (1)$$

Compound (**1**) was characterized by its melting point, elemental analysis, FT-IR spectroscopy, mass spectrometry and its structure was established by single-crystal X-ray diffraction. In the FT-IR spectrum, an absorption band at 3421 cm^{-1} is due to the O–H group in the complex. The three strong absorption bands between 1400 and 1700 cm^{-1} for the carboxylate group indicate the presence of different coordination modes for the acetate ligand [20–23]. The absorptions at low frequency are due to the ν(M–O) and ν(M–N) vibrations, those at 595 and 528 cm^{-1} are characteristic of Ba–OAc derivatives, whereas those at 503 and 480 cm^{-1} more likely belong to Cu(μ,η^2dmae) [24]. The atmospheric pressure chemical ion-

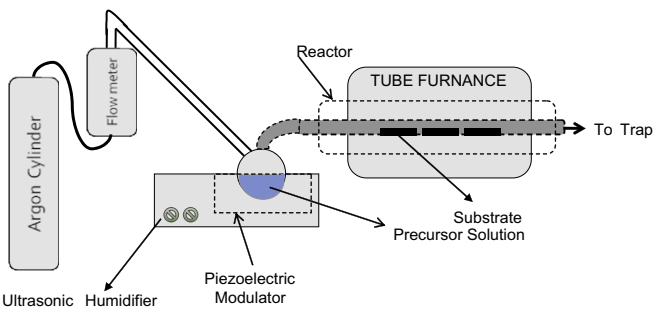


Fig. 1. Schematic diagram of the aerosol-assisted chemical vapour deposition process.

ization (APCI) negative scan mass spectrum does not exhibit a molecular ion peak for the complex. The complex breaks down under MS conditions and gives various fragments of different m/z ratios. The heaviest fragment observed is for $[Ba_2Cu_4(dmae)_4(OAc)_6(OH)]^+$ at m/z (1251.7), with the base peak at m/z (423.7) corresponding to $[BaCu(dmae)(OAc)_2(OH)]^+$, thus showing the instability of the complex under the MS conditions.

3.2. Structural analysis

Selected bond lengths and bond angles for (**1**) are listed in Table 1 and its molecular structure is shown in Fig. 2. The six metal atoms are linked together by oxygens belonging to the chelating-bridging dmae and acetate groups. The coordination sphere of the metal atoms in the complex is satisfied by the donor oxygen and nitrogen atoms of dmae and acetate ligands. The geometric environment of each metal centre is shown in Fig. 3.

Table 1
Selected bond distances (Å) and angles (°) for complex (**1**).

Ba(1)–O(5)	2.573(13)	O(2)–Cu(1)–O(6)	100.1(5)
Ba(1)–O(1)A	2.580(10)	O(2)–Cu(1)–O(1)	170.6(4)
Ba(1)–O(4)A	2.771(12)	O(6)–Cu(1)–O(1)	78.0(4)
Ba(1)–O(7)A	2.955(12)	O(2)–Cu(1)–N(1)	94.9(5)
Ba(1)–O(4)	2.969(11)	O(6)–Cu(1)–N(1)	160.2(5)
Cu(1)–O(2)	1.922(11)	O(1)–Cu(1)–N(1)	85.1(5)
Cu(1)–O(6)	1.962(10)	O(2)–Cu(1)–O(4)	101.1(4)
Cu(1)–O(1)	1.969(10)	O(6)–Cu(1)–O(4)	96.8(4)
Cu(1)–N(1)	2.048(13)	O(1)–Cu(1)–O(4)	88.3(4)
Cu(1)–O(4)	2.262(11	N(1)–Cu(1)–O(4)	92.8(5)
Cu(1)-Cu(2)	2.857(3)	O(6)–Cu(2)–O(8)	169.8(5)
Cu(2)–O(6)	1.931(10)	O(6)–Cu(2)–O(1)	78.7(4)
Cu(2)–O(8)	1.937(10)	O(8)–Cu(2)–O(1)	94.8(4)
Cu(2)–O(1)	1.973(10)	O(6)–Cu(2)–N(2)	84.3(5)
Cu(2)-N(2)	2.000(12)	O(8)–Cu(2)–N(2)	101.0(5)
Cu(2)–O(9)	2.295(11)	O(1)–Cu(2)–N(2)	161.5(5)
Cu(2)–O(7)	2.763(12)	O(6)–Cu(2)–O(9)	94.3(4)
		O(8)–Cu(2)–O(9)	94.2(4)
O(5)–Ba(1)–O(1)A	79.8(3)	O(1)–Cu(2)–O(9)	95.7(4)
O(5)–Ba(1)–O(4)A	94.9(4)	N(2)–Cu(2)–O(9)	92.6(5)
O(1)A–Ba(1)–O(4)A	67.0(3)	Cu(1)–O(1)–Ba(1)A	103.2(4)
O(5)–Ba(1)–O(7)A	92.3(4)	Cu(2)–O(1)–Ba(1)A	97.0(4)
O(1)A–Ba(1)–O(7)A	72.4(3)	Cu(1)-O(4)-Ba(1)A	90.3(4)
O(4)A–Ba(1)–O(7)A	136.6(3)	Ba(1)A–O(4)–Ba(1)	89.4(3)
O(5)–Ba(1)–O(4)	46.3(3)	Cu(2)–O(6)–Cu(1)	94.4(4)
O(1)A–Ba(1)–O(4)	120.2(3)	Cu(1)–O(4)–Ba(1)	144.0(5)
O(4)A–Ba(1)–O(4)	90.6(3)	Cu(1)–O(1)–Cu(2)	92.9(4)
O(7)A–Ba(1)–O(4)	123.5(3)		

Cu(1) is almost square pyramidal in geometry, having a coordination number of five, with a CuO_4N ligation set composed of a chelating-bridging dmae group [N(1),O(1)], {the oxygen of which is triply bridged to Cu(1), Cu(2) and Ba(1)}, an oxygen atom of the bridged dmae ligand [O(6)], connecting Cu(1) with the Cu(2) atom, an oxygen atom of the triply bridged acetate group [O_4], acting as bridge between Cu(1) and both Ba atoms, and an oxygen atom of the monodentate acetate group [O(2)]. The geometry of Cu(1) is not perfectly square pyramidal due to an O(2)–Cu(1)–O(4) angle of 101.1(4)° (greater than 90°) and O(6)–Cu(1)–O(4) 'bite' angle of 96.8(4)° (greater than 90°). Also the copper- oxygen bond distance of Cu(1) to the apical oxygen atom O(4) is much longer (2.262(11) Å) than all the other Cu–O bond lengths around Cu(1), which range from 1.922(11) to 1.969(10) Å, and they are close in value to the sum of the ionic radii, 1.92 Å. The coordination environment of Cu(1) is further augmented by a weak Cu···Cu interaction with Cu(2), with a metal–metal separation of 2.857(3) Å.

If the Cu···Cu interaction is omitted, Cu(2) has a coordination number of six with a coordination environment close to octahedral, with a CuO_5N core made up of a chelating-bridging dmae group [N(2), O(6)], (the oxygen of which acts as a bridge to both Cu atoms), an oxygen atom of the bridged dmae ligand [O(1)] (connecting Cu(2) with the Cu(1) and Ba(1)A atoms), two oxygen atoms of the chelating-bridging acetate group [O(7),O(8)], (O(7) of which also binds Cu(2) with the Ba(1)A atom), and an oxygen atom of a terminal hydroxyl anion [O(9)]. The coordination environment of Cu(2) is a tetragonally elongated octahedron with an O(9)–Cu(2)–O(7) angle of 146.97° (less than 180°), O(8)–Cu(2)–O(7) 'bite' angle of 55.88° (less than 90°), and an O(8)–Cu(2)–N(2) angle of 101.0(5)° (greater than 90°). Again the copper- oxygen bond distances of Cu(2) to the apical oxygen atoms O(9) and O(7) are much longer (2.295(11) and 2.763(12) Å, respectively) than all the other Cu–O bond lengths around Cu(2), which compare well with the sum of the ionic radii, 1.92 Å. A distortion in the octahedral geometry around Cu^{II}(2), expected from the Jahn–Teller theorem [25], is

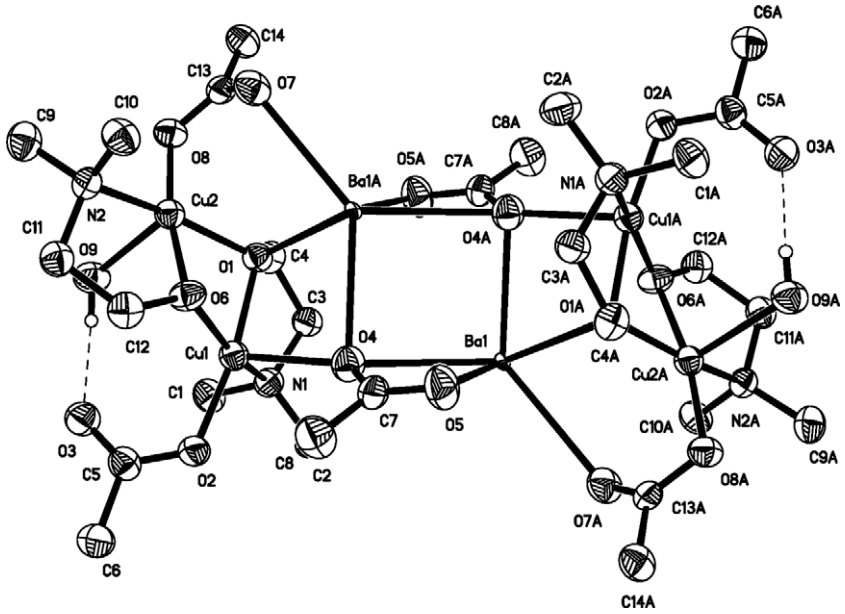


Fig. 2. ORTEP drawing showing the molecular structure of $[Ba_2(\mu\text{-}OAc)_4(OAc)_2Cu_4(\mu\text{-}dmae)_4(OH)_2]$ (**1**). Symmetry operation: #1, $-x+1$, $-y$, $-z+2$. All hydrogen atoms and the Cu···Cu interaction is omitted for clarity.

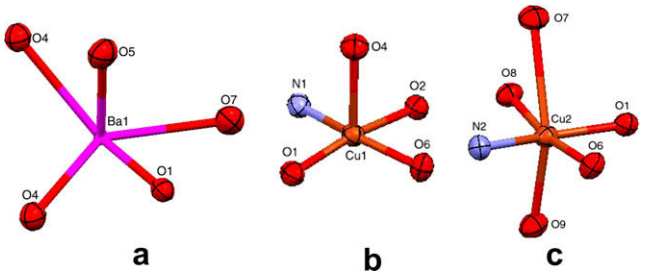


Fig. 3. The (a) distorted square pyramidal of Ba, (b) square pyramidal of Cu(1) and (c) octahedral of Cu(2) geometric spheres in complex (**1**).

due to the unequally occupied e_g (d_{z^2} and $d_{x^2-y^2}$) orbitals, the two axial oxygens O(7) and O(9) are repelled more strongly than the other four coordinating ligands.

Two different ligand sets with different 'bite' angles render the coordination sphere of the barium metal atoms irregular. Both the Ba atoms in the complex have identical geometries and the same coordination number of five, with a BaO_5 set of ligating atoms, composed of one chelating-bridging acetate group [O(4),O(5)] (the oxygen atom O(4) acts as a bridge between Cu(1), Ba(1) and Ba(1)A), the oxygen atom of a triply bridging acetate ligand [O(4)A] (connecting Cu(1)A, Ba(1) and Ba(1)A), the oxygen atom of a doubly bridged acetate ligand [O(7)A] (binding Ba(1) with Cu(2)A) and the oxygen atom of a triply bridging dmae ligand [O(1)A] (connecting Ba(1), Cu(1)A and Cu(2)A). The bonding environment around barium may be described as a distorted square pyramidal with the oxygen atom [O(5)] capping the square face. The average Ba–O distance of 2.769 Å is almost same in value as the sum of the ionic radii, 2.77 Å. All the Cu–N bond distances in the complex, ranging from 2.00 to 2.049 Å, are in good agreement with the reported values [26–28].

Both ligands coordinate in a range of coordination modes. The acetate groups are either monodentate [O(5), O(5)A], or both chelating-bridging two metals [O(7), O(8); O(7)A, O(8)A] and three metals [O(4), O(5); O(4)A, O(5)A]. As for the dmae ligands, they are chelating-bridging two metals [O(6), N(2); O(6)A, N(2)A] and chelating-bridging three metals [O(1), N(1); O(1)A, N(1)A].

Additional stability for the complex is provided by the intramolecular hydrogen bonding [O(9)–H(9)···O(3)] between the oxygen atom O(3) of the monodentate acetate group and the hydroxyl group hydrogen H(9).

3.3. Thermal decomposition studies and characterization of thin films

The thermal behaviour of complex (**1**) has been studied by thermogravimetric analysis over the range 50–500 °C, performed under an inert atmosphere of flowing nitrogen gas. The thermogram of the compound, obtained with a scanning rate of 10 °C/min is shown in the Fig. 4. The decomposition starts at 90 °C and is completed at 367 °C. The decomposition of the precursor proceeds in three steps and the maximum weight loss (approximately 26.15%) takes place between 210 and 367 °C. The residual weight of 48.96% for complex (**1**) is slightly less, but close to the expected composition for CuO–$Ba_2Cu_3O_{5+x}$ (49.2% for **1**), showing that the complex has poor sublimation properties and decomposes quantitatively to the oxide mixture according to following equation.

$$Ba_2(dmae)_4Cu_4(OAc)_6(OH)_2 \xrightarrow[400^\circ C]{AACVD} Ba_2Cu_3O_{5+x} + CuO + Volatiles$$

Coordinative saturation of each metal is obtained by the oxygen atoms of the chelating-bridging acetate and dmae ligands, thus there is no need of additional oxygen to form oxides. So, the new

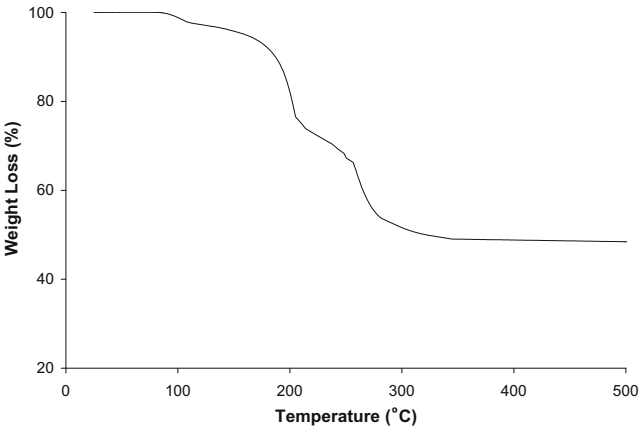


Fig. 4. Thermogravimetric plot of complex (**1**).

precursor has the potential application for deposition of mixed-metal oxide films at relatively low temperatures.

Thin films of mixed-metal oxide were characterized using XRPD, SEM and EDX. The X-ray powder pattern of the thin film obtained from complex (**1**) (Fig. 5) showed the formation of tetragonal $Ba_2Cu_3O_{5+x}$ and CuO phases. The relative peak intensities and the position of the diffraction peaks in the XRPD patterns are very similar to those reported in ICDD Card Nos. [00-040-312] [29] and [01-080-1916] [30], respectively.

The surface of the deposited films was analyzed by scanning electron microscopy (Fig. 6). The SEM image of the mixed-metal oxide thin film shows a smooth and compact film morphology. The particles are homogenously dispersed with clearly well defined grain boundaries and size ranges from 0.08 to 0.4 μm. The different sized particles are uniformly dispersed indicating two distinct phases, which was also proved by XRD analysis. The overall EDX analysis indicates that the metallic ratio of Ba:Cu in the films is close to 1:2, which also confirms the retention of same metallic ratio as that in the complex. The film exhibits a good adhesion to the substrate, which qualifies the "scotch tape test" and is stable towards air and moisture. Overall, the film seems to be of good quality with a slight reflecting nature.

The *V–I* curve is linear, as shown in the graph of voltage–current (Fig. 7), which indicates the sample prepared is found to be ohmic. From the slope of the curve, the resistance is $2.5 \times 10^3\ \Omega$ for the thin film deposited at 400 °C. The resistivity of the film was found to be 0.91 Ω cm, using $\rho = 4.532(V/I) \times d$, where ρ is the resistivity in Ω cm, 4.532 is the instrument constant, *V*/*I* is the slope of curve

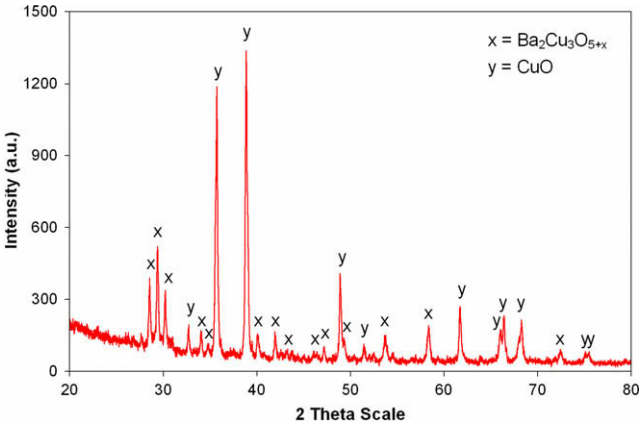


Fig. 5. X-ray powder diffractogram of CuO–$Ba_2Cu_3O_{5+x}$ thin films deposited at 400 °C from (**1**).

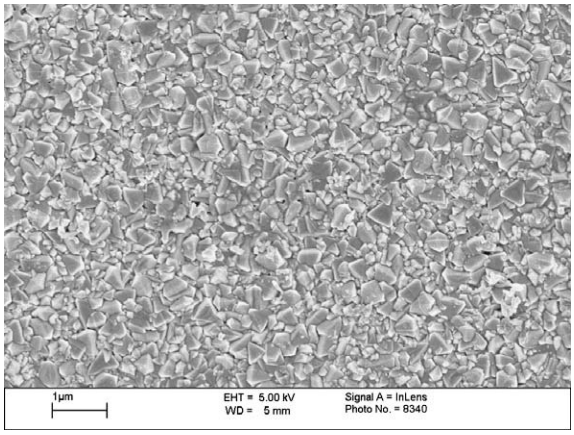


Fig. 6. SEM micrograph of films deposited from complex (**1**) at 400 °C.

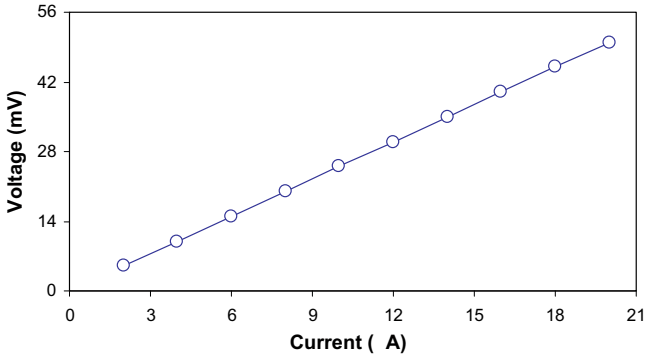


Fig. 7. *V–I* curve of the $CuO–Ba_2Cu_3O_{5+x}$ film deposited from complex **1**.

in Ω and d is the film's thickness (0.8 μm). The resistivity measurement, which is coherent to literature values (10^{-2}–10^{9}), suggests that the material deposited is of a semiconductor nature.

4. Conclusion

Heterobimetallic complex $[Ba_2(\mu\text{-}OAc)_4(OAc)_2Cu_4(\mu\text{-}dmae)_4(OH)_2]$ (**1**) has been synthesized by the direct reaction between $Ba(dmae)_2$ and $Cu(OAc)_2 \cdot H_2O$ in toluene under mild conditions. The complex has been characterized by spectroscopic and X-ray single crystal analysis. The high solubility of (**1**) in organic solvents and its low decomposition temperature makes it an attractive single-source precursor for the deposition of $CuO–Ba_2Cu_3O_{5+x}$ composite thin films.

Acknowledgement

M.S. and M.M. would like to thank the "Higher Education Commission and Pakistan Science Foundation Islamabad, Pakistan for financial support through the "Indigenous 5000 Ph.D. Scholarship Scheme".

Appendix A. Supplementary data

CCDC 654335 contains the supplementary crystallographic data for compound (**1**). These data can be obtained free of charge via http://www.ccdc.cam.ac.uk/conts/retrieving.html, or from the Cambridge Crystallographic Data Centre, 12 Union Road, Cambridge CB2 1EZ, UK; fax: (+44) 1223-336-033; or e-mail: deposit@ccdc.cam.ac.uk. Supplementary data associated with this article can be found, in the online version, at doi:10.1016/j.poly.2008.12.041.

References

[1] M.F. Yan (Ed.), Ceramic Superconductors, American Ceramic Society, Westerville, OH, 1988.
[2] D.L. Nelson, N.S. Whittingham, T.F. George (Eds.), Chemistry of High Temperature Superconductors, ACS Symposium Series 351, American Chemical Society, Washington, DC, 1987.
[3] D.R. Ulrich, Chem. Eng. News (January I) (1990) 28.
[4] M.W. Rupich, B. Lagos, J.P. Hachey, Appl. Phys. Lett. 55 (1989) 2447.
[5] N.N. Sauer, E. Garcia, K.V. Salazar, R.R. Ryan, J.A. Martin, J. Am. Chem. Soc. 112 (1990) 1524. and references therein.
[6] W. Bidell, H.W. Bosh, D. Veghini, H.U. Hund, J. Doring, H. Berke, Helv. Chim. Acta 76 (1993) 596.
[7] W. Bidell, V. Shklover, H. Berke, Inorg. Chem. 31 (1992) 5561.
[8] L.G. Hubert-Pfalzgraf, Inorg. Chem. Commun. 6 (2003) 102.
[9] F. Labrize, L.G. Hubert-Pfalzgraf, J. Vaissermann, C.B. Knobler, Polyhedron 15 (1996) 577.
[10] S.C. Goel, K.S. Kramer, M.Y. Chiang, W.E. Buhro, Polyhedron 9 (1990) 611.
[11] S. Wang, S.T. Trepanier, M.J. Wagner, Inorg. Chem. 32 (1993) 833.
[12] C.P. Love, C.C. Torardi, C.J. Page, Inorg. Chem. 31 (1992) 1784.
[13] O.V. Pryma, S.R. Petrusenko, V.N. Kokozay, B.W. Skelton, O.V. Shishkin, T.S. Teplytsa, Eur. J. Inorg. Chem. (2003) 1426. and references therein.
[14] V.N. Kokozay, O.Y. Vassilyeva, Transition Met. Chem. 27 (2002) 693.
[15] S. Wang, Inorg. Chem. 30 (1991) 2252.
[16] A.P. Purdy, C.F. George, Inorg. Chem. 30 (1991) 1969.
[17] S. Wang, Z. Pang, M.J. Wagner, Inorg. Chem. 31 (1992) 5381.
[18] J. Zhang, L.G. Hubert-Pfalzgraf, D. Luneau, Inorg. Chem. Commun. 7 (2004) 979.
[19] A.A. Tahir, K.C. Molloy, M. Mazhar, G. Kociok-Kohn, M. Hamid, S. Dastgir, Inorg. Chem. 44 (2005) 9207.
[20] K. Nakamoto, Infrared and Raman Spectra of Inorganic and Coordination Compounds, 4th Ed., Wiley, New York, 1986.
[21] G.B. Deacon, R.J. Phillips, Coord. Chem. Rev. 33 (1980) 251.
[22] W.A. Wojtczak, P. Atanassova, M.J. Hampden-Smith, E. Duesler, Inorg. Chem. 35 (1996) 6995.
[23] W.A. Wojtczak, M.J. Hampden-Smith, E.N. Duesler, Inorg. Chem. 37 (1998) 1781.
[24] H. Guillion, L.G. Hubert-Pfalzgraf, J. Vaissermann, Eur. J. Inorg. Chem. (2000) 1243.
[25] J.D. Lee, Concise Inorganic Chemistry, 5th Ed., Chapman and Hall, London, 1996.
[26] M. Shahid, M. Mazhar, M.A. Malik, P. O' Brien, J. Raftery, Polyhedron 27 (2008) 3337.
[27] A.A. Tahir, M. Hamid, M. Mazhar, M. Zeller, A.D. Hunter, M. Nadeem, M.J. Akhtar, J. Chem. Soc., Dalton Trans. (2008) 1224.
[28] M. Shahid, M. Mazhar, M. Helliwell, J. Akhtar, K. Ahmad, Acta Crystallogr. E64 (2008) m1139.
[29] I. Halasz, V. Fulop, I. Kirschner, T. Porjesz, J. Cryst. Growth 91 (1988) 444.
[30] S. Asbrik, A. Waskowska, J. Condens. Matter 3 (1991) 8173.

We synthesized this compound in our laboratory, but also were unable to grow suitable crystals for analysis. However, mass spectrometric studies and elemental analysis confirmed the structure as reported by Costes et al. [10]. We attempted to isolate complexes of the symmetric ligand prepared from two molecules of diacetylmonoxime with these two diamines by various routes. With both amines, however, the desired complexes could not be isolated, instead the complexes isolated were of the tridentate monocondensed diamines (complexes **1**, $[Ni(HL^1)_2](ClO_4)_2$ and **2**, $[Ni(HL^2)_2](ClO_4)_2$).

2. Experimental

2.1. Physical measurements

Elemental analyses (carbon, hydrogen and nitrogen) were performed using a Perkin–Elmer 240C elemental analyzer. IR spectra in KBr (4500–500 cm^{-1}) were recorded using a Perkin–Elmer RXI FT-IR spectrophotometer. Electronic spectra in acetonitrile (1200–350 nm) were recorded on a Hitachi U-3501 spectrophotometer. The magnetic susceptibility measurements were done with an EG&PAR vibrating sample magnetometer, model 155 at room temperature and diamagnetic corrections were made using Pascal's constants. Electrochemical measurements were performed under a dry nitrogen atmosphere in a three-electrode configuration using Pt disc working electrode, Pt auxiliary electrode and SCE (reference electrode) on a Sycopel model AEW2 1820F/S instrument in this work and were uncorrected for junction contribution. The value for the ferrocenium–ferrocene couple under our conditions is 0.40 V.

2.2. Materials

All chemicals were of reagent grade and used without further purification.

Caution! Metal perchlorates in the presence of organic ligands are potentially explosive. Only a small amount of the material should be prepared and it should then be handled with care.

2.3. Synthesis of the complexes

2.3.1. $[Ni(HL^1)_2](ClO_4)_2$ (**1**)

A mixture of diacetylmonoxime (10 mmol, 1.011 g) and ethylenediamine (10 mmol, 0.8 cm^3) in methanol (25 cm^3) was refluxed for about 3 h. It was then cooled and a solution of $Ni(ClO_4)_2{\cdot}6H_2O$ (5 mmol, 1.828 gm) in methanol (20 cm^3) was added with continuous stirring. An orange–red compound precipitated out and was then recrystallised from acetonitrile solution to obtain single crystals suitable of **1** suitable for X-ray diffraction. Yield: (~70%). Anal. *Calc*. for $C_{12}H_{26}N_6O_2Ni(ClO_4)_2$: C, 41.77; N, 24.35; H, 7.59; Ni, 17.01. Found: C, 40.88; N, 23.94; H, 7.75; Ni, 16.52%.

2.3.2. $[Ni(HL^2)_2](ClO_4)_2$ (**2**)

Complex **2** was prepared by the same procedure as complex **1** but using 1,2-diaminopropane instead of 1,2-diaminoethane. An orange yellow compound separated out and was recrystallized from acetonitrile solution to provide single crystals of **2** suitable for X-ray diffraction. Yield: (~74%). Anal. *Calc*. For $C_{14}H_{30}N_6O_2Ni(ClO_4)_2$: C, 45.07; N, 22.52; H, 8.10; Ni, 15.73. Found: C, 44.23; N, 21.85; H, 7.52; Ni, 15.92%.

2.3.3. $[Ni(HL^3)]ClO_4$ (**3**)

A solution of 2,4-pentanedione (10 mmol, 1.1 cm^3) in chloroform (50 cm^3) was added drop-wise to a solution of 1,2-diaminopropane (10 mmol, 0.8 cm^3) in chloroform (50 cm^3). After completion of addition, the solution was stirred for an additional 3 h and chloroform was evaporated under reduced pressure, yielding the monocondensed 4-(2-aminopropylimino)pentan-2-one as a viscous liquid. It was dissolved in methanol (10 cm^3). Solid diacetylmonoxime (10 mmol, 1.011 g.) was added and the mixture was stirred for 24 h. A solution of $Ni(ClO_4)_2{\cdot}6H_2O$ (10 mmol, 3.657 g) in methanol (20 cm^3) was added to the resulting solution with continuous stirring to precipitate an orange-red solid. It was recrystallized from acetonitrile solution to obtain single crystals of **3** suitable for X-ray diffraction. Yield: (~70%). Anal. *Calc*. *for* $C_{12}H_{20}N_3O_2Ni(ClO_4)$: C, 48.53; N, 14.15; H, 6.79; Ni, 19.76. Found: C, 47.63; N, 14.85; H, 6.52; Ni, 19.62%.

Table 1
Crystal data and refinement details of complexes **1**, **2** and **3**.

Crystal data	**1**	**2**	**3**
Formula	$C_{12}H_{26}Cl_2N_6NiO_{10}$	$C_{14}H_{30}Cl_2N_6NiO_{10}$	$C_{12}H_{22}ClN_3NiO_7$
f_w	544.00	572.05	414.49
Temperature (K)	150	150	150
Space group	monoclinic	orthorhombic	triclinic
Crystal system	I_2/a	*Pbca*	$P\bar{1}$
Crystal dimensions (mm)	0.27 × 0.20 × 0.18	0.14 × 0.14 × 0.11	0.30 × 0.05 × 0.05
a (Å)	14.8402(8)	12.0844(5)	8.2510(6)
b (Å)	7.1411(3)	16.0605(8)	10.3773(15)
c (Å)	20.9677(12)	25.3905(12)	11.6828(9)
α (°)	(90)	(90)	109.475(10)
β (°)	109.065(6)	(90)	104.318(11)
γ (°)	(90)	(90)	101.832(14)
V (Å^3)	2100.18(19)	4927.8(4)	867.4(2)
Z	4	8	2
$D_{calc.}$ (gm/cm^3)	1.720	1.542	1.587
μ (mm^{-1})	1.242	1.063	1.311
F(000)	1128	2384	432
Total reflections	6230	32450	5566
Unique reflections	3006	7175	4460
Observed data [$I > 2\sigma(I)$]	2271	2466	3223
No. of parameters refined	146	296	230
R_{int}	0.0235	0.1049	0.0292
R indices (all data)	R_1 = 0.0475, wR_2 = 0.1235	R_1 = 0.1511, wR_2 = 0.2073	R_1 = 0.0890, wR_2 = 0.2107
R indices [$I > 2\sigma(I)$]	R_1 = 0.0328, wR_2 = 0.0963	R_1 = 0.0675, wR_2 = 0.1716	R_1 = 0.0670, wR_2 = 0.1935

2.4. X-ray crystallography

Crystal data are given in Table 1. Intensity data were measured at 150 K using the Oxford X-Calibur CCD System with Mo Kα radiation. The crystals were positioned at 50 mm from the CCD. Three hundred and twenty-one frames were measured with a counting time of 10 s. Data analyses were carried out with the CRYSALIS program [11]. The structures were solved using direct methods with the SHELXS97 program [12]. The two carbon atoms in the saturated chelating ring of complex **3** were disordered over two sites as was the substituent methyl group. All disordered atoms were refined with distance constraints, 50% occupancy and isotropic thermal parameters. The other non-hydrogen atoms were refined with anisotropic thermal parameters. The hydrogen atoms bonded to carbon were included in geometric positions and given thermal parameters equivalent to 1.2 times those of the atom to which they were attached. Absorption corrections were carried out using the ABSPACK program [13]. The structures were refined on F^2 using SHELXL97 [12].

3. Results and discussion

3.1. Spectral studies

The presence of oxime –OH bond in these compounds (**1**–**3**) can be detected by IR bands which occur at 3337, 3334, and 3389 cm^{-1}, respectively. The bands for azomethine (C=N) groups present in all the compounds are distinct and occur within 1639–1603 cm^{-1}. Here also the lowering of the positions of the bands demonstrates their coordination to the metal centre. Single peaks with some slight splitting appear in the range 1108–1080 cm^{-1} indicating the presence of perchlorate with a slight distortion from ideal tetrahedral geometry which is substantiated in all the compounds from their crystal structures in which the perchlorate anion is shown to be involved in hydrogen bonding. The IR spectrum of the square planar compound **3** shows the absence of $\nu_{(NH_2)}$. For compound **1**, $\nu_{(NH_2)}$ appears at 3337, 3288 cm^{-1} along with NH_2 bending at 1673 cm^{-1}. For compound **2**, one peak at 3334 cm^{-1} with a shoulder shows the overlapping appearance of $-NH_2$ and –OH peaks along with NH_2 bending at 1660 cm^{-1}.

The electronic spectra of all the complexes were recorded in acetonitrile solution. The square planar arrangement of complex **3** is characterized by a broad band at 454 nm [14]. No other absorption peaks were observed in the higher wavelength region consistent with the square planar geometry found in the crystal structure. Complexes **1** and **2** show an absorption band in the region 610–580 and a broad band above 750 nm, assigned to υ_1 and υ_2 in the octahedral geometry of Ni(II) [14]. Other high energy bands below 350 nm are assigned as CT bands.

3.2. Magnetic properties

The effective magnetic moments 3.03 and 3.12 BM of the complexes **1** and **2**, respectively, confirm the presence of two unpaired electrons ($S = 1$) in a pseudo-octahedral environment, in agreement with a high-spin configuration ($t_{2g}^6 e_g^2$). Compound **3** is diamagnetic in accordance with the square planar Ni(II).

Table 2
Cyclic voltammetric data of the synthesized complexes **1**, **2** and **3** in acetonitrile solution vs. SCE.

Complex	E_a/V	E_c/V	$(E_a - E_c)/V$	$E_{1/2}/V = 1/2(E_a + E_c)/V$
$[Ni(HL^1)_2](ClO_4)_2$ (**1**)	0.443	0.280	0.163	0.361
$[Ni(HL^2)_2](ClO_4)_2$ (**2**)	0.453	0.310	0.143	0.381
$[Ni(HL^3)]ClO_4$ (**3**)	0.836	–	–	–

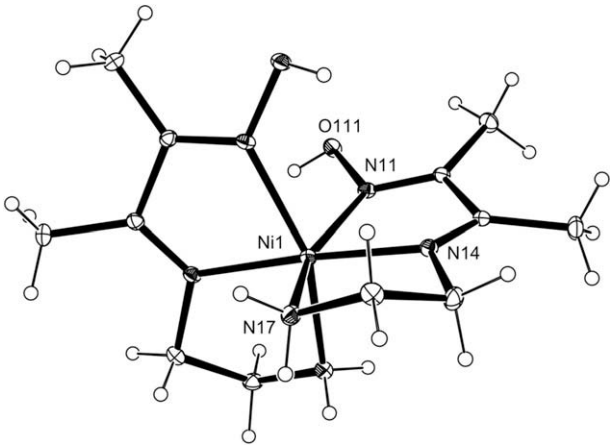


Fig. 1. ORTEP-3 picture for complex **1** with the atom numbering scheme. Thermal ellipsoids are shown at 30% probability. The perchlorate ion is not shown.

Table 3
Selected bond lengths (Å) and bond angles (°) for complex **1**.

Ni(1)–N(11)	2.127(2)
Ni(1)–N(14)	2.005(2)
Ni(1)–N(17)	2.121(2)
N(14)–Ni(1)–N(14)*	175.8(1)
N(14)–Ni(1)–N(17)	81.5(1)
N(14)–Ni(1)–N(11)	75.8(1)
N(14)–Ni(1)–N(17)*	95.6(1)
N(17)–Ni(1)–N(17)*	94.0(1)
N(14)–Ni(1)–N(11)*	107.4(1)
N(17)–Ni(1)–N(11)	156.4(1)
N(17)–Ni(1)–N(11)*	94.6(1)
N(11)–Ni(1)–N(11)*	86.1(1)

* Symmetry element = 0.5 − *x*, *y*, 1 − *z*.

Table 4
Hydrogen bond distances (Å) and angles (°) for complex **1**.

D–H···A	D···A	H···A	∠D–H···A
O(1 1 1)–H(1)···O24	2.71	1.91	157
N(17)–H(17B)···O(1 1 1′)	3.10	2.34	141
N(17)–H(17A)···O(21″)	3.21	2.33	167

Symmetry element ′ = 1/2 − *x*, −1 + *y*, 1 − *z*; ″ = 1/2 + *x*, 1 − *y*, *z*.

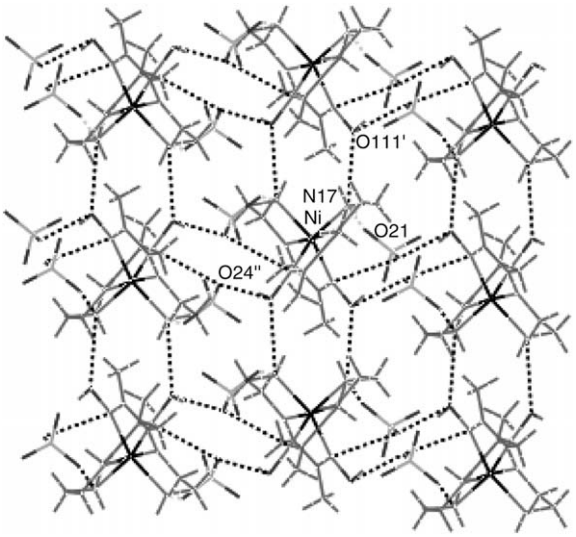


Fig. 2. H-bonded network of complex **1**. Only the major fraction of the disordered perchlorate anion is shown.

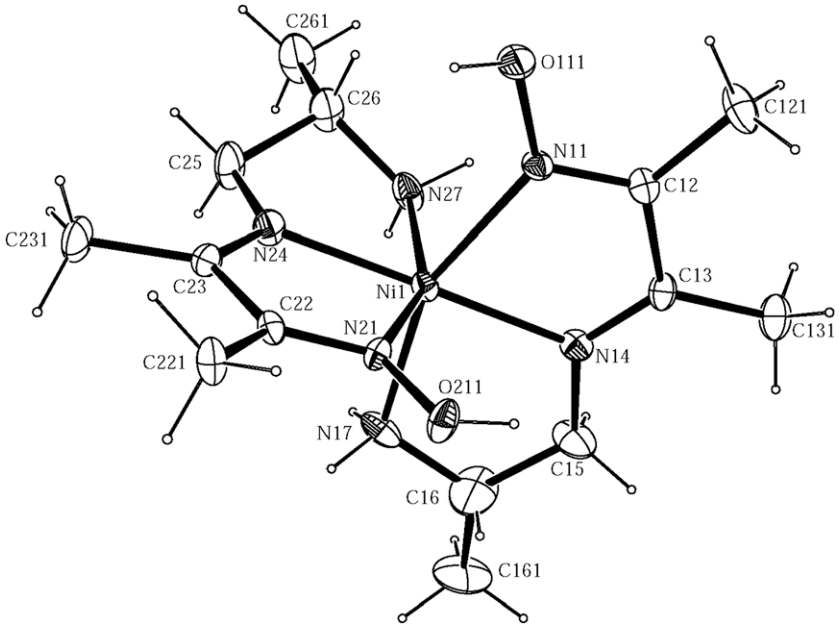


Fig. 3. ORTEP-3 picture for complex **2** with 30% ellipsoid probability. The perchlorate ion is not shown for clarity.

3.3. Cyclic voltammetric studies

Cyclic voltammetric studies of the complexes in acetonitrile solution versus SCE (scan rate 100 mV s^{-1}) reveal that the octahedral complexes **1** and **2** are quasi-reversible with the formal potential values ($E_{1/2}$) of 0.361 and 0.381 V, respectively. The low values of the redox potentials indicate that the higher oxidized species namely Ni^{3+} is stabilized in the presence of amine and oxime donor atoms as was previously established by Chakraborty and co-workers [9]. The formal potentials observed for ligand with oxime and amine as donors have higher values than is observed by us [15]. The anodic peak of complex **3** appears at 0.836 V but no reductive response is observed during the reverse scan. The higher value of the oxidation peak indicates that in the square planar geometry Ni(II) become more stabilized than the corresponding octahedral species **1** and **2**. Moreover, it seems that the oxidized complex undergoes decomposition or ligand rearrangement as no reduction peak is observed in the cathodic scan. Data from electrochemical studies are given in Table 2.

3.4. Structure description

3.4.1. Complex *1*

The structure of **1** contains discrete $[Ni(HL^1)_2]^{2+}$ cations together with perchlorate anions which contains a crystallographic twofold axis, and is shown in Fig. 1. The nickel atom is six-coordinate with a distorted octahedral environment being bonded to two tridentate ligands. The coordination polyhedron around nickel atom is best described as a distorted octahedron with the nickel atom bonded to N11, N14 and N17 of one terdentate ligand and N11∗, N14∗ and N17∗ of another (∗ designates symmetry element $0.5 - x, y, 1 - z$) with both ligands coordinating in the mer conformation.. The saturated five-membered ring, Ni(1)–N(14)–C(15)–C(16)–N(17), exhibits a half-chair conformation with puckering parameters $Q(2) = 0.418(3)$, and $\Phi(2) = 274.3(3)^\circ$ and is twisted around the C(15)–(16) bond. The N(17)–Ni(1)–N(14) angle is 81.5(1)° and is typical of a five-membered chelating ring. The Ni(1)–N bond lengths are Ni(1)–N(11) 2.121(2), Ni(1)–N(14) 2.005(2), and Ni(1)–N(17) 2.121(2) Å. Selected bond lengths and bond angles are given in Table 3.

The amine and hydroxyl (oxime) hydrogen atoms are involved in H-bonding (Table 4). The amine hydrogen, H(17B) forms an inter-molecular H-bond with symmetry related $(1/2 - x, y, 1 - z)$ hy-

Table 5
Bond lengths (Å) and bond angles (°) for complex **2**.

Ni(1)–N(11)	2.129(4)
Ni(1)–N(14)	2.017(4)
Ni(1)–N(17)	2.096(4)
Ni(1)–N(21)	2.128(4)
Ni(1)–N(24)	2.006(4)
Ni(1)–N(27)	2.100(4)
N(24)–Ni(1)–N(14)	178.3(2)
N(24)–Ni(1)–N(27)	80.6(2)
N(14)–Ni(1)–N(27)	98.4(2)
N(24)–Ni(1)–N(17)	97.3(2)
N(14)–Ni(1)–N(17)	81.4(2)
N(27)–Ni(1)–N(17)	94.6(2)
N(24)–Ni(1)–N(21)	75.5(2)
Ni(14)–Ni(1)–N(21)	105.6(1)
N(27)–Ni(1)–N(21)	155.8(2)
N(17)–Ni(1)–N(21)	92.4(1)
N(24)–Ni(1)–N(11)	106.0(2)
N(14)–Ni(1)–N(11)	75.4(2)
N(27)–Ni(1)–N(11)	91.9(2)
N(17)–Ni(1)–N(11)	156.6(2)
N(21)–Ni(1)–N(11)	90.9(1)

Table 6
Hydrogen bond distances (Å) and angles (°) for complex **2**.

D–H···A	D···A	H···A	∠D–H···A
N(17)–H(17A)···O(74′)	3.31	2.47	155
N(17)–H(17B)···O(81″)	3.23	2.44	147
N(17)–H(17B)···O(83″)	3.12	2.28	156
N(27)–H(27A)···O(82)	3.14	2.36	145
N(27)–H(27A) .. O(84)	3.06	2.23	152
N(27)–H(27B)···O(81″)	3.05	2.17	165
O(111)–H(111)···O(73)	2.75	2.08	139
O(111)–H(111)···O(74)	3.11	2.36	152
O(211)–H(211)···O(71‴)	2.76	2.05	146

Symmetry element ′ = $x + 1/2, -y + 1/2, -z$; ″ = $1/2 + x, y, 1/2 - z$; ‴ = $x + 1, -y - 1/2, z + 1/2$.

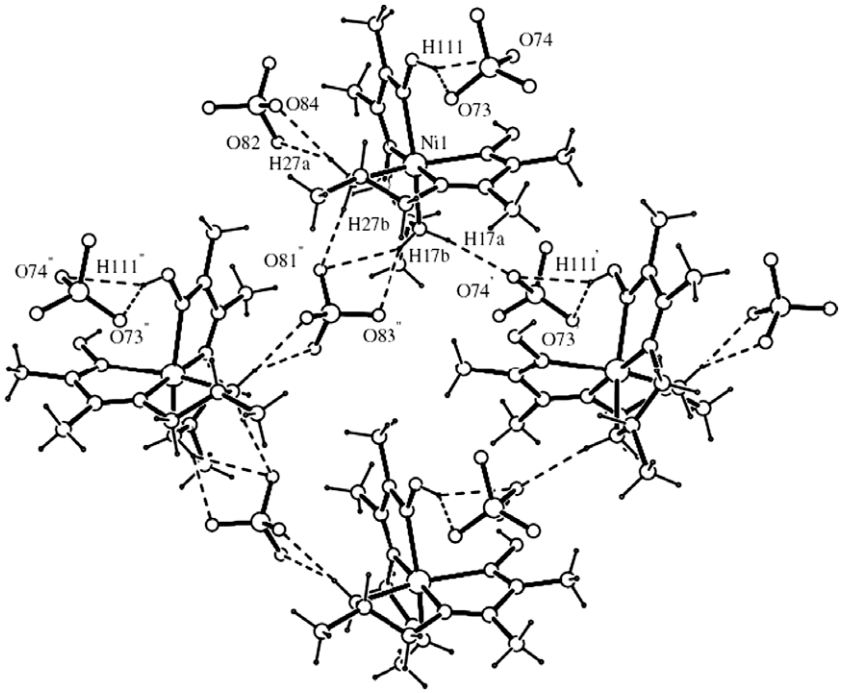


Fig. 4. Intra and inter-molecular H-bonding in complex **2**.

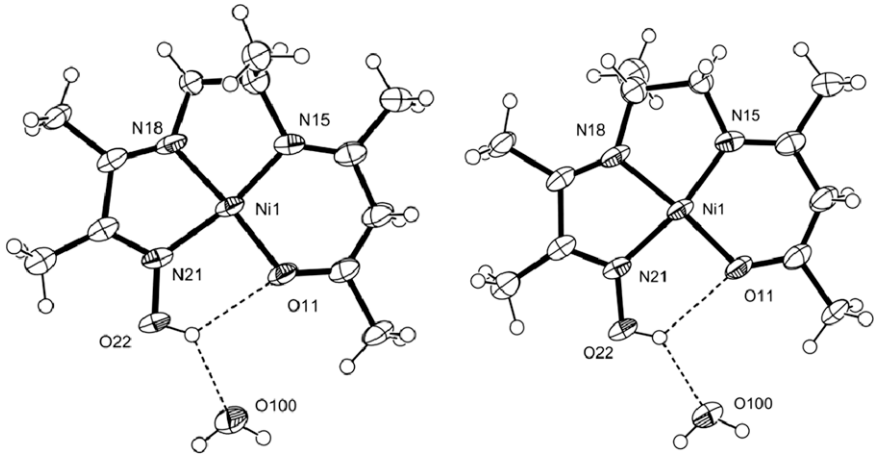


Fig. 5. The two structures, in **3** with ellipsoids at 50% probability. The structures only differ in the positions of the three carbon atoms in the N–CH_2–CH(Me)–N moiety which were refined with 50% occupancy. Hydrogen bonds shown as dotted lines.

droxyl oxygen atom, O(1 1 1) from a second molecule of $[Ni(HL^1)]^{2+}$ at 3.09 Å giving rise to a one-dimensional chain. The O(21) and O(24) atoms of the perchlorate ion form H-bonds with the amine hydrogen atom H(17A) and the hydroxyl hydrogen H(1 1 1) of two neighboring chains to form a 2-D H-bonded network (Fig. 2).

Table 7
Bond lengths (Å) and bond angles (°) for complex **3**.

Ni(1)–N(15)	1.835(3)
Ni(1)–N(18)	1.838(3)
Ni(1)–O(11)	1.821(3)
Ni(1)–N(21)	1.891(4)
O(11)–Ni(1) N(15)	98.54(15)
O(11)–Ni(1) N(18)	174.35(14)
N(15)–Ni(1) N(18)	86.84(16)
O(11)–Ni(1) N(21)	92.27(14)
N(15)–Ni(1) N(21)	168.79(15)
N(18)–Ni(1) N(21)	82.27(15)

The involvement of perchlorate ion in the H-bonded network has been observed in several other complexes [16,17].

3.4.2. Complex *2*

The structure consists of discrete $[Ni(HL^2)_2]^{2+}$ cations together with perchlorate anions. The metal atom is in a six-coordinate distorted octahedral environment being bonded to two tridentate ligands which coordinate meridionally. The structure of **2** is shown

Table 8
Hydrogen bond distances (Å) and angles (°) for complex **3**.

D–H···A	D···A	H···A	∠D–H···A
O(22)–H(22)···O(11)	2.904	2.32	127
O(22)–H(22)···(100)	2.643	2.01	132
O(100)–H(1)···O(43)′	2.886	2.21	136
O(100)–H(1)···O(44)′	2.958	2.12	173

Symmetry element ′ = $-x + 1, -y - 1, -z$.

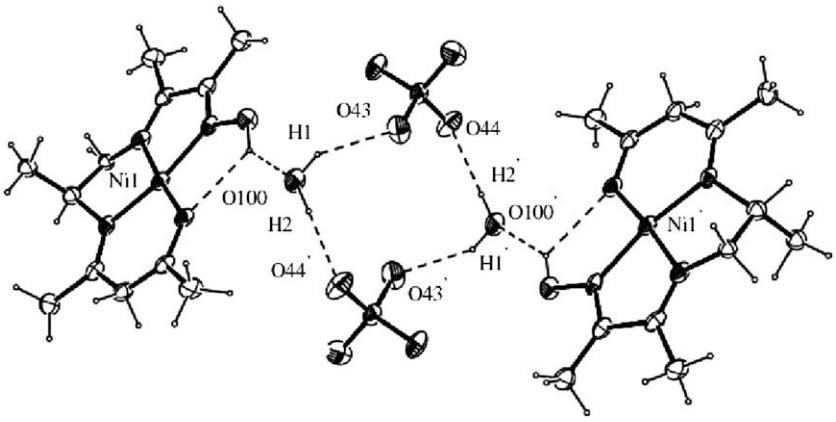


Fig. 6. The H-bonded dimeric structure of **3**.

in Fig. 3 together with the atom numbering scheme. The bond lengths from the metal are equivalent with Ni(1)–N(11), Ni(1)–N(21) at 2.129(4), 2.128(4) Å, slightly longer than Ni(1)–N(17), Ni(1)–N(27) 2.096(4), 2.100(4) Å but significantly longer than Ni(1)–N(14), Ni(1)–N(24) at 2.017(4), 2.006(4) Å. Selected bond lengths and bond angles are given in Table 5.

In this structure, one of the two independent perchlorates is disordered so that two independent tetrahedra of oxygen atoms were refined with 50% occupancy. Both O(1 1 1) and O(2 1 1) are involved in weak hydrogen bonds to disordered oxygen atoms; O(1 1 1) 2.76, 2.78 Å to O(73), O(76) and O(211) 2.77, 2.79 to O(71), O(77). In addition, all four hydrogen atoms on N(17) and N(27) form weak hydrogen bonds to perchlorate oxygen atoms at distances in the range 3.05–3.14 Å (Table 6) giving a closed tetranuclear H-bonded structure (Fig. 4).

*3.4.3. Complex **3***

The two molecules that make up the structure of **3** are shown in Fig. 5 together with the numbering scheme in the metal coordination sphere. The only significant difference between the two molecules is the position of the two carbon atoms in the saturated chelating ring of complex **3** which were disordered over two sites as was the substituent methyl group. Dimensions are given in Table 7. As is apparent from Fig. 5, the methyl group in the five-membered chelating ring is attached either to C(16) or C(17) in the two disordered molecules. It was found that the positions of C(16) and C(17) differed slightly in the two molecules and they were therefore refined independently.

The coordination of the metal is a square plane with an r.m.s. deviation of 0.01 Å for the four donor atoms. The nickel atom is 0.03 Å from this plane. There are no atoms bonding in axial positions. The Ni–N(21) bond is longer at 1.891(4) Å than the other three bonds from nickel which are 1.835(3) Å to N(15), 1.838(3) Å to N(18) and 1.821(3) Å to O(11). The hydrogen on O22 forms weak hydrogen bonds to both O(11) in the complex and the solvent water molecule (Table 8). Dimensions to O(1 0 0) are H···O 2.00, O–H···O 132° and O···O 2.64 Å while dimensions to O(11) are 2.32 Å, 126°, 2.90 Å, respectively. O(1 0 0) also forms donor hydrogen bonds to O(44) $(1-x, -y, -z)$ (2.11 Å, 173°, 2.96 Å) and O(43) $(x, y-1, z)$ (2.21 Å, 136°, 2.89 Å). Thus a dimeric structure of the complex is formed via a perchlorate anion and the water molecule (Fig. 6).

4. Conclusions

Three new Ni(II) compounds have been isolated and characterized by physico-chemical and structural studies. The aim of the work was to prepare symmetrical and unsymmetrical compounds of Schiff base ligands involving 1,2-diaminoethane or 1,2-diaminopropane and 2,4-pentanedione or diacetylmonoxime. Symmetrical compounds with two diacetylmonoxime functions could not be isolated but instead the monocondensed tridentate Schiff base yielded the bis six-coordinate complex. Two compounds with unsymmetrical ligand varieties involving 2,4-pentanedione and diacetylmonoxime were isolated and characterized. One of these involving 1,2-diaminoethane was previously reported by Costes et al. [10]. In our observation, we have concluded that symmetrical ligands which would involve three fused five-membered rings in the complex cation makes it compressed and strained as observed by Fritsky et al. [15] and the more stable, bis-ligand varieties were isolated as the sole products. The introduction of a six membered chelate in the form of 2,4-pentanedione gives a stable, less strained square planar environment around Ni(II).

Acknowledgments

We thank EPSRC and the University of Reading for funds for the X-Calibur system.

Appendix A. Supplementary data

CCDC 679612, 679613 and 695122 contain the supplementary crystallographic data for complex **1**, **2** and **3**, respectively. These data can be obtained free of charge via http://www.ccdc.cam.ac.uk/conts/retrieving.html, or from the Cambridge Crystallographic Data Centre, 12 Union Road, Cambridge CB2 1EZ, UK; fax: (+44) 1223-336-033; or e-mail: deposit@ccdc.cam.ac.uk. Supplementary data associated with this article can be found, in the online version, at doi:10.1016/j.poly.2008.12.015.

References

[1] G.H. Jeffery, J. Bassett, J. Mendham, R.C. Dennney (Eds.), Vogel's Textbook of Quantitative Chemical Analysis, 5th Ed., Longman Group UK Limited, 1989.
[2] M.S. Ray, G. Mukhopadhyay, R. Bhattacharya, S. Chaudhuri, L. Righi, G. Bocelli, A. Ghosh, Polyhedron 22 (2003) 617.
[3] S. Chattopadhyay, M.S. Ray, S. Chaudhuri, G. Mukhopadhyay, G. Bocelli, A. Cantoni, A. Ghosh, Inorg. Chim. Acta 359 (2006) 1367.
[4] M.S. Ray, A. Ghosh, R. Bhattacharya, G. Mukhopadhyay, M.G.B. Drew, J. Ribas, Dalton Trans. (2004) 252.
[5] M.S. Ray, G. Mukhopadhyay, M.G.B. Drew, T.-H. Lu, S. Chaudhuri, A. Ghosh, Inorg. Chem. Commun. 6 (2003) 961.
[6] M.S. Ray, A. Ghosh, S. Chaudhuri, M.G.B. Drew, J. Ribas, Eur. J. Inorg. Chem. 15 (2004) 3110.
[7] D. Maity, P. Mukherjee, A. Ghosh, M. G.B. Drew, G. Mukhopadhyay, Inorg. Chim. Acta 361 (2008) 1515.
[8] O.I. Fritsky, H. Kozlowski, V. Prisyazhnaya, Z. Rzaczynska, A. Karaczyn, Y.T. Sliva, T. Glowiak, J. Chem. Soc., Dalton Trans. (1998) 3629.

[9] A.N. Singh, R.P. Singh, J.G. Mohanty, A. Chakraborty, Inorg. Chem. 10 (1977) 2597.
[10] J.P. Costes, F. Dahan, A. Dupuis, J.P. Laurent, J. Chem. Soc., Dalton Trans. (1998) 1307.
[11] CRYSALIS, Oxford Diffraction Ltd., Version 1, 20012.
[12] SHELXS97 and SHELXL97, G.M. Sheldrick, Programs for Crystal Structure Calculations, University of Gottingen, 1997.
[13] ABSPACK, Oxford Diffraction Ltd., 2005.
[14] A.B.P. Lever, Inorganic Electronic Spectroscopy, 2nd Ed., Elsevier Science Publishers, 1984.
[15] O.M. Kanderal, H. Koziowski, A. Dobosz, J.S. Kozlowska, F. Meyer, I.O. Fritsky, Dalton Trans. (2005) 1428.
[16] M. Sinha Ray, G. Mukhopadhyay, M.G.B. Drew, T.-H. Lu, S. Chaudhuri, A. Ghosh, Inorg. Chem. Commun. 6 (2003) 961.
[17] P. Mukherjee, M.G.B. Drew, A. Ghosh, Eur. J. Inorg. Chem. (2008) 3372.

establish interesting magneto-structural correlations. The d^9 configuration of the Cu^{II} ion has one unpaired electron ($S = 1/2$), and the nearly quenched orbital angular momentum of the Cu^{II} ion provides a g factor close to 2, suggesting the absence of any large internal magnetic fields. A comparison of key structural parameters and exchange integrals for the phenoxo-bridged copper(II) complexes reveals the dependence of J on (i) the Cu–O(phenolate)–Cu angle, (ii) the Cu—Cu distance, (iii) the geometry around the phenolate oxygen atom, and (iv) the deviation of the copper coordination geometry [29].

As an extension of our earlier works with phenoxo-bridged multinuclear transition metal complexes [30–32], we report herein a novel tetra(μ_3-phenoxo) bridged cubane core copper(II) complex, $[Cu_4L_4] \cdot Na \cdot ClO_4$ (**1**) using a potentially multidentate Schiff base ligand *N′*-(2-hydroxy-3-methoxybenzylidene)benzohydrazide (**H_2L**) which can be utilised with both bridging and chelating capacities. In this paper we describe the synthesis, characterizations, X-ray crystal structure and variable temperature magnetic (VTM) susceptibility measurements of this new copper complex. We also present here an appropriate magneto-structural correlation in order to explain the observed magnetic coupling showing both ferro- and antiferromagnetic interactions [$J_{11} = +13.6(4)\ cm^{-1}$ and $J_{12} = -34.9(4)\ cm^{-1}$].

2. Experimental

2.1. Materials

All the chemicals and solvents used for the syntheses were of analytical grade. Benzhydrazide, 3-methoxysalicylaldehyde and sodium hydroxide were purchased from Aldrich Chemical Co. Inc. and used without any further purification. Copper(II) perchlorate hexahydrate was prepared by the treatment of basic copper(II) carbonate, $CuCO_3 \cdot Cu(OH)_2$ (E. Merck, India) with 80% perchloric acid (E. Merck, India) followed by slow evaporation on a steam bath. It was then filtered through a fine glass-frit and preserved in $CaCl_2$ desiccator.

Caution! *Perchlorate salts in presence of organic materials are potentially explosive. It should be prepared in small amounts and handled with extreme care.*

2.2. Syntheses

2.2.1. Synthesis of the Schiff base ligand (**H_2L**)

The Schiff base chelator, *N′*-(2-hydroxy-3-methoxybenzylidene)benzohydrazide (**H_2L**), was prepared by following a method already reported in literature [33]. Benzhydrazide (1.36 g, 10 mmol) was refluxed with 3-methoxysalicylaldehyde (1.52 g, 10 mmol) in 50 ml methanol at 65 °C. After 2.5 h, a deep orange yellow solution was obtained. It was subjected to TLC which revealed the presence of some unreacted starting materials along with the Schiff base product. The Schiff base ligand was isolated by column chromatography in order to get it in the purified form. The purified ligand was then evaporated under reduced pressure to yield a gummy mass, which was dried and stored *in vacuo* over $CaCl_2$ for subsequent use. Yield: 2.35 g (87%). *Anal.* Calc. for $C_{15}H_{14}N_2O_3$: C, 66.66; H, 5.22; N, 10.36. Found: C, 65.82; H, 5.19; N, 10.40%. FT-IR (KBr, cm^{-1}): ν(CH=N) 1627.

2.2.2. Synthesis of $[Cu_4L_4] \cdot Na \cdot ClO_4$ (**1**)

The appropriate quantity of solid Schiff base ligand **H_2L** (0.27 g, 1 mmol) was dissolved in 20 ml methanol. This ligand solution was added dropwise to a 10 ml methanolic solution of $Cu(ClO_4)_2 \cdot 6H_2O$ (0.37 g, 1 mmol) with constant stirring. After addition of 5 ml aqueous NaOH solution (0.40 g, 1 mmol) the reaction mixture was refluxed for 2 h at 65 °C. The resulting deep green solution was then left undisturbed. After 7 days green plate shaped X-ray diffraction quality single crystals were separated out. Yield: 80%. *Anal.* Calc. for $Cu_4H_{48}C_{60}N_8ClO_{16}Na$: C, 49.71; H, 3.34; N, 7.73. Found: C, 49.68; H, 3.31; N, 7.76%.

2.3. Physical measurements

The Fourier transform infrared spectra (4000–200 cm^{-1}) of the ligand and the complex were recorded on a Perkin–Elmer Spectrum RX I FT-IR spectrophotometer in the range 4000–200 cm^{-1} as solid KBr disc and electronic spectrum (800–200 nm) on a Perkin–Elmer Lambda 40 (UV–Vis) spectrometer using HPLC grade acetonitrile as solvent. Elemental analysis was carried out on a Perkin–Elmer 2400 II Elemental Analyser. Cyclic voltammetric measurement was performed using a PAR VersaStat-Potentiostat/Galvanostat II electrochemical analysis system under a dry Argon atmosphere using conventional, three electrode configurations in acetonitrile (HPLC grade) with tetrabutylammonium perchlorate as the supporting electrolyte. A platinised platinum milli electrode was used as the working electrode in cyclic voltammetry at a scan rate of $\nu = 50\ mV\ s^{-1}$. Cryomagnetic susceptibility measurement for the complex was carried out with a Quantum Designed SQUID MPMS-XL susceptometer apparatus, which works in the range 2–300 K under magnetic field of approximately 0.5 T on the polycrystalline sample. Diamagnetic corrections were estimated from Pascal's tables.

2.4. X-ray crystal structure determination

X-ray data of a green single crystal with dimension ($0.19 \times 0.32 \times 0.36$ mm) were collected at 150 K on a Nonius KAPPACCD diffractometer equipped with graphite monochromated focused X-ray tube bearing a molybdenum target (λ/Mo Kα = 0.71069 Å). Data collection was performed with COLLECT. The scaling as well as the global refinement of crystal parameters was performed by DENZO and SCALEPACK. Whole data processing was carried out using the KAPPACCD analysis software [34]. The structure was solved by direct methods with SIR-97 program [35] combined to Fourier difference syntheses and refined against F using reflections with $[I/\sigma(I) > 3]$ by CRYSTALS program [36]. The hydrogen atoms were initially refined with soft restraints on the bonds to regularize their geometry after which they were refined with riding constraints only. Those attached to carbon atoms were repositioned geometrically on the basis of the conformation of the supporting atom and also found by Fourier difference analysis. All non-hydrogen atoms were successfully refined with anisotropic thermal parameters. All calculations and graphical works were done using CAMERON [37] and WINGX [38] programs. Selected crystallographic data and refinement parameters are given in Table 1.

3. Results and discussion

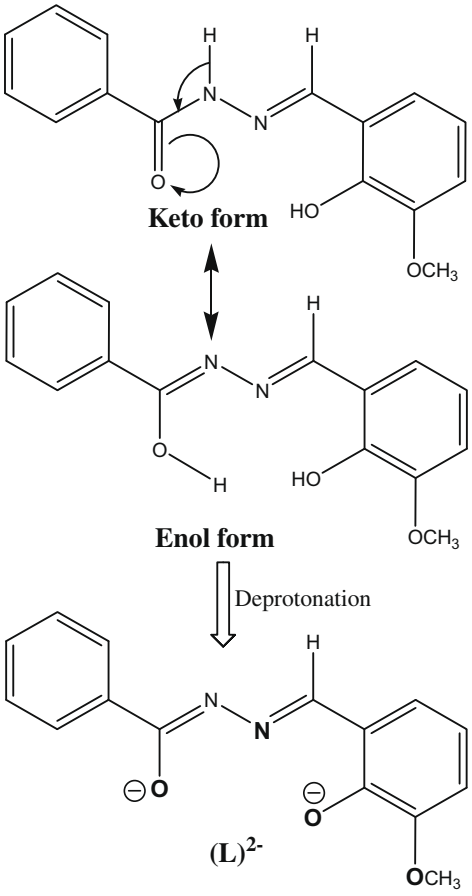
3.1. Infrared spectra

The IR spectrum of the complex **1** has been analyzed in comparison with that of the free hydrazone ligand in the region 4000–200 cm^{-1}. The stretching frequency of the imine (CH=N) group in the uncomplexed hydrazone ligand is observed near 1627 cm^{-1}. It is shifted to the lower frequency value (~1590 cm^{-1}) upon complexation [39] with the metal by 37 cm^{-1} suggesting coordination via the imine group. The increase in ν(N–N) from 1005 to 1020 cm^{-1} in the IR spectrum of the complex is due to the increase in the double bond character of N–N, offsetting the loss of electron density via donation to the metal ion and is a further evidence of

Table 1
Summary of crystal data and refinement details for **1**.

Empirical formula	$Cu_4H_{48}C_{60}N_8ClO_{16}Na$
Formula weight	1449.70
Crystal dimension (mm)	0.19 × 0.32 × 0.36
Crystal system	trigonal
Space group	$P3_221$
a (Å)	14.801(5)
b (Å)	14.801(5)
c (Å)	26.376(5)
β (°)	120
V (Å^3)	5004(3)
Z	3
Temperature (K)	150
D_{calc} (g cm^{-3})	1.443
μ (mm^{-1})	1.374
$F(000)$	2208
θ (°)	1.6–28.0
Total data	11 359
Unique data	7789
Observed data [$I > 3\sigma(I)$]	4843
R^a	0.0972
$R_w{}^b$	0.1475
Goodness-of-fit on F^2, S	1.07
R_{int}	0.038
$\Delta\rho_{max}$ (e Å^{-3})	2.39
$\Delta\rho_{min}$ (e Å^{-3})	−1.22

[a] $R = \Sigma(|F_o - F_c|)/\Sigma|F_o|$.
[b] $R^w = \{\Sigma[w(|F_o - F_c|)^2]/\Sigma[w|F_o|^2]\}^{1/2}$.



Scheme 1.

coordination of the ligand through the imine nitrogen atom. In the complex, sharp bands appearing nearly at 425 and 395 cm^{-1} may be correlated to the Cu–N and Cu–O stretching frequencies respectively. The characteristic spectral band for ν_{str}(N–H) of the hydrazone ligand appears sharply at 3242 cm^{-1}. Interestingly this band disappears in the complex confirming the coordination via enol form instead of keto by deprotonation of N–H proton during the tautomerisation process [40]. A sharp band at ~1500 cm^{-1} indicates the newly formed uncomplexed C=N by enolisation. It further confirms that the coordination of hydrazone takes place in the form of the enol rather than the keto. The loss of the enolic proton is indicated by the absence of a band at ~3400 cm^{-1} in the complex [41,42]. The ν_{str}(C–O) also reduces from 1289 to ~1240 cm^{-1} in the complex when compared to the uncomplexed ligand.

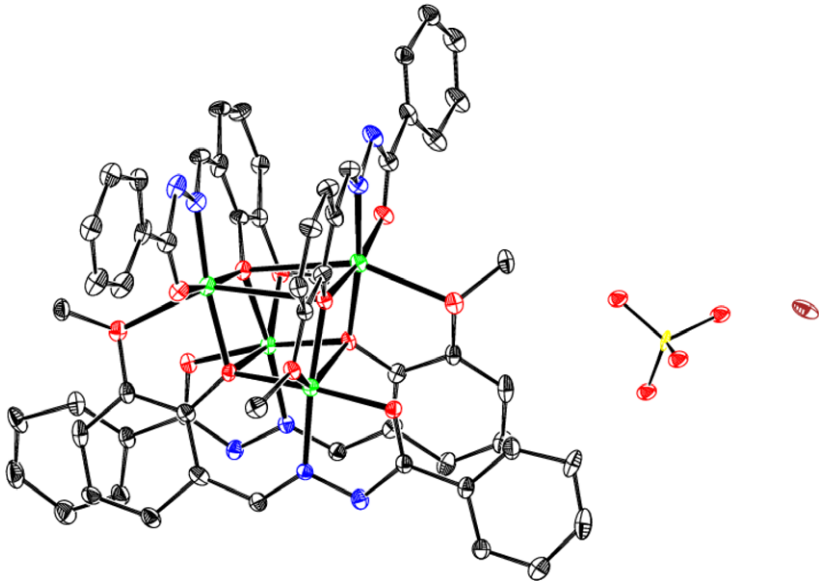


Fig. 1. ORTEP representation of the unit cell of complex **1** (hydrogen atoms are omitted for clarity). Thermal ellipsoids have been drawn at the 40% probability level. Colour code: copper – green, oxygen – red, nitrogen – blue, chlorine – yellow and sodium – brown. (For interpretation of the references to colour in this figure legend, the reader is referred to the web version of this article.)

3.2. Electronic spectra

A low intensity broad band appearing at 626 nm may be attributed to the *d*–*d* transition of the copper(II) ion [43]. The intense band in the region of 300–450 nm can be assigned for the $n \rightarrow \pi^*$ transition of the imine group and the higher energy bands below 300 nm may be correlated to the $\pi \rightarrow \pi^*$ intraligand charge transfer transitions. The complex displays strong absorption bands in the high energy range which are clearly charge transfer in origin. The LMCT band at 315–375 nm range can be assigned for the charge transfer transition from the coordinated unsaturated ligand to the metal ion [44].

3.3. Crystal structure description

The complex crystallizes in trigonal space group $P3_221$ and the unit cell consists of tetrameric Cu_4L_4 cubane moiety along with lattice sodium and perchlorate ions. The ORTEP representation of the unit cell of complex **1** is shown in Fig. 1. In the main structural unit of the complex it is seen that the Cu_4O_4 core consists of four phenoxo-bridged copper atoms, giving an approximately cubic array of alternating copper and oxygen atoms occupying the corners of the cube. The cubic core contains two crystallographically independent metal ions, and the two sets of metal ions are related by the crystallographic twofold axis passing through the middle of Cu1–Cu1* and Cu2–Cu2* vectors. The asymmetric unit, thus, consists of the half of the tetramer.

Although transition metal complexes having cubane structures are well studied class of complexes, to the best of our knowledge the case of complex **1** is an exclusive one as such kind of systems are quite rare especially with the tetradentate dianionic hydrazone ligand with $N_{azo}(O_{phenoxo})(O_{methoxo})(O_{enolato})$ donor set. Under the reaction condition the ligand molecule tautomerises from ketonic to enolic form (Scheme 1). After double deprotonation of the enolic and the phenolic OH groups, the dianionic form of the ligand ($\mathbf{L^{2-}}$) coordinates to the copper(II) center. Four such monomeric CuL entities eventually interconnect through the phenoxo bridges to produce the tetranuclear cubane core. A labeled representation of the chelating modes of the hydrazone ligands connected to copper atoms is presented in Fig. 2a and b. The most striking feature of the complex remains in the presence of unique type of μ_3-bridging phenoxo oxygen atoms carrying out the aggregation of the cubane core. Here each of the four phenoxo oxygens located at the four corners of the cube bridges the metal centers in a μ_3-fashion [O9: Cu1, Cu1*, Cu2; O29: Cu1*, Cu2, Cu2*; O9*: Cu1, Cu1*, Cu2* and O29*: Cu1, Cu2, Cu2*]. The occurrence of this kind of bridging mode in constructing the transition metal cubane core complexes is not very frequent and only limited examples are obtained in the literature [27]. Earlier in 2000, Yamashita et al. reported tetranuclear complexes of reduced Schiff base type tridentate dianionic ligands H_2L2X (X: H, Me, and Cl) derived from condensation reaction of the appropriate *o*-aminobenzyl alcohol and salicylaldehyde [27b]. The crystal structure of the complex $[CuL2H]_4$ (**A**) reported in that paper shows that the complex has a cubane like tetranuclear core attributed to the dimer-of-dimers structure by the stacking of alkoxo-bridged dicopper units.

In case of complex **1**, each copper atom is coordinated to three deprotonated bridging phenoxo oxygens, one enolate, one methoxy oxygen and one azo nitrogen atom to give an octahedral geometry. A detailed analysis of the coordination environment of each of

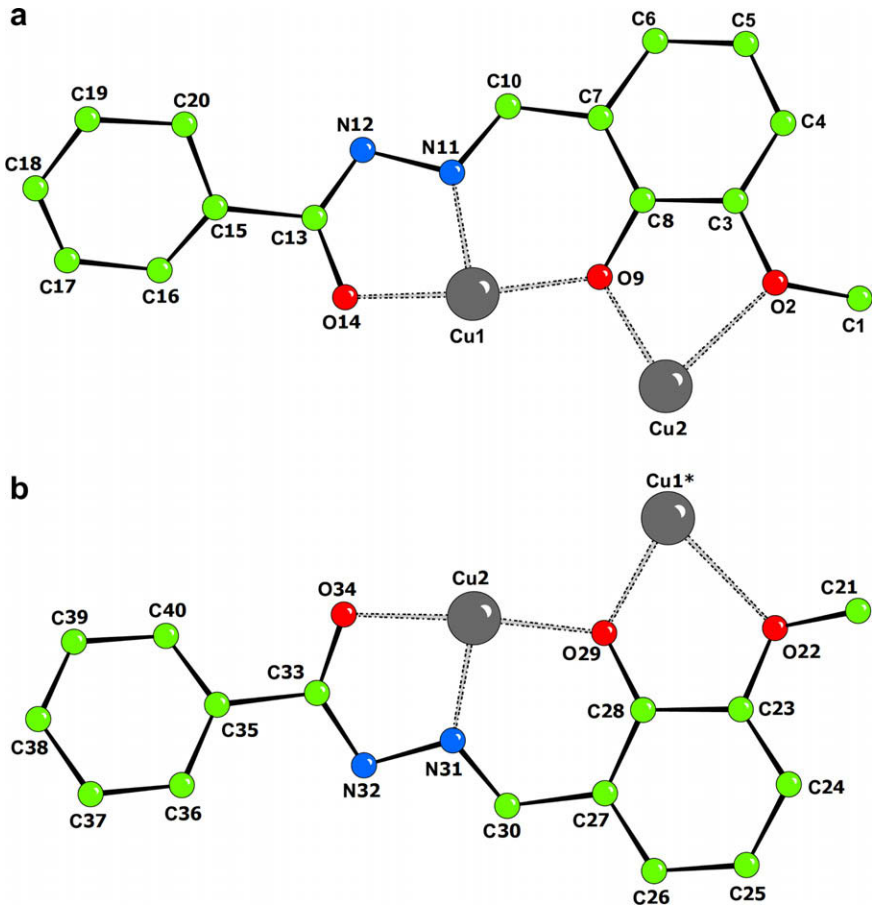


Fig. 2. (a) and (b) Labeled representation of the chelating modes of the hydrazone ligands connected to copper atoms.

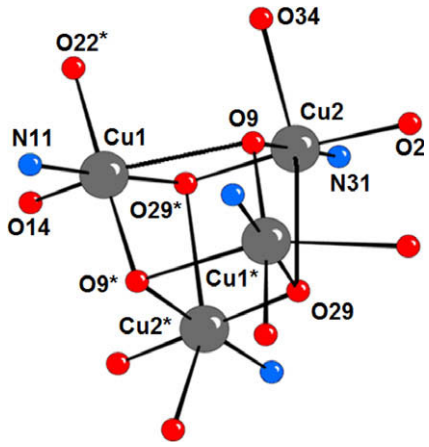


Fig. 3. Environments of copper atoms by oxygen and nitrogen atoms in the $[Cu^{II}_4L_4]$ cluster (only donor sites have been included). Symmetry code: * = *y*, *x*, −*z*.

the metal ions participating in the construction of the tetra(μ_3-phenoxo) bridged cubane core is given in Fig. 3. For Cu1 center the basal plane of the octahedron is constructed by two phenoxo oxygens (O9, O29*), one enolato oxygen (O14) and an azo nitrogen (N11), while the axial positions are occupied by another phenoxo oxygen (O9*) and a methoxy oxygen (O22*). The octahedron around Cu2 center can be described in a similar way where the two phenoxo oxygens (O9, O29), one enolato oxygen (O34) and an azo nitrogen (N31) are in the basal plane and the other phenoxo oxygen (O29*) and a methoxy oxygen (O2) occupy the axial positions (Fig. 3). The geometry of the metal center is considerably distorted from an ideal octahedron and can be best described as elongated octahedral which is clearly reflected from the different bond lengths and angles around the same. The mean lengths of the equatorial bonds around Cu1 are in the range of 1.910(10)–1.964(10) Å while the axial bond distances range from 2.242(7) to 2.679(6) Å owing to the Jahn–Teller effect which is typical for Cu^{II} d^9 system. The slight distortion in the basal plane may be attributed for the strain imposed by the ligand to the metal center during coordination. All the relevant bond lengths and angles are summarized in Table 2. Each pair of Cu atoms located at the corners of the cube is linked through double phenoxo bridges. The bridging bond angles of Cu–O(phenoxo)–Cu are in the range 86.2(3)–112.1(3)° (Table 3). It is evident from the different Cu–O body diagonal distances [Cu1–O29, 3.746; Cu2–O9*, 3.800 Å] as well as from the unequal metal–metal distances (Table 2) that

Table 2
Selected bond distances and bond angles for **1**.

Bond distances (Å)			
Cu1–N11	1.910(10)	Cu2-N31	1.892(11)
Cu1–O14	1.934(9)	Cu2–O29	1.958(6)
Cu1–O9	1.959(8)	Cu2–O34	1.962(9)
Cu1–O29*	1.964(10)	Cu2–O9	1.971(8)
Cu1–O22*	2.242(7)	Cu2–O2	2.279(10)
Cu1–O9*	2.679(6)	Cu2–O29*	2.698(10)
Cu1–Cu2 (or, Cu1*–Cu2*)	3.229	Cu1–Cu1*	3.435
Cu1–Cu2* (or, Cu1*–Cu2)	3.253	Cu2–Cu2*	3.486
Bond angles (°)			
O14–Cu1–N11	82.4(4)	O9–Cu2–O29*	71.7(3)
O9–Cu1–N11	91.1(4)	O2–Cu2–O29	100.7(3)
O14–Cu1–O22*	90.1(3)	O2–Cu2–N31	111.0(5)
O9*–Cu1–O29*	71.0(3)	O9–Cu2–O34	96.8(3)
O9–Cu1–O14	170.3(3)	O9–Cu2–N31	172.2(4)
O9*–Cu1–O22*	146.7(3)	O2–Cu2–O29*	147.9(3)

Symmetry transformations used to generate the equivalent atoms.
* *y*, *x*, −*z*.

Table 3
Length (*D*) of the Cu–Cu pathway (Å) with corresponding angles (°).

Pathway	[a]*D* (Å)	Cu–O–Cu (°)
Cu1 O9 Cu1* (or, Cu1 O9* Cu1*)	4.638	94.3(3)
Cu2 O29 Cu2* (or, Cu2 O29* Cu2*)	4.656	95.7(2)
Cu1 O29* Cu2	4.662	86.2(3)
Cu1 O9 Cu2	3.930	110.5(4)
Cu1 O9* Cu2*	4.650	87.4(2)
Cu1 O29* Cu2*	3.922	112.1(3)

[a] *D* is the sum of the Cu–O bond lengths making the Cu–O–Cu bridge.

the cubane core is not a regular one, but rather distorted in shape. No significant π–π stacking interaction is observed in the crystal packing in spite of the presence of several planar moieties within the structure.

3.4. Electrochemical studies

Cyclic voltammogram of **1** shows two reductive responses on the negative side of SCE (at −0.40 and −1.16 V), both of which are irreversible in nature. The observed potential gap (620 mV) between the two reductions is moderately large and is believed to be due to the effective communication between the two adjacent paramagnetic Cu^{II} metal centers through the bridging ligands. The reduction may be assigned to copper(II) → copper(I) reduction. One irreversible oxidative response is observed on the positive side of SCE at +1.11 V and this is tentatively assigned to the oxidation of the coordinated ligands.

3.5. Magneto-structural correlations

The temperature dependence of the magnetic susceptibility, χ_M in the 2–300 K range, is shown in Fig. 4 and that of $\chi_M T$ in the Fig. 5. The overall behaviour is characteristic of a moderate antiferromagnetically coupled system. At 300 K, $\chi_M T$ is equal to 1.41 $cm^3\,K\,mol^{-1}$ which is close to the value expected for four non-interacting Cu^{II} ions. Upon cooling, this value decreases rather rapidly to reach zero below 20 K. The magnetic susceptibility shows a maximum at 85 K which is also a characteristic of dominant antiferromagnetic interactions. The low temperature behaviour of the magnetic susceptibility showing a minimum hump at 15 K goes on increasing which is indicative of a few paramagnetic impurities.

On the basis of the changes found in the magnetic susceptibility values on changing the temperature from 2 to 300 K, a sound

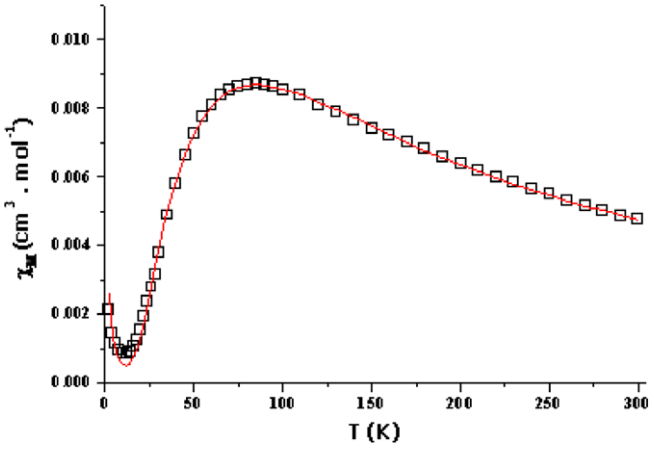


Fig. 4. Temperature dependence of the magnetic susceptibility (χ_M). The solid lines hold for the best fit of the data.

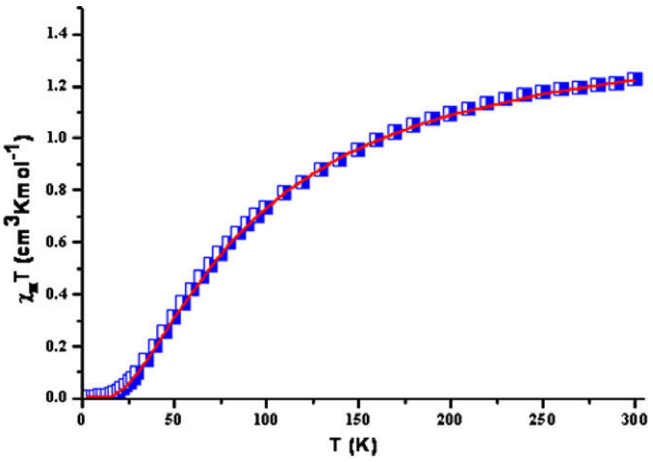


Fig. 5. Temperature dependence of $\chi_M T$ for **1**. The solid line corresponds to the best data fit.

magneto-structural correlation may be drawn successfully. A structural analysis carried out with the help of the Cambridge Structural Database [45] reveals the existence of three major types of cubane structures if they are classified according to the distribution of long Cu–Cu distances: (1) complexes with two short and four long Cu–Cu distances, and we call them 2 + 4 (2) complexes with four short and two long Cu–Cu distances, and may be labeled as 4 + 2 and finally (3) complexes where all six Cu–Cu distances are similar, and they will be termed 6 + 0. Magneto-structural correlations for the hydroxo- and μ-alkoxo-bridged Cu^{II} complexes were proposed earlier by Hatfield and co-workers [46]. From all the above works it is quite clear that the crucial geometrical parameters which can influence the magnetic susceptibility values are the Cu–O–Cu angles and the out-of-plane shift of the atom coordinated to the bridging oxygen [47]. Hence, in the case of the hydroxo-bridged complexes an angle of 98.5° marks the border between ferro- and antiferromagnetic complexes. Ferromagnetism is found in complexes with smaller angles, and antiferromagnetism for larger ones. Alkoxo-/phenoxo-bridged complexes show a similar trend: the larger the Cu–O–Cu angle, the stronger the antiferromagnetic coupling. We can therefore expect ideal cubanes with Cu–O–Cu angles close to 90° to be good candidates for being ferromagnetic.

In the reported complex, the analysis of the structural features within the tetranuclear Cu_4O_4 cubane core (Fig. 3) shows that the bridging system between the Cu^{II} ions is quite asymmetric. As may be anticipated for hexacoordinated Cu^{II} ions, there are short Cu–O(μ_3-phenoxo) bond lengths corresponding to the equatorial plane and long Cu–O(μ_3-phenoxo) bonds in the axial position. This

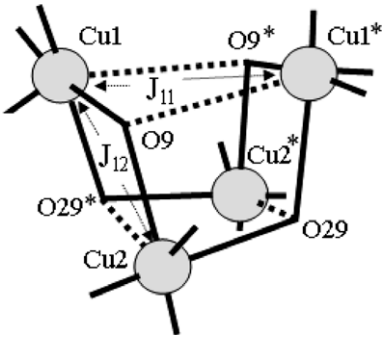


Fig. 6. Schematic representation of the exchange pathways [J_{11} = +13.6(4) cm^{-1}, J_{12} = −34.9(4) cm^{-1}].

asymmetry is also obvious from the Cu–Cu separations with the Cu1–Cu2, Cu1–Cu2* (and their symmetry related counterparts Cu1*–Cu2*, Cu1*–Cu2) distances being significantly shorter [3.229–3.253 Å] than the Cu1–Cu1* and Cu2–Cu2* distances [3.435–3.486 Å]. Therefore complex **1** clearly belongs to 4 + 2 category and the magnetic data have been analyzed considering two different magnetic coupling parameters such as J_{12} for the Cu1–Cu2 and Cu1–Cu2* interactions and J_{11} for the Cu1–Cu1* and Cu2–Cu2* interactions (Fig. 6).

From the following Hamiltonian operator:

$$\hat{\boldsymbol{H}} = -2J_{12}(\boldsymbol{S}_{Cu1}\cdot\boldsymbol{S}_{Cu2} + \boldsymbol{S}_{Cu1}\cdot\boldsymbol{S}_{Cu2*} + \boldsymbol{S}_{Cu1*}\cdot\boldsymbol{S}_{Cu2*} + \boldsymbol{S}_{Cu1*}\cdot\boldsymbol{S}_{Cu2}) - 2J_{11}(\boldsymbol{S}_{Cu1}\cdot\boldsymbol{S}_{Cu1*} + \boldsymbol{S}_{Cu2}\cdot\boldsymbol{S}_{Cu2*}).$$

The energies of the different spin states are then given by equation:

$$E(S_T) = -J_{12}[S_T(S_T+1)] + (J_{12}-J_{11})[S_{11*}(S_{11*}+1) + S_{22*}(S_{22*}+1)]$$
with $\boldsymbol{S}_T = \boldsymbol{S}_{11*} + \boldsymbol{S}_{22*}, \boldsymbol{S}_{11*} = \boldsymbol{S}_1 + \boldsymbol{S}_{1*}$ and $\boldsymbol{S}_{22*} = \boldsymbol{S}_2 + \boldsymbol{S}_{2*}$.

It leads to the following Van–Vleck equation [48]:

$$\chi_M = \frac{2N\beta^2 g^2}{kT} \times \left(\frac{2\exp(-2y) + \exp(-2x) + 5\exp(+2x)}{\exp(-4y) + 6\exp(-2y) + \exp(-4x) + 3\exp(-2x) + 5\exp(2x)}\right),$$

where, $x = J_{12}/kT$ and $y = J_{11}/kT$. The fitting of the experimental data have been carried out using this equation and taking in account an additional intermolecular interactions (zJ') in the molecular field approximation [49] and a paramagnetic impurity (S_{para} = 1/2).

$$\chi_{fit} = (1-P)\frac{\chi_M}{1 - \frac{2zJ'}{Ng^2\beta^2}\chi_M} + P\chi_{para}.$$

The best fit of the experimental data is obtained with J_{11} = +13.6(4) cm^{-1},

$$J_{12} = -34.9(4)\ cm^{-1},\quad g = 2.19(4),$$
$$zJ' = -7(2)\ cm^{-1} \text{ and } P = 1.4(3)\%.$$

The magnetic couplings thus found are in very good agreement with the structural features and also with earlier reported magneto-structural correlations in Cu^{II}-alkoxo-bridged polynuclear systems [50]. In case of the magnetic system with J_{11} exchange coupling parameter, i.e. Cu1–Cu1* and Cu2–Cu2*, the double phenoxo bridges between the Cu centers are made of one long and one short Cu–O bond lengths resulting in two long pathways [for Cu1–Cu1* system: Cu1–O9–Cu1* (or, symmetry related Cu1–O9*–Cu1*), 4.638 Å; for Cu2–Cu2* system: Cu2–O29–Cu2* (or, symmetry related Cu2–O29*–Cu2*), 4.656 Å] with the Cu–O–Cu angles in the range 94.3(3)–95.7(2)°. These structural parameters are not suitable for overlap and thus responsible for the ferromagnetic coupling [J_{11} = +13.6(4) cm^{-1}]. In contrast, both the bridges in the J_{12} type of magnetically coupled system, which includes Cu1–Cu2 (or, Cu1*–Cu2*) and Cu1–Cu2* (or, Cu1*–Cu2), are different from each other. Like the previous case, here also one bridge is made of one short and one long Cu–O bond lengths resulting in a long pathway [Cu1–O29*–Cu2, 4.662 Å; Cu1–O9*–Cu2*, 4.650 Å] with Cu–O–Cu angles in the range 86.2(3)-87.4(2)°. As mentioned before, this does not favour overlap. But here the second bridge is made of two short Cu–O bond lengths resulting in short pathway [Cu1–O9–Cu2, 3.930 Å, Cu1–O29*–Cu2*, 3.922 Å] with Cu–O–Cu angles comprising in the range 110.5(4)–112.1(3)° (Table 3). This certainly favours the overlap and explains well the antiferromagnetic coupling [J_{12} = −34.9(4) cm^{-1}].

Thus the magnetic susceptibilities have been fitted both with ferromagnetic and antiferromagnetic exchange couplings showing

a characteristic of overall antiferromagnetic behaviour due to the predominance of the antiferromagnetic interaction over the ferromagnetic one.

4. Conclusion

A novel tetranuclear Cu^{II} complex has been synthesized exploiting the tetradentate donor set of a dianionic hydrazone ligand. Single crystal X-ray diffraction analysis of the complex reveals the presence of four μ_3-phenoxo bridges connecting four different copper(II) centers in order to form an interesting Cu_4O_4 cubane core with an alternating array of copper and oxygen atoms. This kind of tetra(μ_3-phenoxo) bridged transition metal cubane core is quite rare and therefore needs further exploration. The cryomagnetic susceptibility measurements (2–300 K) demonstrate both ferromagnetic and antiferromagnetic interactions in a 2*J* model resulting in an overall antiferromagnetic behaviour of the magnetically coupled system. Here we have successfully drawn interesting magneto-structural correlations relating the bonding parameters with the magnetic exchange coupling parameters.

Acknowledgements

J. Chakraborty is thankful to the University Grants Commission, New Delhi, for a Senior Research Fellowship. S. Thakurta gratefully acknowledges the Council of Scientific and Industrial Research, New Delhi, India, for the award of a Junior Research Fellowship to her (CSIR Sanction No. 09/096(0519)/2007-EMR-I). D. Luneau thanks the CEA-Grenoble for magnetic measurements carried at in the frame of a "Laboratoire de Recherche Conventionné" (LRC No. DSM-03-31). The work is also financially supported by the research grant from All India Council for Technical Education (AICTE), New Delhi, India.

Appendix A. Supplementary data

CCDC 626145 contains the supplementary crystallographic data for complex **1**. These data can be obtained free of charge via http://www.ccdc.cam.ac.uk/conts/retrieving.html, or from the Cambridge Crystallographic Data Centre, 12 Union Road, Cambridge CB2 1EZ, UK; fax: (+44) 1223-336-033; or e-mail: deposit@ccdc.cam.ac.uk.

References

[1] (a) D. Gatteschi, Adv. Mater. 6 (1994) 635;
(b) K. Takeda, K. Awaga, Phys. Rev. 56 (1997) 14560;
(c) A. Bhattacharjee, Y. Miyazaki, Y. Nakazawa, S. Koner, S. Iijima, M. Soria, Physica B 305 (2001) 56.
[2] E. Coronado, F. Palacio, J. Veciana, Angew. Chem., Int. Ed. Engl. 42 (2003) 2570.
[3] (a) R. Neumann, M. Dahan, Nature 388 (1997) 353;
(b) O. Yaghi, G. Li, H. Li, Nature 378 (1995) 703.
[4] S. Yamada, Coord. Chem. Rev. 190–192 (1999) 537.
[5] K.S. Murray, in: A.G. Sykes (Ed.), Advances in Inorganic Chemistry, vol. 43, Academic Press, San Diego, CA, 1995, pp. 261–358.
[6] S. Rao, D.D. Mishra, R.V. Mourya, N. Nageswara, Polyhedron 16 (1999) 1825.
[7] D.X. West, A.E. Liberta, S.B. Padhye, R.C. Chikate, P.B. Sonawane, A.S. Kumbhar, R.G. Yerande, Coord. Chem. Rev. 123 (1993) 49.
[8] D. Wester, G.J. Palenik, Inorg. Chem. 15 (1976) 755.
[9] K. Andjelković, I. Ivanović, B. Prelesnik, V.M. Leovac, D. Poketi, Polyhedron 15 (1996) 4361.
[10] S. Abram, C. Maichle-Mössmer, U. Abram, Polyhedron 17 (1998) 131.
[11] M. Carcelli, S. Ianelli, P. Pelagatti, G. Pelizzi, Inorg. Chim. Acta 292 (1999) 121.
[12] J. Zhou, Z.-F. Chen, X.-W. Wang, Y.-S. Tan, H. Liang, Y. Zhang, Acta Crystallogr., Sect. E 60 (2004) m568.
[13] H. Ali, N.A. Khamis, W.J. Basirun, B.M. Yamin, Acta Crystallogr., Sect. E 60 (2004) m1351.
[14] G.G. Mohamed, Z.H.A. El-Wahab, J. Thermal Anal. Cal. 73 (2003) 347.
[15] Y. Song, Y. Xu, D.-R. Zhu, X.-Z. You, Acta Crystallogr., Sect. C 56 (2000) 430.
[16] G.F. de Sousa, C.A.L. Filgueiras, A. Abras, S.S. Al-Juaid, P.B. Hitchcock, J.F. Nixon, Inorg. Chim. Acta 218 (1994) 139.
[17] K. Andjelković, I. Ivanović, S.R. Niketić, B. Prelesnik, V.M. Leovac, Polyhedron 16 (1997) 4221.
[18] K. Andjelković, G. Jakovljević, M. Zlatović, Ž. Tešić, D. Sladić, J. Howing, R. Tellgren, J. Serb. Chem. Soc. 69 (2004) 651.
[19] A. Bonardi, C. Merlo, C. Pelizzi, G. Pelizzi, P. Tarasconi, F. Vitali, F. Cavatorta, J. Chem. Soc., Dalton Trans. (1991) 1063.
[20] G.J. Palenik, D.W. Wester, Inorg. Chem. 17 (1978) 864.
[21] (a) R. Acevedo-Chavez, M.E. Costas, S. Bernes, G. Medina, L. Gasque, J. Chem. Soc., Dalton Trans. (2002) 2553;
(b) Z.Q. Xu, L.K. Thompson, D.O. Miller, Chem. Commun. (2001) 1170;
(c) M. Murugesu, R. Clerac, B. Pilawa, A. Mandel, C.E. Anson, A.K. Powell, Inorg. Chim. Acta 337 (2002) 328;
(d) R.H. Bode, W.L. Driessen, F.B. Hulsbergen, J. Reedijk, A.L. Spek, Eur. J. Inorg. Chem. (1999) 505;
(e) R. Ziessel, L. Charbonniere, M. Cesario, T. Prange, H. Nierengarten, Angew. Chem., Int. Ed. Engl. 41 (2002) 975.
[22] (a) B. Graham, M.T.W. Hearn, P.C. Junk, C.M. Kepert, F.E. Mabbs, B. Moubaraki, K.S. Murray, L. Spiccia, Inorg. Chem. 40 (2001) 1536;
(b) J. Sletten, A. Sørensen, M. Julve, Y. Journaux, Inorg. Chem. 29 (1990) z 5054.
[23] A.E. Landers, D.J. Phillips, Inorg. Chim. Acta 32 (1979) 53.
[24] S.-F. Si, J.-K. Tang, D.-Z. Liao, Z.-H. Jiang, S.-P. Yan, Inorg. Chem. Commun. 5 (2002) 76.
[25] Y. Xie, H. Jiang, A.S.C. Chan, Q.L. Liu, X.L. Xu, C.X. Du, Y. Zhu, Inorg. Chim. Acta 333 (2002) 138.
[26] M. Koikawa, H. Yamashita, T. Tokii, Inorg. Chim. Acta 357 (2004) 2635.
[27] (a) C. Lopes, M. Håkansson, S. Jagner, Inorg. Chem. Acta 254 (1997) 361;
(b) H. Yamashita, M. Koikswa, T. Tokii, Mol. Cryst. Liq. Cryst. 342 (2000) 63;
(c) B. Gustafsson, M. Håkansson, G. Westman, S. Jagner, J. Organomet. Chem. 649 (2002) 204.
[28] U. Schollwöck, J. Richter, D.J.J. Farnell, R.F. Bishop (Eds.), Quantum Magnetism, Springer-Verlag, New York, 2004.
[29] D.J. Hodgson, Prog. Inorg. Chem. 19 (1975) 173.
[30] A. Datta, C.R. Choudhury, P. Talukder, S. Mitra, L. Dahlenburg, T. Matsushita, J. Chem. Res. (S) (2003) 642.
[31] P. Talukder, A. Datta, S. Mitra, G. Rosair, M.S. El Fallah, J. Ribas, Dalton Trans. (2004) 4161.
[32] C.R. Choudhury, S.K. Dey, R. Karmakar, C.-D. Wu, C.-Z. Lu, M.S. El Fallah, S. Mitra, New J. Chem. 27 (2003) 1360.
[33] B. Samanta, J. Chakraborty, S. Shit, S.R. Batten, P. Jensen, J.D. Masuda, S. Mitra, Inorg. Chim. Acta 360 (2007) 2471.
[34] Nonius COLLECT, DENZO, SCALEPACK, SORTAV, KAPPACCD Program us B.V., Delft, The Netherlands, 1999.
[35] G. Cascarano, A. Altomare, C. Giacovazzo, A. Guagliardi, A.G.G. Moliterni, D. Siliqi, G. Polidori, M. Camalli, Acta Crystallogr., Sect. A 52 (1996) C79.
[36] D.J. Watkin, C.K. Prout, J.R. Carruthers, P.W. Betteridge, CRYSTALS, Issue 11, Chemical Crystallography Laboratory, Oxford, UK, 1999.
[37] D.J. Watkin, C.K. Prout, L.J. Pearce, CAMERON, Chemical Crystallography Laboratory, Oxford, UK, 1996.
[38] L.J. Farrugia, WINGX, J. Appl. Crystallogr. 32 (1999) 837.
[39] (a) P. Bindu, M.R.P. Kurup, T.R. Satyakeerthy, Polyhedron 18 (1999) 321;
(b) R.P. John, A. Sreekanth, M.R.P. Kurup, A. Usman, A.R. Ibrahim, H.K. Fun, Spectrochim. Acta A59 (2003) 1349;
(c) P. Bindu, M.R.P. Kurup, Transit. Metal Chem. 22 (1997) 578.
[40] P.B. Sreeja, M.R.P. Kurup, A. Kishore, C. Jasmin, Polyhedron 23 (2004) 575.
[41] K. Nakamoto, Infrared and Raman Spectra of Inorganic and Coordination Compounds, Part A and B, 5th Ed., John Wiley, New York, 1997.
[42] R.T. Conley, Infrared Spectroscopy, Allyn and Bacon, Boston, 1966.
[43] P.V. Bernhardt, E.G. Moore, M.J. Riley, Inorg. Chem. 40 (2001) 5799.
[44] A.B.P. Lever, Inorganic Electronic Spectroscopy, 2nd Ed., Elsevier Science Publishers B.V., Amsterdam, 1984. p. 161.
[45] F.H. Allen, O. Kennard, Chem. Des. Autom. News 8 (1993) 31.
[46] V.H. Crawford, H.W. Richardson, J.R. Wasson, D.J. Hodgson, W.E. Hatfield, Inorg. Chem. 15 (1976) 2107.
[47] (a) E. Ruiz, P. Alemany, S. Alvarez, J. Cano, J. Am. Chem. Soc. 119 (1997) 1297;
(b) E. Ruiz, P. Alemany, S. Alvarez, J. Cano, Inorg. Chem. 36 (1997) 3683.
[48] (a) L. Merz, W. Haase, Z. Naturforsch A 31 (1976) 177;
(b) J. Jones, S. Gupta, L.J. Theriot, F.T. Helm, W.A. Baker Jr., Inorg. Chem. 17 (1978) 87;
(c) O. Kahn, Molecular Magnetism, VCH Publishers, New York, 1993.
[49] A.P. Ginsberg, M.E. Lines, Inorg. Chem. 11 (1972) 2289.
[50] (a) W.E. Hatfield, in: R.D. Willet, D. Gatteschi, O. Kahn (Eds.), Magneto-structural Correlations in Exchange Coupled Systems, NATO ASI Series 140, Reidel, Dordrecht, The Netherlands, 1985, p. 555;
(b) E. Ruiz, S. Alvarez, A. Rodriguez-Fortea, P. Alemany, Y. Pouillon, C. Massobrio, in: J. Miller, M. Drillon (Eds.), Magnetism: Molecules to Materials II, Wiley-VCH Verlag GmbH, Weinheim, Germany, 2001, p. 227.

manifests an uncommon four-fold interpenetrated $4^2 6^3 8$–**sra** topology [15]. In these materials and other dpa-containing coordination polymer solids [16–19], the kinked orientation of the nitrogen donor atoms of the dpa and the hydrogen-bonding imparted by the central N–H group tend to act together as structure-directing agents during coordination polymer self-assembly.

In the present study, we report the significant effects of the presence of interstitial perchlorate ions on the topology of dual-ligand succinate or 2,2-dimethylsuccinate coordination polymers incorporating hydrogen-bonding capable dpa tethers. The structures of $\{[Co(suc)(Hdpa)_2(H_2O)_2](ClO_4)_2 \cdot 7.5H_2O\}_n$ (**1**), $\{[Cd_3(suc)_{2.5}(dpa)_2]\ (ClO_4)\}_n$ (**2**) and $\{[Cd_2(dmsuc)_2(dpa)(Hdpa)](ClO_4) \cdot 6H_2O\}_n$ (**3**) all vary very greatly from their perchlorate-free congeners. Complexes **1** and **3** adopt 1D straight chain and 2D (6,3) herringbone layer motifs, respectively; the structure of **2** manifests a unique 3D binodal coordination polymer lattice. Luminescent behavior within the d^{10} derivatives **2** and **3** are also discussed herein.

2. Experimental

2.1. General considerations

Hydrated metal perchlorates, succinic acid, and 2,2-dimethylsuccinic acid were obtained commercially from Aldrich. 4,4′-dipyridylamine (dpa) was prepared via a published procedure [16]. Water was deionized above 3 MΩ in-house. Elemental Analysis was carried out using a Perkin Elmer 2400 Series II CHNS/O Analyzer. IR spectra were recorded on powdered samples on a Perkin Elmer Spectrum One spectrum one instrument.

Caution! Perchlorate compounds can be explosive. Although no issues occurred during this work, minimum quantities were used and the materials were not subject to heating above the temperature of their synthesis.

2.1.1. Preparation of $\{[Co(suc)(Hdpa)_2(H_2O)_2](ClO_4)_2 \cdot 7.5H_2O\}_n$ (1)

$Co(ClO_4)_2 \cdot 6H_2O$ (100 mg, 0.273 mmol), dpa (94 mg, 0.54 mmol) and succinic acid (44 mg, 0.37 mmol) were added to 10 mL of distilled H_2O in a 23 mL Teflon lined Parr acid digestion bomb. The bomb was sealed and heated to 120 °C for 48 h at which point the bomb was gradually cooled to 23 °C. Pink crystals of **1** (63 mg, 0.071 mmol, 26% yield based on Co) were obtained after vacuum filtration and washing with distilled water and acetone, followed by air drying. Crystals of **1** were stable indefinitely in air. *Anal.* Calc. for $C_{24}H_{42}Cl_2CoN_6O_{21.5}$: C, 32.37; H, 4.98; N, 9.44. Found: C, 33.22; H, 4.70; N, 9.67%. IR (cm^{-1}): 3047m vbr, 1647w, 1606m, 1519s, 1483m, 1428w, 1411m, 1365m, 1230w, 1206m, 1087s, 1017m, 902w, 844w, 815s, 718w, 669m, 622s.

2.1.2. Preparation of $\{[Cd_3(suc)_{2.5}(dpa)_2](ClO_4)\}_n$ (2)

$Cd(ClO_4)_2 \cdot 6H_2O$ (150 mg, 0.358 mmol), dpa (165 mg, 0.963 mmol) and succinic acid (77 mg, 0.652 mmol) were added to 10 mL of distilled H_2O in a 23 mL Teflon lined Parr acid digestion bomb. The bomb was sealed and heated to 120 °C for 48 h at which point the bomb was gradually cooled to 23 °C. Colorless crystals of **2** (62 mg, 0.058 mmol, 49% yield based on Cd) were obtained. *Anal.* Calc. for $C_{30}H_{28}Cd_3ClN_6O_{14}$: C, 33.70; H, 2.64; N, 7.86. Found: C, 33.29; H, 2.55; N, 7.79%. IR (cm^{-1}): 3050w br, 1591m, 1524s, 1443w, 1388s, 1342w, 1218m, 1170w, 1094m, 1019w, 899w, 818w, 668m, 617w.

2.1.3. Preparation of $\{[Cd_2(dmsuc)_2(dpa)(Hdpa)](ClO_4) \cdot 6H_2O\}_n$ (3)

$Cd(ClO_4)_2 \cdot 6H_2O$ (100 mg, 0.238 mmol), dpa (110 mg, 0.642 mmol) and 2,2-dimethylsuccinic acid (47 mg, 0.322 mmol) were added to 10 mL of distilled H_2O in a 23 mL Teflon lined Parr acid digestion bomb. The bomb was sealed and heated to 120 °C for 48 h at which point the bomb was gradually cooled to 23 °C. Colorless crystals of **3** (55 mg, 0.052 mmol, 44% yield based on Cd) were obtained. *Anal.* Calc. for $C_{32}H_{45}Cd_2ClN_6O_{18}$: C, 36.19; H, 4.27; N, 7.91. Found: C, 36.40; H, 4.25; N, 7.94%. IR (cm^{-1}): 3291w br, 1595s, 1481m, 1443w, 1432m, 1404m, 1358m, 1301w, 1281w, 1257m, 1206m, 1094s, 1016m, 952w, 918w, 899m, 842w, 813s, 795m, 765w, 728w, 671w, 623s.

Table 1
Crystal and structure refinement data for **1**–**3**.

Compound	**1**	**2**	**3**
Empirical formula	$C_{24}H_{42}Cl_2CoN_6O_{21.5}$	$C_{30}H_{28}Cd_3ClN_6O_{14}$	$C_{32}H_{45}Cd_2ClN_6O_{18}$
Formula weight	888.46	1069.23	1061.99
Collection T (K)	173	173	173
λ (Å)	0.71073	0.71073	0.71073
Crystal system	Triclinic	Triclinic	Monoclinic
Space group	$P\bar{1}$	$P\bar{1}$	$P2_1/n$
a (Å)	7.290(3)	9.3318(18)	12.926(3)
b (Å)	10.062(3)	13.676(3)	25.454(6)
c (Å)	26.152(7)	14.702(3)	13.907(3)
α (°)	98.21(2)	115.426(2)	90
β (°)	91.56(5)	100.074(2)	113.523(3)
γ (°)	106.92(5)	97.313(2)	90
V (Å^3)	1811.8(10)	1624.6(6)	4195.4(17)
Z	2	2	4
D_{calc} (g cm^{-3})	1.632	2.210	1.681
μ (mm^{-1})	0.716	2.113	1.157
Min./max. transmission	0.496	0.798	0.924
hkl ranges	$-9 \le h \le 9$, $-13 \le k \le 12$, $0 \le l \le 34$	$-12 \le h \le 11$, $-18 \le k \le 16$, $0 \le l \le 18$	$-16 \le h \le 16$, $-33 \le k \le 33$, $-18 \le l \le 17$
Unique reflections	8051	7149	9594
R (int)	0.0214	0.0302	0.0681
Parameters/ restraints	571/36	488/2	589/20
R_1 (all data)[a]	0.0505	0.0430	0.0837
R_1 ($I > 2\sigma(I)$)[a]	0.0448	0.0366	0.0459
wR_2 (all data)[b]	0.1185	0.0962	0.1204
wR_2 ($I > 2\sigma(I)$)[b]	0.1157	0.0925	0.1061
Max./min. residual (e$^-$/Å^3)	1.011/−1.016	1.384/−1.140	1.116/−1.099
Goodness-of-fit	1.049	1.071	1.036

[a] $R_1 = \sum||F_o| - |F_c||/\sum|F_o|$.
[b] $wR_2 = \{\sum[w(F_o^2 - F_c^2)^2]/\sum[wF_o^2]^2\}^{1/2}$.

2.1.4. X-ray crystallography

A pink block of **1** (with dimensions 0.40 × 0.25 × 0.15 mm), a colorless block of **2** (0.25 × 0.20 × 0.16 mm) and a colorless plate of **3** (0.35 × 0.25 × 0.05 mm) were subjected to single-crystal X-ray diffraction using a Bruker-AXS SMART 1k CCD instrument. Reflection data was acquired using graphite–monochromated Mo-Kα radiation (λ = 0.71073 Å). Crystals of **1** and **2** were non-merohedral twins, with twin laws determined by CELLNOW [20]. The reflection data were integrated with SAINT [21]. Lorentz and polarization effect and empirical absorption corrections were applied with TWINABS or SADABS [22]. The structures were solved using direct methods and refined on F^2 using SHELTXL [23]. All non-hydrogen atoms were refined with anisotropic thermal parameters. Hydrogen atoms bound to carbon atoms were placed in calculated positions and refined with isotropic thermal parameters using a riding model. The hydrogen atoms bound to any water molecules (except for the disordered cases in **1** and **3**) were found via Fourier difference maps, then restrained at fixed positions and refined with isotropic thermal parameters. One of the dmsuc carboxylate oxygen atoms in **3** is disordered over two positions in a 60/40 ratio. Relevant crystallographic data for **1**–**3** are listed in Table 1.

3. Results and discussion

3.1. Synthesis and spectral characterization

The coordination polymers **1–3** were obtained cleanly through the hydrothermal reaction of the appropriate metal perchlorate, either succinic acid or dimethylsuccinic acid, and dpa in a 1:1:2 mole ratio. The infrared spectra of **1–3** were consistent with their single-crystal structures. Medium intensity bands in the range of ~1600 to ~1200 cm^{-1} arise from stretching modes of the pyridyl rings of the dpa ligands. Features corresponding to pyridyl ring puckering exist in the region between ~930 and ~600 cm^{-1}. Asymmetric and symmetric C–O stretching modes of the fully deprotonated suc or dmsuc ligands were present at ~1520 and ~1360 cm^{-1}. The lack of bands in the region of ~1710 cm^{-1} indicates complete deprotonation of all carboxylate groups in **1–3**. Broad bands in the area of ~3400 to ~3200 cm^{-1} represent O–H stretching modes within water molecules of crystallization (**1** and **3**) and N–H stretching mdoes within the dpa or Hdpa ligands (all cases). The breadth of these features is attributed to hydrogen-bonding pathways (*vide infra*). Strong, broadened bands in the vicinity of 1090 cm^{-1} corroborate the presence of uncoordinated perchlorate anions in **1–3**.

3.1.1. Structural description of $\{[Co(suc)(Hdpa)_2(H_2O)_2](ClO_4)_2 \cdot 7.5H_2O\}_n$ (*1*)

Compound **1** contains an asymmetric unit of two crystallographically independent divalent cobalt atoms on inversion centers, two halves of two crystallographically distinct suc ligands, two singly protonated $Hdpa^+$ ligands, two aqua ligands, two uncoordinated perchlorate ions, and seven and a half water molecules of crystallization (Fig. 1). Operation of the inversion centers creates a $\{CoO_4N_2\}$ coordination environment at each cobalt ion, with trans nitrogen donor atoms from pendant, monodentate Hdpa ligands, trans aqua ligands and trans oxygen donor atoms belonging to *anti* conformation suc ligands. Bond lengths and angles about the cobalt ions are standard for a non-chelated octahedral coordination geometry (Table S1 in the Supplementary data).

The succinate ligands link adjacent cobalt ions with a bis(monodentate) bridging mode, to form two crystallographically independent 1D cationic $[Co(suc)(Hdpa)_2(H_2O)_2]_n^{2n+}$ coordination polymer chains arranged parallel to the *b* crystal direction (Fig. 2), heretofore denoted as chain-A (based on Co1) and chain-B (based on Co2). The Co···Co contact distances in both chain-A and chain-B are 10.062 Å, marking the *b* lattice parameter. Crystallographic distinction between the chains is provided by differences in the interring torsion angles within the Hdpa ligands (26.9° in chain-A, 29.0° in chain-B). Covalent connectivity within the chain-A and chain-B motifs is supplemented by hydrogen-bonding involving the central amine groups and protonated termini of the $Hdpa^+$ ligands and water molecules of crystallization. The unligated water molecules themselves form decorated short hydrogen-bonded chains with D3 classification [24], resembling the connectivity pattern of methylpropane. Uncoordinated perchlorate ions are anchored to the chains via hydrogen-bonding involving the water molecules of crystallization.

Aggregation of chain-A motifs into pseudolayers occurs through hydrogen-bonding involving water molecules of crystallization (O5W) bridging aqua ligands in one chain with unligated succinate oxygen atoms in an adjacent chain. Other interstitial water molecule of crystallization (O7W) links unligated succinate oxygen atoms with ligated succinate oxygen donors in a second chain-A motif (Fig. S1 in the Supporting Information). Interchain hydrogen-bonding patterns conjoining chain-B motifs are different. Here, water molecules of crystallization (O10W) located between the chains link unligated succinate oxygen atoms in both chains, and other unligated water molecules (O2W) bridge aqua ligands and ligated succinate oxygen atoms (Fig. S2). The pendant $Hdpa^+$ ligands permit interdigitation of neighboring pseudolayers and establishment of the three-dimensional structure of **1** through π–π stacking interactions with ring centroid-to-ring centroid distances of 3.721(2) and 3.744(2) Å (Fig. 3). Geometric parameters for the extensive hydrogen-bonding patterns in **1** are listed in Table S2 in the Supplementary data.

The structure of **1** contrasts greatly with that of its perchlorate-free congener $[Co(suc)(dpa)_2]_n$ despite the presence of *anti* conformation suc ligands in both cases. In the latter phase, the suc ligands adopt a bis(chelating) binding mode, made possible by the lack of any aqua ligands, thereby promoting homochiral 1D helical motifs which are connected to six others via dpa-mediated hydrogen-bonding [14]. The pendant dpa ligands in $[Co(suc)(dpa)_2]_n$ are not required to be protonated because of the absence of any unligated anionic species.

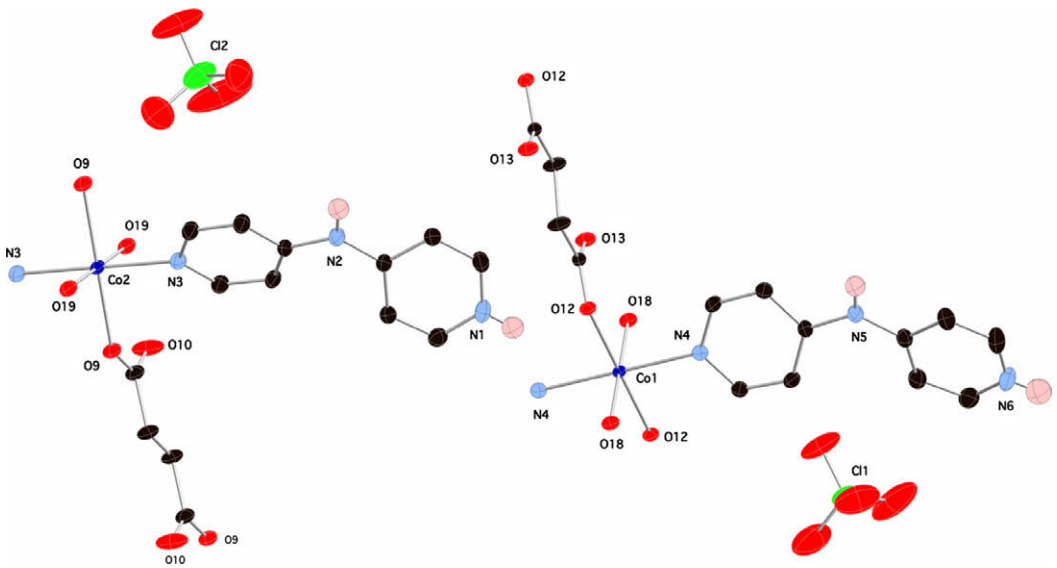


Fig. 1. Coordination environments in **1**. Thermal ellipsoids are drawn at 50% probability. Water molecules of crystallization are not shown.

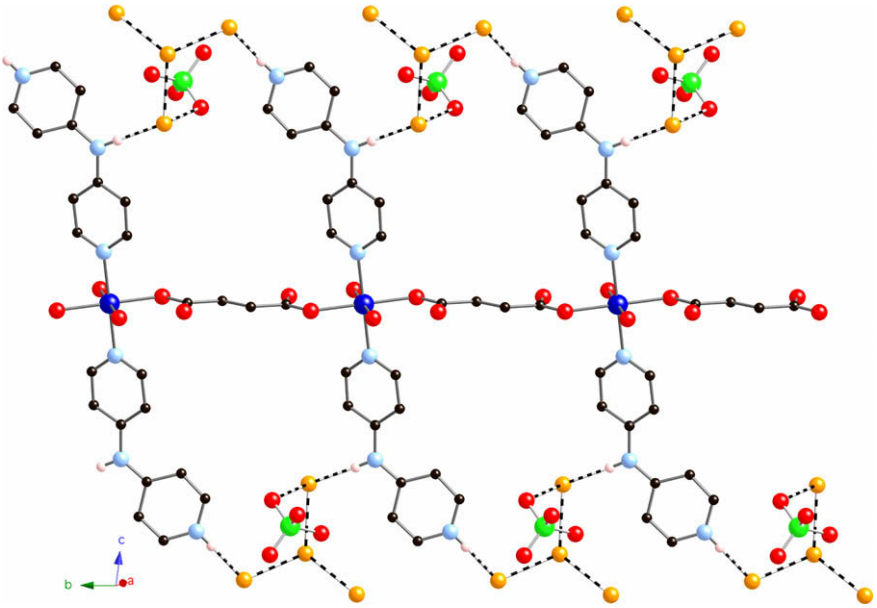


Fig. 2. A single chain-A motif in **1**, with neighboring perchlorate ions and water molecules of crystallization. Hydrogen-bonding is indicated as dashed lines. The chain-B motif is virtually identical except for a greater torsion within the pendant $Hdpa^+$ ligands.

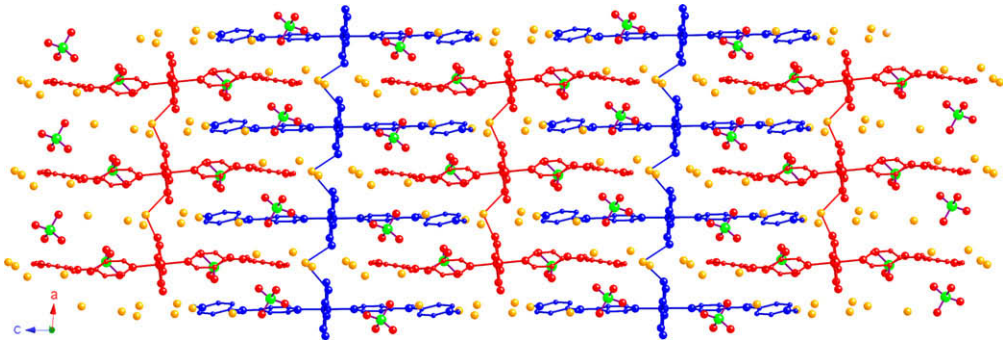


Fig. 3. Interdigitation of pseudolayers in **1**, shown in blue and red, respectively. (For interpretation of the references to colour in this figure legend, the reader is referred to the web version of this article.)

*3.1.2. Structural description of $\{[Cd_3(suc)_{2.5}(dpa)_2](ClO_4)\}_n$ (**2**)*

The asymmetric unit of compound **2** consists of three crystallographically distinct cadmium ions [Cd1–Cd3], two dpa ligands [dpa-A, N1–N3; dpa-B, N4–N6], two and one half succinate dianions [suc-A, O5–O8; suc-B, O11–O14; suc-C, O9–O10], and one unligated perchlorate anion (Fig. 4). The coordination environment at Cd1 is a distorted $\{CdO_6\}$ octahedron, with two oxygen donors from a chelating terminus of suc-C ligands, and four oxygen donor atoms from two different suc-A and suc-B ligands. The coordination environments at Cd2 and Cd3 are both $\{CdN_2O_5\}$ pentagonal bipyramids with axially disposed nitrogen donor ligands from crystallographically distinct dpa ligands. The equatorial plane at Cd2 is defined by two oxygen donors from a chelating suc-B dicarboxylate group, two oxygen atoms from another suc-B ligand in a 1,4-chelating binding mode, and one oxygen atom donor from a suc-A ligand. Similarly, the equatorial plane at Cd3 is marked by two oxygen donors from a chelating suc-A dicarboxylate group, two oxygen atoms from another suc-A ligand in a 1,4-chelating binding mode, and one oxygen atom donor from a suc-B ligand. Relevant bond lengths and angles for **2** are listed in Table S3 in the Supplementary data.

Cd2 and Cd3 atoms are linked by the *gauche* conformation suc-A and suc-B (four-C atom torsion angles = 69.5° and 71.1°, respectively) dianions to construct a $[Cd_2(suc)_2]_n$ chain motif, which contains an "infinite" string of corner-shared $[Cd_2O_2]$ rhomboids (Fig. 5). The Cd2···Cd2, Cd2···Cd3, and Cd3···Cd3 contact distances across these $[Cd_2O_2]$ rhomboids are 3.938, 3.793 and 4.128 Å, respectively. The $[Cd_2(suc)_2]_n$ chain motifs based on Cd2 and Cd3 atoms are linked together by Cd1 atoms, each bound to two suc-A and two suc-B ligands, thus forming a cationic $[Cd_3(suc)_2]_n^{2n+}$ layer as seen in Fig. 5.

Neighboring $[Cd_3(suc)_2]_n^{2n+}$ layers are connected into the overall cationic $[Cd_3(suc)_{2.5}(dpa)_2]_n^{n+}$ 3D coordination polymer network of **3** (Fig. 6) through tethering dpa ligands which bridge Cd2 and Cd3 atoms, and also through *anti* conformation bis(chelating) suc-C ligands that link Cd1 atoms. The through-ligand interlayer Cd···Cd contacts are 12.058, 11.940 and 9.240 Å for dpa-A, dpa-B and suc-C, respectively. The different bridging distances for the dpa ligands are caused by variances in their inter-ring torsion angles (28.8° for dpa-A, 41.3° for dpa-B). Wider inter-ring torsion angles appear to promote shorter metal–metal through dpa contact distances. Covalent connectivity in **2** is supplemented by π–π ∗stacking of the dpa pyridyl rings in the interlayer region (ring centroid-to-ring centroid distances = 3.670(3) and 3.823(3) Å).

Unligated perchlorate ions are anchored to the cationic coordination polymer framework by hydrogen-bonding interactions

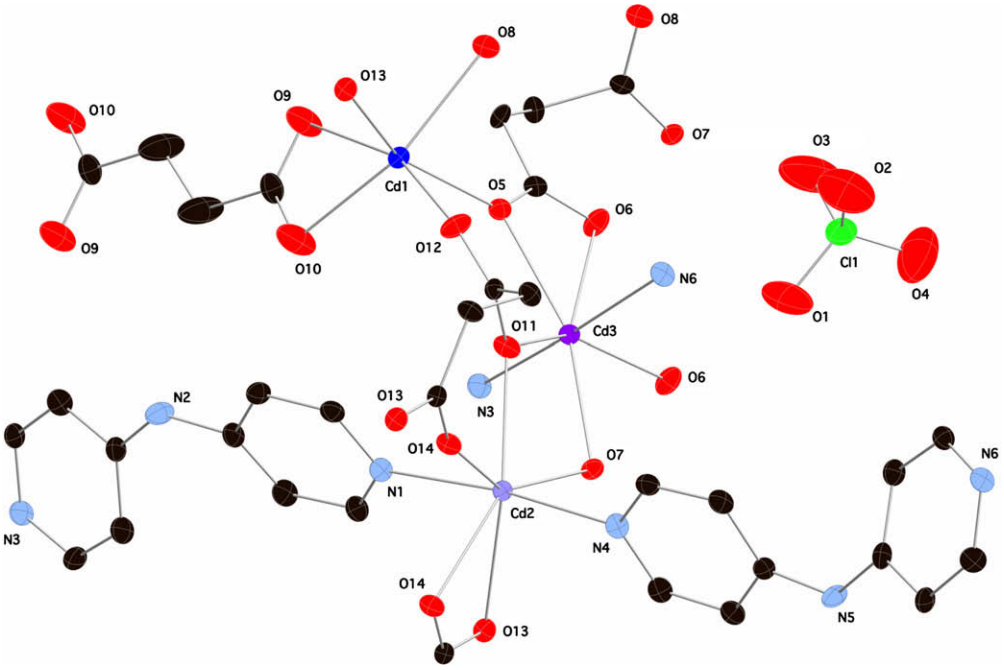


Fig. 4. Coordination environments in **2**. Thermal ellipsoids are drawn at 50% probability.

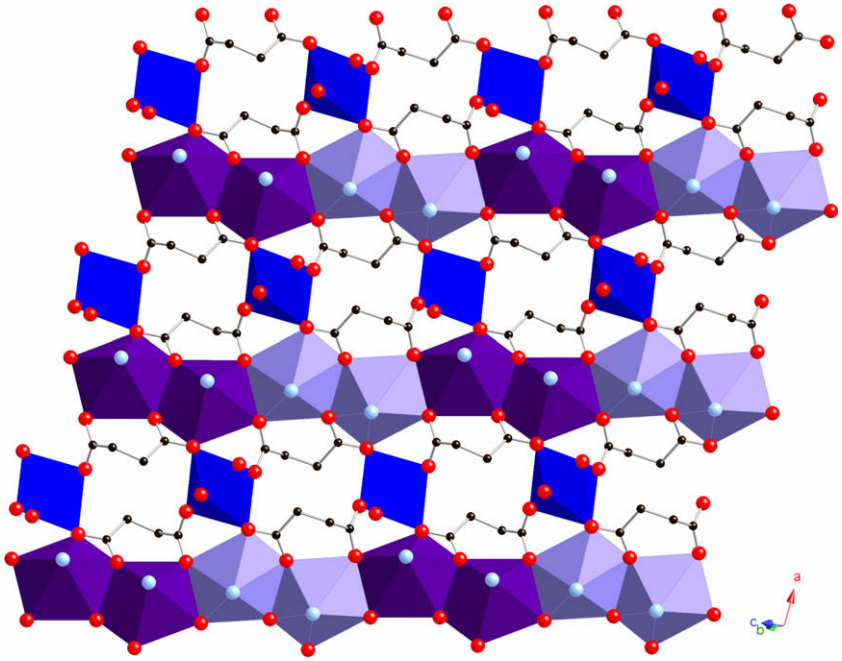


Fig. 5. A single $[Cd_3(suc)_2]_n^{2n+}$ layer in **2**. Cd1, Cd2 and Cd3 coordination spheres are shown as dark blue, light purple and dark purple polyhedra, respectively. (For interpretation of the references to colour in this figure legend, the reader is referred to the web version of this article.)

fostered by the dpa central amine groups. Hydrogen-bonding parameters for **2** are given in Table S2 in the Supplementary data. According to a calculation performed with PLATON [25], the perchlorate ions occupy 10.7% of the unit cell volume of **2**.

Each Cd1 atom can be considered a 5-connected node, with connections within a single $[Cd_3(suc)_2]_n^{2n+}$ layer subunit to two Cd1 atoms and two $[Cd_2O_2]$ dimers through suc-A and suc-B ligands, and one connection to a Cd1 atom in an adjacent layer via the bis(chelating) suc-C ligands. The centroids of the $[Cd_2O_2]$ dimers can be treated as 6-connected nodes, linking two Cd1 atoms and two other $[Cd_2O_2]$ dimers within a single $[Cd_3(suc)_2]_n^{2n+}$ layer via suc-A and suc-B ligands, and two other $[Cd_2O_2]$ dimers in adjacent layers through dpa ligands. Thus the coordination polymer framework of **2** can be represented as a binodal (5,6)-connected lattice, whose topological symbol is $(4^6 6^4)(4^{10}6^5)$ as calculated by TOPOS software (Fig. 7) [26]. The long Vertex Symbol for this net is $(4.4.4.4.4.4.6_3.6_4.6_7.6_7)(4.4.4.4.4.4.4.4.4.4.6_2.6_3.6_4.6_7.6_7)$. To the best of our knowledge **2** is the first example of this binodal

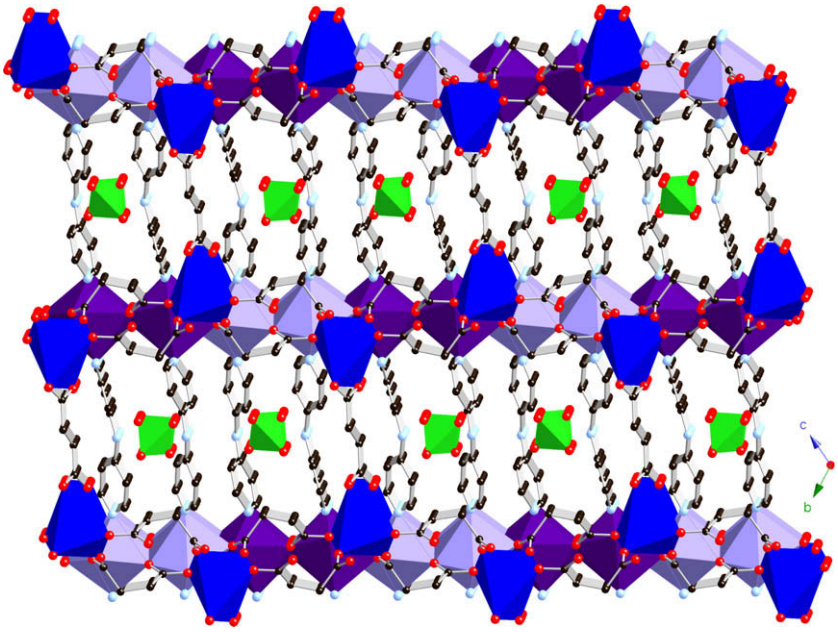


Fig. 6. The 3D coordination polymer network of **2**. Perchlorate ions can be seen in the incipient voids.

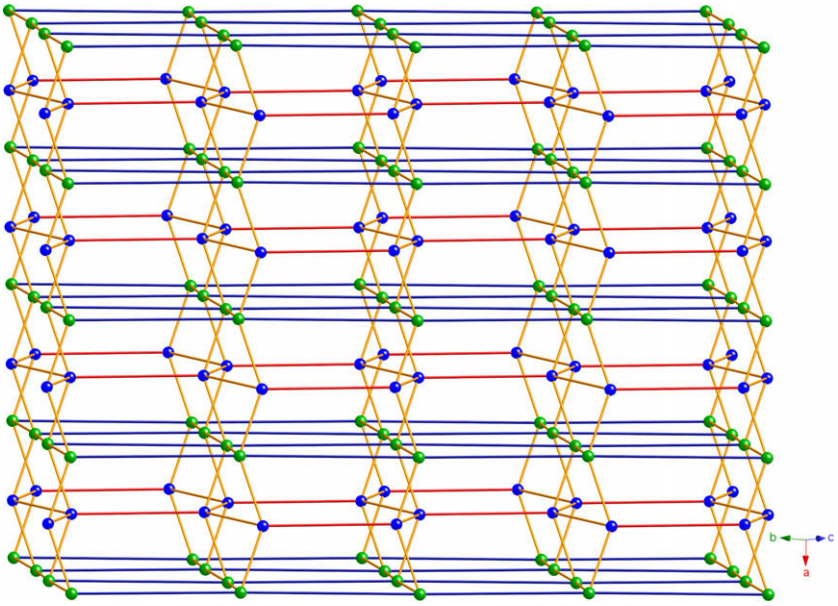


Fig. 7. Framework perspective of the $(4^6 6^4)(4^{10}6^5)$ (5,6)-connected binodal network in 2. Blue and green spheres represent the Cd1 atoms and $[Cd_2O_2]$ dimer centroids. (For interpretation of the references to colour in this figure legend, the reader is referred to the web version of this article.)

topology. The network can also be viewed as alternating (4,4) rectangular and (6,3) hexagonal grids parallel to the *bc* crystal plane being joined by pillaring ligands along the *a* crystal direction.

The structure of **2** contrasts with that of its perchlorate-free analog, $\{[Cd(suc)(dpa)] \cdot H_2O\}_n$ [14], which possesses a twofold interpenetrated primitive cubic lattice formed from $[Cd(suc)]_n$ flat layers pillared by dpa ligands. In this material all of the suc ligands adopt strict *anti* conformations, with their carbon atoms resting on a crystallographic mirror plane. It is plausible that the necessity of accommodating the "spherical" perchlorate ligands into the framework forces the adjustment of some of the suc ligands into a more curved gauche conformation, resulting in a different 3D coordination polymer connectivity during self-assembly.

3.1.3. Structural description of $\{[Cd_2(dmsuc)_2(dpa)(Hdpa)](ClO_4) \cdot 6H_2O\}_n$ (3)

The asymmetric unit of compound **3** (Fig. 8) contains two divalent cadmium atoms, two dmsuc dianions [dmsuc-A, O1–O4; dmsuc-B, O5–O8], one dpa molecule, one protonated $Hdpa^+$ cation, one unligated perchlorate anion, and six water molecules of crystallization, one of which is split equally over two positions. The coordination environment at Cd1 is a distorted $\{CdO_6N\}$ pentagonal bipyramid, with a chelating carboxylate terminus from a dmsuc-B ligand occupying one axial and one equatorial position, a chelating carboxylate belonging to dmsuc-A filling two equatorial positions, and a chelating carboxylate group from a second dmsuc-A ligand taking up another equatorial site and the second

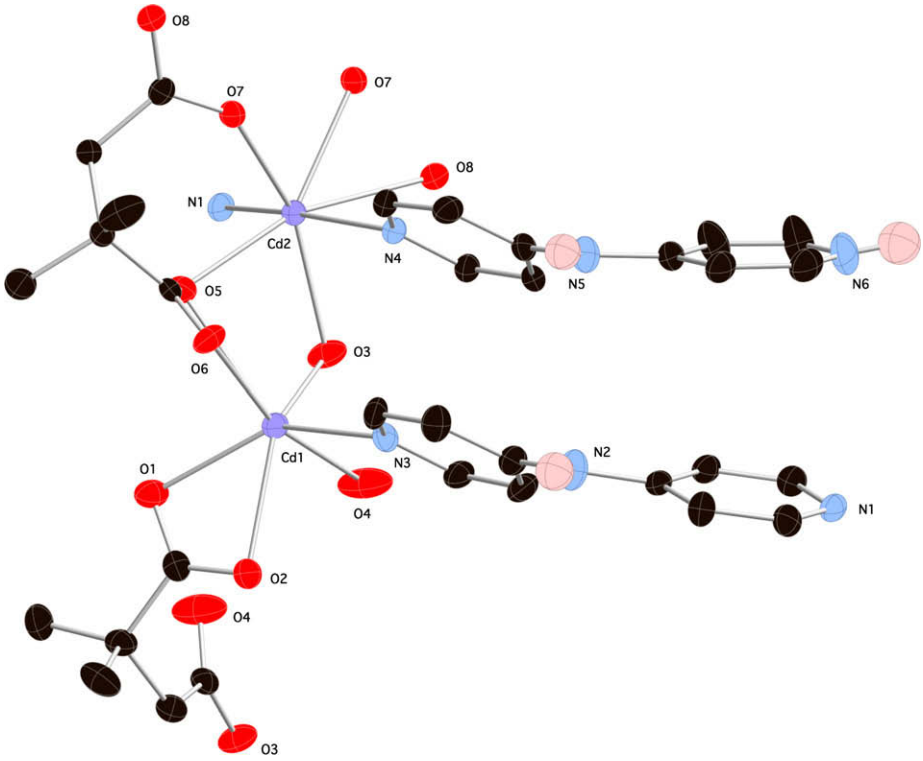


Fig. 8. Coordination environment of **3**, with thermal ellipsoids drawn at 50% probability. The perchlorate ion and water molecules of crystallization have been omitted.

axial position. The remaining equatorial site is defined by a nitrogen donor atom from an unprotonated dpa ligand. The divalent Cd2 atom also adopts a distorted pentagonal bipyramidal coordination geometry, but with a $\{CdO_5N_2\}$ arrangement. Its axial sites are occupied by nitrogen donor atoms from dpa and $Hdpa^+$ ligands. The equatorial positions at Cd2 are filled by two atoms from a dmsuc-B ligand in a 1,4-chelating binding mode, a chelating carboxylate endgroup of a second dmsuc-B ligand, and an oxygen donor atom belonging to a dmsuc-A ligand. Pertinent bond lengths and angles at the cadmium atoms are listed in Table S4 in the Supplementary data.

Each *gauche* conformation dmsuc-A ligand (four-C atom torsion angle = 57.9°) bridges two Cd1 atoms with a bis(chelating) binding mode, and also connects to a Cd2 atom via one of its carboxylate oxygen atoms. The dmsuc-B ligands also adopt a *gauche* conformation (66.8° torsion angle), and bridge Cd1 and Cd2 atoms in a bis(chelating) fashion, while binding to a second Cd2 via a 1,4-chelating arrangement. The dmsuc ligands with their divergent binding modes thus connect the cadmium atoms into a 1D $[Cd_2(dmsuc)_2]_n$ chain motif (Fig. 9). This chain contains an alternating pattern of three 4-membered{CdOCdO} and 14-membered $\{Cd(OC_4O)Cd(OC_4O)\}$ rings, across which the respective Cd···Cd contact distances measure 3.692, 3.846, 3.692 and 6.338 Å.

Conterminous $[Cd_2(dmsuc)_2]_n$ chains are connected into a 2D grid motif through tethering dpa ligands, forming (6,3) herringbone grid $[Cd_2(dmsuc)_2(dpa)(Hdpa)]_n^{n+}$ cationic layers (Fig. 10), which stack in an *AAA* pattern along the [101] crystal direction (Fig. S1). The pendant, monoprotonated $Hdpa^+$ ligands project across the grid apertures and engage in hydrogen-bonding to dmsuc-A carboxylate oxygen atoms through their protonated pyridyl termini. The water molecules of crystallization are situated between these layers, anchored to the coordination polymer framework by hydrogen-bonding donation to carboxylate oxygen atoms and hydrogen-bonding acceptance from dpa and $Hdpa^+$ central amine groups. Uncoordinated perchlorate anions are also situated in the interlamellar regions and engage in hydrogen-bonding with water molecules of crystallization. Hydrogen-bonding data for **3** is given in Table S2 in the Supplementary data. The water molecules of crystallization aggregate into a hydrogen-bonded six molecule cluster with a decorated D5 discrete five-molecule chain [24], with an additional water molecule positioned off the third molecule in the chain in a connectivity pattern reminiscent of 3-methylpentane (Fig. 11).

In contrast to **3**, its perchlorate-free analog $[Cd(dms)(dpa)]_n$ manifests a twofold interpenetrated (4,4)-grid acentric layered topology [16]. The presence of the protonated $Hdpa^+$ ligands lying

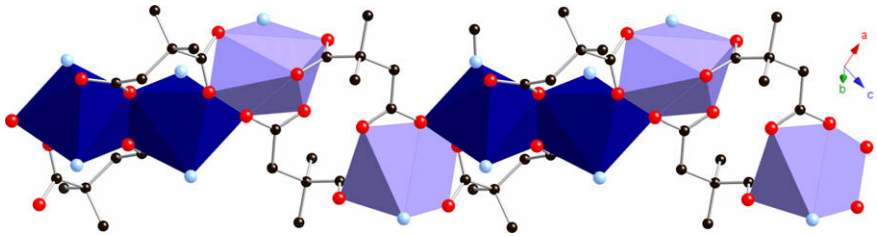


Fig. 9. A single $[Cd_2(dmsuc)_2]_n$ chain motif in **3**.

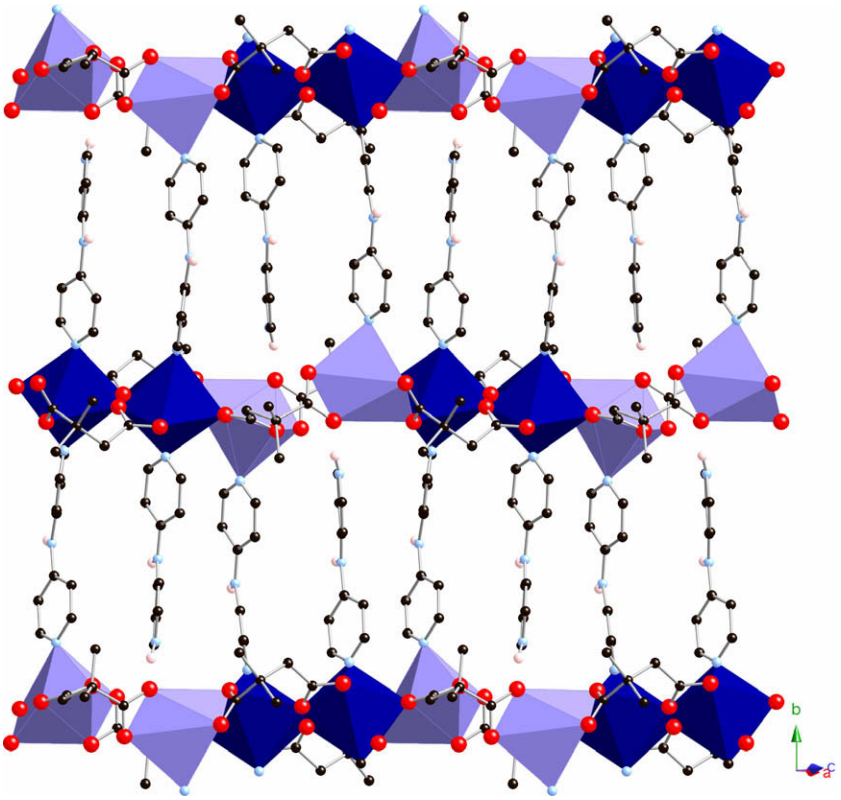


Fig. 10. A single (6,3) hexagonal grid $[Cd_2(dmsuc)_2(dpa)(Hdpa)]_n^{n+}$ cationic layer in **3**. Hydrogen-bonding is indicated as dashed lines.

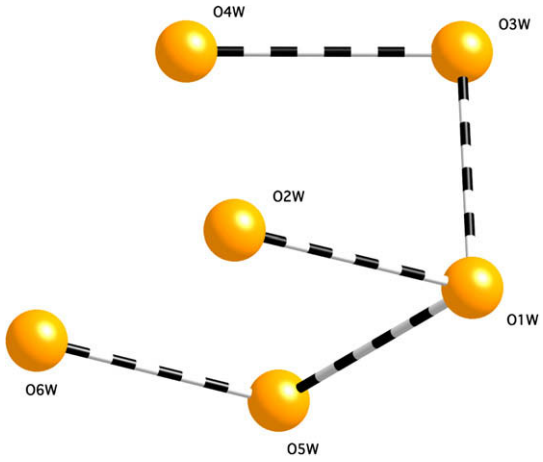


Fig. 11. The decorated D5 water molecule discrete chain in **3**.

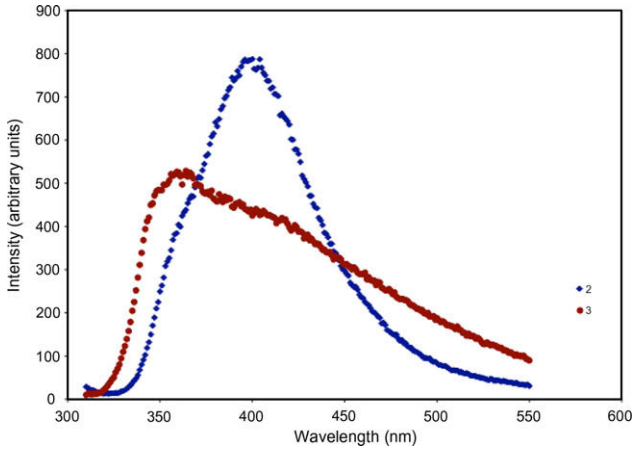


Fig. 12. Luminescence spectra of **2** and **3**.

within the grid apertures in **3** prevents interpenetration in the present case. These ligands also obviate the formation of a covalent (4,4)-grid because of their lack of covalent bridging via the distal pyridyl nitrogen atoms.

*3.1.4. Luminescent properties of **2** and **3***

In the solid state at room temperature both **2** and **3** exhibited blue-violet luminescence upon ultraviolet excitation (λ = 300 nm) (Fig. 12). The luminescent behavior of **2** and **3** is most likely attributable to ligand-centered $\pi \rightarrow \pi*$ or $\pi \rightarrow$ n orbital transitions within the aromatic rings of the dpa/Hdpa+ ligands, by comparison with other luminescent d^{10} coordination polymers [27]. The emission maximum for **2** (λ_{max} = 400 nm) is redshifted relative to that of **3** (λ_{max} = 360 nm). The spectral profile for **3** is much broader, plausibly a result of more energy loss due to radiative non-emissive pathways in the pendant $Hdpa^+$ ligands, which have greater vibrational degrees of freedom because of the absence of a metal atom at one terminus.

4. Conclusions

Incorporation of perchlorate ions into succinate/dpa dual-ligand coordination polymers has resulted in dramatic alterations in overall topology from those observed in prior anion-free derivatives. These changes are promoted either by the protonation of dpa ligands (in **1**) or the formation of a cationic 3D network (in **2**). While the perchlorate-free derivative of **2** possesses a common twofold interpenetrated primitive cubic lattice, **2** itself manifests a novel

binodal 3D cationic lattice featuring alternating (4,4) rectangular grid and (6,3) hexagonal grid layers linked through dpa ligands. Increasing the steric requirements of the dicarboxylate component resulted in a decrease in dimensionality from 3D in **2** to 2D in **3**, with concomitant protonation of the dpa ligands. The use of dipyridyl ligands containing hydrogen-bonding donating functional groups can assist in the inclusion of oxoanions during self-assembly, forcing the aliphatic α,ω-dicarboxylate ligands into different conformations and thus adjusting overall coordination polymer topology. Further efforts in this direction are currently underway.

Acknowledgements

The authors gratefully acknowledge Michigan State University and the donors of the American Chemical Society Petroleum Research for financial support of this work. We thank Dr. Rui Huang for performing the elemental analysis. E.S. thanks the MSU High School Honors Science Program and Dr. Gail Richmond for his participation in this research.

Appendix A. Supplementary data

CCDC 704778–704780 contains the supplementary crystallographic data for complexes **1**–**3**. These data can be obtained free of charge via http://www.ccdc.cam.ac.uk/conts/retrieving.html, or from the Cambridge Crystallographic Data Centre, 12 Union Road, Cambridge CB2 1EZ, UK; fax: (+44) 1223 336 033; or e-mail: deposit@ccdc.cam.ac.uk. Supplementary data associated with this article can be found, in the online version, at doi:10.1016/j.poly.2008.12.026.

References

[1] (a) H. Li, M. Eddaoudi, M. O'Keeffe, O.M. Yaghi, Nature 402 (1999) 276;
(b) R. Matsuda, R. Kitaura, S. Kitagawa, Y. Kubota, R.U. Belosludov, T.C. Kobayashi, H. Sakamoto, T. Chiba, M. Takata, Y. Kawazoe, Y. Mita, Nature 436 (2005) 238;
(c) L. Pan, D. Holson, L.R. Ciemnolonski, R. Heddy, J. Li, Angew. Chem., Int. Ed. 45 (2006) 616;
(d) N.L. Rosi, J. Eckert, M. Eddaoudi, D.J. Vodak, J. Kim, M. O'Keeffe, O.M. Yaghi, Science 300 (2003) 1127;
(e) M. Dinca, A.F. Yu, J.R. Long, J. Am. Chem. Soc. 128 (2006) 8904;
(f) G. Férey, M. Latroche, C. Serre, F. Millange, T. Loiseau, A. Percheron-Guegan, Chem. Commun. (2003) 2976;
(g) X. Zhao, B. Xiao, A.J. Fletcher, K.M. Thomas, D. Bradshaw, M.J. Rosseinsky, Science 306 (2004) 1012;
(h) J.L.C. Roswell, O.M. Yaghi, Angew. Chem., Int. Ed. 44 (2005) 4670;
(i) M. Kondo, T. Okubo, A. Asami, S.I. Noro, T. Yoshitomi, S. Kitagawa, T. Ishii, H. Matsuzaka, Angew. Chem., Int. Ed. 38 (1999) 140;
(j) A.C. Sudik, A.R. Millward, N.W. Ockwig, A.P. Cote, J. Kim, O.M. Yaghi, J. Am. Chem. Soc. 127 (2005) 7110.
[2] (a) J.S. Seo, D. Whang, H. Lee, S.I. Jun, J. Oh, Y.J. Jeon, K. Kim, Nature 404 (2000) 982;
(b) A. Cingolani, S. Galli, N. Masciocchi, L. Pandolfo, C. Pettinari, A. Sironi, J. Am. Chem. Soc. 127 (2005) 6144.
[3] (a) Q.-R. Fang, G.-S. Zhu, M. Xue, J.-Y. Sun, S.-L. Qiu, Dalton Trans. (2006) 2399;
(b) X.-M. Zhang, M.-L. Tong, H.K. Lee, X.-M. Chen, J. Solid State Chem. 160 (2001) 118;
(c) O.M. Yaghi, H. Li, T.L. Groy, Inorg. Chem. 36 (1997) 4292.
[4] (a) N. Guillou, P.M. Forster, Q. Gao, J.S. Chang, M. Nogues, S.-E. Park, A.K. Cheetham, G. Férey, Angew. Chem., Int. Ed. 40 (2001) 2831;
(b) C.-D. Wu, A. Hu, L. Zhang, W. Lin, J. Am. Chem. Soc. 127 (2005) 8940;
(c) H. Han, S. Zhang, H. Hou, Y. Fan, Y. Zhu, Eur. J. Inorg. Chem. 8 (2006) 1594;
(d) W. Mori, S. Takamizawa, C.N. Kato, T. Ohmura, T. Sato, Micropor. Mesopor. Mater. 73 (2004) 15;
(e) S.G. Baca, M.T. Reetz, R. Goddard, I.G. Filippova, Y.A. Simonov, M. Gdaniec, N. Gerbeleu, Polyhedron 25 (2006) 1215.
[5] (a) L.G. Beauvais, M.P. Shores, J.R. Long, J. Am. Chem. Soc. 122 (2000) 2763;
(b) H. Jianghua, Y. Jihong, Z. Yuetao, P. Qinhe, X. Ruren, Inorg. Chem. 44 (2005) 9279.
[6] (a) S. Zang, Y. Su, Y. Li, Z. Ni, Q. Meng, Inorg. Chem. 45 (2006) 174;
(b) L. Wang, M. Yang, G. Li, Z. Shi, S. Feng, Inorg. Chem. 45 (2006) 2474;
(c) S. Wang, Y. Hou, E. Wang, Y. Li, L. Xu, J. Peng, S. Liu, C. Hu, New J. Chem. 27 (2003) 1144.
[7] (a) L.A. Borkowski, C.L. Cahill, Cryst. Growth Des. 6 (2006) 2248;
(b) J. Baier, U. Thewalt, Z. Anorg. Allg. Chem. 628 (2002) 315.
[8] (a) R. Vaidhyanathan, S. Natarajan, C.N.R. Rao, Inorg. Chem. 41 (2002) 5226;
(b) C. Livage, C. Egger, G. Férey, Chem. Mater. 13 (2001) 410;
(c) C. Livage, C. Egger, M. Nogues, G. Férey, Chem. Mater. 11 (1999) 1546;
(d) C. Livage, C. Egger, M. Nogues, G. Férey, J. Mater. Chem. 8 (1998) 2743;
(e) P.M. Forster, A.K. Cheetham, Angew. Chem., Int. Ed. 41 (2002) 457;
(f) S.-M. Ying, J.-G. Mao, Y.-Q. Sun, H.-Y. Zen, Z.-C. Dong, Polyhedron 22 (2003) 3097;
(g) Y.Q. Zheng, Z.P. Kong, Z. Anorg. Allg. Chem. 629 (2003) 1469.
[9] L. Han, Y. Zhou, W.N. Zhao, Cryst. Growth Des. 8 (2008) 2052.
[10] L. Xu, G.-C. Guo, B. Liu, M.-S. Wang, J.-S. Huang, Inorg. Chem. Commun. 7 (2004) 1145.
[11] H.-P. Jia, W. Li, Z.-F. Ju, J. Zhang, Eur. J. Inorg. Chem. (2006) 4264.
[12] B. Chen, C. Liang, J. Yang, D.S. Contreras, Y.L. Clancy, E.B. Lobkovsky, O.M. Yaghi, S. Dai, Angew. Chem., Int. Ed. 45 (2006) 1390.
[13] M.R. Montney, S. Mallika Krishnan, N.M. Patel, R.M. Supkowski, R.L. LaDuca, Inorg. Chem. 46 (2007) 7362.
[14] M.R. Montney, S. Mallika Krishnan, N.M. Patel, R.M. Supkowksi, R.L. LaDuca, Cryst. Growth Des. 7 (2007) 1145.
[15] K.A. Brown, D.P. Martin, R.M. Supkowksi, R.L. LaDuca, Cryst. Eng. Commun. 10 (2008) 846.
[16] P.J. Zapf, R.L. LaDuca, R.S. Rarig, K.M. Johnson, J. Zubieta, Inorg. Chem. 37 (1998) 3411.
[17] S. Mallika Krishnan, N.M. Patel, W.R. Knapp, R.M. Supkowski, R.L. LaDuca, Cryst. Eng. Commun. 9 (2007) 503.
[18] M.A. Braverman, R.M. Supkowski, R.L. LaDuca, J. Solid State Chem. 180 (2007) 1852.
[19] D.P. Martin, R.M. Supkowski, R.L. LaDuca, Inorg. Chem. 46 (2007) 7917.
[20] G.M. Sheldrick, CELLNOW, University of Göttingen, Göttingen, Germany, 2003.
[21] SAINT, Software for Data Extraction and Reduction, Version 6.02 Bruker AXS Inc., Madison, WI, 2002.
[22] SADABS, Software for Empirical Absorption Correction, Version 2.03 Bruker AXS Inc., Madison, WI, 2002.
[23] G.M. Sheldrick, SHELXTL, Program for Crystal Structure Refinement, University of Göttingen, Göttingen, Germany, 1997.
[24] (a) L. Infantes, S. Motherwell, Cryst. Eng. Commun. 4 (2002) 454;
(b) L. Infantes, J. Chisholm, S. Motherwell, Cryst. Eng. Commun. 5 (2003) 480.
[25] A.L. Spek, PLATON, A Multipurpose Crystallographic Tool Utrecht University, Utrecht, The Netherlands, 1998.
[26] V.A. Blatov, A.P. Shevchenko, V.N. Serezhkin, J. Appl. Crystallogr. 33 (2000) 1193.
[27] (a) J.C. Dai, X.T. Wu, Z.Y. Fu, C.P. Cui, S.M. Hu, W.X. Du, L.M. Wu, H.H. Zhang, R.Q. Sun, Inorg. Chem. 41 (2002) 1391;
(b) W. Chen, J.Y. Wang, C. Chen, Q. Yue, H.M. Yuan, J.S. Chen, S.N. Wang, Inorg. Chem. 42 (2003) 944;
(c) N. Hao, E. Shen, Y.B. Li, E.B. Wang, C.W. Hu, L. Xu, Eur. J. Inorg. Chem. (2004) 4102.

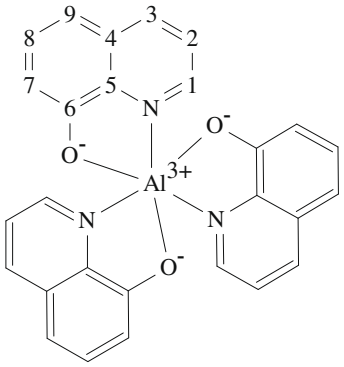


Fig. 1. Molecular structure of Alq_3, tris(quinolin-8-olato)aluminum(III). Carbon atom numbering is shown on one of the ligands.

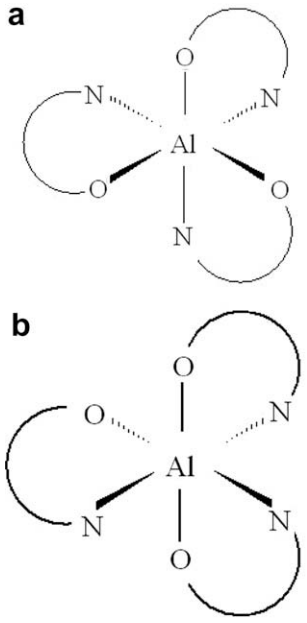


Fig. 2. (a) *Facial* and (b) *meridional* isomers of Alq_3.

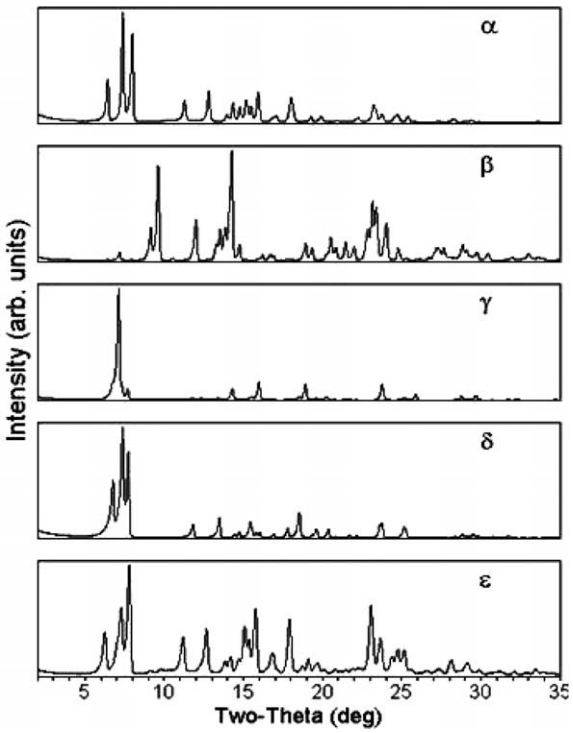


Fig. 3. Room-temperature X-ray powder diffraction patterns for α, β, γ, δ, and ε Alq_3.

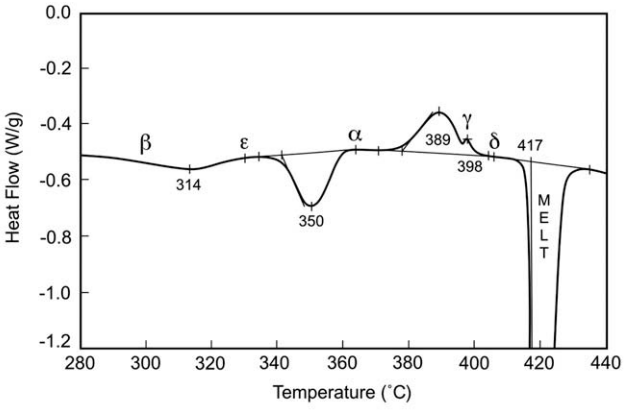


Fig. 4. Differential scanning calorimetry (DSC) curve for Alq_3. Temperatures of phase transitions are indicated on the plot. Labels indicate crystalline forms identified by *in situ* high-temperature XRD after heating to preset temperatures (β, 290 °C; ε, 330 °C; α, 365 °C; γ, 389 °C; δ, 405 °C).

2.1. Identification of Alq_3 phases by X-ray powder diffraction

X-ray powder diffraction (XRPD) is the primary technique used to assess polymorphism (same molecular species, different crystal structure) in crystalline materials. Five crystalline phases (α, β, γ, δ, and ε) of Alq_3 have been identified using XRPD [2–6] and their diffraction patterns are shown in Fig. 3.

2.2. Determination of the effect of thermal processing on Alq_3 phase transitions

To better understand thermal factors involved with the generation of the Alq_3 phases identified by XRPD, differential scanning calorimetry (DSC) was utilized. In Fig. 4, a DSC curve (heating rate 10 °C/min) for an Alq_3 sample (starting phase β Alq_3, Eastman Kodak Company) is shown. Multiple phase transitions that result from thermal processing of Alq_3 are evident.

At the temperatures where the endotherm (valley) and exotherm (peak) transitions occur in the DSC pattern, high-temperature X-ray powder diffraction (HTXRD) patterns were collected to identify the corresponding Alq_3 phase. Based on the HTXRD data, the five crystalline phases of Alq_3 identified previously are noted on the DSC pattern in Fig. 4. Each phase was identified by collecting XRD patterns immediately upon reaching a defined temperature slightly beyond the DSC transition temperature. As-received β Alq_3 was heated from 20 to 365 °C at a rate of 50 °C/min. At 365 °C 0 min (collected immediately after reaching temperature), the diffraction pattern shows Alq_3 as the α form (Fig. 5). This result is consistent with the DSC endotherm at 350 °C. After 5 min, there are small changes in the diffraction pattern that become better defined in the 15 min annealing data set, where the diffraction pattern for γ Alq_3 begins to emerge. After 1 h, γ Alq_3 is the only phase detected. Continued annealing (up to 14 h) does not produce any further change in the diffraction pattern. Upon cooling this specimen back to room temperature, XRPD data indicated that γ Alq_3 is still present.

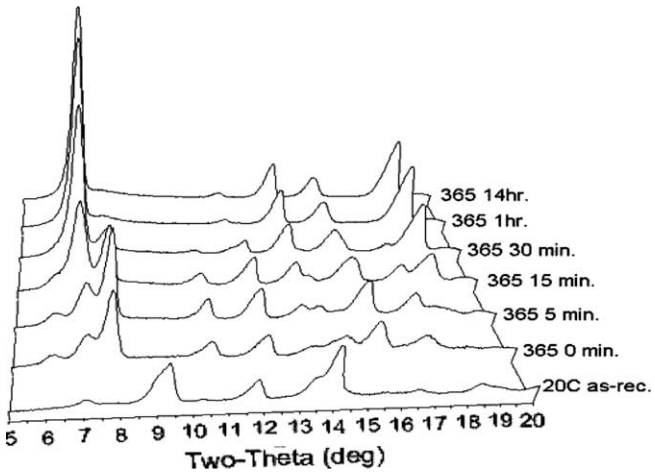


Fig. 5. High-temperature X-ray diffraction patterns for Alq_3 heated to 365 °C.

In thin films deposited using vapor deposition (VD) process, Alq_3 powder is heated at a defined temperature for a prolonged period of time, similar to what is shown in Fig. 5. The XRD patterns in Fig. 5 indicate that the phase conversion process in Alq_3 is dependent not only on the temperature but also on the time held at that temperature. We often use DSC as a method to define phase transition temperatures, noting the temperature for an observed endotherm or exotherm occurring at a specified heating or cooling rate. However, in some materials the kinetics are sluggish and, with time, phase transitions can take place at temperatures below those indicated by DSC data. A similar result was observed by HTXRD for annealing at 305 °C. Initially the sample was β Alq_3; however, upon reaching 305 °C, the sample was observed to convert to ε Alq_3. After 15 min, α Alq_3 was observed to be present, and after 1 h, the sample was completely converted to α Alq_3, even though the phase transition is observed by DSC at 350 °C. Observing the patterns for both ε Alq_3 and α Alq_3 at different temperatures during HTXRD experiments is evidence that these are two distinct Alq_3 phases. Further, contrary to the appearance of the DSC trace, α Alq_3 is thermodynamically the more stable of these two phases at temperatures as low as 305 °C.

Another important observation made during the thermal annealing studies of Alq_3 is that once the β and ε phases have been converted to the α, γ, or δ forms, or taken beyond the Alq_3 melting point (417 °C), β and ε Alq_3 will not be observed again after thermal processing by any means. In OLEDs, facial isomers are particularly desirable due to their blue-shifted fluorescence [11–13] and high quantum yield [11]. Procedures to convert from one crystalline form to another are described in detail in several patents and references [4,5,11,13]. Currently the most common method for depositing Alq_3 in OLED devices is VD, which results in formation of the α form in thin films. Efforts to make OLEDs with blue fluorescent Alq_3 films using solution processed deposition methods are being explored.

2.3. Determination of the crystal structures by single-crystal X-ray diffraction

Single-crystal X-ray diffraction was used to investigate four of the five crystalline phases of Alq_3 and the isomers that they contain. Crystals of ε Alq_3 were obtained using the HTXRD heating stage by heating β Alq_3 at 350 °C for 5 min while the Alq_3 sample on a platinum heating strip was covered with a beryllium foil [5]. The molecules in the crystal structure of ε Alq_3 are *meridional* as detailed in Ref. [5]. Crystals of δ Alq_3 for single-crystal structure determination were grown in our laboratory by a combination of sublimation and annealing in vacuum. This rather complicated procedure was developed, based upon our accumulated understanding of phase interconversions in Alq_3. The procedure is described in detail in Ref. [4]. Although thin, these crystals were found to be of acceptable quality for single-crystal data collection. The structure of δ Alq_3 was found to contain exclusively the *facial* isomer [3,4]. Although the γ phase has been identified [2] using powder XRD, to the best of our knowledge, a single-crystal XRD investigation of this phase has not been published. We too were unable to grow single crystals of the γ crystalline phase of Alq_3. Recent spectroscopic evidence (NMR, see below) has shown unambiguously that γ Alq_3 is *facial*. Chunky, excellent quality single crystals of β Alq_3 with perfectly formed surfaces can be easily obtained by subliming β Alq_3 powder in a tube furnace at 280 °C. The β Alq_3 structure was determined to contain exclusively the *meridional* isomer [2].

A structure of the α form, containing the *meridional* isomer, has been proposed on the basis of powder XRD data [2]. In the course of our HTXRD studies a thin beryllium foil is usually placed on top of the analyzed powder to prevent loss of sample through sublimation. When beryllium foil was not used, needle-like crystals identified as α Alq_3 were found to form on the cooler region of the platinum heating strip. The single crystals of α Alq_3 appeared to have the same unit-cell parameters as reported previously [2] using XRPD. The Alq_3, however, appeared to be present mostly as the *facial* isomer, with a high degree of disorder [5]. Powder XRD patterns were calculated for the present disordered structure of α Alq_3 and for the structure that was previously proposed [2]. The predictions are compared with experimental data in Figs. 6 and 7. Although both calculated patterns show rather good agreement with the observed data, upon close inspection the present

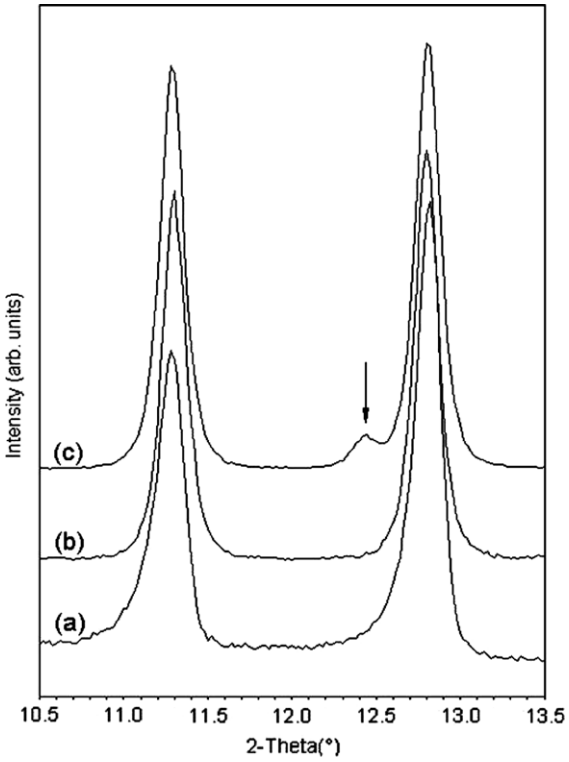


Fig. 6. Comparison of selected range powder XRD patterns for α Alq_3. (a) Observed pattern from Fig. 3; (b) calculated pattern based on the present disordered structure (c) calculated pattern based on the prior, fully ordered structure [2]. Arrow indicates an hkl (0–12) peak that is predicted only for the prior structure and is absent in the observed pattern.

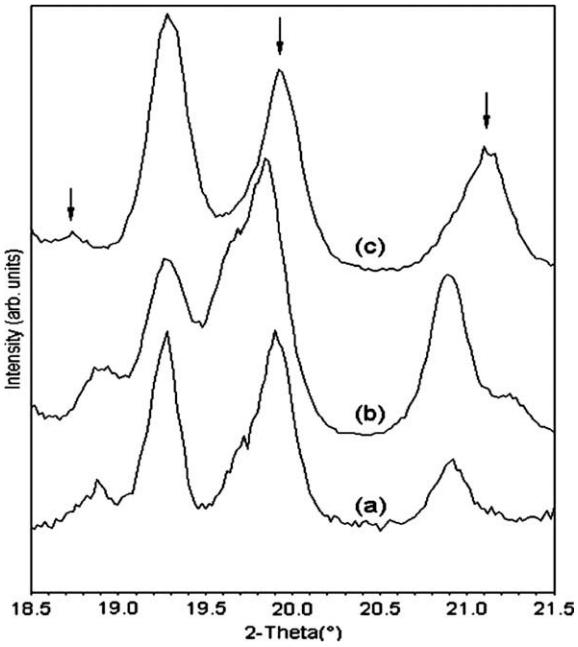


Fig. 7. Comparison of selected range powder XRD patterns for α Alq_3. (a) Observed pattern from Fig. 3; (b) calculated pattern based on the present disordered structure, (c) calculated pattern based on the prior, fully ordered structure [2]. Arrows indicate peaks that are predicted for the prior structure but are absent or shifted in both the predicted pattern for the present structure and in the observed pattern: hkl (1–21) at 18.7° 2θ, hkl (0–23) at 20.0° 2θ, and hkl (−112) at 21.1° 2θ.

disordered structure better reproduces the observed powder pattern.

Although the structure obtained by XRD appears to be predominantly or entirely *facial*, various spectroscopies are more consistent with a *meridional* composition (particularly NMR; see later sections). To resolve this contradiction, we have reconsidered the structural conclusions that can be drawn from the XRD. Somewhat overstated, our hypothesis is that α Alq_3 could be a disordered analog of ε Alq_3, with *meridional* conformation. A conclusive test of this model is not possible at present because of the difficulties involved in analyzing a disordered structure with weakly diffracting, imperfect, tiny crystals.

The unit-cell parameters for all five crystalline phases are compared in Table 1, and molecular packing is compared in Fig. 8. As illustrated in the packing diagrams (Fig. 8), the Alq_3 molecules in α, δ, and ε crystalline phases form stacks, and the propeller axes are approximately aligned with the stacking direction. As shown in Table 1 and Fig. 8, the unit-cell parameters and packing in α Alq_3 are also similar to those in δ Alq_3, even though the two forms contain different isomers. The structure of γ Alq_3 is unknown, but the packing in the β form is quite different from that in the other

Table 1
Unit cell parameters for different crystalline forms of Alq_3.

	α Alq_3	β Alq_3	γ[a] Alq_3	δ Alq_3	ε Alq_3
Space group	$P\bar{1}$	$P\bar{1}$	$P\bar{3}$	$P\bar{1}$	$P\bar{1}$
a (Å)	6.2455(10)	8.4433(6)	14.335(3)	6.1810(12)	13.5190(5)
b (Å)	12.8710(18)	10.2522(8)	14.335(3)	13.268(3)	15.8550(6)
c (Å)	14.739(3)	13.1711(10)	6.194(2)	14.430(3)	18.7110(8)
α (°)	69.890(6)	71.422(1)	90	66.06(3)	95.4940(19)
β (°)	89.464(5)	82.936(1)	90	88.56(3)	109.774(2)
γ (°)	82.52(2)	89.743(1)	120	84.03(3)	114.6270(16)
Volume	1102.1(4)	1071.7(2)	1102.3(4)	1075.5(4)	3296.8(2)
Z	2	2	2	2	6

[a] Unit-cell parameters obtained from powder XRD.

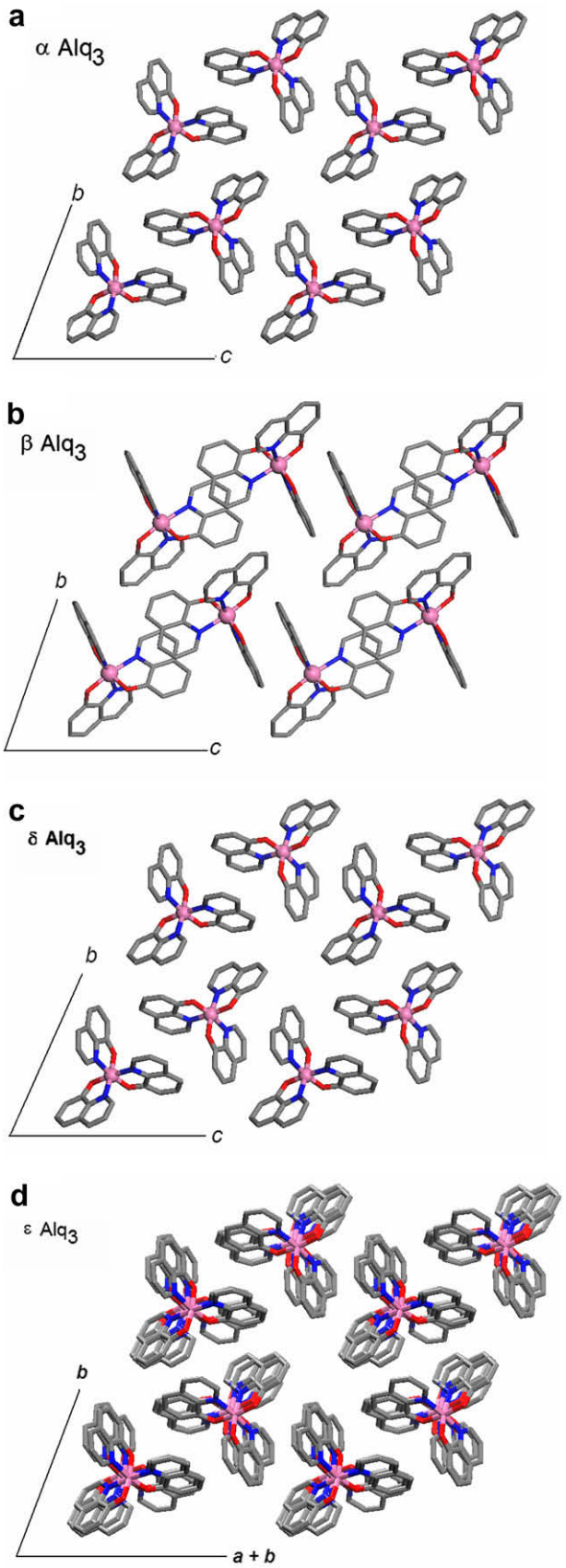


Fig. 8. Molecular packing in (a) α, (b) β, (c) δ, and (d) ε crystalline forms of Alq_3, all viewed down a crystallographic axis close to the Alq_3 stacking axis. For simplicity, the molecules of α Alq_3 are represented by the apparent majority *facial* structure. The structure of γ Alq_3 is not yet known.

crystal forms (see Fig. 8b). The molecules still form stacks along a crystallographic axis, but the propeller axes are far from parallel to the stack axis (~30°).

2.4. Raman, fluorescence, and NMR spectra for the isolated crystalline phases

Characterization of the Alq_3 crystalline phases by XRPD and single-crystal XRD allowed us to establish reference materials. These materials were then used to obtain Raman, fluorescence, and NMR spectra for each of the isolated phases.

2.4.1. Powder micro-Raman spectra of Alq_3 phases

The Raman spectra in Fig. 9 show features that are identifiable as unique for each Alq_3 crystalline phase in this study. These spectra were collected from polycrystalline powders at 4-cm^{-1} resolution. Where there are single-crystal Raman data in the literature, our powder spectra generally agree within their more limited resolution [2,11,14,15].

The spectra in Fig. 9 have been stacked in an order that juxtaposes different crystalline phases with similar Raman spectra. Overall, the spectra appear to fall into three groups: {β}, {α,ε}, and {δ,γ}. This grouping correlates with the assignment of β Alq_3 as a *meridional* structure, ε and (according to our hypothesis) α Alq_3 as *meridional* structures that are relatively similar to each other but markedly different from β Alq_3, and δ and γ Alq_3 as *facial* structures that may contain similar stacks of Alq_3 molecules. Although there are differences within each group, there are also differences within each group. The Raman data, taken together, indicate that there are observable signature differences among the five forms of Alq_3 in the 100–600 cm^{-1} region of the Raman spectra.

The similar Raman spectra of α and ε Alq_3 support the hypothesis that α Alq_3, like ε Alq_3 is *meridional*, and is similar in structure to ε Alq_3. The bigger differences between these two crystalline forms and β Alq_3 might be taken to indicate that α and ε Alq_3 are more similar to each other than to β Alq_3, which is also *meridional* but packs differently from either α or ε Alq_3. Although the unit-cell parameters of δ are similar to those of γ Alq_3 [2,3], the differences between their spectra must be attributed to significant differences in the packing of their *facial* Alq_3 molecules. The differences among the five crystalline forms are mostly rather subtle. Even with the very close similarity between the spectra of α and ε Alq_3, it would be risky to use the Raman spectra alone to identify the isomer in any of the crystalline phases.

2.4.2. Fluorescence spectra of Alq_3 phases

Interestingly, when exposed to UV light, all *facial* polymorph samples (δ and γ) exhibited blue-shifted fluorescence [11–13] relative to the yellow-green fluorescence of *meridional* polymorphs (β and ε) of Alq_3, whereas, α Alq_3 exhibits yellow-green fluorescence. Fig. 10 is a plot of the excitation and emission spectra of powders of Alq_3 crystalline forms, with the emission and excitation spectra from each crystalline form identified at their crossing point. As seen in Fig. 10, the fluorescence spectra of solid samples of different forms of Alq_3 exhibit substantial differences in emission band position [2,6,11].

The crossing points in Fig. 10, as well as red edges of the excitation and the blue edges of the emission spectra, exhibit a characteristic ordering in energy γ + δ > δ > ε > α > β (The nominal γ sample always contained a small fraction of δ in powder; hence the designation γ + δ). While the energies at the crossing points are dependent on the peak chosen for normalization of the excitation spectra, we have observed that this choice of normalization does not change the ordering in energy among the crystalline forms. Generally, the forms α and β are at lower energy, and γ and δ are at higher energy, with the form ε falling approximately midway in energy. The spectra also retain this order through repetition of the measurement on different packings of the crystalline powders in the sample holder, and on different batches of material. This suggests that the spectra are characteristic of the crystalline phase, and we have used them in other studies to identify the crystalline phases. The spectra of α Alq_3 lie between those of the unquestionably *meridional* β and ε phases, and all three occur at longer wavelengths than those of the *facial* γ and δ Alq_3. It is tempting to use these groupings as independent evidence that α Alq_3 contains the same isomer as β and ε Alq_3. Nevertheless, the spectra of β and ε Alq_3 themselves are significantly different, and so are those of γ and δ Alq_3. Evidently, it would be risky to assign the isomer in α Alq_3 on the basis of these spectra.

2.4.2.1. Fluorescence spectra of Alq_3 phases in solution. The maximum of the emission band varies from ~470 to ~515 nm, giving quite different perceived colors to the fluorescence, ranging from light blue (γ and δ) to yellowish green (α, β, and ε Alq_3). There are two fundamentally different explanations for the band shifts, attributing them to (i) molecular properties, i.e., distinctive spectra of *facial* and *meridional* isomers, or (ii) bulk material properties, where solid-state structure determines the absorption and

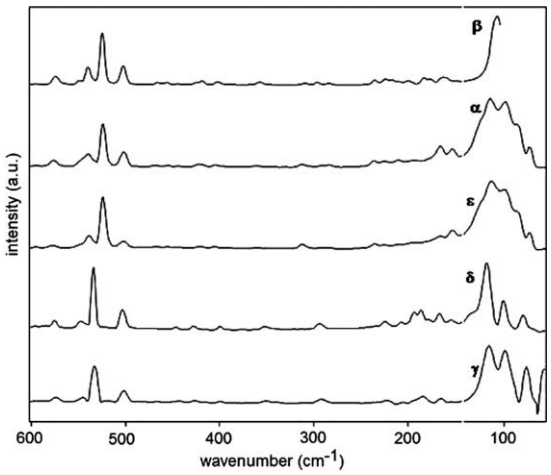


Fig. 9. Micro-Raman spectra for crystalline powders of five Alq_3 phases. The order of presentation is chosen to emphasize the similarities and differences among the crystalline forms.

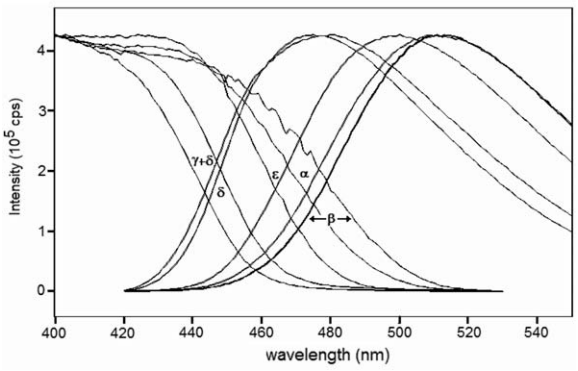


Fig. 10. Fluorescence excitation and emission spectra of Alq_3 powders of different crystalline forms. The spectra of each phase are labeled at their crossing point (as indicated by the double-headed arrow for the case of β Alq_3), without attributing a precise physical significance to that point.

emission band positions. These explanations are not mutually exclusive, and it is reasonable to expect that both molecular and bulk properties affect the optical spectra of Alq_3 samples. The differences between the two crystal forms of a single isomer (β and ε Alq_3) already indicate that solid-state effects can be important. Nonetheless, both *facial* polymorphs (γ and δ) exhibit blue shifts relative to the unequivocally *meridional* polymorphs (β and ε), and those shifts between isomers are considerably larger than the shifts between *meridional* isomers. Hence, it is important to understand whether differences between the isolated molecules also make a major contribution to the shifts.

To answer this question it is logical to examine the spectra of both isomers in solution. If molecular properties are playing a major role in the solid state, it is logical to expect comparable differences between the spectra in solution. Unlike the solution spectrum for *meridional* Alq_3, which is quite straightforward to obtain, measurements for the *facial* isomer are made difficult by the very low solubility of the available crystalline phase (δ) and the rapid conversion of the dissolved *facial* to the *meridional* isomer at room temperature. The low solubility not only decreases the intensity of the emission signal, but also requires precautions to avoid possible contamination with the *meridional* isomer, which can enrich the solution because of its higher solubility. It is also necessary to perform low-temperature filtration of the sample to exclude a relatively intense light blue fluorescence contribution originating from the Alq_3 solid particles.

In a typical experiment, ca. 1 mg of δ crystalline phase powder was placed into a vial cooled to −78 °C by a dry ice-methanol mixture. After 20 min, 15 ml of CD_2Cl_2, precooled by a dry ice-methanol mixture, was added. The sample was allowed to dissolve with occasional shaking while the temperature was maintained at −40 °C. After 1 h, the sample was cooled to −78 °C and ~2 ml was filtered through the precooled 0.25 μm PTFE membrane filter. The resultant solution was transferred into a precooled fluorimetric cuvette. The spectra were acquired using a Fluorolog-3 instrument with the right-angle geometry and 380 nm excitation wavelength. After acquiring the spectra, part of the solution was transferred into a precooled NMR tube and confirmed by proton NMR to contain a virtually pure *facial* isomer of Alq_3 (see below). The remaining solution in the fluorimetric cuvette was allowed to warm up to room temperature, kept at room temperature for 20 min to ensure complete conversion into the *meridional* isomer, and recooled before acquiring spectra to compare *facial* and *meridional* isomer spectra in identical conditions. Incidentally, we found that the spectrum of the *meridional* isomer obtained via solution conversion of the *facial* isomer, as described above, is virtually identical to the spectrum of a sample obtained directly by dissolution of a solid sample of the *meridional* isomer at room temperature and cooling to −40 °C.

The acquired fluorescence spectra are shown in Fig. 11. In notable contrast with the substantial *short*-wavelength shift observed for a solid sample of the *facial* δ crystalline phase relative to a solid sample of any *meridional* crystalline phase, the solution spectrum of *facial* Alq_3 is shifted to slightly *longer* wavelengths relative to that of *meridional* Alq_3. The emission maxima are 534 and 526 nm, respectively. Neither spectrum resembles that of the light blue emission from the solid δ phase. Not unlike the emission spectra, the excitation spectra of the *meridional* and *facial* isomers in solution are virtually identical (shifts <2 nm).

This finding appears contrary to a recent report by Muccini et al. [16] that the optical emission of *facial* Alq_3 in $CDCl_3$ solution is centered at 479 nm and has a bright blue color. However, the experimental procedure described by Muccini et al. does not include a filtration step and, therefore, yields a suspension of solid particles rather than a true solution. Considering the very low solubility of *facial* Alq_3, it is quite clear that the bright blue emission comes

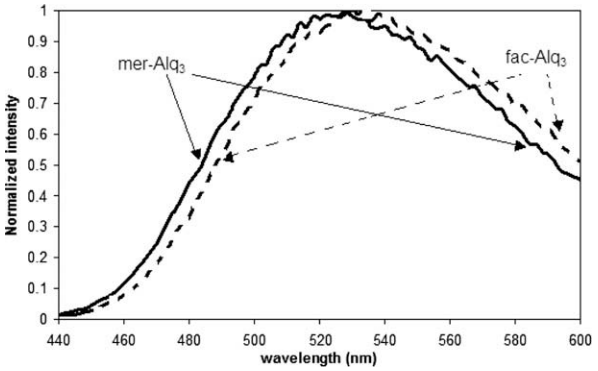


Fig. 11. Fluorescence spectra of *facial* and *meridional* isomers of Alq_3 in cold CD_2Cl_2.

from solid particles of the δ crystalline phase of *facial* Alq_3 material. In contrast, the visual appearance of emission of a solution of *facial* Alq_3 obtained by low-temperature filtration is neither bright nor blue. The present finding also disagrees with the stated conclusion of a recent study of Alq_3 molecules in an SiO_2 matrix by Levichkova et al. [17]. Emission spectra were analyzed into two components, and the bluer and greener components were identified with the *facial* and *meridional* isomers, respectively. No independent assay of the *facial* and *meridional* content of the samples was offered, nor was direct evidence that the Alq_3 is present as isolated molecules. Therefore, intriguing as the observations are, the identification of the emitting species must be regarded as speculative.

2.4.2.2. Fluorescence spectra of Alq_3 phases in powder form. It is now clear that the blue shifts of the spectra of γ and δ Alq_3 are not a consequence of distinctive spectra of the individual *facial* molecules but, rather, are largely a result of solid-state effects. Crystal packing may cause the geometry of the individual molecules to differ somewhat between the crystal and the solution, and their spectra could be shifted to an extent that depends on the isomer. There are, however, many other solid-state effects that may vary from one crystalline phase to another. Crystal packing fixes the alignment of neighboring static molecular dipoles, potentially causing the microscopic local field seen by the ground and excited states to be different for different isomers (and different polymorphs). The orientation of the ground- and excited-state dipole moments of an individual molecule, relative to the local field, probably also depend on the isomer (and the polymorph). The excitonic couplings [18,19] among the Alq_3 molecules probably vary as a consequence of differences between crystal structures and differences in the electronic structure of the *meridional* and *facial* isomers. Any of these effects might change the relative energies of the ground and excited states, leading to a shift in the absorption and emission spectra, as is evidently the case among the *meridional* crystalline phases. These solid-state factors can still be affected by differing properties of the two isomers, e.g., the ground- and excited-state dipole moments (both the magnitudes and the directions) or details of the ground- and excited-state wavefunctions (e.g., degree of delocalization of the excited state) that determine the excitonic coupling parameters. Thus, it is still possible that single-molecule properties contribute to the systematic hypsochromic shifts of the *facial* isomers relative to the *meridional*. Further, it is quite possible that the Alq_3 molecules may form similar stacks in the γ and δ crystalline phases. If so, the "systematic" shifts observed in the γ and δ crystalline phases may also be related to similarities in the molecular environments. In any case, however, it would have been demonstrably incorrect to argue that those shifts result from spectral shifts between isolated *facial* and *meridional* molecules, and to identify the isomer in α Alq_3 on that basis.

2.4.3. NMR spectra for Alq_3 crystalline phases

2.4.3.1. ^{27}Al solid-state NMR. Insight into the structures of Alq_3 crystalline phases can be gained from very-high-field ^{27}Al solid-state NMR experiments [20,21]. Spectra of three crystalline forms collected at 217.6 MHz are shown in Fig. 12. The spectrum for the β form, known from single-crystal XRD to comprise the *meridional* isomer with no disorder, is shown in Fig. 12a. This appears to be the first ^{27}Al spectrum of an unambiguously *meridional* Alq_3. The spectrum of the Alq_3 δ form *facial* isomer (Fig. 12b) is similar to spectra reported previously and is roughly as expected from the nominal molecular symmetry [20,21]. The reported spectrum of the γ form unambiguously identifies it with the *facial* isomer [21]. The spectrum of the α form (Fig. 12c) is similar to that of β Alq_3, but differs both in shape and central frequency. It is difficult to interpret this spectrum in terms of a mostly *facial* composition. On this basis, previous workers have identified the α form, instead, as *meridional* [2]. *Prima facie*, the observed difference between β and α forms could be ascribed to differences in molecular environment, as in the case of γ and δ Alq_3 [2].

2.4.3.2. Solid-state ^{13}C NMR spectra for Alq_3 isomers and polymorphs. ^{13}C NMR spectra and assignments are shown in Fig. 13. For the *facial* isomer we would expect one chemical environment, and for the *meridional*, three. Therefore, for each carbon nucleus in the quinolinolate group, naively we might expect one resonance for the *facial* and three resonances for the *meridional* isomer. However, the observed resonances are rather broad, and much of the anticipated structure is probably hidden in composite, overlapping resonances. ^{13}C is sensitive to intermolecular packing, as illustrated by the different spectra obtained for the β and ε forms. Both forms contain exclusively *meridional* Alq_3, but the molecules are arranged quite differently in their two structures. Because of the sensitivity to intermolecular interactions, a positive determination of the isomerism cannot readily be made on the basis of solid-state ^{13}C NMR spectra alone. Nevertheless, qualitative similarities and differences among the spectra are informative. The δ form, determined to be *facial* by other methods, has the narrowest resonances. The β form, determined to be *meridional* by other methods, appears to be the most complex. Thus, for the β and δ forms, the appearance of the spectra offers support for the isomer assignments. The spectra for the α and ε forms are nearly identical, while the comparison of the β with δ, and ε forms indicates the extent to which different isomers and different crystal structures can influence the spectra. Thus, while the spectra do not help to identify the isomers individually in the α and ε forms, they suggest structural similarities between the two.

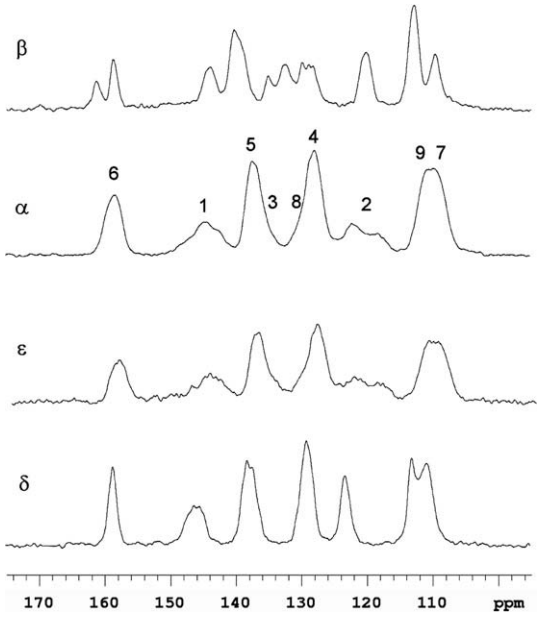


Fig. 13. ^{13}C CPMAS NMR spectra. The atom numbering is shown in Fig. 1. Assignments were not made directly on the solid samples, but are based on solution state spectra.

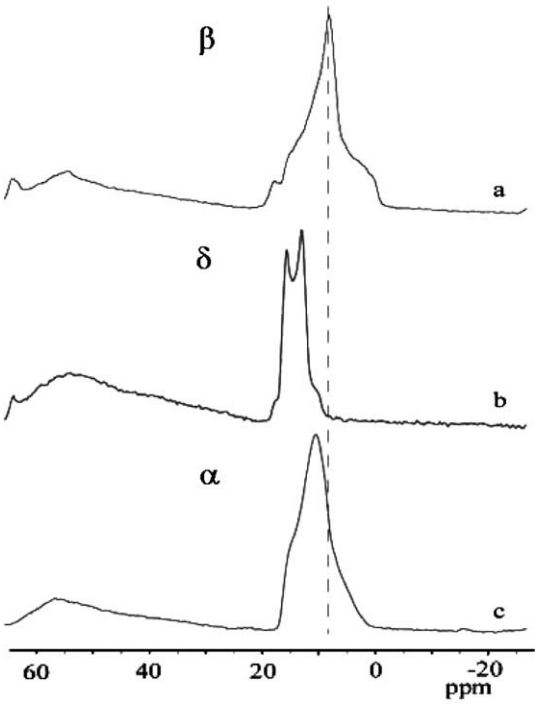


Fig. 12. ^{27}Al MAS NMR spectra of three Alq_3 crystalline forms: (a) β (*meridional*), (b) δ (*facial*), and (c) α polymorph.

Kaji et al. have reported solid-state ^{13}C NMR spectra for the α, γ, and δ crystalline forms [22]. Their spectra of α and δ Alq_3 are similar to ours. Their spectra of γ and δ Alq3 indicate that both comprise the *facial* isomer. They report modest differences between the γ and δ forms, again illustrating the sensitivity of ^{13}C NMR to molecular environment. Corresponding resonances in γ Alq_3 are split in δ Alq_3. Intermolecular packing must be responsible, as all ligands in the crystal are chemically equivalent. In fact, because of the low symmetry of the crystal structure, the three ligands in a δ Alq_3 molecule do occupy different environments.

For α Alq_3, Kaji et al. interpret the breadth of the resonances in terms of structural disorder. Clearly, if a crystal structure is ordered but possesses multiple molecular environments, and if the resolution of the spectra is limited, the result can also be the appearance of broad resonances. This point is illustrated by the generally broader resonances in our spectrum of ε Alq_3 relative to those for β Alq_3. While both polymorphs are fully ordered and comprise the same isomer, ε Alq_3 has three distinct molecular environments and β Alq_3 has only one.

2.4.3.3. ^{1}H NMR solution spectra obtained by low-temperature dissolution. When ^{1}H NMR spectra are acquired at 23 °C, solutions obtained by dissolving any of the five crystalline phases of Alq_3 (α, β, γ, δ, and ε) yield spectra consistent with the *meridional* isomer. However, if both dissolution in CD_2Cl_2 and subsequent acquisition of NMR spectra are performed at −35 °C, the α, β, and ε crystalline phases yield spectra consistent with the *meridional* isomer, while the δ and γ polymorphs yield spectra consistent with the *facial*

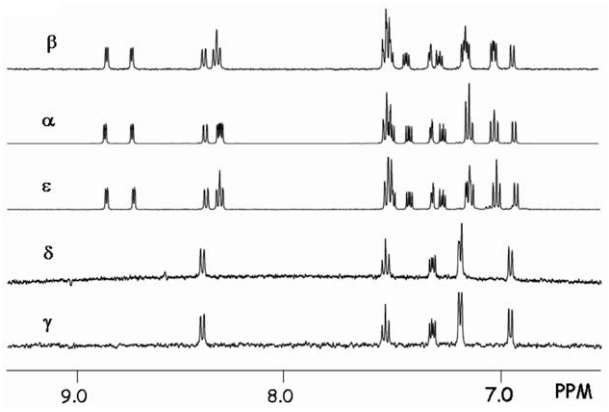


Fig. 14. Comparison of ^{1}H NMR spectra at −35 °C for solutions prepared from different crystalline forms of Alq_3.

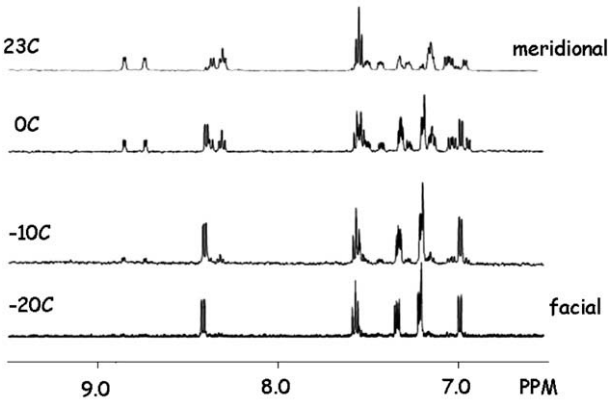


Fig. 15. ^{1}H NMR spectra for δ phase of Alq_3 dissolved in CD_2Cl_2, indicating isomerization (*facial* to *meridional* conversion) with increasing temperature.

isomer (see Fig. 14). It is known that the *meridional* isomer is the more stable in solution at room temperature, that isomerization is rapid at room temperature, and that the rate is strongly temperature-dependent [16]. To illustrate, a series of ^{1}H NMR spectra for the δ crystalline phase (*facial* isomer), dissolved in CD_2Cl_2 at −40 °C, was acquired (∼15 min/spectrum) in a step-wise fashion through a temperature range of −20 to 23 °C, as shown in Fig. 15. The *meridional* isomer begins to form at approximately −10 °C, and complete conversion to the *meridional* isomer is achieved by 23 °C. Therefore, the spectra obtained by dissolution and spectroscopy at −35 °C are most probably indicative of the isomeric state in each crystalline phase. In particular, the spectra in Fig. 14 strongly suggest that α Alq_3 is *meridional* and confirm that γ Alq_3 is *facial*. Incidentally, a solution of *meridional* Alq_3, upon cooling from room temperature to −30 °C, remained *meridional*.

3. Summary and conclusions

Five crystalline phases of Alq_3 have been identified using X-ray diffraction techniques. Single-crystal structures of four (α, β, δ, and ε) have been determined. High-quality single-crystal data indicate that β and ε Alq_3 contain the *meridional* isomer and that δ Alq_3 contains the *facial* isomer. Suitable crystals of γ Alq_3 have not been obtained, and the structure of this crystalline phase is unknown, although unit-cell parameters have been evaluated by powder XRD. Spectroscopic evidence identifies γ Alq_3 as a *facial* form. Only crystals of mediocre quality have ever been obtained for α Alq_3. As solved by conventional single-crystal XRD methods, the structure of these crystals appears to contain predominantly the *facial* isomer with a high degree of disorder. The fractional occupancies in this structure, however, combined with spectroscopic evidence point to a very different hypothesis. Most probably, α Alq_3 consists of the *meridional* isomer; the apparent disorder represents three orientations of the *meridional* molecules in the asymmetric unit; and, fortuitously, most of the atoms for each orientation occupy approximately the same location as the atoms in the apparent *facial* structure [23]. The asymmetric unit of ε Alq_3 also contains *meridional* molecules in three orientations, but with a regular ∼120° rotation between neighboring molecules. Both the crystallographic and the spectroscopic evidence suggest that the α and ε forms are structurally very similar, but that the ordered orientations in ε Alq_3 are supplanted by some form of disorder in α Alq_3.

Perhaps the simplest and most unambiguous indicator of the isomers present in α and γ Alq_3 is the characteristic proton NMR obtained by dissolving the various crystalline phases at low temperature. Strong additional evidence is provided by solid-state ^{13}C and ^{27}Al NMR. Raman spectra are consistent with the identifications. Although both γ and δ Alq_3 exhibit blue-shifted fluorescence and excitation (or absorption) spectra relative to α, β, and ε Alq_3, this comparison does not help to identify the isomers in each form. Hence, the spectral shifts are largely consequences of solid-state effects controlled by crystal packing.

Spectroscopic reference patterns for different crystalline phases were established. The Raman spectra clearly show features that are identifiable as unique for different crystalline forms. Nevertheless, the Raman spectra of α and ε Alq_3 are very similar, suggesting that the crystal structures of the two are also similar. The Raman spectra of γ and δ Alq_3 are also rather similar, providing some additional support for the conclusion that γ is a *facial* form.

The fluorescence and fluorescence-excitation spectra of powder samples exhibit substantial short-wavelength shifts for the *facial* crystalline species relative to the *meridional*. There are smaller, but still substantial shifts between the *meridional* β and ε polymorphs and between the *facial* γ and δ polymorphs, indicating the magnitude of solid-state effects. In solution, the fluorescence spectrum of *facial* Alq_3 is only slightly shifted, and is shifted to *longer* wavelengths relative to that of *meridional* Alq_3. The excitation spectra of the two isomers in solution are virtually identical. Evidently, the shifts seen in solid-state emission spectra are dominated by solid-state, intermolecular effects rather than by differences between the spectra of the individual molecules. Evidently, too, the powder spectra cannot be used to identify the isomer in α Alq_3. The apparently systematic spectral shifts of the *facial* polymorphs relative to the *meridional* polymorphs might even be misleading. If γ Alq_3 contains stacks of molecules similar to those in δ Alq_3, the shifts could be similar for this reason rather than because the two crystalline species contain the same isomer.

Solid-state ^{27}Al NMR spectra of an unambiguous *meridional* form, β, have been obtained for the first time. The spectrum of α is rather similar to that of β, and quite different from that of the unambiguously *facial* δ form. Unlike the spectrum of β Alq_3, the exact shape of the α spectrum cannot be modeled in terms of a *meridional* species in a single environment. These observations are consistent with an assignment of α Alq_3 as *meridional* with multiple molecular environments.

Solid-state ^{13}C NMR spectra of four crystalline phases have been presented. The spectra of β and δ Alq_3 support the crystallographic assignments as *meridional* and *facial*, respectively. The spectra of the α and ε forms cannot be used directly to identify the isomers, but they are very similar to each other. In view of the sensitivity of solid-state ^{13}C NMR to both the isomer and the molecular environment, the similar spectra of α and ε Alq_3 again suggests a close similarity of the two phases.

According to the ^{1}H NMR spectra, dissolution of any of the five crystalline forms of Alq_3 (α, β, γ, δ, and ε) yields a solution of the *meridional* isomer at room temperature. In contrast, when the experiment is repeated at −35 °C, the α, β, and ε crystalline forms yield solutions of the *meridional* isomer, while the γ and δ crystalline forms yield solutions of the *facial* isomer. At room temperature, the results are determined by a rapid conversion to the more stable (in solution) isomer. At low temperature, isomerization is suppressed, and the solution spectra report the isomers present in the respective solids.

Combined powder XRD and DSC studies indicate that some phase conversion processes in Alq_3 are so sluggish that the transition temperatures obtained by DSC exceed the thermodynamic values by 80° or more. In fact, γ can be converted to δ Alq_3 even at room temperature, ~380 °C below the DSC transition temperature, by solvent processing. The phase obtained by heating depends strongly on the incubation time. Once the β and ε phases have been converted to α, γ, or δ Alq_3, or taken beyond the melting point (~417 °C), the β and ε forms are not observed again after any means of thermal processing. A *facial* phase (δ) is the most stable form at high temperature. The progression of crystalline species observed upon heating is an indication of the relative stabilities of the different forms, but not at a common temperature. Because the phase transformations are sluggish, it has not been possible to determine which isomer forms the most stable phase at room temperature. It would be interesting to determine, perhaps calorimetrically, the relative stabilities of the five crystalline phases at a common temperature. For instance, is the *facial* δ form actually the most stable phase at room temperature? Dissolved in CD_2Cl_2 around room temperature, *meridional* Alq_3 is the more stable isomer. It would be interesting to learn whether the greater stability of *facial* Alq_3 in the solid state at high temperature and the greater stability of *meridional* Alq_3 in the solution at room temperature are consequences of packing and solvation forces in the two phases or a finely poised, temperature-dependent difference in the stability of the two isomers as isolated molecules.

4. Experimental

Powder diffraction data were collected using a Rigaku D2000 Bragg-Brentano diffractometer with graphite-monochromated Cu Kα radiation (1.54184 Å). To reduce peak asymmetry, incident-beam and diffracted-beam Soller slits were used. Using MDI JPOWD [24], powder XRD patterns were calculated for comparison to the observed pattern of α Alq_3.

Micro-Raman spectra were generated using a JY-Horiba LabRam spectrometer at an excitation wavelength of 633 nm and an MSPLAN 50X microscope objective. Micro-Raman spectra were collected for multiple crystallites of each sample to determine variability within and between crystallites.

Fluorescence excitation and emission spectra of polymorph powders were obtained using a Tau 3 Spex Fluorolog from JY/Horiba. A powder was either pressed or smeared against a quartz cover, and then measured in a "front-face" orientation in which the excitation light is normal to the surface of the powder, and the emission is collected at 22° relative to this normal.

^{27}Al solid-state NMR data were obtained at the National High Magnetic Field Laboratory (NHMFL) in Tallahassee, Florida. A field strength of 19.6 T, a magic angle spinning (MAS) rate of 10 kHz, and a sweep width of 40 kHz were used. ^{13}C NMR spectra were obtained on a Varian INOVA spectrometer operating at 100 MHz using MAS, cross polarization (CP), and high-power ^{1}H decoupling. Typical parameters used for acquisition were 12 kHz spinning speed, TPPM (Two Pulse Phase Modulation) decoupling, 60 s recycle delay, and 512 transients averaged.

All ^{1}H NMR spectra were obtained on a Varian Inova NMR spectrometer operating at ^{1}H observation frequency of 500 MHz, using a variable temperature 5 mm Indirect PFG (Pulse Field Gradient) probe. Solutions were prepared in CD_2Cl_2 at a consistent concentration, as well as referenced with respect to Tetramethylsilane, TMS (0.00 ppm).

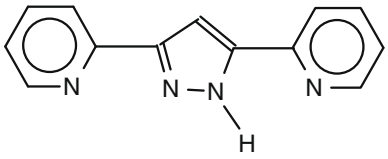
Acknowledgements

The authors thank A. Lanzafame, C. Barnes, P. Reuter, R. Schultz, M. Robbins, J. Lippert, and J. Putrelo of Eastman Kodak Company for spectral measurements. We thank Drs. Zhehong Gan and Hyung-Tae Kwak of the National High Magnetic Field Laboratory (NHMFL) in Tallahassee, FL, for obtaining the ^{27}Al spectra. We thank Dr. Raymond Scaringe of Bristol Myers Squibb for useful discussions and Dr. Michael Cölle of Philips Research, The Netherlands, for useful discussions and help with some references.

References

[1] C.W. Tang, S.A. Van Slyke, Appl. Phys. Lett. 51 (1987) 913.
[2] M. Brinkmann, G. Gadret, M. Muccini, C. Taliani, N. Masciocchi, A. Sironi, J. Am. Chem. Soc. 122 (2000) 5147.
[3] M. Cölle, R.E. Dinnebier, W. Brütting, Chem. Commun. (2002) 2908.
[4] M. Rajeswaran, T.N. Blanton, K. Klubek, Z. Kristallogr. NCS 218 (2003) 439.
[5] M. Rajeswaran, T.N. Blanton, J. Chem. Cryst. 35 (1) (2005) 71.
[6] M. Cölle, W. Brütting, Phys. Stat. Sol. (a) 201 (6) (2004) 1095.
[7] S.H. Simonsen, D.W. Bechtel, Am. Crystallogr. Assoc. Ser. 2 (7) (1980) 23.
[8] M. Ul-Haque, W. Horne, W.J. Lyle, J. Crystallogr. Spectrosc. Res. 21 (4) (1991) 411.
[9] H. Schmidbaur, J. Lettenbauer, D.L. Wilkinson, G. Müller, O. Kumberger, Z. Naturforsch., B: Chem. Sci. 46 (7) (1991) 901.
[10] I. Fujii, N. Hirayama, J. Ohtani, K. Kodama, Anal. Sci. 12 (1996) 153.
[11] M. Braun, J. Gmeiner, M. Tzolov, M. Cölle, F.D. Meyer, W. Milius, H. Hillebrecht, O. Wendland, J.U. von Schutz, W. Brütting, J. Chem. Phys. 114 (2001) 9625.
[12] M. Cölle, J. Gmeiner, W. Milius, H. Hillebrecht, W. Brütting, in: Proceedings of the EL2002, Ghent, 2002, p. 133.
[13] M. Cölle, J. Gmeiner, W. Milius, H. Hillebrecht, W. Brütting, Adv. Funct. Mater. 13 (2003) 108.
[14] M.D. Halls, R. Aroca, Can. J. Chem. 76 (1998) 1730.
[15] A. Degli Esposito, M. Brinkmann, G. Ruani, J. Chem. Phys. 116 (2002) 798.
[16] M. Muccini, M.A. Loi, K. Kenevey, R. Zamboni, N. Masciocchi, A. Sironi, Adv. Mater. 16 (2004) 861.
[17] M.M. Levichkova, J.J. Assa, H. Fröb, K. Leo, Appl. Phys. Lett. 88 (2006) 20912.
[18] M. Pope, C.E. Swenberg, Electronic Processes in Organic Crystals and Polymers, 2nd Ed., Oxford Science Publications, 1999.
[19] D.P. Craig, S.H. Walmsley, Excitons in Molecular Crystals, W.A. Benjamin, 1968.
[20] M. Utz, M. Nandagopal, M. Mathai, F. Papadimitrakopoulos, Appl. Phys. Lett. 83 (2003) 4023.
[21] H. Kaji, Y. Kusaka, G. Onoyama, F. Horii, Jpn. J. Appl. Phys. 44 (6A) (2005) 3706.
[22] H. Kaji, Y. Kusaka, G. Onoyama, F. Hori, J. Am. Chem. Soc. 128 (2006) 4292.
[23] M. Rajeswaran, T.N. Blanton, R.H. Young, W. Brennessel, J. Chem. Crystallogr., submitted for publication.
[24] JPOWD, Materials Data Inc., Livermore, California, 2001.

a bidentate as well as tetradentate ligand depending on the ratio of metal-to-ligand used. The molecular structures of representative compounds are reported as well.



Ligand used in this study

2. Experimental

2.1. Physical measurements

Elemental analyses were performed on a Perkin–Elmer-2400 CHN/O analyzer. Infrared spectra were recorded on a Perkin–Elmer Model 983 spectrophotometer with the sample prepared as KBr pellets. The ^{1}H NMR spectra were recorded on a Bruker ACF-400 (400 MHz) spectrometer in $CDCl_3$ solvent with TMS as the internal reference. All chemicals used were of reagent grade. All reactions were carried out in distilled and dried solvents. Ruthenium trichloride trihydrate, iridium trichloride, rhodium trichloride and osmium tetraoxide (OsO_4) were purchased from Arora Matthey Ltd. The 3,5-bis(2-pyridyl)pyrazole (bpp-H) was prepared by following a literature procedure [40,41]. The precursor complexes [(η^5-C_5H_5)Ru(PPh_3)$_2$Cl] [33,42,43], [(η^5-C_5H_5)Os(PPh_3)$_2$Br] [44,45], [(η^5-C_5Me_5)Ir(μ-Cl)Cl]$_2$, [(η^5-C_5Me_5)Rh(μ-Cl)Cl]$_2$ [46], [(η^5-C_5Me_5)Ru(PPh_3)$_2$Cl] [47], [(η^6-C_6H_6)Ru(μ-Cl)Cl]$_2$ and [(η^6-*p*-^{i}PrC_6H_4Me)Ru(μ-Cl)Cl]$_2$ [48–50], were prepared by following the reported literature methods.

2.2. Single-crystal X-ray structure analyses

Crystals suitable for X-ray diffraction studies for compounds [**1**]PF_6 and [**5**]PF_6 were grown by slow diffusion of wet diethylether into a dichloromethane solution of [**1**]PF_6, and [**5**]PF_6, respectively. Whereas in the case of compound [**8**]BF_4, crystals were grown by slow diffusion of wet diethylether into an acetonitrile solution of [**8**]BF_4. A bright red crystal of [**1**]$PF_6 \cdot H_2O$ and a pale green crystal of [**5**]PF_6 were mounted on a Stoe-Image Plate Diffraction System equipped with a ϕ circle goniometer, using Mo Kα graphite monochromated radiation (λ = 0.71073 Å) with the ϕ range 0–200°, increment of 1.2°, $D_{max} - D_{min}$ = 12.45–0.81 Å. Whereas a crystal of [**8**]$BF_4 \cdot H_2O$ was mounted on a Bruker Apex CCD diffractometer in the full reciprocal sphere equipped with a CCD detector, X-ray intensity data were collected with Mo Kα graphite monochromated radiation at 120 (2) K, with a 0.3°ω scan mode and 10 s per frame. The intensity data were corrected for Lorenz and polarization effects. The structures were solved by direct methods using the program SHELXS-97 [51]. Refinement and all further calculations were carried out using SHELXL-97 [52]. The H-atoms were included in calculated positions and were treated as riding atoms using the SHELXL default parameters. The non-H atoms were refined anisotropically, using weighted full-matrix least-squares on F^2. The data collection parameters and bond lengths and angles are presented in Tables 1 and 2, respectively.

2.3. Preparation of [(η^5-C_5H_5)M(bpp-H)(PPh_3)]PF_6 {M = Ru [**1**]PF_6, Os [**2**]PF_6}

A mixture of [(η^5-C_5H_5)M(PPh_3)$_2$X] {M = Ru, X = Cl and M = Os, X = Br} (100 mg, 0.11 mmol), 3,5-bis(2-pyridyl)pyrazole (bpp-H) (50 mg, 0.22 mmol) and NH_4PF_6 (36 mg, 0.22 mmol) in dry methanol (15 ml) were refluxed under dry nitrogen for 8 h until the color of the solution changed from pale yellow to orange. The solvent was removed under vacuum, the residue was dissolved in dichloromethane (10 ml) and the solution was filtered to remove ammonium halide. The orange solution was concentrated to 5 ml, and upon addition of diethylether the orange–yellow complex precipitated, which was separated and dried under vacuum.

*Complex [(η^5-C_5H_5)Ru(bpp-H)(PPh_3)]PF_6 [**1**]PF_6:* Yield: 75 mg, 68.4%. Elemental *Anal*. Calc. for $C_{36}H_{30}N_4P_2F_6Ru$: C, 54.3; H, 3.7; N, 7.1. Found: C, 54.87; H, 4.13; N, 7.94%. IR (KBr pellets, cm^{-1}): 3429 (ν_{N-H}); 1460 ($\nu_{C=N}$); 850 (ν_{P-F}). ^{1}H NMR ($CDCl_3$, δ): 9.31 (d,

Table 1
Crystallographic and structure refinement parameters for complexes [**1**]$PF_6 \cdot H_2O$, [**5**]PF_6 and [**8**]$BF_4 \cdot H_2O$.

	[**1**]PF_6	[**5**]$PF_6 \cdot H_2O$	[**8**]$BF_4 \cdot H_2O$
Chemical formula	$C_{36}H_{30}F_6N_4P_2Ru$	$C_{23}H_{27}ClF_6IrN_4OP$	$C_{25}H_{23}BCl_2F_4N_4ORu_2$
Formula weight	795.65	748.11	755.32
Crystal system	monoclinic	monoclinic	monoclinic
Space group	$P2_1/n$ (no. 14)	Pc (no. 7)	$P2_1/c$ (no. 14)
Crystal color and shape	green block	red block	orange plate
Crystal size	0.32 × 0.20 × 0.20	0.25 × 0.24 × 0.21	0.22 × 0.13 × 0.04
a (Å)	13.663(1)	8.760(1)	14.229(7)
b (Å)	14.426(1)	13.903(2)	11.265(6)
c (Å)	17.172(1)	13.706(2)	16.008(8)
β (°)	104.284(8)	129.18(1)	95.750(5)
V (Å^3)	3280.1(4)	1293.8(3)	2553(2)
Z	4	2	4
T (K)	173(2)	173(2)	120(2)
D_{calc} (g cm^{-3})	1.611	1.920	1.965
μ (mm^{-1})	0.644	5.393	1.451
Scan range (°)	2.09 < θ < 26.00	2.41 < θ < 26.02	2.21 < θ < 28.21
Unique reflections	6310	4670	5885
Reflections used [$I > 2\sigma(I)$]	5334	3109	5452
R_{int}	0.0542	0.1067	0.0230
Flack parameter		−0.06(3)	
Final R indices [$I > 2\sigma(I)$]*	0.0324, wR_2 0.0854	0.0715, wR_2 0.1780	0.0252, wR_2 0.0622
R indices (all data)	0.0414, wR_2 0.0940	0.0942, wR_2 0.1872	0.0282, wR_2 0.0647
Goodness-of-fit	1.008	0.932	1.026
Max., min. $\Delta\rho$/e (Å^{-3})	0.662, −1.640	4.068, −4.524	0.758, −0.415

* Structures were refined on F_0^2: $wR_2 = [\Sigma[w(F_0^2 - F_c^2)^2]/\Sigma w(F_0^2)^2]^{1/2}$, where $w^{-1} = [\Sigma(F_0^2) + (aP)^2 + bP]$ and $P = [\max(F_0^2, 0) + 2F_c^2]/3$.

Table 2
Selected bond lengths and angles for complexes [**1**]PF_6, [**5**]$PF_6 \cdot H_2O$ and [**8**]$BF_4 \cdot H_2O$.

Distances (Å)	[**1**]PF_6	[**5**]$PF_6 \cdot H_2O$	[**8**]$BF_4 \cdot H_2O$
N(1)–M(1)	2.188(2)	2.07(8)	2.103(2)
N(2)–M(1)	2.085(2)	2.01(5)	2.096(2)
Cl(1)–M(1)		2.398(17)	2.403(13)
N(2)–N(3)	1.342(3)	1.37(8)	1.350(3)
M(1)–CNT(1)	1.830	1.786	1.685
N(3)–M(2)			2.090(2)
N(4)–M(2)			2.090(2)
Cl(2)–M(2)			2.4339(14)
M(2)–CNT(2)			1.681
Angles (°)			
N(3)–N(2)–M(1)	135.60(15)	135(4)	135.49(14)
N(2)–M(1)–N(1)	75.75(8)	77(2)	76.63(8)
N(2)–M(1)–Cl(1)		83.1(15)	87.4
N(1)–M(1)–Cl(1)		87.9(15)	87.1
N(2)–N(3)–M(2)			136.49(15)
N(3)–M(2)–N(4)			76.83(8)
N(4)–M(2)–Cl(2)			82.77(6)
N(3)–Ru(2)–Cl(2)			87.43(5)

1H); 8.55 (d, 1H); 8.06 (s, 1H); 7.8 (td, 1H); 7.75 (d, 2H); 7.62 (m, 2H); 7.45 (m, 2H); 4.75 (s, 5H, C_5H_5); 7.32–7.2 (m, 15H, PPh_3). ^{31}P {^1H} NMR ($CDCl_3$, δ): 50.83 (s, PPh_3). ESI-MS (*m*/*z*): 651.1 [M−PF_6], 650.1 [M−PF_6−H], 389.0 [M−PF_6−PPh_3]. UV–vis [(CH_3CN; λ_{max}, nm (ε, M^{-1} cm^{-1})]: 329 (24000).

*Complex [(η^5-C_5H_5)Os(bpp-H)(PPh_3)]PF_6 [**2**]PF_6:* Yield: 65 mg, 66.7%. Elemental *Anal*. Calc. for $C_{36}H_{30}N_4P_2F_6Os$: C, 48.9; H, 3.4; N, 6.3. Found: C, 49.2; H, 3.91; N, 6.87%. IR (KBr pellets, cm^{-1}): 3425 (ν_{N-H}); 1474 ($\nu_{C=N}$); 850 (ν_{P-F}). ^1H NMR ($CDCl_3$, δ): 9.2 (d, 1H); 8.55 (d, 1H); 8.45 (s, 1H); 7.81 (td, 1H); 7.78 (d, 1H); 7.7 (m, 2H); 7.38 (m, 1H); 6.9 (t, 2H); 4.69 (s, 5H, C_5H_5); 7.3–7.25 (m, 15H, PPh_3). ESI-MS (*m*/*z*): 740.3 [M−PF_6], 739.2 [M−PF_6−H], 478.3 [M−PF_6−PPh_3].

2.4. Preparation of [(η^5-C_5Me_5)Ru(bpp-H)(PPh_3)]PF_6 [**3**]PF_6

A mixture of [(η^5-C_5Me_5)Ru(PPh_3)$_2$Cl] (100 mg, 0.125 mmol), 3,5-bis(2-pyridyl)pyrazole (bpp-H) (56 mg, 0.25 mmol) and NH_4PF_6 (40 mg, 0.25 mmol) in dry methanol (15 ml) were refluxed under dry nitrogen for 12 h until the color of the solution changed from pale yellow to orange. The solvent were removed in a rotary evaporator under reduced pressure, the residue was dissolved in dichloromethane (10 ml), and the solution filtered to remove ammonium chloride. The orange solution was concentrated to 5 ml, when addition of excess hexane gave the orange–yellow complex, which was separated and dried under vacuum. Yield: 70 mg, 64.3%. Elemental *Anal*. Calc. for $C_{41}H_{45}N_4P_2F_6Ru$: C, 56.6; H, 5.2; N, 6.4. Found: C, 57.0; H, 5.9; N, 6.8%. IR (KBr pellets, cm^{-1}): 3424(ν_{N-H}); 1613 ($\nu_{C=N}$); 850 (ν_{P-F}). ^1H NMR ($CDCl_3$, δ): 11.92 (s,1H); 8.7 (d, 1H); 8.5 (s, 1H); 7.8 (td, 1H); 7.6 (d, 1H); 7.28 (t, 2H); 7.1 (m, 1H); 6.89 (t, 2H); 1.45 (s, 15H); 7.33–7.18 (m, 15H, PPh_3). ^{31}P {^1H} NMR ($CDCl_3$, δ): 49.72 (s, PPh_3). ESI-MS (*m*/*z*): 722.3 [M−PF_6], 460.3 [M−PF_6−PPh_3]. UV–vis [(CH_3CN; λ_{max}, nm (ε, M^{-1} cm^{-1})]: 358 (17000).

2.5. Preparation of [(η^5-C_5Me_5)M(bpp-H)Cl]PF_6 {M = Rh [**4**]PF_6, Ir [**5**]PF_6}

A mixture of [(η^5-C_5Me_5)M(μ-Cl)Cl]$_2$ (M = Rh, Ir) (Rh dimer = 100 mg, 0.16 mmol and Ir dimer = 125 mg, 0.16 mmol), 3,5-bis(2-pyridyl)pyrazole (bpp-H) (70 mg, 0.325 mmol) and NH_4PF_6 (50 mg, 0.325 mmol) in dry methanol (15 ml) were stirred at room temperature for 6 h until the color of the solution changed from pale yellow to pale green. The solvents were removed in a rotary evaporator under reduced pressure, the residue was dissolved in dichloromethane (5 ml), and the solution filtered to remove ammonium chloride. The pale green solution was concentrated to 2 ml, when addition of excess hexane gave the orange–yellow complex, which was separated and dried under vacuum.

*Complex [**4**]PF_6*: Yield: 70 mg, 76%. Elemental *Anal.* Calc. for $C_{23}H_{25}N_4PClF_6Rh$: C, 37.8; H, 3.4; N, 7.7. Found: C, 38.0; H, 3.9; N, 7.0%. IR (KBr pellets, cm^{-1}): 3426 (ν_{N-H}); 1612 ($\nu_{C=N}$); 850 (ν_{P-F}). ^1H NMR ($CDCl_3$, δ): 11.80 (s, 1H); 8.9 (d, 1H); 8.6 (d, 1H); 8.2 (td, 1H); 8.0 (s,1H); 7.5 (t, 2H); 7.4 (t, 1H); 7.2 (t, 2H); 1.48 (s, 15H). ESI-MS (*m*/*z*): 494.2 [M−PF_6], 459.2 [M−PF_6−Cl]. UV–vis [(CH_3CN; λ_{max}, nm (ε, M^{-1} cm^{-1})]: 308 (26000).

*Complex [**5**]PF_6*: Yield: 68 mg, 74.1%. Elemental *Anal*. Calc. for $C_{23}H_{25}N_4ClPF_6Ir$: C, 43.1; H, 3.9; N, 8.7. Found: C, 43.6; H, 4.2; N, 8.0%. IR (KBr pellets, cm^{-1}): 3429 (ν_{N-H}); 1613 ($\nu_{C=N}$); 850 (ν_{P-F}). ^1H NMR ($CDCl_3$, δ): 11.86 (s,1H); 8.75 (d,1H); 8.58 (d, 1H); 8.45 (td, 1H); 8.24 (s, 1H); 7.5 (t, 2H); 7.4 (t, 2H); 7.2 (t, 1H); 1.45 (s, 15H). ESI-MS (*m*/*z*): 583.2 [M−PF_6], 548.2 [M−PF_6−Cl].

2.6. Preparation of [(η^6-C_6H_6)Ru(bpp-H)Cl]BF_4 [**6**]BF_4

A mixture of [(η^6-C_6H_6)Ru(μ-Cl)Cl]$_2$ (50 mg, 0.1 mmol), 3,5-bis(2-pyridyl)pyrazole (bpp-H) (88 mg, 0.395 mmol) and NH_4BF_4 (52 mg, 0.496 mmol) was stirred in dry methanol (15 ml) for 4 h at room temperature. The solvent was rotary evaporated. The solid was dissolved in dichloromethane and then filtered to remove ammonium chloride. The solution was concentrated to 2 ml and excess of diethylether was added for precipitation. The light brown color product was separated out, washed with ether and dried in vacuum. Yield: 70 mg, 67.3%. Elemental *Anal.* Calc. for $C_{19}H_{16}N_4BClF_4Ru$: C, 42.75; H, 4.91; N, 10.50. Found: C, 42.6; H, 5.0; N, 10.41%. IR (KBr pellets, cm^{-1}): 3416 (ν_{N-H}); 1613 ($\nu_{C=N}$); 1082 (ν_{B-F}). ^1H NMR ($CDCl_3$, δ): 9.2 (d, 1H), 8.79 (d, 1H), 8.65 (s, 1H), 7.98 (t, 2H), 7.84 (d, 2H), 7.45 (m, 2H), 7.38 (m, 1H), 6.25 (s, 6H). ESI-MS (*m*/*z*): 437 [M−BF_4], 435.9 [M−BF_4−H]. UV–vis [(CH_3CN; λ_{max}, nm (ε, M^{-1} cm^{-1})]: 318 (14000).

2.7. Preparation of [(η^6-p-^{i}PrC_6H_4Me)Ru(bpp-H)Cl]BF_4 [**7**]BF_4

A mixture of [(η^6-$C_{10}H_{14}$)Ru(μ-Cl)Cl]$_2$ (100 mg, 0.163 mmol), 3,5-bis(2-pyridyl) pyrazole (bpp-H) (144 mg, 0.65 mmol) and NH_4BF_4 (85 mg, 0.81 mmol) was stirred in dry methanol (15 ml) for 4 h at room temperature. The yellow compound which formed was filtered, washed with ethanol and diethylether, and dried under vacuum. Yield: 140 mg, 74%. Elemental *Anal.* Calc. for $C_{23}H_{24}N_4BClF_4Ru$: C, 47.65; H, 4.17; N, 9.66. Found: C, 47.5; H, 4.1; N, 9.61%. IR (KBr pellets, cm^{-1}): 3416 (ν_{N-H}); 1613 ($\nu_{C=N}$); 1082 (ν_{B-F}). ^1H NMR ($CDCl_3$, δ): 9.2 (d, 1H), 8.64 (d, 1H), 8.53 (d, 1H), 7.95 (t, 2H), 7.84 (d, 2H), 7.8 (m, 2H), 7.36 (t, 1H), 6.51 (d, 1H, Ar_{p-cy}), 6.1 (d, 1H, Ar_{p-cy}), 5.88 (d, 1H, Ar_{p-cy}), 5.78 (d, 1H, Ar_{p-cy}), 2.63 (sep, 1H), 2.32 (s, 3H), 1.03 (d, 6H). ESI-MS (*m*/*z*): 492.1 [M−BF_4], 491.1 [M−BF_4−H], 457.1[M−BF_4−Cl]. UV–vis [(CH_3CN; λ_{max}, nm (ε, M^{-1} cm^{-1})]: 430 (10000).

2.8. Preparation of [(η^6-C_6H_6)$_2$$Ru_2(bpp)Cl_2$]$BF_4$ [**8**]BF_4

A mixture of [(η^6-C_6H_6)Ru(μ-Cl)Cl]$_2$ (50 mg, 0.10 mmol), 3,5-bis(2-pyridyl)pyrazole (bpp-H) (22 mg, 0.10 mmol) and NH_4BF_4 (51 mg, 0.49 mmol) was stirred in dry methanol (15 ml) for 4 h at room temperature. The brown compound which formed was filtered, washed with methanol and diethylether, and dried under vacuum. Yield: 50 mg, 67.9%. Elemental *Anal.* Calc. for $C_{25}H_{23}N_4BCl_2F_4ORu_2$: C, 39.75; H, 3.07; N, 7.42. Found: C, 39.6; H, 3.0; N, 7.38%. IR (KBr pellets, cm^{-1}): 3416 (ν_{N-H}); 1613 ($\nu_{C=N}$); 1082 (ν_{B-F}). ^1H NMR ($CDCl_3$, δ): 8.91 (d, 1H), 8.5 (d, 1H), 8.35 (t, 2H), 8.12 (s, 1H), 7.92 (m, 2H), 7.7 (d, 1H), 7.55 (d, 1H), 6.35 (s, 6H), 6.1 (s, 6H). ESI-MS (*m*/*z*): 650.9 [M−BF_4], 649.9 [M−BF_4−H].

UV–vis [(CH_3CN; λ_{max}, nm (ε, $M^{-1}\,cm^{-1}$)]: 328 (18000), 424 (3000).

2.9. Preparation of $[(\eta^6\text{-}p\text{-}^iPrC_6H_4Me)_2Ru_2(bpp)Cl_2]BF_4$ [**9**]BF_4

A mixture of $[(\eta^6\text{-}C_{10}H_{14})Ru(\mu\text{-}Cl)Cl]_2$ (100 mg, 0.163 mmol), 3,5-bis(2-pyridyl)pyrazole (bpp-H) (36 mg, 0.16 mmol) and NH_4BF_4 (85 mg, 0.81 mmol) was stirred in dry methanol (15 ml) for 4 h at room temperature. The pale yellow compound which formed was filtered, washed with methanol and diethylether, and dried under vacuum. Yield: 95 mg, 68.44%. Elemental *Anal* . Calc. for $C_{33}H_{37}N_4BCl_2F_4Ru_2$: C, 46.66; H, 4.39; N, 6.60. Found: C, 46.5; H, 4.4; N, 6.7%. IR (KBr pellets, cm^{-1}): 3416 (ν_{N-H}); 1613 ($\nu_{C=N}$); 1082 (ν_{B-F}). ^1H NMR ($CDCl_3$, δ): 9.1 (s,1H); 8.8 (d, 1H); 8.77 (d, 1H); 8.37 (t, 1H); 7.95 (t, 2H); 7.93 (s, 1H); 7.68 (t, 1H); 6.46 (d, 1H); 6.09 (d, 1H, Ar_{p-cy}), 6.01 (d, 1H, Ar_{p-cy}), 5.99 (d, 2H, Ar_{p-cy}); 2.67 (sep, 1H), 2.17 (s, 3H), 1.04 (d, 6H). ESI-MS (*m*/*z*): 763 [$M-BF_4$], 762.0 [$M-BF_4-H$]. UV–vis [(CH_3CN; λ_{max}, nm (ε, $M^{-1}\,cm^{-1}$)]: 322 (19000), 425 (3000).

3. Results and discussion

The mononuclear η^5-cyclic hydrocarbon complexes $[(\eta^5\text{-}C_5H_5)Ru(PPh_3)_2Cl]$, $[(\eta^5\text{-}C_5H_5)Os(PPh_3)_2Br]$ and $[(\eta^5\text{-}C_5Me_5)Ru(PPh_3)_2Cl]$ react with 3,5-bis(2pyridyl)pyrazole (bpp-H) in the presence of ammonium hexafluorophosphate in methanol to form the mononuclear cationic cyclopentadienyl ruthenium and cyclopentadienyl osmium complexes having the general formula $[(\eta^5\text{-}C_5H_5)M(bpp\text{-}H)PPh_3]^+$ (M = Ru [**1**]PF_6; M = Os [**2**]PF_6) and pentamethylcyclopentadienyl ruthenium complex having the formula $[(\eta^5\text{-}C_5Me_5)Ru(bpp\text{-}H)PPh_3]^+$ ([**3**]PF_6) (Chart 1). The complexes are orange–yellow, non-hygroscopic, air stable, crystalline solids. They are soluble in polar solvents such as methanol, dichloromethane, chloroform and acetone, but insoluble in hexane, petroleum ether and diethylether.

3.1. Cyclopentadienyl ruthenium [**1**]PF_6 and osmium [**2**]PF_6 complexes

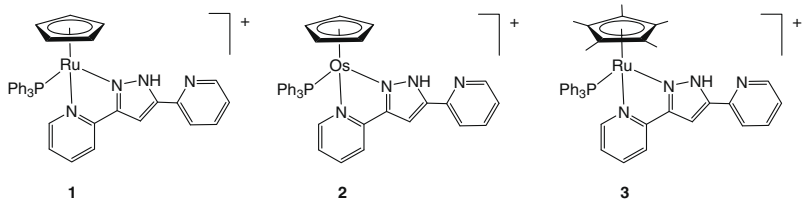
The analytical data of these compounds are consistent with the formulations (Chart 1). These complexes are formed by the reaction of metal complexes with the bpp-H ligand, irrespective of the metal-to-ligand ratio, yielding only mononuclear compounds. Attempts to make dinuclear complexes by increasing the metal complex ratio were unsuccessful, which might be due to the steric bulkiness of the complex due to the presence of the triphenylphosphine group. The infrared spectra of the complexes [**1**]PF_6 and [**2**]PF_6 exhibit a chelated *N*,*N*′-bidentate ligand with strong bands at 3429, 3425, 1460 and 1474 cm^{-1} corresponding to the stretching frequencies of the N–H bond of the pyrazole ring and the C–N bond of the pyridine ring of the ligand. In addition, the infrared spectra contained a strong band at 850 cm^{-1} due to the stretching frequency of the P–F bond of PF_6 for both the complexes. The proton NMR spectra of these complexes exhibit a singlet at 4.75 and 4.69 ppm for the cyclopentadienyl ring protons, indicating a downfield shift from the starting complexes $[(\eta^5\text{-}C_5H_5)Ru(PPh_3)_2Cl]$ and $[(\eta^5\text{-}C_5H_5)Os(PPh_3)_2Br]$ [42,45]. The downfield shift in the position of the cyclopentadienyl protons might result from a change in the electron density on the metal center due to chelation of the 3,5-bis(2-pyridyl)pyrazole (bpp-H) ligand through two nitrogen atoms. In addition to the other ligand peaks, as mentioned in the Section 2, a multiplet in the range 7.3–7.2 ppm, which corresponds to the phenyl protons of the triphenylphosphine group of these complexes, is observed.

The 3,5-bis(2-pyridyl)pyrazole (bpp-H) ligand reacts with the pentamethylcyclopentadienyl ruthenium(II) complexes in the presence of NH_4PF_6 in methanol, to yield the mononuclear cationic complex $[(\eta^5\text{-}C_5Me_5)Ru(PPh_3)(bpp\text{-}H)]PF_6$ ([**3**]PF_6) (Chart 1). The complex is an orange crystalline solid, soluble in polar solvents and air stable. The infrared spectrum displays a sharp band at 3424, 1613 and 850 cm^{-1}, corresponding to the stretching frequencies of the N–H bond of the pyrazole ring, the C–N bond of the pyridine ring and the P–F bond of the counter ion of the complex. In addition to the proton peaks of the ligand, as mentioned in the Section 2, the proton NMR spectrum also displays a singlet peak at 1.45 ppm corresponding to the methyl protons of the pentamethylcyclopentadienyl ring and a multiplet in the range 7.3–7.2 ppm which corresponds to the phenyl protons of the triphenylphosphine group. The $^{31}P\{^1H\}$ NMR spectra of the complexes [**1**]PF_6 and [**3**]PF_6 exhibit a single sharp resonance for triphenylphosphine at 50.8 and 49.7 ppm, respectively, whereas for the starting complexes $[(\eta^5\text{-}C_5H_5)Ru(PPh_3)_2Cl]$ and $[(\eta^5\text{-}C_5Me_5)Ru(PPh_3)_2Cl]$ the signals appear at 42.0 and 38.5 ppm, respectively [33,42,43,47]. The structure of a representative complex, [**1**]PF_6, was solved by a single crystal X-ray diffraction study (Fig. 1).

3.2. Pentamethylcyclopentadienyl rhodium [**4**]PF_6 and iridium complexes [**5**]PF_6

The dinuclear complexes $[(\eta^5\text{-}C_5Me_5)M(\mu\text{-}Cl)Cl]_2$ (M = Rh or Ir) undergo a bridge cleavage reaction with the *N*,*N*′-bidentate nitrogen base (bpp-H) ligand in methanol at room temperature, leading to the formation of the chloride displaced complexes [**4**]PF_6 and [**5**]PF_6, respectively (Scheme 1).

These complexes were isolated as their hexafluorophosphate salts. Here also we were only able to isolate the mononuclear complexes, despite the lack of triphenylphosphine groups. Change in concentration and longer reaction times do not change the reaction pathways. The orange–yellow complexes are air stable, soluble in polar solvents but insoluble in hexane, petroleum ether and diethylether. Complex [**4**]PF_6 exhibits a pale green color when dissolved in solution. The infrared spectra of the complexes [**4**]PF_6 and [**5**]PF_6 exhibit for the chelated *N*,*N*′-bidentate ligand, strong bands at 3426, 1612, 3429 and 1613 cm^{-1}, corresponding to the stretching frequencies of the C–N bond of the pyridine group and the N–H bond of the pyrazole ring. In addition, the infrared spectra contain a strong band at 850 cm^{-1} due to the ν_{P-F} stretching frequency of PF_6. The proton NMR spectra of compounds [**4**]PF_6 and [**5**]PF_6 displays a singlet at 1.48 and 1.45 ppm, corresponding to the protons



1 2 3

Chart 1.

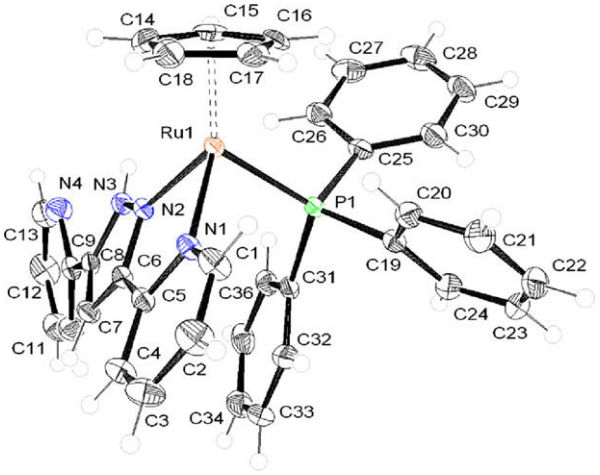
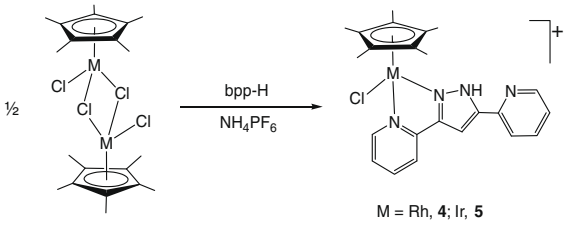


Fig. 1. ORTEP diagram with the labeling scheme for $[(Cp)Ru(bpp\text{-}H)(PPh_3)]^+$ ([**1**]PF_6), at the 50% probability level, the PF_6 anion is omitted for clarity.



Scheme 1.

of the pentamethylcyclopentadienyl group. The molecular structure of the complex [**5**]PF_6 was solved by single crystal X-ray crystallography and the structure is presented in Fig. 2.

3.3. Mononuclear arene ruthenium complexes [6]BF_4 and [7]BF_4 and dinuclear complexes [8]BF_4 and [9]BF_4

The dinuclear arene ruthenium complexes $[(\eta^6\text{-arene})RuCl_2]_2$ (arene = benzene and *p*-cymene) react with the *N*,*N*′-based ligand (bpp-H) in methanol to produce the mononuclear cationic complexes [**6**]BF_4 and [**7**]BF_4 (Scheme 2) and the dinuclear cationic complexes [**8**]BF_4 and [**9**]BF_4 (Scheme 3). The complexes [**6**]BF_4

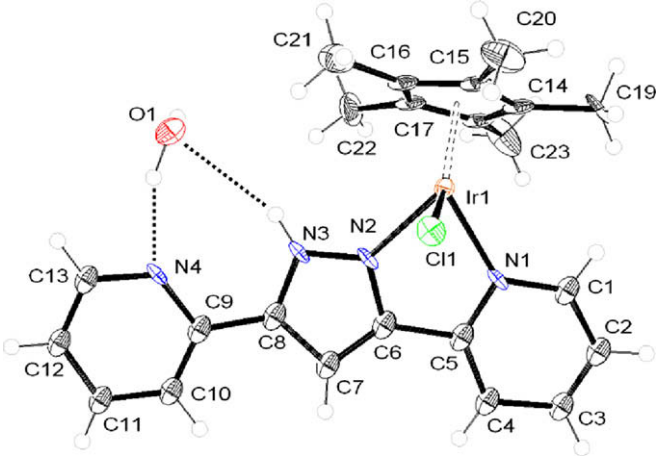
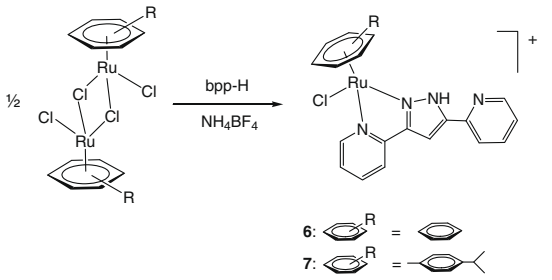


Fig. 2. ORTEP diagram with the labeling scheme for $[(\eta^5\text{-}C_5Me_5)Ir(bpp\text{-}H)Cl]^+$ ([**5**]$PF_6 \cdot H_2O$), at the 50% probability level, the PF_6 anion is omitted for clarity.



Scheme 2.

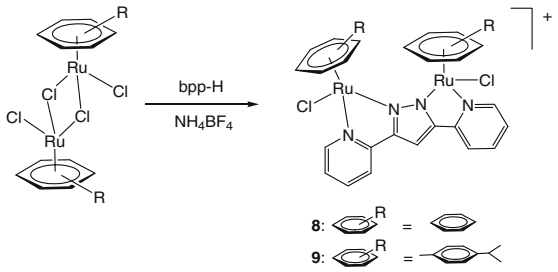
and [**7**]BF_4 are brown in color in solution, while they are yellow, non-hygroscopic, air stable solids. The complexes [**8**]BF_4 and [**9**]BF_4 are also yellow, non-hygroscopic, air stable solids, but they are sparingly soluble in polar solvents like dichloromethane, chloroform, acetone and acetonitrile, and are insoluble in non-polar solvents like hexane, diethylether and petroleum ether.

These complexes display strong bands at 3416 and 1613 cm^{-1} corresponding to the stretching frequencies of the N–H bond of the pyrazole ring and the C–N bond of the pyridine ring. In addition, the IR spectra of all these complexes contain a strong band at 1082 cm^{-1} due to the stretching frequency of the B–F bond of the counter ion of these complexes. In complex [**6**]BF_4, in addition to the proton peaks of the ligand, the NMR spectra also displays a singlet at around 6.25 ppm which corresponds to the six protons of the benzene ring. Whereas in the case of the dinuclear complex [**8**]BF_4, in addition to the ligand peaks, the spectra displays two singlet in the range of 6.3–6.1 ppm which corresponds to the protons of the two benzene rings. The formation of these compounds is also confirmed by ESI-MS spectrometry. The presence of peaks at m/z = 651.1, 740.3, 722.3, 658.5, 748.2, 437.2, 650.9, 492.1 and 763, which coincides with the molecular mass of the cationic complexes [**1**]PF_6 to [**9**]BF_4, also confirms the formation of these compounds.

An interesting point to make here is when the starting dimers $[(\eta^6\text{-arene})RuCl_2]_2$ (arene = benzene, *p*-cymene and hexamethylbenzene) are treated with terpyridine in methanol, rapid displacement of the arene group with terpyridine takes place to form a ruthenium terpyridine complex. In contrast, when [**8**]BF_4 or [**9**]BF_4 is treated with terpyridine, the reaction does not occur, i.e., the direct displacement of the arene group by terpyridine is not possible [53,54]. This could be due to the following reasons: (i) The formation of a mononuclear complex, as a solvated cationic complex in the case of $[(\eta^6\text{-arene})RuCl_2]_2$, is not possible in the case of [**8**]BF_4 or [**9**]BF_4. (ii) In these complexes the arene binds to the metal with *fac*-coordination, it is difficult then to replace this with *mer*-coordinating ligands such as terpyridine due to the frozen free rotation of ligands, unlike in the starting dimers. These complexes are prepared by different methods [38,39]. The dinuclear structure of representative complex [**8**]BF_4 was further confirmed by its molecular structure determination from a single crystal X-ray study (Fig. 3).

4. UV–vis spectroscopy

The UV–vis spectra of the representative complexes [**1**]PF_6, [**3**]PF_6, [**4**]PF_6, [**6**]BF_4, [**7**]BF_4, [**8**]BF_4 and [**9**]BF_4 were acquired in acetonitrile, and spectral data are summarized in the Section 2. Mononuclear complexes [**1**]PF_6, [**3**]PF_6, [**4**]PF_6 and [**6**]BF_4 displayed an intense transition in the UV region. The high energy absorption bands in the electronic spectra of [**1**]PF_6, [**3**]PF_6, [**4**]PF_6 and [**6**]BF_4 in the UV region at ~308–358 nm and have been assigned to ligand-centered $\pi \rightarrow \pi^*/n \rightarrow \pi^*$ transitions [55], whereas in the case of [**7**]BF_4, it shows a low energy absorption band in the visible



Scheme 3.

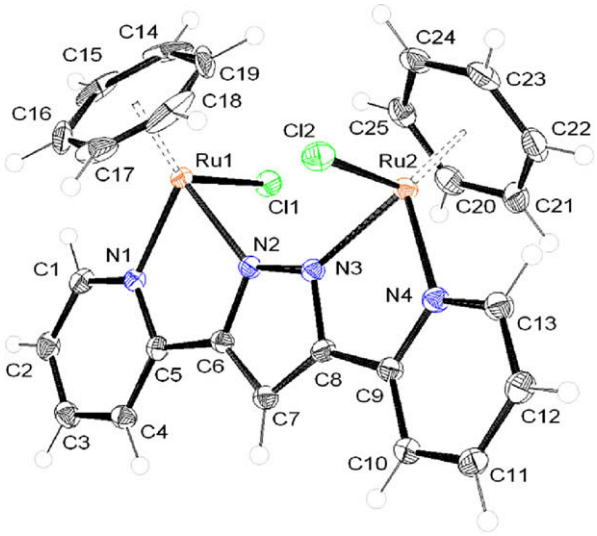


Fig. 3. ORTEP diagram with the labeling scheme for $[(\eta^6\text{-}C_6H_6)_2Ru_2(bpp)Cl_2]^+$ ([**8**]$BF_4 \cdot H_2O$), at the 50% probability level, the water and BF_4 anion are omitted for clarity.

region at ~430 nm which can be assigned to a MLCT transition. The dinuclear complexes [**8**]BF_4 and [**9**]BF_4 exhibited similar trends, with an additional band at ~425 nm that can be assigned to the MLCT band due to a $d\pi$M-arene → π^*_{bpp} transition [55], and they exhibit significant red shifts. In general, these complexes follow the normal trends observed in the electronic spectra of nitrogen bonded metal complexes, which display ligand based $\pi \rightarrow \pi^*/n \rightarrow \pi^*$ transitions in the UV region and metal-to-ligand charge transfer transitions in the visible region. The electronic spectra of these complexes are shown in Fig. 4.

5. Molecular structures

The molecular structures of $[(\eta^5\text{-}C_5H_5)Ru(bpp\text{-}H)PPh_3]PF_6$ ([**1**]PF_6) $[(\eta^5\text{-}C_5Me_5)Ir(bpp\text{-}H)Cl]PF_6 \cdot H_2O$ ([**5**]PF_6) and $[(\eta^6\text{-}C_6H_6)_2Ru_2(bpp)Cl_2]BF_4 \cdot H_2O$ ([**8**]BF_4) have been established by single-crystal X-ray analysis of their hexafluorophosphate and tetrafluoroborate salts. The complexes show a typical piano–stool geometry with the metal center coordinated by the cyclopentadienyl or arene ligand, a terminal chloride in complexes [**5**]PF_6 and [**8**]BF_4, triphenylphosphine in complex [**1**]PF_6 and the chelating bpp-H ligand. The metal atom is in an octahedral arrangement with two *cis*-nitrogen atoms of the bpp-H ligand acting as a bidentate chelating ligand through the neighboring pyridyl and pyrazolyl nitrogen atoms. In this study, the mononuclear complexes [**1**]PF_6 and [**5**]PF_6 were found to be coordinated to N1 and N2, and the dinuclear complex [**8**]BF_4 was found to have the first metal center coordinated to N1 and N2 and the second metal center coordinated

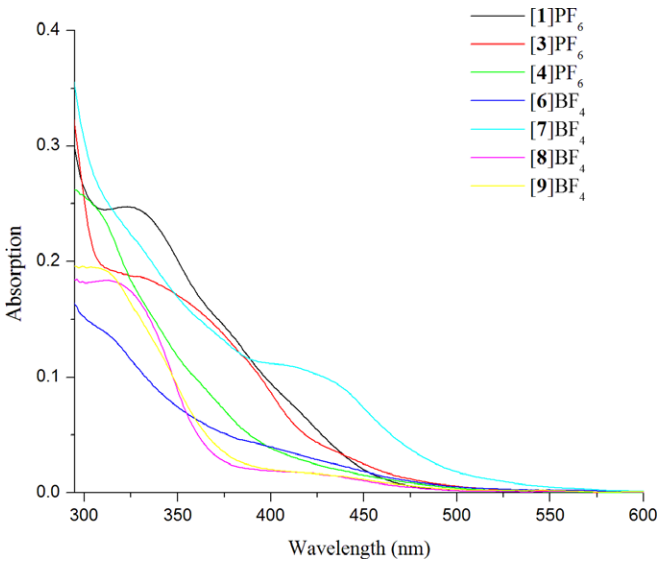


Fig. 4. UV–Visible spectra of the complexes [**1**]PF_6, [**3**]PF_6, [**4**]PF_6, [**6**]BF_4, [**7**]BF_4, [**8**]BF_4 and [**9**]BF_4 in acetonitrile at 298 K.

to N3 and N4 in a five-membered ring chelating fashion involving nitrogen atoms of the pyridine and the pyrazolyl moiety, respectively. The aromatic ring occupies three coordinate sites in these complexes to complete the octahedral geometry around the metal center. The molecular structures of complexes [**1**]PF_6, [**5**]PF_6 and [**8**]BF_4 are shown in Figs. 1–3, respectively. Selected bond lengths and angles are presented in Table 2.

The distances between the iridium atom and the centroid of the η^5-C_5Me_5 ring is 1.786 Å in complex [**5**]PF_6, whereas the distance betwen the ruthenium atom and the centroid of the η^5-C_5H_5 ring is 1.830 Å in complex [**1**]PF_6. These bond distances are comparable to those in the related complex cations $[(\eta^5\text{-}C_5Me_5)IrCl(C_5H_4\ N\text{-}2\text{-}CH{=}N\text{–}C_6H_4\text{–}p\text{–}X)]^+$, where X = NO_2 and Cl [56] and $[Ru(\eta^5\text{-}C_5H_5)(PPh_3)(\kappa^2\text{-paa})]^+$ and $[Ru(\eta^5\text{-}C_5H_5)(\kappa^1\text{-dppm})(\kappa^2\text{-paa})]^+$ [57]. Whereas in the complex [**8**]BF_4, the distances between the metal and the centeriod of the arene rings are 1.685 and 1.681 Å, which are in accordance with the values reported in other related complexes [58].

All these complexes crystallize in monoclinic space groups. The complexes [**5**]PF_6 and [**8**]BF_4 crystallize with a molecule of water per asymmetric unit. The M–N distance in complex [**5**]PF_6 appears to be significantly shorter than the M–N distances in complexes [**1**]PF_6 and [**8**]BF_4. There are no significant differences in the C–C bond lengths in the pentamethylcyclopentadienyl ring, all being about 1.337 Å and pointing to uniform π-electron delocalization in the ring. Furthermore, the five-membered ring is planar as evident in the nearly equal bond distances between metal atom and the ring carbons. The Ir–Cl bond distance is 2.398 Å, which is close to that in related iridium and rhodium complexes with two-coordinated chelating *N,N′*-based ligands [56]. An interesting structural feature of the homodinuclear complex [**8**]BF_4 is the presence of an orientational disorder for the location of the benzene ring C14–C19 (occupancy factor of 75). The ring C14–C19 is the major contribution of the disordered system, whereas the corresponding minor contribution is the orientational disorder ring C26–C31 (occupancy factor of 25) (not shown in Fig. 3). The refined site distribution of C14–19 to C26–31 is 75/25. The Ru(1)···Cl(1) 2.403(13) Å and Ru(2)···Cl(2) 2.4339(14) Å bond lengths are comparable to mononuclear complexes. However, the bond length of Ru(2)···Cl(2) is much longer than the other metal to chloride Ru(1)···Cl(1) distance despite there being no significant change in their environments.

6. Conclusion

The 3,5-bis(2-pyridyl)pyrazole (bpp-H) ligand, which posses two contiguous binding sites for metal ions, has been found to form mono- and binuclear complexes with metal precursors. However, arene ruthenium complexes yielded bimetallic complexes with bpp-H, whereas (η^5-C_5Me_5)M dimers and mononuclear triphenylphosphine complexes do not yield bimetallic complexes with bpp-H, and this could be due to the steric effect of the η^5-C_5Me_5 and PPh_3 ligands. The mononuclear complexes can be made available to bind with other less steric metal precursors to form homo or hetero bimetallic complexes through the other two nitrogen atoms of bpp-H and this work is still in progress and will be reported in the near future.

Acknowledgements

K.M. Rao greatly acknowledges the Department of Science and Technology, New Delhi, (Sanction Order No. SR/S1/IC-11/2004) for financial support. We also thank the Sophisticated Instruments Facility (SIF), Indian Institute of Science, Bangalore, for Providing the NMR facility.

Appendix A. Supplementary data

CCDC 700916, 702728 and 702729 contain the supplementary crystallographic data for [**1**]PF_6, [**5**]$PF_6 \cdot H_2O$ and [**8**]$BF_4 \cdot H_2O$. These data can be obtained free of charge via http://www.ccdc.cam.ac.uk/conts/retrieving.html, or from the Cambridge Crystallographic Data Center, 12 Union Road, Cambridge CB2 1EZ, UK; fax: (+44) 1223 336 033; or e-mail: deposit@ccdc.cam.ac.uk. Supplementary data associated with this article can be found, in the online version, at doi:10.1016/j.poly.2008.12.050.

References

[1] A.M.W.C. Thompson, Coord. Chem. Rev. 160 (1997) 1.
[2] J.P. Sauvage, J.P. Collin, J.C. Chambron, S. Guillerez, C. Coudret, V. Balzani, F. Barigelletti, L.D. Cola, L. Flamigni, Chem. Rev. 94 (1994) 993.
[3] E.C. Constable, Adv. Inorg. Chem. 34 (1989) 1.
[4] E.C. Constable, Adv. Inorg. Radiochem. 30 (1986) 69.
[5] E.C. Constable, Prog. Inorg. Chem. 42 (1994) 67.
[6] F. Fagalde, N.E. Katz, J. Chem. Soc., Dalton Trans. (1993) 571.
[7] J.A. Bailey, V.M. Miskowsky, H.B. Gray, Inorg. Chem. 32 (1993) 369.
[8] H.K. Yip, L.K. Cheng, K.K. Cheung, C.M. Che, J. Chem. Soc., Dalton Trans. (1993) 2933.
[9] M.S. Wrighton, Comment Inorg. Chem. 4 (1985) 269.
[10] L.A. Worl, G.F. Strouse, J.N. Younathan, S.M. Baxter, T.J. Meyer, J. Am. Chem. Soc. 112 (1990) 7571.
[11] J.J. Hopfield, J.N. Onuchic, D.N. Beratan, Science 241 (1988) 817.
[12] J.J. Hopfield, J.N. Onuchic, D.N. Beratan, J. Phys. Chem. 93 (1989) 6350.
[13] J.P. Sauvage, J.P. Collin, J.C. Chambron, S. Guillerez, C. Coudret, V. Balzani, F. Barigelletti, L. Decola, L. Flamigni, Chem. Rev. 94 (1994) 993.
[14] F.L. Carter, L.E. Saitkowski, H. Wohltjen (Eds.), Molecular Electronic Devices, Amsterdam, The Netherlands, 1988.
[15] F.H. Kohnke, J.P. Mathias, J.F. Stoddart, Angew Chem., Int. Ed. Engl. 28 (1989) 1103.
[16] J.M. Lehn, Angew. Chem., Int. Ed. Engl. 29 (1990) 1304.
[17] P. Ball, L. Garwin, Nature 355 (1992) 761.
[18] R.A. Metcalfe, E.S. Dodsworth, A.B.P. Lever, W.J. Pietro, D.J. Stufkens, Inorg. Chem. 32 (1993) 3581.
[19] L.F. Joulie, E. Schatz, M.D. Ward, F. Weber, F. Yellowlees, J. Chem. Soc., Dalton Trans. (1994) 799.
[20] J.M. Lehn, Supramolecular Chemistry, VCH, Weinheim, Germany, 1995.
[21] M. Hitoshi, A.L. Freda, M.C. Zerner, A.B.P. Lever, Inorg. Chem. 39 (2000) 141.
[22] V. Balzani, S. Campagna, D. Denti, A. Juris, S. Serroni, M. Venturi, Acc. Chem. Res. 31 (1998) 26.
[23] W.I. Sundquist, S.J. Lippard, Coord. Chem. Rev. 100 (1990) 293.
[24] T. Yukata, I. Mori, M. Kurihari, J. Mizutani, K. Kubo, S. Furusho, K. Matsumura, N. Tanai, H. Nishihara, Inorg. Chem. 40 (2001) 4986.
[25] A. Dovletoglou, S.A. Adeyemi, T.J. Meyer, Inorg. Chem. 35 (1996) 4120.
[26] S.M. Zakeeruddin, M.K. Nazeeruddin, P. Pechy, F.P. Rotzinger, R. Humphry-Baker, K. Kalyanasundaram, M. Gratzel, Inorg. Chem. 36 (1997) 5937.
[27] A.B.P. Lever, Inorg. Chem. 32 (1990) 1271.
[28] H. Brunner, Adv. Organomet. Chem. 18 (1980) 151.
[29] S.G. Davies, Pure Appl. Chem. 60 (1988) 13.
[30] J.W. Faller, M.R. Mazzieri, J.T. Nguyen, P. Parr, M. Tokunaga, Pure Appl. Chem. 66 (1994) 1463.
[31] E.P. Kundig, A. Quettropani, M. Inage, A. Ripa, C. Dupre, A.F.J. Cunningham, B. Bourdin, Pure Appl. Chem. 68 (1996) 97.
[32] V.I. Sokolov, Chirality and Optical Activity in Organometallic compounds, Gordon and Breach, 1990.
[33] G. Consiglio, F. Morandini, Chem. Rev. 87 (1987) 761.
[34] H. Aneetha, P.S. Zacharias, B. Srinivas, G.H. Lee, Y. Wang, Polyhedron 18 (1999) 299.
[35] S.C. Rasmussen, M.M. Richter, E. Yi, H. Place, K.J. Brewer, Inorg. Chem. 29 (1990) 3926.
[36] D.M. D'Alessandro, P.H. Dinolfo, M.S. Davies, J.T. Hupp, F.R. Keene, Inorg. Chem. 45 (2006) 3261.
[37] M. Harlos, I. Ott, R. Gust, H. Alborzinia, S. Wolfl, A. Kromm, W.S. Sheldrick, J. Med. Chem. 51 (2008) 3924.
[38] C. Sens, I. Romero, M. Rodriguez, A. Llobet, T. Parella, J. Benet-Buchholz, J. Am. Chem. Soc. 126 (2004) 7798.
[39] I. Romero, M. Rodriguez, C. Sens, J. Mola, K. Mohan Rao, L. Francas, E.M. Marza, L. Escriche, Antoni Llobet, Inorg. Chem. 47 (2008) 1824.
[40] F. Teixidor, R. Garcia, J. Pons, J. Casabó, Polyhedron 7 (1988) 43.
[41] J. Pons, X. López, E. Benet, J. Casabó, F. Teixidor, F.J. Sánchez, Polyhedron 9 (1990) 2839.
[42] M.I. Bruce, N.J. Windsor, Aust. J. Chem. 30 (1977) 1601.
[43] C. White, A. Yates, P.M. Maitlis, Inorg. Synth. 29 (1992) 228.
[44] P.W. Wanandi, T.D. Tilley, Organometallics 16 (1997) 4299.
[45] M.I. Bruce, P.J. Low, B.W. Skelton, E.R.T. Tiekink, A. Werth, A.H. White, Aust. J. Chem. 48 (1995) 1887.
[46] J.W. Kang, K. Moseley, P.M. Maitlis, J. Am. Chem. Soc. 91 (1969) 5970.
[47] M.I. Bruce, B.C. Hall, N.N. Zaitseva, B.W. Skelton, A.H. White, J. Chem. Soc., Dalton Trans. (1998) 1793.
[48] M.A. Bennett, T.N. Huang, T.W. Matheson, A.K. Smith, Inorg. Synth. 21 (1982) 74.
[49] M.A. Bennett, T.W. Matheson, G.B. Robertson, A.K. Smith, P.A. Tucker, Inorg. Chem. 19 (1980) 1014.
[50] M.A. Bennett, A.K. Smith, J. Chem. Soc., Dalton Trans. (1974) 233.
[51] M. Sheldrick, Acta Crystallogr., Sect. A 46 (1990) 467.
[52] M. Sheldrick, SHELXL-97, University of Göttingen, Göttingen, Germany, 1999.
[53] D.A. Freedman, S. Kruger, C. Roosa, C. Wymer, Inorg. Chem. 45 (2006) 9558.
[54] Q. Major, A.J. Lough, D.G. Gusev, Organometallics 24 (2005) 2492.
[55] S. Sharma, S.K. Singh, D.S. Pandey, Inorg. Chem. 47 (2008) 1179.
[56] P. Govindaswamy, B. Therrien, G. Süss-Fink, P. Štěpnička, J. Ludvík, J. Organomet. Chem. 692 (2007) 1661.
[57] K. Pachhunga, B. Therrien, K.A. Kreisel, G.P.A. Yap, M.R. Kollipara, Polyhedron 26 (2007) 3638.
[58] K.T. Prasad, B. Therrien, K. Mohan Rao, J. Organomet. Chem. 693 (2008) 3049.

introduction of a blocking ligand. So, the tetracyano derivatives with general formula $[M(AA)(CN)_4]^-$ (M = Fe, Cr and Co; AA = bidentate ligand) have been proved to be well-suited building blocks to obtain low-dimensional cyano-bridged systems [9]. Taking the $[Fe(bipy)(CN)_4]^-$ entity as an illustrative example, its reaction with fully solvated transition metal ions, has led to single- and double-4,2-ribbon like $Fe^{III}_2M^{II}$ bimetallic chains (M = Mn, Ni, Co and Cu) [10a–e] as well as to heterometallic bi- [9], tri- [10a] and tetranuclear [10f] compounds. The extension of the coordination ability of the $[M(AA)(CN)_4]^-$ complex anion to 4f elements or conducting organic cations seems very appealing and it is a practically unexplored research area. The first attempts involving charged salts of TTF (tetrathiafulvalene) and the $[M(phen)(CN)_4]^-$ anion have led to metal-organic supramolecular systems $TTF[M(phen)(CN)_4]$ (M = Fe and Cr) with a semiconducting behaviour [11]. Also the structure and magnetic properties of the hexanuclear complex of formula $\{[Nd^{III}(NO_3)(H_2O)_3]_2[Fe^{III}(phen)(CN)_4]_4\} \cdot 2H_2O$ have been subject of a recent report [9a].

Stimulated by these preliminary results, we have tested the reactivity of the $[Fe(bipy)(CN)_4]^-$ complex toward lanthanide cations in the presence of the bpym ligand. It is worth to mention that non-covalent interactions are favoured in this type of association. At one hand, the oxophilic and highly coordinated lanthanide cations may incorporate several water molecules in their coordination sphere and, on the other hand, the cyanometallate anions are also good hydrogen acceptors. Consequently, hydrogen bonds may easily occur therein and even compete with the coordinative bonds to build supramolecular structures [12]. Bipy–bipy, bipy–bpym and bpym–bpym inter-ring stacking interactions are also possible.

These features have been checked in the 3d–4f heterobimetallic supramolecular systems $[Ln(bpym)(NO_3)_2(H_2O)_3][Fe(bipy)(CN)_4] \cdot H_2O \cdot CH_3CN$ [Ln = Sm (**1**), Gd (**2**), Tb (**3**), Dy (**4**) and Ho (**5**)] and $[Ln(bpym)(NO_3)_2(H_2O)_4][Fe(bipy)(CN)_4]$ [Ln = Pr (**6**), Nd (**7**), Sm (**8**) and Gd) (**9**)] whose preparation and structural characterization are presented here.

2. Experimental

2.1. General

All the chemicals were purchased from commercial sources as reagents pure for analysis and they were used as received. $PPh_4[Fe(bipy)(CN)_4] \cdot H_2O$ was prepared as described in the literature [10a]. The IR spectra of **1**–**9** as KBr pellets were registered on a Bruker IF S55 spectrometer. Elemental analysis (C, H, N) were performed at the Centro de Microanálisis Elemental from the Universidad Complutense de Madrid. The value of the Fe:Ln molar ratio (1:1) for **1**–**9** was determined by electron probe X-ray microanalysis at the Servicio Interdepartamental of the University of Valencia.

2.2. Synthesis

2.2.1. Preparation of $[Ln(bpym)(NO_3)_2(H_2O)_3][Fe(bipy)(CN)_4] \cdot H_2O \cdot CH_3CN$ [Ln = Sm (*1*), Gd (*2*), Tb (*3*), Dy (*4*) and Ho (*5*)]

Compounds **1**–**5** were obtained by the same general method: an acetonitrile solution (10 cm^3) of $PPh_4[Fe(bipy)(CN)_4] \cdot H_2O$ (0.05 mmol) was poured into another acetonitrile solution (10 cm^3) containing bpym (0.05 mmol) and the corresponding lanthanide salt as $Ln(NO_3)_3 \cdot nH_2O$ (0.05 mmol). The orange solid which separated immediately was removed by filtration. Slow evaporation of the filtered solution at room temperature afforded orange prisms of **1**–**5** after a few days. The yield is about 85%. *Anal.* Calc. for $C_{24}H_{25}N_{13}O_{10}FeLn$ [Ln = Sm (**1**), Gd (**2**), Tb (**3**), Dy (**4**) and Ho (**5**)]: C, 33.41; H, 2.90; N, 21.11 (**1**); C, 33.15; H, 2.87; N, 20.95 (**2**); C, 33.09; H, 2.87; N, 20.91 (**3**); C, 32.95; H, 2.86; N, 20.82 (**4**); C, 32.86; H, 2.85; N, 20.76 (**5**). Found: C, 33.20; H, 2.88; N, 20.87 (**1**); C, 33.11; H, 2.82; N, 20.62 (**2**); C, 32.93; H, 2.74; N, 20.65, (**3**); C, 32.87; H, 2.82; N, 20.72 (**4**); C, 32.95; H, 2.81; N, 20.51% (**5**). IR (cm^{-1}): 3418(m), 2927(w), 2856(w), 2128(m), 2057(m), 1636(s), 1560(m), 1519(w), 1470(w), 1444(m), 1382(s), 1310(w), 1280(w), 1032(m), 774(m), 739(w).

2.2.2. Preparation of $[Ln(bpym)(NO_3)_2(H_2O)_4][Fe(bipy)(CN)_4]$ [Ln = Pr (*6*), Nd (*7*), Sm (*8*) and Gd) (*9*)]

Compounds **6**–**9** were synthesized also following the same general method: slow inter-diffusion of mixed acetonitrile/water 1:1 (v/v) solutions of $PPh_4[Fe(bipy)(CN)_4] \cdot H_2O$ (0.03 mmol) and $Ln(NO_3)_3 \cdot nH_2O$ (0.03 mmol) and bpym (0.03 mmol) afforded X-ray quality crystals as red-orange prisms. The yield is about 90%. *Anal.* Calc. for $C_{22}H_{22}N_{12}O_{10}FeLn$ [Ln = Pr (**6**), Nd (**7**), Sm (**8**) and Gd (**9**)]: C, 32.54; H, 2.71; N, 20.70 (**6**); C, 32.40; H, 2.70; N, 22.34 (**7**); C, 32.16; H, 2.68; N, 20.46 (**8**); C, 33.09; H, 2.87; N, 20.91 (**9**). Found: C, 32.36; H, 2.70; N, 20.55 (**6**); C, 32.28; H, 2.65; N, 22.17, (**7**); C, 32.36; H, 2.61; N, 20.31, (**8**); C, 32.98; H, 2.79; N, 20.80% (**9**). IR (cm^{-1}): 3443(m), 2927(w), 2852(w), 2128(m), 2062(m), 1639(s), 1560(m), 1541(w), 1521(w), 1470(w), 1444(m), 1382(s), 1310(w), 1227(w), 1036(m), 778(m), 739(w).

2.3. X-ray data collection and structure refinement

Diffraction data set on single crystals of **1**–**9** were collected at 293(2) K (**1**–**7** and **9**) and 150(2) K (**8**) on a Nonius Kappa CCD diffractometer with graphite-monochromated Mo Kα radiation (λ = 0.71073 Å). Orientation matrix and lattice parameters were determined by least-squares refinements of the reflections obtained by a $\theta-\chi$ scan (Dirac/lsq method). Data collection was done with the COLLECT [13] and the data reduction was done with EVALCCD [14] (**2**–**5** and **7**–**9**) and HKL2000 [15] (**1** and **6**) programs. Empirical absorption corrections were carried out using SADABS [16]. No significant variations were observed in the intensities of two checked reflections during data scaling. All the measured independent reflections were used in the analysis. The values of the minimum and maximum transmission factors were 0.6046/0.7159 (**1**), 0.6366/0.8859 (**2**), 0.6794/0.8587 (**3**), 0.6097/0.8103 (**4**), 0.7614/0.8460 (**5**), 0.5650/0.6732 (**6**), 0.6350/0.7127 (**7**), 0.6056/0.8230 (**8**) and 0.6050/0.6794 (**9**).

The structures of **1**–**9** were solved by direct methods through the SHELXS97 [17] computational program. All non-hydrogen atoms were refined anisotropically by full-matrix least-squares technique on F^2 by using the SHELXL97 [17] program. The hydrogen atoms of bipy, bpym and acetonitrile molecules were placed in calculated positions and refined as riding atoms with a common fixed isotropic thermal parameter. The hydrogen atoms of the coordinated water molecules were neither found nor considered in the refinement. The values of the maximum and minimum final electron density peaks are 1.125/−1.468 (**1**), 0.830/−0.592 (**2**), 0.771/−0.686 (**3**), 0.832/−0.694 (**4**), 0.627/−0.395 (**5**), 0.708/−0.864 (**6**), 1.738/−0.842 (**7**), 0.953/−2.352 (**8**) and 0.651/−0.573 e $Å^{-3}$ (**9**). The final geometrical calculations and the graphical manipulations were carried out with the PARST97 [18], PLATON [19] and DIAMOND [20] programs. Information concerning the crystallographic data collection and structure refinement is summarized in Tables 1 (**1**–**5**) and 2 (**6**–**9**).

3. Results and discussion

3.1. Synthetic aspects and IR characterization

The versatility of the $[M(AA)(CN)_4]^-$ unit as a ligand is illustrated by Scheme 1. One can see therein the different low-dimensional species which have been materialized up to now, the ionic

Table 1
Crystal data and structure refinement for $[Ln(bpym)(NO_3)_2(H_2O)_3][Fe(bipy)(CN)_4] \cdot H_2O \cdot CH_3CN$ [Ln = Sm (**1**), Gd (**2**), Tb (**3**), Dy (**4**) and Ho (**5**)].

Compound	**1**	**2**	**3**	**4**	**5**
Empirical formula	$C_{24}H_{25}FeSmN_{13}O_{10}$	$C_{24}H_{25}FeGdN_{13}O_{10}$	$C_{24}H_{25}FeTbN_{13}O_{10}$	$C_{24}H_{25}FeDyN_{13}O_{10}$	$C_{24}H_{25}FeHoN_{13}O_{10}$
Formula weight	861.77	868.67	870.34	873.92	876.35
Crystal system	monoclinic	monoclinic	monoclinic	monoclinic	monoclinic
Space group	$P2_1/c$	$P2_1/c$	$P2_1/c$	$P2_1/c$	$P2_1/c$
a (Å)	16.2930(8)	16.2627(11)	16.2280(12)	16.222(2)	16.2080(16)
b (Å)	14.2662(5)	14.2120(14)	14.1941(14)	14.1750(8)	14.1510(10)
c (Å)	15.5971(7)	15.5568(10)	15.5713(13)	15.570(3)	15.5710(17)
β (°)	112.357(3)	112.184(7)	112.044(6)	112.136(10)	112.015(8)
V (Å^3)	3352.9(3)	3329.4(5)	3324.5(5)	3316.3(8)	3311.0(5)
Z	4	4	4	4	4
D_{calc} (g cm^{-3})	1.707	1.733	1.739	1.750	1.758
μ (mm^{-1})	2.238	2.482	2.618	2.745	2.883
Reflections collected/unique	8280*/8280	18858/7556	43637/7618	23653/7556	42446/7463
R_{int}	0.0742	0.0428	0.0475	0.0283	0.0308
Reflections observed [$I > 2\sigma(I)$]	7419	5782	5779	5907	6063
Data/restraints/parameters	8280/443/0	7556/443/0	7618/443/0	7556/443/0	7463/443/0
Goodness-of-fit on F^2	1.115	1.042	1.111	1.161	1.066
Final R indices	$R_1 = 0.0443$	$R_1 = 0.0360$	$R_1 = 0.0359$	$R_1 = 0.0313$	$R_1 = 0.0243$
[$I > 2\sigma(I)$]	$wR_2 = 0.1227$	$wR_2 = 0.0784$	$wR_2 = 0.0789$	$wR_2 = 0.0813$	$wR_2 = 0.0489$
R indices (all data)	$R_1 = 0.0514$	$R_1 = 0.0584$	$R_1 = 0.0610$	$R_1 = 0.0528$	$R_1 = 0.0403$
	$wR_2 = 0.1355$	$wR_2 = 0.0889$	$wR_2 = 0.0876$	$wR_2 = 0.0904$	$wR_2 = 0.0548$

* Reflections merged during the integration process.

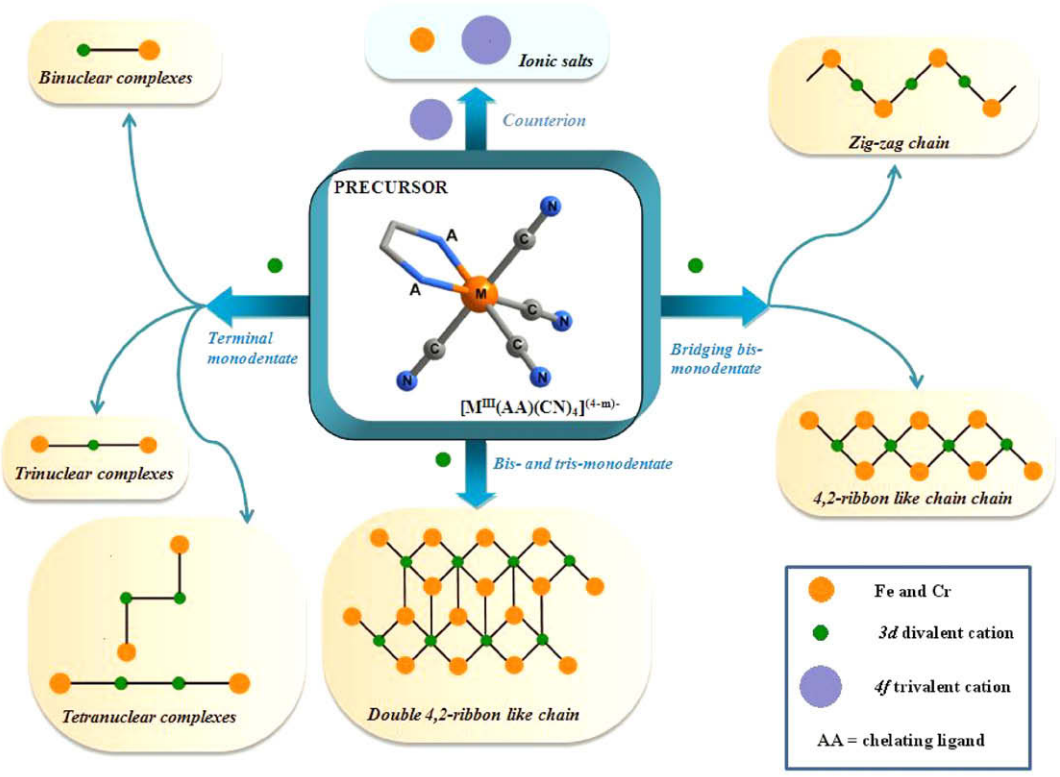
Table 2
Crystal data and structure refinement for $[Ln(bpym)(NO_3)_2(H_2O)_4][Fe(bipy)(CN)_4]$ [Ln = Pr (**6**), Nd (**7**), Sm (**8**) and Gd (**9**)].

Compound	**6**	**7**	**8**	**9**
Empirical formula	$C_{22}H_{22}FePrN_{12}O_{10}$	$C_{22}H_{22}FeNdN_{12}O_{10}$	$C_{22}H_{22}FeSmN_{12}O_{10}$	$C_{22}H_{22}FeGdN_{12}O_{10}$
Formula weight	811.28	814.61	820.72	827.62
Space group	$P2/c$	$P2/c$	$P2/c$	$P2/c$
Crystal system	monoclinic	monoclinic	monoclinic	monoclinic
a (Å)	13.2560(10)	13.2289(12)	13.20190(10)	13.1707(8)
b (Å)	9.1460(10)	9.1268(6)	9.05790(10)	9.0717(6)
c (Å)	13.8950(10)	13.8561(7)	13.7479(2)	13.7871(17)
β	116.347(10)	116.370(5)	116.0010(1)	116.346(6)
V (Å^3)	1509.6(2)	1498.87(18)	1477.60(3)	1476.2(2)
Z	2	2	2	2
D_{calc} (g cm^{-3})	1.785	1.805	1.845	1.862
μ (mm^{-1})	2.148	2.271	2.533	2.793
Reflections collected/unique	3713*/3713	17505/3429	23164/3676	16073/3338
R_{int}	0.0432	0.0431	0.1123	0.0275
Reflections observed [$I > 2\sigma(I)$]	3651	3274	3646	3223
Data/parameters/restraints	3713/204/0	3429/209/0	3676/209/0	3338/209/0
Goodness-of-fit on F^2	1.301	1.160	1.385	1.152
Final R indices	$R_1 = 0.0254$	$R_1 = 0.0254$	$R_1 = 0.0257$	$R_1 = 0.0171$
[$I > 2\sigma(I)$]	$wR_2 = 0.0853$	$wR_2 = 0.0682$	$wR_2 = 0.0887$	$wR_2 = 0.0446$
R indices (all data)	$R_1 = 0.0267$	$R_1 = 0.0274$	$R_1 = 0.0288$	$R_1 = 0.0184$
	$wR_2 = 0.0933$	$wR_2 = 0.0698$	$wR_2 = 0.1142$	$wR_2 = 0.0451$

* Reflections merged during the integration process.

salts on the top corresponding to the present work. Focusing on the reaction of the $[Fe(bipy)(CN)_4]^-$ anion with lanthanide cations in the presence of bpym as coligand, two types of 3D supramolecular heterobimetallic systems have been achieved, namely compounds **1**–**5** and **6**–**9**. The bpym molecule usually coordinates to the d and f type metal ions in a *bis*-chelating fashion [21–30], but this is not the case here where it exerts two structural functions: it acts as a bidentate ligand toward the Ln(III) ions and it is also a receptor of hydrogen atoms from the neighbouring water molecules.

The composition of the solvent induces changes in the coordination sphere of the lanthanide ions and also on the overall pattern of hydrogen bonds. So, if the reaction takes place in acetonitrile, the lanthanide ion is nine-coordinated (series **1**–**5**) whereas it is 10-coordinated (compounds **6**–**9**) when the synthesis is performed in an acetonitrile–H_2O 1:1 (v/v) mixture, the resulting three-dimensional supramolecular assemblies having different trends of the H-bonds. It is also possible that the distinct coordination geometries in complexes **1**–**5** and **6**–**9** are related to the different radii of the lanthanide ions, the smaller (Tb, Dy and Ho) being nine-coordinate and the larger (Pr and Nd) being 10-coordinate (Sm and Gd being intermediate). The infrared spectra of the compounds **1**–**9** exhibit two sharp absorptions characteristic of terminal cyanide groups at 2128 and 2057 cm^{-1}. The ring-stretching modes of coordinated bpym and bipy ligands overlap in the 1640–1560 cm^{-1} region. The medium intensity band at ca. 770 cm^{-1} is assigned to the chelating bipy ligand. Finally, the broad band observed in the high frequency region (ca. 3500–3200 cm^{-1}) is due to the presence of crystallization and coordinated water molecules which are interlinked by an extensive network of hydrogen bonds [31]. A weak intensity peak at ca. 2300 cm^{-1} in the IR spectra of **1**–**5** is assigned to the stretching vibration of the C≡N bond of the acetonitrile molecule. The spectral features of all nine compounds correspond with their single crystal X-ray structures (see below).



Scheme 1.

3.2. Description of the structure of $[Ln(bpym)(NO_3)_2(H_2O)_3][Fe(bipy)(CN)_4] \cdot H_2O \cdot CH_3CN$ [Ln = Sm (**1**), Gd (**2**), Tb (**3**), Dy (**4**) and Ho (**5**)]

Compounds **1**–**5** are isostructural and isomorphous and their structure consists of univalent $[Ln(bpym)(NO_3)_2(H_2O)_3]^+$ cations and $[Fe(bipy)(CN)_4]^-$ anions together with uncoordinated water and acetonitrile molecules which are interlinked through electrostatic forces and supramolecular interactions to afford a neutral three-dimensional network (see below). Bond lengths and angles around the Fe and Ln atoms are listed in Table 3 whereas the hydrogen bonds are given in Table 4.

The $[Ln(bpym)(NO_3)_2(H_2O)_3]^+$ cations are grouped by pairs which are interlinked through hydrogen bonds involving one coordinated water molecule [O(2w)], the crystallization water [O(4w)] and one coordinated nitrate-oxygen [O(1)] to afford a (4,4) layered motif extending in the *bc*-plane (Fig. 1a). $O_w \cdots N_{bpym}$ hydrogen bonds and slightly off-set π–π bpym–bpym interactions occur within each pair of cations, as shown in Fig. 1b. Dealing with these last interactions, the values of the centroid–centroid distance are 3.8910(2) (**1**), 3.8883(3) (**2**), 3.8838(4) (**3**), 3.8785(7) (**4**) and 3.8785(4) (**5**) Å and those of the angle between the normal of each bpym ring and the centroid–centroid vector are 19.87(11) (**1**), 19.68(11) (**2**), 19.88(11) (**3**), 19.67(10) (**4**) and 19.93(8)° (**5**).

The $[Fe(bipy)(CN)_4]^-$ anions are placed above and below the holes of the (4,4) layers (Fig. 2a) defining a *ABA* set of anionic and cationic layers which is repeating along the *a*-axis (Fig. 2b), the cations being anchored to the anions through $N_{cyanide} \cdots O_w$ hydrogen bonds where all the cyanide–nitrogen and coordinated water molecules are involved (see Table 4).

Finally, the *ABA* layers are interlinked along the *a*-axis through π–π type interactions between pairs of bipy ligands from adjacent *ABA* sets leading to a supramolecular three-dimensional network (Fig. 3). The bipy ligands are stacked in an slightly off-set conformation with values of the the centroid–centroid distances of 3.7521(1) (**1**), 3.7526(3) (**2**), 3.7452(4) (**3**), 3.7596(4) (**4**) and 3.7470(4) Å (**5**) and those of the angle between the normal of each pyridyl ring and the centroid–centroid vector being 25.56(8) (**1**), 25.71(10) (**2**), 25.49(9) (**3**), 25.46(9) (**4**) and 25.51(6)° (**5**).

Each crystallographically independent lanthanide atom is nine-coordinated: four oxygen atoms [O(1), O(2), O(4) and O(5)] belonging to two nitrate groups, two bpym-nitrogens [N(21) and N(24)] from a bidentate bpym molecule and three coordinated water molecules [O(1w), O(2w) and O(3w)] build a somewhat distorted monocapped square antiprism [mean bite value $b = 1.09$ (**1**), 1.08 (**2**–**4**) and 1.07 (**5**)] [32] around the rare-earth atom (Fig. 4). The square-planar base of the coordination polyhedron of each lanthanide atom in **1**–**5** is defined by the O(1), O(3w), N(21) and N(24) set of atoms, while the upper square-plane is built by the O(2), O(4), O(1w) and O(2w) atoms. The capping of the antiprism is achieved by the [O(5)] atom from a nitrato group. The largest $Ln–N_{bpym}$ bonds significantly contribute to the distortion polyhedron. The values of the Ln–O bond length cover the ranges 2.456(3)–2.521(3) (**1**), 2.422(3)–2.491(3) (**2**), 2.409(3)–2.479(2) (**3**), 2.392(3)–2.446(3) (**4**) and 2.379(2)–2.450(2) Å (**5**). The average values for the $Ln–O_w$ bond distances are 2.411(3) (**1**), 2.387(3) (**2**), 2.376(3) (**3**), 2.360(3) (**4**) and 2.349(2) Å (**5**), all of them being shorter than those of the mean $Ln–N_{bpym}$ bonds which are 2.619(3) (**1**), 2.596(3) (**2**), 2.575(3) (**3**), 2.564(3) (**4**) and 2.550(2) Å (**5**) (see Table 3).

These last bond lengths which cover the range 2.526(2)–2.632(3) Å are found to be somewhat smaller than those reported for similar coordination bonds in other ionic pair complexes [12b]. All distances concerning the coordination sphere of the trivalent lanthanide cations decrease with the ionic radius in the order Sm(III) (**1**) > Gd(III) (**2**) > Tb(III) (**3**) > Dy(III) (**4**) > Ho(III) (**5**) by following the lanthanide contraction.

Table 3
Bond lengths (Å) and angles (°) of the coordination environments of Fe and Ln in **1**–**5** [Ln = Sm (**1**), Gd (**2**), Tb (**3**), Dy (**4**) and Ho (**5**)].

	1	2	3	4	5
Fe(1)–N(11)	1.985(3)	1.981(3)	1.984(3)	1.987(3)	1.983(2)
Fe(1)–N(12)	1.986(3)	1.988(3)	1.988(3)	1.980(3)	1.984(2)
Fe(1)–C(1)	1.914(4)	1.904(5)	1.909(5)	1.905(5)	1.911(3)
Fe(1)–C(2)	1.920(4)	1.917(4)	1.925(4)	1.919(4)	1.916(3)
Fe(1)–C(3)	1.945(4)	1.937(4)	1.943(4)	1.947(4)	1.947(3)
Fe(1)–C(4)	1.952(4)	1.943(5)	1.948(4)	1.948(4)	1.952(3)
Ln(1)–N(24)	2.604(3)	2.576(3)	2.551(3)	2.542(3)	2.526(2)
Ln(1)–N(21)	2.632(3)	2.615(3)	2.599(3)	2.585(3)	2.576(2)
Ln(1)–O(1)	2.496(3)	2.475(3)	2.462(3)	2.446(3)	2.434(2)
Ln(1)–O(2)	2.521(3)	2.490(3)	2.479(3)	2.467(3)	2.450(2)
Ln(1)–O(4)	2.457(3)	2.422(3)	2.408(3)	2.392(3)	2.379(2)
Ln(1)–O(5)	2.488(3)	2.462(3)	2.450(3	2.444(3)	2.437(2)
Ln(1)–O(1w)	2.393(3)	2.371(3)	2.362(3)	2.341(3)	2.332(2)
Ln(1)–O(2w)	2.397(3)	2.371(3)	2.358(3)	2.348(3)	2.331(2)
Ln(1)–O(3w)	2.441(3)	2.418(3)	2.407(3)	2.396(3)	2.383(2)
N(11)–Fe(1)–N(12)	81.20(13)	80.92(14)	81.09(14)	81.14(13)	81.18(9)
Fe(1)–C(1)–N(1)	177.4(5)	178.2(5)	178.2(5)	177.7(4)	178.1(3)
Fe(1)–C(2)–N(2)	179.0(5)	179.1(5)	178.3(5)	178.5(5)	178.9(3)
Fe(1)–C(3)–N(3)	178.3(4)	178.1(4)	177.9(4)	178.3(4)	178.4(3)
Fe(1)–C(4)–N(4)	178.9(4)	178.5(4)	178.4(4)	178.9(4)	178.7(3)
N(24)–Ln(1)–N(21)	62.12(10)	62.77(11)	63.12(10)	63.21(10)	63.60(7)
O(1)–Ln(1)–O(2)	50.98(11)	51.30(11)	51.63(10)	51.88(10)	52.08(7)
O(4)–Ln(1)–O(5)	51.62(10)	51.90(10)	52.19(10)	52.42(9)	52.65(7)

Table 4
Selected intermolecular contacts (Å) in **1**–**5** [Ln = Sm (**1**), Gd (**2**), Tb (**3**), Dy (**4**) and Ho (**5**)][*].

	1	2	3	4	5
O(1w)···N(1)[a]	2.731(6)	2.712(6)	2.720(6)	2.722(6)	2.718(4)
O(1w)···N(2)[b]	2.760(7)	2.752(6)	2.755(6)	2.761(6)	2.763(4)
O(2w)···O(4w)	2.654(10)	2.656(8)	2.654(8)	2.662(8)	2.663(7)
O(2w)···N(4)	2.751(5)	2.752(5)	2.745(5)	2.746(5)	2.751(3)
O(3w)···N(3)[c]	2.749(5)	2.751(5)	2.746(5)	2.747(5)	2.753(3)
O(3w)···N(22)[d]	2.907(7)	2.903(7)	2.906(6)	2.908(7)	2.902(4)
O(4w)···O(1)[b]	3.127(8)	3.132(7)	3.154(7)	3.160(7)	3.178(5)

[*] Symmetry code: [a] = $-2-x$, $-0.5+y$, $-0.5-z$; [b] = x, $-1.5-y$, $-0.5+z$; [c] = x, $-1+y$, z; [d] = $-2-x$, $-2-y$, $-z$.

Each iron atom in **1**–**5** is six-coordinated with two bipy–nitrogen and four cyanide–carbon atoms building a distorted octahedral surrounding (Fig. 4a). The reduced bite of the bidentate bipy group [(N(11)–Fe(1)–N(12) = 81.2(13) (**1**), 80.92(14) (**2**), 81.09(14) (**3**), 81.14(13) (**4**) and 81.18(9)° (**5**)] being one of the main factors accounting for this distortion. The values of the Fe(1)–N_{bipy} bonds in **1**–**5** [values varying in the range 1.980(3)–1.988(3) Å] compare well with those found in the related low-spin iron(III) complexes $PPh_4[Fe(bipy)(CN)_4]\cdot H_2O$ [1.98(2) and 2.00(2) Å] [10a], $K[Fe(bipy)(CN)_4]\cdot H_2O$ [1.990(3) and 1.991(3) Å] [10d] and $AsPPh_4[Fe(bipy)(CN)_4]\cdot CH_3CN$ [1.997(3) and 1.982(3) Å] [10e]. This agreement is also observed in the values of the Fe(1)–C_{cyano} bond lengths [values covering the range 1.904(5)–1.952(4) Å compared to 1.87(2)–1.91(2) (tetraphenylphosphonium derivative), 1.914(5)–1.958(5) (potassium salt) and 1.911(4)–1.955(4) Å (tetraphenylarsonium compound)]. The iron atom at each cyanide group in **1**–**5** is close to linearity, the values for the angle of the Fe(1)–C–N set of atoms varying in the range 177.4(5)–179.1(5)°.

Both bpym and bipy molecules are close to planarity, the first one exhibiting a somewhat greater deviation with maximum and minimum values of the inter-ring dihedral angle of 6.22(14)° (**4**) and 5.84(15)° (**1**) [the corresponding maximum and minimum values for the twisting between the pyridyl rings of bipy are 1.28(13) (**1**) and 1.69(12)° (**2**)]. The bond lengths and angles within the bipy and bpym ligands are in agreement with those reported for the free molecules [33,34].

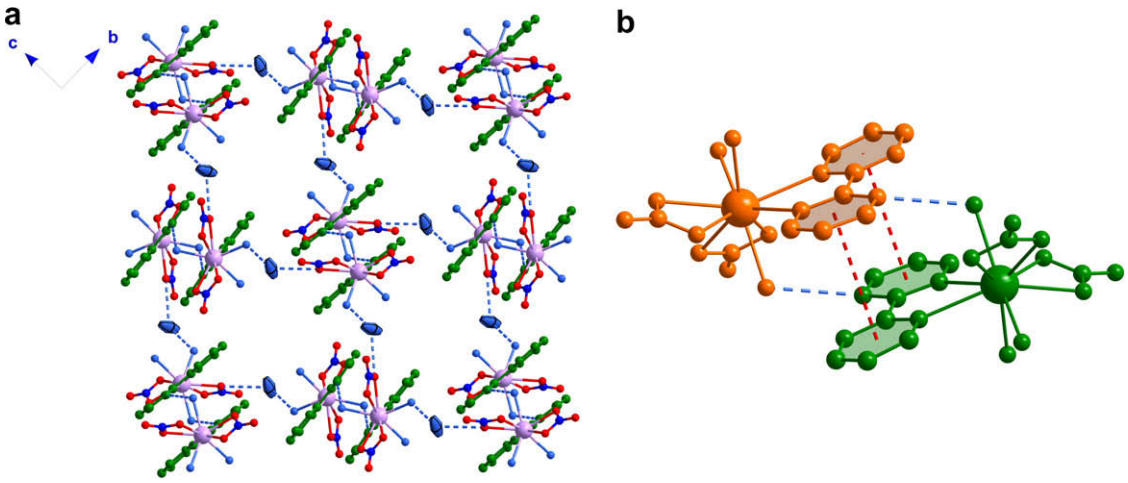


Fig. 1. (a) (4,4) rectangular supramolecular planes built by non-covalent pairs of $[Ln(bpym)(NO_3)_2(H_2O)_3]^+$ cations which are interlinked by $O_w\cdots O_w$ hydrogen bonds and (b) details of the non-covalent interactions between two $[Ln(bpym)(NO_3)_2(H_2O)_3]^+$ cationic synthons showing the $O_w\cdots N_{bpym}$ and intra-ring bpym–bpym contacts.

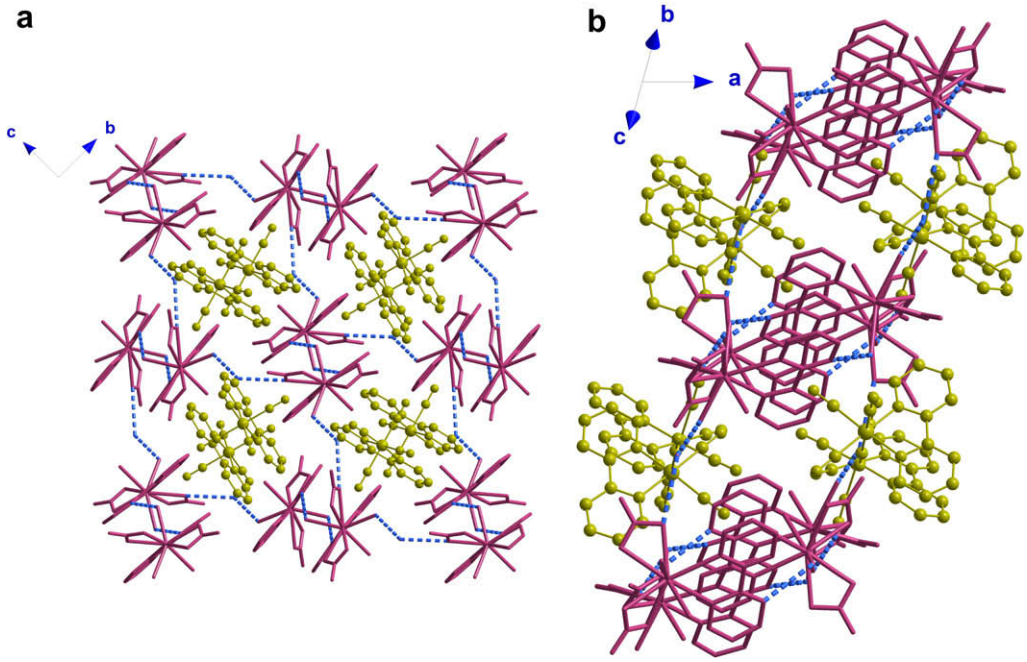


Fig. 2. Details of the crystal packing in the *bc*-plane (a) and along the *a*-axis (b) revealing the anchoring of the $[Fe(bipy)(CN)_4]^-$ anions in the 3D cavities defined by the lanthanide-based cationic synthons.

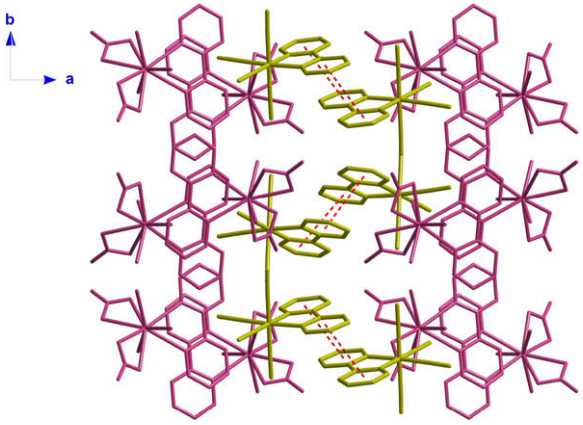


Fig. 3. Details of the crystal packing in the *ab*-plane revealing the inter-ring bipy–bipy interaction between adjacent anionic and cationic planes leading to a three-dimensional structure.

The crystallization acetonitrile molecules are stacked along the *b*-axis and they are located between layers. The shortest intermolecular separations between the iron and the lanthanide atoms occur through the C(3)–N(3)···O(3w) pathway and their values are 7.0359(6) (**1**), 7.0160(9) (**2**), 7.0110(9) (**3**), 7.0037(8) (**4**), 6.9958(7) Å (**5**) [Ln(1)···Fe(1)^d].

*3.3. Description of the structure of [Ln(bpym)(NO$_3$)$_2$(H$_2$O)$_4$][Fe(bipy)(CN)$_4$] [Ln = Pr (**6**), Nd (**7**), Sm (**8**), Gd (**9**)]*

Compounds **6**–**9** are isostructural and their structure is made up by anionic (*A*) and cationic (*B*) layers of $[Fe(bipy)(CN)_4]^-$ and $[Ln(bpym)(NO_3)_2(H_2O)_4]^+$, respectively, each one extending in the *bc*-plane, which are regularly stacked in the *ABAB* sequence along the *a*-axis through $O_w\cdots N_{cyano}$ hydrogen bonds (see Table 6) and off-set π–π bpym–bipy interactions [with values for the centroid–centroid distance of 3.8617(5) (**6**), 3.8506(4) (**7**), 3.8415(1) (**8**) and 3.8242(3) Å (**9**) and those of the angle between the normal

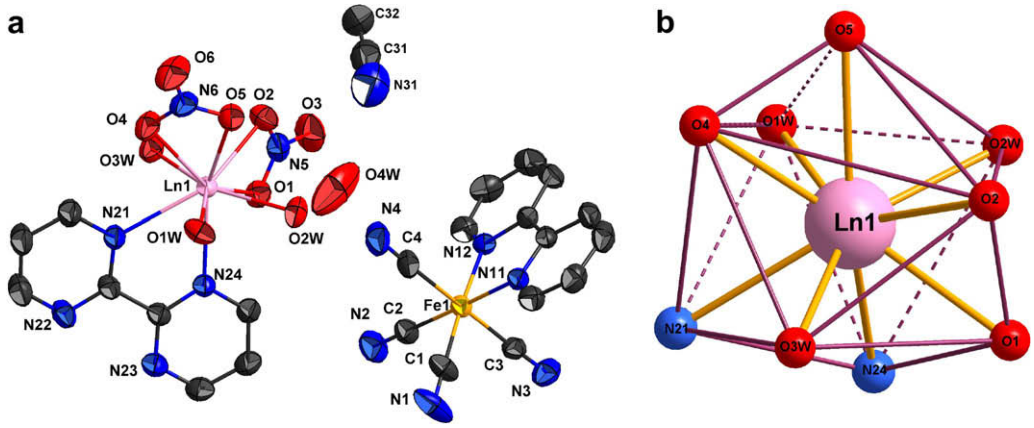


Fig. 4. (a) Perspective drawing of the crystallographically independent units of compounds **1**–**5** with the atom labelling (thermal ellipsoids are plotted at the 50% probability level) and (b) a view of the coordination polyhedron of the lanthanide atom in **1**–**5**. The hydrogen atoms have been omitted for clarity.

of the corresponding pyrimidyl ring and the centroid–centroid vector of 22.57(7) (**6**), 22.60(5) (**7**), 21.94(7) (**8**) and 22.64(5)° (**9**)] (Fig. 5). Both the anion and the cation have a C_{2v} symmetry.

Within each cationic layer, the $[Ln(bpym)(NO_3)_2(H_2O)_4]^+$ units are interlinked through $O_w\cdots N_{bpym}$ type hydrogen bonds along the *b*-axis and the resulting chains extend along the *c*-axis by means of $O_w\cdots O_{nitrate}$ hydrogen bonds (Fig. 6).

As far as the anionic layers are concerned, their $[Fe(bipy)(CN)_4]^-$ constituents are interlinked along the *c*-axis through π–π type interactions between the bipy ligands [values for the centroid–centroid distance of 3.9908(5) (**6**), 3.9808(3) (**7**), 3.9494(1) (**8**) and 3.9725(5) Å (**9**) and those of the angle between the normal of each pyridyl ring and the centroid–centroid vector of 28.29(8)° (**6**), 28.20(6) (**7**), 27.98(7) (**8**) and 27.89(5)° (**9**)] leading to supramolecular chains of iron atoms (Fig. 7).

The crystallographically independent structural units of **6**–**9** are shown in Fig. 8a. The 10-coordination of the lanthanide atom in **6**–**9** (Fig. 8b) versus the nine-coordination observed in **1**–**5** is the main difference between both families concerning these units and this structural feature determines the different supramolecular arrangement of the anions and cations in the resulting three-dimensional structures (Figs. 3 and 5) for **1**–**5** and **6**–**9**, respectively).

The bond lengths around the iron atom of the $[Fe(bipy)(CN)_4]^-$ anion in **6**–**9** [$Fe–C_{cyano}$ = 1.911(2)–1.948(3) Å and $Fe–N_{bipy}$ = 1.9880(2) and 1.992(2) Å] (see Table 5) compare well with those observed for this entity in **1**–**5**. The values of the Fe–C–N angles concerning the two *trans*-coordinated cyanide groups deviate somewhat from the strict linearity [172.0(3) and 172.5(3)°] whereas those coordinated in *cis* are very close to the linearity [177.7(2) and 177.9(3)°]. The lanthanide atoms in **6**–**9** are located on a twofold rotation axis and they are 10-coordinated with one chelating bpym, two bis-bidentate nitrato and four water molecules building a distorted bicapped square antiprism [*b*-mean value = 1.10 (**6**), 1.10 (**7**), 1.09 (**8**) and 1.09 (**9**)] [32]. The square-planar base of the polyhedron is defined by the O(1w), O(1), $O(2w)^b$ and $N(21)^b$ set of atoms while the upper square-plane is built by $O(1w)^b$, $O(1)^b$, O(2w) and N(21) atoms [(*b*) = $-x$, y, $1.5 - z$]. The O(2) and the symmetry-related $O(2)^b$ oxygen atoms cap the base and upper face of the square antiprism, respectively. The largest Ln–O bond distances concern these oxygen atoms [2.695(2) (**6**), 2.680(2) (**7**), 2.670(2) (**8**) and 2.678(2) Å (**9**)].

The bond lengths related with the trivalent lanthanide cations also decrease with the ionic radius, Pr(III) > Nd(III) > Sm(III) > Gd(III), as a result of the lanthanide contraction. The values of the $Ln–O_{nitrate}$ distances cover the range 2.4464(15)–2.695(2) Å, while those of the $Ln–O_w$ bonds are comprised between 2.3962(15) and 2.486(2) Å. The largest bond lengths at the coordination sphere of the lanthanide atom are observed for the $Ln–N_{bpym}$ bonds [2.774(3) (**6**), 2.756(2) (**7**), 2.741(3) (**8**) and 2.712(2) Å (**9**)] (see Table 5) and they are one of the sources of distortion of the coordination polyhedron of the rare-earth atom.

Focusing on the bidentate bipy and bpym ligands of **6**–**9**, their deviation from the planarity here is more accentuated than in the previous family. Although the bipy ligand is still quasi-planar [the values for the inter-ring dihedral angle vary in the range 3.63(9)–4.17(12)°], the bpym molecule is strongly distorted with values for the inter-ring dihedral angle covering the range 18.42(8)–23.32(12)°. Three factors contribute to create this significant distortion of the bpym molecule: its bidentate coordination, the $O_w\cdots N_{bpym}$ hydrogen bonds between $[Ln(bpym)(NO_3)_2(H_2O)_4]^+$ moieties (see Fig. 6) and the weak inter-ring bipy–bpym interactions [the values of the interplanar distances varying in the range 3.82–3.86 Å]. The large values for the inter-ring separation preclude any π–π bipy–bipy [interplanar distances above 3.96 Å] or bpym–bpym stacking interactions [ca. 4.2 Å].

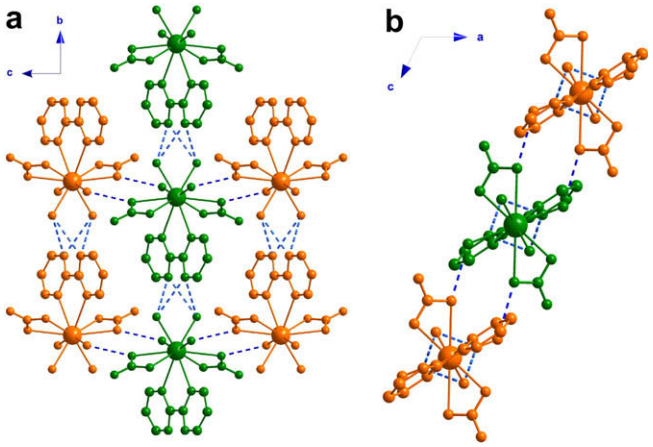


Fig. 6. Views in the (a) *bc* and (b) *ac*-planes of the supramolecular cationic layer in **6**–**9** which is built up by $O_{nitrate}\cdots O_w$ and and $N_{bpym}\cdots O_w$ hydrogen bond interactions. The hydrogen bonds are represented as blue dashed lines. (For interpretation of the references to color in this figure legend, the reader is referred to the web version of this article.)

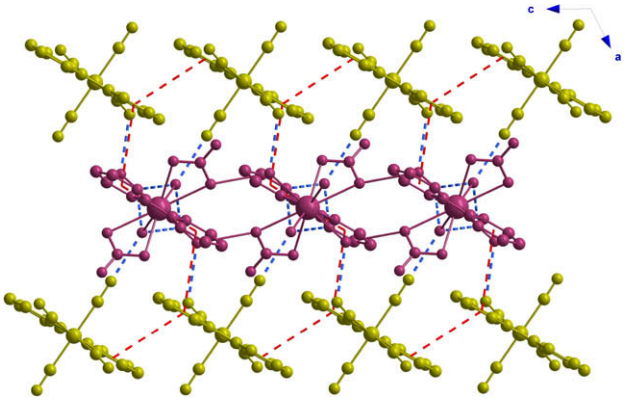


Fig. 5. A view of the crystal packing of **6**–**9** built up from H-bonds and π–π interactions. The hydrogen bonds and the π–π interactions are represented as blue and red dashed lines, respectively. (For interpretation of the references to color in this figure legend, the reader is referred to the web version of this article.)

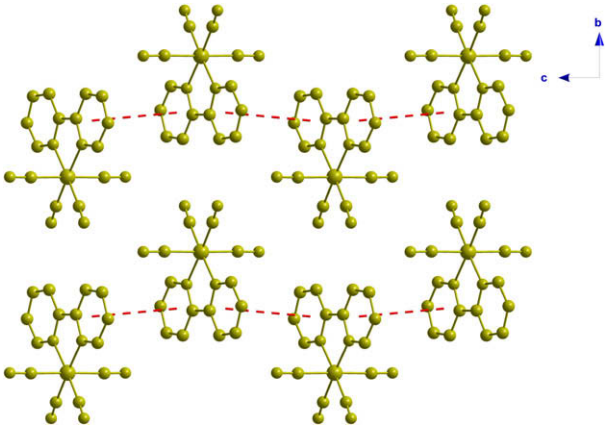


Fig. 7. A view of the supramolecular anionic sheets of **6**–**9** which are built up by π–π interactions among bipy ligands. The π–π bonds are represented as red dashed lines. (For interpretation of the references to color in this figure legend, the reader is referred to the web version of this article.)

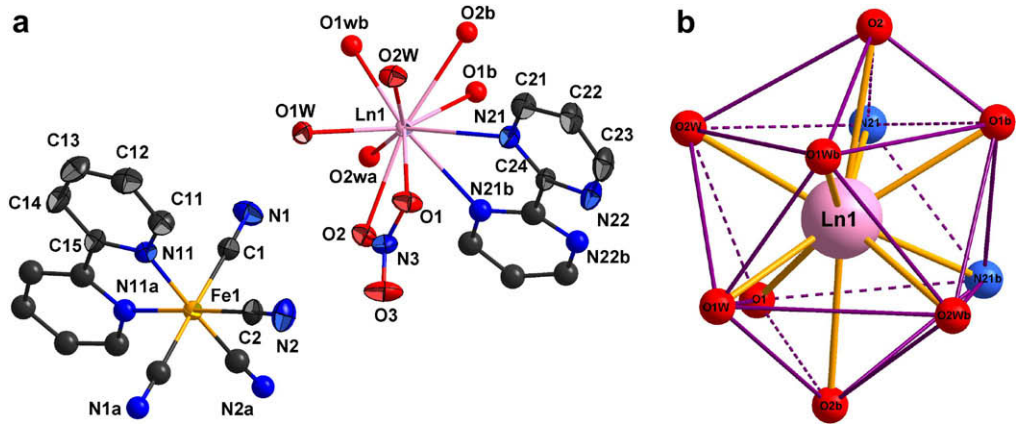


Fig. 8. (a) Perspective drawing of the ionic pair of compounds **6–9** complexes with the atom numbering scheme (thermal ellipsoids are plotted at the 50% probability level) and (b) a view of the coordination polyhedron of the lanthanide atom of **6–9**. The hydrogen atoms were omitted for clarity.

Table 5
Bond lengths (Å) and angles (°) of the coordination environments of Fe and Ln in **6–9** [Ln = Pr (**6**), Nd (**7**), Sm (**8**) and Gd (**9**)]*.

	6	7	8	9
Fe(1)–N(11)	1.991(3)	1.992(2)	1.990(3)	1.988(2)
Fe(1)–C(1)	1.944(3)	1.945(2)	1.948(3)	1.937(2)
Fe(1)–C(2)	1.916(3)	1.916(3)	1.913(4)	1.911(2)
Ln(1)–N(21)	2.774(3)	2.756(2)	2.741(3)	2.712(2)
Ln(1)–O(1)	2.537(2)	2.511(2)	2.483(2)	2.4464(15)
Ln(1)–O(2)	2.695(2)	2.680(2)	2.670(2)	2.678(2)
Ln(1)–O(1W)	2.463(2)	2.445(2)	2.412(2)	2.3962(15)
Ln(1)–O(2W)	2.486(2)	2.467(2)	2.427(2)	2.4028(14)
N(11)–Fe(1)–N(11)[a]	81.08(15)	81.23(13)	81.33(16)	81.31(10)
Fe(1)–C(1)–N(1)	177.5(3)	177.9(3)	177.5(3)	177.7(2)
Fe(1)–C(2)–N(2)	172.5(3)	172.4(3)	172.0(3)	172.2(2)
N(21)–Ln(1)–N(21)[a]	59.82(11)	59.96(9)	60.76(12)	60.75(7)
O(1)–Ln(1)–O(2)	48.62(7)	48.86(6)	49.52(7)	49.25(5)

* Symmetry code: [a] = $-1-x, y, 0.5-z$.

Table 6
Selected intermolecular contacts (Å) in **6–9***.

	6	7	8	9
O(1w)···N(1)	2.709(3)	2.705(3)	2.706(3)	2.7021(2)
O(1w)···N(22)[d]	2.960(4)	2.973 (3)	2.935(4)	3.013(3)
O(1w)···N(22)[e]	3.120(4)	3.117(3)	3.118(4)	3.109(3)
O(2w)···N(2)[f]	2.848(4)	2.844 (4)	2.845(4)	2.836(3)
O(2w)···O(2)[g]	2.860(4)	2.864(3)	2.832(4)	2.868(3)

* Symmetry code: [d] = $x, 1+y, z$; [e] = $-x, 1+y, 1.5-z$; (f) = $-1-x, 1-y, 1-z$; [g] = $x, 1-y, 0.5+z$.

The shortest intermolecular iron···lanthanide separations are 6.7520(6) (**6**), 6.7350(6) (**7**), 6.7118(1) (**8**) and 6.6971(4) Å (**9**) [Fe(1)···Ln(1)[c]; (c) = $-x, 1-y, 1-z$], values which are close to those observed in **1–5.**

4. Conclusions

Two new families of 3d–4f three-dimensional supramolecular systems (compounds **1–5** and **6–9**; **1–9**) containing the ion pair $[Fe(bipy)(CN)_4]^-$ and $[Ln(bpym)(NO_3)_2(H_2O)_n]^+$ [Ln = Sm (**1**), Gd (**2**), Tb (**3**), Dy (**4**), Ho (**5**), Pr (**6**), Nd (**7**), Sm (**8**) and Gd (**9**)] with $n = 3$ (**1–5**) and 4 (**6–9**)] as constituents have been prepared and structurally characterized. The extensive network of hydrogen bonds and π–π type interactions which have their origin in the presence of coordinated water, terminally bound cyanide groups and aromatic rings, contribute to the stabilization of the resulting supramolecular three-dimensional architectures. In fact, both families can be seen as built by alternating cationic and anionic layers and their structural knowledge will orientate the future synthetic attempts to prepare cyanide-bridged 3d–4f heterometallic assemblies. For that, the nitrate anion has to be avoided in order to increase the positive charge on the lanthanide fragment and to make possible coordinative bond between the cyanide–nitrogen and the lanthanide atom. At that respect, it deserves to be noted that this coordinative bond is very common in the previous attempts where these cyanide-bearing units have been used as ligands toward first-row transition metal ions.

Acknowledgements

Funding for this work was provided by the Spanish Ministerio de Ciencia y Tecnología (CTQ2007-61690, MAT2007-60660 and Consolider Ingenio2010 "Factoria de Cristalización CSD2006-00015), the European Union through the Network QuEMolNa (Project MRTN-CT-2003-504880) and the Magmanet Network of Excellence (Contract 515767-2). O.F thank to the Spanish Ministerio de Ciencia y Tecnología for a predoctoral fellowship.

Appendix A. Supplementary data

CCDC 696695–696703 contain the supplementary crystallographic data for **1–9**. These data can be obtained free of charge via http://www.ccdc.cam.ac.uk/conts/retrieving.html, or from the Cambridge Crystallographic Data Centre, 12 Union Road, Cambridge CB2 1EZ, UK; fax: (+44) 1223-336-033; or e-mail: deposit@ccdc.cam.ac.uk. Supplementary data associated with this article can be found, in the online version, at doi:10.1016/j.poly.2008.12.032.

References

[1] (a) Z. He, C. He, E.Q. Gao, Z.M. Wang, X.F. Yang, C.S. Liao, C.H. Yan, Inorg. Chem. 42 (2006) 2206;
(b) Y. Yukawa, G. Aromi, S. Igarashi, J. Ribas, S.A. Zvyagin, J. Krzystek, Angew. Chem., Int. Ed. 44 (2005) 1997;
(c) H.Z. Kou, Y.B. Jiang, A.L. Cui, Cryst. Growth Des. 5 (2005) 77;
(d) T. Yamaguchi, Y. Sunatsuki, M. Kojima, H. Akashi, M. Tsuchimoto, N. Re, S. Osa, N. Matsumoto, Chem. Commun. 9 (2004) 1048;
(e) J.P. Costes, G. Novitchi, S. Shova, F. Dahan, B. Donnadieu, J.P. Tuchagues, Inorg. Chem. 43 (2004) 7792;
(f) A.D. Cutland, R.G. Malkani, J.W. Kampf, V.L. Pecoraro, Angew. Chem., Int. Ed. 39 (2000) 2689;
(g) Y.C. Liang, R. Cao, W.P. Su, M.C. Hong, W.J. Zhang, Angew. Chem., Int. Ed. 39

(2000) 3304;
(h) A. Bencini, C. Benelli, A. Caneschi, A. Dei, D. Gatteschi, Inorg. Chem. 25 (1986) 572.
[2] (a) V. Chandrasekhar, B.M. Pandian, R. Boomishankar, A. Steiner, J.J. Vittal, A. Houri, R. Clerac, Inorg. Chem. 47 (2008) 4919;
(b) A. Okazawa, T. Nogami, H. Nojiri, T. Ishida, Chem. Mater. 20 (2008) 3110;
(c) C. Aronica, G. Chastanet, G. Pilet, B. Guennic, L.V. Robert, W. Wernsdorfer, D. Luneau, Inorg. Chem. 46 (2007) 6108;
(d) W.T. Chen, M.S. Wang, L. Cai, G. Xu, T. Akitsu, A.T. Motoko, G.C. Guo, J.S. Huang, Cryst. Growth Des. 6 (2006) 1738;
(e) J.J. Zhang, S.M. Hu, S.C. Xiang, T.L. Sheng, X.T. Wu, Y.M. Li, Inorg. Chem. 45 (2006) 7173;
(f) F.C. Liu, Y.F. Zeng, J. Jiao, J.R. Li, X.H. Bu, J. Ribas, S.R. Batten, Inorg. Chem. 45 (2006) 6129;
(g) C. Beneli, D. Gatteschi, Chem. Rev. 102 (2002) 2369;
(h) M. Sakamoto, K. Manseki, H. Okawa, Coord. Chem. Rev. 219–221 (2001) 379.
[3] (a) B. Zhao, P.X. Cheng, Y. Chen, C. Cheng, W. Shi, D.Z. Liao, S.P. Yan, Z.H. Jiang, J. Am. Chem. Soc. 126 (2004) 3012;
(b) B. Zhao, P. Cheng, Y. Dai, C. Cheng, D.Z. Liao, S.P. Yan, Z.H. Jiang, G.L. Wang, Angew. Chem., Int. Ed. 42 (2003) 934.
[4] (a) B. Zhao, X.Y. Chen, P. Cheng, D.Z. Liao, S.P. Yan, Z.H. Jiang, J. Am. Chem. Soc. 126 (2004) 15394;
(b) N. Sabatini, M. Guardigli, J.M. Lehn, Coord. Chem. Rev. 123 (1993) 201;
(c) G. Blasse, Mater. Chem. Phys. 31 (1992) 3.
[5] (a) H. Deng, S.G. Shore, J. Am. Chem. Soc. 113 (1991) 8538;
(b) H. Deng, S. Chun, P. Florian, P.J. Grandinetti, S.G. Sore, Inorg. Chem. 35 (1996) 3891.
[6] (a) M. Ohba, H. Okawa, Coord. Chem. Rev. 198 (2000) 313. and references therein;
(b) J. Cernak, M. Orendac, I. Potocnak, J. Chomic, A. Orendacova, J. Skorsepa, A. Feher, Coord. Chem. Rev. 224 (2002) 51. and references therein.
[7] S. Tanase, J. Reedjik, Coord. Chem. Rev. 250 (2006) 2501. and references therein.
[8] (a) A. Figuerola, J. Ribas, D. Casanova, M. Maestro, S. Alvarez, C. Díaz, Inorg. Chem. 44 (2005) 6949;
(b) A. Figuerola, J. Ribas, M. Llunell, D. Casanova, M. Maestro, S. Alvarez, C. Díaz, Inorg. Chem. 44 (2005) 6939;
(c) A. Figuerola, J. Ribas, X. Solans, M. Font-Bardía, M. Maestro, C. Díaz, Eur. J. Inorg. Chem. 9 (2006) 1846;
(d) A. Figuerola, C. Díaz, M.S. El Fallah, J. Ribas, M. Maestro, J. Mahía, Chem. Commun. (2001) 1204;
(e) Ba.-Q. Ma, S. Gao, G. Su, G.X. Xu, Angew. Chem., Int. Ed. 40 (2001) 434;
(f) T. Yi, S. Gao, X.-W. Chen, C.-H. Yan, B.-G. Li, Acta Crystallogr. C54 (1998) 41.
[9] (a) R. Lescouëzec, L.M. Toma, J. Vaissermann, M. Verdaguer, F.S. Delgado, C. Ruiz-Pérez, F. Lloret, M. Julve, Coord. Chem. Rev. 249 (2005) 2691;
(b) L.M. Toma, R. Lescouëzec, J. Pasán, C. Ruiz-Pérez, J. Vaissermann, J. Cano, R. Carrasco, W. Wernsdorfer, J. Am. Chem. Soc. 128 (2006) 4842.
[10] (a) R. Lescouëzec, F. Lloret, M. Julve, J. Vaissermann, M. Verdaguer, Inorg. Chem. 41 (2002) 818;
(b) L.M. Toma, R. Lescouëzec, F. Lloret, M. Julve, J. Vaissermann, M. Verdaguer, Chem. Commun. (2003) 1850;
(c) R. Lescouëzec, J. Vaissermann, C. Ruiz-Pérez, F. Lloret, R. Carrasco, M. Julve, M. Verdaguer, Y. Dromzée, D. Gatteschi, W. Wernsdorfer, Angew. Chem., Int. Ed. 42 (2003) 1483;
(d) L.M. Toma, R. Lescouëzec, L.D. Toma, F. Lloret, M. Julve, J. Vaissermann, M. Andruh, J. Chem. Soc., Dalton Trans. (2002) 3171;
(e) L.M. Toma, R. Lescouëzec, S. Uriel, R. Llusar, C. Ruiz-Pérez, J. Vaissermann, F. Lloret, M. Julve, Dalton Trans. (2007) 3690;
(f) L.M. Toma, F.S. Delgado, C. Ruiz-Pérez, R. Carrasco, J. Cano, F. Lloret, M. Julve, Dalton Trans. (2004) 2836.
[11] S. Wang, P. Day, L.M. Toma, M. Julve, J.D. Wallis, Inorg. Chim. Acta 359 (2006) 3283.
[12] (a) R. Koner, M. Nayak, G. Ferguson, J.N. Low, C. Glidewell, P. Misra, S. Mohanta, Cryst. Eng. Commun. 7 (2005) 129;
(b) B.-Q. Ma, H.-L. Sun, S. Gao, Chem. Commun. (2005) 2336.
[13] R.W.W. Hooft, COLLECT, Nonius BV, Delft, The Netherlands, 1999.
[14] A.J.M. Duisenberg, L.M.J. Kroon-Batenburg, A.M.M. Schreurs, J. Appl. Crystallogr. 36 (2003) 220 (EVALCCD).
[15] Z. Otwinowski, W. Minor, in: C.W. Carter Jr., R.M. Sweet (Eds.), Processing of X-ray Diffraction Data Collected in Oscillation Mode Methods in Enzymology, Macromolecular Crystallography Part A, vol. 307, 1997, pp. 307–326.
[16] SADABS, Version 2.03, Bruker AXS Inc., Madion, WI, 2000.
[17] G.M. Sheldrick, SHELX97, Programs for Crystal Structure Analysis, Release 97-2, Institüt für Anorganische Chemie der Universität, Tammanstrasse 4, D-3400 Göttingen, Germany, 1998.
[18] M. Nardelli, J. Appl. Crystallogr. 28 (1995) 659.
[19] A.L. Spek, PLATON, The University of Utrecht, Utrecht, The Netherlands, 1999.
[20] K. Brandenburg, H. Putz, DIAMOND 2.1d, Crystal Impact, GbR, Postfach 1251, D-53002 Bonn, Germany, 2000.
[21] (a) G. De Munno, G. Bruno, Acta Crystallogr. C40 (1984) 2030;
(b) M. Julve, G. De Munno, G. Bruno, M. Verdaguer, Inorg. Chem. 27 (1988) 3160;
(c) M. Julve, M. Verdaguer, G. De Munno, J.A. Real, G. Bruno, Inorg. Chem. 32 (1993) 795;
(d) G. De Munno, M. Julve, F. Nicolò, F. Lloret, J. Faus, R. Ruiz, E. Sinn, Angew. Chem., Int. Ed. Engl. 32 (1993) 613;
(e) G. De Munno, M. Julve, F. Lloret, J. Faus, M. Verdaguer, A. Caneschi, Angew. Chem., Int. Ed. Engl. 32 (1993) 1046;
(f) G. De Munno, M. Julve, F. Lloret, A. Derory, J. Chem. Soc., Dalton Trans. (1993) 1179;
(g) E. Andrés, G. De Munno, M. Julve, J.A. Real, F. Lloret, J. Chem. Soc., Dalton Trans. (1993) 2169;
(h) G. De Munno, M. Julve, F. Lloret, J. Faus, A. Caneschi, J. Chem. Soc., Dalton Trans. (1994) 1175;
(i) I. Castro, J. Sletten, L.K. Glærum, F. Lloret, J. Faus, M. Julve, J. Chem. Soc., Dalton Trans. (1994) 2777;
(j) I. Castro, J. Sletten, L.K. Glærum, J. Cano, F. Lloret, J. Faus, M. Julve, J. Chem. Soc., Dalton Trans. (1995) 3207;
(k) G. De Munno, M. Julve, F. Lloret, J. Faus, M. Verdaguer, A. Caneschi, Inorg. Chem. 34 (1995) 157;
(l) G. De Munno, R. Ruiz, F. Lloret, J. Faus, R. Sessoli, M. Julve, Inorg. Chem. 34 (1995) 408;
(m) G. De Munno, M. Julve, F. Lloret, J. Cano, A. Caneschi, Inorg. Chem. 34 (1995) 2048;
(n) G. De Munno, T. Poerio, G. Viau, M. Julve, F. Lloret, Y. Journaux, E. Rivière, Chem. Commun. (1996) 2587;
(o) G. De Munno, M. Julve, G. Vaiu, F. Lloret, J. Faus, D. Viterbo, Angew. Chem., Int. Ed. Engl. 35 (1996) 1807;
(p) G. De Munno, M. Julve, J.A. Real, Inorg. Chim. Acta 255 (1997) 185;
(q) J. Sletten, H. Daraghmeh, F. Lloret, M. Julve, Inorg. Chim. Acta 279 (1998) 127;
(r) G. De Munno, D. Armentano, M. Julve, F. Lloret, R. Lescouëzec, J. Faus, Inorg. Chem. 38 (1999) 2234;
(s) Y. Rodríguez-Martín, J. Sanchiz, C. Ruiz-Pérez, F. Lloret, M. Julve, Inorg. Chim. Acta 326 (2001) 20;
(t) G. Marinescu, R. Lescouëzec, D. Armentano, G. De Munno, M. Andruh, S. Uriel, R. Llusar, F. Lloret, M. Julve, Inorg. Chim. Acta 336 (2002) 46;
(u) D. Armentano, G. De Munno, F. Lloret, M. Julve, J. Curély, A.M. Babb, J.Y. Lu, New J. Chem. 27 (2003) 161;
(w) J.M. Herrera, D. Armentano, G. De Munno, F. Lloret, M. Julve, M. Verdaguer, New J. Chem. 27 (2003) 128.
[22] (a) A. Real, J. Zarembowitch, O. Kahn, X. Solans, Inorg. Chem. 26 (1987) 2939;
(b) A.B. Gaspar, V. Ksenofontov, V. Martínez, M.C. Muñoz, J.A. Real, P. Gütlich, Eur. J. Inorg. Chem. (2004) 4770.
[23] (a) R. Cortés, L. Lezama, J.L. Pizarro, M.I. Arriortua, T. Rojo, Angew. Chem., Int. Ed. Engl. 35 (1996) 1810;
(b) R. Cortés, M.K. Urtiaga, L. Lezama, J.L. Pizarro, M.I. Arriortua, T. Rojo, Inorg. Chem. 36 (1997) 5016;
(c) S. Martín, M.G. Barandika, J.I. Ruiz de Larramendi, R. Cortés, M. Font-Bardía, L. Lezama, Z.E. Serna, X. Solans, T. Rojo, Inorg. Chem. 40 (2001) 3687;
(d) S. Martín, M.G. Barandika, R. Cortés, J.I. Ruiz de Larramendi, M.K. Urtiaga, L. Lezama, M.I. Arriortua, T. Rojo, Eur. J. Inorg. Chem. (2001) 2107.
[24] (a) F. Bérézovsky, A.A. Hajem, S. Triki, J. Sala Pala, P. Molinié, Inorg. Chim. Acta 284 (1999) 8;
(b) S. Triki, F. Thétiot, J.R. Galán-Mascarós, J. Sala Pala, K.R. Dunbar, New J. Chem. 25 (2001) 954;
(c) F. Thétiot, S. Triki, J. Sala Pala, J.R. Galán-Mascarós, J.M. Martínez-Agudo, K.R. Dunbar, Eur. J. Inorg. Chem. (2004) 3783;
(d) F. Thétiot, S. Triki, J. Sala Pala, S. Golhen, Inorg. Chim. Acta 358 (2005) 3277.
[25] S. Decurtins, H.W. Schmalle, P. Schneuwly, L.-M. Zheng, J. Ensling, A. Hauser, Inorg. Chem. 34 (1995) 5501.
[26] S.R. Marshall, C.D. Incarvito, J.L. Manson, A.L. Rheingold, J.S. Miller, Inorg. Chem. 39 (2000) 1969.
[27] S. Kawata, S. Kitagawa, M. Enomoto, H. Kumagai, M. Katada, Inorg. Chim. Acta 283 (1998) 80.
[28] E. Colacio, F. Lloret, M. Navarrete, A. Romerosa, H. Stoeckli-Evans, J. Suárez-Varela, New J. Chem. 29 (2005) 1189.
[29] F. Pointillart, P. Herson, K. Boubekeur, C. Train, Inorg. Chim. Acta 361 (2008) 373.
[30] (a) A. Fratini, G. Richards, E. Larder, S. Swavey, Inorg. Chem. 48 (2008) 1030;
(b) A. Fratini, S. Swavey, Inorg. Chem. Commun. 10 (2007) 636;
(c) S. Swavey, J.A. Krause, D. Collins, D. D'Cunha, A. Fratini, Polyhedron 27 (2008) 1061;
(d) H. Jang, C.H. Shim, B.-J. Jung, D.-h. Kim, H.-K. Shim, Y. Do, Eur. J. Inorg. Chem. (2006) 718.
[31] K. Nakamoto, Infrared and Raman Spectra of Inorganic and Coordination Compounds, 4th Ed., vol. 228, Wiley, New York, 1986.
[32] J. Ribas (Ed.), Química de Coordinacion, Omega, Barcelona, 2000.
[33] L.L. Merrit, E.D. Schroeder, Acta Crystallogr. 9 (1956) 801.
[34] L. Fernholdt, C. Rømming, S. Samdal, Acta Chem. Scand. A35 (1981) 707.

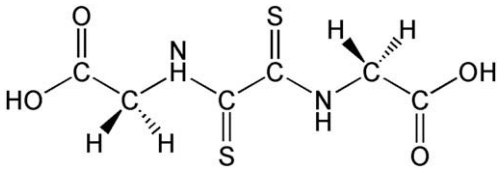


Fig. 1. N,N′-bis(carboxymethyl)dithiooxamide (H_4GLYDTO).

KBr pellets on a Perkin–Elmer 597 spectrophotometer and in the 700–100 cm^{-1} range using polyethylene-sandwiched Nujol mulls on a Bruker IFS-66v spectrophotometer. TGA analyses (25–750 °C) were recorded under an inert atmosphere (N_2) on a Hi-Res TGA 2950 TA Instruments. Evolved gases were detected by IR spectroscopy on a Bruker FTIR TENSOR-27 spectrophotometer. The electronic spectra of microcrystalline samples were obtained by the diffuse reflectance method on Shimadzu UV-3101PC spectrophotometers over the range 900–250 nm. EPR spectra were recorded between room temperature and 120 K on a Bruker ESP 300 spectrometer operating at X-band. The magnetic susceptibilities of polycrystalline samples were measured in the temperature range 2–300 K using a SQUID (Quantum Design) magnetometer. Diamagnetic corrections were made with Pascal's constants.

Caution: although difficulties were not encountered while working with metal perchlorates, they are potentially explosive and should be handled with care.

2.2. Synthesis

$[Mn(H_2GLYDTO)(H_2O)_2]_n$. A mixture of H_4GLYDTO (1.25 mmol, 0.30 g) and $Mn(ClO_4)_2 \cdot 6H_2O$ (2.25 mmol, 0.80 g) in water (50 ml) was stirred at room temperature for 30 min and then NaOH (1.25 mmol, 0.05 g) was added to the solution. The resulting pale brown powder was filtered off and washed with water and ethanol. Single crystals suitable for X-ray diffraction were obtained by slow evaporation (over a week) of the yellow mother liquor at room temperature. Their IR spectra show that the crystals and the original crystalline powder are the same compound. The yield for this reaction was 0.572 g (>95% based on total Mn). Mp. 141 °C (Dec). *Anal.* Calc. for $C_6H_{10}MnN_2O_6S_2$ (325.22): C, 22.2; H, 3.1; N, 8.6; S, 19.7. Found: C, 21.8; H, 3.1; N, 8.5; S, 20.4%. IR (ν_{max}/cm^{-1}): 3469m ν(OH), 3137m ν(NH), 1591s $\nu_{as}(COO^-)$, 1527s, 1437m, 1395s $\nu_s(COO^-)$, 1368s, 1301s, 1258w, 1078s, 980m, 923w, 879s, 865s, 763m, 711w, 646w, 547w, 502w, 468w, 394vw, 319w, 231w, 168w, 116w.

2.3. Crystal structure determination

A yellow plate crystal of $[Mn(H_2GLYDTO)(H_2O)_2]_n$ was mounted on a glass fibre and used for data collection. Crystal data were collected at 293(2) K using a Bruker SMART CCD 1000 diffractometer. Graphite monochromated Mo Kα radiation (λ = 0.71073 Å) was used throughout. The data were processed with SAINT [11] and corrected for absorption using SADABS (transmissions factors: 1.000–0.792) [12]. The structure was solved by direct methods using the program SHELXS-97 [13] and refined by full-matrix least-squares techniques against F^2 using SHELXL-97 [14]. Positional and anisotropic atomic displacement parameters were refined for all non-hydrogen atoms. Hydrogen atoms were located in difference maps and included as fixed contributions riding on attached atoms, with isotropic thermal parameters 1.2 times those of their carrier atoms. Criteria for a satisfactory complete analysis were ratios of *rms* shift to standard deviation of less than 0.001 and no significant features in final difference maps. Atomic scattering factors were obtained from "International Tables for Crystallography" [15]. A summary of the crystal data, experimental details and refinement results is given in Table 1.

Table 1
Crystal data and structure refinement for $[Mn(H_2GLYDTO)(H_2O)_2]_n$.

Empirical formula	$C_6H_{10}MnN_2O_6S_2$
Formula weight	325.22
Temperature (K)	293(2)
Wavelength (Å)	0.71973
Crystal system	monoclinic
Space group	$P2_1/c$ (No. 14)
Unit cell dimensions	
a (Å)	11.526(2)
b (Å)	6.080(1)
c (Å)	8.726(2)
α (°)	90
β (°)	119.695(4)
γ (°)	90
Volume ($Å^{-3}$)	572.4(2)
Z	2
D_{calc} (Mg/m^3)	1.887
Absorption coefficient (mm^{-1})	1.535
F(000)	330
Crystal size	0.25 × 0.23 × 0.06
θ range (°)	1.89–28.28
Limiting indices (h, k, l)	−13/15, 0/7, −11/0
Reflections collected/unique (R_{int})	5458/1376 (0.0228)
Completeness θ (°)	96.8/28.28
Absorption corrected	SADABS
Max./min. transmission	0.9135/0.7002
Data/parameters	1376/79
Goodness-of-fit on F^2	1.119
Final R indices	R_1 = 0.0257, wR_1 = 0.0656
R indices (all data)	R_1 = 0.0397, wR_1 = 0.0684
Largest difference peak/hole	0.271/−0.278

3. Results and discussion

$[Mn(H_2GLYDTO)(H_2O)_2]_n$ was prepared using manganese(II) perchlorate hexahydrate as the metal source and $[H_2GLYDTO]^{2-}$ as a dianionic ligand in an aqueous medium. The product is air stable and is insoluble in common organic solvents.

An exhaustive comparison of the IR spectra of the ligand [10] and complex gave information about the mode of bonding of the ligand in the manganese(II) complex. The IR spectrum of the complex shows a broad absorption at 3469 cm^{-1}, corresponding to ν(OH) vibrations of the coordinated water molecules, and another medium intensity band at 3137 cm^{-1} that can be assigned to the –NH– vibrations. Three absorption bands at 1527, 1300 and 1078 cm^{-1} are the so-called thioamide bands, which are essentially related to the C=S stretching vibration strongly coupled to that of the C–N part of the thioamide group. The ν(C=S) band appears at 879 cm^{-1}. The band due to the carbonyl group at 1710 cm^{-1}, which is present in the spectrum of H_4GLYDTO, is absent in the spectrum of the complex and two bands due to asymmetric and symmetric stretching vibrations of COO^- are observed at 1591 and 1394 cm^{-1}, respectively. The $\Delta\nu = \nu_{as} - \nu_s$ separation value is 197 cm^{-1}, indicating that the carboxyl groups of the complex are coordinated with the manganese(II) ions in a *syn-anti* carboxylato-bridging mode [16]. The band at 335 cm^{-1} is assigned to the Mn–O stretching frequency.

Thermogravimetric analysis revealed that, under an inert atmosphere, the compound is stable up to 141 °C and undergoes the first weight loss (12.4%) from 141 to 231 °C, which may be due to the release of the coordinated water molecules (calcd. 11.1%) and partial decomposition of the ligand. The relatively high temperature for the loss of water molecules implies that hydrogen-bonding interactions occur in the crystal packing. The weight loss upon further heating to 740 °C occurs in three stages. This is due

to complete decomposition of the compound and corresponds to the production of CO, CH_3CHO and HNCS. However, other gases such as CO_2, CH_4 or NH_3 were also identified depending on the stage in question. The final residue of 24.9% is close to the calculated value of 21.9% based on MnO.

The diffuse reflectance spectrum of $[Mn(H_2GLYDTO)(H_2O)_2]_n$ showed absorption bands at around 15000, 20850 and 21900 cm^{-1}, which can be assigned to $^6A_{1g} \rightarrow {}^4T_{1g}$, $^6A_{1g} \rightarrow {}^4A_{1g}$ and $^4E_g(G)$ transitions, respectively. Other absorption bands at 25440, 28530 and 30210 cm^{-1} can also be assigned to $^6A_{1g} \rightarrow {}^4T_{2g}(D)$, $^4E_g(D)$ and $^4T_{1g}(P)$ transitions. These transitions are compatible with a distorted octahedral geometry around high-spin Mn(II) [17].

The X-band EPR spectrum of $[Mn(H_2GLYDTO)(H_2O)_2]_n$ shows an isotropic signal with a *g*-value of 2.0 at room temperature. This signal increases in intensity and becomes broad upon cooling to 120 K.

4. Structure description

A single-crystal X-ray diffraction study revealed that the asymmetric unit consists of one Mn^{II}, half a $H_2GLYDTO^{2-}$ dianion and one water molecule (Fig. 2). Each Mn^{II} ion is six-coordinated to four carboxylate oxygen atoms from four different $H_2GLYDTO^{2-}$ ligands and two symmetrically related water oxygen atoms (Fig. 3). As shown in Figs. 2 and 3, the Mn centre assumes a slightly distorted octahedral coordination geometry with the Mn–O bond distances in the range 2.169(1)–2.188(2) Å (Table 2). The carboxylate oxygen atoms are nearly coplanar and define the equatorial plane of the octahedron, with the bond angles around the neighbouring atoms close to 90° (89.26–90.74°). The oxygen atoms from symmetrically related aqua ligands occupy the axial positions of the octahedron, with bond angles to equatorial oxygen atoms in the range from 87.65(6)° to 92.36(6)°. $H_2GLYDTO^{2-}$ acts as a tetradentate ligand and the carboxylate functionality links the metal centres in a *syn-anti* fashion (Fig. 4). The carboxylate groups link the neighbouring manganese centres to form infinite one-dimensional helical channels that run along the crystallographic *b*-axis with an intrachannel Mn···Mn separation of 5.3176(9) Å (Fig. 5). These Mn atoms are shared by neighbouring helical channels that are alternately left- and right-handed. In addition, these channels are interconnected by the $O_2C–C–N–C–C–N–C–CO_2$ groups of $H_2GLYDTO^{2-}$ to form new alternate left- and right-handed helical chains, both with a distance between Mn atoms of 11.213 Å, and this gives rise to an infinite three-dimensional framework (Fig. 6). When viewed along the *a*-axis, such a 3D framework can also be viewed

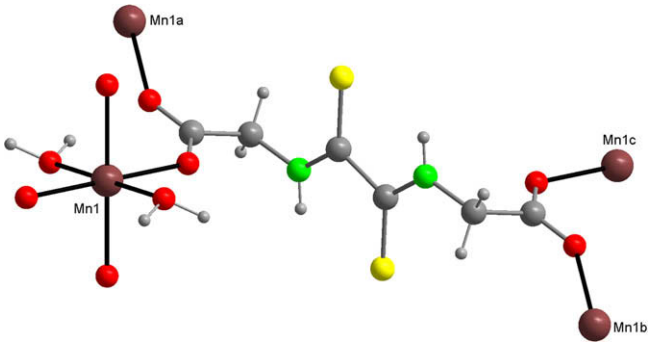


Fig. 3. Perspective view of the $H_2GLYDTO^{2-}$ anion in $[Mn(H_2GLYDTO)(H_2O)_2]_n$ illustrating its tetradentate character as a ligand. Symmetry transformations: *a* = −*x*, −½ + *y*, ½ − *z*; *b* = 1 − *x*, ½ + *y*, 3/2 − *z*; *c* = 1 + *x*, *y*, *z*.

Table 2
Selected bond distances and angles (Å/°) for $[Mn(H_2GLYDTO)(H_2O)_2]_n$.

Distances	
Mn(1)–O(12)[a]	2.1688(13)
Mn(1)–O(12)[b]	2.1688(13)
Mn(1)–O(11)	2.1860(13)
Mn(1)–O(11)[c]	2.1860(13)
Mn(1)–O(1)[c]	2.1883(15)
Mn(1)–O(1)	2.1883(15)
Mn(1)···Mn(1)[a]	5.3176(9)
Mn(1)···Mn(1)[b]	5.3176(9)
Mn(1)···Mn(1)[d]	5.3176(9)
Angles	
O(12)[a]–Mn(1)–O(12)[b]	180.0
O(12)[a]–Mn(1)–O(11)	90.73(5)
O(12)[b]–Mn(1)–O(11)	89.26(5)
O(12)[a]–Mn(1)–O(11)[c]	89.26(5)
O(12)[b]–Mn(1)–O(11)[c]	90.74(5)
O(11)–Mn(1)–O(11)[c]	180.0
O(12)[a]–Mn(1)–O(1)[c]	87.65(6)
O(12)b–Mn(1)–O(1)[c]	92.35(6)
O(11)–Mn(1)–O(1)[c]	88.90(5)
O(11)[c]–Mn(1)–O(1)[c]	91.10(5)
O(12)[a]–Mn(1)–O(1)	92.35(6)
O(12)[b]–Mn(1)–O(1)	87.65(6)
O(11)–Mn(1)–O(1)	91.10(5)
O(11)[c]–Mn(1)–O(1)	88.90(5)
O(1)[c]–Mn(1)–O(1)	180.0

Symmetry transformations: [a] = *x*, −*y* + 3/2, *z* + 1/2; [b] = −*x*, *y* + 1/2, −*z* + 1/2; [c] = −*x*, −*y* + 2, -*z* + 1; [d] = −*x*, −*y* + 1/2, −*z* + 1/2.

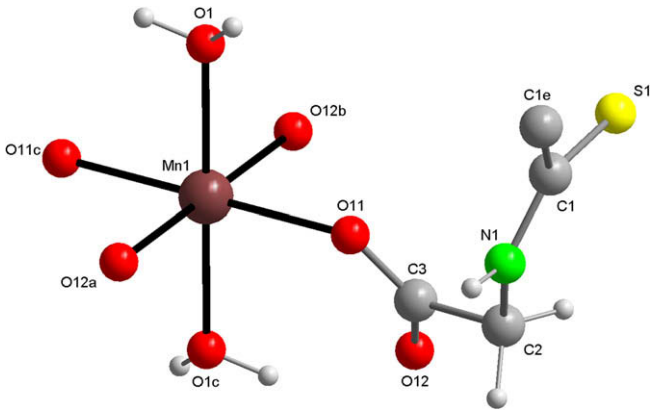


Fig. 2. Perspective view of the asymmetric unit of $[Mn(H_2GLYDTO)(H_2O)_2]_n$, showing the local coordination environment of the manganese. Symmetry transformations: *a* = *x*, 3/2 − *y*, ½ + *z*; *b* = −*x*, ½ + *y*, ½ − *z*; *c* = −*x*, 2 − *y*, 1 − *z*; *e* = 1 − *x*, 2 − *y*, 1 − *z*.

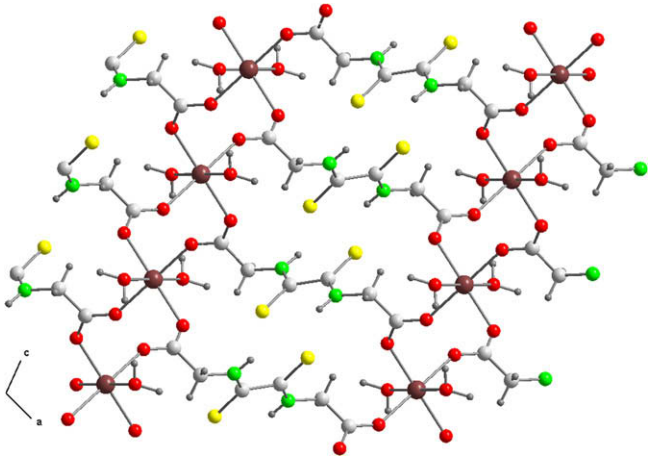


Fig. 4. Cross-sectional view down the *b*-axis showing the carboxylate functionality linking the Mn^{II} in a *syn-anti* fashion.

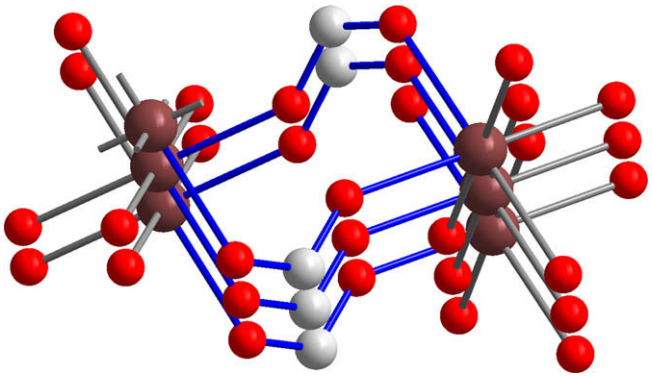


Fig. 5. View of a fragment of the structure illustrating the helical channels.

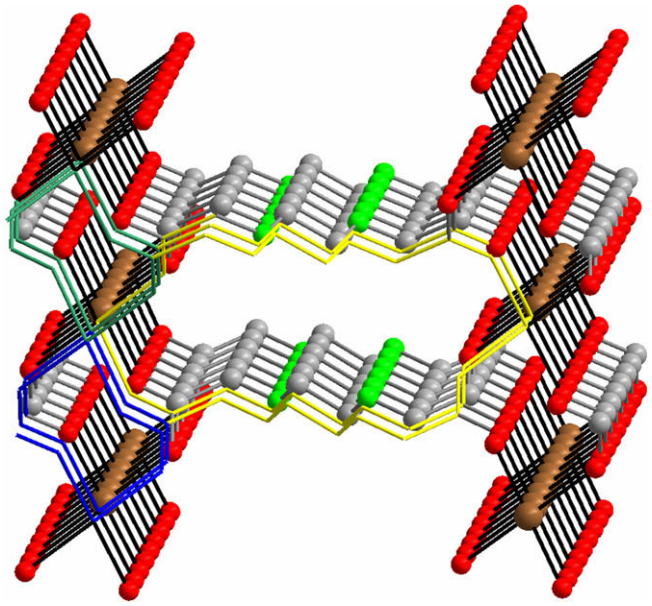


Fig. 6. Perspective view, along the *b*-axis, of a fragment of the 3D structure showing left-handed (blue) and right-handed (green) helical channels. The gross helical pores are marked in yellow. (For interpretation of the references to color in this figure legend, the reader is referred to the web version of this article.)

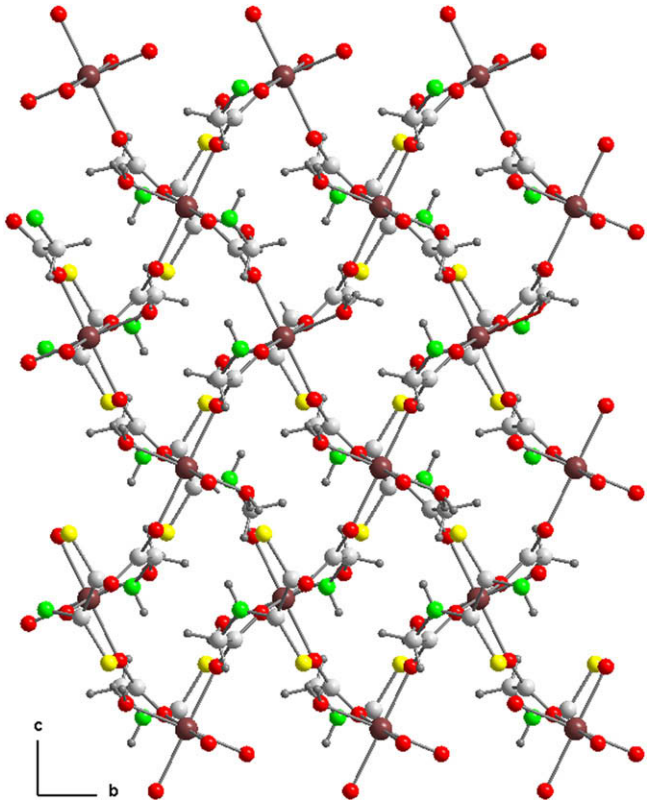


Fig. 7. View of the 3D porous framework along the *a*-axis in $[Mn(H_2GLYDTO)(H_2O)_2]_n$.

Table 3
Hydrogen bonding interactions for $[Mn(H_2GLYDTO)(H_2O)_2]_n$.

D–H···A	d(D–H) (Å)	d(H···A) (Å)	d(D···A) (Å)	∠(DHA) (°)
O(1)–H(1A)···S(1)^{f}	0.96	2.34	3.292(2)	171.7
O(1)–H(1B)···O(12)^{c}	0.87	2.00	2.755(2)	144.0
N(1)–H(1)···S(1)^{e}	0.88	2.42	2.930(2)	116.9
N(1)–H(1)···S(1)^{a}	0.88	2.72	3.469(2)	144.0

Symmetry transformations: $^{a} = x, y - 3/2, z + 1/2$; $^{c} = -x, -y + 2, -z + 1$; $^{e} = -x + 1, -y + 2, -z + 1$; $^{f} = x, -y + 5/2, z + 1/2$.

as a 3D porous coordination polymer containing new rectangular-shaped channels with Mn–Mn distances of 6.060 and 8.726 Å (Fig. 7). Each Mn atom is therefore connected to four neighbouring Mn atoms through four $H_2GLYDTO^{2-}$ units in an undulated shape and the metal centres thus serve as linkers to produce 2D layers parallel to the (1 0 0) plane. Consequently, the carboxylate groups also act as pillars to support these layers, leading to an extended open 3D framework. In addition, an X-ray crystallographic study revealed a supramolecular assembly that is the result of hydrogen-bonding interactions between coordinated water molecules and the organic ligands, and between organic ligands (Table 3).

4.1. Magnetic properties

The magnetic susceptibility, χ, of $[Mn(H_2GLYDTO)(H_2O)_2]_n$ was investigated between 2 and 300 K. The room temperature effective magnetic moment μ_{eff} $[=(8\chi_M T)^{1/2}]$ is 5.93μ_B/Mn, which is consistent with the value of 5.92μ_B/Mn expected for a magnetically isolated high-spin Mn^{II} ($S = 5/2$) ion with $g = 2.00$. From the magnetic point of view, the complex can be considered as dinuclear, where two Mn(II) ions are linked by one carboxylate bridge. The magnetic susceptibilities are represented as a plot of $\chi_M T$ and χ_M versus T in Fig. 8. The experimental value at room temperature (4.40 cm^3 K mol^{-1}) decreases on decreasing the temperature, first slowly and then more rapidly. This behaviour is consistent with the presence of a weak antiferromagnetic interaction between the Mn(II) ions.

In order to quantitatively evaluate these magnetic interactions the data were fitted to an $S = 5/2$ dinuclear spin model (Eq. (1)) based on the isotopic Heisenberg exchange Hamiltonian $H = -2JS_1S_2$ (where $S_1 = S_2 = 5/2$ for Mn^{II} high-spin d^5 ion systems) [18]. N is Avogadro's number, β is Bohr magneton, g is the Landé g-value, k is the Boltzmann constant.

$$\chi_M = \frac{Ng^2\beta^2}{3kT}\frac{A}{B} \quad (1)$$

$$A = 6\exp[2J/kT] + 30\exp[6J/kT] + 84\exp[12J/kT] + 180\exp[20J/kT] + 330\exp[30J/kT]$$

$$B = 1 + 3\exp[2J/kT] + 5\exp[6J/kT] + 7\exp[12J/kT] + 9\exp[20J/kT] + 11\exp[30J/kT]$$

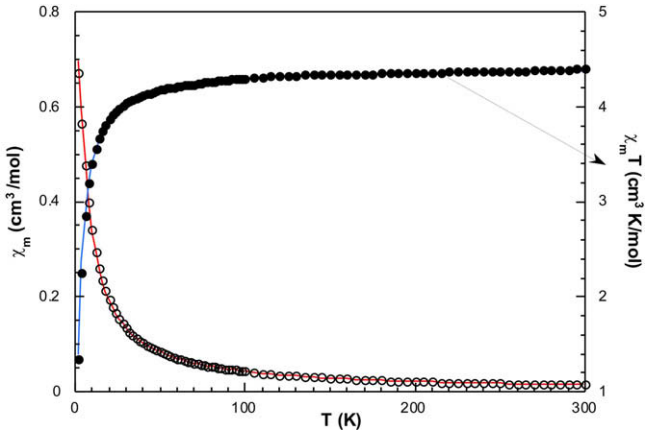


Fig. 8. Temperature dependence of χ_m and $\chi_m T$ for $[Mn(H_2GLYDTO)(H_2O)_2]_n$, solid lines represent the theoretical curves (see text).

The least-squares analysis of magnetic susceptibility data led to $J/k = -0.12$ K (-0.08 cm^{-1}) for $g = 2.01$. The agreement factor is around 6.58×10^{-5}, which corresponds to an excellent agreement between theory and experiment. This J value suggests that weak antiferromagnetic interactions between neighbouring Mn(II) ions are mediated through the double μ^2-carboxylate bridges. The J value is comparable to those reported for other manganese(II) complexes with the *syn-anti* bridging nature of the carboxylate, which generally mediates very weak magnetic interactions [19]. Due to the long superexchange pathway, the coupling through the compound is negligible.

5. Conclusions

A novel hexa-coordinate 3D manganese(II) polymer containing alternate left- and right-handed helical channels was synthesized and structurally characterized. Weak antiferromagnetic interactions between Mn^{II} ions were found with $J = -0.18$ K and $g = 2.00$. Further investigations are currently underway into magnetic materials based on N,N′-disubstituted dithiooxamide derivatives of amino acids as ligands with transition metals.

Acknowledgements

This work was supported by ERDF (EU) and DGI-MCYT (Spain) (Ref. CTQ2006-15329-C02), and by an Isidro Parga Pondal contract awarded to I.G.-S. by the Xunta de Galicia. We thank Dr. T. Rojo (País Vasco) for helping with the magnetic studies.

Appendix A. Supplementary data

CCDC 705437 contains the supplementary crystallographic data for $[Mn(H_2GLYDTO)(H_2O)_2]_n$. These data can be obtained free of charge via http://www.ccdc.cam.ac.uk/conts/retrieving.html, or from the Cambridge Crystallographic Data Centre, 12 Union Road, Cambridge CB2 1EZ, UK; fax: (+44) 1223-336-033; or e-mail: deposit@ccdc.cam.ac.uk. Supplementary data associated with this article can be found, in the online version, at doi:10.1016/j.poly.2008.12.030.

References

[1] (a) J.L. Serrano, T. Sierra, Coord. Chem. Rev. 242 (2003) 73;
(b) Y.F. Zhou, F.L. Jiang, D.Q. Yuan, B.L. Wu, R.H. Wang, Z.Z. Lin, M.C. Hong, Angew. Chem., Int. Ed. 43 (2004) 5665.
[2] F. Wieghardt, Angew. Chem., Int. Ed. Engl. 28 (1989) 1153.
[3] G.C. Dismukes, Chem. Rev. 35 (1996) 2024.
[4] R.E.P. Winpenny, Coord. Chem. Rev. 216–217 (2001) 1 (SMMs).
[5] S.M.J. Aubin, M.W. Wemple, D.M. Adams, H.-L. Tsai, G. Christou, D.N. Hendrickson, J. Am. Chem. Soc. 118 (1996) 7746.
[6] R. Wang, D. Yuan, F. Jiang, L. Han, S. Gao, M. Hong, Eur. J. Inorg. Chem. (2006) 1649.
[7] M. Tong, J. Wang, S. Hu, J. Solid. State Chem. 178 (2005) 1518.
[8] M.C.F. Vidal, I. Lens, A. Castiñeiras, A. Matilla, J.M. Tercero, J. Niclós, Polyhedron 18 (1999) 3313.
[9] (a) A. Castiñeiras, M.C.F. Vidal, J. Romero, R. Sáez, A. Matilla, J. Niclós, J.M. Tercero, Z. Anorg. Allg. Chem. 627 (2001) 1553;
(b) J. Borrás, R. Carballo, A. Castineiras, M.C. Gómez-Conde, M.C. Fernández-Vidal, J. Niclós, Z. Anorg. Allg. Chem. 631 (2005) 2221.
[10] A. Castiñeiras, M.C.F. Vidal, R. Carballo, Transition Met. Chem. 20 (1995) 477.
[11] Bruker, SMART and SAINT, Area Detector Control and Integration Software, Bruker Analytical X-ray Instruments Inc., Madison, Wisconsin, USA, 1997.
[12] G.M. Sheldrick, SADABS, Program for Empirical Absorption Correction of Area Detector Data, University of Göttingen, Germany, 1997.
[13] G.M. Sheldrick, Acta Crystallogr. A46 (1990) 467.
[14] G.M. Sheldrick, SHELXL-97, Program for the Refinement of Crystal Structures, University of Göttingen, Germany, 1997.
[15] A.J.C. Wilson, International Tables for Crystallography, vol. C, Kluwer Academic Publishers, Dordrecht, The Netherlands, 1995.
[16] K. Nakamoto, Infrared Spectra of Inorganic and Coordination Compounds, Wiley, New York, 1997.
[17] A.B.P. Lever, Inorganic Electronic Spectroscopy, 2nd Ed., Elsevier, Amsterdam, 1986.
[18] R.L. Carlin, Magnetochemistry, Springer-Verlag, Berlin, 1986.
[19] (a) S. Konar, S.C. Manna, E. Zangrando, T. Mallac, J. Ribas, N.R. Chaudhuri, Eur. J. Inorg. Chem. (2004) 4202;
(b) J.-Y. Yhang, Y. Ma, A.-L. Cheng, Q. Yue, Q. Sun, E.-Q. Gao, Dalton Trans. (2008) 2061.

play an important role for structural holding via a hydrogen bonding interactions in proteins [35–39]. The role of hydrogen bonding in the stabilization of structures as well as in the functions of various metalloproteins is also well known in biochemistry [40–44]. In order to investigate the influence of different carboxylic acids on the geometrical structure of the central vanadium and probe into the importance of hydrogen bonding in this system, we designed and synthesised a series of vanadium complexes with poly(pyrazolyl)borate and carboxylic acid as ligands: TpVO(pzH)(2,4-Cl–C_6H_3–OCH_2COO) (**1**), TpVO(pzH)(C_6H_5–OCH_2-COO) (**2**), TpVO(pzH)(*p*-Cl–C_6H_4–COO) (**3**), TpVO(pzH)(3,5-NO_2–C_6H_3–COO) (**4**), Tp*VO(pzH*)(*p*-Cl–C_6H_4–COO) (**5**) and Tp*VO(pzH*)(*p*-Cl–C_6H_4–COO) · CH_3OH (**6**). Herein, we will report their spectra, crystal structures and thermal decomposition results. Particularly, the hydrogen bonding will be discussed in detail. In addition, the catalytic activities for bromoperoxidation have been determined and discussed by the UV–Vis spectra absorption method.

2. Experimental

2.1. Materials and methods

All the chemicals used were of analytical grade and were used without further purification. KTp and KTp* were synthesized according to the literature method [45,46] and all the other reactants were used as purchased. All synthetic manipulations were carried out in the atmosphere at room temperature. Elemental analyses (C, H and N) were performed on a PE 240C automatic analyzer. IR spectra were recorded with a JASCO FT/IR-480 spectrometer in the spectral range 4000–220 cm^{-1} with the samples in the form of potassium bromide pellets. The UV–Vis spectra were recorded on a PE Lambda 35 spectrometer.

2.2. Synthesis

2.2.1. Preparation of TpVO(pzH)(L) (L = 2,4-Cl–C_6H_3–OCH_2COO (**1**), C_6H_5–OCH_2COO (**2**), *p*-Cl–C_6H_4–COO (**3**) and 3,5-NO_2–C_6H_3–COO (**4**))

To a 10 ml solution of 2,4-dichlorophenoxyacetic acid (0.22 g, 1 mmol) (**1**) (phenoxyacetic acid (0.15 g, 1 mmol) (**2**), 4-chlorobenzoic acid (0.16 g, 1 mmol) (**3**) and 3,5-dinitrobenzoic acid (0.21 g, 1 mmol) (**4**)) in methanol, $VOSO_4 \cdot nH_2O$ (0.08 g, 0.3 mmol, based on 71% $VOSO_4$) in methanol (5 ml) was added, and the mixture was stirred for 30 min at room temperature to give a clear cyan solution, then a solution of KTp (0.09 g, 0.3 mmol) and pyrazole (0.02 g) in methanol (5 ml) was added to the cyan solution, and this reaction mixture was stirred at room temperature for 4 h to give a purple suspension. The precipitate was filtered out, the purple filtrate stored at room temperature for several days and violet-blue crystals suitable for X-ray diffraction were obtained from mother liquor. Yield (based on V): 0.12 g, 70.41% (**1**); 0.09 g, 60.10% (**2**); 0.11 g, 72.81% (**3**); and 0.14 g, 83.46% (**4**). *Anal.* Calc. for $C_{20}H_{19}BCl_2N_8O_4V$ (**1**): C, 42.29; H, 3.37; N, 19.72. Found: C, 42.27; H, 3.32; N, 19.75%; for $C_{20}H_{21}BN_8O_4V$ (**2**): C, 48.12; H, 4.24; N, 22.45. Found: C, 48.10; H, 4.27; N, 22.47%; for $C_{19}H_{18}BClN_8O_3V$ (**3**): C, 45.31; H, 3.60; N, 22.25. Found: C, 45.27; H, 3.52; N, 22.23%; for $C_{19}H_{17}BN_{10}O_7V$ (**4**): C, 40.81; H, 3.06; N, 25.05. Found: C, 40.77; H, 3.04; N, 25.04%. IR (KBr, cm^{-1}) for **1**: 3429 (ν_{O-H}), 3130 (ν_{N-H}), 2512 (ν_{B-H}), 1616 (ν_{asCOO^-}), 1481 (ν_{sCOO^-}), 975 ($\nu_{V=O}$), 452 (ν_{V-O}), 372, 345 (ν_{V-N}); for **2**: 3421 (ν_{O-H}), 3138 (ν_{N-H}), 2509 (ν_{B-H}), 1613 ((ν_{asCOO^-}), 1501 (ν_{sCOO^-}), 975 ($\nu_{V=O}$), 447 (ν_{V-O}), 374, 350 (ν_{V-N}); for **3**: 3462 (ν_{O-H}), 3140 (ν_{N-H}), 2512 (ν_{B-H}), 1600 ((ν_{asCOO^-}), 1403 (ν_{sCOO^-}), 972 ($\nu_{V=O}$), 475 (ν_{V-O}), 374, 349 (ν_{V-N}); for **4**: 3431 (ν_{O-H}), 3126 (ν_{N-H}), 2513 (ν_{B-H}), 1622 ((ν_{asCOO^-}), 1456 (ν_{sCOO^-}), 970 ($\nu_{V=}$), 433 (ν_{V-O}), 377, 340 (ν_{V-N}).

2.2.2. Preparation of Tp*VO(pzH*)(*p*-Cl–C_6H_4–COO) (**5**) and Tp*VO(pzH*)(*p*-Cl–C_6H_4–COO) · CH_3OH (**6**)

Complexes **5** and **6** were synthesized by a method similar to that of complex **1**, except that 4-chlorobenzoic acid (0.16 g, 1 mmol), KTp* (0.11 g, 0.3 mmol) and 3,5-dimethylpyrazole (0.03 g) replaced 2,4-dichlorophenoxyacetic acid, KTp and pzH. Violet crystals suitable for X-ray analysis were obtained from the mother liquor. Yield (based on V): 0.16 g, 86.61% (**5**) and 0.08 g, 41.2% (**6**). *Anal.* Calc. for $C_{27}H_{34}BClN_8O_3V$ (**5**): C, 52.66; H, 5.56; N, 18.20. Found: C, 52.61; H, 5.52; N, 18.19%; for $C_{28}H_{37}BClN_8O_4V$ (**6**): C, 51.99; H, 5.77; N, 17.32. Found: C, 51.94; H, 5.69; N, 17.30%. IR (KBr, cm^{-1}) for **5**: 3429 (ν_{O-H}), 3127 (ν_{N-H}), 2533 (ν_{B-H}), 1608 ((ν_{asCOO^-}), 1446 (ν_{sCOO^-}), 965 ($\nu_{V=O}$), 473 (ν_{V-O}), 372, 336 (ν_{V-N}); for **6**: 3447 (ν_{O-H}), 3133 (ν_{N-H}), 2521 (ν_{B-H}), 1591 ((ν_{asCOO^-}), 1449 (ν_{sCOO^-}), 967 ($\nu_{V=O}$), 473 (ν_{V-O}), 371, 338 (ν_{V-N}).

Table 1
Crystallographic data and structure refinement for **1**–**6**.

	1	**2**	**3**	**4**	**5**	**6**
Formula	$C_{20}H_{19}BCl_2N_8O_4V$	$C_{20}H_{21}BN_8O_4V$	$C_{19}H_{18}BClN_8O_3V$	$C_{19}H_{17}BN_{10}O_7V$	$C_{27}H_{34}BClN_8O_3V$	$C_{28}H_{37}BClN_8O_4V$
M (g mol^{-1})	568.08	499.20	503.61	559.18	615.82	646.86
Crystal system	monoclinic	monoclinic	monoclinic	monoclinic	orthorhombic	monoclinic
Space group	$P2_1/c$	$P2_1/c$	$P2_1/c$	$C2/c$	$Pna2_1$	$P2_1/n$
a (Å)	11.940(2)	11.905(7)	9.0394(18)	18.558(4)	19.052(3)	16.101(5)
b (Å)	13.628(3)	13.057(8)	19.572(4)	13.503(3)	10.9837(17)	11.353(4)
c (Å)	16.152(3)	15.449(9)	15.744(5)	20.021(4)	14.661(2)	18.757(6)
β (°)	109.71(3)	109.099(9)	124.52(2)	107.98(3)		107.929(4)
V ($Å^3$)	2474.2(9)	2269(2)	2295.0(10)	4771.8(17)	3068.1(8)	3262.2(17)
Z	4	4	4	8	4	4
D_{calc} (g cm^{-3})	1.525	1.461	1.458	1.557	1.333	1.317
Crystal size (mm)	0.16 × 0.13 × 0.13	0.24 × 0.14 × 0.09	0.21 × 0.13 × 0.10	0.20 × 0.20 × 0.08	0.21 × 0.17 × 0.10	0.29 × 0.08 × 0.05
F(000)	1156	1028	1028	2280	1284	1352
μ(Mo Kα) (cm^{-1})	6.61	4.82	5.87	4.79	4.52	4.31
Reflections collected	20707	9714	16974	22967	18328	18258
Independent reflections ($I > 2\sigma(I)$)	4835	3334	3969	5417	6768	6901
Parameters	329	311	316	347	374	393
$\Delta(\rho)$ (e $Å^{-3}$)	0.339 and −0.332	0.604 and −0.455	0.328 and −0.356	0.256 and −0.325	0.348 and −0.265	0.622 and −0.347
Goodness-of-fit	0.964	1.040	0.973	1.026	1.045	1.059
R[a]	0.0575 (0.1496)[b]	0.0547 (0.0845)[b]	0.1061 (0.2377)[b]	0.0578 (0.1105)[b]	0.0469 (0.0619)[b]	0.0571 (0.0841)[b]
wR_2[a]	0.1208 (0.1581)[b]	0.1297 (0.1486)[b]	0.2353 (0.2786)[b]	0.1063 (0.1224)[b]	0.1233 (0.1332)[b]	0.1621 (0.1808)[b]

[a] $R = \sum||F_o| - |F_c||/\sum|F_o|$, $wR_2 = [\sum(w(F_o^2 - F_c^2)^2/[\sum(w(F_o^2)^2]^{1/2}$; $[F_o > 4\sigma(F_o)]$.
[b] Based on all data.

2.3. Single-crystal structure determination

The crystal data, data collection and refinement details are summarized in Table 1. Reflection data were collected at room temperature on a Bruker AXS SMART APEX II CCD diffractometer with graphite-monochromated Mo Kα radiation ($\lambda = 0.71073$ Å) and $\omega-2\theta$ scan mode. All the measured independent reflections ($I > 2\sigma(I)$) were used in the structural analyses and semi-empirical absorption corrections were applied using the SADABS program [47].

The structures were solved by direct methods for **1**, **3**, **4**, **5** and **6**, respectively, and by the heavy-atom Patterson method for **2** and refined with the SHELXTL software package [48]. All non-hydrogen atoms were refined anisotropically. All hydrogen atoms, except for the boron hydrogen atoms, were fixed at calculated positions with isotropic thermal parameters.

2.4. Thermal analysis

Thermogravimetric analyses (TGA) experiments were carried out on a Perkin–Elmer Diamond TG/DTA instrument. During the simple gradient experiment, weight changes were recorded as a function of temperature for a 20 °C/min temperature gradient between 50 and 1000 °C in a nitrogen environment.

2.5. Measurement of bromination activity in solution

The method of introducing four bromine atoms into the molecule of phenol red to form bromophenol blue was used to monitor bromination activity under peroxide conditions. Spectral changes were recorded in 1 cm path length quartz cells using a PE Lambda 35 UV−Vis spectrometer. Phenol red acts as an efficient trap of active bromine species without influencing the rate of reaction until it is exhausted. The reaction mixture contained phosphate buffer (50 mM, pH 5.8), KBr (2 M), phenol red (20 μM) and the vanadium complex (0.50 mM). The redox activity was tested by adding a solution containing the vanadium complex. Cells were transferred to the spectrophotometer immediately after mixing to record spectra in the range 375–650 nm.

3. Results and discussion

3.1. Synthesis

Although the coordination modes of the vanadium atoms in complexes **1**–**6** are similar to those of Tp*VO(pzH*)(C_6H_5COO) · 0.4toluene (**7**) [29] and Tp*VO(pzH*){(μ-η^5-$C_5H_4CO_2$)-Fe(η^5-C_5H_5)} (**8**) [30], their synthetic processes are different. The reaction courses of the complexes are presented as follows:

It is found that the order of addition of the reactants and the stoichiometric ratios can affect the final product. When the poly(pyrazolyl)borate and pyrazole are in excess, it is hard for the carboxylic acids to coordinate to the vanadium. All the compounds are air-stable and soluble in CH_2Cl_2, CH_3CN, THF, etc., and are insoluble in hexane and ether.

3.2. IR spectroscopy

The IR spectra of complexes **1**–**6** reveal B–H stretching vibrations of tris(pyrazolyl)borate in the range 2509–2533 cm^{-1}. For complexes **1**–**6**, the bands in the 1591–1622 cm^{-1} and 1403–1501 cm^{-1} regions are assigned to the asymmetric vas(COO^-) and symmetric vs(COO^-) vibrations of monodentate coordinated, deprotonated carboxylate groups, respectively. The calculated Δ values {vas(COO^-)–vs(COO^-)} of **1**–**6** are 135, 112, 197, 166, 162 and 142 cm^{-1}, respectively, which are all lower than the values expected for monodentate carboxylate ligands (larger than 200 cm^{-1}) but the relative reductions in the Δ values are typical where such carboxylate groups are involved in hydrogen bonding [49,50]. The bands of V=O were observed in the range 962–971 cm^{-1}, V–O in the range 433–475 cm^{-1} and V–N in the range 336–377 cm^{-1} [51].

3.3. UV–Vis spectroscopy

The electronic absorption spectra for complexes **1**–**6** were recorded in CH_2Cl_2 solution. As shown in Fig. 1, the two weak bands in the range 542–767 nm are assigned to d–d transitions within the oxovanadium(IV) moiety [30]. The strong bands in the range

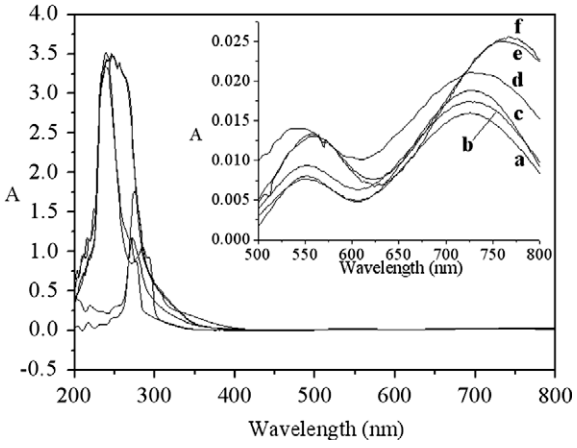
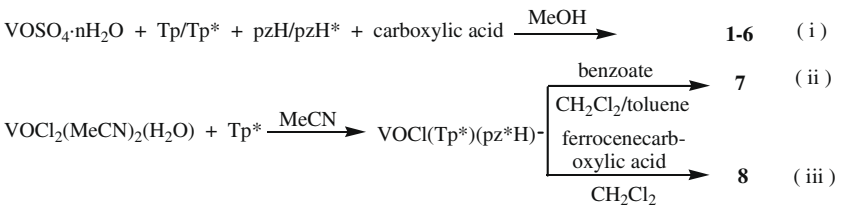


Fig. 1. UV–Vis spectra in CH_2Cl_2 solution: **1** (a); **2** (b); **3** (d); **4** (c); **5** (e); **6** (f).



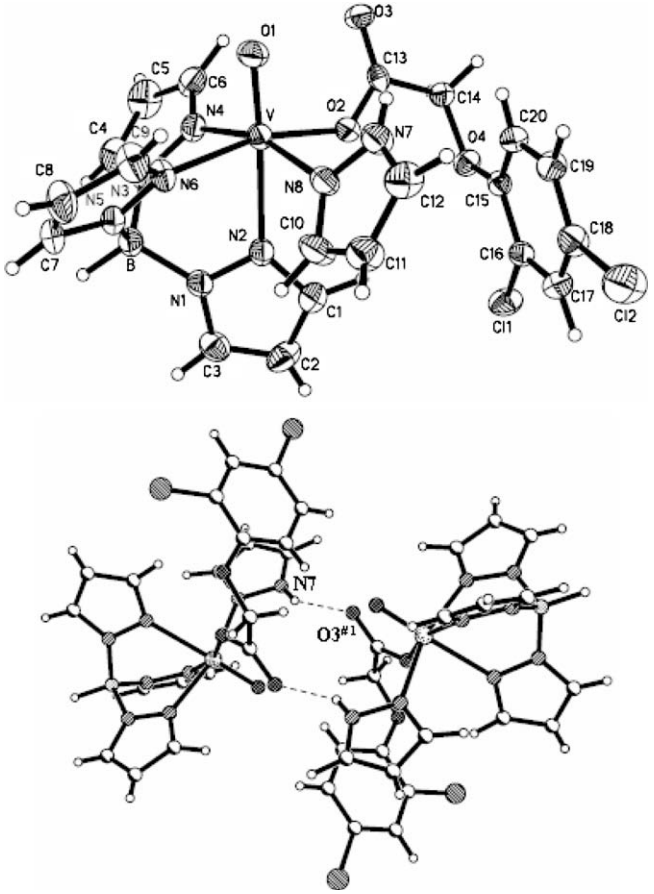


Fig. 2. The molecular structure and atom-numbering scheme for complex **1** with thermal ellipsoids drawn at the 30% probability level and a view of the hydrogen-bonded dimer of complex **1**.

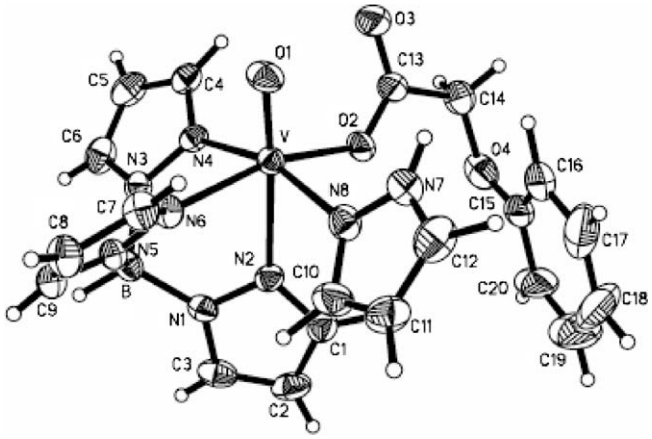


Fig. 3. The molecular structure and atom-numbering scheme for complex **2** with thermal ellipsoids drawn at the 30% probability level.

240–286 nm are related to intraligand charge transfer transitions [19].

3.4. Crystal structures

The X-ray structure analyses reveal that **1**–**4** are neutral complexes of VO–Tp–pz–carboxylate, and **5** and **6** are neutral complexes of VO–Tp*–pzH*–carboxylate. The molecular structures of complexes **1**–**5** are depicted in Figs. 2, 3 and 5–7 (the structure of complex **6** is the same as **5**, except for a lattice methanol molecule, and its structure is depicted in Fig. 1S). In all cases the vanadium atom is six-coordinated with a N_4O_2 donor set in a distorted-octahedral geometry. In complex **1**, two nitrogen atoms (N4, N6) from Tp^-, one nitrogen (N8) from a neutral pyrazole and one oxygen (O2) from carboxylate group of 2,4-dichlorophenoxyacetic acid in *cis* positions form the equatorial plane, and the axial positions

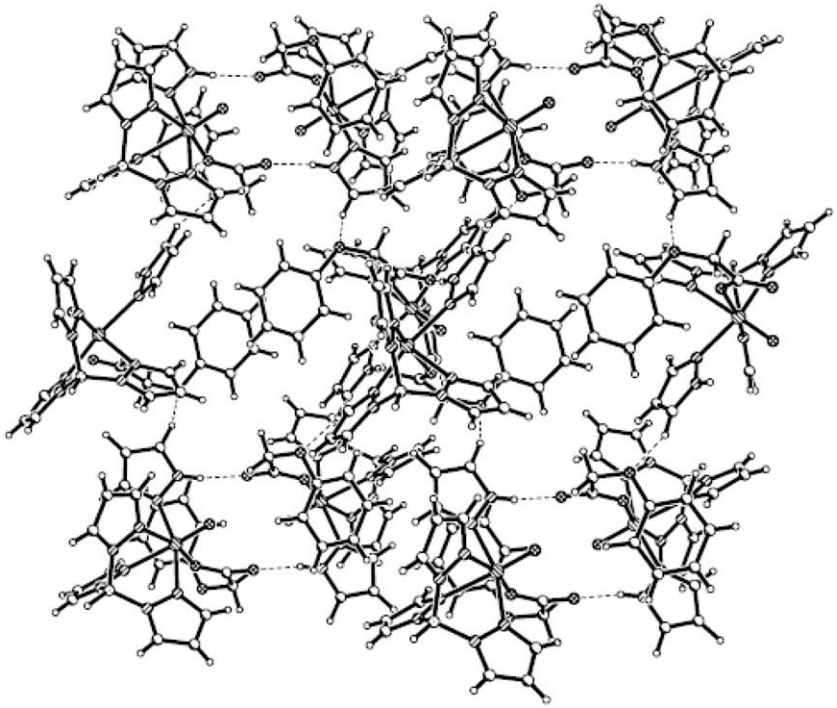


Fig. 4. Molecular packing of complex **2**.

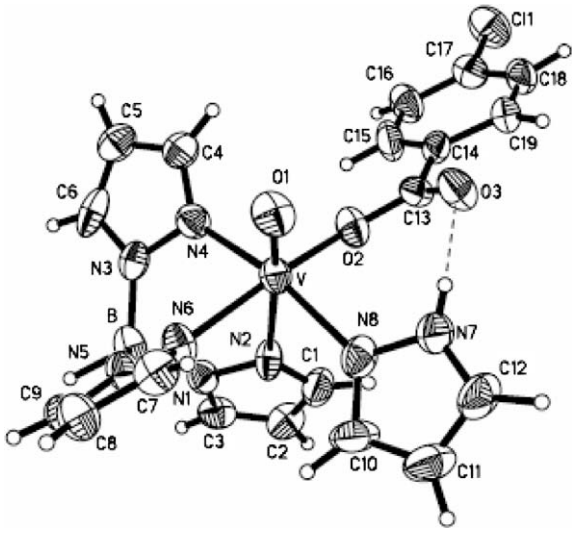


Fig. 5. The molecular structure and atom-numbering scheme for complex **3** with thermal ellipsoids drawn at the 30% probability level.

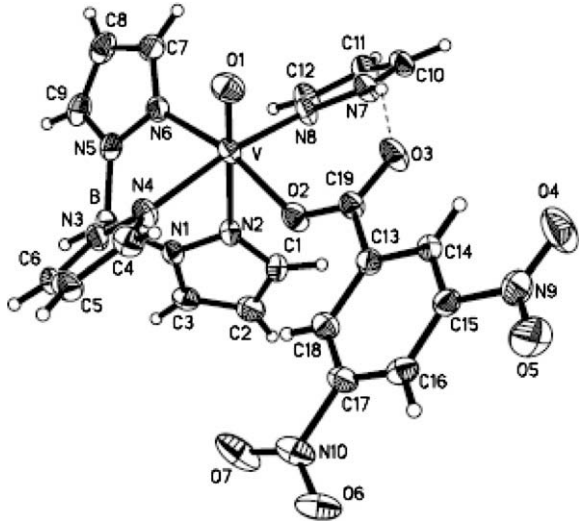


Fig. 6. The molecular structure and atom-numbering scheme for complex **4** with thermal ellipsoids drawn at the 30% probability level.

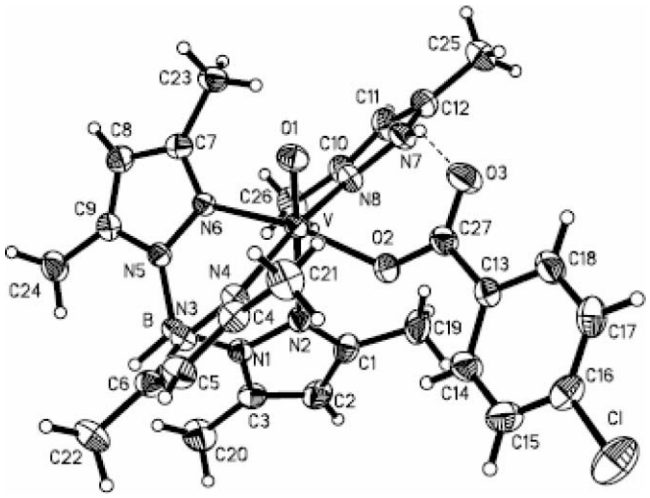


Fig. 7. The molecular structure and atom-numbering scheme for complex **5** with thermal ellipsoids drawn at the 30% probability level.

are occupied by the remaining nitrogen (N2) from Tp^- and a terminal oxygen atom (O1).

The deviations from the least-squares plane through the O2, N4, N6 and N8 atoms comprising the square plane are 0.0055(23), −0.0057(23), 0.0059(24) and −0.0057(23) Å, respectively, showing that these atoms are almost on one plane. The V, O1 and N2 from the apical positions lie 0.2859(24), 1.8702(48) and −2.0050(50) Å out of this plane, respectively, indicating that the vanadium atom is displaced towards the oxo oxygen O1. The V–O(terminal) bond length [V–O1, 1.594(3) Å] agrees well with those reported oxovanadium(IV) complexes containing poly(pyrazolyl)borate [14–16,26–33]. Because of the *trans* effect of the terminal oxo group, the bond length of V–N2 (2.291(4) Å) is considerably longer than those of V–N4, V–N6 and V–N8 (2.115(4), 2.109(4) and 2.136(4) Å, respectively). Such elongation is similar to that observed in comparable complexes [14–16,26–33]. The short V–N average bond length is 2.120(4) Å, which is comparable with V–N in V–BrPO (2.110 Å) [8]. The V–N(pz) and V–O(carboxylate) bond lengths are 2.136(4) and 1.996(3) Å, respectively, which are close to those of similar relevant complexes [29,30]. In addition, the two mononuclear molecules are held together by inter-molecular hydrogen bonds involving the N–H protons and O3 to form a quasi-dimeric structure as shown in Fig. 2. The corresponding hydrogen bonds lengths and angles of N7–H7A···O3$^{\#1}$ [#1: $-x$, $2-y$, $-z$] are 2.864(6) Å and 166.0(1)°.

As shown in Figs. 3 and 5–7, the structures of complexes **2**–**5** are similar to that of **1**, in each complex, the vanadium atom is in a distorted-octahedral environment with the Tp^- or Tp^{*-} occupying three facial sites. The other three sites are occupied by a terminal oxo group (O1), an oxygen atom (O2) from the carboxylate group and a nitrogen atom (N8) from a neutral pyrazole or 3,5-dimethylpyrazole ligand. Two nitrogen atoms (N4, N6) from Tp^- or Tp^{*-}, one nitrogen atom (N8) and one oxygen (O2), occupy the equatorial positions. The deviations of V, O1 and N2 out of the equatorial plane for complexes **2**–**6** are listed in Table 1S, indicating that the vanadium atoms are displaced toward the oxo oxygen O1. The *trans* effect of this terminal oxo group is responsible for the increased length of the V–N2 bond (2.266(9)–2.283(3) Å), which are slightly shorter than those of **7** and **8** (2.355(4) Å for **7**, and 2.3184(4) Å for **8**) and similar to those found in VO(κ^2-B(pz)$_4$)(κ^3-B(pz)$_4$)) and TpVO(Bp). The V–O(terminal) and V–N*cis* bond lengths are in the ranges 1.582(7)–1.593(2) and 2.086(10)–2.134(3) Å, respectively. Both the bond lengths for V–O(terminal) and V–N*cis* agree well with those reported oxovanadium complexes containing poly(pyrazolyl)borate (Table 2). As depicted in Fig. 4, two independent molecules of complex **2** form a dimer by inter-molecular hydrogen bonding as follows: N7–H7B···O3$^{\#2}$ [#2: $-x$, $1-y$, $1-z$; 2.777(6) Å, 164.7(3)°]. These dimeric units are connected to one another via weak inter-molecular C–H···O interactions between the phenoxyl oxygen atoms (O4) and C12 from the neutral pyrazole of an adjacent molecule to form a 2D network on the *bc*-face (Fig. 4). In complexes **3**–**5**, the intramolecular hydrogen bond N7–H7A···O3 [2.71(4) Å, 159.4(9)° for **3**; 2.70(2) Å, 142.3(2)° for **4** and 2.720(4) Å, 146.6(2)° for **5**] exists in each complex.

3.5. Thermal stability analyses

The TG–DTG–DTA curves of decomposition of **1** show two stages of thermal decomposition (Fig. 8). The first stage occurs within the temperature range 155–400 °C with a mass loss of 50.79% corresponding to the loss of a pyrazole molecule and a 2,4-dichlorophenoxyacetate moiety (theoretical value 50.68%). The DTA curve indicates an endothermic process. The second stage, in the temperature range 400–540 °C, was observed as mass loss of 13.69%, corresponding to the loss of $C_3H_4N_2B$, namely one pz moi-

Table 2
Comparison of key bond lengths (Å) and angles (°) for oxovanadium (IV) complexes containing poly(pyrazolyl)borate.

	V–O (terminal)	V–N (*trans*)	V–N (*cis*)	N–V–N (bite)	Reference
1	1.593(3)	2.292(4)	2.119(4)	80.1(2)–84.5(2)	this work
2	1.585(3)	2.273(3)	2.111(3)	80.8(1)–84.5(1)	this work
3	1.582(7)	2.266(9)	2.086(10)	81.0(4)–85.0(4)	this work
4	1.586(2)	2.269(3)	2.109(2)	80.9(1)–85.6(1)	this work
5	1.592(2)	2.282(2)	2.111(3)	80.92(9)–85.5(1)	this work
6	1.593(2)	2.283(3)	2.118(3)	81.4(1)–86.0(1)	this work
7	1.590(8)	2.355(4)	2.117(5)	80.9(3)–85.4(3)	[29]
8	1.598(3)	2.318(4)	2.123(5)	82.0(1)–85.7(1)	[30]
Tp^{*i-Pr2}VO(acac)	1.626(4)	2.329(4)	2.108(5)	81.7(2)–86.9(2)	[31]
Tp* VO(acac)	1.596(2)	2.328(2)	2.116(2)	81.0(1)–87.4(1)	[32]
TpVO(Me-acac)	1.590(5)	2.361(5)	2.122(4)	79.8(1)–86.0(2)	[14]
Tp* VO(Me-acac)	1.597(2)	2.352(2)	2.099(2)	80.90(6)–87.1(1)	[14]
TpVO(Bp)	1.592(2)	2.298(2)	2.104(2)	80.4(1)–87.3(1)	[16]
VO(κ^2-B(pz)$_4$)(κ^3-B(pz)$_4$))	1.588(3)	2.274(3)	2.0995(3)	80.9(1)–85.4(11)	[16]

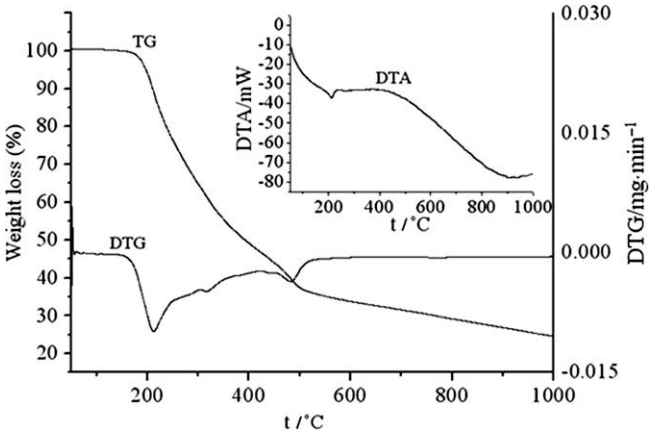


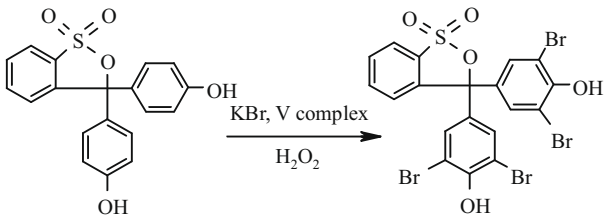
Fig. 8. The TG/DTG/DTA curves for complex **1**.

ety and one BH moiety (theoretical value 13.89%). The DTA curve of the complex indicates an exothermic process.

The TG–DTG–DTA curves of decomposition of **2**, **4** and **5** are shown in Figs. 3S–5S. The thermal decomposition of **2** also exhibits a two-step process. In the range 145–354 °C, there is a 44.05% weight loss, which is attributed to the release of one pyrazole moiety and one phenoxyacete moiety (43.84% theoretical weight loss). This step is followed by a weight loss of 22.30%, which can be attributed to the release of $C_5H_5N_3$, namely 1.6 pz moieties (theoretical value 21.46%) in the range 354–551 °C. As shown in Fig. 4S, the thermal decomposition process of complex **4** can be divided into three stages. The first weight loss corresponds to the release of one CO_2 and two NO_3 moieties and occurs in the temperature range 206–288 °C, the weight loss is 24.99% (calc. 24.32%). The second stage, in the temperature range 288–379 °C, was observed as a mass loss of 14.06%, corresponding to loss of one C_6H_3 moiety (theoretical value 13.41%). The third stage, in the temperature range 379–501 °C, was observed as a mass loss of 11.68% corresponding to loss of one pyrazole moiety (theoretical value 12.16%). As shown in Fig. 5S, the thermal decomposition of complex **5** exhibits a three-step process too. In the range 145–261 °C, there is a 15.95% weight loss, which is attributed to the release of one 3,5-dimethylpyrazole moiety (15.75% theoretical weight loss). In the temperature range 261–357 °C, about a 26.26% weight loss is observed, which may correspond to the release of one 4-chlorobenzoate moiety (theoretical value 25.33%). In the third stage, it experiences a 29.21% weight loss in the temperature range 357–700 °C, which is attributed to the release of two pz* moieties (theoretical value 30.85%).

3.6. Catalytic activity of the complexes in bromination reactions

It has been confirmed that vanadium compounds are able to mimic the reaction in which vanadium-dependent bromoperoxidases catalyze the bromination of organic substrates in the presence of H_2O_2 and bromide, for example, the bromination of trimethoxybenzene [52], salicylaldehyde, benzene and phenol by the VO_2^+ ion [53,54], and the bromination of phenol red by $[VO(O_2)H_2O]^+$ and related species [55]. Herein, we investigate the bromination reaction activity of the complexes using phenol red as the organic substrate, the reactive process as follows:



Addition of a solution of complex **2** to the standard reaction of bromide in phosphate buffer with phenol red as a trap for oxidized bromine resulted in a color change of the solution from yellow to blue. Fig. 9 shows the electronic absorption spectra collected during such a color change using **2** as a catalyst. The spectrum recorded showed

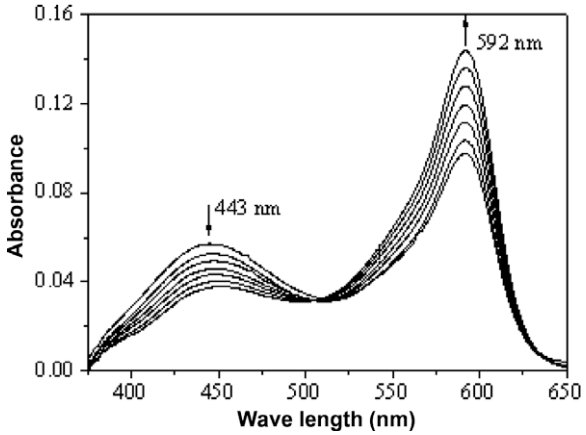


Fig. 9. Oxidative bromination of phenol red catalyzed by complex **2** (spectral changes at 10 min intervals. The reaction mixture contained phosphate buffer (50 mM, pH 5.8), KBr (2 M) and phenol red (20 μM)).

a decrease in absorbance of the peak at 443 nm due to loss of phenol red and a peak at 592 nm characteristic of the product bromophenol blue, showing that complex **2** possess obvious catalytic activity.

In addition, the results of the mimic catalytic activities for **1** and **3**–**6** are similar to that of **2**. It is probably due to the coordination environments of the vanadium atoms in **1** and **3**–**6** which are the same as **2**. Based on the information obtained from spectroscopic and catalytic experiments, we found that during the mimic catalysis reaction course, the concentration of KBr and vanadium, the pH value of the medium and the temperature are the main influencing factors. More detailed research for mimicking catalysis activities is in progress.

4. Conclusions

In order to mimic model complexes of V-HPOs, we designed and synthesized a series of oxovanadium complexes containing tris(pyrazolyl)borate as a supporting ligand and carboxylic acids as the second ligand. The one-step reaction of $VOSO_4 \cdot nH_2O$, pyrazole or 3,5-dimethylpyrazole, potassium poly(pyrazolyl)borate and carboxylic acids in methanol resulted in six new complexes, **1**–**6**. The synthetic process described here is different from those in the literature reports. Structural analyses show that in all of these complexes, the vanadium atoms are six-coordinated with a N_4O_2 donor set in a distorted-octahedral geometry, the carboxylate groups are coordinated as monodentate and the uncoordinated oxygen atom of the carboxylate groups form intra- or inter-molecular hydrogen bonds with the NH group of the corresponding coordinated neutral pyrazole (pzH/pzH*). Catalytic activity of the complexes in bromination reactions was discussed, which indicated that complexes **1**–**6** are in fact active in the bromination of phenol red in the presence of H_2O_2, Br^- and phosphate buffer, and hence may also be considered as potential functional model complexes.

Acknowledgements

We thank National Natural Science Foundation of China (Grant No. 20771051) and Education Foundation of Liaoning Province in China (Grant No. 2007T093) for financial assistance.

Appendix A. Supplementary data

CCDC 671865, 671897, 671895, 671896, 671898 and 687668 contain the supplementary crystallographic data for **1**–**6**. These data can be obtained free of charge via http://www.ccdc.cam.ac.uk/conts/retrieving.html, or from the Cambridge Crystallographic Data Centre, 12 Union Road, Cambridge CB2 1EZ, UK; fax: (+44) 1223-336-033; or e-mail: deposit@ccdc.cam.ac.uk. Supplementary data associated with this article can be found, in the online version, at doi:10.1016/j.poly.2008.12.055.

References

[1] C.J. Schneider, J.E. Penner-Hahn, V.L. Pecoraro, J. Am. Chem. Soc. 130 (2008) 2712.
[2] A. Butler, Curr. Opin. Chem. Biol. 2 (1998) 279.
[3] D. Rehder, Coord. Chem. Rev. 182 (1999) 297.
[4] C. Wikete, P. Wu, G. Zampetlla, L.D. Gioia, G. Licini, D. Rehder, Inorg. Chem. 46 (2007) 196.
[5] A. Butler, Coord. Chem. Rev. 187 (1999) 17.
[6] M.R. Maurya, A. Kumar, M. Ebel, D. Rehder, Inorg. Chem. 45 (2006) 5924.
[7] D.C. Crans, J.J. Smee, E. Gaidamauskas, L. Yang, Chem. Rev. 104 (2004) 849.
[8] M. Weyand, H.J. Hecht, M. Kieβ, M.F. Liaud, H. Vilter, D.J. Schomburg, Mol. Biol. 293 (1999) 595.
[9] J.S. Martinez, G.L. Carroll, R.A. Tschirret-Guth, G. Altenhoff, R.D. Little, A. Butler, J. Am. Chem. Soc. 123 (2001) 3289.
[10] G.J. Colpas, B.J. Hamstra, J.W. Kampf, V.L. Pecoraro, J. Am. Chem. Soc. 118 (1996) 3469.
[11] M.J. Clague, N.L. Keder, A. Butler, Inorg. Chem. 32 (1993) 4754.
[12] C. Slebodnick, B.J. Hamstra, V.L. Pecoraro, Struct. Bonding 89 (1997) 51.
[13] Y.H. Xing, F.Y. Bai, K. Aoki, Z. Sun, M.F. Ge, Syn. React. Inorg. Met. 37 (2007) 203.
[14] Y.H. Xing, K. Aoki, Z. Sun, M.F. Ge, S.Y. Niu, J. Chem. Res. 2 (2007) 100.
[15] Y.H. Xing, Y.H. Zhang, Z. Sun, L. Ye, Y.T. Xu, M.F. Ge, B.L. Zhang, S.Y. Niu, J. Inorg. Biochem. 101 (2007) 36.
[16] Y.H. Xing, B.L. Zhang, Y.H. Zhang, H.Q. Yuan, Z. Sun, M.F. Ge, Polyhedron 26 (2007) 3037.
[17] E. Kime-Hunt, K. Spartalian, M. DeRusha, C.M. Nunn, C.J. Carrano, Inorg. Chem. 28 (1989) 4392.
[18] P. Dapporto, F. Mani, C. Mealli, Inorg. Chem. 17 (1978) 1323.
[19] M. Mohan, S.M. Holmes, R.J. Butcher, J.P. Jasinski, C.J. Carrano, Inorg. Chem. 31 (1992) 2029.
[20] C.C. McLauchlan, K.J. McDonald, Acta Crystallogr. E62 (2006) m588.
[21] D. Rehder, H. Gailus, H. Schmidt, Acta Crystallogr. C54 (1998) 1590.
[22] C.J. Carrano, M. Mohan, S.M. Holmes, R. de la Rosa, A. Butler, J.M. Charnock, C.D. Garner, Inorg. Chem. 33 (1994) 646.
[23] M. Herberhold, G. Frohmader, T. Hofmann, W. Milius, J. Darkwa, Inorg. Chim. Acta 267 (1998) 19.
[24] S. Scheuer, J. Fischer, J. Kress, Organometallics 14 (1995) 2627.
[25] M. Kosugi, S. Hikichi, M. Akita, Y. Moro-oka, J. Chem. Soc., Dalton Trans. (1999) 1369.
[26] N.S. Dean, M.R. Bond, C.J. O'Connor, C.J. Carrano, Inorg. Chem. 35 (1996) 7643.
[27] C.C. McLauchlan, K.J. McDonald, Acta Crystallogr. E61 (2005) m2379.
[28] N.E. Heimer, W.E. Cleland Jr., Acta Crystallogr. C46 (1990) 2049.
[29] D. Collison, D.R. Eardley, F.E. Mabbs, A.K. Powell, S.S. Turner, Inorg. Chem. 32 (1993) 664.
[30] D. Collison, F.E. Mabbs, S.S. Turner, A.K. Powell, E.J.L. McInnes, L.J. Yellowlees, J. Chem. Soc., Dalton Trans. (1997) 1201.
[31] M. Kosugi, S. Hikichi, M. Akita, Y. Moro-oka, Inorg. Chem. 38 (1999) 2567.
[32] R.L. Beddoes, D. Collison, F.E. Mabbs, M.A. Passand, Polyhedron 9 (1990) 2483.
[33] S.M. Holmes, C.J. Carrano, Inorg. Chem. 30 (1991) 1231.
[34] D. Qiu, L.T. Kilpatrick, N. Kitajima, T.G. Spiro, J. Am. Chem. Soc. 116 (1994) 2585.
[35] S. Trofimenko, Polyhedron 23 (2004) 197.
[36] D. Badura, H. Vahrenkamp, Inorg. Chem. 41 (2002) 6020.
[37] Y.J. Sun, L.Z. Zhang, P. Cheng, H.K. Lin, S.P. Yan, W. Sun, D.Z. Liao, Z.H. Jiang, P.W. Shen, Inorg. Chem. 42 (2003) 508.
[38] U.P. Singh, R. Singh, S. Hikichi, M. Akita, Y. Moro-oka, Inorg. Chim. Acta 310 (2000) 273.
[39] M.N. Isupov, A.R. Dalby, A.A. Brindley, Y. Izumi, T. Tanabe, G.N. Murshudov, J.A. Littlechild, J. Mol. Biol. 299 (2000) 1035.
[40] R.H. Holm, P. Kennepohl, E.I. Solomon, Chem. Rev. 96 (1996) 2237.
[41] C. Kimblin, X. Bu, A. Butler, Inorg. Chem. 41 (2002) 161.
[42] S. Sarmah, P. Hazarika, N.S. Islam, Mol. Cell. Biochem. 236 (2002) 95.
[43] M. Casny, D. Rehder, Chem. Commun. (2001) 921.
[44] W. Plass, Coord. Chem. Rev. 237 (2003) 205.
[45] S. Trofimenko, J. Am. Chem. Soc. 89 (1967) 6288.
[46] P. Jesson, S. Trofimenko, D.R. Eaton, J. Am. Chem. Soc. 89 (1967) 3148.
[47] G.M. Sheldrick, SADABS, Program for Empirical Absorption Correction for Area Detector Data, University of Göttingen, Göttingen, Germany, 1996.
[48] G.M. Sheldrick, Program for Crystal Structure Refinement, University of Göttingen, Göttingen, Germany, 1997.
[49] G.B. Deacon, R.J. Philips, Coord. Chem. Rev. 33 (1980) 227.
[50] M. Devereux, D.O. Shea, A. Kellett, M. McCann, M. Walsh, D. Egan, C. Deegan, K. Kedziora, G. Rosair, H. Müller-Bunz, J. Inorg. Biochem. 101 (2007) 881.
[51] B.J.A. Jeragh, A. El-Dissouky, Transition Met. Chem. 29 (2004) 579.
[52] R.I. de la Rosa, M.J. Clague, A. Butler, J. Am. Chem. Soc. 114 (1992) 760.
[53] M.R. Maurya, S. Agarwal, C. Bader, M. Ebel, D. Rehder, J. Chem. Soc., Dalton Trans. (2005) 537.
[54] M.R. Maurya, A. Kumar, P. Manikandan, S. Chand, Appl. Catal. A: Gen. 277 (2004) 45.
[55] R.M. Tóltaro, P.A.M. Williams, M.C. Apella, M.A. Blesa, E.J. Baran, J. Chem. Soc., Dalton Trans. (2000) 4403.

Electronic absorption spectra were measured on a Shimadzu (UV-310PC) spectrometer. Luminescence spectra were recorded using a Perkin Elmer (LS 50 B) spectrometer.

2.1. Synthesis of $[(AgCN)_2 \cdot bpy]$ (1)

Seventy eight milligram (0.5 mmol) of bpy in 10 mL MeCN was added to 33 mg (0.25 mmol) of AgCN in 10 mL H_2O. The resulting mixture was heated at about 70°, while concentrated ammonia solution was added dropwise with stirring until the solution became clear. Prismatic colorless crystals appeared after standing at room temperature for two weeks. The crystals were recovered by filtration, washed with H_2O and dried in air (the yield was 65.5% with respect to AgCN).

Anal. Calcd for **1** ($C_{12}H_8N_4Ag_2$): C, 33.96; H, 1.88; N, 13.20. Found: C, 33.56; H, 1.79; N, 13.46. IR (KBr, cm^{-1}): 3048 (ν_{CH}), 2135 ($\nu_{C\equiv N}$), 1594 ($\nu_{C=N}$), 1529, 1481 ($\nu_{C=C}$), 1404, 1317 (δ_{CH}), 1218, 1063, 995, 803, 726, 618, 571, 471.

2.2. Synthesis of $[(AgCN)_3 \cdot (tbpe)_2 \cdot H_2O]$ (2)

Ninety one milligram (0.5 mmol) of tbpe in 10 mL MeCN was added to 33 mg (0.5 mmol) of KCN in 5 mL H_2O. The resulting mixture was added to 85 mg (0.5 mmol) of $AgNO_3$ in 10 mL H_2O. Concentrated ammonia solution was added dropwise with stirring to the previous mixture until the solution became clear. Yellow needle crystals appeared after standing at room temperature for two weeks. The crystals were recovered by filtration, washed with H_2O and dried in air (the yield was 85.6% with respect to $AgNO_3$).

Anal. Calc. for **2** ($C_{27}H_{22}N_7OAg_3$): C, 41.32; H, 2.80; N, 12.49. Found: C, 41.21; H, 2.37; N, 11.47%. IR (KBr, cm^{-1}): 3440 (ν_{H_2O}), 3046 (ν_{CH}), 2117 ($\nu_{C\equiv N}$), 1601 ($\nu_{C=N}$), 1555, 1498 ($\nu_{C=C}$), 1421, 1349 (δ_{CH}), 1219, 1067, 971, 826, 669, 550, 468.

2.3. Synthesis of $[(AgCN)_4 \cdot bpe]$ (3)

Ninety two milligram (0.5 mmol) of bpe in 10 mL MeCN was added to 33 mg (0.5 mmol) of KCN in 10 mL H_2O. The resulting mixture was added to 85 mg (0.5 mmol) of $AgNO_3$ in 10 mL H_2O and then concentrated ammonia solution was added dropwise with stirring to the previous mixture until the solution became clear. A colorless polycrystalline precipitate appeared after standing at room temperature for two weeks. The precipitate was recovered by filtration, washed with H_2O and dried in air (the yield was 70% with respect to $AgNO_3$).

Anal. Calc. for **3** ($C_{16}H_{12}N_6Ag_4$): C, 26.69; H, 1.66; N, 11.67. Found: C, 27.10; H, 1.59; N, 11.44%. IR (KBr, cm^{-1}): 3060, 2938, 2861 (ν_{CH}), 2130, 2160 ($\nu_{C\equiv N}$), 1600 ($\nu_{C=N}$), 1558, 1492, ($\nu_{C=C}$), 1453, 1416, 1339 (δ_{CH}), 1210, 1070, 830, 722, 610, 570 and 469.

2.4. X-ray structural determination

Structural measurements for SCPs **1**–**3** were performed on a Kappa CCd Enraf Nonius FR 90 four cycle geniometer with graphite monochromatic Mo Kα radiation {[λ Mo Kα] = 0.71073 Å} at 25 ± 2 °C. All the structures were resolved using direct-methods and all of the non-hydrogen atoms were located from the initial solution or from subsequent electron density difference maps during the initial stages of the refinement. After locating all of the non-hydrogen atoms in each structure the models were refined against F^2, first using isotropic and finally using anisotropic thermal displacement parameters. The positions of the hydrogen atoms were then calculated and refined isotropically, and then the final cycle of refinements was performed. The cyano groups of all structures were ordered unless otherwise stated. Crystallographic data for **1–3** are summarized in Table 1. Selected bond distances and bond angles are given in Tables 2–4. The C9 atom and N11 atom of the two bridging cyanide groups in **3** were located at inversion centers and were modeled as disordered over a pair of sites of equal occupancy. The disorder of these cyano groups in the asymmetric unit of **3** reflects the observation that R_w remains constant upon adopting a C atom or N atom at these sites.

Table 1
Crystal data and structure refinement parameters of the SCPs **1**–**3**.

	1	**2**	**3**
Empirical formula	$C_{12}H_8N_4Ag_2$	$C_{27}H_{22}N_7OAg_3$	$C_{16}H_{12}N_6Ag_4$
Formula weight	423.944	784.101	719.794
T (K)	298	298	298
Crystal system	monoclinic	triclinic	monoclinic
Space group	$P2_1/c$	$P\bar{1}$	$P2_1/c$
a (Å)	9.0565 (4)	9.8431 (4)	10.1872 (5)
b (Å)	16.0063 (8)	10.3592 (4)	9.1610 (5)
c (Å)	9.1361 (4)	14.0880 (6)	14.4862 (6)
α (°)	90.00	98.873 (2)	90.00
β (°)	110.516 (3)	101.739 (2)	130.0 (18)
γ (°)	90.00	95.506 (3)	90.00
V (Å^3)	1240.38 (10)	1377.54 (10)	974.01 (8)
Z	4	2	2
μ (Mo Kα) (mm^{-1})	3.14	2.14	3.97
Calculated density (Mg m^{-3})	2.270	1.818	2.454
Goodness-of-fit on F^2	2.014	2.127	1.704
F(000)	808	730	676
R indices [$I>3\sigma$ (I)] R_1/wR_2	0.035/0.072	0.039/0.078	0.033/0.076
R indices (all data)	0.121/0.094	0.081–0.087	0.077/0.084
R_{int}	0.031	0.028	0.033
Data/restraints/parameters	1370/0/163	3452/0/343	1049/0/113

Table 2
Selected bond distances (Å) and bond angles (°) for SCP **1**.

Ag1–C7	2.085 (3)	Ag1–Ag2[d]	3.2550 (4)
Ag1–N5[a]	2.570 (2)	Ag2–N6	2.249 (2)
Ag1–C8[b]	2.080 (3)	Ag2–N3	2.129 (3)
Ag2–N4	2.387 (3)	N4–C8	1.127 (4)
C7–N3	1.124 (4)		
C7–Ag1–N5[a]	91.26 (9)	Ag1[c]–N5–C13	127.0 (2)
C7–Ag1–C8[b]	164.85 (11)	Ag1[c]–N5–C12	117.2 (2)
N5[a]–Ag1–C8[b]	103.39 (9)	Ag2–N4–C8	161.7 (3)
N4–Ag2–N6	94.86 (9)	Ag2–N6–C16	125.9 (2)
N4–Ag2–N3	110.43 (9)	Ag2–N6–C14	173.80 (11)
N6–Ag2–N3	151.13 (10)	Ag2–N6–C15	154.03 (13)
Ag1–C7–N3	163.3 (3)	Ag2–N6–C18	146.26 (13)
Ag1[c]–N5–C9	154.10 (14)	Ag2–N6–C17	117.6 (2)
Ag1[c]–N5–C10	170.35 (13)	Ag2–N3–C7	166.0 (3)
Ag1[c]–N5–C11	144.60 (13)		
Hydrogen bonding			
Intra-layer H-bonding		Inter–layer H-bonding	
C7–H16[e]	2.989 (3)	C8–H15	3.065 (3)
C7–H15[e]	2.840 (3)	N3–H18[f]	2.978 (3)
C7–H13[a]	3.047 (3)		
N4–H13[a]	2.895 (3)		
N4–H17	2.583 (3)		
N3–H16[e]	2.841 (3)		
C8–H9[a]	2.923 (3)		
N3–H13[a]	3.031 (3)		
C17–H12[e]	3.056 (3)		
C8–H17	3.033 (3)		

Symmetry codes: [a] $x-1, 1/2-y, 1/2+z$; [b] $-1-x, 1/2+y, 3/2-z$; [c] $1+x, 1/2-y, z-1/2$; [d] $-1-x, -y, 1-z$; [e] $-x, -y, 1-z$; [f] $x, 1/2-y, 1/2+z$.

3. Results and discussion

The novel SCPs **1–3** exhibit variable stoichiometries. The molar ratios of AgCN:L are 2:1 for **1**, 3:2 for **2** and 4:1 for **3** in MeCN/H_2O/NH_3 solution. It seems that self-assembly of either authentic or in situ prepared AgCN and the bipodal ligand takes place at the appropriate stoichiometry required by the extended framework

Table 3
Selected bond distances (Å) and bond angles (°) for SCP **2**.

Ag1–Ag2[a]	3.0415 (5)	Ag2–N33	2.409 (3)
Ag1–N4	2.496 (3)	Ag2–N34	2.487 (4)
Ag1–C31	2.076 (4)	Ag3–N25	2.211 (4)
Ag1–C32	2.078 (4)	Ag3–C26	2.062 (5)
Ag2–N30	2.330 (3)	Ag3–N33	2.716 (4)
Ag2–N18	2.294 (3)	Ag3–N34	2.590 (5)
Ag2[a]–Ag1–N4	117.89 (8)	Ag2–N30–C14	170.1 (2)
Ag2[a]–Ag1–C31	74.39 (11)	Ag2–N30–C12	130.0 (3)
Ag2[a]–Ag1–C32	95.26 (11)	Ag2–N30–C13	158.3 (2)
N4–Ag1–C31	96.80 (14)	Ag2–N30–C15	141.8 (2)
N4–Ag1–C32	99.83 (14)	Ag2–N30–C16	114.0 (3)
C31–Ag1–C32	163.2 (2)	Ag2–N18–C22	176.8 (2)
Ag1[a]–Ag2–N30	89.22 (8)	Ag2–N18–C21	148.9 (2)
Ag1[a]–Ag2–N18	74.84 (8)	Ag2–N18–C29	120.1 (2)
Ag1[a]–Ag2–N33	138.25 (9)	Ag2–N18–C23	151.8 (2)
Ag1[a]–Ag2–N34	130.54 (10)	Ag2–N18–C19	123.7 (3)
N30–Ag2–N18	164.01 (12)	Ag3–N25–C24	170.2 (2)
N30–Ag2–N33	93.56 (12)	Ag3–N25–C40	149.4 (2)
N30–Ag2–N34	90.55 (13)	Ag3–N25–C38	120.4 (3)
N18–Ag2–N33	99.18 (12)	Ag3–N25–C39	148.5 (2)
N18–Ag2–N34	98.78 (13)	Ag3–N25–C37	122.3 (3)
N33–Ag2–N34	91.12 (14)	Ag1–C31–N33	172.3 (4)
N25–Ag3–C26	158.9 (2)	Ag2–N33–Ag3	92.56 (12)
N25–Ag3–N33	83.78 (13)	Ag2–N33–C31	148.6 (3)
N25–Ag3–N34	86.52 (14)	Ag3–N33–C31	118.0 (3)
C26–Ag3–N33	109.8 (2)	Ag1–C32–N34	176.8 (4)
C26–Ag3–N34	110.7 (2)	Ag2–N34–Ag3	93.87 (13)
N33–Ag3–N34	82.38 (11)	Ag2–N34–C32	132.8 (4)
Ag1–N4–C9	172.6 (2)	Ag3–N34–C32	132.5 (4)
Ag1–N4–C6	118.4 (3)	Ag3–C26–N27	176.0 (5)
Ag1–N4–C5	124.6 (3)	Ag1–N4–C8	152.6 (2)
Ag1–N4–C7	146.8 (2)		

Intra-layer H-bonds		Water H-bonds		Inter-layer H-bonds	
C31–H6	2.878 (4)	C7–H35A	2.710 (4)	C37–H37[c]	3.061 (4)
C31–H37	2.982 (4)	C15–H35B	3.037 (4)	C26–H13	3.053 (5)
N33–H16	3.008 (4)	N27–H35A	2.809 (5)		
N34–H16	2.952 (4)	N27–H35B	2.839 (5)		
N34–H38	2.862 (5)	N27–H35B[b]	2.847 (4)		
N27–H13	2.945 (6)	O35–H11	2.770 (4)		
C26–H16	2.955 (5)	O35–H17[b]	2.735 (4)		
N30–H29[c]	2.812 (3)	O35–H7	2.689 (4)		
C12–H19[b]	3.045 (4)	O35–H15	2.490 (4)		
C17–H23[b]	2.865 (4)				
C14–H23[b]	2.729 (4)				

Symmetry codes: [a] $1-x,-y,1-z$; [b] $-x,-y,-z$; [c] $1-x,-y,-z$.

Table 4
Selected bond distances (Å) and bond angles (°) for SCP **3**.

Ag2–C4	3.031 (3)	Ag1–Ag2	3.0565 (4)
Ag2–C9	2.060 (4)	Ag1–N3	2.253 (3)
Ag2–N11	2.068 (3)	Ag1–C4	2.064 (4)
Ag1–N8[a]	2.301 (4)		
Ag2–Ag1–N3	125.84 (7)	Ag1–C4–N8	177.9 (3)
Ag2–Ag1–C4	69.52 (9)	Ag1[a]–N8–C4	152.0 (3)
Ag2–Ag1–N8[a]	71.35 (7)	Ag2–C9–C9[b]	178.1 (5)
N3–Ag1–C4	139.58 (11)	Ag2–N11–N11[c]	176.8 (5)
N3–Ag1–N8[a]	96.94 (11)	Ag1–N3–C5	122.6 (2)
C4–Ag1–N8[a]	123.10 (12)	Ag1–N3–C7	121.6 (2)
C9–Ag2–N11	165.58 (14)		
Hydrogen bonding			
C6–H5[d]	2.918 (3)		
C7–H13[d]	3.064 (3)		
N8–H7[a]	2.813 (3)		

Symmetry codes: [a] $-x,1/2+y,-1/2-z$; [b] $-x,-y,-1-z$; [c] $1-x,-y,-z$; [d] $1-x,1/2+y,1/2-z$.

structure to adopt enough space demanded by the bipodal bridging ligand. The increased ratio of AgCN as the size specificity of the bridging ligand is increased can be considered as an essential requirement for the construction of unique $(AgCN)_n$ building blocks which create extended networks suitable for accommodating such long bridging ligands. In addition, these ligands behave as non-rigid spacers which are capable of displaying a variety of conformations. SCPs **1–3**, which are prepared at room temperature, can be also considered as unprecedented SCPs that may be compared with those prepared by hydrothermal reactions, described for $[(CuCN)_2.\ \mu\text{-L}]$ with L = bpy and tbpe [8] and $(CuCN)_2[(CuCN)_2(\mu\text{-}4,4'\text{-bpy})]$ [9]. Hydrothermal reactions, in spite of being exploited to prepare numerous SCPs, afford mostly the formation of mixtures of undesirable materials. The present procedure, in spite of being surprisingly simple, affords the formation of precipitates of **1–3** which consist exclusively of one discrete species and never of mixtures of different assemblies.

3.1. Crystal Structures

3.1.1. Crystal structure of $[(AgCN)_2 \cdot bpy]$ (1)

The asymmetric unit of **1** contains one fragment which consists of two silver atoms, two cyanide groups and one bpy molecule, Fig. 1a. The two silver atoms assume a distorted trigonal planar geometry where each is coordinated to two ordered cyanide groups and to the nitrogen atom of the bpy ligand. The two silver atoms are crystallographically different. Ag1 is strongly bonded to the cyanide groups, Ag1–C = 2.08 Å, but it is weakly coordinated to the bpy ligand, Ag1–N5 = 2.570 Å, which in spite of being weak is only slightly longer than those of previously reported silver complexes [5,7]. In this case the bpy ligand is at right angles to the C7–Ag1–C8 plane, N5–Ag1–C7 = 91.26°. On the other hand, whereas the Ag1–C distances are in the normal range, the bonds from the nitrogen atoms of the cyanide ligands to Ag2 are second-

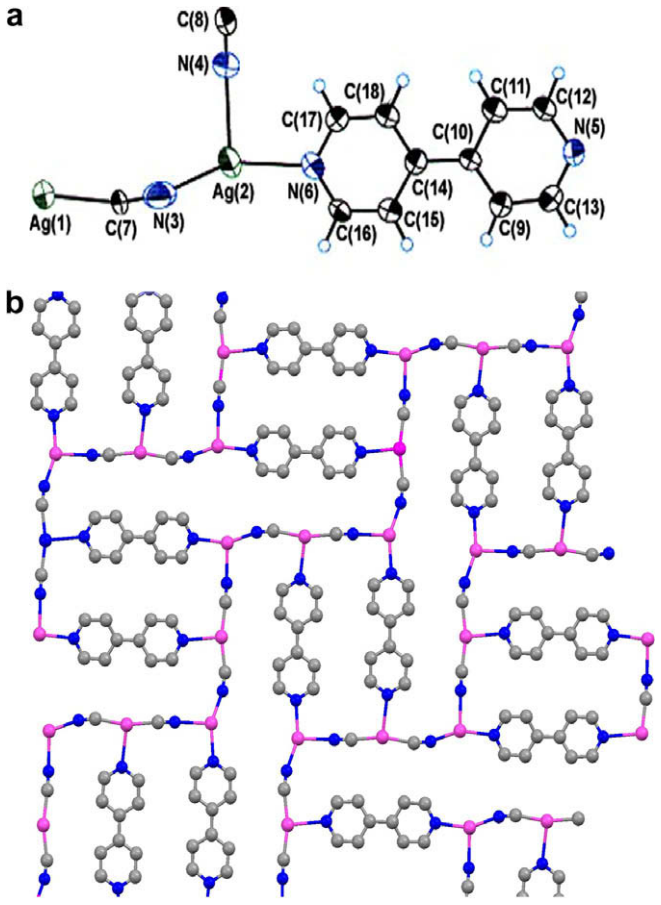


Fig. 1. (a) ORTEP plot of the asymmetric unit of **1**. (b) Structure of the 2D-layer of **1** along the diagonal of the unit cell. H-atoms have been omitted for clarity.

ary with a much longer range of distances, Ag2–N = 2.129–2.387 Å, while the Ag2–N6(bpy) bond is relatively strong with a distance equals to 2.249 Å. The extended structure of **1** consists of infinite puckered 1D-AgCN chains exhibiting a wave-like structure with a separation distance between the successive chains of 5.8093 Å, Fig. 1b. The wave-like appearance of the individual $[AgCN]_\infty$ chains results not only from the wide N(C)–Ag–C(N) angles at Ag1 and Ag2 (C7–Ag1–C8 = 164.85° and N3–Ag2–N4 = 110.43°) but also from the pronounced deviation from linearity for N3–C7–Ag1 = 163.3°, C7–N3–Ag2 = 166.0° and C8–N4–Ag2 = 161.7°. This deviation from linearity at the silver atoms in the $[AgCN]_\infty$ chains is in order to allow the coordination of the silver ions with the bidentate organodiimine ligand. These puckered chains are connected in a unique way by the bpy ligand via the Ag1 and Ag2 atoms creating corrugated 2D-layers with two types of fused rectangular rings; the first one consists of $Ag_8(CN)_6(bpy)_2$ with dimensions of 6.804 × 23.39 Å, while the second ring consists of $Ag_4(CN)_2(bpy)_2$ with dimensions of 6.526 × 12.142 Å, Fig. 1b. Analogous connectivity patterns in which infinite $[CuCN]_\infty$ chains are bridged by bpy have also been reported for [(CuCN)$_2$(μ-4,4′-bpy)], [{CuCN(μ-4,4′-bpy)}·2(μ-4,4′-bpy)] [8,10] and (CuCN)$_2$[(CuCN)$_2$(μ-4,4′-bpy)] [9]. Interestingly, only one type of hexagonal ring, $\{Cu_4(CN)_4(bpy)_2\}$, exists in the sheets forming the lamellar structure of [(CuCN)$_2$(μ-4,4′-bpy)], which differs however from those realized in **1**. Also, the layer's structure is stabilized by extensive H-bonding between the cyanide groups and hydrogen atoms of the bpy ligands, 2.583–3.056 Å, Table 2. The corrugated layers are arranged in parallel positions along the *b*-axis with a separation distance of almost 3.901 Å, creating channels, Fig. 2. These corrugated layers are interwoven along the *c*-axis causing stacking of the layers via interconnections of Ag–Ag interactions, Ag1–Ag2 = 3.2548 Å, meanwhile they are further packed by hydrogen bonding, N3–H18^d = 2.975 Å and C8–H15 = 3.056 Å, and π–π stacking, 3.120–3.379 Å, creating a novel 3D-network structure, Figs. 2 and 3. The Ag–Ag bonding interactions look like pillars between the layers. The argentophilic interaction as well as the close inter-layers Ag2–N5 and Ag1–N4 contacts of 3.120 and 3.236 Å, respectively, cause pyramidalisation of the silver atoms in such way that the angles of the planar trigonal geometry around the silver sites deviate significantly from 120° in spite of the sum of the angles being 360°, Table 2. Such behavior is also observed for Cu(I) in CuCN complexes [8].

3.1.2. Crystal structure of $[(AgCN)_3 \cdot (tbpe)_2 \cdot H_2O]$ (2)

The reaction of the ternary system $AgNO_3$, tbpe and KCN in H_2O/MeCN/NH_3 media affords yellow needle crystals of $[Ag_3(CN)_3(\mu\text{-tbpe})_2 \cdot H_2O]$, (**2**). One molecule of **2** comprises the asymmetric unit of the structure which consists of two independent fragments containing three chemically and crystallographically different Ag(I)

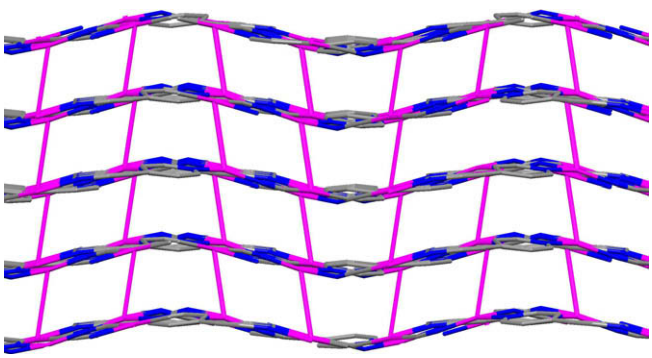


Fig. 2. 3D-dimensional structure of **1** showing the argentophilic interaction. H-atoms have been omitted for clarity.

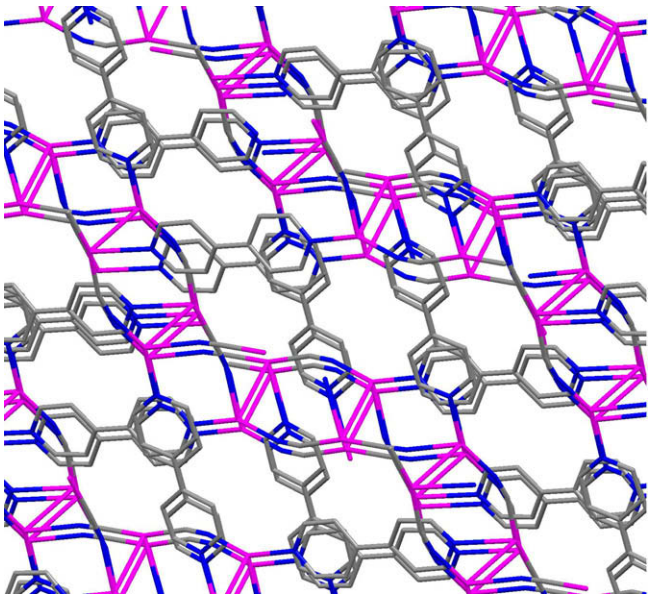


Fig. 3. 3D-structure of **1** along the *c*-axis showing the interwoven layers. H-atoms have been omitted for clarity.

atoms, Fig. 4a. The Ag(I) atoms are coordinated to ordered cyanide groups in a unique way representing the main building blocks of the structure of **2**. These building blocks form parallel ribbons connected by the tbpe ligands via silver atoms, Fig. 4b. Ag2 and Ag3 atoms are coordinated in tetrahedral fashion, while Ag1 atom exhibits a distorted planar trigonal configuration. Ag1 is strongly coordinated to two cyanide groups, Ag1–C31 = 2.076 Å, Ag1–C32 = 2.078 Å, and one nitrogen atom of the tbpe ligand, Ag1–N4 = 2.496 Å. The angles of the trigonal configuration at Ag1 assume a large deviation from the ideal value of 120° causing substantial pyramidal distortion which results essentially from the strong argentophilic interaction between Ag1 and Ag2, Table 3. The Ag2 atom exhibits a tetrahedral configuration via coordination to two cyanide groups and two tbpe ligands. On the other hand, the Ag3 atom assumes a strong coordination to the nitrogen atom of the tbpe ligand, Ag3–N25 = 2.211 Å, and to one cyanide group, Ag3–C26 = 2.062 Å, while it is weakly coordinated to the other cyanide groups that complete the distorted tetrahedral surroundings, Ag3–N33 = 2.716 Å, Ag3–N34 = 2.590 Å. The tetrahedral geometry around Ag3 is more distorted than that around Ag2 in consequence of the small chelate angles of 82.38° and 91.120°. In this case, two cyanide groups are asymmetrically bonded to three silver atoms, resulting in the μ_3-CN coordination mode forming a quadro minicycle $[Ag_2(\mu_3\text{-}CN)_2]$ motif, Fig. 5, similar to that found in the prototype CuCN coordination polymers [11].

Alternatively, the $(AgCN)_\infty$ building blocks create unusual parallel infinite ribbons which consist of fused hexagonal rings, $Ag_4(CN)_2$, with two double edge sides of the quadro minicyle $[Ag_2(\mu_3\text{-}CN)_2]$ motifs, Figs. 4b and 5. Surprisingly, the ribbons contain free terminal cyanide unit at Ag3, Ag3–C26–N27 = 176.0°. Four cyanide angles exhibit significant deviation from linearity, Ag2–N34–C32 = 132.8°, Ag2–N33–C31 = 148.6°, Ag3–N33–C31 = 118.0°, Ag3–N34–C32 = 132.5°, while the other Ag1–CN bonds are nearly linear, Table 3. The cyanide ligands turn out to be free of any disordered. **2** is the first example containing the minicycle $[Ag_2(\mu_3\text{-}CN)_2]$ motif, thus a comparison to CuCN complexes containing a similar type of the unusual minicycle $[Cu_2(\mu_3\text{-}CN)_2]$ motif is particularly pertinent. The minicycle $[Cu_2(\mu_3\text{-}CN)_2]$ motif is now realized as being the basic building block of an increasing number of 2D or 3D supramolecular assemblies [11,12]. The unusual character of the $[Cu_2(\mu_3\text{-}CN)_2]$ motif

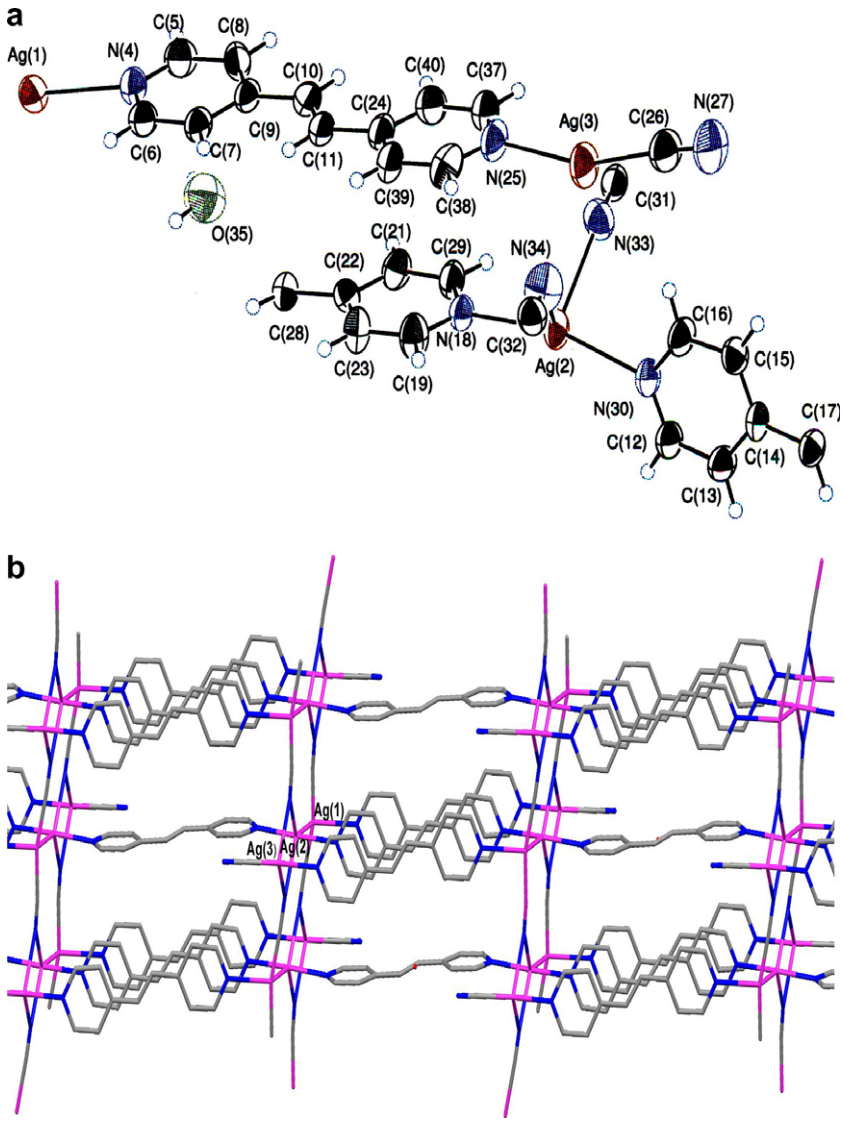


Fig. 4. (a) ORTEP plot of the asymmetric unit of **2**. (b) Structure of the layer of **2** along the *b*-axis showing the parallel ribbons. H-atoms have been omitted for clarity.

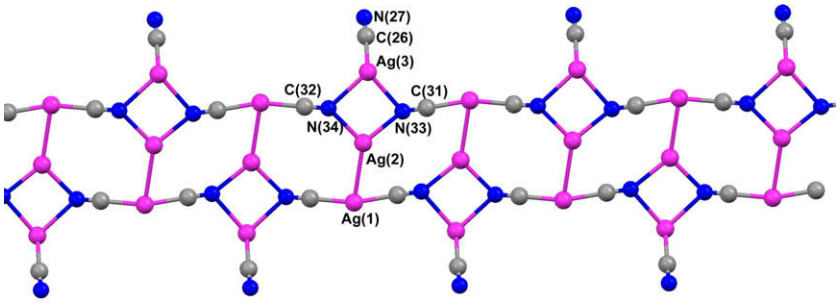
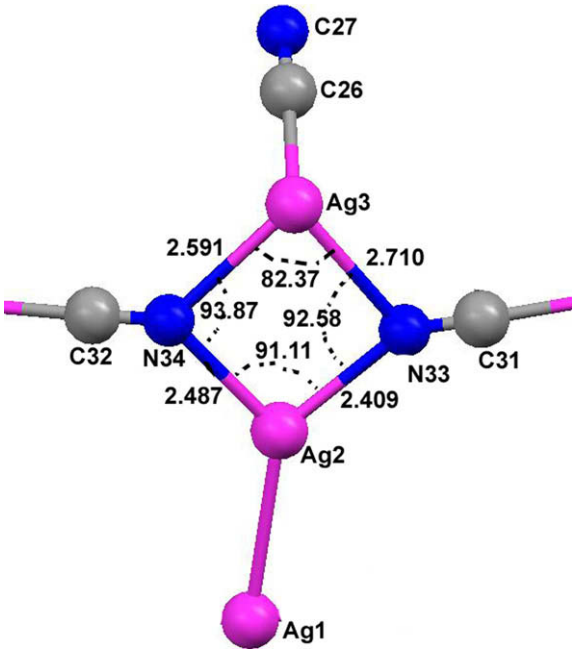


Fig. 5. View of the $(AgCN)_n$ ribbon showing the minicyclic $[Ag_2(\mu_3\text{-}CN)_2]$ motif along the *c*-axis.

comes from the fact that the carbon atoms bridge two copper atoms while the nitrogen atoms coordinate to one copper atom. In contrast, the nitrogen atoms in the $[Ag_2(\mu_3\text{-}CN)_2]$ motif act as μ_2-bridges, as should be expected. However, while the bifurcation of cyanide groups is no longer unusual, it greatly exceeds that in CuCN SCPs [12], while the Ag–N distances are not equal leading to the formation of a distorted rhombus with the sum of the internal angles being quite close to 360°, scheme 1. The bifurcated cyanide ligands can be considered as a consequence of the formation of the quadro minicycle $[Ag_2(\mu_3\text{-}CN)_2]$ motifs. Also, the $(AgCN)_\infty$ building blocks create a cluster-like structure consisting of three silver atoms exhibiting a strong Ag1–Ag2 interaction with a distance of 3.0145 Å and a weak Ag2–Ag3 interaction with a distance of 3.715 Å. Examples of weak Ag–Ag interactions with intermetallic distances from 3.40 to 3.724 Å are known [13]. The parallel ribbons are connected in a unique way by the tbpe molecules. One set of three nearly parallel tbpe



Scheme 1. Distorted $[Ag_2(\mu_3\text{-}CN)_2]$ rhombus in **2**.

ligands, with separation distances of 3.617–3.81 Å, and one tbpe ligand lying at right angles to the other ligands and to the plane defined by the $(AgCN)_n$ ribbon connect these ribbons in an alternate manner along the *a*-axis forming layers, Fig. 6. These layers contain polygons with dimensions of 9.843 × 14.602 Å. On the other hand, one type of the tbpe molecules fill the space of the hexagonal rings along the *c*-axis, alternatively one being vertical while the other one is horizontal, Fig. 7. The second type of tbpe ligands intermingle around both sides of the ribbon in horizontal positions while the terminal cyanide groups are directed to the space between the layers which form the 3D-network structure of **2**, Figs. 6 and 7. The structure of the layer is also stabilized by a wide range of intra-layer hydrogen bonding between the cyanide groups and the H-atoms of the pyridyl rings, 2.729–3.045 Å, Table 3. These parallel layers exhibit large channels in which water molecules thread, acting as guest molecules. The water molecules play an essential role in connecting the layers as they thread along the sides of the layers, H-bonding with the terminal cyanide groups belonging to one layer, tbpe ligand in the same layer and with the terminal cyanide groups of the adjacent layer, Table 3 and Fig. 6. This was further confirmed by TGA as SCP **2** starts decomposition by the loss of water molecules between 120 and 160 °C. The layers close packing was also achieved by weak but not negligible inter-layer hydrogen bonding, C37–H37^d = 3.061 Å and C26–H13 = 3.053 Å, as well as π–π stacking interactions between the pyridyl ring of tbpe from one layer and the ethylenic group from the adjacent layer, C10–C7 = 3.394 Å.

3.1.3. Crystal structure of $[(AgCN)_4 \cdot bpe]$ (3)

Half of the formula unit comprises the asymmetric unit of the structure of **3**, which contains two crystallographically different silver atoms, two cyanide groups and half of a bpe molecule, Fig. 8. Ag1 is coordinated to two ordered cyanide groups and to the nitrogen atom of the bpe ligand. Ag1 assumes a distorted trigo-

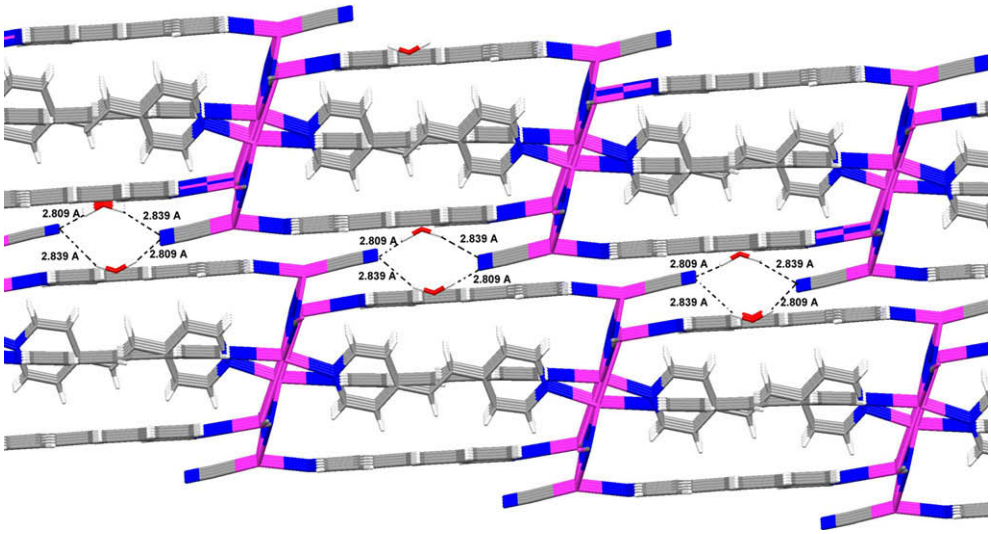


Fig. 6. View of packing of **2** along the *a*-axis showing H-bonding through water molecules.

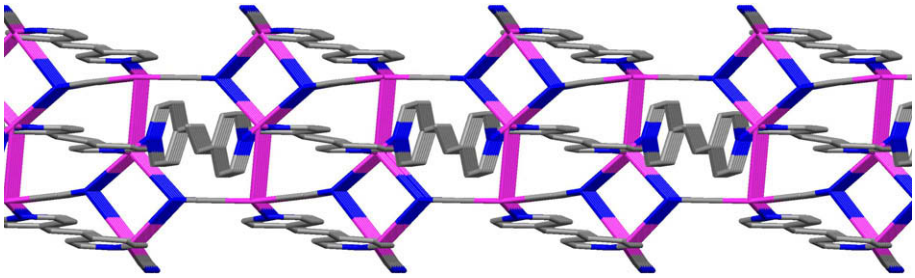


Fig. 7. View of one layer of **2** along the *c*-axis. H-atoms have been omitted for clarity.

nal planar geometry with the sum of bond angles equal to 360°, Table 4. The substantial pyramidal distortion of the essentially trigonal planar coordination sphere results mainly from the argentophilic interaction between Ag1 and Ag2, Table 4. Ag2 is coordinated to two disordered cyanide groups where it adopts a quasi-linear geometry, N(C)–Ag2–N(C) = 165.58°. This loss of linearity results from close Ag1–Ag2 and Ag2...C4 (3.031 Å) contacts.

The structure of **3** consists of two types of $(AgCN)_n$ chains, Fig. 9a and b. The first type, which runs in the ac-plane, is nearly linear and is composed of $\{Ag2–CN\}_n$ fragments. The second type, that runs along the *b*-axis, consists of corrugated chains of $\{Ag1CN\}_n$ and exhibits a wave-like structure with a separation distance between the chains of 11.132 Å. These chains are interconnected by the bpe ligands creating a 3D-network structure, while the two types of $(AgCN)_n$ chains are interconnected by the argentophilic interaction, Fig. 10. On the other hand, the 3D-structure is stabilized by extensive π–π stacking between the cyanide groups at both of the silver atoms and the pyridyl rings, 3.03 and 3.756 Å, and H-bonding between hydrogen atoms of the pyridyl rings and the cyanide groups at the silver atoms, 2.813, 3.159, 2.975 and 3.228 Å. The directions of propagation of the two chains are perpendicular to each other along the *a*-axis, Fig. 9b. The planes of the pyridyl rings are completely parallel in each set of the spacer ligands along the *b*-axis, while in the ac-plane each two sets of the spacer bpe ligands are interwoven in different conformations to accommodate a box-like structure of dimensions 9.161 × 11.132 Å, of intersecting $(AgCN)_n$ chains, Fig. 11.

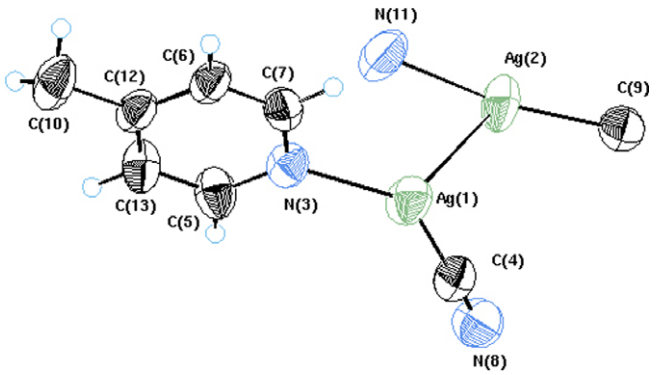


Fig. 8. ORTEP plot of the asymmetric unit of **3**.

3.2. Electronic absorption spectra and emission spectra of SCPs 1–3

The electronic absorption spectra of SCPs **1–3** display, generally, the absorption bands of the bipodal ligands in addition to the CT bands, Table 5. The bands due to $n–\pi^*$ transitions of the bipodal ligands disappear in the spectra of SCPs **1–3** due to the participation of the bipodal ligands in the coordination sphere of the silver(I) ions. The absorption spectra of SCPs **1** and **2** exhibit an additional broad band at 301–350 nm, respectively, corresponding to

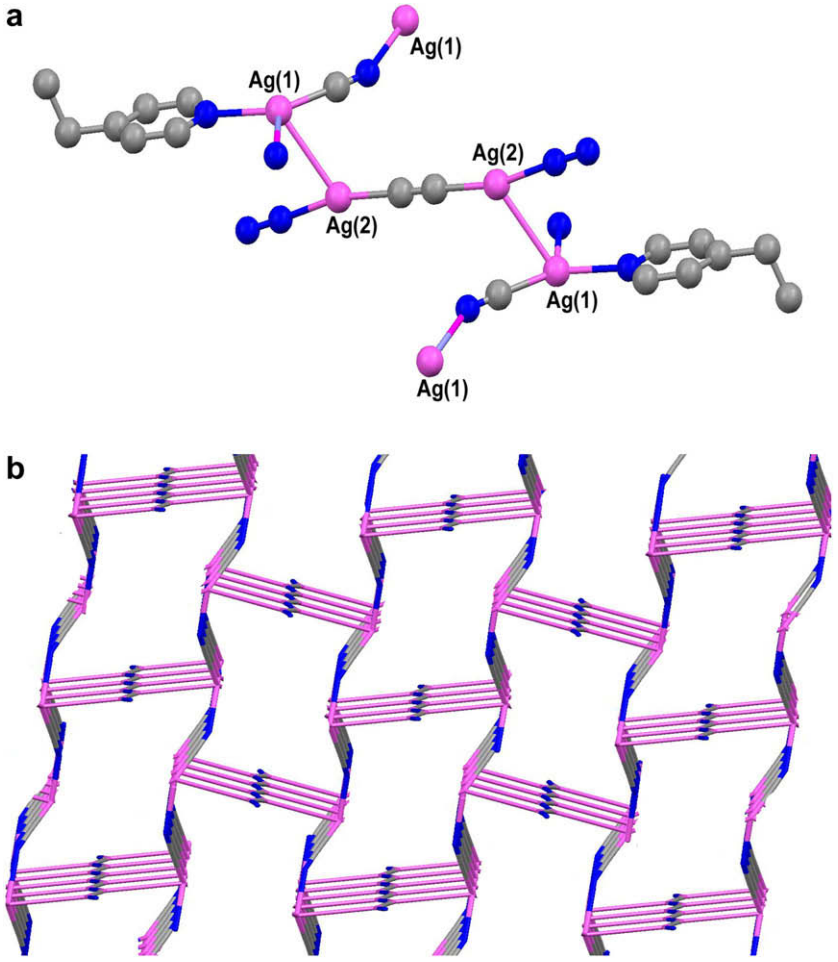


Fig. 9. (a) View of the basic building block of **3**. H-atoms have been omitted for clarity. (b) View of the connection of $(AgCN)_n$ chains in **3** to form a 3D-network, neglecting the bpe ligand.

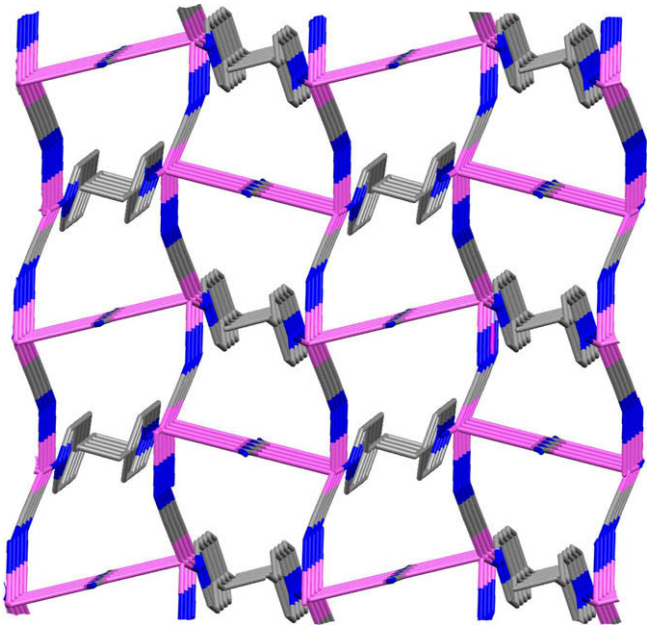


Fig. 10. View of the 3D-framework of **3** showing the argentophilic interaction. H-atoms have been omitted for clarity.

metalto-ligand charge transfer (MLCT), where the charge is transferred from the silver(I) center to the unoccupied π^*-orbital of the ligand. The emission spectra of the SCPs **1–3** together with the emission spectra of the bipodal ligands were measured in the solid state at room temperature and using the same excitation wavelength in each case, Fig. 12, Table 5. The emission spectra of the bipodal ligands display structural bands which correspond to the lowest (π–π^*) and close lying (n–π^*) states. On the other hand, the emission spectra of SCPs **1–3** display the structural bands of the bipodal ligands as well as additional bands at 600–640 nm, 584–624 nm and 600 nm, respectively. These bands may be attributed to MLCT or metal centered transitions of the type $4d^{10} \rightarrow 4d^9\,5s^1$ and $4d^{10} \rightarrow 4d^9\,5p^1$ on the silver(I) center. The emission spectra of SCPs **1–3** exhibit a slight red shift compared to those of the corresponding ligands, whereas the intensities of the bands of SCPs **2** and **3** increase significantly from those of the ligands.

3.3. Thermogravimetric analysis of SCPs *1–3*

The thermal decomposition bahaviour of SCPs **1–3** show broad similarity, but they are not identical, Table 6. They show the usual trend of similar early reported compounds [14]. Firstly dehydration occurs, followed by loss of the bipodal ligand and finally removal of the inorganic anions. After complete thermolysis the calculated and observed percentages of the residues are coincident with metallic silver. The loss of water molecules at 120–160 °C, for SCP **2**, confirms the involvement of the water molecules in hydrogen bonding with the cyanide groups, as depicted in the crystal structure (vide supra). The cyanide groups are lost in the form of cyanogen molecules at relatively high temperatures, indicating the bridging capability of the cyanide groups forming stable $(AgCN)_n$ frameworks.

4. General discussion

The SCPs **1–3** illustrate the rich diversity of structures that can be achieved by variation of the spacer bipodal ligand. The length and the molecular conformation of the spacer ligands affect significantly the self-assembly of the $(AgCN)_n$ building blocks to produce enough wide space to accommodate the spacer ligands via the formation of different rings and polygons. The bipodal ligands play the role of bridging the $(AgCN)_n$ building blocks creating 2D-layers which are interwoven, **1** and **2**, or intersecting, **3**, to produce 3D-structures via extensive H-bonding and π–π stacking, as well as Ag···Ag interactions. The structures of **1** and **2** are completely different from those of the analogous $[(Cu_2(CN)_2(\mu\text{-}4,4'\text{-bpy})]$, **1′** and $[(CuCN)_2(\mu\text{-tbpe})]$, **2′**. **1** exhibits an interwoven but non-interpenetrating open framework while **1′** contains two identical non-intersecting but interpenetrating frameworks with a rhombic (Cu_2X_2) motif. In spite of both **2** and **2′** containing the minicycle (Cu_2X_2) and (Ag_2N_2) motifs, **2′** contains large void spaces in the framework which results in interpenetration by a second independent framework, while **2** contains a cluster-like structure of $(AgCN)_n$ ribbons which are connected in a unique way by the tbpe ligands creating

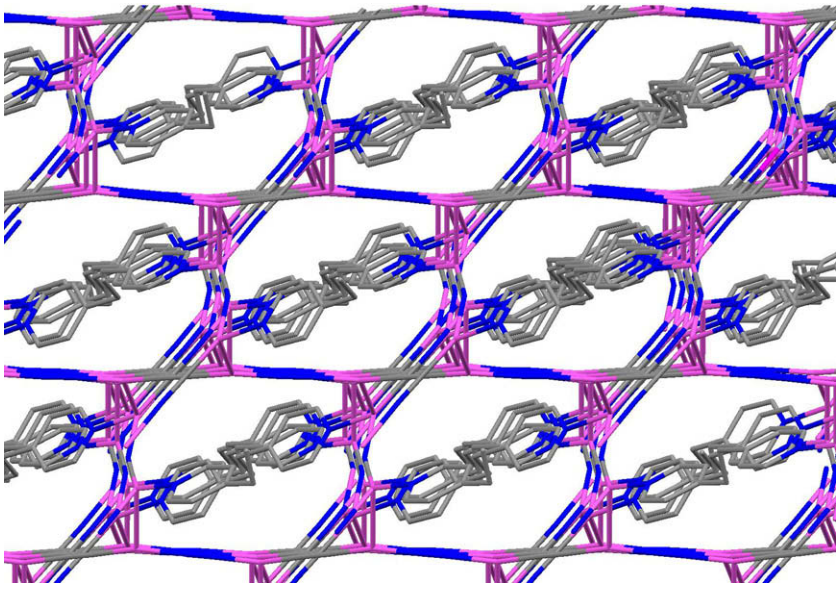


Fig. 11. View of the box-like structure in **3**.

Table 5
Absorption and emission bands for bpy, tbpe, bpe and SCPs **1**–**3**.

	Ligand				SCP			
	λabs (nm)	Assignment	λem (nm)		λabs (nm)	Assignment	λem (nm)
bpy	218	^1L_a	400	**1**	220	^1L_a	405
	278	^1L_b	452		255	^1L_b	428
	390	$n-\pi^*$	481		301	CT	454
			516				484
			660				525
							600
							640
tbpe	232	^1L_a	390	**2**	220	^{1}La	433
	265	^1L_b	478		252	^1L_b	454
	325	$n-\pi^*$	529		350	CT	485
	450	$n-\pi^*$					524
							584
							624b
bpe	201	^1L_a	401	**3**	201	^1L_a	405
	258	^1L_b	432		268	^1L_b	425
	315	$n-\pi^*$	452				444
	392		482				487
			522				527
			600				600b

* b = Broad.

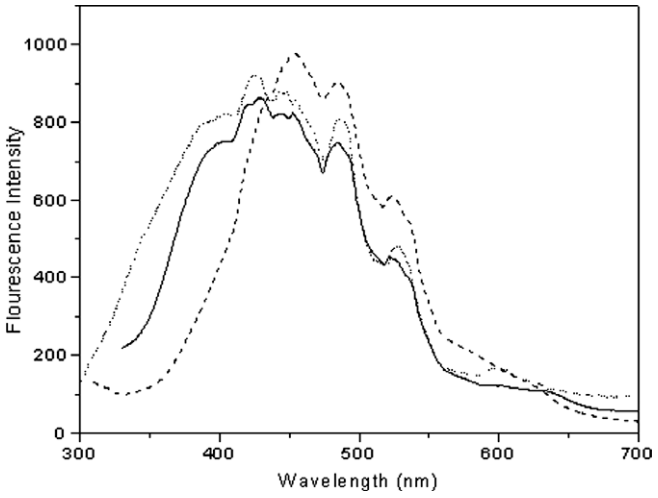


Fig. 12. Emission Spectra of SCPs **1**–**3**; **1** (solid line), **2** (dashed line), **3** (doted line), (λ_{ex} is 320 nm for **1**, 300 nm for **2** and 270 nm for **3**).

a non-interpenetrating 3D-network with terminal cyanide ligands and threaded water molecules. The unprecedented structure of **3** consists of intersecting $(AgCN)_n$ chains forming a box-like structure with wide voids containing the interwoven bridging bpe ligands. In **1** and **2**, the Ag1–Ag2 and Ag1–N4 (in **1**) and Ag2–C4 (in **2**) contacts produce a distorted geometry at the silver sites. The coordination versatility of the silver atom is also in evidence as quasi-linear, [AgNC], distorted trigonal planar, [AgN_3], [AgC_2 N], [AgN_2C], and tetrahedral [AgN_4], [AgN_3C] geometries have been observed, in addition to the influence of the argentophilic interaction on the distortion of the geometry around the silver sites.

5. Conclusion

The results reinforce the observation that the cyanide group is an effective bridging ligand which can link together two or three silver centers, μ_2-1,2-CN or μ_3-1,2,2-CN. Ligand length and flexibility affect the AgCN–ligand ratio, where the proportion of the ligand decreases as the length and flexibility of the ligand increase. It is also clear that the organic ligands may be introduced as structural components of composite inorganic–organic materials and used, in addition to conventional and unconventional interactions, to propagate 3D-topologies.

Appendix A. Supplementary data

CCDC 682258, 682259 and 682260 contain the supplementary crystallographic data for **1**, **2** and **3**. These data can be obtained free of charge via http://www.ccdc.cam.ac.uk/conts/retrieving.html, or from the Cambridge Crystallographic Data Centre, 12 Union Road, Cambridge CB2 1EZ, UK; fax: (+44) 1223 336 033; or e-mail: deposit@ccdc.cam.ac.uk. Supplementary data associated with this article can be found, in the online version, at doi:10.1016/j.poly.2008.12.053.

Table 6
Thermogravimetric analysis data for SCPs **1**–**3**.

Comp.	First step			Second step			Third step			Residue		
	Trans. temp. (°C)	Δm% obs. (cal.)	Assig. (%)	Trans. temp. (°C)	Δm% obs. (cal.)	Assig. (%)	Trans. temp. (°C)	Δm% obs. (cal.)	Assig.	Form. Temp. (°C)	Δm% obs. (cal.)	Assig. (%)
1	150–300	36.5 (36.8)	1 bpy	380–480	6.00 (6.13)	0.5 $(CN)_2$	500–700	7.0 (6.13)	0.5 $(CN)_2$%	700	50.5 (50.1)	2 Ag
2	120–160	2.19 (2.20)	1 H_2O	170–360	45.84 (46.4)	2 tbpe	450–730	9.00 (9.9)	1.5 $(CN)_2$%	750	42.9 (41.2)	3 Ag
3	150–300	26.1 (25.6)	1 bpe	320–600	13.8 (14.4)	2 $(CN)_2$				620	60.1 (59.9)	4 Ag

References

[1] P. Ball, Nature 371 (1994) 202;
J.W. Steed, D.R. Turner, K.J. Wallace, Core Concepts in Supramolecular Chemistry and Nanochemistry, John Wiley and Sons Ltd., 2007. (Chapter 1).

[2] W.-P. Wu, Y.-Y. Wang, C.-J. Wang, Y.-P. Wu, P. Liu, Q.-Z. Shi, Inorg. Chem. Commun. 9 (2006) 645;
A.T. Blanke, N.R. Champness, P. Hubberstey, W.S. Li, M.A. Withersby, M. Schröder, Coord. Chem. Rev. 183 (1999) 117;
H.L. Zhu, Y.X. Tong, X.M. Chen, J. Chem. Soc., Dalton Trans. (2000) 4182–4186;
L. Zhang, X.-Q. Lü, C.-L. Chen, H.-Y. Tan, H.-X. Zhang, B.-S. Kang, Cryst. Growth Des. 5 (2005) 283;
G.A. Bowmaker, Effendy, S. Marfuah, B.W. Skelton, A.H. White, Inorg. Chim. Acta 358 (2005) 4371.

[3] M.L. Tong, X.M. Chen, B.H. Ye, L.N. Ji, Angew. Chem. Int. Ed. 38 (1999) 2237;
M.L. Tong, X.M. Chen, S.W. Ng, Inorg. Chem. Commun. 3 (2000) 436;
M.L. Tong, S.L. Zheng, X.M. Chen, Chem Eur. J. 6 (2000) 3729;
S. Hamamci, V.T. Yilmaz, W.T.A. Harrison, J. Mol. Struct. 734 (2005) 191;
D.J. Eisler, R.J. Puddphatt, Cryst. Growth Des. 5 (2005) 57.

[4] H.-B. Zhou, W. Dong, M. Liang, D.-Z. Liao, Z.-H. Jiang, S.-P. Yan, P. Cheng, Z. Anorg. Allg. Chem. 630 (2004) 498;
F.B. Stocker, D. Britton, V.C. Young, Inorg. Chem. 39 (2000) 3479.

[5] T. Pretsch, H. Hartl, Inorg. Chim. Acta 358 (2005) 1179;
J.-D. Lin, Z.-H. Li, J.-R. Li, S.-W. Du, Polyhedron 26 (2007) 107;
A.A. Isab, M.I.M. Wazeer, M. Fettouhi, B.A. Al-Maythalony, A.R. Al-Arfaj, N.O. Al-Zamil, Inorg. Chim. Acta 360 (2007) 3719;
G.A. Bowmaker, Effendy, P.C. Junk, B.W. Skelton, A.H. White, Z. Naturforsch. 59b (2004) 1277.

[6] G.A. Bowmaker, B.J. Kennedy, J.C. Reid, Inorg. Chem. 37 (1998) 3968.

[7] C.-X. Ren, H.-L. Zhu, G. Yang, X.-M. Chen, J. Chem. Soc., Dalton Trans. (2001) 85–90;
N.K. Mills, A.H. White, J. Chem. Soc., Dalton Trans. (1984) 229;
H. Krautscheid, N. Emig, N. Klaassen, P. Seringer, J. Chem. Soc., Dalton Trans. (1998) 3071;
G.A. Bowmaker, Effendy, B.W. Skelton, N. Somers, A.H. White, Inorg. Chim. Acta 358 (2005) 4307;
C.-X. Ren, B.-H. Ye, W.-H. Feng, X.-M. Chen, S.W. Ng, Acta Crystallogr. E60 (2004) 652.

[8] D.J. Chesnut, D. Plewak, J. Zubieta, J. Chem. Soc., Dalton Trans. (2001) 2567.

[9] S.J. Hibble, A.M. Chippindale, Z. Anorg. Allg. Chem. 631 (2005) 542.

[10] O. Teichert, W.S. Sheldrick, Z. Anorg. Allg. Chem. 626 (2000) 1509.

[11] F.B. Stocker, T.P. Staeva, C.M. Rienstra, D. Britton, Inorg. Chem. 38 (1999) 984;
D. Britton, F.B. Stocker, T.P. Staeva, Acta Crystallogr. C55 (1999) 2014;
H. Hanika-Heidl, S.H. Etaiw, M. Sh. Ibrahim, A.S. Badr El-din, R.D. Fischer, J. Organomet. Chem. 684 (2003) 329;
B. Liu, L. Xu, G.-C. Guo, J.-S. Huang, Inorg. Chem. Commun. (2005) 796.

[12] N.S. Persky, J.M. Chow, K.A. Poschmann, N.N. Lacuesta, S.L. Stoll, Inorg. Chem. 40 (2001) 29;
X. He, C.-Z. Lu, C.-D. Wu, L.-J. Chen, Eur. J. Inorg. Chem. (2006) 2491.

[13] B. Wu, X.-T. Wu, X. Tian, W.-H. Sun, J. Organomet. Chem. 640 (2001) 57;
P. Chiu, C.Y. Chen, J.Y. Zeng, C.Y. Lu, H.M. Lee, J. Organomet. Chem. 690 (2005) 1682.

[14] L. Triščiková, I. Potočňák, J. Chomic, T. Müller, Themochim. Acta 419 (2004) 231.

aqueous interactions and ensuing chemistry of Ni(II) with the α-hydroxycarboxylate binder D-(−)-quinic acid. This chemistry is expected to (a) enlighten the type and nature of interactions emerging into the structural speciation of the requisite binary Ni(II)–hydroxycarboxylate cellular systems, and (b) provide insight into the chemical and physical properties on new Ni(II) species emerging as potential metallo(bio)targets in cellular physiology or toxicity. To this end, we, herein, report on the pH-specific synthesis, spectroscopic and structural characterization, and magnetic susceptibility studies of a new binary Ni(II)–quinate species $Na[Ni(C_7H_{11}O_6)_3] \cdot 2.75H_2O$ **(1)** closely tied to the aqueous speciation of the binary system and its significance in Ni(II) biologically relevant chemistry.

2. Experimental

2.1. Materials and methods

All manipulations were carried out under aerobic conditions. $NiCl_2 \cdot 6H_2O$ and D-(−)-quinic acid (purity 98%) were purchased from Fluka. Nano-pure quality water was used for all reactions run. NaOH and NaCl were supplied by Fluka.

2.2. Physical measurements

FT-IR measurements were taken on a 1760X FT-IR spectrometer from Perkin–Elmer, using KBr pellets. UV–Visible measurements were carried out on a Hitachi U2001 spectrophotometer in the range from 190 to 1000 nm. A ThermoFinnigan Flash EA 1112 CHNS elemental analyzer was used for the simultaneous determination of carbon and hydrogen (%). The analyzer is based on the dynamic flash combustion of the sample (at 1800 °C) followed by reduction, trapping, complete GC separation and detection of the products. The instrument is (a) fully automated and controlled by PC via the Eager 300 dedicated software and (b) capable of handling solid, liquid or gaseous substances. Magnetic susceptibility data were collected on powdered samples of **1** with a Quantum Design SQUID susceptometer in the 2–300 K temperature range, under various applied magnetic fields. Magnetization measurements were carried out at three different temperatures in the field range 0–5 T.

2.3. pH-potentiometric measurements

The protonation constants of quinic acid were determined by pH-potentiometric titrations of 30.0(1) ml samples in the pH range 2.8–11.4 under a purified argon atmosphere. The concentration of quinic acid was in the range of 1.3–5.0 mmol dm^{-3}. The stability constants of the Ni(II) complexes of quinic acid were determined by pH-potentiometric titrations of 30.0(1) ml samples in the pH range 2.4–8.7 under a purified argon atmosphere. Precipitation was observed at pH ~8.7, as in the case of the aqueous binary system of Co(II) with 2′-deoxyguanosine 5′-monophosphate [9].

All solutions were prepared using Fluka reagent grade quinic acid, $NiCl_2 \cdot 6H_2O$, and ultra-pure deionized water. The purity of quinic acid and the exact concentration of quinate and Ni(II) solutions, were determined by the Gran method [10–12]. The exact concentration of Ni(II) was checked by EDTA complexometric titrations as previously described [13]. The ionic strength was adjusted to 0.15 M with NaCl. The temperature was maintained at 25.0 ± 0.1 °C during the measurements. The titrations were carried out with a carbonate-free NaOH solution of known concentration (ca. 0.15 M). The base solution was prepared following a standard procedure: NaOH pellets were dissolved in nano-pure quality water under an argon atmosphere. Carbon dioxide was removed from water by boiling and cooling under a stream of purified argon. The NaOH solution was standardized using potassium hydrogen iodate ($KH(IO_3)_2$). The nickel concentration was 1.0 mM, and the employed metal:ligand ratios were 1:2, 1:3, and 1:4. In order to collect solution data at pH values lower than 3.0, a known amount of nitric acid was initially added. The pH was measured with a computer-controlled Crison titration system elaborated for titrations at such low concentrations [14] and a Mettler Toledo-Inlab 412 combined glass-electrode, calibrated for hydrogen ion concentration according to Irving et al. [15] by using the GLEE program [16]. The ionic product of water was found to be $pK_w = 13.76$ [17].

The one step protonation constants of quinic acid are given as $\log K_1$, consistent with the equilibrium $L^- + H^+ \rightleftarrows HL$, where $K_1 = [HL]/[L^-] \rightleftarrows [H^+]$. The stepwise protonation constants of quinic acid are given as $\log K_n$, consistent with the equilibrium $H_{n-1}L + H \rightleftarrows H_nL$, where $K_n = [H_nL]/[H_{n-1}L]\,[H]$. The initial computations were obtained in the form of overall protonation constants $\beta_n = [H_nL]/[L]\,[H]^n$, taking into account that $\beta_n = \prod K_n$. The concentration stability constants $\beta_{pqr} = [M_pL_qH_r]/[M]^p[L]^q[H]^r$ for quinic acid were calculated with SUPERQUAD [18], and those for Ni(II)–quinate complexes, arising in the investigated system, with the PSEQUAD computer program [19]. The pH-dependent species distribution curves and simulated titration curves were derived from the overall formation constants measured with the program HYSS [20].

Formation of Ni(II)–hydroxo complexes was taken into consideration in the employed calculations leading to the most plausible speciation model. The hydroxo species considered include the following: (a) $[NiH_{-1}]^+$ ($\log\beta_{1-1} = -9.74$), (b) $[Ni_2H_{-1}]^{3+}$ ($\log\beta_{2-1} = -9.6$), and (c) $[Ni_4(OH)_4]^{4+}$ ($\log\beta_{4-4} = -27.4$). Relevant information on the above species was taken from Plyasunova et al. [21] and corrected for an ionic strength of 0.15 M by use of the Davies equation [22].

2.4. Synthesis of sodium [tris(quinato)nickel(II)] hydrate: $Na[Ni(C_7H_{11}O_6)_3] \cdot 2.75H_2O$ (**1**)

$NiCl_2 \cdot 4H_2O$ (0.50 g, 2.1 mmol) and D-(−)-quinic acid (0.80 g, 4.2 mmol) were placed in a 25 mL round bottom flask and dissolved in 6 mL of water. The reaction mixture was then stirred at room temperature until both reactants were completely dissolved. Subsequently, the pH of the clear solution was adjusted to 5.5 with NaOH. The resulting reaction mixture was placed in the refrigerator at 4 °C and ethanol was added. Four months later, green crystalline material appeared on the bottom of the flask. The crystalline product was isolated by filtration and dried in vacuo. Yield 0.62 g (36%). *Anal.* Calc. for **1**, $Na[Ni(C_7H_{11}O_6)_3] \cdot 2.75H_2O$ ($C_{21}H_{38.50}O_{20.75}NaNi$, MW = 704.47): C, 35.7; H, 5.5. Found: C, 35.0; H, 5.8%.

2.5. X-ray crystal structure determination

X-ray quality crystals of compound **1** were grown from reaction mixtures upon addition of ethanol. A single crystal with dimensions 0.50 × 0.30 × 0.20 mm (**1**) was mounted on the tip of a glass fiber with epoxy glue. Single crystal analysis was carried out on a Bruker AXS SMART 1K CCD area detector diffractometer. The frame data were acquired at room temperature using the SMART-NT software and Mo Kα radiation ($\lambda = 0.71073$ Å) [23]. A total of 1325 45-s frames were collected in three sets with 0.3° ω-scan. The collected frames were then processed using the SAINT-NT software [24] to provide the *hkl* file corrected for Lorentz and polarization effects. An empirical absorption correction was applied through the program SADABS [23]. The structure was solved by direct methods using the SHELX-90 program and refined by least-squares methods on F^2, SHELXTL-93, incorporated in SHELXTL, Version 5.1 (Table 1) [25].

Table 1
Summary of crystal, intensity collection and refinement data for Na[Ni-($C_7H_{11}O_6$)$_3$] · 2.75H_2O (1).

Formula	$C_{21}H_{38.50}O_{20.75}NaNi$
Formula weight	704.47
T (K)	293(2)
Wavelength	Mo Kα 0.71073
Space group	$P2_12_12_1$
a (Å)	15.330(3)
b (Å)	15.453(3)
c (Å)	16.660(3)
β (°)	90.00
V (Å^3)	3946.9(11)
Z	4
D_{calc}/D_{measd} (Mg m^{-3})	1.186/1.89
Absorbtion coefficient (μ) mm^{-1}	0.570
Range of h, k, l	−18 → 18, −17 → 19, −12 → 20
Goodness-of-fit on F^2	1.147
R indices[a]	R = 0.0653, R_w = 0.2038[b]

[a] R values are based on F values, R_w values are based on F^2. $R = \frac{\sum||F_0|-F_c||}{\sum(|F_0|)}$, $R_w = \sqrt{\sum[w(F_0^2 - F_c^2)^2]/\sum[w(F_0^2)^2]}$.

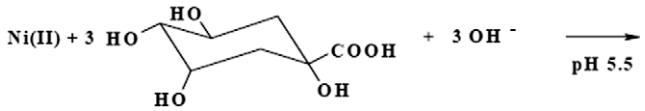
[b] For 7735 reflections with $I > 2\sigma(I)$.

All non-hydrogen atoms were refined anisotropically. Hydrogen atoms on carbon atoms were geometrically positioned and left riding on their parent atoms during structure refinement. Hydrogen atom positions, which belong to oxygen atoms, were first determined from E-maps, brought to reasonable distances from their parent oxygen atoms, and then fixed. The disordered oxygen-atoms of water were left as such (nascent form). The final assignment of hydrogen atoms satisfies the electroneutrality of compound **1**, with the understanding that Ni ions are formally in the +2 oxidation state. The associated CCDC reference number is 644650. Selected crystallographic data appear in Table 1. Further crystallographic details for **1**: $2\theta_{max}$ = 52°; reflections collected/unique/used, 23772/7735 [R_{int} = 0.0471]; 415 parameters refined; $[\Delta\rho]_{max}/[\Delta\rho]_{min}$ = 0.917/−0.399 e/Å^3; R/R_w (for all data), 0.0841/0.2127.

3. Results

3.1. Synthesis

Complex **1** was synthesized through a simple reaction between Ni(II) and D-(−)-quinic acid in a 1:2 molar ratio and isolated by addition of ethanol to the reaction mixture. The presence of NaOH helped to adjust the pH of the reaction mixture, while concurrently providing the appropriate counter ions to balance the arisen charge on the Ni(II)–quinate assembly (vide infra). The same reaction run with a Ni(II):quinic acid a 1:3 molar ratio led to a material identical to **1** by virtue of its FT-IR signature (yield 33%). A major advantage, however, of this reaction was that the crystalline product was obtained faster than that of the 1:2 Ni(II):quinic acid ratio. The stoichiometric reaction leading to the formation of compound **1** is shown below (Reaction 1):



D-(-)-quinic acid

$[Ni(C_7H_{11}O_6)_3]^-$ + 3 H_2O Reaction 1

Elemental analysis of the isolated green-colored crystalline material and FT-IR spectroscopy suggested the molecular formula Na[Ni-($C_7H_{11}O_6$)$_3$] · 2.75H_2O for **1**. Confirmation came from the X-ray crystallographic determination of its structure. Compound **1** is soluble in water, but insoluble in common organic solvents. Crystalline **1** is stable in the air at room temperature for long periods of time.

3.2. Description of X-ray crystallographic structure

Compound **1** emerges from a crystal lattice composed of discrete anionic Ni(II) complexes and Na^+ counter ions. The structure diagram for complex **1** is shown in Fig. 1. A list of selected bond distances and angles for **1** is given in Table 2. Complex **1** crystallizes in the orthorhombic space group $P2_12_12_1$ with four molecules per unit cell. The X-ray crystal structure of **1** reveals a Ni(II) assembly, with three quinate ligands coordinating to the metal ion through the alcoholic and carboxylate oxygens O(1) and O(5), O7 and O11, and O13 and O17, respectively. Each bound ligand is singly deprotonated, with the site of deprotonation being the carboxylic acid group. The three bound quinates formulate a distorted octahedral environment around Ni(II). Unlike other metal ions (e.g. Mn(II)) bound to the quinate ligand, the Ni(II) ion bears quinate ligands, the terminal alcoholic moieties of which do not participate in coordination to abutting metal ions in the crystal lattice of the title compound lattice.

The Ni–O bond distances are in the range from 2.009(4) to 2.069(4) Å for **1**, which are comparable with those in complexes, $(NH_4)_2[Ni_2(C_6H_5O_7)_2(H_2O)_4]_2 \cdot 2H_2O$ (2.020(3)–2.074(2) Å) (**2**) [26], $K_2[Ni(C_6H_5O_7)_2(H_2O)_4] \cdot 4H_2O$ (2.036(3)–2.125(3) Å) (**3**) [27], $[Ni(C_4H_4O_5)(H_2O)] \cdot H_2O$ (2.034(5)–2.101(5) Å) (**4**), $[Ni(C_4H_4O_5)(H_2O)(C_{12}H_8N_2)]$ (2.032(3)–2.048(3) Å) (**5**) [28], and $[(N(CH_3)_4)_5[Ni_4(C_6H_4O_7)_3(OH)(H_2O)] \cdot 18H_2O]_2$ (1.95(1)–2.12(1) Å) (**6**) [29].

The angles are in the range 77.99(15)–102.76(19)° for complex **1** and similar to those observed in (81.53(9)–96.7(2)°) (**2**), (86.8(1)–95.2(1)°) (**3**), (81.1(2)–95.0(2)°) (**4**), (89.2(2)–95.1(2)°) (**5**), (76.5(4)–102.1(4)°) (**6**), and also similar to those in the quinate organic–inorganic hybrid $[Mn_2(C_7H_{11}O_6)_4]_n \cdot nH_2O$ (69.56(15)–96.75(17)° and 73.02(13)–95.41(15)°, respectively) [30].

The octahedral Ni(II) ion in **1** correlates well with other octahedral divalent metal ions such as Zn(II) [31], Cu(II) [32], and Ni(II) [25], in analogous octahedral species bearing citrates. The M–O distances observed in those complexes are in line with those seen

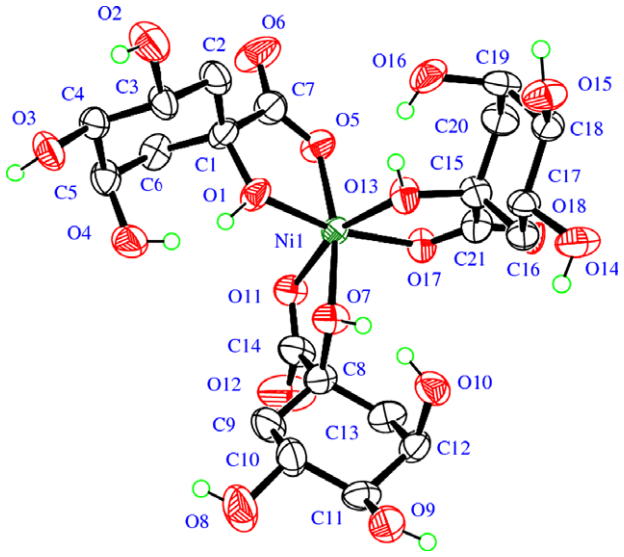


Fig. 1. The structure of the anionic assembly in Na[Ni($C_7H_{11}O_6$)$_3$]·2.75H_2O (**1**) with the atom-labeling scheme (50% thermal probability ellipsoids).

Table 2
Bond lengths (Å) and angles (°) in **1**.

Distances			
Ni(1)–O(1)	2.039(4)	Ni(1)–O(11)	2.041(4)
Ni(1)–O(5)	2.009(4)	Ni(1)–O(13)	2.069(4)
Ni(1)–O(7)	2.031(4)	Ni(1)–O(17)	2.005(4)
Angles			
O(17)–Ni(1)–O(5)	94.62(18)	O(7)–Ni(1)–O(11)	79.58(17)
O(17)–Ni(1)–O(7)	98.70(19)	O(1)–Ni(1)–O(11)	102.76(19)
O(5)–Ni(1)–O(7)	166.49(18)	O(17)–Ni(1)–O(13)	77.99(15)
O(17)–Ni(1)–O(1)	165.95(18)	O(5)–Ni(1)–O(13)	98.3(2)
O(5)–Ni(1)–O(1)	79.16(16)	O(7)–Ni(1)–O(13)	86.78(18)
O(7)–Ni(1)–O(1)	88.32(17)	O(1)–Ni(1)–O(13)	90.36(17)
O(17)–Ni(1)–O(11)	90.52(17)	O(11)–Ni(1)–O(13)	160.67(17)
O(5)–Ni(1)–O(11)	98.10(19)		

in **1** and range from 2.052(2) to 2.164(2) Å (Zn(II)) and from 2.021(3) to 2.072(3) Å (Ni(II)), while a wider range due to Jahn–Teller distortion is observed in the copper analog (1.969(3)–2.341(3) Å). Equally comparable are the M–O distances with those occurring in the congener quinate compounds $[Zn(C_7H_{11}O_6)_2]$ [33], $[Cd(C_7H_{11}O_6)_2]\cdot H_2O$, $[Cu(C_7H_{10}O_6)(H_2O)]_2(H_2O)_2$ [34], $\{[Cu(NO_3)(C_7H_{11}O_6)(H_2O)]\cdot 2H_2O\}_n$, $\{[CuCl(C_7H_{11}O_6)(H_2O)]\cdot H_2O\}_n$ [35], $[Pt(C_6H_{14}N_2)(C_7H_{10}O_6)]$ [36], and the trinuclear $(NH_4)_2\{[V(O)_2]_2[V(O)](\mu\text{-}C_7H_{10}O_6)_2\}\cdot H_2O$ [37].

In the lattice structure, the Na^+ ions counterbalance efficiently the anionic charge. They are in contact with the alcoholic oxygens of the quinate anion at distances in the range of 2.344(6)–2.423(5) Å (six contacts) (Fig. 2B). The crystal structure of **1** is composed of an infinite 3D network, where quinate ligands bridge each Ni-atom with its three neighboring Na-atoms. The three Na-atoms define a triangle, with the Ni-atom located above its center and the Ni–Na distance in the range 8.083(3)–8.096(3) Å (Fig. 2A). Each Na^+ ion is bound to three quinates, all originating from different $[Ni(C_7H_{11}O_6)_3]^-$ units.

3.3. UV–Visible spectroscopy

The UV–Visible spectrum of **1** was recorded in water (Fig. S1). The spectrum exhibits peaks at λ_{max} 725 (ε 2 M^{-1} cm^{-1}) and 662 nm (ε 2 M^{-1} cm^{-1}), and a distant shoulder around 395 nm rising into the UV. The absorption feature around 395 nm (ε 6 M^{-1} cm^{-1}) could be tentatively attributed to the $^3A_{2g} \rightarrow {}^3T_{1g}(P)$ transition. The observed multiple structure containing the 725 and 662 nm features, a region normally corresponding to the $^3A_{2g} \rightarrow {}^3T_{2g}$ transition, is in line with literature reports invoking the presence of an ^1E_g state lying so close to $^3T_{2g}$ that extensive mixing takes place. That mixing leads to the observation of a doublet band, where the spin forbidden transition picks up intensity from the spin-allowed transition, thus accounting for the complexity of the spectrum [38]. The spectrum bears similar features to that of $[Ni(H_2O)_6]^{2+}$ ion, signifying the effect of the O-containing ligands in the electronic structure of Ni(II).

3.4. FT-IR spectroscopy

The FT-IR spectrum of **1** exhibits strong absorptions for the carbonyls of the carboxylate groups in both the antisymmetric and symmetric vibration regions. The antisymmetric stretching vibrations $\nu_{as}(COO^-)$ appear close to 1602 cm^{-1}, whereas the symmetric stretches $\nu_s(COO^-)$ appear in the range 1450–1334 cm^{-1}. The frequencies for the carbonyl stretches in **1** are shifted to lower values compared to those of the free quinic acid. In addition to this, they indicate a change in the vibrational status of the quinate anion upon coordination to the metal ion. The difference between the symmetric and antisymmetric stretches, $\Delta(\nu_{as}(COO^-) - \nu_s(COO^-))$, was greater than 200 cm^{-1}, indicating that the carboxylate groups of the quinate ligand were either free or coordinated to the metal ion in a monodentate fashion [39,40]. The latter contention was further confirmed by the X-ray crystal structure of **1**. Similar trends in the frequencies of the carboxylate carbonyls have also been observed in the FT-IR spectra of other metal–quinate complexes as well as α-hydroxycarboxylate complexes with metal ions [41,42].

3.5. Magnetic susceptibility studies

Magnetic susceptibility measurements were carried out at different magnetic fields and in the temperature range 2–300 K. The data were fitted with the MAGPACK [43] program, employed with a nonlinear least-squares curve-fitting program, DSTEPIT [44]. The temperature dependence of $\chi_M T$ (χ_M being the magnetic suscepti-

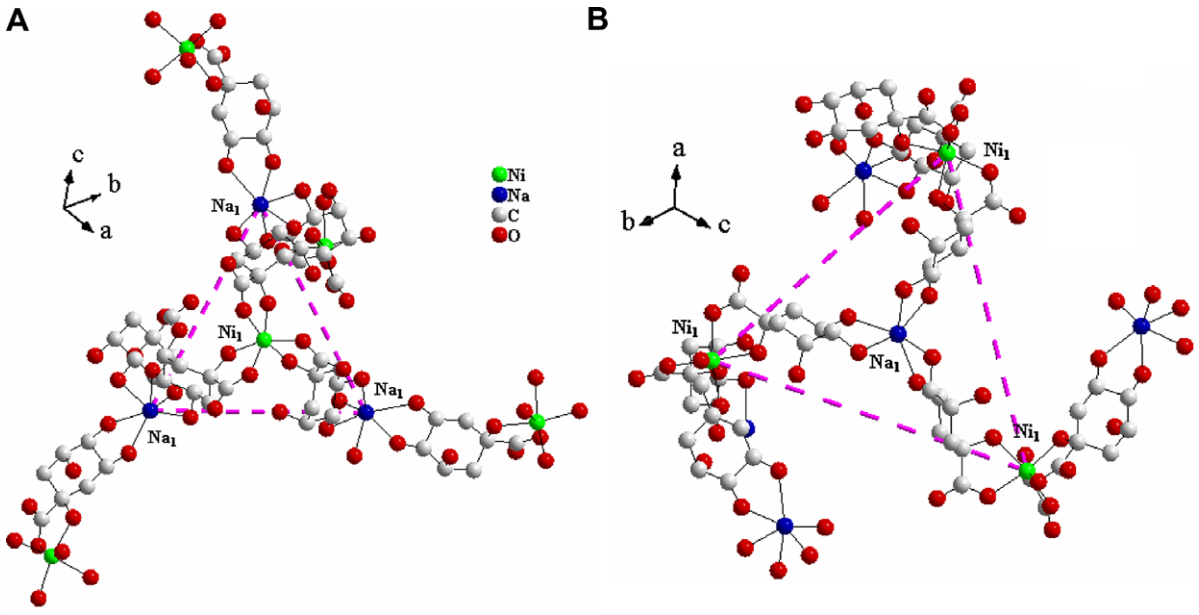


Fig. 2. Structural organization of **1**, showing the relationship between Na- and Ni-atoms (A and B) in the lattice composition (see text).

bility for one Ni(II) ion) for complex **1** is shown in Fig. 3 (solid circles). The $\chi_M T$ value is 1.78 emu mol^{-1} K at 300 K. From that temperature down to 10 K there is a smooth linear decrease, while after that temperature and until 2 K a more pronounced decrease occurs, reaching the value of 0.84 emu mol^{-1} K. The shape of this curve is characteristic of the occurrence of large zero field effects along with the temperature independent paramagnetism effect, TIP, which leads to a linear temperature dependence of the susceptibility data. The susceptibility data were fitted by the following equation:

$$H = D\left[S_z^2 - \frac{1}{3}S(S+1)\right] + E(S_x^2 - S_y^2) + g_z\mu_B H_z S_z + g_x\mu_B H_x S_x + g_y\mu_B H_y S_y, \quad (1)$$

where an isotropic g-value was used. The best fit (solid line in Fig. 3) is given by the parameters $D = 3.4$ cm^{-1} and $g = 2.2$, TIP = 1.8×10^{-3}. In the inset of the figure, simulations of the susceptibility function are shown for different values of the D parameter, where the g value and the TIP were kept at values obtained from the fitting procedure. Both axes are in logarithmic scale.

Isothermal magnetization curves at T 2 K in the applied field 0–5 T are shown in Fig. 4. The curves for the increasing and decreasing fields are identical. The data were fitted using (Eq. (1)) and the best fit (solid line in Fig. 4) is given by the parameters of $D = 2.8$ cm^{-1}, $g = 2.2$. The latter are very close to the values obtained from the susceptibility study, verifying the large zero-field character of the system.

3.6. Speciation studies

pH-potentiometric titrations of the ligand quinic acid alone, and Ni(II) with D-(−)-quinic acid in various metal ion to ligand molar ratios [Ni:L] = [1:2/1:3/1:4] were carried out. The titration curves were evaluated with different potential speciation models. The best fit between the experimental and calculated titration curves for the binary Ni(II)–quinic acid system was obtained by considering the species [Ni(II)], $[NiL_2]^o$ (HL = $C_7H_{12}O_6$; L = $C_7H_{11}O_6^-$), $[NiL_2H_{-1}]^-$, and $[NiH_{-1}]^+$. The fit is reasonably good in the overall pH and concentration range used, demonstrating that the adopted speciation model is satisfactorily defined. Other complexes, such as 1:1 and 1:2 Ni(II):quinate complexes or variably protonated and deprotonated species were rejected by the computer program (PSEQUAD) during the computation process. The species emerging from the speciation distribution of the binary system are in good agreement with the corresponding species synthesized and isolated in the solid state. The stability constants of the complexes formed are listed in Table 3. The uncertainties (3SD values) for the stability constants are given in parentheses. The pH range of the optimal formation of complexes is also reported. For the titratable quinate carboxylate group, the pK_a value of 3.34 was obtained and was found to be very close to the values reported by Clifford (3.40) [45] and Luethy-Krause et al. (3.36) [46]. For shikimic acid (3R, 4S, 5R)-3,4,5-trihydroxy 1-cyclohexanecarboxylic acid) the pK_a value is 4.15 [45]. The presence of an alcoholic moiety in a position α- to the carboxylate group of quinic acid increases its acid strength.

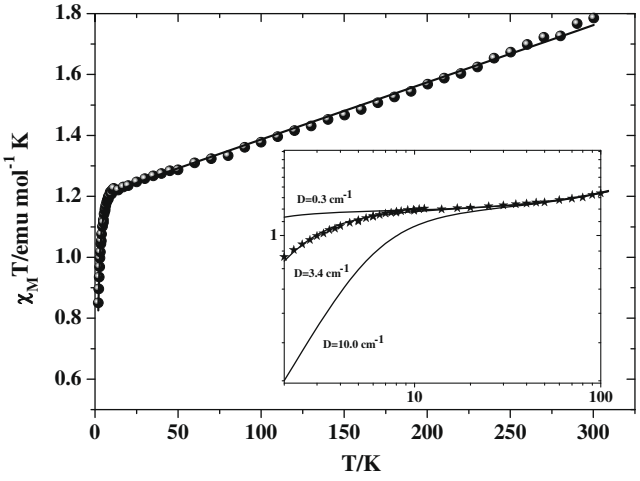


Fig. 3. Temperature dependence of the susceptibility data in the form of $\chi_M T$ vs. T (solid stars) and the fitting results using the theoretical formula discussed in the text (solid line). In the inset, simulations of the susceptibility function are shown, in the form of $\chi_M T$ vs. T, for different values of the D parameter. Both axes are in logarithmic scale.

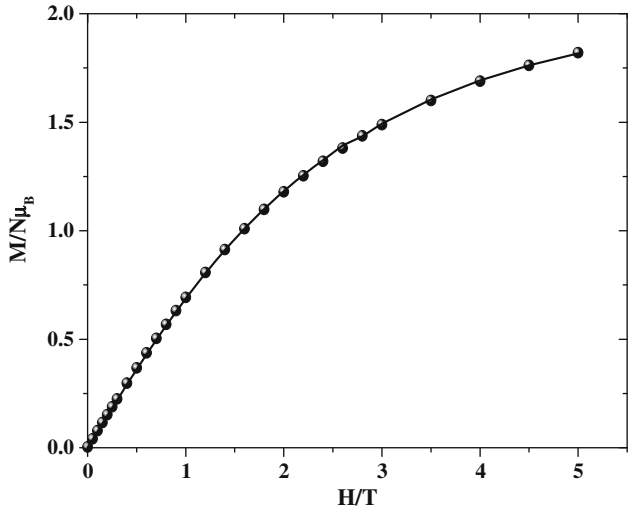


Fig. 4. Magnetization measurements in the field range 0–5 T, at temperature T 2 K, and the fitting results using the theoretical formula discussed in the text (solid line).

The titrimetric data were evaluated on the premise that complex formation between Ni(II) and quinate proceeds through binding of the quinate carboxylate and the α-alcoholic group moieties. The titration curves in the absence and presence of Ni(II) suggest formation of the $[NiL_2]^o$ species in the acidic region up to pH 8, and the $[NiL_2H_{-1}]^-$ species at pH values beyond 7. These studies also suggest that this ligand reacts expediently with Ni(II) ions, forming soluble metal chelate complexes. In the $[NiL_2]^o$ complex, the ligand appears to be deprotonated at the carboxylate moiety and as such both quinate ligands act in a bidentate fashion, coordinating Ni(II). The hexacoordination of Ni(II) ion is consistent with the presence of the $[Ni(H_2O)_6]^{2+}$ complex ion in the entire pH range investigated.

Table 3
Proton (log$K$) and Ni(II)–quinic acid complex formation constants (logβ) at $I = 0.15$ (NaCl) and 25 °C.

	Quinic acid	Ni–quinic acid	pH range for each species
Log$K$(HL)	3.34(1)		
Logβ (NiL_2)		4.95(3)	all domain
Logβ (NiL_2H_{-1})		−4.14(7)	>7.0
pK ($[NiL_2H_{-1}]/[NiL_2]$)		9.09	
Fitting[a]		9.656×10^{-3}	
Number of pts.		191	

Charges from the various species are omitted for clarity.
[a] Goodness-of-fit between the experimental and the calculated titration curves expressed in milliliters of titrant.

The overall stability constant of the mononuclear complex $[NiL_2]^o$ ($\log\beta$ 4.95) is similar yet greater than those in complexes of Ni(II) with some α-hydroxycarboxylic acids, such as 2-hydroxyacetic acid (glycolic acid) ($\log\beta$ 3.77) [47], 2-hydroxypropanoic acid (lactic acid) ($\log\beta$ 2.85) [48], 2-hydroxybutanoic acid ($\log\beta$ 2.89) [49], 2-hydroxy-2-methylpropanoic acid (2-hydroxyisobutyric acid) ($\log\beta$ 2.80) [50], and 2-hydroxy-2-phenylacetic acid (mandelic acid) ($\log\beta$ 2.48) [51].

In the pH range beyond 7 of the binary Ni(II)–quinic acid system, two species emerge, namely $[NiL_2H_{-1}]^-$ and the mononuclear $[NiH_{-1}]^+ = [Ni(OH)]^+$. Quinic acid contains one carboxylic acid group and four alcoholic hydrogens. The pK_a of the latter is >11. The dicationic metal ions (Co(II), Ni(II), etc.) are not sufficiently strong to deprotonate the alcoholic proton of quinic acid. As a consequence, it is very likely that one of the two water molecules coordinated to the nickel ion in the mononuclear species $[NiL_2H_{-1}]^-$ is possibly deprotonated. This is the species arising as the successor participant to the $[NiL_2]^o$ species at higher pH values in the speciation diagram. These two species coexist with the hexa-aquo nickel $[Ni(H_2O)_6]^{2+}$ species in the entire pH range studied, as that is shown in the speciation curves presented in Fig. 5. The maximum% content of $[NiL_2]^o$ appears to be 30% and stays constant in the pH range 4.5–7.5 of the binary Ni(II)–quinic acid system, where $c_{Ni} = 0.000657$ mol dm^{-3}, and $c_{ligand} = 0.002704$ mol dm^{-3}.

Beyond the pH range 8.2–8.8, depending on the molar ratio Ni(II):quinate, a precipitate appears and the pH rise ceases, most likely due to OH^- ions being consumed toward formation of $Ni(OH)_2$. The incipient precipitation at pH beyond 8.5 makes the observation of the next phase of the aqueous speciation doubtful, even in the presence of higher ligand-to-metal molar ratios (Fig. S2).

The presence of the hexa-aquo $[Ni(H_2O)_6]^{2+}$ species over the entire pH range, where the aqueous speciation was investigated, has been noted. In a similar system containing histidinehydroxamic acid, the Ni(II) ion is strongly bound to the ligand in mononuclear NiL ($\log\beta = 10.49$) and NiL_2 ($\log\beta = 18.80$) complexes [52]. From the speciation curves of that system, it can be seen that the hexa-aquo $[Ni(H_2O)_6]^{2+}$ species stays intact up to pH around 11. As was the case of the binary system of Ni(II) in presence of quinic acid, a precipitate appears beyond pH 9 in this system as well. In the Ni(II)–D-glucosamine system [53], the NiL_2 ($\log\beta = 6.43$) complex appears in the pH range 7–10. From the speciation curves of this system, it can be seen that the aquo $[Ni(H_2O)_6]^{2+}$ species stays as such up to pH around 11. Hexa-aquo Ni(II) ions are also the major species present in the binary system of Ni(II) with pycdpnen (a pyridylamido hexadentate ligand) up to pH 7 [54]. In the case of the aqueous binary system of Ni(II) with 2-(4-methylthiazol-2-yl)-2-(hydroxyimino)acetic acid, the binary NiL_2 complex also forms ($\log\beta = 11.83$), while at pH<6.5 hexa-aquo Ni(II) ions are present [55]. The stability constant of the $[NiL_2H_{-1}]^-$ ($\log\beta = -4.14$) species is higher than that of the monohydroxo species $[NiH_{-1}]^+$ ($\log\beta = -9.74$). That could help explain why at pH beyond 7, where both species form, the% content of the $[NiL_2H_{-1}]^-$ species appears to be higher than that of the $[NiH_{-1}]^+$ species in the same pH range [56].

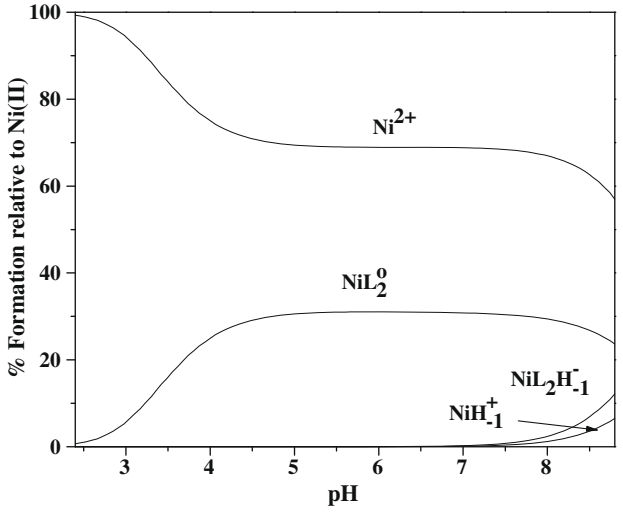


Fig. 5. Speciation curves for complexes forming in the binary Ni(II)–quinic acid system; $c_{Ni} = 0.000657$ mol dm^{-3}, $c_{ligand} = 0.002704$ mol dm^{-3}. Charges are omitted for clarity.

4. Discussion

4.1. The chemistry of the binary Ni(II)–quinate system in aqueous media

The synthesis of $Na[Ni(C_7H_{11}O_6)_3] \cdot 2.75H_2O$ (**1**) through the pH specific reaction of $NiCl_2$ with quinic acid at pH 5.5, emphasizes the distinct interaction of D-(−)-quinic acid with the divalent metal ion Ni(II). The analytical, spectroscopic, structural and magnetic susceptibility characterization of the derived material provided the physical and chemical properties of **1**, revealing a considerable number of structural details related to the reactivity of quinic acid toward Ni(II).

Associated with the distinct structural identity of **1** was the retention of the protonation of the α-alcoholic group in the quinate ligand upon binding to Ni(II). Each binding site around Ni(II) includes the oxygen from the carboxylate moiety bearing 1− charge, thus raising the total charge for the isolated mononuclear complex to 1−. Formation of a five-membered cyclic ring is most likely a source for stability in the isolated complex. The negative charge on the anionic complex $[Ni(C_7H_{11}O_6)_3]^-$ is counteracted by one sodium ion. Retention of the proton of the alcoholic group in the α-position to the carboxylate group has also been observed in the case of the congener α-hydroxycarboxylic acid, citric acid, upon binding of the latter to Ni(II) and Mn(II). In contrast to that behavior, binding of the α-hydroxycarboxylate ligand citrate to the higher oxidation state manganese ion Mn(III), led to a species in which the alcoholic group does not retain the proton despite the fact that citrate employs the same mode of coordination to Mn(III) as in Ni(II), through formation of a five-member cyclic ring [25,57].

Beyond the conventional contributions of the ligand to the reactivity of Ni(II), there appear to be general features potentially involved in the binary Ni(II)–quinic acid system linked to its aqueous chemistry. These include: (a) the coordination mode of all three quinate ligands to Ni(II) in **1**, and (b) the presence of the uncoordinated polyol functionalities in the quinates, signifying the unique chemical reactivity of Ni(II) ions toward α-hydroxycarboxylate ligands (central carboxylate and alcoholic groups) leading to a metal-cyclic motif formation. Even though both the α-hydroxycarboxylate and polyol functionalities in quinate are capable of promoting metal ion binding chemistries, the herein distinctly observed chemical reactivity and structural identity may indicate commensurably diverse chemical reactivity at the biological level. In such an environment, the natural metal ionic binder organic moieties are key molecular targets participating in essential biosynthetic pathways and likely influencing cellular integrity and survival.

Lastly, the employed synthetic strategy for the isolation of complex **1** reflects a chemical reactivity of Ni(II), because of which the title species crystallized out of solution. Key to the achievement of the solid state lattice of **1** appears to be (a) the low solubility of the anionic assembly $[Ni(C_7H_{11}O_6)_3]^-$ in the presence of the counter

ion Na^+, and (b) the involvement of water molecules in the assembly. To that end, solvent water molecules of crystallization contribute to the establishment of extensive hydrogen-bonding interactions throughout the lattice of **1** bestowing to it considerable stability.

4.2. The Ni(II)–quinic acid binary system speciation

A well-defined form of a metal–organic binary species such as **1** requires that an in-depth knowledge of its solution identity and properties is established. To this end, the aqueous solution study on the distribution of species arising in the binary system Ni(II)–quinic acid: (a) aids significantly in the understanding of the nature of various species forming as a function of pH and the stoichiometry of the reagent partners involved, and (b) provides a direct correlation of the physicochemical profile of the proposed species with the structure and properties of the species in the solid state (**1**). In this regard, the species prevailing in the requisite aqueous speciation bear a 1:2 Ni:L stoichiometry. In line with this stoichiometry, mononuclear $[NiL_2]^0$ and $[NiL_2H_{-1}]^-$ species emerge as competent participants in the pH distribution. Beyond that, mononuclear $[Ni(II)]^{2+}$ and $[NiH_{-1}]^+$ species emerge as complementary representative compounds of the aqueous binary distribution in different pH-ranges. Complex $[NiL_2]^0$ dominates in the low to physiological pH range. Its almost constant % fraction of total Ni(II) (30%) in the low and physiological pH range up to pH 8, indicates a preference over other species that could bear quinate ligands. It portrays a species containing a Ni(II) metal ion bearing two quinate ligands and likely two water molecules, thus bestowing an octahedral coordination environment to the central metal ion. In that respect, the $[NiL_2]^0$ species correlates the nature of the proposed solution species with that of **1** in the solid state. That, in turn, implies that compound **1** upon dissolution turns into $[NiL_2]^0$ giving up one quinate ligand. Consequently, **1** is likely not a species existing in solution, but rather one that emerges through favored lattice dynamics upon crystallization from the reaction mixture originally employed. It is worth noting that no 1:1 Ni:L species were proposed through the aqueous solution studies. Collectively, the data of the aqueous speciation relate the existence of the $[NiL_2]^0$ species at pH values around the specific pH value employed for the synthesis of that complex, with **1** ultimately crystallizing out of solution. This thesis is in line with recently isolated complexes of Co(II) with quinic acid at variable pH values in the corresponding binary aqueous speciation [58]. Hence, the idea of (a) synthesizing and isolating the proposed $[NiL_2]^0$ species, and (b) converting the $[NiL_2]^0$ species to **1** upon increasing the quinate:Ni(II) molar ratio (or influencing other factors) in the synthetic reaction mixture, are currently under investigation in our lab.

Moreover, the aqueous speciation studies suggest that other binary species exist at higher pH values (>7.5), including the $[NiL_2H_{-1}]^-$ complex. The composition of that complex presents a synthetic challenge that will shed light into that pH region of the aqueous speciation diagram, pinpointing specific structural features borne by quinate and the bound water molecules to Ni(II). The presence of Ni(II) bearing the same number of quinates at a higher pH as the $[NiL_2]^0$ dominant complex, but with an additional deprotonated aquo ligand (most likely), attests to its significance as a competent partner in the aqueous distribution diagram (albeit at a lower % fraction), explicitly projecting a variable chemical reactivity between Ni(II) and quinate as a function of pH.

4.3. Relevance of Ni(II) aqueous speciation to physiology and/or Ni(II) toxicity

The role of nickel in various structures and compartments in cells has been widely investigated and includes both normal physiological functions as well as toxic effects. As an exogenous inorganic cofactor, Ni(II) has been shown to exhibit physiological and/or aberrant effects (e.g. toxicity) with all the concomitant consequences to the integrity of organisms. As an enzyme metal cofactor and inducer of pathogenic physiologies, Ni(II) could exert influence on biochemical processes in cell structures or intercede in the chemistry of cellular (metal)homeostasis [59] by promoting binary and ternary interactions with cellular organic targets of both low and high molecular mass. Quinic acid is a suitable form of an organic substrate–ligand (a) present in plant fluids and circulating within plant structures, and (b) poised to seek chelation to divalent metal ions, such as Ni(II). In so doing, it establishes a binary Ni(II)–quinic acid system, which in the pH-range of plant physiological functions, generates a distribution of species with distinct physicochemical properties and potential (bio)chemical activity. Metal-linked biochemical activity has been observed in plants, emphasizing the ability of their cells to seek and identify metal ions or organic nutrients (a) essential to maintaining of their physiology [60], and/or (b) competent in combating (phyto)toxicity [61,62] events. To that end, the herein data signify the importance of the form, type and nature of Ni(II)–L (L = hydroxycarboxylate chelator) interactions potentially associated with the maintenance/compromise of cellular physiology or Ni(II) toxicity. In this respect, the well-characterized species **1** relates to the $[NiL_2]$ complex as the dominant species present in the aqueous speciation of the binary Ni(II)–quinic acid system. In plants, the chemistry of Ni(II), represented by well-defined soluble species such as $[NiL_2]^0$, may also reflect critical aspects of its interactive chemistry with other α-hydroxycarboxylic acids.

In humans, on the other hand, aberrant Ni(II) reactivity may influence processes (sister chromatid exchange, signaling pathways, transcription factor chemistry, etc.) linked to various manifestations of Ni(II) toxicity, potentially leading to allergic [63], respiratory and carcinogenic phenotypes [64]. In all of the aforementioned cases, soluble and bioavailable forms of Ni(II) constitute (a) the key to understanding the genetic and epigenetic (bio)chemistry unfolding in cellular compartments, organs and tissues, and (b) targets of ongoing research seeking to comprehend the intricate chemistry of Ni(II) toxicity at the molecular level. In this challenging field, efforts to understand further details of binary and ternary interactions of Ni(II), associated with soluble and bioavailable species currently eluding characterization, are ongoing in our labs.

5. Conclusion

The present endeavor (a) projects the complexity of the Ni(II)–quinic acid solution speciation in aqueous media and the diversity of species expected to arise as a function of pH and molecular Ni(II):quinate stoichiometry, (b) defines the physicochemical properties of a well-defined and characterized Ni(II)–quinate species **1** isolated at a specific pH value and its partner $[NiL_2]^0$ in solution projected through the aqueous speciation studies, and (c) links the pH-dependent bioinorganic chemistry of low molecular mass binary Ni(II)–(O-containing)organic substrate species with further binary and ternary interactions that might promote any potential activity relating to Ni(II) physiology or toxic effects on fundamental structures within cellular fluids.

Acknowledgments

This work was supported by a "Pythagoras" grant from the National Ministry of Education and Religious Affairs, and by a "PENED" grant co-financed by the E.U.-European Social Fund (75%) and the Greek Ministry of Development-GSRT (25%).

Appendix A. Supplementary data

CCDC 644650 contains the supplementary crystallographic data for **1**. These data can be obtained free of charge via http://www.ccdc.cam.ac.uk/conts/retrieving.html, or from the Cambridge Crystallographic Data Centre, 12 Union Road, Cambridge CB2 1EZ, UK; fax: (+44) 1223 336 033; or e-mail: deposit@ccdc.cam.ac.uk. Supplementary data associated with this article can be found, in the online version, at doi:10.1016/j.poly.2008.12.045.

References

[1] E. Denkhaus, K. Salnikow, Crit. Rev. Oncol. Hemat. 42 (2002) 35.
[2] S.O. Moussa, K. Morsi, J. Alloy. Compd. 426 (2006) 136.
[3] A.M. Brennenstuhl, T.S. Gendron, R. Cleland, Corros. Sci. 35 (1993) 699.
[4] G. Winter, T. Buhrke, O. Lenz, A.K. Jones, M. Forgber, B. Friedrich, Fed. Eur. Biochem. Soc. Lett. 579 (2005) 4292.
[5] R.K. Watt, P.W. Ludden, Cell. Mol. Life. Sci. 56 (1999) 604.
[6] E. Haslam, in: Shikimic Acid: Metabolism and Metabolites, Wiley and Sons, New York, 1993.
[7] A.J. Pittard (Ed.), *Escherichia coli* and *Salmonella*: Cellular and Molecular Biology, ASM Press, Washington, DC, 1996.
[8] R. Bentley, Crit. Rev. Biochem. Mol. Biol. 25 (1990) 307.
[9] M. Jezowska-Bojczuk, P. Kaczmarek, W. Bal, K.S. Kasprzak, J. Inorg. Biochem. 98 (2004) 1770.
[10] G. Gran, Acta Chem. Scand. 29 (1950) 559.
[11] G. Gran, Analyst 77 (1952) 661.
[12] F.J.C. Rossotti, H. Rossotti, J. Chem. Educ. 42 (1965) 375.
[13] G. Schwarzenbach, Complexometric Titrations, Interscience, New York, 1960, p. 83.
[14] Micro TT2050 Titrator Quick Guide, Crison Instruments, Alella, Spain, 1985.
[15] H.M. Irving, M.G. Miles, L.D. Petit, Anal. Chim. Acta 38 (1967) 475.
[16] P. Gans, B. O'Sullivan, Talanta 51 (2000) 33.
[17] H.S. Harned, B.B. Owen, The Physical Chemistry of Electrolytic Solutions, 3rd ed., Reinhold Publishing Corp., New York, 1958.
[18] P. Gans, A. Sabatini, A. Vacca, J. Chem. Soc., Dalton Trans. (1985) 1195.
[19] L. Zékány, I. Nagypál, G. Peintler, PSEQUAD for Chemical Equilibria, Technical Software Distributions, Baltimore, 1991.
[20] L. Alderighi, P. Gans, A. Ienco, D. Peters, A. Sabatini, A. Vacca, Coord. Chem. Rev. 184 (1999) 311.
[21] N.V. Plyasunova, Y. Zhang, M. Muhammed, Hydrometallurgy 48 (1998) 43.
[22] B.J. Colston, V.J. Robinson, Analyst 122 (1997) 1451.
[23] SMART-NT, Version 5.0, Brucker AXS, Madison, WI, 1998.
[24] SAINT-NT, Version 5/6.0, Brucker AXS, Madison, WI, 1999.
[25] SHELXTL-NT, Version 5.1, Brucker AXS, Madison, WI, 1998.
[26] Z.H. Zhou, Y.J. Lin, H.B. Zhang, G.D. Lin, K.R. Tsai, J. Coord. Chem. 42 (1997) 131.
[27] E.N. Baker, H.M. Baker, B. Anderson, R.D. Reeves, Inorg. Chim. Acta 78 (1983) 281.
[28] Y. Guo, D. Xiao, E. Wang, Y. Lu, J. Lü, X. Xu, L. Xu, J. Sol, State Chem. 178 (2005) 776.
[29] J. Strouse, S.W. Layten, E. Strouse, J. Am. Chem. Soc. 99 (1977) 562.
[30] M. Menelaou, C.P. Raptopoulou, A. Terzis, V. Tangoulis, A. Salifoglou, Eur. J. Inorg. Chem. (2005) 1957.
[31] R. Swanson, W.H. Ilsley, A.G. Stanislowski, J. Inorg. Biochem. 18 (1983) 187.
[32] R.C. Bott, D.S. Sagatys, D.E. Lynch, G. Smith, C.H.L. Kennard, T.C.W. Mak, Aust. J. Chem. 44 (1991) 1495.
[33] Y. Inomata, T. Haneda, F.S. Howell, J. Inorg. Biochem. 76 (1999) 13.
[34] N. Barba-Behrens, F. Salazar-Garcia, A.M. Bello-Ramirez, E. Garcia-Baez, M.J. Rosales-Hoz, R. Contreras, A. Flores-Parra, Transition Met. Chem. 19 (1994) 575.
[35] I. Bkouche-Walksman, Acta Crystallogr., Sect. C 50 (1994) 62.
[36] G. Hata, Y. Kitano, T. Kaneko, H. Kawai, M. Mutoh, Chem. Pharm. Bull. 40 (1992) 1604.
[37] R. Codd, T.W. Hambley, P.A. Lay, Inorg. Chem. 34 (1995) 877.
[38] A.B.P. Lever, in: Inorganic Electronic Spectroscopy, 2nd ed., Elsevier, Amsterdam, 1984, pp. 507–511.
[39] C. Djordjevic, M. Lee, E. Sinn, Inorg. Chem. 28 (1989) 719.
[40] G.B. Deacon, R.J. Philips, Coord. Chem. Rev. 33 (1980) 227.
[41] M. Matzapetakis, C.P. Raptopoulou, A. Tsohos, B. Papaefthymiou, N. Moon, A. Salifoglou, J. Am. Chem. Soc. 120 (1998) 13266.
[42] M. Matzapetakis, C.P. Raptopoulou, A. Terzis, A. Lakatos, T. Kiss, A. Salifoglou, Inorg. Chem. 38 (1999) 618.
[43] J.J. Borrás-Almenar, J.M. Clemente-Juan, E. Coronado, B.S. Tsukerblat, J. Comput. Chem. 22 (2001) 985.
[44] Program 66, Quantum Chemistry Program Exchange, Indiana University, Bloomington, IN, 1986.
[45] M. Clifford, Tea and Coffee Trade J. 159 (1987) 35.
[46] B. Luethy-Krause, I. Pfenninger, W. Landolt, Trees – Struct. Funct. 4 (1990) 198.
[47] G.V. Bakore, M.S. Bararia, Z. Phys. Chem. (Leipzig) 242 (1969) 102.
[48] Z. Warnke, E. Kwiatkowski, Rocz. Chem. 47 (1973) 467.
[49] B. Mayer, R. Medancic, B. Grabaric, I. Filipovic, Croat. Chem. Acta 51 (1978) 151.
[50] G.H. Thun, W. Guns, F. Verbeek, Anal. Chim. Acta 37 (1967) 332.
[51] T. Matusinovic, I. Filipovic, Croat. Chem. Acta 58 (1985) 227.
[52] M.S. El-Ezaby, N.M. Shuaib, H.M. Marafie, M.M. Hassan, J. Inorg. Biochem. 33 (1988) 161.
[53] J. Lerivrey, B. Dubois, P. Decock, G. Micera, J. Urbanska, H. Kozlowski, Inorg. Chim. Acta 125 (1986) 187.
[54] C. Jubert, A. Mohamadou, C. Gérard, S. Brandes, A. Tabard, J.-P. Barbier, Inorg. Chem. Commun. 6 (2003) 900.
[55] A.A. Mokhir, E. Gumienna-Kontecka, J. Swiatek-Kozlowska, G.E. Petkova, O.I. Fritsky, L. Jerzykiewicz, A.A. Kapshuk, T.Y. Sliva, Inorg. Chim. Acta 329 (2002) 113.
[56] S. Lacour, V. Deluchat, J.-C. Bollinger, B. Serpaud, Talanta 46 (1998) 999–1009.
[57] M. Matzapetakis, N. Karligiano, A. Bino, M. Dakanali, C.P. Raptopoulou, V. Tangoulis, A. Terzis, J. Giapintzakis, A. Salifoglou, Inorg. Chem. 39 (2000) 4044.
[58] M. Menelaou, A. Konstantopai, C. Mateescu, H. Zhao, C. Drouza, N. Lalioti, A. Salifoglou, Inorg. Chem. (2009), submitted for publication.
[59] G.W. Zamponi, E. Bourinet, T.P. Snutch, J. Membrane Biol. 151 (1996) 77.
[60] S.A. Kim, M.L. Guerinot, FEBS Lett. 581 (2007) 2273.
[61] L.P. Weng, A. Wolthoorn, T.M. Lexmond, E.J. Temminghoff, W.H. van Riemsdijk, Environ. Sci. Technol. 38 (2004) 156.
[62] L.P. Weng, T.M. Lexmond, A. Wolthoorn, E.J. Temminghoff, W.H. van Riemsdijk, Environ. Toxicol. Chem. 22 (2003) 2180.
[63] L. Peltonen, Contact Dermatitis 5 (1979) 27.
[64] K.S. Kasprzak, F.W. Sunderman Jr., K. Salnikow, Mutat. Res. 533 (2003) 67.

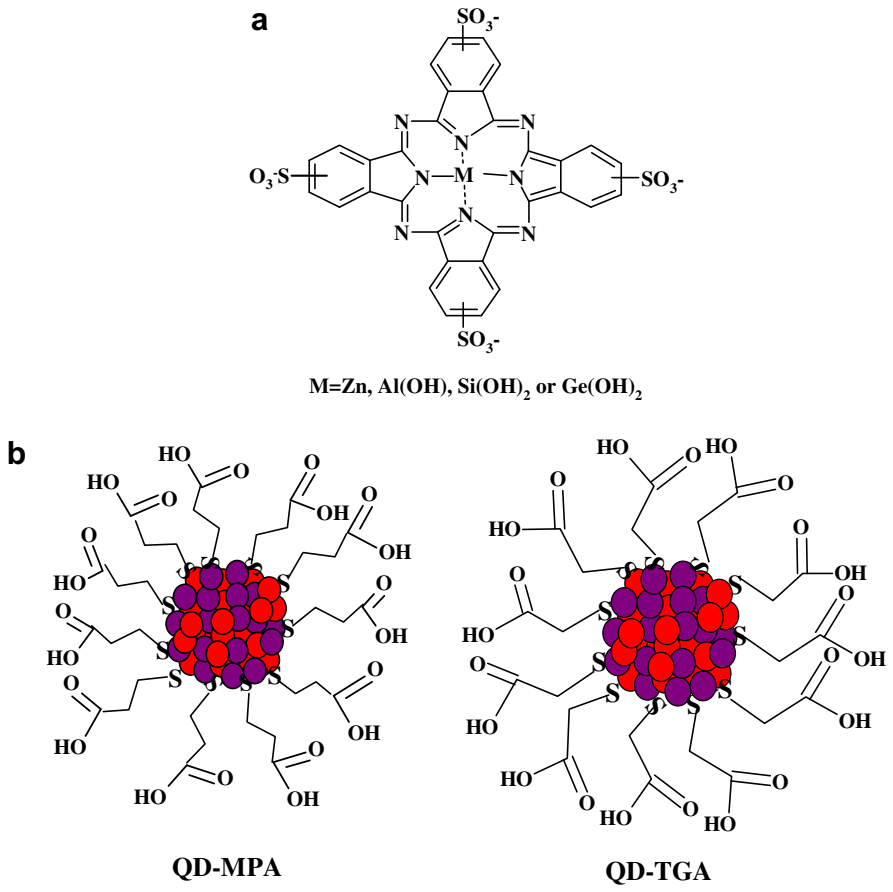


Fig. 1. (a) Molecular structure of the tetrasulfonated metallophthalocyanines ($MPcS_4$) and (b) Representation of the quantum dots studied, QD-MPA or QD-TGA: quantum dots capped with mercaptopropionic acid or thioglycolic acid, respectively.

to obtain QD-MPA of sizes 2.3 and 3.6 nm (represented as MPA1 and MPA2, respectively) and QD-TGA of 3.2 and 3.7 nm (represented as TGA1 and TGA2, respectively) in diameter. The sizes were estimated using a polynomial fitting function (Eq. (1)) derived in literature [30].

$$D = (9.8127 \times 10 - 7)\lambda^3 - (1.7147 \times 10 - 3)\lambda^2 + (1.0064)\lambda - (194.84), \quad (1)$$

where λ is the absorption maxima of the QDs. The fitting function is not valid for sizes of quantum dots outside the size range of 1–9 nm [30].

The QDs absorption maxima were 500, 550, 595 and 600 nm for MPA1, TGA1, MPA2 and TGA2, respectively, while the emission maxima were 550, 587, 649 and 632 nm, respectively. Rhodamine 6G was obtained from Sigma–Aldrich. Ultra pure water was obtained from a Milli-Q Water System (Millipore Corp., Bedford, MA, USA).

2.2. Equipment

Fluorescence excitation and emission spectra were recorded on a Varian Eclipse spectrofluoremeter. UV–Visible spectra were recorded on a Varian 500 UV–Vis/NIR spectrophotometer. Laser flash photolysis experiments were performed with light pulses produced by a Quanta-Ray Nd: YAG laser providing 400 mJ, 90 ns pulses of laser light at 10 Hz, pumping a Lambda-Physik FL3002 dye (Pyridin 1 dye in methanol). Single pulse energy ranged from 2 to 7 mJ. The analyzing beam source was from a Thermo Oriel xenon arc lamp, and a photomultiplier tube was used as detector. Signals were recorded with a digital real-time oscilloscope (Tektronix TDS 360). The triplet life times were determined by exponential fitting of the kinetic curves using the program ORIGINPRO 7.5. The flash photolysis experiments were performed at ±24 °C.

2.3. Photophysical studies

Fluorescence quantum yields (Φ_F) were determined by comparative method [31], (Eq. (2)):

$$\Phi_F = \Phi_{F(R)} \cdot \frac{F.A_R.n^2}{F_R.A.n_R^2}, \quad (2)$$

where F is the fluorescence intensity, A is the optical density at the excitation wavelength, and n is the refractive index of the solvent used. R refers to the reference fluorophore with known quantum yield. Rhodamine 6G ($\Phi_F = 0.94$ [32] in ethanol) and ZnPc ($\Phi_F = 0.20$ [33] in DMSO) were employed as standards for the QDs and MPcs, respectively. At least three independent experiments were performed for the quantum yield determinations. Both the sample and the reference were excited at the same relevant wavelength.

The determined fluorescence quantum yield values of the QDs and $MPcS_4$ were employed in determining the fluorescence quantum yields of $MPcS_4$ and QDs in each mixture ($\Phi^{Mix}_{F(MPcS_4)}$ and $\Phi^{Mix}_{F(QD)}$) using a modified form of Eq. (2) as shown by Eqs. (3a) and (3b).

$$\Phi^{Mix}_{F(QD)} = \Phi_{F(QD)} \frac{F^{Mix}_{QD}}{F_{QD}}, \quad (3a)$$

where $\Phi_{F(QD)}$ is the fluorescence quantum yield of the QDs alone, and was used as standard, F^{Mix}_{QD} is the fluorescence intensity of the

QDs in the mixture and F_{QD} is the fluorescence intensity of the QD in the absence of the respective $MPcS_4$ complexes. (λ_{exc} = 500 nm).

$$\Phi^{Mix}_{F(MPcS_4)} = \Phi_{F(MPcS_4)} \cdot \frac{F^{Mix}_{MPcS_4}}{F_{MPcS_4}}, \quad (3b)$$

where $\Phi_{F(MPcS_4)}$ is the fluorescence quantum yield of the $MPcS_4$ complexes alone, and was used as standard, $F^{Mix}_{MPcS_4}$ is the fluorescence intensity of the $MPcS_4$ complexes in the mixture and $F_{(MPcS_4)}$ is the fluorescence intensity of the $MPcS_4$ complexes alone (λ_{exc} = 620 nm).Triplet quantum yields were determined using a comparative method, Eq. (4):

$$\Phi^{Sample}_T = \Phi^{Std}_T \frac{\Delta A^{Sample}_T \varepsilon^{Std}_T}{\Delta A^{Std}_T \varepsilon^{Sample}_T} \quad (4)$$

where A^{Sample}_T and A^{Std}_T are the changes in the triplet state absorbance of the sample and the standard, respectively. ε^{Sample}_T and ε^{Std}_T are the triplet state extinction coefficients for the sample and standard, respectively. Φ^{Std}_T is the triplet state quantum yield for the standard. $ZnPcS_4$ in aqueous solution, Φ^{Std}_T = 0.56 [34] was used as standard. Solutions of samples in a H_2O:methanol (1:1) solvent mixture for triplet yield and lifetime measurements were purged of oxygen (by bubbling argon) for 20 min before laser irradiation.

2.4. Energy transfer (ET) study

The energy transfer efficiency (*Eff*) was determined experimentally from the fluorescence quantum yields of the donor (QDs) in the absence ($\Phi_{F(QD)}$) and presence ($\Phi^{Mix}_{F(QD)}$) of the acceptor and it is defined by Eq. (5) [12,35]:

$$Eff = 1 - \frac{\Phi^{Mix}_{F(QD)}}{\Phi_{F(QD)}}. \quad (5)$$

The Förster distance (R_0) is the critical distance between the donor and the acceptor molecules for which efficiency of energy transfer is 50% and it depends on the quantum yield of the donor, extinction coefficient of the acceptor, the degree of spectral overlap of the donor's fluorescence emission spectrum and the acceptor's absorption spectrum and a highly fluorescent donor is important [12,36], R_0 is expressed by Eq. (6):

$$R^6_0 = 8.8 \times 10^{23} \kappa^2 n^{-4} \Phi_{F(QD)} J \quad (6)$$

where κ is the dipole orientation factor, assumed to be 2/3; n is the refractive index of the medium; Φ_F is the fluorescence quantum yield of the donor in the absence of the acceptor; and J is the overlap integral calculated as (Eq. (7)):

$$J = \int f_{QD}(\lambda) \varepsilon_{MPc}(\lambda) \lambda^4 d\lambda \quad (7)$$

where f_{QD} is the normalized QDs emission spectrum; and ε_{MPc}, the molar extinction coefficient of the respective $MPcS_4$ complex.

The donor-to-acceptor distance, r is calculated by using Eq. (8) [12,36]:

$$r = R_0 \left(\frac{1}{Eff} - 1 \right)^{1/6}. \quad (8)$$

The above energy transfer parameters (J and R_0) were computed using the program PHOTOCHEMCAD [37] based on Eqs. (6) and (7).

3. Results and discussion

3.1. Electronic absorption and fluorescence spectra

Synthesis of tetrasulfonated metallophthalocyanine (Fig. 1) is known, and in this work, literature methods of synthesis and characterization were employed and gave expected results [28,29]. The CdTe QDs synthesized in this work, gave characteristic spectral behavior [5,16]. Shown in Fig. 2a are the absorption and emission spectra for MPA1 and TGA1 QDs.

Electronic absorption and fluorescence emission spectra of ($(OH)_2GePcS_4$) are shown in Fig. 2b in a mixture of H_2O and methanol (1:1). In this solvent mixture, the $MPcS_4$ complexes are monomeric. It has been documented that aggregation is accompanied by a reduction of photochemical activity in processes involving phthalocyanine excited states [38,39]. It is also known that the addition of organic solvents normally breaks the aggregates, resulting in monomeric species [40], hence the water:methanol solvent mixture was employed in this work. The $MPcS_4$ complexes obeyed Beer's law for concentrations less than 1×10^{-5} mol dm^{-3} in this solvent mixture. The excitation spectra of the $MPcS_4$ complexes were mirror images of the fluorescence emission spectra, Fig. 2b.

3.2. Photophysical behavior of $MPcS_4$ in the presence of QDs

Fluorescence quantum yield (Φ_F) values for the QDs and the $MPcS_4$ complexes were calculated using Eq. (2) and shown in Table 1. The Φ_F value of the QDs ranged from 0.19 to 0.62 at their different emission wavelength maxima (λ_{exc} 500 nm). It is known that the surface structure and the occurrence of charge carrier traps (which affect fluorescence) strongly depend on the size and symmetry of QDs [41]. Thus there is dependence of Φ_F values on the size of the QDs. However, the nature of the QDs (MPA versus TGA) was not found to significantly affect the Φ_F values [41]. The Φ_F values further decreased in the presence of the respective $MPcS_4$ complexes as shown in Table 1 ($\Phi^{Mix}_{F(QD)}$). This decrease in the fluorescence yield of the QDs in the presence of the $MPcS_4$

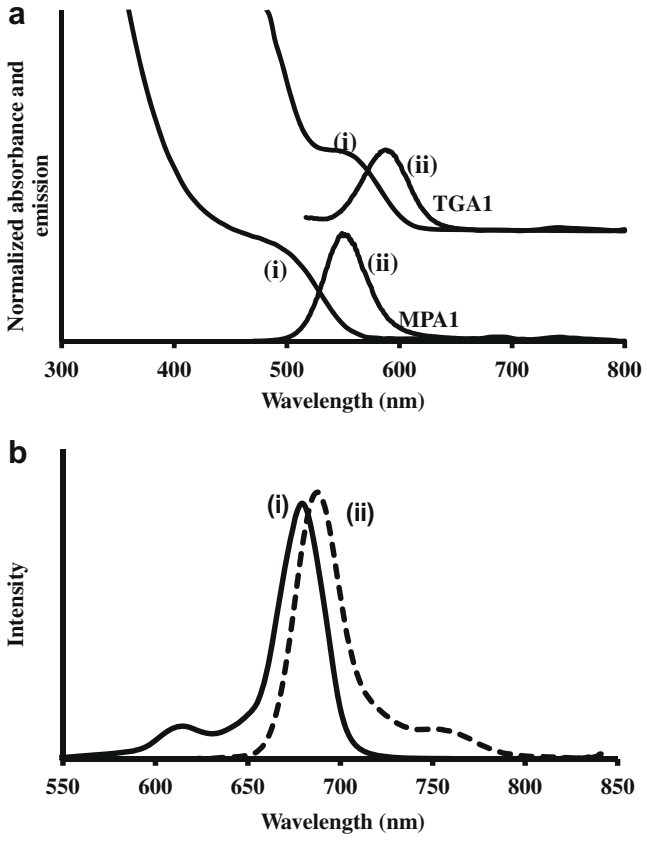


Fig. 2. Absorption (i) and emission (ii) spectra of TGA1 and MPA1 (a) and $(OH)_2GePcS_4$ (b) (λ_{exc} = 500 and 620 nm, respectively).

Table 1
Fluorescence quantum yields of QDs and photophysical parameters of MTSPcs in the presence of QDs in 1:1 methanol: water mixture.[a]

MPc	[b]QD	$\Phi^{Mix}_{T(TSPc)}$	$\tau^{Mix}_{T(TSPc)}$ (μs)	$\Phi^{Mix}_{F(QD)}$	$\Phi^{Mix}_{F(TSPc)}$ 620 nm exc
(OH)AlPcS$_4$	MPA1	0.46 (0.36)	600 (560)	0.17	0.20 (0.18)
	MPA2	0.43	610	0.45	0.22
	TGA1	0.41	610	0.27	0.19
	TGA2	0.46	560	0.49	0.26
ZnPcS$_4$	MPA1	0.51 (0.56)	240 (180)	0.17	0.16 (0.14)
	MPA2	0.42	220	0.33	0.16
	TGA1	0.49	250	0.12	0.16
	TGA2	0.45	290	0.45	0.17
(OH)$_2$SiPcS$_4$	MPA1	0.45 (0.56)	140 (280)	0.18	0.05 (0.10)
	MPA2	0.55	310	0.25	0.09
	TGA1	0.53	340	0.09	0.05
	TGA2	0.54	340	0.32	0.07
(OH)$_2$GePcS$_4$	MPA1	0.85 (0.81)	240 (250)	0.17	0.13 (0.12)
	MPA2	0.87	280	0.32	0.16
	TGA1	0.81	350	0.07	0.12
	TGA2	0.85	360	0.37	0.15

[a] Number in brackets are the quantum yields ($\Phi_{F(MPcS_4)}$ or $\Phi_{T(MPcS_4)}$) or triplet lifetimes $\tau_{T(MPcS_4)}$ of MPcS$_4$ alone.
[b] MPA = 3-mercaptopropionic acid and TGA = thioglycolic acid. Fluorescence quantum yields of quantum dots alone ($\Phi_{F(QD)}$): 0.19 (MPA1) 0.59 (MPA2), 0.30 (TGA1) and 0.62 (TGA2).

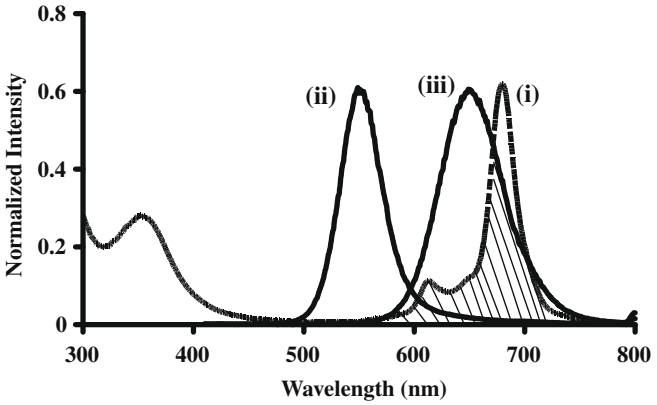


Fig. 3. Normalized absorption spectra of (OH)$_2$SiPcS$_4$ (i) and emission spectra of MPA1 (ii) and MPA2 (ii) (λ_{exc} = 500 nm).

complexes is due to the non-radiative transfer of energy from the QDs to the MPcS$_4$ complexes because as the QD particles fluoresce, the MPc molecules (acceptor) absorb the energy, thus reducing the fluorescence intensity of the QDs (donor) in the QD-MPc mixture. Φ_F values for the MPcS$_4$ complexes are listed in Table 1 (in parenthesis, λ_{exc} 620 nm). Apart from the (OH)$_2$SiPcS$_4$, Φ_F values decreases with the size of the central metal which is consistent with the strengths of spin–orbit (S–O) coupling induced by the respective central metals based on their relative masses.

There was generally a slight increase in the Φ_F values of the MPcS$_4$ complexes, except for (OH)$_2$SiPcS$_4$ (all sizes) and (OH)$_2$GePcS$_4$ (TGA1 and MPA1) in the presence of the QDs ($\Phi^{Mix}_{F(TSPc)}$, λ_{exc} 620 nm) compared to the values of the MPcS$_4$ complexes alone (in parenthesis, Table 1). The increase was more pronounced in the presence of the larger QDs (MPA2 and TGA2). For (OH)$_2$SiPcS$_4$, there was generally a small decrease in the Φ_F values. However, considering experimental errors, the changes in Φ_F values is insignificant in many cases. The decrease in Φ_F values could be due to the heavy atom effect of the QDs on the MPcS$_4$ complexes, and the slight increase in Φ_F values could be attributed to the possible shielding of the Pc by the QDs, thus decreasing quenching of the former.

An efficient overlap occurs between the absorption spectra of the MPcS$_4$ complexes with the emission spectra of QDs, Fig. 3. A decrease in the fluorescence emission intensity (on exciting at 500 nm, where the QDs absorb, but the MPcS$_4$ complexes have negligible absorbance) of the QDs on excitation of a mixture containing the respective QDs and respective MPcS$_4$ complex, and an emergence of the respective MPcS$_4$ complex fluorescence was observed as shown in Fig. 4. This suggests that energy transfer occurs from CdTe QDs to the MPcS$_4$ complexes. No significant fluorescence for the MPcS$_4$ complexes was observed on excitation at 500 nm in the absence of the QDs, so the fluorescence of the MPcS$_4$ complexes that emerged in this case must be due to the fluorescence induced by QDs unto the MPcS$_4$ complexes. The observation of FRET shows different behavior from the aggregation observed for MPcs substituted with alklthio substituted MPc complexes [19]. In this study, it is most likely that the QDs interact with the MPcS$_4$ complexes by adsorption.

The J values obtained as shown in Table 2 are of the order of 10^{-13} cm^6, for some porphyrin based molecules, J values of the order 10^{-14} cm^6 have been observed [35]. The J values were about the same for all the complexes in the presence of the various QDs except for ZnPcS$_4$ in the presence of MPA1 where the value was very low. The center-to-center separation distance between donor and acceptor (r, Å), were calculated using Eq. (8) and values are shown in Table 2. Most of the calculated r values were above the critical distance (R_0) at which energy transfer is 50% except for the complexes in the presence of TGA1 (with exception of (OH)AlPcS$_4$, and (OH)$_2$SiPcS$_4$ in the presence of MPA2). This gives an indication that the energy transfer in these combinations may not be optimum since for efficient energy transfer to occur r should be lower than R_0. The efficiency of energy transfer *Eff* was calculated with values stated in Table 2 and it was highest in each set for the MPcS$_4$ complexes in the presence of TGA1 except with (OH)AlPcS$_4$, as already predicted from the r values obtained. The values of *Eff* obtained for the MPcS$_4$ complexes in the presence of TGA2 and MPA2 were also very reasonable. However, bringing all the results together, TGA1 though exhibited high *Eff*, resulted in low fluorescence yield ($\Phi^{Mix}_{F(QD)}$) in the presence of the MPcS$_4$ complexes (Table 1) while TGA2 and MPA2, though with a lower *Eff*, maintained slightly higher fluorescence yields ($\Phi^{Mix}_{F(QD)}$) in the presence of the individual MPcS$_4$ complexes (Table 1). TGA2 and MPA2 QDs in the presence of MPcS$_4$ complexes may therefore be of better value in photosensitization reactions where detections will be needed since their fluorescence intensities will still be high enough to help in visualization.

Φ_T values provide a measure of the fraction of absorbing molecules that undergoes intersystem crossing to the triplet state (Φ_T). The efficiency of a phthalocyanine as a photosensitizer is determined by its triplet quantum yield (Φ_T) and lifetime (τ_T). The variation of Φ_T among the MPcS$_4$ complexes in Table 1 depends on heavy atom effect which encourages intersystem crossing to the triplet state. The observed trend for Φ_T corresponds to the increase in atomic masses of the central metals. (OH)$_2$SiPcS$_4$ behaves differently again in this case having a triplet yield that is of the same value with ZnPcS$_4$ even though there is a large difference in their relative atomic masses. This, however, explains the low Φ_F value obtained for the complex since most of the excited species were able to undergo ISC to the triplet state leading to a low Φ_F. The variation of Φ_T values of the MPcS$_4$ complexes in the presence of the QD is shown in Table 1. For (OH)AlPcS$_4$ and (OH)$_2$GePcS$_4$ slight increase in the Φ_T was observed compared to the respective MPcS$_4$ complexes alone. This slight increase in Φ_T in the presence of the QDs is attributed to the heavy atom effects of the QDs which contain heavy Cd and Te atoms. The increase in Φ_T of the MPcS$_4$

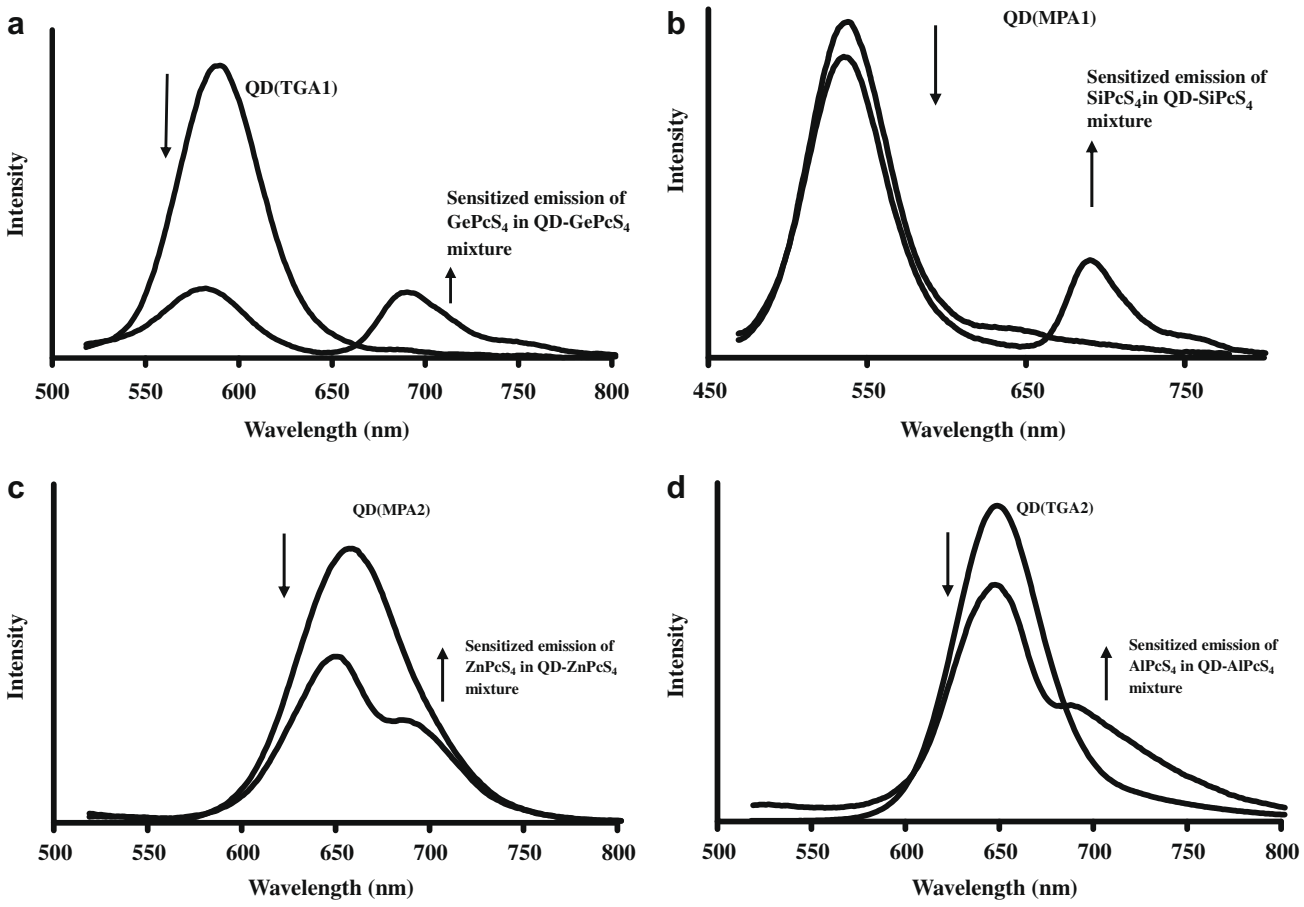


Fig. 4. Indirect activation of (a) $(OH)_2GePcS_4$ ($\sim 1 \times 10^{-5}$ mol dm^{-3}) by TGA1, (b) $(OH)_2SiPcS_4$ ($\sim 1 \times 10^{-5}$ mol dm^{-3}) by MPA1, (c) $ZnPcS_4$ ($\sim 1 \times 10^{-5}$ mol dm^{-3}) by MPA2 and (d) $(OH)AlPcS_4$ (6×10^{-6} mol dm^{-3}) by TGA2 through energy transfer, (λ_{exc} = 500 nm). [QD] = $\sim 1 \times 10^{-6}$ mol dm^{-3}.

complexes may be an advantage since it means the triplet state will be highly populated, thereby creating higher photosensitizing effect in photoactive reactions. The Φ_T values for $ZnPcS_4$ and $(OH)_2SiPcS_4$ complexes in the presence of QDs either decreased or remained the same, behaving contrary to what is expected on the basis of the heavy atom effect.

Table 2
Energy transfer parameters for TSPc-QD interactions in 1:1 water:methanol mixture.

MPc	QD	[a]J (10^{-13} cm^6)	[a]R_0 (Å)	r (Å)	*Eff*
$(OH)AlPcS_4$	MPA1	1.02	32.84	46.53	0.11
	MPA2	1.31	60.71	73.57	0.24
	TGA1	2.38	40.68	58.67	0.10
	TGA2	1.18	59.58	72.20	0.24
$ZnPcS_4$	MPA1	0.68	30.71	43.51	0.11
	MPA2	7.44	55.21	57.47	0.44
	TGA1	1.73	38.70	36.17	0.60
	TGA2	7.33	55.54	65.55	0.27
$(OH)_2SiPcS_4$	MPA1	1.13	33.39	54.54	0.05
	MPA2	1.13	59.19	56.09	0.58
	TGA1	2.61	41.52	36.05	0.70
	TGA2	1.01	58.50	59.29	0.48
$(OH)_2GePcS_4$	MPA1	0.44	28.57	40.48	0.11
	MPA2	5.73	52.87	54.30	0.46
	TGA1	1.11	35.90	29.35	0.77
	TGA2	4.83	51.81	55.43	0.40

[a] Using Eqs. (5)–(8), J and R_0 were determined using the program PHOTOCHEMCAD then r and *Eff* were calculated.

The triplet state lifetime, τ_T values of the $MPcS_4$ complexes ranged from 180 to 560 μs. It was observed that there was a general increase in the τ_T values of the $MPcS_4$ complexes in the presence of the various QDs as seen in Table 1. This observation could be due to the fact that there is a reduction in the exposure of the phthalocyanine to the aqueous medium because of the presence of the QDs, since water is known as a quencher of the triplet states of MPcs [33]. The increase in the τ_T of the $MPcS_4$ complexes in the presence of the QDs contradicts what is expected by the heavy atom effect, whereby when Φ_T increases as observed above, the τ_T decreases but it is justified for the $ZnPcS_4$ and $(OH)_2SiPcS_4$ complexes, where there is a general decrease in Φ_T in the presence of QDs. These long τ_T values, however, shows that the $MPcS_4$ complexes will likely spend more time at the triplet state allowing for increased diffusional interactions which will be an advantage in photosensitized reactions.

4. Conclusion

Energy transfer from mercaptocarboxylic acid capped CdTe quantum dots (QDs) to various tetrasulfonated metallophthalocyanines in a H_2O:MeOH (1:1) solvent mixture occurred and was found to be dependent on the overlap of the absorption spectra of the $MPcS_4$ complexes and the emission spectra of the QDs. High triplet state quantum yields (Φ_T, ranging from 0.41 to 0.87) of the $MPcS_4$ complexes in the presence of the QDs with corresponding long triplet state lifetimes (τ_T, ranging from 140 to 610 μs) to allow for photosensitized reactions to occur was observed. The mixture

of $MPcS_4$ complexes with QDs may find use in photosensitization reactions.

Acknowledgments

This work was supported by the Department of Science and Technology (DST) and National Research Foundation (NRF), South Africa through DST/NRF South African Research Chairs Initiative for Professor of Medicinal Chemistry and Nanotechnology as well as Rhodes University and Medical Research Council of South Africa. MI thanks the Andrew Mellon Foundation for a scholarship.

References

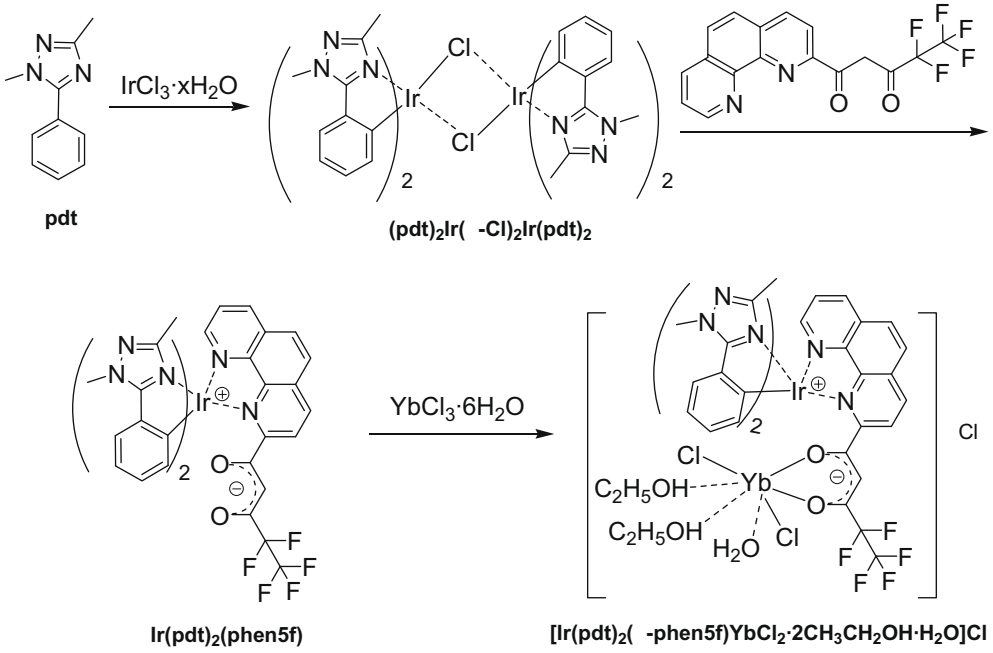
[1] H. Mattoussi, J.M. Mauro, E.R. Goldman, G.P. Anderson, V.C. Sundar, F.V. Mikulec, M.G. Bawendi, J. Am. Chem. Soc. 122 (2000) 12142.
[2] M. Bruchez Jr., M. Moronne, P. Gin, S. Weiss, A.P. Alivasatos, Science 281 (1998) 2013.
[3] W.C.W. Chan, S.M. Nie, Science 281 (1998) 2016.
[4] A.P. Alivisatos, J. Phys. Chem. 100 (1996) 13226.
[5] N. Gaponik, I.L. Radtchenko, G.B. Sukhorukov, H. Weller, A.L. Rogach, Adv. Mater. 14 (2002) 879.
[6] B.J. Battersby, D. Bryant, W. Meutermans, D. Matthews, M.L. Smythe, M. Trau, J. Am. Chem. Soc. 124 (2002) 5782.
[7] A.P. Alivisatos, Science 271 (1996) 933.
[8] R. Wargnier, A.V. Baranov, V.G. Maslov, V. Stsiapura, M. Artemyev, M. Pluot, A. Sukhanova, I. Nabiev, Nanoletters 4 (2004) 451.
[9] I. Roy, T.Y. Ohulchanskyy, H.E. Pudavar, E.J. Bergey, A.R. Oseroff, T. Morgan, T.J. Dougherty, P.N. Prasad, J. Am. Chem. Soc. 125 (2003) 7860.
[10] A.C.S. Samia, X. Chen, C. Burda, J. Am. Chem. Soc. 125 (2003) 15736.
[11] L. Stryer, Ann. Rev. Biochem. 47 (1978) 819.
[12] J.R. Lakowicz, Principles of Fluorescence Spectroscopy, 3rd Ed., Springer, New York, 2006.
[13] L. Shi, N. Rosenzweig, Z. Rosenzweig, Anal. Chem. 79 (2007) 208–214.
[14] L. Shi, B. Hernandez, M. Selke, J. Am. Chem. Soc. 128 (2006) 627.
[15] S. Dayal, R. Krolicki, Y. Lou, X. Qiu, J.C. Berlin, M.E. Kenney, C. Burda, Appl. Phys. B 84 (2006) 309.
[16] M. Idowu, J.Y. Chen, T. Nyokong, New J. Chem. 32 (2008) 290.
[17] J. Ma, J.Y. Chen, M. Idowu, T. Nyokong, J. Phys. Chem. B 112 (2008) 4465.
[18] S. Dayal, Y. Lou, A.C.S. Samia, J.C. Berlin, M.E. Kenney, C. Burda, J. Am. Chem. Soc. 128 (2006) 13974.
[19] S. Moeno, T. Nyokong, J. Photochem. Photobio. A 201 (2009) 228.
[20] M. Idowu, T. Nyokong, J. Lumin., in press.
[21] I.J. Macdonald, T.J. Dougherty, J. Porphyr. Phthalocya. 5 (2001) 105.
[22] R. Bonnett, Chem. Soc. Rev. 24 (1995) 19.
[23] M.S. Xu, J.B. Xu, M. Wang, L. Que, J. Appl. Phys. 91 (2002) 748.
[24] L.E. Norena-Franco, F.K. Vasnik, Analyst 121 (1996) 1115.
[25] M.R. Hamblin, T. Hasan, Photochem. Photobio. Sci. 3 (2004) 436.
[26] A. Minnock, D.I. Vernon, J. Schofield, J. Griffiths, J.H. Parish, S.B. Brown, J. Photochem. Photobio. B 32 (1996) 159.
[27] P. Tau, T. Nyokong, J. Mol. Catal. A: Chem. 273 (2007) 149.
[28] J. Weber, DH. Busch, Inorg. Chem. 4 (1965) 469.
[29] S.K. Saini, A. Jena, J. Dey, A.K. Sharma, R. Singh, Mag. Res. Imag. 13 (1995) 985.
[30] W.W. Yu, L. Qu, W. Guo, X. Peng, Chem. Mat. 15 (2003) 2854.
[31] S. Fery-Forgues, D. Lavabre, J. Chem. Ed. 76 (1999) 1260.
[32] R.F. Kubin, A.N. Fletcher, J. Lumin. 27 (1982) 455.
[33] A. Ogunsipe, J.Y. Chen, T. Nyokong, New J. Chem. 7 (2004) 822.
[34] A. Harriman, M.C. Richoux, J. Chem. Soc. Faraday Trans. 276 (1980) 1618.
[35] J.S. Hsiao, B.P. Krueger, R.W. Wagner, T.E. Johnson, J.K. Delaney, D.C. Mauzerall, G.R. Fleming, J.S. Lindsey, D.F. Bocian, R.J. Donohoe, J. Am. Chem. Soc. 118 (1996) 11181.
[36] T. Forster, Disc. Far. Soc. 27 (1959) 7.
[37] H. Du, R.A. Fuh, J. Li, L.A. Cockan, J.S. Lindsey, Photochem. Photobio. 68 (1998) 141.
[38] J.R. Darwent, P. Douglas, A. Harriman, G. Porter, M.C. Richoux, Coord. Chem. Rev. 44 (1982) 83.
[39] J.R. Wagner, H. Ali, R. Langlois, N. Brasseur, J.E. van Lier, Photochem. Photobio. 45 (1987) 587.
[40] G. Schnurpfeil, A.K. Sobbi, W. Spiller, H. Kliesch, D. Worhle, J. Porphyr. Phthalocya. 1 (1997) 159.
[41] K. Boldt, O.T. Bruns, N. Gaponik, A. Eychmüller, J. Phys. Chem. B. 110 (2006) 1959.

Table 1
Crystallographic data and structure refinement for $Ir(pdt)_2(phen5f)$ and $[(pdt)_2Ir(\mu\text{-}phen5f)YbCl_2 \cdot 2CH_3CH_2OH \cdot H_2O]Cl$.

	$Ir(pdt)_2(phen5f) \cdot 2CH_3CH_2OH \cdot 0.5CH_3CH_2OCH_2CH_3$	$[(pdt)_2Ir(\mu\text{-}phen5f)YbCl_2 \cdot 2CH_3CH_2OH \cdot H_2O]Cl$
Empirical formula	$C_{43}H_{44.50}F_5IrN_8O_{4.50}$	$C_{43}H_{39}Cl_3F_5IrN_8O_6Yb$
Formula weight	1032.57	1330.41
Temperature (K)	113(2)	113(2)
Wavelength (Å)	0.71073	0.71073
Crystal system	Monoclinic	Triclinic
Space group	$P2_1/c$	$P\bar{1}$
Unit cell dimensions, a (Å)	12.801(3)	12.233(2)
b (Å)	9.0698(18)	13.889(3)
c (Å)	37.396(8)	16.970(3)
α (°)	90	82.12(3)
β (°)	95.63(3)	71.14(3)
γ (°)	90	67.31(3)
Volume (Å^3)	4320.9(15)	2517.1(9)
Z	4	2
D_{calc} (g cm^{-3})	1.587	1.755
Absorption coefficient (mm^{-1})	3.164	4.717
$F(000)$	2066	1288
Crystal size (mm)	0.14 × 0.12 × 0.08	0.06 × 0.08 × 0.04
Theta range for data collection (°)	2.02–25.02	1.59–25.02
Reflections collected/unique [R_{int}]	23406/7409 [0.0638]	14768/8878 [0.0532]
Refinement method	Full-matrix least-squares on F^2	Full-matrix least-squares on F^2
Data/restraints/parameters	7409/58/624	8878/95/689
Goodness-of-fit on F^2	1.067	1.118
Final R indices [$I > 2\sigma(I)$]	$R_1 = 0.0535$, $wR_2 = 0.1187$	$R_1 = 0.0570$, $wR_2 = 0.1345$
R indices (all data)	$R_1 = 0.0638$, $wR_2 = 0.1250$	$R_1 = 0.0695$, $wR_2 = 0.1421$
Largest difference peak and hole (e Å^{-3})	2.074 and −2.310	1.818 and −1.126

reaction mixture was poured to 10 ml of water. And the filtered solid was washed with 30 ml of water by three times. Then the solid was dissolved in CH_2Cl_2 (50 ml), and the solution was dried in anhydrate sodium sulfate. After evaporation of the solvent, the crude product was purified via chromatography by using CH_2Cl_2 as eluent, and the Ir^{III} chloro-bridged dimer $(pdt)_2Ir(\mu\text{-}Cl)_2Ir(pdt)_2$ as yellow powder was obtained.

The dimer $(pdt)_2Ir(\mu\text{-}Cl)_2Ir(pdt)_2$ (469 mg, 0.41 mmol), Hphen5f (300 mg, 0.82 mmol) and anhydrous sodium carbonate (435.5 mg, 4.11 mmol) were refluxed in 2-ethoxyethanol (10 ml) under a N_2 atmosphere for 20 h. After cooling to room temperature, the mixture was poured into water. The crude product was obtained by filtration and then dissolved in CH_2Cl_2. The solution was dried in anhydrous sodium sulfate overnight. After evaporation of the solvent, the residue was purified via chromatography, using acetone for the elution. The pure product $Ir(pdt)_2(phen5f)$ was obtained as an orange-yellow powder (yield, 48%). ^1H NMR (400 MHz, DMSO–d_6): δ, ppm 8.80 (d, 1H, J = 8.0 Hz), 8.72 (d, 1H, J = 8.0 Hz), 8.31 (dd, 2H, J = 22, 8.8 Hz), 8.05 (d, 1H, J = 4.7 Hz), 7.89 (dd, 1H, J = 8.0, 5.1 Hz), 7.69 (d, 1H, J = 7.5 Hz), 7.46 (d, 1H, J = 8.0 Hz), 7.37 (d, 1H, J = 7.7 Hz), 7.05–7.01 (m, 1H), 6.97–6.93 (m, 1H), 6.85–6.81 (m, 1H), 6.73–6.70 (m, 1H), 6.25 (d, 1H,



Scheme 1. Synthetic routes of Ir^{III} complex and Ir^{III}–Yb^{III} complex.

J = 7.9 Hz), 6.15 (d, 1 H, J = 7.7 Hz), 4.21–4.14 (m, 4H), 4.04 (s, 3H), 1.58 (s, 3H), 0.83 (s, 3H). MALDI-TOF-MS: observed $[M+H]^+$, 905.2; calculated, 905.20. *Anal.* Calc. for $C_{37}H_{28}F_5IrN_8O_2 \cdot CH_3CH_2OH$: C, 49.31; H, 3.61; N, 11.80. Found: C, 49.39; H, 3.39; N, 11.79%.

2.2.2. Synthesis of Ir^{III}–Yb^{III} bimetallic complex

The complex-ligand $Ir(pdt)_2(phen5f)$ (0.3 mmol, 270 mg), $YbCl_3 \cdot 6H_2O$ (0.1 mmol, 38.8 mg) and ethanol (100 ml) were mixed in a round-bottom flask, and refluxed for 6 h. A crystallization from concentrated EtOH solution by slow diffusion of Et_2O led to microcrystalline $(pdt)_2Ir(\mu\text{-phen5f})YbCl_3$, which was deep-yellow solid. $(pdt)_2Ir(\mu\text{-phen5f})YbCl_3 \cdot 2H_2O$ *Anal.* Calc. for $C_{37}H_{32}N_8F_5O_4Ir$-$YbCl_3$: C, 36.45; N, 9.19; H, 2.65. Found: C, 36.47; N, 9.14; H, 2.65%.

2.3. X-ray crystallographic analyses

The X-ray diffraction data were measured on a Rigaku Micro-Max-007 CCD diffractometer by the ω scan technique at 131 K using graphite-monochromated Mo Kα (λ = 0.71073 Å) radiation. An absorption correction by multi-scan was applied to the intensity data. The structures were solved by direct method and the heavy atoms were located from E-map. The remaining non-hydrogen atoms were determined from the successive difference Fourier syntheses. The non-hydrogen atoms were refined anisotropically, whereas the hydrogen atoms were generated geometrically with isotropic thermal parameters. The structures were refined on F^2 by full-matrix least-squares methods using the SHELXTL-97 program package [17]. Crystallographic data and important refinement parameters for $Ir(pdt)_2(phen5f)$ and $[(pdt)_2Ir(\mu\text{-phen5f})YbCl_2 \cdot 2CH_3CH_2OH \cdot H_2O]Cl$ are summarized in Table 1.

3. Results and discussion

3.1. Synthesis and crystal structure

All synthetic routes for Ir^{III} complex and Ir^{III}–Yb^{III} complex are outlined in Scheme 1. The new cyclometalated ligand pdt was designed as the substitute for the previous used ligand ppy (2-phenylpyridinato-N,$C^{2'}$) in $Ir(ppy)_2(phen5f)$ [14]. The complex $Ir(pdt)_2(phen5f)$ was prepared from the reaction of the chloride-bridged Ir^{III} dimmer $(pdt)_2Ir(\mu\text{-Cl})_2Ir(pdt)_2$ and the ligand Hphen5f [18] under the similar conditions as those for the synthesis of $Ir(C^N)_2(O^O)$ [16]. The reaction conditions of $Ir(pdt)_2(phen5f)$ and $YbCl_3 \cdot 6H_2O$ and the crystal growth condition were similar as those used in the synthesis of bimetallic complex $\{[(dfppy)_2Ir(\mu\mu\text{-phen5f})]_3EuCl\}Cl_2$ [18], but the obtained crystal structure and the corresponding element analysis showed that the formation ratio between Ir^{III} and Yb^{III} was 1:1. This result confirmed that the bimetallic complex containing Ir^{III} and Ln^{III} with the ration of 1:1 could stably exist in such system.

The single crystals of $Ir(pdt)_2(phen5f)$ were grown from slowly evaporating solution of EtOH/acetone, and those of $[(pdt)_2Ir(\mu\text{-phen5f})YbCl_2 \cdot 2CH_3CH_2OH \cdot H_2O]Cl$ were obtained using the EtOH solution by slow diffusion of Et_2O. The two X-ray crystal structures are showed in Fig. 1, and both of the structure and metric parameters are shown in Tables 2 and 3. There was distorted octahedral coordination geometry around Ir^{III} ion. The C^N coordination sites were offered by two cyclometalated ligands and the N^N sites are contributed by the ancillary ligand phen5f. The O^O sites are free and in *trans*-form. Furthermore, the Ir–N bond lengths between Ir^{III} ion and the ancillary ligand phen5f is longer than those between Ir^{III} ion and the cyclometalated ligand pdt, which shows the combination of the Ir^{III} ion and C^N ligand anion was tighter than that of the Ir^{III} ion and N^N ancillary ligand. The bond lengths of O(1)–C(13) and O(2)–C(15) are 1.257(9) and 1.244(9) Å, respectively, which shows that the two carbonyl groups in β-diketone are averaged after the hydrogen was taken off in the reaction of the Ir^{III} dimer and Hphen5f.

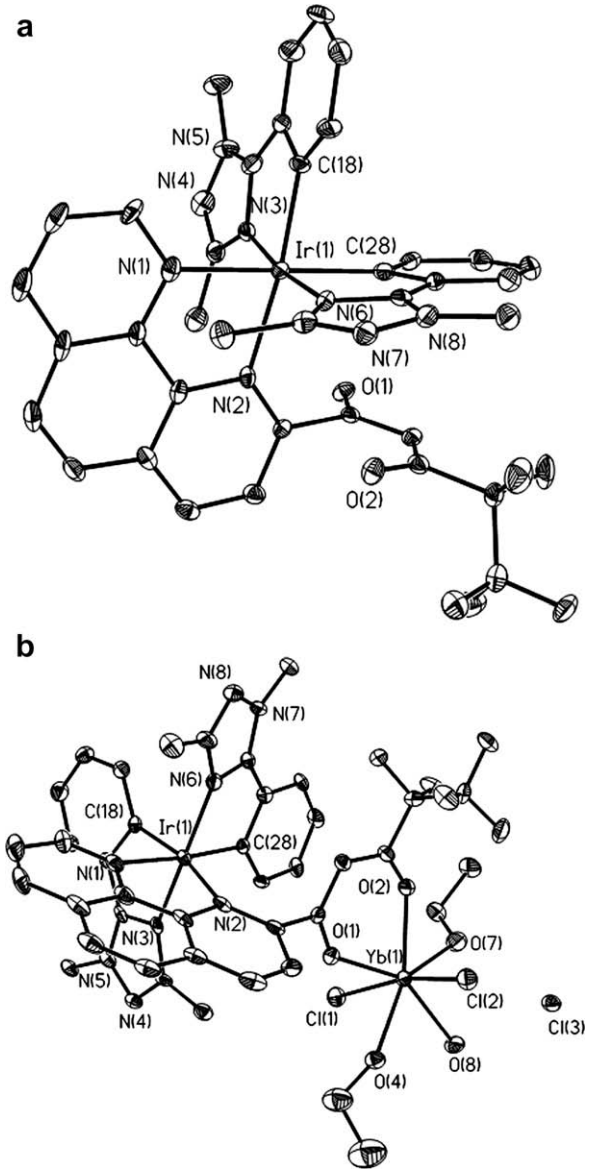


Fig. 1. ORTEP diagrams of $Ir(pdt)_2(phen5f)$ (a) and $[(pdt)_2Ir(\mu\text{-phen5f})Yb\text{-}Cl_2 \cdot 2CH_3CH_2OH \cdot H_2O]Cl$ (b). Thermal ellipsoids are shown in (a) and (b) at 30% probability level and the hydrogen atoms and solvent molecules are omitted for clarity.

Table 2
Selected bond lengths and angles for $Ir(pdt)_2(phen5f)$.

Selected bond lengths (Å)		Selected angles (°)	
Ir(1)–C(28)	2.036(8)	C(28)–Ir(1)–N(6)	79.2(3)
Ir(1)–N(6)	2.049(6)		
Ir(1)–C(18)	2.044(7)	N(3)–Ir(1)–C(18)	80.0(3)
Ir(1)–N(3)	2.043(6)		
Ir(1)–N(1)	2.130(6)	N(1)–Ir(1)–N(2)	77.4(2)
Ir(1)–N(2)	2.165(6)		
O(1)–C(13)	1.257(9)		
O(2)–C(15)	1.244(9)		

Comparing the two bimetallic Ir^{III}–Ln^{III} complexes $[(pdt)_2Ir(\mu\text{-phen5f})YbCl_2 \cdot 2CH_3CH_2OH \cdot H_2O]Cl$ and $\{[(dfppy)_2Ir(\mu\text{-phen5f})]_3EuCl\}Cl_2$, one can find that there is only one Ir^{III} complex-ligand in the former while there are three Ir^{III} complex-ligands in the

Table 3
Selected bond lengths and angles for $[(pdt)_2Ir(\mu\text{-phen5f})Yb\text{-}Cl_2 \cdot 2CH_3CH_2OH \cdot H_2O]Cl$.

Selected bond lengths (Å)		Selected angles (°)		Selected bond lengths (Å)	
Ir(1)–C(28)	2.040(9)	C(28)–Ir(1)–N(6)	79.7(3)	Yb(1)–O(1)	2.237(7)
Ir(1)–N(6)	2.050(7)			Yb(1)–O(2)	2.298(7)
Ir(1)–C(18)	2.008(10)	C(18)–Ir(1)–N(3)	80.0(3)	Yb(1)–O(8)	2.347(7)
Ir(1)–N(3)	2.054(7)			Yb(1)–O(4)	2.350(8)
Ir(1)–N(1)	2.144(8)	N(1)–Ir(1)–N(2)	77.0(3)	Yb(1)–O(7)	2.392(8)
Ir(1)–N(2)	2.210(8)			Yb(1)–Cl(1)	2.575(5)
O(1)–C(13)	1.257(11)			Yb(1)–Cl(2)	2.616(6)
O(2)–C(15)	1.239(13)				

later. This is due to the fact that from Eu^{III} to Yb^{III}, the ionic radii become smaller contributed by the lanthanide contraction. The Yb^{III} ion tends to coordinate with the small molecules, such as ethanol and water, while keeps the coordination number unchanged. The configuration of the two carbonyl groups in the β-diketone has been changed from the *trans*-form to the *cis*-form upon coordination, but the bond length between carbon and oxygen slightly changed solely (Tables 2 and 3). It is obvious that the combination of β-diketone in $Ir(pdt)_2(phen5f)$ and Yb^{III} is tighter than that of EtOH or water and Yb^{III}. The non-bonding distances for Yb···Ir are 6.317 Å.

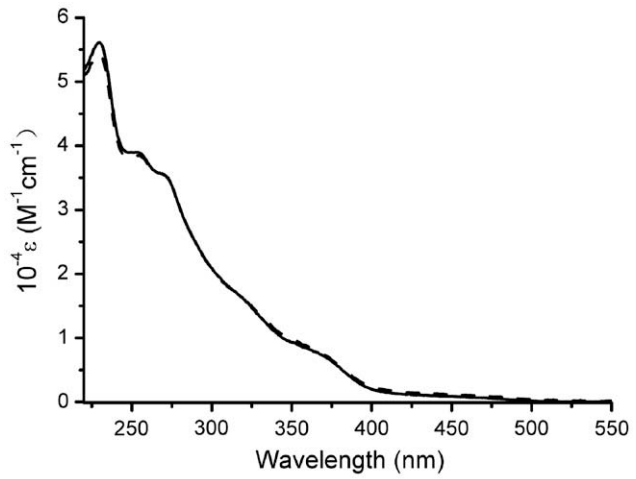


Fig. 2. UV–Vis absorption spectra of $Ir(pdt)_2(phen5f)$ (solid line) and $[(pdt)_2Ir(\mu\text{-phen5f})YbCl_2 \cdot 2CH_3CH_2OH \cdot H_2O]Cl$ (dashed line) in EtOH (1×10^{-5} M) at room temperature.

3.2. Photophysical properties

The absorption spectra of $Ir(pdt)_2(phen5f)$ and $[(pdt)_2Ir(\mu\text{-phen5f})YbCl_2 \cdot 2CH_3CH_2OH \cdot H_2O]Cl$ in ethanol are shown in Fig. 2. For $Ir(pdt)_2(phen5f)$, the short wavelength region below around 280 nm should be due to the π–π^* transitions of the ligands [15], while the longer wavelength region from 400 to 470 nm should be mainly assigned to the mixture of the ^{3}MLCT (metal-to-ligand charge transfer) transition in the $Ir(pdt)^{2+}$ moiety or the transition from Ir^{III} to phen5f. Moreover, $[(pdt)_2Ir(\mu\text{-phen5f})YbCl_2 \cdot 2CH_3CH_2OH \cdot H_2O]Cl$ exhibited such similar absorption properties as $Ir(pdt)_2(phen5f)$ because they had the same absorption ligand while the absorption of $YbCl_3$, ethanol and water in the range were quite small.

However, the complex $Ir(pdt)_2(phen5f)$ showed hardly observed emission in EtOH solution at room temperature. Both of the ^{3}MLCT from Ir^{III} to the cyclometalated ligand pdt [15] and to the ancillary ligand phen [19] should exhibit the corresponding phosphorescence emissions. The absence of emission might be caused by some special radiationless transitions which we have not still understood clearly. It might be induced by the rotation or vibration of the β-diketone part in the phen5f ligand, and this assume was supported by the following fact. When the EtOH solution was cooled down to 77 K, the low-temperature emission spectrum of $Ir(pdt)_2(phen5f)$ was observed in an EtOH rigid matrix as expected (Fig. 3). It showed the main peaks around 507 and 535 nm. This fact implied that the $Ir(pdt)_2(phen5f)$ complex-ligand might be suitable for the sensitization of Yb^{III} for NIR emission.

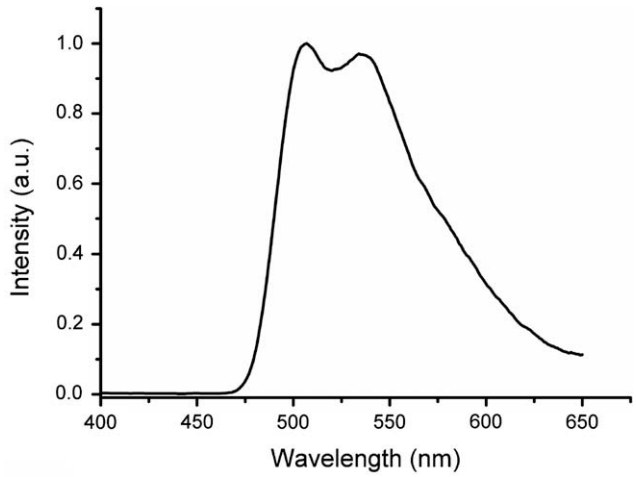


Fig. 3. Emission of $Ir(pdt)_2(phen5f)$ in an EtOH rigid matrix (1×10^{-5} M) at 77 K.

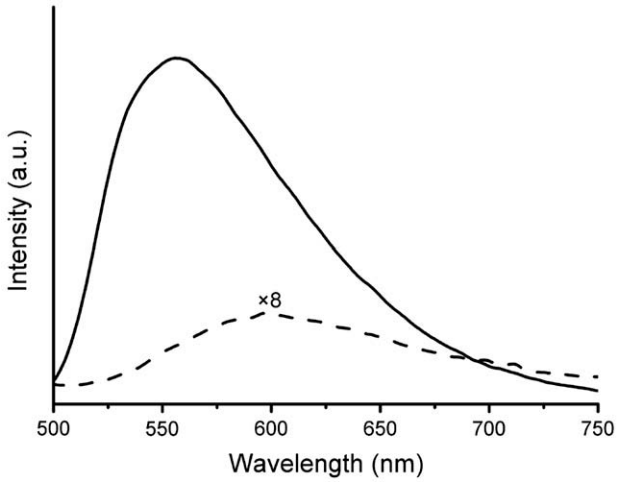


Fig. 4. Solid-state emission spectra (powdered samples) in visible region of $Ir(pdt)_2(phen5f)$ (solid line) and $[(pdt)_2Ir(\mu\text{-phen5f})YbCl_2 \cdot 2CH_3CH_2OH \cdot H_2O]Cl$ (dashed line).

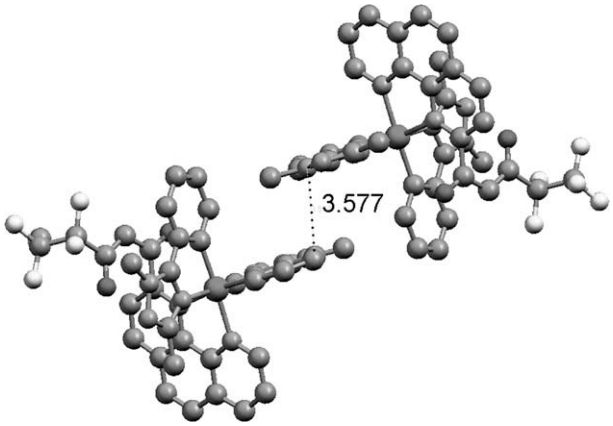


Fig. 5. Intermolecular π–π interaction in the crystal structure of $Ir(pdt)_2(phen5f)$.

The solid emissions at room temperature from $Ir(pdt)_2(phen5f)$ and $[(pdt)_2Ir(\mu\text{-}phen5f)YbCl_2 \cdot 2CH_3CH_2OH \cdot H_2O]Cl$ are shown in Fig. 4. Powdered $Ir(pdt)_2(phen5f)$ luminesced yellow-green with a maximum around 556 nm, which was red shifted when it was compared with what we observed in an EtOH matrix at 77 K (Fig. 3). This result might originate from the face to face π–π overlap interactions between aromatic molecules in the solid state and be ascribed to excimer formation [20], which is confirmed by the crystal packing of $Ir(pdt)_2(phen5f)$. The π–π spacing between the pdt ligands of adjacent molecules is *ca.* 3.58 Å (Fig. 5). Moreover, the solvent effect in the EtOH system should be another important factor for the differences between the emissions. When Yb^{III} ion

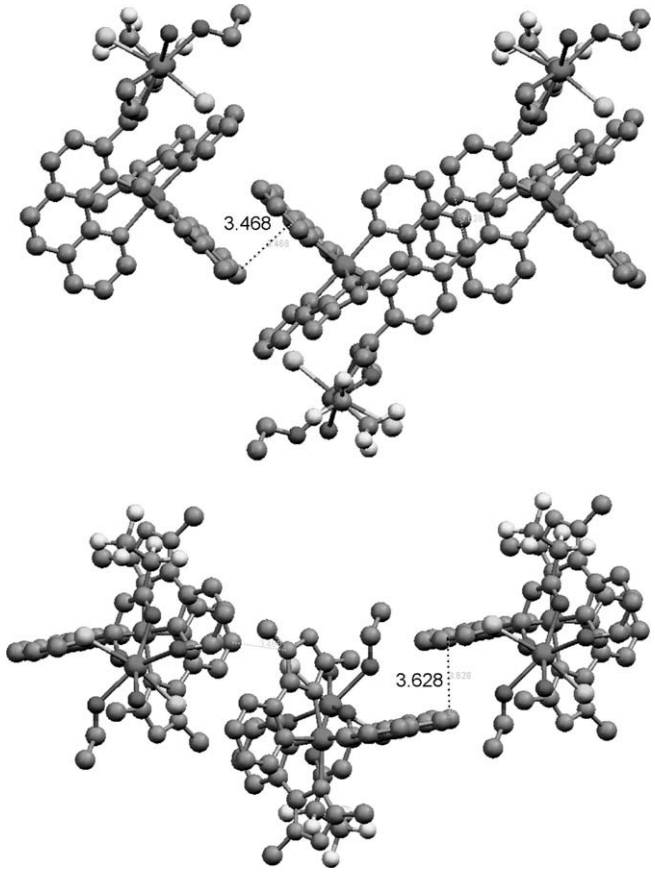


Fig. 6. Intermolecular π–π interaction in the crystal structure of $[(pdt)_2Ir(\mu\text{-}phen5f)YbCl_2 \cdot 2CH_3CH_2OH \cdot H_2O]Cl$.

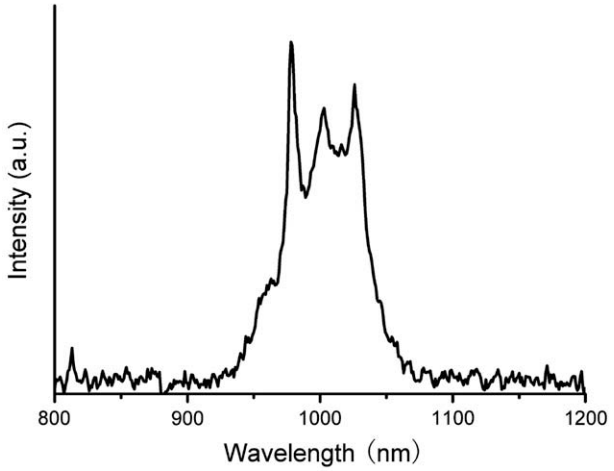


Fig. 7. Solid-state NIR emission spectrum (powdered samples) of $[(pdt)_2Ir(\mu\text{-}phen5f)YbCl_2 \cdot 2CH_3CH_2OH \cdot H_2O]Cl$.

was incorporated in the complex and the bimetallic complex $[(pdt)_2Ir(\mu\text{-}phen5f)YbCl_2 \cdot 2CH_3CH_2OH \cdot H_2O]Cl$ was formed, one could find that the emission around 610 nm was very weak. From the packing of $[(pdt)_2Ir(\mu\text{-}phen5f)YbCl_2 \cdot 2CH_3CH_2OH \cdot H_2O]Cl$, the π–π spacing between the pdt ligands and the phen5f ligands of adjacent molecules is *ca.* 3.47 and 3.63 Å, respectively (Fig. 6). The latter could cause the red shift in the emission maximum for bimetallic complex. Emission quenching implied that the energy transfer occurred in the analogous Ir^{III}–Ln^{III} bimetallic complexes.

Upon irradiation of the MLCT absorption of the Ir complex at 490 nm, the emission spectrum of $[(pdt)_2Ir(\mu\text{-}phen5f)YbCl_2 \cdot 2CH_3\text{-}CH_2OH \cdot H_2O]Cl$ was measured (Fig. 7). There is only one emission band around 978 nm affected by crystal-field splitting which is assigned to the $^2F_{5/2} \rightarrow {}^2F_{7/2}$ transition. The results of emission quenching in visible region and obtained NIR emission indicated that the energy transfer from Ir^{III} moiety to Yb^{III} center occurred.

However, the NIR emission from $[(pdt)_2Ir(\mu\text{-}phen5f)YbCl_2 \cdot 2CH_3CH_2OH \cdot H_2O]Cl$ was not very strong, and the emission from the solution was not obtained under our experiment conditions. The possible factors could be found from the structure of the bimetallic complex $[(pdt)_2Ir(\mu\text{-}phen5f)YbCl_2 \cdot 2CH_3\text{-}CH_2OH \cdot H_2O]Cl$. Firstly, there were ethanol and water molecules in the coordination environment, which might seriously quench the photoluminescence, especially the NIR emission. Secondly, there were only one Ir^{III} complex-ligand $Ir(pdt)_2(phen5f)$ in $[(pdt)_2Ir(\mu\text{-}phen5f)YbCl_2 \cdot 2CH_3CH_2OH \cdot H_2O]Cl$ while there were usually two or more ligands around the center Ln^{III} ion, which indicated that more antennae participating in the light harvesting would be favorable for emission. Moreover, the triplet state level of the complex $Ir(pdt)_2(phen5f)$ was a little higher than the energy level of Yb^{III}, which might make the energy transfer from the Ir^{III} center to the Yb^{III} center less efficient.

4. Conclusions

A new cyclometalated ligand 1,3-dimethyl-5-phenyl-1H-[1,2,4]-triazole (pdt) was synthesized, and the corresponding Ir^{III} complex $Ir(pdt)_2(phen5f)$ was obtained. The bimetallic complex $[(pdt)_2Ir(\mu\text{-}phen5f)YbCl_2 \cdot 2CH_3CH_2OH \cdot H_2O]Cl$ was synthesized by the approach of "complexes as ligands". Meanwhile, the emission quenching was observed in the solid state of the Ir^{III} and Ir^{III}–Yb^{III} complex. Upon irradiation of the MLCT absorption of $Ir(pdt)_2(phen5f)$, the characteristic emission of Yb^{III} was obtained with a peak around 978 nm. And the crystal packing of the Ir^{III}

and Ir^{III}–Yb^{III} complex implied that the similar combination principles between the cyclometalated ligands and bridge ligands might exist in these Ir^{III} systems sensitizing NIR lanthanide emission.

Acknowledgements

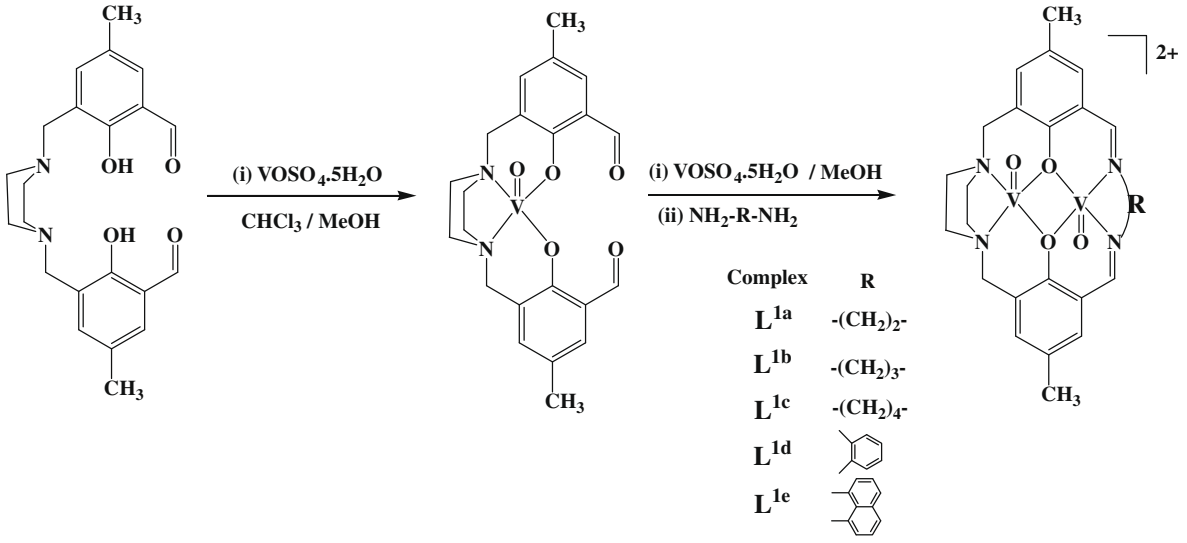
The authors are grateful to the National Basic Research Program (2006CB601103) and the NNSFC (20461002, 20471004, 50772003 and 20671006) for financial support.

Appendix A. Supplementary data

CCDC 694308 and 694309 contains the supplementary crystallographic data for this article. These data can be obtained free of charge via http://www.ccdc.cam.ac.uk/conts/retrieving.html, or from the Cambridge Crystallographic Data Centre, 12 Union Road, Cambridge CB2 1EZ, UK; fax: (+44) 1223-336-033; or e-mail: deposit@ccdc.cam.ac.uk. Supplementary data associated with this article can be found, in the online version, at doi:10.1016/j.poly.2008.12.043.

References

[1] K. Kuriki, Y. Koike, Y. Okamoto, Chem. Rev. 102 (2002) 2347.
[2] T.S. Kang, B.S. Harrison, M. Bouguettaya, T.J. Foley, J.M. Boncella, K.S. Schanze, J.R. Reynolds, Adv. Funct. Mater. 13 (2003) 205.
[3] Y. Kawamura, Y. Wada, Y. Hasegawa, M. Iwamuro, T. Kitamura, S. Yanagida, Appl. Phys. Lett. 74 (1999) 3245.
[4] D. Parker, Chem. Soc. Rev. 33 (2004) 156.
[5] G.R. Motson, J.S. Fleming, S. Brooker, Adv. Inorg. Chem. 55 (2004) 361.
[6] J.-C.G. Bünzli, C. Piguet, Chem. Soc. Rev. 34 (2005) 1048.
[7] S. Comby, J.-C.G. Bünzli, in: K.A. Gschneidner Jr., J.-C.G. Bünzli, V.K. Pecharsky (Eds.), Handbook on the Physics and Chemistry of Rare Earths, vol. 37, Elsevier, Amsterdam, 2007 (Chapter 235).
[8] J. Zhang, P.D. Badger, S.J. Geib, S. Petoud, Angew. Chem., Int. Ed. 44 (2005) 2508.
[9] J.C.G. Bünzli, C. Piguet, Chem. Rev. 102 (2002) 1897.
[10] D. Parker, R.S. Dickins, H. Puschmann, C. Crossland, J.A.K. Howard, Chem. Rev. 102 (2002) 1977.
[11] M.D. Ward, Coord. Chem. Rev. 251 (2007) 1663.
[12] Z.N. Chen, Y. Fan, J. Ni, Dalton Trans. (2008) 573.
[13] M. Mehlstäubl, G.S. Kottas, S. Colella, L. De Cola, Dalton Trans. (2008) 2385.
[14] F.-F. Chen, Z.-Q. Bian, B. Lou, E. Ma, Z.-W. Liu, D.-B. Nie, Z.-Q. Chen, J. Bian, Z.-N. Chen, C.-H. Huang, Dalton Trans. (2008) 577.
[15] S.C. Lo, C.P. Shipley, R.N. Bera, R.E. Harding, A.R. Cowley, P.L. Burn, I.D.W. Samuel, Chem. Mater. 18 (2006) 5119.
[16] S. Lamansky, P. Djurovich, D. Murphy, F. Abdel-Razzaq, H.-E. Lee, C. Adachi, P.E. Burrows, S.R. Forrest, M.E. Thompson, J. Am. Chem. Soc. 123 (2001) 4304.
[17] G.M. Sheldrick, SHELXTL, Version 5.1, Bruker Analytical X-ray System Inc., Madison, WI, 1997.
[18] F.-F. Chen, Z.-Q. Bian, Z.-W. Liu, D.-B. Nie, Z.-Q. Chen, C.-H. Huang, Inorg. Chem. 47 (2008) 2507.
[19] R.J. Watts, G.A. Crosby, J. Am. Chem. Soc. 94 (1972) 2606.
[20] S. Lamansky, P. Djurovich, D. Murphy, F. Abdel-Razzaq, R. Kwong, I. Tsyba, M. Bortz, B. Mui, R. Bau, M.E. Thompson, Inorg. Chem. 40 (2001) 1704.



Scheme 1. Synthesis of mono and binuclear $V^{IV}O$ complexes.

complexes with unsymmetrical bicompartmental macrocyclic ligands (Scheme 1), which have one tetradentate compartment (N2O2) comprising of two piperazinyl nitrogens and two phenolic oxygens, and another tetradentate compartment (N2O2) comprising of two phenolic oxygens and two imine nitrogen atoms. The distance between the two vanadium centers is fixed by the two bridging phenolate ligands, while the distortion in geometry and stability of the complexes is varied by changing one of the compartmental ring sizes by condensing various aliphatic and aromatic diamines.

2. Experimental

2.1. Physical measurements

Elemental analysis was carried out on a Carlo Erba model 1106 elemental analyzer. FT-IR spectra were obtained on a Perkin Elmer FT-IR spectrometer with samples prepared as KBr pellets. UV–Vis spectra were recorded using a Perkin Elmer Lambda 35 spectrophotometer operating in the range 200–1400 nm with quartz cells and ε are given in M^{-1} cm^{-1}. Electrospray ionization mass spectral measurements were made using a Thermo Finnigan LCQ-6000 Advantage Max-ESI mass spectrometer. Cyclic voltammograms were obtained on a CH11008 Electrochemical analyzer using a three- electrode set-up comprising of a glassy carbon working, platinum wire auxiliary and a saturated Ag/AgCl reference electrode under oxygen-free conditions. The concentration of the complexes was 10^{-3} M. TBAP (Tetra(*n*-butyl)ammonium perchlorate) (10^{-1} M) was used as the supporting electrolyte. EPR spectra were recorded on powdered samples of **1a–1e** using a JEOL TES 100 ESR spectrometer. Low temperature measurements were made using a liquid nitrogen Dewar. The room temperature magnetic moment was measured on a PAR vibrating sample magnetometer model 155.

2.2. Materials

5-Methylsalicylaldehyde and the precursor compound 6,6′-piprazine-1,4-diyl-dimethylene bis (4-methyl-2-formyl-phenol) (**I**) were prepared by the literature methods [18,19]. Tetra(*n*-butyl)ammonium perchlorate (TBAP), used as the supporting electrolyte in the electrochemical measurements, was purchased from Fluka and recrystallized from hot methanol (Caution! All perchlorate salts are potentially explosive, hence care should be taken in handling TBAP). All the solvents were purified by the reported procedures [20]. The supercoiled pBR322 DNA and calf thymus (CT) DNA was purchased from Bangalore Genei (India). Superoxide dismutase (SOD), ethidium bromide (EB) and L-histidine were obtained from Sigma (USA). Tris(hydroxymethyl)aminomethane–HCl (Tris–HCl) buffer solution was prepared by using deionized, triple distilled water.

2.3. General methods

2.3.1. DNA binding and cleavage experiments

The DNA binding experiments were performed in Tris–HCl/NaCl buffer (50 mM Tris HCl/1 mM NaCl buffer, pH 7.5) using DMF (dimethylformamide) solution (10%) of the oxidovanadium(IV) complexes **1b**, **1d** and **1e**. The concentration of calf thymus (CT) DNA was determined from the absorption intensity at 260 nm with a ε value [21] of 6600 M^{-1} cm^{-1}. Absorption titration experiments were made using different concentrations of CT DNA, keeping the concentration of the complexes constant, with due correction for the absorbance of the CT DNA itself. Samples were equilibrated before recording each spectrum. The fluorescence spectral method using ethidium bromide (EB) as a reference was used to determine the relative DNA binding properties of the complexes **1d** and **1e** to calf thymus (CT) DNA (50 mM Tris HCl/1 mM NaCl buffer, pH 7.5). Fluorescence intensities of EB at 620 nm with an excitation wavelength of 450 nm were measured at different complex concentrations. Reduction in the emission intensity was observed with addition of the complexes. The relative binding tendency of the complexes to CT DNA was determined from a comparison of the slopes of the lines in the fluorescence intensity versus complex concentration plot. The apparent binding constant (K_{app}) was calculated using the equation $K_{EB}[EB]/K_{app}[complex]$, where the complex concentration was the value at a 50% reduction of the fluorescence intensity of EB and $K_{EB} = 1.0 \times 10^7$ M^{-1} ([EB] = 1.3 μM) [21]. The cleavage of supercoiled pBR322 DNA by the complexes was studied by agarose gel electrophoresis. The gel electrophoresis experiments were performed as follows: pBR322 DNA (0.2 μg, 33 μM) was treated with the complexes **1c** and **1e** in 50 mM Tris–HCl/NaCl buffer (pH 7.2) and H_2O_2, followed by dilution with Tris–HCl buffer to a total volume of 18 μL. All the samples were incubated for 1 h at 37 °C, followed by their addition to the loading buffer containing 25% bromophenol blue, 0.25% xylene cyanol and

30% glycerol (3 μL). The solution was finally loaded on 0.8% agarose gel containing 1.0 μg/mL^{-1} of ethidium bromide. Electrophoresis was done for 1 h at 50 V in TBE (45 mM Tris, 45 mM H_3BO_3, 1 mM-EDTA, pH 8.3) buffer. Bands were visualized by UV light and photographed.

2.3.2. Antibacterial and antifungal assays

The agar diffusion method was followed for antibacterial and antifungal susceptibility tests. Petri plates were prepared by pouring 10 ml of Mueller Hinton Agar for bacteria, and allowed to solidify. These agar plates were inoculated with 0.1 ml of a standardized bacterial suspension (2×10^6 cells/ml) and uniformly spread. A 6 mm well was cut at the center of the agar plate and the well was filled with a solution of the complexes (**1a**–**1e** separately). The diameter of the inhibition zone observed around the well was measure for each bacterium after 24 h of incubation at 37 °C. One well was filled with sterile distilled water to serve as a control. For fungus, Sabouraud Dextrose Agar medium was amended with the complexes (**1a**–**1e** separately) when the medium was warm, and poured into Petri plates. After solidification of the medium, mycelial disks (6 mm diameter) of the test fungi were inoculated at the center of the plates. The diameter of the inhibition zone for each fungus was measured after 48 h of incubation at 28 °C. The mechanism of inhibition was determined by measuring the change in the cell wall permeability. An increase in conductivity of the bacterial and fungal suspension treated with complexes (**1a**–**1e**) indicates an alteration in the cell wall permeability or injury to the cell wall leading to the non-specific release of electrolytes and free amino acids from the cells. The conductivity of the bacterial suspension and fungal mycelial suspension in sterile distilled water without the addition of complexes served as a control. The concentration of the bacterial cells and fresh weight of the fungal mycelia were kept constant. Conductivity was measured using a Conductivity Meter and expressed in micro Siemens.

2.4. Synthesis of mono and binuclear vanadyl complexes

To a solution of the precursor compound (**I**) (4.35 g, 10 mmol) in $CHCl_3$/MeOH (50 ml 1:1), a methanolic solution of vanadyl sulfate (2.52 g, 10 mmol) was added dropwise under constant stirring. A brown colored mononuclear complex precipitated. The solid was separated by filtration and washed with isopropyl alcohol and diethyl ether. Yield: 2.82 g (34%). The binuclear vanadyl complexes were prepared from a general procedure in which to a vigorously stirred suspension of the mononuclear complex (1 g, 2.4 mmol) in methanol (20 ml), a methanolic solution of vanadyl sulfate (0.6 g, 2.4 mmol) was added slowly, and the mixture was stirred for 15 min to obtain a clear solution. Then, a methanolic solution (5 ml) of the corresponding diamine (0.07 g, 1,2-diamino ethane; 0.08 g, 1,3-diaminopropane; 0.1 g, 1,4-diaminobutane; 0.13 g, 1,2-diaminobenzene; 0.19 g, 1,8-diaminonaphthalene; 1.2 mmol) was added dropwise to the above solution and refluxed for 6 h. The resulting solid that separated out on evaporating the solution at room temperature and the resulting compound was washed with ether and dried. All the compounds were recrystallized from acetonitrile solution. [Yield: ~80%]. For **1a**, green solid, Yield: 0.8 g (62%). *Anal.* Calc. for $C_{24}H_{28}N_4O_8SV_2$: C, 45.42; H, 4.41; N, 8.83. Found: C, 45.72; H, 4.61; N, 8.62%. ESI mass in CH_3CN: *m/z* 269.2 $[(VO)_2L^{1a}]^{2+}$. For **1b**, green solid, Yield: 0.86 g (64%). *Anal.* Calc. for $C_{25}H_{30}N_4O_8SV_2$: C, 46.29; H, 4.62; N, 8.64. Found: C, 46.34; H, 4.81; N, 8.73%. ESI mass in CH_3CN: *m/z* 276.3 $[(VO)_2L^{1b}]^{2+}$. For **1c**, pale green solid, Yield: 0.96 g (70%). *Anal.* Calc. for $C_{26}H_{32}N_4O_8SV_2$: C, 47.13; H, 4.83; N, 8.46. Found: C, 47.26; H, 4.96; N, 8.34%. ESI mass in CH_3CN: *m/z* 283.2 $[(VO)_2L^{1c}]^{2+}$. For **1d**, orange solid, Yield: 0.89 g (63%). *Anal.* Calc. for $C_{28}H_{28}N_4O_8SV_2$: C, 49.26; H, 4.11; N, 8.21. Found: C, 49.36; H, 4.28; N, 8.41%. ESI mass in CH_3CN: *m/z* 293.5 $[(VO)_2L^{1d}]^{2+}$. For **1e**, brown solid, Yield: 1.1 g (72%). *Anal.* Calc. for $C_{32}H_{30}N_4O_8SV_2$: C, 52.45; H, 4.09; N, 7.65. Found: C, 52.57; H, 4.15; N, 7.78%. ESI mass in CH_3CN: *m/z* 318.6 $[(VO)_2L^{1e}]^{2+}$.

3. Results and discussion

3.1. Spectral studies

The IR spectrum of the precursor compound shows a peak at 1650–1680 cm^{-1} due to the presence of a CHO group. The formation of an imine group (C = N) in the macrocyclic complexes by Schiff base condensation between CHO and NH_2 is evidenced by the appearance of a strong peak at 1610–1630 cm^{-1}. The strong peak around 1110–1120 cm^{-1} may due to the sulfate ion. The electronic spectra of all the complexes were measured in CH_3CN at 298 K for the range 300–800 nm. They all show a weak band in the range 570–600 nm due to metal centered d–d transitions [22,23]. Moderately intense charge transfer bands appear in the range 350–450 nm. These bands are due to charge transfer from the azomethine nitrogen and phenoxide oxygen to $V^{IV}O$ ion [24]. A strong peak in the range 250–290 nm is due to a intraligand transition (π–π^*). The absorption maxima for the d–d transition suggest that the geometry around the vanadyl ion is approximately square pyramid [25,26]. Further, the complexes reported in the present work show that on moving from **1a** to **1e** increase in λ_{max} (red shift) of the d–d transition of the $V^{IV}O$ ion is observed. It indicates that the coordination geometry of complex **1a** is less distorted [27,28] than that of the later complexes **1b**, **1c**, **1d** and **1e**. ESI mass spectral data of the binuclear $V^{IV}O$ complexes confirm the proposed formula of the complexes. The EPR spectra of the solid complexes **1a**–**1e** were recorded at liquid nitrogen temperature (LNT). All the binuclear complexes showed a single broad-band resonance (Fig. 1) at ca. *g* = 1.98–2.03 (Table 1) with the half field signal at 1500 G (*M* = ±2), which suggest magnetic interactions between two vanadyl ions through the phenolate bridge.

3.2. Cyclicvoltammetric studies

The electrochemical properties of complexes **1a–1e** were studied by cyclic voltammetry. The cyclic voltammogram of **3a** recorded in acetonitrile is given in Fig. 2. The electrochemical data are summarized in Table 2. For all the complexes two quasi-reversible waves were observed. Coulometric experiments indicated that each of the couples is involved in a one electron transfer process.

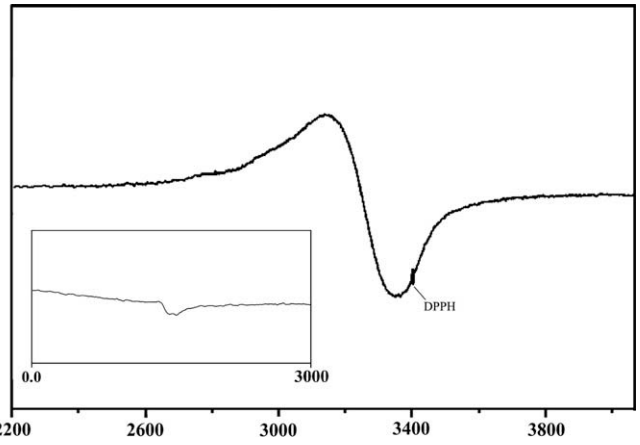


Fig. 1. X-band EPR spectrum of frozen solid (**1c**) at 77 K. Inset gives the EPR spectrum showing the $\Delta M_s = \pm 2$ transition.

Table 1
Characteristic data of the binuclear macrocyclic $V^{IV}O$ complexes.

Complex	IR (cm^{-1}) (KBr disk) (br, broad; s, strong)	λ_{max}/nm ($\epsilon/M^{-1}\,cm^{-1}$) (sh, shoulder)	ESR/magnetic	
			g	μ_{eff}, μ_B at 298 K
1a	3445br, 2923s, 1608s, 985s, 600s	570 sh (220), 370 (10,580), 265 (1,210)	1.97	1.70
1b	3449br, 2926s, 1628s, 975s, 605s	582 sh (250), 380 (10,900), 270 (25,900)	1.99	1.71
1c	3448br, 2928s, 1630s, 980s, 610s	596 sh (222), 385 (10,894), 290 (12,796)	2.01	1.75
1d	3440br, 2921s, 1625s, 962s, 610s	600 sh (230), 370 (11,240), 268 (22,350)	2.03	1.73
1e	3440br, 2921s, 1625s, 962s, 610s	600 sh (230), 370 (11,240), 268 (22,350)	2.04	1.72

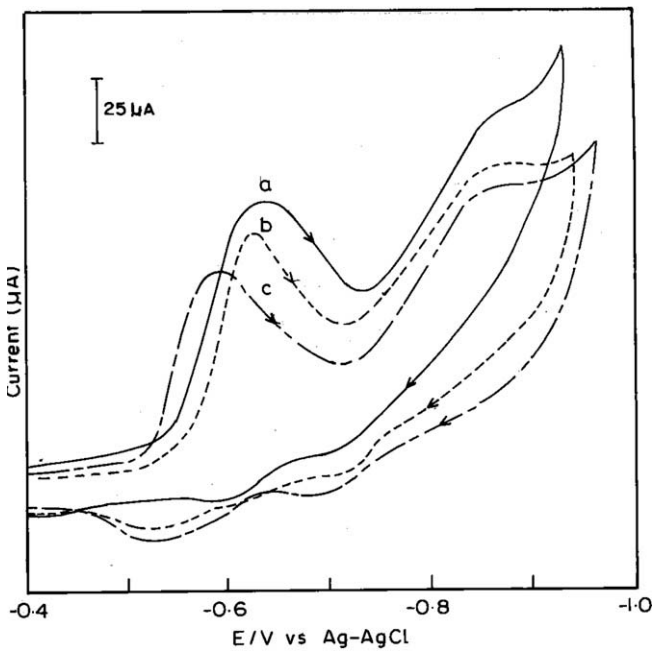


Fig. 2. Cyclicvoltammograms of the macrocyclic binuclear vanadyl(IV) complexes **1a**, **1b** and **1c** (1×10^{-3} M in DMF) in the cathodic region.

Based on these observations, it is reasonable to suggest that the reduction process may involve the stepwise redox processes depicted below:

$$(V^{IV}O)_2 \rightleftharpoons V^{III}OV^{IV}O_2 \rightleftharpoons (V^{III}O)_2.$$

The first redox potentials of the complexes are in the range ($E_{½}$) −0.51 to −0.63 V, and are assigned to the vanadyl ion present in the azomethine moiety. The second redox potentials of all the complexes were observed in the range ($E_{½}$) −0.74 to −0.78 V. The more negative potentials of the second quasi-reversible peaks are assigned to reduction of the vanadyl(IV) ion, which is located in the piperazinyl [29] moiety. As the size of the macrocycle is increased, an anodic shift of first reduction potential is observed for the binuclear $V^{IV}O$ complexes, which is consistent with reported observations [30]. As the chain length of the alkylimine compartment increases, the entire macrocyclic ring becomes more flexible, which enables easier reduction [31,32]. The ΔE_p values of first redox couple of the unsymmetrical $V^{IV}O$ complexes **1a**–**1c** decreases with the increasing chain between the two imine N atoms, easing the reduction process. The same trends were observed for the complexes of ligands **1d** and **1e**, which contain aromatic diimines. As the chelate ring size increases, the reduction potential shifts from $E^1_{pc} = -0.56$ to -0.54 V and $E^2_{pc} = -0.85$ to -0.83 V. From the cyclic voltammetric studies it can be stated that the complexes containing aromatic diimines get reduced at higher negative potentials than the complexes containing aliphatic diimines. The higher reduction potential can be attributed due to the greater planarity and electronic properties that are associated with aromatic rings [33].

In the positive potential region (+0.50 to +1.00 V) two quasi-reversible oxidation couples are observed for all the complexes. The cyclic voltammograms of the complexes are shown in Fig. 3 and the data are summarized in Table 3. A controlled potential electrolysis experiment indicates that the two oxidation peaks

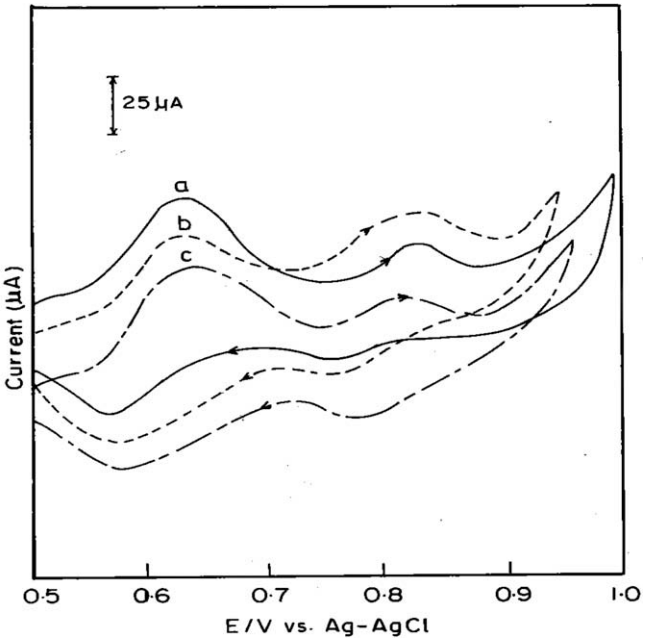


Fig. 3. Cyclicvoltammograms of the macrocyclic binuclear vanadyl(IV) complexes **1a**, **1b** and **1c** (1×10^{-3} M in DMF) in the anodic region.

Table 2
Electrochemical data of the binuclear $V^{IV}O$ complexes in the cathodic potential region.

Complex	E^1_{pc} (V)	E^1_{pa} (V)	$E_{½}$ (V)	ΔE_p (mV)	E^2_{pc} (V)	E^2_{pa} (V)	$E_{½}$ (V)	ΔE_p (mV)
1a	−0.67	−0.59	−0.63	80	−0.85	−0.71	−0.78	140
1b	−0.63	−0.54	−0.59	90	−0.83	−0.72	−0.77	110
1c	−0.59	−0.52	−0.56	70	−0.80	−0.69	−0.74	110
1d	−0.56	−0.49	−0.53	70	−0.85	−0.67	−0.76	180
1e	−0.54	−0.48	−0.51	60	−0.83	−0.66	−0.75	170

Table 3
Electrochemical data of the binuclear $V^{IV}O$ complexes in the anodic potential region.

Complex	E^1_{pc} (V)	E^1_{pa} (V)	$E_{½}$ (V)	ΔE_p (mV)	E^2_{pc} (V)	E^2_{pa} (V)	$E_{½}$ (V)	ΔE_p (mV)
1a	0.63	0.56	0.59	70	0.84	0.78	0.81	60
1b	0.65	0.57	0.61	80	0.85	0.77	0.81	80
1c	0.66	0.58	0.62	80	0.82	0.79	0.80	30
1d	0.72	0.65	0.68	70	0.93	0.81	0.87	120
1e	0.78	0.72	0.75	60	0.97	0.83	0.90	140

are associated with a stepwise oxidation process at the metal center

$$(V^{IV}O)_2 \rightleftharpoons V^{V}OV^{IV}O_2 \rightleftharpoons (V^{V}O)_2.$$

The first and second oxidation potentials of the complexes **1a**–**1c** shift towards more positive values from (E^1_{pc}) +0.63 to +0.78 V and (E^2_{pc}) +0.82 to +0.97 V as the number of methylene groups (chain length) increases in the imine compartment. This is because as the ring size increases, due to flexibility, the geometry around vanadium ion gets more distorted. For example the first oxidation potential of the complex **1c** is +0.66 V (E^1_{pc}). This potential is more positive when compared to the first and second oxidation potentials of complexes **1b** and **1a**. Similar trend has been observed for complexes **1d** and **1e**. This is because for complexes with aromatic diimines, an increase in unsaturation will decrease the electron density on the metal ions through delocalization, which prevents the easy oxidation of the metal ions in the macrocyclic ring.

3.3. DNA binding and cleavage studies

3.3.1. Absorption spectra studies

In the present investigation the interaction of the macrocyclic binuclear oxidovanadium(IV) complexes **1b**, **1d** and **1e** in DMF solutions (10%) with CT DNA have been investigated by UV absorption spectroscopy. Absorption titration experiments of $V^{IV}O$ complexes in buffer were performed by using a fixed complex concentration to which increments of the DNA stock solution were added. The binding ability of the complexes with CT DNA was studied by UV spectroscopy by following the intensity changes of the intraligand π–π^* transition band 200–220 nm. The binding of $V^{IV}O$ complexes to duplex DNA led to a decrease in the absorption intensities (Fig. 4) with a small amount of red shift in the UV–Vis absorption spectra. For the complexes **1b**, **1d** and **1e** the intrinsic binding constant K_b has been determined from the spectral titration data (Fig. 5) using the following equation [34]

$$[DNA]/(\varepsilon_a - \varepsilon_f) = [DNA]/(\varepsilon_b - \varepsilon_f) + 1/K_b(\varepsilon_b - \varepsilon_f).$$

Here, ε_a, ε_f and ε_b correspond to A_{obsd}/[$V^{IV}O$ complex], the extinction coefficient for the free complex, and the extinction coefficient for the complex in the fully bound form, respectively. The binding constants (K_b) of complexes **1b**, **1d** and **1e** are calculated as 3.02×10^4, 5.23×10^4 and 9.18×10^4 M^{-1}, respectively. The K_b values are lower than those reported for the typical classical intercalator ethidium bromide (EB) DNA, 3.3×10^5 M^{-1} in 50 mM Tris–HCl/1.0 mM NaCl buffer, pH 7.5 [35]. After intercalating the base pairs of DNA, the π^* orbital of the intercalated ligand can couple with the π orbital of the base pairs, thus decreasing the transition π–π^* energy and resulting in bathochromism. On the other hand, the coupling π orbital is partially filled by electrons, thus decreasing the transition probabilities and concomitantly resulting in hypochromism. [36]. The appreciable decrease in absorption intensity and significant red shift of the π–π^* band of complexes **1b**, **1d** and **1e** suggest that the complexes bind to DNA strongly. Complex **1e** show a minor bathochromic shift of the spectral band, of ~3 nm, suggesting a groove binding preference of the complex. Structurally, the ligand **1e** should provide an aromatic moiety to overlap with the stacking base pairs of the DNA helix by intercalation, which results in hypochromism and bathochromism. The higher binding propensity of complexes **1d** and **1e** may be probably due to the presence of more aromatic moieties [37] than the other $V^{IV}O$

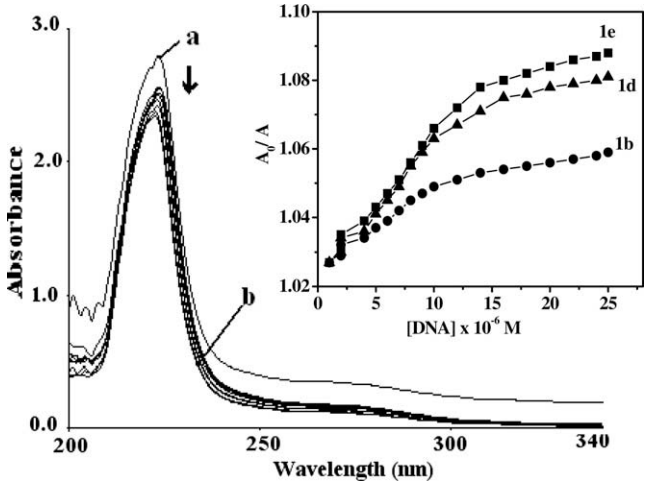


Fig. 4. Absorption spectra of the complex **1e** (1×10^{-5} M) in the absence (a) and presence of increasing amounts (b) of CT DNA (0–2.5×10^{-6} M) at room temperature in 50 mM Tris–HCl/NaCl buffer (pH 7.5). The arrow indicates decreasing absorbance with increasing DNA concentration. Insets shows the saturation in absorption intensity hypochromism (**1b**, **1d** and **1e**) is indicated by the plot of A_o/A versus [DNA].

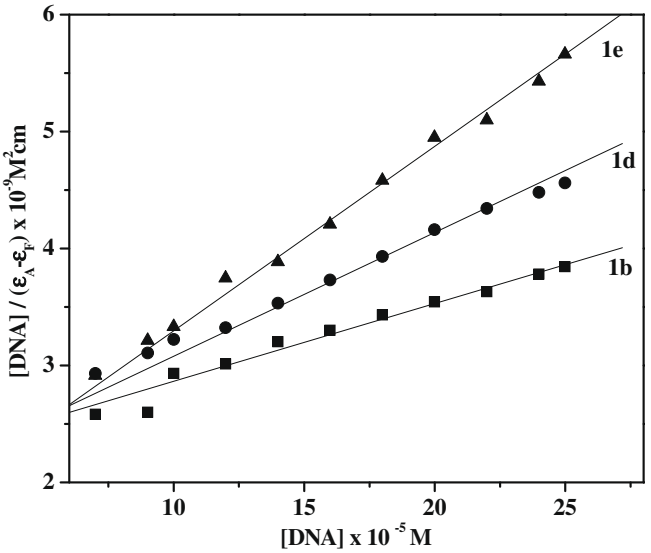


Fig. 5. The plots of [DNA]/(ε_a–ε_f) versus [DNA] for the titration of DNA with vanadyl(IV) complexes **1b**, **1d** and **1e**.

complex, **1b**. The increased aromatic moieties in the macrocyclic ligands of the oxidovanadium(IV) complexes facilitates their potential intercalative and/or DNA major groove binding, while complex **1b** may prefer minor groove binding.

3.4. Fluorescence spectra studies

Fluorescence measurements were performed to study the metal interaction with DNA using a Perkin Elmer spectrofluorimeter. Ethidium bromide (EB) is one of the most sensitive fluorescence probes that can bind with DNA [13]. The fluorescence of EB increases after intercalating into DNA. If the metal intercalates into DNA, it leads to a decrease in the binding sites of DNA available for EB, resulting in a decrease in the fluorescence intensity of the EB–DNA system [38]. The emission spectra of EB bound to DNA in the absence and presence of complex **1e** are shown in Fig. 6. The addition of the complex to DNA pretreated with EB causes an appreciable reduction in fluorescence intensity. This indicates that the complex **1e** binds with DNA. The reduction of the emission intensity gives a measure (Fig. 7) of the DNA binding propensity of the complex and the stacking interaction (intercalation) between the adjacent DNA base pairs [39]. The fluorescence quenching curves of DNA-bound EB by complexes **1d** and **1e** illustrates that the quenching of EB bound to DNA by the complexes are in good agreement with the linear Stern–Volmer equation. In the linear fit plot of I_0/I versus [complex]/[DNA], K is given by the ratio of the slope to intercept. The K values for the complexes **1d** and **1e** are 5.22 ($R = 0.989$) and 4.21 (0.991), respectively (I_0 is the emission intensity of EB–DNA in the absence of complex; I is the emission intensity of EB–DNA in the presence of complex). The concentrations of the complexes are taken when a 50% reduction of emission intensity of EB is observed [40]. From the data in Fig. 7, we know that 50% of the EB molecules were replaced from DNA-bound EB at a concentration ratio of [$V^{IV}O$ complex]/[EB] of 8.43 for **1d** and 9.96 for **1e**. By taking a DNA binding constant of $1.0 \times 10^7\ M^{-1}$ for EB [41], apparent DNA binding constants of 1.0×10^6 and $1.2 \times 10^6\ M^{-1}$ were derived {K_b(EB)/([$V^{IV}O$ complex]/[EB])} for the complexes **1d** and **1e**, respectively. The K_{app} values implies that both complexes can strongly interact with DNA and are protected by DNA efficiently, since the hydrophobic environment inside the DNA helix reduces the accessibility of solvent water molecules to the complex and the complex mobility is restricted at the binding site, leading to a decrease of the vibrational modes of relaxation [42]. The K_{app} value for complex **1e** is greater than the complex **1d**. This may be due to the presence of more aromatic moieties, which enhances the binding propensity of the molecule to DNA through the intercalative mode. The presence of a 4-methylphenol group and also the hydrophobic property of the rigid macrocycle ligands facilitate the DNA binding [43].

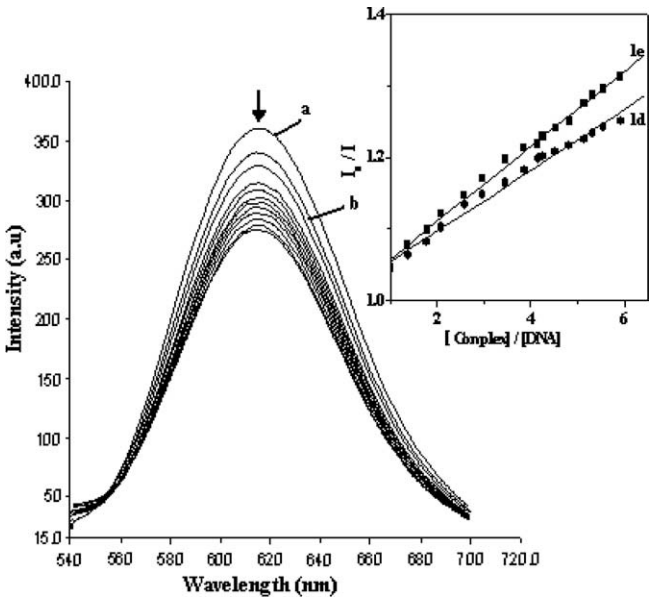


Fig. 6. Emission spectra of EB bound to DNA in the presence of **2e** ([EB] = 3.3 μM, [DNA] = 40 μM, [complex] = 0–25 μM, λ_{ex} = 510 nm). (a) Emission spectrum of DNA-bound EB. (b) The arrow indicates decreasing absorbance with increasing vanadyl(IV) complex (**1e**) concentrations. Inset shows the plots of emission intensity I_o/I versus [DNA]/[complex].

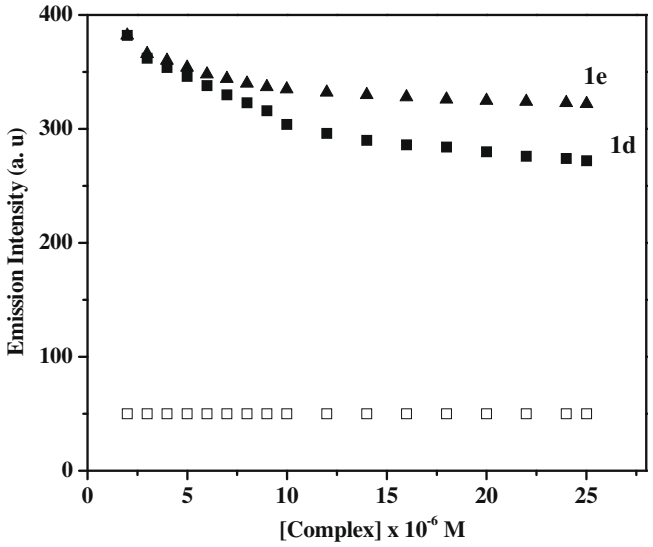


Fig. 7. The effect of addition of complexes **1d** (■) and **1e** (▲) on the emission intensity of 40 μM CT DNA-bound EB in Tris–HCl/NaCl buffer (50 mM, pH 7.5) at 25 °C; (□) on the emission intensity of EB in absence of CT DNA but at different concentrations of **1d** and **1e**.

3.5. DNA cleavage activity

The ability of complexes **1c** and **1e** to perform DNA cleavage in the presence of H_2O_2 has been studied by agarose gel electrophoresis using supercoiled pBR322 DNA (0.2 μg, 33 μM) in a medium of 50 mM Tris–HCl/NaCl buffer (pH 7.2). Both the complexes show considerable DNA cleavage ability at low concentrations (30 μM). When circular plasmid DNA is subjected to electrophoresis, relatively fast migration will be observed for the intact supercoil form (Form I). If scission occurs on one strand (nicking), the supercoil will relax to generate a slower moving open circular form (Form II). If both strands are cleaved, a linear form (Form III) that migrates between Forms-I and -II will be generated [44]. Fig. 8 shows the gel electrophoretic results of complexes **1c** and **1e** interaction with plasmid pBR322 DNA. Under similar conditions no cleavage of pBR322 DNA occurred for free H_2O_2 (Lane 2). In the presence of the $V^{IV}O$ complexes **1c** and **1e** (30 μM) with 60 μM H_2O_2, plasmid DNA was nicked as is evident from the formation of Form II (lanes 3 and 4) and the disappearance of the supercoiled form in the electrophoretic experiment. In lanes 5 and 6, using 50 μM of complexes **1c** and **1e** with 60 μM H_2O_2, bands could not be identified due to smearing. At higher concentrations of the dinuclear complexes (50 μM) the nicked DNA degraded completely into small pieces and only a smear was present and it could not induce the conversion of SC to the linear form at the tested concentrations. The cleavage mechanism of pBR322 DNA induced by complexes **1c** and **1e** was investigated and clarified in the presence of a singlet

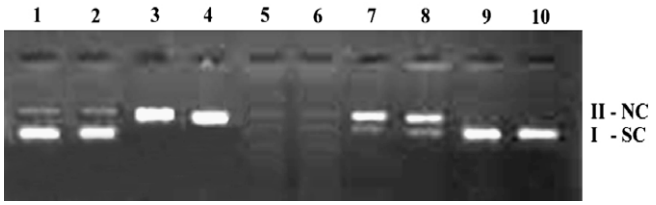


Fig. 8. Cleavage of SC pBR322 DNA (0.2 μg, 33.3 μM) by VO(IV) complexes **1c** and **1e** (0.03–0.05 mM) in the presence of H_2O_2 (60 mM) in 50 mM Tris–HCl/NaCl buffer (pH 7.2). lane 1, DNA control; lane 2, DNA + H_2O_2; lanes 3 and 4, DNA + H_2O_2 + **1c** and **1e** (0.03 mM), respectively; lanes 5 and 6, DNA + H_2O_2 + **1c** and **1e** (0.05 mM), respectively; lanes 7–8, DNA + H_2O_2 + L-histidine (0.04 M) + **1c** and **1e** (0.03 mM), respectively; lanes 9–10, DNA + H_2O_2 + DMSO (2μL) + **1c** and **1e** (0.03 mM), respectively (Gel image showing supercoiled (Form I) and circular relaxed (Form II) DNA).

oxygen quencher L-histidine [45] (lanes 6 and 7) and in the presence of the hydroxyl radical scavenger 0.4 M DMSO (lanes 9 and 10) [46]. Complete inhibition of DNA cleavage was observed from lane 9 to 10. These observations suggest the existence of diffusible radical species in the nuclease mechanism. This can be inferred by monitoring the quenching of DNA cleavage in the presence of DMSO, suggesting the possibility of the formation of HO· radicals as the reactive species [47]. Generation of a HO· radical adduct by the vanadyl(IV)–H_2O_2 system resembles the Fenton reaction (Fe^{2+}–H_2O_2) [48]. In the presence of H_2O_2, the macrocyclic ring containing $V^{IV}O$ ion(s) get oxidized and generates the HO· radicals [49] as follows: ($VO^{2+} + H_2O_2 \rightarrow VO_2^+ + OH + H^+$). These highly reactive hydroxyl radical species can cleave the DNA by abstraction of the hydrogen atom from the deoxyribose sugar [50]. It was also observed that vanadyl(IV) complexes were not able to cleave DNA under an oxygen-free atmosphere. It is remarkable that L-histidine also slightly inhibits the DNA cleaving activity of the complexes. This gives strong evidence of an oxidative process intervening in the DNA cleavage reaction. These results indicate that the presence of oxygen plays a fundamental role in the process of DNA cleavage by the binuclear oxidovanadium(IV) complexes. In the presence of H_2O_2 both the oxidovanadium(IV) complexes **1c** and **1e** degrade pBR322 DNA by oxidative cleavage.

3.6. Antifungal activity

Studies on the antifungal activity of macrocyclic ligands and their complexes are limited in the literature [51–53]. We have evaluated the antifungal activity of all the $V^{IV}O$ complexes against the pathogenic fungus *Aspergillus ochraceous*, *Paecilomyces variotii* and *Botrytis cineraia*. The three fungal species selected for this study are plant pathogens and they indirectly pose health problem in human beings. For example, *A. ochraceous* is a post-harvest fungus infecting the coffee bean and producing ochratoxin. *B. cineraia* infects grape wine and wines prepared from infected grapes yield inferior quality wines. *Paecilomyces variotii* causes paecilomycosis in man. The screening data were reported in Table 4. It is observed from the results that all the tested complexes show some antifungal activity. The activity reported by the present complexes was comparable with the antifungal activities of the macrocyclic ligand containing Cu(II) and Ni(II) ions. [54,55]. It is interesting to notice that the complexes **1d** and **1e** show higher activity than complexes **1a**–**1c**, which contain aliphatic diimines.

3.7. Antibacterial activity

All the binuclear oxidovanadyl complexes have been tested for antibacterial activity against three selected bacteria: *Serratia species*, *Micrococcus luteus* and *Proteus vulgaris*. All these three bacterial species are human pathogens. The screening results are shown in Table 4. *Proteus vulgaris*, used in this study, displayed more resistance to the complexes than the strain of *Serratia* sp. Even though *Serratia* sp. and *P. vulgaris* belongs to the Gram negative group, the difference in their response to oxidovanadium

Table 4
Antibacterial and antifungal activities of the synthesized bimetallic complexes.

Microorganisms	Mean zone of inhibition (mm)[a]					
	1a	**1b**	**1c**	**1d**	**1e**	Stds[b]
Bacteria:						
Serratia species	12.4 ± 0.1	12.7 ± 0.2	19.4 ± 0.3	19.2 ± 0.1	20.3 ± 0.1	27.5 ± 0.3
Micrococcus luteus	11.5 ± 0.1	12.0 ± 0.1	18.8 ± 0.2	19.5 ± 0.3	19.1 ± 0.3	25.6 ± 0.3
Proteus vulgaris	11.6 ± 0.1	11.9 ± 0.1	18.2 ± 0.1	17.2 ± 0.3	17.7 ± 0.2	24.5 ± 0.3
Fungi:						
Aspergillus ochraceous	9.8 ± 0.1	12.3 ± 0.2	19.3 ± 0.1	19.7 ± 0.1	19.8 ± 0.1	36.8 ± 0.2
Pacilomyces variotii	10.3 ± 0.2	12.6 ± 0.2	19.3 ± 0.1	18.3 ± 0.1	19.2 ± 0.5	35.5 ± 0.3
Botrytis cineraia	10.4 ± 0.1	11.6 ± 0.2	18.7 ± 0.1	17.9 ± 0.1	17.7 ± 0.1	38.2 ± 0.1

[a] Values are mean diameter of inhibition zone (mm) and an average of triplicate runs.
[b] Standards: antibacterial studies, ciprofloxacine–5 μg; antifungal studies, cotrimazole–100 μg. **1a** [$C_{24}H_{28}N_4O_8SV_2$], **1b** [$C_{25}H_{30}N_4O_8SV_2$], **1c** [$C_{26}H_{32}N_4O_8SV_2$], **1d** [$C_{28}H_{28}N_4O_8SV_2$] and **1e** [$C_{32}H_{30}N_4O_8SV_2$] each at a concentration of 5 μM.

Table 5
Change in the conductivity of the bacterial and fungal suspensions after treatment with the $V^{IV}O$ complexes (μ Siemens).

Microorganisms	Control	**1a**	**1b**	**1c**	**1d**	**1e**
Bacteria:						
Serratia species	245 ± 5	625 ± 10	670 ± 9	697 ± 10	780 ± 14	838 ± 10
Micrococcus luteus	260 ± 12	550 ± 12	570 ± 10	617 ± 11	690 ± 12	740 ± 12
Proteus vulgaris	230 ± 7	510 ± 10	540 ± 9	575 ± 7	610 ± 12	624 ± 10
Fungi:						
Aspergillus ochraceous	423 ± 14	1122 ± 16	1241 ± 17	1260 ± 16	1305 ± 15	1354 ± 12
Paecilomyces variotii	380 ± 13	1019 ± 11	1114 ± 13	1180 ± 14	1210 ± 11	1278 ± 15
Botrytis cineraia	395 ± 16	940 ± 12	995 ± 14	1042 ± 8	1088 ± 12	1196 ± 9

complexes could be attributed to their resistance pattern decided by the genetic factors. It is common among bacteria that different strains of bacterial species show different responses to a particular toxic material. The inhibition of bacterial and fungal cells by oxidovanadium complexes was due to the alteration in the cell permeability and subsequent injury to the cell membrane which led to leakage of electrolytes from the cells. This leakage caused an increase in conductivity of the suspended medium. The data from conductivity tests (Table 5) of the fungi clearly confirmed this fact. However, further more studies are needed to understand the functions which are responsible for the antifungal and antibacterial activities of the tested complexes.

4. Conclusion

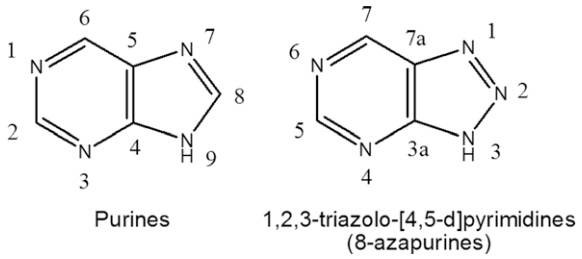
In conclusion, it has been observed that the small variation in the chain length of the imine compartment: (i) shift the reduction potential anodically on increasing the chain length, (ii) shift the oxidation potential to a more positive potential as the chain length increases, (iii) aromatic diimine containing unsymmetrical macrocyclic binuclear $V^{IV}O$ complexes show better DNA binding ability than the aliphatic diimine containing complexes, (iv) these macrocyclic $V^{IV}O$ complexes significantly promote the oxidative cleavage of supercoiled plasmid DNA under physiological conditions in the presence of H_2O_2. All these studies on the complexes agree well with the established trend.

Acknowledgement

L.L. acknowledges the UGC for the financial assistance through the F.I.P. program.

References

[1] D.C. Crans, J.J. Smee, E. Gaidamauskas, L. Yang, Chem. Rev. 104 (2004) 849.
[2] R.K. Narla, Y. Dong, O.J. D'Cruz, C. Navara, F.M. Uckun, Clin. Cancer Res. 6 (2000) 1546.
[3] Y. Dong, R.K. Narla, E. Sudbeck, F.M. Uckun, J. Inorg. Biochem. 78 (2000) 321.
[4] D. Rehder, Bioinorganic Vanadium Chemistry, Wiley, West Sussex, 2008.
[5] R.K. Narla, Y. Dong, O.J. D'Cruz, C. Navara, F.M. Uckum, Clin. Cancer Res. 6 (2000) 1546.
[6] M.A. Abou-Seif, Ann. Clin. Biochem. 35 (1998) 254.
[7] M.M. El-Naggar, A.M., El-Waseef, K.M. El-Halafawy, I.H. El-Sayed, Cancer Lett. 133 (1998) 71.
[8] V.J. Moebus, R. Stein, D.G. Kieback, I.B. Runnebaum, G. Sass, R. Kreienber, Anticancer Res. 17 (1997) 815.
[9] V.L. Pecoraro, M.J. Baldwin, A. Gelasco, Chem. Rev. 94 (1994) 807.
[10] K.K. Nanda, R. Das, M.J. New Lands, R. Hynes, E.J. Gabe, K. Nag, J. Chem. Soc., Dalton Trans. (1992) 897.
[11] J. Nishio, H. Okawa, S. Ohtsuka, M. Tomono, Inorg. Chim. Acta 218 (1994) 27.
[12] H. Furutachi, H. Owaka, Inorg. Chem. 36 (1997) 3911.
[13] P.K. Sasmal, A.K. Patra, M. Nethaji, A.R. Chakravarty, Inorg. Chem. 46 (2007) 11112.
[14] S. Anbu, M. Kandaswamy, Pon Sathya Moorthy, M. Balasubramanian, M.N. Ponnuswamy, Polyhedron 28 (2009) 49.
[15] S. Anbu, M. Kandaswamy, P. Suthakaran, G. Murugan, Babu Varghese, J. Inorg. Biochem., in press, doi:10.1016/j.jinorgbio.2008.12.013.
[16] M.C.B. Oliveira, M.S.R. Couto, P.C. Severino, T. Foppa, G.T.S. Martins, B. Szpoganicz, R.A. Peralta, A. Neves, H. Terenzi, Polyhedron 24 (2005) 495.
[17] K.G. Ragunathan, H.-J. Schneider, Angew Chem., Int. Ed. Engl. 35 (1996) 1219.
[18] S. Karunakaran, M. Kandaswamy. J. Chem. Soc., Dalton Trans. (1994) 1595.
[19] J.C. Duff, J. Chem. Soc. (1941) 547.
[20] M. Thirumavalavan, P. Akilan, M. Kandaswamy, Inorg. Chem. 42 (2003) 3308.
[21] M.E. Reichmann, S.A. Rice, C.A. Thomas, P. Doty, J. Am. Chem. Soc. 76 (1954) 3047.
[22] M. Lee, A.L. Rhodes, M.D. Wyatt, S. Forrow, J.A. Hartley, Biochemistry 32 (1993) 4237.
[23] R.K. Boggeses, J.W. Hughes, W.M. Coleman, L.T. Taylor, Inorg. Chim. Acta 38 (1980) 183.
[24] M. Fujiowara, T. Matsushita, J. Shona, Polyhedron 4 (1985) 1895.
[25] R.S. Drago, Physical Methods in Chemistry, Saunders College Publishing, Philadelphia, 1987.
[26] S. Mohanta, K.K. Nanda, S. Ghosh, M. Mukherjee, M. Helliwell, K. Nag, J. Chem. Soc., Dalton Trans. (1996) 4233.
[27] R. Das, K.K. Nanda, A.K. Mukherjee, M. Mukherjee, M. Helliwell, K. Nag, J. Chem. Soc., Dalton Trans. (1993) 2241.
[28] S.J. Gruber, C.M. Harris, Inorg. Nucl. Chem. 30 (1968) 1805.
[29] M. Hand, Helv. Chim. Acta 40 (1957) 27.
[30] S. Karunakaran, M. Kandaswamy. J. Chem. Soc., Dalton Trans. (1995) 1851.
[31] E.V.R. Akimova, N.W. Alcock, D.H. Busch, Inorg. Chem. 37 (1998) 1563.
[32] W.E. Gao, G. Bu, D. Yang, Z. Liao, S. Jiang, G.Yan, J. Way, J. Chem. Soc., Dalton Trans. (2000) 1431.
[33] J. Manonmani, R. Thirumurugan, M. Kandaswamy, V. Narayanan, Shanmuga Sundara Raj, M.N. Ponnuswamy, G. Shanmugam, H.K. Fun, Polyhedron 20 (2001) 3039.
[34] H. Okawa, M. Tadocara, T.K. Aratake, M. Ohba, K. Shindom, M. Mitsumi, M. Koikawa, M. Tomono, D.E. Fenton, J. Chem. Soc., Dalton Trans. (1993) 253.
[35] A. Wolfe, G.H. Shimer, T. Mechan, Biochemistry 26 (1987) 6392.
[36] L.F. Tan, X.H. Liu, H. Chao, L.N. Ji, J. Inorg. Biochem. 101 (2007) 56.
[37] B. Peng, H. Chao, B. Sun, H. Li, F. Gao, L.-N. Ji, J. Inorg. Biochem. 100 (2006) 1487.
[38] K.G. Strothkamp, R.E. Strothkamp, J. Chem. Edu. 71 (1994) 77.
[39] C.V. Kumar, H. Emma, J. Chem. Soc., Chem. Commun. (1992) 470.
[40] E. Nyarko, N. Hanada, A. Habib, M. Tabata, Inorg. Chim. Acta 357 (2004) 739.
[41] Y. Zhao, J. Zhu, W. He, Z. Yang, Y. Zhu, Y. Li, J. Zhang, Z. Guo, Chem. Eur. J. 12 (2006) 6621.
[42] W. Qian, F. Gu, L. Gao, S. Feng, D. Yan, D. Liao, P. Cheng, J. Chem. Soc., Dalton Trans. (2007) 1060.
[43] D. Koushik, J. Ratha, M. Manassero, X.-Y. Wang, S. Gao, P. Banerjee, J. Inorg. Biochem. 101 (2007) 95.
[44] Q.L. Zhang, J.G. Liu, J.Z. Liu, H. Li, Y. Yang, H. Xu, H. Chao, L.N. Ji, Inorg. Chim. Acta 339 (2002) 34.
[45] H. Kishikawa, Y.P. Jiang, J. Goodisman, J.C. Dabrowiak, J. Am. Chem. Soc. 113 (1991) 5434.
[46] J.A. Cowan, C. Opin, Chem. Biol. 5 (2001) 634.
[47] H. Sakurai, H. Tamura, K. Okatani, Biochem. Biophys. Res. Commun. 206 (1995) 133.
[48] C. Walling, Acc. Chem. Res. 8 (1975) 125.
[49] H.B. Brooks, F. Sicillo, Inorg. Chem. 10 (1971) 2530.
[50] D.S. Sigman, Acc. Chem. Res. 19 (1986) 180.
[51] T.G. Roy, S.K.S. Hazari, B.K. Dey, S. Chakraborty, E.R.T. Tiekink, Met. Based Drugs 6 (1999) 345.
[52] M.A. Ali, A.H. Mirza, A. Monsur, S. Hossain, M. Nazimuddin, Polyhedron 20 (2001) 1045.
[53] M.E. Hossain, M.N. Alam, J. Begum, M.A. Ali, M. Nazimuddin, E.E. Smith, R.C. Haynes, Inorg. Chim. Acta 249 (1996) 207.
[54] S.K.S. Hazari, T.G. Roy, B.K. Dey, S.C. Das, E.R.T. Tiekink, Met. Based Drugs 4 (1997) 255.
[55] T.G. Roy, S.K.S. Hazari, B.K. Dey, H.A. Miah, C. Bader, D. Rehder, Eur. J. Inorg. Chem. (2004) 4115.



Scheme 1.

coordinated counteranion [16]. In the present work, we have extended this study, allowing the presence of the monodentate auxiliary ligand pyridine (py), and six new ternary complexes have been isolated and structurally characterized; for the Mn(II), Zn(II), Cd(II) and Co(II) complexes, only py is bound to the metal ion and $dmax^-$ acts as non-coordinated anion whereas for the Ni(II) and Cu(II) complexes, both ligands are directly bonded to the metal centres.

2. Experimental

2.1. Synthesis of the compounds

The synthesis of 4,6-dimethyl-1,2,3-triazolo[4,5-*d*]pyrimidin-5,7-dione (Hdmax) was carried out according to the published method of Nübel and Pfleiderer [17]. Other reagents were obtained form commercial sources and were used without further purification.

The metal complexes were obtained by mixing two 1:2 pyridine-aqueous solutions, 10 mL each, one containing 2 mmol of Hdmax and the other containing 1 mmol of the appropriate metal salt (sulfate for Mn and nitrate for the remaining metals). The mixture was allowed to evaporate at room temperature and, after several days, crystals suitable for X-ray studies were obtained in each case.

From elemental analyses, the following formulae were deduced for the isolated compounds:

$[Mn(H_2O)_4(py)_2](dmax)_2$ (**1**), colourless crystals. *Anal.* Calc. for $C_{22}H_{30}MnN_{12}O_8$: C, 40.9; H, 4.7; N, 26.0. Found: C, 40.9; H, 5.1; N, 26.8%.

$[Co(H_2O)_4(py)_2](dmax)_2$ (**2**), pale pink crystals. *Anal.* Calc. for $C_{22}H_{30}CoN_{12}O_8$: C, 40.7; H, 4.7; N, 25.9. Found: C, 40.6; H, 4.7; N, 26.1%.

$[Ni(dmax)_2(H_2O)_2(py)_2]\cdot 2H_2O$ (**3**), mauve crystals. *Anal.* Calc. for $C_{22}H_{30}N_{12}NiO_8$: C, 40.7; H, 4.7; N, 25.9. Found: C, 40.7; H, 5.2; N, 26.2%.

$[Cu(dmax)_2(H_2O)_2(py)_2]\cdot 2H_2O$ (**4**), blue crystals. *Anal.* Calc. for $C_{22}H_{30}CuN_{12}O_8$: C, 40.4; H, 4.6; N, 25.7. Found: C, 40.4; H, 4.6; N, 26.0%.

$[Zn(H_2O)_4(py)_2](dmax)_2$ (**5**), colourless crystals. *Anal.* Calc. for $C_{22}H_{30}N_{12}O_8Zn$: C, 40.3; H, 4.6; N, 25.6. Found: C, 40.8; H, 4.8; N, 26.3%.

$[Cd(H_2O)_4(py)_2](dmax)_2$ (**6**), colourless crystals. *Anal.* Calc. for $C_{22}H_{30}CdN_{12}O_8$: C, 37.6; H, 4.3; N, 23.9. Found: C, 37.5; H, 4.4; N, 24.2%.

2.2. Instrumentation

Microanalysis of C, H and N were performed in a Fisons Instruments EA-1008 analyser. Thermal behaviour was studied under an air flow in Shimadzu TGA-50 and Shimadzu DSC-50 equipment, at heating rates of 20 °C min^{-1} and 10 °C min^{-1}, respectively. Reflectance diffuse spectra were made on a VARIAN model CARY-5E spectrophotometer. EPR spectra of the powdered Cu sample was recorded at room temperature on a Bruker ESP-300E spectrometer, operating at X-band (9–10 GHz) (all this equipment is sited at the Centre of Scientific Instrumentation of the University of Granada). IR spectra were recorded on a ThermoNicolet IR 200 spectrometer using KBr pellets.

2.3. Crystallography

Data were collected at room temperature for **1**, **2** and **6** and at 100 K for **3**, **4** and **5**, in a Bruker SMART APEX CCD system with Mo Kα radiation (λ = 0.7107 Å). Data were corrected for absorption (multi-scan, transmission ranges, 0.897–0.789, 0.854–0.759, 0.859–0.743, 0.810–0.744, 0.901–0.781, 0.750–0.644 for **1** to **6,** respectively). The structures were solved by the heavy atom meth-

Table 1
Crystal data.

Compound	**1**	**2**	**3**	**4**	**5**	**6**
Chemical formula	$C_{22}H_{30}MnN_{12}O_8$	$C_{22}H_{30}CoN_{12}O_8$	$C_{22}H_{30}N_{12}NiO_8$	$C_{22}H_{30}CuN_{12}O_8$	$C_{22}H_{30}N_{12}O_8Zn$	$C_{22}H_{30}CdN_{12}O_8$
Formula weight	645.52	649.51	649.29	654.12	655.95	702.98
Crystal size (mm)	0.39 × 0.24 × 0.21	0.46 × 0.38 × 0.24	0.42 × 0.30 × 0.20	0.36 × 0.29 × 0.25	0.29 × 0.20 × 0.11	0.47 × 0.42 × 0.37
Crystal system	triclinic	triclinic	triclinic	triclinic	triclinic	triclinic
Space group	$p-1$	$p-1$	$p-1$	$p-1$	$p-1$	$p-1$
Unit cell dimensions						
a (Å)	8.4735(6)	8.4326(5)	8.4471(4)	8.6913(5)	8.4090(9)	8.5015(4)
b (Å)	9.1517(7)	9.0674(5)	8.6061(4)	11.2673(7)	8.9126(9)	9.1721(5)
c (Å)	10.2500(8)	10.2434(6)	11.4137(6)	14.9465(9)	9.9452(10)	10.1821(5)
α (°)	89.138(1)	89.034(1)	83.422(1)	110.327(1)	86.016(2)	87.250(1)
β (°)	88.455(1)	88.769(1)	69.440(1)	92.400(1)	86.980(2)	87.410(1)
γ (°)	64.069(1)	63.924(1)	61.375(1)	98.579(1)	66.681(1)	65.661(1)
V (Å^3)	714.57(9)	703.32(7)	680.47(6)	1350.22(14)	682.56(12)	722.29(6)
Z	1	1	1	2	1	1
D_{calc} (g/cm^3)	1.500	1.533	1.584	1.609	1.596	1.616
Absorption coefficient (mm^{-1})	0.530	0.679	0.784	0.881	0.971	0.823
θ range for data collection (°)	1.99–28.27	1.99–28.04	1.91–28.10	1.46–28.34	2.05–28.24	2.00–28.24
Reflections collected/unique	8332/3227	8043/3145	7924/3077	15839/6150	8018/3100	8365/3259
Data/restrains/parameters	3227/4/210	3145/4/210	3077/4/210	6150/8/416	3100/4/210	3259/4/210
Goodness-of-fit on F^2	1.011	1.156	1.147	1.065	1.100	1.095
R ($I \geq 2\sigma(I)$)	0.0354	0.0316	0.0284	0.0290	0.0240	0.0229
wR_2 (all data)	0.1007	0.0895	0.0773	0.0820	0.0637	0.0606
Largest difference in peak and hole (e Å^{-3})	0.205/−0.234	0.300/−0.216	0.537/−0.384	0.440/−0.396	0.353/−0.265	0.277/−0.286

od and anisotropically refined in F^2 using SHELXL-97 [18]. Hydrogen atoms of the heterocycles were placed in ideal positions, whereas those of the water molecules were clearly spotted in the ΔF maps and refined with a restrained O–H distance (0.84(1) Å). Isotropic thermal parameters of all H-atoms were fixed to 1.2 times the equivalent isotropic thermal parameter of their parent atoms. Table 1 summarizes the crystallographic data for these compounds.

3. Results and discussion

3.1. X-ray structural studies

3.1.1. Complexes $[M(H_2O)_4(py)_2](dmax)_2$ (M=Mn, Co, Zn, Cd(II))

Compounds **1**, **2**, **5** and **6** are isostructural and therefore, may be discussed jointly. The unit cell of these compounds contains one $[M(H_2O)_4(py)_2]^{2+}$ cation (M = Mn, Co, Zn, Cd(II)) and two 4,6-dimethyl-1,2,3-triazolo[4,5-*d*]pyrimidin-5,7-dionato ($dmax^-$) non-coordinated anions, which have lost the acidic proton present in the free ligand at the N atom at position 2. Fig. 1 displays a view of the basic ionic unit in **5**, almost identical to those in the other three compounds. The metal atoms lie in crystallographic inversion centres and their environments are slightly distorted octahedra defined by two symmetry related py ligands in *trans* dispositions, and four water molecules. Distances and angles in the coordination sphere are listed in Table 2. The plane of the pyridine ligand is almost perpendicular to the $M(H_2O)_4$ plane, the corresponding dihedral angle ranging from 85.2° (**6**) to 87.2° (**1**). The conformation around the M–py bond is established with the projection of the pyridine plane almost bisecting the Ow–M–Ow angles (torsion angles C(py)–N(py)–M–O(w), 45 ± 6°), which probably optimizes the interactions between the aromatic ortho protons and the water oxygens, which may be considered as bifurcated weak intramolecular H-bonds, the corresponding C···O and H···O distances ranging from 3.1 to 3.6 Å and from 2.75 to 3.15 Å, respectively, these values being higher for the Mn and Cd compounds than for the Co and Zn ones. Surprisingly enough, there are very few previous references for $[M(H_2O)_4(py)_2]^{2+}$ cations, in fact for Mn, Zn and Cd, those presented here are the first examples; for Co, the geometrical parameters of the cation are almost identical to those in previous works [19].

The acidic proton of Hdmax is located at the nitrogen atom at position 2 in the crystal structure of the free ligand [20]. The ionization of this proton leads to the closing of the endocyclic angle at N2 (5.1–5.3°) and the opening of the adjacent endocyclic angles at N1 (3.6–3.8°) and N3 (4.5–4.7°). Changes in bond distances are probably less significant (maximum N1-C7a, around 0.02 Å).

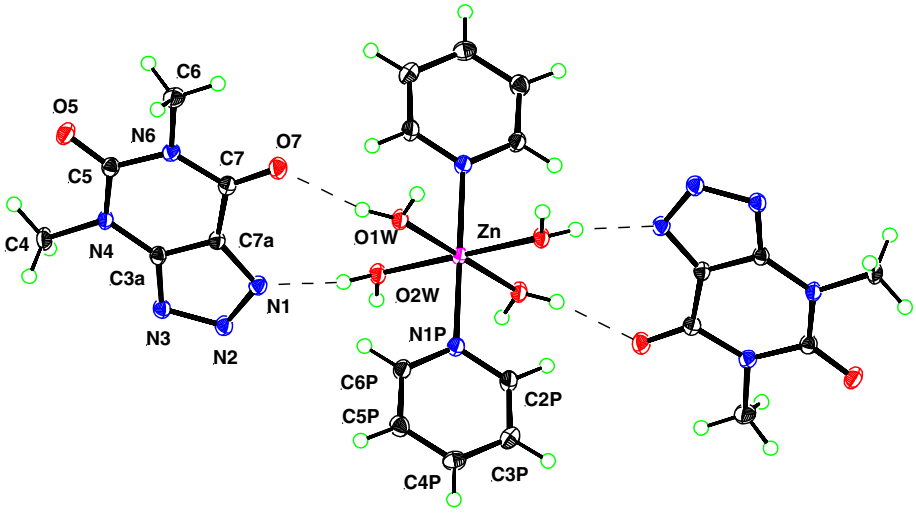


Fig. 1. View of the basic ionic unit of compound **5**.

Table 2
Distances (Å) and cis angles (°) in the first coordination sphere.

	1	2	3	4	5	6
M–N2			2.0637(12)	2.0142(12) 2.0203(12)		
M–N(pyr)	2.2839(14)	2.1595(14)	2.0943(12)	2.0248(12) 2.0281(12)	2.1453(11)	2.3119(16)
M–O(wat)	2.1544(11) 2.1932(11)	2.0757(11) 2.1314(11)	2.0950(10)	2.3675(10) 2.4248(11)	2.1000(10) 2.1456(10)	2.2848(13) 2.3261(13)
N2–M–N(pyr)			91.03(4)	91.91(5) 89.23(5) 88.70(5) 90.17(5)		
N2–M–O(wat)			87.08(4)	91.53(4) 87.76(4) 84.46(4) 96.31(4)		
N(pyr)–M–O(wat)	89.10(5) 91.58(5)	88.67(5) 91.61(5)	87.78(4)	91.55(4) 88.75(4) 85.57(4) 94.17(4)	89.15(4) 92.17(4)	88.72(6) 92.84(6)
O(wat)–M–O(wat)	87.71(4)	88.03(4)			88.09(4)	87.09(5)

Table 3
Hydrogen-bond distances (D–H···A, Å) in compounds **1**, **2**, **5** and **6.**

	1	2	5	6
O(1W)–H(11W)···O(7)	2.7955(17)	2.8084(16)	2.8153(14)	2.800(2)
O(1W)–H(12W)···N(3)#2	2.7658(18)	2.7669(17)	2.7730(15)	2.785(2)
O(2W)–H(21W)···N(2)#3	2.7651(18)	2.7674(17)	2.7609(15)	2.758(2)
O(2W)–H(22W)···N(1)	2.7774(17)	2.7701(17)	2.7792(15)	2.795(2)

Symmetry transformations used to generate equivalent atoms: #2: $x + 1, y, z$ #3: $-x, -y + 1, -z + 1$.

Nevertheless, the main interest of these structures lies probably more in the second coordination sphere than in the first. As it happens with the analogous hexa-aqua salts [16], the topology of the H-bonds are a good example of how concepts usually applied to the first coordination sphere find clear analogies in the second coordination sphere, so we may use terms like "monodentate", "bridging ligand", "chelate" and so on. All hydrogen atoms of coordinated water molecules, clearly spotted in the X-ray analysis, participate as donors in these H-bonds, four of five potential hydrogen acceptor sites (N1, N2, N3 and O7) being involved for the 4,6-dimethyl-1,2,3-triazolo[4,5-*d*]pyrimidin-5,7-dionato anions. The corresponding H-bond geometrical parameters are collected in Table 3.

All H-bond interactions between water molecules and anions take place in the equatorial plane of the complex. N2 and N3 interact with water molecules belonging to the same cation and this closes a ring which may be defined as a "chelate", where the ring includes seven atoms (the metal, two oxygens, two hydrogens and two nitrogens). This pattern may be represented in the condensed way as $R^2_2(7)$ according to the graph set notation proposed by Etter and Bernstein et al. [21,22]: R indicates a ring, the degree (in parentheses) is the number of atoms in the ring, and the super- and subscripts represent the number of hydrogen bond acceptors and donors in the motif, respectively. Likewise, N1 and O7 define another chelate (in this case $R^2_2(9)$) with another $[M(H_2O)_4(py)_2]^{2+}$ cation. These chelating interactions build tape structures that grow in the *a* direction (Fig. 2). A tape is defined as an infinite monodimensional structure in which the components are linked by more than one hydrogen bond, with the hydrogen bonds approximately copla-

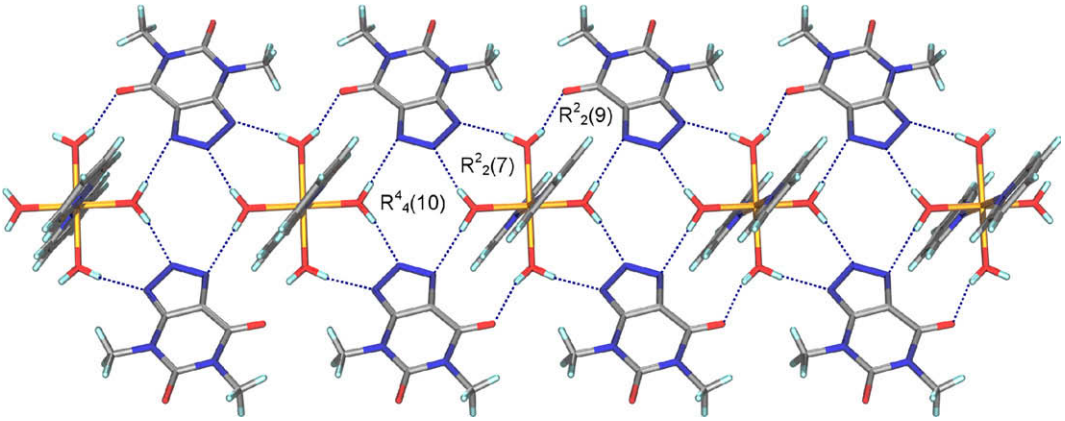


Fig. 2. Tape along the 100 direction built by the hydrogen bond interactions in compound **5**.

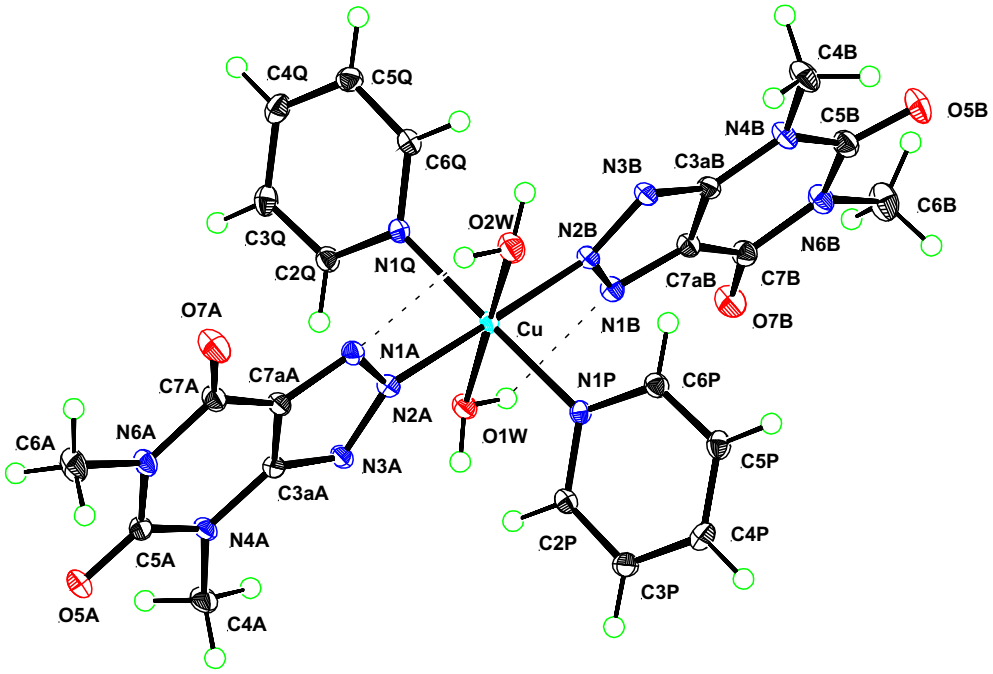


Fig. 3. Molecular structure of compound **4** (that of **3** is analogous to it).

nar [23]. A third ring motif $R_4^4(10)$ involving two cations and two anions appears in the tape around the crystallographic inversion centres. The anion is roughly coplanar with the tape.

Perhaps the most noteworthy feature of these tapes is that they are topologically identical to those present in the above mentioned hexa-aqua salts [16]. This fact prompted us to define this set of H-bond interactions as a case of molecular recognition between the square planar $[M(H_2O)_4]^{2+}$ subunits (M = Mn, Co, Zn, Cd) and the 4,6-dimethyl-1,2,3-triazolo[4,5-*d*]pyrimidin-5,7-dionato anions, letting us predict that in any compound containing these two species it is likely that the tape superstructure will be generated, regardless of the nature of the axial ligands. The stability of this superstructure may also explain, in principle, the surprising fact of the non-direct coordination between the divalent Mn, Co, Zn and Cd centres and the anion dmax$^-$, a species with several binding sites.

The tapes interact each other mainly through two types of π–π interactions: between parallel displaced pyridine moieties (3.4 Å) and between inversion centre related couples of dmax$^-$ anions (3.4 Å). Weak poorly defined H-bonds are also formed between the aromatic meta protons of pyridine and the carbonyl oxygen O5 of neighbouring tapes (C···O distances, around 3.4 Å).

Table 4
Hydrogen-bond distances (D-H···A, Å) in compounds **3** and **4**.

	3	**4**
O(Wc)–H···N(1)	2.7501(16)	2.8167(16)
		2.8328(16)
O(Wc)–H···O(Wi)	2.7286(15)	2.7868(15)
		2.7446(17)
O(Wi)–H···O(5)#1 (3) or O(5A)#2 (4)	2.8809(17)	2.8788(16)
O(Wi)–H···N(3B)		2.8918(17)
O(Wi)–H···O(7)#3 (3) or O(7A)#4 (4) or O(7B)#5 (4)	2.9467(16)	2.8983(16)
		2.8933(16)

O(Wc) = O atom of coordinated water (O1W for **3** and O1W, O2W for **4**).
O(Wi) = O atom of interstitial water (O2W for **3** and O3W, O4W for **4**).
Symmetry transformations used to generate equivalent atoms: #1: *x*, *y*, *z* + 1 #2: −*x* + 1, −*y* + 2, −*z* + 1 #3: −*x* + 2, −*y* + 1, −*z* + 1 #4: −*x*, −*y* + 1, −*z* #5: −*x* + 1, −*y* + 1, −*z* + 1.

3.1.2. Complexes $[M(dmax)_2(H_2O)_2(py)_2] \cdot 2H_2O$ (M=Ni, Cu(II))

In contrast to the compounds described in the previous paragraphs, in the case of Ni and Cu, there is direct coordination between the metal and the anion dmax$^-$. This is not too surprising, since divalent Ni and Cu usually form more stable complexes than Mn, Co and Zn, according to the well known Irving-Williams series. Direct (Ni,Cu)-dmax$^-$ binding seeming to be thermodinamically more favoured than the formation of the tapes described in Section 3.1.1. Both structures are built by neutral $[M(dmax)_2(H_2O)_2(py)_2]$ molecules (Fig. 3) plus two interstitial water molecules per complex unit. Nevertheless, the compounds are not isostructural, in **3** the nickel atom lies in a crystallographic inversion centre whereas the copper atom in **4** is placed in a general position, even if the molecule still presents local approximate C_i symmetry; the disposition of the ligands is therefore all-*trans* in both cases. The distortion of the octahedron is **3** is slight, whereas in **4** the expected tetragonal Jahn-Teller distortion is present, with the water molecules occupying the axial positions (Table 2). As in the previous compounds, the ionization of the acidic proton at position 2 leads to the closing of the endocyclic angle at N2 and the opening of the adjacent endocyclic angles at N1 and N3, but the differences with the free ligand are smaller (3.1–3.6°, 2.2–2.7° and 2.8–3.1°, respec-

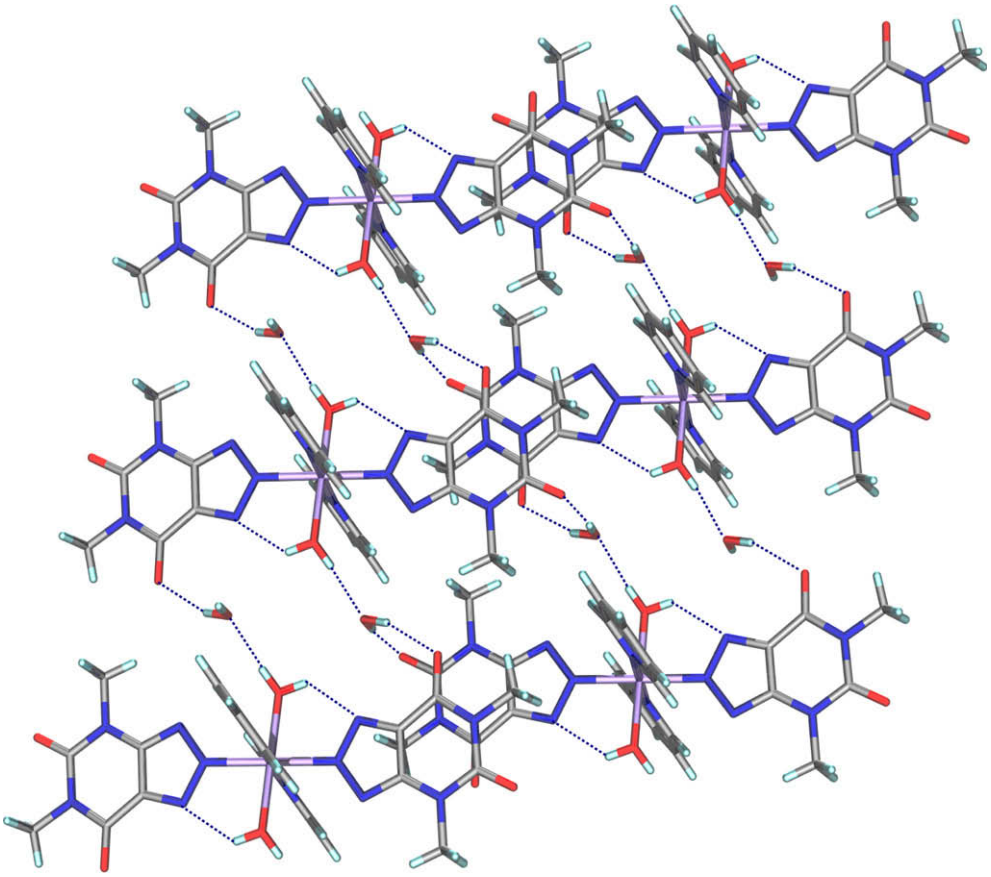


Fig. 4. Bidimensional H-bond superstructure in compound **3**.

tively) showing that the effect of the loss of the proton is partially compensated by the presence of the metal cation.

In both cases, one of the H-atoms of each coordinated water molecule forms an intramolecular H-bond with the N1 atom of one of the neighbouring dmax$^-$ anions (Table 4, Fig. 3), this leaves for each $[M(dmax)_2(H_2O)_2(py)_2]$ unit only two available donor H-atoms which are linked in all cases to interstitial water molecules. Therefore, these interstitial water molecules have the main responsibility for joining the molecules and to build the H-bond network. In the nickel compound, all non-coordinated water molecules are symmetry equivalent (O2W), their H-atoms being linked to carbonyl oxygen atoms of different complex molecules and building in this way a bidimensional corrugated superstructure in the *ac* plane (Fig. 4). For the copper complex, there are two crystallographically different interstitial water molecules (O3W and O4W): the two protons of O3W and one of OW4 also interact with carbonyl oxygens of different neighbouring molecules, whereas the second proton of O4W is linked to the N3 atom of a dmax$^-$ moiety belonging to the same complex as the coordinated water molecule for which O4W acts as a H-bond acceptor: this creates a –Cu–H_2O–H_2O-dmax $R_2^2(7)$ chelate ring. The water–carbonyl interactions also generate a bidimensional superstructure, growing in the $\bar{1}01$ crystallographic plane.

The layers in both compounds interact more weakly through normal Van der Waals contacts, weak C(aromatic)-H···O interactions and π-stacking interactions that take place between pyridine moieties (3.4 Å), but not between the dmax$^-$ anions.

3.2. Spectral, thermal and magnetic studies

The 1700–1500 cm^{-1} region of the infrared spectra of the free heterocycle Hdmax displays three bands at 1717, 1681 and 1604 cm^{-1}, assignable to carbonyl stretching and possibly to $\delta(H_2O)$, these bands being slightly displaced to lower (the first two) or higher (the last one) wavenumbers in the complexes. For all the complexes, a new band appears at 1544 cm^{-1}, characteristic of the anionic form of this ligand [16], and an intense band close to 1310 cm^{-1} is present in the region expected for vibrational modes of the aromatic ring. The main bands of pyridine [24,25] are slightly displaced to higher wavenumbers in the complexes.

The spectra also show broad bands in the 3500–3100 cm^{-1} region, assignable to υ(OH) of water, broadened and lower wavenumber displaced by the hydrogen bonds. The free ligand also displays a broad absorption around 2800 cm^{-1}, which disappears in the complexes, probably related to the acidic proton of the imidazole ring, extensively associated in H-bonding.

The first step of the thermal decomposition of the isolated complexes (except **4**) is the successive loss of four water molecules and two pyridine moieties with a well defined weight loss effect, the corresponding percentage agreeing well with the expected value. For **1**, **5** and **6** this process appears in the DSC diagrams as several overlapped endothermic peaks, and dehydration enthalpies cannot be reliably obtained, whereas for **2** and **3** the endothermic peaks are better defined and separated and, from the integration of the first one (102.4 and 113.0 °C, respectively), we can calculate the dehydration energies (45.5 kJ/mol and 48.7 kJ/mol, respectively). The second step is the pyrolytic decomposition around 400 °C, giving different metal oxides as inorganic residues. For the copper complex, the elimination of water and pyridine are well separated both in the TG and DSC diagrams. Dehydration takes place in a single step (endothermic peak at 80.4 °C) with dehydration energy of 47.4 kJ/mol. After this, the loss of two pyridine moieties takes place (endothermic peak at 176.2 °C) followed by the pyrolysis of the triazolopyrimidine derivative.

The diffuse reflectance spectra of **2–4** are typical of octahedral species [26]. The cobalt compound exhibits two main absorptions: a broad one centred at 8818 cm^{-1}, assigned to the $^4T_{2g}(F) \leftarrow {}^4T_{1g}(F)$ (υ_1) transition and another one at 19380 cm^{-1} assigned to the $^4T_{1g}(P) \leftarrow {}^4T_{1g}(F)$ (υ_3) transition. Ligand field parameters were calculated by Dou equations [27] on the basis of an octahedral geometry, giving $\Delta_o = 9953$ cm^{-1} and $B = 780$ cm^{-1}. The spectrum for the nickel compound shows two of the three typical bands expected for octahedral Ni(II) complexes at 11325 ($^3T_{2g}(F) \leftarrow {}^3A_{2g}(F)$, υ_1) and 17889 ($^3T_{1g}(F) \leftarrow {}^3A_{2g}(F)$, υ_2) cm^{-1}, from which the parameters $\Delta_o = 11325$ cm^{-1} and $B = 835$ cm^{-1} were calculated. Finally, the copper compound presents only one broad and asymmetric band with a maximum at 17153 cm^{-1} that can be assigned to a d–d transition with a d^9 configuration and a distorted octahedral geometry.

The X-band EPR spectrum has been recorded at room temperature for a polycrystalline powdered sample of compound **4**. The spectrum consists of a single very broad asymmetric band attributable to an unresolved anisotropic spectrum with an average *g* value of 2.06.

Acknowledgements

This work was supported by a project of the Ministry of Education and Science of Spain (Project: CTQ-2005-00329/BQU) and the Junta de Andalucía (FQM195). C.R. Maldonado is grateful for a FPU grant from the Ministry of Education and Science of Spain.

Appendix A. Supplementary data

CCDC 709198–709203 contain the supplementary crystallographic data for complexes **1**–**6**. These data can be obtained free of charge via <http://www.ccdc.cam.ac.uk/conts/retrieving.html>, or from the Cambridge Crystallographic Data Centre, 12 Union Road, Cambridge CB2 1EZ, UK; fax: (+44) 1223 336 033; or e-mail: deposit@ccdc.cam.ac.uk. Supplementary data associated with this article can be found, in the online version, at doi:10.1016/j.poly.2008.12.026.

References

[1] B. Lippert, Coord. Chem. Rev. 200–202 (2000) 487.
[2] L.G. Purnell, J.C. Shepherd, D.J. Hodgson, J. Am. Chem. Soc. 97 (1975) 2376.
[3] L.G. Purnell, D.J. Hodgson, Biochim. Biophys. Acta 447 (1976) 117.
[4] L.G. Purnell, E.D. Estes, D.J. Hodgson, J. Am. Chem. Soc. 98 (1976) 740.
[5] L.G. Purnell, D.J. Hodgson, J. Am. Chem. Soc. 99 (1977) 3651.
[6] B.J. Graves, D.J. Hodgson, Inorg. Chem. 20 (1981) 2223.
[7] N. Katsaros, A. Grigoratos, Inorg. Chim. Acta 108 (1985) 173.
[8] V. Ravichandran, G.A. Ruban, K.K. Chacko, M.A.R. Molina, E.C. Rodríguez, J.M. Salas-Peregrín, K. Aoki, H. Yamazaki, J. Chem. Soc., Chem. Commun. (1986) 1780.
[9] W.S. Sheldrick, P. Bell, Inorg. Chim. Acta 123 (1986) 181.
[10] W.S. Sheldrick, P. Bell, Z. Naturforsch. B 41 (1986) 1117.
[11] W.S. Sheldrick, P. Bell, Z. Naturforsch. B 42 (1987) 195.
[12] W.S. Sheldrick, B. Günther, Inorg. Chim. Acta 152 (1988) 223.
[13] W.S. Sheldrick, P. Bell, Inorg. Chim. Acta 160 (1989) 265.
[14] W.S. Sheldrick, B. Günther, J. Organomet. Chem. 375 (1989) 233.
[15] W.S. Sheldrick, G. Heeb, Inorg. Chim. Acta 190 (1991) 241.
[16] C.R. Maldonado, M. Quirós, J.M. Salas, A. Rodríguez-Diéguez, Inorg. Chim. Acta, in press, doi:10.1016/j.ica.2008.07.029.
[17] G. Nübel, W. Pfleiderer, Chem. Ber. 98 (1965) 1060.
[18] G.M. Sheldrick, SHELXL-97, University of Göttingen, Germany, 1997.
[19] E. Suresh, M.M. Bhadbhade, K. Venkatasubramanian, Polyhedron 18 (1999) 657.
[20] M.P. Sánchez, M.A. Romero, J.M. Salas, D.J. Cárdenas, J. Molina, M. Quirós, J. Mol. Struct. 344 (1995) 257.
[21] M.C. Etter, J. Phys. Chem. 95 (1991) 4601.
[22] J. Bernstein, R.E. Davis, L. Shimoni, N.-L. Chang, Angew. Chem., Int. Ed. Engl. 34 (1995) 1555.
[23] A.D. Burrows, Struct. Bond. 108 (2004) 55.
[24] C.H. Kline, J. Turkevich, J. Chem. Phys. 12 (1944) 300.
[25] L. Corrsin, B.J. Fax, R.C. Lord, J. Chem. Phys. 21 (1953) 1170.
[26] A.B.P. Lever, Inorganic Electronic Spectroscopy, Elsevier, Amsterdam, 1986.
[27] Y. Dou, J. Chem. Ed. 67 (1990) 134.

value of the solution was adjusted to 6.0 with ammonium hydroxide. The mixture was kept at room temperature for one week. Red crystals were obtained and washed with water and ethanol, then dried in air with a yield of 1.51 g (76%). C and H elemental Anal. *Calc.* for $C_8H_{20}O_{12}N_2Co$: C, 24.3; H, 5.1; N, 7.1. Found: C, 24.0; H, 5.3; N, 7.4%. UV–Vis λ_{max}: 514 nm, ε = 6.2 L mol^{-1} cm^{-1}. IR (KBr, cm^{-1}): $\nu_{as}(CO_2)$ 1591_{vs}, 1547_{vs}; $\nu_s(CO_2)$ 1422_s. ^{1}H NMR (400 MHz, D_2O, 25 °C, DSS): δ = 4.750 (br, q, 1H, CH), 2.891 (br, q, J = 3.8 Hz, 1H, CH_2), 2.850 (br, q, J = 6.8 Hz, 1H, CH_2) ppm. Similarly, when the pH value of the mixture was adjusted to between 1 and 3, the brown solid of *trans*-[Co(*R*-H_2mal)(*S*-H_2mal)$(H_2O)_2$] · $2H_2O$ (**4**) was obtained as the major product with a yield of 72% [7]. C and H elemental Anal. *Calc.* for $C_8H_{18}O_{14}Co$: C, 24.2; H, 4.6. Found: C, 23.8; H, 4.8%. UV–Vis λ_{max}: 511 nm, ε = 9.2 L mol^{-1} cm^{-1}. IR (KBr, cm^{-1}): $\nu(CO_2H)$ 1680_{vs}; $\nu_{as}(CO_2)$ 1653_{vs}, 1552_{vs}; $\nu_s(CO_2)$ 1450_s.

2.2. Preparation of $[Co_2(R\text{-}Hmal)(S\text{-}Hmal)(H_2O)_4]_n \cdot 2nH_2O$ (**2**)

R,*S*-malic acid (0.74 g, 5.5 mmol) was added to a stirred solution of $CoCl_2 \cdot 6H_2O$ (1.15 g, 5 mmol) in water (10 mL). The pH of the solution was adjusted to 5.0 with ammonium hydroxide. The mixture was heated in a 60 °C water bath for two days. Purple red crystals were obtained, washed with water and ethanol, then dried in air to give **2** in a yield of 0.74 g (60%). C and H elemental Anal. *Calc.* for $C_8H_{20}O_{16}Co_2$: C, 19.6; H, 4.1. Found: C, 19.7; H, 3.8%. IR (KBr, cm^{-1}): $\nu_{as}(CO_2)$ 1596_{vs}, 1567_{vs}; $\nu_s(CO_2)$ 1432_m, 1379_m.

2.3. Preparation of $K_4[Co_4(OH)_2(R\text{-}mal)_2(S\text{-}mal)_2(H_2O)_4] \cdot 10H_2O$ (**3**)

R,*S*-malic acid (0.81 g, 5.5 mmol) was added to a stirred solution of $CoCl_2 \cdot 6H_2O$ (1.18 g, 5 mmol) in 2:1 water–ethanol solution (15 mL). The pH value of the solution was adjusted to 7.0 with potassium hydroxide. Purple red crystals were obtained after standing at room temperature for several days, which were washed with water and ethanol, and dried in air to give **3** in a yield of 0.11 g (7.5%). C, H and N elemental Anal. *Calc.* for $C_{16}H_{42}O_{36}Co_4K_4$: C, 16.0; H, 3.5. Found: C, 15.5; H, 3.7%. IR (KBr, cm^{-1}): $\nu_{as}(CO_2)$ 1593_{vs}, 1564_{vs}; $\nu_s(CO_2)$ 1415_s, 1383_s, 1364_s.

2.4. X-ray structural data collections, structure solutions and refinements

Crystals of **1**–**3** were measured on a Bruker Smart Apex CCD diffractometer with graphite monochromate Mo Kα radiation (λ = 0.71073 Å) at 296 K. The data were corrected for Lorentz and polarization effects. An absorption correction was applied using the SADABS program [19]. The structures were solved by the WINGX package [20] and refined by full-matrix least-squares procedures with anisotropic thermal parameters for all the non-hydrogen atoms using SHELXL-97 [21]. Hydrogen atoms were located from difference Fourier maps and refined isotropically. Crystal data collections and refinement parameters are summarized in Table 1. Selected bond lengths and angles are listed in Table 2.

3. Results and discussion

3.1. Syntheses and conversions

The syntheses of the cobalt malato complexes were carried out in aqueous solutions under different pH values, molar ratios and counterions, as shown in Scheme 1. Complexes **1**–**3** exist in different forms of aggregates, in which **1** is a monomer, **2** forms a two-dimensional layered structure based on a dimeric unit, while **3** is in a tetranuclear species. In the synthesis of **1**, the high molar ratio of malic acid to cobalt chloride of 2:1 was applied to initiate the reaction. The presence of a small excess of malic acid in the reaction mixture was essential, since its deficiency caused the isolation of **2**. With a metal-to-ligand ratio of 1:1, $[Co_2(R\text{-}Hmal)(S\text{-}Hmal)(H_2O)_4]_n \cdot 2nH_2O$ (**2**) was isolated. When the pH value was less than 3.0, *cis*-$[Co(H_2mal)_2(H_2O)_2] \cdot 2H_2O$ or *trans*-$[Co(H_2mal)_2(H_2O)_2] \cdot 2H_2O$ (**4**) was obtained [7,8]. In weakly acidic and neutral conditions, **1** and **2** could be isolated from the solution in the pH ranges of 4.0–7.0 and 3.0–6.0, respectively. Use of various bases like ammonium hydroxide or potassium hydroxide not only supplied the necessary counterions to balance the negative charges of the cobalt malate complexes, but also made a contribution to the formation of monomeric and polymeric structures. As compared to the pH value and molar ratio, the sensitivity of the reactions to produce **1** and **2** with temperature is low under water bath conditions, unlike hydrothermal syntheses [4–6]. The synthesis of **3** is complete with the addition of ethanol at room temperature at pH 7.0. Complex **3** was isolated in a very low yield; this has not been reproduced at present.

Complexes **1** and **4** are soluble in water, while **2** and **3** are difficult to dissolve in water, even with strong heating. The chemical form and the structure of cobalt malate are dependent on the pH value and molar ratio. It is noted that water-soluble **1** exists in a physiological pH range, suggesting that it may serve as a model complex to study the coordination of cobalt with the biological malate system.

3.2. Description of the crystal structures

The X-ray crystal structure of complex **1** comprises two ammonium cations, the mesomeric anion $[Co(R\text{-}Hmal)(S\text{-}Hmal)]^{2-}$ and two water molecules. As illustrated in Fig. 1, the $[Co(R\text{-}Hmal)(S\text{-}Hmal)]^{2-}$ anion is octahedrally coordinated by two equivalent malates. The malato ligands bind in a tridentate fashion through the oxygen atoms of the α-hydroxy, α-carboxy and β-carboxy groups. Compared with the other water-soluble species *cis*-$[Co(H_2mal)_2(H_2O)_2] \cdot 2H_2O$ or *trans*-$[Co(H_2mal)_2(H_2O)_2] \cdot 2H_2O$ under acidic conditions, the deprotonation of the β-carboxylic acid group results in the tridentate coordination between pH 4.0–7.0. This type of coordination is also found in citrate complexes like $(NH_4)_4[M(Hcit)_2]$ (M = Co, Mn, Zn) [22–24], $(NH_4)_5[M(cit)_2] \cdot 2H_2O$ [M = Fe(III), Mn(III), Al(III), Ga(III)] [23,25,26] and $(NH_4)_3[Ga(Hcit)_2] \cdot 2H_2O$ [27]. The citrate ligand coordinates with the α-hydroxy or α-alkoxy, α-carboxy and β-carboxy groups, leaving the other β-carboxy or β-carboxylic acid group free. However, the present structure is a novel dimalato tridentate complex.

As illustrated in Fig. 2a, complex **2** comprises a dimeric unit of $[Co_2(R\text{-}Hmal)(S\text{-}Hmal)(H_2O)_4]$. Each Co^{II} ion in **2** exists in an octahedral environment and is surrounded by three different malates and two water molecules. The sixfold coordination polyhedron is severely removed from idealized octahedral symmetry. Specifically, the six apices of the oxygen coordination octahedron are occupied as follows. One malate ligand employs both of the α-hydroxy and α-carboxy oxygen atoms for two coordination positions, forming a five-membered chelate ring. Two additional malate ligands from two adjacently located octahedral Co^{II} ions coordinate through their β-carboxy oxygen atoms, O(4b) and O(5a). The remaining coordination sites are completed by two water molecules in a *cis*-configuration. Furthermore, both *R*- and *S*-malates exist in the dimeric unit.

In Fig. 2b, the dimeric unit labelled A connects Co(II) ions into macrocyclic loops labelled B. The B loop is formed by four dimeric A units. The two types of loops are arrayed alternately to form a 1D double-chain, which is similar to the one-dimensional structure of $[Zn_2(cpoa)_2(bpe)(H_2O)]$ [H_2cpoa = 4-carboxyphenoxy acetic acid, bpe = 1,2-bis(4-pyridyl)ethane] [28], and each A loop is further surrounded by four B loops, whereas two adjacent B loops are perpendicular to each other in parallel 2D layers.

Table 1
Crystal data summary of intensity data collection and structure refinement for $(NH_4)_2[Co(R\text{-Hmal})(S\text{-Hmal})]\cdot 2H_2O$ (**1**), $[Co_2(R,S\text{-Hmal})_2(H_2O)_4]_n\cdot 4nH_2O$ (**2**) and $[Co_4(OH)_2(R\text{-mal})_2(S\text{-mal})_2(H_2O)_4]\cdot 10H_2O$ (**3**).

	1	2	3
Empirical formula	$C_8H_{20}O_{12}N_2Co$	$C_8H_{20}O_{16}Co_2$	$C_{16}H_{42}O_{36}K_4Co_4$
Formula weight	395.19	490.10	1202.62
Crystal color	red	Purple red	Purple red
Crystal size (mm)	0.41 × 0.24 × 0.19	0.10 × 0.10 × 0.05	0.31 × 0.24 × 0.19
Crystal system	Monoclinic	Monoclinic	Monoclinic
Cell constants			
a (Å)	7.6374(4)	10.1040(1)	9.5955(5)
b (Å)	10.6516(5)	7.4932(7)	10.4076(6)
c (Å)	9.1292(5)	10.704(1)	19.775(1)
β (°)	91.085(1)	93.229(2)	100.784(1)
V (Å3)	742.53(7)	809.1(1)	1940.0(2)
Space group	$P2_1/c$	$P2_1/n$	$P2_1/c$
Formula units/unit cell	2	2	2
D_{calc} (g cm^{-3})	1.768	2.012	2.229
F(000)	410	500	1220
Diffractometer radiation	Smart Apex CCD/Mo Kα (λ = 0.7107 Å)		
Reflections collected/unique/R_{int}	8172/1769/0.096	9063/1913/0.161	10760/3672/0.158
Data/restraints/parameters	1769/14/130	1913/10/139	3672/27/316
θ range (°)	2.67–28.33	2.70–28.33	2.10–26.00
Goodness-of-fit on F^2	1.080	0.994	1.075
R_1, wR_2 $[I > 2\sigma(I)]$[a]	0.036, 0.088	0.064, 0.131	0.090, 0.250
R_1, wR_2 (all data)	0.038, 0.089	0.095, 0.143	0.097, 0.258
Largest difference in peak and hole (e Å^{-3})	0.60, −0.39	1.14, −0.73	1.61, −2.42

[a] $R_1 = \Sigma||F_o| - |F_c||/\Sigma(|F_o|)$, $wR_2 = \Sigma[w(F_o^2 - F_c^2)^2]/\Sigma[w(F_o^2)^2]^{1/2}$.

Table 2
Selected bond distances (Å) and angles (°) for $(NH_4)_2[Co(R\text{-Hmal})(S\text{-Hmal})]\cdot 2H_2O$ (**1**), $[Co_2(R,S\text{-Hmal})_2(H_2O)_4]_n\cdot 4nH_2O$ (**2**) and $[Co_4(OH)_2(R\text{-mal})_2(S\text{-mal})_2(H_2O)_4]\cdot 10H_2O$ (**3**).

1			
Co(1)–O(1)	2.095(1)	Co(1)–O(5)	2.053(1)
Co(1)–O(2)	2.048(1)		
O(1)–Co(1)–O(2)	79.21(5)	O(1)–Co(1)–O(5)	84.63(5)
O(2)–Co(1)–O(5)	88.56(6)	O(1)–Co(1)–O(5a)	95.37(5)
O(2)–Co(1)–O(1a)	100.79(5)		
2			
Co(1)–O(1)	2.138(3)	Co(1)–O(5a)	2.063(3)
Co(1)–O(2)	2.064(4)	Co(1)–O(1w)	2.131(3)
Co(1)–O(4b)	2.063(3)	Co(1)–O(2w)	2.072(4)
O(1)–Co(1)–O(2)	77.2(1)	O(2)–Co(1)–O(2w)	93.9(2)
O(1)–Co(1)–O(4b)	167.0(1)	O(4b)–Co(1)–O(5a)	86.4(1)
O(1)–Co(1)–O(5a)	97.3(1)	O(4b)–Co(1)–O(1w)	93.0(1)
O(1)–Co(1)–O(1w)	99.1(1)	O(4b)–Co(1)–O(2w)	90.6(2)
O(1)–Co(1)–O(2w)	86.3(1)	O(5a)–Co(1)–O(1w)	94.4(1)
O(2)–Co(1)–O(4b)	90.5(1)	O(5a)–Co(1)–O(2w)	175.9(2)
O(2)–Co(1)–O(5a)	88.8(2)	O(1w)–Co(1)–O(2w)	83.0(2)
O(2)–Co(1)–O(1w)	175.4(1)		
3			
Co(1)–O(1)	2.066(5)	Co(2)–O(1a)	1.920(5)
Co(1)–O(2)	2.009(5)	Co(2)–O(4a)	2.053(5)
Co(1)–O(6)	2.014(5)	Co(2)–O(6)	1.919(5)
Co(1)–O(7)	2.044(5)	Co(2)–O(9)	2.052(5)
Co(1)–O(1w)	2.077(7)	Co(2)–O(11)	1.835(5)
Co(1)–O(2w)	2.153(6)	Co(2)–O(11a)	1.860(5)
Co(2)–Co(2a)	2.752(2)		
O(1)–Co(1)–O(2)	79.1(2)		
O(1)–Co(1)–O(6)	103.3(2)	O(6)–Co(2)–O(9)	83.7(2)
O(1)–Co(1)–O(7)	175.6(2)	O(6)–Co(2)–O(11)	99.1(2)
O(1)–Co(1)–O(1w)	91.6(2)	O(6)–Co(2)–O(11a)	90.9(2)
O(1)–Co(1)–O(2w)	89.2(2)	O(6)–Co(2)–O(1a)	166.4(2)
O(2)–Co(1)–O(6)	177.6(2)	O(6)–Co(2)–O(4a)	84.8(2)
O(2)–Co(1)–O(7)	97.2(2)	O(11)–Co(2)–O(11a)	83.7 (2)
O(2)–Co(1)–O(1w)	90.4(3)	O(11)–Co(2)–O(9)	92.8(2)
O(2)–Co(1)–O(2w)	92.0(2)	O(11)–Co(2)–O(4a)	175.5(2)
O(6)–Co(1)–O(7)	80.4(2)	O(11)–Co(2)–Co(2a)	42.2 (2)
O(6)–Co(1)–O(2w)	87.5(2)	O(11a)–Co(2)–O(1a)	97.5(2)
O(6)–Co(1)–O(1w)	90.0(3)	O(11a)–Co(2)–O(9)	173.1(2)
O(6)–Co(2)–Co(2a)	96. 7(2)	O(11a)–Co(2)–O(4a)	94.0(2)
O(7)–Co(1)–O(1W)	90.7(3)	O(11a)–Co(2)–Co(2a)	41.51(14)
O(7)–Co(1)–O(2W)	88.7(2)	O(4a)–Co(2)–Co(2a)	135.4(2)
O(1a)–Co(2)–O(11)	92.5(2)	O(1w)–Co(1)–O(2w)	177.5(3)
O(1a)–Co(2)–O(4a)	84.0(2)	O(9)–Co(2)–Co(2a)	134.8(2)
O(1a)–Co(2)–Co(2a)	96.7(2)	O(9)–Co(2)–O(4a)	89.8(2)
O(1a)–Co(2)–O(9)	88.6(2)	Co(2)–O(11)–Co(2a)	96.3(2)

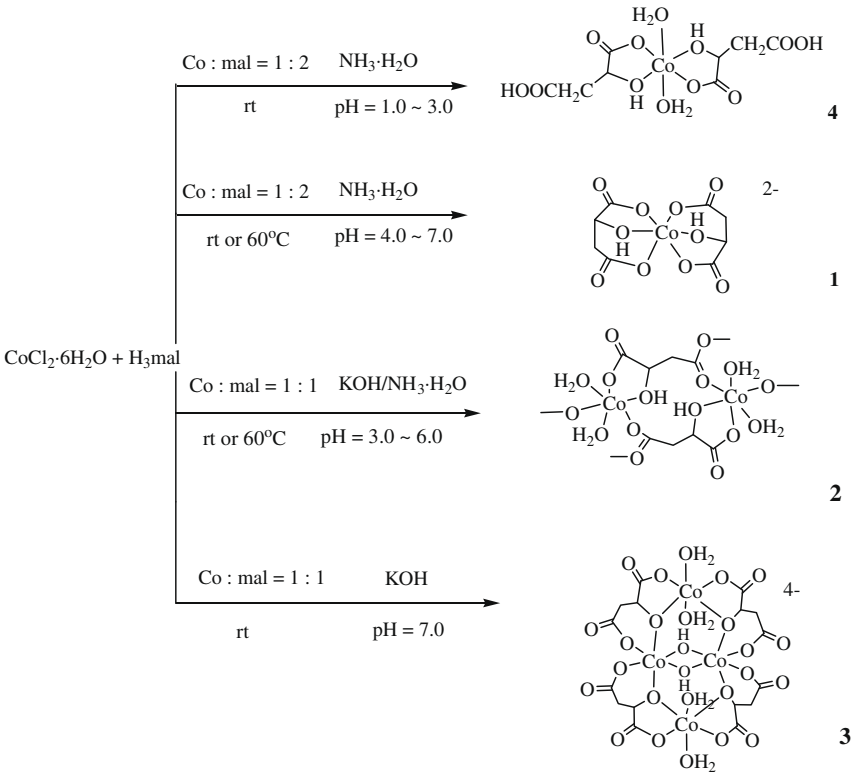
Symmetric transformation for **1**: *a*, −*x* + 2, −*y*, −*z* + 2; **2**: *a*, *x* + ½, −*y* + ½, *z* + ½, *b*, −*x* + 2, −*y*, −*z* + 1; **3**: *a*, −*x* + 1, −*y*, −*z* + 2.

The difference between complex **2** and the other observed transition metal malate complexes, such as the one-dimensional structure of $[M(S\text{-Hmal})(H_2O)_2]_n\cdot nH_2O$ (M = Co, Ni) [3,29,30], is that each biionized malate moiety acts as a bidentate ligand coordinating to the Co^{II} ion *via* its α-hydroxy and α-carboxy groups. While the other β-carboxy group does not participate in the coordination to the same metal ion, instead it acts as a bridged ligand to bind another two Co^{II} ions simultaneously. This coordination mode of the dimeric unit $[Co_2(R\text{-Hmal})(S\text{-Hmal})(H_2O)_4]$ is novel among the cobalt malato complexes, but is similar to citrato cobalt and nickel cyclic dimers, such as $M_2[Co_2(Hcit)_2(H_2O)_4]\cdot 6H_2O$ (M = K or Na) and $M_2[Ni_2(Hcit)_2(H_2O)_4]\cdot nH_2O$ (M = K, *n* = 4; M = NH_4, *n* = 2) [31–33].

With the participation of alcohol, $K_4[Co_4(OH)_2(R\text{-mal})_2(S\text{-mal})_2(H_2O)_4]\cdot 10H_2O$ (**3**) is obtained at pH 7. The crystal structure of **3** comprises potassium cations, a tetranuclear malato cobalt anion and lattice water molecules. As shown in Fig. 3, the mixed-valence $Co^{II/III}$ ions in the cluster are held together by the bridging hydroxy and α-alkoxy groups. In the centrosymmetric tetramer, two types of octahedrally coordinated $Co^{II/III}$ ions can be distinguished as Co1 and Co2, which exist in normal octahedral environments. Two equivalent triionized malate ions coordinate with Co1 both *via* their α-alkoxy O(1) and O(6) atoms and α-carboxy O(2) and O(7) atoms, forming five-membered chelating rings. The oxygen atoms O(1) and O(6) are further coordinated to the adjacent Co^{III} ions. Moreover, the β-carboxy group does not participate in the coordination to the same metal ion, instead it binds the Co^{III} ion in the $Co_2(OH)_2$ unit [Co–O–Co = 96.3(2)°]. The remaining coordination sites of Co1 are completed by two water molecules in a *trans*-configuration. The two adjacent $Co^{II}(mal)_2$ and $Co_2^{III}(OH)_2$ units are further linked into a tetranuclear unit (Fig. 3). The distance between the two Co^{III} ions is 2.752(2) Å, which is close enough to involve metal–metal bonding interactions. This is similar to that [2.793(2) Å] of the dimeric Co^{III} complex $[Co_2(OH)_2(CH_3CO_2)_3(bpy)_2]\cdot ClO_4\cdot H_2O$ [34].

In the case of **3**, the partial aerial oxidation of the cobalt(II) ions is unexpected, which has not been previously observed for malic acid, but it has been found with other Schiff bases, like $[Co_2^{II/III}L(acac)(O_2CCH_2CO_2H)][Co_2^{II/III}L(acac)(OH)]\cdot 7H_2O$ [35]. It seems that this type of ligand favours the isolation of $Co^{II/III}$ mixed-valence complexes in a neutral or acidic medium. The oxidation of the initial cobalt(II) salt by atmospheric oxygen is highly dependent on the pH value of the medium.

The Co–O bond distances in **1**–**3** are summarized in Table 2. For **3**, the bond distances of the malate ligand to the cobalt ion range from 1.919(5) to 2.053(5) Å. The shortest Co–O bond in the malate ligand is observed for the α-alkoxy group with the Co^{III} ion, which is attributed to the deprotonation of the α-hydroxy group and the high valence cobalt ion. For the Co^{III} ion, the Co^{III}–O bond distances vary from 1.835(5) to 2.053(5) Å, which are shorter than the normal Co^{II}–O bonds.



Scheme 1. Syntheses of the cobalt malato complexes at different pH values and molar ratios.

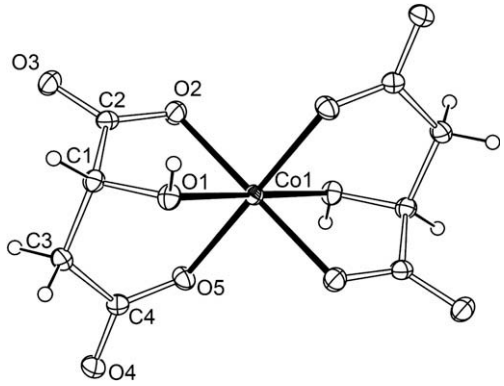


Fig. 1. ORTEP plot of the anion of $(NH_4)_2[Co(R\text{-Hmal})(S\text{-Hmal})] \cdot 2H_2O$ (**1**) with 30% probability thermal ellipsoids.

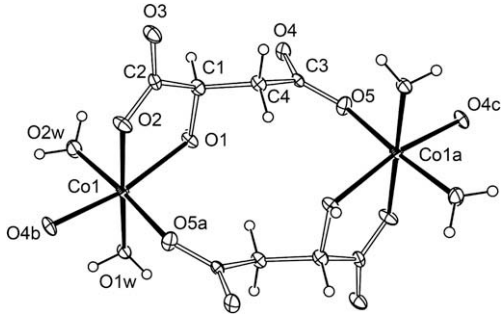


Fig. 2a. ORTEP plot of the molecular structure of $[Co_2(R\text{-Hmal})(S\text{-Hmal})\text{-}(H_2O)_4]_n \cdot 2nH_2O$ (**2**) with 30% probability thermal ellipsoids.

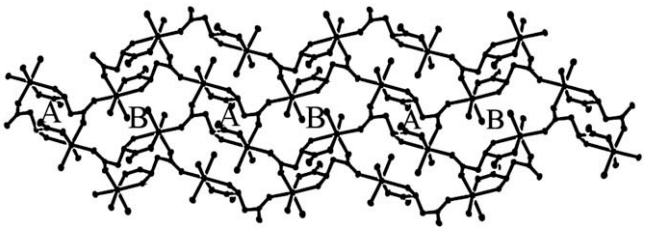


Fig. 2b. ORTEP plot of the structural packing in **2** depicting the 2D layers. Hydrogen atoms were omitted for clarity.

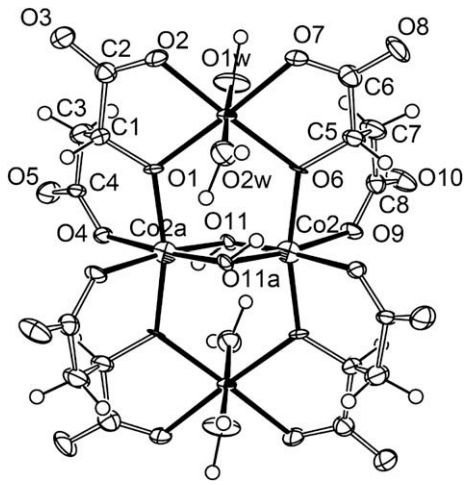


Fig. 3. ORTEP plot of molecular structure of $[Co_4(OH)_2(R\text{-mal})_2(S\text{-mal})_2\text{-}(H_2O)_4] \cdot 10H_2O$ (**3**) with 30% probability thermal ellipsoids.

Table 3
Comparisons of Co–O distances () in malato and citrato cobalt complexes.

Complex	Co–O (hydroxy, α-alkoxy)	Co–O (α-carboxy)	Co–O (β-carboxy)	Ref.
$(NH_4)_2[Co(R\text{-Hmal})(S\text{-Hmal})]\cdot 2H_2O$ (**1**)	2.095(1)	2.048(1)	2.053(1)	
$[Co_2(R\text{-Hmal})(S\text{-Hmal})(H_2O)_4]_n\cdot 4nH_2O$ (**2**)	2.138(3)	2.064(4)	2.063(3)	
$[Co_4(OH)_2(R\text{-mal})_2(S\text{-mal})_2(H_2O)_4]\cdot 10H_2O$ (**3**)				this work
Co^{II}	2.066(5)	2.009(5)		
Co^{III}	1.920(5)		2.053(5)	
$[Co^{III}(S\text{-mal})(NH_3)_3]\cdot 2H_2O$	1.887(2)	1.926(2)	1.926(2)	[37]
$[Co(R\text{-Hmal})(H_2O)]_n\cdot nH_2O$	2.128(2)	2.084(2)	2.080(2)	[4]
$[Co(S\text{-Hmal})(H_2O)]_n\cdot nH_2O$	2.103(2)	2.096(2)	2.113(2)	[5]
$[Co(R\text{-Hmal})(H_2O)]_n$	2.128(2)	2.056(2)	2.029(2)	[6]
trans-$[Co(H_2mal)_2(H_2O)_2]\cdot 2H_2O$	2.066(1)	2.076(1)	/	[7]
cis-$[Co(H_2mal)_2(H_2O)_2]$	2.130(2)	2.045(2)	/	[8]
$[Co^{II}(Hmal)(Im)_3]$	2.120(2)	2.110(2)	2.141(2)	[38]
$(NH_4)_4[Co(Hcit)_2]$	2.157(2)	2.075(2)	2.051(2)	[22]
$[Co(H_2cit)(H_2O)]_n$	2.034(2)	$2.125(2)_{av}$	2.099(2)	[31]
$(NH_4)_{2n}[Co_2(Hcit)_2(H_2O)_2]_n$	2.089(2)	2.073(2)	$2.106(1)_{av}$	[31]
$[Co(H_2O)_4]_n[Co_2(Hcit)_2(H_2O)_4]_n\cdot 6nH_2O$	2.155(2)	2.069(2)	$2.075(2)_{av}$	[31]
$[Co(H_2O)_6]_n[Co(Hcit)(H_2O)_{2n}]\cdot 2nH_2O$	2.116(3)	2.079(3)	$2.070(3)_{av}$	[31]
$Na_2[Co_2(Hcit)_2(H_2O)_4]\cdot 6H_2O$	2.169(2)	2.044(2)	2.052(2)	[33]
$K_2[Co_2(Hcit)_2(H_2O)_4]\cdot 6H_2O$	2.194(2)	2.065(2)	2.044(2)	[33]
$[C(NH_2)_3]_4[Co(Hcit)_2]\cdot 2H_2O$	2.090(2)	2.105(2)	2.087(2)	[39]
$[(NMe_4)_3Na\{Co_4(cit)_4[Co(H_2O)_5]_2\}]\cdot 11H_2O$	2.075–2.142		2.055–2.157	[40]

Comparisons of the Co–O distances for malato and citrate cobalt complexes are given in Table 3. The tetranuclear complex **3** shows the shortest Co^{II}–O (α-carboxy) bond [2.009(5) Å] and **2** has the longest Co–O (α-hydroxy) bond [2.138(3) Å]. Other Co–O distances are shown in Table 3. The Co–O bond distances in malate cobalt are similar to the cobalt lactate $[Co(R\text{-Hlact})(S\text{-Hlact})(H_2O)_2]\cdot H_2O$ [2.018(3)–2.129(3) Å] (H_2lact = lactic acid) [36] and cobalt citrate in Table 3. Moreover, these Co–O distances are also comparable to those in the malato manganese and nickel complexes, for example $[Mn(S\text{-}H_2mal)_2(H_2O)_2]\cdot 4H_2O$ [2.134(1)–2.213(1) Å] [8] and $[Ni(S\text{-Hmal})(H_2O)_2]_n\cdot nH_2O$ [2.021(4)–2.082(5) Å] [29].

Bond valence calculations confirm the following information [41]. In the monomeric and dimeric complexes **1** and **2**, the bond valence values for the Co atoms are 2.19 and 2.06, respectively, indicating the +2 oxidation state for the Co ions. However, the bond valence values in **3** are 2.24 and 3.15 for Co1 and Co2, respectively, suggesting that Co1 has the +2 oxidation state, while the oxidation state for Co2 is +3. It is noted that there is partial oxidation of Co^{II} to Co^{III} in the reaction process, but the detailed mechanism is as yet unclear.

The FT-IR spectra of the title complexes display characteristic features of the coordinated malato ligand, shown in Figs. S1–S4. The absorptions for antisymmetric stretching carboxylate vibrations ν_{as} (COO) appear at 1591 and 1547 for **1**, 1596 and 1567 for **2**, 1593 and 1564 cm^{-1} for **3**, and the corresponding symmetric stretching vibrations ν_s (COO) appeared at 1364–1450 cm^{-1} for **1**–**3**. The frequencies of the coordinated carboxylate are shifted to lower frequencies compared to that of free malic acid, which is consistent with the absence of IR bands between 1700 and 1740 cm^{-1} for a typical undissociated carboxylic acid group. As shown in Figs. S5 and S6, the UV–Vis spectra of **1** and **4** in solution contain broad bands at 514 and 511 nm, respectively, which are assigned to the transition $^4T_{1\,g}(F) \rightarrow {}^4T_{2\,g}(P)$ and $^4T_{1\,g}(F) \rightarrow {}^4A_{2\,g}$ for an octahedral Co^{2+} ion, respectively [42]. The ^{1}H NMR spectra of **1** and **4** were tested in dilute solution. Due to the strong paramagnetic effect of the cobalt complexes, it was difficult to obtain the signals from the methylene and methenyl groups of the malate ligand.

4. Conclusions

From the above results, it was found that due to the flexibility of the H_3mal ligand, the complexes show interesting structures varying from monomer, dimer to tetramer, that are dependent on the pH value and molar ratio. The cobalt(II) malate complexes $(NH_4)_2[Co(R\text{-Hmal})(S\text{-Hmal})]\cdot 2H_2O$ (**1**), $[Co_2(R\text{-Hmal})(S\text{-Hmal})(H_2O)_4]_n\cdot 2nH_2O$ (**2**), $K_4[Co_4(OH)_2(R\text{-mal})_2(S\text{-mal})_2(H_2O)_4]\cdot 10H_2O$ (**3**) and *trans*-$[Co(R\text{-}H_2mal)(S\text{-}H_2mal)(H_2O)_2]\cdot 2H_2O$ (**4**) could be obtained in aqueous solution between pH 1.0 and 7.0. Compared to the other cobalt malate compounds previously reported, there are some remarkable features of these compounds: (a) although the starting malate was racemic, there is no enantiomer of malic acid coordinated with cobalt in these complexes. (b) Complex **2** shows a unique polymer structure with a novel dimeric unit that is different from the other cobalt malate complexes. (c) Complex **3** gives a unique tetranuclear mixed-valence structure, and the space between the two cobalt atoms Co2···Co2a is 2.752(2) Å, which is close enough to involve metal–metal bonding interactions. The solution isolation of the cobalt malates with pH and molar ratio dependence is helpful for the systematic understanding of the precursor method with malic acid.

Acknowledgements

Financial supports provided by the National Science Foundation of China (20423002) and the Ministry of Science and Technology (2005CB221408) are gratefully acknowledged.

Appendix A. Supplementary data

CCDC 703117–03119 contain the supplementary crystallographic data for **1**–**3**. These data can be obtained free of charge via http://www.ccdc.cam.ac.uk/conts/retrieving.html, or from the Cambridge Crystallographic Data Centre, 12 Union Road, Cambridge CB2 1EZ, UK; fax: (+44) 1223-336-033; or e-mail: deposit@ccdc.cam.ac.uk. Supplementary data of the IR spectra of compounds **1**–**4**, UV and ^{1}H NMR spectra of compound **1** associated with this article can be found, in the online version, at doi:10.1016/j.poly.2009.01.017.

References

[1] D. Voet, J.G. Voet, Biochemistry, 3rd Ed., Wiley and Sons, 2004.
[2] S.R. Berger, Kirk–Othmer Encyclopedia of Chemical Technology, Wiley, 1981.
[3] L. Kryger, S.E. Rasmussen, Acta Chem. Scand. 26 (1972) 2349.
[4] A. Beghidja, P. Rabu, G. Rogez, R. Welter, Chem. Eur. J. 12 (2006) 7627.
[5] F.T. Xie, L.M. Duan, J.Q. Xu, L. Ye, Y.B. Liu, X.X. Hu, J.F. Song, Eur. J. Inorg. Chem. 22 (2004) 4375.
[6] A. Beghidja, G. Rogez, P. Rabu, R. Welter, M. Drillon, J. Mater. Chem. 16 (2006) 2715.

[7] A. Karipides, Acta Crystallogr., Sect. B 37 (1981) 1115.
[8] M. Fleck, E. Tillmanns, L. Bohatý, P. Held, Z. Kristallogr. 219 (2004) 101.
[9] E. Campi, Ann. Chim. 53 (1963) 96.
[10] V.V. Grigoreva, S.M. Tsimbler, Z. Neorg. Khim. 13 (1968) 498.
[11] G. Occupati, L. Pratt, J. Inorg, Nucl. Chem. 36 (1974) 1731.
[12] Y. Teraoka, H. Kakebayashi, I. Moriguchi, S. Kagawa, Chem. Lett. (1991) 673.
[13] Y. Teraoka, H. Kakebayashi, I. Moriguchi, S. Kagawa, J. Alloys Compd. 193 (1993) 70.
[14] S. Mueller, K. Striebel, O. Haas, Electrochim. Acta 39 (1994) 1661.
[15] S.K. Tiwari, P. Chartier, R.N. Singh, J. Electrochem. Soc. 142 (1995) 148.
[16] D. Mazas-Brandariz, M.A. Senaris-Rodriguez, S. Castro-Garcia, M.A. Camacho-Lopez, C. Julien, Ionics 5 (1999) 345.
[17] S. Castro-Garcia, C. Julien, M.A. Senaris-Rodriguez, D. Mazas-Brandariz, Ionics 6 (2000) 434.
[18] P.S. Whitfield, S. Niketic, I.J. Davidson, J. Power, Sources 146 (2005) 617.
[19] SADABS, University of Göttingen, Göttingen, Germany, 1997.
[20] L.J. Farrugia, J. Appl. Crystallogr. 32 (1999) 837.
[21] G.M. Sheldrick, SHELXL-97, Program for the Refinements of Crystal Structure, University of Göttingen, Göttingen, Germany, 1997.
[22] M. Matzapetakis, M. Dakanali, C.P. Raptopoulou, V. Tangoulis, A. Terzis, N. Moon, J. Giapintzakis, A. Salifoglou, J. Biol. Inorg. Chem. 5 (2000) 469.
[23] M. Matzapetakis, N. Karligiano, A. Bino, M. Dakanali, C.P. Raptopoulou, V. Tangoulis, A. Terzis, J. Giapintzakis, A. Salifoglou, Inorg. Chem. 39 (2000) 4044.
[24] R. Swanson, W.H. Ilsley, A.G. Stanislowski, J. Inorg. Biochem. 18 (1983) 187.
[25] M. Matzapetakis, C.P. Raptopoulou, A. Tsohos, V. Papaefthymiou, N. Moon, A. Salifoglou, J. Am. Chem. Soc. 120 (1998) 13266.
[26] M. Matzapetakis, M. Kourgiantakis, M. Dakanali, C.P. Raptopoulou, A. Terzis, A. Lakatos, T. Kiss, I. Banyai, L. Iordanidis, T. Mavromoustakos, A. Salifoglou, Inorg. Chem. 40 (2001) 1734.
[27] P. O'Brien, H. Salacinski, M. Motevalli, J. Am. Chem. Soc. 119 (1997) 12695.
[28] W.J. Zhuang, X.J. Zheng, L. Li, D.Z. Liao, H. Mac, L.P. Jin, Cryst. Eng. Commun. 9 (2007) 653.
[29] A.T. Reed, A. Karipides, Acta Crystallogr., Sect. B 32 (1976) 2085.
[30] Z.H. Zhou, J.J. Ye, Y.F. Deng, G. Wang, J.X. Gao, H.L. Wan, Polyhedron 21 (2002) 787.
[31] Z.H. Zhou, Y.F. Deng, H.L. Wan, Cryst. Growth Des. 5 (2005) 1109.
[32] M. Kotsakis, C.P. Raptopoulou, V. Tangoulis, A. Terzis, J. Giapintzakis, T. Jakusch, T. Kiss, A. Salifoglou, Inorg. Chem. 42 (2003) 22.
[33] (a) E.N. Baker, H.M. Baker, B. Anderson, R.D. Reeves, Inorg. Chim. Acta 78 (1983) 281;
(b) Z.H. Zhou, Y.J. Lin, H.B. Zhang, G.D. Lin, K.R. Tsai, J. Coord. Chem. 42 (1997) 131.
[34] K. Dimitrou, K. Folting, W.E. Streib, G. Christou, J. Am. Chem. Soc. 115 (1998) 6432.
[35] M. Fondo, N. Ocampo, A.M. García-Deibe, M. Corbella, M. Salah El Fallah, J. Cano, J. Sanmartìn, M.R. Bermejo, J. Chem Soc., Dalton Trans. (2006) 4905.
[36] R. Carballo, B. Covelo, E.M. Vázquez-López, Anorg. Allg. Chem. 628 (2002) 468.
[37] S. Bunel, C. Ibarra, V. Calvo, A. Blasko, C.A. Bunton, N.L. Keder, Polyhedron 10 (1991) 2495.
[38] Z.M. Jin, L. He, L. Shen, M.C. Li, M.L. Hu, Acta Crystallogr. E59 (2003) m1053.
[39] T.A. Hudson, K.J. Berry, B. Moubaraki, K.S. Murray, R. Robson, Inorg. Chem. 45 (2006) 3549.
[40] M. Murrie, S.J. Teat, H. Stoeckli-Evans, H.U. Gudel, Angew. Chem., Int. Ed. 42 (2003) 4653.
[41] (a) I.D. Brown, D. Altermatt, Acta Crystallogr., Sect. B 41 (1985) 244;
(b) N.E. Brese, M. O'Keefee, Acta Crystallogr., Sect. B 47 (1991) 192.
[42] J.N. Nwabueze, Transition Met. Chem. 22 (1996) 123.

exist predominantly in the G^+G^+ form [29,30], where the R groups are on opposite sides of the S–C–S plane. It is possible to distinguish between the two conformers with opposite helicity, generating the *P*- and the *M*-forms of optical antipodes. These characteristic twisted structures have implicit helicity in the spacer ligands and are of interest in terms of chiral crystal engineering.

The synthesis and structures of four new coordination polymers with 4bpytm, [Ag(4bpytm)](NO_3) (**1**), [Ag(4bpytm)](ClO_4) (**2**) and [Ag(4bpytm)](ClO_4) ½CH_2Cl_2 ½dmf (**2·Solv**), [Ag(CH_3COO)(4bpytm)]·H_2O (**3**) and [Ag(CF_3COO)(4bpytm)] (**4**), are described here. The NO_3^- and ClO_4^- anions do not coordinate to the silver(I) atoms and only act as counterions in complexes **1** and **2·Solv**. However, in complexes **3** and **4**, the carboxylate anions, $CH_3CO_2^-$ and $CF_3CO_2^-$, act as coordinating ligands, giving rise to a different degree of covalent polymerization and allowing the inclusion of crystallization water molecules in **3**.

2. Experimental

2.1. Materials and physical measurements

Bis(4-pyridylthio)methane was prepared as described previously [26]. The other starting materials and solvents were obtained commercially and were used as supplied. Elemental analyses (C, H, N, S) were carried out on a Fisons EA-1108 microanalyser. IR spectra were recorded from KBr discs (4000–400 cm^{-1}) on a Bruker Vector 22 spectrophotometer. A Shimadzu UV-3101PC spectrophotometer was used to obtain electronic spectra in the solid state. TGA analysis was carried out using a TA Instruments Hi-Res TGA2950 Thermobalance coupled to a Bruker Tensor 27 FT-IR apparatus. Powder X-ray diffraction data were obtained using Cu K_α radiation and were collected on a Siemens D-5000 diffractometer over the range 5.0–60.0° in steps of 0.20° (2θ) with a count time per step of 5.0 s.

Caution: Although problems were not encountered in this work, transition metal perchlorates are potentially explosive and should be handled with care.

2.2. Synthesis of the complexes

2.2.1. [Ag(4bpytm)](NO_3) (**1**)

Compound **1** was obtained by reaction of bis(4-pyridylthio)methane (4bpytm) (0.187 g, 0.80 mmol) in MeOH (10 mL) and $AgNO_3$ (0.80 mmol) in H_2O (10 mL). The resulting mixture was stirred for 24 h and the resulting white precipitate was filtered off, washed with EtOH and $CHCl_3$ and dried under vacuum. Single crystals were obtained by slow diffusion in a test tube of a solution of 4bpytm (23 mg, 0.10 mmol) in methanol (10 mL) and a solution of $AgNO_3$ (17 mg, 0.10 mmol) in water (10 mL). The X-ray power diffraction (XRPD) pattern of the resulting material do not show differences compared with that simulated from the crystal structure.

Data for **1**: Yield: 81%. *Anal.* Calc. for $C_{11}H_{10}N_3O_3S_2Ag$: C, 32.6; H, 2.4; N, 10.4; S, 15.9. Found: C, 31.9; H, 2.3; N, 10.0; S, 15.4%. IR (KBr, cm^{-1}): 1590s, 1537m, 1483m, 1361s, 1335s, 1222m, 1066m, 824m, 735m, 495m. UV–Vis (λ_{max}, cm^{-1}): 38 163.

2.2.2. [Ag(4bpytm)](ClO_4) (**2**) and [Ag(4bpytm)](ClO_4) ½CH_2Cl_2 ½dmf (**2·Solv**)

A solution of $AgClO_4$ (0.166 g, 0.80 mmol) in MeOH (10 mL) was added dropwise to a solution of 4bpytm (0.187 g, 0.80 mmol) in $CHCl_3$ (10 mL). The suspension was stirred for 24 h and the resulting white precipitate was filtered off, washed with $CHCl_3$ and dried under vacuum. Single crystals of **2·Solv** were obtained when a solution of bis(4-pyridylthio)methane (4bpytm) (59 mg, 0.25 mmol) in CH_2Cl_2 (3 mL) was slowly added to a solution of $AgClO_4$ (52 mg, 0.25 mmol) in CH_3CN (3 mL) layered with dmf (1.5 mL) in a test tube. The reagents were allowed to mix slowly by diffusion to form colorless crystals of **2·Solv**.

Data for **2**: Yield: 76%. *Anal.* Calc. for $C_{11}H_{10}N_2S_2O_4ClAg$: C, 29.9; H, 2.2; N, 6.3; S, 14.4. Found: C, 29.1; H, 2.0; N, 6.0; S, 13.9%. IR (KBr, cm^{-1}): 1596s, 1537m, 1481m, 1230s, 1144–1084s,b,sh, 797m, 734m, 630s, 492m. UV–Vis (λ_{max}, cm^{-1}): 38 461.

2.2.3. [Ag(CH_3COO)(4bpytm)]·H_2O (**3**)

Compound **3** was obtained by reaction of bis(4-pyridylthio)methane (4bpytm) (0.187 g, 0.80 mmol) in a 1:1 mixture of MeOH/$CO(CH_3)_2$ (10 mL) and Ag(CH_3COO) (0.134 g, 0.80 mmol) in H_2O (10 mL). The resulting mixture was stirred for 24 h and the resulting pale ochre precipitate was filtered off, washed with MeOH and dried under vacuum. Single crystals were obtained by slow evaporation of the colorless mother liquor. The XRPD pattern of the resulting material do not show differences compared with that simulated from the crystal structure.

Data for **3**: Yield: 79%. *Anal.* Calc. for $C_{13}H_{15}N_2S_2O_3Ag$: C, 37.2; H, 3.6; N, 6.7; S, 15.3%. Found: C, 36.6; H, 3.4; N, 6.4; S, 14.9%. IR (KBr, cm^{-1}): 3418m, 1646m, 1576s, 1480m, 1410s, 1228m, 1063m, 797m, 735m, 491m. UV–Vis (λ_{max}, cm^{-1}): 38 461.

2.2.4. [Ag(CF_3COO)(4bpytm)] (**4**)

Compound **4** was obtained by reaction of bis(4-pyridylthio)methane (4bpytm) (0.187 g, 0.80 mmol) in $CHCl_3$ (10 mL) and Ag(CF_3COO) (0.177 g, 0.80 mmol) in MeOH (10 mL). The mixture was stirred for 24 h and the resulting white precipitate was filtered off, washed with $CHCl_3$ and dried under vacuum. Single crystals were obtained by slow evaporation of the colorless mother liquor. Crystals were also obtained by slow diffusion in a test tube of a solution of 4bpytm (70 mg, 0.30 mmol) in $CHCl_3$ (3 mL) and a solution of Ag(CF_3COO) (66 mg, 0.30 mmol) in $CO(CH_3)_2$ (3 mL). The XRPD pattern of the resulting material do not show differences compared with that simulated from the crystal structure.

Data for **4**: Yield: 80%. *Anal.* Calc. for $C_{13}H_{10}N_2S_2O_2F_3Ag$: C, 34.3; H, 2.2; N, 6.1; S, 14.1. Found: C, 34.2; H, 1.9; N, 5.9; S, 13.5%. IR (KBr, cm^{-1}): 1675s, 1578s, 1538m, 1482m, 1413s, 1202s, 1066m, 836m, 721m, 492m. UV–Vis (λ_{max}, cm^{-1}): 39 370.

2.3. Crystallography

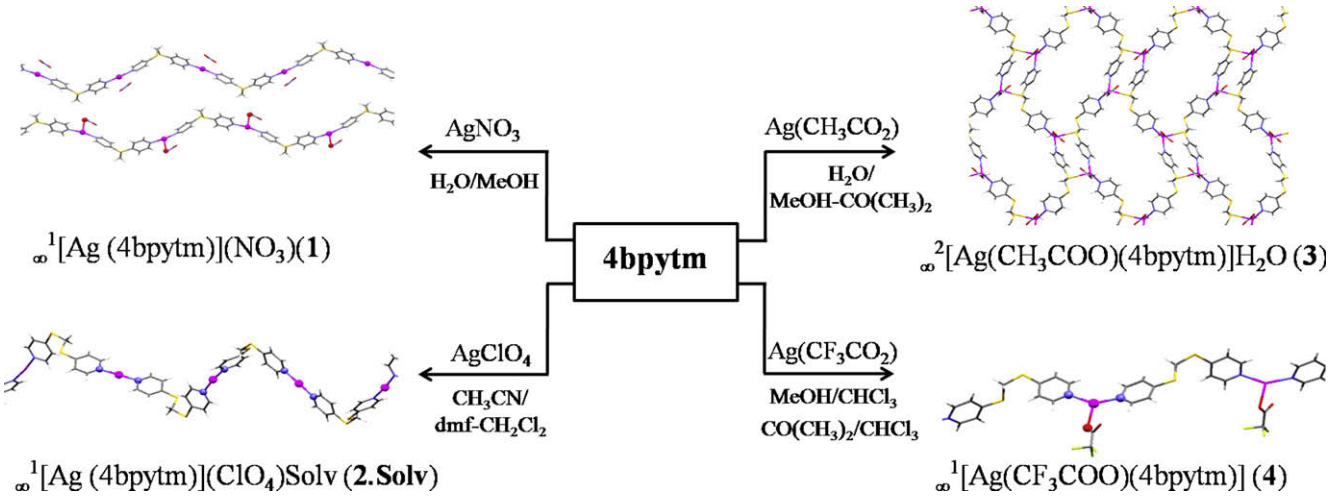
Crystallographic data were collected on a Bruker Smart 1000 CCD diffractometer at 293 K using graphite monochromated Mo K_α radiation (λ = 0.71073 Å) and were corrected for Lorentz and polarization effects. The frames were integrated with the Bruker SAINT [31] software package and the data were corrected for absorption using the program SADABS [32]. The structures were solved by direct methods using the program SHELXS97 [33]. All non-hydrogen atoms were refined with anisotropic thermal parameters by full-matrix least-squares calculations on F^2 using the program SHELXL97 [34]. Hydrogen atoms were inserted at calculated positions and constrained with isotropic thermal parameters. Drawings were produced with MERCURY [35] and special computations for the crystal structure discussions were carried out with PLATON [36]. Crystal data and structure refinement data are listed in Table 1.

3. Results and discussion

All of the complexes were obtained as powders under quite similar reaction conditions in moderate to good yields (76–81%) from equimolar mixtures of silver(I) salts and the *N*,*N*′-ligand. A general reaction scheme is shown in Scheme 1. Single crystals of **1**, **2·Solv** and **4** were prepared by slow diffusion of different solutions of

Table 1
Crystal and structure refinement data.

Compound	**1**	**2·Solv**	**3**	**4**
Empirical formula	$C_{11}H_{10}N_3O_3S_2Ag$	$C_{26}H_{29}Cl_4N_5O_9S_4Ag_2$	$C_{13}H_{15}N_2O_3S_2Ag$	$C_{13}H_{10}F_3N_2O_2S_2Ag$
Formula weight	404.21	1041.32	419.26	455.22
Crystal system	orthorhombic	triclinic	orthorhombic	monoclinic
Space group	$Pca2_1$	$P\bar{1}$	$Pbca$	$C2/c$
Unit cell dimensions				
a (Å)	7.7568(8)	8.063(2)	8.9104(7)	16.306(3)
b (Å)	14.8241(15)	14.558(5)	13.4625(10)	11.961(3)
c (Å)	24.006(2)	16.248(6)	25.651(2)	17.437(3)
α (°)		74.962(7)		
β (°)		87.505(8)		107.338(5)
γ (°)		88.690(9)		
V (Å^3)	2760.4(5)	1840.0(11)	3077.0(4)	3246.1(12)
Z	8	2	8	8
ρ_{calc} (g cm^{-3})	1.945	1.880	1.810	1.863
Absorption coefficient (mm^{-1})	1.772	1.638	1.591	1.537
$F(000)$	1600	1036	1680	1792
Crystal size (mm)	0.13 × 0.17 × 0.19	0.10 × 0.12 × 0.16	0.12 × 0.19 × 0.21	0.10 × 0.11 × 0.12
θ Range (°)	1.70–27.99	1.30–28.09	1.59–28.06	2.15–28.02
Reflections collected	14979	9518	15702	9439
Independent reflections (R_{int})	6139 (0.0929)	6765 (0.1006)	3634 (0.0995)	3663 (0.1591)
Maximum/minimum transmission	1.0000/0.6346	1.0000/0.7146	1.0000/0.8426	1.0000/0.7591
Goodness-of-fit on F^2	0.605	0.733	0.768	0.825
Final R indices [$I > 2\sigma(I)$]	R_1 = 0.0443	R_1 = 0.0667	R_1 = 0.0430	R_1 = 0.0546
	wR_2 = 0.0768	wR_2 = 0.1174	wR_2 = 0.0561	wR_2 = 0.1192



Scheme 1.

the corresponding silver(I) salts into solutions of 4bpytm in MeOH or $CHCl_3$ at room temperature. Single crystals of **3** and **4** were prepared by slow evaporation of the mother liquors. The powder X-ray diffraction experiments of compounds **1**, **3** and **4** were compared with those simulated from the crystal structures to show that the crystals selected for crystallographic analysis are representative of the bulk materials. In almost all cases 1D coordination polymers (**1**, **2·Solv** and **4**) were obtained with the ligand acting in an *N*,*N*′-bis(monodentate) manner but the 2D coordination polymer **3** was obtained with the *N*,*N*′-ligand acting as a tridentate system. To the best of our knowledge, **1** and **2·Solv** are the first examples of 1D cationic coordination polymers with the 4bpytm ligand. All the complexes reported with this ligand are neutral coordination polymers, except the discrete binuclear species $[Cu_2(HmL)_4(4bpytm)]\cdot H_2O$ [28] and $[Cu_2(HL)_4(4bpytm)_3]$ [37]: (HmL = 2-methyllactate and HL = lactate).

The infrared spectra of these compounds show the characteristic absorption bands of the 4bpytm ligand [26], which is barely modified upon formation of the Ag(I) complexes. Intense absorptions at 1361 and 1335 cm^{-1} are observed for compound **1** and these are due to the nitrate anion. Complex **2·Solv** shows an absorption due to the perchlorate group as several bands in the range 1144–1084 and at 630 cm^{-1}, with the spectrum also having an absorption at 1674 cm^{-1} for the ν(C=O) band due to the dmf solvent molecule. The IR spectra of **3** and **4** show ν_{as}(C=O) bands at 1646 and 1675 cm^{-1} and ν_s(C=O) bands at 1410 and 1413 cm^{-1} in **3** and **4**, respectively. The value of the difference $\Delta\nu = (\nu_{as} - \nu_s)$ is greater than 200 cm^{-1}, which indicates that the carboxylate groups behave as monodentate ligands [38].

Microanalysis confirmed that, in each case, the 1:1 4bpytm ligand-to-metal ratio was conserved in these complexes. The diffuse reflectance spectra of the complexes exhibit a band in the range 38 100–39 400 cm^{-1} and this is characteristic of the 4bpytm ligand.

The thermal decomposition of the complexes was studied by thermogravimetric analysis. In the solvated compounds, the initial step is consistent with the escape of solvent molecules: a weight loss of 3.7% between room temperature and 135 °C in compound **3** corresponds to the release of the lattice water molecule (Calc.

4%) and in **2**·**Solv** the 16% loss between room temperature and 247 °C corresponds to the loss of the dmf and CH_2Cl_2 molecules (Calc. 14.3%). The second loss of 16% in **3** and 20% in **2**·**Solv** at 190 °C and 347 °C, respectively, agrees with the loss of weight corresponding to acetate (Calc. 14%) and perchlorate (Calc. 19.4%) anions, respectively. The final loss in both cases corresponds to the 4bpytm ligand. For compound **4** the decomposition occurs in only one step between room temperature and 216 °C, with a weight loss of 63% corresponding to the release of all the ligand content.

3.1. Structure of [Ag(4bpytm)](NO$_3$) (*1*)

Selected interatomic distances and angles and the main hydrogen bonds are listed in Tables 2 and 3. The coordination environment of the silver atom is shown in Fig. 1 together with the atom numbering scheme used. The structure is based on a 1D helical coordination polymer [Ag(4bpytm)](NO_3), which crystallized in the polar space group $Pca2_1$, with the Flack parameter being 0.10(3) [39].

Complex **1** is based on two different helical chains of the same helicity and each chain has silver atoms with a different environment. In one of the chains Ag1 is coordinated by two pyridine nitrogen atoms from different 4bpytm ligands and this gives a linear coordination geometry with an N–Ag–N bond angle of 171.9(3)° (Table 2). In the other chain Ag2 has a coordination close to a "T" shaped geometry [N21–Ag2–N11, 162.6(3)°; N21–Ag2–O31, 88.7(3)° and N11–Ag2–O31, 108.1(3)°] involving the NO_3^- anion in a weak coordination to Ag2, with an Ag···O distance of 2.688(6) Å, as observed in other silver(I) compounds [40,41]. Both silver atoms are bonded to nitrogen atoms of 4bpytm ligands with Ag–N distances in the range 2.144(7)–2.170(7) Å. The Ag···Ag distances in each chain separated by the bridging 4bpytm are 12.527 Å for Ag1 and 12.786 Å for Ag2. The chains run along the *c* axis and the 4bpytm ligands have C–S–C–S torsion angles of 64.3(5)° and 69.2(5)° in one chain and 68.4(5)° and 68.6(5)° in the other, with these values being smaller than those found in the free ligand [26] but in the range reported for other polymeric metal complexes [26–28]. The Ag(1) center presents secondary interactions with two nitrate anions, with Ag–O distances of 2.752(7) and 2.960(8) Å, and with a sulfur atom (S11) belonging to a neighboring chain at a distance of 3.352(2) Å (Table 2). The next closest atoms to the Ag2 center are an oxygen atom (O31) at a distance of 3.049(8) Å and a sulfur atom (S1) belonging to a neighboring chain at 3.234(2) Å. Both metal centers therefore have three secondary interactions at distances shorter than the corresponding sum of the van der Waals radii.

The chains are connected to give a 3D architecture by Ag···O and Ag···S interactions (Fig. 1, right). In this way, the nitrate anions, by means of Ag···O interactions, link chains of opposite helicity based on the same metal center (Ag1 or Ag2), the Ag2–S1 interaction also connects chains of opposite helicity but in this case they are based on a different silver cation and the Ag1–S11 linked chains of the same helicity and a different silver cation. The resulting 3D network is also stabilized by the effect of several hydrogen bonds

Table 2
Selected interatomic bond lengths (Å) and angles (°) and secondary interactions involving the silver(I) centers.

	Lengths		Angles	
1	Ag1–N1	2.161(7)	N1–Ag1–N9	171.9(3)
	Ag1–N9	2.144(7)	N21–Ag2–N11	162.6(3)
	Ag2–N11	2.170(7)		
	Ag2–N21	2.155(8)		
	Ag2–O31	2.688(6)		
Secondary interactions	Ag1–O41^{i}	2.752(7)		
	Ag1–O41^{ii}	2.960(8)		
	Ag1–S11^{iii}	3.352(2)		
	Ag2–O31^{iv}	3.049(8)		
	Ag2–S1^{v}	3.234(2)		
i = $-x+1, -y+1, z-1/2$; ii = $-x+1/2, y+1, z-1/2$; iii = $x+1, y, z$; iv = $x-1/2, -y+1, z$; v = $-x-1/2, y-1, z-1/2$				
2·**Solv**	Ag1–N1	2.142(11)	N1–Ag1–N1^{i}	179.999(1)
	Ag2–N2	2.108(12)	N2–Ag2–N11	172.7(5)
	Ag2–N11	2.157(12)		
	Ag3–N12	2.191(11)		
Secondary interactions	Ag1–S1^{iv}	3.357(4)		
	Ag1–O11^{ii}	2.940(9)		
	Ag2–O21^{vi}	3.097(16)		
	Ag2–O24^{ii}	3.119(16)		
	Ag2–O31	3.107(13)		
	Ag3–S12^{vii}	3.283(4)		
	Ag3–O13^{vii}	3.182(17)		
i = $-x, -y+1, -z$; ii = $-x-1, -y+2, -z+1$; iv = $-x-1, -y+1, -z$; vi = $-x-2, -y+2, -z+1$; vii = $-x-3, -y+2, -z+2$				
3	Ag–N1	2.245(4)	N1–Ag–N2	126.94(15)
	Ag–N2	2.263(4)	N1–Ag–O1	119.37(14)
	Ag–O1	2.295(3)	N2–Ag–O1	103.13(13)
	Ag–S1	2.8304(14)	N1–Ag–S1	99.21(10)
			N2–Ag–S1	101.83(11)
			O1–Ag–S1	101.66(10)
4	Ag–N2	2.220(5)	N2–Ag–N1	139.6(2)
	Ag–N1	2.230(6)	N2–Ag–O1	116.2(2)
	Ag–O1	2.354(6)	N1–Ag–O1	102.7(2)
Secondary interactions	Ag–Ag^{i}	3.2485(15)		
	Ag–S2^{ii}	3.359(2)		
i = $-x+1/2, -y+3/2, -z+1$; ii = $-x, 1-y, 1-z$				

Sum of van der Waals radius: Ag···S = 3.52 Å; Ag···O = 3.24 Å; Ag···Ag = 3.44 Å [46,50].

Table 3
Main hydrogen bond distances (Å) and angles (°).

D–H···A	*d* (D–H)	*d* (H···A)	*d* (D···A)	∠(DHA)	Role
1					
C4–H4···O33^{i}	0.93	2.48	3.363(12)	159	Support the 3D architecture
C5–H5···O42^{ii}	0.93	2.40	3.295(13)	162	Support the 3D architecture
C6–H6A···O33^{iii}	0.97	2.48	3.252(11)	136	Support the 3D architecture
C27–H27A···O42^{iv}	0.97	2.44	3.272(11)	143	Support the 3D architecture
C29–H29···O43^{v}	0.93	2.36	3.236(13)	156	Support the 3D architecture
i = 5/2 − *x*, −1 + *y*, −1/2 + *z*; ii = 1 − *x*, 1 − *y*, 1/2 + *z*; iii = 3/2 − *x*, −1 + *y*, −1/2 + *z*; iv = 2 − *x*, 1 − *y*, 1/2 + *z*; v = 3 − *x*, 1 − *y*, 1/2 + *z*					
2·Solv					
C6–H6B···O31^{i}	0.97	2.38	3.176(17)	139	Fix solvent to chain
C12–H12···O22^{ii}	0.93	2.48	3.369(19)	161	Support the 3D architecture
C16–H16···O22^{iii}	0.93	2.55	3.25(2)	132	Support the 3D architecture
C17–H17B···O23^{iv}	0.97	2.42	3.32(3)	153	Support the 3D architecture
C21–H21···O14^{iv}	0.93	2.53	3.32(2)	143	Support the 3D architecture
i = −2 − *x*, 1 − *y*, 1 − *z*; ii = −1 − *x*, 2 − *y*, 1 − *z*; iii = −2 − *x*, 2 − *y*, 1 − *z*; iv = −1 + *x*, *y*, *z*					
3					
C8–H8···O1^{i}	0.93	2.34	3.242(7)	163	Support the 3D architecture
C10–H10···O1 W	0.93	2.50	3.391(7)	159	Fix solvent to sheets
C2–H2···O1 W	0.93	2.62	3.253(7)	126	Fix solvent to sheets
O1 W···O2^{ii}			2.711(6)		Organize the sheets in 3D
O1 W···O2^{iii}			2.922(6)		Organize the sheets in 3D
i = 1/2 − *x*, 1/2 + *y*, *z*; ii = −*x* + 1/2, *y* − 1/2, *z*; iii = *x* − 1/2, −*y* + 1/2, −*z* + 1					
4					
C4–H4···F3^{i}	0.93	2.20	3.113(8)	165.6	Support the 3D architecture
C6–H6B···F1^{ii}	0.97	2.55	3.395(7)	145.8	Support the 3D architecture
C6–H6A···.O2^{ii}	0.97	2.45	3.294(9)	145.8	Support the 3D architecture
C6–H6B···O2^{iii}	0.97	2.57	3.255(8)	128.0	Support the 3D architecture
C10–H10···O1^{iv}	0.93	2.50	3.200(9)	132.6	Support the 3D architecture
i = −1 + *x*, *y*, *z*; ii = −1/2 + *x*, 1/2 + *y*, *z*; iii = −*x*, 1 − *y*, 1 − *z*; iv = 1/2 − *x*, 3/2 − *y*, 1 − *z*					

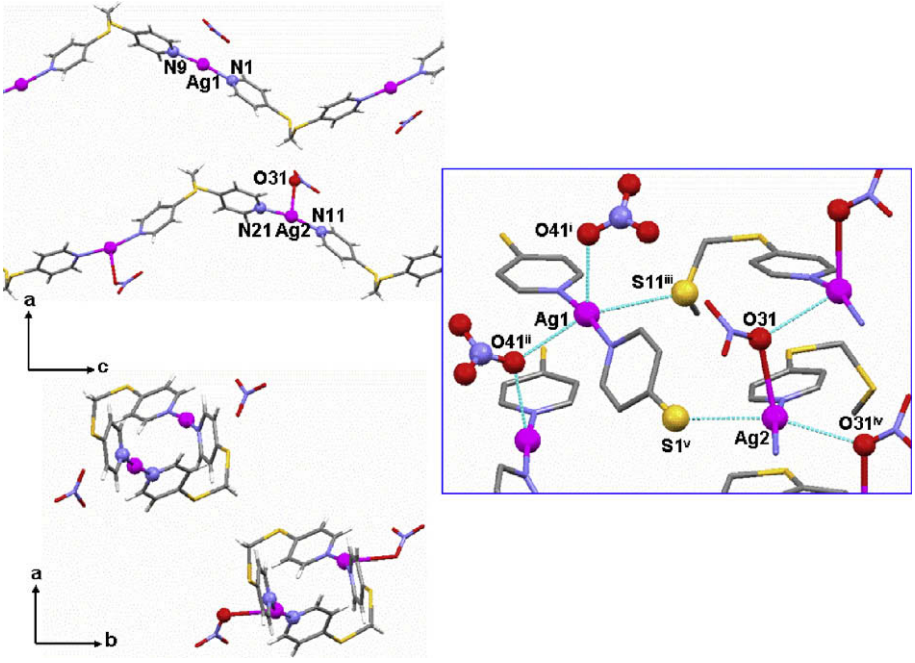


Fig. 1. Structure of [Ag(4bpytm)](NO$_3$) (**1**). Left: pictures showing the helical chains that run along the *c* axis. Right: Ag···S and Ag···O interactions between chains (some parts of the ligand have been omitted for clarity).

involving the –CH$_{py}$ and –CH$_2$ methyl groups of the ligand 4bpytm and the uncoordinated oxygen atom belonging to a nitrate anion (Table 3). The final 3D supramolecular architecture (Fig. 2) is racemic due to the existence of equal amounts of *P*- and *M*-helices.

It is clear that the nitrate anion plays a key role in the supramolecular assembly of **1**, which has a very efficient packing with a Kitaigorodskii packing index [42] of 75.6%, a value that is slightly greater than the index calculated for the coordination polymers previously reported with 4bpytm [26–28]. Although the nitrate anion could be classified as a potential coordinative anion [22], in this case the good solubility of AgNO$_3$ in water could be responsible for the semi-coordination or non-coordination of the anion to silver(I). According to these results it can be suggested that the solubility seems to be a major parameter for the crystallization [20].

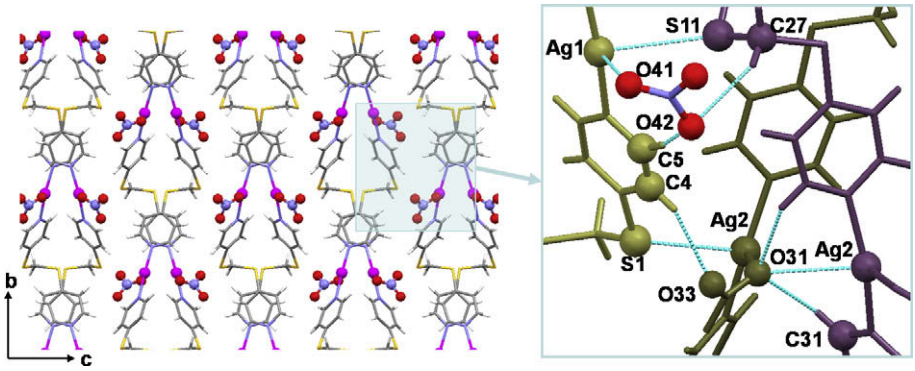


Fig. 2. View in the *bc* plane of the 3D architecture in **1**, showing in detail the main interactions (Ag···O, Ag···S and CH···O) between chains of opposite chirality.

3.2. Structure of [Ag(4bpytm)](ClO$_4$) ½CH$_2$Cl$_2$ ½dmf (**2·Solv**)

The coordination environment of the silver atoms in **2·Solv** is represented in Fig. 3 together with the atom numbering scheme. Selected bond distances and angles are listed in Table 2. The crystal structure of **2·Solv** consists of ClO_4^- anions, molecules of solvents and an $[Ag(4bpytm)]^+$ cationic chain. In the chain there are three crystallographically independent Ag^I centers, which are coordinated by two pyridine nitrogen atoms from two different 4bpytm ligands. Each silver center is in an almost linear coordination environment, with the Ag–N bond distances in the range 2.108(12)–2.191(11) Å, as expected for such coordination bonds [42,43,24], and with N–Ag–N angles of 172.7(5)° and 180.0(1)°. The ligand coordinates to the Ag^I centers in an *N,N*-bis-monodentate bridging mode with both *P*- and *M*-conformations, resulting in an infinite achiral chain with intramolecular Ag···Ag separations of 12.537 Å between Ag2–Ag3 and 12.177 Å between Ag2–Ag1. In the ligand the C–S–C–S torsion angles with values between 71.9(8)° and 174.6(7)° are larger than those found in the free ligand, in complex **1** and in the known polymeric complexes with the 4bpytm ligand [26–28]. These angles correspond to a TG conformation, which is much less common than the GG conformation [30,44]. This kind of conformation has only been observed in the molecular compound $[Cu_2(HL)_4(4bpytm)_3]$ (HL = lactate), where 4bpytm acts as monodentate ligand [37], meaning that **2·Solv** is the first example of a TG conformation in a coordination polymer with the 4bpytm ligand.

Another feature of **2·Solv** is the formation of a 3D network, as in **1**, by means of Ag···S and Ag···O interactions between adjacent chains (Fig. 3). The perchlorate anions are located next to the silver ions and are linked by Ag···O close contacts, with interaction distances in the range 2.940(9)–3.182(17) Å – i.e., shorter than the sum of van der Waals radii of silver and oxygen (3.24 Å) [47]. Ag1–S1 (3.357(4) Å) and Ag3–S12 (3.283(4) Å) are the next closest interactions between two different neighboring chains. The dmf molecule is linked to the Ag2 center at 3.107(13) Å, which indicates the presence of non-bonding Ag–O interactions. Therefore, the environments around the silver centers are different: Ag3 and Ag1 have four secondary interactions that involve two perchlorate anions and two adjacent chains towards semi-coordination with

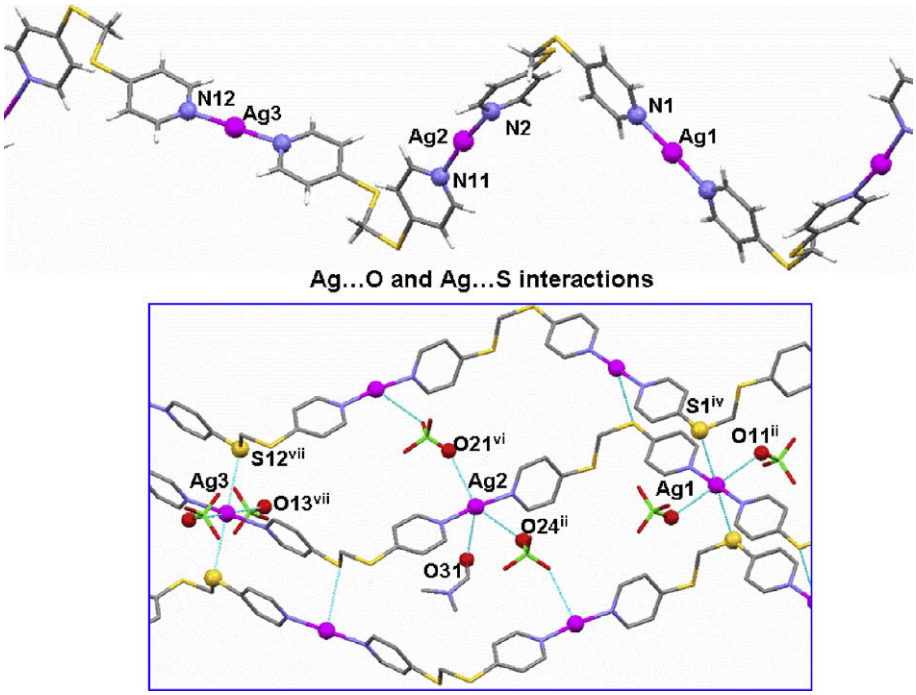


Fig. 3. Structure of [Ag(4bpytm)](ClO$_4$) ½CH$_2$Cl$_2$ ½dmf (**2·Solv**). Top: view of the silver atom environments with the corresponding labeling scheme. Bottom: view of the secondary interactions around each metal center.

the corresponding S atoms, but Ag2 only interacts with two perchlorate anions and one dmf solvent molecule (Fig. 3). The perchlorate anion is also linked to the framework by the effect of CH···O hydrogen bonds involving the pyridine rings and methyl groups of 4bpytm (Table 3, Fig. 4). In addition, the 3D association is reinforced by π–π stacking interactions (Fig. 4) between the [N2/C21/C22/C18/C19/C20] rings (coordinated to Ag3) of adjacent chains in a face-to-face mode with a centroid-to-centroid distance of 3.624(8) Å and an interplanar dihedral angle of 0.02°, which indicates the parallel disposition of the aromatic rings.

The resulting cavities in this network are filled by solvent molecules and perchlorate counterions as guest molecules (Fig. 4). The dmf and CH_2Cl_2 solvent molecules are involved in different weak interactions with the metal–organic framework. CH_2Cl_2 is only weakly linked by CH···Cl (with C–Cl distances greater than 3.5 Å) interactions to the metal–organic framework and, comparatively, this solvent is much more strongly connected to the perchlorate anions ($CH_{dichloromethane}$···$OClO_3$, C–O distance of 3.490(5) Å). On the other hand, dmf is linked to the network by means of several contacts, including Ag···O interactions, CH···O hydrogen bonds (Table 3) and CH···π interactions between one methyl group of dmf and the [N11/C12/C13/C14/C15/C16] ring of the 4bpytm ligand, with a CH···centroid distance of 3.527(18) Å and a CH···centroid angle of 123°. The volume occupied by the solvent is also evident in the corresponding values of the Kitaigorodskii packing index [42]: 59.4% when the solvent is omitted in the calculation and 73.3% when the solvent is included. The counterion and solvents filling the cavities of the network, which are weakly bonded to Ag(I), may act as a template for the formation of the network and consequently may contribute to the stability of the structure.

3.3. Structure of $[Ag(CH_3COO)(4bpytm)]\cdot H_2O$ (**3**)

The coordination environment of the silver atom in compound **3** is shown in Fig. 5 along with the atom numbering scheme used. The structure is based on 2D layers and water of crystallization. The AcO^- anion also acts as a coordinating monodentate anion. The Ag–O bond length (2.295(3) Å) is shorter than the normal range for Ag–O bond distances for silver carboxylate and oxalate complexes [48–50]. It is known that bidentate anions, such as AcO^-, have a higher density of negative charge on their peripheral, and therefore potentially interacting, atoms in comparison to NO_3^-, ClO_4^- and they are therefore able to coordinate more strongly [51]. The silver atom adopts a distorted tetrahedral geometry by coordination to two pyridine nitrogen atoms of each ligand, with $Ag–N_{py}$ distances of 2.245(4) and 2.263(4) Å, to an oxygen atom of acetate and to a sulfur atom from 4bpytm (Ag–O and Ag–S distances of 2.295(3) and 2.830(14) Å, respectively). In this way, each metal center is connected to three different ligand molecules and each ligand molecule is also coordinated by three Ag^I cations, thus generating the 2D network that is schematically represented in Fig. 5. The ligand adopts an *N,N,S*-tridentate bridging mode and it should be pointed out that this kind of coordination mode for 4bpytm has not been documented previously. The values for the C–S–C–S torsion angles in 4bpytm (79.1(3)° and 176.8(2)°) are similar to those found in **2·Solv** and they correspond to a TG conformation. Each Ag^I center is connected to four other Ag^I centers through the bridging ligand and, depending on the coordination mode of the ligand, the Ag···Ag distances are 7.376, 10.093 and 13.035 Å.

The 2D layer can be described as a rhombic grid with a major diagonal Ag···Ag distance of 20.65 Å and a minor diagonal Ag···Ag distance of 10.82 Å (Fig. 5). The crystallization water molecules are located in the void, as shown in Fig. 5, and they are undoubtedly responsible for the resulting 3D supramolecular organization, which is formed through hydrogen bonding involving the uncoordinated oxygen atoms of the carboxylato groups (Table 3). These layers are also linked by two kinds of weak interactions: CH···O hydrogen bonds, involving the water molecule and the coordinated oxygen of the acetate as acceptors (Table 3), and CH···π stacking

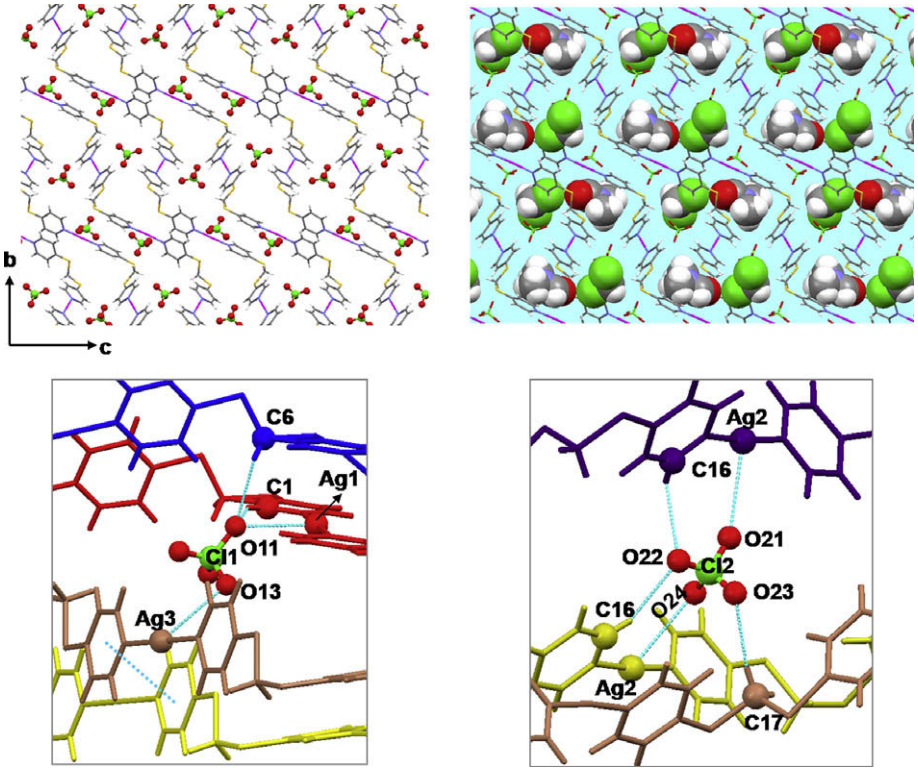


Fig. 4. View of the 3D architecture in **2·Solv** with perchlorate ions represented as "ball and stick" (top left) and solvent molecules shown as space filling representations (top right). Bottom: detail of main interactions that involve perchlorate anions.

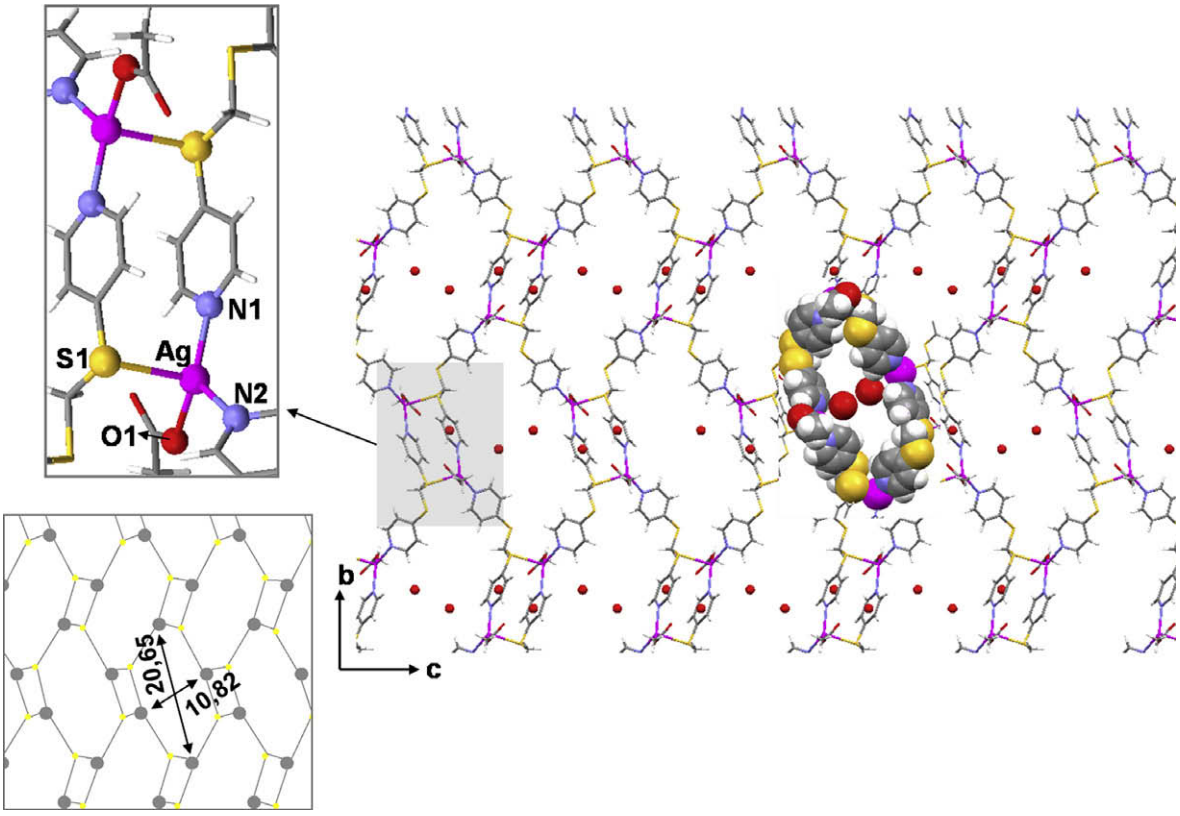


Fig. 5. View of the 2D coordination polymer [Ag(CH_3COO)(4bpytm)]·H_2O (**3**) together with the coordination environment of silver ions (top left) and a metric representation (bottom left).

interactions, involving the –CH belonging to the methyl group of the acetate ligand and the [N1/C1/C2/C3/C4/C5] ring of the 4bpytm ligand (Fig. 6). The CH···centroid distance is 3.884(5) Å with a C–H···centroid angle of 123°. These interactions link the 2D layer described above in an AB stacking mode (Fig. 6). In the resulting 3D network the molecules are packed very efficiently, with a Kitaigorodskii packing index [42] of 74.3%.

3.4. Structure of [Ag(CF_3COO)(4bpytm)] (**4**)

The structure of **4** is based on a 1D arrangement of Ag^I ions linked by 4bpytm ligands and trifluoroacetate anions. In this structure the Ag^I center is three coordinated by one oxygen atom of the organic anion and by two 4bpytm ligands through nitrogen donor atoms [Ag–N2 2.220(5), Ag–N1 2.230(6) Å] with a distorted trigonal planar coordination [N2–Ag–N1 139.6(2)°, N2–Ag–O1 116.2(2)°, N1–Ag–O1 102.7(2)°] (Fig. 7). The trifluoroacetate ion is coordinated to the silver atom in a monodentate manner with silver–oxygen distances of 2.354(6) Å. The Ag atom also interacts with one adjacent Ag atom, with an Ag–Ag distance of 3.2485(15) Å, and with an S atom from a neighboring chain, with an Ag–S distance of 3.359(5) Å. In both cases the distances are shorter than the sum of the corresponding van der Waals radii [47,51]. The Ag···Ag distance across the 4bpytm ligand is 13.903 Å, a slightly higher value than those found in the other complexes reported here. In the 4bpytm ligand the C–S–C–S torsion angle values of 81.5(4)° and 168.3(4)° are in the range reported for the polymeric metal complexes **2**·**Solv** and **3** and these adopt a TG conformation [45]. From the point of view of chirality, the 1D polymer consists of alternate linkages of the *M*- and *P*-forms of the ligand with the Ag^I ions. The chain is thus represented as –*M*–(Ag)–*P*–(Ag)–*M*–, resulting in an achiral structure running along the *b* axis.

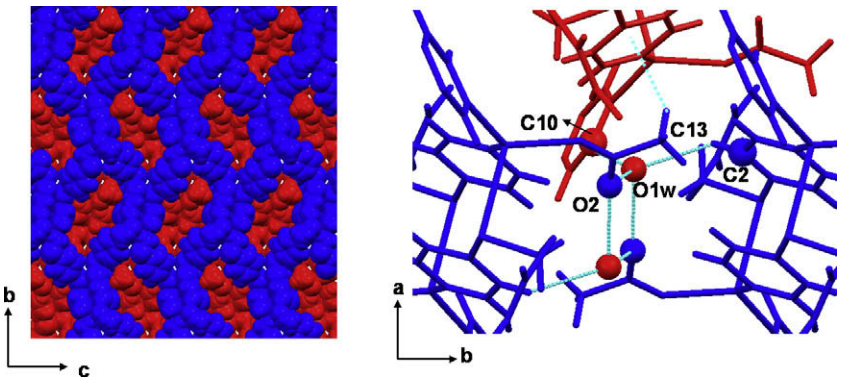


Fig. 6. View of the AB stacking mode of the layers (left) and details of the interactions with water of crystallization (right).

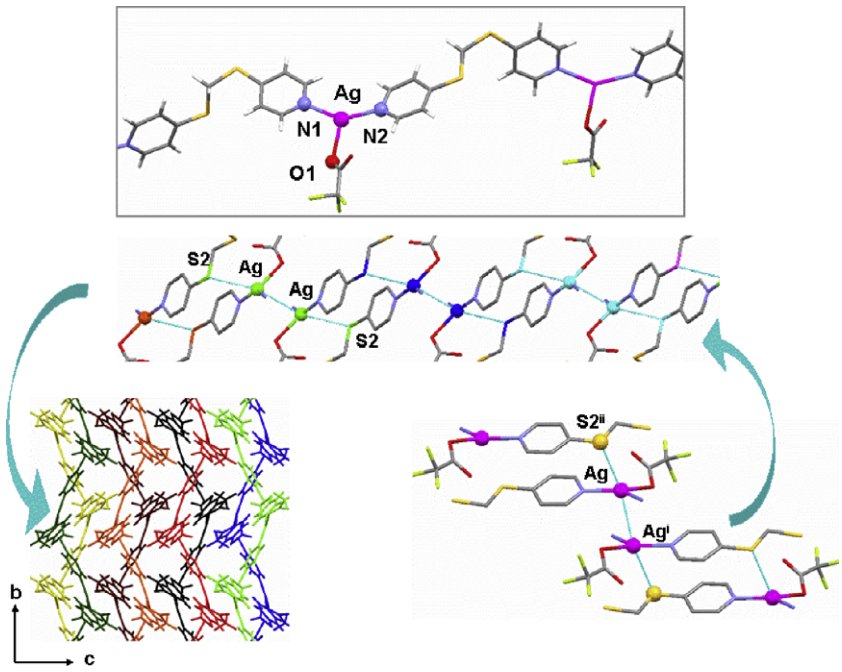


Fig. 7. View (top) of the 1D coordination polymer [Ag(CF_3COO)(4bpytm)] (**4**) together with the coordination environment of silver ions, showing detail of the S···Ag···Ag···S interactions. View in the *ab* plane of the 3D network (bottom left).

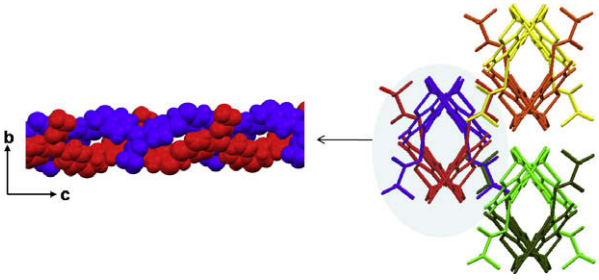


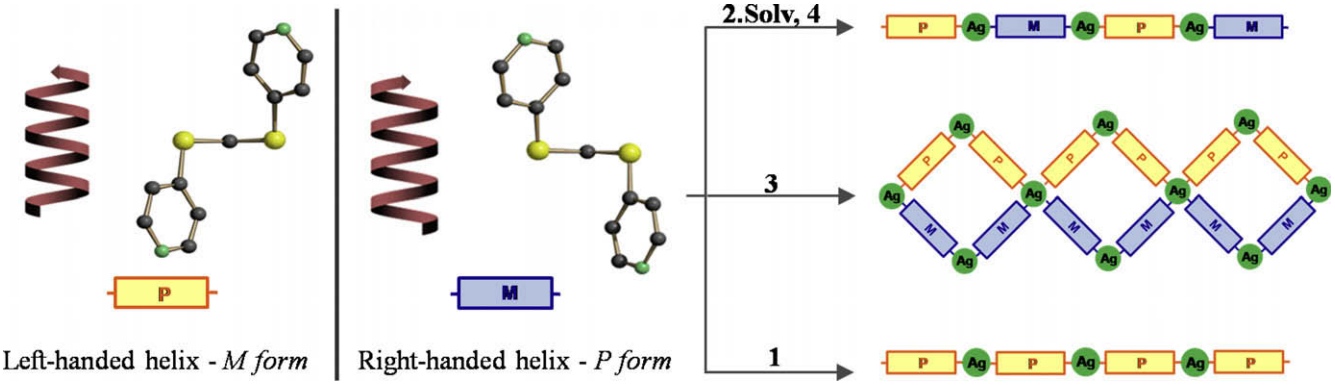
Fig. 8. View of the 3D organization showing details of the arrangement of the chains through Ag···Ag interactions.

The chains are interconnected through Ag–Ag and Ag–S interactions as well as weak CH···O hydrogen bonds (Table 3). Therefore, a specific combination of Ag–Ag and Ag–S contacts produces the pattern S···Ag···Ag···S (Fig. 7), which is mainly responsible for the 3D network. This network involves four chains in different points, as shown schematically in Fig. 7.

Taking into account only the effect of the argentophilic interactions, a double interweaved chain is formed, as shown in Fig. 8, and in turn these double chains are interconnected by means of the Ag···S interactions. In the resulting 3D network, the molecules are packed efficiently, with a Kitaigorodskii packing index [42] of 69.9%. Although electronegative atoms such as fluorine or oxygen, which are hydrogen bond acceptors, are present in the structure, weak CH···F or CH···O interactions do not play a significant role in the supramolecular organization.

4. Conclusions

The Ag(I)/4bpytm system was investigated using inorganic and organic anions. $CH_3CO_2^-$ and $CF_3CO_2^-$ act as coordinating ligands giving rise to neutral coordination polymers, but with NO_3^- and ClO_4^- cationic chains are obtained. In all the compounds the cation is coordinated preferentially by the nitrogen atoms of 4bpytm in an *N*,*N*′-bis(monodentate) bridging mode and, only in one compound, the thioether sulfur is involved in coordination (*N*,*N*,*S*-tridentate bridging mode). From the viewpoint of chirality, the twisted structure of 4bpytm is accompanied by axial chirality (as shown in



Scheme 2.

Scheme 2) but the alternate linkage of the *M*- and *P*-forms affords achiral structures.

In the compounds with lower coordination number, the secondary interactions Ag···S and Ag···O play a crucial role in the self-organization of the supramolecular polymers and in one case the argentophilic interactions are also involved in the supramolecular organization. In one compound the Ag–S and Ag–O bonds are coordinating producing a 2D coordination polymer. When solvent is present, it influences the overall structure through its involvement in weak interactions or its role as a guest molecule in void space in the solid state.

Supplementary data

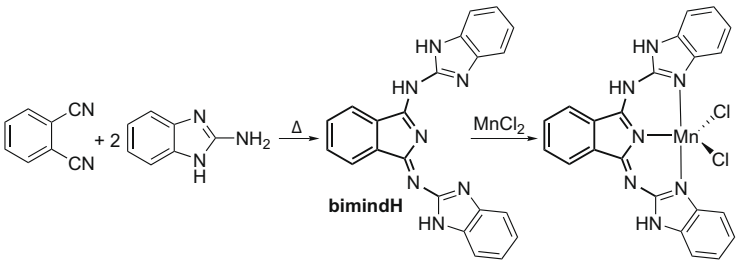
CCDC 702279, 702280, 702281 and 702282 contain the supplementary crystallographic data for **1**, **2**·**Solv**, **3** and **4**. These data can be obtained free of charge via http://www.ccdc.cam.ac.uk/conts/retrieving.html, or from the Cambridge Crystallographic Data Centre, 12 Union Road, Cambridge CB2 1EZ, UK; fax: (+44) 1223-336-033; or e-mail: deposit@ccdc.cam.ac.uk.

Acknowledgements

Financial support from ERDF (EU), MEC (Spain) and Xunta de Galicia (Spain) (research Projects CTQ2006-05642/BQU and PGIDIT06-PXIB314373PR) are gratefully acknowledged.

References

[1] J.M. Lehn, Supramolecular Chemistry: Concepts and Perspectives, VCH, Weinheim, Germany, 1995.
[2] R. Robson, J. Chem. Soc., Dalton Trans. (2000) 3735.
[3] Y. Rodríguez-Martín, M. Hernández-Molina, F.S. Delgado, J. Pasán, C. Ruíz-Pérez, J. Sánchiz, F. Lloret, M. Julve, CrystEngCommun. 4 (2002) 522.
[4] C. Janiak, Dalton Trans. (2003) 2781.
[5] L. Carlucci, G. Ciani, D.M. Proserpio, CrystEngCommun. 5 (2003) 269.
[6] K. Biradha, CrystEngCommun. 5 (2003) 374.
[7] S. Kitagawa, R. Kitaura, S. Noro, Angew. Chem., Int. Ed. 43 (2004) 2334.
[8] M. Du, C.-P. Li, X.-J. Zhao, Cryst. Growth Des. 6 (2006) 335.
[9] T.-T. Luo, H.-L. Tsai, S.-L. Yang, Y.-H. Liu, R.-D. Yadav, C.-C. Su, C.-H. Ueng, L.-G. Lin, K.-L. Lu, Angew. Chem., Int. Ed. 44 (2005) 6063.
[10] G. Peli, S. Rizzato, S. Cassesse, L. Garlaschelli, M. Manassero, CrystEngCommun. 7 (2005) 575.
[11] J.K. Clegg, L.F. Lindoy, B. Moubaraki, K.S. Murray, J.C. McMurtrie, Dalton Trans. (2004) 2417.
[12] M. Albrecht, I. Janser, S. Kamptmann, P. Weis, B. Wibbeling, R. Fröhlich, Dalton Trans. (2004) 37.
[13] D.A. McMorran, Inorg. Chem. 47 (2008) 592.
[14] R. Horikoshi, T. Mochida, N. Maki, S. Yamada, H. Moriyama, J. Chem. Soc., Dalton Trans. (2002) 28.
[15] Y.-P. Ren, X.-J. Kong, L.-S. Long, R.-B. Huang, L.-S. Zheng, Cryst. Growth Des. 6 (2006) 572.
[16] L. Pan, E.B. Woodlock, X. Wang, K.-C. Lam, A.L. Rheingold, Chem. Commun. (2001) 1762.
[17] J. Bourlier, M.W. Hosseini, J.-M. Planeix, N. Kyritsakas, New J. Chem. 31 (2007) 25.
[18] Y. Wang, B. Ding, P. Cheng, D.-Z. Liao, S.-P. Yan, Inorg. Chem. 46 (2007) 2002.
[19] A.Y. Robin, J.L. Sagué, A. Neels, T.V. Slenters, K.M. Fromm, Inorg. Chim. Acta 360 (2006) 212.
[20] A.Y. Robin, J.L. Sagué, K.M. Fromm, CrystEngCommun. 8 (2006) 403.
[21] Y. Zheng, M. Du, L. Jian-Rong, R.H. Zhang, X.H. Bu, Dalton Trans. (2003) 1509.
[22] O.S. Jung, Y.J. Kim, Y.A. Lee, K.M. Park, S.S. Lee, Inorg. Chem. 42 (2003) 844.
[23] Y.B. Xie, X.H. Bu, J. Cluster Sci. 14 (2003) 471.
[24] Y.B. Xie, C. Zhang, J.R. Li, X.H. Bu, Dalton Trans. (2004) 562.
[25] H.C. Chen, H.L. Hu, Z.K. Chan, C.W. Yeh, H.W. Jia, C.P. Wu, J.D. Chen, J.C. Wang, Cryst. Growth Des. 7 (2007) 698.
[26] A. Amoedo-Portela, R. Carballo, J.S. Casas, E. García-Martínez, A.B. Lago-Blanco, A. Sánchez-González, J. Sordo, E.M. Vázquez-López, Z. Anorg. Allg. Chem. 631 (2005) 2241.
[27] R. Carballo, B. Covelo, E. García-Martínez, A.B. Lago, E.M. Vázquez-López, Z. Anorg. Allg. Chem. 633 (2007) 780.
[28] R. Carballo, B. Covelo, N. Fernández-Hermida, E. García-Martínez, A.B. Lago, E.M. Vázquez-López, Cryst. Growth Des. 8 (2008) 995.
[29] M. Korn, A. Haas, H. Oberhammer, Chem. Ber. 128 (1995) 461.
[30] E.M. Page, D.A. Rice, K. Aerset, K. Hagen, A.R.J. Genge, J. Phys. Chem. A 104 (2000) 6672.
[31] Siemens SAINT, Version 4, Software Reference Manual, 1996, Siemens Analytical X-ray Systems, Inc., Madison, WI, USA.
[32] G.M. Sheldrick, SADABS, Program for Empirical Absorption Correction of Area Detector Data, University of Göttingen, Germany, 1996.
[33] G.M. Sheldrick, SHELXS-97, Program for the Solution of Crystal Structures from X-ray Data, University of Göttingen, Germany, 1997.
[34] G.M. Sheldrick, SHELXL-97, Program for the Refinement of Crystal Structures from X-ray Data, University of Göttingen, Germany, 1997.
[35] I.J. Bruno, J.C. Cole, P.R. Edgington, M.K. Kessler, C.F. Macrae, P. McCabe, J. Pearson, R. Taylor, Acta Crystallogr., Sect. B 58 (2002) 389.
[36] A.L. Spek, PLATON, A Multipurpose Crystallographic Tool, Utrecht University, Utrecht, The Netherlands, 2001.
[37] R. Carballo, B. Covelo, N. Fernández-Hermida, E. García-Martínez, A.B. Lago, E.M. Vázquez-López, J. Mol. Struct. 892 (2008) 427.
[38] S.D. Robinson, M.F. Uttley, J. Chem. Soc., Dalton Trans. 18 (1973) 1912.
[39] H.D. Flack, Acta Crystallogr., Sect. A 39 (1983) 876.
[40] Y.-B. Xie, J.-R. Lie, X.-H. Bu, Polyhedron 24 (2005) 413.
[41] S.R. Batten, J.C. Jeffery, M.D. Ward, Inorg. Chim. Acta 292 (1999) 231.
[42] A.I. Kitaigorodskii, Molecular Crystals and Molecules, Academic Press, New York, 1973.
[43] C.L. Chen, Z.Q. Yu, Q. Zhang, M. Pan, J.Y. Zhang, C.Y. Zhao, C.Y. Su, Cryst. Growth Des. 8 (2008) 897.
[44] D.M. Shin, I.N. Lee, Y.A. Lee, Y.K. Chung, Inorg. Chem. 42 (2003) 2977.
[45] G.P. Moss, Pure Appl. Chem. 68 (1996) 2193.
[46] C.Y. Chen, J.Y. Zheng, H.M. Lee, Inorg. Chim. Acta 360 (2007) 21.
[47] A. Bondi, J. Phys. Chem. 68 (1994) 441.
[48] C.-K. Xia, C.-Z. Lu, X.-Y. Wu, Q.-Z. Zhang, J.-J. Zhang, D.-M. Wu, Polyhedron 26 (2007) 941.
[49] M. Jansen, Angew. Chem., Int. Ed. 26 (1987) 1098.
[50] A.J. Blake, G. Baum, N.R. Champness, S.S.M. Chung, P.A. Cooke, D. Fenske, A.N. Khlobystov, D.A. Lemenovskii, W.S. Li, M. Schröder, Dalton Trans. (2000) 4285.
[51] X.-H. Bu, Y.-B. Xie, J.-R. Li, R.-H. Zhang, Inorg. Chem. 42 (2003) 7422.



Scheme 1.

grown from dmf by diethyl ether diffusion. The intensity data were collected with Rigaku R-AXIS Rapid single-crystal diffractometer using Mo Kα radiation (λ = 0.71070 Å) at 130 K. Crystallographic data and details of the structure determination are given in Table 1, whereas selected bond lengths and angles are listed in Table 2. SHELX-97 [17] was used for structure solution and full matrix least squares refinement on F^2. The SQUEEZE function of PLATON was used to eliminate the contribution from the heavily disordered methanol solvent. Crystal structure has been deposited at the Cambridge Crystallographic Data Centre (Deposition no. 688573).

2.3. Synthesis of bimindH

It was prepared by fusing phthalonitrile (1.20 g, 9.4 mmol) and 2-amino-benzimidazole (2.5 g, 18.8 mmol) and maintaining a temperature of 190 °C until ammonia evolution ceased (~19 h). Extraction of the solid, which formed on cooling, into methanol gave yellow crystals on recrystallization (2.62 g, 71%). IR (KBr) cm^{-1}: 3278 m, 1642 m, 1630 s, 1614 vs, 1596 s, 1507 s, 1413 s, 1368 m, 1315 s, 1266 s, 1213 m, 1102 m, 1066 w, 997 w, 915 w, 821 m, 739 s, 694 s, 637 m, 563 w, 506 m. UV–Vis (dmf) λ_{max} ($\log\varepsilon$/$dm^3\ mol^{-1}\ cm^{-1}$): 271 (4.11); 288 (4.30); 303 (4.227); 314.5 (4.200); 347 (4.366); 369 (4.367); 388 (4.353); 412.5 (4.310); 440 (4.303); 470 (4.055). ^{1}H NMR (dmf-d^7), δ (ppm): 2.15 (s, 1H); 3.50 (s, 2H); 7.34 (m, 4H); 7.85 (m, 6H); 8.09 (m, 2H). *Anal.* Calc. for $C_{22}H_{15}N_7$: C, 70.01; H, 4.01; N, 25.98. Found: C, 69.61; H, 4.11.; N, 25.72%.

Table 1
Summary of the crystallographic data and structure parameters for [Mn(bimindH)Cl_2](dmf).

Formula weight	649.44
Crystal system	monoclinic
Crystal description	needle
Space group	*C*2/*c*
Unit cell dimensions	
a (Å)	19.973(9)
b (Å)	12.561(4)
c (Å)	12.180(6)
α (°)	90.00
β (°)	107.980(17)
γ (°)	90.00
V (Å^3)	2907(2)
Z	4
D_{calc} (g cm^{-1})	1.4841
Crystal size (mm^3)	0.55 × 0.18 × 0.18
Index ranges	$-25 \leqslant h \leqslant 25$
	$-14 \leqslant k \leqslant 16$
	$-15 \leqslant l \leqslant 15$
T (K)	130(2)
Radiation	Mo Kα (λ = 0.71070)
Absorption coefficient (mm^{-1})	0.682
F(000)	1340
Reflections collected	3327
Observed reflections [$I > 2\sigma(I)$]	2403
Goodness-of-fit	1.047
Final *R* indices	R_1 = 0.0479, wR_2 = 0.1047
R indices (all data)	R_1 = 0.0710, wR_2 = 0.1121

Table 2
Selected bond lengths (Å) and bond angles (°) for [Mn(bimindH)Cl_2](dmf).

Mn(1)–N(1)	1.959(2)	Mn(1)–Cl(1)	2.3145(9)
N(1)–C(1)	1.347(3)	N(1)–C(2)	1.397(3)
Mn(1)–N(4)	2.007(3)	C(2)–C(7)	1.405(3)
N(2)–C(7)	1.378(3)	N(4)–C(8)	1.390(3)
C(8)–C(9)	1.468(3)	C(9)–C(9^2)	1.403(5)
N(1)–Mn(1)–N(1^2)	175.74(11)	Cl(1)–Mn(1)–Cl(1^2)	119.53(4)
Cl(1)–Mn(1)–N(4)	120.24(2)	N(1)–Mn(1)–N(4)	87.87(5)
N(1)–Mn(1)–Cl(1)	90.53(7)	N(1)–Mn(1)–Cl(1^2)	91.61(7)
N(4)–C(8)–N(3)	128.7(2)		

2.4. Synthesis of [Mn(bimindH)Cl_2](dmf)

A solution of 0.59 g (3 mmol) of $MnCl_2 \cdot 4H_2O$ in 10 cm^3 CH_3OH was added to a suspension of 1.13 g (3 mmol) bimindH in 10 cm^3 CH_3CN and the orange yellow suspension was refluxed for 6 h. The solvent was removed by evaporation and the crude product was washed with cold CH_3OH and diethyl ether, and then dried under vacuum (1.28 g, 85%). The red product was recrystallized from dmf by ether diffusion. M.p. (Dec) 300 °C. IR (KBr) cm^{-1}: 3278 m, 1654 s, 1630 s, 1593 vs, 1569 s,1499 vs, 1421 s, 1315 m, 1283 w, 1184 m, 1091 m, 1037 m, 927 w, 784 w, 743 s, 702 s, 608 m, 522 w. UV–Vis (dmf) λ_{max} ($\log\varepsilon$/$dm^3\ mol^{-1}\ cm^{-1}$): 272 (4.15); 297 (4.23); 346 (4.288); 361 (4.313); 380.5 (4.229); 430 (4.333); 455 (4.394); 485.5 (4.192). ESR (toluene): g = 1.9998, A = 94.0 G. *Anal.* Calc. for $C_{22}H_{15}Cl_2MnN_7$: C, 52.51; H, 3.00; N, 19.48. Found: C, 52.23; H, 3.13; N, 19.28%.

2.5. Catalase-like activity

All reactions were carried out at 20 °C in a ~40 cm^3 reactor containing a stirring bar under air. The stoichiometry of the reaction was measured by simultaneous determination of the amount of O_2 and H_2O_2 concentrations. The evolved dioxygen was measured volumetrically, and amount of H_2O_2 was determined with the help of iodometric titration. In a typical experiment EtCN (30 cm^3) was added to the complex (0.04 mmol) and the flask was closed with a rubber septum. Dihydrogen peroxide (4–14 mmol) was injected through the septum with a syringe. The reactor was connected to a graduated burette filled with oil and dioxygen evolution was measured volumetrically at time intervals of 0.5 min. Observed initial rates were expressed as mol $dm^{-3}\ s^{-1}$ by taking the volume of the solution (30 cm^3) into account and calculated from the maximum slope of curve describing evolution of O_2 versus time.

3. Results and discussion

3.1. Synthesis and characterization of the [Mn(bimindH)Cl_2](dmf)

The synthetic route to the 1,3-bis(2′-benzimidazolylimino)isoindoline ligand involves the direct reaction of phthalonitrile and the 2-aminobenzimidazole at high temperature for 19 h followed

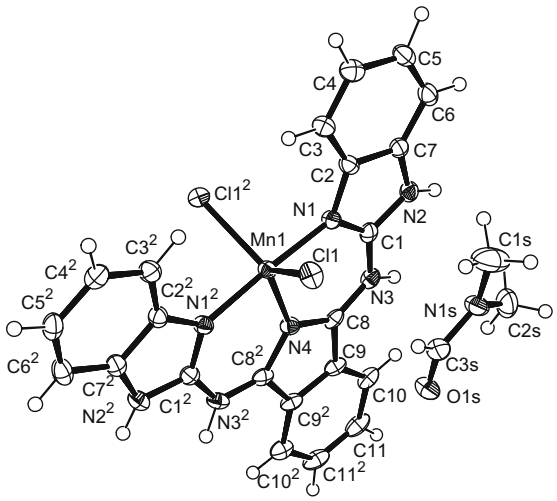


Fig. 1. Ellipsoid drawing of [Mn(bimindH)Cl_2](dmf) with the atom numbering scheme.

by extraction into methanol. This direct fusion method provides good yields and is a more efficient procedure than the syntheses involving 1,3-diiminoisoindoline as starting material. Reaction of equimolar amounts of 1,3-bis(2′-benzimidazolylimino)isoindoline and $MnCl_2 \cdot 4H_2O$ in methanol/acetonitrile resulted in the formation of [Mn(bimindH)Cl_2].

The Mn(II) ion is bound to a neutral tridentate isoindoline ligand and two chloride anions, forming a distorted trigonal bipyramidal environment around the metal ion. Analytical data, the infrared and the electronic spectrum of the complex are all consistent with the presence of a neutral nondeprotonated isoindoline ligand. Infrared spectra of metal complexes with deprotonated ligand versus nondeprotonated ligand show substantial differences in the region 1450–1660 cm^{-1} [18,19]. The infrared spectrum of [Mn(bimindH)Cl_2] has two strong absorptions at 1654 and 1630 cm^{-1}, and one weak at 3278 cm^{-1}, characteristic of a coordinated nondeprotonated isoindoline ligand. Complexes that contain deprotonated isoindoline ligands only exhibit weak bands above 1600 cm^{-1} [20,21]. The electronic spectrum of the [Mn(bimindH)Cl_2] complex is dominated by the π–π* transitions of the neutral ligand bimindH. Deprotonation of the pyrrole nitrogen could be reduced the difference in energy between occupied and unoccupied π–MOs of the ligand and resulted in a red shift of π–π* transitions (50–100 nm) [21].

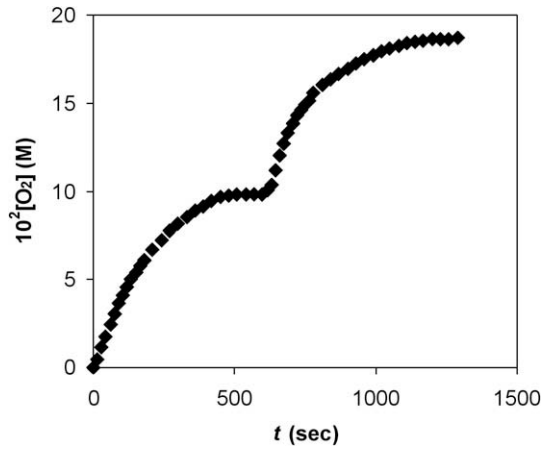


Fig. 2. Disproportionation of H_2O_2 in the presence of Mn(bimind)Cl_2 during the first two cycles at 20 °C in EtCN. [Mn(bimindH)Cl_2]$_0$ = 1.2×10^{-4} M, [H_2O_2]$_0$ = 2.0×10^{-1} M, [H_2O_2]$_{t\,=\,630\ s}$ = 2.0×10^{-1} M.

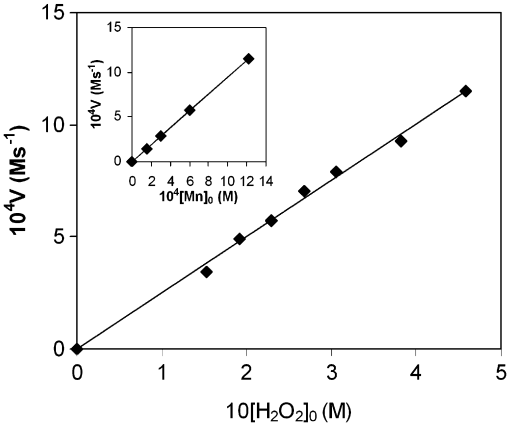


Fig. 3. Effect of the [H_2O_2] and [Mn(bimind)Cl_2] on the initial rate of H_2O_2 disproportionation at 20 °C in EtCN.

X-ray quality crystals of [Mn(bimindH)Cl_2](dmf) were grown from dmf by diethyl ether diffusion. The molecular structure of [Mn(bimindH)Cl_2](dmf) is shown in Fig. 1. The manganese(II) ion has a slightly distorted trigonal–bipyramidal geometry with $\tau = 0.93$ as judged by the method of Addison and co-workers [22]. Two chloride ions and one nitrogen atom of the isoindoline ligand occupy basal positions. The two other nitrogen atoms of the bimindH ligand are in apical positions. The Mn–N distance in the basal plane is shorter than those in apical positions.

3.2. Catalase-like activity

Compound [Mn(bimindH)Cl_2] is stable under ambient conditions and are not oxidized by atmospheric dioxygen. The catalase-like activity of the complex [Mn(bimindH)Cl_2] to disproportionate H_2O_2 into H_2O and O_2 was examined in EtCN at 20 °C by volumetric measurements of evolved dioxygen. Fig. 2 shows typical dioxygen uptake versus time curves for the disproportionation process during the first two cycles, supporting that the activity of the catalyst does not change under the conditions. At constant [H_2O_2]$_0$, the initial rate of H_2O_2 disproportionation varies linearly with the [catalyst], meaning that the reaction is first-order in catalyst (Fig. 3). The slope of the line gives a first-order rate constant (k) = 0.942 s^{-1} for a H_2O_2 concentration of 229 mM.

At low substrate concentrations, the reaction is also first-order in peroxide concentration as shown in Fig. 3, to establish a rate law of $-d[H_2O_2]/dt = k_{cat}[H_2O_2][Mn(bimindH)Cl_2]$. The slope of the line provides the bimolecular rate constant for a second-order reaction of 4.12 $M^{-1}\,s^{-1}$, which is somewhat slower than other published model compounds, but almost three times bigger than that of the Mn(indH)Cl_2–imidazole system (Table 3). This data suggest that the catalytic activity of the Mn(II) complex can be

Table 3
Related kinetics values for synthetic catalase models.

Complex	k ($M^{-1}s^{-1}$)	Solvent	Reference
Mn(bimindH)Cl_2	4.12	EtCN	this work
Mn(indH)Cl_2/imH	1.55	MeCN	[12]
$[Mn_2L^1(CH_3CO_2)](ClO_4)_2$	1.00 (92)	MeOH (+NaOH)	[23]
$[Mn_2L^2(CH_3CO_2)](ClO_4)_2$	8.50 (291)	MeOH (+NaOH)	[23]
$[Fe^{III}(PBMPA)(H_2O)_2]Cl_2$	0.27	H_2O	[24]

L^1 = *N*,*N*,*N*′,*N*′-tetrakis(2-methylenebenzamydzolyl)-1,3-diaminopropan-2-ol; L^2 = *N*,*N*,*N*′,*N*′-tetrakis(2-(1-ethylbenzamidazolyl))-2-hydroxy-1,3-diaminopropane; PBMPA = *N*-propanoate-*N*,*N*-bis(2-pyridylmethyl)-amine.

controlled by the modification of electron donor properties on the ligand. On the basis of kinetic data and the lack of time-lag at the onset of the reaction suggest that the Mn(bimindH)Cl_2 is transformed from Mn(II) to Mn(IV)O on the addition of H_2O_2, which is reduced to its initial active form by another H_2O_2 molecule. Similar mechanism was proposed earlier for the Mn(indH)Cl_2–H_2O_2 system [14].

Acknowledgments

Financial support of the Hungarian National Research Fund (OTKA K67871), COST, Budaconsum Ltd., and Ulrich Trade Ltd. are gratefully acknowledged.

References

[1] A. Messerschmidt, R. Huber, T. Paulos, K. Wieghardt (Eds.), Handbook of Metalloproteins, John Wiley and Sons Ltd., New York, 2001.
[2] J.A. Thomas, D.R. Morris, L.P. Hager, J. Biol. Chem. 245 (1970) 3129.
[3] Y. Kono, I. Fridovich, J. Biol. Chem. 258 (1983) 6015.
[4] W.F. Beyer Jr., I. Fridovich, Biochemistry 24 (1985) 6460.
[5] V.V. Barynin, P.D. Hempstead, A.A. Vagin, S.V. Lamzin, P.M. Harrison, P.J. Artymyuk, J. Inorg. Biochem. 67 (1997) 196.
[6] G.S. Allgood, J.J. Perry, J. Bacteriol. 168 (1986) 563.
[7] Y. Naruta, K. Maruyama, J. Am. Chem. Soc. 113 (1991) 3595.
[8] A.C. Rosenzweig, C.A. Frederick, S.J. Lippard, P. Nordlund, Nature 366 (1993) 537.
[9] E.J. Larson, V.L. Pecoraro, J. Am. Chem. Soc. 113 (1991) 7809.
[10] M.U. Triller, W.-Y. Hsieh, V.L. Pecoraro, A. Rompel, B. Krebs, Inorg. Chem. 41 (2002) 5544.
[11] M.L. Pires dos Santos, A. Faljoni-Alário, A.S. Mangrich, A.M. da Costa Ferreira, J. Inorg. Biochem. 71 (1998) 71.
[12] J. Kaizer, R. Csonka, G. Speier, M. Giorgi, M. Réglier, J. Mol. Catal. A: Chem. 236 (2005) 12.
[13] J. Kaizer, T. Csay, G. Speier, M. Réglier, M. Giorgi, Inorg. Chem. Commun. 9 (2006) 1037.
[14] J. Kaizer, T. Csay, P. Kővári, G. Speier, L. Párkányi, J. Mol. Catal. A: Chem. 280 (2008) 203.
[15] D.F. Shriver, M.A. Drezdzon, The Manipulation of Air-Sensitive Compounds, John Wiley and Sons, New York, 1986.
[16] D.D. Perrin, W.L. Armarego, D.R. Perrin, Purification of Laboratory Chemicals, 2nd Ed., Pergamon, New York, 1990.
[17] G.M. Sheldrick, SHELXL97, Program for the Refinement of Crystal Structures, University of Göttingen, Germany, 1997.
[18] É. Balogh-Hergovich, J. Kaizer, G. Speier, G. Huttner, A. Jacobi, Inorg. Chem. 39 (2000) 4224.
[19] J. Kaizer, J. Pap, G. Speier, M. Réglier, M. Giorgi, Transition Met. Chem. 29 (2004) 630.
[20] J. Kaizer, G. Baráth, G. Speier, M. Réglier, M. Giorgi, Inorg. Chem. Commun. 10 (2007) 292.
[21] R.J. Letcher, W. Zhang, C. Bensimon, R.J. Crutchley, Inorg. Chim. Acta 210 (1993) 183.
[22] A.W. Addison, T.N. Rao, J. Reedijk, J. van Rijn, G.C. Verschoor, J. Chem. Soc., Dalton Trans. (1984) 1349.
[23] A.E.M. Boelrijk, G.C. Dismukes, Inorg. Chem. 39 (2000) 3020.
[24] N.M.F. Carvalho, A. Horn Jr., R.B. Faria, A.J. Bortoluzzi, V. Drago, O.A.C. Antunes, Inorg. Chim. Acta 359 (2006) 4250.

crystal structure and the FTIR spectra of O-ethyl benzoyl thiocarbamate ($R^1 = CH_3CH_2$, $R^2 = H$, $R^3 = C(O)C_6H_5$) were reported very recently, along with the first comparative quantum chemical study of the geometric and vibration properties of this type of compounds [16].

We report here a new method of synthesis for two simple O-alkyl N-methoxycarbonyl thiocarbamates, namely the O-methyl (**I**) and O-ethyl derivatives (**II**) (see Scheme 1), along with a complete characterization through GC–MS analysis and NMR (^1H and ^{13}C) and FTIR and FT-Raman vibration spectroscopy. The low-temperature crystal structure of $CH_3CH_2OC(S)N(H)C(O)OCH_3$ has been determined by X-ray diffraction methods. The experimental data were employed as references for quantum chemical calculations at the B3LYP/6-311++G** level of approximation.

2. Results and discussion

2.1. Synthesis

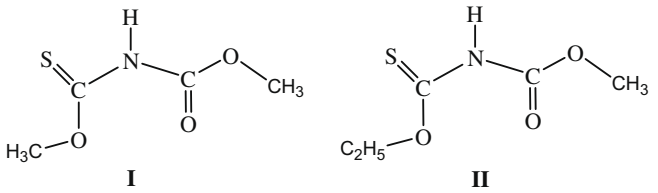
Kulkarni et al. [15,16] have reported a process for preparing N-alkoxy carbonyl isothiocyanate derivatives by reacting methyl chloroformate with metal thiocyanate salts in the presence of an organic solvent and a catalytic amount of a tertiary amine. This intermediate product is then converted to the corresponding thiocarbamate by reacting it with alcohols.

To avoid the use of methyl chloroformate, the $ROC(S)N(H)C(O)OCH_3$ species have been synthesized by the addition reaction between pure methoxycarbonyl isothiocyanate, $CH_3OC(O)NCS$ and the corresponding alcohol (ROH, R = CH_3– and CH_3CH_2–) without the use of solvent nor amine, according to Eq. (1)

$$CH_3OC(O)NCS + ROH \rightarrow ROC(S)N(H)C(O)OCH_3 \quad R = CH_3, CH_3CH_2 \qquad (1)$$

This method is an adaptation of those reported recently by Arslan et al. [16] for O-methyl N-benzyl thiocarbamate. Conventional vacuum techniques were used to condense pure $CH_3OC(O)NCS$ and an excess of methanol/ethanol in a Carius tube closed by a valve with PTFE stems (Young, London, UK). The reactions were performed at room temperature during 2 h. After removing the excess of ethanol in vacuum the remaining solid product was purified by sublimation in a 10^{-2} mbar vacuum at 50 °C, a procedure that afforded pure crystals of **II**. On the other hand, the O-methyl derivative was purified by column chromatography using a mixture of ether ethylic/hexane (3/1, v/v) as eluent solvent. The yield of O-methyl and O-ethyl N-methoxycarbonyl thiocarbamate was nearly quantitative. The final purity of the compounds was checked by IR and (^1H and ^{13}C) NMR spectroscopy.

$CH_3OC(O)NCS$ was prepared by thermal isomerization of $CH_3OC(O)SCN$. $CH_3OC(O)SCN$ was synthesized following the method reported by Haas and Reinke [17] for related XC(O)SCN (X = F and Cl) compounds. Accordingly, $CH_3OC(O)SCl$ (Aldrich, estimated purity better than 97%) was condensed in a tube containing AgCN (Aldrich, 97% purity) previously dried at 70 °C for 4 h. After 24 h at 20 °C, the volatile components were fractionated under dynamic vacuum through traps held at −10, −45 and −196 °C. Pure $CH_3OC(O)SCN$ was collected as a colorless liquid in the −10 °C trap, being the yield of the reaction of 95% (based on the quantity of $CH_3OC(O)SCl$ used). $CH_3OC(O)SCN$ is then heated at 50 °C for 4 h yielding an orange liquid which is further distilled in the same manner as described before. Pure $CH_3OC(O)NCS$ is obtained as a colorless liquid in the −10 °C trap. The yield of this isomerization reaction is *ca.* 60%. The final purity was confirmed by FTIR spectroscopy.



Scheme 1. O-methyl (**I**) and O-ethyl (**II**) N-methoxycarbonyl thiocarbamates.

2.2. Physical properties and spectroscopic characterization

Compounds **I** and **II** are white solids with melting points of 44(1) and 78(1) °C, respectively.

The ^1H NMR spectrum for $CH_3OC(S)N(H)C(O)OCH_3$ shows three singlet bands at $\delta = 8.39$ (*s*, N–H broad), 4.13 (s, $^1J_{HC} = 74.2$ Hz, $CH_3OC(O)$–) and 3.77 (s, $^1J_{HC} = 74.2$ Hz, $CH_3OC(S)$–) ppm, ($^1J_{HC}$ coupling constant values for both O–CH_3 groups were obtained from the ^{13}C satellites). The ^{13}C NMR spectrum shows signals at $\delta = 189.6$ and 149.8 ppm assigned to the C=O and C=S, respectively and signals at 59.5 and 53.4 ppm corresponding to the carbon atoms in the methoxy moieties, –OCH_3, respectively bonded to the C=S and C=O groups.

The ^1H NMR spectrum of $CH_3CH_2OC(S)N(H)C(O)OCH_3$ shows four signals at $\delta = 8.26$ (s, N–H broad), 4.60 (q, $^3J_{HH} = 7.1$ Hz, –CH_2–), 3.76 (s, $^1J_{CH} = 74.0$ Hz, CH_3O–) and 1.41 (t, $^3J_{HH} = 7.2$ Hz, –CH_3). The ^{13}C NMR spectrum shows five signals at $\delta = 188.8$, 149.7, 69.3, 53.3 and 13.9 ppm, assigned to the carbon atoms of the C=O, C=S, CH_2, CH_3O and CH_3 groups, respectively.

These assignments are clearly supported by HSQC (heteronuclear single quantum coherence) 2D-NMR spectroscopy as can be appreciated in the Supplementary data (Figs. S1 and S2). The ^1H and ^{13}C NMR spectral assignments are compatible with those previously reported for thiocarbamate compounds [2,5,18].

GC chromatogram shows a single peak at retention times of 7.3 and 10.6 min for compounds **I** and **II**, respectively. In the GC–MS spectra, both compounds show the molecular ion ($M^{\cdot+}$) peak as a strong intensity signal at *m/z* 149 for O-methyl and 163 for O-ethyl derivative compounds. The mass spectra were assigned to expected ionic fragments from logical ruptures of the corresponding $M^{\cdot+}$ molecular ions as shown in Table 1.

Additional evidences for identifying the synthesized compounds come from the analysis of their IR and Raman spectra in the solid phase (see Figs. 1 and 2 and Tables S2 and S3 of the Supplementary data). Thus, the characteristic broad band for amides assigned to the N–H bond stretching are observed at 3216 cm^{-1} and 3204 cm^{-1} in the IR spectra of the O-methyl and O-ethyl derivatives, respectively. One of the most intense bands observed in the IR and Raman spectra is centered at 1768 (1761 cm^{-1} in Raman)

Table 1
Main peaks observed in the mass spectra (70 eV electron ionization) of $CH_3OC(S)N(H)C(O)OCH_3$ (**I**) and $CH_3CH_2OC(S)N(H)C(O)OCH_3$ (**II**).

m/z	Intensity (%)		Fragments	
	I	**II**	**I**	**II**
135		27		$CH_3OC(O)N(H)C(S)HO^+$
119	25	25	$CH_3OC(O)N(H)C(S)H^+$	$CH_3OC(O)N(H)C(S)H^+$
89	20	20	$CH_3OC(S)N^+$	$CH_3CH_2OC(S)^+$
75	25	40	$CH_3OC(S)^+$	$CH_3OC(O)HNH^+$
59	55	78	$CH_3OC(O)^+$	$CH_3OC(O)^+$
45		65		$CH_3CH_2O^+$
31	10		CH_3O^+	
29		100		$CH_3CH_2^+$
15	100	75	CH_3^+	CH_3^+

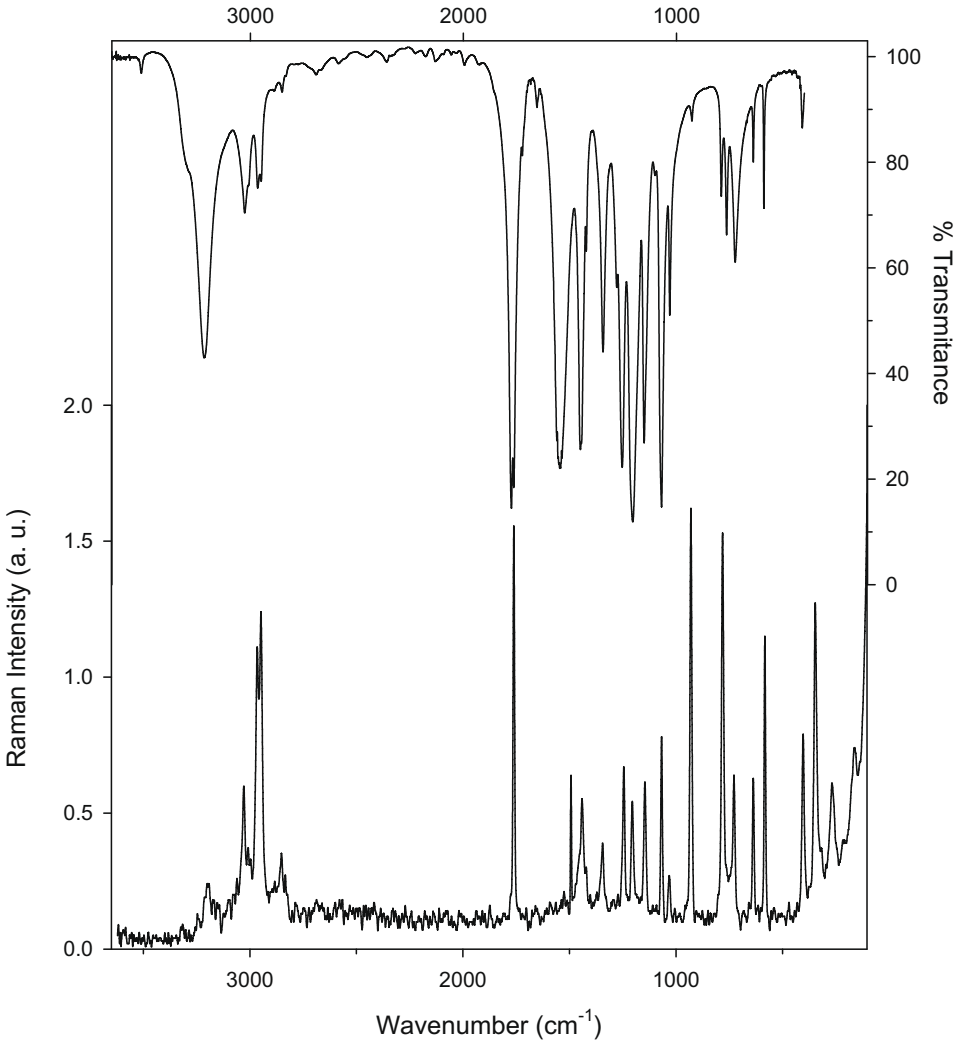


Fig. 1. Solid IR (in KBr pellet) and Raman spectra for $CH_3OC(S)N(H)C(O)OCH_3$.

and 1770 cm^{-1} (1768 cm^{-1} in Raman), characteristic of the carbonyl stretching mode of compounds **I** and **II**. Characteristic strong absorptions due to the stretching mode of the C═S groups appear at 1255 and 1266 cm^{-1} in the IR spectra of compounds **I** and **II**.

2.3. Quantum chemical calculations

Theoretical studies on carbamic acid and thiocarbamic O- and S-acids were undertaken by Remko et. al. [19] One of the important characteristic of these systems is the electronic resonance on the thioamide group [1]. However, there is only one previous work dealing with theoretical studies on thiocarbamate derivatives [16]. Following these works, the molecular geometry and vibrational spectra of $ROC(S)N(H)C(O)OCH_3$ ($R = CH_3-$ and CH_3CH_2-) were calculated by the B3LYP density functional method with 6-31G* and the more extended 6-311++G** basis sets.

In principle, the studied compounds may adopts several conformations, depending on the orientation around each of the C–O, O–C, C–N, N–C and C–O single bonds. Taking into consideration structural studies previously reported for the methoxycarbonyl –$C(O)OCH_3$ moiety [20–26], a *syn* orientation of the δ(O═C–OC) dihedral angle is preferred, being the *anti* form higher in energy. Thus, special attention was dedicated to the ROC(S)N(H)C(O)– moiety of the title compounds.

To analyze the conformational preferences of the compounds studied in the present work, the potential energy functions for internal rotation around the δ(C5C4–O3C3), δ(C4O3–C3S), δ(SC3–NC2) and δ(C3 N–C2O2) dihedral angles were calculated at the B3LYP/6-31G* level by allowing geometry optimizations with the respective dihedral angles (δ) varying from 0° to 360° in steps of 30°. The potential energy functions for compounds **I** and **II** are shown in Fig. 3 (see Fig. 4 for atoms numbering). The curve obtained for the δ(C5C4–O3C3) dihedral angle corresponding to the O-ethyl derivative (Fig. 3A) clearly indicates the presence of two minima, the most stable conformation corresponding to a mutual *anti* orientation of the C5–C4 and O3–C3 bonds in the ethyl group [δ(C5C4–O3C3) = 180°], while a second stable *gauche* form is located slightly higher in energy by *ca.* 0.89 kcal mol^{-1}. The other dihedral angles considered are common for both studied compounds and very similar potential curves are calculated, as shown in Fig. 3. The curve obtained as a function of the dihedral angle around the O3–C3 bond shows a deep minimum at δ(C4O3–C3S) = 0°, corresponding to a mutual *syn* orientation of the C4–O3 and C═S bonds. The potential energy curves for the rotation of the amidic-like groups characterized by the δ(SC3–NC2) and δ(C3 N–C2O2) dihedral angles present minima for both *syn* and *anti* planar forms. The *anti* conformation of the C═S bond with respect to the N–C2 bond is more stable by *ca.* 2.6 kcal mol^{-1} than the *syn* conformer [δ(SC3–NC2) = 0°]. On the other hand, the *syn* form is *ca.* 1.2 kcal mol^{-1} more stable than the *anti* conformation when the δ(C3 N–C2O2) dihedral angle is considered.

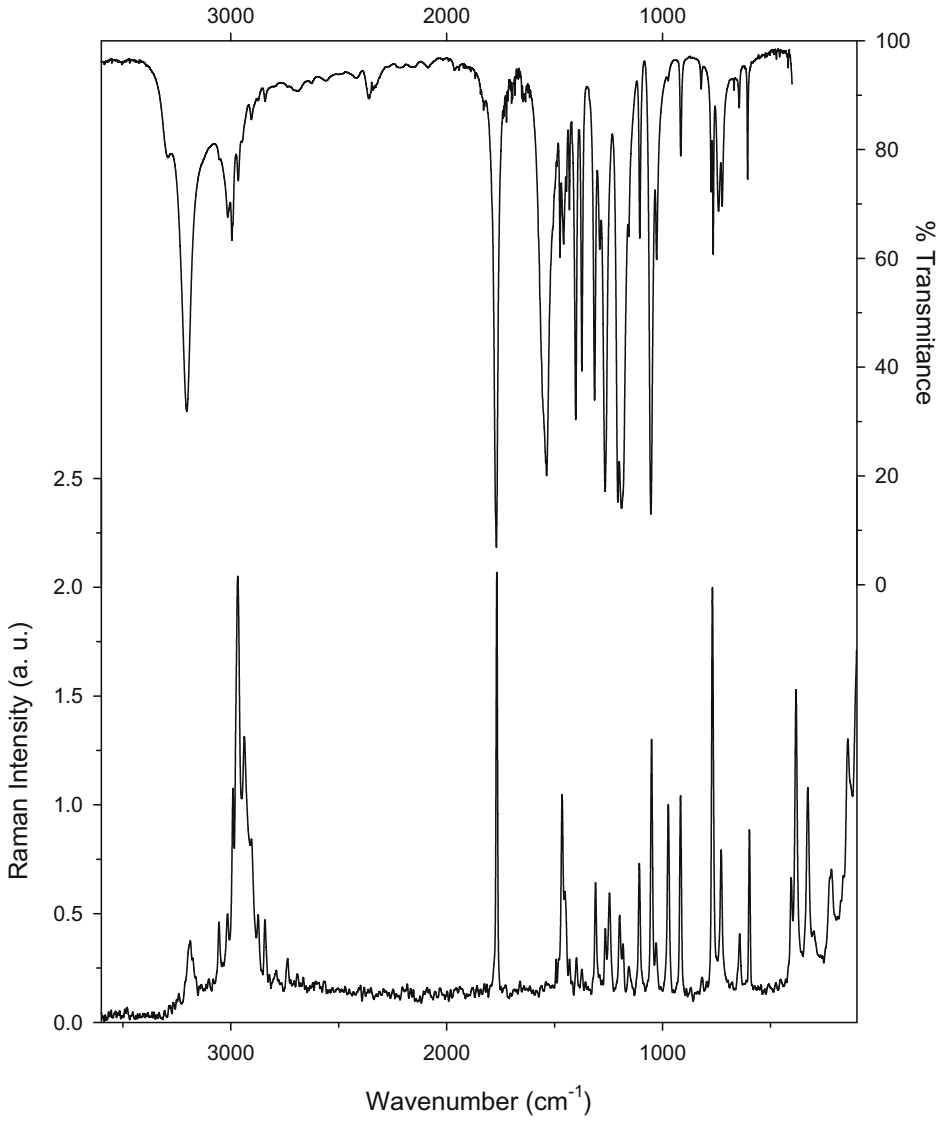


Fig. 2. Solid IR (in KBr pellet) and Raman spectra for $CH_3CH_2OC(S)N(H)C(O)OCH_3$.

Additionally, full geometry optimizations and frequency calculations were computed for each of the more stable structures of both compounds with the B3LYP method and the 6-31G* and 6-311++G** basis sets. Predicted relative energies, ΔE° (corrected by zero-point energy), are given in Table 2. The optimized molecular structures for the main conformers of the studied compounds are shown in Fig. 4. Accordingly, the most stable conformation for compound **II** is the one with alternated *anti–syn–anti–syn* (*a–s–a–s*) mutual orientations around the C4–O3, O3–C3, C3–N and N–C2 single bonds, respectively. The conformation with *syn*, *anti* and *syn* orientation around to the O3–C3, C–N and N–C2 single bonds, respectively –named as *syn–anti–syn* (*s–a–s*) in Fig. 3 is the most stable form of $CH_3OC(S)N(H)C(O)OCH_3$.

The second more stable conformation of compound II, higher in energy by only 0.89 kcal mol^{-1} (B3LYP/6-311++G**) with respect to the most stable form, corresponds to a conformer with *gauche* orientation of the δ(C5C4–O3C3) dihedral angle (*gauche–syn–anti–syn* form in Fig. 4). The next stable conformer (ΔE° = 1.48 kcal mol^{-1}) possesses *anti* orientation of the δ(C3 N–C2O2) dihedral angle (*anti–syn–anti–anti* conformation in Fig. 4). In the case of compound **I**, the second more stable conformer (ΔE° = 1.35 kcal mol^{-1}) exhibits its *anti* orientation of the δ(C3 N–C2O2) dihedral angle (*syn–anti–anti* conformation in Fig. 4).

Other conformers of $ROC(S)N(H)C(O)OCH_3$ (R = CH_3– and CH_3CH_2–) were found to be stable with calculated energies higher than 1.5 kcal mol^{-1} and are also included in the Table 2. Selected geometric parameters calculated (B3LYP/6-311++G**) for the most stable conformers of the title compounds are compared with the experimental values (see below) in Table 3.

2.4. Vibrational analysis

To our knowledge, neither experimental nor theoretical vibration analysis for $ROC(S)N(H)C(O)OCH_3$ (R = CH_3– and CH_3CH_2–) have so far been performed. The IR and Raman spectra of solid $CH_3OC(S)N(H)C(O)OCH_3$ and $CH_3CH_2OC(S)N(H)C(O)OCH_3$ are shown in Figs. 1 and 2, respectively. Experimental and calculated [B3LYP/6-311++G**] frequencies and intensities are given as Supplementary data (Table S2 and S3). A tentative assignment of the observed bands was carried out by comparison with spectra of related molecules [16,18,27–33]. The gas-phase molecular symmetry of the studied species is C*s* for both compounds and therefore all 42 (27A′ + 15A″) and 51 (32A′ + 19A″) normal modes for compounds **I** and **II**, respectively, are active in the IR and Raman spectra. The general features of the vibration spectra of solid $ROC(S)N(H)C(O)OCH_3$ (R = CH_3– and CH_3CH_2–) can be explained by supposing

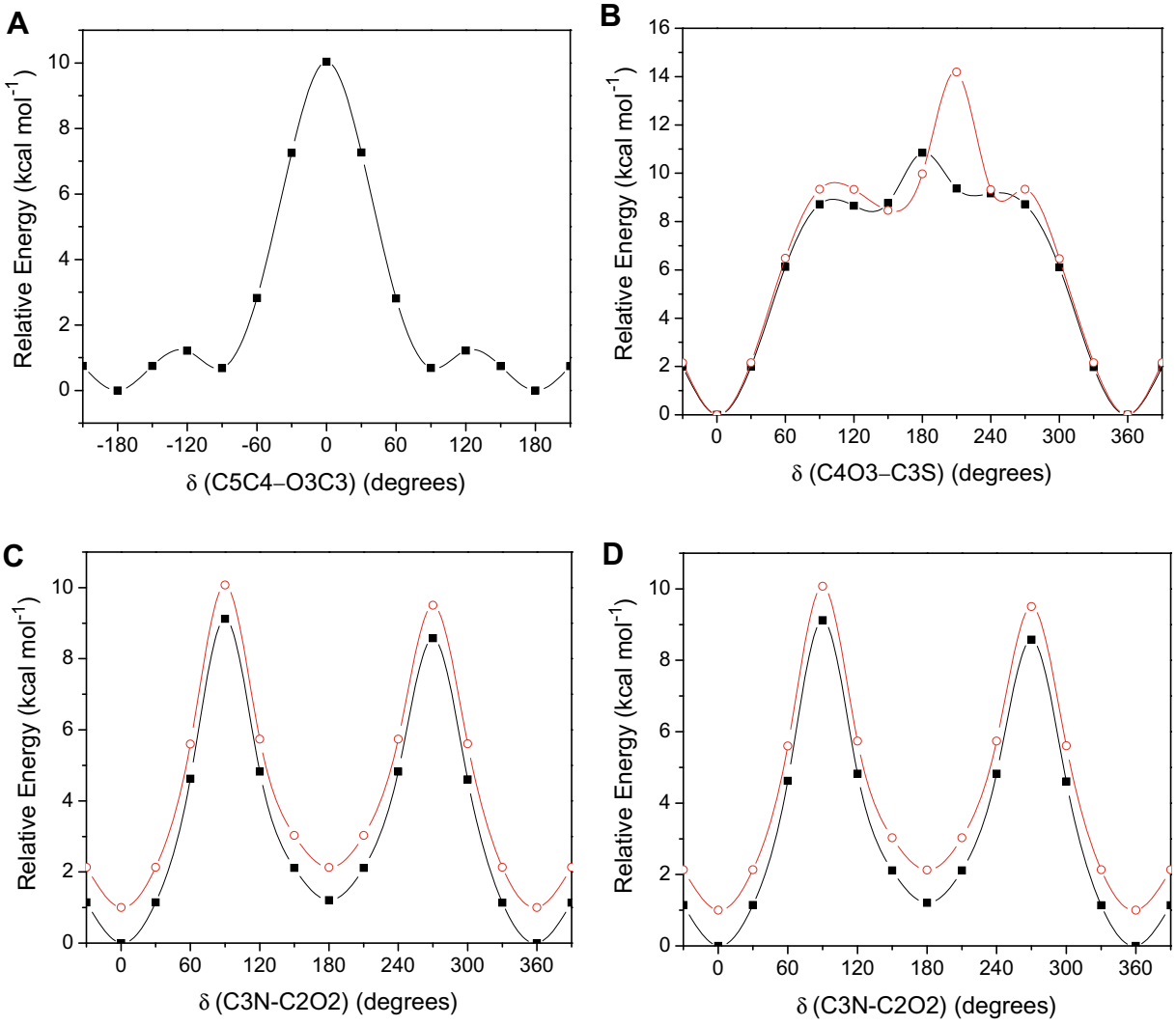


Fig. 3. Calculated (B3LYP/6-31G*) potential function for internal rotation of ROC(S)N(H)C(O)OCH$_3$ (—■— R = CH_3CH_2– and —○— R = CH_3–) as a function of the δ(C5C4–O3C3) (A), δ(C4O3–C3S) (B), δ(SC3–NC2) (C) and δ(C3N–C2O2) (D) dihedral angles. For the last two dihedral angles, the curve corresponding to the compound **I** was shifted by 1 kcal mol^{-1} in energy.

the solely presence of the most stable *syn–anti–syni* and *anti–syn–anti–syn* conformers, respectively. The assignment of the characteristic vibration modes of the main –OC(S)N(H)C(O)O– moiety is summarized in Table 4.

The intense IR absorptions at 3216 cm^{-1} (**I**) and 3204 cm^{-1} (**II**) are assigned to the N–H stretching mode. These values agree with the corresponding ones in the IR spectrum of O-ethyl benzoylthiocarbamate, where this mode is observed at 3256 cm^{-1} [16]. For other related molecule, namely N-(morpholinothiocarbonyl)benzamide, similar results were reported [34]. A single absorption is observed in the carbonyl stretching region for O-methyl and O-ethyl N-methoxycarbonyl thiocarbamates. Thus, the strong IR absorptions at 1768 and 1770 cm^{-1} with counterparts in the Raman spectra at 1761 and 1768 cm^{-1} were assigned to the ν(C=O) modes. Calculated (B3LYP/6-311++G**) frequencies for this mode are slightly higher: 1828 and 1826 cm^{-1} for O-methyl and O-ethyl N-methoxycarbonyl thiocarbamates, respectively. The IR absorptions observed at 1255 and 1266 cm^{-1} were assigned to the ν(C=S) mode for compounds **I** and **II**, in good agreement with the calculated values (Table 4). The formation of C=S···H–X intermolecular hydrogen bonds seems to strongly effect the frequency of the ν(C=S) mode. For example, a strong band at 1203 cm^{-1} was observed in the IR spectra of (E)-O-ethyl N-(4-chlorophenyl)thiocarbamate, a molecule which presents intermolecular hydrogen bonds [27], while the ν(C=S) stretching frequency for some free thioureas are reported lo lay in the region around 1325 cm^{-1} [31]. The relatively low frequency values for the ν(C=S) stretching mode observed in the IR spectra of the title compounds can be related to the formation of intermolecular hydrogen bonds involving the thiocarbonyl group. Indeed, C=S···H–N bonds are observed in the X-ray crystal structure of compound **II**, as will be discussed in the next section.

In connection with the amide- and thioamide-like groups, strong IR absorptions at 1548 and 1537 cm^{-1} of compounds I and II (Figs. 1 and 2) are assigned to the in-plane N–H deformation mode [δ(N–H), A′]. Medium intensity IR absorptions at 1345 and 1315 cm^{-1} (1345 and 1310 cm^{-1} in the Raman) are assigned to the C(S)–N stretching mode. Strong IR absorptions at 1205 and 1190 cm^{-1} are assigned to the N–C(O) stretching mode of O-methyl and O-ethyl N-methoxycarbonyl thiocarbamate, respectively, in agreement with reported data for related species [16,30].

Others clearly defined bands in the IR and Raman spectra (see Table 4) correspond to the C=O and N–H out-of-plane deformation modes, observed as strong Raman dispersions at 781 cm^{-1} (**I**) and

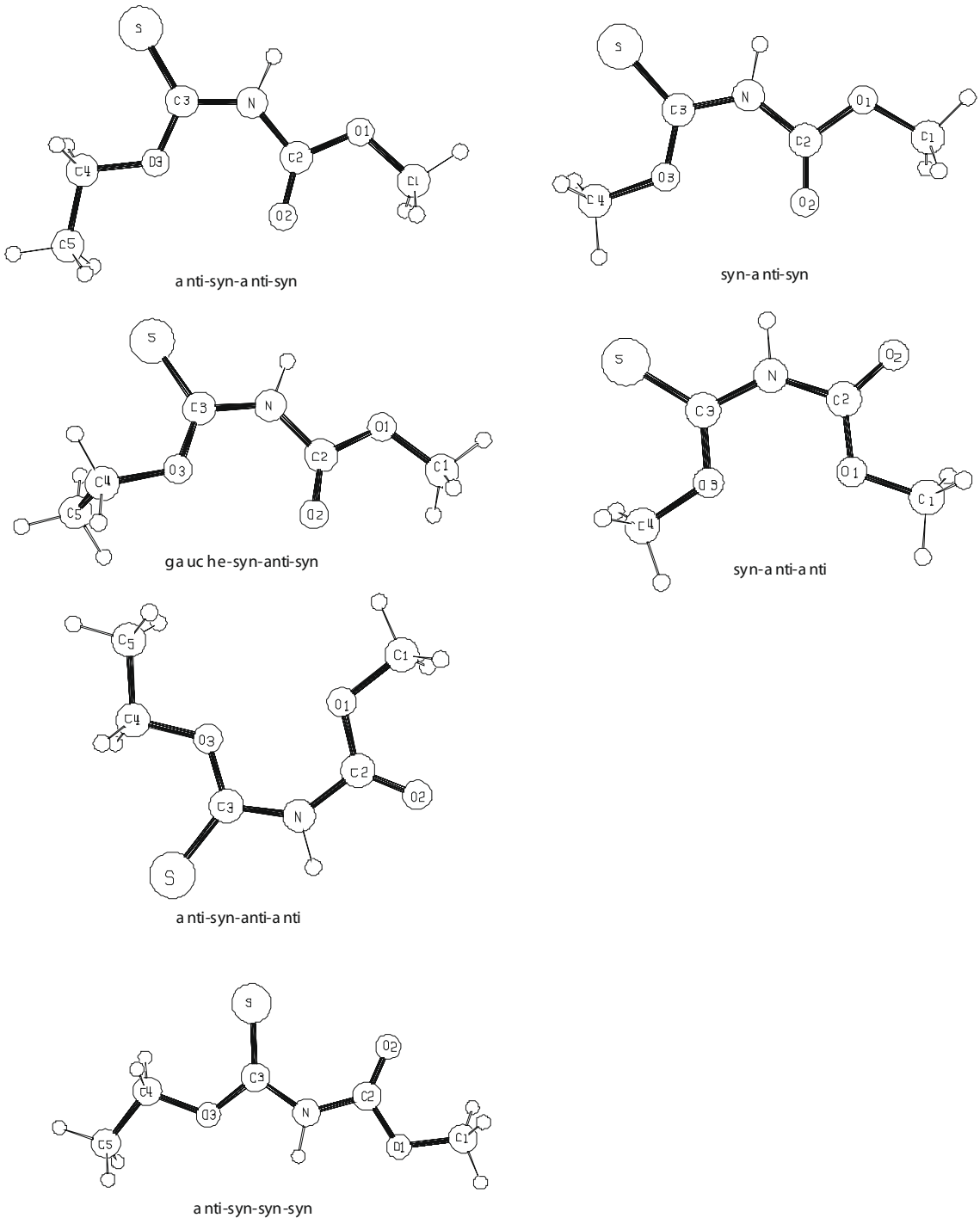


Fig. 4. Molecular structure of the main conformers of O-ethyl N-methoxycarbonyl thiocarbamate (left side) and O-methyl N-methoxycarbonyl thiocarbamate (right side) found theoretically with atom numbering.

766 cm^{-1} (**II**). The corresponding IR absorptions due to C═S out-of-plane deformation mode are observed at 590 and 646 cm^{-1} (583 and 643 cm^{-1} in Raman) for compounds **I** and **II**, respectively.

2.5. X-ray diffraction analysis

Crystal data and structure refinement results for O-ethyl N-methoxycarbonyl thiocarbamate are summarized in Table 5. An ORTEP [35] drawing of the molecule is shown in Fig. 5 and Table 3 includes the main geometric parameters derived from the structure refinement, as well as those obtained from quantum chemical calculations. In general, the parameter computed with theoretical calculations agree fairly well with those refined from the X-ray analysis.

Only molecules of **II** having the *anti–syn–anti–syn* conformation are found in the crystal. Thus, the molecules adopt a conformation with both O and S donor atoms in mutual *trans* orientations relative to each other, with torsion angles almost planar. Thus, experimental studies reported for related thiourea compounds show also an almost planar conformation around the –NC(S)N– unit [36,37]. The *trans* orientation of sulfur and oxygen donor atoms within the –C(S)NHC(O)– moiety has a significant role on the

Table 2
B3LYP calculated relative energies ΔE^o (corrected by zero-point energy) in kcal mol^{-1} for the most stable conformers of the ROC(S)N(H)C(O)OCH$_3$ [R = CH$_3$– (**I**) and CH$_3$CH$_2$– (**II**)] compounds.

Conformation[a]		Basis sets	ΔE^o(**I**)	ΔE^o(**II**)
I	II			
s-a-s	*a-s-a-s*	6-31G*	0.00	0.00
		6-311++G**	0.00	0.00
	g-s-a-s	6-31G*		0.86
		6-311++G**		0.89
s-a-a	*a-s-a-a*	6-31G*	1.22	1.35
		6-311++G**	1.35	1.48
	g-s-a-a	6-31G*		2.13
		6-311++G**		2.30
s-s-s	*a-s-s-s*	6-31G*	2.17	2.41
		6-311++G**	1.58	1.83
	g-s-s-s	6-31G*		3.11
		6-311++G**		2.62
s-s-a	*a-s-s-a*	6-31G*	2.55	2.78
		6-311++G**	2.18	2.40
	g-s-s-a	6-31G*		3.53
		6-311++G**		3.24

[a] *s* = *syn*, *a* = *anti*, *g* = *gauche*.

Table 3
Experimental and calculated (B3LYP/6-311++G**) selected geometric parameters for the most stable conformers of ROC(S)N(H)C(O)OCH$_3$ (R = CH$_3$– and CH$_3$CH$_2$–).

Parameter[a]	CH$_3$CH$_2$OC(S)N(H)C(O)OCH$_3$		CH$_3$OC(S)N(H)C(O)OCH$_3$
	Experimental X-ray	Calculated[b] *anti–syn–anti–syn*	Calculated[b] *syn–anti–syn*
C=O	1.194(2)	1.200	1.200
N–C2	1.401(2)	1.396	1.397
N–C3	1.368(2)	1.383	1.382
S=C	1.654(2)	1.661	1.659
O3–C3	1.318(2)	1.318	1.320
O3–C4	1.464(2)	1.452	1.440
O1–C2	1.343(2)	1.355	1.320
O1–C1	1.451(2)	1.439	1.439
O=C–N	127.2(2)	127.9	127.9
C3–N–C2	128.1(1)	130.1	130.0
O3–C3–N	113.1(1)	112.5	112.3
N–C3–S	121.2(1)	120.5	120.8
O3–C3–S	125.7(1)	127.0	126.8
C3–O3–C4	118.1(1)	119.7	119.2
δ(C1O1–C=O)	–0.8(3)	0.0	0.0
δ(O=C–NC3)	–0.3(3)	0.0	0.0
δ(C2N–C=S)	–175.6(1)	–179.9	–179.9
δ(S=C–O3C4)	4.4(2)	0.0	0.0
δ(C3O3–C4C5)	–177.9(1)	–179.9	

[a] Values in Å and °, for atom numbering see Fig. 3.
[b] Most stable conformer calculated for **I** and **II**.

Table 5
Crystal data and structure refinement results for CH$_3$CH$_2$OC(S)N(H)C(O)OCH$_3$.

Empirical formula	$C_5H_9NO_3S$
Formula weight	163.19
T (K)	150(2)
λ (Å)	0.71073
Crystal system, space group	monoclinic, $P2_1/n$
Unit cell dimensions	
	a (Å) = 4.088(1), α (°) = 90
	b (Å) = 22.346(1), β (°) = 100.687(3)
	c (Å) = 8.284(1), γ (°) = 90
V (Å^3)	743.7(2)
Z	4
D_{Calc} (Mg/m^3)	1.458
Absorption coefficient (mm^{-1})	0.383
F(000)	344
Crystal size (mm)	0.195 × 0.162 × 0.143
θ Range for data collection	2.66–25.99°
Limiting indices	$-4 \leqslant h \leqslant 5$, $-27 \leqslant k \leqslant 25$, $-8 \leqslant l \leqslant 10$
Reflections collected/unique (R_{int})	4183/1422 (0.0442)
Completeness to θ = 25.99°	97.9%
Refinement method	full-matrix least-squares on F^2
Data/restraints/parameters	1422/0/93
Goodness-of-fit on F^2	1.109
Final R indices [$I > 2\sigma(I)$]	R_1[a] = 0.0324, wR_2[b] = 0.0906
R indices (all data)	R_1 = 0.0355, wR_2 = 0.0923
Largest difference in peak and hole (e Å^{-3})	0.318 and −0.303

[a] $R_1 = \Sigma||F_o| - |F_c||/\Sigma|F_o|$.
[b] $wR_2 = [\Sigma w(|F_o|^2 - |F_c|^2)^2/\Sigma w(|F_o|^2)^2]^{1/2}$.

molecular packing of the title compound. This conformation is stabilized in the crystal by the occurrence of intermolecular N–H···S=C hydrogen bonds [d(N···S) = 3.387(1) Å] between adjacent molecules. Pairs of molecules related by a crystallographic inversion center can interact forming a planar dimeric unit (see Fig. 5). This type of hydrogen-bond formation represents an example of π-bond cooperative behavior, frequently called "Resonance-Assisted Hydrogen Bonding" (RAHB) [38], which occurs when XH groups are polarized by charge flow through π-bonds. As a result of the dual donor and acceptor capacity of the thioamide unit, intermolecular N–H···S=C hydrogen bonds are common in thiourea compounds. Additionally, weak C=S···H–C interactions between dimeric structures involving methoxy groups are observed.

Interestingly, X-ray diffraction analysis carried out for the closely related O-ethyl benzoylthiocarbamate species [16] shows that the crystal packing is dominated by endless chains linked by C=O···N–H hydrogen bond interactions. The N–H···S=C intermolecular interaction are absent in the crystal, and the *syn–syn–syn* conformation is the only form observed in the crystal. On the other hand, theoretical studies predict the *syn–anti–syn* form as the most stable conformer of this molecule isolated in a vacuum [16], in

Table 4
Experimental and theoretical (B3LYP/6-311++G**) vibrational data (cm^{-1}) for the –OC(S)N(H)C(O)– moiety of O-methyl (I) and O-ethyl (II) N-methoxycarbonyl thiocarbamates.

Experimental				Calculated[b]		Proposed assignment/symmetry
IR[a]		Raman[a]		B3LYP/6-311++G**		
I	**II**	**I**	**II**	**I**	**II**	
3216m	3204s	3192vvw	3188vw	3622(10)	3621(9)	ν(N–H)/A′
1768vs	1770vs	1761	1768vs	1828(56)	1826(53)	ν(C=O)/A′
1548vs	1537vs			1541(100)	1537(100)	δ(N–H)/A′
1345m	1315m	1345w	1310w	1347(44)	1331(47)	ν(C(S)–N)/A′
1255vs	1266s	1245m	1265vw	1266(43)	1264(46)	ν(C=S)/A′
1205vvs	1190vs	1205w	1183vw	1201(45)	1182(98)	ν(N–C(O)) A′
765w	766w	781vs	769vs	772(3)	772(3)	δoop (O–C(O)N)/A″
639w	724w	638w	728w	646(10)	653(9)	ρ(N–H)/A″
590w	646	583s	643vw	635(1)	633(1)	δoop (N–C(S)O)/A″

[a] Band intensity: vs , very strong; s, strong; m, medium; sh, shoulder; w, weak; vw, very weak; vvw, very very weak.
[b] In parentheses relative calculated values for the more stable forms, IR intensities of compound **I**, 100% ≡ 679.10 Km/mol and for compound **II**, 100% ≡ 705.99 Km/mol.

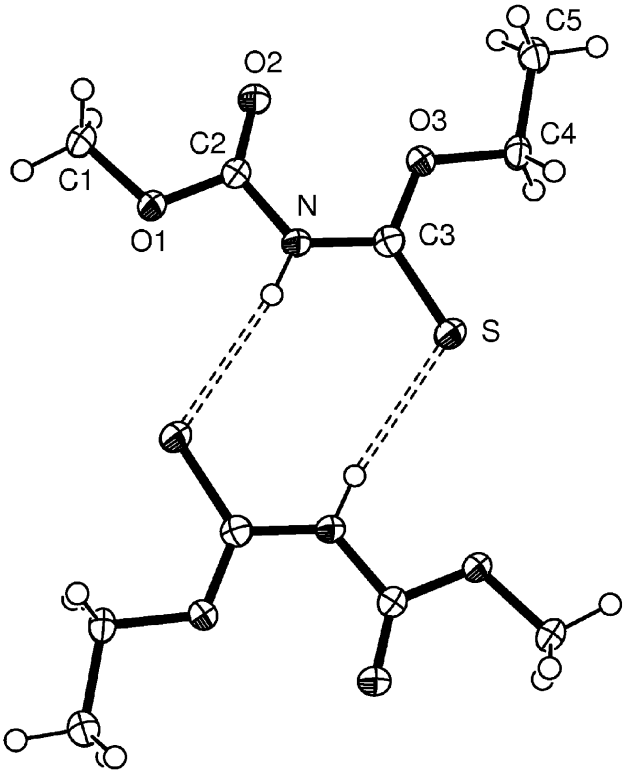


Fig. 5. Molecular plot of dimeric *anti–syn–anti–syn* $CH_3CH_2OC(S)N(H)C(O)OCH_3$ in the solid state showing the labeling of the non-H atoms and their displacement ellipsoids at the 50% probability level. The unlabeled monomer is related to the labeled one by a crystallographic inversion center. H-bonds are indicated by dashed lines.

agreement with the preferred conformation found for both title compounds. Thus, the overall molecular structure of thiocarbamate species seems to be determined by the formation of N–H···X=C (X = O, S) hydrogen bonds between adjacent molecules. Depending on the substituents bonded to the central –OC(O)N(H)C(S)O– moiety, the acceptor group can be either C=S or C=O, leading to different crystal motif –chains or dimers– and to different molecular conformation in the solid thiocarbamate species.

To the best of our knowledge the present work is the first example of a thiocarbamate species forming such an N–H···S=C hydrogen bond network. Similar observations have been made for related compounds, such as thio- [39] and seleno-ureas [40]. The presence of this type of interactions strongly affects the C=S bond length, which is noticeably lengthened [d(C=S) = 1.654(2) Å. The comparison of the C=S bond length for a series of molecules possessing the –C(O)N(H)C(S)– moiety is shown in Table 6. Species

Table 6
Comparison of the C=S bond length in compounds that present and do not present N–H···S=C hydrogen bonds.

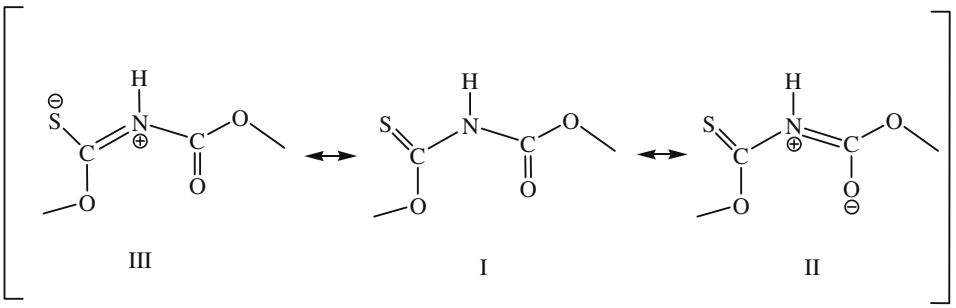
Species	Main moiety	C=S distance (Å)
$CH_3CH_2OC(S)N(H)C(O)OCH_3$	–C(O)N(H)C=SO–	1.654(2)[a]
$CH_3CH_2OC(S)N(H)C_6H_4Cl$ [27]	–C(O)N(H)C=SO–	1.667(2)[b]
ClC_6H_4 N(H)C(S)N(H)C(O)$C_6H_4CH_3$ [36]	–C(O)N(H)C=SN–	1.6696(18)[b]
$[(C_2H_5)_2NC(S)N(H)C(O)]_2(CH_2)_3$ [39]	–C(O)N(H)C=SN–	1.687(3)[b]
$(C_2H_5)_2NC(S)N(H)C(O)C_6H_4OCH_3$ [50]	–C(O)N(H)C=SN–	1.676(4)[b]
$CH_3CH_2OC(S)N(H)C(O)C_6H_5$ [16]	–C(O)N(H)C=SO–	1.619(3)[c]
$[C_2H_5OC(S)N(H)C(O)]_2$-1,4C_6H_4 [51]	–C(O)N(H)C=SO–	1.638(3)[c]
$(CH(CH_3)_2)OC(S)N(H)C(O)C_4OH_4$ [42]	–C(O)N(H)C=SO–	1.636(5)[c]
$[CH_3OC(S)N(H)C(O)]_2$-1,3C_6H_4 [52]	–C(O)N(H)C=SO–	1.637(2)[c]

[a] Experimental results for $CH_3CH_2OC(S)N(H)C(O)OCH_3$.
[b] Related compounds having N–H···S=C hydrogen bonds.
[c] Related compounds which do not present N–H···S=C hydrogen bonds.

displaying N–H···S=C hydrogen bonds have longer C=S bond lengths by *ca.* 0.04 Å than similar species without intermolecular N–H···S=C interactions.

In addition, both C–N bond lengths (Table 3) are shorter than the average value of 1.472(5) Å [41]. In the title compounds, the C–N bond in the thiourea group (S)C–NH [N–C3 = 1.368 (2)°] is considerably shorter than the amide bond (O)C–NH [N–C2 = 1.401 (2)°]. This trend seems to be characteristic for thiocarbamate compounds [16,27,42]. However, for carboxyl substituted thioureas the above trend is the opposite, i.e., the C–N bond in the amidic-like group (O=C–NH–) is shorter than the C–N thiourea bond (S)C–NH [28–30,36,43]. The C=O double bond in compound **II** (1.194(2) Å) is very well reproduced by quantum chemical calculations (1.200 Å) with a value that is to some extent shorter than that reported for O-ethyl benzoylthiocarbamate [1.205(3) Å] [16]. Differences in the (O)C–O and (S)C–O single-bond lengths for the methoxy and ethoxy groups (1.343(2) and 1.318(2) Å for the O1–C2 and C3–O3 bonds, respectively) suggest that resonance interactions are extended over the whole planar structure.

The previous structural features can be rationalized considering that several resonant structures are feasible for the thiocarbamate central moiety. Three of them are showed in the Scheme 2. It is well-known that the traditional picture of amide resonance is more appropriate for thioamides than for oxoamides [44]. Moreover, previous studies showed that amide resonance in H_2 N(C=X)H species increases with a decrease in the electro-negativity of X (X = O, S, Se) [1]. By using *ab initio* molecular orbital calculations, Wiberg and Rablen [44] concluded that amide resonance is dependent on the charge polarization across the C=X double bond, the charge polarization across thiocarbonyl bond is weaker than that in C=O bond, hence the contribution from resonance structure is much more reduced for the oxygen analogs. In perfect agreement with these results, vibration and structural data for compounds **I** and **II** are consistent with a larger π resonant contribution of the thioamide group (structure **III**) when comparing with the amide group structure (structure **II**).



Scheme 2. Main resonance structures for the central thiocarbamate moiety.

3. Conclusions

Two O-alkyl N-methoxycarbonyl thiocabamates have been prepared in high yield and purity by treating $CH_3OC(O)NCS$ with the corresponding alcohols at room temperature. Conformational and structural properties were determined by using experimental techniques which include vibrational spectroscopy (IR and Raman) as well as X-ray diffraction analysis. For both substances, it was determined that the molecular skeleton is essentially planar. Results derived from the quantum chemical calculations show that the central –OC(O)N(H)C(S)– moiety adopts a planar structure with a preferred *syn–anti–syn* orientation around the O–C, C–N and N–C single bonds, respectively. This form is present in crystalline $CH_3CH_2OC(S)N(H)C(O)OCH_3$ (150 K) as centro-symmetric dimeric units held by resonance-assisted N–H···S=C hydrogen bonds.

4. Experimental

4.1. General procedure and reagents

Volatile materials were manipulated in a glass vacuum-line equipped with PTFE system (Young, London, UK) and capacitance pressure gauge (221 AHS-1000, MKS Baratron) for the control of the pressure. The vacuum line has a connection to an IR cell (optical path length 10 cm, Si windows 0.5 mm thick). This arrangement allowed us to observe the course of the isomerization in gaseous phase by FTIR spectroscopy (EQUINOX 55, Bruker). The pure compounds are air stable and they were stored in a glass tube under room temperature conditions.

4.2. Instrumentation

4.2.1. X-ray diffraction

The measurements were performed on an Enraf-Nonius Kappa-CCD diffractometer with graphite-monochromated Mo Kα ($\lambda = 0.71073$ Å) radiation. Diffraction data were collected (φ and ω scans with κ-offsets) with COLLECT [45]. Integration and scaling of the reflections was performed with HKL DENZO-SCALEPACK [46] suite of programs. The unit cell parameters were obtained by least-squares refinement based on the angular settings for all collected reflections using HKL SCALEPACK [46]. The data were corrected numerically for absorption with PLATON [47]. The structure was solved by direct methods with SHELXS-97 [48] and the molecular model refined by full-matrix least-squares procedure on F^2 with SHELXL-97 [48]. The hydrogen atoms were positioned stereo-chemically and refined with the riding model. The methyl hydrogen atoms locations were optimized during the refinement by treating them as rigid bodies which were allowed to rotate around the corresponding C–C or C–O bonds. Crystal structure data have been deposited at the Cambridge Crystallographic Data Centre (CCDC). Enquiries for data can be direct to: Cambridge Crystallographic Data Centre, 12 Union Road, Cambridge, UK, CB2 1EZ or (e-mail) deposit@ccdc.cam.ac.uk or (fax) +44 (0) 1223 336033. Any request to the Cambridge Crystallographic Data Centre for this material should quote the full literature citation and the reference number 695371.

4.2.2. Vibrational spectroscopy

Gas and solid-phase IR spectra were recorded with a resolution of 1 and 2 cm^{-1}, respectively, in the 4000–400 cm^{-1} range on a Bruker EQUINOX 55 FTIR spectrometer. FT-Raman spectra of the solid substances were run on a Bruker 66 with FRA 106 Raman accessory at a resolution of 2 cm^{-1}; the sample fitted in a 2 mm glass capillary was excited by the 1064 nm line of a 5 mW Nd:YAG laser.

4.2.3. NMR spectroscopy

The ^1H and ^{13}C NMR spectra were recorded with a Varian, Mercury Plus spectrometer operating at 200 and 50.3 MHz, respectively. The HSQC 2D-NMR measurement were recorded with observed ^1H at 200 MHz and decouple ^{13}C at 50.3 MHz. Pure sample dissolved in $CDCl_3$ was used as an external reference The spectra were recorded at room temperature in the 0–11 ppm and 0–220 ppm ranges for ^1H and ^{13}C NMR spectra, respectively.

4.2.4. GC–MS determination

The GC–MS measurements were recorded in a GCMS-QP2010 SHIMADZU instrument using gaseous Helium as mobile phase with the pressure in the column head equal to 100 kPa. The column used was a 19091J-433 HP-5 of 30 m × 0.32 mm × 0.25 mm film thickness. A 1-μL volume of the compounds dissolved in $CHCl_3$ was chromatographed under the following conditions: injector temperature was 200 °C, the initial column temperature (70 °C) was held for 2 min, then increased to 200 °C at 7 °C/min and held for 2 min after elevated to 300 °C at 5 °C/min and held for 2 min. In the spectrometer the source was kept at 200 °C.

4.2.5. Melting point determination

The melting points were determined in a capillary tube containing the pulverized sample, which was introduced in a BÜCHI-Glasapparatefabrik-flawil schmlzpunktestimmungsapparat (melting point apparatus) equipped with a thermometer (0–300 ± 1 °C).

4.2.6. Theoretical calculations

All quantum chemical calculations were performed with the GAUSSIAN 03 program package [49]. The molecular geometries were optimized to standard convergence criteria by using a DFT hybrid method with Becke's non local three parameter exchange and the Lee, Young and Parr correction (B3LYP) using 6-31G* and 6-311++G** basis sets.

Acknowledgments

Financial support by the Volkswagen-Stiftung and the Deutsche Forschungsgemeinschaft is gratefully acknowledged. The Argentinean authors thank the ANPCYT-DAAD for the German–Argentinean cooperation Awards (PROALAR) and the DAAD Regional Program of Chemistry for Argentina. They also thank to Consejo Nacional de Investigaciones Científicas y Técnicas (CONICET), the Comisión de Investigaciones Científicas de la Provincia de Buenos Aires (CIC), República Argentina and FAPESP (Brazil). They are indebted to the Facultad de Ciencias Exactas, Universidad Nacional de La Plata for financial support. STV and CODV especially acknowledge the DAAD, which generously sponsors the DAAD Regional Program of Chemistry for the República Argentina supporting Latin–American students to study for their Ph.D. in La Plata.

Appendix A. Supplementary data

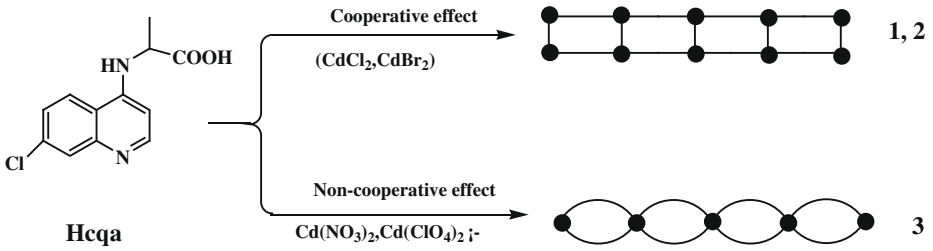
Supplementary data can be obtained free of charge via http://www.ccdc.cam.ac.uk/conts/retrieving.html, or from the Cambridge Crystallographic Data Centre, 12 Union Road, Cambridge CB2 1EZ, UK; fax: (+44) 1223 336 033; or e-mail: deposit@ccdc.cam.ac.uk.

Supplementary data associated with this article can be found, in the online version, at doi:10.1016/j.poly.2009.01.022.

References

[1] D. Kaur, P. Sharma, P.V. Bharatam, J. Mol. Struct. (Theochem) 757 (2005) 149.
[2] S. Faizi, B.S. Siddiqui, R. Saleem, S. Siddiqui, K. Aftab, A.-U.-H. Gilani, J. Chem. Soc., Perkin Trans. 1 (1992) 3237.
[3] S. Faizi, B.S. Siddiqui, R. Saleem, S. Siddiqui, K. Aftab, A.-U.-H. Gilani, J. Chem. Soc., Perkin Trans. 1 (1994) 3035.

[4] S. Faizi, B.S. Siddiqui, R. Saleem, F. Noor, S. Husnain, J. Nat. Prod. 60 (1997) 1317.
[5] S. Faizi, B.S. Siddiqui, R. Saleem, S. Siddiqui, K. Aftab, A.-U.-H. Gilani, Phytochem. 38 (1995) 957.
[6] F.S. Kuan, P. Tadbuppa, E.R.T. Tiekink, Z. Kristallogr. New Cryst. Struct. 220 (2005) 393.
[7] P. Tadbuppa, E.R.T. Tiekink, Z. Kristallogr. New Cryst. Struct. 220 (2005) 395.
[8] R.E. Benson, G.A. Broker, L.M. Daniels, E.R.T. Tiekink, J.L. Wardell, D.J. Young, Acta Crystallogr., Sect. E 62 (2006) O4106.
[9] B. Yang, S.S. Zhang, H. Li, Indian J. Heterocyclic Chem. 15 (2005) 31.
[10] B. Yang, S.S. Zhang, J.Z. Li, J. Chem. Soc. Pakistan 27 (2005) 223.
[11] B. Yang, S.S. Zhang, Y.F. Wang, Chem. Res. Chin. Univ. 21 (2005) 163.
[12] A.M. Plutín, M. Suárez, E. Ochoa, T. Machado, R. Mocelo, J.M. Concellón, H. Rodríguez-Solla, Tetrahedron 61 (2005) 5812.
[13] K. Oyamada, J. Tobitsuka, T. Matsui, M. Nagano, Nippon Nogei Kagaku Kaishi 50 (1976) 23.
[14] S.V. Kulkarni, US Patent 6066754, 2000.
[15] M. Conrad, R. Lantzsch, V.C. Desai, S.V. Kulkarni, US Patent 5917050, 1999.
[16] H. Arslan, U. Florke, N. Külcü, Spectrochim. Acta 67A (2007) 936.
[17] A. Haas, H. Reinke, Chem. Ber. 102 (1969) 2718.
[18] J. Goerdeler, A. Schulze, Chem. Ber. 115 (1982) 1252.
[19] M. Remko, K.R. Liedl, B.M. Rode, J. Mol. Struct. (Theochem) 418 (1997) 179.
[20] M.F. Erben, C.O. Della Védova, R.M. Romano, R. Boese, H. Oberhammer, H. Willner, O. Sala, Inorg. Chem. 41 (2002) 1064.
[21] N.D. Epiotis, R.L. Yates, F. Bernardi, S. Wolfe, J. Am. Chem. Soc. 98 (1976) 5435.
[22] G.I.L. Jones, D.G. Lister, N.L. Owen, M.C.L. Gerry, P. Palmieri, J. Mol. Spectrosc. 60 (1976) 348.
[23] N.V. Belova, H. Oberhammer, G.V. Girichev, J. Phys. Chem. A 108 (2004) 3593.
[24] C.E. Blom, H. Günthard, Chem. Phys. Lett 84 (1981) 267.
[25] C. Mueller, W. Schaefer, A. Schweig, N. Thon, H. Vermeer, J. Am. Chem. Soc. 98 (1976) 5440.
[26] H. Wennerstrom, S. Forsen, B. Roos, J. Phys. Chem. 76 (1972) 2430.
[27] P.P. Tadbuppa, E.R.T. Tiekink, Acta Crystallogr., Sect. E 63 (2007) o1779.
[28] J. Dillen, M.G. Woldu, K.R. Koch, Acta Crystallogr., Sect. E 62 (2006) o4819.
[29] J. Dillen, M.G. Woldu, K.R. Koch, Acta Crystallogr., Sect. E 62 (2006) o5228.
[30] J. Dillen, M.G. Woldu, K.R. Koch, Acta Crystallogr., Sect. E 62 (2006) o5225.
[31] C.G. Overberger, H.A. Friedman, J. Polym. Sci. A 3 (1965) 3625.
[32] S. Torrico Vallejos, M.F. Erben, H. Willner, R. Boese, C.O. Della Védova, J. Org. Chem. 72 (2007) 9074.
[33] S. Torrico Vallejos, M.F. Erben, R. Boese, O.E. Piro, E.E. Castellano, C.O. Della Védova, J. Mol. Struct. 918 (2009) 146.
[34] W. Zhou, L. Zhu, Y. Zhang, Z. Yu, L. Lu, X. Yang, Vib. Spec. 36 (2004) 73.
[35] C.K. Johnson, ORTEP-II, A Fortran Thermal-Ellipsoid Plot Program, Report ORNL-5318, Oak Ridge National Laboratory, Tennessee, USA, 1976.
[36] A. Saeed, U. Floerke, Acta Crystallogr., Sect. E 62 (2006) o2924.
[37] A. Saeed, U. Floerke, Acta Crystallogr., Sect. E 62 (2006) o5036.
[38] T. Steiner, Angew. Chem., Int. Ed. Engl. 41 (2002) 48.
[39] S. Stockmann, J. Bruce, J. Miller, K.R. Koch, Acta Crystallogr., Sect. C 64 (2008) o166.
[40] J.C. Bruce, N. Revaprasadu, K.R. koch, New J. Chem. 31 (2007) 1647.
[41] F.H. Allen, O. Kennard, D.G. Watson, L. Brammer, A.G. Orpen, R. Taylor, J. Chem. Soc., Perkin Trans. 2 (1987) S1.
[42] A.D. Morales, H. Novoa de Armas, N.M. Blaton, O.M. Peeters, C.J. De Ranter, H. Márquez, R. Pomés Hernández, Acta Crystallogr., Sect. C 56 (2000) 1042.
[43] J.C. Bruce, K.R. Koch, Acta Crystallogr., Sect. C 64 (2008) m1.
[44] K.B. Wiberg, P.R. Rablen, J. Am. Chem. Soc. 117 (1995) 2201.
[45] Enraf-Nonius, COLLECT, Nonius BV, Delft, The Netherlands, 1997–2000.
[46] Z. Otwinowski, W. Minor, in: C.W. Carter Jr., R.M. Sweet (Eds.), Methods in Enzymology, vol. 276, Academic Press, New York, 1997, pp. 307–326.
[47] PLATON, A Multipurpose Crystallographic Tool, Utrecht University, Utrecht, The Netherlands, A.L. Spek, 1998.
[48] G. Sheldrick, Acta Crystallogr., Sect. A 64 (2008) 112.
[49] M.J. Frisch, G.W. Trucks, H.B. Schlegel, G.E. Scuseria, M.A. Robb, J.R. Cheeseman, J.A. Montgomery Jr., T. Vreven, K.N. Kudin, J.C. Burant, J.M. Millam, S.S. Iyengar, J. Tomasi, V. Barone, B. Mennucci, M. Cossi, G. Scalmani, N. Rega, G.A. Petersson, H. Nakatsuji, M. Hada, M. Ehara, K. Toyota, R. Fukuda, J. Hasegawa, M. Ishida, T. Nakajima, Y. Honda, O. Kitao, H. Nakai, M. Klene, X. Li, J.E. Knox, H.P. Hratchian, J.B. Cross, V. Bakken, C. Adamo, J. Jaramillo, R. Gomperts, R.E. Stratmann, O. Yazyev, A.J. Austin, R. Cammi, C. Pomelli, J.W. Ochterski, P.Y. Ayala, K. Morokuma, G.A. Voth, P. Salvador, J.J. Dannenberg, V.G. Zakrzewski, S. Dapprich, A.D. Daniels, M.C. Strain, O. Farkas, D.K. Malick, A.D. Rabuck, K. Raghavachari, J.B. Foresman, J.V. Ortiz, Q. Cui, A.G. Baboul, S. Clifford, J. Cioslowski, B.B. Stefanov, G. Liu, A. Liashenko, P. Piskorz, I. Komaromi, R.L. Martin, D.J. Fox, T. Keith, M.A. Al-Laham, C.Y. Peng, A. Nanayakkara, M. Challacombe, P.M.W. Gill, B. Johnson, W. Chen, M.W. Wong, C. Gonzalez, J.A. Pople, GAUSSIAN 03, Revision C.02, Gaussian, Inc., Wallingford CT, 2004.
[50] A.D. Morales, H. Novoa de Armas, N.M. Blaton, O.M. Peeters, C.J. De Ranter, H. Márquez, R. Pomés Hernández, Acta Crystallogr., Sect. C 56 (2000) 503.
[51] G. Blewett, C. Esterhuysen, M.W. Bredenkamp, K.R. Koch, Acta Crystallogr., Sect. C 60 (2004) o862.
[52] G. Blewett, M.W. Bredenkamp, K.R. Koch, Acta Crystallogr., Sect. C 61 (2005) o469.



Scheme 1. Molecular structure of the ligand Hcqa and the topologies of its 1D coordination polymers.

volume) was sealed in a Teflon-lined stainless steel reactor, heated at 100 °C for 3 days and cooled to room temperature. Colorless plate-like single crystals of **1** were obtained and washed with distilled water. Yield: 35%. *Anal.* Calc. for $C_{24}H_{22}CdCl_3N_4O_4$: C, 44.40; H, 3.42; N, 8.63. Found: C, 44.21; H, 2.99; N, 8.86%. IR (KBr, cm^{-1}): 3341(m), 3279(m), 2987(m), 1618(s), 1584(vs), 1557(s), 1453(s), 1403(vs), 1368(s), 1028(w), 949(w), 902(w), 870(m), 812(m), 762(w), 688(m).

2.2.2. $[Cd(cqaH)(cqa)Br]_n$ (**2**)

Compound **2** was prepared by a similar method to **1**, except for using $CdBr_2 \cdot 4H_2O$ instead of $CdCl_2 \cdot 2.5H_2O$. Yield: 22%. *Anal.* Calc. for $C_{24}H_{22}CdCl_2BrN_4O_4$: C, 41.55; H, 3.20; N, 8.08. Found: C, 41.94; H, 3.21; N, 7.86%. IR (KBr, cm^{-1}): 3336(m), 3283(m), 2982(w), 1615(s), 1583(vs), 1559(s), 1453(s), 1402(s), 1367(vs), 1033(w), 949(w), 902(w), 865(m), 812(m), 763(w), 686(m).

2.2.3. $\{[Cd_2(cqa)_4] \cdot 3H_2O\}_n$ (**3**)

Compound **3** was prepared by a similar method to **1**, except for using $Cd(NO_3)_2 \cdot 4H_2O$ instead of $CdCl_2 \cdot 2.5H_2O$. Yield: 26%. *Anal.* Calc. for $C_{48}H_{42}Cd_2Cl_4N_8O_{11}$: C, 45.12; H, 3.31; N, 8.77. Found: C, 44.93; H, 3.07; N, 8.96%. IR (KBr, cm^{-1}): 3448(br), 3276(s), 2986(w), 1579(vs), 1456(m), 1406(s), 1368(s), 1041(w), 950(w), 914(m), 867(m), 812(m), 763(m), 660(w). This compound could also be obtained in various yields under the same hydrothermal conditions, by using $Cd(ClO_4)_2 \cdot 6H_2O$, $Cd(OAc)_2$, $Cd(SCN)_2$, CdI_2 and $CdSO_4 \cdot 8/3H_2O$ instead of $Cd(NO_3)_2 \cdot 4H_2O$.

2.3. Caution

Although we have experienced no problems in handling perchlorate compounds, these should be handled with great caution due to the potential for explosion.

2.4. X-ray structure determinations

X-ray intensity data of **1–3** were collected on a Bruker SMART APEX CCD diffractometer [20] using graphite monochromatized Mo Kα radiation (λ = 0.71073 Å) at 291(2) K. The raw data were reduced and corrected for Lorentz and polarization effects using the SAINT program and for absorption using the SADABS program. The structures were solved by direct methods and refined with the full-matrix least-squares technique using SHELXTL version 5.1 [21]. Anisotropic thermal parameters were assigned to all non-hydrogen atoms. Hydrogen atoms were placed in calculated positions and refined using a riding model. The crystallographic data are shown in Table 1. Selected bond lengths and bond angles are given in Table 2.

Table 1
Crystallographic data and details of refinements for complexes **1**–**3**.

Complexes	**1**	**2**	**3**
Empirical formula	$C_{24}H_{22}CdCl_3N_4O_4$	$C_{24}H_{22}CdBrCl_2N_4O_4$	$C_{48}H_{42}Cd_2Cl_4N_8O_{11}$
Mr	649.21	693.67	1273.50
Crystal system	triclinic	triclinic	trigonal
Space group	$P\bar{1}$	$P\bar{1}$	$R\bar{3}$
a (Å)	9.997(2)	10.039(4)	20.301(4)
b (Å)	11.236 (1)	11.488(5)	20.301(4)
c (Å)	11.871(3)	11.866(5)	32.781(8)
α (°)	106.045(3)	105.983(7)	90
β (°)	106.171(2)	106.705(7)	90
γ (°)	97.565 (1)	98.265(8)	120
V (Å^3)	1198.9(4)	1222.6(9)	11700(4)
Z	2	2	9
D_{calc} (g/cm^{-3})	1.798	1.884	1.627
μ (mm^{-1})	1.287	2.787	1.090
θ range (°)	1.89–26.00	1.90–26.00	1.70–26.00
Reflections collected/ unique (R_{int})	6629/4638 (0.0314)	6563/4660 (0.0344)	21061/5121 (0.0446)
Data/restraints/ parameters	4638/0/327	4660/0/327	5121/0/354
F(000)	650	686	5742
T (K)	291(2)	291(2)	291(2)
R_1[a], wR_2[b] [$I > 2\sigma(I)$]	0.0587, 0.1159	0.0613, 0.1303	0.0451, 0.0946
R_1[a], wR_2[b] [all data]	0.0814, 0.1196	0.0842, 0.1356	0.0628, 0.0988
Goodness-of-fit	1.003	1.014	1.097
Largest difference in peak and hole (e Å^{-3})	1.409, −0.750	0.687, −1.263	0.273, −0.989

[a] $R_1 = \sum||F_o| - |F_c||/\sum|F_o|$.
[b] $wR_2 = [\sum w(|F_o^2| - |F_c^2|)^2/\sum w(|F_o^2|)^2]^{1/2}$.

Table 2
Selected bond lengths (Å) and angles (°) for **1**–**3**.

Complex **1**			
Cd(1)–O(3)	2.228(4)	Cd(1)–N(1a)	2.282(5)
Cd(1)–O(4b)	2.341(4)	Cd(1)–O(2)	2.345(4)
Cd(1)–O(1)	2.514(4)	Cd(1)–Cl(1)	2. 537(1)
O(3)–Cd(1)–N(1a)	100.6(2)	O(3)–Cd(1)–O(4b)	90.7(1)
N(1a)–Cd(1)–O(4b)	87.0(2)	O(3)–Cd(1)–O(2)	154.1(2)
N(1a)–Cd(1)–O(2)	102.4(2)	O(4b)–Cd(1)–O(2)	78.8(1)
O(3)–Cd(1)–O(1)	100.5(1)	N(1a)–Cd(1)–O(1)	151.9(2)
O(4b)–Cd(1)–O(1)	74.4(1)	O(2)–Cd(1)–O(1)	54.0(1)
O(3)–Cd(1)–Cl(1)	92.6 (1)	N(1a)–Cd(1)–Cl(1)	104.7(1)
O(4b)–Cd(1)–Cl(1)	167.0(1)	O(2)–Cd(1)–Cl(1)	92.9(1)
O(1)–Cd(1)–Cl(1)	92.93(9)		
Complex **2**			
Cd(1)–O(3)	2.232(5)	Cd(1)–N(1a)	2.296(6)
Cd(1)–O(4b)	2.342(5)	Cd(1)–O(2)	2.345(5)
Cd(1)–O(1)	2.509(5)	Cd(1)–Br(1)	2.676(1)
O(3)–Cd(1)–N(1a)	99.3(2)	O(3)–Cd(1)–O(4b)	154.2(2)
O(1)–Cd(1)–Br(1)	92.7(1)	N(1a)–Cd(1)–Br(1)	104.6(2)
Complex **3**			
Cd(1)–O(2b)	2.212(3)	Cd(1)–O(4a)	2.257(3)
Cd(1)–O(3a)	2.486(3)	N(1)–Cd(1)	2.285(3)
N(3)–Cd(1)	2.285(3)		
O(2b)–Cd(1)–O(4a)	105.1(1)	O(2b)–Cd(1)–N(3)	108.0(1)
O(4a)–Cd(1)–N(3)	95.5(1)	O(2b)–Cd(1)–N(1)	102.5(1)
O(4a)–Cd(1)–N(1)	134.7(1)	N(3)–Cd(1)–N(1)	109.4(1)
O(2b)–Cd(1)–O(3a)	149.5(1)	O(4b)–Cd(1)–O(3a)	54.1(1)
N(3)–Cd(1)–O(3a)	97.0(1)	N(1)–Cd(1)–O(3a)	84.9(1)

Symmetry codes: (a) $x-1, y, z$; (b) $-x, -y+2, -z$ for **1** and for **2**; (b) $x-1, y, z$ for **2**; (a) #1 $-x+1, -y, -z$; (b) $-x+2/3, -y+1/3, -z+1/3$ for **3**.

3. Results and discussion

3.1. Preparation and IR analysis

Compounds **1–3** were synthesized under similar hydrothermal conditions by the reaction of the corresponding Cd salts and the Hcqa ligand. They are stable in air at ambient temperature and are insoluble in common solvents such as water, alcohol and acetonitrile. In the IR spectra, before the ligand coordinates to the Cd metal, the N–H stretching frequency is 3260 cm^{-1}. After it coordinates to the Cd metal, the N–H stretching frequencies are shifted to 3341 and 3279 cm^{-1} for compound **1**, 3336 and 3283 cm^{-1} for compound **2** and 3276 cm^{-1} for compound **3**. Obviously, additional absorptions at 3341 and 3336 cm^{-1} were observed for **1** and **2**, respectively, while the N–H stretching frequency of compound **3** is still slightly changed after the formation of the metal complex. Meanwhile, **1** and **2** show the characteristic bands of carboxylate groups with asymmetric vibrations at 1584 and 1583 cm^{-1}, and symmetric vibrations at 1403, 1368 and 1402, 1367 cm^{-1}, respectively. The Δ values representing the separation between $\nu_{as(COO)^-}$ and $\nu_{s(COO)^-}$ are all 181 and 216 cm^{-1}, respectively. In the IR spectrum of **3**, characteristic bands of the carboxylate groups are observed at 1579 cm^{-1} for the antisymmetric vibration and at 1406 and 1358 cm^{-1} for the symmetric vibration. The Δ values between $\nu_{as(COO)^-}$ and $\nu_{s(COO)^-}$ are 173 and 221 cm^{-1}, respectively. The results suggest that there exist two different coordination fashions for the carboxylate groups in **1–3**, which are consistent with the X-ray structural analysis results [22].

3.2. Structural description

3.2.1. Structures of $[Cd(cqaH)(cqa)Cl]_n$ (1) and $[Cd(cqaH)(cqa)Br]_n$ (2)

The X-ray crystal structure analyses of **1** and **2** reveal that they are isostructural. Therefore, only the crystal structure of **1** is described in detail. The asymmetric unit of **1** contains one Cd^{2+} cation, one Cl^- anion, one cqaH (the Hcqa ligand where the proton is transferred from the acid group to the imine group) ligand, and one deprotoned cqa^- ligand. As shown in Fig. 1, each Cd^{2+} ion adopts a distorted octahedral geometry and it is coordinated to one Cl^- anion, one nitrogen atom and two carboxylate oxygen atoms from cqaH and two carboxylate oxygens from cqa^-. The coordination fashion of the carboxylate oxygen from cqaH is in accordance with similar reported complexes [23]. The carboxylate oxygen atoms from cqaH (O1, O2), one nitrogen atom (N1A) and one carboxylate oxygen atom (O3) form the basal plane, whereas the axial positions are taken up by one chlorate anion (Cl1) and the other carboxylate oxygen atom (O4B). The carboxylate–oxygen atoms from cqaH join two Cd(II) atoms, yielding a Cd_2O_2 binuclear

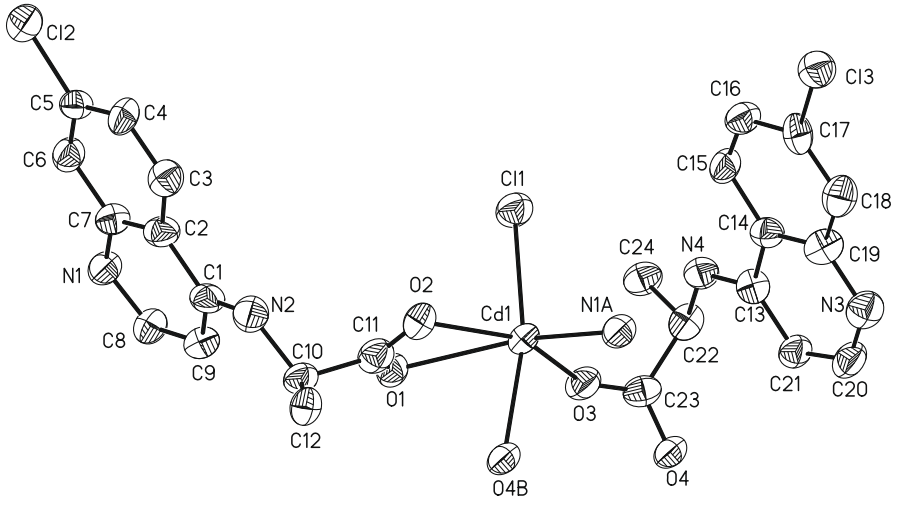


Fig. 1. View of the coordination environment of Cd(II) in complex **1**, thermal ellipsoids are drawn at the 50% probability level. Hydrogen atoms have been omitted for clarity.

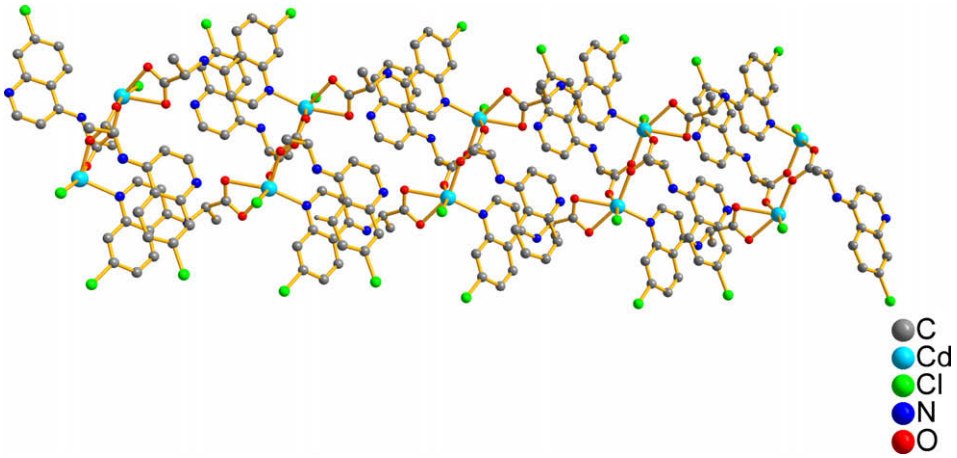


Fig. 2. The ribbon-like chain structure for complex **1**.

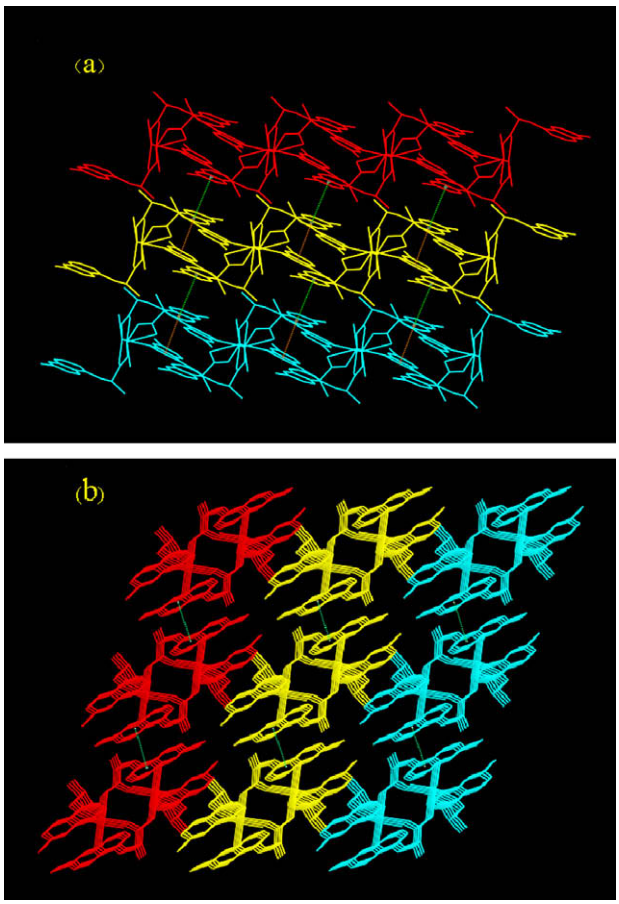


Fig. 3. (a) The 2D layered structure of **1** via π–π stacking interactions; (b) The 3D supramolecular architecture of **1** via π–π stacking interactions.

unit with an 8-membered metallacycle. Each dimer is further linked to give a one-dimensional ribbon-like polymer via one nitrogen atom and the carboxylate oxygen atoms from the cqa^- ligand (Fig. 2). The most remarkable feature of **1** is the existence of three types of π−π stacking interactions which connect the 1D ribbon-like chains into a 3D supramolecular framework. First, there are intrachain π–π stacking interactions of quinolyl rings with centroid–centroid separations of 3.554 Å. Then, the 1D ribbon-like chains are bridged to form a 2D supramolecular sheet through interchain π−π stacking interactions between the quinolyl rings, with centroid–centroid distances of 3.584 Å (Fig. 3a). Finally, every layer interacts with neighboring layers via π−π stacking interactions between quinolyl rings (centroid–centroid distances of 3.593 Å), further extending the 2D layers into a 3D supramolecular framework (Fig. 3b). A similar supramolecular framework formed by π−π stacking interactions can be observed in $[Pb_2(1,4\text{-}bdc)_2(dpdp)_2]\cdot H_2O$ (1,4-H_2bdc = benzene-1,4-dicarboxylic acid, dpdp = dipyrido[3,2-a:2′,3′-c]-phenazine) [24], which only have two types of π–π stacking interactions. Richer π−π stacking interactions are observed in **1** and it provides a practicable method to assembly the supramolecular framework. Additionally, the centroid–centroid distances of the π−π interactions gradually increases, which indicates these interactions gradually decrease when the dimensionality is expanded from one to three.

3.2.2. Structure of $\{[Cd_2(cqa)_4]\cdot 3H_2O\}_n$ (**3**)

In the asymmetric unit of **3** there is one Cd^{2+} ion, two deprotonated Hcqa ligands and one and a half disordered water molecules. Each Cd^{2+} ion sits in a distorted tetragonal–pyramidal arrangement, in which the equatorial plane is completed by one nitrogen atom (N1) and three carboxylate oxygens (O2A, O3B and O4B) from cqa^- and the vertex position is occupied by the other nitrogen atom (N3) from cqa^- (Fig. 4). Each Cd^{2+} center is connected by two ligands into a double-stranded chain with an 18-membered ring. It is noteworthy that there are two different 18-membered rings with Cd···Cd separations of 8.421 and 8.234 Å (Fig. 5). The intriguing structural feature of this compound comprises three sets of double-stranded polymer chains which extend in three non-coplanar directions ([1 1 1], [1 1 $\bar{1}$] and [1 $\bar{1}$ $\bar{1}$]). The chains are organized around the crystallographic 3-fold axes in the [0 0 1] direction and adopt an interwoven arrangement through three types of interchain π–π interactions between quinolyl rings, with centroid–centroid distances of 3.616, 3.644 and 3.669 Å (Fig. 6). The complicated and entangled repeated array ultimately leads to a

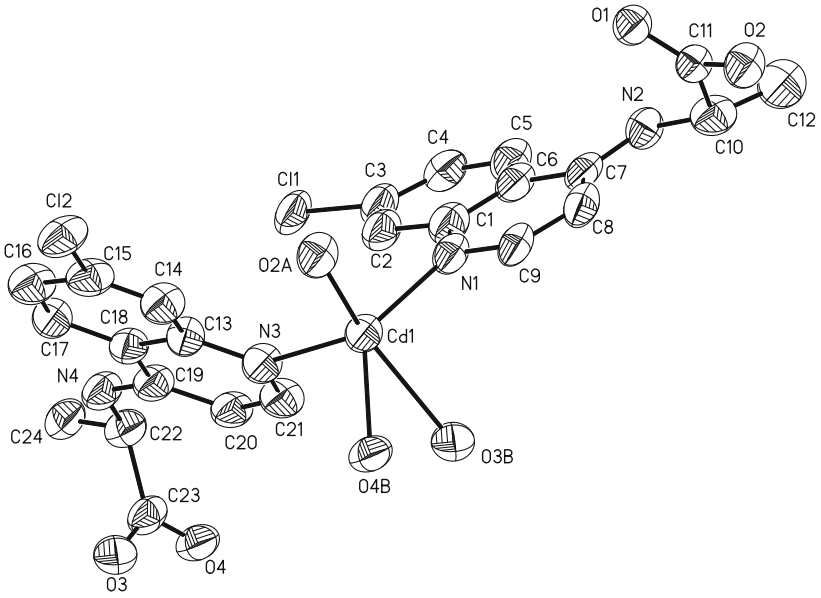


Fig. 4. View of the coordination environment of Cd(II) in complex **3**, thermal ellipsoids are drawn at the 50% probability level. Lattice water molecules and hydrogen atoms have been omitted for clarity.

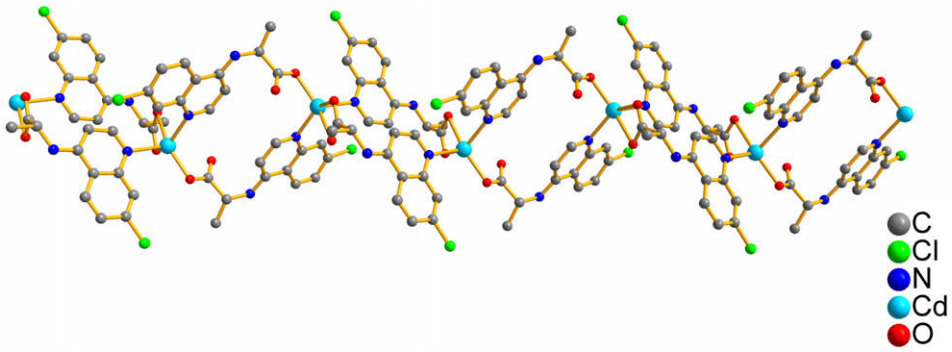


Fig. 5. The double-stranded chain structure in complex **3**.

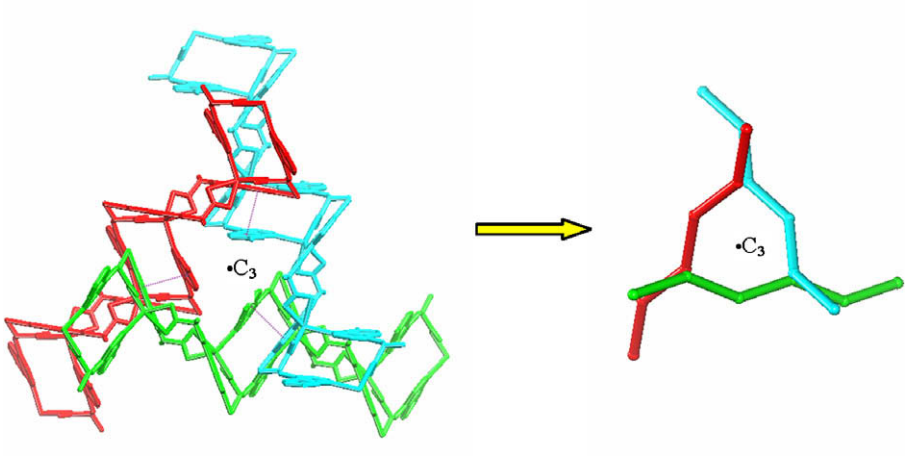


Fig. 6. Views showing four 1D zigzag chains arranged around a 3-fold axis and interchain π–π stacking interactions between the quinolyl rings in complex **3**.

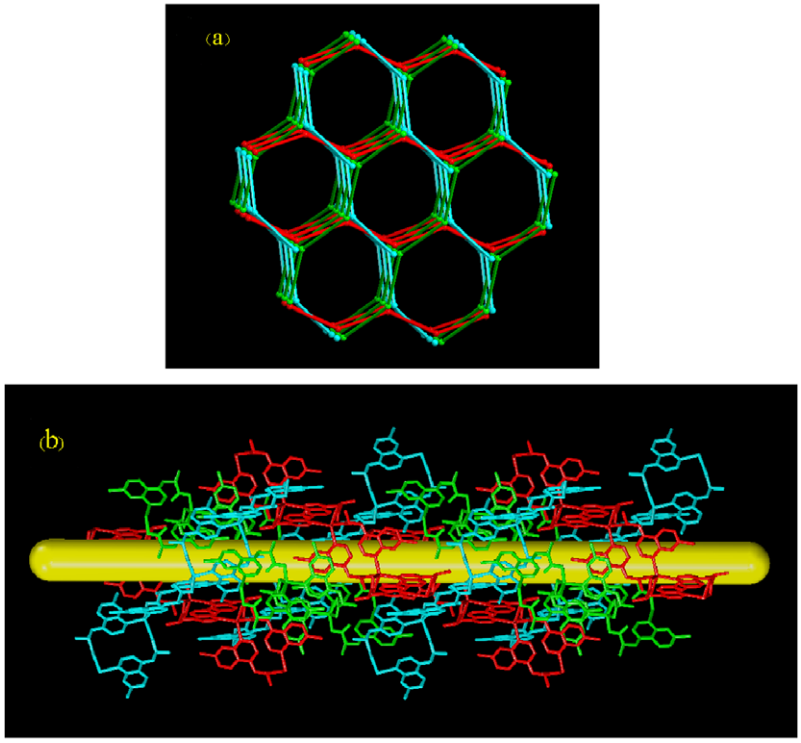


Fig. 7. (a) Simplified picture of the 3D framework with 1D channels; (b) The 1D channel is organized by three series of double-stranded polymer chains.

3D framework with 1D channels in the [001] direction (Fig. 7). Similar topological compounds constructed from three sets of chains have been reported for $[Ni(cyclam)(bpydc)] \cdot 5H_2O$ and $[\{Ni(C_{10}H_{26}N_6)\}_3(bpdc)_3] \cdot 2C_5H_5N \cdot 6H_2O$ (cyclam = 1,4,8,11-tetraazacyclotetradecane, bpydc = 2,2′-bipyridyl-5,5′-dicarboxylate, $C_{10}H_{26}N_6$ = 3,10-dimethyl-1,3,5,8,10,12-hexaazacyclotetradecane, bpdc = 4,4′-biphenyldicarboxylate), containing three sets of rigid chains, or $[Ag(sebn)](AsF_6)$ and $[Ag(sebn)](CF_3SO_3)$ (sebn = 1,10-decanedinitrile) containing three sets of flexible chains [25–27]. In contrast to these compounds, complex **3** is a rare example with both rigid and flexible chains. The chains are helpful for forming stronger π–π stacking interactions. The 1D channels with honeycomb-like windows have a diameter of ca. 7.6 Å (effective size 5.8 Å), which are occupied by disordered water guest molecules. After the removal of these guest solvents, the volume of the effective void, calculated using PLATON, is 11.0% of the unit-cell volume in **3**. The π–π stacking interactions further enhance the stability of this 3D framework.

The results suggest that the architectures of the coordination polymers are not only depended on the organic ligands, but also mediated by the anions and the cooperation effect from the anion and ligand. In our cases, the effects might be attributed to the following contributions: (i) Cl^-/Br^- ions and Cd^{2+} have a stronger electrostatic interaction and affinity than I^- and the other anions owing to the Cl^-/Br^- ions having a smaller ion radius [28]. The Cl^-/Br^- ions are easily involved in the affinity of the Cd centers and its self-organization. (ii) Previous studies suggested that Cl^-/Br^- ions usually cannot act as templating metal ions but they have a stronger capability of coordination than other anions in self-assembly reactions [29,30]. (iii) The cooperative effect of the ligand should also be very important. Generally, a stable metal–organic coordination polymer is good for a neutral framework [31,32]. If the anions show a weaker electrostatic affinity and weaker coordination ability to metal ions, the Hcqa ligand with both pyridyl and carboxylate groups can easily form a neutral and stable framework by itself.

3.3. Thermal stability

TG curves have been obtained under flowing N_2 for crystalline samples of **1–3** in the temperature range 25–750 °C. As shown in Fig. 8, for complex **3** a weight loss of 3.8% in the 75−150 °C range corresponds to the release of the lattice water molecules (calculated 4.2%). The decomposition of the residual components started beyond 500 °C. It can be seen from the TGA curves of **1** and **2**, the networks remain intact until they are heated to 350 °C and then they begin to collapse. The total observed weight loss at 730 °C is 38.9% and 41.3%, respectively, and the final residuals were not characterized.

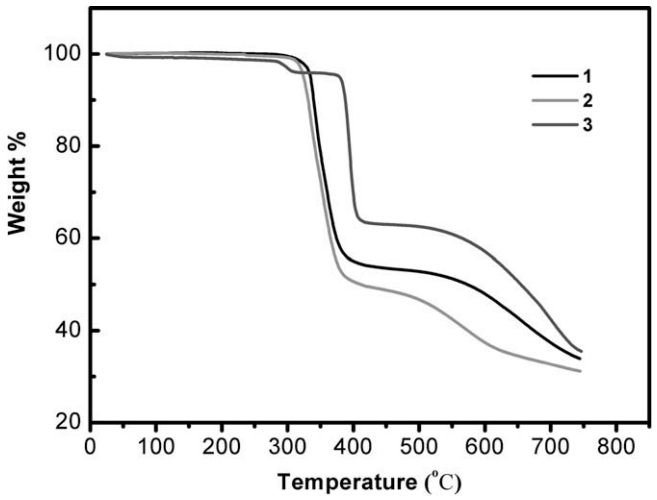


Fig. 8. Thermogravimetric curves for **1–3**.

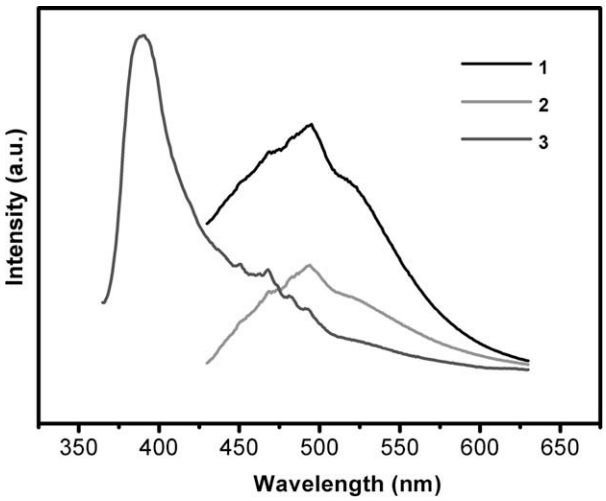


Fig. 9. Emission spectra of **1–3**.

3.4. Fluorescent emission properties

Metal–organic coordination polymers with the cadmium ion usually exhibit photoluminescent properties [33–36]. The photoluminescent properties of compounds **1–3** have been recorded in the solid state at room temperature. As shown in Fig. 9, complex **1** displays an intense emission maxima at 494 nm when excited at 400 nm. A similar emission band at 494 nm is also observed for **2** but the intensity is rather weak, which is reasonable because of the heavy atom (Br^-) that exists in compound **2** [37,38]. Complex **3** shows a very strong emission band located at 390 nm upon excitation at 350 nm. The bathochromic shift of the emission probably results from the differences of the coordination environment around the metal ions, since the photoluminescence behavior is nearly related to the coordination fashion of the ligands [39,40]. All the emissions could be attributed to the $\pi \rightarrow \pi^*$ intraligand fluorescence [41].

4. Conclusions and perspectives

In conclusion, three new coordination polymers based on the 7-chloroquinolin-4-alanine ligand have been successfully synthesized and characterized. The results revealed that the architectures of the coordination compounds are greatly affected by the anion and ligand: the cooperative effect induced the formation of 1D infinite molecular ribbon and the non-cooperative effect drove the generation of a 1D double-stranded chain. Hence, we believe that the cooperative effect of the anion and ligand may be considered in mediating the structure and it can play an important role in supramolecular chemistry and crystal engineering.

Acknowledgments

This work was supported by the National Basic Research Program of China (2006CB806104 and 2007CB925103), and the National Natural Science Foundation of China (20721002 and 20531040).

Appendix A. Supplementary data

CCDC 697466, 697467 and 697468 contains the supplementary crystallographic data for **1**, **2** and **3**. These data can be obtained free of charge via http://www.ccdc.cam.ac.uk/conts/retrieving.html or from the Cambridge Crystallographic Data Centre, 12 Union Road, Cambridge CB2 1EZ, UK; fax: (+44) 1223 336 033; or e-mail: deposit@ccdc.cam.ac.uk. Supplementary data associated with this article can be found, in the online version, at doi:10.1016/j.poly.2008.12.059.

References

[1] C.V.K. Sharma, Cryst. Growth Des. 2 (2002) 465.
[2] J.P. Zhang, X.M. Chen, Chem. Commun. (2006) 1689.
[3] B. Kesanli, W.B. Lin, Coord. Chem. Rev. 246 (2003) 305.
[4] R.E. Morris, P.S. Wheatley, Angew. Chem., Int. Ed. Engl. 47 (2008) 4966.
[5] D.N. Dybtsev, A.L. Nuzhdin, H. Chun, K.P. Bryliakov, E.P. Talsi, V.P. Fedin, K. Kim, Angew. Chem., Int. Ed. Engl. 45 (2006) 916.
[6] R.Q. Zou, H. Sakurai, S. Han, R.Q. Zhong, Q. Xu, J. Am. Chem. Soc. 129 (2007) 8402.
[7] S.Q. Ma, X.S. Wang, D.Q. Yuan, H.C. Zhou, Angew. Chem., Int. Ed. Engl. 47 (2008) 4130.
[8] S.K. Ghosh, S. Bureekaew, S. Kitagawa, Angew. Chem., Int. Ed. Engl. 47 (2008) 3403.
[9] N. Guillou, C. Livage, M. Drillon, G. Férey, Angew. Chem., Int. Ed. Engl. 42 (2003) 5314.
[10] J. Zhang, R. Liu, P.Y. Feng, X.H. Bu, Angew. Chem., Int. Ed. Engl. 46 (2007) 8388.
[11] Y.Y. Liu, J.F. Ma, J. Yang, J.C. Ma, G.J. Ping, Cryst. Eng. Commun. 10 (2008) 565.
[12] Y.Q. Sun, J. Zhang, G.Y. Yang, Chem. Commun. (2006) 4700.
[13] D.A. Hrovat, J. Chen, K.N. Houk, W.T. Borden, J. Am. Chem. Soc. 122 (2000) 7456.
[14] J.A. Bornhorst, J.J. Falke, Biochemistry 39 (2000) 9486.
[15] L.R. MacGillivray, M.M. Siebke, J.L. Reid, Org. Lett. 3 (2001) 1257.
[16] J.G. Planas, C. Vinas, F. Teixidor, A. Comas-Vives, G. Ujaque, A. Lledos, M.E. Light, M.B. Hursthouse, J. Am. Chem. Soc. 127 (2005) 15976.
[17] Y. Inomata, Y. Arai, T. Yamakoshi, F.C. Howell, J. Inorg. Biochem. 98 (2004) 2149.
[18] Q. Ye, Y.M. Song, G.X. Wang, K. Chen, D.W. Fu, P.W.H. Chan, J.S. Zhu, S.D. Huang, R.G. Xiong, J. Am. Chem. Soc. 128 (2006) 9410.
[19] J.J. Cheng, R. Zeidan, S. Mishra, A.J. Liu, S.H. Pun, R.P. Kulkarni, G.S. Jensen, N.C. Bellocq, M.E. Davis, J. Med. Chem. 49 (2006) 6522.
[20] SMART and SAINT, Area Detector Control and Integration Software, Siemens Analytical X-ray Systems, Inc., Madison, WI, 1996.
[21] G.M. Sheldrick, SHELXTL V5.1 Software Reference Manual, Bruker AXS, Inc., Madison, WI, 1997.
[22] K. Nakamoto, Infrared and Raman Spectra of Inorganic and Coordination Compounds, John Wiley and Sons, New York, 1986.
[23] Y.Z. Tang, X.F. Huang, Y.M. Song, P.W.H. Chan, R.G. Xiong, Inorg. Chem. 45 (2006) 4868.
[24] J. Yang, J.F. Ma, Y.Y. Liu, J.C. Ma, S.R. Batten, Inorg. Chem. 46 (2007) 6542.
[25] L. Carlucci, G. Ciani, P. Macchi, D.M. Proserpio, S. Rizzato, Chem. Eur. J. 5 (1999) 237.
[26] E.Y. Lee, M.P. Suh, Angew. Chem., Int. Ed. Engl. 43 (2004) 2798.
[27] H.R. Moon, J.H. Kim, M.P. Suh, Angew. Chem., Int. Ed. Engl. 44 (2005) 1261.
[28] R.G. Pearson, R.J. Mawby, Halogen Chemistry, in: V. Gutmann (Ed.), Academic Press, New York, 1967.
[29] Y. Long, X. Yang, T.B. Lu, P. Cheng, Cryst. Growth Des. 5 (2005) 1215.
[30] G.H. Wang, Z.G. Li, H.Q. Li, N.H. Hu, J.W. Xu, Cryst. Growth Des. 8 (2008) 1932.
[31] M. Eddaoudi, D.B. Moler, H.L. Li, B.L. Chen, T.M. Reineke, M. O'Keeffe, O.M. Yaghi, Acc. Chem. Res. 34 (2001) 319.
[32] O.M. Yaghi, M. O'Keeffe, N.W. Ockwig, H.K. Chae, M. Eddaoudi, J. Kim, Nature 423 (2003) 705.
[33] Q.G. Zhai, C.Z. Lu, X.Y. Wu, S.R. Batten, Cryst. Growth Des. 7 (2007) 2332.
[34] Z.Y. Du, X.L. Li, Q.Y. Liu, J.G. Mao, Cryst. Growth Des. 7 (2007) 1501.
[35] C. Janiak, J. Chem. Soc., Dalton Trans. (2003) 2781.
[36] H. Zhao, Z.R. Qu, H.Y. Ye, R.G. Xiong, Chem. Soc. Rev. 37 (2008) 84.
[37] R.S. Drago, Physical Methods in Chemistry, Saunders, Philadelphia, 1977 (Chapter 5).
[38] K.J. Wei, Y.S. Xie, J. Ni, M. Zhang, Q.L. Liu, Cryst. Growth Des. 6 (2006) 1634.
[39] X.L. Wang, C. Qin, Y.G. Li, N. Hao, C.W. Hu, L. Xu, Inorg. Chem. 43 (2004) 1850.
[40] Y. Su, S.Q. Zang, Y.Z. Li, H.Z. Zhu, Q.J. Meng, Cryst. Growth Des. 7 (2007) 1277.
[41] X.F. Wang, Y. Lv, T. Okamura, H. Kawaguchi, G. Wu, W.Y. Sun, N. Ueyama, Cryst. Growth Des. 7 (2007) 1125.

agents and solvents employed were commercially available and were used as received without further purification.

UV–Vis spectra were recorded on a SHIMADZU UV-2401 spectrometer and Fourier-transformer IR data on a SHIMADZU FTIR-8400 spectrometer. Mössbauer measurements were performed on a constant acceleration spectrometer from 20 to 150 K with an optional small field (Knox College).

2.2. Synthesis of [Na(2,2,2-crypt)][Fe^{II}(TpivPP)(N$_3$)] · 3C$_6$H$_5$Cl

[Fe^{III}(TpivPP)(SO$_3$CF$_3$)(H$_2$O)] [4] (100 mg, 0.081 mmol) and 1 mL of zinc amalgam were stirred for 1 h under argon in 10 mL of C$_6$H$_5$Cl. This deep red solution of [Fe^{II}(TpivPP)] was then filtered into a second solution that was made by stirring for 2 h a mixture of 150 mg (0.39 mmol) of cryptand-222 and 200 mg of NaN$_3$ (3.08 mmol) in 10 mL of C$_6$H$_5$Cl. The solution was filtered and crystals of the complex were prepared by slow diffusion of hexanes into the chlorobenzene solution. UV–Vis [C$_6$H$_5$Cl, λ_{max} in nm]: 359, 440, 568. IR (KBr disk, cm^{-1}): ν(N$_3$) 2024, 1996.

2.3. X-ray crystallography

Single crystal X-ray diffraction measurements were carried out at 223 K on a Bruker Nonius FR590 Kappa CCD area detector diffractometer employing graphite monochromatized Mo Kα radiation (λ = 0.71073 Å) in the ϕ scan mode. Final unit cell dimensions were obtained and refined on the entire data set. Integration and scaling resulted in the data set, corrected for Lorentz and polarization effects using DENZO/SCALEPACK [5]. The trial structure was obtained by direct methods using SIR-2004-1.0 [6], which revealed the position of the iron and sodium atoms, most atoms of the porphinato ligand, and the cryptand-222. The remainder of the structure was found in the subsequent difference Fourier syntheses. There are one [Fe^{II}(TpivPP)(N$_3$)]$^-$ anion, one sodium cryptand-222 counterion and three chlorobenzene solvent molecules in the asymmetric unit of the structure. The final structural refinement was made with F^2 data with the program SHELXL-97 [7].

A *tert*-butyl group of the picket occupies two alternative positions with converged occupancies of 0.58(1) and 0.42(1). Two oxygen atoms O5 and O6 of the cryptand-222 present two major positions with refined occupancy coefficients converged to 0.60(1) and 0.40(1) (for O5A and O5B) and 0.68(1) and 0.32(1) (for O6A and O6B). All non-hydrogen atoms were refined anisotropically, except the minor component of the disordered *tert*-butyl group as well as the two disordered oxygen atoms O5 and O6 of the cryptand-222. The hydrogen atoms were geometrically fixed and allowed to refine using a riding model. The crystal data and structural refinement parameters are given in Table 1 and selected bond lengths and angles are given in Table 2.

3. Results and discussion

3.1. UV–Vis and IR

The electronic spectrum of the [Fe^{II}(TpivPP)(N$_3$)]$^-$ species exhibits a Soret band at 443 nm in chlorobenzene. The position of the Soret band is red-shifted, as seen for Fe(II) pentacoordinate *meso*-porphyrin complexes with ionic axial ligands (see Table 3). So, the UV–Vis spectrum of the azido-Fe(II) derivative alone suggests the formation of a five-coordinate iron(II) porphyrin species. The question of the spin state, however, remains. As shown in Table 3, the high-spin (S = 2) iron(II) halide and oxyanionic (RO$^-$) species have Soret maxima around 440 nm [8,9]. Interestingly, however, the Soret maximums for five-coordinated low-spin (S = 0) iron(II) porphyrinates [Fe^{II}(TpivPP)(NO$_2$)]$^-$ [10] and [Fe^{II}(TpivPP)(CN)]$^-$ [11] are also in the 435–450 nm area [10].

Table 1
Crystal data and structural refinement for [Na(2,2,2-crypt)][Fe^{II}(TpivPP)(N$_3$)] · 3C$_6$H$_5$Cl.

Empirical formula	C$_{100}$H$_{115}$Cl$_3$FeN$_{13}$NaO$_{10}$
Formula weight (M)	1844.24
Crystal system	triclinic
Space group	$P\bar{1}$
Lattice constants	
a (Å)	13.3325(2)
b (Å)	14.5655(2)
c (Å)	24.7510(4)
α (°)	87.391(6)
β (°)	87.4748(5)
γ (°)	84.7848(6)
Volume, V (Å^3)	4777.82(12)
Z	2
D_{calc} (g/cm^3)	1.282
Absorption coefficient, μ (mm^{-1})	0.312
F(000)	1948
Crystal size (mm^3)	0.50 × 0.50 × 0.15
T (K)	223(2)
θ range for data collection	3.08–26.25
Limiting indices	$-16 \leqslant h \leqslant 16$, $-15 \leqslant k \leqslant 15$, $-30 \leqslant l \leqslant 30$
Unique reflections (R_σ)	17353 (0.0432)
Data/restraints/parameters	17353/0/1176
Goodness-of-fit on F^2	1.053
Final R indices [$I > 2\sigma(I)$]	R_1[a] = 0.0603, wR_2[b] = 0.1414
R indices (all data)	R_1 = 0.0780, wR_2 = 0.1556
Largest difference in peak and hole (e Å^{-3})	0.524 and −0.593

[a] $R_1 = \sum||F_o| - |F_c||/\sum|F_o|$.
[b] $wR_2 = [\sum w(F_o^2 - F_c^2)^2/\sum w(F_o^2)^2]^{1/2}$ and $w = 1/[\sigma^2(F_o^2) + (0.0604P)^2 + 4.14P]$, where $P = (F_o^2 + 2F_c^2)/3$.

Table 2
Selected bond lengths (Å) and bond angles (°) of [Na(2,2,2-crypt)][Fe^{II}(TpivPP)(N$_3$)] · 3C$_6$H$_5$Cl.

Iron coordination polyhedron			
Fe–N1	2.091(2)	N1–Fe–N2	87.89(7)
Fe–N2	2.093(2)	N1–Fe–N3	154.06(8)
Fe–N3	2.092(2)	N1–Fe–N4	86.46(7)
Fe–N4	2.099(2)	N1–Fe–N9	108.87(9)
Fe–N9	2.077(2)	N2–Fe–N3	86.95(7)
Azido ligand			
N9–N10	1.194(3)	Fe–N9–N10	116.8(2)
N10–N11	1.169(4)	N9–N10–N11	178.0(3)
Sodium-cryptand-222			
Na–N12	2.770(3)	N12–Na–N13	177.70(10)
Na–N13	2.750(3)	N12–Na–O7	68.80(8)
Na–O7	2.426(2)	N12–Na–O10	110.71(8)
Na–O8	2.521(2)	N13–Na–O8	67.26(8)
Na–O9	2.511(2)	N13–Na–O10	67.00(9)

Table 3
Electronic spectra data[a] for selected iron(II) *meso*-porphyrins.

Complex	λ_{max} (nm)			Spin S	Reference
	Soret region	α, β region			
[Fe^{II}(TpivPP)(N$_3$)]$^-$	443	572	612	2	this work
[Fe^{II}(TpivPP)(Cl)]$^-$	446	571	609	2	[8]
[Fe^{II}(TpivPP)(OMe)]	456	580	622	2	[9]
[Fe^{II}(TpivPP)(OAc)]	448	572	611	2	[9]
[Fe^{II}(TpivPP)(OPh)]$^-$	450	576	616	2	[9]
[Fe^{II}(TpivPP)(NO$_2$)]$^-$	444	567	608	0	[10]
[Fe^{II}(TpivPP)(CN)]$^-$	455	565	601	0	[11]
[Fe^{II}(TpivPP)(NO$_3$)]	438	564	604	2	[12]

[a] Solvent: chlorobenzene.

The [Na(2,2,2-crypt)][Fe^{II}(TpivPP)(N_3)] · $3C_6H_5Cl$ complex shows a strong band in the IR spectrum at 1102 cm^{-1} which is attributed to the counterion (cryptand-222)sodium(+). The same spectrum exhibits a strong band at 1996 cm^{-1} and a weak band at 2024 cm^{-1} attributed to the asymmetric stretching frequency ν_{as} of the N_3^- ligand. Thus, the IR data are consistent with a Fe(II) mono-azido picket fence porphyrin species. IR data for azido-porphyrin and azido-hemoprotein iron(III) species are available in the literature [3]. McCoy and Caughey [13] observed infrared bands for MetMb-N_3 at 2045 and 2023 cm^{-1} and at 2047 and 2025 cm^{-1} for MetHb-N_3 in aqueous solution; both of these hemoprotein systems are spin-equilibrium systems with azide and histidine as the ligand set. These authors assigned the high frequency bands to the high-spin iron(III) forms and the low frequencies to the low-spin iron(III) forms. The bis-azide Fe(III) complex [Fe^{III}(TPP)(N_3)$_2$]$^-$ [3] presents two bands at 2014 and 2036 cm^{-1} attributed to ν_{as} of the N_3^- groups. These absorption bands are assigned to high and low-spin Fe(III) forms, respectively. The cobalt(III) bis-azide derivative: [Co^{III}(TpivPP)(N_3)$_2$]$^-$ [14] also exhibits two stretching frequencies attributed to the N_3^- ligands: a strong band at 1993 cm^{-1} and a weak band at 2019 cm^{-1}. This d^6 metal complex was found to be a low-spin species. Our iron(II) derivative [Fe^{II}(TpivPP)(N_3)]$^-$ (with a d^6 configuration), shows, as was mentioned above, two $\nu_{as}(N_3)$ bands at 1996 cm^{-1} (the strongest) and 2024 cm^{-1} for the weak band. Thus, both azido d^6 metals (Fe^{2+} and Co^{3+}) complexes present very similar $\nu_{as}(N_3)$ values but the Fe(II) derivative, as will be shown by the molecular structure and by Mössbauer spectroscopy, is high-spin ($S = 2$).

3.2. Crystal structure

The structure of the [Na(2,2,2-crypt)][Fe^{II}(TpivPP)(N_3)] · $3C_6H_5Cl$ compound was determined at 223 K. Fig. 1 is an ORTEP diagram of the [Fe^{II}(TpivPP)(N_3)]$^-$ complex ion. The iron(II) atom is coordinated to the N_3^- ligand from the pocket side of the TpivPP porphyrin.

The coordinated azide ion is linear with a N9–N10–N11 angle value of 178.0(3)°, the two N–N distances are definitely inequivalent: N9–N10 and N10–N11 bond lengths are, respectively, 1.194(3) and 1.169(4) Å. This difference is not unusual and reflects one resonance form of bound azide. The Fe–azide plane makes a dihedral angle of 28.0(1)° with the plane define by Fe, N9 and N3. This value is smaller than the one found in the related iron(III)

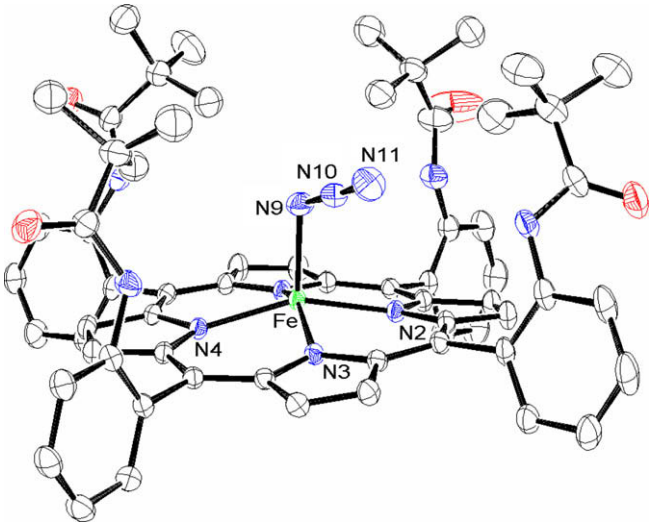


Fig. 1. ORTEP view of the ion complex [Fe^{II}(TpivPP)(N_3)]$^-$, thermal ellipsoids are drawn at the 30% probability level. Only the major positions of the disordered atoms are shown and hydrogen atoms have been omitted for clarity.

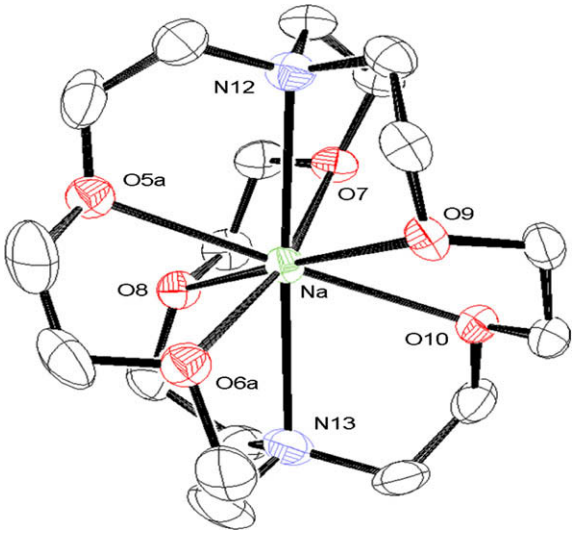


Fig. 2. ORTEP diagram of the [Na(2,2,2-crypt)]$^+$ cation. Thermal ellipsoids are drawn at the 30% probability level. Only the major positions of the disordered atoms are shown and hydrogen atoms have been omitted for clarity.

species [Fe^{III}(TPP)(N_3)$_2$]$^-$ (32°). The 116.8(2)° Fe–N9–N10 angle is significantly smaller than in either the five-coordinate [Fe^{III}(TPP)(N_3)] [15] species (121.8°) or the six-coordinate [Fe^{III}(TPP)(N_3)$_2$]$^-$ [3] ion complex (118.01°) but is within the range for the angle of a trigonally hybridized nitrogen. The negative charge of the [Fe^{II}(TpivPP)(N_3)]$^-$ anion is balanced by a [Na(2,2,2-crypt)]$^+$ counterion. An ORTEP drawing of this cation is given in Fig. 2. The eight-coordinate Na^+ ion is bonded to six O atoms and two N atoms. The average Na–O(2,2,2-crypt) distance is 2.500(3) Å, and the average Na–N(2,2,2-crypt) bond length is 2.760(3) Å.

As a consequence of the decreased charge, there is a small increase in the radius of Fe(II) compared to Fe(III), and this leads to increased bond lengths in the coordination group. Thus, the axial Fe–N(azide) bond length is 2.078(2) Å for our iron(II) species [Fe^{II}(TpivPP)(N_3)]$^-$, which is longer than those of all the reported iron(III) azido-porphyrin derivatives (see Table 4). The average equatorial Fe–N_p distance for the [Fe^{II}(TpivPP)(N_3)]$^-$ ion complex is 2.094(3) Å, and falls within the range found for five-coordinate high-spin iron(II) porphyrins (2.072–2.115 Å) [16]. This is a stereochemical proof that our synthetic compound is high-spin ($S = 2$). In order to accommodate the high-spin iron(II) atom, the porphinato cores undergo a significant radial expansion. This is very well illustrated by the long Fe–P_C (P_C = plane made by the 24-atom core of the porphyrin) and Fe–P_N (P_N = plane made by the four nitrogens of the porphyrin ring) distances shown by Fe(II) high-spin [Fe^{II}(Porph)(X)]$^-$ complexes (X is an anionic ligand). The values of these distances for the iron(II) azide species and for other iron porphyrinates are summarized in Table 4. As shown in Fig. 3, the porphyrin ring for [Fe^{II}(TpivPP)(N_3)]$^-$ exhibits a non-planar conformation that is domed and also shows major ruffling. The core conformation has also been analyzed by the normal structural decomposition (NSD) method provided by Shelnutt and co-workers [20]. These calculations confirm the major ruffling and doming distortions: *ruf* = 0.401 Å (~47%), *dom* = 0.190 Å (~22%), *sad* = 0.115 Å (~13%), *wav*(*x*) = 0.086 Å (~10%) and *wav*(*y*) = 0.069 Å (~8%) for a total out-plane-distortion D_{oop} = 0.471 Å.

3.3. Mössbauer spectrum

Fig. 4 represents the Mössbauer spectrum, taken at 20 K, of a sample of the azido-Fe(II) porphyrinate which shows one quadrupole doublet. The isomer shift (δ_{Fe}) and quadrupole splittings (ΔEq)

Table 4
Porphinato core parameters (Å) for selected Fe(III) high-spin ($S = 5/2$) and Fe(II) high-spin ($S = 2$) porphyrin complexes.

Complex	Fe–N_p[a]	Fe–X_L[b]	Fe–P_C[c]	Fe–P_N[d]	Spin S	Reference
Iron(III) complex						
$[Fe^{III}(TPP)(N_3)]$	2.066(3)	1.953(5)	–	–	5/2	[15]
$[Fe^{III}(OEP)(N_3)]$[e]	2.056(2)	1.9618(14)	–	–	5/2	[17]
$[Fe^{III}(TPP)(N_3)_2]^-$	2.010(4)	1.998(2)			(5/2, 1/2)	[3]
$[Fe^{III}(TTP)(OAc)]$[f]	2.067	1.898(4)	0.520	0.485	5/2	[18]
$[Fe^{III}(TpivPP)(NCO)]$	2.069(5)	1.970(5)	0.540(1)	0.486(1)	5/2	[19]
Iron(II) complex						
$[Fe^{II}(TpivPP)(N_3)]^-$	2.094(3)	2.078(2)	0.525	0.459	2	this work
$[Fe^{II}(TpivPP)(OAc)]^-$	2.107(2)	2.034(3)	0.64	0.55	2	[9]
$[Fe^{II}(TpivPP)(Cl)]^-$	2.108(15)	2.301(2)	0.59	0.53	2	[8]
$[Fe^{II}(TpivPP)(NO_3)]^-$	2.070(16)	2.069(4)	0.49	0.42	2	[12]

[a] Average equatorial iron–nitrogen pyrrole distance.
[b] Iron–axial ligand distance.
[c] Distance between the iron atom and the mean plane made by the 24-atom core of the porphyrin.
[d] Distance between the iron centre and the mean plane of the four pyrrole N atoms.
[e] OEP, octaethylporphyrin.
[f] TTP, tetratoluylporphyrin.

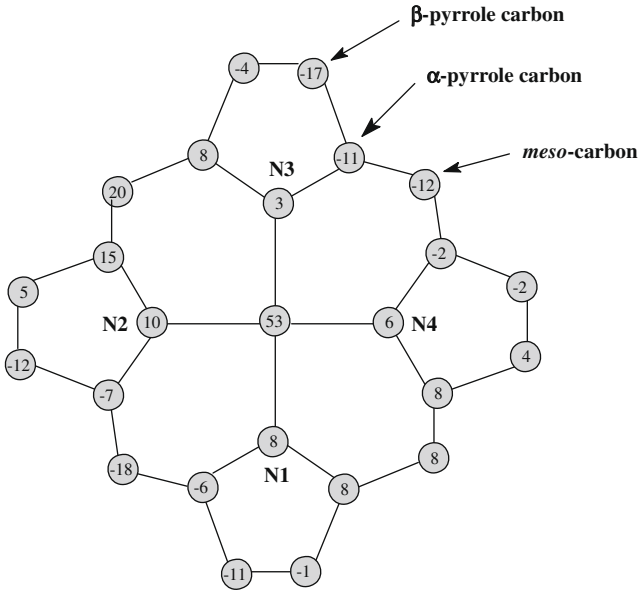


Fig. 3. Formal diagram of the porphinato core of $[Fe^{II}(TpivPP)(N_3)]^-$ illustrating the displacement, in units of 0.01 Å, of each atom from the mean plane of the 24-atom porphinato core. Positive values of displacement are toward the azide axial ligand.

values have been obtained by fitting these data to a set of two Lorentzian lines.

Mössbauer data for the complex ion $[Fe^{II}(TpivPP)(N_3)]^-$ are summarized in Table 5, along with some five-coordinated ferrous high-spin ($S = 2$) porphyrin complexes. As seen in this table, the ΔEq and δ_{Fe} values of the iron(II) azido-porphyrinate derivative are practically the same at 20, 77 and 150 K.

Porphyrin species with isomer shift values of ~0.8–1 mm/s are expected for high-spin iron(II) [21]. Indeed, the isomer shift for $[Fe^{II}(TpivPP)(N_3)]^-$ of 1.07 mm/s at 77 K strongly supports a high-spin-state assignment for this species. Previous studies (see Table 5) suggest that high-spin iron(II) porphyrinates of the general formula $[Fe^{II}(Porph)(X)]^-$, where X is a monodentate anionic ligand, have distinctively large quadrupole splittings (ΔEq ~ 3.5–4.5 mm/s). Indeed, the quadrupole splitting for $[Fe^{II}(TpivPP)(N_3)]^-$ of 4.22(1) mm/s (at 77 K) is consistent with their findings. These unusually large quadrupole splitting values arise from a significant bonding orbital contribution to the electric-field gradient from the anionic axial ligand, d_{xy} becomes the lowest d orbital in energy and

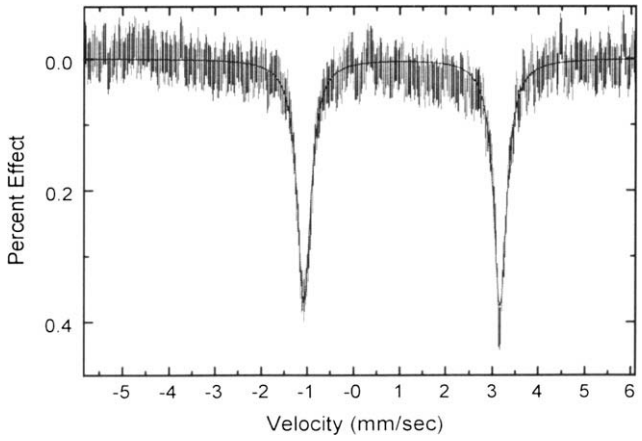


Fig. 4. Mössbauer spectrum of $[Fe^{II}(TpivPP)(N_3)]^-$ at 20 K in a weak applied field of 500 G.

Table 5
Mössbauer parameters for some five-coordinate high-spin ($S = 2$) iron(II) porphyrin complexes.

Complex	ΔEq (mm/s)	δ_{Fe} (mm/s)	T (K)	Reference
$[Fe^{II}(TpivPP)(N_3)]^-$	4.23(1)	1.08(1)	20	this work
	4.22(1)	1.07(1)	77	
	4.17(1)	1.04(1)	150	
$[Fe^{II}(TpivPP)(Cl)]^-$	4.36	1.01	77	[8]
$[Fe^{II}(TpivPP)(OMe)]^-$	3.64	1.00	77	[9]
$[Fe^{II}(TpivPP)(OAc)]^-$	4.19	1.03	77	[9]
$[Fe^{II}(TpivPP)(NO_3)]^-$	3.59	0.98	77	[12]

hence is doubly occupied. We believe that the electronic repulsion of the iron(II) in-plane d_{xy} orbital by the negative charge of the pyrrole nitrogens is thus expected to increase the magnitude of the iron atom displacement from the porphyrin plane with a concomitant increase in the values of the Fe–N_p, Fe–P_C and Fe–P_N distances, as is observed for our azido iron(II) porphyrin derivative.

4. Conclusion

The synthesis and characterization of the anionic iron(II) azido-porphyrin derivative, $[Na(2,2,2\text{-crypt})][Fe^{II}(TpivPP)(N_3)] \cdot 3C_6H_5Cl$, is described. Structural and Mössbauer data for this high-spin iron(II) species is consistent with a $(d_{xy})^2(d_{xz})^1(d_{yz})^1(d_{z^2})^1(d_{x^2-y^2})^1$

ground state electronic configuration. This study confirms the fact that the unusually large quadrupole splitting values found in the Mössbauer spectra for five-coordinate high-spin iron(II) $[Fe^{II}(Porph)(X)]^-$ species are structurally related to the large out-of-plane Fe displacement and the concomitant long $Fe–N_p$ bond lengths.

Acknowledgement

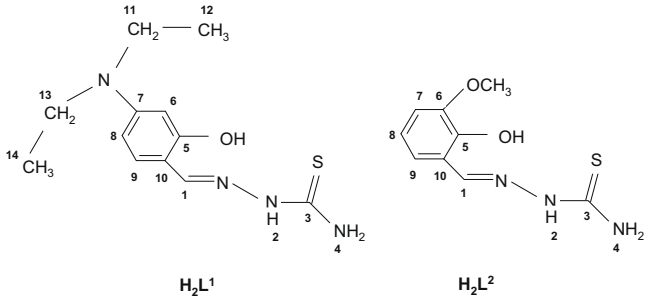
We gratefully acknowledge Prof. W.R. Scheidt, from the University of Notre Dame, 46556 Notre Dame IN, USA, for the gift of the cryptand-222.

Appendix A. Supplementary data

CCDC 680459 contains the supplementary crystallographic data for this paper. These data can be obtained free of charge via http://www.ccdc.cam.ac.uk/conts/retrieving.html, or from the Cambridge Crystallographic Data Centre, 12 Union Road, Cambridge CB2 1EZ, UK; fax: (+44) 1223-336-033; or e-mail: deposit@ccdc.cam.ac.uk. Supplementary data associated with this article can be found, in the online version, at doi:10.1016/j.poly.2008.12.054.

References

[1] C. Hu, A. Roth, M.K. Ellison, J. An, CM. Ellis, C.E. Schulz, W.R. Scheidt, J. Am. Chem. Soc. 127 (2005) 5675. and references cited therein.
[2] C. Hu, B.C. Noll, C.E. Schulz, W.R. Scheidt, J. Am. Chem. Soc. 127 (2005) 15018.
[3] M.K. Ellison, H. Nasri, Y.-M. Xia, J.-C. Marchon, C.E. Schulz, P.G. Debrunner, W.R. Scheidt, Inorg. Chem. 36 (1997) 4804. and references cited therein.
[4] A. Gismelseed, E.I. Bill, A.X. Trautwein, H. Winkler, H. Nasri, P. Doppelt, D. Mandon, J. Fischer, R. Weiss, Inorg. Chem. 29 (1990) 2741.
[5] Z. Otwinowski, W. Minor, Processing of X-rays diffraction data collected in oscillation mode, Methods in enzymology, in: C.W. Carter Jr., R.M. Sweet (Eds.), Macromolecular Crystallography, Part A, vol. 276C, Academic Press, New York, 1997, p. 307.
[6] M.C. Burla, R. Calinandro, M. Camalli, B. Carrozzini, G.L. Cascarano, L. De Caro, C. Giacovazzo, G. Polidori, R. Spagna, J. Appl. Crystallogr. 38 (2005) 381.
[7] G.M. Scheldrick, SHELXL-97, Program for Crystal Structure Refinement, Göttingen, 1997.
[8] M. Schappacher, L. Ricard, R. Weiss, Inorg. Chem. Acta (1983) L9.
[9] H. Nasri, J. Fischer, R. Weiss, J. Am. Chem. Soc. 109 (1987) 2549.
[10] H. Nasri, M.K. Ellison, C. Krebs, H.B. Scheidt, W.R. Scheidt, J. Am. Chem. Soc. 122 (2000) 10795.
[11] H. Ben Abbes, H. Nasri, unpublished results.
[12] H. Nasri, M.K. Ellison, B. Shaevitz, G.P. Gupta, W.R. Scheidt, Inorg. Chem. 45 (2006) 5284.
[13] S. McCoy, W.S. Caughey, Biochemistry 9 (1970) 2387.
[14] B. Bel Haj, M.S. Belkhiria, M. Giorgi, H. Nasri, unpublished results.
[15] Y. Zhang, W.A. Hallows, W.J. Ryan, J.G. Jones, G.B. Carpenter, D.A. Sweigart, Inorg. Chem. 33 (1994) 3306.
[16] (a) W.R. Scheidt, C.A. Reed, Chem. Rev. 81 (1981) 543;
(b) W.R. Scheidt, in: K.L. Kadish, K.M. Smith, R. Guilard (Eds.), The Porphyrin Handbook, vol. 3, Academic Press, 2000, p. 49.
[17] W.R. Scheidt, unpublished results.
[18] H. Oumous, C. Lecombe, J. Protas, P. Cocolios, R. Guilard, Polyhedron 3 (1984) 651.
[19] M.S. Belkhiria, M. Dhifet, H. Nasri, J. Porphyrins Phthalocyanines 9 (2005) 575.
[20] W. Jensen, J.-G. Ma, J.A. Shelnutt, Biophys. J. 74 (1998) 753.
[21] P.G. Debrunner, in: A.B.P. Lever, H.B. Gray (Eds.), Iron Porphyrin, Part 3, Academic Press, New York, 1983 (Chapter 2).



Scheme 1. Thiosemicarbazonato ligands used in the reactions.

2.2. IR spectra

All IR spectra were recorded as KBr pellets using a Perkin–Elmer Fourier-Transform Spectrum RX1 spectrophotometer in the region 4500–450 cm^{-1}.

2.3. Thermogravimetric analyses

All experiments were performed on a Mettler TG 50 thermobalance using aluminum crucibles under oxygen atmosphere with a heating rate of 5 °C min^{-1}. For all experiments the temperature ranged from 25 to 600 °C. The results were developed by applying the Mettler STAR^e 6.1. program.

Elemental analyses, yields, selected IR and thermal analysis data are given in Tables 1 and 2.

2.4. NMR experiment

All one-dimensional (^{1}H and APT) and gradient-selected two-dimensional (gCOSY, gHSQC and gHMBC) NMR spectra were recorded at ambient temperature on Bruker Avance DRX500 and Bruker Avance DPX 300 spectrometers equipped with a 5 mm inverse detection probe and a dual probe, respectively. The sample concentration in DMSO–d_6 was 20 mg ml^{-1}. TMS was used as the internal standard. The typical spectral conditions for one-dimensional ^{1}H and ^{13}C (APT) spectra were as follows. The spectra were recorded using 64 K data points and spectral widths of 7700 Hz and 32 000 Hz for ^{1}H and ^{13}C experiments, respectively. Digital resolution was 0.12 and 0.48 Hz per point, respectively. The number of scans was 16 for ^{1}H and 500–1000 for APT spectra. The COSY spectra were recorded under the following conditions: spectral width was 7700 Hz in both dimensions, 2 K data points were applied in the time domain and 512 increments were collected for each data set with linear prediction and zero filling to 2 K. Eight scans were applied for each increment. The digital resolution was 6.50 Hz per point in both dimensions. The gradient-selected inverse ^{1}H–^{13}C correlation experiments, gHSQC and gHMBC were recorded using the acquisition matrix of 1 K × 256 with 16 and 32 scans, respectively, and processed with a 2 K × 1 K transformed matrix. The spectral width was 6600 Hz in f2 dimension and 32000 Hz in f1 dimension for both experiments. The digital resolution was 3.25 Hz per point and 30.70 Hz per point in f2 and f1, respectively. HMBC spectra were recorded using a low-pass *J*-filter (3.4 s) and a delay for long-range coupling of 65 ms.

The NMR data of complexes are given in Table 3.

Table 1
Analytical and spectral data for the $[MoO_2LD]$ and $[(MoO_2L)_2bpy]$ complexes.

Formula (Mr)		Color	Analysis found (calculated)						Selected IR data (cm^{-1})		
			%C	%H	%N	%S	%Mo	Yield (%)	C=N	Mo–O	C–O
$[MoO_2(C_{12}H_{16}N_4OS)(C_5H_5N)]$ (471.39)	**1a**	dark red	43.03 (43.32)	4.70 (4.49)	14.76 (14.86)	7.01 (6.80)	20.12 (20.35)	66	1607 1570	920 892	1510
$[MoO_2(C_{12}H_{16}N_4OS)(C_6H_7N)]$ (485.42)	**1b**	dark red	44.31 (44.54)	4.31 (4.78)	14.03 (14.43)	6.52 (6.61)	20.15 (19.76)	81	1613 1578	932 902	1512
$[MoO_2(C_{12}H_{16}N_4OS)(C_3H_4N_2)]$ (460.37)	**1c**	dark red	38.66 (39.13)	4.39 (4.38)	17.82 (18.26)	7.07 (6.97)	21.01 (20.84)	51	1613 1581	923 898	1512
$[\{MoO_2(C_{12}H_{16}N_4OS)\}_2(C_{10}H_8N_2)]$ (940.77)	**1d**	dark red	42.72 (43.41)	4.59 (4.29)	14.36 (14.89)	6.54 (6.82)	20.15 (20.40)	72	1613 1579	933 901	1512
$[MoO_2(C_9H_9N_3O_2S)(C_5H_5N)]$ (430.29)	**2a**	light orange	39.18 (39.08)	3.39 (3.28)	13.01 (13.02)	7.57 (7.45)	21.98 (22.30)	71	1599 1562	927 903	1513
$[MoO_2(C_9H_9N_3O_2S)(C_6H_7N)]$ (444.32)	**2b**	orange	40.39 (40.55)	3.49 (3.63)	12.50 (12.61)	7.29 (7.22)	21.40 (21.59)	26	1596 1560	932 904	1507
$[MoO_2(C_9H_9N_3O_2S)(C_3H_4N_2)]$ (419.27)	**2c**	orange	34.24 (34.38)	3.15 (3.13)	16.56 (16.70)	7.69 (7.65)	23.00 (22.88)	67	1592 1562	925 896	1518
$[\{MoO_2(C_9H_9N_3O_2S)\}_2(C_{10}H_8N_2)]$ (858.56)	**2d**	dark red	38.98 (39.17)	3.42 (3.05)	12.84 (13.05)	7.46 (7.47)	22.61 (22.35)	36	1608 1563	922 897	1525

Table 2
Thermoanalytical data for the $[MoO_2LD]$ and $[(MoO_2L)_2bpy]$ complexes.

Formula	Complex	Loss of N-donor			Decomposition		
		Temperature range (°C)	Δm (%) found	(calculated)	Temperature range (°C)	Δm (%) found	(calculated)
$[MoO_2(C_{12}H_{16}N_4OS)(C_5H_5N)]$	**1a**	101–153	16.24	(16.78)	219–489	51.90	(52.22)
$[MoO_2(C_{12}H_{16}N_4OS)(C_6H_8N)]$	**1b**	159–193	19.10	(19.30)	232–463	51.41	(51.05)
$[MoO_2(C_{12}H_{16}N_4OS)(C_3H_4N_2)]$	**1c**				188–504	69.14	(68.73)
$[\{MoO_2(C_{12}H_{16}N_4OS)\}_2(C_{10}H_8N_2)]$	**1d**				196–512	69.77	(69.40)
$[MoO_2(C_9H_9N_3O_2S)(C_5H_5N)]$	**2a**	169–206	18.13	(18.38)	251–470	48.40	(48.20)
$[MoO_2(C_9H_9N_3O_2S)(C_6H_8N)]$	**2b**	163–197	20.73	(20.96)	253–487	46.54	(46.65)
$[MoO_2(C_9H_9N_3O_2S)(C_3H_4N_2)]$	**2c**				199–511	65.96	(65.67)
$[\{MoO_2(C_9H_9N_3O_2S)\}_2(C_{10}H_8N_2)]$	**2d**				198–530	65.87	(66.47)

Table 3
^1H and ^{13}C chemical shifts (ppm) of the ligands H_2L^1 and H_2L^2 and their molybdenum(VI) complexes **1** and **2**.

Compound atom	H_2L^1		**1**		H_2L^2		**2**	
	^1H	^{13}C	^1H	^{13}C	^1H	^{13}C	^1H	^{13}C
1	8.19 (s)	142.45	8.21 (s)	151.19	8.40 (s)	139.83	8.43 (s)	150.47
2	11.07 (s)				11.39 (s)			
3		176.55		162.60		178.05		166.01
4	7.87 (s)		6.66 (s)		8.10 (s)			
	7.66 (s)				7.88 (s)			
5		158.26		160.38		146.34		148.57
6	6.09 (s)	97.40	6.06 (s)	98.64		148.26		148.16
7		150.20		151.88	6.96 (dd)	113.19	7.10 (dd)	115.15
8	6.21 (d)	104.08	6.34 (d)	105.18	6.77 (t)	119.33	6.92 (t)	120.37
9	7.52 (d)	129.12	7.28 (d)	134.60	7.53 (dd)	118.52	7.15 (dd)	124.41
10		107.51		108.96		121.14		121.20
11	3.33 (q)	43.94	3.70 (q)	43.84	3.81 (s)	56.25	3.77 (s)	55.60
12	1.10 (t)	12.69	1.10 (t)	12.47				
13								
14								
OH	9.61 (s)				9.17 (s)			

2.5. Reagents and apparatus for spectrophotometric determination of molybdenum

An aqueous solution of ammonium molybdate (c = 0.01 mol L^{-1}) was standardized gravimetrically with 8-hydroxyquinoline [6]. Working samples of lower concentrations were prepared by diluting aliquots of the stock solution. Cationic surfactants (benzethonium chloride (hyamine), cetyltrimethylammonium bromide (CTMA) or cetylpyridinium chloride (CPC)) were dissolved in reagent grade chloroform. All chemicals used were of the p.a. purity grade. A Varian double-beam spectrophotometer, Model Cary 3, equipped with 1-cm quartz cells, was used to determine absorption spectra and perform absorbance measurements. A Griffin flask shaker with a time switch served for extraction.

2.6. X-ray crystallography

Data were collected on an Oxford Diffraction Xcalibur CCD diffractometer with graphite-monochromated Mo K_α radiation at 293 K. Details of data collection and crystal structure refinement are presented in Table 4.

Programs CRYSALIS CCD and CRYSALIS RED [7] were employed for data collection, cell refinement and data reduction. The structures were solved by direct methods. The refinement procedure by full-matrix least squares methods based on F^2 values against all reflections included anisotropic displacement parameters for all non-H atoms. Calculations were performed with SHELXS97 [8] and SHELXL97 [9] (both operating under the WINGX [10] program package). Geometry calculations were done using PLATON [11] and PARST [12], and the molecular graphics were done with ORTEP [13] and MERCURY [14]. Selected bond distances and valence angles are listed in Table 5.

2.6.1. General procedure for the synthesis of $[MoO_2LD]$ D = pyridine (**1a** and **2a**) or γ-picoline (**1b** and **2b**) or imidazole (**1c** and **2c**)

The complex $[MoO_2(C_{12}H_{16}N_4OS)]_n$ (**1**) or $[MoO_2(C_9H_{11}N_3O_2S)]_n$ (**2**) (0.26 mmol) was suspended in dry methanol (10 mL) and an appropriate amine (pyridine, γ-picoline or imidazole) (2 mmol) was added in excess. The mixture was heated for 2 h. The solution was evaporated to one third of its volume under reduced pressure and left for 5–7 days at room temperature. The obtained products were filtered off, washed with tetrachloromethane and dried.

Table 4
Crystallographic data for compounds **2a**, **2b** and **2c**.

	2a	**2b**	**2c**
Empirical formula	$C_{14}H_{14}MoN_4O_4S$	$C_{15}H_{16}MoN_4O_4S$	$C_{12}H_{12}MoN_5O_4S$
Formula weight	430.29	444.32	418.27
Crystal system	monoclinic	monoclinic	triclinic
Space group	$P2_1/n$	$P2_1/n$	$P\bar{1}$
Unit cell dimensions			
a (Å)	10.7619(16)	10.9868(5)	7.0611(12)
b (Å)	14.545(2)	13.9059(5)	9.2401(16)
c (Å)	11.1880(16)	11.5416(5)	11.897(2)
α (°)	90.00	90.00	85.103(14)
β (°)	110.765(14)	107.299(5)	88.414(14)
γ (°)	90.00	90.00	81.410(14)
V (Å^3)	1630.7(4)	1683.58(12)	764.6(2)
Z	4	4	2
D_{calc} (g cm^{-3})	1.753	1.753	1.817
μ (mm^{-1})	0.959	0.932	1.022
$F(000)$	864	896	418
Reflections collected/unique	10500/3011	15036/5306	5040/2679
Data/restraints/parameters	3011/0/218	5306/0/226	2679/0/208
Goodness-of-fit on F^2	1.096	1.078	1.086
R/wR $[I > 2\sigma(I)]$[a]	0.0523/0.0719	0.0355/0.0848	0.0293/0.0652
Largest difference peak and hole (e Å^3)	0.579 and −0.480	1.249 and −0.626	0.548 and −0.363

[a] $R = \sum||F_o| - |F_c||/\sum F_o$, $w = 1/[\sigma^2(F_o^2)+(g_1P)^2 + g_2P]$ where $P = (F_o^2 + 2F_c^2)/3$, $S = \Sigma[w(F_o^2 - F_c^2)^2/(N_{obs} - N_{param})]^{1/2}$.

Table 5
Selected bond lengths (Å) and angles (°).

	2a	2b	2c
Mo1–O1	1.707(3)	1.7087(16)	1.702(2)
Mo1–O2	1.703(4)	1.7082(16)	1.710(2)
Mo1–O3	1.967(3)	1.9582(15)	1.9589(19)
Mo1–N3	2.309(4)	2.3151(16)	2.304(3)
Mo1–S1	2.4316(14)	2.4513(5)	2.4334(10)
Mo1–N4	2.456(4)	2.4123(19)	2.344(2)
O1–Mo1–O2	105.90(18)	105.58(8)	105.71(11)
O1–Mo1–O3	106.52(16)	103.48(7)	106.38(10)
O1–Mo1–N3	162.33(16)	165.24(7)	160.37(10)
O1–Mo1–N4	83.56(16)	84.52(8)	86.21(10)
O1–Mo1–S1	90.53(14)	93.10(6)	91.60(8)
O2–Mo1–O3	97.67(17)	100.17(7)	95.83(9)
O2–Mo1–N3	88.25(16)	86.35(7)	90.42(10)
O2–Mo1–N4	170.06(15)	169.87(7)	167.81(10)
O2–Mo1–S1	101.00(14)	98.00(6)	96.93(8)
O3–Mo1–N3	81.38(13)	82.43(6)	82.49(9)
O3–Mo1–N4	76.32(14)	77.71(6)	77.98(8)
O3–Mo1–S1	150.15(11)	150.99(5)	154.18(6)
N3–Mo1–N4	83.04(13)	83.55(6)	78.44(9)
N3–Mo1–S1	76.15(10)	76.36(4)	75.08(7)
N4–Mo1–S1	81.63(10)	80.43(4)	85.06(7)

*2.6.2. General procedure for synthesis of [{MoO_2L}$_2$ D] D = bpy (**1d** and **2d**)*

The complex $[MoO_2(C_{12}H_{16}N_4OS)]_n$ (**1**) or $[MoO_2(C_9H_{11}N_3O_2S)]_n$ (**2**) (0.26 mmol) was suspended in dry ethanol (10 mL) and 4,4′-bipyridine (0.16 mmol) was added. The mixture was warmed up for 2 h. The solution was evaporated to one third of its volume under reduced pressure and left for several days at room temperature. The obtained products were filtered off, washed with tetrachloromethane and dried.

2.6.3. Procedure for spectrophotometric determination of molybdenum

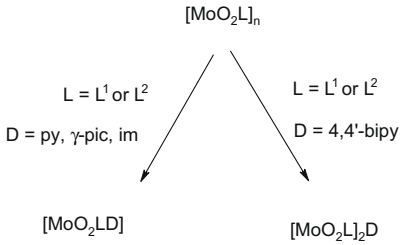
The solution for spectrophotometric determination of molybdenum was obtained by wet ashing. An appropriate amount of the thiosemicarbazonato complexes containing 2–5 mg of molybdenum was weighed and transferred to a Kjeldahl flask. Concentrated sulfuric acid (1–2 cm^3) and a few drops of concentrated nitric acid were added and the solution was heated slowly at the beginning with constant swirling, and then it was boiled. The addition of concentrated nitric acid was repeated until all organic matter completely decomposed. After cooling, the digest was quantitatively transferred into a volumetric flask.

To an aliquot of solution containing the $Mo^{VI}O_2^{2+}$ ion (1×10^{-5} mol L^{-1}), hydrochloric acid, ascorbic acid and potassium thiocyanate were added in amounts to achieve the desired conditions in a final volume of 5 mL (HCl, 2 mol L^{-1}; ascorbic acid, 2%; KSCN, 0.2–0.6 mol L^{-1}). After 20 min, a solution of the cationic surfactant cetylpyridinium chloride (CPC) in chloroform (5.0 mL) was added in excess (molar ratio 1:200) to the previously prepared aqueous solution. Both phases were shaken with a mechanical shaker for 20 min and after separation of the phases the resulting solution was used for spectrophotometric determination of molybdenum. The absorbance of the organic phase was measured at 465 nm against a reagent blank prepared under the same experimental conditions.

3. Results and discussion

3.1. Synthesis of the complexes

New mononuclear [MoO_2L(py)] (**1a** and **2a**), [MoO_2L(γ-pic)] (**2a** and **2b**) and [MoO_2L(im)] (**1c** and **2c**) and dinuclear [{MoO_2L}$_2$D] (**1d** and **2d**) molybdenum(VI) complexes were obtained by the reaction of polimeric $[MoO_2L]_n$ (**1** or **2**) thiosemicarbazonato complexes with an appropriate amine (pyridine, γ-picoline, imidazole or 4,4′-bipyridine) (Scheme 2). In all the isolated complexes the thiosemicarbazonato ligands are coordinated to molybdenum as tridentate *ONS*-donors through phenolic–oxygen, imine–nitrogen and thiol–sulfur. The octahedral coordination around the Mo atom is completed by a N-donor molecule. The IR spectra of all the complexes showed a doublet characteristic of the presence of the *cis*-MoO_2 group in the range 892–932 cm^{-1}. Absence of an intensive band in the region 850–800 cm^{-1} in the spectra of the dinuclear complexes (**1d** and **2d**) indicates that the [{MoO_2L}$_2$D] complexes are formed by a simple linkage of two mononuclear species through the bridging 4,4′-bypiridine ligand ($LO_2Mo–NC_5H_5–C_5H_5N–MoO_2L$), and not *via* metal–oxygen bridging. The stretching frequencies found in that region in the IR spectra of **1d** and **2d** have a very small intensity and are not characteristic of the presence of a Mo_2O_b group [15]. All other frequencies characteristic for coordinated thiosemicarbazonato ligands are in accordance to the literature data [16] and are given in the Table 1.



Scheme 2. Reactions of polymeric $[MoO_2L]_n$ and amine, pyridine (py), γ-picoline γ-pic), imidazole (im) and 4,4′-bipyridine (bpy).

The thermal analysis data (Table 2) of the mononuclear complexes [MoO_2L(py)] (**1a** and **2a**) and [MoO_2L(γ-pic)] (**2a** and **2b**) exhibit two main processes. The first step is related to the loss of the coordinated N-donor molecule and conversion into stable species of the formula [MoO_2L]. The second step is associated with complex decomposition resulting in a solid residue identified as MoO_3. The decomposition of the complexes coordinated with imidazole [MoO_2L(im)] (**1c** and **2c**) or 4,4′-bipyridine [{MoO_2L}$_2$D] (**1d** and **2d**), proceeded without a stable intermediate product.

3.2. Structural studies

The structures of **2a**, **2b** and **2c** are shown in Fig. 1. In all the compounds the molybdenum atom has a distorted octahedral coordination, with two oxo groups *cis* to each other and the doubly deprotonated tridentate ligand equatorially oriented *via* O, N and S atoms. The octahedral coordination is completed by the N atom of the donor molecule (pyridine, γ-picoline or imidazole, in **2a**, **2b** and **2c**, respectively).

The interatomic distances Mo1–O1 and Mo1–O2 (Table 5) are typical of Mo–O double bonds. The corresponding bond angles O1–Mo1–O2 (which are significantly larger than 90°) indicate the greater repulsion between two oxygen atoms closely attached to the central metal atom. Repulsion between the terminal oxo atoms is accompanied by a contraction of the opposite angle N3–Mo1–N4. Values of the other coordination angles are in agreement with those found in similar structures [17,18], and with the fact that the ligand geometry, together with the donor atom size, has an influence on the final angle value. Such a sterically crowded environment in all the complexes causes a shift of the molybdenum atom from the equatorial plane towards the O2 atom (distances from the mean plane defined by S1, N3, O1 and O3 range from 0.2815(3) to 0.3439(5) Å). Also, the other bond distances of Mo1–S1, Mo1–O3 and Mo1–N3 resemble those found in other (similar) thiosemicarbazonato molybdenum complexes [4,5,19]. Owing to

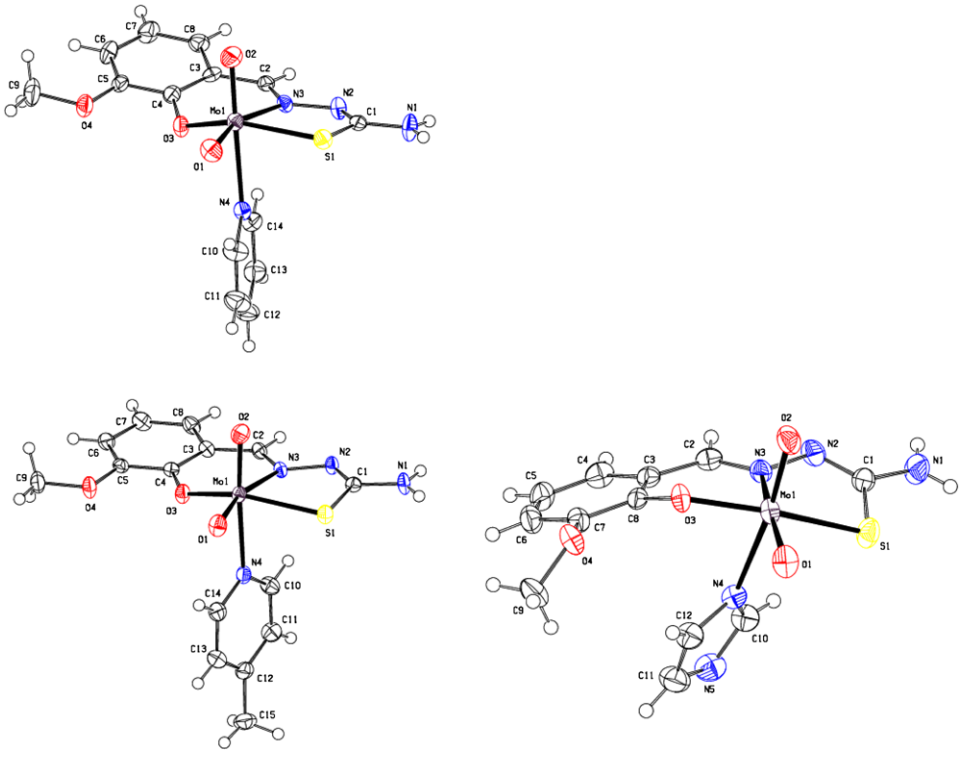


Fig. 1. View of the molecular structures of **2a**, **2b** and **2c** with the atom labelling scheme. Thermal ellipsoids are shown at the 50% probability level.

the *trans* influence of the terminal oxo ligands, the Mo–N4 bond from the amine donor ligand and the Mo–N3 bond from the thiosemicarbazonato ligand are longer than Mo–N bonds that are not under such an influence. A Cambridge Structural Database [20] survey gave 31 structures with similar *NOS* donors and with M=O *trans* to the Mo–N bond. The Mo-N bond lengths in those structures are in the range 2.224–2.325 Å. In contrast, the Mo–N bond distance is in the range 2.115–2.180 Å when the *trans* effect is not present (3 hits). The Mo–N bond to pyridine, γ-picoline or imidazole ligands is always longer, ranging from 2.372 to 2.475 Å in nine structures.

Ligand deprotonation and chelation causes the collapse of the intramolecular O–H···O and N–H···N hydrogen bonds which contribute to the planarity of the molecular skeleton (compared with the free ligand form in the solid state) [21]. As in many previously described cases, the *trans* configuration of the S1 atoms with respect to N3 changes upon chelation into a *cis* configuration [18,19]. In addition, the *cis* configuration of the N1 atom with respect to N3, which favors an intramolecular hydrogen bond in the free ligand form, changes to a *trans* configuration. This event is also associated with rotation around the C1–N2 and C2–C3 bonds together with lengthening of the C1–S1, C1–N1, N2–N3, C2–N3 and C3–C4 bonds and shortening of the C1–N2, C2–C3 and C4–O3 bonds in comparison with the ligand in the free form [19]. Other bond lengths and angles within the bound ligand are in agreement with the fact that, upon complexation to the metal atom, the system of conjugated bonds extends over the five- and six-membered chelate heterocycles. The conformations of the five-membered chelate rings in **2b** and **2c** are very flat envelopes on Mo1, whereas in **2a** the five-membered ring is planar. The six-membered chelate rings are found to be more puckered, with conformations near to envelope on Mo1 in **2a**, half-boat in **2b** and with the conformation close to screw-boat in **2c** (with Mo1 and O3 atoms found on the opposite sides of the mean plane [22,23]. The bound ligand in **2a** and **2c** is not planar. The angles between the planes of the salycilaldiminic and thiosemicarbazone

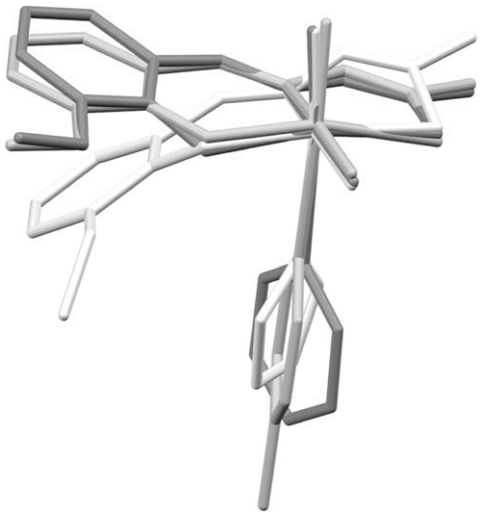


Fig. 2. Superposition of the molecules of **2a** (dark grey), **2b** (grey) and **2c** (light grey).

parts of the ligand [18.36(10)° and 32.93(6)° in **2a** and **2c**, respectively] indicate non-planarity of the ligand. These two planes are mutually coplanar in **2b**. Fig. 2 depicts the conformational changes between the molecules of **2a**, **2b** and **2c**.

The crystal structures of all the complexes are characterized with strong hydrogen bonding interactions of the N–H···N type. This type of structural motif, denoted with the graph-set notation $R_2^2(8)$ [24] is very usual in crystal structures of salicylthiosemicarbazone derivatives, as well as in their complexes. In addition to that, a great variety of weaker intermolecular interactions of the N–H···O, C–H···O, T shaped N–H···π and π···π type (Figs. 3–5) is also present.

In the crystal structure of **2a**, centrosymmetric dimers are held together by strong N–H···N^{i} (i = $x - 1/2$, $-y$, $1 - z$) hydrogen bonds

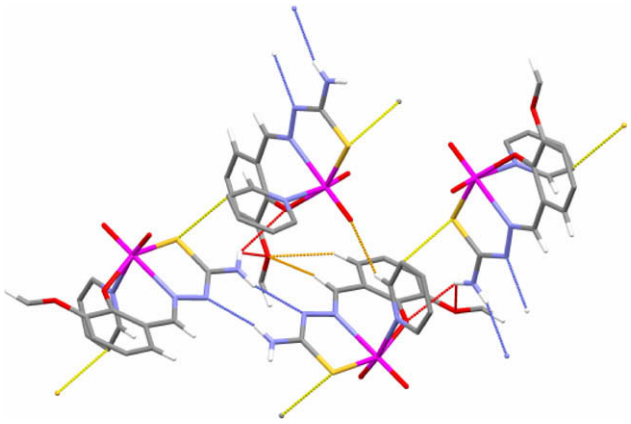


Fig. 3. Intermolecular interactions in **2a** are shown by dashed lines: N–H···N are blue, C···S yellow, N–H···O red and C–H···O orange colored. The molecules are projected down the [1 0 1] direction. (For interpretation of the references to color in this figure legend, the reader is referred to the web version of this article.)

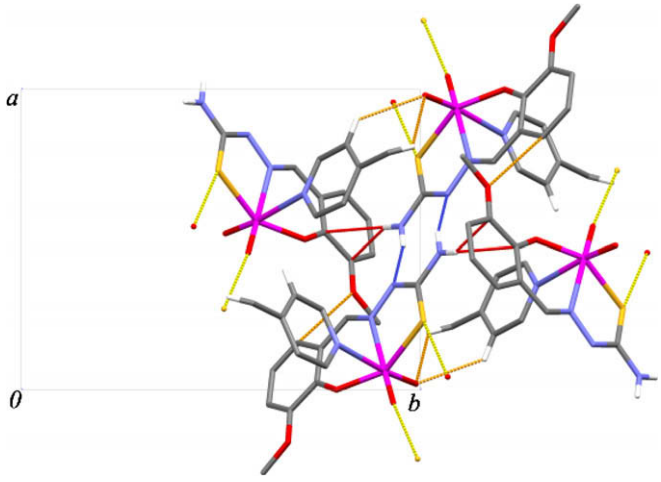


Fig. 4. Crystal packing of **2b**. The same color scheme as in Fig. 2 is applied, except that O···S is now yellow. The molecules are projected down the crystallographic *c*-axis. (For interpretation of the references to color in this figure legend, the reader is referred to the web version of this article.)

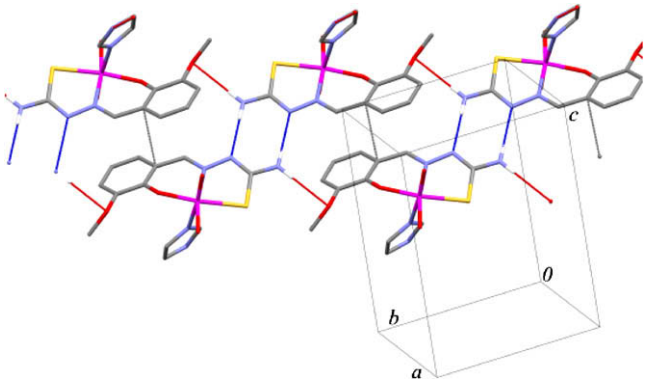


Fig. 5. Crystal packing of (**2c**). Same color scheme as in Fig. 2 is applied.

of the $R_2^2(8)$ type. Such dimers are further connected through N–H···O, C–H···O and S···π interactions forming zig-zag-like sheets of molecules with relatively close H···H contacts (Table 6, Fig. 3).

Table 6
Hydrogen bonding geometry in structures **2a**, **2b** and **2c**.

D–H···A	*d*(D–H) (Å)	*d*(H···A) (Å)	*d*(D···A) (Å)	∠(D–H···A) (°)
Compound ***2a***				
N1–H1A···N2^{i}	0.86	2.27	3.104(6)	164
N1–H1B···O3^{ii}	0.86	2.47	3.153(5)	136
N1–H1B···O4^{ii}	0.86	2.60	3.181(6)	126
C14–H14···O2^{iii}	0.93	2.48	3.267(6)	142
Compound ***2b***				
Nl–H1A···N2^{iv}	0.86	2.30	3.126(3)	161
C8–H8···O4^{V}	0.93	2.51	3.215(3)	133
C9–H9A···O2^{vi}	0.96	2.49	3.085(4)	120
C11–H1···O2^{vii}	0.93	2.56	3.260(4)	132
C15–H15C···O2^{viii}	0.96	2.52	3.203(5)	128
Compound ***2c***				
Nl–H1A···N2^{ix}	0.86	2.14	2.996(4)	174
N1–H1B···O4^{X}	0.86	2.47	3.165(4)	139
C9–H9C···O2^{xi}	0.96	2.36	3.249(4)	154
C12–H12···O1^{xii}	0.93	2.51	3.404(4)	161

Symmetry codes: i = l − *x*, −*y*, 1 − *z*; ii = 3/2 − *x*, −1/2 + *y*, 3/2 − *z*; iii = −1/2 + x, 1/2 − *y*, −1/2 + *z*; iv = l − *x*, 2 − *y*, 1 − *z*; v = 1/2 + *x*, 3/2 − *y*, 1/2 + *z*; vi = −1/2 − *x*, −1/2 + *y*, 1/2 − *z*: vii = 1/2 − *x*, −l/2 + *y*, 1/2 − *z*; viii = 1/2 + *x*, 3/2 − *y*, −1/2 + *z*, ix = 2 − *x*, 1 − *y*, 2 − *z*; *x* = 1 + *x*, −1 + *y*, *z*; xi = *x*, 1 + *y*, *z*; xii = l − *x*, 2 − *y*, 1 − *z*.

Similarly to **2a**, in the crystal structure of **2b**, there are also centrosymmetric dimers connected by weak hydrogen bonds of the N–H···N^{ii} type (ii = 1 − *x*, 2 − *y*, 1 − *z*). Chains of dimers are held together by van der Waals O···S contacts, similar to those found in the literature [25]. Like in the crystal structure of **2c**, one of the hydrogen atoms bound to N1 (the one not involved in N–H···N hydrogen bonding) is involved in T shaped N–H···π interactions, which together with the C–H···O interactions form a three dimensional network (Table 6, Fig. 4).

Molecules in the crystal structure of **2c**, like in the previously described structures, are connected with strong N–H···N hydrogen bonds forming dimers which are arrayed into chains through π···π stacking interactions. Single chains are held together by weaker interactions of the van der Waals (N···O) and C–H···O type (Table 6, Fig. 5).

3.3. NMR spectroscopy

The complete ^{1}H and ^{13}C atom assignments in DMSO–d_6 were made on the basis of the combined use of several one-dimensional (^{1}H and APT sequences) and two-dimensional homo- and heteronuclear experiments (COSY, HSQC and HMBC sequences). The proton and carbon chemical shifts of the ligands H_2L^1 and H_2L^2 (Scheme 1) and the polymeric complexes **1** and **2** are given in Table 3. The observed chemical shift values are similar to those reported previously for the related thiosemicarbazone ligands and their molybdenum(VI) complexes [4,5].

3.4. Spectrophotometric measurements

After decomposition of each molybdenum(VI) complex and addition of hydrochloric acid, the obtained solution containing the $Mo^{VI}O_2^{2+}$ ion was reduced to $[Mo^{V}O(SCN)_4]^-$ by addition of potassium thiocyanate and ascorbic acid. The formed thiocyanato molybdenum(V) complex was extracted using an excess of the extractant in chloroform. Three cationic surfactants were used to study the extraction behavior of the thiocyanato molybdenum(V) complex: benzethonium chloride (hyamine), cetyltrimethylammonium bromide (CTMA) or cetylpyridinium chloride (CPC). Among them CPC had the highest sensitivity and was selected for the study.

The optimum conditions for extractions of the thiocyanato molybdenum(V) complex (1×10^{-5} mol L^{-1}) were found to be:

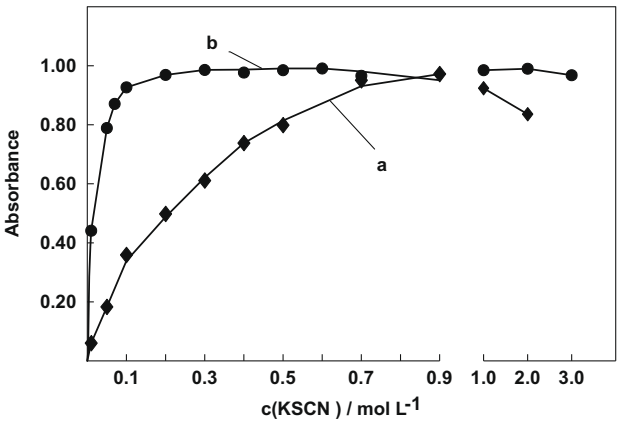


Fig. 6. The dependence of the absorbance of the $[MoO(SCN)_4]^-$ complex on thiocyanate concentration after extraction in the organic phase: (a) without ascorbic acid and (b) in the presence of 2% ascorbic acid.

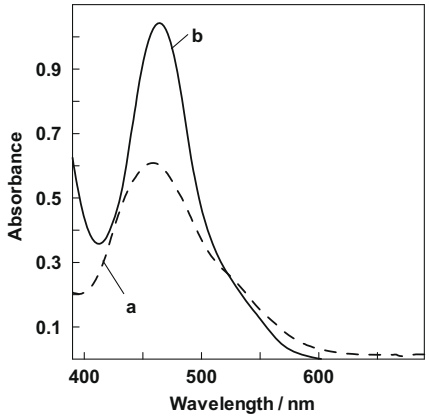


Fig. 7. Absorption spectra of the $[MoO(SCN)_4]^-$ complex *vs* reagent blank: (a) in water and (b) in chloroform after extraction with CPC.

2 mol L^{-1} hydrochloric acid, 2% solution ascorbic acid and an excess of CPC (molar ratio of at least 200:1). For the maximal and constant absorbances the required concentration of potassium thiocyanate depends on the presence of the reducing agent: the concentration was 0.2–0.6 mol L^{-1} in presence of 2% ascorbic acid, whereas in its absence the concentration was 0.9 mol L^{-1} (Fig. 6).

The composition of the ion pair formed by CPC and the thiocyanato molybdenum(V) complex was confirmed spectrophotometrically in the organic phase. The results obtained by the Job's method of continuous variation showed that the molar ratio of the cationic surfactant and the thiocyanato molybdenum(V) complex CPC was 1:1, with the most probable formula (CPC) $[MoO(SCN)_4]$.

The $[MoO(SCN)_4]^-$ complex formed in the aqueous hydrochloric acid solution has a sharp absorption maximum at 460 nm, whereas when extracted with CPC in chloroform a change in position, as well as in the value, of the molar absorptivity was observed (Fig. 7). The molar absorptivity of the complex was found to be 2.5×10^4 mol^{-1} dm^3 cm^{-1} at 465 nm.

The absorbance of the (CPC)$[MoO(SCN)_4]$ complex at 465 nm remained stable for at least 6 h. The results show that Beer's Law is verified for the range of concentrations from 5×10^{-6} to 7×10^{-5} mol L^{-1}. The relative standard deviation of the method was found to be ±0.9 for five repeated experiments.

The proposed method has been successfully applied for the determination of Mo in the new thiosemicarbazones complexes. The results obtained by the proposed method were in good agreement with calculated values and were comparable to those obtained by the thermogravimetric method. The anions used for wet ashing, sulfate and nitrate, were tolerated for a Mo(VI) to anion mole ratio exceeding 1:2500.

Supplementary data

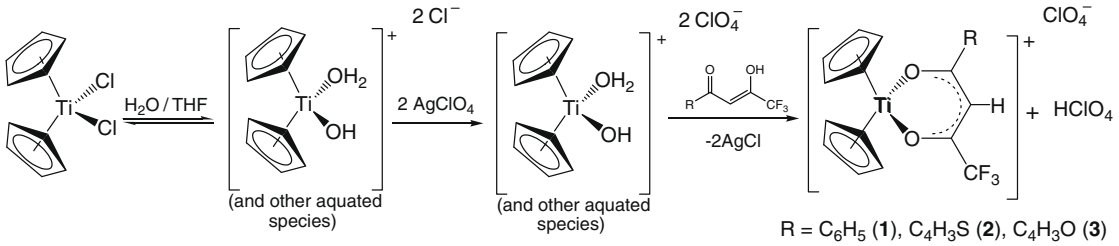
CCDC 706547–706549 contains the supplementary crystallographic data for the structures 2a, 2b and 2c. These data can be obtained free of charge via http://www.ccdc.cam.ac.uk/conts/retrieving.html, or from the Cambridge Crystallographic Data Centre, 12 Union Road, Cambridge CB2 1EZ, UK; fax: (+44) 1223 336 033; or e-mail: deposit@ccdc.cam.ac.uk. Supplementary data associated with this article can be found, in the online version, at doi:10.1016/j.poly.2008.12.026.

Acknowledgments

Financial support for this research was provided by the Ministry of Science and Technology of the Republic of Croatia (Grant Nos. 119-1101342-1082, 119-1191342-1083, 119-1193079-1084, and 119-1191342-2959).

References

[1] E.I. Stiefel, Met. Ions Biol. Syst. 39 (2002) 727.
[2] R.H. Holm, J.M. Berg, J. Am. Chem. Soc. 107 (1985) 917.
[3] L.J. Laughlin, C.G. Young, Inorg. Chem. 35 (1996) 1050.
[4] (a) M. Cindrić, V. Vrdoljak, N. Strukan, B. Kamenar, Polyhedron 24 (2005) 369; (b) V. Vrdoljak, M. Cindrić, D. Matković-Čalogović, B. Prugovečki, P. Novak, B. Kamenar, Z. Anorg. Allg. Chem. 631 (2005) 928.
[5] V. Vrdoljak, M. Cindrić, D. Milić, D. Matković-Čalogović, P. Novak, B. Kamenar, Polyhedron 24 (2005) 1717.
[6] Z. Marczenko, Spectrophotometric Determination of Elements, Ellis Harwood Ltd., John Wiley and Sons, 1976. p. 362.
[7] Oxford Diffraction, Oxford Diffraction Ltd., Xcalibur CCD system, CRYSALIS Software System, Version 1.170, 2003.
[8] G.M. Sheldrick, SHELXS97, Program for the Solution of Crystal Structures, University of Göttingen, Germany, 1997.
[9] G.M. Sheldrick, SHELXL-97, Program for the Refinement of Crystal Structures, University of Göttingen, Germany, 1997.
[10] L.J. Farrugia, J. Appl. Crystallogr. 32 (1999) 837.
[11] A.L. Spek, Acta Crystallogr., Sect. A 46 (1990) C34;
A.L. Spek, PLATON, A Multipurpose Crystallographic Tool, Utrecht University, Utrecht, The Netherlands, 1998.
[12] M. Nardelli, Comput. Chem. 7 (1983) 95;
M. Nardelli, J. Appl. Crystallogr. 28 (1995) 659.
[13] L.J. Farrugia, J. Appl. Crystallogr. 30 (1997) 565.
[14] C.F. Macrae, P.R. Edgington, P. McCabe, E. Pidcock, G.P. Shields, R. Taylor, M. Towler, J. van de Streek, J. Appl. Crystallogr. 39 (2006) 453.
[15] M. Cindrić, N. Strukan, V. Vrdoljak, T. Kajfež, B. Kamenar, Z. Anorg. Allg. Chem. 628 (2002) 2113.
[16] S. Purohit, A.P. Koley, L.S. Prasad, P.T. Manoharan, S. Ghosh, Inorg. Chem. 28 (1989) 3735.
[17] (a) E.B. Seena, M.R.P. Kurup, Polyhedron 26 (2007) 3595;
(b) N.R. Pramanik, S. Ghosh, T.K. Raychaudhuri, S. Chaudhuri, M.G.B. Drew, S.S. Mandal, J. Coord. Chem. 60 (2007) 2177;
(c) M. Cindrić, M. Rubčić, I. Đilović, G. Giester, B. Kamenar, Croat. Chem. Acta 80 (2007) 583;
(d) M. Rubčić, I. Đilović, M. Cindrić, D. Matković-Čalogović, Acta Crystallogr., Sect. C 64 (2008) 570;
(e) S.K. Dutta, S. Samanta, D. Ghosh, R.J. Butcher, M. Chandhury, Inorg. Chem. 41 (2002) 5555.
[18] A.B. Ilyukhin, V.L. Abramenko, V.S. Sergienko, Koord. Khim. (Russ.) Coord. Chem. 20 (1994) 653.
[19] A. Rana, R. Dinda, P. Sengupta, S. Ghosh, L.R. Falvello, Polyhedron 21 (2002) 1023.
[20] F.H. Allen, C.A. Baalham, J.P.M. Lommerse, P.R. Raithby, Acta Crystallogr., Sect. B 54 (1998) 320.
[21] R.-G. Zhao, W. Zhang, J.-K. Li, L.-Y. Zhang, Acta Crystallogr., Sect. E 64 (2008) o1113.
[22] D. Cremer, J.A. Pople, J. Am. Chem. Soc. 97 (1975) 1354.
[23] D. Cremer, Acta Crystallogr., Sect. B 40 (1984) 498.
[24] M.C. Etter, J.C. MacDonald, J. Bernstein, Acta Crystallogr., Sect. B 46 (1990) 256.
[25] X. Ma, Z. Yang, C. Schulzke, A. Ringe, J. Magull, Z. Anorg. Allg. Chem. 633 (2007) 1320.



Scheme 1. Synthesis of $[Cp_2Ti(CF_3COCHCOR)]^+ClO_4^-$ complexes.

[10]. Addition of silver perchlorate ($AgClO_4$) removes the Cl^- ions by precipitating silver chloride (AgCl) while the hydrolysed perchlorate titanium salt, *e.g.* $[Cp_2Ti(H_2O)(OH)]^+ClO_4^-$ remains in solution. Finally, the β-diketone replaces the hydrolysed leaving groups, forming an ionic species, $[Cp_2Ti(\beta\text{-diketonato})]^+ClO_4^-$, with ClO_4^- as the counter-ion. The problem of the insolubility of the β-diketones in water was overcome by means of a mixed solvent system, using a 1:2 ratio of H_2O and THF. It was found that these salts could also be synthesized in anhydrous THF, in which case, instead of hydrolysis in water, a similar solvated species could be formed by displacement of the two Cl^- ligands in Cp_2TiCl_2 with OC_4H_4 instead of OH_2.

All the synthesized salts are insoluble in water, hexane and ether, slightly soluble in organic solvents such as chloroform, dichloromethane and are soluble in acetone, THF and ethanol. However, dissolving the product in ethanol caused it to decompose. The $[Cp_2Ti(\beta\text{-diketonato})]^+$ cation is very sensitive to moisture in solution, but has been found to be stable in the solid state.

2.2. X-ray structure analysis

The molecular diagrams showing the atomic labelling, accompanied by diagrams showing the molecular packing of **1**, **2** and **3**, respectively, are presented in Fig. 1. Crystal data and details of data collection and refinement are summarized in Table 1. Selected bond lengths and angles for the molecules are listed in Table 2. Structural data for similar complexes are also included in Table 2.

Geometrical aspects: The crystal structures of complexes **1**–**3** revealed a *pseudo*-tetrahedral structure with the centroids of the cyclopentadienyl rings and the two oxygen atoms of the β-diketonato ring in the ancillary positions of the central titanium(IV) atom. It is evident, from examination of the bond angles (see Table 2), that the coordination tetrahedron is distorted. The (centroid Cp1)–Ti–(centroid Cp2) angle is on average *ca.* 134° for complexes **1**–**3**, which is a significant deviation from the ideal tetrahedral bond angle of 109.5°. This large angle is attributed to steric hindrance between the Cp ligands. In contrast, the O1–Ti–O2 angle is on average *ca.* 86°, which is considerably smaller than the standard 109.5° angle. This small angle is attributed to constraints in accommodating the chelated β-diketonato ligand. The other angles around the Ti atom, ranging from 103.4° to 108.4°, approach those for an ideal tetrahedral geometry.

Typical C–C and C–O single and double bond lengths are: C–C (1.54 Å), C=C (1.34 Å), C–O (1.43 Å), C=O (1.23 Å) [11]. The large double bond character of the C–C and C–O bonds in the chelate ring of the β-diketonato ligand (see Table 2) emphasize effective electron delocalization in the *pseudo*-aromatic core of the β-diketonato ligand. This electron delocalization enhances electronic communication between the R-groups of the β-diketonato ligand and the Ti centre. The β-diketonato ligand in $[Cp_2Ti(\beta\text{-diketonato})]^+$ binds, within experimental error (taken as three times the bond e.s.d.), symmetrically to the titanium core in **1** and **2** and asymmetrically in **3**, with a difference between the two Ti–O bond lengths of 0.014, 0.000 and 0.023 Å, respectively. This implies that the electron donating properties of the substituted non-CF_3 groups Ph, C_4H_3S, C_4H_3O ($\chi_R = 2.21$ [12], 2.10 [13], unknown) of the β-diketonato ligand do not show an observed effect on the Ti–O bond length in the solid state compared to the stronger electron withdrawing property of the CF_3 group ($\chi_{CF_3} = 3.01$ [12]). The Ti–O bond lengths are shorter in the Ti^{IV} complexes (average 1.996 Å) compared to the Ti^{III} analogues (average 2.076 Å), see Table 2, and this indicates that the more electron deficient Ti^{IV} centre binds oxygen more strongly than Ti^{III}. The same trend is observed in the Ti–Cp bonds: the Ti–(centroid Cp) bonds (average 2.036 Å) for the Ti^{IV} complexes are *ca.* 0.03 Å shorter than those for the Ti^{III} complexes (average 2.062 Å).

The Cp rings of all the complexes tabulated in Table 2 are in a staggered conformation. From an examination of the Cambridge Structural Database (CSD) [14] it can be seen that the staggered sandwich conformation in bent metallocene $Cp_2Ti^{IV}(O\text{-ligand})_2$ and $Cp_2Ti^{IV}(O,O'\text{-ligand})$ complexes is highly favored, although in many cases it was found that the energy barrier to cyclopentadienyl rotation is very small [15]. It has been shown that the choice of conformation is attributed largely to crystal packing effects [16] highlighted in the crystals of Cp_2NbCl_2 and Cp_2MoCl_2, where both the staggered and eclipsed conformations are found in the same crystal.

Crystallographic aspects: The structures **1**–**3** are isomorphous, *i.e.* they crystallize in the same space group, $P2_1/n$, $Z = 4$, with unit cell parameters varying slightly to accommodate the differences in the substituted R-groups and are situated on fairly similar coordinates within the unit cell. The refinements of $[Cp_2Ti(tfba)]^+$ (**1**) and $[Cp_2Ti(tfth)]^+$ (**2**) showed large thermal vibrations on parts of the periphery of the molecules, such as the Cp ring and the CF_3 and ClO_4^- groups. These large thermal vibrations may be attributed to the fact that the collections were done at room temperature and possibly also to loose packing environments in the periphery of the molecules. The thermal vibrations were treated by disordered refinement techniques, involving geometric and anisotropic restraints to obtain more satisfactory refinement results. In the data collection of **3**, where sub-zero temperatures were utilized, these disorders became less pronounced and were considered negligible in the final refinements. Site occupancies for both disordered parts of **1** and **2** (indicated as A and B in Fig. 1) were refined freely but restricted to add up to one. These refined to ratios which are shown in Table 3.

Hydrogen-interactions, although relatively weak, also play a part in site occupation ratios. There are H-interactions between the atoms in the higher occupied site, *e.g.* the interactions C_2–$H_2\cdots F_{1A}$ have higher occupation rates of 56.9% and 83.7% (position A) for the disordered F atoms in $[Cp_2Ti(tfba)]^+$ (**1**) and $[Cp_2Ti(tfth)]^+$ (**2**), respectively. Similarly, H-interactions with perchlorate exist, which lead to the higher occupation rates of 80.0% and 58.9% (position A) for the disordered O atoms in the perchlorate ion.

The fact that the Cp ring, marked C_{21} to C_{26} in the molecular diagram of Fig. 1, is not disordered in all three cases, while the other

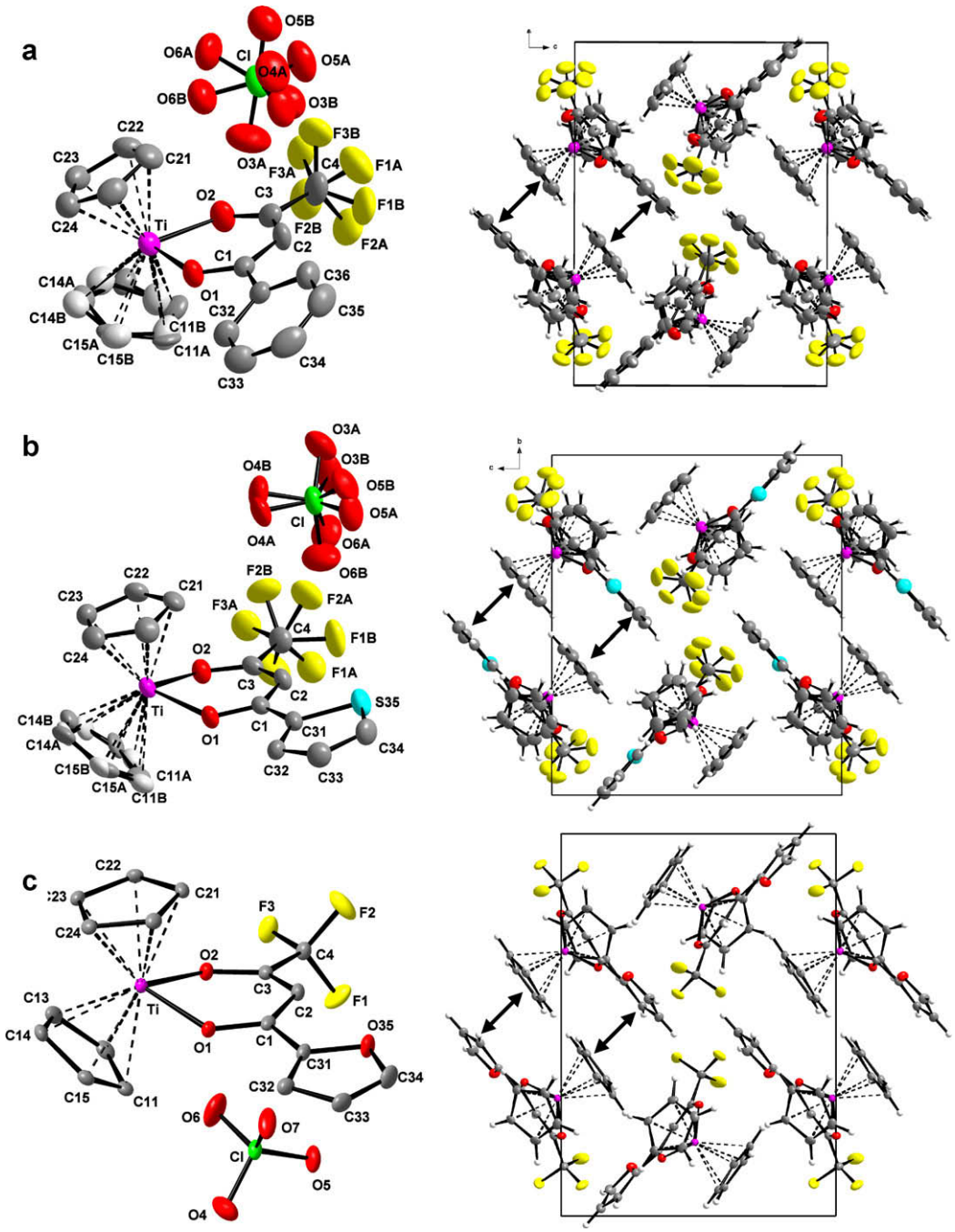


Fig. 1. Molecular structure indicating the numbering scheme (with 30% probability displacement ellipsoids, left) and packing viewed along the *a*-axis (right) of (a) $[Cp_2Ti(tfba)]^+ClO_4^-$ and (b) $[Cp_2Ti(tfth)]^+ClO_4^-$ at $T = 20°$ and (c) $[Cp_2Ti(tffu)]^+ClO_4^-$ at $T = -123°$. Monomeric cationic entities in the crystal are linked by π–π stacking interactions (indicated by double-headed arrows) forming dimeric units (perchlorate ions have been removed for the sake of clarity).

Cp ring (marked C_{11} to C_{16}) is disordered in $[Cp_2Ti(tfba)]^+$ (**1**) and $[Cp_2Ti(tfth)]^+$ (**2**) may be attributed to the fact that the non-disordered Cp rings are involved in the observed π-stacking as described below, forcing this ring (C_{21} to C_{26}) into a more restricted packing environment.

Packing features. The isomorphous complexes **1**–**3** have very similar packing arrangements, with π–π stacking between one Cp ring and the R-group ring of the β-diketonato ligand, *i.e.* the C_6H_5, C_4H_3S and C_4H_3O fragments of tfba, tfth and tffu, respectively. The π–π stacking interactions are between pairs of Ti complexes, forming dimeric units, see Fig. 1 (right).

The planes of the π–π stacked rings are nearly parallel in $[Cp_2Ti(tfth)]^+$ (**2**), with only a small deviation of 0.9° between the planes, compared to 7.4° and 11.0° in the corresponding complexes **3** and **1**, respectively. Geometrical parameters describing the π–π stacking [17] are given in Fig. 2. In all three cases (tfba, tfth and tffu), the rings are displaced from each other, in a slipped or offset alignment. The centroid–centroid separation, R_{cen}, of 3.724, 3.590 and 3.667 Å and the displacement (centre-normal) angle, θ, of 14.4°, 10.4° and 12.6° corresponds to a horizontal displacement of the ring centroids, *d*, of 0.926, 0.648 and 0.800 Å, respectively. The shortest C–H separations between the rings are 3.264, 3.486 and 3.217 Å. These parameters fall well within those required for effective π–π stacking [18]. The packing pattern observed here appears to be unique to the Ti^{IV} bis(cyclopentadienyl) mono(β-diketonato) complexes because the Ti^{III} analogues, *i.e.*

Table 1
Crystal data and structure refinement for $[Cp_2Ti(CF_3COCHCOR)]^+ClO_4^-$ with R = C_6H_5, C_4H_3S and C_4H_3O.

	$[Cp_2Ti(tfba)]^+ClO_4^-$	$[Cp_2Ti(tfth)]^+ClO_4^-$	$[Cp_2Ti(tffu)]^+ClO_4^-$
Formula	$TiO_6C_{20}H_{16}ClF_3$	$TiO_6C_{18}H_{14}ClF_3S$	$TiO_7C_{18}H_{14}ClF_3$
Formula weight	492.68	498.70	482.64
Crystal colour/habit	red, cubic	red, plate	red, plate
Crystal system	monoclinic	monoclinic	monoclinic
Space group	$P2_1/n$	$P2_1/n$	$P2_1/n$
Unit cell dimension			
a (Å)	10.088(2)	9.872(2)	10.0303(5)
b (Å)	16.613(3)	15.346(3)	16.0338(9)
c (Å)	12.443(3)	13.134(3)	11.6124(6)
α (°)	90	90	90
β (°)	96.86(3)	97.46(3)	97.046(2)
γ (°)	90	90	90
Volume (Å^3)	2060.4(7)	1973.1(7)	1853.45(17)
Z	4	4	4
D_{calc} (Mg m^{-3})	1.588	1.679	1.730
Temperature (°C)	20	20	−123
Wavelength (Å)	0.71073	0.71073	0.71073
Absorption coefficient (mm^{-1})	0.607	0.737	0.677
F(000)	1000	1008	976
Crystal size (mm^3)	0.12 × 0.12 × 0.12	0.20 × 0.14 × 0.06	0.27 × 0.11 × 0.07
Theta range for data collection (°)	2.06–25.00	2.05–28.30	2.41–28.32
Index ranges	$-11 \leqslant h \leqslant 11$, $-11 \leqslant k \leqslant 19$, $-14 \leqslant l \leqslant 14$	$-13 \leqslant h \leqslant 9$, $-20 \leqslant k \leqslant 18$, $-17 \leqslant l \leqslant 13$	$-13 \leqslant h \leqslant 13$, $-21 \leqslant k \leqslant 20$, $-15 \leqslant l \leqslant 15$
Reflections collected	11213	13654	17806
Independent reflections [R_{int}]	3622 [0.1037]	4871 [0.0727]	4606 [0.0316]
Completeness to θ = 28.35 (%)	100.0	99.3	99.4
Absorption correction	semi-empirical from equivalents	semi-empirical from equivalents	semi-empirical from equivalents
Max. and min. transmission	0.9307 and 0.9307	0.9571 and 0.8666	0.9542 and 0.8384
Refinement method	full-matrix least-squares on F^2	full-matrix least-squares on F^2	full-matrix least-squares on F^2
Data/restraints/parameters	3622/367/391	4871/319/383	4606/0/271
Goodness-of-fit on F^2	1.010	0.969	1.046
Final R indices [$I > 2\sigma(I)$]	R_1 = 0.0601, wR_2 = 0.1294	R_1 = 0.0517, wR_2 = 0.1166	R_1 = 0.0339, wR_2 = 0.0787
R indices (all data)	R_1 = 0.1852, wR_2 = 0.1812	R_1 = 0.1628, wR_2 = 0.1555	R_1 = 0.0465, wR_2 = 0.0858
Largest difference in peak and hole (e Å^{-3})	0.355 and −0.385	0.300 and −0.427	0.586 and −0.364

Table 2
Selected bond lengths (Å) and angles (°) for $[Cp_2Ti^{IV}(\beta\text{-diketonato})]^+$ and $Cp_2Ti^{III}(\beta\text{-diketonato})$ complexes.

β-Diketonato ligand	$[Cp_2Ti^{IV}\beta]^+$				$Cp_2Ti^{III}\beta$		
	tfba	tfth	tffu	acac[5a]	acac[6a]	ba[7a]	dbm[7a]
Ti–O1	1.979(4)	1.996(3)	1.9914(12)	1.969	2.068	2.085	2.067
Ti–O1	1.979(4)	1.996(3)	1.9914(12)	1.969	2.068	2.085	2.067
Ti–O2	1.993(5)	1.996(3)	2.0144(13)	1.981	2.068	2.078	2.087
O1–C1	1.281(7)	1.277(4)	1.283(2)	1.295	1.287	1.261	1.261
O2–C3	1.283(8)	1.283(5)	1.281(2)	1.279	1.260	1.268	1.286
C1–C2	1.389((9)	1.408(6)	1.411(3)	1.344	1.360	1.388	1.401
C2–C3	1.350(9)	1.359(6)	1.369(3)	1.404	1.390	1.385	1.388
Ct1–Ti[b,c]	2.007(13)	2.000(2)	2.0333(9)	2.033	2.066	2.067	2.060
Ct1–Ti[b,c]	2.059(15)	2.033(2)					
Ct2–Ti[b]	2.023(3)	2.037(2)	2.0333(8)	2.036	2.052	2.070	2.064
O1···O2	2.705	2.720	2.729	2.710	2.775	2.758	2.740
O1–Ti–O2	85.91(19)	85.98(12)	85.90(5)	86.6	84.3	83.0	82.5
Ct1–Ti–Ct2[b]	136.3	133.4	133.3	133.8	134.4	135.2	134.3
O1–C1–C2	120.7(6)	121.8(4)	123.06(16)	123.4	126.8	123.8	124.8
C1–C2–C3	124.7(6)	123.0(4)	121.79(16)	126.1	123.4	124.9	122.8
O2–C3–C2	127.1(6)	127.8(4)	128.15(17)	123.4	125.7	125	125.4
φ[d]	46.6	48.4	47.4	47.5	45.9	46.6	44.9
ω[e]	7.9	19.4	19.9	16.8	4.6	1.0	13.3

[a] acac, $CH_3COCHCOCH_3^-$; ba, $CH_3COCHCOC_6H_5^-$; dbm, $C_6H_5COCHCOC_6H_5^-$.
[b] Ct1, centroid of plane defined by C11–C15; Ct2, centroid of plane defined by C21–C25.
[c] Cp1 disordered, two positions.
[d] φ, angle between the two Cp planes.
[e] ω, dihedral angle between the β-diketonato ligand plane (through atoms O1–C1–C2–C3–O2) and the O1–Ti–O2 plane.

$[Cp_2Ti^{III}(CH_3COCHCOC_6H_5)]$ [6] and $[Cp_2Ti^{III}(C_6H_5COCHCOC_6H_5)]$ [7], display no π–π stacking. These $Cp_2Ti^{III}(\beta)$ complexes do not have a counter-ion such as ClO_4^- in the case of Ti^{IV} which might influence the observed packing.

2.3. Theoretical studies

Density functional theory (DFT) calculations were carried out on complexes **1**–**3** and $[Cp_2Ti^{IV}(CH_3COCHCOCH_3)]^+$ (**4**) to study

Table 3
Site occupancies (%) for disordered parts (marked A and B in Fig. 1) of the Cp_1-ring and the CF_3 and ClO_4^- groups in $[Cp_2Ti(tfba)]^+ClO_4^-$ (**1**) and $[Cp_2Ti(tfth)]^+ClO_4^-$ (**2**). Crystal data collected at $T = 20°$.

Complex	Disordered group		
	CF_3 $F_A:F_B$	ClO_4^- $O_A:O_B$	Cp_1 $C_A:C_B$
$[Cp_2Ti(tfba)]^+$ (**1**)	56.9:43.1	80.0:20.0	42.0:58.0
$[Cp_2Ti(tfth)]^+$ (**2**)	83.7:16.3	58.9:41.1	80.0:20.0

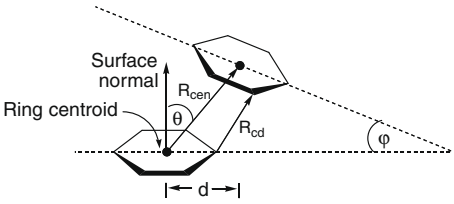


Fig. 2. Definition of the π–π stacking geometrical parameters, R_{cen} (centroid–centroid separation), R_{cd} (closest contact distance) and θ (centre-normal angle) between the two aromatic rings involved in slipped or offset non-parallel alignment of π–π stacking. *Note:* The two benzene rings displayed in the figure can be any aromatic ring, *e.g.* C_6H_5, C_4H_3O or C_4H_3O.

the ground state geometrical and electronic properties of the β-diketonato interactions with the titanium centre in monomeric complexes of the type $[Cp_2Ti^{IV}(R^1COCHCOR^2)]^+$. Since these density functional methods are applied to β-diketonato titanocenyl complexes for the first time and reported here, some measure on the reliability of the approach was obtained by comparing the calculated data with the known single crystal X-ray diffraction structural data of **1**–**4**. The root-mean-square distances (RMSD) calculated for non-hydrogen atoms for the best three-dimensional superposition of calculated structures on experimental structures give a qualitative measurement of the accuracy of the ground state geometry of the calculated structures. Excellent agreement between experimental and theoretical structures is obtained, as reflected by the RMSD values of 0.20, 0.08, 0.07 and 0.04 Å for **1**–**4**, respectively. For **1** and **2**, containing disordered parts, the parts with the highest site occupancy were used in the RMSD calculation. The largest deviation from the experimental structure was found for **1**, containing a large % of disordered parts. Fig. 3 displays the optimized structures of **1**–**4** with selected calculated geometrical parameters. All the bonds in the Ti-β-diketonato ring structure of **1**–**4** were reproduced by DFT calculations to within 0.01–0.03 Å of the experimental values. Since comparisons of experimental metal–ligand bond lengths with calculated bond lengths below a threshold of 0.02 Å are considered as meaningless [19], the computational method used thus gives a good account of the experimental bond lengths. The O1–Ti–O2 angles were calculated accurately to within 1°. The DFT optimized structures containing titanocene with the Cp rings in the staggered or in the eclipsed conformation are approximately equi-energetic, with no preference for either conformation. This result is in agreement with the experimental observation that the choice of conformation is attributed to crystal packing effects and is counter-ion dependant [16].

An interesting observation for experimental structure **2** is that the sulfur on the aromatic thienyl group is orientated towards the methine hydrogen of the β-diketonato ligand; this is in contrast to the orientation in the uncoordinated Htfth ligand [20]. The same result was found for the orientation of the O atom of the furyl group in the crystal structure of **3** [21]. Theoretical calculations, however, did not give any preference for the orientation of the thienyl or furyl group in the optimized ground state structure of **2** or **3**, respectively. The energy needed for rotation between the orientations is 11.3 kcal/mol for **2**, showing that this rotation may easily occur at room temperature [22], see Fig. 4.

Electronic structure: A bent Cp_2Ti^{2+} fragment has C_{2v} symmetry if the Cp ligands have an eclipsed geometry, and C_s symmetry if the

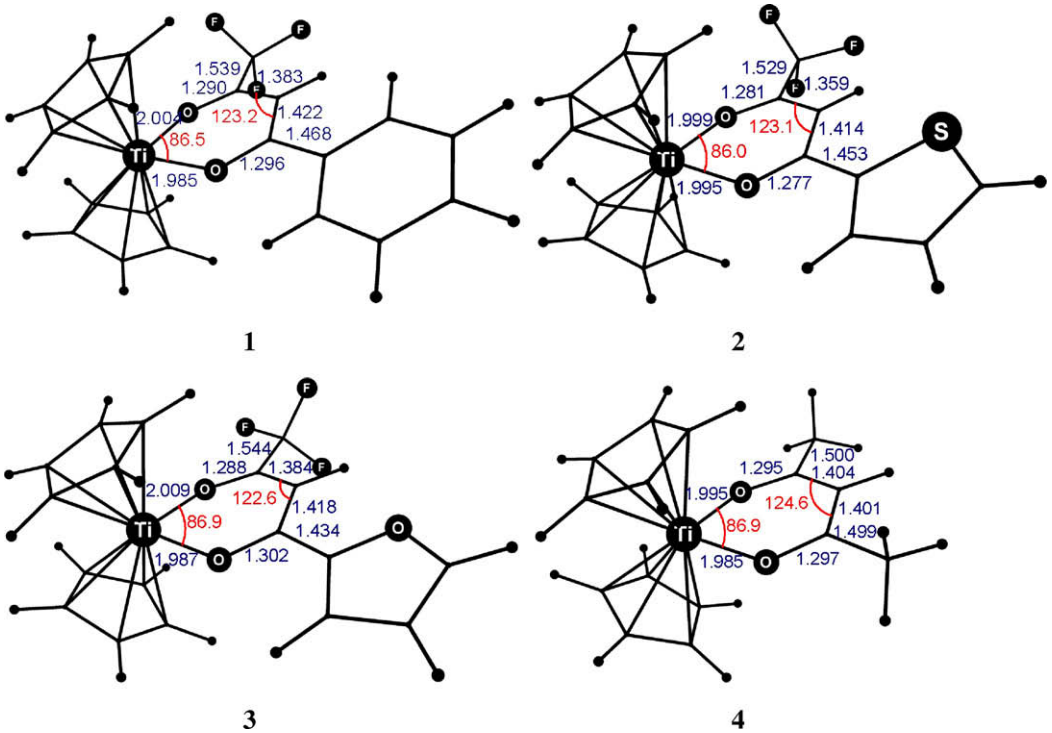


Fig. 3. The PW91/TZP calculated minimum energy geometries of **1**–**4**. Angles (°) and bond lengths (Å) are as indicated.

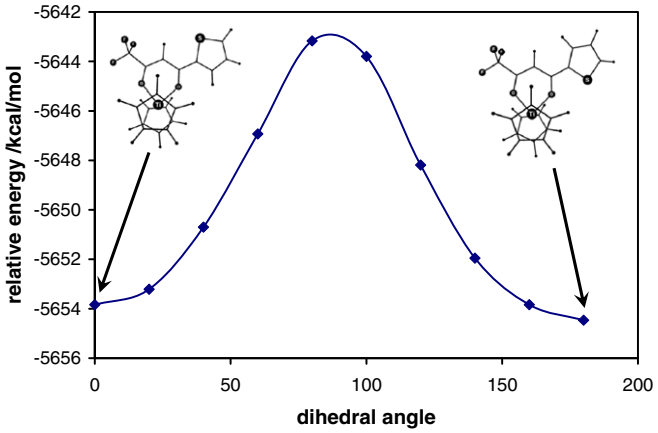


Fig. 4. Rotation of **2** from the isomer with the S orientated towards the methine H to the isomer with S orientated in the same direction as the O, as a function of the O1–C1–C31–S dihedral angle where all other internal coordinates have been optimized at each point.

rings are staggered. The C_s symmetry is preserved when a symmetrical β-diketonato ligand is complexed to Cp_2Ti^{2+}. The electronic structure of $[Cp_2Ti(acac)]^+$ with C_s symmetry is thus presented here as a representative example of the $[Cp_2Ti(\beta\text{-diketonato})]^+$ complexes **1**–**4**. To understand the way in which the acac$^-$ ligand binds, the interaction between the frontier orbitals of a bent Cp_2Ti^{2+} fragment [8] and the HOMOs of the acac$^-$ ligand is schematically illustrated in Fig. 5. The usual in-plane σ-type Ti–O interaction is observed where the unoccupied b_2 LUMO+1 of Cp_2Ti^{2+} interacts with the occupied b_2 HOMO of acac$^-$ (forming HOMO−5 of $[Cp_2Ti(acac)]^+$) and the unoccupied $2a_1$ LUMO+2 of Cp_2Ti^{2+} interacts with the occupied a_1 HOMO−2 of acac$^-$ (forming HOMO−6 of $[Cp_2Ti(acac)]^+$). The $[Cp_2Ti(acac)]^+$ complex is formally a 16-electron d^0 complex if only Ti–O σ-bonding is considered. The electron count is increased by Ti ← O π donation. A moderate to weak π-type interaction is observed in the HOMO−2 and HOMO−7 of the $[Cp_2Ti(acac)]^+$ complex, see Fig. 5 for a schematic presentation of the interaction and Fig. 6 for presentation of the orbitals involved in Ti–O bonding. The above described Ti–O interactions result in Ti–O bonds of an average 1.99 Å for **1**–**4**, slightly longer than that for determined for $Cp_2Ti^{IV}(OR)_2$ complexes containing two monodentate OR ligands, *i.e.* 1.96 Å for $Cp_2Ti(cyanoacetato)_2$ [23] and 1.93 Å for $Cp_2Ti(benzoato)_2$ [9] and comparable to the Ti–O bond length of 1.97 Å in $[\eta^2\text{-OC(Ph)=C(Ph)O]TiCp_2}$, containing a dioxolate bidentate ligand [24].

One interesting feature of the $[Cp_2Ti(\beta\text{-diketonato})]^+$ structures is the degree of out-of-plane folding of the β-diketonato ligand, as schematically shown in Fig. 7. The folding of $[Cp_2Ti(\beta\text{-diketonato})]^+$ along the O···O axis is $\omega = 7.9°$, 19.4°, 19.9° and 16.8° for **1**–**4**, respectively. Similar folding is observed in the series of d^0 penta metallacyclic structures, *i.e.* Cp_2Ti(dioxolene) [24], Cp_2Ti(dithiolene) [25] and Cp_2Ti(diselenolene) [26] complexes, with an increasing degree of folding along the O···O, S···S and Se···Se axes of 38°, 42–50° and 48–52°, respectively. It was rationalized by Lauher and Hoffmann [8] using extended Hückel (EH) calculations that the folding in the Cp_2Ti(dithiolene) complexes was due to a stabilizing interaction between the empty acceptor LUMO $1a_1$ orbital of the Cp_2Ti^{2+} fragment and the HOMO b_1 orbital of the dithiolene ligand, which was only possible by a symmetry lowering of the Cp_2Ti(dithiolene) complex to the C_2 conformation and associated folding of the TiS_2C_2 metallacycle. In this study we confirmed this Ti ← L (L = O, S, Se) π interaction (between the empty acceptor $1a_1$ LUMO of the Cp_2Ti^{2+} and the b_1 HOMO of the ligand) with DFT calculations for the above pentacyclic series, $Cp_2(TiO_2C_2R_2)$,

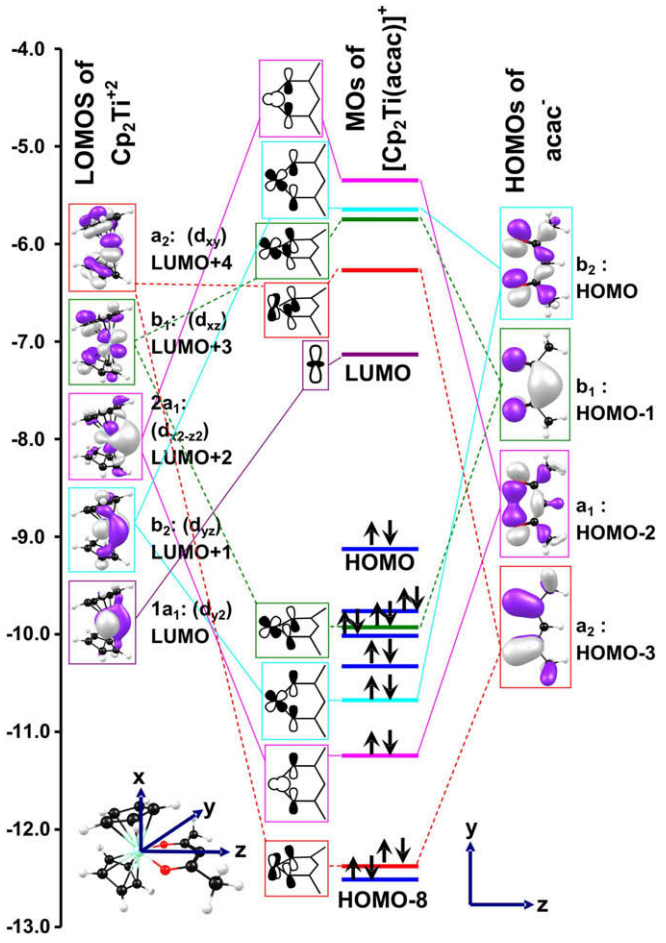


Fig. 5. A schematic molecular orbital (MO) diagram for the interaction between Cp_2Ti^{2+} and the acac$^-$ unit in **4**. The *y*-axis denotes the relative energy in eV for the molecular orbitals of the $[Cp_2Ti(acac)]^+$ complex **4**. The MO energy levels indicated in blue do not have any Ti–O interaction.

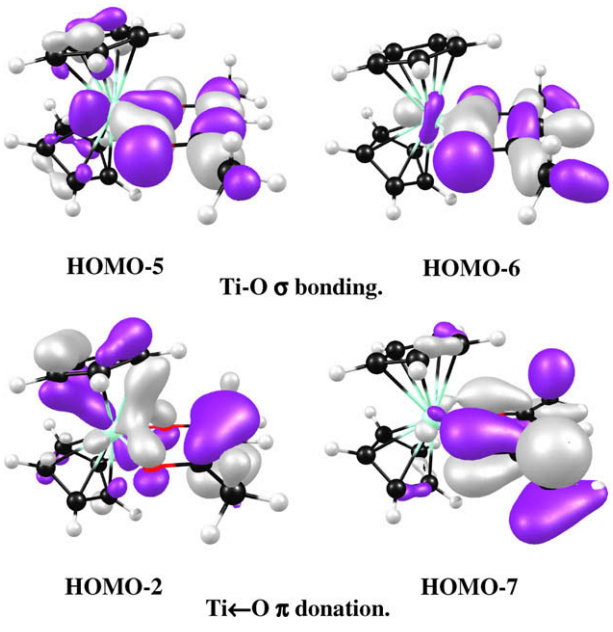


Fig. 6. Selected occupied MO's of **4**, illustrating the Ti–O σ and Ti ← O π interaction.

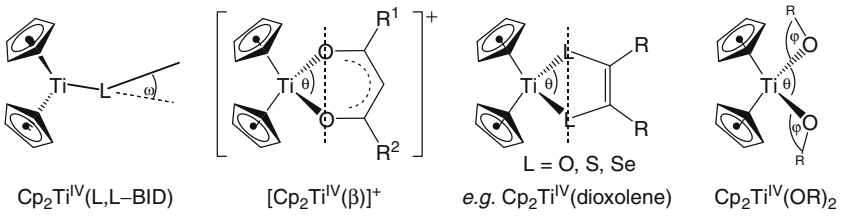


Fig. 7. Folding round the L···L axis in the Cp_2Ti(LL-BID) complexes (LL-BID = bidentate ligand with donor atoms L, L = O, S or Se) is described by the dihedral angle, ω, between the cyclic ligand plane and the L–Ti–L plane. In the $Cp_2Ti(OR)_2$ complexes containing monodentate ligands OR, the large θ and φ angles describe the degree of bending along Ti–O–R.

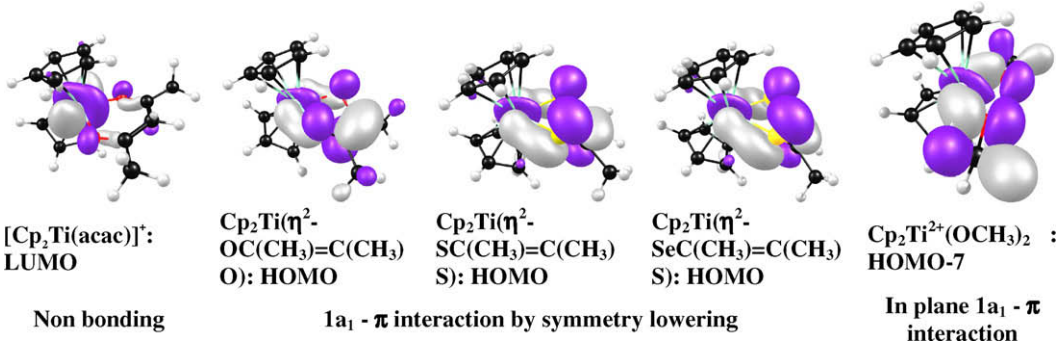


Fig. 8. The $1a_1$ type MO of the $[Cp_2Ti(\beta\text{-diketonato})]^+$, Cp_2Ti(dioxolene), Cp_2Ti(dithiolene), Cp_2Ti(diselenolene) and $Cp_2Ti(OR)_2$ complexes illustrating the $1a_1$–π interaction.

$Cp_2(TiS_2C_2R_2)$ and $Cp_2Ti(Se_2C_2R_2)$ (R = CH_3), see Fig. 8. However, no such Ti ← O π interaction was observed for the hexacyclic $[Cp_2Ti(\beta\text{-diketonato})]^+$ complexes **1–4** where the $1a_1$ LUMO of the Cp_2Ti^{2+} fragment remains non-bonding in $[Cp_2Ti(acac)]^+$, see Fig. 7. Thus we conclude that the folding in the $[Cp_2Ti(\beta\text{-diketonato})]^+$ complexes is not due to the stabilization of the same electronic interaction as in the Cp_2Ti(dioxolene) [24], Cp_2Ti(dithiolene) [25] and Cp_2Ti(diselenolene) [26] series.

Bending along Ti–O–R, stabilized by Ti ← O π interactions, is observed in $Cp_2Ti^{IV}(OR)_2$ complexes. Extended Hückel (EH) calculations [9] revealed that the in-plane Ti ← O π interaction involving the $1a_1$ LUMO of Cp_2Ti^{2+} and the b_1 HOMO of the ligand was made possible by the large O–Ti–O (θ = 89–91°) and Ti–O–R (φ = 143–148°) angles [9,23, 27]. The in-plane Ti ← O π interaction was reproduced with DFT in the present study for $Cp_2Ti^{IV}(OCH_3)_2$ and is illustrated in Fig. 8. The strain of the β-diketonato ring structure in $[Cp_2Ti(\beta\text{-diketonato})]^+$ complexes with a O–Ti–O angle of *ca.* 86°, however, makes large O–Ti–O and Ti–O–C angles impossible. Thus stabilization through in-plane Ti ← O π interaction is thus geometrically not possible for $[Cp_2Ti^{IV}(\beta\text{-diketonato})]^+$ complexes.

The potential energy as a function of the folding along the O···O, S···S and Se···Se axes, with all other internal coordinates being optimized at each point, was calculated for the model complexes $[Cp_2Ti(\beta\text{-diketonato})]^+$, Cp_2Ti(dioxolene), Cp_2Ti(dithiolene) and Cp_2Ti(diselenolene). A plot of potential energy as a function of folding indicates that it takes less than 1 kcal/mol to fold the $[Cp_2Ti(acac)]^+$ complex from the minimum energy conformation, with a folding angle of 17°, to planar. This energy is substantially increased in the pentacyclic series, where the energy needed is 7.4, 16.7 and 16.0 kcal/mol for the $Cp_2Ti(O_2C_2(CH_3)_2)$, $Cp_2Ti(S_2C_2(CH_3)_2)$ and $Cp_2Ti(Se_2C_2(CH_3)_2)$ complexes, respectively.

3. Conclusions

New titanocenyl complexes of the type $[Cp_2Ti(CF_3COCHCOR)]^+ClO_4^-$ with R = C_6H_5, C_4H_3S and C_4H_3O were synthesized and characterized. Crystallographic studies showed that all complexes exhibit π–π stacking between one Cp ring and the aromatic R-group ring, *i.e.* the C_6H_5, C_4H_3S and C_4H_3O fragments, respectively. DFT calculations show that $[Cp_2Ti^{IV}(\beta\text{-diketonato})]^+$ complexes behave differently to $Cp_2Ti^{IV}(OR)_2$ and Cp_2Ti^{IV}(dioxolene) complexes in that no significant bonding interaction between the $1a_1$ LUMO of the Cp_2Ti^{2+} fragment and the coordinating ligand is observed.

4. Experimental

4.1. Materials and apparatus

Solid reagents (Merck, Aldrich and Sigma) were used without further purification. Liquid reactants and solvents were distilled prior to use using standard purification techniques [28] and water was double distilled. Melting points were determined with a Reichert Thermopan microscope equipped with a Kofler hot-stage and are uncorrected. NMR measurements were recorded on a Bruker Advance DPX 300 NMR spectrometer. Chemical shifts are reported as δ values relative to $SiMe_4$ (0 ppm). IR spectra were recorded from neat samples on a Digilab FTS 2000 Fourier transform spectrometer utilizing a He–Ne laser at 632.6 nm.

4.2. Synthesis

Safety note: Perchlorate complexes are potentially explosive, should be treated with caution and handled in small quantities.

4.2.1. Preparation of $[Cp_2Ti(tfba)]^+ClO_4^-$ (*1*)

Titanocene dichloride, Cp_2TiCl_2 (249.0 mg, 1.0 mmol) was dissolved in H_2O/THF, 1:2 mixture (9 ml) and stirred under nitrogen for ½ h. The solution was cooled down on an ice-bath before silver perchlorate, $AgClO_4$ (406 mg, 1.96 mmol), dissolved in water (2 ml) was added. The cooled mixture was stirred for a further ½ h. $AgClO_4$ is light sensitive and the reaction must be shielded from light. Silver chloride, a white precipitate, was filtered off and washed with H_2O/THF (2 ml). Trifluorobenzoylacetone, Htfba (432 mg,

2.0 mmol), dissolved in cold THF (2 ml, *ca.* 4 °C) was added dropwise to the orange filtrate while stirring, causing a slight colour change. After ½ h of stirring the solution was removed and left for 7 days to precipitate (turned dark brown/black). The dark sticky precipitate was collected and washed with water (2 × 100 ml) and diethyl ether (4 × 50 ml). Recrystallisation from DCM/hexane afforded the pure product. Spectroscopically pure crystals suitable for single X-ray analysis were obtained by recrystallisation from DCM/hexane. Yield 51% (246 mg). M.p. = 200 °C. Colour: metallic brown. ν_{CO} = 1554 cm^{-1}. NMR: δ_H (300 MHz, acetone–d_6)/ppm: 7.16 (s, 10H, 2 × C_5H_5), 7.55 (s, 1H, CH), 7.68 (t, 2H, C_6H_5), 7.86 (t, 1H, C_6H_5), 8.35 (d, 2H, C_6H_5). *Anal.* Calc. for $TiC_{20}H_{16}O_6ClF_3$: C, 48.75; H, 3.27. Found: C, 48.13; H, 3.22%.

4.2.2. Preparation of $[Cp_2Ti(tfth)]^+ClO_4^-$ (**2**)

Preparation as for **1**, but replacing the trifluorobenzoylacetone with trifluorothenoylacetone, Htfth (461 mg, 2.0 mmol). Yield 48% (235 mg). M.p. = 191 °C. Colour: dark brown. ν_{CO} = 1566 cm^{-1}. NMR: δ_H (300 MHz, acetone–d_6)/ppm 7.13 (s, 10H, 2 × C_5H_5), 7.38 (s, 1H, CH), 7.50 (t, 1H, C_4H_3S), 8.42 (d, 1H, C_4H_3S), 8.56 (d, 1H, C_4H_3S). *Anal.* Calc. for $TiC_{18}H_{14}SO_6ClF_3$: C, 43.35; H, 2.83. Found: C, 43.77; H, 2.87%.

4.2.3. Preparation of $[Cp_2Ti(tffu)]^+ClO_4^-$ (**3**)

Preparation as for **1**, but replacing the trifluorobenzoylacetone with trifluorofuroylacetone, Htffu (412 mg/2.0 mmol). Yield 43% (203 mg). M.p. = 195 °C. Colour: brown. ν_{CO} = 1568 cm^{-1}. NMR: δ_H (300 MHz, acetone–d_6)/ppm: 7.00 (t, 1H, C_4H_3O), 7.13 (s, 10H, 2 × C_5H_5), 7.18 (s, 1H, CH), 8.07 (d, 1H, C_4H_3O), 8.28 (d, 1H, C_4H_3O). *Anal.* Calc. for $TiC_{18}H_{14}O_7ClF_3$: C, 44.79; H, 2.92. Found: C, 44.71; H, 2.87%.

4.3. X-ray crystal structure determination

The X-ray intensity data for **1** and **2** were measured on a Bruker SMART 1K CCD area detector and that for **3** on a Bruker X8 Apex II 4K CCD area detector. Both instruments were equipped with a graphite monochromator and a Mo Kα fine-focus sealed tube (λ = 0.71073 Å) operated at 1.5 kW power (50 kV, 30 mA). The detector was placed at a distance of 4.00 cm from the crystal. Data collection temperature for **1** and **2** was room temperature (293 K), whereas the temperature during the collection of **3** was 150(2) K, using an Oxford 700 series cryostream cooler.

The initial unit cell and data collection of **3** were achieved by the APEX2 software [29] utilizing COSMO [30] for optimum collection of more than a hemisphere of reciprocal space. A total of 948 frames were collected with a scan width of 0.5° in φ and ω with an exposure time of 20 s per frame. The initial unit cell and data collection for **1** and **2** were achieved by the SMART-NT software [31], set up for data collection of more that a hemisphere of reciprocal space. A total of 1350 frames were collected with a scan width of 0.3° in φ and exposure times of 10 s per frame. The frames were integrated using a narrow frame integration algorithm and reduced with the Bruker SAINTPLUS and XPREP software [32] packages, respectively. Analysis of all of the data collections showed no significant decay during the data collection. Data were corrected for absorption effects using the multi-scan technique SADABS [33].

All the structures were solved by the direct methods package SIR97 [34] and refined using the WINGX software package [35] incorporating SHELXL [36]. The largest peaks on the final difference electron densities and the deepest holes were all within 1 Å from non-hydrogen atoms and presented no physical meaning in the final refinements. Aromatic protons were placed in geometrically idealized positions (C–H = 0.93–0.98 Å) and constrained to ride on their parent atoms with $U_{iso}(H) = 1.2U_{eq}(C)$. Disorders on the perchlorate ions, CF_3 moieties and those on the Cp rings were treated with various geometrical and vibrational restraints.

Atomic scattering factors were taken from the International Tables for Crystallography Volume C [37]. The molecular plot was drawn using the DIAMOND program [38] with a 30% thermal envelope probability for non-hydrogen atoms. Hydrogen atoms were drawn as arbitrary sized spheres with a radius of 0.135 Å.

4.4. Quantum computational methods

Pure Density Functional Theory (DFT) calculations were carried out using the Amsterdam Density Functional 2007 (ADF) program system [39] with the PW91 (Perdew–Wang, 1991) exchange and correlation functional [40]. The TZP (Triple ζ polarized) basis set, a fine mesh for numerical integration (5.2 for geometry optimizations), a spin-restricted formalism and full geometry optimization (gas-phase) with tight convergence criteria, as implemented in the ADF 2007 program, were used. The accuracy of the computational method was evaluated by comparing the root-mean-square deviations (RMSD's) between the optimized molecular structure and the crystal structure, using the non-hydrogen atoms in the molecule. RMSD values were calculated using the "RMS Compare Structures" utility in CHEMCRAFT Version 1.5 [41]. Whether artificially generated atomic coordinates or coordinates obtained from X-ray crystal data were used in the input files, optimizations for each compound resulted in the same optimized geometry. The optimized structures were verified as a minimum through frequency calculations. Unless indicated, no symmetry limitations were imposed in the calculations.

Acknowledgements

Financial assistance from the South African National Research Foundation under Grant No. 61093 and the Central Research Fund of the University of the Free State is gratefully acknowledged.

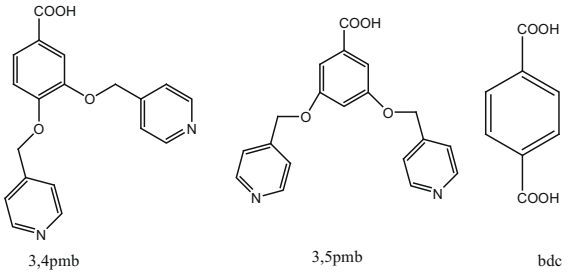
Appendix A. Supplementary data

CCDC 693411, 693410 and 6934 contains the supplementary crystallographic data for $[(C_5H_5)_2Ti(CF_3COCHCOR)]^+ClO_4^-$ with R = C_6H_5 (**1**), C_4H_3S (**2**) and C_4H_3O (**3**), respectively. These data can be obtained free of charge via http://www.ccdc.cam.ac.uk/conts/retrieving.html, or from the Cambridge Crystallographic Data Centre, 12 Union Road, Cambridge CB2 1EZ, UK; fax: (+44) 1223-336-033; or e-mail: deposit@ccdc.cam.ac.uk. Supplementary data associated with this article can be found, in the online version, at doi:10.1016/j.poly.2008.12.060.

References

[1] N.J. Long, Metallocenes: An Introduction to Sandwich Complexes, Blackwell Science, London, 1998. p. 23.
[2] P. Köpf-Maier, Eur. J. Clin. Pharmacol. 47 (1994) 1.
[3] B.K. Keppler, C. Friesen, H.G. Moritz, H. Vongerichten, E. Vogel, Struct. Bonding 78 (1991) 97.
[4] (a) G. Doyle, R.S. Tobias, Inorg. Chem. 6 (1967) 1111;
(b) G. Doyle, R.S. Tobias, Inorg. Chem. 7 (1968) 2484.
[5] M. Casado, J.J. Perez-Torrente, M.A. Ciriano, A.J. Edwards, F.J. Lahoz, L.A. Oro, Organometallics 18 (1999) 5299 (CSD Ref.: LIHDUB).
[6] A.M. Bond, R. Colton, U. Englert, H. Hűgel, F. Marken, Inorg. Chim. Acta 235 (1995) 117 (CSD Ref.: HIDPOZ).
[7] S.S. Yun, I. Suh, E.H. Kim, S. Lee, J. Coord. Chem. 51 (2000) 219 (CSD Ref.: MOYJEP, MOYJIT).
[8] J.W. Lauher, R. Hoffmann, J. Am. Chem. Soc. 98 (1976) 1729.
[9] D.M. Hoffman, N.D. Chester, R.C. Fay, Organometallics 2 (1983) 48.
[10] J.H. Toney, T.J. Marks, J. Am. Chem. Soc. 107 (1985) 947.
[11] R.C. Weast, Handbook of Chemistry and Physics, 63rd Ed., The Chemical Rubber Co., Ohio, p. F180.
[12] W.C. Du Plessis, J.C. Erasmus, G.J. Lamprecht, J. Conradie, T.S. Cameron, M.A.S. Aquino, J.C. Swarts, Can. J. Chem. 77 (1999) 378.

[13] M.M. Conradie, A.J. Muller, J. Conradie, S. Afr. J. Chem. 61 (2008) 13.
[14] Cambridge Structural Database (CSD), Version 5.27, August 2007 update.
[15] (a) B.E. Mann, C.M. Spencer, B.F. Taylor, J. Chem. Soc., Dalton Trans. (1984) 2027;
(b) L.N. Mulay, A. Attalla, J. Am. Chem. Soc. 85 (1963) 702.
[16] C.K. Prout, G.B. Allison, L.T.J. Delbaere, E. Gore, Acta Crystallogr. B28 (1972) 3043.
[17] G.B. McGaughey, M. Gagne, A.K. Rappe, J. Biol. Chem. 273 (1998) 15458.
[18] C. Janiak, J. Chem. Soc., Dalton Trans. (2000) 3885.
[19] W.J. Hehre, A Guide to Molecular Mechanisms and Quantum Chemical Calculations, Wavefunction Inc., 2003. p. 153.
[20] R.D.G. Jones, Acta Crystallogr., Sect. B: Struct. Crystallogr. Cryst. Chem. 32 (1976) 1224 (CSD Ref.: THTFBD).
[21] R. Boese, M. Yu Antipin, D. Blaser, K.A. Lyssenko, J. Phys. Chem. 102 (1998) 8654 (CSD Ref.: LIWPIQ).
[22] J.S. Lomas, J. Phys. Org. Chem. 20 (2007) 221.
[23] D.A. Edwards, M.F. Mahon, T.J. Paget, Polyhedron 16 (1997) 25.
[24] L.C. Song, P.C. Liu, C. Han, Q.M. Hu, J. Org. Chem. 648 (2002) 119.
[25] F. Guyon, M. Fourmigue, P. Audebert, J. Amaudrut, Inorg. Chim. Acta 239 (1995) 117.
[26] O. Jeannin, M. Nomura, M. Fourmigué, J. Organomet. Chem. 692 (2007) 4113.
[27] M.A.A.de C.T. Carrondo, M.J. Calhorda, M.B. Hursthouse, Acta Crystallogr. C43 (1987) 880.
[28] B.S. Furniss, A.J. Hannaford, P.W.G. Smith, A.R. Tatchell, Vogel's Textbook of Practical Organic Chemistry, 5th Ed., Longman Scientific and Technical, John Wiley and Sons, New York, p. 395 (Chapter 4).
[29] APEX2, Version 1.0–27, Bruker AXS Inc., Madison, Wisconsin, USA, 2005.
[30] COSMO, Version 1.48, Bruker AXS Inc., Madison, Wisconsin, USA, 2003.
[31] Bruker SMART-NT, Version 5.050, Bruker AXS Inc., Madison, Wisconsin, USA, 1998.
[32] SAINTPLUS, Version 7.12 including XPREP, Bruker AXS Inc., Madison, Wisconsin, USA, 2004.
[33] SADABS, Version 2004/1, Bruker AXS Inc., Madison, Wisconsin, USA, 1998.
[34] A. Altomare, M.C. Burla, M. Camalli, G.L. Cascarano, C. Giacovazzo, A. Guagliardi, A.G.G. Moliterni, G. Polidori, R. Spagna, J. Appl. Crystallogr. 32 (1999) 115.
[35] L.J. Farrugia, J. Appl. Crystallogr. 32 (1999) 837 (WINGX 1.70.01).
[36] G.M. Sheldrick, SHELXL97, Program for Crystal Structure Refinement, University of Göttingen, Germany, 1997.
[37] International Tables for Crystallography, Kluwer Academic Publishers, Dordrecht, The Netherlands, vol. C, 2002.
[38] K. Brandenburg, H. Putz, DIAMOND Release 3.1a, Crystal Impact GbR, Bonn, Germany, 2005.
[39] G.T. Velde, F.M. Bickelhaupt, E.J. Baerends, C.F. Guerra, S.J.A. van Gisbergen, J.G. Snijders, T.J. Ziegler, J. Comp. Chem. 22 (2001) 931.
[40] J.P. Perdew, J.A. Chevary, S.H. Vosko, K.A. Jackson, M.R. Perderson, D.J. Singh, C. Fioihais, Phys. Rev. B46 (1992) 6671.
[41] G.A. Zhurko, D.A. Zhurko, CHEMCRAFT, Version 1.5 (build 282), 2007.



Scheme 1. Schematic views of ligands.

excitation spectra were recorded on a Varian Cary Eclipse spectrometer.

2.2. Syntheses of the ligands and the complexes

2.2.1. Synthesis of 3,5-pmb and 3,4-pmb

3,5-Dihydroxybenzoic acid (15.4 g), ethanol (53 ml) and sulfuric acid (4 ml) were mixed and refluxed for 6–7 h. The excess ethanol was removed under vacuum, and then the reaction mixture was extracted with ethylacetate. The extracted solution was washed once with water, and then with $NaHCO_3$ aqueous solution. After drying with Na_2SO_4, the solvent was evaporated. To 20 mmol (3.64 g) of the product, 40 mmol (6.5 g) of 4-pycolyl chloride hydrochloride and 120 mmol (4.8 g) of NaOH and 10 ml DMF were added. The mixture was heated at 70 °C for 10 h, and then the product was washed with ethanol and filtered. The solid product was transferred to a 100 ml round bottom flask, 50 ml of 5% NaOH solution was added and the resulting solution was refluxed at 70 °C for 5 h, then the mixture was transferred into a 400 ml beaker. After adding 50 ml of distilled and concentrated HCl drop by drop, a light brown precipitate was obtained at about pH 6, which was washed with ethanol and filtered. Yield: 72%. *Anal.* Calc. for $C_{19}H_{16}N_2O_4$ (336.11): C, 67.85; H, 4.79; N, 8.33%. Found: C, 67.91; H, 4.98; N, 8.26%. M.p. for the crude product is 128 °C.

The synthetical method of 3,4-pmb was similar to the synthesis of 3,5-pmb, except that 3,4-dihydroxybenzoic acid was used instead of 3,5-dihydroxybenzoic acid. Yield: 60%. *Anal.* Calc. for $C_{19}H_{16}N_2O_4$ (336.11): C, 67.85; H, 4.79; N, 8.33. Found: C, 67.91; H, 4.98; N, 8.26%.

2.2.2. [Ni(3,4-pmb)(bdc)$_{0.5}$] (**1**)

Compound **1** was prepared from a mixture of $NiCl_2 \cdot 6H_2O$ (0.3 mmol, 0.066 g), 3,4-pmb (0.2 mmol, 0.073 g), bdc (0.2 mmol, 0.033 g) and NaOH (0.6 mmol, 0.024 g) in 8 ml distilled water. This mixture was heated in a sealed Teflon lined steel autoclave at 150 °C for three days. After the mixture was slowly cooled to room temperature at a rate of 10 °C/h, green crystals of **1** were obtained (yield: 58% based on Ni). *Anal.* Calc. for $C_{23}H_{15}N_2O_{10}Ni$ (538.08): C, 51.34; H, 2.81; N, 5.21. Found: C, 50.69; H, 2.79; N, 5.20%.

2.2.3. [Co(3,5-pmb)(bdc)$_{0.5}$] (**2**)

A mixture of $Co(OAc)_2 \cdot 2H_2O$ (0.3 mmol, 0.075 g), 3,5-pmb (0.2 mmol, 0.073 g), bdc (0.2 mmol, 0.033 g) and NaOH (0.6 mmol,0.024 g) was dissolved in 8 ml distilled water. The mixture was heated in sealed Teflon lined steel autoclave at 150 °C for three days. After cooling to room temperature at a rate of 10 °C/h, crystals of the product were obtained (yield: 52% based on Co). *Anal.* Calc. for $C_{23}H_{17}N_2O_6Co$ (476.32): C, 58.00; H, 3.60; N, 5.88. Found: C, 57.96; H, 3.20; N, 5.79%.

2.2.4. [Cd(3,5-pmb)(bdc)$_{0.5}$] (**3**)

The procedure was similar to the synthesis of complex **2** except that $Cd(OAc)_2 \cdot 2H_2O$ (0.3 mmol, 0.08 g) was used instead of $Co(OAc)_2 \cdot 2H_2O$. Yield: 64% based on Cd. *Anal.* Calc. for $C_{23}H_{17}N_2O_6Cd$ (529.79): C, 54.91; H, 3.41; N, 5.57. Found: C, 54.85; H, 3.32; N, 5.55%.

2.3. X-ray crystallography analysis

A suitable single crystal of each complex was mounted on a glass fiber and used for X-ray diffraction analyses. Data were collected at 293(2) K on a Bruker ApexII CCD diffractometer using the scan technique with Mo Kα radiation (λ = 0.71069 Å). Absorption corrections were applied using the multi-scan technique [30]. The structures were solved by the direct method and refined by full-matrix least-square techniques on F^2 using SHLXL-97 [31]. Further details of the X-ray structural analysis for compounds **1**–**3** are given in Table 1. Selected bond lengths and angles for **1**–**3** are listed in Table 2.

3. Results and discussion

3.1. Description of the structures

The hydrothermal reactions of H_2bdc and the corresponding metal salt with the pyridyl-containing ligands at 150 °C have afforded crystals of complexes **1**–**3**. H_2bdc is completely deprotonated to coordinate to the metal center. In each complex, the carboxylate groups of bdc and the carboxylate group of the pmb ligands adopt similar coordination modes.

3.1.1. [Ni(3,4-pmb)(bdc)$_{0.5}$] (**1**)

Single crystal X-ray diffraction analysis reveals that **1** has a 3D threefold interpenetrated adamantanoid structure. As is shown in Fig. 1, each Ni(II) center adopts a distorted octahedral geometry, supplied by two nitrogen atoms from different 3,4-pmb ligands (the average Ni–N distance is 2.037 Å and the N–Ni–N angle is 94.82°), and four oxygen atoms from two carboxylate groups of bdc and pmb in a chelating mode. The Ni–O bond distances are in the range 2.07–2.14 Å, and the O–Ni–O bond angles range from 62.3° to 98.1°. If each chelating carboxylate groups is treated as one connecting point, the nickel center has a pseudotetrahedral geometry [32]. Each Ni(II) atom is thus connected to four other Ni(II) centers, resulting in the formation of a diamondoid network. The

Table 1
Crystal data and structure refinement for **1**–**4**.

	1	**2**	**3**
Empirical formula	$C_{23}H_{15}N_2O_{10}Ni$	$C_{23}H_{17}N_2O_6Co$	$C_{23}H_{17}N_2O_6Cd$
Formula weight	538.08	476.32	529.79
T (K)	293(2)	293(2)	293(2)
λ (Å)	0.71069	0.71069	0.71069
Crystal system	monoclinic	monoclinic	triclinic
Space group	$C2/c$	$P2_1/c$	$P\bar{1}$
a (Å)	23.343(1)	9.985(4)	7.285(3)
b (Å)	12.032(1)	21.438(5)	10.405(4)
c (Å)	17.308(1)	10.936(9)	14.356(5)
α (°)	90.0	90.0	83.810(6)
β (°)	104.744(1)	110.570(9)	76.997(6)
γ (°)	90.0	90.0	77.190(6)
V (Å^3)	4701(3)	2192(2)	1032.0(9)
Z	8	4	2
D_{calc} (g cm^{-3})	1.520	1.444	1.705
μ (mm^{-1})	0.886	0.825	1.103
F(000)	2200	976	530
Data/restraints/parameters	4161/0/343	4129/0/289	3604/0/289
Goodness-of-fit on F^2	1.034	0.977	1.026
R_1[a]	0.0458	0.0458	0.0244
wR_2[b]	0.1702	0.1030	0.0862

[a] $R_1 = \sum||F_o| - |F_c||/\sum|F_o|$.
[b] $wR_2 = \sum[w(F_o^2 - F_c^2)^2]/\sum[w(F_o^2)^2]^{1/2}$.

Table 2
Selected bond lengths (Å) and angles (°) for compounds **1**–**3**.

1			
Ni(1)–N(1)	2.018(3)	Ni(1)–N(2)#1	2.057(4)
Ni(1)–O(4)#2	2.074(3)	Ni(1)–O(1)	2.102(3)
Ni(1)–O(3)#2	2.126(3)	Ni(1)–O(2)	2.147(3)
N(1)–Ni(1)–N(2)#1	94.8(2)	N(1)–Ni(1)–O(4)#2	98.6(1)
N(2)#1–Ni(1)–O(4)#2	99.7(1)	N(1)–Ni(1)–O(1)	98.7(1)
N(2)#1–Ni(1)–O(1)	99.3(1)	O(4)#2–Ni(1)–O(1)	153.0(1)
N(1)–Ni(1)–O(3)#2	161.3(1)	N(2)#1–Ni(1)–O(3)#2	90.7(1)
O(4)#2–Ni(1)–O(3)#2	62.7(1)	O(1)–Ni(1)–O(3)#2	98.1(1)
N(1)–Ni(1)–O(2)	91.8(2)	N(2)#1–Ni(1)–O(2)	161.2(1)
O(4)#2–Ni(1)–O(2)	96.6(1)	O(1)–Ni(1)–O(2)	62.3(1)
2			
Co(1)–O(2)#1	1.947(2)	Co(1)–O(6)	1.957(3)
Co(1)–N(1)	2.036(3)	Co(1)–N(2)#2	2.067(3)
O(2)#1–Co(1)–O(6)	105.3(1)	O(2)#1–Co(1)–N(1)	113.3(1)
O(6)–Co(1)–N(1)	124.4(1)	O(2)#1–Co(1)–N(2)#2	94.7(1)
O(6)–Co(1)–N(2)#2	113.3(1)	N(1)–Co(1)–N(2)#2	102.7(1)
3			
Cd(1)–O(1)#1	2.228(2)	Cd(1)–O(6)#2	2.234(2)
Cd(1)–O(5)	2.234(3)	Cd(1)–N(2)	2.239(3)
Cd(1)–O(2)#3	2.257(3)	Cd(1)–Cd(1)#2	3.121(1)
O(1)#1–Cd(1)–O(6)#2	89.9(1)	O(5)–Cd(1)–O(2)#3	88.6(1)
O(1)#1–Cd(1)–O(5)	87.9(1)	N(2)–Cd(1)–O(2)#3	92.9(1)
O(6)#2–Cd(1)–O(5)	156.9(1)	O(1)#1–Cd(1)–Cd(1)#2	87.04(7)
O(1)#1–Cd(1)–N(2)	110.2(1)	O(6)#2–Cd(1)–Cd(1)#2	75.65(8)
O(6)#2–Cd(1)–N(2)	104.5(1)	O(5)–Cd(1)–Cd(1)#2	81.31(8)
O(1)#1–Cd(1)–O(2)#3	156.9(1)	N(2)–Cd(1)–Cd(1)#2	162.73(7)
O(6)#2–Cd(1)–O(2)#3	84.5(1)	O(2)#3–Cd(1)–Cd(1)#2	69.84(8)

Symmetry transformations: for **1**: #1 $x-1/2, y-1/2, z$; #2 $x-1/2, y+1/2, z$; for **2**: #1 $x, y+1/2, -z+1/2$; #2 $-x+1, -y+2, -z$; for **3**: #1 $x, y, z-1$; #2 $-x, -y, -z$; #3 $-x, -y, -z+1$.

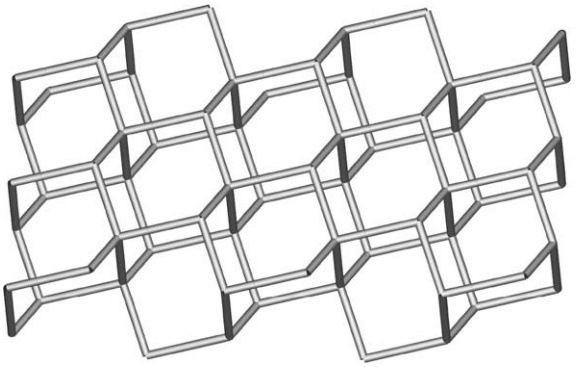


Fig. 2. The three-dimensional adamantanoid cages in complex **1**.

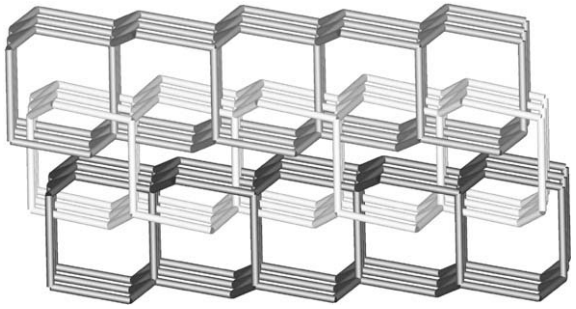


Fig. 3. The threefold interpenetrated adamantanoid architecture of **1**.

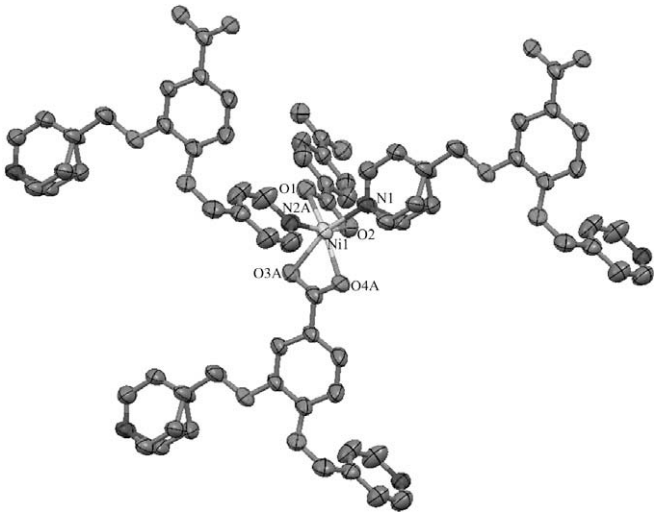


Fig. 1. The coordination environment of Ni(II) in complex **1**.

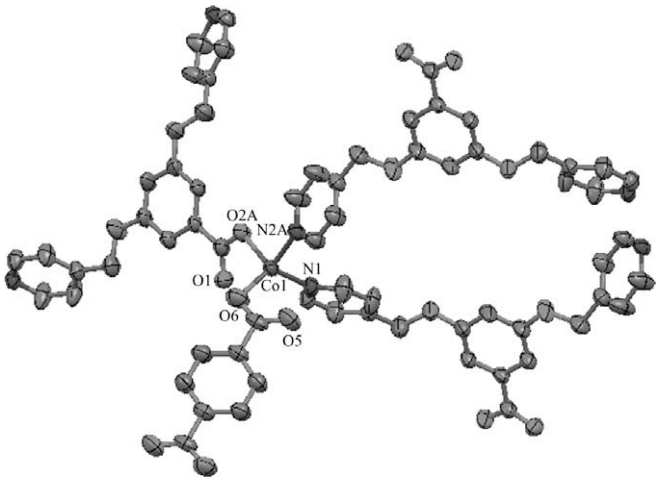


Fig. 4. The coordination environment of Co(II) in complex **2**.

Ni···Ni separations observed were in the range 10.65–13.13 Å. The long spacers between the coordination sites result in large cavities with adamantanoid cages (Fig. 2). In order to minimize the big void cavities and to stabilize the framework naturally, the potential voids are effectively filled by mutual interpenetration of other two independent equivalent frameworks, generating a threefold network (Fig. 3).

*3.1.2. [Co(3,5-pmb)(bdc)$_{0.5}$] (**2**)*

Unlike compound **1**, compound **2** has a 3D fourfold polyrotaxane structure. The network is constructed by binuclear molecules, in which each Co ion is tetrahedraly coordinated to two nitrogen atoms of different 3,5-pmb ligands (Co–N = 2.04 Å and N–Co–N = 102.06°) and two oxygen atoms of two different carboxylate groups in the monodentate mode from pmb and bdc ligands (Co–O = 1.95 Å and O–Co–O = 105.29°) (Fig. 4). The whole network is constructed from four equivalent independent fragments. Each individual fragment consists of a ring and rod chains, in which the ring is constituted by two metal atoms bridged by two pmb ligands. These rings connect with each other via bdc (the rod) to form a chain, and then two adjacent chains are linked by the monodentate carboxylic group of the pmb ligand to form a 3D network. Interestingly, each chain is entangled with one chain from another equivalent independent fragment through the rod to form the polyrotaxane topology (Fig. 5).

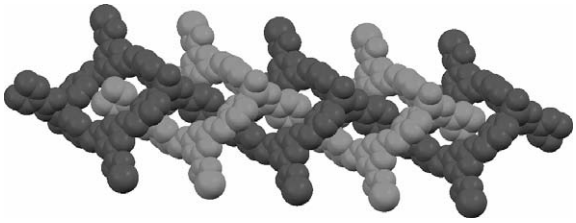


Fig. 5. The polyrotaxane architecture in complex **2**.

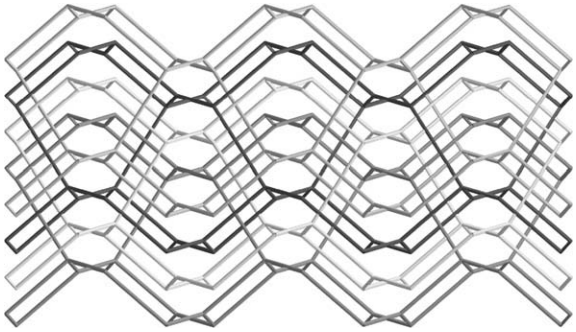


Fig. 6. The 3D fourfold interpenetrated structure of complex **2**.

The most fascinating structural feature of **2** is that four equivalent networks with rotaxane entanglement are then interwoven with each other to give a 3D fourfold structure (Fig. 6).

*3.1.3. [Cd(3,5-pmb)(bdc)$_{0.5}$] (**3**)*

For complex **3**, the X-ray diffraction analysis reveals that it has a unique 2D coordination network consisting of [$Cd_2(CO_2)_4$] units bridged by bdc and pmb ligands (Fig. 7). Each Cd(II) atom is coordinated by one nitrogen atom of a pmb ligand and four oxygen atoms from the carboxylate group of pmb and bdc, in which the four carboxylate oxygen atoms comprise the equatorial plane and the N atom occupies the vertex of square-pyramidal structure to give a square-pyramidal coordinated geormetry. The average Cd–O bond length is 2.233 Å and the Cd–N bond length is 2.239 Å. Two adjacent Cd(II) atoms are bridged equivalently by four carboxylate groups of different pmb and bdc ligands, forming a paddle wheel secondary building unit (SBU). The Cd···Cd separation is 3.12 Å, which is significantly shorter than those in reported discrete dimeric cadmium–tetracarboxylate complexes (3.278–3.452 Å) [33,34], but slightly longer than the sum of the van der Waals radii 3.04 Å [35,36], suggesting that there should be no Cd···Cd bond in the SBU. There exits a crystallographic inversion center between the two Cd cores in each dinuclear unit.

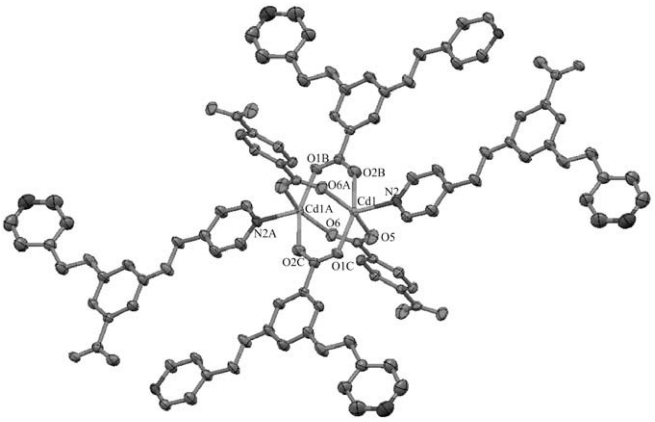


Fig. 7. The coordination environment of Cd(II) in complex **3** highlighting the dinuclear unit.

Two pmb ligands conect with two SBU units like arms to form a four membered ring with a Cd···Cd separation in the intersecting ring of 12.13 Å The rings are extended to form 1D fragments along the *c*-axis, which are extended into a ladder-like 2D network via the bdc ligand (Fig. 8). The arms of each fragment intervene with ones of adjacent fragments without any interlocking (Fig. 9).

3.2. Properties

3.2.1. IR spectroscopy

The IR spectrum of complex **1** shows typical antisymmetric and symmetric stretching bands of carboxylate groups at 1585 and 1384 cm^{-1}, respectively. The separation (Δ) $\upsilon_{asym}(CO_2) - \upsilon_{sym}(CO_2)$ is 200 cm^{-1}, which is consistent with the type of coordination of the carboxylate groups. The peaks of compound **2** centered at 1617 and 1389 cm^{-1} should be assigned to antisymmetric and symmetric stretching bands of carboxylate groups, respectively. The separation (Δ) value is 227 cm^{-1}, indicating the existence of a monodentate coordination mode [37]. In complex **3**, the characteristic bands of the carboxylate groups are shown at 1550 and 1390 cm^{-1} for the for the antisymmetric and symmet-

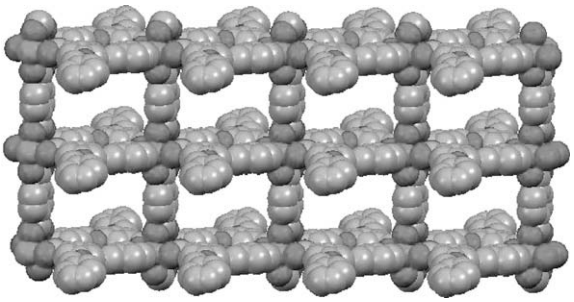


Fig. 8. The 2D ladder-like network of complex **3**.

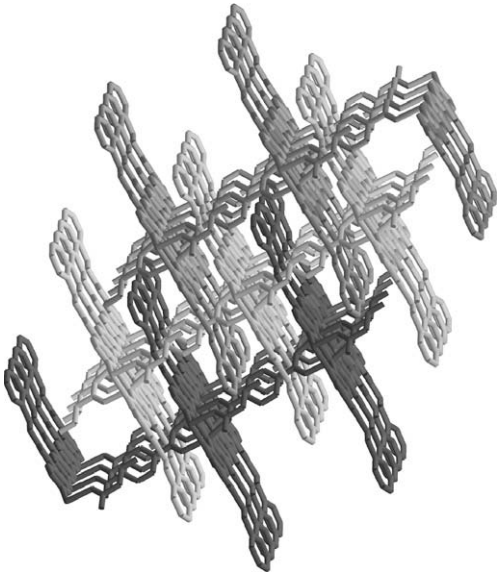


Fig. 9. The intervening fragments of **3**.

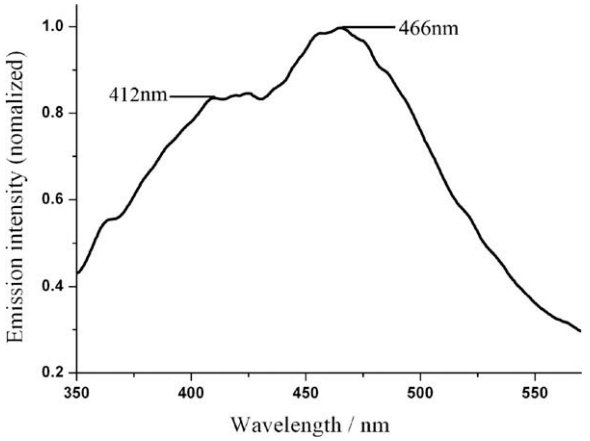


Fig. 10. The emission spectra of **3** in the solid state at room temperature.

ric stretching bands, respectively, with a Δ value of ca. 160 cm^{-1}, indicating the presence of a bis-bidentate coordination mode [37].

3.2.2. Luminescent properties

The solid-state luminescence property of complex **3** was investigated at room temperature. Interestingly, the emission spectrum for complex **3** shows a main peak at 466 nm with a shoulder at about 410 nm upon excitation at 373 nm (Fig. 10). In order to understand the nature of this emission band, we analyzed the photoluminescent property of the pmb ligand and found that the strongest emission peak for pmb apears at 406 nm upon excitation at 346 nm, whereas the emission peak for H_2bdc apears at 390 nm upon excitation at 350 nm [38]. So the shoulder peak of the emission spectrum at 410 nm of complex **3** is probably due to an intraligand energy transition, while the emission band at 466 nm may be assigned to a metal–ligand charge transfer.

4. Conclusion

Three new Ni(II), Co(II) and Cd(II) coordination polymers with different structural motifs based on mixed bdc and dipyridylbenzoates ligands (pmb) have been hydrothermally synthesized and structurally characterized. Complex **1** has a 3D threefold interpenetrated adamantanoid architecture, **2** has a 3D fourfold with rotaxane topology, and **3** is a 2D network with paddle wheel dimeric cadmium tetracarboxylate building units. In summary, our research demonstrates that the dipyridylbenzoates ligand (pmb) could be a potential bridging ligand to construct novel supramolecular architectures with different structures.

Acknowledgements

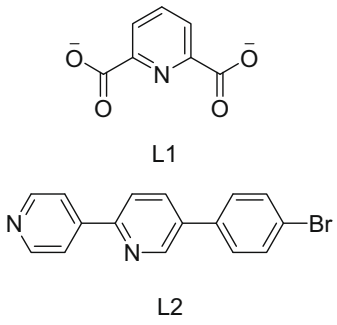
We are thankful for financial support from the National Natural Science Foundation of China (Project Nos. 20373009 and 20703008), the Chang Jiang Scholars Program (2006), the Program for Changjiang Scholars and the Innovative Research Team in the University (IRT0714), the Specialized Research Fund for the Doctoral Program in the Higher Education Institution of the Ministry of Education of China (No. 20030183063), and the Science Foundation for Young Teachers of Northeast Normal University (20080502).

Appendix A. Supplementary data

CCDC 670735–670737 contains the supplementary crystallographic data for **1**–**3**, respectively. These data can be obtained free of charge via http://www.ccdc.cam.ac.uk/conts/retrieving.html, or from the Cambridge Crystallographic Data Centre, 12 Union Road, Cambridge CB2 1EZ, UK; fax: (+44) 1223-336-033; or e-mail: deposit@ccdc.cam.ac.uk. Supplementary data associated with this article can be found, in the online version, at doi:10.1016/j.poly.2008.12.056.

References

[1] R. Robson, B.F. Abrahams, S.R. Batten, R.W. Gable, B.F. Hoskins, J. Liu, Supramolecular Architecture, American Chemical Society, Washington, DC, 1992.
[2] M. Moulton, L.P. Wu, T. Kuroda-Sowa, Adv. Inorg. Chem. 46 (1999) 173.
[3] X.J. Li, R. Cao, W.H. Bi, Y.Q. Wang, Y.L. Wang, X. Li, Polyhedron 24 (2005) 2955–2962.
[4] X.L. Wang, C. Qin, E.B. Wang, L. Xu, Z.M. Su, C.W. Hu, Angew. Chem., Int. Ed. 43 (2004) 5036–5040.
[5] M.J. Zaworotko, Chem. Soc. Rev. 23 (1994) 283.
[6] P.J. Hagrman, D. Hagrman, J. Zubieta, Angew. Chem., Int. Ed. Engl. 38 (1999) 2639.
[7] L. Carlucci, G. Ciani, D.M. Proserpio, Coord. Chem. 246 (2003) 247.
[8] O.R. Evans, W.B. Lin, Acc. Chem. Res. 35 (2002) 511.
[9] K. Biradha, M. Fujita, Chem. Commun. (2002) 1866.
[10] M. Konodo, T. Joshitomi, K. Seki, H. Matsuzaka, S. Kitagawa, Angew. Chem., Int. Ed. Engl. 36 (1997) 1844.
[11] K.N. Power, T.L. Hennigar, M.J. Zaworotko, New J. Chem. 22 (1998) 177.
[12] F.A.A. Paz, Y.Z. Khimyak, A.D. Bond, J. Rocha, J. Klinowski, Eur. J. Inorg. Chem. (2002) 2823.
[13] X.H. Bu, W. Chen, S.L. Lu, R.H. Zhang, D.Z. Liao, W.M. Bu, F. Shionoya, M. Brisse, J. Ribas, Angew. Chem., Int. Ed. 40 (2001) 3201.
[14] F.A.A. Paz, Y.Z. Khimyak, A.D. Bond, J. Rocha, J. Klinowski, Eur. J. Inorg. Chem. (2002) 2823.
[15] T.M. Reineke, M. Eddaoudi, D.M. Moler, M. O'Keeffe, O.M. Yaghi, J. Am. Chem. Soc. 122 (2002) 4843.
[16] D.M. Proserpio, R. Hoffman, P. Preuss, J. Am. Chem. Soc. 116 (1994) 9634.
[17] O. Ermer, Adv. Mater. 3 (1991) 608.
[18] J.S. Miller, Adv. Mater. 13 (2001) 525.
[19] L. Carlucci, G. Ciani, D.M. Proserpio, CrysEngCommun. 5 (2003) 269.
[20] S.A. Bourne, J.J. Liu, B. Moulton, M.J. Zaworotko, Chem. Commun. (2001) 861.
[21] X.H. Bu, M.L. Tong, H.C. Chang, S. Kitagawa, S.R. Batten, Angew. Chem., Int Ed. 43 (2004) 192.
[22] D.R. Xiao, Y.G. Li, E.B. Wang, L.L. Fan, H.Y. An, Z.M. Su, L. Xu, Inorg. Chem. 46 (2007) 4158.
[23] J.P. Sauvage, Acc. Chem. Res. 31 (1998) 611.
[24] K. Kim, Chem. Soc. Rev. 31 (2002) 96.
[25] M. Fujita, O. Sasaki, K. Watanabe, K. Ogura, K. Yamaguchi, New J. Chem. 22 (1998) 189.
[26] L. Carlucci, G. Ciani, M. Moret, D.M. Proserpio, S. Rizzato, Angew. Chem., Int. Ed. 39 (2000) 1506.
[27] X. Shi, G.S. Zhu, X.H. Wang, G.H. Li, Q.R. Fang, X.J. Zhao, G. Wu, G. Tian, M. Xue, R.W. Wang, S.L. Qiu, Cryst. Growth Des. 5 (2005) 314.
[28] B.H. Ye, B.B. Ding, Y.Q. Weng, XM. Chen, Cryst. Growth Des. 5 (2005) 801.
[29] A. Thirumurugan, C.N.R. Rao, J. Mater. Chem. 15 (2005) 3852.
[30] T. Higashi, Program for Absorption Correction, Rigaku Corporation, Tokyo, Japan, 1995.
[31] SHELXTL, Version 5.1, Siemens Industrial Automation Inc., 1997.
[32] Y.H. Liu, C.S. Lin, H.L. Tsai, C.H. Ueng, K.L. Lu, Solid State Chem. 157 (2001) 166.
[33] T. Allman, R. Goel, N.K. Jha, A.L. Beauchamp, Inorg. Chem. 23 (1984) 914.
[34] S.L. Li, T.C.W. Mak, J. Chem. Soc., Dalton Trans. (1995) 1519.
[35] A. Bond, J. Chem. Phys. 98 (1964) 441.
[36] R. Wang, L. Han, F. Jiang, Y. Zhou, D. Yuan, M. Hong, Cryst. Growth Des. 5 (2005) 129.
[37] P.K. Chen, Y.X. Che, L. Xue, J.M. Zheng, Cryst. Growth Des. 6 (2006) 2517.
[38] W. Chen, J.Y. Wang, C. Chen, Q. Yue, H.M. Yuan, J.S. Chen, S.N. Wang, Inorg. Chem. 42 (2003) 944.



Scheme 1.

Magana 560 spectrometer with samples prepared as KBr pellets. A PE TGA thermogravimetric analyzer was used to obtain the TGA curve at a heating rate of 10 °C min^{-1}. Elemental analyses were carried out using the Perkin–Elmer elemental analyzer 2400CHN. The magnetic susceptibilities of the nickel and copper complexes were measured in the temperature range of 2–300 K with an applied field of 1000 Oe, as well as *M* versus H (0–6 T) at 2 K on a SQUID magnetometer by using polycrystalline sample. Experimental data were corrected for diamagnetic contributions employing both the subtraction of the sample holder and Pascal's constants [45]. 5-(4-Br)-ph-2,4′-bpy and the Co(II) complex were prepared as previously reported [43].

2.2. Synthesis

2.2.1. $[Ni(L1)(L2)_2 \cdot H_2O]_n$

This complex was prepared as light blue block crystals in *ca.* 40% yield according to a previously described procedure using $NiSO_4 \cdot 6H_2O$ in place of $CoSO_4 \cdot 7H_2O$ [43]. Brown powder was also obtained as reaction product. Elemental *Anal.* Calc. for $C_{39}H_{27}Br_2NiN_5O_5$: C, 54.20; H, 3.15; N, 8.10. Found: C, 54.71; H, 3.25; N, 7.95%. IR (KBr, cm^{-1}): 3413 s, 3066 s, 1653 s, 1567 vs, 1464 s, 1346 s.

2.2.2. $[Cu_4(L1)_4(L2)_4 \cdot 2H_2O$

Compound **$[Cu_4(L1)_4(L2)_4] \cdot 2H_2O$** was isolated as blue block crystals following the above procedure using $CuSO_4 \cdot 5H_2O$ in place of $NiSO_4 \cdot 6H_2O$, black powder was obtained as by product. Yield: ~45%. Elemental *Anal.* Calc. for $C_{92}H_{58}N_{12}O_{18}Br_4Cu_4$: C, 50.38; H, 2.67; N, 7.66. Found: C, 50.79; H, 2.99; N, 7.32%. IR (KBr, cm^{-1}): ν = 3422 m, 3081 m, 1632 s, 1465 m, 1427 m, 1368 m, 1270 m, 1213 m.

2.3. Crystal structure analysis

All diffraction data were collected at room temperature on a Bruker SMART APEX CCD area detector diffractometer using graphite a monochromated Mo Kα radiation (λ = 0.71073 Å). Intensity data were collected by ω scan technique. All data were corrected for Lorentz polarization effects [46]. The structures were solved by the direct method using SIR97 [47] and were refined on F^2 by full-matrix least-squares technique using the SHELXL-97 [48] program package. The non-hydrogen atoms were refined anisotropically. In **$[Ni(L1)(L2)_2 \cdot H_2O]_n$** and **$[Cu_4(L1)_4(L2)_4] \cdot 2H_2O$**, it was not practical to assign hydrogen atoms on the disordered water molecules. The other H atoms were added in ideal positions (C–H = 0.93 Å, U_{iso}(H) = 1.2U_{eq} (C)) and were not refined. The crystallographic parameters are listed in Table 1.

2.4. Theoretical calculations

DFT calculations were carried out for each nearest neighboring binuclear Cu complex with the B3LYP gradient-corrected density functional [49–51] and the Ahlrich's pVDZ [52] basis set, as implemented in GAUSSIAN 03 [53]. The broken-symmetry [54] procedure was used to evaluate the singlet state energy for each binuclear Cu complex. The value of the exchange parameter *J* was obtained as $J = [E(BS) - E(T)]$, where $E(T)$ is the energy for the triplet state, and $E(BS)$ is the energy for the broken symmetry singlet.

Table 1
Crystallographic data for complexes **$[Ni(L1)(L2)_2 \cdot H_2O]_n$** and **$[Cu_4(L1)_4(L2)_4] \cdot 2H_2O$**.

	$[Ni(L1)(L2)_2 \cdot H_2O]_n$	$[Cu_4(L1)_4(L2)_4] \cdot 2H_2O$
Empirical formula	$C_{39}H_{29}Br_2NiN_5O_5$	$C_{92}H_{58}N_{12}O_{18}Br_4Cu_4$
Formula weight	866.19	2193.34
Temperature (K)	293(2)	293(2)
Crystal system	monoclinic	triclinic
Space group	$P2(1)/c$	$P\bar{1}$
a (Å)	17.499(5)	12.858(5)
b (Å)	10.432(5)	17.972(5)
c (Å)	38.525(5)	19.026(5)
α (°)	90	92.239(5)
β (°)	102.62(0)	92.670(5)
γ (°)	90	98.692(5)
V (Å^3)	6862.71(4) Å	4337(2)
Z	8	2
D_{calc} (Mg m^{-3})	1.669	1.677
μ (mm^{-1})	2.949	2.888
F(000)	3456	2180
Reflections collected	34880	24518
Independent reflection	12135	16706
Refined parameters	937	1321
Goodness-of-fit (F^2)	0.982	0.964
R indices [$I > 2\sigma(I)$]	R_1 = 0.0604, wR_2 = 0.1360	R_1 = 0.0548, wR_2 = 0.1179
R indices (all data)	R_1 = 0.1312, wR_2 = 0.1665	R_1 = 0.1144, wR_2 = 0.1408

3. Results and discussion

We have previously reported the synthesis and the X-ray crystallographic studies of the Co^{II} complex **$[Co(L1)(L2)_2 \cdot H_2O]_n$** [43]. The structural analysis indicates that there are two crystallographically independent cobalt ions (Co1 and Co2) in **$[Co(L1)(L2)_2 \cdot H_2O]_n$**, and each cobalt ion exists in a distorted octahedral coordination environment. The two kinds of Co^{II} ions are bridged by pdc^{2-} anions to form two kinds of 1D coordination polymeric zigzag chains (the Co1 chain and the Co2 chain). The analytical data of **$[Ni(L1)(L2)_2 \cdot H_2O]_n$** suggests that the nickel(II) complex is analogous to the cobalt complex. However, the analytical data of the copper complex suggests that it is a tetranuclear cluster with formula **$[Cu_4(L1)_4(L2)_4] \cdot 2H_2O$**. Thus, a simple change of the metal center has yielded completely different nuclearity, structure, and magnetic behavior. The scheme for the above transformation is as following:

$$M^{2+} + pdc^{2-}\ (L1) + 5\text{-}(4\text{-}Br)\text{-}ph\text{-}2,4'\text{-}bpy\ (L2) + nH_2O \longrightarrow \begin{cases} \text{antiferromagnetic } [M(L1)(L2)_2 \cdot H_2O]_n\ (M=Ni \text{ or } Co) \\ \text{ferromagnetic } [M_4(L1)_4(L2)_4] \cdot 2H_2O\ (M=Cu) \end{cases}$$

3.1. Crystal structures

The crystal structure of **$[Ni(L1)(L2)_2 \cdot H_2O]_n$** (Fig. 1) is similar to the cobalt complex **$[Co(L1)(L2)_2 \cdot H_2O]_n$** [43]. There are two crystallographically independent nickel ions in the nickel complex, and each nickel ion exists in distorted octahedral coordination environment. The Ni^{II} ions are bridged by the bridging ligands pdc^{2-} to form 1D coordination zigzag polymeric chains along the *b*-axis. Thus, two kinds of 1D coordination zigzag polymeric chains (the Ni1 chain and Ni2 chain) exist in the nickel complex. In the

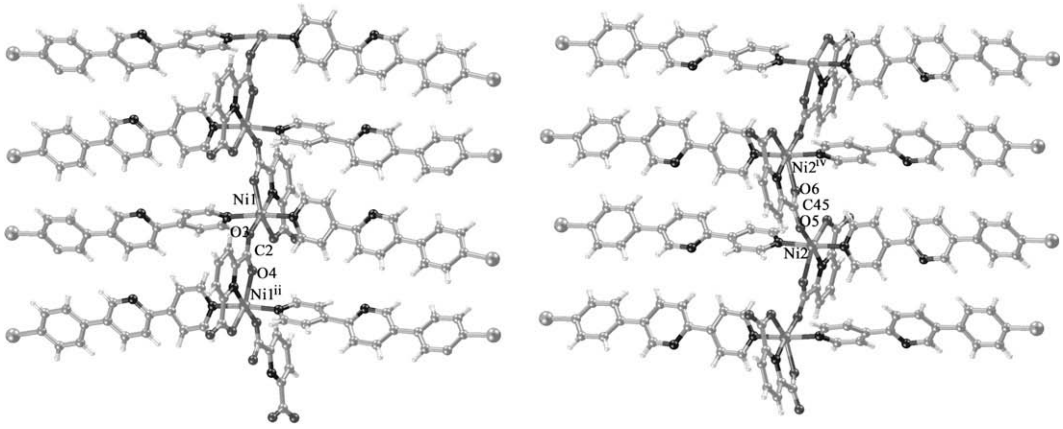


Fig. 1. The perspective view 1D zigzag polymeric chains in the complex $\mathbf{[Ni(L1)(L2)_2 \cdot H_2O]_n}$.

Ni1 chain, the equatorial Ni–N (1.990(8) Å) and Ni–O (2.052(7)–2.187(6) Å) (Table 2) bond distances are close (±0.01 Å) to those of the similar system with 5-ph-2,4′-bpy ligand [40], the two axial Ni–N distances (2.096(6) and 2.098(6) Å) are almost in the same length. For the Ni2 chain, the equatorial Ni–N bond distance is 2.000(7) Å, the equatorial Ni–O bond distances are in the range 2.044(7)–2.234(6) Å. The two axial Ni–N distances are unequal (2.082(5) and 2.096(6) Å), which is different from that of the Ni1 chain. Furthermore, Ni1 or Ni2 centered neighboring chains associate into a 2D layer by hydrogen bonds interactions, Ni1 and Ni2 layers are alternately arranged. Interestingly, in the Ni2 layer of $\mathbf{[Ni(L1)(L2)_2 \cdot H_2O]_n}$, both C–H groups and uncoordinated nitrogen atoms contribute to the hydrogen bonds formation (H···π, *ca.* 2.88 Å), whereas in the Ni1 layer only C–H groups form hydrogen bonds (H···π, *ca.* 2.78 Å) (see *Fig.* S1 in the Supplementary data). The intra-chain Ni1···Ni1 and Ni2···Ni2 distances are 5.57 and 5.61 Å, respectively. The torsion angle Ni1–O3–O4–Ni1^{iii} and Ni2–O6–O5–Ni2^{iv} (Symmetry codes: (iii) $1-x, -0.5+y, 1.5-z$; (iv) $-x, -0.5+y, 1.5-z$) are 177.2° and 172.9°, respectively. Therefore, the Ni2 chains are more twisted compared to those of the similar system with 5-ph-2,4′-bpy as L2 (Ni1–O3–O2–Ni1^{ii}, 175.3°) [40] by the introduction of bromide substituent on the pendant, though the Ni1 chains are less twisted.

The complex $\mathbf{[Cu_4(L1)_4(L2)_4] \cdot 2H_2O}$ can be engineered with the same ligands (L1 and L2) as in $\mathbf{[Ni(L1)(L2)_2 \cdot H_2O]_n}$ or $\mathbf{[Co(L1)(L2)_2 \cdot H_2O]_n}$, in the presence of the copper ions. Unlike the nickel or cobalt complex, there are two centrosymmetric $[Cu_4(L1)_4(L2)_4]$ tetramers in the unit cell of the copper complex. These two tetramers, **A** and **B**, have similar coordination spheres (see Fig. 2). In each tetramer, the two crystallographically independent copper ions possess distorted square pyramidal coordination. In the tetramer **A**, the four Cu^{II} ions are arranged symmetrically in a quadrilateral, in which neighboring Cu^{II} (Cu1···Cu2 or Cu1···Cu2A) ions are bridged alternately by the carboxylate group of two different pdc^{2-} ligands. Both Cu1 and Cu2 are penta-coordinated with same square-pyramidal coordinational mode. The basal plane is constructed by one N and two O atoms offered by one pdc^{2-} and one N atom from bpy ligand in trans position with pdc^{2-}, with normal Cu–O (2.014(6)–2.049(7) Å) and Cu–N (1.905(6)–1.966(7) Å) bond distances (Table 2) [24]. The apical sites are occupied by the O atom from other pdc^{2-} ligand, and Cu–O bond lengths are 2.182(7) and 2.164(6) Å, respectively, which are longer than those in the basal plane. In the tetramer **B**, the basal plane Cu–O (2.026(5)–2.053(6) Å) and the Cu–N (1.898(6)–1.950(5) Å) bond distances are similar to those in the tetramer **A**. The apical Cu–O distances are 2.192(5) and 2.195(7) Å, which are longer than the corresponding ones in the tetramer **A**. The length of each tetramer measured by the distance between the Br atoms in the trans position in $\mathbf{[Cu_4(L1)_4(L2)_4] \cdot 2H_2O}$ is ca. 32 Å. The tetramers **A** associate into a 1D chain through intercluster π···π stacking interactions (the face to face distance, 3.74 Å) between the pyridine rings of neighboring clusters (see *Fig. S2 in the Supplementary data*), while the tetramers **B** associate into a 1D chain through C–H···O hydrogen bonds (C···O, 3.269 Å) along the *a*-axis. The neighboring chains, **A** and **B**, self-assemble into a 2D layer by hydrogen bonds C–H···O (C···O, 2.641–3.442 Å) along the b-axis. In addition, the C–H···Br hydrogen bonds (C···Br, 3.624 Å) only exist in the chain **A**, which link the neighboring layers to form a 3D network (see *Fig. S3 in the Supplementary data*). The intercluster metal–metal distances are 5.138 Å, 8.643 Å, 9.045 Å, and 10.683 Å for Cu1···Cu1, Cu3···Cu4, Cu1···Cu4, and Cu2···Cu3, respectively. Obviously, 5.138 Å of intercluster Cu1···Cu1 distance is shorter than all intracluster Cu···Cu distances due to π···π stacking interactions between the pyridine rings of neighboring **A** clusters. This indicates that the intercluster π···π supramolecular interactions in the copper complex play a crucial role in the stabilization of the structure. The different coordination sphere around Ni (Co) and Cu is due to the fact that the weaker John–Teller effect in Ni^{II} (Co^{II}) than that of Cu^{II}, corresponding to distorted octahedral and distorted square pyramidal coordination structure in the complex $\mathbf{[Ni(L1)(L2)_2 \cdot H_2O]_n}$ ($\mathbf{[Co(L1)(L2)_2 \cdot H_2O]_n}$) and $\mathbf{[Cu_4(L1)_4(L2)_4] \cdot 2H_2O}$, respectively, therefore, 1D coordinational polymer and tetranuclear complex is obtained, respectively. Very recently we have obtained three mononuclear

Table 2
Selected bond distances (Å) in $\mathbf{[Ni(L1)(L2)_2 \cdot H_2O]_n}$ and $\mathbf{[Cu_4(L1)_4(L2)_4] \cdot 2H_2O}$.

[Ni(L1)(L2)$_2$ · H$_2$O]$_n$[a]			
Ni2–N4	2.000(7)	Ni1–N3^{ii}	1.990(8)
Ni2–O5^{i}	2.044(7)	Ni1–O3	2.052(7)
Ni2–N6	2.082(5)	Ni1–N2	2.096(6)
Ni2–N5	2.096(6)	Ni1–N1	2.098(6)
Ni2–O8	2.101(8)	Ni1–O1^{ii}	2.106(7)
Ni2–O6	2.234(6)	Ni1–O4^{ii}	2.187(6)
[Cu$_4$(L1)$_4$(L2)$_4$] · 2H$_2$O			
Cu3–N7	1.904(5)	Cu1–N1	1.906(6)
Cu3–N8	1.950(5)	Cu1–N2	1.966(7)
Cu3–O12	2.026(5)	Cu1–O2	2.014(6)
Cu3–O10	2.035(7)	Cu1–O3	2.031(5)
Cu3–O11	2.192(5)	Cu1–O4	2.182(7)
Cu4–N12	1.898(6)	Cu2–N4	1.905(6)
Cu4–N11	1.944(6)	Cu2–N5	1.947(6)
Cu4–O14	2.030(5)	Cu2–O7	2.046(7)
Cu4–O16	2.053(6)	Cu2–O5	2.049(5)
Cu4–O13	2.195(7)	Cu2–O6	2.164(6)

[a] (i) $-x, 0.5+y, 1.5-z$; (ii) $1-x, 0.5+y, 1.5-z$.

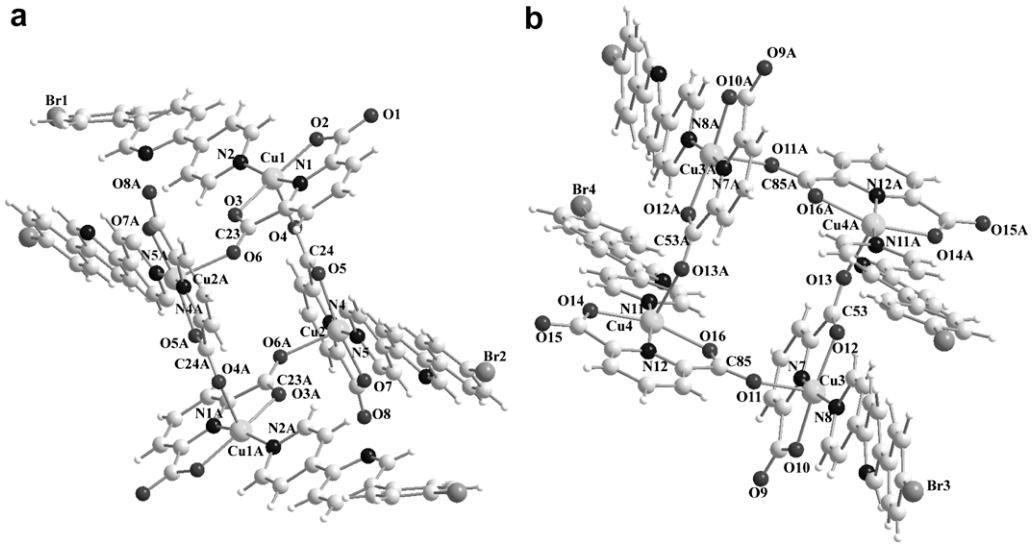


Fig. 2. The perspective view of tetramer **A** (a) and **B** (b) in the complex **[Cu$_4$(L1)$_4$(L2)$_4$]**. Cu1···Cu2, 5.608 Å; Cu1···Cu2A, 5.565 Å; Cu1···Cu1A, 9.135 Å; Cu2···Cu2A, 7.159 Å; Cu3···Cu4, 5.602 Å; Cu3···Cu4A, 5.628 Å; Cu3···Cu3A, 8.214 Å; Cu4···Cu4A, 7.658 Å. Atoms labeled 'A' are generated with $[1-x, -y, 1-z]$.

copper complexes constructed by pdc^{2-}, water molecule, and 2,4′-bipyridine as well as its derivative 5-phenyl-2,4′-bipyridine or 5-chloro-2,4′-bipyridine [55], where the copper ions also exhibit pentacoordinated environment with distorted square pyramidal geometry. Thus, both the Cu^{2+} and the pendant 5-(4-Br)-ph-2,4′-bpy ligand contribute to the formation of the tetranuclear complex **[Cu$_4$(L1)$_4$(L2)$_4$] · 2H$_2$O**.

3.2. Magnetic properties

The global feature of $\chi_M T$ versus T curve of **[Ni(L1)(L2)$_2$ · H$_2$O]$_n$** suggests a weak intramolecular antiferromagnetic interaction between Ni(II) ions as shown in Fig. 3, which is similar to that of **[Co(L1)(L2)$_2$ · H$_2$O]$_n$** [43]. The value of $\chi_M T$ at 300 K is 1.41 cm^3 mol^{-1} K and thus higher than the spin-only value of 1.00 cm^3 mol^{-1} K expected for uncoupled high-spin Ni^{II} ion ($S = 1$, $g = 2$), in accordance with the well-documented orbital contribution of the octahedral Ni^{II} ion [56,57]. As the sample is cooled from room temperature, the $\chi_M T$ value smoothly decreases from 1.41 cm^3 mol^{-1} K to 1.37 cm^3 mol^{-1} K at 50 K and then decreases more rapidly at low temperatures, reaching a value of 0.26 cm^3 mol^{-1} K at 2 K. The low-temperature drop may be due to secondary effects such as inter-chain interactions and/or zero-field splitting effects. The magnetic data for **[Ni(L1)(L2)$_2$ · H$_2$O]$_n$** can be fitted to the Curie–Weiss law with $C = 1.44$ cm^3 mol^{-1} K, $\theta = -10.2$ K. The negative θ value for the nickel complex indicates the antiferromagnetic interactions between Ni^{II} ions. An empirical (Weng's) formula has been reported in the literature to analyze 1-D systems with $S = 1$, using numerical procedures [45,58]:

$$\chi_{chain} = \frac{N\beta^2 g^2}{kT}\frac{2.0 + 0.019x + 0.777x^2}{3.0 + 4.346x + 3.232x^2 + 5.834x^3}$$

where $x = |J|/kT$. Considering the weak inter-chain interactions, the susceptibility can be corrected by the mean-field, (zJ') [59].

$$\chi_M = \chi_{chain}/[1 - (zJ'/Ng^2\beta^2)\chi_{chain}]$$

The best-fit parameters for **[Ni(L1)(L2)$_2$ · H$_2$O]$_n$** are found to be $g = 2.0$ (fixed), $J = -3$ cm^{-1}, $zJ' = -0.5$ cm^{-1}, and $R = 1.44 \times 10^{-4}$. The J value of -3 cm^{-1} for the nickel complex indicates that the coupling between the Ni(II) centers through the syn-anti carboxylate bridge is weakly antiferromagnetic. Furthermore, the J value of the nickel complex is close to that of the similar carboxylate systems with 5-ph-2,4′-bpy as pendant (-3.99 cm^{-1}) [40], and less negative than the reported *syn–syn* carboxylate system (-13.3 cm^{-1}) [60].

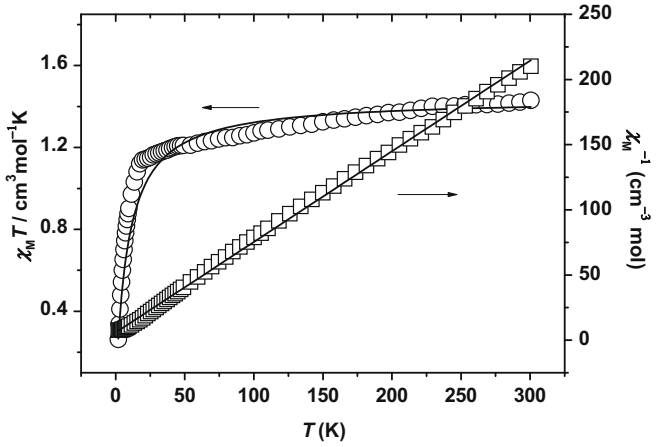


Fig. 3. Plots of $\chi_M T$ vs T and χ_M^{-1} vs T for the complex **[Ni(L1)(L2)$_2$ · H$_2$O]$_n$**. The solid line shows the best fit to the model (see text).

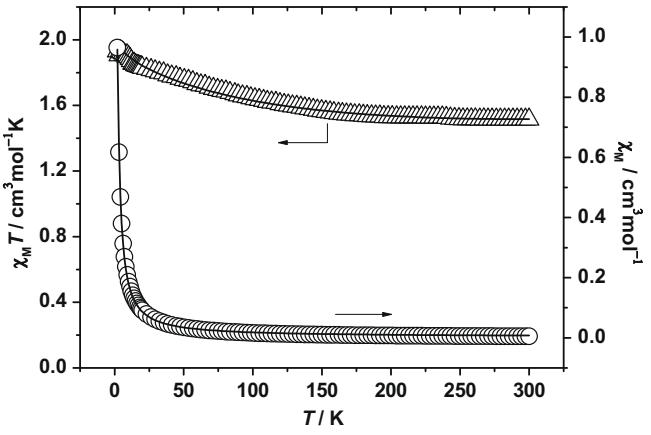


Fig. 4. Plots of $\chi_M T$ vs T and χ_M vs T for the complex **[Cu$_4$(L1)$_4$(L2)$_4$] · 2H$_2$O**. The solid lines represent the best fit of the data (see text for details).

The magnetic behavior for the complex **[Cu$_4$(L1)$_4$(L2)$_4$] · 2H$_2$O** is shown in Fig. 4. As the sample is cooled from room temperature, the value of $\chi_M T$ smoothly increases from 1.52 cm^3 mol^{-1} K to 1.53 cm^3 mol^{-1} K at 200 K and then increases rapidly at low temperatures, reaching a value of 1.93 cm^3 mol^{-1} K at 2 K, indicating the presence of intracluster ferromagnetic interactions. Taking into account the compound topology, three coupling parameters J_1, J_2, and J_3 can be considered to interpret the magnetic interactions in the copper complex, using the Hamiltonian:

$$H = -J_1(S_1 \cdot S_2 + S_3 \cdot S_4) - J_2(S_1 \cdot S_4 + S_2 \cdot S_3) - J_3(S_1 \cdot S_3 + S_2 \cdot S_4)$$

On the basis of the structural data of the tetramer, we set $J = J_1 = J_2$ and $J_3 = 0$ (see Chart 1). For this square disposition, the E_n value can be obtained by using the Kambe method [61,32] from the Hamiltonian:

$$H = -J(S_1 \cdot S_2 + S_3 \cdot S_4 + S_1 \cdot S_4 + S_2 \cdot S_3)$$

The analysis of the experimental susceptibility data has been performed by the use of the expression:

$$\chi_M T = Ng^2\beta^2 T(f(J,T)/3kT)$$

$$\text{where } f(J,T) = \frac{6\exp(J/kT) + 12\exp(2J/kT) + 30\exp(3J/kT)}{1 + 3\exp(J/kT) + 7\exp(2J/kT) + 5\exp(3J/kT)}.$$

The best-fit parameters are: $g = 2$, $J = 3$ cm^{-1}, and $R = 2.00\times10^{-5}$. The J value of 3 cm^{-1} for the copper complex suggests that the coupling between the Cu(II) ions through the *syn–anti* (basal–apical) O–C–O bridge is weakly ferromagnetic. In addition, the J value of copper complex is larger than that found in related structure [25], and smaller than those reported square Cu$_4$ systems [24,32]. Previous studies showed that the magnetic behaviors of a basal–apical O–C–O bridging complex related to the Addison parameter (τ) [62] of each square-pyramidal copper(II) center, representing the mixture of the magnetic $x^2 - y^2$ and z^2 orbitals. It is known that for $\tau = 0$ (pure square pyramidal), the interaction is strongly ferromagnetic but strongly antiferromagnetic when $\tau = 1$ (pure trigonal bipyramidal). In the copper complex, τ values for Cu1–Cu4 are 0.18, 0.12, 0.15, and 0.19, respectively. However, the basal–apical pathway was antiferromagnetic in similar system, where τ values were 0.14 and 0.25 [24].

DFT calculations are used in order to obtain insights into intracluster magnetic interactions in **[Cu$_4$(L1)$_4$(L2)$_4$] · 2H$_2$O**. Four binuclear copper(II) models (**a1**, **a2**, **b1**, and **b2**) are selected in our calculations to compute J value corresponding to each carboxylate bridging neighboring Cu ions in tetramers **A** or **B**. The model **a1** (**a2**) is obtained from the tetramer **A**, by taking the Cu1 and Cu2 (Cu2A) atoms, two pyridine ligands based on the structure of 5-(4-Br)-ph-2,4′-bpy, two pyridine-2,6-dicarboxylate ligands among which one serves as a bridge connecting the two copper atoms and the other one binds to Cu2 (Cu1), the formic acid molecule derived from the structure of pyridine-2,6-dicarboxylate binds to Cu1 (Cu2). Similarly, the model **b1** (**b2**) corresponding to the dimer containing atoms Cu3 and Cu4 (Cu3 and Cu4A) is taken from the tetramer **B**, where the 5-(4-Br)-ph-2,4′-bpy ligand is also replaced by a pyridine molecule for computational cost reasons. The J value obtained from [E(BS)−E(T)] (where E(BS) or E(T) denotes for the energy of broken symmetry singlet or triplet state, respectively) is 0.46 cm^{-1}/0.48 cm^{-1} for model **a1**/**a2**, and the J value is 0.54 cm^{-1}/0.48 cm^{-1} for **b1**/**b2**. These positive J values also demonstrate that the coupling between the Cu(II) ions through the basal–apical O–C–O bridge is weakly ferromagnetic, which differs from the antiferromagnetic coupling in similar system [24].The calculated J values of four model binuclear copper(II) complexes are similar to those found by the same DFT strategy in related structures (0−1.4 cm^{-1}) [63].

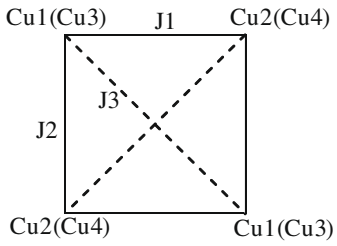


Chart 1. Schematic representation of the magnetic model in the tetramer **A** or **B** of **[Cu$_4$(L1)$_4$(L2)$_4$] · 2H$_2$O**.

The selected atom Mulliken spin populations obtained from our calculations in the triplet states for models **a1** and **a2** are presented in Table 3. In the triplet state of **a1**, the spin population on Cu1 is 0.596, and the spin populations on the directly coordinated atoms (N1, N2, O2, O3, O4) have the same sign as that on Cu1, corresponding to the spin delocalization from the spin center Cu^{II}. Furthermore, the spin population on Cu2 is 0.595, and the spin population on the directly coordinated atoms (N4, N5, O6A, O5, O7) also have the same sign as that on Cu2. The spin population on C24 atom of the bridging carboxylate ligand is negative. Obviously, the spin population distribution on the bridging carboxylate can be rationalized by the spin polarization mechanism. Thus, the path Cu1−O4−C24−O5−Cu2 is ferromagnetic in **a1**. Meanwhile, the spin population in **a2** indicates that Cu1−O3−C23−O6−Cu2A is also a ferromagnetic pathway. This behavior can also be observed for **b1** and **b2** (see *Table* S1 in the Supplementary data). Therefore, the paths Cu3−O11−C85−O16−Cu4 and Cu3−O12−C53−O13−Cu4A for **b1** and **b2**, respectively, are ferromagnetic. According to our DFT calculations, the O–C–O bridges in the basal–apical mode are responsible for the intracluster Cu^{II}···Cu^{II} ferromagnetic exchange which is reasonable for complex **[Cu$_4$(L1)$_4$(L2)$_4$] · 2H$_2$O**.

The X-ray crystallographic study suggests that the intercluster Cu1···Cu1 distance (5.138 Å) is shorter than all intracluster Cu···Cu distances due to the π···π stacking of Cu1 centered fragments of neighboring **A** clusters. Therefore, with the aim to understand the intercluster magnetic interactions in the copper complex, the Cu1 centered fragment was selected as model in our DFT calculation for the spin density distribution. As shown in Fig. 5, Cu1 and the directly coordinated atoms (N1, N2, O2, O3) have the positive density, demonstrating the spin delocalization from Cu1 to the ligands for the Cu1 centered fragment. For each Cu centered fragment, the alternating sign of the spin density is found on the ligand L1 and the bipyridine of L2. This is ascribed to the spin polarization effect to stabilize the high-spin state. The analysis of the spin densities shows opposite signs on two atoms in the face to face positions (C11 and C20, C15 and Cu1, C22 and C10) on

Table 3
Mulliken spin populations on the selected atoms of models **a1** and **a2** in the HS state for [**Cu$_4$(L1)$_4$(L2)$_4$] · 2H$_2$O**.

Model **a1**		Model **a2**	
Cu1	0.596	Cu1	0.589
Cu2	0.595	Cu2A	0.588
N1	0.113	N1	0.115
N2	0.054	N2	0.057
N4	0.114	N4A	0.116
N5	0.064	N5A	0.057
O2	0.121	O2	0.138
O3	0.011	O3	0.078
O4	0.094	O4	0.001
O5	0.086	O5A	0.102
O6A	0.002	O6	0.010
O7	0.118	O7A	0.110
C24	−0.002	C23	−0.001

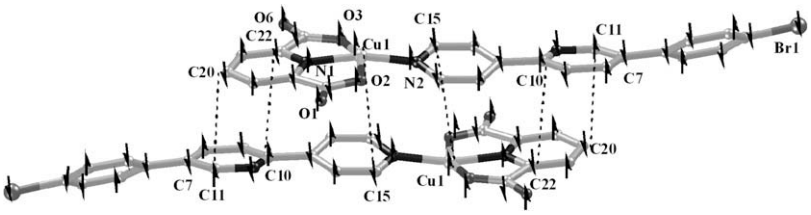


Fig. 5. The spin densities for stacked Cu1 centered fragments of neighboring **A** clusters for $\mathbf{[Cu_4(L1)_4(L2)_4]\cdot 2H_2O}$. The arrow upward denotes positive spin density and the arrow downward denotes negative spin density (hydrogen atoms have been omitted for clarity).

neighboring Cu1 centered fragments (*Fig.* 5 and Table S2 in the Supplementary data), which favors for the intermolecular ferromagnetic coupling according to the McConnell Model I [64]. Because the spin density on each interacting site except Cu1 (0.539) is pretty small (C11: 0.001, C20: −0.004, C15: −0.002, C22: −0.005, C10: 0.001), the intercluster interaction may also slightly contribute to the weakly ferromagnetic coupling for $\mathbf{[Cu_4(L1)_4(L2)_4]\cdot 2H_2O}$.

4. Conclusions

A series of complexes containing the identical bridging ligand and pendants and different metals such as Ni^{2+}, Co^{2+}, and Cu^{2+} was synthesized and characterized. In the nickel and cobalt complexes $\mathbf{[M(L1)(L2)_2\cdot H_2O]_n}$ (M = Ni^{2+} or Co^{2+}, L1 = pdc^{2-}, L2 =5-(4-Br)-ph-2,4′-bpy), the metal ions are hexa-coordinated with distorted octahedral geometries, and bridged by the L1 pdc^{2-} forming 1D backbone with L2 5-(4-Br)-ph-2,4'-bpy as pendants. However, in the copper complex $\mathbf{[Cu_4(L1)_4(L2)_4]\cdot 2H_2O}$, the metal ions adopt a distorted square pyramidal geometry and the O–C–O bridge of pdc^{2-} adopts a basal–apical disposition between metal ions to give a square planar backbone with L2 pendants. Antiferromagnetic coupling between metal ions in the nickel and cobalt complexes has been observed, the copper complex possesses weakly ferromagnetic coupling due to its tetranuclear cluster structure. DFT calculations suggested that the O–C–O bridges in a basal–apical mode are responsible for intermetallic ferromagnetic exchange for the tetranuclear copper cluster. The successful transform of magnetic property from antiferromagnetic $\mathbf{[Ni(L1)(L2)_2\cdot H_2O]_n}$ or $\mathbf{[Co(L1)(L2)_2\cdot H_2O]_n}$ to ferromagnetic coupling $\mathbf{[Cu_4(L1)_4(L2)_4]\cdot 2H_2O}$ can be simply traced back to the tuning of metal ions with investigated ligands. As a result, the metal ion plays the key role in the magnetic transform. This report may provide a reasonable way in the design and exploitation of new magnetic compounds for useful applications.

Acknowledgments

We thank the Natural Science Foundation of China (50473032; 20773022), NCET-06-0321, NENU-STB07007, the JLSDP (20082212), and the analysis and testing foundation of Northeast Normal University for financial support.

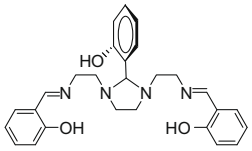
Appendix A. Supplementary data

CCDC 652700 and 621386 contain the supplementary crystallographic data for $\mathbf{[Ni(L1)(L2)_2\cdot H_2O]_n}$ and $\mathbf{[Cu_4(L1)_4(L2)_4]\cdot 2H_2O}$. These data can be obtained free of charge via http://www.ccdc.cam.ac.uk/conts/retrieving.html, or from the Cambridge Crystallographic Data Centre, 12 Union Road, Cambridge CB2 1EZ, UK; fax: (+44) 1223-336-033; or e-mail: deposit@ccdc.cam.ac.uk. Supplementary data associated with this article can be found, in the online version, at doi:10.1016/j.poly.2008.12.051.

References

[1] M. Cavallini, J. Gomez-Segura, D. Ruiz-Molina, M. Massi, C. Albonetti, C. Rovira, F. Biscarini, Angew. Chem., Int. Ed. 44 (2005) 888.
[2] O. Waldmann, G. Carver, C. Dobe, D. Biner, A. Sieber, U. Güdel, H.H. Mutka, J. Ollivier, N.E. Chakov, Appl. Phys. Lett. 88 (2006) 042507.
[3] A. Vindigni, A. Rettori, L. Bogani, A. Caneschi, D. Gatteschi, R. Sessoli, M.A. Novak, Appl. Phys. Lett. 87 (2005) 073102.
[4] H. Ohno, D. Chiba, F. Matsukura, T. Omiya, E. Abe, T. Dietl, Y. Ohno, K. Ohtani, Nature 408 (2000) 944.
[5] R.L. Edelstein, C.R. Tamanaha, P.E. Sheehan, M.M. Miller, D.R. Baselt, L.J. Whitman, R.J. Colton, Biosens. Bioelectron. 14 (2000) 805.
[6] B. Zhang, Z. Wang, H. Fujiwara, H. Kobayashi, M. Kurmoo, K. Inoue, T. Mori, S. Gao, Y. Zhang, D. Zhu, Adv. Mater. 17 (2005) 1988.
[7] E. Coronado, P. Delhaes, D. Gatteschi, J.S. Miller, Molecular Magnetism: From Molecular Assemblies to the Devices, Kluwer Academic Publishers, Dordrecht, The Netherlands, 1996.
[8] G. DeMunno, F. Lloret, M. Julve, in: O. Kahn (Ed.), Magnetism: A Supramolecular Function, Kluwer Academic Publishers, Dordrecht, The Netherlands, 1996.
[9] A.L. Feig, S.J. Lippard, Chem. Rev. 94 (1994) 759.
[10] E.I. Solomon, T.C. Brunold, M.I. Davis, J.N. Kemsley, S.-K. Lee, N. Lehnert, F. Neese, A.J. Skulan, Y.S. Yang, J. Zhou, Chem. Rev. 100 (2000) 235.
[11] S. Saito, Y. Yamamoto, Chem. Rev. 100 (2000) 2901.
[12] T.Y. Luh, M.K. Leung, K.T. Wong, Chem. Rev. 100 (2000) 3187.
[13] L. Jiang, H.J. Choi, X.-L. Feng, T.-B. Lu, J.-R. Long, Inorg. Chem. 46 (2007) 2181.
[14] S.S.Y. Chui, S.M.F. Lo, J.P.H. Charmant, A.G. Orpen, I.D. Williams, Science 283 (1999) 1148.
[15] S.-I. Noro, S. Kitagawa, M. Kondo, K. Seki, Angew. Chem., Int. Ed. 39 (2000) 2081.
[16] E. Colacio, M. Ghazi, R. Kivekäs, M. Klinga, F. Lloret, J.M. Moreno, Inorg. Chem. 39 (2000) 2770.
[17] L. Gutierrez, G. Alzuet, J.A. Real, J. Cano, J. Borrás, A. Castiñeiras, Inorg. Chem. 39 (2000) 3608.
[18] F. Karadas, E.J. Schelter, M. Shatruk, A.V. Prosvirin, J. Bacsa, D. Smirnov, A. Ozarowski, J. Krzystek, J. Telser, K.R. Dunbar, Inorg. Chem. 47 (2008) 2074. and references cited therein.
[19] L.M. Field, M.C. Morón, P.M. Lahti, F. Palacio, A. Paduan-Filho, N.F. Oliveira Jr., Inorg. Chem. 45 (2006) 2562.
[20] A. Caneschi, D. Gatteschi, N. Lalioti, C. Sangregorio, R. Sessoli, G. Venturi, A. Vindigni, A. Rettori, M.G. Pini, M.A. Novak, Angew. Chem., Int. Ed. 40 (2001) 1760.
[21] S. Subramanian, M.J. Zaworotko, Angew. Chem., Int. Ed. 34 (1995) 2127.
[22] P. Losier, M.J. Zaworotko, Angew. Chem., Int. Ed. 35 (1996) 2779.
[23] S.M.-F. Lo, S.S.-Y. Chui, L.-Y. Shek, Z. Lin, X. Zhang, G. Wen, I.D. Williams, J. Am. Chem. Soc. 122 (2000) 6293.
[24] M.S. Ray, A. Ghosh, A. Das, M.G.B. Drew, J. Ribas-Ariño, J. Novoa, J. Ribas, Chem. Commun. (2004) 1102.
[25] P.K. Nanda, G. Aromý, D. Ray, Chem. Commun. (2006) 3181.
[26] P. Mialane, C. Duboc, J. Marrot, E.R.A. Dolbecq, F. Sécheresse, Chem. Eur. J. 12 (2006) 1950.
[27] S. Konar, P.S. Mukherjee, M.G.B. Drew, J. Ribas, N.R. Chaudhuri, Inorg. Chem. 42 (2003) 2545.
[28] M. Murugesu, R. Clérac, B. Pilawa, A. Mandel, C.E. Anson, A.K. Powell, Inorg. Chim. Acta 337 (2002) 328.
[29] Y. Zhang, H.C. Liang, L.N. Zakharov, S.K. Das, M.M. Hetu, A.L. Rheingold, Inorg. Chim. Acta 360 (2007) 1691.
[30] C. Ruiz-Pérez, M. Hernández-Molina, P. Lorenzo-Luis, F. Lloret, J. Cano, M. Julve, Inorg. Chem. 39 (2000) 3845.
[31] S.K. Dey, B. Bag, K.M.A. Mali, M.S. El Fallah, J. Ribas, S. Mitra, Inorg. Chem. 42 (2003) 4029.
[32] S. Roy, T.N. Mandal, A.K. Barik, S. Gupta, R.J. Butcher, M.S. El Fallah, J. Tercero, S.K. Kar, Polyhedron 27 (2008) 105.
[33] A. Burkhardt, E.T. Spielberg, H. Görls, W. Plass, Inorg. Chem. 47 (2008) 2485.
[34] S.K. Ghosh, P.K. Bharadwaj, Inorg. Chem. 42 (2003) 8250.
[35] S.K. Ghosh, J. Ribas, P.K. Bharadwaj, CrystEngCommun 6 (2004) 250.
[36] S.K. Ghosh, J. Ribas, P.K. Bharadwaj, Cryst. Growth Des. 5 (2005) 623.
[37] B. Zhao, P. Cheng, Y. Dai, C. Cheng, D.-Z. Liao, S.-P. Yan, Z.H. Jiang, G.-L. Wang, Angew. Chem., Int. Ed. 42 (2003) 934.

[38] B. Zhao, P. Cheng, X. Chen, C. Cheng, W. Shi, D.-Z. Liao, S.-P. Yan, Z.-H. Jiang, J. Am. Chem. Soc. 126 (2004) 3012.
[39] H.-L. Gao, L. Yi, B. Zhao, X.-Q. Zhao, P. Cheng, D.-Z. Liao, S.-P. Yan, Inorg. Chem. 45 (2006) 5980.
[40] Y.-L. Zhao, S.-X. Cui, B. Li, J.-P. Zhang, Q. Liu, J. Mol. Struct. 873 (2008) 191.
[41] E.A. Boudreaux, L.N. Mulay, Theory and Applications of Molecular Paramagnetism, John Wiley & Sons, London, 1976. Chapter 7 and references cited therein.
[42] R.D. Willet, D. Gatteschi, O. Kahn (Eds.), Magneto-Structural Correlations in Exchange Coupled Systems, NATO Advanced Study Institute Series 140, Reidel Publishing, Dordrecht, Germany, 1983.
[43] S.-X. Cui, Y.-L. Zhao, B. Li, J.-P. Zhang, Q. Liu, Y. Zhang, Polyhedron 27 (2008) 671.
[44] R.G. Parr, W. Yang, Density Functional Theory of Atoms and Molecules, Oxford University Press, New York, 1989.
[45] O. Kahn, Molecular Magnetism, VCH, New York, 1993.
[46] P. Starynowicz, COSABS99, Program for Absorprtion Correction, University of Wroclaw, Wroclaw, Poland, 1999.
[47] A. Altomare, M.C. Burla, M. Camalli, G.L. Cascarano, C. Giacovazzo, A. Guagliardi, A.G.G. Moliterni, G. Polidori, R. Spagna, J. Appl. Crystallogr. 32 (1999) 115.
[48] G.M. Sheldrick, SHELXL97, University of Göttingen, Germany, 1997.
[49] A.D. Becke, Phys. Rev. A: Atom. Mol. Opt. Phys. 38 (1988) 3098.
[50] C. Lee, W. Yang, R.G. Parr, Phys. Rev. B: Condens. Mat. Mater. Phys. 37 (1988) 785.
[51] P.J. Stephens, F.J. Devlin, C.F. Chabalowski, M.J. Frisch, J. Phys. Chem. 98 (1994) 11623.
[52] A. Schater, H. Horn, R. Ahlrichs, J. Chem. Phys. 97 (1992) 2571.
[53] M.J. Frisch, G.W. Trucks, H.B. Schlegel, G.E. Scuseria, M.A. Robb, J.R. Cheeseman, J.A. Jr. Montgomery, T. Vreven, K.N. Kudin, J.C. Burant, J.M. Millam, S.S. Iyengar, J. Tomasi, V. Barone, B. Mennucci, M. Cossi, G. Scalmani, N. Rega, G.A. Petersson, H. Nakatsuji, M. Hada, M. Ehara, K. Toyota, R. Fukuda, J. Hasegawa, M. Ishida, T. Nakajima, Y. Honda, O. Kitao, H. Nakai, M. Klene, X. Li, J.E. Knox, H.P. Hratchian, J.B. Cross, V. Bakken, C. Adamo, J. Jaramillo, R. Gomperts, R.E. Stratmann, O. Yazyev, A.J. Austin, R. Cammi, C. Pomelli, J.W. Ochterski, P.Y. Ayala, K. Morokuma, G.A. Voth, P. Salvador, J.J. Dannenberg, V.G. Zakrzewski, S. Dapprich, A.D. Daniels, M.C. Strain, O. Farkas, D.K. Malick, A.D. Rabuck, K.J.B. Raghavachari, Foresman, J.V. Ortiz, Q. Cui, A.G. Baboul, S. Clifford, J. Cioslowski, B.B. Stefanov, G. Liu, A. Liashenko, P. Piskorz, I. Komaromi, R.L. Martin, D.J. Fox, T. Keith, M.A. Al-Laham, C.Y. Peng, A. Nanayakkara, M. Challacombe, P.M.W. Gill, B. Johnson, W. Chen, M. .W. Wong, C. Gonzalez, J.A. Pople, GAUSSIAN 03, Revision B.05, Gaussian, Inc., Wallingford, CT, 2004.
[54] L. Noodlemann, J. Chem. Phys. 74 (1981) 5737.
[55] S.-X. Cui, Y.-L. Zhao, J.-P. Zhang, Q. Liu, Y. Zhang, Cryst. Growth Des. 8 (2008) 3803.
[56] F.E. Mabbs, D.J. Machin, Magnetism and Transition Metal Complexes, Chapman and Hall, London, 1973.
[57] B.N. Figgis, M.A. Hitchman, Ligand Field Theory and Its Applications, Wiley-VCH, New York, 2000.
[58] C.Y. Weng, Thesis, Carnegie Mellon University, Pittsburgh, PA, 1969.
[59] C.J. O'Connor, Prog. Inorg. Chem. 29 (1982) 203.
[60] B.-B. Ding, Y.-Q. Weng, Z.-W. Mao, C.-K. Lam, X.-M. Chen, B.-H. Ye, Inorg. Chem. 44 (2005) 8836.
[61] K. Kambe, J. Phys. Soc. Jpn. 5 (1950) 48.
[62] A.W. Addison, T.N. Rao, J. Reedjik, J. Rijn, C.G. Verschoor, J. Chem. Soc., Dalton Trans. (1984) 1349.
[63] A. Rodriguez-Fortea, P. Alemany, S. Alvarez, E. Ruiz, Chem. Eur. J. 7 (2001) 627.
[64] H.M. McConnell, J. Chem. Phys. 39 (1963) 1910.



Scheme 1.

without attacking the 2-imidazolidinyl and imine carbon atoms, which would lead to ligand hydrolysis. The complex shows binding of the catechol molecule by replacement of the labile aqua bridge and its oxidation in air.

2. Experimental

2.1. Materials and instrumentation

All the starting chemicals and solvents were analytically pure and were used without further purification. Copper(II) carbonate, triethylenetetramine and salicylaldehyde were obtained from S.D. Fine Chem, India. The ligand H_3L was prepared according to a modified literature procedure [8]. ^1H and ^{13}C NMR spectra of the ligand were obtained on a Bruker AC 200 NMR spectrometer using TMS as the internal standard. The ^1H NMR spectrum of the complex was collected on a 250 MHz Bruker DXR 250 spectrometer. Infrared spectra were recorded as KBr pellets on a Nicolet Nexus-870 FT-IR spectrometer. The solution electrical conductivity and UV–Vis spectra were obtained using a Unitech type U131C digital conductivity meter with a solute concentration of about 10^{-3} M and a Shimadzu UV 3100 UV–Vis–NIR spectrophotometer, respectively. The room temperature magnetic susceptibilities in the solid state were measured using a home built Gouy balance fitted with a polytronic d.c. power supply. The experimental magnetic susceptibilities were corrected for the diamagnetic response using Pascal's constants [13]. Variable temperature magnetic measurements were carried out at the "Servei de Magnetoquímica (Universitat de Barcelona)" on polycrystalline samples (ca. 40 mg) using a Quantum Design MPMS XL-5 SQUID susceptometer operating at a constant magnetic field of 1T between 2 and 300 K. The experimental magnetic moment was corrected for the diamagnetic contribution from the sample holder. EPR experiments were performed on a Bruker ESR 300E (X-Band, 9.45 GHz) spectrometer, and spectra were collected at room temperature and ca. 77 K on powdered samples working with an Oxford make liquid helium cryostat for variable temperature measurements. Elemental analyses (C, H and N) were performed on a Perkin–Elmer model 240 C elemental analyzer.

Caution! Perchlorate salts are potentially explosive, only a small amount should be prepared, and handled with proper care.

2.2. Synthesis

2.2.1. $[\{Cu_2(\mu\text{-}L)(\text{-}H_2O)\}_2](ClO_4)_2 \cdot 4.5H_2O$ ($\mathbf{1} \cdot 4.5H_2O$)

To the ligand solution (0.50 g, 1.09 mmol) in 15 ml of DCM, a methanolic solution of triethylamine (0.55 ml, 4 mmol) was added dropwise to give a solution of pH 7–8. Then, a methanolic solution of $Cu(ClO_4)_2 \cdot 6H_2O$ (0.80 g, 2.18 mmol) was added slowly to the ligand solution with magnetic stirring at ambient temperature for 10 min. The reaction mixture was then stirred for 2 h and the solvent was removed in air. The deep green precipitate obtained was filtered through a glass frit and washed with water followed by methanol and hexane, and finally dried in vacuum over P_4O_{10}. Yield: 1.16 g (72%). *Anal.* calc. for $C_{54}H_{67}N_8O_{20.5}Cu_4Cl_2$: C, 43.78; H, 4.55; N, 7.56; Cu, 17.16. Found: C, 43.62; H, 4.57; N, 7.46; Cu, 17.28%. Infrared spectrum, $\nu(cm^{-1}$, KBr disk) 3388(b), 2936(m), 1627(s), 1595(s), 1537(s), 1447(s), 1312(s), 1094(s), 914(s), 722(s). Molar conductance, Λ_M ($ohm^{-1}\,cm^2\,mol^{-1}$, MeCN solution) 130.3. UV–Vis spectra [λ_{max}, nm (ε, $l\,mol^{-1}\,cm^{-1}$), DMF solution] 640 (290), 380 (10365), 273 (22040). μ_{eff} (tot.): 2.43 μ_B; μ_{eff}/Cu: 1.71 μ_B at 298 K.

2.3. X-ray crystallography

Green block-like single crystals of $\mathbf{1} \cdot 4.5H_2O$ suitable for single-crystal diffraction were grown from a saturated MeCN-DCM solution mixture. The X-ray intensity data were collected at 295 K on a Nonius Kappa CCD diffractometer using a crystal of dimensions $0.48 \times 0.28 \times 0.10\,mm^3$ and with graphite monochromated Mo Kα radiation ($\lambda = 0.71073$ Å) by the ω-scan method. A total of 6816 reflections were recorded with Miller indices $h_{min} = -14$, $h_{max} = 14$, $k_{min} = -15$, $k_{max} = 12$, $l_{min} = -29$, $l_{max} = 29$. In the final cycles of full-matrix least-squares on F^2 all non-hydrogen atoms were assigned anisotropic thermal parameters and refinement converged at $R = 0.0665$. The residual electron density is in the range +0.99 to −0.54 e $Å^{-3}$. The structure was solved using the program SIR97 [14]. The refinement was performed using full-matrix least-squares with all non-hydrogen atoms treated anisotropically and hydrogens included in calculated positions, riding on their carrier atoms. The asymmetric unit of $\mathbf{1} \cdot 4.5H_2O$ contains two crystallographic independent dinuclear cationic units $[\{Cu_2(\mu\text{-}L)(\mu\text{-}H_2O)\}_2]$ with significant geometric differences. The water molecule bridging the Cu(II) atoms in the cation **1**b displays a greater disorder than that in the cation **1**a, and was refined over two positions with occupancies of 0.7 and 0.3, respectively. The other non-coordinated water molecules display a high degree of disorder and most of them were refined over two positions. The hydrogen positions of the water molecules could not be determined. The disordered oxygens of the ClO_4^- anions were refined over two positions. All calculations were performed using SHELXL-97 [15] and PARST [16] implemented in the WINGX [17] system of programs. The crystallographic data are given in Table 1 and the bond lengths and bond angels are given in Table 2.

2.4. Catecholase activity

The catecholase activity was studied in MeCN at 25 °C by the reaction of $\mathbf{1} \cdot 4.5H_2O$ with 3,5-di-*tert*-butylcatechol (3,5-DTBC). For this purpose a 1.1×10^{-4} mol dm^{-3} solution of $\mathbf{1} \cdot 4.5H_2O$ in oxygen saturated MeCN was treated with 30 equiv of 3,5-DTBC under aerobic conditions. The increase in the absorption band at 395 nm, characteristic of the absorption band of the quinone

Table 1
Crystallographic data for $\mathbf{1} \cdot 4.5H_2O$.

Molecular formula	$C_{54}H_{67}N_8O_{20.5}Cu_4Cl_2$
Molecular weight	1481.22
Crystal system	monoclinic
Space group	*Pc* (No. 7)
a (Å)	11.1383(2)
b (Å)	12.2998(2)
c (Å)	23.0325(4)
β (°)	90.6342(8)
U ($Å^3$)	3155.23(9)
D_{calc} ($g\,cm^{-3}$)	1.559
Z	2
F(000)	1522
Crystal size (mm)	$0.48 \times 0.28 \times 0.10$
μ (mm^{-1})	1.494
Range (°)	3.76–27.00
R_1, wR_2 [$I > 2\sigma(I)$]	0.0665, 0.1927
Goodness-of-fit on F^2	1.070
Final difference map max., min. (e $Å^{-3}$)	0.99, −0.54

$R_1 = \Sigma(||F_o| - |F_c||)/\Sigma|F_o|$. $wR_2 = [\Sigma w(|F_o| - |F_c|)^2/\Sigma w(F_o)^2]^{1/2}$.
$w = 0.75/(\sigma^2(F_o) + 0.0010F_o^2)$.

Table 2
Selected bond distances [Å] and angles [°] in **1** · 4.5H_2O.

	1a	1b
Bond distances		
Cu1–O1	1.892(8)	1.889(9)
Cu1–O2	1.974(6)	1.975(6)
Cu1–N1	1.922(8)	1.950(8)
Cu1–N2	2.063(7)	2.092(7)
Cu1–O1w	2.496(9)	2.491(13)/2.768(30)
Cu2–O2	1.960(6)	1.951(6)
Cu2–O3	1.898(8)	1.894(8)
Cu2–N3	2.063(8)	2.053(8)
Cu2–N4	1.930(10)	1.928(9)
Cu2–O1w	2.802(10)	2.571(14)/2.860(30)
Cu1···Cu2	3.335(2)	3.355(1)
Bond angles		
O1–Cu1–O2	89.4(3)	90.6(3)
O1–Cu1–N1	94.5(3)	93.6(3)
O1–Cu1–N2	176.3(3)	177.1(3)
O1–Cu1–O1w	92.2(3)	85.1(4)/100.1(8)
O2–Cu1–N1	158.6(3)	160.6(3)
O2–Cu1–N2	91.3(3)	90.6(3)
O2–Cu1–O1w	81.2(3)	71.7(4)/82.6(7)
N1–Cu1–N2	83.5(3)	84.4(3)
N1–Cu1–O1w	119.5(4)	127.5(3)/115.1(7)
N2–Cu1–O1w	91.5(3)	97.8(4)/82.6(8)
O2–Cu2–O3	90.5(3)	91.7(3)
O2–Cu2–N3	91.7(3)	91.2(3)
O2–Cu2–N4	160.3(3)	162.8(3)
O2–Cu2–O1w	73.8(3)	70.2(3)/80.6(7)
O3–Cu2–N3	176.8(3)	177.0(3)
O3–Cu2–N4	93.4(4)	94.1(4)
O3–Cu2–O1w	88.7(4)	82.7(4)/97.0(8)
N3–Cu2–N4	85.2(4)	83.5(3)
N3–Cu2–O1w	89.3(3)	97.4(4)/82.6(7)
N4–Cu2–O1w	125.6(4)	126.6(4)/114.7(7)
Cu1–O2–Cu2	115.9(3)	117.4(3)
Cu1–O1w–Cu2	77.8(3)	83.0(4)/73.3(8)

formed, was followed spectrophotometrically at various time intervals from 3 to 60 min.

3. Results and discussion

3.1. Synthesis and characterization

The ligand H_3L used in this work was prepared following a modified literature procedure [8] and was characterized by FTIR, ^1H and ^{13}C NMR spectra. The reaction in methanol of H_3L with $Cu(ClO_4)_2 \cdot 6H_2O$ in the presence of NEt_3 in a 1:2:3 molar ratio yielded the green complex $[\{Cu_2(\mu\text{-}L)(\mu\text{-}H_2O)\}_2](ClO_4)_2 \cdot 4.5H_2O$ (**1** · 4.5H_2O). The process was conducted in air and at room temperature. The complex was characterized by analytical, spectroscopic and single-crystal X-ray diffraction techniques. The molar conductivity value of **1** · 4.5H_2O in MeCN is 130 $ohm^{-1}cm^2\ mol^{-1}$ (28 °C), consistent with a 1:1 type electrolyte in solution. The FTIR spectrum of **1** · 4.5H_2O (Fig. S1) is in agreement with the coordination of the Schiff base and exhibits a broad medium band at 3388 cm^{-1} characteristic of ν_{OH} of an aqua bridge [18]. For the uncoordinated ClO_4^-, the stretching vibration appears at ~1094 cm^{-1}.

3.2. UV–Vis spectroscopy

The electronic spectrum of **1** · 4.5H_2O in DMF solution (Fig. S2) shows several intense absorption bands in the visible region that are assigned to allowed d–d and charge-transfer transitions. It exhibits a broad band at 640 nm (290 $lmol^{-1}\ cm^{-1}$) due to a d–d transition. Higher intensity charge-transfer transitions are obtained at 380 and 273 nm, with molar extinction coefficients of 10365 and 22040 $l\ mol^{-1}\ cm^{-1}$, respectively, attributed to $PhO^- \rightarrow Cu(II)$, $\sigma(amino) \rightarrow Cu(II)$ LMCT and intraligand charge-transfer transitions [19].

3.3. ^1H NMR spectroscopy

^1H NMR spectroscopy has been shown to be applicable for the characterization of the structure and reactivity of Cu_2 complexes with magnetic coupling that ranges from weakly ferromagnetic to strongly antiferromagnetic [20]. Therefore, few reports have described copper complexes that produce narrow ^1H NMR resonances [21–26]. Paramagnetic NMR spectra of Cu_2 complexes have been used extensively in order to establish their relevance as models for metal sites in copper enzymes [27]. Construction of a library of a compounds along with their NMR properties is beneficial in the context of bioinorganic modeling of naturally occurring metalloenzymes. 250 MHz ^1H NMR data of complex **1** · 4.5H_2O were collected in d_4-methanol at room temperature. This study benefited from an extensive investigation made with the related compound $[Cu_2(\mu\text{-}L')(\mu\text{-}OAc)]$, where L′ is a ligand very similar to the dinucleating ligand used here, possessing three methyl substituents in place of hydrogen atoms [9a]. The spectrum of **1** · 4.5H_2O shows a total of 17 hyperfine shifted peaks, as expected from the idealized C_s symmetry of the compound, spread over a very large window of chemical shift, spanning about 250 ppm. This reflects the fact that at room temperature the system remains largely paramagnetic as a result of the very weak nature of the observed antiferromagnetic coupling. In addition, peaks attributed to MeOH and free ligands were detected. The signals from the solvent were used as an internal reference. Inspection of the intensity integrals of these 17 resonances allowed their grouping into five sets of one (a), one (b), 10 (c), four (d) and one (e) signals, respectively, integrating for two, one, two, one and two protons, as predicted from the structure of **1** · 4.5H_2O (Fig. 1, top) consisting of two chemically identical $[Cu_2(\mu\text{-}L)(\mu\text{-}H_2O)]^+$ cations **1**a and **1**b. These groups correspond to the following categories of protons: group 'a', only one signal, which integrates to two protons, corresponding to the two equivalent hydrogens α to

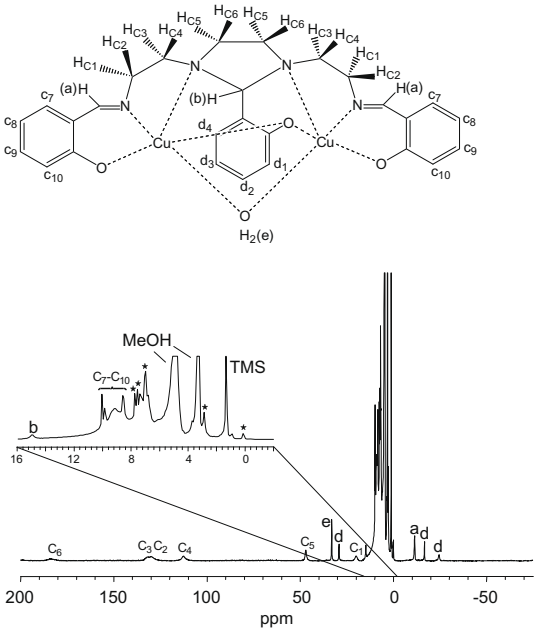


Fig. 1. Complex **1** · 4.5H_2O where all the protons have been labeled according to the groups a, b, c, d and e. At the bottom is a labeled 250 MHz ^1H NMR spectrum of **1** · 4.5H_2O as a mixture of two chemically equivalent $[Cu_2(\mu\text{-}L)(\mu\text{-}H_2O)]^+$ cations, **1**a and **1**b. * denote signals from the free ligand.

the imine N-atoms, and which was readily assigned; group 'b', one signal with an intensity equivalent to one proton, arising from the imidazolidinyl hydrogen; group 'c' is the most numerous. It includes 10 signals with intensity ratios for two H-nuclei. These results from the hydrogen atoms attached to the amine groups (six signals) and from those attached to the two external phenyl rings (which are equivalent). The peaks from the first sub-group are broader than these of the second, since the protons causing the former are crystallographically closer to the metal centers. The resonances of the other sub-group are sharper and show the alternation of chemical shifts characteristic of a π-delocalization mechanism [22]. Group 'd' includes the four peaks from the central phenyl ring of the ligand (one proton per signal). The mechanism of π-delocalization of the electronic spin is also evident here, which was useful in the assignment of the peaks. Group 'e' is the last set of signals, arising from the bridging water molecule. With this study, complex **1** · $4.5H_2O$ enters the small group of binuclear [Cu_2] complexes of which the ^1H NMR spectrum could be explained almost unambiguously and it is a valuable contribution to the growing body of spectroscopic data which can be useful in the functional and structural studies of the metalloenzymes.

3.4. Description of structure

Crystals of **1** · $4.5H_2O$ suitable for X-ray structure determination were obtained from mixtures of MeCN–DCM solvents. An ORTEP view of the cation **1**a is shown in Fig. 2. The crystallographic data are given in Table 1 the selected bond distances and angles are given in Table 2. The asymmetric part of the unit cell contains two crystallographically independent and chemically identical [Cu_2-(μ-L)(π-H_2O)]$^+$ cations (**1**a and **1**b), two perchlorate anions and 4.5 uncoordinated water molecules.

The cations represent the first example of a Cu_2 complex bridged by phenolate oxygen ($O_{ph}{}^b$), imidazolidinyl nitrogen (N_{md}) and water oxygen (O_{aq}) atoms. Several Cu(II) dimeric complexes containing an aquo-bridge between the metallic centers, sometimes coupled with a further hydroxo-bridge, can be retrieved from the recent structural literature [28]. Depending of the position, axial or equatorial, in the square-pyramidal coordination environment, the Cu–μ(OH_2) bond distances vary within the long range of about 1.99–2.74 Å, while the corresponding Cu–μ(OH) ones exhibit shorter values, from 1.88 to 1.99 Å. Accordingly, only on the basis of the bond lengths, the oxygens bridging the copper atoms in both **1**a and **1**b cations can be ascribed to water molecules, even if the positions of the hydrogen atoms could not be determined from X-ray data. The coordination from imine nitrogens (N_{im}) and terminal phenolate oxygens (O_{ph}) complete the distorted N_2O_3 square-pyramidal environments around each copper ions. The shared bi-square-pyramidal arrangement is assembled from two non-coplanar tetradentate coordination pockets of the ligand. This angular arrangement of the binding sites arises from the non-planar structure of the imidazolidinyl spacer, which in turn is responsible for aqua bridging instead of coordination of two monodentate ligands, as observed with phenolate spacer containing binucleating ligands. The bridging H_2O completes the triply bridging motif leading to intramolecular Cu···Cu separations of 3.335(2) and 3.355(1) Å in **1**a and **1**b, respectively. For each metal atom, two nitrogen atoms, one terminal and one bridging phenolate oxygen atoms give one five-membered (N–Cu–N) and two six-membered (N–Cu–O) terminal and bridging chelate rings. The average bite angles for the five-membered (N–Cu–N) chelate rings are 84.3(3)° and 83.9(3)° for **1**a and **1**b, respectively. The average bite angles for the six-membered (N–Cu–O) terminal chelate rings are 93.9(3)° and 93.8(3)°, whereas the average angles for the six-membered (N–Cu–O) bridging chelate rings are 91.5(3)° and 90.9(3)° for **1**a and **1**b, respectively.

The Cu(1)–O_{aq}–Cu(2) angles are 77.8(3)° for **1**a and 83.0(4)°/73.3(8)° for both the disordered bridging water molecules in **1**b. Small variations in the distances in Cu–$O_{ph}{}^b$ indicate that the monatomic phenolate oxygen bridges are nearly symmetric. The reported dinuclear complex [Cu_2(OH)(H_2O)L^1(ClO_4)$_2$]$^+$ (L^1 = a binucleating macrocyclic ligand) also has long Cu–O_{aq} linkages (2.519(12) Å) and an acute Cu–O_{aq}–Cu angle of 77.3(4)° [29]. The calculation of the least-square planes defined by the equatorial atoms around Cu(II) together with the metal atom shows the copper ions to be displaced from the basal planes toward the axial water molecule by 0.207(1) [Cu(1)] and 0.142(1) Å [Cu(2)] for **1**a and 0.181(1) [Cu(1)] and 0.126(1) Å [Cu(2)] for **1**b, respectively. As a result, the Cu centers could be considered to be in a square planar coordination environment, each with a weak axial bond to the water oxygen. The angles between the two CuN_2O_2 basal planes are 144.54(4)° for **1**a and 143.61(4)° for **1**b.

The central phenolate oxygen atom adopts a trigonal–pyramidal geometry (sum of the angles around O(2) is 331.6(4)° and 332.0(4)° for **1**a and **1**b, respectively. The symmetry of the coordination sphere around the two copper(II) ions in the dinuclear units, measured by the Addison parameter (τ) [30], are best described by distorted square pyramids with τ for Cu(1) and Cu(2) of 0.295 and 0.276, respectively for **1**a, and 0.275 and 0.236, respectively for **1**b. Based on the coordination sphere symmetry, it was proposed that in the square pyramid coordination limit (τ = 0) the magnetic orbitals are mainly $d_{x^2-y^2}$ and weak ferromagnetic interactions should result [31]. The Cu–N_{imd} distances (average 2.063(7) Å for **1**a and 2.072(7) Å for **1**b) are longer than the Cu–N_{im} distances (average 1.926(9) Å for **1**a and 1.939(9) Å for **1**b) [32–34]. The Cu–O_{ph} distances (av. 1.895(8) Å for **1**a and 1.891(8) Å for **1**b) are in the normal range for similar dicopper complexes, with longer average Cu–$O_{ph}{}^b$ distances of 1.967(6) and 1.963(6) Å for **1**a and **1**b, respectively.

The complex shows intricate unsymmetrical hydrogen bonding between an uncoordinated water molecule and two terminal phenolate oxygen atoms with average hydrogen binding distances of 2.687 Å for **1**a and 2.776 Å for **1**b. A second uncoordinated water molecule is hydrogen bonded to the first one at a distance of 2.794 Å for **1**a and 2.761 Å for **1**b, which is quite comparable to the O···O distance in ice (about 2.74 Å) [35]. The assignment of the apical bridge as water is supported by the long Cu–O distances [2.496(10) and 2.802(10) Å for **1**a, 2.491(13) and 2.571(14) Å (and 2.768(30) and 2.860(30) Å) for **1**b]. The variations in the distances in Cu–O_{aq} indicate that the monatomic aqua oxygen bridges are not symmetric. The long apical bridging bonds reflect weak axial interactions, as expected for copper complexes in a square-

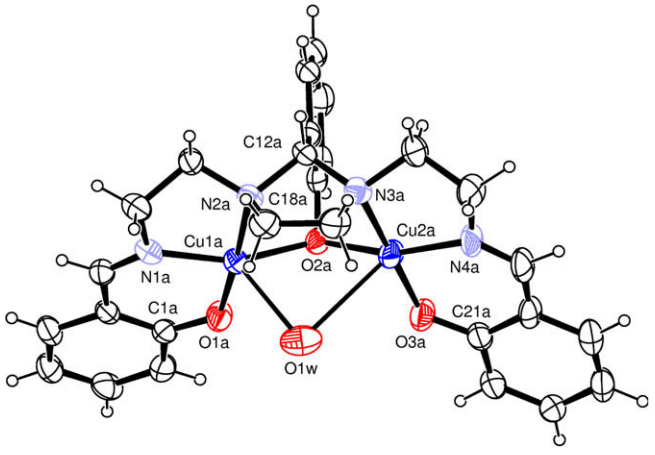


Fig. 2. An ORTEP view of the cation **1**a with the atom numbering scheme and thermal ellipsoids drawn at the 50% probability level.

pyramidal geometry. The geometry around the bridging water oxygen atom is distorted tetrahedral with a Cu(1)–O(W)–Cu(2) bond angle of 77.8(3)° and 83.0(4)°/73.3(8)° for **1**a and **1**b, respectively. The ClO_4^- counter anions in **1** · 4.5H_2O are disordered [36]. The average Cl–O distances are in the normal range, being 1.417 Å. The unit cell-packing pattern of **1** · 4.5H_2O indicates π–π interactions of the terminal phenyl rings of the ligand and the stacked cationic layers are uniformly separated by the ClO_4^- anions.

3.5. Magnetic behavior and EPR studies

The degree of the magnetic super-exchange interaction within the dinuclear complex [{Cu_2(μ-L)(μ-H_2O)}$_2$](ClO_4)$_2$ · 4.5H_2O (**1** · 4.5H_2O) was evaluated by means of variable temperature bulk magnetic susceptibility measurements under the influence of a constant magnetic field of 1T in the 2–300 K temperature range. The results are shown in Fig. 5 as a $\chi_m T$ versus T plot, after subtraction of diamagnetic contributions and a temperature independent paramagnetism (TIP) term of 120×10^6 cm^3 K mol^{-1}. The product $\chi_m T$ remains almost constant during practically the whole temperature range at a value very close to that expected for two independent Cu^{II} ions, and only experiences a decrease at very low temperatures (near 10 K) down to a value of 0.60 cm^3 K mol^{-1} at 2 K. This corroborates the fact that the coupling between the metal ions in complex **1** · 4.5H_2O is very weak and antiferromagnetic. This behavior could be modeled by fitting to the experimental data an expression of the type $\chi_m T = f(T)$ derived from the Bleaney–Bowers equation (Eq. (1)) where the g value obtained by EPR (2.09) was used

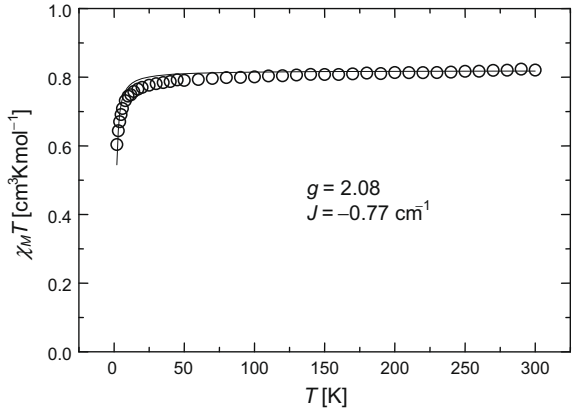


Fig. 3. Plot of $\chi_m T$ versus T for complex **1** · 4.5H_2O. The solid line is a fit of the data to the Bleaney–Bowers equation.

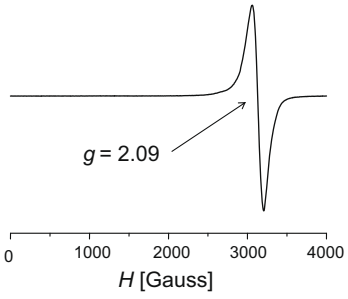


Fig. 4. X-band EPR spectrum for a powdered sample of **1** · 4.5H_2O at 4 K.

$$\chi_m = \frac{N_a g^2 \mu_B}{kT} \cdot \frac{2e^{2J/kT}}{1+3e^{2J/kT}}. \quad (1)$$

This equation is derived after considering the following Heisenberg spin-Hamiltonian (Eq. (2)) to describe the exchange within the complex

$$\hat{H} = -2J\hat{S}_1\hat{S}_2. \quad (2)$$

The best fit (Fig. 3, solid line) was obtained for $J = -0.77$ cm^{-1}. This result is in contrast with that observed for various analogous complexes featuring the same kind of dinucleating ligand as in **1** · 4.5H_2O, and various other exogenous ligands, such as AcO^-, HO^- or MeO^- [9e,f]. In all these cases moderately strong ferromagnetic coupling between the metals was found and this was attributed, following DFT calculations, to the counter-complementarity existing between the N–C–N bridge provided by the central ring of the ligand (always coordinated in basal positions of Cu^{II}) and the O-donors also bound to basal positions. In the present case, however, the geometry of the complex is different to any of the studied compounds and thus comparisons are hard to make. In addition, other examples of complexes featuring a phenoxide-type bridge together with an aqua bridge are non-existent. It was established, however, by DFT calculations that exchange of an OH^- bridge by an H_2O bridge has very drastic consequences from a magnetic point of view [37], and this could explain the disparity of behaviors observed here.

X-band (9.45 GHz) powder EPR spectra of complex **1** · 4.5H_2O were recorded at 4, 77 and 295 K. The spectra at each of these temperatures were very similar (Fig. 4), consisting of a broad isotropic signal centered at $g = 2.09$. This is consistent with the fact that the coupling between both Cu^{II} ions is very weak and thus the compound behaves apparently as the sum of two mononuclear independent $S = 1/2$ entities rather than a system experiencing super-exchange of the electronic magnetic moments.

3.6. Catecholase activity

Complex **1** · 4.5H_2O shows oxidation of 3,5-di-*tert*-butylcatechol (3,5-DTBC) in oxygen saturated acetonitrile solution at pH 7·5. The ability of the complex towards oxidation of catechol to quinone was examined and the time dependent growth of

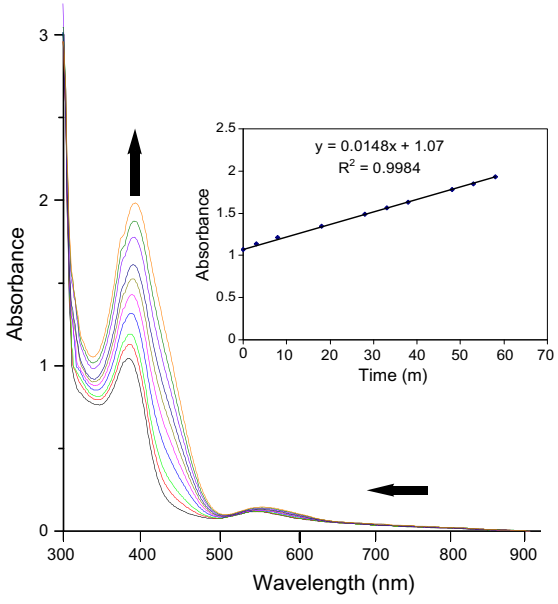


Fig. 5. Time dependent growth of 3,5-DTBQ at 395 nm in MeCN at 25 °C. Inset shows absorbance versus time plot.

3,5-DTBQ is shown in Fig. 5. The oxidation of 3,5-DTBC to the corresponding *o*-quinone was followed by the growth of a strong absorption band of the product at 395 nm, using UV–Vis spectroscopy. The complex simulates the short copper–copper distance of about ~3 Å in CO, as well as the N_2O_2 donor set from the binucleating ligand, which is formed in the enzymes by the pendant imidazoles of the amino acid histidine. The UV–Vis spectra of the original solution immediately after the addition of 3,5-DTBC and at regular intervals of time up to 1 h were recorded. The course of the oxidation of 3,5-DTBC and the reaction rate were determined by monitoring the time dependent increase of the quinone absorption band at 395 nm, which indicates the catechol oxidation ability of the aqua bridged complex [38]. The initial reaction rate obtained from the slope of the absorption versus time plot was found to be $2.46 \times 10^4\ h^{-1}$ (inset of Fig. 5), which is comparable to other exogenous μ-hydroxo and endogenous μ-phenoxo bridged dinuclear copper complexes [39]. This also points to the role of the angular and labile aqua bridging ligands for efficient catechol binding in the apical sites of two non-coplanar N_2O_2 chelated copper sites in $\mathbf{1} \cdot 4.5H_2O$.

4. Conclusion

Basal N,N′-imidazolidinyl (NCN) and *apical* aqua bridging moieties have been identified in a non-planar Cu_2 complex incorporating a N_4O_3 coordinating heptadenate ligand with a low $Cu{-}O_{aq}{-}Cu$ angle and an elongated $Cu{-}O_{aq}$ bond. The copper centers are at an average distance of 3.34 Å and show a weak antiferromagnetic interaction identified from variable temperature magnetic moment data. In a simulated copper–copper distance and N_2O_2 coordination environment, the complex shows catecholase like activity. The present study provides valuable insight into the biologically relevant coordination chemistry of copper. Currently we are engaged in synthesizing analogous complexes of other 3d and 4d metal ions to explore the role of bridging imidazolidine moiety and variety of apical groups in the molecular structure, the magnetic interactions and substrate reactivity.

Acknowledgments

We are thankful to DST, New Delhi, for the Single Crystal X-ray Diffractometer facility in the Department of Chemistry, IIT Kharagpur under its FIST program. We also thank Dr. Alok Ranjan Paital for growing the single crystals used in this study. We are very thankful to the reviewers at the revision stage.

Appendix A. Supplementary data

CCDC 695278 contains the supplementary crystallographic data for $\mathbf{1} \cdot 4.5H_2O$. These data can be obtained free of charge via http://www.ccdc.cam.ac.uk/conts/retrieving.html, or from the Cambridge Crystallographic Data Centre, 12 Union Road, Cambridge CB2 1EZ, UK; fax: (+44) 1223 336 033; or e-mail: deposit@ccdc.cam.ac.uk.

Supplementary data associated with this article can be found, in the online version, at doi:10.1016/j.poly.2008.12.063.

References

[1] D.E. Wilcox, Chem. Rev. 96 (1996) 2435.
[2] N. Strater, W.N. Lipscomb, T. Klabunde, B. Krebs, Angew. Chem., Int. Ed. Engl. 35 (1996) 2024.
[3] F. Meyer, H. Pritzkow, Angew. Chem., Int. Ed. Engl. 39 (2000) 2112.
[4] (a) L.K. Thompson, F.L. Lee, E.J. Gabe, Inorg. Chem. 27 (1988) 39;
(b) W.M.E. Koomen-van Oudenniel, R.A.G. de Graaff, J.G. Haasnoot, R. Prins, J. Reedijk, Inorg. Chem. 28 (1989) 1128;
(c) C.A. Salata, M.T. Youinou, C.J. Burrows, Inorg. Chem. 3 (1991) 3454;
(d) L.K. Thompson, S.S. Tandon, M.E. Manuel, Inorg. Chem. 34 (1995) 2356;
(e) J.L. Chou, D.N. Horng, J.P. Chyn, K.M. Lee, F.L. Urbach, G.H. Lee, H.L. Tsai, Inorg. Chem. Commun. 2 (1999) 392;
(f) C. He, S.J. Lippard, Inorg. Chem. 39 (2000) 5225;
(g) C.J. Sumby, P.J. Steel, Inorg. Chem. Commun. 6 (2003) 127.
[5] (a) P.A. Vigato, S. Tamburini, D. Fenton, Coord. Chem. Rev. 106 (1990) 25;
(b) J.E. Bol, W.L. Driessen, J. Reedijk, J. Chem. Soc., Chem. Commun. (1995) 1365;
(c) S. Torelli, C. Belle, I. Gautier-Luneau, J.L. Pierre, Inorg. Chem. 39 (2000) 3526;
(d) Y.C. Chou, S.F. Huang, R. Koner, G.H. Lee, Y. Wang, S. Mohanta, H. Wei, Inorg. Chem. 43 (2004) 2759.
[6] T. Klabunde, C. Eicken, J.C. Sacchettini, B. Krebs, Nat. Struct. Biol. 5 (1998) 1084.
[7] (a) A. Sánchez-Ferrer, J.N. Rodriguez-Lopez, F. García-Cánovas, F. Garcíacarmona, Biochim. Biophys. Acta 1247 (1995) 1;
(b) E.I. Solomon, U.M. Sundaram, T.E. Machonkin, Chem. Rev. 96 (1996) 2563;
(c) C. Eicken, B. Krebs, J.C. Sacchettini, Curr. Opin. Struct. Biol. 9 (1999) 677;
(d) C. Gerdemann, C. Eicken, B. Krebs, Acc. Chem. Res. 35 (2002) 183.
[8] E. Wong, S. Liu, T. Liigger, F.E. Hahn, C. Orvig, Inorg. Chem. 34 (1995) 93.
[9] (a) M. Bera, W.T. Wong, G. Aromí, D. Ray, Eur. J. Inorg. Chem. (2005) 2526;
(b) A.R. Paital, C.S. Hong, H.C. Kim, D. Ray, Eur. J. Inorg. Chem. (2007) 1644;
(c) P.K. Nanda, G. Aromí, D. Ray, Chem. Commun. (2006) 3181;
(d) P.K. Nanda, G. Aromi, D. Ray, Inorg. Chem. 45 (2006) 3143;
(e) M. Fondo, A.M. García-Deibe, M. Corbella, E. Ruiz, J. Tercero, J. Sanmartín, M.R. Bermejo, Inorg. Chem. 44 (2005) 5011;
(f) M. Fondo, N. Ocampo, A.M. García-Deibe, M. Corbella, M.R. Bermejo, J. Sanmartín, J. Chem. Soc., Dalton Trans. (2005) 3785;
(g) M. Fondo, A.M. Garcia-Deibe, J. Sanmartin, M.R. Bermejo, L. Lezama, T. Rojo, Eur. J. Inorg. Chem. (2003) 3703;
(h) M. Fondo, N. Ocampo, A.M. Garcia-Deibe, R. Vicente, M. Corbella, M.R. Bermejo, J. Sanmartin, Inorg. Chem. 45 (2006) 255.
[10] M. Bera, U. Mukhopadhyay, D. Ray, Inorg. Chim. Acta 358 (2005) 437.
[11] M. Bera, K. Biradha, D. Ray, Inorg. Chim. Acta 357 (2004) 3556.
[12] P.K. Nanda, M. Bera, G. Aromí, D. Ray, Polyhedron 25 (2006) 2791.
[13] R.L. Carlin, Magnetochemistry, Springer-Verlag, New York, 1986.
[14] A. Altomare, M. C. Burla, M. Camalli, G.L. Cascarano, C. Giacovazzo, A. Guagliardi, A.G. Moliterni, G. Polidori, R. Spagna, SIR97, J. Appl. Crystallogr. 32 (1999) 115.
[15] G. M. Sheldrick, SHELXS-97, Program for the Refinement of Crystal Structures, University of Göttingen, Germany, 1997.
[16] M. Nardelli, J. Appl. Crystallogr. 28 (1995) 659.
[17] L.J. Farrugia, J. Appl. Crystallogr. 32 (1999) 837.
[18] K. Nakamoto, Infrared and Raman Spectra of Inorganic and Coordination Compounds, 4th Ed., Wiley, New York, 1986. pp. 147–150, 227–233, 251–253.
[19] A.B.P. Lever, in: Inorganic Electronic Spectroscopy, 2nd Ed., Elsevier, Amsterdam, 1984, p. 355.
[20] J.H. Satcher Jr., A.L. Balch, Inorg. Chem. 34 (1995) 3371.
[21] M. Maekawa, S. Kitigawa, M. Munakata, H. Masuda, Inorg. Chem. 28 (1989) 1904.
[22] A.L. Balch, M. Mazzanti, B.C. Noll, M.O. Olmstead, J. Am. Chem. Soc. 115 (1993) 12206.
[23] R.C. Holz, J.M. Brink, Inorg. Chem. 33 (1994) 4609.
[24] R.A. Zelonka, M.C. Baird, Inorg. Chem. 11 (1972) 134.
[25] S. Wang, Z. Pang, J.C. Zheng, M.J. Wagner, Inorg. Chem. 32 (1993) 5975.
[26] R.C. Holz, J.M. Brink, F.T. Gobena, C.J. O'Connor, Inorg. Chem. 33 (1994) 4609.
[27] J.M. Brink, R.A. Rose, R.C. Holz, Inorg. Chem. 35 (1996) 2878.
[28] (a) L.C. Porter, R.J. Doedens, Inorg. Chem. 24 (1985) 1006;
(b) G. Christou, S.P. Perlepes, E. Libby, K. Folting, J.C. Huffman, R.J. Webb, D.N. Hendrickson, Inorg. Chem. 29 (1990) 3657;
(c) D.J. Elliot, L.L. Martin, M.R. Taylor, Acta Crystallogr., Sect. C 54 (1998) 1259;
(d) P. Sgarabotto, F. Bisceglie, G. Pelosi, L. Abdel-Rahman, Polyhedron 18 (1999) 2505;
(e) J. Barreira Fontecha, S. Goetz, V. McKee, Angew. Chem., Int. Ed. Engl. 41 (2002) 4553;
(f) I. Chadjistamatis, A. Terzis, C.R. Raptopoulou, S.P. Perlepes, Inorg. Chem. Commun. 6 (2003) 1365;
(g) M. Salah el Fallah, A. Escuer, R. Vicente, F. Badyine, X. Solans, M. Font-Bardia, Inorg. Chem. 43 (2004) 7218;
(h) O. Svajlenova, J. Vančo, J. Marek, Acta Crystallogr., Sect. C 60 (2004) m275;
(i) I. Gautier-Luneau, D. Phanon, C. Duboc, D. Luneau, J.-L. Pierre, J. Chem. Soc., Dalton Trans. (2005) 3785;
(j) M. Barquin, M.J. Gonzalez Garmendia, L. Larrinaga, E. Pinilla, M.R. Torres, Z. Anorg. Allg. Chem. 631 (2005) 2151;
(k) E. Aznar, S. Ferrer, J. Borras, F. Lloret, M. Liu-Gonzalez, H. Rodriguez-Prieto, S. Garcia-Granda, Eur. J. Inorg. Chem. (2006) 5115;
(l) P. Talukder, S. Sen, S. Mitra, L. Dahlenberg, C. Desplanches, J. -P. Sutter, Eur. J. Inorg. Chem. (2006) 329;
(m) C. Chailuecha, S. Youngme, C. Pakawatchai, N. Chaichit, G.A. van Albada, J. Reedijk, Inorg. Chim. Acta 359 (2006) 4168.
[29] M.G.B. Drew, J. Nelson, F. Esho, V. McKee, S.M. Nelson, J. Chem. Soc., Dalton Trans. (1982) 1837.
[30] A.W. Addison, T.N. Rao, J. Reedijk, J. Van Rijn, G.C. Verschoor, J. Chem. Soc., Dalton Trans. (1984) 1349.
[31] C. Escuer, M. Font-Bardia, S.S. Massoud, F.A. Mautner, E. Peñalba, X. Solans, R. Vicente, New J. Chem. 28 (2004) 681.
[32] E.P. Copeland, I.A. Kahwa, J.T. Mague, G.L. Mcpherson, J. Chem. Soc., Dalton Trans. (1997) 2849.

[33] U. Mukhopadhyay, L. Govindasamy, K. Ravikumar, D. Velmurugan, D. Ray, Inorg. Chem. Commun. 1 (1998) 152.
[34] B. Chiari, O. Piovesana, T. Tarantelli, P.F. Zanazzi, Inorg. Chem. 21 (1982) 2444.
[35] R. Ludwig, Angew. Chem., Int. Ed. Engl. 40 (2001) 1808.
[36] S.Y. Li, Z.L. You, B. Chen, Y.S. Lin, Z.D. Ziong, H.L. Zhu, Acta. Crystallogr., Sect. E 60 (2004) 999.
[37] A. Rodríguez-Fortea, E. Ruiz, S. Alvarez, P. Alemany, J. Chem. Soc., Dalton Trans. (2005) 2624.
[38] (a) A. Neves, L.M. Rossi, A.J. Bortoluzzi, B. Szpoganicz, C. Wiezbicki, E. Schwingel, Inorg. Chem. 41 (2002) 1778;
(b) S. Torelli, C. Belle, S. Hamman, J.L. Pierre, Inorg. Chem. 41 (2002) 3983;
(c) P. Kamau, R.B. Jordan, Inorg. Chem. 41 (2002) 3076;
(d) C.T. Yang, M. Vetrichelvan, X. Yang, B. Moubaraki, K.S. Murray, J.J. Vittal, J. Chem. Soc., Dalton Trans. (2004) 113.
[39] K.S. Banu, T. Chattopadhyay, A. Banerjee, S. Bhattacharya, E. Suresh, M. Nethaji, E. Zangrando, D. Das, Inorg. Chem. 47 (2008) 7083.

The $[VO(acac)_2]$ complex has already been directly immobilised on several solid matrixes, namely alumina, silica gel, mesoporous silicas and clays [16–19]. It has also been immobilised by microencapsulation in polystyrene [20] and by covalent grafting onto amine functionalised activated carbon [21] and clays [16] through Schiff base condensation between surface amine groups and the carbonyl groups of the acetylacetonate ligand.

Hexagonal mesoporous silicas are ordered mesoporous materials with wormlike pore structure [22,23]. Unlike the well-known MCM-41 materials, which are prepared using an anionic template, the HMS type materials are synthesised using a neutral template (long-chained alkylamines) [23,24]. The surface functionalisation of HMS materials with amine groups via reaction with APTES has been previously reported in the literature [25–29]. Both unmodified and amine functionalised HMS materials have already been used as supports for several transition metal catalysts such as manganese, copper and titanium [26–30].

Herein we report the immobilisation of $[VO(acac)_2]$ onto a synthetic HMS using three different methodologies, as depicted in Scheme 1: method A, direct complex immobilisation onto the parent material; method B, functionalisation of HMS with APTES followed by covalent complex grafting; and method C, reaction between the APTES modified HMS prepared in method B and TMS to deactivate eventually unreacted surface silanol groups and subsequent complex grafting. The novel $[VO(acac)_2]$ based materials were tested as heterogeneous catalysts in the epoxidation of geraniol, at room temperature, in dichloromethane, using *t*-BuOOH as the oxygen source; furthermore, the reusability of these heterogeneous catalysts was tested for four times. The main purpose of this work was to correlate different grafting methodologies for the immobilisation of $[VO(acac)_2]$ catalyst onto HMS with the corresponding catalytic activity and stability in the reaction media.

2. Experimental

2.1. Materials and solvents

All the reagents and solvents used in the preparation and modification of the HMS material were used as received. $[VO(acac)_2]$, APTES, TMS, *t*-BuOOH solution in decane (5 mol dm^{-3}) and chlorobenzene were from Aldrich, tetraethoxysilane was from Lancaster, dichloromethane was from Romil (HPLC grade) and toluene and other solvents used in the synthesis procedures were from Fischer Scientific (analytical reagent grade).

2.2. Preparation of the heterogeneous catalysts

Synthesis of HMS: The HMS material was synthesised following a reported procedure [23]. Briefly, tetraethoxysilane (37.0 cm^3, 0.166 mol) was added to a stirred solution of ethanol (88.1 cm^3, 1.51 mol), water (88.5 cm^3, 4.91 mol) and 1-dodecylamine (10.3 cm^3, 0.0448 mol). The mixture was stirred at room temperature for 24 h. The white precipitate obtained was vacuum-filtered and washed with deionised water (100 cm^3) and ethanol (100 cm^3). In order to remove the template (1-dodecylamine), the precipitate was calcined at 600 °C for 24 h.

Immobilisation of $[VO(acac)_2]$: The immobilisation of $[VO(acac)_2]$ was performed by three different methodologies described below and summarised in Scheme 1.

Method A: A mixture of HMS (0.5 g) in dry toluene (50.0 cm^3) and $[VO(acac)_2]$ (0.0261 g, 0.09843 mmol) was refluxed for 24 h. The material was vacuum-filtered, washed by reflux in dichloromethane (50.0 cm^3) and methanol (50.0 cm^3) and dried overnight in an oven at 120 °C; the resulting material is denoted as A1.

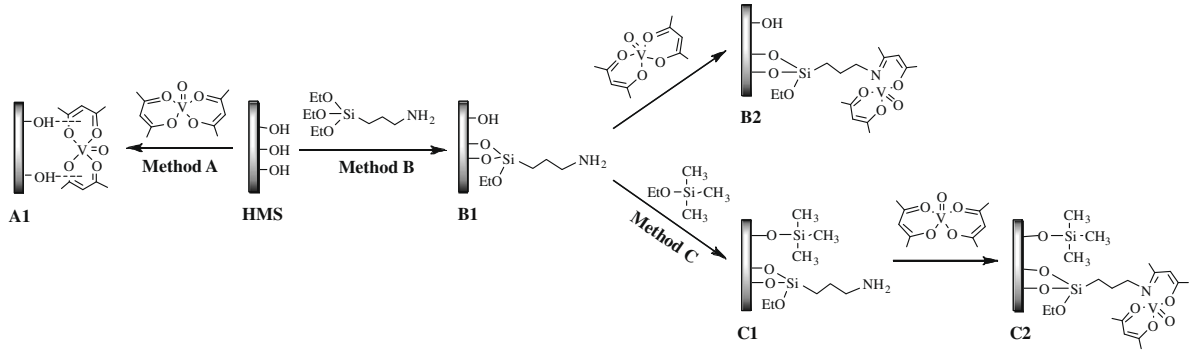
Method B: A mixture of HMS (1.6 g) in dry toluene (100.0 cm^3) and APTES (0.80 mmol) was refluxed for 24 h and the resulting material (B1) was vacuum-filtered, washed with toluene (2 × 100 cm^3) and dried overnight in an oven at 120 °C. Afterwards, a mixture of B1 (0.6 g) in dry toluene and $[VO(acac)_2]$ (0.0322 g, 0.1214 mmol) was refluxed for 24 h and the resulting material was vacuum-filtered, washed by reflux in dichloromethane (50.0 cm^3) and methanol (50.0 cm^3) and dried overnight in an oven at 120 °C; the resulting material is denoted as B2.

Method C: A mixture of B1 (0.6 g) and TMS (1 mmol) was refluxed in dry toluene for 24 h and the resulting material (C1) was vacuum-filtered, washed with toluene (2 × 50 cm^3) and dried overnight in an oven at 120 °C. Afterwards, a mixture of C1 (0.4 g) and $[VO(acac)_2]$ (0.0233 g, 0.0879 mmol) was refluxed in dry toluene for 24 h and the final material was vacuum-filtered, washed by reflux in dichloromethane (50.0 cm^3) and methanol (50.0 cm^3) and dried overnight in an oven at 120 °C; the resulting material is denoted as C2.

2.3. Physico-chemical measurements

Vanadium bulk contents obtained by inductively coupled plasma emission spectrometry (ICP-AES) and nitrogen elemental analysis (EA) were performed at 'Laboratório de Análises', IST, Lisbon (Portugal). X-ray photoelectron spectroscopy (XPS) was performed at "Centro de Materiais da Universidade do Porto" (Portugal), in a VG Scientific ESCALAB 200A spectrometer using non-monochromatised Al Kα radiation (1486.6 eV). The materials were compressed into pellets prior to the XPS studies. To correct possible deviations caused by electric charge of the samples, the C 1s band at 285.0 eV was taken as internal standard. The surface atomic percentages were calculated from the corresponding peak areas and using the sensitivity factors provided by the manufacturer.

The nitrogen adsorption isotherms at −196 °C were measured in an automatic apparatus (ASAP 2010; Micromeritics). Before



Scheme 1. Methodologies for $[VO(acac)_2]$ immobilisation onto HMS materials.

the adsorption experiments the samples were outgassed under vacuum during 2.5 h at 150 °C.

The FTIR spectra of the materials were obtained with a Jasco FT/IR Plus spectrophotometer in the 400–4000 cm^{-1} region, with a resolution of 4 cm^{-1} and 32 scans, using pellets of the materials diluted with KBr.

Gas chromatography (GC) experiments were performed with a Varian CP-3380 chromatograph equipped with a FID detector and using helium as carrier gas and a fused silica Varian Chrompack capillary column CP-Sil 8 CB Low Bleed/MS (30 m × 0.25 mm i.d.; 0.25 μm film thickness). The chromatographic conditions were: 40 °C (3 min), 5 °C min^{-1}, 170 °C (2 min), 20 °C min^{-1}, 200 °C (10 min); injector temperature, 200 °C; detector temperature, 300 °C. The reaction parameters geraniol conversion (%C), 2,3-epoxygeraniol selectivity ($\%S_{2,3\text{-epoxygeraniol}}$) and 6,7-epoxygeraniol selectivity ($\%S_{6,7\text{-epoxygeraniol}}$) were calculated using the following formula, where A stands for chromatographic peak area: $\%C = \{[A(\text{geraniol})/A(\text{chlorobenzene})]_{t=0h} - [A(\text{geraniol})/A(\text{chlorobenzene})]_{t=xh}\} \times 100/[A(\text{geraniol})/A(\text{chlorobenzene})]_{t=0h}$, $\%S_{2,3\text{-epoxygeraniol}} = A(2,3\text{-epoxygeraniol}) \times 100/[A(2,3\text{-epoxygeraniol}) + A(6,7\text{-epoxygeraniol})]$, $\%S_{6,7\text{-epoxygeraniol}} = A(6,7\text{-epoxygeraniol}) \times 100/[A(2,3\text{-epoxygeraniol}) + A(6,7\text{-epoxygeraniol})]$.

2.4. Catalysis experiments

The reactions were carried out in 5.00 cm^3 of dichloromethane, at room temperature with constant stirring, and the composition of the reaction medium was 1.00 mmol of geraniol, 0.50 mmol of chlorobenzene (internal standard) and 0.10 g of heterogeneous catalyst. The oxidant, 1.50 mmol of *t*-BuOOH, was progressively added to the reaction medium using a Bioblock Scientific Syringe Pump at a rate of 0.5 cm^3 h^{-1}. For each material the %C was determined by withdrawing periodically 0.1 cm^3 aliquots from the reaction mixture. The reaction media composition was determined by GC, with geraniol, *t*-BuOOH, 2,3-epoxygeraniol, 6,7-epoxigeraniol and decane being quantified by the internal standard method (chlorobenzene). After the reaction, the catalysts were washed by reflux with 100 cm^3 of dichloromethane, and dried in an oven at 120 °C for 13 h, under vacuum. The catalysts were then reused for four times using the same experimental conditions. Control experiments using HMS, B1 and C1 materials as well as with $[VO(acac)_2]$ complex in the homogeneous phase were also performed under identical reaction conditions.

3. Results and discussion

3.1. Textural and chemical characterisation

The nitrogen adsorption–desorption isotherms at −196 °C for the different materials are depicted in Fig. 1. The curves do not show any hysteresis cycle, but the data analysis by the *t*-method [31] confirms the inexistence of microporosity. The isotherms can be considered of type IVc according to the IUPAC classification [31], being characteristic of mesoporous materials (pore widths between 2 and 50 nm). As described in more detailed elsewhere [32], type IVc isotherms, although they are obtained in mesoporous materials, they are completely reversible, that is, they do not present hysteresis. This type of isotherms was found by other authors in materials that are similar to those studied in this work, such as some samples of MCM-41 [32,33] and HMS type materials [34]. The specific surface areas (A_{BET}) and mesoporous volumes of the samples are given in Table 1. From this table it can be seen that the subsequent modifications performed on the parent HMS material lead to a concomitant decrease of the A_{BET} values. However, it is rather noticeable that after the immobilisation of the complex onto

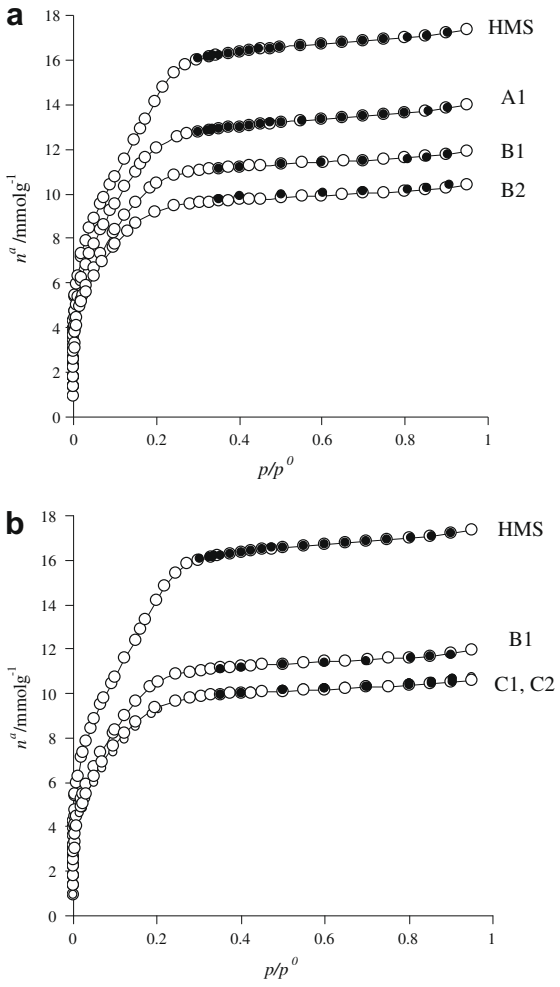


Fig. 1. Nitrogen adsorption–desorption isotherms at −196 °C of the materials prepared by: (a) methods A and B and (b) method C. Closed points are desorption points.

the supports even the lowest A_{BET} value (obtained for the B2 sample) is as high as 792 m^2 g^{-1}

In Fig. 2 the mesopore size distributions, obtained by the Broekhoff–de Boer method [35], are presented. As noticed from the HMS sample distribution, the mesopores present widths in the range of 2.4 and 3 nm. The direct complex immobilisation (A1) leads to an increase of the intensity of the peaks at the lowest pore diameter values (near 2.4 nm) and this effect is also observed for the remaining materials containing the vanadium complex (B2 and C2). In the case of C2, that is, the $[VO(acac)_2]$ based material where TMS was added, besides the peaks shift to lower values, the distribution seems to be more regular, that is, the different maxima become closer, suggesting that the TMS molecules, after reacting with the remaining silica OH groups, produce more uniform porous materials.

In Table 1 are also collected the N and V contents obtained by elemental and ICP-AES analysis, respectively, and by XPS. From the N bulk analysis and taking into account the initial amount of alkoxysilane used, it was possible to calculate the APTES grafting efficiency (amount of reacted alkoxysilane/amount in original solution × 100) for B1, which is 90%. Furthermore, the bulk (EA) and surface nitrogen (XPS) contents are similar, suggesting that APTES is uniformly grafted onto this material.

Upon complex immobilisation, the ICP-AES vanadium analysis in association with the peaks observation in the V $2p_{3/2}$ region of

Table 1
Chemical analysis and textural properties of HMS based materials.

Material	N (μmol g^{-1})		V (μmol g^{-1})			Textural properties	
	EA	XPS[a]	ICP	XPS[b]	ICP after catalysis[c]	A_{BET} (m^2 g^{-1})	V_{meso} (cm^3 g^{-1})
HMS	n.d.	59	–	–	–	1138	0.52
A1	n.d.	194	4	84	–	1020	0.41
B1	450	446	–	–	–	908	0.36
B2	364	170	128	25	35	792	0.31
C1	378	248	–	–	–	793	0.32
C2	293	237	51	51	41	808	0.32

[a] μmol N/weight of sample = at% N/[at% C × Ar(C) + at% N × Ar(N) + at% O × Ar(O) + at% Si × Ar(Si) + at% V × Ar(V)].
[b] μmol V/weight of sample = at% V/[at% C × Ar(C) + at% N × Ar(N) + at% O × Ar(O) + at% Si × Ar(Si) + at% V × Ar(V)].
[c] Vanadium ICP-AES content after five catalytic cycles.

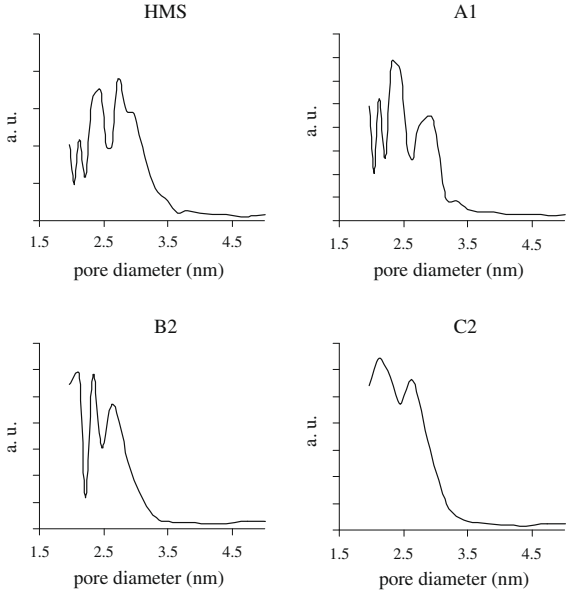


Fig. 2. Mesopore size distributions for HMS and for samples with anchored complex, obtained from the low temperature nitrogen adsorption data using the Broekhoff–de Boer method.

the high resolution XPS spectra of A1, B2 and C2 materials, confirm the presence of the metal complex in the HMS materials. From the vanadium contents determined by ICP-AES it was possible to determine the complex loadings for A1, B2 and C2 materials, which are 4, 128 and 51 μmol g^{-1}, respectively (Table 1), corresponding to complex immobilisation efficiencies (amount of immobilised complex/amount in original solution × 100) of 2%, 65% and 25%, respectively. As can be seen, the direct immobilisation of the complex onto the parent HMS (method A) leads to the lowest complex immobilisation efficiency, whereas the highest value is achieved for complex immobilisation onto the APTES functionalised HMS (method B). This is a consequence of the absence of chemical adsorption sites for the complex immobilisation in the parent HMS in contrast with the NH_2-functionalised HMS (B1), where the grafted NH_2 groups can act as specific sites for complex covalent anchorage. C1 material shows lower V content than B1, probably because the grafted TMS molecules hinder the reaction between APTES and the complex molecules.

Moreover, the comparison between the vanadium ICP-AES and XPS values can also provide some insights about the complex localisation within the HMS materials. In A1 material, [$VO(acac)_2$] is mainly immobilised in the outer pores of the parent HMS, since the total amount of vanadium per weight of material is lower than the vanadium surface content. On the other hand, in B2 material the VO complex is mainly grafted in the inner pores, since the bulk content is higher than the surface loading and finally, in C2, the metal complex appears to be homogeneously distributed throughout the HMS pores, since the vanadium bulk and surface contents are similar.

Analysis of A_{BET} values as a function of vanadium surface (XPS) and bulk (ICP-AES) contents for A1, B2 and C2 materials, Table 1, can give some interesting relations concerning the functionalised materials. In the case of the vanadium surface contents, the sample with higher complex loading (A1) is also the one which presents higher A_{BET} value since the surface inside the pores remains unoccupied to a large extent. More relevant, however, is the relation between the A_{BET} values and the vanadium bulk contents: in this case, as can be expected, the A_{BET} decreases with the increase in the vanadium total content: $A_{BET}(A1) > A_{BET}(C2) > A_{BET}(B2)$. However, for vanadium values of 51 and 128 μmol g^{-1} (for C2 and B2, respectively), the A_{BET} values only decrease from 808 to 792 m^2 g^{-1}, that is, in this vanadium content range, when the vanadium bulk amount increases 2.5 times the decrease in the surface area is only of 2%.

3.2. FTIR measurements

The infrared spectrum of the HMS parent material, Fig. 3, shows the typical Si–O lattice vibrations: two low intensity broad bands between 2100 and 1750 cm^{-1}, a broad and strong band in the 1390–900 cm^{-1} region and two strong bands between 900 and 400 cm^{-1} [26–29]. Moreover, it can also be observed a broad band at 3450 cm^{-1} assigned to O–H stretching vibrations and a very sharp peak at 3745 cm^{-1}, with medium intensity, due to stretching vibrations of isolated silanol groups [26–29]. A band at 1630 cm^{-1} is also observed in the spectrum and is attributed to H–O–H bending vibrations of physisorbed water [26–29].

Upon HMS functionalisation with APTES (B1), Fig. 3b, several changes can be observed in all the frequency range. The peak at 3745 cm^{-1} disappears, indicating the reaction between the surface silanol groups and the ethoxyl functionalities of APTES. A decrease in the broad band centred at 3450 cm^{-1} can also be observed due to a decrease in the adsorbed water content, as a consequence of the APTES grafting reaction. Furthermore, new bands due to N–H and C–H stretching vibrations can be observed in the 2970–2850 cm^{-1} region and the H–N–H and H–C–H bending vibrations are also observed in the range of 1560–1430 cm^{-1} [26–29].

Upon treatment of the APTES modified HMS with TMS (C1), Fig. 3c, no significant changes are detected; nevertheless a small decrease in the broad band centred at 3450 cm^{-1} due to OH stretching vibrations can be observed, suggesting the reaction between the remaining free silanol groups of the support and the ethoxyl groups of the TMS molecules. The presence of TMS in the material is also demonstrated by a small increase in the peaks corresponding to C–H stretching vibrations.

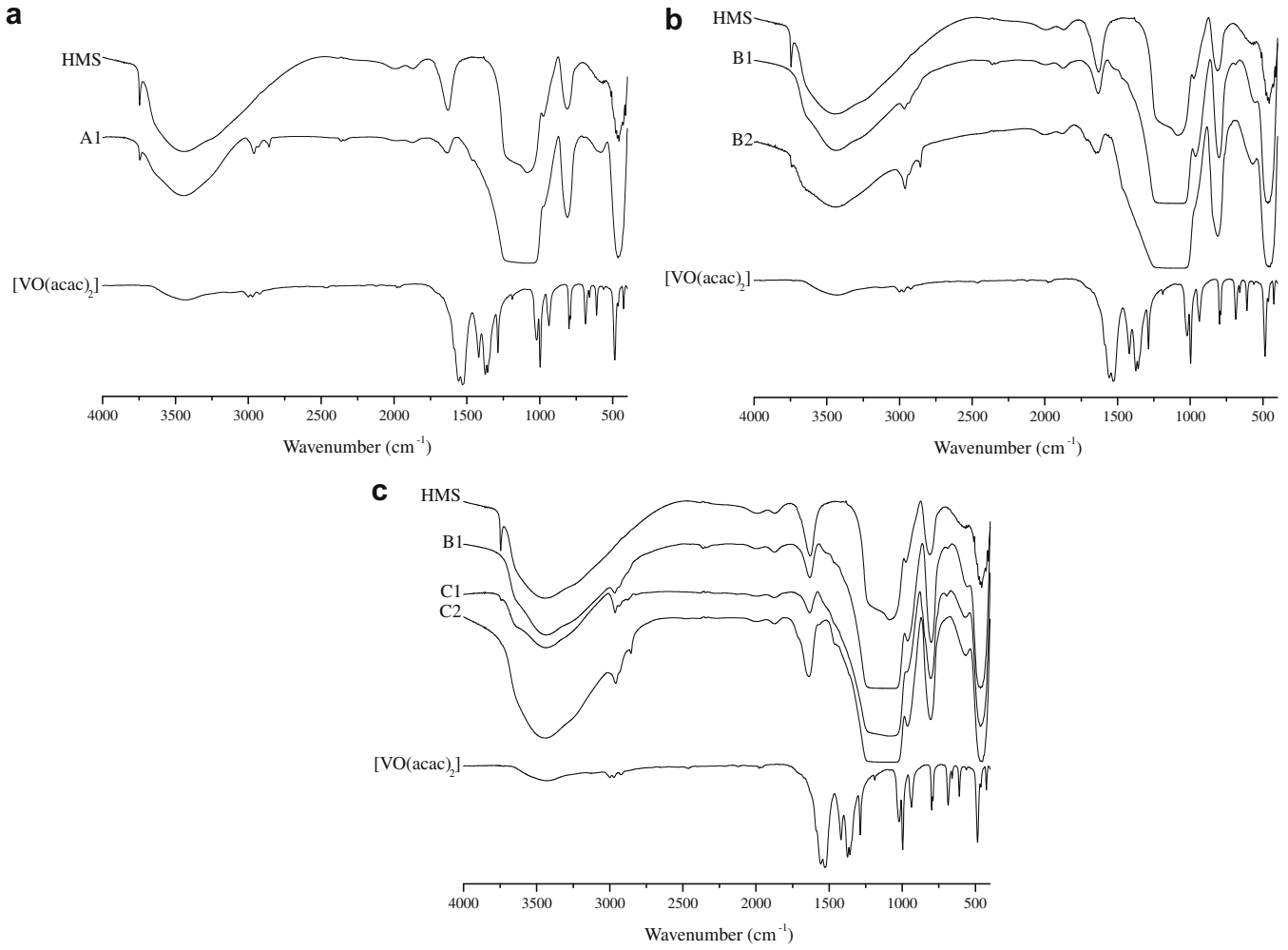


Fig. 3. FTIR spectra of the free [VO(acac)$_2$] complex and of parent and modified HMS materials prepared by methods: (a) A, (b) B and (c) C.

The FTIR spectra of the materials after complex immobilisation (A1, B2 and C2), Fig. 3a–c, present some changes in the ranges of 2970–2850 cm^{-1} and of 1780–1350 cm^{-1}, that can be unambiguously assigned to the immobilised complex; however, in all these spectra, the band due to the V=O stretching vibration, which appears at 997 cm^{-1} in the free complex could not be observed probably because it is masked by the strong and broad Si–O–Si band positioned in the 1390–900 cm^{-1} range. In fact, the free complex spectrum exhibits the most relevant bands in the ranges 3000–2920 cm^{-1} (C–H stretching vibrations), 1560–1350 cm^{-1} (stretching vibrations associated with the chelate ring) and at 997 cm^{-1} corresponding to the VO stretching vibrations [36].

The FTIR spectrum of A1, Fig. 3a, presents three new bands in the C–H stretching vibrations range, at 2960, 2932 and 2857 cm^{-1}, which are consistent with a band shift of the free complex bands situated at 3000, 2971 and 2923 cm^{-1}. This result, combined with the observed decreases in both the intensity of the broad band centred at 3450 cm^{-1} and the sharp peak at 3745 cm^{-1}, suggest that the HMS hydroxyl surface groups may be involved in the complex immobilisation through hydrogen bonds with the delocalised π-system of the acetylacetonate ligand, Scheme 1, as observed in the direct immobilisation of [VO(acac)$_2$] onto alumina, clays, silica gel and other mesoporous silicas [16,18,19].

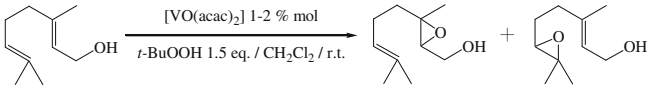
When comparing the spectra of B2 and C2 with the correspondent parent materials (B1 and C1, respectively) it is possible to see several changes which are attributed to the grafted VO complex: (i) increase in the intensity of the C–H stretching vibrations in the 2970–2850 cm^{-1} region and a change in their profile, (ii) increase in the intensity and broadness of the band at 1630 cm^{-1} and (iii) the appearance of a shoulder on the latter band in the high energy side, at approximately 1710 cm^{-1}. The broadening of the band at 1630 cm^{-1} can be due to the presence of overlapped bands assigned to the grafted complex, as already seen in the grafting of the same VO(IV) complex and Cu(II) analogue in Laponite and K10-montmorillonite, using the same immobilisation procedure [16,37]. These new bands are assigned to chelate stretching vibrations, now containing the new C=N bond formed by Schiff condensation reaction between the amine groups of the grafted APTES and the C=O group from the coordinated acetylacetonate ligand, Scheme 1 [16,37]. Due to the high APTES grafting efficiency onto the parent HMS, no significant direct immobilisation of [VO(acac)$_2$] may occur in materials B1 and C1.

3.3. Epoxidation of geraniol catalysed by [VO(acac)$_2$] heterogeneous catalysts

The results obtained in the epoxidation of geraniol at room temperature using [VO(acac)$_2$] based materials as catalysts and *t*-BuOOH as the oxygen source, in dichloromethane, are summarised in Table 2. Data from homogeneous phase and blank experiments ran under identical conditions are also included.

The geraniol conversions for 48 h of reaction are 100%, 35% and 17% using B2, C2 and A1 materials, respectively (Table 2). This sequence follows the order of vanadium loadings obtained by

Table 2
Epoxidation of geraniol catalysed by $[VO(acac)_2]$ in homogeneous and heterogeneous phases.[a]



geraniol 2,3-epoxygeraniol 6,7-epoxygeraniol

Catalyst	*t* (h)	Cycle	%C[b]	% Selectivity (% yield)[c]	
				2,3-Epoxygeraniol	6,7-Epoxygeraniol
$[VO(acac)_2]$	1	first	100	99 (99)	1 (0.7)
HMS	48	first	7	49 (3)	51 (4)
A1	48	first	17	92 (16)	8 (1)
B1	48	first	4	50 (2)	50 (2)
B2	48	first	100	98 (98)	2 (2)
	48	second	100	98 (98)	2 (2)
	48	third	99	99 (98)	1 (1)
	48	fourth	100	99 (98)	1 (1)
	48	fifth	100	99 (99)	1 (1)
C1	48	first	4	57 (2)	43 (2)
C2	48	first	35	99 (35)	1 (0)
	48	second	93	100 (93)	0 (0)
	48	third	66	99 (66)	1 (0)
	48	fourth	77	99 (76)	1 (1)
	48	fifth	34	99 (34)	1 (0)

[a] *Typical reaction conditions:* 1.00 mmol geraniol, 0.50 mmol chlorobenzene (internal standard), 0.10 g heterogeneous catalyst and 1.50 mmol *t*-BuOOH.
[b] Based on geraniol consumption.
[c] Selectivity of the geraniol epoxides; yield calculated as: (%C × %S)/100.

ICP-AES (Table 1) onto the HMS materials: B2 ≫ C2 > A1. The regioselectivity towards the allylic double bond remains identical to the homogeneous counterpart for all the heterogeneous $[VO(acac)_2]$ based catalysts, being nearly 100% for 2,3-epoxygeraniol (Table 2). From the control experiments with the parent materials it is possible to conclude that the silica surface both unmodified and functionalised with APTES/TMS does not have relevant catalytic activity on its own, as can be confirmed by the geraniol conversion percentages of HMS, B1 and C1 materials, of only 7% and 4%, respectively.

All the reactions in the heterogeneous phase have higher reaction times when compared to the homogeneous reaction. This effect is due to diffusion constraints imposed to the substrate and reagents by the specific localisation of the active catalytic centres within the porous matrix [16,21,27].

With the exception of A1 which presents high catalyst leaching after the first cycle, detected by visual inspection of the colour of the reaction medium, the new heterogeneous catalysts were reused for further four catalytic cycles. During the catalytic cycles, B2 shows similar %C and $\%S_{2,3\text{-epoxygeraniol}}$ to those exhibited in the first cycle, but C2 shows some change in %C. In order to understand these different behaviours, leaching of the catalytic active phase was determined by measurement of vanadium contents by ICP-AES after the five catalytic cycles; the values are presented in Table 1. Materials B2 and C2 have complex leaching percentages of 73% and 20%, respectively, and thus it can be concluded that the constant high catalytic activity of B2 in all cycles may have a significant homogeneous component. In this context, C2 can be considered the most stable catalyst upon reuse, presenting a satisfactory geraniol conversion, but showing high selectivity for the desired product even after four reuse cycles.

As a summary, in terms of catalyst stability, the most effective immobilisation method is the one which uses TMS in combination with APTES (method C: covalent grafting, Scheme 1), leading to a homogeneous distribution of the complex throughout the support.

4. Conclusions

New heterogeneous catalysts were prepared by immobilisation of $[VO(acac)_2]$ onto HMS supports both directly and after functionalisation with amine groups. In the case of APTES functionalised supports, the effect of TMS addition before complex grafting was also studied.

The ICP-AES and XPS results of the final materials showed that the $[VO(acac)_2]$ immobilisation was achieved in all cases, with B2 presenting the highest grafting efficiency (highest complex loading). In the case of A1 (method A), the metal complex was mainly immobilised on the outer silica surface by hydrogen bonds between the HMS hydroxyl surface groups and the delocalised π-system of the acetylacetonate ligand. Complex immobilisation by methods B and C (materials B2 and C2) occurred by covalent bond formed by the reaction between the surface NH_2 grafted groups and the C=O group of the acetylacetonate ligand. In B2 the VO complex was mainly grafted in the inner pores of the solid matrix, but in the case of C2, the complex distribution in HMS pores was more homogeneous.

In the geraniol epoxidation, the material which led to the highest geraniol conversion was B2. One of the reasons that could justify the highest values for this material, in particular when compared with C2, could be its highest vanadium content for comparable specific surface area values. However, B2 material also resulted in a higher leaching percentage after five catalytic cycles when compared with C2. It could be concluded that the grafting process leading to C2 catalyst, although resulting in lower $[VO(acac)_2]$ content, was the most efficient one, giving rise to a heterogeneous catalyst with satisfactory substrate conversion, high regioselectivity until the fourth catalytic cycle and high stability,

corresponding to a leaching percentage of 20% after five consecutive catalytic cycles. Material A1 showed the lowest %C and the highest active phase leaching; this was a consequence of the lowest V content, determined by the absence of specific immobilisation sites and by weak non-covalent support interactions through hydrogen bonds, which can easily be disrupted by the oxidative nature of the catalytic reaction medium.

Acknowledgements

This work was funded by FCT Fundação para a Ciência e a Tecnologia (FCT) and FEDER, through the Project Refs. POCI/CTM/56192/2004 and PTDC/CTM/65718/2006. C.P. thanks FCT for a Ph.D. fellowship.

References

[1] T. Katsuki, Coord. Chem. Rev. 140 (1995) 189.
[2] V. Conte, F. Di Furia, G. Licini, Appl. Catal. A 157 (1997) 335. and references therein.
[3] M.N. Sheng, J.G. Zajacek, J. Org. Chem. 35 (1970) 1839.
[4] (a) K.B. Sharpless, R.C. Michaelson, J. Am. Chem. Soc. 95 (1973) 6136;
(b) S. Tanaka, H. Yamamoto, H. Nozaki, K.B. Sharpless, R.C. Michaelson, J.D. Cutting, J. Am. Chem. Soc. 96 (1974) 5254;
(c) K.B. Sharpless, T.R. Verhoeven, Aldrichim. Acta 12 (1979) 63.
[5] C. Bolm, Coord. Chem. Rev. 237 (2003) 245.
[6] B.E. Rossiter, T.R. Verhoeven, K.B. Sharpless, Tetrahedron Lett. 20 (1979) 4733.
[7] A.G.J. Ligtenbarg, R. Hage, B.L. Feringa, Coord. Chem. Rev. 237 (2003) 89.
[8] L. Canali, D.C. Sherrington, Chem. Soc. Rev. 28 (1999) 85.
[9] Q.-H. Fan, Y.-M. Li, A.S.C. Chan, Chem. Rev. 102 (2002) 3385.
[10] N.E. Leadbeater, M. Marco, Chem. Rev. 102 (2002) 3217.
[11] D. Brunel, N. Belloq, P. Sutra, A. Cauvel, M. Laspéras, P. Moreau, F. Di Renzo, A. Galarneau, F. Fajula, Coord. Chem. Rev. 178–180 (1998) 1085.
[12] C. Freire, C. Pereira, in: J.L. Figueiredo, M.M. Pereira, J. Faria (Eds.), Catalysis from Theory to Application – An Integrated Course, Imprensa da Universidade de Coimbra, Portugal, 2008, p. 213 (Chapter A.9).
[13] D.E. de Vos, I.F.J. Vankelecom, P.A. Jacobs (Eds.), Chiral Catalyst Immobilisation and Recycling, Wiley-VCH Verlag, Weinheim, 2000, p. 19.
[14] D.E. de Vos, M. Dams, B.F. Sels, P.A. Jacobs, Chem. Rev. 102 (2002) 3615.
[15] Q.-H. Xia, H.-Q. Ge, C.-P. Ye, Z.-M. Liu, K.-X. Su, Chem. Rev. 105 (2005) 1603.
[16] C. Pereira, A.R. Silva, A.P. Carvalho, J. Pires, C. Freire, J. Mol. Catal. A: Chem. 283 (2008) 5.
[17] S. Shylesh, A.P. Singh, J. Catal. 244 (2006) 52.
[18] A.-M. Hanu, S. Liu, V. Meynen, P. Cool, E. Popovici, E.F. Vansant, Micropor. Mesopor. Mater. 95 (2006) 31.
[19] M. Baltes, O. Collart, P. Van der Voort, E.F. Vansant, Langmuir 15 (1999) 5841.
[20] A. Lattanzi, N.E. Leadbeater, Org. Lett. 4 (2002) 1519.
[21] B. Jarrais, A.R. Silva, C. Freire, Eur. J. Inorg. Chem. (2005) 4582.
[22] X.S. Zhao, F. Su, Q. Yan, W. Guo, X.Y. Bao, L. Lv, Z. Zhou, J. Mater. Chem. 16 (2006) 637.
[23] P.T. Tanev, T.J. Pinnavaia, Science 267 (1995) 865.
[24] K. Wilson, J.H. Clark, Pure Appl. Chem. 72 (2000) 1313.
[25] P.M. Price, J.H. Clark, D.J. Macquarrie, J. Chem. Soc., Dalton Trans. (2000) 101.
[26] A.R. Silva, K. Wilson, J.H. Clark, C. Freire, Micropor. Mesopor. Mater. 91 (2006) 128.
[27] A.R. Silva, K. Wilson, A.C. Whitwood, J.H. Clark, C. Freire, Eur. J. Inorg. Chem. (2006) 1275.
[28] A.R. Silva, K. Wilson, J.H. Clark, C. Freire, Stud. Surf. Sci. Catal. 158 (2005) 1525.
[29] Z. Fu, D. Yin, W. Zhao, Y. Chen, D. Yin, J. Guo, L. Zhang, Catal. Lett. 90 (2003) 205.
[30] Z. Fu, D. Yin, Q. Xie, W. Zhao, A. Lv, D. Yin, Y. Xu, L. Zhang, J. Mol. Catal. A: Chem. 208 (2004) 159.
[31] F. Rouquerol, J. Rouquerol, K. Sing, Adsorption by Powders and Porous Solids, Academic Press, 1999.
[32] M. Grün, K.K. Unger, A. Matsumoto, K. Tsutsumi, in: B. McEnaney, T.J. Mays, J. Rouquerol, F. Rodríguez-Reinoso, K. Sing, K.K. Unger (Eds.), Characterisation of Porous Solids IV, The Royal Society of Chemistry, London, 1997.
[33] R. Schmidt, M. Stöcker, E. Hansen, D. Akporiaye, O.H. Ellestad, Micropor. Mater. 3 (1995) 443.
[34] A.P. Fotopoulos, K.S. Triantafyllidis, Catal. Today 127 (2007) 148–156.
[35] W.J. Lukens Jr., P. Schmidt-Winkel, D. Zhao, J. Feng, G.D. Stucky, Langmuir 15 (1999) 5403.
[36] P. Van der Voort, I.V. Babitch, P.J. Grobet, A.A. Verbeckmoes, E.F. Vansant, J. Chem. Soc., Faraday Trans. 92 (1996) 3635.
[37] C. Pereira, S. Patrício, A.R. Silva, A.L. Magalhães, A.P. Carvalho, J. Pires, C. Freire, J. Colloid Interf. Sci. 316 (2007) 570.

The SCPs **1**–**3**, were prepared by the same procedure under the same conditions. A solution of 85 mg (0.5 mmol) of $AgNO_3$ in 10 mL H_2O was being added at room temperature to the mixture of (0.5 mmol) of the bipodal ligand; **L**, in 10 mL MeCN and of 48 mg (0.5 mmol) of KSCN in 10 mL H_2O. White turbidity appeared then after concentrated ammonia solution was added to the hot mixture dropwise with stirring till clearness. The mixture was filtered off and the filtrate was left to stand for some days. Prismatic colorless crystals of **1** appeared after two weeks. After filtration, subsequent washing with small portions of water and MeCN and overnight drying, about 109 mg of [$(AgSCN)_2 \cdot$ bpy] **1** were obtained. *Anal.* Calc. for **1** ($C_{12}H_8N_4S_2Ag_2$): C, 29.50; H, 1.63; N, 11.47. Found: C, 29.32; H, 1.60; N, 11.55%. IR (KBr, cm^{-1}): 3045w, 2117s, 2090s, 1597s, 1528m, 1409s, 1372m, 1214m, 1067m, 799s, 622s, 562m, 508s, 452w and 431w. Also, brown prismatic crystals of [$(AgSCN)_2 \cdot$ (tbpe)], **2**, were formed after two weeks and filtered off then after washed with small portions of water and MeCN and dried overnight. Ninety-six milligrams of **2** were obtained. *Anal.* Calc. for **2** ($C_{14}H_{10}N_4S_2Ag_2$): C, 32.67; H, 1.94; N, 10.89. Found: C, 32.63; H, 1.97; N, 10.75%. IR (KBr, cm^{-1}): 3047w, 2925w, 2862w, 2099s, 1599m, 1419s, 1319m, 1295m, 1250m, 1207m, 980s, 827s, 754s, 552s, 448m. Brown needle crystals of **3** were formed after one week and filtered off then after washed with small portions of water and MeCN and dried overnight. Sixty-two milligrams of [$(AgSCN)_2 \cdot$ phenz], **3**, were obtained. *Anal.* Calc. for **3** ($C_{14}H_8N_4S_2Ag_2$): C, 32.80; H, 1.56; N, 10.93. Found: C, 32.64; H, 1.55; N, 11.09%. IR (KBr, cm^{-1}): 3048w, 3006w, 2867w, 2131s, 1513s, 1466m, 1432m, 1360m, 1119m, 905m, 823m, 748s, 654m, 594m, 439m.

2.2. X-ray structural determination

Structural measurements for the SCPs **1**–**3** were performed on a Kappa CCd Enraf Nonius FR 90 four cycle geniometer with graphite monochromatic Mo Kα radiation {[λMo Kα] = 0.71073 Å} at 25 ± 2 °C. All structures were resolved using direct-methods and

Table 1
Crystal data and structure refinement parameters of the SCPs **1**–**3**.

	1	2	3
Empirical formula	$C_{12}H_8Ag_2N_4S_2$	$C_{14}H_{10}Ag_2N_4S_2$	$C_{14}H_8Ag_2N_4S_2$
Formula weight	488.072	514.110	512.114
Temperature (K)	298	298	298
Crystal system	monoclinic	triclinic	monoclinic
Space group	C_2/c	$P\bar{1}$	$P2_1/c$
a (Å)	18.3525 (7)	5.9315 (2)	4.1453 (2)
b (Å)	6.2310 (3)	7.3747 (3)	20.6722 (9)
c (Å)	12.1581 (4)	9.6990 (4)	9.3478 (4)
α (°)	90.00	99.676 (2)	90.00
β (°)	99.836 (3)	106.843 (2)	110. 00(18)
γ (°)	90.00	97.072 (2)	90.00
V (Å^3)	1369.89 (10)	393.59 (3)	760.36 (6)
Z	4	1	2
μ(Mo Kα) (mm^{-1})	3.16	2.75	2.85
R_1	0.044	0.029	0.033
wR_2	0.212	0.060	0.079
R_{int}	0.024	0.022	0.026
Data/restraints/parameters	925/0/91	1251/0/100	1085/0/106
Calculated density (mg/m^3)	2.367	2.169	2.237
Goodness-of-fit on F^2	2.506	1.026	1.316

Table 2
Selected bond distances (Å) and bond angles (°) for the SCP **1**.

Ag1–S2	2.7742 (6)	S2–N15	2.797 (2)
Ag1–S2^a	3.0637 (6)	S2–C14	1.660 (2)
Ag1–N8	2.247 (2)	C14–N15	1.138(2)
Ag1–N15^b	2.158 (2)	Ag1–Ag1^a	3.2431 (5)
Ag1^a–S2	3.3939(6)		
S2–Ag1–S2^a	92.95 (2)	Ag1–S2–C14	103.06 (7)
S2–Ag1–N8	99.45 (4)	Ag1^a–S2–N15	94.34 (4)
S2–Ag1–N15^b	98.98 (5)	Ag1^a–S2–C14	94.73 (6)
S2^a–Ag1–N8	88.88 (4)	Ag1–N8–C10	153.18 (9)
S2^a–Ag1–N15^b	91.53 (4)	Ag1–N8–C12	145.15 (9)
N8–Ag1–N15^b	161.52 (7)	Ag1–N8–C9	125.21 (12)
Ag1–S2–Ag1^a	87.05 (2)	Ag1–N8–C11	170.53 (8)
Ag1–S2–N15	103.30 (4)	Ag1–N8–C13	116.99 (13)
Ag1^c–N15–S2	172.81 (9)	S2–C14–N15	178.9 (2)
Ag1^c–N15–C14	172.2 (2)		
Interlayer H-bonding			
S2–H9^a	2.8667 (5)		
S2–H13^a	3.0163 (4)		
N15–H13^d	2.657 (2)		
C14–H13^d	2.907 (2)		

Symmetry codes: (a) 1/2 − x, 1/2 − y, −z; (b) x, −y, z − 1/2; (c) x, −y, 1/2 + z; (d) 1/2 − x, −1/2 − y, −z.

Table 3
Selected bond distances (Å) and bond angles (°) for the SCP **2**.

Ag1–S2	2.7534 (8)	S2–H6	2.9547 (7)
Ag1–S2^a	2.7722 (8)	C10–N5	1.154 (3)
Ag1–N3	2.248 (2)	S2–C10	1.652 (3)
Ag1–N5	2.173 (3)	Ag1–Ag1^a	3.3638 (6)
S2–Ag1–S2^a	105.00 (2)	Ag1^a–S2–C10	98.57 (10)
S2–Ag1–N3	103.72 (6)	Ag1–N3–C4	173.91 (12)
S2–Ag1–N5	100.08 (7)	Ag1–N3–C7	154.34 (14)
S2^a–Ag1–N3	95.27 (6)	Ag1–N3–C8	145.69 (12)
S2^a–Ag1–N5	103.02 (8)	Ag1–N3–C9	125.3 (2)
N3–Ag1–N5	144.95 (10)	Ag1–N3–C11	117.5 (2)
Ag1–S2–Ag1^a	75.00 (2)	Ag1–N5–S2	155.98 (13)
Ag1–S2–N5	96.58 (6)	Ag1–N5–C10	155.6 (2)
Ag1–S2–C10	96.37 (10)	Ag1^a–S2–N5	98.91 (6)
S2-C10-N5	179.1(3)		
Hydrogen-bonding			
Inter-layer		Intra-layer	
S2–H6	2.9547 (7)	N5–H11^c	2.927 (3)
S2–H7^b	3.0761 (7)	C10–H11^c	2.869 (3)
N5–H7^b	3.202 (7)		
N5–H6^b	3.292 (7)		
C10–H7^b	2.838 (3)		

Symmetry codes: (a) −x, −y, 1−z; (b) −x, −y, −z; (c) 1 − x, −y, 1 − z.

Table 4
Selected bond distances (Å) and bond angles (°) for the SCP **3**.

Ag1–S2	2.6020 (8)	Ag1–N11^a	2.219 (3)
S2–C6	1.652 (3)	C6–N11	1.141 (3)
Ag1–N4	2.438 (2)	Ag1–S2^a	2.5942 (8)
S2–Ag1–S2	105.82 (3)	Ag1–N4–C3	122.1 (2)
S2–Ag1–N4	115.69 (5)	Ag1–N4–C3^b	150.78 (12)
S2–Ag1–N11^a	108.30 (7)	Ag1–N4–N4^b	179.2 (2)
S2–Ag1–N4	87.82 (5)	Ag1–N4–C5	90.95 (10)
S2–Ag1–N11^a	121.83 (7)	Ag1–N4–C8	120.4 (2)
N4–Ag1–N11^a	116.26 (9)	Ag1–N4–C8^b	152.51 (11)
Ag1–S2–Ag1	105.82 (3)	Ag1–N4–C9	89.49 (10)
Ag1–S2–C6	110.23 (10)	Ag1^c–N11–S2	176.83 (13)
Ag1–S2–N11	100.18 (6)	Ag1^c–N11–C6	177.7 (3)
S2–C6–N11	178.5 (3)		
Hydrogen-bonding			
S2–H5	2.84 (3)	N11–H7	3.014 (3)
S2–H10^b	2.97 (3)	N11–H9^c	2.997 (3)
C6–H7	3.037 (3)	N11–H9^d	2.728 (3)

Symmetry codes: (a) x − 1, 1/2 − y, z − 1/2; (b) −x, −y, 1 − z; (c) 1 + x, 1/2 − y, 1/2 + z; (d) 1 + x, 1/2 − y, 1/2 + z.

all of the non-hydrogen atoms were located from the initial solution or from subsequent electron density difference maps during the initial stages of the refinement. After locating all of the non-hydrogen atoms in each structure the models were refined against F^2, first using isotropic and finally using anisotropic thermal displacement parameters. The positions of the hydrogen atoms were then calculated and refined isotropically, and the final cycle of refinements was performed. The cyano groups of all structures were ordered. Crystallographic data for the SCPs **1**–**3** are summarized in Table 1. Selected bond distances and bond angles are given in Tables 2–4.

3. Results and discussion

3.1. Crystal structures

3.1.1. Crystal structure of $[(AgSCN)_2 \cdot bpy]$ (*1*)

The ORTEP plot of the novel SCP **1** shows one half of the chemical formula; Fig. 1a, while the formula unit contains two crystallographically identical silver atoms, two thiocyanate ligands and one bpy ligand. Each silver atom is bound to one S atom and one N atom of two thiocyanate ligands and one N atom of bpy ligand forming distorted trigonal planar geometry with N8–Ag1–N15

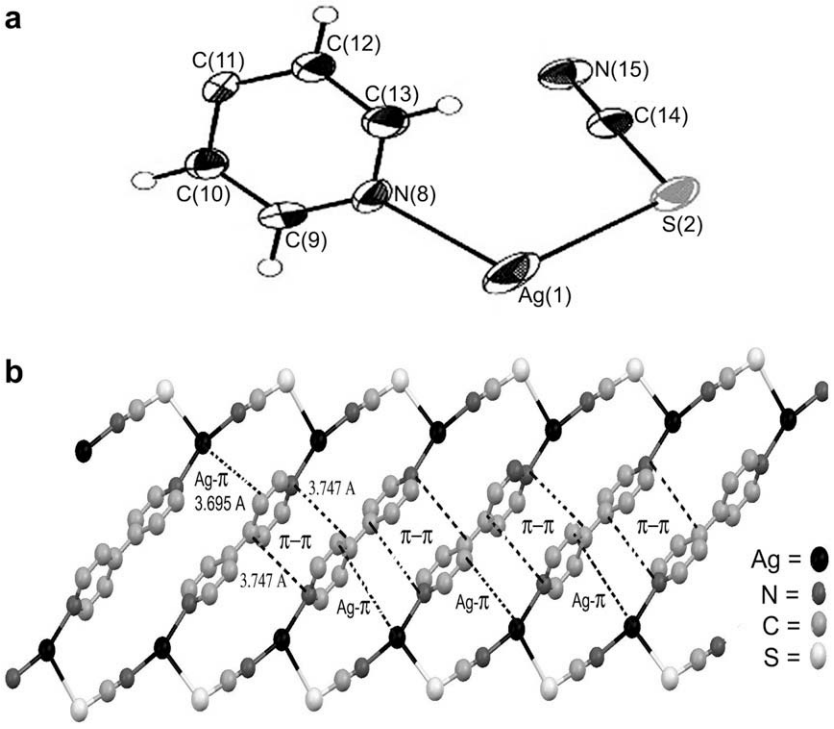


Fig. 1. (a) An ORTEP view of the asymmetric unit of the SCP **1**. (b)View of the ribbon structure of the SCP **1** along the *b*-axis; H-atoms are omitted for clarity.

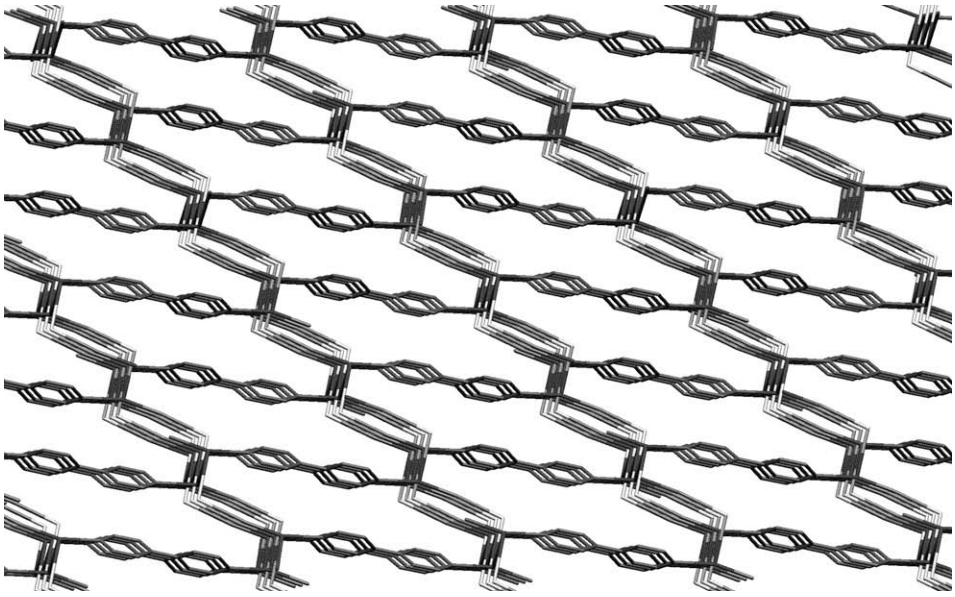


Fig. 2. View of the 3D-structure of the SCP **1** along the *b*-axis showing the crossing of the 2D-layers.

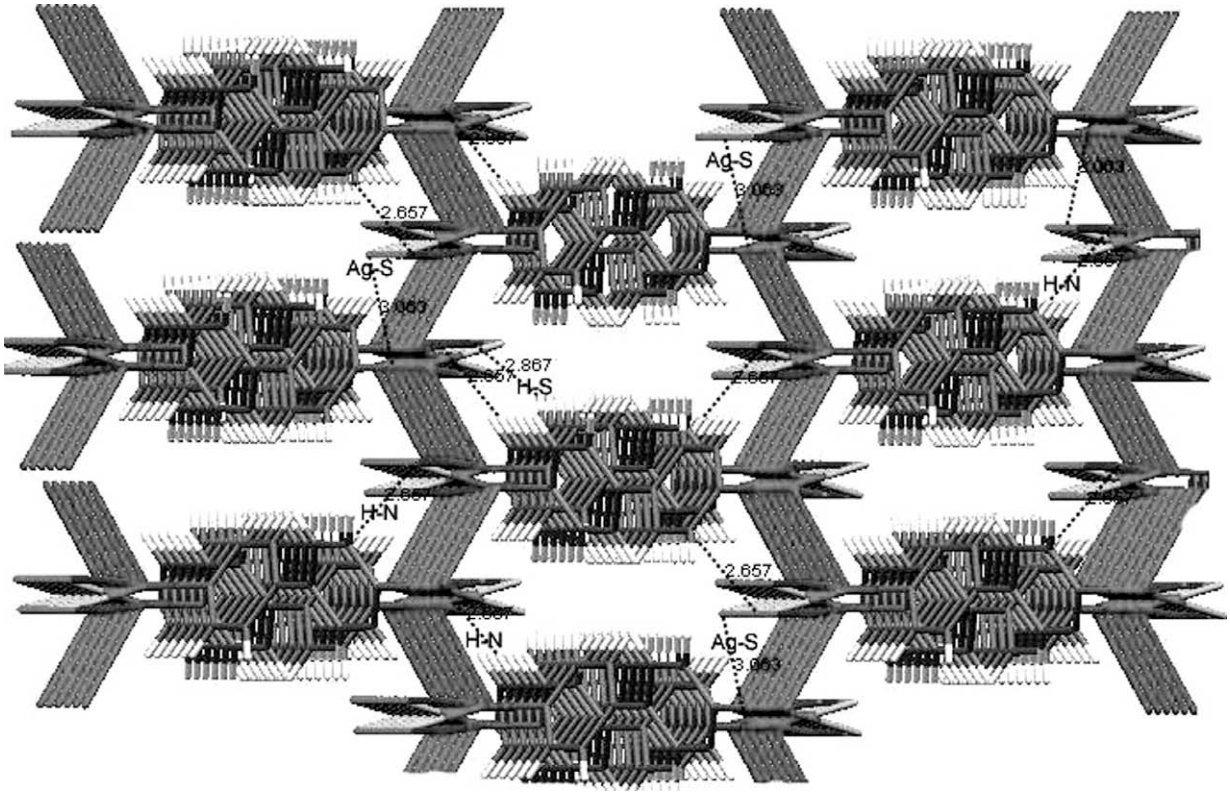


Fig. 3. View of the 3D-structure of the SCP **1** along the *c*-axis showing the Ag–Ag, Ag–S interactions and hydrogen-bonding.

angle equals to 161.52°, Table 2 and Fig. 1b. The thiocyanate ligand acts as μ_2-1,3-ligand connecting the silver atoms, Ag1–N15 = 2.158 Å, Ag1–S2 = 2.774 Å, which are in the range of the reported values [10,14]. On the other hand, the AgNC angle is nearly linear, while AgSC angle is nearly perpendicular; Table 2. The AgSCN building blocks create infinite parallel zig-zag chains with S2–Ag1–N15 = 98.99° and Ag1–S2–C14 = 103.06°. These zig-zag chains are bridged by the bpy bipodal ligand forming extended vertical 2D-ribbons along the *b*-axis, Fig. 1b. In this case, a polygon consisting of $[(Ag_4(SCN)_2(bpy)_2]$, of dimensions of 6.096 Å × 16.632 Å, is recognized as a typical fragment of **1**. These polygons are arranged in unique way that one pyridyl ring of the bpy ligand in one polygon is parallel to another pyridyl ring of bpy in the adjacent polygon with a separation distance of 3.74 Å suggesting the presence of weak but not negligible stacking interactions, between the pyridine rings, as well as Ag–π interaction between the silver(I) ion and the neighboring pyridyl ring; 3.695 Å; Fig. 1b. It is worth mentioned here that one pyridyl ring in each bpy ligand is tilted out of the plane defined by the other bpy ring by an angle of 43.93°. Alternatively, these ribbons can be considered as infinite non-interpenetrating 2D-layers that cross each other along the *b*-axis via the AgSCN fragments, Fig. 2. On the other hand, each ribbon can be considered as a compressed spring along the *c*-axis creating a unique shape, Fig. 3.

The ribbons are arranged parallel in unique way where one layer connect two ribbons above and two ribbons below by Ag–Ag interactions; Ag–Ag = 3.242 Å and by H-bonds between H-atoms of the pyridyl rings in one layer and thiocyanate groups in the neighboring layers; H–S = 2.867 and 3.016 Å, C–H = 2.907 Å and N–H = 2.657 Å, as well as considerable contacts between Ag atoms and S2 atoms in the adjacent layers Ag–S2[a] = 3.0627 and 3.393 Å forming 3D-network structure; Fig. 3. The Ag–Ag and Ag–S2 contacts cause pyramidalisation of Ag(I) sites.

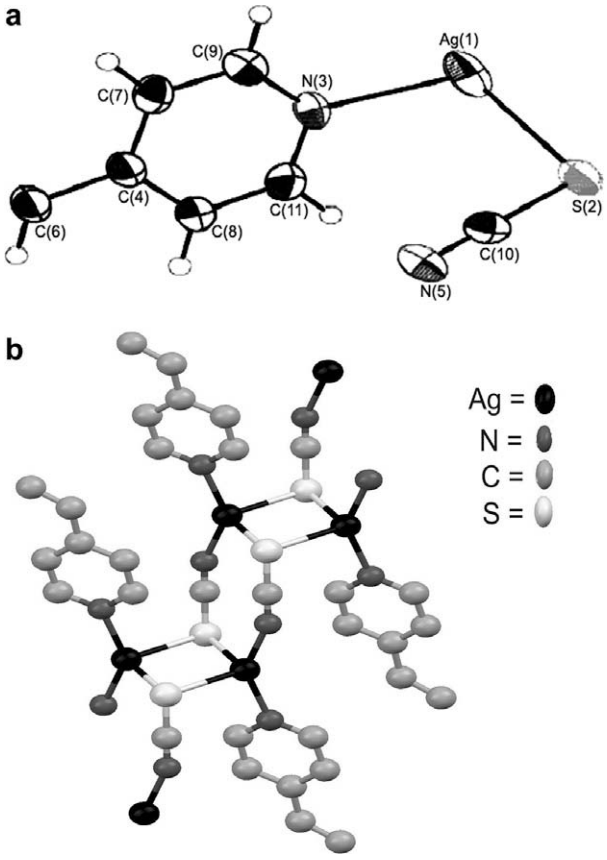


Fig. 4. (a) An ORTEP plot of the asymmetric unit of the SCP **2**. (b) The basic building block of the SCP **2**; H-atoms are omitted for clarity.

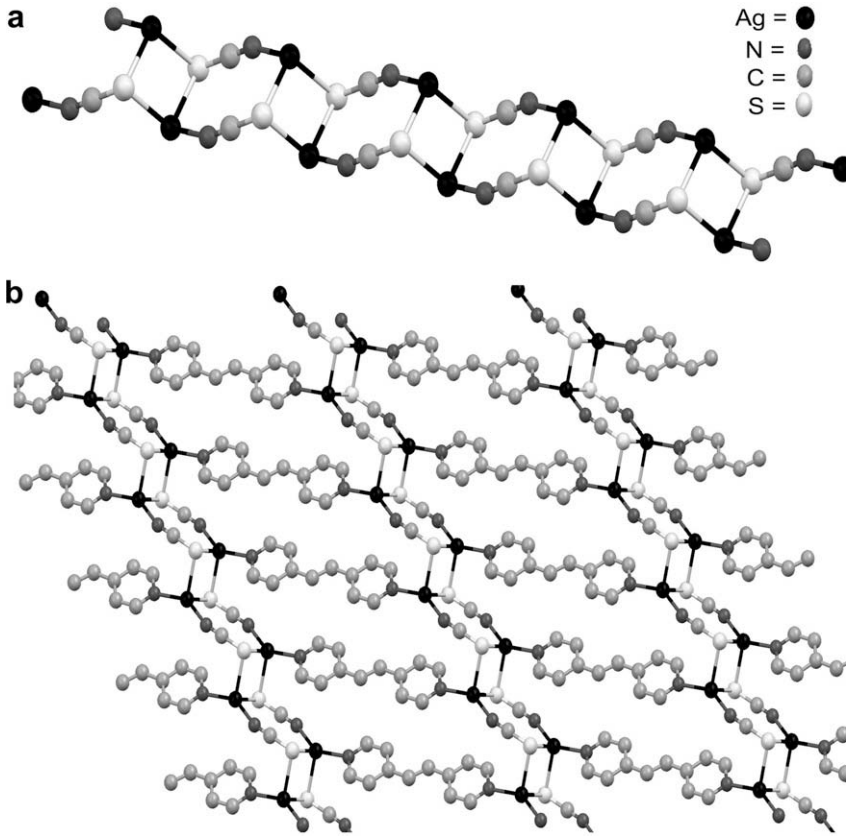


Fig. 5. (a) Stair-case-like ribbon of the SCP **2** along the *a*-axis. (b) View of the 2D-layer of the SCP **2** along the *b*-axis; H-atoms are omitted for clarity.

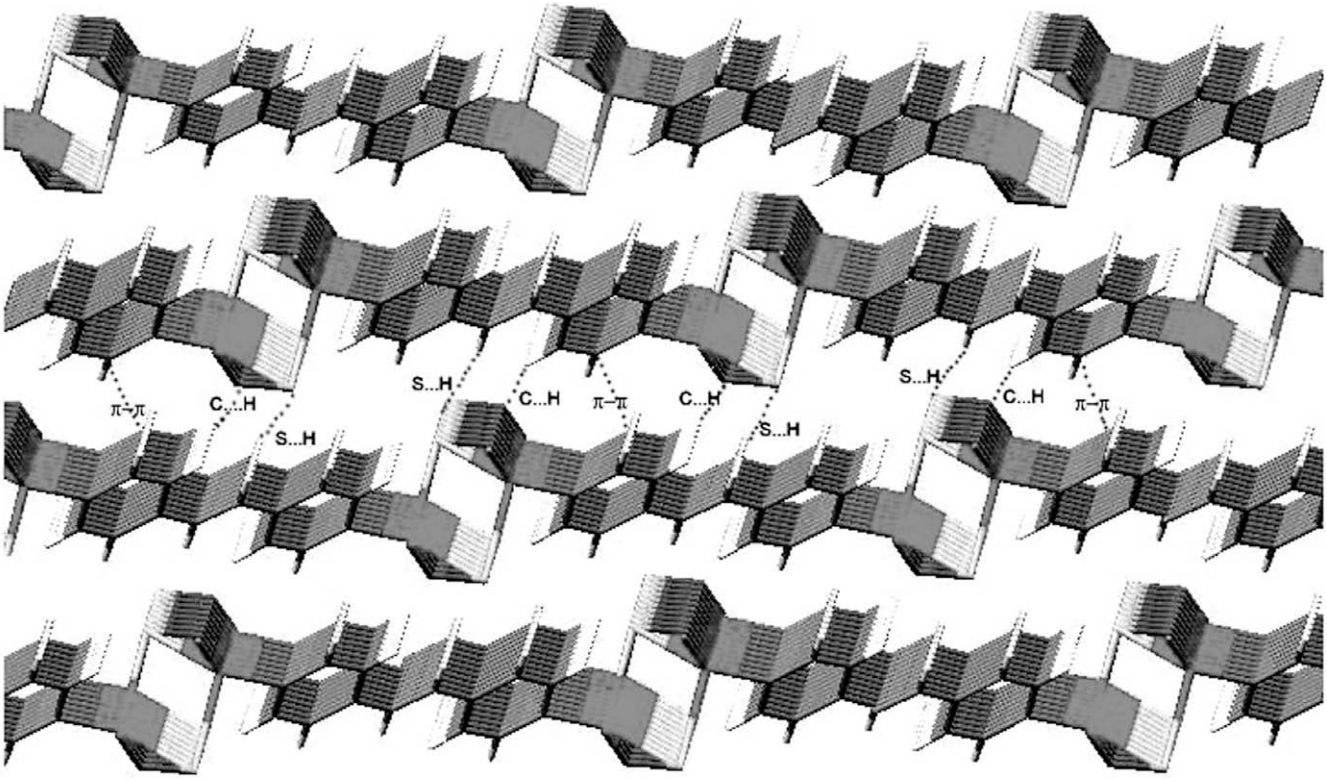


Fig. 6. View of the layer stacking of the SCP **2** along the *a*-axis showing H-bonding and π–π stacking.

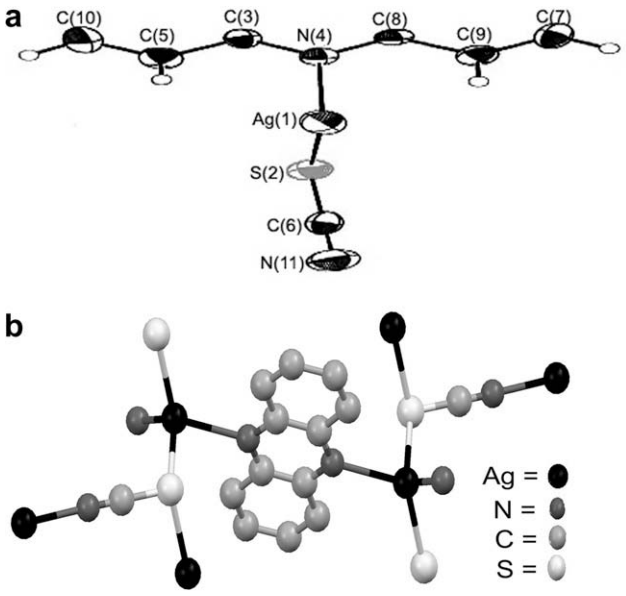


Fig. 7. (a) An ORTEP plot the asymmetric unit of the SCP **3**. (b) The basic building block of the SCP **3**; H-atoms are omitted for clarity.

*3.1.2. Crystal structure of [(AgSCN)$_2$ · tbpe] (**2**)*

The crystal structure of **2** consists of silver(I) thiocyanate and tbpe fragments in a 2:1 molar ratio creating a three-dimensional network formulated as $\infty^3[(AgSCN)_2 \cdot tbpe] \equiv \infty^3[Ag_2(\mu_3\text{-}SCN)_2(\mu\text{-}tbpe)]$. The asymmetric unit of **2** consists of only one Ag(I) ion, one SCN group and half of the tbpe ligand, Fig. 4a. Each Ag(I) ion is pseudo-tetrahedrally four-coordinated by a tbpe nitrogen atom; Ag1–N3 = 2.248 Å, two thiocyanate sulfur atoms Ag1–S2 = 2.753 Å, Ag1–S2^a = 2.772 Å and one nitrogen atom of another thiocyanate ligand; Ag1–N5 = 2.173 Å, with the bond angles at the silver atom in the range of 95.27–144.95°; Fig. 4b, Table 3. The extended structure of **2** consists of infinite parallel AgSCN zig-zag chains bonded at the sulfur atom; Ag1–S2–C10 = 96.37° and contains the unusual bifurcated cyanide fragment which exhibits bent AgCN angle, where Ag1–N5–C10 = 155.6°; Table 3. Each two close parallel AgSCN zig-zag chains are connected via two silver atoms and two sulfur atoms forming an array of fused polymer rings containing the unique quadro minicycle (Ag_2S_2) motif, in addition to the usual hexagonal rings of $Ag_2(SCN)_2$ with dimensions of 3.776 Å × 5.577 Å; Fig. 4b. These fused rings create stair-case like $\infty^1[Ag_2(SCN)_2]$ ribbons in which the minicycle (Ag_2S_2) motif represents the steps along the *a*-axis, Fig. 5a. The S–S distance in the minicycle is equal to 4.383 Å while the Ag–Ag distance is equal to 3.364 Å which is shorter than the sum of the van der Waals radii of two silver atoms (3.44 Å [26]),

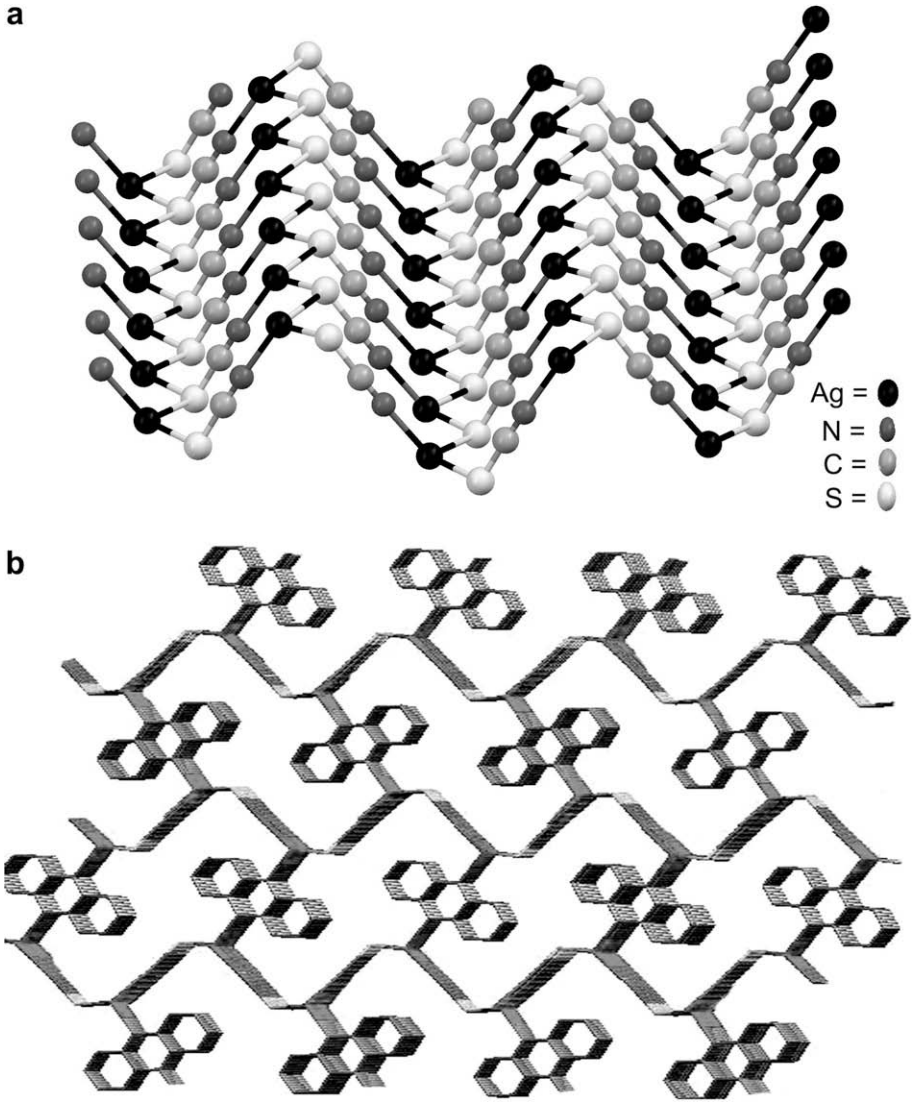


Fig. 8. (a) View of the parallel zig-zag $(AgSCN)_n$ chains showing the hexagonal $Ag_3(SCN)_3$ rings. (b) 3D-dimensional structure of the SCP **3** along the *a*-axis. H-atoms are omitted for clarity.

Table 5
Absorption and emission bands for bpy, tbpe, phenz and the SCPs **1**–**3**.

	Ligand			SCP			
	λ_{abs} (nm)	Assignment	λ_{em} (nm)		λ_{abs} (nm)	Assignment	λ_{em} (nm)
bpy	218	$^1L_a \leftarrow {}^1A$	400	**1**	219	$^1L_a \leftarrow {}^1A$	430
	278	$^1L_b \leftarrow {}^1A$	452		278	$^1L_b \leftarrow {}^1A$	450
	390	$n–\pi^*$	481		345	CT	487
			516				528
			660				
tbpe	232	$^1L_a \leftarrow {}^1A$	390	**2**	214	$^1L_a \leftarrow {}^1A$	425
	265	$^1L_b \leftarrow {}^1A$	478		272	$^1L_b \leftarrow {}^1A$	450
	325	$\pi–\pi^*$	529		352 b	CT	490
	450	$n–\pi^*$					519
							543
phenz	220	$^1C_b \leftarrow {}^1A$	390	**3**	218	$^1C_b \leftarrow {}^1A$	428
	275	$^1B_b \leftarrow {}^1A$	464		252	$^1B_b \leftarrow {}^1A$	493
	340	$^1L_a \leftarrow {}^1A$	490		366	$^1L_a \leftarrow {}^1A$	528
	394		522		412	$^1L_b \leftarrow {}^1A$	583
	414	$^1L_b \leftarrow {}^1A$			442	CT	
	510	$n–\pi^*$					

* b, broad.

indicating argentophilic interaction. The bifurcated silver-SCN fragment can be considered as a consequence of the formation of the minicycle (Ag_2S_2) motif which represents the essential building block in the structure of **2**.

These infinite parallel stair-case-like ribbons are arranged in a quasi-parallel fashion in the cell and separated by a distance of 13.606 Å. They are bridged by the tbpe ligands via silver atoms along the diagonal of the unit cell, forming infinite two-dimensional layered structure; Fig. 5b. In this case, one tbpe is directed to the space of the hexagonal ring $Ag_2(SCN)_2$ and the ethylenic moiety locates toward the quadro minicycle (Ag_2S_2) motif while the other pyridyl ring is directed to the next hexagonal ring in the adjacent stair-case chain. The bridging tbpe molecules are arranged in a parallel way with a distance between two successive tbpe ligands equal to 5.932 Å forming distorted polygon structure consisting of $[Ag_4(SCN)_2(tbpe)_2]$ with dimensions of 5.415 Å × 18.348 Å. It is interesting that the network structure of **2** consists of adjacent parallel infinite 2D-layers which are all related by translation in the *a*-axis direction in the solid state, being stacked in an ...AAAA... fashion to build up the three-dimensional structure with the inter-layer separation of about 6.5 Å; Fig. 6. The 3D-network structure of **2** is stabilized by extensive π–π stacking between the pyridyl rings, 3.360 Å, as well as hydrogen bonds between H-atoms of the ethylenic group and the sulfur atoms, 2.955 Å, and between the H-atom of the pyridyl rings and C10 of the thiocyanate group, 2.838 Å; see Table 3.

3.1.3. Crystal structure of $[(AgSCN)_2 \cdot phenz]$ (**3**)

The reaction of in situ prepared AgSCN with phenazine in aqueous ammonical solution affords the brown needle crystals $\infty^3[(AgSCN)_2 \cdot phenz]$, **3**. The crystal structure of **3** confirms the assignment of 2:1 stoichiometry for the silver(I) thiocyanate phenazine complex while the asymmetric unit of **3** comprises half of the formula unit, Fig. 7a. The asymmetric unit consists of one type of silver(I) which is four-coordinated assuming distorted tetrahedral geometry with angles in the range of 87.82–121.83°; Table 4. The silver site is coordinated to two sulfur atoms; Ag–S = 2.594 and 2.602 Å, a nitrogen atom of the thiocyanate ligand; Ag–N = 2.219 Å and nitrogen atom of the phenazine ligand; Ag–N = 2.438 Å, Fig. 7b. In this case, two silver atoms are bridged almost symmetrically by the S atom of the μ_3-1,1,3-SCN ligand. The structure of **3** is best described as AgSCN infinite chains which significantly perturbed at S atom to assume zig-zag conformation arranged parallelly to the crystallographic *c*-axis, Fig. 8a. The angles of the thiocyanate ligand are almost linear while the Ag1–S2–C6 acquires bent conformation, 110.80°; Table 4. These parallel zig-zag chains are bridged by the sulfur atoms where each S atom connects two silver atoms, one from its own chain and the other silver atom is from the adjacent chain, creating 2D-sheet containing fused hexagonal rings, 4.145 Å × 7.194 Å, that adopt chair conformation leading to the formation of corrugated layers consisting of $Ag_3(SCN)_3$ fragments, Fig. 8a. These hexagonal rings are interwoven along the *b*-axis.

The 2D-sheets of $(AgSCN)_n$ are further linked by the planar phenazine ligands creating distorted polygons consisting of $[Ag_6(SCN)_4(phenz)_2]$ with enough space to accommodate the phenyl rings of the phenazine ligand forming 3D-network structure. It is worth noting here that the phenazine ligands as well as the thiocyanate bridges are completely parallel assuming weak stacking interactions; 3.618 Å, while hydrogen bonds with S2; 2.84 and 2.97 Å, and the CN unit; 2.728–3.014 Å; Table 4, as well as short contacts between silver atom and carbon atoms of phenz and SCN ligands, 3.347 and 3.339 Å, lead to further stabilization of the 3D-network of **3**, Fig. 8b.

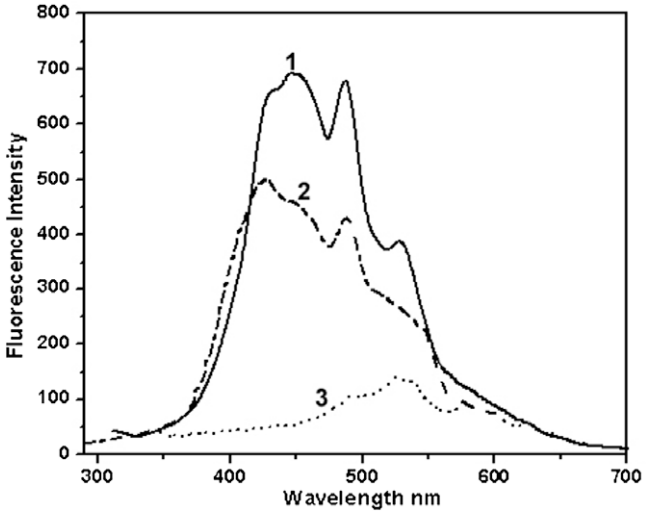


Fig. 9. Emission Spectra of the SCPs **1**–**3**; (λ_{ex} is 300 nm for **1**, 270 nm for **2** and 300 nm for **3**).

Table 6
Thermogravimetric analysis data of the SCPs **1**–**3**.

Compound	First step			Second step			Third step			Residue		
	Transition temperature (°C)	Δm% observed (calculated)	Assignment (%)	Transition temperature (°C)	Δm% observed (calculated)	Assignment (%)	Transition temperature (°C)	Δm% observed (calculated)	Assignment (%)	Formation temperature (°C)	Δm% observed (calculated)	Assignment (%)
1	180–250	32.5 (31.9)	1 bpy	380–480	6.5 (6.5)	1 S	500–750	10.5 (10.5)	1 $(CN)_2$	750	50.5 (50.7)	Ag_2S
2	200–300	35.5 (35.4)	1 tbpe	350–450	6.0 (6.22)	1 S	480–750	10.5 (10.1)	1 $(CN)_2$	750	47.5 (48.1)	Ag_2S
3	150–250	35.5 (35.6)	1 phenz	270–350	6.4 (6.19)	1 S	400–750	10.0 (10.0)	1 $(CN)_2$	750	48.0 (48.0)	Ag_2S

Table 7
Geometry of the thiocyanate group in the SCPs **1**–**3**.

Angle (°)/bond (Å)	**1**	**2**	**3**
Ag–N–C	172.2	155.6	177.7
Ag–S–C	103.6–94.73	96.37–98.53	110.23–100.17
S–C–N	178.9	179.1	178.5
S–C	1.660	1.652	1.652
C–N	1.138	1.154	1.150

3.2. Electronic absorption spectra and emission spectra of SCPs *1*–*3*

The electronic absorption spectra of the ligands and the SCPs **1**–**3** were measured in the solid state at room temperature as reflectance spectra. The absorption spectra of the SCPs **1**–**3** display, generally, the absorption bands of ligands in addition to the CT bands. Thus, investigating the absorption spectra of the bpy and tbpe ligands reveals that the spectra display mainly three absorption bands at 218–232 nm ($^1L_a \leftarrow {}^1A$), 265–278 nm ($^1L_b \leftarrow {}^1A$), and 325 nm (π–π^*), in addition to a band at 390–450 nm (n–π^*), Table 5. On the other hand, the spectrum of phenazine shows several bands at 220, 275, 340, 394, 414, 510 nm; Table 5. It is a matter of fact that replacement of the methine group in anthracene by nitrogen atom in phenazine ligand results in relatively little changes in the spectrum of phenazine. This is especially true due to the fact that the replacement of N for CH of anthracene occurs at positions that it does not seriously affect the symmetry of anthracene. Thus, the phenz and anthracene are isoelectronic. In spite of the fact that transition ($^1C_b \leftarrow {}^1A$) in anthracene is forbidden the ($^1C_b \leftarrow {}^1A$) band in phenz is observed at 220 nm which is surprisingly intense for a forbidden transition [27]. The band at 270 nm exhibits red shift than $^1B_b \leftarrow {}^1A$ band of anthracene [27]. The bands at 340 and 394 nm should be assigned to $^1L_a \leftarrow {}^1A$ transition, whereas the band of phenz at 414 nm should be assigned to $^1L_b \leftarrow {}^1A$ transition. The relatively low intensity band at the long wavelength side is assigned to n–π^* transition. The bands due to n–π^* transitions disappear in the spectra of SCPs **1**–**3** due to participation of the bipodal ligands in the coordination sphere of silver(I) ions. The absorption spectra of the SCPs **1**–**3** exhibit an additional broad band at 345, 352 and 442 nm, respectively, corresponding to metal-to-ligand charge transfer (MLCT) where the charge is transferred from the silver(I) center to the unoccupied π^*-orbital of the ligand.

The emission spectra of the SCPs **1**–**3**, Fig. 9, together with the emission spectra of their ligands were measured using the same excitation wavelength in each case. The emission spectra of the bipodal ligands display structural bands, Table 5, which correspond to the lowest (π, π^*) and close lying (n, π^*) states. On the other hand, the emission spectra of the SCPs **1**–**3** display structural peaks of the bipodal ligands as well as additional bands which may assigned to MLCT or metal-centered transitions of the type $4d^{10} \rightarrow 4d^9\ 5s^1$ and $4d^{10} \rightarrow 4d^9\ 5p^1$ on the silver(I) center. The emission spectra of the SCPs **1**–**3** exhibit red shift compared to those of the corresponding ligands.

3.3. Thermogravimetric analysis of the SCPs *1*–*3*

The SCPs **1**–**3** are thermally stable until 150–200 °C, then after they start decomposition with the loss of ligand in the temperature range 150–300 °C, Table 6. The second decomposition step involves removal of one sulfur atom in the temperature rang 350–480 °C, for the SCP **1** and **2** and at 270–360 °C for the SCP **3**. The third step occurs at slow rate and over relatively large temperature range, 400–750 °C, where two cyanide groups are lost as cyanogen, Table 6. Finally above 750 °C the residue is obtained which is coincident with the silver sulfide. The relatively high temperature at which the SCN groups are released supporting the bridging capability of this group forming stable $(AgSCN)_n$ chains.

4. Conclusions

The general features of the structure of the SCPs **1**–**3** are the formation of AgSCN-L adducts in a 2:1 molar ratio forming 3D-networks containing the AgSCN building blocks connected via μ_2-1,3-SCN in **1** and μ_3-1,1,3-SCN in **2** and **3**. These AgSCN building blocks form zig-zag AgSCN chains which are bridged by the bipodal ligands creating polygons consisting of $[Ag_4(SCN)_2(L)_2]$; L = bpy or tbpe, and $[Ag_6(SCN)_4(phenz)_2]$. However, the parallel zig-zag chains assume different modes of interaction where in **1** they are bridged by Ag–Ag bonding interactions, in **2** via the formation of quaro minicycle Ag_2S_2 motif with weaker Ag–Ag interaction and in **3** by S atoms creating hexagonal rings which adopt chair conformation without any interaction between the silver atoms. The mode of bridging depends on the nature of the bipodal ligand, whereas the longest bipodal ligand tbpe; 9.412 Å, acquire wide space in the network structure of **2** which should be achieved by the formation of the minicycle motif and the bifurcated AgNC fragment which assumes quasi-linear fashion in **1**; 172.2° while it is almost linear in **2**; 177.7°. In the same direction, the AgSCN zig-zag chains are more puckered in **2** than in **1** and **3**; Table 7. The S–C–N fragment tends to be linear in all cases, whereas the Ag–N–C–S fragment is quasi-linear in **1** and **3** but nonlinear in **2**. On the other hand, the Ag–S distances in **1** and **2** are longer than that in molecular AgSCN (2.648 Å) [22], while they assume shorter distance in **3**. Thus, using bipodal ligands which would not be constrained to a planar conformation like bpy and tbpe which exhibit the two pyridyl rings in two parallel planes separated by ethylenic bond or the bulky planar phenazine ligand, would change the shape and geometry of the $(AgSCN)_n$ chains and allow the interconnection of chains and propagation of the microstructure in three dimensions.

Appendix A. Supplementary data

CCDC 682261–682263 contain the supplementary crystallographic data for SCPs **1**–**3**. These data can be obtained free of charge via http://www.ccdc.cam.ac.uk/conts/retrieving.html, or from the Cambridge Crystallographic Data Centre, 12 Union Road, Cambridge CB2 1EZ, UK; fax: (+44) 1223-336-033; or e-mail: deposit@ccdc.cam.ac.uk. Supplementary data associated with this

article can be found, in the online version, at doi:10.1016/j.poly.2009.01.005.

References

[1] J.W. Steed, D.R. Turner, K.J. Wallace, Core Concepts in Supramolecular Chemistry and Nanochemistry, John Wiley and Sons Ltd., 2007.
[2] H.-F. Zhu, J. Fan, T.-a. Okamura, W.-Y. Sun, N. Ueyama, Cryst. Growth Des. 5 (2005) 289. and references therein.
[3] M. Munakata, L.P. Wu, T. Kuroda-Sowa, Adv. Inorg. Chem. 46 (1999) 173.
[4] F.-C. Liu, Y.-F. Zeng, J.-P. Zhao, B.-W. Hu, X.-H. Bu, J. Ribas, J. Cano, Inorg. Chem. 46 (2007) 1520.
[5] Y. Song, Y. Xu, T.-W. Wang, Z.-X. Wang, X.-Z. You, J. Mol. Struct. 796 (2006) 36.
[6] R. Robson, B.F. Abrahams, S.R. Batten, R.W. Gable, B.F. Hoskins, J. Lieu, Supramolecular architecture, in: T. Bein (Ed.), ACS, Washington, DC, 1992, p. 256.
[7] H. Gudbjartson, K. Biradha, K.M. Poirier, M.J. Zaworotko, J. Am. Chem. Soc. 121 (1999) 2599.
[8] M.-L. Tong, B.-H. Ye, J.-W. Cai, X.-M. Chen, S.W. Ng, Inorg. Chem. 37 (1998) 2645.
[9] H.-L. Zhu, Y.-X. Tong, X.-M. Chen, J. Chem. Soc., Dalton Trans. (2000) 4182.
[10] N.K. Mills, A.H. White, J. Chem. Soc., Dalton Trans. (1984) 229.
[11] C. Pettinari, Polyhedron 20 (2001) 2755.
[12] G.A. Bowmaker, Effendy, B.W. Skelton, N. Somers, A.H. White, Inorg. Chim. Acta 358 (2005) 4307.
[13] M. Amirnasr, A.D. Khalaji, L.R. Falvello, T. Soler, Polyhedron 25 (2006) 1967.
[14] F.B. Stocker, D. Britton, V.G. Young Jr., Inorg. Chem. 39 (2000) 3479.
[15] C.-X. Ren, H.-L. Zhu, G. Yang, X.-M. Chen, J. Chem. Soc., Dalton Trans. (2001) 85.
[16] T. Pretsch, H. Hartl, Inorg. Chim. Acta 358 (2005) 1179.
[17] A.A. Isab, M.I.M. Wazeer, M. Fettouhi, B.A. Al-Maythalony, A.R. Al-Arfaj, N.O. Al-Zamil, Inorg. Chim. Acta 360 (2007) 3719.
[18] E.C. Constable, C.E. Housecroft, B.M. Kariuki, N. Kelly, C.B. Smith, Inorg. Chem. Commun. 5 (2002) 199.
[19] R.S. Rarig Jr., J. Zubieta, Inorg. Chim. Acta 319 (2001) 235.
[20] W.-H. Sun, T. Zhang, L. Wang, Y. Chen, R. Froehlich, J. Organomet. Chem. 689 (2004) 43. and references therein.
[21] H. Krautscheid, N. Emig, N. Klaassen, P. Seringer, J. Chem. Soc., Dalton Trans. (1998) 3071.
[22] F.A. Cotton, G. Wilkinson, Advanced Inorganic Chemistry, 5th Ed., Wily-Interscience, Singapore, 1988. pp. 940–941 (Chapter 18).
[23] G.A. Bowmaker, Effendy, B.W. Skelton, A.H. White, J. Chem. Soc., Dalton Trans. (1998) 2123. and reference therein.
[24] C. Stockheim, K. Wieghardt, B. Nuber, J. Weiss, U. Flöurke, H.-J. Haupt, J. Chem. Soc., Dalton Trans. (1991) 1487.
[25] J.-D. Lin, Z.-H. Li, J.-R. Li, S.-W. Du, Polyhedron 26 (2007) 107.
[26] A. Bondi, J. Phys. Chem. 68 (1964) 441.
[27] E.S. Stern, C.J. Timmons, Electronic Absorption Spectroscopy in Organic Chemistry, Edward Arnold Publishers Ltd., London, 1970. p. 113 (Chapter 6).

search Institute, Lucknow, India. The electronic spectra were recorded (in 10^{-5} M $CHCl_3$ solution) using a Simadzu UV-1601 spectrophotometer and Emission spectra were recorded in Perkin–Elmer L52 spectrophotometer using 10^{-5} M $CHCl_3$ solution at room temperature. Infrared spectral data were collected (KBr pellets) using a Perkin–Elmer L120-000A spectrophotometer and ^{1}H NMR spectra of the samples were measured in DMSO-d_6 at the Indian Institute of Chemical Biology, Kolkata, West Bengal, India using a Bruker-400 MHz instrument at room temperature.

2.1. Synthesis of ligands

The ligands, Hsmth and Hapmth, were synthesized by condensation of salicylaldehyde and 2-hydroxy acetophenone with morpholine *N*-thiohydrazide, respectively, using our previously published method [55].

2.2. Synthesis of the phenylmercury(II) complexes

[PhHg(Hsmth)] ***(1)***: Phenylmercury(II) acetate (0.676 g, 0.002 mol) was dissolved in dry ethanol (25 ml) and filtered directly into an ethanolic solution (15 ml) of the ligand, H_2smth (0.530 g, 0.002 mol). The mixture was heated under gentle reflux for about half an hour and filtered while hot. The filtrate, on concentration to ~20 ml and cooling, yielded a light yellow brown compound. It was recrystallized from dry ethanol to get suitable light yellow crystals for X-ray diffraction. Yield, 0.840 g, 70%; m.p. 168–170 °C. *Anal.* Calc. for $C_{18}H_{19}HgN_3O_2S$: C, 39.89; H, 3.53; N, 7.75. Found: C, 40.11; H, 3.45; N, 7.68%. νC=N, 1615 (m); λ_{max} = 243, 299, 343 nm; δ_{ph} 6.90–7.43 ppm.

[PhHg(Hapmth)] ***(2)***: Synthesized following the method similar that used for the compound (**1**) above using equimolecular portions of phenylmercury(II) acetate (0.676 g, 0.002 mol) and the ligand, H_2apmth (0.676 g, 0.002 mol) and recrystallized from dry ethanol to produce light yellow crystals for X-ray diffraction. Yield, 0.778 g, 70%; m.p. 175–180 °C. *Anal.* Calc. for $C_{19}H_{21}HgN_3O_2S$: C, 41.04; H, 3.81; N, 7.56. Found: C, 41.11; H, 3.75; N, 7.68%. νC=N, 1560 (m); λ_{max} = 244, 301, 344 nm; δ_{ph} 6.90–7.43 ppm, δ_{methyl} = 2.32 ppm.

2.3. Crystallography

Crystallographic data and refinement details are given in Table 1. Diffraction intensities were measured at 100 K for both complexes **1** and **2** using a Bruker APEX CCD based diffractometer (Mo Kα radiation, λ 0.71073 Å) in the θ range (a) 1.82–28.31 for **1** (b) 1.93–28.33 for **2** using ω scans. Data processing was done using SAINT and absorption corrections using SADABS [56]. The structures were solved by direct methods [56]. Refinement (anisotropic displacement parameters, hydrogen atoms in riding model approximation and weighting scheme of the form $w = 1/[\sigma^2(F_o^2) + (0.0434P)^2]$, where $P = (F_o^2 + 2F_c^2)/3$) was on F^2. Graphics were obtained with ORTEP 3 for Windows and thermal ellipsoid plots are at the 50% probability level [57]. Additional figures were drawn with PLATON for Windows [58].

3. Results and discussion

The reactions of salisylaldehyde and 2-hydroxy acetophenone with morpholine *N*-thiohydrazide in 1:1 molar ratio in ethanol yielded the thiohydrazone ligands, which may remain in equilibrium with their thiol forms I and II, respectively, in solution [59,60].

The treatment of phenylmercury(II) acetate with salicylaldehyde morpholine *N*-thiohydrazone and 2-hydroxyacetophenone morpholine *N*-thiohydrazone (Fig. 1) in dry ethanol under gentle refluxing conditions resulted in deprotonation of the NH proton and formed light yellow to light yellow brown complexes [PhHg(Hsmth)] (**1**) and [PhHg(Hapmth)] (**2**). These two complexes are generally soluble in DMSO, acetonitrile and nitromethane, and partially soluble in acetone and chloroform. The crystal structures and spectroscopic properties of the complexes are described below.

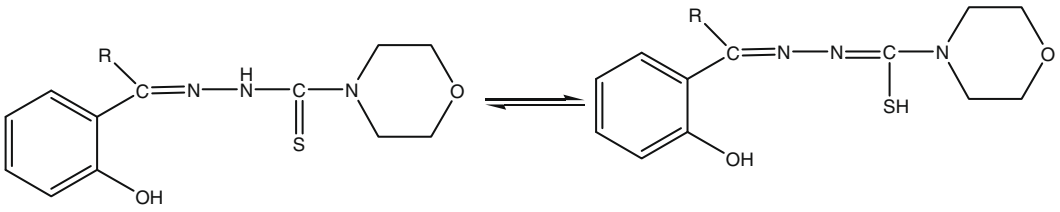
3.1. Crystal and molecular structure of [PhHg(Hsmth)] (1)

The ORTEP drawing and the atomic numbering scheme of [PhHg(Hsmth)] (**1**) are shown in Fig. 2, and selected bond lengths and bond angles are given in Table 2. The X-ray analysis reveals that the complex (**1**) adopts a distorted T-shaped geometry around mercury(II) by the ligand (I) through the phenyl carbon, thiol sulfur and azomethine N atom of the ligand H_2smth.

Phenylmercury(II) makes bonds to thiol sulfur and azomethine N atoms of the ligand H_2smth. This N, S-chelate has a bite angle of 74.15(8)° with the result that azomethine N atom does not lie at 90° to the C_{ph}–Hg–S axis of PhHg(Hsmth). Due to the small bite, the C_{ph}–Hg–S angle is 166.83(10)°. Thus, the Hg complex does not acquire a T-shaped structure and is rather severely distorted

Table 1
Crystal data and structure refinement parameters of phenylmercury(II) complexes.

Empirical formula	$C_{18}H_{19}HgN_3O_2S$	$C_{19}H_{21}HgN_3O_2S$
Formula weight	542.02	556.04
Crystal size (mm)	0.10 × 0.20 × 0.30	0.15 × 0.23 × 0.30
Crystal system	triclinic	monoclinic
Space group	*P*1(2)	*P*21(4)
Temperature (K)	293	100
a (Å)	8.6240(17)	8.1659(19)
b (Å)	9.935(2)	16.506(4)
c (Å)	11.792(2)	13.687(3)
α (°)	77.30(3)	90
β (°)	72.82(3)	92.817(4)
γ (°)	70.29(3)	90
V (Å^3)	900.5(4)	1842.7(7)
F(000)	520	1120
Z	2	4
D_{calc} (Mg m^{-3})	1.999	2.004
μ (mm^{-1})	8.678	8.485
θ Range for data collection (°)	1.8–28.3	1.9–28.3
T_{max}, T_{min}	0.4774, 0.1805	0.8089, 0.7289
Goodness-of-fit on F^2	1.060	1.124
Final *R* indices [$I > 2\sigma(I)$]	R_1 = 0.0239, wR_2 = 0.0614	R_1 = 0.0323, wR_2 = 0.0797
R indices (all data)	R_1 = 0.0250, wR_2 = 0.0619	R_1 = 0.0340, wR_2 = 0.0802



(I) H_2smth when R = H
(II) H_2apmth when R = CH_3

Fig. 1. Tautomerism between thioketo and thiol form of the Schiff base ligands.

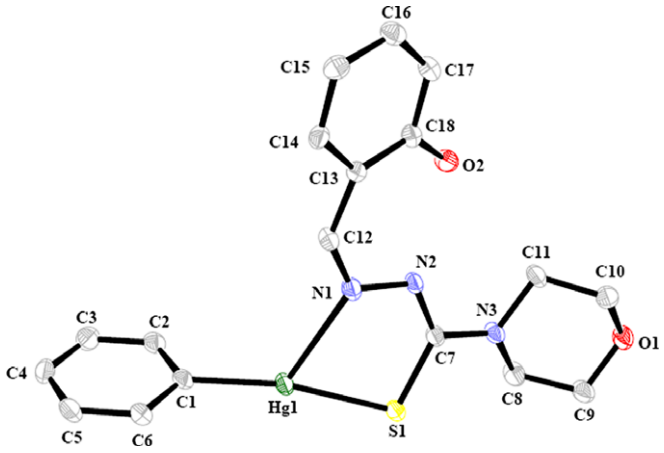


Fig. 2. Perspective view of complex [PhHg(Hsmth)] (**1**) with the numbering scheme. The thermal ellipsoids are drawn at the 50% probability level.

Table 2
Selected bond lengths and bond angles of phenylmercury(II) complexes.

Bond lengths		Bond angles	
Complex ***1***			
Hg1–S1	2.3779(11)	S1–Hg1–N1	74.15(8)
Hg1–N1	2.561(3)	S1–Hg1–C1	166.83(10)
Hg1–C1	2.070(4)	N1–Hg1–C1	118.93(12)
S1–C7	1.759(4)		
Complex ***2***			
Hg1–S1	2.357(2)	S1–Hg1–C1	173.6(2)
Hg2–S2	2.350(2)	S2–Hg2–C20	175.68(19)
Hg1–C1	2.068(8)		
Hg2–C20	2.063(7)		
S1–C7	1.768(8)		
S2–C26	1.785(8)		

[61,62]. It can be seen from earlier reported value that C–Hg–S angles vary (ca. 165–170°) [63–66] with the nature of the thiosemicarbazone. Variation in bite angle S–Hg–N1 and the angles at S, viz. Hg–S–C, do not show significant changes.

The Hg–C_{ph} bond length 2.070(4) Å in complex (1) is in the range of unperturbed Hg–C bonds (2.05–2.09 Å) [63]. This distance is slightly shorter than the Hg–C_{Me} bond distance (2.09 Å) but close to the values of Hg–C_{ph} bond lengths of previously reported similar phenylmercury(II) complexes [64–66]. The back donation of an electron from mercury(II) to the π^* orbital of phenyl ring is the key factor for shortening of this bond length. The Hg–S distance, 2.3779(11) Å and Hg–N bond distance 2.561(3) Å of complex (**1**) are similar to earlier reported values [67]. The coordination of the azomethine nitrogen and thiol sulfur atom to the mercury(II) atom leads to the formation of a stable five-membered chelate ring.

The complex (**1**) shows a C–S bond distance of 1.759 (4) Å which is shorter than the C–S single bond (1.81 Å) [68,69] but longer than the C–S double bond (1.62). This suggests partial double bond character of the C–S bond in this complex similar to the related thiosemicarbazonates of methylmercurey(II) and dimethylthallium(III) [67,70,71].

The intramolecular hydrogen bond O2–H2A····N2 leads to the formation of stable six-member ring with a H2A····N2 separation of 2.557(4) Å and O2–H2A····N2 angle 136°. The combination of C–H····π and Hg····π weak interactions form two-dimensional extended structure. The mercury(II) ion interacts with Cg3 (mid point of phenyl ring) with the formation of 1D square-box in which the Hg····Cg^a separation is 3.937 Å ($a = 1 - x, -y, -z$). The structure is further extended to 1D by the formation of edge to face C–H····π interaction. The Hg····π interaction forms supramolecular dimer which are joined through C6–H6····$Cg4^b$ ($b = 1 - x, -y, 1 - z$) stacking with the formation of 1D supramolecular chain. The C6–H6····Cg4 distance is 2.95 Å. The two-dimensional supramolecular structure is completed with the formation of C9–H9B····$Cg3^c$ weak bond ($c = -1 + x, 1 + y, z$) (Fig. 3) with H····Cg separation of 2.68 Å. The H6····Cg4 separation is slightly larger than the H9B····Cg3 separation.

3.2. Crystal and molecular structure of [PhHg(Hapmth)] (2)

The molecular structure of the complex [PhHg(Hapmth)] (**2**) is shown in Fig. 4 and selected bond lengths and bond angles are given in Table 2. The complex (**2**) crystallizes in space group $P2_1$.

The crystal structure of the complex [PhHg(Hapmth)] (**2**) adopts a familiar linear coordination geometry. The complex has two independent molecules comprising the asymmetric unit. Both the mercury atoms are coordinated by the thiol sulfur of the H_2apmth ligand and a carbon atom of the phenyl ring. Little difference in bond lengths and bond angles is shown by the two units. The

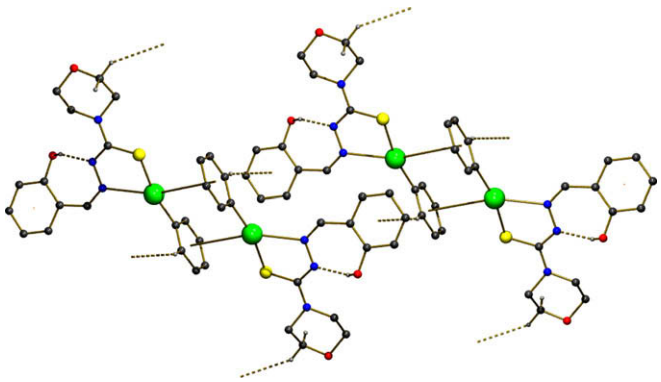


Fig. 3. Two-dimensional C–H–π and Hg–π interactions of the complex [PhHg(Hsmth)] (**1**).

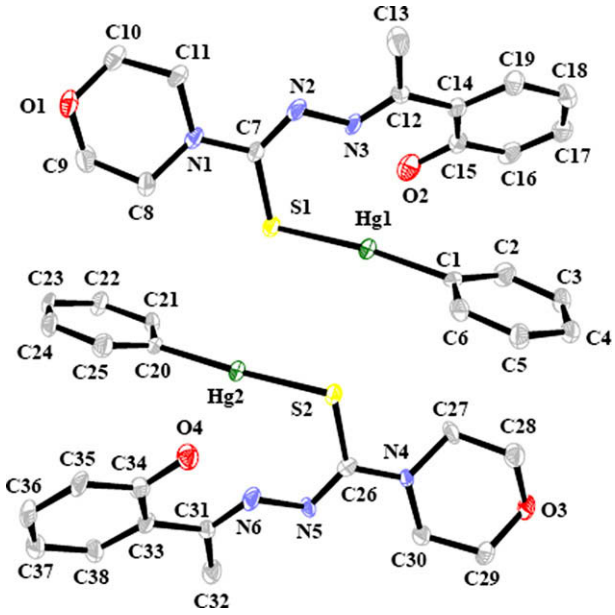


Fig. 4. Perspective view of complex [PhHg(Hapmth)] **(2)** with the numbering scheme. The thermal ellipsoids are drawn at the 50% probability level.

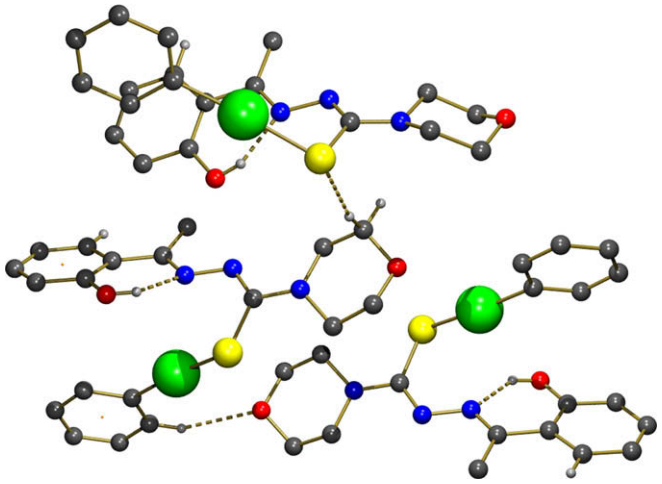


Fig. 5. Two-dimensional hydrogen bonding network of the complex [PhHg(Hapmth)] **(2)**.

$C_{ph}(1)$–Hg(1)–S(1) and $C_{ph}(20)$–Hg(2)–S(2) bond angles, 173.6(2)° and 175.68(19)°, respectively, are close to linear.

The Hg(1)–$C(1)_{ph}$ and Hg(2)–$C(20)_{ph}$ distances, 2.068(8) and 2.063(7) Å, respectively, are similar to the analogous phenylmercury(II) compound [65-67]. The average Hg–S bond length of 2.354(2) Å is within the range of Hg–S bonds of similar sulfur containing ligands [64–66].

The C(7)–S(1) bond distance [1.768(8) Å] is slightly shorter than the C(26)–S(2) distance [1.785(8) Å], but both are shorter than a C–S single bond (1.81 Å) [67–71] and longer than a C–S double bond (1.62). This small difference in C–S bond length may be due to C(10)–H(10B)–S(2) (see latter discussion) which is absent in the case of S(1). This observation suggests that both C–S bonds contain partial double bond character in the complex [67,70,71]. The C(7)–N(2) (1.301(11) Å) and C(26)–N(5) (1.269(11) Å) bond distances are close to the C–N double bond which confirms the deprotonation of the hydrazinic proton.

Both the unit form stable six-member rings via intramolecular O–H····N hydrogen bonding with O2–H2A····N3 and O4–H4A····N6 bond distances 2.550(8) and 2.542(8) Å and bond angles 145° and 144°, respectively. Several intermolecular weak interactions such as C–H····S, C–H····O hydrogen bonding, C–H····π and Hg····Hg form a two-dimensional extended structure. The intermolecular hydrogen bonding network of this compound forms a 2D supramolecular sheet which consists of C–H····S and C–H····O interactions (Fig. 5). This C6–H6····$O3^d$ hydrogen bond forms 1D supramolecular chain ($d = -1 + x, -1 + y, z$) with the D····A separation is 3.348(10) Å and D–H····A angle is 147°. This 1D chain is further extended to 2D extended structure by the formation of C10–H10B····$S2^e$ hydrogen bond ($e = -x, -1/2 + y, 1-z$) Two asymmetric units of the compound [PhHg(Hapmth)] (**2**) are joined together by the C10–H10B····S2 bond (Fig. 4). The D····A separation of this C–H····S hydrogen bond is 3.830(9) Å with the D–H····A angle 168°.

The two independent asymmetric units of the molecule [PhHg(Hapmth)] (**2**) are further interconnected by a weak Hg1····Hg2 interaction (Fig. 6). The Hg1····$Hg2^f$ [$f = x,-1 + y, z$] distance of 4.0216(10) Å is smaller than the sum of the van der Waal radius (5.0 Å) [72]. In addition to this Hg····Hg contact, the C–H····π interactions (Fig. 5) between C19–H19····$Cg5^g$ and C38–H38····$Cg2^h$ [$g = x, -1 + y, 1 + z$ and $h = x, 1 + y, -1 + z$] forms a three-dimensional ladder. The H····Cg distance is the same for both C–H····π interactions (2.94 Å), but the angle (C19–H19····Cg5) is 129° compared to 140° for C38–H38····Cg2.

3.3. Infrared and ^1H NMR spectra

The infrared spectra of the free ligands H_2smth and H_2apmth do not show any *ν*SH bands at 2570 cm^{-1} (Ref. [74–77]), but instead an intense band for *ν*C=S at 800 cm^{-1} is observed. This band disappears in the complexes and a new band around 760–750 cm^{-1} is observed for *ν*C–S suggesting mercury coordination through thiol sulfur. This mode is supported by the presence of a medium band around 350 cm^{-1} assignable to *ν*Hg–S.

The bands due to *ν*NH of the free ligands are located in the region 3300–3100 cm^{-1} but the *ν*OH band at 3500 cm^{-1} is not observed possibly due to strong hydrogen bonding which causes a

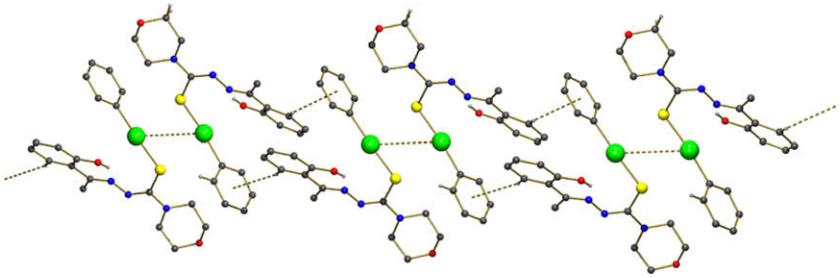


Fig. 6. Two-dimensional Hg–Hg and C–H–π interactions of the complex [PhHg(Hapmth)] **(2)**.

shift to a lower frequency. The νNH band of the free ligands disappeared in both complexes as a consequence of deprotonation.

Moreover, the νC=N stretching mode is at a slightly higher wave number in complex (**1**) and shows a similar spectroscopic pattern to previously reported phenylmercury(II) complexes with similar coordination modes. This band remains unchanged in complex (**2**) [70,71,77]. These observation for the two complexes suggests a similar S,N coordination mode for complex (**1**) and only S coordination for complex (**2**).

The bands at 1589 (sh), 1475 (m), 1015 (m), 995 (m), 720 (vs), 440 (s), 230 (s) and 180 (sh) for both of these complexes are characteristic of a phenylmercury ring [73–76].

The ^{1}H NMR spectra for the two phenylmercury(II) complexes do not show any chemical shift due to a NH proton in $CDCl_3$. The phenolic –OH signals of the ligands shift to lower field for both complexes but there is no deprotonation possibly due to strong hydrogen bonding. Thus both ligands coordinate to the phenylmercury(II) as singly charged anionic ligands. The phenyl ring proton signals appear in the range 6.90–7.43 ppm for both complexes. The methyl protons of complex (**2**) are observed at δ = 2.32 ppm. The chemical shifts of N–CH_2 (4 H) and O–CH_2 (4H) of the morpholine ring are observed at δ 3.17 ppm and δ 3.6 ppm, respectively [73–76].

3.4. Electronic and luminescent properties

Measured data for the electronic spectra of the free ligands, H_2smth, H_2apmth and their metal complexes are given in Table 3. The free ligands show absorption bands in the region 340–347 nm, 298–301 nm and 240–241 nm. The bands in the region 340–347 nm and 298–301 nm may be due to n–π^* and π–π^* transition, respectively [76,78]. The phenylmercury(II) complexes exhibit these bands but slightly shifted. The dependence of the solution absorption spectra on original Schiff bases suggests that the transitions are mainly ligand-centered transitions. Therefor, the electronic absorption spectra are probably dominated by intraligand π–π^* transitions possibly mixed with a small contribution from the metal in the HOMO and the LUMO [53,79].

The luminescent properties of the ligand and the complexes were studied in solution and solid state using different wavelengths. There is little change in emission spectra with variation of excitation wavelength, indicating that a single emissive state or multiple steps in equilibrium, is/are responsible for the observed emission. The emission energy is dependent on the nature of the Schiff bases but does not vary much with respect to the substituent. The similarity of the emission band shapes of the complexes and the parent Schiff bases are suggestive of a ligand dominated emissive state and the lowest emissive states in these complexes can be assigned as a metal perturbed intraligand π–π^* transition. In $CHCl_3$ solution, the free ligand H_2smth shows emission bands at 412 and 431 nm upon excitation with λ_{ex} = 343 nm. With respect to the free ligand H_2smth, the complex (**1**) in $CHCl_3$ shows similar peaks at 415 and 435 nm upon excitation with a similar wavelength. Besides these similar emission bands, the complex also shows a broad emission band at λ_{max} = 489 (λ_{ex} = 343 nm) as shown in Fig. 7. The luminescent spectra of the ligand, H_2apmth and corresponding phenylmercury(II) complex (**2**) are show in Fig. 8. The luminescent properties of H_2apmth and its corresponding phenylmercury(II) complex (**2**) is the same as that of H_2smth and its complex (**1**). The ligand, H_2apmth shows emission bands at λ_{max} = 412 and 434 nm, while the respective phenylmercury(II) complex shows emission bands at 410 and 430 nm. Like complex (1), complex (2) also shows an emission peak at 489 nm upon excitation with same wavelength. The emission bands near the 412 and 434 nm region of both complexes and the corresponding Schiff bases should be attributed to ligand center π–π^* transitions. The striking feature of the emission spectra in $CHCl_3$ (10^{-5} M) is the appearance of a new band at λ_{max} = 489 nm for complex (**1**) and λ_{max} = 500 nm for complex (**2**). The appearance of these new bands may result from an intermolecular interaction in $CHCl_3$ like solid state luminescence spectra [42–49,53,79].

In solution, both ligands and complexes show strongly solvent-dependent emission properties. The emission maxima shift toward shorter wavelength with an increase in the polarity of the solvent. The emission maxima of (**1**) are 415, 435 and 489 nm in $CHCl_3$ but is 427 nm in the polar solvent DMSO (λ_{ex} = 343 nm); for complex (**2**), the emission maxima in DMSO is 427 nm. This type of lumines-

Table 3
Photophysical data of phenylmercury(II) complexes.

	Absorbed λ (nm)	Excited λ (nm)	Emitted λ (nm)	Quantum yield	Conditions
Hsmth	244, 299, 343	343	412, 431, 519	0.035	$CHCl_3$ solid state
Hapmth	244, 301, 345	343	412, 434, 516	0.084	$CHCl_3$ solid state
Complex **1**	244, 299, 343	343	415, 435, 489, 488	0.041	$CHCl_3$ solid state
Complex **2**	244, 302, 347	343	410, 430, 500, 500	0.081	$CHCl_3$ solid state

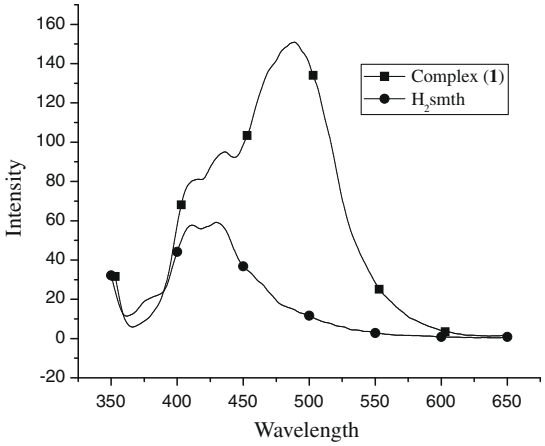


Fig. 7. Emission spectra of Ligand I, H_2smth and the complex (1) in $CHCl_3$ (λ_{ex} = 343 nm) at room temperature.

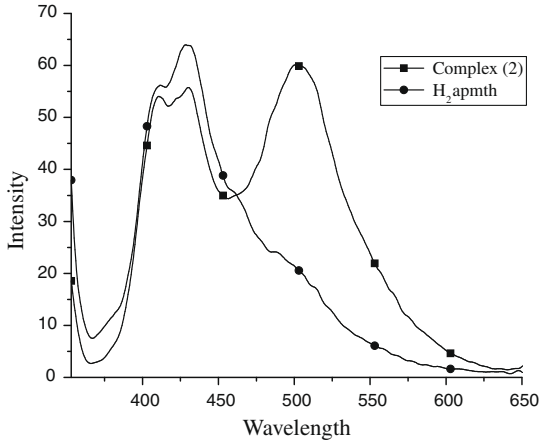


Fig. 8. Emission spectra of Ligand II, H_2apmth and the complex (2) in $CHCl_3$ (λ_{ex} = 343 nm) at room temperature.

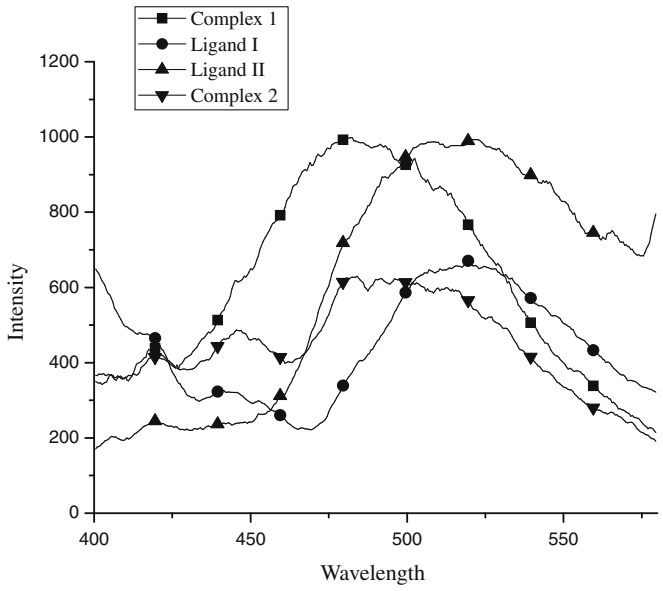


Fig. 9. Solid state emission spectra of the ligands, H_2smth, H_2apmth and the complexes (1) and (2) at room temperature (λ_{ex} = 343 nm).

cent property is a rare case as a red shift of the maxima is expected for most compounds when polarity increases. The observed blue-shift may be due to the presence of a highly polarized ground state [80,81].

The emission property of both complexes was also studied in solid state. The emission maxima of H_2smth, H_2apmth, complexes (**1**) and (**2**) are 519, 516, 488 and 500 nm, respectively (Fig. 9). The emission maxima of complexes (**1**) and (**2**) are blue-shifted in the solid state compared to emission maxima of the corresponding free ligands. This blue-shift may be due to the result of Hg····π and Hg····Hg stacking in solid state as shown in Figs. 3 and 6.

4. Conclusion

The thiohydrazone ligands used in the present investigation were previously used in this laboratory for the preparation of transition metal complexes. Based on the reaction conditions, the ligands were either found monobasic tridentate (NSO donor) or dibasic tridentate (NSO) donors [55]. However, in the present investigation with phenylmercury(II) species, the ligands either behave as monobasic bidentate NS or monobasic monodentate S-donor ligands. Depending on the nature of the ligands and the steric properties of Schiff bases, we are able to isolate two-dimensional solid state aggregate through Hg····π, Hg····Hg and C–H····π interactions. The Hg····Hg distance between adjacent molecules is such that both mercuriophilic and Hg····π interaction appear to be contributing to supramolecular aggregation. The emission properties of the complexes are dominated by mercury-perturbed organic π–π* transitions.

Acknowledgements

One of us (K.D.) is thankful to the University Grants Commission, New Delhi for Emeritus Fellowship and financial grants to conduct this work. We are also thankful to the Sophisticated Instrumentation Facility, Central Drug Research Institute, Lucknow, India for elemental analysis and spectroscopic data. Facilities provided by the DST, Govt. of India, New Delhi under FIST are also gratefully acknowledged.

Appendix A. Supplementary data

CCDC 677407 and 677408 contain the supplementary crystallographic data for [PhHg(Hsmth)] and [PhHg(Hapmth)]. These data can be obtained free of charge via http://www.ccdc.cam.ac.uk/conts/retrieving.html, or from the Cambridge Crystallographic Data Centre, 12 Union Road, Cambridge CB2 1EZ, UK; fax: (+44) 1223 336 033; or e-mail: deposit@ccdc.cam.ac.uk. Supplementary data associated with this article can be found, in the online version, at doi:10.1016/j.poly.2009.01.002.

References

[1] G.B. Cunningham, Y.T. Li, S.X. Liu, K.S. Schanze, J. Phy. Chem. B 107 (2003) 12569.
[2] Q.S. Zhang, Q.G. Zhou, Y.X. Cheng, L.X. Wang, D.G. Ma, X.B. Jing, F.S. Wang, Adv. Mater. 16 (2004) 432.
[3] F. Li, M. Zhang, G. Cheng, J. Feng, Y. Zhao, Y.G. Ma, S.Y. Liu, J.C. Shen, Appl. Phys. Lett. 84 (2004) 148.
[4] C.H. Chen, J. Shi, Coord. Chem. Rev. 171 (1998) 161.
[5] S.N. Wang, Coord. Chem. Rev. 215 (2001) 79.
[6] C.W. Tang, S.A. Vanslyke, Appl. Phys. Lett. 51 (1987) 913.
[7] T.H. Kwon, H.S. Cho, M.K. Kim, J.W. Kim, J.J. Kim, K.H. Lee, S.J. Park, I.S. Shin, H. Kim, D.M. Shin, Y.K. Chung, J.I. Hong, Organometallics 24 (2005) 1578.
[8] F.M. Hwang, H.Y. Chen, P.S. Chen, C.S. Liu, Y. Chi, C.F. Shu, F.L. Wu, P.T. Chou, S.M. Peng, G.H. Lee, Inorg. Chem. 44 (2005) 1344.
[9] J. Li, P.I. Djurovuch, B.D. Alleyne, M. Yousufuddin, N.N. Ho, J.C. Thomas, J.C. Peters, R. Bau, M.E. Thomson, Inorg. Chem. 44 (2005) 1713.
[10] X.M. Liu, W. Gao, Y. Mu, G.H. Li, L. Ye, H. Xia, Y. Ren, S.H. Feng, Organometallics 24 (2005) 1614.
[11] V.A. Montes, G. Li, R. Pohl, J. Shinar, P. Anzenbacher Jr., Adv. Mater. 16 (2004) 2001.
[12] R. Pohl, V.A. Montes, J. Shinar, P. Anzenbacher Jr., J. Org. Chem. 69 (2004) 1723.
[13] R. Pohl, P. Anzenbacher Jr., Org. Lett. 5 (2003) 2769.
[14] Q.G. Wu, J.A. Lavigne, Y. Tao, M. D'Iorio, S.N. Wang, Inorg. Chem. 39 (2000) 5248.
[15] Q.G. Wu, A. Hook, S.N. Wang, Angew. Chem., Int. Ed. Engl. 39 (2000) 3933.
[16] D.T. Song, S.N. Wang, Eur. J. Inorg. Chem. (2003) 3774.
[17] Q.G. Wu, J.A. Lavigne, Y. Tao, M. D'Iorio, S.N. Wang, Chem. Mater. 13 (2001) 17.
[18] Y. Liu, J.H. Guo, H.D. Zhang, Y. Wang, Angew. Chem., Int. Ed. Engl. 41 (2002) 182.
[19] Y.Q. Li, Y. Liu, W.M. Bu, J.H. Guo, Y. Wang, Chem. Commun. (2000) 1551.
[20] Y.K. Chan, P.K. Ng, X. Gong, S.J. Hou, Appl. Phys. Lett. 75 (1999) 3920.
[21] K.Z. Wang, L. Huang, L.H. Gao, L.P. Jin, C.H. Huang, Inorg. Chem. 41 (2002) 3353.
[22] S. Ranjan, S.Y. Lin, K.C. Hwang, Y. Chi, W.L. Ching, C.S. Liu, Y.T. Tao, C.H. Chien, S.M. Peng, G.H. Lee, Inorg. Chem. 42 (2003) 1248.
[23] Y.L. Tung, S.W. Lee, Y. Chi, L.S. Chen, C.F. Shu, F.I. Wu, A.J. Carty, P.T. Choi, S.M. Peng, G.H. Lee, Adv. Mater. 17 (2005) 1059.
[24] H. Xia, C. Zhang, X. Liu, S. Qiu, P. Lu, F. Shen, J. Zhang, Y. Ma, J. Phys. Chem. B 108 (2004) 3185.
[25] H. Xia, C. Zhang, X. Liu, S. Qiu, P. Lu, J. Zhang, Y. Ma, Appl. Phys. Lett. 84 (2004) 290.
[26] B. Carlson, G.D. Phelan, W. Kaminsky, L. Dalton, X.Z. Jiang, S. Liu, A.K.-Y. Jen, J. Am. Chem. Soc. 124 (2002) 14162.
[27] Y.L. Chen, S.W. Lee, Y. Chi, K.C. Hwang, S.B. Kumar, Y.H. Hu, Y.M. Cheng, P.T. Chou, S.M. Peng, G.H. Lee, S.J. Yeh, C.T. Chen, Inorg. Chem. 44 (2005) 4287.
[28] Y.L. Tung, P.C. Wu, C.S. Liu, Y. Chi, J.K. Yu, Y.H. Hu, P.T. Chou, S.M. Peng, G.H. Lee, Y. Tao, J.C. Arthur, C.F. Shu, F.I. Wu, Organometallics 23 (2004) 3745.
[29] Y.G. Ma, C.M. Che, H.Y. Chao, X.M. Zhou, W.H. Chan, J.C. Shen, Adv. Mater. 11 (1999) 852.
[30] X.M. Zhang, M.L. Tong, M.L. Gong, H.K. Lee, L. Luo, K.F. Li, Y.X. Tong, X.M. Chen, Chem. Eur. J. 8 (2002) 3187.
[31] G. Yu, S.W. Yin, Y.Q. Liu, Z.G. Shuai, D.B. Zhu, J. Am. Chem. Soc. 125 (2003) 14816.
[32] W.K. Lo, W.K. Wong, W.Y. Wong, J.P. Guo, Eur. J. Inorg. Chem. (2005) 3950.
[33] M.R. Haneline, M. Tsunoda, F.P. Gäbbai, J. Am. Chem. Soc. 124 (2002) 3737.
[34] R.Q. Fan, D.S. Zhu, Y. Mu, G.H. Li, Y.L. Yang, Q. Su, Eur. J. Inorg. Chem. (2004) 4891.
[35] V.W.W. Yam, K.K.W. Lo, W.K.M. Fung, C.R. Wang, Coord. Chem. Rev. 171 (1998) 17.
[36] H.H. Patterson, S.M. Kanan, M.A. Omary, Coord. Chem. Rev. 128 (2000) 227.
[37] W.-Y. Wong, G.-L. Lu, L. Liu, J.-X. Shi, Z. Lin, Eur. J. Inorg. Chem. (2004) 2066.
[38] (a) X.-Y. Liu, X.-Y. Mu, H. Xia, L. Ye, W. Gao, H.-Y. Wang, Y. Mu, Eur. J. Inorg. Chem. (2006) 4317;
(b) W.-Y. Wong, Coord. Chem. Rev. 251 (2007) 2400.
[39] S.J. Faville, W. Henderson, T.J. Mathienson, B.K. Nicholson, J. Orgmet. Chem. 580 (1999) 363.
[40] L. Liu, S.-Y. Poon, W.-Y. Wong, J. Orgmet. Chem. 690 (2005) 363.
[41] W.-Y. Wong, L. Liu, J.-X. Shi, Angew. Chem., Int. Ed. Engl. 42 (2003) 4064.
[42] R.J. Puddephatt, Chem. Commun. (1998) 1055.
[43] R.J. Puddephatt, Coord. Chem. Rev. 216–217 (2001) 313.

[44] H. Schmidbaur, Chem. Soc. Rev. 24 (1995) 391.
[45] C.-M. Che, H.-Y. Chao, V.M. Miskowski, Y. Li, K.-K. Cheung, J. Am. Chem. Soc. 123 (2001) 4985.
[46] W. Lu, H.-F. Xiang, N. Zhu, C.-M. Che, Organometallics 21 (2002) 2343.
[47] H.-Y. Chao, W. Lu, Y. Li, M.C.W. Chan, C.-M. Che, K.-K. Cheung, N. Zhu, J. Am. Chem. Soc. 124 (2002) 14696.
[48] M.I. Bruce, B.C. Hall, B.W. Skelton, M.E. Smith, A.H. White, J. Chem. Soc., Dalton Trans. (2002) 995.
[49] P. Li, B. ahrens, K.-H. Choi, M.S. Khan, P.R. Raithby, P.J. Khan, M.S. Wilson, W.-Y. Wong, Cryst. Eng. Commun. 4 (2002) 405.
[50] B.C. Tzeng, A. Schier, H. Schmidbaur, Inorg. Chem. 38 (1999) 3978.
[51] B.C. Hollatz, A. Schier, H. Schmidbaur, J. Am. Chem. Soc. 119 (1997) 8115.
[52] C. King, J.C. Wang, M.N.I. Kham, J.P. Fackler Jr., Inorg. Chem. 28 (1989) 2145.
[53] M.J. Irwin, J.J. Vittal, R.J. Puddephatt, Organometallics 16 (1997) 3541.
[54] W.J. Hunks, M.A. MacDonals, M.C. Jennings, J. Puddephatt, Organometallics 19 (2000) 5063.
[55] K. Dey, D. Bandyopadhyay, Indian J. Chem. 31A (1992) 34.
[56] G.M. Sheldrick, SHELXS-97, SHELXL-97 Programs for Crystal Structure Analysis, University of Göttingen, Germany, 1997.
[57] (a) L.J. Farrugia, ORTEP 3 for Windows, Version 1.076, University of Glasgow, 1997–2002;
(b) L.J. Farrugia, J. Appl. Crystallogr. 30 (1997) 565.
[58] (a) A.L. Spek, Acta Crystallogr., Sect. A C34 (1990) 46;
(b) A.L. Spek, PLATON Version 29-11-98.
[59] B. Singh, U. Srivastava, Syn. React. Inorg. Met. 18 (1988) 515.
[60] S. Biswas, S. Sarkar, B.B. Bhaumik, K. Dey, J. Coord. Chem. 61 (2008) 605, and references cited therein.
[61] T.S. Lobana, Coord. Chem. Rev. 63 (1985) 161.
[62] T.S. Lobana, Rekha, R.J. Butcher, T.W. Failes, P. Turner, J. Coord. Chem. 58 (2005) 1369.
[63] L.G. Kuz'mina, Y.T. Struchkov, Croat. Chem. Acta 57 (1984) 701.
[64] S. Biswas, S. Sarkar, I.M. Steele, S. Sarkar, G. Mostafa, B.B. Bhaumik, K. Dey, Polyhedron 26 (2007) 5061.
[65] T.S. Lobana, A. Sánchez, J.S. Casas, A. Castiñeiras, J. Sordo, M.S. García-Tasende, E.M. Vázquez-lópez, J. Chem. Soc., Dalton Trans. (1997) 4289, and references cited therein.
[66] C.S. Lai, E.R.T. Tiekink, Cryst. Eng. Commun. 5 (2003) 253.
[67] J. Zukerman-Schpector, M.C. Rodrìguez-Argüelles, M.I. Suárez, A. Sánchez, J.S. Casas, J. Sordo, J. Coord. Chem. 24 (1991) 177.
[68] L. Pauling, The Nature of Chemical Bond, 3rd Ed., Cornell University Press, New York, 1960.
[69] J.D. Curry, R.J. Jandacer, J. Chem. Soc., Dalton Trans. (1972) 1123.
[70] A. Macias, M.C. Rodrìguez-Argüelles, M.I. Suárez, A. Sánchez, J.S. Casas, J. Sordo, U. Englert, J. Chem. Soc., Dalton Trans. (1989) 1787.
[71] J.S. Casas, M.V. Castaño, M.S. García-Tasende, I. Martinez-Santamarta, A. Sánchez, J. Sordo, E.E. Castellano, J. Zukerman-Schpector, J. Chem. Res. (1992) 324.
[72] S.J. Faville, W. Henderson, T.J. Mathieson, B.K. Nicholson, J. Organomet. Chem. 580 (1999) 363. and references cited therei.
[73] S. Sarkar, S. Biswas, K. Dey, B.B. Bhaumik, J. Coord. Chem. 60 (2007) 1057.
[74] K. Dey, S. Sarkar, S. Mukhopadhyay, S. Biswas, B.B. Bhaumik, J. Coord. Chem. 59 (2006) 565.
[75] K. Dey, S. Sarkar, S. Mukhopadhyay, A.K. Mallik, S. Biswas, B.B. Bhaumik, J. Coord. Chem. 59 (2006) 1233.
[76] N.B. Colthup, L.H. Dally, S.E. Wiberly, Introduction to Infrared and Raman Spectroscopy, Academic Press, New York, 1964, p. 305.
[77] J.S. Casas, M.V. Castaño, T.S. Lobana, A. Sánchez, A. Castiñeiras, M.C. Rodrìguez-Argüelles, A. Sánchez, J. Sordo, J. Chem. Soc., Dalton Trans. (1993) 1253.
[78] A. Syamal, O.P. Singhal, J. Inorg. Nucl. Chem. 43 (1981) 2821.
[79] W.-Y. Wong, G.-L. Lu, L. Liu, J.-X. Shi, Z. Lin, Eur. J. Inorg. Chem. (2004) 2066.
[80] E.M. Kosower, J. Am. Chem. Soc. 80 (1958) 3253.
[81] X.-M. Liu, X.-Y. Mu, H. Xia, L. Ye, W. Gao, H.-y. Wang, Y. Mu, Eur. J. Inorg. Chem. (2006) 4317.

KBr pellets. Elemental analyses were performed at the Ecole d'ingénieurs de Fribourg, Switzerland.

2.1. Synthesis

2.1.1. [$Ph_2PCH_2PPh_2CH_2C(O)Ph$]Br (**1**)

The phosphonium salt was prepared following the literature procedure [10] using $BrCH_2COPh$ (1.55 g, 7.8 mmol) and $PPh_2CH_2PPh_2$ (3.00 g, 7.8 mmol). Yield: 4.10 g (90%). M.p. 194–196 °C (Reported: 195–197 °C). IR (cm^{-1}): 1667 (νC=O). ^{1}H NMR ($CDCl_3$): δ 4.32 (d, 2H, PCH_2P, $^2J_{P-H}$ = 14.6), 5.93 (d, 2H, PCH_2COPh, $^2J_{P-H}$ = 12.5), 7.20–8.13 (m, 25H, Ph). ^{31}P NMR ($CDCl_3$): δ −26.18 (d, PPh$_2$, $^2J_{P-P}$ = 63.2), 24.07 (d, PCH$_2$COPh, $^2J_{P-P}$ = 63.2).

2.1.2. [$HgCl_2(Br)(PPh_2CH_2PPh_2CH_2C(O)Ph)$] (**2**)

A mixture of $HgCl_2$ (0.09 g, 0.34 mmol) and [$PPh_2CH_2PPh_2CH_2C(O)Ph$]Br (0.18 g, 0.34 mmol) in methanol (15 ml) was stirred for 3 h. The white precipitate obtained was isolated, washed twice with 15 ml methanol and recrystallised in dichloromethane. Yield: 0.25 g (86%). M.p. 158–160 °C. *Anal.* Calc. for $C_{33}H_{29}BrCl_2HgOP_2$: C, 46.36; H, 3.42. Found. C, 46.34; H, 3.35%. IR (cm^{-1}): 1672 (νC=O). ^{1}H NMR (DMSO–d_6): δ 4.43 (d, 2H, PCH_2P, $^2J_{P-H}$ = 15.5), 5.68 (d, 2H, PCH_2COPh, $^2J_{P-H}$ = 12.2), 7.26–7.99 (m, 25H, Ph). ^{31}P NMR (DMSO–d_6): δ −19.79 (d, PPh$_2$, $^2J_{P-P}$ = 63.2), 23.43 (d, PCH$_2$COPh, $^2J_{P-P}$ = 56.6).

2.1.3. [$HgBr_3(PPh_2CH_2PPh_2CH_2C(O)Ph)$] (**3**)

This complex was obtained using the same procedure as adopted for the preparation of **2** using $HgBr_2$ (0.12 g, 0.34 mmol). The product was recrystallized using dichloromethane containing a few drops of hexane. Yield: 0.29 g (90%). M.p. 135–137 °C. *Anal.* Calc. for $C_{33}H_{29}Br_3HgOP_2$: C, 41.99; H, 3.10. Found. C, 41.49; H, 3.00%. IR (cm^{-1}): 1671 (νC=O). ^{1}H NMR (DMSO–d_6): δ 4.27 (d, 2H, PCH_2P, $^2J_{P-H}$ = 15.4), 5.58 (d, 2H, PCH_2COPh, $^2J_{P-H}$ = 12.2), 7.26–7.97 (m, 25H, Ph). ^{31}P NMR (DMSO–d_6): δ −26.72 (d, PPh$_2$, $^2J_{P-P}$ = 65.4), 23.74 (d, PCH$_2$COPh, $^2J_{P-P}$ = 65.4).

2.1.4. [$HgBr_2(I)(PPh_2CH_2PPh_2CH_2C(O)Ph)$] (**4**)

A mixture of HgI_2 (0.08 g, 0.17 mmol) and [$PPh_2CH_2PPh_2CH_2C(O)Ph$]Br (0.10 g, 0.17 mmol) in methanol (15 ml) was stirred for 3 h. The clear colourless solution was evaporated to dryness giving an oily residue. Addition of diethyl ether (30 ml) resulted in the formation of a pale yellow solid. It was recrystallized in a mixture of dichloromethane–pentane and dried. Yield: 0.075 g (44%). M.p. 103–105 °C. *Anal.* Calc. for $C_{33}H_{29}Br_2HgIOP_2$: C, 40.00; H, 2.95. Found. C, 39.53; H, 2.90%. IR (cm^{-1}): 1675 (νC=O). ^{1}H NMR (DMSO–d_6): δ 4.24 (d, 2H, PCH_2P, $^2J_{P-H}$ = 15.4), 5.57 (d, 2H, PCH_2COPh, $^2J_{P-H}$ = 12.3), 7.24–7.97 (m, 25H, Ph). ^{31}P NMR (DMSO–d_6): δ −28.29 (d, PPh$_2$, $^2J_{P-P}$ = 67.0), 23.39 (d, PCH$_2$COPh, $^2J_{P-P}$ = 67.0).

2.1.5. [$HgCl_3(PPh_2CH_2PPh_2CH_2C(O)Ph)$] (**5**)

To a suspension of $HgCl_2$ (0.10 g, 0.36 mmol) in dichloromethane (10 ml) a solution of $Ph_2PCH_2PPh_2$=C(H)C(O)Ph [10] (0.21 g, 0.36 mmol) in dichloromethane (10 ml) was added dropwise. The clear suspension immediately turned turbid. After completion of the addition the solution became clear and the stirring was continued for two hours. The solution was reduced to about 5 ml and the addition of excess n-pentane resulted in a white precipitate. The solid was dissolved in CH_2Cl_2 and layered with n-pentane. After two days colourless diffraction quality crystals were obtained. Yield: 0.06 g (21% based on ylide). M.p. 184–186 °C. *Anal.* Calc. for $C_{33}H_{29}Cl_3HgOP_2$: C, 48.90; H, 3.61. Found. C, 48.84; H, 3.58%. IR (cm^{-1}): 1674 (νC=O). ^{1}H NMR (400 MHz, DMSO–d_6): δ 4.34 (d, 2H, PCH_2P, $^2J_{P-H}$ = 15.7), 5.64 (d, 2H, PCH_2COPh, $^2J_{P-H}$ = 12.2), 7.27–8.05 (m, 25H, Ph). ^{31}P NMR (162 MHz, DMSO–d_6): δ −22.78 (br, PPh$_2$), 23.55 (d, PCH$_2$COPh, $^2J_{P-P}$ = 60.2).

2.2. X-ray crystallography

All the crystallizations were carried out under aerobic conditions. Single crystals of **2**, **3** and **4** were obtained by slow evaporation of dichloromethane, dichloromethane/hexane and dichloromethane/pentane solutions, respectively. Well formed crystals of **5** were grown by layering pentane over a dichloromethane solution. The intensity data were collected at 173 K (−100 °C) on a Stoe Mark II-Image Plate Diffraction System [15] equipped with a two-circle goniometer and using Mo Kα graphite monochromated radiation. The structures were solved by direct methods using the programme SHELXS-97 [16]. The refinement and all further calculations were carried out using SHELXL-97 [16]. The H-atoms were included in calculated positions and treated as riding atoms using SHELXL default parameters. The non-H atoms were refined anisotropically, using weighted full-matrix least-squares on F^2. Further crystallographic data are given in Table 1. The molecular structure and crystallographic numbering schemes are illustrated in ORTEP [17] drawings, Figs. 1–3.

3. Results and discussion

3.1. Synthesis

The reactions of mercury(II) halides with the phosphine–phosphonium salt, [$Ph_2PCH_2PPh_2CH_2C(O)Ph$]Br in 1:1 molar ratio in methanol afford the zwitterionic complexes **2**–**4** as shown in Scheme 1.

While **2** and **3** are simple complexation products, the formation of **4** involves a halogen exchange followed by complexation as shown below,

$$2[Ph_2PCH_2PPh_2CH_2C(O)Ph]Br + HgI_2 \rightarrow [Br_2(I)Hg(PPh_2CH_2PPh_2CH_2C(O)Ph)] + [Ph_2PCH_2PPh_2CH_2C(O)Ph]I$$

The stability of **4** consisting of the $HgIBr_2$ moiety can be traced to the softness of Hg(II) and I^-. The non-formation of HgI_2Br^- or HgI_3^- may be ascribed to steric effects caused by I^- ion. Complex **5** has been obtained by the reaction of the ylide, $Ph_2PCH_2PPh_2$=C(H)C(O)Ph with $HgCl_2$ in dichloromethane and subsequent crystallization. The preferential formation of zwitterionic complexes as opposed to the formation of phosphonium metalates can be ascribed to the strength of Hg–P bond.

3.2. Spectroscopy

In the IR spectra of complexes **2**–**5**, a strong absorption around 1675 cm^{-1}, which is close to the same frequency in free phosphonium salt (1667 cm^{-1}) indicates the non involvement of the –$PCH_2C(O)Ph$ group in the reactions. The ^{31}P NMR spectra of complexes **2**–**5** exhibit two mutually coupled doublets corresponding to 'phosphonium' and 'phosphine' groups. The former peak remains sharp and unaltered, while the latter peak is relatively broad. In contrast to the ^{31}P NMR of Hg(II)–phosphine complexes [18], the coordination of phosphine to mercury in the present cases did not cause significant downfield shifts. Complexes **2** and **5** show downfield shifts (−19.79 and −22.78 ppm, respectively) compared to that of phosphine of the phosphonium salt (−26.18 ppm). The chemical shift for **3** (−26.72 ppm) appears close to that of the free ligand whereas **4** (−28.29 ppm) shows a slight upfield shift. These data indicate that the presence of a formal negative charge on the metal may effectively reduce the deshielding experienced by the phosphorus due to complexation. In the ^{1}H NMR spectra, the dou-

Table 1
Crystal data and refinement details for compounds **2** · CH_2Cl_2, **3** · CH_2Cl_2, **4** · CH_2Cl_2, **5** · $2CH_2Cl_2$.

	2 · CH_2Cl_2	**3** · CH_2Cl_2	**4** · CH_2Cl_2	**5** · $2CH_2Cl_2$
Empirical formula	$C_{33}H_{29}BrCl_2HgOP_2$, CH_2Cl_2	$C_{33}H_{29}Br_3HgOP_2$, CH_2Cl_2	$C_{33}H_{29}Br_2HgIOP_2$, CH_2Cl_2	$C_{33}H_{29}Cl_3HgOP_2$, $2(CH_2Cl_2)$
Formula weight	939.83	1028.75	1075.74	980.29
Temperature (K)	173(2)	173(2)	173(2)	173(2)
Wavelength (Å)	0.71073	0.71073	0.71073	0.71073
Crystal size (mm)	0.50 × 0.15 × 0.10	0.50 × 0.40 × 0.30	0.40 × 0.30 × 0.25	0.50 × 0.50 × 0.29
Crystal system	monoclinic	monoclinic	monoclinic	monoclinic
Space group	$P2_1/c$	$P2_1/c$	$P2_1/c$	$P2_1/n$
a (Å)	10.1464(4)	10.2043(4)	10.451(2)	10.5390(4)
b (Å)	21.7503(10)	21.7893(10)	21.771(4)	22.6369(8)
c (Å)	15.8516(7)	16.1032(6)	16.265(3)	16.4398(6)
β (°)	96.702(3)	96.698(3)	96.299(16)	106.031(3)
V (Å^3)	3474.3(3)	3556.0(3)	3678.4(12)	3769.5(2)
Z	4	4	4	4
$F(000)$	1824	1968	2040	1920
μ (mm^{-1})	6.007	7.966	7.454	4.693
Reflections measured	42556	47650	19814	53038
Independent reflections	6175	9578	6572	10137
R_{int}	0.0555	0.0642	0.0695	0.0287
Observed reflections [$I > 2\sigma(I)$]	5272	7728	3974	9669
R_1 ($I > 2\sigma(I)$)	0.0399	0.0339	0.0492	0.0310
wR_2 (all data)	0.1107	0.0723	0.1278	0.0674

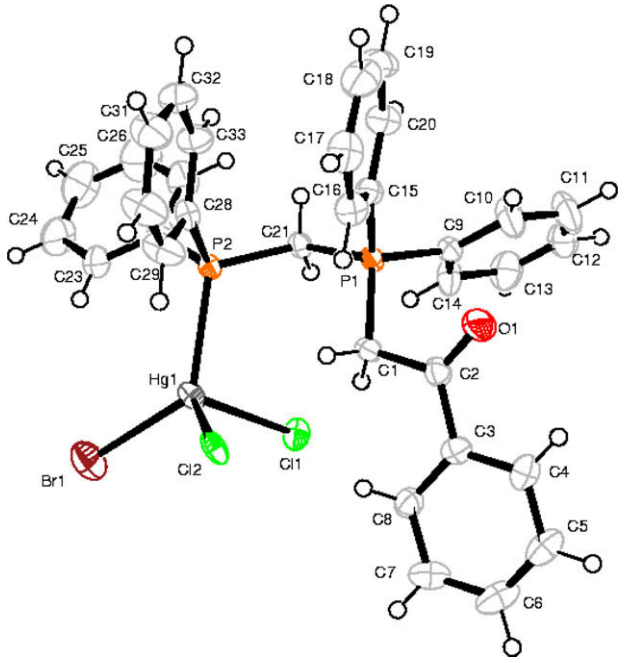


Fig. 1. Molecular structure of [$HgCl_2$(Br)($PPh_2CH_2PPh_2CH_2COPh$)] (**2**) with 30% probability ellipsoids. The dichloromethane solvent has been omitted for clarity.

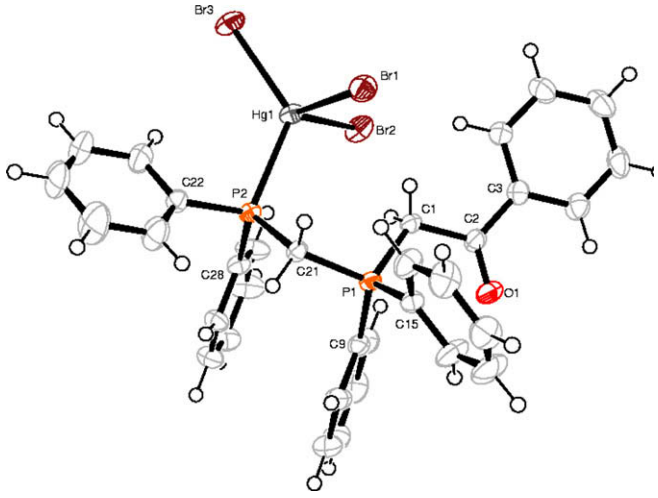


Fig. 2. Molecular structure of [$HgBr_3$($PPh_2CH_2PPh_2CH_2COPh$)] (**3**) with 30% probability ellipsoids. The dichloromethane solvent has been omitted for clarity.

blet in the region of 4.30 ppm attributed to PCH_2P, and the doublet in the region of 5.62 ppm attributed to PCH_2COPh, remains unaffected due to complexation.

3.3. Molecular structures of complexes **2**–**5**

The crystal structures of **2** · CH_2Cl_2, **3** · CH_2Cl_2, **4** · CH_2Cl_2 and **5** · $2CH_2Cl_2$ have been determined and the relevant bond parameters are given in Table 2. The molecular structures of **2**, **3**, **4** are represented in Figs. 1–3, respectively. The structure of **5** is given as Supplementary data (Fig. S1). The Hg atom in all four structures is in a distorted tetrahedral environment with one P, and three halide ligands. The Hg–P distances in all of these zwitterionic complexes fall within the range of 2.39(1)–2.606(3) Å observed in

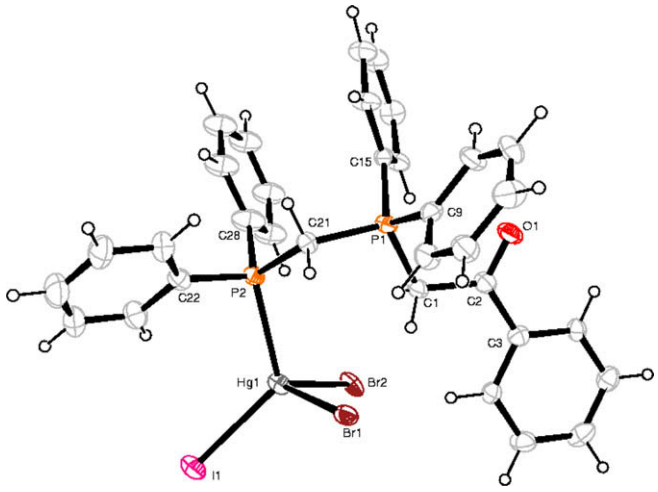
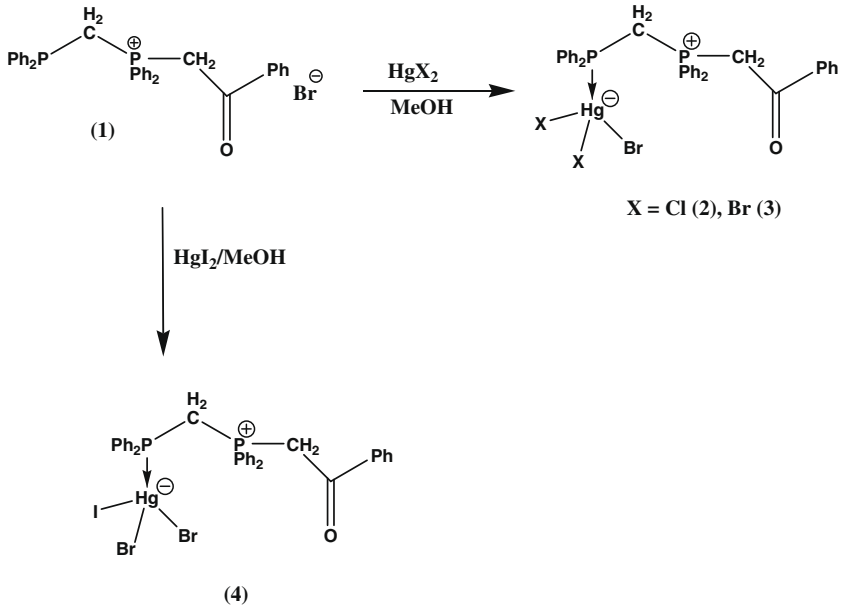


Fig. 3. Molecular structure of [$HgBr_2$(I)($PPh_2CH_2PPh_2CH_2COPh$)] (**4**) with 30% probability ellipsoids. The dichloromethane solvent has been omitted for clarity.



Scheme 1. Reactions of mercuric halides with phosphonium salt **1**.

Table 2
Selected bond distances (Å) and angles (°) in **2**–**5**.[a]

	2	3	4	5
Hg(1)–P(2)	2.4868(15)	2.5077(9)	2.550(3)	2.4465(7)
Hg(1)–X(*l*)	2.5221(8)	2.6545(4)	2.7030(9)	2.5197(8)
Hg(1)–X(*m*)	2.5743(15)	2.6474(4)	2.7038(13)	2.6210(8)
Hg(1)–X(*n*)	2.5792(14)	2.5504(4)	2.7084(13)	2.4263(8)
P(1)–C(1)	1.810(6)	1.806(4)	1.813(10)	1.803(3)
C(1)–C(2)	1.511(9)	1.522(5)	1.510(15)	1.518(4)
O(1)–C(2)	1.230(8)	1.220(5)	1.230(12)	1.213(4)
P(1)–C(21)	1.816(6)	1.816(3)	1.811(10)	1.815(3)
P(2)–C(21)	1.839(6)	1.841(3)	1.836(10)	1.843(3)
X(*n*)–Hg(1)–P(2)	109.81(5)	124.51(2)	112.10(7)	133.53(3)
X(*n*)–Hg(1)–X(*l*)	106.30(4)	107.656(15)	108.67(3)	99.16(3)
P(2)–Hg(1)–X(*l*)	126.85(4)	99.77(2)	121.83(7)	113.45(3)
X(*n*)–Hg(1)–X(*m*)	104.90(5)	106.554(14)	108.55(4)	107.90(3)
P(2)–Hg(1)–X(*m*)	100.50(5)	109.85(2)	95.30(7)	92.71(2)
X(*l*)–Hg(1)–X(*m*)	106.39(4)	107.300(15)	109.05(3)	108.36(3)
P(1)–C(1)–C(2)–O(1)	21.7(8)	24.7(5)	−14.6(15)	9.3(4)

[a] For **2** read *l* = Br(1), *m* = Cl(1), *n* = Cl(2). For **3** read *l* = Br(1), *m* = Br(2), *n* = Br(3). For **4** read *l* = I(1), *m* = Br(1), *n* = Br(2). For **5** read *l* = Cl(1), *m* = Cl(2), *n* = Cl(3).

Hg(II)–phosphine complexes [19]. The Hg–Cl distances in **5** and **2** are comparable to those reported in the literature [20,21]. In complex **3**, one of the Hg–Br distances is shorter [2.550(1) Å] than the other two. It is worth mentioning that in **4**, both the Hg–Br and Hg–I [2.703(1) Å] distances are very similar. One of the P–Hg–halogen bonds in the complexes exhibits a major deviation from an ideal tetrahedral angle. The most striking feature is the large distortion shown by P–Hg–Cl bond angle in complex **5** (which contains three chlorides). It has been observed previously [22] that the weaker bonding of chlorine to mercury compared to that of bromine and iodine, allows the Hg–P bonding to be strengthened leading to a linear P–Hg–Cl arrangement. In accordance with this fact the Hg–P bond length is much shorter in complex **5** (containing three chlorides) and **2** (containing two chlorides) compared to that in **3** and **4** (containing no chloride). The structural features in the phosphonium moiety are very similar in all four complexes. The significant shortening of the C2–O1 bond, as well as the elongation of the P1–C1 and C1–C2 bonds in all four complexes, compared with ylide, $PPh_2CH_2PPh_2CHCOPh$ [12] indicates the absence of any significant additional resonance delocalization in the ylide moiety.

4. Conclusions

The reactions of the phosphine–phosphonium salt, $[PPh_2CH_2PPh_2CH_2COPh]Br$ with mercury(II) halides offers an easy method for the preparation of zwitterionic mixed halogen mercurates. Formation of the above complexes can be ascribed to the strength of Hg–P bond. In the ^{31}P NMR spectra the absence of significant downfield shifts due to complexation could be ascribed to the presence of formal negative charge on the metal which effectively reduces the desheilding experienced by the phosphine phosphorus atom. The crystal structures of the above complexes reveal a distorted tetrahedral geometry around the mercury atom.

Acknowledgements

M.M.E. thanks the Swiss Federal Commission for a scholarship to study at the University of Neuchâtel. K.P. thanks Department of Science and Technology, New Delhi, India, for financial assistance (SERC-SR/S1/IC-29/2003).

Appendix A. Supplementary data

CCDC 662097, 662098, 662099 and 662096 contain the supplementary crystallographic data for **2** · CH_2Cl_2, **3** · CH_2Cl_2, **4** · CH_2Cl_2 and **5** · $2CH_2Cl_2$, respectively. These data can be obtained free of charge via http://www.ccdc.cam.ac.uk/conts/retrieving.html, or from the Cambridge Crystallographic Data Centre, 12 Union Road, Cambridge CB2 1EZ, UK; fax: (+44) 1223-336-033; or e-mail: deposit@ccdc.cam.ac.uk. Supplementary data associated with this article can be found, in the online version, at doi:10.1016/j.poly.2009.01.001.

References

[1] G.M. Kosolapoff, L. Maier, Organophosphorus Compounds, Wiley Interscience, New York, 1972.
[2] T. Toneri, F. Sanda, T. Endo, J. Photopolym. Sci. Technol. 12 (1999) 159.
[3] T. Toneri, K.-I. Watanabe, F. Sanda, T. Endo, Macromolecules 32 (1999) 1293.

[4] T. Toneri, F. Sanda, T. Endo, Macromolecules 34 (2001) 1518.
[5] R. Navarro, E.P. Urriolabeitia, J. Chem. Soc., Dalton Trans. (1999) 4111.
[6] M. Kalyanasundari, K. Panchanatheswaran, W.T. Robinson, H. Wen, J. Organomet. Chem. 491 (1995) 103.
[7] B. Kalyanasundari, K. Panchanatheswaran, V. Parthasarathi, W.T. Robinson, Bull. Chem. Soc. Jpn. 72 (1999) 33.
[8] E.C. Spencer, M.B. Mariyatra, J.A.K. Howard, A.M. Kenwright, K. Panchanatheswaran, J. Organomet. Chem. 692 (2007) 1081.
[9] E.C. Spencer, B. Kalyanasundari, M.B. Mariyatra, J.A.K. Howard, K. Panchanatheswaran, Inorg. Chim. Acta 359 (2006) 35.
[10] Y. Oosawa, H. Urabe, T. Saito, Y. Sasaki, J. Organomet. Chem. 122 (1976) 113.
[11] M.M. Ebrahim, H. Stoeckli-Evans, K. Panchanatheswaran, Polyhedron 26 (2007) 3491.
[12] M.M. Ebrahim, K. Panchanatheswaran, A. Neels, H. Stoeckli-Evans, J. Organomet. Chem., in press. doi:10.1016/j.jorganchem.2008.11.051.
[13] E. Fatuzzo, R. Nitsche, H. Roetschi, S. Zingg, Phys. Rev. 125 (1962) 514.
[14] W.L.F. Armarego, D.D. Perrin, Purification of Laboratory Chemicals, 4th Ed., Butterworth-Heinemann, Oxford, 1996.
[15] Stoe, X-AREA V1.17 and X-RED32 V1.04 Software, Stoe and Cie GmbH, Darmstadt, Germany, 2002.
[16] G.M. Sheldrick, SHELXS-97 and SHELXL-97, Universität Göttingen, Göttingen, Germany, 1999.
[17] L.J. Farrugia, J. Appl. Crystallogr. 30 (1997) 565.
[18] E.C. Alyea, S.A. Dias, R.G. Goel, W.O. Ogini, P. Pilon, D.W. Meek, Inorg. Chem. 17 (1978) 1697.
[19] M. Kubicki, S.K. Hadjikakou, M.N. Xanthopoulou, Polyhedron 20 (2001) 2179.
[20] N.A. Bell, S.J. Coles, C.P. Constable, M.B. Hursthouse, M.E. Light, R. Mansor, N.J. Salvin, Polyhedron 21 (2002) 1845.
[21] N.A. Bell, T.D. Dee, P.L. Goggin, M. Goldstein, R.J. Goodfellow, T. Jones, K. Kessler, D.M. McEwan, I.W. Nowell, J. Chem. Res (1981) (S) 2, (M) 201.
[22] N.A. Bell, T.D. Dee, M. Goldstein, P.J. McKenna, I.W. Nowell, Inorg. Chim. Acta 71 (1983) 135.

phthalocyanine. These substituted platinum phthalocyanines have been prepared for the first time by using a novel route, with high purity. These compounds were characterized by elemental analysis, UV–Vis and infrared spectral analysis, magnetic susceptibility, powder X-ray diffraction and thermogravimetric studies. The electrical conductivity measurements of these compounds were analysed in the temperature range from ambient to 473 K.

2. Materials and methods

Platinic(IV) chloride, phthalonitrile, nitrophthalonitrile were of AR grade, obtained from Fluka, USA and were used as received. All the other reagents used were of analytical grade and were used as such without purification, unless otherwise mentioned.

2.1. Physico-chemical measurements

A domestic L.G. microwave oven, model MG-555F (max. 900 W, min. 180 W, L.G. electronics, India) with five select power levels was used for carrying out the reactions. Elemental analysis for carbon, hydrogen and nitrogen were done using a Vario EL-III CHN & S Elemental Analyser, Analytikjena, Germany. Electronic spectra in the UV–Vis region were recorded in analytical grade 28 M sulfuric acid using a Systronics type – 117 model spectrophotometer with 1 cm silica cells, Systronics, Ahmedabad, India. IR spectra were recorded in potassium bromide using a Shimadzu 8201 PC FT-IR spectrometer, Japan. Magnetic susceptibility measurements were done using a Gouy magnetic balance consisting of a NP-53 electromagnet with a DC power supply, type NP 1053, and a Keroy semimicro balance, supplied by the Universal Scientific Company, Mumbai, India. Pure mercury tetrathiocyanato cobaltate(II) was synthesized and used as a calibration standard [21]. Thermogravimetric analyses were done at the National Institute of Technology, Tiruchirapalli, India, using a TGA 7 Analyser, Perkin–Elmer, USA. Two to five milligram of the sample was used for the analysis and a heating rate of 10 °C/min was used in air atmosphere at a flow rate of 100 ml/min. A JEOL-JDX-8P X-ray diffractometer with Cu Kα radiation (λ = 1.934 Å) was used to study the powder X-ray diffraction pattern of the samples. Powdered complexes were compressed into pellets of 1.3 cm diameter and thickness ranging from 0.15 to 0.25 cm, using a Perkin–Elmer KBr Die under a pressure of 500 kg/cm^2. A KBr press, Techno Search Instruments, Thane, India, was used for applying the pressure. The diameter and thickness of the pellets were determined by using a screw gauge, readable up to 0.005 cm. Conducting silver paint (ELTECKS preparation No. 1228-C) was coated on both flat surfaces of the pellets and the electrical contacts to the samples were made using the same silver paint to the electrodes. The electrical contacts were checked to verify the ohmic connection and resistance measurements were done from room temperature to 473 K using a DOT 402 Digital Milli Ohm Meter and a DOT 425 Insulation Resistance Tester, Bhandari Electronics and Electricals, Bangalore, India.

2.2. Platinum phthalocyanine

One gram (7.8 mmol) of phthalonitrile and 0.5 g (1.5 mmol) of platinic(IV) chloride were mixed well and then placed in a vessel with a small opening at the top. This vessel was then placed in a microwave and irradiated with at a power of 360 W for 2 min, whereupon the compound started to turn a slight bluish color, and then at 720 W for 3 min to complete the reaction. The compound turned totally to a bluish black color. The crude compound was ground well and washed with ethanol and water, and then with acetone in a Soxhlet extractor with 25 mL volume three times to remove the unreacted impurities. The product was then dried at 45 °C in an oven.

Anal. Calc. for platinum phthalocyanine, $C_{32}H_{16}N_8Pt$: C, 54.32; H, 2.26; N, 15.84. Found: C, 54.76; H, 2.35; N, 15.69%. IR absorption bands (cm^{-1}): 717 (s), 724 (w), 736 (s), 752 (w), 869 (s), 949 (w), 1068 (w), 1093 (m), 1118 (s), 1319 (s), 1359 (m), 1437 (w), 1481 (s), 1520 (s), 3061 (m). Yield: 93%.

2.3. Platinum tetranitro phthalocyanine

One gram (5.8 mmol) of nitrophthalonitrile and 0.45 g (1.34 mmol) of platinic(IV) chloride were mixed well and then placed in a vessel with a small opening at the top. This vessel was then placed in a microwave and irradiated with at a power of 540 W for 2 min, whereupon the compound started to turn a slight bluish color, and then at 720 W for 3 min to complete the reaction. The compound turned totally to a bluish black color. The crude product was ground well and washed with ethanol and water, and then with acetone in a Soxhlet extractor with 25 mL volume three times to remove the unreacted impurities. The product was then dried at 45 °C in an oven.

Anal. Calc. for platinum(II) tetranitro phthalocyanine, $C_{32}H_{12}N_{12}O_8Pt$: C, 43.29; H, 1.35; N, 18.94. Found: C, 42.97; H, 1.38; N, 19.15%. IR absorption bands (cm^{-1}): 3068 (m), 1610 (m), 1524 (s), 1483 (m), 1338 (s), 1252 (m), 1132 (s), 1084 (s), 931 (m), 846 (s), 748 (s), 730 (s), 671 (m). Yield: 90%.

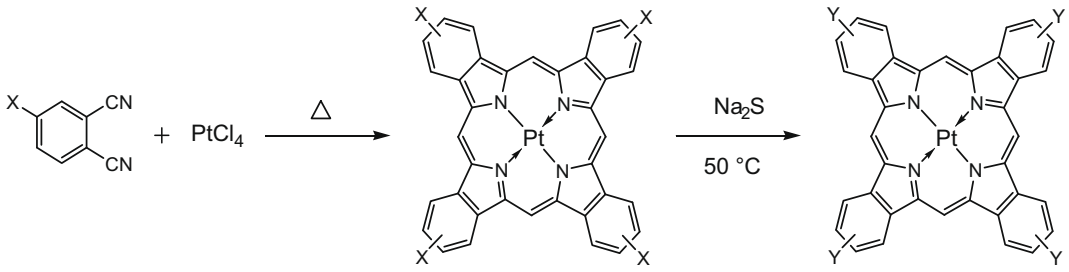
2.4. Platinum tetramino phthalocyanine

For the preparation of the amino derivative of platinum, a similar procedure as used by Achar et al. to synthesize cobalt tetramino phthalocyanine [8] was followed, with a slight modification. 1.0 g (1.13 mmol) of platinum tetranitro phthalocyanine was dissolved in a 50 ml aqueous solution containing 2.5 g (10.42 mmol) of sodium sulfide nonahydrate. The slurry was stirred at 50 °C for 3 h. Then, the bluish complex was separated and washed repeatedly with 0.5 M hydrochloric acid, 1 M sodium hydroxide solution and finally with distilled water until the filtrate was neutral to litmus paper. The dark bluish green product was dried in an oven at 363 K.

Anal. Calc. for platinum(II) tetramino phthalocyanine, $C_{32}H_{20}N_{12}Pt$: C, 50.07; H, 2.61; N, 21.90. Found: C, 50.38; H, 2.54; N, 21.76%. IR absorption bands (cm^{-1}): 3354 (w), 3225 (w), 3057 (w), 1613 (s), 1490 (s), 1328 (s), 1122 (m), 1101 (m), 1033 (w), 962 (m), 867 (w), 745 (s). Yield: 88%.

3. Results and discussion

Platinum phthalocyanine and the tetranitro and tetramino derivatives were synthesized with very good quantitative yields, 88–93%. These phthalocyanines are dark bluish to greenish in color. The elemental analysis for carbon, hydrogen and nitrogen agreed very well with the theoretical calculations, indicating the very good purity of the synthesized compounds. The microwave radiations were carried out at different power levels, ranging from 180 to 900 W for different periods of time to evaluate the optimum conditions for the synthetic procedures. Completion of the reaction under the given microwave power was followed by recording FT-IR spectra at different time intervals. The reactions were carried in a microwave oven until the C≡N group stretching around 2230 cm^{-1} disappeared. The basic reaction and the structure of the synthesized complexes are as shown in Scheme 1. It is clear from the reaction conditions that microwave synthesis is considerably more advantageous with respect to the time required for the completion of the reaction compared to the conventional method. The synthetic yields are also found to be fairly good. Achar et al.



Scheme 1. Synthetic route and structure of the platinum phthalocyanine complexes.

have compared the synthesis of lead phthalocyanine and its derivatives by microwave irradiation and conventional synthesis and found that products obtained in both methods have similar purity, structure and properties [22]. These complexes are soluble in quinoline and chloronaphthalene. These complexes are even soluble in sulfuric acid without undergoing any degradation.

3.1. Electronic spectral study

Electronic absorption spectroscopy is an excellent tool for phthalocyanine investigation and characterization. The electronic spectral data for the three platinum complexes were recorded in the range 250–800 nm using 28 M sulfuric acid as the solvent. The UV–Vis absorption spectra for 1×10^{-5} M solutions of platinum phthalocyanine and the nitro and amino substituted derivatives in sulfuric acid are shown in Fig. 1. The absorption peaks observed for these complexes are shown in Table 1. These complexes showed a major Q-band absorption around 665–680 nm and a shoulder like absorption around 595–615 nm. Interpretation of the spectra is possible by using the analogy of the 18 π electron configuration of the porphyrin system and the mapping of the electronic molecular orbitals of standard metallophthalocyanines by using extended Huckel calculations [23]. The deep bluish to greenish color of the complexes are due to the absorption peaks in the Q-band region which may be assigned to $6e_g \rightarrow 2a_{1u}$ transitions [24]. A small shoulder peak observed at lower wavelengths than the main Q-band are additional components of the Q-band resulting from either vibronic fine structure or dimeric species in solution [25]. It is known that the vibronic structure in phthalocyanines is sensitive to the deviation of the phthalocyanine ring from the ring planarity [14,26]. Coordination of a metal to the phthalocyanine ring, compared to free base phthalocyanine, shifts the Q-band to shorter wavelengths. This is due to the interaction between the d-orbital of the metal and the phthalocyanine, i.e. strong metal to ligand π back-bonding [27]. This interaction increases the separation between the phthalocyanine HOMO and LUMO orbitals. The peaks obtained in the B-band region are around 275–295 nm. The broad absorption peaks observed around 425–450 nm may be due to the C_{4v} symmetry of the complexes [28].

3.2. Infrared spectral study

IR spectra of PtPc, PtTNPc and PtTAPc were recorded in the fundamental region 400–4000 cm^{-1} using the KBr disk technique. The IR spectra recorded for the three complexes are presented in Fig. 2. All the complexes showed absorption peaks around 745, 860, 950, 1060, 1095 and 1120 cm^{-1} which may be assigned to phthalocyanine skeletal vibrations [29]. The vibrational bands of PtPc match well with the reported values for PtPc in the literature [30]. The absorption bands at 1524 and 1338 cm^{-1} observed in the IR spectrum of PtTNPc complex may be assigned to the asymmetric (υ_{as}) and symmetric (υ_s) stretching due to the nitro groups present in the structure of the complex. Two weak absorption bands are ob-

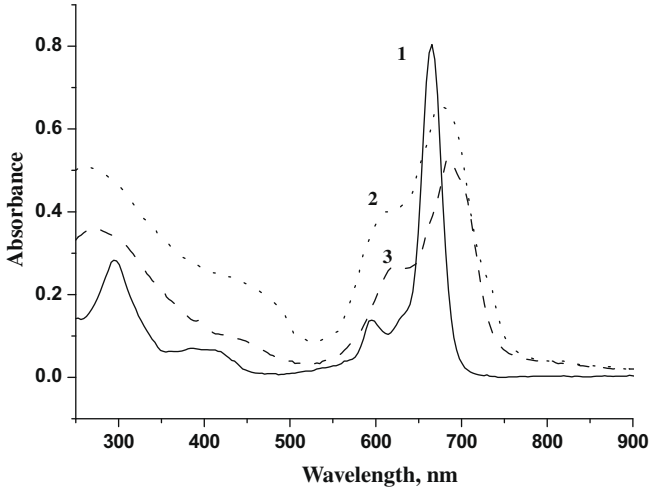


Fig. 1. UV–Vis absorption spectra of 1×10^{-5} M solutions of (1) PtPc, (2) PtTNPc and (3) PtTAPc in 28 M sulfuric acid.

Table 1
Electronic spectral, X-ray diffraction and electrical conductivity data for the platinum complexes.

Compound	Electronic spectral data (nm)	X-ray lattice constants, *a*,*b*,*c* (Å),	Electrical conductivity (S cm^{-1})	
		β (°), V (Å)^3	303 K	473 K
PtPc	295 411 595 665	a = 22.5023 b = 4.0423 c = 16.0905 β = 126.432 V = 1158.74	6.72×10^{-11}	7.06×10^{-8}
PtTNPc	266 435 611 676	a = 24.0678 b = 3.9274 c = 15.1539 β = 124.482 V = 1124.365	8.44×10^{-10}	8.89×10^{-6}
PtTAPc	272 446 623 686	a = 27.7896 b = 3.9285 c = 19.8453 β = 119.827 V = 1268.3	1.43×10^{-7}	4.45×10^{-4}

served at 3354 and 3225 cm^{-1} for the PtTAPc complex which can be assigned to the asymmetric and symmetric stretching of the amino group. All the spectra showed absorption peaks in the range around 3060 cm^{-1} due to the aromatic C–H stretching as well as absorption bands around 1480 cm^{-1}, assignable to C–C bonds.

3.3. Magnetic susceptibility measurements

Magnetic susceptibility measurements of PtPc, PtTNPc and PtTAPc were investigated in the solid state at ambient temperature and varying magnetic field strengths ranging from 1.02 to 3.58 kG. A plot of magnetic susceptibility versus field strength is shown in Fig. 3. The experimental data are in agreement with the diamagnetic nature of the platinum complexes. The magnetic susceptibility values of these complexes showed a decreasing trend with the increase in the magnetic field strength. This may be due to a intermolecular effect [31]. Differences in magnetic susceptibility values and their variations may be due to the differences in intermolecular interactions which in turn may be due to the differences in spacing and inclination of the molecules in the crystal lattice.

3.4. Powder X-ray diffraction

The powder X-ray diffraction spectra of PtPc, PtTNPc and PtTAPc were obtained using Cu Kα radiation (λ = 1.934 Å). The X-ray powder diffraction spectra obtained are shown in Fig. 4. X-ray diffraction studies for the complexes were carried out for the 2θ angle ranging from 2° to 70°. The X-ray diffraction pattern of the complexes showed many sharp peaks in the spectra, indicating the crystalline nature of the sample. The 2θ values corresponding to the sharp peaks were noted down for all the complexes and analysed for the possible crystal structures of the compounds using the procedure DICVOL 91, as outlined elsewhere [32,33]. The crystal data obtained from this method for PtPc compared well with the lattice parameters obtained by Robertson for the single crystal of PtPc [12], which also indicates the superiority of the method used.

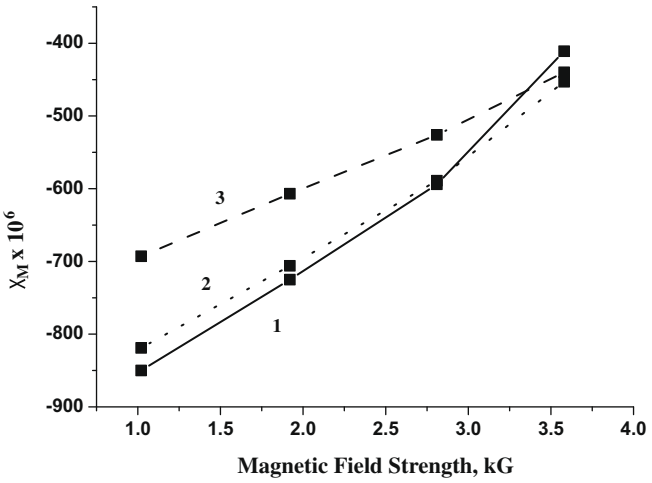


Fig. 3. Plot of magnetic susceptibility vs magnetic field strength.

The lattice constants obtained and the probable crystal structures are given in Table 1. The results obtained from the diffraction study indicated that all the three complexes have the monoclinic structure with different lattice constants and parameters.

3.5. Thermogravimetric studies

Thermal studies performed on platinum phthalocyanine by Konoshita et al., showed it is thermally stable up to 400 °C in air [34]. The dynamic thermogravimetric analyses were carried out in an oxidizing atmosphere for the PtPc, PtTNPc and PtTAPc complexes. The TGA curves are shown in Fig. 5a. All these complexes showed exceptional thermal stability. The nature of the analytical curves indicated that these complexes are degraded in one step in the temperature range 690–750 K. The weight losses are catastrophic in nature for these phthalocyanine complexes. The final

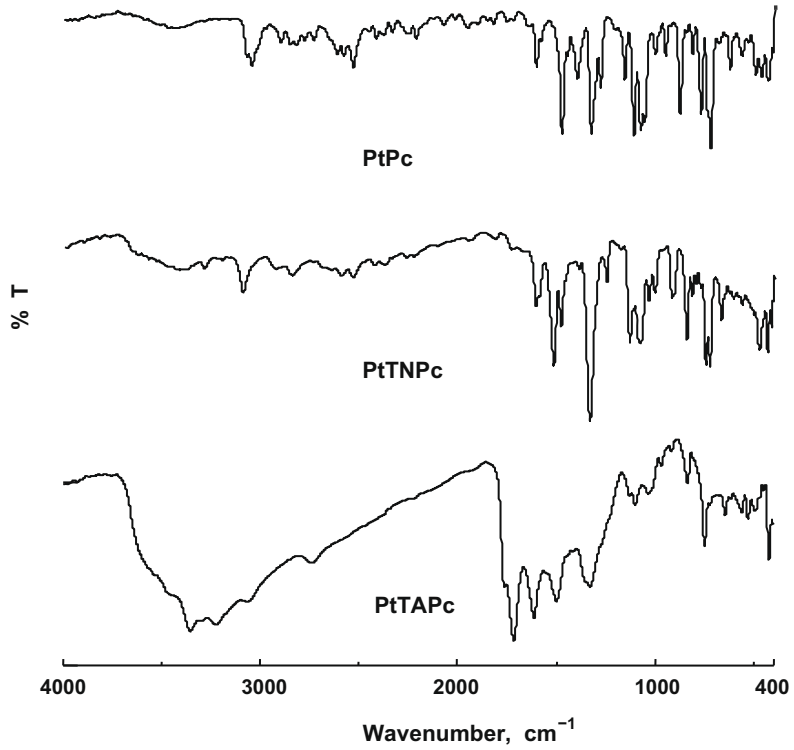


Fig. 2. FT-IR spectra of the complexes as KBr pellets.

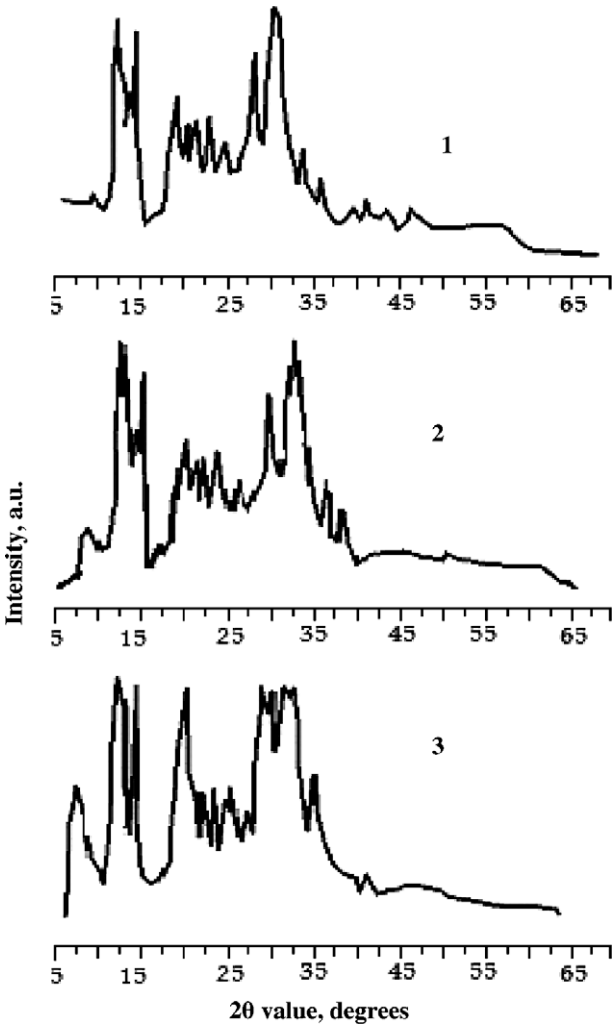


Fig. 4. Powder X-ray diffraction profiles of (1) PtPc, (2) PtTNPc and (3) PtTAPc.

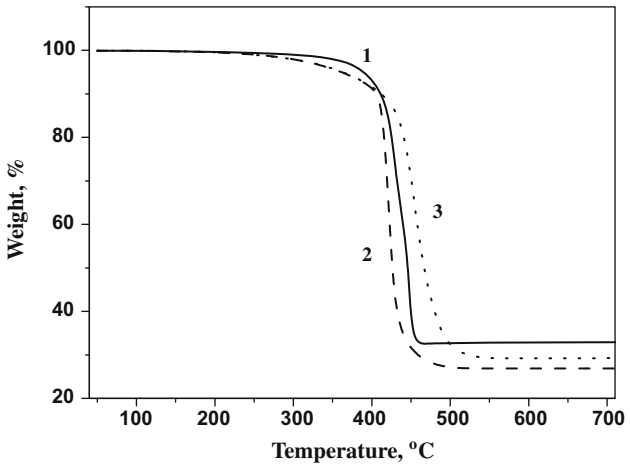


Fig. 5a. Thermogravimetric curves for (1) PtPc, (2) PtTNPc and (3) PtTAPc.

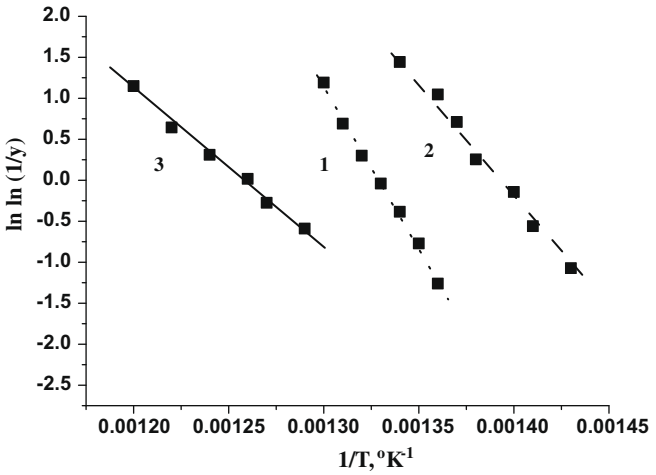


Fig. 5b. Plots of ln $(1/y)$ vs. $1/T$ for the thermal degradation of the phthalocyanine complexes: (1) PtPc, (2) PtTNPc and (3) PtTAPc.

residual weights in the TGA curves corresponded to platinum oxide, which agree very well with the theoretical calculations. The stabilities of these complexes in the oxidizing atmosphere are in the order PtTAPc > PtPc > PtTNPc. The greater thermal stability observed for PtTAPc may be due to the substituted electron donor amino groups which may enhance the resonance stability.

3.6. Kinetic parameters

Kinetic parameters were deduced using Broido's graphical procedure for the straight line decomposition portion of the thermogravimetric analytical curves [35]. Broido's equation is given by:

$$\ln(-\ln y) = -Ea/RT \quad \text{for } n = 1 \tag{1}$$

where y = fraction unreacted; E_a = activation energy (J/mol); R = universal gas constant (8.3145 J/mol K); T = absolute temperature (K).

The graphical plots of $\ln(1/y)$ versus $1/T$ obtained for the three complexes are shown in Fig. 5b. The plots indicate that all the three complexes undergo degradation through a first-order process. The slopes of the plots were used to evaluate the activation energies and the data are presented in Table 2. The activation energies are in the order PtTNPc > PtPc > PtTAPc. The activation energy depends on the chemical structure and the crystalline nature of the complex. If the crystallinity of the material is higher, then the activation energy will also be higher. The thermodynamic properties, like change in enthalpy (ΔH), entropy (ΔS), free energy (ΔG) and frequency factor A, are calculated using the equations as explained elsewhere [36,37]. The kinetic and thermodynamic parameters obtained are summarized in Table 2. The first-order rate constant is determined based on the weight change with time in the linear degradation range of the thermogravimetric curve. The rates of degradation for these complexes are of the same order as their activation energies. The degradation mechanism seems to be similar for all these complexes.

Table 2
Kinetic and thermodynamic parameters for the thermal degradation process of platinum phthalocyanine complexes using Broido's method.

Kinetic parameters	PtPc	PtTNPc	PtTAPc
n	1.0	1.0	1.0
E_a (kJ mol^{-1})	214.65	436.71	168.90
$\Delta H^{\neq}$ (kJ mol^{-1})	249.83	401.75	136.37
$\Delta S^{\neq}$ (J K^{-1} mol^{-1})	47.63	381.92	−78.38
$\Delta G^{\neq}$ (kJ mol^{-1})	209.66	134.57	232.18
A (s^{-1})	5.93×10^{16}	5.63×10^{19}	4.52×10^{8}

3.7. Electrical conductivity

A literature survey revealed that PtPc behaves like a semiconductor, like copper phthalocyanine, in the temperature range 300–500 K, with a room temperature conductivity $\sim 10^{-11}$ S cm^{-1} [20]. The partially oxidized salts of $PtPc(ClO_4)_{0.5}$ and $PtPc(AsF_6)_x$ showed an electrical resistivity of 10^{-2}–10^{-3} Ω cm at room temperature [19]. Electrical conducting properties of phthalocyanines are very sensitive to the presence of impurities. So, care has been taken to synthesize the complexes in a very pure form. The intrinsic electrical conductivity data of the synthesized PtPc, PtTNPc and PtTAPc were recorded from 298 to 473 K and $\log\sigma$ versus $1/T$ was plotted, Fig. 6. The relevant data are presented in Table 1. The plots indicate that these complexes are semiconducting in behavior and showed a linear relationship in the temperature range studied. The thermally activated varying conductivity with temperature was found to obey the expression:

$$\sigma = \sigma_0 e^{-E/KT} \quad (2)$$

where E is the activation energy, σ is the specific conductivity at T (K), σ_0 is a constant and 'K' is the Boltzmann constant. The room temperature specific conductivities of PtPc, PtTNPc and PtTAPc are 6.71×10^{-11}, 8.44×10^{-10} and 1.45×10^{-7} S cm^{-1}, respectively. The substitution of electron withdrawing $-NO_2$ groups increased the electrical conductivity by more than 10 times, whereas the amino substitution increased the electrical conductivity by more than 10^4 times, compared to the parent PtPc. The variations in electrical conductivities for these complexes are due to the nature of the substituent groups on the peripheral benzene ring of the phthalocyanine, the overlap of the π-electron system between the molecules and the differences in the stacking arrangement of phthalocyanine molecules. The improvement in the intrinsic electrical conductivity of substituted phthalocyanines may be due to the favorable stacking arrangement of the molecules with improved overlap of the π-electron systems. Decreasing the electron density on the phthalocyanine ring facilitates greater intermolecular contact because of decreased repulsion between the phthalocyanine rings. The highest increase in electrical conductivity for the electron donor amine substituted complexes is due to the smaller size of the amino group in comparison to the nitro group which is expected to stack the molecule with the smallest intermolecular distance resulting in greater intermolecular contact and increased interactions of 3d-orbitals with the π-orbitals of the neighboring phthalocyanine units. This greater intermolecular interaction provides a better pathway for the charge carriers, resulting in the improved electrical conductivity. The order of electrical conductivities observed for these complexes is PtTAPc > PtTNPc > PtPc. The small change in the slope and activation energy at different temperature ranges may be due to some phase transformations and variations in the intermolecular interactions.

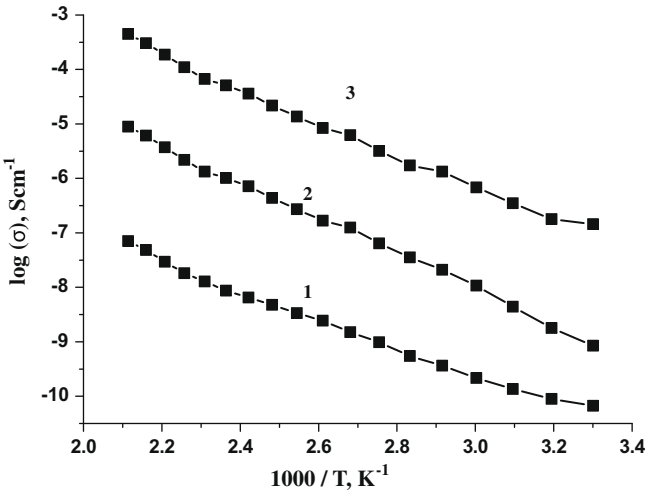


Fig. 6. Variations of electrical conductivities of (1) PtPc, (2) PtTNPc and (3) PtTAPc with temperature.

The electrical conductivity data of PtPc obtained here is similar to the data reported in literature for PtPc and CuPc [20] and the conductivity data obtained here for the substituted platinum phthalocyanines is similar to that of copper and other substituted phthalocyanines [8]. This leads to the conclusion that the angle with the (b) plane – which governs how the atoms in one molecule line up with those in another, behind or in front of it – has no important influence on the mobility of the charge carriers [20].

4. Conclusion

The PtPc, PtTNPc and PtTAPc complexes have been synthesized in the pure state with high yields for the first time by a novel route. The first two complexes were synthesized in dry conditions without using any solvent, urea or catalyst. The purification procedure used was very simple and not time consuming. These complexes have been characterized using elemental analysis, UV–Vis, FT-IR spectroscopy, powder X-ray diffraction and thermogravimetric analytical studies. Kinetic and thermodyanamic parameters associated with the thermal decomposition were calculated using the thermogravimetric data. PtTAPc showed an improvement in the intrinsic electrical conductivity by 4 orders of magnitude and PtTNPc by 1 order of magnitude greater than that of the parent complex.

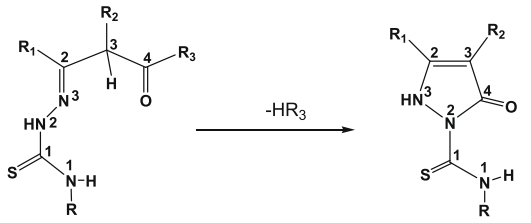
Acknowledgement

One of the authors, K.S. Lokesh, thanks CSIR, New Delhi, for awarding a CSIR – Senior Research Fellowship.

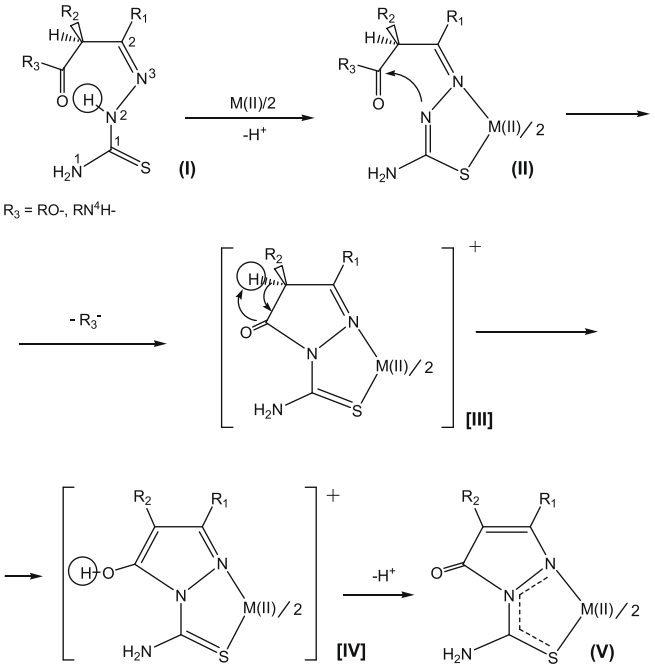
References

[1] F.H. Moser, A.L. Thomas, The Phthalocyanines, vols. I–II, CRC Press Inc., Boca Raton, Florida, 1983.
[2] H. Chen, W. Wang, L. Feng, J. Polym. Sci. Part A: Polym. Chem. (1995) 1165.
[3] D. Wohrle, D. Meissner, Adv. Mater. 3 (1991) 129.
[4] N.B. Mckeown, J. Mater. Chem. 10 (2000) 1979;
W. Freyer, M. Hill, H. Stiel, D. Leupold, J. Inform. Rec. 24 (1998) 95.
[5] D.D. Eley, Nature 162 (1948) 819.
[6] A.T. Vartanyan, Zh. Fiz. Khim. 22 (1948) 769.
[7] B.N. Achar, P.K. Jayasree, Can. J. Chem. 77 (10) (1999) 1690.
[8] B.N. Achar, K.S. Lokesh, J. Organomet. Chem. 689 (2004) 2601, 3357.
[9] M. Hanack, L.R. Subramanian, in: H.S. Nalwa (Ed.), Handbook of Organic Conductive Molecules and Polymers, vol. 1, Wiley, New York, 1997, p. 687 (Chapter 13).
[10] K.S. Lokesh, N. Uma, B.N. Achar, J. Non-Cryst. Solids 353 (2007) 384.
[11] B.N. Achar, T.M. Mohan Kumar, K.S. Lokesh, J. Coord. Chem. 60 (2007) 1833.
[12] J.M. Robertson, J. Chem. Soc. (1935) 615;
J.M. Robertson, J. Chem. Soc. (1936) 1195.
[13] P.A. Barrett, C.E. Dent, R.P. Linstead, J. Chem. Soc. (1936) 1719.
[14] R.J.C. Brown, A.R. Kucernak, N.J. Long, C. Mongay-Batalla, New J. Chem. 28 (2004) 676.
[15] A. Shaabani, F. Bahadoran, N. Safari, Ind. J. Chem. 40A (2001) 195.
[16] A. Shaabani, R. Maleki-Moghaddam, A. Maleki, A.H. Rezayan, Dyes and Pigments 74 (2007) 279.
[17] N. Safari, P.R. Jamaat, M. Pirouzmand, A. Shabani, J. Porphyr. Phthalocyan. 8 (2004) 1209.
[18] D. Villemin, M. Hammadi, M. Hachemi, N. Bar, Molecules 6 (2001) 831.
[19] H. Yamakado, K. Yakushi, N. Kosugi, H. Kuroda, A. Kawamoto, J. Tanaka, T. Sugano, M. Kinoshita, S. Hino, Bull. Chem. Soc. Jpn. 62 (1989) 2267.
[20] Wolfgang Felmayer, Irving Wolf, J. Electrochem. Soc. 105 (1958) 141.
[21] B.N. Figgis, R.S. Nyholm, J. Chem. Soc. (1958) 4190.
[22] B.N. Achar, T.M. Mohan Kumar, K.S. Lokesh, J. Porphyr. Phthalocyan. 9 (2005) 872.
[23] A.M. Schaffer, M. Gouterman, E.R. Davidson, Theor. Chim. Acta 30 (1973) 9.
[24] A.B.P. Lever, Adv. Inorg. Chem. Radichem. 7 (1965) 27.
[25] D.W. Boyd, T.D. Smith, J. Chem. Soc., Dalton Trans. (1972) 839.
[26] F.L. Plows, A.C. Jones, J. Mol. Spectrosc. 194 (1999) 163.

[27] L.M. Mink, M.L. Neitzel, L.M. Bellomy, R.E. Falvo, R.K. Boggess, B.T. Trainum, P. Yeaman, Polyhedron 16 (1997) 2809.
[28] I. Edwards, M. Gouterman, J. Mol. Spectrosc. 33 (1970) 292.
[29] A.N. Sidorov, M.P. Kotliar, Opt. Spektrosk. 11 (1961) 175.
[30] R. Aroca, Z.Q. Zeng, J. Mink, J. Phys. Chem. Solids 51 (1990) 135.
[31] J.H. Weber, D.H. Busch, Inorg. Chem. 4 (1965) 469.
[32] D. Louer, M. Louer, J. Appl. Crystallogr. 5 (1972) 271.
[33] A. Boultif, D. Louer, J. Appl. Crystallogr. 24 (1991) 987.
[34] K. Konoshita, K. Routsis, J.A.S. Bett, Thermochim. Acta 10 (1974) 109.
[35] A. Broido, J. Polym. Sci. A 2 (7) (1969) 1761.
[36] K.J. Laidler, Chemical Kinetics, 2nd Ed., Tata McGraw Hill, 1972.
[37] F. Daniels, R.A. Alberty, Physical Chemistry, John Wiley and sons, New York, 1995.



Scheme 1.



Scheme 2.

interference of other factors, we maintained the same experimental conditions used in the Pb(II) reactions: namely, the same solvent, identical counter-ion (AcO^-) and similar temperature. As described below, if there is a direct relationship between cyclization capacity and acid behaviour in terms of the HSAB principle, then Ph_2Pb(IV) seems to be "harder" than Pb(II).

2. Experimental

2.1. Physical measurements

Elemental analyses were performed on a Fisons instruments EA1108CHNS-O microanalyser. Melting points (m.p.), uncorrected, were determined with a Büchi apparatus. The electrospray mass spectra of the complexes were measured on a Hewlett–Packard model LC-MSD 1100 instrument (positive ion mode, 98:2 MeOH/HCOOH as mobile phase, 20–100 V). IR spectra were recorded from KBr discs on a Bruker IFS66V FT-IR spectrometer and are reported in cm^{-1}. The ^1H, ^{13}C and ^{207}Pb NMR spectra of DMSO-d_6 solutions were recorded on Bruker DPX 250, AMX 300 or AMX 500 instruments; chemical shifts are expressed on the δ scale (downfield shifts positive) relative to tetramethylsilane using the solvent signal for ^1H and ^{13}C NMR spectra and using a saturated solution of Ph_4Pb in $CDCl_3$ (−178 ppm) as the external reference for ^{207}Pb spectra. All spectroscopic measurements were carried out at the RIAIDT services of the University of Santiago de Compostela.

2.2. Materials

Thiosemicarbazide (Merck), N^1-ethylthiosemicarbazide (Merck), methyl acetoacetate (Aldrich), ethyl benzoylacetate (Aldrich), methyl 4-methoxyacetoacetate (Aldrich), methyl propionoylacetate (Aldrich), ethyl 2-methylacetoacetate (Aldrich), ethyl 2-ethylacetoacetate (Aldrich), acetoacetanilide (Merck), *o*-acetoacetanisidide (Aldrich), *p*-acetoacetanisidide (Aldrich), *o*-acetoacetotoluidide (Aldrich), silver acetate (Probus), and diphenyl- lead(IV) chloride (ABCR) were used as received. Diphenyllead(IV) acetate was prepared *in situ* by stirring diphenyllead(IV) chloride and silver acetate in methanol for 5 h. The resulting AgCl precipitate was filtered off and the solution containing the organolead(IV) acetate was used immediately in the preparation of the complexes.

2.3. Synthesis of ligands

The thiosemicarbazone ligands derived from β-dicarbonyl compounds (β-keto esters and β-keto amides) were prepared according to the method described by Jayasree and Aravindakshan [6]. Physical and analytical properties of $HTSC^n$ (n = 1–10) and HL^n (n = 1–7) have been reported elsewhere [3,7]. Recrystallization of $HTSC^{10}$ from EtOH gave crystals suitable for X-ray analysis.

The synthesis and physical and spectroscopic properties of $HTSC^{11}$ are described below.

$HTSC^{11}$. A mixture of *0*-acetoacetotoluidide (1.90 g, 10 mmol) and thiosemicarbazide (0.90 g, 10 mmol) in ethanol (125 ml) was heated under reflux for 1 h. The resulting white solid was filtered off and dried under vacuum. M.p.: 158 °C. *Anal.* Calc. for $C_{12}H_{16}N_4OS$: C, 54.5; H, 6.1; N, 21.2; S, 12.1. Found: C, 54.6; H, 6.0; N, 20.8; S, 11.9%. IR (cm^{-1}): 3443 s, 3280 s, 3163 m, ν(N–H); 1651 s, ν(C=O); 1600 s, ν(C=N); 1497 s, 1247 w, ν(NH–Ph); 1023 m, 850 w, ν(C=S). ^1H NMR: 10.43 s, 10.15 s, 9.67 s, 9.44 s [(2), $N_{(2/4)}H$]; 8.14 s, 7.67 s, 7.63 s [(2), $N_{(1)}H_2$]; 7.36–7.08 m [(4), $H_{8\text{-}11}$]; 3.56 s, 3.40 s [(2), $C_{(3)}H_2$]; 2.20 s, 2.17 s [(3), $C_{(12)}H_3$]; 2.03 s, 1.99 s [(3), $C_{(5)}H_3$]. ^{13}C NMR: 178.8 [$C_{(1)}$]; 167.1 [$C_{(4)}$]; 149.0 [$C_{(2)}$]; 136.0–125.1 [$C_{(6-11)}$]; 46.0 [$C_{(3)}$]; 17.8 [$C_{(12)}$]; 16.7 [$C_{(5)}$].

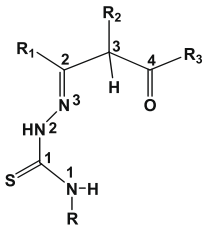
2.4. Synthesis of complexes

General procedure [*Caution! Organolead(IV) compounds are very toxic*] [8]. A solution of freshly prepared $PbPh_2(OAc)_2$ in methanol was mixed in 1:2 or 1:1 molar ratio with a solution or suspension of the thiosemicarbazone ligand in the same solvent. The resulting mixtures were stirred for 6 h at room temperature or under reflux. The experimental conditions and the complexes obtained are summarized in Table 1. Only the reaction between $PbPh_2(OAc)_2$ and $HTSC^4$ gave unidentified products under all conditions. Details for each reaction are described in Supplementary data.

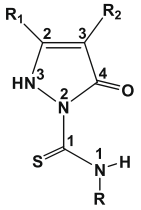
The analytical, physical and spectroscopic data for the complexes obtained are listed below.

$[PbPh_2Cl(L^2)]$. Colour: yellow. M.p.: 191 °C (d). *Anal.* Calc. for $C_{22}H_{18}N_3OSClPb$: C, 42.96; H, 2.95; N, 6.83; S, 5.21. Found: C, 42.79; H, 3.10; N, 6.82; S, 5.09%. IR (cm^{-1}): 3283 s, 3111 w, 3058 s, ν(N–H); 1612 s, ν(C=O); 1578 s, ν(ring); 1402 s, ν(C–N); 922 m, 764 m, ν(C=S). ^1H NMR: 11.80 bs, 9.93 bs [(2) $N_{(1)}H_2$]; 8.03 d (4) [H_oPh_2Pb]; 7.63 t (4) [H_mPh_2Pb]; 7.47 t (2) [H_pPh_2Pb]; 7.38 m (2) [$C_{(6,10)}H$]; 7.28 m (3) [$C_{(7-9)}H$]; 5.87 s, 5.45 br s [(1) $C_{(3)}H$].

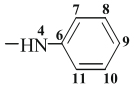
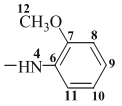
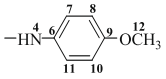
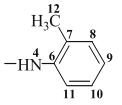
$[PbPh_2(L^2)_2]$. Colour: yellow. M.p.: 163 °C (d). *Anal.* Calc. for $C_{30}H_{28}N_6O_2S_2Pb$: C, 46.44; H, 3.64; N, 10.83; S, 8.26. Found: C, 47.45; H, 3.31; N, 10.74; S, 8.78%. MS (electrospray), m/z (%): 161 (100) [(H_2B)+H−{$NH_2C(S)$}]. IR (cm^{-1}): 3295 s, 3160 w, 3118 s,



I (HTSC^n)



II(HL^n)

I/II	R	R_1	R_2	R_3
HTSC^1/HL^1	-H	$-\overset{5}{C}H_3$	-H	$-O\overset{6}{C}H_3$
HTSC^2/HL^2	-H		-H	$-O\overset{11}{C}H_2\overset{12}{C}H_3$
HTSC^3/HL^3	-H	$-\overset{5}{C}H_2O\overset{6}{C}H_3$	-H	$-O\overset{7}{C}H_3$
HTSC^4/HL^4	-H	$-CH_2CH_3$	-H	$-OCH_3$
HTSC^5/HL^5	-H	$-\overset{5}{C}H_3$	$-\overset{6}{C}H_3$	$-O\overset{7}{C}H_2\overset{8}{C}H_3$
HTSC^6/HL^6	-H	$-\overset{5}{C}H_3$	$-\overset{6}{C}H_2\overset{7}{C}H_3$	$-O\overset{8}{C}H_2\overset{9}{C}H_3$
HTSC^7/HL^7	$-\overset{5}{C}H_2\overset{6}{C}H_3$	$-\overset{7}{C}H_3$	-H	$-O\overset{8}{C}H_3$
HTSC^8/HL^1	-H	$-\overset{5}{C}H_3$	-H	
HTSC^9/HL^1	-H	$-\overset{5}{C}H_3$	-H	
HTSC^{10}/HL^1	-H	$-\overset{5}{C}H_3$	-H	
HTSC^{11}/HL^1	-H	$-\overset{5}{C}H_3$	-H	

Scheme 3. Ligands used in this work or obtained by cyclization (see Scheme 1).

3064 w, *ν*(N–H); 1652 s, *ν*(C=O); 1369 s, *ν*(C–N); 1590 sh, *ν*(ring); 918 w, 765 m, *ν*(C=S). ^{1}H NMR: 12.19 br s, 9.96 br s [(4) $N_{(1)}H_2$]; 7.96 d [H_oPh_2Pb], $^3J(^1H–^{207}Pb)$ = 206.5 Hz; 7.85 s (4) [$C_{(6,10)}H$]; 7.67 t [H_mPh_2Pb]; 7.63 [H_oPh_2Pb]; 7.50 t [H_pPh_2Pb]; 7.45 s (6) [$C_{(7-9)}H$]; 7.37 t [H_mPh_2Pb]; 7.27 t [H_pPh_2Pb]; 6.06 bs, 5.87 s [(2) $C_{(3)}H$]. ^{13}C NMR: 175.8 [$C_{(1)}$]; 165.9 [$C_{(4)}$]; 160.9 [$C_{ipso}(Ph_2Pb)$]; 143.3 [$C_{(2)}$]; 135.8 [$C_o(Ph_2Pb)$], $^2J(^{13}C–^{207}Pb)$ = 90.0 Hz; 132.9 [$C_o(Ph_2Pb)$], $^2J(^{13}C–^{207}Pb)$ = 132.9 Hz; 130.3 [$C_m(Ph_2Pb)$]; 130.2 [$C_p(Ph_2Pb)$]; 130.0–124.5 [$C_{(5-10)}$]; 86.7 [$C_{(3)}$].

[PbPh$_2$(OAc)(L^2)]. Colour: yellow. M.p.: 135 °C (d). *Anal.* Calc. for $C_{24}H_{21}N_3O_3SPb$: C, 45.13; H, 3.31; N, 6.58; S, 5.02. Found: C, 44.62; H, 3.45; N, 6.18; S, 4.82%. MS (electrospray), *m*/*z* (%): 580 (25) [M–(OAc)]; 485 (47) [M–(2Ph)] ≡ [Pb(OAc)(L^2)]; 288 (63) [Pb(L^2)]–{(Ph)+(C(S)NH$_2$)}; 242 (22) HL^2+Na; 185 (23) (HL^2)+H+Na–{C(S)NH$_2$}; 161 (100) (HL^2)+H–{NH$_2$C(S)}. IR (cm^{-1}): 3138 w, 3053 m, *ν*(N–H); 1609 s, *ν*(C=O); 1567 s, 1398 s, *ν*(CH$_3$COO), (Δ*ν*: 169); 1385 s, *ν*(C–N); 1575 h, *ν*(ring); 921 m, 754 m, *ν*(C=S). ^{1}H NMR: 12.00–9.00 (2) [$N_{(1)}H_2$]; 8.30–7.00 m (15) [R_1(Ph)+H(Ph_2Pb)]; 5.87 s, 5,19 s [(1), $C_{(3)}H$]; 1.80 s (3) [CH$_3$COO]. ^{13}C NMR: 175.5 [$C_{(1)}$]; 166.5 [$C_{(4)}$]; 161.0 [$C_{ipso}(Ph_2Pb)$]; 143.3 [$C_{(2)}$]; 136.1 [$C_o(Ph_2Pb)$], $^2J(^{13}C–^{207}Pb)$ = 87.2 Hz; 132.9 [$C_o(Ph_2Pb)$], $^2J(^{13}C–^{207}Pb)$ = 128.0 Hz; 130.2 [$C_m(Ph_2Pb)$]; 130.0 [$C_p(Ph_2Pb)$]; 130.0–124.7 [$C_{(5-10)}$]; 86.8, 83.7 [$C_{(3)}$]; 23.2 [*C*H$_3$COO].

[PbPh$_2$Cl(TSC^3)]. Colour: white. M.p.: 135 °C. *Anal.* Calc. for $C_{19}H_{22}N_3O_3SClPb$: C, 37.10; H, 3.60; N, 6.83; S, 5.21. Found: C, 37.41; H, 3.60; N, 7.03; S, 5.27%. IR (cm^{-1}): 3478 s, 3358 s, 3170 w, 3053 w, *ν*(N–H); 1725 s, *ν*(C=O); 1597 s, *ν*(C=N); 1432 s, 1453 w, *δ*(OCH$_2$); 1247 w, *ν*(C–O); 1014 m, 744 s, *ν*(C=S). ^{1}H NMR: 7.92 d (4) [$H_o(Ph_2Pb)$], $^3J(^1H–^{207}Pb)$ = 110 Hz; 7.55 t (4) [$H_m(Ph_2Pb)$]; 6.93 s (2) [$N_{(1)}H_2$]; 3.97 s (2) [$C_{(5)}H_2$]; 3.61 s, 3.51 s [(2) $C_{(3)}H_2$]; 3.60 s (3) [$C_{(7)}H_3$]; 2.91 s (3) [$C_{(6)}H_3$]. ^{13}C NMR: 168.4 [$C_{(4)}$]; 159.8 [$C_{(2)}$]; 136.7 [$C_o(Ph_2Pb)$], $^2J(^{13}C–^{207}Pb)$ = 88 Hz; 129.9 [$C_m(Ph_2Pb)$]; 129.2 [$C_p(Ph_2Pb)$]; 74.7 [$C_{(5)}$]; 58.8 [$C_{(6)}$]; 52,1 [$C_{(7)}$]; 32.8 [$C_{(3)}$].

[Pb(L^3)$_2$]. See Ref. [2].

[PbPh$_2$(L^3)$_2$]. Colour: beige. M.p.: 121 °C. *Anal.* Calc. or $C_{24}H_{26}N_6O_4S_2Pb$: C, 39.28; H, 3.57; N, 11.45; S, 8.72. Found: C, 37.55; H, 3.73; N, 11.56; S, 9.05%. MS (electrospray), *m*/*z* (%): 548

Table 1
Reactions of $PbPh_2(OAc)_2$ with $HTSC^n$ in MeOH: conditions used and compounds obtained.

Ligand	M:L (mol ratio)	*T*	Compounds
$HTSC^1$	1:2	r.t.	HL[1a]
	1:1	r.t.	HL[1a]
$HTSC^2$	1:2	r.t.	unidentified product
		under reflux	$[PbPh_2(L^2)_2]$
	1:1	r.t.	$[PbPh_2Cl(L^2)]$
		under reflux	$[PbPh_2(OAc)(L^2)]$
$HTSC^3$	1:2	r.t.	$[PbPh_2Cl(TSC^3)]$
		under reflux	first fraction, $[Pb(L^3)_2]$
			second fraction, $[PbPh_2(L^3)_2]$
	1:1	r.t.	$[PbPh_2Cl(TSC^3)]$[b]
$HTSC^4$	1:1 and 1:2	r.t.	unidentified products
		under reflux	
$HTSC^5$	1:2	r.t.	first fraction, $[Pb(L^5)_2]$
			second fraction, $[PbPh_2(L^5)_2]\cdot H_2O$
		under reflux	$[Pb(OAc)(L^5)]$
	1:1	r.t.	unidentified product
		under reflux	first fraction, $[Pb(OAc)(L^5)]$
			second fraction, $[PbPh_2(OAc)(L^5)]\cdot MeOH$
$HTSC^6$	1:2	r.t.	$[PbPh_2(L^6)_2]$[c]
	1:1	r.t.	$[PbPh_2(OAc)(L^6)]$
$HTSC^7$	1:2 or 1:1	r.t.	$[PbPh_2(OAc)(L^7)]$[c]
$HTSC^8$	1:2 or 1:1	r.t.	$[PbPh_2(OAc)(TSC^8)]\cdot 2MeOH$[c]
$HTSC^9$	1:2	r.t.	$[PbPh_2(TSC^9)_2]$
	1:1	r.t.	first fraction, $[PbPh_2(TSC^9)_2]$[d]
			second fraction, $[PbPh_2(OAc)(TSC^9)]$[e]
$HTSC^{10}$	1:2 or 1:1	r.t.	$[PbPh_2(OAc)(TSC^{10})]\cdot H_2O$[c]
$HTSC^{11}$	1:2 or 1:1	r.t.	$[PbPh_2(OAc)(TSC^{11})]\cdot 0.75MeOH$[c]

[a] The same compound was obtained when the reaction mixture was heated under reflux for 6 h.
[b] The reaction of this ligand under reflux afforded unidentified products when a 1:1 molar ratio was used.
[c] The same compound was obtained when 1:2 or 1:1 molar ratios were heated under reflux for 6 h.
[d] The same compound was obtained when 1:2 or 1:1 (second fraction) molar ratios were heated under reflux for 6 h.
[e] The same compound was obtained when a 1:1 (first fraction) molar ratio was heated under reflux for 6 h.

(98) [M–(L^3)]. IR (cm^{-1}): 3277 s, 3094 w, 3055 w, *ν*(N–H); 1663 m, *ν*(C=O); 1369 s, *ν*(C–N); 1580 s, 1517 m, *ν*(ring); 903 m, 760 w, *ν*(C=S). ^{1}H NMR: 11.59 s, 9.64 s [(4) $N_{(1)}H_2$]; 7.98 d (4) [H_oPh_2Pb], $^3J(^1H–^{207}Pb)$ = 208 Hz; 7.57 t (4) [H_mPh_2Pb]; 7.42 t (2) [H_pPh_2Pb]; 4.60 s (2) [$C_{(3)}H$]; 4.37 s (4) [$C_{(5)}H_2$]; 3.30 s (6) [$C_{(6)}H_3$]. ^{13}C NMR: 175.7 [$C_{(1)}$]; 167.3 [$C_{(4)}$]; 157.6 [$C_{(2)}$]; 132.7 [$C_o(Ph_2Pb)$]; 130.2 [$C_m(Ph_2Pb)$]; 129.6 [$C_p(Ph_2Pb)$]; 81.9 [$C_{(3)}$]; 68.2 [$C_{(5)}$]; 58.5 [$C_{(6)}$]. ^{207}Pb NMR: −738.1.

[Pb(L^5)$_2$]. Colour: yellow. M.p.: 154 °C (d). *Anal*. Calc. for $C_{12}H_{16}N_6O_2S_2Pb$: C, 26.32; H, 2.94; N, 15.35; S, 11.71. Found: C, 26.14; H, 2.64; N, 15.24; S, 11.50%. ^{1}H NMR: 11.82 s, 9.65 s [(4) $N_{(1)}H_2$]; 2.08 s (6) [$C_{(5)}H_3$]; 1.61 s (6) [$C_{(6)}H_3$]. ^{13}C NMR: 175.2 [$C_{(1)}$]; 166.0 [$C_{(4)}$]; 90.7 [$C_{(3)}$]; 13.3 [$C_{(5)}$]; 6.4 [$C_{(6)}$].

[PbPh$_2$(L^5)$_2$] · H$_2$O. Colour: yellow. M.p.: 175 °C. *Anal*. Calc. or $C_{24}H_{28}N_6O_3S_2Pb$: C, 40.05; H, 3.92; N, 11.67; S, 8.91. Found: C, 40.63; H, 3.80; N, 10.9; S, 8.49%. IR (cm^{-1}): 3411 m, 3071 w, *ν*(N–H); 1645 s, *ν*(C=O); 1367 s, *ν*(C–N); 1576 m, 1518 m, *ν*(ring); 992 m, 762 w, *ν*(C=S). ^{1}H NMR: 11.75 s, 9.76 s [(4) $N_{(1)}H_2$]; 7.81 (4) [H_oPh_2Pb], $^3J(^1H–^{207}Pb)$ = 210 Hz; 7.56 (4) [H_mPh_2Pb]; 7.43 (2) [H_pPh_2Pb]; 2.07 s, 2.00 s [(6) $C_{(5)}H_3$]; 1.63 s (6) [$C_{(6)}H_3$].

[Pb(OAc)(L^5)]. See Ref. [2].

[PbPh$_2$(OAc)(L^5)]. Colour: yellow. M.p.: 138 °C (d). *Anal*. Calc. for $C_{20}H_{21}N_3O_3SPb$: C, 40.67; H, 3.58; N, 7.11; S, 5.43. Found: C, 40.36; H, 3.95; N, 6.52; S, 5.38%. MS (electrospray), *m*/*z* (%): 532 (18) [M+H–(C(S)NH_2)]; 485 (93) [M+H–{Ph+2CH_3}]; 407 (100) [M–{2Ph+2CH_3}] ≡ [Pb(OAc)(L^5–2CH_3)]. IR (cm^{-1}): 3295 m, 3053 m, *ν*(N–H); 1631 s, *ν*(C=O); 1559 m, 1401 m, *ν*(CH_3COO), (Δ*ν*: 158); 1368 m, *ν*(C–N); 1586 h, 1518 m, *ν*(ring); 909 w, 750 h, *ν*(C=S). ^{1}H NMR: 11.72 bs, 9.74 br s [(2) $N_{(1)}H_2$]; 7.84 d (4) [H_oPh_2Pb], $^3J(^1H–^{207}Pb)$ = 204 Hz; 7.55 t (4) [H_mPh_2Pb]; 7.41 m (2) [H_pPh_2Pb]; 2.03 s (3) [$C_{(5)}H_3$]; 1.82 s (3) [CH_3COO]; 1.62 s (3) [$C_{(6)}H_3$]. ^{13}C NMR: 175.2, 174.3, [$C_{(1)}$]; 167.7 [$C_{ipso}(Ph_2Pb)$]; 166.5, 165.6 [$C_{(4)}$]; 159.7, 158.2 [$C_{(2)}$]; 136.1–128.3 [C_o–$C_p(Ph_2Pb)$]; 95.5, 91.8 [$C_{(3)}$]; 23.1, 21,0 [CH_3COO]; 13.1, 9.8 [$C_{(5)}$]; 6.5, 6.3 [$C_{(6)}$]. ^{207}Pb NMR: −575.3, −871.9.

[PbPh$_2$(L^6)$_2$]. Colour: yellow. M.p.: 184 °C (d). *Anal*. Calc. for $C_{26}H_{30}N_6O_2S_2Pb$: C, 42.79; H, 4.14; N, 11.51; S, 8.78. Found: C, 42.41; H, 4.17; N, 11.28; S, 8.72%. MS (electrospray), *m*/*z* (%): 485 (100) [M–{L^6+C(S)NH_2}]; 407 (87) [PbMe(L^6)]. IR (cm^{-1}): 3414 w, *ν*(N–H); 1616 s, *ν*(C=O); 1369 s, *ν*(C–N); 1586 h, 1518 m, *ν*(ring); 967 m, 748 m, *ν*(C=S). ^{1}H NMR: 11.83 br s, 9.63 s [(4), $N_{(1)}H_2$]; 7.87 d (4) [H_oPh_2Pb]; 7.55 t (4) [H_mPh_2Pb]; 7.43 m (2) [H_pPh_2Pb]; 2.11 m (4) [$C_{(6)}H_2$]; 2.08 s (6) [$C_{(5)}H_3$]; 0.94 t (6) [$C_{(7)}H_3$]. ^{13}C NMR: 155.2 [$C_{(2)}$]; 136.9–128.1 [C_o–$C_p(Ph_2Pb)$]; 104.6 [$C_{(3)}$]; 15.0 [$C_{(6)}$]; 14.7 [$C_{(7)}$]; 13.4 [$C_{(5)}$]. ^{207}Pb NMR: −706.4.

[PbPh$_2$(OAc)(L^6)]. Colour: yellow. M.p.: 132 °C. *Anal*. Calc. for $C_{21}H_{23}N_3O_3SPb$: C, 41.71; H, 3.83; N, 6.93; S, 5.30. Found: C, 41.03; H, 3.62; N, 6.34; S, 5.13%. IR (cm^{-1}): 3138 m, 3055 m, *ν*(N–H); 1611 s, *ν*(C=O); 1564 s, 1405 m, *ν*(CH_3COO), (Δ*ν*: 159); 1370 h, *ν*(C–N); 1585 h, 1521 s, *ν*(ring); 938 w, 773 w, *ν*(C=S). ^{1}H NMR: 11.64 s, 9.71 s [(2), $N_{(1)}H_2$]; 7.81 d (4) [H_oPh_2Pb]; 7.60 m (4) [H_mPh_2Pb]; 7.46 m (2) [H_pPh_2Pb]; 2.11 m (2) [$C_{(6)}H_2$]; 2.02 s (3) [$C_{(5)}H_3$]; 1.81 s (3) [CH_3COO]; 0.95 t, 0.97 t [(3) $C_{(7)}H_3$]. ^{207}Pb NMR: −869.5.

[PbPh$_2$(OAc)(L^7)]. Colour: yellow. M.p.: 146 °C. *Anal*. Calc. for $C_{21}H_{23}N_3O_3SPb$: C, 41.71; H, 3.83; N, 6.93; S, 5.30. Found: C, 41.66; H, 3.74; N, 6.95; S, 5.38%. MS (electrospray), *m*/*z* (%): 578 (35) [M+H–(CH_2CH_3)]; 546 (100) [M–(OAc)]; 407 (18) [M–{2Ph+(NHCH_2CH_3)}] ≡ [Pb(OAc)(L^7–NHCH_2CH_3)]. IR (cm^{-1}): 3437 m, 3052 w, *ν*(N–H); 1609 s, *ν*(C=O); 1568 s, 1415 m, *ν*(CH_3COO), (Δ*ν*: 153); 1345m, *ν*(C–N); 1580 h, *ν*(ring); 947 m, 776 s, *ν*(C=S). ^{1}H NMR: 12.71 br s (2) [$N_{(1)}H_2$]; 7.81 d (4) [H_oPh_2Pb], $^3J(^1H–^{207}Pb)$ = 208 Hz; 7.56 m (4) [H_mPh_2Pb]; 7.41 m (2) [H_pPh_2Pb]; 4.70 s (1) [$C_{(3)}H$]; 3.50 br s (2) [$C_{(5)}H_2$]; 2.06 s (3) [$C_{(7)}H_3$]; 1.84 s (3) [CH_3COO]; 1.11 (3) [$C_{(6)}H_3$]. ^{13}C NMR: 179.6 [CH_3COO]; 174.4 [$C_{(1)}$]; 167.5 [$C_{(4)}$]; 167.1 [$C_{ipso}(Ph_2Pb)$]; 158.7

[$C_{(2)}$]; 132.2 [$C_o(Ph_2Pb)$]; 130.1 [$C_m(Ph_2Pb)$]; 129.7 [$C_p(Ph_2Pb)$]; 86.7 [$C_{(3)}$]; 23.4 [CH_3COO]; overlapped with the signal of DMSO-d_6 [$C_{(5)}$]; 14.6 [$C_{(6)}$]; 13.7 [$C_{(7)}$].

[$PbPh_2(OAc)(TSC^8)$] · 2MeOH. Colour: yellow. M.p.: 126 °C. *Anal.* Calc. for $C_{27}H_{34}N_4O_5SPb$: C, 44.19; H, 4.67; N, 7.63; S, 4.37. Found: C, 44.03; H, 4.62; N, 7.63; S, 4.00%. MS (electrospray), *m/z* (%): 611 (100) [M−(OAc)]; 407 (30) [$PbPh_2(HCOO)$]. IR (cm^{-1}): 3424 m, 3358 m, 3277 m, 3172 w, 3132 w, 3057 m, *ν*(N–H); 1651 s, *ν*(C=O); 1597 s, *ν*(C=N); 1566 sh, 1330 s, *ν*(CH_3COO), (Δ*ν*: 226); 1552 s, 1246 w, *ν*(NH–Ph); 1082 w, 872 w, *ν*(C=S). ^{1}H NMR: 10.25, 10.15, 10.04 [(1), $N_{(4)}H$]; 7.82 d (4) [H_oPh_2Pb], $^3J(^1H–^{207}Pb)$ = 111.4 Hz; 7.55 (2) [$C_{(7,11)}H$]; 7.52 t (4) [H_mPh_2Pb]; 7.35 m (2) [H_pPh_2Pb]; 7.29 (2) [$C_{(8,10)}H$]; 7.04 (1) [$C_{(9)}H$]; 7.00 s (2) [$N_{(1)}H_2$]; 4.09 m (2) [CH_3OH]; 3.16 d (6) [CH_3OH]; 1.98 s (3) [$C_{(5)}H_3$]; 1.74 s (3) [CH_3COO]. ^{13}C NMR: 167.3 [$C_{(4)}$]; 160.9 [$C_{ipso}(Ph_2Pb)$]; 155.3 [$C_{(2)}$]; 138.9–119.2 [C_{7-11}]; 136.3 [$C_o(Ph_2Pb)$], $^2J(^{13}C–^{207}Pb)$ = 88.5 Hz; 129.6 [$C_m(Ph_2Pb)$], $^3J(^{13}C–^{207}Pb)$ = 111.4 Hz; 128.8 [$C_p(Ph_2Pb)$]; 46.5 [$C_{(3)}$]; 23.7 [CH_3COO]; 18.5, 16.9 [$C_{(3)}$]. ^{207}Pb NMR: −294.5, −863.3.

[$PbPh_2(TSC^9)_2$]. Colour: white. M.p.: 181 °C (d). *Anal.* Calc. for $C_{36}H_{40}N_8O_4S_2Pb$: C, 47.00; H, 4.38; N, 12.18; S, 6.97. Found: C, 46.86; H, 4.40; N, 12.12; S, 7.08%. MS (electrospray), *m/z* (%): 943 (13) [M+Na]; 867 (4) [M+H+Na−(Ph)]; 641 (100) [M−(TSC^9)]. IR (cm^{-1}): 3439 w, 3408 w, 3338 m, 3301 m, 3189 m, 3051 m, *ν*(N–H); 1675 s, *ν*(C=O); 1602 s, *ν*(C=N); 1542 s, 1254 s, *ν*(NH–Ph); 1434m, *δ*(OCH_3); 1046 m, 897 w, *ν*(C=S). ^{1}H NMR: 10.08 br s, 9.80 br s, 9.52 br s, 9.28 s [(2) $N_{(4)}H$]; 8.00–7.00 m (10) [$H(Ph_2Pb)$]; 7.80–6.80 m (8) [$C_{(8-11)}H$]; 3.81 s (6) [$C_{(12)}H_3$]; 2.15 s, 1.98 s, 1.94 s [(6) $C_{(5)}H_3$]. ^{207}Pb NMR: −294.5.

[$PbPh_2(OAc)(TSC^9)$]. Colour: white. M.p.: 162 °C (d). *Anal.* Calc. for $C_{26}H_{28}N_4O_4SPb$: C, 44.63; H, 4.03; N, 8.01; S, 4.58. Found: C, 44.44; H, 4.26; N, 7.83; S, 4.41%. MS (electrospray) *m/z* (%): 641 (100) [M−(OAc)]; 518 (42) [M−{(OAc)+Ph+OCH_3+CH_3}]; 285 (55) [PbPh]. IR (cm^{-1}): 3437 w, 3404 m, 3380 m, 3300 m, 3189 m, *ν*(N–H); 1674 s, *ν*(C=O); 1602 s, *ν*(C=N); 1581 s, 1330, *ν*(CH_3COO), (Δ*ν*: 251); 1544 s, 1257 s, *ν*(NH–Ph); 1433 m, *δ*(OCH_3); 1024 m, 897 w, *ν*(C=S). ^{1}H NMR: 9.55 br s, 9.29 br s [(1) $N_{(4)}H$]; 7.88 m (1) [$C_{(11)}H$]; 7.80 d (4) [$H_o(Ph_2Pb)$], $^3J(^1H–^{207}Pb)$ = 112 Hz; 7.51 t (4) [$H_m(Ph_2Pb)$]; 7.35 t (2) [$H_p(Ph_2Pb)$]; 7.03 m (2) [$C_{(8,9)}H$]; 6.88 m (1) [$C_{(10)}H$]; 3.81 s (3) [$C_{(12)}H_3$]; 3.83 s, 3.73 s, 3.63 s, 3.38 s [(2) $C_{(3)}H_2$]; 2.00 s, 1.96 s [(3) $C_{(5)}H_3$]; 1.74 s (3) [CH_3COO]. ^{13}C NMR: 166.9 [$C_{(4)}$]; 160.6 [$C_{ipso}(Ph_2Pb)$]; 154.4 [$C_{(2)}$]; 149–110 [C_{7-11}]; 136.1 [$C_o(Ph_2Pb)$], $^2J(^{13}C–^{207}Pb)$ = 86.5 Hz; 129.3 [$C_m(Ph_2Pb)$], $^3J(^{13}C–^{207}Pb)$ = 111.2 Hz; 128.6 [$C_p(Ph_2Pb)$]; 55.6 [$C(_{12})H_3$]; 46.2 [$C_{(3)}$]; 16.9 [$C_{(5)}$]. ^{207}Pb NMR: −294.5.

[$PbPh_2(OAc)(TSC^{10})$] · H_2O. Colour: yellow. M.p.: 148 °C. *Anal.* Calc. for $C_{26}H_{30}N_4O_5SPb$: C, 43.51; H, 4.21; N, 7.81; S, 4.47. Found: C, 43.99; H, 4.44; N, 7.69; S, 4.45%. MS (electrospray). *m/z* (%): 641 (100) [M−(OAc)]; 485 (32) [$PbPh_3(HCOO)$+H]. IR (cm^{-1}): 3410 m, 3351 m, 3284 m, 3052 m, *ν*(N–H); 1646 s, *ν*(C=O); 1604 s, *ν*(C=N); 1580 s, 1331 m, *ν*(CH_3COO), (Δ*ν*: 249); 1552 s, 1237 s, *ν*(NH–Ph); 1434 m, *δ*(OCH_3); 1032 m, 836 m, *ν*(C=S). ^{1}H NMR: 10.20 s, 9.90 s [(1) $N_{(4)}H$]; 7.82 d (4) [$H_o(Ph_2Pb)$], $^3J(^1H–^{207}Pb)$ = 112.8 Hz; 7.52 t (4) [$H_m(Ph_2Pb)$], $^4J(^1H–^{207}Pb)$ = 58.4 Hz; 7.40 m (2) [$C_{(7,11)}H$]; 7.37 m (2) [$H_p(Ph_2Pb)$]; 6.86 d (2) [$C_{(8,10)}H$]; 3.70 s (3) [$C_{(12)}H_3$]; 1.98 s, 1.96 s [(3) $C_{(5)}H_3$]; 1.73 s (3) [CH_3COO]. ^{13}C NMR: 178.2 [$C_{(1)}$]; 166.7 [$C_{(4)}$]; 155.3–113.8 [$C_{(7-11)}$]; 136.2 [$C_o(Ph_2Pb)$]; 129.7 [$C_m(Ph_2Pb)$]; 129.0 [$C_p(Ph_2Pb)$]; 55.2 [$C_{(12)}$]; 46.3 [$C_{(3)}$]. ^{207}Pb NMR: −294.3.

[$PbPh_2(OAc)(TSC^{11})$] · 0.75MeOH. Colour: yellow. M.p.: 132 °C. *Anal.* Calc. for $C_{26.75}H_{31}N_4O_{3.75}SPb$: C, 45.39; H, 4.41; N, 7.92; S, 4.53. Found: C, 44.83; H, 4.65; N, 7.53; S, 4.17%. MS (electrospray). *m/z* (%): 625 (100) [M−(OAc)]. IR (cm^{-1}): 3432 m, 3368 w, 3267 m, 3157 m, 3053 m, *ν*(N–H); 1642 s, *ν*(C=O); 1602 h, *ν*(C=N); 1577 s, 1329 s, *ν*(CH_3COO), (Δ*ν*: 248); 1535 s, 1248 w, *ν*(NH–Ph); 1016 m, 850 w, *ν*(C=S). ^{1}H NMR: 10.15 br s, 9.64 br s, 9.42 s [(1) $N_{(4)}H$]; 7.82 d (4) [$H_o(Ph_2Pb)$], $^3J(^1H–^{207}Pb)$ = 113.2 Hz; 7.53 t (4) [$H_m(Ph_2Pb)$], $^4J(^1H–^{207}Pb)$ = 58.4 Hz; 7.37 m (2) [$H_p(Ph_2Pb)$]; 7.35–7.05 m (4) [$C_{(8-11)}H$]; 4.10 q (0.75) [CH_3OH]; 3.16 d (2.25) [CH_3OH]; 2.19 s, 2.17 s [(3) $C_{(12)}H_3$]; 2.03 s, 1.98 s [(3) $C_{(5)}H_3$]; 1.74 s (3) [CH_3COO]. ^{13}C NMR: 176.3 [$C_{(1)}$]; 167.2 [$C_{(4)}$]; 160.9 [$C_{ipso}(Ph_2Pb)$]; 157.7 [$C_{(2)}$]; 136.4–125.2 [$C_{(7-11)}$]; 136.3 [$C_o(Ph_2Pb)$], $^2J(^{13}C–^{207}Pb)$ = 87.2 Hz; 129.6 [$C_m(Ph_2Pb)$]; 128.9 [$C_p(Ph_2Pb)$]; 48.6 [$C_{(3)}$]; 17.8 [$C_{(12)}$]; 16.9 [$C_{(5)}$]. ^{207}Pb NMR: −191.9, −670.9, −862.8.

The following crystals, which were suitable for X-ray diffractometry, were obtained from the mother liquors of the specified reactions: [$PbPh_2Cl(L^2)$] ($PbPh_2(OAc)_2$/$HTSC^2$ reaction, 1:1 molar ratio, room temperature), [$PbPh_2(OAc)(L^5)$] · MeOH ($PbPh_2(OAc)_2$/TSC^5 reaction, 1:1 molar ratio, under reflux), [$PbPh_2(OAc)$-(TSC^8)] · 2MeOH ($PbPh_2(OAc)_2$/$HTSC^8$ reaction, 1:1 molar ratio, room temperature), [$PbPh_2(OAc)(TSC^{10})$] · H_2O ($PbPh_2(OAc)_2$/$HTSC^{10}$ reaction, 1:1 molar ratio, room temperature) and [$PbPh_2$-$(OAc)(TSC^{11})$] · 0.75MeOH ($PbPh_2(OAc)_2$/$HTSC^{11}$ reaction, 1:2 molar ratio, room temperature).

2.5. X-ray crystallography

Crystal data for $HTSC^{10}$, [$PbPh_2(OAc)(TSC^{10})$] · H_2O, [$PbPh_2$-$(OAc)(TSC^{11})$] · 0.75MeOH, [$PbPh_2Cl(L^2)$] and [$PbPh_2(OAc)(L^5)$] · MeOH were collected on a Nonius Kappa CCD (São Carlos Institute of Physics, University of São Paulo), and data for [$PbPh_2$-$(OAc)(TSC^8)$] · 2MeOH were obtained on a Bruker SMART CCD-1000 (RIAIDT, University of Santiago de Compostela). Structures were solved using direct methods for the ligand and the Patterson method for the complexes, followed by normal difference Fourier techniques and refined using SHELXS-97 [9]. Data were corrected for absorption by multi-scan [10] or SADABS [11]. All hydrogen atoms were introduced in calculated positions. Molecular graphics were obtained with ORTEP-3 [12], PLATON [13] and MERCURY [14]. Experimental details and crystal and refinement data are listed in Table 2.

3. Results and discussion

3.1. Syntheses and physical properties of the complexes

Diphenyllead(IV) reacts with TSCs derived from β-keto esters through cyclization processes similar to those induced by Pb(II). Differences in the complexes obtained (Table 1) can be related to the apparently slightly higher tendency of $PbPh_2^{2+}$ to form heteroleptic [$PbPh_2(OAc)(L)$] compounds instead of the homoleptic [$PbPh_2(L)_2$] type, suggesting a somewhat lower affinity of $PbPh_2^{2+}$ for the pyrazolonate anion than the Pb(II) cation. This lower affinity is particularly evident in the reaction with $HTSC^1$, which leads to free pyrazolone (HL^1) with the organometallic cation under all of the conditions tested, whereas with Pb(II) the [$Pb(L^1)_2$] complex is formed. However, the dephenylation reactions in which the organometallic cation take part, which transform $PbPh_2^{2+}$ into Pb(II), paradoxically contribute most to the differences between the products obtained when these TSCs are cyclized in the presence of $PbPh_2^{2+}$ and Pb(II) cations. Although these dephenylation processes can give rise to lead(II) pyrazolonates, very often these reactions are incomplete and lead to mixed compounds that are very difficult to separate and identify. Similar but fully evolved processes have previously been observed for the $PbPh_3^+$ and $PbMe_2^{2+}$ cations in the presence of ferrocenyl TSCs [15] and these results were related to the weakness of the Pb–C bonds [16]. It is worth noting that, in some cases, a minimal amount of the heteroleptic complexes containing Cl^- ligands were also isolated, probably because the $PbPh_2(OAc)_2$ used in the reaction was contaminated with some $PbPh_2Cl_2$ used in the synthesis of the former species (see Section 2).

Table 2
Crystallographic data for ligand and complexes.

	HTSC^{10}	[$PbPh_2(OAc)(TSC^8)$] · 2MeOH	[$PbPh_2(OAc)(TSC^{10})$] · H_2O	[$PbPh_2(OAc)(TSC^{11})$] · 0.75MeOH	[$PbPh_2(OAc)(L^5)$] · MeOH	[$PbPh_2Cl(L^2)$]
Empirical formula	$C_{12}H_{16}N_4O_2S$	$C_{27}H_{34}N_4O_5PbS$	$C_{26}H_{30}N_4O_5PbS$	$C_{26.75}H_{31}N_4O_{3.75}PbS$	$C_{21}H_{25}N_3O_4SPb$	$C_{22}H_{18}ClN_3OPbS$
Molecular weight	280.35	733.83	717.79	707.81	622.69	615.09
T (K)	140(2)	293(2)	140(2)	120(2)	120(2)	120(2)
λ (Å)	0.71073	0.71073	0.71073	0.71073	0.71073	0.71073
Crystal system	triclinic	orthorhombic	monoclinic	orthorhombic	triclínico	monoclínico
Space group	$P\bar{1}$	$Pna2_1$	$P2_1/n$	$Pna2_1$	$P\bar{1}$	$P2_1/n$
a (Å)	4.864(6)	19.539(4)	10.0550(2)	19.4506(4)	7.68970(10)	9.6303(8)
b (Å)	8.815(7)	9.7859(18)	18.7710(6)	10.0005(2)	11.7006(2)	14.3190(10)
c (Å)	16.657(15)	14.957(3)	15.0200(4)	14.9527(2)	12.7776(3)	97.727(4)
α (°)	102.12(5)	90	90	90	96.8530(10)	90
β (°)	90.76(7)	90	95.7340(10)	90	105.8530(10)	15.9170(10)
γ (°)	102.87(13)	90	90	90	90.4740(10)	90
V (Å^3)	679.40(12)	2859.9(9)	2820.73(13)	2908.54(9)	1097.02(3)	2175.0(3)
Z	2	4	4	4	2	4
D_{calc} (Mg/m^3)	1.370	1.704	1.690	1.616	1.885	1.878
μ (mm^{-1})	0.242	6.015	6.096	5.908	7.817	7.994
F(000)	296	1448	1408	1390	604	1176
Crystal size (mm)	0.60 × 0.40 × 0.12	0.27 × 0.13 × 0.11	0.06 × 0.04 × 0.02	0.18 × 0.17 × 0.12	0.30 × 0.11 × 0.05	0.11 × 0.08 × 0.07
θ range(°)	1.25–24.99	2.33–28.28	1.74–25.00	2.29–24.99	3.20–27.53	3.43–25.00
h; k; l range	−3, 5; −10, 10; −19, 19	0, 26; 0, 12; −9, 19	−11, 11; −22, 22; −17, 17	−23, 22; −11, 11; −17, 17	−9, 9; −15, 15; 0, 16	−11, 11; −15, 17; −18, 18
Max. and Min. transmission	0.9715–0.8682	0.407–0.516	0.715–0.544	0.5374–0.4161	0.6772–0.3730	0.6046–0.4734
Measured reflections	3086	16806	16655	23250	10112	9774
Unique reflections	2124	4985	4964	5021	5020	3816
R_{int}	0.0749	0.0392	0.0659	0.0748	0.0683	0.0958
R_1 ($I > 2\sigma I$)	0.1069	0.0258	0.0808	0.0438	0.0299	0.0512
wR_2 ($I > 2\sigma I$)	0.2681	0.0492	0.1941	0.1142	0.0677	0.1148
Goodness-of-fit	1.038	1.054	1.204	1.077	1.072	1.021
Deposit no.	712077	712078	712079	712080	712081	712082

Regarding the reactions of diphenyllead(IV) acetate with TSCs derived from β-keto amides, cyclization did not occur in any case and only thiosemicarbazonates were isolated. Note that Pb(II) forms the corresponding pyrazolonate with HTSC[8], although not with HTSC[9] or HTSC[10] [2]. Thus, if there is a relationship between cyclization and "soft" character, then $PbPh_2^{2+}$, although a "borderline" ion, might be a little "harder" than Pb(II).

The complexes are all solids and are mostly yellow in colour. The complexes are insoluble in water, soluble in DMSO and DMF but only sparingly soluble in ethanol and acetone.

3.2. X-ray studies

3.2.1. HTSC[10]

The atomic numbering scheme for this TSC ligand is shown in Fig. 1 and selected bonds lengths and angles are listed in Table 3. The structure shows some disorder that affects the atoms of the ring [C(7), C(8), C(10) and C(11)], which are delocalized between two equally populated positions.

The thiosemicarbazone chain adopts the E configuration around the C(2)–N(3) and C(1)–N(2) bonds with the sulfur atom trans to the N–N bond. The bonds lengths and angles are similar to those previously found for this type of compound [17]. The atoms of the molecule are distributed in two planes, SN(1)C(1)N(2)-N(3)C(2)C(5)C(3) [rms = 0.0668] and C(4)N(4)C(6)C(7)C(8)C(9)-C(10)C(11) [rms = 0.0976] which form a dihedral angle of 76.94(0.42)°.

There is an intermolecular hydrogen bond [N(1)–H(1A)···N(3)] that limits the free rotation of the $-N(1)H_2$ group around the N(1)–C(1) bond (see below) and there is also a weak intermolecular N(1)–H(1B)···S^i interaction that associates the molecules into pairs. Another intramolecular hydrogen bond [N(4)–H(4)···$O(1)^{ii}$] connects the pairs to give parallel chains along the *a* axis (Table 4, Fig. 1S).

3.2.2. Complexes

The molecular structures of the complexes $[PbPh_2(OAc)(TSC^8)] \cdot 2MeOH$, $[PbPh_2(OAc)(TSC^{10})] \cdot H_2O$ and $[PbPh_2(OAc)(TSC^{11})] \cdot 0.75MeOH$ are shown in Figs. 2–4 together with the numbering schemes. Selected bonds lengths and angles are listed in Table 5. The three structures include solvent molecules (MeOH or H_2O) in the lattice. In $[PbPh_2(OAc)(TSC^{10})] \cdot H_2O$, the water molecule is disordered over two positions with occupancies of 0.75:0.25. Only the molecule in the high-occupancy position has been included in Table 4. This disorder is probably responsible for the low quality of the collected data.

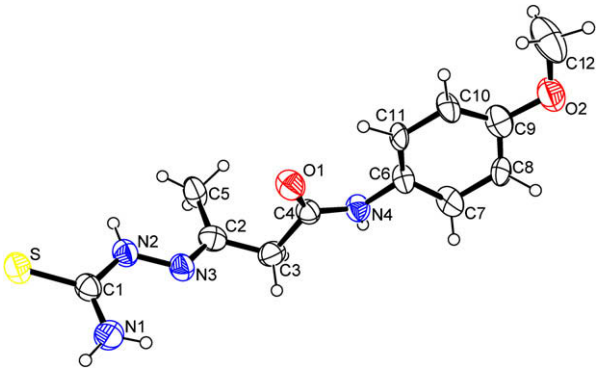


Fig. 1. Molecular structure of HTSC[10].

Table 3
Bond distances (Å) and angles (°) for HTSC[10].

S–C(1)	1.693(9)	C(1)–N(2)–N(3)	118.6(7)
O(1)–C(4)	1.239(10)	C(2)–N(3)–N(2)	117.5(7)
N(1)–C(1)	1.323(10)	N(1)–C(1)–N(2)	117.3(8)
N(2)–N(3)	1.403(10)	N(1)–C(1)–S(1)	124.2(7)
N(2)–C(1)	1.360(11)	N(2)–C(1)–S(1)	118.6(7)
N(3)–C(2)	1.295(11)	N(3)–C(2)–C(3)	115.0(7)
C(2)–C(3)	1.509(12)	C(2)–C(3)–C(4)	111.3(7)
C(3)–C(4)	1.545(11)	O(1)–C(4)–C(3)	120.7(8)

Table 4
Hydrogen bonds (Å, °) in ligand and complexes.

D–H···A	d(D–H)	d(H···A)	d(D···A)	<(DHA)
HL[10a]				
N(1)–H(1A)···N(3)	0.88	2.27	2.638(11)	105.1
N(1)–H(1B)···S^i	0.88	2.66	3.537(8)	175.9
N(4)–H(4)···$O(1)^{ii}$	0.88	2.02	2.884(10)	168.7
$[PbPh_2(OAc)(TSC^8)] \cdot 2MeOH$[b]				
N(1)–H(1B)···$O(4)^i$	0.86	2.34	3.188(8)	166.7
N(4)–H(4)···$O(2)^{ii}$	0.86	2.01	2.843(6)	163.9
O(4)–H(4A)···O(3)	0.82	1.86	2.679(6)	172.1
O(5)–H(5)···$O(4)^{iii}$	0.82	2.03	2.841(9)	170.8
$[PbPh_2(OAc)(TSC^{10})] \cdot H_2O$[c]				
N(1)–H(1B)···$O(1W)^i$	0.88	2.00	2.88(2)	173.6
N(4)–H(4)···$O(4)^i$	0.88	1.95	2.827(19)	174.1
O(1W)–H(12W)···$O(3)^{ii}$	0.80	2.13	2.755(19)	136.1
$[PbPh_2(OAc)(TSC^{11})] \cdot 0.75MeOH$[d]				
N(1)–H(1A)···N(3)	0.88	2.34	2.645(13)	100.7
N(1)–H(1B)···$O(1S)^i$	0.88	2.07	2.903(14)	156.8
O(1S)–H(1S)···O(2)	0.84	1.92	2.712(13)	157.8
N(4)–H(4)···$O(3)^{ii}$	0.88	1.95	2.782(11)	156.1
$[PbPh_2Cl(L^2)]$[e]				
N(1)–H(1A)···O	0.88	1.94	2.650(11)	136.4
N(1)–H(1B)···Cl^{ii}	0.88	2.50	3.355(9)	165.4
$[PbPh_2(OAc)(L^5)] \cdot MeOH$[f]				
N(1)–H(1A)···O(1)	0.88	1.93	2.633(4)	135.6
N(1)–H(1B)···$O(1S)^{ii}$	0.88	1.92	2.783(5)	166.9
O(1S)–H(1S)···O(1)	0.84	1.95	2.718(4)	151.1

[a] i: $-x+1, -y+1, -z$; ii: $x+1, y, z$.
[b] i: $-x+1/2, y-1/2, z+1/2$; ii: $-x+1/2, y-1/2, z-1/2$; iii: $x-1/2, -y+3/2, z$.
[c] i: $x-1/2, -y+1/2, z-1/2$; ii: $x, y, z+1$.
[d] i: $-x-1/2, y+1/2, z-1/2$; ii: $-x-1/2, y+1/2, z+1/2$.
[e] ii: $-x+3/2, y+1/2, -z+1/2$.
[f] ii: $-x, -y, -z+1$.

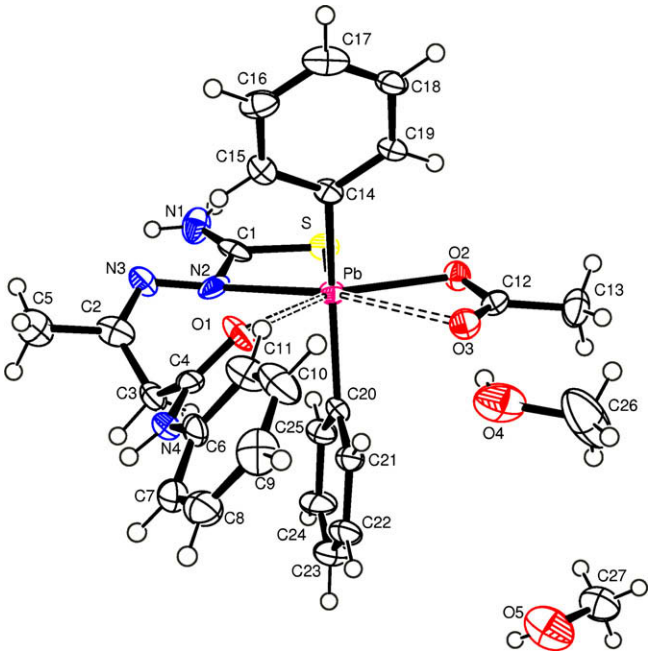


Fig. 2. Molecular structure of $[PbPh_2(OAc)(TSC^8)] \cdot 2MeOH$.

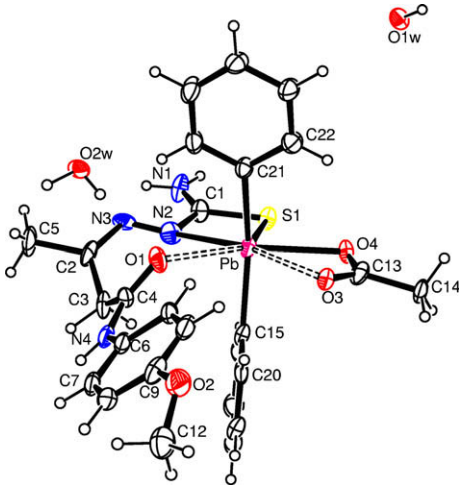


Fig. 3. Molecular structure of $[PbPh_2(OAc)(TSC^{10})] \cdot H_2O$.

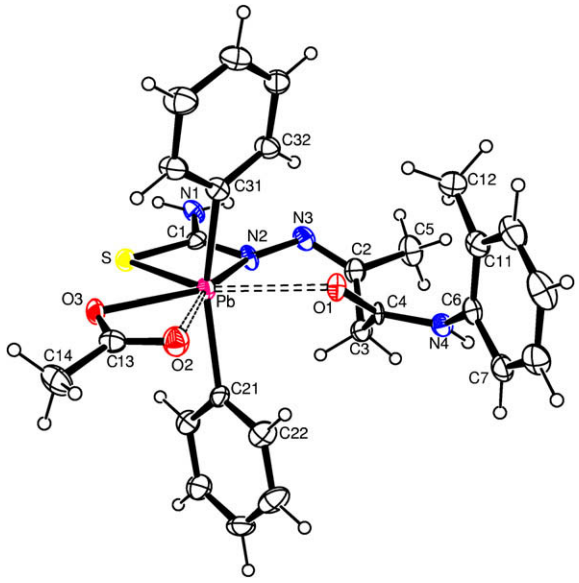


Fig. 4. Molecular structure of $[PbPh_2(OAc)(TSC^{11})] \cdot 0.75MeOH$ (methanol have been omitted for clarity).

As can be seen from the figures, in all three heteroleptic complexes the diphenyllead(IV) cation is bound to a TSC^- ligand and to an anisobidentate acetate. The thiosemicarbazonate interacts via its S, N(2) and O(1) donor atoms, with the last interaction probably being a weak one. Similarly, one of the lead–acetate bonds [Pb–O(3)] seems to be even weaker than Pb–O(1) judging by the bond distance (cf. 2.83–2.77 Å). If these weak Pb–O bonds are taken into account, then lead has a pentagonal bipyramidal coordination, with the donor atoms of both TSC^- and AcO^- ligands equatorial and the carbon atom of the phenyl groups apical.

The deprotonation and coordination of the thiosemicarbazonate to the metal give rise to some changes with respect to the structure of the free $HTSC^8$ and $HTSC^{10}$ ligands [7a]. In both cases the bonding to the metal increases the carbon–sulfur bond distances, suggesting a thione to thiol evolution of the thioamide group. Also, in order to achieve the coordination of O(4) along with that of S and N(2), the ligands must change its conformation about the C(2)═N(3) bond in the free state from E to Z.

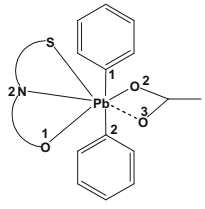
The most conspicuous characteristic of these structures is the N(2),S-coordination mode adopted by the TSC^- anion in place of the more usual N(3),S-coordination (see, e.g. Ref. [7b]). This leads to a four-membered chelate ring (see Figs. 2–4) instead of the five-membered ring that is formed when the thiosemicarbazonate binds in the usual N(3),S-mode. The N(2),S-coordination, initially observed in a dimethylthallium complex [18], is now well documented in more than thirty structures [19] and has been the subject of some experimental and theoretical discussion [20]. Nevertheless, in the present context, the relevance of the $[PbPh_2(OAc)(TSC^n)]$ structures resides not in the unusual character of the coordination mode of the TSC^- ligand, but in the fact that the involvement of the electron pair of N(2) in the bonding to the metal prevents its participation in the nucleophilic attack on the

Table 5
Selected bond distances (Å) and angles (°) for thiosemicarbazonate complexes.

Bond[a]	$[PbPh_2(OAc)(TSC^8)] \cdot 2MeOH$	$[PbPh_2(OAc)(TSC^{10})] \cdot H_2O$	$[PbPh_2(OAc)(TSC^{11})] \cdot 0.75MeOH$
Pb–C1	2.185(5)	2.172(18)	2.188(9)
Pb–C2	2.186(6)	2.164(17)	2.188(10)
Pb–O2	2.419(4)	2.403(10)	2.456(6)
Pb–N2	2.423(4)	2.473(16)	2.445(7)
Pb–S	2.6134(16)	2.620(5)	2.638(2)
Pb–O1	2.617(4)	2.647(12)	2.634(6)
Pb–O3	2.831(4)	2.793(11)	2.772(8)
S–C	1.736(7)	1.736(18)	1.737(9)

C(14)–Pb–C(20)	154.3(2)	C(21)–Pb–C(15)	157.5(7)	C(21)–Pb–C(31)	157.7(4)
N(2)–Pb–S	63.5(3)	N(2)–Pb–S(1)	62.5(4)	N(2)–Pb–S	60.8(2)
O(2)–Pb–S	77.79(10)	N(2)–Pb–O(1)	73.4(5)	O(3)–Pb–S	80.14(18)
N(2)–Pb–O(1)	74.3(3)	O(4)–Pb–S(1)	78.6(3)	O(3)–Pb–O(2)	49.1(2)
O(1)–Pb–O(3	96.09(13)	O(3)–Pb–O(1)	96.3(4)	O(1)–Pb–O(2)	92.8(2)
O(2)–Pb–O(3)	48.54(13)	O(3)–Pb–O(3)	49.5(4)	N(2)–Pb–O(1)	77.4(3)

[a]



$C(O)R_3$ group and the subsequent ring formation (see Section 1, the (II) → [III] evolution).

It is interesting to compare these structures with that of $[Zn(^TSC^9)_2]$ [7b]. In the zinc complex the ligand behaves in the more usual way and exhibits N(3),S-coordination; there is also an N(4)–H···N(2) hydrogen bond that involves the N(2) electron pair and the O(1) atom is located away from the metal centre, making any Zn–O(1) interaction impossible. Thus, it seems that, as suggested previously [21], small differences in weak interactions or in the steric requirements of the packing may determine which of the N(2),S- or N(3),S-coordination modes is adopted.

In the three complexes an intermolecular $[N(4)–H(4)\cdots O_{acetate}]$ hydrogen bond (Table 4) associates the molecules into chains; other bonds involving the solvent molecules (MeOH or H_2O) link these chains to form a layered network (Figs. 2S–7S).

With respect to the complexes containing the cyclized ligand, the arrangement of the dimers of $[PbPh_2(OAc)(L^5)]\cdot MeOH$ is shown in Fig. 5 and the asymmetric unit of $[PbPh_2Cl(L^2)]$ is represented in Fig. 6. Both figures include a numbering scheme in keeping with that used above for the uncyclized ligands. Selected bond lengths and angles are listed in Table 6.

In the former complex, the metallic atom is coordinated to the S and N(3) atoms of the monodeprotonated pyrazolone, to one oxygen atom of the acetate group [Pb–O(2) = 2.343(3) Å] and, more weakly, to the $O(3)^i$ (i = x, $-y+1$, $-z$) atom belonging to an acetate from a neighbouring molecule [$Pb–O(3)^i$ = 2.721(4) Å]. Thus, the acetate is bis-monodentate and bridges between the two diphenyllead(IV) units to give the dimeric arrangement displayed in Fig. 5. The intramolecular Pb···O(3) distance in the monomer (3.08 Å) is too long to represent a significant interaction.

The geometry around the metal is distorted octahedral and the pyrazolonate shows, in comparison to the free ligand [22], the expected structural evolution [2]. The intermolecular hydrogen bonds $N(1)–H(1B)\cdots O(1S)^{ii}$ and O(1S)–H(1S)···O(1), involving the solvent molecule and the amino and carbonyl groups of the L^- ligand (see Table 4), link the dimers to form a chain (Figs. 8S and 9S).

In $[PbPh_2Cl(L^2)]$ (Fig. 6) the monodeprotonated pyrazolone is N(3),S-coordinated to one diphenyllead(IV) cation and O(1)-bound to another, bridging between the metal centres and connecting the molecules to form a chain (Figs. 10S and 11S). The $Pb–O(1)^i$ distance [2.581(7) Å] is shorter than that in $[Pb(L^7)_2]$ [2.727(3) Å] [2], in which two intermolecular $Pb\cdots O(1)^x$ interactions also exist but the repulsive effect of a stereochemically active lone electron pair on Pb(II) also hinders the intermolecular approach. It is remarkable that the adopted structure contains only bridging pyrazolonates but not bridging chlorides, thus confirming the significant affinity of the diphenyllead(IV) cation with the oxygen donor centres.

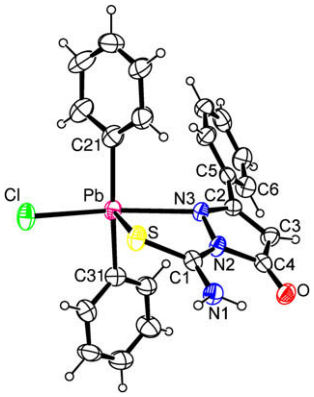
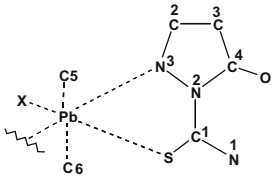


Fig. 6. Asymmetric unit of $[PbPh_2Cl(L^2)]$.

Table 6
Selected bond distances (Å) and angles (°) for pyrazolonate complexes.

Bond[a]	$[PbPh_2Cl(L^2)]$[b]		$[PbPh_2(OAc)(L^5)]\cdot MeOH$[c]
Pb–C(5)	2.173(13)		2.178(4)
Pb–C(6)	2.171(12)		2.166(4)
Pb–N(3)	2.562(8)		2.516(3)
Pb–S	2.686(3)		2.7031(10)
Pb–O(2)	–		2.343(3)
$Pb–O(3)^i$	–		2.721(4)
$Pb–O^i$	2.581(7)		–
Pb–Cl	2.625(3)		–
C–S	1.704(11)		1.710(4)
C(31)–Pb–C(21)	164.6(4)	C(15)–Pb–C(9)	162.67(16)
$N(3)–Pb–O^i$	104.5(2)	O(2)–Pb–S	72.72(8)
N(3)–Pb–S	70.35(18)	$O(2)–Pb–O(3)^i$	106.48(12)
O^i–Pb–Cl	101.07(18)	N(3)–Pb–S	70.33(8)
Cl–Pb–S	84.15(9)	$N(3)–Pb–O(3)^i$	110.36(12)

[a]


[b] i: $-x+3/2$, $y-1/2$, $-z+1/2$.
[c] i: $-x$, $-y+1$, $-z$.

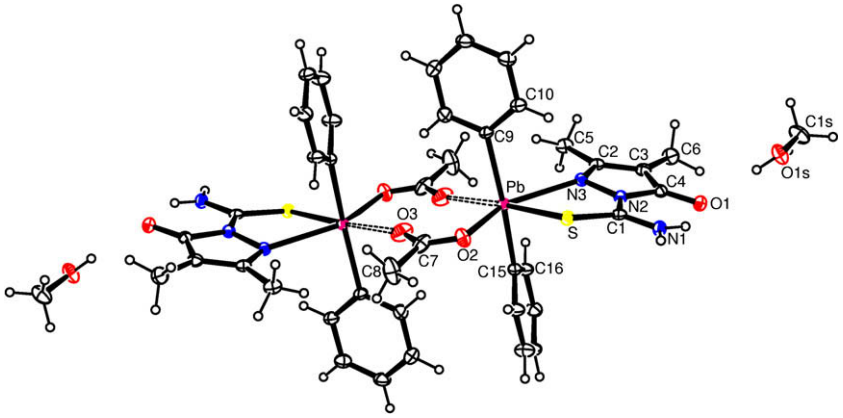


Fig. 5. Dimers of $[PbPh_2(OAc)(L^5)]\cdot MeOH$.

Once again the metal has octahedral coordination, with the main distortion caused by the C(21)–Pb–C(31) angle, which is 164.6(4)° rather than 180°, and the short N(3),S-bite of the ligand [N(3)–Pb–S = 70.35(18)°], which clearly differs from the ideal 90°.

In the crystal lattice, the chains interact via the N(1)–H(1B)···Cl^{ii} intermolecular hydrogen bond (Table 4) to give a layered arrangement (Figs. 10S and 11S).

3.3. IR spectroscopy

The most significant IR bands of the complexes are listed in Section 2 and were assigned according to a previous study [2].

In the spectra of the thiosemicarbazonates [$PbPh_2(OAc)(TSC^n)$] and [$PbPh_2(TSC^n)_2$], the ν(C=N) vibration remains close to its position in the spectra of the free ligands, which is consistent with N(3) not participating in the coordination to the metal. However, the ν(C=S) vibration is shifted to lower wavenumbers, as one would expect if there is a thione to thiol evolution due to the formation of a Pb–S bond. Thus, in this type of complex the TSC^- ligand is probably N(2),S-bound. The acetate ν_{as}(COO) and ν_s(COO) vibration modes lie at positions in keeping with a general anisobidentate OAc^- coordination [23].

In the pyrazolonate complexes the position of the band associated with the ν(C=S) changes upon metallation to lower wavenumber with respect to the free HL^n, suggesting the coordination of the sulfur atom to the metal in all of these pyrazolone complexes. The behaviour of the ν(C=N) mode is similar in all derivatives (a shift to higher wavenumber with respect to the free pyrazolone) and this is consistent with the coordination of N(3) as in [$PbPh_2(OAc)(L^5)$] · MeOH and [$PbPh_2Cl(L^2)$]. As indicated previously [7b], coordination of the oxygen atom of the carbonyl group to the metal cannot be confirmed by the modification of the band associated with ν(C=O) because this mode is also sensitive to the metallation of N(3) and to the changes in the hydrogen bonding interactions involving the carbonyl group. Thus, in [$PbPh_2(OAc)(L^5)$] · MeOH this signal is shifted by approximately 30 cm^{-1} to lower wavenumbers with respect to its position in HL^5, although the X-ray study showed (Fig. 5) that the C=O group is not involved in the coordination to the metal. However, in [$PbPh_2Cl(L^2)$], in which an O(1)–Pb bond exists, ν(C=O) was shifted to lower wavenumbers compared to the corresponding absorption in HL^2 and this shift was only marginally larger (*ca.* 40 cm^{-1}).

As far as the acetate ligand in the heteroleptic [$PbPh_2(OAc)(L^n)$] complexes is concerned, the value of $\Delta\nu$ (=[ν_{as}(COO)– ν_s(COO)]) (150–170 cm^{-1}) suggests a coordination behaviour similar to that described for [$PbPh_2(OAc)(L^5)$] [23].

3.4. ^{1}H, ^{13}C and ^{207}Pb NMR spectra

The ^{1}H, ^{13}C and ^{207}Pb NMR data for the complexes in DMSO–d_6 solution are included in Section 2. The corresponding data for the ligands $HTSC^n$ (n = 1–10) and HL^n (n = 1–7) have been published previously [3,7]. In cases where a long acquisition time was necessary to obtain a spectrum, some of the complexes decomposed to give a black precipitate (possibly PbS), benzene (as shown by new signals at 7.35 and 128.3 ppm in the ^{1}H and ^{13}C NMR spectra, respectively) and, in the case of heteroleptic complexes, diphenyllead acetate (according to the observed ^{207}Pb NMR signal at −863 ppm). This phenomenon was not explored further.

In the ^{1}H and ^{13}C NMR spectra of the thiosemicarbazonate complexes the signals belonging to the TSC^- moiety change with respect to those of the free ligand in the expected way: (i) that of the N(2)H group disappears due to deprotonation; (ii) the two bands associated with the –N(1)H_2 group [2] evolve to give a broad signal, in accordance with the free rotation of this group around the N(1)–C(S) bond as a result of the HTSC deprotonation and metallation; (iii) the C(2) signal is displaced to lower field (by between 6 and 16 ppm) upon complexation, probably due to the bonding of N(3) to the lead atom [7b].

In cases where the signals of the organometallic moiety did not overlap with the aromatic proton signals of the ligand, and therefore could be located, they showed chemical shifts that were very similar in all the complexes and also $^3J(^1H–^{207}Pb)$ values close to 112 Hz. In the ^{13}C NMR spectra the $^2J(^{13}C–^{207}Pb)$ coupling constants are between 87 and 88 Hz. These values are lower than those obtained for diphenyllead compounds with CN = 6 and even lower than those with CN = 5 [24,25], which suggests that in these compounds CN = 4. This low CN is also supported by the ^{207}Pb chemical shift (δ = −294 ppm), which is identical in all compounds and is displaced to lower field by almost 200 ppm with respect to the values reported for other diphenyllead complexes with CN 6 or 5 [24,25].

All of these data suggest that the solid state structures of the complexes [$PbPh_2(OAc)(TSC^n)$] (n = 8, 10 and 11), in which the metal exhibits a CN = 7, are modified in DMSO solution to form species in which the diphenyllead is probably only bound to the TSC^- anion via its S and N(3) atoms. If this is the case, it must be concluded that the NMR parameters of the diorganolead moiety are sensitive, as can been expected, to the CN of the metal and to the identity of the donor atoms, but is rather insensitive to the donor strength of these atoms.

In the pyrazolonate complexes, the main changes in the ^{1}H and ^{13}C NMR spectra of the pyrazolone moiety regarding the free HL^n ligands are: (i) the absence of the signal associated with the N(3)H group; (ii) the slight shielding of C(1) and (iii) the significant deshielding of C(2). The former modification is a consequence of the deprotonation of the ligand and the latter two suggest that the S,N(3)–Pb bonding is retained in DMSO solution.

The values of the $^3J(^1H–^{207}Pb)$ constants, in cases where they could be observed, are in the range 204–210 Hz and this is consistent with a CN of 6 or higher [24]. The limited availability of ^{207}Pb chemical shift data precludes any general conclusions, but this parameter in the cases of [$PbPh_2(L^3)_2$] (−738.1) and [$PbPh_2(L^6)_2$] (−706.4) also suggests a CN of 6 or higher [25–27]. However, the chemical shift value in [$PbPh_2(OAc)(L^6)$] (−869.5) indicates that during the acquisition of the spectrum this complex evolved to give diphenyllead acetate. The complex [$PbPh_2(OAc)(L^5)$] shows two signals, one at −575 and another at −871.9, and this underwent a partial or total displacement of the AcO^- ligand in solution to give a new complex with a lower CN and $PbPh_2(OAc)_2$.

Acknowledgements

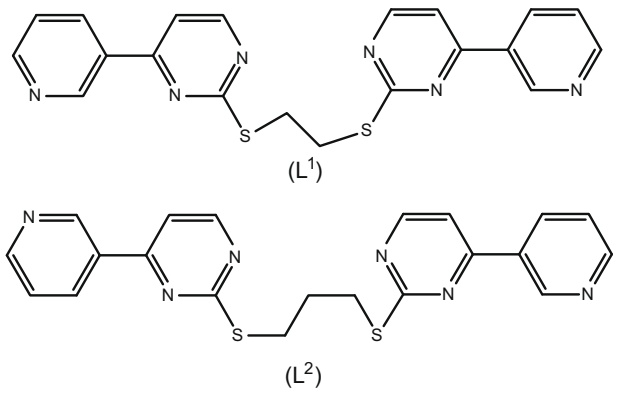
We thank the Secretariat General for Research and Development of the Xunta de Galicia (Spain) and the Spanish Ministry of Science and Technology for financial support under Projects PGIDIT03PXIC20306PN, CTQ2006-11805-BQU and BQU2002-04524-C02-01.

Appendix A. Supplementary data

CCDC 712077, 712078, 712079, 712080, 712081 and 712082 contains the supplementary crystallographic data for $HTSC^{10}$, [$PbPh_2(OAc)(TSC^8)$]·2MeOH, [$PbPh_2(OAc)(TSC^{10})$]·H_2O, [$PbPh_2(OAc)(TSC^{11})$]·0.75MeOH, [$PbPh_2(OAc)(L^5)$]·MeOH and [$PbPh_2Cl(L^2)$], respectively. These data can be obtained free of charge via http://www.ccdc.cam.ac.uk/conts/retrieving.html, or from the Cambridge Crystallographic Data Centre, 12 Union Road, Cambridge CB2 1EZ, UK; fax: (+44) 1223-336-033; or e-mail: deposit@ccdc.cam.ac.uk. Supplementary data associated with this article can be found, in the online version, at doi:10.1016/j.poly.2009.01.004.

References

[1] K.N. Zelenin, V.V. Alekseyev, Top. Heterocycl. 1 (1996) 141.
[2] J.S. Casas, E.E. Castellano, J. Ellena, M.S. García-Tasende, A. Sánchez, J. Sordo, A. Touceda, S. Vázquez-Rodríguez, Polyhedron 26 (2007) 4228.
[3] J.S. Casas, M.V. Castaño, M.S. García-Tasende, E. Rodríguez-Castellón, A. Sánchez, L.M. Sanjuán, J. Sordo, Dalton Trans. (2004) 2019.
[4] R.D. Hancock, A.E. Martell, J. Chem. Ed. 73 (1996) 654.
[5] J.S. Casas, E.E. Castellano, J. Ellena, M.S. García-Tasende, A. Sánchez, J. Sordo, A. Touceda, Polyhedron 27 (2008) 1.
[6] S. Jayasree, K.K. Aravindakshan, Polyhedron 12 (1993) 1187.
[7] (a) J.S. Casas, M.V. Castaño, E.E. Castellano, M.S. García-Tasende, A. Sánchez, M.L. Sanjuán, J. Sordo, Eur. J. Inorg. Chem. (2000) 83;
(b) J.S. Casas, M.V. Castaño, E.E. Castellano, J. Ellena, M.S. García-Tasende, A. Gato, A. Sánchez, L.M. Sanjuán, J. Sordo, Inorg. Chem. 41 (2002) 1550;
(c) J.S. Casas, M.V. Castaño, M.S. García-Tasende, A. Sánchez, J. Sordo, A. Touceda, Polyhedron 24 (2005) 3057.
[8] S.G. Schäfer, R.L.F. Davies, B. Elsenhans, W. Forth, K. Schümann, in: H. Marquardt, S.G. Schäfer, R.O. McClellan, F. Welsch (Eds.), Toxicology, Academic Press, San Diego, CA, 1999 (Chapter 32).
[9] G.M. Sheldrick, SHELX-97, An Integrated System for Solving and Refining Crystal Structures from Diffraction Data, University of Göttingen, Göttingen, Germany, 1997.
[10] R.H. Blessing, Acta Crystallogr. A51 (1995) 33.
[11] G.M. Sheldrick, SADABS, Program for Empirical Absorption Correction of Area Detector Data, University of Göttingen, Göttingen, Germany, 1997.
[12] L.J. Farrugia, ORTEP III for Windows, J. Appl. Crystallogr. 30 (1997) 565.
[13] A.L. Spek, PLATON 99, A Multipurpose Crystallographic Tool, University of Utrecht, Utrecht, The Netherlands, 1999.
[14] I.J. Bruno, J.C. Cole, P.R. Edgington, M.K. Kessler, C.F. Macrae, P. McCabe, J. Pearson, R. Taylor, MERCURY, New Software for Searching the Cambridge Structural Database and Visualising Crystal Structures, Acta Crystallogr. B58 (2002) 389.
[15] J.S. Casas, M.V. Castaño, M.C. Cifuentes, J.C. García-Monteagudo, A. Sánchez, J. Sordo, A. Touceda, J. Organomet. Chem. 692 (2007) 2234.
[16] K.A. Jensen, in: P. Grandjean, E.C. Grandjean (Eds.), Biological Effects of Organolead Compounds, CRC Press, Boca Raton, Florida, 2000, p. 3.
[17] J.S. Casas, M.S. García-Tasende, J. Sordo, Coord. Chem. Rev. 209 (2000) 197.
[18] J.S. Casas, E.E. Castellano, A. Macías, M.C. Rodríguez-Argüelles, A. Sánchez, J. Sordo, J. Chem. Soc., Dalton Trans. (1993) 353.
[19] F.H. Allen, Acta Crystallogr. B58 (2002) 380.
[20] D. Mishra, S. Naskar, M.G.B. Drew, S.K. Chattopadhyay, Polyhedron 24 (2005) 1861 and references therein.
[21] J.S. Casas, E.E. Castellano, J. Ellena, M.S. García-Tasende, A. Sánchez, J. Sordo, A. Touceda-Varela, Inorg. Chem. Commun. 7 (2004) 1109.
[22] R. Carballo, J.S. Casas, E. García-Martínez, G. Pereiras-Gabián, A. Sánchez, J. Sordo, E.M. Vázquez-López, Acta Crystallogr. E58 (2002) o787.
[23] K. Nakamoto, Infrared and Raman Spectra of Inorganic and Coordination Compounds, 5th Ed., John Wiley and Sons, New York, 1997.
[24] N. Ólafsson, C.N. Flensburg, P. Andersen, J. Chem. Soc., Dalton Trans. (2000) 4360.
[25] D.G. Calatayud, E. López-Torres, A. Mendiola, Inorg. Chem. 46 (2007) 10434.
[26] M. Schürmann, H. Friedo, J. Organomet. Chem. 530 (1997) 121.
[27] D. Weber, S.H. Hausner, A. Eisengräber-Pabst, S. Yun, J.A. Kraese-Bauer, H. Zimmer, Inorg. Chim. Acta 357 (2004) 125.



Scheme 1.

2.2. Synthesis of ligand

L^2 was synthesized in an analogous way to L^1, which was described previously [17]. An ethanol solution (50 mL) of 1,3-dibromopropane (2.02 g, 10 mmol) was added to a dry ethanol solution (300 mL) containing 4-(pyridin-3-yl) pyrimidine-2-thiol (3.78 g, 20 mmol) and sodium hydroxide (0.80 g, 20 mmol). The solution was stirred and refluxed for 8 h. Yellow precipitates were filtered out, washed by water and ethanol, and dried in vacuum. Yield (3.12 g) 74.6%, M.p. 117–118 °C. *Anal. Calc.* for $C_{21}H_{18}N_6S_2$: C, 60.26; H, 4.33; N, 20.08. Found: C, 60.29; H, 4.27; N, 19.82%. IR (KBr, cm^{-1}): 1589 (m), 1562 (vs), 1533 (m), 1480 (w), 1440 (w), 1428 (w), 1419 (m), 1402 (m), 1343 (m), 1323 (s), 1206 (s), 1192 (m), 1023 (w), 824 (m). ESI-MS: 858.7 (100%) $[2L^2+Na]^+$, 441.2 (28%) $[L^2+Na]^+$, 419.3 (26%) $[L^2+H]^+$. ^1H NMR (δ, $CDCl_3$): 9.29 (s, 2H, pyridyl–H), 8.76 (d, 2H, pyrimidyl–H), 8.62 (d, 2H, pyridyl–H), 8.47 (d, 2H, pyridyl–H), 7.51 (t, 2H, pyridyl–H), 7.41 (d, 2H, pyrimidyl–H), 3.46 (t, 4H, methylene–H), 2.35 (m, 2H, methylene–H). Single crystals of L^2 suitable for X-ray diffraction were grown from its methanol solution by slow evaporation in air at room temperature.

2.3. Synthesis of complexes

*$[ZnL^2I_2]$ (**1**):* A solution of ZnI_2 (16.0 mg, 0.05 mmol) in methanol (5 mL) was very slowly dropped on the top of a solution of L^2 (20.9 mg, 0.05 mmol) in chloroform (5 mL) in a tube. Pale yellow crystals formed after 6 days (yield: 42%). *Anal.* Calc. for $C_{21}H_{18}I_2N_6S_2Zn$: C, 34.19; H, 2.46; N, 11.39. Found: C, 34.21; H, 2.51; N, 11.36%. IR (KBr, cm^{-1}): 1608 (w), 1559 (s), 1544 (s), 1482 (w), 1431 (m), 1406 (m), 1347 (m), 1325 (m), 1202 (m), 1180 (w), 1052 (w), 810 (w).

*$\{[CdL^2I_2]_2 \cdot CH_3OH\}_n$ (**2**):* **2** was prepared in a way like **1**. Yield, 40%. *Anal.* Calc. for $C_{43}H_{40}I_4N_{12}OS_4Cd_2$: C, 32.24; H, 2.51; N, 10.49. Found: C, 32.30; H, 2.57; N, 10.38%. IR (KBr, cm^{-1}): 3406 (w), 1602 (w), 1599 (s), 1543 (s), 1482 (w), 1430 (m), 1407 (m), 1348 (m), 1325 (w), 1202 (m), 1181 (w), 10468 (w), 809 (w).

*$\{[ZnL^2(H_2O)_4](ClO_4)_2\}_2$ (**3**):* A solution of $Zn(ClO_4)_2 \cdot 6H_2O$ (37.2 mg, 0.10 mmol) in methanol (10 mL) was added to a solution of L^2 (41.8 mg, 0.10 mmol) in methanol (20 mL). The mixture was refluxed for half an hour and then cooled to room temperature. The solution was filtered, then complex **3** was obtained by slow evaporation of the filtrate at room temperature in 52% yield. *Anal.* Calc. for $C_{42}H_{52}N_{12}O_{24}S_4Cl_4Zn_2$: C, 33.41; H, 3.47; N, 11.13. Found: C, 33.28; H, 3.54; N, 11.08%. IR (KBr, cm^{-1}): 3460 (m), 1654 (m), 1608 (m), 1566 (vs), 1546 (s), 1484 (m), 1430 (m), 1403 (s), 1354 (s), 1332 (m), 1265 (w), 1206 (s), 1181 (m), 1110 (vs), 845 (w), 820 (m), 626 (s).

*$\{[CdL^2(H_2O)_4](ClO_4)_2\}_2$ (**4**):* Complex **4** was prepared by a similar way to complex **3**. Yield, 58%. *Anal.* Calc. for $C_{42}H_{52}N_{12}O_{24}S_4Cl_4Cd_2$: C, 31.45; H, 3.27; N, 10.48. Found: C, 31.40; H, 3.42; N, 10.41%. IR (KBr, cm^{-1}): 3449 (m), 1605 (m), 1566 (vs), 1546 (s), 1485 (w), 1432 (w), 1411 (m), 1355 (m), 1333 (w), 1306 (w), 1207 (m), 1119 (vs), 1048 (s), 813 (m), 623 (s).

*$[ZnL^1I_2]_n$ (**5**):* A solution of ZnI_2 (16.0 mg, 0.05 mmol) in methanol (5 mL) was very slowly dropped on the top of solution of L^1 (20.2 mg, 0.05 mmol) in chloroform (5 mL) in a tube. Pale yellow crystals formed after 6 days (yield: 45%). *Anal.* Calc. for $C_{20}H_{16}I_2N_6S_2Zn$: C, 33.19; H, 2.23; N, 11.61. Found: C, 33.20; H, 2.30; N, 11.58%. IR (KBr, cm^{-1}): 1608 (w), 1562 (s), 1540 (s), 1481 (w), 1430 (m), 1416 (m), 1346 (s), 1329(w), 1199 (m), 1178 (w), 1052 (w), 805 (w).

*$[CdL^1I_2]_n$ (**6**):* Complex **6** was prepared in an analogous way to complex **5**. Yield, 40%. *Anal.* Calc. for $C_{20}H_{16}I_2N_6S_2Cd$: C, 31.17; H, 2.09; N, 10.90. Found: C, 31.20; H, 2.04; N, 10.80%. IR (KBr, cm^{-1}): 1604 (w), 1560 (s), 1541 (s), 1481 (w), 1429 (m), 1416 (m), 1404 (w), 1346 (m), 1199 (m), 1181 (w), 1048 (w), 806 (w).

*$\{\{[ZnL^1_2(H_2O)_4](ClO_4)_2L^1\}_{0.5} \cdot CH_3OH\}$ (**7**):* A solution of $Zn(ClO_4)_2 \cdot 6H_2O$ (37.2 mg, 0.10 mmol) in methanol (15 mL) was added to a solution of L^1 (40.4 mg, 0.1 mmol) in methanol (20 mL). The mixture was refluxed for half an hour, and then cooled to room temperature. The solution was filtered, and complex **7** was obtained by slow evaporation of the filtrate at room temperature in 73% yield. *Anal.* Calc. for $C_{31}H_{32}N_9O_7S_3ClZn_{0.50}$: C, 46.14; H, 4.00; N, 15.62. Found: C, 46.20; H, 3.94; N, 15.56%. IR (KBr, cm^{-1}): 3456 (m), 3066 (m), 1599 (w), 1565 (vs), 1539 (s), 1480 (m), 1430 (m), 1403 (s), 1358 (m), 1345 (m), 1323 (s), 1224 (w), 1206 (m), 1195 (s), 1120 (s), 1088 (s), 832 (m), 809 (m).

*$\{\{[Cd_{0.5}L^1(H_2O)_2](ClO_4) \cdot CH_3OH\}_2L^1\}$ (**8**):* Complex **8** was prepared similarly to complex **7**. Yield, 48%. *Anal.* Calc. for $C_{62}H_{64}N_{18}O_{14}S_6Cl_2Cd$: C, 44.83; H, 3.88; N, 15.18. Found: C, 44.80; H, 3.97; N, 15.15%. IR (KBr, cm^{-1}): 3469 (m), 3063 (w), 1600 (w), 1564 (vs), 1540 (s), 1479 (w), 1429 (w), 1403 (s), 1357 (m), 1346 (m), 1323 (m), 1224 (m), 1205 (m), 1196 (s), 1121 (s), 1105 (s), 1086 (s), 832 (m), 809 (m).

2.4. Crystallographic analyses

Diffraction data for L^2 and complexes **1**–**8** were measured on a Bruker SMART 1K CCD diffractometer [18] at 291 K using graphite mono-chromated Mo Kα radiation (λ = 0.71073 Å). Lorentz polarization and absorption corrections were applied. The structures were solved by direct methods and refined with the full-matrix least-squares technique using SHELXTL version 5.1 [19]. Anisotropic thermal parameters were assigned to all non-hydrogen atoms. The hydrogen atoms were geometrically fixed and allowed to ride on the attached atoms. The summary of the crystal data, experimental details and refinement results are listed in Table 1, while selected bond distances and bond angles are given in Table 2.

3. Results and discussion

3.1. Synthesis and characterization

Similar to solubility of L^1, L^2 is soluble in common polar organic solvents. Reactions of L^2 or L^1 with MI_2 (M = Zn^{2+} and Cd^{2+}) yielded the neutral species $[ZnL^2I_2]$ (**1**), $[CdL^2I_2]_n$ (**2**), $[ZnL^1I_2]_n$ (**5**) and $[CdL^1I_2]_n$ (**6**) by diffusion between solutions of the corresponding ligand and the metal salt. The other compounds were produced by refluxing L^2 or L^1 with metal salts in methanol. All complexes were prepared in 1:1 metal/ligand molar ratio, and it is found that the relative ratio between the two reagents will not affect the final products.

Table 1
Crystal and structure refinement data for L^2 and complexes **1**–**8**.

Complex	L^2	1	2	3	4	5	6	7	8
Empirical formula	$C_{21}H_{18}N_6S_2$	$C_{21}H_{18}N_6S_2ZnI_2$	$C_{43}H_{40}N_{12}OS_4Cd_2I_4$	$C_{42}H_{52}Cl_4N_{12}O_{24}S_4Zn_2$	$C_{42}H_{52}Cl_4N_{12}O_{24}S_4Cd_2$	$C_{20}H_{16}N_6S_2ZnI_2$	$C_{20}H_{16}N_6S_2CdI_2$	$C_{31}H_{32}N_9O_7S_3ClZn_{0.50}$	$C_{62}H_{64}N_{18}O_{14}S_6Cl_2Cd$
Formula weight	418.55	737.74	1601.57	1509.82	1603.86	723.72	770.74	830.52	1661.04
Crystal size (mm)	0.10 × 0.10 × 0.60	0.04 × 0.10 × 0.10	0.05 × 0.20 × 0.20	0.15 × 0.18 × 0.20	0.10 × 0.15 × 0.20	0.20 × 0.20 × 0.40	0.08 × 0.20 × 0.20	0.12 × 0.18 × 0.20	0.08 × 0.18 × 0.20
Crystal system	triclinic	orthorhombic	monoclinic	triclinic	triclinic	monoclinic	monoclinic	triclinic	triclinic
Space group	$P\bar{1}$	*Pbca*	$P2_1/n$	$P\bar{1}$	$P\bar{1}$	*C*2/*c*	*C*2/*c*	$P\bar{1}$	$P\bar{1}$
a (Å)	5.0318(14)	24.7031(18)	14.5484(10)	11.456(3)	11.728(3)	16.392(4)	16.419(3)	10.2089(14)	10.213(3)
b (Å)	13.164(4)	9.0682(6)	11.1144(7)	11.712(3)	11.779(3)	6.8226(16)	6.8503(14)	10.4503(14)	10.431(3)
c (Å)	14.528(4)	22.0420(17)	33.732(2)	11.998(4)	12.081(3)	22.404(5)	22.834(5)	17.267(2)	17.334(5)
α (°)	92.317(5)	90	90	74.346(5)	74.248(5)	90	90	101.934(3)	101.834(6)
β (°)	92.858(5)	90	100.9660(10)	76.801(5)	76.576(5)	103.024(4)	102.607(4)	101.832(3)	102.198(5)
γ (°)	92.013(5)	90	90	73.668(5)	72.983(5)	90	90	92.802(3)	92.593(6)
V (Å^3)	959.7(5)	4937.7(6)	5354.8(6)	1467.2(7)	1514.6(7)	2441.1(10)	2506.3(9)	1756.0(4)	1759.0(9)
Z	2	8	4	1	1	4	4	2	1
D_{calc} (Mg/m^3)	1.448	1.985	1.987	1.709	1.758	1.969	2.043	1.526	1.568
μ (mm^{-1})	0.299	3.687	3.301	1.233	1.105	3.726	3.521	0.643	0.642
F(000)	436	2832	3048	772	808.0	1384	1456	834	852
Reflections collected/ unique [R_{int}]	4721/3304 [0.023]	23271/4347 [0.095]	30441/11677 [0.078]	7500/5218 [0.024]	7535/5239 [0.050]	6302/2396 [0.050]	5992/2203 [0.041]	8422/909 [0.088]	8538/6043 [0.092]
Parameters	262	289	596	397	397	141	141	466	466
R_1[a]	0.0456	0.0411	0.0755	0.0497	0.0659	0.1014	0.0402	0.1117	0.1165
wR_2[b]	0.1078	0.0541	0.1356	0.1223	0.1680	0.2730	0.0808	0.1984	0.1961
Goodness-of-fit	0.95	0.75	1.01	0.96	0.92	1.08	0.94	1.10	1.09
Min./max. $\Delta\rho$ (e Å^{-3})	−0.21/0.29	−0.43/0.60	−0.85/1.09	−0.35/0.61	−1.16/1.56	−0.90/6.88	−0.85/1.23	−0.68/0.59	−1.23/0.82

[a] $R_1 = \sum||F_o| - |F_c||/\sum|F_o|$.
[b] $wR_2 = [\sum[w(F_o^2 - F_c^2)^2]/\sum w(F_o^2)^2]^{1/2}$.

Table 2
Selected bond lengths (Å) and angles (°) for complexes **1**–**8**.

*Complex **1***			
I1–Zn1	2.5657(9)	I2–Zn1	2.5207(9)
Zn1–N3	2.057(5)	Zn1–N6	2.049(5)
I1–Zn1–I2	119.72(3)	I1–Zn1–N3	106.03(14)
I1–Zn1–N6	108.84(13)	I2–Zn1–N3	107.43(13)
I2–Zn1–N6	111.08(14)	N3–Zn1–N6	102.2(2)
*Complex **2***			
I1–Cd1	2.6631(11)	I2–Cd1	2.6775(10)
I3–Cd2	2.7106(11)	I4–Cd2	2.6981(11)
Cd1–N6#1	2.286(7)	Cd1–N3	2.277(7)
Cd2–N12#2	2.335(8)	Cd2–N9	2.272(7)
I1–Cd1–I2	126.58(4)	I1–Cd1–N3	104.36(19)
I1–Cd1–N6#1	113.1(2)	I2–Cd1–N3	107.5(2)
I2–Cd1–N6 #1	106.9(2)	N3–Cd1–N6#1	92.9(3)
I3–Cd2–N9	107.7(2)	I3–Cd2–N12#2	100.65(19)
I4–Cd2–N9	108.3(2)	I4–Cd2–N12#2	102.53(19)
N9–Cd2–N12#2	92.8(3)	I3–Cd2–I4	135.78(4)
*Complex **3***			
Zn1–O1	2.082(3)	Zn1–O2	2.153(4)
Zn1–O3	2.166(3)	Zn1–O4	2.103(3)
Zn1–N3	2.111(4)	Zn1–N4	2.124(4)
O1–Zn1–O2	91.52(14)	O1–Zn1–O3	88.19(11)
O1–Zn1–O4	176.38(12)	O1–Zn1–N3	89.90(14)
O1–Zn1–N4	90.13(13)	O2–Zn1–N3	167.49(15)
O3–Zn1–N4	170.55(13)	N3–Zn1–N4	100.93(14)
*Complex **4***			
Cd1–O2	2.275(6)	Cd1–O3	2.261(6)
Cd1–O4	2.320(6)	Cd1–N3	2.304(6)
Cd1–N6	2.300(6)	Cd1–O1	2.307(7)
O2–Cd1–O3	177.5(2)	O2–Cd1–O4	88.4(2)
O2–Cd1–N3	91.4(2)	O2–Cd1–N6	93.3(2)
O1–Cd1–O2	83.0(3)	O4–Cd1–N6	170.4(2)
N3–Cd1–N6	102.7(2)	O3–Cd1–O4	89.5(2)
*Complex **5***			
Zn1–I1	2.5416(15)	Zn1–N1	2.059(9)
I1–Zn1–N1	108.3(2)	I1–Zn1–I1a	120.45(9)
I1–Zn1–N1a	108.9(2)	I1a–Zn1–N1	108.9(2)
N1–Zn1–N1a	100.2(4)	I1a–Zn1–N1a	108.3(2)
*Complex **6***			
Cd1–I1	2.6764(8)	Cd1–N3	2.275(5)
I1–Cd1–N3	106.39(11)	I1–Cd1–I1a	126.59(3)
I1–Cd1–N3a	108.61(12)	I1a–Cd1–N3	108.61(12)
N3–Cd1–N3a	96.01(17)	I1a–Cd1–N3a	106.39(11)
*Complex **7***			
Zn1–O1W	2.054(7)	Zn1–O2W	2.118(7)
Zn1–N1	2.153(7)	Zn1–O1Wa	2.054(7)
Zn1–O2Wa	2.118(7)	Zn1–N1a	2.153(7)
O1W–Zn1–O2W	89.1(3)	O1W–Zn1–N1	92.7(3)
O1W–Zn1–O1Wa	180.00	O1W–Zn1–O2Wa	90.9(3)
O1W–Zn1–N1a	87.3(3)	O2W–Zn1–N1	90.8(3)
O2W–Zn1–O2Wa	180.00	N1–Zn1–N1a	180.00
*Complex **8***			
Cd1–O1W	2.253(9)	Cd1–O2W	2.265(9)
Cd1–N1	2.304(8)	Cd1–O1Wa	2.253(9)
Cd1–O2Wa	2.265(9)	Cd1–N1a	2.304(8)
O1W–Cd1–O2W	88.9(3)	O1W–Cd1–N1	93.8(3)
O1W–Cd1–O1Wa	180.00	O1W–Cd1–O2Wa	91.1(3)
O1W–Cd1–N1a	86.2(3)	O2W–Cd1–N1	91.8(3)
O2W–Cd1–O2Wa	180.00	N1–Cd1–N1a	180.00

Symmetry code: 1 = *x*, 1 + *y*, *z* and 2 = *x*, −1 + *y*, *z* for **2**; a = −*x*, *y*, 1/2 − *z* for **5**; a = 1 − *x*, *y*, 1/2 − *z* for **6**; a = 2 − *x*, −*y*, −*z* for **7**; a = 2 − *x*, −*y*, −*z* for **8**.

Infrared spectra of **2**, **3**, **4**, **7** and **8** display middle peaks characteristic of the O–H stretching vibration in the 3470–3450 cm^{-1} region. In the 1400–1602 cm^{-1} region, the absorption bands are in accordance with the skeletal vibrations of aromatic rings for these five complexes. The weak absorption band appearing in the 800–820 cm^{-1} region can be assigned to the C–S stretching vibration. The strong bands of ClO_4^- appear near 1100 cm^{-1} in the IR spectra of **3**, **4**, **7** and **8**.

3.2. X-ray crystallographic studies of ligand and complexes

3.2.1. L^2

L^2 crystallizes in a triclinic system of a non-centrosymmetric space group $P\bar{1}$ (molecular structure shown in Supplementary data S1).

In the crystal structure of this ligand, pyrimidyl rings and pyridyl rings are slightly twisting, in which the dihedral angle between the neighboring two heterocyclic rings is ca. 8.4°. Adjacent molecules of L^2 are connected with each other via hydrogen bonds [C(18)–H(18)···N(6) (2 − *x*, −*y*, 2 − *z*), C(18)···N(6), 3.441(4) Å, C–H···N, 157.0°], as a consequence, forming dimers. These dimers are again stitched together to form a 3D supramolecular structure through π···π stacking interactions of 3.571 Å between the parallel neighboring dimers (see Supplementary data S2).

3.2.2. $[ZnL^2I_2]$ (**1**)

Single-crystal XRD study has revealed that $[ZnL^2I_2]$ (**1**) crystallizes in an orthorhombic system with space group *Pbca*. The asymmetric unit of **1** contains one ligand, one Zn(II) ion, and two coordinated iodide anions (shown in Fig. 1a).

The Zn(II) ion is coordinated by two iodide anions and two pyridyl N atoms of one ligand in a distorted tetrahedral configuration. The full dithioether molecule acts as an effectively bidentate ligand to link the metal atom and produce an 18-membered chelating metallomacrocycle. Probably owing to the steric requirement, the whole molecule adopts a distorted boat conformation. The ligand wraps around the Zn(II) ion, in which the dihedral angle between two pyridyl rings is ca. 83.6°. Bond angles of N–Zn–N and I–Zn–I are 102.2(2)° and 119.7(3)°, respectively, which are far from an ideal tetrahedral angle. It is worthy noting that two heterocyclic rings of the ligand, pyrimidyl and pyridyl rings, are not coplanar either, the dihedral angle between them is ca. 10.2° and 13.3°, respectively.

Additionally, as shown in Fig. 1b, effective π···π stacking is observed between the aromatic rings within the neighboring macrocycles with the centroid–centroid separation of 3.572 or 3.770 Å. Furthermore there are forces of van der Waals S···I contacts [S···I = 3.93 Å] [20,21]. So the adjacent modules are cemented together primarily with these "glue" leading to the formation of a 3D supramolecular structure (see Supplementary data S3).

3.2.3. $[CdL^2I_2]_n$ (**2**)

By replacing ZnI_2 with CdI_2 in the reaction with L^2, $[CdL^2I_2]_n$ (**2**) were obtained. Complex **2** crystallizes in a monoclinic system of

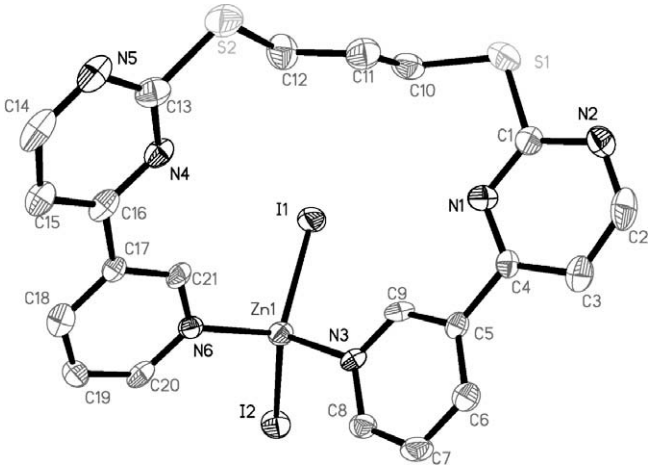


Fig. 1a. Molecular structures of **1** showing the numbering scheme and displacement ellipsoids at the 30% probability level, hydrogen atoms are omitted for clarity.

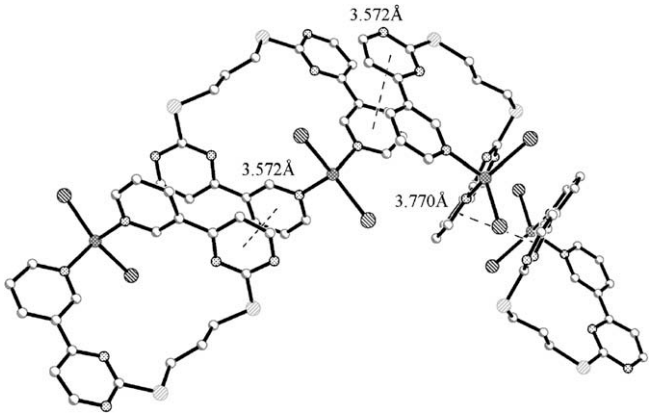


Fig. 1b. Perspective view of the macrocycles held by π···π stacking interactions.

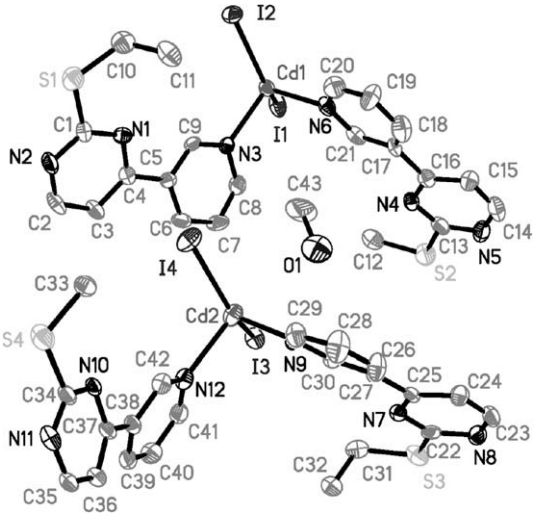


Fig. 2a. Molecular structure of **2** showing the numbering scheme and displacement ellipsoids at the 30% probability level, hydrogen atoms are omitted for clarity.

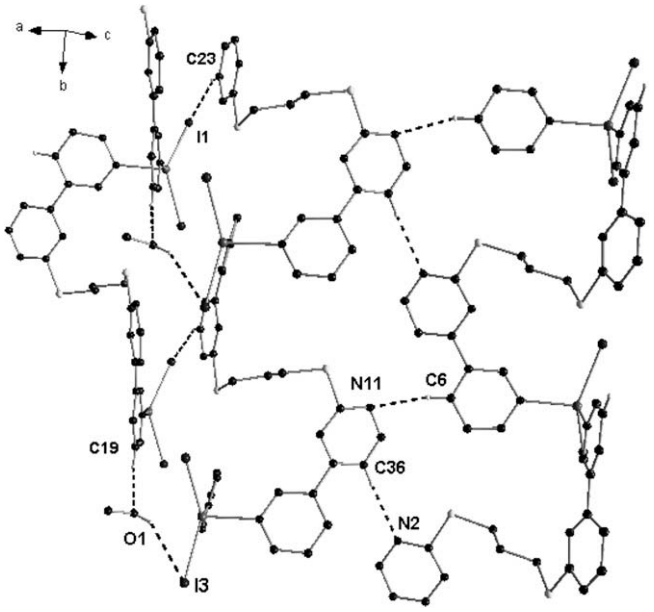


Fig. 2b. View of the structure of 2D planes of **2** showing the intermolecular and intramolecular hydrogen bonding.

space group $P2_1/n$. The asymmetric unit of **2** contains two *N,N′*-bidentate bridging ligands, two Cd ions, four iodide anions and one methanol molecule (Fig. 2a), which form two independent zig-zag polymers.

In complex **2** each Cd(II) ion is coordinated by two N donors from different ligands and two coordinated iodide anions, yielding a distorted tetrahedral coordination sphere with Cd–N and Cd–I distance in the range of those found in the other complexes [22,23]. Additionally, pyrimidyl and pyridyl units, are obviously not coplanar, the dihedral angles between the two heterocyclic units are ca. 17.7° and 17.2° for Cd1 chain, and 28.9° and 22.6° for Cd2 chain.

It is interesting to observe that C–H···N and C–H···I intermolecular hydrogen bonds are formed between adjacent 1D chains, resulting in a 2D fluctuant plane. As shown in Fig. 2b, two pyrimidine nitrogen atoms of L^2 and iodide anions serve as the acceptors to form two kinds of hydrogen bonds ($d_{C6\cdots N11}$ = 3.43 Å, C6–H···N11 = 153.0°; $d_{C36\cdots N2}$ = 3.53 Å, C36–H···N2 = 171.0°; $d_{C23\cdots I1}$ = 3.88 Å, C23–H···I1 = 150.0°). Then methanol molecules not only as hydrogen bonding donors take part in intramolecular hydrogen bonding pattern with iodide anions, but also as hydrogen bonding acceptors, participate in intermolecular hydrogen bonding pattern with C–H. As a result, methanol molecules, acting as glue, cemented the fluctuant planes to give rise to a 3D network.

3.2.4. $\{[ZnL^2(H_2O)_4](ClO_4)_2\}_2$ (**3**) and $\{[CdL^2(H_2O)_4](ClO_4)_2\}_2$ (**4**)

Interaction of $Zn(ClO_4)_2$ or $Cd(ClO_4)_2$ with L^2 led to the generation of dinuclear macrocyclic complexes, $\{[ZnL^2(H_2O)_4](ClO_4)_2\}_2$ (**3**) and $\{[CdL^2(H_2O)_4](ClO_4)_2\}_2$ (**4**). Both complexes **3** and **4** crystallize in a non-chiral space group $P\bar{1}$. Complex **3** contains a $\{[ZnL^2(H_2O)_4]^{2+}\}_2$ 36-numbered cation macrocycle (Fig. 3a), and four free ClO_4^- anions. Each Zn(II) ion exhibits a slightly distorted octahedral coordination geometry, which is completed by two pyridyl nitrogen atoms from different ligands and four water molecules. The basal plane consists of two water oxygen atoms and two nitrogen atoms, while the axial positions are occupied by other two water oxygen atoms with a bond angle (O1–Zn–O4) of 176.4°, which is much close to the linearity, as displayed in Fig. 3a.

In **3**, the Zn–O bond lengths are in the range from 2.082(3) to 2.166(3) Å, and the Zn–N bond lengths are 2.111(4) and 2.124(4) Å, respectively. Zn–O1 and Zn–O4 axial bond lengths are shorter than the equatorial ones, which mean that the metal ions are located in a compressed octahedral coordination geometry. In order to reduce steric hindrance, the adjacent coordinated pyridyl

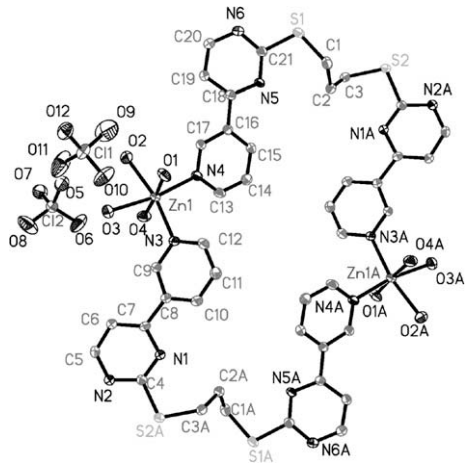


Fig. 3a. Molecular structure of **3** showing the numbering scheme and displacement ellipsoids at the 30% probability level, hydrogen atoms are omitted for clarity [symmetry code: 2 − *x*, −*y*, −*z* for **3**].

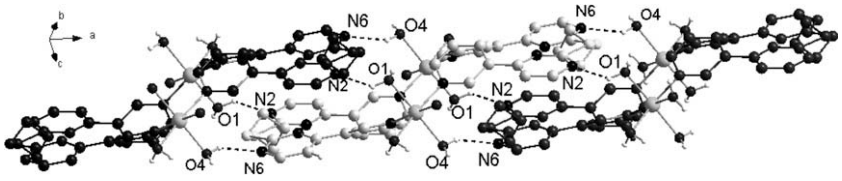


Fig. 3b. View of the structure of 1D chains of **3** showing the intermolecular hydrogen bonding along *a*-axis.

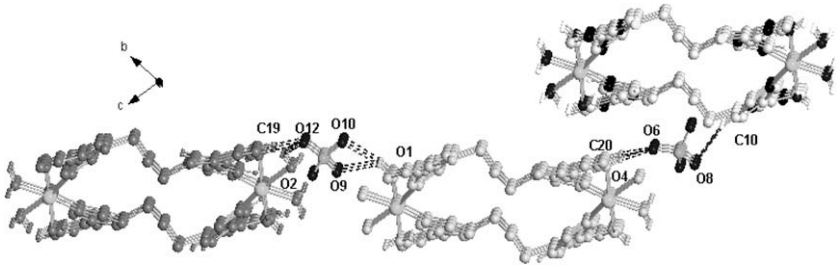


Fig. 3c. View of the structure of a 3D supramolecular framework of **3** showing the intermolecular and intramolecular hydrogen bonding.

rings are inclined to each other with a dihedral angle of 51.6° and a N–Zn–N bond angle of 100.9(2)°, and the dihedral angle between the adjacent pyridyl ring and the pyrimidine ring is 28.5°. In addition, the coordinated pyridyl rings in the symmetrical positions are parallel to each other. By adopting a *N*,*N*′-bidentate bridging coordination pattern, two ligands bridge two Zn(II) ions via N atoms of pyridyl ring in a *cis* conformation to form a M_2L_2 36-numbered macrocycle structure with a Zn···Zn distance of 10.938 Å [24–26].

Complex **4** takes a similar molecular structure to **3** (see Supplementary data S4). The coordination geometry around a Cd(II) atom is analogous to that of a Zn atom in **3**, which is surrounded by four water molecules and two nitrogen atoms from different L^2. The Cd–O bond lengths fall in the range from 2.261(6) to 2.320(6) Å and Cd–N are 2.300(6) and 2.304(6) Å, respectively. The axial bond lengths are also shorter than the equatorial bond lengths with an axial angle of 177.5(2)°. The neighboring coordinated pyridyl rings are inclined to each other with a dihedral angle of 49.9° and a N–Cd–N bond angle of 102.7(2)°. In the macrocycle, the Cd···Cd distance is 10.993 Å.

Although the actual assembly process may happen all at once rather than stepwise, it is particularly interesting and more convenient to describe the 3D structure of **3** or **4** formed by hydrogen bonds in a three-step procedure.

For complex **3**, two independent macrocycle units are linked each other via intermolecular hydrogen bonds O1–H···N2 and O4–H···N6 [O1–H···N2 ($-1+x, y, z$), O1···N2, 2.735(5) Å, O1–H···N2, 137.0°; O4–H···N6 ($1+x, y, z$), O4···N6, 2.835(5) Å, O4–H···N6, 144.0°], forming a tiled chain along *a*-axis. As shown in Fig. 3b, the hydrogen bonds are involved with *cis* nitrogen atoms of pyrimidine rings and the hydrogen of coordinated water molecules, O1 and O4. On the other hand, free perchlorate anions are moored to chains *via* intermolecular hydrogen bonds, O1–H···O9, O1–H···O10, O4–H···O6 and C10–H···O8 [O1–H···O9, O1···O9, 2.970(6) Å, O1–H···O9, 114.0°; O1–H···O10, O1···O10, 3.067(5) Å, O1–H···O10, 169.0°; O4–H···O6, O4···O6, 2.917(5) Å, O4–H···O6, 168.0°, C10–H···O8 ($x, y, -1+z$), C10···O8, 3.481(7) Å, C10–H···O8, 163.0°]. Then the neighboring chains self-assemble through intermolecular hydrogen bonds, O2–H···O12 [O2···O12, 2.886(5) Å, O2–H···O12, 107.0° ($1-x, 1-y, 1-z$)] and C19–H···O12 [C19···O12, 3.305(5) Å, O1–H···O9, 166.0° ($1-x, 1-y, 1-z$)] interactions forming fluctuant layers along *b*-axis.

Furthermore another interesting feature of **3** is the 3D network, formed by intermolecular hydrogen bonds of the adjacent layers between oxygen atoms of anions and hydrogen atoms of aryl rings through C20–H···O6 [C···O6, 3.411(6) Å, C20–H···O6, 1148.0° ($-1+x, y, z$)] and C10–H···O8 [C10···O8, 3.481(7) Å, C10–H···O8, 163.0° ($x, y, -1+z$)] interactions along *c*-axis (as shown in Fig. 3c).

Analogously, complex **4** takes the same molecular packing stack model in a supramolecular structure to **3**.

3.2.5. $[ZnL^1I_2]_n$ (**5**) and $[CdL^1I_2]_n$ (**6**)

Both **5** and **6** pack into the same centrosymmetric space group *C2/c*. The X-ray structures show clearly that **5** (shown in Fig. 4a) and **6** (see Supplementary data S5) are one-dimensional architectures. Each metal atom is bound to two pyridyl N atoms and two iodide anions to attain a pseudo-tetrahedral coordination geometry with M–N distances of 2.059(9)–2.275(5) Å and M–I 2.5416(15)–2.6764(8) Å. The dihedral angles for the two coordination pyridyl rings about Zn1 and Cd1 are 86.3° and 89.1°, respectively. Coordination to the metal center forces serious twisting

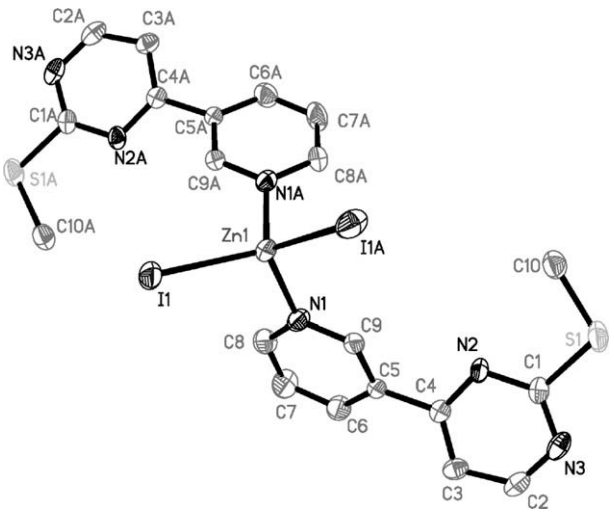


Fig. 4a. ORTEP diagrams (30% thermal probability) of the molecular structure of **5** with the atom-numbering scheme; hydrogen atoms are omitted for clarity.

between the pyridyl ring and the pyrimidyl unit with dihedral angles of 33.2° in **5** and 35.3° in **6**. Compared with the free ligand [17], the ligand in these complexes is much more contorted (see Fig. 4b).

In the crystal packing of **5** and **6**, there are effective face-to-face π···π interactions among the aromatic rings. In **5** the centroid–centroid distances of the π···π interactions are 3.389–3.445 Å. While in **6**, the centroid–centroid distances range from 3.389 to 3.483 Å.

Furthermore there are forces of van der Waals S···I contacts [S···I = 3.776 Å] among adjacent modules to build a supramolecular structure in **6** (see Supplementary data S6).

3.2.6. $\{\{[ZnL^1_2(H_2O)_4](ClO_4)_2\}_{0.5} \cdot L^1_{0.5} \cdot CH_3OH\}$ (**7**) and $\{\{[Cd_{0.5}L^1(H_2O)_2](ClO_4)\}_2 \cdot CH_3OH \cdot L^1\}$ (**8**)

Complexes **7** and **8** pack into the same centrosymmetric space group $P\bar{1}$ with similar crystal structures (molecular structure of **7** as the example shown in Fig. 5a). Two ligands and one metal ion, lattice methanol molecules and counter-anions as well as a free ligand are present in a symmetric unit of **7**. In these two complexes, the metal center is coordinated by four water molecules and two pyridyl N atoms from different ligands, adopting slightly distorted octahedral coordination geometry. Notedly different from the coordination model of L^1 in **5**–**6** or other complexes [17], L^1 is monodentate coordinated to a metal atom in **7**. Intermolecular face-to-face π···π contacts are observed between the heterocycle rings of the free ligand and the ligand binding to metal atom, although they are not strictly coplanar (mean plane angles between the corresponding heterocycle rings are 3.6° and 6.8° in **7**). The centroid–centroid distance of these π···π interactions are 3.754 and 3.787 Å in **7**.

It is also noted that hydrogen binding caused by free anions and methanol molecules with ligands or water molecules play important roles to connect with near molecules in **7** (shown in Fig. 5b).

It is found that L^1 in **7** or **8** only adopts a monodentate coordination pattern, while both L^1 and L^2 through nitrogen atoms from pyridyl rings adopt a *N, N′*-bidentate bridging coordination pattern to connect metal atoms in other complexes. This bidentate coordination fashion is similar to those of Hg(II) complexes with L^1 [17]. For complexes **1** and **2**, systematic variation in dimensionality may be due to the different size of metal atoms, indicating a metal-directed synthesis. Compared complexes **3** and **4** with complexes **1** and **2**, perchlorate anions probably play an important template role in the formation of macrocyclic complexes, indicating an anion-directed synthesis. Complexes resulted from L^1 and L^2 with different molecular structures prove that the role of ligands is much more important than other factors in the assembly process, minor modifications of the ligands will lead to conspicuous changes of the molecular structures of their metal complexes.

3.3. Thermogravimetric properties

Thermogravimetric analysis data for all complexes are given in Fig. 6. For complex **1**, a stable region is observed between RT and 198 °C, while it is between RT and 285 °C for complex **2**. The thermal model of complex **3** shows that the thermal decomposition takes place in two distinct stages. In the first stage, the weight loss corresponds to the loss of eight coordinated water molecules per

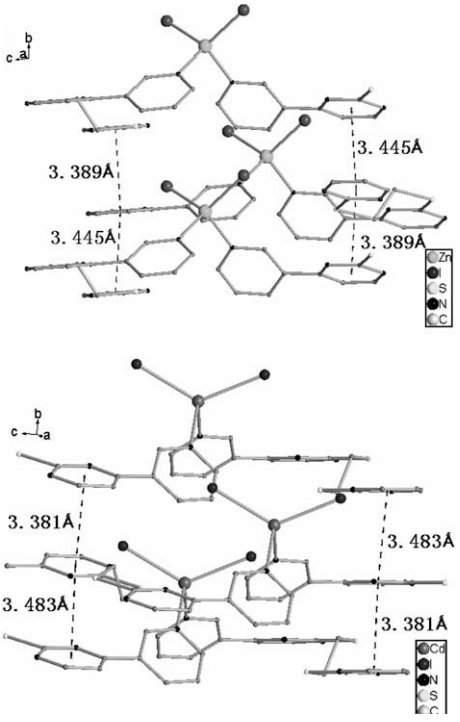


Fig. 4b. Perspective views of the π···π stacking interactions in **5** (top) and **6** (bottom).

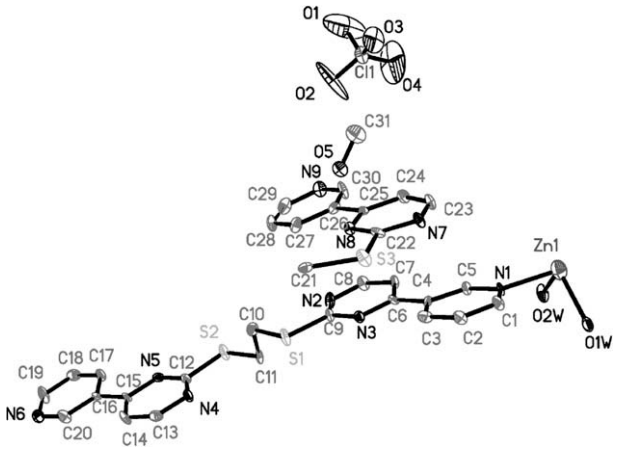


Fig. 5a. ORTEP diagrams (30% thermal probability) of the molecular structure of **7** with the atom-numbering scheme, hydrogen atoms are omitted for clarity.

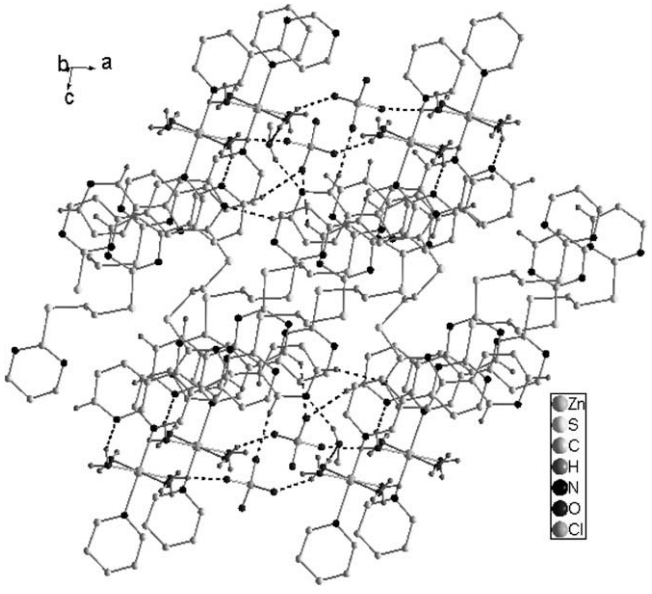


Fig. 5b. View of a 3D supramolecular framework of **7** showing the intermolecular and intramolecular hydrogen bonding.

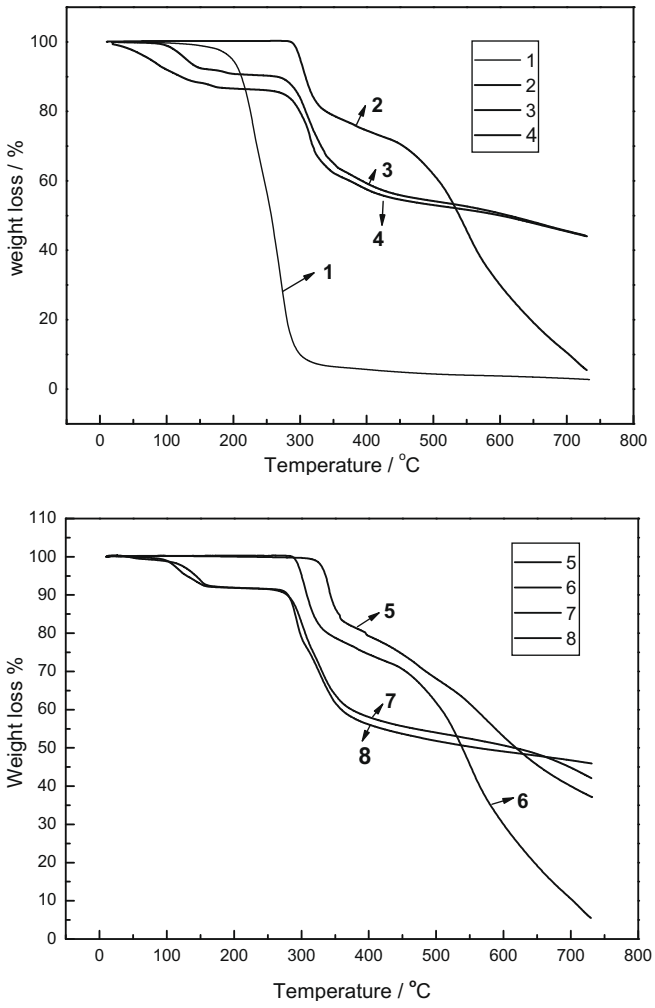


Fig. 6. *Top:* TGA curves of complexes **1**–**4**; *bottom:* TGA curves of complexes **5**–**8**. Heating rate: 20 °C min^{-1}.

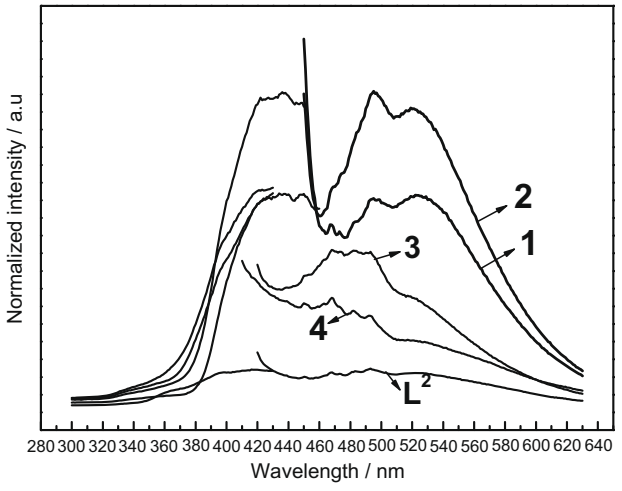


Fig. 7. Excitation and emission spectra of **1**, **2**, **3**, **4** and $\mathbf{L^2}$ in the solid state at room temperature.

formula between 25 and 230 °C. Then the complex begins to decompose. As for the decomposition of complex **4**, the weight loss attributed to the gradual release of eight-coordinated water molecules is observed between RT and 240 °C, then the decomposition happens. As for **5** and **6**, they are very stable in a temperature region between RT and 310 °C. For complexes **7** and **8**, the TGA curves show that the thermal decomposition takes place in two distinct stages. Thermal decompositions first occur to lose water molecules or free solvent molecules between 25 and 250 °C, then the subsequent decomposition starts.

3.4. Luminescence properties

The excitation and emission spectra of complexes **1**–**4**, and L^2 in the solid state at room temperature are shown in Fig. 7. These complexes exhibit intense blue fluorescence emission bands at ca. 494 and 521 nm for **1**, 495 and 520 nm for **2**, 468 and 493 nm for **3**, 467 and 493 nm for **4**, respectively, while weaker blue-fluorescent emission bands are observed at 467 and 493 nm for L^2, under the same conditions. These emissions are neither metal-to-ligand charge transfer nor ligand-to-metal charge transfer in nature, because Zn(II) or Cd(II) ions are difficultly oxidized or reduced due to their d^{10} configurations. These emissions are assigned to the intraligand $\pi\cdots\pi_*$ fluorescence emission since the corresponding ligand also shows a similar emission, i.e., they belong to ligand-to-ligand charge transfer (LLCT) [27,28]. Compared with those of L^2, the increase of emission occurred in complexes **1**–**4** may be ascribed to effective increase of the rigidity and asymmetry of the ligand due to its chelation to the metal atom, which reduces the loss of energy by radiationless decay process [29–32]. Furthermore in complexes **1**–**4** and the free ligand, existences of $\pi\cdots\pi$ interactions between the adjacent aromatic rings may be favorable for reduction of the energy of the $\pi\cdots\pi_*$ transition to some extent and thus help the luminescence [33]. However, complexes **5**–**8** and L^1 did not show any luminescence properties under the same conditions, this is probably due to the short alkyl chain of L^1, which leads to the weak $\pi\cdots\pi$ stacking interactions between neighboring molecules in the crystal structure. As a result, it is inferred that complexes **1** and **2** may be suitable as candidates for blue fluorescent materials.

4. Conclusion

In summary, eight novel complexes with different architectures were constructed from 1,3-bis (4-(pyridin-3-yl) pyrimidin-2-ylthio) propane (L^2) and 1,2-bis (4-(pyridin-3-yl) pyrimidin-2-ylthio) ethane (L^1). Although the difference of L^2 from L^1 lies in the length of alkyl chains, complexes derived from L^2 showed quite distinct coordination architectures and excellent fluorescent properties compared with those derived from L^1. The present study proves that a minor modification about the ligand can give rise to great changes not only in structures but also in properties. Meanwhile, geometric needs of metal atoms and anion effects also play important roles in the formation of the supramolecular architectures. In addition, complexes **1**–**4** exhibit blue fluorescence emissions, and complexes **1** and **2** may be suitable as candidates for potential photoactive materials.

Acknowledgements

The authors are grateful to the financial supports from National Natural Science of Foundation of China (Project No. 20801011) and China Postdoctoral Research Fund (Project No. 20070411010).

Appendix A. Supplementary data

CCDC 679979–679987 contain the supplementary crystallographic data for this article. These data can be obtained free of

charge via http://www.ccdc.cam.ac.uk/conts/retrieving.html, or from the Cambridge Crystallographic Data Centre, 12 Union Road, Cambridge CB2 1EZ, UK; fax: (+44) 1223-336-033; or e-mail: deposit@ccdc.cam.ac.uk. Supplementary data associated with this article can be found, in the online version, at doi:10.1016/j.poly.2009.01.009.

References

[1] B.F. Abrahams, S.R. Batten, H. Hamit, B.F. Hoskins, R. Robson, Angew. Chem., Int. Ed. Engl. 35 (1996) 1690.
[2] C. Janiak, Dalton Trans. (2003) 2781.
[3] S. Kitagawa, R. Kitaura, S.I. Noro, Angew. Chem., Int. Ed. 43 (2004) 2334.
[4] R.J. Hill, D.L. Long, N.R. Champness, P. Hubberstey, M. Schröder, Acc. Chem. Res. 38 (2005) 335.
[5] F. Yamashita, H. Kuniyasu, J. Terao, N. Kambe, Inorg. Chem. 45 (2006) 1399.
[6] M. Bardajı, M.J. Calhorda, P.J. Costa, P.G. Jones, A. Laguna, M.R. Pérez, M.D. Villacampa, Inorg. Chem. 45 (2006) 1059.
[7] R. Peng, D. Li, T. Wu, X.P. Zhou, S.W. Ng, Inorg. Chem. 45 (2006) 4035.
[8] X.H. Bu, Y.B. Xie, J.R. Li, R.H. Zhang, Inorg. Chem. 42 (2003) 7422.
[9] Y.B. Xie, C. Zhang, J.R. Li, X.H. Bu, J. Chem. Soc., Dalton Trans. (2004) 562.
[10] Y. Zheng, M. Du, J.R. Li, R.H. Zhang, X.H. Bu, J. Chem. Soc., Dalton Trans. (2003) 1509.
[11] Y. Zheng, J.R. Li, M. Du, R.Q. Zou, X.H. Bu, Cryst. Growth Des. 5 (2005) 215.
[12] M.C. Hong, Y.J. Zhao, W.P. Su, R. Cao, M. Fujita, Z.Y. Zhou, J. Am. Chem. Soc. 122 (2000) 4819.
[13] W.P. Su, M.C. Hong, J.B. Weng, R. Cao, S.F. Lu, Angew. Chem., Int. Ed. 39 (2000) 2911.
[14] L. Han, M.C. Hong, R.H. Wang, B.L. Wu, Y. Xu, B.Y. Lou, Z.Z. Lin, Chem. Commun. (2004) 2578.
[15] C.H. Huang, S.H. Gou, H.B. Zhu, W. Huang, Inorg. Chem. 46 (2007) 5537.
[16] C.H. Huang, G. Xu, H.B. Zhu, Y. Song, S.H. Gou, Inorg. Chim. Acta 361 (2008) 5.
[17] H.Z. Dong, J. Yang, G. Xu, S.H. Gou, Inorg. Chem. 47 (2008) 2913.
[18] SMART and SAINT, Area Detector Control and Integration Software, Siemens Analytical X-ray Systems Inc., Madison, WI, 1996.
[19] G.M. Sheldrick, SHELXTL V5.1, Software Reference Manual, Bruker AXS Inc., Madison, WI, 1997.
[20] A.M. Beatty, Coord. Chem. Rev. 246 (2003) 131.
[21] H.W. Roesky, M. Andruh, Coord. Chem. Rev. 236 (2003) 91.
[22] Z. Liu, P. Liu, Y. Chen, J. Wang, M.H. Huang, Inorg. Chem. Commun. 8 (2005) 212.
[23] R. Maech, J. Pons, J. Ros, W. Clegg, Inorg. Chem. 42 (2003) 7403.
[24] C.Y. Su, Y.P. Cai, C.L. Chen, H.X. Zhang, B.S. Kang, J. Chem. Soc., Dalton Trans. (2001) 359.
[25] C.Y. Su, Y.P. Cai, C.L. Chen, M.D. Smith, W. Kaim, H.C. Loye, J. Am. Chem. Soc. 125 (2003) 8595.
[26] D.K. Chand, K. Biradha, M. Fujita, Chem. Commun. (2001) 1652.
[27] P.C. Ford, A. Vogler, Acc. Chem. Res. 26 (1993) 220.
[28] D.J. Casadonte, D.R. McMillin, J. Am. Chem. Soc. 109 (1987) 331.
[29] L.Y. Zhang, G.F. Liu, S.L. Zheng, B.H. Ye, X.M. Zhang, X.M. Chen, Eur. J. Inorg. Chem. (2003) 2965.
[30] J.C. Dai, X.T. Wu, Z.Y. Fu, C.P. Cui, S.M. Wu, W.X. Du, L.M. Wu, H.H. Zhang, Q. Sun, Inorg. Chem. 41 (2002) 1391.
[31] X.L. Wang, C. Qin, Y.G. Li, N. Hao, C.W. Hu, L. Xu, Inorg. Chem. 43 (2004) 1850.
[32] H. Yersin, A. Vogler, in: Photochemistry and Photophysics of Coordination Compounds, Springer-Verlag, Berlin, 1987.
[33] S.N. Wang, J.F. Bai, H. Xing, Y.Z. Li, Y. Song, Y. Pan, M. Scheer, X.Z. You, Cryst. Growth Des. 7 (2007) 747.

2.2. Methods

2.2.1. Product analysis

HPLC was employed to detect the reaction products under the conditions used in the kinetic measurements (excess of Glc3Me over Cr^{VI}). The chromatograms were obtained on a KNK-500 A chromatograph provided with a 7125 HPLC pump. The separation was carried out on a Supelcogel C-610H HPLC column (300×7.8 mm, Bio-Rad Laboratories) using 0.1% P/V H_3PO_4 as eluent and a flow rate of 0.5 mL/min, at 30 °C. The effluent was monitored with refractive index (ERC-7522, ERMA INC) and UV (115 UV Gilson, $\lambda = 220$ nm) detectors. The $[H^+]$ of the reaction mixtures (Glc3Me:Cr^{VI} ratios of 25:1, 50:1 and 100:1) was adjusted to 0.2 mol/L by addition of 2 mol/L $HClO_4$ and then the samples were filtered through a 0.2 μm membrane prior to injection into the chromatographic system.

Standard samples of 2-methyl-D-arabinose (Ara2Me), 3-methyl-D-gluconic acid (Glc3MeA) – prepared following published procedures [19,20] – and formic acid were prepared individually and the chromatographic retention times determined separately.

Chromatograms of the reaction mixtures showed two peaks with retention times (t_R) of 13′ 44″ and 17′ 11″, in addition to the peak of unreacted Glc3Me at t_R = 11′ 55″. The retention times of the new peaks are coincident with those of the standard solutions of Ara2Me and formic acid, respectively. No peak corresponding to Glc3MeA was detected in the reaction mixture. Furthermore, co-chromatography of a Cr^{VI}/Glc3Me reaction mixture and Ara2Me or formic acid resulted in the increase of peaks at 13′ 44″ or 17′ 11″, respectively. Additionally, the presence of HCO_2H acid was confirmed through the $HgCl_2$ reaction [21].

For the Glc3Me to Cr^{VI} ratios used in the kinetic studies (higher than 50:1), carbon dioxide was never detected as a reaction product.

2.2.2. Glc3Me stability

The stability of Glc3Me under conditions used in the kinetic studies was checked by monitoring the optical rotation changes on a JENA polarimeter with thermostated 20-cm tubes using the sodium D line. Reactant solutions were previously thermostated and transferred into the cell immediately after mixing. The optical rotations were recorded at different times after the preparation of the solutions and were identical to that of freshly prepared Glc3Me solutions. The specific rotation of Glc3Me was found to be $[\alpha]^{33}_D = +54.1° \pm 0.5°$ ($c = 3.88$ g/100 mL, 1.0 M $HClO_4$, $t = 10$ min to 30 h), a value similar to that measured for Glc3Me in aqueous solution: $[\alpha]^{20}_D = +55.7° \pm 0.5°$ ($c = 4.51$ g/100 mL).

The stability of the Glc3Me at 33 °C was also confirmed by HPLC after incubation of the solutions at fixed $[H^+]$.

2.2.3. Polymerization test

Polymerization of acrylamide was investigated during the reaction of Glc3Me with Cr^{VI} as a test for free radical generation. Acrylamide (0.6 g) was added to a reaction mixture containing $K_2Cr_2O_7$ (3×10^{-3} mmol) and Glc3Me (0.3 mmol) in 2 mL of 0.5 mol/L $HClO_4$, at 33 °C. When the color of Cr^{VI} disappeared, 1 mL of the mixture was diluted with 1 mL of methanol and a white polymer precipitated. Control experiments showed that no polymerization of acrylamide takes place under the experimental conditions with either $HCrO_4^-$ or the Glc3Me alone. The possible reaction of Cr^V or Cr^{IV} with acrylamide was tested with $Na[Cr^VO(ehba)_2]$ and $Na_2[Cr^{IV}O(ehba)_2]$. No precipitation occurred on mixing the Cr^V or Cr^{IV} complexes with acrylamide under the same conditions as those used in the Cr^{VI} + Glc3Me reaction.

2.2.4. Spectrophotometric measurements

Kinetic measurements were performed by monitoring absorbance changes using a Jasco V-550 UV/VIS spectrophotometer with a fully thermostated cell compartment (±0.2 °C). The reactions were followed under pseudo-first-order conditions, at 33 °C, using at least a 50-fold molar excess of Glc3Me over Cr^{VI} and different $[HClO_4]$. Reactant solutions were previously thermostated at 33 °C and transferred into a 1-cm pathlength cell immediately after mixing.

The disappearance of Cr^{VI} was followed spectrophotometrically at 350 nm until at least 80% conversion. In the kinetic measurements, the initial concentration of Cr^{VI} and I were kept constant at 8.0×10^{-4} mol/L and 1.02 mol/L, respectively, while $[HClO_4]$ was varied from 0.15 to 1.02 mol/L, at various [Glc3Me].

The experimental pseudo-first-order rate constants (k_{exp}), determined from the absorbance versus time curves at 350 nm, were deduced from multiple determinations and were within ±5% of each other. The first-order dependence of the rate upon $[Cr^{VI}]$ was verified in a set of experiments where the $[Cr^{VI}]_0$ was varied between 4.0×10^{-4} and 8.0×10^{-4} mol/L but T, $[Glc3Me]_0$, $[H^+]$ and I were kept constant.

The formation of Cr^{III} was monitored by following changes in the 570 nm absorption band. In these experiments the $[Cr^{VI}]_0$ was kept constant at 8.0×10^{-3} mol/L, (Glc3Me:Cr^{VI} ratio of 50) and the $[H^+]$ was varied between 0.40 and 1.02 mol/L. Rate constants obtained at this wavelength are in agreement with those calculated from data at 350 nm for the same experimental conditions.

Cr(VI) esters were investigated by UV–Vis spectrophotometry in the 350–500 nm region in which chromate esters show characteristic absorption bands. Reactions were performed at pH 3.52, where the redox reaction is slow enough to enable the observation of the ester formation. The instrument was zeroed to an arrangement of the reference and sample beams passing through matched cuvettes, both containing 6×10^{-4} mol/L Cr^{VI} at pH 3.52. The solution in the sample cell was replaced with the reaction solution containing 6×10^{-4} mol/L Cr^{VI} and 0.30–0.60 mol/L Glc3Me at pH 3.52, I = 1.02 M, and T = 33 °C. Spectra obtained within 40 min after mixing revealed a distinctive absorption at 373 nm.

The possible formation of Cr^{II} was examined by UV–Vis spectrophotometry in the 200–500 nm region in which CrO_2^{2+} show characteristic absorption bands. This experiment was performed at 22 °C, by periodic scanning of solutions containing 0.21 mol/L Glc3Me, 0.049 mmol/L Cr^{VI} and 1.26 mmol/L O_2, in 0.84 mol/L $HClO_4$. Under these conditions, the Cr^{VI} absorption band at 350 nm decreased in intensity, while new peaks at 293 nm and 247 nm, characteristic of CrO_2^{2+} [22], grew in.

2.2.5. EPR measurements

The EPR spectra were obtained on a Bruker EMX spectrometer operating at X-band frequencies (9–10 GHz). The microwave frequency was generated with a Bruker 04 ER and measured with a Bruker EMX 048T frequency meter. The magnetic field was measured with a Bruker EMX 035M NMR-probe gaussmeter. Spectra were recorded as first derivatives of the microwave absorption in 1024 points at ambient temperature (20 ± 1 °C). g-Values were determined by reference to diphenylpicryhydrazyl radical ($g = 2.0036$) as an external standard. Reactions were carried out by mixing Glc3Me and $K_2Cr_2O_7$ (ratio 49:1, $[Cr^{VI}] = 0.025$ mol/L) in 0.3 and 0.5 mol/L $HClO_4$; and by addition of $Na[Cr^VO(ehba)_2]$ (1.0 mmol/L), or Na_2CrO_4 (1.0 mmol/L) + glutathione (1.0 mmol/L), to solutions of Glc3Me (100 mmol/L) in acetate buffer (0.1 mol/L, pH 5.5) or HEPES buffer (0.1 mol/L, pH 7.5). Stock solution of $Na[Cr^VO(ehba)_2]$ (0.1 mol/L) was prepared in *N*,*N*-dimethylformamide. All of the EPR spectra were simulated using the program PEST WINSIM [23], assuming 100% Lorentzian line shapes.

The spectral parameters for each Cr^{V} species were consistent within all simulation, with maximum deviations in the g_{iso} values being ±0.0001 units. In the simulations, values for ^{1}H superhyperfine coupling constant a_H were included only where the a_H value was greater than the LW (line width) of the Cr^{V} species, since the signal is not significantly affected where the a_H value is ⩽LW.

3. Results and discussion

3.1. Products of the reaction of Glc3Me with Cr^{VI}

Under conditions used in the kinetic studies, excess of Glc3Me over Cr^{VI} in acid medium, HCO_2H and Ar2Me were identified by HPLC as the oxidation products of Glc3Me, while EPR and UV–Vis spectroscopies showed that aqueous Cr^{III} was the final Cr species in the reaction mixture. Thus, the reaction of Glc3Me and Cr^{VI} can be written as in Scheme 1.

This result implies that, in this reaction, C1–C2 bond break prevails over C1–H cleavage. A fact that differentiates the reactivity of the 3-*O*-methyl derivative towards Cr^{VI} from glucose that yields the corresponding aldonic acid as the only reaction product [10].

3.2. Detection of an intermediate Cr^{VI}-ester

At pH 3.52, the redox reaction of Cr^{VI} with Glc3Me proceeds very slowly, with negligible reduction of Cr^{VI} in the first 40 min. Thus, at this pH, the ester formation can be distinguished clearly from the electron transfer reaction. Differential UV–Vis spectra of mixtures of Cr^{VI} and Glc3Me exhibit, immediately after mixing, a distinctive absorption band with λ_{max} = 373 nm consistent with that ascribed to Cr^{VI} oxo-esters [24] that can be assigned to Glc3Me–Cr^{VI} species. Continued scanning over 40 min showed no further change in the spectra. The absorbance of this band increased with the increasing concentration of Glc3Me when the [Glc3Me] was varied at pH 3.5 (Fig. 1), probably as a result of a shift toward the ester in the esterification equilibrium.

3.3. Intermediacy of Cr^{II}

Involvement of Cr^{II} in the mechanism of the oxidation of a number of alcohols, saccharides and hydroxyacids by Cr^{IV} and Cr^{VI} in $HClO_4$ has been demonstrated by conversion into CrO_2^{2+} upon reaction with molecular oxygen [22,25–27]. At high [O_2] and low [Cr^{VI}] the reaction of Cr^{II} with O_2 can compete successfully with the reaction of Cr^{II} with Cr^{VI} and the autocatalytic consumption of CrO_2^{2+} by Cr^{II}, and if formed, Cr^{II} should yield the CrO_2^{2+} product [25,26,28,29]. We examined the presence of intermediate Cr^{II} in the reaction of Glc3Me with Cr^{VI}, by monitoring the formation of CrO_2^{2+}, using $[Cr^{VI}]_0$ low enough to avoid the Cr^{VI} + Cr^{II} competitive reaction. A periodic scanning of the O_2-saturated solution (1.26×10^{-3} mol/L O_2) of a Cr^{VI} + Glc3Me reaction mixture in 0.84 mol/L $HClO_4$ over a period of 3 h, showed that the band at 350 nm, characteristic of Cr^{VI}, decreased in intensity while two absorption bands at λ_{max} = 247 and 293 nm appeared (Fig. 2). These two bands are characteristic of CrO_2^{2+} formed as a long-lived intermediate [22] that then slowly transforms into the final Cr^{III}. Since

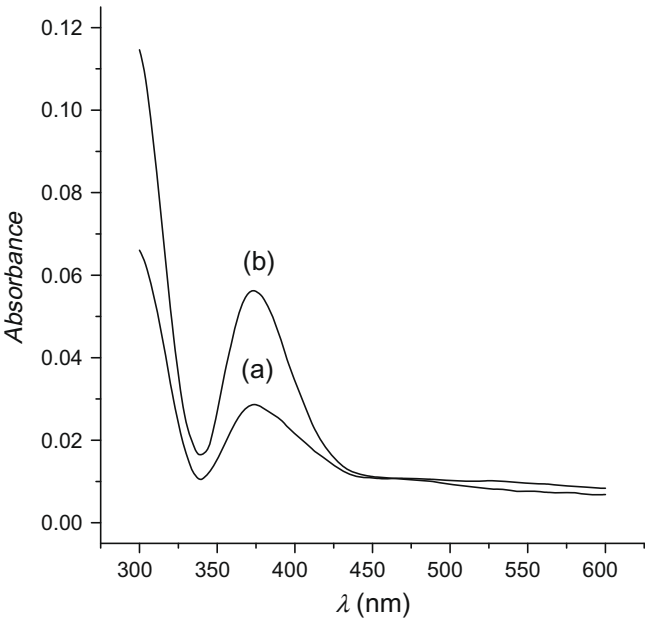


Fig. 1. UV–Vis difference spectra of Glc3Me/Cr^{VI} solutions at pH 3.52, showing the increasing band at 373 nm with increasing [Glc3Me]: (a) 0.30 and (b) 0.60 mol/L. $[Cr^{VI}] = 6.0 \times 10^{-4}$ mol/L, I = 1.02 mol/L, T = 33 °C. Spectra taken 30 min after preparation of the reaction mixture.

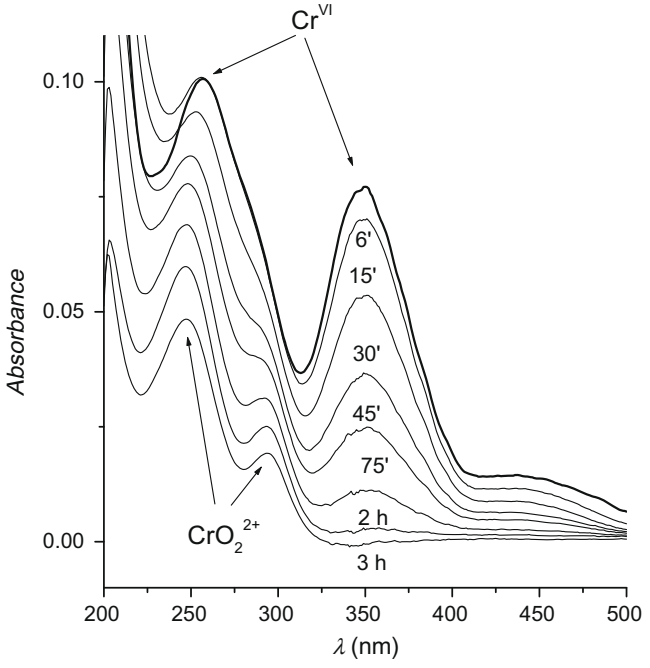
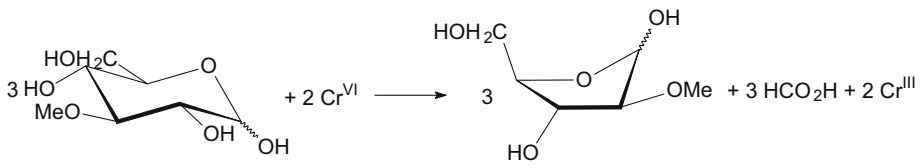


Fig. 2. Formation of CrO_2^{2+} (λ_{max} 293, 247) from the reaction between 0.21 mol/L Glc3Me, 1.26 mmol/L O_2 and 4.9×10^{-2} mmol/L Cr^{VI}, in 0.84 mol/L $HClO_4$. T = 22 °C.



Scheme 1.

CrO_2^{2+} can be exclusively formed by reaction of Cr^{II} with O_2, and, in turn, Cr^{II} had previously been demonstrated to form exclusively through two-electron reduction of Cr^{IV} [26,28], our spectroscopic results provide evidence that Cr^{II} and Cr^{IV} are involved in the redox mechanism of the reaction between Cr^{VI} and Glc3Me.

3.4. Detection of intermediate Cr^V

The most common means of detecting Cr^V complexes in solution is EPR spectroscopy, where strong isotropic signals are observed at room temperature in X-band spectra. The reduction of Cr^V by Glc3Me is $[H^+]$ dependent, and at the high $[H^+]$ used in the kinetic measurements, Cr^V–Glc3Me redox processes are fast and, consequently, high modulation amplitude is required to observe Cr^V. With a modulation amplitude of 4 G, the EPR spectra of solutions from the reaction between Cr^{VI} and 50-times excess of Glc3Me in 0.3–0.5 mol/L $HClO_4$, consisted of two signals: a major one centered at g_{iso1} 1.9788, and an additional weak signal at g_{iso2} 1.9712 (Fig. 3) with relative intensity ⩽10% of the main signal. The high modulation amplitude used to observe Cr^V species at this $[H^+]$, disabled the resolution of the signal superhyperfine (shf) pattern (the ^1H shf splitting (a_H) for Cr^V–alcoholato species is usually <1 G [4,9]). Given that the g values of Cr^V species are very sensitive to the co-ordination number and the nature of the donor groups bound to Cr^V [4,9,30], an estimation of the intermediate Cr^V species formed in the reaction of Cr^{VI} with Glc3Me was made based on g_{iso} values of the EPR signals. The g_{iso} value of 1.9788 is typical of five-coordinate oxochromate(V) complexes formed with *O*-donor ligands, while the value of 1.9712 is typical of a six-co-ordinate oxo-Cr^V complex with two alcoholato donor sites and three water molecules, and can be assigned to $[Cr(O)(O^1,O^2\text{-Glc3Me})(H_2O)_3]^+$ (**I**, Fig. 4) [4,9,30]. The positive charge of this species is also consistent with its appearance at high $[H^+]$ and it is possibly responsible for the higher rates observed for the Cr^V–Glc3Me redox reactions at pH < 1.

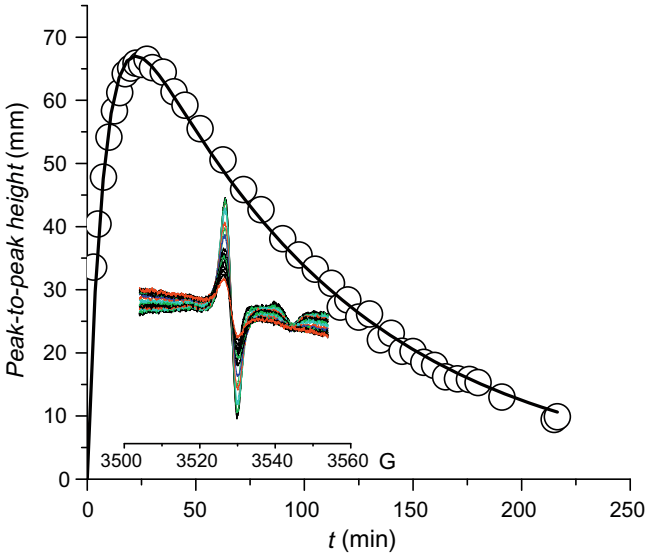


Fig. 3. Peak-to-peak heights of Cr^V EPR signals *vs.* time. $[Cr^{VI}] = 0.025$ mol/L, [Glc3Me] = 1.225 mol/L, $[H^+] = 0.3$ mol/L, $I = 1.02$ mol/L, $T = 20$ °C. Inset: time evolution of X-band EPR spectra from the reaction mixture in 0.3 mol/L $HClO_4$. $\nu = 9.766887$, mod. ampl. = 4 G.

At pH > 3 the redox reaction between Cr^V with Glc3Me becomes slow, Cr^V species remain in solution for longer periods of time and the shf pattern of the Cr^V EPR signals can be resolved using a modulation amplitude lower than the ^1H shf splitting. With this in mind, Cr^V–Glc3Me complexes formed upon addition of 100-times molar excess of Glc3Me to Cr^V generated in either the one-electron reduction of Cr^{VI} by glutathione or the ligand-exchange reaction of $[Cr^VO(ehba)_2]$ were investigated in the 5.5–7.5 pH range by EPR spectroscopy. The Cr^V EPR signals are more intense at pH 5.5 than at pH 7.5, probably because Cr^V disproportionation is slower at the lower pH [31]. In this pH range, the EPR spectra taken at the beginning of the reaction were dominated by a triplet at g_{iso1} 1.9792 ($a_H = 1.0 \times 10^{-4}$ cm^{-1}), with a minor component at g_{iso2} 1.9794 (quintet, $a_H = 0.9 \times 10^{-4}$ cm^{-1}). Fifteen minutes after mixing, the two components at g_{iso1} and g_{iso2} were present in 71% and 29%,

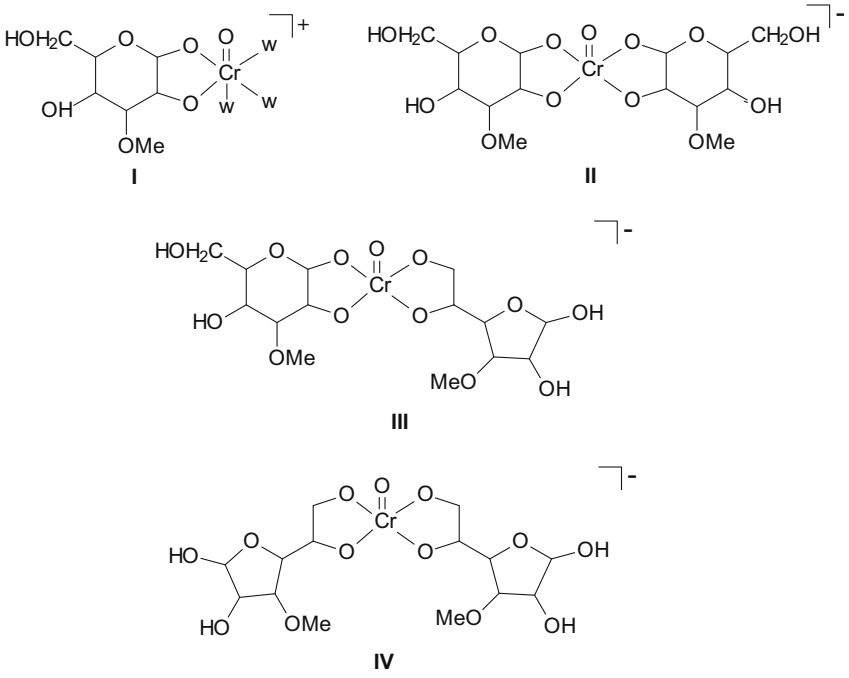


Fig. 4. Structures of Cr^V complexes formed with Glc3Me.

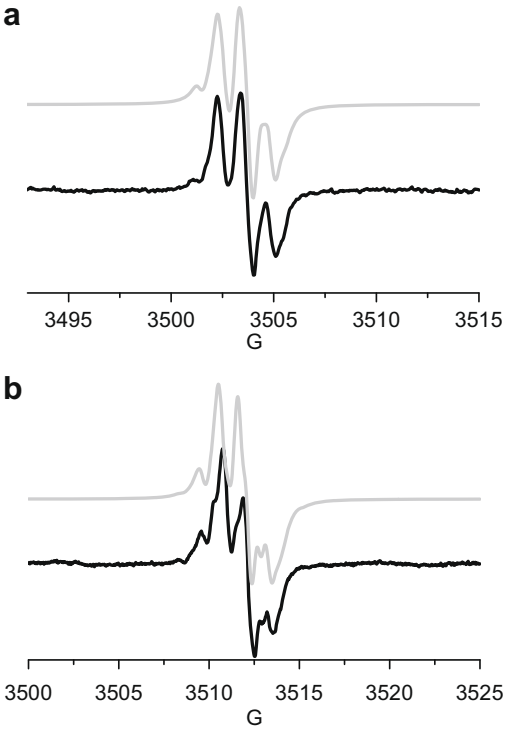


Fig. 5. Experimental (——) and simulated (——) X-band EPR spectra from mixtures of 1 mmol/L glutathione + 1mmol/L Cr^{VI} and 100 mmol/L Glc3Me, pH 5.5; taken (a) 15 min (ν = 9.705912 GHz) and (b) 1 h (ν = 9.728655) after mixing. Mod. ampl. = 0.2 G. T = 20 °C.

respectively (Fig. 5a). It is known that the EPR spectrum of a Cr^{V}-diolato species of six-membered ring *cis*-diols yields a doublet, since only one proton is in the plane of the unpaired electron density of the Cr^{V} ion. Consequently, the EPR spectral multiplicity of bis-chelate Cr^{V}-diolato$_2$ species formed between Cr^{V} and pyranosic *cis*-diols exhibit a triplet with two (one from each chelate ring) carbinolic protons coupled to the Cr^{V} electronic spin. In the present case, the major component of the EPR signal can be attributed to the bis-chelate [Cr(O)(*cis*-O^1,O^2-Glc3Me)$_2$] (**II**, Fig. 4). This result is in line with the reported higher ability of the *cis*- versus the *trans*-diolato for binding Cr^{V} [4,9,32]. The minor component at g_{iso2} 1.9794 can be attributed to the bis-chelate formed with the pyranose and furanose forms of Glc3Me: [Cr(O)(*cis*-O^1,O^2-Glc3Me)(O^5,O^6-Glc3Me-furanose)] (**III**, Fig. 4), with four protons coupled to the electronic spin of Cr^{V}. The assignment of the minor component to [Cr(O)(*cis*-O^1,O^2-Glc3Me-furanose)$_2$] was disregarded based on the a_H values – a_H values expected for Cr^{V}-diolato$_2$ species of five-membered ring *cis*-diols are lower than found here [33,34]. With time, the EPR spectral pattern slowly changed, the proportion of the components varied and a third component appeared. The EPR spectrum taken 1 h after mixing, shown in Fig. 5b, could be deconvoluted into a triplet at g_{iso1} 1.9792 ($a_H = 1.0 \times 10^{-4}$ cm^{-1}), a quintet at g_{iso2} 1.9794 ($a_H = 0.9 \times 10^{-4}$ cm^{-1}) and a septuplet at g_{iso3} 1.9793 ($a_H = 1.0 \times 10^{-4}$ cm^{-1}), in 6:3:1 ratio. Other minor species were also present, but they were not included in the simulations to avoid over-parameterization. Based on the shf coupling, the three components could correspond to [Cr(O)(*cis*-O^1,O^2Glc3Me)$_2$] (**II**), [Cr(O)(*cis*-O^1,O^2-Glc3Me)(O^5,O^6-Glc3Me-furanose)] (**III**) and [Cr(O)(O^5,O^6-Glc3Me-furanose)$_2$] (**IV**) (Fig. 4). At longer times, the proportion of the species at g_{iso1} decreased and the spectra were dominated by species at g_{iso2} and g_{iso3}. These five-coordinate Cr^{V} bis-chelates were still observed 15 h after mixing. Thus, initially, Cr^{V} bis-chelate is formed with Cr^{V} bound to the 1,2-*cis*-diolato moiety of the pyranose form of Glc3Me (kinetic control); but, with time, it transforms into bis-chelates with Cr^{V} bound to the 5,6-*vic*-diolato moiety of the furanose form of the ligand.

3.5. Rate studies

The kinetics of the reaction of Glc3Me with Cr^{VI} was examined by monitoring the [Cr^{VI}] consumption under conditions of excess of Glc3Me over Cr^{VI}, in the 0.15–1.02 mol/L $HClO_4$ range. UV–Vis spectra of the reaction mixtures showed an absorbance band at 350 nm and a shoulder at 420–500 nm, characteristic of Cr^{VI} in acidic medium. At 350 nm, the absorbance versus time curves exhibited a monotonic decrease and the rate constants were calculated from the absorbance changes at this wavelength. As stated before, Cr^{V} species are formed in the chromic oxidation of Glc3Me, and it is known that these species absorb at 350 nm and may superimpose Cr^{VI} absorbance [35]. However, if Cr^{V} reacts faster than Cr^{VI} and exists in solution in a sufficiently small concentration, changes in absorbance at 350 nm essentially reflect changes in Cr^{VI} concentration. The relative values of the Cr^{VI} versus Cr^{V} reduction rate constants obtained from the Cr^{V} EPR signal intensity variation during the reaction course demonstrated this is the case for the reaction studied here (discussed below).

The kinetic profiles at 350 nm could be adequately described by a single exponential decay from which Cr^{VI} pseudo-first order rate constants (k_{exp}) were calculated. Table 1 summarizes values of k_{exp} for various concentrations of Glc3Me and $HClO_4$. Plots of k_{exp} versus [Glc3Me] at constant [H^+] gave good straight lines (Fig. 6) from which values of k_h were determined (Table 1, right). Values of k_h showed quadratic dependence on [H^+] (Fig. 6, inset), and the rate constant k_6, calculated by non-linear least-square fit of {k_h, [H^+]} data pairs, was found to be $(6.35 \pm 0.02) \times 10^{-4}$ mol^{-3} L^3 s^{-1}. Consequently, the complete rate law for the Cr^{VI} consumption can be expressed as in Eq. (1):

$$-d[Cr^{VI}]/dt = k_6[H^+]^2[Glc3Me][Cr^{VI}]. \quad (1)$$

Table 1
Experimental pseudo-first-order rate constants (k_{exp})[a] for different concentrations of Glc3Me and $HClO_4$.

[$HClO_4$] (mol/L)	10^5 k_{exp} (s^{-1}) for [Glc3Me] (mol/L)					
	0.04	0.08	0.12	0.16	0.20	10^4 k_h (mol^{-1} L s^{-1})
0.15		1.94(1)	2.58(3)	2.94(3)	4.09(8)	2.0(1)
0.31	3.12(1)	6.19(3)	8.23(9)	10.4(3)	14.4(1)	7.0(2)
0.46	6.51(4)	12.4(1)	17.7(1)	22.0(4)	28.4(1)	14.3(3)
0.61	10.9(2)	20.1(1)	31.0(2)	40.2(1)	49.9(9)	25.2(2)
0.77	15.8(4)	29.9(3)	44.4(6)	59.2(1)	72.4(2)	36.7(3)
0.92	22.8(3)	44.5(1)	63.6(9)	84.0(7)	106(1)	53.1(5)
1.02	27.0(4)	53.2(1)	78.5(4)	104(1)	135(1)	66.4(6)

[a] Mean values from multiple determinations. $[Cr^{VI}]_0 = 6 \times 10^{-4}$ mol/L, T = 33 °C; I = 1.02 M, λ_{350}.

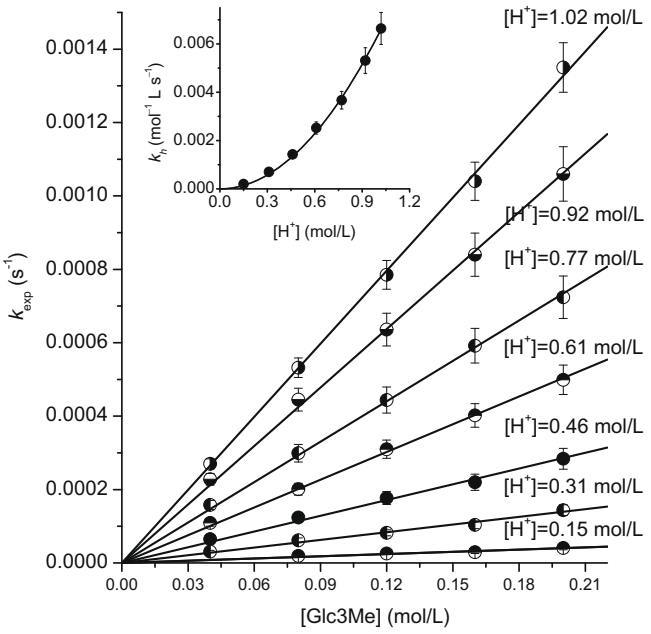


Fig. 6. Effect of [Glc3Me] on k_{exp} at 33 °C, I = 1.02 mol/L, λ = 350 nm and different [H$^+$]. Inset: dependence of k_h on [H$^+$].

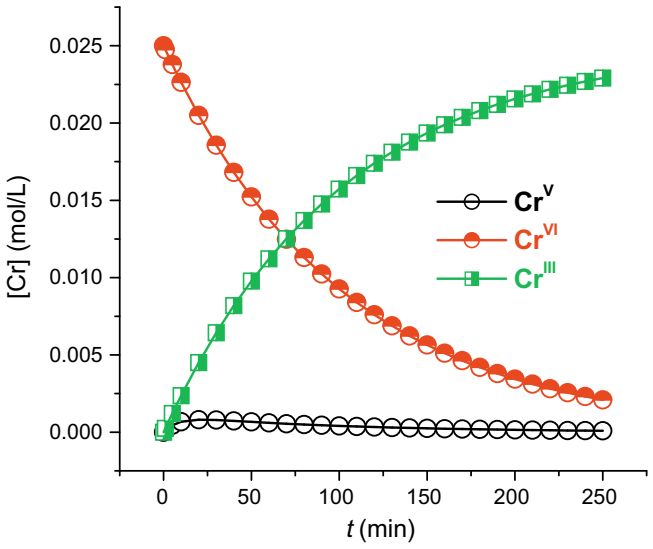


Fig. 7. Simulated kinetic profiles for Cr species. [Cr] calculated using k_a = 0.00496 min^{-1} and k_b = 0.1224 min^{-1} obtained from EPR data in 0.3 mol/L $HClO_4$. [Cr]$_T$ = 0.025 mol/L.

The kinetic results were independently confirmed by following the redox reaction by EPR spectroscopy. Fig. 3 shows a typical curve for the growth and decay of the Cr^V EPR signal peak-to-peak height as a function of time. The kinetic profiles could be adequately fitted with the rate expression derived from a two-step reaction sequence involving two consecutive first-order reactions (Scheme 2 and Eq. (2)) [11,36]:

$$EPR_{area} = Ak_a\{\exp(-2k_at) - \exp(-k_bt)\}/(k_b - 2k_a), \quad (2)$$

where A depends on the spectrometer settings, and k_a and k_b refer to the rate of disappearance of Cr^{VI} and Cr^V, respectively, and were evaluated from a non-linear least-squares fit of Eq. (2). In the 0.3 to 0.5 mol/L $HClO_4$ range, the calculated values of k_a were more than ten-times lower than k_b. For conditions in Fig. 3, k_a = 0.00496 min^{-1} and k_b = 0.1224 min^{-1}. The fact that $k_b > k_a$ implies that the slow redox step involves the reduction of Cr^{VI}. The simulation of the kinetic profiles employing k_a and k_b values obtained from EPR data in 0.3 mol/L $HClO_4$ (Fig. 7), shows that the maximal [Cr^V] represents 3% of the total Cr in solution. These results confirm that [Cr^V] is low throughout the reaction and should not interfere absorbance at 350 nm, which essentially reflects changes in [Cr^{VI}]. Rate constants calculated by this technique were consistent with those obtained from the spectrophotometric measurements at 350 nm, under the same experimental conditions. For 1.225 mol/L Glc3Me and 0.3 mol/L $HClO_4$, the value determined spectrophotometrically for k_{exp} was 1.90×10^{-4} s^{-1}, that compares well with $2k_a = 1.65 \times 10^{-4}$ s^{-1} obtained from EPR measurements.

Sequential absorption spectra of the reaction mixture showed the appearance and growth of two d–d bands at λ_{max} = 409 and 572 nm (Fig. 8). Kinetics traces at 570 nm showed that at this wavelength, the absorbance grew to intensities higher than expected for the free Cr^{3+} and then slowly decayed to the value corresponding to $[Cr(H_2O)_6]^{3+}$ (409 nm, ε = 17.7 mol^{-1} L cm^{-1} and 572 nm, ε = 15.2 mol^{-1} L cm^{-1}) [37], as shown in the inset of Fig. 8. This behavior suggests the formation of an intermediate Cr^{III}–Glc3Me complex, which then hydrolyzes to the final product [30,38]. EPR spectra taken at the end of the reaction confirm that Cr^{3+} is the final Cr species in the reaction of Cr^{VI} with excess Glc3Me in acid medium.

In order to determine the rate of Cr^{III} formation relative to that of the Cr^{VI} consumption, the formation of Cr^{III} was followed at 570 nm, in the presence of excess of Glc3Me in the 0.40–1.02 mol/L $HClO_4$ concentration range. Under these conditions, the first order dependence of the rate upon [Cr^{VI}] was verified. For [Glc3Me]$_0$ = 0.4 mol/L, values of k_{exp} calculated at this wavelength

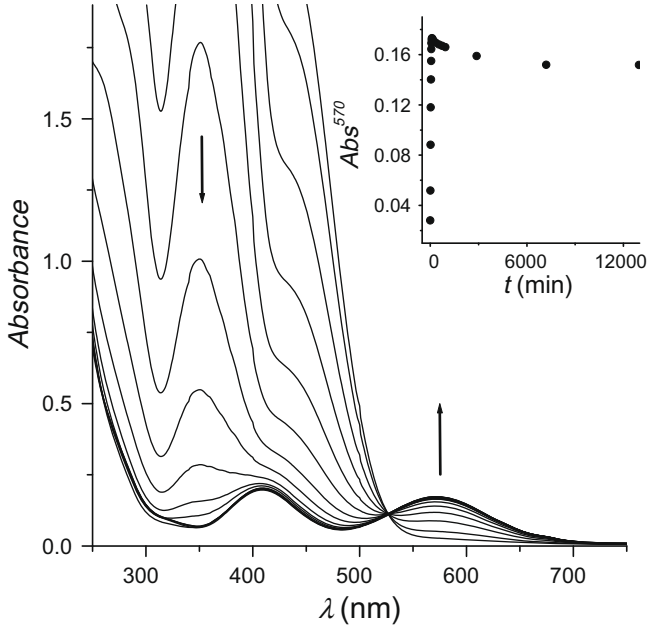
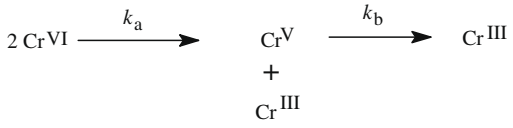


Fig. 8. Time evolution of the UV–Vis spectra of a mixture of 0.4 mol/L Glc3Me and 0.01 mol/L Cr^{VI} over a period of 16 h. [$HClO_4$] = 1.02 mol/L, T = 33 °C. Inset: growth and slow decay of Abs^{570} over a period of 9 days.



Scheme 2.

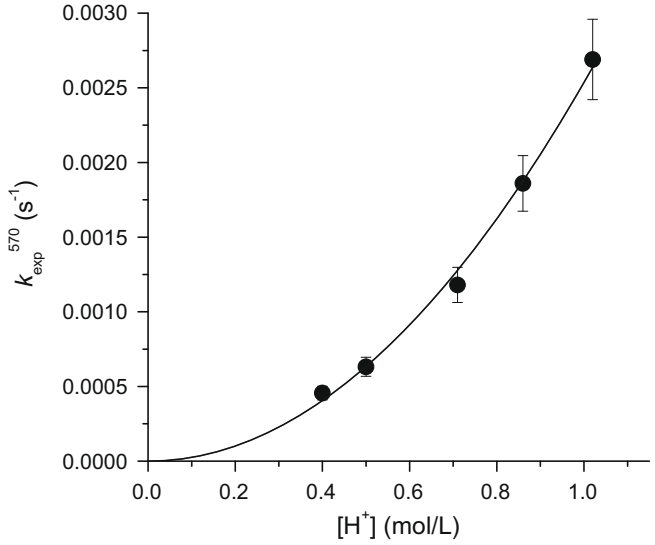


Fig. 9. Effect of acidity on k_{exp} calculated from absorbance data at 570 nm. $[Cr^{VI}] = 8 \times 10^{-3}$ mol/L, [Glc3Me] = 0.4 mol/L, I = 1.02 mol/L, T = 33 °C.

were plotted against $[H^+]$ (Fig. 9). The rate constant calculated by non-linear least-square fit of $\{k_{exp}, [H^+]\}$ data pairs was found to be 25.4×10^{-4} mol^{-2} L^2 s^{-1}, which is the same as that calculated from data at 350 nm. This indicates that the rate of formation of Cr^{III} equals the rate of consumption of Cr^{VI} and that the slow redox path effectively implies the reduction of Cr^{VI}, which should react slower than Cr^V does. This is also consistent with the observation of an isosbestic point at 527 nm (Fig. 8) and implies a low Cr^V concentration throughout the reaction in the $[H^+]$ range used in the kinetics studies.

3.6. Mechanism of the Glc3Me + Cr^{VI} reaction

In the range of substrate and acid concentration used in the kinetics measurements, the oxidation of Glc3Me by Cr^{VI} is a complex reaction that yields Cr^{III}, HCO_2H and Ara2Me as final redox products. The fact that CrO_2^{2+} is detected in the reaction of Glc3Me with Cr^{VI} together with the observation of Cr^V species and the successful trap of organic radicals using acrylamide indicates that the reaction occurs through both one- and two-electron pathways involving Cr^{IV} and Cr^V intermediate species. However, under conditions used in the kinetic measurements, Cr^{IV} and Cr^V react with Glc3Me faster than Cr^{VI} and do not accumulate in the reaction mixture. Therefore, Cr^{IV} and Cr^V, although formed in the Cr^{VI} + Glc3Me, should be involved in fast steps of the reaction pathway. Thus, the absorbance-time profiles reflect the $[Cr^{VI}]$ monotonic decay (at 350 nm) or the $[Cr^{III}]$ monotonic growth (at 570 nm) without interference of $[Cr^{IV}]$ or $[Cr^V]$. In Scheme 3, we propose a mechanism that combines $Cr^{VI} \rightarrow Cr^{IV} \rightarrow Cr^{II}$ and $Cr^{VI} \rightarrow Cr^{IV} \rightarrow Cr^{III}$ pathways, and takes into account: (a) kinetic results, (b) the polymerization of acrylamide added to the reaction mixture, (c) detection of intermediate of Cr^{VI} esters and oxochromate(V) species, (d) observation of CrO_2^{2+} and (e) the reaction products.

The first step of the mechanism proposed in Scheme 3 involves the formation of a Glc3Me–Cr^{VI} mono-chelate (Eq. 3), in agreement with the observation of the absorption band at 373 nm characteristic of chromate oxo-ester, immediately after mixing Glc3Me and Cr^{VI} under conditions where the redox reaction is extremely slow. Therefore, such a chromate ester should be formed rapidly prior to the redox steps. The formation of the chromate ester is followed by the slow redox step where the C–C bond cleavage is proposed to occur through an acid catalyzed two-electron redox process to

$$\text{Glc3Me} + Cr^{VI} \underset{}{\overset{\text{fast}}{\rightleftharpoons}} \text{Glc3Me-}Cr^{VI} \quad (3)$$

$$\text{Glc3Me-}Cr^{VI} \xrightarrow{k_6,\ 2\,H^+} Cr^{IV} + HCO_2H + \text{Ara2Me} \quad (4)$$

$$Cr^{IV} + \text{Glc3Me} \xrightarrow{\text{fast}} Cr^{III} + HCO_2H + \text{Glc3Me}^{\bullet} \quad (5)$$

$$Cr^{IV} + \text{Glc3Me} \xrightarrow{\text{fast}} Cr^{II} + HCO_2H + \text{Ara2Me} \quad (6)$$

$$Cr^{II} + Cr^{VI} \xrightarrow{\text{fast}} Cr^{V} + Cr^{III} \quad (7)$$

$$Cr^{VI} + \text{Glc3Me}^{\bullet} \xrightarrow{\text{fast}} Cr^{V} + \text{Ara2Me} + HCO_2H \quad (8)$$

$$\text{Glc3Me} + Cr^{V} \xrightarrow{\text{fast } (k_b)} Cr^{III} + HCO_2H + \text{Ara2Me} \quad (9)$$

$$Cr^{II} + O_2 \xrightarrow{\text{fast}} CrO_2^{2+} \longrightarrow Cr^{III} \quad (10)$$

$$O_2 + \text{Glc3Me}^{\bullet} \xrightarrow{\text{fast}} \text{Glc3Me}_{ox} \quad (11)$$

Scheme 3.

yield Cr^{IV}, HCO_2H and Ara2Me (Eq. 4). The initial two-electron reduction of Cr^{VI} by Glc3Me is in agreement with previous reports on a number of oxygenated compounds that were selectively oxidized by Cr^{VI} to the lower homolog [30,35]. In the mechanism, we have included two competitive one- and two-electron reductions of Cr^{IV} by Glc3Me. Thus, Cr^{IV} is proposed to react with excess Glc3Me to yield Cr^{III}, HCO_2H and Glc3Me$^{\bullet}$, or Cr^{II}, HCO_2H and Ara2Me, through two alternate fast steps (Eqs. 5 and 6). The first is supported by the observed polymerization of acrylamide when it is added to the Cr^{VI}/Glc3Me reaction mixture, while the second, by the observation of CrO_2^{2+} (the product of the reaction of Cr^{II} with O_2). Cr^V can form by fast reaction of Cr^{II} with Cr^{VI} (Eq. 7) and, alternatively, by rapid reaction of the Glc3Me$^{\bullet}$ with Cr^{VI} (Eq. 8). Cr^V can further oxidize Glc3Me to yield Cr^{III}, HCO_2H and Ara2Me as final redox products (Eq. 9). In the mechanism, one half of the Cr^{VI} reaches Cr^{III} through the Cr^V intermediate, in accordance with Scheme 2 used to fit the time evolution of the Cr^V EPR signal.

In O_2-saturated solutions (1.26 mmol/L) and $[Cr^{VI}]_0 < 0.1$ mmol/L, reactions 7 and 8 can be neglected because Glc3Me$^{\bullet}$ and Cr^{II} intermediates formed in reactions 5 and 6 should be rapidly trapped by O_2 (reactions 10 and 11) [39]. The proposed mechanism is in accordance with the observation that O_2 has not kinetic effect on this reaction, because when $[Cr^{VI}]_0 \geqslant 0.5$ mmol/L (as employed in the kinetic measurements), both Cr^{II} and Glc3Me$^{\bullet}$ react with Cr^{VI} faster than they do with O_2, and reactions 10 and 11 can be neglected [27,40,41].

4. Conclusion

The reaction of Glc3Me with Cr^{VI} strongly depends on pH. In acid medium, redox reaction occurs and reactive Cr^V, Cr^{II} and Cr^{IV} intermediate species are generated in the redox process, together with free radicals, HCO_2H and Ara2Me. At pH > 3, Glc3Me oxidation by Cr^{VI} or Cr^V is very slow and long-lived oxo-Cr^{VI} or oxo-Cr^V–Glc3Me species form. EPR spectroscopy shows that at pH 5.5–7.5 Glc3Me is able to trap Cr^V through the 1,2-diolato moiety to yield

a Cr^V bis-chelate that then slowly converts into species with Cr^V bound to the 5,6-diolato moiety of its furanose form. The selective C1–C2 bond cleavage of Glc3Me upon reaction with high valent chromium in acid medium, distinguishes the 3-OMe derivative from glucose that, under the same experimental conditions, is oxidized to the gluconic acid at comparable rate [10].

Acknowledgments

We thank the National Research Council of Argentina (CONICET), the National University of Rosario (UNR), the National Agency for Sciences Promotion (FONCyT) and the ALFA Program (CROCON Network, Project ALR/B7-30.11/94-7.0064.9) for financial support. MIF thanks V. Andreu for helping with the kinetic measurements.

References

[1] J. Barnhart, J. Soil Contam. 6 (1997) 561 (special issue).
[2] S.A. Katz, H. Salem, in: The Biological and Environmental Chemistry of Chromium, VCH Publishers, Inc., New York, 1994.
[3] C.B. Klein, in: L.W. Chang (Ed.), Toxicology of Metals, CRC-Lewis Publishers, New York, 1996, p. 205.
[4] R. Codd, C.T. Dillon, A. Levina, P.A. Lay, Coord. Chem. Rev. 216–217 (2001) 537.
[5] R. Codd, J.A. Irwin, P. Lay, Curr. Opin. Chem. Biol. 7 (2003) 213.
[6] A.K. Das, Coord. Chem. Rev. 248 (2004) 81.
[7] M. Ciéslak-Golonka, M. Daszkiewicz, Coord. Chem. Rev. 249 (2005) 2391.
[8] B. Gyurcsik, L. Nagy, Coord. Chem. Rev. 203 (2000) 81.
[9] S. Signorella, J.C. González, L.F. Sala, J. Argentine Chem. Soc. 90 (2002) 1.
[10] S. Signorella, V. Daier, S. García, R. Cargnello, J.C. González, M. Rizzotto, L.F. Sala, Carbohydr. Res. 316 (1999) 14.
[11] V. Daier, S. Signorella, M. Rizzotto, M. Frascaroli, C. Palopoli, C. Brondino, J.M. Salas-Peregrin, Can. J. Chem. 77 (1999) 57.
[12] M. Rizzotto, S. Signorella, M.I. Frascaroli, V. Daier, L.F. Sala, J. Carbohyd. Chem. 14 (1995) 45.
[13] S. Signorella, M. Rizzotto, V. Daier, M.I. Frascaroli, C. Palopoli, D. Martino, A. Bousseckson, L.F. Sala, J. Chem. Soc., Dalton Trans. (1996) 1607.
[14] M. Rizzotto, M. Frascaroli, S. Signorella, L. Sala, Polyhedron 15 (1996) 1517.
[15] M. Krumpolc, J. Rocek, Inorg. Synth. 20 (1980) 63.
[16] M.C. Ghosh, E.S. Gould, Inorg. Chem. 30 (1991) 491.
[17] International Agency for Research on Cancer (IARC), IARC Monogr. Eval. Carcinog. Risk Chem. Hum. (Suppl. 7) (1987) 165.
[18] R.Feldam, in: Occupational and Environmental Neurotoxicology, Lippincott-Raven Publishers, Philadelphia, 1999, p. 337.
[19] L.F. Sala, A. Fernández Cirelli, R.M. Lederkremer, Anales Asoc. Química Arg. 66 (1978) 57.
[20] H.S. Isbell, J. Res. Nat. Bur. Stand. (US) 14 (1935) 305.
[21] A.G. Fadnis, S.K. Kulshrestha, Rev. Roumaine Chim. 28 (1983) 99.
[22] S.L. Scott, A. Bakac, J.H. Espenson, J. Am. Chem. Soc. 113 (1991) 7787.
[23] WINSIM EPR Calculations for MS-Windows NT, Version 0.96, National Institute of Environmental Health Sciences, 1995.
[24] M. Mitewa, P. Bontchev, Coord. Chem. Rev. 61 (1985) 241.
[25] J.C. González, S. García, N. Mamana, L.F. Sala, S. Signorella, Inorg. Chem. Commun. 9 (2006) 437.
[26] S.L. Scott, A. Bakac, J.H. Espenson, J. Am. Chem. Soc. 114 (1992) 4205.
[27] S. Signorella, M.I. Frascaroli, S. García, M. Santoro, J.C. González, C. Palopoli, N. Casado, L.F. Sala, J. Chem. Soc., Dalton Trans. (2000) 1617.
[28] A. Al-Ajlouni, A. Bakac, J. Espenson, Inorg. Chem. 33 (1994) 1011.
[29] S. Signorella, M. Santoro, C. Palopoli, C. Brondino, J.M. Salas Peregrin, M. Quiroz, L. Sala, Polyhedron 17 (1998) 2739.
[30] G. Barr-David, M. Charara, R. Codd, R.P. Farrell, J.A. Irwin, P.A. Lay, R. Bramley, S. Brumby, J.Y. Ji, G.R. Hanson, J. Chem. Soc., Faraday Trans. 91 (1995) 1207.
[31] A. Levina, P.A. Lay, Coord. Chem. Rev. 249 (2005) 281.
[32] M. Rizzotto, A. Levina, M. Santoro, S. García, M.I. Frascaroli, S. Signorella, L.F. Sala, P. Lay, J. Chem. Soc., Dalton Trans. (2002) 3206.
[33] S. Signorella, V. Daier, M. Santoro, S. García, C. Palopoli, L. Korecz, A. Rockenbauer, L.F. Sala, Eur. J. Inorg. Chem. (2001) 1829.
[34] S. Signorella, S. García, M. Rizzotto, A. Levina, P. Lay, L.F. Sala, Poyhedron 24 (2005) 1079.
[35] G. Haight, G. Jwisich, M. Kelso, P. Merril, Inorg. Chem. 24 (1985) 2740.
[36] V. Roldán, M. Santoro, J.C. González, J.M. Salas Peregrin, S. Signorella, L.F. Sala, J. Inorg. Biochem. 98 (2004) 347.
[37] A.B.P. Lever, in: Inorganic Electronic Spectroscopy, 2nd Ed., Elsevier, Amsterdam, 1984, p. 419.
[38] S. Signorella, M. Santoro, A. Frutos, G. Escandar, J.M. Salas-Peregrin, V. Moreno, M. González Sierra, L.F. Sala, J. Inorg. Biochem. 73 (1999) 93.
[39] A. Bakac, S.L. Scott, J.H. Espenson, K.R. Rodgers, J. Am. Chem. Soc. 117 (1995) 6483.
[40] O. Pestovsky, A. Bakac, J.H. Espenson, J. Am. Chem. Soc. 120 (1998) 13422.
[41] P.A. Lay, A. Levina, J. Am. Chem. Soc. 120 (1998) 6704.

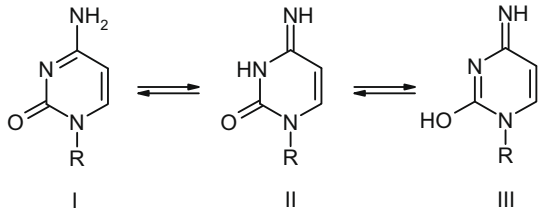


Fig. 1. Tautomers of *N*-1-substituted cytosine.

2.2. ESI-MS

Mass spectral data were acquired on a LCQ Deca ion trap mass spectrometer from ThermoFinnigan (San Jose, CA, USA) equipped with an electrospray ionization (ESI) interface operated in the positive and negative ion modes, mass range 150–2000. Stock samples were prepared in CH_3OH or DMSO, further diluted to a concentration of about 0.05 mg/mL in CH_3CN, CH_3OH or water, and directly injected. Infusion into the mass spectrometer was performed by the built-in syringe pump at a flow rate of 5 μL/min. Nitrogen was used as the auxiliary and sheath gas. Helium was used as the collision gas in the ion trap. The sheath gas flow was set at 85 and the auxiliary gas flow at 30 (arbitrary units). The spray voltage was set at 4.5 kV, while the capillary temperature was 250 °C and the capillary voltage 17 V. Full mass spectra were acquired over the mass range *m/z* 150–2000. Additional solvent cluster studies were performed by varying the capillary voltage (10 V) and temperature (250 °C). For MS/MS investigations, characteristic molecular ions were isolated in the ion trap and collisionally activated with different collision energies (CE) to find the optimal CE for a distinct fragmentation. Product ions in the MS/MS spectra were chosen to perform further MS^3 and MS^4 experiments, relevant to the confirmation of investigated compounds.

2.3. Synthesis

2.3.1. Preparation of ligand *1*

Synthesis of the ligand 1-(*p*-toluenesulfonyl)cytosine (**1**) was performed according to the procedure reported by Kašnar-Šamprec et al. [11]. 1-(*p*-Toluenesulfonyl)cytosine (**1**) had been synthesized previously by the reaction of silylated cytosine and *p*-toluenesulfonyl chloride in acetonitrile, according to Scheme 1. The phenyl-proton (Ph) assignments were confirmed by carbon-proton connectivity in $^1H/^{13}C$ heteronuclear correlation spectra (HETCOR). Additionally, in the NOESY spectrum of **1**, the assignment of Ph-c protons was proved by their interaction with methyl-protons. IR (KBr) ν_{max}/cm^{-1}: 3369 (m), 3100 (m), 3074(m), 1703 (m), 1673 (s), 1524 (s), 1489 (m), 1376 (m), 1353 (m), 1285 (m), 1236 (w), 1184 (m), 1173 (s), 1138 (w), 1116 (m), 1088 (m), 1023 (w), 967 (m), 806 (w), 765 (m), 707 (m), 689 (m), 657 (w), 602 (w), 585 (w), 555 (m), 542 (m); ^1H NMR (DMSO–d_6) δ/ppm: 8.14 (d, 1H, $J_{6,5}$ = 7.8 Hz, H-6), 7.95 (brs, 2H, NH_2), 7.87 (d, 2H, $J_{b,c}$ = 8.1 Hz, Ph-b), 7.46 (d, 2H, $J_{c,b}$ = 8.1 Hz, Ph-c), 5.98 (d, 1H, $J_{5,6}$ = 7.8 Hz, H-5), 2.42 (s, 3H, CH_3); ^{13}C NMR (DMSO–d_6) δ/ppm: 166.27 (s, C-4), 151.22 (s, C-2), 145.61 (s, Ph-d), 139.73 (d, C-6), 134.47 (s, Ph-a), 129.80 (d, Ph-c), 129.02 (d, Ph-b), 97.50 (d, C-5), 21.20 (q, CH_3); MS (EI) exact mass calculated for $C_{11}H_{11}N_3O_3S$: *m/e* 265.051565 ($[M]^+$), found: 265.040053.

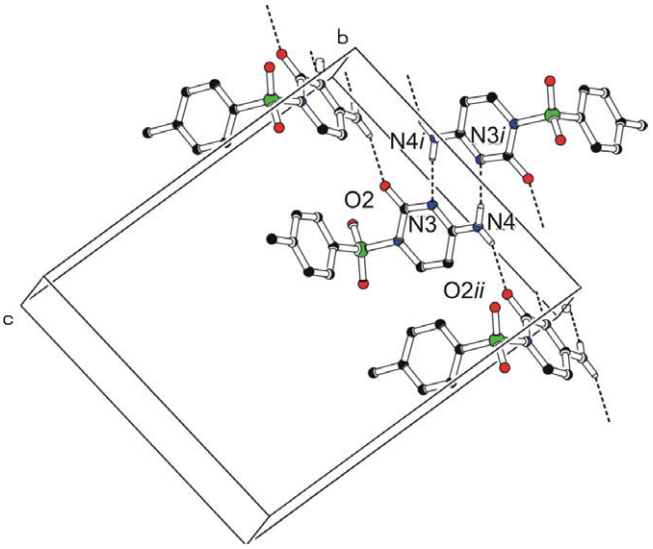


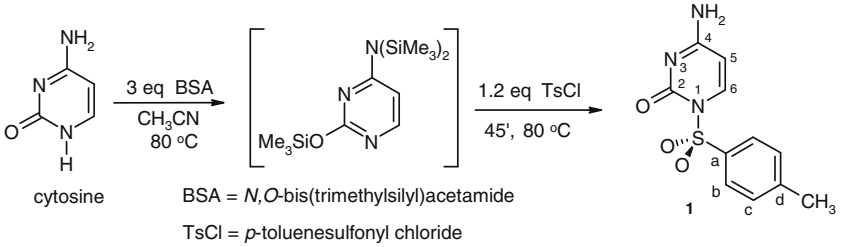
Fig. 2. Packing diagram of **1**.

2.3.2. Preparation of the complex Pd(1-TosC–N3)$_2$Cl$_2$ (*2*)

To a solution of 1-(*p*-toluenesulfonyl)cytosine (**1**) (0.1061 g, 0.4 mmol) in methanol (9 mL), K_2PdCl_4 (0.0653 g, 0.2 mmol) was added. The reaction mixture was stirred and refluxed for 2 h. The red suspension was cooled to room temperature and a pale yellow solid product was filtered off, washed with methanol and dried over vacuo to give 102 mg (76%) of a pale yellow powder **2**: IR (KBr) ν_{max}/cm^{-1}: 3406 (s), 3313 (s), 3288 (s), 3247 (m), 3207 (m), 3107 (m), 3067 (m), 1686 (s), 1650 (s, br), 1613 (s), 1609 (s), 1514 (s), 1503 (s), 1380 (s), 1363 (s), 1276 (s), 1252 (m), 1191 (s), 1171 (s), 1145 (m), 1122 (m), 1107 (m), 1084 (s), 1045 (s), 1017 (m), 974 (m), 815 (m), 792 (s), 766 (s), 706 (s), 695 (s), 673 (s), 613 (s), 590 (s), 552 (s), 541 (s), 480 (m), 361 (m). *Anal.* Calc. for $C_{22}H_{22}Cl_2N_6O_6PdS_2$ xH_2O (M_r = 725.91): C, 36.40; H, 3.33; N, 11.58; S, 8.83. Found: C, 36.05; H, 2.93; N, 11.55; S, 8.54%.

2.3.3. Complex *2* in DMSO-d_6 solution

The first set of signals (marked o in Fig. 4): ^1H NMR (DMSO–d_6) δ/ppm: 8.10 (d, 1H, $J_{6,5}$ = 8.0 Hz, H-6), 7.88 (d, 2H, J = 8.7 Hz, NH_2), 7.84 (d, 2H, $J_{b,c}$ = 8.1 Hz, Ph-b), 7.44 (d, 2H, $J_{c,b}$ = 8.0 Hz, Ph-c), 5.94 (d, 1H, $J_{5,6}$ = 7.9 Hz, H-5), 2.41 (s, 3H, Ph–CH_3); ^{13}C NMR (DMSO–d_6) δ/ppm: 165.90 (s, C-4), 150.87 (s, C-2), 145.28 (s, Ph-d), 139.41 (d, C-6), 134.19 (s, Ph-a,), 129.51 (d, Ph-c), 128.72 (d, Ph-b), 97.25 (d, C-5), 21.11 (q, Ph–CH_3).



Scheme 1. Synthesis of 1-(*p*-toluenesulfonyl)cytosine (**1**).

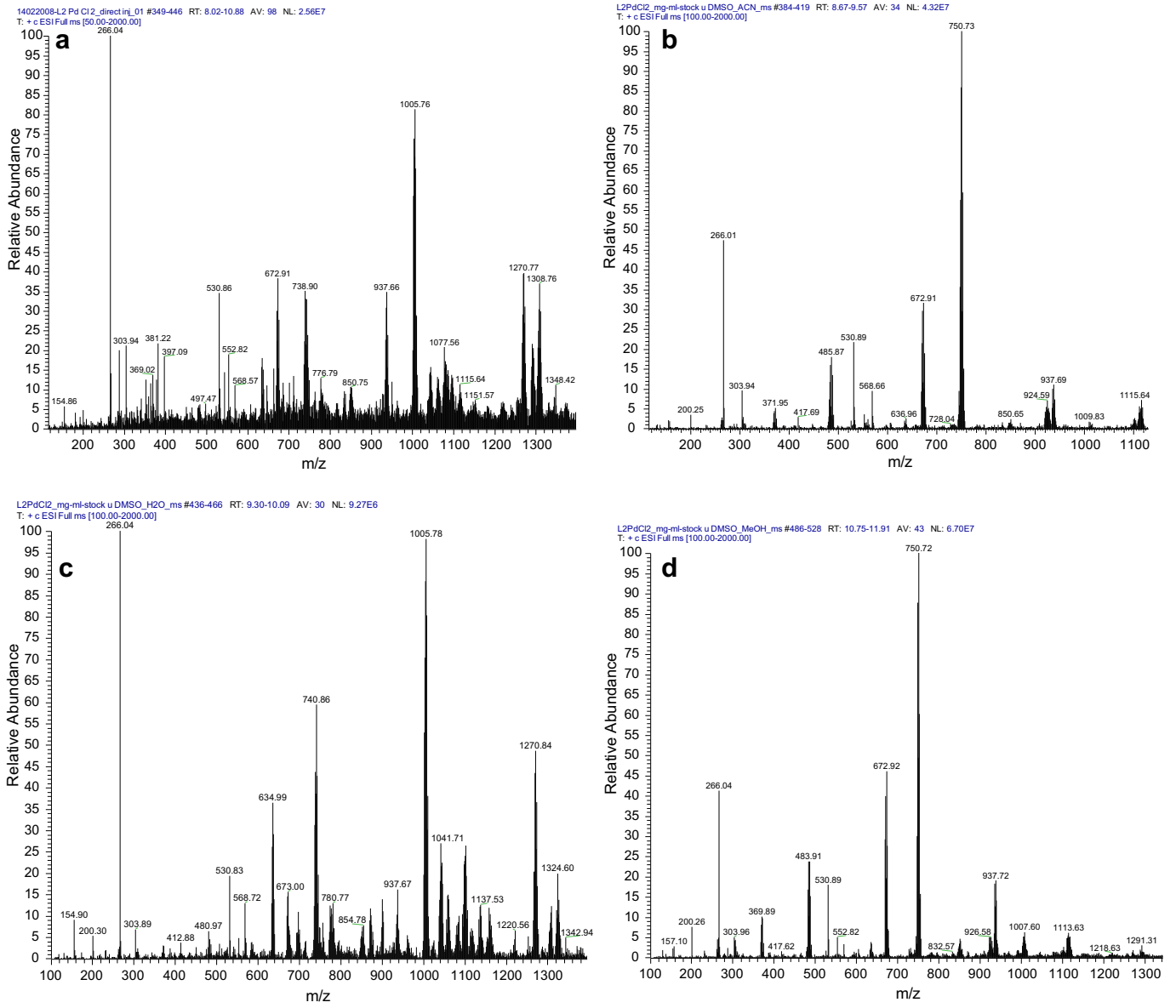


Fig. 3. ESI-MS spectra of the yellow solid Pd**L**$_2$Cl$_2$ (**2**): (a) dissolved in CH_3OH; (b) dissolved in DMSO and diluted with CH_3CN; (c) dissolved in DMSO and diluted with water and (d) dissolved in DMSO and diluted with CH_3OH.

The second set of signals (marked x in Fig. 4): ^{1}H NMR (DMSO–d_6) δ/ppm: 9.34, 9.25, 9.21, 8.89 (4 x brs, 2H, NH), 8.22 (m, 1H, H-6), 7.94 (m, 2H, Ph-b), 7.50 (m, 2H, Ph-c), 6.07 (m, 1H, H-5), 2.43 (s, 3H, Ph–CH_3); ^{13}C NMR (DMSO–d_6) δ/ppm: 163.82 (s, C-4), 148.99 (s, C-2), 146.39 (s, Ph-d), 139.46 (d, C-6), 132.64 (s, Ph-a), 129.92 and 129.77 (d, Ph-c), 129.23 and 129.20 (d, Ph-b), 97.20 (d, C-5), 21.22 (q, Ph–CH_3).

2.3.4. Preparation of complexes *3* and *4*

Slow evaporation of the DMF solution of solid material **2** at room temperature gave, after 10 days, orange needles of complex **3**, whereas a 60-day-long crystallization from the DMSO solution of solid material **2** at room temperature gave crystals of complex **4**. Single crystals of **3** and **4** were characterized by X-ray crystallography.

Complex Pd$_2$(1-TosC$^-$–N3,N4)$_2$DMSO$_2$Cl$_2$ (***4***): IR (KBr) ν_{max}/cm^{-1}: 3407 (w), 3247 (w), 3103 (w), 3012 (w), 2919 (w), 1670 (s), 1648 (s), 1569 (s), 1475 (m), 1396 (m), 1354 (m), 1282 (s), 1236 (m), 1188 (s), 1172 (s), 1148 (s), 1128 (s), 1087 (s), 1043 (s), 1025 (s), 954 (w), 808 (w), 757 (w), 723 (m), 680 (m), 651 (w), 607 (vw), 560 (s), 546 (m), 491 (m), 426 (m), 370 (br, m), 360 (m, sh), 249 (m); ^{1}H NMR (DMSO–d_6) δ/ppm: 7.85 (d, 2H, $J_{b,c}$ = 8.3 Hz, Ph-b), 7.52 (d, 1H, $J_{6,5}$ = 8.0 Hz, H-6), 7.45 (d, 2H, $J_{c,b}$ = 8.2 Hz, Ph-c), 7.26 (brs, 1H, NH-4), 5.92 (d, 1H, $J_{5,6}$ = 8.0 Hz, H-5), 2.93 (s, 3H $(CH_3)_2SO$–Pd), 2.54 (s, 3H $(CH_3)_2SO$–Pd), 2.42 (s, 3H, Ph–CH_3).

2.4. X-ray structural analysis

Crystal data, data collection and refinement parameters for compounds **1**, **3** and **4** are summarized in Table 1. Data collections were performed on an Enraf Nonius CAD4 diffractometer using graphite monochromated Cu Kα radiation (λ = 1.54179 Å). Data reduction and cell refinement were carried out using the procedures incorporated into the WINGX package [12]. Intensities were measured at room temperature. All structures were solved using direct methods with SIR2002 [13] and refined using the full matrix least-squares refinement based on F^2 with SHELXL [14]. Molecular illustrations were prepared using ORTEP-III [15]. All non-hydrogen

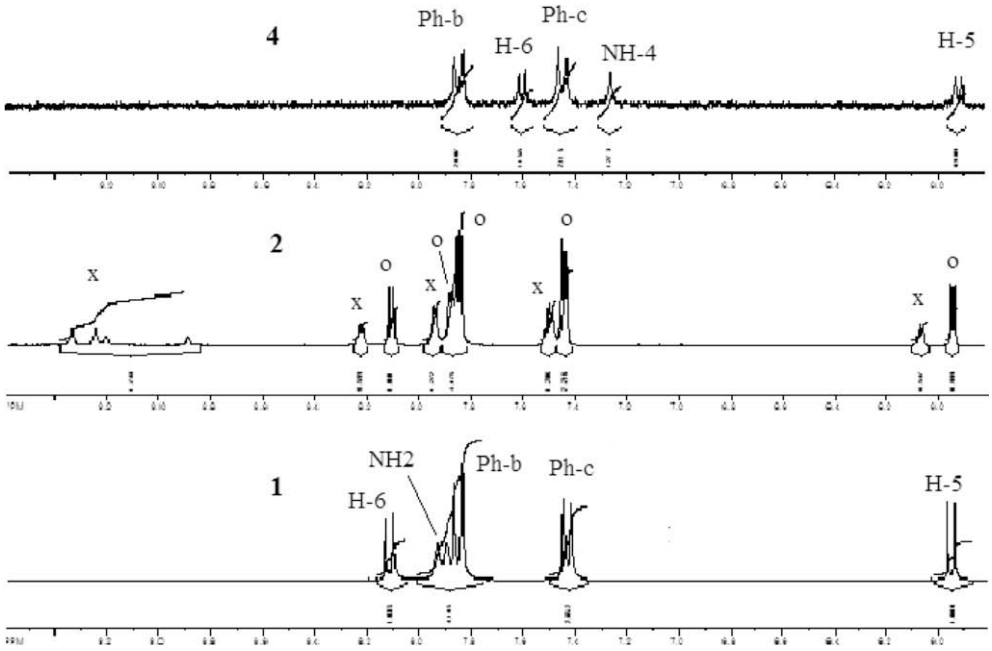


Fig. 4. (DMSO–d_6) ^{1}H NMR spectra of ligand **1** (bottom), complex Pd**L**$_2$Cl$_2$ (**2**) at room temperature (middle) and complex Pd$_2$(1-TosC$^-$–*N*3,*N*4)$_2$DMSO$_2$Cl$_2$ (**4**) (top).

atoms in the structures were refined anisotropically; hydrogen atoms were included in their geometrically calculated positions (except for some hydrogen atoms included in hydrogen bonding) and refined according to the riding model. In the structure of **3**, the substantial residual electron density due to the unresolvable disorder of solvent molecules was reduced by the SQUEEZE [16] routine incorporated into PLATON [17].

3. Results and discussion

3.1. Synthesis and crystal structure of ligand *1*

The synthesis of the ligand 1-(*p*-toluenesulfonyl)cytosine (**1**), (1-TosC), was performed according to the procedure reported by Kašnar-Šamprec et al. [11]. Silylation of cytosine was accomplished with *N*,*O*-bis(trimethylsilyl)acetamide in acetonitrile at 80 °C. Condensation of silylated cytosine with *p*-toluenesulfonyl chloride in acetonitrile gave ligand **1** in 80% yield after recrystallization from methanol (Scheme 1).

In our previous report, we have shown that *N*-1-sulfonyluracil derivatives can adopt chiral conformations, possessing *M* and *P* helicities in the crystalline state [18]. A partial and a total spontaneous resolution upon crystallization was observed for 1-(*p*-toluenesulfonyl)uracil and 1-(1-naphthylsulfonyl)uracil, respectively, while the structurally closely related 1-(*p*-toluenesulfonyl)thymine crystallized as a racemic compound. Unlike its uracil counterpart, 1-tosylcytosine (ligand **1**) does not exhibit *à la Pasteur* separation of conformational enantiomers upon crystallization,

Table 1
Crystallographic data for compounds **1**, **3** and **4**.

Compound	**1**	**3** (squeezed)	**4**
Formula	$C_{11}H_{11}N_3O_3S$	$C_{44}H_{36}N_{12}O_{12}Pd_2S_4$	$C_{30}H_{44}Cl_2N_6O_{10}Pd_2S_6$
Formula weight (g mol^{-1})	265.00	1269.92	1124.77
Crystal color and habit	colorless plate	yellow needle	yellow plate
Crystal dimensions (mm)	0.25 × 0.20 × 0.07	0.3 × 0.07 × 0.07	0.2 × 0.15 × 0.05
Crystal system	monoclinic	orthorhombic	monoclinic
Space group	$P2_1/c$	*Pnab*	*C*2/*n*
a (Å)	13.166 (2)	17.372(3)	42.122(8)
b (Å)	5.660 (3)	17.882(2)	12.5940(9)
c (Å)	15.95 (1)	21.570(5)	16.6390(7)
β (°)	96.02 (5)	90.	97.12(4)
V (Å^3)	1182 (1)	6701(2)	8759(2)
Z	4	4	8
ρ_{calc} (g cm^{-1})	1.491	1.295	1.706
μ (Cu Kα) (mm^{-1})	2.503	5.969	10.915
Absorption correction	none	ψ-scan	ψ-scan
F(000)	552	2560	4544
θ max. (°)	76.46	76.07	76.4
No. of reflections collected	3126	6976	9308
No. of reflections observed [$I > 2\sigma(I)$]	1966	1607	6889
Parameters	120	337	515
R_1	0.0444	0.0777	0.0915
wR_2	0.1234	0.2320	0.2717
ρ_{max}, ρ_{min} (e Å^{-3})	0.71, −0.58	1.13, −1.80	2.62, −2.32

and crystallizes in the centrosymmetric space group $P2_1/a$. However, it exhibits analogous conformational chirality in the solid state with respect to the S–N bond. This is due to the enhanced hydrogen bonding potential of the cytosine, where the presence of a double hydrogen bond donor (amino nitrogen N4) instead of a single H bond donor (endocyclic N3–H) in the case of the uracil derivative, enables the formation of centrosymmetric dimers and tetramers, and finally leads to a centrosymmetric crystal arrangement. The crystal structure of the ligand **1** is characterized by hydrogen-bonded centrosymmetric dimers of the graph set motif $R_2^2(8)$ [19], formed by hydrogen bonds N4–H4b···N3*i*, and centrosymmetric tetramers of the graph set motif R_4^4 including hydrogen bonds N4–H4b···N3*i* and N4–H4a···O2*ii* (Fig. 2). Thus, these two hydrogen-bonded centrosymmetric rings share the common edge made by the hydrogen bond N4–H4B···N3*i* and form an infinite double layer along the crystallographic *a*-axis.

3.2. Synthesis and characterization of complexes **2**, **3** and **4**

3.2.1. Synthesis

1-(*p*-Toluenesulfonyl)cytosine (**1**) and K_2PdCl_4 in a 2:1 molar ratio were refluxed for 2 h in methanol and, upon cooling to room temperature, the pale yellow solid **2** was obtained. Solid **2** is soluble in polar coordinative solvents like DMF and DMSO, and insoluble in most other organic solvents and in water. The same solid product **2** was obtained using DMF instead of methanol, as proved by the X-ray powder diffraction method (data not shown). Slow evaporation of a DMF solution of solid material **2** over 10 days at room temperature gave orange needles of complex **3**, whereas a 60 day crystallization of the DMSO solution at room temperature gave crystals of complex **4** (Scheme 2). The structures of complexes **3** and **4** were confirmed by X-ray structural analysis.

The molecular formula of the pale yellow solid **2** ($Pd\mathbf{L}_2Cl_2$, where **L** = 1-(*p*-toluenesulfonyl)cytosine) (**1**) was confirmed by elemental analysis and ESI-MS spectrometry.

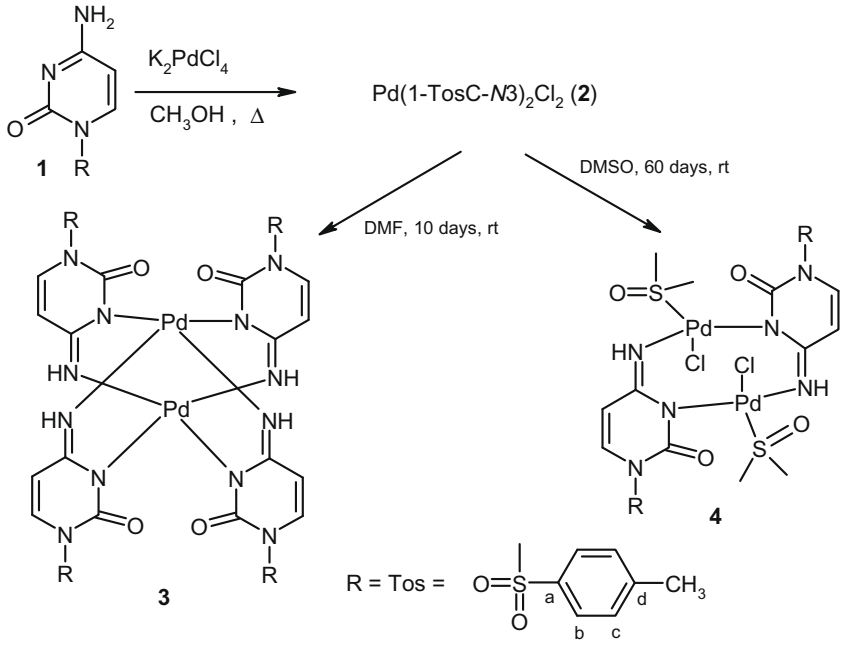
3.2.2. ESI-MS studies

Since ESI-MS is the softest desorption/ionization method, it is ideally suited to investigate the coordination behaviour of transition metal complexes [20,21]. The mass spectrum reflects the composition of the species present in the solution. Franska studied cytosine platinum(II) complexes by ESI-MS in DMSO and observed the formation of cationic complexes with Pt(II). Singly charged [cytosine + PtCl + 2DMSO]$^+$ ions were detected at a low cone voltage [22].

Our MS studies (ESI-MS and HRMS) confirmed the molecular formula of complex **2**. The spectra were taken at a low cone voltage (10 V). Molecular ions containing palladium gave rise to a number of peaks showing the characteristic natural isotope percent distribution of the compounds containing one or two palladium atoms. Masses of the complexes reported in this paper are those containing the most abundant stable isotope of each element in the complex. Since the examined solid, complex **2**, had a low solubility in CH_3OH or CH_3CN, these being the common solvents used for ESI-MS studies, it was dissolved in DMSO and then diluted with CH_3OH, water or CH_3CN in our experiments (Fig. 3). The obtained spectra were compared with the theoretical spectra, matching completely the molecular peak percent distribution caused by the Pd isotopes.

The presence of the complex $Pd\mathbf{L}_2Cl_2$ (**2**) was confirmed by detection of the ions from CH_3OH solutions: at *m/z* 635.00 assigned as the [Pd**L**(**L**–H)]$^+$ ion and at *m/z* 672.91 assigned as [Pd$\mathbf{L}_2$Cl]$^+$, or DMSO solutions: at *m/z* 730.78 assigned as the [(Pd$\mathbf{L}_2Cl_2$)Na]$^+$ ion and at *m/z* 748.75 assigned as the [(Pd$\mathbf{L}_2Cl_2$)K]$^+$ ion, in the ES$^+$ mode. The mononuclear complex $Pd\mathbf{L}_2Cl_2$ exchanged chloride quickly with another ligand forming a $Pd\mathbf{L}_3Cl$ type complex. The presence of that complex was confirmed after detection of the ions from CH_3OH solution: at *m/z* 937.75 assigned as the (Pd$\mathbf{L}_3$Cl)$^+$ ion. Dissolving complex **2** in DMSO and further diluting with water, methanol or acetonitrile showed clearly that the species present in the solutions depend strongly on the added solvent properties. The formation and stability of the formed species were monitored by ESI-MS and LC–MS. Interaction between complex **2** and DMSO was detected as a new species eluted at a retention time of 48.67 minutes with *m/z* 1086 and assigned as [Pd$_2\mathbf{L}_3$(DMSO)]$^+$.

It was also found that when complex $Pd\mathbf{L}_2Cl_2$ was dissolved in DMSO, new dinuclear Pd(II) complexes **4** containing two DMSO molecules in the structure were detected (complex **4** at *m/z*



Scheme 2. Synthesis of complexes: Pd(1-TosC–*N*3)$_2$Cl$_2$ (**2**), Pd$_2$(1-TosC$^-$–*N*3,*N*4)$_4$ (**3**) and Pd$_2$(1-TosC$^-$–*N*3,*N*4)$_2$DMSO$_2$Cl$_2$ (**4**).

992.59 assigned as the $[Pd_2(\mathbf{L}–H)_2(DMSO)_2Cl_2Na]^+$ ion or at *m/z* 1009.46 assigned as the $[Pd_2(\mathbf{L}–H)_2(DMSO)_2Cl_2K]^+$ ion, and its fragments). Complex **3** or its fragments were detected by MS at *m/z* 1268.77 assigned as the $[Pd_2(\mathbf{L}–H)_4]^+$ ion or at *m/z* 1290.80 assigned as the $[Pd_2(\mathbf{L}–H)_4]Na^+$ ion or at *m/z* 1308.76 assigned as the $[Pd_2(\mathbf{L}–H)_4]K^+$. A detailed MS study of the complex $Pd\mathbf{L}_2Cl_2$ will be described elsewhere.

3.2.3. Solution studies

Compound **2** is generally insoluble in common organic solvents, except DMF and DMSO. The molar conductivity value in DMSO proves that complex **2** is a non-electrolyte. This finding indicates that both the chloride anions and the organic ligands are located in the internal coordination sphere of the Pd(II) complex. Despite the fact that most palladium complexes (PdL_2Cl_2) exhibit a fast exchange of axial ligands with solvent molecules, **2** is stable in DMSO–d_6 for several days at room temperature.

With respect to the ^{1}H NMR spectrum of ligand **1**, the spectrum (DMSO–d_6) of complex **2** exhibits two pairs of signals for each proton in a 2:1 ratio (Fig. 4). The first set of resonances of **2** (marked o in Fig. 4) displays two sets of doublets in the aromatic region, corresponding to the H-6 and H-5 protons (δ 8.10 and 5.94 ppm) and phenyl Ph-b and Ph-c protons (δ 7.84 and 7.44 ppm). Two amino protons at N-4, readily exchangeable with deuterium by addition of D_2O, appear as a broadened doublet at δ 7.88 ppm. These data are in accord with the keto-amino form of the ligand in the complex Pd(1-TosC–*N*3)$_2$Cl$_2$ (**2**). On the other hand, all the protons of the second set of resonances in the DMSO solution of **2** (marked x in Fig. 4) were shifted upfield. Signals of the H-6 and H-5 (δ 8.22 and 6.07 ppm) and Ph-b and Ph-c protons (δ 7.94 and 7.50 ppm) show significant additional splitting of the H-5, H-6 and Ph doublets and the broadened singlets at δ 9.34, 9.25, 9.21 and 8.89 ppm are assigned to NH protons. The latter observations may be explained by the existence of two possible rotamers in **2**, which is also evident from the infrared spectra.

The ^{1}H NMR spectrum of the dipalladium complex Pd_2(1-TosC$^-$–*N*3,*N*4)$_2$DMSO$_2$Cl$_2$ (**4**) is considerably different and shows only one signal for each H5, H6, Ph-b, Ph-c and NH-4 proton, due to the high symmetry of the complex and large upfield shifts for the H-6 (δ 7.60 ppm, doublet $J_{6,5}$ = 8 Hz) and the NH-4 (δ 7.26 ppm, broad singlet) protons.

Table 2
IR frequencies for cytosine (Cy), ligand **1** and complexes **2** and **4**.

ν (cm^{-1})	Cy	**1**	**2**	**4**
N–H	3387	3369	3406	3407
	3174	3100	3313	3247
			3288	3103
			3247	
			3207	
			3107	
C=O	1664	1703	1686	1670
C=C	1640	1673	1650	1648
C=N	1617	1524	1613	1569
NH_2 ring	1537	1489	1609	1475
	1504		1514	
	1466		1503	
SO_2	–	1376	1380	1396
		1353	1363	1354
		1184	1191	1188
		1173	1171	1172
		1184	1191	1025
		1173	1171	
		1138	1145	
S–N	–	967	974	1018
ν(Pd–N)	–	–	478	490–426
			453	
			417	
ν(Pd–Cl)	–	–	361	370
			305	360
			280	

3.2.4. Infrared spectra

The infrared spectra with tentative band assignments (ν/cm^{-1}) for cytosine, according to the literature [23], some characteristic changes in ligand **1** and the bands in the spectra of complexes **2** and **4** are shown in Table 2. The strong to weak bands, observed between 3407 and 3100 cm^{-1}, are associated with ν(N–H). Ligand **1** (keto-amino tautomer) shows characteristic $\nu_{as}(NH_2)$ and $\nu_s(NH_2)$ vibrations at 3369 and 3100 cm^{-1} for the C4 amino group, while the ketoimino form of the ligand anion in **4** shows the N–H stretching of the imine group at 3407, 3247 and 3103 cm^{-1}, which is also indicated by the ^{1}H NMR spectrum.

Solid $Pd\mathbf{L}_2Cl_2$ (**2**) shows six bands between 3406 and 3107 cm^{-1}, supporting the existence of two rotamers [24]. The band assigned to ν(C(2)=O), which appears around 1703 cm^{-1} in the free ligand spectrum, is appreciably shifted to lower frequencies. This modification and changes in the zone between 1700 and 1400 cm^{-1}, involving the stretching of ν(C=O, C=C, C=N, ring, C–N, etc.), are related to the new charge distribution in the ring of the complexes. For the palladium complex $Pd\mathbf{L}_2Cl_2$ (**2**), three bands at 280, 306 and 360 cm^{-1}, and for complex **4** one split band within 360–370 cm^{-1} are attributed to the ν(Pd–Cl) vibrations, while the bands within the 426–480 cm^{-1} range are assignable to the ν(Pd–N) stretching vibrations [25].

3.2.5. Crystal structure of *3*

The molecular structure of **3** includes two Pd atoms, 2.6210(15) Å apart, with the interatomic Pd1–Pd2 vector along the twofold symmetry axis parallel to the crystallographic *b*-axis. The relatively short interpalladium distance is probably caused by steric hindrance of the bulky ligands. The coordination spheres of both Pd atoms inside the binuclear metal complex are virtually identical. They both consist of two exocyclic imino N4 [Pd1–N4, 1.970(9) Å; Pd2–N4, 2.039(12) Å] and two endocyclic N3 [Pd1–N3, 2.067(10) Å; Pd2–N3, 2.090(9) Å] atoms. The coordination spheres of the two palladium atoms are inseparable since they involve four ligand molecules, each of which binds to one Pd atom through its endocyclic N3 and to the other one through the exocyclic N4; hence each of the four ligand molecules bridges two palladium atoms *via* its N–C–N moiety. The asymmetric unit contains two ligand molecules (**A** and **B**), as well as two Pd atoms with half-site occupancy. The asymmetric unit is then repeated by a twofold symmetry axis operation to give a paddlewheel binuclear structure where the adjacent ligand molecules are head-to-tail oriented with respect to the twofold axis, *i.e.* with respect to the interpalladium vector (Fig. 5).

The complete geometries of both coordination spheres of complex **3** are given in Table 3. The atom numbering in the ligand molecule **B** is composed of a prefix "2" and the second digit, corresponds to the numbering scheme defined for the ligand molecule **A**. Thus, for example, N3 of the ligand molecule **A** corresponds to N23 of the ligand molecule **B**. It is evident that the Pd–N3 (endocyclic nitrogen) contacts are somewhat longer than the Pd–N4 (exocyclic imino-nitrogen) ones. The four nitrogens forming the first coordination sphere around Pd1 (N23, N23*i*, N4 and N4*i*) are in an almost perfect square-planar arrangement. The maximum deviation from the least square plane defined by Pd1 and the four nitrogen atoms is only 0.0891(11) Å, whereas the least square plane defined only by these four nitrogen atoms reveals a maximum deviation of 0.025(11) Å.

Similarly, the Pd2 coordination sphere least square plane including palladium reveals a maximum deviation of 0.0878(9) Å, excluding Pd2, 0.013(11) Å. In addition, remarkable planarity is re-

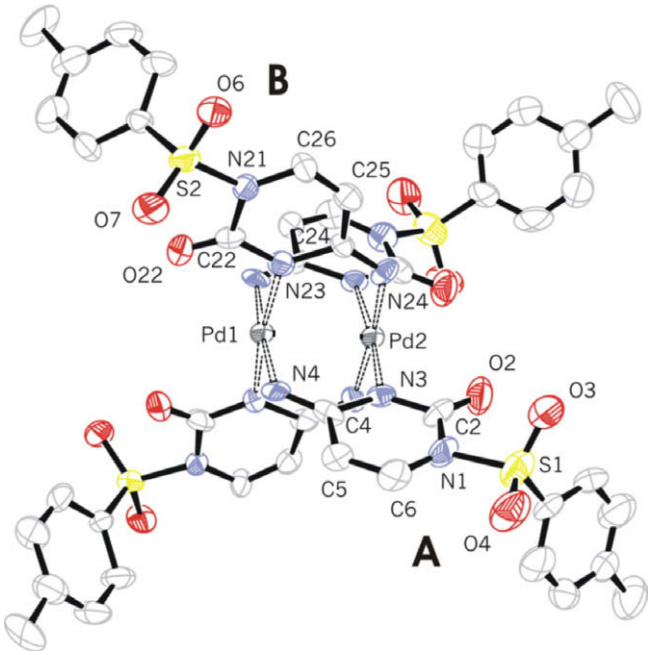


Fig. 5. ORTEP drawing of complex **3** with a partial atom numbering scheme and 30% ellipsoid probability. Hydrogen atoms are omitted for clarity.

vealed by the two planes defined by N3, C4, N4, Pd1, N4*i*, C4*i*, N3*i* and Pd2 [max. deviation of the least square plane, 0.038(10) Å] and N23, C24, N24, Pd1, N24*i*, C24*i*, N23*i* and Pd2 [max. deviation of the least square plane, 0.061(9) Å]. These two planes intersect at the Pd1–Pd2 vector, forming an interplanar angle of 89.3(3)°. This class of ligands reveals a conformational chirality along the N–S bond, as previously described by us [17]. Although **3** crystallizes in the centrosymmetric space group *Pnab*, discrete complex molecules do not contain an intramolecular inversion centre, and all the ligand molecules present inside the single complex molecule are of the same chirality. However, the crystal structure contains complex molecules of both chiralities, related by the extramolecular inversion centers.

The cytosine ring geometries for ligand **1** as well as for complexes **3** and **4** are given in Table 4. In both symmetrically independent ligand molecules **3A** and **3B**, the bond distances inside the cytosine rings reveal remarkable alterations compared to the analogous values in the structure of ligand **1**. This is due to the stabilization of the iminooxo form of the ligand anion upon Pd coordination. While the length of the N3–C4 bond in ligand **1** clearly reflects its double bond character, this bond is significantly longer in both coordinated ligand molecules in complex **3**, suggesting an increase of its single bond character. This implies that the

Table 3
Coordination sphere geometries in **3** (*i*; 1/2 − *x*, *y*, −*z*).

Bond lengths (Å)			
Pd1–N23	2.067(10)	Pd2–N3	2.090(9)
Pd1–N23*i*	2.067(10)	Pd2–N3*i*	2.090(9)
Pd1–N4	1.970(9)	Pd2–N24	2.039(12)
Pd1–N4*i*	1.970(9)	Pd2–N24*i*	2.039(12)
Bond angles (°)			
N23–Pd1–N23*i*	172.4(4)	N3–Pd2–N3*i*	173.3(4)
N23–Pd1–N4	90.9(4)	N3–Pd2–N24	86.3(4)
N23–Pd1–N4*i*	88.8(4)	N3–Pd2–N24*i*	93.4(4)
N23i–Pd1–N4	88.8(4)	N3i–Pd2–N24	93.4(4)
N23i–Pd1–N4*i*	90.9(4)	N3i–Pd2–N24*i*	86.3(4)
N4–Pd1–N4i	175.0(4)	N24–Pd2–N24*i*	174.5(4)

Table 4
Bond distances (Å) inside the cytosine ring in **1**, **3** and **4**.

	1	3A	3B	4A	4B
N1–C2	1.432(3)	1.382(16)	1.504(16)	1.417(12)	1.407(11)
C2–N3	1.339(3)	1.389(16)	1.380(16)	1.334(12)	1.380(12)
N3–C4	1.340(2)	1.421(14)	1.443(14)	1.386(10)	1.374(11)
C4–N4	1.312(3)	1.308(15)	1.279(15)	1.307(12)	1.291(12)
C4–C5	1.436(3)	1.440(15)	1.461(17)	1.429(11)	1.452(12)
C5–C6	1.317(3)	1.351(17)	1.290(15)	1.329(14)	1.308(14)
C6–N1	1.396(3)	1.369(17)	1.381(15)	1.393(13)	1.396(11)

negative charge at the endocyclic N3 atoms compensates the positive charge of the Pd atom in the complex structure.

3.2.6. Crystal structure of *4*

Molecular structure of **4** is given in Fig. 6 as an ORTEP drawing. Complex **4** is a dinuclear bridging molecule where two palladium atoms, being 2.9358(10) Å apart, are each coordinated by one exocyclic imino-nitrogen N4 and one endocyclic nitrogen N3. The coordination spheres are each completed by one DMSO molecule (through its sulfur atom) and one chlorine atom. Two ligand molecules bridge two Pd atoms in such a manner that each ligand complexes one Pd atom with its exocyclic imino-nitrogen N4 and the other one with its endocyclic N3. The positive charge of the Pd atoms (+2) is compensated by one chlorine and one deprotonated endocyclic nitrogen, bearing a negative charge, as a consequence of the iminooxo form stabilization upon Pd complexation (*vide supra*).

The geometry of the cytosine ring is given in Table 4. A comparison with the analogous values observed in the ligand structure reveals an increase of the single bond character of the N3–C4 bond, similarly to the case of complex **3**. In both cases, stabilization of the iminooxo form took place upon the coordination of Pd(II). The two bridging rings involve both palladium atoms, as well as N3, C4 and N4 of both ligand molecules, and the corresponding planes form an interplanar angle of 89.9(2)°. The molecule contains two DMSO molecules coordinated to the Pd atoms through their sulfur atoms. A search of the current version of *CSD* (2007 release) shows that the abundance of O-bonded and S-bonded Pd–DMSO adducts is almost equal. Details of the coordination sphere geometries are given in Table 5. The maximum deviation from the coordination sphere least square plane, defined by Pd1, S3, Cl1, N3 and

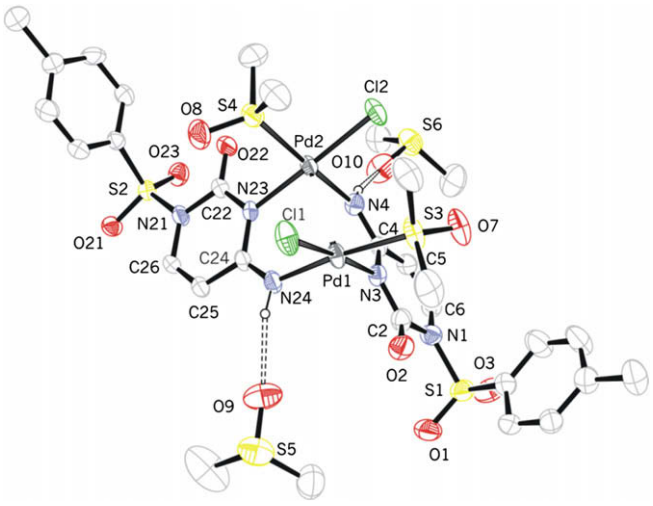


Fig. 6. ORTEP drawing of **4**. Ellipsoids are given on a 30% probability scale. The atom numbering is provided partially and hydrogens are omitted for clarity, except for those included in hydrogen bonding. The solvent molecule connected by the hydrogen bond N24–H···O9 is included.

Table 5
Geometry of the coordination spheres around Pd1 and Pd2 in **4**.

	Pd1	Pd2
Bond lengths (Å)		
Pd–S	2.263(3)	2.252(3)
Pd–Cl	2.292(3)	2.299(2)
Pd–N3 (N23)	2.029(7)	2.034(7)
Pd–N4 (N24)	2.028(8)	2.020(7)
Angles (°)		
S–Pd–Cl	91.10(10)	90.29(10)
S–Pd–N3 (N23)	89.7(2)	89.1(2)
S–Pd–N4 (N24)	173.8(2)	172.5(2)
Cl–Pd–N3 (N23)	176.1(2)	178.5(2)
Cl–Pd–N4 (N24)	90.7(2)	90.3(2)
N3 (N23)–Pd–N4 (N24)	88.1(3)	90.2(3)

N24, is 0.0722(6) Å, whereas in the case of the one defined by Pd2, S4, Cl2, N4 and N23, it is 0.076(7) Å.

The crystal structure is characterized by discrete complex molecules, each of which is connected to two DMSO molecules (in addition to those included in the coordination around Pd), *via* the imino-nitrogens N4 and N24 and the oxygen atoms of the neighbouring non-coordinated solvent molecules [N4–H···O10, 2.965(12) Å, 166°; N24–H···O9, 3.074(15) Å, 146°] (Fig. 6).

4. Conclusions

Complexation of Pd(II) with 1-(*p*-toluenesulfonyl)cytosine ligand (**1**) leads initially to the formation of a kinetically favoured mononuclear complex **2**, regardless of the solvent used. This, initially formed complex undergoes rearrangements in aprotic polar solvents, resulting in the formation of two different dinuclear bridging species (**3** from DMF and **4** from DMSO), where the ligand anion (1-TosC$^-$) exists in a rare iminooxo form and is coordinated to Pd(II) through both its exocyclic (N4) and endocyclic nitrogen atom (N3).

Supplementary data

CCDC 695234, 695235 and 695236 contains the supplementary crystallographic data for compounds **1**, **3** and **4**, respectively. These data can be obtained free of charge via http://www.ccdc.cam.ac.uk/conts/retrieving.html, or from the Cambridge Crystallographic Data Centre, 12 Union Road, Cambridge CB2 1EZ, UK; fax: (+44) 1223-336-033; or e-mail: deposit@ccdc.cam.ac.uk.

Acknowledgments

We thank Dr. sc. Ljerka Tušek-Božić for conductometric measurements. We appreciate the financial support of the Ministry of Science, Education and Sports of the Republic of Croatia through Grants No. 098-0982914-2935, 098-1191344-2943 and 098-0982904-2927.

References

[1] K.A. Hartman, A. Rich, J. Am. Chem. Soc. 87 (1965) 2033.
[2] R.B. Inman, J. Mol. Biol. 9 (1964) 624.
[3] P. Rajagopal, J. Feigon, Nature 339 (1989) 637.
[4] L.C. Sowers, G.V. Fazakerley, R. Eritja, B.E. Kaplan, M.F. Goodman, Proc. Natl. Acad. Sci. USA 83 (1986) 5434.
[5] (a) B. Lippert, H. Schöllhorn, U. Thewalt, J. Am. Chem. Soc. 108 (1986) 6616;
(b) W. Saenger, in: Principles of Nucleic Acid Structure, Springer Verlag, New York, 1982;
(c) M. Monshi, K. Al-Farhan, S. Al-Resayes, G. Ghaith, A.A. Hasanein, Spectrochim. Acta, Part A 53 (1997) 2669.
[6] D. Montagner, E. Zangrando, B. Longato, Inorg. Chim. Acta (2008), doi:10.1016/j.ica.2008.04.030.
[7] (a) F. Zamora, M. Kunsman, M. Sabat, B. Lippert, Inorg. Chem. 36 (1997) 1583;
(b) A.H. Velders, B. van der Geest, H. Kooijman, A.L. Spek, J.G. Haasnoot, J. Reedijk, Eur. J. Inorg. Chem. (2001) 369;
(c) L.Y. Kuo, M.G. Kanatzidis, M. Sabat, A.L. Tipton, T.J. Marks, J. Am. Chem. Soc. 113 (1991) 9027.
[8] P.J.S. Miguel, P. Lax, M. Willermann, B. Lippert, Inorg. Chim. Acta 357 (2004) 4552.
[9] J. Müller, E. Zangrando, N. Pahlke, E. Freisinger, L. Randaccio, B. Lippert, Chem. Eur. J. 4 (1998) 397.
[10] (a) Lj. Glavaš-Obrovac, I. Karner, B. Žinić, K. Pavelić, Anticancer Res. 21 (2001) 1979;
(b) B. Žinić, M. Žinić, I. Krizmanić, EP 0 877 022 B1, Synthesis of the Sulfonylpyrimidine Derivatives with Anticancer Activity, 2003.;
(c) F. Supek, M. Kralj, M. Marjanović, L. Šuman, T. Šmuc, I. Krizmanić, B. Žinić, Invest. New Drugs 26 (2008) 97.
[11] J. Kašnar-Šamprec, Lj. Glavaš-Obrovac, M. Pavlak, I. Mihaljević, V. Mrljak, N. Štambuk, P. Konjevoda, B. Žinić, Croat. Chem. Acta 78 (2005) 261.
[12] L.J. Faruggia, J. Appl. Cryst. 32 (1999) 837.
[13] M.C. Burla, M. Camalli, B. Carrozzini, G.L. Cascarano, C. Giaccovazzo, G. Polidori, R. Spagna, SIR2002, Version 1.0, A Program for Automatic Solution and Refinement of Crystal Structures, University of Bari, Bari, Italy, 2002.
[14] G.M. Sheldrick, SHELX97: Program for the Refinement of Crystal Structures, Universität Göttingen, Germany, 1997.
[15] L.J. Farrugia, J. Appl. Crystallogr. 30 (1997) 565.
[16] P. van der Sluis, A.L. Spek, Acta Crystallogr., Sect. A 46 (1990) 194.
[17] A.L. Spek, PLATON – A Multipurpose Crystallographic Tool, Version 40607, University of Utrecht, Utrecht, The Netherlands, 1998–2007.
[18] A. Višnjevac, M. Žinić, M. Luić, D. Žiher, T. Kajfež Novak, B. Žinić, Tetrahedron 63 (2007) 86.
[19] J. Bernstein, R.E. Davies, L. Shimani, N.-L. Chang, Angew. Chem. 107 (1995) 1689.
[20] J.H. Gross, Mass Spectrometry, Springer, Berlin, 2004.
[21] L.C. Gatlin, F. Tureček, in: R.B. Cole (Ed.), Electrospray Ionization Mass Spectrometry: Fundamentals, Instrumentation, and Applications, Wiley, New York, 1997, p. 527.
[22] M. Franska, Intern. J. Mass Spectrometry 261 (2007) 86.
[23] (a) M. Tsuboi, S. Takahasha, I. Harada, in: J. Duchesene (Ed.), Physicochemical Properties of Nucleic Acids, vol. 2, Academic Press, London, 1973, p. 91;
(b) H. Susi, J.S. Ard, J.M. Purcell, Spectrochim. Acta 29A (1973) 725;
(c) E.D. Radchenko, G.G. Sheina, N.A. Smorygo, Y.P. Blagoi, J. Mol. Struct. 116 (1984) 387;
(d) Y. Nishimura, T. Tsuboi, Chem. Phys. 98 (1985) 71.
[24] E. Nir, I. Huenig, K. Kleinermanns, M.S. de Vries, Phys. Chem. Chem. Phys. 5 (2003) 4780.
[25] (a) L. Szučova, Z. Travniček, M. Zatloukal, I. Popa, Bioorg. Med. Chem. 14 (2006) 479;
(b) I.A. Efimenko, A.P. Kurbakova, Transition Met. Chem. 19 (1994) 539;
(c) P.-C. Kong, F.D. Rochon, Can. J. Chem. 59 (1981) 3293.

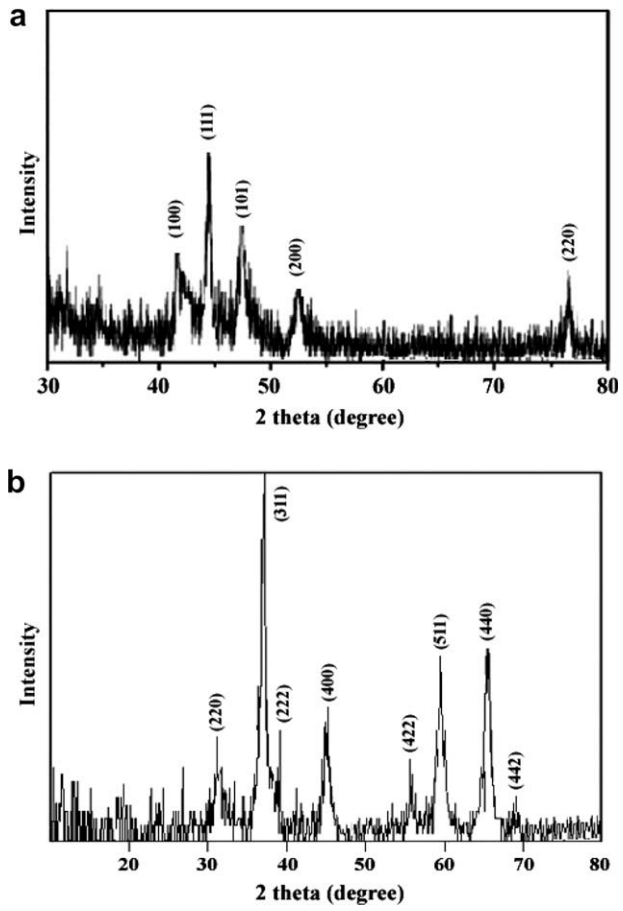


Fig. 1. X-ray diffraction patterns of (a) fresh Co and (b) Co_3O_4 nanoparticles.

2. Experimental

2.1. Materials and physical measurements

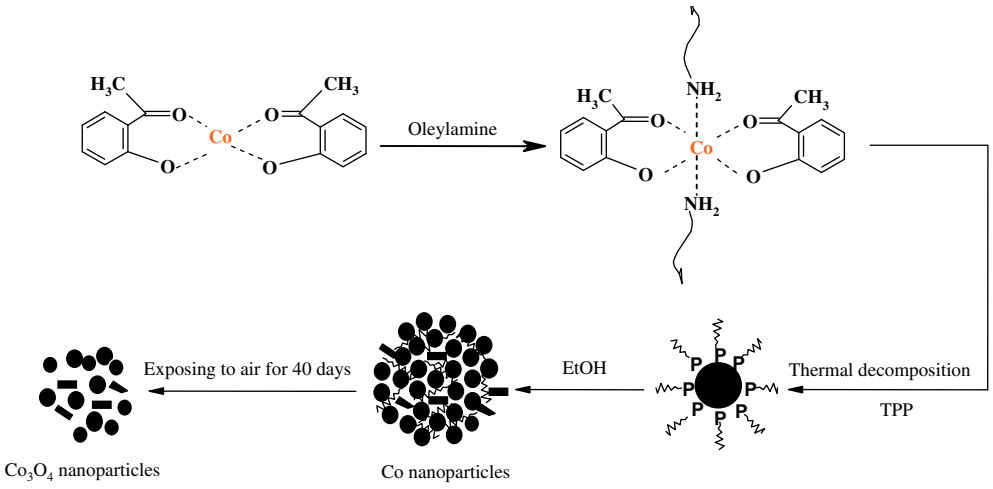
The precursor complex [bis(2-hydroxyacetophenato)cobalt(II)], [Co(aceto)$_2$], was prepared according to the procedure described previously [17]. Oleylamine, triphenylphosphine (TPP), toluene, hexane, and ethanol were purchased from Aldrich and used as received. XRD patterns were recorded by a Rigaku D-max C III, X-ray diffractometer using Ni-filtered Cu Kα radiation. Transmission electron microscopy (TEM) and energy dispersive X-ray (EDX) images were obtained on a Philips EM208 transmission electron microscope with an accelerating voltage of 200 kV. The high-resolution transmission electron microscopy (HRTEM) image was recorded on a JEOL-2010 TEM at an acceleration voltage of 200 kV. Fourier transform infrared (FT-IR) spectra were recorded on Shimadzu Varian 4300 spectrophotometer in KBr pellets. The magnetic measurement was carried out in a vibrating sample magnetometer (VSM) (BHV-55, Riken, Japan) at room temperature.

2.2. Synthesis of Co nanoparticles

The current synthetic procedure is a modified version of the method developed by Hyeon group for the synthesis of various nanoparticles of metals and oxides, which employ the thermal decomposition of metal-surfactant complexes in hot surfactant solution [19]. The synthetic pathway is shown in Scheme 1. In the typical synthesis, a stock solution of co-surfactant complex, prepared by reacting 0.6 g of [Co(aceto)$_2$] with 5 mL of oleylamine at 140 °C, was injected into 5 g of triphenylphosphine (TPP) under vigorous stirring at 250 °C under argon atmosphere. The color of the solution changed from orange to black, indicating that colloidal nanoparticles were generated and then the black solution was aged at 240 °C for 60 min. The reaction mixture was then cooled to room temperature in air and the black products were retrieved by adding 30 mL of anhydrous ethanol, followed by centrifugation. The final product was washed with ethanol for at least three times to remove impurities, if any. The retrieved powder of the nanoparticles could be easily redispersed in nonpolar organic solvents such as hexane or toluene (Scheme 1).

3. Results and discussion

Fig. 1 presents the XRD patterns of the as-prepared samples. The discernible peaks in Fig. 1a can be indexed to (100), (111), (101), (200) and (220) planes of hcp-Co (JCPDS: 89-4308). It is well known that nanometer sized cobalt particles are easy to be oxidized in air. However, from XRD pattern, except for pure hcp-Co, no other cobalt oxide phase were detected, which might result from the protection of oleylamine and TPP on the surface of nanoparticles. The diffraction peaks are clearly broadened, which can be the result of the reduced particle size. This indicates that the Co is all nanoparticle. The average particle diameter can be estimated using Scherrer's formula. The average sizes calculated is 13 nm.



Scheme 1. The overall synthetic procedure of the formation Co_3O_4 nanoparticles.

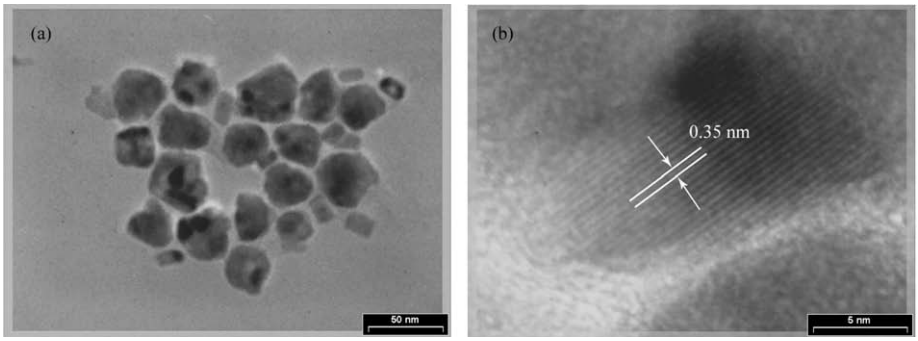


Fig. 2. (a) TEM image and (b) HRTEM image of Co nanoparticles.

The diffractogram shown in Fig. 1b presents the XRD pattern of nanoparticles after exposing the nanoparticles to air; no peak was related to the cobalt element in the XRD pattern. All the reflection peaks can be indexed to a cubic phase of Co_3O_4 spinel with lattice parameter $a = 8.0850$ Å, which is consistent with the reported value (JCPDS: 78-1969). No other peaks for impurities were detected. The spectrum consists of well-defined diffraction peaks indicating that very thin crystalline single phase is formed with cubic crystal structure.

Fig. 2a is TEM image of the Co nanoparticles. Most of the Co particles are irregular (Fig. 2a). The mean size of Co nanoparticles is 20 nm. In the HRTEM (high-resolution transmission electron microscopy) image (Fig. 2b), the distance between the two adjacent planes, d, is measured to be 0.355 nm.

Time-dependent FT-IR studies indicate that oxidation of the as-synthesized cobalt nanoparticles in air is slow. Fig. 3a is the FT-IR spectrum of the freshly prepared cobalt nanoparticles. Characteristic peaks of oleylamine (CH stretching) are observed. Because cobalt is the only product of the decomposition reaction and all the residual surfactant is removed by washing the precipitate with ethanol several times, the characteristic peaks of the oleylamine are introduced from the oleylamine coated surface of cobalt nanoparticles. According to the literature oleylamine should react or coordinate with the surface atoms of the Co nanoparticles to prevent oxidation or aggregation of the Co nanoparticles. Also, adding amounts of hexane at the end of the reaction helps to coat any exposed crystal surface, improving passivation against oxidation. The weak peaks at 3417 cm^{-1} are assigned to the stretching vibration of absorption water. Fig. 3b and c is the FT-IR spectrum of the cobalt nanoparticles from dispersion kept under air for 30 days (curve b) and 40 days (curve c). FT-IR on cobalt nanoparticles kept in hexane under air for 30 days shows the same peaks with Fig. 3a, without any peaks in the 400–600 related to Co–O stretching, from the typical valence state of Co^0, indicating that the Co nanoparticles in hexane are very stable against further oxidation. However, after it is kept in hexane under air for 40 days (Fig. 3c) we observed a valency change of cobalt from the Co nanoparticle sample. The spectra (Fig. 3c) also contained two strong absorption bands at 662 and 581 cm^{-1} which confirm the spinel structure of Co_3O_4. The former peak at 662 cm^{-1} is attributed to the stretching vibration mode of M–O in which M is Co^{2+} and is tetrahedrally coordinated. The band at 581 cm^{-1} can be assigned to the M–O in which M is Co^{3+} and so coordinates octahedrally [20]. Also, Fig. 3 shows two weak stretch vibrations at 2923 and 2852 cm^{-1} attributing to the C–H stretching models of the oleylamine carbon chain, indicating oleylamine molecules are absorbed on the surface of Co_3O_4 nanocrystals. If there is adsorption of $[Co(aceto)_2]$ on the surface of the Co_3O_4 particles, a distinct carbonyl peak around 1640 cm^{-1} should appear in the FT-IR spectrum. Moreover, this peaks which also indicates a change in the valency of the cobalt nanoparticles. Chemical purity and stoichiometry of the Co_3O_4 (the Co nanoparticles kept for 40 days) was tested by EDX. The strong peaks related to Co and O is found in the spectrum Fig. 4. EDX spectrometry for nanoparticles shown oxygen that confirm sample was oxidize in air for 40 days. The Cu peaks are due to the 300 mesh copper grid.

In the presence work as shown in Scheme 1 because of the symmetry of precursor we have sites with same potential energy levels

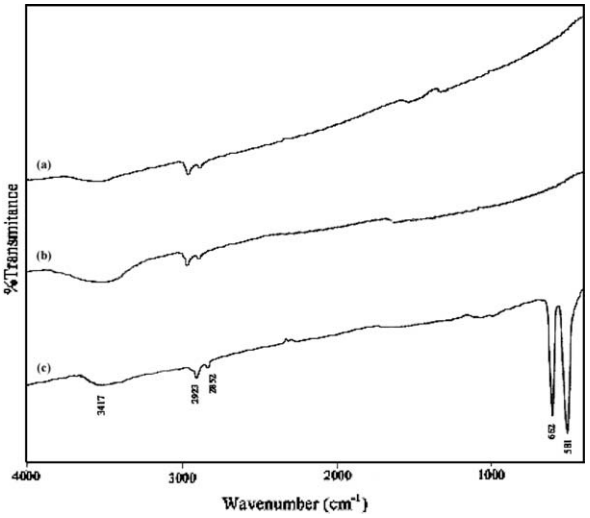


Fig. 3. FT-IR spectra of (a) fresh Co nanoparticles, (b) Co nanoparticles kept for 30 days and (c) Co_3O_4 (the Co nanoparticles kept for 40 days).

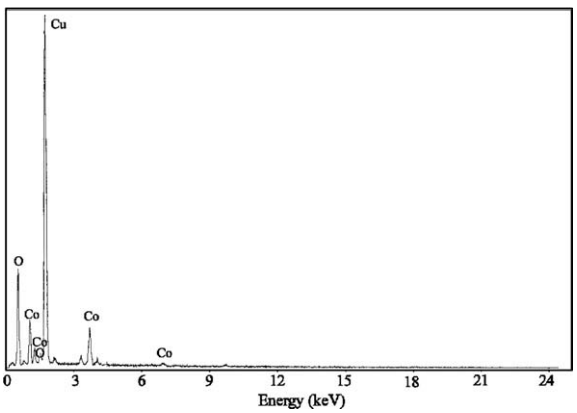


Fig. 4. EDX spectrum of the Co_3O_4 nanoparticles.

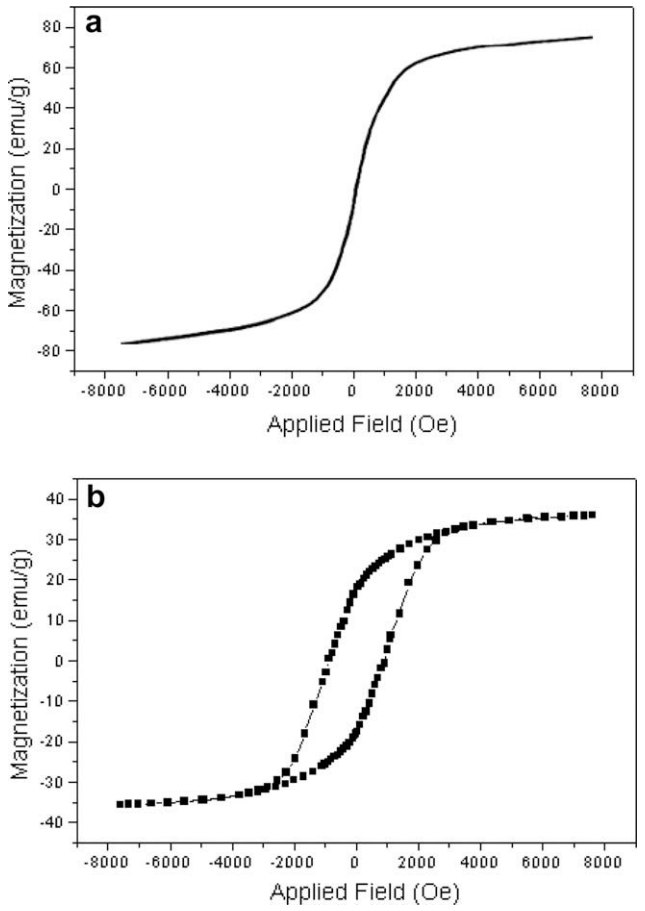


Fig. 5. Magnetization versus applied at 300 K for (a) fresh Co and (b) Co_3O_4 nanoparticles.

on the surface of metallic core. TPP is a high-boiling point surfactant with three phenyl groups providing great steric hindrance to control the size of nanomagnetic metal nanoparticles. The addition of TPP into the mixture of oleylamine and complex as an additional surfactant reduced the particle size much further and resulted in nanoparticles. Oleylamine is known as a ligand that binds tightly to the metal nanoparticles surface. The combined effects of TPP and oleylamine were much more profound than those of individual contributions.

The superparamagnetic behavior is documented by the hysteresis loop measured at 300 K as shown in Fig. 5a. There is almost immeasurable coercivity for Co nanoparticles at room temperature, which is a very typical behavior for a soft magnet. This indicates that the Co particles are superparamagnetic and nanosized. The saturation magnetization, M_s, is 63.9 emu/g for Co nanoparticles, which is lower than that of bulk Co particles (M_{bulk} = 166 emu/g) [21]. The decrease in M_s of Co nanoparticles is due to superparamagnetism of magnetite particles that occurs when the particle size decreases below 8 or 20 nm [12] and oleylamine that coated on the surface of Co nanoparticles. The hysteresis loops (Fig. 5b) measured at room temperature shows a ferromagnetic behavior of the Co_3O_4 nanoparticles. At 25 °C the remanent magnetization, (M_r) is 12.23 emu/g, the coercive field (H_c), is 911.34 Oe and the magnetization at saturation (M_s) is estimated to be only 24.94 emu/g (the saturation magnetization M_s was determined from the extrapolation of curve of H/M versus H). Cobalt oxide nanoparticles are made of small crystalline domains. Each crystalline domain is characterized by its own magnetic moment oriented randomly. The total magnetic moment of the nanoparticles is the sum of these magnetic domains coupled by dipolar interactions. As a result, a low value of M_s is obtained. The magnetic properties of nanomaterials have been believed to be highly dependent on the sample shape, crystallinity, magnetization direction, and so on.

4. Conclusion

In summary, Co and Co_3O_4 nanoparticles were successfully prepared using thermal decomposition of [Co(aceto)$_2$] as new precursor in the presence of TPP and oleylamine. The as-synthesized cobalt particles show very good crystallinity and are stable in hexane as solvent against air oxidation. This method is nontoxic, facile and inexpensive. Co nanoparticles have common features of superparamagnetic at room temperature. This work is easily extended to other metals.

Acknowledgement

Authors are grateful to council of University of Kashan for providing financial support to undertake this work.

References

[1] A.P. Alivisatos, Science 271 (1996) 933.
[2] P. Poizot, S. Laruelle, S. Grugeon, L. Dupont, J.M. Tarascon, Nature 407 (2000) 496.
[3] X. Duan, Y. Huang, R. Agarwal, C.M. Lieber, Nature 421 (2003) 241.
[4] H. Kim, D.W. Park, H.C. Woo, J.S. Chung, Appl. Catal. B 19 (1998) 233.
[5] W.Y. Li, L.N. Xu, J. Chen, Adv. Funct. Mater. 15 (2005) 851.
[6] D.W. Elliott, W.-X. Zhang, Environ. Sci. Technol. 35 (2001) 4922.
[7] V.F. Puntes, K.M. Krishnan, A.P. Alivisatos, Science 291 (2001) 2115.
[8] C.B. Murray, S. Sun, W. Gaschler, IBM J. Res. Dev. 45 (2001) 47.
[9] X.L. Dong, C.J. Choi, B.K. Kim, Scripta Mater. 47 (2002) 857.
[10] Z.H. Wang, C.J. Choi, B.K. Kim, Z.D. Zhang, J. Alloys Compd. 351 (2003) 319.
[11] S. Sun, C.B. Murray, J. Appl. Phys. 85 (1999) 4325.
[12] C. Luna, M.P. Morales, C.J. Serna, M. Vazquez, Mater. Sci. Eng. C 23 (2003) 1129.
[13] Y. Ichiyanagi, S. Yamada, Polyhedron 24 (2005) 2813.
[14] H. Shao, Y. Huang, H. Lee, Y.J. Suh, C.O. Kim, J. Magn. Magn. Mater. 304 (2006) e28.
[15] D.K. Lee, Y.H. Kim, X.-L. Zhang, Y.S. Kang, Current Appl. Phys. 6 (2006) 786.
[16] H.T. Yang, Y.K. Su, C.M. Shen, T.Z. Yang, H.J. Gao, Surf. Interface Anal. 36 (2004) 155.
[17] M. Salavati-Niasari, F. Davar, M. Mazaheri, M. Shaterian, J. Magn. Magn. Mater. 320 (2008) 575.
[18] M. Salavati-Niasari, F. Davar, M. Mazaheri, Mater. Lett. 62 (2008) 1890.
[19] H.M. Park, E. Kang, S.U. Son, H.M. Park, M.K. Lee, J. Kim, K.W. Kim, H. Noh, J. Park, C.J. Bae, J. Park, T. Hyeon, Adv. Mater. 17 (2005) 429.
[20] M. Herrero, P. Benito, F.M. Labajos, V. Rives, Catal. Today 128 (2007) 129.
[21] E.P. Wohlfarth, in: E.P. Wohlfarth (Ed.), Ferromagnetic Materials, North-Holland, Amsterdam, 1980, p. 20.

dried according to the standard literature procedures [10], freshly distilled, and saturated with nitrogen prior to use. All starting reagents were purchased from commercial sources and used without further purification or synthesised from published methods. The 4-(4-pyridyl)-1,3-dithiol-2-one was synthesised according to literature reports [8,11].

Elemental analyses of the compounds isolated in theses studies were performed at ITN analytical services using an EA 110 CE Instruments automatic analyser. Melting points were performed on a Stuart Scientific SMP2.

2.2. Synthesis

2.2.1. Tetraphenylphosphonium salt of bis[1-(4-pyridin-4-yl)-1,2-ethylenedithiolato]nickel, $PPh_4[Ni(4\text{-}pedt)_2]$ (**1**)

The 4-(4-pyridyl)-1,3-dithiol-2-one (0.50 g; 2.56 mmol) was added to a sodium methoxide solution (0.147 g; 6.40 mmol; 13 mL) After 45 min of stirring, $Ni(NO_3) \cdot 6H_2O$ (0.37 g, 1.28 mmol) was added. One hour later the red solution was filtered to an aqueous PPh_4Cl solution (0.96 g, 2.56 mmol, 100 mL). A black precipitate appeared immediately from the brown solution. The solid was recovered by filtration, washed with water and recrystallised from acetonitrile to afford black crystals of the nickel salt suitable for X-ray diffraction. 50% yield (0.47 g, 0.64 mmol); m.p. 217–218 °C. $C_{38}H_{30}NiN_2PS_4$ (Mol. Wt.: 732.59). Elemental *Anal.* Calc.: C, 62.30; H, 4.13; N, 3.82; S, 17.51. Found: C, 62.09; H, 4.06; N, 3.77; S, 17.31%.

2.2.2. Tetraphenylphosphonium salt of bis[1-(4-pyridin-4-yl)-1,2-ethylenedithiolato]copper $PPh_4[Cu(4\text{-}pedt)_2]$ (**2**)

The oxo compound (0.10 g; 0.51 mmol) was added to a freshly made sodium methoxide solution (0.023 g; 1.02 mmol, 3 mL) and stirred at room temperature, until total dissolution, followed by drop wise addition of a solution of $CuCl_2 \cdot 2H_2O$ (0.043 g; 0.25 mmol) in methanol (2 mL). The solution was stirred for 1 h and filtered to a PPh_4Br methanol solution (0.214 g, 0.51 mmol, 3 mL). No precipitate formation was observed. The reaction vial was opened to the air, a few H_2O drops were slowly added until start of incipient precipitation and the mixture was left overnight at 4 °C. The oil that formed was separated from the mixture by centrifugation, dried under vacuum (P_2O_5) and recrystallised from dichloromethane/hexane to be recovered as a microcrystalline precipitate. 48% yield (0.089 g, 0.12 mmol); m.p. 162–163 °C. $C_{38}H_{30}N_2CuS_4$ (Mol. Wt.:737.44). Elemental *Anal.* Calc.: C, 61.89; H, 4.10; N, 3.80; S, 17.39. Found: C, 61.72; H, 4.92; N, 3.84; S, 18.03%.

2.2.3. Tetrabutylammonium salt of bis[1-(4-pyridyl)-1,2-ethylenedithiolato]nickel $n\text{-}Bu_4N[Ni(4\text{-}pedt)_2]$ (**3**)

The procedure was similar to the described above. The oxo compound was added (0.10 g; 0.51 mmol) to a freshly made sodium methoxide solution (0.023 g; 1.02 mmol, 3 mL) and stirred at room temperature, until total dissolution, followed by dropwise addition of a solution of $NiCl_2 \cdot 6H_2O$ (0.061 g; 0.25 mmol) in methanol (2 mL). The red solution was stirred for 1 h and then filtered into n-Bu_4NBr methanol solution (0.165 g, 0.51 mmol, 3 mL). No precipitate formation was observed. The reaction vial was opened to the air, a few H_2O drops were slowly added until start of incipient precipitation and the mixture was left overnight at 4 °C. The reddish oil formed was separated from the mixture by centrifugation, dried under vacuum (P_2O_5) and recrystallised from acetone to be recovered as a microcrystalline precipitate. 65% yield (0.105 g, 0.16 mmol); m.p. 133–134 °C. $C_{30}H_{46}N_3NiS_4$ (Mol. Wt.: 635.66) Elemental *Anal.* Calc.: C, 56.68; H, 7.29; N, 6.61; S, 20.18. Found: C, 56.01; H, 7.89; N, 6.12; S, 19.75%.

2.2.4. Tetrabutylammonium salt of bis[1-(4-pyridyl)-1,2-ethylenedithiolato]copper, $n\text{-}Bu_4N[Cu(4\text{-}pedt)_2]$ (**4**)

Following the same general procedure used for n-$Bu_4N[Ni(4\text{-}pedt)_2]$, the oxo compound was added (0.10 g; 0.51 mmol) to a freshly made sodium methoxide (0.023 g; 1.02 mmol, 3 mL) stirred until total dissolution, followed by drop wise additio of a solution of $CuCl_2 \cdot 2H_2O$ (0.043 g; 0.25 mmol) in methanol (2 mL). The solution was stirred for 1 h and afterwards filtered onto an n-Bu_4NBr methanol solution (0.165 g, 0.51 mmol, 3 mL). No precipitate formation was observed. A few H_2O drops were slowly added until start of incipient precipitation and the mixture was left overnight at 4 °C. The oil formed was separated from the mixture by centrifugation, dried under vacuum (P_2O_5) and recrystallised from dichloromethane/hexane to be recovered as a microcrystalline precipitate. 41% yield (0.065 g, 0.10 mmol); m.p. 160–162 °C. $C_{30}H_{46}N_3CuS_4$ (Mol. Wt.: 640.51) Elemental *Anal.* Calc.: C, 56.26; H, 7.24; N, 6.56; S, 20.02. Found: C, 55.83; H, 7.01; N, 6.12; S, 19.84%.

2.2.5. Tetrabutylammonium salt of bis[1-(4-pyridyl)-1,2-ethylenedithiolato]gold $n\text{-}Bu_4N[Au(4\text{-}pedt)_2]$ (**5**)

Following the same general procedure used for n-$Bu_4N[Ni(4\text{-}pedt)_2]$, the oxo compound (0.10 g; 0.51 mmol) was dissolved in a freshly prepared methoxide solution (0.024 mg; 1.02 mmol, 3 mL). The total dissolution of the oxo compound was followed by drop wise addition of a $KAuCl_4 \cdot 4H_2O$ methanol solution (0.097 g; 0.25 mmol, 2 mL). The brown solution was filtered into an n-Bu_4NBr methanol solution (0.165 g, 0.51 mmol, 3 mL). After the addition of a few milliliters of water, the reaction vial was kept for several hours at 4 °C. The brown oil formed was recovered by centrifugation, dried under vacuum (P_2O_5) and recrystallised from diclorometha/hexane to be recovered as a microcrystalline precipitate. 60% yield (0.115 g, 0.15 mmol); m.p. 127–129 °C. $C_{30}H_{46}N_3AuS_4$ (Mol. Wt.: 773.93). Elemental *Anal.* Calc.: C, 46.56; H, 5.99; N, 5.43; S, 16.57. Found: C, 46.21; H, 5.52; N, 5.25; S, 16.39%.

2.2.6. Crown ether [Na(18C6)] salt of bis[1-(4-pyridyl)-1,2-ethylenedithiolato]nickel $[Na(18C6)][Ni(4\text{-}pedt)_2]$ (**6**)

The oxo compound (0.20 g; 1.03 mmol) was added to a freshly prepared methoxide solution (0.047 g, 2.05 mmol, 5 mL). After stirring until total dissolution, $NiCl_2 \cdot 6H_2O$ methanol solution (0.122 g; 0.51 mmol, 5 mL) was added. The red solution was stirred for 1 h and then filtered into an 18-crown-6 methanol solution (0.271 g, 1.03 mmol, 1 mL). The mixture was left at 4 °C for two weeks. A mixture of amorphous brown and darker polycrystalline precipitate was recovered by vacuum filtration. The mixture was dissolved in dichloromethane and an insoluble precipitate was removed. By slow diffusion of hexane into the dichloromethane solution, it was possible to recover compound **6** as a dark brown polycrystalline material. 58% yield (0.197 g; 0.29 mol) m.p. 260–261 °C. $C_{26}H_{34}N_2NaNiO_6S_4$ (Mol. Wt.: 680.5). Elemental *Anal.* Calc.: C, 45.89; H, 5.04; N, 4.12; S, 18.85. Found: C, 45.43; H, 5.35; N, 4.12; S, 18.30%.

2.2.7. Crown ether [Na(18C6)] salt of bis[1-(4-pyridyl)-1,2-ethylenedithiolato] gold $[Na(18C6)][Au(4\text{-}pedt)_2]$ (**7**)

The oxo compound (0.10 g, 0.51 mmol) was added to a freshly prepared sodium methoxide solution (0.0235 g, 1.02 mmol, 5 ml) and stirred for 45 min. The dark red solution was removed from the inert atmosphere and solid $KAuCl_4 \cdot 4H_2O$ (0.097 g, 0.25 mmol) was added. The mixture was stirred for 2 h, filtered over Celite to a solution of 18C6 (0.0677 g, 0.25 mmol) in methanol (1 ml), layered with pentane and left at 4 °C. A few days later, an amorphous brown precipitate was recovered by vacuum filtration. From an attempt to recrystallise from dichloromethane/hexane, an oil was

obtained which was dried and characterised. Yield 0.088 g, 0.11 mmol (44%); m.p. 145–146 °C. $C_{26}H_{34}O_6N_2S_4AuNa$ (Mol. Wt.: 818.08). Elemental *Anal.* Calc.: C, 38.14; H, 4.19; N, 3.42; S, 15.63. Found: C, 38.38; H, 4.91; N, 3.50; S, 15.28%.

2.3. Physical characterisation

Cyclic voltammetry data were obtained using a BAS C3 Cell Stand. The measurements were performed at room temperature in CH_2Cl_2 solutions, containing [*n*-Bu_4]PF_6 (0.1 M) as supporting electrolyte, with a scan rate of 100 mV/s using platinum wire working and counter electrodes and a Ag/AgCl reference electrode. The $[(Me_5C_5)_2Fe]^+/[Me_5C_5)_2Fe]$ ($[Fc^*]^+/[Fc^*]$) couple was used as the internal reference and the potentials of the redox couples observed were referenced to that.

Single crystals suitable for X-ray crystallographic analyses were obtained by recrystallisation in acetonitrile, for compound **1**, and by slow diffusion of hexane into a saturated solution of dichloromethane, for compounds **2**, **3**, **5** and **6**. In compound **6** two water molecules were incorporated in the crystal structure to yield compound **6** · **2H$_2$O**, due to the presence of air humidity.

The data for compounds **1**, **2**, **3**, **5** and **6** · **2H$_2$O** were collected on a Bruker AXS APEX CCD area detector X-ray diffractometer equipped with an Oxford Cryosystems low-temperature device at 150 K in the ω and φ scans mode. A semi empirical absorption correction was carried out using SADABS [12]. Data collection, cell refinement and data reduction were done with the SMART and SAINT programs [13]. The structures were solved by direct methods using SIR97 [14] and refined by fullmatrix least-squares methods with the SHELXL97 [15] program using the WINGX software package [16]. Non-hydrogen atoms were refined with anisotropic thermal parameters whereas H-atoms were placed in idealised positions and allowed to refine riding on the parent C atom. In **3** and **5** one of the butyl groups on the cation show disorder that was modelled over two positions with the following occupation factors: 52%:48% and 55%:45%, respectively. The final difference Fourier map revealed the existence of residual electron densities of: 2.4/−0.89 e A^{-3} for compound **5**, which are located near the Au atom. Molecular graphics were prepared using ORTEP3 [17] and MERCURY 1.4.2 [18]. A summary of the crystal data, structure solution and refinement is listed in Table 1.

EPR spectra were obtained at room temperature on powders using a conventional X-band spectrometer (Bruker ESP 300E) equipped with a microwave bridge ER041XK, a rectangular cavity operating in T102 mode and a field controller ER 032M system. The modulation amplitude was kept well below the linewidth and the microwave power well below saturation.

Static magnetic susceptibility measurements in the range 2–300 K were performed using a superconducting longitudinal Faraday system (Oxford Instruments) under a magnetic field of 5 T and field gradient of 1 T/m. A polycrystalline sample (~20 mg) was placed inside a previous calibrated thin-wall Teflon bucket. The force was measured with a microbalance (Sartorius S3D-V), applying forward and reverse field gradients. Magnetisation data were corrected for contributions due to the core diamagnetism, estimated from tabulated Pascal constants as -385×10^{-6}, -379×10^{-6} and -348×10^{-6} emu/mol for **1**, **3** and **6**, respectively.

Table 1
Crystallographic data and refinement parameters for complexes $Ph_4P[Ni(4\text{-pedt})_2]$ (**1**), $Ph_4P[Cu(4\text{-pedt})_2]$ (**2**), *n*-$Bu_4N[Ni(4\text{-pedt})_2]$ (**3**), *n*-$Bu_4N[Au(4\text{-pedt})_2]$ (**5**) and $[Na(18C6)][Ni(4\text{-pedt})_2] \cdot 2H_2O$ (**6** · **2H$_2$O**).

Compound	**1**	**2**	**3**	**5**	**6** · **2H$_2$O**
Formula	$C_{38}H_{30}N_2NiPS_4$	$C_{38}H_{30}CuN_2PS_4$	$C_{30}H_{46}N_3NiS_4$	$C_{30}H_{46}AuN_3S_4$	$C_{26}H_{38}N_2NaNiO_8S_4$
Formula weight (g mol^{-1})	732.58	737.39	635.65	773.90	712.49
Wavelength (Å)	0.71073	0.71073	0.71073	0.71073	0.71073
Crystal system, space group	monoclinic, *C*2/*c*	monoclinic, *C*2/*c*	triclinic, $P\bar{1}$	triclinic, $P\bar{1}$	monoclinic, $P2_1/n$
a (Å)	26.8750(5)	26.9179(8)	9.0033(2)	8.6211(1)	11.7067(14)
b (Å)	17.3528(3)	17.3541(6)	11.2258(2)	11.1196(2)	9.7243(12)
c (Å)	18.1609(3)	18.1969(5)	16.9070(3)	17.6962(3)	14.3179(18)
α (°)	90	90	107.7870(10)	74.646(1)	90
β (°)	127.5650(10)	127.3820(10)	90.3960(10)	88.829(1)	96.103(2)
γ (°)	90	90	98.3450(10)	80.336(1)	90
V (Å^3), *Z*	6713.4(2), 8	6754.5(4), 8	1607.48(5), 2	1612.14(4), 2	1620.7(3), 2
ρ_{calc} (Mg/m^3), μ (mm^{-1})	1.450, 0.906	1.450, 0.973	1.313, 0.887	1.594, 4.846	1.468, 0.918
F(000)	3032	3040	678	780	750
Crystal size (mm)	0.4 × 0.3 × 0.08	0.30 × 0.20 × 0.16	0.28 × 0.24 × 0.20	0.38 × 0.30 × 0.28	0.20 × 0.12 × 0.10
θ range (°)	2.83–25.03	2.74–25.68	3.21–25.35	2.64–25.68	2.73–25.68
Collected *hkl*	$-31 \le h \le 31$ $-20 \le k \le 20$ $-21 \le l \le 21$	$-32 \le h \le 32$ $-21 \le k \le 21$ $-20 \le l \le 22$	$-10 \le h \le 10$ $-13 \le k \le 13$ $-20 \le l \le 20$	$-10 \le h \le 10$ $-13 \le k \le 13$ $-21 \le l \le 21$	$-14 \le h \le 12$ $-11 \le k \le 11$ $-17 \le l \le 17$
Reflections collected	41666	23618	13680	17908	7273
Independent reflections [R_{int}]	5910 [0.0424]	6409 [0.0656]	5821 [0.0422]	6122 [0.0306]	3051 [0.0414]
Completeness to θ (%)	25.03 (99.7)	25.68 (99.7)	25.35 (98.9)	25.68 (99.7)	25.68 (99.3)
Absorption correction	semi-empirical from equivalents	semi-empirical from equivalents	semi-empirical from equivalents	semi-empirical from equivalents	semi-empirical from equivalents
Max. and min. transmission	0.8052 and 0.7133	0.8599 and 0.7590	0.8425 and 0.7893	0.3440 and 0.2603	0.9139 and 0.8378
Refinement method	full-matrix least-squares on F^2	full-matrix least-squares on F^2	full-matrix least-squares on F^2	full-matrix least-squares on F^2	full-matrix least-squares on F^2
Data/restraints/parameters	5910/0/418	6409/0/418	5821/6/370	6122/2/370	3051/2/201
Goodness-of-fit on F^2	1.069	1.049	1.079	1.071	1.035
Final *R* indices [$I > 2\sigma(I)$]	$R_1 = 0.0276$, $wR_2 = 0.0711$	$R_1 = 0.0396$, $wR_2 = 0.0868$	$R_1 = 0.0366$, $wR_2 = 0.0899$	$R_1 = 0.0254$, $wR_2 = 0.0590$	$R_1 = 0.0376$, $wR_2 = 0.0791$
R indices (all data)	$R_1 = 0.0341$, $wR_2 = 0.0740$	$R_1 = 0.0644$, $wR_2 = 0.0945$	$R_1 = 0.0482$, $wR_2 = 0.0947$	$R_1 = 0.0401$, $wR_2 = 0.0630$	$R_1 = 0.0659$, $wR_2 = 0.0853$
Largest difference in peak and hole (e Å^{-3})	0.416 and −0.355	0.422 and −0.473	0.556 and −0.280	2.348 and −0.895	0.392 and −0.502

3. Results and discussion

3.1. Synthesis

The synthesis of the nickel, copper and gold complexes **1**–**7** were performed following standard procedures for complexes with this type of dithiolene ligands (Scheme 1). The dithiolate ligand (**L**) was obtained from the corresponding oxo compound by hydrolytic cleavage with sodium methoxide and without intermediate isolation it was reacted with the selected metal salt to give an anionic complex which is precipitated as a salt in the presence of the selected cation. The presence of water was necessary to precipitate the bisdithiolene complex from the solution. In case of **1**, a water solution of the cation was added and the bisdithiolene complex precipitated immediately as a black precipitate. In the case of compounds **2**, **3**, **4** and **5** a few drops of water were added at the end of the reaction until the start of incipient precipitation and after keeping the reaction mixture at 4 °C it was possible to collect the product as fine precipitate which tends to form an oil. Compounds **6** and **7** were obtained without adding water after keeping the solution a few days at 4 °C until complexes precipitated. These complexes were obtained after recrystallisation from acetonitrile, acetone or dichloromethane/hexane in overall yields between 41% and 65%.

Complexes **1**–**7** were characterised by elemental analyses and cyclic voltammetry studies. The elemental analyses after the recrystallisations are consistent with a 1:1 cation:anion stoichiometry, in agreement with the X-ray crystal structure determination of the diffracting single crystals. While this is expected for M = Au, for Cu and Ni even though starting from a $Ni^{II}Cl_2$ or $Cu^{II}Cl_2$ salt, the dianionic bisdithiolene complexes could not be obtained, even under nitrogen atmosphere and the monoanionic dithiolene complexes were obtained as evidenced by the X-ray structure determination or by the electronic paramagnetic resonance (EPR) spectroscopy. Whereas complexes **1**, **2**, **3**, **5** and **6** · **2H$_2$O** were unambiguously characterised by single X-ray structure determination, compounds **4**, **6** and **7** could not be studied by single X-ray diffraction due to their poor crystal quality.

3.2. Crystal structure

Compounds **1**, **2**, **3**, **5** and **6** · **2H$_2$O** have been characterised by single crystal X-ray diffraction technique. The ORTEP views of these compounds are shown in Figs. 1–5. Selected bond angles and distances are given in Table 2.

The monoanionic Ph_4P salts **1** and **2** are isostructural and crystallise in the monoclinic system, space group $C2/c$, $Z = 8$, the asymmetric unit comprising one cation $[PPh_4]^+$ located in a general position and two independent half-anions $[M(4\text{-pedt})_2]^-$ (M = Ni and Cu for compounds **1** and **2**, respectively) both with the metals located at an inversion centre. The angle between the two $[M(4\text{-pedt})_2]^-$ units mean planes is about 49.47° and 49.52° for compounds **1** and **2**, respectively.

The monoanionic *n*-Bu_4N salts **3** and **5** are isostructural and crystallise in the triclinic system, $P\bar{1}$ space group, $Z = 2$. The asymmetric unit comprises two independent half-anion units. Both the metal atoms located at inversion centres and with one cation unit located at a general position. The angle between the anionic units mean planes is between 88.98° and 89.81° for **3** and **5**, respectively.

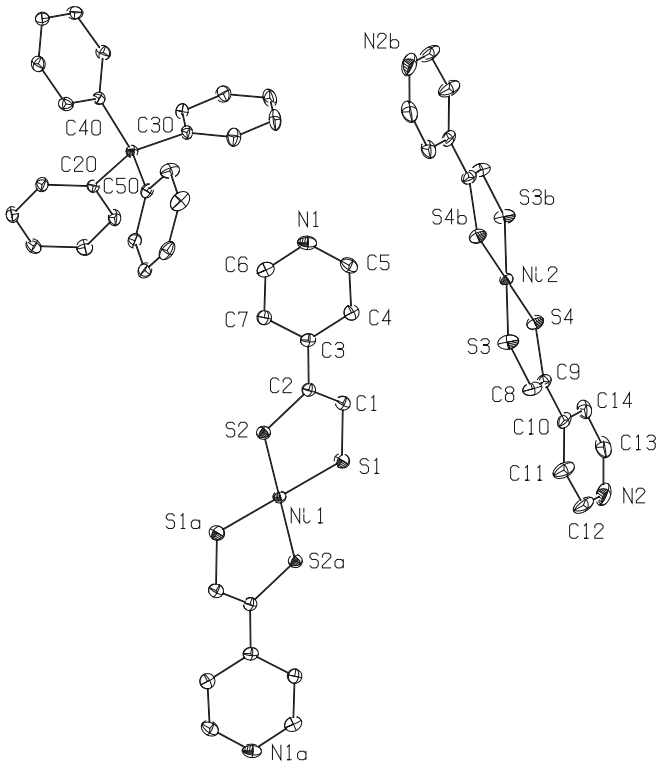
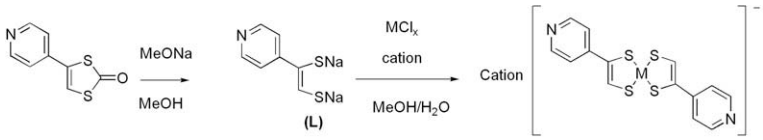


Fig. 1. ORTEP views of the cation and the two independent anion units of $Ph_4P[Ni(4\text{-pedt})_2]$, (**1**), showing the atomic numbering scheme. Displacement ellipsoids are drawn at the 30% probability level. H atoms have been omitted for clarity. [Symmetry codes: (a) $2 - x$, $1 - y$, $1 - z$; (b) $1.5 - x$, $1.5 - y$, $1 - z$].

The compound **6** · **2H$_2$O** crystallises in the monoclinic system, space group $P2_1/n$, $Z = 2$. The asymmetric unit comprises one independent half-anion unit and one independent half-cation unit located at inversion centres.

In all complexes, the centrosymmetric anion $[M(4\text{-pedt})_2]^-$ (M = Ni, Cu or Au) adopts a square-planar coordination geometry and a *trans* conformation. The central core of the anions, constituted by the metal atom, the four sulfur atoms and the four carbon atoms, is essentially planar (rms deviations of fitted atoms are 0.0091 and 0.0057 Å for compound **1**; 0.0182 and 0.0237 Å for compound **2**; 0.0152 and 0.0268 Å for compound **3**; 0.0537 and 0.0250 Å for compound **5**; 0.0125 Å for compound **6** · **2H$_2$O**).

Important bond lengths within the MS_2C_2 metallocycle are collected in Table 2. The average M–S bond lengths are in good agreement with values found in other Ni, Cu and Au monoanionic bisdithiolene complexes, respectively [1c,19–21]. While the central core of the complexes is planar, the two pyridine rings are rotated out of the central core plane with dihedral angles between



(Ph_4P)[Ni(4-pedt)$_2$] (**1**) 50% yield; (Ph_4P)[Cu(4-pedt)$_2$] (**2**) 48% yield; (*n*-Bu_4N)[Ni(4-pedt)$_2$] (**3**) 65% yield; (*n*-Bu_4N)[Cu(4-pedt)$_2$] (**4**)41% yield; (*n*-Bu_4N)[Au(4-pedt)$_2$] (**5**) 60% yield; [Na(18c6)][Ni(4-pedt)$_2$] (**6**) 58% yield; [Na(18c6)][Au(4-pedt)$_2$] (**7**) 44% yield

Scheme 1.

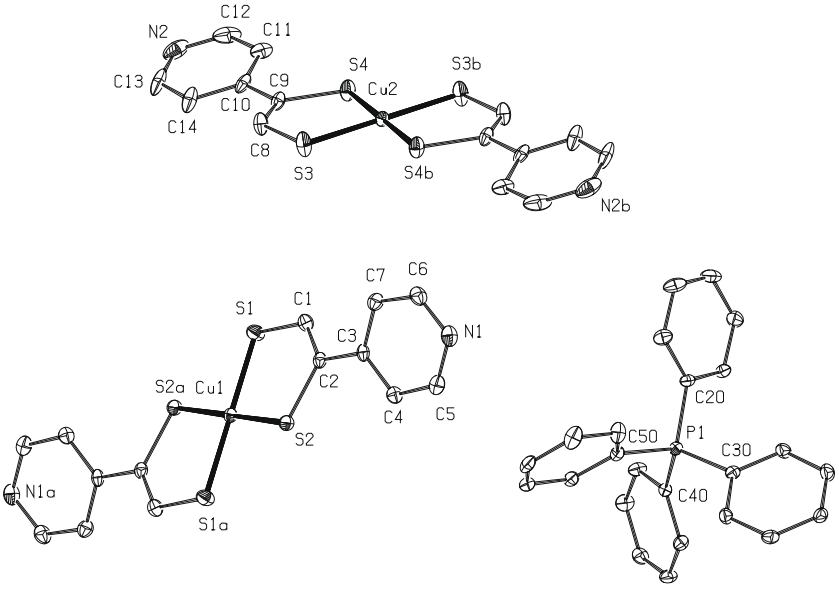


Fig. 2. ORTEP views of the cation and the two independent anion units of $Ph_4P[Cu(4\text{-pedt})_2]$, (**2**), showing the atomic numbering scheme. Displacement ellipsoids are drawn at the 30% probability level. H atoms have been omitted for clarity. [Symmetry codes: (a) $1-x, 1-y, z$; (b) $0.5-x, 1.5-y, -z$].

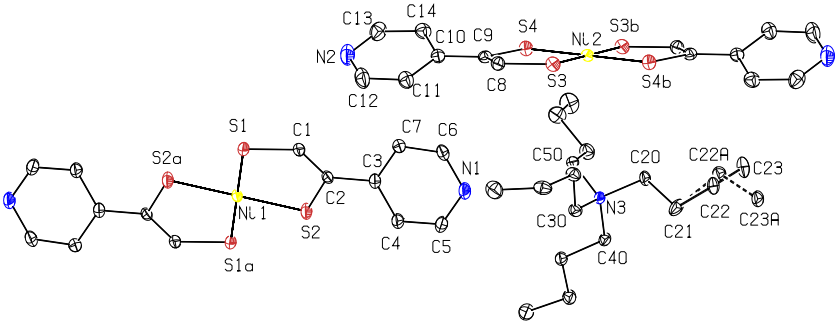


Fig. 3. ORTEP views of the cation and the two independent anion units of $n\text{-}Bu_4N[Ni(4\text{-pedt})_2]$, (**3**), showing the atomic numbering scheme. Displacement ellipsoids are drawn at the 30% probability level. H atoms have been omitted for clarity. [Symmetry codes: (a) $-x, -y, -z$; (b) $1-x, 1-y, 1-z$].

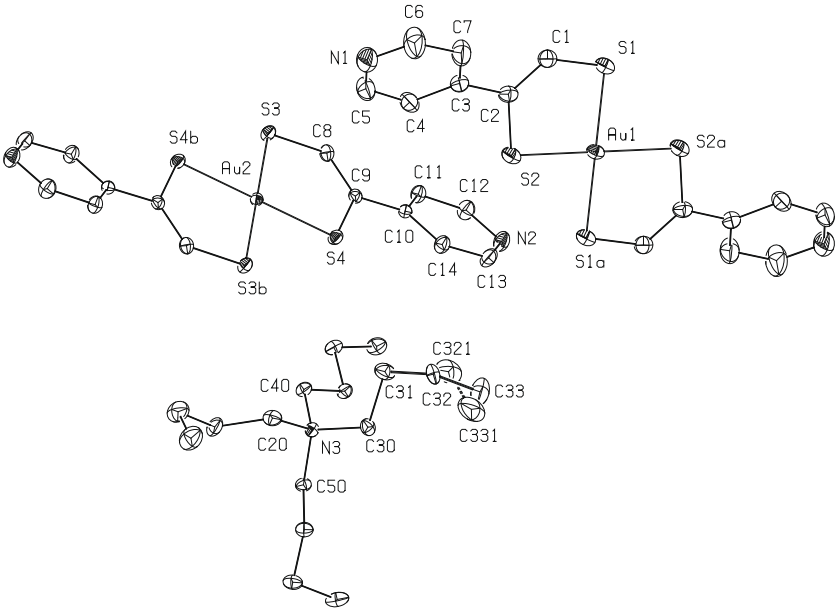


Fig. 4. ORTEP views of the cation and the two independent anion units of $n\text{-}Bu_4N[Au(4\text{-pedt})_2]$, (**5**), showing the atomic numbering scheme. Displacement ellipsoids are drawn at the 30% probability level. H atoms have been omitted for clarity. [Symmetry codes: (a) $-x, -y, -z$; (b) $1-x, 1-y, 1-z$].

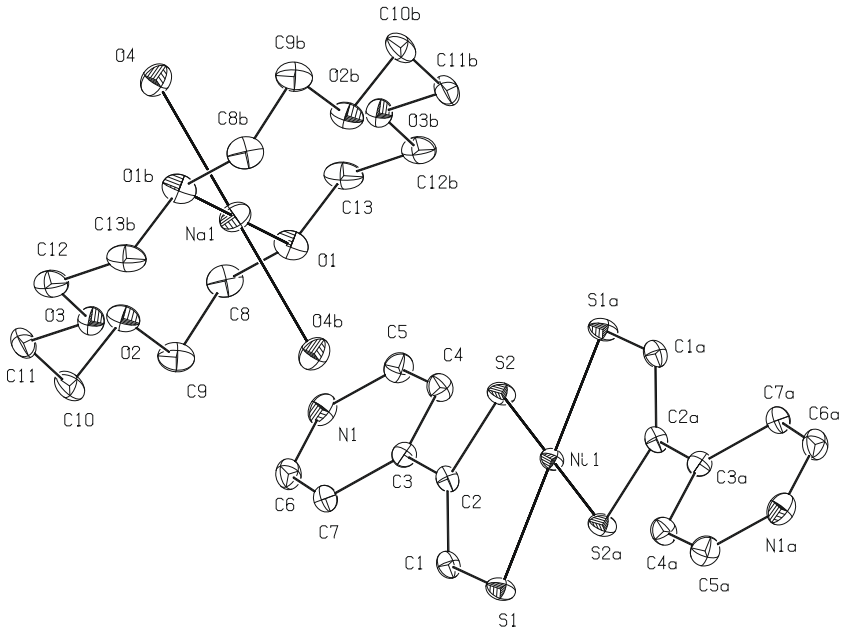
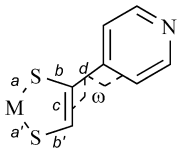


Fig. 5. ORTEP views of the cation and anion units of $[Na(18C6)][Ni(4\text{-pedt})_2] \cdot 2H_2O$, (**6** · **2H$_2$O**), showing the atomic numbering scheme. Displacement ellipsoids are drawn at the 30% probability level. H atoms have been omitted for clarity. [Symmetry codes: (a) $-x, -y, -z$; (b) $2-x, 1-y, 1-z$].

Table 2
Important bond lengths (in Å) within the metallocycle, the torsion angle ω (in °) between the pyridine group plane and the metallocycle plane and δ-parameter (defined below) for compounds **1**, **2**, **3**, **5** and **6** · **2H$_2$O**.



Compound	**1**		**3**		**6** · **2H$_2$O**	**2**		**5**	
	M = Ni2	M = Ni1	M = Ni1	M = Ni2	M = Ni	M = Cu1	M = Cu2	M = Au2	M = Au1
M–S (*a*)	2.1293(5)	2.1507(5)	2.1383(5)	2.1549(6)	2.1375(7)	2.1871(7)	2.1626(7)	2.3078(10)	2.3183(13)
M–S (*a*′)	2.1474(5)	2.1416(5)	2.1463(6)	2.1478(7)	2.1531(7)	2.1797(8)	2.1812(8)	2.3053(11)	2.3082(11)
S–C (*b*)	1.737(2)	1.742(2)	1.739(2)	1.740(3)	1.738(3)	1.771(3)	1.765(3)	1.768(4)	1.771(4)
S–C (*b*′)	1.715(2)	1.715(2)	1.713(2)	1.715(2)	1.714(3)	1.735(3)	1.740(3)	1.742(4)	1.735(5)
C=C (*c*)	1.353(3)	1.351(3)	1.364(3)	1.351(3)	1.354(4)	1.335(4)	1.328(4)	1.345(6)	1.336(6)
C–C (*d*)	1.478(3)	1.476(3)	1.474(3)	1.476(3)	1.469(4)	1.481(4)	1.483(4)	1.477(5)	1.476(7)
ω	13.14(6)	28.50(8)	29.51(8)	28.64(7)	33.56(7)	28.92(12)	13.90(8)	21.83(13)	33.44(17)
δ	1.26	1.55	1.49	1.44	1.38	2.03	1.42	1.47	2.03

$\delta = 100(b - b')/b$.

13° and 33°; depending on the complex, with the majority of them between 21° and 33°, only one of the anionic units in the Ph_4P salts **1** and **2** presents a smaller angle of about 13°. The rotation of the pyridine rings is induced by steric hindrance between hydrogen atoms at the 2-position of the pyridine ring and in the metallocycle carbon but this rotation is also assisted by the interaction with neighbouring molecular units in the solid. The salts **5** and **6** · **2H$_2$O** present the higher pyridine rotation values (~33°) and this large value can be ascribed to cation interactions (and also anion interactions in the case of complex **5**) as denoted by several short contacts (see Tables S1 and S2 and Figs. S1 and S2).

The smaller pyridine rotations of only ~13°, in **1** and **2**, are associated with anionic and cationic interactions, including π–π interactions between the pyridine groups of the $[M(4\text{-pedt})_2]^-$ units: (see Tables S3 and S4 and Fig. S3). The two pyridine rings involved are coplanar with distances close to the sum of the van der Waals radii, clearly denoting significant π–π interactions (Fig. S3c).

A feature related to the unsymmetrical nature of the 4-pedt ligand, is the S–C bond length difference within the metallocycle (Table 2). The shortening of the **b**′ bond when compared with the **b** bond can be evaluated in terms of a parameter $\delta = 100(b - b')/b$, as previously done on other unsymmetrical bisdithiolene complexes such as the $[Ni(adt)_2]^-$ (adt = acrylonitrile-1,2-dithiolate) or $[Ni(tfadt)_2]^-$ (tfadt = 2-(trifluoromethyl)acrylonitrile-1,2-dithiolate) [6,22]. In our case δ values are between 1.26% and 2.03% in the four structures analysed and it can be attributed to the mesomeric effect of the pyridine group.

A long debated aspect of the dithiolene complexes is the so called "non-innocence" of the ligands, which may lead to formal ambiguities in the description of the different oxidation sates of

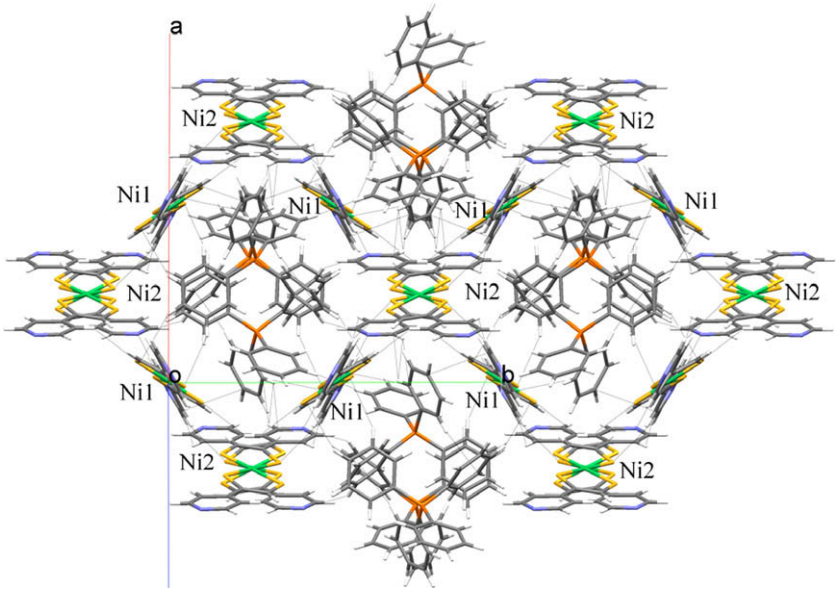


Fig. 6. Crystal structure of **1**, viewed along the cation stacking axis.

these complexes [19]. In these monoanionic complexes the ligand may have a significant contribution to the frontier orbitals and can be viewed as being present in one of two extreme forms: the dianionic ene-1,2-dithiolate or the neutral dithioketone [1a,19]. In this particular case of the $[M(4\text{-pedt})_2]^-$ dithiolenes where the dithiole ring is not fused to any aromatic ring the lengths of the C–C and C–S bonds provide a direct indication on the nature of a dithiolene ligand. In all complexes studied the C=C (1.32–1.36 Å) and C–S (1.71–1.77 Å) bond lengths were found in the range typical of sp^2 C hybridisation [23] indicative of the ene-1,2-dithiolate form of the dithiolene and M(III) oxidation state. In the solid state, the monoanionic $[M(4\text{-pedt})_2]^-$ species with M = Ni, Cu and Au,

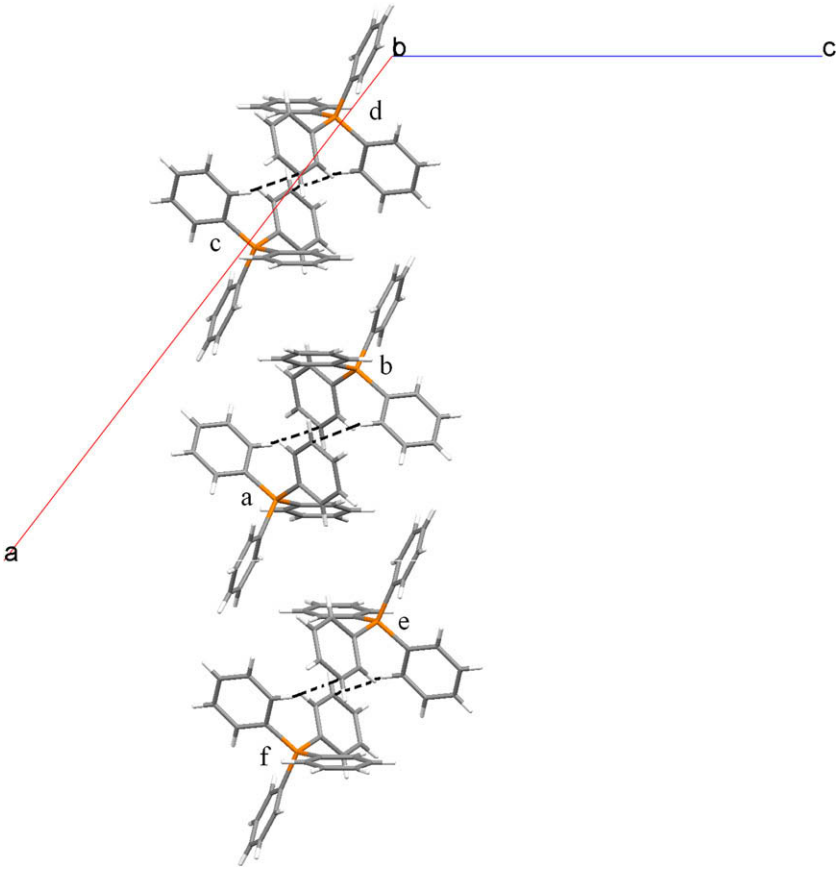


Fig. 7. Chain of $[PPh_4]^+$ cations in compound **1** viewed along *b*. [Symmetry codes: (a) *x*, *y*, *z*; (b) 1.5 − *x*, ½ − *y*, 1 − *z*; (c) −1/2 + *x*, 1/2 − *y*; −½ + *z*; (d) 1 − *x*, *y*, 1/2 − *z*; (e) 2 − *x*, *y*, 1.5 − *z*; (f) 1/2 + *x*, 1/2 − *y*, 1/2 + *z*].

present different packing patterns and interactions depending on the cation type complexes. The compounds **1** and **2** are isostructural with the previously reported $(PPh_4)[Au(4\text{-pedt})_2]$ [9]. A characteristic of their crystal structure is the occurrence of cation columns along $b + c$, isolated by a alveolar anion arrangement (Fig. 6). As **1** and **2** are isostructural, we will only focus our structural analysis on the compound **1**. In the cation column, it is possible to observe cation pairs and the only intra column short contact is H25···C54 (2.785(3) Å) (Fig. 7). Such inversion-centred arrangements of PPh_4^+ cations are a recurrent feature among molecules bearing at least three phenyl rings on the same atoms [24]. In the alveolar anionic arrangement there are no S–S short contacts, but there are several other N···H, S···H, H···H short contacts and π–π interactions (Table S3). Of particular note are the C52–H52···N2 (3.514(4) Å) and C6–H6···N2 (3.537(3) Å) weak hydrogen bonding interactions.

The crystal structure of the two tetrabutylammonium salts (**3** and **5**) can be seen as made from parallel mixed chains constituted by pairs of cations alternating with an anion. The parallel chains alternate with sheets of anions (Fig. 8). These two compounds have several short intermolecular contacts but none of them corresponds to S–S interactions (for compound **5** Table S1).

The crystal structure of compound **6** · **2H$_2$O** can be described in terms of parallel alternated layers of $[Ni(4\text{-pedt})_2]^-$ anions and $Na(18C6)^+$ cations. The coordination sphere of the sodium cation is completed by two water molecules, one on each side (Fig. 9). The angle between the anionic units mean plan is about 44.53. Only between anions and cations, there are relevant interactions. Besides several N···O, N···H, C···H, O···S, S···H short contacts a hydrogen bond N1···H4A–O4 (2.916(4) Å) is present, which is the most important, governing the chain-like arrangement anion–cation–anion(...) as depicted in Fig. 10.

3.3. Redox behaviour

The redox behaviour of the different complexes was studied by cyclic voltammetry in CH_2Cl_2 solution containing $[n\text{-}Bu_4N]PF_6$ (0.1 M) as electrolyte. Each of the compounds **1**, **3** and **6** containing the Ni complex (cyclic voltammogram of compound **6**, Supplementary data, Fig. 4S) exhibit two quasi reversible redox waves, at circa −0.52 V and 0.30 V versus $[Fc]^+/[Fc]$ which are ascribed to the couples $[Ni(4\text{-pedt})_2]^{2-}/[Ni(4\text{-pedt})_2]^-$ and $[Ni(4\text{-pedt})_2]^-/[Ni(4\text{-pedt})_2]^0$ (Table 3). The $E^{1/2}$ potentials for the Ni complexes in these three compounds are identical. The variation in the scan rate (from 10 to 200 mV s^{-1}) monitoring the wave profile, the separation of the peak potentials ($\delta E > 59$ mV), and the ratio of the cathodic and anodic currents ($-I_p^c/I_p^a \approx 1$) indicate that the processes are quasi reversible. The low values of the first process explain the difficulty in preparing the dianionic complex, which can be spontaneously oxidised by minor amounts of oxygen or other oxidising agents. On the other hand the low value of the second process predicts that the neutral complex can be prepared. However attempts to isolate it were so far not successful.

The compounds **2** and **4** containing the Cu complex (cyclic voltammogram of compound **2**, Supplementary data, Fig. 5S) show also identical cyclic voltammograms with one quasi reversible redox process at ca −0.38 V, ascribed to the couples $[Cu(4\text{-pedt})_2]^{2-}/[Cu(4\text{-pedt})_2]^-$ (Table 3). Scans to higher positive potentials

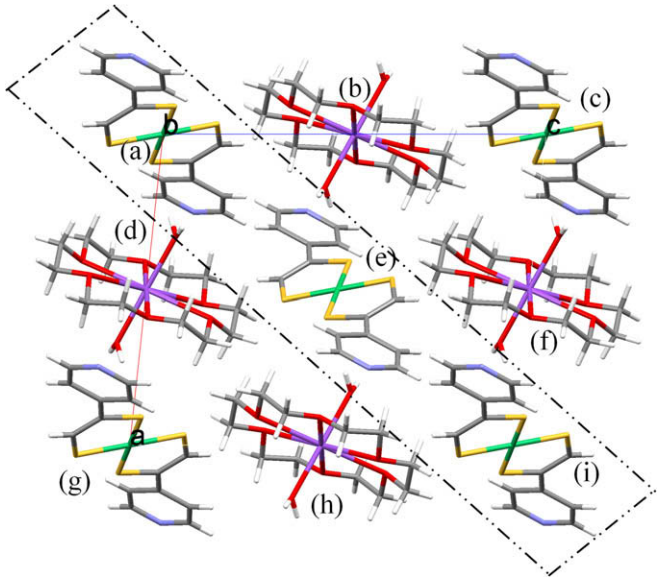


Fig. 9. Crystal structure of **6** · **2H$_2$O**, viewed along the *b*-axis. The dashed box marks a layer of $[Ni(4\text{-pedt})_2]^-$ anions. [Symmetry codes: (a) x, y, z; (b) $-1 + x, y, z$; (c) $x, y, 1 + z$; (d) $1.5 - x, -1/2 + y, 1/2 - z$; (e) $1/2 - x, 1/2 + y, 1/2 - z$; (f) $1.5 - x, -1/2 + y, 1.5 - z$; (g) $1 + x, y, z$; (h) $x, -1 + y, z$; (i) $1 + x, y, 1 + z$].

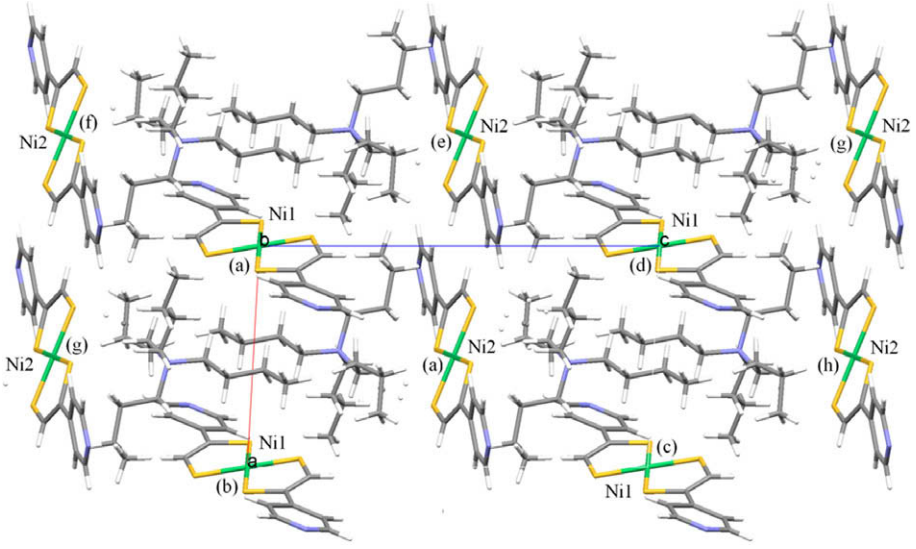


Fig. 8. Crystal structure of **3**, viewed along the *b*-axis. [Symmetry codes: (a) x, y, z; (b) $1 + x, y, z$; (c) $1 + x, 1 + y, 1 + z$; (d) $x, 1 + y, 1 + z$; (e) $-1 + x, y, z$; (f) $-1 + x, -1 + y, -1 + z$; (g) $x, -1 + y, -1 + z$; (h) $x, 1 + y, 1 + z$; (i) $-1 + x, 1 + y, 1 + z$].

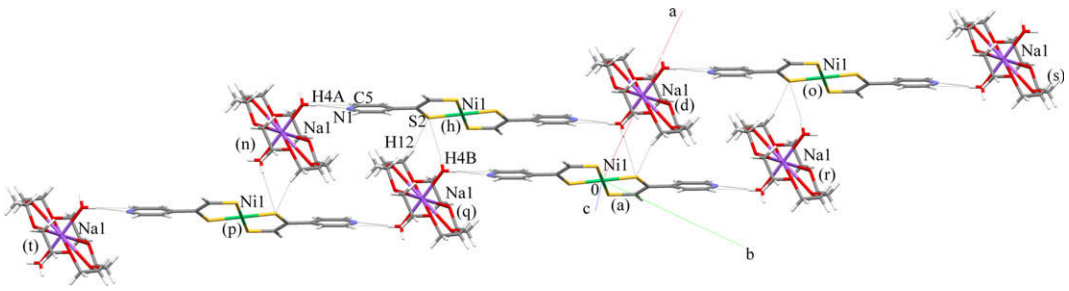


Fig. 10. Detail of the mixed layer in **6** · **2H$_2$O**, two adjacent mixed chains. [Symmetry codes: (a) *x*, *y*, *z*; (d) 1.5 − *x*, −1/2 + *y*, 1/2 − *z*; (n) 1/2 − *x*, −2.5 + *y*, 1/2 − *z*; (o) 1 + *x*, 1 + *y*, *z*; (p) −1 + *x*, −2 + *y*, *z*; (q) 1/2 − *x*, −1.5 + *y*, 1/2 − *z*; (r) 1.5 − *x*, 1/2 + *y*, 1/2 − *z*; (s) 2.5 − *x*, 1.5 + *y*, ½ − *z*; (t) −1/2 − *x*, −3.5 + *y*, ½ − *z*].

Table 3
Redox potentials (mV, vs. $[Fc]^+/[Fc]$) of **1**–**6** at room temperature in CH_2Cl_2 containing $[n\text{-}Bu_4N]PF_6$ (0.1 M) with a 100 mV s^{-1} scan rate.

Compound	$[ML_2]^{2-}/[ML_2]^-$	$[ML_2]^-/[ML_2]^0$
[*n*-Ph$_4$P][Ni(4-pedt)$_2$] (**1**)	−519	297
[*n*-Ph$_4$P][Cu(4-pedt)$_2$] (**2**)	−374	676
[*n*-Bu$_4$N][Ni(4-pedt)$_2$] (**3**)	−523	303
[*n*-Bu$_4$N][Cu(4-pedt)$_2$] (**4**)	−379	771
[*n*-Bu$_4$N][Au(4-pedt)$_2$] (**5**)		585
[Na(18C6)][Ni(4-pedt)$_2$] (**6**)	−518	298
[Na(18C6)][Au(4-pedt)$_2$] (**7**)		588

(∼0.6 V versus $[Fc]^+/[Fc]$) reveal the existence of an irreversible process which should correspond to the couple $[Cu(4\text{-pedt})_2]^-/[Cu(4\text{-pedt})_2]^0$.

Compounds **5** and **7** containing the $[Au(4\text{-pedt})_2]^-$ complex (cyclic voltammogram of compound **7**, Supplementary data, Fig. 6S) both exhibit one oxidation and a reduction process, assigned to the couples $[Au(4\text{-pedt})_2]^-/[Au(4\text{-pedt})_2]^0$ (Table 3). For both gold compounds, the $E^{1/2}$ potentials are very similar. A variation in the scan rate (from 10 to 200 mV s^{-1}) monitoring the wave profile, the separation of the peak potentials ($\delta E > 59$ mV), and the ratio of the cathodic and anodic currents ($-I_p^c/I_p^a = 1$) indicate that the oxidation is not electrochemically reversible.

It is known that the nature of the R substituent in the complexes $Ni(S_2C_2R_2)_2$ affects the redox potentials and even a small variation in the electron withdrawing substituent can tune the redox potential [1a,25]. In this case we observe that the pyridine groups, which are only partially rotated relatively to the central bisdithiolene plane, thus retaining the possibility of interacting via their π systems, make the 4-pedt complexes easier to oxidise than phenyl substituted or even unsubstituted edt ligands [5].

3.4. EPR measurements

While the monoanionic Cu and Au complexes are diamagnetic the monoanionic Ni, complexes, as d^7 system in a square planar coordination are expected to be paramagnetic $S = 1/2$ systems. Indeed the EPR spectra of **1**, **3** and **6** as powders, show a signal typical of monoanionic Ni dithiolene complexes [1,26,27,28] with rhombic symmetry, with $g_1 = 2.1035$, $g_2 = 2.0518$, $g_3 = 2.0128$ compound **1** and $g_1 = 2.1153$, $g_2 = 2.0480$, $g_3 = 2.0087$ for the compound **6**. In the case of compound **3** the EPR spectrum denotes the existence of two Ni sites with different g_1 (2.0849 and 2.0834) and g_3 (2.0183 and 2.0113) values but with the same (or very close) g_2 value (2.0701). This should be related with the different crystallographic environments of the two anionic Ni units in the asymmetric unit of the compound **3**. In fact Ni1 unit besides quite asymmetric Ni–S bonds lengths has several short S···H–C contacts with cations which are absent in unit Ni2. In spite of the existence of two different anionic Ni^{III} units in the asymmetric unit of **1**, the two sets of g principal values for this compound are not distinguishable within experimental error in agreement with the fact that the two Ni units present comparable short contacts between the S atoms.

3.5. Magnetic susceptibility

The magnetic susceptibility measurements of the compounds **1** and **3** in the range 2–300 K indicate a paramagnetic behaviour with effective magnetic moments essentially temperature independent down to ∼15 K with values at room temperature of 1.72 and 1.79 BM, respectively. For compound **6**, the room temperature magnetic moment is 1.67 BM, but it slightly increases upon cooling down to 11 K (1.85 BM), denoting weak ferromagnetic interactions that are not effective at lower temperature (confirmed by magnetisation versus magnetic field at 3.1 K – see Supplementary data). These values are consistent with a $S = 1/2$ state, due to an unpaired electron of a d^7 system in an quadrangular coordinating geometry. The calculated magnetic moment for the three compounds assuming a Curie law for $S = ½$ and g values g_{av} from EPR is 1.78 BM.

4. Conclusion

The new paramagnetic complex, $[Ni(4\text{-pedt})_2]^-$, with the dithio-azo 4-pedt ligand has been synthesised, and isolated as the $[PPh_4]^+$, $[n\text{-}Bu_4N]^+$ and Na^+(18C6) salts, which were characterised by single crystal X-ray diffraction, cyclic voltametry EPR and magnetic susceptibility. These three compounds present three distinct crystal structures and similar magnetic and redox behaviour, characteristic of monoanionic Ni complexes with quadrangular coordinating geometry and exhibit two quasi reversible redox waves, attributed to the $[Ni(4\text{-pedt})_2]^{2-}/[Ni(4\text{-pedt})_2]^-$ and $[Ni(4\text{-pedt})_2]^-/[Ni(4\text{-pedt})_2]^0$ redox processes.

Two other complexes with the same dithio-azo ligand have been synthesised, $[Au(4\text{-pedt})_2]^-$ and $[Cu(4\text{-pedt})_2]^-$, isolated as the $[n\text{-}Bu_4N]^+$ and Na^+(18C6) salts in case Au and as the $[PPh_4]^+$ and $[n\text{-}Bu_4N]^+$ salts in case Cu, all of them exhibiting diamagnetic behaviour.

The $[n\text{-}Bu_4N]^+$ and $[PPh_4]^+$ salts of Au and Cu complexes are isostructural with the correspondent Ni ones. Both Ni and Cu complexes present a similar quasi reversible redox process corresponding to the couple $[ML_2]^{2-}/[ML_2]^-$ but they differ in the couple $[ML_2]^-/[ML_2]^0$ which is a quasi reversible process for Ni and an irreversible one for Cu. For the Au complexes only the couple $[ML_2]^-/[ML_2]^0$ is observed.

The ability of the pyridine groups of these complexes to coordinate other metals is presently under study and will be reported subsequently.

Acknowledgements

This work was partially supported by FCT trough Contract (PTDC/QUI/64967/2006) and by GRICES-Ministère des Affaires Etrangères (France) Pessoa No. 07981RL bilateral agreement and it also benefited from the ESF COST action D35.

Appendix A. Supplementary data

CCDC 698755, 698756, 698757, 698758 and 698759 contain the supplementary crystallographic data for **1**, **2**, **3**, **5** and **6** · **2H$_2$O**. These data can be obtained free of charge via http://www.ccdc.cam.ac.uk/conts/retrieving.html, or from the Cambridge Crystallographic Data Centre, 12 Union Road, Cambridge CB2 1EZ, UK; fax: (+44) 1223-336-033; or e-mail: deposit@ccdc.cam.ac.uk. Supplementary data associated with this article can be found, in the online version, at doi:10.1016/j.poly.2009.01.015.

References

[1] (a) J.A. McCleverty, Prog. Inorg. Chem. 10 (1968) 49;
(b) D. Coucouvanis, Prog. Inorg. Chem. 11 (1970) 233;
(c) R. Eisenberg, Prog. Inorg. Chem. 12 (1970) 295;
(d) L. Alcácer, H. Novais, in: J.S. Miller (Ed.), Extended Linear Chain Compounds, vol. 3, Springer, New York, 1983, p. 319 (Chapter 6);
(e) S. Alvarez, R. Vicente, R. Hoffmann, J. Am. Chem. Soc. 107 (1985) 6253;
(f) T.B. Rauchfuss, Prog. Inorg. Chem. 52 (2004) 1;
(g) N. Robertson, L. Cronin, Coord. Chem. Rev. 227 (2002) 93.
[2] (a) N. Bendellat, Y. Le Gal, S. Golhen, A. Gouasmina, L. Ouahab, J.M. Fabre, Eur. J. Inorg. Chem. (2006) 4237;
(b) J.D. Wallis, J.P. Griffiths, J. Mater. Chem. 15 (2005) 347.
[3] (a) Y. Xu, D. Zhang, H. Li, D. Zhu, J. Mater. Chem. 9 (1999) 1245;
(b) F. Iwarhori, S. Golhen, L. Ouahab, R. Carlier, J.-P. Sutter, Inorg. Chem. 40 (2001) 6541;
(c) F. Setifi, L. Ouahab, S. Golhen, Y. Yoshida, G. Saito, Inorg. Chem. 42 (2003) 1791;
(d) A. Ota, L. Ouahab, S. Golhen, O. Cador, Y. Yoshida, G. Saito, New J. Chem. 29 (2005) 1135;
(e) L. Wang, B. Zhang, J. Zangh, Inorg. Chem. 45 (2006) 6860;
(f) M. Chahma, N. Hassan, A. Alberola, H. Stoeckli-Evans, M. Pilkington, Inorg. Chem. 46 (2007) 3807;
(g) M. Moshimann, S.-X. Liu, G. Labat, A. Neels, S. Decurtins, Inorg. Chim. Acta 360 (2007) 3848;
(h) Q. Zhu, Y. Lu, Y. Zhang, G.K. Bian, G.-Y. Niu, J. Dai, Inorg. Chem. 46 (2007) 10065;
(i) S.I.G. Dias, A.I.S. Neves, S. Rabaça, I.C. Santos, M. Almeida, Eur. J. Inorg. Chem. (2008) 4728.
[4] S. Rabaça, M.C. Duarte, I.C. Santos, M. Fourmigué, M. Almeida, Inorg. Chim. Acta 360 (2007) 3797.
[5] V. Madhu, S.K. Das, Inorg. Chem. 47 (2008) 5055.
[6] (a) M. Fourmigué, J.N. Bertran, Chem. Commun. (2000) 2111;
(b) L.N. Dawe, J. Miglioi, L. Turnbow, M.L. Taliaferro, W.W. Shum, J.D. Bagnato, L.V. Zakharov, A.L. Rheingold, A.M. Arif, M. Fourmigué, J.S. Miller, Inorg. Chem. 44 (2005) 7530.
[7] S. Shi, in: D.M. Roundhill, J.P. Fackler Jr. (Eds.), Optoelectronic Properties of Inorganic Compounds, Plenum, New York, 1999, p. 52.
[8] E. Cerrada, J. Garrido, M. Laguna, N. Lardiés, I. Romeo, Synth. Metals 102 (1999) 1709.
[9] J.M. Tunney, A.J. Blake, E.S. Davies, J. McMaster, C. Wilson, C.D. Garner, Polyhedron 25 (2006) 591.
[10] D.D. Perrin, W.L.F. Armarego, Purification of Laboratory Chemicals, Pergamon, Oxford, 1988.
[11] O.P. Levi, J.Y. Becker, A. Ellern, V. Khodorkovsky, Tetrahedron Lett. 42 (2001) 1571.
[12] G.M. Sheldrick, SADABS, Bruker AXS Inc., Madison, Wisconsin, USA, 2004.
[13] Bruker, SMART and SAINT, Bruker AXS Inc., Madison, Wisconsin, USA, 2004.
[14] A. Altomare, M.C. Burla, M. Camalli, G. Cascarano, G. Giacovazzo, A. Guagliardi, A.G.G. Moliterni, G. Polidori, R. Spagna, J. Appl. Crystallogr. 32 (1999) 115.
[15] G.M. Sheldrick, SHELXL97, Program for Crystal Structure Refinement, University of Goettingen, Germany, 1997.
[16] L.J. Farrugia, J. Appl. Crystallogr. 32 (1999) 837.
[17] L.J. Farrugia, J. Appl. Crystallogr. 30 (1997) 565.
[18] C.F. Macrae, P.R. Edgington, P. McCabe, E. Pidcock, G.P. Shields, R. Taylor, M. Towler, J. van de Streek, J. Appl. Crystallogr. 39 (2006) 453.
[19] B.S. Lim, D.V. Fomitchev, R.H. Holm, Inorg. Chem. 40 (2001) 4257.
[20] K. Ray, T. Weyhermüller, A. Goossens, M.W.J. Crajé, K. Wieghardt, Inorg. Chem. 42 (2003) 4082.
[21] (a) H. Alves, D. Simão, H. Alves, D. Belo, S. Rabaça, E.B. Lopes, V. Gama, M.T. Duarte, R.T. Henriques, H. Novais, M. Almeida, Eur. J. Inorg. Chem. (2001) 3119;
(b) H. Alves, D. Simão, I.C. Santos, V. Gama, R.T. Henriques, H. Novais, M. Almeida, Eur. J. Inorg. Chem. (2004) 1318;
(c) E.B. Lopes, H. Alves, I.C. Santos, D. Graf, J.S. Brooks, E. Canadell, M. Almeida, J. Mater. Chem. 18 (2008) 2825.
[22] O. Jeannin, J. Delaunay, F. Barrière, M. Fourmigué, Inorg. Chem. 44 (2005) 9763.
[23] F.H. Allen, O. Kennard, D.G. Watson, J. Chem. Soc., Perkin Trans. II (1987) S1.
[24] I. Dance, M. Scudder, Chem. Eur. J. 2 (1996) 481.
[25] (a) D.C. Olson, V.P. Mayweg, G.N. Schrauzer, J. Am. Chem. Soc. 86 (1966) 4876;
(b) E. Hoyer, Chem. Industry 10 (1965) 652.
[26] (a) A. Davison, N. Edelstein, R.H. Holm, A.H. Maki, Inorg. Chem. 2 (1963) 1227;
(b) D. Belo, H. Alves, S. Rabaça, L.C. Pereira, M.T. Duarte, V. Gama, R.T. Henriques, M. Almeida, E. Ribera, C. Rovira, J. Veciana, Eur. J. Inorg. Chem. (2001) 3127.
[27] (a) R.P. Burns, C.A. McAuliffe, Adv. Inorg. Chem. Radiochem. 22 (1979) 303;
(b) R. Kirmse, J. Stach, W. Dietzsch, G. Steimecke, E. Hoyer, Inorg. Chem. 19 (1980) 2679.
[28] R. Kirmse, J. Stach, U. Abram, W. Dietzsch, B. Bottcher, M.C.M. Gribnau, C.P. Keijzers, Inorg. Chem. 23 (1984) 3333.

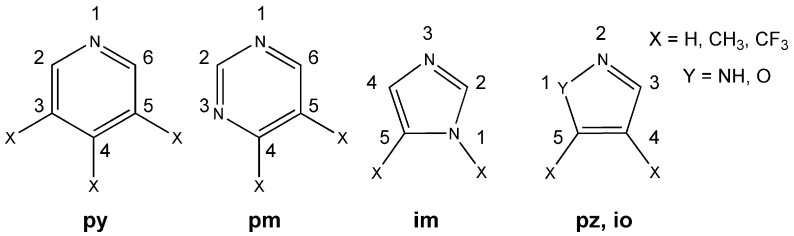


Fig. 1. Pyridine-, pyrimidine-, pyrazole-, isoxazole- and imidazole-based ligand skeletons and positional numbering.

the reactivity of $AuCl_3$(4R-py) {4R-py = *para*-substituted pyridines} are highlighted. Moreover, to avoid mixing of the electronic effects on the stability of the M–N bond with well-known steric effects, no group was put in an α-position with respect to the coordinating nitrogen atom [2,3].

The proton affinities (PA) of the ligands have been computed on the basis of Eq. (1) as the total energy difference between the heterocycle L (E_L) and its protonated counterpart $[LH]^+$ ($E_{[LH]^+}$). These energy values have been corrected for zero-point vibrational energies (ZPVE) and the thermal contributions to enthalpy at 298 K ($\Delta H^{0\rightarrow 298}$). Finally, the pressure–volume work term $-RT$, where R is the gas constant, which is equal to -0.6 kcal mol^{-1} at 298 K, has been added to Eq. (1) [10]. All the energy data, obtained using the DFT B3LYP/6-31G** method, are reported in Table 1:

$$PA = E_L + ZPVE_L + \Delta H_L^{0\rightarrow 298} - E_{[LH]^+} - ZPVE_{[LH]^+} - \Delta H_{[LH]^+}^{0\rightarrow 298} - RT \quad (1)$$

Hwang et al. studied the correlation between experimental and B3LYP/6-31G** computed proton affinities for 16 N-heterocycles, constituted by pyridine, imidazole and pyrazole derivatives [11], observing that the PA variations are correctly predicted by the *ab initio* simulations, even if the calculated absolute values are about 3% too large.

In our case the maximum PA value, 238.0 kcal mol^{-1}, corresponds to 1,5-dimethyl-1*H*-imidazole, 1,5-$(CH_3)_2$-im, while the lowest, 189.2 kcal mol^{-1}, is that of 4,5-bis-trifluoromethyl-isoxazole, 4,5-$(CF_3)_2$-io. Even if the considered PA range is relatively wide, about 49 kcal mol^{-1}, the computed N–H bond lengths of the protonated species are all quite similar, falling in a range between 1.011 and 1.019 Å. Also the difference of the zero-point vibrational energy (ZPVE) between $[LH]^+$ and L, attributable to the N–H vibrations in the protonated form of the ligands, is rather constant for all the considered heterocycles, ranging between 7.9 and 9.0 kcal mol^{-1}. The difference between the thermal contributions to enthalpy ($\Delta H^{0\rightarrow 298}$) of L and $[LH]^+$ is quite small, affecting the PA to a maximum of 1.3 kcal mol^{-1}.

2.2. Mulliken charges and charge-proton affinity relationship

Once the desired proton affinities of the various ligands L were computed, the geometries of the corresponding $AuCl_3L$ complexes were optimised using the hybrid B3PW91 density functional. The Mulliken charges of the $AuCl_3$ fragment (Q_{AuCl_3}), which are simply the sums of the Mulliken charges of the three chlorine atoms and the gold centre, were computed and the values are reported in Table 2.

Very good linear relationships between the Mulliken charge of the $AuCl_3$ fragment in the $AuCl_3L$ complexes and the computed proton affinity of L have been found for all the groups of the considered monodentate nitrogen ligands (pyridines, pyrimidines, imidazoles, pyrazoles and isoxazoles), as depicted in Figs. 2–6. The PA values are, in all cases, referred to the nitrogen atom that coordinates the metal centre.

Besides the $AuCl_3$ charge, the PA variation of the ligands also affects the geometry of the considered compounds. On reducing the ligand proton affinity, the coordinated heterocycle tends to be more perpendicular with respect to the $AuCl_3$ plane. In the pyridine-complexes the Cl_{cis}–Au–N–C_α dihedral angle ranges from 130.8° for the 3,4,5-$(CH_3)_3$-py derivative to 138.2° for {3,4,5-$(CF_3)_3$-py}. In the isoxazole-complexes the same angle ranges between 143.4° {4,5-$(CH_3)_2$-io} and 153.6° {4,5-$(CF_3)_2$-io}, while in the imidazole derivatives it varies between 159.4° {1,5-$(CH_3)_2$-im} and 164.0° {1,5-$(CF_3)_2$-im}. The Cl_{cis}–Au–N–C_α dihedral angle is scarcely affected by the PA in the pyrimidine-complexes, where it is around 136.5°, and in the pyrazole-complexes, where the heterocycle is on about the same plane as $AuCl_3$.

The general equation describing the linear correlation between the ligand proton affinity PA and the $AuCl_3$ charge Q_{AuCl_3} is Eq. (2):

$$Q_{AuCl_3}^L = \alpha^L PA^L + \beta^L \quad (2)$$

Both the α^L and β^L parameters, reported in Table 3, depend upon the nature of the considered class of the ligands. The slopes α^L represent the variations of electron density on the $AuCl_3$ fragment on varying the proton affinity of L, that is, on changing the σ-donor ability of the considered ligands. The β^L values formally represent the $AuCl_3$ Mulliken charges in complexes where the coordinated N-ligand has zero proton affinity. From these two parameters it is easy to compute the proton affinity value corresponding to a zero charge of the $AuCl_3$ fragment, PA_0^L, on the basis of Eq. (3):

$$PA_0^L = -\beta^L/\alpha^L \quad (3)$$

This last parameter represents the ligand minimum basicity for a charge variation in $AuCl_3$, and therefore it can be considered as the minimum proton affinity to have a meaningful bond between the heterocycle and the metal ion. Table 3 reports the α^L, β^L and PA_0^L values for the five groups of considered ligands.

The increasing basicity of the free ligands L, expressed by the PA values, corresponds to a rise of the σ-donor ability, which leads to a more negative Mulliken charge on the $AuCl_3$ fragment. From Table 3 it is observable that the slopes of the plots corresponding to different types of N-ligands, α^L, are not the same: the pyridine and pyrimidine ligands show the greatest $AuCl_3$ charge variations on changing the basicity of L, while the other N-donors show lower variations. This means that the different slopes found on changing the N-donor type represent a measure of the π-acidity of these nitrogen ligands once coordinated to $AuCl_3$. In fact, the π-acceptor ability tends to keep the charge on the $AuCl_3$ fragment as constant as possible on varying the σ-donation: the greater the π-acidity, the lower the charge variation on changing the proton affinity. The α^L gradients are therefore representative of the relative π-back-donation potential of a group of coordinated ligands: lower values correspond to poorer π-acidities. On this basis, on comparing the slopes of the linear relationships a new π-acidity scale can be built:

Pyridines ≈ pyrimidines < imidazoles < pyrazoles ≈ isoxazoles.

The α^L values are compared in the histogram in Fig. 7. From Table 3 and Fig. 7 it is to be stressed that this theoretical approach

Table 1
Total energies (E_L and $E_{[LH]^+}$), zero-point vibrational energies ($ZPVE_L$ and $ZPVE_{[LH]^+}$) and thermal contributions to enthalpy at 298 K ($\Delta H_L^{0\rightarrow 298}$ and $\Delta H_{[LH]^+}^{0\rightarrow 298}$) of the ligands L and their conjugated acids $[LH]^+$ and computed proton affinities (PA). L = pyridines, pyrimidines, imidazoles, pyrazoles and isoxazoles.

Heterocycle	E_L (a.u.)	$ZPVE_L$ (kcal mol^{-1})	$\Delta H_L^{0\rightarrow 298}$ (kcal mol^{-1})	$E_{[LH]^+}$ (a.u.)	$ZPVE_{[LH]^+}$ (kcal mol^{-1})	$\Delta H_{[LH]^+}^{0\rightarrow 298}$ (kcal mol^{-1})	PA (kcal mol^{-1})
Pyridines							
3,4,5-$(CH_3)_3$-py	−366.2542	108.0	5.8	−366.6454	116.7	5.3	236.6
3,4-$(CH_3)_2$-py	−326.9354	90.5	4.7	−327.3225	99.3	4.8	233.4
3,5-$(CH_3)_2$-py	−326.9350	90.3	4.9	−327.3207	99.1	5.0	232.5
4-CH_3-py	−287.6146	73.0	3.2	−287.9972	81.8	3.3	230.5
3-CH_3-py	−287.6139	73.0	3.8	−287.9947	81.9	3.8	229.4
py	−248.2926	55.8	2.7	−248.6681	64.7	2.7	226.1
3-CF_3-4-CH_3-py	−624.6490	76.2	5.4	−625.0188	84.8	5.5	222.7
3-CH_3-4-CF_3-py	−624.6475	76.2	5.4	−625.0160	84.9	5.4	221.8
4-CF_3-py	−585.3264	58.8	4.9	−585.6891	67.6	5.0	218.1
3-CF_3-py	−585.3264	58.8	4.3	−585.6883	67.5	4.4	217.7
3,4-$(CF_3)_2$-5-CH_3-py	−961.6703	79.4	8.0	−962.0274	88.0	8.0	214.8
3,4-$(CF_3)_2$-py	−922.3522	61.9	6.4	−922.7042	70.5	6.5	211.5
3,4,5-$(CF_3)_3$-py	−1259.3735	64.8	9.2	−1259.7153	73.3	9.3	205.2
Pyrimidines							
4,5-$(CH_3)_2$-pm	−342.9749	83.0	4.2	−343.3480	91.4	4.8	224.5
4-CH_3-pm	−303.6546	65.5	3.2	−304.0212	73.9	3.3	221.0
5-CH_3-pm	−303.6515	65.6	3.2	−304.0153	74.1	3.9	218.5
pm	−264.3296	48.4	2.6	−264.6870	56.9	2.7	215.1
4-CF_3-5-CH_3-pm	−640.6806	68.8	5.3	−641.0347	77.1	5.4	213.2
4-CH_3-5-CF_3-pm	−640.6867	68.7	5.3	−641.0417	77.5	5.6	213.1
4-CF_3-pm	−601.3601	51.3	4.3	−601.7059	59.7	4.4	207.9
5-CF_3-pm	−601.3616	51.4	4.8	−601.7063	59.7	4.4	207.8
4,5-$(CF_3)_2$-pm	−938.3846	54.3	6.4	−938.7202	62.6	6.6	201.6
Imidazoles							
1,5-$(CH_3)_2$-im	−304.8593	79.7	4.4	−305.2535	88.4	4.4	238.0
1-CH_3-im	−265.5354	62.1	2.9	−265.9245	71.0	3.4	234.2
5-CH_3-im	−265.5465	62.2	3.4	−265.9344	70.9	3.4	234.0
im	−266.2231	44.7	2.4	−266.6043	53.6	2.4	229.7
1-CH_3-5-CF_3 -im	−602.5728	65.5	5.5	−602.9461	74.1	5.6	225.0
1-CF_3-5-CH_3-im	−602.5751	65.1	5.4	−602.9482	73.7	5.5	224.9
1-CF_3-im	−563.2501	47.6	3.9	−563.6173	56.2	4.5	220.5
5-CF_3-im	−563.2579	47.8	4.0	−563.6234	56.5	4.0	220.0
1,5-$(CF_3)_2$-im	−900.2783	50.7	6.0	−900.6343	59.2	6.1	214.2
Pyrazoles							
4,5-$(CH_3)_2$-pz	−304.8506	79.5	4.6	−305.2256	87.5	4.8	226.5
5-CH_3-pz	−265.5305	61.1	4.5	−265.8999	70.1	3.2	223.5
4-CH_3-pz	−265.5273	62.1	2.9	−265.8942	70.3	3.7	220.7
pz	−266.2070	44.8	2.4	−266.5681	53.0	2.4	217.7
4-CF_3-5-CH_3-pz	−602.5678	65.2	4.6	−602.9222	73.1	5.4	213.1
4-CH_3-5-CF_3-pz	−602.5619	65.1	4.6	−602.9146	73.2	5.9	211.3
5-CF_3-pz	−563.2400	47.8	4.0	−563.5856	55.9	4.2	208.0
4-CF_3-pz	−563.2424	48.0	3.9	−563.5876	56.0	4.1	207.8
4,5-$(CF_3)_2$-pz	−900.2724	51.0	6.7	−900.6054	59.0	6.9	200.2
Isoxazoles							
4,5-$(CH_3)_2$-io	−324.6869	71.1	4.0	−325.0453	79.2	4.1	216.0
5-CH_3-io	−285.3668	53.8	3.3	−285.7189	61.9	3.5	212.1
4-CH_3-io	−285.3613	53.9	3.3	−285.7096	62.2	3.5	209.5
io	−246.0397	36.4	2.2	−246.3810	44.8	2.4	205.1
4-CF_3-5-CH_3-io	−622.4004	56.8	4.8	−622.7380	64.8	5.2	202.9
4-CH_3-5-CF_3-io	−622.3908	56.8	5.0	−622.7255	65.0	5.2	201.1
5-CF_3-io	−583.0687	39.5	4.4	−583.3963	47.7	4.6	196.6
4-CF_3-io	−583.0720	39.6	4.4	−583.3980	47.8	4.0	196.2
4,5-$(CF_3)_2$-io	−920.0965	42.5	6.7	−920.4121	50.6	6.8	189.2

highlights the greater π-acceptor ability of the five-membered N-donor heterocycles compared to the six-membered ligands, a different behavior which was already supposed on the basis of kinetic measurements. In particular, in a previous work regarding the displacement of N-donors by chloride from $AuCl_3$ (N-ligands) [3d] a difference of about 1 kcal mol^{-1} between the free energies of activation of pyridines and five-membered N-donors with equivalent pK_a values was found, the pyridines showing a greater lability. The lower reactivity of the coordinated five-membered heterocycles was mainly attributed to the enforcement of the Au–N bond caused by π-back-donation, in agreement with the results reported in this paper.

Finally, some words should be given on the PA_0^L values reported in Table 3. As already described, PA_0^L represents the ligand minimum proton affinity for a charge variation in $AuCl_3$, therefore it is interpretable as the minimum ligand basicity for a meaningful bond between the heterocycle and the metal ion. Surprisingly, the PA_0^L values are substantially comparable for all the groups of ligands considered in this work, falling around 150 kcal mol^{-1}. Therefore, PA_0^L seems a parameter more related to the electronic features of $AuCl_3$ than those of the coordinating nitrogen donors. In particular, it is presumable that PA_0^L could be related to the electrophilicity of the metal fragment, but further experiments must be carried out to strengthen this hypothesis.

Table 2
Computed $AuCl_3$ Mulliken charges (Q_{AuCl_3}) in $AuCl_3L$ complexes. L = pyridines, pyrimidines, imidazoles, pyrazoles and isoxazoles.

Complex N-ligand	Q_{AuCl_3}
Pyridines	
3,4,5-$(CH_3)_3$-py	−0.357
3,5-$(CH_3)_2$-py	−0.349
3,4-$(CH_3)_2$-py	−0.347
4-CH_3-py	−0.337
3-CH_3-py	−0.333
py	−0.321
3-CF_3-4-CH_3-py	−0.300
3-CH_3-4-CF_3-py	−0.300
4-CF_3-py	−0.287
3-CF_3-py	−0.281
3,4-$(CF_3)_2$-5-CH_3-py	−0.265
3,4-$(CF_3)_2$-py	−0.253
3,4,5-$(CF_3)_3$-py	−0.219
Pyrimidines	
4,5-$(CH_3)_2$-pm	−0.306
4-CH_3-pm	−0.296
5-CH_3-pm	−0.289
pm	−0.273
4-CH_3-5-CF_3-pm	−0.259
4-CF_3-5-CH_3-pm	−0.259
4-CF_3-pm	−0.243
5-CF_3-pm	−0.239
4,5-$(CF_3)_2$-pm	−0.211
Imidazoles	
1,5-$(CH_3)_2$-im	−0.305
1-CH_3-im	−0.295
5-CH_3-im	−0.291
im	−0.275
1-CF_3-5-CH_3-im	−0.260
1-CH_3-5-CF_3-im	−0.255
1-CF_3-im	−0.244
5-CF_3-im	−0.237
1,5-$(CF_3)_2$-im	−0.213
Pyrazoles	
4,5-$(CH_3)_2$-pz	−0.262
5-CH_3-pz	−0.251
4-CH_3-pz	−0.241
pz	−0.228
4-CF_3-5-CH_3-pz	−0.213
4-CH_3-5-CF_3-pz	−0.211
5-CF_3-pz	−0.199
4-CF_3-pz	−0.190
4,5-$(CF_3)_2$-pz	−0.169
Isoxazoles	
4,5-$(CH_3)_2$-io	−0.254
5-CH_3-io	−0.242
4-CH_3-io	−0.233
io	−0.218
4-CF_3-5-CH_3-io	−0.209
4-CH_3-5-CF_3-io	−0.201
5-CF_3-io	−0.189
4-CF_3-io	−0.187
4,5-$(CF_3)_2$-io	−0.163

3. Conclusions

On the basis of the linear relationships between the $AuCl_3$ Mulliken charges in $AuCl_3L$ complexes and the proton affinities of several groups of N-donor heterocycles L, it has been possible to build a new theoretical π-acidity scale for pyridines, pyrimidines, imidazoles, pyrazoles and isoxazoles referred to a specific metal fragment. A different π-back-bonding ability between five- and six-membered ligands has been highlighted, in perfect agreement with already reported experimental evidences. Finally, the minimum proton affinity value to have a meaningful bond between $AuCl_3$ and N-donor heterocycles, like those considered in this work, has been estimated.

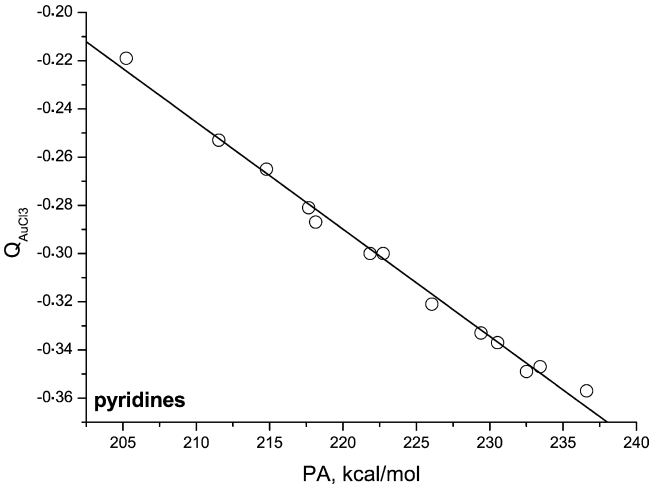


Fig. 2. $AuCl_3$ Mulliken charge (Q_{AuCl_3}) against the ligand proton affinity PA for $AuCl_3L$ complexes, L = pyridines.

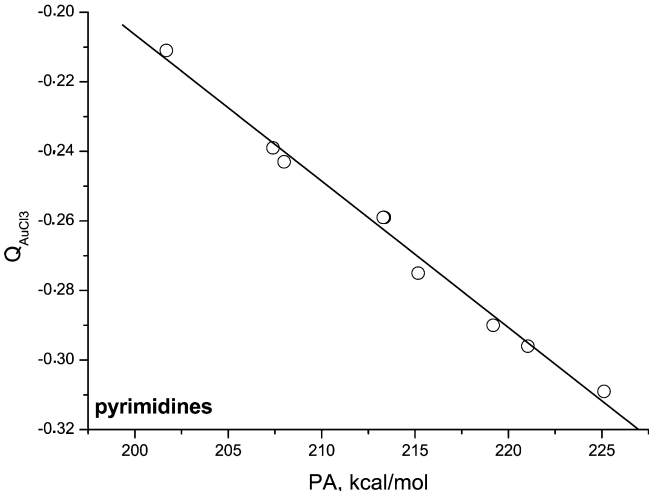


Fig. 3. $AuCl_3$ Mulliken charge (Q_{AuCl_3}) against the ligand proton affinity PA for $AuCl_3L$ complexes, L = pyrimidines.

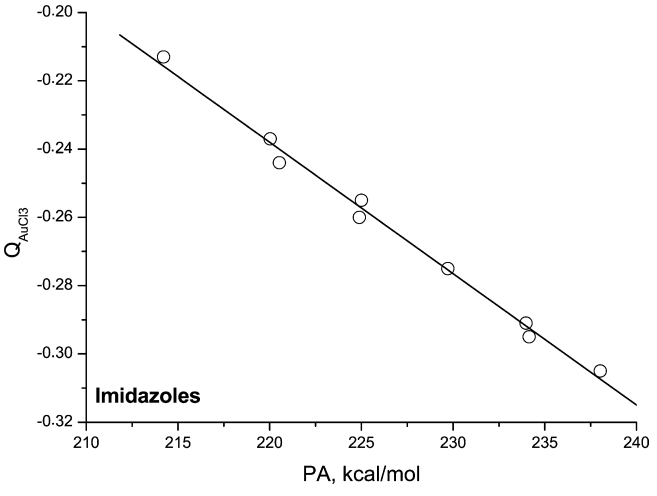


Fig. 4. $AuCl_3$ Mulliken charge (Q_{AuCl_3}) against the ligand proton affinity PA for $AuCl_3L$ complexes, L = imidazoles.

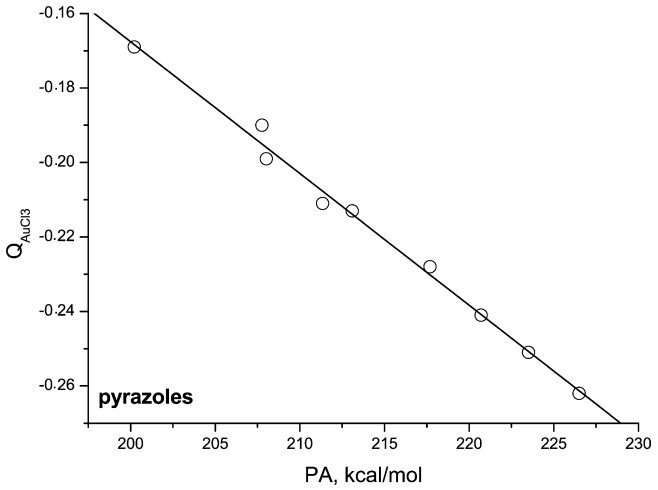


Fig. 5. $AuCl_3$ Mulliken charge (Q_{AuCl_3}) against the ligand proton affinity PA for $AuCl_3L$ complexes, L = pyrazoles.

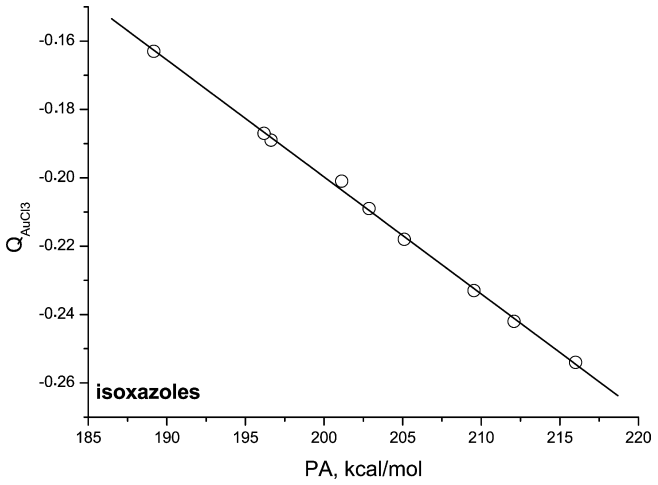


Fig. 6. $AuCl_3$ Mulliken charge (Q_{AuCl_3}) against the ligand proton affinity PA for $AuCl_3L$ complexes, L = isoxazoles.

Table 3
α^L, β^L and PA_0^L values for the five groups of considered ligands.

Ligand	α^L (mol kcal^{-1})	β^L	PA_0^L (kcal mol^{-1})
Pyridines (py)	−0.0045 ± 0.0001	0.69 ± 0.03	150 ± 10
Pyrimidines (pm)	−0.0042 ± 0.0002	0.64 ± 0.04	150 ± 10
Imidazoles (im)	−0.0039 ± 0.0001	0.61 ± 0.03	160 ± 10
Pyrazoles (pz)	−0.0035 ± 0.0001	0.54 ± 0.02	150 ± 10
Isoxazoles (io)	−0.00342 ± 0.00005	0.48 ± 0.01	142 ± 5

These studies will continue, changing both the metal centre and the ancillary ligands, in order to discover if this kind of computational approach could be a useful tool to gain more information on the role of π-back-bonding in d^8 metal complexes and on the relative electrophilicity of different metal fragments.

4. Computational details

The ground-state computational geometry optimisations of the $AuCl_3L$ complexes {L = pyridines (py), pyrimidines (pm), imidazoles (im), pyrazoles (pz) and isoxazoles (io)} were carried out using the hybrid DFT B3PW91 method [12] without symmetry constrains, in combination with the Dunning's split-valence double-ζ D95V basis set on the light atoms [13] and the ECP-based SDD basis set on Au and Cl [14]. The geometry optimisations of

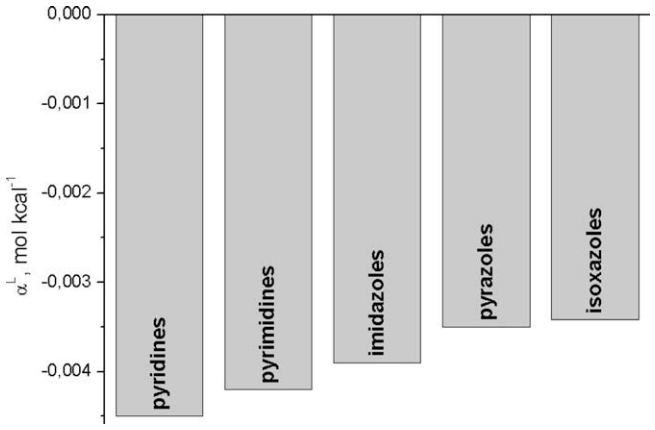


Fig. 7. α^L values of the $AuCl_3$-coordinated ligands.

the free ligands L and of their conjugate acids $[LH]^+$ were carried out with the hybrid B3LYP functional [15] using Pople's split-valence double-ζ polarised 6-31G** basis set [16]. The "restricted" formalism was applied in all calculations and no solvation model was added. A standard accuracy of 10^{-3} Å and 10^{-1}° was used in all the geometry optimisations and all the resulting stationary points were characterized as true minima (*i.e.*, no imaginary frequencies). From the IR simulations, carried out with the harmonic oscillator approximation, the zero-point vibrational energies (ZPVEs) were computed. The thermal contributions to enthalpy have been calculated on the basis of statistical mechanical standard formulas (rigid-rotor approximation). Charge distributions were derived from Mulliken population analysis [17]. Mulliken charges are reported, as usual, as the differences between the number of protons and the number of electrons. Unfortunately, as already observed in a previous work [9], the Natural Bond Orbitals analysis [18] does not properly work for the systems considered in this paper: the software separates the $AuCl_3L$ complexes into three different fragments, $[AuCl_2]^{x+}$, $[Cl]^{y-}$ and $[L]^{(y-x)+}$, leading to wrong results, including an apparent d^{10} configuration of the gold centre. We did not succeed in obtaining any useful results by trying to perform Bader's atoms-in-molecules (AIM) analysis [19] on the $AuCl_3L$ complexes.

All calculations were carried out at CINECA (Centro Italiano di Supercalcolo, Bologna, Italy) using IBM p5-575 computers with 64-bit IBM Power5 processors operating at 1.9 GHz frequency. The software used was GAUSSIAN'03 [20].

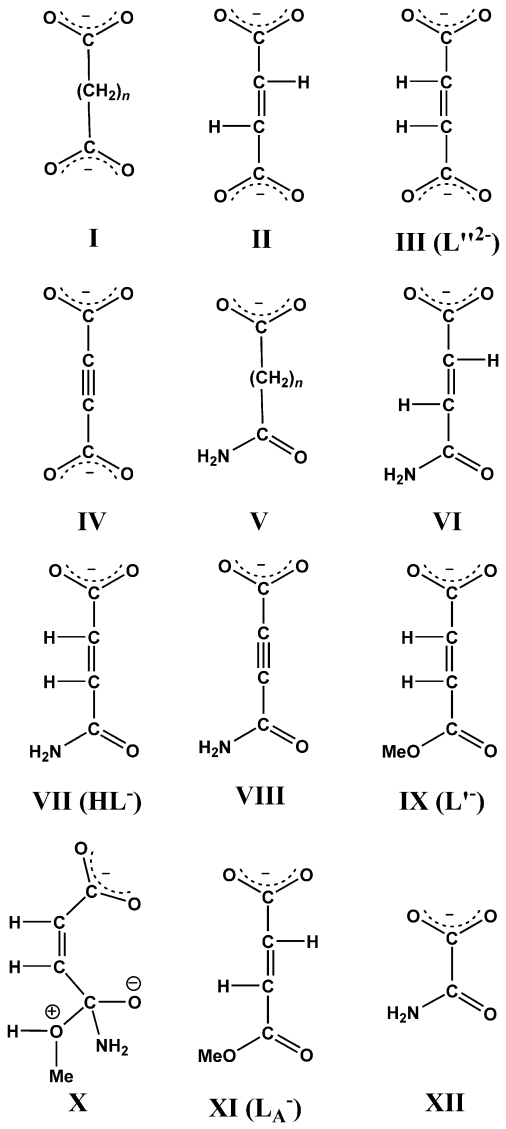
Acknowledgements

Financial support of Ca' Foscari University of Venice (Ateneo Fund 2007) is gratefully acknowledged. We sincerely thank CINECA (Centro Italiano di Supercalcolo, Bologna, Italy) for technical support.

References

[1] (a) J. Reedijk, in: G. Wilkinson, R.D. Gillard, J. McCleverty (Eds.), Comprehensive Coordination Chemistry, vol. 2, Pergamon, Oxford, 1987, p. 73;
(b) R.J. Puddephatt, in: G. Wilkinson, R.D. Gillard, J. McCleverty (Eds.), Comprehensive Coordination Chemistry, vol. 5, Pergamon, Oxford, 1987, p. 894;
(c) D.M. Roundhill, in: G. Wilkinson, R.D. Gillard, J. McCleverty (Eds.), Comprehensive Coordination Chemistry, vol. 5, Pergamon, Oxford, 1987, p. 429;
(d) A.P. Sadimenko, S.S. Basson, Coord. Chem. Rev. 147 (1996) 247;
(e) A.P. Sadimenko, Adv. Heterocycl. Chem. 86 (2004) 293;
(f) A.P. Sadimenko, Adv. Heterocycl. Chem. 80 (2001) 157;
(g) A.P. Sadimenko, Adv. Heterocycl. Chem. 83 (2002) 117;
(h) C.E. Housecroft, Coord. Chem. Rev. 164 (1997) 667;

(i) M. Bortoluzzi, G. Annibale, G. Marangoni, G. Paolucci, B. Pitteri, Polyhedron 25 (2006) 1979.
[2] (a) L. Cattalini, M.L. Tobe, Inorg. Chem. 5 (1966) 1145;
(b) L. Cattalini, A. Orio, M.L. Tobe, Inorg. Chem. 6 (1967) 75;
(c) L. Cattalini, M. Nicolini, A. Orio, Inorg. Chem. 5 (1966) 1674;
(d) L. Cattalini, A. Orio, A. Doni, Inorg. Chem. 6 (1967) 280;
(e) B. Pitteri, G. Marangoni, L. Cattalini, F. Visentin, V. Bertolasi, P. Gilli, Polyhedron 20 (2001) 869;
(f) B. Pitteri, G. Marangoni, L. Cattalini, Polyhedron 14 (1995) 2331.
[3] (a) B. Pitteri, G. Marangoni, L. Cattalini, J. Chem. Soc., Dalton Trans. (1994) 3539;
(b) M. Bellicini, L. Cattalini, G. Marangoni, B. Pitteri, J. Chem. Soc., Dalton Trans. (1994) 1805;
(c) B. Pitteri, M. Bortoluzzi, Polyhedron 25 (2006) 2698;
(d) B. Pitteri, M. Bortoluzzi, Transition Met. Chem. 31 (2006) 1028;
(e) M. Bonivento, L. Cattalini, G. Marangoni, B. Pitteri, T. Bobbo, Transition Met. Chem. 22 (1997) 46.
[4] (a) A.S.K. Hashmi, M. Rudolph, J.P. Weyrauch, M. Wölfle, W. Frey, J.W. Bats, Angew. Chem., Int. Ed. 44 (2005) 2798;
(b) A.S.K. Hashmi, J.P. Weyrauch, M. Rudolph, E. Kurpejovic, Angew. Chem., Int. Ed. 43 (2004) 6545;
(c) A.S.K. Hashmi, F. Ata, J.W. Bats, M.C. Blanco, W. Frey, M. Hamzic, M. Rudolph, R. Salathé, S. Schäfer, M. Wölfle, Gold Bull. 40 (2007) 31;
(d) A.S.K. Hashmi, G.J. Hutchings, Angew. Chem., Int. Ed. 45 (2006) 7896;
(e) A.S.K. Hashmi, Chem. Rev. 107 (2007) 3180.
[5] (a) M. Dolg, in: J. Grotendorst (Ed.), Modern Methods and Algorithms of Quantum Chemistry, NIC Series, vol. 1, John Neumann Institute for Computing, Jülich, 2000, p. 479;
(b) E.R. Davidson, D. Feller, Chem. Rev. 86 (1986) 681;
(c) G. Frenking, I. Antes, M. Böhme, S. Dapprich, A.W. Ehlers, V. Jonas, A. Nauhaus, M. Otto, R. Stegmann, A. Veldkamp, S.F. Vyboishchikov, Rev. Comp. Chem. 8 (1996) 63;
(d) T.R. Cundari, M.T. Benson, M.L. Lutz, S.O. Sommerer, Rev. Comp. Chem. 8 (1996) 145.
[6] (a) C.J. Cramer, Essentials of Computational Chemistry, 2nd Ed., John Wiley and Sons, Chichester, 2004;
(b) F. Jensen, Introduction to Computational Chemistry, 2nd Ed., John Wiley and Sons, Chichester, 2007;
(c) D.C. Young, Computational Chemistry: A Practical Guide for Applying Techniques to Real-World Problems, John Wiley and Sons, Chichester, 2001.
[7] (a) R.G. Parr, W. Yang, Density-Functional Theory of Atoms and Molecules, Oxford University Press, Oxford, 1989;
(b) J.K. Labanowski, J. Andzelm, Density Functional Methods in Chemistry, Springer-Verlag, New York, 1991;
(c) P. Geerlings, F. De Proft, W. Langenaker, Chem. Rev. 103 (2003) 1793.
[8] See for example the articles included in Quantum Inorganic Chemistry, Faraday Discuss, vol. 124, 2003, p. 1.
[9] B. Pitteri, M. Bortoluzzi, Eur. J. Inorg. Chem. (2007) 4456.
[10] A. El Hammadi, M. El Mouhtadi, J. Mol. Struct. (THEOCHEM) 497 (2000) 241.
[11] S. Hwang, Y.H. Jang, D.S. Chung, Bull. Korean Chem. Soc. 26 (2005) 585.
[12] (a) A.D. Becke, J. Chem. Phys. 98 (1993) 5648;
(b) A.D. Becke, Phys. Rev. A 38 (1988) 3098;
(c) J.P. Perdew, in: P. Ziesche, H. Eschrig (Eds.), Electronic Structure of Solids, Akademie Verlag, Berlin, 1991, p. 11.
[13] (a) T.H. Dunning, P.J. Hay, in: H.F. Schafter (Ed.), Modern Theoretical Chemistry, vol. 3, Plenum Press, New York, 1976, p. 1;
(b) T.H. Dunning, J. Chem. Phys. 55 (1971) 716.
[14] (a) A. Bergner, M. Dolg, W. Kuechle, H. Stoll, H. Preuss, Mol. Phys. 80 (1993) 1431;
(b) P. Schwerdtfeger, M. Dolg, W.H.E. Schwarz, G.A. Bowmaker, P.D.W. Boyd, J. Chem. Phys. 91 (1989) 1762.
[15] P.J. Stephens, F.J. Devlin, C.F. Chabalowski, M.J. Frisch, J. Phys. Chem. 98 (1994) 11623.
[16] W.J. Hehre, R. Ditchfield, J.A. Pople, J. Chem. Phys. 56 (1972) 2257.
[17] (a) R.S. Mulliken, J. Chem. Phys. 23 (1955) 1833;
(b) R.S. Mulliken, J. Chem. Phys. 23 (1955) 1841;
(c) R.S. Mulliken, J. Chem. Phys. 23 (1955) 2338;
(d) R.S. Mulliken, J. Chem. Phys. 23 (1955) 2343.
[18] (a) NBO 3.1, E.D. Glendening, A.E. Reed, J.E. Carpenter, F. Weinhold, Part of GAUSSIAN 03 Software Package, see Ref. [20].;
(b) A.E. Reed, L.A. Curtiss, F. Weinhold, Chem. Rev. 88 (1988) 899.
[19] R.F.W. Bader, Atoms in Molecules: A Quantum Theory, Oxford University Press, Oxford, 1990.
[20] M.J. Frish, G.W. Trucks, H.B. Schlegel, G.E. Scuseria, M.A. Robb, J.A. Montgomery Jr., T. Vreven, K.N. Kudin, J.C. Burant, J.M. Millam, S.S. Ivengar, J. Tomasi, V. Barone, B. Mennucci, M. Cossi, G. Scalmani, N. Rega, G.A. Petersson, H. Nakatsuji, M. Hada, M. Ehara, K. Toyota, R. Fukuda, J. Hasegawa, M. Ishida, T. Nakajima, Y. Honda, O. Kitao, H. Nakai, M. Klene, X. Li, J.E. Knox, H.P. Hratchian, J.B. Cross, V. Bakken, C. Adamo, J. Jaramillo, R. Gomperts, R.E. Stratmann, O. Yazyev, A.J. Austin, R. Cammi, C. Pomelli, J.W. Ochterski, P.Y. Ayala, R. Morokuma, G.A. Voth, P. Salvador, J.J. Dannenberg, V.G. Zakrewski, S. Dapprich, A.D. Daniels, M.C. Strain, O. Farkas, D.K. Malick, A.D. Rabuck, K. Raghavachari, J.B. Foresman, J.V. Ortiz, Q. Cui, A.G. Baboul, S. Clifford, J. Cioslowski, B.B. Stefanov, G. Liu, A. Liashenko, P. Piskorz, I. Komaromi, R.L. Martin, D.J. Fox, T. Keith, M.A. Al-Laham, C.Y. Peng, A. Nanayakkara, M. Challacombe, P.M.W. Gill, B. Johnson, W. Chen, M.W. Wong, C. Gonzales, J.A. Pople, GAUSSIAN 03, Revision D.02, Gaussian Inc., Wallingford, CT, 2004.



Scheme 1. Some of the ligands discussed in the text. The ligand used in this work is the maleamate(−1) ion (**VII**, HL^-).

instead of a carboxylate group, is expected – due to different charge, electronic properties and hydrogen bonding capabilities – to significantly affect the chemical and structural identity of the resultant metal complexes in comparison with that of the α,ω-dicarboxylate complexes.

With the above considerations in mind, we had explored "ligand blend" reaction systems involving the succinamate(−1) ligand ($n = 2$ in **V** of Scheme 1; $Hsucm^-$) and various aromatic chelating *N*,*N*′-donors as a means to dinuclear and polymeric copper(II) complexes [4]. In a subsequent step we used the maleamate(−1) (**VII** in Scheme 1; HL^-)/phen ligand combination in copper(II) chemistry [5]. The coordination chemistry of maleamic acid (H_2L) was unknown before those studies. It was expected that the presence of the double bond between the central carbon atoms would alter the coordination chemistry of H_2L as compared to that of succunamic acid (H_2sucm). The HL^-/phen ligand "blend" led to interesting mononuclear, dinuclear and polymeric copper(II) complexes containing intact HL^-. We also reported that the $Cu(ClO_4)_2 \cdot 6H_2O/H_2L$/phen reaction systems in MeOH, in the absence of external OH^- ions, affords complex $[Cu_2(L')_2(ClO_4)(phen)_2(MeOH)](ClO_4)$ in which the maleamate(−1) ion has been transformed to the monomethyl maleate(−1) ligand L'^- (**IX** in Scheme 1) via a novel, Cu^{II}-promoted process and through the intermediate formation of the HL^--free coordination polymer $[Cu(ClO_4)(phen)(MeOH)_2]_n$ [5b].

We illustrate herein how the reactions of $Cu(ClO_4)_2 \cdot 6H_2O$ with H_2L *and* bpy yield a series of interesting complexes containing the intact HL^- or ligands derived from the metal ion-assisted transformation of the primary amide group. The use of bpy allows direct structural comparison with the complexes featuring the corresponding α,ω-dicarboxylate (**III** in Scheme 1; maleate) and the succinamate(−1) ligand ($n = 2$ in **V** of Scheme 1; $Hsucm^-$), i.e. the $Cu^{II}/^-OOC–CH{=}CH–COO^-$/bpy and $Cu^{II}/Hsucm^-$/bpy complexes. We have also wondered if isostructural bpy analogues of the Cu^{II}/HL^-/phen complexes [5] could be prepared and if the bpy versus phen difference would lead to different Cu^{II}-assisted reactivity chemistry on HL^-. The answers of these questions are provided in this work.

2. Experimental

2.1. General and spectroscopic measurements

All manipulations were performed under aerobic conditions using materials as received (Aldrich Co.). All chemicals and solvents were of reagent grade. Elemental analyses for C, H and N were performed on a Perkin–Elmer 2400/*II* automatic analyzer. IR spectra were recorded from KBr pellets in the range 4000–400 cm^{-1} on a Bruker Equinox 55/S FT-IR spectrophotometer.

Safety note: Perchlorate salts are potentially explosive; such compounds should be synthesized and used in small quantities, and treated with utmost care at all times.

2.2. Compound preparation

2.2.1. $[Cu_2(HL)_2(bpy)_2(H_2O)_2](ClO_4)_2$ (**1**) and $[Cu(L'')(bpy)]_n \cdot 2nH_2O$ (**2** $\cdot 2nH_2O$) in a mixture

A colorless aqueous solution (1.5 ml) of $LiOH \cdot H_2O$ (0.018 g, 0.44 mmol) was added to a colorless solution of H_2L (0.049 g, 0.43 mmol) in MeCN (20 ml) to give a white suspension. Solid bpy (0.045 g, 0.29 mmol) was then added to afford a colorless solution. A blue solution of $Cu(ClO_4)_2 \cdot 6H_2O$ (0.107 g, 0.29 mmol) in MeCN (10 ml) was finally added to obtain a blue solution. X-ray quality blue prismatic crystals and light blue long plate-like crystals in an approximate ratio of 1:1 formed by layering of the blue solution with a mixture of Et_2O/*n*-hexane (40 ml, 1:1 v/v). The crystals were separated manually and dried in air. X-ray crystallography revealed that blue prisms correspond to complex **1** and light blue plates correspond to complex **2** $\cdot 2nH_2O$. FT-IR for **1** (KBr pellet, cm^{-1}): 3442sb, 3354sb, ~3190mb, 2922w, 2850w, 1676s, 1640s, 1603vs, 1598vs, 1496m, 1473s, 1447vs, 1382m, 1308m, 1249w, 1198w, 1177w, 1112vs, 1082vs, 1022vw, 877w, 820m, 764s, 728s, 655m, 624s, 490w, 478w. *Anal.* Calc. for $C_{28}H_{28}N_6O_{16}Cl_2Cu_2$ (902.56): C, 37.26; H, 3.12; N, 9.31. Found: C, 36.97; H, 3.63; N, 9.16%. FT-IR for **2** $\cdot 2nH_2O$ (KBr pellet, cm^{-1}): 3385mb, 3109w, 3072w, 3032vw, 2360w, 1648w, 1591vs, 1560vs, 1542sh, 1494w, 1474w, 1448m, 1432m, 1404m, 1315m, 1286w, 1249w, 1199w, 1175w, 1160vw, 1112vw, 1055w, 1031w, 1017w, 987w, 913w, 875vw, 859w, 836w, 782m, 732w, 679vw, 650w, 596w, 448vw. *Anal.* Calc. for $C_{14}H_{14}N_2O_6Cu$ (369.82): C, 45.47; H, 3.82; N, 7.57. Found: C, 45.35; H, 3.74; N, 7.64%.

2.2.2. $[Cu_2(HL)_2(bpy)_2(H_2O)_2](ClO_4)_2$ (**1**)

Solid $LiOH \cdot H_2O$ (0.018 g, 0.43 mmol) was added to a colorless solution of H_2L (0.049 g, 0.43 mmol) in MeOH (20 ml) to give again a colorless solution. Solid $Cu(ClO_4)_2 \cdot 6H_2O$ (0.159 g, 0.43 mmol) was then added to obtain a light blue solution. A colorless solution

of bpy (0.067 g, 0.43 mmol) in MeOH (5 ml) was then added to give a final blue solution, which was layered with a mixture of Et_2O/*n*-hexane (30 ml, 1:1 v/v) to afford X-ray quality blue prismatic crystals. The crystals were collected by filtration under vacuum, washed with cold MeOH (2 ml) and Et_2O (2 ml), and dried in air. Typical yields were in the 55–60% range. The identity of the blue crystals was established as **1** by unit cell determination (a = 7.421(4), b = 10.273(5), c = 11.868(6) Å, α = 83.43(2), β = 87.90(2), γ = 77.59(2)°; see Table 1). The IR spectrum of the crystals was identical to that of the authentic material prepared in a mixture with **2** · 2*n*H_2O. *Anal.* Calc. for $C_{28}H_{28}N_6O_{16}Cl_2Cu_2$ (902.56): C, 37.26; H, 3.12; N, 9.31. Found: C, 36.87; H, 3.32; N, 9.28%.

*2.2.3. [$Cu_2(HL)_2(bpy)_2(H_2O)_2$]($ClO_4$)$_2$ · 2H_2O (**1** · 2H_2O)*

A colorless aqueous solution (2 ml) of LiOH · H_2O (0.018 g, 0.44 mmol) was added to a colorless solution of H_2L (0.049 g, 0.43 mmol) in MeCN (20 ml) to give a white suspension. Solid $Cu(ClO_4)_2 \cdot 6H_2O$ (0.159 g, 0.43 mmol) was then added to give a light blue suspension, which was stirred for 30 min. A colorless solution of bpy (0.067 g, 0.43 mmol) in MeCN (6 ml) was finally added to obtain a blue mixture, which was filtered to give a clear blue solution. X-ray quality blue prismatic crystals of **1** · 2H_2O were obtained by layering of the blue solution with a mixture of Et_2O/*n*-hexane (40 ml, 1:1 v/v). The crystals were collected by filtration under vacuum, washed with cold MeCN (2 ml) and Et_2O (2 ml), and dried in air. Typical yields were in the 55–60% range. FT-IR for **1** · 2H_2O (KBr pellet, cm^{-1}): 3394sb, 3197sb, 2359w, 1679s, 1641m, 1602vs, 1496m, 1473m, 1445vs, 1374m, 1303s, 1250w, 1196w, 1171w, 1098vs, 932vw, 907vw, 890vw, 863vw, 822m, 776s, 730m, 658w, 625s, 503w, 479w. *Anal.* Calc. for $C_{28}H_{32}N_6O_{18}Cl_2Cu_2$ (938.59): C, 35.83; H, 3.44; N, 8.95. Found: C, 35.96; H, 3.28; N, 8.77%.

*2.2.4. [Cu(L″)(bpy)]$_n$ · 2nH_2O (**2** · 2nH_2O)*

2.2.4.1. Method A. Solid LiOH · H_2O (0.018 g, 0.43 mmol) was added to a colorless aqueous solution (25 mL) of H_2L (0.049 g, 0.43 mmol). A solution of bpy (0.034 g, 0.22 mmol) in MeOH (5 mL) was then added to the above solution. An aqueous light blue solution (5 mL) of $Cu(ClO_4) \cdot 6H_2O$ (0.080 g, 0.22 mmol) was finally added to afford a light blue solution. Slow evaporation of the final solution yielded turquoise needle-like crystals of **2** after one week. The identity of the crystals was confirmed by unit cell determination (a = 7.352(3), b = 19.945(9), c = 10.099(5) Å, β = 98.39(1)°) and IR spectroscopy. The crystals were collected by filtration under vacuum and dried in air. Typical yields were 60%. *Anal.* Calc. for $C_{14}H_{14}N_2O_6Cu$ (369.82): C, 45.47; H, 3.82; N, 7.57. Found: C, 45.65; H, 3.94; N, 7.74%.

2.2.4.2. Method B. A colorless aqueous solution (3 ml) of LiOH · H_2O (0.037 g, 0.88 mmol) was added to a colorless solution of H_2L'' (0.051 g, 0.44 mmol) in MeCN (25 ml) to give a white suspension. Solid bpy (0.069 g, 0.44 mmol) was then added to give a new white suspension. A light blue solution of $Cu(ClO_4)_2 \cdot 6H_2O$ (0.163 g, 0.44 mmol) in MeCN (15 ml) was finally added to obtain a blue suspension which was filtered to give a final blue solution. Turquoise needle-like crystals of **2** · 2*n*H_2O were obtained in closed vials at ~4 °C after *ca* 30 days. The identity of the product was revealed by IR spectroscopy. The crystals were collected by filtration under vacuum and dried in air.

*2.2.5. [$Cu_2(L'')(bpy)_2(H_2O)_2$]$_n$(ClO_4)$_{2n}$ · 0.5*n*H_2O (**3** · 0.5*n*H_2O)*

The procedure is identical to that of Method B above. X-ray quality blue prismatic crystals of **3** · 0.5*n*H_2O were obtained by layering of the blue solution with Et_2O (50 ml). The crystals were collected by filtration under vacuum and dried in air. Typical yields were ~55%. FT-IR for **3**: (KBr pellet, cm^{-1}): 3446mb, 3114w, 3087w, 1647w, 1601m, 1583vs, 1561vs, 1496m, 1473s, 1446vs, 1416m, 1320s, 1282w, 1270w, 1250m, 1209m, 1176sh, 1162sh, 1089vs, 1033w, 1017w, 930w, 912w, 857w, 830m, 771vs, 730s, 702w, 664w, 623vs, 576w, 457vw, 441w, 418w. The dried product analyzed as **3**. *Anal.* Calc. for $C_{24}H_{22}N_4O_{14}Cl_2Cu_2$ (788.45): C, 36.56; H, 2.81; N, 7.11. Found: C, 36.38; H, 2.79; N, 7.07%. Vapor diffusion of Et_2O (10 ml) into the blue reaction solution yielded light blue needle-like crystals of **4**, which were not suitable for X-ray crystallography. The FT-IR spectrum of this material is identical to that of **7b** (vide infra).

*2.2.6. [$Cu_2(L'')_2(bpy)_2$] · 2MeOH (**5** · 2MeOH)*

2.2.6.1. Method A. Solid LiOH · H_2O (0.036 g, 0.86 mmol) was added to a colorless solution of H_2L'' (0.050 g, 0.43 mmol) in MeOH

Table 1
Crystallographic data for complexes **1**, **1** · 2H_2O, **3** · 0.5*n*H_2O, **5** · 2MeOH, **6** and **7b**.

	1	**1** · 2H_2O	**3** · 0.5*n*H_2O	**5** · 2MeOH	**6**	**7b**
Formula	$C_{28}H_{28}Cl_2Cu_2N_6O_{16}$	$C_{28}H_{32}Cl_2Cu_2N_6O_{18}$	$C_{24}H_{23}Cl_2Cu_2N_4O_{14.5}$	$C_{30}H_{28}Cu_2N_4O_{10}$	$C_{30}H_{26}Cl_2Cu_2N_4O_{16}$	$C_{14}H_{14}Cl_2CuN_4O_8$
Fw	902.54	938.58	797.44	731.64	896.52	500.74
Space group	$P\bar{1}$	$P\bar{1}$	$P2_1/n$	$C2/c$	$C2/c$	$P2_1/m$
a (Å)	7.380(3)	9.773(4)	16.5319(4)	18.49(1)	11.506(8)	8.8949(9)
b (Å)	10.266(4)	10.115(4)	9.3947(2)	7.881(5)	15.161(9)	12.4848(12)
c (Å)	11.874(5)	11.519(6)	19.0116(4)	21.30(2)	21.21(1)	8.7524(11)
α (°)	83.13(1)	66.29(1)				
β (°)	87.90(1)	78.72(2)	95.3380(10)	98.28(2)	104.31(3)	97.825(6)
γ (°)	77.69(1)	62.05(2)				
V (Å^3)	872.6(6)	920.9(7)	2939.93(11)	3071(4)	3585(4)	962.91(18)
Z	1	1	4	4	4	2
T (°C)	25	25	−93	25	25	25
Radiation	Mo Kα	Mo Kα	Cu Kα	Mo Kα	Mo Kα	Cu Kα
ρ_{calc} (g cm^{-3})	1.718	1.692	1.802	1.582	1.661	1.727
μ (mm^{-1})	1.455	1.386	4.176	1.449	1.414	4.640
R_1[a]	0.0315[b]	0.0609[c]	0.0568[d]	0.0310[e]	0.0590[f]	0.0781[g]
wR_2[a]	0.0782[b]	0.1771[c]	0.1647[d]	0.0800[e]	0.1649[f]	0.1777[g]

[a] $w = 1/[\sigma^2(F_o^2) + (\alpha P)^2 + bP]$ and $P = (\max F_o^2, 0) + 2(F_c^2)/3$, $R_1 = \Sigma(|F_o| - |F_c|)/\Sigma(|F_o|)$ and $wR_2 = \{\Sigma[w(F_o^2 - F_c^2)^2]/\Sigma[w(F_o^2)^2]\}^{1/2}$.
[b] For 2748 reflections with $I > 2\sigma(I)$.
[c] For 2798 reflections with $I > 2\sigma(I)$.
[d] For 4209 reflections with $I > 2\sigma(I)$.
[e] For 2239 reflections with $I > 2\sigma(I)$.
[f] For 2688 reflections with $I > 2\sigma(I)$.
[g] For 1053 reflections with $I > 2\sigma(I)$.

(20 ml) to give a white suspension. Solid bpy (0.067 g, 0.43 mmol) was added and the resultant new suspension was stirred under heating for 30 min. Finally a light blue solution of $Cu(ClO_4)_2 \cdot 6H_2O$ (0.159 g, 0.43 mmol) in MeOH (10 ml) was added to give a dark blue suspension, which was filtered to obtain a dark blue solution. Layering of the final reaction solution with a mixture of Et_2O/*n*-hexane (50 ml, 1:1 v/v) gave large blue prismatic crystals, which were collected by filtration under vacuum, washed with cold MeOH (5 ml) and Et_2O (5 ml), and dried in air. Typical yields were in the 65–70% range. FT-IR (KBr pellet, cm^{-1}): 3385sb, 3108m, 3072vw, 3061vw, 3033vw, 2031vw, 1826vw, 1647vs, 1590vsb, 1561vsb, 1541ssh, 1494m, 1474m, 1446s, 1423m, 1402vs, 1314s, 1286m, 1250m, 1223w, 1193m, 1176m, 1157m, 1113w, 1100w, 1073vw, 1057m, 1037m, 1018m, 988w, 911m, 860, 836m, 781s, 732s, 681w, 664wsh, 650w, 643wsh, 601mb, 448vw. The dried product was analyzed as solvent free. *Anal.* Calc. for $C_{28}H_{20}N_4O_8Cu_2$ (667.58): C, 50.38; H, 3.02; N, 8.39. Found: C, 50.22; H, 3.21; N, 8.19%.

2.2.6.2. Method B. Solid $LiOH \cdot H_2O$ (0.036 g, 0.86 mmol) was added to a colorless solution of H_2L'' (0.050 g, 0.43 mmol) in MeOH (20 ml) to give a white suspension. Solid bpy (0.067 g, 0.43 mmol) was then added and the new resultant suspension was stirred under heating for 30 min. Finally a light blue solution of $Cu(NO_3)_2 \cdot 2.5H_2O$ (0.100 g, 0.43 mmol) in MeOH (10 ml) was added to give a blue suspension, which was filtered to obtain a blue solution. Layering of the final solution with Et_2O (30 ml) gave cubic blue crystals, which were collected by filtration under vacuum, washed with cold MeOH (5 ml) and Et_2O (5 ml), and dried in air. Typical yields were in the 65–70% range. The identity of the crystals was confirmed by unit cell determination (a = 18.49(1), b = 7.885(5), c = 21.31(1) Å, β = 98.26(2)°; see Table 1) and by IR comparison with the authentic material prepared using Method A. *Anal.* Calc. for $C_{28}H_{20}N_4O_8Cu_2$ (667.58): C, 50.38; H, 3.02; N, 8.39. Found: C, 50.52; H, 3.18; N, 8.31%.

*2.2.7. $[Cu_2(L')_2(bpy)_2(ClO_4)_2]$ (**6**)*

Solid bpy (0.045 g, 0.29 mmol) was dissolved in a colorless solution of H_2L (0.050 g, 0.43 mmol) in MeOH (20 ml). A light blue solution of $Cu(ClO_4)_2 \cdot 6H_2O$ (0.107 g, 0.29 mmol) in MeOH (8 ml) was then added to obtain a light blue solution which was layered with a mixture of Et_2O/*n*-hexane (30 ml, 1:1 v/v). Slow mixing initially gave a light blue polycrystalline solid (**7a**). Upon storage of the closed layering tube at room temperature for two weeks, the polycrystalline powder was transformed into blue, X-ray quality crystals of the product (**6**). The crystals were collected by filtration under vacuum and dried in air. Typical yields were >55%. FT-IR (KBr pellet, cm^{-1}): 3414mb, 3118w, 3088w, 3036vw, 2959w, 2856vw, 2027vw, 1719vs, 1648sh, 1601sb, 1568s, 1497m, 1474m, 1447s, 1432s, 1361m, 1324sh, 1317m, 1237s, 1174m, 1162m, 1117vs, 1046s, 995w, 967w, 926m, 900w, 828m, 817w, 771s, 746w, 728s, 684w, 666w, 651w, 624s, 493w. The IR spectrum of the light blue powder is completely different compared to that of **6**. *Anal.* Calc. for $C_{30}H_{26}N_4O_{16}Cl_2Cu_2$ (896.55): C, 40.19; H, 2.92; N, 6.25. Found: C, 40.30; H, 2.87; N, 6.17%.

*2.2.8. $[Cu(ClO_4)_2(bpy)(MeCN)_2]$ (**7b**)*

A colorless solution of bpy (0.069 g, 0.44 mmol) in MeCN (12 ml) was added to a light blue solution of $Cu(ClO_4)_2 \cdot 6H_2O$ (0.163 g, 0.44 mmol) in the same solvent (40 ml) to give a light blue-turquoise solution. X-ray quality, light blue crystals of the product formed by layering of the final solution with a mixture of Et_2O/*n*-hexane (50 ml, 1:1 v/v). The crystals were collected by filtration under vacuum, washed with cold MeCN (2 ml) and Et_2O (3 ml), and dried in air. Typical yields were in the 55–60% range. FT-IR (KBr pellet, cm^{-1}): 3440mb, 3106w, 2362vw, 1869vw, 1742vw, 1636w, 1609sh, 1600s, 1566m, 1496m, 1472s, 1443s, 1326m, 1317m, 1285w, 1246m, 1144vsb, 1091vsb, 1023s, 1013sh, 940m, 904m, 774s, 728s, 658w, 653sh, 627vs, 472vw, 417m. *Anal.* Calc. for $C_{14}H_{14}N_4O_8Cl_2Cu_2$ (564.29): C, 29.80; H, 2.50; N, 9.93. Found: C, 29.67; H, 2.64; N, 9.86%.

2.3. Single-crystal X-ray crystallography

A blue prismatic crystal of **1** (0.10 × 0.20 × 0.40 mm) and a light blue prismatic crystal of **2** · $2nH_2O$ (0.18 × 0.25 × 0.45 mm) were mounted in air. Blue prismatic crystals of **1** · $2H_2O$ (0.20 × 0.30 × 0.45 mm), **5** · 2MeOH (0.20 × 0.30 × 0.55 mm), **6** (0.25 × 0.35 × 0.50 mm) and **7b** (0.10 × 0.10 × 0.45 mm) were mounted in capillaries. A blue prismatic crystal of **3** · $0.5nH_2O$ (0.08 × 0.13 × 0.51 mm) was taken directly from the mother liquor and immediately cooled to −93 °C. Diffraction measurements for **3** · $0.5nH_2O$ and **7b** were made on a Rigaku R-AXIS SPIDER Image Plate diffractometer using graphite monochromated Cu Kα radiation. Data for **1**, **1** · $2H_2O$, **5** · 2MeOH and **6** were collected on a Crystal Logic Dual Goniometer diffractometer using graphite monochromated Mo Kα radiation. Unit cell dimensions (for **1**, **1** · $2H_2O$ **2** · $2nH_2O$, **5** · 2MeOH, **6**) were determined and refined by using the angular settings of 25 automatically centred reflections in the range $11 < 2\theta < 23°$. Intensity data were recorded using a $\theta-2\theta$ scan. Three standard reflections monitored every 97 reflections showed less than 3% variation and no decay. Lorentz, polarization corrections were applied using CRYSTAL LOGIC software. For **3** · $0.5nH_2O$ and **7b**, data collection (ω-scans) and processing (cell refinement, data reduction and empirical absorption correction) were performed using the CRYSTALCLEAR program package [6]. Important crystallographic and refinement data are listed in Table 1. Compound **2** · $2nH_2O$ has been reported earlier [7] and will not be further discussed from the crystallographic point of view.

The structures were solved by direct methods using SHELXS-97 [8] and refined by full-matrix least-squares techniques on F^2 with SHELXL-97 [9]. Further crystallographic details for **1**: $2\theta_{max} = 50°$; reflections collected/unique/used, 3238/3075 [R_{int} = 0.0126]/3075; 337 parameters refined; $(\Delta/\sigma)_{max}$ = 0.009; $(\Delta\rho)_{max}/(\Delta\rho)_{min}$ = 0.351/−0.304 e/Å^3; R/R_w (for all data), 0.0369/0.1082. Further crystallographic details for **1** · $2H_2O$: $2\theta_{max} = 50°$; reflections collected/unique/used, 3449/3241 [R_{int} = 0.0208]/3241; 317 parameters refined; $(\Delta/\sigma)_{max}$ = 0.003; $(\Delta\rho)_{max}/(\Delta\rho)_{min}$ = 0.954/−1.392 e/Å^3; R/R_w (for all data), 0.0689/0.1858. Further crystallographic details for **3** · $0.5nH_2O$: $2\theta_{max} = 130°$; reflections collected/unique/used, 19328/4944 [R_{int} = 0.0471]/4944; 499 parameters refined; $(\Delta/\sigma)_{max}$ = 0.002; $(\Delta\rho)_{max}/(\Delta\rho)_{min}$ = 0.891/−0.760 e/Å^3; R/R_w (for all data), 0.06256/0.1713. Further crystallographic details for **5** · 2MeOH: $2\theta_{max} = 50°$; reflections collected/unique/used, 2785/2696 [R_{int} = 0.0082]/2696; 264 parameters refined; $(\Delta/\sigma)_{max}$ = 0.002; $(\Delta\rho)_{max}/(\Delta\rho)_{min}$ = 0.266/−0.281 e/Å^3; R/R_w (for all data), 0.0416/0.0864. Further crystallographic details for **6**: $2\theta_{max} = 50°$; reflections collected/unique/used, 3228/3135 [R_{int} = 0.0595]/3135; 287 parameters refined; $(\Delta/\sigma)_{max}$ = 0.014; $(\Delta\rho)_{max}/(\Delta\rho)_{min}$ = 0.744/−0.911 e/Å^3; R/R_w (for all data), 0.0682/0.1769. The crystals of **7b** had poor quality with large ω-widths, which probably came from two different domains. As a result, the data set contained reflections with large F_o^2 compared to the expected F_c^2 value; these reflections have been omitted during the refinement. Further crystallographic details for **7b**: $2\theta_{max} = 130°$; reflections collected/unique/used, 4987/1405 [R_{int} = 0.1150]/1405; 144 parameters refined; $(\Delta/\sigma)_{max}$ = 0.001; $(\Delta\rho)_{max}/(\Delta\rho)_{min}$ = 1.198/−0.799 e/Å^3; R/R_w (for all data), 0.0881/0.1869. In all structures, all non-H atoms were refined anisotropically. Hydrogen atoms were located by difference maps and were refined isotropically, except those of the methyl group in **6** and those in **7b** which were introduced at calculated positions as riding on bonded atom.

3. Results and discussion

3.1. Syntheses

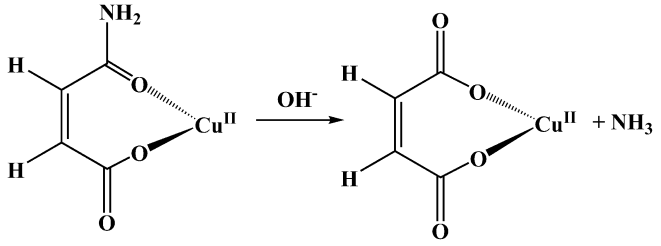
Our previous investigation of the tertiary Cu^{II}/H_2L/phen reaction system [5] has led to interesting results concerning the chemical and structural properties of the compounds isolated. In order to examine to what extent the nature of the aromatic ligand might affect the identity of the products isolated, we have expanded our research on the investigation of the Cu^{II}/H_2L/bpy reaction system. The influence of the same synthetic parameters, i.e., the solvent, the absence or presence of external hydroxides, the inorganic anion in the copper(II) salts and the stoichiometry of the reactants, has been investigated. In the present work we have kept constant the inorganic anion of the copper(II) source; we have explored reactions employing $Cu(ClO_4)_2 \cdot 6H_2O$ which contains an anion with a weak coordinating capability.

Our initial efforts involved the reaction of $Cu(ClO_4)_2 \cdot 6H_2O$ with 1.5 equivalents of H_2L and one equivalent of bpy in the presence of 1.5 equivalents of $LiOH \cdot H_2O$ in MeCN/H_2O (20:1 v/v). Blue prismatic crystals of **1** and light blue plate-like crystals of the known [7] polymeric complex **2** have been simultaneously isolated in an approximate 1:1 ratio (Scheme 3). Assuming the formation of equimolar quantities of the two products, the preparation of **1** and **2** can be summarized in the balanced Eq. (1):

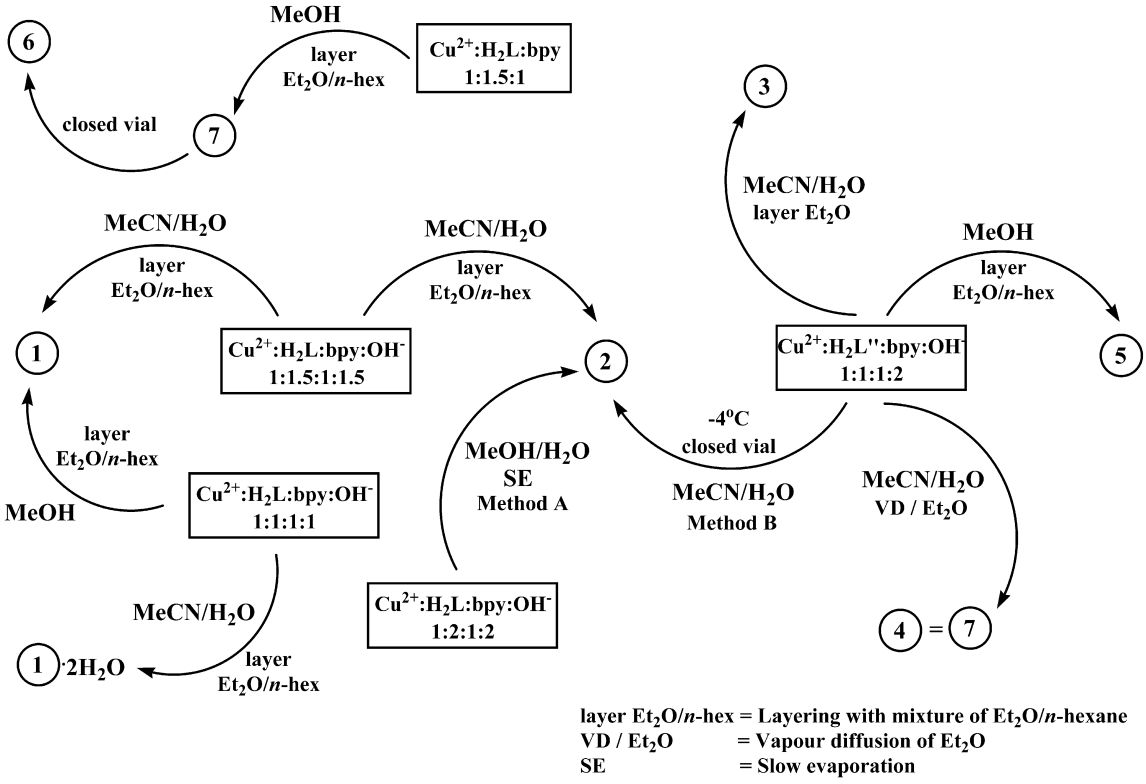
$$3n\mathrm{Cu(ClO_4)_2 \cdot 6H_2O} + 3n\mathrm{H_2L} + 3n\mathrm{bpy} + 4n\mathrm{LiOH \cdot H_2O} \xrightarrow{\mathrm{MeCN/H_2O}} \underset{\mathbf{1}}{n[\mathrm{Cu_2(HL)_2(bpy)_2(H_2O)_2](ClO_4)_2}} + \underset{\mathbf{2}}{[\mathrm{Cu(L'')(bpy)}]_n} \cdot 2n\mathrm{H_2O} + 4n\mathrm{LiClO_4} + n\mathrm{NH_3} + 21n\mathrm{H_2O} \quad (1)$$

The dianion L''^{2-} in **2** is the maleate(−2) ligand (**III** in Scheme 1) that formed in situ by the hydrolysis of the primary amide group to carboxylate function, accompanied by simultaneous release of ammonia. It is well known that such hydrolysis reactions are accelerated by metal ions [10]. Coordination of the oxygen atom of the amide group to the Cu^{II} centre in solution modifies the reactivity of that group. The metal ion polarizes the carbonyl group increasing the $\delta+$ character of the amide carbon, and the OH^- ion can attack this carbon to generate the tetrahedral intermediate, which collapses – with loss of NH_3 – to give the maleate(−2) ligand containing two carboxylate groups. Avoiding any detailed mechanistic scheme and assuming the formation of a seven-membered chelating ring, the $HL^- \rightarrow L''^{2-}$ transformation is depicted in Scheme 2. We believe that the little amount of water added in the reaction mixture – in order to dissolve $LiOH \cdot H_2O$ and to prevent contamination of the product by $LiClO_4$ which is insoluble in anhydrous MeCN – or contained in the starting materials is beneficial to the hydrolysis of the primary amide group and the formation of the maleate(−2) ligand followed by its subsequent coordination affording **2**.

With the identity of compound **1** established by crystallographic studies, we have employed the 'correct' stoichiometric ratio of the reactants to obtain pure **1**. However, from the strictly 1:1:1:1 $Cu(ClO_4)_2 \cdot 6H_2O/H_2L$/bpy/$LiOH \cdot H_2O$ reaction mixture in MeCN/H_2O (20:1 v/v) we have isolated compound **1** · $2H_2O$ upon



Scheme 2. The maleamate(−1) to maleate(−2) transformation observed during the preparation of complex **2** from the $Cu(ClO_4) \cdot 6H_2O/H_2L$/bpy/$OH^-$ reaction system in MeCN/H_2O.



Scheme 3. Diagram of the reaction pathways, showing the various combinations of stoichiometries and crystallization methods, and the products obtained by each.

layering of the resultant blue solution with mixture of Et_2O/*n*-hexane (Scheme 3). The structure of the dinuclear cation in **1** · $2H_2O$ is completely similar to that of the corresponding cation in **1**, see Eq. (2). The presence of two water solvate molecules in the structure of the former leads to a completely different crystal structure due to hydrogen bonding interactions. In order to study the influence of the solvent on the reaction that leads to **1** · $2H_2O$, we have performed the above stoichiometric reaction in MeOH and have isolated pure **1** [Eq. (3)]; its identity was established by unit cell determination:

$$2Cu(ClO_4)_2 \cdot 6H_2O + 2H_2L + 2bpy + 2LiOH \cdot H_2O \xrightarrow{MeCN/H_2O} \underset{\mathbf{1} \cdot 2H_2O}{[Cu_2(HL)_2(bpy)_2(H_2O)_2](ClO_4)_2 \cdot 2H_2O} + 2LiClO_4 + 12H_2O \quad (2)$$

$$2Cu(ClO_4)_2 \cdot 6H_2O + 2H_2L + 2bpy + 2LiOH \cdot H_2O \xrightarrow{MeOH} \underset{\mathbf{1}}{[Cu_2(HL)_2(bpy)_2(H_2O)_2](ClO_4)_2} + 2LiClO_4 + 14H_2O \quad (3)$$

The next question addressed was whether, and in what manner, changes in the reactants' ratio might affect the product identity. Thus, reaction of $Cu(ClO_4)_2 \cdot 6H_2O$ with two equivalents of H_2L and one equivalent of bpy in the presence of two equivalents of $LiOH \cdot H_2O$ in MeOH/H_2O (1:6 v/v) afforded a blue solution, which yielded light blue crystals of **2**, see Eq. (4). The identity of the crystals was confirmed by unit cell determination (see preparation of **2**, Method A, Scheme 3):

$$Cu(ClO_4)_2 \cdot 6H_2O + nH_2L + nbpy + 2nLiOH \cdot H_2O \xrightarrow{MeOH/H_2O} \underset{\mathbf{2} \cdot 2nH_2O}{[Cu_2(L'')(bpy)]_n \cdot 2nH_2O} + 2nLiClO_4 + nNH_3 \uparrow + 7nH_2O \quad (4)$$

Three features of the reaction represented by Eq. (4) deserve comments: First, the isolation of complex **2** containing the maleate(−2) ligand is in agreement with our previous conclusion that the presence of water in the reaction mixture is responsible (together with the presence of OH^- ions) for the hydrolysis of the maleamate(−1) ligand to maleate(−2). Second, the 'wrong' Cu^{II} to HL^- ($H_2L + OH^-$) reaction ratio (1:2) employed for the preparation of **2** (see Section 2), compared to that required by Eq. (4) (1:1), did not prove detrimental to the clean isolation of the product. And third, our inability to isolate complexes containing HL^- from the above reaction solution does not corroborate its quantitate hydrolysis to L''^{2-}; other more soluble species could be present in the reaction mixture, although not isolated in the solid state.

In order to prepare pure **2** in a rational manner we have used maleic acid, H_2L'' as starting material. Reaction of $Cu(ClO_4)_2 \cdot 6H_2O$ with one equivalent of H_2L'' and one equivalent of bpy in the presence of two equivalents of $LiOH \cdot H_2O$ in MeCN/H_2O (20:1 v/v) gave a blue solution which upon standing in closed vials at −4 °C afforded a turquoise microcrystalline solid which was characterized as **2** by infrared spectroscopy [Eq. (5)]. Layering of the blue reaction solution with Et_2O afforded blue crystals of **3** · 0.5*n*H_2O [Eq. (6)], whereas vapor diffusion of Et_2O onto the above blue solution afforded light blue microcrystals of **4** – not suitable for X-ray analysis – which were characterized by infrared spectroscopy as complex **7b** (vide infra). The isolation of **2**, **3** and **4** from the same reaction solution is an impressive example of the dramatic influence of the crystallization method on the product identity (Scheme 3):

$$nCu(ClO_4)_2 \cdot 6H_2O + nH_2L'' + nbpy + 2nLiOH \cdot H_2O \xrightarrow{MeCN/H_2O(-4\ ^\circ C)} \underset{\mathbf{2} \cdot 2nH_2O}{[Cu(L'')(bpy)]_n \cdot 2nH_2O} + 2nLiClO_4 + 8nH_2O \quad (5)$$

$$2nCu(ClO_4)_2 \cdot 6H_2O + nH_2L'' + 2nbpy + 2nLiOH \cdot H_2O \xrightarrow{MeCN/H_2O} \underset{\mathbf{3} \cdot 0.5nH_2O}{[Cu_2(L'')(bpy)_2(H_2O)_2]_n \cdot (ClO_4)_{2n} \cdot 0.5nH_2O} + 2nLiClO_4 + 13.5nH_2O \quad (6)$$

In a next step, we wondered whether the reaction solvent might affect the isolation of **2** prepared by the direct use of H_2L'' and we performed a reaction analogous to (5) in MeOH (Scheme 3). The resultant blue solution was layered with a mixture of Et_2O/*n*-hexane to afford blue crystals of **5** (as its MeOH solvate) according to Eq. (7). In our efforts to further investigate the parameter space of the above reaction, we employed $Cu(NO_3)_2 \cdot 2.5H_2O$ as starting material keeping all the other reaction parameters unchanged. We thought that the presence of the more coordinatively active NO_3^- in the reaction mixture might lead to new chemical and structural types. However, we isolated only compound **5**; the presence of other more soluble nitrate-containing species in the reaction solution cannot be ruled out [Eq. (8)]:

$$2Cu(ClO_4)_2 \cdot 6H_2O + 2H_2L'' + 2bpy + 4LiOH \cdot H_2O + 2MeOH \xrightarrow{MeOH} \underset{\mathbf{5} \cdot 2MeOH}{[Cu_2(L'')_2(bpy)_2] \cdot 2MeOH} + 4LiClO_4 + 20H_2O \quad (7)$$

$$2Cu(NO_3)_2 \cdot 2.5H_2O + 2H_2L'' + 2bpy + 4LiOH \cdot H_2O + 2MeOH \xrightarrow{MeOH} \underset{\mathbf{5} \cdot 2MeOH}{[Cu_2(L'')_2(bpy)_2] \cdot 2MeOH} + 4LiNO_3 + 13H_2O \quad (8)$$

Our final efforts involved the study of the influence of the externally added OH^-s on product identity, based on our previous experience with the $Cu(ClO_4)_2$? $6H_2O$/H_2L/phen reaction system, where the absence of external OH^-s leads to a novel transformation of HL^- in alcohols [5b]. Thus, reaction of $Cu(ClO_4)_2$? $6H_2O$ with two equivalents of H_2L and one equivalent of bpy in MeOH afforded a light blue solution which was layered with a mixture of Et_2O/*n*-hexane to yield a light blue polycrystalline solid (**7a**). This solid completely transformed to blue crystals upon storage of the closed layering tube for two weeks. X-ray crystallography revealed (vide infra) that the blue crystals had the formula $[Cu_2(L')_2(bpy)_2(ClO_4)_2]$ (**6**) [Eq. (9)] (Scheme 3), where L'^- is the monoanion of monomethyl maleate, $^-$OOC–CH=CH–COOMe (**IX** in Scheme 1). This $H_2L \rightarrow HL'$ ligand transformation had been established crystallographically for the first time during our previous work on phen-containing $Cu(ClO_4)_2 \cdot 6H_2O$/H_2L reaction mixtures in MeOH in the absence of OH^-s. This process is metal-ion promoted/assisted as we have shown by certain 'blind' experiments [5b]. We have performed numerous experiments in order to obtain X-ray quality crystals of the 'intermediate' compound **7a**, which were all unsuccessful. The IR spectrum of this material showed the typical bpy and ClO_4^- bands, and the ν(OH) band of MeOH at ~3440 cm^{-1}; no bands attributable to amide, carboxylate or ester groups of HL^- or/and L'^- ligands were visible. Analytical data repeatedly indicated the empirical formula $Cu(ClO_4)_2(bpy) \cdot x$MeOH (x = 2–3). As expected, the polycrystalline product **7a** could be isolated by the direct 1:1 reaction of $Cu(ClO_4)_2 \cdot 6H_2O$ and bpy in MeOH in high yields (>60%). With the goal to obtain better crystals of a compound that would be structurally analogous to **7a**, we performed the 1:1 reaction between $Cu(ClO_4)_2 \cdot 6H_2O$ and bpy in MeCN. We were lucky enough to obtain X-ray quality, light blue crystals of $[Cu(ClO_4)_2(bpy)(MeCN)_2]$ (**7b**) by layering of the light blue-turquoise reaction solution with a mixture of Et_2O/*n*-hexane [Eq. (10)]. The IR spectra of **7a** and **7b** are almost identical – except the bands due to the coordinated solvent – suggesting that the former is structurally similar to the latter:

$$2Cu(ClO_4)_2\cdot 6H_2O + 2H_2L + 2bpy + 2MeOH \xrightarrow{MeOH} \times [Cu_2(L')_2(bpy)_2](ClO_4)_2 + 2NH_4ClO_4 + 12H_2O \quad (9)$$
6

$$Cu(ClO_4)_2\cdot 6H_2O + bpy + 2MeCN \xrightarrow{MeCN} \times [Cu(ClO_4)_2(bpy)(MeCN)_2] + 6H_2O \quad (10)$$
7b

The fact that complex **7a** does not contain HL^- or any ligand derived from H_2L does not allow us to draw direct mechanistic conclusions for the Cu^{II}-assisted/promoted [5b] transformation of HL^- to L'^- in MeOH. Again coordination of the oxygen atom of the amide group in solution is likely to modify the reactivity of that group [10]. The metal centre polarizes the carbonyl group and MeOH can attack the amide carbon to generate the tetrahedral intermediate **X** (Scheme 1), which may collapse after intramolecular proton transfer to the amido group and loss of NH_3 to give the ligand L'^- that contains both an ester and a carboxylate group. In accordance with our belief that the observed ligand transformation does not take place through hydrolysis of the amide group and esterification of one of the carboxylate groups, the Cu^{II}/L''^{2-}/bpy reaction systems in MeOH or MeOH/H_2O ([7b], this work) give ternary complexes containing only the maleate (L''^{2-}, **III** in Scheme 1) ligand and not complexes of L'^-; however, a strict comparison between our system that led to **6** and the other reaction mixtures (which use H_2L'' as starting material) is not possible, because the latter contained a considerable OH^- concentration.

Alcoholysis of free amides in organic chemistry is possible but it is seldom observed, except for the imidazolide type of amide [11]. Czarnik has reported [12] that Ni^{II} can be used to accelerate the conversion of a pyridyl substituted acrylamide to the corresponding ethyl acrylate at 78 °C, i.e., the ethanolysis of a primary amide. Although no mechanistic details were reported, the study provided strong evidence that preactivation of the amide group, through O-coordination, is necessary for the conversion of the amide group to the corresponding ester in EtOH, i.e., for the ethanolysis reaction. A similar activation is possible for the observed $HL^- \rightarrow L'^-$ tranformation during the preparation. Metal ion (Zn^{II}, Cd^{II}, Hg^{II})-assisted alcoholysis reactions of *secondary* amides *in the presence of external OH^-s* have been reported [13]. The proposed mechanism [13c] involves reaction of the deprotonated-amide intermediate complex with MeOH to yield a structure involving both amide and methoxide nucleophile coordination to the metal centre; attack of the nucleophile at the amide carbonyl carbon and breakdown of the resulting intermediate initiates the amide cleavage which produces the free ester and the corresponding amine-ligated complex.

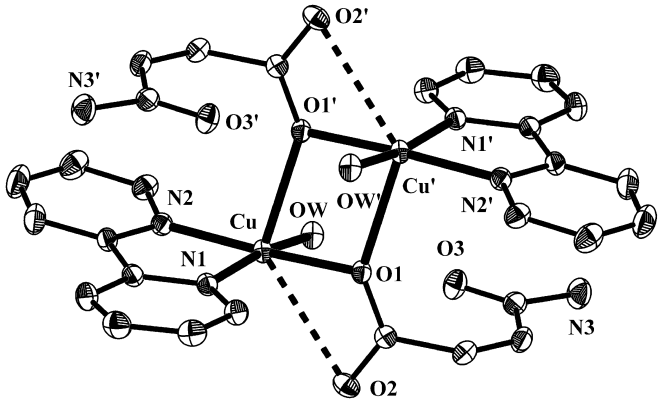


Fig. 1. Partially labeled ORTEP plot of the cation of **1** with ellipsoids drawn at the 30% probability level. H atoms have been omitted for clarity. Primed atoms are generated by symmetry (′) = 1 − *x*, 2 − *y*, −*z*.

We believe that this mechanism is not possible in our case because amide deprotonation of the coordinated HL^- is unlikely due to the absence of external OH^-s in the reaction mixture.

To investigate the possible role of bpy in the Cu^{II}-assisted/promoted $HL^- \rightarrow L'^-$ tranformation, 1:2 reactions between $Cu(ClO_4)_2\cdot 6H_2O$ and H_2L in MeOH, and in the absence of external OH^-s, were performed. No crystalline solids suitable for single-crystal X-ray crystallography could be isolated. Analytical results were not reproducable, but the IR spectra of the isolated powders all exhibit the characteristic strong $\nu(C{=}O)_{ester}$ band at 1718 cm^{-1}, which is the diagnostic spectral feature of L'^-. Thus, the bpy co-ligand does not seem to be crucial for the amide–ester transformation.

3.2. Description of structures

The molecular structures of the dinuclear cations that are present in complexes **1** and **1** · $2H_2O$ are very similar. We give below a comparative structural description for the cations of **1** (Fig. 1, Table 2) and **1** · $2H_2O$ (Fig. S1, Table 2). The structure of the cation in both complexes consists of two centrosymmetrically related Cu^{II} ions bridged by the carboxylate groups of two HL^- ligands which present the less common η^2 coordination mode. A chelating bpy and a water molecule complete five-coordination around each Cu^{II} atom. The neutral primary amide groups of the HL^- ligands remain uncoordinated. The Cu···O(2) distance of 2.847 Å (dashed line in Fig. 1) provides evidence for weak interaction, as has sometimes [14] (but not always [15]) observed for monoatomic bridging carboxylate groups. The coordination geometry about each metal ion in both complexes is well described as square pyramidal with the bridging carboxylate oxygen atoms occupying the apical positions for the two Cu^{II} centres; for example, in **1**, atoms O(1′) and O(1) occupy the apical positions for Cu and Cu′, respectively. Analysis of the shape-determining angles using the approach of Reedijk and coworkers [16] yields trigonality index, τ, values of 0.09 and 0.26 for the Cu^{II} ions in **1** and **1** · $2H_2O$, respectively (τ = 0 and 1 for perfect *sp* and *tbp* geometries, respectively). As expected, the axial bonds are the longest.

In the crystal lattice of **1**, the cations are hydrogen bonded and form chains extending parallel to the *a*-axis [Ow···O(2) (−*x*, 2 − *y*, −*z*)], which are further associated through ClO_4^- ions to form a 2D network parallel to the (0 1 1) plane (Fig. 2, Table 5).

Table 2
Selected interatomic distances (Å) and angles (°) for complexes **1** and **1** · $2H_2O$.

1		**1** · $2H_2O$	
Distances			
Cu–O(1)	1.958(2)	Cu(1)–O(1)	1.963(3)
Cu–N(2)	1.974(2)	Cu(1)–N(2)	1.973(4)
Cu–OW	1.975(2)	Cu(1)–OW1	1.982(4)
Cu–N(1)	1.987(2)	Cu(1)–N(1)	1.990(4)
Cu–O(1′)	2.365(2)	Cu(1)–O(1′)	2.332(3)
Cu···Cu′	3.347(2)	Cu(1)···Cu(1′)	3.345(2)
Angles			
O(1)–Cu–N(2)	175.20(7)	O(1)–Cu(1)–N(2)	177.2(2)
O(1)–Cu–OW	86.58(9)	O(1)–Cu(1)–OW1	89.2(2)
N(2)–Cu–OW	96.4(1)	N(2)–Cu(1)–OW1	92.6(2)
O(1)–Cu–N(1)	95.77(8)	O(1)–Cu(1)–N(1)	96.6(2)
N(2)–Cu–N(1)	81.96(9)	N(2)–Cu(1)–N(1)	82.4(2)
OW–Cu–N(1)	169.85(8)	OW1–Cu(1)–N(1)	161.4(2)
O(1)–Cu–O(1′)	78.92(7)	O(1)–Cu(1)–O(1′)	78.0(1)
N(2)–Cu–O(1′)	97.34(7)	N(2)–Cu(1)–O(1′)	99.6(2)
OW–Cu–O(1′)	88.55(8)	OW1–Cu(1)–O(1′)	96.1(2)
N(1)–Cu–O(1′)	101.59(8)	N(1)–Cu(1)–O(1′)	102.4(2)

Symmetry transformations used to generate equivalent atoms: in **1**, (′) = 1 − *x*, 2 − *y*, −*z*; in **1** · $2H_2O$, (′) = 1 − *x*, −*y*, 2 − *z*.

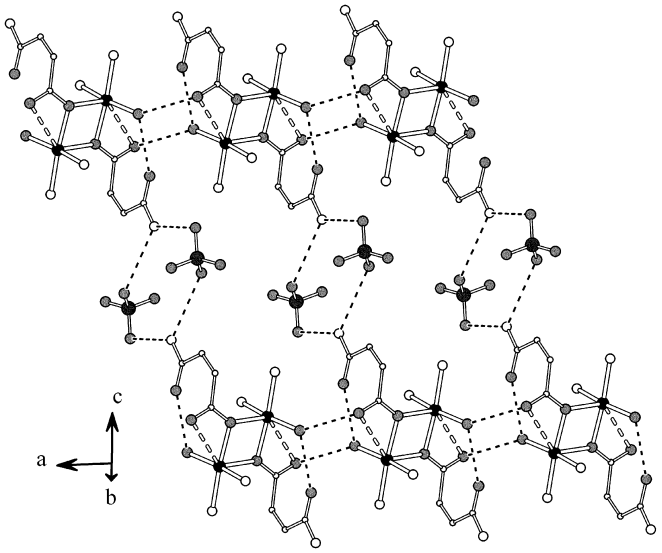


Fig. 2. A part of the 2D structure of **1** due to H-bonding interactions. Colour code: Cu, black; O, medium grey; N, large white; C, small white; Cl, dark grey. H bonds are presented by dashed lines. Only the N atoms of the bpy ligands are shown.

In the crystal lattice of **1** · $2H_2O$, the cations are hydrogen bonded and form chains extending parallel to the *b*-axis [N(3)···O(3) $(1-x, 1-y, 2-z)$], which are further associated to form a 2D network parallel to the (001) plane (Fig. 3, Table 5).

The crystal structure of **3** · $0.5nH_2O$ consists of 1D polymeric chains based on dinuclear $[Cu_2(L'')(bpy)_2(H_2O)_2]^{2+}$ cations (L''^{2-} = the dianion of maleic acid) (Fig. 4, Table 3), perchlorate counterions and H_2O solvate molecules; the latter two will not be further discussed. The structure of the dinuclear repeating unit in **3** consists of two Cu^{II} atoms bridged by two *syn,syn* $\eta^1:\eta^1:\mu_2$ carboxylate groups belonging to two L''^{2-} anions. Each L''^{2-} anion bridges two neighboring $[Cu_2^{II}]$ units through its two carboxylato groups thus promoting the formation of a helical chain along the *b*-axis. A chelating bpy molecule and an aquo ligand complete five-coordination around each Cu^{II} atom. The coordination geometry about each metal ion is well described as square pyramidal with a coordinated H_2O molecule occupying the apical position. Analysis of the shape-determining angles using the approach of Reedijk and co-workers [16] yields trigonality index, τ, values of 0.21 and 0.11 for Cu(1) and Cu(2), respectively. As expected, the axial bonds are the longest. There is a significant intramolecular stacking interaction

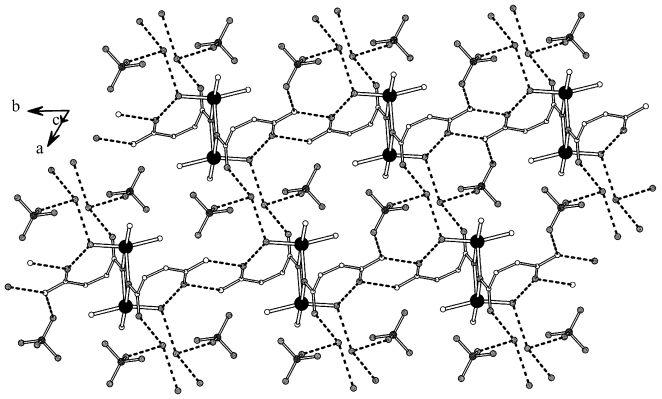


Fig. 3. A part of the 2D structure of **1** · $2H_2O$ due to H-bonding interactions. Colour code as in Fig. 2. H bonds are presented by dashed lines. Only the N atoms of the bpy ligands are shown.

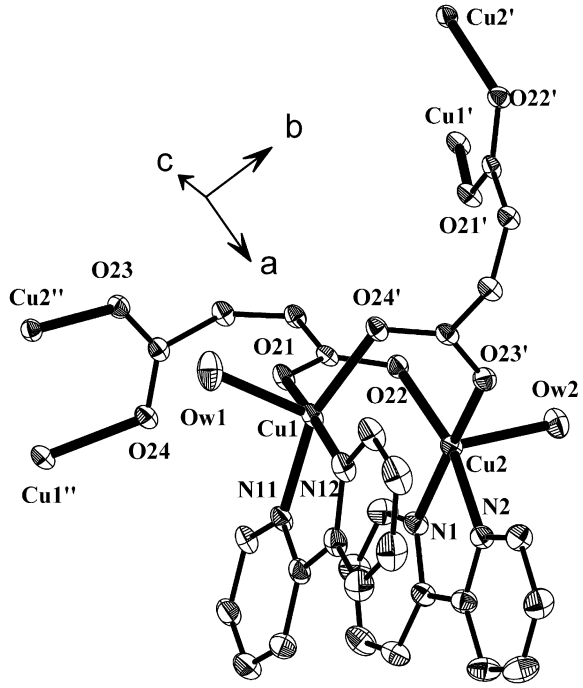


Fig. 4. Partially labeled ORTEP plot of a very small fragment of the 1D structure of **3** · $0.5nH_2O$ with ellipsoids drawn at the 30% probability level. H atoms have been omitted for clarity. Primed atoms are generated by symmetry: (′) = $0.5-x, 0.5+y, 0.5-z$; (″) = $0.5-x, -0.5+y, 0.5-z$.

Table 3
Selected interatomic distances (Å) and angles (°) for **3** · $0.5nH_2O$.

Distances			
Cu(1)–O(21)	1.946(3)	Cu(2)–O(23′)	1.961(3)
Cu(1)–O(24′)	1.989(3)	Cu(2)–O(22)	1.965(3)
Cu(1)–N(12)	1.989(4)	Cu(2)–N(2)	1.997(3)
Cu(1)–N(11)	1.993(4)	Cu(2)–N(1)	2.001(4)
Cu(1)–Ow(1)	2.176(5)	Cu(2)–Ow(2)	2.235(4)
Cu(1)···Cu(2)	3.090(1)	Cu(2)···Cu(1′)	5.489(1)
Cu(1)···Cu(1″)	6.103(1)	Cu(2)···Cu(2′)	7.806(2)
Angles			
O(21)–Cu(1)–O(24′)	93.7(1)	O(23′)–Cu(2)–O(22)	93.0(1)
O(21)–Cu(1)–N(12)	172.7(2)	O(23′)–Cu(2)–N(2)	92.8(1)
O(24′)–Cu(1)–N(12)	91.1(1)	O(22)–Cu(2)–N(2)	166.3(1)
O(21)–Cu(1)–N(11)	92.0(1)	O(23′)–Cu(2)–N(1)	173.1(1)
O(24′)–Cu(1)–N(11)	160.0(2)	O(22)–Cu(2)–N(1)	92.3(1)
N(12)–Cu(1)–N(11)	81.6(2)	N(2)–Cu(2)–N(1)	81.2(2)
O(21)–Cu(1)–Ow(1)	90.5(2)	O(23′)–Cu(2)–Ow(2)	90.4(1)
O(24′)–Cu(1)–Ow(1)	96.9(2)	O(22)–Cu(2)–Ow(2)	91.9(1)
N(12)–Cu(1)–Ow(1)	94.3(2)	N(2)–Cu(2)–Ow(2)	100.5(2)
N(11)–Cu(1)–Ow(1)	102.3(2)	N(1)–Cu(2)–Ow(2)	93.9(2)

Symmetry transformations used to generate equivalent atoms: (′) = $0.5-x, 0.5+y,$

between the aromatic ligands; the mean distance and the angle between the two bpy planes in *syn* positions are 3.83 Å and 5.2°, respectively. We strongly believe that the structure of the dinuclear subunit is maintained by these intramolecular, attractive interactions [4,17]. For a detailed discussion of such structural phenomena in complexes containing the $\{M_2^{II,II}(\eta^1:\eta^1:\mu_2\text{-}O_2CR)_2\}^{2+}$ core, see Ref. [17]. In the crystal lattice of **3**, there are intra-chain hydrogen bonding interactions, as well as intermolecular interactions which lead to the connection of the chains through the solvate water and the perchlorate oxygen atoms (Table 5).

The structure of the dinuclear molecule that is present in complex **5** · 2MeOH consists of two centrosymmetrically related Cu^{II} ions bridged by two carboxylato groups from two maleate(−2)

ligands (Fig. 5, Table 4). The bridging carboxylate group adopts the rather rare η^2 coordination mode. The second carboxylate group of each L''^{2-} ligand is monodentately coordinated to Cu^{II} giving rise to a remarkable seven-membered $CuO_{carboxylate}C–C=C–CO_{carboxylate}$ chelating ring. A chelating bpy completes five-coordination around each metal ion, creating an almost perfect square pyramidal geometry ($\tau = 0.04$). The apical position of the square pyramid is occupied by a bridging carboxylate oxygen atom; thus, O3 and O3′ occupy the apical positions of Cu1′ and Cu1, respectively. In the crystal lattice of **5**, each dinuclear complex is hydrogen bonded to two adjacent methanol solvate molecules (Table 5). Complex **5** bears striking similarity to the various solvates of $[Cu_2(L'')_2(phen)_2]$ [18].

The structure of the dinuclear complex **6** (Fig. 6, Table 4) consists of centrosymmetrically related Cu^{II} ions bridged by the carboxylato group of two L′ anions, where L'^- is the monomethyl maleate(−1) ligand (**IX** in Scheme 1) formed by the Cu^{II}-assisted/promoted transformation of HL^-. The L'^- ion behaves as a carboxylate-type ligand, i.e., the ester group remains uncoordinated in accordance with the known weak coordinating capacity of the ester function. In the molecule of **6**, the carboxylate group of the L'^- ligands is in the familiar *syn,syn* $\eta^1:\eta^1:\mu_2$ coordination mode. A chelating bpy molecule and one coordinated ClO_4^- complete five-coordination at each Cu^{II} centre. The metal coordination geometry is well described as square pyramidal with the terminal monodentate ClO_4^- occupying the apical position; the parameter τ is 0.14. Perchlorate coordination is rare in copper(II) chemistry; however, there exist examples of structurally characterized copper(II) perchlorato complexes [17,19]. There is a significant intramolecular stacking interaction between the aromatic ligands; the mean distance and the angle between the two bpy planes in *syn* positions are 3.61 Å and 2.1°, respectively. As in the dinuclear subunits of **3** · 0.5*n*H_2O, we do believe that the structure of the dinuclear molecule is maintained by these intramolecular, attractive aromatic stacking interactions [17]. Complex **6** joins a small family of structurally characterized compounds possessing the $\{Cu_2(\eta^1:\eta^1:$

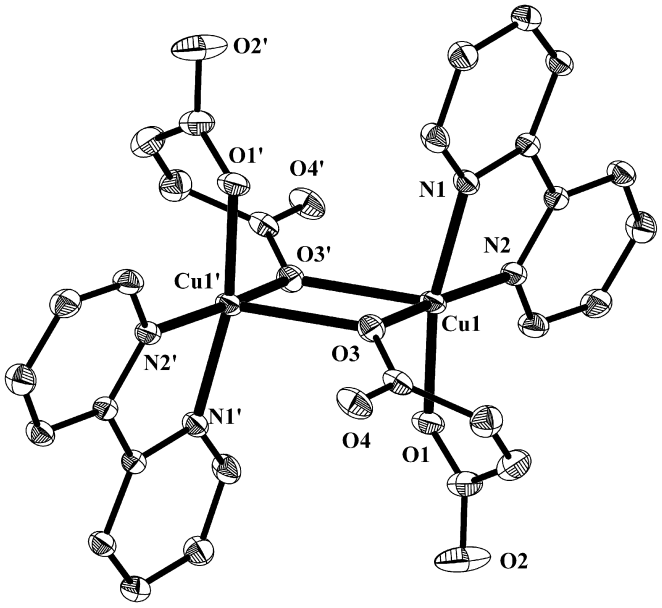


Fig. 5. Partially labeled ORTEP plot of the dinuclear molecule present in **5** · 2MeOH with ellipsoids drawn at the 30% probability level. H atoms have been omitted for clarity. Primed atoms are generated by symmetry (′) = 0.5 − *x*, 0.5 − *y*, 1 − *z*.

Table 4
Selected interatomic distances (Å) and angles (°) for **5** · 2MeOH and **6**.

5 · 2MeOH		**6**	
Distances			
Cu(1)–O(1)	1.932(2)	Cu(1)–O(2′)	1.957(3)
Cu(1)–O(3)	1.9680(19)	Cu(1)–O(1)	1.958(3)
Cu(1)–N(2)	1.998(2)	Cu(1)–N(2)	1.976(3)
Cu(1)–N(1)	2.005(2)	Cu(1)–N(1)	1.984(4)
Cu(1)–O(3′)	2.281(2)	Cu(1)–O(11)	2.293(4)
Cu(1)···Cu(1′)	3.362(2)	Cu(1)···Cu(1′)	3.089(5)
Angles			
O(1)–Cu(1)–O(3)	91.42(9)	O(2′)–Cu(1)–O(1)	89.4(1)
O(1)–Cu(1)–N(2)	91.6(1)	O(2′)–Cu(1)–N(2)	93.4(2)
O(3)–Cu(1)–N(2)	169.83(8)	O(1)–Cu(1)–N(2)	175.1(1)
O(1)–Cu(1)–N(1)	167.15(9)	O(2′)–Cu(1)–N(1)	166.7(1)
O(3)–Cu(1)–N(1)	94.18(9)	O(1)–Cu(1)–N(1)	94.6(2)
N(2)–Cu(1)–N(1)	81.02(9)	N(2)–Cu(1)–N(1)	81.8(2)
O(1)–Cu(1)–O(3′)	93.41(9)	O(2′)–Cu(1)–O(11)	91.0(1)
O(3)–Cu(1)–O(3′)	75.7(1)	O(1)–Cu(1)–O(11)	89.9(1)
N(2)–Cu(1)–O(3′)	113.85(9)	N(2)–Cu(1)–O(11)	94.1(2)
N(1)–Cu(1)–O(3′)	99.17(9)	N(1)–Cu(1)–O(11)	101.7(2)

Symmetry transformations used to generate equivalent atoms: (′) = 0.5 − *x*, 0.5 − *y*, 1 − *z* (for **5** · 2MeOH) and (′) = 1 − *x*, *y*, 0.5 − *z* (for **6**).

Table 5
Hydrogen bonding interactions in **1**, **1** · 2H_2O, **3** · 0.5*n*H_2O and **5** · 2MeOH.

Interaction	D···A (Å)	H···A (Å)	D–H···A (°)	Symmetry operation
1				
Ow–HwA···O(2)	2.684	1.980	162.2	−*x*, 2 − *y*, −*z*
N(3)–HN(3)A···O(4)	3.199	2.466	157.3	−*x*, 2 − *y*, −*z*
N(3)–HN(3)B···O(5)	3.029	2.274	160.8	*x*, 1 + *y*, −1 − *z*
1 · *2H₂O*				
N(3)–HN(3)A···O(3)	2.998	2.177	176.1	1 − *x*, 1 − *y*, 2 − *z*
N(3)–HN(3)B···O(6)	3.272	2.531	165.6	1 − *x*, 1 − *y*, 2 − *z*
Ow(1)–Hw(1)A···Ow(2)	2.677	1.955	170.8	*x*, *y*, *z*
Ow(1)–Hw(1)B···O(3)	2.686	2.015	147.4	*x*, *y*, *z*
Ow(2)–Hw(2)A···O(2)	2.774	1.806	165.8	−*x*, 1 − *y*, 2 − *z*
Ow(2)–Hw(2)B···O(7)	2.739	2.004	149.9	*x*, *y*, *z*
3 · 0.5*n*H_2O				
Ow(1)–Hw(1)B···O(22)	2.822	2.251	147.7	0.5 − *x*, −0.5 + *y*, 0.5 − *z*
Ow(1)–Hw(1)A···Ow(3)	2.492	1.763	171.9	*x*, *y*, *z*
Ow(2)···O(47)	2.763			1.5 − *x*, 0.5 + *y*, 0.5 − *z*
Ow(2)···O(46)	2.844			−0.5 + *x*, 0.5 − *y*, −0.5 + *z*
Ow(3)···O(41)	2.872			−0.5 + *x*, 0.5 − *y*, 0.5 + *z*
5 · *2MeOH*				
Om(1)–Hom(1)···O(2)	2.734	1.622	172.8	0.5 − *x*, 0.5 − *y*, 1 − *z*

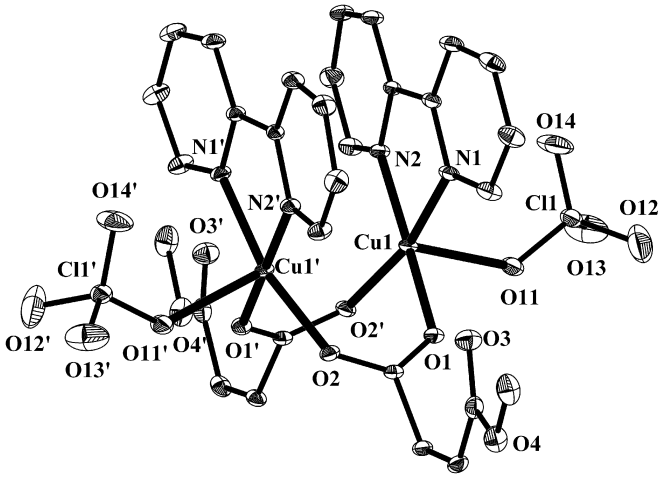


Fig. 6. Partially labeled ORTEP plot of **6** with ellipsoids drawn at the 30% probability level. H atoms have been omitted for clarity. Primed atoms are generated by symmetry (′) = 1 − *x*, *y*, 0.5 − *z*.

μ_2-$O_2CR)_2\}^{2+}$ core (R = H, CH_3, C_2H_5, $CH_2CH_2C_6H_5$) and stacked aromatic ligands in *syn* positions [4,17,20].

The structure of **7b** consists of mononuclear molecules [Cu(bpy)$(ClO_4)_2$(MeCN)$_2$] (Fig. 7, Table S1). The coordination sphere of the Cu^{II} ion consists of four N atoms belonging to one bpy and two coordinated *cis* MeCN molecules and two O atoms from two *trans* perchlorate ions. The coordination geometry can be described as distorted octahedral with the perchlorate oxygen atoms in the apical positions at Cu(1)–O(1) = 2.515(1) and Cu(1)–O(4) = 2.548(7) Å. The Cu–N bond distances in the equatorial plane are Cu(1)–N(1) = 1.971(5) and Cu(1)–N(2) = 1.988(6) Å. There is a mirror plane of symmetry passing through Cu(1), Cl(1), Cl(2), O(1), O(2), O(4) and O(6) which is perpendicular to the equatorial plane of the distorted octahedron.

Compounds **1** and **1** · $2H_2O$ join a small family of structurally characterized maleamate complexes. In all the previously reported complexes, the aromatic co-ligands were 1,10-phenanthroline (phen) [5] or 2,6-bis(pyrazol-1-yl)pyridine (bppy). It should be mentioned at this point that few metal complexes of *N*-substituted

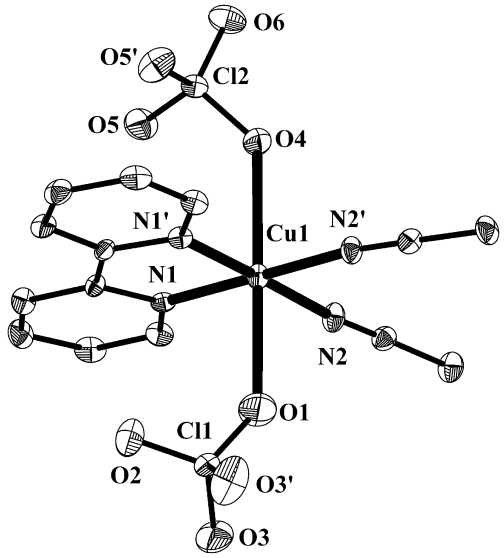


Fig. 7. Partially labeled ORTEP plot of **7b** with ellipsoids drawn at the 30% probability level. H atoms have been omitted for clarity. Primed atoms are generated by symmetry (′) = *x*, 0.5 − *y*, *z*.

maleamate ligands have been structurally characterized [21]. These are $[Bu^n_3Sn^{IV}(L1)]_n$ [21a], where $L1^-$ is the *N*-(1-naphthyl)maleamate(−1) ligand, and $[Mo^{II}(\eta^3\text{-}C_3H_4\text{-Me-2})L2)(CO)_2$(phen)] [21b], where $L2^-$ is the *N*-(*p*-tolyl)maleamate(−1) ligand. $L1^-$ behaves as an O(carboxylate)O(amide) bidentate bridging ligand leading to polymeric chains, while $L2^-$ acts as an O(carboxylate) monodentate ligand.

Complex **6** is the third structurally and *published* complex of any metal containing the anionic L'^- ligand (**IX** in Scheme 1). The two previously reported complexes are $[Cu_2(L')_2(ClO_4)$(phen)$_2$(MeOH)](ClO_4) and $[Cu_2(L')_2$(bppy)$_2](ClO_4)_2$ [5b]. All the three compounds have been prepared using maleamic acid (H_2L) as one of the starting materials and MeOH as solvent. However, search in the CCDC database reveals that Winpenny and co-workers have deposited [22] the structure of $[Co^{II,II,II}_3$(cpyol)$_4(L'_2)_2$(MeOH)$_6$] · 2MeOH, where cpyol$^-$ is the 6-chlropyridine-2-olate(−1) ligand; the monomethyl maleate(−1) ligand L'^- exhibits a *syn*,*syn* η^1:η^1:μ_2 carboxylate-type coordination in the four compounds. It is worth mentioning that the polymeric compound $[Sr_2(L_A)_3(H_2O)_4]_n(L_A)_n$, where L_A^- is the monomethyl fumarate(−1) (**XI** in Scheme 1), i.e., the isomer of L'^-, has recently been structurally characterized [23]. The complex was prepared from the reaction of $SrCO_3$ and methyl fumarate (HL_A) in H_2O; the L_A^- ions exhibit no less than three different ligation modes (μ_2, μ_3, μ_4) in this compound.

Complexes **3** · 0.5*n*H_2O and **5** · $2H_2O$ are the third and fourth members of a small group that has Cu^{II}/L''^{2-}/bpy complexes as members. The previously characterized members are the mononuclear complex [Cu(L″)(bpy)(H_2O)] · $2H_2O$ [24] and the coordination polymer [Cu(L″)(bpy)]$_n$ · 2*n*H_2O [7]. The latter has also been obtained in the present work (complex **2** · 2*n*H_2O) using either H_2L (Sections 2.2.1 and 2.2.4 – Method A) or H_2L' (Section 2.2.4 – Method B) as starting materials.

3.3. IR spectra

Dried samples of complexes **1**, **1** · $2H_2O$, **3**, **5**, **6**, **7a** and **7b** were characterized by IR spectroscopy. Complexes **1**, **1** · $2H_2O$ and **3** exhibit a very broad band covering the whole 3450–3150 cm^{-1} range, assignable to ν(OH) vibrations of lattice or/and coordinated H_2O [25]. The broadness and relatively low frequency of this band are both indicative of H-bonding.

The ν(C⋯C) and ν(C⋯N) bands of free bpy in the 1600–1400 cm^{-1} region are sensitive to chelation [26]. The 1578 and 1556 cm^{-1} bands of free bpy shift to higher frequencies in the complexes. Other characteristic vibrations of free bpy are the C–H out-of-plane deformations which appear as a strong band at 756 cm^{-1} and a weak satellite at 739 cm^{-1}; upon chelation two strong bands appear at ~770 and ~730 cm^{-1} [26].

In the spectra of **1**, **1** · $2H_2O$ and **3**, the strong band at 1080–1100 cm^{-1} and the medium-intensity band at ~625 cm^{-1} are attributed to the $\nu_3(F_2)$ [ν_d(ClO)] and $\nu_4(F_2)$ [δ_d(OClO)] modes, respectively, of the uncoordinated T_d ionic perchlorates [27]. The large number of ClO_4^- bands at around 1100 and 630 cm^{-1} in the spectra of **6**, **7a** and **7b** are consistent with the presence of coordinated ClO_4^- groups in these compounds [27].

The strong band at 1719 cm^{-1} in the spectrum of **6** is assigned to the carbonyl stretching vibration of the ester group [28].

The IR spectra of **1** and **1** · $2H_2O$ exhibit the typical bands of the primary amide and carboxylate groups [28]. Tentative assignments of few diagnostic bands attributed to these groups are given in Table 6. The assignments have been given in comparison with the data obtained for sodium maleamate, Na(HL), assumed to contain a "free" carboxylate group [29], oxamato(−1) [**XII** in Scheme 1] [30], malonamato(−1) [**V** in Scheme 1; *n* = 1] [31] and succinamato(−1) [**V** in Scheme 1; *n* = 2] [4] metal complexes. As a general remark, we must emphasize that some of the vibrational modes

Table 6
Diagnostic amide and carboxylate IR bands (cm^{-1}), and their tentative assignments for sodium maleamate[a] and complexes **1** and **1** · $2H_2O$.

Vibration	Na(HL)	**1**	**1** · $2H_2O$
$\nu_{as}(NH_2)$	3385sb	3354sb[c]	3394sb[c]
$\nu_s(NH_2)$	3160mb	3180mb[c]	3197sb[c]
$\nu(C{=}O)_{amide}$	1677s	1676s	1679s
$\delta(NH_2)$	1636m[b]	1640s[b]	1641m[b]
$\nu(C{=}C)$	1636m[b]	1640s[b]	1641m[b]
$\nu_{as}(CO_2)$[d]	1576s	1603vs	1602vs
$\nu(CN)_{amide}$	1449s	1447vs	1445vs
$\nu_s(CO_2)$	1407m	1382m	1374m

Abbreviations: b, broad; m, medium; s, strong; v, very.
[a] Prepared from the 1:1 reaction between H_2L and NaOH in EtOH, followed by precipitation with Et_2O.
[b] Overlapping bands.
[c] These bands are components of the ν(OH) manifold.
[d] These vibrations may include an aromatic stretching character.

Table 7
The carboxylate stretching IR bands (cm^{-1}) for complexes **3**, **5** and **6**.

Compound[a]	$\nu_{as}(CO_2)$	$\nu_s(CO_2)$
3	1561vs	1416m
5	1647vs[b], 1590vsb[c]	1423m, 1402vs
6	1568s[c]	1432s

[a] Solvate molecules have not been included.
[b] This vibration has also a ν(C=C) character.
[c] This vibration may include an aromatic stretching character.

shown in Table 6 are strongly coupled and thus the proposed assignments must be regarded as approximate descriptions of the vibrations [28]. The typical bands of the neutral amide group, i.e., $\nu_{as}(NH_2)$, $\nu_s(NH_2)$, ν(C=O) and ν(CN), in the spectra of **1** and **1** · $2H_2O$ are situated at the same wavenumber to those in the spectrum of Na(HL), confirming the crystallographically established non-participation of the amide group in coordination. The difference Δ, where $\Delta = \nu_{as}(CO_2) - \nu_s(CO_2)$, for **1** (221 cm^{-1}) and **1** · $2H_2O$ (228 cm^{-1}) is more than that of Na(HL), as expected for the crystallographically confirmed, essentially monoatomic bridging mode of the carboxylate ligation [29,32].

The carboxylate stretching vibrations for **3**, **5** and **6** are listed in Table 7. The difference Δ for **3** (145 cm^{-1}) is less than that of the "free" maleate(−2) ion (200 cm^{-1} [7a]), as expected for the bidentate bridging mode of the carboxylate ligation [29]. Owing to the presence of two different types (monodentate, monoatomic bridging) of carboxylate ligation in **5**, two $\nu_{as}(CO_2)$ and two $\nu_s(CO_2)$ appear in its spectrum. The 1647, 1402 cm^{-1} pair (Δ = 245 cm^{-1}) are assigned to the monoatomically bridging carboxylate groups, while the 1590, 1402 cm^{-1} pair (Δ = 188 cm^{-1}) to the monodentate carboxylate groups.

4. Concluding comments and perspectives

The initial use of the HL^-/bpy "ligand blend" in reactions with $Cu(ClO_4)_2 \cdot 6H_2O$ has yielded the new complexes **1**, **1** · $2H_2O$ and **6**, and the known [7] coordination polymer **2** · $2nH_2O$. The HL^- ion has been tranfrormed to L''^{2-} and L'^- in **2** · $2nH_2O$ and **6**, respectively, via Cu^{II}-assisted hydrolysis (**2** · $2nH_2O$) and methanolysis (**6**) of the primary amide group. The reaction that yields **6** takes place through the formation of **7a**, whose structure has been assigned on the basis of its spectral similarity with the structurally characterized complex **7b**. The $Cu(ClO_4)_2 \cdot 6H_2O/L''^{2-}$/bpy reaction system has also led to the new complexes **3** · $0.5nH_2O$ and **5** · 2MeOH. The dinuclear complexes **1**, **1** · $2H_2O$, **5** · 2MeOH and **6** have bridging carboxylate units that rarely appear in $Cu_2^{II,II}$ chemistry, while **3** · $0.5nH_2O$ is an interesting 1D polymer composed of dinuclear subunits.

The chemistry of the $Cu(ClO_4)_2 \cdot 6H_2O/HL^-$/bpy system, as detailed in the above discussion for **1**, **1** · $2H_2O$, **6**, **7a** and **7b**, shows similarities and differences to that of the corresponding $Cu(ClO_4)_2 \cdot 6H_2O/HL^-$/phen system [5].The HL^- to L'^- transformation occurs for both systems in MeOH in the absence of external OH^-s. Complexes $[Cu_2(L')_2(bpy)_2(ClO_4)_2]$ (**6**) and $[Cu_2(L')_2(phen)_2(ClO_4)(MeOH)](ClO_4)$ have similar structural motifs based on the $\eta^1{:}\eta^1{:}\mu_2$ mode of the carboxylate ligation and on intramolecular stacking interactions between the *syn* aromatic ligands. However, the intermediates to this transformation have different structures; complex $[Cu(ClO_4)_2(bpy)(MeOH)_2]$ is mononuclear, whereas compound $[Cu(ClO_4)(phen)(MeOH)_2]_n(ClO_4)_n$ is an 1D coordination polymer. Both $Cu(ClO_4)_2 \cdot 6H_2O/HL^-$/bpy and $Cu(ClO_4)_2 \cdot 6H_2O/HL^-$/phen systems favour the formation of dinuclear cationic complexes. However, in the phen-containing cation $[Cu_2(HL)_3(phen)_2]^+$, bridging of the two Cu^{II} centres is achieved through three HL^- ligands, whereas complexes **1** and **1** · $2H_2O$ have only two HL^- bridges with one H_2O ligand completing five-coordination at each metal centre. A final difference between the two reaction systems is that the HL^- to L''^{2-} transformation established in **2** · $2nH_2O$ was not observed in the phen-containing [5] reaction mixtures.

The reactivity and structural chemistry of the $Cu(ClO_4)_2 \cdot 6H_2O/HL^-$/bpy system is different to that of the $Cu(ClO_4)_2 \cdot 6H_2O/Hsucm^-$ (n = 2 in **V** of Scheme 1)/bpy system [4,33]. The dinuclear complex $[Cu_2(Hsucm)_3(bpy)_2](ClO_4)$ [33], which is structurally similar with complex $[Cu_2(HL)_3(bpy)_2](ClO_4)$ [5b], is the main product from the $Hsucm^-$-containing reaction mixture. No esterification of the primary amide group of $Hsucm^-$ was observed during our synthetic investigations in the $Cu(ClO_4)_2 \cdot 6H_2O/Hsucm^-$/bpy reaction system [4,33]. We attribute this difference to the ability of HL^- to form a seven-membered $CuO_{carboxylate}C{-}C{=}C{-}CO_{amide}$ chelating ring (see left part of Scheme 2) in solution; such a ring, whose formation is not possible in $Hsucm^-$ (due to free rotation), activates strongly the amide carbon atom towards nucleophilic attack in the case of HL^-.

Finally, the structural chemistry of the $Cu(ClO_4)_2 \cdot 6H_2O/HL^-$/bpy system, as detailed in the above discussion for **1** and **1** · $2H_2O$, does not show similarities to the corresponding L''^{2-} system (see Refs. [7,24], and complexes **3** and **5** of this work), due to the different nature (charge, donor groups) of HL^- and the maleate(−2) [L''^{2-}] ligand.

Complexes of other 3d- or 4f-metal perchlorates with the HL^-/bpy ligand combination are not known to date, and it is currently not evident whether the chemical identity and structure of such compounds, and the $HL^- \rightarrow L'^-$, L''^{2-} transformations are dependent on the particular nature of the metal ion. It is also clear that the metal ion/HL^- chemistry warrants expansion to monodentate and tridentate aromatic *N*-heterocycles. Of particular interest would be the synthetic investigation of the metal ion/monoamide of acetylenedicarboxylate (**VIII** in Scheme 1)/aromatic *N*-donors. We currently study these matters. Experimental work at the time of writing also reveals that replacement of ClO_4^- with NO_3^- in the Cu^{II}/HL^-/bpy system has a dramatic influence on the identity of the products and it is an excellent source of polynuclear and polymeric complexes with interesting structures and magnetic properties; our results will be reported soon.

Acknowledgement

S.P.P. thanks the Research Committee of the University of Patras for support (K. Caratheodory Program No. 03016).

Appendix A. Supplementary data

CCDC 713991, 713992, 713993, 713994, 713995 and 713996 contain the supplementary crystallographic data for **1**, **1** · $2H_2O$,

3 · 0.5$n$$H_2O$, **5** · 2MeOH, **6** and **7b**, respectively. These data can be obtained free of charge via http://www.ccdc.cam.ac.uk/conts/retrieving.html, or from the Cambridge Crystallographic Data Centre, 12 Union Road, Cambridge CB2 1EZ, UK; fax: (+44) 1223-336-033; or e-mail: deposit@ccdc.cam.ac.uk. Supplementary data associated with this article can be found, in the online version, at doi:10.1016/j.poly.2009.01.023.

References

[1] (a) For reviews see: D.-K. Bucar, G.S. Papaefstathiou, T.D. Hamilton, Q.L. Chu, I.G. Georgiev, L.R. McGillivray, Eur. J. Inorg. Chem. (2007) 4559;
(b) A.Y. Robin, K.M. Fromm, Coord. Chem. Rev. 250 (2006) 2127;
(c) S. Kitaqawa, S. Noro, J.A. McClevert, T.J. Meyer (Eds.), Comprehensive Coordination Chemistry II, vol. 7, Elsevier, Amsterdam, 2004, pp. 231–261;
(d) C. Janiak, Dalton Trans. (2003) 2781.

[2] (a) For reviews see: A.J. Tasiopoulos, S.P. Perlepes, Dalton Trans. (2008) 5537;
(b) G. Christou, Polyhedron 24 (2005) 1809;
(c) E.K. Brechin, Chem. Commun. (2005) 5141;
(d) R.E.P. Winpenny, in: J.A. McCleverty, T.J. Meyer (Eds.), Comprehensive Coordination Chemistry II, vol. 7, Elsevier, Amsterdam, 2004, pp. 125–175.

[3] (a) For example see: D. Ghoshal, T.K. Maji, G. Mostafa, S. Sain, T.-H. Lu, J. Ribas, E. Zangrando, N.R. Chaudhuri, Dalton Trans. (2004) 1687;
(b) Y.Y. Wang, X. Wang, Q.Z. Shi, Y.C. Gao, Transition Met. Chem. 27 (2002) 481;
(c) M. Geraghty, M. McCann, M.T. Casey, M. Curran, M. Devereux, V. McKee, J. McCrea, Inorg. Chim. Acta 277 (1998) 257;
(d) M. McCann, M.T. Casey, M. Devereux, M. Curran, V. McKee, Polyhedron 16 (1997) 2741.

[4] I. Chadjistamatis, A. Terzis, C.P. Raptopoulou, S.P. Perlepes, Inorg. Chem. Commun. 6 (2003) 1365.

[5] (a) K.N. Lazarou, S.P. Perlepes, V. Psycharis, C.P. Raptopoulou, Polyhedron 27 (2008) 2131;
(b) K.N. Lazarou, I. Chadjistamatis, V. Psycharis, S.P. Perlepes, C.P. Raptopoulou, Inorg. Chem. Commun. 10 (2007) 318.

[6] Rigaku/MSC, CRYSTALCLEAR, Rigauk/MSC Inc., The Woodlands, Texas, USA, 2005.

[7] (a) C. Zhang, J. Sun, X. Kong, C. Zhao, J. Coord. Chem. 49 (2000) 181;
(b) K.-L. Zhang, Y. Xu, J.-G. Lin, X.-Z. You, J. Mol. Struct. 703 (2004) 63.

[8] G.M. Sheldrick, SHELXS-97, Structure Solving Program, University of Göttingen, Germany, 1997.

[9] G.M. Sheldrick, SHELXL-97, Crystal Structure Refinement Program, University of Göttingen, Germany, 1997.

[10] E.C. Constable, Metals and Ligand Reactivity, VCH, Weinheim, 1996. p. 46.

[11] J. March, Advanced Organic Chemistry, 4th Ed., Wiley, New York, 1992. p. 398.

[12] A.W. Czarnik, Tetrahedron Lett. 25 (1984) 4875.

[13] (a) L.M. Berreau, M.M. Makowska-Crzyska, A.M. Arif, Inorg. Chem. 39 (2000) 4390;
(b) M.M. Makowska-Crzyska, K. Doyle, R.A. Allred, A.M. Arif, D.C. Bedout, L.M. Berreau, Eur. J. Inorg. Chem. (2005) 822;
(c) E. Szajna, M.M. Makowska-Crzyska, C.C. Wasden, A.M. Arif, L.M. Berreau, Inorg. Chem. 44 (2005) 7595.

[14] G. Christou, S.P. Perlepes, E. Libby, K. Folting, J.C. Huffman, R.J. Webb, D.N. Hendrickson, Inorg. Chem. 29 (1990) 3657.

[15] J.-P. Costes, F. Dahan, J.-P. Laurent, Inorg. Chem. 24 (1985) 1018.

[16] A.W. Addison, T.N. Rao, J. Reedijk, J. Rijn, G.C. Verschoor, J. Chem. Soc., Dalton Trans. (1984) 1349.

[17] S.P. Perlepes, J.C. Huffman, G. Christou, Polyhedron 11 (1992) 1471. and references cited therein.

[18] (a) Y.-Q. Zheng, J. Sun, J.-L. Lin, Z. Anorg. Allg. Chem. 628 (2002) 1397;
(b) Z.-Q. Li, D.-J. Xu, J.-Y. Wu, M.Y. Chiang, J. Chem. Cryst. 35 (2005) 615;
(c) C.-G. Zhang, C.-X. Zhao, Z. Ma, D.-Y. Yan, J. Coord. Chem. 52 (2000) 87.

[19] (a) I. Castro, J. Faus, M. Julve, F. Lloret, M. Verdaguer, O. Kahn, S. Jeannin, Y. Jeannin, J. Vaisserman, J. Chem. Soc., Dalton Trans. (1990) 2207;
(b) M. Li, J.-Z. Zou, Z. Xu, X.-Z. You, X.-Y. Huang, Polyhedron 14 (1995) 639;
(c) C.-C. Su, S.-P. Wu, C. -Y Wu, T.-Y. Chang, Polyhedron 14 (1995) 267.

[20] (a) E. Dubler, U.K. Häring, K.H. Scheller, P. Baltzer, H. Sigel, Inorg. Chem. 23 (1984) 3785;
(b) T. Tokii, N. Watanabe, M. Nakashima, Y. Muto, M. Morooka, S. Ohba, Y. Saito, Bull. Chem. Soc. Jpn. 63 (1990) 364;
(c) M. Mikuriya, S. Kida, I. Veda, T. Tokii, Y. Muto, Bull. Chem. Soc. Jpn. 50 (1977) 2464;
(d) D.B.W. Yawney, J.A. Moreland, R.J. Doedens, J. Am. Chem. Soc. 95 (1973) 1164.

[21] (a) M. Parvez, S. Ali, S. Ahmad, M.H. Bhatti, M. Mazhar, Acta Crystallogr., Sect. C 58 (2002) m334;
(b) D. Morales, J. Pérez, L. Riera, V. Riera, D. Miguel, m.E.G. Mosquera, S. Garcia-Granda, Chem. Eur. J. 9 (2003) 4132.

[22] S. Parsons, A. Cantlay, R. Winpenny, P. Wood, private communication.

[23] K. Stahl, J.E.T. Andersen, H. Nilsson, Acta Crystallogr., Sect. E 62 (2006) m1677.

[24] M.-T. Li, X.-C. Fu, C.-G. Wang, Acta Crystallogr., Sect. E 62 (2006) m916.

[25] C. Papatriantafyllopoulou, C.P. Raptopoulou, A. Terzis, J.F. Janssens, E. Manesssi-Zoupa, S.P. Perlepes, J.C. Plakatouras, Polyhedron 26 (2007) 4053.

[26] A.K. Boudalis, V. Nastopoulos, S.P. Perlepes, C.P. Raptopoulou, A. Terzis, Transition Met. Chem. 26 (2001) 276.

[27] K. Nakamoto, Infrared and Raman Spectra of Inorganic and Coordination Compounds, 4th Ed., Wiley, New York, 1986.

[28] H.O. Desseyn, in: S. Patai (Ed.), The Chemistry of Acid Derivatives, vol. 2, Wiley, New York, 1992, pp. 271–303.

[29] G.B. Deacon, R.J. Phillips, Coord. Chem. Rev. 33 (1980) 227.

[30] C. Vansant, H.O. Desseyn, S.P. Perlepes, Transition Met. Chem. 20 (1995) 454.

[31] C. Vansant, H.O. Desseyn, V. Tangoulis, C.P. Raptopoulou, A. Terzis, S.P. Perlepes, Polyhedron 14 (1995) 2115.

[32] S.P. Perlepes, E. Libby, W.E. Streib, K. Folting, G. Christou, Polyhedron 8 (1992) 923.

[33] I. Chadjistamatis, S.P. Perlepes, C.P. Raptopoulou, unpublished results.

AFCBP1 bipotentiostat [17]. Solutions of the compounds were 2 mM in anhydrous acetonitrile (Aldrich, used as received) with 0.1 M tetra-*n*-butylammonium hexafluorophosphate. Data are reported from cyclic voltammograms recorded at a 0.5 mm Pt disc working electrode at a scan rate of 100 mV s^{-1}. Electrochemical potentials are quoted relative to the ferrocene–ferrocenium couple measured under the same experimental conditions (same concentrations, solvent, support electrolyte, electrodes, temperature and scan rate).

2.2. Synthesis of ligands, HL^1–H_2L^3 and their precursors

2.2.1. (3-Indolyl-2-ethyl)[bis(2-pyridylmethyl)]amine (HL^1)

Tryptamine (1.6 g, 0.01 mol) in tetrahydrofuran (10 mL) was combined with pyridine-2-carboxaldehyde (2.14 g, 0.02 mol) and sodium triacetoxyborohydride (4.87 g, 0.02 mol). After diluting with tetrahydrofuran (50 mL), the reaction mixture was stirred under dinitrogen for 3 days. Then, the reaction mixture was quenched by adding aqueous saturated sodium bicarbonate, and the product extracted with diethylether. The extract was dried over magnesium sulfate and the solvent removed on a rotary evaporator. The residue was purified by column chromatography (silica gel; eluent 1:9 methanol/dichloromethane). The major yellow band afforded a brown oil (2.5 g, 75%).

m/z (ESI-MS) 345 (M^+, 2%), 252 (100), 248 (4); δ_H ($CDCl_3$) 8.56 (2H, d, Py), 8.12 (1H, br s, NH), 7.58 (2H, d, Py), 7.52 (2H, d, Py), 7.45 (1H, d, Ind), 7.35 (1H, d, Ind), 7.13 (2H, t, Py), 7.02 (1H, t, Ind), 6.94 (1H, t, Ind), 6.90 (1H, s, Ind), 4.03 (4H, s, CH_2-CH_2), 3.01 (4H, s, CH_2); ν/cm^{-1} (KBr disc) 1592s, 1569m, 1474m, 1455m, 1434s, 1360m, 1149w, 1002w.

2.2.2. (3-Indolyl-2-ethyl)[bis(2-pyridyl-2-ethyl)]amine (HL^2)

2-Vinylpyridine was purified by passing through a short silica column with diethylether as eluent followed by removal of the diethylether by rotary evaporation. To 2-vinylpyridine (1.64 g, 15.6 mmol) in methanol (20 mL) was added tryptamine (0.5 g, 3.12 mmol) in methanol along with glacial acetic acid (15 mL). The mixture was stirred and heated at reflux under dinitrogen for 5 days. The mixture was then cooled and the solvent removed using a rotary evaporator. The residue was re-dissolved in chloroform. This solution was washed with saturated sodium carbonate and saturated brine solutions, and then dried over magnesium sulfate. The solvent was removed on a rotary evaporator and the oily residue purified by column chromatography (silica support; eluent 2:8 methanol–dichloromethane) to afford the product as a brown oil (0.84 g, 72%).

m/z (ESI-MS) 371 (M^+, 50%), 332 (100), 266 (90), 252 (30); δ_H ($CDCl_3$) 9.47 (1H, br s, NH), 8.43 (2H, d, Py), 7.49 (3H, m, Ar), 7.28 (1H, d, Ind), 7.04 (6H, m, Ar), 6.89 (1H, d, Ind), 3.01 (2H, t, CH_2), 2.97 (2H, t, CH_2), 2.89 (4H, s, CH_2).

2.2.3. (3-Indolyl-2-ethyl)(4-imidazolylmethyl)(2-pyridylmethyl)amine (H_2L^3)

2.2.3.1. (3-Indolyl-2-ethyl)(2-pyridylmethyl)amine. To tryptamine (6.5 g, 0.04 mol) dissolved in methanol (10 mL), was combined with pyridine-2-carboxaldehyde (4.3 g, 0.04 mol). After diluting the mixture with methanol (70 mL), the solution was hydrogenated under hydrogen (1 atm) in the presence of 10% Pd–C catalyst (0.6 g) over night. After removal of the catalyst by filtration through a silica plug, the solvent was removed by rotary evaporation to give a pale yellow oil (8.24 g, 82%), which was used without further purification in the synthesis of H_2L^3.

2.2.3.2. H_2L^3. (3-Indolyl-2-ethyl)(2-pyridylmethyl)amine (410 mg, 1.63 mmol) dissolved in 1,2-dichloroethane (10 mL) was added 4(5)-imidazolylcarboxaldehyde (156 mg, 1 eq.) and sodium triacetoxyborohydride (800 mg). Additional 1,2-dichloroethane (30 mL) was added and the reaction mixture was stirred under dinitrogen for 3 days. The mixture was quenched by adding aqueous saturated sodium bicarbonate, and the product was extracted with diethylether. The combined extracts were dried over anhydrous magnesium sulfate and the solvents removed on a rotary evaporator; the residue was placed under high vacuum to afford a light brown oil (0.46 g, 85%).

m/z (ESI-MS) 334 (M^+, 25%), 252 (100); δ_H (D_2O) 8.42 (1H, s, Im), 8.23 (1H, d, Py), 8.03 (1H, d, Py), 7.52 (2H, d, Ind), 7.34 (2H, m, Py & Ind), 7.12 (2H, t, Ind), 7.04 (1H, s, Im), 6.91 (1H, t, Py), 4.17 (2H, s, CH_2), 4.11 (2H, s, CH_2), 3.09 (2H, d, CH_2), 2.84 (2H, d, CH_2).

2.3. $[Cu(L)Cl_2]$ ($L = HL^1$–H_2L^3) complexes

2.3.1. $[Cu(HL^1)Cl_2]$ (**1**)

$CuCl_2 \cdot 2H_2O$ (25 mg, 1 eq.) in iso-propanol (10 mL) was layered on HL^1 (50 mg, 0.14 mmol) in dichloromethane (2 mL). After several days, a deep green crystalline solid (47.7 mg, 71%) deposited from the mixture.

(Found: C, 54.85; H, 4.90; N, 11.49%. $C_{22}H_{22}Cl_2CuN_4 \cdot 0.5H_2O$ requires C, 54.38; H, 4.77; N, 11.53%); λ_{max}/nm (MeOH) 219 (ε/$dm^3\ mol^{-1}\ cm^{-1}$ 14833), 256 (12472), 282 (9722), 676 (148); EPR (frozen MeOH solution, 77 K) $g_{||} = 2.23$, $g_{\perp} = 2.04$, $A_{||} = 178$ G; $\overline{\nu}$/cm^{-1} (KBr disc) 1608s, 1573w, 1480w, 1459m, 1443s, 1471m, 1343m, 1284m, 1092m, 1055m, 1024m.

2.3.2. $[Cu(HL^2)Cl_2]$ (**2**)

HL^2 (94.4 mg, 0.255 mmol) in iso-propanol (2 mL) was layered on $CuCl_2 \cdot 2H_2O$ (43 mg, 1 eq.) in iso-propanol (10 mL); upon standing for several days a dark green precipitate formed (92.3 mg, 72%).

(Found: C, 49.63; H, 5.81; N, 9.37%. $C_{24}H_{26}Cl_2CuN_4 \cdot 4H_2O$ requires C, 49.96; H, 5.94; N, 9.71%); λ_{max}/nm (MeOH) 214 (ε/$dm^3\ mol^{-1}\ cm^{-1}$ 12382), 263 (8470), 674 (158); EPR (frozen MeCN solution, 77 K) $g_{||} = 2.35$, $g_{\perp} = 2.09$, $A_{||} = 159$ G; $\overline{\nu}$/cm^{-1} (KBr disc) 3335br, 1607s, 1570m, 1484m, 1445s, 1313w, 1108w, 1027w.

2.3.3. $[Cu(H_2L^3)Cl_2]$ (**3**)

H_2L^3 (100 mg, 0.227 mmol) in methanol (5 mL) was added slowly to a solution of $CuCl_2 \cdot 2H_2O$ (38.7 mg, 1 eq.) in methanol (5 mL). After stirring for 10 min, the solution was left to stand under a diethylether atmosphere for a few days; a green crystalline solid (74 mg, 75%) formed.

(Found: C, 49.71; H, 4.87; N, 13.87%. $C_{20}H_{21}Cl_2CuN_5 \cdot H_2O \cdot 0.5CH_3OH$ requires C, 49.25; H, 5.04; N, 14.01%); λ_{max}/nm (MeOH) 220 (ε/$dm^3\ mol^{-1}\ cm^{-1}$ 14222), 263 (10444), 280 (911), 653 (100); EPR (frozen MeOH solution, 77 K) $g_{||} = 2.23$, $g_{\perp} = 2.05$, $A_{||} = 175$ G; $\overline{\nu}$/cm^{-1} (KBr disc) 3248br, 2895s, 1609s, 1572w, 1503w, 1456s, 1445s, 1350m, 1271m, 1104m.

2.4. X-ray crystallography

As good quality crystals of complexes **1**–**3** were not obtained, each complex was separately treated with an excess $K[PF_6]$, $Na[BF_4]$ or $Li(ClO_4)$ in methanol and the resulting green solutions left to stand under an atmosphere of diethylether. Single crystals of $[Cu(HL^1)Cl](ClO_4).0.5Et_2O \cdot 0.25H_2O$ (**4**), $[Cu(HL^2)F]_2[BF_4]_2$ (**5**) and $[Cu(H_2L^3)Cl][PF_6]$ (**6**) were obtained. X-ray reflection data for **4**–**5** were measured with an Enraf-Nonius CAD-4 diffractometer in ω–2θ scan mode at 294 K. Crystal structure and refinement data are collected in Table 1. A summary of key bond lengths and bond angles is given in Table 2. The CIF files have been deposited at the Cambridge Crystallographic Data Centre and allocated the deposition numbers CCDC 710201–710203.

Table 1
X-ray crystal structure collection and refinement data.

	$[Cu(HL^1)Cl](ClO_4)\cdot 0.5C_4H_{10}O\cdot 0.25H_2O$ (**4**)	$[Cu(HL^2)F]_2[BF_4]_2$ (**5**)	$[Cu(H_2L^3)Cl][PF_6]$ (**6**)
Formula	$C_{24}H_{27.5}Cl_2Cu\ N_4O_{4.75}$	$C_{24}H_{26}BCuF_5N_5$	$C_{20}H_{21}ClCuF_6N_5P$
Formula mass	582.5	539.8	575.4
Crystal size	0.26 × 0.21 × 0.05	0.24 × 0.17 × 0.10	irregular
Space group	*C*2/*c*	$P\bar{1}$	$P2_1/c$
a (Å)	23.077(9)	10.885(6)	11.761(6)
b (Å)	14.427(4)	11.067(7)	15.157(4)
c (Å)	15.600(7)	12.225(6)	14.866(7)
α (°)	90	63.91(3)	90
β (°)	94.43(4)	64.32(3)	119.70(2)
γ (°)	90	81.29(3)	90
T (°C)	21	21	21
Z	8	2	4
D_{calc} (g cm^{-3})	1.49	1.51	1.66
Radiation λ (Å)	Mo Kα, 0.71073	Mo Kα, 0.71073	Mo Kα, 0.71073
μ (cm^{-1})	1.096	0.975	1.205
F (000)	2404.0	554.0	1164.0
Maximum, minimum transmission factors	0.89, 0.77	0.87, 0.78	
θ_{max}	23	24	25
Number of intensity measurements	3693	3928	4207
R_{merge} for number of equivalent reflections	0.037	0.025	0.026
Number of observed reflections in final refinement [$I/\sigma(I) > 3$]	1460	3342	2168
Number of variables in final refinement	171	265	186
R	0.093	0.051	0.071
R_w	0.104	0.077	0.082
Goodness-of-fit	2.04	1.64	1.71
Maximum, minimum peak in final difference map (e Å^{-3})	1.13, 1.69	1.11, −0.67	1.26, −1.17

Table 2
Selected key bond length (Å) and angle (°) data for complexes **4**–**6**.

4		**5**		**6**	
Cu1–Cl1	2.241(5)	Cu1–F1	1.911(2)	Cu1–Cl1	2.249(2)
Cu1–N1	1.909(12)	Cu1–F1*	2.212(2)	Cu1–N1	1.933(7)
Cu1–N2	1.907(11)	Cu1–N1	2.064(3)	Cu1–N3	1.940(7)
Cu1–N4	2.052(13)	Cu1–N2	2.013(3)	Cu1–N5	2.091(7)
Cl1–Cu1–N1	97.181(5)	Cu1–N3	2.011(3)	Cl1–Cu1–N1	95.386(2)
Cl1–Cu1–N2	96.472(4)	Cu1–Cu1*	3.125(2)	Cl1–Cu1–N3	98.691(2)
Cl1–Cu1–N4	178.512(4)	F1–Cu1–F1*	81.706(8)	Cl1–Cu1–N5	177.012(2)
N1–Cu1–N2	165.611(6)	F1–Cu1–N1	88.602(1)	N1–Cu1–N3	164.628(3)
N1–Cu1–N4	83.211(7)	F1–Cu1–N2	89.141(1)	N1–Cu1–N5	81.723(3)
N2–Cu1–N4	83.028(7)	F1–Cu1–N3	176.011(1)	N3–Cu1–N5	84.266(3)
		F1*–Cu1–N1	101.047(1)		
		F1*–Cu1–N2	96.576(1)		
		F1*–Cu1–N3	101.190(1)		
		N1–Cu1–N2	161.712(1)		
		N1–Cu1–N3	88.146(1)		
		N2–Cu1–N3	93.226(1)		
		Cu1–F1–Cu1*	98.294(8)		

3. Results and discussion

3.1. Syntheses

Two new indole-substituted ligands, HL^1 and H_2L^3, were easily synthesized by reductive amination using an appropriate aldehyde and tryptamine with sodium triacetoxyborohydride in dry 1,2-dichloroethane [18]. HL^2 was produced by reaction of excess 2-vinyl pyridine with tryptamine. Copper(II) complexes, $[Cu(L)Cl_2]$ (**1**: L = HL^1, **2**: L = HL^2; **3**: L = H_2L^3) were obtained by adding the ligand (L) in dichloromethane to $CuCl_2\cdot 2H_2O$ in iso-propanol. After several days, the green–blue microcrystalline complexes **1**–**3** precipitated. Unfortunately, none of the complexes gave crystals of sufficient quality for an X-ray crystal structure determination.

3.2. X-ray crystallography

As crystals of **1**–**3** were unavailable, in separate reactions, each of these complexes was treated with excess $K[PF_6]$, $Na[BF_4]$ or $Li(ClO_4)$ in methanol and the resulting green solutions were left to stand under an atmosphere of diethylether. Single crystals of $[Cu(HL^1)Cl](ClO_4)\cdot 0.5Et_2O\cdot 0.25H_2O$ (**4**), $[Cu(HL^2)F]_2[BF_4]_2$ (**5**) and $[Cu(H_2L^3)Cl][PF_6]$ (**6**) were obtained that were satisfactory for X-ray structure determinations. Fig. 1 presents views of the structures and selected bond length and angle data are gathered in Table 2.

Complex **4** exhibits a distorted square planar copper(II) centre formed by the binding of the two pyridine and amine nitrogen atoms, and a chloro co-ligand, Fig. 1a. The sum of the six less-than-180° angles about the Cu centre is 704°, which compares with 720° (and 645°) for perfect square planar (and tetrahedral) centre(s) [19,20]. The Cu–Cl1 (2.241(5) Å), Cu–N(amine) (2.052(13) Å), and Cu–N(py) (1.907(11) and 1.909(12) Å) distances are all in the anticipated range for copper(II) complexes. The indole substituent does not bind to the copper(II) centre and lies offset π-stacked with the pyridine ring containing N2. The inter-ring separation of the offset π-stacked pyridinyl and indolyl rings is 3.38 Å, which is comparable to the Trp 236···His 291 separation in cyto-

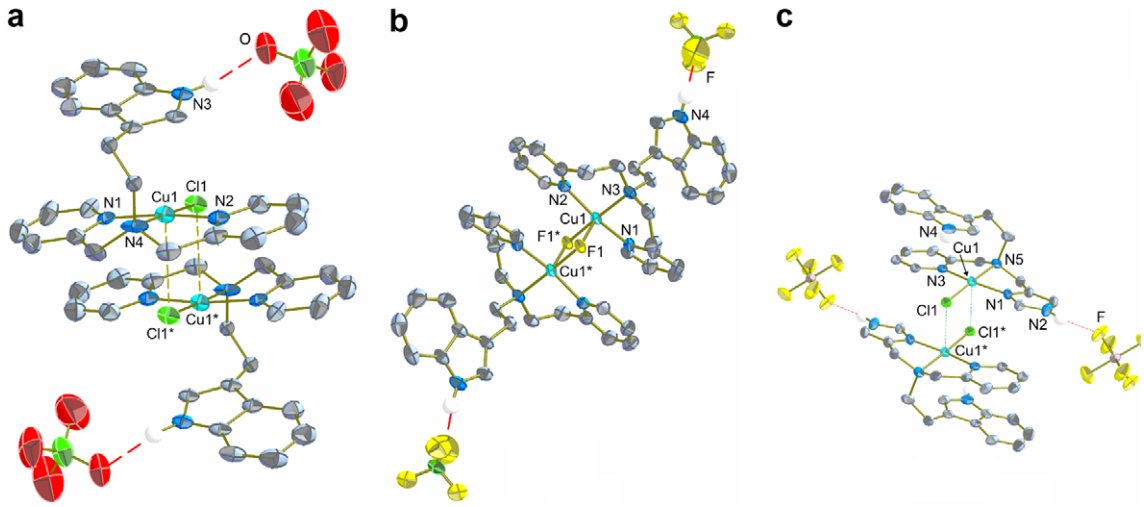


Fig. 1. Views of the paired cations and closely associated anions in the X-ray crystal structures of: (a) $[Cu(HL^1)Cl](ClO_4)$, **4**; (b) $[Cu(HL^2)F]_2[BF_4]_2$, **5**; (c) $[Cu(H_2L^3)Cl][PF_6]$, **6**. In all views, 50% thermal ellipsoids are shown and hydrogen atoms bonded to carbon have been omitted for clarity; in each case, atoms labelled with an asterisk are related by a crystallographic inversion to the corresponding atom labelled without the asterisk.

chrome *c* oxidases (see above) [1]. In the crystal structure, adjacent cation pairs of **4** are connected by weak (3.10 Å) Cu···Cl1 interactions. The inter-copper distance between neighbouring cations is 3.75 Å. The indole N–H forms a hydrogen bond to the perchlorate counterion (N3···O 2.97 Å).

Fig. 1b shows the centrosymmetric $[Cu(HL^2)F]_2^{2+}$ dimers and associated $[BF_4]^-$ counterions in the crystal structure of **5**. Fluoride abstraction reactions in transition metal complexes containing the tetrafluoroborate anion are well-known [21]. The copper(II) centre in **5** has a typical distorted square pyramidal geometry with a trigonality index [22] $\tau = 0.25$ [F1–Cu1–N3 = 176.011(1)° is the largest bond angle and N1–Cu1–N2 = 161.712(1)° the next largest]. Axial Cu–F1* bonds (2.212(2) Å) link to the adjacent Cu* to give a dimeric structure. The axial Cu–F1* bond is longer than the in-plane Cu–F1 (1.911(2) Å) and Cu–N bonds (2.029 Å average). The Cu···Cu* distance in the dimer is 3.125(2) Å. The indole substituent of HL^2 is not coordinated to the copper centre and is without any π-stacking interactions within the complex ion. There is an hydrogen bond between the indole N–H and F on tetrafluoroborate (N···F 3.04 Å).

The molecular structure of **6**, Fig. 1c, reveals the copper(II) ion to be distorted square planar bound by the amine, imidazolyl and pyridyl nitrogen atoms and by a chloro co-ligand. The sum of the six less-than-180° bond angles about the copper(II) centre is 701.7° [19,20]. The indolyl ring is offset π-stacked with the pyridyl ring consistent with the larger π-surface area and electron density of pyridyl *cf.* imidazolyl rings. The separation between the π-stacked indolyl and pyridyl rings is 3.11 Å. The Cu1–Cl1 and Cu1–Cu1* (adjacent cation) distances are 3.14 and 3.72 Å, respectively. The $[PF_6]^-$ counterion forms a F···H–N hydrogen bond (2.94 Å) with the coordinated imidazolyl N–H rather than with the pendant indole.

3.3. Physicochemical data for complexes *1*–*3* in solution

Numerous studies reveal $[Cu(N_3\text{–}L)Cl_2]$ complexes, analogous to **1**–**3**, to contain five-coordinate $Cu^{II}Cl_2N_3$ centres that display characteristic EPR and UV–Vis spectra [17–22,24–26]. Available data are indicative for five-coordinate $Cu^{II}Cl_2N_3$ centres in **1**–**3**. The FTIR of spectrum of each complex (see Supplementary data) shows characteristic pyridyl stretches at ~1604 and 1571 cm^{-1} indicative for all pyridines binding to the Cu(II) ion. The fingerprint regions of the IR spectra show characteristic indole peaks between 1400 and 1500 cm^{-1} [23]. The Vis/NIR spectra of **1**–**3** in methanol solution show a broad band having a maximum at ~640–750 nm and a prominent tail to lower energy, consistent with each complex adopting a tetragonally-elongated, square pyramidal ($CuCl_2N_3$) structure, Table 3. Likewise EPR spectra of complexes **1**–**3** in frozen

Table 3
Electronic and X-band EPR spectroscopic data for the Cu(II) complexes in methanol.

	UV-NIR (297 K) [λ_{max}/nm] (ε/dm^3 mol^{-1} cm^{-1})	EPR (77 K)
1	676 (148)	$g_{\|\|} = 2.23$, $g_\perp = 2.04$, $A_{\|\|} = 178$ G
2	674 (158)	$g_{\|\|} = 2.35$, $g_\perp = 2.09$, $A_{\|\|} = 159$ G
3	653 (100)	$g_{\|\|} = 2.23$, $g_\perp = 2.05$, $A_{\|\|} = 175$ G

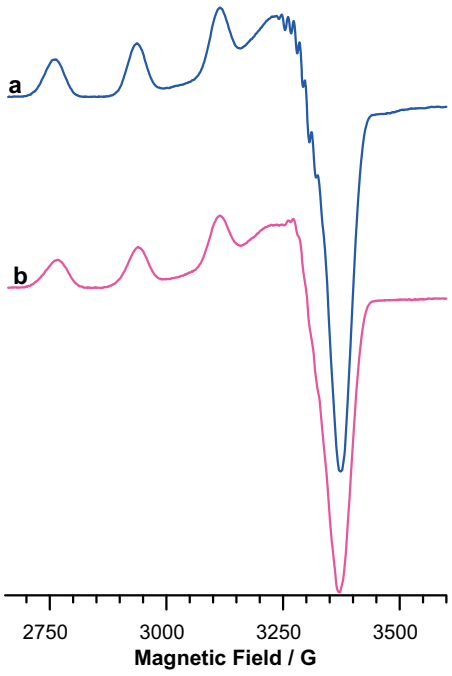


Fig. 2. X-band EPR spectra of complexes **1** (a) and **3** (b) in frozen methanol solution at 77 K; ν/GHz = 9.448.

methanol at 77 K are axial ($d_{x^2-y^2}$ ground-state) fully consistent with square pyramidal $CuCl_2N_3$ structures, *e.g.* Fig. 2 and Table 3. *N*-Superhyperfine coupling is also apparent in the spectra: *e.g. N*-superhyperfine peaks ($A_{N-Cu} \approx 12$ G) from three Cu(II)-bound *N*-donors are clearly discerned in the spectrum of **1**, Fig. 2a.

3.4. Electrochemistry of complexes 1–3

Cyclic voltammograms (CVs) of **1**–**3** in acetonitrile were acquired to characterize the redox properties of the indole and copper centres in each complex. The CVs show quasi-reversible Cu(II)/Cu(I) couples, at −0.57 V for the methylene-bridged amine complexes **1** and **3** and at −0.25 V for the ethylene-linked amine complex **2** (*e.g.* see Fig. 3). Lower potential Cu(II)/Cu(I) couples are expected for complexes of bis(pyridylmethyl)amine ligands compared to complexes of bis(pyridylethyl)amines [24–26]. On scanning to positive potentials, the CVs of **1**–**3** all show a broad anodic peak at +0.64 V followed closely by an peak at +0.77 V for an oxidation process that appears to have some reversibility (a broad cathodic peak is discernable ca. at +0.71 V in the return scan: $i_{p,c}/i_{p,a} = 1.1$). The broad anodic peak at +0.64 V is found in CVs of both bis(triphenylphosphoranylidene)ammonium chloride (PPNCl) and [(Bz-bpa)$CuCl_2$] and, therefore, may be attributed to oxidation of 'free' chloride anion (in the complexes, from dissociation of chloro ligand) [27–29]. The second peak at +0.77 V in the CVs of **1**–**3** is absent in the CVs of PPNCl and [(Bz-bpa)$CuCl_2$] and therefore must be an indole substituent-centred oxidation. For comparison, CVs of indole, Fig. 3a, reveal a broad anodic peak at +0.80 V and CVs of 3-methylindole, Fig. 3b, show a sharp anodic peak at +0.57 V that is followed by a broad peak at +0.80 V; the irreversibility arises from rapid coupling reactions of the indolyl radical [30,31]. Thus, the peaks in this region for **1**–**3** can be attributed to oxidation of the indole substituent. Notably, although the merging of chloride- and indole-centred oxidation processes complicates the electrochemistry, the potential of the indole oxidation is only slightly, if at all, affected by coordination of the indole-substituted ligand to the copper(II) centre.

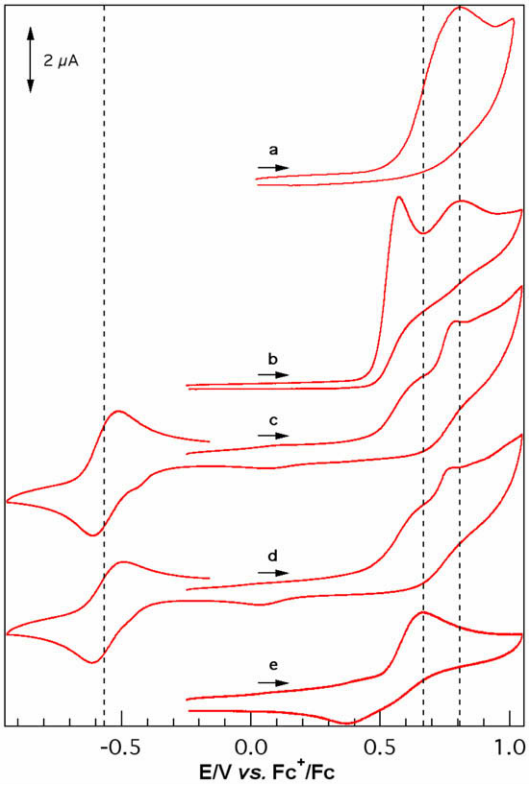


Fig. 3. Cyclic voltammograms of indole (a), 3-methylindole (b), **1** (c), **3** (d) and PPNCl (e) in acetonitrile with 0.1 M [Bu_4N][PF_6] at 295 K; 1.0 mm Pt disc working electrode; scan rate = 100 mV s^{-1}.

4. Conclusions

Three new indole-substituted ligands (HL^1–H_2L^3) were synthesized from tryptamine and copper(II) complexes (**1**–**6**) were successfully obtained from them. The results of the electrochemistry for complexes **1**–**3** show coordination of the ligands to a copper centre and the proximity of the indole and copper(II) centres does not affect the Cu^{II}/Cu^{I} couples or the indole-centred oxidation processes. This finding contrasts with our previous results for some complexes wherein copper(II) centres closely related to those reported here were substituted with ferrocenyl (Fc) substituents; in these Fc ∼ Cu(II) complexes significant mutual perturbations of the electron donor properties of each centre were observed that lead to new reactivity [26]. The crystal structures of **4** and **6** reveal offset π-stacking between the indolyl group and the ring of a pyridinyl or imidazolyl donor bound to the Cu(II) ion. The inter-ring separation is ca. 3.1–3.3 Å, which is analogous to that observed for the Trp 236···His 291 sidechains within CcO. In solution, π-stacking of the indolyl and ligand heterocyclic donor rings in complexes **1**–**6** is possible, but much less likely due to the disrupting effect(s) of solvent molecules. Thus model systems of considerably more sophistication will be needed if the effects of π-stacking between an indolyl group and a Cu(II)-bound heterocyclic ligand donor are to be explored further.

Acknowledgement

This research was supported by the Australian Research Council.

Appendix A. Supplementary data

CCDC 710201, 710202, 710203 contain the supplementary crystallographic data for **4**, **5**, **6**. These data can be obtained free of charge via http://www.ccdc.cam.ac.uk/conts/retrieving.html, or from the Cambridge Crystallographic Data Centre, 12 Union Road, Cambridge CB2 1EZ, UK; fax: (+44) 1223 336 033; or e-mail: deposit@ccdc.cam.ac.uk. Supplementary data associated with this article can be found, in the online version, at doi:10.1016/j.poly.2009.01.025.

References

[1] S. Yoshikawa, K. Shinzawa-Itoh, R. Nakashima, R.Yaono, E. Yamashita, N. Inoue, M. Yao, M.J. Fei, C.P. Libeu, T. Mizushima, H. Yamaguchi, T. Tomizaki, T. Tsukihara, Science 280 (1998) 1723.
[2] T. Tsukihara, E. Yamashita, H. Aoyama, T. Tomizaki, H. Yamaguchi, K. Shinzawai-Itoh, R. Nakashima, R. Yaono, S. Yoshikawa, Science 269 (1995) 1069.
[3] S.Iwata.C. Ostermeier, B.Ludwig.H. Michel, Nature 376 (1995) 660.
[4] C. Ostermeier, A. Harrenga, U. Ermler, H. Michel, Proc. Natl. Acad. Sci. USA 94 (1997) 10547.
[5] T. Soulimane, G. Buse, G.P. Bourenkov, H. Bartunik, R. Huber, E.T. Manuel, EMBO J. 19 (2000) 1766.
[6] K. Kamaraj, E. Kim, B. Galliker, L.N. Zakharov, A.L. Rheingold, A.D. Zuberbuehler, K.D. Karlin, J. Am. Chem. Soc. 125 (2003) 6028.
[7] J.-G. Liu, Y. Naruta, F. Tani, Chem. Eur. J. 13 (2007) 6365.
[8] K.N. White, I. Sen, I. Szundi, Y.R. Landaverry, L.E. Bria, J.P. Konopelski, M.M. Olmstead, O. Einarsdottir, Chem. Commun. 31 (2007) 3252.
[9] J.P. Collman, R.A. Decréau, Y. Yan, J. Yoon, E.I. Solomon, J. Am. Chem. Soc. 129 (2007) 5794.
[10] D.G. Lonnon, S.T. Lee, S.B. Colbran, J. Am. Chem. Soc. 129 (2007) 5800.
[11] T. Motoyama, Y. Shimazaki, T. Yajima, Y. Nakabayashi, Y. Naruta, O. Yamauchi, J. Am. Chem. Soc. 126 (2004) 7378.

[12] Y. Shimazaki, T. Nogami, F. Tani, A. Odani, O. Yamauchi, Angew. Chem., Int. Ed. Engl. 40 (2001) 3859.
[13] Y. Shimazaki, H. Yokoyama, O. Yamauchi, Angew. Chem., Int. Ed. Engl. 38 (1999) 2401.
[14] H. Masuda, T. Sugimori, A. Odani, O. Yamauchi, Inorg. Chim. Acta 180 (1991) 73.
[15] À. García-Raso, J.J. Fiol, F. Bádenas, E. Lago, E. Molins, Polyhedron 20 (2001) 2877.
[16] T.A. Smith, J.E. Penner-Hahn, M.A. Berding, S. Doniach, K.O. Hodgson, J. Am. Chem. Soc. 107 (1985) 5945.
[17] Z. He, S.B. Colbran, D.C. Craig, Chem.-Eur. J. 9 (2003) 116.
[18] A.F. Abdel-Magid, K.G. Carson, B.D. Harris, C.A. Maryanoff, R.D. Shah, J. Org. Chem. 61 (1996) 3849.
[19] Z. He, P.J. Chaimungkalanont, D.C. Craig, S.B. Colbran, J. Chem. Soc., Dalton Trans. (2000) 1419.
[20] S.E. Watkins, D.C. Craig, S.B. Colbran, J. Chem. Soc., Dalton Trans. (2002) 2423.
[21] R.R. Jacobson, Z.T. Tyeklár, K.D. Karlin, J. Zubieta, Inorg. Chem. 30 (1991) 2035.
[22] A.W. Addision, T.N. Rao, J. Reedijk, J.V. Rijn, G.C. Verschoor, J. Chem. Soc., Dalton Trans. (1984) 1349.
[23] S.V. Tsukerman, A.I. Bugai, Y.N. Surov, V.F. Lavrushin, N.S. Pivenko, J. Appl. Spectr. (1980) 1526.
[24] I. Sanyal, M. Mohammad-Tahir, M.S. Nasir, P. Ghosh, B.I. Cohen, Y. Gultneh, R.W. Cruse, A. Farooq, K.D. Karlin, S. Liu, J. Zubieta, Inorg. Chem. 31 (1992) 4322.
[25] K.D. Karlin, S.E. Sherman, Inorg. Chim. Acta 64 (1982) L39.
[26] A.J. Evans, S.E. Watkins, D.C. Craig, S.B. Colbran, J. Chem. Soc., Dalton Trans. (2002) 983.
[27] P. Catellonese, G. Launay, Bull. Soc. Chim. 7-8 (1978) I317.
[28] D.M. Novak, B.E. Conway, J. Chem. Soc., Faraday Trans. 77 (1981) 2341.
[29] B.E. Conway, Y. Phillips, S.Y. Qian, J. Chem. Soc., Faraday Trans. 91 (1995) 283.
[30] P.G. Keech, N.J. Bunce, J. Appl. Electrochem. 33 (2003) 79.
[31] G.L. Skiles, J.D. Adams, G.S. Yost, Chem. Res. Toxicol. 2 (1989) 254.

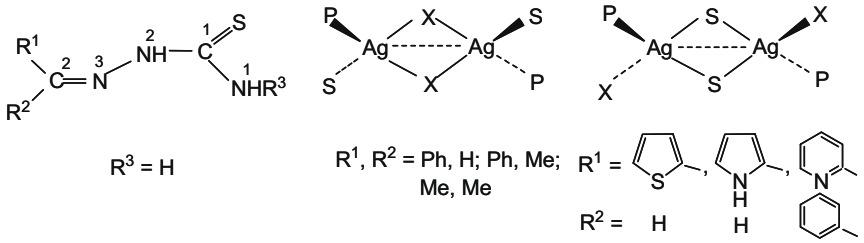


Chart 1.

4000–200 cm^{-1} on a Pye-Unicam SP-3-300 spectrophotometer. Melting points were determined with an electrically heated Gallenkamp apparatus. ^1H NMR were recorded on a JEOL AL-300 FT spectrometer operating at a frequency of 300 MHz using $CDCl_3$ as the solvent with TMS as an internal standard. ^{31}P NMR spectra were recorded on a Bruker ACP-300 spectrometer operating at a frequency of 121.5 MHz with H_3PO_4 as an external standard with $\delta = 0$.

2.2. Synthesis of the complexes

2.2.1. $[Ag_2(\mu\text{-}Cl)_2(\eta^1\text{-}S\text{-}HttsMe)_2(PPh_3)_2]$ (**1**)

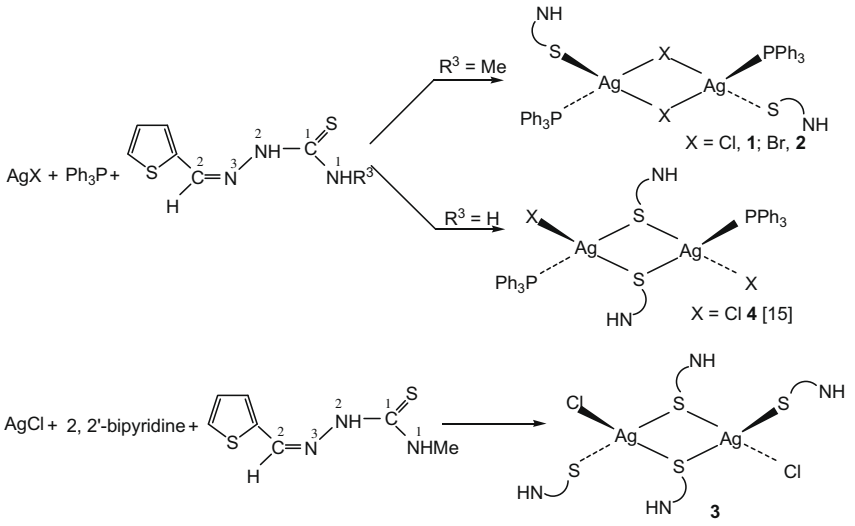
To AgCl (0.025 g, 0.17 mmol) suspended in acetonitrile (15 mL) was added solid Ph_3P (0.046 g, 0.17 mmol), and the reaction mixture was stirred for 2 h. The white precipitates that formed were filtered to remove acetonitrile, and to the white solid suspended in chloroform was added the solid HttscMe ligand (0.035 g, 0.17 mmol). The contents stirred for a further period of 10 min and the yellow colored clear solution thus formed was allowed to crystallize. Slow evaporation at room temperature yielded crystals of $[Ag_2(\mu\text{-}Cl)_2(\eta^1\text{-}S\text{-}HttsMe)_2(PPh_3)_2]$ (**1**) (**1** yellow, 72%, m.p. 175–177 °C). *Anal.* Calc. for $C_{50}H_{48}Ag_2Cl_2N_6P_2S_4$: C, 49.26; H, 4.35; N, 6.92. Found: C, 49.67; H, 4.0; N, 6.95%. IR data (KBr, cm^{-1}): ν(N–H) 3340(s); ν(–NH–) 3160(m); $\nu(C\text{–}H)_{Ph}$ 2951(m); $\nu(C\text{–}H)_{Me}$ 2733(w); ν(C=N) + ν(C=C) 1620(m), 1565(m), 1530(m); $\nu(P\text{–}C_{Ph})$ 1093(s); ν(C–N) 1031(s); ν(C=S) 854(s). ^1H NMR ($CDCl_3$, δ ppm): 12.42s ($-N^2H$), 8.66s (C^2H), 7.32–7.52m ($C^{4,6}H$ + 15H, PPh_3 + N^1H), 7.05dd (C^5H), 3.23d ($-CH_3$). ^{31}P NMR ($CDCl_3$, δ ppm): 10.5, $\Delta\delta$ (δ complex – δ ligand) 14.7.

2.2.2. $[Ag_2(\mu\text{-}Br)_2(\eta^1\text{-}S\text{-}HttsMe)_2(PPh_3)_2]$ (**2**)

To AgBr (0.025 g, 0.13 mmol) suspended in acetonitrile (15 mL) was added solid Ph_3P (0.035 g, 0.13 mmol), and the reaction mixture was stirred for 2 h. The white precipitates that formed were filtered to remove acetonitrile, and to the white solid suspended in chloroform was added the solid HttscMe ligand (0.027 g, 0.13 mmol). The contents were stirred for a further period of 10 min and the yellow colored clear solution thus formed was allowed to crystallize. Slow evaporation at room temperature yielded crystals of $[Ag_2(\mu\text{-}Br)_2(\eta^1\text{-}S\text{-}HttsMe)_2(PPh_3)_2]$ (**2**) (**2** yellow, 69%, m.p. 195–198 °C). *Anal.* Calc. for $C_{50}H_{48}Ag_2Br_2N_6P_2S_4$: C, 46.47; H, 3.92; N, 6.92. Found: C, 46.28; H, 3.70; N, 6.47%. IR data (KBr, cm^{-1}): ν(N–H) 3345(s); ν(–NH–) 3150(m); $\nu(C\text{–}H)_{Ph}$ 2975(m); $\nu(C\text{–}H)_{Me}$ 2753(w); ν(C=N) + ν(C=C) 1632(m), 1555(m), 1532(m); $\nu(P\text{–}C_{Ph})$ 1094(s); ν(C–N) 1029(s); ν(C=S) 853(s). ^1H NMR ($CDCl_3$, δ ppm): 11.59s ($-N^2H$), 8.61s (C^2H), 7.32–7.52m ($C^{4,6}H$ + 15H, PPh_3 + N^1H), 7.06dd (C^5H), 3.23d ($-CH_3$). ^{31}P NMR ($CDCl_3$, δ ppm): 6.2, $\Delta\delta$ (δ complex – δ ligand) 10.9.

2.2.3. $[Ag_2Cl_2(\mu\text{-}S\text{-}HttscMe)_2(\eta^1\text{-}S\text{-}HttscMe)_2] \cdot 2CHCl_3$ (**3**)

To AgCl (0.025 g, 0.17 mmol) suspended in acetonitrile (15 mL) was added solid 2,2′-bipyridine (0.034 g, 0.17 mmol) and the reaction mixture was stirred for 2 h. The light purple precipitates that formed were filtered to remove acetonitrile, and to the purple precipitates suspended in chloroform was added the solid ligand HttscMe (0.035 g, 0.17 mmol). The contents were stirred for a further period of 10 min and the solution was allowed to crystallize. Slow evaporation at room temperature yielded crystals of $[Ag_2Cl_2(\mu\text{-}S\text{-}HttscMe)_2(\eta^1\text{-}S\text{-}HttscMe)_2]$ (**3**) (yellow, 65%, decomposed at 180–185 °C). *Anal.* Calc. for $C_{28}H_{36}Ag_2Cl_8N_{12}S_8$: C, 27.86; H, 3.20; N, 19.0. Found: C, 27.23; H, 2.90; N, 19.4%. IR data (KBr, cm^{-1}): ν(N–H) 3347(s); ν(–NH–) 3142(m); $\nu(C\text{–}H)_{Ph}$ 2981(m); $\nu(C\text{–}H)_{Me}$ 2757(w); ν(C=N) + ν(C=C) 1638(m), 1566(m), 1530(m); ν(C–N) 1029(s); ν(C=S) 854(s). ^1H NMR ($CDCl_3$, δ ppm): 11.68s ($-N^2H$), 8.56s (C^2H), 7.86sb (N^1H) 7.32–7.39m ($C^{4,6}H$), 7.06dd (C^5H), 3.24d ($-CH_3$).



Scheme 1.

Table 1
Crystallographic data of complexes **1**–**3**.

Empirical formula	$C_{50}H_{48}Ag_2Cl_2N_6P_2S_4$	$C_{50}H_{48}Ag_2Br_2N_6P_2S_4$	$C_{28}H_{36}Ag_2Cl_8N_{12}S_8$
M	1209.80	1298.70	1296.51
T (K)	100(2)	100(2)	200(2)
Crystal system	monoclinic	monoclinic	monoclinic
Space group	$P2_1/n$	$P2_1/n$	$P2_1/n$
Unit cell dimensions			
a (Å)	10.7279(13)	10.8211(8)	15.6035(10)
b (Å)	16.153(2)	16.3962(13)	9.9952(5)
c (Å)	14.9158(18)	14.8555(11)	17.5911(11)
α (°)	90.00	90.00	90.00
β (°)	102.864(2)	102.868(2)	109.667(7)
γ (°)	90.00	90.00	90.00
V (Å^3)	2519.8(5)	2569.5(3)	2583.5(3)
Z	2	2	2
D_{calc} (g cm^{-3})	1.594	1.679	1.667
μ (mm^{-1})	1.155	2.583	1.531
Reflections collected	6680	15505	18520
Unique reflections	6217	6299	8418
R_{int}	0.0399	0.0520	0.0449
Reflections with $[I > 2\sigma(I)]$	5088	4991	6138
Final *R* indices $[I > 2\sigma(I)]$	$R = 0.0506$, $wR = 0.0977$	$R = 0.0648$, $wR = 0.1246$	$R = 0.0960$, $wR = 0.1993$

3. X-ray crystallography

The data for **1** and **2** were measured on a Bruker AXS SMART APEX CCD diffractometer. Data were reduced and corrected for absorption using SMART and SAINT [42]. The structures were solved by direct methods and refined by full matrix least squares based on F^2 with anisotropic thermal parameters for non-hydrogen atoms using SHELXTL (structure solution, refinement and some molecular graphics). All non-hydrogen atoms were refined anisotropically. All hydrogen atoms were placed in calculated positions and were refined with an isotropic displacement parameter 1.5 (methyl) or 1.2 (all others) times that of the adjacent carbon or oxygen atom.

A prismatic crystal of complex **3** was mounted on an automatic Enraf–Nonius CAD-4 diffractometer equipped with a graphite monochromator and Mo Kα radiation (λ = 0.71073 Å). The unit cell dimensions and intensity data were measured at 200 K. The structure was solved by direct methods and refined by full matrix least squares based on F^2 with anisotropic thermal parameters for non-hydrogen atoms using XCAD-49 (data reduction), and SHELXL (absorption correction, structure solution refinement and molecular graphics) [43]. The thiophene rings of the terminally bonded HttscMe ligand in complex **3** are disordered and the data is 99% complete to a theta value of 25° (2θ of 50°), which meets the criterion. The reason for the 90% completion figure is that data was collected out to a theta value of 32.51°, but at this angle the data is incomplete due to the shape of the detector (this is normal for area detector data).

4. Results and discussion

4.1. Synthesis

Scheme 1 gives a pictorial representation of formation of the silver(I) halide complexes with thiophene-2-carbaldehyde N^1-methylthiosemicarbazone (HttscMe). To silver(I) chloride suspended in acetonitrile was added triphenylphosphine, and the contents were stirred for 2 h, which formed white precipitates. The ligand HttscMe was added to these precipitates suspended in chloroform and stirred for 10 min. The clear solution was allowed to evaporate at room temperature, which formed crystals of the stoichiometry, $[Ag_2(\mu\text{-}Cl)_2(\eta^1\text{-}S\text{-}HttsMe)_2(PPh_3)_2]$ **1**. A similar reaction with silver(I) bromide yielded $[Ag_2(\mu\text{-}Br)_2(\eta^1\text{-}S\text{-}HttsMe)_2(PPh_3)_2]$ **2**. The use of 2,2′-bipyridine in lieu of Ph_3P in the reaction of silver(I) chloride with HttscMe yielded $[Ag_2(\mu\text{-}S\text{-}HttscMe)_2(\eta^1\text{-}HttsMe)_2] \cdot 2CHCl_3$ **3**. There was no coordination by 2,2′-bipyridine in this reaction. Reactions of silver(I) halides with thiosemicarbazones in the absence of Ph_3P or 2,2′-bipyridine yield insoluble complexes. Thus the presence of the co-ligand is necessary to get crystalline compounds.

It was reported earlier that thiophene-2-carbaldehyde thiosemicarbazone (Httsc, R^3 = H) with silver(I) chloride formed a sulfur-bridged complex, $[Ag_2Cl_2(\mu\text{-}S\text{-}Httsc)_2(Ph_3P)_2] \cdot 2CH_3CN$ **4** [15], and the replacement of one hydrogen at the N^1 nitrogen with a methyl group has changed the nature of bonding from sulfur-bridging (**4**) to halogen-bridging (**1** and **2**). Complex **3** shows S-bridging, as in **4**, and probably is dominated by the presence of four

Table 2
Bond lengths (Å) and bond angles (°).

$[Ag_2(\mu\text{-}Cl)_2(\eta^1\text{-}HttsMe)_2(Ph_3P)_2]$ ***1***			
Ag(1)–P(1)	2.4258(8)	C(2)–S(1)	1.700(3)
Ag(1)–S(1)	2.5693(8)	C(2)–N(2)	1.348(4)
Ag(1)–Cl(1)	2.6335(8)	C(2)–N(1)	1.322(4)
Ag(1)–Cl(1)	2.6493(8)	N(2)–N(3)	1.379(4)
Ag–Ag$^{\#1}$	3.734(4)		
P(1)–Ag(1)–S(1)	112.32(3)	S(1)–Ag(1)–Cl(1)	105.84(3)
P(1)–Ag(1)–Cl(1)	114.88(3)	Cl(1)–Ag(1)–Cl(1)	90.15(2)
S(1)–Ag(1)–Cl(1)	109.81(3)	Ag(1)–Cl(1)–Ag(1)	89.85(2)
P(1)–Ag(1)–Cl(1)	121.58(3)	C(2)–S(1)–Ag(1)	109.00(11)
$[Ag_2(\mu\text{-}Br)_2(\eta^1\text{-}HttsMe)_2(Ph_3P)_2]$ ***2***			
Ag(1)–P(1)	2.4414(11)	C(2)–S(1)	1.699(5)
Ag(1)–S(1)	2.5625(12)	C(2)–N(2)	1.361(5)
Ag(1)–Br(2)	2.7357(5)	C(2)–N(1)	1.324(6)
Ag(1)–Br(2)	2.7422(5)	N(2)–N(3)	1.374(5)
Ag–Ag$^{\#1}$	3.746(5)		
P(1)–Ag(1)–S(1)	113.10(4)	S(1)–Ag(1)–Br(2)	112.08(3)
P(1)–Ag(1)–Br(2)	122.13(3)	Br(2)–Ag(1)–Br(2)	93.717(15)
S(1)–Ag(1)–Br(2)	105.60(3)	Ag(1)–Br(2)–Ag(1)	86.284(15)
P(1)–Ag(1)–Br(2)	108.68(3)	C(2)–S(1)–Ag(1)	109.38(15)
$[Ag_2(\mu\text{-}S\text{-}HttscMe)_2(\eta^1\text{-}HttsMe)_2] \cdot 2CHCl_3$ ***3***			
Ag–S(1B)	2.5168(7)	Ag–S(1A)	2.6259(8)
Ag–Cl	2.5770(8)	S(1A)–C(2A)	1.721(3)
Ag–S(1A)	2.5969(7)	S(2A)–C(7A)	1.722(3)
Ag–Ag$^{\#1}$	3.4867 (5)	N(1A)–C(2A)	1.327(4)
S(1B)–Ag–Cl	111.31(2)	Cl–Ag–S(1A)	108.46(2)
S(1B)–Ag–S(1A)	109.49(2)	S(1A)–Ag–S(1A)	96.24(2)
Cl–Ag–S(1A)	116.71(2)	C(2A)–S(1A)–Ag	100.25(8)
S(1B)–Ag–S(1A)	113.94(2)	Ag–S(1A)–Ag	83.76(2)

S-donor atoms in this dimer, and this also enhances the argentophilicity with a relatively short Ag···Ag contact.

The presence of two ν(N–H) bands in the ranges 3340–3347 cm^{-1} (due to $-N^1HR$) and 3142–3160 cm^{-1} (due to $-N^2H$) in complexes

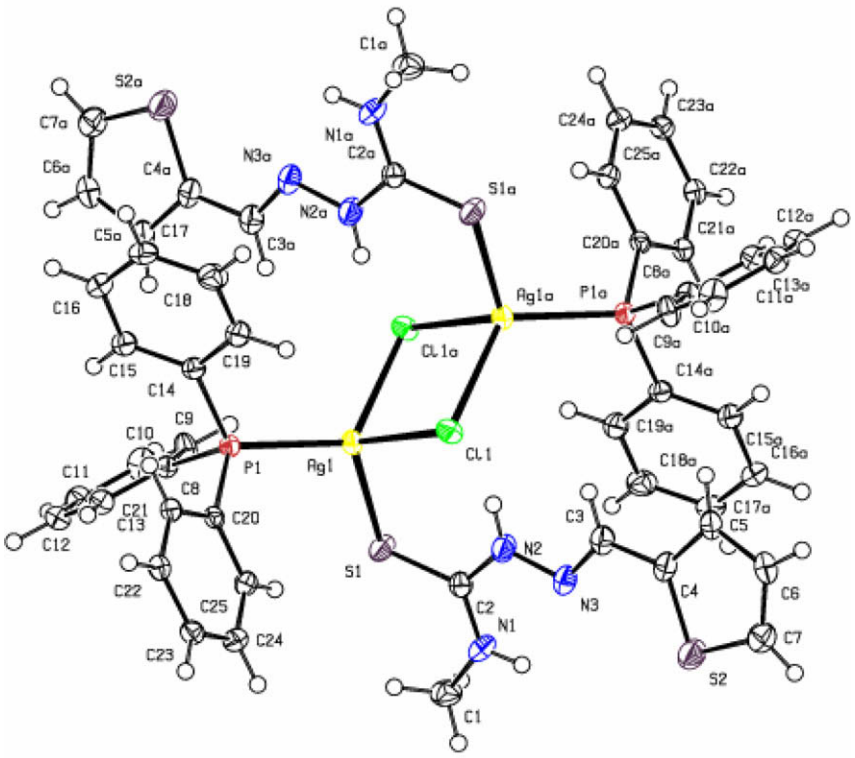


Fig. 1. ORTEP drawing of $[Ag_2(\mu\text{-}Cl)_2(\eta^1\text{-}HttsMe)_2(Ph_3P)_2]$, **1**, showing thermal ellipsoids at the 50% probability level.

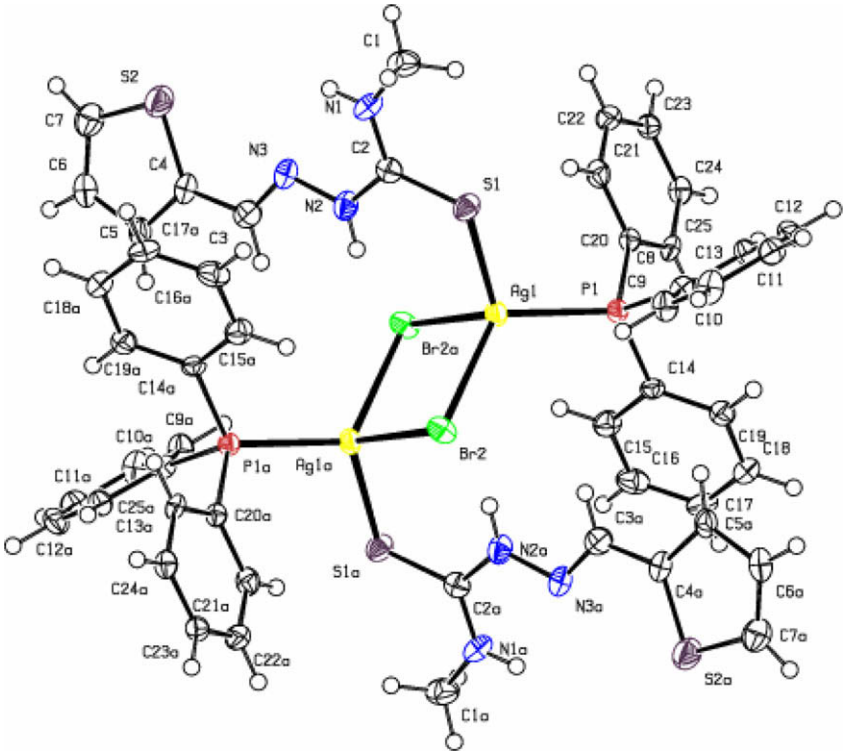


Fig. 2. ORTEP drawing of $[Ag_2(\mu\text{-}Br)_2(\eta^1\text{-}HttsMe)_2(Ph_3P)_2]$, **2**, showing thermal ellipsoids at the 50% probability level.

Table 3
Comparison of bond parameters of dimers **1**–**8**.

R^1, R^2, R^3 (No.)	Ag–S	Ag–X	Ag–X–Ag	X–Ag–X	Ag···Ag	Ref.
Ag(μ-X)$_2$Ag cores						
 , H Me (**1**)	2.5693(8)	2.6335(8); 2.6493(8)	89.85(2) (Cl)	90.15(2)	3.734(4)	this work
 , H Me (**2**)	2.5625(12)	2.7357(5); 2.7422(5)	86.284(15) (Br)	93.717(15)	3.746(5)	this work
Me, Me H (**5**)	2.507(2)	2.6454(7); 2.8378(7)	82.24(2) (Br)	97.75(2)	3.6089(9)	[16]
 ,Me H (**6**)	2.5881(6)	2.7252(3); 2.7914(3)	78.004(8) (Br)	101.997(8)	3.4722(3)	[16]
 ,Me H (**7**)	2.5851(8)	2.6254(8); 2.7056(8)	78.01(2) (Cl)	101.99(2)	3.3558(5)	[16]
 , H H (**8**)	2.5927(6)	2.7210(3); 2.8115(3)	73.2.27(8) (Br) Ag–S–Ag	106.721(8) S–Ag–S	3.3023(3)	[15]
Ag(μ-S)$_2$Ag cores						
 , H Me (**3**)	2.5967(11); 2.6259(12)	2.5771(12)	83.77(3) (Cl)	96.23(3)	3.4867(5)	this work
 , H H (**4**)	2.611(2); 2.876(2)	2.520(2)	68.33(6) (Cl)	111.67(6)	3.0902(15)	[15]

$R^1R^2C{=}NNHC(=S)NHR^3$.

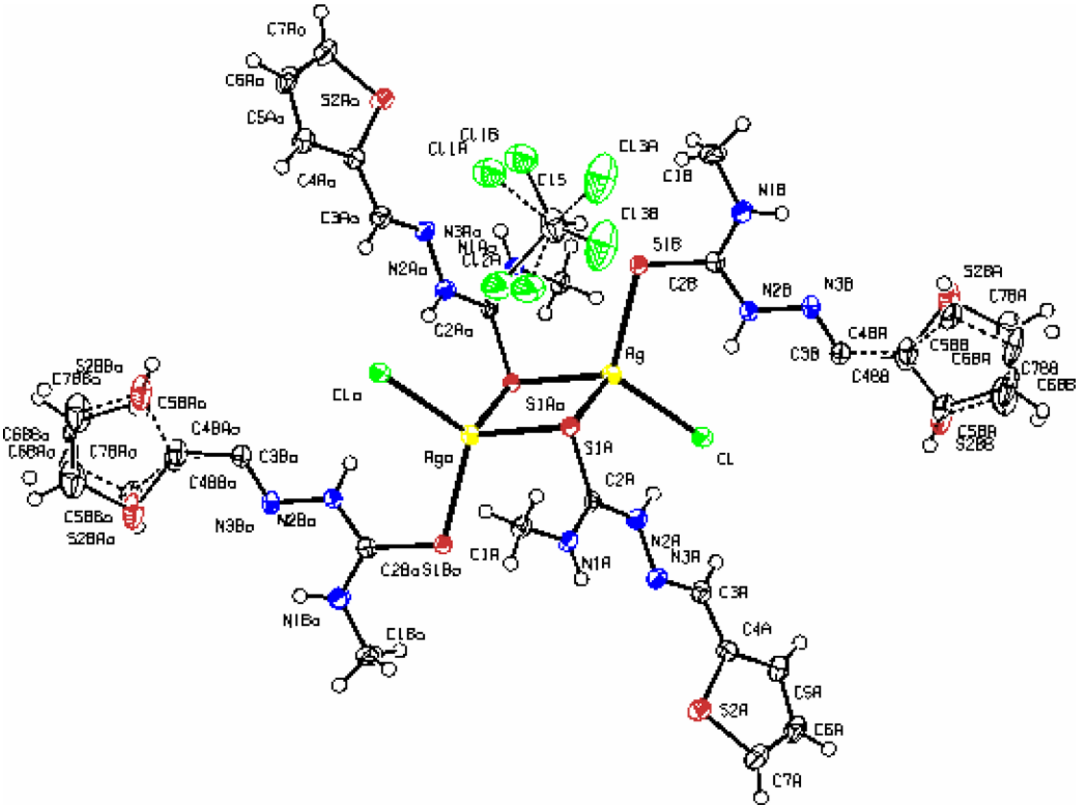


Fig. 3. ORTEP drawing of $[Ag_2(\mu\text{-S-HttscMe})_2(\eta^1\text{-HttsMe})_2] \cdot 2CHCl_3$ **3**, showing thermal ellipsoids at the 50% probability level.

1–**3** supports the coordination of HttscMe as a neutral ligand. The (N–H) band of the –N^1HR group showed a high-energy shift in the complexes vis-à-vis the free ligand (3326 cm^{-1}). The most characteristic thioamide band due to ν(C=S) lies in the range 852–854 cm^{-1} in complexes **1**–**3** and is at a somewhat low energy region (free ligand, 860 cm^{-1}). This indicates the coordination of sulfur to the silver center. The $\nu(P–C_{Ph})$ bands in complexes **1** and **2** at 1093 and 1094 cm^{-1}, respectively, support the presence of coordinated triphenylphosphine in these complexes [15,16].

4.2. Structures of the complexes

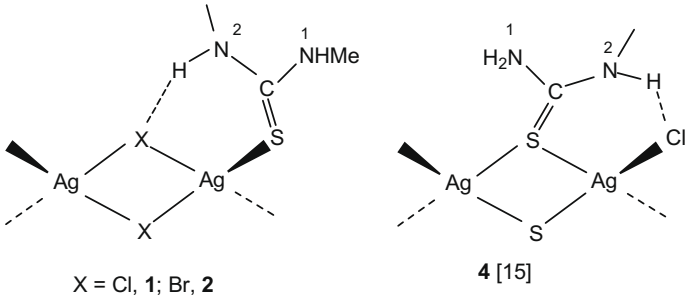
The crystallographic data and important bond parameters (bond lengths and bond angles) of complexes **1**–**3** are given in Tables 1 and 2, respectively. The molecular structures along with the numbering scheme are given in Figs. 1–3, respectively. All the three complexes crystallized in the monoclinic crystal system with space group $P2_1/n$.

4.3. Structures of the dimers *1*–*3*

Complexes **1** and **2** have similar structures. In each complex, silver(I) is coordinated to two bridging halogen atoms, one terminal S atom and one terminal P atom. The central $Ag(\mu\text{-}X)_2Ag$ cores of these dimers are almost square planar as the X–Ag–X and Ag–X–Ag angles are close to 90° (90.15(12), 89.85(2)° **1**; 93.717(15), 86.284(15)° **2**), while similar cores of complexes **5**–**8** form parallelograms (Table 3). In complex **3**, two bridging sulfurs, one terminal sulfur and one terminal chloride atom are coordinated to the silver(I) centers. The central core $Ag(\mu\text{-}S)_2Ag$ is a parallelogram (S–Ag–S, Ag–S–Ag, 109.49°, 83.76°). The geometries around each silver atom in complexes **1**–**3** can be treated as distorted tetrahedral. The Ag–X–Ag and X–Ag–X or Ag–S–Ag and S–Ag–S bond angles vary in a complementary fashion, the larger the angle at the bridging halogen/sulfur, the greater is the Ag···Ag contact. The Ag···Ag separation (3.487 Å) in sulfur-bridged complex **3** is close to twice the sum of the van der Waal's radius of silver atoms (3.40 Å [44]) and this separation is less than that (3.734(4) Å for **1**; 3.746(5) Å for **2**) in the halogen-bridged dimers.

4.4. H-bonded networks

Scheme 2 shows the intra-molecular interactions in complexes **1** and **2**. Complex **4** has S-bridging and the imino group is H-bonded to the terminal chlorine. The presence of the methyl group at the N^1 atom modulates the bonding property of HttscMe, probably by way of higher steric crowding if it was in a sulfur-bridged dimer. This paves way for halogen-bridging and the imino group now H-bonds to this halogen (N^2H···Cl, 2.45 Å **1**; N^2H···Br, 2.614 Å **2**). The two chloro-bridged dimeric units of **1** are interconnected



Scheme 2.

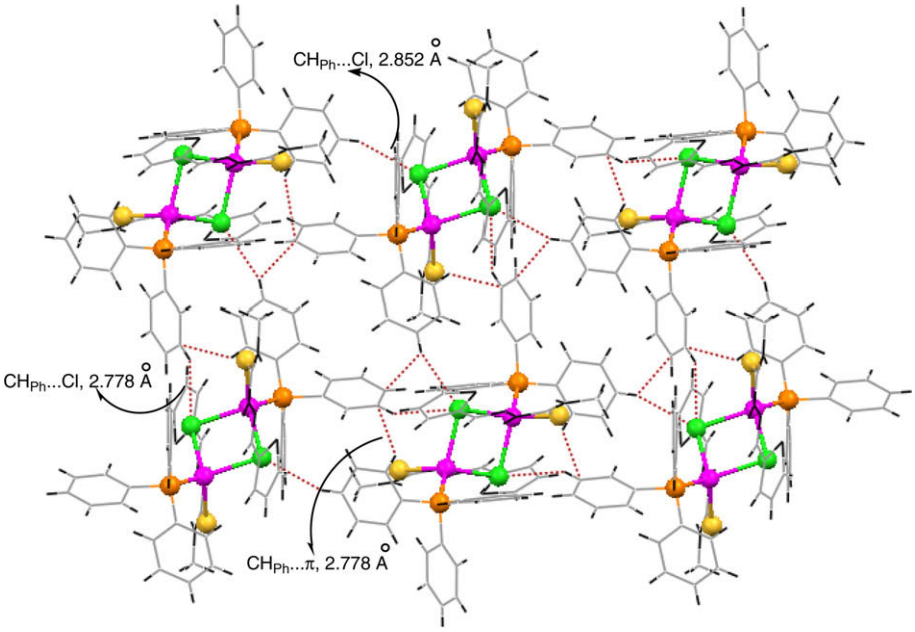


Fig. 4. Packing diagram of $[Ag_2(\mu\text{-}Cl)_2(\eta^1\text{-}HttsMe)_2(Ph_3P)_2]$ **1**.

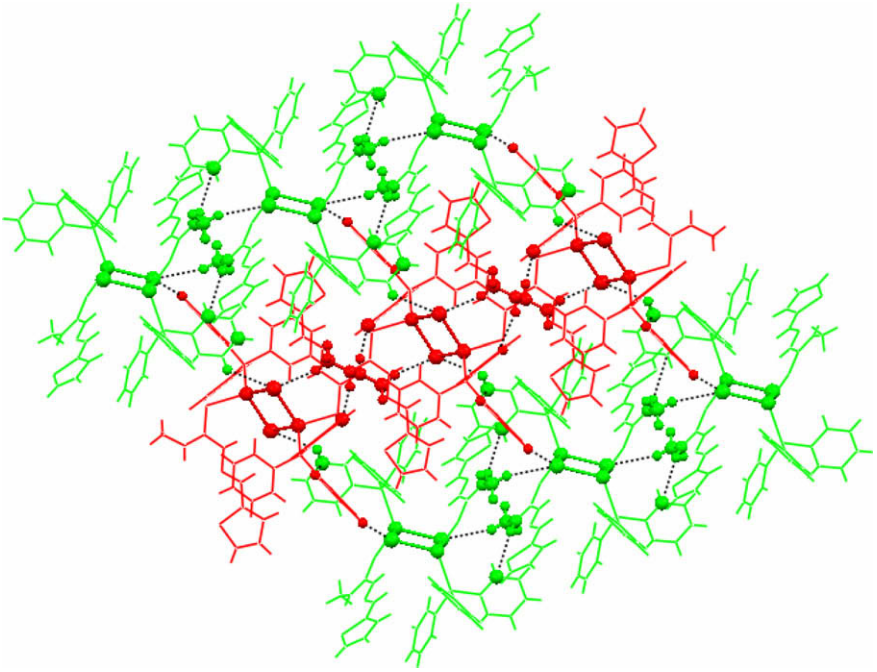


Fig. 5. Packing diagram of $[Ag_2(\mu\text{-}Br)_2(\eta^1\text{-}HttsMe)_2(Ph_3P)_2]$ **2**.

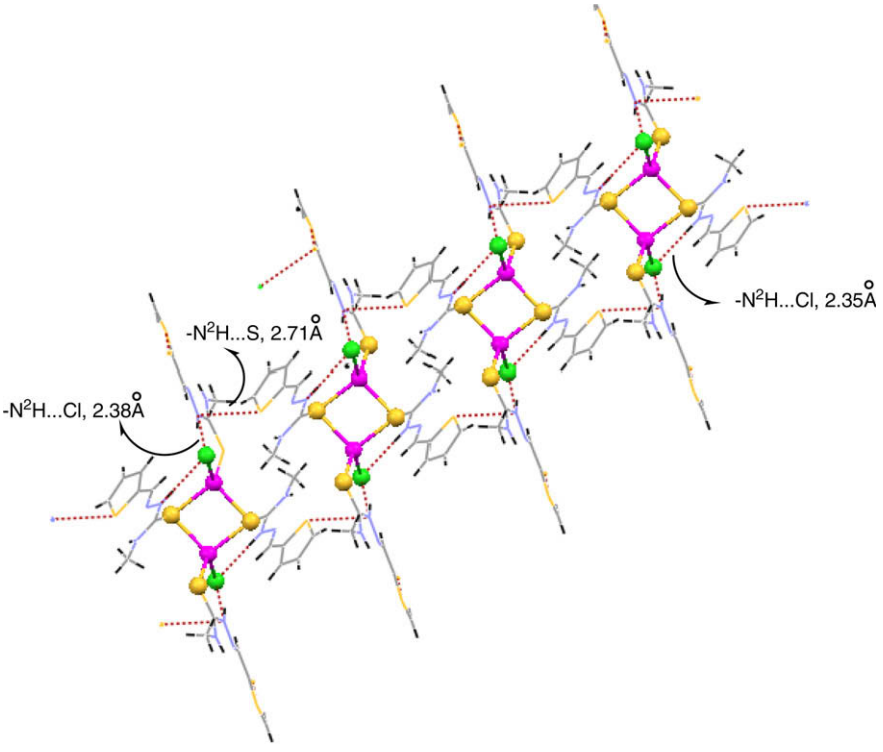


Fig. 6. Packing diagram of $[Ag_2(\mu\text{-}S\text{-}HttscMe)_2(\eta^1\text{-}HttsMe)_2] \cdot 2CHCl_3$ **3**.

via phenyl hydrogen–chlorine ($CH_{Ph}\cdots Cl^{\#1}$, 2.852 Å) and phenyl hydrogen–π, ($CH_{Ph}\cdots\pi$, 2.626 Å) interactions to form a linear chain along the *a*-axis (Fig. 4). Two such linear chains are further interconnected by a phenyl hydrogen–chlorine ($CH_{Ph}\cdots Cl^{\#2}$, 2.778 Å) interaction which forms a H-bonded 2D polymer. In the dimer **2**, two units are H-bonded via MeN^1H–π (2.768 Å) and methyl-bromine, ($H_2CH\cdots Br$, 2.972 Å) interactions, which form a H-bonded linear chain. Two linear chains are connected via phenyl hydrogen–bromine ($CH_{Ph}\cdots Br^{\#1}$, 2.996 Å) interaction and form a H-bonded 2D polymer (Fig. 5).

The imino hydrogen atom of terminal as well as bridging ligands forms a strong intra-molecular H-bond with the chlorine

atom (–N^2H_{ter}···Cl, 2.38 Å; –N^2H_{bri}···Cl, 2.35 Å) in complex **3**. Two dimeric units are interconnected via the imino hydrogen of a terminal ligand of one unit and the sulfur atom of a bridging ligand of the second unit (–N^2H_{ter}···S_{bri}, 2.71 Å), which forms a linear chain polymer (Fig. 6). The lack of Ph_3P, which provides CH–π interactions, limits the dimensionality of **3** to 1D.

4.5. Solution phase behaviour

The ^{1}H NMR spectra of complexes **1**–**3** show shifts in the N^2H proton signal to low field (δ 12.42, 11.60 and 11.68 ppm, respectively) relative to the free ligand (δ 9.15 ppm). The presence of the N^2H proton signals in these complexes ensures that no deprotonation occurred during complexation. The C^2H proton signals also appear shifted to low field: δ 8.66 (**1**), 8.61 (**2**) and 8.56 ppm (**3**) (free ligand, 7.93 ppm). The ring protons of Ph_3P in complexes **1** and **2** appear in the range δ *7.32–7.51* ppm and appear to have obscured the N^1HMe proton signals. The methyl protons of –N^1HCH_3 appear as a doublet in the range, δ *3.22–3.25* ppm in **1**–**3**. The C^5H protons of the thiophene ring appeared as a doublet of doublets in the range, δ *7.07–7.1* ppm in these complexes, while the other ring protons are obscured by proton signals for triphenyl phosphine in complexes **1** and **2** and N^1HMe proton signals (δ 7.34–7.86 ppm) in complex **3**.

Complexes **1** and **2** showed ^{31}P NMR bands at δ 10.05 and 6.2 ppm, respectively. The coordination shifts, ($\Delta\delta = \delta_{complex} - \delta_{ligand}$) are 14.7 (**1**) and 10.9 ppm (**2**). These coordination shifts are similar to those found in halogen-bridged dimers in silver(I)–thiosemicarbazone chemistry [15].

5. Conclusion

For the mixed ligand complexes $[AgX_2(Htsc)_2(Ph_3P)_2]$ it is interesting to note that for R = H at N^1HR of (C_4H_4S)CH=N–NH–C(=S)–N^1HR, a sulfur-bridged dimmer, **4**, was formed [15], while for R = Me at N^1HR, halogen-bridged dimers **1** and **2** have been obtained. It demonstrates the influence of methyl substituents at the N^1 nitrogen on the bonding properties of thiophene-2-carbaldehyde thiosemicarbazones, which would enhance the steric crowding if the ligand were sulfur-bridged. In the absence of a co-ligand, as in compound **3**, the presence of four sulfur donor atoms prefers S-bridging over chloride-bridging. This also enhances the argentophilicity, with a relatively short Ag···Ag contact induced by the S-bridging. It is the first example of a complex of the stoichiometry $[Ag_2Cl_2(HttscMe)_4]$ among thiosemicarbazone/heterocyclic thioamide chemistry of coinage metals. Compounds **1**–**3** present the first report of complexes of N^1-substituted thiosemicarbazones with silver(I).

Acknowledgement

Financial assistance from CSIR (Scheme No. 01(1993)/05/EMR-II), New Delhi, is gratefully acknowledged.

Appendix A. Supplementary data

CCDC 705112–705114 contains the supplementary crystallographic data for **1–3**, respectively. These data can be obtained free of charge via http://www.ccdc.cam.ac.uk/conts/retrieving.html, or from the Cambridge Crystallographic Data Centre, 12 Union Road, Cambridge CB2 1EZ, UK; fax: (+44) 1223-336-033; or e-mail: deposit@ccdc.cam.ac.uk. Supplementary data associated with this article can be found, in the online version, at doi:10.1016/j.poly.2009.01.041.

References

[1] D.X. West, S.B. Padhye, P.B. Sonaware, Struct. Bond. (Berlin) 76 (1991) 4.
[2] D.X. West, A.E. Liberta, S.B. Padhye, R.C. Chilate, P.B. Sonaware, A.S. Kumbhar, R.G. Yerande, Coord. Chem. Rev. 123 (1993) 49.
[3] D.X. West, J.S. Ives, J. Krejci, M.M. Salberg, T.L. Zumbahlen, G.A. Bain, A.E. Liberta, J. Valdes-Martinez, S. Hernadez-Ortiz, R.A. Toscano, Polyhedron 14 (1995) 2189.
[4] M. Joseph, M. Kuriakose, M.R.P. Kurup, E. Suresh, A. Kishore, S.G. Bhat, Polyhedron 25 (2006) 61.
[5] M.A. Ali, A.H. Mirza, A.M.S. Hossssian, M. Nazimuddin, Polyhedron 20 (2001) 1045.
[6] S. Lhuachan, S. Siripaisarnpipat, N. Chaichat, Eur. J. Inorg. Chem. (2003) 263.
[7] L.A. Ashfield, A.R. Cowley, J.R. Dilworth, P.S. Donnely, Inorg. Chem. 43 (2004) 4121.
[8] T.S. Lobana, Rekha, R.J. Butcher, Transition Met. Chem. 29 (2004) 291. and references therein.
[9] T.S. Lobana, S. Khanna, R.J. Butcher, A.D. Hunter, M. Zeller, Polyhedron 25 (2006) 2755.
[10] T.S. Lobana, Rekha, R.J. Butcher, A. Castineiras, E. Bermejo, P.V. Bharatam, Inorg. Chem. 45 (2006) 1535.
[11] T.S. Lobana, S. Khanna, R.J. Butcher, A.D. Hunter, M. Zeller, Inorg. Chem. 46 (2007) 5826.
[12] T.S. Lobana, S. Khanna, R.J. Butcher, Z. Anorg. Allg. Chem. 633 (2007) 1820.
[13] T.S. Lobana, Rekha, B.S. Sidhu, A. Castineiras, E. Bermejo, T. Nishioka, J. Coord. Chem. 58 (2005) 803.
[14] T.S. Lobana, Rekha, A.P.S. Pannu, G. Hundal, R.J. Butcher, A. Castineiras, Polyhedron 26 (2007) 2621.
[15] T.S. Lobana, S. Khanna, R. Sharma, G. Hundal, R. Sultana, M. Chaudhary, R.J. Butcher, A. Castineiras, Cryst. Growth Design 8 (2008) 1203.
[16] T.S. Lobana, S. Khanna, G. Hundal, B.-J. Liaw, C.W. Liu, Polyhedron 27 (2008) 2251.
[17] T.S. Lobana, S. Khanna, A. Catineiras, Inorg. Chem. Commun. 10 (2007) 1307.
[18] K. Onodera, N.C. Kasuga, T. Takashima, A. Hara, A. Amano, H. Murakami, K. Nomiya, J. Chem. Soc., Dalton Trans. (2007) 3646.
[19] I.G. Santos, A. Hagenbach, U. Abram, J. Chem. Soc., Dalton Trans. (2004) 677.
[20] A. Sreekanth, H.-K. Fun, M.R.P. Kurup, Inorg. Chem. Commun. 7 (2004) 1250.
[21] J.S. Casas, E.E. Catellano, M.D. Couce, J. Ellena, A. Sanchez, J. Sordo, C. Taboada, J. Inorg. Biochem. 100 (2006) 1858.
[22] U. Abram, K. Ortner, R. Gust, K. Sommer, J. Chem. Soc., Dalton Trans. (2000) 735.
[23] K. Ortner, U. Abram, Inorg. Chem. Commun. 1 (1998) 251.
[24] F. Bigoli, E. Leporati, M.A. Pellinghetti, Cryst. Struct. Commun. 4 (1975) 127.
[25] S. Knapp, T.P. Keenean, J. Liu, J.A. Potonza, H.J. Schugar, Inorg. Chem. 29 (1990) 2189.
[26] A.A. Duorkin, Y.A. Simonov, L.I. Budarin, E.V. Fesento, V.N. Kalinin, Kristallographie 35 (1990) 1460.
[27] D. Paekar, A.S. Craig, G. Ferguson, A.J. Lough, Polyhedron 8 (1989) 2951.
[28] A.J. Blake, G. Reid, M. Schroder, J. Chem. Soc., Dalton Trans. (1991) 615.
[29] J.L. Wang, M. Sin, F.M. Miao, S. Yu, F.S. Gong, X.H. Duan, Acta Crystallogr., Sect. C 47 (1991) 2203.
[30] N.K. Mills, A.H. White, J. Chem. Soc., Dalton Trans. 229 (1985) 4.
[31] P.J. Reddy, V. Raichandran, K.K. Chacko, E. Weber, W. Saenger, Acta Crystallogr., Sect. C 45 (1989) 1871.
[32] C.E. Halloway, M. Melnik, W.A. Nevin, W. Liu, J. Coord. Chem. 35 (1995) 85.
[33] (a) P.J. Blower, J.A. Clarkson, S.C. Rawle, J.A.R. Hartmom, R.E. Wolf Jr., R. Yagbasan, S.G. Bott, S.R. Cooper, Inorg. Chem. 28 (1989) 4040;
(b) P. Karagiannidis, P. Aslanidis, S. Kokkov, C.J. Cheer, Inorg. Chim. Acta 172 (1990) 247.
[34] (a) A.B. Corradi, G.G. Fava, M.B. Ferrari, M. Nardelli, Acta Crystallogr., Sect. C 43 (1987) 407;
(b) B. Norrin, A. Oskarsson, Acta Chem. Scand., Ser. A 39 (1985) 701.
[35] (a) M. Nardelli, G.G. Fava, G.G. Batlistini, A. Musatti, J. Chem. Soc., Chem. Commun. (1965) 187;
(b) M. Nardelli, G.G. Fava, I. Chierici, Ricierca Sci., Sect. A (1965) 480.
[36] C.E. Holloway, M. Melnik, W.A. Nevin, W. Liu, J. Coord. Chem. (Rev.) 35 (1995) 85.
[37] K. Nomiya, S. Takahashi, R. Noguchi, J. Chem. Soc., Dalton Trans. (2000) 2091.
[38] K. Nomiya, S. Takahashi, S.R. Noguchi, S. Nemoto, T. Takayama, M. Oda, Inorg. Chem. 39 (2000) 3301.
[39] (a) K. Nomiya, K. Tsuda, T. Sudoh, M. Oda, J. Inorg. Biochem. 68 (1997) 39;
(b) W. Su, M. Hong, J. Weng, Y. Liang, Y. Zhao, R. Cao, Z. Zhou, A.S.C. Chan, Inorg. Chim. Acta 331 (2002) 8.
[40] (a) M. Munakata, L.-P. Wu, T. Kuroda-Sowa, Adv. Inorg. Chem. 46 (1999) 173;
(b) T.S. Lobana, R. Sharma, R.J. Butcher, Polyhedron 27 (2008) 1375.
[41] B. Liu, G.-W. Zhou, M.-L. Fu, L. Xu, G.-C. Guo, J.-S. Huang, Bull. Korean Chem. Soc. 25 (2004) 1937.
[42] Bruker, SMART, SAINT and XREP, Area Detector Control, and Data Integration and Reduction Software, Bruker Analytical X-ray Instruments Inc., Madison, Wisconsin, USA, 1995.
[43] G.M. Sheldrick, SHELXL-97, Program for the Refinement of Crystal Structures, University of Goettingen, Germany, 1997.
[44] J.E. Huheey, E.A. Keiter, R.L. Keiter, Inorganic Chemistry: Principals of Structure and Reactivity, 4th Ed., Harper Collins College Publishers, New York, 1993.

position of $[Ni(O_4C_2)(H_2O)_4]$, without any additional reducing agents. This precursor is a cheap and easy prepared complex with low toxicity.

2. Experimental

All the chemical reagents used in our experiments were of analytical grade and were used as received without further purification. XRD patterns were recorded by a Rigaku D-max C III, X-ray diffractometer using Ni-filtered Cu Kα radiation. Transmission electron microscopy (TEM) images were obtained on a Philips EM208 transmission electron microscope with an accelerating voltage of 200 kV. Fourier transform infrared (FT-IR) spectra were recorded on Shimadzu Varian 4300 spectrophotometer in KBr pellets. The elemental analysis (carbon, hydrogen and nitrogen) of the materials was obtained from Carlo ERBA Model EA 1108 analyzer. Thermogravimetric-differential thermal analysis (TG-DTA) were carried out using a thermal gravimetric analysis instrument (Shimadzu TGA-50H) with a flow rate of 20.0 mL min^{-1} and a heating rate of 10 °C min^{-1}. The electronic spectra of the complexes were taken on a Shimadzu UV–visible scanning spectrometer (Model 2101 PC).

Nickel oxalate precursor was synthesized according to this procedure: the $Ni(COOCH_3)_2 \cdot 4H_2O$ was dissolved in 10 mL of distilled water to form a homogeneous solution. A stoichiometric amount of potassium oxalate dissolved in an equal volume of distilled water, was dropwise added into the above solution under magnetic stirring. The solution was stirred for about 15 min and a green precipitate was isolated, washed and dried at 50 ℃. The obtained product was characterized by FT-IR, elemental analyses and thermogravimetric analysis (TGA) [5]. *Anal.* Calc. for $[Ni(O_4C_2)(H_2O)_4]$: C, 10.98; H, 3.69; Ni, 26.83. Found: C, 10.89; H, 3.57; Ni, 26.74%.

The main synthetic procedure in order to approach to final products is a modified version of the method developed by Hyeon and others for the synthesis of metal nanocrystals that employ the thermal decomposition of transition metal complexes [23,24]. In current synthesis, NiO nanoclusters were prepared by the thermal decomposition of nickel oxalate as precursor. First 0.6 g of $[Ni(O_4C_2)(H_2O)_4]$ and 5 mL of $C_{18}H_{37}N$ were mixed to produce $[Ni(O_4C_2)(H_2O)_2]$–oleylamin as suggested intermediate precursor. The solution was placed in a 50 mL three-neck distillation flask and heated up to 140 ℃ for 60 min. Then 5 g of $C_{18}H_{15}P$ was injected into the resulting metal-complex solution at 240 ℃. The color of the solution changed from green to black, indicating generation of colloidal products. The black solution was aged at 240 ℃ for 45 min, and was then cooled to room temperature. The black products were precipitated by adding excess C_2H_5OH to the solution. The NiO nanoclusters were washed with C_2H_5OH. These products could easily be re-dispersed in nonpolar organic solvents, such as C_6H_{12} (Scheme 1). The synthesized nanoclusters were characterized by XRD, TEM, FT-IR and UV–Vis techniques.

3. Results and discussion

In order to make sure of the precursor composition, elemental analysis was done. The TGA curve of the as-prepared precursor is shown in Fig. 1. It can be seen that there are two distinct weight loss steps. The first weight loss occurs at 110–190 ℃, which corresponds to the evaporation of crystallized water, that is to say, nickel oxalate in the stage. The second weight loss step occurs at the temperature range 210–370 ℃. The weight loss at 210–370 ℃ may be ascribed to the decomposition of the oxalate. The weight loss of two steps is about 17.80% and 41.18%, which is close to the theoretical value.

The XRD diffraction patterns of the sample of nickel oxides were recorded for the identification of the products (Fig. 2). The main diffraction peaks were observed at 37.18°, 43.42°, 62.82°, 74.20° and 79.2° in the XRD pattern of the nickel oxide which confirm that the formed material is nickel oxide. The diffraction peaks match with the standard values and they can be indexed to pure cubic phase of NiO (*Fm3 m*) with lattice parameter $a = 4.1771$ Å (JCPDS: 78-0429). The crystal size of the NiO nanoclusters was estimated by Debye–Scherrer equation ($d = 0.9\lambda/\beta\cos\theta$) and it was about 2.7 nm, which is in agreement with the other observation results. The diffraction peaks are clearly broadened, which can be the result of the reduced particle size.

To investigate whether the surface of the nanoparticles was capped with organic surface, the Fourier transformed infrared (FT-IR) of the as-synthesized samples was performed. Fig. 3 shows the FT-IR spectra of NiO nanoclusters and progressive formatted

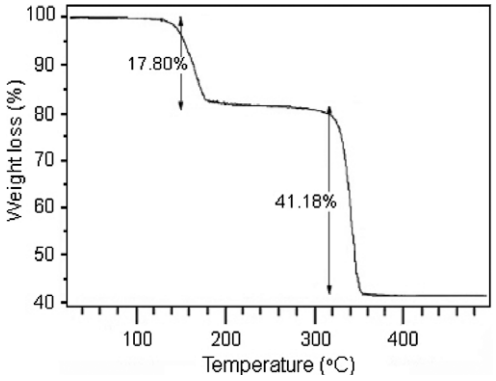
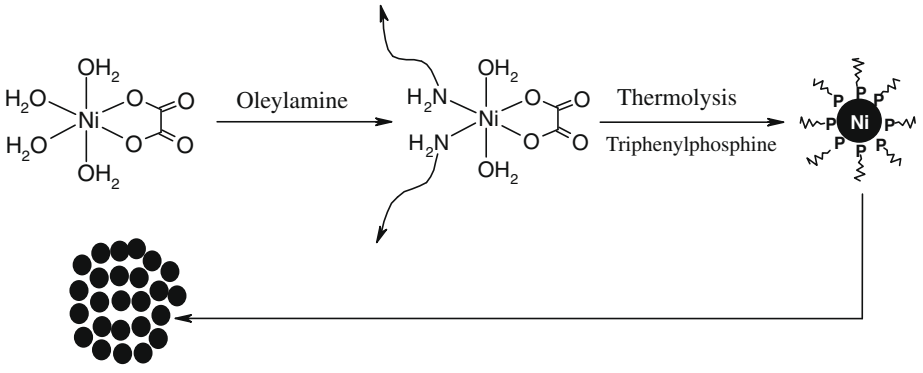


Fig. 1. TGA of the nickel oxalate precursor.



Scheme 1. Schematic diagram illustrating the formation of NiO nanoclusters.

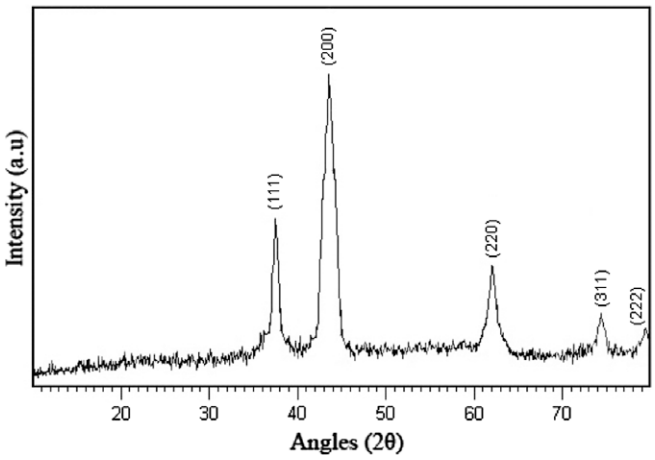


Fig. 2. XRD pattern of the NiO nanoclusters.

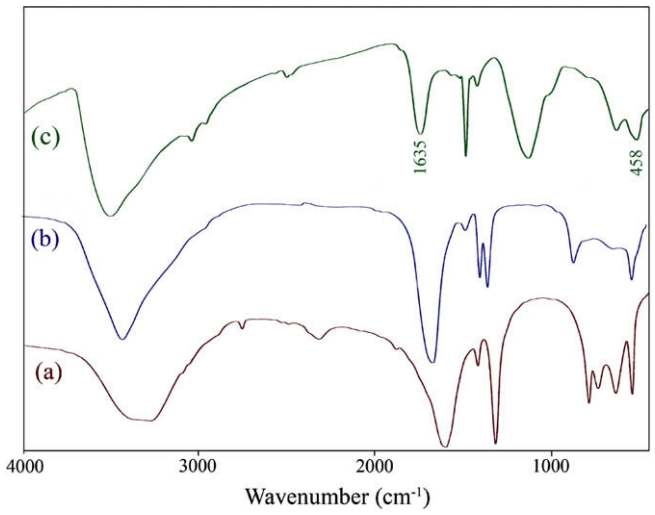


Fig. 3. FT-IR spectra of (a) $K_2C_2O_4 \cdot H_2O$, (b) $[Ni(O_4C_2)(H_2O)_4]$ and (c) NiO nanoclusters.

materials within the procedure. The board peaks at ca. 3350–3400 cm^{-1} in all three spectra are representative of H_2O. Curve c shows that the surface was hydroxylated because the sample was exposed to the ambient after calcinations and some water was adsorbed probably on the external surface of the samples during handling to record the spectra. In our measurement, number of weak peaks between ν1000–1400 and ν2800–3000 cm^{-1} are attributable to the symmetric and asymmetric stretching of the $-CH_2$ groups, terminal $-CH_3$ and $=CH$ of $C_{18}H_{37}N$. The H–OH bending vibration appears at 1635 cm^{-1}. The sharp peak at 1430 cm^{-1} can be assigned to the phenyl stretching mode υ(P–ph) (curve c). Also a characteristic broad band due to the C–N stretching mode was present at about 1150 cm^{-1}. So the oleylamine and TPP serves as the capping ligand that controls growth. Triphenylphosphine (TPP) was widely used in the synthesis of phosphine-stabilized metal nanoparticles [25]. Finally, the peak at 458 cm^{-1} in spectrum (curve c), showing Ni–O bonds, gave clear evidence about the presence of the crystalline NiO. In curve a, the narrow band at 465 cm^{-1} is attributed to the bending mode of –COO group [26]. The spectra of NiO nanoclusters shows two weak stretch vibrations at 2921 and 2865 cm^{-1} attributing to the C–H stretching modes of the $C_{18}H_{37}N$ carbon chain, indicating that $C_{18}H_{37}N$ molecules have been absorbed on the surface of NiO nanoclusters. So, the $C_{18}H_{37}N$ serves as the capping ligand that controls growth [24].

The surface morphological study of the nickel oxide nanoclusters was carried out using SEM images. Fig. 4a shows the SEM images of the nickel oxide samples. From the SEM analyses, one can conclude the formation of nanoclusters flower-like structure (Fig. 4a). The transmission electron microscopic (TEM) photographs and selected area electron diffraction (SAED) pattern of the product have been given in Fig. 4b and c. The size of nanoclusters obtained from the XRD diffraction patterns are in close agreement with the TEM studies which show sizes of 2–10 nm (Fig. 4c). The particle size distributions are shown as insets in Fig. 4b and c. Most of the particles in Fig. 4b and c have diameters of 3 and 5 nm, respectively, which compare well with the values calculated from the XRD pattern. These sizes are nearly spherical. Some loose spheres formed by aggregation of small particles can be observed in TEM images. We may consider that when the reaction was carried out at 240 ℃, most organic molecules such as oleylamine and triphenylphosphine were decomposed. Since only a few $C_{18}H_{37}N$ molecules were adsorbed on NiO nanoclusters loose solid was finally produced. The SAED pattern in the inset in Fig. 4b reveals that the NiO nanoclusters are crystalline.

Since the surface areas of metal nanoclusters are enormously relative to their masses, they have an excess free energy surface comparable to the lattice energy, making them thermodynamically unstable. Protective agents are therefore essential in order to be able to outweigh the attractive van der Waals forces by the repulsive steric forces. To achieve sufficient inter-particle separation, it can be helpful to use sterically demanding substituents [22]. In this work we have used $C_{18}H_{15}P$, (TPP) and as a ligand stabilizing agent to make nanoclusters stable and prevent their agglomeration. $C_{18}H_{15}P$ is a high-boiling point surfactant with a patulous structure providing greater steric hindrance. So, this agent might slow down the rate of agglomeration of the nanoparticles during their growth, resulting in much smaller nanoclusters. Also we have used $C_{18}H_{37}N$ as an additional surfactant in order to reduce the particle size much further and resulted in uniform size distribution (Fig. 4).

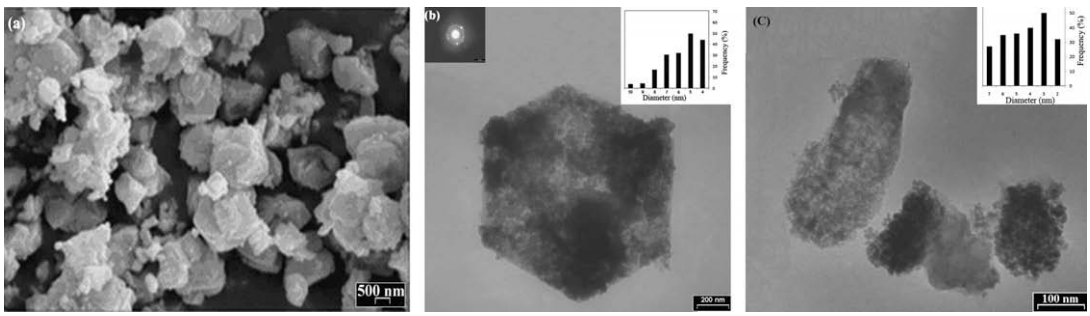


Fig. 4. (a) SEM; (b) and (c) TEM images of NiO nanoclusters (the inset shows the SAED pattern and the histograms of the particle size distributions).

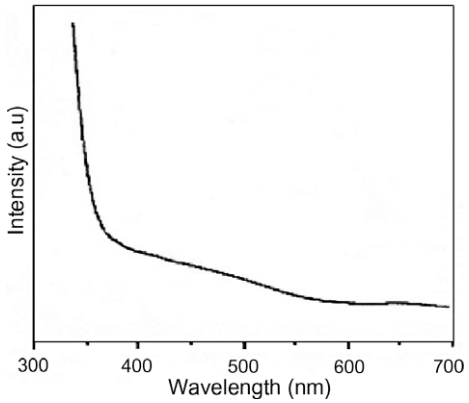


Fig. 5. UV–Vis absorption spectrum of the NiO nanoclusters dispersed in C_2H_5OH.

Table 1
Preparation of NiO under different conditions.

Sample	Capping agent	Temperature (℃)	Time	Particles size
1		450	2 h	9 nm [5]
2	oleylamine	240	45 min	agglomeration
3	TPP	240	45 min	no product
4	oleylamine + TPP	240	45 min	2.7 nm

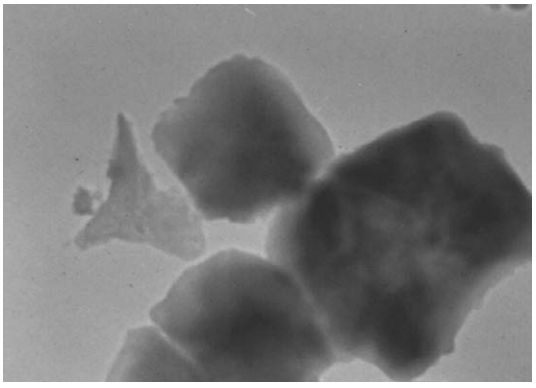


Fig. 6. NiO agglomerations (sample 2) synthesized in presence of oleylamine.

$C_{18}H_{37}N$ has been known as a ligand that binds tightly to the metal nanoparticles surface. The combined effects of TPP and $C_{18}H_{37}N$ were much more profound than those of individual contributions. Furthermore, as capping agents, TPP and oleylamine surround initial nuclei and result in decomposition of precursor in lower temperature (240 ℃). However, the decomposition without these capping agents (see Fig. 1) occurs in higher temperature (370 ℃) [27,28].

Fig. 5 is the UV–Vis spectrum of the as-synthesized NiO nanoclusters dispersed in ethanol. A strong absorption in the UV region is observed at wavelengths about 365 nm, while a broad absorption appears in the visible region. These absorptions can be attributed to intra-3d transition of Ni^{2+} in the cubic structure of NiO [29,30].

In addition, the nickel oxide nanoparticles have been prepared under different condition (Table 1). By controlling the quality of nanoparticles, NiO with various sizes can be formed. $[Ni(O_4C_2)(H_2O)_4]$ calcined at 450 ℃ for 2 h and resulted 9 nm nanoparticles (sample 1) [5], 0.5 g $[Ni(O_4C_2)(H_2O)_4]$ and 5 mL of oleylamine were mixed and heated in 240 ℃ for 45 min so led to NiO agglomerations which show size of more than 1000 nm (sample 2) (Fig. 6). Also 0.5 g $[Ni(O_4C_2)(H_2O)_4]$ and 5 g of TPP were heated together in 240 ℃ for 45 min, after washing with ethanol no precipitations were obtained. To prepare NiO nanoclusters (sample 4), the procedure mentioned in Section 2, including $C_{18}H_{37}N$ and TPP, was done. Considering different condition employed to prepare these samples, it is obvious that using both $C_{18}H_{37}N$ and TPP as capping agent is preferred for NiO nanoclusters synthesis.

4. Conclusion

NiO nanoclusters have been successfully synthesized through a thermal decomposition of new precursor $[Ni(O_4C_2)(H_2O)_4]$ in the presence of TPP and $C_{18}H_{37}N$. The as-synthesized nickel oxide nanoclusters show NiO with cubic structure without any other impurities. From the results of XRD, FT-IR and TEM, the NiO nanoclusters show good morphologies corresponding to nanosize about 2–10 nm, relatively.

Acknowledgement

Authors are grateful to council of University of Kashan for providing financial support to undertake this work.

References

[1] C.C. Chen, A.B. Herhold, C.S. Johnson, A.P. Alivisatos, Science 276 (1997) 398.
[2] Y. Wang, J. Zhu, X. Yang, L. Lu, X. Wang, Thermochim. Acta 437 (2005) 106.
[3] Y.R. Uhma, J.H. Park, W.W. Kima, C.H. Chob, C.K. Rhee, Mater. Sci. Eng. B 106 (2004) 224.
[4] S.H. Lin, F.R. Chen, J.J. Kai, Appl. Surf. Sci. 254 (2008) 3357.
[5] X. Wang, J. Song, L. Gao, J. Jin, H. Zheng, Z. Zhang, Nanotechnology 16 (2005) 37.
[6] H. Sato, T. Minami, S. Takata, T. Yamada, Thin Solid Films 236 (1993) 27.
[7] V. Srinivasan, J. Weidner, J. Electrochem. Soc. 144 (1997) L210.
[8] J. He, H. Lindström, A. Hagfeldt, S.E. Lindquist, J. Phys. Chem. B 103 (1999) 8940.
[9] R. Cinnsealach, G. Boschloo, S.N. Rao, D. Fitzmaurice, Sol. Energy Mater. Sol. Cells 57 (1999) 107.
[10] K. Yoshimura, T. Miki, S. Tanemura, Jpn. J. Appl. Phys. 34 (1995) 2440.
[11] C. Natarajan, H. Matsumoto, G. Nogami, J. Electrochem. Soc. 144 (1997) 121.
[12] C.S. Carney, C.J. Gump, A.W. Weimer, Mater. Sci. Eng. A 431 (2006) 1.
[13] A. Surca, B. Orel, B. Pihlar, P. Bukovec, J. Electroanal. Chem. 408 (1996) 83.
[14] J.H. Liang; Y.D. Li, Chem. Lett. 32 (2003) 1126.
[15] Z.H. Liang, Y.J. Zhu, X.L. Hu, J. Phys. Chem. B 108 (2004) 3488.
[16] D.N. Yang, R.M. Wang, J. Zhang, Z.F. Liu, J. Phys. Chem. B 108 (2004) 7531.
[17] R.H. Kodama, S.A. Makhlouf, A.E. Berkowitz, Phys. Rev. Lett. 79 (1997) 1393.
[18] M.H. Shah, Nanoscale Res. Lett. 3 (2008) 255.
[19] P. Palanisamy, A.M. Raichur, Mater. Sci. Eng. C 29 (2009) 199.
[20] X. Song, L. Gao, J. Am. Ceram. Soc. 91 (2008) 3465.
[21] S. Rodríguez-Llamazares, J. Merchán, I. Olmedo, H.P. Marambio, J.P.Muñoz, P. Jara, J.C. Sturm, B. Chornik, O. Peña, N. Yutronic, M.J. Kogan, J. Nanosci. Nanotech. 8 (2008) 3820.
[22] B. Corain, G. Schmid, N. Toshima (Eds.), Catalysis and Materials Science: The Issue of Size Control, Elsevier Publishers, Oxford, 2008, p. 21.
[23] J. Park, E. Kang, S.U. Son, H.M. Park, M.K. Lee, J. Kim, et al., Adv. Mater. 17 (2005) 429.
[24] M. Salavati-Niasari, F. Davar, M. Mazaheri, M. Shaterian, J. Magn. Magn. Mater. 320 (2008) 575.
[25] H.T. Yang, Y.K. Su, C.M. Shen, T.Z. Yang, H.J. Gao, Surf. Interf. Anal. 36 (2004) 155.
[26] K. Nakamoto, Infrared and Raman spectra of Inorganic and Coordination Compounds, 4th Ed., Wiley, VCH, 1986, p. 245.
[27] M. Salavati-Niasari, Z. Fereshteh, F. Davar, Polyhedron 28 (2009) 126.
[28] M. Salavati-Niasari, F. Davar, N. Mir, Polyhedron 27 (2008) 3514.
[29] G. Boschloo, A. Hagfeldt, J. Phys. Chem. B 105 (2001) 3039.
[30] T. Tsuboi, W. Kleeman, J. Phys.: Condens. Matter 6 (1994) 8625.

carrying ortho hydroxy naphthaldimine parts **(3)**, and present the complexation properties of the ligand with a series of metal cation. The complex stability constants and complex compositions of metal cations with the ligand were determined by using spectrofluorimetric titrations in acetonitrile-dichloromethane (9.5/0.5).

2. Experimental

2.1. Chemicals

Acetonitrile and dichloromethane from Merck (spectrometric grade) were the solvents for absorption and fluorescence measurements. All metal perchlorates purchased from Acros were of the highest quality available and vacuum dried over blue silica gel before use.

2.2. Apparatus

^{1}H NMR and ^{13}C NMR spectra were recorded on a Varian 200 A spectrometer, using $CDCl_3$ with TMS as the internal reference. IR spectra were recorded on a Perkin–Elmer 1600 FTlR spectrophotometer using KBr pellets. The absorption spectra of the solutions were recorded using a Unicam UV2 spectrophotometer. Mass spectra of the ligand was measured on a Micromass Quattro LC-MS/MS spectrometer. Elemental analysis was performed on Costech 4010 CHNS instrument. A Photon Technologies International Quanta Master Spectrofluorimeter (model QM-4/2006) was used for all fluorescence measurements.

2.3. Measurements

Absorption spectra of fluoroionophore **(3)** with a concentration of 2.58×10^{-5} M in acetonitrile-dichloromethane solution (9.5/0.5) containing 100 molar equivalents of appropriate metal perchlorate salt were measured using 1-cm long absorption cell. Fluorescence spectra of the ligand solutions of 2.58×10^{-6} M were measured in 1-cm quartz cell. Excitation wavelength was 380 nm for **(3)**. Fluorescence emission spectra were recorded in the range 400–600 nm with slit width 1.0 nm.

The stoichiometry of the complexes was determined by using the molar-ratio method. The stability constants were calculated according to the procedure described in literature [25].

2.4. Synthesis

2.4.1. Synthesis of ligand *(3)*

Compound **(1)** [26] (0.195 g, 0.37 mmol) was dissolved in dry dioxane (15 mL) and purged under nitrogen atmosphere in a Schlenk system connected to a vacuum line. A solution of 2-hydroxy-1-naphthaldehyde **(2)** (0.128 g, 0.74 mmol) in dry dioxane (15 mL) was added dropwise to this solution for 30 min. at 40 °C. The reaction mixture was refluxed and stirred at reflux temperature for 32 h, monitored by TLC [silica gel (ethyl alcohol)]. At the end of this period, the red solution was concentrated on an evaporator to 10 mL and the dark red solid formed was filtered off, washed with hot ethanol and cold diethyl ether, then dried *in vacuo*. The dark red solid product (yield 96%) was obtained by recrystallization from ethanol, mp 233–235 °C. *Anal.* Calc. for $C_{50}H_{46}N_4O_4S_2$: C, 72.26; H, 5.58; N, 6.74; S, 7.72. Found: C, 72.69; H, 5.75; N, 6.52; S, 7.08%. IR (KBr pellets, cm^{-1}): 3433 (O–H), 3053 (Ar–H), 2928–2797 (C–H), 1620 (C=N). ^{1}H NMR ($CDCl_3$): (δ) 15.26 (s, 2H, O–H), 9.35 (s, 2H, CH=N), 7.51–8.16 (m, 12H, napht.-H), 6.80–7.47 (m, 10H, macrocyc.-H) 4.25 (s, 4H, Ar–CH_2), 3.41 (t, 4H, O–CH_2), 3.35–2.61 (m, 8H, N–CH_2), 2.57 (t, 4H, S–CH_2). ^{13}C NMR ($CDCl_3$): (δ) 167.68, 155.30, 148.01, 140.81, 135.93, 135.25, 135.01, 132.98, 132.49, 132.44, 132.01, 129.34, 127.82, 127.48, 123.44, 121.72, 119.14, 109.36, 103.17, 66.22, 59.97, 53.25, 51.26, 33.65, MS (EI): m/z = 831.32 $[M]^+$.

3. Results and discussion

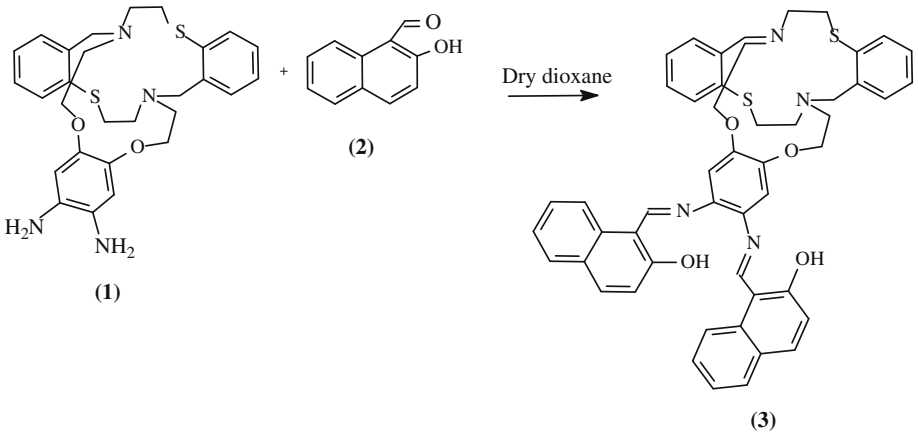
3.1. Characterization of the ligand *(3)*

The synthetic pathway to new Schiff base ligand **(3)** is summarized in Scheme 1. Compound **(1)** was prepared according to the previous papers [26].

Compound **(3)** was synthesized by reaction of compound **(1)** with 2-hydroxy-1-naphthaldhyde **(2)** in dry dioxane. IR spectra of the diamine Schiff base naphthaldimine **(3)** show a broad band at 3435 cm^{-1} for OH stretching vibration. This band shifts towards 2791 cm^{-1} due to the increasing strength of the OH···N hydrogen bond. In the IR spectrum of compound **(3)**, the C=N stretching vibration was observed at 1620 and 1602 cm^{-1} as a strong absorption. The coexistence of two different hydrogen bond types within Schiff base molecule can be possible. There is such example of diamine Schiff base naphtaldimine molecule in which one naphtaldimine part exists in enol-imine (A form), while the other exists in keto-amine (H form) [17]. The bands at about 1541 and 1507 cm^{-1} stems from the stretching vibrations of the skeleton NH–C=C–C=O, which belongs to the keto-amine tautomer. The absence of primary aromatic amine groups belonging to compound **(1)** and carbonyl groups belonging to compound **(2)** has also supported the structure. In the ^{1}H NMR spectrum of **(3)**, the chemical shifts belong to HC=N protons at δ = 9.35 ppm. The absence of the singlet at δ = 5.23 ppm belonging to primary aromatic amine groups of the starting material, supports the formation of compound **(3)**. The resonance of moving hydroxyl group was observed at δ = 15.26 ppm for this compound. ^{13}C NMR spectral data is also in good agreement with this structure. For ligand **(3)**, the value of the chemical shift of the phenolic carbon atom at δ = 167.68 ppm suggests the coexistence of enol-imine and keto-amine forms. The carbon resonance of azomethine group was observed at δ = 155.30 ppm. The result of the mass spectral data at m/z = 831.06 $[M]^+$ confirms the formation of compound **(3)**.

3.2. Absorption spectra

As seen from Fig. 1, ligand **(3)** possesses five absorption bands with maximums at 200, 260, 323, 377 and 475 nm in acetonitrile-dichloromethane (9.5/0.5). Molar absorption coefficients are 7.5×10^4, 1.8×10^4, 8.7×10^3, 1.0×10^4 and 4.8×10^3 cm^{-1} M^{-1} in these wavelengths, respectively. The presence of 100 equivalents of Mn^{2+}, Ni^{2+} and Co^{2+} cations produces modest changes in the absorption of the ligand (Fig. 1c and d). These metal cations caused a decrease of absorption at 377 nm. On the other hand, there was a red shift in this wavelength for Mn^{2+}. These results suggest that the mentioned cations affected the keto–enol tautomeric equilibrium of the ligand (Scheme 2). Especially, that new broad band at about 450 nm caused by Mn^{2+} may have resulted from the shifting of the tautomeric equilibrium from the enol to the keto form. The effects of Fe^{2+} and Fe^{3+} ions on the absorption spectra of the ligand are pronounced. As seen from Fig. 1a, the interaction of Fe^{3+} with the ligand markedly increased absorptions in all parts of the spectrum except for the one at about 475 nm. However, Fe^{2+} caused a decrease of absorption above 220 nm. Similar effect was also observed for Pb^{2+} (Fig. 1b). Fe^{3+} gives a new strong absorption band at 344 nm with the molar absorptivity coefficient of 1.6×10^5 cm^{-1} M^{-1}. Namely, there was a blue shift by 33 nm in the 377 nm absorption band for



Scheme 1. Synthetic pathway to new macrocyclic ligand **(3)** used in this study.

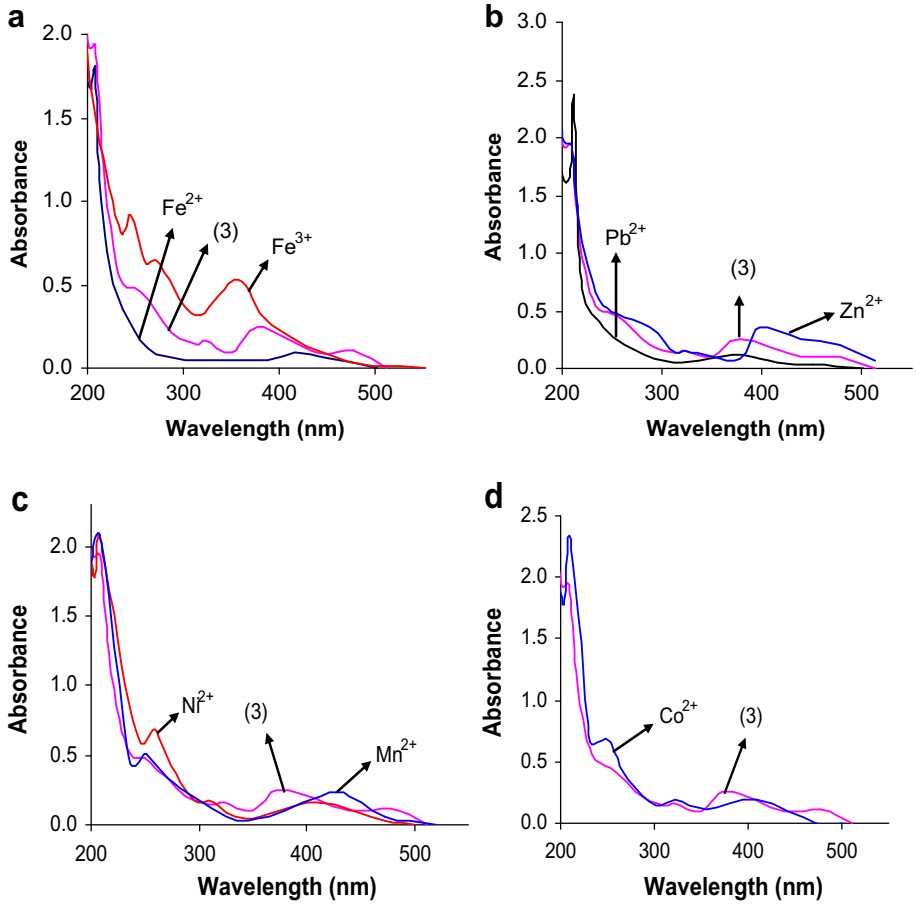
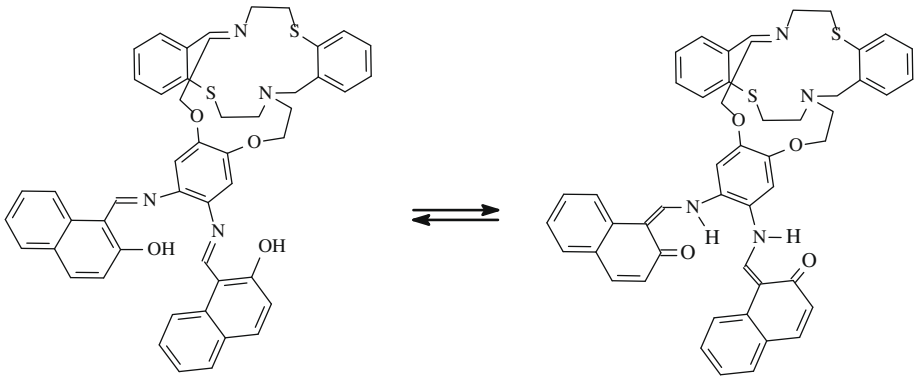


Fig. 1. The effect of metal cations on the absorption spectra of **(3)** in acetonitrile-dichloromethane solution (9.5/0.5): (a) for Fe^{2+} and Fe^{3+}; (b) for Zn^{2+} and Pb^{2+}; (c) Mn^{2+} and Ni^{2+}; (d) for Co^{2+}. Ligand concentration: 2.58×10^{-5} M. Metal perchlorate concentrations: 2.58×10^{-3} M.

Fe^{3+} cation. The absence of the 475 nm absorption band shows that Fe^{3+} caused the tautomeric equilibrium shift to the enol-imine form.

The absorption spectrum around 260 nm, attributed to the benzo-cryptand moiety, showed an enhancement of absorbance for Fe^{3+}, Co^{2+} and Ni^{2+}. This result can be explained by the disruption of the π-conjugated system between benzene and naphthaldimine groups. Similar changes in the absorption spectrum of benzo-15-crown-5 possessing 1-naphthaleneacetamide moiety in the binding of cation were observed in literature [27].

The change in the absorption spectra of ligand **(3)** with increasing concentrations of Zn^{2+} is shown in Fig. 2. Fig. 2a shows the change in the absorption spectra between 190 and 320 nm. There were two isobestic points at 215 and 240 nm. This result indicates that there were two equilibriums during the complexation. The decrease of absorbance at 220 nm provided the determination of the complex composition of Zn^{2+}-ligand **(3)**. There was a good relationship between $A_o - A$ and $[M]/[L]$ at 220 nm. A_o and A are the absorbance of free ligand and the absorbance of the solution involving Zn^{2+} cation, respectively. As seen from Fig. 2a (inset), the complex



Enol-imine (A form) Keto-amine (H form)

Scheme 2. Tautomeric forms (enol-imine and keto-amine) of the new macrobicyclic Schiff base ligand **(3)**.

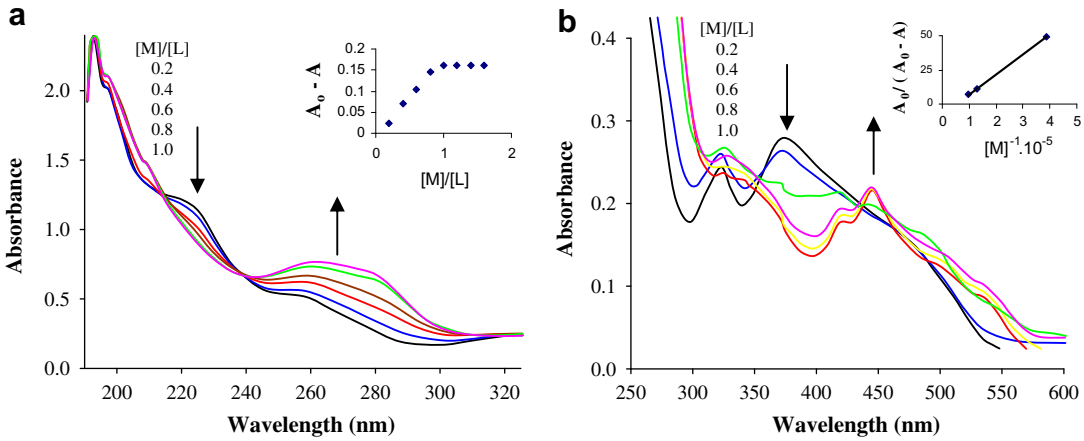


Fig. 2. Absorption spectra of **(3)** complexed with Zn^{2+}. (a) Between 190 and 320 nm and (b) between 250 and 600 nm. The spectral changes during the addition of 0–1 equivalent of $Zn(ClO_4)_2$. Ligand concentration: 2.58×10^{-5} M. Insets: measurements were carried out at 220 nm.

composition was 1:1 (*M*:*L*). The absorbance around 280 nm resulted from the naphthalene moieties accordingly increased during the complexation. This result suggests that a large conformational change occurred around the naphthalene groups. Fig. 2b shows the change in the absorption spectra between 250 and 500 nm with increasing amounts of Zn^{2+} ions. There was no isobestic point observed between these wavelengths. However, there were regular absorption changes at 377 and 450 nm. Pronounced decreases of absorbance with increases of the Zn^{2+} ion concentration was observed at 377 nm. On the contrary, there was regular absorption increases at 425 nm with increases of the Zn^{2+} ion concentration. This shows that the complexation shifts the equilibrium from the enol-imine form to keto-amine form.

The change in the absorption spectra of ligand **(3)** with increasing concentrations of Co^{2+} is shown in Fig. 3. Fig. 3a shows the change in the absorption spectra between 190 and 320 nm. The changes in the absorption spectra were very similar to that in the case of Zn^{2+} ion. The absorption decrease was observed at 220 nm with increases of the Co^{2+} ion concentration. Fig. 3a (inset) shows the molar-ratio plot for Co^{2+}. A_o and A are the absorbance of free ligand and the absorbance of the solution involving Co^{2+} cation, respectively. The inflection point was 1.0 ([*M*]/[*L*]). It can thus be concluded that ligand **(3)** formed a stable 1:1 (*M*:*L*) complex with Co^{2+}. The isobestic point at 237 nm was not clear when it was observed in detail. This seems to be due to the presence of small amounts of free ligand. Fig. 3b shows the change in the absorption spectra between 250 and 500 nm with increasing amounts of Co^{2+} ions. As seen from the Fig. 3b, two well-pronounced isobestic points were observed at 350 and 400 nm. Totally, three isobestic points were found in the absorption spectrum as a result of the Co^{2+} binding. These results indicate that there were three equilibriums during the complexation.

In order to determine the complex stability constant, the ratio of $A_o/(A_o - A)$ was plotted versus $[M]^{-1}$, as in Figs. 2b and 3b, which gave a good straight line. The stability constant was calculated from the ratio intercept/slope [25]. The values of Log *K* were 4.87 and 4.22 for the Zn^{2+}- and Co^{2+} complex, respectively. The calculations were carried out at 220 nm (Table 1).

3.3. Fluorescence spectra

Excitation at 380 nm gives an emission band with a maximum 463 nm for the ligand **(3)**. Fig. 4 shows the effects of the metal cations on the fluorescence spectra of ligand **(3)**. As seen from Fig. 4, the maximum emission band intensities of the ligand **(3)** accordingly reduced over the interaction with the metal cation except for Fe^{3+} and Zn^{2+}. There is a blue shift and an enhancement in the fluorescence intensity upon the addition of guest cations Fe^{3+} and Zn^{2+}. PET (photo-induced electron transfer) is hindered by the use of one electron pair of N of the imine group because of the complexation of these cations. Namely, fluorescence intensity is enhanced upon cation binding. Similar fluorescence enhance-

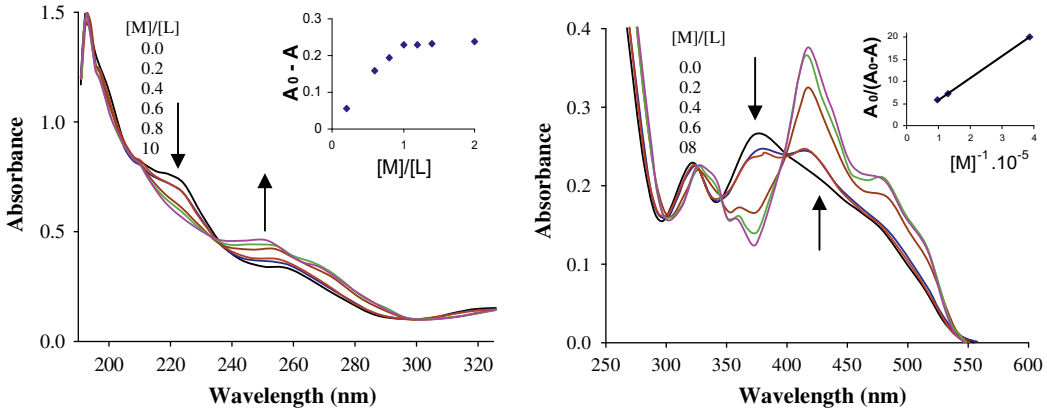


Fig. 3. Absorption spectra of **(3)** complexed with Co^{2+}. (a) Between 190 and 320 nm and (b) between 250 and 600 nm. The spectral changes during the addition of 0–1 equivalent of $Co(ClO_4)_2$. Ligand concentration: 2.58×10^{-5} M. Insets: Measurements were carried out at 220 nm.

ments were observed in the complexation of the Schiff base derived from salicylaldehyde with Zn^{2+} cation [28].

The transition metal cations such as Pb^{2+}, Co^{2+}, Ni^{2+}, Mn^{2+} and Fe^{2+} caused strong quenching of the fluorescence emission of the ligand. A decrease of the fluorescence intensity caused by these cations is probably a result of the "heavy atom effect" [29]. The incorporation of heavy metal cation into the structure leads to increase the rate of intersystem crossing (ISC) by spin-orbit coupling. This effect is known as "heavy atom effect". Especially, there was an important quenching for Ni^{2+} and Co^{2+}. The quenching effect after the formation of the Co^{2+} and Ni^{2+}-complex can be ascribed to either a naphthyl-to-metal energy transfer (ET) or a metal-to-naphthyl electron transfer (et) mechanism [30].

The effect of Fe^{2+} and Fe^{3+} is opposite on the fluorescence spectra of the ligand. While Fe^{2+} causes a strong quenching, Fe^{3+} causes an enhancement with a blue shift by 30 nm on the spectra. This result shows that the emission mechanism occurring through the complexation is different for these cations. The blue shift was about 13 nm for Zn^{2+} cation. This result shows that increasing the charge density of the transition metal cation causes more blue shift.

The complex formation was monitored by the effect of gradual addition of perchlorate salts to the solution of the ligand. The successive decrease of the emission intensity with addition of Co^{2+} was observed for the fluorimetric titrations. Fig. 5 shows the decrease of the emission of ligand **(3)** with addition of Co^{2+} ion. The values of $I_o - I$ at 463 nm was plotted against the ratio of [metal]/[ligand]. I_o and I are the fluorescence intensity of free ligand and the fluorescence intensity of the solution involving Co^{2+} cation, respectively. The curve obtained (Fig. 5 inset) clearly shows the formation of a 1:1 (M:L) complex for the ligand **(3)** with Co^{2+}.

Similarly, the decrease of the emission intensity with addition of Ni^{2+} was observed for the fluorimetric titrations. Fig. 6 shows

Table 1
Complex stability constants and complex composition of ligand **(3)** with metal cations in acetonitrile-dichloromethane (9.5/0.5).

Cation	Complex composition[a] (M:L)	Stability constant[a]	
		(Log K)[b]	(Log K)[c]
Zn^{2+}	1:1		4.87 ± 0.30
Co^{2+}	1:1	4.22 ± 0.14	4.22 ± 0.41
Ni^{2+}	2:1	4.68 ± 0.04	

[a] Averages calculated from the data obtained from four independent absorbance and fluorescence measurements.
[b] Obtained from the fluorescence measurements.
[c] Obtained from the absorbance measurements.

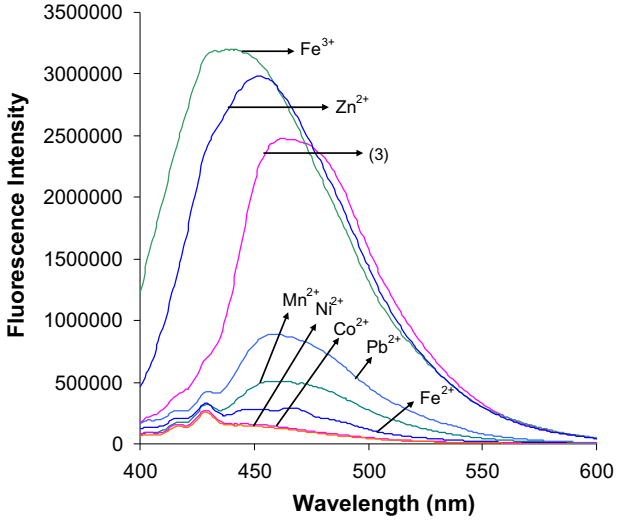


Fig. 4. Effects of metal cations on fluorescence spectra of ligand **(3)** in acetonitrile-dichloromethane solution (9.5/0.5). (Ligand concentration = 2.58×10^{-6} M. Metal perchlorate concentrations = 2.58×10^{-3} M. Excitation at 380 nm.)

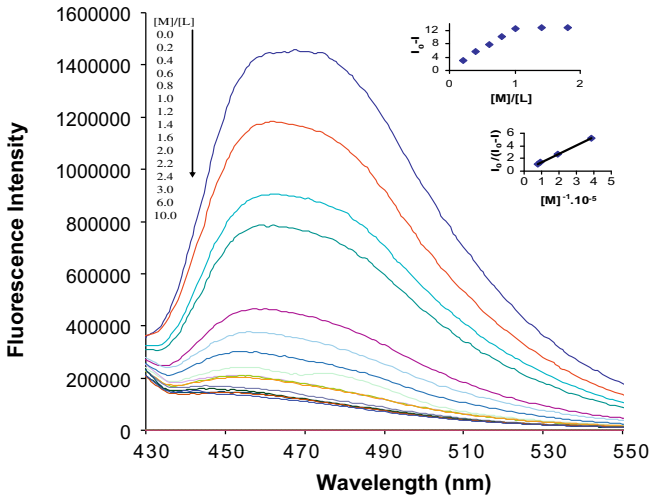


Fig. 5. Fluorescence spectra (λ_{exc}: 380 nm, λ_{em}: 463 nm) of ligand **(3)** in acetonitrile-dichloromethane (9.5/0.5) with increasing amounts of Co^{2+} ions. [L]: 2.58×10^{-6} M.

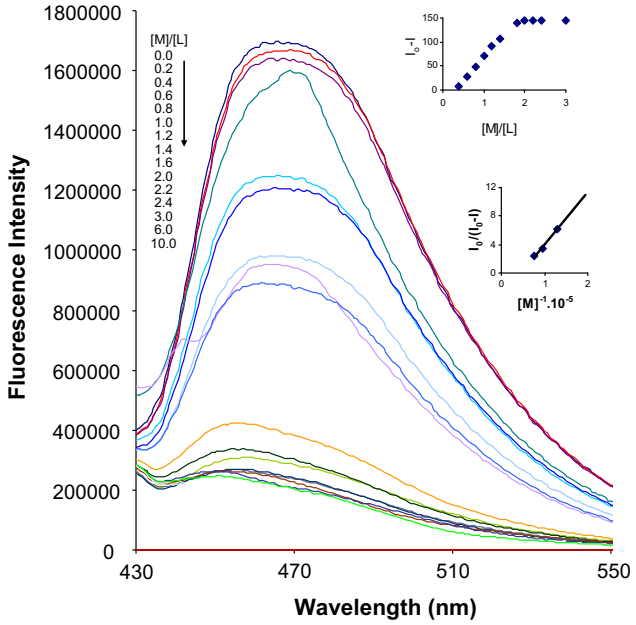


Fig. 6. Fluorescence spectra (λ_{exc}: 380 nm, λ_{em}: 463 nm) of ligand **(3)** in acetonitrile-dichloromethane (9.5/0.5) with increasing amounts of Ni^{2+} ions. [*L*]: 2.58×10^{-6} M.

the decrease of the emission of ligand **(3)** with addition of Ni^{2+} ion. The $I_o - I$ values at 463 nm was plotted against the ratio of [metal]/[ligand]. I_o and I are the fluorescence intensity of free ligand and the fluorescence intensity of the solution involving Ni^{2+} cation, respectively. The curve obtained (Fig. 6 inset) clearly shows the formation of a 2:1 (*M*:*L*) complex for the ligand **(3)** with Ni^{2+}. We did not observe a regular change in the fluorescence spectra of the ligand in the titrations with other tested metal cations. As seen from Table 1, the values of Log *K* were 4.68 and 4.22 for the Ni^{2+}- and Co^{2+} complex, respectively. The values of stability constant from obtained absorption and emission measurements for the Co^{2+} complex with 4.22 were in agreement (Table 1).

Acknowledgment

This work was supported by the Scientific and Technological Research Council of Turkey (TUBITAK).

References

[1] John C. Crano, Robert J. Guglielmetti (Eds.), Organic Photochromic and Thermochromic Compounds, Springer, 1999.
[2] M. Irie, Chem. Rev. 100 (2000) 1685.
[3] E. Hadjoidis, A. Rontoyianni, K. Ambroziac, T. Dziembowska, I.M. Marvidis, J. Photochem. Photobiol. A: Chem. 162 (2004) 521.
[4] A. Oshima, A. Momotake, T. Arai, J. Photochem. Photobiol. A: Chem. 162 (2004) 473.
[5] P. Fita, E. Luzina, T. Dziembowska, Cz. Radzewicz, A. Grabowska, J. Chem. Phys. 125 (2006) 184508.
[6] Y. Huisen, X. Xinfu, Chem. J. Internet 5 (2) (2003) 052017.
[7] A.C. Olivieri, R.B. Wilson, I.C. Paul, D.Y. Curtin, J. Am. Chem. Soc. 111 (1989) 5525.
[8] H. Josi, F.S. Kamounah, C. Gooijer, G. Zwan, L. Antonov, J. Photochem. Photobiol. A: Chem. 152 (2002) 183.
[9] P. Fita, E. Luzina, T. Dziembowska, D. Kopec, P. Piatkowski, Cz. Radzewicz, A. Grabowska, Chem. Phys. Lett. 416 (2005) 305.
[10] S. Mahanta, R.B. Singh, S. Kar, N. Guchait, Chem. Phys. 324 (2006) 742.
[11] H. Ünver, M. Kabak, D.M. Zengin, T.N. Durlu, J. Chem. Crystallogr. 31 (2001) 203.
[12] M. Yıldız, H. Ünver, D. Erdener, N. Ocak, A. Erdönmez, T.N. Durlu, Cryst. Res. Technol. 41 (2006) 600.
[13] Z. Rozwadowski, W. Schlif, B. Kamienski, Magn. Reson. Chem. 43 (2005) 573–577.
[14] J. Matijevic-Sosa, M. Vinkovic, D. Vikic-Topic, Croat. Chem. Acta 79 (2006) 489.
[15] S.H. Alarcon, A.C. Olivieri, D. Sanz, R.M. Claramunt, J. Elguero, J. Mol. Struct. 705 (2004) 1.
[16] K. Ambroziak, Z. Rodwadowski, T. Dziembowska, B. Bieg, J. Mol. Struct. 615 (2002) 109.
[17] Z. Popovic, V. Roje, G. Pavlovic, D. Matkovic-Calogovic, G. Giester, J. Mol. Struct. 597 (3) (2001) 9.
[18] P.V. Rao, C.P. Rao, E.K. Wegelius, K. Rissanen, J. Chem. Crystallogr. 33 (2003) 139.
[19] W.M.F. Fabian, L. Antonov, D. Nedeltcheva, F.S. Kamounah, P.J. Taylor, J. Phys. Chem. A 108 (2004) 7603.
[20] L. Antonov, W.M.F. Fabian, D. Nedeltcheva, F.S. Kamounah, J. Chem. Soc., Perkin Trans. 2 (2000) 1173.
[21] A.M. Asiri, K.O. Badahdah, Molecules 12 (2007) 1796.
[22] W. Zeng, J. Li, Z. Mao, Z. Hong, S. Qin, Adv. Synth. Catal. 346 (2004) 1385.
[23] Z. Hayvali, N. Gündüz, Z. Kiliç, E. Weber, J. Pract. Chem. 341 (1999) 568.
[24] X. Wei, Z. Mao, J. Li, S. Qin, Synthetic Commun. 34 (2004) 1237.
[25] J. Bourson, B. Valeur, J. Phys. Chem. 93 (1989) 3871.
[26] H. Kantekin, Ü. Ocak, Y. Gök, H. Alp, Polyhedron 21 (2002) 1865.
[27] H. Hama, T. Morozumi, H. Nakamura, Tetrahedron Lett. 48 (2007) 1859.
[28] L. Gao, Y. Wang, J. Wang, L. Huang, L. Shi, X. Fan, Z. Zou, T. Yu, M. Zhu, Z. Li, Inorg. Chem. 45 (2006) 6844.
[29] H. Warmke, W. Wiczk, T. Ossowski, Talanta 52 (2000) 449.
[30] J.S. Kim, D.T. Quang, Chem. Rev. 107 (2007) 3780.

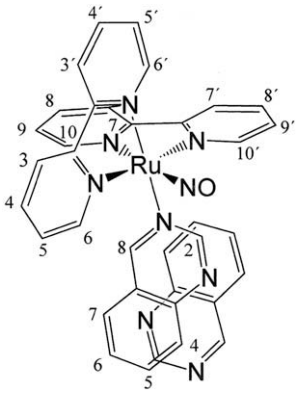


Fig. 1. Pictorial view of the *cis*-$[Ru(bpy)_2(qui)NO](PF_6)_3 \cdot (qui)$ structure and NMR labels.

Then, 303 mg of *cis*-$[Ru(bpy)_2(qui)(NO_2)]PF_6$ were dissolved in 20 mL of methanol. Next, 4 mL of HPF_6 were added to this solution and the reaction mixture was allowed to react for 1 h. The resulting yellowish solid was collected by filtration, washed with methanol and diethyl ether, and dried under vacuum. Yield 311 mg (74%). FT-IR (KBr): ν(NO) = 1944 cm^{-1}. *Anal.* Calc. for $RuC_{36}H_{28}N_9OP_3F_{18}$: C, 38.3; H, 2.7; N, 11.2. Found: C, 38.0; H, 2.5; N, 11.1% (*Caution:* The compound must be handled with care because it appears to be hygroscopic and sensitive to light exposure).

2.2. Physical measurements

All the UV–Vis spectra were recorded on a Hitachi U-3501 spectrophotometer in different solvents, at solution concentrations of approximately 10^{-5} mol L^{-1}. The infrared spectra were registered on an FT-IR/Nicolet spectrometer, model Protegé 460, from KBr pellets. The ^1H and COSY NMR measurements were performed from a 10^{-2} mol L^{-1} CD_3CN solution, in a Bruker DRX 500 MHz spectrometer and the NOESY spectrum were recorded on a Bruker DPX 300 MHz, under the same solution conditions, with mixing time t_m = 700 ms. The ESI MS mass spectrum were acquired using a high-resolution hybrid quadrupole (q) and orthogonal time-of-flight (TOF) mass spectrometer (QTOF from Waters Micromass, UK) operating in the positive ion mode at ca. 5000 resolving power. The temperature of the nebulizer was 150 °C, the cone voltage was 30 V and the sample were dissolved in a water/ethanol 1:1 (v:v) mixture. Photolysis of the complex was carried out in a water/ethanol 1:1 (v:v) deaerated mixture. The light source was the output from a 200 mW high-pressure mercury lamp and a 400 nm interference filter, to enable selection of the desired irradiation wavelength range. A sample of known volume was placed in a 1-cm quartz cuvette at 25 °C and maintained under continuous stirring while irradiated. UV–Vis spectra were recorded after pre-defined time intervals. NO release from the complex during visible irradiation was measured using a specific NO-selective electrode (ISO-NOP NO meter, World Precision Instruments, Sarasota, FL, USA). The calibration curve of the NO-selective electrode was prepared by using several dilutions of a known volume of a saturated NO solution in 10.0 mL of deaerated acetate buffer solution (pH 7.4). The current value in nA was recorded for each added volume. NO concentration was calculated according to the NO molar fraction solubility of NO (2.1×10^{-3} mol L^{-1} at 25 °C). The sensitivity of this apparatus ranged from 1 nM to 20 μM, with a 2-mm sensor, which directly detected NO concentration by an amperometric technique. Photolysis in aqueous media under physiological conditions was carried out as described above, using a solution of complex in PBS buffer.

pH values were recorded on a Labmeter pH meter model PH2. In order to evaluate the pK_a of the quinazoline ligand in the complex and the pH for the conversion of coordinated NO^+ into NO_2^-, absorption spectra of the complex solutions at different pH values were registered. Variations in the absorbance values of the bands, recorded in the visible region, were plotted against the pH. The curves were differentiated for determination of the pK_a values. Mcllvaine buffer solutions were used for the pH range 2.5–7.5 while the Kolthoff buffer was used for pH 10 [19]. For the pH range 0–2.5, trifluoroacetic acid and NaOH 0.1 mol L^{-1} solutions were employed. Other pH values were obtained by combinations of NaOH and HCl solutions. All solutions were prepared from KCl 0.1 mol L^{-1} solutions.

3. Results and discussion

3.1. NMR and ESI MS structural characterization

Compound *cis*-$[Ru(bpy)_2(qui)NO](PF_6)_3 \cdot (qui)$ was obtained following a synthetic procedure previously reported for analogous nitrosyl complexes [18]. Elemental analysis results suggest that the complex was isolated with an additional *qui* molecule. Contamination was excluded on the basis of the apparent 1:1 stoichiometric relation between the complex and non-coordinated *qui*, not to mention the fact that the complex was washed with methanol after filtration, a solvent in which the ligand is fully soluble. To verify whether the investigated complex was associated with this additional quinazoline molecule in solution, its structural characterization was performed by ^1H 1D and COSY 2D NMR. Table 1 summarizes the tentative assignment of the signals observed in the ^1H NMR spectrum of the *cis*-$[Ru(bpy)_2(qui)NO](PF_6)_3 \cdot (qui)$ complex. Assignments are based on literature data for related species [20], and comparison with chemical shift values (δ) of the free ligands was carried out [21]. Correlations observed in the COSY

Table 1
Tentative assignment of the ^1H chemical shift values δ (ppm) for the compound $[Ru(bpy)_2(qui)(NO)](PF_6)_3 \cdot qui$ (spectrum acquired from 1×10^{-2} mol dm^{-3} CD_3CN solutions).

Proton	δ (ppm)[a]		qui[b]
	Coordinated qui	Associated qui	
Quinazoline			
H_2	9.19 br	8.94 br	9.08
H_4	8.62–8.42 m	8.32 t	8.84
H_5	7.99 t	7.83 m	7.62
H_6	7.83 t sp	7.71 m	7.59
H_7	8.24–8.17 m	8.24–8.17 m	7.85
H_8	8.24–8.17 m	8.10 m	7.76
2,2′-Bipyridine			
H_3	8.62–8.42 m	–	–
H'_3	8.71 d	–	–
H_7	8.75 d sp	–	–
H'_7	8.89 d	–	–
H_4	8.62–8.42 m	–	–
H'_4	8.62–8.42 m	–	–
H_8	8.62–8.42 m	–	–
H'_8	8.62–8.42 m	–	–
H_5	7.67 t sp	–	–
H'_5	7.79 t sp	–	–
H_9	8.10 m	–	–
H'_9	8.24–8.17 m	–	–
H_6	8.62–8.42 m	–	–
H'_6	8.62–8.42 m	–	–
H_{10}	8.77 d sp	–	–
H'_{10}	9.40 s	–	–

[a] Data obtained in this work.
[b] Data from Ref. [21]; s, singlet; d, doublet; t, triplet; m, multiplet; br, broad signal; sp, superimposed signal.

spectra also aided the characterization (see Supplementary material for the spectra).

The spectrum of the compound *cis*-[Ru(bpy)$_2$(qui)NO](PF$_6$)$_3$ · (*qui*) displays a large number of peaks as a consequence of the non-equivalence of the aromatic rings of the quinazoline and bipyridine ligands. As seen in Fig. 1, the ring labeled (2–3–4–5–6) should exert direct influence (from ring current effects) on proton **10**, while the (7′–8′–9′–10′–11′) ring should affect the signal of proton **6**′. In turn, the coordinated quinazoline ring should affect proton **6**, while proton **10**′ would be subjected to induced current effects of the nitrosyl ligand. The δ values of the protons belonging to the [Ru(bpy)$_2$] moiety follow the same pattern observed for the [Ru(bpy)$_3$]$^{2+}$ complex [22,23]. Due to coordination to the ruthenium ion, free rotation of the bpy rings is not possible. In addition, protons **3**, **3**′, **7** and **7**′ are sterically strained, so the van der Waals interaction between them causes a deshielding effect, shifting their signals to lower field compared with other protons in that ligand [23]. An interesting feature is the signal at 9.40 ppm, ascribed to proton **10**′. This large shift to lower field has also been observed in other mononuclear ruthenium complexes. It arises from the close proximity of that proton with the adjacent NO ligand and has been attributed to inductive effects from the latter ligand. This kind of anisotropy is known to occur from chemical units such as NO or CN, where the π electrons of the multiple bond are disturbed by the applied magnetic field. These electrons respond to this external perturbation by circulating in order to generate an opposed magnetic field in the axis of the multiple bond. In the region below and above this bond there is an induced magnetic field adding to the applied one, causing a deshielding effect on protons near this region [24–27]. Finally, protons **6**, **6**′, and **10** are subjected to *ring current* effects, since they are located in the shielding region of the pyridinic aromatic rings and therefore have their signals shifted to higher field compared with the free ligand. As expected, protons **5**, **5**′, **9**, and **9**′ appear as triplets, with δ values varying from 7.67 to 8.24 ppm due to the non-equivalence of the bpy rings. The same discussion can be applied to protons **4**, **4**′, **8** and **8**′, except that the signals of **4**, **4**′ are superimposed.

However, the most important feature emerging from these measurements is that the experimental value of I (the sum of the integral value of the signals observed in the ^{1}H spectrum) is 28.2, which matches the calculated value of 28, obtained when one considers the total number of H nuclei present in the complex structure (22) plus an additional molecule of *qui*, which contributes with 6 protons. Moreover, it was possible to assign the signals of both the coordinated and the non-coordinated *qui* ligands, which leads to the conclusion that there is an interaction sustaining the complex:*qui* association in solution in 1:1 stoichiometry.

The analysis of the NOESY spectrum (Supplementary material) was rather inconclusive, since there is a large superimposition of signals in the aromatic region of the spectrum and, consequently, large superimpositions of the observed correlations. However, the spectrum presents some inter – molecular correlations, such as between protons Hq5–Hq2 and Hq6–Hq2 (coordinated and un-coordinated quinazoline protons, respectively) that suggest the interaction between the coordinated and the un-coordinated quinazoline molecule in the compound. Although in solution a dynamic equilibrium for that interaction is expected, the observed correlations also suggest that the main site of interaction of the unbound *qui* is the coordinated *qui* molecule.

Under the experimental conditions employed in this work for the acquisition of the ESI MS spectrum (30 eV for cone voltage), it is not expected to detect the molecular peak corresponding to the charged species [Ru(bpy)$_2$(qui)(NO)]$^{3+}$ · (*qui*), in which the ruthenium complex is weakly associated to the additional *qui* molecule. Actually, the compound suffered an extensive fragmentation process at the source, and consequently the MS spectrum displayed peaks corresponding to fragments originated from the cleavage of stronger bonds such as Ru–NO or Ru–qui (coordinated molecule) (the ESI MS spectrum as well as the assignment of the main peaks observed are available as Supplementary material).

3.2. UV–Vis spectroscopy and solvent effect

The absorption spectrum of the *cis*-[Ru(bpy)$_2$(qui)NO](PF$_6$)$_3$ · (*qui*) complex in acetonitrile solution displays absorption bands in the UV region ($\pi \rightarrow \pi^*$ intraligand and Ru$_{d\pi} \rightarrow$ NO$_\pi^*$) [18] and a lower energy band centered at 430 nm (ε = 5741 cm^{-1} mol^{-1} L). This last band could be assigned to a metal to ligand charge transfer transition (MLCT, possibly Ru$_{d\pi}$–qui$_\pi^*$), to a low lying nπ transition of the quinazoline ligands or even to a transition related to the association of the additional quinazoline molecule to the complex. To probe these hypothesis, the absorption spectrum of the compound *cis*-[Ru(bpy)$_2$(qui)NO](PF$_6$)$_3$ · (*qui*) was acquired in aqueous medium, in two different pH values (Fig. 2), assuming that the protonation of the nitrogen heteroatoms of both the coordinated and non-coordinated *qui* molecules could contribute to the association disassembly. In fact, at pH 1 the sites available in the complex are protonated (pK_{a1} = 3.5 and pK_{a2} = 3.2 for free quinazoline, and pK_a = 2.75 for the coordinated *qui* ligand) and, under this condition, there is no absorption in the visible region of the UV–Vis spectrum. At pH 3.7, the lower energy absorption band is restored.

Both Ru$_{d\pi}$–qui$_\pi^*$ MLCT or a low lying nπ transition would respond to the protonation of the non-coordinated N heteroatoms. The MLCT band would be red shifted since the protonation would stabilize to some extent the π^* levels of the quinazoline, lowering the transition energy. Such shift is not observed (Fig. 2). Alternatively, the involvement of the non-ligand electron pair of the quinazoline nitrogen atoms in the bond with the protons would further stabilize the non-ligand levels, promoting a hypsochromic shift of a nπ transition. This is observed (Fig. S9, Supplementary material), however, the quinazoline transitions occur in a higher energy region of the spectrum than the observed for the complex transitions (Fig. 2). Thus, the assignment of the 430 nm band as a MLCT or as a nπ transition was ruled out.

Based on the previous discussion and considering that this kind of mononuclear ruthenium–nitrosyl complex typically presents transitions in the higher energy region of the UV–Vis spectrum, it was concluded that the 430 nm band is due to the association of the *qui* molecule with the complex. As shown in Fig. 2, this absorption, and most probably the kind of interaction that sustains the assembly of the complex, is dependent on the protonation of the quinazoline nitrogen heteroatoms.

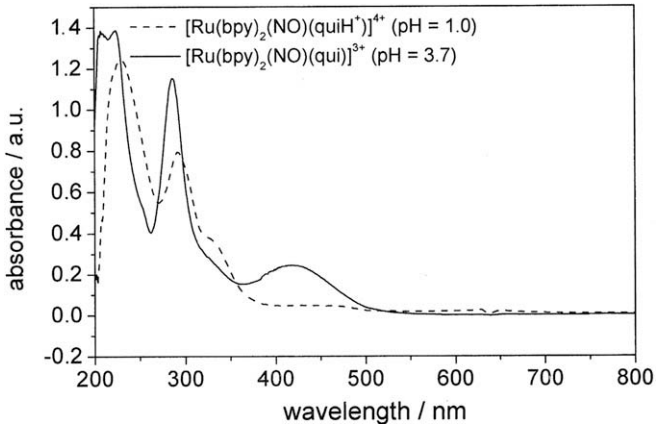


Fig. 2. Electronic spectra of the *cis*-[Ru(bpy)$_2$(qui)NO](PF$_6$)$_3$ · (*qui*) compound in aqueous medium, at pH 1.0 and 3.7.

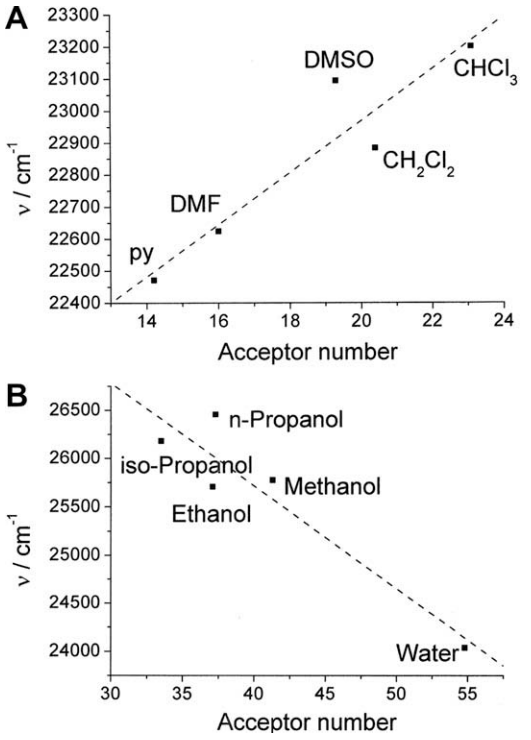


Fig. 3. CT absorption energy of the *cis*-[Ru(bpy)$_2$(qui)NO](PF$_6$)$_3$ · (*qui*) complex vs. the acceptor number of (A) an aprotic and (B) a protic group of solvents.

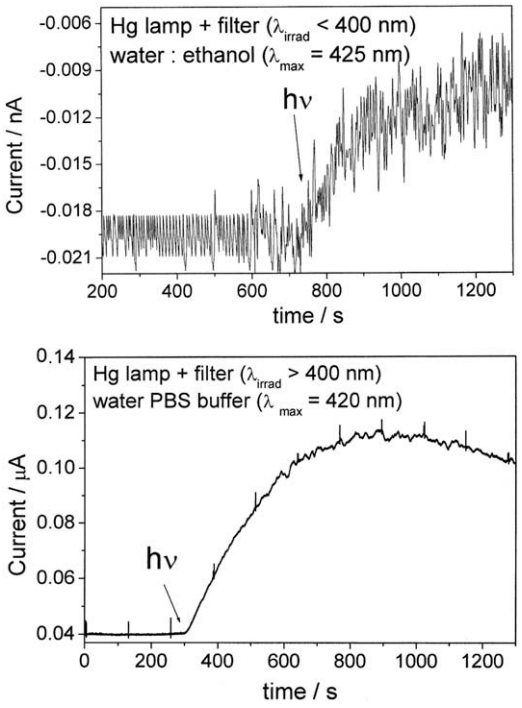


Fig. 4. Chronoamperogram of *cis*-[Ru(bpy)$_2$(qui)NO](PF$_6$)$_3$ · (*qui*) solutions in different conditions, irradiated with visible light.

It is worth mentioning that the coordinated NO^+ ligand constitutes a site for nucleophilic attack in higher pH values (pH 6.63 for the conversion of coordinated NO^+ to NO_2^-), but at pH 3.7 it is actually coordinated in the form of NO^+, as probed by its typical IR stretching band at 1935 cm^{-1} (see Supplementary material for the pK_a determination curves, the IR and UV–Vis spectra at pH 7.4).

Aiming at further characterizing this visible absorption band, a solvent effect experiment was carried out. In the solvents used in this work, the lower energy band in the spectra of the complex displays a well behaved correlation with the solvent parameter "acceptor number" (AN, Fig. 3) [28,29]. This shows that the complex sites that probably interact with the solvent are the nitrogen electron lone-pairs of the quinazoline ligands, which should be involved in a "donating type" interaction with the solvent molecules. This kind of solvatochromism is characteristic of charge transfer transitions that require a large reorganization of the solvation sphere because of the charge density redistribution over the molecule. This result, together with the spectral region of the studied transition and its ε value (in the order of 10^3), suggests that this is a charge transfer transition (CT). Interestingly, the dependence of the band energy on the AN of the solvent features a different correlation pattern ongoing from an aprotic to a protic group of solvents. This reveals that protonation or a proton donating interaction, such as the formation of hydrogen bond (a possible event in protic solvents), plays an important role in the spectral behavior of the compound [Ru(bpy)$_2$(qui)NO]PF$_6$ · (*qui*).

Therefore, the observed spectral dependence on pH and solvent leads to the conclusion that the assembly of the aggregate complex:*qui* in solution is a reversible event. Additionally, due to the hydrophobic and planar nature of the quinazoline ligand, this aggregation is possibly driven by π-stacking interactions between the ligands. The most dramatic effect is seen when the protonation of the quinazoline ligands is promoted. This creates charge on these ligands, what would disrupt the π-stacking interaction that holds the solution arrangement.

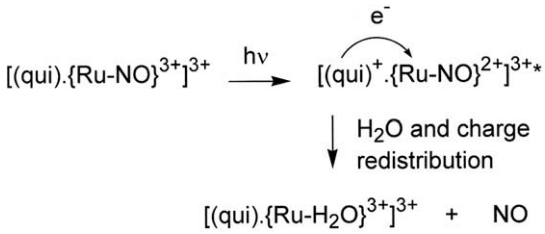
Preliminary molecular modeling results based on DFT calculations[1] suggest that the HOMO is a molecular orbital centered at the non-coordinated quinazoline ligand, with a little contribution from the {RuNO}^{6} moiety [30]. The LUMO, in turn, has a large metal character, with its major contribution from the metallic unit {RuNO}^{6}. Therefore, this result strongly suggests that the lower energy band of absorption spectrum of the complex (430 nm in acetonitrile), that is the HOMO–LUMO transition, has a charge transfer character, corroborating the spectroscopic results discussed above.

On a qualitative basis, at this point it is interesting to further analyze the assignment of this transition. Keeping in mind that the HOMO has a ligand character and the LUMO has a metal character, this CT band could be considered as belonging to a ligand-to-metal charge transfer (LMCT) transition type, even though the quinazoline ligand involved in the transition is not coordinated to the central metal ion, in other words this transitions is an outer sphere charge transfer [31–34]. On the other hand, it would be counter-intuitive, if one thinks that the complex is formally a Ru(II) com-

[1] All calculations were performed using the GAUSSIAN 03 (Multiprocessor Version) package. Geometry optimizations were carried out without any symmetry constraints, using the double-ζ LANL2DZ basis set with the relative pseudopotential for ruthenium, and the DGDZVP basis set of double-ζ and polarization quality, for the other atoms. The B3LYP hybrid functional was employed in all the calculations. The TD-DFT excitation spectrum was computed for 40 excited states in vacuum only. In this case, the DGDZVP basis set was substituted with the larger DGDZVP2, of double polarization. The stabilization energy, without corrections, for the formation of the stacked complex was calculated by the relation:

$$E(complex + quinazoline) = E(complex) - E(quinazoline),$$

where E(complex + quinazoline) is the total stabilization energy (in atomic units) calculated for the stacked complex (−88 kJ/mol), E(complex) is the total energy for the complex without an additional quinazoline, and E(quinazoline) is the total energy calculated for an isolated quinazoline molecule. For the geometry optimization of the complex without the additional quinazoline, the same atomic basis sets used for optimization of the stacked complex were employed. The geometry optimization of quinazoline was carried out using the DGDZVP basis set for all the atoms. Further details focusing on the molecular modeling results are the subject of another work that is being carried out in our laboratories.



Scheme 1.

pound. Nevertheless, it has already been discussed that ruthenium ions might have an ambiguous behavior, regarding its oxidation state, when coordinated to nitrogen species (especially NO) [35–38]. Thus, a Ru(II) ion coordinated to NO^+ has its Lewis acidity increased to such a limit that it might behave as Ru(III). This seems to be the case here, so it is reasonable to assign the 430 nm band as an outer sphere LMCT transition.

3.3. Photophysics

A simple way to test the CT nature of this transition is to evaluate its ability to promote the photorelease of the coordinated NO. Fig. 4 presents the photolysis results when aqueous/ethanolic or PBS buffered (pH 7.4) aqueous solutions of the complex are irradiated with visible light ($\lambda > 400$ nm).

Irradiation of this complex in both conditions is effective to release NO, which is detected by an amperometric measurement. It has already been described that the NO^+ ligand must be reduced to NO^0, so that it can be released from ruthenium compounds [2–6,10–16]. One way to do this is to irradiate the compound in a CT transition, usually the $Ru_{d\pi} \rightarrow NO_{\pi}^{*}$, a photoredox state that leads to NO^0 generation in the excited state. This seems to be the case in the present work. Assuming that the 430 nm band is an LMCT transition that directly addresses a molecular orbital with {RuNO} character, one possible mechanism is presented in Scheme 1. Irradiation on this CT band generates the reduced NO form, which is released. The complex further decays, suffering a charge redistribution where the Ru^{2+} ion is oxidized to Ru^{3+}, in order to restore the neutral form of the adjacent quinazoline ligand. The aquation reaction then takes place.

It is worth mentioning that the proposed mechanism holds for the nitrosyl species and, at physiological pH, the species actually present in the solution has a NO_2^- ligand coordinated to the ruthenium ion ($pK_a = 6.63$). Although the photolysis carried out in this work is a qualitative experiment, chronoamperometric curve in Fig. 4B demonstrates that NO release seems to be more efficient, considering that the conditions of both experiments were the same, except for the reaction medium. Probably this is so because other mechanisms of NO release should be involved in this second experiment. In fact, it has already been demonstrated that nitro bipyridine ruthenium compounds are also able to release nitric oxide, due to a photoinduced homolytic dissociation of NO from a coordinate NO_2^-, yielding a Ru^{2+}–H_2O complex and NO as photoproducts [39].

4. Conclusions

In summary, the use of the quinazoline ligand has led to the isolation of a ruthenium–nitrosyl complex that delivers NO under visible light irradiation. The visible absorption band has a charge transfer nature, involving a second quinazoline molecule which is associated with the ruthenium complex by means of weak interactions, possibly of the π-stacking nature. Spectroscopic experiments, such as solvent effect and pH dependence of the spectral behavior, corroborate the charge transfer assignment of the transition. Therefore, the interaction of the complex ion with a *qui* molecule in solution introduces new spectroscopic features into the compound, constituting an example of the use of weak interactions (non-covalent interactions) to create interesting properties in inorganic/organic molecular systems.

Acknowledgements

The authors would like to thank the Brazilian agencies FAPESP, FAPEMIG, and CNPq (IM-INOFAR) for financial support. Prof. Roberto Santana da Silva for the essential discussions and the use of various equipments, Prof. Luiz Alberto Beraldo de Moraes (FFCLRP, Universidade de São Paulo) and Prof. Marcos N. Eberlin (IQ – UNICAMP, Universidade Estadual de Campinas) for the ESI MS spectrum and Dr. Ana Paula Landi Librandi and Maria Perpétua F.M. Del Lama for the help with some spectroscopic experiments.

Appendix A. Supplementary data

Supplementary data associated with this article can be found, in the online version, at doi:10.1016/j.poly.2009.01.027.

References

[1] For example: L.J. Ignarro, Nitric Oxide Biology and Pathobiology, Academic Press, San Diego, 2000.
[2] E. Tfouni, M. Krieger, B.R. McGarvey, D.W. Franco, Coord. Chem. Rev. 236 (2003) 57.
[3] F. Roncaroli, L.M. Baraldo, L.D. Slep, J.A. Olabe, Inorg. Chem. 41 (2002) 1930.
[4] M.G. Sauaia, F.S. Oliveira, A.C. Tedesco, R.S. Silva, Inorg. Chim. Acta 355 (2003) 191.
[5] H.E. Toma, A.D.P. Alexiou, A.L.B. Formiga, M. Nakamura, S. Dovidauskas, M.N. Eberlin, D.M. Tomazela, Inorg. Chim. Acta 358 (2005) 2891.
[6] P.C. Ford, S. Wecksler, Coord. Chem. Rev. 249 (2005) 1382.
[7] D. Bonaventura, R.G. Lima, J.A. Vercesi, R.S. Silva, L.M. Bendhack, Vasc. Pharmacol. 46 (2007) 215.
[8] D. Bonaventura, F.S. Oliveira, C.N. Lunardi, J.A. Vercesi, R.S. Silva, L.M. Bendhack, Nitric Oxide – Biol. Chem. 15 (2006) 387.
[9] N. Paolocci, M.I. Jackson, B.E. Lopez, K. Miranda, C.G. Tocchetti, D.A. Wink, A.J. Hobbs, J.M. Fukuto, Pharmacol. Therapeut. 113 (2007) 442.
[10] R.S. Silva, M.S.P. Marchesi, C. Khin, C.N. Lunardi, L.M. Bendhack, P.C. Ford, J. Phys. Chem. B 111 (2007) 6962.
[11] M.J. Rose, M.M. Olmstead, P.K. Mascharak, J. Am. Chem. Soc. 129 (2007) 5342.
[12] R.G. Lima, M.G. Sauaia, D. Bonaventura, A.C. Tedesco, L.M. Bendhack, R.S. Silva, Inorg. Chim. Acta 359 (2006) 2543.
[13] Z.N. Da Rocha, R.G. de Lima, F.G. Doro, E. Tfouni, R.S. da Silva, Inorg. Chem. Commun. 11 (2008) 737.
[14] M.J. Rose, N.L. Fry, R. Marlow, L. Hinck, P.K. Mascharak, J. Am. Chem. Soc. 130 (2008) 8834.
[15] M.G. Sauaia, R.G. Lima, A.C. Tedesco, R.S. Silva, Inorg. Chem. 44 (2005) 9946.
[16] M.G. Sauaia, R.G. Lima, A.C. Tedesco, R.S. Silva, J. Am. Chem. Soc. 125 (2003) 14718.
[17] E. Buisine, K. Villiers, T.J. Egan, C. Biot, J. Am. Chem. Soc. 128 (2006) 12122.
[18] M.G. Sauaia, R.S. Silva, Transition Met. Chem. 28 (2003) 254.
[19] T. Morita, R.M.V. Assumpção, Manual de Soluções, Reagentes e Solventes, Edgard and Blücher Ltd., Brazil, 1968.
[20] S. Nikolaou, M. Uemi, H.E. Toma, Spec. Lett. 34 (2001) 267.
[21] J. Kunes, J. Bazant, M. Pour, K. Waisser, M. Slosarek, J. Janota, Il Farmaco 55 (2000) 7250.
[22] E.C. Constable, K.R.A. Seddon, J. Chem. Soc., Chem. Commun. (1982) 34.
[23] E.C. Constable, J. Lewis, Inorg. Chim. Acta 70 (1983) 251.
[24] R.A. Leising, S.A. Kubow, M.R. Churchill, L.A. Buttrey, J.W. Ziller, K.J. Takeuchi, Inorg. Chem. 29 (1990) 1306.
[25] M. Heijden, P.M. van Vliet, J.G. Haasnoot, J.J. Reedijk, Chem. Soc., Dalton Trans. (1993) 3675.
[26] M. Maruyama, H. Matsuzawa, Y. Kaizu, Inorg. Chim. Acta 237 (1995) 159.
[27] J.H. Malin, C.F. Shmidt, H.E. Toma, Inorg. Chem. 14 (1975) 2924.
[28] V. Gutmann, Pure Appl. Chem. 51 (1979) 2197.
[29] U. Mayer, Pure Appl. Chem. 51 (1979) 1697.
[30] For the $\{MNO\}^n$ notation see: J.H. Enemark, R.D. Feltham, J. Am. Chem. Soc. 96 (1974) 5002.
[31] H.M.A. Salman, M.R. Mahmoud, M.H.M. Abou-El-Wafa, U.M. Rabie, R.H. Crabtree, Inorg. Chem. Commun. 7 (2004) 1209.

[32] H. Kunkely, A. Vogler, Inorg. Chem. Commun. 11 (2008) 413.
[33] J.F. Endicott, Y.-J. Chen, P. Xie, Coord. Chem. Rev. 249 (2005) 343.
[34] S.V. Rosokha, J.K. Kochi, Acc. Chem. Res. 41 (2008) 641.
[35] K.Q. Ferreria, L.N. Cardoso, S. Nikolaou, Z.N. Rocha, R.S. Silva, E. Tfouni, Inorg. Chem. 44 (2005) 5544.
[36] K.Q. Ferreira, A.M. Lucchesi, Z.N. Rocha, R.S. Silva, Inorg. Chim. Acta 328 (2002) 147.
[37] A. Walstrom, M. Pink, H. Fan, J. Tomaszewisk, K.G. Caulton, Inorg. Chem. 46 (2007) 7704.
[38] A.V. Marchenko, A.N. Vedernikov, D.F. Dye, M. Pink, J.M. Zaleski, K.G. Caulton, Inorg. Chem. 41 (2002) 4087.
[39] R.G. Lima, M.G. Sauaia, D. Bonaventura, A.C. Tedesco, R.F.V. Lopez, L.M. Bendhack, R.S. da Silva, Nitric Oxide 358 (2004) 2643.

NEt_3 (15 mL) in THF (30 mL) was added a solution of ethynylferrocene (300 mg, 1.43 mmol) in THF (10 mL) at 5 °C and the resulting solution was refluxed for 13 h. The mixture was cooled to room temperature, and then diethyl ether (50 mL) was added. The suspension was filtered in celite, and the filtrate was dried under vacuum to afford a black solid. The black solid was redissolved in CH_2Cl_2 and the solution mixed with silica gel. The solvent was removed under vacuum and the resulting coated silica gel was loaded on the top of a silica gel column packed in dry hexane. The mixture was chromatographed using hexane/ethyl acetate (50:50) affording **1** as a dark solid. Yield: 470 mg (78%). *Anal. Calc.* for $C_{21}H_{14}CrFeO_3$: C, 59.74; H, 3.34. Found: C, 59.67; H, 3.28%. ^1H NMR ($CDCl_3$, 298 K, 200 MHz): δ 5.50 (d, 2H, $^3J_{HH}$ = 5.6, H_oPh), 5.40 (t, 1H, $^3J_{HH}$ = 5.6, H_pPh), 5.23 (d, 2H, $^3J_{HH}$ = 5.5, H_mPh), 4.52 (s, 4H, C_5H_4), 4.27 (s, 5H, C_5H_5). $^{13}C\{^1H\}$ ($CDCl_3$, 298 K, 200 MHz): δ 232.7 (C≡O), 94.5 (aromatic, CH, Ph), 92.7 (C_{ipso}), 92.3, 90.2 (aromatic, CH, Ph), 85.4, 81.3 (C≡C), 71.8 (2C, C_5H_4), 70.2 (2C, C_5H_4), 69.5 (5C, C_5H_5), 63.7. (1C, C_5H_4). IR (KBr, cm^{-1}): $\nu_{C\equiv C}$: 2225 (vw); ν_{CO}: 1960(s), 1882(s), 1868(s).

2.3. Synthesis of $[Cr(CO)_3(\eta^6\text{-}C_6H_5)\{Co_2(CO)_6\text{-}\mu^2\text{-}\eta^2\text{-}C\equiv C\text{-}\}(\eta^5\text{-}C_5H_4)\text{-}Fe(\eta^5\text{-}C_5H_5)]$ (**2**)

To a Schlenk flask containing $Co_2(CO)_8$ (58 mg, 0.17 mmol) and **1** (72 mg, 0.17 mmol) was added THF (50 mL) at −40 °C and the resulting solution was stirred for 10 min. The mixture was allowed to warm to 25 °C, and stirred for 12 h. The solvent was removed under vacuum and crude product was mixed with silica gel in CH_2Cl_2. The solvent was removed under vacuum and the resulting coated silica gel was loaded on the top of a silica gel column packed in dry hexane. The mixture was chromatographed using hexane/diethyl ether (90:10) affording **2** as a dark green solid. Yield: 96 mg (80%). *Anal. Calc.* for $C_{27}H_{14}Co_2CrFeO_9$: C, 45.80; H, 1.99. Found: C, 45.74; H, 1.93%. ^1H NMR ($CDCl_3$, 298 K, 300 MHz): δ 6.14 (d, 2H, $^3J_{HH}$ = 5.7, H_oPh), 5.54 (t, 1H, $^3J_{HH}$ = 5.7, H_pPh), 5.23 (t, 2H, $^3J_{HH}$ = 5.9, H_mPh), 4.46 (s, 2H, C_5H_4), 4.40 (s, 2H, C_5H_4), 4.18 (s, 5H, C_5H_5). $^{13}C\{^1H\}$($CDCl_3$, 298 K, 300 MHz): δ 232.2 (C≡O, Cr), 199.2 (C≡O, Co), 107.5 (*C*≡C), (C≡C) not observed, 96.7, 94.7, 88.8 (aromatic, CH, Ph), 85.0(C_{ipso}), (1C, C_5H_4) not observed, 76.3, 70.1 (C_5H_4), 69.8 (C_5H_5). IR (KBr, cm^{-1}): ν_{CO} 2085(s), 2052(s), 2020(s), 1963(s), 1900(s), 1870(s).

2.4. Synthesis of $[Cr(CO)_3(\eta^6\text{-}C_6H_5)\{Mo_2Cp_2(CO)_4\text{-}\mu^2\text{-}^2\text{-}C\equiv C\text{-}\}(^5\text{-}C_5H_4)Fe(^5\text{-}C_5H_5)]$ (**3**)

To a solution of $Mo_2Cp_2(CO)_6$ (490 mg, 1.00 mmol) in *n*-butyl ether (50 ml) previously refluxed for 7 h (to generate the starting complex $Mo_2Cp_2(CO)_4$) was added dropwise over a period of 10 min at 0 °C a solution **1** (300 mg, 1.00 mmol) in THF (40 ml). The mixture was allowed to warm to room temperature, and stirred for 12 h. The solvent was removed under vacuum and the residue subjected to chromatography on silica gel. Elution with ether/hexane (80:20) gave the desired compound as a dark red solid. Yield: 350 mg (41%). *Anal. Calc.* for $C_{35}H_{24}CrFeMo_2O_7$: C, 49.09; H, 2.83. Found: C, 49.01; H, 2.79%.^1H NMR ($CDCl_3$, 298 K, 300 MHz): δ 6.40 (d, 2H, $^3J_{HH}$ = 4.5, H_oPh), 5.52 (t, 1H, $^3J_{HH}$ = 4.5, H_pPh), 5.31 (t, 2H, $^3J_{HH}$ = 4.0, H_mPh), 5.24 (s, 10H, C_5H_5–Mo), 4.40 (s, 2H, $H_oC_5H_4$), 4.30 (s, 2H, $H_mC_5H_4$), 4.23 (s, 5H, C_5H_5–Fe). $^{13}C\{^1H\}$ ($CDCl_3$, 298 K, 300 MHz): δ 234.2 (C≡O, Cr), 230.2 e 229.7 (C≡O, Mo), 129.9, 128.0, 126.0 (C_5H_5–Mo), (C_{ipso}, C_5H_5–Mo) not observed, 122.0 (C_5H_4–*C*≡C), 108.8 (C_6H_5–C≡C), 96.1 (C_{ipso}, C_6H_5), 96.1, 94.0, 93.9, 92.4, 90.1 (aromatic, CH, C_6H_5), 69.7 (CH, C_5H_5–Fe), 69.3, 68.9, 68.7, 67.9, 67.8 (CH, C_5H_4–Fe). IR (KBr, cm^{-1}): ν_{CO} 2004(s), 1994(s), 1959(s), 1931(s), 1882(s), 1865(s), 1846(s).

2.5. X-ray diffraction analysis

The structure of **1** was determined by Robert Burrow (Universidade de Santa Maria, RS, Brazil). The structure of **3** was determined by V.G. Young Jr. (University of Minnesota, USA). Crystal data, data collection details, and solution and refinement procedures are provided in Table 1 [27–29]. For complex **3** all non-H atoms were refined with anisotropic displacement parameters unless stated otherwise. All hydrogen atoms were placed in ideal positions and refined as riding atoms with relative isotropic displacement parameters [27,28].

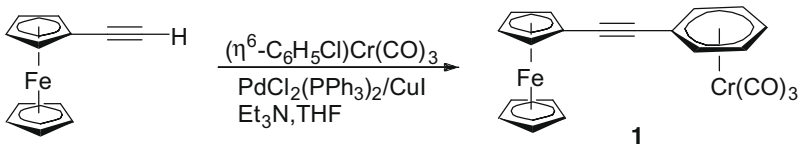
On p. 6, line 19, the description of the treatment of the hydrogen atoms is correct only for **3**. For structure **1**, the cif file indicates that all of the hydrogen atom coordinates were refined and their Uiso values were fixed. The term in the cif file for **3** which describes the hydrogen treatment (_refine_ls_hydrogen_treatment) should be changed from "mixed" to "constr" for **3** and to "refxyz" for **1**. The reference 29 (Otwinowski & Minor) is not applicable to hydrogen atoms.

3. Results and discussion

The reaction of $Cr(CO)_3(\eta^6\text{-}C_6H_5Cl)$ with 1.4 equiv of ethynylferrocene in the presence of a catalytic amount of $Pd(PPh_3)_2Cl_2$/CuI in a gently refluxing THF/NEt_3 for 13 h affords the corresponding starting heterobimetallic compound $[Cr(CO)_3(\eta^6\text{-}C_6H_5)C\equiv C\text{-}\{(\eta^5\text{-}C_5H_4)Fe(\eta^5\text{-}C_5H_5)\}]$(**1**) [22], which was isolated as a dark solid (78%, Scheme 1). The identity of **1** was confirmed on the basis of elemental analysis, multinuclear (^1H, ^{13}C) NMR data, and by an X-ray diffraction study.

Table 1
Crystal data and structure refinement for **1** and **3**.

	1	**3**
Empirical formula	$C_{21}H_{14}CrFeO_3$	$C_{35}H_{24}CrFeMo_2O_7$
Formula weight (g mol^{-1})	422.17	856.27
T (K)	193(2)	173(2)
λ (Å)	0.71073	0.71073
Crystal system	monoclinic	orthorhombic
Space group	$P2_1/c$	$P2_12_12_1$
Unit cell dimensions		
a (Å)	12.081(2)	10.609(3)
b (Å)	19.6295(10)	12.554(4)
c (Å)	7.4011(10)	23.789(7)
α (°)	90	90
β (°)	103.235(14)	90
γ (°)	90	90
V (Å^3)	1708.6(4)	3168.3 (15)
Z	4	4
Diffractometer	Enraf-Nonius CAD4	Bruker SMART
D_{calc} (Mg m^{-3})	1.641	1.795
Absorption coefficient (mm^{-1})	1.502	1.605
F(000)	856	1696
Crystal size (mm)	0.50 × 0.30 × 0.10	0.120 × 0.040 × 0.004
θ Range for data collection (°)	2.70–25.07	1.71–24.92
Index ranges	$-14 \leqslant h \leqslant 14$, $0 \leqslant k \leqslant 0$, $0 \leqslant l \leqslant 8$	$-12 \leqslant h \leqslant 12$, $0 \leqslant k \leqslant 14$, $0 \leqslant l \leqslant 28$
Reflections collected	3279	27940
Refinement method	full-matrix least-squares on F^2	full-matrix least-squares on F^2
Completeness to θ (%)	(25.07°) 96.8	(24.92°) 99.7
Independent reflections [R_{int}]	3028 [0.0162]	5514 [0.0942]
Data/restraints/parameters	3028/0/250	5514/0/416
Final R indices [$I > 2\sigma(I)$]	R_1 = 0.0269, wR_2 = 0.0683	R_1 = 0.0440, wR_2 = 0,0978
R indices (all data)	R_1 = 0.0398, wR_2 = 0.0727	R_1 = 0.0647, wR_2 = 0.1091
Largest difference in peak and hole (e Å^{-3})	0.296 and −0.370	0.562 and −1.152



Scheme 1.

The IR spectrum of **1** shows three bands of the carbonyl stretching frequencies determined by a splitting of the asymmetric mode (E), which can be rationalized in terms of a small perturbation of C_{3v} symmetry by alkyne–ferrocene fragment on the benzene ring [30,31]. The ^{1}H NMR spectrum of **1** contains three sets of arene resonances in the region between 5.50 and 5.23 ppm, and two singlets at 4.52 and 4.27 ppm attributable to the cyclopentadienyl protons of ferrocene unit. As expected, the resonances of the alkyne carbons appear at 85.4 and 81.3 ppm.

Crystals of complex **1** suitable for an X-ray diffraction study were grown from slow diffusion of hexane into the CH_2Cl_2 solution containing **1** at −20 °C. Details of crystal and refinement data are reported in Table 1. Selected bond distances and angles are listed in Table 2. The crystal structure of **1** consists of two structural sub-units "$Cr(CO)_3((\eta^6\text{-}C_6H_5\text{–})$", and "$(\text{-}C{\equiv}C\text{–}C_5H_4)Fe(C_5H_5)$", which adopts a *cisoid* conformation as displayed in Fig. 1.

The $Cr(CO)_3$ group shows the well-known piano-stool conformation found in half-sandwich tricarbonyl complexes. The bond angles OC–Cr–CO (88.8° average) and Cr–C bond distances (1.848 Å average) are comparable to the (η^6-arene)tricarbonylchromium complexes $YCH_2C{\equiv}CPh[Cr(CO)_3]$ (Y = NMe_2, 88.4°, 1.841 Å; Y = N(Me)(CH_2Ph), 88.8°, 1.840 Å) [23]. On the other hand, the Cr–Ct(1) distance (1.723 Å, Ct(1) = centroid of C31–C36) is slightly longer than in (η^6-arene)tricarbonylchromium compounds incorporating propargyl amine units (average 1.701 Å) [23], which can be associate to the presence of an electron-donating ferrocenyl group. The C≡C bond distance (1.194 Å) falls in normal range for similar arene tricarbonyl chromium complexes [32,33]. The $Cr(CO)_3$ tripod is arranged in a nearly staggered conformation with the dihedral angles of the projected Cr-CO with respect to the aromatic carbon atoms varying from 37° to 40° (Figs. 2 and 4). The alkyne fragment is found lying in the mean plane of the arene and cyclopentadienyl rings, whereas the C_{ipso}–C≡C linkages are almost linear (C(31)–C(2)–C(1) = 174.2 (2)°; C(21)–C(1)–C(2) = 176.3 (2)°). The ferrocene unit shows an almost eclipsed conformation (average torsion angle 13.9°) with characteristic Fe–Ct distances (Fe–Ct(2) = 1.654 Å, Ct(2) = centroid of C21–C25); Fe–Ct(3) = 1.649 Å, Ct(3) = centroid of C11–C15) [34–36].

Table 2
Selected bond lengths [Å] and angles [°] for **1**.

Cr(1)–(34)	2.220 (2)	Cr(1)–(33)	2.220 (2)
Cr(1)–(36)	2.227 (2)	Cr(1)–(32)	2.224 (2)
Cr(1)–(35)	2.207 (2)	Cr(1)–(31)	2.246 (2)
Cr(1)–(41)	1.849 (2)	Cr(1)–(51)	1.851 (2)
Cr(1)–(61)	1.844 (2)	C(41)–(41)	1.150 (3)
C(51)–(51)	1.152 (3)	C(61)–(61)	1.154 (3)
Fe–(24)	2.032 (2)	Fe–(25)	2.034 (2)
Fe–(14)	2.039 (2)	Fe–(13)	2.044 (2)
Fe–(11)	2.046 (2)	Fe–(15)	2.047 (2)
Fe–(21)	2.052 (2)	Fe–(23)	2.052 (2)
Fe–(23)	2.052	(2) Fe–(12)	2.054 (2)
C(1)–(2)	1.193 (3)	C(2)–(31)	1.440 (3)
C(1)–(21)	1.424 (3)		
C(2)–(1)–(21)	176.3 (2)	C(1)–(2)–(31)	174.2 (2)
C(1)–(21)–(22)	127.8 (2)	C(1)–(21)–(25)	124.7 (2)
C(36)–(31)–(2)	122.3 (2)	C(32)–(31)–(2)	118.4 (2)
O(41)–C(41)–Cr	178.2 (2)	O(51)–C(51)–Cr	179.3 (2)
O(61)–C(61)–Cr	179.5 (2)	C(41)–Cr–C(51)	90.27 (10)
C(41)–Cr–C(61)	88.09 (10)	C(51)–Cr–C(61)	88.18 (10)

Selected bond distances and angles are listed in Table 2. The crystal structure of **1** consists of two structural sub-units "$Cr(CO)_3((\eta^6\text{-}C_6H_5\text{–})$", and "$(\text{-}C{\equiv}C\text{–}C_5H_4)Fe(C_5H_5)$", which adopts a *cisoid* conformation as displayed in Fig. 1.

The 1-(ferrocenylethynyl)(η^6-arene)tricarbonylchromium (**1**) reacts with an equimolar amount of $[Co_2(CO)_8]$ in THF at room temperature to give, after workup, the heterotetrametallic complex $[Cr(CO)_3(\eta^6\text{-}C_6H_5)\{Co_2(CO)_6\text{-}\mu^2\text{-}\eta^2\text{-}C{\equiv}C\text{-}\}(\eta^5\text{-}C_5H_4)Fe(\eta^5\text{-}C_5H_5)\}]$ (**2**) as dark solid in 80% yield (Scheme 2). The structure of **2** was assigned based on elemental analysis, IR, and multinuclear (^{1}H, ^{13}C) NMR data.

The characterization of **2** was first provided by the IR ν(CO) spectrum. In solid state, complex **2** shows six bands of the carbonyl stretching frequencies. The three CO stretching bands at higher frequencies are attributed to the carbonyl bonded to cobalt atoms [37]. In the case of the (η^6-arene)$Cr(CO)_3$ unit, three bands are expected: the A_1 band at higher frequency and the E band, split due to the deviation from idealised C_{3v} symmetry [30,31]. In addition, the IR spectrum of **2** displays the vibration mode of the C≡C unit at 1564 cm^{-1}, indicating a weakening of the C≡C bond upon coordination of the dicobalt compound [38,39]. From IR data we can assume that the $Co_2(CO)_6$ moiety coordinated to alkyne moiety acts as an electron-withdrawing substituent. The positive value of the

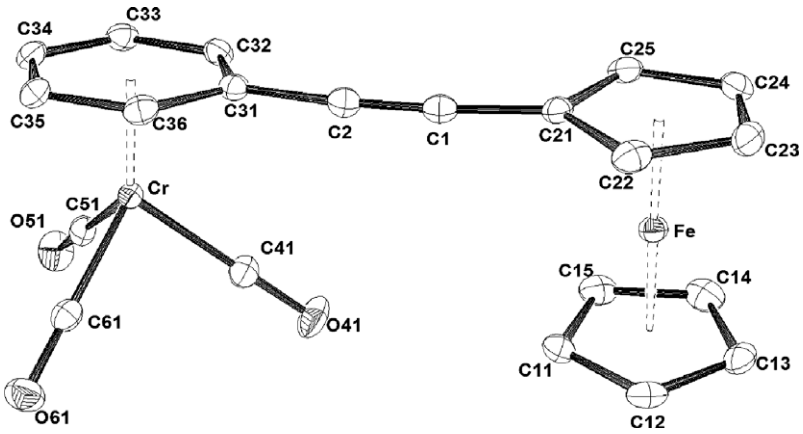


Fig. 1. Molecular structure of **1** (H atoms omitted) with thermal ellipsoids at the 30% probability level.

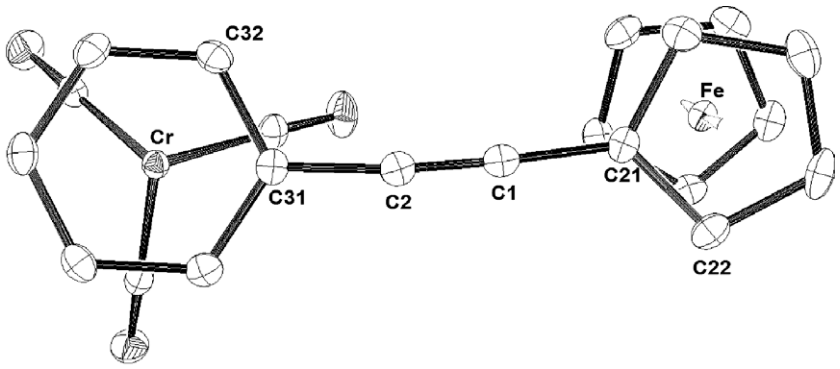


Fig. 2. Ortep view of complex **1** with the $Cr(CO)_3$ tripod projected onto the arene ring.

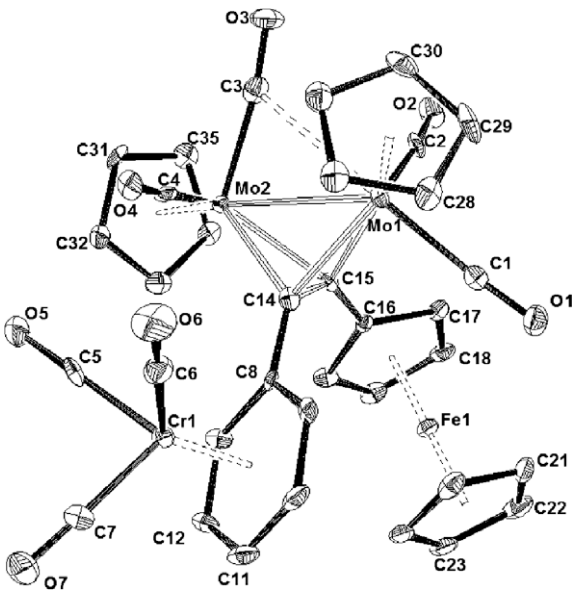


Fig. 3. Molecular structure of **3** (H atoms omitted) with thermal ellipsoids at the 30% probability level.

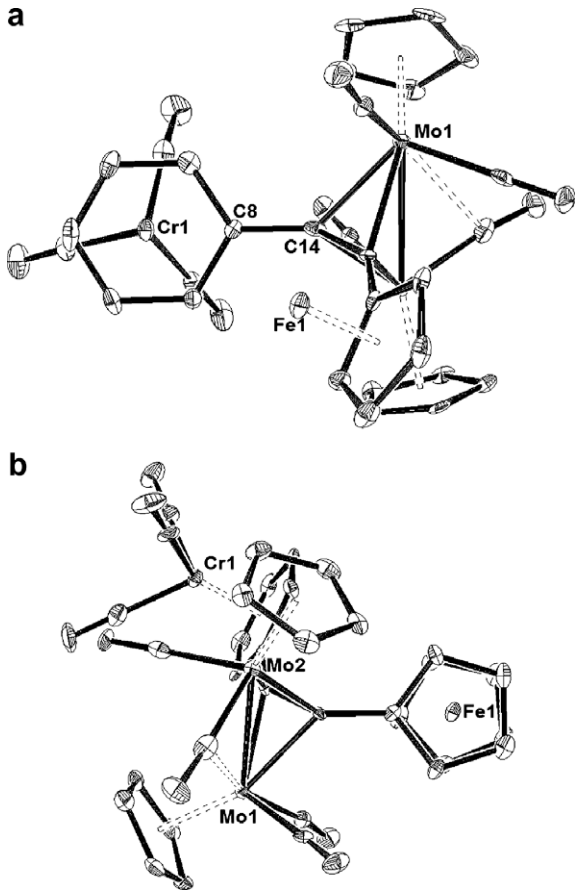
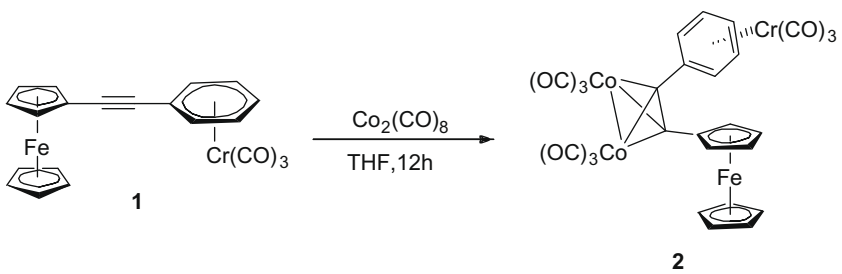


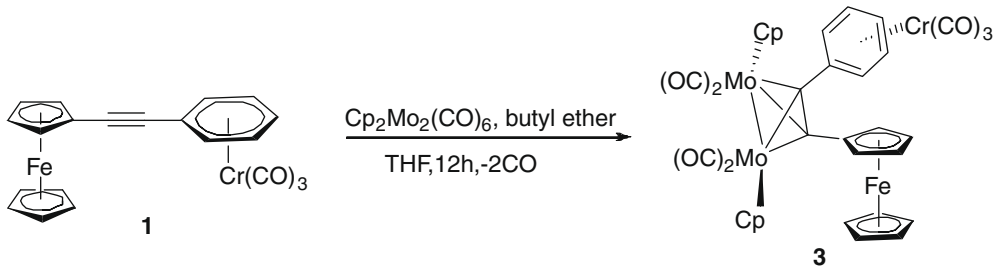
Fig. 4. Ortep view of complex **3** with: (a) the $Cr(CO)_3$ tripod projected onto the arene ring (one Cp ring coordinated to Fe omitted for clarity), (b) projected onto the Cp rings of the ferrocene unit.

parameter $\Delta\nu_M$ (10 cm^{-1}) [40] calculated for E-mode carbonyl absorption bands strongly suggests a slight electronic density transfer from the chromium fragment to the dicobalt-alkyne unit.

As expected, the ^1H NMR spectrum of **2** shows the usual three set of resonances in the range of 6.14–5.23 ppm attributable to the arene protons, and three singlets at 4.46, 4.40 and 4.18 ppm corresponding to the cyclopentadienyl protons of the ferrocene unit. In addition, the ^1H NMR spectrum of **2** displays the low frequency shift of the arene protons with respect to those of the cor-



Scheme 2.



Scheme 3.

responding complex **1** as result of electron-withdrawing characteristic of $Co_2(CO)_6$ fragment. The $^{13}C\{^1H\}$ NMR spectrum of **2** contains one sharp peak at 232.2 ppm related to the carbonyl groups bound to the chromium atom and a typical broad shape resonance at 199.2 ppm corresponding to the two equivalent sets of carbonyl ligands coordinated to the cobalt metal centres.

The 1:1 reaction of **1** with "$Mo_2Cp_2(CO)_4$" in di-*n*-butyl ether/CH_2Cl_2 at room temperature for 12 h affords the corresponding heterotetrametallic complex $[Cr(CO)_3(\eta^6\text{-}C_6H_5)\{Mo_2Cp_2(CO)_4\text{-}\mu^2\text{-}\eta^2\text{-}C{\equiv}C\text{-}\}(\eta^5\text{-}C_5H_4)Fe(\eta^5\text{-}C_5H_5)]$ (**3**) (Scheme 3), which was isolated as dark red solid in moderate yield (41%). The identity of **3** was established on the basis of elemental analysis, IR, multinuclear (^1H, ^{13}C) NMR data, and by an X-ray diffraction study.

The IR spectrum of **3** shows six ν(CO) bands in the range of 2004–1865 cm^{-1} corresponding to the terminal CO groups coordinated to molybdenum and chromium metal centres, and one lower-frequency band at 1846 cm^{-1} assigned to the semi-bridging carbonyl group. In this case the value of the parameter $\Delta\nu_M$ cannot be calculated due to difficulty assigning precisely the carbonyl stretching E band related to the $Cr(CO)_3$ moiety.

The ^1H NMR spectrum of **3** shows three set of arene resonances at 6.40, 5.52 and 5.31 ppm in a 2:1:2 intensity ratio, one singlet at 5.24 ppm assigned to the molybdenum cyclopentadienyl protons, and three singlets at 4.40, 4.30 and 4.23 ppm in a 2:2:5 intensity ratio related to the cyclopentadienyl protons of the ferrocene unit. Similarly found for complex **2**, the flow of electronic density from arene ligand to the "$Mo_2Cp_2(CO)_4$" fragment is reflected by the low field of the ^1H NMR signals of the arene group. The $^{13}C\{^1H\}$ NMR spectrum displays one singlet at 234.2 ppm related to the carbonyl groups coordinated to chromium metal center, and two weak singlets at 230.2 and 229.7 corresponding to the carbonyl groups bonded to molybdenum metal center as result of a fluxional process these ligands.

Crystals of complex **3** suitable for an X-ray diffraction study were grown from slow diffusion of hexane into the CH_2Cl_2 solution containing **3** at 25 °C. Crystal data and structure refinement for **3** are summarized in Table 1, and selected bond distances and angles are listed in Table 3. The molecular geometry and atom-labeling scheme is shown in Fig. 3. The compound **3** consists in three structural sub-units "$Cr(CO)_3(\eta^6\text{-}C_6H_5\text{-})$", "$Mo_2Cp_2(CO)_4(\eta^2, \mu^2\text{-}C{\equiv}C\text{-})$", and "$(\text{-}C_5H_4)Fe(C_5H_5)$". The Cr–Ct(1) (Ct(1) = centroid of C8–C13) and CrC–O bond distances in **3** (1.763 Å, average 1.173 Å(10)) are slightly longer than those observed in complex **1** (1.723 Å, average 1.152 Å(3)); this is likely due to the electron-withdrawing capacity of the "$Mo_2Cp_2(CO)_4$" as already indicated by the ^1H and ^{13}C NMR data.

As a general trend, the cluster core $Mo_2(\text{-}C{\equiv}C\text{-})$ shows the common tetrahedron geometry where the alkyne unit is almost perpendicular to the Mo–Mo bond. The Mo(1)–Mo(2) bond distance of 3.0036 (12) Å is comparable to those found in similar molybdenum complexes [41]. The coordination of the alkyne ligand to the Mo_2 unit is quite symmetrical, which can be evidenced by similar Mo–C bond distances [Mo(1)–C(14) = 2.220 (8) Å, Mo(1)–C(15) = 2.230 (7) Å; Mo(2)–C(14) = 2.251 (8) Å, Mo(2)–C(15) = 2.230 (7) Å]. The smallish Mo(1)–Mo(2)–C(3) angle of 69.5 (2)°, slightly bent Mo(2)–C(3)–O(3) angle (171.0 (7)°), away from Mo(1), and close non-bonding Mo(1)–C(3) bond distance (2.969(8)Å) are characteristic of a weakly interacting type II semi-bridging carbonyl [24,42]. The angle between the Mo(1)–Mo(2) and C(14)–C(15) vectors is 90.6°. The cyclopentadienyl rings, which have an average C-C bond distance of 1.442 Å are in the *trans*-position with respect to each other (pseudo torsion angle Ct(1)–Mo(1)–Mo(2)–Ct(2) = 152.2° (Ct(1) = centroid of C26–C30; Ct(2) = centroid of C31–C35). The Mo(1)–Ct(1) distance (2.037 Å) is slightly shorter than the Mo(2)–Ct(2) distance (2.059 Å), which can be attributable to the donation of electronic density from Mo(1) to the semi-bridging carbonyl of Mo(2). Neither ring shows slippage and both distances are in agreement with values observed for similar compounds [43].

Table 3
Selected bond lengths [Å] and angles [°] for **3**.

Mo(1)–Mo(2)	3.0036 (12)	Mo(1)–C(1)	2.022 (9)
Mo(1)–C(2)	2.035 (9)	Mo(2)–C(3)	1.997 (9)
Mo(2)–C(4)	2.002 (9)	Mo(1)–C(14)	2.220 (8)
Mo(1)–C(15)	2.230 (7)	Mo(2)–C(14)	2.251 (8)
Mo(2)–C(15)	2.230 (7)	Mo(1)–C(26)	2.412 (9)
Mo(1)–C(27)	2.414 (8)	Mo(1)–C(28)	2.363 (8)
Mo(1)–C(29)	2.335 (8)	Mo(1)–C(30)	2.371 (8)
Mo(2)–C(31)	2.348 (7)	Mo(2)–C(32)	2.368 (8)
Mo(2)–C(33)	2.415 (8)	Mo(2)–C(34)	2.433 (8)
Mo(2)–C(35)	2.409 (8)	C(14)–C(15)	1.399 (10)
C(8)–C(14)	1.479 (10)	C(15)–C(16)	1.487 (11)
O(1)–C(1)	1.176 (10)	O(2)–C(2)	1.160 (9)
O(3)–C(3)	1.185 (10)	O(4)–C(4)	1.164 (10)
Cr(1)–C(8)	2.336 (7)	Cr(1)–C(9)	2.271 (8)
Cr(1)–C(10)	2.256 (8)	Cr(1)–C(11)	2.256 (8)
Cr(1)–C(12)	2.236 (8)	Cr(1)–C(13)	2.260 (8)
Cr(1)–C(5)	1.844 (9)	Cr(1)–C(6)	1.884 (10)
Cr(1)–C(7)	1.868 (9)	O(5)–C(5)	1.191 (10)
O(6)–C(6)	1.161 (11)	O(7)–C(7)	1.166 (10)
Fe(1)–C(16)	2.132 (7)	Fe(1)–C(17)	2.078 (7)
Fe(1)–C(18)	2.060 (8)	Fe(1)–C(19)	2.050 (8)
Fe(1)–C(20)	2.069 (8)	Fe(1)–C(21)	2.064 (8)
Fe(1)–C(22)	2.088 (9)	Fe(1)–C(23)	2.091 (8)
Fe(1)–C(24)	2.076 (8)	Fe(1)–C(25)	2.070 (9)
C(8)–C(14)–C(15)	129.5 (7)	C(14)–C(15)–C(16)	140.2 (7)
C(15)–C(16)–C(17)	126.9(7)	C(15)–C(16)–C(20)	126.8(7)
C(14)–C(8)–C(13)	120.8 (6)	C(14)–C(8)–C(9)	123.2 (7)
O(1)–C(1)–Mo(1)	171.4 (7)	O(2)–C(2)–Mo(1)	174.3 (7)
O(3)–C(3)–Mo(2)	171.0 (7)	O(4)–C(4)–Mo(2)	177.9 (6)
C(14)–Mo(1)–C(15)	36.6 (3)	C(14)–Mo(2)–C(15)	36.4 (3)
Mo(1)–C(14)–Mo(2)	48.2 (2)	Mo(1)–C(15)–Mo(2)	47.66 (19)
C(8)–C(14)–Mo(1)	134.6 (5)	C(8)–C(14)–Mo(2)	137.2 (5)
C(16)–C(15)–Mo(1)	134.4 (5)	C(16)–C(15)–Mo(2)	129.3 (5)
C(1)–Mo(1)–C(2)	90.9 (3)	C(1)–Mo(1)–Mo(2)	129.3 (2)
C(3)–Mo(2)–C(4)	85.7 (3)	O(5)–C(5)–Cr(1)	178.8 (8)
O(6)–C(6)–Cr(1)	177.3 (8)	O(7)–C(7)–Cr(1)	177.7 (9)
C(5)–Cr(1)–C(6)	89.3 (4)	C(5)–Cr(1)–C(7)	88.6 (4)
C(6)–Cr(1)–C(7)	90.4 (4)	C(16)–C(15)–Fe(1)	133.4 (5)

In alkyne–dimolybdenum cluster, the R_1–C≡C–R_2 [R_1 = $Cr(CO)_3$-(η^6-C_6H_5–), R_2 = (–C_5H_4)Fe(C_5H_5)] moiety is no longer linear [C(16)–C(15)–C(14) = 140.2 (7)°, and C(8)–C(14)–C(15) = 129.5 (7)°] and the substituents are bent back by *ca.* 45°. In addition, the presence of substituents leads a twisting of the C(8)–C(14) bond relative to the C(15)–C(16) vector to give a dihedral angle of 4.8(15)°. As expected, the coordinated triple bond C(14)–C(15) = 1.399(10) Å) is significantly longer than the uncoordinated one in **1** (1.193(3) Å) indicating the reduction of the C≡C bond to a C=C bond upon coordination to the two molybdenum metal centers. In the ferrocene unit, the Fe-centroid distances are essentially equal (Fe–Ct(1) = 1.674, Fe–Ct(2) = 1.675 Å)(Ct(1) = centroid of C16–C20; Ct(2) = centroid of C21–C25), and the Ct(1)–Fe(1)–Ct(2) angle is almost linear (177.6(7)°). The average Fe–C separations for both rings are identical at 2.08 Å and slightly longer than those found in **1** (average 2.04 Å).

Comparing the molecular structures of **1** and **3** it was observed that the coordination of dimolybdenum moiety to the alkyne unit changes the orientation of the carbonyl groups coordinated to the chromium metal center [from 38.6° (staggered) in **1** to 12.2° (eclipsed) in **3**] as well as the torsion angle of the Cp rings bounded to the iron metal center [from 13.9° in **1** to 4.7° in **3**]. Furthermore, the Cr–C_{ipso} and Fe–C_{ipso} bond lengths in **3** (Cr(1)–C(8) = 2.336(7) Å; Fe(1)–C(16) (2.132(7) Å) are longer than those ones found in **1** (Cr–C(31) = 2.246(2) Å; [**1**, Fe–C(21) = 2.052(2) Å). These results are consistent with the ability of "$Mo_2Cp_2(CO)_4$" moiety to withdraw some electronic density from the arene and Cp rings.

It is interesting to note that the *cisoid* conformation presented in **1** (torsion angle defined by Cr–C(31)–C(21)–Fe of 6.4°) no longer exist after the coordination of the alkyne ligand to the Mo_2 unit. In **3**, the torsion angle of 94.8° (defined by Cr(1)–C(8)–C(16)–Fe(1)) indicates that **1** has twisted in order to form the alkyne–dimolybdenum cluster, maybe by rotation about the C(2)–C(31) bond and/or rotation about the C(1)–C(21) bond.

4. Conclusion

We have shown that two novel heterotetrametallic complexes (**2 and 3**) are readily synthesized by reacting **1** with the respective binuclear compounds [$Co_2(CO)_8$] and [$Mo_2Cp_2(CO)_4$]. Structural data from **1** reveal that the two structural sub-units $Cr(CO)_3$((η^6-C_6H_5–) and (–C≡C–C_5H_4)Fe(C_5H_5) adopts a *cisoid* conformation. The X-ray structural analysis of **3** shows that the conformation of the tricarbonyl tripod with respect to the aromatic ring as well as the disposition of the Cp rings bounded to the iron metal centre changes significantly after the coordination of the Mo_2 unit to the alkyne ligand.

Acknowledgments

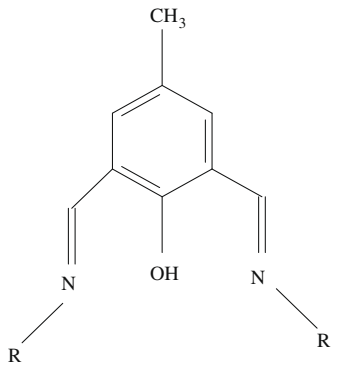
We gratefully acknowledge financial support from the CNPq and Pronex/FAPERGS (Brazil). Elton L.S. Gomes thanks CNPq for PhD fellowship. The X-ray structural analysis of **1** was performed by Dr. Robert Burrow (Universidade de Santa Maria, RS, Brazil). The X-ray structural analysis of **3** was performed by Dr. V.G. Young, Jr (University of Minnesota, USA).

Appendix A. Supplementary data

Supplementary data associated with this article can be found, in the online version, at doi:10.1016/j.poly.2009.01.032.

References

[1] J.L. Oudar, D.S. Chemla, J. Chem. Phys. 66 (1977) 2664.
[2] D.S. Chemla, J. Zyss (Eds.), Nonlinear Optical Properties of Organic Molecules and Crystals, vols. 1–2, Academic Press, San Diego, CA, 1987.
[3] S.R. Marder, D.N. Beratan, L.T. Cheng, Science 252 (1991) 103.
[4] E. Goovaerts, W.E. Wenseleers, M.H. Garcia, G.H. Cross, in: H.S. Nalwa (Ed.), Handbook of Advanced Electronic and Photonic materials and Devices, vol. 9, chapter 3, Academic Press, New York, 2001, pp. 127–191.
[5] J. Heck, S. Dabek, T. Meyer-Fridrieschen, H. Wong, Coord. Chem. Rev. 190–192 (1999) 1217.
[6] S. Di Bella, Chem. Soc. Rev. 30 (2001) 355.
[7] R. Germaneau, R. Chavignon, J.-Ph. Tranchier, F. Rose-Munch, E. Rose, M. Collot, C. Duhayon, Organometallics 26 (2007) 6139.
[8] T.-Y. Dong, M.-C. Lin, S.-W. Chang, C.-C. Ho, S.-F. Lin, L. Lee, J. Organomet. Chem. 692 (2007) 2324.
[9] G. Vives, A. Carella, S. Sistach, J.P. Launay, G. Rapenne, New J. Chem. 30 (2006) 1429.
[10] M.J.L. Tschan, B. Therrien, J. Ludvík, P, Stepnicka andG. Süss-Fink, J. Organomet. Chem. 691 (2006) 4304.
[11] Z. Li, A.M. Beatty, T.P. Fehlner, Inorg. Chem. 42 (2003) 5707.
[12] G.L. Xu, M.C. DeRosa, R.J. Crutchley, T. Ren, J. Am. Chem. Soc. 126 (2004) 3728.
[13] G.L. Xu, R.J. Crutchley, M.C. DeRosa, Q.J. Pan, H.X. Zhang, X. Wang, T. Ren, J. Am. Chem. Soc. 127 (2005) 13354.
[14] J.H.K. Yip, J. Wu, K.Y. Wong, K.W. Yeung, J.J. Vittal, Organometallics 21 (2002) 1612.
[15] A. Albinati, F.F. de Biani, P. Leoni, L. Marchetti, M. Pasquali, S. Rizzato, P. Zanello, Angew. Chem., Int. Ed. Engl. 44 (2005) 5701.
[16] N.D. Jones, M.O.Wolf, D.M. Giaquinta, Organometallics 16 (1997) 1352.
[17] T.J.J. Müller, A. Netz, Organometallics 17 (1998) 3609.
[18] A. Netz, T.J.J. Müller, Tetrahedron 56 (2000) 4149.
[19] A. Netz, K. Polborn, T.J.J. Müller, J. Am. Chem. Soc. 123 (2001) 3441.
[20] A. Netz, K. Polborn, T.J.J. Müller, Organometallics 20 (2001) 376.
[21] Z.F. Plyta, D. Prim, J.-Ph. Tranchier, F. Rose-Munch, E. Rose, Tetrahedron Lett. 40 (1999) 6769.
[22] T.J.J. Müller, M. Ansorge, J. Lindner, Chem. Ber. 129 (1996) 1433.
[23] E.L.S. Gomes, V. Caliman, M. Horner, V.G. Young Jr., J. Dupont, O.L. Casagrande Jr., Organometallics 18 (1999) 3898.
[24] E.L.S. Gomes, R. Burrow, A.J. Lough, J. Dupont, O.L. Casagrande Jr., J. Chem. Soc., Dalton Trans. (2001) 1634.
[25] J. Polin, H. Schottenberger, Org. Synth. 73 (1996) 262.
[26] C.A.L. Mahaffy, P. Pauson, Inorg. Synth. 28 (1990) 137.
[27] SHELXTL-Plus V 5.0, Siemens Industrial Automation, Inc., Madison, WI.
[28] G.M. Sheldrick, SHELXS97 and SHELXS97, University of Göttingen, Germany, 1997.
[29] Z. Otwinowski, W. Minor, Methods Enzymol. 276 (1997) 307.
[30] R.D. Fisher, Chem. Ber. 93 (1960) 165.
[31] D.A. Brown, J.R. Raju, J. Chem. Soc. A. (1966) 1617.
[32] T.J.J. Müller, J. Lindner, Chem. Ber. 129 (1996) 607.
[33] T.J.J. Müller, M. Ansorge, J. Lindner, Chem. Ber. 130 (1997) 1135.
[34] H. Fink, N.J. Long, A.J. Martin, G. Opromolla, A.J.P. White, D.J. Williams, P. Zanello, Organometallics 16 (1997) 2646.
[35] P. Debroy, S. Roy, Coord. Chem. Rev. 251 (2007) 203.
[36] R.D. Adams (Ed.), 50th Anniversary of the Discovery of Ferrocene, J. Organomet. Chem. (2001) (special issue) 637, and references cited therein.
[37] S.P. Tunik, A.V. Vlasov, A.B. Nikolskii, G.L. Starova, S. Ooi, H. Nakai, T. Sato, J. Organomet. Chem. 464 (1994) 71.
[38] R.S. Dickson, P.J. Fraser, Adv. Organomet. Chem. 12 (1974) 323.
[39] D. Seyferth, T. Kugita, A. Rheingold, G.P.A. Yap, Organometallics 14 (1995) 5632.
[40] Determination of $\Delta\nu$ was done with Average Values of νE, $\Delta\nu M = (\nu E$ of Heterotetrametallic Complex 2 – νE of the Corresponding Starting (η^6-Arene)Tricarbonylchromium–Ferrocenylethynyl Complex **1**).
[41] L.T. Byrne, C.S. Griffith, G.A. Koutsantonis, B.W. Skelton, A.H. White, J. Chem. Soc., Dalton Trans. (1998) 1575.
[42] R.H. Crabtree, M. Lavin, Inorg. Chem. 25 (1996) 805.
[43] N.A. Ustynyuk, V.N. Vinogradova, V.N. Korneva, D.N. Kravtsov, V.G. Andrianov, Yu T. Struchkov, J. Organomet. Chem. 277 (1984) 285.



HL[1], R = cyclohexylmethyl
HL[2], R = 1-naphthylylmethyl

Scheme 1.

studied on a Perkin–Elmer LS 55 Luminescence spectrometer. Fluorescence life times were determined from time-resolved intensity decay by the method of time-correlated single-photon counting using a picosecond diode laser at 403 nm as the light source.

2.2. Synthesis of 4-methyl-2,6-bis(cyclohexylmethyliminomethyl)-phenol (*HL*[1])

The Schiff-base ligand **HL**[1] has been prepared by following the published procedure with a slight modification [16]. To a solution of 4-methyl-2,6-diformylphenol (0.821 g, 5 mmol) in 20 mL of acetonitrile was added cyclohexanemethylamine (1.132 g, 10 mmol) in 5 mL acetonitrile. The reaction mixture was refluxed for 4 h. The mixture was filtered, concentrated on rotary evaporator to dryness. The solid compound was obtained after keeping it at 4 °C overnight. It was recrystallized from toluene (yield = 95%). Data for **HL**[1]: *Anal*. Calc. for $C_{23}H_{34}N_2O$: C, 77.92; H, 9.67; N, 7.90. Found: C, 77.88; H, 9.56; N, 7.96%; FT-IR (KBr phase) (cm^{-1}): 2920 vs, 2849 s, 1637 vs, 1599 s, 1465 s, 1448 s, 1309 m, 1037 w, 889 w, 844 w (w, weak; m, medium; s, strong; vs, very strong). ^1H NMR (300 MHz, $CDCl_3$; δ): 0.94–1.05 (t, 4H), 1.14–1.32 (m, 8H), 1.65–2.0 (m, 10H), 2.29 (s, 3H), 3.47 (t, 4H), 7.41 (s, 2H), 8.48 (s, 2H); HRMS [$(M+H^+)/z$ (%)]: simulated for $C_{23}H_{34}N_2O$; 355.53; found 355.53.

2.3. Synthesis of 4-methyl-2,6-bis(1-naphthalylmethyliminomethyl)-phenol (*HL*[2])

HL[2] was synthesized according to a similar process as that followed for **HL**[1]. In this case 1-naphthalenemethylamine was used instead of cyclohexanemethylamine (yield = 92%). Data for **HL**[2]: *Anal*. Calc. for $C_{31}H_{26}N_2O$: C, 84.13; H, 5.92; N, 6.33. Found: C, 84.06; H, 5.87; N, 6.30%; FT-IR (KBr phase) (cm^{-1}): 2914 w, 2864 w, 1635 vs, 1596 vs, 1460 s, 1436 m, 1392 m, 1307 m, 1256 s, 1027 w, 875 w, 795 vs, 777 vs, 731 w, 663 w. ^1H NMR (300 MHz, $CDCl_3$; δ): 2.26 (s, 3H), 5.27 (s, 4H), 7.42–7.58 (m, 12H), 7.79–7.93 (m, 4H), 8.12 (d, 2H); HRMS [$(M+H^+)/z$ (%)]: simulated for $C_{31}H_{26}N_2O$; 443.56; found 443.56.

2.4. Synthesis of $[Zn_6(L^1)_2(OH)_2(CH_3COO)_8] \cdot CH_3CN$ (**1** · CH_3CN)

Zinc(II) acetate dihydrate (0.198 g, 0.9 mmol) in 10 mL acetonitrile was added slowly to a magnetically stirred 10 mL acetonitrile solution of the ligand (**HL**[1]) (0.106 g, 0.3 mmol). The mixture was stirred in air for 45 min and then refluxed for 1 h. It was filtered and kept in air at ambient temperature. Crystals of **1** suitable for a structure determination by X-ray crystallography were obtained by slow evaporation of the filtrate within few days (yield: 70%). *Anal*. Calc. for $C_{64}H_{95}N_5O_{20}Zn_6$: C, 45.55; H, 5.67; N, 4.15. Found: C, 45.49; H, 5.63; N, 4.19%. FT-IR (KBr phase) (cm^{-1}): 2925 s, 2851 s, 1626 s, 1593 vs, 1556 s, 1446 s, 1423 vs, 1342 m, 1043 w, 823 w, 667 m.

2.5. Synthesis of $[Zn_6(L^2)_2(OH)_2(CH_3COO)_8] \cdot 4CH_3CN$ (**2** · $4CH_3CN$)

Complex **2** · $4CH_3CN$ was also prepared similarly as for the previous procedure. To a 10 mL acetonitrile solution of **HL**[2] (0.133 g, 0.3 mmol) was added 10 mL acetonitrile solution of zinc(II) acetate dihydrate (0.198 g, 0.9 mmol). The mixture was stirred for 45 min and refluxed for 1.5 h. It was cooled, filtered and the filtrate was kept at room temperature. Yellow colored single crystals of **2** · $4CH_3CN$ were obtained from the filtrate within 2 days (yield: 60%). *Anal*. Calc. for $C_{78}H_{76}N_4O_{20}Zn_6$: C, 52.58; H, 4.30; N, 3.14. Found: C, 52.49; H, 4.26; N, 3.19%. FT-IR (KBr phase) (cm^{-1}): 3049 w, 2925 w, 1595 vs, 1578 s, 1414 s, 1342 m, 1232 w, 1020 w, 794 m, 777 m, 669 m.

2.6. X-ray data collection and structure determination

The crystal data of both complexes are summarized in Table 1. The structures of the complexes were determined by the single crystal X-ray diffraction method. The diffraction experiments were carried out on a Bruker SMART CCD area-detector diffractometer at 295 K for **1** · CH_3CN and at 150 K for **2** · $4CH_3CN$. No crystal decay was observed, so that no time-decay correction was needed. The collected frames were processed with the software SAINT [17], and an empirical absorption correction was applied (SADABS) [18] to the collected reflections. The calculations were performed using the Personal Structure Determination Package [19] and the physical constants tabulated therein [20]. The structure was solved by direct methods (SHELXS) [21] and refined by full-matrix least-squares using all reflections and minimising the function $\sum w(F_o^2 - F_c^2)^2$ (refinement on F^2). All the non-hydrogen atoms were refined with anisotropic thermal factors. The hydrogen atoms of the acetato ligands were detected in the final Fourier maps and were not refined. All the other hydrogen atoms were placed in their

Table 1
Crystal data for the complexes.

Complex	**1**	**2**
Empirical formula	$C_{66}H_{98}N_6O_{20}Zn_6$	$C_{94}H_{100}N_{12}O_{20}Zn_6$
Formula weight	1687.77	2110.13
Crystal system	triclinic	monoclinic
Space group	$P\bar{1}$	$C12/c1$
a (Å)	12.5002(7)	30.9334(16)
b (Å)	12.6085(8)	14.4096(7)
c (Å)	13.4821(8)	25.5004(13)
α (°)	102.839(1)	90
β (°)	109.119(1)	121.739(1)
γ (°)	97.340(1)	90
V (Å^3)	1910.5(2)	9666.6(9)
Z	1	4
D_{calc} (g cm^{-3})	1.467	1.450
μ (Mo Kα) (mm^{-1})	1.969	1.573
$F(000)$	876	4352
T (K)	295	150
λ (Mo Kα)	0.71073	0.71073
Max. and min. θ range (°)	23.0, 3.0	27.0, 3.0
Total data, unique data	29164, 10772	89646, 12546
R_{int}	0.0304	0.0280
R_2 (F^2, all reflections)	0.052	0.038
Final R indices (R_1, wR_2)	0.030, 0.062	0.023, 0.067
Goodness-of-fit	0.924	1.007
Largest difference in peak and hole (e Å^{-3})	0.64(36) and −0.51(36)	0.47(11) and −0.39(11)

ideal positions (C–H or O–H = 0.97 Å), with a thermal parameter U 1.10 times that of the atom to which they are attached, and were not refined.

3. Results and discussion

The crystals of the complexes **1** · CH_3CN and **2** · $4CH_3CN$ are highly unstable. They contain solvent molecules, i.e. acetonitrile, in the crystal. The crystal looses its solvent molecules when they are dry. This is also evident from the elemental analysis, where the results show the absence of any acetonitrile molecule(s).

The electronic spectra of the ligands along with complexes **1** and **2** were recorded in acetonitrile at room temperature. Both of the ligands exhibit similar behavior. They show bands at around 320 and 387 nm. These may be assigned to π–π*/n–π* transitions. The complexes show an intense band at around 390 nm which may be assigned due to π–π*/n–π* transitions. A relatively weak transition at around 440–445 nm is assigned to a MLCT band [6].

3.1. Description of the structure of $[Zn_6(L^1)_2(OH)_2(CH_3COO)_8] \cdot CH_3CN$ (**1** · CH_3CN)

Complex **1** crystallizes in the triclinic system, space group $P\bar{1}$ from acetonitrile solvent. A perspective view of the complex is shown in Fig. 1. The selected bond distances and bond angles are listed Table 2. The molecule is a hexametallic neutral monomer, lying on a crystallographic inversion center. The asymmetric unit of the complex comprises three Zn^{2+} ions, one binucleating ligand 4-methyl-2,6-bis(cyclohexylmethyliminomethyl)-phenolate ($\mathbf{L^{1-}}$), one μ_3-hydroxo anion (bonded to the three metal atoms) and four acetato anions. The Zn1 atom is linked by a μ_2-phenoxo oxygen atom (O2) and the N1 atom of the ligand $\mathbf{HL^1}$, a μ_3-hydroxo oxygen atom (O1) and two μ_2-acetato oxygen atoms (O3, O5). It has an almost perfect square pyramidal geometry, as is evident from the τ value of Zn1 which is found to be 0.04. The value of τ is defined as the difference between the two largest donor–metal–donor angles divided by 60, a value which is 0 for an ideal square pyramid geometry and 1 for a trigonal bipyramidal geometry [22]. The Zn1 atom is displaced out the best plane formed by O2, O1, O5 and N1 by 0.226 Å. The O2, O1, O5 and N1 atoms are coplanar to within 0.018 Å. On the other hand, the Zn2 atom is coordinated to a μ_2-phenoxo oxygen atom (O2) and the N2 atom of the ligand $\mathbf{HL^1}$, a μ_3-hydroxo oxygen atom (O1) and two μ_2-acetato oxygen atoms (O6 and O7). The Zn2 atom has a distorted square pyramidal geometry. This is clear from the value of the trigonal index of Zn2, which is found to be 0.38. The square plane is formed by O2, O1, O7 and N2, and the O6 atom occupies the apical position. These atoms are coplanar to within 0.234 Å, whereas the Zn2 atom is out the square plane by 0.488 Å. The apical Zn–O6 bond distance is slightly shorter than the other bond distances. The Zn3 atom is connected to a μ_3-hydroxo oxygen atom (O1) and three μ_2-acetato oxygen atoms (O3, O8 and O9). It has a distorted tetrahedral geometry. The bond angles vary from 104.1(1)° to 124.9(1)°. The two Zn3 units are bridged by two acetato ions. Thus it may be summarized that out the three Zn atoms, two are five-coordinated (one almost perfect square pyramidal and one distorted trigonal bipyramidal) and the third has a tetrahedral four-coordinated geometry. All the bond distances are in good agreement with previously reported values [8,23].

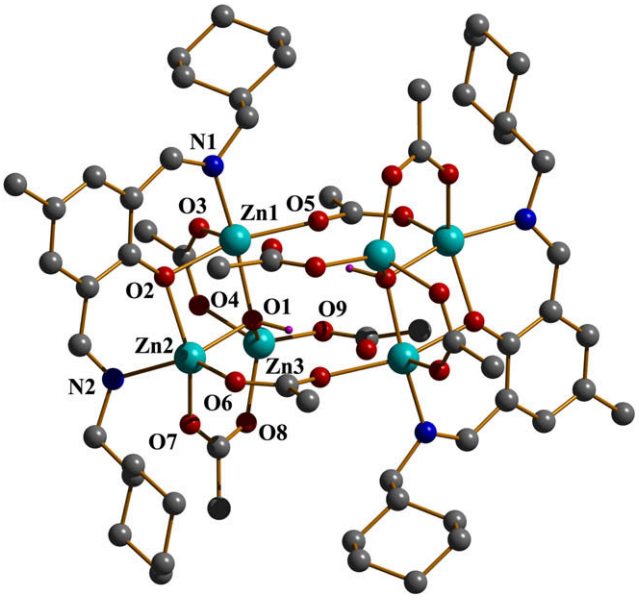


Fig. 1. A perspective view of complex **1** with partial atom numbering scheme and color codes (carbon, grey; oxygen, red; nitrogen, blue; hydrogen, pink; zinc, cyan). All the hydrogen atoms (except the hydrogen atoms of hydroxo ions) and solvent molecule are omitted for clarity. (For interpretation of the references to color in this figure legend, the reader is referred to the web version of this article.)

Table 2
Selected bond lengths (Å) and bond angles (°) of complex **1**.

Zn1–O1	2.012(1)	Zn1–O2	2.097(1)
Zn1–O3	2.084(2)	Zn1–O5	2.129(1)
Zn1–N1	2.018(1)	Zn2–O1	2.047(1)
Zn2–O2	2.070(1)	Zn2–O6	1.988(1)
Zn2–O7	2.047(1)	Zn2–N2	2.059(2)
Zn3–O1	1.949(1)	Zn3–O4	1.964(1)
Zn3–O8	1.964(1)	Zn3–O9	1.931(2)
O1–Zn1–O2	78.9(1)	O1–Zn1–O3	96.4(1)
O1–Zn1–O5	89.0(1)	O1–Zn1–N1	165.3(1)
O2–Zn1–O3	93.4(1)	O2–Zn1–O5	162.9(1)
O2–Zn1–N1	91.2(1)	O3–Zn1–O5	99.9(1)
O3–Zn1–N1	95.1(1)	O5–Zn1–N1	98.2(1)
O1–Zn2–O2	78.7(1)	O1–Zn2–O6	96.2(1)
O1–Zn2–O7	92.6(1)	O1–Zn2–N2	162.4(1)
O2–Zn2–O6	115.6(1)	O2–Zn2–O7	139.8(1)
O2–Zn2–N2	87.6(1)	O6–Zn2–O7	104.3(1)
O6–Zn2–N2	99.7(1)	O7–Zn2–N2	90.6(1)
O1–Zn3–O4	105.3(1)	O1–Zn3–O8	108.5(1)
O1–Zn3–O9	124.9(1)	O4–Zn3–O8	108.7(1)
O4–Zn3–O9	104.5(1)	O8–Zn3–O9	104.1(1)
Zn1–O1–Zn2	102.5(1)	Zn1–O1–Zn3	114.4(1)
Zn2–O1–Zn3	114.1(1)		

3.2. Description of the structure of $[Zn_6(L^2)_2(OH)_2(CH_3COO)_8] \cdot 4CH_3CN$ (**2** · $4CH_3CN$)

The crystals of $[Zn_6(\mathbf{L^2})_2(\mu_2\text{-}OH)_2(\mu_2\text{-}CH_3COO)_8] \cdot 4CH_3CN$ (**2** · $4CH_3CN$) were obtained in the in monoclinic crystal system, *C 12/c*1 space group from acetonitrile. A perspective view of the complex is shown in Fig. 2. Selected bond lengths and bond angles are listed in Table 3. The complex is a hexanuclear monomer lying on a crystallographic twofold axis. The asymmetric unit comprises three Zn^{2+} ions, one binucleating ligand, 4-methyl-2,6-bis(1-naphthalylmethyliminomethyl)-phenolate ($\mathbf{L^{2-}}$), four acetato ligands and one μ_3-hydroxo anion (bonded to the three metal atoms). The Zn1 atom is coordinated to the N1 and O2 atoms of the binucleating ligand, O1 (μ_3-hydroxo oxygen atom) and two oxygen atoms (O3 and O5) of two acetato ions. It is in a distorted octahedral geometry. The *cis* angles around Zn1 range from 79.1(1)° to 98.7(1)°. The Zn1–O3 distance (2.241(1) Å) is quite a lot longer compared to the other Zn1–O or Zn1–N bond distances. The Zn2 atom is linked to one μ_2-phenoxo oxygen atom (O2) and the N2 atom of the ligand $\mathbf{HL^2}$, one μ_3-hydroxo oxygen atom (O1) and two oxygen atoms (O4 and O9) of two acetato ions. Zn2 has a 4 + 1 distorted square pyramidal geometry, whose basal plane is constructed by O1, O2, N2 and O9. O4 occupies the apical position

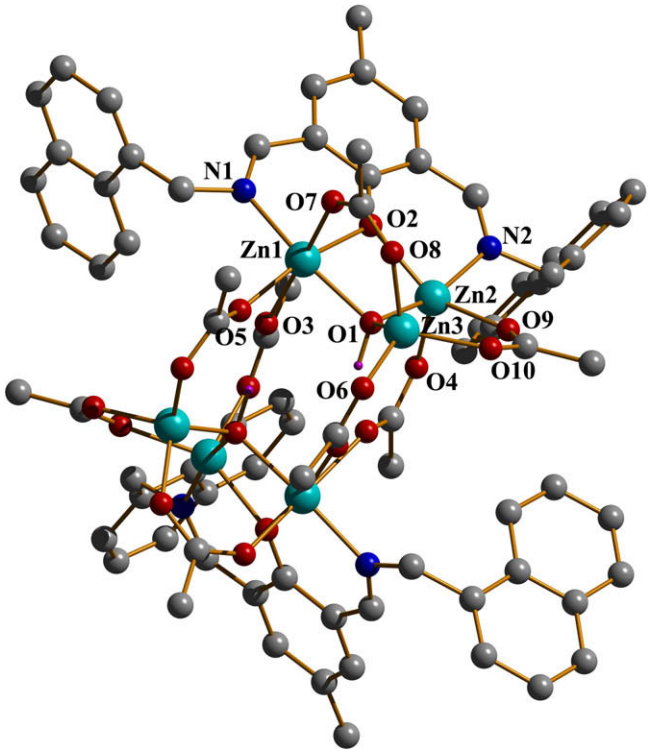


Fig. 2. A perspective view of complex **2** with partial atom numbering scheme and color codes (carbon, grey; oxygen, red; nitrogen, blue; hydrogen, pink; zinc, cyan). All the hydrogen atoms (except the hydrogen atoms of hydroxo ions) and solvent molecules are omitted for clarity. (For interpretation of the references to color in this figure legend, the reader is referred to the web version of this article.).

Table 3
Selected bond lengths (Å) and bond angles (°) of complex **2**.

Zn1–O1	2.027(1)	Zn1–O2	2.082(1)
Zn1–O3	2.241(1)	Zn1–O5	2.094(1)
Zn1–O7	2.120(1)	Zn1–N1	2.042(1)
Zn2–O1	2.055(1)	Zn2–O2	2.064(1)
Zn2–O4	1.988(1)	Zn2–O9	2.036(1)
Zn2–N2	2.061(1)	Zn3–O1	1.935(1)
Zn3–O6	1.960(1)	Zn3–O8	1.957(1)
Zn3–O10	1.960(1)		
O1–Zn1–O2	79.1(1)	O1–Zn1–O3	86.1(1)
O1–Zn1–O5	92.6(1)	O1–Zn1–O7	94.3(1)
O1–Zn1–N1	169.2(1)	O2–Zn1–O3	91.6(1)
O2–Zn1–O5	169.0(1)	O2–Zn1–O7	92.4(1)
O2–Zn1–N1	90.4(1)	O3–Zn1–O5	80.6(1)
O3–Zn1–O7	176.0(1)	O3–Zn1–N1	91.7(1)
O5–Zn1–O7	95.4(1)	O5–Zn1–N1	97.5(1)
O7–Zn1–N1	88.6(1)	O1–Zn2–O2	78.9(1)
O1–Zn2–O4	98.7(1)	O1–Zn2–O9	94.1(1)
O1–Zn2–N2	163.3(1)	O2–Zn2–O4	115.6(1)
O2–Zn2–O9	142.5(1)	O2–Zn2–N2	87.8(1)
O4–Zn2–O9	101.9(1)	O4–Zn2–N2	96.1(1)
O9–Zn2–N2	90.4(1)	O1–Zn3–O6	120.8(1)
O1–Zn3–O8	110.9(1)	O1–Zn3–O10	107.3(1)
O6–Zn3–O8	100.5(1)	O6–Zn3–O10	109.2(1)
O8–Zn3–O10	107.3(1)	Zn1–O1–Zn2	101.5(1)
Zn1–O1–Zn3	115.4(1)	Zn2–O1–Zn3	118.6(1)

of the square pyramid. The O1, O2, N2 and O9 atoms are coplanar to within 0.222 Å, whereas the Zn2 atom is out of basal plane by 0.453 Å. The distortion in the square pyramidal geometry is supported by the trigonal index value of Zn2 which is calculated to be 0.35. The Zn2–O4 distance (1.988(1) Å) is the shortest distance among all the Zn2–donor distances. Zn3 is connected to one μ_3-hydroxo oxygen atom (O1) and three oxygen atoms (O6, O8 and O10)

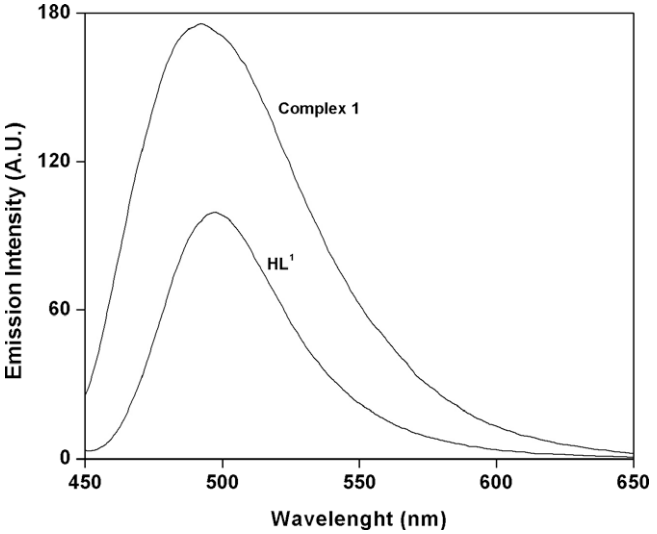


Fig. 3. Emission spectra of equimolar solutions (1×10^{-3} M) of **HL^1** and complex **1** in acetonitrile with an excitation wavelength of 395 nm.

of three different acetato moieties. It is in a distorted tetrahedral geometry. The donor–metal–donor angles range from 100.5(1)° to 120.8(1)°. The Zn3–O bond distances are in the range 1.935(1)–1.960(1) Å. All the metal–donor bond distances are in good agreement with the reported values [8,23]. It may be summarized that of these three independent Zn atoms, one is octahedrally six coordinated, one irregularly five coordinated and one distorted tetrahedrally four coordinated. This is a rare occasion in chemistry when all the three Zn atoms in a complex have different coordination environments [8].

3.3. Fluorescence properties

The fluorescence spectra of the ligands and their zinc(II) complexes are recorded in acetonitrile at room temperature on excitation at 395 nm. The ligands **HL^1** and **HL^2** show emission bands at 497 and 503 nm, respectively. Complexes **1** and **2** exhibit their emission maxima at 492 and 474 nm, respectively. The complexes, having the same molar concentrations as the ligands, display enhanced emission intensities compared to their corresponding ligands when excited with the same amount of energy. Fig. 3 shows the emission of **HL^1** together with its complex as a representative case. The peak of emission band of the complex, as compared to that of the free ligand, is quite unexpected, as one would expect the emission band of the free ligand to be at a higher energy related to that of the complex because of its relatively high energy excitation band. This anomaly can be explained by the fact that excited states resulting from complexes of Zn^{2+} are typically ligand-centered (LC) in nature, owing to the inability of the d^{10} metal center to participate in low-energy charge-transfers for metal-centered transitions [24]. Therefore, the emission from the complex is believed to arise from an excited state centered on the ligand which contains a phenolic proton [8,25]. It is well known that 4-methyl-2,6-diformylphenol undergoes a blue shift of its own band (from 530 to 445 nm) in the presence of a base B (e.g. piperidine or triethylamine), and this observation is believed to support the existence of an equilibrium between the phenol and a proton-transferred species of phenol with the formation of phenoxide and BH^+ ions [26,27]. The same analogy can be applied to the present system because the phenolic proton of the ligand is removed upon complexation with Zn^{2+}, and this proton should be transferred to the anion of the precursor zinc(II) acetate in the solution. We performed an emission experiment on the free ligand in the presence

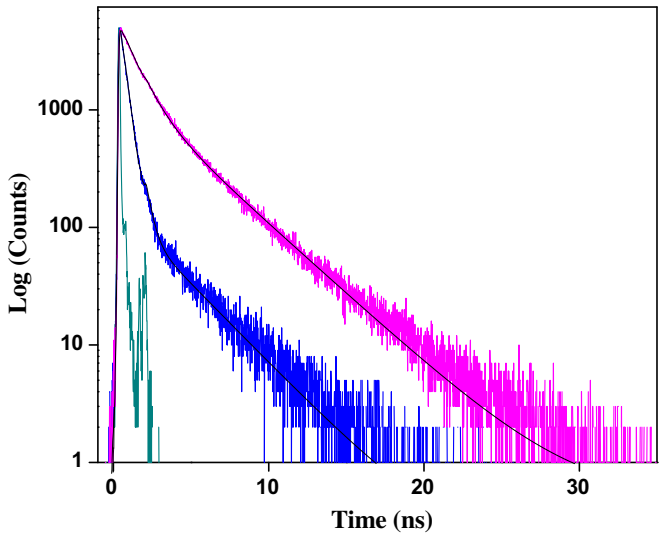


Fig. 4. Time-resolved fluorescence decay of **HL**[1] (blue) and its complex (magenta) in acetonitrile at room temperature (λ_{ex} = 403 nm). The sharp profile on the left (olive) is the lamp profile. (For interpretation of the references to color in this figure legend, the reader is referred to the web version of this article.)

Table 4
Fluorescence quantum yields[a] and radiative and total non-radiative rate data of the ligands and their complexes with Zn^{2+}.

Compounds	Quantum yield	τ_f (ns)	k_r (10^7 s^{-1})	k_{nr} (10^7 s^{-1})
HL[1]	0.05	1.14	4.4	83.3
Complex **1**	0.12	1.68	71.1	58.5
HL[2]	0.03	0.96	3.1	103.8
Complex **2**	0.15	1.37	10.9	71.9

[a] Standard used is Cumarin 343, Φ = 0.63.

of an added base, e.g. triethylamine, in acetonitrile and found that on addition of triethylamine, a new band appeared at around 445 nm. This indicates the existence of an equilibrium between undissociated **HL**[1] and a proton-transferred species of **HL**[1].

The quantum yields measured for all the ligands and complexes are listed in Table 1. The results clearly reveal that the quantum yields of complexes **1** and **2** are increased by 2.4 and 5 times compared to that of the free ligands.

We have also studied the fluorescence decay behavior of the ligands and their complexes (Fig. 4, Supplementary data, Fig. S1). The fluorescence lifetimes (τ) of the ligands and their corresponding complexes in acetonitrile are given in Table 4. The results of fluorescence lifetime measurements indicate that changes in the lifetime would be associated with any number of possible mechanisms for fluorescence enhancement, not only PET (photo-induced electron transfer). The time-resolved spectrum appears to display at least two components. Since the mechanism of fluorescence enhancement is a change in the rigidity upon binding of the zinc ion, a different mechanism other than PET may be of significance. According to the equation [28] $\tau^{-1} = k_r + k_{nr}$ and $k_r = \Phi_f/\tau$, the radiative rate constant k_r and the total non-radiative rate constant k_{nr} of the ligands and their complexes with Zn^{2+} were calculated and listed in Table 4. The data suggest that k_{nr} is just changed by a small amount, but the factor that induces fluorescent enhancement is mainly ascribed to the increase of k_r. Thus, the enhancement in the emission intensity of the complex compared to free ligand may be assigned to the fact that complexation would impose rigidity to the ligand and hence increase the value of the radiative rate constant.

4. Conclusion

We have prepared two hexanuclear zinc(II) complexes with N_2O donor Schiff-base ligands and the complexes have been characterized by single crystal X-ray analysis along with elemental analysis and spectroscopic methods. Three zinc atoms are present in both the complexes. In complex **1**, two zinc atoms are five-coordinated (one distorted square pyramidal and one distorted trigonal bipyramidal) whereas the third is tetrahedrally four-coordinated. In complex **2**, three zinc atoms are present in three different coordination environments (distorted octahedral, irregularly five coordination and distortedly tetrahedral geometry) leading to a rare situation in chemistry. Both complexes showed greater emission intensity compared to their ligands. They emit at around 470–490 nm on excitation at 395 nm.

Appendix A. Supplementary data

CCDC 703376 and 703377 contains the supplementary crystallographic data for this article. These data can be obtained free of charge via http://www.ccdc.cam.ac.uk/conts/retrieving.html, or from the Cambridge Crystallographic Data Centre, 12 Union Road, Cambridge CB2 1EZ, UK; fax: (+44) 1223-336-033; or e-mail: deposit@ccdc.cam.ac.uk. Supplementary data associated with this article can be found, in the online version, at doi:10.1016/j.poly.2009.01.042.

References

[1] P. Roy, K. Dhara, M. Manassero, P. Banerjee, Inorg. Chem. Commun. 11 (2008) 265.
[2] J. Chakraborty, M. Nandi, H. Mayer-Figge, W.S. Sheldrick, L. Sorace, A. Bhaumik, P. Banerjee, Eur. J. Inorg. Chem. (2007) 5033.
[3] A. Erxleben, J. Hermann, J. Chem. Soc., Dalton Trans. (2000) 569.
[4] M. Ghiladi, F.B. Larsen, C.J. McKenzie, I. Søtofte, J.-P. Tuchagues, J. Chem. Soc., Dalton Trans. (2005) 1687.
[5] P. Biswas, M. Ghosh, S.K. Dutta, U. Flörke, K. Nag, Inorg. Chem. 45 (2006) 4830.
[6] P. Roy, J. Coord. Chem., 2009, doi:10.1080/00958970902751888.
[7] K. Dhara, S. Karan, J. Ratha, P. Roy, G. Chandra, M. Manassero, B. Mallik, P. Banerjee, Chem. Asian J. 2 (2007) 1091.
[8] P. Roy, K. Dhara, M. Manassero, J. Ratha, P. Banerjee, Inorg. Chem. 46 (2007) 6405.
[9] G.S. Papaefstathiou, Z. Zhong, L. Geng, L.R. MacGillivray, J. Am. Chem. Soc. 126 (2004) 9158.
[10] B. Dutta, P. Bag, U. Flörke, K. Nag, Inorg. Chem. 45 (2005) 147.
[11] T.Z. Yu, W.M. Su, W.L. Li, Z.R. Hong, R.N. Hua, M.T. Li, B. Chu, B. Li, Z.Q. Zhang, Z.Z. Hu, Inorg. Chim. Acta 359 (2006) 2246.
[12] T.Z. Yu, K. Zhang, Y. Zhao, C. Yang, H. Zhang, D. Fan, W. Dong, Inorg. Chem. Commun. 10 (2007) 401.
[13] T. Kawamoto, M. Nishiwaki, Y. Tsunekawa, K. Nozaki, T. Konno, Inorg. Chem. 47 (2008) 3095.
[14] R.R. Gagne, C.L. Spiro, T.J. Smith, C.A. Hamann, W.R. Thies, A.K. Schiemke, J. Am. Chem. Soc. 103 (1981) 4073.
[15] D.D. Perrin, W.L. Armarego, D.R. Perrin, Purification of Laboratory Chemicals, 2nd Ed., Pergamon, Oxford, UK, 1980.
[16] J.J. Grzybowski, F.L. Urbach, Inorg. Chem. 19 (1980) 2604.
[17] SAINT Reference Manual, Siemens Energy and Automation, Madison, W1, 1994–1996.
[18] G.M. Sheldrick, SADABS, Empirical Absorption Correction Program, University of Gottingen, 1997.
[19] B.A. Frenz, Comput. Phys. 2 (1988) 42.
[20] Crystallographic Computing, vol. 5, Oxford University Press, Oxford, UK, 1991, p. 126 (Chapter 11).
[21] G.M. Sheldrick, SHELXS 86, Program for the Solution of Crystal Structures, University of Gottingen, Germany, 1985.
[22] A.W. Addison, T.N. Rao, J. Reedijk, J. Vanrijn, G.C. Verschoor, J. Chem. Soc., Dalton Trans. (1984) 1349.
[23] Y. Zhao, S. Zhu, M. Shao, X. He, M. Li, W. Lu, Inorg. Chem. Commun. 11 (2008) 239.
[24] C.L. Dollberg, C. Turro, Inorg. Chem. 40 (2001) 2484.
[25] M. Prabhakar, P.S. Zacharias, S.K. Das, Inorg. Chem. 44 (2005) 2585.
[26] S. Mukherjee, Indian J. Chem. 26A (1987) 1002.
[27] R. Das, S. Mitra, S. Mukherjee, Bull. Chem. Soc. Jpn. 66 (1993) 2492.
[28] N.J. Turro, Modern Molecular Photochemistry, Benjamin/Cummings Publishing Co., Inc., Menlo Park, CA, 1978.

reduction to dihydrogen. In this work, we prepared and characterized two diiron dithiolate complexes [{μ-SC(NBn)CH(NHBn)S-μ}$Fe_2(CO)_5$L] (L = PPh_3, **2**; P(Pyr)$_3$, **3**) containing a functionalized C_2 bridge with two vicinal basic sites. We found that the reaction of the complex [{μ-SC(NBn)CH(NHBn)S-μ}$Fe_2(CO)_6$] (**1**) with two equivalents of bis(diphenylphosphino)methane (dppm) in refluxing toluene afforded a desulfurized complex [(μ-S)(μ-dppm)$_2Fe_2(CO)_4$] (**6**) via a dppm mono-dentate intermediate [{μ-SC(NBn)CH(NHBn)S-μ}$Fe_2(CO)_5(\kappa^1$-dppm)] (**4**) and a dppm μ-bridging species [{μ-SC(NBn)CH(NHBn)S-μ}$Fe_2(CO)_4$(μ-dppm)] (**5**). The complexes **2** and **3** can be protonated by mild acids CCl_3COOH and CF_3COOH in acetonitrile, resulting in a 610–650 mV anodic shift of the Fe^IFe^I/Fe^IFe^0 reduction potentials. Here, we report the preparation and characterization of **2**–**6**, the molecular structures of **2**, its protonated species [(**2**H$_N$)(OTf)], and **6**, the protophilicity of **2** and **3**, as well as the electrochemical properties of **2** and **3** compared with the analogous diiron azadithiolate complex [{(μ-$SCH_2)_2N(CH_2C_6H_5)$}$Fe_2(CO)_5$P(Pyr)$_3$] (**7**).

2. Experimental

2.1. General procedures and materials

All reactions and operations related to organometallic complexes were carried out under dry, oxygen-free dinitrogen with standard Schlenk techniques. Solvents were dried and distilled prior to use according to the standard methods. Commercially available chemicals, $Me_3NO\cdot 2H_2O$, HOTf, CCl_3COOH, CF_3COOH, PPh_3, and dppm, were of reagent grade and used as received. Ligand P(Pyr)$_3$, diiron carbonyl complexes [{μ-SC(NBn)CH(NHBn)S-μ}$Fe_2(CO)_6$] (**1**) and [{(μ-$SCH_2)_2N(CH_2C_6H_5)$}$Fe_2(CO)_5$P(Pyr)$_3$] (**7**) were prepared following the literature methods [20–22].

Infrared spectra were recorded on JASCO FT/IR 430 spectrophotometer. Proton and ^{31}P NMR spectra were collected with a Varian INOVA 400 NMR Instrument. Mass spectra were recorded on an HP1100 MSD mass spectrometer. Elemental analyses were performed with a Thermoquest-Flash EA 1112 elemental analyzer.

2.2. Synthesis of [{μ-SC(NBn)CH(NHBn)S-μ}$Fe_2(CO)_5$L] (L = PPh_3, **2**; P(Pyr)$_3$, **3**)

CO-Removing reagent $Me_3NO\cdot 2H_2O$ (0.11 g, 1.0 mmol) was added to a solution of **1** (0.58 g, 1.0 mmol) in MeCN (20 ml). The red solution was stirred for 5 min and the color turned dark red. Triphenylphosphine (0.27 g, 1.0 mmol) was added to the solution, and it was stirred for 30 min. The solvent was removed under reduced pressure. The residue was purified by chromatography on a silica gel column with hexane/CH_2Cl_2 (2:1, v/v) as eluent. The complex **2** was obtained as red powder from the collected red band after removal of solvent. Yield: 0.70 g (86%). *Anal.* Calc. for $C_{39}H_{31}Fe_2N_2O_5PS_2$: C, 53.99; H, 3.71; N, 3.15. Found. C, 53.78; H, 3.78; N, 3.07%. IR (KBr): ν(CO) 2048 (s), 1988 (s), 1938 (m) cm^{-1}. ^{1}H NMR ($CDCl_3$): δ 7.00–7.52 (25H, 5Ph), 4.54, 4.39 (2d, J_{H-H} = 15.8 Hz, 2H, C=NCH_2), 3.87, 3.59 (2d, J_{H-H} = 13.8 Hz, 2H, NHCH_2) 3.11 (s, 1 H, SC*H*), 2.10 (s, 1 H, N*H*) ppm. ^{31}P NMR ($CDCl_3$): δ 60.24 ppm.

The complex **3** was prepared according to the above-described protocol. Yield: 0.50 g (80%). IR (KBr): ν(CO) 2059 (s), 2007 (s), 1991 (s) cm^{-1}. ^{1}H NMR ($CDCl_3$): δ 7.13–7.27 (10H, 2Ph), 6.63, 6.21 (2s, 12H, 3Pyr), 4.79, 4.73 (2d, J_{H-H} = 14.4 Hz, J_{H-H} = 27.2 Hz, 2H, C=NCH_2), 3.94, 3.70 (2d, J_{H-H} = 8.8 Hz, 2H, NHCH_2), 3.28 (s, 1H, SC*H*), 2.21 (s, 1H, N*H*) ppm. ^{31}P NMR ($CDCl_3$): δ 140.01 ppm.

2.3. Synthesis of [{μ-SC(NBn)CH(NHBn)S-μ}$Fe_2(CO)_5PPh_3$](OTf)

HOTf (1.5 equivalents) was added to a solution of **2** (0.81 g, 1.0 mmol) in diethyl ether (50 ml). The red solution was stirred for 5 min and stood for 3 h. Protonated species [(**2**H$_N$)(OTf)] was precipitated as red powder from the solvent and washed three times with cold diethyl ether. Yield: 0.83 g (87%). *Anal.* Calc. for $C_{40}H_{32}F_3Fe_2N_2O_8PS_3$: C, 49.81; H, 3.34; N, 2.90. Found: C, 49.43; H, 3.42; N, 2.65%. IR (KBr): ν(CO) 2061 (s), 2009 (s), 1948 (s) cm^{-1}. ^{1}H NMR ($CDCl_3$): δ 7.09–7.43 (25H, 5Ph), 4.77, 4.58 (2d, J_{H-H} = 13.2 Hz, 2H, C=NCH_2), 4.40–4.80 (br, 2H, NH_2), 4.10, 3.87 (2d, J_{H-H} = 12.8 Hz, 2H, NHCH_2), 3.59 (s, 1H, SC*H*) ppm. ^{31}P NMR ($CDCl_3$): δ 59.10 ppm.

2.4. Synthesis of [{μ-SC(NBn)CH(NHBn)S-μ}$Fe_2(CO)_5$(dppm)] (**4**)

Ligand dppm (0.39 g, 1.0 mmol) was added to a solution of **1** (0.58 g, 1.0 mmol) in toluene (20 ml). The mixture was refluxed for 0.5 h. The resulting solution was evaporated to dryness under reduced pressure, and the residue was chromatographed on an alumina column with hexane/CH_2Cl_2 (2:1, v/v) as eluent. The complex **4** was obtained as red powder from the collected red band after removal of solvent. Yield: 0.66 g (69%). IR (KBr): ν(CO) 2045 (s), 1986 (vs), 1934 (m) cm^{-1}. ^{1}H NMR ($CDCl_3$): δ 7.10–7.35 (30H, 6Ph), 4.52, 4.20 (2d, J_{H-H} = 15.8 Hz, 2H, C=NCH_2), 3.92, 3.61 (2d, J_{H-H} = 13.2 Hz, 2H, NHCH_2), 3.40 (s, 1H, SC*H*), 3.18 (d, J_{H-H} = 8.0 Hz, 2H, PCH_2P), 2.17 (s, 1H, N*H*) ppm. ^{31}P NMR ($CDCl_3$): δ 53.18 (d, J_{P-P} = 91.5 Hz, coordinated dppm), −26.31 (d, J_{P-P} = 91.5 Hz, non-coordinated dppm) ppm. ESI-MS: *m/z* 937.1 [M+H]$^+$.

2.5. Synthesis of [{μ-SC(NBn)CH(NHBn)S-μ}$Fe_2(CO)_4$(μ-dppm)] (**5**)

The toluene solution (20 ml) of **1** (0.58 g, 1.0 mmol) and dppm (0.39 g, 1.0 mmol) was refluxed for 1.5 h. Complex **5** was obtained by chromatography of the residue on an alumina column with hexane/CH_2Cl_2 (1:1, v/v) as eluent. Yield: 0.60 g (66%). IR (KBr): νCO 1995 (s), 1964 (vs), 1931 (s) cm^{-1}. ^{1}H NMR ($CDCl_3$): δ 7.11–7.55 (30H, 6Ph), 4.92, 4.73 (2br, 2H, C=NCH_2), 4.35, 4.01 (2br, 2H, NHCH_2), 4.10 (s, 2H, PCH_2P), 3.46 (s, 1H, SC*H*), 2.20 (br, 1H, N*H*) ppm. ^{31}P NMR ($CDCl_3$): δ 57.23 (d, J_{P-P} = 59.9), 56.31 (br), 56.03 (br), 54.30 (d, J_{P-P} = 53.4) ppm. ESI-MS: *m/z* 909.1 [M+H]$^+$.

2.6. Synthesis of [(μ-S)(μ-dppm)$_2Fe_2(CO)_4$] (**6**)

Ligand dppm (0.78 g, 2.0 mmol) was added to a solution of **1** (0.58 g, 1.0 mmol) in toluene (20 ml). The solution was refluxed for 6 h. The complex **6** was precipitated as red powder from the solution and washed three times with acetone. Yield: 0.72 g (70%). *Anal.* Calc. for $C_{54}H_{44}Fe_2O_4P_4S$: C, 63.30; H, 4.33. Found: C, 63.27; N, 4.35%. IR (KBr): νCO 1967 (m), 1925 (s), 1898 (m), 1875 (w) cm^{-1}. ^{31}P NMR (CH_2Cl_2): δ 44.20 ppm.

2.7. X-ray crystal structure determination

Single crystals of **2**, [(**2**H$_N$)(OTf)], and **6** were obtained by recrystallization from dichloromethane/hexane. All of the single crystal X-ray diffraction data were collected on a Bruker Smart Apex II CCD diffractometer with graphite monochromated Mo Kα radiation (λ = 0.71073 Å) at 298 K using the $\omega-2\theta$ scan mode. Data processing was accomplished with the SAINT program. Intensity data were corrected for absorption by the SADABS program. The structures were solved by direct methods and refined on F^2 against full-matrix least-squares methods by using the SHELX-97 program package. All non-hydrogen atoms were refined anisotropically. Hydrogen atoms were placed by geometrical calculation and refined in a riding model, and the proton on the N atom of [(**2**H$_N$)(OTf)] was

Table 1
Crystallographic data and processing parameters for **2**, [(**2**H_N)(OTf)], and **6**.

Complex	**2**	[(**2**H_N)(OTf)]	**6**
Empirical formula	$C_{40}H_{33}Cl_2Fe_2N_2O_5PS_2$	$C_{41}H_{34}Cl_2F_3Fe_2N_2O_9PS_3$	$C_{54}H_{44}Fe_2O_4P_4S$
M_w	899.37	1065.45	1024.53
Crystal system	monoclinic	triclinic	triclinic
Space group	$P2(1)/n$	$P\bar{1}$	$P\bar{1}$
a (Å)	13.412(3)	11.5545(7)	12.242(2)
b (Å)	15.090(3)	12.2831(8)	12.453(2)
c (Å)	20.288(5)	19.086(1)	18.658(3)
α (°)	90.00	71.785	108.06(1)
β (°)	94.815(3)	86.715	97.30(1)
γ (°)	90.00	64.865	108.486(8)
V (Å^3)	4092(2)	2320.4(3)	2483.3(6)
Z	4	2	2
ρ_{calc} (g cm^{-3})	1.460	1.525	1.370
$F(000)$	1840	1088	1056
Crystal size (mm^3)	0.06 × 0.49 × 0.52	0.09 × 0.13 × 0.22	0.07 × 0.10 × 0.17
$\theta_{Min./Max.}$ (°)	2.21/27.16	2.17/18.65	1.81/25.00
Reflections collected/unique	19849/7145	17183/7943	18416/8400
Parameters refined	472	584	586
Goodness-of-fit on F^2	1.057	1.011	0.932
Final R_1 [$I > 2\sigma(I)$]	0.0629	0.0437	0.0704
Final wR_2	0.1833	0.1164	0.1341
Residual electron density (e Å^{-3})	1.236, −1.094	0.651, −0.487	0.665, −0.543

located by the difference Fourier map. Crystal data and parameters for data collections and refinements of complexes **2**, [(**2**H_N)(OTf)], and **6** are listed in Table 1. The quality of the single crystal of the complex **6** containing solvent was not good, resulting in the large R_{int} value (0.1613).

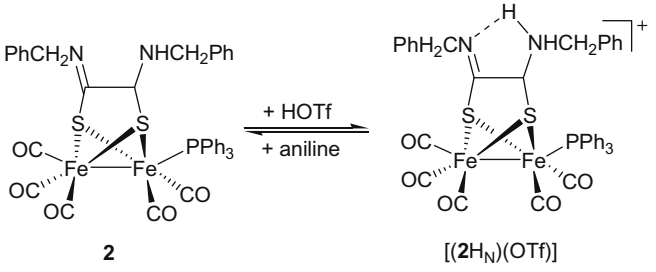
2.8. Electrochemistry

Acetonitrile (Aldrich, spectroscopy grade) used for electrochemical measurements was dried with molecular sieves and then freshly distilled from CaH_2 under N_2. A solution of 0.05 M n[NBu_4][PF_6] (Fluka, electrochemical grade) in CH_3CN was used as electrolyte, which was degassed by bubbling with dry argon for 10 min before measurement. Electrochemical measurements were recorded using a BAS-100W electrochemical potentiostat at a scan rate of 100 mV/s. Cyclic voltammograms were obtained in a three-electrode cell under argon. The working electrode was a glassy carbon disc (diameter 3 mm) successively polished with 3 and 1 μm diamond pastes and sonicated in ion-free water for 10 min. The reference electrode was a non-aqueous Ag/Ag^+ electrode (0.01 M $AgNO_3$ in CH_3CN) and the auxiliary electrode was a platinum wire. All potentials are reported relative to the Fc^+/Fc potential.

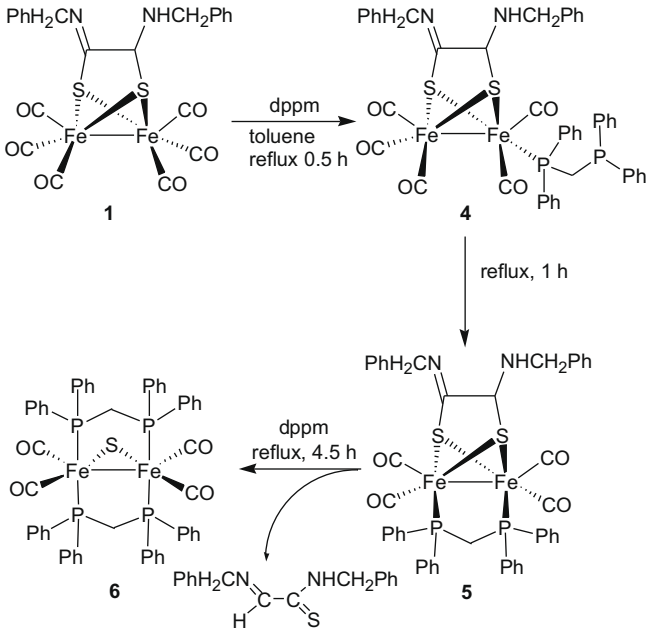
3. Results and discussion

3.1. Preparation and spectroscopic characterization of the complexes **2**, **3**, and [(**2**H_N)(OTf)]

The parent complex [{μ-SC(NBn)CH(NHBn)S-μ}$Fe_2(CO)_6$] (**1**) was prepared according to the literature method [20], which is an oil and very sensitive to air and moisture. More stable diiron complexes [{μ-SC(NBn)CH(NHBn)S-μ}$Fe_2(CO)_5PPh_3$] (**2**) and [{μ-SC(NBn)CH(NHBn)S-μ}$Fe_2(CO)_5P(Pyr)_3$] (**3**) were obtained by treating **1** with a phosphine ligand in the presence of the CO-removing reagent $Me_3NO \cdot 2H_2O$ in CH_3CN. The complexes **2** and **3** are stable in the solid state and in the solution. They were characterized by IR, ^1H and ^{31}P NMR spectroscopy, and the elementary analysis. The complex **2** displays three ν(CO) bands at 2048, 1988, and 1938 cm^{-1} in the IR spectrum, and the ν(CO) bands of **3** appear at 2059, 2007, and 1991 cm^{-1}. Comparison of the ν(CO) bands of **2** and **3** is clearly indicative of the weaker electron donating capability of the $P(Pyr)_3$ ligand as compared to the PPh_3 ligand. The ^1H



Scheme 1.



Scheme 2.

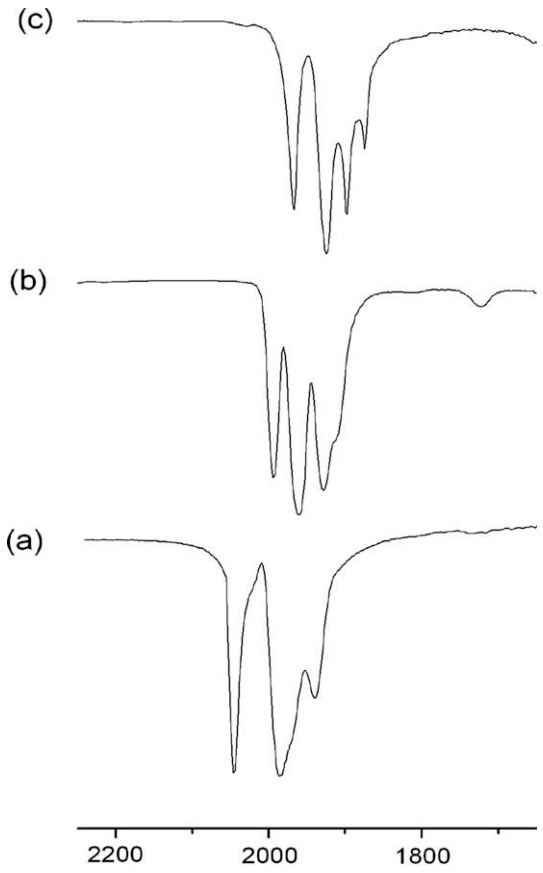


Fig. 1. The IR spectra of complexes **4** (bottom), **5** (middle), and **6** (top).

signals for the two CH_2 groups, the CH, and the NH group in the complex **3** are all move to down-field by 0.11–0.17 ppm compared to the corresponding signals of **2**. The complexes **2** and **3** display ^{31}P signals at 60.2 and 140.0 ppm, respectively.

Protonation of **2** in diethyl ether with addition of 1.5 equivalents HOTf afforded the N-protonated species [(**2**H_N)(OTf)] as red precipitate in a good yield (87%) after being washed with cold diethyl ether and recrystallization in hexane/CH_2Cl_2. In comparison to the ν(CO) bands of **2**, the ν(CO) bands of [(**2**H_N)(OTf)] is shifted to higher frequencies by ca. 15 cm^{-1} in average, indicating that protonation of the amino-N atom on the C_2 bridge has apparent influence on the electron density of the iron atoms. This shift value of the ν(CO) bands is comparable to those reported for N-protonation of other analogous diiron complexes [8–15]. The proton resonance of the SCH group directly attached to the protonated-N atom is moved down-field by ca. 0.31 ppm in the ^1H NMR spectrum of [(**2**H_N)(OTf)]. The spectroscopic evidence strongly supports the protonation of the N atom in the complex **2**. Upon addition of an equivalents of aniline to the solution of [(**2**H_N)(OTf)], the ^{31}P signal at 58.0 ppm for the N-protonated species completely disappeared, and in the same time the signal at 60.2 ppm for the complex **2** appeared as the only peak in the ^{31}P NMR spectrum, indicating a reversible protonation and deprotonation process between **2** and [(**2**H_N)(OTf)] (Scheme 1).

3.2. CO-displacement of *1* by dppm

The reaction of the complex **1** with an equivalents of bis(diphenylphosphino)methane (dppm) in refluxing toluene for 0.5 h afforded the complex [{μ-SC(NBn)CH(NHBn)S-μ}Fe_2-$(CO)_5$(κ^1-dppm)] (**4**), in which dppm acts as a simple monodentate ligand. When the toluene solution of **4** was further refluxed for 1 h, an intramolecular CO-displacement occurred to form a μ-dppm bridging complex [{μ-SC(NBn)CH(NHBn)S-μ}Fe_2-$(CO)_4$(μ-dppm)] (**5**). The complex with a chelating dppm ligand was not detected during the reaction by ^{31}P NMR monitoring, which is different from the reaction of (μ-pdt)[$Fe_2(CO)_6$] and dppm [23,24]. If another equivalents of dppm was added to the toluene solution of **5**, an unexpected complex [(μ-S)(μ-dppm)$_2Fe_2(CO)_4$] (**6**) was obtained after 4.5 h reflux. The complex **6** was formed by simultaneous CO-displacement and desulfurization of **5** (Scheme 2). Sulfur-containing organic compound $PhCH_2N{=}CHC(S)NHCH_2Ph$ was detected in the reaction solution by HPLC–MS analysis. The first two steps for the reaction of **1** and dppm to form the complexes **4** and **5** are just similar to the reaction of (μ-pdt)[$Fe_2(CO)_6$] and dppm [23,24], while the third step, desulfurization reaction, is special for **1**. The complex (μ-pdt)[$Fe_2(CO)_4$(μ-dppm)], in analogy to **5**, did not react with dppm even in refluxing toluene for 72 h. The results show that the [μ-SC=NBnCH(NHBn)(μ-S)] bridge in **1** is apparently less stable than the pdt bridge. The complexes **4**–**6** were characterized by IR, MS, ^1H and ^{31}P NMR spectroscopy, and the molecular structure of **6** was determined by X-ray diffraction study.

Except for the additional ^1H signals of dppm, the complex **4** displays a similar ^1H NMR spectrum with that of **2**. In addition to the signals at 7.10–7.35 ppm for phenyl groups of dppm and the C_2 bridge, a typical doublet at 3.18 ppm (J = 8.0 Hz) for the CH_2 group of dppm is found in the ^1H NMR spectrum of **4**. Two doublets, at 53.2 ppm for the coordinate phosphorus and −26.3 ppm for the non-coordinate one, appear in the $^{31}P\{1H\}$ NMR spectrum of **4**. As the free phosphorus of dppm in **4** is coordinated to the other iron atom by replacement of a CO ligand, the ^1H signal for the

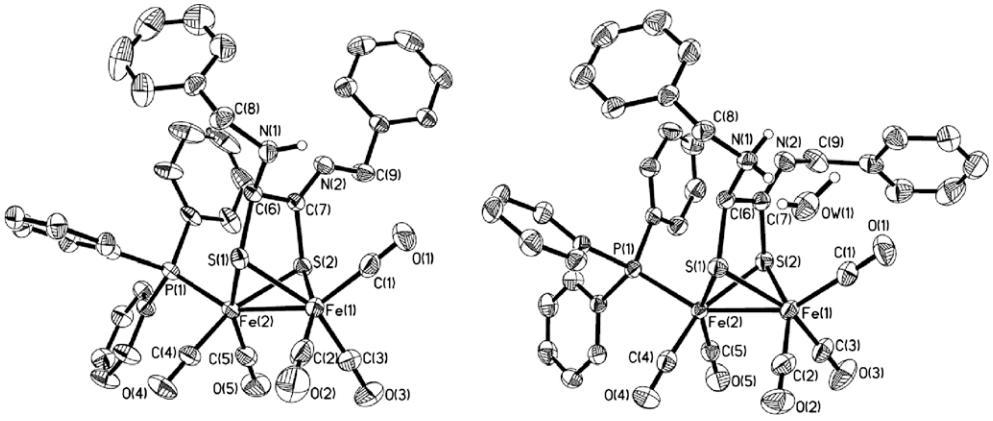


Fig. 2. Molecular structures of **2** (left) and $(2H_N)^+/H_2O$ with the thermal ellipsoids at 30% probability.

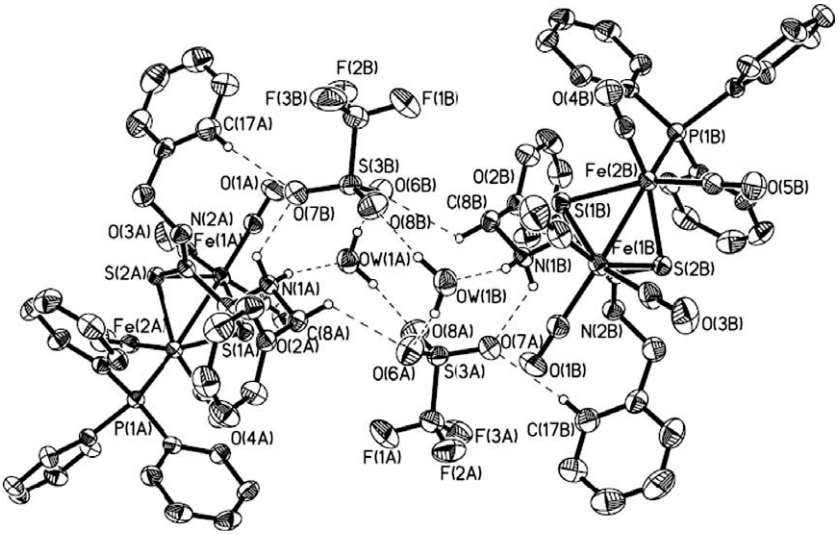


Fig. 3. Diagram of the dimeric structure of [(**2**H_N)(OTf)] encircling two water molecules by hydrogen bonds (ellipsoids at 30% probability).

CH_2 group of dppm ligand is moved from 3.18 to 4.10 ppm. There are two doublets at 57.23 ppm (J_{P-P} = 59.9) and 54.30 ppm (J_{P-P} = 53.4) as well as two broad signals at 56.31 and 56.03 ppm in the ^{31}P spectrum of **5**, indicative of existence of two conformation isomers for the complex **5** in solution in an approximate equal ratio. The isomerization caused by swing of the μ-bridging dppm ligand is similar as that found for (μ-pdt)(μ-PNP)[Fe(CO)PMe_3]-[$Fe(CO)_2$] in our previous studies [25]. Because of the non-symmetric bridge of **5**, the chemical shifts should be different for the two phosphorus centers of the μ-dppm ligand. Therefore four ^{31}P signals are observed, and the two broad signals at 56.31 and 56.03 ppm result from the overlap of two doublets. The complex **6** displays only one ^{31}P signal at 44.2 ppm for four coordinate phosphorus atoms, indicating that **6** has a symmetric molecular structure.

Table 2
Selected bond lengths (Å) and angles (°) for **2** and [(**2**H_N)(OTf)] · H_2O.

Complex	**2**	(**2**H_N)$^+$
Bond lengths		
Fe(1)–Fe(2)	2.527(1)	2.5109(7)
Fe(1)–S(1)	2.256(1)	2.2651(9)
Fe(1)–S(2)	2.269(2)	2.274(1)
Fe(2)–S(1)	2.249(1)	2.250(1)
Fe(2)–S(2)	2.266(1)	2.263(1)
Fe(2)–P(1)	2.253(1)	2.260(1)
S(1)–C(6)	1.847(4)	1.816(3)
S(2)–C(7)	1.803(5)	1.788(3)
N(1)–C(6)	1.437(6)	1.474(4)
N(1)–C(8)	1.468(6)	1.502(4)
N(2)–C(7)	1.260(6)	1.250(4)
N(2)–C(9)	1.456(6)	1.455(5)
N(1)···N(2)	2.728	2.704
Bond angles		
S(1)–Fe(1)–S(2)	80.64(5)	81.14(3)
S(1)–Fe(2)–S(2)	80.87(5)	81.72(3)
P(1)–Fe(2)–Fe(1)	151.23(4)	151.05(3)
C(6)–N(1)–C(8)	114.7(4)	114.6(3)
C(7)–N(2)–C(9)	121.3(4)	121.5(3)
N(1)–C(6)–C(7)	110.8(4)	109.8(3)
N(1)–C(6)–S(1)	111.1(3)	112.0(3)
C(7)–C(6)–S(1)	107.9(3)	110.2(2)
N(2)–C(7)–S(2)	125.2(4)	127.5(3)
N(2)–C(7)–C(6)	119.4(4)	118.3(3)
C(6)–C(7)–S(2)	115.3(3)	114.1(2)

The complex **4** displays three ν(CO) bands in the region of 2061–1948 cm^{-1} (Fig. 1), which are shifted by ca. 50 cm^{-1} in average to lower frequency as compared to the ν(CO) bands of the complex **1**. The subsequent intramolecular CO/phosphine replacement results in a further red-shift of the ν(CO) bands to 1995–1931 cm^{-1}. The complex **6** with two μ-bridging dppm ligands exhibits four ν(CO) bands in the region of 1967–1875 cm^{-1}. The IR, MS, ^1H and ^{31}P NMR data give clear evidence for the formation of phosphine mono-, di-, and tetra-substituted complexes **4**, **5**, and **6**, in the different stages of the CO-displacement of **1**.

3.3. Molecular structures of *2*, *[(2H$_N$)(OTf)]*, and *6*

To obtain unambiguous evidence for the N-protonation of **2**, the molecular structures of **2** and its N-protonated species [(**2**H_N)(OTf)] were determined by X-ray analyses of single crystals, which are depicted in Figs. 2 and 3. The selected bond lengths and angles are summarized in Table 2. The central 2Fe2S skeletons of **2** and (**2**H_N)$^+$ are both in the butterfly framework and each Fe atom is coordinated in the pseudo-square-pyramidal geometry similar to previously reported 2Fe2S models [9–14,23,26]. The protonation of **2** occurs at the nitrogen atom [N(1)] of the secondary amine. The N···N distance (2.704 Å) is proper for intramolecular N–H···N interaction, which can considerably promote the stability of the N-protonated species. After protonation, both the bond lengths of N(1)–C(6) and N(1)–C(8) are elongated by 0.037 and 0.034 Å, respectively, while the bond length of N(2)–C(7) is shortened by 0.01 Å.

Fig. 3 shows that two molecules of water are caged by two [(**2**H_N)(OTf)] molecules through hydrogen bonds. In the solid state of [(**2**H_N)(OTf)], each asymmetric unit contains a molecule of [(**2**H_N)(OTf)] and a molecule of water. The molecule of water is close to the iron atom of the [$Fe(CO)_3$] unit with the Fe(1)···O(H_2O) distance of 4.199 Å. It is proposed that H_2O is coordinated to the distal iron atom in the H_{ox} state of the natural H-cluster [2,24]. The bond lengths and angles related to hydrogen bonds are given in Table S1 (see Supplementary data).

The molecular structure of **6** was also determined by single crystal X-ray analyses, which is shown in Fig. 4, and selected bond lengths and angles are given in Table 3. The central iron atoms of **6** are coordinated in the trigon-bipyramidal geometry, consistent with the structure of [(μ-CO)(μ-dppm)$_2$$Fe_2(CO)_4$] [27]. Each iron atom is coordinated with two terminal carbonyls, which are

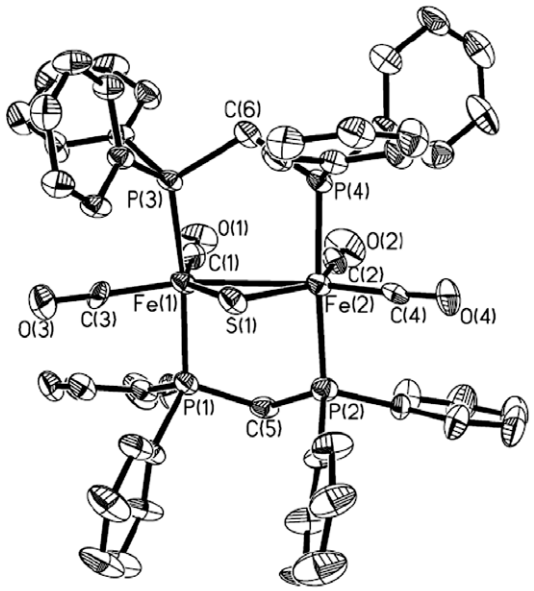


Fig. 4. Molecular structure of **6** with the thermal ellipsoids at 30% probability.

Table 3
Selected bond lengths (Å) and angles (°) for **6**.

Bond lengths			
Fe(1)–Fe(2)	2.838(2)	Fe(1)–P(1)	2.229(2)
Fe(1)–S(1)	2.267(2)	Fe(1)–P(3)	2.204(2)
Fe(2)–S(1)	2.240(2)	Fe(2)–P(2)	2.230(2)
		Fe(2)–P(4)	2.215(2)
Bond angles			
Fe(1)–S(1)–Fe(2)	77.98(8)	P(3)–Fe(1)–Fe(2)	93.16(9)
S(1)–Fe(1)–Fe(2)	50.60(7)	P(4)–Fe(2)–Fe(1)	93.25(9)
S(1)–Fe(2)–Fe(1)	51.42(7)	P(1)–Fe(1)–S(1)	97.22(9)
P(1)–Fe(1)–P(3)	174.3(1)	P(2)–Fe(2)–S(1)	93.1(1)
P(2)–Fe(2)–P(4)	172.4(1)	P(3)–Fe(1)–S(1)	85.23(9)
P(1)–Fe(1)–Fe(2)	92.40(9)	P(4)–Fe(2)–S(1)	84.8(1)
P(2)–Fe(2)–Fe(1)	91.19(9)		

Table 4
Redox potentials of complexes **3** and **7** vs. Fc^+/Fc.[a]

Complex	E_{pa} (V) $Fe^IFe^I/Fe^{II}Fe^I$	E_{pc} (V) Fe^IFe^I/Fe^0Fe^I
2	+0.60	−1.66
[(**2**H_N)(OTf)]	–	−1.01
3	+0.83	−1.51
[(**3**H_N)(OTf)]	–	−0.90
7	+0.59	−1.62
[(**7**H_N)(OTf)]	–	−1.17

[a] $[NBu_4][PF_6]$ (0.05 M) in CH_3CN under Ar; scan rate 0.1 V s^{-1}.

essentially co-planar with the bridging-sulfur atom. This plane is perpendicular to the plane defined by the four phosphorus atoms and the two iron atoms. The Fe(1)–Fe(2) bond length of 2.8383(16) Å in **6** is notably longer than that (2.742 Å) in [(μ-CO)(μ-dppm)$_2$Fe$_2$(CO)$_4$], resulting from the replacement of the μ-CO bridge by μ-S bridge [28].

3.4. Cyclic voltammograms of the complexes *2*, *3*, and *7*

To compare the electrochemical property and the protophilicity of **2** and **3** with the azadithiolate-bridging complex, [{(μ-$SCH_2)_2N(CH_2C_6H_5)$}Fe$_2$(CO)$_5$P(Pyr)$_3$] (**7**) was prepared. The cyclic voltammograms (CVs) of **2**, **3**, and **7** were studied in CH_3CN using 0.05 M $[NBu_4][PF_6]$ as electrolyte. The redox potentials versus Fc^+/Fc are summarized in Table 4. The first reduction peaks of **2** and **3** appear at −1.66 and −1.51 V, respectively, using ferrocene as an internal standard. The approximately equal current height in the CVs of complexes **2** and **3** and ferrocene with an identical molar concentration suggests that the primary reduction of complexes **2** and **3** is a one-electron process (Fe^IFe^I/Fe^IFe^0). The reduction potential of **3** is 110 mV more positive than that (−1.62 V) found for the analogous diiron azadithiolate complex **7**. The oxidation peaks, at +0.60 and +0.83 V for **2** and **3**, respectively, and +0.59 V for **7**, are attributed to the Fe^IFe^I to $Fe^{II}Fe^I$ process [29,30].

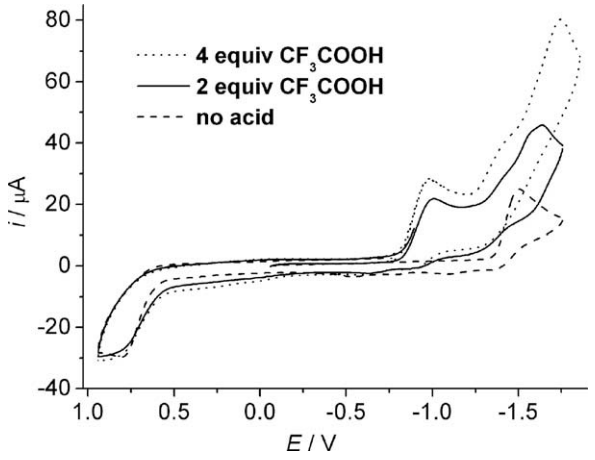


Fig. 5. Cyclic voltammograms of **3** (1.0 mM) in the presence of CF_3COOH in CH_3CN.

Upon addition of one equivalents of HOTf to the CH_3CN solution of **3**, a new peak is observed at −0.90 V in the CV, attributed to the reduction of the protonated species [(**3**H_N)(OTf)] (*Fig.* S1, Supplementary data). Essentially identical CVs were obtained for protonation of **2** with a new peak at −1.01 V. In comparison, the reduction peak of [(**7**H_N)(OTf)] appears at −1.11 V (*Fig.* S1). Protonation of **2** and **3** leads to the 610–650 mV anodic shifts of the reduction peaks, while after protonation, the reduction peak of **7** is shifted by 450 mV. It shows that protonation of the internal base of **2** and **3** exhibits a larger influence on the reduction potential of the iron atoms compared to that displayed by the protonation of the azadithiolato bridge of **7**. It is noteworthy that the complexes **2** and **3** can be protonated by mild acids CCl_3COOH and CF_3COOH (Fig. 5). In contrast, no new peak is detected in the CV when CF_3COOH is added to the solution of **7** (*Fig.* S2). The protonation of **2** and **3** is further verified by in situ ^{31}P NMR spectroscopy with stepwise addition of CCl_3COOH to the $CDCl_3$ solution of **2** or **3** (*Fig.* S3). The results indicate that the complexes **2** and **3** are more protophilic than the diiron azadithiolate the complex **7**. In fact, in organic solvents the internal bases of the FeFe-Hase mimics reported so far can be protonated only in the presence of strong acids, such as $HClO_4$ [11,13], HBF_4 [12,16,19], and HOTf [10,14,18].

4. Conclusion

The ^{31}P NMR spectra and CVs show that the complexes **2** and **3** with a C_2 bridge containing two basic sites are more protophilic than other internal bases in the FeFe-Hase mimics reported so far. The omplexes **2** and **3** can be protonated by CCl_3COOH and CF_3COOH in organic solvent. Protonation and deprotonation

processes between **2** and [(**2**H_N)(OTf)], as well as **3** and [(**3**H_N)(OTf)], are instant and reversible. The protonated species [(**2**H_N)(OTf)] is relatively stable because of the proper distance for intramolecular N–H···N interaction, which is structurally characterized. It is noteworthy that each asymmetric unit of [(**2**H_N)(OTf)] containing a molecule of water close to the iron atom of the [Fe(CO)$_3$] subunit (Fe(1)···O(H_2O) 4.199 Å), which reminds us of H_2O coordinating to the distal iron atom in the H_{ox} state of the natural H-cluster. The reduction potential of the complex **3** is 110 mV more positive than that of the analogous azadithiolate complex **7**, and protonation of the internal base of **2** and **3** exhibits a larger influence on the reduction potential of the iron atoms than that displayed by the protonation of the azadithiolato bridge of **7**. In addition, a desulfurization reaction is found in the reaction of the complex **1** and two equivalents of dppm ligand to afford the complex **6** in refluxing toluene. The reaction undergoes by three steps via a dppm mono-dentate intermediate **4** and a dppm μ-bridging species **5**.

Acknowledgments

We are grateful to the National Natural Science Foundation of China (Grant No. 20633020), the National Basic Research Program of China (Grant No. 2009CB220009), the Program for Changjiang Scholars and Innovative Research Team in University (IRT0711), the Swedish Energy Agency, the Swedish Research Council, and K&A Wallenberg Foundation for financial support of this work.

Appendix A. Supplementary data

CCDC 693477, 693476 and 693475 contain the supplementary crystallographic data for complexes **2**, [(**2**H_N)(OTf)], and **6**, respectively. These data can be obtained free of charge via http://www.ccdc.cam.ac.uk/conts/retrieving.html, or from the Cambridge Crystallographic Data Centre, 12 Union Road, Cambridge CB2 1EZ, UK; fax: (+44) 1223-336-033; or e-mail: deposit@ccdc.cam.ac.uk. Supplementary data associated with this article can be found, in the online version, at doi:10.1016/j.poly.2009.01.006.

References

[1] J.W. Peters, W.N. Lanzilotta, B.J. Lemon, L.C. Seefeldt, Science 282 (1998) 1853.
[2] Y. Nicolet, C. Piras, P. Legrand, C.E. Hatchikian, J.C. Fontecilla-Camps, Structure 7 (1999) 13.
[3] Y. Nicolet, B.J. Lemon, J.C. Fontecilla-Camps, J.W. Peters, Trends Biochem. Sci. 25 (2000) 138.
[4] Y. Nicolet, A.L. Lacey, X. Vernède, V.M. Fernandez, E.C. Hatchikian, J.C. Fontecilla-Camps, J. Am. Chem. Soc. 123 (2001) 1596.
[5] A.S. Pandey, T.V. Harris, L.J. Giles, J.W. Peters, R.K. Szilagyi, J. Am. Chem. Soc. 130 (2008) 4533.
[6] H. Fan, M.B. Hall, J. Am. Chem. Soc. 123 (2001) 3828.
[7] T. Zhou, Y. Mo, A. Liu, Z. Zhou, K.R. Tsai, Inorg. Chem. 43 (2004) 923.
[8] B.E. Barton, M.T. Olsen, T.B. Rauchfuss, J. Am. Chem. Soc. 130 (2008) 16834.
[9] S. Ezzaher, J.-F. Capon, F. Gloaguen, F. Pétillon, P. Schollhammer, J. Talarmin, Inorg. Chem. 48 (2009) 2.
[10] J.D. Lawrence, H. Li, T.B. Rauchfuss, M. Bénard, M. Rohmer, Angew. Chem., Int. Ed. 40 (2001) 1768.
[11] S. Ott, M. Kritikos, B. Åkermark, L. Sun, R. Lomoth, Angew. Chem., Int. Ed. 43 (2004) 1006.
[12] P. Das, J. Capon, F. Gloaguen, F.Y. Pétillon, P. Schollhammer, J. Talarmin, Inorg. Chem. 43 (2004) 8203.
[13] F. Wang, M. Wang, X. Liu, K. Jin, W. Dong, G. Li, B. Åkermark, L. Sun, Chem. Commun. (2005) 3221.
[14] L. Schwartz, G. Eilers, L. Eriksson, A. Gogoll, R. Lomoth, S. Ott, Chem. Commun. (2006) 520.
[15] G. Eilers, L. Schwartz, M. Stein, G. Zampella, L. de Gioia, S. Ott, R. Lomoth, Chem. Eur. J. 13 (2007) 7075.
[16] B.E. Barton, T.B. Rauchfuss, Inorg. Chem. 47 (2008) 2261.
[17] N. Wang, M. Wang, T. Zhang, P. Li, J. Liu, L. Sun, Chem. Commun. (2008) 5800.
[18] F. Gloaguen, J.D. Lawrence, T.B. Rauchfuss, M. Bénard, M.-M. Rohmer, Inorg. Chem. 41 (2002) 6573.
[19] F. Xu, C. Tard, X. Wang, S.K. Ibrahim, D.L. Hughes, W. Zhong, X. Zeng, Q. Luo, X. Liu, C.J. Pickett, Chem. Commun. (2008) 606.
[20] R. Siebenlist, H. Frühaufa, H. Kooijman, N. Veldman, A.L. Spek, K. Goubitz, J. Fraanje, Inorg. Chim. Acta 327 (2002) 66.
[21] K.G. Moloy, J.L. Petersen, J. Am. Chem. Soc. 117 (1995) 7696.
[22] Y. Na, M. Wang, J. Pan, P. Zhang, B. Åkermark, L. Sun, Inorg. Chem. 47 (2008) 2805.
[23] F. Adam, G. Hogarth, I. Richards, J. Organomet. Chem. 692 (2007) 3957.
[24] W. Gao, J. Ekstrom, J. Liu, C. Chen, L. Eriksson, L. Weng, B. Åkermark, L. Sun, Inorg. Chem. 46 (2007) 1981.
[25] N. Wang, M. Wang, T. Liu, P. Li, T. Zhang, M.Y. Darensbourg, L. Sun, Inorg. Chem. 47 (2008) 6948.
[26] Z. Gao, M.B. Hall, J. Am. Chem. Soc. 123 (2001) 3734.
[27] K.G. Moodley, D.W. Engel, J.S. Field, R.J. Haines, Polyhedron 12 (1993) 533.
[28] P. Thometzek, K. Zenkert, H. Werner, Angew. Chem., Int. Ed. 24 (1985) 516.
[29] D. Chong, I.P. Georgakaki, R. Mejia-Rodriguez, J. Sanabria-Chinchilla, M.P. Soriaga, M.Y. Darensbourg, Dalton Trans. (2003) 4150.
[30] P. Li, M. Wang, C. He, G. Li, X. Liu, C. Chen, B. Åkermark, L. Sun, Eur. J. Inorg. Chem. (2005) 2506.

2. Experimental

2.1. General

Standard techniques for handling of air- and moisture-sensitive materials were used [1,3]. $HBBr_2 \cdot SMe_2$ and $H_2BBr \cdot SMe_2$ (1 M solutions in CH_2Cl_2), as well as $HBCl_2 \cdot SMe_2$ (in excess Me_2S) were purchased from Sigma–Aldrich, and were used as supplied. 4-Octene (Sigma–Aldrich) was dried with 3 Å molecular sieves prior to use. 1-Octene (Sasol Ltd.) and CH_2Cl_2 (Merck), used as solvent for preparation of solutions, were dried as mentioned elsewhere [1,3].

2.2. Kinetic measurements

^{11}B NMR spectra were recorded on Varian Unity Inova 500 spectrometer, using 5 mm quartz tubes, at 160 MHz and referenced externally against $BF_3 \cdot OEt_2$. The kinetic reactions were monitored as previously reported, as was the product characterization [1,3].

All kinetic runs were carried out under pseudo-first-order conditions with respect to the haloboranes. The concentration of $HBBr_2 \cdot SMe_2$ was kept constant at 0.025 M, whilst that of $HBCl_2 \cdot SMe_2$ and $H_2BBr \cdot SMe_2$ was fixed at 0.05 and 0.0125 M, respectively. All haloborane solutions were prepared by diluting known concentrations from the stock solution with freshly distilled CH_2Cl_2, the same solvent that was used to prepare the nucleophile solutions. The nucleophile employed in concentration-dependence studies ranged from 10 to 50 times that of the haloborane concentration. In the case of $H_2BBr \cdot SMe_2$ complex, concentrations of the nucleophile were doubled due to the presence of two hydroboration sites on the boron complex.

The observed pseudo-first-order rate constants, k_{obs}, were obtained by fitting a first-order exponential decay equation, through the data points using Origin 5.0 statistical software. Activation parameters, $\Delta H^{\neq}$ and $\Delta S^{\neq}$, were determined from temperature dependence studies over the temperature range of 15–30 °C, at 5 °C intervals. A wider temperature range could not be investigated because of the constraint imposed by the boiling point (40 °C) of the solvent, CH_2Cl_2.

3. Results and discussion

On hydroboration with $HBBr_2 \cdot SMe_2$ and $HBCl_2 \cdot SMe_2$ the disappearance of the ^{11}B NMR doublet peaks ($\delta^{11}B = -7$ ppm at 25 °C, $J_{B\text{-}H} = 162$ Hz and $\delta^{11}B = 2$ ppm at 25 °C, $J_{B\text{-}H} = 158$ Hz) and the emergence of singlet peaks ($\delta^{11}B = 6.3$ ppm and $\delta^{11}B = 14.8$ ppm), respectively, correspond to a reaction that can be described by Eq. (1). The doublet represents the $HBX_2 \cdot SMe_2$, whilst the singlet represents BX_2-octyl·SMe_2.

$$HBX_2 \cdot SMe_2 + \underset{X_2=Br_2 \text{ or } Cl_2}{4\text{-octene}} \rightarrow BX_2\text{-octyl} \cdot SMe_2 \quad (1)$$

In the case of $H_2BBr \cdot SMe_2$, the conversion of the ^{11}B NMR triplet peak ($\delta^{11}B = -10.5$ ppm, at 25 °C, $J_{B\text{-}H} = 134$ Hz) into a singlet peak at $\delta^{11}B = 33.5$ ppm is an indication that the reaction monitored can be described by Eq. (2). The triplet peak represents the $H_2BBr \cdot SMe_2$, whilst the singlet peak represents BBr-$(octyl)_2 \cdot SMe_2$.

$$H_2BBr \cdot SMe_2 + 2\ 4\text{-octene} \rightarrow BBr\text{-}(octyl)_2 \cdot SMe_2 \quad (2)$$

Representative ^{11}B NMR arrays are similar to those reported previously [1,3]. In all the three cases, the products of hydroboration were confirmed by quenching the reactions using H_2O_2/NaOH mixture to form the alcohol, which was characterised using GC, as before [1].

Integration of ^{11}B NMR spectral arrays allowed for the determination of pseudo-first-order rate constants, k_{obs}. First-order exponential decay curves were fitted over the data points to generate the k_{obs}. A representative plot of concentration against time is shown in Fig. 1.

The k_{obs} values, obtained were plotted against the concentration of the entering nucleophile, [Nu], *i.e.* 4-octene. Linear dependence on [Nu] with insignificant *y*-intercepts was observed for both $HBBr_2 \cdot SMe_2$ and $HBCl_2 \cdot SMe_2$. In the case of $H_2BBr \cdot SMe_2$, significant *y*-intercepts were observed, indicative of the presence of a back or parallel reaction. Representative plots are shown in Figs. 2 and 3, for the dihaloboranes and the monohaloborane, respectively. These graphs demonstrate that the reactions are first-order with respect to incoming nucleophile.

For $HBBr_2 \cdot SMe_2$ and $HBCl_2 \cdot SMe_2$, the overall process can be described by the rate law given in Eq. (3):

$$K_{obs} = k_2'[Nu] \quad (3)$$

In the case of $H_2BBr \cdot SMe_2$, the overall process is described by Eq. (4):

$$K_{obs} = k_2'[Nu] + k_{-2} \quad (4)$$

To account for the observed results, a mechanism (Eq. (5)) similar to that already reported [1], is applicable in these investigations. The hydroboration involving the $H_2BBr \cdot SMe_2$ goes through the same

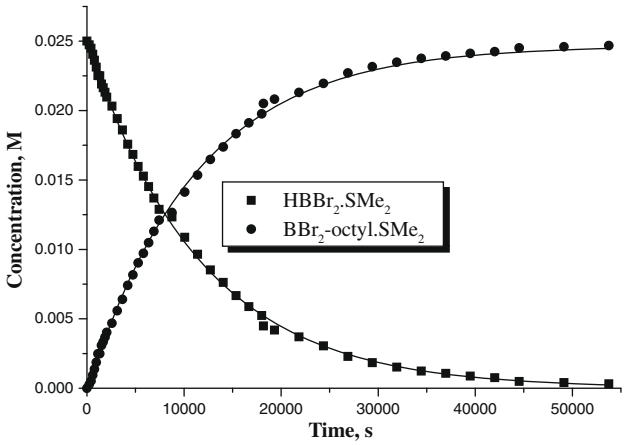


Fig. 1. Exponential decay curve for hydroboration of 4-octene with $HBBr_2 \cdot SMe_2$ in CH_2Cl_2 at 25 °C.

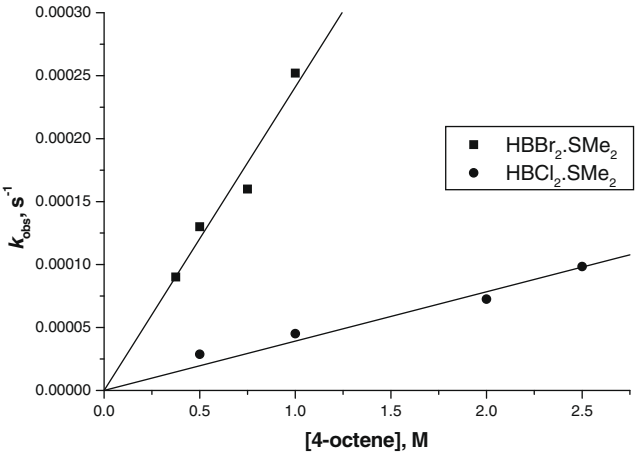


Fig. 2. Dependence of k_{obs} on [4-octene] in the hydroboration reactions of 4-octene with $HBBr_2 \cdot SMe_2$ and $HBBr_2 \cdot SMe_2$ in CH_2Cl_2 at 25 °C.

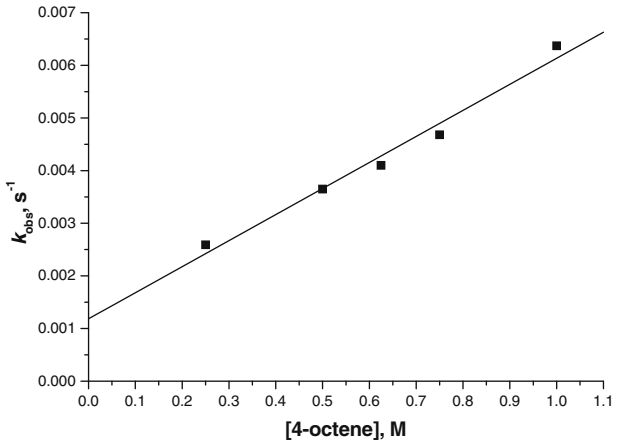


Fig. 3. Dependence of k_{obs} on [4-octene] in the hydroboration reaction of 4-octene with $H_2BBr \cdot SMe_2$ in CH_2Cl_2 at 25 °C.

process twice, with the second hydroboration step being too fast to be monitored within the NMR time.

$$BH_iX_j \cdot SMe_2 \underset{k_{-1}}{\overset{k_1}{\rightleftharpoons}} BH_iX_j + SMe_2$$

$$BH_iX_j + nR \underset{k_{-2}}{\overset{k_2}{\rightleftharpoons}} R_nBX_j \quad (5)$$

$$R_nBX_j + Me_2S \overset{Fast}{\rightleftharpoons} R_nBX_j \cdot SMe_2$$

where i,j and n represent the number of that particular atom(either 1 or 2) and X represents the type of halogen atom (either Br or Cl).

Overall, the mechanism of hydroboration of 4-octene with haloborane addition complexes involves prior dissociation of the complex into the Me_2S and either HBX_2 or H_2BX, which is followed by the reaction of the free HBX_2 or H_2BX with entering nucleophile to, respectively, form RBX_2 or R_2BX. The rate law emanating from the proposed mechanism is that given in Eq. (6):

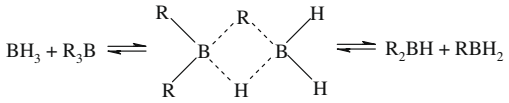
$$K_{obs} = \frac{k_1k_2[R] + k_{-1}k_{-2}[Me_2S]}{k_{-1}[Me_2S] + k_2[R]} \quad (6)$$

Due to the presence of excess Me_2S in the system, $k_{-1}[Me_2S] > k_2[R]$, reducing Eq. (6) to Eq. (7):

$$K_{obs} = \frac{k_1k_2[R] + k_{-1}k_{-2}[Me_2S]}{k_{-1}[Me_2S]} \quad (7)$$

The reactions involving dihaloboranes do not undergo any reverse or parallel reaction, implying that $k_{-2} = 0$, thus resulting into Eq. (3). The opposite is true for the monohaloborane, describing Eq. (4). This means that k_2' in both instances is a composite parameter made up of $k_1k_2/k_{-1}[Me_2S]$.

It can be agued that the mechanism should include an exchange between $R_2BBr \cdot SMe_2$, once it is formed, and $H_2BBr \cdot SMe_2$, resulting into $RHBBr \cdot SMe_2$ as the most active hydroborating reagent in the system. This is not possible because of a number of reasons when one looks at the mechanistic pathway through which such redistribution would occur. A generally accepted mechanistic pathway for the redistribution equilibria that involve boron-containing species, *e.g.* BH_3 as shown in Eq. (8), proceed through formation of hydrogen-bridge dimer that eventually go through dispropotionation by means of a four-centre transition state as shown in Scheme 1 [19]:



Scheme 1. A boron-based four-centred transition state for the disproportionation process.

$$\left.\begin{aligned} &BH_3 + R_3B \rightleftharpoons R_2BH + RBH_2 \\ &2RBH_2 \rightleftharpoons R_2BH + BH_3 \\ &2R_2BH \rightleftharpoons RBH_2 + R_3B \end{aligned}\right\} \quad (8)$$

In our case, such a route was not possible as the boron complex is stabilised by the coordination of the Lewis base as well as π-back donation from the halogen into the boron, which impedes the formation of dimeric adducts. This is supported by the thermodynamic stability of haloboranes in the presence of a donor (Lewis base) which is well documented in literature [19]. Moreover, Pasto et al. [20] have established that the dissolution of diborane in THF produces a solution of $BH_3 \cdot THF$ in THF. In addition, on reacting tetramethylethylene (TME) with borane in THF they observed that the possibility of TME reacting with diborane, which might have been formed through dimer–monomer equilibrium, and could have lead to redistribution complications, was non-existent.

To further invalidate the possibility of formation of a hydrogen-bridged centred transition state that would facilitate the redistribution, it is important to note that in the current systems of haloborane addition complexes, after hydroboration no hydrogen is available to allow for such a bridge to form since all the hydrogens will have been used in the hydroboration process.

The other reason that must be taken into consideration is whether a dehydroboration process is possible under the experimental conditions employed. Based on literature information, under the current conditions it is not possible to have dehydroboration taking place, since the temperature range investigated (15–30 °C) was too low to allow for the breakage of a B–C bond whose energy has been approximated to be 84 kcal mol^{-1} [2].

For the purposes of determining the activation parameters, the composite second order rate constants (k_2'), given in Table 1, were determined by least-square analysis of the plots for different temperatures, ranging from 15–30 °C. These values were used in plotting the Erying plots shown as in Fig. 4. Using the slope and the

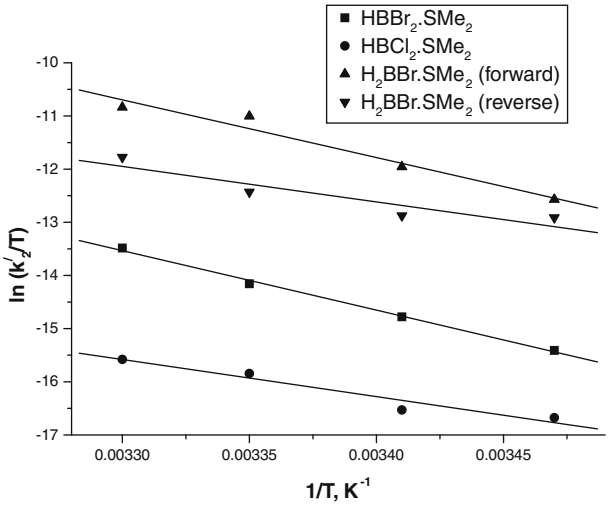


Fig. 4. Erying plots for hydroboration of 4-octene with $HBBr_2 \cdot SMe_2$, $HBCl_2 \cdot SMe_2$ and $H_2BBr \cdot SMe_2$ in CH_2Cl_2 under pseudo-first-order conditions.

Table 1
Kinetic data for hydroboration of 1-octene and 4-octene with $HBBr_2 \cdot SMe_2$, $HBCl_2 \cdot SMe_2$ and $H_2BBr \cdot SMe_2$ in CH_2Cl_2 under pseudo-first-order conditions.

T (°C)	$HBBr_2 \cdot SMe_2$		$HBCl_2 \cdot SMe_2$		$H_2BBr \cdot SMe_2$		
	1-Octene [1]	4-Octene	1-Octene [1]	4-Octene	1-Octene [1]	4-Octene	
	$k_2'/10^{-3}$ ($M^{-1}s^{-1}$)	$k_2'/10^{-5}$ ($M^{-1}s^{-1}$)	$k_2'/10^{-3}$ ($M^{-1}s^{-1}$)	$k_2'/10^{-5}$ ($M^{-1}s^{-1}$)	$k_2'/10^{-2}$ ($M^{-1}s^{-1}$)	$k_2'/10^{-3}$ ($M^{-1}s^{-1}$)	$k_{-2}/10^{-3}$ (s^{-1})
15	1.01 ± 0.02	5.85 ± 0.19	0.16 ± 0.003	1.01 ± 0.13	0.800 ± 0.08	1.00 ± 0.10	0.71 ± 0.07
20	1.86 ± 0.07	11.2 ± 0.52	0.32 ± 0.004	1.94 ± 0.21	1.56 ± 0.09	1.88 ± 0.40	0.75 ± 0.70
25	3.47 ± 0.04	21.2 ± 0.93	0.83 ± 0.006	3.92 ± 0.21	3.30 ± 0.43	4.95 ± 0.42	1.19 ± 0.28
30	5.66 ± 0.84	42.2 ± 0.22	1.36 ± 0.04	6.71 ± 0.04	5.92 ± 0.85	5.96 ± 0.24	2.33 ± 0.14
$\Delta H^{\neq}$ (kJ mol^{-1})	82 ± 1	94 ± 4	104 ± 5	91 ± 1	98 ± 2	90 ± 13	83 ± 13
$\Delta S^{\neq}$ (J K^{-1} mol^{-1})	−18 ± 4	−3 ± 13	+43 ± 16	−26 ± 4	+56 ± 7	+12 ± 44	−24 ± 45

intercepts of the graphs, we were able to calculate the entropies and enthalpies of activation, shown in Table 1.

In our previous work, we compared the rates of hydroboration of different haloboranes using 1-octene and making sure that the amount of the Lewis base was the same. In this paper, our main interest is to compare the hydroboration reaction of 4-octene and that of 1-octene [1,3] with different haloboranes. Therefore, it is important to mention that this paper compares the reactivity between 4-octene and 1-octene with a specific haloborane and not the differences among haloboranes. Consequently, making sure that the different haloborane systems were at same level of excess Lewis base was of no necessity. Even so, the reactivity between $HBBr_2 \cdot SMe_2$ and $H_2BBr \cdot SMe_2$ can be compared since these two systems had the same amount of excess Me_2S.

3.1. Reactivity of 1-octene and 4-octene

Looking at the data in Table 1, the composite second order rate constants, k_2' for hydroboration of 1-octene are larger than those of the hydroboration of 4-octene. This implies that the rate of hydroboration of 1-octene is faster than that of 4-octene, which is in agreement with what Brown et al. [16–18] discovered through relative reactivity studies.

A quantitative analysis of the rate constants, reveal that on average hydroboration of 1-octene with $HBBr_2 \cdot SMe_2$ and $HBCl_2 \cdot SMe_2$ is 16 times faster than that of the 4-octene, whilst in the case of $H_2BBr \cdot SMe_2$ this factor is reduced to 8 times. This difference is due to the difference in the reactivity of the haloboranes, as reported in our previous work [1,3] where we showed that the rate-controlling step on hydroboration with dimethyl sulfide haloborane addition complexes is the dissociation of the Me_2S. The comparison between the mono- and the dihaloborane showed that the rate of dissociation of Me_2S from $H_2BBr \cdot SMe_2$ is 34 times faster than that from $HBBr_2 \cdot SMe_2$. This was accounted for in terms of the magnitude of the inductive effect the boron atom experiences due to the presence of bromine atoms in the two environments.

The difference in reactivity between 1-octene and 4-octene within a haloborane is due to the contribution of k_2 to the k_2' term. This value is controlled by the steric hindrance of the incoming nucleophile, with the internal double bond being more sterically hindered than the terminal one.

Hydroboration reactions involving $H_2BBr \cdot SMe_2$ were observed to have a y-intercept, as shown in Eq. (4), which resulted in k_{-2} values that are given in Table 1. From the mechanism, these values represent a rearrangement process which has previously been proposed [21] to occur (either through dehydroboration or through a stereospecific migration by means of a π-complex or three-centred intermediate) as a means of isomerization. In this study, the temperatures employed were much lower than those at which dehydroboration is expected to occur as already explained above [22], therefore we can assume that the k_{-2} values observed represent the stereospecific migration of boron from one carbon to the next, as opposed to complete dehydroboration.

3.2. Activation parameters

In analysing the activation parameters, as previously stated [1,3], it is important that caution is exercised since the values originate from the composite rate constants, k_2'. This is because the values obtained are a sum of two processes taking place, *i.e.* dissociation of the Me_2S from the boron atom and subsequently the hydroboration reaction.

Therefore, the moderate $\Delta H^{\neq}$ values, accompanied by small $\Delta S^{\neq}$ values imply a process that is dissociatively dominated. However, the magnitude of the $\Delta S^{\neq}$ values is indicative of an overall interchange (I) mechanism. The large errors associated with entropy values are due to the intrinsic extrapolation involved in their determination. The activation enthalpy values are similar in magnitude, an indication that these reactions go through a similar mechanistic process. The rearrangement process (which is means of isomerization) has small values of $\Delta S^{\neq}$. These can also be interpreted to represent an interchange (I) mode of activation. This further supports the proposal that at lower temperatures, isomerization may occur by means of stereospeific rearrangement through a π-complex [21].

4. Summary

The results reported in this paper show that hydroboration of 1-octene with dimethyl sulfide dihaloborane addition complexes ($HBBr_2 \cdot SMe_2$ and $HBCl_2 \cdot SMe_2$) is 16 times faster than hydroboration of 4-octene. This factor is reduced to 8 times when a monohaloborane ($H_2BBr \cdot SMe_2$) is used. This certainly is in agreement and in support of the findings reported by previous workers, *i.e.* hydroboration of internal olefins is sluggish compared to that of terminal olefins. Steric hindrance accounts for the difference in hydroboration reactivities of 1-octene and 4-octene.

The activation parameters obtained for hydroboration of both 1-octene and 4-octene with $HBX_2 \cdot SMe_2$ and $H_2BBr \cdot SMe_2$ are indicative of a mechanistic mode that is dominated by the dissociation of the Me_2S as opposed to the associative nature of the coming in of the nucleophile. The overall mode of activation is interchange (I) in nature. The observed k_{-2} values for $H_2BBr \cdot SMe_2$ is an indication of a rearrangement process most probably through a π-complex, which facilitates isomerization.

Acknowledgements

The authors wish to acknowledge the funding of this project by Sastech R&D, DTI/Thrip, as well as the University of KwaZulu Natal. Our special gratitude goes to Mr. C.D. Grimmer for recording the NMR spectra, as well as assistance with regard to NMR queries. Dr. A. de Klerk of Sasol Ltd. is also acknowledged for his contribution.

References

[1] D. Jaganyi, N. Xaba, A. Mzinyati, C. Grimmer, J. Organomet. Chem. 692 (2007) 1150.
[2] A. de Klerk, S.W. Hadebe, J.R. Govender, D. Jaganyi, A.B. Mzinyati, R.S. Robinson, N. Xaba, Ind. Eng. Chem. Res. 46 (2) (2007) 400.
[3] N. Xaba, D. Jaganyi, J. Organomet. Chem. 692 (2007) 4052.
[4] H.C. Brown, J. Chandrasekharan, J. Organomet. Chem. 53 (1988) 4811.
[5] H.C. Brown, N. Ravindran, S.U. Kulkarni, J. Organomet. Chem. 53 (1988) 4811.
[6] H.C. Brown, L.T. Murray, Inorg. Chem. 23 (1984) 2746.
[7] (a) H.C. Brown, J.J. Chandrasekhan, J. Am. Chem. Soc. 106 (1984) 1863; (b) H.C. Brown, J.J. Chandrasekhan, J. Gazz. Chim. Ital. 117 (1987) 377.
[8] H.C. Brown, J.A. Sikorski, S.U. Kulkarni, H.D. Lee, J. Organomet. Chem. 47 (1982) 863.
[9] H.C. Brown, J. Chandrasekharan, J. Organomet. Chem. 2 (1983) 1261.
[10] H.C. Brown, N. Ravindran, J. Am. Chem. Soc. 98 (1976) 1785.
[11] H.C. Brown, N. Ravindran, J. Am. Chem. Soc. 98 (1976) 1798.
[12] H.C. Brown, N. Ravindran, J. Am. Chem. Soc. (1977) 7097.
[13] H.C. Brown, D.J. Nelson, J. Am. Chem. Soc. 106 (1977) 4907.
[14] H.C. Brown, N. Ravindran, S.U. Kulkarni, J. Organomet. Chem. 44 (1977) 2417.
[15] H.C. Brown, N. Ravindran, S.U. Kulkarni, J. Organomet. Chem. 45 (1980) 384.
[16] H.C. Brown, R. Liotta, C.G. Scouten, J. Am. Chem. Soc. (1976) 5297.
[17] H.C. Brown, J. Chandrasekharan, J. Organomet. Chem. 48 (1983) 644.
[18] H.C. Brown, J. Chandrasekharan, J. Organomet. Chem. 48 (1983) 5080.
[19] D.J. Pasto, V. Balsubramaniyan, P.W. Wojtkowski, Inorg. Chem. 8 (1969) 594.
[20] D.J. Pasto, B. Lepeska, T.C. Cheng, J. Am. Chem. Soc. 94 (1972) 6083.
[21] L.D. Field, S.P. Gallagher, Tetrahendron Lett. 26 (1985) 6125.
[22] H.C. Brown, B.C. Subba Rao, J. Am. Chem. Soc. 81 (1959) 6434.

2.2. Synthesis

In a typical synthesis, a solution of $Ni(NO_3)_2 \cdot 6H_2O$ (0.67 mmol) in 10 ml formamide for **1**, or $Ni(NO_3)_2 \cdot 6H_2O$ (0.67 mmol) and 4,4′-bipyridine (1.34 mmol) in 10 ml formamide for **2** was transferred into a Teflonlined autoclave and then heated under autogenous pressure at 70 °C for 72 h, followed by cooling to room temperature naturally. Green large single crystals in regular cubic shape were collected and washed with ethanol several times, yield 75% for **1** and **2** upon Ni. *Anal.* Calc. for **1**: N, 23.08. Found: N, 23.05%. *Anal.* Calc. for **2**: C, 39.13; H, 2.63; N, 18.26. Found: C, 39.03; H, 2.93; N, 18.32%.

2.3. Characterization

Elemental analyses for C, H, and N were performed on an EA 1110 elemental analyzer. The IR spectra were obtained on a FT/IR-6100 (JASCO) spectrometer. The variable temperature magnetic susceptibilities were measured using a PPMS 6000 (Quantum Design Inc., USA) instrument.

2.4. X-ray crystallography

Data for compounds were collected on a Bruker SMART AXS diffractometer equipped with a monochromator in the Mo Kα (λ = 0.71073 Å) incident beam. The crystals were mounted on a glass fiber. The CCD data were integrated and scaled using the Bruker-SAINT software package, and the structures were solved and refined using SHEXTL V6.12 [32]. Hydrogen atoms were located in the calculated positions. The crystallographic data for **1** and **2** is listed in Table 1.

3. Results and discussion

3.1. Synthesis

Recently, hydro(solvo)thermal synthesis has gained impressive progress. This technique provides a powerful tool for the construction of materials containing unique structures and special properties. In this work, using solvothermal reaction between $Ni(NO_3)_2 \cdot 6H_2O$ and formamide for **1**, $Ni(NO_3)_2 \cdot 6H_2O$ and 4,4′-bipyridine in formamide for **2** at 70 °C for 72 h yields green cubic crystals. This synthetic procedure gave a good yield of about 75% based on nickel in the both cases. Anion NO_2^- in the compounds may come from reduction of NO_3^- by formamide [33]. Indeed, at high temperature and pressure of the solvothermal condition, the reaction is suggested to be as follows:

$$NO_3^- + NH_2{-}CHO \rightarrow NO_2^- + NH_2{-}COOH.$$

To evidence the reaction mechanism above, the analysis of nitrite anion was carried out by a standard method, spectrophotometric determination. A liquid part of the reaction products was isolated and analyzed by using sulfanilamide and *N*-(1-naphthyl)ethylenediamine as indicators with using light at 543 nm. The analysis results showed that almost NO_3^- was reduced to NO_2^-. The oxidation of *N*,*N*-dimethylformamide to form carbamic acid by oxidant such as Ag^+ was also reported in the previous literature [33]. Compounds **1** and **2** can be obtained in a wide temperature range from 70 to 150 °C.

Table 1
Crystallographic data for compounds **1** and **2**.

Empirical formula	N_4NiO_8 (**1**)	$C_{10}H_8N_4NiO_4$ (**2**)
Formula weight	242.75	306.91
T (K)	293(2)	293(2)
Crystal system	monoclinic	tetragonal
Space group	$C2/c$	$P4_32_12$
a (Å)	12.7799(16)	7.9101(7)
b (Å)	8.3600(10)	7.9101(7)
c (Å)	8.2511(10)	17.457(2)
α (°)	90.00	90.00
β (°)	93.167(2)	90.00
γ (°)	90.00	90.00
V (Å^3)	880.20(19)	1092.27(19)
Z	4	4
Absorption coefficient (mm^{-1})	2.231	1.794
Number of data collected	2252	5961
Number of unique data	811	1307
R_{int}	0.1821	0.1151
Goodness-of-fit	1.025	1.054
Final R indices [$I > 2\sigma(I)$]	R_1 = 0.0569, wR_2 = 0.1416	R_1 = 0.0643, wR_2 = 0.1828
Final R indices (all data)	R_1 = 0.0691, wR_2 = 0.1544	R_1 = 0.0867, wR_2 = 0.2306

3.2. Structure description

Compound **1** crystallizes in monoclinic space group $C2/c$ with two-dimensional framework (Fig. 1). In this structure, there is only one crystallographical type of Ni^{2+} ion with a nearly octahedral environment surrounded by six oxygen atoms. Each Ni^{2+} ion is bridged with four neighboring Ni^{2+} ions through NO_2^- ligands. The Ni1–O1, O1–N1, N1–O2($0.5 - x$, $-0.5 + y$, $0.5 - z$) and O2–Ni1 lengths are 2.075(3), 1.273(6), 1.256(5), and 2.083(3) Å; and the Ni1–O1–N1, O1–N1–O2($0.5 - x$, $-0.5 + y$, $0.5 - z$) and N1($0.5 - x$, $0.5 + y$, $0.5 - z$)–O2–Ni1 angles are 123.6(3)°, 122.6(4)°, and 22.0(3)°, respectively. The distance between two neighboring Ni^{2+} ions is 5.873(1) Å. These bond lengths and angles may play an important role to the magnetic coupling between the Ni^{2+} ions. The relative Ni1–O1–N1–O2 and O1–N1–O2–Ni1 torsion angles are 177.7(1)° and 174.06(1)°. This means that Ni1, O1, N1, and O2 atoms are arranged nearly in a plane. Linking Ni^{2+} ions and bridging NO_2^- ligands forms a two-dimensional framework. In addition, each Ni^{2+} ion also coordinates with two NO_2 molecules with bond lengths Ni–O3 (2.080(3) Å), N2–O3 (1.251(7) Å), N2–O4 (1.192(11) Å). Compared with N2–O3 bond, shorter length of N2–O4 may be due to double bond of this terminal link. The double bond can be evidenced further by a comparison of the IR data for 4,4′-bipyridine, **1**, and **2** (Fig. S1). Compound **2** crystallizes in tetragonal space group $P4_32_12$. Asymmetric unit contains half metal atom, half 4,4′-bipy ligand, and a NO_2^- ligand. Symmetry operations ($x - 1$, $y - 1$, z), ($x - 1/2$, $-y+1/2$, $-z + 1/4$), ($-y + 1/2$, $x - 1/2$, $z - 1/4$), (y, x, $-z$), ($x + 1$, $y + 1$, z), and ($y + 1/2$, $-x + 1/2$, $z + 1/4$) generate three-dimensional structure (Fig. 2). There is only one type of Ni^{2+} ion in the structure, coordinated by six atoms. The coordination environment of Ni can be considered as a octahedron compressed along N1–Ni1–N2($x - 1$, $y - 1$, z) axis with Ni–N bond lengths for Ni1–N1 (2.051(8) Å) and Ni1–N2($x - 1$, $y - 1$, z) (2.063(7) Å) are shorter than those of four equatorial bonds Ni–O (2.124(5)–2.126(5) Å). Each Ni^{2+} ion is bridged with four neighboring Ni^{2+} ions via NO_2^- ligands. The Ni1–O1, O1–N3, N3–O2 and O2–Ni1($y + 1/2$, $-x + 1/2$, $Z + 1/4$) lengths are 2.126(5), 1.236(7), 1.275(8), and 2.124(5) Å; and the Ni1–O1–N3, O1–N3–O2 and N3–O2–Ni1($y + 1/2$, $-x + 1/2$, $Z + 1/4$) angles are 126.6(5)°, 127.8(8)°, and 120.0(5)°, respectively. The distance between two neighboring Ni^{2+} ions bridged by NO_2^- is 5.893(1) Å. The relative Ni1–O1–N3–O2 and O1–N3–O2–Ni1($y + 1/2$, $-x + 1/2$, $Z + 1/4$) torsion angles are −178.1(5)° and −156.6(6)°. This shows that the configuration of NO_2^- for **2** is different from that for **1**. Along direction N1–Ni1–N2, two neighboring Ni^{2+} ions are bridged by a ligand 4,4′-bipy molecule with a torsion angle of two pyridine rings to be 47.7(2)°. The distance between these two Ni^{2+} ions is 11.187(1) Å. Two 4,4′-bipyridine molecules of two neighboring Ni^{2+} ions bridged by NO_2^- have perpendicular N–N directions.

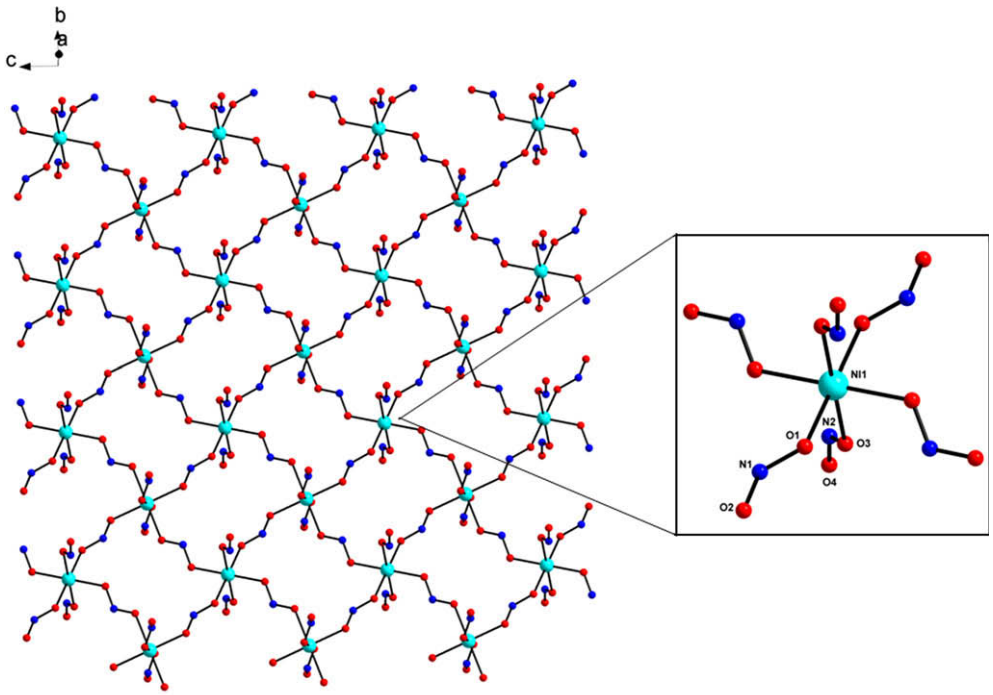


Fig. 1. Two-dimensional structure of **1**.

3.3. Magnetic properties

The $\chi_M T$ versus T plots for **1** and **2** are shown in Figs. 3 and 4 with χ_M being the molar magnetic susceptibility per Ni^{II} ion. At room temperature, the $\chi_M T$ values for **1** and **2** are 1.36 and 1.21 $cm^3\ K\ mol^{-1}$, respectively, which exceed the spin-only value for uncorrelated Ni^{II} ($S = 1$) center (1.0 $cm^3\ K\ mol^{-1}$). The observed $\chi_M T$ values are similar to that found in the end-to-end azide-bridged Ni(II) chain [34]. Upon cooling, a decrease in the $\chi_M T$ product was observed at temperatures down to 20 K (0.62 $cm^3\ K\ mol^{-1}$) for **1** and 26 K (0.53 $cm^3\ K\ mol^{-1}$) for **2**. This suggests the presence of antiferromagnetic interactions in the both compounds. The

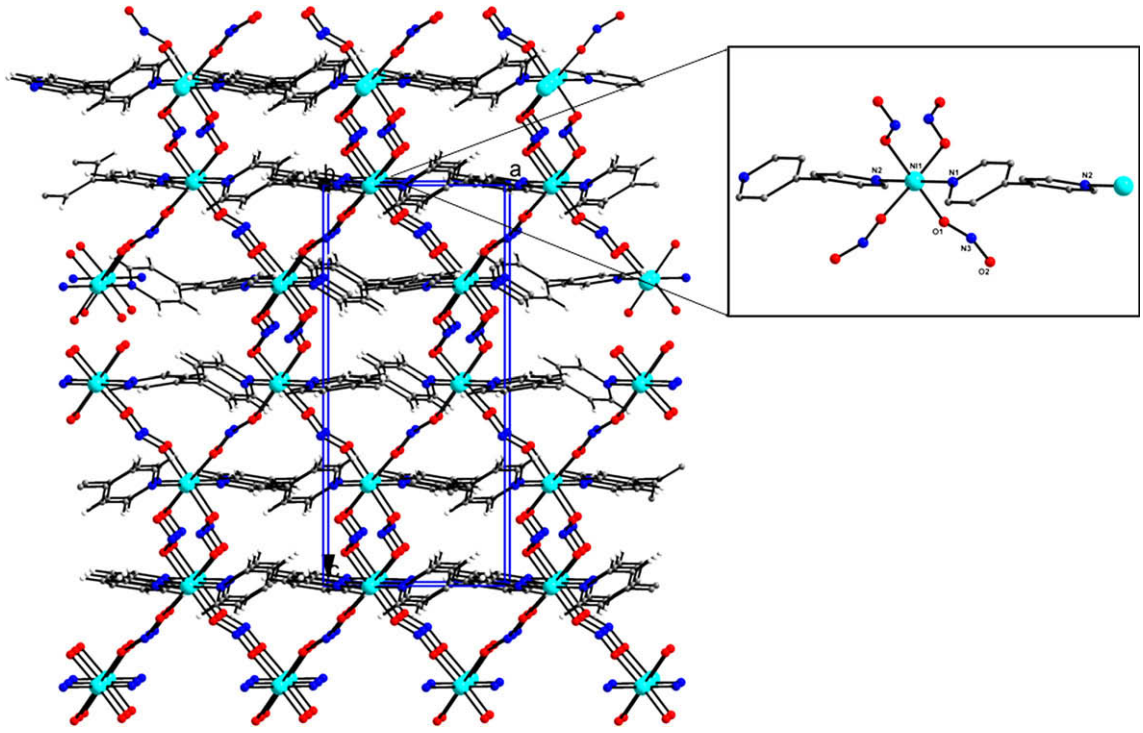


Fig. 2. Three-dimensional structure of **2**.

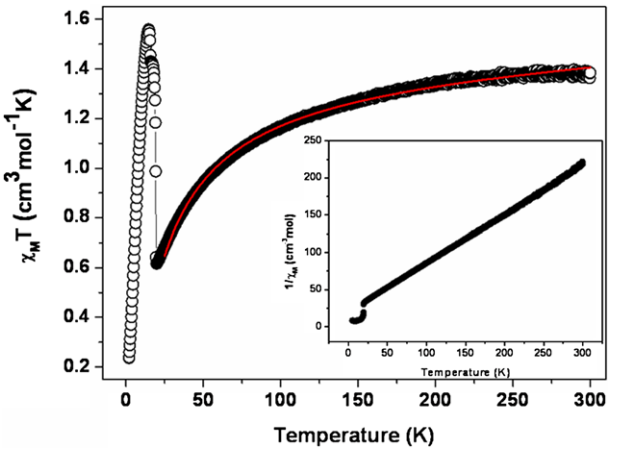


Fig. 3. Plots of the temperature dependence of $\chi_M T$ and $1/\chi_M$ (inset) for **1** at 500 Oe field, with the solid line representing the best fit (see the text).

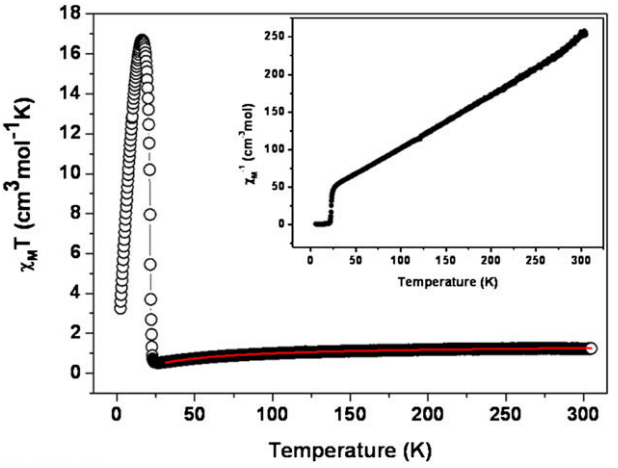


Fig. 4. Plots of the temperature dependence of $\chi_M T$ and $1/\chi_M$ (inset) for **2** at 500 Oe field.

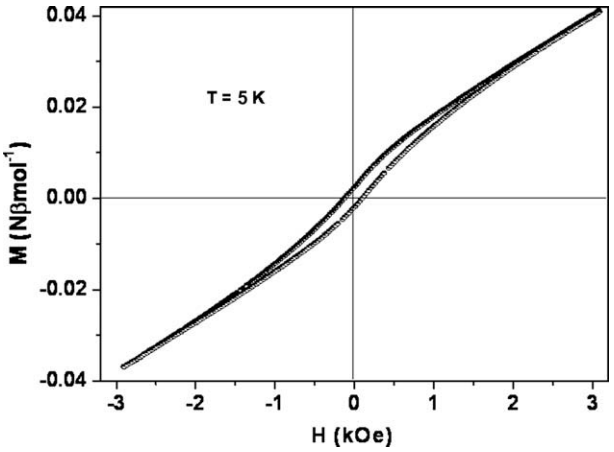


Fig. 5. Hysteresis loop of **1** at $T = 5$ K.

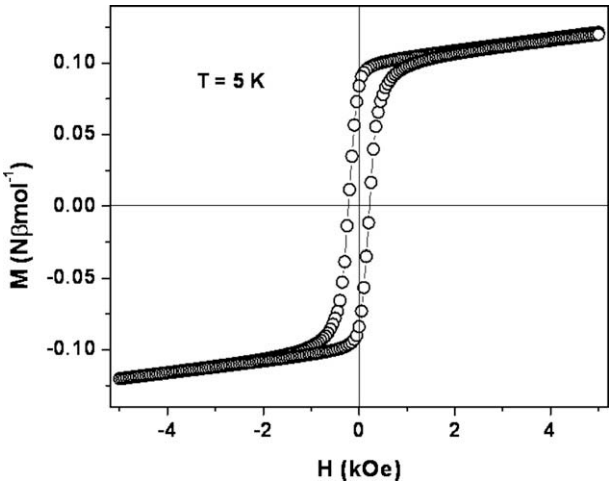


Fig. 6. Hysteresis loop of **2** at $T = 5$ K.

subsequent cooling leads to a abrupt increase to a maximum at 15 K (1.55 cm^3 K mol^{-1}) and 16 K (16.69 cm^3 K mol^{-1}), followed by a drop down to 0.60 cm^3 K mol^{-1} and 7.70 cm^3 K mol^{-1} at 5 K for **1** and **2**, respectively. This overall magnetic behavior is related to the occurrence of spin-canting [34]. Fit of the data ($T > 50$ K) with the Curie–Weiss law [$\chi_M = C/(T - \theta)$] provides parameters of $C = 1.54$ cm^3 K mol^{-1}, $\theta = -31$ K for **1**; and $C = 1.39$ cm^3 K mol^{-1}, $\theta = -41$ K for **2**. Based on the structural feature, we adopted the equation of the Heisenberg model ($H = -2J\Sigma_{ij}S_i - S_j$) for a two-dimensional plane square derived by Rushbrooke and Wood [35]. The deduced expression for $S = 1$ is given by

$$\chi_M = (2Ng^2\beta^2/3kT)[\Sigma_{n=0^6}(p_n/x^n)]^{-1}$$

where $p_0 = 1$, $p_1 = 5.3333$, $p_2 = 9.7778$, $p_3 = 9.4815$, $p_4 = 19.0617$, $p_5 = 45.0897$, $p_6 = 25.4639$, and $x = kT/J$. From the structural considerations of **1** showing a two-dimensional lattice, the high-temperature magnetic data of **1** at $T > 25$ K were fitted to the equation, giving parameters of $g = 2.37$, $J = -2.84$ cm^{-1}. In χ_M versus T plots (Figs. S2 and S3) a long-range magnetic phase transition was observed at low temperature. The critical temperatures are present at 19 K for **1** and 21 K for **2** as evidenced by the peak in the $d\chi_M/dT$ versus T curve (the inset of Figs. S2 and S3). Because four $\mu_{1,3}$-nitrito bridges around each Ni center link four neighboring Ni atoms and then forms the three-dimensional network, the equation for a two-dimensional square lattice was not applied for **2**. The magnetic couplings via 4,4′-bipy can be ignored due to the long mediating distance. Using the mean-field approximation, $T_N = 2z|J|S(S + 1)/3k_B$ with $T_N = 21$ K, $z = 4$, and $S = 1$, J through the nitrite bridges is calculated to be -2.74 cm^{-1}. The obtained J value is compatible with those of **1** and $[Co(pyrazine)_2NO_2]ClO_4$ [11]. Characteristic hysteresis loops are observed at 5 K with a remnant magnetization (M_r) of 0.0025 Nβ mol^{-1} and a coercive field (Hc) of 127 Oe for **1** (Fig. 5), and M_r of 0.084 Nβ mol^{-1} and Hc of 220 Oe for **2** (Fig. 6).

4. Conclusion

We successfully synthesize molecule-based magnetic materials with two- (for $Ni(NO_2)_2(NO_2)_2$) and three- (for $Ni(4,4'\text{-bipyridine})(NO_2)_2$) dimensional coordination polymer frameworks by solvothermal method in formamide using salt $Ni(NO_3)_2 \cdot 6H_2O$ as a precursor. Both complexes mark the first two- and three-dimensional examples constructed from purely nitrite bridges. Magnetic measurements show weak ferromagnetism within framework of the two compounds, in which the magnetization of **2** with 3D network is much stronger than that of **1** with 2D structure. Bridging ligand NO_2^- formed by reducing NO_3^- in the presence of formamide may play an important role in the observed weak ferromagnetism generating T_N values of 19 K for **1** and 21 K for **2**.

Acknowledgement

Financial support from the SRC program of the Korea Science and Engineering Foundation (KOSEF) through the Center for Intelligent Nano-Bio Materials at Ewha Womans University (Grant R11-2005-008-00000-0) is gratefully acknowledged.

Appendix A. Supplementary data

These data can be obtained free of charge via http://www.ccdc.cam.ac.uk/conts/retrieving.html, or from the Cambridge Crystallographic Data Centre, 12 Union Road, Cambridge CB2 1EZ, UK; fax: (+44) 1223 336 033; or e-mail: deposit@ccdc.cam.ac.uk. Supplementary data associated with this article can be found, in the online version, at doi:10.1016/j.poly.2009.01.019.

References

[1] S. Zang, Y. Su, Y. Song, Y. Li, Z. Ni, H. Zhu, Q. Meng, Cryst. Growth Des. 6 (2006) 2369.
[2] D. Bradshaw, J.B. Claridge, E.J. Cussen, T.J. Prior, M.J.J. Rosseinsky, Acc. Chem. Res. 38 (2005) 273.
[3] N.W. Ockwig, O. Delgado-Friedrichs, M. O'Keeffe, O.M. Yaghi, Acc. Chem. Res. 38 (2005) 176.
[4] A. Comotti, S. Bracco, P. Sozzani, S. Horike, R. Matsuda, J. Chen, M. Takata, Y. Kubota, S. Kitagawa, J. Am. Chem. Soc. 130 (2008) 13664.
[5] S. Kitagawa, R. Kitaura, S. Noro, Angew. Chem., Int. Ed. Engl. 43 (2004) 2334–2375.
[6] R.C. Stephen, G.W. Antek, J.M. Adam, J. Am. Chem. Soc. 130 (2008) 10870.
[7] K.G. Sujit, B.S. Sareeya, S. Kitagawa, Angew. Chem., Int. Ed. Engl. 47 (2008) 3403.
[8] S. Tanase, Reedijk, J. Coord. Chem. Rev. 250 (2006) 2501.
[9] M. Mikuriya, D. Yoshioka, M. Handa, Coord. Chem. Rev. 250 (2006) 2194.
[10] M.A. Hitchman, G.L. Rowbottom, Coord. Chem. Rev. 42 (1982) 55.
[11] T. Liu, Y.-H. Chen, Y.-J. Zhang, Z.-M. Wang, S. Gao, Inorg. Chem. 45 (2006) 9148.
[12] H.W. Park, S.M. Sung, K.S. Min, H. Bang, M.P. Suh, Eur. J. Inorg. Chem. (2001) 2857.
[13] J.Y. Xu, W. Gu, H.D. Bian, F. Bian, S.P. Yan, D.Z. Liao, Z.H. Jiang, P.W. Shen, Inorg. Chem. Commun. 6 (2003) 513.
[14] K.N. Power, T.L. Hennigar, M.J. Zaworotko, New J. Chem. 22 (1998) 177.
[15] M.L. Tong, X.M. Chen, S.W. Ng, Inorg. Chem. Commun. 3 (2000) 436.
[16] Y. Sun, Z. Wang, H. Zhang, Y. Cao, S. Zhang, Y. Chen, C. Huang, X. Yu, Inorg. Chim. Acta 360 (2007) 2565.
[17] J. Tao, X.M. Chen, R.B. Huang, L.S. Zheng, J. Solid State Chem. 170 (2003) 130.
[18] M. Du, S.T. Chen, X.H. Bu, Ribas, J. Inorg. Chem. Commun. 5 (2002) 1003.
[19] X.J. Zheng, L.C. Li, S. Gao, L.P. Jin, Polyhedron 23 (2004) 1257.
[20] S.K. Ghosh, J. Ribas, P.K. Bharadwaj, Cryst. Growth Des. 5 (2005) 623.
[21] O. Teichert, W.S.Z. Sheldrick, Anorg. Allg. Chem. 626 (2000) 1509.
[22] F.A.A. Paz, F.N. Shi, J. Klinowski, J. Rocha, T. Trindade, Eur. J. Inorg. Chem. (2004) 2759.
[23] S. Noro, M. Kondo, S. Kitagawa, T. Ishii, H. Matsuzaka, Chem. Lett. 28 (1999) 727.
[24] S. Noro, S. Kitagawa, M. Kondo, K. Seki, Angew. Chem., Int. Ed. Engl. 39 (2000) 2081.
[25] J. Tao, X. Yin, R.B. Huang, L.S. Zheng, Inorg. Chem. Commun. 5 (2002) 1000.
[26] K. Seki, Phys. Chem. Chem. Phys. 4 (2002) 1968.
[27] C.V.K. Sharma, J. Chem. Educ. (2001) 617.
[28] A. Sarkar, S. Kapoor, T. Mukherjee, J. Phys. Chem. B 109 (2005) 7698.
[29] S. Feng, R. Xu, Acc. Chem. Res. 34 (2001) 239.
[30] S. Konar, P.S. Mukherjee, E. Zangrando, F. Lloret, N.R. Chaudhuri, Angew. Chem., Int. Ed. Engl. 41 (2002) 1561.
[31] K.C. Mondal, O. Sengupta, M. Nathaji, P.S. Mukherjee, Dalton Trans. (2008) 767.
[32] Bruker, SHELXTL/PC, Version 6.12 for Windows XP., Bruker AXS Inc., Madison, Wisconsin, USA, 2001.
[33] I.P. Santos, L.M.L. Marzan, Langmuir 15 (1999) 948.
[34] X.-T. Liu, X.-Y. Wang, W.-X. Zhang, P. Cui, S. Gao, Adv. Mater. 18 (2006) 2852.
[35] G.S. Rushbrooke, P.J. Wood, Mol. Phys. 1 (1958) 257.

2. Results and discussion

HL^1P was synthesized adopting a previously published procedure [14]. Some modifications in the experimental conditions, however, increased the yield significantly. The ^{31}P NMR spectrum of the yellow solid shows a resonance at −12.9 ppm. A doublet at 9.1 ppm (J_{PH} = 4.88 Hz) in the ^1H NMR spectrum suggests the presence of the HC=N unit. Oxidation of HL^1P with H_2O_2 in THF results in the formation of HL^1PO in good yields. The ^{31}P NMR signal of the phosphorus atom in the phosphine oxide is found at 31.6 ppm, which corresponds to a low-field shift of 44 ppm compared to the value for HL^1P. The aminophosphine H_2L^2 was prepared by the reduction of HL^1P with an excess of $NaBH_4$ in boiling EtOH. The course of the reaction can readily be tracked by ^1H NMR, where signal of the CH=N protons disappears and a doublet of the methylene protons appears at 4.4 ppm (J_{HH} = 5.24 Hz).

HL^1P reacts with oxorhenium(V) precursors such as $[ReOCl_3(PPh_3)_2]$ or $(NBu_4)[ReOCl_4]$ by almost immediate changes of the colors of the reaction mixtures. However, all our attempts to isolate crystalline products from such mixtures failed. ^{31}P NMR studies of the reaction solutions showed several new signals at negative and positive chemical shift values for each reaction. Number and positions of the signals were strongly dependent on the solvent and the reaction time, which indicates an ongoing decomposition of HL^1P and/or oxidation of the phosphine under formal reduction of the metal ion. The latter type of reaction is not without precedent and has frequently been observed during the interaction of oxorhenium(V) compounds and phosphines, and can principally simply be initiated by released PPh_3 [7]. A detailed analysis of such oxygen transfer reactions has been carried out by Conry and Mayer [15].

In order to simplify the reaction and to minimize the risk of the formation of Re(III) products by a reaction of HL^1P with the oxo oxygen and subsequent formation of HL^1PO in the reaction mixture, we used the phosphine oxide directly. While the course of even this reaction with $(NBu_4)[ReOCl_4]$ remained unclear, HL^1PO reacted within 1 h in boiling THF with the sparingly soluble $[ReOCl_3(PPh_3)_2]$ under formation of a clear green solution. The heating was stopped after 2 h and two crystalline products, the red $[ReOCl_2(PPh_3)(L^1PO–O,N)]$ (**1**) and the green $[Re(NC_6H_4OH)Cl_3(PPh_3)_2]$ (**2**) could be isolated in an approximate ratio of 1:2 (Scheme 1). The amount of compound **2** can be increased by a prolonged reaction time.

The ^{31}P NMR spectrum of **1** exhibits two resonances at 26.8 and 29.4 ppm indicating the presence of L^1PO^- and coordinated PPh_3. The $\nu_{C=N}$ band of the uncoordinated imine compound is bathochromically shifted in the spectrum of the complex and appears at 1566 cm^{-1}. Single crystals of the complex were studied by X-ray diffraction. Fig. 1 shows an ellipsoid representation of **1**. Selected bond lengths and angles are summarized in Table 1. The coordination sphere of the complex is a distorted octahedron with the Schiff base as a singly deprotonated O,N chelate ligand binding via the imine nitrogen and the phenolic oxygen atoms. The oxygen atom O2 is found in *trans* position to the oxo ligand. Such a coordination mode is typical for chelating ligands systems with oxygen donor atoms [7] and goes along with a considerable transfer of electron density from the terminal Re=O bond into the relatively short Re-O2 bond of 1.958(6) Å. The phosphine oxide unit does not contribute to the coordination of the metal atom. This results in a bulky complex molecule, which produces relatively large voids between the molecules, which is also expressed by the relatively low density of the rhenium complex of 1.48 g/cm^3. These holes are almost unoccupied. The highest peaks of electron density located there count approximately 1 $e^-/Å^3$. A refinement with each one water molecule which is disordered in over four positions in such a void improves the *R* value only marginally and is not justified by other experimental data.

The formation of the green phenylimido complex **2** is an unexpected feature of the reaction, but confirms the decomposition of HL^1PO during the reaction with $[ReOCl_3(PPh_3)_2]$. The fact that the amount of **2** formed increases with a prolonged reaction time, also indicates a considerable instability of **1**. The presence of the metal complex is mandatory for the observed ligand decomposition, and all our attempts to decomposed pure HL^1PO in boiling THF failed. The compound resisted such a treatment for 5 h without degradation as has been proven by ^{31}P NMR and TLC experiments. The released 2-aminophenol finally reacts with the oxorhenium core under formation of a phenylimido unit. It is interesting to note that the isolated complex **2** contains two PPh_3 ligands and, consequently, the triphenylphosphine released from $[ReOCl_3(PPh_3)_2]$ is not oxidized immediately by a secondary reaction with the oxo

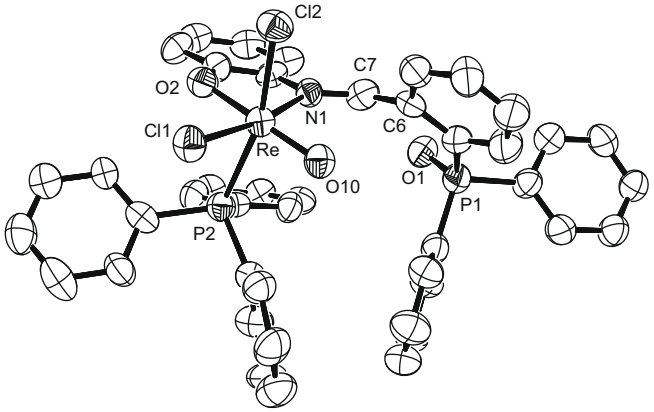
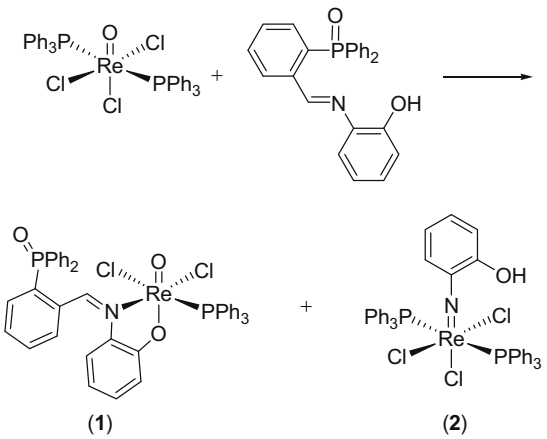


Fig. 1. Ellipsoid representation [21] of $[ReOCl_2(PPh_3)(L^1PO)]$. Thermal ellipsoids represent 50% probability. H atoms have been omitted for clarity.

Table 1
Selected bond lengths (Å) and angles (°) in the $[ReOCl_2(PPh_3)(L^1PO)]$ (**1**).

Re–O10	1.657(6)	Re–O2	1.958(6)
Re–Cl1	2.346(2)	Re–P2	2.469(2)
Re–Cl2	2.386(2)	N1–C7	1.29(1)
Re–N1	2.192(7)	N1–C11	1.44(1)
O10–Re–Cl1	102.4(2)	O10–Re–O2	161.2(3)
O10–Re–Cl2	103.8(3)	N1–Re–O2	76.3(3)
O10–Re–P2	89.7(2)	Re–N1–C7	130.0(6)
O10–Re–N1	87.9(3)		



Scheme 1.

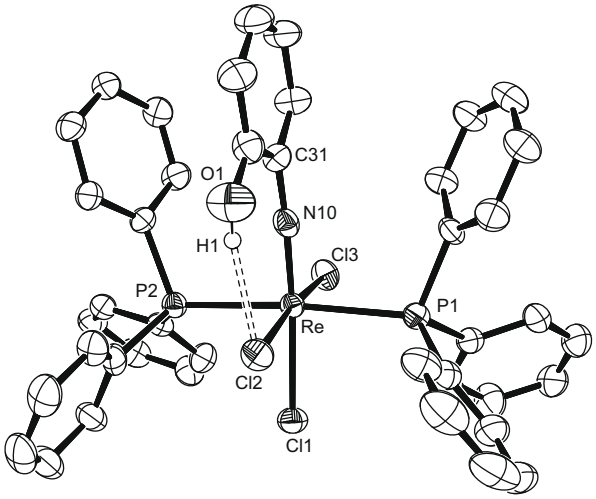
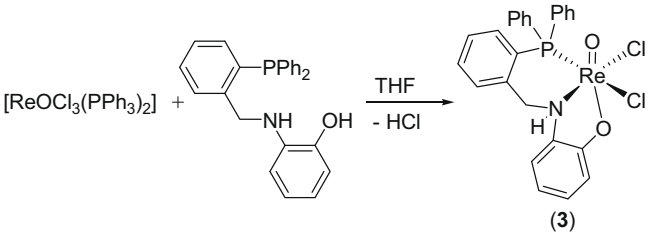


Fig. 2. Ellipsoid representation [21] of $[Re(NC_6H_4OH)Cl_3(PPh_3)_2]$. Thermal ellipsoids represent 50% probability. H atoms (except of H1) have been omitted for clarity.

Table 2
Selected bond lengths (Å) and angles (°) in $[Re(NC_6H_4OH)Cl_3(PPh_3)_2]$.

Re–N10	1.722(6)	Re–P1	2.501(2)
Re–Cl1	2.403(2)	Re–P2	2.490(2)
Re–Cl2	2.425(2)	N10–C31	1.369(9)
Re–Cl3	2.406(2)		
N10–Re–Cl1	173.6(2)	N10–Re–P2	92.1(2)
N10–Re–Cl2	91.3(2)	P1–Re–P2	174.18(5)
N10–Re–Cl3	95.8(2)	Cl2–Re–Cl3	172.92(6)
N10–Re–P1	93.6(2)	Re–N10–C31	174.9(5)



Scheme 2.

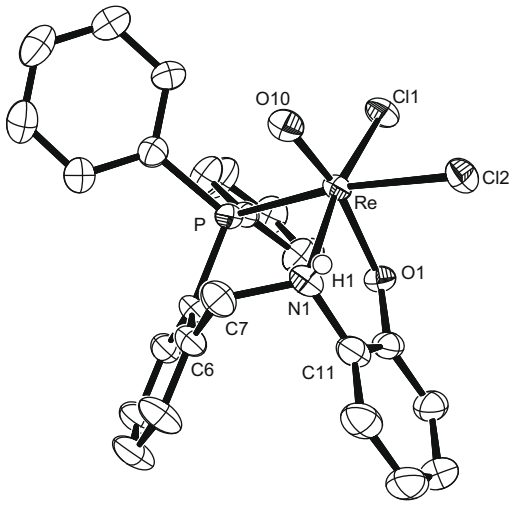


Fig. 3. Ellipsoid representation [21] of *fac*-$[ReOCl_2(HL^2P)]$. Thermal ellipsoids represent 50% probability. H atoms have been omitted for clarity.

Table 3
Selected bond lengths (Å) and angles (°) in *fac*-$[ReOCl_2(HL^2P)]$ (**3**).

Re–O10	1.679(4)	Re–N1	2.195(4)
Re–Cl1	2.344(1)	Re–O1	1.976(3)
Re–Cl2	2.429(1)	N1–C7	1.500(7)
Re–P	2.414(1)	N1–C11	1.469(7)
O10–Re–Cl1	104.1(1)	P–Re–N1	91.0(1)
O10–Re–Cl2	95.7(1)	N1–Re–O1	77.2(2)
O10–Re–P	91.8(1)	Re–N1–C7	115.0(3)
O10–Re–N1	86.4(2)	Re–N1–C11	109.3(3)
O10–Re–O1	163.2(2)	C7–N1–C11	112.1(4)

ligand as has been observed previously, but remains in the solution. This fact is supported by ^{31}P NMR spectra of the reaction mixture. Reactions of anilines with oxo complexes are common and many phenylimido complexes have been prepared in this way, but there are only a few structurally characterized examples of rhenium compounds with (2-hydroxyphenylimido) ligands [16]. Fig. 2 depicts an ellipsoid representation of **2**, selected bond lengths and angles are given in Table 2. Main structural features of the compound are similar to the corresponding 'parent complex' $[Re(NPh)Cl_3(PPh_3)_2]$ [17]. The only remarkable feature in the molecular structure of **2** is an intramolecular hydrogen bond (O1–H1: 0.82 Å, H1–Cl2: 2.25 Å, O1–Cl2: 3.037(7) Å, O1–H1–Cl2: 161.3°), which is established between the phenolic oxygen atom and one of the chloro ligands.

Cleavage of the backbone of the organic ligand is avoided, when the Schiff base is reduced prior reaction with the metal complex. The resulting phosphine amine H_2L^2P is a robust chelating system, which readily reacts with $[ReOCl_3(PPh_3)_2]$ under formation of *fac*-$[ReOCl_2(HL^2P)]$ (**3**) (Scheme 2). The same product is obtained by heating a reaction mixture of H_2L^2P and $(NBu_4)[ReOCl_4]$ in MeOH. The coordination of the phosphorus atom is confirmed by a single resonance in the ^{31}P NMR spectrum at −4.6 ppm, which corresponds to a 12 ppm shift compared to the resonance of uncoordinated H_2L^2P. The IR spectrum contains a medium intense absorption at 968 cm^{-1} related to the Re=O vibration. The broad band at 3452 cm^{-1} is consistent with the stretching vibrations of the NH unit and indicates that the amine donor function is not deprotonated.

The conclusions of the spectroscopic studies are confirmed by an X-ray structure determination of the compound. Fig. 3 depicts the molecular structure of **3** with a facially coordinated HL^2P^- ligand. Expectedly, the oxygen atom occupies the position *trans* to the oxo ligand, and the Re–O1 bond length of 1.973(3) Å is shorter than expected for a rhenium–oxygen single bond. More bond lengths and angles of **3** are summarized in Table 3. The coordination sphere around the metal atom is a distorted octahedron. Main distortions from an ideal octahedron come from the requirements of the four- and five-membered chelate rings, as can clearly be seen at the N1–Re–O1 angle of 77.2°. The Re–Cl2 bond is slightly longer than the Re–Cl1 bond, which is in accord with the stronger structural *trans* influence of the phosphine function compared with the amine.

Concluding it can be stated that a stable tridentate ligand is obtained by the reduction of a Schiff base derived from (2-formylphenyl)diphenylphosphine, while the imine itself undergoes a rapid hydrolysis when reacted with rhenium(V) oxo complexes. This concept can be extended to ligand systems of higher denticity starting from the Schiff bases derived from bis(2-formylphenyl)phenylphosphine or tris(2-formylphenyl)phosphine. Such studies are currently done in our laboratory.

3. Experimental

$(NBu_4)[ReOCl_4]$ [18] and $[ReOCl_3(PPh_3)_2]$ [19] were prepared by literature procedures. IR spectra were measured as KBr pellets on a Shimadzu FTIR-spectrometer 8300. FAB^+ mass spectra were recorded with a TSQ (Finnigan) instrument using a nitrobenzyl alcohol matrix. Elemental analysis of carbon, hydrogen and nitrogen were determined using a Heraeus (vario EL) elemental analyzer. ^1H, ^{13}C and $^{31}P\{^1H\}$ NMR spectra were taken with a JEOL 400 MHz multinuclear spectrometer.

3.1. Synthesis of HL^1P

A mixture of (2-formylphenyl)diphenylphosphine (1.5 g, 5.2 mmol) and 2-aminophenol (0.57 g, 5.2 mmol) were suspended in 10 mL of ethanol and heated under reflux for 1.5 h. The product precipitated as a yellow powder, which was filtered off and washed with cold ethanol. Yield 1.8 g (93%). Elemental *Anal.* Calc. for $C_{25}H_{20}NOP$ (381.13): C, 78.73; H, 5.29; N, 3.67%. Found: C, 78.92; H, 5.29; N, 3.51%. ^1H NMR (400 MHz, DMSO-d_6, ppm): δ 6.72–8.30 (m, 18H, aromatic), 8.78 (s, 1H, OH), 9.14 (d, 1H, HC=N, J_{PH} = 4.88 Hz). ^{13}C NMR (DMSO-d_6, ppm): δ 115–136 (aromatic), 156 (HC=N). ^{31}P NMR (DMSO-d_6, ppm): δ −12.9 s. IR (KBr, cm^{-1}): 3283 (st), 3043 (m), 3013 (w), 2881 (w), 1632 (st), 1581 (m), 1481 (st), 1431 (m), 1369 (w), 1281 (w), 1250 (st), 1270 (m), 1122 (w), 1026 (w), 968 (w), 883 (w), 856 (w), 744 (st), 698 (st), 602 (w), 509 (m), 482 (m). MS (EI): *m/z* 381 ($[M]^+$, 83%), 304 ($[M-Ph]^+$, 100%).

3.2. Synthesis of HL^1PO

HL^1P (1 g, 2.6 mmol) was dissolved in 5 mL of THF and H_2O_2 (0.3 mL, 30% wt.) was added. After stirring the reaction mixture for 10 min, 10 mL brine solution was added. The organic phase was separated and dried over $MgSO_4$. HL^1PO was isolated as an analytically pure, yellow powder after removal of the solvent. Yield 0.98 g (95%). Elemental *Anal.* Calc. for $C_{25}H_{20}NO_2P$ (397.41): C, 75.56; H, 5.07; N, 3.52%. Found: C, 75.68; H, 5.05; N, 3.61%. ^1H NMR (400 MHz, DMSO-d_6, ppm): δ 6.55–8.30 (m, 18H, aromatic), 8.9 (s, 1H, HC=N), 10.05 (s, 1H, OH). ^{31}P NMR (DMSO-d_6, ppm): δ 31.6 s. ^{13}C NMR (DMSO-d_6, ppm): δ 164.1 (s, HC=N). IR (KBr, cm^{-1}): 3420 (w), 3058 (m), 3024 (m), 1632 (m), 1578 (m), 1485 (s), 1435 (m), 1377 (w), 1354 (w), 1292 (m), 1223 (m), 1257 (st), 1157 (m), 1130 (m), 1111 (m), 1072 (m), 1029 (w), 968 (w), 767 (m), 748 (st), 702 (s), 578 (m), 540 (st).

3.3. Synthesis of H_2L^2

HL^1P (1.4 g, 3.6 mmol) and $NaBH_4$ (0.91 g, 24 mmol) were suspended in 20 mL of EtOH and heated for 10 min. After the reaction solution became colorless, the solvent was removed under vacuum and the product was extracted with 15 mL of Et_2O. The organic phase was washed with water and dried over $MgSO_4$. A colorless solid was obtained after removing the solvent under vacuum. Yield 1.2 g (88%). Elemental *Anal.* Calc. for $C_{25}H_{22}NOP$ (383.4): C, 78.31; H, 5.78; N, 3.65%. Found: C, 77.05; H, 5.42; N, 3.14%. ^1H NMR (400 MHz, DMSO-d_6, ppm): δ 4.36 (d, 2H, CH_2, J_{HH} = 5.24 Hz), 5.4 (t, 1H, NH J_{HH} = 5.84 Hz), 6.05–7.6 (m, 18H, aromatic), 9.2 (s, 1H, OH). ^{31}P NMR (DMSO-d_6, ppm): δ −16.6. IR (KBr, cm^{-1}): 3514 (w), 3425 (m), 3055 (m), 2866 (w), 1604 (st), 1515 (st), 1438 (m), 1242 (m), 1192 (m), 1041 (w), 737 (st), 698 (m).

3.4. Synthesis of $[ReOCl(PPh_3)(L^1PO)]$ (**1**) and $[Re(NC_6H_4OH)Cl_3(PPh_3)_2]$ (**2**)

$[ReOCl_3(PPh_3)_2]$ (0.17 g, 0.2 mmol) and HL^1PO (79 mg, 0.2 mmol) were dissolved in 20 mL of THF and heated under reflux for 2 h. The volume of the solution was reduced to 3 mL and cooled to −10 °C. Two different types of crystalline products, red **1** and green **2**, deposited and were separated mechanically. Overall yield of both compounds: 74 mg (ca. 80%). After a reaction time of 2 h an approximate ratio of 1:2 between the compounds **1** and **2** was obtained. The relative amount of **2** increased with prolonged reaction times.

3.4.1. Data for **1**

Elemental *Anal.* Calc. for $C_{43}H_{34}Cl_2NO_3P_2Re$ (1·THF) (931.7): C, 55.43; H, 3.68; N, 1.50%. Found: C, 53.87; H, 3.66; N, 1.62%. ^1H NMR (400 MHz, DMSO-d_6, ppm): δ 6.85–8.04 (m, 38H, aromatic), 10.58 (s, 1H, HC=N). ^{31}P NMR (DMSO-d_6, ppm): δ 26.08 (s, PPh_3), 29.44 (s, $OPPh_3$). IR (KBr, cm^{-1}): 3055 (m), 2851 (w), 1697 (w), 1589 (w), 1566 (w), 1477 (m), 1431 (st), 1194 (m), 1161 (m), 1095 (m), 1068 (w), 1026 (w), 941 (w), 748 (st), 694 (st), 517 (st). MS (FAB^+): *m/z* 896 ($[M-Cl]^+$, 1%), 635 ($[M-C_{18}H_{14}PCl]^+$, 3%).

3.4.2. Data for **2** · *THF*

Elemental *Anal.* Calc. for $C_{42}H_{35}Cl_3NOP_2Re$ (924.2): C, 54.58; H, 3.82; N, 1.52%. Found: C, 55.18; H, 4.19; N, 1.27%. ^1H NMR (400 MHz, $CDCl_3$, ppm): δ 6.17−7.87 (m, 34H, aromatic). ^{13}C NMR ($CDCl_3$, ppm): δ 127.8–138.7 (aromatic). ^{31}P NMR ($CDCl_3$, ppm): δ −20.68 s. IR (KBr, cm^{-1}): 3132 (w), 3055 (w), 2970 (w), 2851 (w), 1593 (w), 1473 (m), 1431 (m), 1342 (w), 1238 (w), 1200 (m), 1153 (w), 1092 (m), 1061 (w), 1030 (w), 999 (w), 744 (m), 694 (st), 652 (w), 517 (st).

3.5. Synthesis of fac-$[ReOCl_2(HL^2P)]$ (**3**)

$[ReOCl_3(PPh_3)_2]$ (83 mg, 0.1 mmol) was dissolved in 20 mL of THF and H_2L^2P (38 mg, 0.1 mmol) was added as solid. The mixture was stirred under reflux for 1 h, whereupon an olive-green suspension was obtained. The solvent was removed under reduced pressure and the residue was suspended in 5 mL of MeOH. The olive-green solid was filtered through a Celite pad and washed twice with MeOH. Recrystallization from CH_2Cl_2/MeOH gave green plates. Yield: 46 mg (71%). Elemental *Anal.* Calc. for $C_{25}H_{21}NO_2Cl_2PRe$ (656.5): C, 45.74; H, 3.38; N, 2.13%. Found: C,

Table 4
X-ray structure data collection and refinement parameters.

	1	**2** · THF	**3** · MeOH
Formula	$C_{43}H_{34}Cl_2NO_3P_2Re$	$C_{46}H_{43}Cl_3NO_2P_2Re$	$C_{26}H_{23}Cl_2NO_3PRe$
M_w	931.75	996.37	687.54
Crystal system	monoclinic	triclinic	triclinic
a (Å)	9.5913(7)	10.874(1)	9.496(1)
b (Å)	14.0170(7)	12.198(1)	10.733(1)
c (Å)	31.379(3)	16.772(1)	13.209(1)
α (°)	90	73.12(1)	81.49(1)
β (°)	97.62(1)	75.09(1)	78.66(1)
γ (°)	90	82.03(1)	74.98(1)
V (Å^3)	4181.4(5)	2052.4(2)	1268.1(2)
Space group	$P2_1/c$	$P\bar{1}$	$P\bar{1}$
Z	4	2	2
D_c (g cm^{-3})	1.480	1.612	1.801
μ (mm^{-1})	3.148	3.274	5.094
Absorption correction	integration	integration	integration
T_{min}/T_{max}	0.8554/0.7745	0.8172/0.6807	0.5527/0.4470
Number of reflections	24050	20987	14474
Number of independent	8732	10926	6753
Number parameters	470	543	294
R_1/wR_2	0.0608/0.1200	0.0547/0.1203	0.0381/0.1951
Goodness of fit	0.919	1.022	1.053
Deposit umber (ccdc)	715062	715063	715064

45.91; H, 3.34; N, 1.91%. ^{1}H NMR (400 MHz, DMS-d_6, ppm): δ 5.0 (d, 1H, CH_2, J_{HH} = 11 Hz), 5.6 (d, 1H, CH_2, J_{HH} = 11 Hz), 6.0 (t, 1H, NH), 6.3–7.8 (m, 18H, aromatic). ^{31}P NMR (DMSO-d_6, ppm): δ −4.6. IR (KBr, cm^{-1}): 3452 (m), 3058 (m), 2943 (w), 2846 (w), 1485 (st), 1435 (m), 1257 (m), 188 (w), 1099 (w), 968 (m), 771 (m), 752 (m), 694 (m), 633 (m), 517 (m). MS (FAB$^+$): 654.9 ([M]$^+$, 7%), 620 ([M−Cl]$^+$, 48%).

3.6. X-ray structure determinations

The intensities for the X-ray determinations were collected on a STOE IPDS with Mo Kα radiation. The structures were solved by direct methods using SHELXS-86 [20] or SHELXS-97 [20]. Subsequent Fourier-difference map analyses yielded the positions of the non-hydrogen atoms. Refinement was performed using SHELXL-97 [20]. Hydrogen atom positions were calculated for idealized positions and treated with the 'riding model' option of SHELXL. Crystal data and more details of the data collections and refinements are contained in Table 4.

Acknowledgment

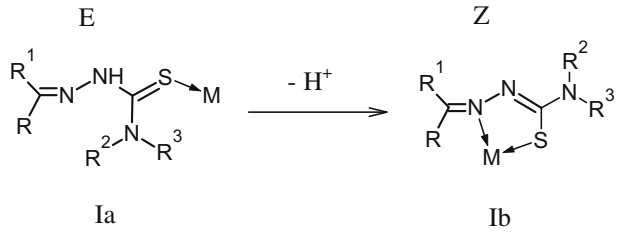
Ali Barandov gratefully acknowledges a PhD scholarship of the German Academic Exchange Service (DAAD).

Appendix A. Supplementary data

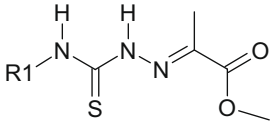
Supplementary crystallographic data can be obtained free of charge via http://www.ccdc.cam.ac.uk/conts/retrieving.html, or from the Cambridge Crystallographic Data Centre, 12 Union Road, Cambridge CB2 1EZ, UK; fax: (+44) 1223 336 033; or e-mail: deposit@ccdc.cam.ac.uk. Supplementary data associated with this article can be found, in the online version, at doi:10.1016/j.poly.2009.01.016.

References

[1] R. Hernandez-Molina, A. Mederos, in: J.A. McCleverty, T.J. Meyer (Eds.), Comprehensive Coordination Chemistry II, vol. 1, Elsevier, Amsterdam, 2003, p. 411.
[2] P. Guerriero, S. Tamburini, P.A. Vigato, U. Russo, C. Benelli, Inorg. Chim. Acta 213 (1993) 279.
[3] H. Okawa, H. Furutachi, D.E. Fenton, Coord. Chem. Rev. 174 (1998) 51.
[4] P. Guerriero, S. Tamburini, V.A. Vigato, Coord. Chem. Rev. 139 (1995) 17.
[5] L. Canali, D.C. Sherrington, Chem. Soc. Rev. 28 (1999) 85.
[6] D.E. Fenton, Chem. Soc. Rev. 17 (1988) 69.
[7] U. Abram, in: J.A. McCleverty, T.J. Mayer (Eds.), Comprehensive Coordination Chemistry II, vol. 5, Elsevier, Amsterdam, 2003, p. 271.
[8] R. Alberto, Rhenium, in: J.A. McCleverty, T.J. Mayer (Eds.) Comprehensive Coordination Chemistry II, vol. 5, Elsevier, Amsterdam, 2003, p. 128.
[9] (a) S. Liu, D.S. Edwards, Chem. Rev. 99 (1999) 2235;
(b) R. Alberto, U. Abram, in: A. Vértes, S. Nagy, Z. Klencsár (Eds.), Handbook of Nuclear Chemistry, vol. 4, Kluwer, Amsterdam, 2003, p. 211;
(c) U. Abram, R. Alberto, Braz. J. Chem. Soc. 17 (2006) 1486.
[10] (a) S.S. Jurisson, K. Dancey, M. McPartlin, P.A. Tasker, E. Deutsch, Inorg. Chem. 23 (1984) 4743;
(b) M.E. Marmion, S.R. Woulfe, W.L. Neumann, D.L. Nosco, E. Deutsch, Nucl. Med. Biol. 26 (1999) 755.
[11] (a) S. Liu, L. Gelmini, S.J. Rettig, R.C. Thompson, C. Orvig, J. Am. Chem. Soc. 114 (1992) 6081. and references cited therein;
(b) D. Voss, L. Butterey-Thomas, T. Janik, R.M. Churchill, R.J. Morrow, Inorg. Chim. Acta 317 (2001) 149.
[12] H. Luo, S. Liu, S.J. Rettig, C. Orvig, Can. J. Chem. 73 (1995) 2272.
[13] J. Grewe, A. Hagenbach, B. Stromburg, R. Alberto, E. Vazquez-Lopez, U. Abram, Z. Anorg. Allg. Chem. 629 (2003) 303.
[14] G. Sanchez, F. Momblona, J.L. Serrano, L. Garcia, E. Perez, J. Perez, G. Lopez, J. Coord. Chem. 55 (2002) 917.
[15] R.R. Conry, J.M. Mayer, Inorg. Chem. 29 (1990) 911.
[16] (a) T.I.A. Gerber, D. Luzipo, P. Mayer, Inorg. Chim. Acta 357 (2004) 429;
(b) G. Bandoli, T.I.A. Gerber, J. Perils, J.G.H. du Preez, Inorg. Chim. Acta 278 (1998) 96;
(c) T.I.A. Gerber, D. Luzipo, P. Mayer, J. Coord. Chem. 59 (2006) 1055.
[17] (a) E. Forsellini, U. Casellato, R. Graziani, M.C. Carletti, L. Magon, Acta Crystallogr., Sect. C 40 (1984) 1795;
(b) U. Wittern, J. Strähle, U. Abram, Z. Naturforsch. B 50 (1995) 997.
[18] R. Alberto, R. Schibli, A. Egli, P.A. Schubiger, W.A. Herrmann, G. Artus, U. Abram, T.A. Kaden, J. Organomet. Chem. 217 (1995) 492.
[19] N.P. Johnson, C.J.P. Lock, G. Wilkinson, Inorg. Synth. (1967) 145.
[20] (a) G.M. Sheldrick, Acta Crystallogr., Sect. A 46 (1990) 467;
(b) G.M. Sheldrick, SHELX97 – A Programme Package for the Solution and Refinement of Crystal Structures, University of Göttingen, Germany, 1997.
[21] L.J. Farrugia, J. Appl. Crystallogr. 30 (1997) 565.



Scheme 1. R^1, R^2 and R^3 can be either H or organic radicals.



Scheme 2. Chemical drawing of Hmpt ligand (R1 = ethyl, phenyl and 3-methylphenyl).

These ligands were then reacted with bis(triphenylphosphine)copper (I) nitrate and acetate and the complexes so obtained, $[Cu(PPh_3)_2(Et\text{-}Hmpt)]_2(NO_3)_2$ **1**, $[Cu(PPh_3)_2(Ph\text{-}Hmpt)]NO_3$ **2**, $[Cu(PPh_3)_2(MePh\text{-}Hmpt)]NO_3$ **3**, $[Cu_2(O_2CCH_3)(Et\text{-}pt)(PPh_3)_2]\cdot H_2O$ **4**, $[Cu(Ph\text{-}mpt)(PPh_3)]$ **5** and $[Cu_2(MePh\text{-}mpt)_2(PPh_3)_2]$ **6**, are reported here. All of them have been characterized by elemental analysis, IR, ^1H NMR spectroscopy and compounds **1**, **2**, **4**, and **6** also by X-ray crystallography. Compound **4** contains two copper atoms with two totally different geometries suggesting, together with the charge balance, the presence of two different oxidation states. For this compound also an EPR spectroscopy analysis was carried out.

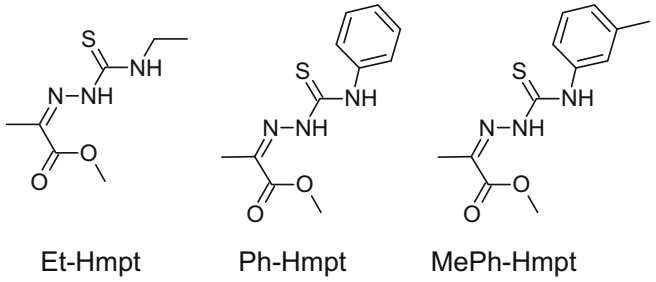
2. Experimental

2.1. Materials and techniques

$[Cu(PPh_3)_2NO_3]$ and $[Cu(PPh_3)_2(CH_3COO)]$ were prepared by reduction of the corresponding Cu(II) salt using a fourfold excess of PPh_3 in CH_3OH at reflux temperature for 1 and 3 h, respectively. The white powder formed in the reaction flask was filtered to separate the product from Ph_3PO and washed first with EtOH and then with diethyl ether. $Cu(NO_3)_2\cdot 3H_2O$ and $Cu(CH_3COO)_2\cdot H_2O$ were procured from Carlo-Erba, while PPh_3 was purchased from Aldrich. C, H, N, S analyses were obtained with a Carlo-Erba 1108 instrument. IR spectra were recorded using KBr pellets on a Nicolet 5PC FT-IR spectrophotometer in the 4000–400 cm^{-1} range. ^1H NMR spectra were recorded on a Bruker AC300 spectrometer at 300 MHz in d_6–DMSO with TMS as the internal reference. EPR spectra, both at room and liquid nitrogen temperature, were recorded in phase-sensitive detection by a X-band (9-GHz) Varian V-4502 spectrometer with a 100 kHz field modulation.

2.2. Preparation of the ligands

Methylpyruvate thiosemicarbazones were prepared by condensation of methylpyruvate with N^1-substituted thiosemicarbazides in a 1:1 molar ratio in methanol using the procedure reported in the literature [24]. In this way methylpyruvate-N^1-ethylthiosemicarbazone (Et-Hmpt $\cdot H_2O$, used to prepare complexes **1** and **4**), methylpyruvate-N^1-phenylthiosemicarbazone (Ph-Hmpt, used to prepare complexes **2** and **5**) and methylpyruvate-N^1-(3-methyl)phenylthiosemicarbazone (MePh-Hmpt, used to prepare complexes **3** and **6**) were synthesised. Scheme 3 reports the structure of the used ligands.



Scheme 3. Schematic view of the used ligands.

2.3. Synthesis of the complexes

To a hot stirred methanolic 40 mL solution of the proper ligand was added an amount of solid $[Cu(PPh_3)_2NO_3]$ for **1** (0.502 g of the ligand, 2.47 mmol, and 1.606 g of metal salt, 2.47 mmol), for **2** (0.610 g of the ligand, 2.43 mmol, and 1.580 g of metal salt, 2.43 mmol), for **3** (0.484 g of the ligand, 1.82 mmol, and 1.187 g of metal salt, 1.82 mmol) together with additional 40 mL of methanol. Similarly, to a hot stirred methanolic 40 mL solution of the proper ligand was added an amount of solid $[Cu(PPh_3)_2CH_3COO]$ for **4** (0.610 g of the ligand, 3.00 mmol, and 3.890 g of metal salt, 6.00 mmol), for **5** (0.480 g of the ligand, 1.91 mmol, and 1.238 g of metal salt, 1.91 mmol), for **6** (0.505 g of the ligand, 1.91 mmol, and 1.233 g of metal salt, 1.91 mmol) together with additional 40 mL of methanol. The mixture was allowed to reach the reflux temperature. When the inorganic salt was completely dissolved, the resulting solution appeared dark yellow and was left under magnetic stirring for 2 h. The solution was then cooled down to room temperature and by slow evaporation of the solvent, crystals suitable for X-ray diffraction were obtained for complexes **1**, **2**, **4** and **6**.

2.3.1. $[Cu(PPh_3)_2(Et\text{-}Hmpt)]_2(NO_3)_2$ ***1***

Yield: 2.01 g, 75% (based on metal). Mp: 166 °C. FT-IR (KBr, cm^{-1}) 3443, m, 3214, m, ν (NH); 3053, m, ν ($CH_{aromatic}$); 2980, m, ν ($CH_{aliphatic}$); 1725, s, ν (CO); 1570, s, ν (CN); 1435, s, ν (NCS); 1384, s, ν (NO); 774, m, ν (CS). *Anal.* Calc. for $C_{86}H_{86}N_8O_{10}P_4S_2Cu_2$: C, 60.52; H, 5.08; N, 6.56; S, 3.76. Found: C, 60.52; H, 5.08; N, 6.56; S, 3.76%. ^1H NMR data (δ, ppm; DMSO–d_6): 1.14 (t, 3H, CH_3CH_2–), 2.12 (s, 3H, CH_3CN–), 3.60 (m, 2H, CH_3CH_2–), 3.76 (s, 3H, CH_3O–), 7.25 (t, b, 18H, PPh_3 $H_p + H_o$); 7.37 (t, 12H, PPh_3 H_m); 8.53 (bs, 1H, N*H*); 11.61 (s, 1H, C(S)NH).

2.3.2. $[Cu(PPh_3)_2(Ph\text{-}Hmpt)]NO_3$ ***2***

Yield: 1.69 g, 77% (based on metal). Mp: 168 °C. FT-IR (KBr, cm^{-1}) 2970, mw, ν ($CH_{aliphatic}$); 1731, s, ν (CO); 1563, s, ν (CN); 1435, s, ν (NCS); 1384, s, ν (NO); 743, m, ν (CS). *Anal.* Calc. for $C_{47}H_{43}N_4O_5P_2SCu$: C, 62.62; H, 4.81; N, 6.21; S, 3.55. Found: C, 62.54; H, 4.91; N, 6.52; S, 2.83%. ^1H NMR data (δ, ppm; DMSO–d_6): 2.25 (s, 3H, CH_3CN–), 3.75 (s, 3H, CH_3O–), 7.25 (t, b, 18H, PPh_3 $H_p + H_o$); 7.37 (t, 12H, PPh_3 H_m); 7.50–7.72 (m, 5H, aromatic ligand H), 10.05 (bs, 1H, N*H*); 11.46 (s, 1H, C(S)NH).

2.3.3. $[Cu(PPh_3)_2(MePh\text{-}Hmpt)]NO_3$ ***3***

Yield: 1.20 g, 72% (based on metal). Mp: 183 °C. FT-IR (KBr, cm^{-1}) 3052, m, ν ($CH_{aromatic}$); 2970, mw, ν ($CH_{aliphatic}$); 1720, s, ν (CO); 1567, s, ν (CN); 1435, s, ν (NCS); 1384, s, ν (NO); 744, m, ν (CS). *Anal.* Calc. for $C_{48}H_{45}N_4O_5P_2SCu$: C, 62.98; H, 4.95; N, 6.12; S, 3.50. Found: C, 63.16; H, 4.87; N, 6.45; S, 2.85%. ^1H NMR data (δ, ppm; DMSO–d_6): 2.18 (s, 3H, CH_3CN–), 2.31 (s, 3H, CH_3Ph), 3.76 (s, 3H, CH_3O–), 7.25 (t, b, 18H, PPh_3 $H_p + H_o$); 7.37 (t, 12H, PPh_3 H_m); 7.50–7.70 (m, 5H, aromatic ligand H), 10.11 (bs, 1H, N*H*); 11.40 (s, 1H, C(S)NH).

2.3.4. $[Cu_2(O_2CCH_3)(Et\text{-}pt)(PPh_3)_2] \cdot H_2O$ **4**

Yield: 5.38 g, 75% (based on metal). Mp: 178 °C. FT-IR (KBr, cm^{-1}) 3442, m, ν (NH); 1650, s, ν (C=O) pyruvate; 1618, m, ν (CN); 1567, m, ν (CO) coordinated carboxylates; 695, m, ν (CS). *Anal.* Calc. for $C_{44}H_{44}N_3O_5P_2SCu_2$: C, 57.70; H, 4.84; N, 4.59; S, 3.50. Found: C, 57.11; H, 4.76; N, 4.44; S, 3.50%.

2.3.5. $[Cu(Ph\text{-}mpt)(PPh_3)]$ **5**

Yield: 0.72 g, 65% (based on metal). Mp: 158 °C. FT-IR (KBr, cm^{-1}) 3400, mb, ν (NH); 3048, m, ($CH_{aromatic}$); 1735, m, ν (CO); 1564, m, ν (CN); 746, ms, ν (CS). *Anal.* Calc. for $C_{29}H_{27}N_3O_2PSCu$: C, 60.46; H, 4.72; N, 7.29; S, 5.57. Found: C, 59.98; H, 4.96; N, 7.01; S, 5.23%. ^{1}H NMR data (δ, ppm; DMSO–d_6): 2.20 (s, 3H, CH_3CN–), 3.75 (s, 3H, CH_3O–), 7.25 (t, b, 9H, PPh_3 $H_p + H_o$); 7.37 (t, 6H, PPh_3 H_m); 7.55–7.72 (m, 5H, aromatic ligand H), 10.08 (bs, 1H, N*H*).

2.3.6. $[Cu_2(MePh\text{-}mpt)_2(PPh_3)_2]$ **6**

Yield: 0.68 g, 60% (based on metal). Mp: 197 °C. FT-IR (KBr, cm^{-1}) 3400, mb, ν (NH); 3025, m, ($CH_{aromatic}$); 1715, m, ν (CO); 1610, m, ν (CN); 742, ms, ν (CS). *Anal.* Calc. for $C_{60}H_{58}N_6O_4P_2S_2Cu_2$: C, 61.06; H, 4.95; N, 7.12; S, 5.43. Found: C, 61.18; H, 4.87; N, 7.13; S, 5.73%. ^{1}H NMR data (δ, ppm; DMSO–d_6): 2.21 (s, 3H, CH_3CN–), 2.35 (s, 3H, CH_3Ph), 3.80 (s, 3H, CH_3O–), 7.25 (t, b, 9H, PPh_3 $H_p + H_o$); 7.35 (t, 6H, PPh_3 H_m); 7.55–7.70 (m, 5H, aromatic ligand H), 10.17 (bs, 1H, N*H*).

2.4. X-ray crystallography

Relevant data concerning data collection and details of structure refinement are summarized in Tables 1a and 1b. Intensity data for **1** were collected on a CAD4 diffractometer with Cu Kα radiation, those of **2** on a Philips PW1100 and those of **4** and **6** on a SMART 1000 Bruker AXS diffractometers with Mo Kα radiation. Data from crystals of compound **1** were affected by twinning and were not corrected for absorption, while for compounds **2, 4** and **6** absorption corrections were carried out using the psi-scan procedure for the first and the SADABS [25] procedure for **4** and **6**. The crystals of compounds **4** and **6** gave very poor diffraction and data could be collected only up to 23.30° of theta. The structures were solved using direct methods (SIR-97 [26]). Refinements were carried out by full matrix least-squares cycles SHELXL97 [27] for all compounds. Most hydrogen atoms were calculated with standard geometry and refined in riding position. The program PARST [28] was employed for the geometrical description and PLUTON [29] and MERCURY [30] for the drawings.

Table 1a
Selected crystal data.

Compound	(**1**)	(**2**)
Formula	$C_{86}H_{86}Cu_2N_8O_{10}P_4S_2$	$C_{47}H_{43}Cu_1N_4O_5P_2S_1$
Molecular mass	1706.71	901.39
Space group	$Pca2_1$	$P2_1/n$
a (Å)	19.057(4)	14.205(4)
b (Å)	18.376(3)	32.117(8)
c (Å)	24.365(8)	9.952(2)
α (°)	90	90
β (°)	90	90.40(2)
γ (°)	90	90
V (Å^3)	8532(4)	4540(2)
Z	4	4
F(000)	3552	1872
D_{calc} (Mg/m^3)	1.329	1.319
μ (mm^{-1})	2.28	0.647
λ (Å)	1.54184	0.71069
Radiation	Cu Kα	Mo Kα
θ range (°)	3–67.02	3–30.05
hkl range	0, 21; 0, 20; −27, 27	−19, 19; −45, 45; 0, 14
Crystal size (mm)	0.4, 0.5, 0.5	0.3, 0.4, 0.5
No. of measured reflections	12779	26205
No. of unique reflections	12772	13240
No. of refined parameters	867	560
Max. and min. resolutions ΔF map (e Å^{-3})	0.55, −0.43	0.62, −0.77
$R = \Sigma\|\|F_o\| - \|F_c\|\|/\Sigma\|F_o\|$	0.0678	0.0473
Rw_2	0.1811	0.1532
Weighting scheme	$1/[\sigma^2(F_o^2) + (0.125P)^2]$	$1/[\sigma^2(F_o^2) + (0.0741P)^2]$

$P = (\max(F_o^2, 0) + 2F_c^2)/3$.

Table 1b
Selected crystal data.

Compound	(**4**)	(**6**)
Formula	$C_{44}H_{44}Cu_2N_3O_5P_2S_1$	$C_{120}H_{116}Cu_4N_{12}O_8P_4S_4$
Molecular mass	915.90	2360.53
Space group	$P\bar{1}$	$P\bar{1}$
a (Å)	11.841(3)	11.561(3)
b (Å)	12.276(3)	19.518(3)
c (Å)	16.896(4)	26.054(5)
α (°)	72.40(2)	94.61(1)
β (°)	79.65(3)	96.22(1)
γ (°)	68.23(2)	90.10(1)
V (Å^3)	2167.8(9)	5825(2)
Z	2	2
F(000)	944	2448
D_{calc} (Mg/m^3)	1.402	1.346
μ (mm^{-1})	1.15	0.91
λ (Å)	0.71069	0.71069
Radiation	Mo Kα	Mo Kα
θ range(°)	3–23.29	3–23.31
hkl range	−13, 13; −13, 13; −18, 18	−12, 12; −21, 21; −28, 28
Crystal size (mm)	0.1, 0.1, 0.4	0.2, 0.2, 0.5
No. of measured reflections	17480	44871
No. of unique reflections	6228	16694
No. of refined parameters	514	1225
Max. and min. resolutions ΔF map (e Å^{-3})	0.75, −0.38	0.93, −0.30
$R = \Sigma\|\|F_o\| - \|F_c\|\|/\Sigma\|F_o\|$	0.0467	0.0650
Rw_2	0.1429	0.1431
Weighting scheme	$1/[\sigma^2(F_o^2) + (0.0963P)^2]$	$1/[\sigma^2(F_o^2) + (0.0383P)^2]$

$P = (\max(F_o^2, 0) + 2F_c^2)/3$.

3. Results and discussion

3.1. Synthesis and spectroscopy

Ligands were synthesized according to the procedure reported in [24] and complexes by reacting these ligands with bis(triphenylphosphine)copper(I) nitrate and with bis(triphenylphosphine) copper(I) acetate. Both ligands and complexes were produced in good yields. In complexes **1**, **2** and **3**, obtained from the nitrate salt, the ligand is protonated while in complexes **4**, **5** and **6**, that are obtained from the acetate salt, it is deprotonated. The syntheses were carried out in methanol in order to deter possible problems arising from transesterification or hydrolysis processes that could modify the ligands. Compound **4** was isolated with difficulty and only after many attempts. The best conditions were found using a 2:1 ratio of ligand with respect to the metal content. Moreover, in comparison with the syntheses of the other complexes, compound **4** was exposed to atmospheric oxygen and moisture more than the other ones being recalcitrant to crystallize. The higher acetate content stabilizing the anionic form of the ligand, together with the increased acidity of the hydrazine nitrogen due to copper(I) oxidised to copper(II), promoted the hydrolysis of the methyl group from the ester improving the electrophilicity of the carboxyl carbon and speeding up the process of demethylation.

The ^{1}H NMR spectrum of complex **1** exhibits the NHC=S signal at about 11.40 ppm, showing that the ligand is present in its neutral

form and the structure of the complex in the solid state persists in DMSO solution; the deshielded N*H*CH_2CH_3 signal at 8.53 ppm upon complexation can be related to the change from an *E* to a *Z* conformation of the ligand and the coordination to the metal of the S and N3 atoms of the ligand [24]. Even for complexes **2** and **3** the signal attributed to NHC=S and the deshielded resonance of the N*H*R nucleus reveals that the ligands are in their neutral form and in a *Z* conformation showing that the three complexes behave in a similar way. The ^{1}H NMR spectra of complexes **4** and **5** show the lack of the signal of the N*H*C=S group confirming that in solution the ligand is deprotonated. The resonances at *ca* 10.10 ppm, downfield with respect to the resonances of the same N*H* group in the free ligand, show that also these compounds are in a *Z* conformation. Due to its paramagnetism, it was not possible to record the ^{1}H NMR spectra of complex **4**. As regards as IR spectra, the absorptions in the region 3510–3150 cm^{-1} usually attributed to ν(OH) and ν(NH) stretching frequencies are assigned with difficulty, because of numerous hydrogen bonding interactions involving amino and imino groups (NH···S, NH···ONO_2^- and NH···OH_2). No relevant shifts are observed by the comparison of the vibrational stretching C=O bonds of complexes with the absorption of the free ligands [24], showing that the metal centre does not bind via pyruvate oxygen. An exception is reported for complex **4**, where the C=O absorption at 1650 cm^{-1} (*ca* 70 cm^{-1} at lower frequencies with respect the free ligand) shows that the C=O group is involved in coordination. For all complexes ν(C=N) and ν(C=S) are significantly shifted at lower frequencies showing that every ligand bind the metal ion via N,S. For complexes **1**, **2** and **3** the nitrate group vibration can be easily find at 1384 cm^{-1} with a strong absorption, while for complex **4**, the typical stretching bands (symmetrical and asymmetrical) for CH_3COO^- are identified. In agreement with diffraction and/or NMR data, no counterion can be observed in the IR spectra of compounds **5** and **6**.

An electron paramagnetic resonance study was also performed for compound **4** in order to provide information about the electronic structure of the metal and its immediate surrounding. The sample was in polycrystalline form because we experienced some difficulty to find single crystals of dimensions large enough to give an acceptable signal to noise ratio. The resulting derivative absorptions, with superimposed a DPPH (diphenyl-β-picrylhydrazyl) marker (g = 2.0036), are shown in Fig. 1a and b. The two spectra are quite similar, apart from the observation at the liquid nitrogen temperature of a more intense signal with some emphasization of a number of not completely resolved weak peaks of a possible superhyperfine nature, see below. The increase of the peak-to-peak intensity in decreasing temperature is usual in EPR, reminiscent of the fact that a simple isolated paramagnetic centre follows the $1/T$ Curie's law.

Both resonance signals appear typical for a Cu^{2+} ion in octahedral field with tetragonal distortion and show a well resolved four lines hyperfine pattern in the low field range. They may be described by a spin Hamiltonian of the form:

$$\mathscr{H} = \mu_B \vec{S} \cdot \overleftrightarrow{g} \cdot \vec{H} + \vec{S} \cdot \overleftrightarrow{A} \cdot \vec{I}, \quad \text{with } S = 1/2,\ I_{Cu} = 3/2. \tag{1}$$

Here the first term represents the Zeeman interaction of the copper unpaired spin S = 1/2 with the applied static magnetic field H (μ_B = Bohr magneton) and the second one describes the hyperfine interaction of the unpaired electron with the copper nucleus (I = 3/2).

The $\overleftrightarrow{g}$ and $\overleftrightarrow{A}$ tensors are approximately axial with maximum values:

$$g_{//} = 2.274 \pm 0.002 \quad \text{and} \quad |A_{//}| = (104 \pm 2) \times 10^{-4}\ cm^{-1} \tag{2}$$

However, the presence of a rhombic contribution is also evident, more pronounced in the high temperature spectrum, but the overlap of various non-resolved hyperfine peaks prevents a precise determination of the in-plane constants.

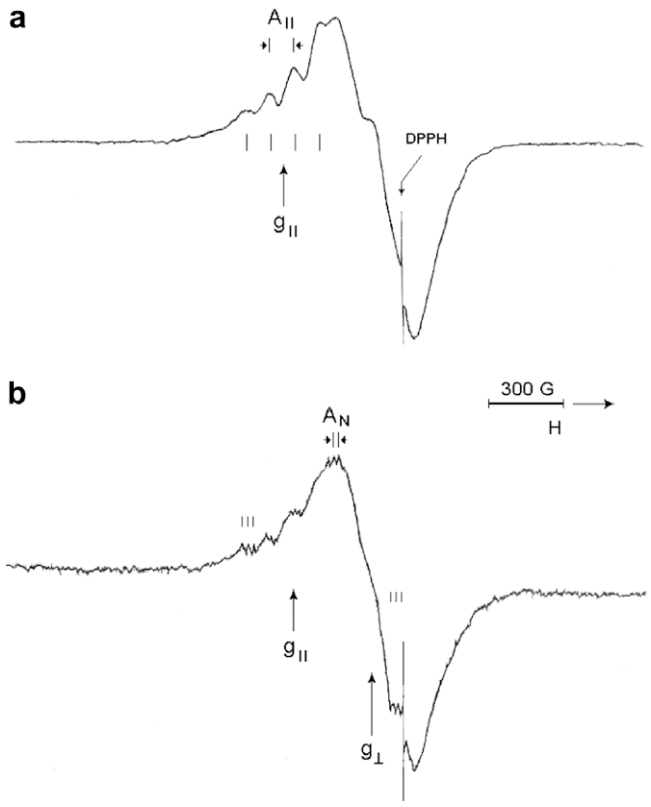


Fig. 1. Derivative X-band EPR spectra of a polycrystalline sample of **4** at room temperature (a) and at T = 77 K (b). The observed intensities of the signals a and b were in the approximate ratio 1:4.

Assuming complete axial symmetry, we estimate:

$$g_\perp \approx 2.065 \pm 0.007 \quad \text{and} \quad |A_\perp| \leqslant 30 \times 10^{-4}\ cm^{-1} \tag{3}$$

Although in general the measured g values may not coincide with the local single-ion values if exchange is present, here we have no doubt about this because the $\overline{1}$ point symmetry makes the two copper(II) per unit cell magnetically undistinguishable.

The g values are strongly indicative of a magnetically isolated Cu^{2+} ion with unpaired spin in a substantially $d_{x^2-y^2}$ ground state orbital. In this case, in fact, it should roughly be [31]:

$$\begin{aligned} g_{//} &= g_0 - 8\alpha^2\lambda/\Delta_1, \\ g_\perp &= g_0 - 2\alpha^2\lambda/\Delta_2, \end{aligned} \tag{4}$$

where g_0 is the free electron g value 2.0023, λ is the spin-orbit coupling constant for the free copper ion with a vale close to $-828\ cm^{-1}$, and Δ_1 and Δ_2 stand for the optical energy splittings due to the crystal-field between the ground state and the d_{xy} and $d_{xz,yz}$ orbitals, respectively.

The reducing α^2 factor measures the fraction of time spent by the unpaired electron at the copper ion and is directly related to the covalence of the bonds [32–34]. A light anisotropy of this factor arising from the excited orbitals d_{xy} and $d_{xz,yz}$ in (Eq. (4)) has been neglected for simplicity.

The value $|A_{//}|$ appears somewhat low as compared with usual axial values for copper(II) complexes, frequently found in the range $150–200 \times 10^{-4}\ cm^{-1}$. The reduced value has possibly to be related to the strong spin delocalization due to the Cu(II)–S very covalent bond. In fact, this should result in two distinct effects. A low presence of the unpaired spin at the copper nucleus with reduction of both the dipolar and Fermi-contact terms of the hyperfine interaction, and an induced in-plane rhombic distortion with mixing between the $d_{x^2-y^2}$

and $d_{3z^2-r^2}$ orbitals which should also reduce the axial dipolar term [34].

As a further experimental fact, we observe that the powder spectrum at liquid nitrogen temperature shows the presence of several groups of three equiintense weak peaks, see Fig. 1b. The measured splittings correspond to energies in the range 13–16 $\times 10^{-4}$ cm^{-1}. Both the number of peaks and the energy splitting involved seem to suggest the presence of a superhyperfine interaction between the magnetic copper and one nitrogen nucleus ($I_N = 1$), in line with the structure of Fig. 5.

In conclusion, all the results of this EPR study on a polycrystalline sample of compound **4** appear to strictly support the proposed crystallographic view based on two copper centres in different oxidation states.

3.2. Crystal structures of the complexes

A PLUTON drawing representing complex $[Cu(PPh_3)_2(Et\text{-}Hmpt)]_2(NO_3)_2$ **1** is reported in Fig. 2. The structure can be described as formed by two cationic complex molecules with two bridging nitrates that act as counterions. The copper(I) ion coordinates two triphenylphosphines and an N^1-ethyl methylpyruvate thiosemicarbazone molecule in its neutral form. The thiosemicarbazones bind to the metal through the sulfur and the iminic nitrogen and form a five-term chelation ring. The coordination bonds have distances of 2.165(6) and 2.148(6) Å for the Cu–N bonds and 2.365(2) and 2.368(2) Å for the Cu–S bonds. The Cu–P bonds range instead from 2.254(2) to 2.281(2) Å. The angles N–Cu–S of 82.3(2)° and 82.9(2)° are fairly small, while the P–Cu–P angles are wide (129.60(8)° and 130.54(8)°). The copper coordination is slightly distorted from the ideal tetrahedron but less than expected in the presence of a potentially terdentate planar ligand. The non-methylated oxygens of the ligand and the copper atom are 2.802(6) and 2.799(6) Å apart and do not seem to influence the copper coordination geometry. Noteworthy in both molecules that the centroids between the coordinated N and S atoms lie on the plane defined by P–Cu–P, as in a typical tetrahedral coordination geometry.

The thiosemicarbazone moieties, expected to be planar because of the extended conjugated system of double bonds, in one of the cations are in fact fairly planar with a distortion of only 9.8(4)° between the average thiosemicarbazide plane and that of the terminal carboxylate, but in the other the molecule are significantly distorted: the angle between the average plane of the terminal carboxylate and that of the thiosemicarbazide fragment is 23.0(4)°.

Table 2
Selected parameters of the hydrogen bonds involving the nitrate ions in compound **1**.

Donor···acceptor (Å)	Angle (°)	Donor···acceptor (Å)	Angle (°)
N1···O4	N1–H1···O4	N1A···O4	N1A–H1A···O4
3.01(2)	149.5(6)	3.18(1)	131.6(6)
N1···O6	N1–H1···O6	N1A···O6	N1A–H1A···O6
2.87 (1)	134.0(6)	3.17(2)	139.3(6)
N2···O4	N2–H2···O4	N2A···O4	N2A–H2A···O4
3.18(2)	135.9(5)	3.13(1)	137.4(5)
N2···O6	N2–H2···O6	N2A···O6	N2A–H2A···O6
3.19(1)	131.6(4)	2.85(1)	142.6(5)

A peculiarity of this structure is the way the two nitrate ions link the two cationic moieties. A system of loose bifurcated hydrogen bonds binds each thiosemicarbazone amino and hydrazine NH groups to two different oxygen atoms from the nitrate ions (see Fig. 2). These interactions are quite loose and this is reflected in the long bond distances (see Table 2) observed in the structure and also in the high thermal parameters presented by the nitrate ions.

Another feature that characterizes the packing of these molecules is a sixfold phenyl embrace (6PE) [35–38] (P1···P1^I $I = (x, 1 + y, z)$ distance 7.354 Å) (see Fig. 3) between molecules related by a translation along y. More precisely the phenyls of the triphenylphosphines involved in this interaction present what the aforementioned paper calls an "offset sextuple phenyl embrace" (OSPE) conformation. To complete the description of the packing it is noteworthy to observe that the hydrogen bonds with the nitrate ions together with these OSPE create a ribbon of molecules that develops along the y-axis.

The structure of compound **2**, $[Cu(PPh_3)_2(Ph\text{-}Hmpt)]NO_3$, is reported in Fig. 4. The asymmetric unit is formed by a complex cation, $[Cu(PPh_3)_2(Ph\text{-}Hmpt)]^+$, and a disordered nitrate anion bound through a loose charge-assisted hydrogen bond. In the cation complex, the copper(I) ion coordinates two triphenylphosphines and an N^1-phenyl methylpyruvate thiosemicarbazone molecule in its neutral form. Also in this case the thiosemicarbazone binds to the metal through the sulfur and the iminic nitrogen and forms a five-term chelation ring. The angle N–Cu–S is 81.70(7)° while the

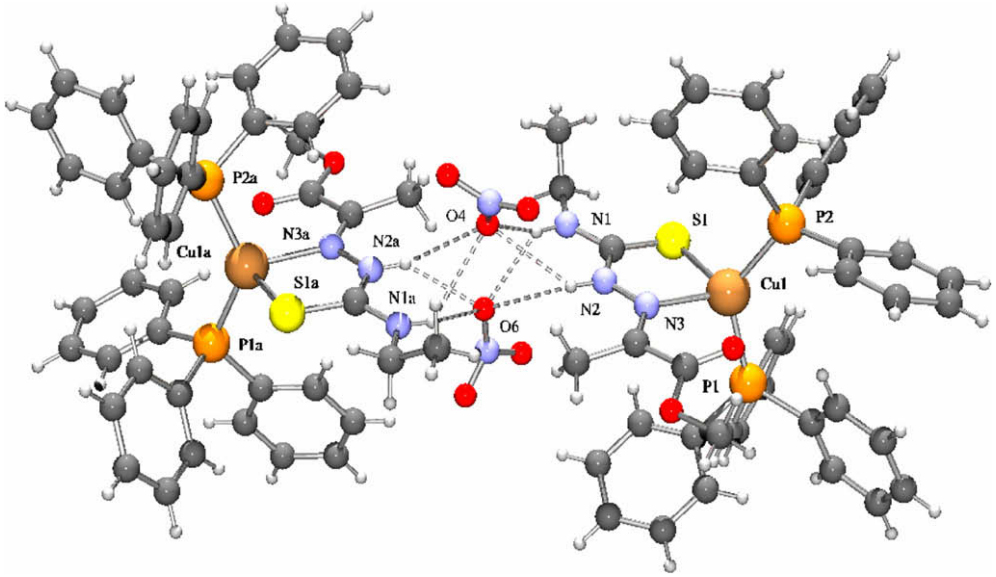


Fig. 2. PLUTON rendering of complex $[Cu(PPh_3)_2(Et\text{-}Hmpt)]_2(NO_3)_2$ **1**.

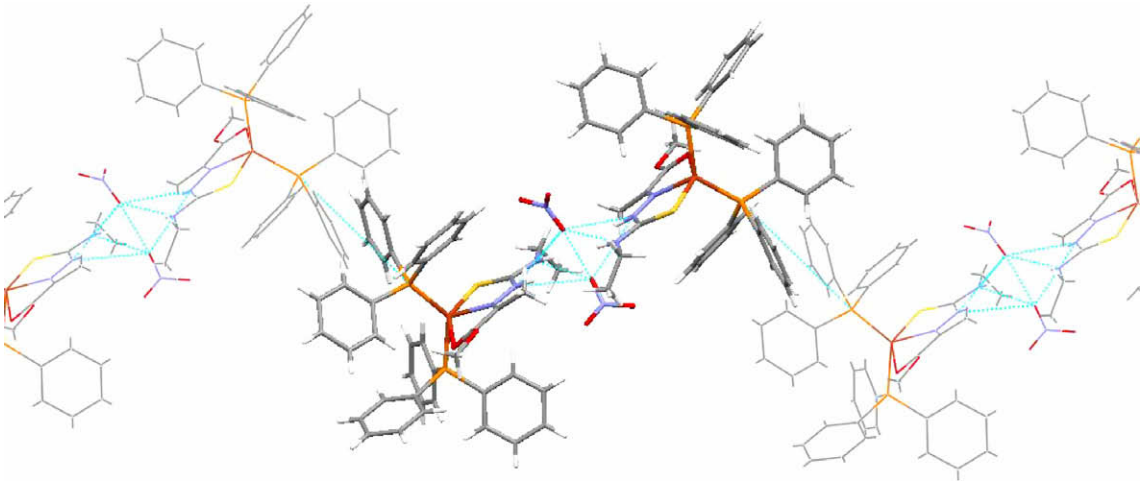


Fig. 3. MERCURY drawing showing compound **1** with two adjacent molecules linked through the six phenyl embrace.

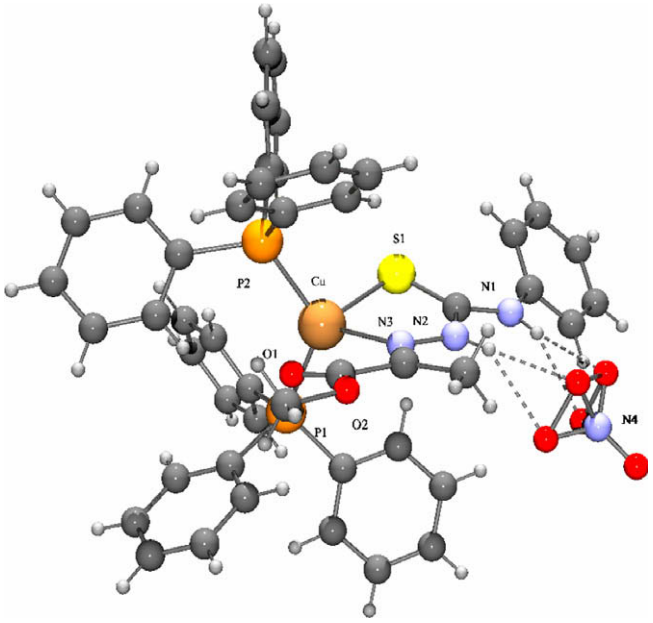


Fig. 4. PLUTON rendering of complex $[Cu(PPh_3)_2(Ph\text{-}Hmpt)]NO_3$ **2** showing the disordered nitrate hydrogen bond interaction (on the right-hand side).

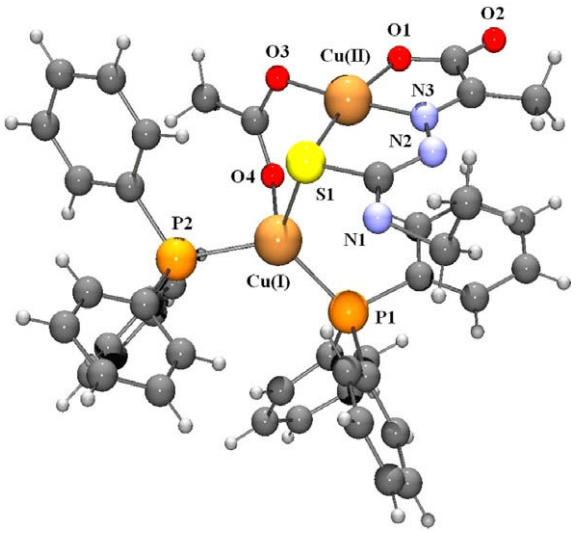


Fig. 5. PLUTON rendering of compound **4** complex fragment $[Cu_2(O_2CCH_3)(Et\text{-}pt)(PPh_3)_2]$.

P–Cu–P is slightly narrower than the previous ones, being 124.28(3)°. Compared to compound **1** the copper tetrahedral coordination is therefore slightly more regular. The coordination bonds have values of 2.156(2) Å for Cu–N, 2.400(1) Å for Cu–S and the Cu–P bonds are of 2.282(1) and 2.277(1) Å.

The thiosemicarbazone ligand is strongly distorted from the expected planarity and the angle between the thiosemicarbazide average plane and that of the carboxylate fragment is of 24.10(9)°; also the average plane of the phenyl ring is tilted of 36.3(1)° with respect to the thiosemicarbazide group. Also here, one carboxylate oxygen is oriented in the direction of the copper atom but presents a long distance Cu–O of 2.780(2) Å.

The crystal structure of compound **4** $[Cu_2(O_2CCH_3)(Et\text{-}pt)(PPh_3)_2] \cdot H_2O$ is reported in Fig. 5. The solution of this structure shed light on the anomalies that were observed in the elemental analysis and the IR spectra. This compound was particularly recalcitrant to crystallise and, probably due to the long exposure to oxygen and to air moisture, copper(I) has been partially oxidised to copper(II) and the ligand has hydrolysed and lost the ester methyl group and has become a carboxylic acid. The asymmetric unit, as a consequence, contains two metal centres in two different oxidation states. The two copper atoms are bridged by an acetate ion and by a shared sulfur from the thiosemicarbazone. The copper(II) atom coordinates in a square planar fashion the thiosemicarbazone ligand. In this case the ligand behaves as O,N,S terdentate using also its carboxylic oxygen. The fourth position site is occupied by an acetate oxygen atom. The coordination distances are: Cu(II)–N 1.912(4), Cu(II)–S 2.267(1), Cu(II)–O 1.949(3) and Cu(II)–O(ac) 1.895(3) Å. Those of the tetrahedral copper(I) fragment are: Cu(I)–O(ac) 2.248(4), Cu(I)–S1 2.351(1) Å, and the two with the phosphorus atoms of the tpp ligands are Cu–P1 2.238(1) and Cu–P2 2.277(1) Å.

The packing is formed by ribbons of molecules held together by hydrogen bonds involving the water molecule [N1–H···O1 W 2.936(7) Å 158.8(4)° and O1 W···O1W^{i} 2.982(7) Å i = $-x, -y, -z + 2$] and by a weak interaction between the copper(II) atom with the hydrazine nitrogen atom of a nearby molecule (Cu2···N2^{i} 3.406(5) Å i = $-x + 1, -y, -z + 2$) as can be seen in Fig. 6. These ribbons are then joined together by a 6PE (sixfold phenyl embrace)

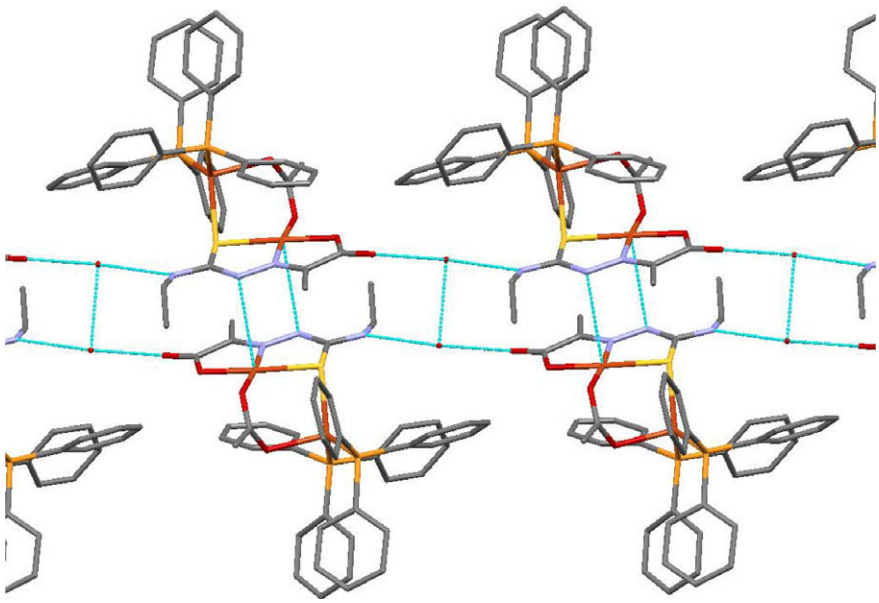


Fig. 6. MERCURY drawing of the packing of compound **4** showing the ribbon of complex molecules held together through hydrogen bonds formed by water molecules and by a long interaction between copper(II) and the hydrazine nitrogen of an adjacent molecule.

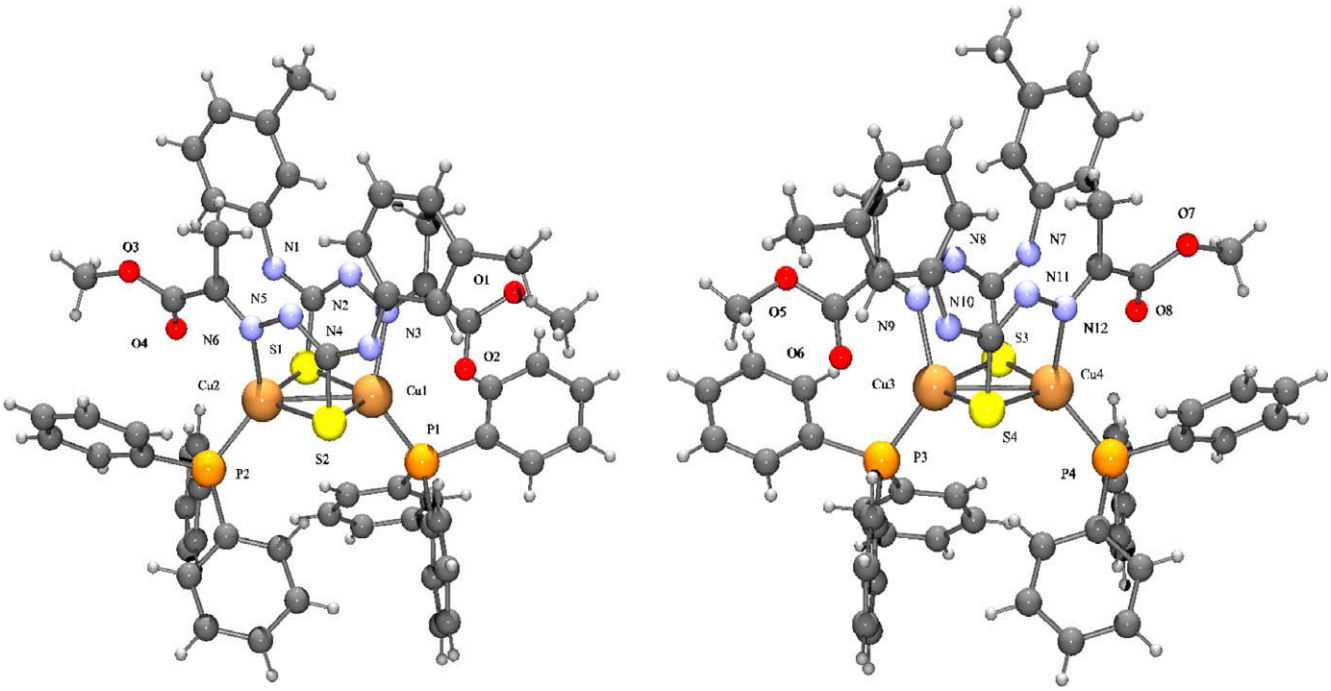


Fig. 7. PLUTON rendering of the two independent molecules of complex $[Cu_2(MePh\text{-}mpt)_2(PPh_3)_2]$ **6**.

Table 3
Selected bond distances for compound **6**.

Bond	Distance (Å)	Bond	Distance (Å)
Cu1–Cu2	2.845(1)	Cu3–Cu4	2.845(1)
Cu1–S1	2.347(3)	Cu3–S3	2.343(3)
Cu1–S2	2.379(3)	Cu3–S4	2.386(3)
Cu1–P1	2.213(3)	Cu3–P3	2.207(3)
Cu1–N3	2.102(7)	Cu3–N9	2.084(7)
Cu2–S1	2.385(3)	Cu4–S3	2.395(3)
Cu2–S2	2.343(3)	Cu4–S4	2.343(3)
Cu2–P2	2.217(3)	Cu4–P4	2.213(3)
Cu2–N6	2.124(7)	Cu4–N12	2.115(8)

interaction with a distance P···P of 7.234 Å that involves the triphenylphosphines.

The crystal structure of compound **6** $[Cu_2(MePh\text{-}mpt)_2(PPh_3)_2]$ is reported in Fig. 7. The asymmetric unit contains two independent enantiomeric complex molecules. Both are planar 2Cu–2S clusters made up of two copper ions with interatomic distances of 2.845(1) and 2.844(1) Å, bridged by two sulfur atoms belonging to two thiosemicarbazone ligands. These ligands are deprotonated and located on the same face of the cluster plane, bind through the sulfur and the iminic nitrogen (see Table 3) and are perpendicular to each other and oriented head to tail (see Fig. 7). The triphenylphosphines are on the opposite side and two phenyls interact edge

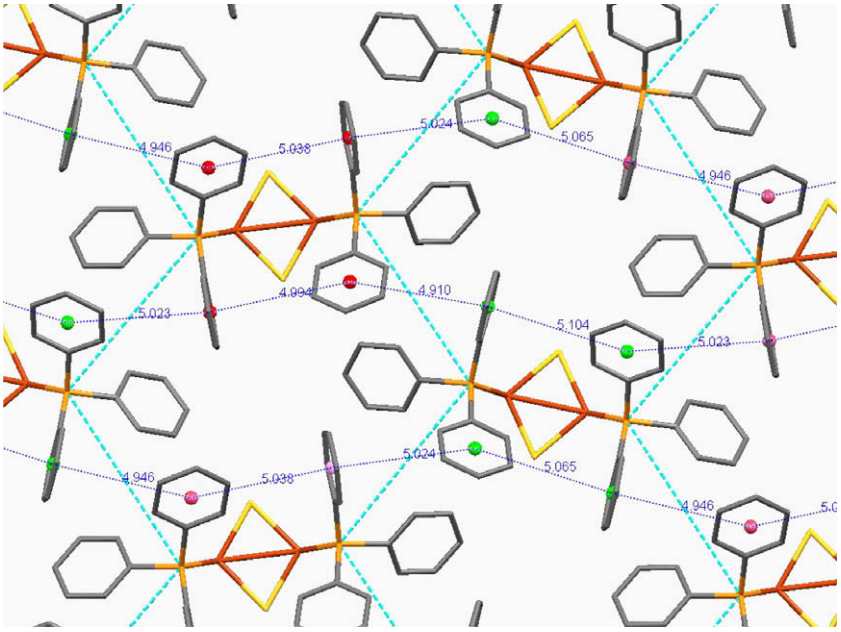


Fig. 8. MERCURY drawing of the packing of compound **6** showing the phenyl–phenyl edge to face interactions extending in the *xy* plane.

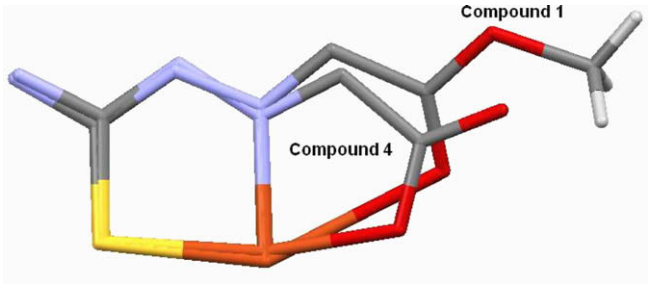


Fig. 9. PLUTON rendering of the methylpyruvate thiosemicarbazone group deformation observed passing from a Cu(I) in **1** to a Cu(II) coordination in **4**.

to face with those of an adjacent molecule forming parallel quadruple phenyl embrace (PQPE) [35–38] (see Fig. 8).

4. Conclusions

Copper(I) ions, with their d^{10} electronic configuration, do not have an energetically preferred geometry and their coordination is therefore mainly governed by steric repulsions. Aside from the two donor species P and S, the remaining space around the copper ion, in bistriphenylphosphine complexes present in the Cambridge Structural Database [39], is usually occupied by a fourth ligand, usually a halide. In previous experiments we have verified that the absence of other soft species can influence the coordination and in particular that the imino nitrogen can become a suitable donor for coordination on a soft metal ion in the absence of softer competitors. What is apparent in the structures reported in this paper is that the control on the coordinating behaviour of a ligand is tuned by a series of factors among which the predominant is the hard soft nature of the atoms involved in the interactions with the metal centre. In our case it is striking the comparison between compounds **1** and **4**. Compound **4** was recalcitrant to crystallisation and the crystals were obtained after many attempts leaving the compound exposed to atmospheric oxygen and moisture. The copper(I) oxidised to copper(II) increases both the acidity of the hydrazine nitrogen stabilizing the anionic form and promotes the hydrolysis of the methyl group from the esther improving the electrophilicity of the carboxyl carbon and speeding up the process of demethylation. This phenomenon of demethylation had been previously observed in a work where an analogous ligand was coordinated by zinc(II) [40]. The ligand is therefore the same but the effects are dramatically different in the coordination of copper(I) versus copper(II). The fairly rigid ligand is markedly deformed upon coordination on copper(II) in **4** (see Fig. 9) to allow the carboxylic oxygen to bind to the metal ion, while it remains almost unaltered upon coordination of copper(I) in **1**.

Acknowledgment

Thanks are due to Dr. Mario Ghillani for his valuable contribution in the recording of EPR spectra.

Appendix A. Supplementary data

CCDC 690657, 690658, 690659 and 690660 contains the supplementary crystallographic data for compounds **1**, **2**, **4** and **6**. These data can be obtained free of charge via http://www.ccdc.cam.ac.uk/conts/retrieving.html, or from the Cambridge Crystallographic Data Centre, 12 Union Road, Cambridge CB2 1EZ, UK; fax: (+44) 1223-336-033; or e-mail: deposit@ccdc.cam.ac.uk. Supplementary data associated with this article can be found, in the online version, at doi:10.1016/j.poly.2009.01.013.

References

[1] T.S. Lobana, Rekha, A.P.S. Pannu, G. Hundal, R.J. Butcher, A. Castineiras, Polyhedron 26 (2007) 2621.
[2] T.S. Lobana, Rekha, R.J. Butcher, Transition Met. Chem. 29 (2004) 291.
[3] T.S. Lobana, Rekha, R.J. Butcher, A. Castineiras, E. Bermejo, P.V. Bharatam, Inorg. Chem. 45 (2006) 1535.
[4] D.X. West, S.B. Padhye, P.B. Sonawane, Struct. Bond. (Berlin) 76 (1991) 1.
[5] D.R. Smith, Coord. Chem. Rev. 164 (1997) 575.
[6] A.R. Cowley, J.R. Dilworth, P.S. Donnelly, E. Labisbal, A. Sousa, J. Am. Chem. Soc. 124 (2002) 5270.
[7] D.B. Lovejoy, D.R. Richardson, Blood 100 (2002) 666.
[8] L.-J. Ming, Med. Res. Rev. 23 (2003) 697.
[9] M. Belicchi-Ferrari, G. Gasparri-Fava, C. Pelizzi, P. Tarasconi, Inorg. Chim. Acta 97 (1985) 99.
[10] M. Belicchi-Ferrari, G. Gasparri-Fava, M. Lanfranchi, C. Pelizzi, P. Tarasconi, Inorg. Chim. Acta 181 (1991) 253.
[11] J.S. Casas, M.S. Garcia-Tasende, J. Sordo, Coord. Chem. Rev. 209 (2000) 197.

[12] M.J.M. Campbell, Coord. Chem. Rev. 15 (1975) 279.
[13] S. Padhye, G.B. Kauffman, Coord. Chem. Rev. 63 (1985) 127.
[14] D.X. West, A.E. Liberta, S.B. Padhye, R.C. Chikate, P.B. Sonawane, A.S. Kumbhar, R.G. Yerande, Coord. Chem. Rev. 123 (1993) 49.
[15] R.L. De Lima, L.R.D. Teixeira, T.M.G. Carneiro, H. Beraldo, J. Braz. Chem. Soc. 10 (1999) 184.
[16] N.T. Akinchan, R. Akinchan, P.M. Drozdewski, Y.H. Yang, T.L. Klein, D.X. West, Synth. React. Inorg. Met.-Org. Chem. 26 (1996) 1735.
[17] H.G. Zheng, D.X. Zeng, X.Q. Xin, W.T. Wong, Polyhedron 16 (1997) 3499.
[18] S. Lhuachan, S. Siripaisarnpipat, N. Chaichit, Eur. J. Inorg. Chem. (2003) 263.
[19] L.J. Ashfield, A.R. Cowley, J.R. Dilworth, P.S. Donnelly, Inorg. Chem. 43 (2004) 4121.
[20] M. Belicchi-Ferrari, A. Bonardi, G. Gasparri-Fava, C. Pelizzi, P. Tarasconi, Inorg. Chim. Acta 223 (1994) 77.
[21] T.S. Lobana, B.S. Sidhu, A. Castineiras, E. Bermejo, T. Nishioka, J. Coord. Chem. 58 (2005) 803.
[22] T.S. Lobana, S. Khanna, R.J. Butcher, A.D. Hunter, M. Zeller, Polyhedron 25 (2006) 2755.
[23] M. Belicchi-Ferrari, F. Bisceglie, C. Cavalieri, G. Pelosi, P. Tarasconi, Polyhedron 26 (2007) 3774.
[24] M. Belicchi-Ferrari, F. Bisceglie, G. Pelosi, P. Tarasconi, R. Albertini, S. Pinelli, J. Inorg. Biochem. 87 (2001) 137.
[25] G.M. Sheldrick, Acta Crystallogr. A64 (2008) 112.
[26] A. Altomare, M.C. Burla, M. Cavalli, G. Cascarano, C. Giacovazzo, A. Gagliardi, A.G.G. Moliterni, G. Polidori, R. Spagna, J. Appl. Crystallogr. 32 (1999) 115.
[27] G. Sheldrick, SHELXL97, A Program for Structure Refinement, University of Goettingen, Germany, 1997.
[28] M. Nardelli, J. Appl. Crystallogr. 28 (1995) 659.
[29] (a) A.L. Spek, Acta Crystallogr. A46 (1990) C34;
(b) A.L. Spek, PLATON, A Multipurpose Crystallographic Tool, Utrecht University, Utrecht, The Netherlands, 1998.
[30] C.F. Macrae, P.R. Edgington, P. McCabe, E. Pidcock, G.P. Shields, R. Taylor, M. Towler, J. van de Streek, J. Appl. Crystallogr. 39 (2006) 453.
[31] A. Abragam, B. Bleaney, Electron Paramagnetic Resonance of Transition Ions, Clarendon Press, Oxford, 1970.
[32] D. Kivelson, R. Neiman, J. Chem. Phys. 35 (1961) 149.
[33] A.H. Maki, B.R. McGarvey, J. Chem. Phys. 29 (1958) 31.
[34] E. Buluggiu, A. Vera, A.A.G. Tomlinson, J. Chem. Phys. 36 (1972) 5602.
[35] I.G. Dance, M.L. Scudder, J. Chem. Soc., Chem. Commun. (1995) 1039.
[36] I.G. Dance, M.L. Scudder, Chem. Eur. J. 2 (1996) 481.
[37] I. Dance, M. Scudder, J. Chem. Soc. Dalton Trans. 10 (2000) 1579.
[38] I. Dance, M. Scudder, J. Chem. Soc., Dalton Trans. 10 (2000) 1587.
[39] F.H. Allen, Acta Crystallogr. B58 (2002) 380.
[40] M. Belicchi Ferrari, G. Gasparri Fava, G. Pelosi, P. Tarasconi, Polyhedron 19 (2000) 1895.

investigations may be of interest for the multi-purpose rational theoretical design of new magnetic high-spin compounds.

The compound $[Cr_{10}(OCH_3)_{20}(CH_3COO)_{10}]$ ($n = 10$) is well known because of its highly unusual magnetic properties, which were experimentally evaluated [10]. The results of the study show that this compound possesses a very high-spin ground state ($S = 15$). The authors argue that very few examples of ferromagnetic Cr···Cr exchange in such molecular systems had been reported previously [13,14] and, furthermore, there are only four examples of ferromagnetically coupled cyclic complexes of metal ions [15]. From this point of view, compounds that are similar to the above mentioned compounds may serve to obtain a better understanding of some nano-properties of molecular magnets.

The main aim of our study is to investigate the relative stability of $[Cr_n(OCH_3)_{2n}(CH_3COO)_n]$ depending on the number n of its interior groups by means of calculations that are carried out in accordance with well known quantum-chemistry methods such as the HF and DFT approaches.

2. Calculational methods

Carboxylate methoxy clusters of the 'wheel'-type, $[Cr_n(OCH_3)_{2n}(CH_3COO)_n]$ ($n = 4$, 6, 8, 10, 12 and 14), were studied theoretically in order to determine the most stable compound, first. Then the results obtained from the theoretical study were compared with the corresponding experimental data reported previously. All the calculations on their geometries and electronic properties have been performed with the aim of finding the total energy, E_{tot}, and then to determine the ratio E_{tot}/n. The latter value corresponds to one Cr-containing coordination section of these compounds and is considered as a measure of the *relative stability* for the compounds. All the complexes were studied in their ferromagnetic state, which was found as the ground state for the experimentally obtained compound with $n = 10$ [10,12] (spins of all the chromic ions were considered as parallel).

Their geometries were obtained on the basis of the molecular mechanics MM+ method from the GAUSSIAN-03 computational package [19]; for $n = 10$, the data calculated were found to be very close to the known X-ray data [10]. Their electronic properties were calculated by means of the MO LCAO Hartree–Fock–Roothaan and DFT (hybrid B3LYP functional) methods, using the STO-3G and 6-31G(d) basis sets.

3. Results and discussion

The X-ray structure of the molecule $[Cr_{10}(OCH_3)_{20}(CH_3COO)_{10}]$ and the structure found from the MM+ method are both shown in Fig. 1, in two different projections. The values of the geometrical parameters for the model molecule and its X-ray analogue are presented in Table 1.

As one can see from Fig. 1, both projections are very similar to each other except for the positions of the CH_3 groups belonging to the $-OCH_3$ bridges. The CH_3 groups of the X-ray structure are insufficiently oriented inside the ring. However, the data of Table 1 indicate that the average length of the Cr–O bonds found from the MM method correlates with the experimental value well enough. It should be noted that the most substantial difference in bond lengths exists for the Cr–O bonds whose oxygen atoms belong to CH_3COO groups. The average value of the bond lengths is equal to 1.82 Å in the calculated model structure; in the X-ray structure, the lengths considered vary from 1.98 to 2.01 Å. At the same time, different valence and torsion angles, found by means of the MM+ method, are very close to the corresponding experimental values (see the values given in Table 1).

Our package of programs was chosen for the reason that it contains a generic model (in the frameworks of the force field MM+), which can be applied even when some required parameters of the force field are absent. This is a typical situation in coordination compound modeling. When comparing various series of related molecules, this approach gives fully reasonable results and does not require great calculation efforts. However, the *ab initio* HF and DFT methods used in our case for the calculation of the single point energy and especially for the optimization of molecular geometry of large systems that contain transition metal ions and

Table 1
Comparison of the molecular mechanics force field results with the experimental X-ray data [10] for the structure $[Cr_{10}(OCH_3)_{20}(CH_3COO)_{10}]$.

Geometry characteristics	Found by MM+	X-ray data
$Cr-O_{(CH_3COO)}$ (Å)	1.82	1.98–2.01
$Cr-O_{(CH_3O)}$ (Å)	1.87	1.94–1.98
Cr···Cr (Å)	2.90	2.99
$Cr-O_{(OCH_3)}$···Cr (°)	101.50	98.41–99.91
Cr···Cr···Cr (°)	143.99	142.81

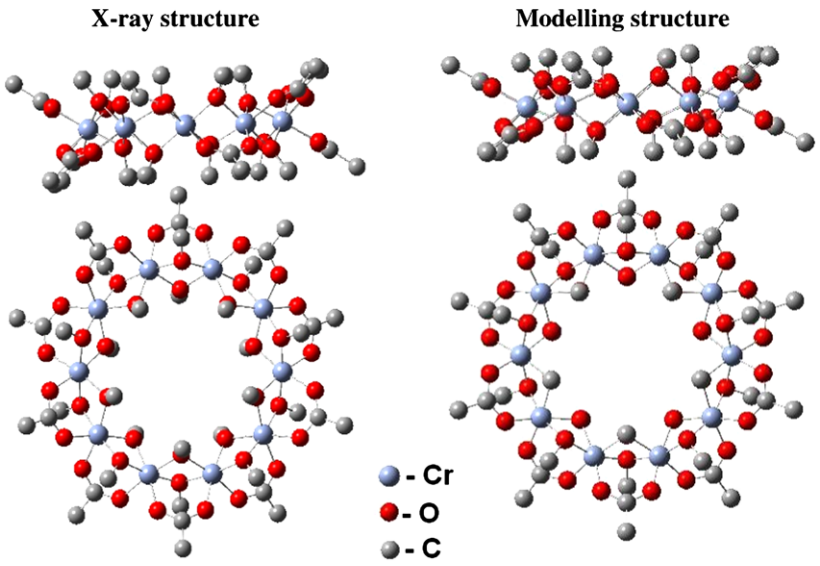


Fig. 1. Two projections of the chromic wheel $[Cr_{10}(OCH_3)_{20}(CH_3COO)_{10}]$ structure (hydrogen atoms omitted for clarity).

labile organic ligands, require huge computational efforts (even for the minimal basis set STO-3G). There is no guarantee that the molecular geometries found from these two methods are better than the geometries obtained on the basis of an adequately selected MM method (see [20]). The electronic characteristics of the compound with $n = 10$ were calculated by both the HF method and DFT from its X-ray geometry, and the geometries obtained by means of the MM+ method and DFT are given in Table 2.

A comparison of the total energies and charge distributions, which have been obtained by means of the two quantum-chemistry methods indicated above, tells us that these values are in good agreement with each other. The charges on the chromium ions vary in the ranges 1.09–1.12 for HF and B3LYP (6-31G(d)) and 0.81–0.87 for B3LYP (STO-3G) basis set, and thus they are far from the formal charge of +3 for the chromium(III) ions. This tells us about the electron density delocalization in the molecular system. The values of the local magnetic moments correspond to three unpaired electrons on any chromium center, which possesses the $3d\uparrow^3 d\downarrow^0$ spin configuration.

Some theoretical electronic characteristics of the compounds with $n = 4$, 6, 8, 10, 12 and 14 calculated by both MO LCAO methods, i.e. HF and DFT (B3LYP), are presented in Table 3. The table contains data on the total molecular energy per one Cr-containing coordination section, E_{tot}/n, and the difference $E_{tot}/n - E_{tot}/10$. $E_{tot}/10$ is the minimal value of the energy of one coordination section for the most stable 'wheel' with $n = 10$. Previously obtained data [10] show that this compound is really being formed under the experimental conditions. It should be noted that calculations with the 6-31G(d) basis also give a lower minimum of energy for $n = 10$ than those with the STO-3G basis. One of the significant advantages of the DFT method, being based on unrestricted determinants for open-shell systems, is that the method is not very prone to "spin contamination", i.e. (S^2) is normally close to $s_z(s_z + 1)$. This is mainly a consequence of electron correlation being included in the single determinantal wave function.

It follows from the calculations that for our systems with three unpaired electrons on each Cr atom, the system multiplicity increases with the growth of number of Cr atoms. Thus, in the series of complexes $[Cr_n(OCH_3)_{2n}(CH_3COO)_n]$ with $n = 4$, 6, 8, 10, 12 and 14, the multiplicity takes the corresponding values equal to 9, 19, 25, 31, 37, 43, and calculated values of S^2 are 22, 90, 156, 240, 342 and 462. The distribution of the spin density in the system with $n = 10$ is shown in Fig. 2.

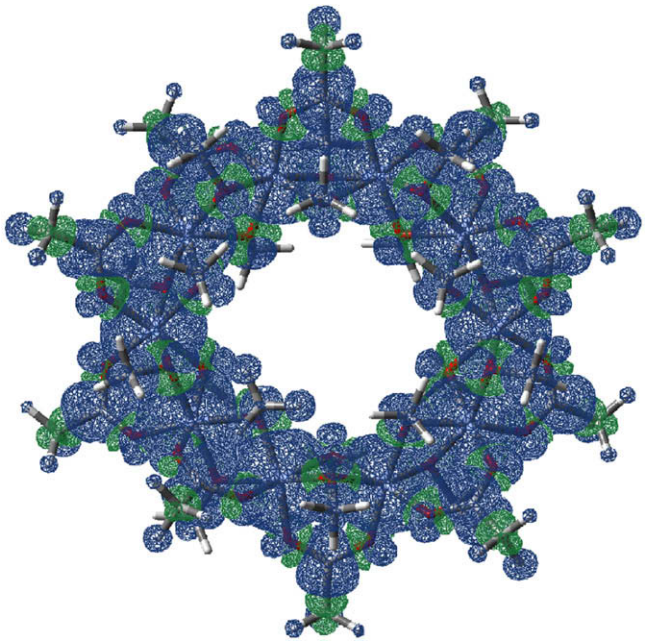


Fig. 2. Spin density distribution for the $[Cr_{10}(OCH_3)_{20}(CH_3COO)_{10}]$ molecule.

To estimate the stability of the systems under study, an analysis of some energy parameters is needed. As follows from Table 3, the E_{tot}/n values that have been calculated by both of the above mentioned methods agree very well with the above given experimental data on the stability of our complexes.

In Fig. 3, one can see the dependence of E_{tot}/n on the number n. It should be noted that the energy values of the compounds with $n = 10$ and $n = 12$ are very close to each other. It means that by changing either the experimental conditions of their syntheses or the molecular volumes of their organic ligands, one can shift the chemical equilibrium to the formation of the desired compound.

In order to understand the reason for the relative stability of $[Cr_n(OCH_3)_{2n}(CH_3COO)_n]$ with $n = 10$ we have compared various electron characteristics of the compounds under study. However, a comparison of characteristics such as atomic charges, spin densities, energies and energy gaps of the MO's of the active zones of the complexes (including their HOMO, LUMO and all the singly occu-

Table 2
Comparison of some electronic characteristics of the structure with $n = 10$, based on the MM+ and X-ray [10] geometries.

Geometry, method	E_{tot} (kcal/mol)	Average charge Q, $\|e\|$ on the atoms			Local magnetic moments at Cr
		Cr	O_{CH_3COO}	O_{CH_3O}	
Modelled, HF	−9306036.46	1.12	−0.40	−0.43	3.10
X-ray, HF	−9306184.48	1.10	−0.40	−0.45	3.12
Modelled, DFT(STO-3G)	−9327404.53	0.87	−0.31	−0.34	2.94
X-ray, DFT(STO-3G)	−9327455.85	0.82	−0.29	−0.34	3.05
Modelled, DFT(6-31G(d))	−9432547.93	1.17	−0.53	−0.63	3.10

Table 3
Total energies and their relative differences per one Cr-containing coordination section for systems of the type $[Cr_n(OCH_3)_{2n}(CH_3COO)_n]$ with $n = 4$, 6, 8, 10, 12 and 14.

E (kcal/mol)	n					
	4	6	8	10	12	14
E_{tot}/n(HF)	−930456.96	−930562.16	−930594.72	−930603.65	−930601.18	−930578.07
$E_{tot}/n - E_{tot}/10$	146.71	41.54	8.97	0	2.51	25.60
E_{tot}/n(DFT-STO-3G)	−932672.44	−932709.40	−932734.69	−932740.46	−932737.89	−932725.73
$E_{tot}/n - E_{tot}/10$	68.08	31.12	5.84	0	2.64	14.81
E_{tot}/n(DFT-6-31G(d))	−943180.58	−943219.29	−943244.47	943254.79	943248.05	943239.69
$E_{tot}/n - E_{tot}/10$	74.21	35.50	10.32	0	6.74	15.10

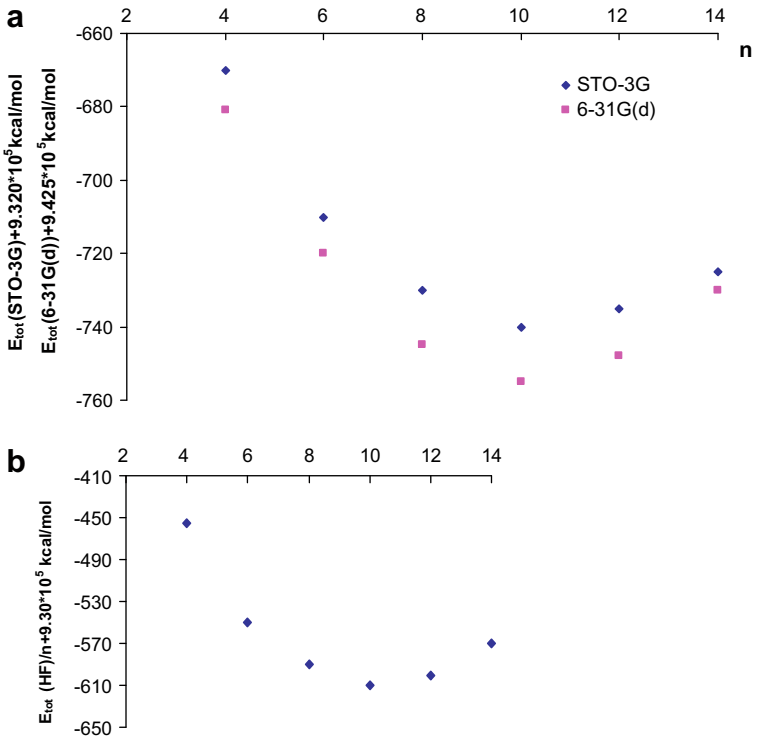


Fig. 3. The values of n and E_{tot}/n exposed for: (a) DFT and (b) Hartree–Fock calculations.

pied MO's, containing the 3d-electrons of the Cr atoms) does not allow us to find any correlations between the above parameters and the relative stability of these compounds.

Luckily, we paid attention to the following circumstance. The X-ray data show [10] that the varying oxygen surroundings of the Cr ions in the structure $[Cr_{10}(OCH_3)_{20}(CH_3COO)_{10}]$ violate the octahedral form. In this connection, we have supposed that possible geometrical distortions of the 'CrO_6' octahedrons in the structures with $n \neq 10$ are more significant than those in the structure with $n = 10$.

As the first stage of our investigation, the following expression was used for the description of the degree of geometrical distortion (δ) of the octahedrons:

$$\delta = 3 * 180 - (\varphi 1 + \varphi 2 + \varphi 3) \quad (1)$$

where φ_i ($i = 1$–3) are the values of the three O–Cr–O angles taken along the three main axes of the octahedrons. A comparison of the data presented in the first line of Table 4 with the data of Table 3 shows, however, that there is no clear-cut correlation between the δ and E_{tot}/n values.

It should be noted that the quantity δ describes geometrical distortions within any coordination octahedron, which must be caused by the electronic repulsion which exists between the electronic pairs belonging to the six Cr–O bonds of the octahedrons. At the same time, there is one more type of electronic repulsion between neighboring coordination units, which belong to any pair of neighboring Cr ions in the compounds under study. In other words, this repulsion exists within any pair of the neighboring coordination sections.

Table 4
The values of the parameters δ and ξ, depending on n.

n	4	6	8	10	12	14
δ (°)	122.163	49.741	34.948	40.001	47.530	55.289
ξ (°)	182.193	109.747	80.008	76.005	77.517	81.006

The total number of such pairs (taken along the wheels considered) equals the number of all Cr-containing coordination sections for any investigated structure. Thus, the influence of this repulsion may be properly taken into account as an addendum to the value of δ that describes the deposit of the above repulsion type relative to one coordination section.

Fig. 4 and Table 1 show that the average repulsion of the coordination units belonging to a pair of their neighboring Cr ions will depend on the average value of the angle $\varphi 4$: Cr–Cr–Cr, where all Cr ions are neighbors. As the Cr–Cr distance remains practically constant (~2.90 Å) for all the investigated structures, it is clear that any decrease in the value of $\varphi 4$ (from the value of 180) will lead to a corresponding increase in the above mentioned repulsion between these coordination units. Thus, bearing in mind all these reasons, we have applied to the description of the total electronic repulsion per coordination section the following quantity, ξ:

$$\xi = 4 * 180 - (\varphi 1 + \varphi 2 + \varphi 3 + \varphi 4) \quad (2)$$

From Table 4 (line 2) and also from a comparison of Figs. 3 and 5, it is seen that the main reason for the compound $[Cr_{10}(OCH_3)_{20}(CH_3COO)_{10}]$ to be relatively stable is that its electronic repulsion per one coordination section takes a minimal

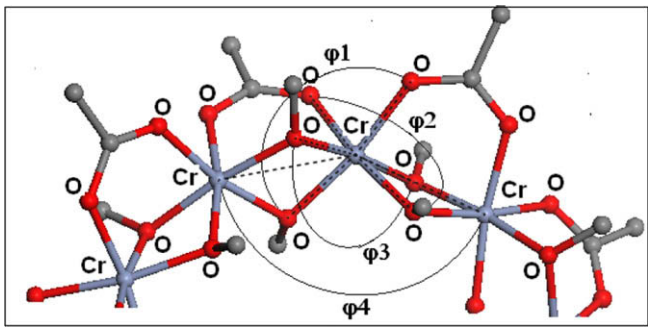


Fig. 4. Angles $\varphi 1$–$\varphi 4$ in a molecular fragment selected for the ξ value calculation.

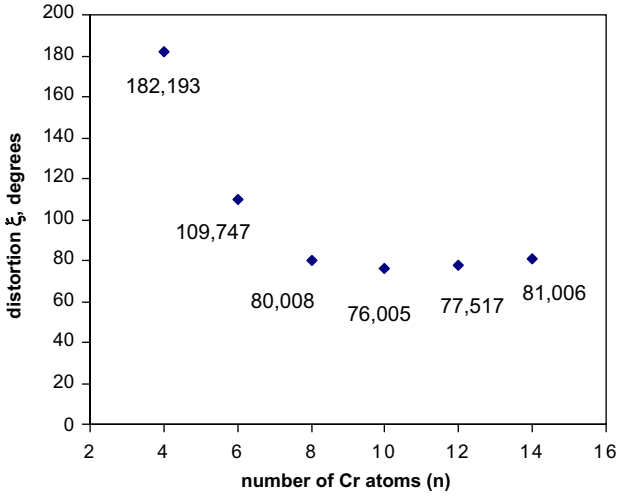


Fig. 5. The ξ vs. n dependence curve.

value. In turn, the electronic repulsion per $\{Cr(OCH_3)_2CH_3COO\}$ coordination section can be properly taken into account for any compound by means of the above given simple geometrical parameter ξ.

4. Conclusion

The results obtained from the study of a series of macro-coordination compounds show that both the HF and DFT methods describe the known experimental data adequately. The values of a simple structural (geometrical) parameter ξ determined from the results of the MM+ method, and data obtained from the quantum-chemistry calculations of the above mentioned nano-clusters, are both in very good agreement with the experimentally known data on the stability of chromic wheels. Hopefully, the parameter ξ can be used in future to forecast the relative stability of different coordination compounds of the wheels type from the nature of their ligands and, perhaps, the nature of their metal ions (i.e. without using voluminous quantum-chemistry calculation methods). However, this assumption requires additional research applied to new series of similar compounds of the wheel-type.

Acknowledgment

This work was supported by INTAS (No. 03-51-4532).

References

[1] D. Gatteschi, A. Caneschi, L. Pardi, R. Sessoli, Science 265 (1994) 1054.
[2] A. Muller, F. Peters, M.T. Pope, D. Gatteschi, Chem. Rev. 98 (1998) 239.
[3] W. Wernsdorfer, R. Sessoli, Science 284 (1999) 133.
[4] M.N. Leuenberger, D. Loss, Nature 410 (2001) 789.
[5] S. Hill, R.S. Edward, N. Aliaga-Alcalde, G. Christou, Science 302 (2003) 1015.
[6] R.E.P. Winpenny, Compreh. Coord. Chem. 7 (2004) 125.
[7] F.L. Meier, D. Loss, Phys. Rev. B 64 (2001) 224411.
[8] J. Slageren, R. Sessoli, D. Gatteschi, A.A. Smith, M. Helliwell, R.E.P. Winpenny, A. Gornia, A.-L. Barra, A.G.M. Jansen, E. Rentschler, G.A. Timko, Chem. Eur. J. 8 (2002) 271.
[9] M. Atkinson, C. Benelli, M. Murrie, S. Parsons, R.E.P. Winpenny, Chem. Commun. (1999) 285.
[10] E. McInnes, Ch. Anson, A. Powell, A. Thomson, R. Sessoli, Chem. Commun. (2001) 89.
[11] N.V. Gerbeleu, Y.T. Struchkov, G.A. Timko, A.S. Batsanov, K.M. Indrichan, G.A. Popovic, Dokl. Akad. Nauk SSSR 313 (1990) 1459.
[12] N.V. Gerbeleu, Y.T. Struchkov, G.A. Timko, A.S. Batsanov, K.M. Indrichan, G.A. Popovic, Dokl. Akad. Nauk SSSR 313 (1990) 232.
[13] R.H. Laye, E.J.L. McInnes, Eur. J. Inor. Chem. 14 (2004) 2811.
[14] E.J.L. McInnes, C. Anson, A.K. Powell, A.J. Thomson, S. Poussereau, R. Sessoli, Chem. Commun. (2001) 89.
[15] D.M. Low, G. Rajaraman, M. Helliwell, G. Timco, J. van Slageren, R. Sessoli, S.T. Ochsenbein, R. Bircher, C. Dobe, O. Waldmann, H.U. Güdel, M.A. Adams, E. Ruiz, S. Alvarez, E.J.L. McInnes, Chem. Eur. J. 12 (2006) 1385.
[16] Le Sun, Jingping Zhang, Shuxin Cui, Polyhedron 26 (2007) 2169.
[17] R. Carrasco, J. Cano, T. Mallah, L.F. Jones, D. Collison, E.K. Brechin, Inorg. Chem. 43 (2004) 5410.
[18] A.V. Postnikov, J. Kortus, M.R. Pederson, Phys. Stat. Sol. (b) 243 (2006) 2533.
[19] J.M. Frisch, G.W. Trucks, H.B. Schlegel, G.E. Scuseria, M.A. Robb, J.R. Cheeseman, V.G. Zakrzewski, J.A. Montgomery, R.E.J., Stratmann Jr., C. Burant, S. Dapprich, J.M. Millam, A.D. Daniels, K.N. Kudin, M.C. Strain, O. Farkas, J. Tomasi, V. Barone, M. Cossi, R. Cammi, B. Mennucci, C. Pomelli, C. Adamo, S. Clifford, J. Ochterski, G.A. Petersson, P.Y. Ayala, Q. Cui, K. Morokuma, D.K. Malick, A.D. Rabuck, K. Raghavachari, J.B. Foresman, J. Cioslowski, J.V. Ortiz, A.G. Baboul, B.B. Stefanov, G. Liu, A. Liashenko, P. Piskorz, I. Komaromi, R. Gomperts, R.L. Martin, D.J. Fox, T. Keith, A. Al-Laham, C.Y. Peng, A. Nanayakkara, M.P. Challacombe, M.W. Gill, B. Johnson, W. Chen, M.W. Wong, J.L. Andres, C. Gonzalez, M. Head-Gordon, E.S. Replogle, J.A. Pople, GAUSSIAN-03, Gaussian Inc., Pittsburgh, PA, 2003.
[20] R.J. Deeth, Struct. Bond. 82 (1995) 1.

2.3. Synthesis of [(μ-O){ReOCl(amp)}$_2$] (**1**)

To a suspension of 0.100 g (120 μmol) of *trans*-[ReOCl$_3$(PPh$_3$)$_2$] in 20 cm^3 of acetone was added 0.053 g (243 μmol) of Hamp. After the mixture was heated under reflux for 4 h, it was cooled to room temperature and a brown precipitate was removed by filtration. Recrystallization from acetonitrile gave red crystals, which were suitable for X-ray diffraction study. Yield = 71% (0.039 g), m.p. 249 °C. *Anal.* Found: C, 33.92; H, 3.81; N, 6.15. $C_{26}H_{34}Cl_2N_4O_5Re_2$ requires C, 33.73; H, 3.70; N, 6.05%. IR (cm^{-1}): ν(Re=O) 961w, ν(Re–O–Re) 692vs, ν(NH$_2$) 2911 m, 2963 m, ν(Re–NH$_2$) 422 m, ν(Re–N(2)) 449 m, ν(Re–Cl) 312 m. ^{1}H NMR (ppm): 7.82(m, 2H, Ph), 7.38(m, 3H, Ph), 5.64(s, 1H, H(4)), 1.18(d, 1H, H(1)), 1.39(d, 2H, H(2)), 2.03(s, 3H, H(12)), 2.09(s, 3H, H(13)).

2.4. Synthesis of [ReOCl$_2$(ada)] (**2**)

A mass of 0.041 g (240 μmol) of Hada was added to *trans*-[ReOCl$_3$(PPh$_3$)$_2$] (0.100 g, 120 μmol) in 20 cm^3 of methanol under a nitrogen atmosphere. The resulting suspension was heated under reflux for an hour, and then cooled to room temperature. A red-brown precipitate was filtered off. The solvent was reduced to about 3 cm^3, and dark red crystals (unsuitable for X-ray diffraction) appeared upon standing overnight. Recrystallization of the precipitate from dichloromethane/diethyl ether gave dark red plates, which were of a poor quality and an X-ray measurement was not possible. Yield = 48% (0.026 g), m.p. 241 °C. *Anal.* Found: C, 24.83; H, 3.91; N, 6.68. $C_9H_{17}Cl_2N_2O_2Re$ requires C, 24.44; H, 3.87; N, 6.33%. IR (cm^{-1}): ν(Re=O) 966vs, ν(NH$_2$) 2941 m, 2992 m, ν(C=N) 1605vs, ν(Re–N) 451 m, 459 m, ν(Re–Cl) 328 m. ^{1}H NMR (ppm): 3.24(s, 2H, C(6)H$_2$), 2.44(s, 3H, C(4)H$_3$), 1.88(s, 3H, C(9)H$_3$), 1.95(s, 2H, C(7)H$_2$, 1.28(s, 3H, C(11)H$_3$), 0.79 (s, 3H, C(12)H$_3$), 4.22(d, 1H, N(2)H), 4.14(d, 1H, N(2)H).

2.5. Synthesis of fac-[Re(CO)$_3$Br(Hada)] (**3**)

Hada (0.084 g, 493 μmol) was dissolved in 10 cm^3 of ethanol, and added to 0.100 g (246 μmol) of [Re(CO)$_5$Br] in 5 cm^3 of ethanol. The resulting solution was heated under reflux for an hour and then cooled to room temperature. It was filtered and left to evaporate slowly at room temperature. After 4 days light yellow crystals, suitable for X-ray diffraction studies, were collected by filtration. Yield = 62% (0.079 g), m.p. 217–219 °C. *Anal.* Found: C, 27.83; H, 3.61; N, 5.44. $C_{12}H_{18}BrN_2O_4Re$ requires C, 27.70; H, 3.49; N, 5.38%. IR (cm^{-1}): ν(C≡O)$_{fac}$ 2010s, 1902s, ν(NH$_2$) 2937 m, 2980 m, ν(Re–N(1)) 435 m, ν(Re–N(2)) 408 m, ν(C=O) 1622 m. ^{1}H NMR (ppm): 3.34 (s, 2H, C(6)H$_2$), 2.52(s, 3H, C(4)H$_3$), 1.96(s, 3H, C(7)H$_3$), 1.86(s, 2H, C(9)H$_2$), 1.28(s, 3H, C(11)H$_3$), 0.76(s, 3H, C(12)H$_3$), 4.08(d, 1H, N(2)H), 3.90(d, 1H, N(2)H).

Table 1
Crystallographic data for complexes **1** and **3**.

	1	**3**
Formula	$C_{26}H_{34}Cl_2N_4O_5Re_2$	$C_{12}H_{18}BrN_2O_4Re$
Formula weight	925.89	520.39
Crystal system	orthorhombic	monoclinic
Space Group	*Pbcn*	$P2_1/c$
a (Å)	21.2813(4)	10.7486(4)
b (Å)	10.4160(2)	9.5778(4)
c (Å)	13.8811(3)	16.1477(7)
β (°)		96.961(2)
V (Å^3)	3077.0(1)	1650.1(1)
Z	4	4
D_{calc} (g cm^{-3})	1.999	2.095
μ (mm^{-1})	8.075	9.798
F(000)	1768	984
Crystal size (mm)	0.02 × 0.05 × 0.06	0.20 × 0.13 × 0.09
θ Range (°)	3.5–27.5	3.2–25.4
Index ranges	$-27 \leqslant h \leqslant 27$	$-12 \leqslant h \leqslant 12$
	$-11 \leqslant k \leqslant 13$	$-11 \leqslant k \leqslant 10$
	$-17 \leqslant \ell \leqslant 18$	$-19 \leqslant \ell \leqslant 19$
Reflection/unique	45304/3529	19335/3033
Observed data [$I > 2\sigma(I)$]	2577	2693
Parameters	179	185
Goodness-of-fit on F^2	1.10	1.16
Final *R* indices: *R*	0.0297	0.0312
wR_2	0.0664	0.0716
Largest difference in peak/hole (e Å^{-3})	1.98/−1.29	0.59/−1.29

Table 2
Selected bond lengths (Å) and angles (°) for **1** and **3**.

Re–O(1)	2.028(3)	Re–N(1)	2.144(4)
Re–O(2)	1.9098(2)	Re–N(2)	2.042(4)
Re–O(3)	1.706(3)	Re–Cl	2.446(1)
C(1)–N(1)	1.482(6)	C(2)–N(2)	1.479(6)
C(5)–O(1)	1.298(5)	C(3)–N(2)	1.320(7)
C(3)–C(4)	1.410(6)	C(4)–C(5)	1.370(6)
O(2)–Re–O(3)	172.2(2)	Re–O–Re	179.7(3)
O(1)–Re–N(1)	169.9(1)	Cl–Re–N(2)	171.3(1)
O(3)–Re–Cl	91.8(1)	O(3)–Re–N(1)	89.7(2)
O(3)–Re–O(1)	99.2(1)	O(3)–Re–N(2)	96.6(2)
C(2)–N(2)–C(3)	121.1(4)	C(4)–C(5)–O(1)	127.2(4)
C(4)–C(5)–C(6)	120.7(4)	N(1)–Re–N(2)	81.3(2)
O(1)–Re–N(2)	92.9(1)	Cl–Re–O(1)	87.69(9)
Re–Br	2.6386(7)	Re–C(1)	1.910(6)
Re–N(1)	2.218(5)	C(7)–N(1)	1.292(8)
Re–N(2)	2.194(5)	C(5)–O(4)	1.22(1)
C(9)–N(1)	1.475(8)	C(1)–O(1)	1.155(8)
C(5)–C(6)	1.50(1)	C(10)–N(2)	1.499(8)
C(1)–Re–N(2)	174.1(3)	C(2)–Re–N(1)	170.6(2)
C(3)–Re–Br	178.7(2)	N(1)–Re–N(2)	77.0(2)
Br–Re–N(1)	83.9(1)	Br–Re–N(2)	84.1(1)
Br–Re–C(1)	90.3(2)	Br–Re–C(2)	92.6(2)
C(7)–N(1)–C(9)	118.2(5)	C(6)–C(5)–O(4)	121.9(7)
C(5)–C(6)–C(7)	113.4(6)	Re–N(2)–C(10)	113.4(4)

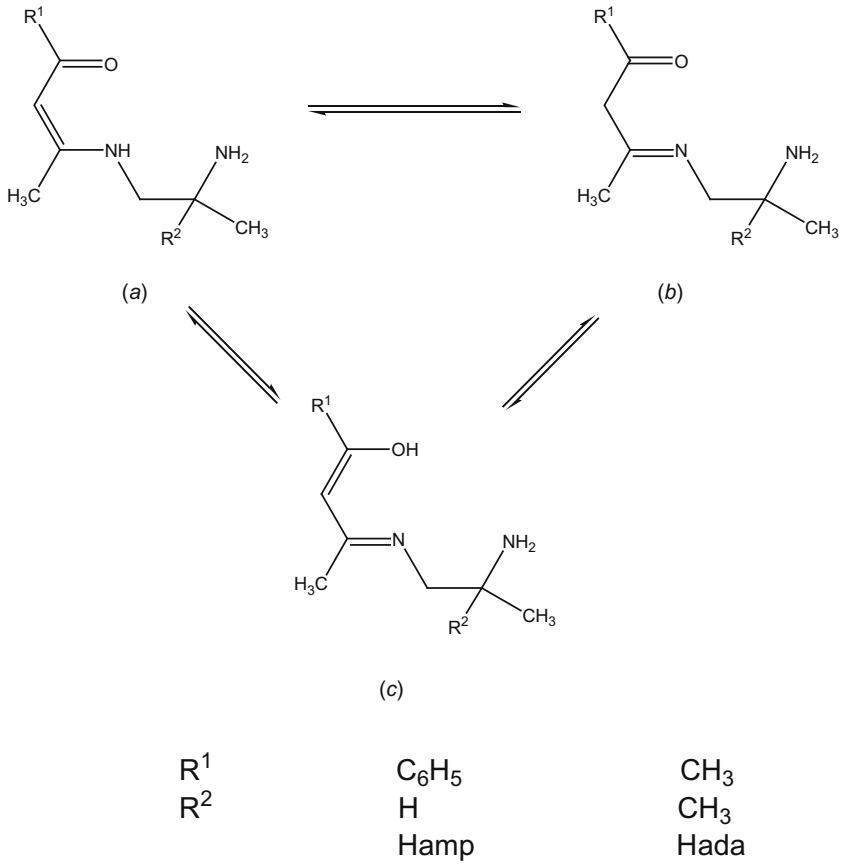
2.6. X-ray crystallography

Intensity data collection was performed at 200 K on a Nonius Kappa CCD detector system using the ω scan technique with Mo Kα radiation. Intensities were corrected for Lorentz and polarization effects. The structures were solved by direct methods and were refined by full-matrix least-squares procedures using the SHELXL-97 package [17]. Crystal and structure refinement data for **1** and **3** are given in Table 1. Non-hydrogen atoms were refined with anisotropic displacement parameters; hydrogen atoms were idealized and fixed. Selected bond lengths and angles are given in Table 2.

3. Results and discussion

3.1. [(μ-O){ReOCl(amp)}$_2$] (**1**)

The complex was synthesized by the reaction of *trans*-[ReOCl$_3$(PPh$_3$)$_2$] with two molar equivalents of Hamp in refluxing acetone in air with trace amounts of water present. It is an established fact that monomeric octahedral oxorhenium(V) complexes prefer the position *trans* to the oxo group to be occupied by an anionic oxygen donor atom like an alcoxide or phenoxide [12,18,19]. Tautomer *c* of amp (Scheme 1) can provide such an oxygen donor (after deprotonation) to produce a monomeric complex of formula [ReOCl$_2$(amp)], as was observed previously with NNO-donor chelates [20–22]. However, the fact that the μ-oxo dimer **1** is formed therefore precludes the existence of amp as the tautomer *c*. Complex **1** is possibly formed *via* the intermediate [ReOCl$_2$(amp)] (with



Scheme 1. Schematic representation and tautomerization of the ligands.

amp in a deprotonated form of tautomer *a* or *b*), with a labile chloride *trans* to the oxo group, which is then substituted by a water molecule, the double deprotonation of which leads to the formation of **1**. The initial occupation of the *trans* site by the anionic oxygen atom of amp would prevent this process of formation. Complex **1** is diamagnetic and a non-electrolyte in DMF, and is only soluble in acetonitrile, DMSO and DMF.

The infrared spectrum of **1** displays the Re=O stretch as a weak band at 961 cm^{-1}. Weak intensity absorptions corresponding to ν(Re=O) have been observed previously for dimeric Re(V) species [23,24]. However, the dominant feature of the spectrum is the presence of a strong and intense absorption at 692 cm^{-1}, ascribed to the asymmetric Re–O–Re stretch [23,24]. The tridentate coordination of amp is manifested by the medium intensity peaks at 449 [ν(Re–N(2)], 422 [ν(Re–NH_2)] and 378 cm^{-1} [ν(Re–O)]. The ^1H NMR spectrum consists of sharp, well-resolved peaks with no detectable paramagnetic shifts or line broadening of signals. The most informative aspect of the spectrum is a one-proton singlet at 5.64 ppm, which is assigned to a single proton on C(4) (see Fig. 1 for atom labelling), implying a C(3)=C(4) double bond and the presence of tautomer *a* in complex **1**. The phenyl protons appear as two multiplets at 7.82 and 7.38 ppm, and the signals of the two methyl groups occur at 2.03 and 2.09 ppm. In addition, there are a two proton signal at 1.39 ppm [C(2)H_2] and a one-proton peak at 1.18 ppm [C(1)H].

The molecular structure of **1** is illustrated in Fig. 1. The axis of the molecule is formed by the O=Re–O–Re=O moiety, with an improper rotation (rotation of 98.93° followed by a reflection) depicting the symmetry of the two halves relative to each other. The corresponding bond lengths and angles of the two [ReOCl(amp)] halves are identical. The Re–O–Re angle is 179.7(3)°, and the two O–Re=O are equal [172.2(2)°], showing significant deviation from linearity (Table 2). Each rhenium atom is centred in an octahedron with the equatorial plane formed by a N_2OCl donor set. The octahedron is severely distorted, with the N(2) and O(1) donor atoms being displaced significantly away from the Re=O(3) bond [O(3)–Re–N(2)=96.6(2)°, O(3)–Re–O(1)=99.2(1)°], while the O(3)–Re–N(1) [89.7(2)°] and O(3)–Re–Cl [91.8(1)°] angles are close to orthogonality. The result of these distortions is an O(3)–Re–O(2) angle of 172.2(2)°, with the Re atom displaced from the mean equatorial plane by 0.162 Å towards the O(3) oxo atom. The axial Re=O(3) and Re–O(2) distances of 1.706(3) and 1.9098(2) Å, respectively, are typical of this backbone. The Re–N(1) bond length of 2.144(4) Å is typical of Re(V)–NH_2 bonds, which vary in the range 2.12–2.20 Å [13]. The Re–N(2) length of 2.042(4) Å falls within the range observed [1.94(1)–2.05(1) Å] for rhenium(V)–amide bonds [27–30], implying that N(2) is deprotonated. Bond lengths of neutral secondary amine and imine nitrogens to rhenium(V) fall in the range 2.08–2.15 Å, with an average value of 2.11(1) Å [23–32]. The amp ligand therefore acts as a monoanionic tridentate chelate, with coordination through the neutral amino group N(1)H_2, the deprotonated amido nitrogen N(2), and the neutral ketonic oxygen O(1) [Re–O(1) = 2.028(3) Å], as depicted as tautomer *a* in Scheme 1.

The intraligand bond distances illustrate π-delocalization in the phenyl rings [average C–C distance = 1.384(9) Å]. The C(1)–N(1) bond is single [1.482(6) Å], with the bond angles around C(1) typical of sp^3 hybridization. There is considerable π-delocalization over the N(2)–C(3)–C(4)–C(5) backbone of amp, with bond lengths longer than formal double bonds, but shorter than typical C–C and C–N single bonds. The C(5)–O(1) bond length of 1.298(5) Å is considerably shorter than single C–O^- bond lengths in octahedral

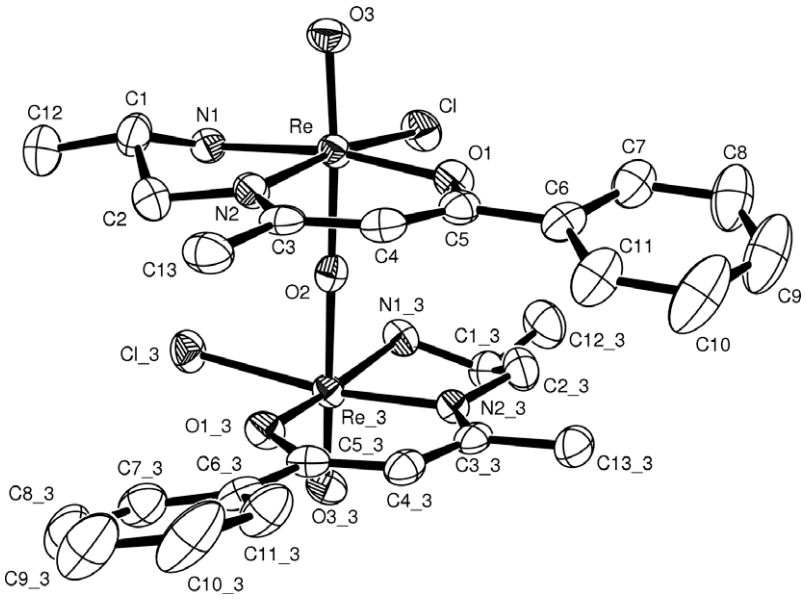


Fig. 1. Structure of complex **1**. Thermal ellipsoids are shown at 50% probability, and hydrogen atoms are omitted for clarity.

rhenium(V) complexes with the oxygen coordinated *cis* to the oxo group [average 1.35(1) Å] [10–15], but longer than the uncoordinated ketonic C=O group in complex **3** [1.22(1) Å]. The bite angle formed by the six-membered metallocycle [O(1)–Re–N(2) = 92.9(1)°] is, as expected, larger than the bite angle of the five-membered one [N(1)–Re–N(2) = 81.3(2)°]. The spatial arrangement of the phenyl rings is governed by the intramolecular hydrogen bond C(7)H···O(1) and the intermolecular bonds C(8)H···Cl and C(10)H···Cl (see Table 3).

A previous study of an oxorhenium(V) complex with the acetylacetone-derived Schiff base, the tridentate ONS-donor ligand 4-[2-(methylthio)aniline]-3-penten-2-one (Hmap), had led to the isolation of the product (n-Bu_4 N)[$ReOCl_3$(map)] (**4**) [12c]. The X-ray crystal structure shows that the map ligand is coordinated bidentately as a monoanionic N,O-donor, with a dangling thioether functionality. This result corresponds to the existence of tautomer *c* in **4,** in which the phenolate group is deprotonated.

3.2. [$ReOCl_2$(ada)] (**2**)

Complex **2** was prepared by the reaction of *trans*-[$ReOCl_3(PPh_3)_2$] with a twofold molar excess of Hada in methanol. With equimolar ratios of reactants, only the product [$ReOCl_2$(OMe)$(PPh_3)_2$] was isolated.

Table 3
Hydrogen bonding distances (Å) and angles (°) for **1** and **3**.

D–H···A	D–H	H···A	D···A	∠D–H···A
1				
N(1)–H(1A)···O(3)	0.92	2.23	3.144(5)	174
N(1)–H(1B)···Cl	0.92	2.51	3.388(4)	160
C(7)–H···O(1)	0.95	2.32	2.659(7)	100
C(8)–H···Cl	0.95	2.81	3.665(7)	149
C(10)–H···Cl	0.95	2.73	3.497(6)	138
3				
N(2)–H(2A)···O(3)	0.92	2.50	3.243(8)	138
N(2)–H(2B)···Br	0.92	2.58	3.491(5)	171
C(6)–H(6A)···Br	0.99	2.93	3.859(8)	157
C(6)–H(6B)···O(4)	0.99	2.57	2.97(1)	104
C(9)–H(9A)···Br	0.99	2.92	3.474(7)	116

Spectroscopic evidence suggests that ada acts as a tridentate N_2O-donor chelate, with deprotonation of the alcoholate oxygen to coordinate as tautomer *c* (Scheme 1) in the complex. In the infrared spectrum the asymmetric Re=O stretching frequency appears as a very strong band at 966 cm^{-1}, which falls in the range (947–968 cm^{-1}) normally observed for neutral six-coordinate monooxorhenium(V) complexes with an anionic oxygen atom coordinated *trans* to the oxo group [11,12,18–22]. An absorption at 328 cm^{-1}, with a shoulder at 322 cm^{-1}, is observed for ν(Re–Cl), which falls outside the range of 295−310 cm^{-1} observed for complexes with the chloride coordinated *trans* to the oxo group. A very strong band at 1605 cm^{-1} is typical of ν(C=N), and medium intensity bands at 2941 and 2992 cm^{-1} indicates the presence of the neutral amino group.

3.3. *fac*-[$Re(CO)_3Br$(Hada)] (**3**)

The rhenium(I) complex was prepared by the reaction of [$Re(CO)_5Br$] with two equivalents of Hada in refluxing ethanol. The infrared spectrum exhibits a sharp, strong band at 2010 cm^{-1} and a broad, intense absorption at 1902 cm^{-1}, attributed to ν(C–O) of the *fac*-$[Re(CO)_3]^+$ unit [33,34]. Two medium intensity peaks at 435 and 408 cm^{-1} are assigned to ν(Re–N(1)) and ν(Re–N(2)H_2), respectively. In the ^{1}H NMR spectrum four three-proton singlets are observed for the methyl groups, and two two-proton singlets appear at 3.34 and 1.86 ppm for the methylene groups. Interestingly, two one-proton doublets are observed for the N(2)H_2 protons, which are hydrogen-bonded to O(3) and Br in the solid state (see Table 3).

A perspective view of the asymmetric unit is shown in Fig. 2. The X-ray results show that the complex contains the chemically robust *fac*-$[Re(CO)_3]^+$ core in a distorted octahedral geometry. The metal is coordinated to three carbonyl donors in a *facial* orientation, to the neutral amino nitrogen N(2), the imino nitrogen N(1), and a bromide. The ketonic oxygen O(4) is uncoordinated. The Re–CO bond distances [average of 1.911(8) Å] fall in the range observed [1.900(2)–1.928(2) Å] for similar complexes [35,36]. The Re–N(1) bond [2.218(5) Å] is marginally longer than the Re–N(2) one [2.194(5) Å], and they are typical to other similar bonds [25,26,37]. The distortion from octahedral ideality in the complex is mainly the result of the *trans* angles, which fall in the range

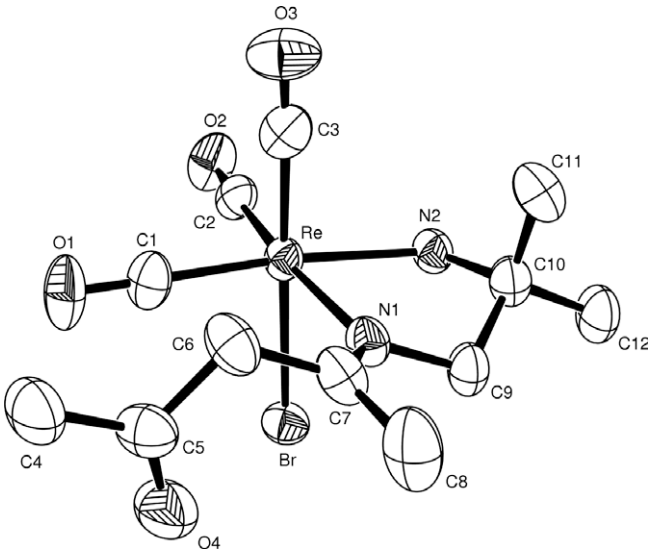


Fig. 2. ORTEP drawing of complex **3** with numbering scheme.

170.6(2)–178.7(2)° (Table 2). These distortions are mainly the result of the constraints imposed by the bidentate coordination of Hada, which has a bite angle of 77.0(2)°. As a result the bromide distorts the two nitrogen atoms less [average Br–Re–N angle is 84.0(1)°] than the two carbonyl carbons [average Br–Re–C angle is 91.5(2)°].

The Hada intraligand bonding distances confirm its coordination to the metal as the neutral tautomeric form *b* in Scheme 1. The two double bonds in Hada are C(5)–O(4) [1.22(1) Å] and C(7)–N(1) [1.292(8) Å], with the O(4)–C(5)–C(6) and C(7)–N(1)–C(9) bond angles equal to 121.9(7)° and 118.2(5)°, respectively. All the other bonds are single, and all the carbon atoms (except C(5) and C(7)) are sp^3 hybridized.

In addition to those formed by the amine group, there are also the intramolecular hydrogen bonds C(6)H(A)···Br, C(6)H(A)···O(4) and C(9)H···Br (see Table 3).

Previously, the reaction of $[Re(CO)_5Cl]$ with the potential tridentate ligand 1-amino-1'-hydroxybinaphthyl (H_2ahb) produced $[Re(CO)_3(Hahb)(H_2O)]$, in which Hahb acts as a monoanionic bidentate N,O-donor chelate *via* the coordination of an imine nitrogen and deprotonated oxygen atom [1d].

4. Conclusion

The characterization of the product $[(\mu\text{-}O)\{ReOCl(amp)\}_2]$ from the reaction of *trans*-$[ReOCl_3(PPh_3)_2]$ with the benzoylacetone-derived ketoamine ligand Hamp shows that the latter is coordinated as a monoanionic NNO-donor chelate in the tautomeric form *a* (Scheme 1). By repeating this reaction with Hada in methanol under nitrogen, $[ReOCl_2(ada)]$ was isolated as product, in which ada is coordinated tridentately as tautomer *c*, with an anionic alcoholate oxygen atom *trans* to the oxo group. However, the reaction of $[Re(CO)_5Br]$ and Hada gives *fac*-$[Re(CO)_3Br(Hada)]$, with Hada coordinated as a neutral bidentate NN-donor as tautomer *b*.

Supplementary data

CCDC 708330 and 708331 contain the supplementary crystallographic data for **1** and **3**. These data can be obtained free of charge via http://www.ccdc.cam.ac.uk/conts/retrieving.html, or from the Cambridge Crystallographic Data Centre, 12 Union Road, Cambridge CB2 1EZ, UK; fax: (+44) 1223-336-033; or e-mail: deposit@ccdc.cam.ac.uk.

References

[1] (a) S. Goyal, K. Lal, J. Indian Chem. Soc. 66 (1989) 477;
(b) A.R. Middleton, A.F. Masters, G. Wilkinson, J. Chem. Soc. (1979) 542;
(c) F. Fulop, J. Mattinen, K. Pihlaja, Tetrahedron 46 (1990) 6545;
(d) Z. Li, Y. Li, L. Lei, C. Che, X. Zhou, Inorg. Chem. Commun. 8 (2005) 307.
[2] C. Qian, C. Zhu, T. Huang, J. Chem. Soc., Perkin Trans. 1 14 (1998) 2131.
[3] K. Maruoka, T. Itoh, T. Shirasaka, H. Yamamoto, J. Am. Chem. Soc. 110 (1988) 310.
[4] V. Ratovelomanana-Vidal, J.-P. Genet, J. Organomet. Chem. 567 (1998) 163. and references therein.
[5] N. Hoshino, Coord. Chem. Rev. 174 (1998) 77.
[6] L. Canali, D.C. Sherrington, Chem. Soc. Rev. 28 (1999) 85.
[7] X. Lin, D.M.J. Doble, A.J. Blake, C. Harrison, C. Wilson, M. Schröder, J. Am. Chem. Soc. 125 (2003) 9476.
[8] J.R. Dilworth, S.J. Parrott, Chem. Soc. Rev. 27 (1998) 43.
[9] J.C. Reubi, J. Nucl. Med. 36 (1995) 1825.
[10] S. Jurisson, D. Berning, J. Wei, M. Dangshe, Chem. Rev. 93 (1993) 1137.
[11] G. Rouschias, Chem. Rev. 74 (1974) 531.
[12] (a) C. Bolzati, M. Porchia, G. Bandoli, A. Boschi, E. Malago, L. Uccelli, Inorg. Chim. Acta 315 (2001) 205;
(b) J.Y. Kim, Y.J. Ji, H.-J. Ha, H.K. Chae, Bull. Korean Chem. Soc. 24 (2003) 504;
(c) A. Sachse, N.C. Mösch-Zanetti, G. Lyashenko, J.W. Wielandt, K. Most, J. Magull, F. Dall'Antonia, A. Pal, R. Herbst-Irmer, Inorg. Chem. 46 (2007) 7129.
[13] B.S. Furniss, A.J. Hannaford, P.W.G. Smith, A.R. Tatchell (Eds.), in: Vogel's Textbook of Practical Organic Chemistry, 5th Ed., Logman Scientific and Technical, England, 1989.
[14] N.P. Johnson, C.J.L. Lock, G. Wilkinson, Inorg. Synth. 9 (1967) 145.
[15] S. Chattopadhyay, G. Bocelli, A. Cantoni, A. Ghosh, Inorg. Chim. Acta 359 (2006) 4441.
[16] J.-P. Costes, M.I. Fernandez-Garcia, Inorg. Chim. Acta 237 (1995) 57.
[17] G.M. Sheldrick, SHELXL-97, Programs for Structure Solution and Refinement, University of Göttingen, Germany, 1997.
[18] A. Marchi, A. Duatti, R. Rossi, L. Magon, U. Mazzi, A. Pasquetto, Inorg. Chim. Acta 81 (1984) 15.
[19] T.I.A. Gerber, D. Luzipo, P. Mayer, J. Coord. Chem. 58 (2005) 1505.
[20] A. Abrahams, I. Booysen, T.I.A. Gerber, P. Mayer, Bull. Chem. Soc. Ethiop. 22 (2008) 247.
[21] V. Bertolasi, M. Sacerdoti, G. Gilli, U. Mazzi, Acta Crystallogr., Sect. B 38 (1982) 426.
[22] A. Abrahams, T.I.A. Gerber, D.R. Luzipo, P. Mayer, J. Coord. Chem. 60 (2007) 2207.
[23] P.D. Benny, C.L. Barnes, P.M. Piekarski, J.D. Lydon, S.S. Jurisson, Inorg. Chem. 42 (2003) 6519.
[24] T.I.A. Gerber, Z.R. Tshentu, S. Garcia-Granda, P. Mayer, J. Coord. Chem. 56 (2003) 1093.
[25] C. Melián, C. Kremer, L. Suescun, A. Mombrú, R. Mariezcurrena, E. Kremer, Inorg. Chim. Acta 306 (2000) 70.
[26] T.I.A. Gerber, D. Luzipo, P. Mayer, J. Coord. Chem. 57 (2004) 1419.
[27] L. Wei, J.W. Babich, J. Zubieta, Inorg. Chem. 43 (2004) 6445.
[28] F. Refosco, F. Tisato, C. Bolzati, G. Bandoli, J. Chem. Soc., Dalton Trans. (1993) 605. and references therein.
[29] I. Booysen, T.I.A. Gerber, P. Mayer, H.J. Schalekamp, J. Coord. Chem. 60 (2007) 1755.
[30] T.I.A. Gerber, D. Luzipo, P. Mayer, J. Coord. Chem. 57 (2004) 1345.
[31] W.A. Herrmann, M.U. Rauch, G.R.J. Artus, Inorg. Chem. 35 (1996) 1988.
[32] U. Mazzi, E. Roncari, R. Rossi, V. Bertolasi, O. Traverso, L. Magon, Transition Met. Chem. 5 (1980) 289.
[33] J. Granifo, Polyhedron 18 (1999) 1061.
[34] D.R. Gamelin, M.W. George, P. Glyn, F.W. Grevek, K. Schaffner, J.J. Turner, Inorg. Chem. 33 (1995) 3246.
[35] L. Maria, C. Moura, A. Paulo, I.C. Santos, J. Orgmet. Chem. 691 (2006) 4773.
[36] L. Wei, S.R. Banerjee, M.K. Levadala, J. Babich, J. Zubieta, Inorg. Chim. Acta 357 (2004) 1499.
[37] T.I. A Gerber, P. Mayer, Z.R. Tshentu, J. Coord. Chem. 58 (2005) 1271.

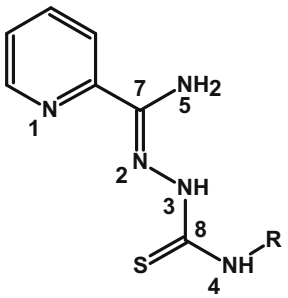


Fig. 1. Generic structure of 2-pyridineformamide thiosemicarbazones.

source at room temperature. The samples were analyzed at 80 K. All spectra were computer-fitted assuming Lorentzian curves.

Tin tetrachloride (Sigma–Aldrich), 2-cyanopyridine (Sigma–Aldrich), thiosemicarbazide (Sigma–Aldrich) and its *N*(4)-methyl (Sigma–Aldrich), *N*(4)-ethyl (Sigma–Aldrich) and *N*(4)-phenyl (Merck) derivatives were purchased and used without further purification. All other chemicals and solvents were of analytical grade.

2.2. Synthesis of [Sn(2Am4DH)Cl_3] (**1**), [Sn(2Am4Me)Cl_3] (**2**), [Sn(2Am4Et)Cl_3] (**3**) and [Sn(2Am4Ph)Cl_3] (**4**)

The 2-pyridineformamide thiosemicarbazones were prepared as described in the literature [15]. The tin(IV) complexes were obtained by stirring an ethanol solution of the desired ligand (3.0 mmol) with a slight excess of $SnCl_4$. The solids were washed with diethylether and then dried *in vacuo*. Crystals of complexes **1** and **2** suitable for X-ray diffraction were obtained by crystallization from ethanol.

2.2.1. Trichloro(2-pyridineformamide-thiosemicarbazonato)tin(IV) [Sn(2Am4DH)Cl_3] (**1**)

Yellow solid. *Anal. Calc. for* $C_7H_8Cl_3N_5SSn$ (419.30): C, 20.05; H, 1.92; N, 16.70. Found: C, 20.07; H, 1.77; N, 16.37%. Molar conductivity (1×10^{-3} mol L^{-1} DMF): 16.0 Ω^{-1} cm^2 mol^{-1}. Melt point: 283–284 °C. IR (CsI/nujol, cm^{-1}): *ν*(NH) 3456s, *ν*(C=N) 1652s, *ν*(CS) 718 m, ρ(py) 645 m, *ν*(M–N) 383 m, *ν*(M–S) 339 m, *ν*(M–Npy) 326 m, *ν*(M–Cl) 290w 258w. The main signals in ^{1}H NMR (DMSO-d_6): *δ* (ppm) = 9.09 (1H, d, H6), 8.16 (1H, t, H5), 8.61 (1H, t, H4), 8.70 (1H, d, H3), 7.23 (2H, s, N4H), 8.6–8.0 (2H, broad, N5H). ^{13}C NMR (DMSO-d_6): *δ* (ppm) = 162.30 (C8), 138.10 (C7), 144.26 (C6), 129.07 (C5), 144.11 (C4), 123.61 (C3), 141.70 (C2). ^{119}Sn NMR (DMSO-d_6): *δ* (ppm) = −480 (s). Yield 65%.

2.2.2. Trichloro(N(4)-methyl-2-pyridineformamide-thiosemicarbazonato)tin(IV) [Sn(2Am4Me)Cl_3] (**2**)

Yellow solid. *Anal.* Calc. for $C_8H_{10}Cl_3N_5SSn$ (433.33): C, 22.17; H, 2.33; N, 16.16. Found: C, 22.25; H, 2.22; N, 16.08%. Molar conductivity (1×10^{-3} mol L^{-1} DMF): 17.1 Ω^{-1} cm^2 mol^{-1}. Melt point: 291–292 °C. IR (CsI/nujol, cm^{-1}): *ν*(NH) 3437 m, *ν*(C=N) 1652 m, *ν*(CS) 768 m, ρ(py) 612 m, *ν*(M–N) 391w, *ν*(M–S) 329w, *ν*(M–Npy) 326w, *ν*(M–Cl) 290w, 279w. The main signals in ^{1}H NMR (DMSO-d_6): *δ* (ppm) = 9.08 (1H, d, H6), 8.15 (1H, t, H5), 8.62 (1H, t, H4), 8.72 (1H, d, H3), 7.71 (1H, q, N4H), 8.8–7.9 (2H, broad, N5H), 2.97 (3H, d, H9). ^{13}C NMR (DMSO-d_6): *δ* (ppm) = 29.09 (C9), 161.06 (C8), 138.15 (C7), 144.28 (C6), 129.07 (C5), 144.11 (C4), 123.55 (C3), 141.94 (C2). ^{119}Sn NMR (DMSO-d_6): *δ* (ppm) = −486 (s). Yield 68%.

2.2.3. Trichloro(N(4)-ethyl-2-pyridineformamide-thiosemicarbazonato)tin(IV) [Sn(2Am4Et)Cl_3] (**3**)

Yellow solid. *Anal.* Calc. for $C_9H_{12}Cl_3N_5SSn$ (447.36): C, 24.16; H, 2.70; N, 15.65. Found: C, 24.20; H, 2.48; N, 15.25%. Molar conductivity (1×10^{-3} mol L^{-1} DMF): 15.3 Ω^{-1} cm^2 mol^{-1}. Melt point: 296–297 °C. IR (CsI/nujol, cm^{-1}): *ν*(NH) 3425 m, *ν*(CN) 1655 m, *ν*(CS) 782 m, ρ(py) 605w, *ν*(M–N) 402w, *ν*(M–S) 345w, *ν*(M–Npy) 315w, *ν*(M–Cl) 288w. The main signals in ^{1}H NMR (DMSO-d_6): *δ* (ppm) = 9.10 (1H, d, H6), 8.16 (1H, t, H5), 8.61 (1H, t, H4), 873 (1H, d, H3), 7.71 (1H, t, N4H), 8.33 (2H, broad, N5H), 3.53 (2H, m, H9), 1.18 (3H, t, H10). ^{13}C NMR (DMSO-d_6): *δ* (ppm) = 14.61 (C10), 37.36 (C9), 160.65 (C8), 138.56 (C7), 144.68 (C6), 129.44(C5), 144.29 (C4), 123.94 (C3), 142.20 (C2). ^{119}Sn NMR (DMSO-d_6): *δ* (ppm) = −483(s). Yield 74%.

2.2.4. Trichloro(N(4)-phenyl-2-pyridineformamide-thiosemicarbazonato)tin(IV) [Sn(2Am4Ph)Cl_3] (**4**)

Yellow solid. *Anal.* Calc. for $C_{13}H_{12}Cl_3N_5SSn$ (495.40): C, 31.52; H, 2.44; N, 14.14. Found: C, 31.82; H, 2.52; N, 14.08%. Molar conductivity (1×10^{-3} mol L^{-1} DMF): 13.2 Ω^{-1} cm^2 mol^{-1}. Melt point: 296–297 °C. IR (CsI/nujol, cm^{-1}): *ν*(NH) 3424 m, *ν*(CN) 1655 m, *ν*(CS) 761 m, ρ(py) 653w, *ν*(M–N) 411w, *ν*(M–S) 355w, *ν*(M–Npy) 305w, *ν*(M–Cl) 290w. The main signals in ^{1}H NMR (DMSO-d_6): *δ* (ppm) = 9.15 (1H, d, H6), 8.22 (1H, t, H5), 8.68 (1H, t, H4), 8.86 (1H, d, H3), 9.80 (1H, s, N4H), 8.55 (2H, broad, N5H), 7.79 (2H, d, H10,14), 7.34 (2H, t, H11,13), 7.04 (1H, t, H12). ^{13}C NMR (DMSO-d_6): *δ* (ppm) = 119.89 (C14, C10), 128.79 (C13, C11), 122.42 (C12), 139.79 (C9), 157.66 (C8), 137.82 (C7), 144.33 (C6), 129.58 (C5), 144.33 (C4), 124.22 (C3), 143.44 (C2). ^{119}Sn NMR (DMSO-d_6): *δ* (ppm) = −491(s). Yield 71%.

2.3. X-ray crystallography

Crystals of [Sn(2Am4DH)Cl_3] (**1**) and [Sn(2Am4Me)Cl_3] (**2**) were mounted on a glass fiber and used for data collection. Crystal data were collected at 293(2) K, using a Bruker SMART CCD 1000 diffractometer [25]. Graphite monochromated Mo Kα radiation (*λ* = 0.71073 Å) was used throughout. The data were processed with SAINT [25], and corrected for absorption [26]. The structures were solved by direct methods using the program SHELXS-97 [27] and refined by full-matrix least-squares techniques againts F^2 using SHELXL-97 [28]. Positional and anisotropic atomic displacement parameters were refined for all non hydrogen atoms. Hydrogen atoms were located in difference maps and included as fixed contributions riding on attached atoms with isotropic thermal parameters 1.2 times those of their carrier atoms. Criteria of a satisfactory complete analysis were the ratios of rms shift to standard deviation less than 0.001 and no significant features in final difference maps. Molecular graphics were obtained from PLATON [29] and SCHAKAL [30]. A summary of the crystals data, experimental details and refinement results are listed in Table 1.

2.4. In vitro antimicrobial activity

Antifungal activity was evaluated by minimum inhibitory concentration (MIC) using the macrodilution test [31]. *Candida albicans* ATCC18804 stored in Sabouraud broth was subcultured for testing in the same medium and grown at 37 °C. Then, the yeast cells were suspended according to the McFarland protocol [31] in saline solution, to produce a suspension of about 10^5 CFU (colony-forming units) mL^{-1}. Serial dilutions of the compounds, previously dissolved in dimethyl sulfoxide (DMSO), were prepared in test tubes to final concentrations of 512, 256, 128, 64, 32, 16, 8, 4, 2 and 1 mg mL^{-1}. A 24-h old inoculum (100 μL) was added to each tube. The MIC, defined as the lowest concentration of the compound which inhibits the visible growth after 18 h, was determined visu-

Table 1
Crystal data and refinement results for [Sn(2Am4DH)Cl_3] (**1**) and [Sn(2Am4Me)Cl_3] (**2**).

Compound	[Sn(2Am4DH)Cl_3]	[Sn(2Am4Me)Cl_3]
Empirical formula	$C_7H_8Cl_3N_5SSn$	$C_8H_{10}Cl_3N_5SSn$
Formula weight	419.28	433.31
Temperature, K	293(2)	293(2)
Crystal system	triclinic	monoclinic
Space group	$\bar{P}$	$P2_1/n$
Unit cell dimensions		
a (Å)	7.0869(6)	12.790(1)
b (Å)	7.8035(6)	8.6308(7)
c (Å)	13. 092(1)	13.849(1)
α (°)	99.509(1)	90
β (°)	96.281(1)	104.178(1)
γ (°)	107.027(1)	90
V (Å^3)	673.2(1)	1482.1(2)
Z, density calculated (Mg/m^3)	2, 2.069	4, 1.942
Absorption coefficient, mm^{-1}	2.632	2.394
F(000)	404	840
Crystal size, mm	0.23 × 0.17 × 0.09	0.28 × 0.27 × 0.14
Crystal color, shape	yellow, prism	yellow, prism
θ range for data collection (°)	1.60–28.04	1.94–23.28
Index range, θ	$-9 \leqslant h \leqslant 7$ $-10 \leqslant k \leqslant 9$ $-17 \leqslant l \leqslant 16$	$-13 \leqslant h \leqslant 14$ $-9 \leqslant k \leqslant 9$ $-15 \leqslant l \leqslant 12$
Completeness	92.6% to θ = 28.04°	98.4% to θ = 23.28°
Absorption correction	SADABS [26]	SADABS [26]
Maximum and minimum transmission	0.7976, 0.5827	0.7304, 0.5537
Goodness-of-fit on F^2	0.970	0.931
Reflection collected/unique [R_{int}]	4330/3021 (0.0214)	6169/2100 (0.0443)
Data/restraints/parameters	3021/0/154	2100/0/163
Final R indices [$I > 2\sigma(I)$]	R_1 = 0.0314, wR_2 = 0.0659	R_1 = 0.0239, wR_2 = 0.0457
R indices (all data)	R_1 = 0.0384, wR_2 = 0.0678	R_1 = 0.0343, wR_2 = 0.0478
Largest differences in peak and hole, e Å^{-3}	0.949, −1.134	0.401, −0.492

ally after incubation for 18 h at 37 °C. Tests using fluconazole as reference and DMSO as negative control were carried out in parallel. No inhibition was observed with 5% v/v DMSO. All tests were performed in triplicates with full agreement between the results.

Antibacterial activity was evaluated by minimum inhibitory concentration (MIC) using the macrodilution test [32]. *Pseudomonas aeruginosa* ATCC27853 stored in Brain Heart Infusion (BHI) broth were subcultured for testing in the same medium and grown at 37 °C. Then the bacterial cells were suspended, according to the McFarland protocol [32] in saline solution, to produce a suspension of about 10^5 CFU mL^{-1}. Serial dilutions of the compounds, previously dissolved in DMSO, were prepared in test tubes to final concentrations of 512, 256, 128, 64, 32, 16, 8, 4, 2 and 1 mg mL^{-1}. A 24-h old inoculum (100 μL) was added to each tube. The MIC, defined as the lowest concentration of the test compound, which inhibits the visible growth after 20 h, was determined visually after incubation for 20 h at 37 °C. Tests using tetracycline as reference and DMSO as negative control were carried out in parallel. All tests were performed in triplicates with full agreement between the results.

2.5. Assay of toxicity against Artemia salina

The *A. salina* (brine shrimp) lethality test was employed as an antitumor prescreen. Lethality towards brine shrimp was assayed using procedures related in the literature [33,34]. Lethal dose (LD_{50}) is the amount of a substance which causes the death of 50% of a group of test animals. Determination of LD_{50} is an indication of the short-term poisoning potential (acute toxicity) of a compound.

Artemia salina encysted eggs (10 mg) were incubated in 500 mL of seawater under artificial light at 28 °C, pH 7–8. After incubation for 24 h, nauplii were collected with a Pasteur pipette and kept for an additional 24 h under the same conditions to reach the metanauplii stage. The samples to be assayed were dissolved in 1% DMSO (dimethylsulfoxide) and diluted in five different concentrations in seawater. About 10 nauplii were added to each set of tubes containing the samples. Controls containing 1% DMSO in seawater were included in each experiment. Forty-eight hours later, the number of survivors was counted, recorded and the lethal dose 50% (LD_{50} value) and 95% confidence intervals were calculated by Probit analysis [35]. The repeatability of the method was evaluated using nine replicates of concentration of each sample.

3. Results and discussion

Microanalyses and molar conductivity data suggest the formation of the following complexes: [Sn(2Am4DH)Cl_3] (**1**), [Sn(2Am4Me)Cl_3] (**2**), [Sn(2Am4Et)Cl_3] (**3**) and [Sn(2Am4Ph)Cl_3] (**4**), in which an anionic thiosemicarbazone is attached to the metal centre and the remaining coordination sites are occupied by three chloride ions. Diffraction X-ray analysis confirms the structures of **1** and **2.**

3.1. Spectroscopic characterization

The vibrations attributed to ν(C=N) at 1663–1587 cm^{-1} in the infrared spectra of the free thiosemicarbazones shift to 1655–1652 cm^{-1} in the spectra of complexes **1–4**, in agreement with coordination of the azomethine nitrogen [10,11,13,14]. The ν(C=S) absorption which lays at 860–854 cm^{-1} in the spectra of the ligands shifts to 768–718 cm^{-1} in the spectra of complexes **1–4**, hence indicating coordination of the sulfur. The 92–136 cm^{-1} shift is compatible with complexation upon deprotonation and formation of a thiolate sulfur [10,13,14]. The in-plane deformation mode of the pyridine ring at 618–600 cm^{-1} in the spectra of the uncomplexed thiosemicarbazones shifts to 653–605 cm^{-1} in complexes **1–4** suggesting coordination of the hetero-aromatic nitrogen [10,11,13,14].

In the spectra of **1–4** the absorptions at 383 and 411 cm^{-1} were assigned to the ν(Sn–N_{imine}) vibration mode. Bands at 329 and 355 cm^{-1} were attributed to ν(Sn–S), and the absorptions at 305–326 cm^{-1} and 258–290 cm^{-1} were attributed to the ν(Sn–Npy) and ν(Sn–Cl) modes, respectively [10,14].

Therefore, the thiosemicarbazones are attached to the metal through the N_{py}–N–S chelating system and chloride ions occupy the remaining coordination positions.

NMR spectra of the thiosemicarbazones and their tin(IV) complexes were recorded in DMSO-d_6 because this is the only solvent in which the free thiosemicarnazones and complexes are soluble. The ^{1}H resonances were assigned on the basis of chemical shifts, multiplicities and coupling constants. The carbon type (C, CH) was determined by using distortionless enhancement by polarization transfer (DEPT135) experiments. The assignments of the protonated carbons were made by 2D hetero-nuclear multiple quantum coherence experiments (HMQC). A ^{119}Sn NMR study was performed for all complexes.

In the ^{1}H spectra of the uncomplexed thiosemicarbazones the N3–H chemical shifts in DMSO-d_6 occur at δ 10.45–10.05 ppm, indicating hydrogen bonding with the solvent [10–14]. This signal is absent in the spectra of **1–4**, according to deprotonation and formation of an anionic ligand. Upon coordination the signals of the pyridine hydrogens undergo significant shifts. Variations also occur in the ^{13}C NMR spectrum for the signals of C8, C7 and the pyridine carbons, in accordance with coordination of the sulfur, the imine nitrogen and the hetero-aromatic nitrogen, leading to

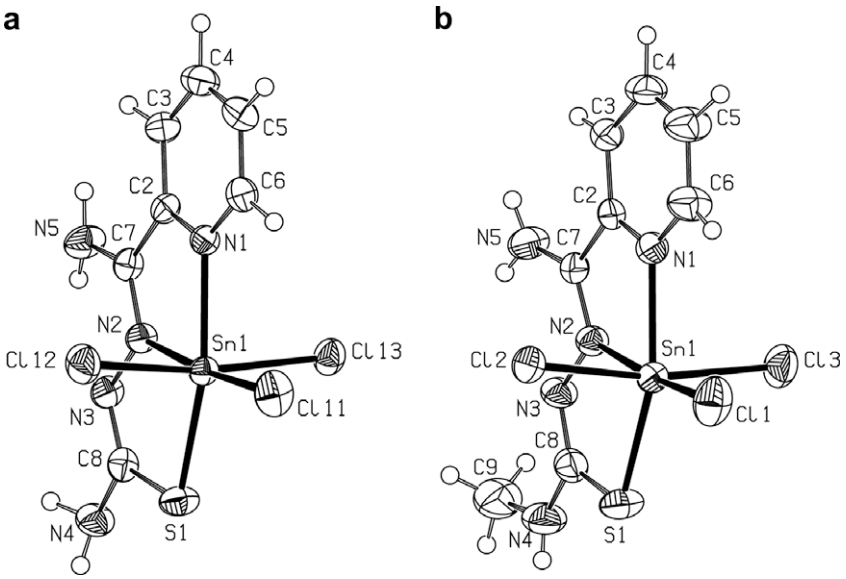


Fig. 2. Molecular plot of [Sn(2Am4DH)Cl_3] (**1**) and [Sn(2Am4Me)Cl_3] (**2**) showing the labeling scheme of the non-H atoms and their displacement ellipsoids at the 50% probability level.

compounds in which the thiosemicarbazone adopts the *E* configuration in relation to the C7–N2 bond.

In the ^{119}Sn NMR spectra of complexes **1**–**4** (DMSO-d_6) only one signal was observed at $\delta = -480$ (**1**), $\delta = -486$ (**2**), $\delta = -483$ (**3**) and $\delta = -491$ (**4**) ppm, compatible with the presence of one tin site. The values of the ^{119}Sn signal are in agreement with data reported in the literature for hexa-coordinated tin complexes [6]. In previous works, we found δ in the –(471–491) ppm range in the same solvent for [Sn(L)Cl_3] (HL = 2-benzoylpyridine-derived thiosemicarbazones) [6,7,13] which also contain an anionic tridentate thiosemicarbazone along with three chloride ions in the metal coordination sphere.

The Mössbauer isomer shifts are very similar for the four complexes, in agreement with the similar s-density around the metal centre in the three compounds. The isomer shifts decrease upon coordination due to the variation in the percentage of s-character as tin changes from approximately sp^3 hybridization (25% s-character) in the tin salt to sp^3d^2 (17% s-character) in the octahedral complexes **1**–**4** [6,7,13]. Hence, δ-values are 0.82(1) mm s^{-1} for $SnCl_4$ [7] and 0.58(5), 0.61(5), 0.63(5) and 0.55(5) mm s^{-1} for **1**–**4,** respectively.

Table 2
Selected bond lengths and angles for [Sn(2Am4DH)Cl_3] (**1**) and [Sn(2Am4Me)Cl_3] (**2**).

Bond	(**1**) (Å)	(**2**) (Å)	Angle	(**1**) (°)	(**2**) (°)
C2–C7	1.483(5)	1.479(5)	C2–C7–N2	115.2(3)	115.7(3)
C7–N5	1.328(4)	1.323(4)	N2–N3–C8	115.1(3)	114.6(3)
C7–N2	1.306(4)	1.301(4)	N3–C8–N4	117.3(3)	118.0(3)
N2–N3	1.379(4)	1.383(3)	N3–C8–S1	127.4(3)	127.5(3)
N3–C8	1.302(4)	1.306(4)	N4–C8–S1	115.3(3)	114.5(3)
N4–C8	1.354(4)	1.330(4)	N1–Sn–N2	73.77(10)	73.42(10)
C8–S1	1.768(4)	1.771(4)	N1–Sn–S1	153.19(8)	153.38(8)
Sn–S1	2.466(1)	2.451(1)	N1–Sn–Cl1	100.38(8)	99.43(7)
Sn–N1	2.240(3)	2.234(3)	N1–Sn–Cl2	88.32(8)	84.27(7)
Sn–N2	2.136(3)	2.148(3)	N1–Sn–Cl3	83.32(8)	85.93(7)
Sn–Cl1	2.368(1)	2.358(1)	N2–Sn–S1	79.81(8)	79.97(7)
Sn–Cl2	2.414(1)	2.4614(9)	N2–Sn–Cl1	174.13(8)	171.88(8)
Sn–Cl3	2.464(1)	2.4297(9)	N2–Sn–Cl2	89.04(9)	87.43(7)
			N2–Sn–Cl3	90.88(9)	94.30(7)
			Cl1–Sn–Cl2	90.35(4)	88.01(3)
			Cl1–Sn–Cl3	88.85(4)	88.93(4)
			Cl2–Sn–Cl3	171.32(3)	169.11(3)

The quadrupole splitting values for **1**–**4** were 0.46(5), 0.55(5), 0.58(5) and 0.67(5) mm s^{-1}, respectively, suggesting an increase in asymmetry of charge distribution with increasing the volume of the substituent attached to N4. This variation is probably due to spatial effects but differences in the electronic contribution among the three groups could also take place.

3.2. X-ray diffraction analysis

In Fig. 2 are perspective views of [Sn(2Am4DH)Cl_3] (**1**) and [Sn(2Am4Me)Cl_3] (**2**)**.** Selected intra-molecular bond distances and angles for **1** and **2** are given in Table 2. The distances and angles observed for the two compounds are very similar (see Table 2). In the two complexes tin(IV) is coordinated by a tridentate anionic ligand and three chloride ions in a distorted octahedral environment.

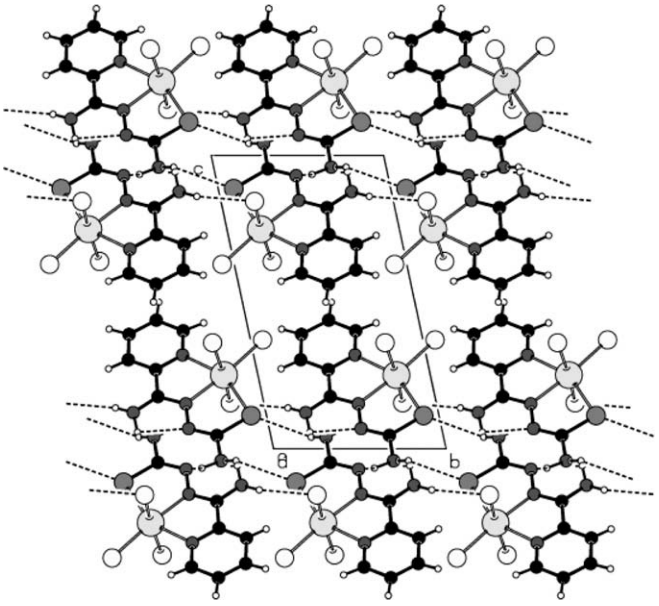


Fig. 3. Molecular packing of [Sn(2Am4DH)Cl_3] (**1**) showing the labeling scheme of the non-H atoms and their displacement ellipsoids at the 50% probability level.

Table 3
Hydrogen bonds distances (Å) and angles (°) for [Sn(2Am4DH)Cl_3] (**1**), [Sn(2Am4-Me)Cl_3] (**2**), with d(H···A) < *r* (Å) + 2.00 Å and <D–H···A> 110°.

	D–H···A	d(D–H)	d(H···A)	d(D···A)	(D–H···A)	Symmetry operation
	N4–H4A···N3	1.01	2.64	3.402(4)	132.4	[−*x* + 2, −*y* + ½, −*z*]
	N4–H4A···Cl3	1.01	2.93	3.672(4)	131.2	[−*x* + 1, −*y* + 1, −*z*]
(**1**)	N4–H4B···S1	0.88	2.78	3.482(3)	138.4	[−*x* + 2, −*y* + 2, −*z*]
	N5–H5A···Cl3	0.92	2.95	3.873(3)	174.5	[−*x* + 1, −*y* + 1, −*z*]
	N5–H5B···Cl3	0.89	2.51	3.316(3)	151.9	[*x*, *y* − 1, *z*]
(**2**)	N4–H4A···Cl2	0.77	2.70	3.381(3)	148.7	[−*x* + 1, −*y* + 1, −*z* + 1]
	N5–H5A···Cl1	0.79	2.84	3.511(3)	143.0	[*x*, *y* − 1, *z*]
	N5–H5B···Cl3	0.80	2.83	3.474(3)	139.5	[−*x*, −*y* + 1, −*z* + 1]
	N5–H5B···Cl2	0.80	2.91	3.577(3)	142.4	[−*x* + 1/2, *y*−1/2, −*z* + 3/2]

Molecular structures of H2Am4DH and H2Am4Me have been determined previously [15,17]. The expected lengthening of the C8–S bonds from 1.698 Å in H2Am4DH [15] to 1.768(4) Å in **1** and from 1.699 Å in H2Am4Me [17] to 1.753(2) Å in **2**, together with the shortening of the N3–C8 bonds from 1.340 Å and 1.358 Å in H2Am4DH and H2Am4Me to 1.302(4) and 1.306(4) Å in **1** and **2,** respectively were observed. Therefore, the C8–S bond changes from a double to a predominantly single bond whereas N3–C8 acquires some double bond character. The bond distances between tin and the imine nitrogens, 2.136(3) Å in **1** and 2.148(3) Å in **2**, are slightly shorter than the distance between tin and the pyridine nitrogen, 2.240(3) Å in **1** and 2.234(3) Å in **2**.

A twisting of approximately 180° in the N3–C8 bond of the thiosemicarbazone to match the steric requirements of tridentate coordination was evidenced. Hence, some angles undergo significant changes on complexation. The C8–N3–N2 angle goes from 118.4° in H2Am4DH [15] to 115.1(3)° in **1** and from 117.2° in H2Am4Me [17] to 114.6(3)° in **2**; N3–C8–S goes from *ca.* 120.1° in the free bases [15,17] to 127.4(2)° in **1** and to 127.5(3)° in **2**; N4–C8–S varies from *ca.* 123.5° in the free bases [15,17] to 115.3(3)° in **1** and to 114.5(3)° in **2**. In complexes **1** and **2,** the metal is located in a pseudo-octahedral environment in which the N1–Sn–S1 angle (*ca.* 153°) deviates markedly from the ideal value of 180°. The N2–Sn–Cl1 and Cl2–Sn–Cl3 angles are aproximately 170°.

The molecular packing of [Sn(2Am4DH)Cl_3] (**1**) (Fig. 3) reveals that a number of weak inter-molecular hydrogen bonds occur between N4–H and different atoms: Cl3, N3 and S1, and N5–H and Cl3 (see Table 3). In the molecular packing of [Sn(2Am4Me)Cl_3] (**2**) (Fig. 4) only inter-molecular hydrogen bonds involving N4–H, N5–H and chlorine atoms of neighboring chains occur (see Table 3). In both cases these interactions give rise to bi-dimensional networks.

3.3. Antimicrobial activity

The minimum inhibitory concentrations (MICs) against *P. aeruginosa* and *C. albicans* of the thiosemicarbazones and their tin(IV) complexes are reported in Table 4. Upon coordination to tin(IV) the activities against *C. albicans* and *P. aeruginosa* substantially increase. Although the antimicrobial activity of $SnCl_4$ could not be evaluated due to its extreme reactivity in air, a synergistic effect

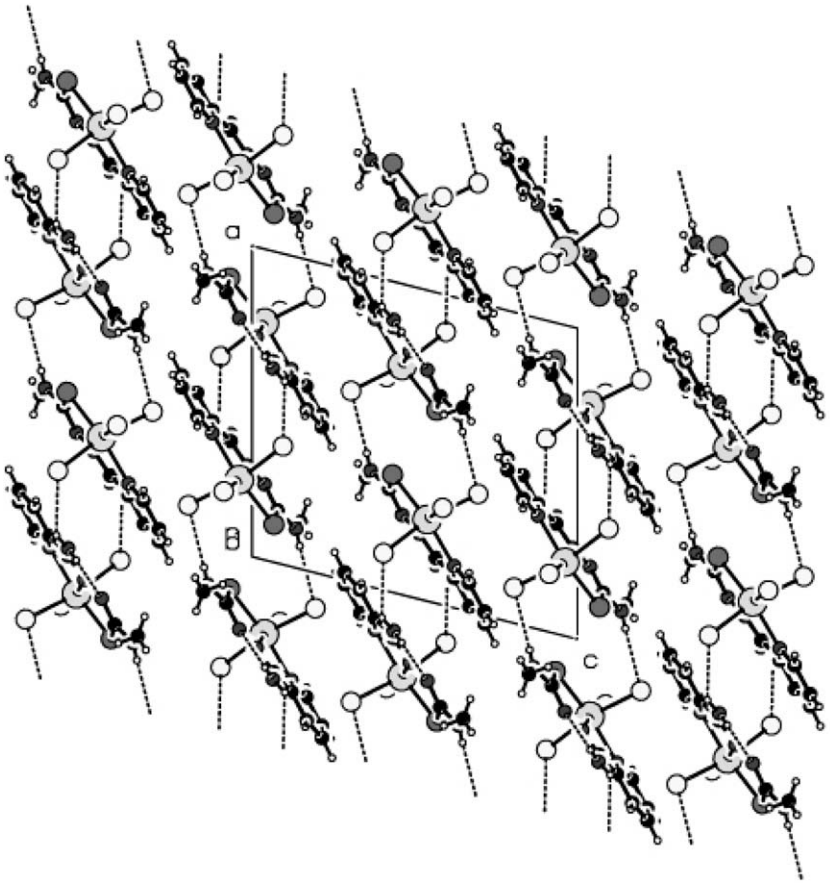


Fig. 4. Molecular packing of [Sn(2AmMe)Cl_3] (**2**) showing the labeling scheme of the non-H atoms and their displacement ellipsoids at the 50% probability level.

Table 4
Minimum inhibitory concentration (MIC) against *Candida albicans* and *Pseudomonas aeruginosa* for 2-pyridineformamide-derived thiosemicarbazones and their tin(IV) complexes.

Compound	MIC/μmol L^{-1} *C. albicans*	MIC/μmol L^{-1} *P. aeruginosa*
H2Am4DH	1312	1320
[Sn(2Am4DH)Cl_3] (**1**)	611	604
H2Am4Me	2448	1330
[Sn(2Am4Me)Cl_3] (**2**)	295	581
H2Am4Et	2294	1220
[Sn(2Am4Et)Cl_3] (**3**)	267	534
H2AmPh	1887	>2060
[Sn(2Am4Ph)Cl_3] (**4**)	>1014	>1022
Tetracycline		29
Fluconazole	18	

involving the metal and the thiosemicarbazone probably takes place. Also, the rigid structure of the thiosemicarbazone in the complexes could facilitate its interaction with the biological target. Finally, changes in lipophilicity upon coordination could also be in part responsible for the activity improvement in the complexes. It is worth comparing the values of MIC against *C. albicans* obtained in the present work for [Sn(2Am4DH)Cl_3] (**1**) (MIC = 611 μM), [Sn(2Am4Me)Cl_3] (**2**) (MIC = 295 μM) and [Sn(2Am4Et)Cl_3] (MIC = 267 μM) (**3**) with those previously determined for [(*n*-Bu)Sn(2Am4DH)Cl_2] (MIC = 290 μM), [(*n*-Bu)Sn(2Am4Me)Cl_2] (MIC = 281 μM) and [(*n*-Bu)Sn(2Am4Et)Cl_2] (MIC = 273 μM) (*n*-Bu stands for the *n*-butyl group) [14]. In both cases upon coordination to tin the antimicrobial activity increases. However, the presence of a chloride instead of the *n*-butyl group does not appreciably affect the antifungal activity.

3.4. Toxicity against Artemia salina

LD_{50} average values for the thiosemicarbazones and their tin(IV) complexes are reported in Table 5. We obtained LD_{50} in the 36.6–2.2 μM range for the free thiosemicarbazones and in the 25.5–1.6 μM range for the tin(IV) complexes. The tested compounds were found to be more active than lapachol (LD_{50} = 281 μM), which is known as reference compound [36]. Among the free thiosemicarbazones H2Am4Ph proved to be the most toxic against *A. salina*. Upon coordination the values of LD_{50} decrease, indicating higher toxicity for the complexes.

The toxicity against *A. salina* bioassay has a good correlation with cytotoxic activity in some human tumors [37]. The low values of LD_{50} obtained for the studied compounds in this assay indicate that they could present antineoplastic properties. H2Am4Ph and its tin complex (**4**) proved to be the most promising compounds.

Table 5
LD_{50} values for 2-pyridineformamide-derived thiosemicarbazones and their tin(IV) complexes against *Artemia salina*.

Compound	LD_{50}[a], μmol L^{-1} ± SD
H2Am4DH	36.6 ± 4.4
[Sn(2Am4DH)Cl_3] (**1**)	25.5 ± 1.7
H2Am4Me	30.0 ± 3.8
[Sn(2Am4Me)Cl_3] (**2**)	13.8 ± 1.3
H2Am4Et	26.0 ± 5.3
[Sn(2Am4Et)Cl_3] (**3**)	12.9 ± 0.6
H2Am4Ph	2.2 ± 0.5
[Sn(2Am4Ph)Cl_3] (**4**)	1.6 ± 0.5

[a] LD_{50}, lethal dose which causes the death of 50% of a group of test animals; SD, standard deviation.

4. Conclusions

Coordination to tin(IV) could be an interesting strategy for increasing the antimicrobial or cytotoxic activity of 2-pyridineformamide thiosemicarbazones. The very low LD_{50} values determined for H2Am4Ph and its tin(IV) complex (**4**) against *A. salina* suggest that the cytotoxicity of these compounds should be further investigated against human tumor cell lines.

Acknowledgement

This work was supported by CNPq and Instituto do Milênio e Inovação e Desenvolvimento de Novos Fármacos e Medicamentos (IM-INOFAR) (Proc. CNPq 420015/05-1), Brazil.

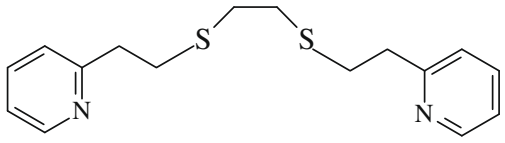
Appendix A. Supplementary data

CCDC 702257 and 702258 contain the supplementary crystallographic data for compounds (**1**) and (**2**). These data can be obtained free of charge via <http://www.ccdc.cam.ac.uk/conts/retrieving.html>, or from the Cambridge Crystallographic Data Centre, 12 Union Road, Cambridge CB2 1EZ, UK; fax: (+44) 1223 336 033; or e-mail: deposit@ccdc.cam.ac.uk. Supplementary data associated with this article can be found, in the online version, at doi:10.1016/j.poly.2008.12.047.

References

[1] H. Beraldo, D. Gambino, Mini. Rev. Med. Chem. 4 (2004) 159.
[2] D.X. West, A. Liberta, S.B. Padhye, R.C. Chikate, P.B. Sonawane, A.S. Kumbhar, R.G. Yerande, Coord. Chem. Rev. 123 (1993) 49.
[3] D.X. West, S.B. Padhye, P.B. Sonawane, Struct. Bond. 76 (1991) 1.
[4] J.S. Casas, M.S. Garcia-Tasende, J. Sordo, Coord. Chem. Rev. 209 (2000) 197.
[5] R.H. Borges, E. Paniago, H. Beraldo, J. Inorg. Biochem. 65 (1997) 267.
[6] A. Perez-Rebolledo, J.D. Ardisson, G.M. de Lima, W.A.A. Macedo, H. Beraldo, Hyperfine Interact. 163 (2005) 89.
[7] A. Perez-Rebolledo, G.M. de Lima, L.N. Gambi, N.L. Speziali, D.F. Maia, C.B. Pinheiro, J.D. Ardisson, M.E. Cortés, H. Beraldo, Appl. Organomet. Chem. 17 (2003) 945 (and references therein).
[8] R.F.F. Costa, A.P. Rebolledo, T. Matencio, H.D.R. Calado, J.D. Ardisson, M.E. Cortès, B.L. Rodrigues, H. Beraldo, J. Coord. Chem. 58 (2005) 307.
[9] A. Pérez-Rebolledo, J.D. Ayala, G.M. de Lima, N. Marchini, G. Bombieri, C.L. Zani, E.M. Souza-Fagundes, H. Beraldo, Eur. J. Med. Chem. 40 (2005) 467.
[10] A.P. Rebolledo, M. Vieites, D. Gambino, O.E. Piro, E.E. Castellano, C.L. Zani, E.M. Souza-Fagundes, L.R. Teixeira, A.A. Batista, H. Beraldo, J. Inorg. Biochem. 99 (2005) 698.
[11] I.C. Mendes, J.P. Moreira, L.N. Speziali, A.S. Mangrich, J.A. Takahashi, H. Beraldo, J. Braz. Chem. Soc. 17 (8) (2006) 1571.
[12] I.C. Mendes, J.P. Moreira, J.D. Ardisson, S.P. Balena, B.L. Rodrigues, H. Beraldo, Polyhedron 26 (2007) 3263.
[13] A. Perez-Rebolledo, G.M. de Lima, N.L. Speziali, O.E. Piro, E.E. Castellano, J.D. Ardisson, H. Beraldo, J. Organomet. Chem. 691 (18) (2006) 3919.
[14] I.C. Mendes, J.P. Moreira, J.D. Ardisson, R.G. Santos, P.R.O. Silva, I. Garcia, A. Castiñeiras, H. Beraldo, Eur. J. Med. Chem. 43 (2008) 1454.
[15] A. Castiñeiras, I. Garcia, E. Bermejo, D.X. West, Z. Naturforsch. B: Chem. Sci. 55 (2000) 511.
[16] E. Bermejo, A. Castiñeiras, I. Garcia-Santos, D.X. West, Z. Anorg. Allg. Chem. 631 (2005) 2011 (and references therein).
[17] D.X. West, J.K. Swearingen, J. Valdes-Martinez, S. Hernandez-Ortega, A.K. El-Sawaf, F. Van Meurs, A. Castineiras, I. Garcia, E. Bermejo, Polyhedron 18 (1999) 2919.
[18] I. Garcia, E. Bermejo, A.K. El Sawaf, A. Castiñeiras, D.X. West, Polyhedron 21 (2002) 729 (and references therein).
[19] E. Bermejo, A. Castiñeiras, L.M. Fostiak, I. Garcia-Santos, J.K. Swearingen, D.X. West, Polyhedron 23 (2004) 2303.
[20] E. Bermejo, A. Castineiras, I. Garcia-Santos, L.M. Fostiak, J.K. Swearingen, D.X. West, Z. Anorg. Allg. Chem. 631 (2005) 728.
[21] D. Kovala-Demertzi, P. Tairidou, U. Russo, M. Gielen, Inorg. Chim. Acta 239 (1995) 177.
[22] M. Gielen, M. Biesemans, R. Willen, Appl. Organomet. Chem. 19 (2005) 440.
[23] A.H. Jacobson, G.L. Willingham, Sci. Total Environ. 258 (2000) 103.
[24] A. Abbott, P.D. Abel, D.W. Arnold, A. Milne, Sci. Total Environ. 258 (2000) 5.
[25] SMART and SAINT, Area Detector Control and Integration Software, Sage, Madison, Wisconsin, USA, 1997.
[26] G.M. Sheldrick, SADABS, Program for empirical Absorption Correction of Area Detector Data, University of Göettingen, Germany, 1997.

[27] G.M. Sheldrick, Acta Cryst. A 46 (1990) 467.
[28] G.M. Sheldrick, SHELXL-97, Program for Crystal Structures Analysis, University of Göettingen, Germany, 1997.
[29] A.L. Spek, PLATON: A Multipurpose Crystallographic Tool, Utrecht University, Utrecht, The Netherlands, 2003.
[30] E. Keller, SCHAKAL-97, Computer Program for the Graphic Representation of Molecular and Crystallographic Models, University of Freiburg, Breisgau, Germany, 1997.
[31] National Committee for Clinical Laboratory Standards, Reference method for broth dilution antifungal susceptibility testing of yeasts, in: NCCLS Document M27eMA2 NCCLS, Pennsylvania, USA, 2002, ISBN: 1-56238-469-4.
[32] National Committee for Clinical Laboratory Standards, Method for dilution antimicrobial susceptibility tests for bacteria that grow aerobically, in: NCCLS Document M7-A6, Pennsylvania, USA, 2003, ISBN: 1-56238-486-4.
[33] B.N. Meyer, N.R. Ferrigni, J.E. Putnam, L.B. Jacobsen, D.E. Nichols, J.L. McLaughlin, J. Med. Plant Res. 45 (1982) 31.
[34] I.A. Nascimento, M.M.S. Araújo, Ecotoxicol. Environ. Restor. 2 (1999) 41.
[35] D.J. Finney, Probit Analysis, Cambridge University Press, Cambridge, 1971.
[36] L.P. Santos Pimenta, G.B. Pinto, J.A. Takahashi, L.G.F. Silva, M.A.D. Boaventura, Phytomedicine 10 (2003) 209.
[37] A.E. Graminha, F.S. Vilhena, A.A. Batista, S.R.W. Louro, R.L. Ziolli, L.R. Teixeira, H. Beraldo, Polyhedron 27 (2008) 547.



Scheme 1. Structure of the ligand = 1,8-bis-(2-pyridyl)-3,6-dithiaoctane (***pdto***).

2. Experimental

2.1. Chemicals

All chemicals and solvents for the synthesis and electrochemical studies were purchased from Aldrich Chemical Co. and were used without further purification.

2.2. Synthesis

Ligand 1,8-bis(2-pyridyl)-3,6-dithioctane (***pdto***) was prepared by the method described by Goodwin and Lions. Yield 70% [6]. Elemental *Anal.* Calc. for $C_{16}H_{20}N_2S_2$: C, 63.1; H, 6.6; N, 9.2; S, 20.1. Found: C, 63.1; H, 6.2; N, 9.7; S, 20.5%.

Aquo 1,8-bis(2-pyridyl)-3,6-dithiaoctane copper(II) hexafluorophosphate, [Cu(***pdto***)(H_2O)](PF_6)$_2$ 0.304 g (1.0 mmol) of ***pdto*** was added to 0.294 g of $Cu(NO_3)_2 \cdot 2.5H_2O$ (1.0 mmol) previously dissolved in 50 mL of methanol. The solution was stirred strongly and a deep blue color was observed. This solution was treated with two equivalents of ammonium hexafluorophosphate (0.0088 g). A blue precipitate was isolated. Elemental *Anal.* Calc. for $CuC_{16}H_{21}N_2S_2OP_2F_{12}$: C, 28.4; H, 3.1; N, 4.2; S, 9.5. Found: C, 28.1; H, 3.0; N, 4.7; S, 9.3%.

2.3. Measurement of cell growth inhibition

The antiproliferative effect was analyzed on cervix human tumor cell line HeLa obtained from American Type Culture Collection (ATCC, Rockville (MD) USA). Once the cells reached a constant rate of proliferation, approximately 2×10^4 cells/well were plated in a 96-well microplate with Dulbecco's modified eagle medium (DMEM) supplemented with 10% of fetal bovine serum (FBS), and allowed to attach, incubating at 37 °C and 5% CO_2 for 24 h. At the end of incubation timing the medium was removed and cells were exposed to drugs in five different concentrations (0, 1, 10, 100 and 300 μg/mL) with fresh supplemented media for 24 h. *cis*-platin was employed as drug control at same mentioned concentrations. Cell growth was determined according to the sulforhodamine B assay, described by Skehan et al. [7,8]. Absorbance was measured at 564 nm (*Microplate reader BIO-RAD 550*) and percentage cell growth by each concentration of drug was calculated as: percentage growth = $100 * [T/C]$; where T is the absorbance of treated wells and C is the absorbance of untreated wells. The software PROBIT (*Log Probit Analysis by Maximum Likelihood/Novartis)* was used to calculate the concentration to inhibit the proliferation of the cells in a 50% (IC_{50}).

2.4. Elemental analysis

Fissons Instruments Analyzer model EA 1108 was used for elemental analysis determination, using a sulfanilamide standard.

2.5. Electrochemistry

All electrochemical measurements were performed in acetonitrile, MeCN, (HPLC grade) solution containing 0.1 M tetra-N-butylammonium tetrafluoroborate ($TBABF_4$) as supporting electrolyte. All electrochemical experiments were obtained at sample concentrations of 1×10^{-3} M in the presence of supporting electrolyte. A potentiostat/galvanostat EG&G PAR model 263 controlled by a PC software was used. A typical three-electrode array was employed for all electrochemical measurements: platinum disk as working electrode $\phi = 2$ mm, platinum wire as counter-electrode, and a silver wire as pseudo reference electrode. The silver electrode was immersed in a MeCN solution with 0.1 M tetra-N-butylammonium chloride (TBACl) in a separate compartment that was connected to the working cell through a BAS vycor™ tip. All potentials were reported versus the couple Fc/Fc^+ according to IUPAC.

Cyclic voltammetry was initiated from open circuit potential (E_{ocp}), the scan rate employed was 0.1 V/s. One step chronoamperometry experiments were performed, initiating at $E_1 = E_{ocp}$ to different potential values, E_2, using a pulse width of 3 s. Electrochemical impedance spectra were measured using a BAS-ZAHNER IM6 potentiostat–galvanostat which was controlled by the software THALES SYSTEM™ version 3.0 previously installed in a PC Pentium III. All the spectra were obtained at open circuit potential and applying to the electrochemical cell an alternant perturbation having an amplitude of 10 mV and frequencies, f, between 100 kHz and 1 Hz. Fitting data to the Randles equivalent circuit were carried out by means of the spectra simulator SIM, which is a routine also supplied by the THALES SYSTEM software.

3. Results and discussion

3.1. Cell growth inhibition studies of [Cu(*pdto*)H_2O]$^{2+}$ complex

The antiproliferative effect of the compound [Cu(***pdto***)H_2O]$^{2+}$ was determined as IC_{50} in human cervix tumor cell line HeLa. From Table 1 it can be seen the similarity between the IC_{50} value of [Cu(***pdto***)H_2O]$^{2+}$ (41.8 ± 1.2 μM) and *cis*-platin (40.1 ± 0.9 μM). An inspection of values, show that the biological activity is due to [Cu(***pdto***)H_2O]$^{2+}$ complex, and not to its precursors. This fact can be related to redox properties, which may correspond to possible Cu-SOD dismutase reactions. In order to explain how the redox properties affect the biological activity, in the next sections we present a complete electrochemical characterization of the [Cu(***pdto***)H_2O]$^{2+}$ complex, and $Cu(NO_3)_2 \cdot 2.5H_2O$.

3.2. Electrochemical behavior of $Cu(NO_3)_2 \cdot 2.5H_2O$

Cyclic voltammogram of a 1×10^{-3} M $Cu(NO_3)_2 \cdot 2.5H_2O$ acetonitrile solution is shown in Fig. 1. When the scan was initiated in negative direction two reduction signals **Ic** and **IIc**, and two oxidation signals **Ia** and **IIa** are observed. The dependence of the signals **Ic** with **Ia** and **IIc** with **IIa** was established by modifying the switching potentials E_{-i}. The cathodic and anodic peak potential values for signals **Ic**, **IIc**, **Ia** and **IIa** are: E_{pc}(**Ic**) = 0.401 V, E_{pc}(**IIc**) = −0.914 V, E_{pa}(**Ia**) = 0.615 V and E_{pa}(**IIa**) = −0.667 V, respectively.

The electrochemical processes **I** and **II** can be attributed to the consecutive reductions Cu(II) + 1e → Cu(I) and Cu(I) + 1e → Cu(0).

Table 1
IC_{50} mean values (μM) and standard deviation (SD) obtained for [Cu(***pdto***)H_2O]$^{2+}$, $Cu(NO_3)_2 \cdot 2.5H_2O$, and *cis*-platin against tumor cell line HeLa.

	IC_{50} (μM) ± SD
cis-Platin	40.1 ± 0.9
[Cu(***pdto***)H_2O]$^{2+}$	41.8 ± 1.2
$Cu(NO_3)_2 \cdot 2.5H_2O$	No activity
pdto	No activity

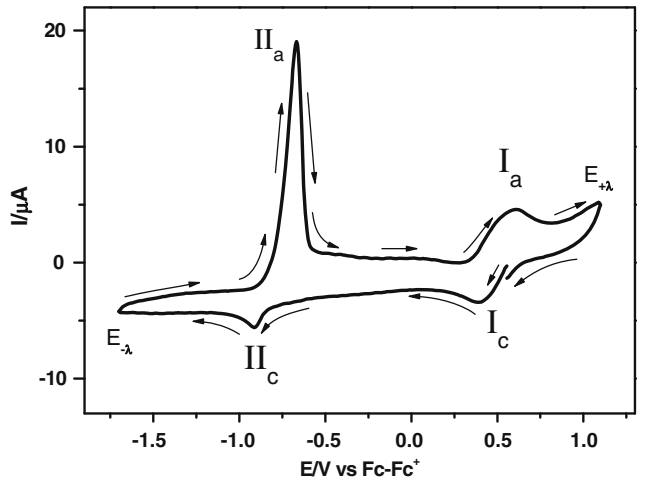


Fig. 1. Cyclic voltammogram of 1×10^{-3} M $Cu(NO_3)_2 \cdot 2.5H_2O$ in MeCN in presence of 0.1 M $TBABF_4$. The scan potential was initiated from E_{ocp} to negative direction. Scan rate 0.1 V s^{-1}. Platinum electrode was used.

However, to confirm this idea one step chronoamperometry experiments were also carried out.

From current-sampled versus potential plot $I(t) - E$, at current sampling time of 1.5 s, two reduction and one oxidation diffusion controlled limit zones are detected: $Id_{Ic}(t)$, $Id_{IIc}(t)$ and $Id_{Ia}(t)$ (see Fig. 2). This is a typical current–potential curve when soluble species of a redox couple are initially presented. Using the ratio $Id_{Ic}(t)/Id_{Ia}(t)$, it was established 90% of Cu(II) and 10% of Cu(I) in solution. The presence of the last species is attributed to its stability in acetonitrile solution [9,10].

The equation that describes the voltammogram in sampled-current voltammetry in the semi-infinite linear diffusion region with two soluble species of a redox couple is:

$$E = E_{1/2} + \frac{RT}{nF}\ln\frac{[Id_{OX}(t) - I(t)]}{[I(t) - Id_{RED}(t)]} \quad (3)$$

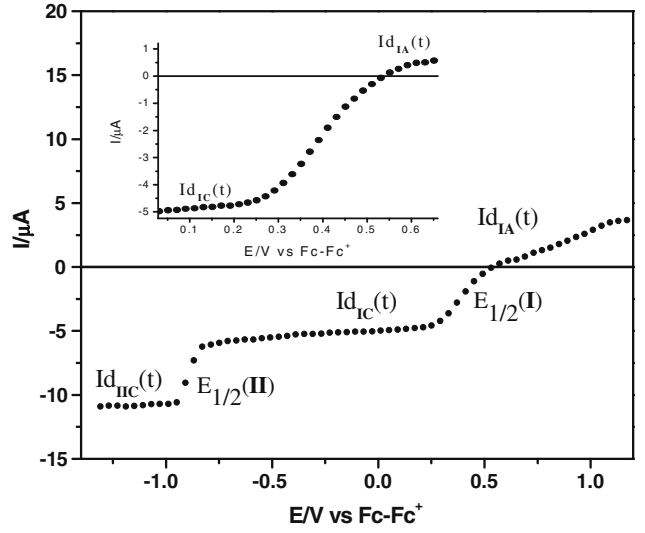


Fig. 2. Current-potential curves $I(t)$–E, constructed from chronoamperograms at different potentials E_2 from −1.560 to 1.571 V/Fc − Fc^+, corresponding to the electrochemical behavior of the copper salt $Cu(NO_3)_2 \cdot 2.5H_2O$. The $I(t)$–E plot was constructed for current sampling times 1.5 s. Inset corresponds to an expanded $I(t)$–E scale.

For a reversible system the slope value should be 0.059/n V at 25 °C and the intercept corresponds to the half wave potential $E_{1/2}$. The half wave potential is usually a very good approximation of E^0 for a reversible couple, whenever the diffusion coefficients ratio is close to the unity Eq. (4):

$$E_{1/2} = E^0 + \frac{RT}{nF}\ln\frac{D_R^{1/2}}{D_O^{1/2}} \quad (4)$$

The slope and the intercept of E versus $\log[Id_{OX}(t) - I(t)]/[I(t) - Id_{RED}(t)]$ plot were found to be 0.122 and 0.387 ($r = 0.999$) for process **I**, and 0.047 and −0.892 ($r = 0.999$) for process **II**. The slope values suggest that non-reversible behavior for processes **I** and **II** is observed.

Due to the non-reversible behavior of both processes, no formal potential E^0, can be evaluated. Instead of E^0, the values of $E_{1/2}$ for processes **I** and **II** were obtained, $E_{1/2}(I) = 0.387$ V and $E_{1/2}(II) = -0.892$ V. Considering the preferential geometry of Cu(II) and Cu(I) complexes and with all arguments presented above, the following electrochemical reactions in MeCN solution are proposed:

I $[Cu^{II}(MeCN)_n]^{2+} + 1e \rightarrow [Cu^{I}(MeCN)_{n-1}]^{+} + MeCN$
$E_{1/2}(I) = 0.387$ V

II $[Cu^{I}(MeCN)_{n-1}]^{+} + 1e \rightarrow Cu(0) + (n-1)MeCN$
$E_{1/2}(II) = -0.892$ V

4. Electrochemical behavior of the complex $[Cu(\textit{pdto})H_2O]^{2+}$

Fig. 3 shows a typical cyclic voltammogram of $[Cu(\textbf{\textit{pdto}})H_2O]^{2+}$ in acetonitrile solution, started from open circuit potential to negative direction. Before the potential switch, $E_{-\lambda}$, two reduction signals **Ic′** and **IIc′** can be observed. When the scan was completed four oxidation signals (**IIa′**, **IIa′*** , **Ia′** and **IIIa′**) and one additional reduction signal (**IIIc′**) were detected. The cathodic peak potential values E_{pc}(**Ic′**), E_{pc}(**IIc′**) and E_{pc}(**IIIc′**) for signals **Ic′**, **IIc′** and **IIIc′** are: 0.180, −1.106 and 0.340 V, respectively. On the other hand, the values of anodic peaks potentials E_{pa}(**Ia′**), E_{pa}(**IIa′**) and E_{pa}(**IIIa′**) for signals **Ia′**, **IIa′** and **IIIa′** were 0.268, −0.650 and 0.543 V.

A comparison of these peak potential values, and those obtained from Fig. 1, suggests that the signals **IIIa′** and **IIIc′** are attributed to

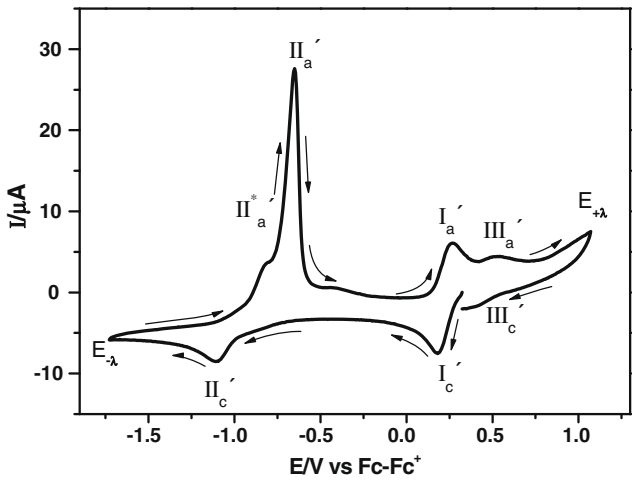


Fig. 3. Cyclic voltammogram of 1×10^{-3} M $[Cu(\textbf{\textit{pdto}})H_2O](PF_6)_2$ in MeCN in presence of 0.1 M $TBABF_4$. The scan potential was initiated from E_{ocp} to negative direction. Scan rate 0.1 V s^{-1}. Platinum electrode was used.

non-coordinated Cu(II) that comes form the dissociation of the complex. The signal **IIa**′* can be explained as the dissolution of deposited elemental copper in the presence of the ligand [11].

In order to obtain the number of electrons exchanged in the principal processes **I**′ and **II**′, current-sampled versus potential plot $I(t) - E$ was constructed from chronoamperometric experiments at current sampling time of 1.5 s. Two diffusion controlled limit zones $Id_{I}(t)$ and $Id_{II}(t)$ with their corresponding half wave potential $E_{1/2}$(I) and $E_{1/2}$(II) are observed.

For a reversible system when only one oxidized species is present in solution, a plot E versus $\log[I_d(t) - I(t)/I(t)]$ should be linear with a slope value of 0.059/n V and with an intercept value that corresponds to the formal potential E^0. Using linear fit with correlation coefficient of 0.999 for both processes, the calculated slopes were 0.065 for process **I**′, and 0.069 for process **II**′. These values clearly suggest that both systems are practically reversible with a value of one electron exchanged in both cases. From the intercept, the obtained values of formal potentials E^0(I′) and E^0(II′) for processes **I**′ and **II**′ were 0.165 and −1.110 V, respectively.

To confirm the number of exchanged electrons in these processes, Cottrell's analysis is presented. It is well known that for a two consecutive electron transfer, the diffusion limit currents are established with the Cottrell Equations: for the first step, Eq. (5), the slope is proportional to n_1, Eq. (7), and for the second step, Eq. (6), the slope is proportional to $(n_1 + n_2)$, Eq. (8) [12]:

$$Ox_1 + n_1 \rightarrow Red_1 \quad (5)$$

$$Red_1 + n_2 \rightarrow Red_2 \quad (6)$$

$$Id(t) = n_1 FAD_o^{1/2}\pi^{1/2}Co^* t^{-1/2} \quad (7)$$

$$Id(t) = (n_1 + n_2)FAD_o^{1/2}\pi^{-1/2}Co^* t^{-1/2} \quad (8)$$

Two linear relationships of current $I(t)$ and $t^{-1/2}$ were obtained within the two diffusion controlled zones, with the equations $I(t) = -4.9t^{-1/2} + 0.36$ ($r = 0.999$) and $I(t) = -10.0t^{-1/2} + 0.9$ ($r = 0.999$) for processes **I**′ and **II**′, respectively. Considering the same value of diffusion coefficient in Eqs. (7) and (8), the ratio $Id_{II}(t)/Id_{I}(t) = 2$ confirms the values $n_1 = 1$ and $n_2 = 1$. With all the evidences the electrochemical processes **I**′ and **II**′ can be attributed to:

I′ $[Cu^{II}(\boldsymbol{pdto})H_2O]^{2+} + 1e \rightarrow [Cu^{I}(\boldsymbol{pdto})]^{+} + H_2O$

$E^0(I') = 0.165\ V/Fc - Fc^+$

II′ $[Cu^{I}(\boldsymbol{pdto})]^{+} + 1e \rightarrow Cu(0) + \boldsymbol{pdto}$ $E^0(II') = -1.110\ V/Fc - Fc^+$

The coordination spheres for Cu(I) and Cu(II) complexes are proposed based on previously reported X-ray structures. [13]. The reversibility presented in the electrochemical processes Cu(II)/Cu(I) is in agreement with the high flexibility of the ligand ***pdto*** towards the preferential geometry of the central atom [4–6,13–24].

In order to complete the electrochemical characterization of the complex $[Cu(\boldsymbol{pdto})H_2O]^{2+}$, and its precursor $Cu(NO_3)_2 \cdot 2.5H_2O$, electrochemical impedance spectroscopy experiments were performed. These results are discussed in the next section.

4.1. Electrochemical impedance spectroscopy studies of $[Cu(\boldsymbol{pdto})H_2O]^{2+}$ $Cu(NO_3)_2 \cdot 2.5H_2O$

Fig. 4 shows typical Nyquist plots for $Cu(NO_3)_2 \cdot 2.5H_2O$ and $[Cu(\boldsymbol{pdto})H_2O]^{2+}$. The presence of a semi-loop at high frequencies in these plots indicates that an electrochemical reaction exists at the open circuit potential (E_{ocp}). This reaction is attributed to the Cu(II)/Cu(I) equilibrium. But, according to the shape of the spectra at the low frequency range, the main contribution to the impedance is due to a semi-infinite diffusion process, which controls the overall reaction rate. It seems that the species involved in this equilibrium diffuse at the interface metal–solution. However these species remains unidentified.

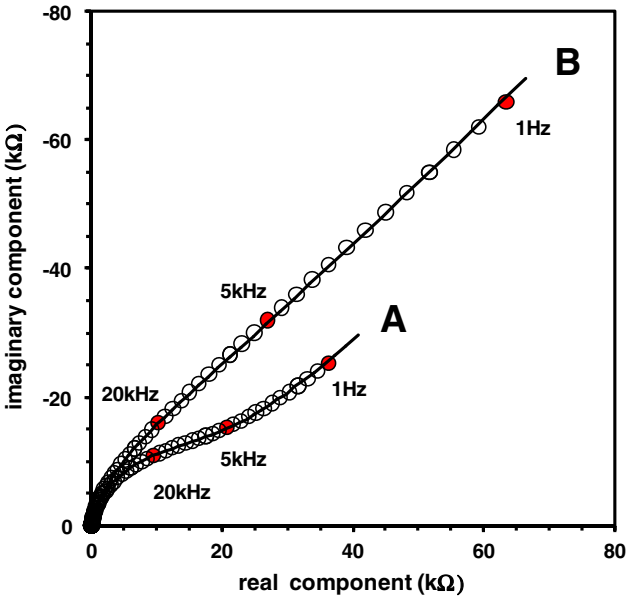


Fig. 4. Nyquist diagram for (A) $Cu(NO_3)_2 \cdot 2.5H_2O$ and (B) $[Cu(\boldsymbol{pdto})H_2O](PF_6)_2$. The concentration of samples was 1×10^{-3} M, in supporting electrolyte (0.1 M $TBABF_4$ in MeCN). EIS spectra were obtained at open circuit potential $E_{i=0}$ vs. $Fc - Fc^+$ couple with alternant perturbation 10 mV.

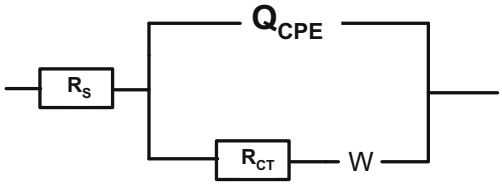
Both impedance spectra have been analyzed using a classical Randles equivalent circuit, displayed on Scheme 2. In this circuit, R_s stands for the resistance of the electrolyte, R_{tc} is the charge transfer resistance of the electrochemical reaction, *CPE* (constant phase element) and n are related to the double layer capacitance C_{dl} (see Eq. (9)) and, W is the Warburg parameter, related to diffusion processes (see Eq. (10)) [25,26]:

$$Z_{CPE} = \frac{1}{Q_{CPE}}(j\omega)^{-n} \quad (9)$$

where $\omega = 2\pi f$, $j = \sqrt{-1}$, and $0 \leqslant n \leqslant 1$ If $n = 1$ $Z_{CPE} = Z_{C_{dl}}$

$$Z_W = W(j\omega)^{-1/2} \quad (10)$$

Fig. 4 shows a good fitting (continuous line) of the Randless circuit to the experimental spectra in both cases. Fitted parameters are presented in Table 2. It is seen that R_{tc} is similar for both $Cu(NO_3)_2 \cdot 2.5H_2O$ and $[Cu(\boldsymbol{pdto})H_2O]^{2+}$ spectra, showing no significant difference in the kinetics of charge transfer of both species. In contrast, there is a significant difference in the Warburg parameter, being more important the diffusion process for the $[Cu(\boldsymbol{pdto})H_2O]^{2+}$ complex. This means that a deeper concentration gradient is built in this case, as a result of a faster electrochemical reaction. Such behavior is related to a more reversible Cu(II)/Cu(I) equilibrium, thus confirming the voltammetric and chronoamperometric results.



Scheme 2. Randles-type equivalent circuit used for fitting EIS spectra.

Table 2
Parameters of the Randles circuit fitted to the impedance spectra.

Compound	Proposed parameters
$Cu(NO_3)_2 \cdot 2.5H_2O$	$R_s = 212.4 \pm 5.5\ \Omega$, $R_{ct} = 17.9 \pm 0.2\ k\Omega$, $C_{dl} = 0.336 \pm 0.005\ \mu F$ $n = 0.933 \pm 0.002$, $W = 86.57 \pm 1.59\ k\Omega/s^{1/2}$
$[Cu(\textbf{\textit{pdto}})H_2O](PF_6)_2$	$R_s = 213.8 \pm 16.3\ \Omega$, $R_{ct} = 18.7 \pm 0.6\ k\Omega$, $C_{dl} = 0.258 \pm 0.007\ \mu F$ $n = 0.924 \pm 0.004$, $W = 246.30 \pm 2.88\ k\Omega/s^{1/2}$

It is totally clear that the complex $[Cu(\textbf{\textit{pdto}})H_2O]^{2+}$ presents more reversible electrochemical behavior than its precursor $Cu(NO_3)_2 \cdot 2.5H_2O$, due to the high flexibility of the ***pdto*** ligand towards the preferential geometry of the central atom. This is in good agreement with the fact that the value of the self-exchange electron transfer rate constant for the couple Cu(II)L/Cu(I)L (L = tetradentate ligands N_2S_2) is larger than the corresponding value of the non-coordinated couple Cu^{2+}/Cu^{+} [27]. In a simple way, we proposed that the electrochemical reversibility presented in the complex $[Cu(\textbf{\textit{pdto}})H_2O]^{2+}$ increases the reaction of electron exchange with superoxide molecule (Eqs. (1) and (2)). According to the Marcus theory, the π system in the ligand ***pdto*** and the smaller molecular reorganization in the couple $[Cu(\textbf{\textit{pdto}})H_2O]^{2+}/[Cu(\textbf{\textit{pdto}})H_2O]^{+}$ support the idea of an easy transfer of electrons from $[Cu(\textbf{\textit{pdto}})H_2O]^{2+}$ to other chemical species in solution [28]. A correlation between the antiporoliferative effect and electrochemical reversibility of the Fe(II)/Fe(III) couple in Fe(II) complexes with thiohydrazones has been recently proposed by Kalinowski et al. [29].

Due to the nature of the studies presented in this work, it cannot be neglected that the biological activity of the complex $[Cu(\textbf{\textit{pdto}})H_2O]^{2+}$ is also related with other properties, like intercalation properties with DNA [3]. But, by simple electrochemical techniques, it is possible to proposed that electrochemical reversibility is an important factor in the antitumoral activity of the $[Cu(\textbf{\textit{pdto}})H_2O]^{2+}$ complex.

5. Conclusion

The similar antiproliferative effects of the complexes $[Cu(\textbf{\textit{pdto}})H_2O]^{2+}$ and *cis*-platin in human cervix tumor cell line HeLa, suggest that the copper compound could be used against other tumor cell lines. We have established, by using cyclic voltammetry chronoamperometry and electrochemical impedance spectroscopy, an electrochemical reversibility for complex $[Cu(\textbf{\textit{pdto}})H_2O]^{2+}$, and irreversibility for the starting material $Cu(NO_3)_2 \cdot 2.5H_2O$ in acetonitrile solution. This fact confirms the flexibility of the ***pdto*** ligand, towards the preferential geometry of Cu (II) and Cu(I) in their corresponding complexes. It can be proposed that antitumoral activity of the complex $[Cu(\textbf{\textit{pdto}})H_2O]^{2+}$ is related with electrochemical reversibility. Due to the studies performed in this work, additional effects like the interaction of $[Cu(\textbf{\textit{pdto}})H_2O]^{2+}$ with DNA reported before, cannot be neglected in the full understanding of the biological activity of this copper complex.

Acknowledgements

The authors thank DGAPA-UNAM (IN212500) (IN209907) and CONACyT proyecto bilateral (CNR Italaia México) (3700PE) for financial support. The authors also thank Guadalupe Osorio-Monreal for all the kind comments done to this work.

References

[1] L.W. Oberley, G.R. Buettner, Cancer Res. 39 (1979) 114.
[2] C. Urquiola, D. Gambino, M. Cabrera, M.L. Lavaggi, H. Cerecetto, M. González, A.L. Cerain, A. Monge, A.J. Costa-Filho, M.H. Torre, J. Inorg. Biochem. 102 (2008) 119.
[3] S. Mahadevan, M. Palaniandavar, Inorg. Chim. Acta 254 (1997) 291.
[4] M. Thompson, J. Whelan, D.J. Zemon, B. Bosnich, E.I. Solomon, H.B. Gray, J. Am. Chem. Soc. 101 (1979) 2482.
[5] U. Sakaguchi, A.W. Addison, J. Chem. Soc., Dalton Trans. (1979) 600.
[6] H.A. Goodwin, F. Lions, J. Am. Chem. Soc. 82 (1960) 5013.
[7] P. Skehan, R. Storeng, D. Scudeiro, A. Monks, J. McMahon, D. Vistica, J.T. Warren, H. Bokesch, S. Kenney, M.R. Boyd, J. Nat. Cancer Inst. 82 (1990) 1107.
[8] L.V. Rubistein, K.D. Shoemaker, K.D. Paul, R.M. Simon, S. Tosini, P. Skehan, D.A. Scudeiro, A. Monks, M.R. Boyd, J. Nat. Cancer Inst. 82 (1990) 1113.
[9] A.J. Parker, Search 4 (1973) 426.
[10] F.A. Cotton, G. Wilkinson, Advanced Inorganic Chemistry, 5th Ed., John Wiley and Sons, New York, 1988. p. 967.
[11] C. Nila, I. González, J. Electroanal. Chem. 401 (1996) 171.
[12] A.J. Bard, L.R. Faulkner, Electrochemical Methods, Fundamentals and Applications, 2nd Ed., John Wiley and Sons, New York, 2001 (Chapter 5).
[13] G.R. Brubaker, J.N. Brown, M.K. Yoo, R.A. Kinsey, T.M. Kutchan, E.A. Mottel, Inorg. Chem. 18 (1979) 299.
[14] A.R. Amundsen, J. Whelan, B. Bosnich, J. Am. Chem. Soc. 99 (1977) 6730.
[15] J.H. Worrell, J.J. Genova, T.D. Dubois, J. Inorg. Nucl. Chem. 40 (1978) 441.
[16] A. Castineiras, M.V. Paredes, W. Hiller, Acta Crystallogr., Sect.C 40 (1984) 2078.
[17] A. Castineiras, W. Hiller, M.V. Paredes, J. Sordo, J. Strähle, Acta Crystallogr., Sect. A 40 (1984) C302.
[18] A. Castineiras, W. Hiller, M.V. Paredes, J. Sordo, J. Strähle, Acta Crystallogr., Sect. C 41 (1985) 41.
[19] D.G. Humphery, G.D. Fallon, K.S. Murray, J. Chem. Soc., Chem. Commun. (1988) 1356.
[20] A. Castineiras, G. Diaz, F. Florencio, S. García-Blanco, S.J. Martínez-Carrera, Cristallogr. Spectrosc. Res. 18 (1988) 395.
[21] A. Castineiras, G. Diaz, F. Florencio, S. García-Blanco, S.Z. Martínez-Carrera, Anorg. Allg. Chem. 101 (1988) 567.
[22] E. Bermejo, A. Castineiras, A.R. Domínguez, J. Strähle, W. Hiller, Acta Crystallogr., Sect. C C49 (1993) 324.
[23] V.V. Pavlischchuk, S.V. Koltilov, E.S. Michael, J. Prushan, A.W. Addison, Inorg. Chim. Acta 278 (1998) 217.
[24] E. Bermejo, A. Castineiras, A.R. Domínguez, J. Strähle, W. Hiller, Acta Crystallogr., Sect. C 49 (1993) 1918.
[25] J.R. Macdonald, W.B. Johnson, in: Impedance Spectroscopy: Emphazing Solid Materials and Systems, John Wiley and Sons, New York, 1987 (Chapter 1).
[26] A. Lasia, in: B.E. Conway et al. (Eds.), Modern Aspects of Electrochemistry, no. 32, Kluwer Academic/Plenum Publishers, New York, 1999 (Chapter 2).
[27] K.M. Davies, B. Guilani, Inorg. Chim. Acta 127 (1987) 223.
[28] J.E. Huheey, E.A. Keiter, R.L. Keiter, Inorganic Chemistry, 4th Ed., Harper Collins College Editions, New York, 1999. p. 557 (Chapter 2).
[29] D.S. Kalinowski, P.C. Sharpe, P.V. Bernhardt, D.S. Richardson, J. Med. Chem. Soc. 50 (2007) 6212.

$CDCl_3$ δ = 77.55). Infrared spectra were collected on Bruker Vector 22 in KBr at room temperature. Elemental analysis was performed on a Perkin–Elmer 240 C elemental analyzer. ThermoGravimetric (TG) and Differential Scanning Calorimetric (DSC) studies were carried out with a NETZSCH STA 449 C with a constant heating rate of 10 °C min^{-1} under Argon (1.0 cm^3 min^{-1}). Melting points were observed in sealed capillaries and are uncorrected.

2.2. Synthesis

2.2.1. Synthesis of $AgNC_4H_4O_2$ (**1**)

Silver oxide (5.0 g, 22 mmol) was added in one portion to a boiling solution of succinimide (3.8 g, 38 mmol) in 100 ml water. The reaction vessel was wrapped with aluminum foil in order to exclude as much light as possible. After the stirred solution was heated to reflux for 45 min and the silver oxide disappeared, the suspension was filtered through a heated Büchner funnel into a filter flask, also wrapped with aluminum foil. The filtrate was allowed to stand at room temperature overnight, during which time *N*-silver(I) succinimide crystallized. The *N*-silver(I) succinimide was separated on a Büchner funnel, dried in a vacuum oven for 1 h at 110 °C. The product was stored under nitrogen and kept in dark place. Yield: 3.1 g (40%, based on Ag_2O) [33].

2.2.2. Synthesis of $Ph_3P \cdot AgNC_4H_4O_2$ (**2a**)

Triphenylphosphine (0.1318 g, 0.5 mmol) dissolved in 20 mL of CH_2Cl_2 was added dropwise into a stirred solution of *N*-silver(I) succinimide (0.1029 g, 0.5 mmol) suspended in 20 mL of CH_2Cl_2 at 0 °C. A clear solution was obtained by filtration through a pad of celite after stirring the reaction mixture for 6 h at 0 °C. A white solid product was obtained after removing all the volatiles with an oil-pump vacuum, yield: 0.22 g (94% based on *N*-silver(I) succinimide). Mp.: 182–183 °C dec. *Anal. Calc.* for $C_{22}H_{19}O_2AgPN$: C, 56.43; H, 4.09. Found: C, 56.36; H, 4.04%. ^{1}H NMR ($CDCl_3$): δ 2.7 (s, 4 H, CH_2–H), 7.4–7.6 (m, 15 H, Ph-H). ^{13}C{H} NMR ($CDCl_3$): δ 32.1 (CH_2), δ 191.4 (C), 134.0 (J_{PC} = 16.0 Hz, C_6H_5), 131.3 (C_6H_5), 129.9 (C_6H_5), 129.2 (J_{PC} = 10.9 Hz, C_6H_5). IR (KBr) data (cm^{-1}): 3049 (m), 2963 (m), 1709 (m), 1611 (s), 1436 (s), 1348 (s), 1282 (s), 1157 (m), 1096 (s), 1026 (m), 806 (m), 745 (s), 693 (s), 507 (s), 451 (m).

2.2.3. Synthesis of $(Ph_3P)_2 \cdot AgNC_4H_4O_2$ (**2b**)

Complex **2b** was obtained by following the above procedure, only using *N*-silver(I) succinimide (0.1379 g, 0.67 mmol) and triphenylphosphine (0.3515 g, 1.34 mmol) instead. Yield: 0.47 g (96% based on *N*-silver(I) succinimide). Mp.: 196–197 °C. *Anal. Calc.* for $C_{40}H_{34}O_2AgP_2N$: C, 65.77; H, 4.69. Found: C, 65.63; H, 4.63%. ^{1}H NMR ($CDCl_3$): δ 2.6 (s, 4 H, CH_2–H), 7.3–7.5 (m, 30 H, Ph-H). ^{13}C{H} NMR ($CDCl_3$): δ 32.5 (CH_2), δ 192.4 (C), 133.9 (J_{PC} = 16.8 Hz, C_6H_5), 132.6 (J_{PC} = 24.1 Hz, C_6H_5), 130.0 (C_6H_5), 128.7 (J_{PC} = 9.5 Hz, C_6H_5). IR (KBr) data (cm^{-1}): 3655 (m), 3049 (m), 2962 (m), 2361 (w), 1700 (m), 1603 (s), 1583 (m), 1478 (m), 1434 (s), 1345 (s), 1285 (s), 1247 (s), 1183 (w), 1095 (s), 1026 (m), 996 (m), 803 (m), 746 (s), 695 (s), 512 (s), 436 (m).

2.2.4. Synthesis of $(Ph_3P)_3 \cdot AgNC_4H_4O_2$ (**2c**)

Complex **2c** can be synthesized in the same manner as **2a** (Section 2.2.2). In this respect, triphenylphosphine (0.4328 g, 1.65 mmol) was reacted with *N*-silver(I) succinimide (0.1132 g, 0.55 mmol). After appropriate work-up (see Section 2.2.1), complex **2c** was obtained as a white solid. Yield: 0.51 g (93% base on *N*-silver(I) succinimide). Mp.: 194–196 °C dec. *Anal. Calc.* for $C_{58}H_{49}AgO_2P_3N$: C, 70.17; H, 4.98. Found: C, 69.91; H, 4.73%. ^{1}H NMR ($CDCl_3$): δ 2.5 (s, 4 H, CH_2–H), 7.3–7.5 (m, 45 H, Ph-H). ^{13}C{H} NMR ($CDCl_3$): δ 32.5 (CH_2), δ 192.5 (C), 134.0 (J_{PC} = 4.8 Hz, C_6H_5), 133.8 (J_{PC} = 8.6 Hz, C_6H_5), 129.6 (C_6H_5), 128.6 (J_{PC} = 8.8 Hz, C_6H_5). IR (KBr) data (cm^{-1}): 3047 (m), 1703 (m), 1598 (s), 1477 (m), 1434 (s), 1344 (s), 1282 (s), 1245 (s), 1157 (m), 1096 (s), 1026 (m), 998 (m), 806 (m), 743 (s), 694 (s), 513 (s), 465 (m).

2.2.5. Synthesis of $(EtO)_3P \cdot AgNC_4H_4O_2$ (**2d**)

Complex **2d** can be synthesized by a similar procedure used for the synthesis of **2a** (Section 2.2.1). In this respect, [$(EtO)_3P$] (1.87 g, 11.27 mmol) was reacted with *N*-silver(I) succinimide (2.32 g, 11.27 mmol). After appropriate work-up, complex **2d** was isolated as a white solid. Yield: 3.81 g (91% based on *N*-silver(I) succinimide). Mp.: 53–54 °C. *Anal. Calc.* for $C_{10}H_{19}O_5AgPN$: C, 32.28; H, 5.15. Found: C, 32.16; H, 5.02%. ^{1}H NMR ($CDCl_3$): δ 1.3 (t, 9H, CH_3/CH_3CH_2–, J_{HH} = 7.0 Hz), δ 2.6 (s, 4H, CH_2–H), 4.0 (m, 6 H, CH_2/CH_3CH_2–). ^{13}C{H} NMR ($CDCl_3$): δ 31.9 (CH_2), δ 191.0 (C), 16.1 (J_{PC} = 6.7 Hz, CH_3/CH_3CH_2–), 61.3 (J_{PC} = 3.8 Hz, CH_2/CH_3CH_2–). IR (KBr) data (cm^{-1}): 3437 (m), 2981 (m), 2926 (m), 1701 (m), 1613 (s), 1441 (m), 1358 (s), 1296 (s), 1248 (s), 1163 (s), 1021 (s), 935 (s), 774, (s), 669 (s), 535 (s), 475 (m).

2.2.6. Synthesis of $[(EtO)_3P]_2 \cdot AgNC_4H_4O_2$ (**2e**)

Complex **2e** can be synthesized in the same manner as **2a** (Section 2.2.2). In this respect, [$(EtO)_3P$] (1.4044 g, 8.46 mmol) was reacted with *N*-silver(I) succinimide (0.8708 g, 4.23 mmol). After appropriate work-up (see Section 2.2.1) complex **2e** was obtained as a colorless liquid. Yield: 2.09 g (92% based on *N*-silver(I) succinimide). *Anal. Calc.* for $C_{16}H_{34}O_8AgNP_2$: C, 35.70; H, 6.37. Found: C, 35.57; H, 6.38. ^{1}H NMR ($CDCl_3$): δ 1.2 (t, 18 H, CH_3/CH_3CH_2–, J_{HH} = 7.0 Hz), δ 2.5 (s, 4 H, CH_2–H), 3.9 (m, 12 H, CH_2/CH_3CH_2–). ^{13}C{H} NMR ($CDCl_3$): δ 31.8 (CH_2), δ 191.0 (C), 16.1 (J_{PC} = 6.1 Hz, CH_3/CH_3CH_2–), 60.0 (J_{PC} = 5.7 Hz, CH_2/CH_3CH_2–). IR (KBr) data (cm^{-1}): 3440 (m), 2979 (s), 2934 (m), 2901 (m), 2358 (w), 1715 (m), 1612 (s), 1477 (m), 1441 (m), 1391 (s), 1348 (s), 1287 (s), 1245 (s), 1162 (m), 1097 (m), 1022 (s), 937 (s), 771 (s), 669 (m), 536 (s), 442 (m).

2.2.7. Synthesis of $[(EtO)_3P]_3 \cdot AgNC_4H_4O_2$ (**2f**)

Complex **2f** was synthesized in a similar procedure to that used for the synthesis of **2a** (Section 2.2.1). In this respect, [$(EtO)_3P$] (1.5538 g, 9.36 mmol) was reacted with *N*-silver(I) succinimide (0.6423 g, 3.12 mmol). After appropriate work-up, complex **2d** was isolated as a colorless liquid. Yield: 2.03 g (92% based on *N*-silver(I) succinimide). *Anal. Calc.* for $C_{22}H_{49}O_{11}AgP_3N$: C, 37.51; H, 7.01. Found: C, 37.32; H, 6.89%. ^{1}H NMR ($CDCl_3$): δ 1.3 (t, 27H, CH_3/CH_3CH_2–, J_{HH} = 7.0 Hz), δ 2.6 (s, 4 H, CH_2–H), 4.0 (m, 18 H, CH_2/CH_3CH_2–). ^{13}C{H} NMR ($CDCl_3$): δ 32.1 (CH_2), δ 191.5 (C), 16.2 (J_{PC} = 5.9 Hz, CH_3/CH_3CH_2–), 59.5 (J_{PC} = 6.6 Hz, CH_2/CH_3CH_2–). IR (KBr) data (cm^{-1}): 3414 (m), 2979 (s), 2926 (m), 2898 (m), 1701 (m), 1598 (s), 1437 (m), 1441 (w), 1391 (m), 1348 (s), 1295 (s), 1252 (s), 1162 (m), 1097 (m), 1023 (s), 933 (s), 773, (s), 669 (m), 556 (m), 454 (m).

2.3. Single crystal structure of $(Ph_3P)_3 \cdot AgNC_4H_4O_2$ (**2c**)

Single crystals of **2c** could be obtained by cooling a saturated dichloromethane solution to −20 °C. Suitable crystals for X-ray determination were placed in glue under N_2 due to their sensitive nature to oxygen and moisture. The X-ray structure measurement was performed on a BRUKER SMART Apex CCD, detector equipped with graphite monochromatic Mo Kα radiation (λ = 0.71073 Å), at room temperature. The program SMART [34] was used for determination of the unit cell. Data reduction and integration was carried out with SAINT [34] and absorption corrections were applied using the program SADABS [35]. The structure was solved using direct methods and refined by full-matrix least-squares procedures on

Table 1
Crystallographic data and analysis parameters for $(Ph_3P)_3 \cdot AgNC_4H_4O_2 \cdot 3CH_2Cl_2$.

Formula	$C_{58}H_{49}AgNO_2P_3 \cdot 3(CH_2Cl_2)$
Formula weight	1247.54
Space group	$P\bar{1}$
Crystal size (mm)	$0.6 \times 0.5 \times 0.4$
Crystal system	triclinic
Z value	2
a (Å)	13.070(3)
b (Å)	13.496(3)
c (Å)	20.073(4)
α (°)	94.283(4)
β (°)	105.502(4)
γ (°)	116.693(3)
D_{calc} [g/cm^3]	1.395
Index ranges	$-15 \leqslant h \leqslant 15$, $-16 \leqslant k \leqslant 10$, $-23 \leqslant l \leqslant 20$
Crystal shape/color	block/colorless
$F(000)$	1276
μ (Mo Kα) (mm^{-1})	0.73
λ (Mo Kα) (Å)	0.71073
Temperature (K)	295(2)
θ Range (°)	1.9–25.0
Independent reflections $[(I) > 2\sigma(I)]$	10274
R_1 $[I > 2\sigma(\theta)]$[a]	0.066
wR_2 $[I > 2\sigma(\theta)]$[b]	0.160
Goodness-of-fit (GOF) on F^2[c]	1.18
$\Delta\rho_{max}$ (e Å^{-3})	1.10
$\Delta\rho_{min}$ (e Å^{-3})	−0.78

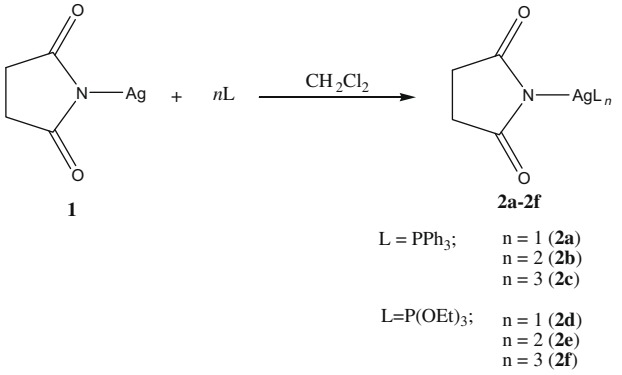
[a] $R_1 = \sum(||F_o| - |F_c||)/\sum|F_o|$; $wR_2 = [\sum(w(F_o^2 - F_c^2)^2)/\sum(wF_o^4)]^{1/2}$.
[b] $w = 1/[\sigma^2(F_o^2) + (0.064P)^2]$, $P = (F_o^2 + 2F_c^2)/3$.
[c] $S = [\sum w(F_o^2 - F_c^2)^2]/(n-p)^{1/2}$, n = number of reflections, p = parameters used.

F^2 (SHELX-97) [36]. All of the non-hydrogen atoms were refined with anisotropic displacement parameters. Crystallographic data and details on refinement are presented in Table 1. The crystal structure of **2c** is drawn using ORTEP [37].

3. Results and discussion

3.1. Synthesis

The phosphine/phosphite stabilized *N*-silver(I) succinimide complexes of the type $[L_n \cdot AgNC_4H_4O_2]$ (L = PPh_3, n = 1, **2a**; n = 2, **2b**; n = 3, **2c**; L = $P(OEt)_3$; n = 1, **2d**; n = 2, **2e**; n = 3, **2f**) were prepared by reacting $Ph_3P/(EtO)_3P$ with *N*-silver(I) succinimide in dichloromethane in stoichiometric amounts at 0 °C in high yield (Scheme 1). The complexes were isolated as white solids (**2a**–**2c**) or colorless liquids (**2d**–**2f**). They are very sensitive to moisture, oxygen as well as light. The complexes are insoluble in cold non-polar solvents such as petroleum, whereas they are highly soluble in polar or unsaturated hydrocarbons such as methylenechloride, benzene and tetrahydrofuran. All the products obtained gave satisfactory elemental analysis results and were characterized by FT-IR, ^{1}H NMR and ^{13}C {H} NMR spectroscopy.



Scheme 1. Synthesis of complexes **2a**–**2f**.

The spectra of succinimide were investigated by Woldbaek, Klaeboe and Christensen [38]. Assignments are proposed by comparison with the normal-coordinate interpretation presented by the authors mentioned above. So far, discussion of the IR spectra of the metal complexes has been restricted to the stretching carbonyl band (1700 cm^{-1}) [39].

In the IR spectra, the broad N–H stretching band (~3170 cm^{-1}) in succinimide disappears in the complexes obtained, as well as the sharp band at 820 cm^{-1} assigned to the out-of-plane N–H bending mode [38]. The in-plane N–H bending vibration has been tentatively associated with a sharp peak at 1418 cm^{-1} in succinimide, with an overtone at ~2800 cm^{-1}. The overtone is absent from the spectra of the complexes. This illustrates the formation of a Ag–N bond.

In the 1600–1800 cm^{-1} region, succinimide contains sharp peaks at 1773 and 1695 cm^{-1} for the in-phase and out-of-phase stretching motions of the C=O groups [38]. In the *N*-silver(I) succinimide complexes, these bands are found at 1700–1710 and 1580–1615 cm^{-1}, respectively. These changes, which are correlated with those found for the uracil moiety [38], could be ascribed to the delocalization of the anionic charge to the ring and carbonyl groups, thus decreasing the C=O bond order (Scheme 2). The (C=O) region is very sensitive to proton substitution, but rather insensitive to whether the C=O groups are involved in metal coordination [38]. A weak band at 420 cm^{-1}, believed to involve the C=O in-plane bending vibration, was shifted to 436–475 cm^{-1} in the complexes. However, the weakness of these bands in the infrared spectra complicates their use for diagnostic purposes.

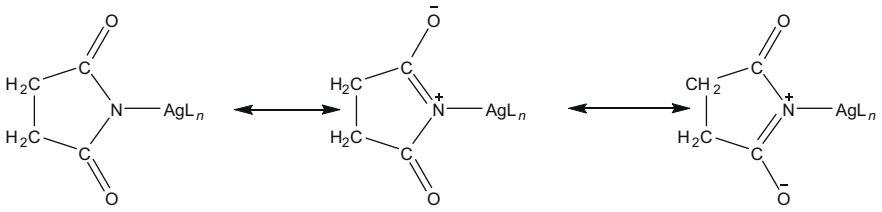
The NMR spectra (^{1}H and ^{13}C{H}) were recorded for all six complexes (see Section 2) at room temperature, The ^{1}H NMR spectra are consistent with the stoichiometries of the complexes. The protons of complexes **2a**–**2c** in the aryl proton region were in the range 7.2–7.6 ppm. The complexes (**2d**–**2f**) are easily distinguished because the resonances of the protons show only two groups. The proton of $-CH_2-$ in $C_4H_4NO_2-$ appeared at 2.5–2.7 ppm, which agrees well with that previously reported [40]. In the ^{13}C{H} NMR spectra, the triphenylphosphine carbon resonances of **2a**–**2c** are easily distinguished (128.6–134.1 ppm) from the resonance of $-CH_2-$ on $C_4H_4NO_2-$ (31.8–32.1 ppm).

3.2. Single crystal structure of *2c*

Single crystals of $[(Ph_3P)_3 \cdot AgNC_4H_4O_2]$ (**2c**) could be grown by slowly cooling a saturated dichloromethane solution containing **2c** to −20 °C. The molecular structure of **2c** is depicted in Fig. 1. Selected bond distances (Å) and bond angles (°) are given in Table 2.

Complex **2c** crystallizes in the triclinic space group $P\bar{1}$, and is composed of one molecule of $[(Ph_3P)_3 \cdot AgNC_4H_4O_2]$ and three molecules of dichloromethane (Fig. 1). In the complex, a four-coordinated silver(I) ion is present with three PPh_3 ligands occupying three of the coordination sites (PPP) and the nitrogen atom of succinimide occupying the fourth site, forming a distorted tetrahedral geometry around silver. The N–Ag–P(1) (107.29(1)°) and N–Ag–P(3) (94.95(1)°) angles are smaller than that of the ideal tetrahedral angle, while the P(1)–Ag–P(2) (113.70(5)°) and P(2)–Ag–P(3) (113.32(5)°) angles are larger (Table 2).

The succinimide ring is roughly planar; the N atom is 0.027 Å above the C(55)–C(56)–C(57)–C(58) plane, producing a slight "envelope" distortion in the ring. The succinimide ring is similar to the reported complex $[Li(Ag(Suc)_2) \cdot H_2O]$ [38]. The carbonyl oxygen, however, show different distances to the plane, implying the no coordinating interactions with silver.



Scheme 2. Delocalization of the anionic charge into the ring and carbonyl groups, decreasing the C=O bond order.

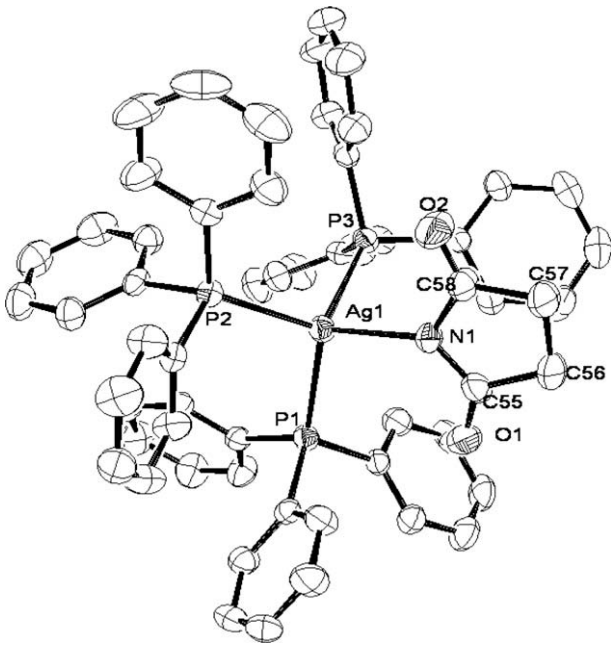


Fig. 1. ORTEP drawing of **2c**, showing 30% probability displacement ellipsoids. The hydrogen atoms and solvent molecules are omitted for clarity.

Table 2
Selected bond lengths (Å) and bond angles (°) for the $(Ph_3P)_3 \cdot AgNC_4H_4O_2 \cdot 3CH_2Cl_2$.

Bond lengths (Å)			
Ag(1)–P(1)	2.619(2)	Ag(1)–P(2)	2.561(1)
Ag(1)–P(3)	2.575(2)	Ag(1)–N(1)	2.313(4)
N(1)–C(55)	1.342(7)	N(1)–C(58)	1.354(8)
O(1)–C(55)	1.216(7)	O(2)–C(58)	1.205(7)
C(55)–C(56)	1.524(8)	C(57)–C(56)	1.490(9)
C(57)–C(58)	1.511(9)	P(1)–C(1)	1.830(5)
P(1)–C(7)	1.824(6)	P(1)–C(13)	1.831(5)
P(2)–C(19)	1.818(6)	P(2)–C(31)	1.821(6)
P(2)–C(25)	1.830(5)	P(3)–C(37)	1.820(5)
P(3)–C(49)	1.823(5)	P(3)–C(43)	1.824(6)
Bond angles (°)			
N(1)–Ag(1)–P(2)	116.5(1)	C(32)–C(31)–P(2)	119.7(5)
N(1)–Ag(1)–P(3)	94.9(1)	C(36)–C(31)–P(2)	121.7(5)
P(2)–Ag(1)–P(3)	113.3(5)	C(38)–C(37)–P(3)	118.0(4)
N(1)–Ag(1)–P(1)	107.3(1)	C(42)–C(37)–P(3)	123.0(4)
P(2)–Ag(1)–P(1)	113.7(5)	C(44)–C(43)–P(3)	124.1(5)
P(3)–Ag(1)–P(1)	109.5(5)	C(48)–C(43)–P(3)	116.6(5)
C(7)–P(1)–C(1)	102.8(2)	O(1)–C(55)–N(1)	126.1(6)
C(7)–P(1)–C(13)	101.9(2)	O(1)–C(55)–C(56)	122.6(6)
C(7)–P(1)–Ag(1)	113.9(2)	N(1)–C(55)–C(56)	111.2(6)
C(1)–P(1)–Ag(1)	116.9(2)	C(57)–C(56)–C(55)	103.8(5)
C(13)–P(1)–Ag(1)	117.7(2)	C(8)–C(7)–P(1)	118.2(4)
C(19)–P(2)–C(31)	103.3(3)	C(20)–C(19)–P(2)	119.0(4)
C(19)–P(2)–C(25)	102.8(2)	C(24)–C(19)–P(2)	123.3(5)
C(19)–P(2)–Ag(1)	115.2(2)	C(55)–N(1)–Ag(1)	123.5(4)
C(31)–P(2)–Ag(1)	121.1(2)	C(58)–N(1)–Ag(1)	124.1(4)
C(25)–P(2)–Ag(1)	111.1(2)	C(6)–C(1)–P(1)	122.6(4)
C(37)–P(3)–C(49)	102.6(2)	C(2)–C(1)–P(1)	117.7(4)
C(37)–P(3)–C(43)	103.0(3)	C(12)–C(7)–P(1)	124.1(4)
C(37)–P(3)–Ag(1)	114.7(2)	O(2)–C(58)–N(1)	125.6(6)
C(49)–P(3)–Ag(1)	111.7(2)	O(2)–C(58)–C(57)	122.6(7)
C(56)–C(57)–C(58)	103.4(6)	N(1)–C(58)–C(57)	111.9(6)
C(55)–N(1)–C(58)	109.6(5)	C(43)–P(3)–Ag(1)	120.6(2)

The C–N–C and N–C–C angles, depending on the substituent on nitrogen, are roughly correlated with the electrophilic character of the substituent. For instance, the C–N–C angle progressively decreases with decreasing substituent electrophilic character (115.0(15)°, C1; 111.6(7)°, Br; 112.6(6)°, H; 109.6(5)°, Ag; 108.3(4)°, Ni), whereas the adjacent N–C–C angles increase, but to a lesser extent (106.5(15)°, C1; 107.4(8)°, Br; 108.3(6)°, H; 111.9(6)°, Ag; 112.1(5)°, Ni) [38].

The Ag–P distances [2.619(2), 2.561(1), 2.575(2) Å] are longer than the sum of covalent radii of the P and Ag atoms (2.44 Å) [40] and that of $[(R_3P)_2AgPI]$ (PI = $C_8H_4NO_2$) [2.4944(7) Å] [41]. The Ag–N distance [2.313(4) Å] is much longer than that of $[(R_3P)_2AgPI]$ (PI = $C_8H_4NO_2$) [2.223(3) Å] [41] and the angles of P–Ag–P [113.70(5)° and 109.46(5)°] are much smaller than that of $[(Ph_3P)_2AgPAZ]$ [130.88(5)° and 125.49(8)°] (PAZ = $C_8H_5N_2O$) [41].

3.3. Thermal analysis

The complex was studied by ThemoGravimetry (TG) to obtain information on transition, decomposition temperatures and frequencies and then by Differential Scanning Calorimetry (DSC) to determine the change of entropy during thermolysis. These studies are also required to optimize the temperature at which the respective single silver precursor should be maintained during the CVD experiments. For an example, the TG and DSC curves of complex **2d** are shown in Fig. 2. It can be seen from the DSC curve that there

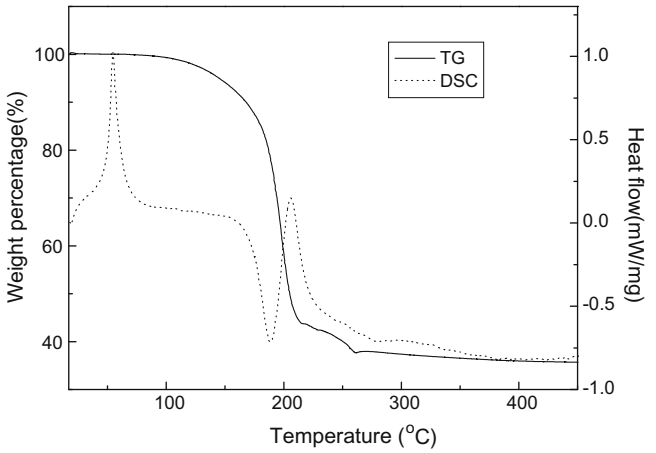


Fig. 2. TG and DSC curves of **2d** (heating rate 10 °C min^{-1}, argon atmosphere).

is one apparent endothermic process with a peak temperature of 55 °C, which could be attributed to the melting process of complex

2d. There are two continuous exothermic/endothermic processes from 163 to 210 °C, with peak temperatures of 189 and 207 °C. As seen from the TG curve, it is very difficult to distinguish from one step to another and know the sequence of decomposition of $P(OEt)_3$ and succinimide. The total weight losses are about 65.09%. The final percentage of the residue is 34.91%, which is higher than the theoretical value of silver (29.01%), which may be due to the some impurities in the complex. The complex exhibits a proper thermal decomposition temperature indicating that it could be a promising candidate as a precursor for growing silver films using the chemical vapor deposition technique.

4. Supplementary data

CCDC 687312 contains the supplementary crystallographic data for **2c**. These data can be obtained free of charge via http://www.ccdc.cam.ac.uk/conts/retrieving.html, or from the Cambridge Crystallographic Data Centre, 12 Union Road, Cambridge CB2 1EZ, UK; fax: (+44) 1223-336-033; or e-mail: deposit@ccdc.cam.ac.uk.

Acknowledgement

We gratefully acknowledge the National 863 Research Project (2006AA03Z219), Natural Science Foundation of Jiangsu province (BK2007199); The Foundation for "Liu Da Ren Cai" of Jiangsu Province (06-E-021) is also acknowledged.

References

[1] M. Dennehy, O.V. Quinzani, M. Jennings, J. Mol. Struct. 841 (2007) 110.
[2] I.G. Dance, Polyhedron 5 (1986) 1037.
[3] B. Krebs, G. Henkel, Angew. Chem. Int. Ed. Engl. 30 (1991) 769.
[4] C. Housecroft, Coord. Chem. Rev. 115 (1992) 141.
[5] R.H. Holm, P. Kennepohl, E.I. Solomon, Chem. Rev. 96 (1996) 2239.
[6] M. Hong, W. Su, R. Cao, W. Zhang, W.T. Wong, J. Lu, Inorg. Chem. 38 (1999) 600.
[7] F. Colombo, R. Annunziata, M. Benaglia, Tetrahedron Lett. 48 (2007) 2687.
[8] K. Ozawa, F. Iso, Y. Nakao, Z.X. Cheng, H. Fujii, M. Hase, H. Yamaguchi, J. Eur. Chem. Soc. 27 (2007) 2665.
[9] H. Schmidt, Y. Shen, M. Leschke, Th. Haase, K. Hohse-Hoeinghaus, H. Lang, J. Organomet. Chem. 669 (2003) 25.
[10] G.V. Samsonov, Handbook of the Physicochemical Properties of the Elements, IFI-Plenum, New York, 1968.
[11] A. Jain, K. Chi, T.T. Kodas, M.J. Hampden-Smith, J. Electrochem. Soc. 140 (1993) 1434.
[12] N. Awaya, Y. Arita, in: Proceedings of the 1991 Symposium on VLSI Thchnology, Orso, Japan, 1991, p. 37.
[13] J.E. Parmeter, G.A. Petersen, P.M. Smith, C.A. Apblett, J.S. Reid, J.A.T. Norman, A.K. Hochberg, D.A. Roberts, T.R. Omstead, J. Vac. Sci. Technol. B13 (1995) 130.
[14] G. Braeckelmann, D. Manger, A. Burke, G.G. Peterson, A.E. Kaloyeros, C. Reidsema, T.R. Omstead, J.F. Loan, J.J. Sullivan, J. Vac. Sci. Technol. B14 (1996) 1828.
[15] S. Kim, D.J. Choi, K.R. Yoon, K.H. Kim, S.K. Koh, Thin Solid Films 311 (1997) 218.
[16] J. Rickerby, J.H.G. Steinke, Chem. Rev. 102 (2002) 1525.
[17] H.K. Shin, K.M. Chi, J. Farkas, M.J. Hampden-Smith, T.T. Kodas, E.N. Duesler, Inorg. Chem. 31 (1992) 424.
[18] D.B. Beach, F.K. LeGoues, C.K. Hu, Chem. Mater. 2 (1990) 216.
[19] T.L. Alford, J. Li, J.W. Mayer, S.Q. Wang, Thin Solid Films 262 (1995) R7.
[20] P.L. Pai, C.H. Ting, IEEE Electron Dev. Lett. 10 (1989) 423.
[21] T.T. Kodas, M.J. Hampden-Smith, The Chemistry of Metal CVD, VCH, Weinheim, 1994.
[22] F.R. Hartley, Chem. Res. 73 (1973) 163.
[23] J. Li, R.S. Blewer, J.W. Mayer, MRS Bull. 18 (1993) 18.
[24] H.K. Shin, M.J. Hampden-Smith, E.N. Duesler, T.T. Kodas, Can. J. Chem. 70 (1992) 2954.
[25] R.J.H. Voorhoeve, J.W. Merewether, J. Electrochem. Soc. 119 (1972) 364.
[26] N.A. Clinton, J.K. Kochi, J. Organomet. Chem. 42 (1972) 229.
[27] D.J. Darensbourg, M.W. Holteamp, B. Khandelwal, J.H. Reibenspies, Inorg. Chem. 33 (1994) 531.
[28] J.K. Kochi, Acc. Chem. Res. 7 (1974) 351.
[29] T. Miyaji, Z. Xi, K. Nakajima, T. Takahashi, Organometallics 20 (2001) 2859.
[30] A. Bayler, A. Schier, H. Schmidbaur, Inorg. Chem. 37 (1998) 4353.
[31] M.B. Dines, Inorg. Chem. 11 (1972) 2949.
[32] B.G. Lor, M. Iglesias, C. Cascales, E.G. Puebla, M.A. Monge, Chem. Mater. 13 (2001) 1364.
[33] H.E. Baumgarten, Organic Synthesis, coll. vol. 5, New York, 1973, p. 663.
[34] Bruker AXS Inc., SAINT, Area Detector Control and Data Integration and Reduction Software, Madison, WI, USA, 1997.
[35] G.M. Sheldrick, SADABS, Program for Empirical Absorption Correction of Area Detector Data, University of Gottingen, Germany, 1997.
[36] G.M. Sheldrick, SHELX-97, Programs for Crystal Structure Analysis (Release 97-2), University of Gottingen, Germany, 1997.
[37] L. Zsolnai, G. Huttner, ORTEP, University of Heidelberg, Germany, 1994.
[38] (a) T. Woldbaek, P. Klaeboe, D.H. Christensen, Acta Chem. Scand. Ser. A. A30 (1976) 531;
(b) J. Perron, A.L. Beauchamp, Inorg. Chem. 23 (1984) 2853.
[39] D.M. Roundhill, Inorg. Chem. 9 (1970) 254.
[40] B.K. Teo, J.C. Calabrese, Inorg. Chem. 15 (1976) 2467.
[41] D.R. Whitcomb, M. Rajeswaran, J. Chem. Crytallogr. 36 (2006) 587.

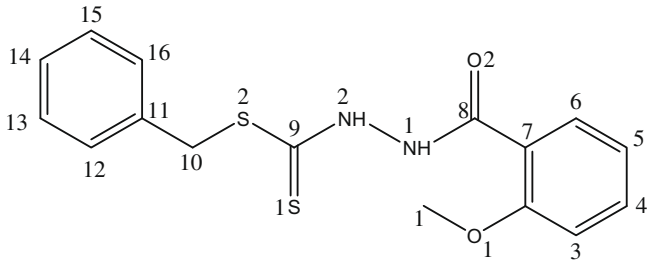


Fig. 1. Benzyl *N*′-(2-methoxybenzoyl)hydrazinecarbodithioate.

3.65 (m, 3H, $-OCH_3$), 7.76–7.10 (9H, aromatic protons). ^{13}C NMR (d_6-DMSO, δ ppm): 56.25 ($-OC^1H_3$), 157.25 (C^2), 112.31 (C^3), 136.97 (C^4), 121.09 (C^5), 129.08 (C^6), 119.21 (C^7), 164.55 (>C^8=O), 202.22 (>C^9=S), 38.04 (>$C^{10}H_2$), 133.91 (C^{11}), 128.42 (C^{12}, C^{16}), 130.63 (C^{13}, C^{15}), 127.26 (C^{14}). UV–Vis [λ_{max}, DMSO, nm]: 330, 301, 278, 242.

2.3. Preparation of the complexes

2.3.1. Preparation of $[M(Hmbhcd)_2]_n$ {M = Mn(II) **2**, Co(II) **5** and Ni(II) **6**}

The complexes **2**, **5** and **6** were prepared by stirring a solution of H_2mbhcd (2 mmol) in MeOH/$CHCl_3$ (25 ml) with a solution of $M(OAc)_2 \cdot XH_2O$ (1 mmol) in MeOH for 3–4 h at room temperature. The resulting precipitate was filtered off, washed with an ethanol–chloroform mixture and dried at room temperature under vacuum. The yield ranged from 58% to 67%.

*2.3.1.1. $[Mn(Hmbhcd)_2]_n$ (**2**).* Mustard yellow, yield 58%; M.p. 190 °C, μ_{eff} = 5.98 BM. *Anal. Calc.* for $C_{32}H_{30}MnN_4O_4S_4$ (717.39): C, 53.55; H, 4.21; N, 7.81; S, 17.87; Mn, 7.65. Found: C, 53.12; H, 4.37; N, 8.01; S, 17.69; Mn, 7.99%. IR (νcm^{-1}, KBr): ν(NH) 3179 m; ν(>C=O) 1601s; thioamide I [β(NH) + ν(CN)] 1511s; thioamide II [ν(CN) + β(NH)] 1299s; ν(N–N) 1102 m; ν(>C=S) 842; ν(CH_2) 2958. UV–Vis [λ_{max}, DMSO, nm]: 550, 335, 311, 288. MS(FAB) *m*/*z* = 718 $[M]^{+\cdot}$.

*2.3.1.2. $[Co(Hmbhcd)_2]_n$ (**5**).* Dark yellow, yield 62%; M.p. 233 °C (d); μ_{eff} = 5.11 BM. *Anal.Calc.* for $C_{32}H_{30}CoN_4O_4S_4$ (721.79): C, 53.25; H, 4.19; N, 7.76; S, 17.77; Co, 8.16. Found: C, 53.07; H, 4.18; N, 7.56; S, 16.99; Co, 7.78%. IR (ν cm^{-1}, KBr): ν(NH) 3179 m; ν(>C=O) 1598s; thioamide I [β(NH) + ν(CN)] 1514s; thioamide II [ν(CN) + β(NH)] 1301s; ν(N–N) 1102 m; ν(>C=S) 842; ν(CH_2) 2925. UV–Vis [λ_{max}, DMSO, nm]: 592, 445, 320. MS(FAB) *m*/*z* = 722 $[M]^{+\cdot}$.

*2.3.1.3. $[Ni(Hmbhcd)_2]_n$ (**6**).* Green, yield 64%; M.p. 225 °C; μ_{eff} = 2.99 BM. *Anal. Calc.* for $C_{32}H_{30}NiN_4O_4S_4$ (721.54): C, 53.27; H, 4.19; N, 7.76; S, 17.77; Ni, 8.13. Found: C, 52.37; H, 4.19; N, 7.63; S, 17.49; Ni, 8.02%. IR (ν cm^{-1}, KBr): ν(NH) 3177 m; ν(>C=O) 1601s; thioamide I [β(NH) + ν(CN)] 1513s; thioamide II [ν(CN) + β(NH)] 1295s; ν(N–N) 1105 m; ν(>C=S) 847; ν(CH_2) 2846. UV–Vis [λ_{max}, DMSO, nm]: 668, 457, 331, 298, 259. MS(FAB) *m*/*z* = 721 $[M]^{+\cdot}$.

2.3.2. Preparation of $[Mn(Hmbhcd)_2(o\text{-phen})] \cdot DMSO$ (**3**)

Complex **2**, as prepared above, was stirred with a solution of *o*-phen (0.198 g, 1 mmol) in methanol (15 ml) for 1 h. The yellowish turbid suspension obtained was made clear after adding a few drops of DMSO. The clear yellow solution of the complex was kept for crystallization which yielded light yellow transparent crystals of **3** after 16 days.

Light yellow, yield 67%; M.p. 200 °C, μ_{eff} = 6.10 BM. *Anal. Calc.* for $C_{46}H_{44}MnN_6O_5S_5$ (976.11): C, 56.60; H, 4.54; N, 8.61; S, 16.42; Mn, 5.63. Found: C, 56.12; H, 4.07; N, 8.11; S, 16.40; Mn, 6.01%. IR (ν cm^{-1}, KBr): ν(NH) 3181 m; ν(>C=O) 1602s; thioamide I [β(NH) + ν(CN)] 1501s; thioamide II [ν(CN) + β(NH)] 1300s; ν(N–N) 1101 m; ν(>C=S) 910; ν(CH_2) 2933; (*o*-phen) 1240; ν(SO) of DMSO 1018. UV–Vis [λ_{max}, DMSO, nm]: 585, 461, 338, 317, 289.

2.3.3. Preparation of $[Mn_2(Hmbhcd)_2(2,2'\text{-bpy})_2(\mu\text{-OAc})_2]$ (**4**)

Complex **4** was prepared by stirring a solution of H_2mbhcd (2 mmol) in MeOH/$CHCl_3$ (25 ml) with a solution of $Mn(OAc)_2 \cdot 4H_2O$ (1 mmol) in MeOH for 2 h at room temperature followed by the addition of 2,2′-bpy (0.156 g, 1 mmol) to yield a clear yellow solution. This solution was filtered and kept for crystallization for 25 days, which gave yellow transparent crystals of **4**.

Light yellow, yield 61%; M.p. 245 °C, μ_{eff} = 5.90 BM. *Anal.Calc.* for $C_{56}H_{52}Mn_2N_8O_8S_4$ (1203.18): C, 55.90; H, 4.36; N, 9.31; S, 10.66; Mn, 9.13. Found: C, 55.48; H, 4.30; N, 9.89; S, 10.59; Mn, 9.96%. IR (ν cm^{-1}, KBr): ν(NH) 3181 m; ν(>C=O) 1601s; thioamide I [β(NH) + (CN)] 1512s; thioamide II [ν(CN) + β(NH)] 1312s; ν(N–N) 1106 m; ν(>C=S) 905; ν(CH_2) 2922; (bpy) 1181; $\nu_{as}(CH_3COO)^-$ 1561; $\nu_s(CH_3COO)^-$ 1480. UV–Vis [λ_{max}, DMSO, nm]: 632, 343, 234.

3. Analyses and physical measurements

Carbon, hydrogen, nitrogen and sulfur contents were estimated on a CHN Model CE-440 Analyzer and on an Elementar Vario EL III Carlo Erbo 1108. By following standard procedures, the complexes were analyzed for their metal content, after decomposition with a mixture of conc. HNO_3 and HCl, followed by conc. H_2SO_4 [22]. Magnetic susceptibility measurements were performed at room temperature on a Cahn Faraday balance using $Hg[Co(NCS)_4]$ as the calibrant and electronic spectra were recorded on an UV-1700 Pharmaspec spectrophotometer. IR spectra were recorded in the 4000–400 cm^{-1} region as KBr pellets on a Varian Excalibur 3100 FT-IR spectrophotometer. ^1H and ^{13}C NMR spectra were recorded in DMSO-d_6 and on a JEOL AL300 FT NMR spectrometer using TMS as an internal reference. The FAB mass spectra were recorded on a Jeol SX 102/Da-600 mass spectrometer/data system with argon/xenon (6 kv, 10 m A0) as the FAB gas and *m*-nitrobenzyl alcohol (NBA) was used as the matrix.

4. Crystallographic data collection and structure refinement

X-ray single crystal refinement, diffraction data collection and data reduction for complexes **3** and **4** were performed at 200(2) K with a graphite monochromated Mo Kα (λ = 0.71073 Å) radiation source using standard methods [23]. The MERCURY package was used for molecular graphics [24]. Crystal structure diagrams were generated by use of the ORTEP-3 for Windows program [25]. The structures were solved by direct methods (SHELX-97) [26] and refined against all data by full-matrix least-squares on F^2 using anisotropic displacement parameters for all non-hydrogen atoms. Crystallographic data and refinement details for the structural analysis of the complexes are summarized in Table 1 and selected bond lengths and bond angles for complexes **3** and **4** are given in Tables 2 and 4, respectively. The hydrogen bonds are listed in Tables 3 and 5 for complexes **3** and **4**, respectively.

5. Results and discussion

The ligand H_2mbhcd reacts with $M(OAc)_2 \cdot XH_2O$ in a $CHCl_3$–MeOH mixture to give polymer complexes with a metal:ligand composition of 1:2. The CHNS elemental analyses and mass spectrometry results are in full agreement with the calculated values of mass percent of elements and molecular weights. In the case of the ligand, the presence of the thioamide functional group –

Table 1
Crystal refinement parameters of the complexes [Mn(Hmbhcd)$_2$(*o*-phen)] · DMSO (**3**) and [Mn$_2$(Hmbhcd)$_2$(2,2′-bpy)$_2$(μ-CH$_3$COO)$_2$] (**4**).

Parameters	**3**	**4**
Empirical formula	$C_{46}H_{44}MnN_6O_5S_5$	$C_{56}H_{52}Mn_2N_8O_8S_4$
Formula weight	976.11	1203.18
Space group	$P\bar{1}$	$P2_1/c$
Crystal system	triclinic	monoclinic
T (K)	200(2)	200(2)
λ (Mo Kα)	0.71073	0.71073
a (Å)	11.5011(4)	9.7502(4)
b (Å)	14.2290(5)	28.1656(11)
c (Å)	15.6479(4)	10.0010(4)
α (°)	74.828(3)	90
β (°)	82.874(3)	100.662(4)
γ (°)	66.705(3)	90
V (Å^3)	2269.43(13)	2699.06(19)
Z	2	2
ρ_{calc} (Mg/m^3)	1.428	1.480
M (mm^{-1})	0.574	0.686
F(000)	1014	1244
Crystal size (mm^3)	0.52 × 0.46 × 0.39	0.47 × 0.42 × 0.31
θ Range for data collection	4.73–32.40	4.61–34.67
Index ranges	$-17 \le h \le 14$ $-20 \le k \le 19$ $-22 \le l \le 22$	$-15 \le h \le 12$ $-44 \le k \le 40$ $-15 \le l \le 15$
Reflections collected	35710	28540
Independent reflections	14822	10840
Data/restraints/parameters	14822/0/572	10840/0/330
Goodness-of-fit on F^2	1.070	0.932
R_1[a], wR_2[b] [$I > 2\sigma(I)$]	0.0354, 0.0897	0.0657, 0.1361
R_1[a], wR_2[b] (all data)	0.0651, 0.1046	0.1551, 0.1562
Largest difference in peak and hole (e Å^{-3})	0.499, −0.422	0.842, −0.561

Table 2
Selected bond lengths and bond angles for complex **3** (Å and °).

Bond lengths			
Mn–O(2B)	2.1988(10)	Mn–N(1)	2.2842(12)
Mn–O(2A)	2.2697(10)	Mn–N(2)	2.2903(12)
Mn–N(2B)	2.2154(12)	S(1S)–O(1S)	1.484(2)
Mn–N(2A)	2.2319(13)	S(1S)–C(2S)	1.761(3)
		S(1S)–C(1S)	1.770(3)
Bond angles			
O(2B)–Mn–N(2B)	71.75(4)	N(2B)–Mn–N(2A)	137.49(4)
		O(2B)–C(8B)–N(1B)	119.58(12)
O(2B)–Mn–N(2A)	83.69(4)		
O(2B)–Mn–O(2A)	114.90(4)	N(2A)–Mn–O(2A)	71.61(4)
O(1S)–S(1S)–C(2S)	105.33(15)	C(8A)–O(2A)–Mn	115.66(9)
O(1S)–S(1S)–C(1S)	105.25(13)	C(8B)–O(2B)–Mn	117.92(9)
C(2S)–S(1S)–C(1S)	98.28(17)	C(11)–N(2)–Mn	115.77(9)
C(8A)–N(1A)–N(2A)	118.41(12)	N(2A)–C(9A)–S(1A)	127.05(11)
C(9B)–N(2B)–N(1B)	115.11(11)	N(2A)–C(9A)–S(2A)	109.72(11)
N(1B)–N(2B)–Mn	113.56(9)	C(8B)–N(1B)–N(2B)	117.16(12)

NH–C(=S)SR, indicates that the ligand can exhibit thione–thiol tautomerism. The solid state IR spectrum and XRD of H$_2$mbhcd do not reveal the presence of –(SH), indicating that in the solid state it remains in the thione form. The ^{1}H NMR spectrum in DMSO-d_6 is devoid of any signal attributed to the SH proton, indicating that in solution also it remains as the thione form. The ligand behaves as uninegative tridentate/bidentate and facilitates the formation of the metal complexes [M(Hmbhcd)$_2$]$_n$ {where M = Mn(II) **2**, Co(II) **5** and Ni(II) **6**}, [Mn(Hmbhcd)$_2$(*o*-phen)] · DMSO (**3**) and [Mn$_2$(Hmbhcd)$_2$(2,2′-bpy)$_2$(μ-OAc)$_2$] (**4**). These are stable towards air and moisture for several days. All the compounds are soluble in a methanol–chloroform mixture and other polar solvents such as DMF and DMSO.

5.1. IR spectra

The IR spectrum of H$_2$mbhcd in KBr shows two bands at 3127 and 3068 cm^{-1} due to the presence of two –NH groups. The presence of the thioamide functional group –NH–(C=S)SR gives rise to characteristic bands associated with thioamide I [β(NH) + ν(CN)] [mainly due to βNH], thioamide II [ν(CN) + β(NH)] [high ν(CN)] and thioamide IV [mainly due to ν(C=S)]. The bands at 1641, 1467, 1250, 1046 and 905 cm^{-1} are assigned to ν(C=O), thioamide I, thioamide II, ν(N–N) and ν(C=S), respectively. The bands at 2938 cm^{-1} correspond to ν(CH$_2$) of the benzyl ring. An exhaustive comparison of the IR spectra of the ligand and the complexes gave information about the mode of bonding of the ligand in the metal complexes **2–6**. The IR spectra of the complexes [Mn(Hmbhcd)$_2$]$_n$ (**2**), [Co(Hmbhcd)$_2$]$_n$ (**5**) and [Ni(Hmbhcd)$_2$]$_n$ (**6**) show only one peak at 3177–3179 cm^{-1}, suggesting the loss of one hydrazinic proton and participation of the resulting deprotonated nitrogen in bonding with the metal ion. A negative shift of 40–43 cm^{-1} in amide I indicates the involvement of the carbonyl oxygen in bonding for complexes **2**, **5** and **6**. A negative shift of 58–63 cm^{-1} in the ν(C=S) band indicates the involvement of the thione sulfur in bonding for complexes **2, 5** and **6**. Furthermore, the bands at 1511–1514, 1295–1301 and 1102–1105 cm^{-1} due to thioamide I, thioamide II and ν(N–N) undergo a shift to higher frequencies of 44–47, 45–51 and 56–59 cm^{-1}, respectively, showing the involvement of the thione sulfur and hydrazinic nitrogen in bonding.

In the IR spectra of complexes **3** and **4**, the bands at 3180–3181, 1601–1603, 1501–1512, 1300–1312, 1101–1106, 906–910 and 2922–2933 cm^{-1} are assigned to ν(NH), ν(C=O), thioamide I, thioamide II, ν(N–N), ν(C=S) and ν(CH$_2$), respectively. The ν(C=S) band at 906–910 cm^{-1} remains practically unchanged in the complexes in comparison to the ligand, suggesting non-involvement of the thione sulfur in bonding, while a negative shift of 38–40 cm^{-1} for ν(C=O) indicates the involvement of this group in bonding. A positive shift in ν(N–N) indicates the involvement of the hydrazinic nitrogen in bonding. This is also supported by the positive shift in thioamide I and II. The IR spectra of each of complexes **3** and **4** show a band at 1240 and 1181 cm^{-1}, respectively, for coordinated *o*-phen and 2,2′-bpy [27]. The peak corresponding to the SO stretching of non-bonded DMSO occurs at 1018 as a strong and broad band [28]. Thus, H$_2$mbhcd behaves as a uninegative bidenate ligand in complexes **3** and **4** and a uninegative tridentate ligand in complexes **2**, **5** and **6**. The symmetric (1480 cm^{-1}) and asymmetric (1561 cm^{-1}) stretching bands of the acetate anion in complex **4** indicate its bridging bidentate nature [29].

5.2. Magnetic moments and electronic spectra

The μ_{eff} values of 5.98, 6.10 and 5.90 B.M. for complexes **2**, **3** and **4**, respectively show the presence of a high spin Mn^{2+} ion having five unpaired electrons with the $^6A_{1g}$ ground state. Their UV–Vis spectra exhibit one d–d band at 632–550 nm due the $^6A_{1g} \rightarrow {}^4T_{1g}(G)$ transition, suggesting an octahedral geometry around Mn(II) [30]. An additional band at 461 nm in [Mn(Hmbhcd)$_2$(*o*-phen)] · DMSO (**3**) is assigned to an intraligand/charge transfer transition. The magnetic moment of 5.11 B.M. and the presence of two well resolved bands at 592 and 445 nm corresponding to the $^4T_{1g} \rightarrow {}^4A_{2g}$ and $^4T_{1g}$ transitions, respectively, is indicative of a cobalt(II) ion in an octahedral environment for complex **5** [30]. An absorption band at 320 nm in the high-energy region is assigned to an intraligand transition. The magnetic moment of 2.99 B.M. for [Ni(Hmbhcd)$_2$]$_n$ (**6**) is typical of a high spin octahedral Ni(II) complex and the presence of two bands at 668 and 457 nm are considered to arise from the $^3A_{2g} \rightarrow {}^3T_{2g}(F)$ and $^3T_{1g}(P)$ transitions in an octahedral geometry around Ni(II). The high-energy bands at 331, 298 and 259 nm in the spectrum of [Ni(Hmbhcd)$_2$]$_n$ are probably due to charge transfer/intraligand transitions [30].

Table 3
Hydrogen bonds for complex **3** (Å and °).

D–H···A	d(D–H)	d(H···A)	d(D···A)	<(DHA)
N(1A)–H(1AD)···O(1A)	0.88	1.94	2.5950(16)	130.0
N(1B)–H(1BD)···O(1B)	0.88	2.00	2.6541(15)	130.5
C(1A)–H(1AB)···O(1S)	0.98	2.55	3.339(3)	138.0

Symmetry transformations used to generate equivalent atoms.

5.3. ^1H and ^{13}C NMR spectra

The ^1H NMR spectrum of H_2mbhcd shows two signals at 10.73 and 10.55 ppm due to the presence of –NH(CO)– and –NH(CS)– protons, respectively. The peaks at 4.45 and 3.91 ppm correspond to $–CH_2$ and $–OCH_3$ protons. The protons due to the two aromatic rings, i.e. the 2-methoxybenzene ring and the benzyl ring, appear as multiplets between 7.76 and 7.10 ppm. The ^{13}C NMR spectrum of H_2mbhcd shows 16 signals due to the presence of 16 carbon atoms. The peaks at δ 202.22 and 164.14 ppm are attributed to the >C=S and >C=O carbons, respectively. The ^1H and ^{13}C NMR of complexes could not be recorded due to their paramagnetic nature.

5.4. Mass spectrometry

FAB mass spectral analyses of $[Mn(Hmbhcd)_2]_n$ (**2**), $[Co(Hmbhcd)_2]_n$ (**4**) and $[Ni(Hmbhcd)_2]_n$ (**6**) show the presence of the molecular ion peaks at m/z = 718 $[M]^{+\cdot}$, 722 $[M]^{+\cdot}$ and 721 $[M]^{+\cdot}$, respectively which correspond to the molecular weight of one unit of the polymer. Other peaks at higher m/z values indicate their polymeric nature. Complex **2** gave several important peaks at m/z 684 (45% intensity), 610 (35% intensity), 593 (25% intensity), 509 (35% intensity), 470 (98% intensity) and 386 (75% intensity) corresponding to fragments formed from $[Mn(Hmbhcd)_2]_n$ after release of H_2S, $C_6H_4(–OCH_3)$, $PhCH_2S–$, $[C_6H_4(OCH_3)–C(O)–NHN–C(S)–]$, $2(PhCH_2S–)$ and $[C_6H_4(OCH_3)C(O)NH–N–C(S)–S–]$, respectively. The fragments at m/z = 689 (12.5% intensity), 598 (25% intensity), 571 (25% intensity) and 390 (35% intensity) correspond to the fragments formed from $[Co(Hmbhcd)_2]_n$ (**4**) after release of HS, $PhCH_2S–$, $[C_6H_4(OCH_3)–C(O)–NH)–]$ and $C_6H_4(OCH_3)–C(O)–NH–N–C(S)S–]$, respectively from one unit of the complex. Complex **6** gave important peaks at m/z = 597 (50% intensity), 473 (48% intensity) and 389 (75% intensity), corresponding to the fragments formed from one unit of $[Ni(Hmbhcd)_2]_n$ after release of $PhCH_2S–$, $2PhCH_2S–$ and $[C_6H_4(OCH_3)C(O)NH–N–C(S)–S–]$, respectively.

On the basis of the analytical data and spectroscopic studies, tentative structures of the complexes $[M(Hmbhcd)_2]_n$ are given in Fig. 2.

Table 4
Selected bond lengths and bond angles for complex **4** (Å and °).

Bond lengths			
Mn–O(12) 1	2.0931(17)	Mn–N(1A)	2.238(2)
Mn–O(11)	2.1738(18)	Mn–N(2A)	2.277(2)
Mn–O(2)	2.1889(17)	Mn–N(1)	2.382(2)
O(12)–C(11A)	1.260(3)	O(11)–C(11A)	1.253(3)
		O(12)–Mn 1	2.0931(17)
Bond angles			
O(12) 1–Mn–O(11)	101.22(7)	O(12) 1–Mn–O(2)	88.97(7)
O(11)–Mn–O(2)	90.78(7)	O(12) 1–Mn–N(1A)	167.74(8)
O(11)–Mn–N(1A)	89.09(7)	O(2)–Mn–N(1A)	97.60(7)
O(12) 1–Mn–N(2A)	99.37(7)	O(11)–Mn–N(2A)	94.37(7)
O(2)–Mn–N(2A)	169.15(7)	N(1A)–Mn–N(2A)	72.97(7)
O(12) 1–Mn–N(1)	86.93(7)	O(11)–Mn–N(1)	160.86(7)
O(2)–Mn–N(1)	71.93(7)	C(8)–O(2)–Mn	115.49(15)
N(1A)–Mn–N(1)	85.29(7)	C(11A)–O(12)–Mn 1	138.68(16)
C(11A)–O(11)–Mn	120.96(17)	C(9)–N(1)–Mn	141.72(18)
N(2)–N(1)–Mn	105.58(13)		

Symmetry transformations used to generate equivalent atoms.
1 $-x+1,-y,-z$.

Table 5
Hydrogen bonds for complex **4** (Å and °).

D–H···A	D(D–H)	D(H···A)	d(D···A)	<(DHA)
N(2)–H(2A)···O(1)	0.88	1.93	2.614(3)	132.9
C(10)–H(10B)···O(11) 2	0.99	2.39	3.331(3)	157.9

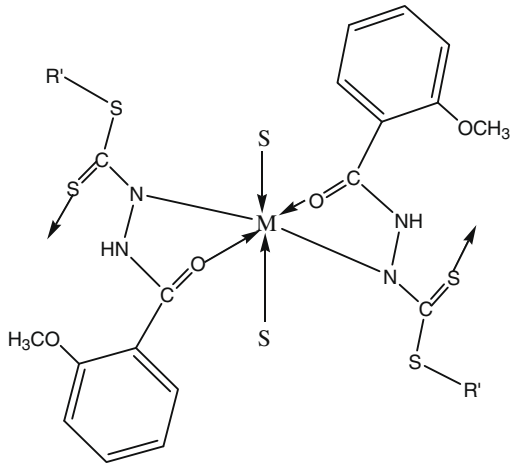
Symmetry transformations used to generate equivalent atoms.
2 $x-1,y,z$.

6. Crystal structure description

6.1. Crystal structure description of complex 3

Fig. 3 shows a Mercury view of the Mn(II) complex together with the atom numbering scheme. The metal center in complex **3** is coordinated by an N_4O_2 core from two uninegative bidentate ligands using the hydrazinic nitrogens (N2, after loss of a proton) and carbonyl oxygens. Various bond distances found within the chelate rings are intermediate between single and double bond lengths and shorter or longer than the corresponding bond lengths in comparison to the ligand. The average bond lengths in complex **3** are: O(2A)–C(8A) = 1.2503(18); O(2B)–C(8B) = 1.2569(17), N(1A)–C(8A) = 1.3363(19), N(1B)–C(8B) = 1.3303(19), N(1A)–N(2A) = 1.3872(16), N(1B)–N(2B) = 1.3851(15) Å, which suggest considerable delocalization of charge [31] in the chelate ring.

Transition metal complexes in which bonding of the ligand takes place through a carbonyl oxygen and nitrogen and also bonded with N-heterocyclic bases such as *o*-phen or 2,2′-bpy are prone to exhibit metalloaromaticity [32–36]. The above criteria of metalloaromaticity are fulfilled in complex **3**. The most noteworthy structural feature of complex **3** is that two *ortho*-H atoms from the *o*-phen ring point towards the center of the corresponding Mn–OCN1N2 chelate rings [37]. This delocalized charge in the chelate ring forms an unusual intramolecular C–H···π interaction with the *ortho* hydrogen of the adjacent *o*-phen ring [19,37] (Fig. 4).



$[M(Hmbhcd)_2]_n$ {M = Mn(II) (2), Co(II) (5), Ni(II) (6), R' = CH_2Ph

Fig. 2. Tentative structure of the complexes $[M(Hmbhcd)_2]_n$ {M = Mn(II), Co(II) and Ni(II)}.

The shortest centroid to centroid separation found between parallel benzyl and *o*-phen rings is 4.038 Å within the molecule, which rules out the possibility of intramolecular face to face (π···π) interactions in **3**. The chelate rings around Mn(II) formed by $(Hmbhcd)^-$ display a dihedral angle of 73.50° (between the mean planes MnN2AN1AC8AO2A and MnO2BC8BN1BN2B) and indicate strain in both chelate rings. This strain between the chelate rings is also supported by the dihedral angle between the 2-methoxy benzene ring and the chelate rings. The chelate ring O2BMnN2BN1BC8B and the corresponding 2-methoxy benzene ring lie in the same plane while another chelate ring O2AMnN2AN1AC8A and its corresponding 2-methoxy benzene ring are nearly planar with a dihedral angle of 14.11°. The dihedral angle between a benzyl ring (mean plane C16BC15BC14BC13BC12BC11B) and one chelate ring (mean plane MnO2BC8BN1BN2B) is 24.30° and between another chelate ring (mean plane MnN2AN1AC8AO2A) and benzyl ring (mean plane C14AC13AC12AC11AC16AC15A) is 62.81°.

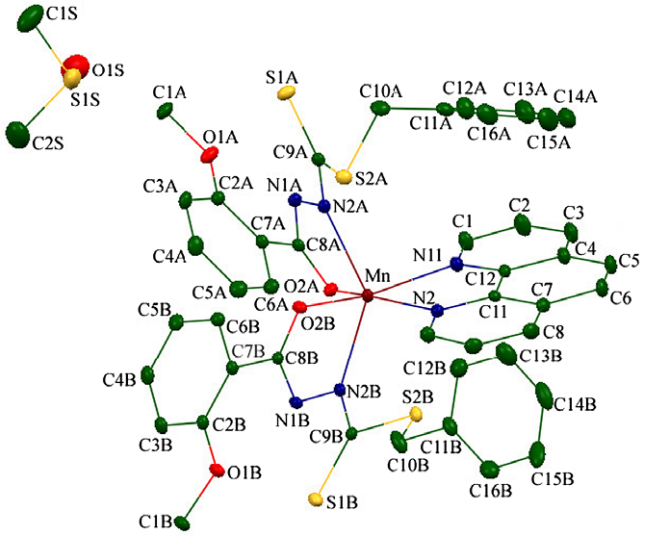


Fig. 3. Mercury view of $[Mn(Hmbhcd)_2(o\text{-phen})]\cdot DMSO$ showing the atomic numbering scheme with ellipsoids of 20% probability. Hydrogen atoms are omitted for clarity.

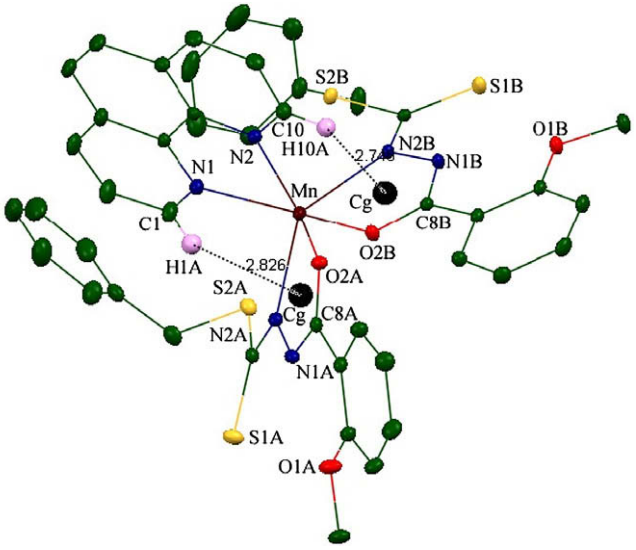


Fig. 4. Crystal structure of $[Mn(Hmbhcd)_2(o\text{-phen})]$, showing an unusual intramolecular C–H···π interaction with the Mn(II) chelate ring. For clarity other hydrogen atoms and the DMSO molecule are omitted.

6.2. Crystal packing of complex **3**

The weak intermolecular interactions are listed in Table 6. The presence of intramolecular hydrogen bonding, N(1B)–H(1BD)···O(1B) = 1.99 Å and N(1A)–H(1AD)···O(1A) = 1.94 Å, provide stability to complex **3**. The two-dimensional framework is formed with the help of intermolecular hydrogen bonding, C10–H10A···O1S (2.604 Å), C1A–H1AB···O1S (2.546 Å) and C3A–H3AA···S1B (2.908 Å). The whole arrangement of molecules in the crystal packing creates channels which enclose DMSO molecules (Fig. 5).

6.3. Crystal structure description of complex **4**

Each Mn(II) center is six coordinately bonded through two N atoms of one 2,2′-bpy, one deprotonated nitrogen from a hydrazinic moiety and three oxygen atoms, belonging to two different acetates and one carbonyl oxygen of the ligand **1** (Fig. 6). The two neighboring Mn(II) centers are connected by two bridging acetate ions which results in the formation of a distorted rectangular shaped cavity of size 3.151 × 3.017 $Å^2$, labeled as [Mn–O12–C12A–O11–Mn–O12–C12A–O11] (Fig. 6). One molecular unit of $[Mn_2(Hmbhcd)_2(2,2'\text{-bpy})_2(\mu\text{-OAc})_2]$ shows the presence of an intramolecular N–H···O hydrogen bond, with a distance and angle of 2.614(3) Å and 111.2°, respectively. The $Mn–O_{acetate}$ bond lengths of 2.0929(17) and 2.1737(18) Å are relatively shorter than the reported bond length values for bridged Mn–OAc = 2.144(2)–2.203(2) Å, indicating relatively stronger bonding between Mn(II) and oxygen in this system [38]. The bond distance of $Mn–O_{carbonyl}$ = 2.1890(17) Å is comparable to the bond lengths found for $[Mn(Hpchc)_2(o\text{-phen})]$ [19]. The $Mn–N_{bpy}$ distances [2.238(2) and 2.277(2) Å] are slightly longer than the reported values for $Mn–N_{bpy}$, 2.038(3)–2.254(3) Å [39], but the bite angle N(1A)–Mn–N(2A) = 72.96(7)° is close to 73°, as observed for chelating 2,2′-bpy complexes [39]. The C–O, C–N and N–N bond distances of 1.262(3), 1.326(3) and 1.406(3) Å, respectively, are intermediate between single and double bond character. All these intermediate distances suggest extensive delocalization of charge in the five-membered chelate ring of complex **4** [31] and is the basis of metalloaromaticity.

6.4. Crystal packing of **4**

A view of the crystal packing along the b axis gives a linear arrangement of Mn(II) centers and increases the chain in one dimension with a Mn···Mn separation of 10.001 Å in

Table 6
Intermolecular interactions (Å) for complexes **3** and **4**.

Complex **3**		Complex **4**			
D–H···A	d(H···A)	D–H···A	D(H···A)	D–H···A	d(H···A)
C10–H10A···O1S	2.60	C–H···Cg	2.90	C4A–H4AA···O11	2.64
C3A–H3AA···S1B	2.90	C1–H1C···S1	2.93	$Cg_{(bpy)}\cdot\cdot\cdot Cg_{(bpy)}$	3.26
C1H–H1A···Cg	2.82	C10–H10B···O11	2.39	C4A–H4AA···C11A	2.56

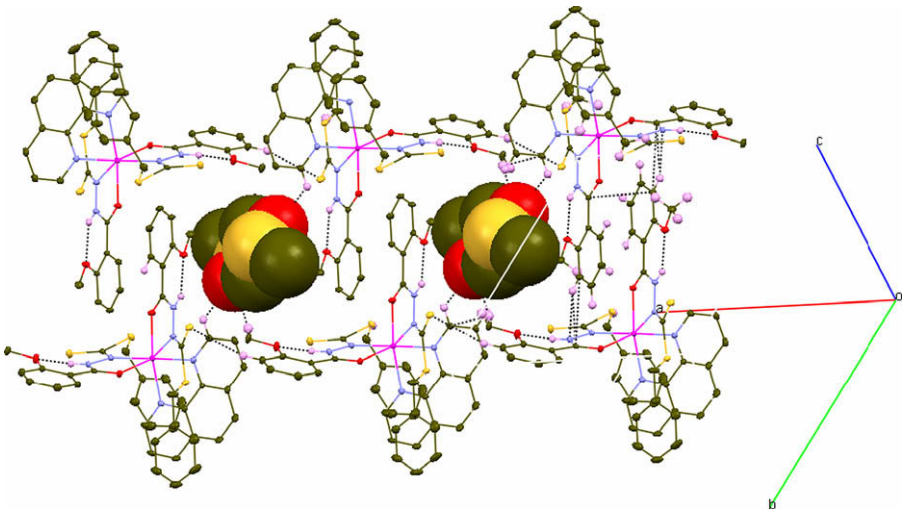


Fig. 5. Molecular packing of complex **3** showing intermolecular hydrogen bonding and the enclosed DMSO (hydrogen atoms are omitted except those taking part in hydrogen bonding).

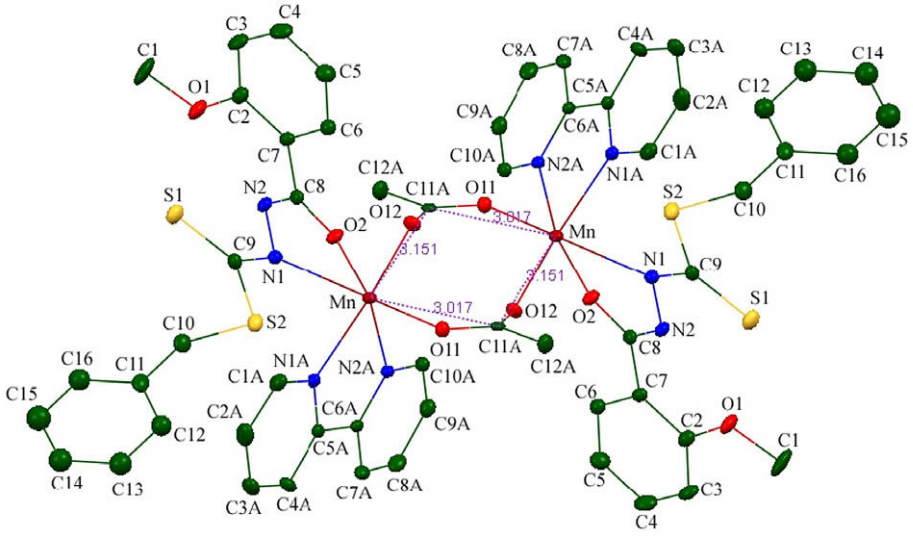


Fig. 6. Distorted rectangular cavity in the structure of $[Mn_2(Hmbhcd)_2(2,2'\text{-bpy})_2(\mu\text{-OAc})_2]$. Mercury view of $[Mn_2(Hmbhcd)_2(2,2'\text{-bpy})_2(\mu\text{-OAc})_2]$ (**4**) showing the atomic numbering scheme with an ellipsoidal plot at 20% probability.

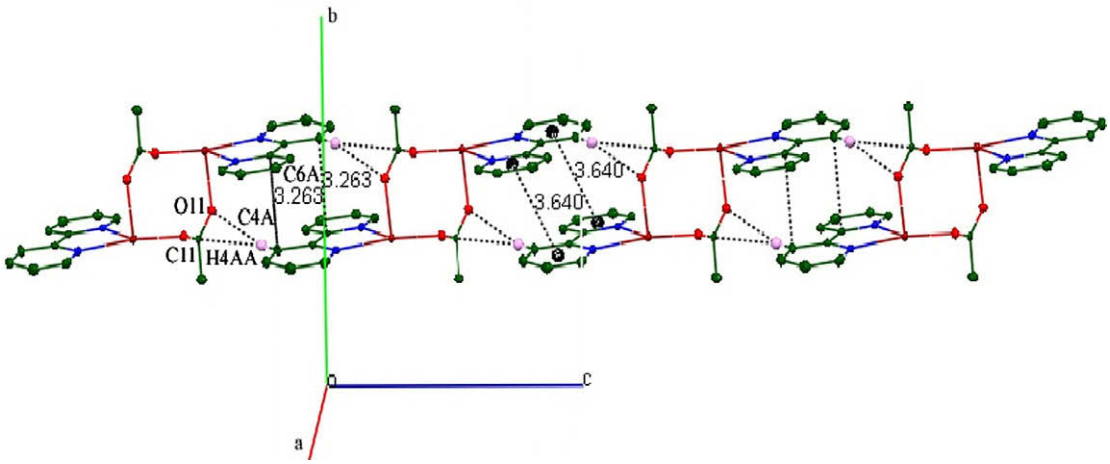


Fig. 7. One-dimensional chain due to the presence of face to face interactions and C4A–H4AA···O11 hydrogen bonds. For more clarity the $(Hmbhcd)^-$ ligand and hydrogen atoms are omitted (except H4AA).

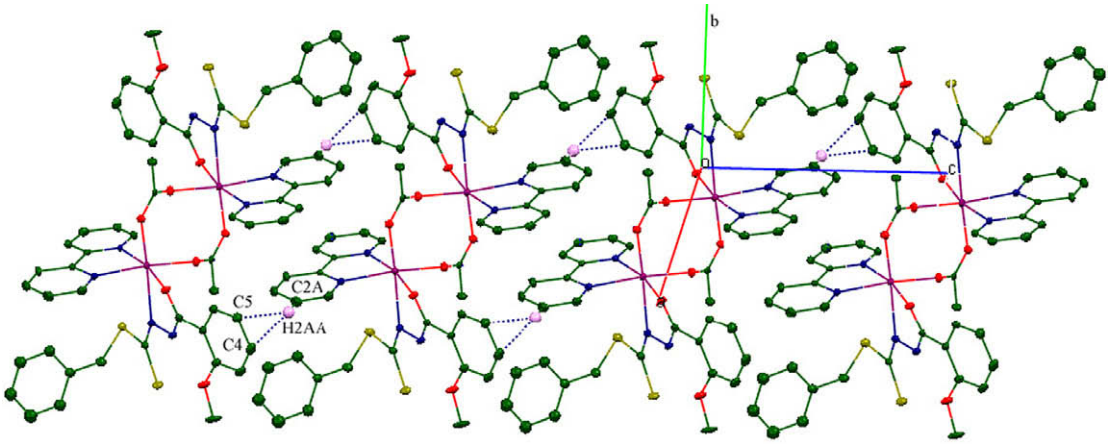


Fig. 8. Molecular packing of complex **4** showing C–H···π interactions (hydrogen atoms except H2AA are omitted for clarity).

Table 7
Comparative bond lengths, bond angles and torsional angles for H_2mbhcd and complexes **3** and **4**.

H_2mbhcd	[Mn(Hmbhcd)$_2$(*o*-phen)] · DMSO	[Mn(Hmbhcd)$_2$(2,2′-bpy)(μ-OAc)$_2$]
S(1)–C(9) 1.656(2)	S(1A)–C(9A) 1.6907(16) S(1B) –C(9B) 1.6849(14)	S(1)–C(9) 1.689(3)
S(2)–C(9) 1.740(2)	S(2A)–C(9A) 1.7833(15) S(2B)–C(9B) 1.7827(14)	S(2)–C(9) 1.786(3)
S(2)–C(10) 1.807(3)	S(2A)–C(10A) 1.8160(16) S(2B)–C(10B) 1.8083(17)	S(2)–C(10) 1 .810(3)
O(2)–C(8) 1.222(3)	O(2A)–C(8A) 1.2503(18) O(2B)–C(8B) 1.2569(17)	O(2)–C(8) 1.262(3)
N(1)–C(8) 1.340(3)	N(1A)–C(8A) 1.3363(19) N(1B)–C(8B) 1.3303(19)	N(2)–C(8) 1.326(3)
N(1)–N(2) 1.372(3)	N(1A)–N(2A) 1.3872(16) N(1B)–N(2B) 1.3851(15)	N(1)–N(2) 1.406(3)
N(2)–C(9) 1.323(3)	N(2A)–C(9A) 1.3151(19) N(2B)–C(9B) 1.3189(18)	N(1)–C(9) 1.316(3)
Bond angles		
C(9)–S(2)–C(10) 104.13(12)	C(9A)–S(2A)–C(10A) 101.91(7) C(9B)–S(2B)–C(10B) 102.45(7)	C(9)–S(2)–C(10) 102.98(13)
O(2)–C(8)–N(1) 120.48(19)	O(2A)–C(8A)–N(1A) 120.35(13) O(2B)–C(8B)–N(1B) 119.58(12)	O(2)–C(8)–N(2) 122.0(2)
O(2)–C(8)–C(7) 122.33(19)	O(2A)–C(8A)–C(7A) 121.17(13) O(2B)–C(8B)–C(7B) 119.91(13)	
N(1)–C(8)–C(7) 117.18(17)	N(1A)–C(8A)–C(7A) 118.46(13) N(1B)–C(8B)–C(7B) 120.50(12)	N(2)–C(8)–C(7) 117.9(2)
N(2)–C(9)–S(1) 123.36(17)	N(2A)–C(9A)–S(1A) 127.05(11) N(2B)–C(9B)–S(1B) 127.90(10)	N(1)–C(9)–S(1) 127.6(2)
N(2)–C(9)–S(2) 110.94(15)	N(2A)–C(9A)–S(2A) 109.72(11) N(2B)–C(9B)–S(2B) 108.55(10)	N(1)–C(9)–S(2) 109.89(19)
S(1)–C(9)–S(2) 125.69(13)	S(1A)–C(9A)–S(2A) 123.04(9) S(1B)–C(9B)–S(2B) 123.41(8)	S(1)–C(9)–S(2) 122.36(15)
C(11)–C(10)–S(2) 104.53(17)	C(11A)–C(10A)–S(2A) 111.47(12) C(11B)–C(10B)–S(2B) 107.88(11)	C(11)–C(10)–S(2) 115.8(2)
Torsional angles		
C(8)–N(1)–N(2)–C(9)–173.7(2)	C(8A)–N(1A)–N(2A)–C(9A) 179.61(12) C(8B)–N(1B)–N(2B)–C(9B)–172.22(12)	C(9)–N(1)–N(2)–C(8) 172.7(2)
N(2)–N(1)–C(8)–O(2)5.8(4)	N(2A)–N(1A)–C(8A)–O(2A)–4.93(19) N(2B)–N(1B)–C(8B)–O(2B) 1.16(19)	N(1)–N(2)–C(8)–O(2)–1.4(4)
N(2)–N(1)–C(8)–C(7)–173.3(2)	N(2A)–N(1A)–C(8A)–C(7A) 173.73(11) N(2B)–N(1B)–C(8B)–C(7B) 178.31(12)	N(1)–N(2)–C(8)–C(7) 176.8(2)
N(1)–N(2)–C(9)–S(1) 4.9(3)	N(1A)–N(2A)–C(9A)–S(1A)–6.76(18) N(1B)–N(2B)–C(9B)–S(1B) 5.76(19)	N(2)–N(1)–C(9)–S(1)–2.5(3)
N(1)–N(2)–C(9)–S(2)–174.10(18)	N(1A)–N(2A)–C(9A)–S(2A) 168.31(9) N(1B)–N(2B)–C(9B)–S(2B)–169.88(9)	N(2)–N(1)–C(9)–S(2) 173.66(16)
C(10)–S(2)–C(9)–N(2) 170.75(19)	C(10B)–S(2B)–C(9B)–N(2B)–142.08(12) C(10A)–S(2A)–C(9A)–N(2A) 142.23(11)	C(10)–S(2)–C(9)–N(1) 155.33(18)
C(10)–S(2)–C(9)–S(1)–8.2(2)	C(10A)–S(2A)–C(9A)–S(1A)–42.46(11) C(10B)–S(2B)–C(9B)–S(1B) 42.04(13)	C(10)–S(2)–C(9)–S(1)–28.3(2)
C(9)–S(2)–C(10)–C(11)–173.74(19)	C(9A)–S(2A)–C(10A)–C(11A)–93.19(12) C(9B)–S(2B)–C(10B)–11B) 177.94(14)	C(9)–S(2)–C(10)–C(11) 80.3(2)

$[Mn_2(Hmbhcd)_2(2,2'\text{-bpy})_2(\mu\text{-OAc})_2]$. The chain grows infinitely in 1 D along the a axis with the help of C4A–H4AA···O11 and π···π interactions between two successive 2,2′-bpy rings (Fig. 7). The distance between the centroids (Cg) of two 2,2′-bpy ligands of two adjacent units of $[Mn_2(Hmbhcd)_2(2,2'\text{-bpy})_2(\mu\text{-OAc})_2]$ is 3.262 Å, which is within the range of π···π stacking interactions (3.3–3.7 Å). The π···π stacking interactions between the two units of molecules, intermolecular hydrogen bonding, C4A–H4AA···O11 = 2.641 Å, and short contact of C4A–H4AA···C11A = 2.562 Å connect the sheets into a 1D coordination framework (Fig. 7).

The 2,2′-bpy ligand forms C–H···π interactions with the phenyl ring of the 2-methoxy benzene ring with a distance of C–H···$Cg_{(2\text{-methoxy ring})}$ of 2.907 Å (Fig. 8). There is intermolecular hydrogen bonding, C1–H1$C_{(2\text{-methoxy benzene ring})}$···S1 = 2.931 Å and C10–H10B···O11 (CH_2 of benzyl ring) = 2.394 Å, which extends the crystal packing and gives a three dimensional framework. The weak intermolecular interactions are listed in Table 6.

Looking at the crystal data and structure of the complexes, it is found that the bond lengths and bond angles in the ligand H_2mbhcd are very similar, but the torsional angles of compounds **3** and **4** differ widely (Table 7). The basic change observed in the structure of the ligand due to metal coordination is in the orientation of the benzyl ring. One benzyl ring, C11A–C12A–C13A–C14A–C15A–C16A, in complex **3** and both benzyl rings, C11–C12-C13–C14–C15–C16, in complex **4** show major deviation in torsional angles [C9A–S2A–C10A–C11A = −93.19°, C9B–S2B–C10B–C11B = 177.96° for complex **3**, C9–S2–C10–C11 = –80.34°, C9–S2–C10–C11 = 80.34° for complex **4**] in comparison to the ligand H_2mbhcd [C9–S2–C10–C11 = −173.79°]. The O(2)–C(8) bond length in the ligand, 1.222(3) Å, is shorter than the corresponding length {O(2A)–C(8A) = 1.2503(18) Å (**3**), O(2B)–C(8B) = 1.2569(18) Å (**3**) and O(2)–C(8) = 1.262(3) (**4**)} in the complexes, indicating that the single bond character of the C–O bond has increased due to delocalization of charge. There are slight variations in the N(1)–C(8), N(1)–N(2) and N(2)–C(9) bond lengths in complexes **3** and **4** as compared to the respective bond lengths of H_2mbhcd.

The C–N and N–N bond lengths in the ligand and the complexes show intermediate between single and double bond character, which is also indicative of considerable delocalization of charge in the chelate ring formed by the coordination of the deprotonated hydrazinic nitrogen and carbonyl oxygen in complexes **3** and **4**. This delocalization generates aromaticity in the chelate ring of both complexes.

7. Conclusion

In this work, the synthesis and spectral studies of Mn(II), Co(II) and Ni(II)} complexes derived from benzyl *N*′-(2-methoxybenzoyl)hydrazine carbodithioate (H_2mbhcd) are presented. $[Mn(Hmbhcd)_2(o\text{-phen})]\cdot DMSO$ (**3**) and $[Mn_2(Hmbhcd)_2(2,2'\text{-bpy})_2(\mu\text{-OAc})_2]$ (**4**) have been studied by single crystal X-ray crystallography, which indicate that the complexes involve delocalization of charges in the chelate ring.

Acknowledgement

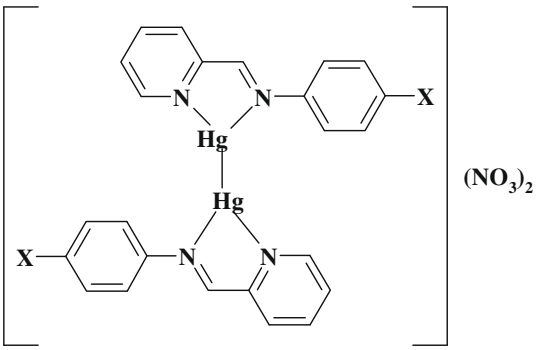
One of the authors (M. Singh) is thankful to CSIR, New Delhi, India for the award of SRF, supported by Grant No. 9/13(160)2008/EMR-I.

Appendix A. Supplementary data

CCDC 656090, 677286 and 701544 contain the supplementary crystallographic data for **1**, **3** and **4**. These data can be obtained free of charge via http://www.ccdc.cam.ac.uk/conts/retrieving.html, or from the Cambridge Crystallographic Data Centre, 12 Union Road, Cambridge CB2 1EZ, UK; fax: (+44) 1223 336 033; or e-mail: deposit@ccdc.cam.ac.uk. Supplementary data associated with this article can be found, in the online version, at doi:10.1016/j.poly.2008.12.061.

References

[1] M. Akbar Ali, A.H. Mirza, C.W. Voo, A.L. Tan, P.V. Bernhardt, Polyhedron 22 (2003) 3433.
[2] M. Akbar Ali, A.H. Mirza, M. Nazimuddin, Raju Ahmed, L.R. Gahan, P.V. Bernhardt, Polyhedron 22 (2003) 1471.
[3] S. Roy, T.N. Mandal, A.K. Barik, S. Pal, S. Gupta, A. Hazra, R.J. Butcher, A.D. Hunter, M. Zeller, Polyhedron 26 (2007) 2603.
[4] M.T.H. Tarafdar, N. Saravanan, K.A. Crouse, Transition Met. Chem. 28 (2003) 241.
[5] M.A. Ali, C.M. Haroon, M. Nazimuddin, S.M.H. Majumder, M.T.H. Tarafder, M.A. Khair, Transition Met. Chem. 17 (1992) 133.
[6] M.E. Hossain, M.N. Alam, M.A. Ali, M. Nazimuddin, F.E. Smith, R.C. Hynes, Polyhedron 15 (1996) 973.
[7] C.Y. Duan, Y.P. Tian, X.Z. Yu, T.C.W. Mak, Polyhedron 16 (1997) 4097.
[8] H.L. Singh, S. Varshney, A.K. Varshney, Appl. Organomet. Chem. 13 (1999) 637.
[9] H.L. Singh, B. Khunger, U.D. Triphathi, A.K. Varshney, Main Group Met. Chem. 24 (2001) 5.
[10] M.B. Ferrari, S. Capacchi, G. Pelosi, G. Reffo, P. Tarasconi, R. Albertini, S. Pinelli, P. Lunghi, Inorg. Chim. Acta 286 (1999) 134.
[11] D.L. Klayman, J.P. Scovill, J. Bruce, J.F. Bartosevich, J. Med. Chem. 27 (1984) 84.
[12] J.P. Scovill, D.L. Klayman, D.L. Franchino, J. Med. Chem. 25 (1982) 1261.
[13] G.M. de Lima, J.L. Neto, H. Beraldo, H.G.L. Siebald, D.J. Duncalf, J. Mol. Struct. 604 (2002) 287.
[14] C. Klofutar, S. Paljk, F. Krasovec, P. Suhae, Kem. Ind. 24 (1975) 361.
[15] C. Klofutar, S. Paljk, F. Krasovec, P. Suhae, Chem. Abstr. 84 (1976) 84739.
[16] R.A. Sanchez-Delgado, K. Lazardi, L. Rincon, J.A. Urbina, J. Med. Chem. 36 (1993) 2041.
[17] D.F. Xiang, C.Y. Duan, X.S. Tan, Q.W. Hang, W.X. Tang, J. Chem. Soc., Dalton Trans. (1998) 1201.
[18] B.J. Day, Drug Discov. Today 13 (9) (2004) 557.
[19] M. Singh, R.J. Butcher, N.K. Singh, Polyhedron 27 (17) (2008) 3451.
[20] M. Singh, V. Aggrwal, U.P. Singh, N.K. Singh, Polyhedron 28 (1) (2009) 107.
[21] N.K. Singh, M. Singh, R.J. Butcher, Acta Crystallogr., Sect. E 63 (2007) o4679.
[22] A.I. Vogel, A Text Book of Quantitative Inorganic Analysis, 3rd Ed., ELBS, Longman, London, 1969.
[23] Oxford Diffraction, CrysAlis RED and CrysAlis CCD Versions 1.171.31.8 Oxford Diffraction Ltd., Abingdon, Oxfordshire, England, 2007.
[24] I.J. Bruno, J.C. Cole, P.R. Edgington, M. Kessler, C.F. Macrae, P. McCabe, J. Pearson, R. Taylor, Acta Crystallogr., Sect. B 58 (2002) 389.
[25] L.J. Farrugia, J. Appl. Crystallogr. 30 (1997) 565.
[26] G.M. Sheldrick, SHELXL97, University of Göttingen, Germany, 1997.
[27] Asma EI-Said, Transition Met. Chem. 28 (2003) 749.
[28] I.P. Evans, A. Spencer, G. Wilkinson, J. Chem. Soc., Dalton Trans. 2 (1973) 204.
[29] K. Nakamoto, Infrared and Raman Spectra of Inorganic and Coordination Compounds, 4th Ed., Wiley Press, 1986.
[30] A.B.P. Lever, Inorganic Electronic Spectroscopy, Elsevier, Amsterdam, 1984.
[31] J.R. Dilworth, J. Hyde, P. Lyford, P. Vella, K. Venkatasubramaman, J.A. Zubieta, Inorg. Chem. 18 (1979) 268.
[32] G.A. Bogdanovic, A.S.-De Bire, S.D. Zaric, Eur. J. Inorg. Chem. (2002) 1599.
[33] Z.D. Tomic, V.M. Leovac, S.V. Pokorni, D. Zobel, S.D. Zaric, Eur. J. Inorg. Chem. (2003) 1222.
[34] S.D. Zaric, Eur. J. Inorg. Chem. (2003) 2197.
[35] V.B. Medakovic, M.K. Milicic, G.A. Bogdanovic, S.D. Zaric, J. Inorg. Biochem. 98 (2004) 1867.
[36] A. Castin-eiras, A.G. Sicilia-Zafra, J.M. González-Pèrez, D. Choquesillo-Lazarte, J. Niclós-Gutièrrez, Inorg. Chem. 41 (2002) 6956.
[37] M. Trivedi, D.S. Pandey, Q. Xu, Inorg. Chim. Acta 360 (2007) 2492.
[38] L.-F. Chen, J. Zhang, L.-J. Song, Z.-F. Ju, Inorg. Chem. Commun. 8 (2008) 555.
[39] E. Coronado, J.R.G. Mascarós, C.M. -Gastaldo, Polyhedron 26 (2007) 2101.



Complex	X
1	F
2	Cl
3	Br
4	I

Fig. 1. Chemical formula of Hg(I) complexes **1**–**4**.

(200 mg, 1 mmol) in methanol (10 ml). The resulting precipitate that formed immediately was dissolved in hot absolute methanol (20 ml). The filtered solution was cooled in the dark, giving the complex as light yellow needles, which were washed successively with ice-cooled absolute methanol (5 ml) and ether (25 ml), and dried in a vacuum desiccator overnight. Yield: 92%. *Anal.* Calc. for $C_{24}H_{18}F_2Hg_2N_6O_6$: C, 31.14; H, 1.96; N, 9.08. Found: C, 31.17; H, 1.95; N, 9.05%. UV–Vis: $\lambda(\log\varepsilon)$ (DMSO): 243(4.11), 275(3.92), 295(3.91). IR (KBr/ν, cm^{-1}): 1596 (C=N).

*2.2.2. Synthesis of $[Hg_2(B)_2](NO_3)_2$ (**2**)*

This complex was prepared by a procedure similar to that for **1** using 21.7 mg (0.1 mmol) of **B**. Light yellow crystals were collected by filtration and dried in *vacuo*. Yield: 93%. *Anal.* Calc. for $C_{24}H_{18}Cl_2Hg_2N_6O_6$: C, 30.07; H, 1.89; N, 8.77. Found: C, 30.09; H, 1.87; N, 8.74%. UV–Vis: $\lambda(\log\varepsilon)$ (DMSO): 240(4.21), 273(3.84), 297(3.71). IR (KBr/ν, cm^{-1}): 1601 (C=N).

*2.2.3. Synthesis of $[Hg_2(C)_2](NO_3)_2$ (**3**)*

This complex was prepared by a procedure similar to that for **1** using 26.1 mg (0.1 mmol) of **C**. Light yellow crystals were collected by filtration and dried in *vacuo*. Yield: 86%. *Anal.* Calc. for $C_{24}H_{18}Br_2Hg_2N_6O_6$: C, 27.52; H, 1.73; N, 8.02. Found: C, 27.50; H, 1.72; N, 8.05%. UV–Vis: $\lambda(\log\varepsilon)$ (DMSO): 239(4.23), 269(3.86), 298(3.86). IR (KBr/ν, cm^{-1}): 1599 (C=N).

*2.2.4. Synthesis of $[Hg_2(D)_2](NO_3)_2$ (**4**)*

This complex was prepared by a procedure similar to that for **1** using 30.8 mg (0.1 mmol) of **D**. Light yellow crystals were collected by filtration and dried in *vacuo*. Yield: 89%. *Anal.* Calc. for $C_{24}H_{18}Hg_2I_2N_6O_6$: C, 25.25; H, 1.59; N, 7.36. Found: C, 25.28; H, 1.56; N, 7.34%. UV–Vis: $\lambda(\log\varepsilon)$ (DMSO): 238(4.20), 272(3.81), 296(3.95). IR (KBr/ν, cm^{-1}): 1602 (C=N).

2.3. X-ray analyses

Crystals of **1** and **3**, which were suitable for X-ray crystallography, were obtained as described above. A summary of the key crystallographic information is given in Table 1. Diffraction data for **1** was collected on a Bruker–Nonius Kappa-CCD diffractometer using monochromated Mo Kα radiation and measured using a combination of ϕ scans and ω scans with κ offsets to fill the Ewald sphere. The data was processed using the Denzo-SMN package [21]. Absorption corrections were carried out using SORTAV [22]. The structure was solved and refined using SHELXTL V6.1 [23] for full-matrix least-squares refinement based on F^2. All H-atoms were included in calculated positions and allowed to refine in a riding-motion approximation with U_{iso} tied to the carrier atom. Diffraction data for **3** collected on a Bruker SMART APEX2 CCD area detector using graphite monochromated Mo Kα radiation (λ = 0.71073 Å). Preliminary orientation matrices were obtained from the first frames using APEX2 [24]. The structures were solved using direct methods and refined by the full-matrix least-squares method on F^2 data using SHELXTL [25]. All H-atoms were geometrically positioned and refined using a riding model with d (C–H) = 0.93 Å, U_{iso} = 1.2U_{eq}(C).

Table 1
Crystal data and structure refinements for **1** and **3**.

Complex	**1**	**3**
Empirical formula	$C_{24}H_{18}F_2Hg_2N_6O_6$	$C_{24}H_{18}Br_2Hg_2N_6O_6$
Formula weight	925.62	1047.44
Temperature (K)	150(1)	100(2)
Wavelength (Å)	0.71073	0.71073
Crystal system	triclinic	monoclinic
Space group	$P\bar{1}$	$C2/c$
a (Å)	7.2680(2)	35.571(1)
b (Å)	8.8507(2)	7.1888(2)
c (Å)	10.202(2)	26.781(8)
α (°)	97.52(3)	90
β (°)	97.19(3)	129.554(1)
γ (°)	102.04(3)	90
V (A^3)	628.4(2)	5280(3)
Z	1	8
Density (g cm^{-3})	2.446	2.635
μ (mm^{-1})	12.270	14.696
F(000)	430	3856
Crystal size (mm^3)	0.14 × 0.11 × 0.03	0.23 × 0.12 × 0.11
θ range for data collection (°)	2.88–27.47.	1.48–30.03
Index ranges	$-9 \leqslant h \leqslant 9$, $-11 \leqslant k \leqslant 11$, $-12 \leqslant l \leqslant 13$	$-49 \leqslant h \leqslant 50$, $-10 \leqslant k \leqslant 10$, $-37 \leqslant l \leqslant 37$
Reflections collected	5778	32 124
Independent reflections [R_{int}]	2832 [0.0788]	7667 [0.0917]
Completeness to θ = 27.47°	98.1%	99.4%
Absorption correction	semi-empirical from equivalents	semi-empirical from equivalents
Maximum and minimum transmission	0.696 and 0.313	0.1948 and 0.1331
Refinement method	Full-matrix least-squares on F^2	Full-matrix least-squares on F^2
Data/restraints/parameters	2832/0/181	7667/0/361
Goodness-of-fit (GOF) on F^2	1.055	0.990
Final R indices [$I > 2\sigma(I)$]	R_1 = 0.0577, wR_2 = 0.1404	R_1 = 0.0427, wR_2 = 0.0712
R indices (all data)	R_1 = 0.0739, wR_2 = 0.1518	R_1 = 0.0908, wR_2 = 0.0837
Largest difference in peak and hole (e $Å^{-3}$)	4.521 and −4.235	2.518 and −2.406

3. Results and discussion

3.1. Synthesis and spectral properties

The mercury(I) complexes were prepared by reacting equimolar quantities of mercury(I) nitrate and the ligands in methanol. These complexes are light yellow solids, which are insoluble in chloroform, methanol, ethanol and acetone, and are stable under ambient conditions. While most mercury(I) complexes containing nitrogen donor ligands undergo disproportionation reactions, some imines are known to form stable mercury(I) complexes [4,13]. The existence of stable iminopyridine complexes of mercury(I), which have

Table 2
Selected bond lengths (Å) and bond angles (°) for **1** and **3**.

1		**3**	
Hg1–Hg1a	2.5334(11)	Hg1–Hg1′	2.5190(7)
Hg1–N1	2.317(9)	Hg1–N1	2.219(6)
Hg1–N2	2.427(8)	Hg1–N2	2.565(7)
Hg1–O1	2.490(9)	Hg1–O1	2.698(6)
		Hg1–N1′	2.292(6)
		Hg1–N2′	2.429(6)
		Hg1–O1′	2.569(6)
N1–Hg1–N2	70.4(3)	N1–Hg1–N2	70.9(2)
N1–Hg1–O1	81.9(3)	N1–Hg1–O1	83.2(2)
N2–Hg1–O1	75.3(3)	N2–Hg1–O1	91.45(19)
N1–Hg1–Hg1a	145.7(3)	N1–Hg1–Hg1′	163.48(16)
N2–Hg1–Hg1a	134.9(2)	Hg1′–Hg1–N2	122.56(15)
O1–Hg1–Hg1a	122.6(2)	Hg1′–Hg1–O1	104.62(14)
N3–O1–Hg1	119.2(7)	N3–O1–Hg1	108.9(5)
		N1′–Hg1′–N2	70.7(2)
		N1′–Hg1′–O1′	72.0(2)
		N2′–Hg1′–O1′	88.7(2)
		N1′–Hg1′–Hg1	144.60(16)
		N2′–Hg1′–Hg1	133.72(14)
		Hg1–Hg1′–O1′	124.29(14)
		N3′–O1′–Hg1′	110.1(4)

been confirmed in this study, is consistent with an earlier suggestion that mercury(I) complexes should favor π-acceptor ligands. The IR spectra of the free ligands exhibit the characteristic band of the imine group in the 1621–1631 cm^{-1} region [20]. This band is shifted to lower frequencies in the IR spectra of the corresponding complexes due to the coordination of the imine nitrogen, and appears in the 1596–1602 cm^{-1} region.

The absorption spectra of the complexes **1–4** have absorption bands in the 200–300 nm range (see experimental section) attributed to ligand-centered $\pi \rightarrow \pi^*$ or/and charge transfer transitions.

3.2. Crystal structures

The crystallographic data of compounds **1** and **3** are summarized in Table 1 and selected bond distances and angles are given in Table 2.

3.2.1. $[Hg_2(A)_2](NO_3)_2$ (**1**)

A view of the complex $[Hg_2(A)_2](NO_3)_2$, **1**, along with the atom-numbering scheme is shown in Fig. 2. Complex **1** has crystallographic $\bar{1}$ symmetry and the inversion center is located at the midpoint of the Hg–Hg bond. Each mercury atom has essentially four nearest neighboring atoms, namely the other mercury atom, two nitrogen atoms of the diimine molecule and one oxygen atom belonging to a nitrate ion. The Hg atoms in **1** have an irregular coordination environment. The N1–Hg1–O1 and the intraligand N1–Hg1–N2 angles are only 81.9(3)° and 70.4(3)°, respectively. On the contrary, the Hg1a–Hg1–N1 and Hg1a–Hg1–N2 angles are 145.7(3)° and 134.9(2)°, respectively.

The average Hg–N bond distance (2.372 Å) is similar to that found in structurally related complexes ($[L^2HgHgL^2]^{2+}$ with two N-donor atoms per Hg); for example: 2.335 Å for $[Hg_2(phen)_2](OTf)_2$, 2.39 Å for $Hg_2(phen)(NO_3)_2$ [12], 2.356 Å for $[Hg_2(L^{pPh})][ClO_4]_2$, (L^{pPh} = terdentate ligand, [bis(pyrazol-3-yl)pyridine] derivative) [16] and 2.335 Å for $[Hg_2(phen)_2](OTf)_2$ and 2.352 Å for $Hg_2(4\text{-benzyl-py})_4ClO_4)_2$ [13,14]. However, the Hg–N bond lengths in complexes of the type $[L^2HgHgL^2]^{2+}$ lie between the same bond lengths in complexes of the type $[L^1HgHgL^1]^{2+}$ and $[(L^2)_2HgHg(L^2)_2]^{2+}$. The Hg–N bond lengths observed for complexes of the type $[L^1HgHgL^1]^{2+}$ exhibit values in the 2.10–2.20 Å range [4]. A mean value of 2.521 Å is observed for the complex $[Hg_2(phen)_4]^{2+}$ with four N-donor atoms per Hg [13]. The diimine ligands in **1** are coordinated in a slightly asymmetric bidentate manner: The difference between the bond lengths of Hg1–N1 and Hg1–N2 is 0.11 Å. A similar asymmetry has been reported for $[Hg_2(phen)_2](OTf)_2$, with a difference of 0.14 Å [13].

The Hg1–O1 distance is 2.490(9) Å, compared to the sum of the van der Waals radii of 3.02–3.25 Å. This distance is slightly shorter than those in $Hg_2(phen)(NO_3)_2$, (2.59 and 2.91 Å) [12] and in $Hg_2(quinoline)_2(NO_3)_2$, (2.818, 2.786 and 2.802 Å) [26–29].

The Hg–Hg bond length of **1** is 2.5334(11) Å, compared to 2.513(5) Å for $[Hg_2(phen)_2](OTf)_2$, 2.516(7) Å for $Hg_2(phen)(NO_3)_2$ and 2.551(2) Å for $Hg_2(quinoline)_2(NO_3)_2$ [12,13,27].

The geometry of imine and pyridine nitrogen atoms is planar. The planarity is measured by three N atom bond angles. The sums

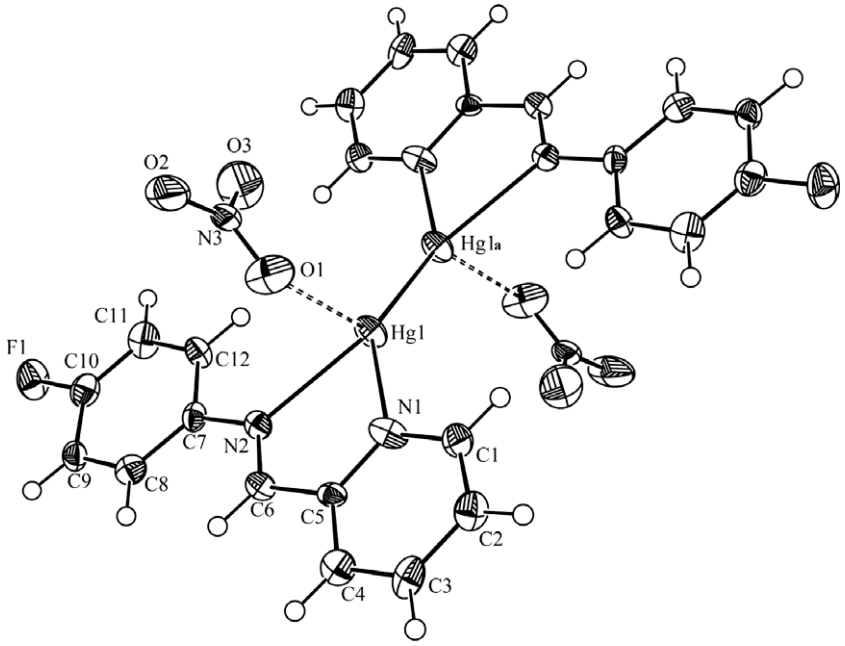


Fig. 2. Structure of **1** in the crystal, showing the atom-labelling scheme. Thermal ellipsoids are at 50% probability.

Table 3
Geometry of the pyridine, chelate and benzene ring in compounds **1** and **3**.

	1	**3**	
		Ligand 1	Ligand 2
Planes 1 (pyridine ring)	N1–C5–C6–N2	N1–C5–C6–N2	N1′–C5′–C6′–N2′
Planes 2 (chelate ring)	N1–C2–C3–C4–C5.– N2	N1–C2–C3–C4–C5	N1′–C2′–C3′–C4′–C5′
Planes 3 (benzene ring)	C7–C8–C9–C10–C11–C12	C7–C8–C9–C10–C11–C12	C7′–C8′–C9′–C10′–C11′–C12′
Dihedral angle/° between planes 1 and 2	1.29(4)	5.88(3)	5.20(4)
Dihedral angle/° between planes 2 and 3	2.10(3)	9.45(3)	7.59(3)
Dihedral angle/° between planes 1 and 3	2.65(4)	6.19(3)	11.21(3)
Distance/Å of Hg (1) to the plane 1	0.1091(5)	0.1193(5)	0.0492(4)
Distance/Å of Hg (1a) to the plane 1	1.089(5)	0.127(4)	0.816(4)
Torsion angle/° N–C=C–N (lig 1)	4.848(2)	4.197(2)	−9.073(2)
Angel between plane 1 and Hg–Hg line	67.25(4)	84.35(3)	69.90(3)

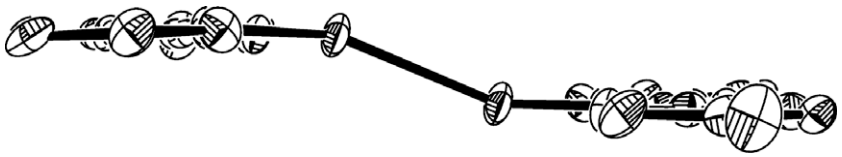


Fig. 3. View of the $[Hg_2(A)_2]^{2+}$ cation of complex **1** perpendicular to the Hg–Hg bond.

of these angles (ΣN) are 359.5° and 360° for N1 and N2, respectively. Despite the fact that the imine nitrogen atoms in **1** are sp^2 hybridized, some strain in the chelate ring is suggested by the deviation from the 120° angle about the nitrogen, Hg1–N2–C6 (114.6(7)°), Hg1–N2–C7 (124.3(7)°), and C6–N2–C7 (121.1(9)°).

Surprisingly, the dihedral angles between the planes of the pyridine ring, chelate ring and the benzene ring (best plane of 1, 2 and 3, Table 3) in **1** show coplanarity of these planes, leading to a considerable planarity of the ligands. The coplanarity of the pyridine and chelate ring results in a bite size of 2.74 Å for d(N1–N2).

While the ligand is planar, the $[L^2HgHgL^2]^{2+}$ cation of **1**, as a whole, is not coplanar. The mercury atom is closely within the plane of the corresponding chelate diimine ligand (max. deviation from this plane is 0.11 Å). However, the inversion-related mercury is displaced by 1.1 Å out of this plane, so that the $[L^2HgHgL^2]^{2+}$ unit has an appreciable 'step' in the Hg–Hg bond (Fig. 3).

$[Hg_2(A)_2](NO_3)_2$, **1**, exhibits a supramolecular structure as a result of the π–π stacking of the diimine ligands, and this may be responsible for the insolubility of the complex. Each diimine ligand has two diimine neighbors within the stacks, which are oriented along the crystallographic, 1 1 1 plane (Fig. 4). The mean inter-ring distances between corresponding atoms of the diimine ligands and the two neighboring ligands are almost equal and amount to 3.42 Å for the stacks involving the rings formed by the pyridine ring and the neighboring benzene ring. A related stacking of the phenanthroline ligands was observed for $[Hg_2(phen)_2](OTf)_2$ with separations of approximately 3.45 Å [13] and 3.50 Å for $Hg_2(phen)(NO_3)_2$ [12].

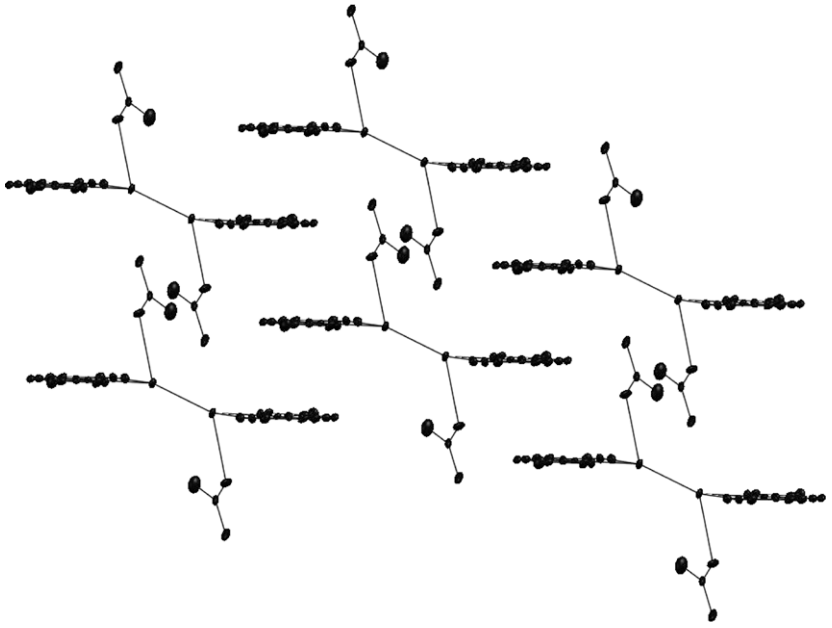


Fig. 4. Packing of $[Hg_2(A)_2](NO_3)_2$, **1**.

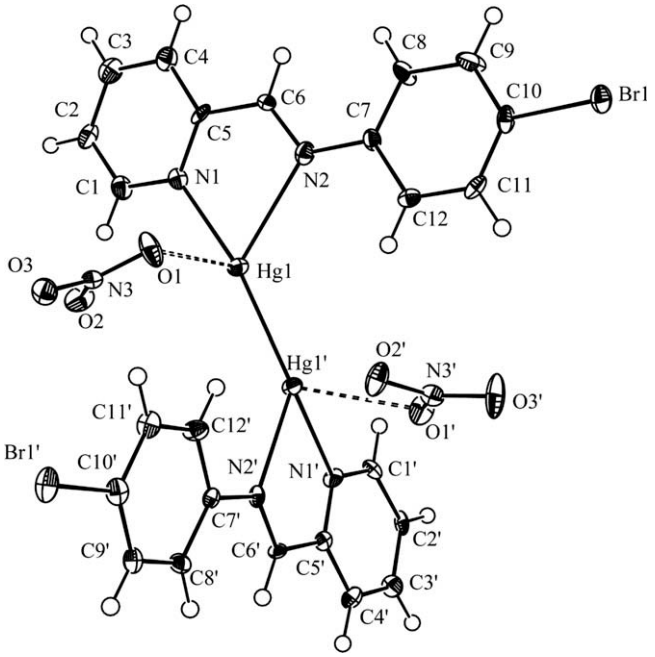


Fig. 5. Structure of **3** in the crystal, showing the atom-labelling scheme. Thermal ellipsoids are at 50% probability.

3.2.2. $[Hg_2(C)_2](NO_3)_2$ (**3**)

The molecular structure of **3** is illustrated in Fig. 5, where each mercury atom is coordinated by the bidentate diimine ligand and another mercury atom. The Hg–N distances of **3** cover the range 2.219(6)–2.565(7) Å, which is well within the van der Waals limit of 3.05–3.28 Å, depending on the van der Waals radius of mercury (1.50–1.73 Å) [28,29], while the Hg–N distances of **1** cover a shorter range (2.317–2.427 Å). The diimine ligands in **3** are coordinated in a considerably asymmetric bidentate manner: The difference between the bond lengths Hg1–N1 and Hg1–N2 is 0.346 and 0.137 Å between Hg1′–N1′ and Hg1′–N2′ (Table 2). However, the average Hg–N bond length of 2.376 Å agrees well with the same distance in the **1** ($Hg–N_{ave}$ = 2.372 Å).

The Hg–Hg bond length of 2.5190(7) Å in **3** is slightly shorter than the same bond length in complex **1**. However, the average Hg–Hg bond distance of **1** and **3** is 2.526 Å, and the Hg–Hg bond lengths in these complexes ($[L^2HgHgL^2]^{2+}$) lie between the same bond lengths in complexes of the type $[L^1HgHgL^1]^{2+}$ (2.51 Å with the exception of $Hg_2(quinoline)_2(NO_3)_2$, exhibiting a value of 2.551(2) Å) and complexes of the type $[(L^2)_2HgHg(L^2)_2]^{2+}$ (2.549 Å).

The environment of each mercury atom differs in terms of mercury–oxygen contacts. The Hg–O distances are 2.698(6) and 2.569(6) Å for Hg1–O1 and Hg1′–O1′, respectively. Whereas Hg1 is four coordinate, Hg1′ has an additional relatively weak interaction with another oxygen of the same nitrate atom [Hg1′···O2′, 3.03 Å]. However, the Hg–O distances are longer than those in **1**.

The dihedral angle between the plane of the chelate ring and the pyridine ring (Table 3) indicate the coplanarity of these moieties, resulting in a bite size of 2.788 and 2.735 Å for d(N1–N2) and d(N1′–N2′).

A comparison of the dihedral angles between the planes of the pyridine, chelate and the benzene ring (best plane of 1, 2 and 3, Table 3) in **3** indicate that the ligand is distorted from planarity, with an average twist of 8.5° between the chelate and the benzene planes.

In contrast with complex **1**, the chelate ring of ligand 1 in complex **3** twists around the Hg–Hg bond, such that it is approximately perpendicular to the chelate ring of ligand 2, resulting in a dihedral angle of 84.58° between the chelate rings (Fig. 6).

The mercury atom, Hg1 is closely coplanar with the diimine ligand. Deviation of the Hg (1) atom from this plane is 0.05 Å. However, Hg1′ deviates considerably from this plane, by 0.816 Å.

As in complex **1,** a related stacking of diimine ligands was observed for **3** with separations of approximately 3.50 Å [13]. In the structure of **3**, each of the two diimine ligands is stacked with one diimine ligand of a neighboring complex.

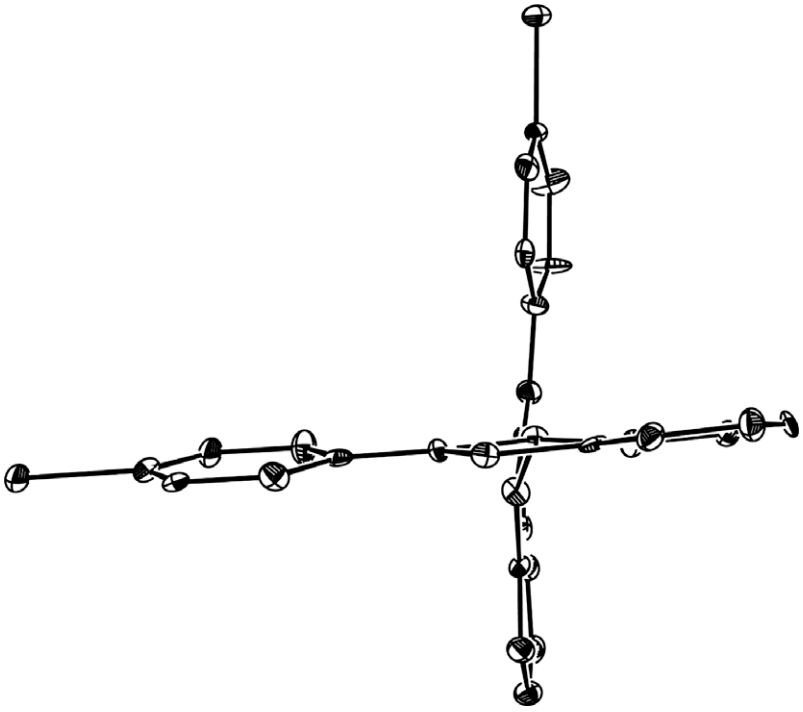


Fig. 6. View of the $[Hg_2(B)_2]^{2+}$ cation of complex **3** along the Hg–Hg bond.

4. Supplementary data

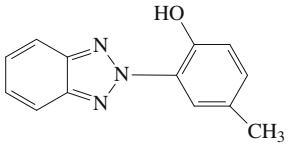
CCDC 714916 and 714917 contain the supplementary crystallographic data for this paper. These data can be obtained free of charge via http://www.ccdc.cam.ac.uk/conts/retrieving.html, or from the Cambridge Crystallographic Data Centre, 12 Union Road, Cambridge CB2 1EZ, UK; fax: (+44) 1223-336-033; or e-mail: deposit@ccdc.cam.ac.uk.

Acknowledgment

Financial support by the Alzahra University is gratefully acknowledged.

References

[1] D.K. Breitinger, in: J.A. McCleverty, T.J. Meyer (Eds.), Cadmium and Mercury in Comprehensive Coordination Chemistry II, Elsevier, Oxford, 2004.
[2] W. Levason, C.A. McAuliffe, in: C.A. McAuliffe (Ed.), The Chemistry of Mercury, McMillan, London, 1977.
[3] M.J. Taylor, Metal-to-Metal Bonded States of the Main Group Elements, Academic Press, London, 1975.
[4] K. Brodersen, Comment. Inorg. Chem. 1 (1981) 207.
[5] K. Brodersen, G. liehr, N. Hacke, Z. Anorg. Allg. Chem. 1 (1974) 409.
[6] K. Brodersen, J. Hofmann, Z. Naturforsch B 47 (1992) 460.
[7] K. Brodersen, J. Hofmann, Z. Naturforsch B 46 (1991) 1684.
[8] D.L. Kepert, D. Taylor, A.H. White, Inorg. Chem. 11 (1972) 1639.
[9] G. Anderegg, Helv. Chim. Acta 42 (1959) 344.
[10] J. Limmer, N. Hacke, K. Brodersen, Chem. Ber. 106 (1973) 2185.
[11] D.L. Kepert, D. Taylor, A.H. White, J. Chem. Soc., Dalton Trans. (1973) 893.
[12] R.C. Elder, J. Halpern, J.S. Pond, J. Am. Chem. Soc. 89 (1967) 6877.
[13] R. Malleier, W. Schuh, H. Kopacka, K. Wurst, P. Peringer, Inorg. Chim. Acta 361 (2008) 195.
[14] D. Taylor, Aust. J. Chem. 30 (1977) 2647.
[15] J.C. Dewan, D.L. Kepert, A.H. White, J. Chem. Soc., Dalton Trans. (1975) 490.
[16] S.P. Argent, H. Adams, T.R. Johannessen, J.C. Jeffery, L.P. Harding, W. Clegg, R.W. Harrington, M.D. Ward, J. Chem. Soc., Dalton Trans. (2006) 4996.
[17] R.N. Dominey, B. Hauser, J. Hubbard, J. Dunham, Inorg. Chem. 30 (1991) 4754.
[18] S. Dehghanpour, N. Bouslimani, R. Welter, F. Mojahed, Polyhedron 26 (2007) 154.
[19] D.D. Perrin, W.L. Armarego, D.R. Perrin, Purification of Laboratory Chemicals, second ed., Pergamon, New York, 1990.
[20] S. Dehghanpour, A. Mahmoudi, Main Group Chem. 6 (2007) 121.
[21] Z. Otwinowski, W. Minor, Methods in Enzymology, in: C.W. Carter, R.M. Sweet (Eds.), Macromolecular Crystallography, Part A, vol. 276, Academic Press, London, 1997.
[22] R.H. Blessing, Acta Cryst. A51 (1995) 33.
[23] G.M. Sheldrick, Acta Cryst. A64 (2008) 112.
[24] Bruker SMART, Bruker Molecular Analysis Research Tool, v. 5.059, Bruker AXS, Madison, Wisconsin, USA, 1998.
[25] G.M. Sheldrick SHELXTL v. 5.10, Structure Determination Software Suite, Bruker AXS, Madison, Wisconsin, USA, 1998.
[26] E.L. Torres, M.A. Mendiola, J.R. Procopio, M.T. Sevilla, E. Colacio, J.M. Moreno, I. Sobrados, Inorg. Chim. Acta 323 (2001) 130.
[27] K. Brodersen, N. Hacke, G. Liehr, Z. Anorg. Allg. Chem. 414 (1975) 1.
[28] A. Bondi, J. Phys. Chem. 68 (1964) 441.
[29] A.J. Canty, G.B. Deacon, Inorg. Chim. Acta 45 (1980) L225.



Scheme 1. Structure of 2-(2′-hydoxy-5′-methylphenyl)benzotriazole (Hhmpbta).

phenyl)benzotriazole in the presence of PPh_3 resulted in failure. In contrast to 8-hydroxyquinoline and quinoline-2-carboxylic acid, the both above mentioned reactions lead to the monosubstituted chelates. Only few crystals of $[ReOCl(hmpbta)_2]$ were isolated from the reaction of $[ReOCl_3(AsPh_3)_2]$ with ligand excess in acetonitrile.

Here, we present the synthesis, structural and spectroscopic characterization of $[ReOCl_2(hmpbta)(AsPh_3)] \cdot MeCN$ (**1** · MeCN), $[ReOBr_2(hmpbta)(AsPh_3)] \cdot MeCN$ (**2** · MeCN), $[ReOCl_2(hmpbta)(PPh_3)] \cdot MeCN$ (**3** · MeCN), $[ReOBr_2(hmpbta)(PPh_3)] \cdot MeCN$ (**4** · MeCN) and $[ReOBr_2(hmpbta)(PPh_3)] \cdot MeCN$ (**4** · Me_2CO) complexes. The paper reports also X-ray structure of $[ReOCl(hmpbta)_2]$ (**5**) and DFT calculations for **1** and **5**.

Currently density functional theory (DFT) is commonly used to examine the electronic structure of transition metal complexes. It meets with the requirements of being accurate, easy to use and fast enough to allow the study of relatively large molecules of transition metal complexes [14]. Gancheff et al. [15] have performed extended tests of the ability of the B3LYP method in LANL2DZ basis set for rhenium compounds in a geometry optimization and calculation of spectral properties. Although this is not a very extended basis set, its use with DFT has shown to be sufficient for the geometry optimization and calculation of spectral properties. The correctness of B3LYP method with LANL2DZ basis set for rhenium complexes has been also proven in this paper. The experimental geometries of **1** and **5** are well reproduced and the calculated electronic spectrum of **1** is in good accordance with the experimental one.

2. Experimental

2.1. General procedure

All the reagents used to the synthesis were commercially available and were used without further purification. The $[ReOX_3(PPh_3)_2]$ and $[ReOX_3(AsPh_3)_2]$ complexes were prepared according to the literature methods [16].

IR spectra were recorded on a Nicolet Magna 560 spectrophotometer in the spectral range 4000–400 cm^{-1} with the samples in the form of KBr pellets. Electronic spectra were measured on a spectrophotometer Lab Alliance UV–Vis 8500 in the range 1100–180 nm in acetonitrile solution. Elemental analyses (CHN) were performed on a Perkin–Elmer CHN-2400 analyzer.

2.2. Preparation of $[ReOCl_2(hmpbta)(AsPh_3)] \cdot MeCN$ (**1** · MeCN)

$[ReOCl_3(AsPh_3)_2]$ (0.5 g, 0.54 mmol) was added to 2-(2′-hydoxy-5′-methylphenyl)benzotriazole (0.125 g, 0.55 mmol) in acetonitrile (50 ml) and the reaction mixture was refluxed for 2 h. The resulting solution was allowed to cool to room temperature and reduced in volume to ~10 ml. A greenish-brown crystalline precipitate of [Re-

Table 1
Crystal data and structure refinement for $[ReOX_2(hmpbta)(EPh_3)] \cdot MeCN$, $[ReOX_2(hmpbta)(EPh_3)] \cdot Me_2CO$ (X = Cl, Br; E = P, As) and $[ReOCl(hmpbta)_2]$ complexes.

	1 · MeCN	**2** · MeCN	**3** · MeCN	**4** · MeCN	**4** · Me_2CO	**5**
Empirical formula						
$C_{33}H_{28}AsCl_2N_4O_2Re$						
$C_{33}H_{28}AsBr_2N_4O_2Re$	$C_{33}H_{28}PCl_2N_4O_2Re$	$C_{33}H_{28}PBr_2N_4O_2Re$		$C_{34}H_{31}PBr_2N_3O_3Re$	$C_{26}H_{20}ClN_6O_3Re$	
Formula weight	844.61	933.53	800.66	889.58	906.61	686.13
Temperature (K)	291.0(3)	291.0(3)	293(2)	293(2)	293(2)	293(2)
Wavelength (Å)	0.71073	0.71073	0.71073	0.71073	0.71073	0.71073
Crystal system	triclinic	triclinic	triclinic	triclinic	triclinic	orthorhombic
Space group	$P\bar{1}$	$P\bar{1}$	$P\bar{1}$	$P\bar{1}$	$P\bar{1}$	*Pbca*
Unit cell dimensions (Å, °)	a = 11.3671(9)	a = 11.4867(3)	a = 11.23761(5)	a = 11.4304(3)	a = 11.5541(6)	a = 15.5760(3)
	α = 81.544(6)	α = 86.016(2)	α = 80.885(3)	α = 86.340(2)	α = 85.804(4)	
	b = 11.4937(8)	b = 11.5198(2)	b = 11.2594(4)	b = 11.5647(3)	b = 11.6407(6)	b = 15.6522(3)
	β = 87.203(6)	β = 80.689(2)	β = 87.458(3)	β = 80.129(2)	β = 81.455(4)	
	c = 13.5044(8)	c = 13.5428(3)	c = 13.4622(4)	c = 13.7003(3)	c = 13.5171(7)	c = 20.1927(4)
	γ = 67.316(7)	γ = 66.135(2)	γ = 66.978(4)	γ = 66.171(2)	γ = 67.831(5)	
Volume ($Å^3$)	1610.11(19)	1617.22(6)	1547.60(10)	1632.10(7)	1664.64(15)	4922.95(17)
Z	2	2	2	2	2	8
D_{calc} (Mg/m^3)	1.742	1.917	1.718	1.810	1.809	1.851
Absorption coefficient (mm^{-1})	4.995	7.279	4.188	6.256	6.137	5.087
$F(000)$	824	896	788	860	880	2672
Crystal size (mm)	0.183, 0.047, 0.045	0.288, 0.103, 0.009	0.036, 0.092, 0.26	0.107, 0.049, 0.012	0.107, 0.104, 0.008	0.358, 0.089, 0.085
θ range for data collection (°)	1.52–25.05	1.52–25.03	2.52–25.00	1.51–25.02	1.52–25.03	2.02–25.03
Index ranges	$-13 \leqslant h \leqslant 13$	$-13 \leqslant h \leqslant 13$	$-9 \leqslant h \leqslant 13$	$-13 \leqslant h \leqslant 13$	$-13 \leqslant h \leqslant 13$	$-18 \leqslant h \leqslant 18$
	$-13 \leqslant k \leqslant 13$	$-13 \leqslant k \leqslant 11$	$-12 \leqslant k \leqslant 13$	$-13 \leqslant k \leqslant 13$	$-13 \leqslant k \leqslant 11$	$-17 \leqslant k \leqslant 18$
	$-16 \leqslant l \leqslant 16$	$-16 \leqslant l \leqslant 16$	$-15 \leqslant l \leqslant 15$	$-16 \leqslant l \leqslant 15$	$-16 \leqslant l \leqslant 16$	$-24 \leqslant l \leqslant 24$
Reflections collected	15750	16075	15052	15906	16241	46479
Independent reflections [R_{int}]	5713 [0.0835]	5705 [0.0246]	5366 [0.0196]	5753 [0.0235]	5862 [0.0470]	4358 [0.0347]
Completeness to 2θ = 50° (%)	100	100	98.4	100	99.8	100.0
Min. and max. transmission	0.751, 0.804	0.382, 0.950	0.640, 0.853	0.703, 0.922	0.520, 0.951	0.580, 0.657
Data/restraints/parameters	5713/0/390	5705/0/390	5366/0/390	5753/0/390	5862/0/417	4358/0/337
Goodness-of-fit on F^2	1.040	0.986	1.005	1.100	1.053	1.055
Final R indices [$I > 2\sigma(I)$]	R_1 = 0.0738	R_1 = 0.0185	R_1 = 0.0183	R_1 = 0.0227	R_1 = 0.0310	R_1 = 0.0162
	wR_2 = 0.1732	wR_2 = 0.0444	wR_2 = 0.0441	wR_2 = 0.0632	wR_2 = 0.0770	wR_2 = 0.0428
R indices (all data)	R_1 = 0.1008	R_1 = 0.0236	R_1 = 0.0205	R_1 = 0.0265	R_1 = 0.0400	R_1 = 0.0222
	wR_2 = 0.2007	wR_2 = 0.0452	wR_2 = 0.0444	wR_2 = 0.0648	wR_2 = 0.0834	wR_2 = 0.0441
Largest difference in peak and hole (e $Å^{-3}$)	1.273 and −1.009	0.397 and −1.025	0.967 and −0.702	0.486 and −1.547	0.991 and −0.877	0.669 and −0.529

OCl_2(hmpbta)($AsPh_3$)] · MeCN was filtered off and dried in the air. Yield 80%.

Single crystals of **1** · MeCN were obtained by recrystallization from acetonitrile.

Anal. Calc. for $C_{33}H_{28}AsCl_2N_4O_2Re$: C, 46.93; H, 3.34; N, 6.63. Found: C, 47.35; H, 3.73; N, 6.47%.

IR (KBr; ν/cm^{-1}): 1568 (m) and 1504 (s) ν_{CN} and $\nu_{C=C}$; 965(vs) $\nu_{Re=O}$.

2.3. Preparation of [$ReOBr_2$(hmpbta)($AsPh_3$)] · MeCN (**2** · MeCN)

A procedure similar to that for **1** · MeCN was used with [$ReOBr_3(AsPh_3)_2$] (0.5 g, 0.47 mmol) and Hhmpbta (0.11 g, 0.49 mmol). Greenish-brown crystals of **2** · MeCN were collected in 85% yield, respectively.

IR (KBr; ν/cm^{-1}): 1578 (m) and 1502(s) ν_{CN} and $\nu_{C=C}$; 965(vs) $\nu_{Re=O}$.

UV–Vis of **2** (CH_3CN; λ_{max} [nm] (ε; [dm^3 mol^{-1} cm^{-1}])): 630.0 (80), 372.5 (11200), 315.4 (21900), 245.8 (41500) and 207.5 (122000).

Anal. Calc. for $C_{33}H_{28}AsBr_2N_4O_2Re$: C, 42.46; H, 3.02; N, 6.00. Found: C, 42.84; H, 3.36; N, 6.30%.

Table 2
Short intra- and intermolecular contacts detected in **1** · MeCN, **2** · MeCN, **3** · MeCN, **4** · MeCN, **4** · Me_2CO and **5** complexes.

D–H···A	D–H	H···A	D···A	D–H···A
1 · *MeCN*				
C6 H6 O2	0.93	2.73	3.521(15)	143.4
C5 H5 O2#1	0.93	2.61	3.390(16)	142.4
C24 H24 O1	0.93	2.46	3.025(14)	119.3
C27 H27 Cl2#1	0.93	2.79	3.539(11)	138.0
C30 H30 N3	0.93	2.42	2.762(15)	101.6
C31 H31B Cl1#2	0.96	2.73	3.578(15)	147.4
2 · *MeCN*				
C14 H14 O2	0.93	2.68	3.474(3)	143.4
C15 H15 O2#3	0.93	2.61	3.403(4)	143.9
C24 H24 O1	0.93	2.40	2.966(3)	118.8
C27 H27 Br2#3	0.93	2.90	3.604(3)	133.5
C30 H30 N3	0.93	2.45	2.766(4)	99.9
C31 H31A Br1#4	0.96	2.99	3.610(3)	123.2
3 · *MeCN*				
C14 H14 O2	0.93	2.51	3.300(3)	143.5
C15 H15 O2#5	0.93	2.56	3.363(3)	144.7
C27 H27 O1	0.93	2.38	2.944(3)	118.7
C20 H20 Cl2#5	0.93	2.73	3.454(3)	135.0
C23 H23 N3	0.93	2.45	2.774(4)	100.2
C32 H32C Cl1#6	0.96	2.67	3.565(3)	155.9
4 · *MeCN*				
C14 H14 O2	0.93	2.52	3.312(5)	143.2
C15 H15 O2#3	0.93	2.63	3.445(5)	146.8
C24 H24 O1	0.93	2.39	2.964(5)	119.5
C27 H27 Br2#3	0.93	2.89	3.598(4)	133.4
C30 H30 N3	0.93	2.47	2.783(5)	99.9
C31 H31A Br1#4	0.96	2.87	3.627(5)	136.4
4 · *Me_2CO*				
C3 H3 O99′#7	0.93	2.49	3.258(14)	139.5
C8 H8 O2	0.93	2.47	3.272(6)	144.3
C9 H9 O2#6	0.93	2.63	3.385(6)	139.2
C24 H24 O1	0.93	2.36	2.954(6)	121.1
C27 H27 Br2#6	0.93	2.88	3.614(5)	136.9
C30 H30 N3	0.93	2.45	2.765(6)	99.7
C31 H31C Br1#2	0.96	2.73	3.654(6)	160.9
5				
C12 H12 N3	0.93	2.40	2.744(3)	101.9
C19 H19 Cl1#8	0.93	2.77	3.508(3)	136.9

Symmetry transformations used to generate equivalent atoms: #1: $-x+1, -y, -z$; #2: $-x, -y, -z$; #3: $-x+1, -y+2, -z+1$; #4: $-x+1, -y+1, -z+1$; #5: $-x+1, -y+1, -z$; #6: $-x, -y+1, -z$; #7: $-x-1, -y-1, -z-1$; #8: $-x+2, -y, -z+1$.

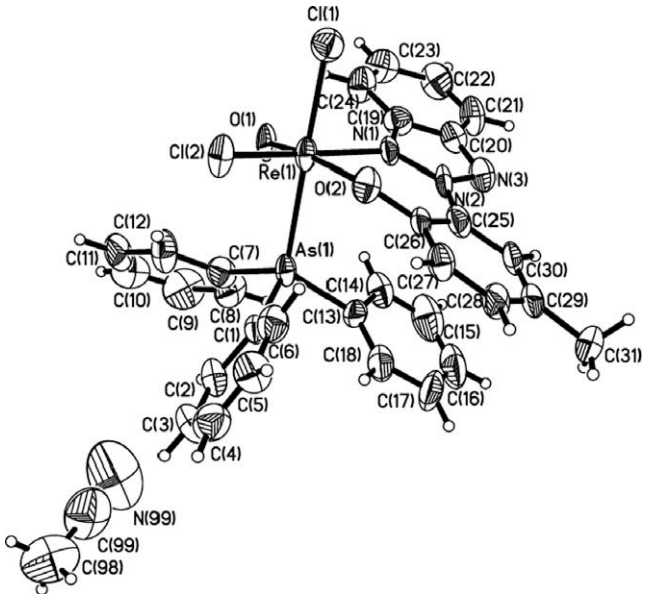


Fig. 1. The molecular structure of **1** · MeCN. Displacement ellipsoids are drawn at 50% probability.

2.4. Preparation of [$ReOCl_2$(hmpbta)(PPh_3)] · MeCN (**3** · MeCN)

A procedure similar to that for **1** · MeCN was used with [$ReOCl_3(PPh_3)_2$] (0.50 g, 0.6 mmol) and Hhmpbta (0.135 g, 0.6 mmol). Greenish-brown crystals of **3** · MeCN were collected in 80% yield, respectively.

IR (KBr; ν/cm^{-1}): 1569 (m) and 1505(s) ν_{CN} and $\nu_{C=C}$; 966(vs) $\nu_{Re=O}$.

UV–Vis of **3** (CH_3CN; λ_{max} [nm] (ε; [dm^3 mol^{-1} cm^{-1}])): 618.7 (90), 379.5 (6700), 328.7 (14300), 246.1 (29600) and 201.6 (98600).

Anal. Calc. for $C_{33}H_{28}PCl_2N_4O_2Re$: C, 49.50; H, 3.52; N, 7.00. Found: C, 48.84; H, 3.16; N, 7.42%.

2.5. Preparation of [$ReOBr_2$(hmpbta)(PPh_3)] · MeCN (**4** · MeCN)

A procedure similar to that for **1** · MeCN was used with [$ReOBr_3(PPh_3)_2$] (0.50 g, 0.52 mmol) and Hhmpbta (0.12 g, 0.53 mmol). Greenish-brown crystals of **4** · MeCN were collected in 80% yield, respectively.

IR (KBr; ν/cm^{-1}): 1567 (m) and 1505(s) ν_{CN} and $\nu_{C=C}$; 966(vs) $\nu_{Re=O}$.

UV–Vis of **4** (CH_3CN; λ_{max} [nm] (ε; [dm^3 mol^{-1} cm^{-1}])): 621.0 (80), 369.9 (9800), 329.0 (20550), 244.6 (40100) and 205.6 (115900).

Anal. Calc. for $C_{33}H_{28}PBr_2N_4O_2Re$: 44.56; H, 3.17; N, 6.30. Found: C, 43.95; H, 3.43; N, 6.63%.

2.6. Preparation of [$ReOBr_2$(hmpbta)(PPh_3)] · MeCN (**4** · Me_2CO)

[$ReOBr_3(PPh_3)_2$] (0.50 g, 0.52 mmol) was added to 2-(2′-hydoxy-5′-methylphenyl)benzotriazole (0.12 g, 0.53 mmol) in acetone (80 ml) and the reaction mixture was refluxed for 2 h. The resulting solution was allowed to cool to room temperature and reduced in volume to ~10 ml. A greenish-brown crystalline precipitate of [$ReOBr_2$(hmpbta)(PPh_3)] · Me_2CO was filtered off and dried in the air. Yield 80%.

IR (KBr; ν/cm^{-1}): 1567 (m) and 1505(s) ν_{CN} and $\nu_{C=C}$; 966(vs) $\nu_{Re=O}$.

Anal. Calc. for $C_{34}H_{31}PBr_2N_4O_2Re$: C, 45.04; H, 3.45; N, 4.63. Found: C, 45.92; H, 3.14; N, 4.35%.

2.7. Crystal structures determination and refinement

The X-ray intensity data of **1** · MeCN, **2** · MeCN, **3** · MeCN, **4** · MeCN, **4** · Me_2CO and **5** were collected on a KM-4-CCD automatic diffractometer equipped with CCD detector and graphite monochromated Mo Kα radiation (λ = 0.71073 Å) at room temperature. Details concerning crystal data and refinement are given in Table 1. Lorentz, polarization and numerical absorption correction [17] were applied. The structures were solved by the Patterson method and subsequently completed by the difference Fourier recycling. All the non-hydrogen atoms were refined anisotropically using full-matrix, least-squares technique. The hydrogen atoms were treated as "riding" on their parent carbon atoms and assigned isotropic temperature factors equal 1.2 (non-methyl) and 1.5 (methyl) times the value of equivalent temperature factor of the parent atom. The methyl groups were allowed to rotate about their local threefold axis. SHELXS97 [18], SHELXL97 [19] and SHELXTL [20] programs were used for all the calculations. Atomic scattering factors were those incorporated in the computer programs.

2.8. Computational details

The gas phase geometries of **1** and **5** were optimized without any symmetry restrictions in the singlet ground-state with the DFT method using the hybrid B3LYP functional of GAUSSIAN03 [21–23]. The calculations were performed by using ECP basis set on the rhenium atom, the standard 6–31+G** basis for chlorine, arsine, oxygen and nitrogen, 6–31G* for carbon and 6–31G for hydrogen atoms [24,25]. The Xe core electrons of Re were replaced by an effective core potential and DZ quality Hay and Wadt Los Alamos ECP basis set (LANL2DZ) [26] was used for the valence electrons. Additional d function with exponent α = 0.3811 and *f* function with exponent α = 2.033 on the rhenium atom were added [27]. All vibrations in the calculated vibrational spectrum of **1** and **5** were real, thus the both geometries correspond to true energy minimum.

The electronic spectrum of **1** was calculated with the TDDFT method, and the solvent effect was simulated using the polarizable continuum model with the integral equation formalism (IEF-PCM) [28].

Natural bond orbital (NBO) calculations were performed with the NBO code [29,30] included in GAUSSIAN03.

3. Results and discussion

3.1. Preparation and infrared data

The $[ReOX_2(hmpbta)(EPh_3)] \cdot MeCN$ (X = Cl, Br; E = As, P) and $[ReOBr_2(hmpbta)(PPh_3)] \cdot Me_2CO$ complexes were prepared in high yield by a route analogous to that used for the synthesis of the $[ReOX_2(hqn)(EPh_3)_2]$ and $[ReOX_2(quin\text{-}2\text{-}c)(EPh_3)_2]$, namely by ligand exchange reactions starting from $[ReOX_3(EPh_3)_2]$ complexes and 2-(2′-hydoxy-5′-methylphenyl)benzotriazole in molar ratio 1:1 [9–12]:

$$[ReOX_3(EPh_3)_2] + Hhmpbta \rightarrow [ReOX_2(hmpbta)(EPh_3)] + HX + EPh_3 \quad X = Cl, Br; \quad E = As, P$$

Table 3
The experimental and optimized bond lengths (Å) and angles (°) for **1** · MeCN.

Bond lengths	Experimental	Optimized	Bond angles	Experimental	Optimized
Re(1)–O(1)	1.695(7)	1.684	O(1)–Re(1)–O(2)	165.0(3)	162.01
Re(1)–O(2)	1.934(7)	1.979	O(1)–Re(1)–N(1)	88.4(3)	88.07
Re(1)–N(1)	2.166(8	2.170	O(2)–Re(1)–N(1)	81.4(3)	80.00
Re(1)–Cl(1)	2.402(3)	2.431	O(1)–Re(1)–Cl(2)	100.1(3)	100.77
Re(1)–Cl(2)	2.344(3)	2.413	O(2)–Re(1)–Cl(2)	90.7(2)	92.24
Re(1)–As(1)	2.5847(12)	2.655	N(1)–Re(1)–Cl(2)	171.2(2)	170.38
			O(1)–Re(1)–Cl(1)	99.2(3)	101,31
			O(2)–Re(1)–Cl(1)	91.3(2)	91.14
			N(1)–Re(1)–Cl(1)	87.1(2)	85.28
			Cl(2)–Re(1)–Cl(1)	89.19(11)	89.24
			O(1)–Re(1)–As(1)	84.2(3)	83.73
			O(2)–Re(1)–As(1)	85.6(2)	84.39
			N(1)–Re(1)–As(1)	94.1(2)	96.89
			Cl(2)–Re(1)–As(1)	89.16(9)	87.92
			Cl(1)–Re(1)–As(1)	176.42(8)	174.61

Table 4
The experimental bond lengths (Å) and angles (°) for $[ReOX_2(hmpbta)(EPh_3)] \cdot MeCN$.

Bond lengths	**2** · MeCN E = As; X = Br	**3** · MeCN E = P; X = Cl	**4** · MeCN E = P; X = Br	**4** · Me_2CO E = P; X = Br	Bond angles	**2** · MeCN	**3** · MeCN	**4** · MeCN	**4** · Me_2CO
Re(1)–O(1)	1.6765(19)	1.6938(18)	1.691(2)	1.669(3)	O(1)–Re(1)–O(2)	164.50(9)	165.05(8)	165.24(12)	164.74(15)
Re(1)–O(2)	1.9227(18)	1.9458(18)	1.940(2)	1.931(3)	O(1)–Re(1)–N(1)	88.74(9)	88.54(8)	88.50(12)	88.16(15)
Re(1)–N(1)	2.145(2)	2.155(2)	2.164(3)	2.160(4)	O(2)–Re(1)–N(1)	80.30(8)	80.34(8)	80.26(10)	80.31(13)
Re(1)–X(1)	2.5103(3)	2.4019(7)	2.5470(4)	2.5332(6)	O(1)–Re(1)–X(2)	99.92(7)	100.30(6)	99.99(9)	99.75(12)
Re(1)–X(2)	2.4798(3)	2.3409(6)	2.4923(4)	2.4868(5)	O(2)–Re(1)–X(2)	91.60(5)	91.63(5)	92.09(7)	92.68(9)
Re(1)–E(1)	2.5711(3)	2.4839(7)	2.4935(10)	2.4877(12)	N(1)–Re(1)–X(2)	171.05(6)	170.24(6)	170.29(8)	170.76(10)
					O(1)–Re(1)–X(1)	99.67(7)	98.96(7)	98.95(10)	99.29(12)
					O(2)–Re(1)–X(1)	90.88(5)	90.37(6)	89.95(8)	90.00(9)
					N(1)–Re(1)–X(1)	87.81(6)	86.55(6)	86.57(8)	86.38(10)
					X(2)–Re(1)–X(1)	88.529(11)	87.99(2)	87.462(15)	87.619(19)
					O(1)–Re(1)–E(1)	84.43(7)	85.35(7)	85.57(10)	85.53(12)
					O(2)–Re(1)–E(1)	85.34(5)	85.65(6)	85.88(8)	85.61(9)
					N(1)–Re(1)–E(1)	93.52(6)	94.76(6)	94.82(8)	95.25(10)
					X(2)–Re(1)–E(1)	89.569(10)	90.10(2)	90.55(2)	90.17(3)
					X(1)–Re(1)–E(1)	175.719(10)	175.53(2)	175.31(2)	174.98(3)

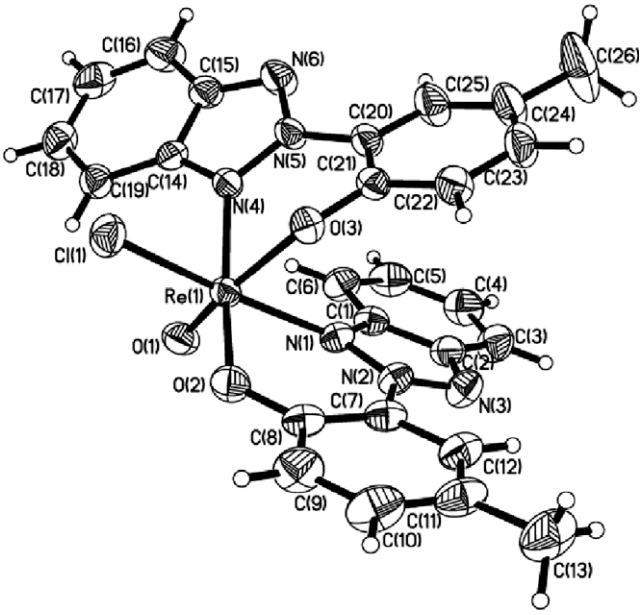


Fig. 2. The molecular structure of **5**. Displacement ellipsoids are drawn at 50% probability.

Formation of the monosubstituted chelates were also observed in the reactions of NH_4ReO_4 with 2-(2′-hydoxy-5′-methylphenyl)benzotriazole in the presence of PPh_3 as reductant.

Attempts of preparation of the disubstituted $[ReOX(hmpbta)_2]$ chelates by refluxing of $[ReOX_3(EPh_3)_2]$ with ligand excess or in the reactions of NH_4ReO_4 with excess of 2-(2′-hydoxy-5′-methylphenyl)benzotriazole in the presence of PPh_3 resulted in failure. In contrast to 8-hydroxyquinoline and quinoline-2-carboxylic acid, the both mentioned above reactions lead to the monosubstituted chelates. We managed to isolate only few crystals of $[ReOCl(hmpbta)_2]$ from the reaction of $[ReOCl_3(AsPh_3)_2]$ with ligand excess refluxed in acetonitrile for two days.

The $[ReOX_2(hmpbta)(EPh_3)]$ · solvent (solvent = MeCN, acetone) complexes are air stable and slightly soluble in acetonitrile, dichloromethane, chloroform, acetone, sparingly soluble in benzene and toluene. In general, the elemental analyses of the examined complexes are in good agreement with their formulation, some discrepancies of the hydrogen and nitrogen percentages between the calculated and found values are likely due to the solvate nature of the oxocompounds.

The selected frequencies observed in the IR spectra of $[ReOX_2(hmpbta)(EPh_3)]$ complexes are given in Section 2. The strong ν(Re=O) stretching bands of the $[ReOX_2(hmpbta)(EPh_3)]$ compounds are found in the narrow range 965–970 cm^{-1}. They are in the higher end of the range observed for $\{ReO\}^{3+}$ core complexes. It suggests that the Re–hydoxy bond *trans* to the oxo ligand does not compete effectively for the d_{Re} orbitals and indicates the presence of the {O≡Re–O} structural subunit in the examined structures. A similar trend is observed for the $[ReOX_2(hqn)(EPh_3)_2]$ and $[ReOX_2(quin\text{-}2\text{-}c)(EPh_3)_2]$ [9–12].

Table 6
Atomic charges from the Natural Population Analysis (NPA) for **1** and **5**.

Atom	1	5
Re(1)	1.014	1.445
O(1)	−0.461	−0.486
O(2)	−0.667	−0.652
O(3)		−0.676
N(1)	−0.293	−0.298
N(4)		−0.294
Cl(1)	−0.415	−0.404
Cl(2)	−0.389	
As(1)	1.375	

3.2. Crystal structures

The crystallographic data of **1** · MeCN, **2** · MeCN, **3** · MeCN, **4** · MeCN, **4** · Me_2CO, and **5** complexes are summarized in Table 1. All the $[ReOX_2(hmpbta)(EPh_3)]$ complexes are isostructural, crystallise as acetonitrile or acetone solvates in the triclinic $P\bar{1}$ space group, whereas the disubsituted $[ReOCl(hmpbta)_2]$ chelate – in the orthorhombic *Pbca* space group. In both solvates of **4** the complex molecule atoms occupy the same (in the range of experimental error) positions of unit cell, and MeCN/Me_2CO occupies the same solvent accessible void. The short intra- and intermolecular contacts [31,32] detected in the **1** · MeCN, **2** · MeCN, **3** · MeCN, **4** · MeCN, **4** · Me_2CO, and **5** are gathered in Table 2.

The perspective drawing of $[ReOCl_2(hmpbta)(AsPh_3)]$ · MeCN (**1** · MeCN) is presented in Fig. 1, and the selected bond distances and angles of **1** · MeCN, **2** · MeCN, **3** · MeCN, **4** · MeCN, and **4** · Me_2CO are collected in Tables 3 and 4. Fig. 2 presents the molecular structure of $[ReOCl(hmpbta)_2]$ (**5**), and the selected bond distances and angles of **5** are gathered in Table 5.

The geometry of $[ReOX_2(hmpbta)(EPh_3)]$ and $[ReOCl(hmpbta)_2]$ compounds reveal typical features of quasi-octahedral oxorhenium(V) complexes with oxygenated bidentate ligands. In each $[ReOX_2(hmpbta)(EPh_3)]$ complex, the rhenium atom is coordinated by a terminal oxygen atom (O_t), two halide ions in *cis* arrangement, the phosphorus or arsine atom from EPh_3 molecule, and the biden-

Table 5
The experimental and optimized bond lengths (Å) and angles (°) for **5**.

Bond lengths	Experimental	Optimized	Bond angles	Experimental	Optimized
Re(1)–O(1)	1.6860(18)	1.689	O(1)–Re(1)–O(2)	103.08(8)	104.81
Re(1)–O(2)	1.9707(16)	1.970	O(1)–Re(1)–O(3)	162.15(8)	161.60
Re(1)–O(3)	1.9792(16)	2.003	O(2)–Re(1)–O(3)	88.41(7)	86.95
Re(1)–N(1)	2.116(2)	2.115	O(1)–Re(1)–N(1)	86.84(8)	85.54
Re(1)–N(4)	2.1300(19)	2.165	O(2)–Re(1)–N(1)	87.91(7)	87.40
Re(1)–Cl(1)	2.3383(6)	2.405	O(3)–Re(1)–N(1)	79.88(7)	80.85
			O(1)–Re(1)–N(4)	89.17(8)	89.64
			O(2)–Re(1)–N(4)	167.51(7)	164.94
			O(3)–Re(1)–N(4)	80.32(7)	80.17
			N(1)–Re(1)–N(4)	95.33(7)	98.142
			O(1)–Re(1)–Cl(1)	102.30(7)	100.90
			O(2)–Re(1)–Cl(1)	87.52(5)	87.10
			O(3)–Re(1)–Cl(1)	91.68(5)	93.67
			N(1)–Re(1)–Cl(1)	170.52(5)	172.43
			N(4)–Re(1)–Cl(1)	87.44(5)	85.97

tate N,O-donors of the 2-(2′-hydoxy-5′-methylphenyl)benzotriazolato ligand. The oxygen atom of 2-(2′-hydoxy-5′-methylphenyl)benzotriazolato ligand occupies *trans* position to the terminal oxo ion. The rhenium atom of $[ReOCl(hmpbta)_2]$ is coordinated by two bidentate $hmpbta^-$ ligands, one chloride ion and terminal oxo (O_t) ligand. Clear distortions of the pseudooctahedral environment of Re center in $[ReOX_2(hmpbta)(EPh_3)]$ and $[ReOCl_2(hmpbta)_2]$ are induced by the multiple bonding ligand (O_t) and narrow bite angle of the chelating ligand. The high concentration of electronic density along the Re–O_t axis strongly influences the positions of the adjacent atoms (two halogen atoms in $[ReOX_2(hmpbta)(EPh_3)]$ and Cl(1), O(2) in $[ReOCl(hmpbta)_2]$), which are pushed away.

In complexes **1** · MeCN, **2** · MeCN, **3** · MeCN, **4** · MeCN, **4** · Me_2CO the rhenium atom is displaced, respectively, 0.1153(25), 0.1268(6), 0.1252(7), 0.1273(8), 0.1238(11) Å from the plane formed by the two halogen, one nitrogen and one P or As atoms (plane A), 0.0697(26), 0.0708(6), 0.0752(7), 0.0741(9), 0.0735(12) Å from the plane formed by the two oxygen, one halogen and one P or As atoms (plane B) and 0.0526(34), 0.0521(9), 0.0267(9), 0.0162(12), 0.0181(14) Å from the plane formed by two oxygen, one halogen and one nitrogen atoms (plane C). Least squares plane A is inclined at 89.61(20)°, 89.89(5)°, 89.88(5)°, 89.80(7)°, 89.62(8)° to plane B and at 87.89(20)°, 87.82(5)°, 87.99(5)°, 87.83(7)°, 87.90(9)° to plane C; planes B and C are inclined at 88.66(12)°, 89.49(3)°, 89.06(3)°, 89.55(4)°, 89.29(8)°, respectively.

For complex **5** the rhenium atom is displaced 0.1896(9) Å from the equatorial plane formed by the two nitrogens, one oxygen and one chloride atoms (plane A) and 0.0749(9) and 0.0562(8) Å from the axial planes formed, respectively, by the three oxygen, one

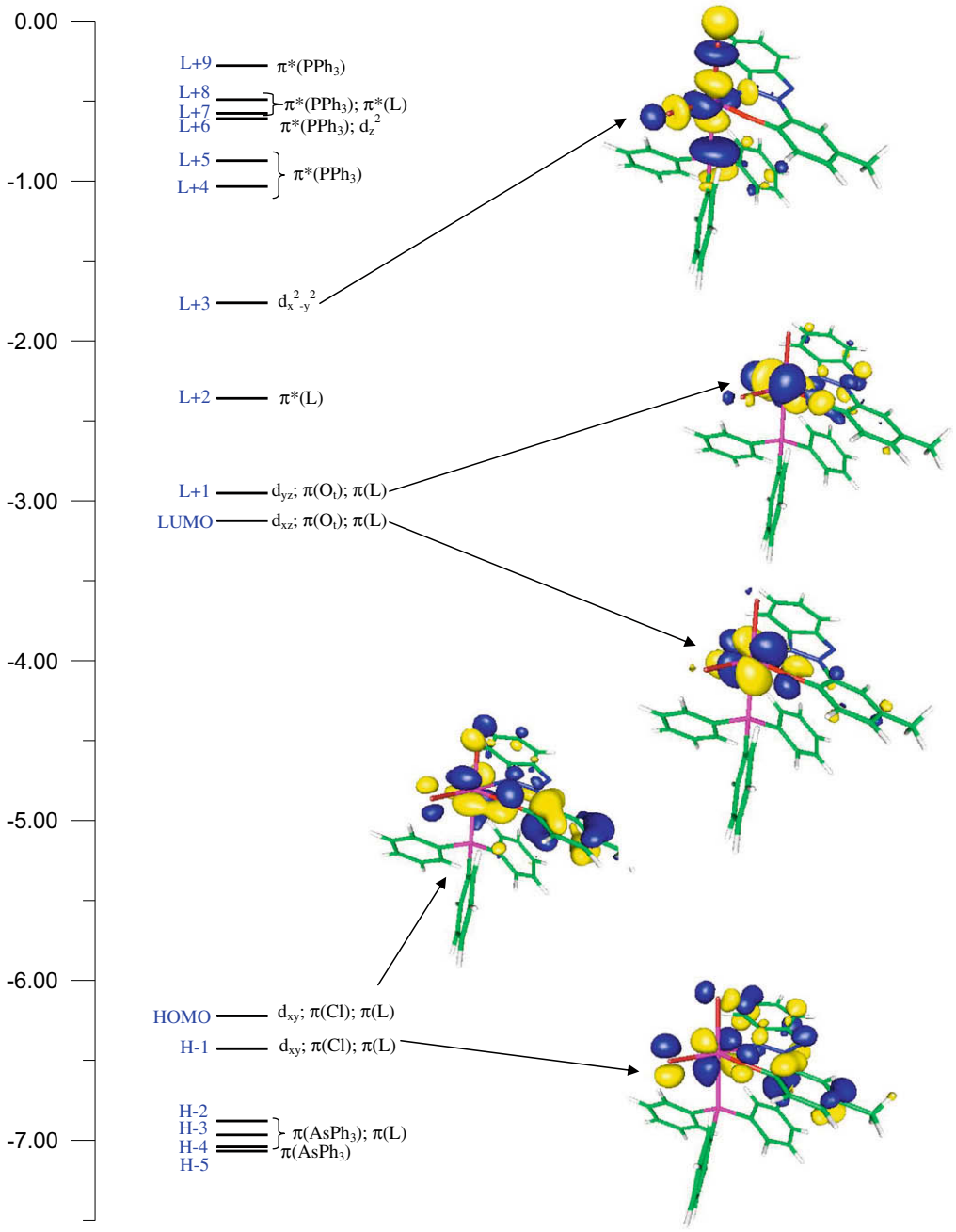


Fig. 3. The energy (eV), character and some contours of the unoccupied molecular orbitals of **1**. Positive values of the orbital contour are represented in blue (0.04 au) and negative values – in yellow (−0.04 au). (For interpretation of the references to colour in this figure legend, the reader is referred to the web version of this article.)

nitrogen atoms (plane B) and two oxygens, one chloride and one nitrogen atoms (plane C). Least squares plane A is inclined at 89.24(5)° to the plane B and at 89.19(4)° to the plane C. The planes B and C are inclined at 88.76(4)°.

The Re–O_t bond lengths of [$ReOX_2$(hmpbta)(EPh_3)] and [ReOCl(hmpbta)$_2$] complexes fall in the range 1.639–1.76 Å, typical of mononuclear complexes of rhenium(V) having $[ReO]^{3+}$ core, and indicate the presence of a triple bond Re≡O [33]. The interatomic distances between the rhenium atom and the oxygen atom of 2-(2′-hydoxy-5′-methylphenyl)benzotriazolato ligand are somewhat shorter than an ideal single Re–O bond length (*ca.* 2.04 Å) [34], It indicates small delocalization in the O(2)–Re(1)–O(1) moi-

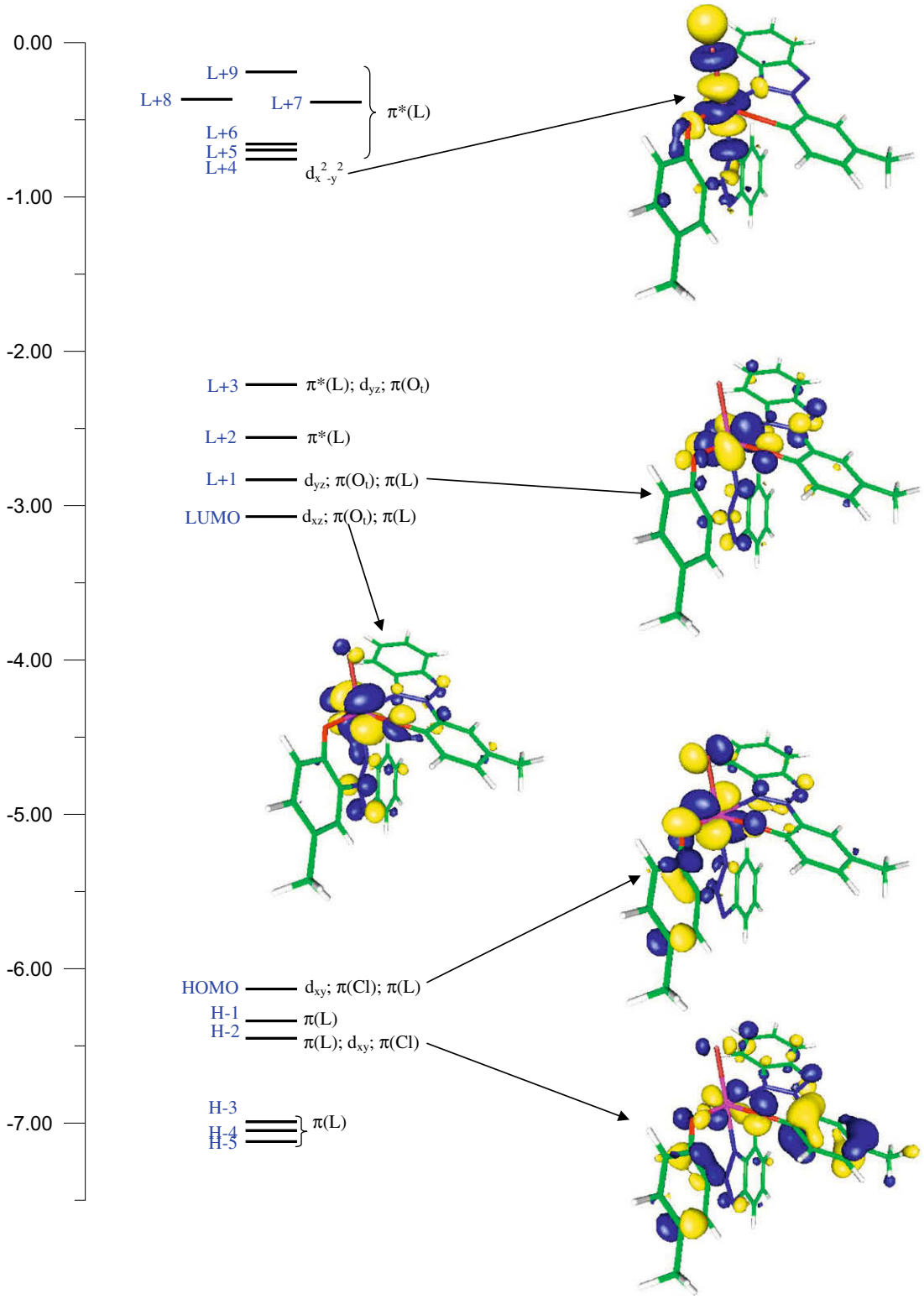


Fig. 4. The energy (eV), character and some contours of the unoccupied molecular orbitals of **5**. Positive values of the orbital contour are represented in blue (0.04 au) and negative values – in yellow (−0.04 au). (For interpretation of the references to colour in this figure legend, the reader is referred to the web version of this article.)

Table 7
The occupancy and composition of the calculated natural bond orbitals (NBOs) between the rhenium and the oxo ligand for **1** and **5**.

BD	Occupancy	Composition of NBO	BD*	Occupancy
1				
Re–O_t	1.993	$0.567(d)_{Re} + 0.824(p)_O$	$0.824(d)_{Re} - 0.567(p)_O$	0.270
Re–O_t	1.987	$0.571(d)_{Re} + 0.821(p)_O$	$0.821(d)_{Re} - 0.571(p)_O$	0.313
5				
Re–O_t	1.991	$0.558(d)_{Re} + 0.830(p)_O$	$0.830(d)_{Re} - 0.558(p)_O$	0.284
Re–O_t	1.990	$0.569(d)_{Re} + 0.822(p)_O$	$0.822(d)_{Re} - 0.569(p)_O$	0.322

BD denotes two-center bond.
* Denotes antibond NBO.

ety. The similar trend is observed for many Re(V)-oxo complexes with an monoanionic oxygen *trans* to the oxo group.

In the [ReOCl(hmpbta)$_2$] complex, the interatomic distance between the rhenium atom and the oxygen atom of 2-(2′-hydoxy-5′-methylphenyl)benzotriazolato ligand in *trans* position to the terminal oxo ion is somewhat longer than the corresponding Re–O bond in the equatorial plane. This structural *trans* influence is common in mononuclear six-coordinate oxo Re(V) complexes with an monoanionic oxygen *trans* to the oxo group [9–12].

The elongation of the Re(1)–X(1) distances *trans* to the phosphorus or arsine atom of EPh_3 molecule in comparison with Re(1)–X(2) bonds *trans* to the nitrogen atom of the 2-(2′-hydoxy-5′-methylphenyl)benzotriazolato ligand in the [$ReOX_2$(hmpbta)(EPh_3)] complexes is a consequence of *structural trans* effect of the EPh_3 ligands.

3.3. Geometry optimization, charge distribution, electronic structure and NBO analysis

The geometries of **1** and **5** were optimized in a singlet state by the DFT method with the B3LYP functional. The optimized geometric parameters of **1** and **5** are gathered in Tables 3 and 5, respectively. In general, the predicted bond lengths and angles are in agreement with the values based upon the X-ray crystal structure data, and the general trends observed in the experimental data are well reproduced in the calculations. The largest differences are found for the Re–As and Re–Cl bond distances. It may come from the basis sets which are approximated to a certain extent or may indicate the influence of the crystal packing on the values of the experimental bond lengths. The theoretical calculations do not consider the effects of chemical environment.

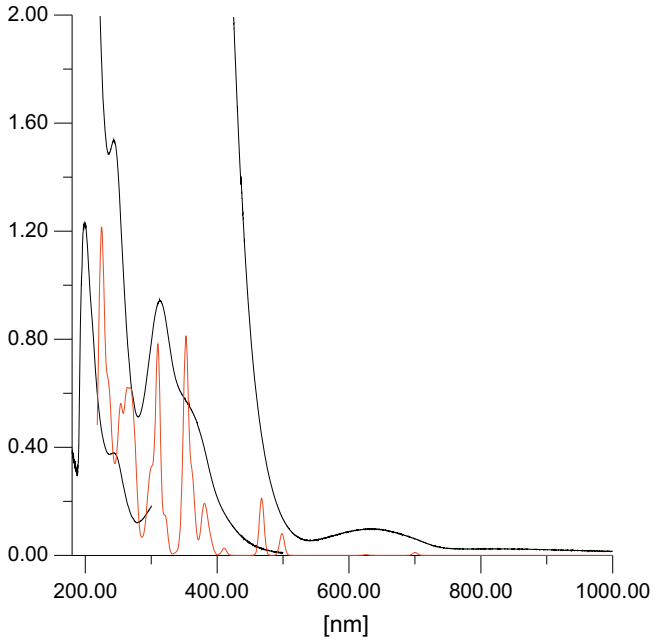


Fig. 5. The experimental (black) and calculated (red) electronic absorption spectra of **1**. (For interpretation of the references to colour in this figure legend, the reader is referred to the web version of this article.)

Table 6 presents the atomic charges from the Natural Population Analysis (NPA) for **1** and **5**. The calculated charge on the rhenium atom in complex **5** is somewhat larger in comparison with the monosubstituted compound. However, the both values are considerably lower than the formal charge +5, which results from significant charge donation from the oxygen atoms, chloride ions and triphenylarsine. In both complexes **1** and **5**, the considerable differences in values of charges are observed for the terminal oxo ligand and the oxygen atom of hmpbta$^-$ ligand – less negative are the terminal oxo ligands, which indicates the higher electron density delocalization from the terminal ligands towards the rhenium centers and corresponds to differences in the Re–O_t and Re–O_{hmpbta} bonds lengths.

The **1** and **5** are closed-shell structures. Their partial molecular orbital diagrams with several highest occupied and lowest unoccupied molecular orbital contours are presented in Figs. 3 and 4, respectively.

Two highest occupied MOs of **1**, are of d_{xy} type with some contributions from pπ chloride and hmpbta$^-$ orbitals. The LUMO and LUMO + 1 are predominately localized on the rhenium atom (d_{xz} and d_{yz} orbitals) with some contribution of pπ oxygen orbitals. The LUMO + 3 is of $d_{x^2-y^2}$ character, and d_{z^2} rhenium orbital contributes mainly to the LUMO + 12. The value of the energy separation between the highest occupied molecular orbital (HOMO) and the lowest unoccupied molecular orbital (LUMO) equals to 3.10 eV. This value is considerable higher in comparison with the HOMO–LUMO gap of [$ReOX_2$(hqn)(EPh_3)$_2$] and [$ReOX_2$(quin-2-c)(EPh_3)] {[$ReCl_2$(quin-2-c)(PPh_3)] – 2.93 eV; [$ReOX_2$(hqn)(EPh_3)$_2$] – 2.87 eV}. The bigger absolute value of the energy gap means better stability, and explains high stability of the title monosubstituted chelates.

The qualitative molecular orbitals scheme of **5** is almost the same as for **1**. HOMO and HOMO−2 of **5** are of d_{xy} type with some contributions from pπ chloride and hmpbta$^-$ orbitals. The LUMO and LUMO + 1 are predominately localized on the rhenium atom (d_{xz} and d_{yz} orbitals) with some contribution of pπ oxygen orbitals. The LUMO + 4 is of $d_{x^2-y^2}$ character, and d_{z^2} rhenium orbital contributes to the higher unoccupied MO. The HOMO–LUMO gap of **5** is equal to 3.06 eV, and is somewhat smaller in comparison with value calculated for **1**. It seems to explain difficulty in synthesis of the disubstituted chelates.

The nature of rhenium-terminal oxygen interaction in **1** and **5** has been studied by NBO analysis. The occupancy and composition of the calculated Re–O_t natural bond orbitals (NBOs) are given in Table 7.

Each natural bond orbital (NBO) σ_{AB} can be written in terms of two directed valence hybrids (NHOs) h_A and h_B on atoms A and B:

Table 8
The energy and molar absorption coefficients of experimental absorption bands and the electronic transitions calculated with the TDDFT method for **1**.

The most important orbital excitations	Character	λ (nm)	E (eV)	f	Experimental Λ (nm) (E (eV)) ε
H → L	d/π(Cl)/π(L) → d	700.4	1.77	0.0027	630.0 (1.97) 70
H-1 → L					
H → L	d/π(Cl)/π(L) → d	625.8	1.98	0.0006	
H-1 → L					
H-1 → L + 1	d/π(Cl)/π(L) → d	476.4	2.65	0.0530	346.2 (3.58) 10650
H → L + 1					
H-2 → L + 1	π(L)/π($AsPh_3$) → d	378.2	3.28	0.0325	
H-3 → L + 1	π ($AsPh_3$)/π (L) → d	362.8	3.42	0.0460	
H-1 → L + 2	d/π(Cl)/π(L) → π* (L)	353.2	3.51	0.1403	
H-8 → L	π($AsPh_3$) → d				
H-8 → L	π($AsPh_3$) → d	351.4	3.53	0.0405	
H → L + 3	d/π(Cl)/π(L) → d	321.3	3.86	0.0327	315.4 (3.93) 16700
H-1 → L + 3					
H-10 → L + 1	π(Cl)/n(As) → d	310.8	3.99	0.0845	
H-2 → L + 2	π(L)/π($AsPh_3$) → π*(L)				
H-2 → L + 2	π(L)/π($AsPh_3$) → π* (L)	309.7	4.00	0.1076	
H-10 → L + 1	π(Cl)/n(As) → d				
H-4 → L + 2	π($AsPh_3$)/π(L) → π* (L)	301.2	4.12	0.0588	
H-5 → L + 2	π($AsPh_3$) → π* (L)	296.0	4.19	0.0383	
H-2 → L + 3	π(L)/π($AsPh_3$) → π* (L)	276.0	4.49	0.0373	243.2 (5.10) 34450
H-3 → L + 3	π($AsPh_3$)/π(L) → d	268.9	4.61	0.0893	
H-6 → L + 3	π($AsPh_3$)/π(L) → d	263.1	4.71	0.0743	
H-10 → L + 2	π(Cl)/n(As) → π*(L)	253.5	4.89	0.0527	
H → L + 6	d/π(Cl)/π(L) → π*(PPh_3)	251.9	4.92	0.0380	
H-3 → L + 4	π(PPh_3)/π(L) → π* ($AsPh_3$)	236.0	5.25	0.0461	200.8 (6.17) 1 10500
H-11 → L + 3	π(Cl)/π(L)./π(O)/n(As) → d	227.4	5.45	0.0478	
H-2 → L + 5	π(L)/π($AsPh_3$) → π* ($AsPh_3$)	226.1	5.48	0.0492	
H-7 → L + 4	π($AsPh_3$) → π* ($AsPh_3$)	224.4	5.52	0.0337	
H-3 → L + 5	π(PPh_3)/π(L) → π* ($AsPh_3$)	223.5	5.55	0.0686	

ε, molar absorption coefficient ($dm^3\ mol^{-1}\ cm^{-1}$); f, oscillator strength; H, highest occupied molecular orbital; L, lowest unoccupied molecular orbital.

$$\sigma_{AB} = c_A h_A + c_B h_B$$

where c_A and c_B are polarization coefficients. Each valence bonding NBO must in turn be paired with a corresponding valence *anti*-bonding NBO:

$$\sigma^*_{AB} = c_B h_A + c_A h_B$$

to complete the span of the valence space. The Lewis-type (donor) NBOs are thereby complemented by the non-Lewis-type (acceptor) NBOs that are formally empty in an idealized Lewis picture. The interactions between 'filled' Lewis-type NBOs and 'empty' non-Lewis NBOs lead to loss of occupancy from the localized NBOs of the idealized Lewis structure into the empty non-Lewis orbitals, and they are referred to as 'delocalization' corrections to the zeroth-order natural Lewis structure [29,30].

The detected natural Re–O_t bond orbitals of **1** and **5** are π orbitals – the p_x and p_y oxygen orbitals and d_{xz} and d_{yz} rhenium orbitals are involved in their formation. Not detected σ_{Re-O_t} bond has character of predominant Coulomb-type interactions between the central ion and ligands [35]. The terminal oxo ligand of **1** and **5** has two lone pair orbitals, and electron density from one of them is strongly delocalized into non-Lewis rhenium orbital. Accordingly, NBO analysis confirms a triple bond between the rhenium and the terminal oxygen ligand in **1** and **5**.

3.4. Electronic spectra

The experimental and calculated electronic spectra of **1** are presented in Fig. 5. Each calculated transition is represented by a gaussian function $y = ce^{-bx^2}$ with the height (c) equal to the oscillator strength and b equal to 0.04 nm^{-2}. The positions and molar absorption coefficients of electronic bands for the other [ReOX_2(hmpbta)(EPh_3)] complexes are given in Experimental part. The electronic spectra of [ReOX_2(hmpbta)(EPh_3)] complexes are very similar in terms of the position, intensity and shape of the bands in the whole region 1000–180 nm.

Table 8 presents the most important electronic transitions calculated with the TDDFT method assigned to the observed absorption bands of **1**. The assignment of the calculated orbital excitations to the experimental bands was based on an overview of the contour plots and relative energy to the orbitals HOMO and LUMO involved in the electronic transitions. The simplified molecular orbital diagram of **1** with several contours of occupied and unoccupied MOs (active in the electronic transitions) is presented in Fig. 3.

The TDDFT/PCM calculations show that the longest wavelength experimental band of **1** at 630.0 nm originates in the HOMO → LUMO and HOMO−1 → LUMO transitions. As can be seen from the Fig. 3, the LUMO orbital is mainly formed from rhenium d atomic orbital, the HOMO−1 and HOMO orbitals are delocalized among rhenium ion, chloride and hmpbta$^-$ ligands. Accordingly, the transitions assigned to the longest wavelength experimental band can be seen as mixed chloride/hmpbta → Re (*Ligand–Metal Charge Transfer; LMCT*) and d → d (*Ligand Field; LF*) transitions.

The experimental absorption band at 346.2 nm can be assigned to *Ligand–Metal Charge Transfer* transitions occurring from the chloride, triphenylarsine and hmpbta$^-$ ligands to d rhenium orbitals.

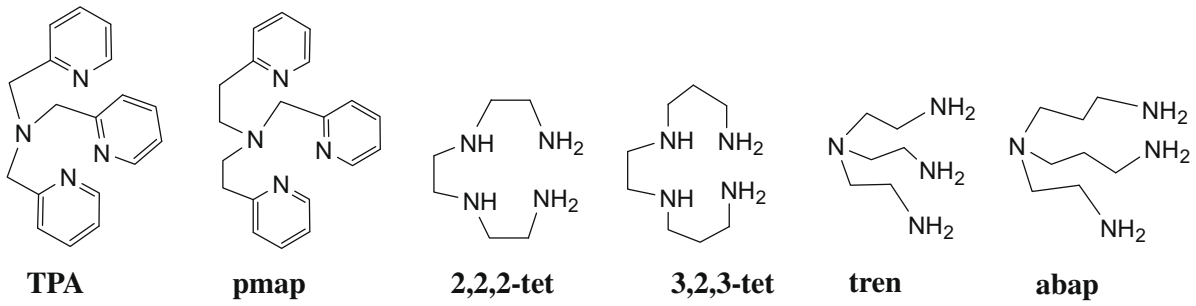
The absorption bands at 315.2, 243.2 and 200.8 nm result mainly from *Ligand–Ligand Charge Transfer* and interligand (*IL*) transitions. However, some contribution of the *Ligand–Metal Charge Transfer* from the chloride, triphenylarsine and hmpbta$^-$ orbitals to the d rhenium orbitals in these bands is also confirmed by the calculations.

Acknowledgement

The GAUSSIAN03 calculations were carried out in the Wrocław Centre for Networking and Supercomputing, WCSS, Wrocław, Poland under calculational grant No51/96.

References

[1] C.C. Romão, F.E. Kühn, W.A. Hermann, Chem. Rev. 97 (1997) 3197.
[2] A.A. Shteinman, Russ, Chem. Bull., Int. Ed. 50 (2001) 1795.
[3] F.E. Kühn, A. Scherbaum, W.A. Herrmann, J. Organomet. Chem. 689 (2004) 4149.
[4] G.S. Owens, J. Arias, M.M. Abu-Omar, Catal. Today 55 (2000) 317.
[5] A.M. Kirillov, M. Haukka, M.V. Kirillova, A.J.L. Pombeiro, Adv. Synth. Catal. 347 (2005) 1435.
[6] A. Deloffre, S. Halut, L. Salles, J.-M. Brégeault, J.R. Gregorio, B. Denise, H. Rudler, J. Chem. Soc., Dalton Trans. (1999) 2897.
[7] J.R. Dilworth, S.J. Parrott, Chem. Soc. Rev. 27 (1998) 43.
[8] P. Blower, Dalton Trans. (2006) 1705.
[9] B. Machura, R. Kruszynski, Polyhedron 26 (2007) 3686.
[10] B. Machura, R. Kruszynski, Polyhedron 26 (2007) 2957.
[11] B. Machura, S. Michalik, R. Kruszynski, J. Kusz, Polyhedron 26 (2007) 2837.
[12] B. Machura, J. Kusz, Polyhedron 27 (2008) 366.
[13] T. Carofiglio, E. Solari, C. Floriani, A. Chiesi-Villa, C. Rizzoli, Polyhedron 15 (1996) 4435.
[14] H. Chermette, Coord. Chem. Rev. 178–180 (1998) 699.
[15] J. Gancheff, C. Kremer, E. Kremer, O.N. Ventura, J. Mol. Struct. (Theochem) 580 (2002) 107.
[16] G. Rouschias, G. Wilkinson, J. Chem. Soc. A (1966) 465.
[17] (a) STOE and Cie, X-RED, Version 1.18, STOE and Cie GmbH, Darmstadt, Germany, 1999.;
(b) CRYSALIS RED, Oxford Diffraction Ltd., Version 1.171.29.2.
[18] G.M. Sheldrick, Acta Crystallogr. A46 (1990) 467.
[19] G.M. Sheldrick, SHELXL97, Program for the Refinement of Crystal Structures, University of Gttingen, Germany, 1997.
[20] G.M. Sheldrick, SHELXTL: Release 4.1 for Siemens Crystallographic Research Systems, 1990.
[21] M.J. Frisch, G.W. Trucks, H.B. Schlegel, G.E. Scuseria, M.A. Robb, J.R. Cheeseman, J.A. Montgomery Jr., T. Vreven, K.N. Kudin, J.C. Burant, J.M. Millam, S.S. Iyengar, J. Tomasi, V. Barone, B. Mennucci, M. Cossi, G. Scalmani, N. Rega, G.A. Petersson, H. Nakatsuji, M. Hada, M. Ehara, K. Toyota, R. Fukuda, J. Hasegawa, M. Ishida, T. Nakajima, Y. Honda, O. Kitao, H. Nakai, M. Klene, X. Li, J.E. Knox, H.P. Hratchian, J.B. Cross, C. Adamo, J. Jaramillo, R. Gomperts, R.E. Stratmann, O. Yazyev, A.J. Austin, R. Cammi, C. Pomelli, J.W. Ochterski, P.Y. Ayala, K. Morokuma, G.A. Voth, P. Salvador, J.J. Dannenberg, V.G. Zakrzewski, S. Dapprich, A.D. Daniels, M.C. Strain, O. Farkas, D.K. Malick, A.D. Rabuck, K. Raghavachari, J.B. Foresman, J.V. Ortiz, Q. Cui, A.G. Baboul, S. Clifford, J. Cioslowski, B.B. Stefanov, G. Liu, A. Liashenko, P. Piskorz, I. Komaromi, R.L. Martin, D.J. Fox, T. Keith, M.A. Al-Laham, C.Y. Peng, A. Nanayakkara, M. Challacombe, P.M.W. Gill, B. Johnson, W. Chen, M.W. Wong, C. Gonzalez, J.A. Pople, GAUSSIAN03, Revision B.03, Gaussian Inc., Pittsburgh, PA, 2003.
[22] A.D. Becke, J. Chem. Phys. 98 (1993) 5648.
[23] C. Lee, W. Yang, R.G. Parr, Phys. Rev. B 37 (1988) 785.
[24] P.C. Hariharan, J.A. Pople, Theor. Chim. Acta 28 (1973) 213.
[25] V.A. Rassolov, M.A. Ratner, J.A. Pople, P.C. Redfern, L.A. Curtiss, J. Comp. Chem. 22 (2001) 976.
[26] P.J. Hay, W.R. Wadt, J. Chem. Phys. 82 (1985) 299.
[27] K. Eichkorn, F. Weigend, O. Treutler, R. Ahlrichs, Theor. Chem. Acc. 97 (1997) 119.
[28] M.E. Casida, in: J.M. Seminario (Ed.), Recent Developments and Applications in Modern Density Functional Theory, Theoretical and Computational Chemistry, vol. 4, Elsevier, Amsterdam, 1996.
[29] E.D. Glendening, A.E. Reed, J.E. Carpenter, F. Weinhold, NBO, Version 3.1.
[30] E. Reed, L.A. Curtiss, F. Weinhold, Chem. Rev. 88 (1988) 899.
[31] G.A. Jeffrey, W. Saenger, Hydrogen Bonding in Biological Structures, Springer-Verlag, 1994.
[32] G.R. Desiraju, T. Steiner, The Weak Hydrogen Bond in Structural Chemistry and Biology, Oxford University Press, 1999.
[33] J.M. Mayer, Inorg. Chem. 27 (1988) 3899.
[34] S.R. Flechter, A.C. Skapski, J. Chem. Soc., Dalton Trans. (1972) 1073.
[35] M.L. Kuznestov, A.J.L. Pombeiro, J. Chem. Soc., Dalton Trans. (2003) 738.



Scheme 1.

supplement, tris(picolinato)chromium(III), [Cr(pic)$_3$] showed nicking of DNA in absence of oxidant [22].

Careful inspection of the literature data reveals that most of the hydrolytic activity of DNA and RNA were produced with Cu(II) and Co(III) complexes. Therefore, we believe that it would be interesting to perform a systematic study on the catalytic cleavage of DNA using a series of Co(III) complexes derived from tetraamine ligands of varied skeletal structures to see how the nature of the blocking amine ligands might enhance or prohibit the DNA hydrolysis. In other words, to determine the structural features in the Co(III) complexes that rapidly and efficiently promote the cleavage of DNA. For this reason, three categories of tetradentate-N-donor ligands were synthesized as well as their Co(III) complexes. These include: linear tetradendate amines (2,2,2-tet, 3,2,3-tet),[1] tripod amines with three aliphatic amine arms (tren, abap) and with three pyridyl arms (TPA, pmap). The structures of these amines are illustrated in Scheme 1.

The common feature between TPA, tren and 2,2,2-tet is the presence of three ethylenic groups between the N-donor atoms of these ligands and hence their ability to form five-membered chelate rings upon their coordination with Co^{III} center whereas the pmap, abap and 3,2,3-tet contain two arms with three methylene groups and one with an ethylenic group. These will lead to the formation of one five- and two flexible six-membered chelate rings when bind Co^{III} center. This study should allow us to evaluate the role of the pyridyl groups and the length of arms between the N-donor atoms of the coordinated amines in promoting the cleavage of the double-stranded DNA.

2. Experimental

2.1. Materials and methods

The compounds 2-(2-aminoethyl)pyridine, 2-picolylchloride hydrochloride, N-(2-bromoethyl)-phthalimide and 2-vinylpyridine were obtained from Aldrich Chemical Co., USA, 4,7-diaza-1,10-decanediamine (3,2,3-tet) was purchased from Strem Chemical Company, USA whereas 2-pyridylmethylamine and di-(2-pyridylmethyl)amine (DPA) were obtained from TCI, America. All other materials were reagent grade quality. Infrared spectra were recorded on JASCO FT/IR-480 plus spectrometer as KBr pellets. Electronic spectra were recorded on an Agilent 8453 HP diode UV–Vis spectrophotometer. Mass spectra were obtained on a HP 5890 series II GC spectrometer coupled to a HP 5972 Mass Selective Detector (MSD). Elemental analyses were performed at the Atlantic Microlaboratory, Norcross, Georgia USA.

Caution: Salts of perchlorate and their metal complexes are potentially explosive and should be handled with great care and in small quantities.

2.2. Synthesis of the compounds

2.2.1. Synthesis of the amine ligands

The three triopd amine ligands tris(2-pyridylmethyl)amine (TPA), bis[2-(2-pyridyl)ethyl]-(2-pyridylmethyl)amine (pmap) and N-(2-aminoethyl)-N,N-bis(3-aminopropyl)amine tetrahydrochloride trihydrate (abap · 4HCl · 3H$_2$O) were synthesized and characterized following the procedures described elsewhere [42–45].

2.2.2. Synthesis of Co(III) complexes

[Co(pmap)CO$_3$]ClO$_4$. A cold aqueous solution of bis[2-(2-pyridyl)ethyl]-(2-pyridylmethyl)amine (3.20 g, 10 mmol dissolved in 10 mL H$_2$O) was neutralized with 5 M HClO$_4$ to pH ~ 7 and then added drop-wise to an ice cold mixture of a well stirred slurry of Na$_3$[Co(CO$_3$)$_3$] · 3H$_2$O [46] (3.62 g, 10 mmol) in H$_2$O (50 mL). The temperature of the solution was gradually raised to 75 °C over a period of 1 h and stirring was continued at this temperature for 3 h, during which volume of the solution was reduced to ca 30 mL. The resulting reddish-orange solution was allowed to cool to room temperature, filtered through celite and left to crystallize at ambient temperature. After one week, the red precipitate which separated was collected by filtration, washed with absolute ethanol, then air dried and re-crystallized from H$_2$O (overall yield: 3.78 g, 71%). Slow evaporation of the dilute aqueous solution of the complex at room temperature afforded well-shaped crystals suitable for X-ray analysis. Characterization: *Anal.* Calc. for C$_{21}$H$_{22}$N$_4$ClCoO$_7$ (MM = 536.82 g/mol): C, 46.99; H, 4.13; N, 10.44. Found: C, 46.89; H, 4.12; N, 10.41%. UV–Vis. in H$_2$O (λ_{max} in nm, ε in M^{-1} cm^{-1}): 515 nm (144) and ~365 nm (sh). Selected IR bands (KBr, cm^{-1}): ν(C–O) 1665 (s); ν(C=C) 1637 (s); ν(Cl–O) (ClO$_4^-$) 1102 (vs) cm^{-1}.

The carbonato complexes [Co(tren)CO$_3$]ClO$_4$ and [Co(3,2,3-tet)-CO$_3$]ClO$_4$ · H$_2$O were synthesized using a procedure similar to that described above for [Co(pmap)CO$_3$]ClO$_4$ and were characterized according to the published procedures [47,48]. The remaining complexes [Co(abap)Cl$_2$]ClO$_4$ · H$_2$O, [Co(abap)(H$_2$O)Cl]Cl(ClO$_4$), [Co(TPA)Cl$_2$]ClO$_4$, *cis*-β-[Co(2,2,2-tet)Cl$_2$]-ClO$_4$ and [Co(tren)-(H$_2$O)$_2$](ClO$_4$)$_3$ were synthesized and characterized as reported elsewhere [43,49,50].

2.2.3. Preparation of aqua–Co(III) solutions

Aquahydroxo complex ions, [Co(N$_4$)(OH)(H$_2$O)]$^{2+}$ (N$_4$ = TPA, **1**; pmap, **2**; 2,2,2-tet, **3**; 3,2,3-tet, **4**; tren, **5** and abap, **6**) used for studying the hydrolytic cleavage of DNA were generated in aqueous solutions by two methods:

[1] *Ligand abbreviations:* TPA, tris(2-pyridylmethyl)amine; pmap, bis[2-(2-pyridylethyl)]-(2-pyridylmethyl)amine; 2,2,2-tet, triethylenetetraamine; 3,2,3-tet, 4,7-diaza-1,10-decanediamine; tren, tris(2-aminoethyl)amine; abap, N-(2-aminoethyl)-N,N-bis(3-aminopropyl)amine; cyclen, 1,4,7,10-tetraazacyclododecane.

(1) From the carbonato complexes by treating a weighed amount of the corresponding carbonato compound with 0.12 mL of 1.0 M $HClO_4$ solution. The resulting mixture was warmed for 5 min at 60 °C to expel CO_2 [19a,51]. This was then diluted with deionized water and transferred to 10.0 mL volumetric flask where $NaClO_4$ was added to adjust the ionic strength to 0.1 M and completed to the mark to give a solution of final concentration of 3.00 mM. The pH of these solutions were adjusted to 7.0 with 1 M NaOH or 1 M $HClO_4$ solution using glass stick "dotting" where the volume changes were negligible [52].
(2) From the chloro complexes by dissolving a weighed sample of the complex in 0.01 M $HClO_4$ solution, and allowing them to hydrolyze by heating on a steam-bath for 30 min, then ionic strength and pH 7.0 were adjusted as described above.

The stock solutions of the aquahydoxo–cobalt(III) complexes (3.00 mM of complex, pH 7.0, I = 0.1) were prepared and stored in the refrigerator at −20 °C. These solutions were used within period of two weeks.

2.3. X-ray structure determination of [Co(pmap)(CO_3)]ClO_4

The single crystal data were collected on a Bruker-AXS SMART APEX CCD diffractometer with graphite crystal-monochromatized Mo Kα radiation (λ = 0.71073 Å) at 100(2) K. The data were corrected for Lorentz-polarization effects, and for absorption by using the SADABS program [53]. The structure was solved by direct methods and refined by full-matrix least-squares techniques on $|F|^2$ using SHELX system of programs [54]. In case of disordered oxygen atoms of perchlorate counter ion split occupancies of 0.555(4) for O(4) to O(7) and 0.445(4) for O(8) to O(11), respectively, were applied. All hydrogen atoms belonging to the complex were in their calculated positions and refined using a riding model. All non-hydrogen atoms were refined anisotropically [total 344 parameters, R_1 = 0.0643, wR_2 (all data) = 0.2072, *S = 1.190,* largest difference peak and hole: 0.698 and −0.593 e/Å^3]. The crystallographic parameters are: $C_{21}H_{22}ClCoN_4O_7$ (formula weight = 536.74), monoclinic, space group *C*2/*c*, *a* = 17.617(3), *b* = 18.028(4), *c* = 14.515(3) Å, β = 109.72(1)°, *V* = 4340(2) Å^3, *Z* = 8, D_{calc} = 1.643 Mg/m^3, μ = 0.968 mm^{-1}, 15417 reflections measured (Θ_{max} = 24.99°), 3813 unique (R_{int} = 0.0389), and of these 3548 had $I > 2\sigma(I)$.

2.4. DNA study

2.4.1. Plasmid DNA isolation

pUC19 plasmid was introduced into DH5α competent cells based on manufactory protocol (Invitrogen Corporation, Carlsbad, California 92008, USA). Single colony was selected from standard Luria Bertani (LB) plate and cultured in 5 mL of LB medium at 37 °C in a shaker at speed of 300 rpm for overnight. This starter cell culture was diluted 1:500 using freshly prepared LB medium and grew at 37 °C in a shaker at speed of 300 rpm for 16–18 h. Cells were harvested at 4000 rpm for 5 min. The plasmid DNAs were purified from the cell culture using Qiagen plasmid purification column based on manufactory protocol (QIAGEN Inc., Valencia, CA 91355, USA). All the LB medium and LB plate contained 100 μg/mL ampicillin. The plasmid DNA concentrations were determined spectrophotometrically by measuring the absorbance at 260 nm.

2.4.2. Plasmid DNA hydrolysis by Co(III) complexes and agarose gel electrophoresis

Approximately 1.0 μg of pUC19 plasmid DNA was incubated with Co(III) complexes with indicated concentrations in a total volume of 20 μL at 37 °C water-bath for a varying of incubation time. At the end of incubation, bromophenol blue loading buffer was added. The samples were then loaded on a 1.0% agarose gel containing approximately 2.0 μg/mL ethidium bromide. Electrophoresis was carried out at 150 V for approximately 20 min in Tris–Borate–EDTA (TBE) buffer. Bands were visualized by UV light and photographed by a Bio-Rad gel documentation system (Bio-Rad Laboratories, Hercules, CA 94547). The intensity of the different forms (**I**, **II** and **III**) of plasmid DNA was quantified using Quantity One software (Bio-Rad Laboratories). Experimental data were analyzed using graphic and statistical software PRISM 4.0. Differences of $p < 0.05$ by analysis of variance (ANOVA) and Dunnett's post test were considered to be significantly different from controls.

2.4.3. Kinetic measurements for the DNA cleavage by aquahydroxo–cobalt(III) complexes ***1*** and ***3***

DNA cleavage rates at varying concentration of cobalt(III)–tetraamine complexes {0 (control), 50, 100, 150, 300 and 450 μM} were carried out in 1.0 mM Tris–Cl buffer, pH 7.0 and I = 0.1 M ($NaClO_4$) at 37 °C for different interval of time. The percentage of form **II** quantified by QUANTITY ONE software was plotted against time for each catalyst concentration. The data were fitted with single-exponential curve (pseudo-first-order kinetics) using ORIGIN 7.5 and Eq. (1) to extract the hydrolysis rate or apparent rate constant, k'_{obs} [34]:

$$y = (100 - y_0)(1 - \exp(-k'_{obs}t)) \quad (1)$$

$$k'_{obs} = V'_{max}[\text{catalyst}]/(K_M + [\text{catalyst}]) \quad (2)$$

where y_0 and y represent the percentages of DNA form **II** at zero time and at any time t, respectively. The values of k'_{obs} were then plotted against the concentrations of cobalt(III) complexes (catalyst = [Co(III]) (Eq. (2)) allowing a pseudo-Michaelis–Menten analysis and the determination of the maximal reaction velocity V'_{max} and K_M [34]. It is important to emphasize here that Cowan and co-workers indicated that for comparison of rates of reactions, the pseudo-Michaelis–Menten rate constant, k'_{cat} which represents the rate at saturation levels (i.e., V'_{max}) would be used [34].

Similar experiments with constant Co(III) concentration (150 μM) and varying DNA (substrate) concentrations (8.53, 25.6, 76.8 and 203.4 μM DNA bps) were also performed ("true" Michaelis–Menten kinetics). Experimental data were analyzed using graphic and statistical software PRISM 4.0. Differences of $p < 0.05$ by analysis of variance (ANOVA) and Dunnett's post test were considered to be significantly different from controls.

3. Results and discussion

3.1. Syntheses the complexes

One general method was used to synthesize the carbonato complexes, [Co(N_4)CO_3]ClO_4 where N_4 = pmap, tren and 3,2,3-tet. They were obtained in reasonably good yield (60–80%) by the reaction of an aqueous solution of the tetraamine (pre-neutralized to pH ~ 7 with 5 M $HClO_4$ solution) with to an equimolar amount of $Na_3[Co(CO_3)_3] \cdot 3H_2O$. Re-crystallization of these compounds from

Table 1
UV–Vis spectral data for the carbonato–tetraamine–cobalt(III) complexes in H_2O.[a]

Complex	λ_{max}, nm (ε_{max}, M^{-1} cm^{-1})
[Co(pmap)CO_3]ClO_4	515 (144), ~365 (sh)
[Co(tren)CO_3]ClO_4	504 (132), 354 (110)
[Co(3,2,3-tet)CO_3]$ClO_4 \cdot H_2O$	518 (136), 360 (133)

[a] Values are comparable to those reported in Refs. [47,48].

aqueous solutions afforded the complexes in high pure forms. The purity of the complexes was checked by comparing their electronic spectra in H_2O (Table 1) with literature values [47,48]. However, it should be noted that $[Co(3,2,3\text{-tet})CO_3]ClO_4$ and $[Co(tren)CO_3]ClO_4$ complexes were previously prepared by $PbO_2/NaHCO_3$ method [49]. The chloro complexes $[Co(abap)Cl_2]ClO_4 \cdot H_2O$, $[Co(abap)(H_2O)Cl]Cl(ClO_4)$ and $[Co(TPA)Cl_2]ClO_4$ were synthesized and characterized according to the literature methods [43,47,50].

3.2. Characterization of the carbonato-Co(III) complexes

The electronic spectra of the carbonato complexes under investigation $[Co(N_4)CO_3]ClO_4$ display two bands over the wavelength range 550–360 nm. These spectral features are consistent with octahedral *cis*-geometry and the bands arise from $^1T_{1g}$ (Oh) ← $^1A_{1g}$ (Oh) and $^1T_{2g}$ (Oh) ← $^1A_{1g}$ (Oh) transitions. Although the actual field is of lower symmetry (C_{4v}), this has a small effect upon the model and the $^1T_{1g}$ state is split into $^1E_{1g}$ and $^1A_{2g}$ (octahedral labels were retained for simplicity) [56]. Inspection of the data in Table 1 clearly indicates that λ_{max} of the low energy d–d band increases in the order: tren < pmap < 3,2,3-tet. This is due to the reduction in the ligand field strength on going from tren to 3,2,3-tet.

3.3. Crystal structure of $[Co(pmap)CO_3]ClO_4$ complex

The complex $[Co(pmap)CO_3]ClO_4$ was structurally characterized by single crystal X-ray diffraction technique. The structure of the complex consists of a discrete monomeric $[Co(pmap)(CO_3)]^+$ cation and a disordered perchlorate counter ion. A perspective view of the complex cation is shown in Fig. 1. Selected bond distances and angles are given in Table 2. The Co(1) center is octahedrally coordinated by the four nitrogen donor atoms of the pmap blocking ligand and by O(1) and O(2) of the chelating carbonato group. The Co–N bond distances are in the range from 1.925(4) to 1.991(5) Å, the Co(1)–O(1) and Co(1)–O(2) bond lengths are 1.902(3) and 1.906(3) Å, respectively. The cobalt center lies only 0.015 Å out of the plane of the carbonato group, which forms dihedral angles of 9.8°, 84.2° and 95.3°, respectively, with the planes of the three pyridyl rings of the pmap ligand. The shortest separation between Co(1) centers of monomeric complex cations is 7.6779(19) Å. It should be noted that although the crystal structure of $[Co(pmap)CO_3]ClO_4$ was determined by Blackman and his group [48], more details for the structural parameters are reported here. The O–Co–O bond angle of $[Co(pmap)CO_3]^+$ (69°) is comparable to that observed in the corresponding carbonato complexes of tren (68.5°), cyclen (68.4°) and trpn (68.4°) [11a,49].

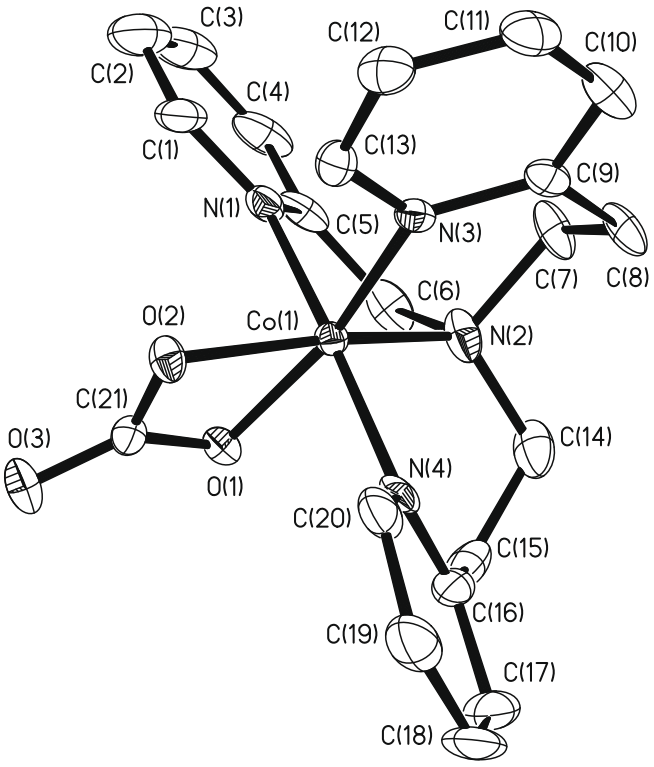


Fig. 1. Perspective view of $[Co(pmap)(CO_3]^+$ cation showing the atom labeling scheme and 50% probability displacement ellipsoids.

Table 2
Selected bond lengths (Å) and angles (°) for $[Co(pmap)CO_3]ClO_4$.

Co(1)–O(1)	1.902(3)	Co(1)–O(2)	1.906(3)
Co(1)–N(1)	1.925(4)	Co(1)–N(4)	1.944(4)
Co(1)–N(3)	1.972(4)	Co(1)–N(2)	1.991(5)
O(1)–C(21)	1.336(6)	O(2)–C(21)	1.315(5)
O(3)–C(21)	1.222(6)		
O(1)–Co(1)–O(2)	69.09(14)	O(1)–Co(1)–N(1)	87.7(2)
O(2)–Co(1)–N(1)	91.5(2)	O(1)–Co(1)–N(4)	88.1(2)
O(2)–Co(1)–N(4)	89.1(2)	N(1)–Co(1)–N(4)	175.2(2)
O(1)–Co(1)–N(3)	165.1(2)	O(2)–Co(1)–N(3)	96.0(2)
N(1)–Co(1)–N(3)	92.7(2)	N(4)–Co(1)–N(3)	92.0(2)
O(1)–Co(1)–N(2)	96.4(2)	O(2)–Co(1)–N(2)	164.84(14)
N(1)–Co(1)–N(2)	83.2(2)	N(4)–Co(1)–N(2)	95.0(2)
N(3)–Co(1)–N(2)	98.4(2)	C(21)–O(1)–Co(1)	90.7(2)
C(21)–O(2)–Co(1)	91.2(3)	O(3)–C(21)–O(2)	126.7(5)
O(3)–C(21)–O(1)	124.2(4)	O(2)–C(21)–O(1)	109.1(4)

3.4. Aquaamine–Co(III) complexes

The diaqua complex ions, $[Co(N_4)((H_2O)_2]^{3+}$ which were used for DNA studies after adjusting their pHs to 7.0, were generated in the acidic medium by hydrolyzing the corresponding carbonato- or the chloro-Co(III) compounds [43,47–50]. Phosphate buffers were not used to avoid their possible interaction with the aqua complex species [58]. The electronic spectra of the prepared diaqua solutions displayed two absorption maxima, almost at the same positions as their parent carbonato compounds which indicates the formation of complexes with *cis*-geometry [57] and were also identical to those obtained for the corresponding isolated diaqua compounds [10,57,58]. Moreover, the solutions adjusted to pH 7.0, showed no sign of significant spectral changes due to hydrolysis and/or redox reactions during the entire period of preservation in the refrigerator (four weeks), except in the case of 3,2,3-tet compound which reveals pronounced tendency for isomerization to the *trans* isomer. The two λ_{max} detected at 360 and 520 nm in the fresh solution of *cis*-$[Co(3,2,3\text{-tet})(H_2O)_2]^{3+}$ (pH ~ 7.0) were disappeared and instead, three new bands of lower intensities, typical for *trans*-disubstituted tetraamine–cobalt(III) complexes [56] were observed at ca 442, 614 and 742 nm. The process was also associated with color change from red to green.

In the neutral pH region, the acid–base equilibrium studies performed on the aqua–tetraamine–cobalt(III) complexes, reveal that the predominant species under these conditions is the aquahydroxo complex ion, $[Co(N_4)(H_2O)(OH)]^{2+}$ [11a,19a,57,59,60]. The tripodal nature of the amine ligands (TPA, Pmap, abap and tren) encountered in the Co(III) complexes used in this study presents some advantages which make them suitable candidates for studying the hydrolytic cleavage of DNA. They provide two available coordination sites that are relatively rapid towards substitution reactions [7,11,12,19,61]. Also, the geometrical nature of these amines enforces the formation of complexes with *cis*-geometry. On the other hand, in the linear tetraamines 2,2,2-tet and 3,2,3-tet the *cis*/*trans* isomerization may occur where this tendency is

higher in case of 3,2,3-tet as indicated above. Consequently, the presence of high proportion of *trans*-[Co(3,2,3-tet)(OH)(H_2O)]$^{2+}$ in solution reduces the hydrolytic efficiency of **4** to catalyze the DNA cleavage.

3.5. Hydrolytic cleavage of plasmid DNA by aqua–Co(III) complexes

3.5.1. Hydrolysis of plasmid DNA

A wide range of octahedral *cis*-aquahydroxo–tetraamine–Co(III) complexes of different structural amine skeletons were used to test the hydrolytic cleavage of DNA at pH 7.0, I = 0.1 M ($NaClO_4$) and at 37 °C. Among the six complexes used in this study, only three complex ions [Co(TPA)(OH)(H_2O)]$^{2+}$ (**1**), [Co(pmap)(OH)(H_2O)]$^{2+}$ (**2**) and [Co(2,2,2-tet)(OH)(H_2O)]$^{2+}$ (**3**) showed significant DNA cleavage where the supercoiled DNA (form I) was cleaved to the relaxed open circular DNA (form II) over a period of 24 h as illustrated in Fig. 2. During this long incubation period, complex **1** showed pronounced capability to further cleave form II to linear DNA (form III) while significant changes of form III were not observed for **2** and **3**. The cleavage ability of the complexes decreases in the order **1** > 3 ≫ 2, where very low catalytic cleavage was obtained in complex **2** (pmap). On the other hand, the remaining Co(III) complexes did not exhibit any detectable DNA cleavage as indicated by the fact that the percentages of all forms were almost unchanged with each complex over a period of 24 h (Fig. 1S in the Supplementary data).

As a result of the very low efficiency of the complex ion [Co(pmap)(OH)(H_2O)]$^{2+}$ (**2**) in hydrolyzing the plasmid DNA, no more study was performed on this complex but instead the two aqua complexes [Co(TPA)(OH)(H_2O)]$^{2+}$ (**1**) and [Co(2,2,2-tet)(OH)(H_2O)]$^{2+}$ (**3**) were the subject of further detailed kinetics studies in order to explore their activities in the catalytic cleavage of plasmid DNA. The migration position of the form III cleaved by **1** was confirmed by the EcoRI digestion of pUC19, which is known to contain only one site in pUC19 plasmid and expected to produce one linearized DNA (Fig. 3).

3.5.2. Kinetics of plasmid DNA hydrolysis

The kinetics of DNA cleavage by complexes [Co(TPA)(OH)(H_2O)]$^{2+}$ (**1**) and [Co(2,2,2-tet)(OH)(H_2O)]$^{2+}$ (**3**) were carried out by following the conversion of form **I** to form **II** over various concentrations of the complexes (50–450 μM) and constant pUC19 DNA concentration (76.8 μM) at different time intervals at pH 7.0, I = 0.1 M ($NaClO_4$) and 37 °C. The percentages of form **II** were plotted against time and plots are represented in Figs. 4 and 5 for complexes **1** and **3**, respectively. It should be noted that significant increase of form **III** was not observed until 16 h of DNA incubation with **1** therefore form **III** cleaved by **1** was not included in Fig. 4. However, longer incubation (Fig. 2) results in cleavage of form **I** into form **II** first by **1**, and then continues to cleave form **II** to form **III**. Each of these plots follows pseudo-first-order kinetic

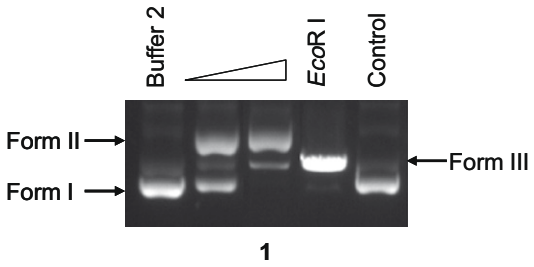


Fig. 3. Electrophoretic separations of pUC19 plasmid DNA cleavage by complex **1** and by EcoRI. Plasmid DNA (76.8 μM) was incubated with Co(III) complexes (50 and 150 μM) or 2.0 U EcoRI for 24 h in 1 × buffer 2 (NEB), I = 0.1 M ($NaClO_4$) at 37 °C.

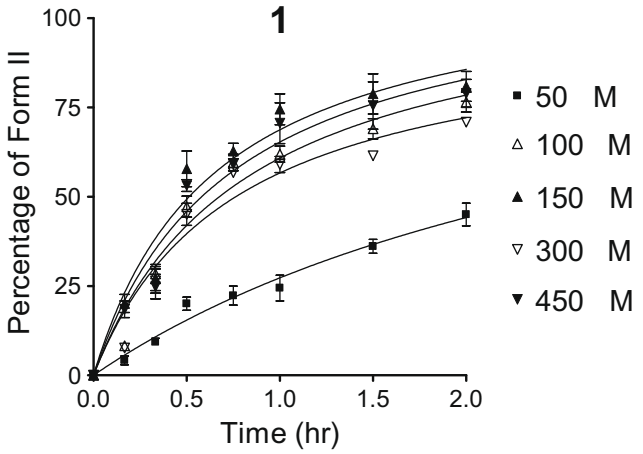


Fig. 4. Cleavage profile of pUC19 plasmid DNA by **1**. DNA (76.8 μM) was incubated with varying concentrations of **1** in 1.0 mM Tris–Cl buffer pH 7.0, I = 0.1 M ($NaClO_4$) at 37 °C.

profile and was fitted well to a single-exponential curve using Eq. (1). From these curves, the cleavage rate constant, k'_{obs} at each complex concentration was calculated and data are collected in Table 3. The kinetic parameters for the pseudo-Michaelis–Menten conditions were derived from the plots of k'_{obs} versus [Co(III)] (=[catalyst]) and fit to Eq. (2). Under these experimental conditions, values of $k''_{cat} = 3.49 \times 10^{-4}\ s^{-1}$ and $K_M = 159$ μM for **1** and $k''_{cat} = 5.08 \times 10^{-5}\ s^{-1}$ and $K_M = 296$ μM for **3** were obtained (Table 3), where these values represent pseudo-Michaelis–Menten conditions. The calculated values of K_M and k'_{cat} fall into the range reported for the cleavage of DNA by other metal complexes ($K_M = 3.0 \times 10^2$–2.0×10^3 μM, and $k'_{cat} = 5.0 \times 10^{-5}$–$2.0 \times 10^{-4}\ s^{-1}$) [16,31,37,55,62–64]. The DNA cleavage by [Co(TPA)(OH)(H_2O)]$^{2+}$, **1** is about six times much faster than the corresponding complex [Co(2,2,2-tet)(OH)(H_2O)]$^{2+}$, **3**. Interestingly, the rate

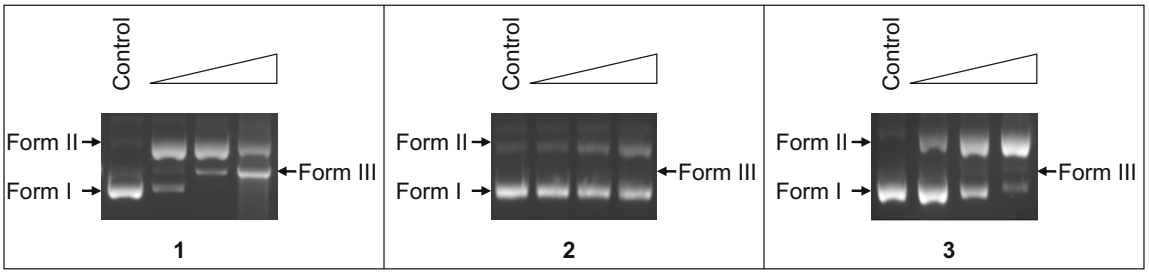


Fig. 2. Electrophoretic separations of pUC19 plasmid DNA cleavage by aquaamine–cobalt(III) complexes: (**1**) TPA (left panel), (**2**) pmap (middle panel) and (**3**) 2,2,2-tet (right panel). Plasmid DNA (76.8 μM) was incubated with varying [Co(III)] (0, 50, 150 and 450 μM, from left lane to the right lane) for 24 h in 1.0 mM Tris–Cl buffer pH 7.0, I = 0.1 M ($NaClO_4$) at 37 °C.

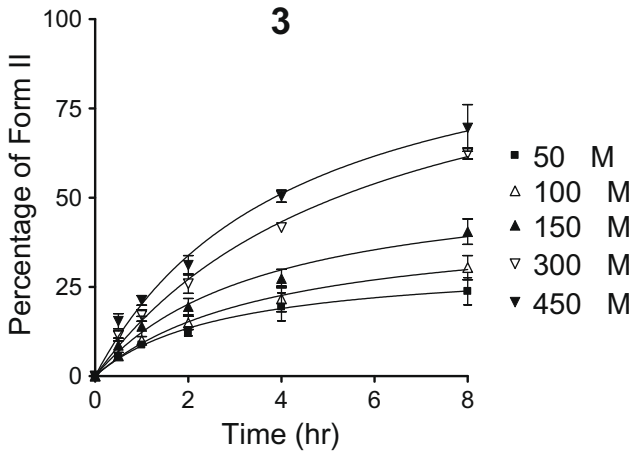


Fig. 5. Cleavage profile of pUC19 plasmid DNA by complex **3**. DNA (76.8 μM) was incubated with varying Co(III) concentrations of **3** in 1.0 mM Tris–Cl buffer pH 7.0, I = 0.1 M ($NaClO_4$) at 37 °C.

Table 3
Pseudo-Michaelis–Menten kinetic data for the cleavage of pUC19 plasmid DNA by aquahydroxo–amine–Co(III) complexes.

Complex	[DNA] (μM)	[Co(III)] (μM)	k'_{obs} (s^{-1})	V'_{max} [a] (s^{-1})	K_M (μM)
1 (TPA)	76.8	50	7.99×10^{-5}	3.49×10^{-4}	159
		100	1.54×10^{-4}		
		150	1.89×10^{-4}		
		300	2.09×10^{-4}		
		450	2.20×10^{-4}		
3 (2,2,2-tet)	76.8	50	7.77×10^{-6}	5.08×10^{-5}	296
		100	1.08×10^{-5}		
		150	1.52×10^{-5}		
		300	3.17×10^{-5}		
		450	3.81×10^{-5}		

[a] At the saturation level, $V'_{max} = k'_{cat}$ [34].

enhancements obtained here with **1** and **3** correspond to 3.5×10^7 and 5.1×10^6, respectively, over the non-catalyzed DNA ($k = 1.0 \times 10^{-11}$ s^{-1} at 37 °C [1]) clearly reveals the efficiency of these complexes to cleave the double-stranded DNA. Comparable rate enhancements by cobalt(III)–polyamine complexes derived from cyclen ($k'_{cat} = 2.2 \times 10^{-4}$ s^{-1}) [7] and tamen ($k'_{cat} = 5.0 \times 10^{-5}$ s^{-1}) [65] have been reported for the hydrolysis of DNA when rates were compared at the saturation levels under pseudo-Michaelis–Menten kinetics.

Plasmid DNA cleavage was also monitored under 'true' Michaelis–Menten kinetic conditions using a constant Co(III) concentration (150 μM) and varying substrate DNA concentration (8.53–203 μM). A typical cleavage profile of pUC19 plasmid DNA by Co(III) complex is shown in Fig. 6 (and in Fig. 2S in the Supplementary data). The cleavage rate constants, k_{obs} were estimated in a similar fashion as that shown by Eq. (1) and the plots of k_{obs} versus [DNA] [34] for the two complexes are depicted in Fig. 7. These

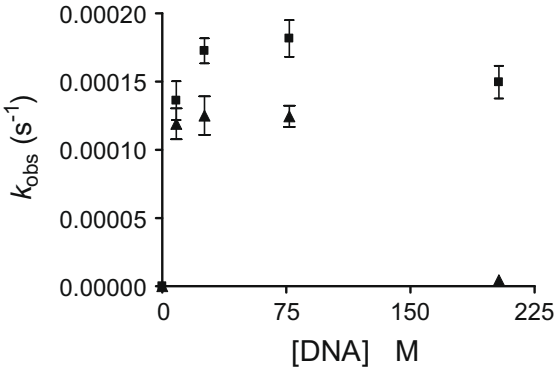


Fig. 7. Kinetics of the cleavage of pUC19 plasmid DNA by **1** (■) and **3** (▲). Varying concentrations of DNA were incubated with 150 μM of **1** or **3** in 1.0 mM Tris–Cl buffer pH 7.0, I = 0.1 M ($NaClO_4$) at 37 °C.

plots did not fit Michaelis–Menten equation. Therefore, K_M and k_{cat} ($k_{cat} = V_{max}/[E]_0$, where $[E]_0$ = [catalyst] = [Co(III)] [34]) were not calculated under these conditions. The data for the two complexes **1** and **3** presented in Fig. 7 show that k_{obs} increases slightly at the very low DNA concentrations reaching a maximum at ca [DNA] = 50 μM and then starts to decrease at higher DNA concentrations. The decrease of k_{obs} in **3** is faster than in **1**. This kinetic behavior is very similar to that reported in some copper complexes [55] and at the same time is different from a perfect saturation behavior observed in other metal complexes [34]. Thus, in order to reach a maximum DNA cleavage activity, a certain number of Co(III) complexes appears to be required to bind to each plasmid DNA; a situation which probably was not achieved with these two complexes. Finally we should indicate that in some of the previous work, V_{max} have been inappropriately used to calculate rate enhancement instead of k_{cat} [7,17a] and this point was addressed by Cowan and co-workers [34].

In order to clarify the DNA cleavage mechanism by the complexes **1** and **3** (hydroxyl radical mechanism, O_2-dependent versus hydrolytic mechanism, O_2-independent), the cleavage of DNA was further investigated in presence and absence of hydrogen peroxide (0.1 mM) and in presence of radical scavengers like DMSO (0.4 M). The DNA cleavage was almost the same as that obtained either with H_2O_2 or with DMSO for both complexes **1** and **3** (Fig. 8). This demonstrates the absence of hydroxyl radical in the cleavage reaction. Therefore, DNA cleavage by the complexes **1** and **3** is most likely proceeding *via* a hydrolytic pathway.

Many of the mononuclear *cis*-diaqua–Co(III) complexes are known to be good promoters in the catalysis of phosphate diesters and of ATP [3,12,19,20]. These complexes also exhibit their highest activity in the neutral pH region (pH ~ 7), where only one of the coordinated water molecule is deprotonated, giving the *cis*-aquahydroxo species [3,12,19]. Therefore, a similar mechanism can be proposed here for the hydrolytic cleavage of the phosphodiester bonds of DNA by the *cis*-aquahydroxo–Co(III) complexes used in this study. The mechanism of reaction involves the coordination

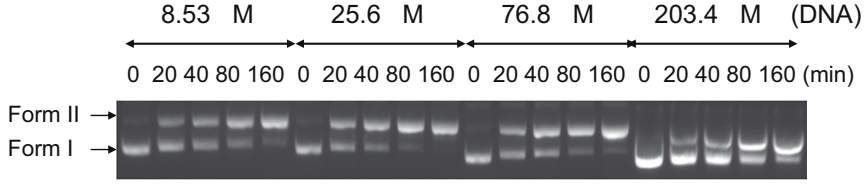


Fig. 6. Cleavage profile of pUC19 plasmid DNA by **1**. Varying concentrations of DNA (8.53, 25.6, 76.8 and 203.4 μM) were incubated with 150 μM of **1** for 0, 20, 40, 80 and 160 min in 1.0 mM Tris–Cl, pH 7.0 at 37 °C.

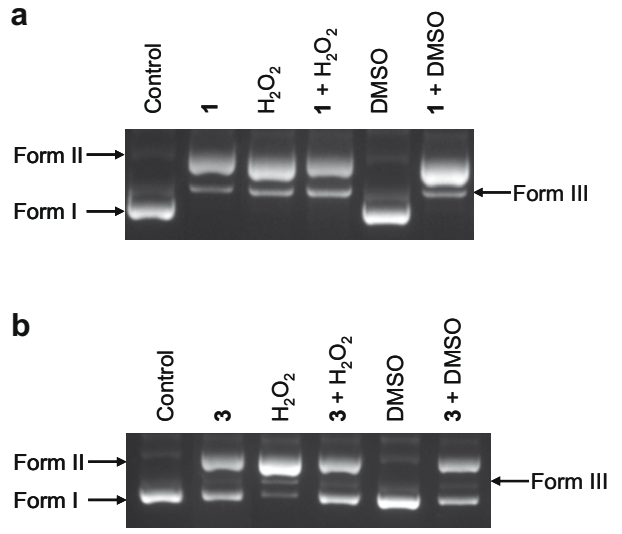


Fig. 8. Electrophoretic separations of pUC19 plasmid DNA cleavage by: (a) complex **1** and (b) complex **3** under the addition of H_2O_2 or of scavenger DMSO. Plasmid DNA (76.8 μM) was incubated with 150 μM of the complex and 0.1 mM H_2O_2 or 0.4 M DMSO for 24 h at 37 °C.

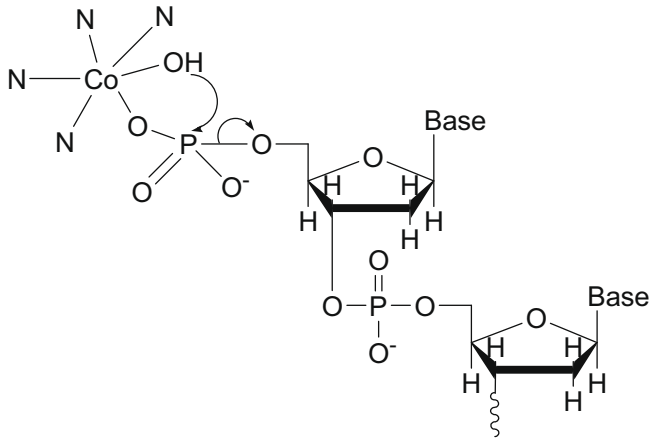


Fig. 9. Proposed intermediate in the DNA cleavage by *cis*-aquahydroxo–tetraamine–cobalt(III) complexes (charge on the cobalt complex cation was omitted for simplicity).

of the phosphate onto the metal followed by an intramolecular nucleophilic attack of the hydroxo ligand on the metal-bound DNA strand, forming a four-membered ring intermediate and hence the cleavage of DNA. It should be emphasized here that this hydroxide ion plays a critical role in the phosphoryl transfer hydrolysis process. The proposed intermediate is illustrated in Fig. 9.

4. Concluding remarks

In this study, we demonstrated the efficiency of the aquahydroxo–Co(III) complexes derived from TPA (**1**) and 2,2,2-tet (**3**) in promoting the hydrolytic cleavage of DNA. Under pseudo-Michaelis–Menten conditions and at the saturation kinetic level, the former complex enhances the rate of cleavage of the double-stranded DNA by a factor that is about 35-million-fold greater than the uncatalyzed DNA. The rate enhancement by **1** compared to **3**, most likely is attributed to the presence of the pyridyl groups in **1** which may undergo ring stacking with the DNA nucleic bases. This interaction was confirmed in the reactions M^{2+}-polypyridyl complexes with AMP, ADP and ATP [66]. Moreover, the stacking interaction is also known to accelerate the rates of hydrolysis of ADP and ATP systems [20a,67]. Small alteration in the ligand skeleton by inserting methylene groups into the arms between the N-donor groups in TPA and 2,2,2-tet to increase the chain lengths as in pmap and 3,2,3-tet, respectively, led to dramatic depression in the cleavage rates of DNA. Very low catalytic activity was observed with **2** and almost no hydrolysis in **4**. This indicates that increasing the arms in these two complexes could be responsible for such reduction in rates. Another interesting conclusion which should be addressed when comparing the rates of DNA cleavage by compounds **1** and **2** is the improper orientation of the pyridyl groups in **3**. This may lead to poor π–π interaction with the N-heterocyclic bases of DNA and hence lowers catalytic efficiency. In summary, the TPA–Co(III) complex is a very promising model to catalyze the hydrolytic cleavage of DNA and more work has to be directed to improve the reactivity of this system by incorporating substituted pyridyl groups into the TPA skeleton.

Acknowledgments

W.X. thanks the start-up funds and 2007 Summer Research Award (College of Sciences) and S.S.M. thanks Dean B. Clark and the Department of Chemistry (UL – Lafayette) for financing this work. The authors also, thank Dr. K. Knierim (UL – Lafayette) for helpful discussion of the kinetic data and the reviewer.

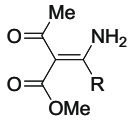
Appendix A. Supplementary data

CCDC 687881 contains the supplementary crystallographic data for $[Co(pmap)CO_3]ClO_4$. These data can be obtained free of charge via http://www.ccdc.cam.ac.uk/conts/retrieving.html, or from the Cambridge Crystallographic Data Centre, 12 Union Road, Cambridge CB2 1EZ, UK; fax: (+44) 1223-336-033; or e-mail: deposit@ccdc.cam.ac.uk. Supplementary data associated with this article can be found, in the online version, at doi:10.1016/j.poly.2009.02.003.

References

[1] A. Radzicka, R. Wolfenden, Science 267 (1995) 90.
[2] E.L. Hegg, J.N. Burstyn, Coord. Chem. Rev. 173 (1998) 133.
[3] G. Pratviel, A. Bernadou, B. Meunier, in: A.G. Sykes (Ed.), Advances in Inorganic Chemistry, vol. 45, Academic Press, London, 1997, p. 251.
[4] J. Stubbe, J. Kozarich, W. Wu, D. Vanderwall, Acc. Chem. Res. 29 (1996) 322.
[5] J. Yan, J.A. Cowan, J. Am. Chem. Soc. 127 (2005) 8408.
[6] (a) F.B.A. El Amrani, L. Perelló, J.A. Real, M. Gonzáles-Alvarez, G. Alzuet, J. Borrás, S. Gracía-Granda, J. Montejo-Bernardo, J. Inorg. Biochem. 100 (2006) 1208;
(b) V. Uma, M. Kanthimathi, T. Weyhermuller, B.U. Nair, J. Inorg. Biochem. 99 (2005) 2299.
[7] R. Hettich, H.-J. Schneider, J. Am. Chem. Soc. 119 (1997) 5638. and references therein.
[8] (a) T. Humphry, M. Forconi, N.H. Williams, A.C. Hengge, J. Am. Chem. Soc. 126 (2004) 11864;
(b) T. Humphry, M. Forconi, N.H. Williams, A.C. Hengge, J. Am. Chem. Soc. 124 (2002) 14860.
[9] (a) D.H. Vance, A.W. Czarnik, J. Am. Chem. Soc. 115 (1993) 12165;
(b) E.U. Akkaya, A.W. Czarnik, J. Am. Chem. Soc. 110 (1988) 8553.
[10] (a) D. Wahnon, A.-M. Lebuis, J. Chin, Angew. Chem., Int. Engl. Ed. 34 (1995) 2412;
(b) J.A. Connolly, M. Banaszczyk, R.C. Hynes, J. Chin, Inorg. Chem. 33 (1994) 665.
[11] (a) J. Chin, M. Banaszczyk, V. Jubian, X. Zou, J. Am. Chem. Soc. 111 (1989) 186;
(b) J. Chin, M. Banaszczyk, V. Jubian, J. Chem. Soc., Chem. Commun. (1988) 735;
(c) J. Chin, X. Zou, J. Am. Chem. Soc. 110 (1988) 223.
[12] P. Hendry, A.M. Sargeson, in: S. Lippard (Ed.), Progress in Inorganic Chemistry: Bioinorganic Chemistry, vol. 38, John Wiley & Sons, Inc, 1990, p. 201.
[13] K.L. Klinkel, A.K. Kiemele, D.L. Gin, J.R. Hagadorn, Chem. Commun. (2006) 2919.
[14] K.A. Deal, G. Park, J. Shao, N.D. Chasteen, M.W. Brechbiel, R.P. Planalp, Inorg. Chem. 40 (2001) 4176.

[15] M.J. Belousoff, M.B. Duriska, B. Graham, S.R. Batten, B. Moubaraki, K.S. Murray, L. Spiccia, Inorg. Chem. 45 (2006) 3746.
[16] M. Scarpellini, A. Neves, R. Hörner, A. Bortoluzzi, B. Szpoganics, C. Zucco, R. Nome Silva, V. Drago, A. Mangrich, W.A. Ortiz, W.A.C. Passos, M.C.B. de Oliveira, M.C.H. Terenzi, Inorg. Chem. 42 (2003) 8343.
[17] (a) K.A. Deal, A.C. Hengge, J.N. Burstyn, J. Am. Chem. Soc. 118 (1996) 1713;
(b) K.A. Deal, J.N. Burstyn, Inorg. Chem. 35 (1996) 2792;
(c) E.L. Hegg, J.N. Burstyn, Inorg. Chem. 35 (1996) 7474.
[18] J.R. Morrow, W.C. Trogler, Inorg. Chem. 28 (1989) 2330.
[19] (a) S.S. Massoud, J. Inorg. Biochem. 55 (1994) 183;
(b) F. Tafesse, S.S. Massoud, R.M. Milburn, Inorg. Chem. 32 (1993) 1864;
(c) S.S. Massoud, R.M. Milburn, J. Inorg. Biochem. 39 (1990) 337;
(d) F. Tafesse, S.S. Massoud, R.M. Milburn, Inorg. Chem. 24 (1985) 2591.
[20] (a) H. Sigel, Pure Appl. Chem. 70 (1998) 969;
(b) H. Sigel, C.A. Blinddauer, A. Holý, H. Dvořáková, Chem. Commun. (1998) 1219.
[21] (a) C. Liu, M. Wang, T. Zhang, H. Sun, Coord. Chem. Rev. 248 (2004) 147;
(b) P. Molenveld, J.F.J. Engbersen, D.N. Reinhoudt, Chem. Soc. Rev. 29 (2000) 75;
(c) G. Pratviel, A. Bernadou, B. Meunier, in: A.G. Sykes (Ed.), Advances in Inorganic Chemistry, vol. 45, Academic Press, London, 1997, p. 251.
[22] S. Chaudhary, J. Pinkston, M.M. Rabile, J.D. Van Horn, J. Inorg. Biochem. 99 (2005) 787.
[23] (a) A. Bencini, E. Berni, A. Bianchi, V. Fedi, C. Giorgi, P. Paoletti, B. Valtancoli, Inorg. Chem. 38 (1999) 6323;
(b) M. Yashiro, A. Ishikubo, M. Komiyama, J. Chem. Soc., Chem. Commun. (1995) 1793.
[24] X.-Y. Wang, J. Zhang, K. Li, N. Jiang, S.-Y. Chen, H.-H. Lin, Y. Huang, L.-J. Ma, X.-Q. Yu, J. Bioorg. Med. Chem. 14 (2006) 6745.
[25] (a) M.S.S. Babu, K.H. Reddy, P.K. Krishna, Polyhedron 26 (2007) 572;
(b) H. Li, X.-Y. Le, D.W. Pang, H. Deng, Z.-H. Xu, Z.-H. Lin, J. Inorg. Biochem. 99 (2005) 2240.
[26] Q.-L. Li, J. Huang, Q. Wang, N. Jiang, C.-Q. Xia, H.-H. Lin, J. Wu, X.-Q. Yu, Bioorg. Med. Chem. 14 (2006) 4151.
[27] (a) T. Kobayashi, S. Tobita, M. Kobayasi, T. Imajy, M. Chikira, M. Yashiro, Y.J. Fujii, Inorg. Biochem. 101 (2007) 348;
(b) Y. Li, Y. Wu, J. Zhao, P. Yang, J. Inorg. Biochem. 101 (2007) 283.
[28] L.M. Rossi, A. Neves, R. Hörner, H. Terenzi, B. Szpoganicz, J. Sugai, J. Inorg. Chim. Acta 337 (2002) 366.
[29] K.M. Deck, T.A. Tseng, J.N. Burstyn, Inorg. Chem. 41 (2002) 669.
[30] Q.-X. Xiang, J. Zhang, P.-Y. Liu, C.-Q. Xia, Z.-Y. Zhou, R.-G. Xie, X.-Q. Yu, J. Inorg. Biochem. 99 (2005) 1661.
[31] J.-L. Garcia-Giménez, G. Alzuet, M. González-Alvarez, A. Castiñeiras, M. Liu-González, J. Borrás, Inorg. Chem. 46 (2007) 7178.
[32] B.L. Griggs, G.A. Lawrance, M. Maeder, M.J. Robertson, P. Turner, Inorg. Chim. Acta 360 (2007) 2403.
[33] S.K. Gupta, P.B. Hitchcock, Y.S. Kushwah, G.S. Argal, Inorg. Chim. Acta 360 (2007) 2145.
[34] A. Sreedhara, J.D. Freed, J.A. Cowan, J. Am. Chem. Soc. 122 (2000) 8814.
[35] (a) A. Sreedhara, J.A. Cowan, J. Biol. Inorg. Chem. 6 (2001) 337;
(b) J.A. Cowan, Curr. Opin. Chem. Biol. 5 (2001) 634.
[36] (a) P.U. Maheswari, M. Ster, S. Smulders, S. Barends, G.P. Wezel, C. Massera, S. Roy, H. Dulk, P. Gamez, J. Reedijk, Inorg. Chem. 47 (2008) 3719;
(b) U. Maheswari, K. Lappalainen, M. Sfregola, S. Barends, P. Gamez, U. Turpeinen, I. Mutikainen, G.P. van Wezel, J. Reedijk, J. Chem. Soc., Dalton Trans. (2007) 3676.
[37] M.E. Branum, A.K. Tipton, S. Zhu, Jr.L. Que, J. Am. Chem. Soc. 123 (2001) 1898.
[38] (a) R.A. Moss, J. Zhang, K.G. Ragunathan, Tetrahedron Lett. (1998) 1529;
(b) R.A. Moss, K. Bracken, J. Zhang, Chem. Commun. (1997) 563;
(c) P. Gómez-Tagle, A.Y. Yatsimirsky, J. Chem. Soc., Dalton Trans. (1998) 2957.
[39] H.-J. Schneider, J. Rammo, R. Hettich, Angew. Chem., Int. Engl. Ed. 32 (1993) 1716.
[40] (a) P.E. Jurek, A.M. Jurek, A.E. Martell, Inorg. Chem. 39 (2000) 1016;
(b) P.E. Jurek, A.E. Martell, Chem. Commun. 39 (1999) 1609.
[41] M.A. Camargo, A. Neves, A.J. Bortoluzzi, B. Szpoganicz, A. Matendal, M. Murgu, F.L. Fischer, H. Terenzi, P.C. Severino, Inorg. Chem. 47 (2008) 2919.
[42] (a) R.L. Fanshawe, A.G. Blackman, Inorg. Chem. 34 (1995) 421;
(b) R.L. Fanshawe, A.G. Blackman, C.R. Clark, Inorg. Chim. Acta 342 (2003) 342;
(c) S.S. Massoud, F.A. Mautner, R. Vicente, A.A. Gallo, E. Ducasse, Eur. J. Inorg. Chem. (2007) 1091.
[43] S.S. Massoud, R.R. Jeanbatiste, T.M. Nguyen, F.R. Louka, A.A. Gallo, J. Coord. Chem. 60 (2007) 2409.
[44] (a) Z. Tyeklár, R.R. Jacobson, N. Wei, N.N. Murthy, J. Zubieta, K.D. Karlin, J. Am. Chem. Soc. 115 (1993) 2677;
(b) U. Mukhopadhyay, I. Bernal, S.S. Massoud, F.A. Mautner, Inorg. Chim. Acta 357 (2004) 3673.
[45] (a) M. Schatz, M. Becker, F. Thaler, F. Hampel, S. Schindler, R.R. Jacobson, Z. Tyeklár, N.N. Murthy, P. Ghosh, Q. Chen, J. Zubieta, K.D. Karlin, Inorg. Chem. 49 (2001) 2312;
(b) R. Vicente, J. Cano, E. Ruiz, S.S. Massoud, F.A. Mautner, Inorg. Chem. 47 (2008) 4648.
[46] H.F. Bauer, W.C. Drinkards, J. Am. Chem. Soc. 74 (1960) 5031.
[47] (a) A.M. Sargeson, G.H. Searle, Inorg. Chem. 6 (1967) 2172;
(b) S.S. Massoud, Polyhedron 13 (1994) 1467.
[48] P.M. Jaffray, L.F. McClintock, K.E. Baxter, A.G. Blackman, Inorg. Chem. 44 (2005) 4215.
[49] (a) J.H. Loehlin, E.B. Fleisher, Acta Crystallogr. B32 (1976) 3063;
(b) E.Q. Schlemper, P.K. Sen Gupta, T.P. Dasgupta, Acta Crystallogr. C39 (1983) 1012.
[50] A.M. Sargeson, G.H. Searle, Nature (London) 200 (1963) 356.
[51] P.R. Norman, R.D. Cornelius, J. Am. Chem. Soc. 104 (1982) 2356.
[52] (a) H. Sigel, S.S. Massoud, R. Tribolet, J. Am. Chem. Soc. 110 (1988) 6857;
(b) S, S. Massoud, H. Sigel, Inorg. Chem. 27 (1988) 1447;
(c) R.M. Milburn, M. Gautam-Basak, R. Tribolet, H. Sigel, J. Am. Chem. Soc. 107 (1985) 3315.
[53] R.H. Blessing, Acta Crystallogr., Sect. A 51 (1995) 33–38.
[54] G.M. Sheldrick, Acta Crystallogr., Sect. A 64 (2008) 112.
[55] Y. An, S.-D. Liu, S.Y. Deng, L.-N. Ji, Z.W. Mao, J. Inorg. Biochem. 100 (2006) 1586.
[56] F. Basolo, C.J. Ballahausen, C.J. Bjerrum, Acta Chim. Scand. 9 (1955) 810.
[57] S.S. Massoud, R.M. Milburn, Inorg. Chim. Acta 163 (1989) 87.
[58] W.V. Miller, S.K. Madan, Inorg. Chem. 9 (1970) 2362.
[59] S.S. Massoud, R.M. Milburn, Inorg. Chim. Acta 146 (1988) 3.
[60] D. Buckingham, J.D. Edwards, G.M. McLaughhlin, Inorg. Chem. 21 (1982) 2770.
[61] (a) S.S. Massoud, R.M. Milburn, Polyhedron 8 (1989) 275;
(b) S.S. Massoud, R.M. Milburn, Polyhedron 8 (1989) 415.
[62] J. Qian, W. Gu, H. Liu, F. Gao, L. Feng, S. Yan, D. Liao, P. Cheng, J. Chem. Soc., Dalton Trans. (2007) 1060.
[63] Y. An, M.L. Tong, L.N. Ji, Z.W. Mao, J. Chem. Soc., Dalton Trans. (2006) 2066.
[64] M. Lanznaster, A. Neves, A.J. Bortoluzzi, V.V. Aires, B. Szpoganicz, H. Terenzi, P.C. Severino, J.M. Fuller, S.C. Drew, L.R. Gahan, G.R. Hanson, M.J. Riley, G. Schenk, J. Biol. Inorg. Chem. 10 (2005) 319.
[65] N.E. Dixon, R.J. Geue, J.N. Lambert, S. Moghaddas, D.A. Pearce, A.M. Sargeson, Chem. Commun. (1996) 1287.
[66] (a) H. Sigel, B.P. Operschall, S.S. Massoud, B. Song, R. Griesser, J. Chem. Soc., Dalton Trans. 46 (2006) 5521;
(b) S.S. Massoud, R. Tribolet, H. Sigel, Eur. J. Biochem. 187 (1990) 387.
[67] (a) H. Sigel, Coord. Chem. Rev. 100 (1990) 453;
(b) R.M. Milburn, M. Gautam-Basak, R. Tripolet, H. Sigel, J. Am. Chem. Soc. 107 (1985) 3315.



HL^{Me} R = methyl
HL^{iBu} R = *i*-butyl
HL^{nBu} R = *n*-butyl
HL^{nHe} R = *n*-hexyl

Chart 1.

VG MM16 operating in electron ionisation mode at 70 eV electron beam energy and an ion source temperature of 180 °C. TGS–DSC analysis were performed with a Perkin–Elmer TGS-2, DSC-4 apparatus.

X-ray photoelectron spectroscopy (XPS) analyses were performed with a Perkin–Elmer Φ 5600ci spectrometer, with monochromatised Al Kα radiation (1486.6 eV), calibrated vs. $Au4f_{7/2}$ at 83.9 eV [10]. XRD data were collected with a Philips diffractometer with thin film equipment (Cu Kα, λ = 1.54 Å, incident angle 1°).

2.2. Synthesis of the ligands

The β-enaminodiones (MeCO)(MeOCO)C=C(NH_2)R (R = Me (**HL^{Me}**); R = *i*-Bu (**HL^{iBu}**); R = *n*-Bu (**HL^{nBu}**); R = *n*-hexyl (**HL^{nHe}**)), were prepared by reaction of methyl acetoacetate with the appropriate nitrile in the presence of a stoichiometric amount of $SnCl_4$, with the same procedure already reported for **HL^{Me}** [11,12].

HL^{nBu}: ^{1}H NMR (in $CDCl_3$): δ = 0.93 (t, 3H, C*H*$_3$), 1.30–1.75 (m, 4H, 2C*H*$_2$), 2.26 (s, 3H, C*H*$_3$CO), 2.45 (m, 2H, C*H*$_2$), 3.76 (s, 3H, C*H*$_3$OCO), 5.68 (s, 1H, N*H*), 11.21 (s, 1H, N*H*). FTIR [cm^{-1}, KBr]: 3370 [ν(NH)], 2959–2872 [δ(CH)], 1709 [ν(MeOC=O)], 1603 [ν(C=O)].

HL^{iBu}: ^{1}H NMR (in $CDCl_3$): δ = 0.91 (d, 6H, CH(C*H*$_3$)$_2$), 1.84 (m, 1H, C*H*), 2.20 (s, 3H, C*H*$_3$CO), 2.32 (d, 2H, CH$_2$), 3.70 (s, 3H, C*H*$_3$OCO), 6.00 (s, 1H, N*H*), 11.18 (s, 1H, N*H*). FTIR [cm^{-1}, KBr]: 3364 [ν(NH)], 2961–2872 [δ(CH)], 1703 [ν(MeOC=O)], 1603 [ν(C=O)].

HL^{nHe}: ^{1}H NMR (in $CDCl_3$): δ = 0.87 (m, 3H, C*H*$_3$), 1.20–1.70 (m, 8H, 4C*H*$_2$), 2.24 (s, 3H, C*H*$_3$CO), 2.44 (m, 2H, C*H*$_2$), 3.75 (s, 3H, C*H*$_3$OCO), 5.64 (s, 1H, N*H*), 11.21 (s, 1H, N*H*).

2.3. Synthesis of the complexes

Complexes **1–6** were obtained by reaction of the metal acetate with the appropriate ligand in 1/2 molar ratio, in anhydrous ethanol, at room temperature under argon; the resulting solutions were left under stirring for variable times and the complexes can either precipitate spontaneously from the reaction mixture or be recovered from the solution evaporated to dryness. In many cases the compounds are isolable in different forms, distinguished as **a** or **b**, which exhibit identical composition but different spectroscopic properties; the symbols **a** and **b** indicate only the order in which the complexes have been isolated.

[Pd(**L^{Me}**)$_2$] (**1a, 1b**). [Pd(OAc)$_2$] (0.17 g, 0.76 mmol) and **HL^{Me}** (0.25 g, 1.60 mmol) were dissolved in anhydrous ethanol (20 ml) and the resulting solution was stirred for 4 h at room temperature, then filtered. The solid was recrystallised from dichloromethane/hexane, affording pure (**1a**) as a bright yellow solid (0.090 g, 27% yield). The yellow alcoholic filtrate was evaporated to small volume under reduced pressure and treated with diethylether (10 ml), giving (**1b**) as a light yellow solid, which was filtered and dried under vacuum (0.157 g, 47% yield). *Anal.* Calc. for $C_{14}H_{20}N_2O_6Pd$ (*MW* = 418.72): C, 40.16; H, 4.81; N, 6.69. Found for (**1a**): C, 40.28; H, 4.71; N, 6.37. Found for (**1b**): C, 39.57; H, 4.76; N, 6.68%. (**1a**). ^{1}H NMR (in $CDCl_3$), two species, labelled **a** and **a′**, in approximately 2/1 ratio are present in solution: δ = 2.09 (s, 3H, C*H*$_3$CO, **1a**), 2.16 (s, 3H, C*H*$_3$, **1a**), 2.18 and 2.19 (2s, 3H, C*H*$_3$CO and C*H*$_3$, **1a′**), 3.76 (s, 4.5H, C*H*$_3$OCO, **1a** and **1a′**), 6.34 (s, 0.5H, N*H*, **1a′**), 6.79 (s, 1H, N*H*, **1a**). ^{13}C NMR (in $CDCl_3$): δ = 25.6 and 26.7 (*C*H$_3$ and *C*H$_3$CO, **1a**), 26.1 and 27.0 (*C*H$_3$ and *C*H$_3$CO, **1a′**), 51.6 (*C*H$_3$OCO, **1a** and **1a′**), 106.0 ((CH$_3$CO)*C*, **1a** and **1a′**), 164.7 (*C*NH, **1a**), 165.4 (*C*NH, **1a′**), 170.9 (CH$_3$O*C*O, **1a′**), 171.1 (CH$_3$O*C*O, **1a**), 179.5 (CH$_3$*C*O, **1a**), 181.4 (CH$_3$*C*O, **1a′**). FTIR [cm^{-1}, KBr]: 3322 [ν(NH)], 1692 [ν(MeOC=O)], 1577 [ν(C⟷O)]. FTIR [cm^{-1}, $CDCl_3$]: 3348, 3316(sh) [ν(NH)], 1702 [ν(MeOC=O)], 1587 [ν(C⟷O)]. UV–Vis (λ_{max}/nm, $CHCl_3$): 328 (ε = 6400 ± 500 dm^3 mol^{-1} cm^{-1}), 260 (ε = 21 100 ± 2100 dm^3 mol^{-1} cm^{-1}). MS-EI: *m/z* 418 ([Pd(**L^{Me}**)$_2$]$^+$). (**1b**). ^{1}H NMR (in $CDCl_3$): δ = 2.15 (s, 3H, C*H*$_3$CO), 2.17 (s, 3H, C*H*$_3$), 3.75 (s, 3H, C*H*$_3$OCO), 6.80 (s, 1H, N*H*). ^{13}C NMR (in $CDCl_3$): δ = 25.9 and 26.7 (*C*H$_3$ and *C*H$_3$CO), 51.6 (*C*H$_3$OCO), 106.0 ((CH$_3$CO)*C*), 165.2 (*C*NH), 171.0 (CH$_3$OCO), 180.7 (CH$_3$CO). FTIR [cm^{-1}, KBr]: 3325 and 3310 [ν(NH)], 1684 and 1675 [ν(MeOC=O)], 1584 and 1576 [ν(C⟷O)]. FTIR [cm^{-1}, $CDCl_3$]: 3348 and 3313 [ν(NH)], 1702 [ν(MeOC=O)], 1576 [ν(C⟷O)]. UV–Vis (λ_{max}/nm, $CHCl_3$): 326 (ε = 7400 ± 500 dm^3 mol^{-1} cm^{-1}), 260 (ε = 22 300 ± 1600 dm^3 mol^{-1} cm^{-1}). MS-EI: *m/z* 418 ([Pd(**L^{Me}**)$_2$]$^+$). Complex (**1a**) decomposes at 178 °C at atmospheric pressure, while it sublimes at 156 °C at 4 × 10^{-2} mbar; FTIR analysis reveals that both the sublimate (FTIR: 3321 [ν(NH)], 1689 [ν(MeOC=O)] and 1576 [ν(C⟷O)]) and the residue are still (**1a**) (FTIR: 3322 [ν(NH)], 1690 [ν(MeOC=O)], 1574 [ν(C⟷O)]). Complex (**1b**) decomposes at 210 °C at atmospheric pressure, while it sublimes at 156 °C at 4 × 10^{-2} mbar; FTIR analysis reveals that the sublimate is (**1a**) (FTIR: 3320 [ν(NH)], 1688 [ν(MeOC=O)] and 1576 [ν(C⟷O)]) while the residue is still (**1b**) (FTIR: 3323 and 3310 [ν(NH)], 1685 and 1673 [ν(MeOC=O)], 1574 [ν(C⟷O)]).

[Pd(**L^{iBu}**)$_2$] (**2a, 2b**). [Pd(OAc)$_2$] (0.17 g, 0.76 mmol) was dissolved in anhydrous ethanol (15 ml) and the resulting solution was additioned with **HL^{iBu}** (0.30 g, 1.50 mmol, in 15 ml anhydrous ethanol). The reaction mixture was left under stirring for 2 h at room temperature, then evaporated under reduced pressure. The residue was dissolved with dichloromethane (15 ml) and filtered through Celite. The filtrate was again evaporated to small volume and finally, treated with diethylether (20 ml), affording a yellow precipitate (**2**), which was filtered and dried under vacuum (0.24 g, 63% yield). *Anal.* Calc. for $C_{20}H_{32}N_2O_6Pd$ (*MW* = 502.88): C, 47.77; H, 6.41; N, 5.57. Found: C, 46.96; H, 6.40; N, 5.38%. (**2**): FTIR [cm^{-1}, KBr]: 3297, 3270 and 3248 [ν(NH)], 1715 [ν(MeOC=O)], 1584 [ν(C⟷O)]. UV–Vis (λ_{max}/nm, $CHCl_3$): 330 (ε = 6600 ± 500 dm^3 mol^{-1} cm^{-1}), 260 (ε = 19 000 ± 1400 dm^3 mol^{-1} cm^{-1}). MS-EI: *m/z* 502 ([Pd(**L^{iBu}**)$_2$]$^+$). The NMR spectra revealed that the isolated solid was a mixture of two isomers (**2a**, **2b**) in 2.5/1 ratio. (**2a**). ^{1}H NMR (in $CDCl_3$): δ = 0.89 (d, 6H, (C*H*$_3$)$_2$CHCH$_2$, $^3J_{HH}$ = 6.6 Hz), 1.83 (m, 1H, (CH$_3$)$_2$C*H*CH$_2$), 2.18 (s, 3H, C*H*$_3$CO), 2.37 (d, 2H, (CH$_3$)$_2$CHC*H*$_2$, $^3J_{HH}$ = 7.4 Hz), 3.74 (s, 3H, C*H*$_3$OCO), 6.34 (s, 1H, N*H*). ^{13}C NMR (in $CDCl_3$): δ = 22.8 ((*C*H$_3$)$_2$CHCH$_2$), 26.6 (*C*H$_3$CO), 28.1 ((CH$_3$)$_2$CHCH$_2$), 49.5 ((CH$_3$)$_2$CHCH$_2$), 52.2 (*C*H$_3$OCO), 106.2 ((CH$_3$CO)*C*), 169.0 (*C*NH), 171.6 (CH$_3$O*C*O), 181.7 (CH$_3$*C*O). ^{15} N NMR (in $CDCl_3$): δ = 145.4. (**2b**). ^{1}H NMR (in $CDCl_3$): δ = 0.92 (d, 6H, (C*H*$_3$)$_2$CHCH$_2$, $^3J_{HH}$ = 6.6 Hz), 1.83 (m, 1H, (CH$_3$)$_2$C*H*CH$_2$), 2.09 (s, 3H, C*H*$_3$CO), 2.33 (d, 2H, (CH$_3$)$_2$CHC*H*$_2$, $^3J_{HH}$ = 7.4 Hz), 3.74 (s, 3H, C*H*$_3$OCO), 6.74 (s, 1H, CN*H*). ^{13}C NMR (in $CDCl_3$): δ = 22.9 ((*C*H$_3$)$_2$CHCH$_2$), 26.2 (*C*H$_3$CO), 27.9 ((CH$_3$)$_2$*C*HCH$_2$), 49.0 ((CH$_3$)$_2$CHCH$_2$), 52.2 (*C*H$_3$OCO), 106.4 ((CH$_3$CO)*C*), 168.0 (*C*NH), 171.8 (CH$_3$O*C*O), 179.9 (CH$_3$*C*O). ^{15} N NMR (in $CDCl_3$): δ = 166.9. Complex (**2**) decomposes at 195 °C at atmospheric pressure, while it sublimes at 155 °C at 6 × 10^{-2} mbar; FTIR analysis reveals that the sublimate is (**2b**) (FTIR [cm^{-1}, KBr]: 3270 and 3248 [ν(NH)], 1713 [ν(MeOC=O)], 1585 [ν(C⟷O)]) while the residue is still a mixture of (**2a**) and (**2b**) (FTIR: 3298, 3270 and 3248 [ν(NH)], 1715 [ν(MeOC=O)], 1584 [ν(C⟷O)]).

[Pd(**L^{nBu}**)$_2$] (**3**). A yellow solid was obtained with the same experimental procedure of complex (**2**) (0.29 g, 77% yield). *Anal.*

Calc. for $C_{20}H_{32}N_2O_6Pd$ (MW = 502.88): C, 47.77; H, 6.41; N, 5.57. Found: C, 46.89; H, 6.30; N, 5.41%. ^{1}H NMR (in $CDCl_3$): δ = 0.87 (t, 3H, $CH_3(CH_2)_3$, $^3J_{HH}$ = 7.2 Hz), 1.28 (m, 2H, $CH_3CH_2(CH_2)_2$), 1.52 (m, 2H, $CH_3CH_2CH_2CH_2$), 2.14 (s, 3H, CH_3CO), 2.42 (t, 2H, $CH_3(CH_2)_2CH_2$, $^3J_{HH}$ = 8.0 Hz), 3.72 (s, 3H, CH_3OCO), 6.38 (s, 1H, N*H*). ^{13}C NMR (in $CDCl_3$): δ = 13.8 ($CH_3(CH_2)_3$), 22.7 (CH_2), 25.6 (CH_3CO), 30.4 (CH_2), 39.3 (CH_2), 51.7 (CH_3OCO), 105.7 ((CH_3CO)*C*), 168.7 (*C*NH), 171.1 (CH_3OCO), 179.3 (CH_3CO). FTIR [cm^{-1}, KBr]: 3295 [ν(NH)], 1719 [ν(MeOC=O)], 1582 [ν(C⟷O)]. UV–Vis (λ_{max}/nm, $CHCl_3$): 328 (ε = 7100 ± 500 dm^3 mol^{-1} cm^{-1}), 260 (ε = 20200 ± 1500 dm^3 mol^{-1} cm^{-1}). MS-EI: *m/z* 503 ([Pd($\mathbf{L^{nBu}}$)$_2$]$^+$). Complex (**3**) decomposes at 195 °C at atmospheric pressure, while it sublimes at 172 °C at 4 × 10^{-2} mbar; FTIR analysis reveals that both the sublimate (FTIR: 3293 [ν(NH)], 1717 [ν(MeOC=O)], 1582 [ν(C⟷O)]) and the residue are complex (**3**) (FTIR: 3293 [ν(NH)], 1719 [ν(MeOC=O)], 1582 [ν(C⟷O)]).

[Pd($\mathbf{L^{nHe}}$)$_2$] (**4**). [Pd(OAc)$_2$] (0.16 g, 0.73 mmol) was dissolved in anhydrous ethanol (15 ml) and the resulting solution was additioned with $\mathbf{HL^{nHe}}$ (0.33 g, 1.45 mmol) dissolved in anhydrous ethanol (15 ml) and ethyl acetate (1 ml). The reaction mixture was left under stirring for 1 h at room temperature, then evaporated to small volume under reduced pressure. The residue was treated with ethanol (20 ml) under stirring for 1 h and the solvent was removed. The residue was dissolved with dichloromethane (15 ml) and filtered through Celite. The filtrate was again evaporated to small volume and finally treated with diethylether (20 ml), affording a yellow precipitate, which was filtered and dried under vacuum (0.25 g, 61% yield). *Anal.* Calc. for $C_{24}H_{40}N_2O_6Pd$ (MW = 558.99): C, 51.57; H, 7.21; N, 5.01. Found: C, 51.61; H, 7.31; N, 4.90%. ^{1}H NMR (in $CDCl_3$): δ = 0.85 (t, 3H, $CH_3(CH_2)_5$, $^3J_{HH}$ = 6.1 Hz), 1.25–1.50 (m, 8H, $CH_3(CH_2)_4CH_2$), 2.15 (s, 3H, CH_3CO), 2.40 (t, 2H, $CH_3(CH_2)_4CH_2$, $^3J_{HH}$ = 7.3 Hz), 3.72 (s, 3H, CH_3OCO), 6.19 (s, 1H, N*H*). ^{13}C NMR (in $CDCl_3$): δ = 14.0 ($CH_3(CH_2)_5$), 22.5 (CH_2), 25.9 (CH_3CO), 28.2 (CH_2), 29.2 (CH_2), 31.4 (CH_2), 39.6 (CH_2), 51.6 (CH_3OCO), 105.6 ((CH_3CO)*C*), 169.0 (*C*NH), 171.1 (CH_3OCO), 180.6 (CH_3CO). FTIR [cm^{-1}, KBr]: 3297 [ν(NH)], 1711 [ν(MeOC=O)], 1580 [ν(C⟷O)]. UV–Vis (λ_{max}/nm, $CHCl_3$): 328 (ε = 7600 ± 500 dm^3 mol^{-1} cm^{-1}), 260 (ε = 20100 ± 1500 dm^3 mol^{-1} cm^{-1}). MS-EI: *m/z* 558 ([Pd($\mathbf{L^{nHe}}$)$_2$]$^+$). Complex (**4**) decomposes at 189 °C at atmospheric pressure, while it sublimes at 180 °C at 5 × 10^{-2} mbar; FTIR analysis reveals that both the sublimate (FTIR: 3295 [ν(NH)], 1713 [ν(MeOC=O)], 1582 [ν(C⟷O)]) and the residue (FTIR: 3297 [ν(NH)], 1711 [ν(MeOC=O)], 1580 [ν(C⟷O)]) are complex (**4**).

[Ni($\mathbf{L^{Me}}$)$_2$] (**5**). A solution of $\mathbf{HL^{Me}}$ (0.63 g, 4.02 mmol) and [Ni(OAc)$_2$]·4H$_2$O (0.50 g, 2.00 mmol) in anhydrous ethanol (20 ml) was stirred for 1 h at room temperature, then evaporated to small volume under reduced pressure. The residue was treated with ethanol (20 ml) and again the solvent was removed. This treatment was continued until the smell of acetic acid disappeared; 3–4 cycles were generally sufficient. Finally, treatment with diethylether (10 ml) gave a light red solid, which was filtered and dried under vacuo (0.47 g, 63%). *Anal.* Calc. for $C_{14}H_{20}N_2NiO_6$ (MW = 371.03): C, 45.32; H, 5.43; N, 7.55. Found: C, 45.34; H, 5.34; N, 7.58%. ^{1}H NMR (in $CDCl_3$): δ = 1.95 (s, 3H, CH_3CO), 2.08 (s, 3H, CH_3CNH), 3.68 (s, 3H, CH_3OCO), 5.37 (s, 1H, N*H*). ^{13}C NMR (in $CDCl_3$): δ = 25.9 and 27.2 (CH_3CNH and CH_3CO), 51.2 (CH_3OCO), 105.8 ((CH_3CO)*C*), 167.7 (*C*NH), 170.3 (CH_3OCO), 181.7 (CH_3CO). FTIR [cm^{-1}, KBr]: 3320 [ν(NH)], 1688 [ν(MeOC=O)], 1570 [ν(C⟷O)]. UV–Vis (λ_{max}/nm, $CHCl_3$): 342 (ε = 3500 ± 300 dm^3 mol^{-1} cm^{-1}), 272 (ε = 30200 ± 2800 dm^3 mol^{-1} cm^{-1}), 244 (ε = 36500 ± 3000 dm^3 mol^{-1} cm^{-1}). MS-EI: *m/z* 370 ([Ni($\mathbf{L^{Me}}$)$_2$]$^+$). Complex (**5**) decomposes at 193 °C at atmospheric pressure, while it sublimes at 130 °C at 4 × 10^{-2} mbar; FTIR analysis reveals that the sublimate is a mixture of (**5**) and another isomer (FTIR: 3342 and 3320 [ν(NH)], 1690 [ν(MeOC=O)], 1591 and 1572 [ν(C⟷O)]), while the residue is complex (**5**) (FTIR: 3320 [ν(NH)], 1688 [ν(MeOC=O)], 1570 [ν(C⟷O)]).

[Ni($\mathbf{L^{iBu}}$)$_2$] (**6**). A solution of $\mathbf{HL^{iBu}}$ (0.25 g, 1.60 mmol) in anhydrous ethanol (20 ml) was added to a solution of [Ni(OAc)$_2$]·4H$_2$O (0.19 g, 0.78 mmol, in 15 ml anhydrous ethanol). The resulting mixture was stirred for 12 h at room temperature and then evaporated to small volume under reduced pressure. The resulting residue was treated with ethanol (20 ml) under stirring for 1 h and the solvent was again removed. Treatment with diethylether (20 ml) afforded a reddish precipitate, which was filtered and dried under vacuum. The solid was recrystallised from dichloromethane/diethylether, affording pure (**6**) as a pink solid (0.26 g, 75% yield). *Anal.* Calc. for $C_{20}H_{32}N_2NiO_6$ (MW = 455.19): C, 52.77; H, 7.09; N, 6.15. Found: C, 51.44; H, 7.01; N, 5.98%. ^{1}H NMR (in $CDCl_3$): δ = 0.90 (d, 6H, $(CH_3)_2CHCH_2$, $^3J_{HH}$ = 6.8 Hz), 1.72 (m, 1H, $(CH_3)_2CHCH_2$), 1.94 (s, 3H, CH_3CO), 2.28 (d, 2H, $(CH_3)_2CHCH_2$, $^3J_{HH}$ = 7.2 Hz), 3.70 (s, 3H, CH_3CO_2), 5.37 (s, 1H, CN*H*). ^{13}C NMR (in $CDCl_3$): δ = 22.8 ((CH_3)$_2$CHCH$_2$), 26.7 (CH_3CO), 27.9 ((CH_3)$_2$CHCH$_2$), 49.0 ((CH_3)$_2$CHCH$_2$), 51.8 (CH_3OCO), 106.1 ((CH_3CO)*C*), 170.7 (*C*NH), 171.1 (CH_3OCO), 181.5 (CH_3CO). ^{15}N NMR (in $CDCl_3$): δ = 162.7. FTIR [cm^{-1}, KBr]: 3279 and 3268 [ν(NH)], 1709 [ν(MeOC=O)], 1582 [ν(C⟷O)]. UV–Vis (λ_{max}/nm, $CHCl_3$): 346 (ε = 3000 ± 200 dm^3 mol^{-1} cm^{-1}), 272 (ε = 26300 ± 1700 dm^3 mol^{-1} cm^{-1}), 244 (ε = 34600 ± 2300 dm^3 mol^{-1} cm^{-1}). MS-EI: *m/z* 454 ([Ni($\mathbf{L^{iBu}}$)$_2$]$^+$). Complex (**6**) decomposes at 180 °C at atmospheric pressure, while it sublimes at 125 °C at 7.5 × 10^{-2} mbar; FTIR analysis reveals that both the sublimate (FTIR: 3279 and 3268 [ν(NH)], 1707 [ν(MeOC=O)], 1582 [ν(C⟷O)] and the residue (FTIR: 3279 and 3268 [ν(NH)], 1709 [ν(MeOC=O)], 1582 [ν(C⟷O)]) are complex (**6**).

2.4. Vapour deposition of complex [Ni($\mathbf{L^{Me}}$)$_2$] (**5**)

All deposition experiments were performed in a cold wall reactor using O_2, N_2, N_2/O_2 or $N_2/O_2/H_2O$ mixtures as gas carrier (purity 99.999%). The precursor was sublimed from a small crucible located close to the reactor (for a similar reactor see Ref. [13]).

Deposition on silicon under N_2: temperature of precursor 132 °C, of substrate 450 °C, total pressure 0.08 mbar, gas flow 8.1 cc min^{-1}; deposition on glass under O_2: temperature of precursor 130 °C, of substrate 450 °C, total pressure 0.08 mbar, gas flow 8.1 cc min^{-1}; deposition on silicon under $O_2 + H_2O$: temperature of precursor 133 °C, of substrate 450 °C, total pressure 0.03 mbar, gas flow 10 cc min^{-1}; deposition on glass under $O_2 + H_2O$: temperature of precursor 133 °C, of substrate 450 °C, total pressure 0.03 mbar, gas flow 10 cc min^{-1}.

The Si(100) substrate before the deposition was degreased using boiling trichloroethylene and rinsed with isopropyl alcohol.

3. Results and discussion

The results obtained in this study confirm the validity of the procedure for the synthesis of β-imino carbonyl enolato complexes starting from metal(II) acetates and β-enaminodiones (Eq. (1)). The factors governing the success of this exchange reaction have been recently fully

$$M(OAc)_2 + 2(R'CO)(R''CO)C{=}C(NH_2)R \rightarrow [M((R'CO)(R''CO)CC(NH)R)_2] + 2HOAc \quad (1)$$

exploited and depend on: (i) the relative stabilities of metal acetates and metal complexes and on (ii) the acidity of the β-enaminodiones compared with that of acetic acid [2a]. The chain length in the series of investigated β-enamino ketoesters (MeCO)(MeOCO)C=C(NH$_2$)R (R = Me, *i*-Bu, *n*-Bu, *n*-hexyl) has practically no effect on the output of the synthetic procedure so that complexes [M$\mathbf{L}_2$] (**1–6: 1**, Pd, $\mathbf{L^{Me}}$;

2, Pd, $\mathbf{L^{iBu}}$; **3**, Pd, $\mathbf{L^{nBu}}$; **4**, Pd, $\mathbf{L^{nHe}}$; **5**, Ni, $\mathbf{L^{Me}}$; **6**, Ni, $\mathbf{L^{iBu}}$) are obtained always in good yields. In most cases the complexes precipitate spontaneously otherwise the reaction is forced toward the desired products by co-distillation from the reaction mixture of solvent and the acetic acid produced in the ligand exchange process.

The results are coherent with those obtained with the ethyl substituent at the imino group [3]. The potentially tridentate N,O,O ligand acts in all cases as bidentate through the nitrogen and the keto oxygen atoms to give monomeric square planar neutral complexes. These are air and moisture stable solids, which can be stored safely under inert atmosphere; they are soluble in common organic solvents, such as ethanol, CH_2Cl_2, and $CHCl_3$, but mostly insoluble in *n*-hexane or diethylether.

The IR spectra in KBr of all complexes are very similar as the whole, being characterised by: (i) the N–H band approximately around 3300 cm^{-1}, (ii) a band at 1570–1585 cm^{-1}, which can be easily attributed to the coordinated acetyl carbonyl, (iii) an absorption in the range 1675–1719 cm^{-1} due to the C=O stretching vibration of the uncoordinated ester. In fact, the wavenumber values for O,O′-chelation in β-diester complexes are always close to 1600 cm^{-1}, as an effect of electronic delocalisation which occurs in the metallocycle ring [14]. These features confirm N,O ligand to metal coordination.

In addition the ^1H and ^{13}C NMR spectra are consistent with the proposed picture; in particular the ketonic carbonyl C signal (179.3–181.7 ppm) is shifted upfield in comparison with the signal of the corresponding carbon in the free ligand [2b,3]. No information can be gained instead from the chemical shift values of the C=N and C(O)OMe carbons which remain practically unchanged. Preferential coordination of the keto group with respect to the ester one has been widely observed in analogous complexes [1–3].

The palladium complexes (**1**) and (**2**) have been isolated in two forms, labelled **a** and **b**, whereas palladium(II) complexes (**3**) and (**4**) and the nickel ones (**5**) and (**6**) have been isolated only in one form.

This explains some small differences between the NMR spectra of samples (**1a**) and (**1b**) or (**2a**) and (**2b**). NOE experiments carried out on sample **2a** revealed a strong dipolar interaction between the protons of the *i*-butyl substituent and the imino hydrogen. Moreover a strong dipolar interaction between the hydrogen atoms of the acetyl and methyl ester groups indicates that they are spatially very close to each other (conformation **A** in Fig. 1). The same experiments carried out on sample (**2b**), indicate that the oxo and methoxy substituents on (**2b**) are turned and the methyl ester is preferentially faced toward the *i*-butyl group (conformation **B**). Thus the small differences observed in the solution NMR spectra of (**2a**) and (**2b**) can be easily attributed to these conformational changes of the ester substituent of the chelate ring. Similar considerations may apply to the solution chemistry of the palladium complex (**1**) for which three different sets of signals relative to **a**, **a**′ and **b** are observed. NOE experiments are not conclusive for this complex; in fact a sample of (**1b**) shows strong dipolar interactions consistent with conformation **B**. However sample (**1a**) shows two N–H proton signals of different intensity relative to the two species labelled **a** and **a**′, both correlating only with the corresponding imino methyl substituent, and no other spatial correlations are evident. The absence of these expected correlations may be due perhaps to a turning away of the methyl oxo. It should be underlined that the position of the N–H signal attributable to the minor species labelled **a**′ strongly depends on the type of solvents and, for example, passing from $CDCl_3$ to anhydrous C_6D_6 moves from 6.34 to 5.10 ppm, thus suggesting the possibility of intermolecular hydrogen bonding. With more sterically demanding groups, like *n*-butyl or *n*-hexyl, only one species has been isolated, thus indicating that the rotation of the ester group is hindered and that acetyl and methyl ester groups are preferentially faced to each other (conformation **A** in Fig. 1)

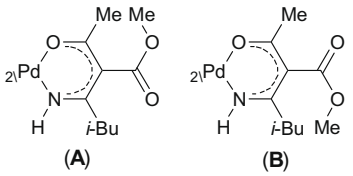


Fig. 1. Proposed conformations of complex (**2**).

In the UV–Vis spectra, palladium(II) complexes (**1**)–(**4**) show two maxima at ca. 330 and 260 nm of medium and strong intensities respectively. The shortest wavelength absorption at 260 nm may be assignable to $\pi \rightarrow \pi^*$ transition of the ligand, while the absorption at 330 nm ca. may be due to metal-to-ligand charge transfer transitions. The nickel compounds (**5**) and (**6**) present a third absorption at 240 nm ca., which is still assigned to a $\pi \rightarrow \pi^*$ transition of the ligand.

The complexes are volatile and remarkably stable as it appears evident from the presence of very intense molecular ions in the mass spectra of all compounds (**1**)–(**6**) (see Supplementary Information). The primary fragmentations are the same for both forms (**a** and **b**) and can be divided in two main categories: fragmentations of the ligand moiety anchored to the metal and those of the "free" ligand. The mass spectra of all the complexes are also characterised by the presence of HML^+ ions containing only one coordinated ligand and related fragmentations.

The high stability of this type of complexes is also confirmed by melting point measurements and TGA analysis (Table 1 and Fig. 2). The effect of the length of R chain on the melting point is rather limited, even if a decrease of the value with the lengthening of the chain is observed, probably due to reduced H-bonding interactions. Comparing palladium(II) and nickel(II) complexes it is evident a greater stability of the former ones, as indicated by the somewhat higher melting point values (215–178 °C versus 193–180 °C). TGA studies of the palladium complexes (**1**)–(**4**) show that they decompose in two steps; the first around 300 °C gives a residue (ca. 30%), which transforms in palladium black upon heating at 950 °C. Also in the case of nickel complexes (**5**)–(**6**) there are two losses of weight: the major one takes place between 110–350 °C and gives a residue that vaporizes almost completely at temperatures below 750 °C.

DSC measurements show a markedly different behaviour for the two metal centres. Nickel complexes are characterised by a strong endothermic peak (31.3 and 54.3 kJ mol^{-1}) at approximately the fusion temperatures 193 (**5**) and 180 (**6**) °C. For the palladium complexes the ΔH versus temperature diagram is much more complicated: low energy endothermic peaks (ca. 3 kJ mol^{-1}), probably associated to conformational processes, are observed, in addition to very intense peaks in the correspondence of state changes like fusion and evaporation.

The nickel complex (**5**) has been tested under MOCVD conditions to verify its suitability as precursor in the formation of thin films over glass or silicon substrates. Its high volatility allows rather accessible temperatures (130–133 °C) and pressures (3×10^{-2}–8×10^{-2} mbar), whereas the substrate was kept at 450 °C to ensure fast decomposition of the complex.

The film surface morphology was investigated by SEM (Fig. 3), confirming a uniform substrate coverage, typical of a three-dimensional growing, characterised by well-interconnected agglomerates with mean sizes around 100 nm.

The nature of the thin films depends on the employed carrier gases: use of N_2 and of O_2 gives nickel metal and nickel oxide respectively, whereas a mixture of water with either N_2 or O_2 affords a co-deposition of both. The presence of nickel oxide in the

Table 1
Thermal data for complexes (**1**)–(**6**) and for [M($\mathbf{L^{Et}}$)$_2$] (M = Pd, Ni).

Complex	m. p.	DSC		TGA	
	(°C)	T (°C)	ΔH (kJmol^{-1})	T (°C) range	Wt.% loss
(**1a**)	178 (dec.)	93	2.9	70–150	2.2
		129	12.9	150–290	58.66
		194	1.9	290–950	12.15
(**1b**)	210-220 (dec.)	196	18.2	110–320	68.63
		216	0.6	320–950	10.73
		242	17.4		
[Pd($\mathbf{L^{Et}}$)$_2$] form **a**[a]	>250	178–301	142.2	150–440	75.44
				440–915	6.16
[Pd($\mathbf{L^{Et}}$)$_2$] form **b**[a]	>250	117	19.9	130–290	68.3
		208–310	101.2	290–935	6.95
(**2**)	194–199 (dec.)	178	0.4	115–300	78.28
		190	3	300–950	13.68
		220	4.8		
		250	17.2		
(**3**)	195–200 (dec.)	223	55.3	130–285	71.83
		246	6.9	285–950	9.25
(**4**)	189 (dec)	148	3.2	185–290	74.95
		212	1.4	290–950	8.79
		220	31.7		
(**5**)	193	197	31.3	210–350	92.42
				350–950	5.61
[Ni($\mathbf{L^{Et}}$)$_2$][a]	183	126	17.3	150–280	92.6
		183	31.2	280–900	6.6
		322	95.7		
(**6**)	178–181 (dec.)	182	54.3	110–310	93.9
				310–950	6.22

[a] The synthesis and characterisation of these complexes have been reported in Ref. [3].

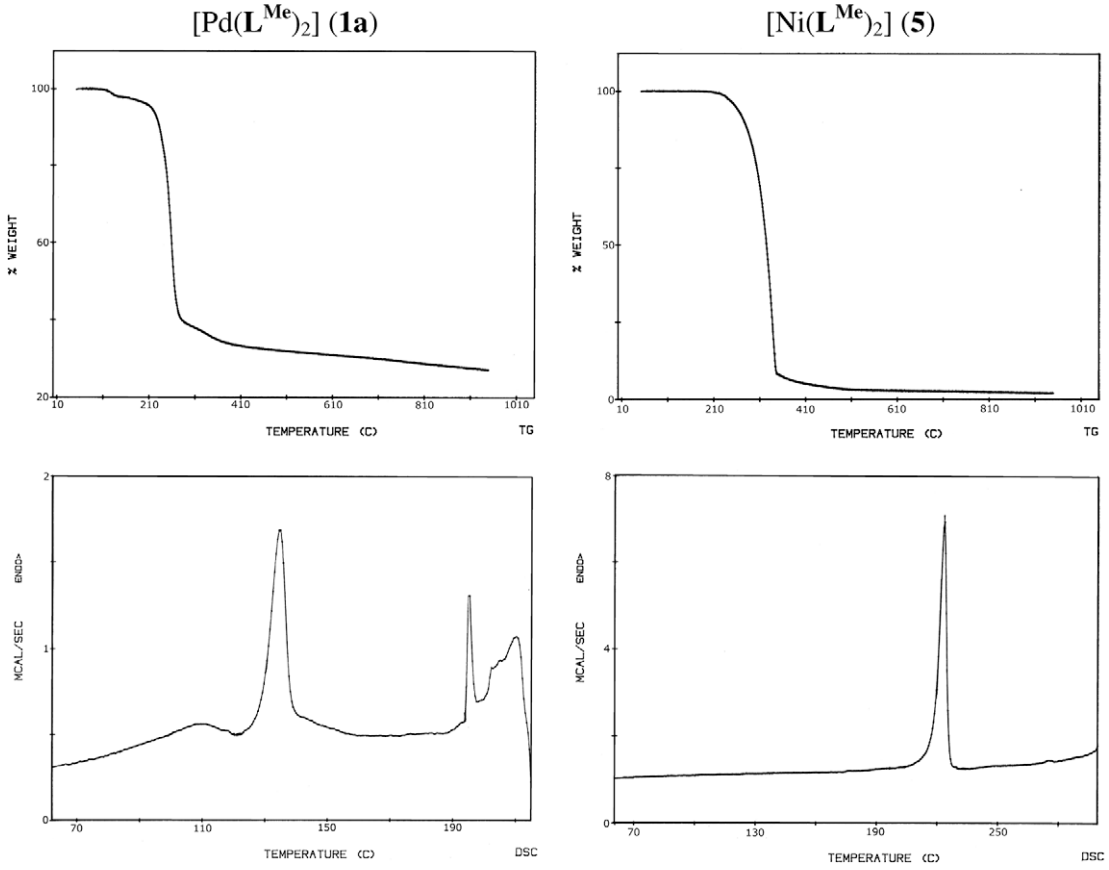


Fig. 2. Comparison of the thermal behaviour (TGA and DSC) of complexes (**1a**) and (**5**).

films obtained under nitrogen can not be detected by X-ray technique, even if ESCA analysis indicates the presence of NiO (see further); these results suggest an amorphous phase for NiO [15]. X-rays analysis on the deposited films reveals a preferential

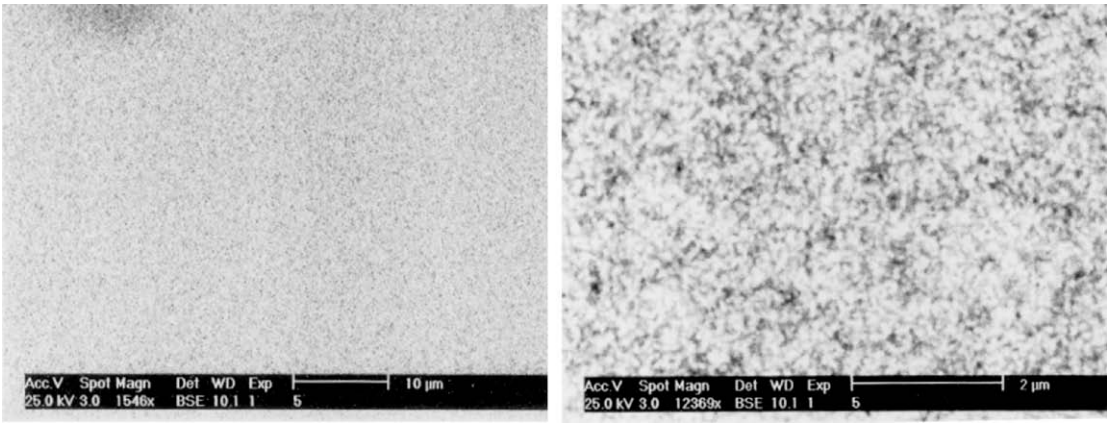


Fig. 3. Selected SEM images of the thin films deposited on glass using $O_2 + H_2O$ carrier.

Table 2
Superficial composition of films obtained by MOCVD of complex [Ni($\mathbf{L^{Me}}$)$_2$] (**5**).

Substrate/carrier	Si/N_2	Glass/O_2	Si/O_2 + H_2O	Glass/O_2 + H_2O
C/%	64.0	21.0	47.7	51.4
O/%	18.3	40.7	26.6	25.4
Ni/%	15.4	32.9	24.7	22.0
N/%	2	0	1	1
Si/%	0	5.0	0	0

orientation (1 1 1) for nickel metal and (2 0 0) plus (1 1 1) for nickel oxide.

The superficial composition determined by ESCA (Table 2) shows in all cases a high carbon content, mostly due to a superficial contamination, and very low quantity of nitrogen derived from ligand decomposition.

Silicon is practically absent in the surface so ensuring a good homogeneity of the deposit. The Ni/O ratio is within the experimental errors close to 1. Analysis of the films deposited in the presence of water reveals two contributions to the O1s peak: the first one at 529.9 eV is attributed to Ni–O bonds in the NiO, whereas the contribution at higher binding energy (531.6 eV) suggest the presence of OH groups present on the NiO surface [16–18]. The Ni2p peaks are found at a value consistent with literature data for NiO with hydroxyl groups on the surface [17]; the NiO (1 1 1) faces can be in fact stabilised by hydroxylation [19].

4. Conclusions

In conclusion, the synthesis of β-imino carbonyl enolato complexes of palladium(II) and nickel(II), by reaction of the acetato salt and the required β-enaminodione, appears rather general. The obtained complexes are square planar, stable and volatile, with a limited effect of the imino alkyl chain on their thermal behaviour. The N,O square planar coordination observed also for nickel(II) complexes is particularly interesting, because it makes possible to utilize, for example, [Ni($\mathbf{L^{Me}}$)$_2$], as convenient MOCVD precursor for the production of Ni or NiO thin films. It should be underlined that O,O coordination to nickel(II), as in β-carbonyl enolato complexes, gives rise to octahedral high melting, non volatile, oligomeric *via* O-bridges structures [20].

Acknowledgement

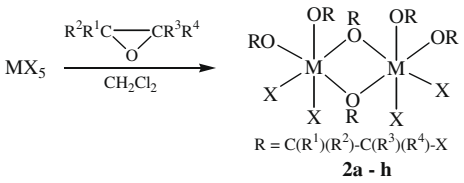
We thank Mr.A. Ravazzolo for skilled technical assistance.

Appendix A. Supplementary data

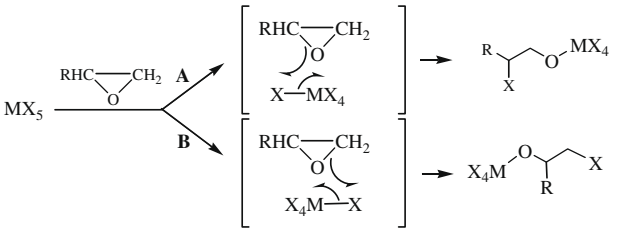
Supplementary data associated with this article can be found, in the online version, at doi:10.1016/j.poly.2009.02.017.

References

[1] M. Basato, B. Corain, G. Zanotti, J. Chem. Soc., Dalton Trans. (1992) 3003.
[2] (a) M. Basato, M. Bortolussi, E. Faggin, C. Tubaro, A.C. Veronese, Inorg. Chim. Acta 362 (2009) 531;
(b) M. Basato, G. Favero, A.C. Veronese, A. Grassi, Inorg. Chem. 32 (1993) 763.
[3] M. Basato, U. Vettori, A.C. Veronese, A. Grassi, G. Valle, Inorg. Chem. 37 (1998) 6737.
[4] A.C. Veronese, C.F. Morelli, R. Callegari, M. Basato, J. Mol. Catal. A: Chem. 124 (1997) 99.
[5] M. Basato, E. Caneva, C. Tubaro, A.C. Veronese, Inorg. Chim. Acta (2008), doi:10.1016/j.ica.2008.11.017.
[6] B. Corain, M. Basato, A.C. Veronese, J. Mol. Catal. 81 (1993) 133.
[7] E.C. Constable, Metals and Ligand Reactivity, VCH, Weinheim, 1995.
[8] N.S. Simpkins (Ed.), 100 Modern Reagents, The Royal Society of Chemistry, London, 1989.
[9] M.L. Hitchman, K.F. Jensen, Chemical Vapor Deposition: Principles and Applications, Academic Press, London, 1993.
[10] E. Brescacin, M. Basato, E. Tondello, Chem. Mater. 11 (1999) 314.
[11] A.C. Veronese, V. Gandolfi, M. Basato, B. Corain, J. Chem. Res. (S) (1988) 246.
[12] A.C. Veronese, V. Gandolfi, M. Basato, B. Corain, J. Chem. Res. (M) (1988) 1843.
[13] G. Carta, N. El Habra, L. Crociani, G. Rossetto, P. Zanella, A. Zanella, G. Paolucci, D. Barreca, E. Tondello, Chem. Vap. Deposition 13 (2007) 185.
[14] D.A. Thornton, Coord. Chem. Rev. 104 (1990) 173.
[15] M. Becht, F. Atamny, A. Baiker, K.-H. Dahemen, Surf. Sci. 371 (1997) 399.
[16] J.F. Moulder, W.F. Stickle, P.E. Sobol, K.D. Bomben, Handbook of X-ray Photoelectron, J. Chastain, Perkin Elmer Corporation, USA, 1992.
[17] (a) R.P. Furstenau, G. McDougall, M.A. Langell, Surf. Sci. 150 (1985) 55;
(b) N.S. McIntyre, M.G. Cook, Anal. Chem. 47 (1975) 2208.
[18] M.M. Natile, A. Glisenti, Chem. Mater. 14 (2002) 4895.
[19] (a) M.A. Langell, M.H. Nassir, J. Phys. Chem. 99 (1995) 4162;
(b) D. Cappus, C. Xu, D. Ehrlich, B. Dillmann, C.A. Ventrice Jr., K. Al Shamery, H. Kuhlenbeck, H.-J. Freund, Chem. Phys. 177 (1993) 533.
[20] R.C. Mehrotra, R.C. Bohra, D.P. Gaur, Metal β-Diketonates and Allied Derivatives, Academic Press, New York, 1978.



Scheme 1. The reactivity of MX_5 (M = Nb, Ta; X = Cl, Br) with epoxides.



Scheme 2. Possible routes of formation of the haloalcoholato fragment.

by studying the reactions of $NbCl_5$ with styrene oxide and epoxycyclohexane (vide infra).

The compounds **2a**–**h** have been characterized spectroscopically (IR and NMR), by elemental analyses, and by X-ray diffraction in the case of **2h** (Fig. 1 and Table 1).

The unit cell contains discrete dinuclear $[TaBr_2(OCH_2CH_2Br)_2(\mu\text{-}OCH_2CH_2Br)]_2$ molecules, which reside on a crystallographic inversion centre. The dimeric species adopts an edge sharing bioctahedral geometry, with four terminal bromide ligands in the axial positions (*trans* geometry). Conversely, the equatorial plane is occupied by four terminal and two bridging haloalcoholates. All bonding distances are comparable with those previously reported for Ta(V)–Br and Ta(V)–OR containing complexes [6]. The bridging ligand is almost symmetric [Ta(1)–O(1) 2.091(11) Å; Ta(1)–O(1)#1 2.107(10) Å], and these contacts are considerably elongated compared to the ones referring to the terminal haloalcoholates [Ta(1)–O(2) 1.818(9) Å; Ta(1)–O(3) 1.822(10) Å].

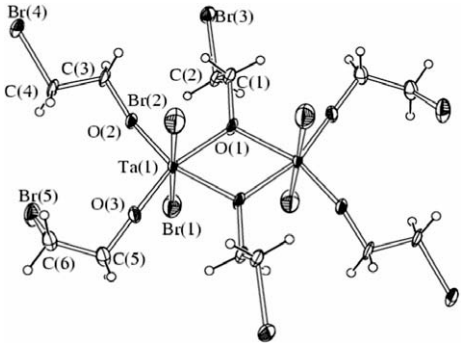


Fig. 1. Molecular structure of $[TaBr_2(OCH_2CH_2Br)_2(\mu\text{-}OCH_2CH_2Br)]_2$, **2h**. Thermal ellipsoids are drawn at the 30% probability level. Only independent atoms are labelled.

Table 1
Selected bond distances (Å) and angles (°) of $[TaBr_2(OCH_2CH_2Br)_2(\mu\text{-}OCH_2CH_2Br)]_2$, **2h**.

Ta(1)–Br(1)	2.459(2)	C(2)–Br(3)	1.97(2)
Ta(1)–Br(2)	2.466(3)	O(2)–C(3)	1.43(2)
Ta(1)–O(1)	2.091(11)	C(3)–C(4)	1.52(3)
Ta(1)–O(1)#1	2.107(10)	C(4)–Br(4)	1.93(2)
Ta(1)–O(2)	1.818(9)	O(3)–C(5)	1.418(19)
Ta(1)–O(3)	1.822(10)	C(5)–C(6)	1.50(2)
O(1)–C(1)	1.50(2)	C(6)–Br(5)	1.950(16)
C(1)–C(2)	1.48(3)		
O(2)–Ta(1)–O(3)	105.8(5)	O(1)–Ta(1)–Br(1)	89.8(3)
O(2)–Ta(1)–O(1)	92.4(4)	O(1)#1–Ta(1)–Br(1)	90.0(3)
O(3)–Ta(1)–O(1)	161.8(4)	O(2)–Ta(1)–Br(2)	88.4(3)
O(2)–Ta(1)–O(1)#1	160.3(4)	O(3)–Ta(1)–Br(2)	91.4(3)
O(3)–Ta(1)–O(1)#1	93.8(4)	O(1)–Ta(1)–Br(2)	89.6(3)
O(1)–Ta(1)–O(1)#1	68.0(5)	O(1)#1–Ta(1)–Br(2)	89.6(3)
O(2)–Ta(1)–Br(1)	91.8(3)	Br(1)–Ta(1)–Br(2)	179.34(8)
O(3)–Ta(1)–Br(1)	89.2(3)	Ta(1)–O(1)–Ta(1)#1	112.0(5)

Symmetry transformations used to generate equivalent atoms: #1 $-x+1/2, -y+1/2, -z+2$.

Compounds **2** add to the family of transition metal alcoholato complexes [7], which have found various applications (film-deposition [8], nanotechnology [9], polymerization catalysis [10] and the preparation of materials with notable properties [11]); and in more detail, cases of structurally characterized metal complexes containing 2-haloalcoholates are available in the literature, including both late [12] and early transition [13] metal species.

Regarding niobium(V) and tantalum(V), although examples of pentaalcoholates are numerous [14a–e], only a few mixed halide-alcoholates $[MX_n(OR)_{5-n}]_2$ have been crystallographically characterized so far [14f–i]. Complexes **2** belong to this rather uncommon class of compounds [15], and represent the first case of structurally characterized coordination compounds of the heavier Group 5 elements containing halo-substituted alcoholates.

The NMR spectra of **2a**, **c**, **e** and **f** exhibit slightly distinct resonances for the terminal and bridging ligands (see Section 4) [13], and agree with the dinuclear structure $[MX_2(OR)_2(\mu\text{-}OR)]_2$. For instance, the methyl units belonging to the $OC(Me)_2$ moieties in **2c** give rise to resonances at 1.70 (bridging ligands) and 1.58 ppm (terminal) in the ^1H NMR spectrum, and at 29.1 (bridging) and 28.9 ppm (terminal) in the ^{13}C NMR spectrum. On the other hand, the ^1H NMR spectra of **2b**, **d** and **g** display only broad resonances, for which discrimination between terminal and bridging ligands has not been possible. In contrast to the previous observations on some niobium or tantalum alkoxides, no dimer–monomer equilibria [13,16] have been detected in solution at room temperature for compounds **2**.[2]

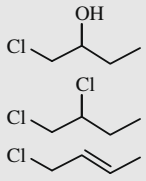
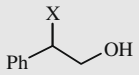
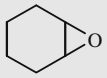
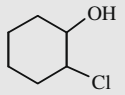
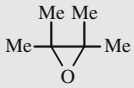
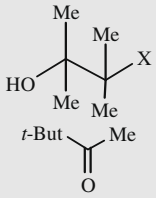
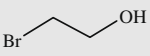
It is worthy noting that the formal insertion of 1,2-epoxybutane into the metal–halide bond could in principle generate two isomeric forms, according to the site of attack of the halide, see Scheme 2.

A careful reading of the 1D and 2D NMR spectra of **2a** and **f** has evidenced the absence of resonances attributable to $-OCH_2$-CH(Et)Cl units [6c,6d], suggesting that multiple 1,2-epoxybutane insertion into the metal–chloride bonds of MCl_5 (M = Nb, Ta) occurs in a highly regioselective mode (Scheme 2, path B), placing the halide on the less hindered carbon atom.

The NMR spectra of **2b** and **d**, obtained by reacting NbX_5 (X = Cl, Br) with styrene oxide, do not allow, unambiguously, the formation of any of the species obtainable by the two potential modes of insertion to be ruled out (see Scheme 2). Nevertheless, the hydrolysis of $CDCl_3$ solutions of complexes **2b** and **d**, and subsequent GC–MS and NMR analyses on the organic phase, have pointed out that either **2b** or **2d** contain the $[OCH_2CH(Cl)Ph]$ fragment (entry 2, Table 2). In other words, the insertion of styrene oxide to give **2b** and **d** seems to proceed, differently from the insertion of 1,2-epoxybutane, according to path A of Scheme 2, the halide going to the more hindered carbon atom. This feature may be attributable to the steric hindrance of the phenyl ring, which would force this ligand to occupy the farthest position from the metal centre.

[2] NMR experiments could not be run on complex **2h**, because of its low solubility in suitable deuterated solvents ($CDCl_3$, CD_2Cl_2).

Table 2
Products of hydrolysis of compounds **2a**–**h**.

Entry	Epoxide	Haloalkoxo derivative	Hydrolysis product
1		**2a**, **f**[a]	
2		**2b**, **d**[b]	
3		**2g**	
4		**2c**, **e**[b]	
5		**2h**	

[a] 1,2-Dichlorobutane and 1-chloro-2-butene have been detected probably due to the action of HCl, product of the hydrolysis, on 1-chloro-2-butanol.
[b] X = Cl, Br.

The identities of products **2a**–**h** have been corroborated by combined GC–MS and NMR analyses on concentrated $CDCl_3$ solutions of these compounds after treatment with H_2O, see Section 4 and Table 2. The addition of water causes the quick precipitation of a white solid (probably metal oxides), and release of the organic material. The hydrolysis of **2c** (entry 4, Table 2) deserves more comment: beside 2,3-dimethyl-3-chloro-2-butanol, minor amounts of *t*-butylmethylketone have been observed by NMR and GC–MS analyses, suggesting that pathways alternative to the insertion (see Scheme 1) may be operating, at least for the reaction of 2,3-dimethyl-2,3-epoxybutane with $NbCl_5$.

With the purpose of extending the series of halo-2-haloalcoholato complexes of type **2**, we studied the reactivity of $NbBr_5$ with 1,2-epoxybutane and with epoxycyclohexane. Unfortunately, these reactions afforded mixtures of compounds which could not be separated and characterized. Nonetheless, GC–MS and NMR analyses on the reaction mixtures treated with water led to the identification of 1,2-dibromobutane and 1-bromo-2-butene from $NbBr_5$ and 1,2-epoxybutane, and of 2-bromocyclohexanol and 1,2-dibromocyclohexane from $NbBr_5$ and epoxycyclohexane. These results indicate that the reactions of 1,2-epoxybutane and epoxycyclohexane with $NbBr_5$ proceed *via* epoxide insertions, analogously to that discussed for **2a**–**h**.

2.2. Reactivity of MF_5 (M = Nb, Ta) with epoxides: isomerisation of 2,3-dimethyl-2,3-epoxybutane to 3,3-dimethyl-2-butanone

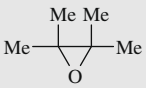
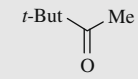
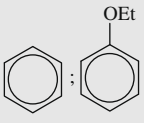
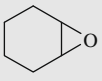
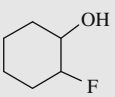
According to our recent reports, the reactivity of niobium and tantalum pentahalides with oxygen-donor ligands is strongly influenced by the metal–halide bond energy [6a,6b], and the fluorides often show a chemistry quite different from that of the other halides. Therefore, we decided to investigate the reactivity of MF_5 (M = Nb, Ta) with epoxides, with the aim to see whether insertion reactions could take place, despite the high value of the metal–fluoride bond energy [17].

Niobium pentafluoride and 2,3-dimethyl-2,3-epoxybutane react to afford the ketone complex $NbF_5[O{=}C(Me)(^tBu)]$, **3**, in *ca.* 90% yield. This reaction is strictly stoichiometric: the same reaction, carried out by using variable epoxide to metal ratios greater than 1, resulted in the formation of **3** in an admixture with the unreacted epoxide. Complex **3**, which belongs to the restricted family of carbonylic adducts of Group 5 pentahalides [6a], has been characterized spectroscopically (^1H, ^{13}C and ^{19}F NMR, IR) and by GC–MS analysis carried out on the organic material obtained by hydrolysis of **3** (entry 1, Table 3). A salient spectroscopic feature is given by a strong IR absorption at 1647 cm^{-1}, ascribed to the carbon–oxygen double bond (uncoordinated *t*-butylmethylketone shows the C=O stretching vibration at 1708 cm^{-1}, recorded as a liquid film). The ^1H NMR spectrum displays one set of two resonances, attributed to the methyl unit (s, 2.84 ppm) and the *t*-butyl group (s, 1.41 ppm). The major ^{13}C NMR aspect is given by the carbonylic resonance, seen at 245.6 ppm, *i.e.* significantly downfield-shifted with respect to the resonance of the uncoordinated ketone (δ = 213.81 ppm). Furthermore, the ^{19}F NMR spectrum shows uniquely a broad resonance at 145.8 ppm, accounting for the five fluorines of the $[NbF_5]$ moiety, and indicating the monomeric, neutral nature of **3**.

In contrast to that discussed about the reaction of $NbCl_5$ with 2,3-dimethyl-2,3-epoxybutane, which affords some *t*-butylmethylketone as result of HCl release and subsequent hydrolysis (vide infra), the formation of *t*-butylmethylketone in the case of NbF_5 is probably the consequence of direct epoxide isomerisation promoted by niobium fluoride. This latter rearrangement has been reported to occur under the assistance of various metal species, including high valent vanadium [18], cobalt [19], erbium [20], bismuth [21] and lithium [22] compounds.

We tried to extend the chemistry of niobium and tantalum pentafluorides to a series of epoxides (1,2-epoxybutane, styrene oxide and epoxycyclohexane). At variance with that reported

Table 3
Reactants and main products (after hydrolysis) of the reactions of MF_5 with epoxides.

Entry	M	Epoxide	Hydrolysis product
1	Nb		
2	Nb, Ta		
3	Ta		
4	Ta		

above about the synthesis of **3**, the reactions of MF_5 with epoxides other than 2,3-dimethyl-2,3-epoxybutane led to complicated mixtures of products. We did not succeed in the characterization of the inorganic species, but we were able to identify some of the organic compounds produced in the course of the reactions, and released from the metallic frames upon hydrolysis (see Table 3). Thus, ethylmethylketone has been recognized in the mixture obtained from NbF_5 or TaF_5 and 1,2-epoxybutane (entry 2, Table 3): accordingly, this reaction proceeds with epoxide rearrangement, similar to that described for 2,3-dimethyl-2,3-epoxybutane (entry 1, Table 3).

Conversely, no traces of acetophenone and cyclohexanone have been found in the hydrolyzed mixtures generated from the reactions of TaF_5 with styrene oxide and epoxycyclohexane, respectively. Therefore, alternative pathways are likely to be operating in these two cases. More precisely, benzene and ethoxybenzene have been recognized (GC–MS and NMR) as the main products from the treatment of TaF_5 with styrene oxide followed by hydrolysis (entry 3, Table 3). Furthermore, GC–MS and NMR analyses on a sample obtained by addition of epoxycyclohexane to TaF_5, and successive hydrolysis, revealed the presence of small amounts of 2-fluorocyclohexanol (entry 4, Table 3). All these organics prove that C–C and C–H bond activation, together with C–O and C–F bond formation, are possible processes taking place in the course of the reactions of MF_5 (M = Nb, Ta) with epoxides.

3. Conclusions

The strong oxophilicity of niobium and tantalum pentahalides is tested in the room temperature reactions with epoxides, in a 1:3 molar ratio, which proceed rapidly, exothermically and regioselectively. Multiple epoxide ring opening and insertion into metal–chloride (or bromide) bonds give novel stable dinuclear species containing both halide and 2-haloalcoholato ligands. Although MF_5 (M = Nb, Ta) are very reactive towards epoxides, the relatively high metal–fluoride bond energy inhibits insertion reactions. Several alternative pathways appear to be operative concurrently; among them, epoxide to ketone isomerization prevails in some cases.

4. Experimental

4.1. General procedures

All manipulations of air and/or moisture sensitive compounds were performed under an atmosphere of pre-purified argon using standard Schlenk techniques. The reaction vessels were oven dried at 150 °C prior to use, evacuated (10^{-2} mm Hg) and then filled with argon. All the reagents, including MX_5 (M = Nb, Ta, X = Cl; M = Nb, Ta, X = F), were commercial products (Aldrich) of the highest purity available. $NbBr_5$ and $TaBr_5$ were prepared according to published procedures [23]. Epoxides were liquid commercial products stored under an argon atmosphere as received. Solvents were distilled before use under an argon atmosphere from appropriate drying agents: CH_2Cl_2 and $CDCl_3$ from P_4O_{10}, pentane from $LiAlH_4$.

Infrared spectra were recorded at 298 K on a FT-IR Perkin–Elmer Spectrometer equipped with a UATR sampling accessory (solid samples). NMR measurements were performed at 298 K on Varian Gemini 200BB and Mercury Plus 400 instruments. The chemical shifts for ^1H, ^{13}C and ^{19}F NMR spectra were referenced to TMS and to $CFCl_3$, respectively. The chemical shifts were assigned *via* DEPT experiments and ^1H, ^{13}C correlation through gs-HSQC and gs-HMBC experiments [24]. NMR assignments related to terminal and bridging ligands have been specified only where a distinction has been possible. GC/MS analyses were performed on a HP6890 instrument, interfaced with a MSD-HP5973 detector and equipped with a Phenonex Zebron column. Carbon and hydrogen analyses were performed at the Dipartimento di Chimica Farmaceutica of the University of Pisa on a Carlo Erba mod. 1106 instrument, paying particular attention to the sensitive compounds, which were weighed and directly introduced into the analyzer. The halide content refers to the metal-bound halides, and was determined by the Volhardt method [25] after exhaustive hydrolysis of the sample. Metals were analyzed as M_2O_5, obtained by hydrolysis of the sample followed by calcination in a platinum crucible. Every elemental analysis was repeated twice in order to get reproducible results.

4.2. Preparation of $[MX_2(OR)_2(\mu\text{-}OR)]_2$ [M = Nb, X = Cl, R = –CH(Et)CH_2Cl, **2a**; M = Nb, X = Cl, R = –CH_2CH(Ph)Cl, **2b**; M = Nb, X = Cl, R = –C(Me)$_2$C(Me)$_2$Cl, **2c**; M = Nb, X = Br, R = –CH_2CH(Ph)Br, **2d**; M = Nb, X = Br, R = –C(Me)$_2$C(Me)$_2$Br, **2e**; M = Ta, X = Cl, R = –CH(Et)CH_2Cl, **2f**; M = Ta, X = Cl, R = –$\overline{CH(CH_2)_4CHCl}$, **2g**; M = Ta, X = Br, R = –CH_2CH_2Br, **2h**]

General procedure: A suspension of MX_5 (M = Nb, Ta; X = Cl, Br; 1.00 mmol), in CH_2Cl_2 (15 mL) inside a Schlenk tube, was treated with the appropriate epoxide (3.00 mmol). In the case of the synthesis of **2h**, ethylene oxide was added as a CH_2Cl_2 solution (50 mg/mL). Dissolution of the solid and a colour change occurred rapidly and exothermically. The mixture was stirred for an additional 30 min, then the final solution was concentrated (3 mL), layered with pentane (15 mL) and stored at −20 °C. The product was obtained as a solid after 48–72 h. In a different experiment, MX_5 (0.50 mmol) was introduced into a NMR tube, then $CDCl_3$ (0.85 mL) and epoxide (1.50 mmol) were added in the order given. The ^1H NMR analysis was performed once the solid dissolved: complete consumption of the epoxide occurred. Afterwards, the mixture was treated with a large excess of H_2O (*ca.* 20 mmol): precipitation of a colourless solid took place nearly instantaneously. The content of the resulting solution was determined by means of ^1H and ^{13}C NMR spectroscopies, and by GC–MS analysis.

2a: orange, from $NbCl_5$ and 1,2-epoxybutane. *Anal.* Calc. for $C_{24}H_{48}Cl_{10}Nb_2O_6$[3]: C, 29.63; H, 4.97; Nb, 19.10; Cl, 14.58. Found: C, 29.44; H, 5.06; Nb, 18.90; Cl, 14.19%. Yield: 0.312 g, 64%. ^1H NMR ($CDCl_3$) δ = 5.05–4.81 (m-br, 6H, CH); 4.74–3.82 (m-br, 12H, $ClCH_2$); 1.95, 1.90, 1.63 (m-br, 12H, CH_2CH_3); 1.06 (m-br, 18H, CH_3) ppm. ^{13}C NMR ($CDCl_3$) δ = 63.4, 62.8 [$(CH)_{terminal}$ and $(CH)_{bridging}$]; 46.3, 45.2 [$(ClCH_2)_{terminal}$ and $(ClCH_2)_{bridging}$]; 27.9, 26.9 [$(CH_2CH_3)_{terminal}$ and $(CH_2CH_3)_{bridging}$]; 10.9 (CH_3) ppm. IR (solid state): ν = 2975w-m, 1448 m, 1378 m, 1051s, 903s, 783vs cm^{-1}. Hydrolysis (entry 1, Table 2): 1-chloro-2-butanol, 1,2-dichlorobutane, 1-chloro-2-butene (NMR and GC–MS); ratio 4:2:1 (^1H NMR).

2b: orange, from $NbCl_5$ and styrene oxide. *Anal.* Calc. for $C_{48}H_{48}Cl_{10}Nb_2O_6$[3]: C, 45.71; H, 3.84; Nb, 14.73; Cl, 11.24. Found: C, 45.66; H, 3.97; Nb, 14.43; Cl, 11.01%. Yield: 0.366 g, 58%. ^1H NMR ($CDCl_3$) δ = 7.69–6.89 (br, 30H, *arom* CH); 5.18 (m-br, 6H, CHCl); 4.16 (br, 12H, CH_2) ppm. ^{13}C NMR ($CDCl_3$) δ = 137.9, 137.2 [(*ipso*-Ph)$_{bridging\ and\ terminal}$]; 128.6, 127.4 (*arom* CH); 65.2 (CHCl); 60.7, 59.9 [$(CH_2)_{terminal}$ and $(CH_2)_{bridging}$] ppm. Hydrolysis (entry 2, Table 2): 2-phenyl-2-chloroethanol (NMR and GC–MS).

2c: yellow, from $NbCl_5$ and 2,3-dimethyl-2,3-epoxybutane. *Anal.* Calc. for $C_{36}H_{72}Cl_{10}Nb_2O_6$[3]: C, 37.89; H, 6.36; Nb, 16.28; Cl, 12.42. Found: C, 37.77; H, 6.19; Nb, 16.10; Cl, 12.23%. Yield: 0.337 g, 59%. ^1H NMR ($CDCl_3$) δ = 1.70 [s, 12H, $(OCMe_2)_{bridging}$]; 1.58 [s, 24H, $(OCMe_2)_{terminal}$]; 1.27 (s, 36H, CMe_2Cl) ppm. ^{13}C NMR ($CDCl_3$) δ = 80.7 ($OCMe_2$); 75.8, 74.4 [$(CMe_2Cl)_{terminal}$ and $(CMe_2Cl)_{bridging}$]; 29.1 [$(OCMe_2)_{bridging}$]; 28.9 [$(OCMe_2)_{terminal}$]; 25.2, 24.2 [$(CMe_2Cl)_{terminal}$ and $CMe_2Cl)_{bridging}$] ppm. IR (solid state):

[3] Due to the fact that the carbon-bonded halide does not precipitate with silver nitrate under the conditions used for the analysis, the halide content refers to the metal-bonded halide ion.

ν = 2979w, 2936w, 2886w, 1447wm, 1384m, 1321wm, 1119m, 1097s, 1072s, 1043vs, 977m, 951s, 932vs, 831s, 811m, 674vs, 661s cm^{-1}. Hydrolysis (entry 4, Table 2): 2,3-dimethyl-3-chloro-2-butanol, *t*-butylmethylketone (NMR and GC–MS); ratio 5:1 (^{1}H NMR).

In a NMR tube, 2,3-dimethyl-2,3-epoxybutane (1.50 mmol) was added to $NbCl_5$ (0.50 mmol) in $CDCl_3$ (0.70 mL). An exothermic reaction took place accompanied by gas (HCl) evolution, and the solid quickly dissolved.

2d: light yellow, from $NbBr_5$ and styrene oxide. *Anal.* Calc. for $C_{48}H_{48}Br_{10}Nb_2O_6$[3]: C, 33.80; H, 2.84; Nb, 10.89; Br, 18.74. Found: C, 33.90; H, 2.88; Nb, 10.71; Br, 18.55%. Yield: 0.512 g, 60%. ^{1}H NMR ($CDCl_3$) δ = 7.69–7.25 (br, 30H, *arom* CH); 5.28 (m-br, 6H, CHCl); 4.67 (br, 12H, CH_2) ppm. Hydrolysis (entry 2, Table 2): 2-phenyl-2-bromoethanol (NMR and GC–MS).

2e: yellow, from $NbBr_5$ and 2,3-dimethyl-2,3-epoxybutane. *Anal.* Calc. for $C_{36}H_{72}Br_{10}Nb_2O_6$[3]: C, 27.27; H, 4.58; Nb, 11.71; Br, 20.16. Found: C, 27.11; H, 4.66; Nb, 11.60; Br, 19.95%. Yield: 0.484 g, 61%. ^{1}H NMR ($CDCl_3$) δ = 1.84 [s, 12H $(OCMe_2)_{bridging}$]; 1.75 [s, 24H, $(OCMe_2)_{terminal}$]; 1.36, 1.32 [s, 36H, $(CMe_2Br)_{terminal}$ and $(CMe_2Br)_{bridging}$] ppm. ^{13}C NMR ($CDCl_3$) δ = 80.7 ($OCMe_2$); 75.8, 74.4 [$(CMe_2Br)_{terminal}$ and $(CMe_2Br)_{bridging}$]; 29.1 [$(OCMe_2)_{bridging}$]; 28.9 [$(OCMe_2)_{terminal}$]; 25.2, 24.2 [$(CMe_2Br)_{terminal}$ and $CMe_2Br)_{bridging}$] ppm. IR (solid state): ν = 2979w, 2936w, 2886w, 1447wm, 1384m, 1321wm, 1119m, 1097s, 1072s, 1043vs, 977m, 951s, 932vs, 831s, 811m, 674vs, 661s cm^{-1}. Hydrolysis (entry 4, Table 2): 2,3-dimethyl-3-bromo-2-butanol (NMR and GC–MS).

2f: dark yellow, from $TaCl_5$ and 1,2-epoxybutane. *Anal.* Calc. for $C_{24}H_{48}Cl_{10}O_6Ta_2$[3]: C, 25.09; H, 4.21; Ta, 31.50; Cl, 12.34. Found: C, 25.21; H, 4.07; Ta, 31.29; Cl, 12.12%. Yield: 0.368 g, 64%. ^{1}H NMR ($CDCl_3$) δ = 5.26–4.78 (m-br, 6H, CH); 4.62–3.53 (m-br, 12H, $ClCH_2$); 1.95, 1.82, 1.67, 1.54 (m-br, 12H, CH_2CH_3); 1.02 [t, $^3J_{HH}$ = 6.59 Hz, 12 H, $(CH_3)_{terminal}$]; 0.90 [*t*, $^3J_{HH}$ = 8.05 Hz, 6 H, $(CH_3)_{bridging}$] ppm. ^{13}C NMR ($CDCl_3$) δ = 62.9, 62.4 [$(CH)_{terminal}$ and $(CH)_{bridging}$]; 46.4, 45.3 [$(ClCH_2)_{terminal}$ and $(ClCH_2)_{bridging}$]; 27.4, 27.3 [$(CH_2CH_3)_{terminal}$ and $(CH_2CH_3)_{bridging}$]; 10.4 [$(CH_3)_{terminal}$]; 9.3 [$(CH_3)_{bridging}$] ppm. Hydrolysis (entry 1, Table 2): 1-chloro-2-butanol, 1,2-dichlorobutane, 1-chloro-2-butene (NMR and GC–MS); ratio 5:2:1 (^{1}H NMR).

2g: orange, from $TaCl_5$ and epoxycyclohexane. *Anal.* Calc. for $C_{36}H_{60}Cl_{10}O_6Ta_2$[3]: C, 33.13; H, 4.63; Ta, 27.73; Cl, 10.86. Found: C, 33.03; H, 4.68; Ta, 27.60; Cl, 10.61%. Yield: 0.359 g, 55%. ^{1}H NMR ($CDCl_3$) δ = 4.92 (m-br, 6H, CHCl); 4.22 (m-br, 6H, OCH); 2.32, 1.74, 1.31 (m-br, 48H, CH_2) ppm. IR (solid state): ν = 2944w, 2863w, 1595m, 1448m, 1362m, 1259s, 1205w, 1079s, 1050s, 1023s, 977ms, 794vs, 738s, 666s cm^{-1}. Hydrolysis (entry 3, Table 3): 2-chlorocyclohexanol (NMR and GC–MS).

2h: light yellow, from $TaBr_5$ and ethylene oxide. *Anal.* Calc. for $C_{12}H_{24}Br_{10}O_6Ta_2$[3]: C, 10.11; H, 1.70; Ta, 25.39; Br, 22.42. Found: C, 10.13; H, 1.66; Ta, 25.23; Br, 22.19%. Yield: 0.499 g, 70%. IR (solid state): ν = 2965w, 2906w, 1470w-m, 1434m, 1414m, 1368w-m, 1278m, 1214w, 1172m-s, 1122s, 1084vs, 1042s, 1014vs, 996m-s, 934vs, 861s, 763m, 737m, 697s, 678vs cm^{-1}. Hydrolysis (entry 5, Table 2): 2-bromoethanol (NMR and GC–MS).

4.3. Reactivity of $NbBr_5$ with 1,2-epoxybutane and epoxycyclohexane

General procedure: A suspension of $NbBr_5$ (1.00 mmol), in $CDCl_3$ (0.80 mL) inside a NMR tube, was treated with the appropriate epoxide (3.00 mmol). The tube was sealed, and left at room temperature overnight. Then, a ^{1}H NMR spectrum revealed that complete consumption of the epoxide had occurred, and formation of a complicated mixture of products had taken place. This mixture was treated with water (*ca.* 30 mmol), resulting in quick formation of a white precipitate. The precipitate was separated from the solution, which was analyzed by both GC–MS and ^{1}H NMR. From $NbBr_5$ and 1,2-epoxybutane: 1-bromo-2-butene, 1,2-dibromobutane (ratio 1:1). From $NbBr_5$ and epoxycyclohexane: 2-bromocyclohexanol, 1,2-dibromocyclohexane (ratio 3:1).

4.4. Preparation of $NbF_5[O{=}C(Me)(Bu^t)]$, **3**

A suspension of NbF_5 (0.120 g, 0.639 mmol) in CH_2Cl_2 was treated with 2,3-dimethyl-2,3-epoxybutane (0.082 mL, 0.64 mmol). The resulting mixture was stirred for 90 min, then the volatile materials were removed *under vacuum*. Compound **3** was obtained as a crystalline colourless solid by storing a CH_2Cl_2 solution (3 mL), layered with pentane (10 mL), at −20 °C for one week. Yield: 0.166 g, 90%. *Anal.* Calc. for $C_6H_{12}F_5NbO$: C, 25.02; H, 4.20; Nb, 32.25. Found: C, 24.90; H, 4.26; Nb, 32.11%. ^{1}H NMR ($CDCl_3$) δ = 2.84 (s, 3H, Me); 1.41 (s, 9H, Bu^t) ppm. ^{13}C NMR ($CDCl_3$) δ = 245.6 (CO); 48.5 (CMe_3); 26.7 (Me); 26.2 (CMe_3) ppm. ^{19}F NMR ($CDCl_3$) δ = 145.8 (br, 5F) ppm. IR (solid state): ν = 2979w-m, 2947w, 2881w, 1647s (C=O), 1482m, 1466m, 1404w-m, 1368m, 1293w, 1226w, 1146vs, 1054m, 994m, 923s, 797vs, 684vs cm^{-1}. In a different experiment, NbF_5 (0.55 mmol), $CDCl_3$ (0.85 mL) and 2,3-dimethyl-2,3-epoxybutane (0.50 mmol) were added in the order given in a NMR tube and the tube was sealed. The ^{1}H NMR spectrum, recorded when the solid dissolved (about 2 h), evidenced the clean formation of **3**. The tube was opened, and an excess of water was introduced (*ca.* 30 mmol). Precipitation of a colourless solid occurred nearly instantaneously. 3,3-Dimethyl-2-butanone was recognized in solution by both ^{1}H NMR and GC–MS.

The reaction of NbF_5 (0.05 mmol) with 2,3-dimethyl-2,3-epoxybutane (0.50 mmol), in $CDCl_3$ inside a sealed NMR tube, resulted in the clean formation of **3**, in an admixture with a large quantity of unreacted epoxide (ratio: 1:80 *ca.*). The ratio did not change on heating the solution at 120 °C for 30 min.

4.5. Reactivity of MF_5 (M = Nb, Ta) with epoxides (1,2-epoxybutane, styrene oxide, cyclohexene oxide)

General procedure: To a suspension of compound MF_5 (M = Nb, Ta; 0.50 mmol) in $CDCl_3$ (0.80 mL) inside a NMR tube, the appropriate epoxide was added (0.50 mmol). The tube was sealed, and left at room temperature overnight. A ^{1}H NMR spectrum revealed the complete consumption of the epoxide and the formation of a complicated mixture of unidentifiable products. The tube was opened, then the mixture was treated with a large excess of water (*ca.* 15 mmol), resulting in the quick precipitation of a solid from the pale yellow solution. The latter was analyzed by both GC–MS and ^{1}H NMR. From NbF_5 or TaF_5 and 1,2-epoxybutane (entry 2, Table 3): ethylmethylketone. From TaF_5 and cyclohexene oxide (entry 3, Table 3): 2-fluorocyclohexanol. From TaF_5 and styrene oxide (entry 4, Table 3): benzene, ethoxybenzene (ratio *ca.* 1:1).

4.6. X-ray crystallographic study

Crystal data and collection details for $[TaBr_2(OCH_2CH_2Br)_2(\mu\text{-}OCH_2CH_2Br)]_2$, **2h**, are reported in Table 4. The diffraction experiments were carried out on a Bruker APEX II diffractometer equipped with a CCD detector using Mo Kα radiation. Data were corrected for Lorentz polarization and absorption effects (empirical absorption correction SADABS) [26]. The structure was solved by direct methods and refined by full-matrix least-squares based on all data using F^2 [27]. The asymmetric unit contains only half of the molecule, whereas the second half is generated by an inversion centre. Hydrogen atoms bonded to C-atoms were fixed at calculated positions and refined by a riding model. All non-hydrogen atoms were refined with anisotropic displacement parameters.

Table 4
Crystal data and experimental details for **2h**.

Complex	**2h**
Formula	$C_{12}H_{24}Br_{10}O_6Ta_2$
Formula weight	1425.31
T (K)	100(2)
λ (Å)	0.71073
Crystal system	monoclinic
Space group	$C2/c$
a (Å)	12.2223(13)
b (Å)	10.4276(12)
c (Å)	23.080(3)
α (°)	90
β (°)	95.602(2)
γ (°)	90
Cell volume (Å^3)	2927.5(6)
Z	4
D_{calc}, g cm^{-3}	3.234
μ (mm^{-1})	21.144
$F(000)$	2560
Crystal size (mm)	0.17 × 0.15 × 0.14
θ limits (°)	2.57–25.03
Reflections collected	13415
Independent reflections [R_{int}]	2595 [0.0379]
Data/restraints/parameters	2595/100/192
Goodness on fit on F^2	1.051
R_1 ($I > 2\sigma(I)$)	0.0561
wR_2 (all data)	0.1835
Largest difference in peak and hole (e Å^{-3})	2.569/−4.554

The bridging $-CH_2CH_2Br$ group and a terminal one are disordered. Disordered atomic positions were split and refined using one occupancy parameter per disordered group and restrained to have similar geometries (SAME line in SHELXTL). Similar U restraints were applied to the C, Br and O atoms.

Supplementary data

CCDC 710805 contains the supplementary crystallographic data for $[TaBr_2(OCH_2CH_2Br)_2(\mu\text{-}OCH_2CH_2Br)]_2$, **2h**. These data can be obtained free of charge via http://www.ccdc.cam.ac.uk/conts/retrieving.html, or from the Cambridge Crystallographic Data Centre, 12 Union Road, Cambridge CB2 1EZ, UK; fax: (+44) 1223-336-033; or e-mail: deposit@ccdc.cam.ac.uk.

Acknowledgments

The authors wish to thank the Ministero dell'Istruzione, dell'Università e della Ricerca (MIUR, Roma), Programmi di Ricerca Scientifica di Notevole Interesse Nazionale, Cofinanziamento 2004–2005, and the Consiglio Nazionale delle Ricerche (C.N.R.) Progetto CNR-MIUR "Sviluppo di microcelle a combustibile", for financial support.

References

[1] (a) Y. Shichijo, A. Migita, H. Oguri, M. Watanabe, T. Tokiwano, K. Watanabe, H. Oikawa, J. Am. Chem. Soc. 130 (2008) 12230;
(b) J. Justicia, A.G. Campaña, B. Bazdi, R. Robles, J.M. Cuerva, J.E. Oltra, Adv. Synth. Catal. 350 (2008) 571.
[2] H.S. Park, D.W. Kwon, K. Lee, Y.H. Kim, Tetrahedron Lett. 49 (2008) 1616.
[3] (a) T. Ollevier, E. Nadeau, Tetrahedron Lett. 49 (2008) 1546;
(b) M. Curini, F. Epifano, M.C. Marcotullio, O. Rosati, Eur. J. Org. Chem. 21 (2001) 4149.
[4] (a) A. Gansäuer, A. Barchuk, F. Keller, M. Schmitt, S. Grimme, M. Gerenkamp, C. Mück-Lichtenfeld, K. Daasbjerg, H. Svith, J. Am. Chem. Soc. 129 (2007) 1359;
(b) A.W. Eppley, N.I. Totah, Tetrahedron 53 (1997) 16545;
(c) K. Fujiwara, T. Tokiwano, A. Murai, Tetrahedron Lett. 36 (1995) 8063;
(d) M. Emziane, P. Lhoste, D. Sinou, J. Mol. Catal. 49 (1988) L23;
(e) A.E. Vougioukas, H.B. Kagan, Tetrahedron Lett. 28 (1987) 6065.
[5] The fluorides of niobium(V) and tantalum(V) have tetranuclear structures in the solid state, while the corresponding heavier halides are dinuclear in the solid state and mononuclear in the vapour phase A.F. Wells, Structural Inorganic Chemistry, 5th Ed., Clarendon Press, Oxford, 1993. For the sake of simplicity, in this paper the general formula MX_5, when dealing with the niobium(V) and tantalum(V) halides, will be used.
[6] (a) F. Marchetti, G. Pampaloni, S. Zacchini, Dalton Trans. (2007) 4343;
(b) F. Marchetti, G. Pampaloni, S. Zacchini, Inorg. Chem. 47 (2008) 365;
(c) F. Marchetti, G. Pampaloni, S. Zacchini, Chem. Commun. (2008) 3651;
(d) F. Marchetti, G. Pampaloni, S. Zacchini, Dalton Trans. (2008) 7026;
(e) F. Marchetti, G. Pampaloni, S. Zacchini, Polyhedron 27 (2008) 1969;
(f) F. Marchetti, G. Pampaloni, S. Zacchini, Eur. J. Inorg. Chem. (2008) 453;
(g) F. Marchetti, G. Pampaloni, T. Repo, Eur. J. Inorg. Chem. (2008) 2107.
[7] (a) As general references see: J.A. McCleverty, T.J. Meyer (Eds.), Comprehensive Coordination Chemistry II, Elsevier Pergamon, London, 2005;
(b) A. Singh, R.C. Mehrotra, Coord. Chem. Rev. 248 (2004) 101.
[8] (a) N. Huesing, B. Launay, G. Kickelbick, S. Gross, L. Armelao, G. Bottaro, M.P. Feth, H. Bertagnolli, G. Kothleitner, Appl. Catal. A 254 (2003) 297;
(b) T.J. Boyle, T.M. Alam, D. Dimos, G.J. Moore, C.D. Buchheit, H.N. Al-Shareef, E.R. Mechenbier, B.R. Bear, J.W. Ziller, Chem. Mater. 9 (1997) 3187;
(c) P.A. Shcheglov, D.V. Drobot, G.A. Seisenbaeva, S. Gohil, V.G. Kessler, Chem. Mater. 14 (2002) 2378.
[9] (a) J.H. Jung, T. Shimizu, S. Shinkai, J. Mater. Chem. 15 (2005) 3979;
(b) M. Niederberger, N. Pinna, J. Polleux, M. Antonietti, Angew. Chem., Int. Ed. 43 (2004) 2270.
[10] (a) Some recent references are: E.C.E. Rosenthal, H. Cui, J. Koch, ACS Symp. Ser. 974 (2007) 70;
(b) T. Gueta-Neyroud, B. Tumanskii, M. Kapon, M.S. Eisen, Macromolecules 40 (2007) 5261;
(c) J. Yamada, K. Nomura, Organometallics 24 (2005) 3621;
(d) E.C.E. Rosenthal, H. Cui, J. Koch, P. Escarpa Gaede, M. Hummert, S. Dechert, J. Chem. Soc., Dalton Trans. (2005) 3108;
(e) A.V. Grafov, C.L. Firme, I.A. Grafova, F. Benetollo, M.L. Dias, M.J.M. Abadie, Polymer 46 (2005) 9626;
(f) B. Lian, Y. Qian, W. Zhou, J. Huang, Appl. Organomet. Chem. 19 (2005) 621;
(g) E.C.E. Rosenthal, H. Cui, K.C.H. Lange, S. Dechert, Eur. J. Inorg. Chem. (2004) 4681;
(h) Z. Janas, L.B. Jerzykiewicz, K. Przybylak, P. Sobota, K. Szczegot, Eur. J. Inorg. Chem. (2004) 1639.
[11] (a) U. Schubert, Acc. Chem. Res. 40 (2007) 730;
(b) G.J.deA.A. Soler-Illia, C. Sanchez, New J. Chem. 24 (2000) 493;
(c) J.H. Thurston, K.H. Whitmire, Inorg. Chem. 41 (2002) 4194.
[12] R.M. Trend, B.M. Stoltz, J. Am. Chem. Soc. 126 (2004) 4482.
[13] (a) A. Decken, G.B. Nikiforov, J. Passmore, Dalton Trans. (2006) 4328;
(b) F. Wolff, R. Choukroun, C. Lorber, B. Donnadieu, Eur. J. Inorg. Chem. (2003) 628;
(c) Y. Li, A. Turnas, J.T. Ciszewski, A.L. Odom, Inorg. Chem. 41 (2002) 6298;
(d) T. Carofiglio, P.G. Cozzi, C. Floriani, A. Chiesi-Villa, C. Rizzoli, Organometallics 12 (1993) 2726;
(e) D.C. Bradley, H. Chudzynska, M.E. Hammond, M.B. Hursthouse, M. Motevalli, W. Rouwen, Polyhedron 11 (1992) 375;
(f) C.H. Winter, P.H. Sheridan, M.J. Heeg, Inorg. Chem. 30 (1991) 1962.
[14] (a) A.A. Pinkerton, D. Schwarzenbach, L.G. Hubert-Pfalzgraf, J.G. Riess, Inorg. Chem. 15 (1976) 1196;
(b) L.N. Lewis, M.F. Garbauskas, Inorg. Chem. 24 (1985) 363;
(c) R.N. Kapoor, F. Cervantes-Lee, C.F. Campana, C. Haltiwanger, K. Abney, K.H. Pannell, Inorg. Chem. 45 (2006) 2203;
(d) S.C. Goel, J.A. Hollingsworth, A.M. Beatty, K.D. Robinson, W.E. Buhro, Polyhedron 17 (1998) 781;
(e) R. Wang, K. Folting, J.C. Huffman, L.R. Chamberlain, I.P. Rotwell, Inorg. Chim. Acta 120 (1986) 81;
(f) J.R. Clark, A.L. Pulvirenti, P.E. Fanwick, M. Sigalas, O. Eisenstein, I.P. Rothwell, Inorg. Chem. 36 (1997) 3623;
(g) T. Matsuo, H. Kawaguchi, Inorg. Chem. 41 (2002) 6090;
(h) H. Kawaguchi, T. Matsuo, J. Organomet. Chem. 690 (2005) 5333;
(i) C. Redshaw, D.M. Homden, M.A. Rowan, M.R.J. Elsegood, Inorg. Chim. Acta 358 (2005) 4067.
[15] Niobium(V) fluoroalkoxides have been reported as being obtained from the reaction of $NbOCl_3$ and the corresponding fluoroalcohols L.G. Hubert-Pfalzgraf, J.G. Riess, Inorg. Chim. Acta 41 (1980) 111.
[16] D.C. Bradley, C.E. Holloway, J. Chem. Soc. (A) (1968) 219.
[17] J.E. Huheey, E.A. Keiter, R.L. Keiter, Inorganic Chemistry, 4th Ed., Principles of Structure and Reactivity, Harper and Collins College Publisher, New York, 1993.
[18] F. Martinez, C. del Campo, E.F. Llama, J. Chem. Soc., Perkin 1 (2000) 1749.
[19] J.-Y. Kim, T. Kwan, Chem. Pharm. Bull. 18 (1970) 1040.
[20] A. Procopio, R. Dalpozzo, A. De Nino, M. Nardi, G. Sindona, A. Tagarelli, Synlett 14 (2004) 2633.
[21] A.M. Anderson, J.M. Blazek, P. Garg, B.J. Payne, R.S. Mohan, Tetrahedron Lett. 41 (2000) 1527.
[22] B. Rickborn, R.M. Gerkin, J. Am. Chem. Soc. 93 (1971) 1693.
[23] F. Calderazzo, P. Pallavicini, G. Pampaloni, P.F. Zanazzi, J. Chem. Soc., Dalton Trans. (1990) 2743.
[24] W. Wilker, D. Leibfritz, R. Kerssebaum, W. Bermel, Magn. Reson. Chem. 31 (1993) 287.
[25] D.A. Skoog, D.M. West, Fundamentals of Analytical Chemistry, 2nd Ed., Holt, Rinehart and Winston, Chatham, UK, 1974. p. 233.
[26] G.M. Sheldrick, SADABS, University of Göttingen, Göttingen, Germany.
[27] G.M. Sheldrick, SHELX97, University of Gottingen, Göttingen, Germany.

by solvent system and metal to ligand ratio. In some cases, a small change in any of these factors can lead to new complexes with different structural topologies and different functions. Through controlling and tuning these effect factors, we have prepared a series of novel coordination polymers from zinc-benzoate [52,53], but metal-organic complexes from various metal ions with mixed-ligand system of benzoate and bipyridyl groups have been seldom reported [54].

As an extension of our previous work, in this study, we have investigated the complex formation of various metal benzoates with the bridging ligand 4,4′-bipyridine (4,4′-bpy) in order to further prepare functional coordination polymers with intriguing structures and potential applications especially in catalysis and to systematically investigate the influence of the metal ion effects less studied on the assembly processes of coordination polymers containing various metal benzoates.

We report here the syntheses and structures of six novel M(II) coordination polymers (**1**-Co, **2**-Ni, **3**-Cu, **4**-Zn, **5**-Zn, and **6**-Cd), comparison of coordination modes of metal ions including the previously known compound **7**-Mn, and their novel catalytic activities for transesterification reactions.

2. Experimental

Materials: Acetone, methanol, ethanol, methylene chloride, DMF, *para*-substituted phenyl acetate, *para*-substituted phenyl benzoate, methylacetate, methylbenzoate, 4,4′-bipyridine (4,4′-bpy), ammonium benzoate, $Cd(NO_3)_2 \cdot 4H_2O$, $Zn(NO_3)_2 \cdot 6H_2O$, $Cu(NO_3)_2 \cdot 5/2H_2O$, $Ni(NO_3)_2 \cdot 6H_2O$, $Co(NO_3)_2 \cdot 6H_2O$, and $Mn(NO_3)_2 \cdot H_2O$ were purchased from Aldrich and were used as received. 4-Fluorophenyl acetate and 4-nitrophenyl benzoate were obtained from Lancaster.

Instrumentation: Elemental analysis for carbon, nitrogen, and hydrogen was carried out by using an EA1108 (Carlo Erba Instrument, Italy) in the Organic Chemistry Research Center of Sogang University, Korea. IR spectra were measured on a BIO RAD FTS 135 spectrometer as KBr pellets. Product analysis for the transesterification reaction was performed on either a Hewlett–Packard 5890 II Plus gas chromatograph interfaced with Hewlett–Packard Model 5989B mass spectrometer or a Donam Systems 6200 gas chromatograph equipped with a FID detector using 30-m capillary column (Hewlett–Packard, HP-1, HP-5, and Ultra 2).

Synthesis of $[Co_2(O_2CPh)_4(4,4'\text{-bpy})_2]_n$ (**1**-*Co):* 37.0 mg (0.125 mmol) of $Co(NO_3)_2 \cdot 6H_2O$ and 36.0 mg (0.25 mmol) of $C_6H_5COONH_4$ were dissolved in 4 mL water and carefully layered by 4 mL ethanol solution of 4,4′-bipyridine ligand (40.0 mg, 0.25 mmol). The yield was 48.0 mg (42.1%) for compound **1**-Co. Slow evaporation of the diffused mixture provided suitable crystals of **1**-Co for X-ray crystallography in two months. *Anal.* Calc. for $C_{48}H_{36}Co_2N_4O_8$ (914.67), **1**-Co: C, 63.03; H, 3.98; N, 6.13. Found: C, 63.25; H, 3.54; N, 5.88%. IR (KBr): $\nu(cm^{-1})$ = 3062(m), 1606(s), 1549(s), 1490(w), 1419(s), 1221(m), 1070(m), 1024(w), 857(m), 813(m), 722(s), 681(m), 630(m), 478(w). The decomposed temperature is 260 °C.

Synthesis of $[Ni(O_2CPh)_4(H_2O)_2(4,4'\text{-bpy})]_n$ (**2**-*Ni):* 36.0 mg (0.125 mmol) of $Ni(NO_3)_2 \cdot 6H_2O$ and 36.0 mg (0.25 mmol) of $C_6H_5COONH_4$ were dissolved in 4 mL water and carefully layered by 4 mL solution of a mixture of acetone, methanol and ethanol (2/2/2) of 4,4′-bipyridine ligand (40.0 mg, 0.25 mmol). The yield was 18.5 mg (31.0%) for compound **2**-Ni. Slow evaporation of the diffused mixture provided suitable crystals of **2**-Ni for X-ray crystallography in a month. *Anal.* Calc. for $C_{24}H_{22}N_2NiO_6$ (479.03), **2**-Ni: C, 60.17; H, 4.64; N, 5.85. Found: C, 59.85; H, 4.48; N, 6.07%. IR (KBr): $\nu(cm^{-1})$ = 3391(br), 3065(w), 1604(s), 1540(s), 1491(w), 1392(s), 1219(m), 1174(w), 1069(m), 1045(w), 1024(w), 858(w), 815(s), 720(s), 676(s), 636(m), 439(w). The decomposed temperature is 250 °C.

Synthesis of $[Cu_2(O_2CPh)_4(4,4'\text{-bpy})]_n$ (**3**-*Cu):* 24.0 mg (0.125 mmol) of $Cu(NO_3)_2 \cdot 5/2H_2O$ and 36.0 mg (0.25 mmol) of $C_6H_5COONH_4$ were dissolved in 4 mL DMF and carefully layered by 4 mL methanol solution of 4,4′-bipyridine ligand (40.0 mg, 0.25 mmol). The yield was 27.0 mg (28.1%) for compound **3**-Cu. Slow evaporation of the diffused mixture provided suitable crystals of **3**-Cu for X-ray crystallography in a few days. *Anal.* Calc. for $C_{38}H_{28}Cu_2N_2O_8$ (767.72), **3**-Cu: C, 59.45; H, 3.68; N, 3.65. Found: C, 59.01; H, 3.94; N, 3.55%. IR (KBr): $\nu(cm^{-1})$ = 3446(br), 1675(w), 1627(s), 1573(s), 1403(s), 1218(m), 1070(w), 813(m), 719(s), 686(s), 631(w), 485(m).

Synthesis of $[Zn_2(O_2CPh)_2(OH)_2(4,4'\text{-bpy})_2]_n$ (**4**-*Zn) and* $[Zn_3(O_2CPh)_4(\mu\text{-}OH)_2(4,4'\text{-bpy})_2]_n$ (**5**-*Zn):* For **4**-Zn, 38.0 mg (0.125 mmol) of $Zn(NO_3)_2 \cdot 6H_2O$ and 36.0 mg (0.25 mmol) of $C_6H_5COONH_4$ were dissolved in 4 mL methanol and carefully layered by 4 mL methylene chloride solution of 4,4′-bipyridine ligand (40.0 mg, 0.25 mmol). The yield was 25.0 mg (28.2%) for compound **4**-Zn. Slow evaporation of the diffused mixture provided suitable crystals of **4**-Zn for X-ray crystallography in two months. *Anal.* Calc. for $C_{34}H_{28}N_4O_6Zn_2$ (719.34), **4**-Zn: C, 56.77; H, 3.93; N, 7.79. Found: C, 56.53; H, 4.12; N, 8.07%. IR (KBr): $\nu(cm^{-1})$ = 3062(br m), 2361(m), 1632(s), 1613(s), 1492(w), 1403(br s), 1221(m), 1173(w), 1072(m), 1047(w), 1024(w), 840(m), 815(s), 717(s), 684(s), 643(m), 457(m). For **5**-Zn, 38.0 mg (0.125 mmol) of $Zn(NO_3)_2 \cdot 6H_2O$ and 36.0 mg (0.25 mmol) of $C_6H_5COONH_4$ were dissolved in 4 mL water and carefully layered by 4 mL acetone solution of 4,4′-bipyridine ligand (40.0 mg, 0.25 mmol). The yield was 43.0 mg (33.6%) for compound **5**-Zn. Slow evaporation of the diffused mixture provided suitable crystals of **5**-Zn for X-ray crystallography in two months. *Anal.* Calc. for $C_{48}H_{36}N_4O_{10}Zn_3$ (1024.98), **5**-Zn: C, 56.24; H, 3.55; N, 5.47. Found: C, 56.30; H, 3.42; N, 5.65%. IR (KBr): $\nu(cm^{-1})$ = 3061(br m), 2363(m), 2341(w), 1611(s), 1570(s), 1493(w), 1419(w), 1375(s), 1226(m), 1074(m), 1045(w), 815(br m), 718(s), 685(s), 641(s). The decomposed temperature of **4**-Zn is 200 °C.

Synthesis of $[Cd_2(O_2CPh)_4(4,4'\text{-bpy})_2]_n$ (**6**-*Cd):* 39.0 mg (0.125 mmol) of $Cd(NO_3)_2 \cdot 4H_2O$ and 36.0 mg (0.25 mmol) of $C_6H_5COONH_4$ were dissolved in 4 mL water and carefully layered by 4 mL methanol solution of 4,4′-bipyridine ligand (40.0 mg, 0.25 mmol). The yield was 37.0 mg (27.2%) for compound **6**-Cd. Slow evaporation of the diffused mixture provided suitable crystals of **6**-Cd for X-ray crystallography in several months. *Anal.* Calc. for $C_{50}H_{44}Cd_2N_4O_{10}$ (1085.7), **6**-Cd: C, 55.30; H, 4.09; N, 5.16. Found: C, 55.19; H, 3.92; N, 5.24%. IR (KBr): $\nu(cm^{-1})$ = 3060(m), 1598(s), 1555(s), 1410(s), 1221(m), 1071(m), 1008(m), 854(m), 809(s), 716(s), 684(s), 628(s), 496(w). The decomposed temperature is 300 °C.

Catalytic activity of compounds ***1*****–*****7****:* Catalytic reaction conditions: ester (0.05 mmol) was dissolved in methanol (1 mL), and the compounds **1**–**7** (1.0 mg, 1.09×10^{-3} mmol for **1**-Co, 1.0 mg, 2.09×10^{-3} mmol for **2**-Ni, 1.0 mg, 1.28×10^{-3} mmol for **3**-Cu, 1.0 mg, 1.39×10^{-3} mmol for **4**-Zn, 1.0 mg, 0.96×10^{-3} mmol for **5**-Zn, 1.0 mg, 0.92×10^{-3} mmol for **6**-Cd, and 1.0 mg, 2.21×10^{-3} mmol for **7**-Mn) were added, respectively, and shaken at 50 °C (450 rpm). Reaction conversion was monitored by GC/mass analysis of 20 μL aliquots withdrawn periodically from the reaction mixture. All reactions were run at least three times and the average conversion yields are presented.

X-ray crystallography: The X-ray diffraction data for all five compounds were collected on a Bruker SMART APX diffractometer equipped with a monochromater in the Mo Kα (λ = 0.71073 Å) incident beam. Each crystal was mounted on a glass fiber. The CCD data were integrated and scaled using the Bruker-SAINT software package, and the structure was solved and refined using SHEXTL V6.12 [55]. All

Table 1
Crystallographic data for compounds **1**–**7**.

	1-Co	**2**-Ni	**3**-Cu	**4**-Zn	**5**-Zn	**6**-Cd	**7**-Mn[a]
Empirical formula	$C_{48}H_{36}Co_2N_4O_8$	$C_{24}H_{13}N_2NiO_6$	$C_{38}H_{28}Cu_2N_2O_8$	$C_{34}H_{28}N_4O_6Zn_2$	$C_{48}H_{36}N_4O_{10}Zn_3$	$C_{50}H_{44}Cd_2N_4O_{10}$	$C_{24}H_{18}MnN_2O_4$
Formula weight	914.67	484.07	767.72	719.34	1024.98	1085.7	453.34
Temperature (K)	293(2)	170(2)	170(2)	170(2)	170(2)	293(2)	170(2)
Wavelength (Å)	0.71073	0.71073	0.71073	0.71073	0.71073	0.71073	0.71073
Space group	$P2_1/c$	$P4_32_12$	$C2/c$	$P2_1/c$	$P\bar{1}$	$P\bar{1}$	$Pbcn$
a (Å)	10.9885(14)	15.025(2)	20.3982(18)	7.5157(13)	9.583(3)	9.990(3)	18.6268(19)
b (Å)	22.643(3)	15.025(2)	18.9865(16)	22.813(4)	11.389(4)	10.774(3)	11.6799(12)
c (Å)	9.3980(12)	27.318(6)	21.4028(18)	24.820(4)	11.396(4)	12.346(4)	9.4348(9)
α (°)	90.00	90.00	90.00	90.00	96.730(7)	105.501(5)	90.00
β (°)	112.458(2)	90.00	118.152(2)	95.732(3)	110.626(6)	92.234(5)	90.00
γ (°)	90.00	90.00	90.00	90.00	108.107(6)	111.667(4)	90.00
Volume (Å^3)	2161.0(5)	6167.1(17)	7308.5(11)	4234.2(13)	1069.8(6)	1176.0(6)	2052.6(4)
Z	2	8	8	4	1	2	4
D_{calc} (Mg/m^3)	1.406	1.043	1.425	1.128	1.616	1.533	1.467
Absorption coefficient (mm^{-1})	0.827	0.660	1.220	1.172	1.738	0.967	0.677
Crystal size (mm^3)	0.15 × 0.08 × 0.05	0.15 × 0.15 × 0.10	0.10 × 0.08 × 0.08	0.10 × 0.03 × 0.03	0.25 × 0.08 × 0.05	0.08 × 0.06 × 0.06	0.25 × 0.20 × 0.20
Reflections collected	10523	33006	20023	20746	5873	6370	10697
Independent reflections [R_{int}]	3747 [0.0693]	5885 [0.1166]	7123 [0.0589]	7226 [0.0783]	4031 [0.0369]	4497 [0.0277]	2018 [0.0346]
Data/restraints/parameters	3747/0/280	5885/0/256	7123/0/461	7226/2/421	4031/0/296	4497/0/300	2018/0/143
Goodness-of-fit on F^2	0.844	0.930	0.945	0.818	0.931	0.944	0.946
Final R indices [$I > 2\sigma(I)$]	R_1 = 0.0439, wR_2 = 0.0977	R_1 = 0.0696, wR_2 = 0.1547	R_1 = 0.0570, wR_2 = 0.1517	R_1 = 0.0705, wR_2 = 0.1656	R_1 = 0.0537, wR_2 = 0.1142	R_1 = 0.0442, wR_2 = 0.0963	R_1 = 0.0286, wR_2 = 0.0723
R indices (all data)	R_1 = 0.0960, wR_2 = 0.1197	R_1 = 0.1673, wR_2 = 0.1997	R_1 = 0.0852, wR_2 = 0.1578	R_1 = 0.1483, wR_2 = 0.1819	R_1 = 0.0953, wR_2 = 0.1270	R_1 = 0.0681, wR_2 = 0.1033	R_1 = 0.0375, wR_2 = 0.0738
Largest difference in peak and hole (e Å^{-3})	0.685 and −0.460	0.299 and −0.211	2.361 and −0.885	0.969 and −0.543	0.631 and −0.818	0.873 and −0.894	0.219 and −0.443

[a] The crystal structure of complex **7**-Mn $[Mn(O_2CPh)_2(4,4'\text{-bpy})]_n$ was re-determined, and all the parameters were same with the results reported by Chen et al. [56].

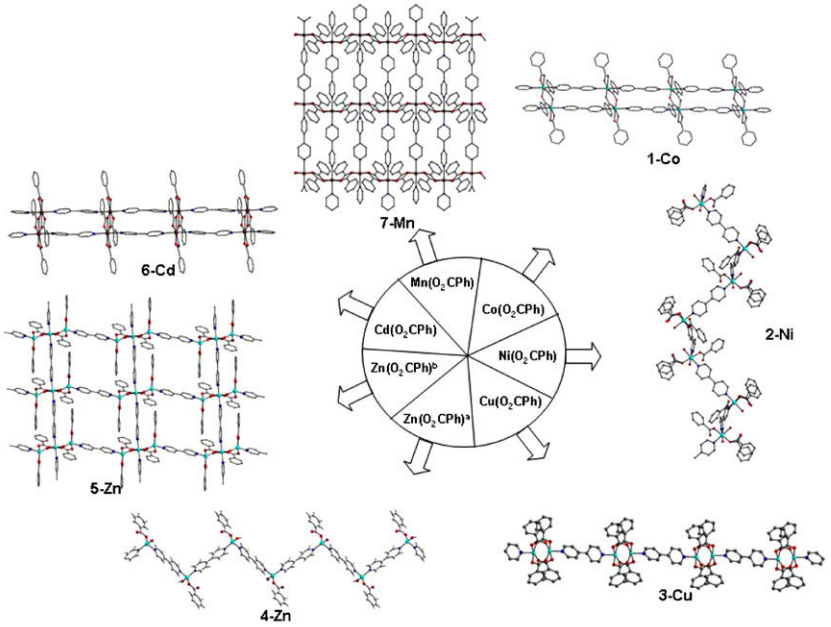
hydrogen atoms were placed in the calculated positions. The crystallographic data for compounds **1**–**7** are listed in Table 1.

3. Results and discussion

Synthesis and spectral characterization: To investigate structures of metal complexes containing 4,4′-bpy and benzoate coligands, six transition metal ions have been chosen: Co(II), Ni(II), Cu(II), Zn(II), Mn(II), and Cd(II) cations. The Mn(II)-benzoate complex with 4,4′-bpy was reported previously [56], but we re-measured the data for the crystal structure of the complex $[Mn(O_2CPh)_2(4,4'\text{-bpy})]_n$ (**7**-Mn) to compare their structures and the coordination modes with those of other metal complexes. We found all the parameters are same with the results reported by Chen et al. [56]. Although we used the same 4,4′-bpy and benzoate coligands, each metal cation provided the different structure, respectively. All seven compounds are shown in Scheme 1. The infrared spectra of **1**–**7** were fully consistent with their formulations. Asymmetric and symmetric C=O stretching modes of the ligated benzoate moieties were evidenced by very strong, slightly broadened bands at ~1600 and ~1400 cm^{-1} [57–59]. The absence of any bands in the area of ~1710 cm^{-1} indicates full deprotonation of all carboxylate groups in **1**–**7** [57–59], which is consistent with the results of the X-ray analysis.

*Structure description of $[Co_2(O_2CPh)_4(4,4'\text{-bpy})_2]_n$ (**1**-Co):* Asymmetric unit contains a Co atoms, two benzoate ligands, and a 4,4′-bpy ligand, and there is a crystallographic inversion center between the cobalt atoms. Symmetry operations $(-x+2,-y,-z+1)$, $(x-1,y,z-1)$, and $(x+1,y,z+1)$ produce a one-dimensional chain **1**-Co. Benzoate groups coordinate to the Co ions in two different ways: bridging mode and chelating mode. Two benzoate ligands bridge two Co ions, and each Co ion has a chelating benzoate ligand. These $Co_2(O_2CPh)_4$ units are connected by two 4,4′-bpy bridging ligands to form a ladder-type double chain (Fig. 1a). The structure of **1**-Co contains no solvent molecules. The packing diagram along *a-axis* is shown in Fig. 1b. The coordination geometry of Co ion is distorted octahedral constructed by four oxygen atoms from benzoate ligands and two nitrogen atoms from 4,4′-bpy ligands. The two pyridyl rings of 4,4′-bpy ligand are nearly coplanar by the dihedral angle of 7.0°. The Co–$O_{bridging}$ bond distances are 2.006(3) and 2.014(3) Å, typical in Co complexes containing 4,4′-bpy ligands [44,60]. These Co–O bond distances for bridging benzoate ligands are shorter than those for chelating benzoate ligands (Co–$O_{chelating}$ 2.170(3) and 2.191(3) Å). The Co–N bond distances are 2.163(3) and 2.158(3) Å (Table 2), similar to those found in the reported Co complexes [44,60]. The Co···Co distance is 4.057(2) Å, similar to that found in the reported Co complex (4.02(1) Å) [44].

*Structure description of $[Ni(O_2CPh)_2(H_2O)_2(4,4'\text{-bpy})]_n$ (**2**-Ni):* Asymmetric unit contains a Ni atom, two benzoate, two water, and a 4,4′-bpy ligand, and symmetry operations $(-y+2, -x+2, -z+1/2)$ and $(y,x,-z)$ produces a helical structure **2**-Ni (Fig. 2a). One of benzoate ligands is disordered with two sets of benzoate. The similar helical structure $[Ni(O_2CPh)_2(CH_3O)_2(4,4'\text{-bpy})]_n$ **2′** has been reported by Biradha et al. [61]. The crystals of **2**-Ni for X-ray analysis were obtained with the similar cell parameters to those of **2′**. Both compounds **2**-Ni and **2′** have a tetragonal cell with the $P4_32_12$ space group (Table 1). The difference between two compounds is the coordination environment around the Ni ion. The Ni ion in **2**-Ni is N2O4 hexa-coordinated from two benzoate oxygen atoms, two water oxygen atoms and two nitrogen atoms to form a distorted octahedral geometry. In **2′**, the geometry of a Ni ion is also distorted octahedral, but methanol molecules coordinate to the Ni ion instead of water molecules in **2**-Ni. The $Ni(O_2CPh)_2(H_2O)_2$ units in **2**-Ni are connected by 4,4′-bpy to form a helical compound. The right-handed and the left-handed helices are packed alternatively to form a racemic mixture (Fig. 2b) while the crystal packing of **2′** induced spontaneous resolution of the helices. Cavities between helices (1912 Å^3 in volume, 31% of unit cell volume) are larger than those of compound **2′**, and there is no guest molecule in **2**-Ni. Two pyridyl rings are tilted by 17.2°



Scheme 1.

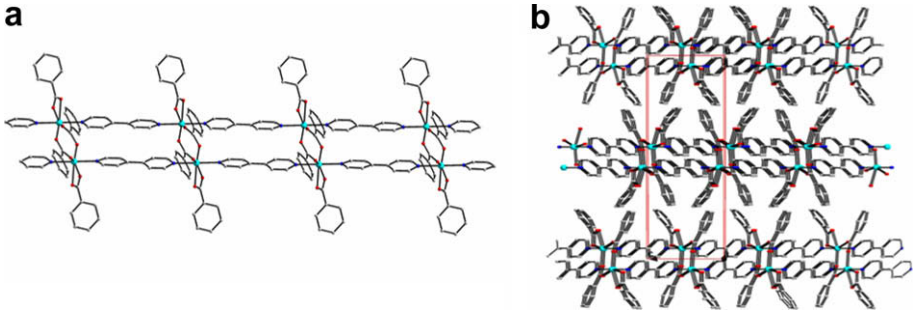


Fig. 1. (a) Structure of ladder-type $[Co_2(O_2CPh)_4(4,4'\text{-bpy})_2]_n$ **1**-Co. All hydrogen atoms were omitted for clarity. (b) Packing diagram of **1**-Co.

and 20.2°. The Ni–$O_{benzoate}$ bond distances are 2.031(5) and 2.042(5) Å, and the Ni–O_{water} bond distances are 2.085(4) and 2.089(4) Å. The Ni–N bond distances are 2.077(5) and 2.097(5) Å (Table 2).

*Structure description of $[Cu_2(O_2CPh)_4(4,4'\text{-bpy})]_n$ (**3**-Cu):* The crystal structure of **3**-Cu is shown in Fig. 3a. The paddle-wheel type units are bridged by 4,4′-bpy ligand to form a one-dimensional polymeric compound **3**-Cu. View along the crystallographic *b-axis* of **3**-Cu is shown in Fig. 3b. The octahedral coordination around the Cu ion consists of four oxygen atoms from benzoate ligands (1.947(4)–2.004(4) Å), a nitrogen atom of the 4,4′-bpy ligand (Cu–N 2.147(4) and 2.150(4) Å) and the second copper atom (Cu···Cu 2.642(1) Å) (Table 2). The Cu–N bond distances are similar to those found in the reported Cu(II) complexes, $[Cu_2(Hsal)_4(4,\text{-bpy})]_n$ (H_2sal = salicylic acid) [62], $[Cu_2(O_2CPh)_4(pyz)]_n$ (pyz = pyrazine) [63], $[Cu_2(OAc)_4(bpe)]\cdot 2H_2O$ (bpe = 1,2-bis(4-pyridyl)ethane) [64]. The Cu···Cu distance in the paddle-wheel unit is comparable with the reported Cu complexes (2.66 Å [62], 2.5899(7) Å [63], 2.6424(7) Å [64]). The Cu–O bond distances are usually observed in the similar Cu complexes [62–64]. The Cu′–Cu–N bond angle (171.3(1)°) shows a nearly linear chain structure. The two pyridyl rings of the 4,4′-bpy ligand are twisted by the dihedral angle of 28.2°. The coordination mode of benzoate shows only bridging type as shown in Fig. 2. It is worthwhile to mention that while $[Cu(maa)_2(bpp)]$ (Hmma = 2-methylcrylic acid and bpp = 1,3-bis(4-pyridyl)propane) system [65] with 1:1 ratio of bpp:$[Cu_2(maa)_4\cdot 2H_2O]$ contains a zigzag chain containing a dinuclear paddle-wheel type structure and with 2:1 ratio do a triple-stranded molecular braid that contains a mononuclear node, our system under 2:1 ratio of 4,4′-bpy:Cu-benzoate generate a 1-D polymer with a dinuclear paddle-wheel type structure. In addition, Long and co-workers showed the pH effects on the structures of Cu complexes containing benzoate and 4,4′-bpy ligands, ranging from a 0-D mononuclear complex to a 2-D network [54]. Therefore, these results suggest that the compound **3**-Cu could be converted to unknown compounds by further change of the reaction conditions such as pH, solvent, and ligand-to-metal ratio.

*Structure description of $[Zn_2(O_2CPh)_2(OH)_2(4,4'\text{-bpy})_2]_n$ (**4**-Zn) and $[Zn_3(O_2CPh)_4(\mu\text{-}OH)_2(4,4'\text{-bpy})_2]_n$ (**5**-Zn):* The reactions of Zn-benzoate with 4,4′-bpy ligands produced two different structures in different solvent systems. The methylene chloride solution of zinc-benzoate can react with the methanol solution of 4,4′-bpy ligand to form a one-dimensional zigzag chain **4**-Zn. The aqua solution of zinc-benzoate can react with the acetone solution of 4,4′-bpy ligand to form two-dimensional compound **5**-Zn. For compound **4**-Zn, asymmetric unit contains two crystallographi-

Table 2
Selected bond distances for compounds **1**–**7**.

1*-*Co			
Co(1)–O(12)	2.006(3)	Co(1)–O(21)	2.170(3)
Co(1)–O(11)	2.014(3)	Co(1)–O(22)	2.191(3)
Co(1)–N(32)	2.158(3)	Co(1)–C(21)	2.516(5)
Co(1)–N(31)	2.163(3)		
O(12)–Co(1)–O(11)	119.42(12)	N(32)–Co(1)–O(21)	96.25(12)
O(12)–Co(1)–N(32)	91.81(12)	N(31)–Co(1)–O(21)	84.82(12)
O(11)–Co(1)–N(32)	92.06(12)	O(12)–Co(1)–O(22)	91.16(12)
O(12)–Co(1)–N(31)	86.97(12)	O(11)–Co(1)–O(22)	149.41(12)
O(11)–Co(1)–N(31)	88.53(12)	N(32)–Co(1)–O(22)	86.78(12)
N(32)–Co(1)–N(31)	178.78(14)	N(31)–Co(1)–O(22)	93.24(12)
O(12)–Co(1)–O(21)	149.12(12)	O(21)–Co(1)–O(22)	59.75(11)
O(11)–Co(1)–O(21)	90.09(12)		
2*-*Ni			
Ni(1)–O(41)	2.031(5)	Ni(1)–O(1)	2.085(4)
Ni(1)–O(31)	2.042(5)	Ni(1)–O(2)	2.089(4)
Ni(1)–N(11)	2.077(5)	Ni(1)–N(21)	2.097(5)
O(41)–Ni(1)–O(31)	179.4(2)	N(11)–Ni(1)–O(2)	179.3(2)
O(41)–Ni(1)–N(11)	89.5(2)	O(1)–Ni(1)–O(2)	92.29(19)
O(31)–Ni(1)–N(11)	90.52(19)	O(41)–Ni(1)–N(21)	90.8(2)
O(41)–Ni(1)–O(1)	91.0(2)	O(31)–Ni(1)–N(21)	88.6(2)
O(31)–Ni(1)–O(1)	91.0(2)	N(11)–Ni(1)–N(21)	89.9(2)
N(11)–Ni(1)–O(1)	88.26(18)	O(1)–Ni(1)–N(21)	178.1(2)
O(41)–Ni(1)–O(2)	90.9(2)	O(2)–Ni(1)–N(21)	89.5(2)
O(31)–Ni(1)–O(2)	89.1(2)		
3*-*Cu			
Cu(1)–O(31)	1.947(4)	Cu(2)–O(42)	1.954(3)
Cu(1)–O(11)	1.963(4)	Cu(2)–O(22)	1.957(3)
Cu(1)–O(41)	1.993(4)	Cu(2)–O(32)	1.999(3)
Cu(1)–O(21)	1.998(3)	Cu(2)–O(12)	2.004(4)
Cu(1)–N(51)	2.150(4)	Cu(2)–N(52)	2.147(4)
Cu(1)–Cu(2)	2.6417(8)		
O(31)–Cu(1)–O(11)	171.85(15)	O(42)–Cu(2)–O(22)	170.92(14)
O(31)–Cu(1)–O(41)	89.51(16)	O(42)–Cu(2)–O(32)	89.32(15)
O(11)–Cu(1)–O(41)	91.54(15)	O(22)–Cu(2)–O(32)	90.40(15)
O(31)–Cu(1)–O(21)	89.18(15)	O(42)–Cu(2)–O(12)	91.31(14)
O(11)–Cu(1)–O(21)	87.75(16)	O(22)–Cu(2)–O(12)	86.47(15)
O(41)–Cu(1)–O(21)	165.23(15)	O(32)–Cu(2)–O(12)	163.99(14)
O(31)–Cu(1)–N(51)	100.53(16)	O(42)–Cu(2)–N(52)	93.69(15)
O(11)–Cu(1)–N(51)	87.43(16)	O(22)–Cu(2)–N(52)	95.38(15)
O(41)–Cu(1)–N(51)	94.86(15)	O(32)–Cu(2)–N(52)	93.12(15)
O(21)–Cu(1)–N(51)	99.84(15)	O(12)–Cu(2)–N(52)	102.80(15)
4*-*Zn			
Zn(1)–O(11)	1.951(5)	Zn(1)–N(31)	2.059(5)
Zn(1)–N(11)	2.052(6)	Zn(1)–O(13)	2.060(11)
O(11)–Zn(1)–N(11)	105.4(2)	O(11)–Zn(1)–O(13)	115.8(5)
O(11)–Zn(1)–N(31)	96.7(2)	N(11)–Zn(1)–O(13)	129.8(7)
N(11)–Zn(1)–N(31)	100.8(2)	N(31)–Zn(1)–O(13)	101.5(5)
5*-*Zn			
Zn(1)–O(3)	2.081(4)	Zn(1)–O(11)#1	2.183(5)
Zn(1)–O(3)#1	2.081(4)	Zn(2)–O(3)	1.922(5)
Zn(1)–N(1)	2.140(5)	Zn(2)–O(21)	1.987(5)
Zn(1)–N(1)#1	2.140(5)	Zn(2)–O(12)	1.992(4)
Zn(1)–O(11)	2.183(5)	Zn(2)–N(2)	2.054(6)
O(3)–Zn(1)–O(3)#1	180.000(2)	O(3)#1–Zn(1)–O(11)#1	85.97(13)
O(3)–Zn(1)–N(1)	89.61(13)	N(1)–Zn(1)–O(11)#1	88.37(13)
O(3)#1–Zn(1)–N(1)	90.39(13)	N(1)#1–Zn(1)–O(11)#1	91.63(13)
O(3)–Zn(1)–N(1)#1	90.39(13)	O(11)–Zn(1)–O(11)#1	179.999(1)
O(3)#1–Zn(1)–N(1)#1	89.61(13)	O(3)–Zn(2)–O(21)	122.45(14)
N(1)–Zn(1)–N(1)#1	180.0(2)	O(3)–Zn(2)–O(12)	104.06(14)
O(3)–Zn(1)–O(11)	85.97(13)	O(21)–Zn(2)–O(12)	106.44(14)
O(3)#1–Zn(1)–O(11)	94.03(13)	O(3)–Zn(2)–N(2)	116.96(15)
N(1)–Zn(1)–O(11)	91.63(13)	O(21)–Zn(2)–N(2)	107.93(15)
N(1)#1–Zn(1)–O(11)	88.37(13)	O(12)–Zn(2)–N(2)	94.46(15)
O(3)–Zn(1)–O(11)#1	94.03(13)		

Symmetry transformations used to generate equivalent atoms: #1 $-x+1,-y+1,-z+2$

6*-*Cd			
Cd(1)–N(32)	2.310(4)	Cd(1)–O(21)	2.362(4)
Cd(1)–N(31)	2.323(3)	Cd(1)–O(22)	2.432(3)
Cd(1)–O(12)#1	2.328(3)	Cd(1)–O(11)#1	2.577(4)
Cd(1)–O(11)	2.341(3)	Cd(1)–C(21)	2.730(5)
N(32)–Cd(1)–N(31)	174.78(13)	N(31)–Cd(1)–O(22)	86.13(13)
N(32)–Cd(1)–O(12)#1	91.02(13)	O(12)#1–Cd(1)–O(22)	83.32(12)
N(31)–Cd(1)–O(12)#1	94.20(12)	O(11)–Cd(1)–O(22)	150.16(12)

(*continued on next page*)

Table 2 (*continued*)

N(32)–Cd(1)–O(11)	89.14(13)	O(21)–Cd(1)–O(22)	54.27(12)
N(31)–Cd(1)–O(11)	87.73(12)	N(32)–Cd(1)–O(11)#1	95.90(12)
O(12)#1–Cd(1)–O(11)	126.27(12)	N(31)–Cd(1)–O(11)#1	87.27(12)
N(32)–Cd(1)–O(21)	92.22(13)	O(12)#1–Cd(1)–O(11)#1	52.35(11)
N(31)–Cd(1)–O(21)	83.96(13)	O(11)–Cd(1)–O(11)#1	74.20(12)
O(12)#1–Cd(1)–O(21)	137.59(12)	O(21)–Cd(1)–O(11)#1	167.17(11)
O(11)–Cd(1)–O(21)	96.05(12)	O(22)–Cd(1)–O(11)#1	134.48(11)
N(32)–Cd(1)–O(22)	94.54(13)		

Symmetry transformations used to generate equivalent atoms: #1 $-x+2,-y+1,-z+1$.

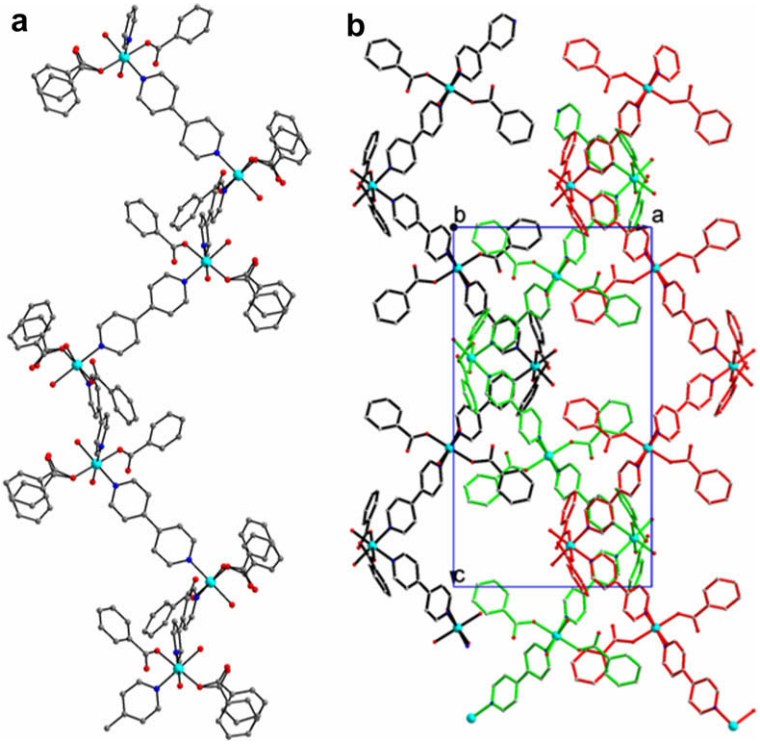


Fig. 2. (a) Helical structure of $[Ni(O_2CPh)_2(H_2O)_2(4,4'\text{-bpy})]_n$ **2**-Ni. One of benzoate ligands is disordered with two sets of benzoate. All hydrogen atoms were omitted for clarity. (b) Crystal packing diagram along *b*-axis.

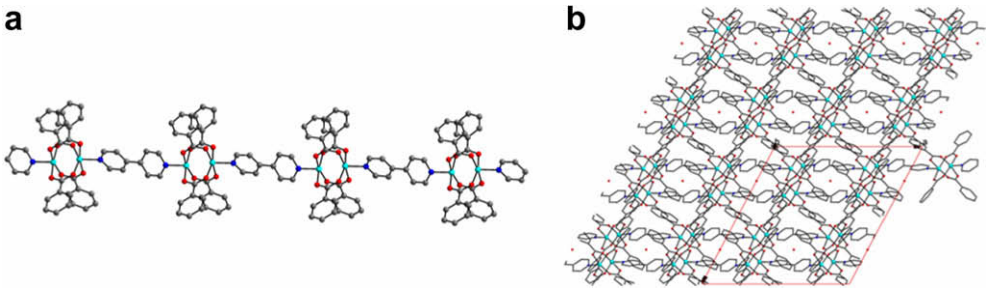


Fig. 3. (a) Structure of $[Cu_2(O_2CPh)_4(4,4'\text{-bpy})]_n$ **3**-Cu containing paddle-wheel type dinuclear Cu units. All hydrogen atoms were omitted for clarity. (b) View along the crystallographic *b*-axis of **3**-Cu.

cally independent Zn atoms, two benzoate ligands, two hydroxyls, and two 4,4′-bpy ligands, and there are inversion centers in the middle of 4,4′-bpy ligands. Symmetry operations $(-x+2,-y+1,-z+1)$ and $(-x+1,-y,-z+2)$ produce a zigzag chain (Fig. 4a). The individual chains are cross each other to form infinite channels as shown in Fig. 4b. The Zn atom is four-coordinated by two nitrogen atoms from 4,4′-bpy ligands and two oxygen atoms from one benzoate and one hydroxyl ligand to form a distorted tetrahedral geometry. One of 4,4′-bpy bridging ligands is nearly planar with the dihedral angle of 3.8°, and others are exactly planar. The Zn–N bond distances range from 2.037(5) to 2.059(5) Å, similar to those found in previously reported Zn compounds $[Zn(OAc)_2(\mu\text{-bpe})]\cdot 2H_2O$ [66], $\{[Zn_2(4,4'\text{-bpy})_2(4\text{-aba})_4](H_2O)_5\}_n$ (4-aba = 4-aminobenzoic acid) [67], and $[\{(F_3CCO_2)(\mu\text{-}O_2CCH_3)Zn\}_2(\mu\text{-bpe})_2]_n$ [47]. The Zn–$O_{benzoate}$ bond distances range from 1.924(5) to 1.951(5) Å (Table 2), similar to

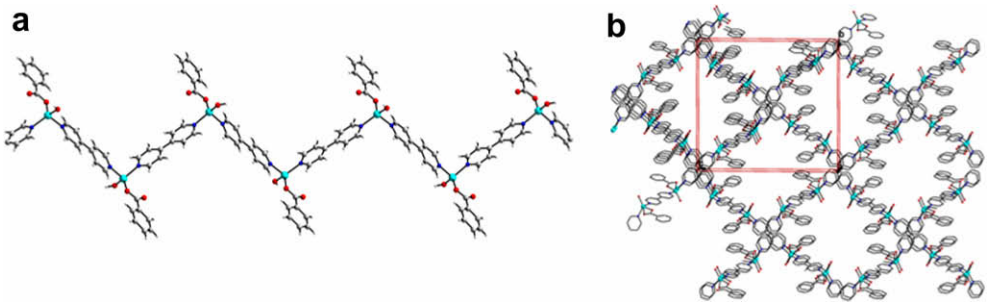


Fig. 4. (a) Structure of $[Zn_2(O_2CPh)_2(OH)_2(4,4'\text{-bpy})_2]_n$ **4**-Zn. All hydrogen atoms were omitted for clarity. (b) View along the crystallographic *a*-axis of **4**-Zn.

those found in the reported Zn compounds [28–30]. The Zn–$O_{hydroxyl}$ bond distances are 2.051(7) and 2.060(1) Å. The Zn···Zn distances in **4**-Zn are 11.190(13) and 11.208(6) Å.

For compound **5**-Zn, asymmetric unit contains one and half Zn atoms, two benzoate ligands, a hydroxyl, a 4,4′-bpy ligand, and a water solvent molecule, and there is an inversion center on central Zn atom. Symmetry operations $(-x+1,-y+1,-z+2)$, $(-x+1,-y,-z+2)$, and $(-x+2,-y+1,-z+1)$ produce a two-dimensional sheet **5**-Zn. The $Zn_3(O_2CPh)_4(\mu\text{-}OH)_2$ units are connected by bridging 4,4′-bpy ligands to form a two-dimensional sheet (Fig. 5a). Out of three Zn centers the central Zn atom is N2O4 coordinated from two bridging benzoate ligands, two bridging hydroxyl ligands, and two bridging 4,4′-bpy ligands to form a distorted octahedral geometry. The other two Zn centers are symmetric to each other, and each is NO3 coordinated from a bridging benzoate, an asymmetric chelating benzoate, a μ-hydroxyl, and a bridging 4,4′-bpy ligand to form distorted trigonal-bipyramidal geometry. View along the crystallographic *b-axis* of **5**-Zn is shown in Fig. 5b. The topological feature of compound **5**-Zn is most unusual because it features a previously unobserved trinuclear motif that is catenated with adjacent ones to form a 2-D supramolecular structure. The Zn–$O_{bridging}$ bond distances are 1.992(3) and 2.183(3) Å, similar to those found in the related Zn(II)-4,4′-bpy coordination polymer, $[Zn_4O(ip)_3(4,4'\text{-bpy})]$ (ip = isophthalate) [68], and the asymmetric Zn–$O_{chelating}$ bond distances are 1.987(4) and 2.62(1) Å. The Zn–$O_{hydroxyl}$ bond distances are 1.922(3) and 2.081(3) Å which can be comparable with those found in a coordination network containing $Zn_3(OH)_3$ units, $[Zn_3(OH)_3(bpp)_3[NO_3]_3\cdot 8.67H_2O$ [69] and our previous 2-D compound containing hexanuclear $Zn_6(OH)_8$ units, $[Zn_6(OH)_8(bpp)_4](OTf)_4\cdot 3H_2O$ (bpp = 1,3-bis(4-pyridyl)propane) [70]. The Zn–N bond distances are 2.054(4) and 2.140(4) Å (Table 2), similar to those found in previously reported compounds $[Zn(OAc)_2(\mu\text{-bpe})]\cdot 2H_2O$ [66], $\{[Zn_2(4,4'\text{-bpy})_2(4\text{-aba})_4](H_2O)_5\}_n$ [67], and $[\{(F_3CCO_2)(\mu\text{-}O_2CCH_3)Zn\}_2(\mu\text{-bpe})_2]_n$ [47]. Two pyridyl rings of the 4,4′-bpy ligand are exactly coplanar with an inversion center in the middle C–C bond between two rings. The Zn···Zn distance in **5**-Zn is 3.326(7) Å, shorter than those found in the related Zn compound containing trinuclear $Zn_3(O_2CPh)_6$ units (3.370(2) and 3.347(2) Å) [53]. It is interesting to note that despite the prevalence of coordination polymers containing 4,4′-bpy and acetate ligands, the structure of the complexes described here has not been previously reported.

*Structure description of $[Cd_2(O_2CPh)_4(4,4'\text{-bpy})_2]_n$ (**6**-Cd):* Asymmetric unit contains a Cd atom, two benzoate ligands, a 4,4′-bpy ligand, and a methanol solvent molecule, and symmetry operations $(-x+2,-y+1,-z+1)$, $(x-1,y-1,z)$, and $(x+1,y+1,z)$ produce an one-dimensional compound. The benzoate-bridged Cd_2 units are connected to form a ladder-type chain **6**-Cd (Fig. 6a). The packing diagram along *a-axis* is shown in Fig. 6b. The structure of **6**-Cd is very similar to that of **1**-Co showing ladder-type double chains. While two benzoate ligands in **1**-Co connect Co atoms with a bridging coordination mode, the benzoate ligands in **6**-Cd connect two Cd atoms with a chelating/bridging bidentate coordination mode in which a benzoate ligand chelates to one Cd atom and simultaneously bridges to the other Cd atom. Each Co atom in **1**-Co or each Cd in **6**-Cd has another chelating benzoate ligand, respectively. The coordination geometry of Co atom in **1**-Co is distorted octahedral, and that of Cd in **6**-Cd can be described as a distorted pentagonal pyramid with five oxygen atoms of benzoate ligands and two nitrogen atoms of 4,4′-bpy ligands (N2O5 coordinated). The Cd–$O_{chelating/bridging}$ distances are 2.328(3) and 2.577(4) Å which can be comparable with those in the related Cd/4,4′-bpy compounds, [Cd(tp)(4,4′-bpy)] (2.287(2)–2.653(2) Å, tp = terphthalate) [71], $[Cd(4,4'\text{-bpy})(oba)]_n$ (2.383(3)–2.749(3) Å, H_2oba = 4,4′-oxybis(benzoic acid)) [72], and $[Cd_6(MeCO_2)(4,4'\text{-bpy})_2(H_2bna)_4]\cdot 3.5H_2O$ (2.262(2)–2.550(3) Å, H_2bna = 2,2′-dihydroxyl-[1]-binaphthalene-3,3′-dicarboxylate) [73]. The Cd–

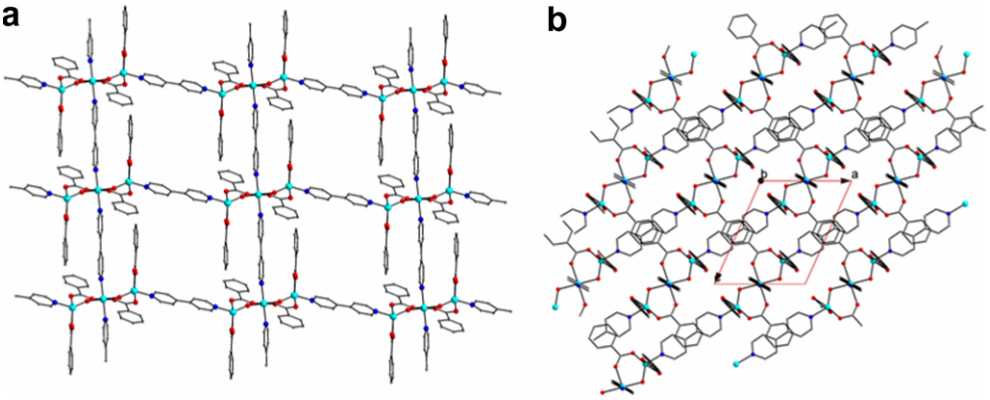


Fig. 5. (a) Structure of $[Zn_3(O_2CPh)_4(\mu\text{-}OH)_2(4,4'\text{-bpy})_2]_n$ **5**-Zn. All hydrogen atoms were omitted for clarity. (b) View along the crystallographic *b*-axis of **5**-Zn.

$O_{chelating}$ distances of 2.362(4) and 2.432(3) Å are similar to those found in Cd related compounds (2.329(3)–2.432(3) Å) [72,73] but different from those found in Cd(tp)(4,4′-bpy) in which two oxygen atoms asymmetrically coordinate to Cd atoms (2.263(2) and 2.608(2) Å) [71]. The Cd–N bond distances are 2.310(4) and 2.323(3) Å (Table 2), similar to those found in the related Cd/4,4′-bpy compounds [71–73]. The Cd···Cd distance is 3.925(10) Å which is also comparable with those found in the related Cd/4,4′-bpy compounds (3.908(1) Å [71], 3.872(2) Å [72], and 3.873(1)–4.514(1) Å [73]), and is shorter than that of Co···Co in **1**-Co since benzoate ligands connect Cd atoms with chelating/bridging bidentate coordination mode in compound **6**-Cd. The two pyridyl rings are twisted by 27.5°, in contrast to those in Co complex in which they are nearly coplanar.

3.1. Coordination geometry around each metal

Six metal cations have been employed to investigate how the change of metal cations influences on construction of metal-benzoate complexes with 4,4′-bpy ligand. Each metal cation provides different structure, respectively (Scheme 1), and so it is clear that selection of appropriate metal ions plays a key role in controlling the structures of the complexes.

The coordination geometries of metal atoms in metal-benzoate complexes are shown in Scheme 2. **1**-Co and **6**-Cd show similar double chain structures, but the coordination around each metal ion is different. The coordination geometry of Co atom in **1** is distorted octahedral constructed by four oxygen atoms from benzoate ligands and two nitrogen atoms from 4,4′-bpy ligands, and that of Cd in **6** is a distorted pentagonal pyramid with five oxygen atoms of benzoate ligands and two nitrogen atoms of 4,4′-bpy ligands. The Ni atom in the helical structure of **2**-Ni is N2O4 hexa-coordinated from two benzoate oxygen atoms, two water oxygen atoms and two nitrogen atoms to form a distorted octahedral geometry. The coordination of Cu atom in **3**-Cu is octahedral with four oxygen atoms in the equatorial plane completed by nitrogen atom of 4,4′-bpy ligand and by the second copper atom. In Zn-benzoate complexes, different solvent systems provide different crystal structures (**4**-Zn and **5**-Zn). The coordination around Zn atom in **4**-Zn is distorted tetrahedral constructed by two nitrogen atoms from 4,4′-bpy ligands and two oxygen atoms from one benzoate and one hydroxyl ligand. In compound **5**-Zn, the central Zn atom has a distorted octahedral geometry formed by two bridging benzoate ligands, two bridging hydroxyl ligands, and two bridging 4,4′-bpy ligands, and the other two symmetric Zn atoms have a distorted tetrahedral geometry formed by one bridging benzoate ligand, one dangling benzoate ligand, and one bridging 4,4′-bpy ligand. The Mn atom in the two-dimensional structure of **7**-Mn is N_2O_4 coordinated by two nitrogen atom from 4,4′-bpy ligands and four oxygen atoms from two benzoate ligands to form a slightly distorted octahedral geometry [56]. These results show the systematic change in the coordination geometries of the metal ions: from a tetrahedral (four-coordinate) **4**-Zn ion, a trigonal-bipyramidal (five-coordinate) **5**-Zn ion, an octahedral (six-coordinate) **1**-Co, **2**-Ni, and **7**-Mn ions to a pentagonal-bipyramidal (seven-coordinate) **6**-Cd ion. Since different structure provides different coordination geometry of each metal ion, it is clear that selection of appropriate metal ions can control the coordination geometry of each metal ion to form different crystal structures.

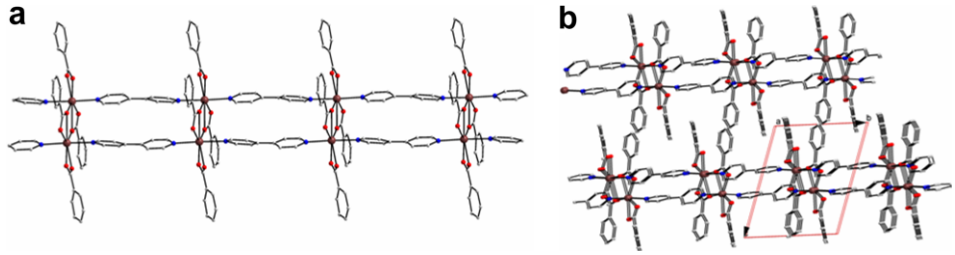
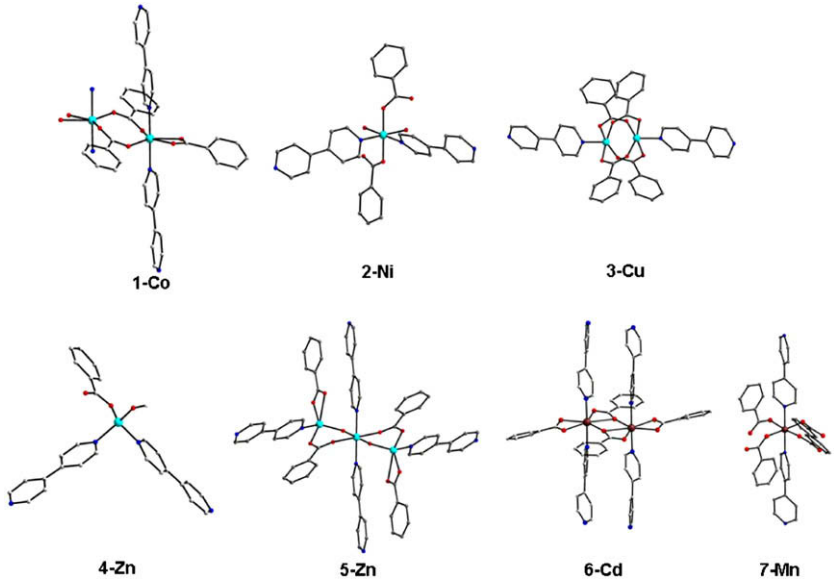
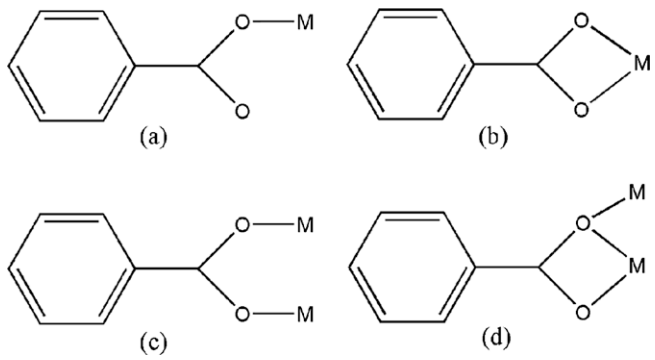


Fig. 6. (a) Structure of $[Cd(O_2CPh)_4(4,4'\text{-bpy})_2]_n$ **6**-Cd. All hydrogen atoms were omitted for clarity. (b) View along the crystallographic *a*-axis of **6**-Cd.



Scheme 2.



Scheme 3.

3.2. Carboxylate coordination modes of each polymer

Benzoate groups can coordinate to the metal atoms in four different ways: monodentate (a), chelating (b), bridging (c), and chelating/bridging (d) modes (Scheme 3) [74–76]. In **1**-Co and **6**-Cd, 4,4′-bpy bridged single chains are connected by benzoate ligands with the bridging mode for **1**-Co and with the chelating/bridging mode for **6**-Cd to form ladder-type double chains, and each metal ion has a chelating benzoate ligand. In the helical structure **2**-Ni, benzoates coordinate to Ni atoms as monodentate ligands. In **3**-Cu, benzoate groups bridge two Cu atoms to form paddle-wheel type dinuclear units, and these units are connected by 4,4′-bpy ligands to form an one-dimensional compound. For Zn-benzoate complexes with 4,4′-bpy ligands, two different structures are obtained in different solvent systems. In zigzag chains **4**-Zn, benzoate groups coordinate Zn atoms as monodentate ligands while in the $Zn_3(O_2CPh)_4(\mu\text{-}OH)_2$ units of **5**-Zn, benzoate and hydroxyl groups bridge Zn atoms and terminal two Zn atoms are also coordinated by monodentate benzoate ligands. In **7**-Mn, benzoate ligands bridge Mn atoms to form double zigzag one-dimensional chains, and 4,4′-bpy ligands connect those double zigzag chains to form two-dimensional sheets.

3.3. Solvent effect

The reactions of Zn-benzoate with 4,4′-bpy ligands produced two different structures in different solvent systems, and Cu-benzoate may also show solvent effect based on this work and the previously reported results [54], while the reactions of other metal benzoates (for Co, Ni, Cd, or Mn ions) with 4,4′-bpy ligands did not show solvent effects. The methylene chloride solution of zinc-benzoate can react with the methanol solution of 4,4′-bpy ligand to form an one-dimensional zigzag chain **4**-Zn. The aqua solution of zinc-benzoate can react with the acetone solution of 4,4′-bpy ligand to form two-dimensional compound **5**-Zn. This phenomenon shows the similar result to that found in the our previous Zn-benzoate complexes with bpe ligands (bpe = 1,4-bis(4-pyridyl)ethane) in which the solvent and the ligand-to-metal ratio are simultaneously playing a controlling role over the structure [53].

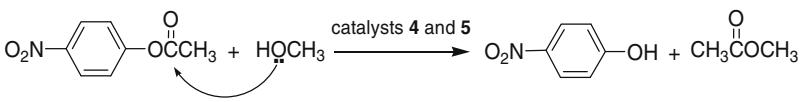
3.4. Conformations of 4,4′-bpy in these seven compounds

Conformations of 4,4′-bpy in these seven compounds are very different depending on crystal structures of different metal ions. Dihedral angles between the two pyridyl rings of 4,4′-bpy are listed in Table 3. The compound **1**-Co and **6**-Cd shows similar structures with different coordination modes of carboxylate ligands, and the dihedral angles between two planes of pyridyl rings are 7.0° and 27.5°, respectively. Two pyridyl rings are nearly coplanar in **1**-Co while those are twisted in **6**-Cd since the chelating/bridging mode of benzoates in **6** may make two pyridyl rings more tilted than those in **1**-Co having the bridging mode. In the helical structure of **2**-Ni, two pyridyl rings are tilted by 17.5° and 20.3°. The bridging 4,4′-bpy ligands in **4**-Zn and **5**-Zn are either nearly planar or exact planar to form a zigzag chain and a two-dimensional structure, respectively. In one-dimensional structure for Cu-benzoate, **3**-Cu containing paddle-wheel type dinuclear units, two pyridyl rings are tilted by 28.2°. In the two-dimensional network of **7**-Mn, two pyridyl rings are much tilted by 39.0°.

3.5. Catalytic transesterification reactions by the compounds **1**–**7**

While an enormous number of the polymeric coordination compounds have been developed and reported over the past 10 years, their application as homogeneous or heterogeneous catalysts is relatively very scarce [18–27]. Therefore, the application of the polymeric compounds as catalysts for various organic reactions is important and meaningful. We have previously reported that the Cu-containing polymeric compounds were found to be a good heterogeneous catalyst for epoxide ring-opening reactions [18,20] that offers the practical advantages of simplifying the separation and isolation of products, and of the potential for catalyst recycling [18–27]. Moreover, we have recently reported that various Zn-containing coordination polymers could carry out the homogeneous and heterogeneous catalytic transesterifications of a range of esters with methanol under the mild conditions [77,78]. While these catalyst systems constitute a promising class of catalysts that appears to be an efficient, mild, and sometimes easily-recyclable method for the alcoholysis of esters and the epoxide ring opening, there is still more demand to develop new type of catalysts that show a high efficiency. Based on the previous results, therefore, we began to examine the reactivity of the Cu-containing polymeric compound **3**-Cu as potential catalysts for the ring opening of epoxides under mild conditions [18,20]. Unfortunately, the reaction was proceeded with only a few percents in several days when a mixture of **3**-Cu and epoxide in methanol was shaken at room temperature. The rest compounds also showed the similar results.

Next, we have tested the catalytic activity of those compounds **1**–**7** for transesterification of phenyl acetate, since we have recently observed that Zn-containing coordination polymers could perform the catalytic transesterification of a variety of esters [77,78]. First of all, the zinc-containing polymeric compounds **4**-Zn and **5**-Zn have been employed as catalysts for transesterification reaction in methanol. The ester, *p*-nitrophenyl acetate, was initially used as a substrate (Eq. (1)):



(1)

Table 3
The dihedral angles (°) between two pyridyl rings of 4,4′-bpy in compounds **1**–**7**.

Compounds	Dihedral angles (°)
1-Co	7.0
2-Ni	17.5, 20.3 (helix)
3-Cu	28.2
4-Zn	3.8, 0.0 (coplanar)
5-Zn	0.0 (coplanar)
6-Cd	27.5
7-Mn	39.0

The polymeric compounds **4**-Zn and **5**-Zn were somewhat soluble in methanol, resulting in a homogeneous condition. Treatment of 4-nitrophenyl acetate and methanol in the presence of **4**-Zn and **5**-Zn at 50 °C produced methyl acetate quantitatively within 0.29 and 0.21 days, respectively, under the neutral conditions (see entry 1 in Table 4). Little transesterification occurred without **4**-Zn and **5**-Zn in the same time period. These efficient reactivities are one of best among the catalytic systems reported previously in Zn-containing coordination and polymeric compounds, to our best knowledge [77–84]. These promising results led us to examine further the transesterification of other esters including *p*-substituted phenyl acetates and benzoates by **4**-Zn and **5**-Zn. The results are also shown in Table 4. The substrates *p*-nitrophenyl acetate and benzoate with the electron-withdrawing substituent at the *para*-position have undergone faster transesterification (entries 1 and 5), while the esters *p*-methylphenyl acetate and benzoate with the electron-donating one such as a methyl group have shown slow reaction (entries 4 and 8). Furthermore, vinyl acetate, which is often used as a precursor for synthesis of various esters [85–87], was converted effectively to the product methyl acetate within 0.5 and 0.5 days, respectively, by **4**-Zn and **5**-Zn. These results suggest that the compounds **4**-Zn and **5**-Zn could be efficient catalysts for ester synthesis by transesterification.

As Zn-containing polymers have shown a good catalytic activity, Cd-containing polymer **6**-Cd, positioned in the same group in the periodic table, was next tested for the transesterification. Surprisingly, the catalyst **6**-Cd catalyzed the conversion of 4-nitrophenyl acetate to the products within 0.62 day. This result is interesting because it is well known that the second period transition metals are much less labile for the substitution reaction [88]. More importantly, this is the first example that a Cd-containing coordination polymer catalyzed the transesterification of esters, to our knowledge. Therefore, this result offers the opportunity to use many Cd-containing polymeric compounds reported to date as a potential catalyst for the transesterification reactions. The catalyst **6**-Cd also catalyzed the transesterification of a variety of substrates including 4-substituted phenyl acetates and 4-substituted benzoates, and its reactivity is comparable to **4**-Zn and **5**-Zn, as shown in Table 4.

After this test, the rest polymeric compounds, **1**-Co, **2**-Ni, **3**-Cu, and **7**-Mn, containing redox-active metals (Co, Ni, Cu, and Mn) were also tested for transesterification reactions of *p*-nitrophenyl acetate. Unexpectedly, **1**-Co, **3**-Cu, and **7**-Mn have shown efficient catalytic reactivities for the transesterification reactions, while **2**-Ni has displayed a very slow conversion (see Table 4). This result suggest that the polymeric compounds **1**-Co, **3**-Cu, and **7**-Mn, well known as redox-active catalysts [89,90], could be employed as a solvolytic catalyst. To our knowledge, this is the first example that redox-active metal-containing coordination polymers catalyzed the transesterification of esters. This result also offers the opportunity to use many redox-active metal-containing polymeric compounds reported to date as a potential catalyst for the transesterification reactions. On the other hand, it deserves to mention the fact that Cu-containing polymeric compound, **3**-Cu, could catalyze transesterification reactions, because we previously reported that Cu-containing polymeric compounds did not catalyze transesterification reactions but do catalyze the epoxide ring-opening reaction [18,20], while our previous Zn-containing polymer-supported catalysts carried out the transesterification reactions efficiently but do not catalyze the epoxide ring-opening reaction [79–84,91]. Therefore, we concluded that the nature of metals plays an important role to perform the specific reactions, for example, transesterification with Zn [79–84,91] versus epoxide ring opening with Fe, Ru, and Cu [18,20,92,93]. However, this observation that **3**-Cu used in this study did catalyze the transesterification reactions suggests that we need more data to have a general conclusion.

These positive results with **1**-Co, **3**-Cu, and **7**-Mn led us to investigate further the transesterification of various *p*-substituted phenyl acetates and benzoates. As shown in Table 4, the substrates with the electron-withdrawing substituents have undergone faster transesterification reactions (entries 1 and 5), while those with the electron-donating ones have shown slow reactions (entries 4 and 8). In addition, *p*-nitrophenyl acetate and *p*-nitrophenyl benzoate, known to be problematic substrates for the transesterification reaction due to undesirable side reactions such as isomerization or polymerization [94], were also converted quantitatively to the corresponding products. Vinyl acetate was used as an acylating agent and, expectedly, converted efficiently to the product methyl acetate within 0.06–1.5 day by **1**-Co, **2**-Ni, **3**-Cu, and **7**-Mn (entry 9), suggesting that these catalytic systems can be useful for preparing various esters by transesterification.

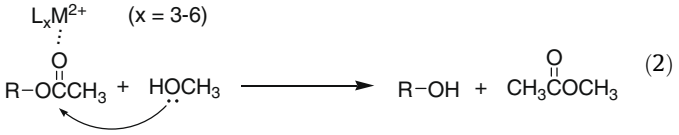
Table 4
Transesterification of esters by methanol in the presence of compounds **1**–**7** at 50 °C.[a]

Entry	Substrate	**1**-Co (time/days)[b]	**2**-Ni (time/days)[b]	**3**-Cu (time/days)[b]	**4**-Zn (time/days)[b]	**5**-Zn (time/days)[b]	**6**-Cd (time/days)[b]	**7**-Mn (time/days)[b]
1	4-nitrophenyl acetate	1	0.71	1.35	0.29	0.21	0.62	0.04
2	4-fluorophenyl acetate	8	39	7	6	2	-	8
3	phenyl acetate	12	44	7	1	1	2	4
4	4-methylphenyl acetate	25	61	10	8	2	-	11
5	4-nitrophenyl benzoate[c]	5	13	6	0.83	1	1	0.08
6	4-chlorophenyl benzoate	20	47	13	4	6	6	7
7	phenyl benzoate	45	55	25	3	3	6	11
8	4-methylphenyl benzoate	50	120	50	8	8	8	20
9	vinyl acetate	1.5	1	1	0.5	0.5	0.5	0.06

[a] All esters were completely converted to the corresponding products, methyl acetate and methyl benzoate. *Reaction conditions:* esters, 0.05 mmol; catalyst, 1.09×10^{-3} mmol for **1**-Co, 2.09×10^{-3} mmol for **2**-Ni, 1.28×10^{-3} mmol for **3**-Cu, 1.39×10^{-3} mmol for **4**-Zn, 0.96×10^{-3} mmol for **5**-Zn, 0.92×10^{-3} mmol for **6**-Cd, and 2.21×10^{-3} mmol for **7**-Mn; solvent, methanol (1 mL). See Section 2 for the detailed reaction conditions.
[b] Time necessary for the complete conversion of substrate to product.
[c] The solvent was a mixture of CH_3OH/CH_2Cl_2 (1/1) because of low solubility of substrate in CH_3OH.

The reactivities of the compounds used in this study are in the order of **5**-Zn > **4**-Zn > **6**-Cd > **7**-Mn ~ **3**-Cu > **1**-Co > **2**-Ni with the consideration of the concentration of each complex (see Section 2), indicating that the non-redox metal-containing compounds, **5**-Zn, **4**-Zn, and **6**-Cd, show better activity than the redox-active metal-containing compounds, **7**-Mn, **3**-Cu, **1**-Co, and **2**-Ni. Based on these results, it is possible to tune the catalytic activities by changing from Zn to those metals such as Cd, a kinetically inert metal, and Cu, Mn, and Co, the redox-active metals.

Though we do not know, at this moment, about the exact reactive species and the reaction mechanism for the transesterification reaction by the catalysts, it has been proposed that the mechanism of metal ion catalyzed transesterification probably involves electrophilic activation of the carbon center of the carbonyl moiety by binding of the metal to the carbonyl oxygen [95–99]. Therefore, Lewis acidity of the metal center may be important in catalytic transesterification. Based on this idea, a possible transesterification mechanism in this catalyst system can be proposed [78]. The substrate phenyl acetate substitutes a labile ligand, maybe benzoate, to give the adduct $L_xM^{2+}\cdots O{=}CR_1(OR_2)R$ (L is 4,4′-bpy or benzoate; x = 3 (**4**-Zn), 4 (**3**-Cu), 5 (**1**-Co, **2**-Ni, **5**-Zn, and **7**-Mn), and 6 (**6**-Cd)) (Eq. (2)). Then, the nucleophile methanol would attack the carbon atom of carbonyl moiety of the adduct to produce the product methyl acetate. Detailed mechanistic studies are currently under investigation:



(2)

4. Conclusions

We have presented a systematic investigation on the coordination polymers assembled from metal benzoates and 4,4′-bpy. Their structures show various coordination modes depending on metal ions: from a tetrahedral (four-coordinate) **4**-Zn ion, a trigonal-bipyramidal (five-coordinate) **5**-Zn ion, an octahedral (six-coordinate) **1**-Co, **2**-Ni, and **7**-Mn ions, a pentagonal-bipyramidal (seven-coordinate) **6**-Cd ion. **1**-Co and **6**-Cd show ladder-type double chains, **2**-Ni does a helical structure, **3**-Cu does a one-dimensional chain containing paddle-wheel units, **4**-Zn does a zigzag chain, **5**-Zn and **7**-Mn do a two-dimensional sheet. Since different structures provide different coordination geometry of each metal ion, it is clear that selection of appropriate metal ions can control the coordination geometry of each metal ion to form different crystal structures.

We have also shown that the compounds **1**–**7** catalyzed the transesterification of a variety of esters. Importantly, the transesterification reactivity shown by the catalysts **4**-Zn and **5**-Zn are very efficient and one of the best among the catalytic efficiencies reported previously with Zn-containing coordination and polymeric compounds. In addition, the catalyst **6**-Cd containing Cd ion, well known as an inert metal ion for the ligand substitution, also catalyzed efficiently the transesterification of a variety of esters, and its reactivity is comparable to **4**-Zn and **5**-Zn. Moreover, the redox-active metal-containing polymers, **1**-Co, **3**-Cu, and **7**-Mn, have shown efficient catalytic reactivities for the transesterification reactions, while **2**-Ni has displayed a very slow conversion. This result suggests that the polymeric compounds **1**-Co, **3**-Cu, and **7**-Mn, well known as redox-active catalysts, could be employed as a solvolytic catalyst. To our knowledge, this is the first example that redox-active metal-containing coordination polymers catalyzed the transesterification of esters. This result also offers the opportunity to use many redox-active metal-containing polymeric compounds reported to date as a potential catalyst for the transesterification reactions.

The reactivities of the compounds used in this study are in the order of **5**-Zn > **4**-Zn > **6**-Cd > **7**-Mn ~ **3**-Cu > **1**-Co > **2**-Ni, indicating that the non-redox metal-containing compounds, **5**-Zn, **4**-Zn, and **6**-Cd, show better activity than the redox-active metal-containing compounds, **7**-Mn, **3**-Cu, **1**-Co, and **2**-Ni. These results suggest that it is possible to tune the catalytic activities by changing from Zn to those metals such as Cd, a kinetically inert metal, and Cu, Mn, and Co, the redox-active metals.

Supplementary data

CCDC 695227–695232 contain the supplementary crystallographic data for **1**-Co, **2**-Ni, **3**-Cu, **4**-Zn, **5**-Zn, and **6**-Cd. These data can be obtained free of charge via http://www.ccdc.cam.ac.uk/conts/retrieving.html, or from the Cambridge Crystallographic Data Centre, 12 Union Road, Cambridge CB2 1EZ, UK; fax: (+44) 1223-336-033; or e-mail: deposit@ccdc.cam.ac.uk.

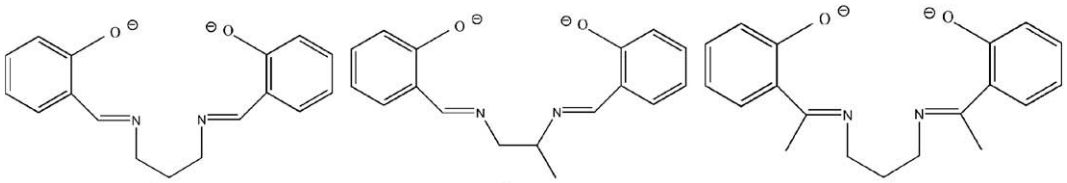
Acknowledgements

Financial support from Korea Ministry Environment "ET – Human Resource Development Project", the Korea Research Foundation (2007-314-C00159), the Korean Science and Engineering Foundation (R01-2008-000-20704-0), The SEOUL R&BD Program, and the SRC program of the Korea Science and Engineering Foundation (KOSEF) through the Center for Intelligent Nano-Bio Materials at Ewha Womans University (Grant R11-2005-008-00000-0) is gratefully acknowledged.

References

[1] S.R. Batten, R. Robson, Angew. Chem., Int. Ed. 37 (1998) 1460.
[2] D.B. Moler, H. Li, B. Chen, T.M. Reineke, M. O'Keeffe, O.M. Yaghi, Acc. Chem. Res. 34 (2001) 319.
[3] B. Moulton, M.J. Zaworotko, Chem. Rev. 101 (2001) 1629.
[4] K. Kim, Chem. Soc. Rev. 31 (2002) 96.
[5] C. Janiak, Dalton Trans. (2003) 2781.
[6] P.J. Hagrman, D. Hagrman, J. Zubieta, Angew. Chem., Int. Ed. 38 (1999) 2638.
[7] S. Noro, R. Kitaura, M. Komdo, S. Kitagawa, T. Ishii, H. Matsuzaka, M. Yamashita, J. Am. Chem. Soc. 124 (2002) 2568. and references therein.
[8] S.L. James, Chem. Soc. Rev. 32 (2003) 276.
[9] K.S. Min, M.P. Suh, J. Am. Chem. Soc. 122 (2000) 6834.
[10] J. Fan, L. Gan, H. Kawaguchi, W.-Y. Sun, K.-B. Yu, W.-X. Tang, Chem. Eur. J. 9 (2003) 3965.
[11] A.J. Fletcher, E.J. Cussen, D. Bradshaw, M.J. Rosseinsky, K.M.J. Thomas, Am. Chem. Soc. 126 (2004) 9750.
[12] D.N. Dybtsev, H. Chun, K. Kim, Angew. Chem., Int. Ed. 43 (2004) 5033.
[13] E.-Y. Choi, K. Park, C.-M. Yang, H. Kim, J.-H. Son, S.W. Lee, Y.H. Lee, D. Min, Y.-U. Kwan, Chem. Eur. J. 10 (2004) 5535.
[14] J.L.C. Rowsell, O.M. Yaghi, Angew. Chem., Int. Ed. 44 (2005) 4670.
[15] B. Kesanli, Y. Cui, M.R. Smith, E.W. Bittner, B.C. Bockrath, W. Lin, Angew. Chem., Int. Ed. 44 (2005) 72.
[16] H. Chun, D.N. Dybtsev, H. Kim, K. Kim, Chem. Eur. J. 11 (2005) 3521.
[17] G.A. Mines, B.-C. Tzeng, K.J. Stevenson, J. Li, J.T. Hupp, Angew. Chem., Int. Ed. 41 (2002) 154.
[18] S.-K. Yoo, J.Y. Ryu, J.Y. Lee, C. Kim, S.-J. Kim, Y. Kim, Dalton Trans. (2003) 1454.
[19] S. Takizawa, H. Somei, D. Jayaprakash, H. Sasai, Angew. Chem., Int. Ed. 42 (2003) 5711.
[20] S.J. Hong, J.Y. Ryu, J.Y. Lee, C. Kim, S.-J. Kim, Y. Kim, Dalton Trans. (2004) 2697.
[21] S. Kitagawa, R. Kitaura, S.-I. Noro, Angew. Chem., Int. Ed. 43 (2004) 2334.
[22] S.J. Hong, J.S. Seo, J.Y. Ryu, J.H. Lee, C. Kim, S.-J. Kim, Y. Kim, A.J. Lough, J. Mol. Struct. 751 (2005) 22.
[23] C.-D. Wu, A. Hu, L. Zhang, W.J. Lin, Am. Chem. Soc. 127 (2005) 8940.
[24] X. Wang, X. Wang, H. Guo, Z. Wang, K. Ding, Chem. Eur. J. 11 (2005) 4078.
[25] H. Han, S. Zhang, H. Hou, Y. Fan, Y. Zhu, Eur. J. Inorg. Chem. (2006) 1594.
[26] D.N. Dybtsev, A.L. Nuzhdin, H. Chun, K.P. Bryliakov, E.P. Talsi, V.P. Fedin, K. Kim, Angew. Chem., Int. Ed. 45 (2006) 916.
[27] S. Hasegawa, S. Horike, R. Matsuda, S. Furukawa, K. Mochizuki, Y. Kinoshita, S.J. Kitagawa, Am. Chem. Soc. 129 (2007) 2607.
[28] M.C. Hong, Y.J. Zhao, W.P. Su, R. Cao, M. Fujita, Z.Y. Zhou, A.S.C. Chan, J. Am. Chem. Soc. 122 (2000) 4819.

[29] J.F. Ma, J.F. Liu, X. Yan, H.Q. Jia, Y.H. Lin, J. Chem. Soc., Dalton Trans. (2000) 2403.
[30] D.M. Shin, I.S. Lee, Y.-A. Lee, Y.K. Chung, Inorg. Chem. 42 (2003) 2977.
[31] C. Richardson, P.J. Steel, D.M. D'Alessandro, P.C. Junk, F.R. Keene, J. Chem. Soc., Dalton Trans. (2002) 2775.
[32] K. Biradha, M.J. Fujita, Chem. Soc., Dalton Trans. (2000) 3805.
[33] O.-S. Jung, S.H. Park, K.M. Kim, H.G. Jang, Inorg. Chem. 37 (1998) 5781.
[34] M.A. Withersby, A.J. Blake, N.R. Champness, P.A. Cooke, P. Hubberstey, W.-S. Li, M. Schroder, Inorg. Chem. 38 (1999) 2259.
[35] W.-X. Chen, S.-T. Wu, L.-S. Long, R.-B. Huang, L.-S. Zheng, Crystal Growth Design 7 (2007) 1171.
[36] R.-Q. Fang, X.-M. Zhang, Inorg. Chem. 45 (2006) 4801.
[37] Y.B. Go, X. Wang, E.V. Anokhina, A.J. Jacobson, Inorg. Chem. 44 (2005) 8265.
[38] Y.-B. Dong, Y.-Y. Jiang, J. Li, J.-P. Ma, F.-L. Liu, B. Tang, R.-Q. Huang, S.R.J. Batten, Am. Chem. Soc. 129 (2007) 4520.
[39] C.-M. Liu, S. Gao, D.-Q. Zhang, D.-B. Zhu, Crystal Growth Design 7 (2007) 1312.
[40] L. Carlucci, G. Ciani, D.M. Proserpio, S. Rizzato, Chem. Eur. J. 5 (1999) 237.
[41] H.-P. Wu, C. Janiak, G. Rheinwald, H.J. Lang, Chem. Soc., Dalton Trans. (1999) 183.
[42] A.J. Blake, N.R. Brooks, N.R. Champness, P.A. Cooke, A.M. Deveson, D. Fenske, P. Hubberstey, M.J. Schroder, Chem. Soc., Dalton Trans. (1999) 2103.
[43] R.W. Saalfrank, I. Bernt, M.M. Chowdhry, F. Hampel, G.B.M. Vaughan, Chem. Eur. J. 7 (2001) 2765.
[44] V.R. Pedireddi, S. Varughese, Inorg. Chem. 43 (2004) 450.
[45] M.-L. Tong, H.-J. Chen, X.-M. Chen, Inorg. Chem. 39 (2000) 2235.
[46] Y.-S. Zhang, G.D. Enright, S.R. Breeze, S. Wang, New J. Chem. 23 (1999) 625.
[47] N.L. Toh, M. Nagarathinam, J.J. Vittal, Angew. Chem., Int. Ed. 44 (2005) 2237.
[48] B. Conerney, P. Jensen, P.E. Kruger, B. Moubaraki, K.S. Murray, CrystEngCommun. 5 (2003) 454.
[49] R. Carballo, B. Covelo, M.S.E. Fallah, J. Ribas, E.M. Vazquez-Lopez, Crystal Growth Design 7 (2007) 1069.
[50] M.V. Marinho, M.I. Yoshida, K.J. Guedes, K. Krambrock, A.J. Bortoluzzi, M. Horner, F.C. Machado, W.M. Teles, Inorg. Chem. 43 (2004) 1539.
[51] B.-H. Ye, X.-M. Chen, F. Xue, L.-N. Ji, T.C.W. Mak, Inorg. Chim. Acta 299 (2000) 1.
[52] H. Kwak, S.H. Lee, S.H. Kim, Y.M. Lee, B.K. Park, E.Y. Lee, Y.J. Lee, C. Kim, S.-J. Kim, Y. Kim, Polyhedron 27 (2008) 3484.
[53] H. Kwak, S.H. Lee, S.H. Kim, Y.M. Lee, B.K. Park, Y.J. Lee, J.Y. Jun, C. Kim, S.-J. Kim, Y. Kim, Polyhedron 28 (2009) 553.
[54] One example has been reported by Wu et al. that the reaction of copper benzoate with 4,4′-bpy is dependent on pH for the formation of the coordination complexes. S.-T. Wu, L.-S. Long, R.-B. Huang, L.-S. Zheng, Crystal Growth Design 7 (2007) 1746.
[55] Bruker, SHELXTL/PC, Version 6.12 for Windows XP, Bruker AXS Inc., Madison, Wisconsin, USA, 2001.
[56] H. Chen, W.-G. Wang, C.-B. Ma, C.-N. Chen, Q.-T. Liu, Jiegou Huaxue 26 (2007) 687.
[57] K. Nakamoto, Infrared and Raman Spectra of Inorganic and Coordination Compounds, John Wiley and Sons, New York, 1986.
[58] J. Tao, M.-L. Tong, X.-M. Chen, J. Chem. Soc., Dalton Trans. (2000) 3669.
[59] W. Chen, J.-Y. Wang, C. Chen, Q. Yue, H.-M. Yuan, J.-S. Chen, S.-N. Wang, Inorg. Chem. 42 (2003) 944.
[60] J. Lu, C. Yu, T. Niu, T. Paliwala, G. Crisci, F. Somosa, A.J. Jacobson, Inorg. Chem. 37 (1988) 4637.
[61] K. Biradha, C. Seward, M. Zaworotko, Angew. Chem., Int. Ed. 38 (1999) 492.
[62] L.-G. Zhu, S. Kitagawa, H. Miyasaka, H.-C. Chang, Inorg. Chim. Acta 355 (2003) 121.
[63] S. Takamizawa, E. Nakata, H. Yokoyama, Inorg. Chem. Commun. 6 (2003) 763.
[64] A.M. Goforth, K. Gerth, M.D. Smith, S. Shotwell, U.H.F. Bunz, H.-C. zur Loye, Solid State Sci. 7 (2005) 1083.
[65] X.-J. Luan, X.-H. Cai, Y.-Y. Wang, D.-S. Li, C.-J. Wang, P. Liu, H.-M. Hu, Q.-Z. Shi, S.-M. Peng, Chem. Eur. J. 12 (2006) 6281.
[66] M.T. Ng, T.C. Deivaraj, W.T. Klooster, G.J. McIntyre, J.J. Vittal, Chem. Eur. J. 10 (2004) 5853.
[67] R. Wang, F. Jiang, Y. Zhou, L. Han, M. Hong, Inorg. Chim. Acta 358 (2005) 545.
[68] J.T. Tao, M.-L. Tong, J.-X. Shi, X.-M. Chen, S.W. Ng, Chem. Commun. (2000) 2043.
[69] M.J. Plater, M.R.St.J. Foreman, T. Gelbrich, M.B. Hursthouse, J. Chem. Soc., Dalton Trans. (2000) 1995.
[70] J.Y. Lee, S.J. Hong, C. Kim, S.-J. Kim, Y. Kim, Inorg. Chem. Commun. 8 (2005) 692.
[71] J. Tao, M.-L. Tong, X-M. Chen, J. Chem. Soc., Dalton Trans. (2000) 3669.
[72] Y. Ma, Y. He, L. Zhang, X. Wang, J. Gao, Z. Han, Struct. Chem. 18 (2007) 1005.
[73] L.-Y. Zhang, J.-P. Zhang, Y.-Y. Lin, X.-M. Chen, Crystal Growth Design 6 (2006) 1684.
[74] M. Casarin, C. Corvaja, C.D. Nicola, D. Falcomer, L. Franco, M. Monari, L. Pandolfo, C. Pettinari, F. Piccinelli, Inorg. Chem. 44 (2005) 6265.
[75] B.-H. Ye, M.-L. Tong, X.-M. Chen, Coord. Chem. Rev. 249 (2005) 545.
[76] F. Li, T. Li, X. Li, X. Li, Y. Wang, R. Cao, Crystal Growth Design 6 (2006) 1458.
[77] Y.M. Lee, S.J. Hong, H.J. Kim, S.H. Lee, H. Kwak, C. Kim, S.-J. Kim, Y. Kim, Inorg. Chem. Commun. 10 (2007) 287.
[78] H. Kwak, S.H. Lee, S.H. Kim, Y.M. Lee, E.Y. Lee, B.K. Park, E.Y. Kim, C. Kim, S.-J. Kim, Y. Kim, Eur. J. Inorg. Chem. (2008) 408.
[79] J.S. Seo, D. Whang, H. Lee, S.I. Jun, J. Oh, Y.J. Jeon, K. Kim, Nature 404 (2000) 982.
[80] J.Y. Ryu, J.H. Han, J.Y. Lee, S.J. Hong, S.H. Choi, C. Kim, S.-J. Kim, Y. Kim, Inorg. Chim. Acta 358 (2005) 3659.
[81] Y. Kim, S.-J. Kim, S.H. Choi, J.H. Han, S.H. Nam, J.H. Lee, H.J. Kim, C. Kim, D.W. Kim, H.G. Jang, Inorg. Chim. Acta 359 (2006) 2534.
[82] J.Y. Kwon, Y. Kim, S.-J. Kim, S.H. Lee, H. Kwak, C. Kim, Inorg. Chim. Acta 361 (2008) 1885.
[83] L. Xu, Y. Kim, S.-J. Kim, H.J. Kim, C. Kim, Inrog. Chem. Commun. 10 (2007) 586.
[84] B.K. Park, S.H. Lee, E.Y. Lee, H. Kwak, Y.M. Lee, Y.J. Lee, J.Y. Jun, C. Kim, S.-J. Kim, Y.J. Kim, Mol. Struct. 890 (2008) 123.
[85] G.W. Nyce, J.A. Lamboy, E.F. Connor, R.M. Waymouth, J.L. Hedrick, Org. Lett. 4 (2002) 3587.
[86] D. Tashiro, Y. Kawasaki, S. Sakaguchi, Y.J. Ishii, Org. Chem. 62 (1997) 8141.
[87] Y. Ishii, M. Takeno, Y. Kawasaki, Y. Muromachi, Y. Nishiyama, S. Sakaguchi, J. Org. Chem. 61 (1996) 3088.
[88] S.J. Lippard, J.M. Berg, Principles of Bioinorganic Chemistry, University Science Books, Mill Valley, CA, 1994.
[89] E.M. McGarrigle, D.G. Gilheany, Chem. Rev. 105 (2005) 1563.
[90] E. Kim, E.E. Chufan, K. Kamaraj, K.D. Karlin, Chem. Rev. 104 (2004) 1077.
[91] D.-W. Yoo, J.-H. Han, S.H. Nam, H.J. Kim, C. Kim, J.-K. Lee, Inorg. Chem. Commun. 9 (2006) 654.
[92] D.-W. Yoo, S.-K. Yoo, C. Kim, J.-K. Lee, J. Chem. Soc., Dalton Trans. (2002) 3931.
[93] S.H. Lee, E.Y. Lee, D.-W. Yoo, S.J. Hong, J.H. Lee, H. Kwak, Y.M. Lee, J. Kim, C. Kim, J.-K. Lee, New J. Chem. 31 (2007) 1579.
[94] V.K. Aggarwal, A. Mereu, Chem. Commun. (1999) 2311.
[95] F.E. Jacobsen, J.A. Lewis, S.M. Cohen, J. Am. Chem. Soc. 128 (2006) 3156.
[96] J. Weston, Chem. Rev. 105 (2005) 2151.
[97] G. Parkin, Chem. Rev. 104 (2004) 699.
[98] W.D. Horrocks Jr., J.N. Ishley, R.R. Whittle, Inorg. Chem. 21 (1982) 3265.
[99] W.D. Horrocks Jr., J.N. Ishley, R.R. Whittle, Inorg. Chem. 21 (1982) 3270.



Scheme 1.

To the resulting solution, NaOCN (0.130 g, 2.00 mmol) dissolved in a minimum amount of water was added, stirring continued for 3 h, to complete the aerial oxidation of Mn^{II}. The filtered solution was kept in a refrigerator (5 °C) for 1 week when dark green crystals deposited. Yield: 0.234 g (0.62 mmol, 62%). *Anal. Calc.* for $C_{36}H_{32}N_6O_6Mn_2$: C, 57.1; H, 4.27; N, 11.14. Found: C, 57.20; H, 4.23; N, 11.23%. Characteristic IR absorptions (cm^{-1}): ν_a(NCO) 2160, ν_s(NCO) 1313, δ(NCO) 615, $\nu_{schiff\ base}$(C=N) 1620. Electronic absorption bands ($\bar{\nu}_{max}/10^3\ cm^{-1}$, $\varepsilon_{max}/100\ cm^{-1}\ M^{-1}$): 17.11, 3.47(sh); 26.34, 66.0; 32.94, 108(sh); 35.65, 180.

2.2.2. [Mn(salmen)N_3]$_2$ (**2**)

In a beaker open to the atmosphere, salicylaldehyde (0.244 g, 1.00 mmol) and 1,2-diaminopropane (0.074 g, 1.0 mmol) were stirred in 40 mL of methanol. $Mn(CH_3COO)_2 \cdot 4H_2O$ (0.245 g, 1.00 mmol) was added, and stirring was continued for about 1 h. To the resulting solution, NaN_3 (0.130 g, 2.00 mmol) dissolved in a minimum amount of water was added and stirring continued for 3 h to complete the aerial oxidation of Mn^{II}. The resulting microcrystalline precipitate was filtered off and dried. Yield: 0.306 g (0.81 mmol, 81%). It was recrystallized by slow evaporation of an acetonitrile solution at room temperature yielding dark-brown X-ray quality crystals. *Anal. Calc.* for $C_{36}H_{32}N_{10}O_4Mn_2$: C, 54.12; H, 4.27; N, 18.57. Found: C, 54.19; H, 4.32; N, 18.98%. Characteristic IR absorptions (cm^{-1}): $\nu_a(N_3)$ 2035, $\nu_s(N_3)$ 1309, $\delta(N_3)$ 599, $\nu_{schiff\ base}$(C=N) 1612. Electronic absorption bands ($\bar{\nu}_{max}/10^3\ cm^{-1}$, $\varepsilon_{max}/100\ cm^{-1}\ M^{-1}$): 20.20, 12.1(sh); 24.44, 45.7; 28.35, 61.5(sh); 32.16, 124, 35.87,192.

2.2.3. [Mn(acphpn)N_3]$_2$ (**3**)

In a beaker open to the atmosphere, $Mn(CH_3COO)_2 \cdot 4H_2O$ (0.245 g, 1.00 mmol) and NaN_3 (0.130 g, 2.00 g) were dissolved in 30 mL methanol and filtered. 2-Hydroxyacetophenone (0.272 g, 2.00 mmol) and 1,3-diaminopropane (0.071 g, 1.0 mmol) were dissolved in 30 mL methanol and filtered. The two solutions were mixed and stirred for 2 h to complete the aerial oxidation of Mn^{II}. The filtered solution was kept at room temperature for three days to obtain dark green crystals. Yield: 0.254 g (0.63 mmol, 63%). *Anal. Calc.* for $C_{38}H_{40}N_{10}O_4Mn_2$: C, 56.25; H, 4.98; N, 17.26. Found: C, 56.45; H, 4.98; N, 17.36%. Characteristic IR absorptions (cm^{-1}): $\nu_a(N_3)$ 2038, $\nu_s(N_3)$ 1300, $\delta(N_3)$ 522, $\nu_{schiff\ base}$(C=N) 1587. Electronic absorption bands ($\bar{\nu}_{max}/10^3\ cm^{-1}$, $\varepsilon_{max}/100\ cm^{-1}\ M^{-1}$): 18.00, 8.04; 26.32, 67.0(sh); 30.01, 89.0; 36.67, 191.

2.3. Magnetic studies

The magnetic susceptibility was measured in the 1.98–300 K temperature range using a Quantum Design MPMS SQUID susceptometer. The samples were pressed into pellets to avoid orientation effects of the microcrystals during magnetic measurements. Diamagnetic corrections were applied using Pascal's constants [24]. The magnetic susceptibilities have been computed both with the program SUSCEP [25] based on the expression derived from the isotropic spin-exchange Hamiltonian, $\hat{H} = -2J\hat{S}_1\hat{S}_2$ ($S1 = S_2 = 2$) and van Vleck's equation [26], and by exact calculations of the energy levels associated to the spin Hamiltonian through diagonalization of the full matrix with a general program for axial symmetry [27]. In the latter case, least-squares fittings were accomplished with an adapted version of the function-minimization program MINUIT [28].

2.4. X-ray crystallography

X-ray data were collected for compounds **1–3** on a Bruker SMART APEX CCD X-ray diffractometer, using graphite-monochromated Mo K radiation ($\lambda = 0.71073$ Å). Data were reduced using SAINTPLUS [29], and a multi-scan absorption correction using SADABS [30] was performed. The structures were solved using SHELXS-97 and full matrix least-squares refinements against F^2 were carried out using SHELXL-97 [31]. All ring hydrogen atoms were assigned on the basis of geometrical considerations and were allowed to ride upon the respective carbon atoms. All hydrogen atoms were assigned fixed U_{iso} values, equal to $1.2U_{eq}$ of the parent atom for ring and $1.5U_{eq}$ for methyl hydrogens. Crystallographic data and structure refinement parameters are presented in Table 1. Selected bond distances and angles are collated in Tables 2–4.

3. Results and discussion

3.1. Crystal structures

All three complexes crystallize in the $P2_1/n$ space group. Complexes **1** and **2** have almost identical formula weights and nearly equal unit cell dimensions, even though their chemical compositions are different. The crystals of all three complexes contain dinuclear Mn^{III} entities (Fig. 1), wherein the two centrosymmetrically related five-coordinate metal centers are held by two weak phenoxo bridges (Mn···O in the 2.49–2.59 Å range). Within each five-coordinate unit, the tetradentate Schiff base ligand chelates in the equatorial mode, while the axial position is occupied by a nitrogen atom from the pseudo-halide ion, azide or cyanate, coordinating in a bent mode. The equatorial donor atoms (O_2N_2) are very nearly coplanar even though the manganese atom deviates significantly from this plane (0.16 Å in **1**; 0.20 Å in **2**; 0.13 Å in **3**). The mean planes of the two halves of the Schiff base ligands (excluding the methylene groups) are inclined with respect to each other by 15° in the three crystals. There are only slight differences in the Mn–(N,O) distances in the three complexes: Mn–O($eq.$)$_{av}$, Mn–N($eq.$)$_{av}$, Mn–N($ax.$) are, respectively, 1.90, 2.01, 2.14 Å in **1**; 1.88, 1.99, 2.14 Å in **2**; 1.89, 2.01, 2.17 Å in **3**. The overall coordination geometry of each Mn^{III} ion is thus distorted octahedral with the Jahn–Teller elongation along the OCN/NNN–Mn···O axis.

Coming to the dimer formed by bridging the five-coordinate complex molecules, the plane of the Mn_2O_2 bridge is nearly perpendicular to the equatorial coordination plane: dihedral angle, 88.5° in **1**, 87.4° in **2**, 89.7° in **3**. The axial N atom deviates only slightly from the bridging plane (0.08 Å in **1**; 0.16 Å in **2**; 0.03 Å in **3**). The most important difference between the three dimers

Table 1
Crystallographic data and structure refinement for **1**, **2** and **3.**

	1	**2**	**3**
Formula	$C_{36}H_{32}Mn_2N_6O_6$	$C_{34}H_{32}Mn_2N_{10}O_4$	$C_{38}H_{40}Mn_2N_{10}O_4$
Formula weight	754.56	754.58	810.68
Crystal system	monoclinic	monoclinic	monoclinic
a (Å)	8.6269(5)	8.6770(17)	8.4760(5)
b (Å)	13.6701(8)	13.731(3)	20.2098(12)
c (Å)	14.3355(8)	14.326(3)	10.3259(6)
α (°)	90	90	90
β (°)	105.1050(10)	104.316(3)	91.2810(10)
γ (°)	90	90	90
V (Å^3)	1632.18(16)	1653.8(6)	1768.37(18)
Space group	$P2_1/n$	$P2_1/n$	$P2_1/n$
Z	2	2	2
T (K)	100(2)	298(2)	298(2)
ρ_{calcd} (g cm^{-3})	1.535	1.515	1.522
μ (mm^{-1})	0.832	0.820	0.772
Reflections collected	18686	18714	20250
θ Range (°)	2.09–28.26	2.09–28.31	2.02–28.24
$h/k/l$ indices	−11,11/−18,18/−18,19	−11,11/−17,18/−18,18	−11,11/−26,26/−13,13
Unique reflection, R_{int}	4047, 0.0218	3969, 0.0536	4221, 0.0280
GOF	1.363	1.058	1.028
R (F_o^2)[a] [$I > 2\sigma(I)$]	0.0351	0.0616	0.0360
R_w (F_o^2)[b] [$I > 2\sigma(I)$]	0.0986	0.1361	0.0916
$\Delta\rho_{max}$, $\Delta\rho_{min}$ (e Å^{-3})	0.328, −0.223	0.583, −0.362	0.348, −0.225

[a] $R = \sum||F_o| - |F_c||/\sum|F_o|$.
[b] $R_w = [\sum w(F_o^2 - F_c^2)^2 / \sum(wF_o^4)]^{1/2}$.

Table 2
Selected bond lengths [Å] and angles [°] for **1**.

Mn–O1	1.9162(11)	Mn–N1	2.0261(13)	Mn–N3	2.1394(15)
Mn–O2	1.8757(11)	Mn–N2	1.9920(13)	Mn–O1#1	2.5130(11)
N3–C18	1.169(2)	C18–O3	1.195(2)		
O1–Mn–N1	87.73(5)	O2–Mn–N1	169.90(5)	O1–Mn–O1#1	79.42(4)
O1–Mn–N2	170.78(5)	O2–Mn–N2	90.58(5)	O2–Mn–O1#1	86.42(4)
O1–Mn–N3	96.07(6)	O2–Mn–N3	95.82(6)	N1–Mn–O1#1	83.50(5)
N1–Mn–N3	94.29(6)	O2–Mn–O1	91.07(5)	N2–Mn–O1#1	91.63(5)
Mn–N3–C18	135.11(14)	N2–Mn–N1	89.06(6)	N3–Mn–O1#1	175.02(5)
N3–C18–O3	178.2(2)	Mn–O1–Mn#1	100.58(4)	#1 $-x+1, -y+1, -z+1$	

Table 3
Selected bond lengths [Å] and angles [°] for **2**.

Mn–O1	1.903(2)	Mn–N1	1.988(3)	Mn–N3	2.137(3)
Mn–O2	1.860(2)	Mn–N2	1.984(3)	Mn–O1#1	2.589(2)
N3–N4	1.183(5)	N4–N5	1.153(5)		
O1–Mn–N1	88.85(11)	O2–Mn–N1	169.18(11)	O1–Mn–O1#1	81.46(9)
O1–Mn–N2	163.55(12)	O2–Mn–N2	92.15(12)	O2–Mn–O1#1	87.61(9)
O1–Mn–N3	96.15(12)	O2–Mn–N3	97.00(13)	N1–Mn–O1#1	82.78(10)
N1–Mn–N3	92.79(13)	O2–Mn–O1	94.65(10)	N2–Mn–O1#1	83.87(10)
Mn–N3–N4	127.8(3)	N2–Mn–N1	81.93(13)	N3–Mn–O1#1	174.99(11)
N5–N4–N3	177.9(5)	Mn–O1–Mn#1	98.55(4)	#1 $-x+1, -y+1, -z+1$	

Table 4
Selected bond lengths [Å] and angles [°] for **3**.

Mn–O1	1.8633(12)	Mn–N1	2.0148(13)	Mn–N3	2.1722(16)
Mn–O2	1.9124(11)	Mn–N2	2.0050(13)	Mn–O2#1	2.4929(12)
N3–N4	1.177(2)	N4–N5	1.157(3)		
O1–Mn–N1	89.51(5)	O2–Mn–N1	169.78(5)	O2–Mn–O2#1	78.77(5)
O1–Mn–N2	174.51(6)	O2–Mn–N2	85.63(5)	O1–Mn–O2#1	88.00(5)
O1–Mn–N3	91.59(6)	O2–Mn–N3	95.91(6)	N1–Mn–O2#1	91.84(5)
N1–Mn–N3	93.52(6)	O1–Mn–O2	94.16(5)	N2–Mn–O2#1	86.58(5)
N2–Mn–N1	89.82(6)	Mn–N3–N4	130.80(14)	N3–Mn–O2#1	174.61(5)
N5–N4–N3	178.5(2)	Mn–O2–Mn#1	101.23(5)	#1 $-x, -y+2, -z$	

arises from the bridging bond lengths (Å) and angles (°): Mn–O, Mn···O, Mn–O···Mn are, respectively, 1.92, 2.51, 100.6 in **1**; 1.90, 2.59, 98.5 in **2**; 1.91, 2.49, 101.2 in **3**. The Mn···Mn distance in the three dimers is 3.43 Å. In summary, the bridge geometry in compound **3** is characterized by a shorter Mn···O distance coupled with a wider Mn–O···Mn angle while the longer Mn···O distance goes with a more acute Mn–O···Mn angle in compound **2**; compound **1** has a bridge geometry intermediate between those of **2**

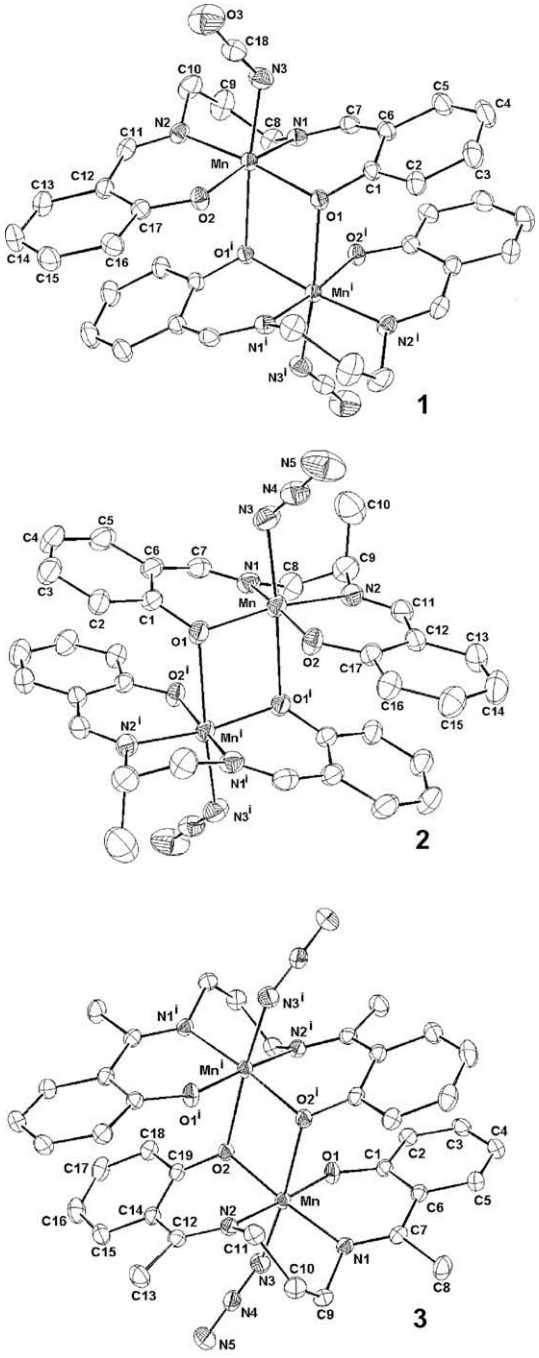


Fig. 1. ORTEP view of the dimers in $[Mn(salpn)NCO]_2$ (**1**) $[Mn(salmen)N_3]_2$ (**2**) $[Mn(acphpn)N_3]_2$ (**3**). Hydrogen atoms are omitted, and the thermal ellipsoids are represented at the 30% probability level. i = $-x+1$, $-y+1$, $-z+1$ for **1**; $-x+1$, $-y+1$, $-z+1$ for **2**; $-x,-y+2,-z$ for **3**.

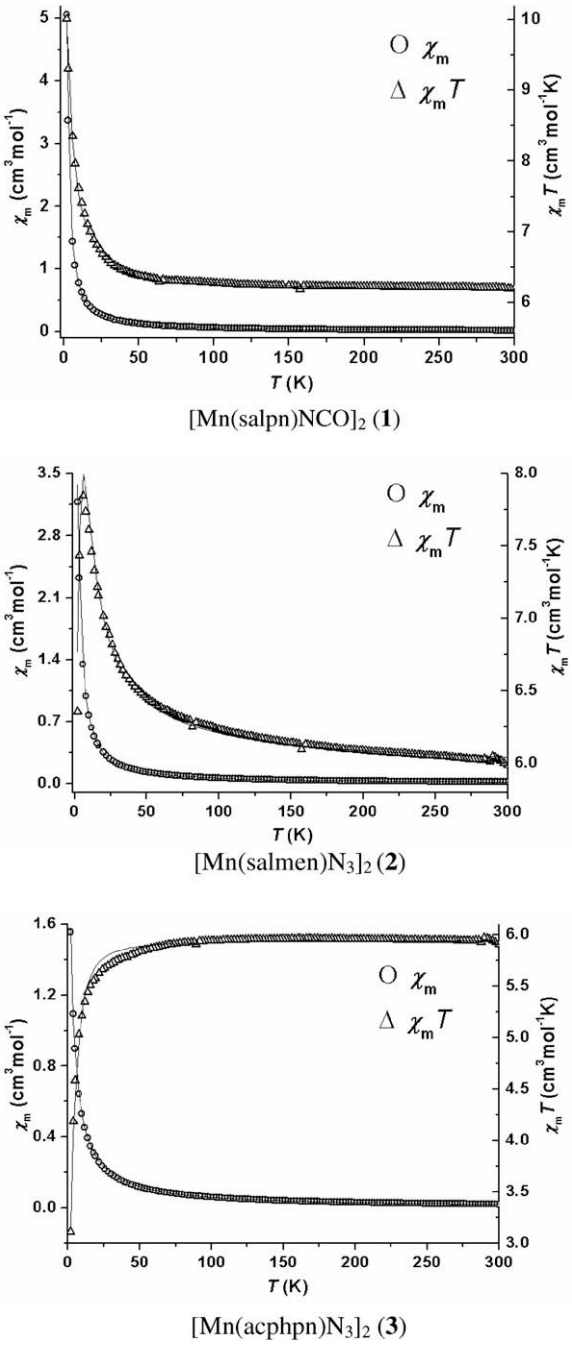


Fig. 2. Temperature variation of the magnetic susceptibility χ_m and $\chi_m T$ product (per dimeric unit) for compounds **1**–**3**. Magnetic field strength used: 1000 Oe (**1**); 5000 Oe (**2**); 3000 Oe (**3**).

and **3**. These differences have an important bearing on the magnetic properties.

3.2. Magnetic properties

The variations of the molar magnetic susceptibility χ_m, and of the product $\chi_m T$ in the temperature range 1.98–300 K for the three complexes are shown in Fig. 2. The room temperature $\chi_m T$ values ($cm^3\ mol^{-1}\ K$) are nearly equal for the three dimers and comparable to the expected spin-only value of 6.00 $cm^3\ mol^{-1}\ K$ per dinuclear Mn^{III} unit: 6.19 for **1**; 5.99 for **2**; 5.90 for **3**. However, the three compounds behave differently when the temperature is lowered. In the case of compound **1**, $\chi_m T$ increases continuously to reach a value of 10.01 $cm^3\ mol^{-1}\ K$ at 1.98 K. Since the expected value for the $S = 4$ ground state is 10.00 $cm^3\ mol^{-1}\ K$, the above result proves the ferromagnetic coupling within the dimer and the absence of significant competing effects from Mn^{III} single ion zero-field splitting and/or antiferromagnetic inter-dimer interactions. Compound **2** also shows an increase upon lowering the temperature. However a maximum $\chi_m T$ of 7.85 $cm^3\ mol^{-1}\ K$ is reached at 5.82 K. Further cooling leads to a rapid decrease to 6.34 $cm^3\ mol^{-1}\ K$ at 2 K. Therefore, while the intra-dimer interaction in compound **2** is ferromagnetic like in **1**, there are competing Mn^{III} single

ion zero-field splitting (zfs) effects and/or antiferromagnetic inter-dimer interactions leading to a rapid fall in $\chi_m T$ below 6 K. In sharp contrast to **1** and **2**, compound **3** is clearly an antiferromagnetically coupled dimer with the $\chi_m T$ value decreasing continuously upon cooling from room temperature to reach a value of 3.11 $cm^3\ mol^{-1}$ K at 2 K.

The magnetic susceptibilities were therefore computed through exact diagonalisation of the spin Hamiltonian including Zeeman and zfs terms and isotropic exchange [27] and fitted to the experimental magnetic data by least-squares techniques [28]. The calculations employed the Hamiltonian, $\beta H \cdot \mathbf{g} \cdot (S_1 + S_2) - 2JS_1 \cdot S_2 + D(S_{z1}^2 + S_{z2}^2)$. Although **g**-tensor was assumed to be axial, the difference between its parallel and perpendicular components was not significant. The single ion zero-field splitting parameter, D is identical for the two centrosymmetrically related Mn^{III} ions in the dimer. The best sets of parameters obtained by least square fitting were: **1**, $J = 0.\ 42(2)\ cm^{-1}$, $D = 0.0006(2)\ cm^{-1}$, $g = 2.022(1)$, LSE (least-squares error) = 0.00007; **2**, $J = 0.58(1)\ cm^{-1}$, $D = -2.32(4)\ cm^{-1}$, $g = 2.000(3)$, LSE = 0.0001; **3**, $J = -0.20(2)\ cm^{-1}$, $D = -0.009(3)\ cm^{-1}$, $g = 1.997(2)$, LSE = 0.00003. The solid lines in Fig. 2 were computed using the above parameters. The differences between the three compounds are further illustrated in Fig. 3, by plotting together their effective magnetic moments as a function of temperature. While the differences in J values are in agreement with the differences in bridge geometry in the molecular structures of **1–3**, the large zfs difference between **1** and **3** on the one hand, and **2** on the other hand, is difficult to explain in view of their very similar coordination geometries. This apparent discrepancy suggests that Mn^{III} zfs may not be the unique effect competing with the isotropic spin–spin interactions, but that possibly inter-dimer magnetic interactions also operate in these complexes. As a first step to check this hypothesis, we also computed the magnetic susceptibilities using the dimer model [26] including inter-dimer interactions within the molecular field approximation [32]. The best sets of parameters obtained by least square fitting were: **1**, $J = 0.364(6)\ cm^{-1}$, $zj = 0.0020(3)\ cm^{-1}$, $g = 2.025$(fixed), LSE = 0.002; **2**, $J = 0.853(9)\ cm^{-1}$, $zj = -0.0576(2)\ cm-^{1}$, $g = 1.99$(fixed), LSE = 0.001; **3**, $J = -0.1385\ (5)\ cm^{-1}$, $zj = -0.0561\ (5)\ cm^{-1}$, $g = 2.00$(fixed), LSE = 0.0004. The quality of the fits, although satisfactory, was not as good as the previous ones, suggesting the operation of both Mn^{III} zfs and antiferromagnetic inter-dimer interactions, at least for **2** and **3**. As a further step, we also computed the magnetic susceptibilities through exact diagonalisation of the spin Hamiltonian including axial Zeeman and zfs terms, isotropic exchange, and inter-dimer interactions within the molecular field approximation. Although the quality of the fits was excellent, D and zj were correlated preventing us to safely estimate independently the respective contribution of these two factors to the magnetic susceptibilities in this series of dimeric Mn^{III} compounds. Considering the similar Jahn–Teller elongation in complexes **1–3** the D is expected to be similar and negative in all the three compounds. Therefore, based on the observed temperature dependence of the magnetic moments and the fitting results, it is reasonable to conclude that the magnitude of D is very small for these compounds so that the variation of the magnetic moment at low temperatures is dominated by inter-dimer interactions.

It is worthwhile to examine the reason for the conspicuous difference in the inter-dimer interactions in compounds **1** and **2**. The intermolecular interactions between dimers are shown in Fig. 4. The shortest Mn···Mn separation between dimers is nearly the same in both compounds: 8.86 Å in **1** and 8.68 Å in **2**. A close examination of the crystal packing shows that the important inter-dimer interactions present in both compounds are (i) =CH···N_c (2.52 Å in **1**; 2.47 Å in **2**), (ii) =CH···O_t/N_t (2.62 Å in **1**; 2.57 Å in **2**) and (iii) Ph-H···Cπ (2.83 Å in **1**; 2.66 Å in **2**) where, suffixes c and t refer to coordinated and terminal atom of the pseudohalide ion. The only difference between the two compounds is the presence of a π-stacking interaction (3.36 Å) [33] in **1** while such an interaction is blocked in **2** by the methyl group. Instead, a hydrogen atom of the methyl group in **2** is involved in a C–H···Phπ interaction (2.88 Å) [34]. The above two contacts which distinguish the packing in the two compounds are shown by red dotted lines in Fig. 4. Correlation of these observations with the magnetic data seems to suggest that the methyl group interaction in **2** is responsible for the antiferromagnetic inter-dimer pathway, while the π-stacking in **1** is ferromagnetic and all other contacts common to both compounds may be of the antiferromagnetic type. This leads to a near-cancellation of the inter-dimer interactions so that the dimer in **1** remains ferromagnetically coupled down to 2 K. The methyl C–H···Phπ interaction is also present in **3** (3.02, 3.13 Å) while the other interactions listed above are absent. The terminal azido in this compound is involved in a Ph-H···N interaction (2.59 Å). As noted above, the inter-dimer exchange interaction determined by the fitting of magnetic susceptibility is antiferromagnetic in this

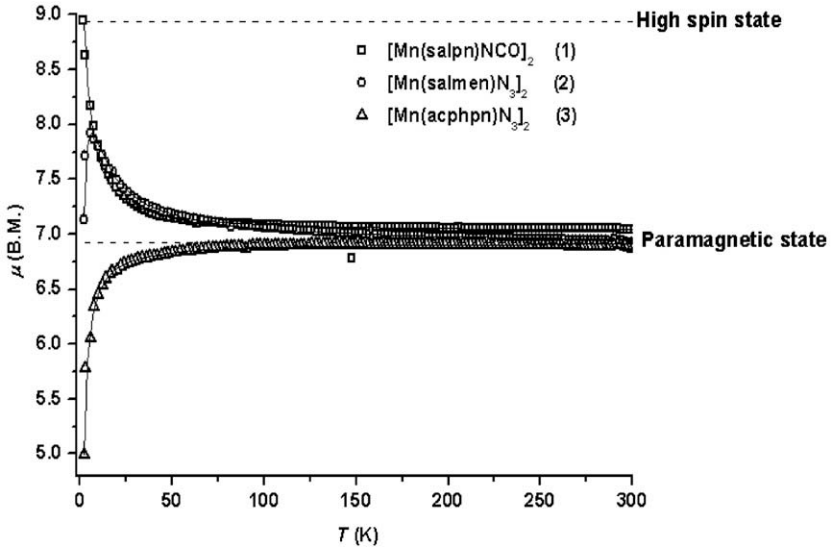


Fig. 3. Temperature variation of magnetic moment (μ_{eff} per dimeric unit) for the three compounds (**1**, **2** and **3**).

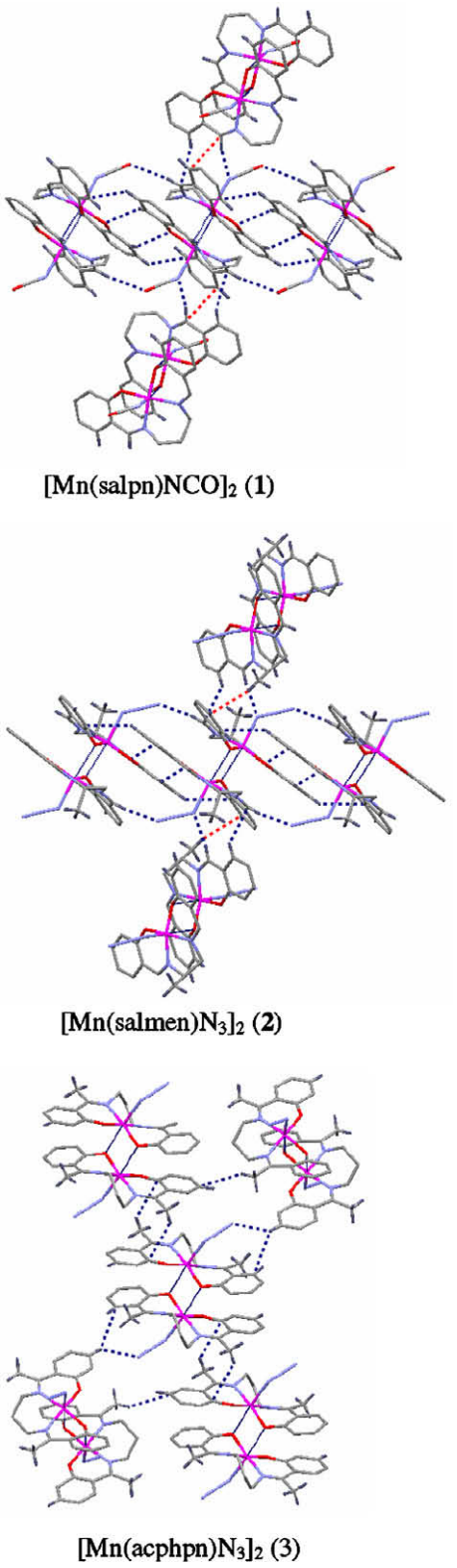


Fig. 4. Intermolecular interactions between dimers in complexes **1**, **2** and **3**.

compound as well. *dc*-Magnetisation measurements were done for **1** and **2** mainly to check for hysteresis. Attempts to fit the magnetisation data (Fig. S1) using the parameters previously derived from temperature variation of molar susceptibility gave satisfactory result only for **2**. It seems that a larger anisotropic term (D) will be needed for **1**. The reason for this discrepancy is not evident. The absence of hysteresis indicates that inter-dimer interactions do not lead to long range order in **1** and **2**, above 1.9 K.

A look at the 20-odd phenoxo-bridged dinuclear Mn^{III} compounds reported [2–21] to date shows that the exchange splitting, $2J$, falls in the range, -3.4 to 12.6 cm^{-1}, with only two instances of $2J > 4$ cm^{-1}. Further, the small magnitude of the interaction energy may reduce the precision with which it can be determined from least-squares analysis when competing influences from zero-field splitting and inter-dimer interactions are present. Therefore, a precise correlation of exchange interactions with molecular structure is difficult to evaluate in this class of compounds. In the case of several dimers having water, thiocyanate or chloride as axial ligands and showing ferromagnetic interaction, it was found that the $2J$ value has a reciprocal correlation with the Mn···O bond distance (2.4–3.7 Å) [5]. However, for the present compounds, the relationship is reversed, with the following respective Mn···O distances (Å) and $2J$ (cm^{-1}) values: 2.49, −0.4 (**3**); 2.51, 0.84 (**1**); 2.59, 1.16 (**2**). Because four magnetic orbitals are involved on each centre, it is unlikely that the exchange interaction may be controlled by just one structural parameter. In this respect, it is worth noting that the increase in $2J$ (cm^{-1}) parallels the decrease in Mn–O···Mn angle (°), with the

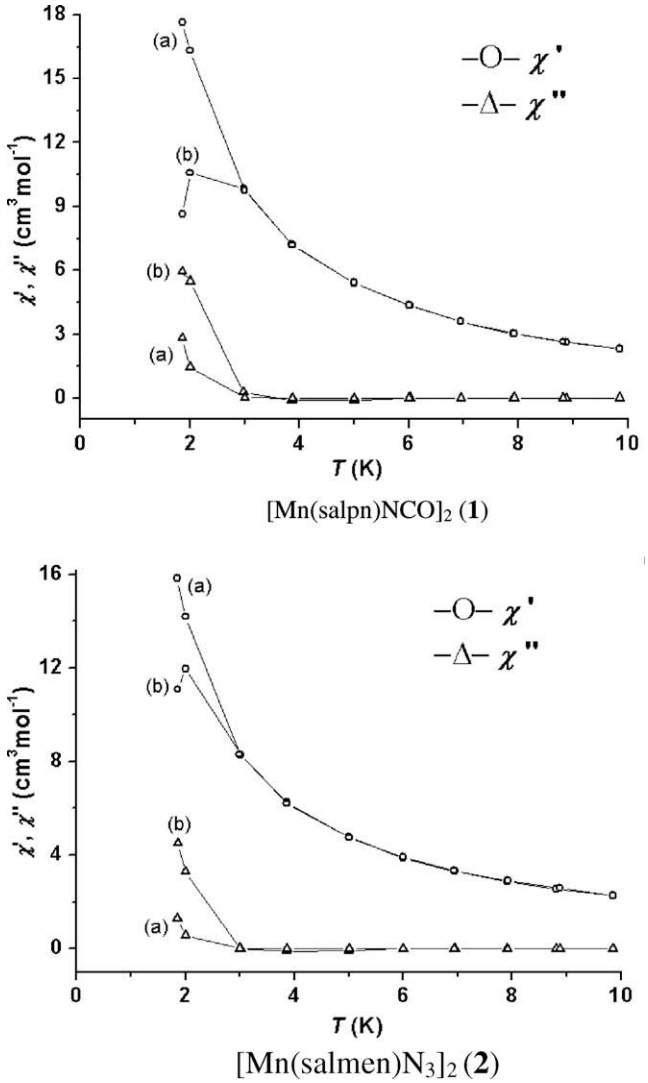


Fig. 5. Temperature variation of the in-phase χ' and out-of-phase χ'' components of the *ac*-magnetic susceptibility in zero static field for complexes **1** and **2** at, (a) 100 Hz and (b) 1000 Hz. Solid lines between the experimental data points are shown as a guide to the eye, they do not result from fitting.

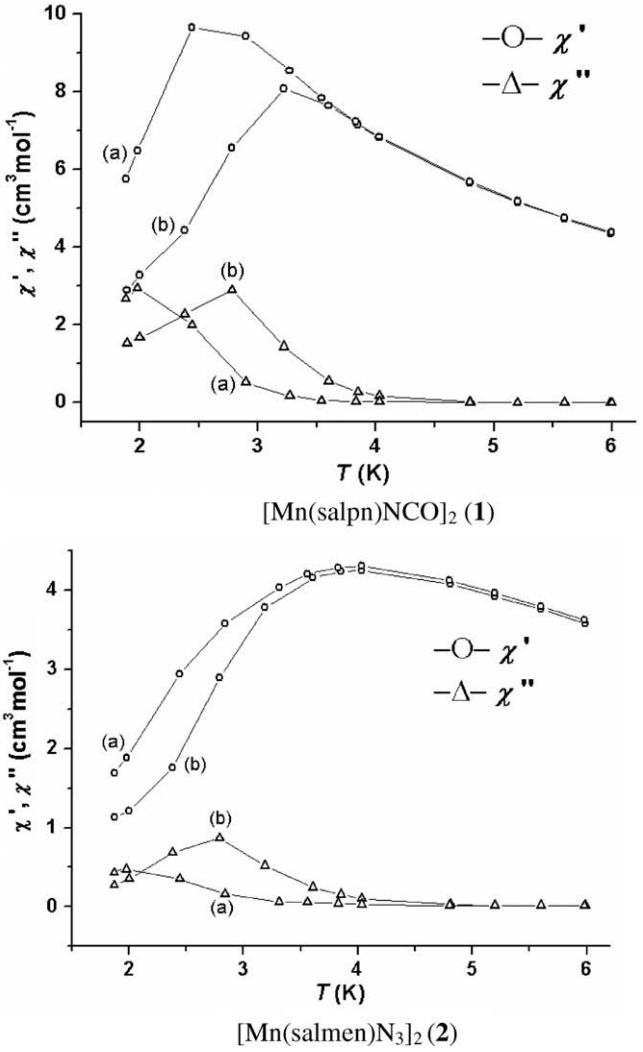


Fig. 6. Temperature variation of the in-phase χ' and out-of-phase χ'' components of the *ac*-magnetic susceptibility for complex **1** at a *dc* field of 0.1 T and for complex **2** at a *dc* field of 0.5 T. The *ac* field fluctuates at a frequency of (a) 100 Hz and (b) 1000 Hz. Solid lines between the experimental data points are shown as a guide to the eye, they do not result from fitting.

following respective values: −0.4, 101.2 in **3**; 0.84, 100.6 in **1**; 1.16, 98.5 in **2**.

In order to check whether compounds **1** and **2** behave as single molecule magnets (SMMs), their *ac* susceptibility was measured in the temperature range 2–10 K at two different frequencies (100 and 1000 Hz). The observation of frequency dependent in-phase χ' and out-of-phase χ'' magnetic susceptibilities (Fig. 5) suggests an SMM behavior for both compounds. Even though no maxima were seen in the above data obtained with zero *dc* field, clear maxima appeared when a *dc* field (0.1 and 0.5 T for complexes **1** and **2**, respectively) was applied (Fig. 6). While the above results are in agreement with observation of an SMM behavior for other phenoxo-bridged Mn^{III} dimers [4,6], further detailed *ac* susceptibility measurements needed for evaluating the relaxation parameters of complexes **1** and **2** is not attempted in the present study.

4. Conclusions

The present results further demonstrate, in line with previous studies [5,6], that a precise correlation of the magnetic exchange parameter with bridge geometry is difficult in the case of phenoxo-bridged dimers due to the weakness of the magnetic coupling and the involvement of several magnetic orbitals in the interaction. An important finding from the present study is that weak inter-dimer interactions like stacking or C–H···π can cause dramatic changes in the overall temperature dependence of the magnetic susceptibility as seen in the case of compounds **1** and **2**, both of which are ferromagnetically coupled dimers. Alkyl substituents on the Schiff base are effective in modulating the inter-dimer interactions causing differences in behavior at lower temperatures. The ferromagnetically coupled dimers, in spite of their very small magnitude of the zero-field splitting do show evidence for single molecule magnetism.

Acknowledgments

The X-ray data were collected at the diffractometer facility at University of Hyderabad, established by the Department of Science and Technology, Government of India. Infrastructure support from UGC (UPE program) is also acknowledged. This work was supported by CSIR, India.

Appendix A. Supplementary data

CCDC 704765, 704766 and 704767 contain the supplementary crystallographic data for **1**, **2** and **3**. These data can be obtained free of charge via http://www.ccdc.cam.ac.uk/conts/retrieving.html, or from the Cambridge Crystallographic Data Centre, 12 Union Road, Cambridge CB2 1EZ, UK; fax: (+44) 1223-336-033; or e-mail: deposit@ccdc.cam.ac.uk. Supplementary data associated with this article can be found, in the online version, at doi:10.1016/j.poly.2009.02.024.

References

[1] Review: S.J. Wezenberg, A.W. Kleij, Angew. Chem., Int. Ed. 47 (2008) 2.
[2] H. Shyu, H. Wei, Y. Wang, Inorg. Chim. Acta 290 (1999) 8.
[3] R. Karmakar, C.R. Choudhury, G. Bravic, J.-P. Sutter, S. Mitra, Polyhedron 23 (2004) 949.
[4] L. Lecren, W. Wernsdorfer, Y.-G. Li, A. Vindigi, H. Miyasaka, R. Clerac, J. Am. Chem. Soc. 129 (2007) 5045.
[5] H. Miyasaka, R. Clerac, R.T. Ishii, H. Chang, S. Kitagawa, M. Yamashita, J. Chem. Soc., Dalton Trans. (2002) 1528.
[6] Z. Lu, M. Yuan, F. Pan, S. Gao, D. Zhang, D. Zhu, Inorg. Chem. 45 (2006) 3538.
[7] H.H. Ko, J.H. Lim, H.C. Kim, C.S. Hong, Inorg. Chem. 45 (2006) 8847.
[8] S. Saha, D. Mal, S. Koner, A. Bhattacherjee, P. Gutlich, S. Mondel, M. Mukherjee, K.-I. Okamoto, Polyhedron 23 (2004) 1811.
[9] N. Matsumoto, Z. Zhong, H. Okawa, S. Kida, Inorg. Chim. Acta 160 (1989) 153.
[10] M.R. Bermejo, A. Castineiras, J.C. Garcia-Montergudo, M. Rey, A. Sousa, M. Watkinson, C.A. McAuliffe, R.G. Pritchard, R.I. Beddose, J. Chem. Soc., Dalton Trans. (1996) 2935.
[11] A. Garcia-Deibe, A. Sousa, M.R. Bermejo, P.P. MacRory, C.A. McAuliffe, R.G. Pritchard, M. Hellowell, J. Chem. Soc., Chem. Commun. (1991) 728.
[12] M. Mikuriya, Y. Yamato, T. Tokii, Bull. Chem. Soc. Jpn. 65 (1992) 1466.
[13] B.J. Kennedy, K. Murray, Inorg. Chem. 24 (1985) 152.
[14] S. Sailaja, M.V. Rajasekharan, C. Hureau, E. Riviere, J. Cano, J.-J. Girerd, Inorg. Chem. 42 (2003) 180.
[15] B. Mabad, D. Luneau, S. Theil, F. Dahan, J.M. Savariault, J.P. Tuchagues, J. Inorg. Biochem. 43 (1991) 373.
[16] B.J. Kennedy, K.S. Murray, Inorg. Chem. 24 (1985) 1552.
[17] N. Matsumoto, N. Takemoto, A. Ohyosi, H. Okawa, Bull. Chem. Soc. Jpn. 61 (1988) 2984.
[18] H. Miyasaka, K. Sugimoto, K. Sugiura, T. Ishii, M. Yamashita, Mol. Cryst. Liq. Cryst. 379 (2002) 197.
[19] H. Miyasaka, K. Mizushima, S. Furukawa, K. Sugiura, T. Ishii, H. Yamasaka, Mol. Cryst. Liq. Cryst. 379 (2002) 171.
[20] Y. Sato, H. Miyasaka, N. Matsumoto, H. Okawa, Inorg. Chim. Acta 247 (1996) 57.
[21] H. Miyasaka, A. Saitoh, S. Abe, Coord. Chem. Rev. 251 (2007) 2622.
[22] K.R. Reddy, M.V. Rajasekharan, J.-P. Tuchagues, Inorg. Chem. 37 (1998) 5978.
[23] S. Nastase, F. Tuna, C. Maxim, C.A. Muryn, N. Avarvari, R.E.P. Winpenny, M. Andruh, Cryst. Growth Des. 7 (2007) 1825.
[24] P. Pascal, Ann. Chim. Phys. 19 (1910) 5.
[25] G.V.R. Chandramouli, C. Balagopalakrishna, M.V. Rajasekharan, P.T. Manoharan, Comput. Chem. 20 (1996) 353.

[26] C.J. O'Connor, Prog. Inorg. Chem. 29 (1982) 203.
[27] P. Garge, R. Chikate, S. Padhye, J.-M. Savariault, P. de Loth, J.-P. Tuchagues, Inorg. Chem. 29 (1990) 3315.
[28] F. James, M. Roos, MINUIT program, a system for function minimization and analysis of the parameters errors and correlations, Comput. Phys. Commun. 10 (1975) 345.
[29] SAINTPLUS, Bruker AXS Inc., Madison, Wisconsin, USA, 2003.
[30] G.M. Sheldrick, SADABS, Program for Empirical Absorption Correction, University of Gottingen, Gottingen, Germany, 1996.
[31] G.M. Sheldrick, SHELX-97, Programs for Crystal Structure Analysis, University of Gottingen, Gottingen, Germany, 1997.
[32] A.P. Ginsberg, M.E. Lines, Inorg. Chem. 11 (1972) 2289.
[33] C.A. Hunter, Chem. Soc. Rev. (1994) 101.
[34] M. Nishio, CrystEngComm 6 (2004) 130.

concentration of $\sim 10^{-3}$ mol L^{-1}. The redox behaviors of the complexes were examined on a computer controlled EG&G PAR model 270 VERSTAT electrochemical instrument using a Ag/AgCl electrode with TBAP as the supporting electrolyte. All the measurements were made at 298 K in dimethylformamide solution for a complex concentration range of 10^{-3}–10^{-4} mol L^{-1} using dry dinitrogen for 3–4 min in order to remove dissolved oxygen.

2.2. Preparation of the complexes

The complexes were synthesized following a common procedure, as described below, using the respective metal(II) chloride salts and 1,3-bis(2-pyridylmethylthio)propane (L) in a 1:1 mole ratio. To a methanolic solution (15 mL) of L (276.0 mg, 1.0 mmol), iron(II) chloride tetrahydrate (1.0 mmol) (for **1**), cobalt(II) chloride hexahydrate (1.0 mmol) (for **2**) or nickel(II) chloride hexahydrate (for **3**) was added dropwise, stirring the mixture for an hour. The reaction mixture was refluxed for 3 h and then kept at room temperature. The pure crystallized product was obtained from this solution by allowing slow evaporation of the solvent. The product was collected by filtration followed by washing with water and methanol, and dried in *vacuo*.

*[Fe(L)Cl$_2$] (**1**):* Yield: 70–75%; *Anal.* Calc. for $C_{15}H_{18}Cl_2FeN_2S_2$: C, 43.15; H, 4.31; N, 6.71; Fe, 13.42. Found: C, 43.18; H, 4.32; N, 6.79; Fe, 13.50%. IR (cm^{-1}): $\nu_{C=N}$ 1468; ν_{C-S} 758. Magnetic moment (μ, B.M.): 5.45. Conductivity (Λ_o, Ω^{-1} cm^2 mol^{-1}) in DMF: 45.

*[Co(L)Cl$_2$] (**2**):* Yield: 71–75%; *Anal.* Calc. for $C_{15}H_{18}Cl_2CoN_2S_2$: C, 42.86; H, 4.29; N, 6.67; Co, 14.03. Found: C, 43.12; H, 4.15; N, 6.5 1; Co, 13.91%. IR (cm^{-1}): $\nu_{C=N}$ 1472; ν_{C-S} 761. Magnetic moment (μ, B.M.): 4.91. Conductivity (Λ_o, Ω^{-1} cm^2 mol^{-1}) in DMF: 52.

*[Ni(L)Cl$_2$] (**3**):* Yield: 80–85%; *Anal.* Calc. for $C_{15}H_{18}Cl_2N_2NiS_2$: C, 42.85; H, 4.29; N, 6.67; Ni, 13.99. Found: C, 42.99; H, 4.18; N, 6.79; Ni, 14.08%. IR (cm^{-1}): $\nu_{C=N}$ 1470; ν_{C-S} 760. Magnetic moment (μ, B.M.): 3.08. Conductivity (Λ_o, Ω^{-1} cm^2 mol^{-1}) in DMF: 42.

2.3. X-ray crystal structure analysis

Single crystals of complexes **1** and **3** suitable for X-ray diffraction analysis were grown by slow evaporation of methanolic solutions at ambient temperature. Crystallographic data and details of the refinements are provided in Table 1. Diffraction data for **1** were collected at 150(2) K using the Oxford Diffraction X-Calibur CCD System (321 frames, counting time of 2 s, the crystal positioned at 50 mm from the CCD). The experiment for **2** was carried out at room temperature on a Nonius DIP-1030H system (45 frames, the crystal positioned at 90 mm from the image plate). Mo Kα radiation (λ = 0.71073 Å) was used for both data collections. Cell refinement, indexing and scaling of the data sets were carried out using programs CRYSALIS [22], DENZO and SCALEPACK [23]. An absorption correction was applied to **1** by the ABSPACK program [24]. Both structures were solved using direct methods with the SHELXS97 program and refined by the full-matrix least-squares method based on F^2 with all observed reflections [25]. Hydrogen atoms were fixed at geometrical positions. As the complexes were located on a crystallographic twofold axis, the central methylene C(8) atom results was disordered over two sites (0.5 occupancy each). All the calculations were performed using the WINGX System, Version 1.70.01 [26].

Table 1
Crystallographic data for **1** and **3**.

	1	**3**
Empirical formula	$C_{15}H_{18}Cl_2FeN_2S_2$	$C_{15}H_{18}Cl_2N_2NiS_2$
Formula weight	417.18	420.04
Temperature (K)	150(2)	293(2)
Crystal system	orthorhombic	
Space group	*Pbcn*	
a (Å)	14.315(2)	14.312(3)
b (Å)	8.4443(9)	8.551(2)
c (Å)	14.5516(18)	14.678(3)
Volume ($Å^3$)	1759.0(4)	1796.3(7)
Z	4	
ρ_{calc} (g/cm^3)	1.575	1.553
F(000)	856	864
θ range (°)	2.80–30.00	2.77–29.64
μ (Mo Kα) (mm^{-1})	1.395	1.606
Unique reflections/data $I > 2\sigma(I)$	2528/1011	2402/1600
Final R_1/wR_2 indices [$I > 2\sigma(I)$]	0.0854/0.2129	0.0348/0.0943
Goodness-of-fit	0.891	0.888
$\Delta\rho$ (e A^{-3})	1.596, −1.604	0.491, −0.476

3. Results and discussion

3.1. Synthesis and characterization

The organic ligand 1,3-bis(2-pyridylmethylthio)propane (L) was synthesized by the reaction of the respective alkyl dithiol compound with 2-picolyl chloride in the presence of sodium ethoxide. The complexes were obtained in good yields from the reaction of the corresponding metal salt with an equimolar amount of the respective organic moiety in methanol medium. All the complexes are monomeric in nature and are sparingly soluble in common organic solvents. The complex conductivity measurements in dimethylformamide show conductance values in range 42–52 Λ_o mol^{-1} cm^{-1}, which suggest that the complexes exist in solution as non-electrolytes. The magnetic moment (μ) at room temperature of iron(II) in (**1**) is 5.45 B.M., which indicates a high-spin octahedral iron(II) complex; the values of μ for the cobalt(II) and nickel(II) complexes are 4.91 and 3.08 B.M., respectively.

3.2. Structures of complexes *1* and *3*

The X-ray structural analyses evidence that the crystals of **1** and **3** are isomorphous, and an ORTEP view of complex **1** is shown in Fig. 1, together with the atom numbering scheme. The metal resides on a crystallographic twofold axis bisecting the Cl–M–Cl and S–M–S angles. Thus the methylene C(8) atom of the organic moiety is disordered over two positions (each of occupancy 0.5), and only one orientation is displayed in Fig. 1. The tetradentate NSSN ligand is wrapped around the metal in such a way that the pyridine rings are in *trans* positions and the metal ion completes the highly distorted octahedral coordination sphere with two chlorides located in *cis* positions. The present coordination pattern of L

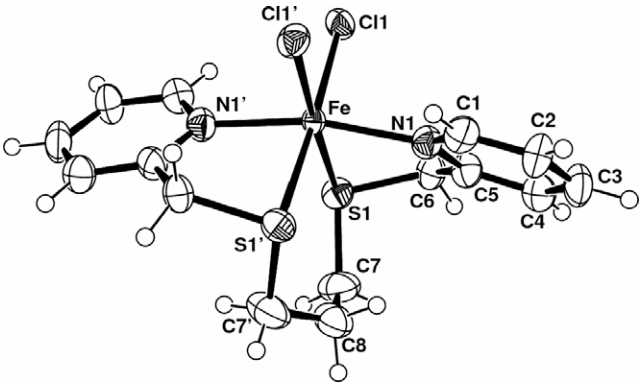


Fig. 1. ORTEP drawing (ellipsoids at 50% probability) of complex [Fe(L)Cl_2] (**1**). The molecule is located on a twofold axis and only one position for the disordered C(8) methylene is shown. The same atom numbering is applied to the isomorphous complex [Ni(L)Cl_2] (**3**), substituting Fe with Ni.

Table 2
Coordination bond distances (Å) and angles (°) for **1** and **3**.

	1, M = Fe	**3**, M = Ni
Bond distance (Å)		
M–N(1)	2.099(5)	2.104(2)
M–S(1)	2.440(2)	2.451(1)
M–Cl(1)	2.384(2)	2.392(1)
Bond angles (°)		
N(1)–M–N(1′)	167.4(3)	166.48(9)
N(1)–M–Cl(1′)	95.35(15)	95.50(5)
N(1)–M–Cl(1)	93.16(15)	93.63(5)
N(1)–M–S(1)	82.40(15)	82.22(5)
N(1)–M–S(1′)	89.23(15)	88.77(5)
Cl(1)–M–Cl(1′)	94.90(9)	94.88(4)
Cl(1)–M–S(1)	84.20(6)	84.38(3)
Cl(1)–M–S(1′)	177.51(5)	177.54(2)
S(1)–M–S(1′)	96.80(9)	96.45(3)

Primed atoms at $-x,y,-z+1/2$.

was also detected in the neutral $[Ni(L)(ONO_2)_2]$ derivative [27], but it is noteworthy that in the trigonal bipyramidal copper(II) complex $[Cu(L)Cl]^+$ [21] a pyridine-N and a thioether-S reside at the axial positions whereas the equatorial sites were occupied by the other N and S donors and by the chloride ligand. The coordination bond lengths and angles of **1** and **3**, listed in Table 2, show only minor differences related to the metal ionic radii. The M–N bond lengths are comparable within their e.s.d.'s (2.099(5) and 2.104(2) Å in **1** and **3**, respectively), while the values of the M–S and M–Cl distances differ by *ca.* 0.01 Å, being of 2.440(1), 2.451(1) Å and 2.384(2), 2.392(1) Å in **1** and **3**, respectively. The bond angles subtended at the metal differ by less than 1° in the two structures, but they deviate considerably from the ideal octahedral values and the N–M–N angle of 167° (mean value for the two structures) shows the highest deviation. In fact the pyridine rings of the ligand are bent with respect to the S_2Cl_2 plane, forming a dihedral angle of 80.57° (mean value), likely induced by ligand constraints upon coordination, while the dihedral angle made by the trans located pyridine planes is 55.3(2)° and 54.9(1)° in **1** and **3**, respectively. The bond distances and geometrical distortions of **3** agree with those found in [Ni(2,2′-(2,5-dithiahexamethylene) dipyridine)Cl_2] [28] while small differences are evidenced when compared with the disordered crystal structure of $[Ni(L)(ONO_2)_2]$ [7].

3.3. Spectroscopic properties

The infrared spectra of all the complexes exhibit characteristic strong to medium intensity bands in the regions 1468–1472 and 758–761 cm^{-1}, which are assignable to $\nu_{C=N}$ and ν_{C-S}, respectively, in addition to the other characteristic bands of the organic moieties. This observation supports the presence of the ligand frame containing the pyridine ring and the C–S bond, and ν_{C-S} is generally observed in the free ligand in the range of 780–790 cm^{-1} [21].

The electronic absorption spectra of complexes **1**–**3** were recorded at room temperature using dimethylformamide as the solvent and the data tabulated in Table 3. All the spectra in the high energy region (below 400 nm) exhibit bands corresponding to intramolecular $\pi \rightarrow \pi^*$ and $n \rightarrow \pi^*$ transitions. In addition, characteristic bands for the complexes were detected as follows.

In the electronic spectrum of $[Fe(L)Cl_2]$, a prominent peak around 475 nm with a shoulder at about 752 nm was observed, corresponding to MLCT and d–d transitions, respectively. The electronic spectrum of **2** shows bands at 425, 560 and 967 nm, assignable to the transitions $^4T_{1g} \rightarrow {}^4T_{1g}(P)$, $^4T_{1g} \rightarrow {}^4A_{2g}(F)$ and $^4T_{1g} \rightarrow {}^4T_{2g}(F)$, respectively. The position of these bands indicates an octahedral geometry about the Co^{II} ion [29]. The spectrum of **3** exhibits bands at 475, 685 and 873 nm, which may be assigned to $^3A_{2g}(F) \rightarrow {}^3T_{1g}(P)$, $^3A_{2g}(F) \rightarrow {}^3T_{1g}(F)$ and $^3A_{2g}(F) \rightarrow {}^3T_{2g}(F)$ transitions, respectively. These observations suggest an octahedral geometry of the Ni^{II} ion [30].

3.4. Electrochemistry

The redox properties of the complexes were examined by cyclic voltammetry using a Pt-disk working electrode and a Pt-wire auxiliary electrode in dry dimethylformamide using $[n\text{-}Bu_4N]ClO_4$ as the supporting electrolyte. Voltammetric data are set out in Table 3.

The voltammetric response for $[Fe(L)Cl_2]$ (**1**) exhibits an oxidative couple at the $E_{1/2}$ value of +0.295 V, assigned to the Fe^{II}/Fe^{III} pair, [29] with a peak potential separation (ΔE_p) of 120 mV and cathodic to anodic current intensity ratio of 0.97. The cyclic voltammogram of $[Co(L)Cl_2]$ (**2**) shows a quasi-reversible peak for the Co^{II}/Co^{III} redox couple at $E_{1/2}$ of 0.795 V with ΔE_p of 195 mV. The cyclic voltammogram of $[Ni(L)Cl_2]$ (**3**) exhibits a quasi-reversible Ni^{II}/Ni^{III} redox couple centered at 0.745 V versus Ag/AgCl. Here, the $E_{1/2}$ value for complex **3** lies at the higher side of the range generally measured, 0.3–0.8 V, for the Ni^{III}/Ni^{III} oxidation potential data for thioether containing nickel(II) complexes, [31] indicating that Ni^{II} is fairly stabilised in **3**. No cathodic response, recommended for $Ni^{II} \rightarrow Ni^{I}$ reduction, was observed for **3** up to −1.51 V. The voltammetric parameters were studied in the scan rate interval 50–400 mV s^{-1}. The ratio between the cathodic peak current and the square root of the scan rate ($I_{pc}/v^{1/2}$) is approximately constant. The peak potential shows a small dependence on the scan rate. The ratio I_{pc} to I_{pa} is close to unity. From these data, it can be deduced that the redox couple is related to a quasi-reversible one-electron transfer process controlled by diffusion.

Table 3
UV–Vis spectral and electrochemical data.[a]

Compound	UV–Vis data[a]	Electrochemical data[b]			
	λ (nm) (ε, $dm^3\ mol^{-1}\ cm^{-1}$)	E_{pc}[a] (V)	E_{pa}[a] (V)	$E_{1/2}$ (V)	Reversibility (I_{pc}/I_{pa})
1	212(9530), 261(8310), 332(3010), 475(975), 752(108)	+0.235	+0.355	+0.295	0.97
2	210(9000), 257(6300), 337(2820), 425(89), 560(186), 967(22)	+0.600	+0.990	+0.795	1.03
3	210(10230), 258(7430), 328(2915), 475(221), 685(520), 873(31)	+0.665	+0.825	+0.745	0.93

[a] In DMF.
[b] Data recorded in mV, at 298 K and scan rate 100 mV s^{-1}; $E_{1/2} = (E_{pc} + E_{pa})/2$; I_{pc}/I_{pa} is constant for scans in the range of 50–400 mV s^{-1}.

4. Conclusion

The synthesis and characterization of three new mononuclear complexes of iron(II), cobalt(II) and nickel(II) with a N_2S_2 donor set have been performed. No inert atmosphere (i.e. dinitrogen) is required for the synthesis of the iron(II) and cobalt(II) complexes, but these are prone to aerial oxidation. Structural characterization of **1** and **3** by X-ray diffraction indicates isomorphous crystals with the metal ion in an octahedral geometry with the chloride and py ligands occupying *cis* and *trans* positions, respectively. All the complexes manifest very similar redox behavior in dimethylformamide solution, showing M^{II}/M^{III} redox couples in the cyclic voltammograms, but no cathodic response for the M^{II}/M^{I} redox process.

Supplementary data

CCDC 697636 and 697637 contain the supplementary crystallographic data for compounds **1** and **3**, respectively. These data can be obtained free of charge via http://www.ccdc.cam.ac.uk/conts/retrieving.html, or from the Cambridge Crystallographic Data Centre, 12 Union Road, Cambridge CB2 1EZ, UK; fax: (+44) 1223-336-033; or e-mail: deposit@ccdc.cam.ac.uk.

Acknowledgements

Financial support from the Council of Scientific and Industrial Research (CSIR), New Delhi, India, is gratefully acknowledged. We thank EPSRC and the University of Reading for funds for the Oxford X-Calibur system. E. Zangrando thanks MIUR-Rome, PRIN 2007HMTJWP_002 for financial support.

References

[1] T.C. Harrop, P.K. Mascharak, Acc. Chem. Res. 37 (2004) 253. and references therein.
[2] D.S. Marlin, P.K. Mascharak, Chem. Soc. Rev. 29 (2000) 69.
[3] (a) E.S. Raper, Coord. Chem. Rev. 165 (1997) 475;
(b) R.L. Richard, Coord. Chem. Rev. 154 (1996) 83.
[4] T.S. Lobana, K. Isobe, H. Kitayama, T. Nishioka, I. Kinoshita, Angew. Chem., Int. Engl. 43 (2004) 213.
[5] J. Hausmann, M.H. Klingele, V. Lozan, G. Steinfeld, D. Siebert, Y. Journaux, J.J. Girerd, B. Kersting, Chem. – A Eur. J. 10 (2004) 1716.
[6] K.A. Crouse, K.B. Chew, M.T.H. Tarafder, A. Kasbollah, A.M. Ali, B.M. Yamin, H.K. Fun, Polyhedron 23 (2004) 161.
[7] L.A. Tyler, J.C. Naveron, M.M. Olmstead, P.K. Mascharak, Inorg. Chem. 39 (2000) 357.
[8] R.H. Prince, in: G. Wilkinson, R.D. Gillard, J. McCleverty (Eds.), Comprehensive Coordination Chemistry, Pergamon Press, Oxford, UK, 1987, p. 925.
[9] R.H. Holm, E.I. Solomon, Chem. Rev. 104 (2004) 347.
[10] R.H. Holm, P. Kennepohl, E.I. Solomon, Chem. Rev. 96 (1996) 2239.
[11] D. Sellmann, J. Sutter, Acc. Chem. Res. 30 (1997) 460.
[12] D. Sellmann, R. Prakash, F.W. Heinemann, M. Moll, M. Klimowicz, Angew. Chem., Int. Eng. 43 (2004) 1877.
[13] P.A.N. Reddy, B.K. Santra, M. Nethaji, A.R. Chakravarty, J. Inorg. Biochem. 98 (2004) 377.
[14] S. Dhar, D. Senapati, P.K. Das, P. Chattopadhyay, M. Nethaji, A.R. Chakravarty, J. Am. Chem. Soc. 125 (2003) 12118.
[15] R.P. Happe, W. Roseboom, A.J. Pierik, S.P. Albracht, K.A. Bagley, Nature 385 (1997) 126.
[16] A. Volveda, E. Gracin, C. Piras, A.L. Delacey, V.M. Fernandez, E.C. Hatchikian, M. Frey, J.C. Fontecilla-Camps, J. Am. Chem. Soc. 118 (1996) 12989.
[17] R. Cammack, Nature 373 (1995) 556.
[18] Z.Z. Ziang, A. Sen, J. Am. Chem. Soc. 117 (1995) 4455.
[19] J.P. Scovill, D.L. Klaymann, C. Lambros, G.E. Childs, J.D. Notsch, J. Med. Chem. 27 (1984) 87.
[20] M. Huang, C.F. Shaw, D.H. Petering, J. Inorg. Biochem. 98 (2004) 639.
[21] S. Sarkar, A. Patra, M.G.B. Drew, E. Zangrando, P. Chattopadhyay, Polyhedron 28 (2009) 1. and references therein.
[22] CRYSALIS, Oxford Diffraction Ltd., Abingdon, UK, 2006.
[23] Z. Otwinowski, W. Minor, in: C.W. Carter Jr., R.M. Sweet (Eds.), Methods in Enzymology, vol. 276, Academic Press, New York, 1997, pp. 307–326.
[24] ABSPACK, Oxford Diffraction Ltd., Oxford, UK, 2005.
[25] G.M. Sheldrick, Acta Crystallogr. A64 (2008) 112.
[26] L.J. Farrugia, J. Appl. Crystallogr. 32 (1999) 837.
[27] J.E. Barclay, S.C. Davies, D.J. Evans, S.A. Fairhurst, C. Fowler, R.A. Henderson, D.L. Hughes, K.E. Oglieve, Transition Met. Chem. 23 (1998) 701.
[28] T. Pandiyan, S. Bernes, C. Duran de Bazua, Acta Crystallogr., Sect. C: Cryst. Struct. Commun. 55 (1999) 318.
[29] J. Simaan, S. Poussereau, G. Blondin, J.J. Girerd, D. Defaye, C. Philouze, J. Guilhem, L. Tchertanov, Inorg. Chim. Acta 299 (2000) 221.
[30] A.B.P. Lever, Inorganic Electronic Spectroscopy, 2nd Ed., Elsevier, Amsterdam, 1984.
[31] S. Karmakar, S.B. Choudhury, D. Ray, A. Chakravorty, Polyhedron 12 (1993) 291.

2. Experimental

2.1. General

All chemicals were of reagent grade purity and were used without further purification. All experiments were carried out in air. Elemental analyses were performed by atomic absorption spectroscopy for copper and spectrophotometrically for chromium (as chromate at λ = 370 nm) at the Department of Chemistry, National Taras Shevchenko University of Kyiv and with a vario EL III Universal CHNOS Elemental Analyzer (for C, H, N, S) at the Faculty of Chemistry, University of Wroclaw.

2.2. Preparation

Copper powder (1.26 mmol for **1**–**3**; 2.5 mmol for **4**), $NH_4[Cr(NCS)_4(NH_3)_2]\cdot H_2O$ (2.52 mmol for **1**, **3**; 1.26 mmol for **2**; 0.625 mmol for **4**), NH_4NCS (1.26 mmol for **2**; 4.375 mmol for **4**), non-aqueous solvent (20 mL, dmf for **1**, CH_3CN for **2**, CH_3OH for **3**, dmso for **4**), acetone (5 mL, for **3** and **4**) and *N*,*N*-dimethylethylenediamine (2.25 mmol for **1**–**3**; 5.0 mmol for **4**) were placed in a flask in the above order, heated to 50–60 °C and magnetically stirred until total dissolution of the copper powder was observed (10–15 min). Crystals suitable for X-ray crystallography were formed after several days (**2**), separated after several days following the successive addition of 5 ml of Pr^iOH (**1** and **4**), deposited after slowly evaporation of the solvent at room temperature (**3**). The crystals were filtered off and dried in vacuo at room temperature. The compounds are soluble in CH_3CN, dmso and dmf.

2.2.1. $[Cu(dmen)_2(dmf)_2][Cr(NCS)_4(NH_3)_2]_2 \cdot 6dmf$ (**1**)

Yield: 1.24 g, 67% (per copper). *Anal. Calc.* for $C_{40}H_{92}N_{24}S_8O_8Cr_2Cu$: C, 32.88; H, 6.34; N, 23.00; S, 17.55; Cr, 7.12; Cu, 4.35. Found: C, 32.7; H, 6.5; N, 22.8; S, 17.7; Cr, 7.3; Cu, 4.4%. IR (KBr, cm^{-1}): 3330(w), 3250(w), 3180(w), 2950(w), 2090(vs), 1665(s), 1595 (m), 1470(m), 1400(m), 1255(s), 1150(m), 1110(m), 1060(m), 1010(m), 950(w), 790(w).

2.2.2. $[Cu(dmen)_2(NCS)][Cr(NCS)_4(NH_3)_2]$ (**2**)

Yield: 0.61 g, 78% (per copper). *Anal. Calc.* for $C_{13}H_{30}N_{11}S_5CrCu$: C, 25.33; H, 4.91; N, 25.00; S, 26.01; Cr, 8.44; Cu, 10.31. Found: C, 25.1; H, 5.1; N, 24.8; S, 26.2; Cr, 8.6; Cu, 10.2%. IR (KBr, cm^{-1}): 3330(w), 3240(w), 3150(w), 2980(w), 2100(vs), 2070(vs), 1660(w), 1590(s), 1465(s), 1410(w), 1260(s), 1190(m), 1140(s), 1120(s), 1060(m), 1030(w), 1010(s), 950(w), 860(w), 840(w), 790(s).

2.2.3. $[Cu(dmenac)(NCS)(\mu\text{-}SCN)Cr(NCS)_3(NH_3)_2]$ (**3**)

Yield: 0.51 g, 65% (per copper). *Anal. Calc.* for $C_{15}H_{29}N_{10}S_5CrCu$: C, 28.81; H, 4.67; N, 22.40; S, 25.64; Cr, 8.32; Cu, 10.16. Found: C, 28.6; H, 4.8; N, 22.2; S, 25.8; Cr, 8.5; Cu, 10.1%. IR (KBr, cm^{-1}): 3300(w), 3240(w), 3160(w), 2980(w), 2140(vs), 2120–2070 (vs), 1660(s), 1600(s), 1480(m), 1415(w), 1380(m), 1260(s), 1195(m), 1130(w), 1110(m), 1030(m), 1020(s), 980(w), 960(m), 910(w), 790(w), 775(w).

2.2.4. $[Cu(dmen_2ac)(NCS)][Cr(NCS)_4(NH_3)_2] \cdot 6dmso$ (**4**)

Yield: 0.52 g, 71% (per copper). *Anal. Calc.* for $C_{31}H_{74}N_{11}S_{11}O_6CrCu$: C, 31.95; H, 6.40; N, 13.22; S, 30.27; Cr, 4.46; Cu, 5.45. Found: C, 31.8; H, 6.6; N, 13.0; S, 30.4; Cr, 4.6; Cu, 5.5%. IR (KBr, cm^{-1}): 3320(w), 3230(w), 3160(w), 2980(w), 2100(vs), 1650(s), 1590(m), 1550(w), 1480(w), 1280(s), 1230(w), 1170(w), 1080(w), 1030(s), 960(w), 845(w), 790(w).

2.3. Physical measurements

Infrared spectra were recorded as KBr discs on a UR-10 spectrophotometer in the 4000–400 cm^{-1} region using conventional techniques. UV/Vis spectra were recorded on a Perkin–Elmer Lambda 900 spectrophotometer using the diffuse-reflectance technique.

Table 1
Crystal data and structure refinement for **1**–**4**.

	1	**2**	**3**	**4**
Empirical formula	$C_{40}H_{92}N_{24}S_8O_8Cr_2Cu$	$C_{13}H_{30}N_{11}S_5CrCu$	$C_{15}H_{29}N_{10}S_5CrCu$	$C_{31}H_{74}N_{11}S_{11}O_6CrCu$
M	1461.40	616.32	625.32	1165.26
Crystal system	triclinic	orthorhombic	orthorhombic	monoclinic
Space group	$P\bar{1}$	$Pna2_1$	*Pbca*	$P2_1/c$
a (Å)	13.9396(8)	16.166(3)	15.4491(6)	17.983(2)
b (Å)	13.9485(8)	12.290(4)	13.3876(4)	14.8012(15)
c (Å)	19.9961(7)	13.952(3)	26.9866(10)	22.371(3)
α (°)	90.635(4)	90.000	90.000	90.000
β (°)	90.167(4)	90.000	90.000	102.532(12)
γ (°)	113.099(3)	90.000	90.000	90.000
V (Å^3)	3575.9(3)	2772.0(12)	5581.5(3)	5812.5(13)
Z	2	4	8	4
D_{calc} (g cm^{-3})	1.357	1.477	1.488	1.332
μ (mm^{-1})	0.886	1.559	1.549	0.993
F(000)	1538	1272	2576	2456
Data collection				
T (K)	294(2)	294(2)	294(2)	294(2)
2θ scan range (°)	2.57–25.00	3.02–30.00	2.52–27.50	2.70–27.50
h, *k*, *l* ranges	−16 + 13, ±16, −23 + 20	−14 + 22, −11 + 17, −17 + 19	−20 + 11, −17 + 9, ±35	±23, −15 + 19, −27 + 29
Reflections collected	24900	10826	21888	29296
Independent reflections [R_{int}]	7366 [0.052]	4847 [0.017]	4342 [0.099]	5546 [0.071]
Refinement				
Final *R* indices	R_1 = 0.0915	R_1 = 0.0334	R_1 = 0.0718	R_1 = 0.0537
[$I > 2\sigma(I)$]	wR_2 = 0.2482	wR_2 = 0.0795	wR_2 = 0.1251	wR_2 = 0.0999
R indices	R_1 = 0.1442	R_1 = 0.0512	R_1 = 0.1172	R_1 = 0.1460
(all data)	wR_2 = 0.2814	wR_2 = 0.0852	wR_2 = 0.1456	wR_2 = 0.1208
Goodness-of-fit (GOF) (*F*)	1.063	0.917	1.103	0.804
$\Delta(\rho)$ (e Å^{-3})	+2.171, −0.750	+0.473, −0.250	+0.513, −0.558	+0.916, −0.540

The EPR spectra were recorded on a Bruker ESP 300E (Bruker, Germany) spectrometer operating at X-band and equipped with a Bruker NMR gaussmeter ER 035 M and a Hewlett–Packard microwave frequency counter HP 5350B. The spectra were measured using typical instrument parameters: microwave frequency, from about 9.5 GHz at 77 K to about 9.7 GHz at 295 K.; microwave power, 20 milliwatts; modulation frequency, 100 kHz; modulation amplitude not greater than 0.5 mT. The EPR parameters were calculated by computer simulation of the experimental spectra using Bruker's WIN-EPR SIMFONIA Software Version 1.25. Magnetic susceptibility data of powdered samples were measured with a SQUID magnetometer (Quantum Design MPMSXL-5) over the temperature range 1.8–300 K at a magnetic induction of 0.5 T. Corrections for diamagnetism of the constituted atoms were calculated from Pascal's constants [15].

2.4. Crystal structure determination

Details of the structure determination and crystallographic data for compounds **1**–**4** are summarized in Table 1. X-ray diffraction data were collected on an XCalibur 3 diffractometer equipped with graphite-monochromated Mo Kα radiation ($\lambda = 0.71073$ Å) and a CCD detector using ω- and ϕ-scans. The structures were solved by direct methods and refined by full-matrix least-squares methods using the SHELXTL package [16]. All non-hydrogen atoms were refined within anisotropic approximation except for the disordered atoms of one of the dmso molecules in **4** [O(6) and O(6A) atoms], which were refined isotropically. In the structure of **2** one of the methylene groups of the dmen ligand was disordered over two positions with populations 40:60%. In **4**, six dmso molecules were found, two of them were disordered over two positions with populations 37:63% and 50:50%. The H atoms were located from the difference maps of electron density and refined by the "riding" model with $U_{iso} = nU_{eq}$ of the carrier non-hydrogen atom ($n = 1.5$ for methyl and 1.2 for other H-atoms).

3. Results and discussion

3.1. Synthesis and spectroscopic characterization

The reaction of copper powder, Reinecke's salt, NH_4NCS (in the case of **2**) with *N*,*N*-dimethylethylenediamine (dmen) in dmf (**1**) or CH_3CN (**2**) in open air, using a Cu:$NH_4[Cr(NCS)_4(NH_3)_2]$:dmen molar ratio of 1:2:2 (for **1**) and 1:1:2 (for **2**), affords heterometallic compounds with a Cu(II):Cr(III) ratios of 1:2 (**1**) and 1:1 (**2**). The reactions proceed by the following pathways:

$$Cu^0 + 2NH_4[Cr(NCS)_4(NH_3)_2] + 2dmen + 1/2O_2 + 8dmf \rightarrow \rightarrow [Cu(dmen)_2(dmf)_2][Cr(NCS)_4(NH_3)_2]_2 \cdot 6dmf + 2NH_3 + H_2O \quad (1)$$

$$Cu^0 + NH_4[Cr(NCS)_4(NH_3)_2] + 2dmen + NH_4NCS + 1/2O_2 \rightarrow \rightarrow [Cu(dmen)_2(NCS)][Cr(NCS)_4(NH_3)_2] + 2NH_3 + H_2O \quad (2)$$

In our previous work, we have shown that the Reinecke's salt could act as a source of ammonia molecules and thiocyanato groups as well as creating favorable conditions for the formation of 2-methyl-2-amino-4-imino-pentan derivatives in the presence of acetone molecules [14]. The one-step reaction of copper powder, Reinecke's salt in acetone/CH_3OH (1:4) (for **3**) or acetone/dmso (1:4) (for **4**) solution of *N*,*N*-dimethylethylenediamine (dmen) with a molar ratio of Cu:$NH_4[Cr(NCS)_4(NH_3)_2]$:dmen of 1:2:1 and 4:1:8, respectively, gave two different compounds with two novel open-chain aliphatic Schiff-base ligands, dmenac and $dmen_2ac$. Their formation can be understood if one considers the following reaction schemes (it should be noted that the molar ratios of the starting reagents in the syntheses differ from those in the reaction schemes):

$$Cu^0 + NH_4[Cr(NCS)_4(NH_3)_2] + dmen + NH_4SCN + 2(CH_3)_2CO + + 1/2O_2 \rightarrow [Cu(dmenac)(NCS)(\mu\text{-}SCN)Cr(NCS)_3(NH_3)_2] + + NH_3 + 3H_2O \quad (3)$$

$$Cu^0 + NH_4[Cr(NCS)_4(NH_3)_2] + 2dmen + + NH_4SCN + 2(CH_3)_2CO + 6dmso + 1/2O_2 \rightarrow \rightarrow [Cu(dmen_2ac)(NCS)][Cr(NCS)_4(NH_3)_2] \cdot 6dmso + + 2NH_3 + 3H_2O \quad (4)$$

The infrared spectra for complexes **1**–**4** show all the characteristic ligands frequencies: $\nu_{as}(NH_2)$, $\nu_s(NH_2)$, ν(N–H), ν(C–H), $\delta(NH_2)$, ν(C–N) and ν(C–C) in the ranges 3330–3300, 3250–3230, 3180–3150, 2980–2950, 1600–1590, 1060–1030 and 980–950 cm^{-1}, respectively, and ν(C=N) for **3** and **4** at 1660 and 1650 cm^{-1}, respectively. The presence of the last two bands in the spectra of **3** and **4** confirms that the condensation process has taken place. The IR spectra show very strong absorption bands in the spectral region characteristic of the NCS ligand (Table 2), suggesting the presence of terminal N-bonded thiocyanate groups in **1**–**4** and bridging thiocyanate groups in **3** [17]. The observed value of ν(CN) at 2100 cm^{-1} for **2**–**4** and the Reinecke's salt, as well as the presence of two bands attributable to ν(CN) in **2** and a very strong and broad band in the region 2120–2070 cm^{-1} in **3** could be a result of the participation of some of NCS groups in hydrogen bonding, which is confirmed by the X-ray analyses of **1**–**4**. The presence of solvent molecules in **1** and **4** can be identified by peaks at 1665 cm^{-1} (dmf, **1**) and 1020 cm^{-1} (dmso, **4**), typical for coordinated dmf and dmso [18]. In our case the shift of ν(CO) and ν(SO) to lower values can be explained by the involvement of the solvate molecules in hydrogen bonding.

The solid-state diffuse-reflectance spectra of **1**–**4** show broad asymmetric bands with maxima in the region 525–545 nm, which probably result from overlapping d–d transitions for the distorted Cu(II) and Cr(III) centers [19–21]. Additionally, the spectra display ligand-to-metal charge transfer bands at *ca.* 300 nm.

3.2. Description of the crystal structures

3.2.1. $[Cu(dmen)_2(dmf)_2][Cr(NCS)_4(NH_3)_2]_2 \cdot 6dmf$ (**1**)

Crystalline samples of **1** represent small grown together crystals with mane defects. All attempts to obtain well defined crystals with bigger size were unsuccessful. This property of **1** results in a relatively low precision of the crystal structure determination. Therefore, we cannot discuss in detail the geometrical parameters of **1**. However, the structural data reflects the coordination pattern of the metals and general organization of the crystals.

The crystal structure of **1** consists of discrete $[Cu(dmen)_2(dmf)_2]^{2+}$ cations, anions of the Reinecke's salt $[Cr(NCS)_4(NH_3)_2]^-$ as counterions and dmf molecules, that are hydrogen bonded into supramolecular sheets. The $[Cr(NCS)_4(NH_3)_2]^-$ anion is structurally similar to previously reported compounds (Table S1) [12–14,22–25]. The copper(II) ions in **1** are in an elongated octahedral (4 + 2) coordination environment with four nitrogen atoms of two dmen bidentate ligands in the equatorial plane and two oxygen atoms of dmf molecules in the axial positions (Fig. 1).

The compound **1** contains six solvate dmf molecules, and hence the crystal architecture is assisted by numerous N–H···O hydrogen

Table 2
Selected infrared spectroscopic data for **1**–**4** and Reinecke's salt.

Compound	ν(CN), cm^{-1}	ν(CS), cm^{-1}
$NH_4[Cr(NCS)_4(NH_3)_2] \cdot H_2O$	2100	830
1	2090	790
2	2100 and 2070	860 and 840
3	2140 and 2120–2070	790 and 775
4	2100	790

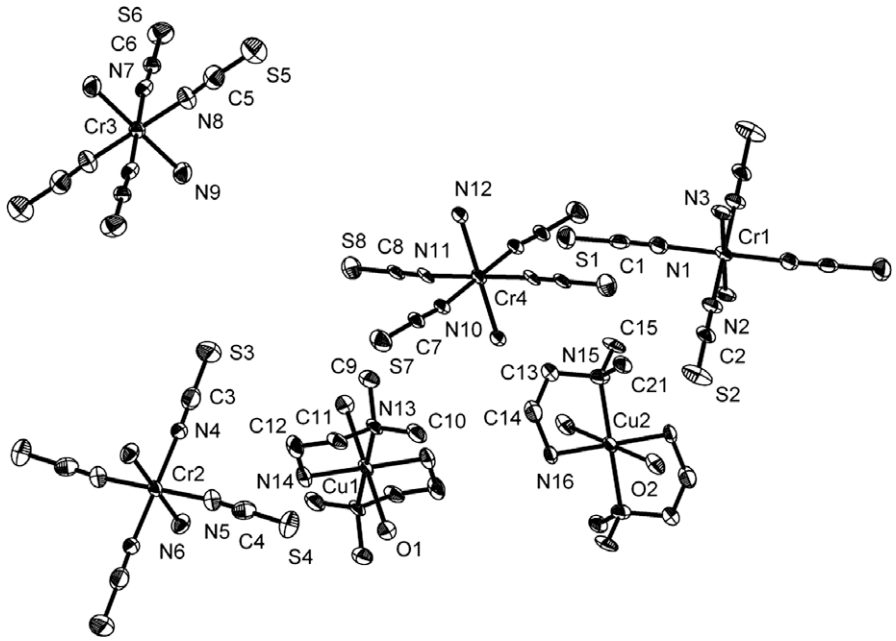


Fig. 1. Fragment of the structure of **1** with 50% probability thermal ellipsoids, showing the atom numbering scheme (H atoms and dmf molecules are omitted for clarity).

bonds (Table S2). The oxygen atoms of dmf molecules are H-bonded by hydrogen atoms of NH_3 molecules of $[Cr(NCS)_4(NH_3)_2]^-$ anions and by hydrogen atoms of primary amine groups of dmen ligands of $[Cu(dmen)_2(dmf)_2]^{2+}$ cations, forming supramolecular sheets. The sheets can be considered as being built up of two types of hydrogen bonded chains, as can be visualized in Fig. 2. It is noteworthy, that there are two types of supramolecular sheets, based on two sets of crystallographically independent atoms [sheet 1, formed by Cu(1), O(4), Cr(4), Cr(2), O(7) and O(9) atoms, and sheet 2, formed by Cu(2), O(3), Cr(1), Cr(3), O(45) and O(5) atoms] (Table S2). The sheets are well separated from each other and finally form the 2D layered supramolecular architecture.

3.2.2. $[Cu(dmen)_2(NCS)][Cr(NCS)_4(NH_3)_2]$ (**2**)

The structure of **2** includes $[Cu(dmen)_2(NCS)]^+$ cations and anions of the Reinecke's salt $[Cr(NCS)_4(NH_3)_2]^-$, that are hydrogen bonded into cationic and anionic chains. These are linked together into 2D supramolecular sheets, which are further stacked by hydrogen bonding to form a three-dimensional supramolecular architecture. In **2**, the chromium(III) ion has the same coordination environment and geometrical parameters as in **1** (Table S1). The coordination geometry of the copper(II) ion in **2** is a slightly distorted square-based pyramid (trigonality index $\tau = 0.054$ [26]); the four N atoms of two dmen ligands form the base and the fifth N atom, from the thiocyanate anion, occupies the apex position (Fig. S1). The $Cu–N_{dmen}$ distances are in the range 1.986(3)–2.104(3) Å, with slightly shorter bond lengths to the primary amine nitrogen atoms than those to the tertiary ones (Table S1), which is usually observed for complexes with the dmen ligand [27–30].

In the crystal lattice of **2**, $[Cu(dmen)_2(NCS)]^+$ cations form cationic chains through N–H···S hydrogen bonds between H(N) atoms of primary amine groups of dmen ligands and S atoms of terminal NCS groups of adjacent cations, while $[Cr(NCS)_4(NH_3)_2]^-$ anions are joined into anionic chains by means of N–H···S bonds between NH_3

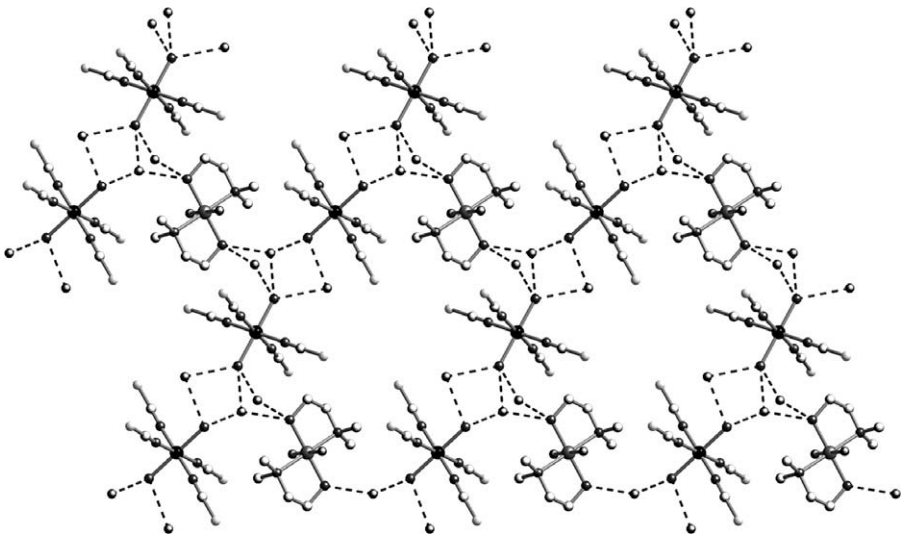


Fig. 2. Fragment of the supramolecular sheet of **1** (hydrogen atoms are omitted for clarity and only oxygen atoms of dmf molecules are shown).

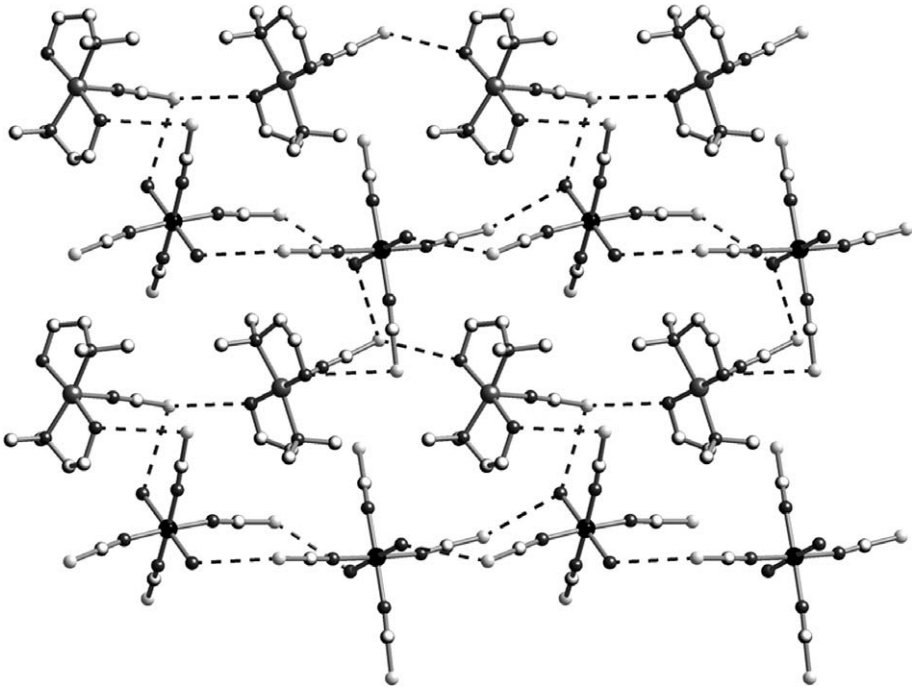


Fig. 3. Fragment of the H-bonded sheet of **2** (H atoms are removed for clarity).

molecules and the S atoms of thiocyanate groups (Fig. 3). The alternating cationic and anionic chains are inter-connected by N–H···S hydrogen bonds (Table S2) to create a three-dimensional supramolecular network.

3.2.3. *[Cu(dmenac)(NCS)(μ-SCN)Cr(NCS)$_3$(NH$_3$)$_2$] (**3**) and [Cu(dmen$_2$ac)(NCS)][Cr(NCS)$_4$(NH$_3$)$_2$] · 6dmso (**4**)*

Fragments of the crystal structures of binuclear complex **3** and solvated ionic complex **4**, with their labelling schemes, are shown in Fig. 4 and Fig. S2, respectively. The crystal structure of **3** is made up of Cu(dmenac)(NCS)$^+$ and Cr(NCS)$_4$(NH$_3$)$_2^-$ moieties, connected by a thiocyanate bridge. The crystal structure of **4** consists of [Cr(NCS)$_4$(NH$_3$)$_2$]$^-$ anions, [Cu(dmen$_2$ac)(NCS)]$^+$ cations and six dmso molecules of crystallization. Three of dmso molecules participate in hydrogen bonds with anions of the Reinecke's salt, forming supramolecular chains, while the cations with the rest of solvate molecules are accommodated in the interchain space.

In the compounds **3** and **4**, all the chromium(III) atoms have the same coordination environment and geometrical parameters as in **1** and **2** (Table S1). The coordination geometries of the five-coordinated copper(II) atoms in **3** and **4** are closely related to a distorted square-based pyramid (τ = 0.243 for **3**, τ = 0.112 for **4**) with the sulfur atom of the bridging thiocyanate group and nitrogen atom of a terminal thiocyanate group at the axial sites in **3** and **4**, respectively. The apical Cu–S distance in **3** has a value of 2.694(4) Å, which is close to those found in other pentacoordinated copper(II) complexes with the sulfur atom at an apical position [31–34]. The basal sites of the copper pyramids are occupied by three nitrogen atoms of the dmenac ligand and one nitrogen atom of a terminal NCS group (**3**), and by four nitrogen atoms of the dmen$_2$ac ligand (**4**). Usually, complexes with Curtis-type ligands have slightly shorter bond lengths to the imine nitrogen than those to the secondary amine nitrogen [35–38], this is the case in **4**, while **3** exhibits a slightly shorter bond to the primary amine nitrogen of the dmenac ligand (Table S1).

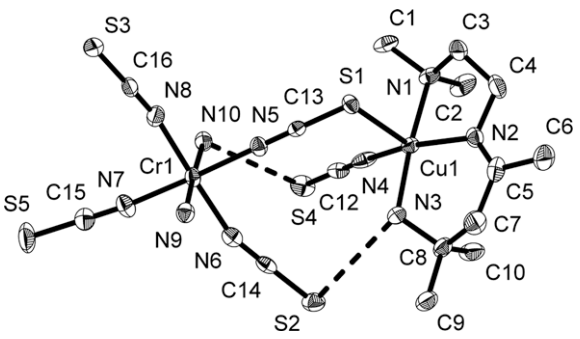


Fig. 4. View of the molecular structure of **3** with the atom numbering scheme showing intramolecular hydrogen bonds. Atom displacement ellipsoids are shown at the 50% probability level (H atoms are omitted for clarity).

The molecular structure of **3** is strengthened by two intramolecular N–H···S bonds (Fig. 4), while adjacent binuclear complexes are connected into two-dimensional sheets by intermolecular hydrogen bonds between thiocyanate ligands and NH$_3$ molecules of [Cr(NCS)$_4$(NH$_3$)$_2$]$^-$ anions (Table S2, Fig. 5).

An interesting feature of the crystal structure of **4**, revealed by analysis of the packing diagram, is the presence of anionic supramolecular chains, built from H-bonded solvate molecules and [Cr(NCS)$_4$(NH$_3$)$_2$]$^-$ anions. The interchain space is filled with [Cu(dmen$_2$ac)(NCS)]$^+$ cations, each of which is bound to the oxygen atom of a dmso molecule through the H(N) atom of the secondary amine group of the dmen$_2$ac ligand, forming a cationic agregate, and two uncoordinated solvate molecules (Fig. 6).

3.3. EPR and magnetic properties

The EPR spectra of polycrystalline samples of compounds **1**, [Cu(dmen)$_2$(dmf)$_2$]$^{2+}$, **3** and **4** at 295 and 77 K are very similar (Fig. 7): they exhibit an almost isotropic and very broad line around g = 2, which seems to be caused by resonance transitions between the electronic levels split by a small zero-field splitting parameter D (according to Spin Hamiltonian due to at least S = 3/2). It is in agreement with the rather high symmetry of the Cr(III) coordination. The parameters of the spectra remain practically

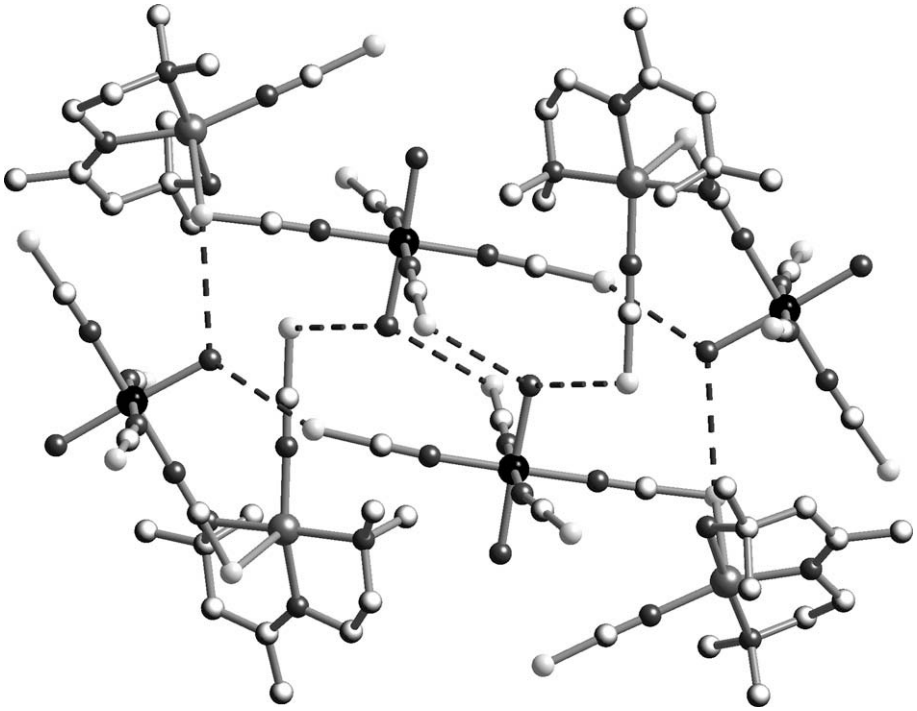


Fig. 5. Fragment of the supramolecular sheets of **3** showing intermolecular hydrogen bonds (H atoms are omitted for clarity).

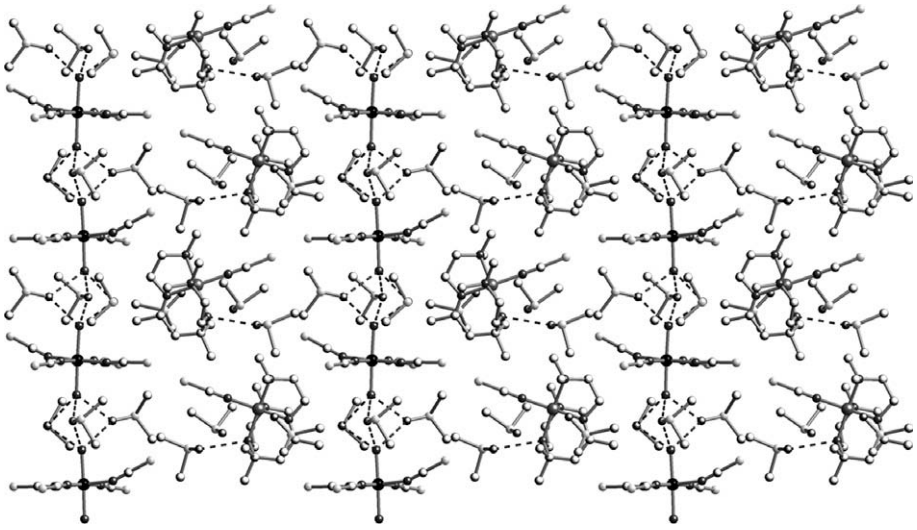


Fig. 6. The arrangement of anionic supramolecular chains, copper(II) cations and solvate molecules of **4** (the hydrogen atoms are omitted for clarity).

unchanged on lowering the temperature down to 77 K. The lack of anisotropy, typical for Cu(II) complexes, and g about 2 indicates that the EPR signal due to copper(II) is overlapped by that from the Cr(III) complex. The spectrum of **2** (295 K) also displays a broad line due to Cr(III), but a strong narrow line of rhombic type is distinctly seen; its simulation gave $g_1 = 2.164$, $g_2 = 2.109$ and $g_3 = 2.055$ which correspond to the Cu(II) complex, but are effective, not molecular.

A comparison of the EPR frozen solution spectra for the compounds dissolved in dmf (Fig. 8) reveals that the spectra of **1** and **2** are the same, but are different from those for **3** and **4**, which in turn are also very close. The following spin Hamiltonian parameters were obtained by computer simulation of the experimental spectra for compounds **1** and **2**: $g_{II} = 2.214$, $g_{\perp} = 2.048$, $A_{II} = 189 \times 10^{-4}\,cm^{-1}$, $A_{\perp} = 22 \times 10^{-4}\,cm^{-1}$ (which are typical for a 4 N donor set around the Cu(II) plane) and for compounds **3** and **4**: $g_z = 2.218$, $g_x = 2.064$, $g_y = 2.040$, $A_z = 178 \times 10^{-4}\,cm^{-1}$, $A_x = 45 \times 10^{-4}\,cm^{-1}$, $A_y = 15 \times 10^{-4}\,cm^{-1}$ (suggesting deviation from the in-plane coordination of the ligands). The tendency of the g and A tensors to change from axial to rhombic may be assign to an increase of axial symmetry distortion of the coordination geometry, indicated by crystal structure studies; for **1** this distortion is absent, for **2** it is very small, and for **3** and **4** it is apparently greater according to the trigonality index τ (see Section 3.2). The second-derivative spectrum for **3** shows in the high field region of the spectrum the resolution of ^{14}N hyperfine splitting of ~12 Gs due to the nitrogen nuclei of the ligands.

A careful inspection of the low field region (Fig. 9) of the frozen solution spectra, measured over a wide range of the magnetic field allows the detection, for all compounds, of a broad slightly resolved line with a dominant signal at $g = 3.86$ and with a relatively weaker signal at about 5.6. The computer simulation of this line,

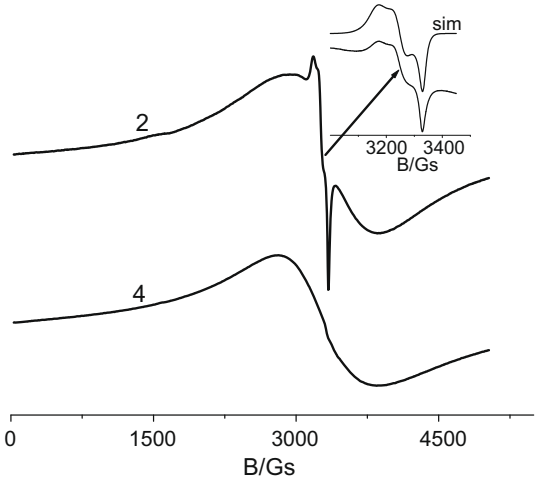


Fig. 7. The EPR spectra of polycrystalline compounds **2** and **4** at 77 K, with a magnified signal due to the Cu(II) centers simulated using the parameters giving in the text.

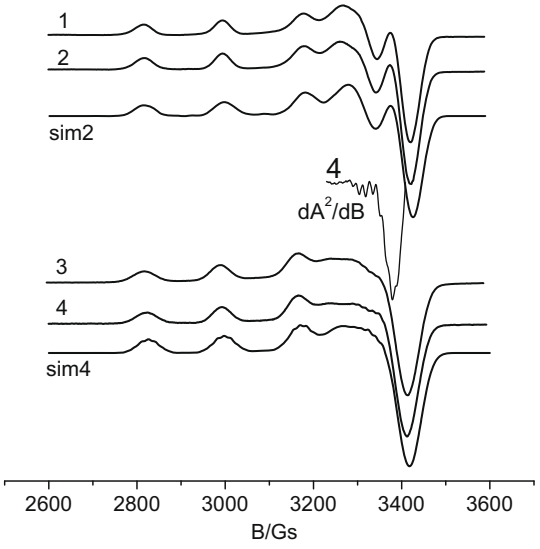


Fig. 8. The EPR spectra of frozen DMF solutions of Cu(II) complexes **1**–**4**, together with the corresponding spectra simulated (sim) for complexes **2** and **4** using the parameters given in the text, at 77 K. In the middle, the fragment of compound **4** spectrum as a second-derivative (in the same magnetic field scale) shows the hyperfine splitting (about 12 G) due to interaction with ^{14}N nuclei of the ligands.

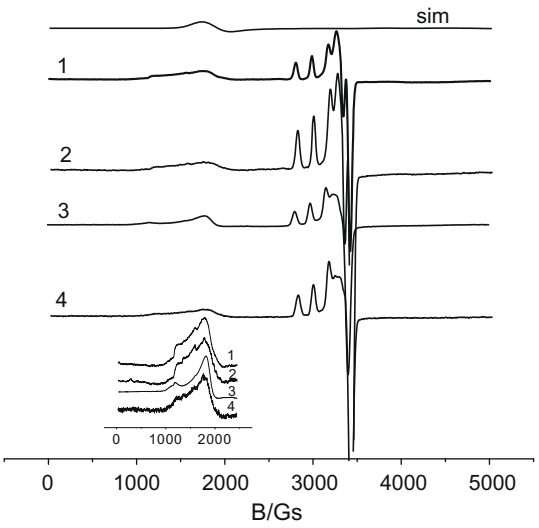


Fig. 9. The EPR spectra of DMF frozen solutions of compounds **1**–**4**, recorded in the magnetic field range of 5000 Gs, with magnified low field lines and with the spectrum simulated (sim) using $S = 3/2$, $D \sim 0.5$ cm^{-1}, $g_x = g_y = g_z = 1.97$.

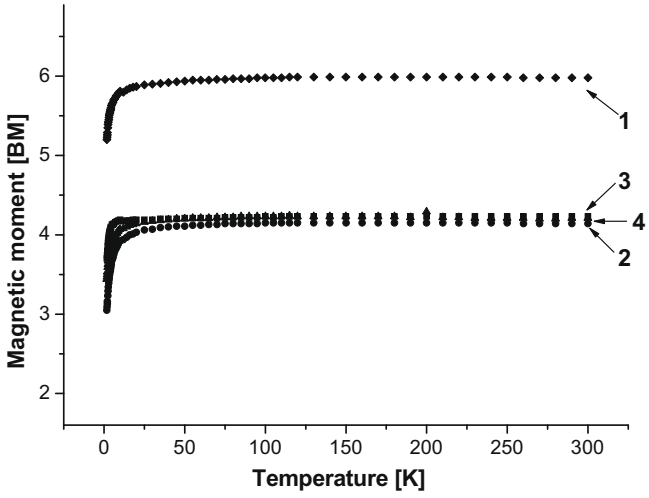


Fig. 10. Temperature dependences of the experimental effective magnetic moments for **1**–**4**.

performed using $S = 3/2$, gives D (the zero-field splitting parameter) of about 0.4 cm^{-1} and $g_x = g_y = g_z = 1.97$. The parameters are similar to those detected for other Cr(III) complexes with $D > h\nu$ [39,40] and suggest that the low field line corresponds to resonance transitions between the spin levels (split in zero magnetic field) of the Cr(III) center.

The results of the magnetic susceptibility measurements for **1**–**4** are plotted as the effective magnetic moment (μ_{eff}) versus temperature in Fig. 10. Compound **1** shows a room temperature magnetic moment of 5.9 μ_B, which is close to the expected one for the non-interaction of the Cu(II) ion and two Cr(III) ions, where the constituent metals have typical μ_{eff} spin-only values of 1.8 and 3.8 μ_B, respectively. Compounds **2**–**4**, with the same formula unit "CuCr", reveal room temperature magnetic moments of 4.14 (**2**), 4.23 (**3**) and 4.21 μ_B (**4**), respectively, in agreement with the expected value for non-interacting Cu(II) and Cr(III) ions. On lowering the temperature, the effective magnetic moments for **1**–**4** remain constant down to *ca.* 20 K and then decrease progressively to 5.26 (**1**), 3.13 (**2**), 3.78 (**3**) and 3.5 μ_B (**4**), respectively, at 2 K. These data indicate the paramagnetic behavior with the Curie–Weiss constants $\Theta = -0.64$ and $C = 4.49$ (**1**), $\Theta = -1.19$ and $C = 2.16$ (**2**), $\Theta = -0.49$ and $C = 2.24$ (**3**), $\Theta = -0.53$ K and $C = 2.23$ cm^3 mol^{-1} K (**4**).

4. Conclusion

Mild direct synthesis conditions, as well as commercially available and relatively simple precursors provide an easy and promising way of synthesizing new heterometallic complexes with primary amines and their Schiff-base derivatives. This research describes the synthesis and structural as well as magnetic characterization of four novel Cu(II)/Cr(III) complexes using a one-pot self-assembly from zerovalent copper, Reinecke's salt, NH_4NCS (in the case of **2** and **4**), acetone (in the case of **3** and **4**) and *N*,*N*-dimethylethylenediamine (dmen) in non-aqueous solvents in the

open air. It has been shown that the presence of acetone in the reaction mixture provides favorable conditions for metal-directed self-assembly condensation, yielding two novel open-chain Schiff-base ligands, dmenac and $dmen_2ac$.

Acknowledgement

This work was supported in part by Fundamental Researches State Fund of Ukraine (project 14.3/005).

Appendix A. Supplementary data

CCDC 682958–682961 contain the supplementary crystallographic data for this paper. These data can be obtained free of charge via http://www.ccdc.cam.ac.uk/conts/retrieving.html, or from the Cambridge Crystallographic Data Centre, 12 Union Road, Cambridge CB2 1EZ, UK; fax: (+44) 1223-336-033; or e-mail: deposit@ccdc.cam.ac.uk.

Supplementary data associated with this article can be found, in the online version, at doi:10.1016/j.poly.2009.02.041.

References

[1] T. Mallah, S. Thiébaut, M. Verdaguer, P. Veillet, Science 262 (1993) 1554.
[2] M. Verdaguer, Science 272 (1996) 698.
[3] M. Ohba, H. Okawa, Coord. Chem. Rev. 198 (2000) 313.
[4] J. Cernák, M. Orendác, I. Potocnák, J. Chomic, A. Orendácová, J. Skorsepa, A. Feher, Coord. Chem. Rev. 224 (2002) 51.
[5] F. Thétiot, S. Triki, J. Sala Pala, C.J. Gómez-García, S. Golhen, Chem. Commun. (2002) 1078.
[6] E. Coronado, M.C. Giménez, C.J. Gómez-García, F.M. Romero, Polyhedron 22 (2003) 3115.
[7] J. Mrozínski, Coord. Chem. Rev. 249 (2005) 2534.
[8] G. Denti, S. Serroni, S. Campagna, A. Juris, M. Ciano, V. Balzani, in: A.F. Williams, C. Floriani, A.E. Merbach (Eds.), Perspectives in Coordination Chemistry, VCH, Basel, Switzerland, 1992.
[9] J.W. Bae, Y.J. Cho, S.H. Lee, C.-O.M. Yoon, C.M. Yoon, Chem. Commun. (2000) 1857.
[10] A.S. Batsanov, M.A. Fox, A.E. Goeta, J.A.K. Howard, A.K. Hughes, J.M. Malget, J. Chem. Soc., Dalton Trans. (2002) 2624.
[11] A. De Nicola, Y. Liu, K.S. Schanze, R. Ziessel, Chem. Commun. (2003) 288.
[12] V.M. Nikitina, O.V. Nesterova, V.N. Kokozay, E.A. Goreshnik, J. Jezierska, Polyhedron 27 (2008) 2426.
[13] V.M. Nikitina, O.V. Nesterova, V.N. Kokozay, R.I. Zubatyuk, V.V. Dyakonenko, O.V. Shishkin, E.A. Goreshnik, C.J. Gómez-García, J.M. Clemente-Juan, J. Jezierska, Inorg. Chim. Acta (2008), doi:10.1016/j.ica.2008.10.003.
[14] V.M. Nikitina, O.V. Nesterova, V.N. Kokozay, V.V. Dyakonenko, O.V. Shishkin, J. Jezierska, Inorg. Chem. Commun. 12 (2009) 101.
[15] E. König, Magnetic Properties of Coordination and Organometallic Transition Metal Complexes, Springer, Berlin, 1966.
[16] G.M. Sheldrick, SHELXTL PLUS. PC Version, A System of Computer Programs for the Determination of Crystal Structure from X-ray Diffraction Data, Rev. 5.1, 1998.
[17] A. Golub, H. Kohler, V. Skopenko (Eds.), Chemistry of Pseudohalides, Elsevier Science, Amsterdam, 1986.
[18] K. Nakamoto, Infrared and Raman Spectra of Inorganic and Coordination Compounds, fifth ed., J. Wiley, New York, 1997.
[19] A.B.P. Lever, Inorganic Electronic Spectroscopy, second ed., Elsevier Science, Amsterdam, Oxford, New York, Tokyo, 1984.
[20] B.J. Hathaway, in: G. Wilkinson, R.D. Gillard, J.A. McCleverty (Eds.), Comprehensive Coordination Chemistry, the Synthesis, Reactions, Properties and Applications of Coordination Compounds, vol. 5, Pergamon, Oxford, 1987, p. 674.
[21] L.F. Larkworthy, K.B. Nolan, P. O'Brien, in: G. Wilkinson, R.D. Gillard, J.A. McCleverty (Eds.), Comprehensive Coordination Chemistry, the Synthesis, Reactions, Properties and Applications of Coordination Compounds, vol. 3, Pergamon, Oxford, 1987, p. 837.
[22] H.M. Colquhoun, K. Henrick, Inorg. Chem. 20 (1981) 4074.
[23] K.-L. Zhang, W. Chen, Y. Xu, Z. Wang, Z.J. Zhong, X.-Z. You, Polyhedron 20 (2001) 2033.
[24] T.G. Cherkasova, I.P. Gorunova, Zh. Neorg. Khim. 48 (2003) 611.
[25] A. Cucos, N. Avarvari, M. Andruh, Y. Journaux, A. Müller, M. Schmidtmann, Eur. J. Inorg. Chem. (2006) 903.
[26] A.W. Addison, T.N. Rao, J. Reedijk, J. Van Rijn, G.C. Verschoor, J. Chem. Soc., Dalton Trans. (1984) 1349.
[27] N. Mondal, M.K. Saha, S. Mitra, V. Gramlich, M.S. El Fallah, Polyhedron 19 (2000) 1935.
[28] Z. Smekal, J. Kamenicek, P. Klasova, G. Wrzeszcz, Z. Sindelar, P. Kopel, Z. Zak, Polyhedron 21 (2002) 1203.
[29] C.J. Shorrock, H. Jong, R.J. Batchelor, D.B. Leznoff, Inorg. Chem. 42 (2003) 3917.
[30] C. López, R. Costa, F. Illas, C. de Graaf, M.M. Turnbull, C.P. Landee, E. Espinosa, I. Mata, E. Molins, J. Chem. Soc., Dalton Trans. (2005) 2322.
[31] C.V. Depree, U. Beckmann, K. Heslop, S. Brooker, J. Chem. Soc., Dalton Trans. (2003) 3071.
[32] A.M. Madalan, V.C. Kravtsov, D. Pajic, K. Zadro, Y.A. Simonov, N. Stanica, L. Ouahab, J. Lipkowski, M. Andruh, Inorg. Chim. Acta 357 (2004) 4151.
[33] Z.-L. You, Z. Anorg. Allg. Chem. 632 (2006) 669.
[34] Y.-F. Wang, L.-Y. Wang, L.-F. Ma, Z. Anorg. Allg. Chem. 634 (2008) 181.
[35] G. Mendoza-Diaz, L. Ruiz-Ramirez, R. Moreno-Esparza, Polyhedron 19 (2000) 2149.
[36] N.F. Curtis, H.K.J. Powell, H. Puschmann, C.E.F. Rickard, J.M. Waters, Inorg. Chim. Acta 355 (2003) 25.
[37] N.F. Curtis, H. Puschmann, Polyhedron 25 (2006) 1204.
[38] N.F. Curtis, K. Flood, W.T. Robinson, Polyhedron 25 (2006) 1579.
[39] K.P. Bryliakov, M.V. Lobanova, E.P. Talsi, J. Chem. Soc., Dalton Trans. (2002) 2263.
[40] L. Jacquamet, Y. Sun, J. Hatfield, W. Gu, S.P. Cramer, M.W. Crowder, G.A. Lorigan, J.B. Vincent, J.-M. Latour, J. Am. Chem. Soc. 125 (2003) 774.

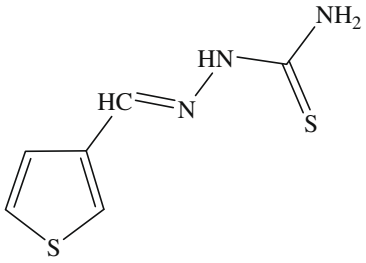


Fig. 1. Chemical structure of the ligand.

tions were estimated from Pascal's constants and magnetic data were corrected for diamagnetic contributions of the sample holder.

2.3. Crystal data collection and processing

Crystals of the ligand 3TTSCH and [Ni(3TTSC)$_2$] are monoclinic with the space group $P2_1/c$. The crystal and instrumental parameters used in the unit-cell determination and data collection are summarized in Table 1. X-ray single-crystal diffraction data were collected at 293 K on a STOE-IPDS diffractometer, equipped with a graphite monochromator using Mo Kα radiation (λ = 0.71073 Å) (CIMA, UMR CNRS 6200, Université d'Angers). The structures were solved by full-matrix least-squares techniques using the SHELX-97 package [15]. Positions of H-atoms were calculated geometrically and the distances N1–H1A and N1–H1B for [Ni(3TTSC)$_2$] were refined. Gaussian absorption corrections were applied.

2.4. Synthesis of the ligand 3TTSCH

The ligand was obtained from thiophene-3-carboxaldehyde and thiosemicarbazide (1:1 molar ratio) in absolute ethanol with the addition of two drops of sulfuric acid [16]. The mixture was refluxed for 1 h and then cooled, filtered and recrystallized from ethanol. Yellow single crystals suitable for X-ray analysis were grown at room temperature by slow evaporation of solution of the ligand in a mixture of ethanol (75%) and water (25%).

Table 1
Crystallographic data.

Formula	$C_6H_7N_3S_2$	$C_{12}H_{12}N_6NiS_4$
Name	3TTSCH	[Ni(3TTSC)$_2$]
Formula weight	185.27	427.23
Crystal system	monoclinic	monoclinic
Space group	$P2_1/c$	$P2_1/c$
a (Å)	18.951(1)	7.4810(9)
b (Å)	5.7911(5)	7.5187(6)
c (Å)	23.551(2)	15.212(2)
α (°)	90	90
β (°)	99.914(8)	101.75(1)
γ (°)	90	90
V (Å^3)	2546.1(3)	837.7(2)
Z	12	2
Color	yellow	yellow-brown
D_{calc} (g cm^{-3})	1.450	1.694
F(000)	1152	436
Crystal size (mm)	0.73 × 0.31 × 0.08	0.69 × 0.23 × 0.08
μ (mm^{-1})	0.564	1.662
hkl limits	$-22 \leqslant h \leqslant 23$	$-9 \leqslant h \leqslant 9$
	$-7 \leqslant k \leqslant 7$	$-9 \leqslant k \leqslant 9$
	$-29 \leqslant l \leqslant 28$	$-18 \leqslant l \leqslant 18$
θ_{min}, θ_{max} (°)	2, 26	3, 26
Reflections collected/unique	23 584/4955	7898/1616
Number of data with $I > 2\sigma(I)$	3708	1317
Number of variables	299	126
R_1 for $I > 2\sigma(I)$	0.0583	0.0295
wR_2 for $I > 2\sigma(I)$	0.1670	0.0744

$w = 1/[\sigma^2(F_o^2) + (0.1414P)^2 + 0.00000P]$ where $P = (F_o^2 + 2F_c^2)/3$ for 3TTSCH.
$w = 1/[\sigma^2(F_o^2) + (0.0440P)^2 + 0.22020P]$ where $P = (F_o^2 + 2F_c^2)/3$ for [Ni(3TTSC)$_2$].

2.5. Preparation of the complexes

All the complexes were prepared starting from 5 mmol (1 g) of 3TTSCH dissolved in EtOH. An ethanolic solution of the metal halide was added slowly while stirring. The complexes were removed by filtration, washed with MeOH and finally dried in vacuum over silica gel.

2.5.1. Bis(3-thiophenaldehyde thiosemicarbazone) cobalt(II) [Co(3TTSC)$_2$]

$CoCl_2 \cdot 6H_2O$ (0.64 g; 2.5 mmol, 10 cm^3) or $CoBr_2$ (0.59 g; 2.5 mmol, 10 cm^3) was added to the 3TTSCH ethanolic solution (20 cm^3) under refluxing conditions. The reflux was maintained for 24 h. The resulting solution was concentrated and a dark-brown precipitate was filtered off.

2.5.2. Bis(3-thiophenaldehyde thiosemicarbazone) nickel(II) [Ni(3TTSC)$_2$]

$NiCl_2 \cdot 6H_2O$ (0.64 g; 2.5 mmol, 10 cm^3) or $NiBr_2 \cdot xH_2O$ (0.59 g; 2.5 mmol, 10 cm^3) was added to the ethanolic solution of 3TTSCH (20 cm^3) under refluxing conditions. An aqueous solution of sodium hydroxide was added dropwise to reach a pH value in the range 6–7 [17]. The reflux was maintained for 3 h.

2.5.3. Bis[chloro (3-thiophenaldehyde thiosemicarbazone) copper(II)] [CuCl(3TTSC)]$_2$

$CuCl_2 \cdot 2H_2O$ (0.91 g; 5 mmol, 10 cm^3) was added to 3TTSCH in EtOH (15 cm^3). Although the complex appeared instantaneously, the reflux was maintained for 1 h in order to complete the reaction. The same compound was obtained when operating at room temperature.

2.5.4. Dibromo (3-thiophenaldehyde thiosemicarbazone) copper(II) [CuBr$_2$(3TTSC)]

$CuBr_2$ (1.2 g; 5 mmol, 10 cm^3) was added to 3TTSCH in EtOH (15 cm^3) at room temperature. The complex appeared instantaneously, however, the reaction was maintained for 3 h.

2.5.5. Bis(bromo (3-thiophenaldehyde thiosemicarbazone) copper(II)) [CuBr(3TTSCH)]$_2$

$CuBr_2$ (1.2 g; 5 mmol, 10 cm^3) was added to 3TTSCH in EtOH (15 cm^3). Although the complex appeared instantaneously, the reflux was maintained for 2 h.

3. Results and discussion

3.1. Crystal structure of the ligand 3TTSCH

The main crystal parameters are reported in Table 1. The monoclinic unit cell (space group $P2_1/c$) contains twelve molecules in four groups of three independent molecules. The three independent molecules, with the numbering scheme, are given in Fig. 2. Each of the three independent molecules is quite planar and the most important deviations are observed for the thiosemicarbazone sulfur atoms as follows: S(1): 0.1838 Å, S(3): 0.1867 Å and S(5): 0.7895 Å. The first and the second molecules lie in quite parallel planes, while the third one is located in a plane forming angles of 54.17(6)° with the first molecule and 53.69(6) with the second one. The sulfur atom S(1) and the hydrazone nitrogen N(3) are in the E position with respect to the C(1)–N(2) bond, the same configuration is observed for S(3) and S(5) with respect to the C(7)–N(5) and C(13)–N(8) bonds, respectively. This configuration is often ob-

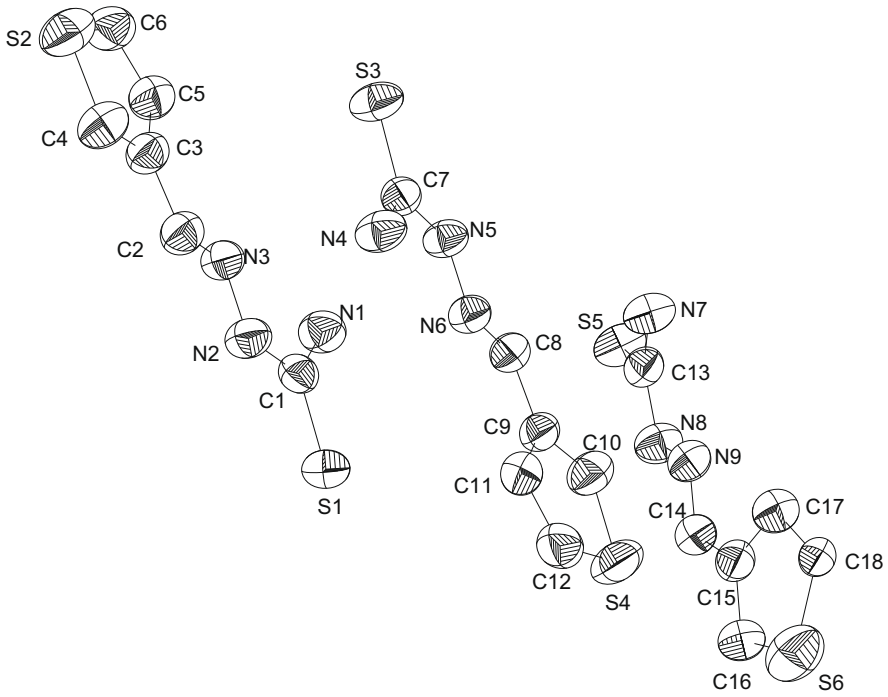


Fig. 2. ORTEP view (50% displacement ellipsoids) of the three independent molecules of the ligand with the numbering scheme.

served in thiosemicarbazones and its stability is due to the presence of an intramolecular hydrogen bond between the N-imino atom and H from NH_2 [5]. In the case of 3TTSCH, the distances N(3)–H, N(6)–H and N(9)–H are 2.358(2), 2.248(2) and 2.290(3) Å, respectively, and consequently these interactions are weak, but sufficient to stabilise the *E* configuration.

There are no significant differences for bond distances and angles in the thiosemicarbazone moiety between the three independent molecules. Representative bond distances and angles for the three independent molecules are shown in Table 2. The C–S bond lengths (1.683(3)–1.691(3) Å) and the dihedral angles around C(1), C(7) and C(13) are typical of a delocalised π electron system [10,18]. The bond length of the C(2)–N(3) bond is 1.268(4) Å, that of N(2)–N(3) is 1.389(4) Å, and these distances are typical of a C=N double bond and an N–N single bond, respectively, and similar values are observed for the two other independent molecules.

The packing arrangement in the unit cell is given in Fig. 3. The third independent molecules in parallel planes are located along the *c* edges and are common to two unit cells. The first and the second independent molecules are grouped in two rows between the planes of the third molecule. The packing of a group of independent molecules is governed by hydrogen bonds (Table 4). Their lengths are consistent with those observed in the case of the furanic analogue thiosemicarbazone [9,19].

Table 2
Selected bond lengths (Å) and angles (°) of the three independent molecules for the ligand 3TTSCH.

Bond lengths		Bond angles	
C(1)–N(1)	1.330(4)	N(1)–C(1)–N(2)	118.2(3)
C(1)–N(2)	1.350(4)	N(1)–C(1)–S(1)	123.0(2)
C(1)–S(1)	1.687(3)	N(2)–C(1)–S(1)	118.8(2)
C(2)–N(3)	1.268(4)	N(3)–C(2)–C(3)	122.2(3)
N(2)–N(3)	1.389(4)	C(1)–N(2)–N(3)	121.2(3)
C(7)–N(4)	1.320(4)	N(4)–C(7)–N(5)	117.2(3)
C(7)–N(5)	1.344(4)	N(4)–C(7)–S(3)	123.6(2)
C(7)–S(3)	1.683(3)	N(5)–C(7)–S(3)	119.2(2)
C(8)–N(6)	1.276(4)	N(6)–C(8)–C(9)	119.0(3)
N(5)–N(6)	1.379(3)	C(7)–N(5)–N(6)	118.6(2)
C(13)–N(7)	1.304(4)	N(7)–C(13)–N(8)	117.4(3)
C(13)–N(8)	1.348(4)	N(7)–C(13)–S(5)	123.5(2)
C(13)–S(5)	1.691(3)	N(8)–C(13)–S(5)	119.1(2)
C(14)–N(9)	1.270(4)	N(9)–C(14)–C(15)	120.8(3)
N(8)–N(9)	1.371(4)	C(13)–N(8)–N(9)	119.9(3)

3.2. Crystal structure of the nickel complex [Ni(3TTSC)$_2$]

The main crystal parameters are reported in Table 1. The bond distances and angles for the thiosemicarbazone moiety are listed in Table 3 and the structure and the numbering scheme are given in Fig. 4. The centrosymmetric structure consists in the neutral complex species [Ni(3TTSC)$_2$], with the nickel at the centre of symmetry. The coordination results in a square-planar geometry involving the thiolato sulfur atoms and the N(3) nitrogen atoms in a *Z* configuration around the C(1)–N(2) bond (Fig. 4). As the ligand is deprotonated, the resulting negative charge is delocalized along the thiosemicarbazone moiety. Due to the free rotation around the C(2)–C(3) bond there are two possible configurations for the thiophene ring, with an almost 50% probability for each one. This phenomenon was not observed in the case of the furan analogue [10]. The complex molecule is quite planar, the highest deviations are due to the S(1) and N(2) atoms, with 0.5477 and −0.2654 Å deviations, respectively (Fig. 5).

The molecular arrangement inside the unit cell is given in Fig. 6. All the nickel ions are located at the midpoint of the *b* and *c* edges (Fig. 6a). The neutral molecules Ni(3TTSC)$_2$ lie in two sets of parallel planes (Fig. 6b) with a 60° angle between them. The packing is governed by hydrogen bonds between S(1) and H(1A), and N(2) and H(1B) (Table 4). Though these interactions are weak, they have already been observed and described for similar compounds [5].

3.3. Structures of the cobalt and copper complexes

3.3.1. Analytical data

The elemental analysis of the ligand and its complexes is summarized in Table 5. A good harmony between the experimental and

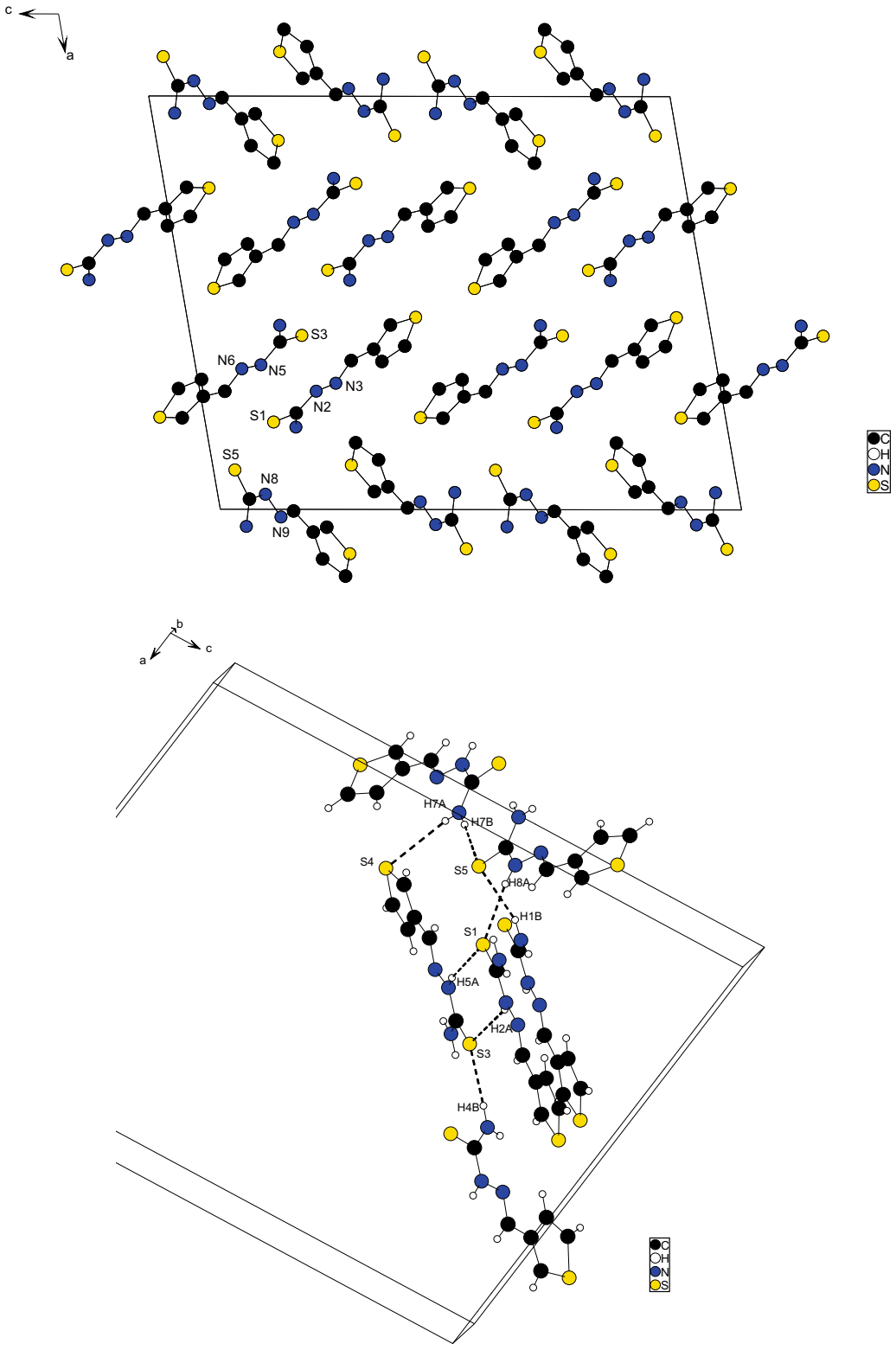


Fig. 3. Packing arrangement and intermolecular hydrogen bonds for the ligand.

calculated values is observed and the formulae of the complexes are $[Co(3TTSC)_2]$, $[Ni(3TTSC)_2]$, $[CuCl(3TTSC)]_2$, $[CuBr(3TTSC)]_2$ and $[CuBr_2(3TTSCH)]$.

The melting points were determined using DSC. In all complexes, decomposition follows the beginning of the melting process.

3.3.2. Infrared spectra

The main infrared vibration bands are reported in Table 6. In principle, since the ligand contains a thioamide –NH–C═S functional group, it can exhibit thione–thiol tautomerism [20]. The ν(S–H) band around 2570 cm^{-1} [21] is absent from IR spectra of the ligand but the ν(N–H) band at 3149 cm^{-1} is present, indicating

Table 3
Bond lengths (Å) and angles (°) for the nickel complex.

Bond lengths		Bond angles	
C(1)–N(2)	1.300(3)	N(2)–C(1)–N(1)	118.9(2)
C(1)–N(1)	1.341(3)	N(2)–C(1)–S(1)	123.29(2)
C(1)–S(1)	1.739(2)	N(1)–C(1)–S(1)	117.83(2)
C(2)–N(3)	1.298(3)	C(1)–N(2)–N(3)	111.97(3)
C(2)–C(3)	1.444(4)	C(2)–N(3)–N(2)	114.7(2)
N(2)–N(3)	1.396(3)	C(2)–N(3)–Ni(1)	125.59(2)
N(3)–Ni(1)	1.912(2)	N(2)–N(3)–Ni(1)	119.67(2)
S(1)–Ni(1)	2.1714(7)	C(1)–S(1)–Ni(1)	95.05(9)

Table 4
Bond lengths (Å), angles (°) and positions of intermolecular hydrogen bonds for the ligand and the Ni(II) complex.

Compound	Hydrogen bonds	Distance (Å)	Angle (°)
3TTSCH	S(1)···H(5A)	2.63	160.2(2)
	S(1)···H(8A)	2.53	162.4(2)
	S(3)···H(2A)	2.55	145.5(2)
	S(3)···H(4B)	2.48	173.7(2)
	S(4)···H(7A)	3.00	144.1(2)
	S(5)···H(1B)	2.61	162.5(2)
	S(5)···H(7B)	2.53	172.5(2)
$[Ni(3TTSC)_2]$	S(1)···H(1A)	2.69	162(1)
	N(2)···H(1B)	2.64	127(1)

that in the solid state the ligand remains as the thione tautomer. The spectrum of the ligand exhibits a strong band at 1603 cm^{-1} due to the C=N stretching vibration.

In the case of the nickel complex, the $\nu(NH_2)$ vibration band is slightly shifted to lower wavenumbers, whereas ν(N–H) is shifted to higher values. The ring breathing remains quite unchanged when passing from ligands to complexes at *ca.* 830 cm^{-1} [22] and ν(C=N) is not significantly modified. There is no significant influence of complexation upon the two bands corresponding to ν(CS), situated at 1165 and 786 cm^{-1} in the ligand spectrum.

In addition, the spectrum of the nickel complex shows the two vibration bands, ν(M–S) and ν(M–N), at 519 and 420 cm^{-1}, respectively, which correspond to coordination bonds [23]. In the spectra of the other complexes, we find the same bands shifts as in the case of the nickel complex. The respiration band of the cycle at *c.a.* 830 cm^{-1} remained unchanged.

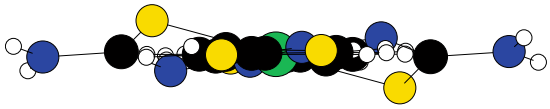


Fig. 5. Atoms deviation with respect to the plane of the molecule of $[Ni(3TTSC)_2]$.

The spectra of all the complexes show the presence of ν(M–S) and ν(M–N) bands, again like in the case of the nickel complex. Thus, in all the complexes the coordination occurs through the sulfur and the nitrogen atom of the imino moiety of the molecule. According to these results, the proposed structures for these new complexes are given in Fig. 6.

3.3.3. Structures of the complexes

The structures of the cobalt(II) and copper(II) complexes are given in Fig. 7. They were determined on the basis of the crystal structure of $[Ni(3FTSC)_2]$ and from their spectroscopic data. In all the species, the coordination occurs through the sulfur (thiosemicarbazone) atom and the N (imino) atom, as in all cases the vibration bands relative to these atoms are identically shifted (Table 5). In addition, the nickel complex was found to be a diamagnetic species.

The elemental analysis for the cobalt(II) complex shows unambiguously that the ligand acts as the deprotonated thiol tautomer. The χT value at 300 K is 0.5 $cm^3\ mol^{-1}$, corresponding to a low spin Co(II) complex and the magnetic moment is 2.13 B.M. This value, much lower than expected for Co(II) tetrahedral complexes, is typical of Co^{II} in a strongly distorted tetrahedral geometry, almost square-planar [24,25]. In addition, there no signal in the EPR spectrum, which is typical of low spin cobalt(II) species.

The two binuclear complexes $[CuX(3TTSC)]_2$ (X = Cl or Br) exhibit the same binuclear structure in which the copper(II) shows a square-planar geometry and bridging halogenides, as has already been reported for 3-furaldehyde thiosemicarbazone [10]. These complexes revealed antiferromagnteic coupling, as is usually observed in binuclear copper(II) complexes with bridging halides [26].

The mononuclear $[CuBr_2(3TTSC)]$ complex is a square-planar species and the copper is coordinated through the sulfur thione atom and the N-imino atom. In this case, the ligand remains protonated and remains as the thione tautomer, like in Ref. [10]. The

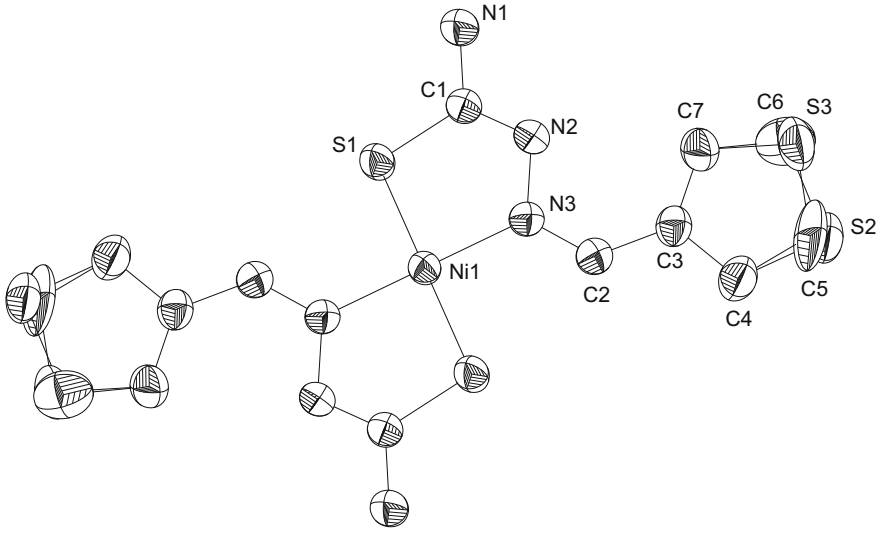


Fig. 4. ORTEP view (50% displacement ellipsoids) and atom numbering for $[Ni(3TTSC)_2]$.

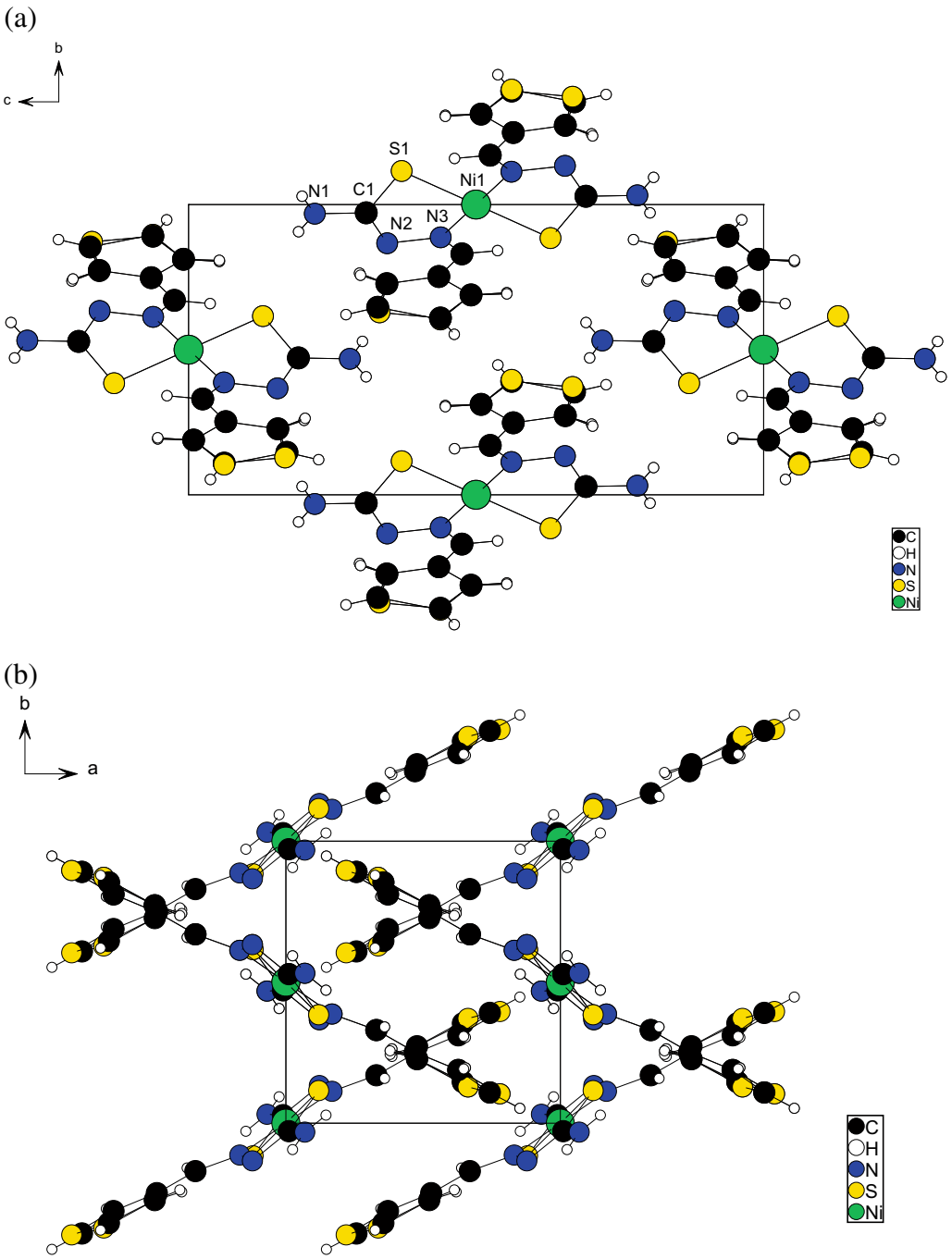


Fig. 6. Packing arrangement for the nickel complex viewed from the *a* axis (a) and *c* axis (b).

Table 5
Analytical data.

Compound	Colour	Yield (%)	MP (°C)	Elemental analysis found (calc.)		
				C (%)	H (%)	N (%)
3TTSCH	yellow	93	165	38.98 (38.87)	3.81 (3.77)	22.68 (22.67)
$[Co(3TTSC)_2]$	dark-brown	44	197d	33.33 (33.56)	3.41 (3.29)	19.35 (19.57)
$[Ni(3TTSC)_2]$	yellow-brown	57	240d	33.89 (33.58)	3.26 (3.29)	19.57 (19.58)
$[CuCl(3TTSC)]_2$	green	72	215d	25.46 (25.35)	2.61 (2.48)	14.36 (14.78)
$[CuBr(3TTSC)]_2$	green	67	223d	20.78 (21.92)	2.31 (2.15)	11.82 (12.78)
$[CuBr_2(3TTSCH)]$	dark-green	58	215d	17.83 (17.64)	2.08 (1.73)	9.46 (10.28)

d, decomposition.

Table 6
Infrared data for the ligand and the complexes (cm^{-1}).

Compound	$\nu(NH_2)$	$\nu(NH)$	$\nu(C{=}N)$	$\nu(CS)$	Ring breath	$\nu(N{-}N)$	$\nu(M{-}S)$	$\nu(M{-}N)$
3TTSCH	3408	3149	1603	1165 786	831	944		
$[Co(3TTSC)_2]$	3406	3150	1603	1164 783	833	944	519	420
$[Ni(3TTSC)_2]$	3372	3168	1608	1163 780	830	945	533	440
$[CuCl(3TTSC)]_2$	3408	3140	1600	1167 780	835	947	528	430
$[CuBr(3TTSC)]_2$	3378	3143	1600sh	1166 784	830	949	525	422
$[CuBr_2(3TTSCH)]$	3403	3138	1600sh	1166 783	831	946	525	420

sh, shoulder.

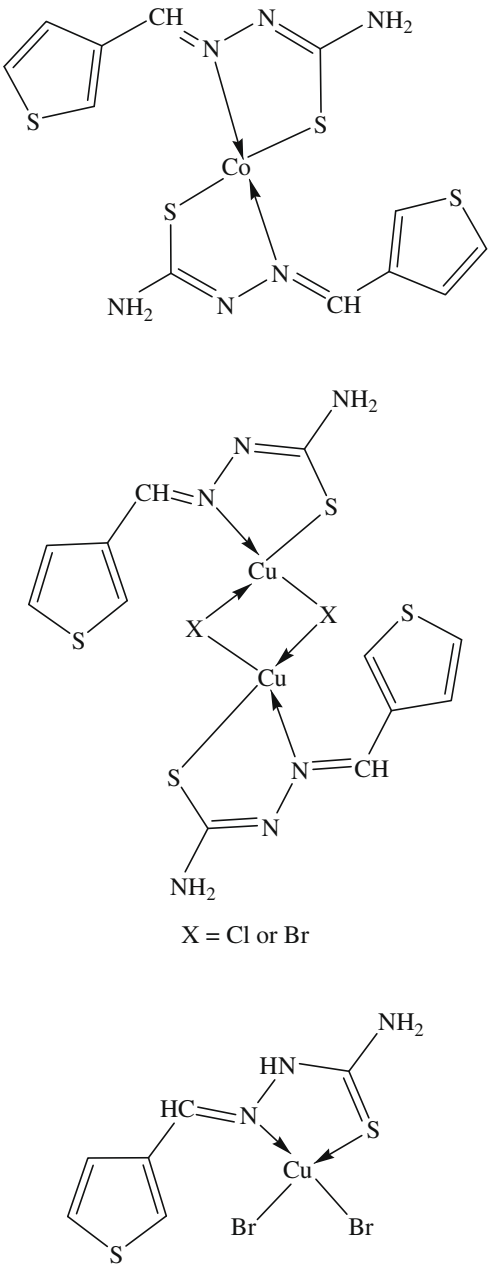


Fig. 7. Chemical structures of the cobalt(II) and copper(II) complexes.

EPR spectrum at room temperature showed typical signals corresponding to the Cu^{2+} ion.

These various structures for complex species have already been observed for other thiosemicarbazones [19,27].

Supplementary data

CCDC 710981 and 710982 contains the supplementary crystallographic data for this article. These data can be obtained free of charge via http://www.ccdc.cam.ac.uk/conts/retrieving.html, or from the Cambridge Crystallographic Data Centre, 12 Union Road, Cambridge CB2 1EZ, UK; fax: (+44) 1223-336-033; or e-mail: deposit@ccdc.cam.ac.uk.

Acknowledgement

The authors wish to thank Eric Rivière, Research Engineer (Equipe Chimie Inorganique, ICMMO, Université Paris-Sud, Orsay, France), for SQUID measurements, EPR spectra recording and useful discussions about the structures of the complexes.

References

[1] H. Beraldo, D. Gambino, Mini-Rev. Med. Chem. 4 (2004) 31.
[2] J.S. Casas, M.S. García-Tasende, J. Sordo, Coord. Chem. Rev. 209 (2000) 197.
[3] H.A. Tang, L.F. Wang, R.D. Yang, Transition Met. Chem. 28 (2003) 395.
[4] T.S. Lobana, P. Kumari, M. Zeller, R.J. Butcher, Inorg. Chem. Commun. 11 (2008) 972.
[5] I.C. Mendes, L.R. Teixeira, R. Lima, H. Beraldo, N.L. Speziali, D.X. West, J. Mol. Struct. 559 (2001) 355.
[6] R.B. de Oliveira, E.M. de Souza-Fagundes, R.P.P. Soares, A.A. Andrade, A.U. Krettli, C.L. Zani, Eur. J. Med. Chem. 43 (2008) 1983.
[7] W.-S. Hong, C.-Y. Wu, C.-S. Lee, W.-S. Hwang, M.Y. Chiang, J. Organomet. Chem. 689 (2004) 277.
[8] S.-G. Teoh, S.-H. Ang, H.-K. Fun, C.-W. Ong, J. Organomet. Chem. 580 (1999) 17.
[9] E.M. Jouad, M. Allain, M.A. Khan, G.M. Bouet, J. Mol. Struct. 604 (2002) 205.
[10] E.M. Jouad, M. Allain, M.A. Khan, G.M. Bouet, Polyhedron 24 (2005) 327.
[11] E.M. Jouad, G. Larcher, M. Allain, A. Riou, G.M. Bouet, M.A. Khan, X.D. Thanh, J. Inorg. Biochem. 86 (2001) 565.
[12] G. Ibrahim, M.A. Khan, P. Richomme, O. Benali-Baïtich, G. Bouet, Polyhedron 16 (1997) 3455.
[13] I. Hall, C. Lee, G. Ibrahim, M.A. Khan, G. Bouet, Appl. Organomet. Chem. 11 (1997) 565.
[14] E.M. Jouad, X.D. Thanh, G. Bouet, N. Ménard, M.A. Khan, Biol. Rhythm Res. 33 (2002) 513.
[15] G.M. Sheldrick, SHELX97 – Program for Crystal Structure Analysis (Release 97-2), G. University of Göttingen, 1998.
[16] D.X. West, J.K. Swearingen, J. Valdés-Martínez, S. Hernández-Ortega, A.K. El-Sawaf, F. van Meurs, A. Castiñeiras, I. Garcia, E. Bermejo, Polyhedron 18 (1999) 2919.
[17] J. Garcia-Tojal, A. Garcia-Orad, J.L. Serra, J.L. Pizarro, L. Lezama, M.I. Arriortua, T. Rojo, J. Inorg. Biochem. 75 (1999) 45.
[18] E.M. Jouad, A. Riou, M. Allain, M.A. Khan, G.M. Bouet, Polyhedron 20 (2001) 67.
[19] E.M. Jouad, Thèse de l'Université d'Angers, Angers, 2002.
[20] Y.-P. Tian, C.-Y. Duan, C.-Y. Zhao, X.-Z. You, T.C.W. Mak, Z.-Y. Zhang, Inorg. Chem. 36 (1997) 1247.

[21] L.J. Bellamy, Advances in Infrared Group Frequencies, Methuen and Co., London, 1968.
[22] S. Gronowitz, A.R. Katritsky, R.E. Reavill, J. Chem. Soc. (1963) 3881.
[23] J.R. Ferraro, Low-Frequency Vibrations of Inorganic and Coordination Compounds, Plenum Press, New York, 1971.
[24] V. Suni, M.R. Prathapachandra Kurup, M. Nethaji, Polyhedron 26 (2007) 5203.
[25] J.R. Anacona, G. Da Silva, J. Chil. Chem. Soc. 50 (2005) 447.
[26] M.d.C. Aguirre, J. Borrás, A. Castiñeiras, J.M. García-Monteagudo, I. García-Santos, J. Niclós, D.X. West, Eur. J. Inorg. Chem. 2006 (2006) 1231.
[27] M. Bellichi Ferrari, G. Gasparri Fava, P. Tarasconi, C. Pelizzi, J. Chem. Soc., Dalton Trans. (1989) 361.

confirmed that $[UO_2Cl_4]^{2-}$ is the most stable chloro complex in [Bmim][Tf_2N] and [$MeBu_3N$][Tf_2N] [26]. The authors have also defined the coordination spheres of the different uranyl-chloro complexes in both ionic liquids and they have studied the influence of the ionic liquid cation on the uranyl solvation. Spectroscopic analysis by Nockemann et al. have also revealed a D_{4h} symmetry for $[UO_2Cl_4]^{2-}$ [27] in Tf_2N-based ionic liquids. Gaillard et al. have confirmed by EXAFS and molecular dynamics simulation that this tetrachloro complex of uranium is the most stable form in various ionic liquids, and they measured a U–Cl distance of 2.69 Å [28]. Few works are also reported on the electrochemical behaviour of uranyl-chloro complexes in both chloro [12] and non-chloroaluminate-based ILs [29,30].

Concerning the complexation of uranyl(VI) by bromide ions in ionic liquids, the electrochemical behaviour is described in a bromoaluminate-based solvent [31] and the luminescence of the tetrabromouranyl complex was recently reported in a pyrrolidinium ionic liquid [32]. However, the coordination of uranyl bromide complexes in ionic liquids has not been investigated so far. UV–Vis absorption spectra of uranyl tetrabromo complexes are only reported in solid state [33] and in anhydrous organic solvents [34], and several crystal structures of uranyl tetrabromo complexes are described [27,34,35].

Within the frame of our work on the fundamental data on uranium in the presence of halide ions in ionic liquids, it is essential to determine which species are present in solution. For that purpose, solid state structural techniques can be coupled with solution spectroscopies. X-ray diffraction allows obtaining information on the structure of crystallized products. However, the collected data do not systematically reflect the coordination environment of the complex in solution [36–38]. To circumvent this problem, UV–Vis and X-ray absorption spectroscopies appear as powerful complementary techniques, allowing to gain further insight into the coordination of the involved species and to determine whether the ligand arrangement of the solution species is preserved or not in the solid state. This is the motivation to study UO_2^{2+} with bromide anions by comparing the crystal structure and the coordination in solution.

In the present work, the coordination of the UO_2^{2+} ion by bromide ions in the ionic liquids [Bmim][Tf_2N] and [$MeBu_3N$][Tf_2N] has been studied by UV–Vis and EXAFS spectroscopies and compared to the crystal structure of $[Bmim]_2[UO_2Br_4]$.

2. Experimental

Yellow single crystals of $[Bmim]_2[UO_2Br_4]$ are obtained by slow evaporation, at room temperature, of an aqueous solution of [Bmim]Br and UO_2Br_2 in the stoechiometry 2:1. One drop of HBr is added to the solution to avoid hydrolysis of the uranyl compounds. X-ray intensity data were collected on a SMART 6000 diffractometer, equipped with a CCD detector, using Cu Kα radiation (λ = 1.54178 Å). The images were interpreted and integrated with the program SAINT from Bruker [39]. Both structures were solved by direct methods and refined by full-matrix least-squares on F^2 using the SHELXTL program package [40]. Non-hydrogen atoms were anisotropically refined and the hydrogen atoms in the riding mode with isotropic temperature factors were fixed at 1.2 times U_{eq} of the parent atoms (1.5 times for methyl groups).

The ionic liquids ([Bmim][Tf_2N] 99.9% and [$MeBu_3N$][Tf_2N] 99.9%) and the bromide salts ([Bmim]Br 98% and [$MeBu_3N$]Br 98%) were commercially available (Solvionic) and used without further purification. The uranyl salt $UO_2(OTf)_2$ (where OTf^- is the triflate anion $CF_3SO_3^-$) was synthesized according to the procedure described in Ref. [41]. Bromide stock solutions (0.3 M) were prepared in both ionic liquids and dried under reduced pressure (~5 mbar) at 70–80 °C during at least 24 h. Prior to addition of bromide salt, the bromide content in the ionic liquids is lower than 8×10^{-5} M. Uranyl stock solutions (0.02 M) were prepared by dissolving $UO_2(OTf)_2$ in both ionic liquids. The water concentration, measured by coulometric Karl–Fisher titration, was found equal to 125 ± 20 ppm in all solutions. The ionic liquids, the bromide salts and the uranyl salt were stocked in an argon-filled dry box and all the samples were prepared in this dry box at least 24 h before analysis.

The samples for UV–Vis absorption spectroscopy (1.2 mL) were either prepared from the above mother solutions or by dissolving a sample of $[Bmim]_2[UO_2Br_4]$ in the ionic liquid [Bmim][Tf_2N]. In all cases the uranyl concentration in the samples is 0.01 M. The absorption spectra were recorded with a Shimadzu UV-2501 PC spectrophotometer using 1 cm path length quartz cells sealed airtight by Teflon stoppers, at 25 °C in [Bmim][Tf_2N] and at 60 °C in [$MeBu_3N$][Tf_2N].

The EXAFS measurements were performed on 200 μL solutions of $UO_2(OTf)_2$ (0.02 M) in presence of four equivalents of [Bmim]Br and [$MeBu_3N$]Br in [Bmim][Tf_2N] and [$MeBu_3N$][Tf_2N], respectively. Uranium L_{III}-edge EXAFS spectra were collected at the Rossendorf Beamline [42] at the ESRF. The measurements were performed using a double crystal Si(1 1 1) monochromator in equidistant k-steps of 0.05 $Å^{-1}$ across the EXAFS region. Higher harmonics were rejected by two platinum-coated mirrors. The measurements were carried out at ambient temperature in transmission mode using argon-filled ionization chambers. For the energy calibration the first inflection point of an yttrium metal foil at 17038 eV was used. The uranium L_{III} threshold energy, $E_{k=0}$, was arbitrarily defined at 17185 eV. EXAFS data extraction and data fit were performed with the program EXAFSPAK [43]. Theoretical phase and amplitude functions were calculated with FEFF 8.2 [44] using the crystal structure of $[NH_4]_2[UO_2Br_4] \cdot 2H_2O$ [35]. The amplitude reduction factor, s_0^2, was defined as 0.9. The multiple scattering paths in the uranyl unit were included in the curve fit by constraining its Debye–Waller factor and its effective path length to twice the values of the corresponding $U–O_{ax}$ single-scattering path. The overall goodness of the fits, F, is given by χ^2 weighted by the magnitude of data.

3. Results and discussion

3.1. Crystal structure

The structure of $[Bmim]_2[UO_2Br_4]$ was determined by single crystal X-ray diffraction (Table 1). The crystal structure of $[Bmim]_2[UO_2Br_4]$ consists of $[Bmim]^+$ cations and $[UO_2Br_4]^{2-}$ anions (Fig. 1). The uranium atom is located on an inversion centre. The geometry of the uranium anion is a tetragonal bipyramid, with four Br^- anions in the equatorial plane perpendicular to the uranyl moiety.

The average U–Br and U–O distances are 2.823(3) and 1.765(6) Å, respectively (Table 2). The U–Br bond lengths are in good agreement with those previously reported [34,35]. In the packing of the crystal structure, which is displayed in Fig. 2, the butyl-methyl-imidazolium cations are arranged into layers parallel to (1 0 0), and the $[UO_2Br_4]^{2-}$ anions into rows along the [0 1 0] direction. Each $[UO_2Br_4]^{2-}$ anion is surrounded by four $[Bmim]^+$ cations, which form weak C–H···Br2 hydrogen bonds with distances ranging from 2.83 to 2.86 Å (C–Br distances range from 3.695(9) to 3.704(9) Å). The formation of such hydrogen bonding between anionic uranium species and $[Bmim]^+$ cations was already described in $[UCl_6]^{2-}$ and $[UO_2Cl_4]^{2-}$ [23,31].

Table 1
Crystallographic data of the $[Bmim]_2[UO_2Br_4]$ complex.

Chemical formula	$C_{16}H_{30}Br_4N_4O_2U$
Formula weight ($g\,mol^{-1}$)	868.07
Crystal symmetry	triclinic
Space group	$P\bar{1}$ (No. 2)
a (Å)	8.806(2)
b (Å)	9.067(2)
c (Å)	9.726(2)
α (°)	114.163(12)
β (°)	102.428(14)
γ (°)	102.632(13)
V (Å^3)	649.6(3)
Z	1
ρ_{calc} ($g\,cm^{-3}$)	2.219
T (K)	298(2)
λ (Cu Kα) (Å)	1.54178
μ (Cu Kα) (mm^{-1})	24.932
$F(000)$	402
Crystal size (mm^3)	0.2 × 0.1 × 0.1
Independent reflections	2393
R_{int}	0.0619
Independent reflections ($I > 2\sigma(I)$)	2288
R ($I > 2\sigma(I)$)	0.0474
ωR_2 (for all data)	0.1150

Table 2
Selected distances (Å) and angles (°) in $[Bmim]_2[UO_2Br_4]$ (symmetry codes: (i) $1-x,2-y,-z$).

U1–O1	1.765(6)	O1–U1–Br1	88.6(2)
U1–Br2	2.8197(10)	O1^i–U1–Br1	91.4(2)
U1–Br1	2.8259(11)	O1–U1–Br2	90.8(2)
		O1^i–U1–Br2	89.2(2)
		Br1–U1–Br2	89.93(3)
		Br1–U1–Br2^i	90.07(3)
		Br1–U1–Br1^i	180.00(3)

3.2. UV–Vis absorption spectroscopy

The absorption spectrum of $[Bmim]_2[UO_2Br_4]$ dissolved in $[Bmim][Tf_2N]$, reported on Fig. 3, shows four main bands at 449.6, 464.2, 480.1 and 497.2 nm. This spectrum displays similarities with that of $[N(C_{10}H_{21})_4]_2[UO_2Br_4]$ measured in anhydrous benzene [34] and of $Cs_2[UO_2Br_4]$ in the solid state [33]. This observation suggests that $[UO_2Br_4]^{2-}$ would present the same symmetry in the ionic liquid as in organic solvents and in the solid state. The tetrabromo complex would thus present a D_{4h} symmetry, like the chloro analogue. Moreover, this spectrum also coincides with those obtained when four equivalents of [Bmim]Br are added to $UO_2(OTf)_2$ in $[Bmim][Tf_2N]$ (Fig. 3). This latter observation indicates that the triflate and Tf_2N^- ligands are easily displaced by bromide ions. An increase in bromide amount (up to 10 equivalents) does not lead to any change in the absorption spectra pattern, neither in the position of the peaks nor in their relative intensities, indicating that the $[UO_2Br_4]^{2-}$ entity is the most stable species in solution.

Similar results are observed in $[MeBu_3N][Tf_2N]$. An increase in $[MeBu_3N]Br$ concentration does not modify the absorption spectrum obtained when four equivalents of $[MeBu_3N]Br$ ions are added to $UO_2(OTf)_2$ in $[MeBu_3N][Tf_2N]$ (Fig. 4). In this ionic liquid the positions of the four characteristic bands are 449.8, 464.3, 479.9 and 497.1 nm. These results tend to demonstrate that, in both ionic liquids, the tetrabromo uranyl complex is the predominant species as soon as a stoichiometric quantity of bromide ions is added to $UO_2(OTf)_2$. Moreover, this complex would present the same D_{4h} symmetry in these media as in organic solvents and in the solid state. UV–Vis absorption spectra do not allow to observe any significant effect of the IL cation, neither on the formation nor on the structure of the tetrabromo uranyl complex. This was already observed in the case of the tetrachloro uranyl complex [25].

The absorption spectrum of $[UO_2Cl_4]^{2-}$ in $[Bmim][Tf_2N]$, described in Ref. [25], is also reported on Fig. 3. Compared to $[UO_2Cl_4]^{2-}$ in the same ionic liquid, the absorption bands of the tetrabromo uranium complex are shifted to longer wavelengths and the intense charge-transfer band due to the bromide ions is observed at higher wavelength than in the case of chloride ions. Moreover, the discrete transitions in the spectrum of the uranyl bromide solution show a larger peak width and a higher molar extinction coefficient (ε) compared with the spectrum of $[UO_2Cl_4]^{2-}$. Due to the interference with the intense charge-transfer band, the UV–Vis absorption spectra of uranyl bromide are difficult to analyze and only a conclusion based on comparison has been drawn. In the uranyl chloride system, it has been observed that the intermediate species show higher extinction coefficients than the limiting species $[UO_2Cl_4]^{2-}$, which is related with a lower complex symmetry [38,45]. To this point of discussion, the possibility of a contribution of lower symmetry uranyl bromide complexes cannot be totally excluded. Furthermore, the remaining water molecules present in the ionic liquids, which are known to be hygroscopic, may coordinate to the UO_2^{2+} ions. Indeed, in the present work, the water concentration in $[Bmim][Tf_2N]$ and in $[MeBu_3N][Tf_2N]$ is 10^{-2} M, which is the same as the concentration of uranium in the samples. The coordinative interaction between uranyl and water may result in an increasing acidity of the water protons, which may lead subsequently to a deprotonation and to the formation of hydrolysis products. The hydrolysis products of UO_2^{2+} show broad featureless absorption bands with high extinc-

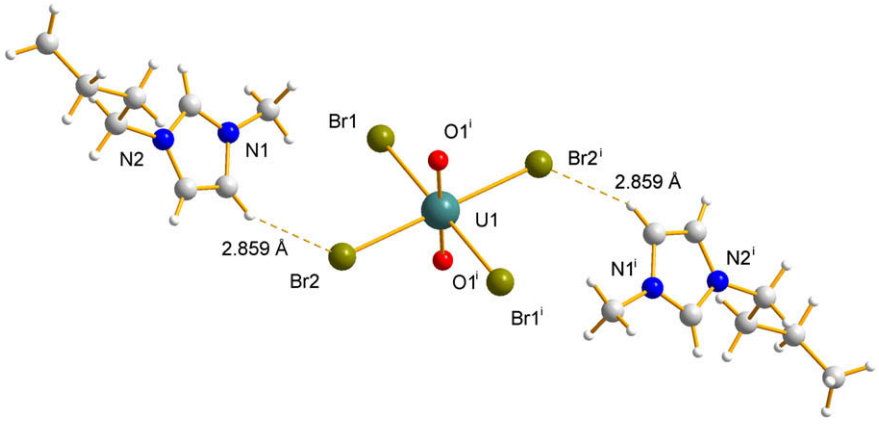


Fig. 1. Part of the crystal structure of $[Bmim]_2[UO_2Br_4]$, showing the $[UO_2Br_4]^{2-}$ anion forming weak hydrogen bonds with the surrounding $[Bmim]^+$ cations (symmetry codes: (i) $1-x,2-y,-z$).

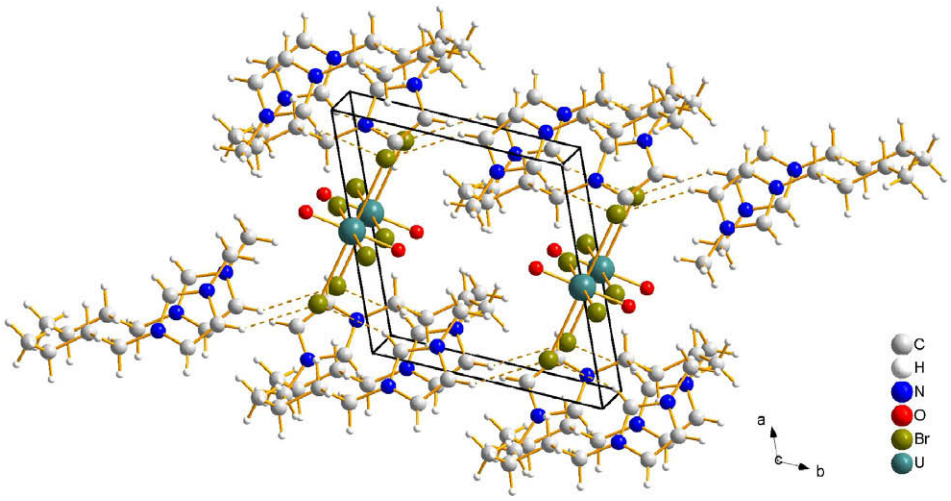


Fig. 2. Packing diagram of the crystal structure of $[Bmim]_2[UO_2Br_4]$, viewed along the *c*-axis.

tion coefficients [27,46]. Contribution of such species may interfere with the charge-transfer band from bromide ligands, and may contribute to explain the enhanced ε coefficient. The UV–Vis spectra do not allow to exclude this possibility. In order to clarify the UO_2^{2+} coordinating environment in more detail EXAFS measurements were performed.

3.3. EXAFS spectroscopy

EXAFS is used to investigate the first coordination sphere of the uranyl(VI) complex and to measure the uranium interatomic distances. Bromide ions are the main coordinating ligands, but beside the solvent, the residual water contained in the ionic liquid may also act as a ligand. Therefore, as discussed previously, the possibility of a participation of oxygen from water in the coordination of U(VI) bromide complex has to be considered. EXAFS spectroscopy suffers from the relative large error for the determination of the coordination number *N*, which is in the range of 15% of the estimated value. A better indicator is therefore often provided by the bond lengths in the first coordination shell, which can be determined within a confidence range of ±0.01 Å, and which are strongly correlated with the coordination number by the bond valence relationship [47].

The crystal structure data show the formation of the tetracoordinate uranyl dianion $[UO_2Br_4]^{2-}$, with the four bromide ions lying in the equatorial plane (equatorial coordination number *N* of 4). In this arrangement, the U–Br distances are usually in the range of 2.80–2.83 Å [48]. Pentacoordinate uranyl complexes are well known; compounds with five identical equatorial ligands are much more scarce but have been reported in $[UO_2(CN)_5]^{3-}$ [49] and $[UO_2(NCS)_5]^{3-}$ [50] for example. The derivative $[UO_2Br_5]^{3-}$ has not been observed up to now in crystal structures, but bromo uranyl complexes with a mixed coordination number $N_{Oeq} + N_{Br}$ of 5 have been reported such as $[UO_2Br_2(OH_2)_3]$ (see Scheme 1) [51].

With the exception of $[UO_2Br_2(THF)_3]$, where the mean U–Br distance is close to 2.85 Å [52], the U–Br distances in pentacoordinate uranyl compounds are notably longer, and are in the range of 2.90–2.91 Å in $[UO_2Br_2(OH_2)_3]$ [51]. The increasing of the U–Cl

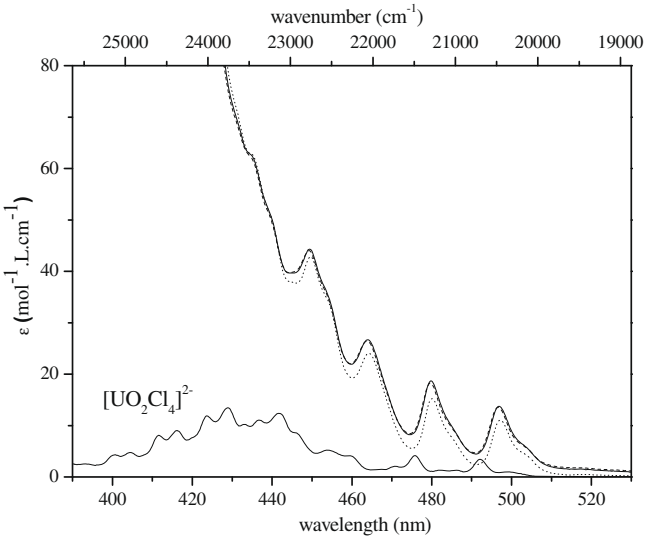


Fig. 3. Absorption spectra of 0.01 M $[Bmim]_2[UO_2Br_4]$ (dotted line) and 0.01 M $UO_2(OTf)_2$ with four (solid line) and seven (dashed line) equivalents of [Bmim]Br in $[Bmim][Tf_2N]$ at 25 °C. The absorption spectra of $UO_2(OTf)_2$ (0.01 M) with four equivalents of [Bmim]Cl in $[Bmim][Tf_2N]$ at 25 °C is added for comparison (Ref. [25]).

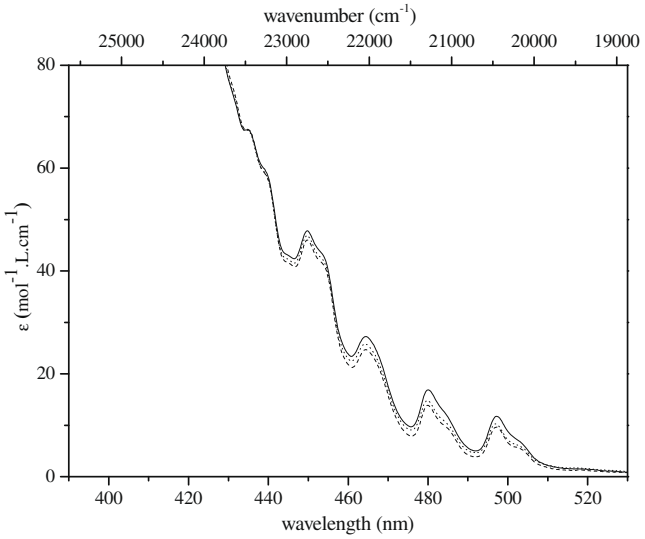
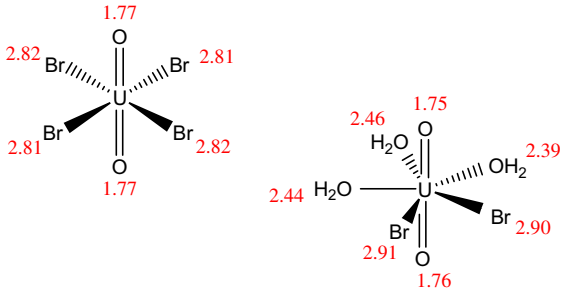


Fig. 4. Absorption spectra of 0.01 M $UO_2(OTf)_2$ with four (solid line), six (dotted line) and 15 (dashed line) equivalents of $[MeBu_3N]Br$ in $[MeBu_3N][Tf_2N]$ at 60 °C.



Scheme 1. References of cluster $[UO_2Br_4]^{2-}$ taken from Ref. [35] and $[UO_2Br_2(OH_2)_3]$ taken from Ref. [51]. The numbers indicate the bond lengths to uranium.

bond length with increasing of the equatorial coordination number can also be illustrated in some aquo-chloro uranyl(VI) compounds. Indeed, the tetracoordinate complex $[UO_2Cl_4]^{2-}$ shows a U–Cl distance of 2.68 Å [53], whereas the U–Cl bond length of several intermediate pentacoordinate species with a mixed equatorial coordination (e.g. $UO_2(H_2O)_4Cl^+$, $UO_2(H_2O)_3Cl_2^0$ and $UO_2(H_2O)_2Cl_3^-$) reaches 2.71–2.74 Å [54]. The lengthening of the U–Br bonds in U(VI) aquo-bromo complexes is in the order of ~0.05–0.1 Å, which is greater than the lengthening occurring in uranyl chloride compounds. This may result from the larger size of the bromide ion. These distance differences are beyond the error limit for distance determination in EXAFS, which is a prerequisite to extract the coordination of U(VI) bromide in [Bmim][Tf_2N] and [$MeBu_3N$][Tf_2N]. The k^3-weighted U L_{III}-edge EXAFS spectra obtained for the 0.02 M $[UO_2Br_4]^{2-}$ solutions in [Bmim][Tf_2N] and [$MeBu_3N$][Tf_2N] at room temperature are shown in Fig. 5.

In both ionic liquids, the first peak of the Fourier transform, also displayed on Fig. 5 in the k range of 4.2–16.2 $Å^{-1}$, corresponds with the two axial oxygen atoms in a U–O distance of 1.77 Å. The second shell indicates bromine atoms in a U–Br distance of 2.82 Å in [Bmim][Tf_2N] and 2.83 Å in [$MeBu_3N$][Tf_2N] (Table 3). These distances are in a good agreement with a fourfold Br coordination, although the determined equatorial coordination numbers are slightly higher than 4. An inclusion of solvent or water molecules does not improve the fit procedure. Therefore, we can conclude from EXAFS spectroscopy that the $[UO_2Br_4]^{2-}$ coordination polyhedron is maintained in [Bmim][Tf_2N] and [$MeBu_3N$][Tf_2N] without any other ligand in the coordination shell. From these results, the ionic liquid cation seems to have no influence on the coordination sphere of the tetrabromo uranyl complex and on the U–Br and U–O distances. Moreover, we can conclude that the crystal structure of $[Bmim]_2[UO_2Br_4]$ can serve in the presented case as a good model for the uranyl bromide coordination in the ionic liquid. Because the hydrogen bonds between Br and $[Bmim]^+$ have only a weak influence on the U–Br distance in the crystal structure, we are not able to draw a conclusion whether they also exist in the liquid sample.

Table 3
EXAFS fit parameters of $[UO_2Br_4]^{2-}$ (0.02 M) in [Bmim][Tf_2N] and [$MeBu_3N$][Tf_2N].

Sample	Scattering path	R (Å)	N	σ^2 (Å^2)	$\Delta E_{k=0}$	F
$[UO_2Br_4]^{2-}$ in [Bmim][Tf_2N]	U–O_{ax}	1.766(2)	2.0(1)	0.0015(3)	−2.6	0.24
	U–Br	2.821(2)	4.4(2)	0.0051(2)		
$[UO_2Br_4]^{2-}$ in [$MeBu_3N$][Tf_2N]	U–O_{ax}	1.768(2)	1.9(1)	0.0013(3)	−1.8	0.24
	U–Br	2.827(2)	4.2(2)	0.0047(2)		

Standard deviations are given in bracket. The threshold energy, $E_{k=0}$, was arbitrarily defined at 17185 eV and varied as a global fit parameter resulting in the energy shift $\Delta E_{k=0}$.

4. Concluding remarks

In the solid state, the $[Bmim]_2[UO_2Br_4]$ complex consists of a tetragonal bipyramid. The average U–Br and U–O distances are 2.823(3) and 1.765(6) Å, respectively. Single crystal XRD also reveals the presence of H-bonding between $[UO_2Br_4]^{2-}$ anions and $[Bmim]^+$ cations.

In [Bmim][Tf_2N] and [$MeBu_3N$][Tf_2N], UV–Vis and EXAFS spectroscopic measurements reveal that addition of four equivalents of bromide ions onto $UO_2(OTf)_2$ leads to the $[UO_2Br_4]^{2-}$ entity. This tetrabromouranyl complex is stable and is the dominating species. The U–Br distances are 2.821(2) and 2.827(2) Å and the U–O distances are 1.766(2) and 1.768(2) Å, respectively, in [Bmim][Tf_2N] and [$MeBu_3N$][Tf_2N]. In those Tf_2N-based ionic liquids, the coordination environment does not depend on the ionic liquid cation and is the same as in the solid state. EXAFS measurements tend to prove that neither solvent nor water molecules are included in the coordination sphere of uranyl.

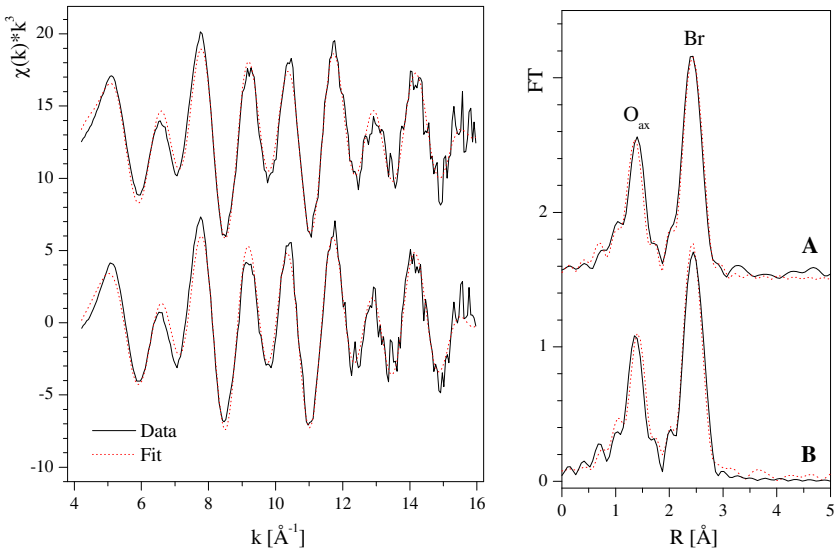


Fig. 5. U L_{III}-edge k^3-weighted EXAFS data (left) and the corresponding Fourier transforms (right) of a 0.02 M $[UO_2Br_4]^{2-}$ solution in [Bmim][Tf_2N] (A) and [$MeBu_3N$][Tf_2N] (B) at 25 °C, with raw data (solid line) and fit results (dotted line).

Further works will be focused on the redox properties of the $[UO_2Br_4]^{2-}$ complex in Tf_2N-based ionic liquids.

Supplementary data

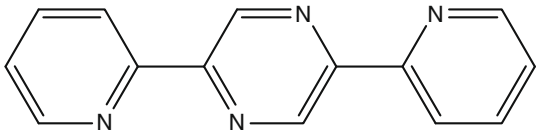
CCDC 690078 contains the supplementary crystallographic data for this paper. These data can be obtained free of charge via http://www.ccdc.cam.ac.uk/conts/retrieving.html, or from the Cambridge Crystallographic Data Centre, 12 Union Road, Cambridge CB2 1EZ, UK; fax: (+44) 1223-336-033; or e-mail: deposit@ccdc.cam.ac.uk.

Acknowledgments

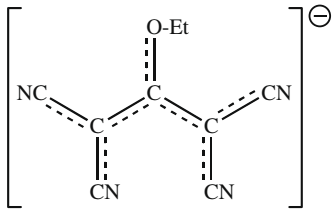
We thank the European Actinet network and the GNR PARIS (French organization) for their financial support.

References

[1] M.J. Earle, K.R. Seddon, Pure Appl. Chem. 72 (2000) 1391.
[2] R. Hagiwara, J.S. Lee, Electrochemistry 75 (2007) 23.
[3] P. Hapiot, C. Lagrost, Chem. Rev. 108 (2008) 2238.
[4] P. Wasserscheid, T. Welton, Ionic Liquids in Synthesis, Wiley-VCH, Weinheim, 2003.
[5] T. Welton, Chem. Rev. 99 (1999) 2071.
[6] R.D. Rogers, K.R. Seddon, Ionic Liquids, Industrial Applications to Green Chemistry, ACS Symposium Series, vol. 818, Washington, 2002.
[7] D. Allen, G. Baston, A.E. Bradley, T. Gorman, A. Haile, I. Hamblett, J.E. Hatter, M.J.F. Healey, B. Hodgson, R. Lewin, K.V. Lovell, B. Newton, W.R. Pitner, D.W. Rooney, D. Sanders, K.R. Seddon, H.E. Sims, R.C. Thied, Green Chem. 4 (2002) 152.
[8] L. Berthon, S.I. Nikitenko, I. Bisel, C. Berthon, M. Faucon, B. Saucerotte, N. Zorz, P. Moisy, Dalton Trans. (2006) 2526.
[9] E. Bossé, L. Berthon, N. Zorz, J. Monget, C. Berthon, I. Bisel, S. Legand, P. Moisy, Dalton Trans. (2008) 924.
[10] R. De Waele, L. Heerman, W. D'Olieslager, J. Electroanal. Chem. 142 (1982) 137.
[11] J.P. Schoebrechts, B. Gilbert, Inorg. Chem. 24 (1985) 2105.
[12] P.B. Hitchcock, T.J. Mohammed, K.R. Seddon, J.A. Zora, C.L. Hussey, E.H. Ward, Inorg. Chim. Acta 113 (1986) L25.
[13] C.J. Anderson, G.R. Choppin, D.J. Pruett, D. Costa, W. Smith, Radiochim. Acta 84 (1999) 31.
[14] C.J. Anderson, M.R. Deakin, G.R. Choppin, W. D'Olieslager, L. Heerman, D.J. Pruett, Inorg. Chem. 30 (1991) 4013.
[15] T.A. Hopkins, J.M. Berg, D.A. Costa, W.H. Smith, H.J. Dewey, Inorg. Chem. 40 (2001) 1820.
[16] S. Dai, Y.S. Shin, L.M. Toth, C.E. Barnes, Inorg. Chem. 36 (1997) 4900.
[17] S. Dai, L.M. Toth, G.R. Hayes, J.R. Peterson, Inorg. Chim. Acta 256 (1997) 143.
[18] V.A. Cocalia, K.E. Gutowski, R.D. Rogers, Coord. Chem. Rev. 250 (2006) 755.
[19] K. Binnemans, Chem. Rev. 107 (2007) 2592.
[20] A.-V. Mudring, A. Babai, S. Arenz, R. Giernoth, Angew. Chem., Int. Ed. 44 (2005) 5485.
[21] D.B. Williams, M.E. Stoll, B.L. Scott, D.A. Costa, W.J. Oldham, Chem. Commun. (2005) 1438.
[22] E. Bossé, C. Den Auwer, C. Berthon, P. Guilbaud, M.S. Grigoriev, S. Nikitenko, C. Le Naour, C. Cannes, P. Moisy, Inorg. Chem. 47 (2008) 5746.
[23] S.I. Nikitenko, C. Cannes, C. Le Naour, P. Moisy, D. Trubert, Inorg. Chem. 44 (2005) 9497.
[24] S.I. Nikitenko, C. Hennig, M.S. Grigoriev, C. Le Naour, C. Cannes, D. Trubert, E. Bossé, C. Berthon, P. Moisy, Polyhedron 26 (2007) 3136.
[25] M.-O. Sornein, C. Cannes, C. Le Naour, G. Lagarde, E. Simoni, J.-C. Berthet, Inorg. Chem. 45 (2006) 10419.
[26] A. Chaumont, G. Wipff, J. Phys. Chem. B 112 (2008) 12014.
[27] P. Nockemann, K. Servaes, R. Van Deun, K. Van Hecke, L. Van Meervelt, K. Binnemans, C. Görller-Walrand, Inorg. Chem. 46 (2007) 11335.
[28] C. Gaillard, A. Chaumont, I. Billard, C. Hennig, A. Ouadi, G. Wipff, Inorg. Chem. 46 (2007) 4815.
[29] N. Asanuma, M. Harada, Y. Yasuike, M. Nogami, K. Suzuki, Y. Ikeda, J. Nucl. Sci. Technol. 44 (2007) 368.
[30] P. Giridhar, K.A. Venkatesan, T.G. Srinivasan, P.R.V. Rao, Electrochim. Acta 52 (2007) 3006.
[31] M. Deetlefs, C.L. Hussey, T.J. Mohammed, K.R. Seddon, J.A. van Den Berg, J.A. Zora, Dalton Trans. (2006) 2334.
[32] K. Goossens, K. Lava, P. Nockemann, K. Van Hecke, L. Van Meervelt, K. Driesen, C. Görller-Walrand, K. Binnemans, T. Cardinaels, Chem. Eur. J. 15 (2009) 656.
[33] C. Görller-Walrand, S. De Jaegere, J. Chim. Phys. 70 (1973) 360.
[34] D. Brown, Compounds of Uranium with Chlorine, Bromine, Iodine, in: Gmelin Handbook of Inorganic Chemistry, System No. 55, Uranium, Supplement vol. C9, Springer, Berlin, 1979, p. 1.
[35] G. Van den Bossche, M.R. Spirlet, J. Rebizant, J. Goffart, Acta Crystallogr., Sect. C 43 (1987) 383.
[36] K.E. Gutowski, N.J. Bridges, R.D. Rodgers, in: L.R. Morss, N.M. Edelstein, J. Fuger (Eds.), The Chemistry of the Actinide and Transactinide Elements, vol. 4, Springer, Dordrecht, The Netherland, 2006, p. 2380.
[37] C. Hennig, W. Kraus, F. Emmerling, A. Ikeda, A.C. Scheinost, Inorg. Chem. 47 (2008) 1634.
[38] C. Hennig, K. Servaes, P. Nockemann, K. Van Hecke, L. Van Meervelt, J. Wouters, L. Fluyt, C. Görller-Walrand, R. Van Deun, Inorg. Chem. 47 (2008) 2987.
[39] SAINT, Version 5/6.0, Bruker Analytical X-ray Systems, Madison, WI, 1997.
[40] SHELXTL-PC, Version 5.1, Bruker Analytical X-ray Systems, Madison, WI, 1997.
[41] J.-C. Berthet, M. Lance, M. Nierlich, M. Ephritikhine, Eur. J. Inorg. Chem. (2000) 1969.
[42] W. Matz, N. Schell, G. Bernhard, F. Prokert, T. Reich, J. Claussner, W. Oehme, R. Schlenk, S. Dienel, H. Funke, F. Eichhorn, M. Betzl, D. Prohl, U. Strauch, G. Huttig, H. Krug, W. Neumann, V. Brendler, P. Reichel, M.A. Denecke, H. Nitsche, J. Synchrotron Rad. 6 (1999) 1076.
[43] G.N. George, I.J. Pickering, EXAFSPAK, a Suite of Computer Programs for Analysis of X-ray Absorption Spectra, Stanford Synchrotron Radiation Laboratory, Stanford, 2000.
[44] A.L. Ankudinov, B. Ravel, J.J. Rehr, S.D. Conradson, Phys. Rev. B 58 (1998) 7565.
[45] C. Görller-Walrand, S. De Houwer, L. Fluyt, K. Binnemans, Phys. Chem. Chem. Phys. 6 (2004) 3292.
[46] G. Meinrath, J. Radioanal. Nucl. Chem. 224 (1997) 119.
[47] P.C. Burns, R.C. Ewing, F.C. Hawthorne, Can. Mineral 35 (1997) 1551.
[48] G. Vandenbossche, M.R. Spirlet, J. Rebizant, J. Goffart, Acta Crystallogr., Sect. C – Cryst. Struct. Commun. 43 (1987) 383.
[49] J.-C. Berthet, P. Thuery, M. Ephritikhine, Chem. Commun. (2007) 604.
[50] G. Bombieri, E. Forsellini, R. Graziani, G.C. Pappalardo, Transition Met. Chem. 4 (1979) 70.
[51] M.J. Crawford, A. Ellern, K. Karaghiosoff, P. Mayer, H. Nöth, M. Suter, Inorg. Chem. 43 (2004) 7120.
[52] J. Rebizant, G. Van den Bossche, M.R. Spirlet, J. Goffart, Acta Crystallogr., Sect. C 43 (1987) 1298.
[53] K. Servaes, C. Hennig, R. Van Deun, C. Görller-Walrand, Inorg. Chem. 44 (2005) 7705.
[54] C. Hennig, J. Tutschku, A. Rossberg, G. Bernhard, A.C. Scheinost, Inorg. Chem. 44 (2005) 6655.



2,5-dpp



tcnoet$^-$

Scheme 1.

boxylato bridges [17,18] the magnetic coupling across the di-μ-chloro and bis-bidentate 2,5-dpp bridges being very weak [15,16].

Curiously the reaction of the $[Cu_2(2,5\text{-dpp})]^{4+}$ dinuclear unit with tricyanomethanide $[N(CN)_3^-$, tcm] in aqueous solution afforded the chain compound of formula $\{[Cu(2,5\text{-dpp})(tcm)]\cdot tcm\}_n$ where the tcm group acts as both terminally bound monodentate ligand and counterion [20]. This is surprising because of the well-known ability of the tcm ligand to act as a bridge in most of its metal complexes [21]. In the present work, we show the results that we obtained when the 1,1,3,3-tetracyano-2-ethoxypropenide anion [tcnoet$^-$; see Scheme 1 (bottom)] is used instead of the tcm$^-$ group. The synthesis and magneto-structural characterization of the new copper(II) complexes $[Cu_2(2,5\text{-dpp})(H_2O)_4(CF_3SO_3)_4]\cdot 2H_2O$ (**1**) and $[Cu_2(2,5\text{-dpp})(H_2O)_2(tcnoet)_4]_n$ (**2**) are described herein.

2. Experimental

2.1. Materials

Copper(II) triflate, copper(II) nitrate trihydrate, tetramethoxysilane and acetonitrile were purchased from commercial sources and used as received. The ligand 2,5-dpp was prepared according to the five-step procedure described previously [16] with a small modification in the last step [20]. The potassium salt of the 1,1,3,3-tetracyano-2-ethoxypropenide was synthesised by a previously reported procedure [22]. Elemental analyses (C, H, N) were carried out by the Microanalytical Service of the University of València.

2.2. Preparation of complexes

2.2.1. $[Cu_2(2,5\text{-dpp})(H_2O)_4(CF_3SO_3)_4]\cdot 2H_2O$ (**1**)

X-ray quality crystals of **1** as pale green parallelepipeds were grown from an acetonitrile solution containing 2,5-dpp (0.2 mmol) and copper(II) trifluoromethanesulphonate (0.4 mmol) by slow evaporation in a hood at room temperature. They were collected by filtration, washed with a small amount cold acetonitrile and diethyl ether and stored over calcium(II) chloride. The yield is practically quantitative. *Anal.* Calc. for $C_{18}H_{22}Cu_2F_{12}N_4O_{18}S_4$ (**1**): C, 20.29; H, 2.07; N, 5.26. Found: C, 20.17; H, 2.02; N, 5.21%.

2.2.2. $[Cu_2(2,5\text{-dpp})(H_2O)_2(tcnoet)_4]_n$ (**2**)

This compound was prepared by using the gel technique. Tetramethoxysilane (1 cm^3) was added under continuous stirring to a warm aqueous solution (10 cm^3) containing $Cu(NO_3)_2\cdot 3H_2O$ (0.22 mmol) and 2,5-dpp (0.11 mmol). The gel was formed on standing after one day at room temperature. An aqueous solution (10 cm^3) containing K(tcnoet) (0.5 mmol) was carefully added on the gel. Single crystals of **2** as brown needles were grown inside the gel on standing at room temperature after several weeks. They were mechanically separated and washed with cold water and dried on filter paper. The yield is *ca.* 80%. *Anal.* Calc. for $C_{50}H_{34}Cu_2N_{20}O_6$ (**2**): C, 52.24; H, 2.96; N, 24.36. Found: C, 52.11; H, 2.88; N, 24.21%.

2.3. Physical techniques

IR spectra were recorded on KBr pellets of **1** and **2** with a Bruker IF S55 spectrophotometer in the 400–4000 cm^{-1} region. Magnetic susceptibility measurements on polycrystalline samples of **1** and **2** were carried out with a Superconducting Quantum Interference Design (SQUID) magnetometer in the temperature range 1.9–300 K and under an applied magnetic field of 1 T ($T > 50$ K) and 1000 G ($T \leqslant 50$ K). The magnetic susceptibility data were corrected for the diamagnetic contribution of the constituent atoms through the Pascal constants [-447×10^{-6} (**1**) and -562×10^{-6} cm^3 mol^{-1} (**2**) per two copper(II) ions] [23] and also for the sample holder. A value of 60×10^{-6} cm^3 mol^{-1} was used for the temperature-independent paramagnetism (tip) of the copper(II) ion. X-band EPR spectrum on a polycrystalline sample of **2** was performed with a Brüker ER 200 spectrometer equipped with a helium continuous-flow cryostat.

2.4. X-ray data collection and structure refinement

Diffraction data on single crystals of **1** and **2** were collected with Bruker–Nonius X8APEXII CCD area detector (**1**) and Oxford Diffraction Xcalibur 2 CCD (**2**) difractometers using graphite-monochro-

Table 1
Summary of crystal data and structure refinement for $[Cu_2(2,5\text{-dpp})(H_2O)_4(CF_3SO_3)_4]\cdot 2H_2O$ (**1**) and $[Cu_2(2,5\text{-dpp})(H_2O)_2(tcnoet)_4]_n$ (**2**).[a]

Compound	**1**	**2**
Empirical formula	$C_{18}H_{22}Cu_2F_{12}N_4O_{18}S_4$	$C_{50}H_{34}Cu_2N_{20}O_6$
Formula weight	1065.72	1138.05
Temperature (K)	273(2)	170(2)
λ (Å)	0.71073	0.71073
Space group	$P\bar{1}$	$P\bar{1}$
a (Å)	9.2283(2)	9.9084(8)
b (Å)	9.2404(2)	11.0461(9)
c (Å)	12.0026(3)	12.9719(12)
α (°)	76.100(1)	65.659(9)
β (°)	70.393(1)	84.796(7)
γ (°)	88.760(1)	80.094(7)
V (Å^3)	933.97(4)	1274.0(2)
Z	1	1
Crystal dimemsions (mm)	0.16 × 0.08 × 0.06	0.15 × 0.12 × 0.05
ρ_{calc} (g cm^{-3})	1.895	1.483
F(000)	532	580
μ (mm^{-1})	1.50	0.906
Max 2θ (°)	56.6	63.5
Reflections collected	20864	13179
Independent reflections [R_{int}]	4869 [0.0205]	7713 [0.0602]
Reflections with $I > 2\sigma(I)$	4033	3524
Data/restraints/parameters	4595/9/280	7713/0/380
Goodness-of-fit, S, on F^2	1.050	0.984
R [$I > 2\sigma(I)$][b]	0.0488	0.0408
R_w [$I > 2\sigma(I)$][c]	0.1375	0.0684
$\Delta\rho_{max,min}$ (e Å^{-3})	+1.844/−0.849	+0.528/−0.419

[a] For compounds **1** and **2**, the asymmetric unit contains 0.5 of the empirical formula.

[b] $R = \sum(|F_o| - |F_c|)/\sum|F_o|$.

[c] $R_w = \{\sum[w(F_o^2 - F_c^2)^2]/\sum[w(F_o^2)^2]\}^{1/2}$ and $w = 1/[\sigma(F_o)^2 + (mP)^2 + nP]$ with $P = [F_o^2 + 2F_o^2]/3$, $m = 0.0794$ (**1**) and 0.0258 (**2**) and $n = 1.261$ (**1**) and 0.0000 (**2**).

Table 2
Selected bond lengths (Å) and angles [°] for $[Cu_2(2,5\text{-dpp})(H_2O)_4(CF_3SO_3)_4]\cdot 2H_2O$ (**1**) with esds in parentheses.[a]

Copper environment			
Cu(1)–N(1)	1.997(3)	Cu(1)–O(2W)	1.979(2)
Cu(1)–N(2)	2.020(2)	Cu(1)–O(1)	2.319(2)
Cu(1)–O(1W)	2.944(2)	Cu(1)–O(4)	2.387(3)
N(1)–Cu(1)–N(2)	80.9(1)	N(2)–Cu(1)–O(4)	83.9(1)
N(1)–Cu(1)–O(2W)	168.4(1)	O(1W)–Cu(1)–O(2W)	92.4(13)
N(1)–Cu(1)–O(1W)	94.5(1)	O(1W)–Cu(1)–O(1)	91.5(1)
N(1)–Cu(1)–O(1)	100.0(1)	O(1W)–Cu(1)–O(4)	93.9(1)
N(1)–Cu(1)–O(4)	87.4(1)	O(2W)–Cu(1)–O(1)	89.1(1)
N(2)–Cu(1)–O(2W)	91.7(1)	O(2W)–Cu(1)–O(4)	82.9(1)
N(2)–Cu(1)–O(1W)	174.9(1)	O(1)–Cu(1)–O(4)	170.5(1)
N(2)–Cu(1)–O(1)	91.3(1)		
2,5-Dpp ligand			
N(1)–C(1)	1.336(4)	C(4)–C(5)	1.374(5)
N(1)–C(5)	1.348(4)	C(5)–C(6)	1.472(4)
C(1)–C(2)	1.368(6)	C(6)–C(7)	1.383(4)
C(2)–C(3)	1.366(7)	N(2)–C(6)	1.348(3)
C(3)–C(4)	1.387(6)	N(2)–C(7a)	1.333(4)
C(1)–N(1)–C(5)	118.7(3)	N(1)–C(5)–C(6)	114.4(3)
C(1)–N(1)–Cu(1)	125.8(3)	C(5)–C(6)–N(2)	158.4(2)
C(5)–N(1)–Cu(1)	115.1(2)	C(5)–C(6)–C(7)	124.8(2)
N(1)–C(1)–C(2)	122.6(4)	C(6)–N(2)–Cu(1)	113.8(2)
C(1)–C(2)–C(3)	118.7(4)	C(6)–N(2)–C(7a)	119.5(2)
C(2)–C(3)–C(4)	119.8(4)	C(7a)–N(2)–Cu(1)	126.6(2)
C(3)–C(4)–C(5)	118.5(4)	C(7)–C(6)–N(2)	120.8(3)
C(4)–C(5)–N(1)	121.7(3)	C(6)–C(7)–N(2a)	120.7(2)
C(4)–C(5)–C(6)	124.0(3)		

D–H···A	D···A (Å)	<D–H···A (°)
Hydrogen bonds[b]		
O(1W)–H(1W)···O(3b)	2.665(4)	171(4)
O(1W)–H(2W)···O(6c)	2.648(5)	139(4)
O(2W)–H(3W)···O(3W)	2.694(4)	170(4)
O(2W)–H(4W)···O(3Wd)	2.831(4)	163(4)
O(3W)–H(6W)···O(2b)	2.839(4)	166(4)
O(3W)–H(5W)···O(5e)	2.842(5)	157(4)

[a] Symmetry transformations used to generate equivalent atoms: (a) $-x+1,-y+1,-z+2$; (b) $-x+1,-y+2,-z+1$; (c) $-x+2,-y+1,-z+1$; (d) $-x+1,-y+1,-z+1$; (e) $x-1,y,z$.
[b] A, acceptor; D, donor.

Table 3
Selected bond lengths (Å) and angles (°) for $[Cu_2(2,5\text{-dpp})(H_2O)_2(tcnoet)_4]_n$ (**2**) with esds in parentheses.[a]

Copper environment			
Cu(1)–N(1)	1.990(2)	Cu(1)–N(11)	1.966(2)
Cu(1)–N(2)	2.010(2)	Cu(1)–N(04b)	2.647(2)
Cu(1)–N(01)	1.958(2)	Cu(1)–O(1W)	2.287(2)
N(1)–Cu(1)–N(2)	81.20(7)	N(2)–Cu(1)–O(1W)	84.40(8)
N(1)–Cu(1)–N(01)	167.46(8)	N(11)–Cu(1)–N(01)	91.10(7)
N(1)–Cu(1)–N(11)	95.71(7)	N(11)–Cu(1)–N(04b)	77.87(8)
N(1)–Cu(1)–N(04b)	78.23(7)	N(11)–Cu(1)–O(1W)	93.17(8)
N(1)–Cu(1)–O(1W)	89.63(7)	N(01)–Cu(1)–N(04b)	91.56(8)
N(2)–Cu(1)–N(01)	92.39(7)	N(01)–Cu(1)–O(1W)	100.51(8)
N(2)–Cu(1)–N(11)	176.07(7)	N(04b)–Cu(1)–O(1W)	167.85(8)
N(2)–Cu(1)–N(04b)	93.86(7)		
Tcnoet$^-$ polynitrile ligands			
N(01)–C(01)	1.150(2)	N(11)–C(11)	1.141(3)
N(02)–C(02)	1.151(3)	N(12)–C(12)	1.147(3)
N(03)–C(03)	1.153(3)	N(13)–C(13)	1.141(3)
N(04)–C(04)	1.147(3)	N(14)–C(14)	1.146(3)
C(01)–C(06)	1.416(3)	C(11)–C(16)	1.405(3)
C(02)–C(06)	1.408(3)	C(12)–C(16)	1.414(3)
C(03)–C(07)	1.421(3)	C(13)–C(17)	1.424(3)
C(04)–C(07)	1.421(3)	C(14)–C(17)	1.428(3)
C(05)–C(07)	1.395(3)	C(15)–C(17)	1.381(3)
C(05)–C(06)	1.402(3)	C(15)–C(16)	1.416(3)
C(08)–C(09)	1.497(3)	C(18)–C(19)	1.483(4)
C(05)–O(01)	1.346(2)	C(15)–O(11)	1.337(2)
C(08)–O(01)	1.450(3)	C(18)–O(11)	1.454(3)
N(01)–C(01)–C(06)	176.8(2)	C(06)–C(05)–C(07)	127.1(2)
N(02)–C(02)–C(06)	177.0(2)	N(11)–C(11)–C(16)	179.3(3)
N(03)–C(03)–C(07)	178.7(3)	N(12)–C(12)–C(16)	178.0(3)
N(04)–C(04)–C(07)	177.2(3)	N(13)–C(13)–C(17)	178.1(3)
C(09)–C(08)–O(01)	106.3(2)	N(14)–C(14)–C(17)	177.6(3)
C(08)–O(01)–C(05)	120.9(2)	C(19)–C(18)–O(11)	107.3(2)
O(01)–C(05)–C(06)	112.6(2)	C(18)–O(11)–C(15)	120.8(2)
O(01)–C(05)–O(07)	120.3(2)	O(11)–C(15)–C(16)	112.3(2)
O(11)–C(15)–C(17)	123.7(2)	C(04)–C(07)–C(05)	119.8(2)
C(16)–C(15)–C(17)	123.8(2)	C(11)–C(16)–C(15)	120.1(2)
C(01)–C(06)–C(05)	118.1(2)	C(11)–C(16)–C(12)	117.0(2)
C(01)–C(06)–C(02)	115.9(2)	C(12)–C(16)–C(15)	122.1(2)
C(02)–C(06)–C(05)	126.0(2)	C(13)–C(17)–C(14)	116.5(2)
C(03)–C(07)–C(04)	118.0(2)	C(13)–C(17)–C(15)	121.4(2)
C(03)–C(07)–C(05)	122.1(2)	C(14)–C(17)–C(15)	122.0(2)

D–H···A	D···A (Å)	<D–H···A (°)
Hydrogen bonds[b]		
(O1W)–H(5)···N(03c)	3.042(4)	164(3)
(O1W)–H(6)···N(12d)	2.907(3)	168(3)

[a] Symmetry transformations used to generate equivalent atoms: (b) $1-x,1-y,2-z$; (c) $1-x,2-y,2-z$; (d) $1-x,2-y,1-z$.
[b] A, acceptor; D, donor.

mated Mo Kα radiation (λ = 0.71073 Å). These data were processed through the SAINT [24] reduction and SADABS [25] absorption software for **1** whereas the data collection and data reduction for **2** were performed with the CRYSALIS-CCD and CRYSALIS-RED programs [26,27]. Scattering factors and corrections for anomalous dispersion were taken from the *International Tables for X-ray Crystallography* [28]. Crystal parameters and refinement results are listed in Table 1. The structures of **1** and **2** were solved by direct methods and successive Fourier-difference synthesis, and they were refined on F^2 by weighted anisotropic full-matrix least-squares methods through the SHELXTL [29] (**1**) and SHELX97 [30] (**2**) software packages. All non-hydrogen atoms of **1** and **2** were refined anisotropically. All hydrogen atoms in **1** and those of the ethyl groups of the two tcnoet anions of **2** were placed in calculated positions and refined as riding atoms, where the hydrogen atoms of the coordinated water molecule [O(1W)] and those of the 2,5-dpp ligand of **2** were located by difference Fourier maps. A common isotropic displacement parameter was allowed for all the hydrogen atoms of **1** and **2**. The residual maximum in the final Fourier-difference maps of **1** was 1.884 and it is near the S(2) atom, which identifies the more thermally disordered triflate anion. The final geometrical calculations were performed with the PARST97 program [31]. The graphical manipulations were carried out with the DIAMOND program [32] and the XP utility of the SHELXTL system. Main interatomic bond lengths and angles are listed in Tables 2 and 3 for **1** and **2**, respectively.

3. Results and discussion

3.1. Synthesis and IR spectroscopy

The bis-bidentate character of the 2,5-dpp molecule accounts for the stability in solution of the dinuclear species $[Cu_2(2,5\text{-dpp})]^{4+}$. The neutralization of its charge by the poorly coordinating triflate anions or the polynitrile tcnoet$^-$ ligand led to the neutral complexes **1** and **2**, respectively. Interestingly, the presence in **1** of terminally bound water molecules and monodentate triflate anions (both of them being easy leaving groups) together with its high solubility in water, would make this complex a good precursor of homo- and heterometallic species when used as a Lewis acid toward preformed complexes that can as ligands.

The IR spectra of **1** and **2** in the high-frequency region have in common the occurrence of a broad and strong absorption centered at ca. 3500 (**1**) and 3450 cm^{-1} (**2**) which are due to the presence of hydrogen bonded water molecules [33]. The shift toward higher wavenumbers of the of the peaks of the ν(C=N) and ν(C=C)

stretchings of the 2,5-dpp group in **1** (a doublet at 1605 and 1570 cm^{-1}) and **2** (1610 and 1565 cm^{-1}) when compared to the free ligand (two peaks at 1580 and 1555 cm^{-1}) supports its coordination to the copper atom [16,20]. Evidence for unidenate sulfonate coordination of the triflate group (C_{3v} symmetry) in **1** is provided by the set of peaks due to this anion [34–36]: two SO_3 stretching modes at 1290s and 1250s cm^{-1} [ν_4(E)], a SO_3 deformation mode at 520m cm^{-1} [ν_5(E)] plus three features at 1035s [$\nu_1(A_1)$], 765w [$\nu_2(A_1)$] and 647s cm^{-1} [$\nu_3(A_1)$]. Finally, the occurrence of a doublet at 2243m and 2203s cm^{-1} in the infrared spectrum of **2** which is assigned to the ν(C≡N) stretching modes of the polynitrile tcnoet ligand [to be compared with the strong absorption at 2205 cm^{-1} in the IR spectrum of the K(tcnoet) salt] strongly supports the presence of coordinated and noncoordinated nitrile-tcnoet groups in this compound, agreement with other structurally characterized tcnoet-containing metal complexes [22,37,38]. All these spectroscopic suggestions of **1** and **2** have been confirmed by the corresponding X-ray structures (see below).

3.2. Description of the structures

3.2.1. Structure of $[Cu_2(2,5\text{-dpp})(H_2O)_4(CF_3SO_3)_4]\cdot 2H_2O$ (**1**)

The structure of **1** is made up of neutral and centrosymmetric dicopper(II) units of formula $[Cu_2(2,5\text{-dpp})(H_2O)_4(CF_3SO_3)_4]$ (Fig. 1) and crystallization water molecules which are interlinked by an extensive network of hydrogen bonds which involve all the water molecules and the uncoordinated triflate-oxygens (see end of Table 2), the whole leading to a three-dimensional network (Fig. 2). Interestingly, the layers shown in Fig. 2a are interconnected by hydrogen bonds through the O(2W) and O(3W) water molecules which form a R4 [39] quasi-planar water ring with a D_{2d} symmetry [graph set notation $R_2^2(8)$] [40] (Fig. 2b). This water ring and its nearest neighbours constitute an aesthetic butterfly-like motif (see center of Fig. 2b) which grows in the *ab* plane.

Each copper(II) ion atom in **1** exhibits an elongated octahedral CuN_2O_4 environment: a pyrazine-[N(2)] and a pyridyl-nitrogen [N(1)] atoms from a 2,5-dpp ligand and two water molecules

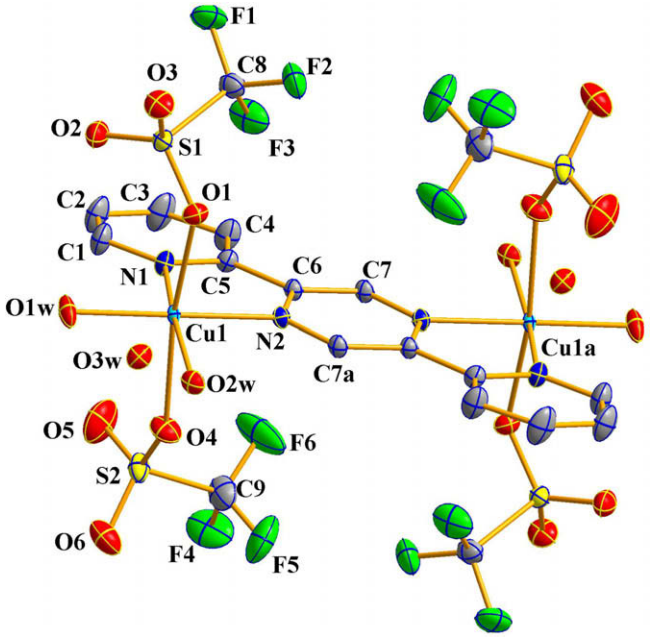


Fig. 1. Crystal structure of the complex $[Cu_2(2,5\text{-dpp})(H_2O)_4(CF_3SO_3)_4]\cdot 2H_2O$ (**1**) showing the atom numbering. Thermal ellipsoids are plotted at the 30% probability level and the hydrogen atoms have been omitted for simplicity. Symmetry code: (a) $-x+1,-y+1,-z+2$.

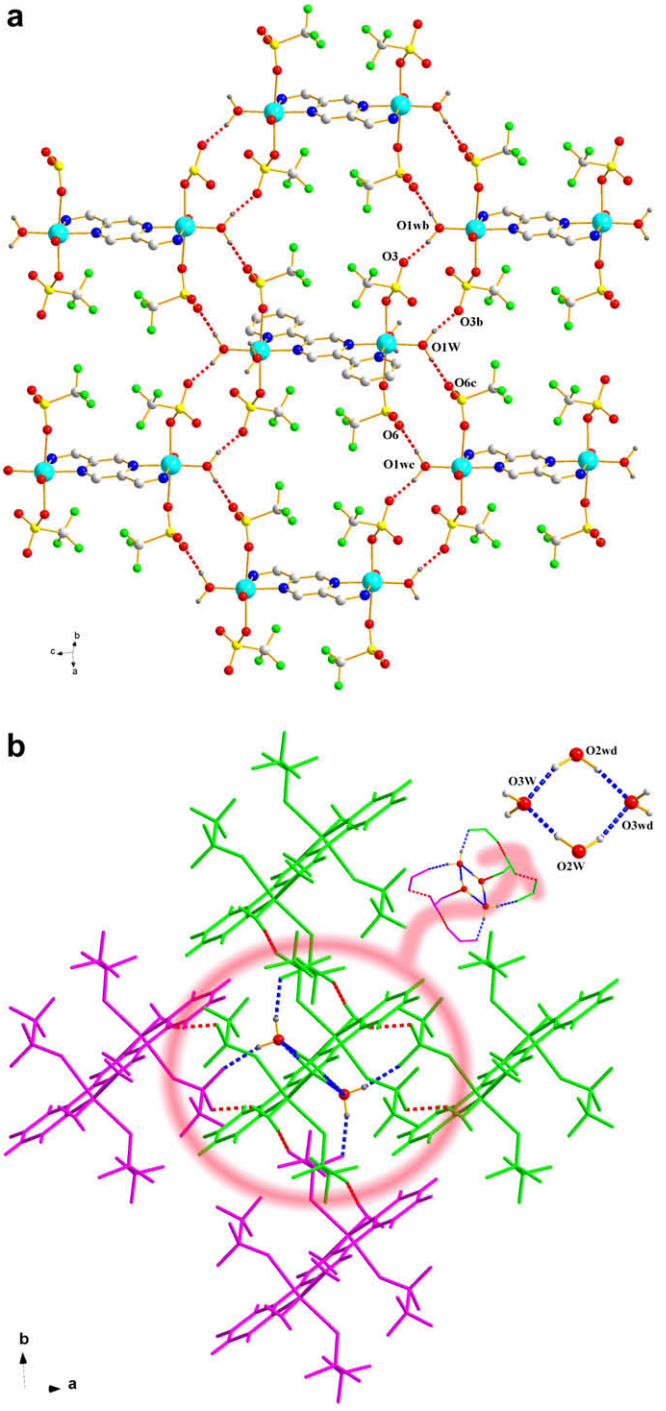


Fig. 2. View of the three-dimensional supramolecular structure of **1** through hydrogen bonds (blue and red dotted lines): (a) layered motif through hydrogen bonds involving the coordinated O(1W) water molecule and the uncoordinated and O(3) and O(6) triflate-oxygens; (b) interlayer connection by hydrogen bonds (blue dotted lines) through the O(3W)O(2W)O(2Wd)O(3Wd) tetrameric ring from the butterfly-shaped motif. Symmetry code: (b) $-x+1,-y+2,-z+1$; (c) $-x+2,-y+1,-z+1$; (d) $-x+1,-y+1,-z+1$. (For interpretation of the references to color in this figure legend, the reader is referred to the web version of this article.)

[O(1W) and O(2W)] build the basal plane whereas two sulfonate-oxygen atoms from two triflate anions [O(1) and O(4)] occupy the axial positions. The equatorial bonds at the copper atom vary in the narrow range 1.944(2)–2.020(2) Å, values which are shorter than the axial interactions [2.319(2) and 2.387(3) Å for Cu(1)–O(1)

and Cu(1)–O(4), respectively]. The main source of distortion of the environment of the copper atom in **1** is due to the short bite of the chelating 2,5-dpp group, the value subtended by this ligand at the metal atom being 80.9(1)° [N(1)–Cu(1)–N(2)]. This value lies with the range of those observed in the other five structurally characterized 2,5-dpp-bridged copper(II) complexes [77.6(2)–81.0(1)°] [2,17,18,20]. The copper(II) ion is shifted by 0.100(1) Å from the equatorial plane through the O(1) axial triflate-oxygen.

The bis-bidentate coordination mode of the 2,5-dpp ligand in **1** is the most common coordination mode of this group in its metal complexes [2,13,15,17–20], the bidentate 2,5-dpp being observed in the mononuclear $[ZnCl_2(2,5\text{-dpp})(dmf)]$ (dmf = dimethylformamide) and trinuclear $[Zn_3(OAc)_6(2,5\text{-dpp})_2]\cdot H_2O$ complexes [19]. The bond lengths and angles within the 2,5-dpp ligand agree with those observed for the free molecule [2] and its metal complexes [13,15,17–20]. The ligand as a whole is close to planarity, the largest deviation from the mean plane being 0.055(5) Å at C(3). The value of dihedral angle between the pyrazine and the pyridyl rings is only 4.3(2)°. The basal plane of the copper atom and the mean planes of the pyridyl and pyrazine rings form dihedral angles of 12.5(2)° and 8.3(2)°, respectively. The copper–copper separation across the 2,5-dpp bridging ligand is 6.763(1) Å [Cu(1)···Cu(1a); (a) = $-x+1,-y+1,-z+2$], whereas the shortest intermolecular metal–metal distance is 7.175(1) Å [Cu(1)···Cu(1d); (x) = $1-x,1-y,1-z$].

The structure of **1** contains monodentate triflate anions which exhibit a staggered-ethane conformation about the S–C bond. They occupy the axial positions at each copper(II) ion in agreement with their poor coordination ability [34,41]. Their structural parameters are very close to those found in other structures containing unidentate triflate groups [35,36,42].

3.2.2. Structure of $[Cu_2(2,5\text{-dpp})(H_2O)_2(tcnoet)_4]_n$ (**2**)

The structure of **2** is made up of zigzag chains of copper(II) ions of formula $[Cu_2(2,5\text{-dpp})(H_2O)_2(tcnoet)_4]_n$ running parallel to the [1–10] (Figs. 3 and 4). Regular alternating bis-bidentate 2,5-dpp and double μ-1,7-tcnoet bridges occurs in them, the electroneutrality being achieved by terminally bound tcnoet groups. The chains are interlinked through hydrogen bonds involving the coordinated water molecule and two of the uncoordinated nitrile-nitrogen atoms (see end of Table 3) to afford a layered structure which grows in the *ab* plane (Fig. 4).

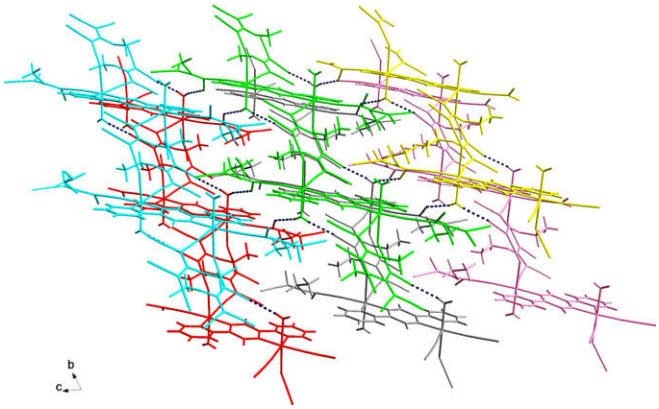


Fig. 4. A view of the packing of adjacent layers in **2** showing the interchain connection by hydrogen bonds (dashed lines) within each layer.

Each copper(II) ion exhibits an elongated octahedral CuN_5O environment: a pyrazine-[N(2)] and a pyridyl-nitrogen [N(1)] atoms from a 2,5-dpp ligand and two nitrile-nitrogen atoms from a terminal [N(11)] and a bridging [N(01)] tcnoet groups build the equatorial plane whereas a water molecule [O(1W)] and a nitrile-nitrogen [N(04b) from a bridging tcnoet ligand occupy the axial positions. The equatorial Cu–N bond distances vary in the narrow range 1.963(2)–2.010(2) Å, values which are shorter than the axial interactions [2.287(2) and 2.647(2) Å for Cu(1)–O(1W) and Cu–N(04b), respectively]. The angle subtended at the copper atom by the chelating 2,5-dpp ligand is 81.20(7)°, a value which is very close to that observed in **1**. The maximum deviation from the equatorial plane is 0.122(2) Å at N(01) and the copper atom is shifted only by 0.071(1) Å toward the O(1W) atom.

The pyridyl and pyrazine fragments of the bis-bidentate 2,5-dpp ligand form a dihedral angle of 7.93(6)°, a value which is practically identical to that of the free 2,5-dpp molecule [7.88(6)°] [2].

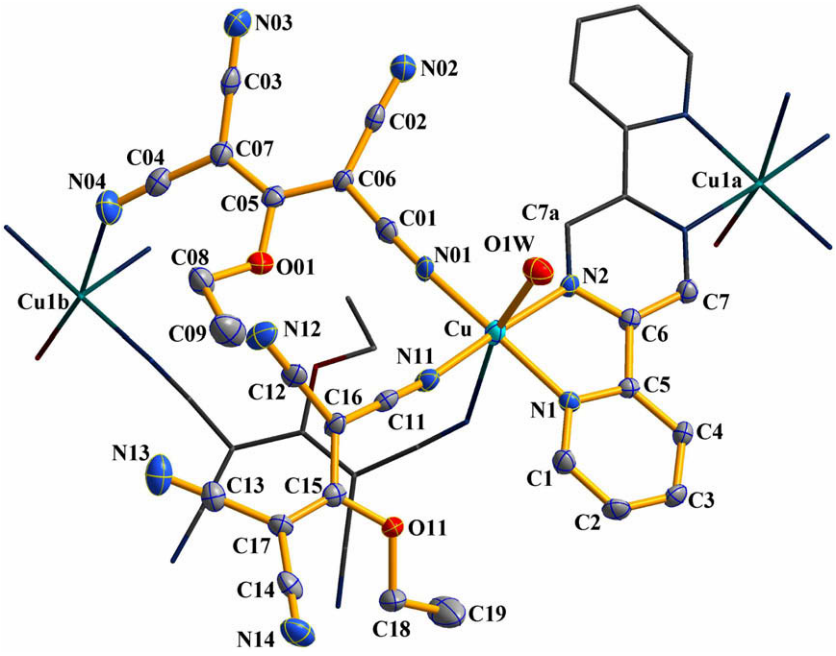


Fig. 3. Perspective view of a fragment of the chain $[Cu_2(2,5\text{-dpp})(H_2O)_2(tcnoet)_4]_n$ (**2**) showing the atom numbering. Thermal ellipsoids are plotted at the 50% probability level and the hydrogen atoms are omitted for the sake of clarity. Symmetry code: (a) $-x,2-y,2-z$; (b) $1-x,1-y,2-z$.

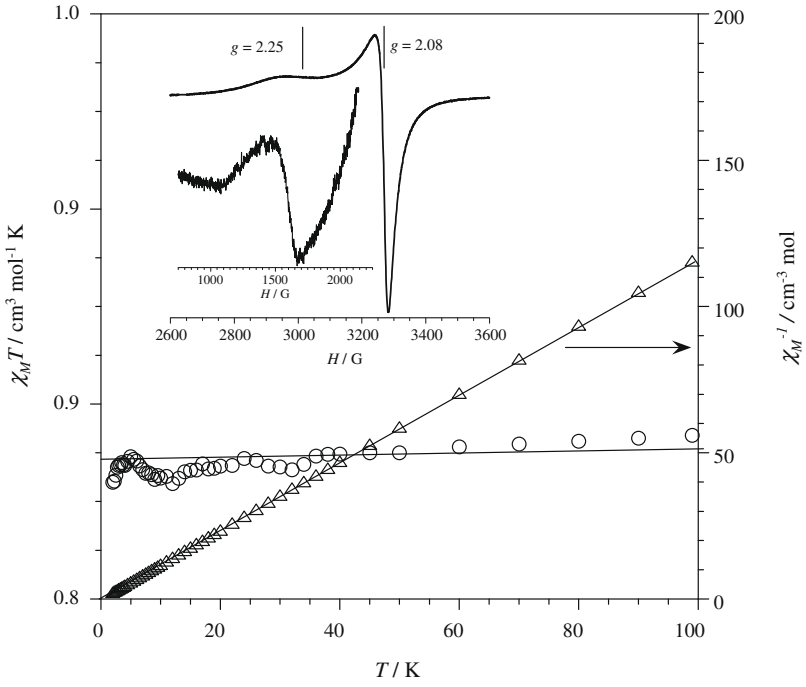


Fig. 5. Thermal dependence of the $\chi_M T$ product (○) and $1/\chi_M$ (△) for **1**. The solid line is the best fit through a Curie law (see text). The inset shows the X-band EPR spectra of a polycrystalline sample of **1** at 4.2 K.

The equatorial plane of the copper(II) ion and the mean planes of the pyridyl and pyrazine rings form dihedral angles of 10.62(6)° and 8.26(5)°, respectively. The central carbon atoms of the terminal [C(16), C(15) and C(17)] and bridging [C(06), C(05) and C(07)] tcnoet ligands have a sp^2-hybridization (sum of the bond angles around each atom being ca. 360°) (see Table 3). Both tcnoet groups exhibit a strong electronic delocalization as indicated by the six nearly equivalent carbon–carbon bond lengths [C–C values ranging in the ranges 1.381(3)–1.428(3) Å (terminal tcnoet) and 1.395(3)–1.421(3) Å (bridging tcnoet)], this delocalization including the C(15)–O(11) and C(05)–O(01) bonds which are approximately 0.10–0.12 Å shorter than the single C(18)–O(11) and C(08)–O(01) bonds [1.454(3) and 1.450(3) Å, respectively]. In spite of this π electronic delocalization, the two types of tcnoet ligands deviate significantly from planarity: the two planar $C(CN)_2$ units are tilted out of the plane containing the central C(16)C(15)C(17)O(11) and C(06)C(05)C(07)O(01) fragments, the values of the tilt angles being 41.51(8) (terminal tcnoet) and 18.27(8)° (bridging tcnoet). These geometrical features of the tcnoet groups in **2** are essentially similar to those observed for this polynitrile anion in a few structures of metal complexes [22,37,38,43].

The copper–copper separation across the bis-bidentate 2,5-dpp is 6.754(1) Å [Cu(1)···Cu(1a); (a) $-x, 2-y, 2-z$], a value which is shorter than that through the double tcnoet bridge [9.559(1) Å for Cu(1)···Cu(1b); (b) $1-x, 1-y, 2-z$] because of the larger size of the 16-membered [$Cu(NCCCCCN)_2Cu$] dimetallacycles involved in this last pathway. The value of the shortest interchain copper–copper distance is 8.275(1) Å [Cu(1)···Cu(1e); (e) $-x, 2-y, 1-z$].

3.3. Magnetic properties of **1** and **2**

The temperature dependence of $1/\chi_M$ and $\chi_M T$ for **1** [χ_M is the magnetic susceptibility per two copper(II) ions] is shown in Fig. 5. At room temperature, $\chi_M T$ is ca. 0.85 $cm^3\ mol^{-1}$ K, a value which is as expected for two magnetically isolated spin doublets. This value remains constant on cooling until 1.9 K. This Curie law behaviour is characterized by the parameters $C = 0.845\ cm^3\ mol^{-1}$ K and $g = 2.12$ where C is the Curie constant in the expression $\chi_M = C/T$. The lack of magnetic interaction between the local doublets through the bis-bidentate 2,5-dpp ligand in **1** is in line with the very poor ability of this molecule to mediate magnetic interactions between the paramagnetic centers that it links [16–20]. The X-band EPR spectra recorded on a polycrystalline sample of **1** show absorption bands of axial symmetry with $g_{\|} = 2.25$ and $g_{\perp} = 2.08$ (see inset of Fig. 5) and no significant variations from room temperature to 4.2 K. At very low temperatures, there appears a very weak half-field transition that could be interpreted as the $\Delta M_S = 2$ forbidden transition in the triplet in agreement with the dinuclear structure of **1**.

The lack of magnetic coupling though the pyrazine ring of 2,5-dpp in its copper(II) complexes is quite surprising. One can see in **1** that the unpaired electron on each copper(II) is described by a $d_{x^2-y^2}$ type magnetic orbital which is mainly located in the basal plane [the x and y axes being roughly defined the Cu(1)–N(1) and Cu(1)–(N(2) bonds]. Consequently, a significant overlap between these magnetic orbitals through the pyrazine ring (σ exchange pathway connecting equatorial bonds at the copper atoms) is predicted and then, an antiferromagnetic coupling would be expected. In fact, values of the antiferromagnetic coupling (J) covering the range -12.4 to $-5.6\ cm^{-1}$ (the Hamiltonian being defined as $(\hat{H} = -J\hat{S}_A \cdot \hat{S}_B)$ have been reported for magneto-structurally characterized pyrazine-bridged copper(II) complexes where the same exchange pathway (that is the one connecting equatorial bonds of adjacent copper atoms) is involved [44–47]. This antiferromagnetic interaction attains larger values in the tppz-bridged copper(II) [tppz = 2,3,5,6-tetrakis(2-pyridyl)pyrazine] with values of J covering the range -61.1 to $-19.9\ cm^{-1}$ [48–51]. These features suggest that the energies of the HOMOs of the appropriate symmetry of the pyrazine (pyz) molecule which interact with the magnetic orbitals of the copper(II) ions in the pyz-bridged copper(II) complexes are dependent on both the degree and substitution pattern of the pyz molecule. Theoretical calculations which are beyond the scope of the present work are needed to give a clearcut answer to this assumption.

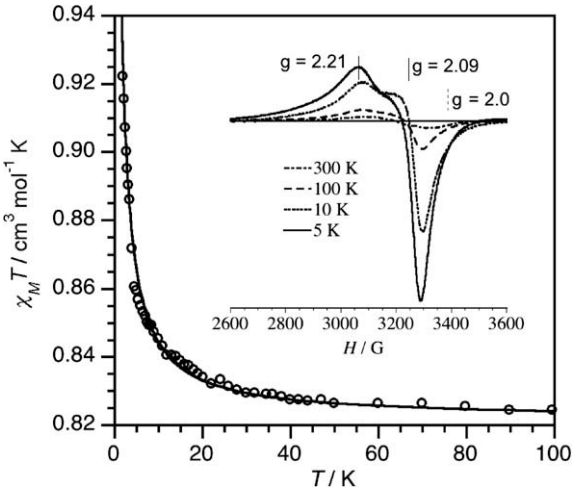


Fig. 6. Thermal dependence of the $\chi_M T$ product for **2** at $T \leqslant 100$ K: (○) experimental data; (–) best-fit curve (see text). The inset shows the X-band EPR spectra of a polycrystalline sample of **2** at different temperatures.

The magnetic properties of **2** under the form of $\chi_M T$ versus T plot [χ_M is the magnetic susceptibility per two copper(II) ions] is shown in Fig. 6. At room temperature, $\chi_M T$ is equal to 0.80 $cm^3\ mol^{-1}$ K, a value which is as expected for two magnetically noninteracting spin doublets. Upon cooling, this value remains constant until $T = 30$ K and it increases further to reach a value of ca. 0.92 $cm^3\ mol^{-1}$ K at 1.9 K. This small increase of $\chi_M T$ of **2** in the low temperature domain indicates the occurrence of a very weak ferromagnetic coupling. Although there are two bridging ligands in **2** (namely the bis-bidentate 2,5-dpp ligand and the double tcnoet bridges) and then two possible intrachain exchange pathways, that through the 2,5-dpp ligand can be discarded in the light of the lack of magnetic coupling which is observed in **1**. Consequently, the exchange pathway for the small ferromagnetic coupling observed in **2** is most likely provided by the double tcnoet bridges. The analysis of the magnetic data of **2** through a simple Bleaney–Bowers expression through the Hamiltonian $H = -JS_1 \cdot S_2$ leads to $J = +0.78\ cm^{-1}$ and $g = 2.13$. Variable-temperature X-band EPR spectra of **2** (see inset of Fig. 6) support the occurrence of a low-lying spin triplet with a very small zero field splitting in agreement with the susceptibility data.

Given the Curie law behaviour observed in **1**, the out-of-plane exchange pathway through the double tcnoet bridges seems to be responsible for the weak ferromagnetic interaction observed in **2**. The unpaired electron (magnetic orbital) on each copper(II) ion of **2** is described by a $d_{x^2-y^2}$ type orbital which is mainly located in the basal plane [the x and y axes corresponding roughly to the Cu(1)–N(01) and Cu(1)–N(11) bonds]. A small spin density is expected in the axial site occupied by the N(04b) atom [Cu(1)–N(04b) = 2.647(2) Å] that is in the tcnoet-nitrogen which connect this axial site with one equatorial position of the symmetry related Cu(1b) atom. So, the overlap between the magnetic orbitals of the adjacent Cu(1) and Cu(1b) atoms is expected to be poor and thus, the magnetic coupling would weak either antiferro- (net overlap) or ferromagnetic [case of accidental orthogonality which depends on some structural parameters such as the angle at the axial bridging atom, that is 134.3(2)° for Cu(1)–N(04b)–C(04b)]. The ferromagnetic coupling in **2** is most likely due to the accidental orthogonality between the magnetic orbitals within the [Cu(1)(NCCCCCN)$_2$Cu(1b)] dimetallacycle (out-of-plane exchange pathway), a situation which has been previously observed in oximato- [52], di-μ-chloro- [53] and double end-on azido/cyanato-dicopper(II) complexes [54].

4. Conclusions

The present study shows that the 2,5-dpp ligand is a suitable connector of metal ions to yield dinuclear species (**1**) that can be used as precursors of alternating chain compounds in the presence of potential bridging coligands such as tcnoet (**2**). The bis-bidentate 2,5-dpp molecule appears as a very poor mediator of magnetic interactions in its copper(II) complexes whereas the polynitrile tcnoet ligand is able to transmit weak ferromagnetic interactions between copper(II) ions separated by more than 9.5 Å through the out-of-plane exchange pathway.

Supplementary data

CCDC 711506 and 711507 contain the supplementary crystallographic data for **1** and **2**, respectively. These data can be obtained free of charge via http://www.ccdc.cam.ac.uk/conts/retrieving.html, or from the Cambridge Crystallographic Data Centre, 12 Union Road, Cambridge CB2 1EZ, UK; fax: (+44) 1223-336-033; or e-mail: deposit@ccdc.cam.ac.uk.

Acknowledgements

This work was supported by the Ministerio Español de Ciencia y Tecnología through the Project CTQ-2007-61690), the Italian MIUR and the French CNRS (Centre National de la Recherche Scientifique). Pre- (C.Y.) and post-doctoral (F.S.) grants from the Ministerio Español de Ciencia y Tecnología (C.Y.) and the Agence Universitaire de la Francophonie (F.S.) are gratefully acknowledged.

References

[1] F.H. Case, E. Koft, J. Am. Chem. Soc. 81 (1959) 905.
[2] A. Neels, H. Stoeckli-Evans, Chimia 47 (1993) 198.
[3] P.J. Steel, Chem. Rev. 106 (1990) 227.
[4] W. Kaim, S. Kohlman, Inorg. Chem. 26 (1987) 68.
[5] W. Kaim, S. Kohlman, Inorg. Chem. 25 (1986) 3306.
[6] S. Ernst, V. Kasack, W. Kaim, Inorg. Chem. 27 (1988) 1146.
[7] S. Ernst, W. Kaim, Inorg. Chem. 28 (1989) 1520.
[8] S. Campagna, G. Denti, G. de Rosa, L. Sabatino, S. Serroni, M. Ciano, V. Balzani, Inorg. Chem. 28 (1989) 2565.
[9] G. Denti, S. Campagna, L. Sabatino, S. Serroni, M. Ciano, V. Balzani, Inorg. Chem. 29 (1990) 4750.
[10] G. Di Marco, A. Bartolotta, V. Ricevuto, S. Campagna, G. Denti, L. Sabatino, G. De Rosa, Inorg. Chem. 30 (1991) 270.
[11] S. Serroni, G. Denti, Inorg. Chem. 31 (1992) 4251.
[12] G. Denti, S. Serroni, S. Campagna, V. Ricevuto, A. Juris, M. Ciano, V. Balzani, Inorg. Chim. Acta 198–200 (1992) 507.
[13] T. Tsubomura, S. Enoto, S. Endo, T. Tamane, K. Matsumoto, T. Tsukuda, Inorg. Chem. 44 (2005) 6373.
[14] L. Ding, M. Wagner, M. Bolte, Acta Crystallogr. C57 (2001) 162.
[15] A. Neels, B.M. Neels, H. Stoeckli-Evans, A. Clearfield, D.M. Poojary, Inorg. Chem. 36 (1997) 3402.
[16] A. Escuer, T. Comas, R. Vicente, J. Ribas, Transition Met. Chem. 18 (1993) 42.
[17] A. Neels, H. Stoeckli-Evans, A. Escuer, R. Vicente, Inorg. Chem. 34 (1995) 1946.
[18] A. Neels, H. Stoeckli-Evans, A. Escuer, R. Vicente, Inorg. Chim. Acta 260 (1997) 189.
[19] A. Neels, H. Stoeckli-Evans, Inorg. Chem. 38 (1999) 6164.
[20] C. Yuste, A. Bentama, S.E. Stiriba, D. Armentano, G. De Munno, F. Lloret, M. Julve, Dalton Trans. (2007) 5190.
[21] S.R. Batten, K.S. Murray, Coord. Chem. Rev. 246 (2003) 103. and references therein.
[22] F. Thétiot, S. Triki, J. Sala Pala, Polyhedron 22 (2003) 1837.
[23] A. Earnshaw, Introduction to Magnetochemistry, Academic Press, London, 1968.
[24] SAINT, Version 6.45, Bruker Analytical X-ray Systems Inc., Madison, WI, USA, 2003.
[25] G.M. Sheldrick, SADABS, Version 2.10, Bruker AXS Inc., Madison, Wisconsin, USA, 2003.
[26] CRYSALIS-CCD 170, Oxford-Diffraction, 2002.
[27] CRYSALIS-RED 170, Oxford-Diffraction, 2002.
[28] International Tables for X-ray Crystallography, vol. 4, Kynoch Press, Birmingham, 1975.
[29] SHELXTL NT, Version 5.10, Bruker Analytical X-ray Inc., Madison, WI, USA, 1998.
[30] M. Sheldrick, SHELX97, Programs for Crystal Structure Analysis, University of Göttingen, Göttingen, Germany, 1997.

[31] M. Nardelli, J. Appl. Crystallogr. 28 (1993) 659.
[32] K. Brandeburg, H. Putz, DIAMOND 2.14, Crystal Impact GbR, GBR, Bonn, Germany, 2000.
[33] K. Nakamoto, Infrared and Raman Spectra of Inorganic and Coordination Compounds, 4th Ed., Wiley, New York, 1986. p. 227.
[34] G.A. Lawrance, Chem. Rev. 86 (1986) 17.
[35] J.S. Haynes, S.J. Rettig, J.R. Sams, R.C. Thompson, J. Trotter, Can. J. Chem. 64 (1986) 429.
[36] I. Castro, J. Faus, M. Julve, C. Bois, J.A. Real, F. Lloret, J. Chem. Soc., Dalton Trans. (1992) 47.
[37] F. Setifi, A. Bouchama, J. Sala Pala, J.Y. Salaün, S. Triki, Inorg. Chim. Acta 359 (2006) 3269.
[38] S. Benmansour, F. Setifi, C. Gómez-García, S. Triki, E. Coronado, Inorg. Chim. Acta 361 (2008) 3856.
[39] (a) L. Infantes, S. Motherwell, CrystEngCommun. 4 (2002) 454;
(b) L. Infantes, J. Chisholm, S. Motherwell, CrystEngCommun. 5 (2003) 480;
(c) M. Mascal, L. Infantes, J. Chisholm, Angew. Chem., Int. Ed. 45 (2006) 32.
[40] J. Bernstein, R.E. Davies, L. Shimoni, N.-L. Chang, Angew. Chem., Int. Ed. 34 (1995) 1555.
[41] D. Armentano, T.F. Mastropietro, M. Julve, R. Rossi, P. Rossi, G. De Munno, J. Am. Chem. Soc. 129 (2007) 2740.
[42] J. Faus, M. Julve, J.M. Amigó, T. Debaerdemaeker, J. Chem. Soc., Dalton Trans. (1989) 1681.
[43] F. Setifi, S. Benmansur, S. Triki, C.J. Gómez-García, M. Marchivie, J.Y. Salaün, M. Mustafa, Inorg. Chim. Acta 360 (2007) 3879.
[44] J. Choi, J.D. Woodward, J.L. Musfeldt, C.P. Landee, M.M. Turnbull, Chem. Mater. 15 (2003) 2797.
[45] H.N. Bordallo, L. Chapon, J.L. Manson, C.D. Ling, J.S. Qualls, D. Hall, D.N. Argyriou, Polyhedron 22 (2003) 2045.
[46] B.R. Jones, P.A. Varughese, I. Olejniczak, J.M. Pigos, J.L. Musfeldt, C.P. Landee, M.M. Turnbull, G.L. Carr, Chem. Mater. 13 (2001) 2127.
[47] J.S. Haynes, S.J. Rettig, J.R. Sams, R.C. Thompson, J. Trotter, Can. J. Chem. 65 (1987) 420.
[48] (a) M. Graf, B. Greaves, H. Stoeckli-Evans, Inorg. Chim. Acta 204 (1993) 239;
(b) M. Graf, H. Stoeckli-Evans, A. Escuer, R. Vicente, Inorg. Chim. Acta 257 (1997) 89.
[49] (a) J. Carranza, C. Brennan, J. Sletten, J.M. Clemente-Juan, F. Lloret, M. Julve, Inorg. Chem. 42 (2003) 8716;
(b) J. Carranza, J. Sletten, C. Brennan, F. Lloret, J. Cano, M. Julve, Dalton Trans. (2004) 3997;
(c) C. Yuste, D. Armentano, N. Marino, L. Cañadillas-Delgado, F.S. Delgado, C. Ruiz-Pérez, D.P. Rillema, F. Lloret, M. Julve, Dalton Trans. (2008) 1583.
[50] G.-Y. Su, C.W. Chen, S.C. Cheng, S.H. Lin, H.H. Wei, C.J. Lee, Polyhedron 24 (2005) 487.
[51] E. Burkholder, V. Golub, C.J. O'Connor, J. Zubieta, Inorg. Chem. 42 (2003) 6729.
[52] B. Cervera, R. Ruiz, F. Lloret, M. Julve, J. Cano, J. Faus, C. Bois, J. Mrozinski, J. Chem. Soc., Dalton Trans. (1997) 395.
[53] H. Grove, J. Sletten, M. Julve, F. Lloret, J. Chem. Soc., Dalton Trans. 8 (2001) 2487.
[54] J. Carranza, J. Sletten, F. Lloret, M. Julve, J. Mol. Struct. 890 (2008) 31. and references therein.

deionized water (50 mL) in a 100 mL beaker with stirring at room temperature or 60 °C for 0.5–15 h. The resulting solid was filtered and washed with deionized water until the supernatant became neutral and then the wet products were dried in an oven at 80 °C overnight. These samples are designated as M^{n+}/K-CoKBL, where the M^{n+} stands for the metal ions.

2.4. Characterization

Powder X-ray diffraction (XRD) patterns were recorded on a Shimadzu XD-D1 diffractometer using Cu Kα radiation and a carbon monochromator. For Rietveld analysis, the XRD pattern was measured on another diffractometer (Rigaku Rint 2500) and analyzed by the RIETAN-FP program [8]. The TCH pseudo-Voigt profile function was used. The parameters were optimized according to the following order: the unit cell parameter [3], the fractional coordinates, the site occupancies, and the isotopic displacement parameters. The morphology of the product was observed with a scanning electron microscope (SEM), Hitachi S-5000H. The specific surface area was calculated using the BET single-point method from nitrogen uptake measured at 77 K. The samples were pretreated in an N_2 flow at 300 °C for 30 min prior to the measurements. The elemental analyses were performed using a Shimadzu ICPS-1000 IV, inductively coupled plasma (ICP) emission spectrometer, after the samples were dissolved in HCl.

2.5. Catalyst test

Catalyst tests were carried out in a fixed-bed flow reactor. The Co_3O_4 catalyst prepared by calcination of the precursor at 400 °C in air for 4 h was tabletted, pulverized into 10–22 mesh, and set in the reactor. The catalyst bed was heated to 500 °C in a helium gas flow and held at that temperature for 30 min. Then, the reaction gas composed of 5000 ppm N_2O, 2% O_2, and He balance was introduced to the catalyst bed at $W/F = 0.3$ g s mL^{-1}. The effluent gases from the reactor were analyzed every 5 min at 500 °C with an on-line micro-gas-chromatograph (CP 2002, Chrompack, Netherlands) (columns: 10-m Molecular Sieve 5A at 80 °C; 10-m Porapak Q at 40 °C). After the steady state was attained, reaction temperature was decreased from 500 °C to the temperature where the catalyst showed negligible N_2O conversion. The catalyst activity is expressed by the T_{50} value, which is defined as the temperature at which the catalyst exhibits 50% N_2O conversion under the above-mentioned conditions.

3. Results and discussion

3.1. Preparation of alkali-metal cobalt kambaldaites (M-CoKBL)

Although Petrov et al. reported the synthesis of sodium or ammonium cobalt kambaldaite (CoKBL), there are no reports on the synthesis of the other alkali-metal analogues of CoKBL. Therefore, we tried to prepare them by the precipitation method.

When the precipitate, obtained by the addition of a cobalt nitrate solution to a potassium bicarbonate solution at 50 °C, was aged at that temperature, the K-CoKBL phase (ideal structure, $K_2Co_8(CO_3)_6(OH)_6{\cdot}6H_2O$) appeared. Similarly, synthesis of M-CoKBL requires aging at relatively high temperatures and transformation of cobalt carbonate into the kambaldaite phase took place during aging. This process is accompanied by the change in color of the precipitate as described in Section 2. The preparation method adopted in this paper is much simpler than that reported previously [3,4].

Fig. 1 shows XRD patterns of the products. All the XRD patterns had kambaldaite-like features. In the case of lithium and sodium, however, cobalt carbonate was formed as a by-product. Although we briefly reported the direct synthesis of Na-CoKBL by precipitation of cobalt nitrate with sodium bicarbonate at 35 °C followed by aging at that temperature for 24 h [5], detailed examination of the XRD patterns by the Reitveld method (vide infra) revealed that these products (Li- and Na-CoKBL) were always contaminated with a small amount of $CoCO_3$ irrespective of the reaction conditions.

The SEM images of NH_4- and alkali-metal-CoKBL are shown in Fig. 2. NH_4-CoKBL was composed of rod-shaped particles. Twined particles and star-burst type particles were also observed. Li-CoKBL had a hexagonal-rod morphology. In the SEM image, small $CoCO_3$ particles were also observed. Na-CoKBL particles are hexagonal prisms. Besides much smaller contaminated $CoCO_3$ particles, well-developed Na-CoKBL particles with faceted surfaces were observed. This morphology is completely different from that of Na-CoKBL prepared by Petrov et al. who reported that the sample consisted of globular crystals with a rough surface [3].

K-CoKBL was composed of unique caterpillar-like spindles. However, close examination of each particle revealed that caterpillar-like morphology was formed by stacking of hexagonal or hexagonal-like plates, indicating that stacking defects frequently occurred during the crystal growth toward the *c*-axis direction. Although many X-shaped twined particles were observed in the SEM photographs of K-CoKBL, particles having morphologies other than caterpillar-like one were not observed, indicating that the product was phase-pure K-CoKBL.

During the course of the preparation of K-CoKBL, a sharp color change of the precipitate in a few minutes was noted after a rather long aging time (~1 h). This observation indicates that nucleation of K-CoKBL crystals occurred in a relatively short period followed by rapid crystal growth. Therefore, the particle-size distributed in a narrow range.

Cs-CoKBL also had the caterpillar-like morphology but overall shape of each particle was hexagonal bipyramidal. For Rb-CoKBL, spindle-like particles without the caterpillar-like morphology and irregularly shaped particles were observed. The latter particles may be due to an amorphous phase.

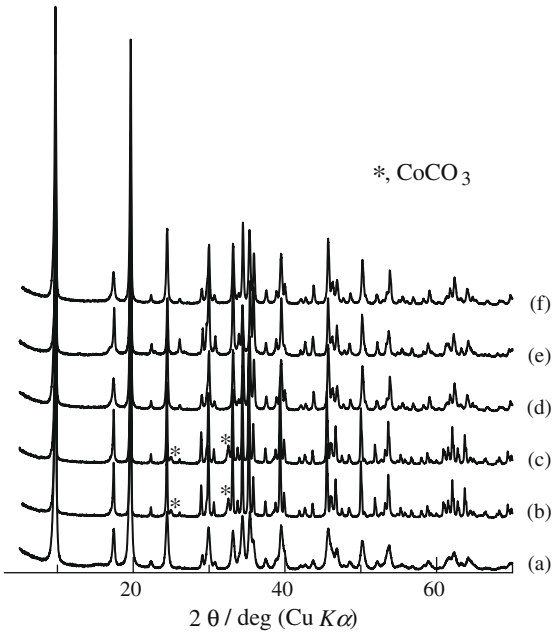


Fig. 1. XRD patterns of: (a), NH_4-CoKBL; (b), Li-CoKBL; (c), Na-CoKBL; (d), K-CoKBL; (e), Rb-CoKBL; and (f), Cs-CoKBL.

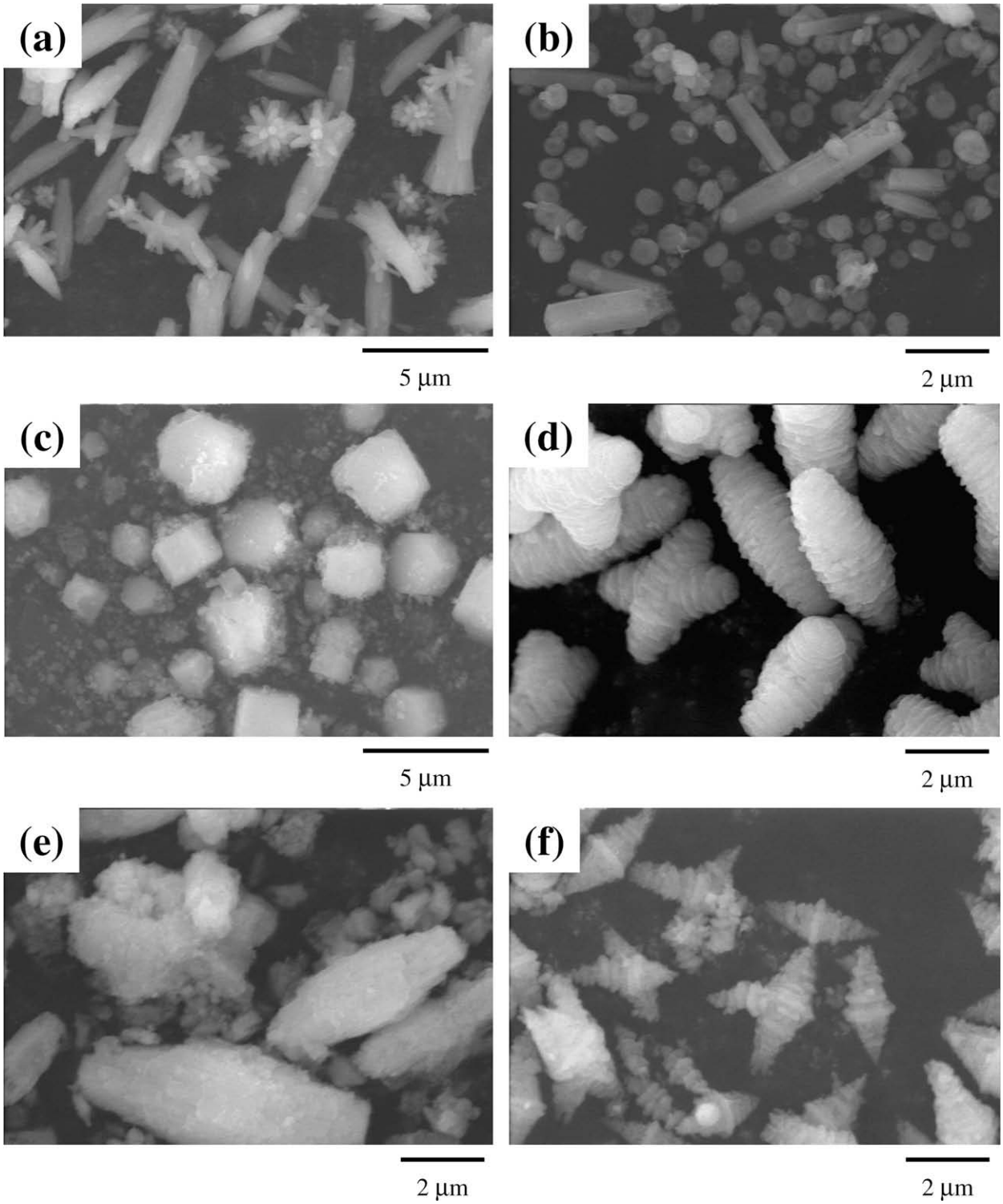


Fig. 2. SEM images of: (a), NH_4-CoKBL; (b), Li-CoKBL; (c), Na-CoKBL; (d), K-CoKBL; (e), Rb-CoKBL; and (f), Cs-CoKBL.

3.2. Rietveld analysis of alkali-metal cobalt kambaldaite

All the XRD peaks of the products (except for Li-CoKBL and Na-CoKBL) can be indexed according to the space group of $P6_3$ [9]. The unit cell parameters, *a* and *c*, and empirical formula of M-CoKBL calculated by Rietveld method are summarized in Table 1.

The unit cell parameters of Na-CoKBL obtained by the precipitation method were slightly larger than the reported values [3]. The empirical formula of Na-CoKBL was $Na_{1.83}Co_{7.99}(CO_3)_6(OH)_{5.82} \cdot 5.35H_2O$, which is much closer to the ideal formula than that reported by Petrov et al. ($Na_{0.84}Co_{4.04}(CO_3)_{2.99}(OH)_{2.81} \cdot 3.32H_2O$) [3]. They attributed this deviation to partial elution of Na^+ ions by washing with water because the Na^+ ions in kambaldaite are relatively mobile, and the absence of distinct smooth crystal faces was attributed to the elution phenomenon. However, the present product had smooth surfaces in spite of the fact that the sample was

Table 1
Crystallographic data of alkali CoKBL obtained by precipitation method.

Notation	R_{wp}, %	Unit cell parameter		By product		Empirical formula	Ref.
		a (Å)	c (Å)	Phase	wt%		
Li-CoKBL	14.4	10.4482(8)	6.0951(4)	$CoCO_3$	27.0	$Li_{1.49}Co_{4.41}(CO_3)_{2.14}(OH)_6 \cdot 1.50H_2O$	
Na-CoKBL	10.3	10.4654(7)	6.1857(3)	$CoCO_3$	6.8	$Na_{1.83}Co_{7.99}(CO_3)_6(OH)_{5.82} \cdot 5.35H_2O$	
K-CoKBL	8.68	10.4100(13)	6.1483(6)			$K_{1.31}Co_8(CO_3)_{5.69}(OH)_{5.93} \cdot 4.40H_2O$	this work
Rb-CoKBL	11.9	10.4541(22)	6.1424(9)			$Rb_{0.06}Co_{7.79}(CO_3)_{4.79}(OH)_6 \cdot 8.07H_2O$	
Cs-CoKBL	11.4	10.4385(26)	6.1482(11)			$Cs_{0.35}Co_{7.02}(CO_3)_{4.20}(OH)_6 \cdot 5.43H_2O$	
Na-CoKBL	7.04	10.4405(5)	6.1663(7)			$Na_{0.84}Co_{4\ 04}(CO_3)_{2.99}(OH)_{2.81} \cdot 3.32H_2O$	[3]
NH_4-CoKBL	7.91	10.4028(5)	6.1250(3)			$(NH_4)_{1.89}Co_{7.88}(CO_3)_6(OH)_6 \cdot 4.27H_2O$	[4]

Space group: CoKBL, $P6_3$ (No. 173); $CoCO_3$, $R\bar{3}c$ (No. 167).

completely washed with water with prolonged immersion of the sample in water. These facts suggest that partial elution of Na^+ ions was prevented by faceted surfaces of Na-CoKBL.

Fig. 3 shows the observed, calculated and difference profiles for the final refinement of XRD of K-CoKBL. The refinement led to residual values of $R_{wp} = 8.68\%$, $R_p = 6.73\%$, $R_e = 5.08\%$ and $S = 1.709$. The empirical formula of K-CoKBL was close to the ideal one. The unit cell parameters, a and c were 10.4100 ± 0.0013 and 6.1483 ± 0.0006 Å, respectively, which were slightly smaller than the reported values for Na-CoKBL [3]. The kambaldaite structure is built by infinite chains of $[Co(1)(OH)_2(OCO_2)_4]$ octahedra sharing opposite edges, parallel to the twofold screw axis. These chains are connected via bridging CO_3^{2-} groups and $[Co(2)(OH)_3(OCO_2)_3]$ octahedra, resulting in formation of tunnels in which $[M(H_2O)_6]$ octahedra are located to cancel the negative charge of the framework. The result maintained above (smaller unit cell volume of K-CoKBL as compared with that of Na-CoKBL) may be due to the fact that hydrated radius of alkali-metal cation decreases with the increase in the period of the periodic table. The site occupancy of potassium in the lattice was low, and the K/Co ratio calculated by the Rietvald method was 0.16 (theoretical value for the ideal structure, 0.25). This value was essentially identical with the K/Co molar ratio determined by ICP analysis (0.13). This result may suggest that elution of K^+ ions took place because the surface of the particle was rather rough. The final positional and thermal parameters for K-CoKBL are listed in Table 2.

For Rb-CoKBL, calculated Rb content was much smaller than ideal one. Since the product particles had rough surfaces, elution of Rb ions accompanied by elimination of a part of counter anions might have occurred during washing the particles.

Because the 2a sites of the $P6_3$ space group where alkali-metal cations are accommodated have O_h-like surroundings, NH_4^+ having the T_d structure cannot locate in the 2a site. Therefore, Rietveld analysis of NH_4-CoKBL was not carried out in this work.

3.3. Ion-exchange of K-CoKBL

Since kambaldaite has a unique one-dimensional channel structure, we tried to ion-exchange the K^+ ions in the channels of K-CoKBL with various metal ions for application of the ion-exchanged K-CoKBL as the precursor of catalysts for direct decomposition of nitrous oxide.

The XRD patterns of the products are shown in Fig. 4 and K/Co molar ratios of M^{n+}/K-CoKBL before/after the ion-exchange treatment analyzed by the ICP emission spectrometry are shown in Table 3. When the samples were treated in the solutions of with aluminum, iron and gallium nitrates, the K/Co molar ratio after the treatment decreased. However, the K-CoKBL phase collapsed and a hydrotalcite-like phase appeared except for Fe^{3+}/K-CoKBL. Although the K-CoKBL phase was maintained in the case of nickel nitrate, K/Co molar ratio after the ion-exchange treatment was almost as same as before ion-exchange; therefore ion-exchange

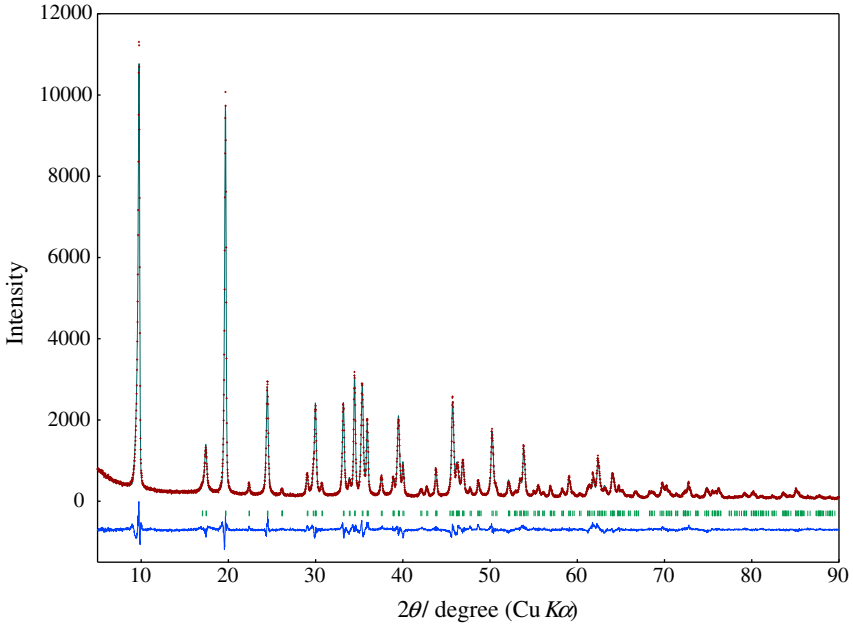


Fig. 3. Observed, calculated, and difference patterns obtained by Rietveld analysis of K-CoKBL as-synthesized by precipitation of cobalt nitrate with potassium bicarbonate at 50 °C followed by aging at that temperature for 3 h.

Table 2
Atomic coordinates of $K_{L31}Co_8(CO_3)_{5.69}(OH)_{5.93} \cdot 4.40H_2O$ obtained by precipitation method.

Atom	Site	g[a]	Atomic coordinates			B[b] (Å^2)
			x	y	z	
K	2a	0.653(6)	0	0	0.3693	8.23
Co(1)	6c	1	0.5143	0.0014	1/4	0.81
Co(2)	2b	1	2/3	1/3	0.6366	0.95
Ow(1)	6c	0.753(5)	0.0802	0.1785	0.1240	0.39
OH(2)	6c	0.988(7)	0.5061	0.1317	0.5073	0.42
C	6c	0.948	0.7607	0.2045	0.0138	0.12
O(3)	6c	0.948	0.7298	0.1514	0.1849	0.13
O(4)	6c	0.948	0.7226	0.1775	-0.1531	3.57
O(5)	6c	0.948	0.9069	0.3200	0.0243	0.72

Space group $P6_3$ (No. 173).
[a] Site occupancy.
[b] Isotrophic displacement parameter.

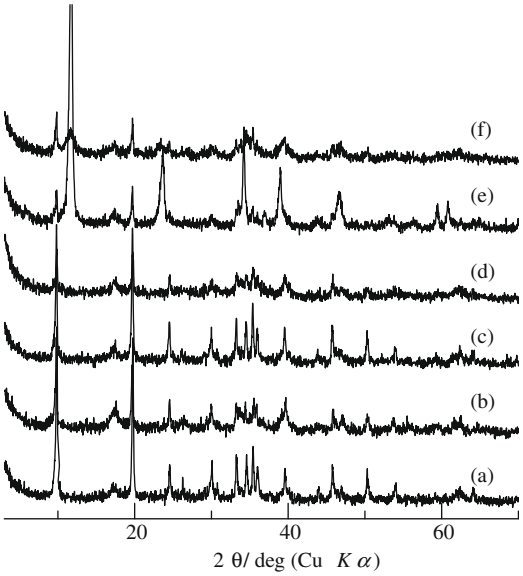


Fig. 4. XRD patterns of (a) K-CoKBL; (b) Li^+/K-CoKBL; (c) Ni^{2+}/K-CoKBL; (d) Fe^{3+}/K-CoKBL; (e) Ga^{3+}/K-CoKBL; and (f) Al^{3+}/K-CoKBL.

reaction might not proceed well. In the case of lithium, ion-exchange might proceed because the solution of lithium acetate is slightly basic. These results suggest that the K-CoKBL structure is weak even in slightly acidic solutions, the K-CoKBL phase dissolving in the ion-exchange solution because of low concentration of hydroxide and carbonate ions. In other words, collapse of the structure took place more quickly than the ion-exchange of K-CoKBL, and the hydrotalcite-like phase seems to be formed by a dissolution–recrystallization mechanism.

The XRD patterns of the samples obtained by calcination of M^{n+}/K-CoKBL at 400 °C for 4 h showed the formation of Co_3O_4 having a spinel structure. Similarly, when the parent K-CoKBL sample was calcined at the same temperature, it transformed into Co_3O_4. The BET surface area of the Co_3O_4 obtained from K-CoKBL (75 $m^2\ g^{-1}$) was larger than that obtained from $CoCO_3$ (57 $m^2\ g^{-1}$) [7]. As mentioned in Section 1, the CoKBL phase was formed by a transformation sequence of: hydrotalcite-like phase → cobalt carbonate → CoKBL phase. This transformation sequence was also observed by increasing the precipitation temperature. Therefore, the CoKBL phase was well crystallized as compared with the $CoCO_3$. However, the BET surface area of Co_3O_4 obtained by decomposition of the CoKBL phase was larger than that obtained from $CoCO_3$. This result can be explained by the disturbance of the development of Co_3O_4 crystals by the K^+ ions present in the precursor, K-CoKBL.

3.4. N_2O decomposition over Co_3O_4 catalysts

The catalytic activities of the modified Co_3O_4 catalysts obtained by calcination of M^{n+}/K-CoKBL are shown in Fig. 5. Although the catalyst obtained from K-CoKBL itself exhibited only a low activity (T_{50} value ~330 °C), all the catalysts obtained from M^{n+}/K-CoKBL by the ion-exchange treatment showed higher activities. Especially, the catalysts obtained from Al^{3+}/K-CoKBL, Fe^{3+}/K-CoKBL, and Ga^{3+}/K-CoKBL showed much higher activity and the T_{50} values of these catalysts were 176 °C, 171 °C, and 178 °C, respectively. Then, we prepared the M^{3+}/K-CoKBL samples (M = Al, Fe, and Ga) having various M^{3+}/Co molar ratios by varying the treatment conditions such as stirring temperature (r.t. or 60 °C) and stirring

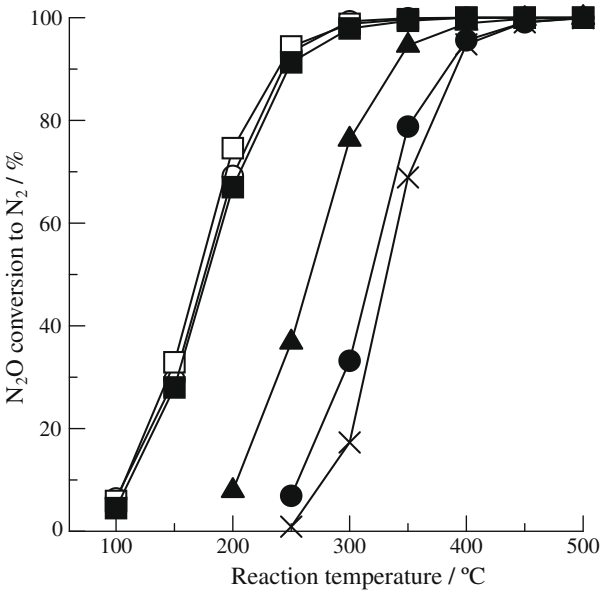


Fig. 5. N_2O decomposition activities of Co_3O_4 catalysts derived from K-CoKBL (×) and K-CoKBL "ion-exchanged" with: (□), Fe^{3+}; (○), Al^{3+}; (■), Ga^{3+}; (▲), Ni^{2+}; (●), Li^+. Reaction conditions: N_2O, 5000 ppm; O_2, 2%; He balance; W/F = 0.3 g s mL^{-1}.

Table 3
Ion-exchange conditions and ICP atomic emission spectrometric analysis of M^{n+}/K-CoKBL.

Source of metal	Initial concentration/mol L^{-1}	Ion-exchange temperature	Ion-exchange time (h)	Notation	K/Co molar ratio of before ion-exchange	K/Co molar ratio of after ion-exchange	M^{n+}/Co molar ratio
$CH_3COOLi \cdot 2H_2O$	0.31	60 °C	10.5	Li^+/K-CoKBL	0.11	0.012	0.21
$Ni(NO_3)_2 \cdot 6H_2O$	0.31	r.t.	15	Ni^{2+}/K-CoKBL	0.13	0.11	0.043
$Al(NO_3)_3 \cdot 9H_2O$	0.062	r.t.	0.5	Al^3+/K-CoKBL	0.13	0.095	0.36
$Fe(NO_3)_3 \cdot 9H_2O$	0.062	60 °C	0.5	Fe^3+/K-CoKBL	0.10	0.044	0.34
$Ga(NO_3)_3 \cdot 1.5H_2O$	0.062	60 °C	0.5	Ga^{3+}/K-CoKBL	0.10	0.045	0.22

Table 4
Dependence of the catalyst activity on the K/Co molar ratio in the "ion-exchanged" K-CoKBL.

Al^{3+}/K-CoKBL				Fe^{3+}/K-CoKBL				Ga^{3+}/K-CoKBL			
K/Co molar ratio		Al^{3+}/Co	T_{50}/°C	K/Co molar ratio		Fe^{3+}/Co	T_{50}/°C	K/Co molar ratio		Ga^{3+}/Co	T_{50}/°C
Before ion-exchange	After ion-exchange			Before ion-exchange	After ion-exchange			Before ion-exchange	After ion-exchange		
0.11	0.063	0.36	328	0.05	0.0079	0.32	292	0.05	0.0085	0.15	306
0.088	0.074	0.096	202	0.1	0.044	0.34	171	0.1	0.045	0.22	178
0.11	0.077	0.34	194	0.11	0.076	0.29	187	0.12	0.063	0.23	186
0.13	0.095	0.36	176	0.11	0.093	0.33	286	0.13	0.091	0.22	228
0.11	0.107	0.36	185	0.13	0.1	0.079	226	0.12	0.097	0.061	307
								0.14	0.13	0.26	303

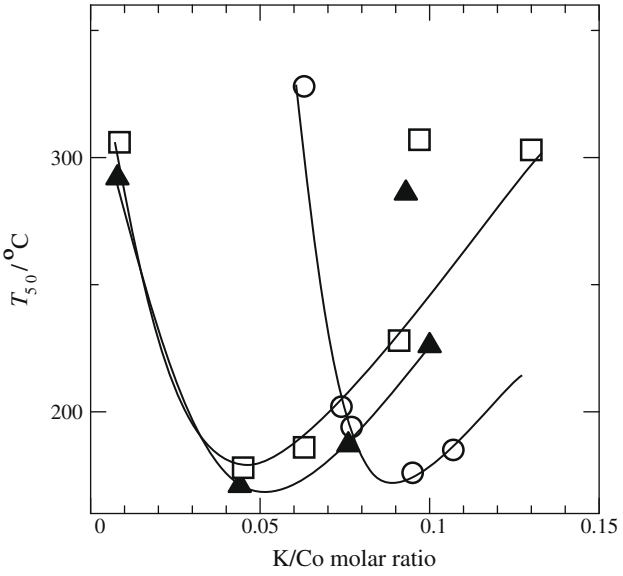


Fig. 6. Temperature of 50% N_2O conversion (T_{50}) versus K/Co molar ratio of the catalyst obtained by calcination of M^{n+}/K-CoKBL. "Ion-exchange" solution: ○, $Al(NO_3)_3$; ▲, $Fe(NO_3)_3$; □, $Ga(NO_3)_3$. Reaction conditions: N_2O, 5000 ppm; O_2, 2%; He balance; W/F = 0.3 g s mL^{-1}.

time (from 0.5 h to overnight), and examined the activities of the modified Co_3O_4 catalysts obtained by calcination of M^{3+}/K-CoKBL. The K/Co and M^{3+}/Co molar ratios and T_{50} values of the catalysts are summarized in Table 4. The catalyst activity was plotted against the K/Co ratio in Fig. 6 which clearly shows that the catalytic activity was closely connected with the K/Co molar ratio. When the catalyst activity was plotted against M^{3+}/Co ratio, no correlation was observed (data not shown), indicating that the amount of M^{3+} ions introduced in the precursor was not connected with the catalytic activity. The T_{50} value of the K-doped Co_3O_4 catalyst prepared by impregnation of commercial $CoCO_3$ with potassium nitrate is about 150 °C [7]. Therefore, the activity of the catalyst obtained by calcination of M^{3+}/K-CoKBL was slightly lower than that of the impregnation catalyst and almost equal to that of the Co_3O_4 catalyst prepared by a precipitation method (172 °C) [5,6].

4. Conclusions

Ammonium- and alkali-metal cobalt kambaldaites (M-CoKBL; ideal formula, $M_2Co_8(CO_3)_6(OH)_6 \cdot 6H_2O$) were directly obtained by precipitation of a cobalt nitrate solution with ammonium or alkali-metal bicarbonate at 50 °C followed by aging at that temperature for 2–3 h. The XRD patterns of the kambaldaites can be simulated by the structure with the $P6_3$ space group. Na-CoKBL had a well-developed hexagonal prism morphology and had an empirical formula close to the ideal one. When K-CoKBL was soaked in the solution of metal nitrate, the collapse of the structure of K-CoKBL took place faster than the ion-exchange by metal ions.

The Co_3O_4 catalysts obtained by calcination of the K-CoKBL "ion-exchanged" with Al^{3+}, Fe^{3+}, and Ga^{3+} exhibited high activities for direct decomposition of nitrous oxide. However, the activity strongly depended on the content of potassium ions remaining in the catalyst but not on the contents of Al^{3+}, Fe^{3+} and Ga^{3+} ions.

Acknowledgment

This work was supported by Grants-in-Aid for Scientific Research (#19310050) from the Ministry of Education, Culture, Sports, Science and Technology, Japan.

Appendix A. Supplementary data

CCDC 420414 contains the supplementary crystallographic data for potassium cobalt kambaldaite (K-CoKBL). Supplementary data associated with this article can be found, in the online version, at doi:10.1016/j.poly.2009.02.026.

References

[1] L.M. Engelhardt, S.R. Hall, A.H. White, Am. Mineral. 70 (1985) 423.
[2] E.H. Nickel, B.W. Robinson, Am. Mineral. 70 (1985) 419.
[3] K. Petrov, E. Mirtcheva, J.L. Martin de Vidales, R. Rojas, O. Garcia-Martinez, Polyhedron 13 (1994) 3269.
[4] K. Petrov, E. Deleva, O. García-Martinez, Solid State Ionics 92 (1996) 303.
[5] C. Ohnishi, K. Asano, S. Iwamoto, M. Inoue, Stud. Surf. Sci. Catal. 162 (2006) 737.
[6] C. Ohnishi, K. Asano, S. Iwamoto, K. Chikama, M. Inoue, Catal. Today 120 (2007) 145.
[7] K. Asano, C. Ohnishi, S. Iwamoto, Y. Shioya, M. Inoue, Appl. Catal. B: Environ. 78 (2008) 242.
[8] F. Izumi, K. Momma, Solid State Phenom. 130 (2007) 15.
[9] T. Hahn, International Tables for Crystallography Vol. A Space-group Symmetry, 4th revised ed., Kluwer Academic, Dordrecht, Netherlands, 1996. p. 548.

Technology. Column chromatographic separations were carried out on neutral Al_2O_3 from Aldrich. Alumina TLC plates D-5160 Duran from Macherey–Nagel were used for selecting eluants and controlling the separation process. The literature procedure was used for the syntheses of the 4-aminophenyl alkyloxybenzoates [49–54].

2.1.1. Ferrocenylketoacetaldehydate sodium (**2**)

Ethyl formate (1.2 mL, 14.9 mmol) and **1** (2.00 g, 8.77 mmol) in absolute benzene (Caution: carcinogen! Consult MSDS) (15 mL) were refluxed for 6 h in the presence of metallic sodium (Caution: highly reactive material! Consult MSDS) (0.60 g, 26.1 mmol) [55]. A precipitate of sodium enolate was filtered off and recrystallized from ethanol. Yield 2.44 g (86%), orange powder. Used without further characterization.

2.1.2. 1-Ferrocenyl-1-{[4-(4-dodecyloxybenzoyloxy) phenyl]amino}propen-2-one (**3a**)

The *p*-aminophenyl ester of *p*-dodecyloxy benzoic acid (1.165 g, 2.93 mmol) and **2** (0.815 g, 2.93 mmol) were dissolved separately in hot ethanol, and then mixed together. Concentrated aqueous HCl (26 μL, 0.30 mmol) was added dropwise to the mixture by a syringe, and then the mixture was refluxed for 30 min. An orange precipitate was filtered out after the mixture cooled down. The precipitate was dissolved in CH_2Cl_2 and filtered through Celite 545. The solvent was evaporated using a rotary evaporator. Recrystallization from *n*-butanol gave 0.472 g (25%) of an orange powder. ^{1}H NMR (250 MHz): δ 0.89 (t, 3H, CH_3), 1.27 (br. s, 16H, CH_2), 1.48 (m, 2H, $OCH_2CH_2CH_2$), 1.82 (quintet, 2H, OCH_2CH_2), 4.04 (t, 2H, OCH_2), 4.19 (s, 5H, C_5H_5), 4.47 (t, 2H, C_5H_4), 4.80 (t, 2H, C_5H_4), 5.61 (d, $J_{H,H}$ = 7.5 Hz, 1H, H1), 6.98 (d, $J_{H,H}$ = 10 Hz, 2H, H6), 7.09 (d, $J_{H,H}$ = 8 Hz, 2H, H3), 7.17 (d, $J_{H,H}$ = 8 Hz, 2H, H4), 7.30 (dd, $J_{H,H}(1)$ = 7.5 Hz, $J_{H,H}(2)$ = 12.5 Hz, 1H, H2), 8.13 (d, $J_{H,H}$ = 10 Hz, 2H, H5), 11.84 (d, $J_{H,H}$ = 12.5 Hz, 1H, NH). FT-IR (cm^{-1}): 2915 (C–H), 2846 (C–H), 1727 (C=O), 1627 (C=O), 1602 (COC=C), 1515 (C=C aryl), 1508 (C=C aryl), 1489 (C=C aryl), 1256, 1199, 1165, 1083, 1072, 1029, 1010, 823, 788, 759, 525, 504, 486. *Anal.* Calc. for $C_{38}H_{45}FeNO_4$: C, 71.81; H, 7.13; N, 2.20. Found: C, 71.81,; H, 7.22; N, 2.45%.

2.1.3. 1-Ferrocenyl-1-{[4-(4-hexadecyloxybenzoyloxy) phenyl]amino}propen-2-one (**3b**)

This compound was prepared in an analogous manner to the previous reaction from 3.295 mmol of the appropriate reagents. Yield 0.64 g (28%). ^{1}H NMR (250 MHz): δ 0.88 (t, 3H, CH_3), 1.26 (br. s, 24H, CH_2), 1.48 (m, 2H, $OCH_2CH_2CH_2$), 1.82 (quintet, 2H, OCH_2CH_2), 4.04 (t, 2H, OCH_2), 4.20 (s, 5H, C_5H_5), 4.47 (t, 2H, C_5H_4), 4.80 (t, 2H, C_5H_4), 5.61 (d, $J_{H,H}$ = 7.5 Hz, 1H, H1), 6.97 (d, $J_{H,H}$ = 10 Hz, 2H, H6), 7.09 (d, $J_{H,H}$ = 9 Hz, 2H, H3), 7.18 (d, $J_{H,H}$ = 9 Hz, 2H, H4), 7.31 (dd, $J_{H,H}(1)$ = 7.5 Hz, $J_{H,H}(2)$ = 12.5 Hz, 1H, H2), 8.13 (d, $J_{H,H}$ = 10 Hz, 2H, H5), 11.84 (d, $J_{H,H}$ = 12.5 Hz, 1H, NH). FT-IR (cm^{-1}): 2917 (ν, C–H), 2849 (ν, C–H), 1727 (ν, C=O), 1626 (ν, C=O), 1603 (ν, COC=C), 1514 (ν, C=C aryl), 1509 (ν, C=C aryl), 1490 (ν, C=C aryl), 1257, 1201, 1164, 1082, 1072, 1030, 1008, 824, 790, 757, 524, 509, 489. *Anal.* Calc. for $C_{42}H_{53}FeNO_4$: C, 72.93; H, 7.72; N, 2.02. Found: C, 72.85; H, 7.69; N, 1.98%.

2.1.4. Bis-{1-ferrocenyl-1-{[4-(4-dodecyloxybenzoyloxy) phenyl]amino}propen-2-onato} copper(II) (**4a**)

The ligand **3a** (104.3 mg, 0.1641 mmol) and $Cu(OAc)_2{\cdot}H_2O$ (17.1 mg, 0.0856 mmol) were dissolved separately in hot ethanol. The solutions were mixed and refluxed for 15 min. A brown precipitate was formed after cooling, which was centrifuged and washed 3 times with ethanol using the centrifugation method. Yield 90.0 mg (82%). FT-IR (cm^{-1}): 2924 (C–H), 2850 (C–H), 1735 (C=O), 1597 (C=N), 1567 (C=C), 1515 (C=C aryl), 1508 (C=C aryl), 1489 (C=C aryl), 1424, 1338, 1333, 1247, 1201, 1199, 1161, 1070, 1014, 1009, 849, 815, 771, 578, 564, 549, 523, 490. *Anal.* Calc. for $C_{76}H_{88}CuFe_2N_2O_8$: C, 68.49; H, 6.65,; N, 2.10. Found: C, 68.59; H, 6.58; N 2.26%.

2.1.5. Bis-{1-ferrocenyl-1-{[4-(4-hexadecyloxybenzoyloxy) phenyl]amino}propen-2-onato} copper(II) (**4b**)

This complex was synthesized in an analogous manner to the previous reaction. Yield 97.0 mg (87%). FT-IR (cm^{-1}): 2923 (C–H), 2848 (C–H), 1734 (C=O), 1599 (C=N), 1568 (C=C), 1513 (C=C aryl), 1509 (C=C aryl), 1490 (C=C aryl), 1425, 1337, 1331, 1250, 1201, 1198, 1160, 1072, 1014, 1009, 847, 811, 770, 579, 564, 550, 524, 489. *Anal.* Calc. for $C_{84}H_{104}CuFe_2N_2O_8$: C, 69.82; H, 7.25; N, 1.94. Found: C, 69.58; H, 7.19; N, 2.04%.

2.1.6. Bis-{1-ferrocenyl-1-{[4-(4-dodecyloxybenzoyloxy) phenyl]amino}propen-2-onato} palladium(II) (**5a**)

The ligand **3a** (98.8 mg, 0.154 mmol) was dissolved completely in freshly distilled 1,4-dioxane (2 mL) in a one-neck 25 mL round flask. $Pd(OAc)_2$ (20.4 mg, 0.091 mmol) was dissolved in 1,4-dioxane (1 mL) in a separate flask. The prepared solutions were mixed and refluxed for 15 min. The product was precipitated by adding ethanol (~4 mL). The precipitate was filtered off and recrystallized from hot ethanol. Yield 48.2 mg (45.5%), brown powder. ^{1}H NMR (250 MHz): δ 0.89 (t, 3H, CH_3), 1.28 (br. s, 16H, CH_2), 1.50 (m, 2H, $OCH_2CH_2CH_2$), 1.83 (quintet, 2H, OCH_2CH_2), 3.96 (m, 2H, C_5H_4), 4.07 (s overlapped with t, 7H, OCH_2 and C_5H_5), 4.23 (t, 2H, C_5H_4), 5.31 (d, $J_{H,H}$ = 7.5 Hz, 1H, H1), 6.91 (d, $J_{H,H}$ = 7.5 Hz, 1H, H2), 7.01 (d, $J_{H,H}$ = 9 Hz, 2H, H6), 7.25 (d overlapped with $CDCl_3$, 2H, H3), 7.44 (d, $J_{H,H}$ = 8 Hz, 2H, H4), 8.20 (d, $J_{H,H}$ = 9 Hz, 2H, H5). FT-IR (cm^{-1}): 2920 (C–H), 2850 (C–H), 1731 (C=O), 1605 (C=N), 1575 (C=C), 1506 (C=C aryl), 1500 (C=C aryl), 1411, 1350, 1251, 1191, 1165, 1074, 1014, 1010, 845, 811, 759, 564, 560, 500, 490. *Anal.* Calc. for $C_{76}H_{88}Fe_2N_2O_8Pd$: C, 66.36; H, 6.45; N, 2.04. Found: C, 65.70; H, 6.43; N, 2.26%.

2.1.7. Bis-{1-ferrocenyl-1-{[4-(4-hexadecyloxybenzoyloxy) phenyl]amino}propen-2-onato} palladium(II) (**5b**)

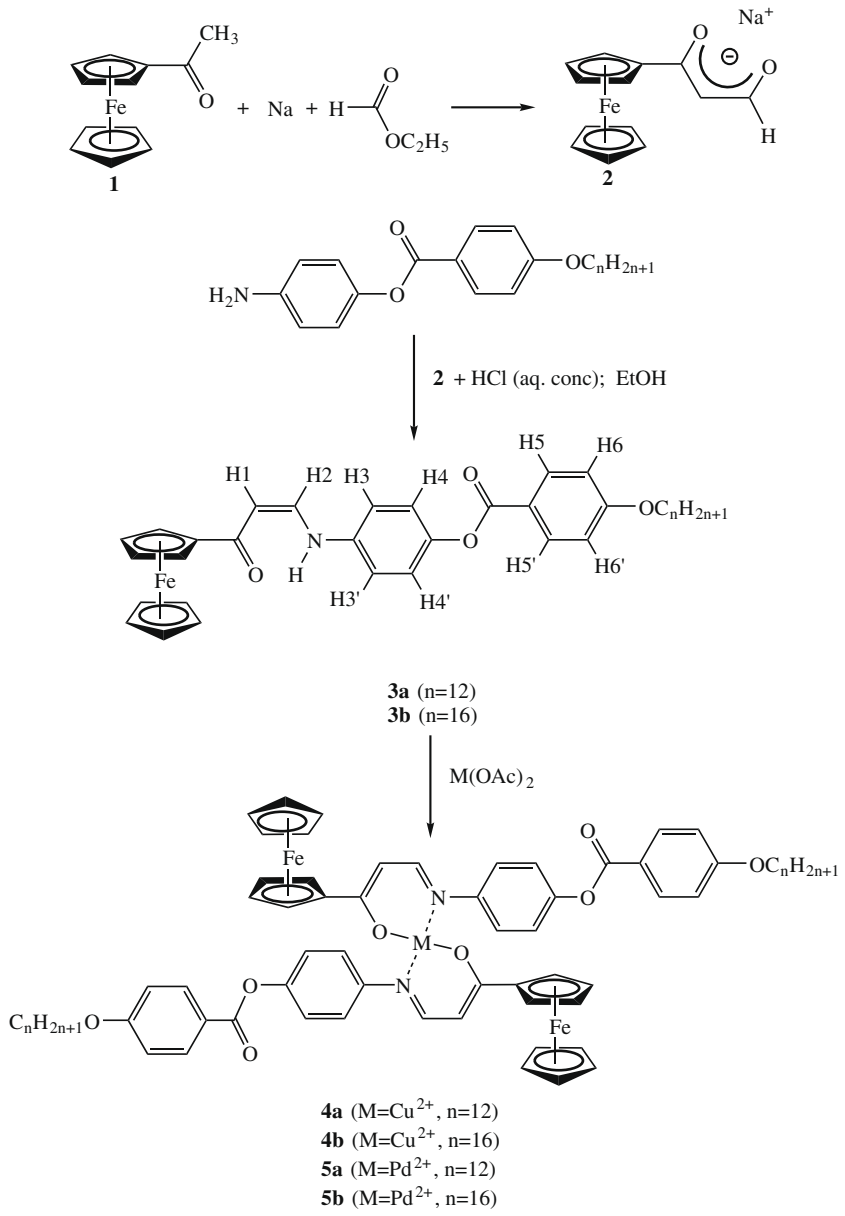
This complex was synthesized in an analogous manner to the previous reaction. Yield 44.0 mg (37%). ^{1}H NMR (250 MHz): δ 0.88 (t, 3H, CH_3), 1.27 (br. s, 24H, CH_2), 1.50 (m, 2H, $OCH_2CH_2CH_2$), 1.84 (quintet, 2H, OCH_2CH_2), 3.96 (m, 2H, C_5H_4), 4.07 (s overlapped with t, 7H, OCH_2 and C_5H_5), 4.23 (t, 2H, C_5H_4), 5.31 (d, $J_{H,H}$ = 7.5 Hz, 1H, H1), 6.91 (d, $J_{H,H}$ = 7.5 Hz, 1H, H2), 7.01 (d, $J_{H,H}$ = 9 Hz, 2H, H6), 7.25 (d overlapped with $CDCl_3$, 2H, H3), 7.44 (d, $J_{H,H}$ = 8 Hz, 2H, H4), 8.19 (d, $J_{H,H}$ = 9 Hz, 2H, H5). FT-IR (cm^{-1}): 2924 (C–H), 2849 (C–H), 1732 (C=O), 1604 (C=N), 1576 (C=C), 1504 (C=C aryl), 1502 (C=C aryl), 1410, 1350, 1250, 1192, 1164, 1074, 1013, 1011, 847, 810, 760, 563, 561, 503, 489. *Anal.* Calc. for $C_{84}H_{104}Fe_2N_2O_8Pd$: C, 67.81; H, 7.05; N, 1.88. Found: C, 67.99; H, 7.01; N, 1.96%.

3. Results and discussion

3.1. Synthesis and characterization

The syntheses of the compounds reported in this paper were performed according to Scheme 1. Acetyl ferrocene **1** can be prepared using a Friedel-Crafts acylation procedure, as was established in the early classical works on ferrocene [55–58]. The addition of $AlCl_3$ catalyst in small portions to equimolar amounts of ferrocene and acetyl chloride allowed the yield of the monoacylated product to increase to over 70%. Compound **1** was separated by column chromatography on Al_2O_3 from the mixture of products.

The crossed Claisen condensation of the acetyl ferrocene **1** with ethyl formate gave the sodium salt of the appropriate ketoalde-



Scheme 1. Syntheses of ligands **3a–b** and heteronuclear complexes **4a–b** and **5a–b**.

hyde **2**. The reaction of compound **2** with *p*-alkoxybenzoyloxy aniline in ethanol in the presence of an equimolar amount of concentrated HCl (aq) led to the β-aminovinyl ketones **3a–b**. The copper(II) complexes **4a–b** and palladium(II) complexes **5a–b** were obtained by treatment of **3a–b** with the corresponding acetate salts in ethanol and 1,4-dioxane, respectively.

The chemical compositions of the synthesized compounds are in good agreement with the data of elemental analyses. The FT-IR spectra of **3a–b** are distinguished by characteristic stretching bands of the ester carbonyl near 1726 cm^{-1}, and ketone carbonyl at 1627 cm^{-1}. In addition, the C=C bond stretching of the ethenyl group is exposed near 1603 cm^{-1}. There is a group of absorption peaks in the area 1480–1515 cm^{-1} which are connected with the deformations of the aromatic rings. Metal-ring vibrations of the ferrocene moiety are displayed in the long-wave area, at 485–525 cm^{-1}. The C=O stretches of the ester group are shifted in the complexes **4a–b** and **5a–b** to a higher frequency region by 8 and 4 cm^{-1}, respectively. The valence vibration of the ketone carbonyl near 1627 cm^{-1} disappears upon complex formation and additional peaks connected with the C=N and C=C bonds in the region 1570–1600 cm^{-1} are generated. In addition vibration modes of the M–O and M–N bonds in the area 560–600 cm^{-1} are displayed in the IR spectra of the metallochelates. Thus, considerable changes occur in the infrared spectra of **4a–b** and **5a–b** in comparison with the free ligands **3a–b**, undoubtedly indicating the successful complex formation.

The UV–Vis spectra of the ligands **3a–b** are represented by three absorption bands (see Table 1). The first band with a maxima near 260 nm is associated with π–π^* electronic transitions of the aromatics rings. The next band is related to the carbonyl chromophore, which is shifted bathochromically to 366 nm due to the conjugational effect of the adjacent ethenyl and cyclopentadienyl groups [59]. The less intensive band at ~465 nm belongs to d–d type transitions of the electrons of the iron atoms [60–62].

An additional shoulder appears near 292–298 nm upon complex formation, which is connected to a ligand-to-metal charge transfer transition in the case of the copper(II) complexes **4a–b** [63], and a metal-to-ligand charge transfer transition in the case

Table 1
UV–Vis spectral data for **3a–b**, **4a–b** and **5a–b**.

Compound	Absorption max, nm (log ε, L × cm^{-1} × mol^{-1})			
	I band	II band (shoulder)	III band	IV band
3a	260 (4.40)		366 (4.36)	465 (3.43)
4a	263 (4.94)	278 (4.39)	383 (4.47)	454 (3.82)
5a	259 (4.75)	295 (4.45)	374 (4.60)	462 (4.08)
3b	260 (4.50)		367 (4.51)	466 (3.50)
4b	262 (4.64)	290 (4.36)	382 (4.47)	450 (3.77)
5b	263 (4.74)	298 (4.25)	388 (4.28)	457 (3.68)

of the palladium(II) complexes **5a–b** [64]. It is noteworthy, that in the metal complexes an absorption band associated with the carbonyl group is bathochromically shifted in comparison with the free ligand. The shift can be explained by the added electronic conjugational effect due to involving this group into the metallochelate cycle. The ferrocenyl group in the complexes **4a–b** and **5a–b** reveals d–d electronic transitions in the same area, 465 nm, as the free ligands **3a–b**.

The ligands **3a–b** and complexes **5a–b** are also characterized by ^{1}H NMR. It is interesting to note that the proton signals of the

Table 2
Data of thermo-optical and DSC studies of **3a–b**, **4a–b** and **5a–b**.

Compound	Phase transitions,[a] °C (ΔH, kJ/mol)	
	Heating process	Cooling process
3a	1st cycle: Cr_1 68(1.5) Cr_2 139(34.3) I	I [99.5(−20.0)][b] X 87(−0.9) Cr_2 67(−1.9) Cr
	2nd cycle: Cr 88(1.9) Cr_1 01(−9.1) Cr_2 138(28.7) I	I [96(−12.0)] X 87(−1.0) Cr_2 67(−2.3) Cr
4a	Cr_1 150.5(−7.0) Cr_2 164.5(50.7) I	I [107][c] X
5a	Cr_1 183.5(24.5) Cr_2 221(58.0) I	I [140] SmC[d]
3b	1st cycle: Cr_1 109(18.4) Cr_2 132(39.5) I	I [114(−21.5)] X 89(−11.0) Cr
	2nd cycle: Cr 100(13.8) Cr_1 119(−16.1) Cr_2 132(38.7) I	I [114(−21.4)] X 88(−13.8) Cr
4b	Cr 145(65.8) I	I [120][c] X
5b	Cr_1 201(64.1) I	I [136] SmC[d]

[a] Cr: crystal; X: soft crystal; SmC: smectic C; I: isotropic liquid phases.
[b] Monotropic mesophase transitions are shown in square brackets.
[c] No peaks were observed on the DSC cooling course in the point where star-like domains were observed under POM.
[d] The mesophase was observed upon rapid cooling in a polarizing microscope, while the corresponding DSC peaks were not resolved.

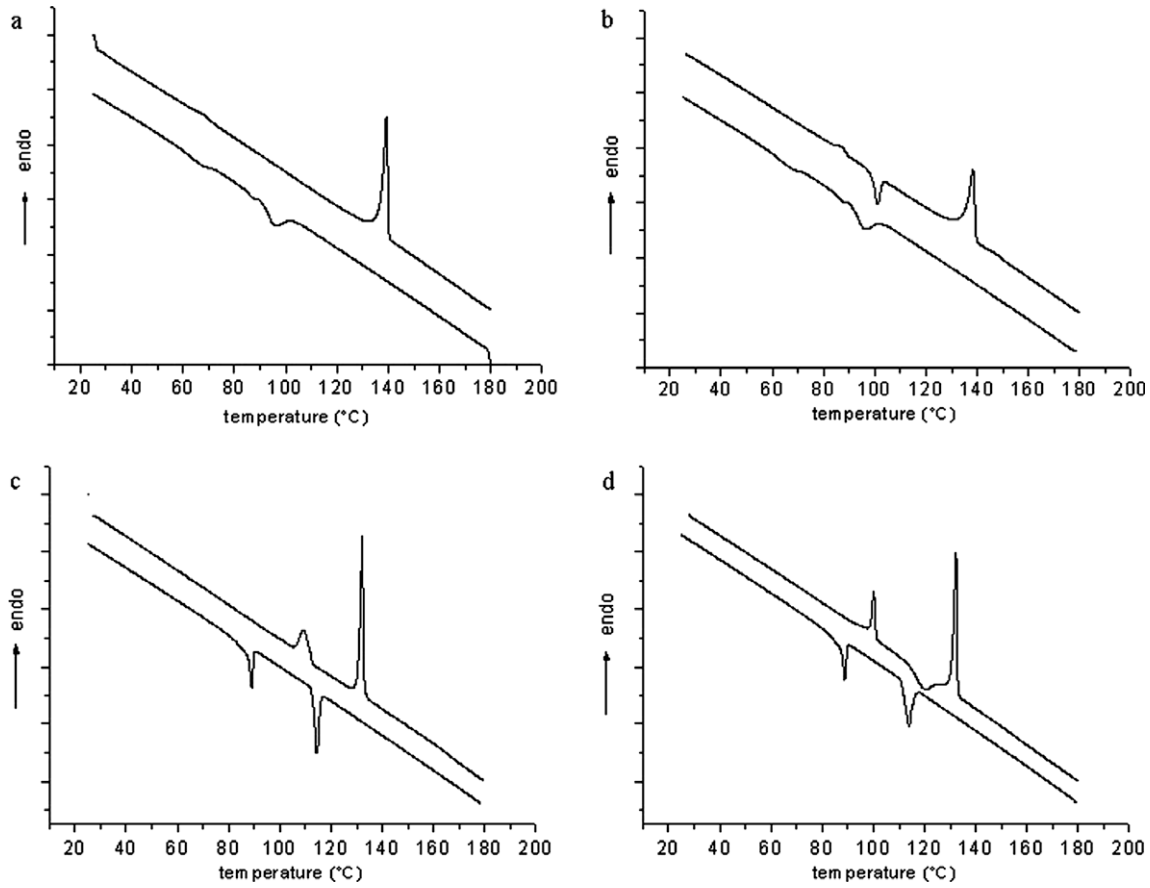


Fig. 1. DSC thermograms of **3a–b**: (a) the first heating and cooling cycle, **3a**; (b) the second heating and cooling cycle, **3a**; (c) the first heating and cooling cycle, **3b**; (d) the second heating and cooling cycle, **3b**.

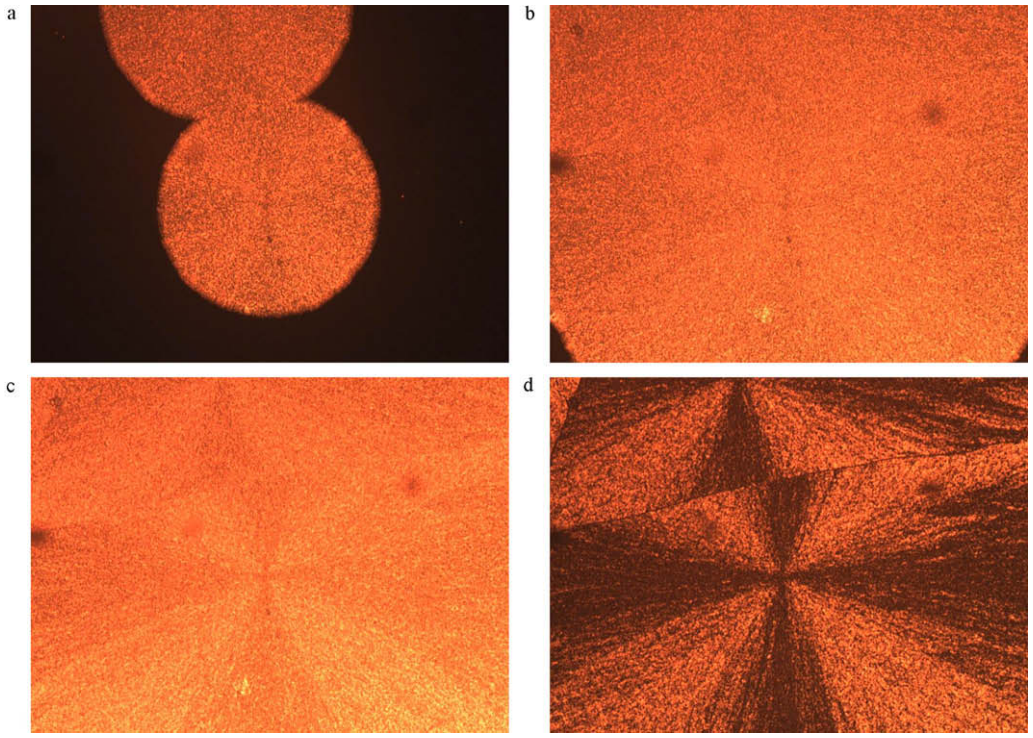


Fig. 2. Optical textures of **3a** under a polarizing microscope: (a) two spherical soft crystal domains growing from the isotropic liquid; (b) the spherical domains mixed with each other; (c and d) development of the spherulitic crystalline structure.

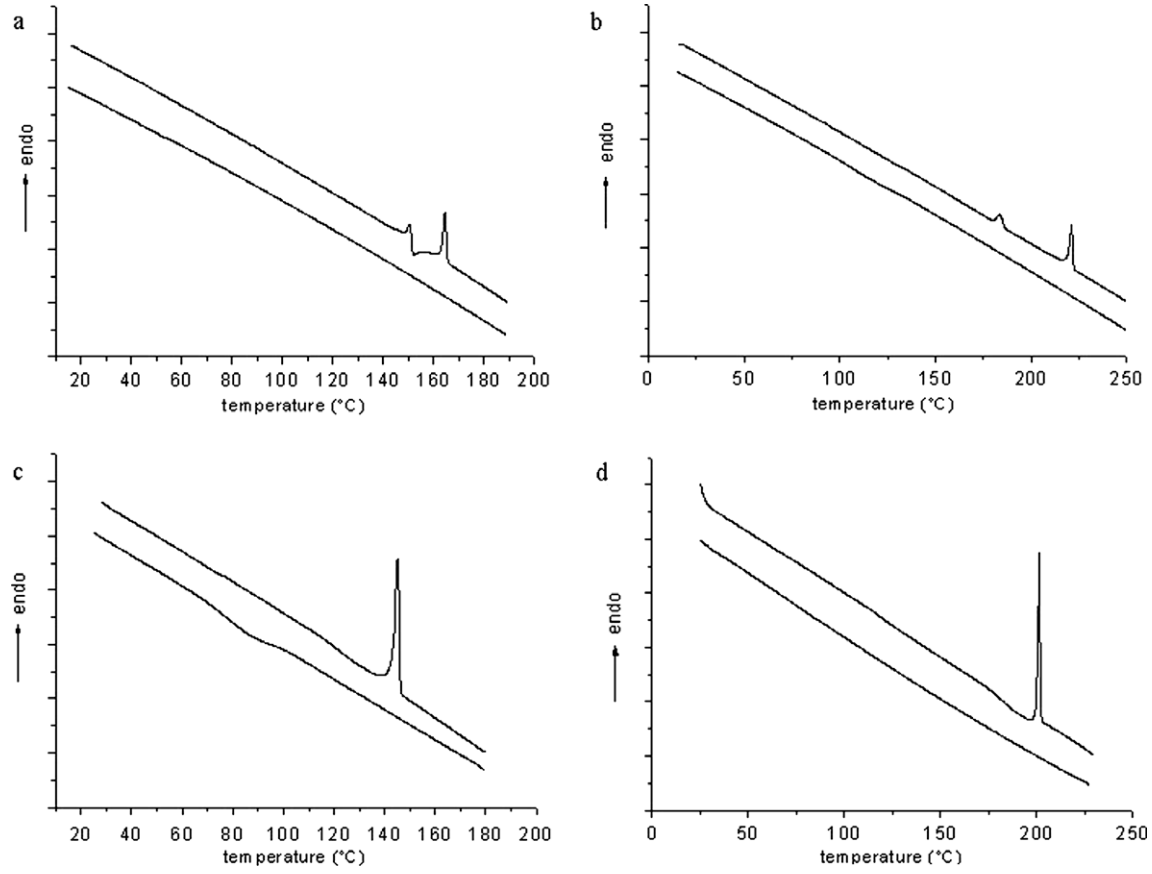


Fig. 3. DSC thermograms of heteronuclear complexes: (a) **4a**; (b) **5a**; (c) **4b** and (d) **5b**.

substituted cyclopentadiene ring of the ferrocene moiety in **5a–b** are high-field shifted by 0.6 ppm in relation to comparable signals in the free ligands **3a–b**. Such a significant shift is due to the fact that the ferrocene unit in these complexes is situated very close to the central chelate core, and there is a considerable electron-donor effect from the Pd(II) ion on it. As for the protons of the ethenyl link, a similar high-field shift is also observed, though the effect is weaker in this case.

3.2. Mesomorphism

Liquid crystal properties of the new synthesized metallomesogens have been investigated by thermal polarizing optical microscopy (POM) and differential scanning calorimetry (DSC). The obtained data on the thermal behaviour of the ligands **3a–b** and two series of heteronuclear complexes **4a–b** and **5a–b** are presented in Table 2.

In the first heating cycle of the DSC measurements, crystal-to-crystal phase transition peaks were observed for the ligands **3a–b** (Fig. 1), although it was small in the case of $n = 12$. In the cooling course, there are several broad responses in the DSC thermogram of **3a** and two sharp peaks in a case of **3b**. During the second heating cycle exothermic peaks appeared in both cases between the first crystal-to-crystal and crystal-to-isotropic liquid phase transitions. This can be explained by partial vitrification of the samples in the first cooling cycle, accomplishing a low energy crystal packing at higher temperatures when increased mobility of molecules allows it to be completed. Enthalpy values of the first DSC peaks after cooling from the isotropic liquid state are relatively high in both **3a** and **3b**. Presumably, these peaks are the result of the transition from the isotropic liquid to a highly disordered soft crystal phase. Two other smaller peaks in the cooling cycle can be assigned to crystal polymorphic phase transitions. A series of microphotographs in Fig. 2 illustrates the development of spherical domains on cooling from the isotropic liquid state in a sample of **3a** under a polarizing microscope. The spherical shape of the domains reveals a possible organization into supramolecular assemblies. The last assumption is founded on the presence of C=O and polar NH groups in **3a–b**, which are capable of forming intermolecular hydrogen bonds. Upon further cooling these spherical formations are transformed into big spherulitic crystals, similar to those observed frequently during crystallization from smectic mesophases. Exactly the same textures were observed under a polarizing microscope in the case of **3b**.

Two DSC peaks corresponding to the crystal-to-crystal and crystal-to-isotropic liquid transitions were observed in the first heating cycle of **4a**, and only one peak from the isotropic liquid phase transition was observed in the case of **4b** (Fig. 3). In the cooling cycle any phase transition peaks were not resolved. The main information about the phase transition behaviour of **4a–b** in the cooling path was obtained from POM observations. Typical optical textures developed from the isotropic liquid state of **4a–b** under a polarizing microscope are presented in Fig. 4. Most likely the observed star-like and flower-like formations are associated with a disordered soft crystal phase. Samples in this state had limited flowability when subjected to stress.

Similar DSC thermograms were obtained for **5a–b** in the heating cycle: two peaks corresponding to the crystal-to-crystal and crystal-to-isotropic liquid transitions in the case of **5a**, and only one peak due to an isotropic liquid transition in the case of **5b**

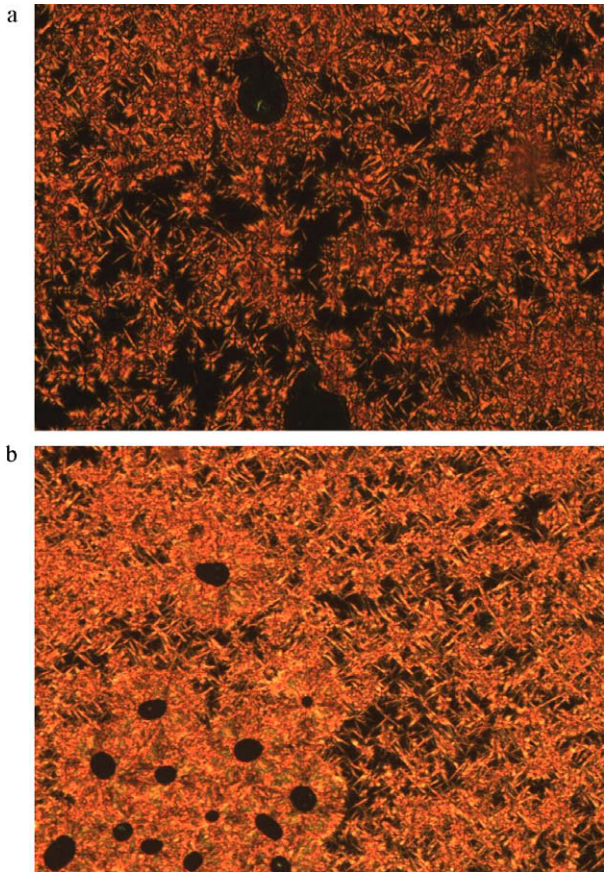


Fig. 4. Emergence of star-like and flower-like domains from the isotropic liquid state in: (a) **4a** and (b) **4b**.

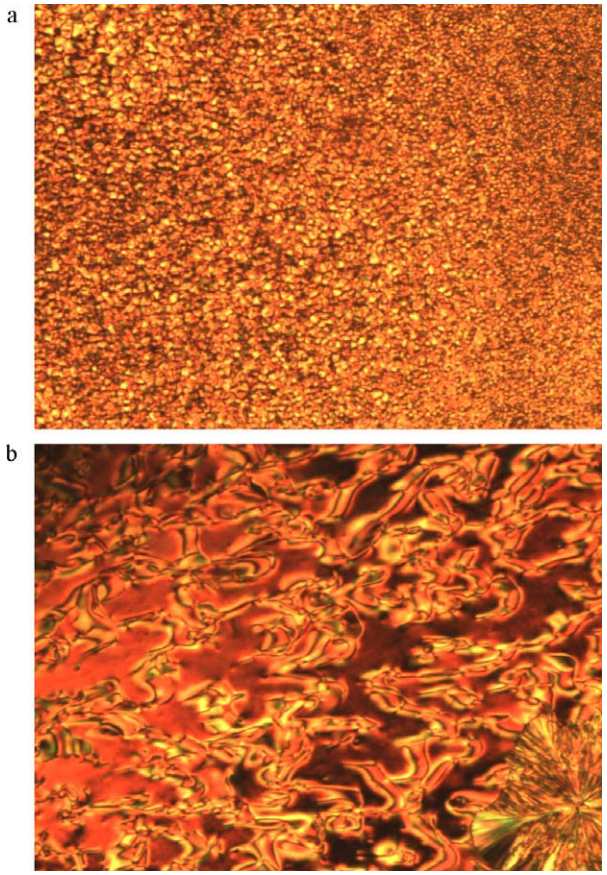


Fig. 5. Optical textures of **5a** under a polarizing microscope: (a) sand-like optical texture and (b) schlieren texture of smectic C.

(Fig. 3). DSC peaks were not revealed on cooling. Monotropic smectic C mesophases were identified for both Pd(II) complexes **5a** and **5b** by polarizing optical microscopy. The typical sand-like and schlieren textures of smectic C were observed upon cooling from the isotropic liquid state (Fig. 5).

Thus, in comparison with the earlier synthesized heteronuclear mesogens with ferrocene- [17] and ferrocenophane-containing [21] β-aminovinylketones, the present compounds exhibited rather poor mesomorphism. In fact the bulky ferrocene moieties in the latter case pile up the central rigid core of a mesogenic molecule rather than being considered as terminal substituents. As a consequence, the geometrical anisotropy of the present complexes is smaller and less favourable for exhibiting liquid crystal properties.

4. Conclusions

Novel ferrocene-containing β-aminovinylketone derivatives containing terminal alkyl chains with 12 and 16 carbon atoms have been synthesized and fully characterized by elemental analyses, ^{1}H NMR, FT-IR and UV–Vis spectroscopies. The synthesized ligands exhibited disordered soft crystal phases. New heteropolynuclear metallomesogen systems were generated from these ligands by incorporating Cu(II) and Pd(II) ions into the enaminoketone chelating site. The synthesized heteronuclear complexes of copper(II), like the free ligands, showed a soft crystal phase. The Pd(II) complexes exhibited a monotropic smectic C mesophase.

Acknowledgements

This work has been supported by a grant from the Korea Science and Engineering Foundation (KOSEF) through the Center for Bioactive Molecular Hybrids (CBMH), and the program Brain Korea 21 (BK-21).

References

[1] A.M. Giroud-Godquin, P.M. Maitlis, Angew. Chem., Int. Ed. Engl. 30 (1991) 375.
[2] P. Espinet, M.A. Esteruelas, L.A. Oro, J.L. Serrano, E. Sola, Coord. Chem. Rev. 117 (1992) 215.
[3] S.A. Hudson, P.M. Maitlis, Chem. Rev. 93 (1993) 861.
[4] J.L. Serrano (Ed.), Metallomesogens, Synthesis Properties and Applications, Wiley-VCH, Weinheim, 1996.
[5] D.W. Bruce, in: D.W. Bruce, D. O'Hare (Eds.), Inorganic Materials, second ed., Wiley, Chichester, 1996, p. 429.
[6] D.W. Bruce, B. Donnio, in: D.M.P. Mingos (Ed.), Structure and Bonding, vol. 95, Springer, Verlag, Berlin-Heidelberg, 1999, p. 193.
[7] R. Giménez, D.P. Lydon, J.L. Serrano, Curr. Opin. Solid State Mat. Sci. 6 (2002) 527.
[8] B. Donnio, D. Guillon, R. Deschenaux, D.W. Bruce, in: J.A. McCleverty, T.J. Meyer (Eds.), Comprehensive Coordination Chemistry II, vol. 7, Elsevier, Oxford, 2003, p. 357.
[9] A.G. Serrette, C.K. Lai, T.M. Swager, Chem. Mater. 6 (1994) 2252.
[10] J. Szydłowska, A. Krowczynski, E. Gorecka, D. Pociecha, Inorg. Chem. 39 (2000) 4879.
[11] K. Binnemans, K. Lodewyckx, B. Donnio, D. Guillon, Chem. Eur. J. 8 (2002) 1101.
[12] K. Binnemans, K. Lodewyckx, Supramol. Chem. 15 (2003) 485.
[13] M. Marcos, A. Omenat, J. Barberá, F. Duran, J.L. Serrano, J. Mater. Chem. 14 (2004) 3321.
[14] K. Binnemans, K. Lodewyckx, B. Donnio, D. Guillon, Eur. J. Inorg. Chem. (2005) 1506.
[15] Yu.G. Galyametdinov, O.N. Kadkin, I.V. Ovchinnikov, Rus. Chem. Bull. 39 (1990) 2235.
[16] Yu. Galyametdinov, O. Kadkin, A. Prosvirin, Rus. Chem. Bull. 43 (1994) 887.
[17] O.N. Kadkin, Yu.G. Galyametdinov, A.I. Rakhmatullin, V.Yu. Mavrin, Rus. Chem. Bull. 48 (1999) 379.
[18] O. Kadkin, Yu. Galyametdinov, A. Rakhmatullin, Mol. Cryst. Liq. Cryst. 332 (1999) 109.
[19] O. Kadkin, H. Han, Yu. Galyametdinov, J. Organomet. Chem. 692 (2007) 5571.
[20] O. Kadkin, J. An, H. Han, Yu. Galyametdinov, Eur. J. Inorg. Chem. (2008) 1682.
[21] H.W. Chae, O.N. Kadkin, M.-G. Choi, Liq. Cryst. 36 (2009) 53.
[22] C. Imrie, P. Engelbrecht, C. Loubser, C.W. McCleland, Appl. Organomet. Chem. 15 (2001) 1.
[23] R. Deschenaux, J.W. Goodby, in: A. Togni, T. Hayashi (Eds.), Ferrocenes: Homogenous Catalysis, Organic Synthesis Materials Science, VCH, Wenheim, New York, 1995, p. 471.
[24] N. Nakamura, T. Nio, T. Okabe, Mol. Cryst. Liq. Cryst. 460 (2006) 85.
[25] W.-C. Shen, Y.-J. Wang, K.-L. Cheng, G.-H. Lee, C.-K. Lai, Tetrahedron 62 (2006) 8035.
[26] D. Apreutesei, G. Lisa, D. Scutaru, N. Hurduc, J. Optoelectron. Adv. Mater. 8 (2006) 737.
[27] S. Campidelli, L. Perez, J. Rodriguez-Lopez, J. Barberá, F. Langa, R. Deschenaux, Tetrahedron 62 (2006) 2115.
[28] J. Brettar, T. Burgi, B. Donnio, D. Guillon, R. Klappert, T. Scharf, R. Deschenaux, Adv. Funct. Mater. 16 (2006) 260.
[29] I. Carlescu, A.M. Scutaru, D. Apreutesei, V. Alupei, D. Scutaru, Appl. Organomet. Chem. 21 (2007) 661.
[30] D. Apreutesei, G.H. Mehl, D. Scutaru, Liq. Cryst. 34 (2007) 819.
[31] I. Carlescu, A.M. Scutaru, D. Apreutesei, V. Alupei, D. Scutaru, Liq. Cryst. 34 (2007) 775.
[32] N. Nakamura, T. Nio, T. Okabe, B. Donnio, D. Guillon, J.-L. Gallani, Mol. Cryst. Liq. Cryst. 466 (2007) 3.
[33] T. Seshadri, H.-J. Haupt, U. Floerke, G. Henkel, Liq. Cryst. 34 (2007) 33.
[34] S. Campidelli, M. Severac, D. Scanu, R. Deschenaux, E. Vazquez, D. Milic, M. Prato, M. Carano, M. Marcaccio, F. Paolucci, G.M.A. Rahman, D.M. Guldi, J. Mater. Chem. 18 (2008) 1504.
[35] I. Carlescu, G. Lisa, D. Scutaru, J. Therm. Anal. Calorim. 91 (2008) 535.
[36] Yu.G. Galyametdinov, G.I. Ivanova, I.V. Ovchinnikov, Zh. Obshch. Khim. 61 (1991) 234 [J. Gen. Chem. USSR 61 (1991) (Engl. Transl.)].
[37] W. Pyzuk, A. Krowczynski, E. Gorecka, Liq. Cryst. 10 (1991) 593.
[38] I. Bikchantaev, Yu.G. Galyametdinov, O. Kharitonova, I.V. Ovchinnikov, D.W. Bruce, D.A. Dunmur, D. Guillon, B. Heinrich, Liq. Cryst. 20 (1996) 489.
[39] W. Pyzuk, E. Gorecka, A. Krowczynski, D. Pociecha, J. Szydłwska, J. Przedmojski, L. Chen, Liq. Cryst. 21 (1996) 885.
[40] C.K. Lai, R. Lin, M.-Y. Lu, K.-C. Kao, J. Chem. Soc., Dalton Trans. (1998) 1857.
[41] U. Pietrasik, J. Szydłwska, A. Krowczynski, D. Pociecha, E. Gorecka, D. Guillon, J. Am. Chem. Soc. 124 (2002) 8884.
[42] C.P. Roll, A.G. Martin, H. Goerls, G. Leibeling, D. Guillon, B. Donnio, W. Weigand, J. Mater. Chem. 14 (2004) 1722.
[43] U. Pietrasik, J. Szydłwska, A. Krowczynski, Chem. Mater. 16 (2004) 1485.
[44] J. Szydłwska, A. Krowczynski, U. Pietrasik, A. Rogowska, Liq. Cryst. 32 (2005) 651.
[45] O.A. Turanova, A.N. Turanov, I.V. Ovchinnikov, Yu.G. Galyametdinov, Russ. J. Coord. Chem. 31 (2005) 757.
[46] O.A. Turanova, Yu.G. Galyametdinov, Russ. J. Gen. Chem. 76 (2006) 1095.
[47] V.N. Kovganko, N.N. Kovganko, Russ. J. Org. Chem. 42 (2006) 907.
[48] U.M. Kauhanka, M.M. Kauhanka, Liq. Cryst. 33 (2006) 213.
[49] D. Soulivong, R. Ziessel, D. Matt, J. Organomet. Chem. 474 (1994) 207.
[50] S. Morrone, D. Guillon, D.W. Bruce, Inorg. Chem. 35 (1996) 7041.
[51] M.-A. Guillevic, M.J. Danks, S.K. Harries, S.R. Collinson, A.D. Pidwell, D.W. Bruce, Polyhedron 19 (2000) 249.
[52] J.-W. Lee, J.-I. Jin, M.F. Achard, F. Hardouin, Liq. Cryst. 28 (2001) 663.
[53] T. Narasimhaswamy, N. Somanathan, D.K. Lee, A. Ramamoorthy, Chem. Mater. 17 (2005) 2013.
[54] K.C. Majumdar, N. Pal, S. Nath, S. Choudhury, N.V.S. Rao, Mol. Cryst. Liq. Cryst. 461 (2007) 37.
[55] R.B. Woodward, M. Rosenblum, M.C. Whiting, J. Am. Chem. Soc. 74 (1952) 3458.
[56] M. Rosenblum, J.O. Santer, W. Glenn Howells, J. Am. Chem. Soc. 85 (1963) 1450.
[57] P.L. Pauson, Quater. Revs. 9 (1955) 391.
[58] M. Vogel, M. Raush, H. Rosenberg, J. Org. Chem. 22 (1957) 1016.
[59] H. George, H.J. Roth, Tetrahedron Lett. 11 (1970) 3361.
[60] D.R. Scott, R.S. Becker, J. Chem. Phys. 35 (1961) 516.
[61] K.I. Grandberg, S.P. Gubin, E.G. Perevalova, Izv. AN SSSR. Ser. Khim. (1966) 549.
[62] K.I. Grandberg, S.P. Gubin, Izv. AN SSSR. Ser. Khim. (1966) 551.
[63] S.V. Sheat, T.N. Waters, J. Inorg. Nucl. Chem. 26 (1964) 1221.
[64] S.R. Allsopp, F. Wilkinson, Chem. Phys. Lett. 19 (1973) 535.

some studies on cyanide-bridged metal complexes and particularly on mixed-valence Cu^{II}/Cu^{I} compounds showed non-negligible exchange interactions between second nearest-neighbor paramagnetic metal ions [15]. We report here the syntheses, structures and magnetic properties of two novel mixed-valence Cu^{II}/Cu^{I} complexes $[Cu^{II}(bpy)Cu^{I}(CN)_3]_n$, (**1**) (bpy = 2,2′-bipyridine) and $\{[Cu^{II}(tn)_2][Cu^{I}_4(CN)_6]\}_n$ (**2**) (tn = 1,3-diaminopropane). The ultimately aim of this work is to assess the effect of the rigidity and volume of the ancillary ligands on the architectures of the Cu^{II}/Cu^{I} mixed-valence polymeric systems, as well as to determine and explain the magnitude of the magnetic coupling through the Cu^{II}–NC–Cu^{I}–CN–Cu^{II} exchange pathway in **1**.

2. Results and discussion

2.1. Syntheses and general characterization

Both compounds (**1** and **2**) were prepared under aerobic conditions, by diffusion through silica gel [16] in a U-tube of aqueous solutions of $K_4[Mo(CN)_8]$ [17] (**1**) or $K_3[Cr(CN)_5(NO)] \cdot H_2O$ [18] (**2**). The opposite positions of the U-tubes were filled by a mixture of a methanolic solution of 2,2′-bipyridyl and $CuCl_2 \cdot 2H_2O$ with an aqueous solution of sodium adipate for **1**, and by an aqueous solution of $CuCl_2 \cdot 2H_2O$ and 1,3-diaminopropane for **2**. Crystal structures determinations of both compounds showed that some of the starting materials ($[Mo(CN)_8]^{4-}$ and $[Cr(CN)_5(NO)]^{3-}$ anions) were not present in the final products and that each asymmetric unit contains a Cu^{I} ion and cyanide anions which were not included as starting materials. This fact indicates that these cyanide metal complexes are acting as source of cyanide anions, as already observed in parent compounds involving copper (II) metal complexes and hexacyanometallate anions [19]. Besides their crucial role as constituent ions in both compounds, these cyanide anions also act as reducing agents for the reduction of a fraction of the aqueous Cu^{II} ions into Cu^{I}, presumably with formation of cyanogen or cyanate as previously reported for other cases [20]. All attempts to obtain compound **1** by direct combination, using aqueous solution of NaCN instead of the cyanometallate complexes, failed. In contrast, when NaCN and $[Cu(tn)_2]^{2+}$ ions were used as starting materials (tn = 1,3-propanediamine), compound **2** was obtained as a mixture with a second phase, of formula $[Cu(tn)_2][Cu_2(CN)_4]$, analogue to the previously reported complexes $[Cu(en)_2(H_2O)][Cu_2(CN)_4]$ [14e] and $[Cu(pn)_2(H_2O)][Cu_2(CN)_4]$ [13d] (pn = 1,2-propanediamine), which exhibit a single diamond-like mixed-valence network. The infrared spectra of **1** and **2** exhibit the bands expected for compounds built with $[Cu(bpy)]^{2+}$ (for **1**), $[Cu(tn)_2]^{2+}$ (for **2**) and CN units (in both compounds). The presence of the CN ligands is clearly indicated by strong absorption bands assignable to ν_{CN} stretching vibrations in the 2080–2187 cm^{-1} range. Previous studies have shown that the positions and number of these absorption bands in compounds involving cyanide bridges can be used as a diagnostic tool for identifying the oxidation state and the coordination of the metal ion, as well as for detecting the presence of cyanide bridges [19,21]. Free CN ion is typically characterized by an absorption band at *ca.* 2080 cm^{-1} [22]; its coordination to on or more metal ions results in an increase for these wave numbers and increase of the metal coordination number can result in a decrease in the ν(CN) band by about 20–40 cm^{-1} [21]. For compound **1**, the three absorption bands observed at 2187, 2114 and 2080 cm^{-1} are in agreement with the presence in **1** of μ_2- and μ_3-cyanide bridges. In contrast, for compound **2**, only one absorption band is observed at 2110 cm^{-1}. It is also well known that IR spectroscopy can be used as a diagnostic tool for identifying the coordination mode of the bpy ligand [23]; chelate coordination mode usually splits the strong γ(CH) absorption observed as an intense and sharp band at 757 cm^{-1} in the free bpy in an asymmetric doublet. The presence of such doublet on the spectrum (764(s) and 729(m) cm^{-1}) clearly indicates that the bpy ligands present their usual chelating coordination mode. Finally, the 1,3-diaminopropane ligand is easily characterized by the presence on the IR spectrum of bands due to ν_{NH} stretching vibrations of the NH_2 groups at 3302 and 3245 cm^{-1} and to the ν_{CH} stretching vibrations of the CH_2 groups around 2900 cm^{-1} [19,24].

2.2. Crystal structures of **1** and **2**

Both compounds **1** and **2** crystallize in the monoclinic space group $P2_1/n$. ORTEP plots and perspective views are shown in Figs. 1–5; selected inter-atomic distances and angles for compounds **1** and **2**, and pertinent crystal data are listed in Tables 1–3, respectively.

*$[Cu^{II}(bpy)Cu^{I}(CN)_3]_n$ (**1**):* The asymmetric unit of compound **1** consists of two Cu atoms, one bpy unit and three CN ions, all in general positions (Fig. 1, Table 1). The two non-equivalent copper ions strongly differ in their environments. Thus, the Cu1 ion, presumably a Cu^{I} centre, presents a CuC_4 coordination involving four carbon atoms from four cyano ligands; the environment is pseudo-tetrahedral as clearly shown by the respective C–Cu–C angles (in the range 102.3–118.3°, with an average value of 109.5°). The C1 carbon atom acts as an almost symmetrical bridge towards two Cu1 ions with Cu1–C1 bond distances of 2.160(9) and

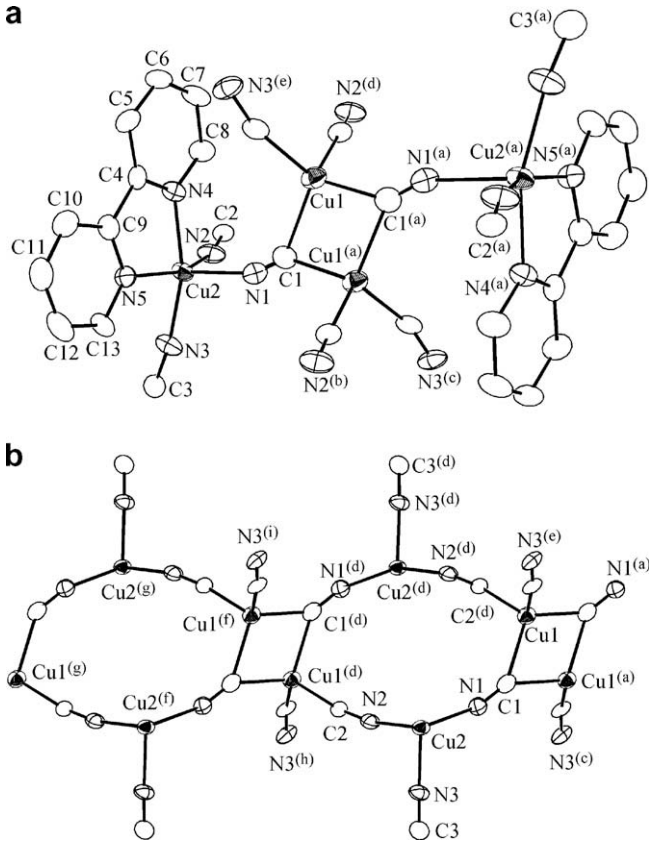


Fig. 1. ORTEP views of compound **1** showing: (a) the atom labelling scheme and the Cu^{I} and Cu^{II} environments and (b) the μ_2- and the μ_3-cyanide bridges (the bpy ligands are omitted for the sake of clarity). The shortest Cu···Cu distances (Å) are: $Cu1\cdots Cu1^{(a)}$ = 2.536(1), Cu1···Cu2 = 4.863(1), $Cu1\cdots Cu2^{(e)}$ = 4.963(1) and $Cu1\cdots Cu2^{(d)}$ = 5.012(1). Symmetry transformations used to generate equivalent atoms: (a) $-x,-y,-z$; (b) $-1+x,y,z$; (c) $-1/2+x,1/2-y,-1/2+z$; (d) $1-x,-y,-z$; (e) $1/2-x,-1/2+y,1/2-z$; (f) $1+x,y,z$; (g) $2-x,-y,-z$; (h) $1/2+x,1/2-y,-1/2+z$; (i) $3/2-x,-1/2+y,1/2-z$.

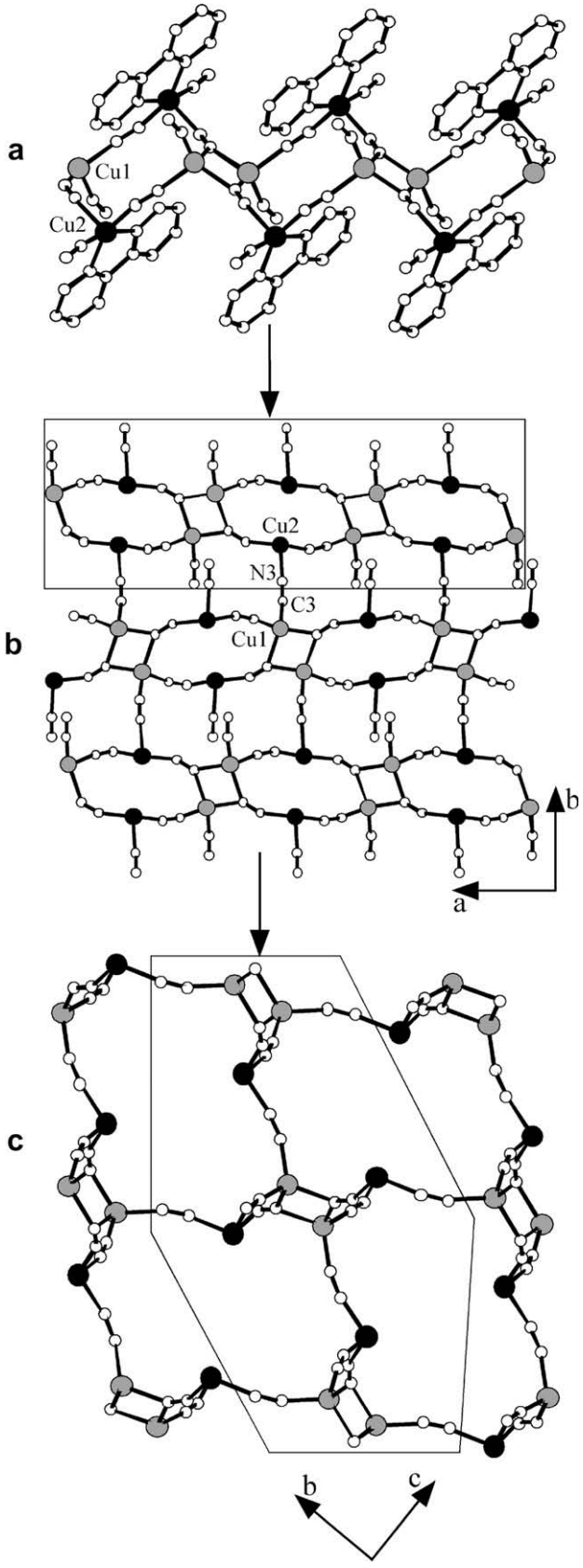


Fig. 2. (a) Schematic view of **1** showing the simplest way to describe the sophisticated three-dimensional structure: 1-D motifs (a) bridged through N3–C3 generates the 2-D units (b) which are connected each other through the N3–C3 bridges to lead to the 3-D structure of **1** (c) Cu1···Cu2 distance through the C3N3 bridges: 4.962 Å. The bpy ligands are omitted for the sake of clarity.

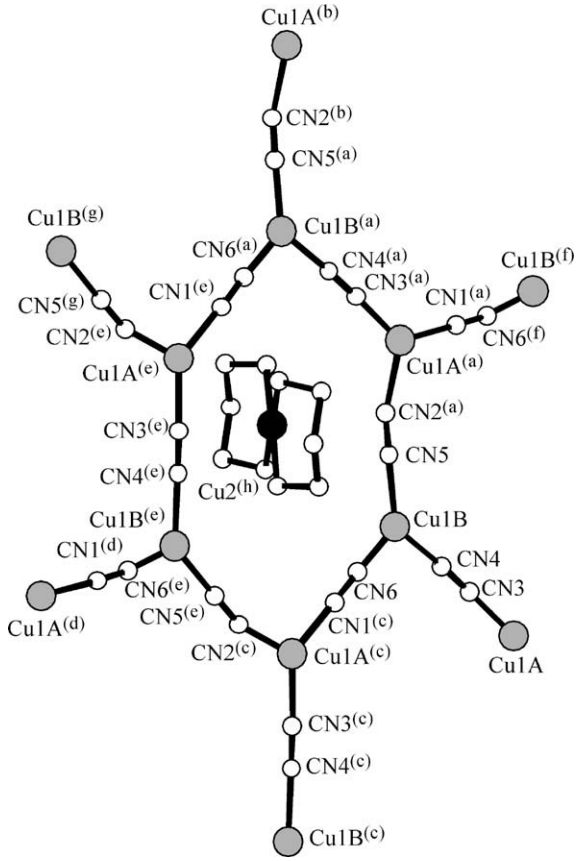


Fig. 3. Perspective view of compound **2** showing the atom labelling scheme and the Cu_6 metallacycles. The shortest Cu···Cu distances (Å) are: Cu^{I}–CN–Cu^{I}: $Cu1A^{(c)}$···Cu1B = 5.008(1), Cu1B···$Cu1A^{(a)}$ = 4.959(1) and $Cu1A^{(a)}$···$Cu1B^{(a)}$ = 4.997(1); Cu^{II}···Cu^{I}: $Cu2^{(h)}$···$Cu1A^{(c)}$ = 6.222(1), $Cu2^{(h)}$···Cu1B = 4.396(1), $Cu2^{(h)}$···$Cu1A^{(a)}$ = 4.133(1), $Cu2^{(h)}$···$Cu1B^{(a)}$ = 5.492(1), $Cu2^{(h)}$···$Cu1A^{(e)}$ = 5.322(1) and $Cu2^{(h)}$···$Cu1B^{(e)}$ = 5.633(1). Symmetry transformations used to generate equivalent atoms: (a) $x, 1+y, z$; (b) $x, 2+y, z$; (c) $1/2+x, -1/2-y, 1/2+z$; (d) $1+x, 1+y, 1+z$; (e) $1/2+x, 1/2-y, 1/2+z$; (f) $-1/2+x, 1/2-y, -1/2+z$; (g) $1/2+x, 3/2-y, 1/2+z$.

2.121(10) Å. These distances are significantly longer than the other two Cu1–C ones (1.951(9) and 1.965(10) Å). The Cu2 ion, presumably a Cu^{II} centre, has a CuN_5 coordination environment involving two nitrogen atoms from a bidentate bpy ligand and three nitrogen atoms from three non-equivalent CN ligands. The metal ion is located in an almost perfect square-pyramidal geometry as indicated by the low value of the trigonality Addison index, τ, of 0.10 [$\tau = (\beta - \alpha)/60$, where α and β are the two greatest basal plane angles ($\beta \geqslant \alpha$) when the polyhedron is viewed as a square-pyramid; for a perfectly square-pyramidal geometry τ is equal to zero and it becomes unity for a perfectly trigonal bipyramidal geometry [25]. For Cu2 α = N2–Cu2–N5 = 158.4(2)° and β = N3–Cu2–N4 = 164.3(2)°]. This slightly distorted square-pyramidal geometry is in good agreement with the structural data which indicate that the four equatorial bond lengths are essentially equivalent (from 1.968(8) to 2.047(6) Å) with the two Cu–N_{bpy} bond lengths only *ca.* 0.02 Å longer than the two basal Cu–NC ones; the Cu2–N1 apical bond length is significantly longer (2.170(8) Å). The three cyano ligands differ in their coordination modes. The C2N2 and C3N3 groups have μ_2 coordination modes with the carbon and nitrogen atoms bonded to Cu1 and Cu2, respectively (Cu1–C and N–Cu2 *ca.* 1.96 and 1.97 Å, respectively). The C1N1 cyano group acts with a μ_3 coordination mode; this ligand, which bridges two Cu1 and one Cu2 ions, involves Cu–C and Cu–N bond lengths longer than those given above (*ca.* 2.14 and 2.17 Å, respectively). These coordination modes lead to the 3-D structure shown in Fig. 2. The sim-

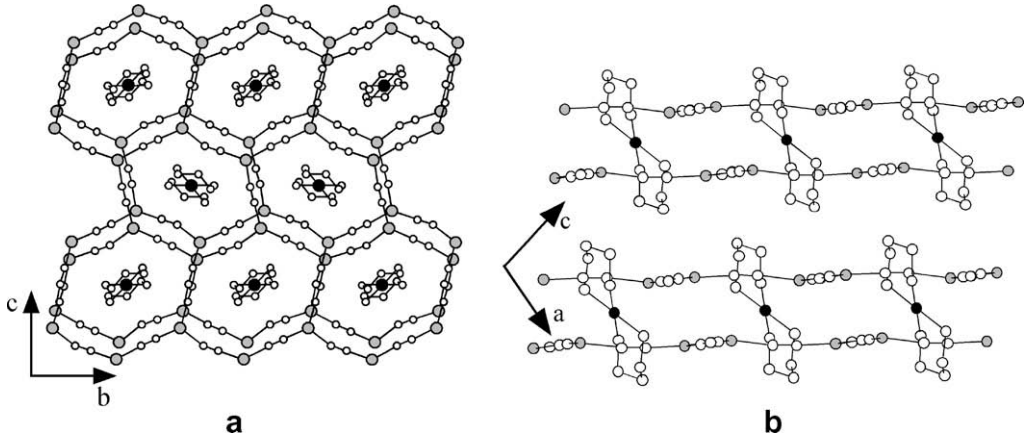


Fig. 4. Extended structure of **2**: (a) 2-D sheets showing the hexagonal infinite cavities and (b) projection of the overall structure in the *ac* plane.

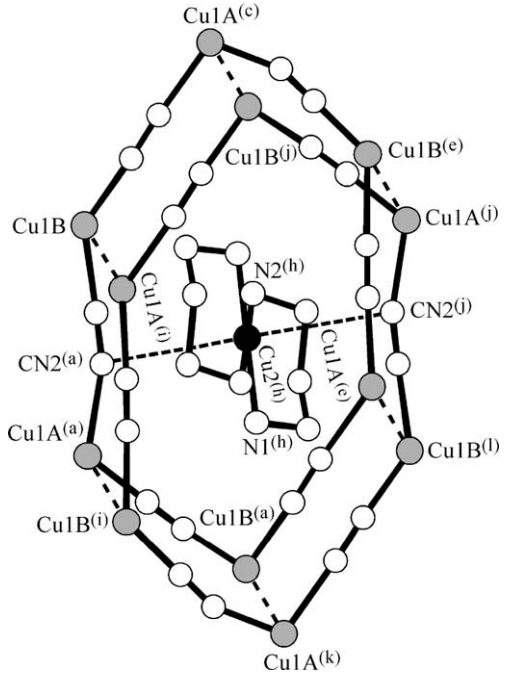


Fig. 5. Compound **2**: perspective view of two adjacent Cu_6 metallacycles showing the tn ligand and the elongated octahedral environment of the Cu2 metal ion as two steric constrains in the molecular arrangement depicted in Fig. 4. Shortest Cu···Cu inter-metallacycle distance: 3.382(1) Å; Cu2(h)···CN2$^{(a)}$ (CN2$^{(j)}$) 3.107(1) Å. Symmetry transformations used to generate equivalent atoms: (a) $x,-1+y,z$; (c) $1/2+x,-1/2-y,1/2+z$; (e) $1/2+x,1/2-y,1/2+z$; (h) $2-x,-y,1-z$; (i) $3/2-x,1/2+y,3/2-z$; (j) $2-x,-y,2-z$; (k) $3/2-x,3/2+y,3/2-z$; (l) $2-x,1-y,2-z$.

Table 1
Selected bond lengths (Å) and angles (°) for **1**.

Cu1–C1	2.160(9)	Cu2–N3	1.968(8)
Cu1–C1$^{(a)}$	2.121(10)	Cu2–N4	2.032(6)
Cu1–C2$^{(d)}$	1.965(10)	Cu2–N5	2.047(6)
Cu1–C3$^{(e)}$	1.951(9)	N1–C1	1.126(10)
Cu2–N1	2.170(8)	N2–C2	1.146(10)
Cu2–N2	1.979(8)	N3–C3	1.155(9)
C1–Cu1–C1$^{(a)}$	107.4(3)	N2–Cu2–N5	158.4(2)
C1–Cu1–C2$^{(d)}$	102.3(3)	N3–Cu2–N4	164.3(2)
C1–Cu1–C3$^{(e)}$	118.3(3)	N3–Cu2–N5	92.3(3)
C1$^{(a)}$–Cu1–C2$^{(d)}$	111.5(3)	N4–Cu2–N5	79.2(2)
C1$^{(a)}$–Cu1–C3$^{(e)}$	109.2(3)	Cu1–C1–Cu1$^{(a)}$	72.6(3)
C2$^{(d)}$–Cu1–C3$^{(e)}$	108.1(3)	Cu1–C1–N1	143.1(7)
N1–Cu2–N2	104.3(3)	Cu1$^{(a)}$–C1–N1	144.0(7)
N1–Cu2–N3	106.2(2)	Cu1–C2$^{(d)}$–N2$^{(d)}$	171.4(7)
N1–Cu2–N4	87.8(2)	Cu1–C3$^{(e)}$–N3$^{(e)}$	163.8(6)
N1–Cu2–N5	95.1(2)	Cu2–N1–C1	154.6(6)
N2–Cu2–N3	91.9(2)	Cu2–N2–C2	164.4(6)
N2–Cu2–N4	91.5(2)	Cu2–N3–C3	168.6(6)

Symmetry transformations used to generate equivalent atoms: (a) $-x,-y,-z$; (d) $1-x,-y,-z$; (e) $1/2-x,-1/2+y,1/2-z$.

Table 2
Selected bond lengths (Å) and angles (°) for **2**.

Cu1A–CN1	1.929(7)	CN1$^{(c)}$–CN6	1.156(8)
Cu1A–CN2	1.957(6)	CN2$^{(a)}$–CN5	1.144(8)
Cu1A–CN3	1.930(7)	CN3–CN4	1.134(7)
Cu1B–CN4	1.936(6)	Cu2–N1	2.033(5)
Cu1B–CN5	1.927(8)	Cu2–N2	1.989(5)
Cu1B–CN6	1.945(5)		
Cu1A$^{(a)}$–CN1$^{(a)}$–CN6$^{(f)}$	174.2(6)	CN1–Cu1A–CN3	130.7(3)
Cu1A$^{(a)}$–CN2$^{(a)}$–CN5	160.3(6)	CN1–Cu1A–CN2	111.4(3)
Cu1A–CN3–CN4	178.0(6)	CN3–Cu1A–CN2	117.8(2)
Cu1B–CN4–CN3	176.1(6)	CN5–Cu1B–CN4	133.1(2)
Cu1B–CN5–CN2$^{(a)}$	177.5(6)	CN5–Cu1B–CN6	117.6(2)
Cu1B–CN6–CN1$^{(c)}$	172.5(6)	CN4–Cu1B–CN6	108.2(2)

Symmetry transformations used to generate equivalent atoms: (a) $x,1+y,z$; (c) $1/2+x,-1/2-y,1/2+z$; (f) $-1/2+x,1/2-y,-1/2+z$.

plest way to describe this complicated 3-D molecular arrangement is to consider as initial building block the infinite chains formed by alternating 12-membered and four-membered cycles (Figs. 1b and 2a). The first cycle, involving four Cu ions (two Cu1 and two Cu2), is a tetranuclear mixed-valence cycle alternating Cu^{I} and Cu^{II} ions which are bridged by end-on cyanide anions, with a shortest Cu···Cu distance of 4.863(1) Å; the second cycle, involving only two Cu1 ions, is generated by the two Cu^{I} ions bridged by the C1 atoms of the μ_3-cyanide anions, the short Cu···Cu distance of 2.536(2) Å is considered nonbonding but shorter than the sum of van der Waals radii for copper (2.8 Å) [26], suggesting significant Cu–Cu interactions. These mixed-valence copper chains are bridged each other through the C3N3 cyano ligand to generate 2-D layers (Fig. 2b) in which the shortest interchain Cu–NC–Cu distance is 4.963(1) Å. The union of adjacent layers by additional C3N3 cyano ligands generates the 3-D structure depicted in Fig. 2c.

*$\{[Cu^{II}(tn)_2][Cu^{I}_4(CN)_6]\}_n$ (**2**):* The asymmetric unit of compound **2** consists of three crystallographically different Cu ions (Cu1A, Cu1B and Cu2) one tn unit and three CN anions (Fig. 3, Table 2); except the Cu2 atom, which lies on an inversion centre in the $[Cu(tn)_2]^{2+}$ units, all these elements are located on general positions. Since there are four Cu^{I} and one Cu^{II} atoms per formula unit, the Cu2

Table 3
Pertinent crystallographic data and structural refinement details for **1** and **2**.

	1	2
Empirical formula	$C_{13}H_8N_5Cu_2$	$C_{12}H_{20}N_{10}Cu_5$[a]
Formula weight	361.32	622.08[a]
Crystal system	monoclinic	monoclinic
Space group	$P2_1/n$ (no. 14)	$P2_1/n$ (no. 14)
a (Å)	8.309(1)	9.838(2)
b (Å)	13.959(2)	8.945(2)
c (Å)	10.815(1)	11.412(2)
β (°)	90.36(1)	97.48(2)
V (Å^3)	1254.4(3)	995.6(2)
Z	4	2[a]
D_{calc} (g cm^{-3})	1.913	2.075
μ (cm^{-1})	33.84	52.72
T (K)	250	170
No. of reflections	3794	4886
Reflections unique [R_{int}]	1063 [0.040]	1510 [0.064]
No. of reflections [$I > 2\sigma(I)$]	965	1011
N_v	181	124
R_1[b]	0.039	0.042
R_w[c]	0.129	0.084
Goodness-of-fit[d]	1.204	1.080
$\Delta\rho_{max,\ min}$ (e Å^3)	+0.158/−0.588	+0.829/−0.628

[a] For compound **2**, the asymmetric unit contains 0.5 of the empirical formula.
[b] $R_1 = \sum|F_o - F_c|/F_o$.
[c] $wR_2 = \{\Sigma[w(F_o^2 - F_c^2)^2]/\Sigma[w(F_o^2)^2]\}^{1/2}$.
[d] Goodness-of-fit = $\{\Sigma[w(F_o^2 - F_c^2)^2]/(N_{obs} - N_{var})\}^{1/2}$.

atoms must be Cu^{II} whereas Cu1A and Cu1B must be Cu^{I} since the asymmetric unit contains two Cu1A, two Cu1B and one Cu2 per formula unit. Nevertheless, the disorder affecting the CN groups (see Section 3) precludes an unambiguous assignment of the oxidation state. The non-equivalent copper ions strongly differ in their environments. Thus, the Cu2 atom presents a centrosymmetric CuN_4 coordination environment involving four nitrogen atoms from two bidentate tn ligands with an almost perfect square planar geometry; while the Cu1A and Cu1B atoms are coordinated to three cyano groups acting as bridging ligands (Fig. 3). The coordination modes of the cyano ligands generate eighteen-membered cycles having six metallic centres (Figs. 3 and 4); the Cu_6 core is a pseudo hexagon with Cu···Cu distances of *ca.* 5.0 Å. Each hexametallacycle forms a cavity in which the $[Cu(tn)_2]^{2+}$ unit is located; the shortest Cu2–Cu1 distance is 4.133(1) Å. The Cu1 atoms lead to essentially planar metallocycles that are connected to their six neighbors to generate hexagonal graphite-like 2-D sheets (Fig. 4); these sheets stack in an eclipsed way forming hexagonal channels as shown in Fig. 4a. These hexagonal sheets are similar to those found in $K[Cu_2(CN)_3]\cdot H_2O$ [27]; the difference is that in $K[Cu_2(CN)_3]\cdot H_2O$ the large hexagonal holes are filled by isolated potassium ions and water molecules, whereas in **2**, the hexagonal channels are filled with planar $[Cu(tn)_2]^{2+}$ units that point their two axial vacant positions towards two CN atoms ($CN2^{(a)}$ and $CN2^{(j)}$ at a distance of 3.107(1) Å) of two adjacent eclipsed hexagonal sheets. The presence of these $[Cu(tn)_2]^{2+}$ units confers electroneutrality to the layers and keeps them at a close distance, with a relatively short inter-planar Cu1···Cu1 distance of 3.382(1) Å, as shown in Fig. 5. Such interaction between the $[Cu(tn)_2]^{2+}$ units and the hexagonal layers suggests that the geometry and size of the cation may play a crucial role in determining the interlayer spacing, the metallacycle topology, the channel dimensions, and therefore, the overall structure of the copper cyanide networks.

2.3. Magnetic properties

The thermal variation of the product of the molar magnetic susceptibility times the temperature ($\chi_m T$) for compound **1** shows at room temperature a value of *ca.* 0.39 emu K mol^{-1} per formula unit, that remains constant when the temperature is decreased down to *ca.* 25 K (Fig. 6). Below *ca.* 25 K the $\chi_m T$ product gradually increases to reach a value of *ca.* 0.44 emu K mol^{-1} at 2 K. The room temperature value confirms the presence of one paramagnetic Cu^{II} ion per formula unit (the spin only value is 0.375 emu K mol^{-1}). Nevertheless, from the structure of compound **1**, it should be expected the absence of any significant magnetic interaction since all the Cu^{II} ions (Cu2) are only connected by long –NC–Cu^{I}–CN– bridges (Figs. 1 and 2). The presence of a weak, although noticeable ferromagnetic interaction in compound **1** suggests that the "diamagnetic" –NC–Cu^{I}–CN– bridge is able to transmit such kind of magnetic interaction, as found in other similar "diamagnetic" –NC–Fe(II)–CN– bridges [28]. Note that this result resembles the coupling found in the Prussian blue derivatives with the "a priori" also "diamagnetic" –NC–Fe(II)–CN– bridges [29]. Since the structure of compound **1** shows the presence of several –NC–Cu^{I}–CN– bridges connecting the Cu^{II} ions in the three directions, we have tried to fit the magnetic properties of compound **1** with a simple Curie–Weiss law: $\chi_m = C/(T-\theta)$. This model reproduces very satisfactorily the magnetic properties of compound **1** with a Curie constant, $C = 0.3872(1)$ emu K mol^{-1}, corresponding to a g value of 2.0323(2) and with a weak and positive Weiss temperature, $\theta = 0.239(1)$ $K = 0.166(1)$ cm^{-1} that confirms the ferromagnetic character of the magnetic coupling (solid line in Fig. 6). Compound **2** also shows at room temperature a $\chi_m T$ value of *ca.* 0.39 emu K mol^{-1} that remains constant down to *ca.* 20 K (Fig. 6). Below *ca.* 20 K the $\chi_m T$ product smoothly decreases to reach a value of *ca.* 0.37 emu K mol^{-1} at 2 K. This tiny decrease suggests the presence of very weak, almost negligible, antiferromagnetic interactions. The structure of compound **2** shows that the Cu^{II} ions are quite well isolated except for the long Cu^{II}–(CN2)–Cu^{II} bridge (Fig. 5). This long monoatomic bridge (C/N) connects the Cu^{II} ions forming regular ···Cu^{II}–(C/N)–Cu^{II}··· chains where the magnetic coupling is expected to be almost negligible given the long bond distance (*ca.* 3.1 Å). Accordingly, we have fit the magnetic properties of compound **2** to a regular $S = 1/2$ antiferromagnetic chain with the model of Hatfield and co-workers [30]. This model reproduces very satisfactorily the magnetic properties of compound **2** with $g = 2.0297(1)$ and a very small intra-chain coupling constant $J = -0.11(1)$ K $= -0.075(1)$ cm^{-1} (solid line in Fig. 6), the Hamiltonian is written as $H = -JS_iS_{i+1}$.

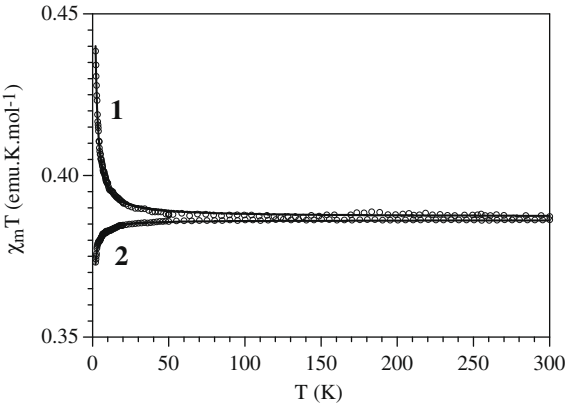


Fig. 6. Thermal variation of the $\chi_m T$ product for compounds **1** and **2**. Solid lines represent the best fit to models (see text).

The isothermal magnetizations at 2 K of the two compounds confirm the presence of very weak magnetic interactions in both compounds (Fig. 7). Thus, the magnetization of compounds **1** and **2** can be well reproduced with a Brillouin function for an $S = 1/2$ spin ground state with g values of 2.085(8) and 2.0262(2), respectively (solid lines in Fig. 7). As expected, the obtained g value is

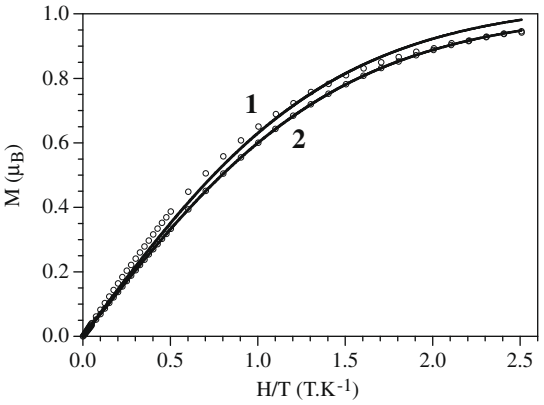


Fig. 7. Isothermal magnetization at 2 K of compounds **1** and **2**. Solid lines show the best fit to the Brillouin function.

slightly higher in compound **1** and the experimental points are above the curve fit at low fields, confirming the presence of a weak ferromagnetic interaction whereas in compound **2** the *g* value is very similar to that found in the fit of the thermal variation of the magnetic susceptibility, confirming the absence of any significant magnetic interaction. Although the magnetic properties of compound **2** could be easily anticipated given the well isolation of the Cu^{II} ions in the structure, those of compound **1** are more surprising. Compound **1** is expected to be paramagnetic since the Cu^{II} ions are connected through the "diamagnetic" –NC–Cu^{I}–CN– bridges. Nevertheless, as for previous Prussian blue and its derivatives containing diamagnetic –NC–Fe(II)–CN– bridges [28,29], such magnetic coupling (even ferromagnetic), can be explained thanks to the presence of some spin density in the Cu^{I} ions.

3. Experimental

3.1. Materials and physical techniques

The reagents 2,2′-bipyridine, 1,3-diaminopropane, copper(II) chloride dihydrate and sodium cyanide were used as received. Silica gel [16], $K_4[Mo(CN)_8] \cdot 2H_2O$ [17] and $K_3[Cr(CN)_5(NO)] \cdot H_2O$ [18] were prepared according to the reported procedures. Infrared spectra were recorded in the range 4000–200 cm^{-1} as KBr pellets on a FT-IR NEXUS NICOLET Spectrometer. Variable temperature susceptibility measurements were carried out in the temperature range 2–300 K with an applied magnetic field of 0.1 T on polycrystalline samples of both compounds with a Quantum Design MPMS-XL-5 SQUID magnetometer. The susceptibility data were corrected for the sample holders previously measured using the same conditions and for the diamagnetic contributions of the salt as deduced by using Pascal's constant tables ($\chi_{dia} = -184 \times 10^{-6}$ and -287.4×10^{-6} emu mol^{-1} for **1** and **2**, respectively). Elemental analyses were obtained from the Service Central d'Analyses (Vernaison).

3.2. Syntheses of compounds *1* and *2*

*$[Cu^{II}(bpy)Cu^{I}(CN)_3]_n$ (**1**):* Under aerobic conditions, a methanolic solution (10 mL) of 2,2′-bipyridine, $C_{10}H_8N_2$ (312 mg, 2.0 mmol) was added, with stirring at room temperature to a methanolic solution (5 mL) of $CuCl_2 \cdot 2H_2O$ (341 mg, 2.0 mmol). A pale green precipitate quickly appeared in the green solution; a 0.2 M aqueous solution of sodium adipate $Na_2O_2C(CH_2)_4CO_2$ was then slowly added with stirring until complete dissolution of the precipitate (*ca.* 10 mL). Silica gel was placed into a U-tube. Diffusion in opposite directions of an aqueous solution (15 mL) of $K_4[Mo(CN)_8]$ (2.048 g, 5.0 mmol) and the blue solution prepared above (15 mL) for two weeks led to dark brown prismatic single crystals of **1** suitable for X-ray structure analysis. For **1**: *Anal.* Calc. for $C_{13}H_8N_5Cu_2$: C, 43.2; H, 2.2; N, 19.4. Found: C, 43.0; H, 2.1; N, 19.7%. Selected IR data: ν/cm^{-1}: 3436sbr, 3081w, 2187m, 2114s, 2080s, 1608m, 1598s, 1575w, 1566w, 1470m, 1444s, 1311w, 1247w, 1172m, 1161m, 1104m, 1065m, 1028m, 1015w, 764s, 729m, 650w, 417w.

*$\{[Cu^{II}(tn)_2][Cu^{I}_4(CN)_6]\}_n$ (**2**):* Under aerobic conditions, 1,3-diaminopropane (2.0 mL, 23.7 mmol) was added with stirring at room temperature to an aqueous solution (30 mL) of $CuCl_2 \cdot 2H_2O$ (4.04 g, 23.7 mmol). A pale green precipitate quickly appeared in the green solution, a 1 M aqueous solution of NaOH was slowly added with stirring until complete dissolution of the precipitate (*ca.* 24 mL) leading to a dark blue solution. Silica gel was placed into a U-tube; diffusion in opposite directions of 15 mL of an aqueous solution of $K_3[Cr(CN)_5(NO)] \cdot H_2O$ (1.737 g, 5 mmol) and 15 mL of the dark blue solution prepared above for four weeks afforded compound **2** as pink prismatic crystals. They were filtered and separated manually from the gel. For **2**: *Anal.* Calc. for $C_{12}H_{20}N_{10}Cu_5$: C, 23.2; H, 3.2; N, 22.5. Found: C, 23.0; H, 3.3; N, 22.7%. Selected IR data: ν/cm^{-1}: 3442br, 3302s, 3245s, 2942w, 2891w, 2110s, 1586s, 1565m, 1285m, 1179m, 1095w, 1028s, 901m, 884w, 668m, 626w, 495m, 362m.

3.3. X-ray crystallography

Data for compounds **1** and **2** were collected on a Xcalibur 2 Diffractometer (Oxford Diffraction) using a graphite monochromated Mo Kα radiation ($\lambda = 0.71073$ Å). The unit cell determination and data reduction were performed using the CRYSALIS program suite [31] on the full set of data. For the two compounds, the crystal structures were solved by direct methods and successive Fourier difference syntheses with the SIR97 program [32] and refined on F^2 by weighted anisotropic full-matrix least-square methods using the SHELXL97 program [33]. Both softwares were used within the WINGX package [34]. After locating all the non-hydrogen atoms in each structure, the models were refined, first using isotropic and finally anisotropic thermal displacement parameters. The position of hydrogen atoms were then calculated and included as isotropic fixed contributors to F_c. Since there is a tendency for the bridging CN groups to have end-for-end disorder in these compounds we have performed several refinements for each structure. For **1**, the best refinement corresponds unambiguously to the model without disorder, the nitrogen atoms of the three CN groups (N1, N2 and N3) were bonded to the Cu^{II} metal ion (Cu2) while the three carbon atoms were bonded to the Cu^{I} metal ion (Cu1). For **2**, the bridging cyano groups were disordered and then each position of the N and C atoms was modeled with a pseudo atom having 50% of C and 50% of N character; the corresponding fictive atom of each position was labelled CN (CN1, CN2, etc.), as reminder of the crystallographic disorder.

4. Conclusion

In summary, we have shown that it is possible to prepare novel mixed-valence Cu^{II}/Cu^{I} cyano compounds with different neutral co-ligands as 2,2′-bipyridine (compound **1**) and 1,3-diaminopropane (compound **2**) presenting extended (3-D in **1** and 2-D in **2**) structures. Compound **1** presents a weak ferromagnetic coupling between the Cu^{II} ions through the "diamagnetic" –NC–Cu^{I}–CN– bridges. This unexpected behavior shows that this kind of bridge is able to transmit weak ferromagnetic coupling, as the –NC–Fe(II)–CN– bridges in the Prussian blue and derivatives.

Supplementary data

CCDC 703838 and 703839 contain the supplementary crystallographic data for compound **1** and **2**, respectively. These data can be obtained free of charge via http://www.ccdc.cam.ac.uk/conts/retrieving.html, or from the Cambridge Crystallographic Data Centre, 12 Union Road, Cambridge CB2 1EZ, UK; fax: (+44) 1223-336-033; or e-mail: deposit@ccdc.cam.ac.uk.

Acknowledgments

This work has been supported by the CNRS (Centre National de la Recherche Scientifique), the European Union (MAGMANet network of excellence, COST Actions D35-WG) and the Spanish Ministerio de Educación y Ciencia (Projects MAT2007-61584 and Consolider-Ingenio 2010 CSD 2007-00010 in Molecular Nanoscience).

References

[1] (a) S. Tanase, F. Tuna, P. Guionneau, T. Maris, G. Rombaut, C. Mathionière, M. Andruh, O. Khan, J.-P. Sutter, Inorg. Chem. 42 (2003) 1625;
(b) H. Kou, S. Gao, J. Zhang, G.-H. Su, R.K. Zheng, X.X. Zhang, J. Am. Chem. Soc. 123 (2001) 11809;
(c) M. Ohba, N. Usuki, N. Fukita, H. Okawa, Angew. Chem., Int. Ed. 38 (1991) 795.
[2] (a) C. Mathoniere, R. Podgajny, P. Guionneau, C. Labrugere, B. Sieklucka, Chem. Mater. 17 (2005) 442;
(b) J.M. Herrera, V. Marvaud, M. Verdaguer, J. Marrot, M. Kalisz, C. Mathonière, Angew. Chem., Int. Ed. 43 (2004) 5468;
(c) Y. Arimoto, S.I. Ohkoshi, Z.J. Zhong, H. Seino, Y. Mizobe, K. Hashimoto, J. Am. Chem. Soc. 125 (2003) 9240;
(d) G. Rombaut, S. Golhen, L. Ouahab, C. Mathonière, O. Kahn, J. Chem. Soc., Dalton Trans. (2000) 3609.
[3] (a) Y. García, V. Niel, M.C. Muñoz, J.A. Real, Top. Curr. Chem. 233 (2004) 229;
(b) V. Niel, A.L. Thompson, A.E. Goeta, C. Enachescu, A. Hauser, A. Galet, M.C. Munoz, J.A. Real, Chemistry 11 (2005) 2047;
(c) C.P. Berlinguette, A. Dragulescu-Andrasi, A. Sieber, J.R. Galán-Mascarós, H.-U. Güdel, C. Achim, K.R. Dunbar, J. Am. Chem. Soc. 126 (2004) 6222;
(d) J.A. Real, A.B. Gaspar, V. Niel, M.C. Muñoz, Coord. Chem. Rev. 236 (2003) 121;
(e) A. Galet, V. Niel, M.C. Muñoz, J.A. Real, J. Am. Chem. Soc. 125 (2003) 14224.
[4] (a) H. Yoshikawa, S. Nishikiori, Dalton Trans. (2005) 3056;
(b) J.Y. Yang, M.P. Shores, J.J. Sokol, J.R. Long, Inorg. Chem. 42 (2003) 1403.
[5] J. Lefebvre, R.J. Batchelor, D.B. Leznoff, J. Am. Chem. Soc. 126 (2004) 16117.
[6] (a) K. Inoue, S. Ohkoshi, H. Imai, in: J.S. Miller, M. Drillon (Eds.), Magnetism: Molecules to Materials, vol. 5, Wiley-VCH, Weinheim, 2005, p. 4;
(b) H. Imai, K. Inoue, K. Kikuchi, Y. Yoshida, M. Ito, T. Sunahara, S. Onaka, Angew. Chem., Int. Ed. 43 (2004) 5618;
(c) E. Coronado, C.J. Gómez-García, A. Nuez, F.M. Romero, E. Rusanov, H. Stoeckli-Evans, Inorg. Chem. 41 (2002) 4615;
(d) F. Bellouard, M. Clemente-León, E. Coronado, J.R. Galán-Mascaros, C.J. Gómez-García, F. Romero, K.R. Dunbar, Eur. J. Inorg. Chem. (2002) 1603;
(e) E. Coronado, C.J. Gómez-García, A. Nuez, F.M. Romero, J.C. Waerenborgh, Chem. Mater. 18 (2006) 2670.
[7] S.S. Kaye, J.R. Long, J. Am. Chem. Soc. 127 (2005) 6506.
[8] F. Ricci, G. Paleschi, Biosen. Bioelec. 21 (2005) 389.
[9] (a) Z.-H. Ni, H.-Z. Kou, L.-F. Zhang, C. Ge, A.-L. Cui, R.-J. Wang, Y. Li, O. Sato, Angew. Chem., Int. Ed. 44 (2005) 7742;
(b) H. Misayaka, H. Takahashi, T. Madanbashi, K. Sugiura, R. Clérac, H. Nojori, Inorg. Chem. 44 (2005) 5969;
(c) D. Li, S. Parkin, G. Wang, G.T. Yee, A.V. Prosvirin, S.M. Holmes, Inorg. Chem. 44 (2005) 4903;
(d) S. Wang, J.-L. Zuo, H.-C. Zhou, H.-J. Choi, Y. Ke, J.-R. Long, X.-Z. You, Angew. Chem., Int. Ed. 43 (2004) 5940;
(e) C.P. Berlinguette, D. Vaughn, C. Cañada-Vilalta, J.R. Galán-Mascarós, K.R. Dunbar, Angew. Chem., Int. Ed. 42 (2003) 1523;
(f) J.J. Sokol, A.G. Hee, J.R. Long, J. Am. Chem. Soc. 124 (2002) 7656.
[10] (a) M. Ferbinteanu, H. Miyasaka, W. Wernsdorfer, K. Nakata, K. Sugiura, M. Yamashita, C. Coulton, R. Clérac, J. Am. Chem. Soc. 127 (2005) 3090;
(b) S. Wang, J.-L. Zuo, S. Gao, Y. Song, H.-C. Zhou, Y.-Z. Zhang, X.-Z. You, J. Am. Chem. Soc. 126 (2004) 8900;
(c) R. Lescouëzec, J. Vaissermann, C. Ruiz-Pérez, F. Lloret, R. Carrasco, M. Julve, M. Verdaguer, Y. Dromzée, D. Gatteschi, W. Wernsdorfer, Angew. Chem., Int. Ed. 42 (2003) 1483;
(d) M.L. Toma, R. Lescouëzec, F. Lloret, M. Julve, J. Vaissermann, M. Verdaguer, Chem. Commun. (2003) 1850.
[11] R. Lescouëzec, L.M. Toma, J. Waisserman, M. Verdaguer, F.S. Delgado, C. Ruiz-Pérez, F. Lloret, M. Julve, Coord. Chem. Rev. 249 (2005) 2691.
[12] (a) E. Colacio, J.M. Domínguez-Vera, F. Lloret, J.M. Moreno Sánchez, R. Kivekäs, A. Rodriguez, R. Sillanpaa, Inorg. Chem. 42 (2003) 4209. and references therein;
(b) D.J. Chesnut, D. Plewak, J. Zubieta, J. Chem. Soc., Dalton Trans. (2001) 2567–2580;
(c) D.J. Chesnut, A. Kusnetzow, R. Birge, J. Zubieta, Inorg. Chem. 38 (1999) 5484;
(d) D.J. Chesnut, J. Zubieta, Chem. Commun. (1998) 1707;
(e) D.J. Chesnut, A. Kusnetzow, J. Zubieta, J. Chem. Soc., Dalton Trans. (1998) 4081.
[13] (a) T. Pretsch, I. Brudgam, H.Z. Hartl, Z. Anorg. Allg. Chem. 629 (2003) 942;
(b) J. Muhle, W.S. Sheldrick, Z. Anorg. Allg. Chem. 629 (2003) 2097;
(c) T. Kromp, W.S. Sheldrick, C. Nather, Z. Anorg. Allg. Chem. 629 (2003) 45. and references therein;
(d) E. Colacio, R. Kivekäs, F. Lloret, M. Sundberg, J. Suárez-Varela, M. Bardají, A. Laguna, Inorg. Chem. 41 (2002) 5141;
(e) G.A. Bowmaker, H. Hartl, V. Urban, Inorg. Chem. 39 (2000) 4548;
(f) O. Teichert, W.S. Sheldrick, Z. Anorg. Allg. Chem. 626 (2000) 1509.
[14] (a) Y. Song, Y. Xu, T.-W. Wang, Z.-X. Wang, X.-Z. You, J. Mol. Struct. 796 (2006) 36;
(b) J.M. Zheng, S.R. Batten, M. Du, Inorg. Chem. 44 (2005) 3371. and references therein;
(c) D. Kim, J. Koo, C.S. Hong, S. Oh, Y. Do, Inorg. Chem. 44 (2005) 4383;
(d) B. Liu, L. Xu, G.-C. Guo, J.-S. Huang, Inorg. Chem. Commun. 8 (2005) 796;
(e) R.J. Williams, A.C. Larson, D.T. Cromer, Acta Crystallogr., Sect. B 28 (1972) 858.
[15] (a) S.-Z. Zhan, W. Li, J.-G. Wang, A.-Q. Liang, Y.-F. Deng, J. Organomet. Chem. 692 (2007) 3568;
(b) T. Pretsch, J. Ostmann, C. Donner, M. Nahorska, J. Mrozinski, H. Hartl, Inorg. Chimi. Acta 358 (2005) 2558;
(c) J. Černák, M. Orendáč, I. Potočňák, J. Chomič, A. Orendáčová, J. Skoršepa, A. Feher, Coord. Chem. Rev. 224 (2002) 51.
[16] H. Zhang, J. Cai, X.-L. Feng, B.-H. Ye, X.-Y. Li, L.-N. Ji, J. Chem. Soc., Dalton Trans. (2000) 1687.
[17] N.H. Furman, C.O. Miller, Inorg. Synth. 3 (1950) 160.
[18] W.P. Griffith, J. Lewis, G. Wilkinson, J. Chem. Soc. (1959) 872.
[19] (a) S. Triki, J. Sala-Pala, F. Thétiot, C.J. Gómez-García, J.-C. Daran, Eur. J. Inorg. Chem. (2006) 185. and references therein;
(b) E. Colacio, A. Debdoubi, R. Kivekäs, A. Rodriguez, J. Inorg. Chem. (2005) 2860.
[20] A.G. Sharpe, in: G. Wilkinson, R. Gillard, J.A. McCleverty (Eds.), Comprehensive Coordination Chemistry, vol. 2, Pergamon Press, Oxford, 1987, pp. 7–14.
[21] (a) H. Huang, K. Alvarez, Q. Lui, T.M. Barnhart, J.P. Snyder, J.E. Penner-Hahn, J. Am. Chem. Soc. 118 (1996) 8808;
(b) K. Nakamoto, in: Infrared and Raman spectra of Inorganic Coordination Compounds, 4th Ed., John Wiley and Sons, New York, 1986, p. 273.
[22] N.S. Persky, J.M. Chow, K.A. Poschmann, N.N. Lacuesta, S.L. Stoll, Inorg. Chem. 40 (2001) 29.
[23] A.A. Schilt, R.C. Taylor, J. Inorg. Nucl. Chem. 9 (1959) 211.
[24] N. Mondal, M.K. Saha, B. Bag, S. Mitra, V. Gramlich, J. Ribas, M.S. El Fallah, J. Chem. Soc., Dalton Trans. (2000) 1601.
[25] A.W. Addison, T.N. Rao, J. Reedijk, J. van Rijn, G.C. Verschoor, J. Chem. Soc., Dalton Trans. (1984) 1349.
[26] J.C. Slater, J. Chem. Phys. 41 (1964) 3199.
[27] D.T. Cromer, A.C. Larson, Acta Crystallogr. 15 (1962) 397.
[28] F. Thétiot, S. Triki, J. Sala-Pala, New J. Chem. 26 (2002) 196.
[29] (a) J.M. Herrera, A. Bachschmidt, F. Villain, A. Bleuzen, V. Marvaud, W. Wernsdorfer, M. Verdaguer, Philos. Trans. A 366 (2008) 127;
(b) M. Verdaguer, G. Girolami, in: J.S. Miller, M. Drillon (Eds.), Magnetoscience: Molecules to Materials, vol. 5, Wiley-VCH, Weinheim, 2005, p. 283;
(c) M. Verdaguer, A. Bleuzen, V. Marvaud, J. Vaissermann, M. Seuleiman, C. Desplanches, A. Scuiller, C. Train, R. Garde, G. Gelly, C. Lomenech, I. Rosenman, P. Veillet, C. Cartier dit Moulin, F. Villain, Coord. Chem. Rev. 190 (1999) 1023.
[30] D.B. Brown, J.A. Donner, J.W. Hall, S.R. Wilson, R.B. Wilson, D.J. Hodgson, W.E. Hatfield, Inorg. Chem. 18 (1979) 2635.
[31] Xcalibur CCD System, CRYSALIS Software System, Version 1.171, Oxford Diffraction Ltd., 2005.
[32] A. Altomare, M.C. Burla, M. Camalli, C. Cascarano, C. Giacovazzo, A. Guagliardi, A.G.G. Moliterni, G. Polidori, R. Spagna, J. Appl. Crystallogr. 32 (1999) 115.
[33] G.M. Sheldrick, SHELX97, Programs for Crystal Structure Analysis, University of Göttingen, Göttingen, Germany, 1997.
[34] L.J. Farrugia, J. Appl. Crystallogr. 32 (1999) 837.

2.2. Zirconium-lactate (henceforth abbreviated as **ZrL**) solution

Zirconium-lactate (henceforth abbreviated as **ZrL**) solution was prepared following a recipe of Halliburton, slightly modified as below: A clear solution of 0.9415 g of $ZrOCl_2 \cdot 8H_2O$ (Fluka) in 1.0 mL water was stirred with 1.895 mL of refluxed lactic acid (90%) (Merck). The white slurry thus formed was dissolved in a minimum volume (~1.0 mL) of conc. NH_3 and quantitatively transferred to a 5 mL volumetric flask, and the volume was made up to the mark with water. This mixture has a molar ratio, $[Zr^{IV}]$:[lactate] = 1:3 and pH 7.5. In all subsequent studies, this was the source for Zr^{IV}.

2.3. Kinetics

The kinetics were determined spectrophotometrically at 25.0 °C in a thermostated cell housing (CPS 240A) of a Shimadzu (UV-1601) spectrophotometer under the conditions: $T_L \gg T_{Zr} \gg T_{HT}$, where the symbols represent the total analytical concentrations of lactic acid, Zr^{IV} and 2-thenoyltrifluoroacetone, respectively. Thus, first-order reaction conditions were maintained, formation of only a 1:1 complex of Zr^{IV} with HT was ensured and the reaction media was efficiently buffered (by excess lactic acid).

pH jump as well as lactate concentration jump experiments were performed to verify the reversible nature of the reactions studied. A sudden pH drop was induced by the addition of two drops of 5.0×10^{-2} mol dm^{-3} $HClO_4$. A jump in lactate concentration was achieved by the rapid addition of lactic acid. All the concentration jumps (H^+ or L^-) were induced under conditions otherwise the same.

The ionic strength (I) of the media was maintained with $NaClO_4$, prepared and standardized as stated before [13].

3. Results and discussion

3.1. Tautomeric equilibrium of HT

It is known that in solution, the keto (HK) and the enolate (E^-) forms of HT coexist in a pH-dependent equilibrium [14–17]:

$$HK \rightleftharpoons H^+ + E^- \quad K_T \tag{1}$$

The UV spectra of a fixed amount of HT in excess lactic acid at different pH (Fig. 1) pass through two isosbestic points [18]. Their existence suggests that the absorption in this region is essentially accounted for by two species. The curve at pH 8 is characteristic of E^- while that at pH 3 is characteristic of HK. The isosbestic points indicate that the system can be described by the species HK and E^- (Eq. (1)) [14,15] and that over the experimental range pH 3–8, there is no other interfering reaction like hydrolysis of HT.

Under such presumptions, Eq. (2) can be derived (see Appendix 1) from Eq. (1):

$$A = \frac{\varepsilon_{HK} T_{HT}[H^+] + \varepsilon_E K_T T_{HT}}{([H^+] + K_T)} \tag{2}$$

A is the absorption measured at 339 nm, ε_{HK} and ε_E, respectively, are the molar extinction co-efficients of the keto (HK) and the enolate (E^-) forms of HT.

But, $\varepsilon_{HK} \sim 0$ at 339 nm, hence at this wavelength,

$$\frac{A}{T_{HT}} = \frac{(\varepsilon_E K_T)}{([H^+] + K_T)} \quad \text{or,} \quad \frac{T_{HT}}{A} = \frac{1}{\varepsilon_E} + \frac{[H^+]}{K_T \varepsilon_E} \tag{3}$$

The absorbance–pH data at 339 nm (Fig. 1), fitted to Eq. (3) yielded an excellent straight line (Fig. 1). The ratio of its intercept to slope yielded $K_T = 7.15 \times 10^{-7}$. Earlier values [15,17,19], measured by pH-potentiometric titration to pH > 9, are imprecise

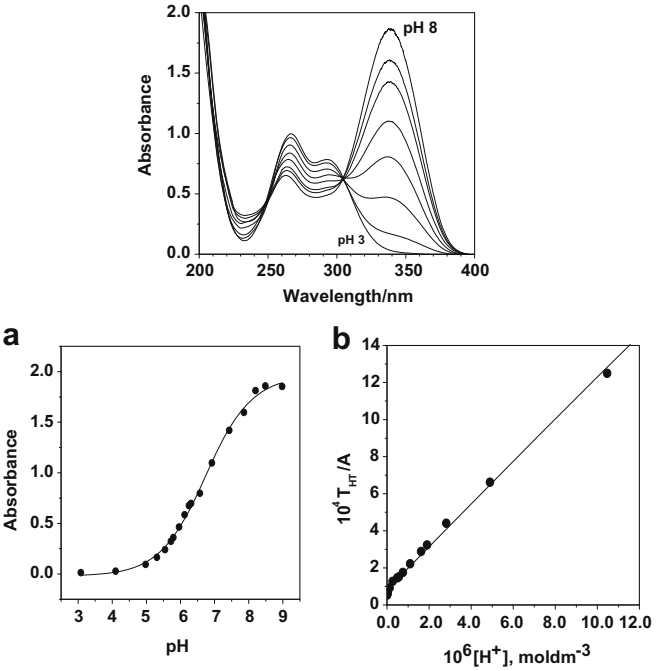


Fig. 1. UV spectra of HT (1.0×10^{-4} mol dm^{-3}), pH 3–8 in lactate buffer (1.0×10^{-2} mol dm^{-3}). (a) Absorption at 339 nm vs. pH. T = 25.0 °C. I = 0. (b) Evaluation of K_T, Eq. (3). T = 25.0 °C. I = 0.

[14] because HT rapidly and nearly completely hydrolyses at pH ⩾ 9. The present spectrophotometric studies carefully avoided the range pH > 8. Hence, HT suffered no hydrolysis and thus no error due to its hydrolysis entered into the measured K_T.

3.2. Reaction between Zr-lactate (ZrL) and HT

Addition of an excess of ZrL at pH 4 to a fixed amount of HT develops a new spectral band at 363 nm, which gains intensity with time, maintaining two isosbestic points (see Fig. 2). The final spectra at equilibrium (Fig. 2) are almost same to those reported [20,21] for ZrE. Evidently, ZrL and HT react to form ZrE. In addition, the existence of the two isosbestic points in Fig. 2 indicates that the absorption in this region is essentially accounted for by two absorbing species, HK (HT at pH 4) and ZrE (represented by the final spectra at equilibrium in Fig. 2):

$$ZrL + HT \rightleftharpoons HL + ZrE; \quad K \tag{4}$$

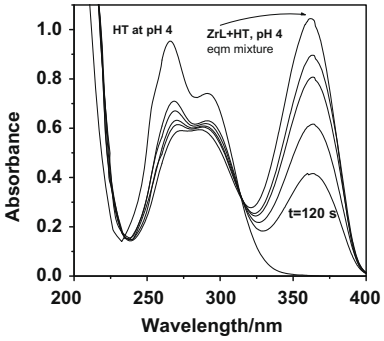


Fig. 2. Kinetic spectra for the reaction between ZrL and HT. T_{Zr} 1.5×10^{-3} mol dm^{-3}, T_{HT} 1.0×10^{-4} mol dm^{-3}, T_L 1.0×10^{-2} mol dm^{-3}, pH 4, T = 25.0 °C, $I = 1.0 \times 10^{-2}$ mol dm^{-3}. Also shown for comparison are the spectra of HT (1.0×10^{-4} mol dm^{-3}) at pH 4.

Within this spectral region, ZrL does not absorb. The rise in absorbance at the peak (363 nm) maintaining the isosbestic points therefore can be interpreted [20] as being due to the gradual formation of ZrE at the expense of HT via the dynamic equilibrium (4).

3.3. The reversible nature of reaction (4)

Fig. 3 illustrates how the absorbance of an equilibrated mixture of ZrL with HT in excess lactate slowly drops if T_L jumps to a higher value under otherwise identical conditions.

Fig. 4 demonstrates that equilibrium (4) can be approached from either direction – forward as well as reverse. Figs. 2–4 together strongly suggest a clean reversible reaction (Eq. (4)).

3.4. Equilibrium study

Absorbances for mixtures of ZrL with HT at equilibrium in excess lactate buffer at different pH are displayed in Table 1. For equilibrium (4), one can derive Eq. (5) (see Appendix 2):

$$\frac{T_{HT}}{A_e} = \frac{T_L[H^+]}{(K_a + [H^+])KT_{Zr}\varepsilon} + \frac{1}{\varepsilon T_{Zr}} \quad (5)$$

where A_e, K_a, ε, K and $[H^+]$, respectively, represent the equilibrium absorbance of the mixture, dissociation constant of lactic acid, molar extinction co-efficient of the absorbing species ZrE, overall equilibrium constant for reaction (4) and molar concentration of the hydrogen ion.

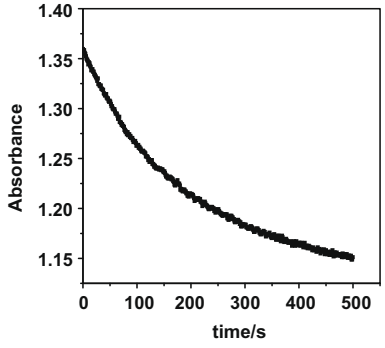


Fig. 3. Effect of T_L jump on the equilibrium absorbance of a mixture of T_{Zr}, 1.5×10^{-3} mol dm^{-3}; T_L, 5.0×10^{-3} mol dm^{-3}and T_{HT}, 1.0×10^{-4} mol dm^{-3} at pH 4.35, $T = 25.0$ °C. Rapid addition of excess lactic acid (T_L, 1.5×10^{-2} mol dm^{-3}) under otherwise the same conditions brings down the absorbance. Least squares fit of absorbance–time data (black points) to first-order decay are shown.

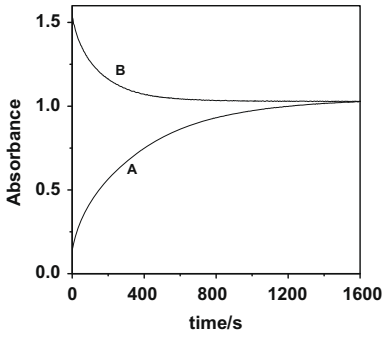


Fig. 4. (A) Rise in absorbance: T_{Zr} 1.5×10^{-3} mol dm^{-3}, T_{HT} 1.0×10^{-4} mol dm^{-3}, T_L 1.0×10^{-2} mol dm^{-3}, $T = 25.0$ °C, pH 4.02. (B) Decay in absorbance: The pH of (A) is suddenly decreased from 5.02 to 4.02. Absorbance decreases from 1.51 to an equilibrium value, the same as that for (A) at pH 4.02.

Table 1
Equilibrium absorbencies at 363 nm of mixtures of ZrL with HT (1.0×10^{-4} mol dm^{-3}). T_L 5.0×10^{-1} mol dm^{-3}; I 1.0 mol dm^{-3}, T 25.0 °C.

[Zr^{IV}] (mol dm^{-3})	pH	Absorbance
0.10	3.97	1.465
0.10	2.33	0.891
0.10	2.99	0.955
0.10	3.41	1.063
0.10	4.07	1.385
0.10	4.56	1.759
0.10	5.01	2.085
0.10	3.98	1.400

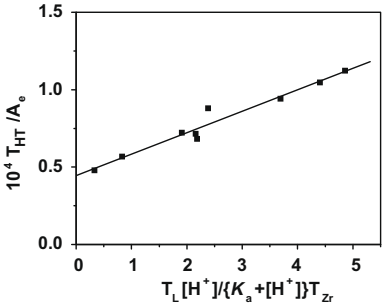


Fig. 5. Evaluation of the equilibrium constant K from Eq. (5).

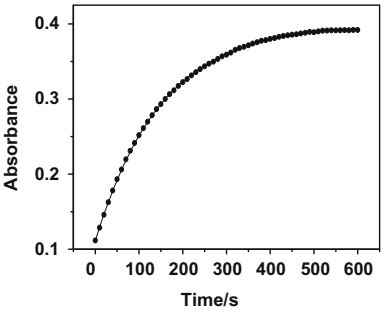


Fig. 6. Abs.–t data (λ, 363 nm) and its fit to the first-order decay equation. T_{Zr}, 5.0×10^{-2} mol dm^{-3}; T_{HT}, 1.0×10^{-4} mol dm^{-3}; T_L, 1.0 mol dm^{-3}; pH 3.5; $I = 2.0$ mol dm^{-3} ($NaClO_4$). The solid line shows the least-squares fit of the experimental data points to Eq. (6).

A plot (Fig. 5) of $\frac{T_{HT}}{A_e}$ versus $\frac{T_L[H^+]}{(K_a+[H^+])T_{Zr}}$ at a constant T_{Zr}, using Table 1 yielded a reasonably good straight line with an equilibrium constant $K = 3.2$ for reaction (4) at 25.0 °C, ionic strength 1.0 mol dm^{-3}.

The tautomerisation equilibrium (1), mentioned above, is attained at a rate much faster [15] than the reactions measured here. This is why the tautomerisation step is kinetically silent in the present reactions, which followed simple first-order kinetics (see below).

3.5. Overall reaction kinetics

The absorbance–time data at 363 nm for reaction (4) under the conditions, $T_{HT} \ll T_{Zr} \ll T_L$ obeyed first-order kinetics for more than 95% to their way to equilibrium (see Figs. 6 and 7). The regression co-efficient in all the cases is better than 0.999.

Representative first-order rate constants, k_0 have been collected in Table 2. Individual values are reproducible to within ±5%.

k_0 increases with increasing pH and T_{Zr} (see Table 2) but decreases with increasing T_L (given below are values for k_0 at differ-

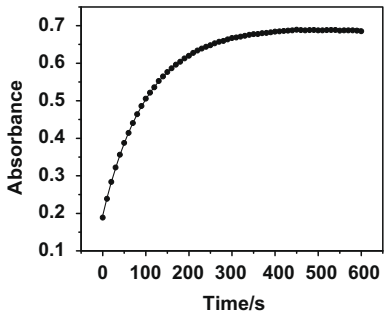


Fig. 7. Abs.–t data (λ, 363 nm) and their fit to Eq. (6), pH 4.5, other conditions the same as for Fig. 6.

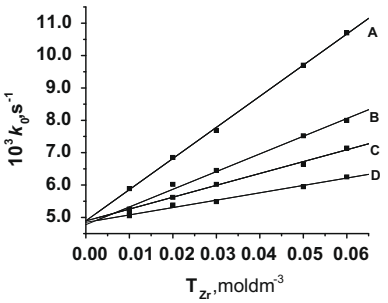


Fig. 8. Variation of k_0 with T_{Zr} at different fixed pHs. T_{HT} 1.0×10^{-4} mol dm^{-3}; T_L 1.0 mol dm^{-3}, I = 2.0 mol dm^{-3}; T = 25.0 °C. pHs are 4.5 (A), 4.0 (B), 3.5 (C) and 3.0 (D).

Table 2
Some representative values of the first-order rate constant k_0 for reaction (4): T_{HT} 1.0×10^{-4} mol dm^{-3}; T_L 1.0 mol dm^{-3}, T 25.0 °C, I 2.0 mol dm^{-3} ($NaClO_4$).

T_{Zr} (mol dm^{-3})	pH	$10^3 k_0$ (s^{-1})	T_{Zr} (mol dm^{-3})	pH	$10^3 k_0$ (s^{-1})
0.01	3.0	5.0	0.01	4.0	5.2
0.02		5.4	0.02		6.0
0.03		5.5	0.03		6.4
0.05		6.0	0.05		7.5
0.06		6.2	0.06		8.0
0.01	3.5	5.3	0.01	4.5	5.9
0.02		5.6	0.02		6.8
0.03		6.0	0.03		7.7
0.05		6.6	0.05		9.7
0.06		7.1	0.06		10.7

ent T_L at pH 3.0 and T_{Zr} 2.0×10^{-2} mol dm^{-3}, I 2.0 mol dm^{-3}, T 25.0 °C):

T_L, mol dm^{-3}:	0.60	0.80	0.90	1.2	1.4
$10^3 k_0$, s^{-1}:	7.2	6.8	6.5	5.1	4.1

These simple kinetic observations clearly indicate (a) fast, reversible replacement of one L with two H_2O molecules and (b) rapid hydrolysis of the diaqua species forming the conjugate base, and (c) a reversible, rate determining (k_1, k_{-1}) entry of the enolate form (E^-) of HT into the coordination sphere of Zr^{IV}.

Unfortunately, the exact composition of "zirconium-lactate" in excess lactate buffer is unknown, but studies by Rose et al. [7] firmly establish that it is mainly the dimer, Zr_2L_6. Accordingly, we propose the following reaction scheme consisting of Eqs. (A)–(C), indeed an abbreviated form of the steps (a)–(c) mentioned above (Scheme 1).

We presume that reactions (A) and (B) precede the rate determining step and none can be the rate steps. This is necessary to explain the inverse dependence of rate on [L] and [H^+]. Assuming kinetic activity of the diaqua species $Zr_2L_5(OH_2)_2^+$ to be negligible compared to that of the hydroxo-aqua species $Zr_2L_5(OH_2)(OH)$, and that $K_AK_B \ll 1$, one can derive from the scheme above (see Appendix 3):

$$k_0 = \frac{k_1 K_{AB} T_{Zr}}{[H^+][L^-]} + k_{-1} \quad (6)$$

As expected from equation (6), k_0 versus T_{Zr} plots are linear (see Fig. 8) with intercepts independent of pH in the range 3.0–4.5. The common intercept of a bunch of four straight lines (Fig. 8) is $k_{-1} = 4.9 \times 10^{-3}$ s^{-1}. Slopes of these lines yielded an average value for $k_1K_{AB} = 2.62 \times 10^{-6}$ dm^6 mol^{-2} s^{-1}; [L] at a given pH was calculated using a pK_a value of lactic acid of 3.86 at T = 25.0 °C [22].

In the absence of any idea of the magnitude for K_{AB} (=K_AK_B), we could not evaluate k_1. Nevertheless, it can be shown (see Appendix 3) that $K_a = \frac{K_{AB}k_1}{k_{-1}}$, where from p$K_a$ is found to be 3.8, in close agreement with the literature [22] value. "ZrL", as prepared by us, most likely contains several oligomeric and polymeric zirconium complexes, [23] along with the main component Zr_2(lactate)$_6$ established by Rose et al. [7]. Nevertheless, the observed simplicity of the kinetic pattern surely indicates that only one Zr^{IV} species (probably the dimer) takes part in the kinetics. Otherwise, much more complex kinetics would have been expected.

4. Conclusion

"Zirconium-lactate" is a transparent mixture containing Zr^{IV} and lactic acid in a 1:3 molar ratio at pH 7.5. It reversibly exchanges one bidentate lactate for the bidentate O,O-donor, 2-thenoyltrifluoroacetone (HT). In excess lactate buffer, this process exhibits simple kinetics and seems to proceed *via* fast dissociation of one lactate, rapid loss of a proton to form the conjugate base and rate determining, reversible entry of HT in its enolate form (E^-) to the coordination sphere of Zr^{IV}. The observance of simple kinetics suggests only one Zr^{IV} species (plausibly the dimer, Zr_2L_6) is kinetically active, though "zirconium-lactate" is a complex mixture of several oligomeric and polymeric Zr^{IV} species. It also appears that replacement of a lactate ligand precedes the entry of HT in the coordination sphere of Zr^{IV}. A similar situation can be expected to happen when "zirconium-lactate" works with guar during the oil-field application. Use of lactate binds and solubilises Zr^{IV} but does not bind it too tightly so that it is easily replaced at the time of necessity. It seems important to control the lactate/guar proportion in oil-field applications.

$$Zr_2L_6 + 2H_2O \rightleftharpoons Zr_2L_5(OH_2)_2^+ + L^- \qquad K_A \text{ (rapid equilibrium)} \qquad (A)$$

$$Zr_2L_5(OH_2)_2^+ \rightleftharpoons Zr_2L_5(OH_2)(OH) + H^+ \qquad K_B \text{ (rapid equilibrium)} \qquad (B)$$

$$Zr_2L_5(OH_2)(OH) + HT \rightleftharpoons Zr_2L_5E + 2H_2O \qquad k_1, k_{-1} \text{ (slow r.d.s)} \qquad (C)$$

Scheme 1.

Acknowledgements

We express our thanks to Halliburton for financial support in terms of a research project and for the award of JRF to Dilip Kumar Chakravorty and subsequently to Rozi Ghosh.

Appendix. Derivation of Eqs. (2), (5), and (6) in the main text

Appendix 1. Derivation of Eq. (2)

$$HK \rightleftarrows H^+ + E^-; \quad K_T = \frac{[H^+][E^-]}{[HK]} \tag{i}$$

$$T_{HT} = [HK] + [E^-] = [HK] + \left(\frac{K_T[HK]}{[H^+]}\right) = [HK]\left([H^+] + \frac{K_T}{[H^+]}\right)$$

$$\text{or, } [HK] = \frac{T_{HT}[H^+]}{([H^+] + K_T)} \text{ and } [E^-] = \frac{K_T T_{HT}}{([H^+] + K_T)}$$

The absorbance, A, at 339 nm (the absorption maximum for the E^- form) of such an equilibrated solution is:

$$A = \varepsilon_{HK}[HK] + \varepsilon_E[E^-] = \frac{\varepsilon_{HK} T_{HT}[H^+]}{([H^+] + K_T)} + \frac{\varepsilon_E K_T T_{HT}}{([H^+] + K_T)}$$

$$= \frac{\varepsilon_{HK} T_{HT}[H^+] + \varepsilon_E K_T T_{HT}}{([H^+] + K_T)} \tag{2}$$

$$\text{or, } \frac{A}{T_{HT}} = \frac{(\varepsilon_{HK}[H^+] + \varepsilon_E K_T)}{([H^+] + K_T)} \tag{ii}$$

ε_{HK} and ε_E are the molar extinction co-efficients of HK and E^-, respectively, at 339 nm.

But $\varepsilon_{HK} \sim 0$ at 339 nm. Hence Eq. (ii) further simplifies to:

$$\frac{A}{T_{HT}} = \frac{(\varepsilon_E K_T)}{([H^+] + K_T)} \text{ or, } \frac{T_{HT}}{A} = \frac{1}{\varepsilon_E} + \frac{[H^+]}{K_T \varepsilon_E} \tag{3}$$

Appendix. 2. Derivation of Eq. (5)

The overall reaction between zirconium-lactate (ZrL) and 2-thenoyltrifluoroacetone (HT) produces lactic acid (HL) along with ZrE, the zirconium complex of the enolate ion (E^-) of HT:

$$ZrL + HT \rightleftharpoons HL + ZrE; \quad K$$

Initial conc.:	T_{Zr}	T_{HT}	T_{HL}	0
Eqm. conc.:	$(T_{Zr} - x)$	$(T_{HT} - x)$	$(T_{HL} + x)$	x

Here, x is the extent of reaction at equilibrium.

Under the conditions: $T_{HL} \gg T_{Zr} \gg T_{HT}$, $K = \frac{[ZrE][HL]}{[ZrL][HT]} = \frac{xT_{HL}}{T_{Zr}(T_{HT} - x)}$.

At a wavelength where only ZrE absorbs, $x = \frac{A_e}{\varepsilon}$. Hence,

$$K = \frac{\frac{A_e T_{HL}}{\varepsilon}}{T_{Zr}\left(T_{HT} - \frac{A_e}{\varepsilon}\right)} = \frac{A_e T_{HL}}{T_{Zr}(T_{HT}\varepsilon - A_e)}; \quad \text{or, } KT_{Zr}T_{HT}\varepsilon - KA_e = A_e T_{HL} \tag{iii}$$

where ε is the molar extinction co-efficient for ZrE at the experimental wavelength. Dividing both sides of Eq. (iii) with $KT_{Zr}\varepsilon A_e$,

$$\frac{T_{HT}}{A_e} = \frac{T_{HL}}{KT_{Zr}\varepsilon} + \frac{1}{\varepsilon T_{Zr}}$$

Now, substituting, $T_{HL} = \frac{T_L[H^+]}{K_a + [H^+]}$, where T_L and K_a are, respectively, the total conc and the deprotonation constant of lactic acid we get,

$$\frac{T_{HT}}{A_e} = \frac{T_L[H^+]}{(K_a + [H^+])KT_{Zr}\varepsilon} + \frac{1}{\varepsilon T_{Zr}} \tag{5}$$

Appendix. 3. Derivation of Eq. (6)

For the scheme consisting of Eqs. (A)–(C)

$$Zr_2L_6 + 2H_2O \rightleftharpoons Zr_2L_5(OH_2)_2{}^+ + L^- \quad K_A \text{ (rapid equilibrium)} \tag{A}$$

$$Zr_2L_5(OH_2)_2{}^+ \rightleftharpoons Zr_2L_5(OH_2)(OH) + H^+ \quad K_B \text{ (rapid equilibrium)} \tag{B}$$

$$Zr_2L_5(OH_2)(OH) + HT \rightleftharpoons Zr_2L_5E + 2H_2O \quad k_1,\ k_{-1} \text{ (slow r.d.s.)} \tag{C}$$

$$K_{AB} = K_A K_B = \frac{[Zr_2L_5(OH_2)(OH)][H^+][L^-]}{[Zr_2L_6]};$$

$$\text{or, } [Zr_2L_5(OH_2)(OH)] = \frac{K_{AB}[Zr_2L_6]}{[H^+][L^-]} \text{ (Assuming, } K_{AB} \ll 1)$$

Hence,

$$\text{Rate} = k_1[Zr_2L_5(OH_2)(OH)][HT] + k_{-1}[Zr_2L_5E]$$

$$= \frac{k_1 K_{AB}[Zr_2L_6]}{[H^+][L^-]} + k_{-1}[Zr_2L_5E] = \frac{k_1 K_{AB} T_{Zr}}{[H^+][L^-]} + k_{-1}[Zr_2L_5E]$$

So that the first-order rate constant,

$$k_0 = \frac{k_1 K_{AB} T_{Zr}}{[H^+][L^-]} + k_{-1} \tag{6}$$

In addition, it can be shown that $\frac{K_A K_B k_1}{k_{-1}} = \frac{K_{AB} k_1}{k_{-1}} = KK_a$. Hence, $K_a = \frac{\frac{K_{AB} k_1}{k_{-1}}}{K}$, where K is the equilibrium constant for reaction (4), and K_a is the deprotonation constant for lactic acid:

$$ZrL + HT \rightleftharpoons ZrE + HL \quad K$$
$$HL \rightleftharpoons H^+ + L^- \quad K_a \tag{4}$$

Substituting known values, $K_a = (2.62 \times 10^{-6}/4.9 \times 10^{-3}) \times (1/3.2) = 1.67 \times 10^{-4}$ or, $pK_a = 3.8$ (reported pK_a 3.86).

References

[1] A. Clearfield, P.A. Vaughan, Acta Crystallogr. 9 (1956) 555.
[2] W. Blumenthal, The Chemical Behavior of Zirconium, van Nostrand, Princeton, NJ, 1958.
[3] A. Clearfield, Rev. Pure Appl. Chem. 14 (1964) 91.
[4] J.-P. Jolivet, in: From Solution to Oxide, John Wiley and Sons, Paris, 2000.
[5] C. Hagfeldt, V. Kessler, I. Persson, J. Chem. Soc., Dalton Trans. (2004) 2142.
[6] D.H. Devia, A.G. Sykes, Inorg. Chem. 20 (1981) 910.
[7] J. Rose, T.J.M. De Bruin, G. Chauveteau, R. Tabary, J.-L. Hazemann, O. Proux, A. Omari, H. Toulhoat, J.-Y. Bottero, J. Phys. Chem. B 107 (2003) 2910.
[8] J. Rose, G. Chauveteau, R. Tabary, S. Moustier, J.-L. Hazemann, Colloid Surf. A: Physicochem. Eng. Asp. 217 (2003) 159.
[9] P.A. Demkowicz, Zirconium Complexes in Lactic Acid in the Solution and Solid States, Ph.D. Thesis, University of Florida, 2001.
[10] S. Banerjee, U. Roy Choudhury, R.N. Banerjee, S. Mukhopadhyay, J. Chem. Soc., Dalton Trans. (2002) 2047.
[11] S. Banerjee, U. Roy Choudhury, B.C. Ray, R. Banerjee, S. Mukhopadhyay, Anal. Lett. 34 (2001) 2797.
[12] H.N. Irving, M.G. Miles, L.D. Pettit, Anal. Chim. Acta 38 (1967) 475.
[13] S.K. Ghosh, S.K. Saha, M.C. Ghosh, R.N. Bose, J.W. Reed, E.S. Gould, Inorg. Chem. 31 (1992) 3358.
[14] E.H. Cook, R.W. Taft, J. Am. Chem. Soc. 74 (1952) 6103.
[15] M.R. Jaffe, D.P. Ray, M. Cefola, N. Sutin, J. Am. Chem. Soc. 93 (1971) 2878.
[16] E.L. King, W.H. Reas, J. Am. Chem. Soc. 73 (1951) 1806.
[17] E. Zebroski, Atomic Energy Commission Report BC-63, Ph.D. Thesis, University of California, 1947.
[18] R.S. Drago, Physical Methods in Inorganic Chemistry, East-West Student Edition, Affiliated East West Press Pvt. Ltd., Madras, 1978. p. 131.
[19] R.E. Connick, W.H. McVey, J. Am. Chem. Soc. 71 (1949) 3182.
[20] A.J. Zielen, R.E. Connick, J. Am. Chem. Soc. 78 (1956) 5785.
[21] E.M. Larseng, G. Terry, J. Leddy, J. Am. Chem. Soc. 75 (1953) 5107.
[22] A.W. Martin, H.V. Tartar, J. Am. Chem. Soc. 59 (1937) 2672.
[23] C. Walther, J. Rothe, M. Fuss, S. Büchner, S. Koltsov, T. Bergmann, Anal. Bioanal. Chem. 388 (2007) 409.

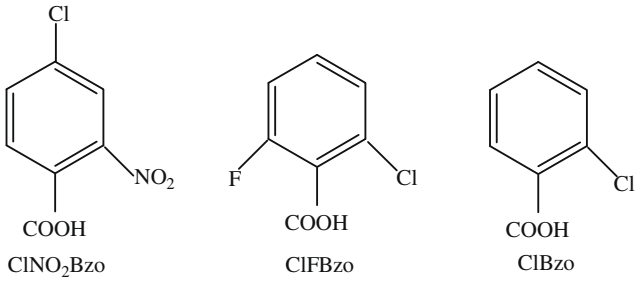


Fig. 1. Chemical structure and abbreviation for the ligands.

synthesis, characterization and nuclease activity of **1**–**3**, together with their antiproliferation and antibacterial activity is reported. The ligands in complexes **1**–**3** are shown in Fig. 1 and the abbreviated formula of the complexes are $[Cu(II)(ClNO_2Bzo)(H_2O)]_2$, $[Cu(II)(ClFBzo)(H_2O)]_2$ and $[Cu(II)(ClBzo)(H_2O)]_2$, respectively.

2. Experimental

2.1. Synthesis of tetrakis(μ-4-chloro-2-nitrobenzoato-κ^2O,O') bis[aquacopper(II)] (*1*)

Copper(II) chloride hydrate (3.00 g, 0.018 mol) was dissolved in ethanol solution (50 ml). To this solution was added 50 ml ethanol solution of 4-chloro-2-nitrobenzoic acid (7.26 g, 0.036 mol). The resultant solution was stirred and refluxed for 2 h. The green solution was then filtered and allowed to cool down to room temperature. Crystals of the title compound were obtained after 3 days of slow evaporation at room temperature. Yield 32.5%. *Anal.* Calc. for **1**: C, 34.84; H, 1.67; N, 5.80. Found: C, 35.19; H, 1.42; N, 5.52%.

2.2. Synthesis of tetrakis(μ-2-chloro-6-fluorobenzoato-κ^2O,O') bis[aquacopper(II)] (*2*)

Copper(II) chloride hydrate (3.00 g, 0.018 mol) was dissolved in ethanol solution (50 ml). To this solution was added 50 ml ethanol solution of 2-chloro-6-fluorobenzoic acid (6.28 g, 0.036 mol). The resultant solution was stirred and refluxed for 2 h. The green solution was then filtered and allowed to cool down to room temperature. Crystals of the title compound were obtained after 3 days of slow evaporation at room temperature. Yield 34.2%. *Anal.* Calc. for **2**: C, 39.23; H, 1.89. Found: C, 39.02; H, 1.46%.

2.3. Synthesis of tetrakis(μ-2-chlorobenzoato-κ^2O,O') bis[aquacopper(II)] (*3*)

Copper(II) chloride hydrate (3.00 g, 0.018 mol) was dissolved in ethanol solution (50 ml). To this solution was added 50 ml ethanol solution of 2-chlorobenzoic acid (5.64 g, 0.036 mol). The resultant solution was stirred and refluxed for 2 h. The green solution was then filtered and allowed to cool down to room temperature. Crystals of the title compound were obtained after 3 days of slow evaporation at room temperature. Yield 35.2%. *Anal.* Calc. for **3**: C, 42.82; H, 2.57. Found: C, 42.51; H, 2.17%.

2.4. Physical measurements

Elemental analyses were performed using a Perkin–Elmer 2400 series-11 CHN/O analyzer. Infrared spectra (KBr pellets) were recorded using a Perkin–Elmer 2000 Infrared Spectrometer. The solution UV–Vis spectra were obtained from a Jasco V-530 Spectrophotometer. The cyclic voltammetric experiments were performed on a BAS-Epsilon electrochemical system. Voltammograms were recorded using a standard three electrode arrangement consisting of a platinum working electrode, a platinum auxiliary electrode and a Ag/AgCl reference electrode. The complexes were dissolved in Tris–NaCl (TN) pH 7.5 buffer prior to measurement.

2.5. X-ray crystallography

Diffraction data were collected using a Bruker APEX2 [30] CCD area-detector, graphite monochromated Mo Kα radiation (λ = 0.71073 Å) at 100(1) K for **1** and 297(2) K for **2** and the Oxford Cyrosystem Cobra low-temperature attachment. The data was reduced using SAINT [31]. A semi-empirical absorption correction was applied to the data using SADABS [31]. The structure was solved by direct methods and refined against F^2 by full-matrix least squares using SHELXTL [32]. Hydrogen atoms were placed in calculated positions. Crystal data and experimental details of the structure determinations are listed in Table 1.

2.6. DNA cleavage experiments

The electrophoresis experiments were performed on a horizontal gel electrophoresis system. Agarose gel electrophoresis experiments were carried out on plasmid pBR322 DNA. All samples in Tris–NaCl buffer at pH 7.5 were incubated at 37 °C for 2 h, and then electrophoresed on 1% agarose gel for 1 h at 80 V. Essentially samples with an increasing concentration of complexes with a given concentration of DNA (0.25 μg/μl) for each sample were incubated in the absence or presence of hydrogen peroxide. The resultant bands for each set of experiments were photographed under UV light by using a Polaroid camera, GelCam, fixed with an electrophoresis hood.

2.7. Cell line and cell culture

Human cancer cell lines, namely MCF-7, DU 145, HeLa, HepG2 and Chang were obtained from the American Type Culture Collection (ATCC, Manassas, VA, USA). The cancer cells were maintained in Dulbecco's modified Eagle's medium (DMEM; Invitrogen Co., Carlsbad, California, USA) supplemented with 10% heat-inactivated fetal calf serum (Invitrogen Co., Carlsbad, California, USA), 100 U/ml penicillin and 100 μg/ml streptomycin (Flowlab, Sydney, Australia). Cells were kept in the logarithmic growth phase by routine passage every 2–3 days using 0.025% trypsin–EDTA treatment.

2.8. In vitro antiproliferation assay

The antiproliferative and cytotoxic activity of **1**–**3** towards MCF-7, DU 145, HeLa, HepG2 and Chang cell lines was evaluated by using the sulforhodamine B (SRB) method, as previously described [33–37]. Cells were seeded 24 h prior to treatment in a 96-well plate at plating densities ranging from 10000 to 20000 cells/well depending on the doubling time of individual cell lines in order to obtain semi-confluent cultures. One plate from each cell line was fixed in situ with sodium trichloroacetate, TCA (Sigma Chemical Co.), to represent a measurement of the cell population for each cell line at the time of drug addition (T_z). Test agents were dissolved in DMSO (Sigma Chemical Co.) and followed by a 2× serial dilution for six points ranging from 6.25 to 200 μg/ml. The final concentration of DMSO used in the corresponding wells did not exceed 1% (v/v), which affect cell viability. Control cultures received the same concentration of solvent alone. Following drug addition, the plates were incubated for an additional 48 h period.

At the end of incubation, cells were fixed in situ with 50 μl of cold 50% (w/v) TCA and incubated for 1 h at 4 °C. The plates were then washed with tap water and air dried. SRB (Sigma Chemical

Table 1
Crystal data, data collection and structure refinement parameters of $[Cu(II)(ClNO_2Bzo)(H_2O)]_2$ and $[Cu(II)(ClFBzo)(H_2O)]_2$.

Complex	$[Cu(II)(ClNO_2Bzo)(H_2O)]_2$	$[Cu(II)(ClFBzo)(H_2O)]_2$
Empirical formula	$C_{28}H_{16}Cl_4Cu_2N_4O_{18}$	$C_{28}H_{16}Cl_4Cu_2F_4O_{10}$
Formula weight	965.33	857.29
Temperature (K)	100(1)	297(2)
Wavelength (Å)	0.71073	0.71073
Crystal system, space group	monoclinic, $C2/c$	triclinic, $P\bar{1}$
Unit cell dimensions		
a (Å)	28.813(3)	7.5638(2)
b (Å)	7.2368(6)	13.0494(4)
c (Å)	17.0053(14)	17.0053(14)
α (°)	90	106.003(2)
β (°)	105.395(6)	90.388(2)
γ (°)	90	91.855(2)
Volume (Å^{-3})	3418.6(5)	1584.17(8)
Z	4	2
D_{calc} (Mg m^{-3})	1.876	1.797
Absorption coefficient (mm^{-1})	1.646	1.759
Crystal size (mm)	0.48 × 0.28 × 0.17	0.43 × 0.37 × 0.35
θ range (°)	1.47–27.50	1.27–35.00
Reflections collected/unique [R_{int}]	30039/3931 [0.0773]	48847/13817 [0.0321]
Data/restraints/parameters	3931/0/261	13817/0/437
Goodness-of-fit on F^2	1.112	1.080
Final R indices [$I > 2\sigma(I)$]	$R_1 = 0.0491$, $wR_2 = 0.1304$	$R_1 = 0.0358$, $wR_2 = 0.0915$
R indices (all data)	$R_1 = 0.0608$, $wR_2 = 0.1479$	$R_1 = 0.0602$, $wR_2 = 0.1131$
Largest difference in peak and hole	2.161 and −1.164	0.936 and −0.647

Co.) solution (100 μl) at 0.4% (w/v) in 1% acetic acid was added to the corresponding wells and further incubated for 10 min at room temperature. After staining, unbound dye was washed out by 1% acetic acid and the bound stain was subsequently solubilised with 10 mM trizma base (Sigma Chemical Co.). The absorbance at 505 nm was read on a spectrophotometric plate reader.

Dose–response curves were constructed to obtain the response parameters which were the GI_{50}, TGI and LC_{50}. Percentage growth is calculated as: $[(T_i - T_z)/(C - T_z)] \times 100$ where (T_z) is time zero, (C) is control growth and (T_i) is test growth in the presence of the drug at the six concentration levels. The GI_{50} value (growth inhibitory activity) corresponds to the concentration of test agents causing 50% decrease in net cell growth which was calculated from $[(T_i - T_z)/(C - T_z)] \times 100 = 50$, the TGI value (cytostatic activity) is the concentration of test agents resulting in total growth inhibition which was calculated from $T_i = T_z$, and the LC_{50} value (cytotoxic activity) is the concentration of the test agents causing net 50% loss of initial cells at the end of the incubation period which was calculated from $[(T_i - T_z)/T_z] \times 100 = (-50)$. All data were derived from three independent experiments.

2.9. Antibacterial screening (inhibition zone)

The antibacterial activity of **1**–**3** was determined by screening against Gram negative bacteria: *Enterobacter aerogenes, Klebsiella pneumoniae, Proteus mirabilis, Pseudomonas aeruginosa, Shigella sonnei* and Gram positive bacteria: *Bacillus cereus, Bacillus subtilis* and *Staphylococus aureus* using the well diffusion method. Sensitivity plates were inoculated with Gram negative bacteria and Gram positive bacteria and the well was loaded with 75 μl of test compound solution using a sterilized micropipette. The incubation was done for 24 h at 37 ± 2 °C. Inhibition was recorded by measuring the diameter of the inhibitory zone after the period of incubation. Three replicas were made for each treatment. To evaluate the effect of concentration on antibacterial activity, three different concentrations (125, 250 and 500 μg/ml) of the test compounds

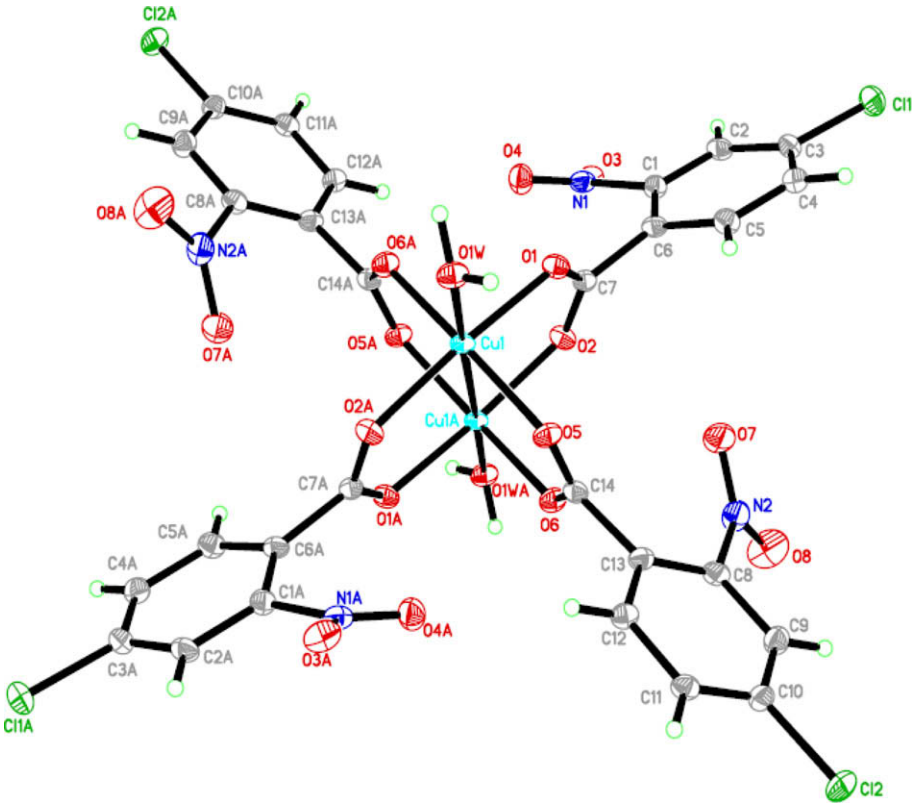


Fig. 2. The molecular structure of **1**, showing 50% probability displacement ellipsoids and the atomic numbering.

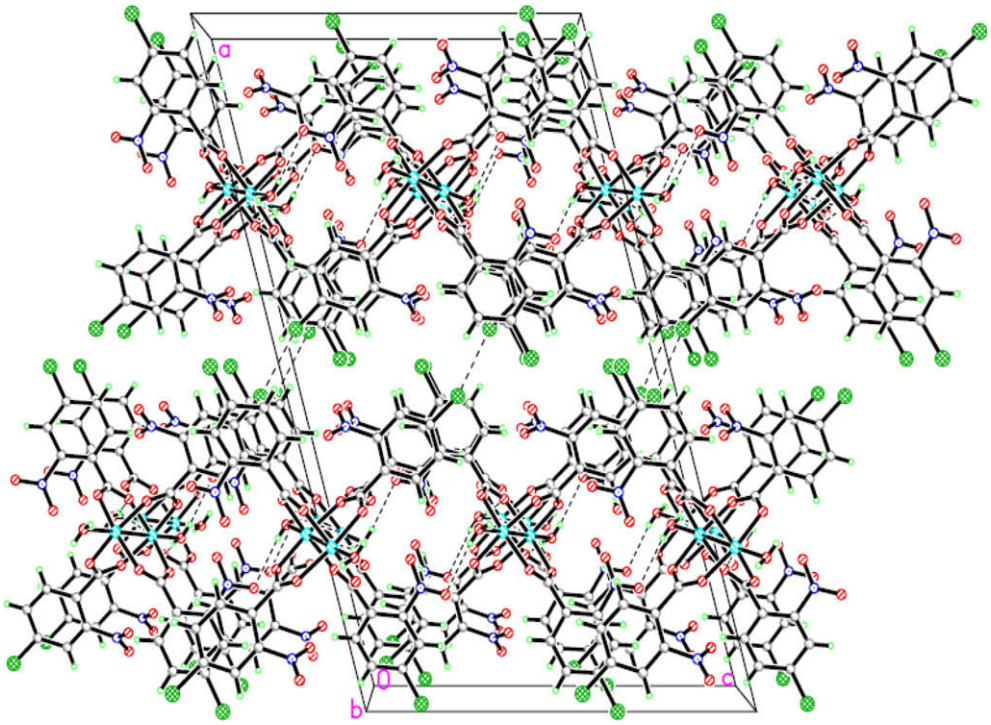


Fig. 3. The crystal packing of **1**.

were used. DMSO, which exhibited no antibacterial activity, was used as a negative control. The stability of the complexes in DMSO medium (2% v/v) were checked by using UV–Vis technique whereby no apparent changes were observed in the absorption peaks of the complexes for two weeks.

2.10. Antibacterial screening (MIC)

The MIC (minimum inhibitory concentration) value for the complexes which showed positive result towards antibacterial activity was further determined using the microdilution broth method. Sample solutions were added to the broth at different concentrations. Measured samples of each bacterial suspension were added to the serial dilution of the test substances. The inoculated test tubes were incubated at 37 ± 2 °C. After 24 h, the turbidity was evaluated. The MIC was defined as the lowest antibacterial concentration of the test samples that inhibit more than 99% of the bacterial population. The experiments were repeated three times and the results were expressed as average values. The solvent showed no antibacterial action.

3. Result and discussion

3.1. Characterization of complex *1*

The crystal structure of **1** is depicted in Fig. 2 and the crystal packing in the solid state is depicted in Fig. 3. Selected interatomic distances and angles are given in Table 2. Complex **1** which is neutral, centrosymmetric and dinuclear consists of two Cu(II) centers bridged by four carboxylate groups of the four ligands. Each Cu(II) center is coordinated by four O atoms of carboxylate groups in the basal plane and the O atom of a water molecule in the apical position, giving a square-pyramidal coordination environment. The Cu···O bond distance of water molecule is markedly longer than the Cu···O bond distance of carboxylate groups. The intramolecular Cu···Cu distance in the dinuclear unit 2.6356(8) Å, which is in the normal range of tetracarboxylatocopper(II) dimers such as diamminetetrakis-μ-(*O*,*O*′-indole-3-carboxylate)dicopper(II), $Cu(L)_4(H_2O)_2$ [LH = (1S, 3R)-3-carbamoyl-2,2,3-trimethylcyclopentane-1-carboxylic acid] and $[Cu_2(taa)_4(dmf)]_2$ [taa = 2-thiopheneacetate anion] [38–40]. The carboxylate bridging angles of O(2)–C(7)–O(1) and O(5)–C(14)–O(6) are similar at 126.7(3)° and 127.3(3)°, respectively. The bond distances of Cu(1)–O(5), Cu(1)–O(6A), Cu(1)–O(2A), Cu(1)–O(1) and Cu(1)–O(1W) are 1.964(2), 1.964(2), 1.967(2), 1.987(2) and 2.130(3) Å, respectively, while the bond angles of O(5)–Cu(1)–O(1W), O(6A)–Cu(1)–O(1W),

Table 2
Selected bond lengths (Å) and bond angles (°) of $[Cu(II)(ClNO_2Bzo)(H_2O)]_2$.

Bond lengths (Å)	
Cu(1)–O(5)	1.964(2)
Cu(1)–O(6A)	1.964(2)
Cu(1)–O(2A)	1.967(2)
Cu(1)–O(1)	1.987(2)
Cu(1)–O(1W)	2.130(3)
Cu(1)–Cu(1)#1	2.6356(8)
O(3)–N(1)	1.235(4)
O(4)–N(1)	1.221(4)
O(7)–N(2)	1.227(4)
O(8)–N(2)	1.219(4)
Bond angles (°)	
O(5)–Cu(1)–O(6A)	168.78(10)
O(5)–Cu(1)–O(2A)	90.45(10)
O(6A)–Cu(1)–O(2A)	89.81(10)
O(5)–Cu(1)–O(1)	89.26(10)
O(6A)–Cu(1)–O(1)	88.29(10)
O(2A)–Cu(1)–O(1)	168.69(10)
O(5)–Cu(1)–O(1W)	94.79(10)
O(6A)–Cu(1)–O(1W)	96.30(10)
O(2A)–Cu(1)–O(1W)	97.28(10)
O(1)–Cu(1)–O(1W)	94.01(10)
O(2A)–C(7)–O(1)	126.7(3)
O(5)–C(14)–O(6A)	127.2(3)

#1: $-x + 1/2, -y + 1/2, -z$.

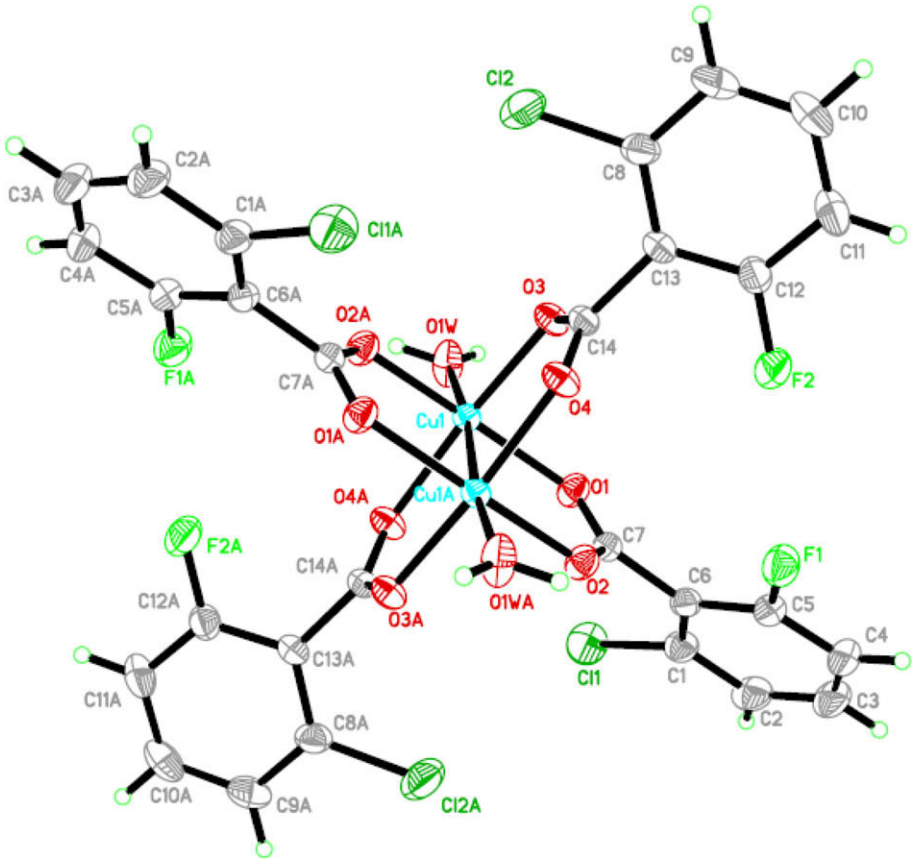


Fig. 4. The molecular structure of **2**, showing 50% probability displacement ellipsoids and the atomic numbering.

O(2A)–Cu(1)–O(1W) and O(1)–Cu(1)–O(1W) are 94.79(10)°, 96.30(10)°, 97.28(10)° and 94.01(10)°, respectively, with a tau value $\tau \approx 0$, indicating a square-pyramidal coordination geometry. The crystal structure of **2** is depicted in Fig. 4 and the crystal packing in the solid state is depicted in Fig. 5. Similar to complex **1**, complex **2** also is neutral, centrosymmetric and dinuclear in which there are two crystallographically independent molecules, both situated over their centers of inversion. Each Cu(II) center displays a square-pyramidal coordination environment where the four O atoms of carboxylate groups from the ligands form the basal plane and the O atom of a water molecule occupies the apical position. The Cu···O bond distance of the water molecule is clearly longer than the Cu···O bond distance of the carboxylate groups. The intramolecular Cu···Cu distance in the dinuclear unit is 2.6334(4) Å, which is almost similar with **1** and also in normal range of tetracarboxylato copper(II) dimers [38–40]. The carboxylate bridging angles of O(1)–C(7)–O(2) and O(4)–C(14)–O(3) show almost parallel values at 126.46(18)° and 126.23(15)°, respectively. The bond distances of Cu(1)–O(1), Cu(1)–O(2A), Cu(1)–O(4A), Cu(1)–O(3) and Cu(1)–O(1W) are 1.9515(14), 1.9584(14), 1.9734(13), 1.9845(13) and 2.1177(14) Å, respectively, and the bond angles of O(1)–Cu(1)–O(1W), O(2A)–Cu(1)–O(1W), O(4A)–Cu(1)–O(1W) and O(3)–Cu(1)–O(1W) are 98.90(6)°, 92.85(7)°, 95.62(6)° and 95.96(6)°, respectively, with a tau value $\tau \approx 0$, indicating a square-pyramidal coordination geometry. The hydrogen bondings that exist in the crystal formation of $[Cu(II)(NO_2Bzo)(H_2O)]_2$ and $[Cu(II)(ClFBzo)(H_2O)]_2$ are shown in Tables 3 and 5. These hydrogen bonding sites could allow the complexes to interact with DNA through hydrogen bonding. In addition, the benzene rings of **1** (interplanar distances = 3.758(2) Å) and **2** (interplanar distances = 3.7936(15) Å) could also allow the complexes to interact with DNA through van der Waals interaction. The crystal structure of **3** was earlier reported elsewhere [41].

The IR spectrum of **1** shows a broad absorption band at 3440 cm^{-1} corresponding to H···O stretching of coordinated water molecules in the complex. The C=C–H absorption band can be observed at 3095 cm^{-1}. The $\nu_{asym}(COO^-)$ and $\nu_{sym}(COO^-)$ absorption can be observed as strong bands at 1614 and 1411 cm^{-1}, respectively [39,42,43].

The $\Delta[\nu_{asym}(COO^-) - \nu_{sym}(COO^-)]$ for **1** is 203 cm^{-1} indicating that the coordination of carboxylate groups are closer to bidentate rather than to monodentate mode [39,42,43]. This result is in agreement with the crystal structure of **1** which shows the carboxylate groups forming bidentate bridging groups in the complex. The strong NO_2 absorption band is not much affected by the complex formation, with ligand and complex showing the NO_2 absorption at 1537 and 1536 cm^{-1}, respectively, indicating that the NO_2 groups are not involved in the coordination to the metal. The IR spectrum of **2** exhibits H···O stretching of coordinated water molecules as a broad absorption band centered at 3419 cm^{-1}. The C=C–H absorption bands can be observed at 3093 and 3065 cm^{-1}. The strong antisymmetric and symmetric carboxylate stretching can be observed as strong bands at 1617 and 1404 cm^{-1}, respectively. The calculated $\Delta[\nu_{asym}(COO^-) - \nu_{sym}(COO^-)]$ for **2** is 213 cm^{-1} indicating the coordination of the carboxylate groups are bidentate in nature. This result concurs with the crystal structure of **2** which shows the carboxylates group forming bidentate bridges in the complex. For complex **3**, the H···O stretching of coordinated water molecules can be seen as a broad absorption band centered at 3416 cm^{-1}. The peaks at 3078 and 3035 cm^{-1} can be assigned to the C=C–H stretching. The $\nu_{asym}(COO^-)$ and $\nu_{sym}(COO^-)$ stretching can be observed as strong bands at 1599 and 1399 cm^{-1}, respec-

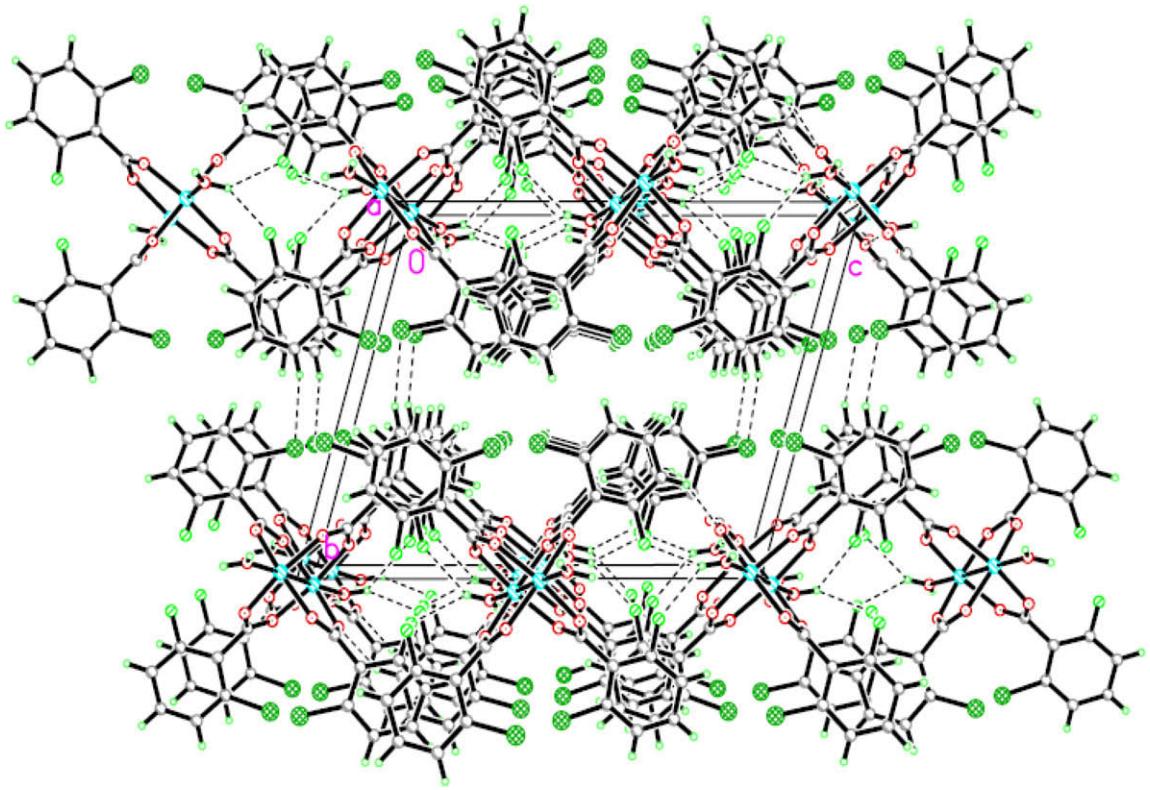


Fig. 5. The crystal packing of **2**.

Table 3
Hydrogen bonding distances and angles of $[Cu(II)(ClNO_2Bzo)(H_2O)]_2$.

D–H···A	Distance (Å) D–H	Distance (Å) H···A	Distance (Å) D···A	Angle (°) D–H–A
O(1W)···H(11W)···O(1)	0.88(5)	1.95(5)	2.822(3)	172(4)
O(1W)···H(21W)···O(3)	0.69(5)	2.28(5)	2.944(3)	163(5)
C(12)···H(12A)···O(4)	0.9297	2.5077	3.231(4)	134.80

D, donor atom; A, acceptor atom.

Table 4
Selected bond lengths (Å) and bond angles (°) of $[Cu(II)(ClFBzo)(H_2O)]_2$.

Bond lengths (Å)	
Cu(1)–O(1)	1.9515(14)
Cu(1)–O(2A)	1.9584(14)
Cu(1)–O(4A)	1.9734(13)
Cu(1)–O(3)	1.9845(13)
Cu(1)–O(1W)	2.1177(14)
Cu(1)–Cu(1)#1	2.6334(4)
Cl(1)–C(1)	1.728(3)
Cl(2)–C(8)	1.727(3)
F(1)–C(5)	1.350(3)
F(2)–C(12)	1.346(3)
Bond angles (°)	
O(1)–Cu(1)–O(2A)	168.02(6)
O(1)–Cu(1)–O(4A)	90.69(7)
O(2A)–Cu(1)–O(4A)	90.48(6)
O(1)–Cu(1)–O(3)	87.64(6)
O(2A)–Cu(1)–O(3)	88.83(6)
O(4A)–Cu(1)–O(3)	168.42(6)
O(1)–Cu(1)–O(1W)	98.90(6)
O(2A)–Cu(1)–O(1W)	92.85(7)
O(4A)–Cu(1)–O(1W)	95.62(6)
O(3)–Cu(1)–O(1W)	95.96(6)
O(1)–C(7)–O(2A)	126.46(18)
O(4A)–C(14)–O(3)	126.23(15)

#1: $-x+1, -y, -z+1$.

tively. The calculated $\Delta[\nu_{asym}(COO^-) - \nu_{sym}(COO^-)]$ for **3** is 200 cm^{-1} indicating a bidentate mode of coordination for the carboxylate groups. This result is in agreements with crystal structure of **3** which shows the carboxylate groups forming bidentate bridges in the complex [41].

As this paper reports the nuclease property of the complexes in the Tris–NaCl pH 7.5 buffer solution, the electronic spectral data of the complexes was obtained in the Tris–NaCl pH 7.5 buffer solution. The UV–Vis spectrum of **1** displays a broad absorption band at λ_{max} = 698 nm which can be assigned to the d–d transition while the bands at 263 and 218 nm in UV region can be assigned to the π–π^* transitions. For complex **2**, a broad d–d transition absorption band occurs at 736 nm while π–π^* transitions occur at 263 and 212 nm. In complex **3**, the d–d transition band can be observed at 732 nm while π–π^* transitions can be observed at 271 and 212 nm.

The cyclic voltammogram of **1**–**3** were recorded in the Tris–NaCl (TN) pH 7.5 buffer solution whereby all the complexes show redox activity. Complex **1** shows two cathodic reduction peaks at −159 and −304 mV and two anodic oxidation peaks at −54 mV and 100 mV which correspond to the $Cu^{II}Cu^{II}$ to $Cu^{II}Cu^{I}$ and $Cu^{II}Cu^{I}$

Table 5
Hydrogen bonding distances and angles of $[Cu(II)(ClFBzo)(H_2O)]_2$.

D–H···A	Distance (Å) D–H	Distance (Å) H···A	Distance (Å) D···A	Angle (°) D–H–A
O(1W)···H(11W)···O(3)	0.8496	1.9436	2.7802(19)	167.99
O(2W)···H(12W)···F(1)	0.8507	2.4619	2.4619	134.40
O(2W)···H(12W)···F(2)	0.8507	2.1610	2.935(2)	151.15
O(1W)···H(21W)···F(3)	0.8495	2.2032	2.919(3)	141.83
O(1W)···H(21W)···F(4)	0.8495	2.3473	3.079(2)	144.57
O(2W)···H(22W)···O(5)	0.8501	1.9213	2.761(2)	169.27
C(11)···H(11A)···O(6)	0.9304	2.5761	2.5761	130.97

D, donor atom; A, acceptor atom.

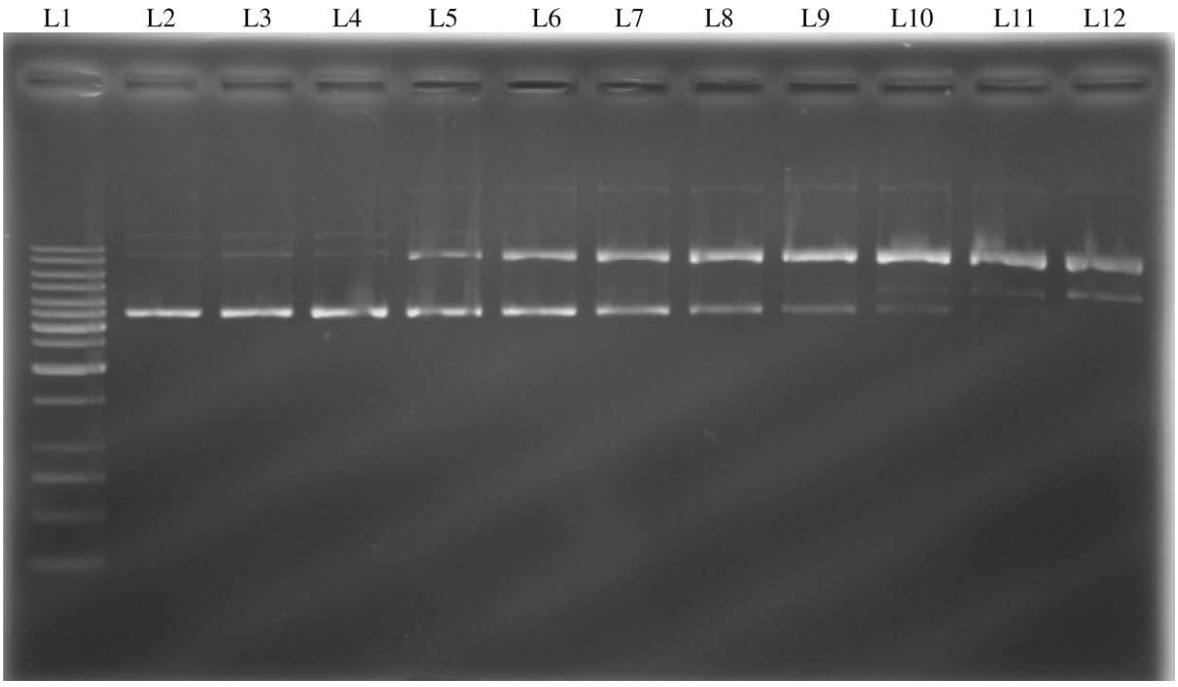


Fig. 6. Cleavage of supercoiled pBR322 by complex **1** at different concentrations in TN buffer pH 7.5. L1 Gene Ruler 1 kb DNA ladder, L2 DNA alone, L3 DNA + H_2O_2 alone, L4 DNA + 40 μM complex **1** alone (without H_2O_2). Lanes 5–12, DNA with increasing concentration of complex **1** + H_2O_2: lane 5, 5 μM; lane 6, 10 μM; lane 7, 15 μM; lane 8, 20 μM; lane 9, 25 μM; lane 10, 30 μM; lane 11, 35 μM; lane 12, 40 μM.

to $Cu^{I}Cu^{I}$ redox process [44–46]. Similar to complex **1**, complex **2** also exhibits two cathodic reduction peaks and two anodic oxidation peaks at −92, −291, −42 and 115 mV, while for complex **3**, the two cathodic reduction peaks and two anodic oxidation peaks can be observed at −77, −274, −26 and 120 mV. All complexes display a quasi-reversible redox behaviour, as judged from the anodic to cathodic peak separation value, ΔEp (=Epa − Epc); ΔEp of **1**–**3** for process $Cu^{II}Cu^{II}$ to $Cu^{II}Cu^{I}$ are 259, 207 and 197 mV, respectively, and ΔEp of **1**–**3** for process $Cu^{II}Cu^{I}$ to $Cu^{I}Cu^{I}$ are 250, 249 and 248 mV, respectively (ΔEp ⩽ 59 mV for reversible process). The $E_{1/2}$ redox potential, taken as the average of Epa and Epc, of **1**–**3** for process $Cu^{II}Cu^{II}$ to $Cu^{II}Cu^{I}$ are −130, −104 and −99 mV, respectively, while $E_{1/2}$ of **1**–**3** for process $Cu^{II}Cu^{I}$ to $Cu^{I}Cu^{I}$ are −179, −167 and −150 mV, respectively. The $E_{1/2}$ values of **1** are at a more negative potential compared to **2** and **3** indicating that **1** has a more stable Cu(II) state compared to **2** and **3**.

3.2. DNA cleavage studies

Fig. 6 shows the result of the plasmid pBR322 DNA cleavage reaction by using an increasing concentration of **1** in the presence of H_2O_2. Control experiments in lanes 3 and 4 show that neither with H_2O_2 alone nor with complex alone (40 μM) can result in any DNA cleavage. However, DNA cleavage can be induced by increasing complex concentration in the presence of H_2O_2, as shown in lanes 5–12, Fig. 6. In general, if scission occurs on one strand of the DNA, the supercoil (Form I) will relax to generate a slow moving open circular or nicked form (Form II) while if scission occurs on both strands, a linear form (Form III) that migrates in between Form I and Form II will be generated. At complex concentration as low as 5 μM (lane 5, Fig. 6), clear cleavage can be observed wherein a small amount of supercoil was converted to the nicked form. Further increases in the complex concentration from 10 to 40 μM (lanes 6–12, Fig. 6), builds up both the more intense band of nicked form and the less intense linear band and diminishes the supercoil band. Formation of the linear band implies that **1** is capable of inducing double strand scission. At 40 μM (lane 12, Fig. 6), the supercoil was completely cleaved. The requirement of H_2O_2 for DNA cleavage indicates an oxidative cleavage mechanism. Similar oxidative cleavage mechanisms have been reported by various Cu(II) complexes with different ligands [20,29,30,47–49]. In contrast, some Cu(II) complexes require a coreductant, such as ascorbate and mercaptoethanol to trigger oxidative DNA cleavage [15,50–53].

Fig. 7 shows the result of the plasmid pBR322 DNA cleavage by an increasing concentration of **2** in the presence of H_2O_2. Once again, no DNA cleavage is observed in the control lanes (lanes 3 and 4, Fig. 7), wherein pBR322 DNA was incubated with H_2O_2 alone or **2** alone. DNA cleavage by **2** occurs in the presence of H_2O_2 and cleavage can be seen at complex concentration as low as 5 μM (lane 5, Fig. 7). On increasing the complex concentration from 10 to 40 μM (lanes 6–12, Fig. 7), the nicked and linear bands build up and the supercoil band diminishes, indicating single and double strand scission. At 40 μM (lane 12, Fig. 7), the supercoiled form was completely cleaved. The necessity of H_2O_2 for DNA cleavage indicates oxidative cleavage. Complex **3** shows a similar DNA cleavage pattern observed in **1** and **2**, with total cleavage occurring at 40 μM.

From the DNA cleavage results of **1**–**3**, it is obvious that **1**–**3** are effective DNA cleavers comparable to other Cu(II) compounds already described in the literature [20,29,30,47–49]. All complexes exhibit similar DNA cleavage efficiency which means different functional groups attached to the benzene ring in **1** (Cl and NO_2), **2** (Cl and F) and **3** (Cl only) do not influence the DNA cleavage efficiency. In addition the DNA cleavage experiment of $CuCl_2$ in the presence of H_2O_2 was carried out and the results show that no DNA cleavage was observed up to 40 μM. This shows that chelation of the benzoate derivative ligands to Cu(II) can lead to the appearance of DNA cleavage activity. Interestingly, research papers on H_2O_2 oxidative DNA cleavage system of water soluble tetracarboxylatocopper(II) dimers with benzoate derivative ligands appear to be scarce.

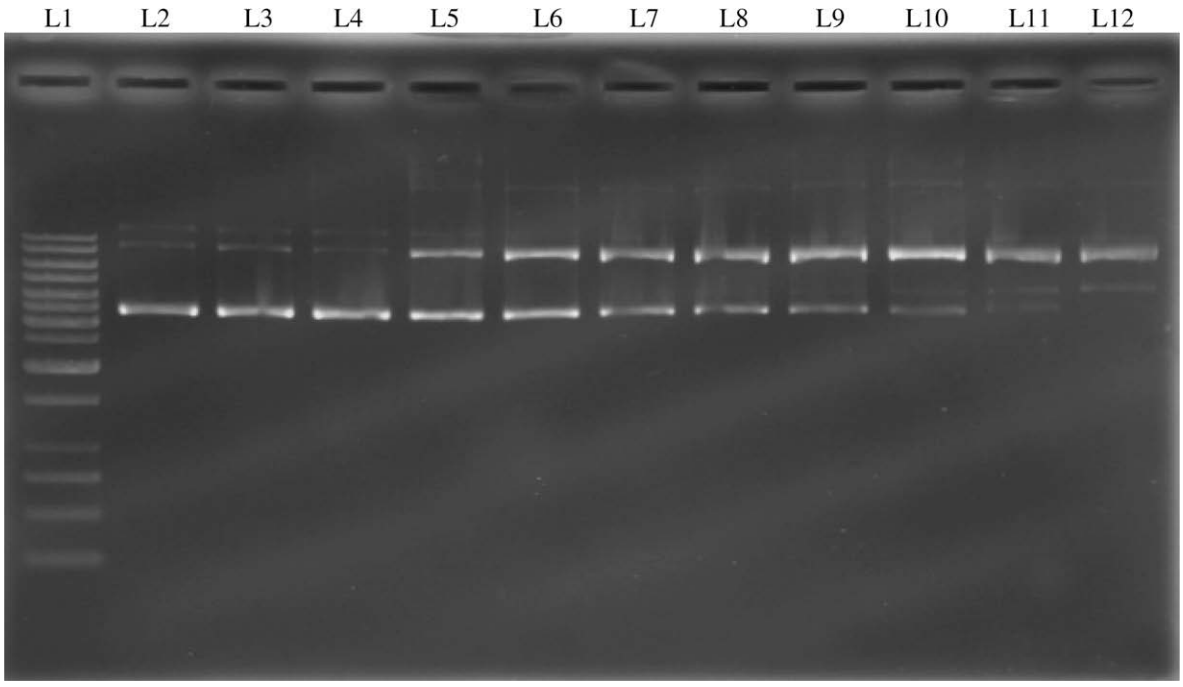


Fig. 7. Cleavage of supercoiled pBR322 by complex **2** at different concentrations in TN buffer pH 7.5. L1 Gene Ruler 1 kb DNA ladder, L2 DNA alone, L3 DNA + H_2O_2 alone, L4 DNA + 40 μM complex **2** alone (without H_2O_2). Lanes 5–12, DNA with increasing concentration of complex **2** + H_2O_2: lane 5, 5 μM; lane 6, 10 μM; lane 7, 15 μM; lane 8, 20 μM; lane 9, 25 μM; lane 10, 30 μM; lane 11, 35 μM; lane 12, 40 μM.

A mechanistic study on the DNA cleavage by **1** and **2** with various inhibiting agents such as *t*-butanol, mannitol, DMSO and NaN_3 has been carried out and the results are depicted in Figs. 8 and 9. The results reveal that hydroxyl radical inhibitors such as *t*-butanol and DMSO (lanes 4 and 6, Figs. 8 and 9) are able to quench the cleavage induced by both complexes to some degree. This suggests that the hydroxyl radical is the reactive oxygen species (ROS) that is involved in the mechanism. Several Cu(II) complexes such as bis(*N*,*N*′-dimethylglycinato)copper(II), bis[*N*-(*N*′-methylacetamido)-L-alaninato)copper(II) and Cu(II) chelated with 1,10-phenantroline-derived ligands have shown the same mechanism in the presence of H_2O_2 [19,29,30]. On the other hand, the cleavage reaction by both complexes are not inhibited by the singlet oxygen inhibitor NaN_3 (lanes 7–12, Figs. 8 and 9) but instead shows an

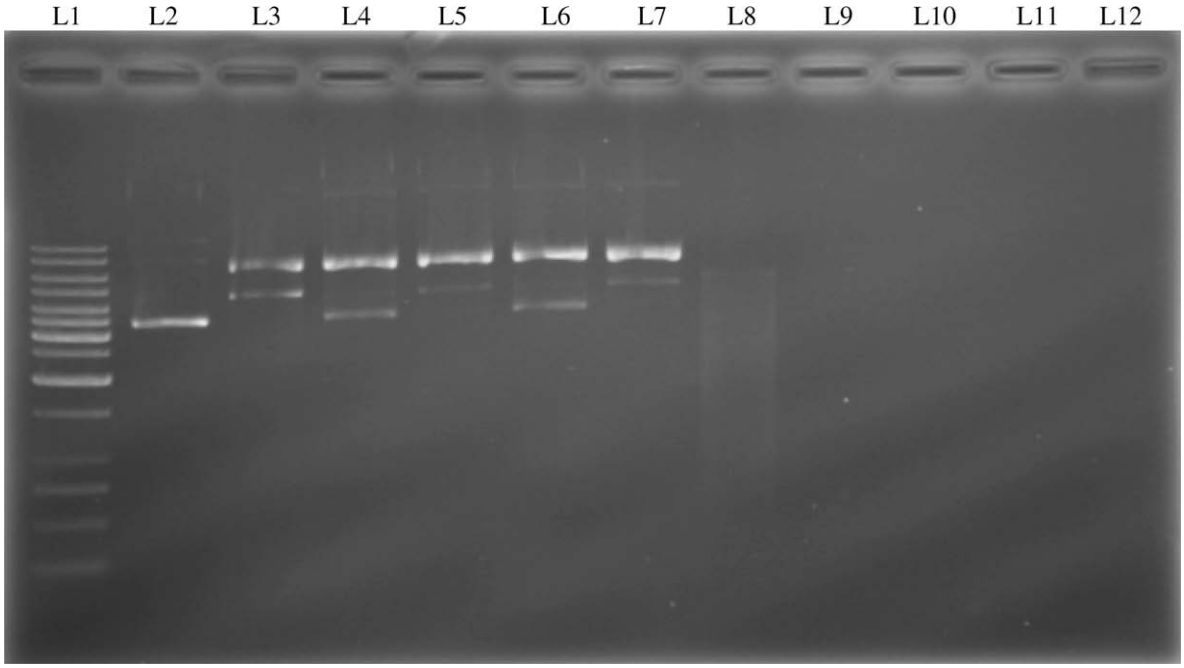


Fig. 8. Effect of various scavengers on the cleavage of pBR322 by 40 μM complex **1**. Lane 1, Gene Ruler 1 kb DNA ladder; lane 2, DNA alone; lane 3, DNA + 40 μM complex **1** + H_2O_2. Lanes 4–12 involve reaction of 40 μM complex **1** + H_2O_2 with DNA in presence of various scavengers; lane 4, *t*-butyl alcohol (1 M); lane 5, 1 mM mannitol; lane 6, DMSO (1 M); lane 7, 1 mM NaN_3; lane 8, 10 mM NaN_3; lane 9, 20 mM NaN_3; lane 10, 30 mM NaN_3; lane 11, 40 mM NaN_3; lane 12, 50 mM NaN_3.

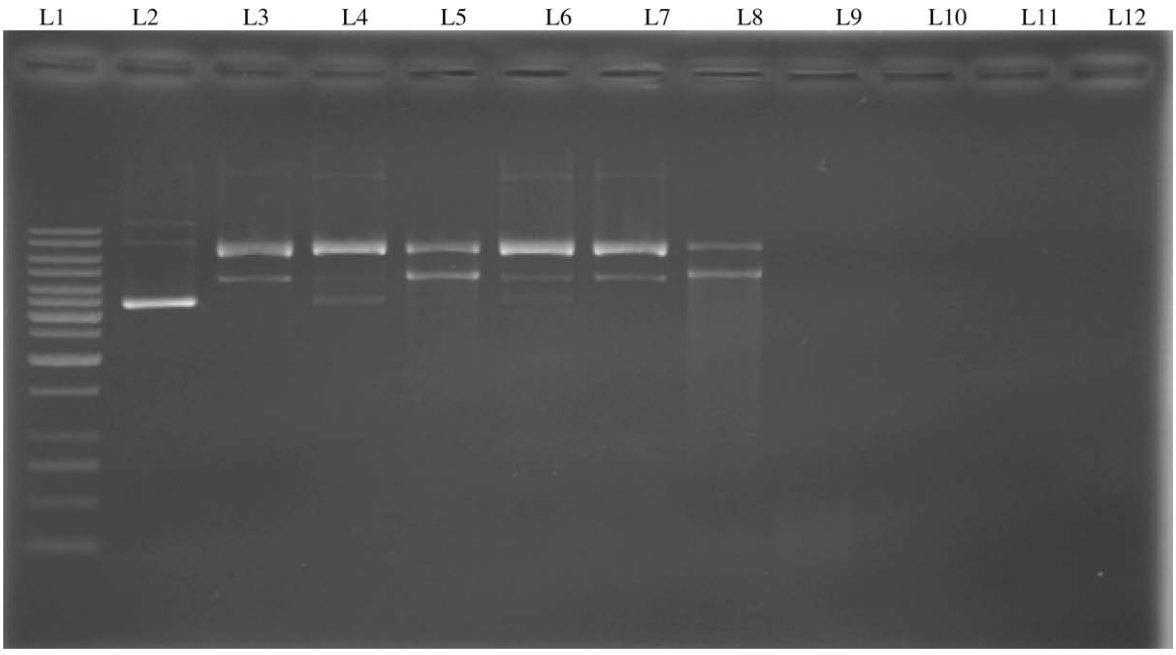


Fig. 9. Effect of various scavengers on the cleavage of pBR322 by 40 μM complex **2**. Lane 1, Gene Ruler 1 kb DNA ladder; lane 2, DNA alone; lane 3, DNA + 40 μM complex **2** + H_2O_2. Lanes 4–12 involve reaction of 40 μM complex **2** + H_2O_2 with DNA in presence of various scavengers; lane 4, *t*-butyl alcohol (1 M); lane 5, 1 mM mannitol; lane 6, DMSO (1 M); lane 7, 1 mM NaN_3; lane 8, 10 mM NaN_3; lane 9, 20 mM NaN_3; lane 10, 30 mM NaN_3; lane 11, 40 mM NaN_3; lane 12, 50 mM NaN_3.

Table 6
Cytotoxic activity of $[Cu(II)(ClNO_2Bzo)(H_2O)]_2$, $[Cu(II)(ClFBzo)(H_2O)]_2$ and $[Cu(II)(ClBzo)(H_2O)]_2$ toward human cancer cell lines.

Cancer cell lines	Cytotoxic activity (μg/ml) of complexes		
	$[Cu(II)(ClNO_2Bzo)(H_2O)]_2$	$[Cu(II)(ClFBzo)(H_2O)]_2$	$[Cu(II)(ClBzo)(H_2O)]_2$
1. MCF-7			
GI_{50} value	174.00 ± 10.51	157.63 ± 10.72	150.72 ± 7.64
TGI value	>200	>200	194.8 ± 6.97
LC_{50} value	>200	>200	>200
2. DU145			
GI_{50} value	>200	165.5 ± 31.02	159.5 ± 12.35
TGI value	>200	>200	>200
LC_{50} value	>200	>200	>200
3. Hela			
GI_{50} value	143.47 ± 8.46	141.20 ± 2.29	142.53 ± 2.48
TGI value	190.77 ± 9.84	>200	>200
LC_{50} value	>200	>200	>200
4. HepG2			
GI_{50} value	68.36 ± 11.32	81.18 ± 9.60	63.50 ± 9.80
TGI value	122.85 ± 14.96	144.80 ± 21.92	126.26 ± 21.75
LC_{50} value	194.22 ± 3.67	194.1 ± 8.35	192.32 ± 10.85

GI_{50}, growth inhibition activity; TGI, cytostatic activity; LC_{50}, cytotoxic activity.

Table 7
Cytotoxic activity of $[Cu(II)(ClNO_2Bzo)(H_2O)]_2$, $[Cu(II)(ClFBzo)(H_2O)]_2$ and $[Cu(II)(ClBzo)(H_2O)]_2$ toward Chang human normal liver cell line.

Normal cell line	Cytotoxic activity (μg/ml) of complexes		
	$[Cu(II)(ClNO_2Bzo)(H_2O)]_2$	$[Cu(II)(ClFBzo)(H_2O)]_2$	$[Cu(II)(ClBzo)(H_2O)]_2$
Chang			
GI_{50} value	178.89 ± 3.44	>200	185.88 ± 16.21
TGI value	>200	>200	>200
LC_{50} value	>200	>200	>200

GI_{50}, growth inhibition activity; TGI, cytostatic activity; LC_{50}, cytotoxic activity.

enhancement. This clearly indicates that singlet oxygen is not the reactive oxygen species (ROS) that is responsible in the cleavage reaction. Complex **3** shows similar results to that observed in **1** and **2**.

Table 8
Antibacterial activity of $[Cu(II)(ClNO_2Bzo)(H_2O)]_2$, $[Cu(II)(ClFBzo)(H_2O)]_2$ and $[Cu(II)(ClBzo)(H_2O)]_2$, results correspond to diameter of the inhibition zone (mm).

Bacteria	Complexes		
	$[Cu(II)(ClNO_2Bzo)(H_2O)]_2$	$[Cu(II)(ClFBzo)(H_2O)]_2$	$[Cu(II)(ClBzo)(H_2O)]_2$
Gram −ve bacteria			
Enterobacter aerogenes (−)			
500 μg/ml	10	12	10
250 μg/ml	7	9	8
125 μg/ml	R	8	R
Klebsiella pneumoniae (−)			
500 μg/ml	R	R	R
Proteus mirabilis (−)			
500 μg/ml	R	R	R
Pseudomonas aeruginosa (−)			
500 μg/ml	R	R	R
Shigella sonnei (−)			
500 μg/ml	R	R	R
Escherichia coli			
500 μg/ml	R	R	R
Gram +ve bacteria			
Bacillus cereus (+)			
500 μg/ml	R	R	R
Bacillus subtilis (+)			
500 μg/ml	R	R	R
Staphylococus aureus (+)			
500 μg/ml	R	R	R

R, resistant; well diameter = 5 mm.

Table 9
Antibacterial activity of $[Cu(II)(ClNO_2Bzo)(H_2O)]_2$, $[Cu(II)(ClFBzo)(H_2O)]_2$, $[Cu(II)(ClBzo)(H_2O)]_2$ and chloramphenicol, the results are expressed as MIC (minimal inhibitory concentration).

Gram −ve bacteria	$[Cu(II)(ClNO_2Bzo)(H_2O)]_2$	$[Cu(II)(ClFBzo)(H_2O)]_2$	$[Cu(II)(ClBzo)(H_2O)]_2$	Chloramphenicol
Enterobacter aerogenes (−) (μg/ml)	250	125	250	3.0

3.3. Cytotoxic studies

The antiproliferative activities of **1**–**3** on human cell lines have been evaluated by obtaining GI_{50}, TGI, and LC_{50} values as shown in Table 4. MCF-7, DU 145, HeLa, HepG2 and Chang cells were exposed to graded concentrations of **1**–**3** for 48 h. All the copper-containing complexes exhibit 50% growth inhibition (GI_{50}) in all cancer cell types at concentration <200 μg/ml. The data reveals an interesting finding in which **1**–**3** show the same selective trend against the cancer cell lines whereby they exhibit higher cytotoxic effect against HepG2 cancer cell lines (GI_{50} = 63–82 μg/ml) compared to MCF-7, DU 145, HeLa (GI_{50} = 140–180 μg/ml) cancer cell lines. Another interesting finding is that **1**–**3** show more than two-fold selective cytotoxicity against HepG2 human liver cancer cells compared to Chang human normal liver cells (GI_{50} = 178–>200 μg/ml). This finding is in contrast with the compound bis(phenanthroline)-4-methylcoumarin-6,7-dioxacetatocopper(II), $[Cu(4\text{-Mecdoa})(phen)_2]$ which shows selective cytotoxic effect against Chang human normal liver cells compared to HepG2 human liver cancer cells [54]. Furthermore, **1**–**3** have almost similar cytotoxic effect against Hela cells and **2**–**3** have slightly higher cytotoxic effect against MCF-7 and DU 145 cells compared to **1**. In HepG2 cells, all GI_{50}, TGI, and LC_{50} values of **1**–**3** can be obtained within the testing concentration range.

3.4. Antibacterial studies

The antibacterial screening of **1**–**3** have been carried out against nine pathogenic bacterial species using disc diffusion method and the results are presented in Table 5. Referring to Table 5, it is noted that **1**–**3** exhibit very selective antibacterial activity, being active against Gram negative *E.* aerogenes while inactive against other tested pathogenic bacteria. This finding is interesting because usually copper complexes which exhibit antibacterial activity against Gram *E.* aerogenes will also exhibit antibacterial activity against other bacteria. For example heterotrinuclear thiocyanato bridged Cu(II)–Hg(II)–Cu(II) complexes and valine-derived Schiff base copper(II) complexes not only show antibacterial activity against *E.* aerogenes but are also active against *Staphylococcus aureus, Escherichia coli, P. aeruginosa* and *Proteus vulgaris* [55,56]. This shows that the antibacterial activity of **1**–**3** is very selective within the testing concentration range. For comparison, **2** appears to be the most active complex against Gram negative bacteria *E.* aerogenes compared to **1** and **3**, as **2** has the widest inhibition zone and can exhibit antibacterial activity at the lowest concentration. Antibacterial tests of $CuCl_2$ against the nine pathogenic bacterial species have also been carried out. The results show that the $CuCl_2$ is inactive against all the tested pathogenic bacterial. From these results it may be inferred that the benzoate derivatives chelated to Cu(II) can induce the antibacterial activity against Gram negative bacteria *E. aerogenes*. The MIC experiments of **1**–**3** against the Gram negative bacteria *E.* aerogenes were further carried out and the results are presented in Table 6. The MIC results consistently show that **2** (MIC = 125 μg/ml) is the most active complex against *E.* aerogenes compared to **1** (MIC = 250 μg/ml) and **3** (MIC = 250 μg/ml). The MIC results of **1**–**3** against *E.* aerogenes show higher activity compared to some cobalt complexes [57] (see Tables 7–9).

4. Conclusion

Three water soluble dicopper(II) complexes, tetrakis(μ-4-chloro-2-nitrobenzoato-*O*,*O*′)bis[aquacopper(II)] (**1**), tetrakis(μ-2-chloro-6-fluorobenzoato-*O*,*O*′)bis[aquacopper(II)] (**2**) and tetrakis(μ-2-chloro-benzoato-*O*,*O*′)bis[aquacopper(II)] (**3**), have been synthesized. All the complexes have been tested for their nucleolytic, antiproliferation and antibacterial activity. For nucleolytic activity, all complexes can induce oxidative DNA cleavage in the presence of H_2O_2. Complexes **1**–**3** show good DNA cleavage ability comparable to other Cu(II) complexes described in the literature. Different functional group attached at the benzene ring in **1** (Cl and NO_2), **2** (Cl and F) and **3** (Cl only) do not influence the DNA cleavage efficiency. Hydroxyl radical is the reactive oxygen species that responsible for the cleavage reactions. In antiproliferation studies, all complexes show the same selective trend exhibiting higher cytotoxic effect against HepG2 cancer cell lines compared to MCF-7, DU 145 and HeLa cancer cell lines. It is interesting to note that **1**–**3** show more than twofold cytotoxic effect against HepG2 human liver cancer cells compared to Chang human normal liver cells, which means **1**–**3** are more potent against cancer cells than normal cells. The antibacterial activity of **1**–**3** exhibit a very selective trend whereby they are active against Gram −ve bacteria *E.* aerogenes while inactive against all other pathogenic bacteria. However, **2** appears to be the most active against the Gram negative bacteria *E.* aerogenes compared to **1** and **3**. The cleavage or fragmentation of DNA by the ROS generated by the complexes could be responsible for the antiproliferative activity exhibited by the complexes.

Acknowledgements

We like to thank the RU Grant from Universiti Sains, Malaysia, and FRGS Grant from Ministry of Higher Education (MOHE), Malaysia, for funding this research.

Appendix A. Supplementary data

CCDC 671169 and 671170 contains the supplementary crystallographic data for complexes **1** and **2**. These data can be obtained free of charge via http://www.ccdc.cam.ac.uk/conts/retrieving.html, or from the Cambridge Crystallographic Data Centre, 12 Union Road, Cambridge CB2 1EZ, UK; fax: (+44) 1223-336-033; or e-mail: deposit@ccdc.cam.ac.uk. Supplementary data associated with this article can be found, in the online version, at doi:10.1016/j.poly.2009.02.006.

References

[1] C. Urquiola, D. Gambino, M. Cabrera, M.L. Lavaggi, H. Cerecetto, M. González, A. López de Cerain, A. Monge, A.J. Costa-Filho, M.H. Torre, J. Inorg. Biochem. 102 (2008) 119.
[2] W. Luo, X.Gao. Meng, J.F. Xiang, Y. Duan, G.Z. Cheng, Z.P. Ji, Inorg. Chim. Acta 361 (2008) 2667.
[3] R.S. Kumar, K. Sasikala, S. Arunachalam, J. Inorg. Biochem. 102 (2008) 234.
[4] M. Devereux, D.O. Shea, A. Kellett, M. McCann, M. Walsh, D. Egan, C. Deegan, K. Kędziora, G. Rosair, H. Müller-Bunz, J. Inorg. Biochem. 101 (2007) 881.
[5] A. Puszko, L. Wasylina, M. Pełczynska, Z. Staszak, A. Adach, M. Cieślak-Golonka, M. Kubiak, J. Inorg. Biochem. 101 (2007) 117.
[6] R.N. Patel, N. Singh, V.L.N. Gundla, U.K. Chauhan, Spectrochim. Acta, Part A 66 (2007) 726.

[7] B.S. Creaven, D.A. Egan, K. Kavanagh, M. McCann, M. Mahon, A. Noble, B. Thati, M. Walsh, Polyhedron 24 (2005) 949.
[8] O. Ibopishak Singh, M. Damayanti, N. Rajen Singh, R.K. Hemakumar Singh, M. Mohapatra, R.M. Kadam, Polyhedron 24 (2005) 909.
[9] D.K. Saha, U. Sandbhor, K. Shirisha, S. Padhye, D. Deobagkar, C.E. Ansond, A.K. Powelld, Bioorg. Med. Chem. Lett. 14 (2004) 3027.
[10] F. Dallavalle, F. Gaccioli, R. Franchi-Gazzola, M. Lanfranchi, L. Marchio, M.A. Pellinghellia, M. Tegonia, J. Inorg. Biochem. 92 (2002) 95.
[11] C.A. Bolosa, K.T. Papazisisb, A.H. Kortsarisb, S. Voyatzib, D. Zamboulib, D.A. Kyriakidisc, J. Inorg. Biochem. 88 (2002) 25.
[12] M.A. Zoroddu, S. Zanetti, R. Pogni, R. Basosi, J. Inorg. Biochem. 63 (1996) 291.
[13] J.D. Ranford, P.J. Sadler, J. Chem. Soc., Dalton. Trans. (1993) 3393.
[14] D.S. Sigman, D.R. Graham, V.D. Aurora, A.M. Stern, J. Biol. Chem. 254 (1979) 12269.
[15] T.B. Thederahn, M.D. Kuwabara, T.A. Larsen, D.S. Sigman, J. Am. Chem. Soc. 111 (1989) 4941.
[16] R. Rao, A.K. Patra, P.R. Chetana, Polyhedron 27 (2008) 1343.
[17] R. Rao, A.K. Patra, P.R. Chetana, Polyhedron 26 (2007) 5331.
[18] A.K. Patra, M. Nethaji, A.R. Chakravarty, J. Inorg. Biochem. 101 (2007) 233.
[19] T. Hirohama, Y. Kuranuki, E. Ebina, T. Sugizaki, H. Arii, M. Chikira, P.T. Selvi, M. Palaniandavar, J. Inorg. Biochem. 99 (2005) 1205.
[20] V. Uma, M. Kanthimathi, T. Weyhermuller, B.U. Nair, J. Inorg. Biochem. 99 (2005) 2299.
[21] S. Zhang, Y. Zhu, C. Tu, H. Wei, Z. Yang, L. Lin, J. Ding, J. Zhang, Z. Guo, J. Inorg. Biochem. 98 (2004) 2099.
[22] M. Pitie, C. Boldron, H. Gornitzka, C. Hemmert, B. Donnadieu, B. Meunier, Eur. J. Inorg. Chem. (2003) 528.
[23] P.G. Sammes, G. Yahioglu, Chem. Rev. (1994) 327.
[24] C.J. Burrows, J.G. Muller, Chem. Rev. 98 (1998) 1109.
[25] M. Scarpellini, A. Neves, R. Horner, A.J. Bortoluzzi, B. Szpoganics, C. Zucco, R.A. Nome Silva, V. Drago, A.S. Mangrich, W.A. Ortiz, W.A. Passos, M.C. de Oliveira, H. Terenzi, Inorg. Chem. 42 (2003) 8353.
[26] S. Dhar, D. Senapati, P.K. Das, P. Chattopadhyay, M. Nethaji, A.R. Chakravarty, J. Am. Chem. Soc. 125 (2003) 12118.
[27] C. Tu, Y. Shao, N. Gan, O. Xu, Z. Guo, Inorg. Chem. 43 (2004) 4761.
[28] Y.L. Wang, Y.C. Liu, Z.S. Yang, G.C. Zhao, Bioelectrochemistry 65 (2004) 77.
[29] C.H. Ng, C.M. Lin, T.M. Chang, S.G. Teoh, S.Y. Yap, S.W. Ng, Polyhedron 25 (2005) 1287.
[30] C.H. Ng, H.K.A. Ong, C.W. Kong, K.K. Su, S.W. Ng, J. Coord. Chem. 59 (2006) 1089.
[31] Bruker, APEX2 (Version 1.27), SAINT (Version 7.12a) and SADABS (Version 2004/1), Bruker AXS Inc., Madison, Wisconsin, USA, 2005.
[32] G.M. Sheldrick, Acta Cryst. A64 (2008) 112.
[33] P. Skehan, R. Storeng, D. Scudiero, A. Monks, J. McMahon, D. Vistica, J.T. Warren, H. Bokesch, S. Kenney, M.R. Boyd, J. Natl. Cancer Inst. 82 (1990) 1107.
[34] R. Albuschat, W.W.M. Lowe, P. Luger, V. Jendrossek, Eur. J. Med. Chem. 39 (2004) 1001.
[35] V. Vichai, K. Kirtikara, Natl. Cent. Genet. Eng. Biotechnol. 1 (2006) 1112.
[36] M.M. Lieberman, G.M.L. Patterson, R.E. Moore, Cancer Lett. 173 (2001) 21.
[37] S.L. Holbeck, Eur. J. Cancer 40 (2004) 785.
[38] M.O. Barbara, R.S. Ewa, J. Mol. Struct. 784 (2006) 69.
[39] W. Huang, H. Qian, S. Gou, C. Yao, J. Mol. Struct. 743 (2005) 183.
[40] P. Drozdzewski, A. Brozyna, M. Kubiak, J. Mol. Struct. 707 (2004) 131.
[41] T. Kawata, S. Ohba, T. Tokii, Y. Muto, M. Kato, Acta Crystallogr., Struct. Commun. 48 (1992) 1590.
[42] W. Huang, D. Hu, S. Gou, H. Qian, H.K. Fun, S. Shanmuga, Q. Meng, J. Mol. Struct. 649 (2003) 269.
[43] G.B. Deacon, R.J. Phillips, Coord. Chem. Rev. 33 (1980) 227.
[44] P. Amudha, P. Akilan, M. Kandaswamy, Polyhedron 19 (2000) 1769.
[45] C. Fernandes, A. Neves, A.J. Bortoluzzi, A.S. Mangrich, E. Rentschler, B. Szpoganicz, E. Schwingel, Inorg. Chim. Acta 320 (2001) 12.
[46] S. Brooker, T.C. Davidson, S.J. Hay, R.J. Kelly, D.K. Kennepohl, P.G. Plieger, B. Moubaraki, K.S. Murray, E. Bill, E. Bothe, Coord. Chem. Rev. 216–217 (2001) 3.
[47] N. Sengottuvelan, D. Saravanakumar, M. Kandaswamy, Polyhedron 26 (2007) 3825.
[48] M.S. Surendra Babu, K. Hussain Reddy, Pitchika G. Krishna, Polyhedron 26 (2007) 572.
[49] T. Kobayashi, M. Kunita, S. Nishino, H. Matsushima, T. Tokoii, H. Masuda, H. Einaga, Y. Nishida, Polyhedron 19 (2000) 2639.
[50] J. Liu, T.-B. Lu, H. Deng, L.-N. Ji, Transition Met. Chem. 28 (2003) 116.
[51] J. Liu, T. Zhang, T. Lu, L. Qu, H. Zhou, Q. Zhang, L. Ji, J. Inorg. Biochem. 9 (2002) 269.
[52] C.A. Detmer III, F.V. Pamatong, J.R. Bocarsly, Inorg. Chem. 35 (1996) 6292.
[53] F.V. Pamatong, C.A. Detmer III, J.R. Bocarsly, J. Am. Chem. Soc. 118 (1996) 5339.
[54] B. Thati, A. Noble, B.S. Creaven, M. Walsh, K. Kavanagh, D.A. Egan, Eur. J. Pharm. 569 (2007) 16.
[55] L.T. Yıldırım, R. Kurtaran, H. Namli, A.D. Azaz, O. Atakol, Polyhedron 26 (2007) 4187.
[56] J. Lv, T. Liu, S. Cai, X. Wang, L. Liu, Y. Wang, J. Inorg. Biochem. 100 (2006) 1888.
[57] M. Poyraz, M. Sari, F. Demirci, M. Kosar, S. Demirayak, O. Büyükgüngör, Polyhedron 27 (2008) 2091.

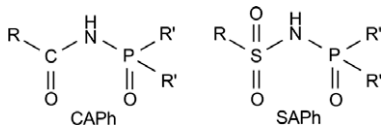


Chart 1. P, N-substituted analogues of β-diketones.

2. Experimental

2.1. Synthesis of H**L** (**1**)

The dimethyl(phenylsulfonyl)amidophosphate was prepared according to the early published procedures [19]. *Anal.* Calc. for $C_8H_{12}NO_5PS$ (M_r = 265.22): C, 36.23; H, 4.56; N, 5.28; S, 12.09. Found: C, 36.12; H, 4.39; N, 5.24; S, 12.1%. IR (KBr, cm^{-1}): 3000(s), 2745(m), 1455(m), 1410(s), 1320(vs), 1260(vs), 1185(vs), 1100(s), 1075(vs), 1060(vs), 955(vs), 885(m), 855(s), 780(s), 695(m), 605(m), 585(s), 535(s), 495(w), 435(w) cm^{-1}. M.p. 121 °C. ^{1}H NMR (DMSO): 3.57 (d, 6H, CH_3, $^3J_{P-H}$ = 12 Hz), 7.58 (m, β-H, 2H, C_6H_5), 7.65 (m, γ-H, 1H, C_6H_5), 7.91 (m, α-H, 2H, C_6H_5) ppm. ^{31}P NMR (DMSO): −2.17 (g, $^3J_{P-H}$=12 Hz) ppm.

2.2. Synthesis of [Cu(**L**)$_2$ · **o-bpe**]$_n$ (**2**)

A solution of H**L** (2 mmol) in isopropanol (10 ml) was mixed with isopropanol solution of sodium (2 mmol). To the resulting sodium salt the methanol solution of $Cu(NO_3)_2 \cdot 6H_2O$ (5 ml) (1 mmol) was added. After 20 min the precipitate of $NaNO_3$ was filtered off and was added to 10 ml of isopropanol solution of **o-bpe** (1 mmol). The resulting clear solution was left at ambient temperature for crystallization in air. The blue/green fine crystals were collected by filtration after 20 min, washed thoroughly with cool isopropanol and finally dried on filter. A well-formed crystal was used for the single X-ray structural analysis. Yield: 0.65 g (85%). *Anal.* Calc. for $C_{28}H_{32}N_4O_{10}P_2S_2Cu$ (M_r = 774.2): C, 43.44; H, 4.17; N, 7.24; S, 8.28. Found: C, 43.31; H, 4.08; N, 7.22; S, 8.49%. IR (KBr, cm^{-1}): 2965(w), 2865(w), 1610(w), 1575(w), 1485(m), 1455(m), 1255(s), 1230(vs), 1185(vs), 1075(s), 1040(vs), 940(w), 840(s), 790(m), 750(m), 740(m), 720(m), 700(m), 615(s), 580(m), 555(s), 510(w), 450(m) cm^{-1}. The compound **2** is soluble in MeOH, EtOH, DMSO and DMF.

2.3. Physical measurements

Elemental analysis (C, H, N and S) were performed using EL III Universal CHNOS Elemental Analyzer.

IR spectra were recorded as KBr pellets using UR-10 spectrometer in the 4000–400 cm^{-1} region using conventional techniques.

NMR spectra were obtained using Varian Mercury 400 NMR spectrometer at 25 °C. ^{1}H and ^{31}P spectra were recorded at 400 and 162.1 MHz, respectively. Chemical shifts are reported with reference to $SiMe_4$ (^{1}H) and H_3PO_4 (^{31}P).

Electron paramagnetic resonance (EPR) spectra were recorded using CMS 8400 spectrometer at X-band frequency (9.38 GHz) at 298 and 77 K. The solid sample for EPR measurements was carefully pounded with pestle.

Variable-temperature magnetic susceptibility data (2–300 K) were acquired on a powdered sample with the use of a Quantum Design MPMS-5 SQUID magnetometer. Corrections for the diamagnetism of the ligand were applied using Pascal's constants [20].

2.4. X-ray structure determination and refinement

The crystals of **1** ($C_8H_{12}NO_5PS$) are orthorhombic. At 293 K a = 7.521(3), b = 8.174(3), c = 18.919(5) Å, V = 1163.09(7) Å^3, M_r = 265.22, Z = 4, space group $P2_12_12_1$, D_{calc} = 1.515 g/cm^3, μ (Mo Kα) = 0.421 mm^{-1}, $F(000)$ = 552. Intensities of 5011 reflections (3154 independent, R_{int} = 0.0198) were measured on the «Xcalibur-3» diffractometer (graphite monochromated Mo Kα radiation, CCD detector, ω-scaning, $2\Theta_{max}$ = 60°).

The crystals of **2** ($C_{28}H_{32}N_4O_{10}P_2S_2Cu$) are monoclinic. At 293 K a = 28.255(2), b = 7.764(6), c = 18.600(6) Å, β = 125.57(3)°; V = 3318.9(3) Å^3, M_r = 774.18, Z = 4, space group $C2/c$, D_{calc} = 1.549 g/cm^3, μ (Mo Kα) = 0.941 mm^{-1}, $F(000)$ = 1596. Intensities of 12 937 reflections (4628 independent, R_{int} = 0.028) were measured on the «Xcalibur-3» diffractometer (graphite monochromated Mo Kα radiation, CCD detector, ω-scaning, $2\Theta_{max}$ = 60°).

The structures were solved by direct method using SHELXTL package [21]. Positions of the hydrogen atoms were located from electron density difference maps and refined by "riding" model with $U_{iso} = nU_{eq}$ of the carrier atom (n = 1.5 for methyl group and n = 1.2 for other hydrogen atoms).

Full-matrix least-squares refinement of the structures against F^2 in anisotropic approximation for non-hydrogen atoms using 3108 (**1**) and 4594 (**2**) reflections was converged to: wR_2 = 0.073 (R_1 = 0.032 for 2500 reflections with $F > 4\sigma(F)$, S = 0.928) for structure **1** and wR_2 = 0.105 (R_1 = 0.040 for 3404 reflections with $F > 4\sigma(F)$, S = 1.028) for structure **2**.

3. Results and discussion

3.1. Synthesis and spectroscopic characterization

Sodium salt Na**L** was obtained by the reaction of *i*-PrONa with *i*-PrOH solution of H**L**. Cu(**L**)$_2$ was prepared by the reaction of Na**L** with $Cu(NO_3)_2$ in alcohol solution. The presence of unsaturated coordination sphere of copper ion in Cu(**L**)$_2$ can be used for obtaining a wide number of mix-ligand compounds by interaction of Cu(**L**)$_2$ with various donor agents. In our work we used **o-bpe** as the bidentate bridging ligand. The reaction of Cu(**L**)$_2$ with an equimolar amount of **o-bpe** in *i*-PrOH leads to the formation of polymeric complex with the general formula [Cu(**L**)$_2$ · **o-bpe**]$_n$ (**2**). Syntheses of all compounds were carried out in air.

The vibration of the amide group ν(N–H) in IR spectra of H**L** appears in the region of 2800–3200 cm^{-1} with the maxima at 3000 cm^{-1}. This band absents in the spectra of Na**L** and [Cu(**L**)$_2$ · **o-bpe**]$_n$, which can be consequence of the ligand's coordination in deprotonated form (**L**$^-$). Two sharp bands which are observed in the spectrum of free ligand with maxima at 1260 and 1320 cm^{-1} are assigned to ν(PO) and ν(SO) vibrations [22]. In the spectra of sodium salt and **2** these bands are shifted to lower frequencies (1185, 1230 and 1250 cm^{-1} for Na**L**, 1180, 1230 and 1250 cm^{-1} for **2**) that can be explained by coordination to the metal ion. The analysis of IR spectra suggests a bidentate coordination of the anionic form **L**$^-$ *via* the oxygen atoms of phosphoryl and sulfonyl groups.

3.2. Crystal structure of **1**

White needle-shaped crystals of H**L** were grown over a period of 5 days from the *i*-PrOH–hexane solution. The molecular structure and the numbering scheme of **1** and crystal packing diagram are shown in Fig. 1, selected bond lengths and angles are listed in Table 1.

Thus as CAPh, namely $CCl_3C(O)NHP(O)(OCH_3)_2$ [23], the geometry around the phosphorus atom in H**L** (**1**) can be described as a distorted tetrahedron. The P(1)–O(3) and P(1)–N(1) bond lengths for **1** have values 1.456(1) and 1.662(2) Å, which are typical for CAPh with ether-type substituents [23–25]. The S(1)–O(1) (1.418(2) Å), S(1)–O(2) (1.428(2) Å) and S(1)–N(1) (1.642(2) Å)

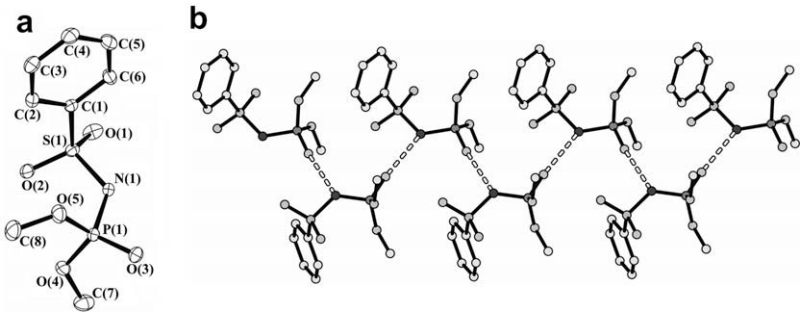


Fig. 1. Structural representation of **1** (a) with atom numbering scheme and 30% probability thermal ellipsoids, and fragments of the crystal packing in the structure of **1** (b). The hydrogen atoms are omitted for clarity. Hydrogen bonds are indicated by dashed lines.

Table 1
Selected geometrical parameters (distances (Å) and angles (°)) for **1**.

P(1)–O(3)	1.456(1)	S(1)–O(2)	1.428(1)
P(1)–O(4)	1.550(1)	S(1)–N(1)	1.642(2)
P(1)–O(5)	1.548(2)	S(1)–C(1)	1.760(2)
P(1)–N(1)	1.662(2)	O(4)–C(7)	1.426(3)
S(1)–O(1)	1.418(2)	O(5)–C(8)	1.433(3)
O(3)–P(1)–O(4)	115.6(1)	O(2)–S(1)–N(1)	107.4(1)
O(3)–P(1)–O(5)	116.0(1)	O(1)–S(1)–C(1)	108.0(1)
O(4)–P(1)–O(5)	103.7(1)	O(2)–S(1)–C(1)	108.7(1)
O(3)–P(1)–N(1)	108.1(1)	N(1)–S(1)–C(1)	105.6(1)
O(4)–P(1)–N(1)	108.4(1)	C(7)–O(4)–P(1)	120.9(1)
O(5)–P(1)–N(1)	104.4(1)	C(8)–O(5)–P(1)	127.7(2)
O(1)–S(1)–O(2)	119.7(1)	S(1)–N(1)–P(1)	125.1(1)
O(1)–S(1)–N(1)	106.6(1)		

bond lengths values depend on the substituent near the sulfur atom and have the typical values for sulfonylamide derivatives [26].

The values of the O–P–N bond angles are 108.4(1)°, 104.4(1)° and 108.1(1)° for the O(4)–P(1)–N(1), O(5)–P(1)–N(1) and O(3)–P(1)–N(1), respectively. It was early published that the presence of small substituents at phosphorus atom possesses a weak effect on the value of the O–P–N angle which falls in the range 107.5–108.9° [27]. Due to the steric effects the O(3)–P(1)–O(4) and O(3)–P(1)–O(5) angles are 115.6(1)° and 116.0(1)°, respectively, which are usually more than those in the ideal tetrahedron. The sulfur atom in the sulfonyl group has a distorted tetrahedral environment too (Table 1).

The O(2) and O(3) oxygen atoms of sulfonyl and phosphoryl groups are located in *anti*-positions to each other similar to most of CAPh [27]. The P═O bond adopts conformation with respect to the N(1)–S(1) bond, O(3)–P(1)–N(1)–S(1) fragment is practically planar (the torsion angle is −167.0(1)°). The deviations of the O(1) and O(2) from the P(1)–N(1)–S(1) plane are 0.583 and 0.579 Å, respectively.

In the crystal packing molecules of **1** are linked to each other by intermolecular hydrogen bonds where amide nitrogen atom of one molecule acts as donor and oxygen atom of phosphoryl group of neighboring molecule acts as acceptor (H···O′ 1.96 Å, N–H···O′ 170°) and form the infinite zigzag chains along [1 0 0] crystallographic direction. Neighboring chains are connected by the C(7)–H(7A)···π′ ($x-1, y-1, z$) hydrogen bonds (H···C′ 2.84 Å, C–H···π′ 153°).

3.3. Crystal structure of *2*

The molecular structure of **2** is shown in Fig. 2 (H atoms are omitted for clarity); selected bond distances and angles are presented in Table 2. The compound has 1D polymer chain structure along [0 1 0] crystallographic direction and consists of Cu(**L**)$_2$ units bridged by **o-bpe** ligands. Two sulfamide ligands are coordinated to metal ion in *trans*-positions because of the presence of steric effects concerning to the asymmetric (chiral) feature of coordinated SO-group. The Cu(1) atom is located in the special position in the center of symmetry. The coordination environment of Cu(II) ion can be described as a distorted square-bipyramidal polyhedron (4 + 2). The CuO_4N_2 chromophore is constructed from two pyridyl nitrogen atoms from two **o-bpe** linkers and four oxygen atoms of phosphoryl and sulfonyl groups from two ligands which are coordinated in bidentate chelate mode forming with central ion six-membered chelate rings. The Cu–O and Cu–N bond distances and O–Cu–O′, O–Cu–N, N–Cu–N′ angles (Table 2) are typical for square-bipyramidal copper complexes with clear presence of

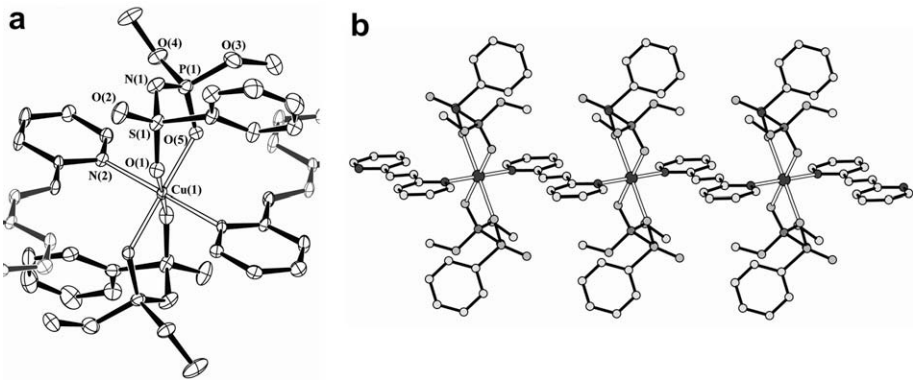


Fig. 2. Structural representation of **2** (a) with atom numbering scheme and 20% probability thermal ellipsoids, and fragments of the crystal packing in the structure of **2** (b). The hydrogen atoms are omitted for clarity.

Table 2
Selected geometrical parameters (distances (Å) and angles (°)) for **2**.

Cu(1)–O(3)	1.950(1)	P(1)–O(5)	1.566(2)
Cu(1)–N(2)	2.053(1)	P(1)–O(4)	1.576(2)
Cu(1)–O(2)	2.589(1)	P(1)–O(3)	1.496(2)
S(1)–O(2)	1.450(2)	P(1)–N(1)	1.591(2)
S(1)–O(1)	1.440(2)	O(4)–C(7)	1.407(3)
S(1)–N(1)	1.554(2)	O(5)–C(8)	1.441(4)
S(1)–C(1)	1.775(2)		
O(3)–Cu(1)–O(3)#1	180.0(1)	N(1)–S(1)–C(1)	107.7(1)
O(3)–Cu(1)–N(2)#1	90.6(1)	O(5)–P(1)–O(4)	107.3(1)
O(3)#1–Cu(1)–N(2)#1	89.4(1)	O(4)–P(1)–O(3)	106.5(1)
O(3)–Cu(1)–N(2)	89.4(1)	O(5)–P(1)–O(4)	107.3(1)
O(3)#1–Cu(1)–N(2)	90.6(1)	O(3)–P(1)–N(1)	119.7(1)
N(2)#1–Cu(1)–N(2)	180.0(1)	O(5)–P(1)–N(1)	106.5(1)
O(2)–Cu(1)–O(3)	82.5(1)	O(4)–P(1)–N(1)	106.8(1)
O(2)#1–Cu(1)–O(3)	97.58(7)	P(1)–O(3)–Cu(1)	129.7(1)
N(2)#1–Cu(1)–O(2)	99.3(1)	S(1)–O(2)–Cu(1)	125.3(1)
N(2)–Cu(1)–O(3)	89.4(1)	C(7)–O(4)–P(1)	123.9(2)
O(2)–S(1)–O(1)	114.8(1)	C(8)–O(5)–P(1)	121.2(2)
O(2)–S(1)–N(1)	111.6(1)	C(9)–N(2)–C(13)	118.5(2)
O(1)–S(1)–N(1)	109.6(1)	C(9)–N(2)–Cu(1)	115.6(1)
O(2)–S(1)–C(1)	106.0(1)	C(13)–N(2)–Cu(1)	125.7(1)
O(1)–S(1)–C(1)	106.9(1)	S(1)–N(1)–P(1)	126.4(1)

Symmetry transformations used to generate equivalent atoms: (#1) <$-x+1/2, -y+1/2, -z+1$>.

Jahn–Teller distortion. The Cu–O(S), Cu–O(P) and Cu–N bond values are 2.588(2), 1.950(1) and 2.053(2) Å, respectively. The six-membered chelate ring adopts a twist-boat conformation (the puckering parameters are $S = 0.67$, $\theta = 86.32$, $\psi = 17.43$) [28]. The deviations of the N(1) and Cu(1) atoms from the O(1)–S(1)–P(1)–O(5) mean plane are 0.40 and 0.74 Å, respectively. The chelate angles values fall in the range 82.5(6)–99.3(6)° which are typical for Cu(II) complexes with octahedral coordination.

The amide nitrogen atom of ligand is deprotonated that leads to the decrease of the S(1)–N(1) and N(1)–P(1) bond length values (Table 2) in comparison with the same values for neutral ligand (structure **1**). In spite of the deprotonation of amide group the O–P–N–S–O backbone is not flat. The P(1)–O(3) and S(1)–O(2) bond values are elongated due to the coordination, the conformation of the O–P–N–S–O fragment is changed owing to the turn of the phosphoryl group relatively the N(1)–S(1) bond (the O(3)–P(1)–N(1)–S(1) is −35.1(2)°).

In the crystal packing neighboring polymer chains are connected by the C(11)–H(11)···π′ ($x, 1-y, z-0.5$) weak hydrogen bonds (H···C′ 2.85 Å, C–H···π′ 130°) and form layers which are parallel to *OYZ* plane. The **o-bpe** ligands are coordinated to the 3d-metals forming *trans*-isomers of complexes which are typical for the ligands of this type [29]. The Cu···Cu′ separations in chain are 7.75 Å.

3.4. EPR studies and magnetochemistry

The X-band EPR spectrum of a solid sample of **2** at 77 K shows the presence of elongated axial symmetry signal with not resolved hyperfine structure (Fig. 3a). The values of anisotropic parameters of the spectrum are $g_{\|} = 2.365$, $g_{\perp} = 2.095$, which are typical for copper(II) ions with $d_{x^2-y^2}$ ground state. The "half-field" signal is not observed which can be suggested as the absence of magnetic exchange interaction between copper(II) ions or the value of it is very weak.

The EPR spectrum of frozen diluted solution at 77 K (Fig. 3b) is not similar to that observed in the solid state with the presence of hyperfine splitting in the parallel orientation region. The values of parameters are $g_{\|} = 2.450$, $g_{\perp} = 2.105$ and $A_{\|} = 126 \cdot 10^{-4}\ cm^{-1}$ which are typical for CuO_6 octahedral coordination environment [30]. Such behavior can be explained by dissociation of polymeric

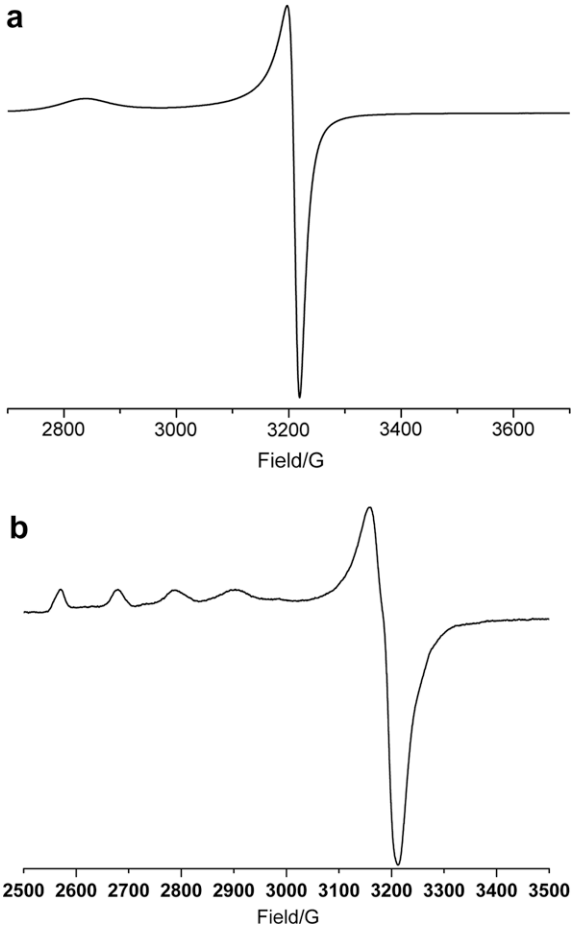


Fig. 3. X-band EPR spectra of compound **2**: (a) solid **2** at 77 K and (b) frozen $CHCl_3$/CH_3OH (1:1, v/v) solution of **2** at 77 K.

complexes in solution and ligand exchange (**o-bpe** molecules to solvent alcohol molecules).

Variable-temperature magnetic susceptibility studies for compound **2** were carried out over the temperature range 2–295 K. The magnetic moment of **2** at room temperature was 1.94μ_B (corresponds to $\chi_M T$ of 0.467 $cm^{-3}\ K\ mol^{-1}$) which is a typical value for copper(II) and slightly greater than the expected spin-only value.

The susceptibility (χ_M) of **2** showed steady increase upon cooling, without maximum (□ in Fig. 4). The plot of $\chi_M T$ (per mole) versus temperature (● in Fig. 4) shows that $\chi_M T$ first negligible decreased from 0.467 $cm^{-3}\ K\ mol^{-1}$ at 295 K to 0.439 $cm^{-3}\ K\ mol^{-1}$ at 10 K (1.94μ_B and 1.88μ_B, respectively), then sharply decreased to 0.404 $cm^{-3}\ K\ mol^{-1}$ at 2 K (1.80μ_B). This is clearly indicative the presence of week antiferromagnetic behavior within the chain. A simulation of these data was based on the Hamiltonian (Eq. (1)) and derived by Bonner and Fisher for infinite chain model with magnetically identical $S = ½$ metal centers (Eq. (2)) [31]:

$$\hat{H} = -J\left(\sum \hat{\mathbf{S}}_i \cdot \hat{\mathbf{S}}_{i+1}\right) \tag{1}$$

$$\chi' = \left(\frac{Ng^2\beta^2}{kT}\right)\left(\frac{0.25 + 0.074975\left(\frac{|J|}{kT}\right) + 0.075235\left(\frac{|J|}{kT}\right)^2}{1 + 0.9931\left(\frac{|J|}{kT}\right) + 0.172135\left(\frac{|J|}{kT}\right)^2 + 0.757825\left(\frac{|J|}{kT}\right)^3}\right) \tag{2}$$

In Eq. (2) J, N, g, β and k have their usual meanings. However, the presence of unlinked copper ions and/or short odd-numbered

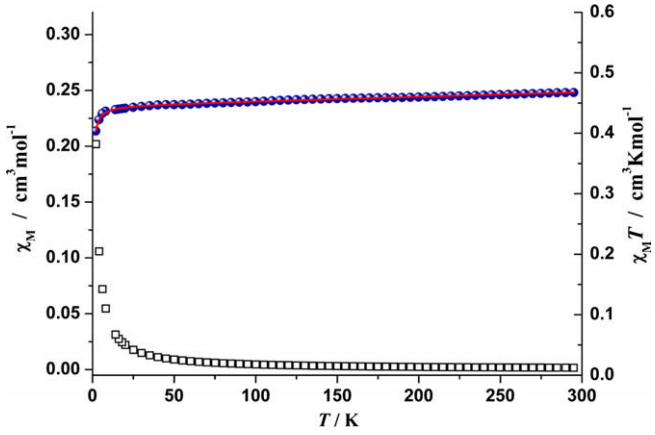


Fig. 4. Plot of χ_M and $\chi_M T$ vs. T for **2**; the solid line represents the simulated curve.

chains was taken into account; the experimental $\chi_M T$ of **2** was fitted using the Eq. (3) in which ρ – the fraction of paramagnetic impurity. Temperature independent paramagnetism (P_{TI}) was also added in calculations:

$$\chi = (1-\rho)\chi' + \frac{Ng^2\beta^2}{4kT}\rho + P_{TI} \quad (3)$$

The best fit calculated for **2** gave the following parameter values: $g = 2.180(1)$, $J = -0.21(1)\,cm^{-1}$, $\rho = 0\%$, $P_{TI} = 74(1)\cdot 10^{-6}$ $cm^3\,mol^{-1}$, $R = 1.49\cdot 10^{-3}$, where $R = [\sum(X_{obs} - X_{calc})^2/\sum X^2_{calc}]^{1/2}$. The small negative value of J confirms the presence of weak predominant antiferromagnetic coupling within the chain. The small decreasing in $\chi_M T$ in the 10–300 K temperature range can be explained by existence of temperature independent paramagnetism. The obtaining value of isotropic g-factor is close to those calculated from EPR spectrum as g_{av} (Eq. (4)):

$$g_{av} = \frac{(g_{\parallel} + 2g_{\perp})}{3} \quad (4)$$

However, the Cu···Cu′ distance in chain is sizeable enough the exchange interaction between copper(II) ions are mediated by the system of conjugated C=C bonds of **o-bpe**. The value of J cannot be compared because there is only one record concerning using **o-bpe** for bridging copper(I) [31] and no records for copper(II) ions reported to date.

4. Conclusion

The paper is devoted to coordination chemistry of sulfonyl phosphoramide ligands and their complex with copper(II). The new copper(II) complex containing deprotonated sulfamide ligands and **o-bpe** as bridging ligand has been obtained. The X-ray crystal structures for H**L** and $[Cu(\mathbf{L})_2\cdot\mathbf{o\text{-}bpe}]_n$ have been determined. In contrast to fully characterized CAPh ligands, which usually form dimer structure by means of hydrogen bonds, the molecules of **1** form a hydrogen bonded chain in which they are linked to each other due to identical (P)O···H–N contacts. The compound **2** has 1D polymeric chain structure. The magnetic study of **2** shows the presence of weak intrachain antiferromagnetic exchange interaction between copper(II) ions.

Supplementary data

CCDC 710779 and 710780 contains the supplementary crystallographic data for **1** and **2**. These data can be obtained free of charge *via* http://www.ccdc.cam.ac.uk/conts/retrieving.html, or from the Cambridge Crystallographic Data Centre, 12 Union Road, Cambridge CB2 1EZ, UK; fax: (+44) 1223-336-033; or e-mail: deposit@ccdc.cam.ac.uk.

Acknowledgement

This work was supported in part by Fundamental Researches State Fund of Ukraine (Project F25/193 – 2008).

References

[1] F.D. Sokolov, V.V. Brusko, N.G. Zabirov, R.A. Cherkasov, Curr. Org. Chem. 10 (2006) 27.
[2] D.A. Safin, F.D. Sokolov, N.G. Zabirov, V.V. Brusko, D.B. Krivolapov, I.A. Litvinov, R.C. Luckay, R.A. Cherkasov, Polyhedron 25 (2006) 3330.
[3] F.D. Sokolov, D.A. Safin, N.G. Zabirov, V.V. Brusko, B.I. Khairutdinov, D.B. Krivolapov, I.A. Litvinov, Eur. J. Inorg. Chem. 10 (2006) 2027.
[4] N.G. Zabirov, O.K. Pozdeev, F.M. Shamsevaleev, R.A. Cherkasov, G.H. Gilmanova, Pharm. Chem. J. 23 (1989) 423.
[5] (a) V. Amirkhanov, C. Janczak, L. Macalik, J. Hanuza, J. Legendziewicz, J. Appl. Spectros. 62 (1995) 5;
(b) V. Amirkhanov, V. Ovchinnikov, J. Legendziewicz, A. Graczyk, J. Hanuza, L. Macalik, Acta Phys. Polon. 90 (1996) 455.
[6] L.G. Shaidarova, A.V. Gedmina, N.A. Ulahovich, G.K. Budnikov, N.G. Zabirov, Zh. Obshch. Khim. 72 (2002) 1662.
[7] O. Navratil, E. Herrmann, N.T.T. Chau, Ch. Tea, J. Smola, Collect. Czech. Chem. Commun. 58 (1993) 798.
[8] K.O. Znovjyak, V.A. Ovchynnikov, S.V. Shishkina, T.Yu. Sliva, V.M. Amirkhanov, Doklady Akademii Nauk 9 (2006) 151.
[9] M.G. Zimin, G.A. Lazareva, N.I. Savelieva, R.G. Islamov, N.G. Zabirov, V.F. Toropova, A.N. Pudovik, Zh. Obshch. Khim. (J. Gen. Chem. USSR) 52 (1982) 1573.
[10] K.E. Gubina, V.A. Ovchynnikov, V.M. Amirkhanov, H. Fischer, R. Stumpf, V.V. Skopenko, Z. Naturforsch. 55b (2000) 576.
[11] V. Skopenko, V. Amirkhanov, T. Sliva, I. Vasilchenko, E. Anpilova, A. Garnovskii, Usp. Khim. 73 (2004) 797.
[12] V.A. Trush, K.V. Domasevitch, V.M. Amirkhanov, Doklady Akademii Nauk 7 (2007) 147.
[13] V.A. Ovchynnikov, T.P. Timoshenko, V.M. Amirkhanov, J. Sieler, V.V. Skopenko, Z. Naturforsch. 55b (2000) 262.
[14] (a) E.A. Trush, V.M. Amirkhanov, V.A. Ovchynnikov, J. Swiatek-Kozlowska, K.A. Lanikina, K.V. Domasevitch, Polyhedron 00 (2003) 1;
(b) V.A. Ovchynnikov, V.M. Amirkhanov, A.A. Kapshuk, T.Yu. Sliva, T. Glowiak, H. Kozlowski, Z. Naturforsch. 53b (1998) 836.
[15] A.V. Kirsanov, Fosfazosoedineniya (Phosphazo Compounds) Naukova Dumka, Kiev, 1965.
[16] K. Xu, C. Angell, Inorg. Chim. Acta 298 (2000) 16.
[17] S. Kishino, S. Saito, US Patent 4 161 524, 1979.
[18] O.V. Moroz, S.V. Shishkina, V.A. Trush, T.Yu. Sliva, V.M. Amirkhanov, Acta Crystallogr., Sect. E 63 (2007) m3175.
[19] A. Kirsanov, V. Shevchenko, Zh. Obshch. Khim. 26 (1956) 504.
[20] G.A. Bain, J.F. Berry, J. Chem. Edu. 85 (2008) 532.
[21] G.M. Sheldrick, SHELXL97 and SHELXS97, University of Göttingen, Germany, 1997.
[22] S. Boudjabi, G. Dewynter, J.-L. Montero, Synlett 5 (2000) 716.
[23] V.M. Amirkhanov, V.A. Trush, Zh. Obsch. Khim. 65 (1995) 1120.
[24] K.E. Gubina, V.M. Amirkhanov, Naturforsch 55b (2000) 1015.
[25] V. Miztahi, T.A. Modro, Cryst. Struct. Commun. 11 (1982) 627.
[26] H.-B. Burgi, J.D. Dunitz, Structure Correlation, vol. 2, VCH, Weinheim, 1997.
[27] V.M. Amirkhanov, V.A. Ovchinnikov, T. Glowiak, H. Kozlowski, Naturforsch 52b (1997) 1331.
[28] N.S. Zefirov, V.A. Palyulin, E.E. Dashevskaya, J. Phys. Org. Chem. 3 (1990) 147.
[29] S. Kitagawa, S. Matsuyama, M. Munakata, T. Emori, J. Chem. Soc., Dalton Trans. (1991) 2869.
[30] (a) B. Kozlevcar, A. Golobic, P. Strauch, Polyhedron 25 (2006) 2824;
(b) V.E. Petrashen, Y.V. Yablokov, R.L. Davidovich, Phys. Status Solids B 101 (1980) 117;
(c) D.K. De, J. Magn. Reson. 47 (1982) 181.
[31] W.E. Estes, D.P. Gavel, W.E. Hatfield, D.J. Hodgson, Inorg. Chem. 17 (1978) 1415.

the reaction. Hence, it is very likely that the mechanism of the OsO_4-catalysed oxidation of any given substrate by $Fe(CN)_6^{3-}$ may prove identical with the mechanism of the oxidation of the same substrate with OsO_4. However, the results of the study of the OsO_4-catalysed oxidation of HPO_3^{2-} by $Fe(CN)_6^{3-}$ [10] and that by OsO_4 [30] did not prove so. The OsO_4-catalysed study did not provide evidence for complex formation between OsO_4 and HPO_3^{2-} ion. The OH^- ion increased the rate which reached a saturation value in the OsO_4-catalysed study [10] whereas the rate decreased with increasing OH^- ion in the OsO_4 oxidation study [30].

It was, therefore, decided to investigate the kinetics of oxidation of $H_2PO_2^-$ and $C_6H_5HPO_2^-$ ions by OsO_4 to compare it with the OsO_4-catalysed oxidation by $Fe(CN)_6^{3-}$ ion [11] and that of HPO_3^{2-} by alkaline OsO_4 [30]. The results described in this paper are identical with those observed in the OsO_4-catalysed oxidation by $Fe(CN)_6^{3-}$ ion [11].

2. Experimental

2.1. Material

Sodium hypophosphite (M.B., AnalaR) is analysed for phosphite ion by published method [31]. It is found that the concentration of HPO_3^{2-} ion <0.1% is present in the sample. The freshly prepared aqueous solution is standardised against a known Ce(IV) solution [32]. Thereafter the solutions are freshly prepared by the dissolution of the required weight of the sample in a known NaOH solution for each set of the experiments. Phenylphosphinic acid (Fluka, Technical) is crystallised twice from hot water. The m.p. of the recrystallised sample is 70–71 °C (lit. 71 °C [33]). The sample is standardised against Ce(IV). The experimental solution is prepared by neutralisation and dilution with a known NaOH solution.

The 50 wt% solution of D_3PO_2 (Aldrich) is used as received. It is suitably diluted in D_2O (99.8 at%, BARC Trombay). The solution is standardised by cerimetry [32]. The experimental solution is prepared by neutralisation and dilution with a known NaOH solution prepared in D_2O just before the start of the rate measurement to avoid any exchange during the course of the experiments.

NaOH (Sarabhai-M, GR) solution is freshly prepared and standardised against a standard potassium hydrogen phthalate (BDH, AnalaR) solution. Solutions of KCl and NaCl (BDH, AnalaR), used for adjusting the ionic strength of the reaction mixtures, are prepared by weighing the respective samples.

The OsO_4 solution is prepared by dissolution of the weighed sample (Johnson Matthey) in 0.1 mol dm^{-3} NaOH and stored in the refrigerator. The solution is standardised by iodometry [10] and spectrophotometrically ($\varepsilon_{316} = 500\ dm^3\ mol^{-1}\ cm^{-1}$) [28]. Suitable dilutions are carried out with standard NaOH solutions as and when needed.

The water is first distilled under mild alkaline conditions using a pinch of potassium permanganate. The first distillate is once again distilled and the second distillate is used for the preparation of the solutions. These solutions, if needed, are purged with nitrogen gas before use.

2.2. Stoichiometry

Several reaction mixtures with different concentration ratios of $RHPO_2^-$ and OsO_4 are prepared at different $[OH^-]$. The OsO_4 is always in excess. The corresponding blanks are also prepared. The optical density of the unreacted OsO_4 in the reaction mixtures is measured at different intervals of time on a HP 8452A diode array spectrophotometer having a band-width of 2 nm and an integration time of 1 s till a constant value is obtained at 320 nm. The blank solutions are similarly treated. The results indicated that mean $\Delta[OsO_4]/\Delta[RHPO_2] = 1 \pm 0.1$. The oxidation product HPO_3^{2-} is identified by TLC [34], $R_f = 0.76$ (lit. value 0.75 [22]). The stoichiometric equation (1) is supported by the quantitative estimation of HPO_3^{2-} [31]. The species OsO_4OH^- is the considered reactive OsO_4 species. The formation of Os(VI) in the reaction mixture is

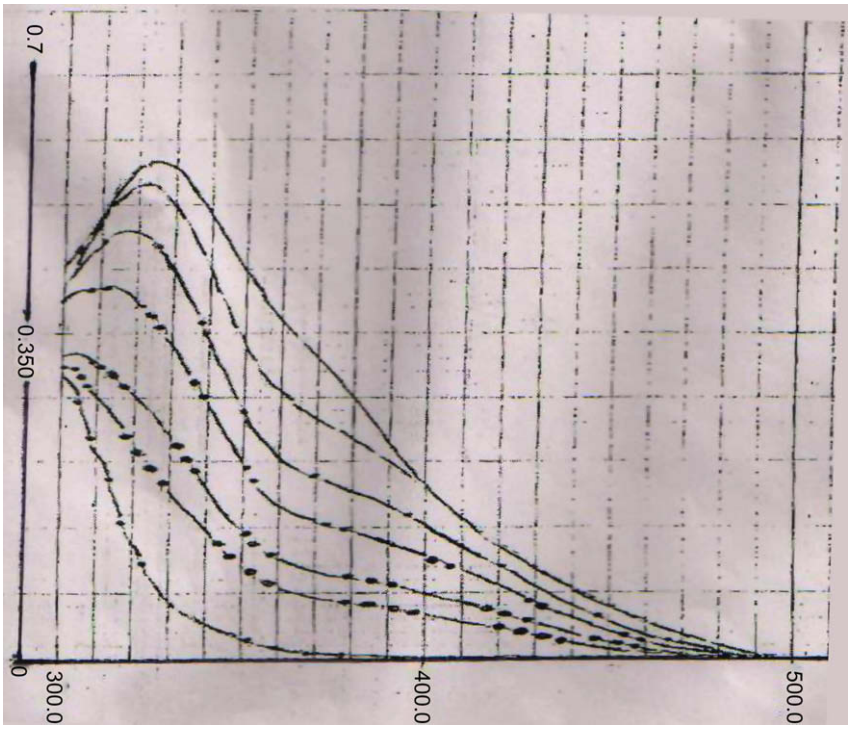


Fig. 1. The spectra of $10^4[OsO_4] = 3.24$ mol dm^{-3} between 300 and 500 nm in $[OH^-] = 0.001$ (---), 0.005 (·····), 0.01 (-·-·-), 0.02 (-··-), 0.05 (-×-) and 0.5 (- - - -) and 2.0 (—) mol dm^{-3} at room temperature.

confirmed by the matching spectra of the spent reaction mixture and that of K_2OsO_4 (Johnson Matthey) in solution of the same alkalinity:

$$OsO_4OH^- + RHPO_2^- \rightarrow OsO_3 + RPO_3^{2-} + H_2O \quad (1)$$

2.3. Spectra of OsO_4 in NaOH

The spectra of $10^4[OsO_4] = 3.24$ mol dm^{-3} in varying [NaOH] solutions is recorded between 300 and 500 nm on a Shimadzu spectrophotometer. The spectra, Fig. 1, show increasing optical densities with the increasing NaOH concentrations. The first and second spectra from bottom corresponding to NaOH = 0.001 and 0.005 mol dm^{-3} have no peaks. The peak starts appearing in the third and fourth spectra from bottom for NaOH = 0.01 and 0.02 mol dm^{-3} and is well defined in the fifth, sixth, and seventh spectra for NaOH = 0.05, 0.5 and 2 mol dm^{-3}. The peaks are slightly red-shifted from 320 nm with increasing [NaOH] which is inconsistent with the observation that alkaline OsO_4 solutions absorb strongly at 316 nm ($\varepsilon_{316} = 500$ dm^3 mol^{-1} cm^{-1}) [35]. The red shift in the peak and increasing ε value with the λ_{max}, $10^{-3}\varepsilon(\lambda_{max}) = 1.43(316)$, 1.58(322) and 1.66(325) at [NaOH] = 0.05, 0.5 and 2.0 mol dm^{-3}, respectively, is consistent with OsO_4 solutions showing a darker hue with increasing alkali concentration.

2.4. Rapid scan of the reaction mixture

The rapid scan spectra of the reaction mixture ($10^4[OsO_4] = 6.0$, $10^3[H_2PO_2^-] = 3.0$ and [NaOH] = 0.1 mol dm^{-3}, and the blank (in the absence of $H_2PO_2^-$) are recorded on an Union-Giken RA-401 stopped-flow spectrophotometer with RA-415 rapid scan attachment. Water is used as the reference and 350 nm is selected as the central wavelength so that the spectral span of the spectra was over 302–398 nm. The gate time (time required for the scan over 96 nm) is 100 ms and interval time (time between two successive scans) is zero. The lower peak in the rapid scan, Fig. 2, is for the OsO_4 solution at 314 nm and the upper peak, which has the higher optical density at 312 nm, is for the reaction mixture. This indicated the likely formation of some newer species probably a complex formed by reactive OsO_4 species and $H_2PO_2^-$ ion. A similar scan was obtained for the reaction of $C_6H_5HPO_2^-$ ion. The height of the peak in case of $C_6H_5HPO_2^-$ happens to be higher than in the case of $H_2PO_2^-$ of the same concentration.

2.5. Spectra of OsO_4 in presence of Cl^- ions

A similar set up as described above is used to study the OsO_4 spectra in presence of Cl^- ions. The spectra of $10^4[OsO_4] = 3$ mol dm^{-3} in 0.1 mol dm^{-3} [NaOH] in presence of Cl^- ions (3.0×10^{-5}–6.0×10^{-3} mol dm^{-3}) does not show any change in λ_{max} indicating that OsO_4 and Cl^- ions do not form any new species.

2.6. Rate measurements

The rates are measured under pseudo-first-order conditions ($[RHPO_2^-] \gg [OsO_4]$) on Union-Giken RA-401 stopped-flow spectrophotometer hooked to a microcomputer which controls the complete operation of the instrument including data acquisition and calculation of the rate constant. The appropriately prepared solutions of OsO_4 and $RHPO_2^-$ at an ionic strength = 1.0 mol dm^{-3} (NaCl) are stored under nitrogen atmosphere in two separate reservoirs that are maintained at the desired temperature (±0.1 °C) by circulating water from a Haake D8G refrigerated circulatory water bath. The rates are measured at 320 nm (disappearance of OsO_4). A total of seven to ten replicate runs for each set of the experiment are studied. The pseudo-first-order rate k_{obs} (s^{-1}) are calculated from the individual runs and the averaged run that are stored in the memory. The two values agreed within ±3%. The k_{obs} values obtained from the averaged runs are reported in the tables.

It is assumed that HPO_3^{2-} ions present as impurity in the $H_2PO_2^-$ sample do not affect the k_{obs} values because the reaction between OsO_4 and HPO_3^{2-} ions is relatively much slower ($10^3 k_{obs} = 4.0$ at 50 °C, $10^4[OsO_4] = 5.0$, $10^3[HPO_3^{2-}] = 5.0$, $[OH^-] = 0.2$ and $\mu = 2.5$ mol dm^{-3} [30]) than the rate of reaction between OsO_4 and $H_2PO_2^-$ ion. The kinetics is studied at temperatures lower than 50 °C because $H_2PO_2^-$ solution undergoes oxidation at high temperatures (50–90 °C) for which the rate law is $-d[H_2PO_2^-]/dt = k[H_2PO_2^-]$ [36].

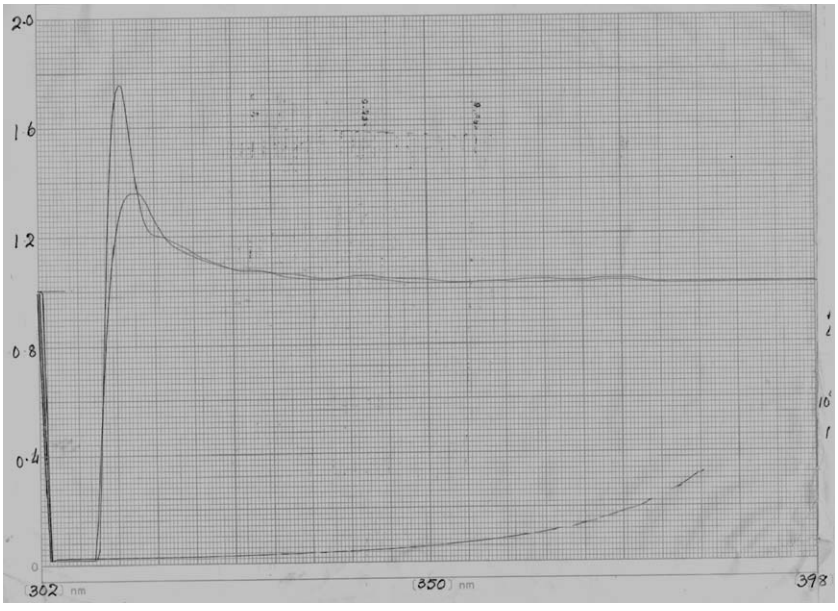


Fig. 2. The rapid scan spectra of the reaction mixture ($10^4[OsO_4] = 6.0$, $10^3[H_2PO_2^-] = 3.0$ and [NaOH] = 0.1 mol dm^{-3}) and the blank ($H_2PO_2^-$ is absent). Water is used as the reference. The gate time (time required for the scan over 96 nm) is 100 ms and interval time (time between two successive scans) is zero. The lower peak is for the blank OsO_4 solution and the upper peak is for the reaction mixture.

Table 1
Dependence of k_{obs} on the initial [OsO_4] at 25 °C. [$RHPO_2^-$] = 0.1, [OH^-] = 0.5 and μ = 1.0 mol dm^{-3}.

	10^3[OsO_4] (mol dm^{-3})							
Substrate	0.3 k_{obs} (s^{-1})	0.6	0.8	1.2	1.6	2.4	3.2	Mean
$H_2PO_2^-$	0.0928	0.0932	0.0917	0.0926	0.0922	0.0928	0.0925	0.0925 ± 0.0005
$C_6H_5HPO_2^-$	0.0602	0.0598	0.0598	0.0604	0.0594	0.0602	0.0590	0.0598 ± 0.0005

3. Results

The first-order dependence in OsO_4 is indicated by the linearity of the log(optical density) against time generated by the computer program from the stored data for the disappearance of OsO_4. The same is confirmed further by studying the k_{obs} values over 10^{-3}[OsO_4] = 0.4–4.2 mol dm^{-3}. The k_{obs} values, Table 1, are independent of the initial OsO_4 concentration. It is further noted that the k_{obs} value for $H_2PO_2^-$ is almost two times the value obtained in the oxidation of $C_6H_5HPO_2^-$ ion. The effect of $RHPO_2^-$, Table 2, indicated that k_{obs} do not increase in the same proportion as the concentration of $RHPO_2^-$ is increased. It is further noted that k_{obs} values are higher for $H_2PO_2^-$ oxidation compared to the k_{obs} values for $C_6H_5HPO_2^-$ oxidation for the same concentration. An analysis of the results indicated that the plots of k_{obs}^{-1} against $[RHPO_2^-]^{-1}$, Fig. 3, were linear with intercepts on the rate ordinates. This behaviour is similar to that observed in the earlier study on OsO_4-catalysed oxidation of $RHPO_2^-$ by $Fe(CN)_6^{3-}$ ion [11]. Hence empirical rate law of the reaction is given by Eq. (2).

Table 2
Dependence of k_{obs} on the initial [$RHPO_2^-$] at different temperatures. 10^3[OsO_4] = 1.6, [OH^-] = 0.5 and μ = 1.0 mol dm^{-3}.

10^2[$RHPO_2^-$] (mol dm^{-3})/ Temperature (°C)	0.5	1.0	2.0	3.0	5.0	8.0	10
	10^2k_{obs} (s^{-1})						
$H_2PO_2^-$							
10	0.555	1.03	1.94	2.66	3.57	4.08	5.29
20	0.99	1.83	3.29	4.18	5.40	7.46	7.75
25	1.34	2.44	4.11	5.46	6.90	8.77	9.26
30	1.89	3.40	5.43	6.94	9.26	10.3	11.4
40	2.90	5.02	7.75	9.52	11.6	14.0	14.6
$C_6H_5HPO_2^-$							
10	0.925	1.54	2.35	2.81	3.42	3.86	3.98
20	1.12	2.06	2.96	3.58	4.27	4.74	5.02
25	1.45	2.42	3.64	4.33	5.05	5.68	5.99
30	1.93	3.32	4.74	5.52	6.41	7.25	7.52
40	2.75	4.37	6.37	7.52	8.47	9.70	10.1

Table 3
Dependence of k_{obs} on the initial [OH^-] at 25 °C. 10^3[Os(VIII)] = 1.6, [$H_2PO_2^-$] = 0.02, [$C_6H_5HPO_2^-$] = 0.03 and μ = 1.0 mol dm^{-3}.

[OH^-]	0.01	0.05	0.10	0.30	0.50	0.70	1.0	Mean
10^2k_{obs} (s^{-1})								
$H_2PO_2^-$	4.11	4.04	4.07	4.15	4.17	4.06	4.08	4.10 ± 0.05
$C_6H_5HPO_2^-$	4.33	4.36	4.37	4.34	4.38	4.35	4.34	4.35 ± 0.02

Table 4
Dependence of k_{obs} on the initial ionic strength of the reaction mixture. 10^3[Os(VIII)] = 1.6, [OH^-] = 0.1, [$H_2PO_2^-$] = 0.02, [$C_6H_5HPO_2^-$] = 0.03 mol dm^{-3} at 25 °C.

[MCl] (mol dm^{-3})	0.1	0.2	0.4	0.7	0.9	1.0
$H_2PO_2^-$						
10^2k_{obs} (s^{-1}, M = Na)	2.58	3.00	3.53	3.91	4.11	4.25
10^2k_{obs} (s^{-1}, M = K)	2.55	3.06	3.54	3.85	4.15	4.23
$C_6H_5HPO_2^-$						
10^2k_{obs} (s^{-1}, M = Na)	2.74	3.16	3.68	4.19	4.34	4.41
10^2k_{obs} (s^{-1}, M = K)	2.77	3.12	3.65	4.21	4.31	4.44

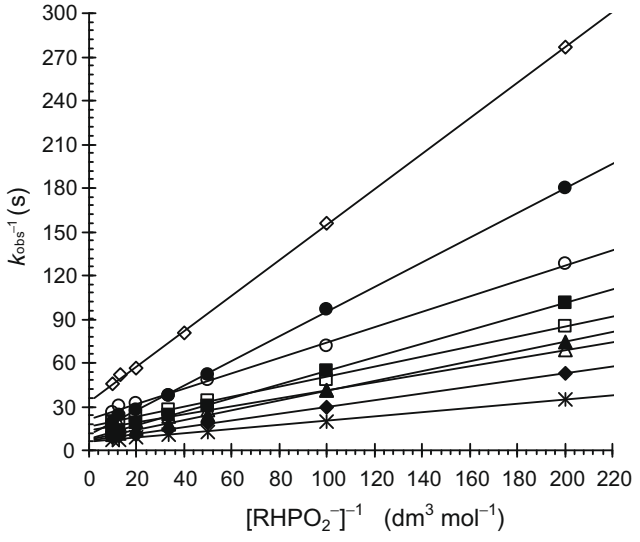


Fig. 3. The plots are between k_{obs}^{-1} and $[RHPO_2^-]^{-1}$ at 10 (●), 20 (■), 25 (▲), 30 (♦) and 40 °C (∗) for $H_2PO_2^-$, 10 (○), 20 (□) and 25 (△) for $C_6H_5HPO_2^-$ and (◇) for $D_2PO_2^-$ at 25 °C. The plots corresponding to 30 and 40 °C for $C_6H_5HPO_2^-$ are excluded for clarity. (10^3[Os(VIII)] = 1.6, [OH^-] = 0.5 and μ = 1.0 mol dm^{-3}).

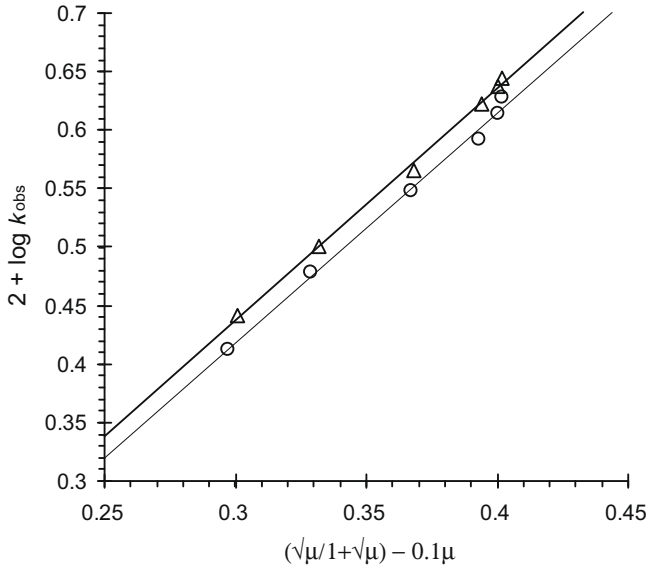


Fig. 4. The plot between log k_{obs} and $\sqrt{\mu}/(1+\sqrt{\mu}) - 0.1\mu$ for $H_2PO_2^-$ (○) and $C_6H_5HPO_2^-$ (△) at 25 °C and 10^3[Os(VIII)] = 1.6, [OH^-] = 0.1, [$H_2PO_2^-$] = 0.02 and [$C_6H_5HPO_2^-$] mol dm^{-3}.

Table 5
Dependence of k_{obs} on the initial $[D_2PO_2^-]$ at 25 °C. $10^3[Os(VIII)] = 1.6$, $[OH^-] = 0.5$ and $\mu = 1.0$ mol dm^{-3}.

$10^2[D_2PO_2^-]$ (mol dm^{-3})	0.5	1.0	2.5	5.0	7.50	10.0
10^2k_{obs} (s^{-1})	0.361	0.641	1.24	1.76	1.93	2.18

The effect of OH^- on the k_{obs}, Table 3, indicated that the k_{obs} is independent of $[OH^-]$. The result is similar to the observation in the earlier study in which one component of the rate is independent of OH^- concentrations [11]. The component dependent on the OH^- concentrations is missed in the present investigation because of the slow nature of the reaction on the stopped-flow scale:

$$k_{obs} = \frac{a[RHPO_2^-]}{1 + b[RHPO_2^-]} \quad (2)$$

The rate increased with the increase in the ionic strength, Table 4, though the k_{obs} had almost the same value in the presence of NaCl and KCl of similar concentrations. This indicated that the reaction does not show specific ion effect. The plot of log k_{obs} against $(\sqrt{\mu}/(1+\sqrt{\mu}) - 0.1\mu)$ is linear, Fig. 4, and consistent with the Davies equation (3) [37]. The slope of the plots for $H_2PO_2^-$ and $C_6H_5HPO_2^-$ oxidations are 1.97 and 2.01, respectively, which is consistent with the disproportionation of the intermediate complex $[OsO_4(OH)\ RHPO_2]^{2-}$ bearing a total charge of two:

$$\log k_{obs} = z_a z_b \left(\frac{\sqrt{\mu}}{1+\sqrt{\mu}} - 0.1\mu\right) + C \quad (3)$$

The rates measured with $D_2PO_2^-$, Table 5, indicated that the k_{obs} is considerably lower than the value obtained with $H_2PO_2^-$. The result is consistent with the empirical rate equation (2) and the plot of k_{obs}^{-1} against $[D_2PO_2^-]^{-1}$ is included in Fig. 3. The intercept of the plot is 33.6 s and the slope is 1.22 mol dm^{-3} s.

4. Discussion

The nature of the OsO_4 spectra in NaOH concentration 0.001–2.0 mol dm^{-3}, Fig. 1, is almost same except that a peak starts appearing for NaOH concentrations > 0.01 mol dm^{-3} which becomes well defined around 315 nm for NaOH concentration > 0.05 mol dm^{-3}. The peak is slightly red-shifted with increasing NaOH concentration. The pale yellow colour of OsO_4 in dilute alkali solution corresponding to the species $[OsO_4(OH_2)OH]^-$ progressively changes to a red coloured solution with increasing alkali concentration because of the formation of red coloured $[OsO_4(OH_2)(OH)_2]^{2-}$ species [38].

The spectra show a peak around 320 nm which is slightly red-shifted with increasing NaOH concentration due to the solution acquiring a dark hue at higher alkali concentrations. The spectra does not show a maximum at 340 nm as reported by Mohan and Gupta [10], who very likely missed the peak around 320 nm since their measurements started from 340 nm onwards only. Since the spectra has no other peak or a shoulder, therefore formation of the species $[OsO_5(OH_2)(OH)]^{3-}$ from $[OsO_4(OH_2)(OH)_2]^{2-}$, equilibrium (4), proposed in the oxidation of phosphite by alkaline OsO_4 [30], is considered unlikely. It might be mentioned that the potassium and cesium salts, $M_2[OsO_4(OH)_2]$, have been prepared by dissolution of OsO_4 in respective strong MOH solutions [39]:

$$[OsO_4(OH_2)(OH)_2]^{2-} + OH^- \overset{K_3}{\rightleftharpoons} [OsO_5(OH_2)(OH)]^{3-} \quad (4)$$

The reaction's first-order dependence in OsO_4, the Michaelis–Menten kinetics with respect to $RHPO_2^-$ and the rapid scan of the reaction mixture, Fig. 2, support the formation of an intermediate complex. The larger consistency in the kinetics of the present reaction and the earlier study is expected because Os(VIII) happened to be the effective oxidant in the earlier study [11]. The reason for the absence of the OH^- ion dependent term, as discussed later, is due to the slow nature of the OH^- ion dependent reaction. The empirical rate law in Eq. (2) is the modified form of the similar equation found in the earlier study [11].

Therefore, the proposed mechanism consisting of reactions (5)–(9) is similar to that considered in the earlier study [11]:

$$OsO_4 + OH^- \overset{K_1}{\rightleftharpoons} [OsO_4OH]^- \quad (5)$$

$$[OsO_4OH]^- + OH^- \overset{K_2}{\rightleftharpoons} [OsO_4(OH)_2]^{2-} \quad (6)$$

$$[OsO_4(OH)]^- + RHPO_2^- \overset{\beta}{\rightleftharpoons} [OsO_4(OH)RHPO_2]^{2-} \quad (7)$$

$$[OsO_4(OH)RHPO_2]^{2-} \overset{k}{\rightarrow} OsO_3 + RPO_3^{2-} + H_2O \quad (8)$$

$$[OsO_4(OH)_2]^{2-} + RHPO_2^- \overset{k_2}{\rightarrow} [OsO_3(OH)]^- + RPO_3^{2-} + H_2O \quad (9)$$

The values of the equilibrium constants K_1 (5.55×10^{13}) and K_2 (16.6) are derived from the relation $K_n = K_{na}/K_w$ where K_{1a} (1×10^{-2}) and K_{2a} (3×10^{-15} mol dm^{-3}) are the first and second ionisation constants [40]. The K_2 value (16.6) is in good agreement with the values (24 ± 4) [10], and (19.5 ± 4) [28] at 25 °C. The consideration of the value of the equilibrium constant K_1 indicates that OsO_4 exists as $[OsO_4(OH_2)OH]^-$ in very dilute alkali solutions viz. ⩽0.01 mol dm^{-3}.

The rate-law derived from the reactions (6)–(9), with the assumption that the analytical $[OsO_4] \cong [OsO_4(OH)^-]$ in view of the very high vale of K_1 mentioned above, is given in Eq. (10), which is same as obtained in the OsO_4-catalysed oxidation by $Fe(CN)_6^{3-}$ ion [11]:

$$k_{obs} = \frac{(k\beta + k_2K_2[OH^-])[RHPO_2^-]}{1 + K_2[OH^-] + \beta[RHPO_2^-]} \quad (10)$$

However, the present reaction is significantly different from the OsO_4-catalysed reaction [11] because k_{obs} is independent of OH^- ions. Eq. (10) has to be suitably modified to make it independent of the hydroxyl terms. The assumption that $1 + \beta[RHPO_2^-] \gg K_2[OH^-]$ might be factually incorrect in view of the derived values of β and K_2 mentioned in the previous study [11]. This problem is rectified by considering the reaction (11) in place of the reaction (9) in the above mechanism:

$$[OsO_4(OH)RHPO_2]^{2-} + OH^- \overset{k_2}{\rightarrow} [OsO_3(OH)]^- + RPO_3^{2-} + H_2O \quad (11)$$

Thus the consideration of the mechanism consisting of the reactions 6, 7, 8, and (11) would give the rate equation (12):

$$k_{obs} = \frac{(k\beta + k_2\beta[OH^-])[RHPO_2^-]}{1 + \beta[RHPO_2^-]} \quad (12)$$

Eq. (12) is reduced to Eq. (13) with the assumption that $k\beta \gg k_2\beta[OH^-]$ because the reaction is independent of OH^- ion concentration. The assumption is rationalised by considering that the reaction (11) is so slow that its contribution to the observed rate is not measured over the timescale of the stopped-flow instrument. The reaction, however, does contribute to the observed rate of the Os(VIII)-catalysed slow reaction with $Fe(CN)_6^{3-}$ ion [11]. Eq. (13) is similar to the empirical rate equation (2) with $a = k\beta$ and $b = \beta$:

$$k_{obs} = \frac{k\beta[RHPO_2^-]}{1 + \beta[RHPO_2^-]} \quad (13)$$

The assumption of the slow nature of the reaction (11) is substantiated by considering the k_2K_2 values, 0.5 and 0.257 dm^3 mol^{-1} s^{-1}, respectively, for $H_2PO_2^-$ and $C_6H_5HPO_2^-$ ions at 30 °C [11]. Since these values are now equivalent to $k_2\beta$, the evaluated value of k_2 is 0.0178 and 0.00459 s^{-1} using presently obtained β values of 28 dm^3 mol^{-1} for $H_2PO_2^-$ and 56 dm^3 mol^{-1} for

$C_6H_5HPO_2^-$ at 30 °C. Thus the k_2 values at 30 °C are about eight times and 19 times less than the k values for $H_2PO_2^-$ and $C_6H_5HPO_2^-$, respectively.

Eq. (13) is consistent with the double reciprocal plots between k_{obs}^{-1} against $[RHPO_2^-]^{-1}$ shown in Fig. 3. The least square values of the intercepts and slopes of the plots in Fig. 3 are in Table 6. The calculated values of k and β, Table 7, are comparable to the values obtained earlier in the OsO_4-catalysed oxidation [11] viz. The present $k = 0.153$ at 30 °C and 0.180 (s^{-1}) at 40 °C is in fair agreement with the values 0.149 and 0.187 (s^{-1}) at the same temperatures in the Os(VIII)-catalysed oxidation of $H_2PO_2^-$ ion by $Fe(CN)_6^{3-}$ ion [11]. The $k = 0.0893$ at 30 °C and 0.114 (s^{-1}) at 40 °C compare well with the values 0.086 and 0.117 at the same temperatures in the oxidation of $C_6H_5HPO_2^-$ ion [11].

The presently obtained β values 28 and 39 $dm^3\ mol^{-1}$ for $H_2PO_2^-$ and 56 and 63 $dm^3\ mol^{-1}$ for $C_6H_5HPO_2^-$ at 30 and 40 °C, respectively, are comparable with the values 25 and 37 $dm^3\ mol^{-1}$ for $H_2PO_2^-$ and 55 and 61 $dm^3\ mol^{-1}$ for $C_6H_5HPO_2^-$ in the previous Os(VIII)-catalysed study [11]. The higher values of β for OsO_4–$C_6H_5HPO_2^-$ complex in comparison to the value for OsO_4–$H_2PO_2^-$ complex is consistent with the larger peak height obtained in the rapid scan spectra of OsO_4–$C_6H_5HPO_2^-$ reaction mixture and is attributed to the stabilising action of phenyl group which is supported by the smaller values of the specific rate constant for the disproportionation of OsO_4–$C_6H_5HPO_2^-$ complex compared to the rate for the disproportionation of OsO_4–$H_2PO_2^-$ complex.

The activation and thermodynamic parameters are calculated from Eqs. (14) and (15), respectively, where k and h are the Boltzmann and Planck constants, respectively, are reported in Table 5. The required plots are in Fig. 5. It might be noted that there is fair agreement between the present values and those obtained previously in the Os(VIII)-catalysed study [11]:

$$k = \frac{\kappa t}{h} \exp\frac{(-\Delta H^{\ddagger})}{RT} \exp\frac{\Delta S^{\ddagger}}{R} \quad (14)$$

$$\log\beta = \frac{-\Delta H^0}{RT} + \frac{\Delta S^0}{R} \quad (15)$$

The rate acceleration with OH^- ion in the $Fe(CN)_6^{3-}$ oxidation of $H_2PO_2^-$ ion has been explained by considering HPO_2^{2-} as the reactive entity [41] which is formed through the equilibrium (16). The species is supported by the conductivity data of sodium hypophosphite [42]. HPO_2^{2-} has been suggested as an intermediate in the base catalysed exchange of hydrogen on hypophosphite anion [43], and is the considered reactive entity in the oxidations by Ru(VII) [22] and $[Ag(OH)_4]^-$ ions [25] in alkaline solution. The equilibrium (14) is not presently considered for the reason that the composite second pK of H_3PO_2 is above 14 which means that the equilibrium amount of HPO_2^{2-} is small under basic conditions used beside OsO_4 forms various species with OH^- ions which are in equilibrium with each other:

$$H_2PO_2^- + OH^- \rightleftharpoons H_3PO_3^{2-} \text{ or } (HPO_2^{2-} + H_2O) \quad (16)$$

Table 6
Values of the slope and intercept of the plots of k_{obs}^{-1} against $[RHPO_2^-]^{-1}$.

Temperature (°C)	10	20	25	30	40
$H_2PO_2^-$					
Intercept (s)	11.1	8.23	7.41	6.55	5.54
Slope (mol dm^{-3} s)	0.845	0.463	0.336	0.231	0.141
$C_6H_5HPO_2^-$					
Intercept (s)	21.6	16.4	14.0	11.2	8.73
Slope (mol dm^{-3} s)	0.525	0.341	0.274.	0.200	0.139

Table 7
Temperature dependence of k and β, and related activation and thermodynamic parameters.

Temperature (°C)	$H_2PO_2^-$ k (s^{-1})	$C_6H_5HPO_2^-$		$H_2PO_2^-$ β ($dm^3\ mol^{-1}$)	$C_6H_5HPO_2^-$
10	0.090	0.0463		13.1	41.1
20	0.121	0.0610		17.8	18.1
25	0.135	0.0714		22.0	51.1
30	0.153	0.0893		28.3	56
40	0.180	0.114		39.3	62.8
$\Delta H^{\ddagger}$ (kJ mol^{-1})	14.6 ± 1	20 ± 1	ΔH^0 (kJ mol^{-1})	27 ± 1	67 ± 1
$-\Delta S^{\ddagger}$ (J K^{-1} mol^{-1})	196 ± 3	182 ± 4	ΔS^0 (kJ mol^{-1})	118 ± 5	258 ± 1
$-\Delta G^{\ddagger}$ (kJ mol^{-1})	73	74	$-\Delta G^0$ (kJ mol^{-1})	8	10

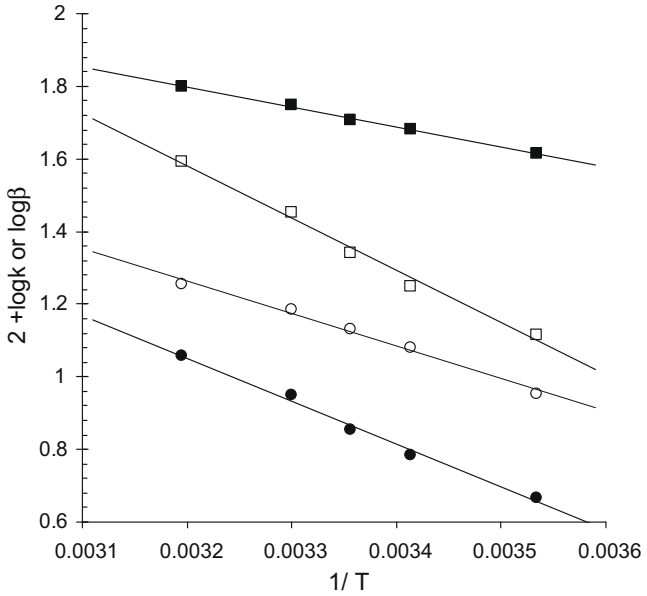
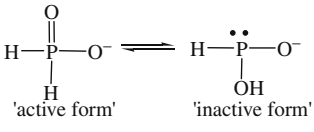


Fig. 5. The plots between log k and $1/T$ for $H_2PO_2^-$ (○) and $C_6H_5HPO_2^-$ (●), and between log β and $1/T$ for $H_2PO_2^-$ (□) and $C_6H_5HPO_2^-$ (■).

The rate constant k_{PH} for the proton exchange of phosphorus-bonded hydrogen in the $H_2PO_2^-$ ion in basic medium is 6×10^{-5} $dm^3\ mol^{-1}\ s^{-1}$ at 25 °C, and the $\Delta H^{\ddagger}$ is 79 kJ mol^{-1} [43]. Thus the net change in enthalpy of the reactions involving HPO_2^{2-} as the reactive species is expected to be greater than the enthalpy change for the reactions proceeding through with $H_2PO_2^-$ species. Alternately, the rate determining constants for the reactions involving HPO_2^{2-} as the reactive species ought to be less than the rate constant for proton exchange mentioned above. The above criterion is well supported by the reactions with RuO_4^- in which the rate determining constant is 248 ± 14 $dm^6\ mol^{-2}\ s^{-1}$ at 24.8 °C ($\Delta H^{\ddagger}$ = 7.8 ± 0.8 kJ mol^{-1} [22], the corresponding value for OH^- independent path is 0.069 ± 0.014 $dm^3\ mol^{-1}\ s^{-1}$ (82 ± 10 kJ mol^{-1}) and 1.13 ± 0.02 $dm^6\ mol^{-2}\ s^{-1}$ (39 ± 5 kJ mol^{-1}) for OH^- dependent path in the oxidation by $Ag(OH)_4^-$ ion at 25 °C [25], and 0.141 ± 0.008 s^{-1} (19 ± 6 kJ mol^{-1}) in the Os(VIII)-catalysed oxidation by $Fe(CN)_6^{3-}$ [11]. In all these reactions the considered reactive entity is $H_2PO_2^-$ ion. Hence in the present reaction with the rate determining constant equal to 0.135 s^{-1} at 25 °C, it is only rational to assume $H_2PO_2^-$ ion as the reactive entity. Since $H_2PO_2^-$ ion is the reactive entity therefore it is the inactive form which is reactive in all these oxidations. The structures of the 'inactive' and 'active' forms are given below:



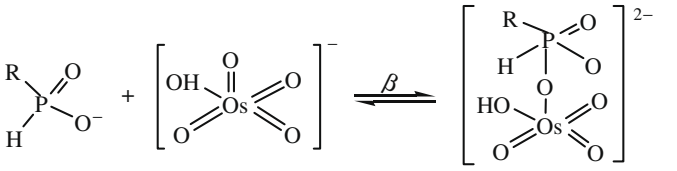
(17)

It might be noted that HPO_2^{2-} is the considered reactive entity in the oxidation with $Fe(CN)_6^{3-}$ in alkaline medium has a $\Delta H^{\ddagger} = 96 \pm 4$ kJ mol^{-1}. The comparison of the rate constant is not made because the same is not available at 25 °C.

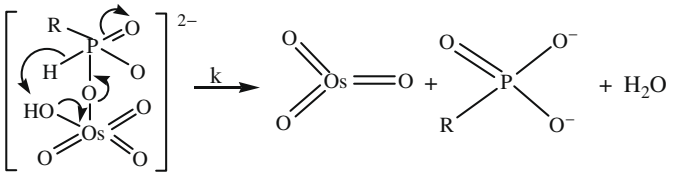
The substantial kinetic isotope effect, $k_H/k_D = 4.53$ at 25 °C, is comparable to $k_H/k_D = 4 \pm 0.5$ obtained in the internal redox of $(NH_3)_5Co(H_2PO_2)^{2+}$ [24] and much different from $k_H/k_D = 2.5 \pm 0.5$ obtained for the OH^- independent path in Ag(III) oxidation [25]. The observed value, suggestive of the fission of P–H bond in the rate determining step, is smaller than the theoretical value 5.5 obtained from Eq. (16) [44] by using $\upsilon_{P-H} = 2400$ cm^{-1} and $\upsilon_{P-D} = 1700$ cm^{-1} for free hypophosphite ion [43]. The smaller value is due to concerted bond making and breaking [45]:

$$\frac{k_H}{k_D} = e\left(\frac{hc(\upsilon_{P-H} - \upsilon_{P-D})}{2\kappa T}\right) \tag{18}$$

The P–H bond fission is heterolytic in nature. A proton and an electron are simultaneously transferred from $H_2PO_2^-$ to the oxidant producing HPO_2^{2-} and Os(VI). The described mode of electron transfer might be equivalent to the transfer of a hydrogen atom. The hydrogen atom transfer is not considered because the energy required for hydrogen atom transfer is expected to be greater than the activation energy obtained for the redox reaction. The probable structure of the Os(VIII)–$RHPO_2^-$ complex and the fission of bonds is considered below:



(19)



(20)

Hence, the oxidation of hypophosphite or phenylphosphinite ion to the corresponding phosphite or phenylphosphonite ion involves a total change of two electrons.

5. Concluding remark

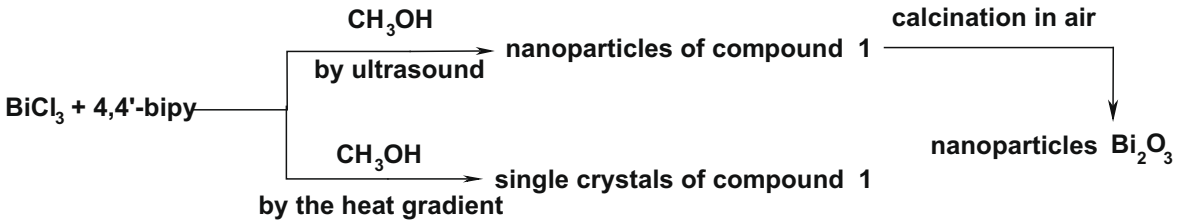
The kinetics of the reaction is similar to the kinetics observed in the OsO_4-catalysed oxidation of the oxo-phosphorus acids with hexacyanoferrate(III) ion [11] except that the present reaction has no OH^- ion dependence. This is attributed to the slow nature of the reaction between OH^- ion and the intermediate and therefore it does not register itself on the time scale of the stopped-flow measurements. The OH^- ion dependent reaction of the previous study [11] has been suitably modified so that the assumption of the inequality is rational. The presently obtained values of k and β are in fair agreement with the values obtained in the earlier study [11]. The result of this study indicates that the alkaline oxidation of hypophosphite ion with different metal ions has different dependence of the rate on [OH^-]. However, the results of the studies so far indicate that the dependence on OH^- is not due to the HPO_2^- ion except in the oxidation of hypophosphite ion by hexacyanoferrate(III) ion because $Fe(CN)_6^{3-}$ does not react with OH^- ions. The rate determining constant for this particular reaction is much slower than the rate for the proton exchange of phosphorus-bonded hydrogen in the $H_2PO_2^-$ ion and the $\Delta H^{\ddagger}$ of the reaction is significantly higher than $\Delta H^{\ddagger}$ for the exchange reaction [43]. This makes this reaction significant in the sense that this is probably the only reaction in alkaline medium in which the active form of hypophosphite ion is the reactive entity.

Acknowledgements

Thanks are due to the Department of Science and Technology (DST) for the grant to purchase the stopped-flow instrument. K.S. was a recipient of Junior Research Fellowship both from the Council of Scientific and Industrial Research (CSIR) and DST.

References

[1] W.H. Latimer, The Oxidation States of Elements and their Potentials in Aqueous Solutions, Prentice Hall, New York, 1952.
[2] L.F. Fieser, M. Fieser, Reagents for Organic Synthesis, vol. 1, Wiley, 1967 (vol. 2, 1969).
[3] B. Sussela, Z. Anal. Chem. 145 (1955) 175.
[4] F. Solymosi, Magy. Kan. Foly. 63 (1957) 294.
[5] F. Solymosi, Naturwissen 44 (1957) 374.
[6] F. Solymosi, Chem. Anal. 51 (1962) 71.
[7] M.C. Agrawal, S.K. Upadhyay, J. Sci. Indus. Res. 42 (1983) 508.
[8] K.K. Sengupta, S. Basu, Indian J. Chem. 15A (1977) 108.
[9] Raj N. Mehrotra, R.C. Kapoor, S.K. Vajpai, J. Chem. Soc., Dalton Trans. (1984) 999.
[10] D. Mohan, Y.K. Gupta, J. Chem. Soc., Dalton Trans. (1977) 1085.
[11] K. Sharma, Raj N. Mehrotra, Polyhedron 27 (2008) 3425.
[12] G.P. Haight Jr., M. Rose, J. Preer, J. Am. Chem. Soc. 90 (1968) 4809.
[13] K.S. Gupta, Y.K. Gupta, J. Chem. Soc. (A) (1970) 256.
[14] A. Viste, D.A. Holm, P.A. Wang, G.D. Veight, Inorg. Chem. 10 (1971) 631.
[15] J.N. Cooper, J. Phys. Chem. 74 (1974) 955.
[16] K.S. Gupta, Y.K. Gupta, Inorg. Chem. 13 (1974) 851.
[17] R.R. Nagori, M. Mehta, Raj N. Mehrotra, J. Chem. Soc., Dalton Trans. (1979) 216.
[18] A.K. Indrayan, S.K. Misra, Y.K. Gupta, Inorg. Chem. 20 (1981) 450.
[19] A.K. Indrayan, S.K. Misra, Y.K. Gupta, Inorg. Chem. 20 (1981) 1924.
[20] K. Sharma, A. Prakash, Raj N. Mehrotra, Bull. Chem. Soc. Jpn. 62 (1989) 4009.
[21] E. Ben-zvi, Inorg. Chem. 6 (1967) 1143.
[22] S.J. Paton, C.H. Brubaker Jr., Inorg. Chem. 12 (1973) 1402.
[23] A.Yu. Prokopchik, J. Liaukonis, G.I. Rozovskii, A. Luneckas, Liet. TSR Mokslu Akad. Darb., Ser. B (1977) 13 (Chem. Abstr. 86 (1977) 195753d).
[24] D.E. Linn Jr., E.S. Gould, Inorg. Chem. 27 (1988) 3140.
[25] Raj N. Mehrotra, L.J. Kirschenbaum, Inorg. Chem. 28 (1989) 4327.
[26] M. Vishnoi, K. Sharma, Raj N. Mehrotra, Int. J. Chem. Kinet. 23 (1991) 377.
[27] B. Singh, A.K. Singh, M.B. Singh, A.P. Singh, Tetrahedron 42 (1986) 715.
[28] R.K. Panda, G. Neogi, D. Ramaswamy, Bull. Chem. Soc. Jpn. 55 (1982) 587.
[29] B.H. Anand, G.D. Menghani, Int. J. Chem. Kinet. 12 (1980) 225.
[30] L. Bhatt, P.D. Sharma, Y.K. Gupta, Indian J. Chem. 23A (1984) 560.
[31] R.T. Jones, E.H. Swift, Anal. Chem. 25 (1953) 1272.
[32] D.N. Bernhart, Anal. Chem. 26 (1954) 1798.
[33] V.M. Plets, Zh. Obsheh. Khim. 6 (1936) 1198.
[34] E. Stahl, Thin Layer Chromatography, Academic, New York, 1965. p. 482.
[35] R.K. Panda, G. Neogi, D. Ramaswamy, Int. J. Chem. Kinet. 13 (1981) 1001.
[36] E.S. Bugenov, O.M. Kletushkina, Kompleksn. Ispol'z. Miner. Syr'ya (1988) 33 (Chem. Abstr. 96 (1987) 41630f).
[37] C.W. Davies, Ion Association, Butterworths, London, 1962.
[38] W.P. Griffith, J. Chem. Soc. (1964) 245.
[39] F. Krauss, D. Wilken, Z. Anorg. Allgem. Chem. 145 (1925) 151.
[40] R.D. Sauerbrum, E.B. Sandell, J. Am. Chem. Soc. 75 (1953) 4170.
[41] D. Mohan, V.K. Chhabra, Y.K. Gupta, J. Chem. Soc., Dalton Trans. (1975) 1737.
[42] W.V. Bhagwat, N.R. Dhar, J. Indian Chem. Soc. 6 (1929) 781.
[43] G.C. Roper, T.E. Hass, H.D. Gilman, Inorg. Chem. 9 (1970) 1049.
[44] T.H. Lowry, K.S. Richardson, Mechanism and Theory in Organic Chemistry, Harper and Row, New York, 1987. p. 234.
[45] L. Melander, W.H. Saunders Jr., Reaction Rates of Isotopic Molecules, Wiley, New York, 1980. p. 130.



Scheme 1. Materials produced and synthetic methods.

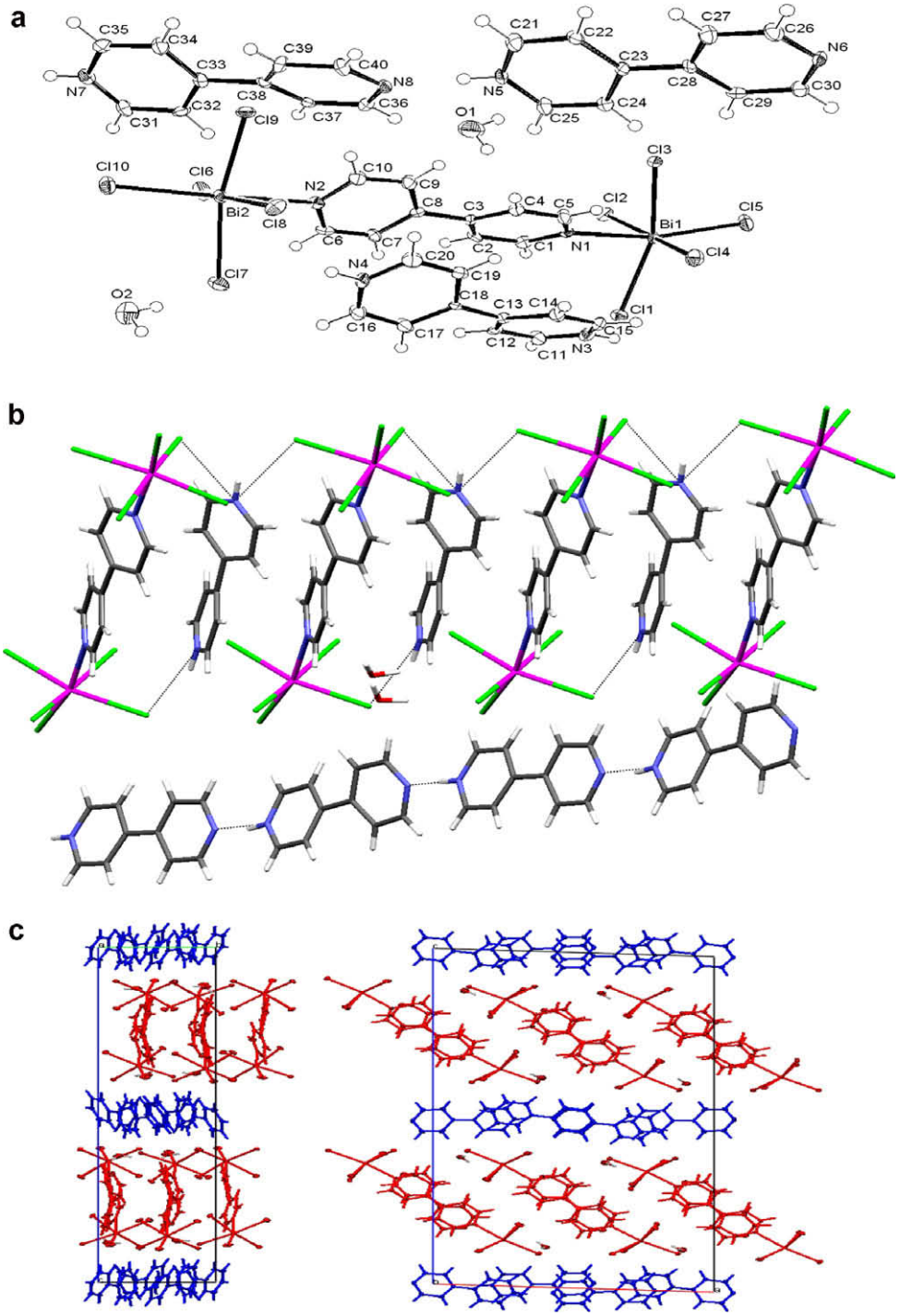


Fig. 1. (a) ORTEP diagram, (b) a fragment of the one-dimensional supramolecular and (c) depiction of the microphase separation of **1** down the *b* and the *a*-axis of the unit cell. Red: stacks of $\{[Bi_2(\mu\text{-}4,4'\text{-bipy})Cl_{10}][4,4'\text{-}H_2bipy](H_2O)_2\}^{4-}$; blue: infinite N–H···N bonded chains of the 4,4′-Hbipy$^+$ cations. (For interpretation of the references to color in this figure legend, the reader is referred to the web version of this article.)

a maximum power output of 600 W, was used for the ultrasonic irradiation. The ultrasonic generator automatically adjusts the power level. The wave amplitude in each experiment was adjusted as needed. IR spectra were recorded using Perkin–Elmer 597 and Nicolet 510P spectrophotometers. Microanalyses were carried out using a Heraeus CHN-O-Rapid analyzer. Melting points were measured on an Electrothermal 9100 apparatus and are uncorrected. X-ray powder diffraction (XRD) measurements were performed using a Philips diffractometer manufactured by X'pert with monochromatized Cu Kα radiation and simulated XRD powder patterns based on single crystal data were prepared using the program Mercury [19]. The crystallite sizes of selected samples were estimated using the Sherrer method. The samples were gold coated for characterization with a scanning electron microscope. The elemental composition of the film was analyzed using energy dispersive X-ray (EDX) spectrometer attached with the JEOL JSM-35 CF SEM instrument. Single crystal diffraction measurements were made at 100(2) K using a Bruker AXS SMART APEX CCD diffractometer. The intensity data were collected using graphite monochromated Mo Kα radiation. The structure was solved by direct methods and refined by full-matrix least-squares techniques on F^2. Crystal data for $\{Bi_2(\mu\text{-}4,4'\text{-bipy})Cl_{10}] \cdot 2(4,4'\text{-bipyH}) \cdot (4,4'\text{-}H_2bipy) \cdot 2H_2O\}$ (**1**): monoclinic space group $P2_1/n$, a = 17.920(4), b = 7.4770(16), c = 36.060(8) Å, β = 92.857(4)°, V = 4825.4(18) Å^3, Z = 4, T = 100(2) K. The refinement of 571 parameters on the basis of 11 944 independent reflections (of a total of 31 180) converged at R_1 = 0.0610, wR_2 = 0.1007. The observed anisotropic thermal parameters, the calculated structure factors, and full lists of bond distances, bond angles and torsion angles are given in the supplementary material.

To prepare nano-particles of $\{Bi_2(\mu\text{-}4,4'\text{-bipy})Cl_{10}] \cdot 2(4,4'\text{-Hbipy}) \cdot (4,4'\text{-}H_2bipy) \cdot 2H_2O\}$ (**1**), 10 ml of a 0.3 M solution of bismuth(III) chloride (0.1 M) in MeOH were positioned in a high-density ultrasonic probe, operating at 20 kHz with a maximum power output of 600 W. Into this solution 10 ml of a 0.3 M solution of the ligand 4,4′-bipy (0.1 M) were added dropwise. The obtained precipitates were filtered off, washed with methanol and then dried in air. m.p. > 300 °C. *Anal.* Calc. for $C_{40}H_{40}Bi_2Cl_{10}N_8O_2$: C, 33.44; H, 2.65; N, 7.80. Found: C, 33.20; H, 2.50; N, 7.54%. IR bands: 476m, 621w, 749s, 805s, 1000m, 1204m, 1479m, 1595s and 3045m.

Different concentrations of metal and ligand solutions (0.02, 0.05 and 0.08 M) with different power settings for the ultrasonic irradiation were tested (60, 120 and 180 W). Appropriate nano-sized particles of compound **1** were obtained only under the above mentioned conditions and the produced nano-particles were used for the thermal analyses.

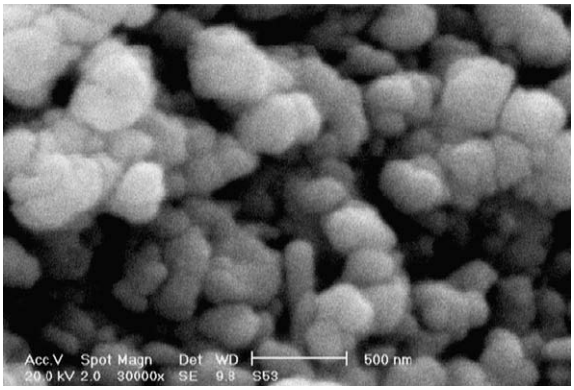


Fig. 3. SEM photographs of $\{Bi_2(\mu\text{-}4,4'\text{-bipy})Cl_{10}] \cdot 2(4,4'\text{-Hbipy}) \cdot (4,4'\text{-}H_2bipy) \cdot 2H_2O\}$ (**1**) nano-particles.

To isolate single crystals of $\{Bi_2(\mu\text{-}4,4'\text{-bipy})Cl_{10}] \cdot 2(4,4'\text{-Hbipy}) \cdot (4,4'\text{-}H_2bipy) \cdot 2H_2O\}$ (**1**), 4,4′-bipy (1 mmol) and bismuth(III) chloride (1 mmol) were placed in the main arm of a branched tube [20]. Methanol was carefully added to fill both arms. The tube was sealed and the ligand-containing arm immersed in an oil bath at 60 °C while the other arm was kept at ambient temperature. After 7–10 days, colorless crystals deposited in the cooler arm were isolated. The single crystals were filtered off, washed with acetone and ether and air dried. Yield: 0.174 g, 40%, m.p. > 300 °C. *Anal.* Calc. for $C_{40}H_{40}Bi_2Cl_{10}N_8O_2$: C, 33.44; H, 2.65; N, 7.80. Found: C, 33.30; H, 2.55; N, 7.54%. IR bands: 476m, 621w, 749s, 805s, 1000m, 1204m, 1479m, 1595s and 3045m.

3. Results and discussion

Scheme 1 gives an overview of the methods used for the synthesis of $\{Bi_2(\mu\text{-}4,4'\text{-bipy})Cl_{10}] \cdot 2(4,4'\text{-Hbipy}) \cdot (4,4'\text{-}H_2bipy) \cdot 2H_2O\}$ (**1**) using two different routes. Nano-particles of **1** were obtained by ultrasonic irradiation of a mixture of 4,4′-bipy and bismuth(III) chloride in a methanolic solution. Single crystalline material was

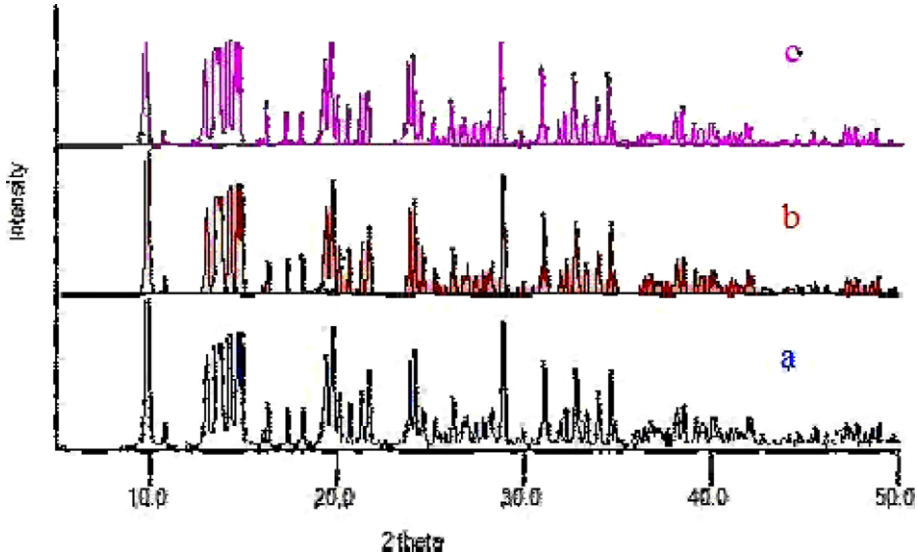


Fig. 2. The XRD patterns of (a) simulated from single crystal X-ray data of compound $\{Bi_2(\mu\text{-}4,4'\text{-bipy})Cl_{10}] \cdot 2(4,4'\text{-Hbipy}) \cdot (4,4'\text{-}H_2bipy) \cdot 2H_2O\}$ (**1**); (b) bulk materials as synthesized of compound $\{Bi_2(\mu\text{-}4,4'\text{-bipy})Cl_{10}] \cdot 2(4,4'\text{-Hbipy}) \cdot (4,4'\text{-}H_2bipy) \cdot 2H_2O\}$ (**1**) by heat gradient, (c) nano-structure of compound $\{Bi_2(\mu\text{-}4,4'\text{-bipy})Cl_{10}] \cdot 2(4,4'\text{-Hbipy}) \cdot (4,4'\text{-}H_2bipy) \cdot 2H_2O\}$ (**1**) by ultrasound.

obtained using a heat gradient applied to a solution of the reagents (the "branched tube method").

The IR spectra of the nano-particles and of the single crystalline material are indistinguishable and show characteristic absorption bands for the 4,4′-bipy ligands. The absorption bands with variable intensity in the frequency range 1400–1580 cm^{-1} correspond to ring vibrations of the pyridyl moieties of the 4,4′-bipy ligands.

The single crystals of **1** were analyzed by X-ray diffraction (Fig. 1a–c). The molecular structure of the complex is built by one $[Bi_2(\mu\text{-}4,4'\text{-bipy})Cl_{10}]^{4-}$ anion, two singly protonated 4,4′-Hbipy$^+$ cations and one doubly protonated 4,4′-H_2bipy^{2+} cation and two H_2O molecules. The 4,4′-bipy ligand in the dinuclear anionic complex is linking the two Bi atoms with each other which have a slightly distorted octahedral $BiCl_5N$ coordination environment. With the $BiCl_3$ starting material as the only chlorine source and protic methanol as the solvent one thus can to assume partial hydrolysis of the bismuth chloride with the HCl released in the process as the source of the chloride anions and protons needed to form the $BiCl_5^{2-}$ dianions and the protonated bipy-cations. In the solid state the 4,4′-Hbipy$^+$ cations are linked by hydrogen bonding. The hydrogen atoms of the uncoordinated and monoprotonated 4,4́-Hbipy$^+$ cations form infinite hydrogen bonded chains via N–H···H hydrogen bonds. The doubly protonated 4,4′-H_2bipy^{2+} cations, on the other hand, are involved in short Cl···H–N interactions (Fig. 1b) with distance around 2.6 Å. The anions and cations thus connected via Cl···H–N hydrogen bonds are also π-stacked atop of each other with alternating 4,4′-H_2bipy^{2+} cations and $[Bi_2(\mu\text{-}4,4'\text{-bipy})Cl_{10}]^{4-}$ anions. The stacks are further connected via O–H···Cl hydrogen bonds of the interstitial water molecule towards chlorine of the same stack, and are laid out in parallel to each other. The $\{[Bi_2(\mu\text{-}4,4'\text{-bipy})Cl_{10}][4,4'\text{-}H_2bipy]\}^{4-}$ stacks and the infinite chains of the monoprotonated 4,4́-Hbipy$^+$ cations, on the other hand, are only loosely connected with each other thus suggesting a microphase separation within the crystal with largely independent layers of each of the two constituent phases.

Fig. 2a shows the XRD patterns simulated from the single crystal X-ray data. Fig. 2b and c shows the XRD patterns of typical samples of compound **1** prepared by the branched tube and the sonochemical process, respectively. Acceptable matches are observed indicating the presence of only one crystalline phase in all samples regardless of the method of preparation. Using the Sherrer formula for the calculation of particle sizes from the broadening of the XRD peaks ($D = 0.891\lambda/\beta\cos\theta$, where D is the average grain size, λ is the X-ray wavelength (0.15405 nm) and θ and β are the diffraction angle and full-width at half maximum of an observed peak, respectively) the average size of the particles prepared via the sonochemical method was found to be around 90 nm, which is in agreement with the value obtained from the SEM images (Fig. 3).

Thermal decomposition of the nano-sized particles of **1** in air produced Bi_2O_3: as established by its powder XRD pattern. The broadening of the peaks indicated that the particles were of nano-

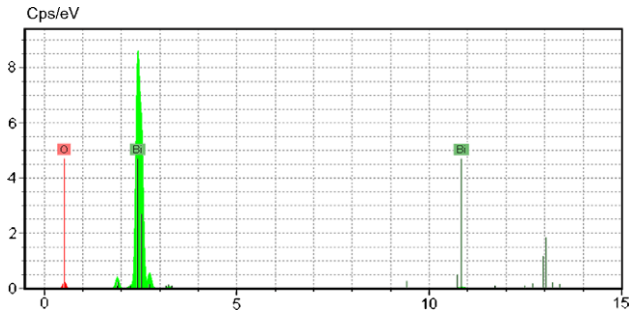


Fig. 4. EDAX analysis of Bi_2O_3 nano-particles (produced by calcination of compound **1** under air atmosphere).

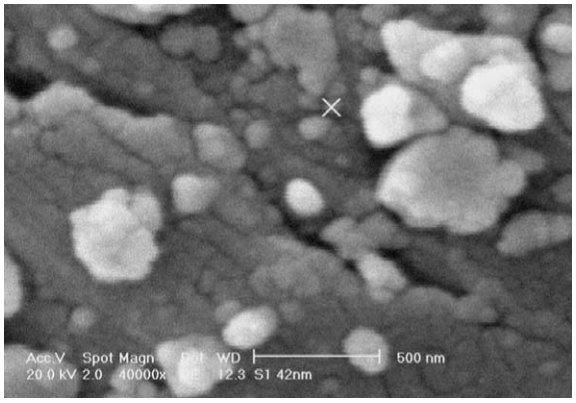


Fig. 5. SEM photographs of Bi_2O_3 nano-particles (produced by calcination of compound **1** under air atmosphere).

meter scale. EDAX was performed in support of XRD observation and to further confirm of the composition of the α-Bi_2O_3 nano-particles produced by calcination of compound **1** under air atmosphere. The EDAX spectrum (Fig. 4) of stoichiometric Bi_2O_3 shows only the bismuth and oxygen peaks appear. The atomic percentage of Bi and O present in the compound are calculated and are found to be 2.00:3.03 showing perfect stoichiometry of the particle surface. Fig. 4 shows that sample Bi_2O_3 nano-particles is composed of Bi and O only, and this spectrum show that there are no impurities within this sample. Fig. 5 shows the SEM images of nano-structured Bi_2O_3 obtained from calcinations of compound **1** under air atmosphere [21]. It is interesting that the calcination of the normal-sized crystals of compound **1** produces Bi_2O_3 but the particle sizes were not at nano-scale.

4. Conclusion

A new Bi(III) supramolecular compound, $\{Bi_2(\mu\text{-}4,4'\text{-bipy})Cl_{10}] \cdot 2(4,4'\text{-Hbipy}) \cdot (4,4'\text{-}H_2bipy)\cdot 2H_2O\}$ (**1**) {4,4′-bipy = 4,4′-bipyridine}, has been synthesized using a thermal gradient approach and by a sonochemical method. In compound **1** similar to its bromo analogue $[4,4'\text{-bipyH}]_n^{n-}[Bi(4,4'\text{-bipy})Bi_4]_n^{n-}$ [22], two of 4,4′-bipy ligands are protonated. Calcination of compound **1** under air atmosphere, produces nano-structured α-Bi_2O_3. There are only three reports discussing the preparation of Bi_2S_3 nano-structures from the solvent thermolysis of bismuth trisxanthate [23], (benzylthiolato)bismuth [24] and bismuth tris(methyl-*n*-hexyldithiocarbamate) [25] precursors. These studies demonstrate supramolecular compounds may be suitable precursors for the preparation of nano-scale materials with interesting morphologies. To the best of our knowledge, this is the first report on the synthesis of nano-structured α-Bi_2O_3 from a supramolecular precursor. From this perspective, further systematic studies of other supramolecular compounds with bismuth(III) and different metal ions are ongoing in our laboratory, which may offer new insight into metal-organic supramolecular assembly and nano-chemistry.

Acknowledgement

This work was supported by the Iran National Science Foundation (INSF).

Appendix A. Supplementary data

CCDC 685221 contains the supplementary crystallographic data for compound **1**. These data can be obtained free of charge via http://www.ccdc.cam.ac.uk/conts/retrieving.html, or from the

Cambridge Crystallographic Data Centre, 12 Union Road, Cambridge CB2 1EZ, UK; fax: (+44) 1223-336-033; or e-mail: deposit@ccdc.cam.ac.uk. Supplementary data associated with this article can be found, in the online version, at doi:10.1016/j.poly.2009.02.004.

References

[1] H.T. Shi, L.M. Qi, J.M. Ma, H.M. Cheng, J. Am. Chem. Soc. 125 (2003) 3450.
[2] H. Zhang, D.R. Yang, D.S. Li, X.Y. Ma, S.Z. Li, D.L. Que, Cryst. Growth Des. 5 (2005) 547.
[3] D.B. Kuang, A.W. Xu, Y.P. Fang, H.Q. Liu, C. Frommen, D. Fenske, Adv. Mater. 15 (2003) 1747.
[4] F. Kim, S. Connor, H. Song, T. Kuykendall, P.D. Yang, Angew. Chem., Int. Ed. 43 (2004) 3673.
[5] K.-T. Wong, J.-M. Lehn, S.-M. Peng, G.-H. Lee, Chem. Commun. (2000) 2259.
[6] A.G. Bunn, P.J. Carroll, B.B. Wayland, Inorg. Chem. 31 (1992) 1297.
[7] A. Caneschi, D. Gatteschi, N. Lalioti, C. Sangregorio, R. Sessoli, G. Venturi, A. Vindigni, A. Rettori, M.G. Pini, M.A. Novak, Angew. Chem., Int. Ed. 40 (2001) 1760.
[8] A. Tanatani, M.J. Moi, J.S. Moore, J. Am. Chem. Soc. 123 (2001) 1792.
[9] M. Fujita, Y.J. Kwon, S. Washizu, K.J. Ogura, J. Am. Chem. Soc. 116 (1994) 1151.
[10] K.S. Suslick, S.B. Choe, A.A. Cichowlas, M.W. Grinstaff, Nature 353 (1991) 414.
[11] J.H. Zhang, Z. Chen, Z.L. Wang, N.B. Ming, J. Mater. Res. 18 (2003) 1804.
[12] P. Zhou, G.J. You, Y.G. Li, T. Han, J. Li, S.Y. Wang, L.Y. Chen, Y. Liu, S.X. Qian, Appl. Phys. Lett. 83 (2003) 3876.
[13] J.W. Medernach, R.L. Snyder, J. Am. Ceram. Soc. 61 (1978) 494.
[14] V.G. Orlov, A.A. Bush, S.A. Ivanov, V.V. Zhurov, Phys. Solid State 39 (1997) 770.
[15] J.A. Switzer, M.G. Shumsky, E.W. Bohannan, Science 284 (1999) 293.
[16] R. Irmawati, M.N.N. Nasriah, Y.H.T. Yap, S.B.A. Hamid, Catal. Today 93 (2004) 701.
[17] Q.B. Yang, Y.X. Li, Q.R. Yin, P.L. Wang, Y.B. Cheng, Mater. Lett. 55 (2002) 46.
[18] Y. Xiong, M. Wu, J. Ye, Q. Chen, Mater. Lett. 62 (2008) 1165.
[19] MERCURY 1.4.1, Copyright Cambridge Crystallographic Data Centre, 12 Union Road, Cambridge CB2 1EZ, UK, 2001–2005.
[20] G. Mahmoudi, A. Morsali, A.D. Hunter, M. Zeller, Cryst. Eng. Commun. 9 (2007) 704.
[21] L. Sillen, Ark. Mineral. Geol. 12A (1937) 1.
[22] A. Morsali, Solid State Sci. 8 (2006) 82.
[23] Y.W. Koh, C.S. Lai, A.Y. Du, E.R.T. Tiekink, K.P. Loh, Chem. Mater. 15 (2003) 4544.
[24] P. Boudjouk, M.P. Remington, D.G. Grier, B.R. Jarabek, G.J. McCarthy, Inorg. Chem. 37 (1998) 3538.
[25] O.C. Monteiro, H.I.S. Nogueira, T. Trindade, Chem. Mater. 13 (2001) 2103.

Table 1
Crystal data and structure refinement for $[Cu(pybzim)_2(NO_3)](NO_3)$.

Empirical formula	$C_{24}H_{18}N_8O_6Cu$
Formula weight	578.00
Temperature (K)	293(2)
Wavelength (Å)	0.71073
Crystal system	monoclinic
Space group	$P2_1/c$
Unit cell dimensions	$a = 17.832(3)$ Å
	$b = 7.455(4)$ Å
	$\beta = 114.985(11)°$
	$c = 19.2683(18)$ Å
Volume (Å^3)	2321.9(13)
Z	4
D_{calc} (Mg/m^3)	1.653
Absorption coefficient (mm^{-1})	1.002
$F(000)$	1180
Crystal size (°)	$0.04 \times 0.06 \times 0.24$
θ range for data collection (°)	2.97–25.00
Index ranges	$-21 \leqslant h \leqslant 21$, $-8 \leqslant k \leqslant 4$,
	$-21 \leqslant l \leqslant 22$
Reflections collected/independent [R_{int}]	14208/4055 [0.0612]
Completeness to $2\theta = 50.0°$	99.3%
Max. and min. transmission	0.964 and 0.926
Data/restraints/parameters	4055/0/352
Goodness-of-fit on F^2	0.804
Final R indices [$I > 2\sigma(I)$]	$R_1 = 0.0350$, $wR_2 = 0.0613$
R indices (all data)	$R_1 = 0.0720$, $wR_2 = 0.0650$
Largest difference in peak and hole (e Å^{-3})	0.393 and −0.489

$Cu(NO_3)_2 \cdot 3H_2O$ in 10 ml of methanol and stirred for 6 h. The resulting precipitate of $[Cu(pybzim)_2(NO_3)](NO_3)$ was filtered off and dried. Yield 60%. The crystals suitable for X-ray investigation were obtained by recrystallization from methanol.

IR (KBr; ν/cm^{-1}): 3060 (ν_{N-H}); 1609, 1594(m), 1494 and 1488(m) ($\nu_{C=C}$, $\nu_{C=N}$), 1462(s), 1446(s), 1409(s), 1384(vs), 1323(s), 1301(s), 1007(m), 988(m), 817(m), 765 and 745 ($\nu_{nitrate}$).

Anal. Calc. for $[Cu(pybzim)_2(NO_3)](NO_3)$: C, 49.87; H, 3.14; N, 19.39. Found: C, 48.98; H, 3.30; N, 18.89%.

2.3. X-ray diffraction studies

A green crystal of $[Cu(pybzim)_2(NO_3)](NO_3)$ was mounted on a KM-4-CCD automatic diffractometer equipped with a CCD detector, and used for data collection. X-ray intensity data were collected with graphite monochromated Mo Kα radiation ($\lambda = 0.71073$ Å) at 293(2) K. Details concerning crystal data and refinement are given in Table 1. Lorentz, polarization and empirical absorption correction using spherical harmonics implemented in SCALE3 ABSPACK scaling algorithm [12,13] were applied. The structure was solved by the Patterson method and subsequently completed by the difference Fourier recycling. All the non-hydrogen atoms were refined anisotropically using full-matrix, least-squares technique. All the hydrogen atoms were found from difference Fourier synthesis after four cycles of anisotropic refinement, and refined as "riding" on the adjacent carbon atom with individual isotropic temperature factor equal 1.2 times the value of equivalent temperature factor of the aromatic parent atom. SHELXS97 [14], SHELXL97 [15] and SHELXTL [16] programs were used for all the calculations. Atomic scattering factors were those incorporated in the computer programs.

2.4. Computational details

The gas phase geometry of the $[Cu(pybzim)_2(NO_3)]^+$ cation was optimized without any symmetry restrictions in the doublet state with the DFT method using the hybrid B3LYP functional of GAUSSIAN-03 [17–19]. The calculations were performed by using the standard 6–311 + G(d,p) basis for Cu atom, 6–31 + G** basis for nitrogen, 6–31G* for carbon and 6–31G for hydrogen atoms. The optimized geometry of the $[Cu(pybzim)_2(NO_3)]^+$ cation was verified by per-

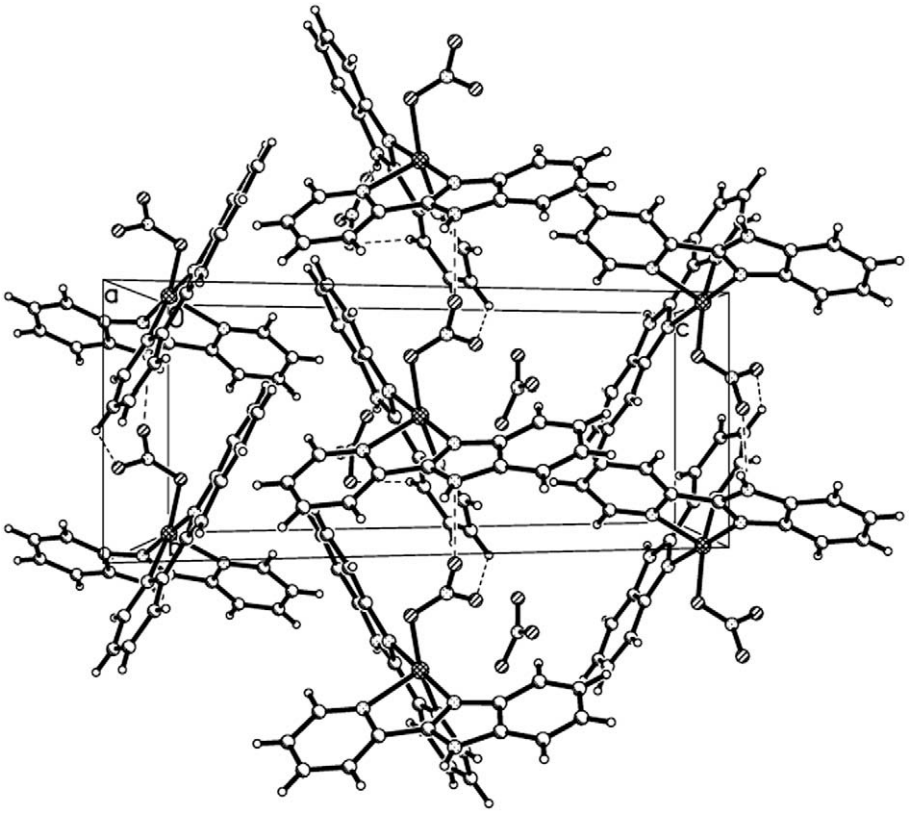


Fig. 1. The cell packing of $[Cu(pybzim)_2(NO_3)](NO_3)$.

forming a frequency calculation. All the vibrations in the calculated vibrational spectrum of $[Cu(pybzim)_2(NO_3)]^+$ were real, thus the optimized geometry corresponds to true energy minimum.

The electronic spectrum of the $[Cu(pybzim)_2(NO_3)]^+$ cation was calculated with the TDDFT method starting from the ground-state geometry optimized in the gas phase. The solvent (methanol) effect was simulated using the polarizable continuum model with the integral equation formalism (IEF-PCM) [20].

Natural bond orbital (NBO) calculations were performed with the NBO code [21] included in GAUSSIAN-03.

3. Results and discussion

The $[Cu(pybzim)_2(NO_3)](NO_3)$ complex was prepared in good yield by the reaction of 2-(2-pyridyl)benzimidazole (pybzim) with copper(II) nitrate trihydrate in molar ratio 2:1. The elemental analysis of the complex is in good agreement with its formulation. The characteristic bands of the C=C and C=N stretching modes of 2-(2-pyridyl)benzimidazole are observed in the range 1610–1480 cm^{-1}. The peak at 3060 cm^{-1} can be attributed to the ν(N–H) stretching frequency of the pybzim ligand. The bands assignable to the coordinated nitrate group of $[Cu(pybzim)_2(NO_3)](NO_3)$ appear at 1462, 1446, 1323, 1301, 1007, 988, 765 and 745 cm^{-1}, whereas the strong band at 1384 and 817 cm^{-1} (of medium intensity) confirm the presence of uncoordinated nitrate ion. The small splitting of in-plane bending NO_3 vibrations (ν_4; at 765 and 745 cm^{-1}, 20 cm^{-1}) indicates the presence of monodentate nitrate group [22].

Table 2
Intermolecular hydrogen bonding contacts detected in the $[Cu(pybzim)_2(NO_3)](NO_3)$ complex.

D–H	A	H···A (Å)	D···A (Å)	D–H···A (°)
N(2)–H(2N)	O(1)#1	2.36	3.004(3)	132
N(2)–H(2N)	O(3)#1	2.19	3.040(3)	172
N(5)–H(5N)	O(6)	1.88	2.713(3)	162
C(10)–H(10)	O(6)#3	2.59	3.339(4)	138
C(12)–H(12)	O(3)#1	2.49	3.392(4)	164
C(22)–H(22)	O(2)#2	2.54	3.043(3)	115
C(24)–H(24)	O(5)	2.48	3.353(4)	156

Symmetry transformations used to generate equivalent atoms: #1: $-x$, $2-y$, $-z$; #2: x, $1+y$, z; #3: $-x$, $0.5+y$, 0, $5-z$.

3.1. Crystal structure

The crystallographic data of $[Cu(pybzim)_2(NO_3)](NO_3)$ are summarized in Table 1. $[Cu(pybzim)_2(NO_3)](NO_3)$ crystallises in the monoclinic space group $P2_1/c$. The cell packing of $[Cu(pybzim)_2(NO_3)](NO_3)$ is given in Fig. 1. A summary of intramolecular hydrogen bonding contacts detected in $[Cu(pybzim)_2(NO_3)](NO_3)$ structure is given in Table 2 [23,24]. The outer sphere nitrate anion is connected to pybzim molecule by N(5)–H(5N)···O(6) hydrogen bonds. Other intermolecular by N–H···O hydrogen bonds links molecules to the cyclic dimers. Additionally in the structure exists short intermolecular C–H···O interactions, which can be classified as weak hydrogen bonds. These interactions expand hydrogen bonded dimer to the three dimensional net.

The asymmetric unit of the title complex consists of the $[Cu(pybzim)_2(NO_3)]^+$ cation and nitrate ion. The molecular structure of the $[Cu(pybzim)_2(NO_3)](NO_3)$ is presented in Fig. 2, and the selected bond distances and angles of $[Cu(pybzim)_2(NO_3)]^+$ are collected in Table 3.

According to the criteria for the assignment for nitrate modes introduced by Kleywegt et al. [25] and presented in Table 4, the nitrate binding mode in the title complex can be classified as monodentate.

The Cu(II) centre of $[Cu(pybzim)_2(NO_3)]^+$ is five-coordinated by four N donors from two 2-(2-pyridyl)benzimidazole ligands and oxygen atom of nitrate anion. The bite angles of 78.70(10)° and 81.23(10)° show no variation from the values reported for $[Cu_2(CN)(2\text{-PyBIm})]n$ – 80.3(2)° [26].

The angular structural index parameter τ [27] expressed here as the difference between the bond angles N(1)–Cu(1)–N(4) and N(6)–Cu(1)–O(1) divided by 60 has a value of 0.16. Compared with the ideal values of 1 for an equilateral bipyramid and 0 for a square pyramid, the τ descriptor of the examined structure indicates a square-pyramidal stereochemistry (Scheme 1).

The equatorial plane of the title complex is defined by three nitrogen and one oxygen atoms. The maximum deviation from the weighted least-squares N(1), N(4), N(6), O(1) plane exists for N(4) atom and it is equal to 0.1000(12) Å. The metal ion Cu is displaced from above mentioned weighted least-squares plane by 0.1083(12) Å. The apical site is occupied by N3 atom with Cu–N distance 2.223(2) Å, ca. 0.25 Å longer than the Cu–N distances in

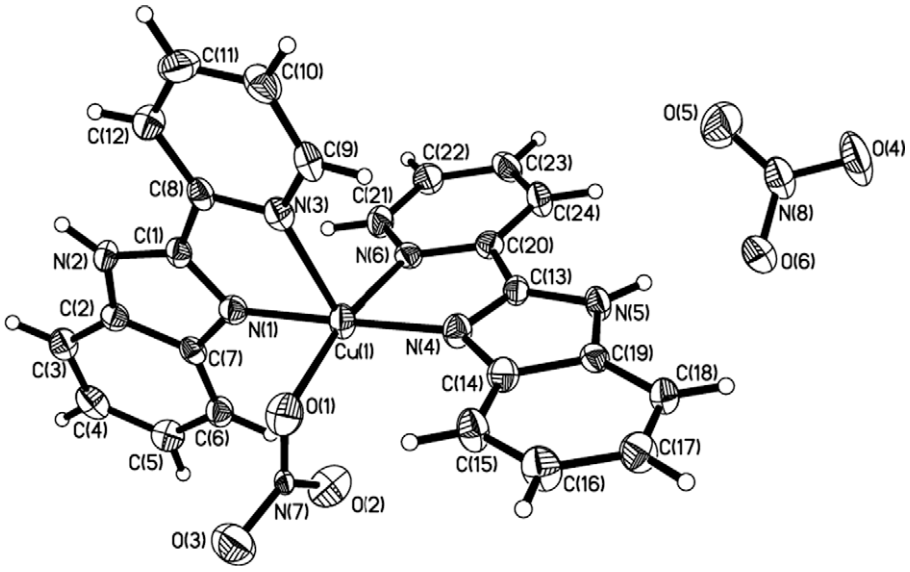
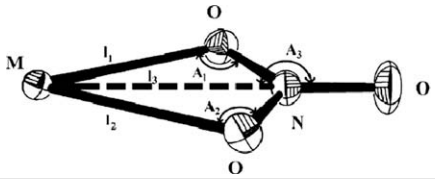


Fig. 2. The molecular structure of the $[Cu(pybzim)_2(NO_3)](NO_3)$. Displacement ellipsoids are drawn at 50% probability.

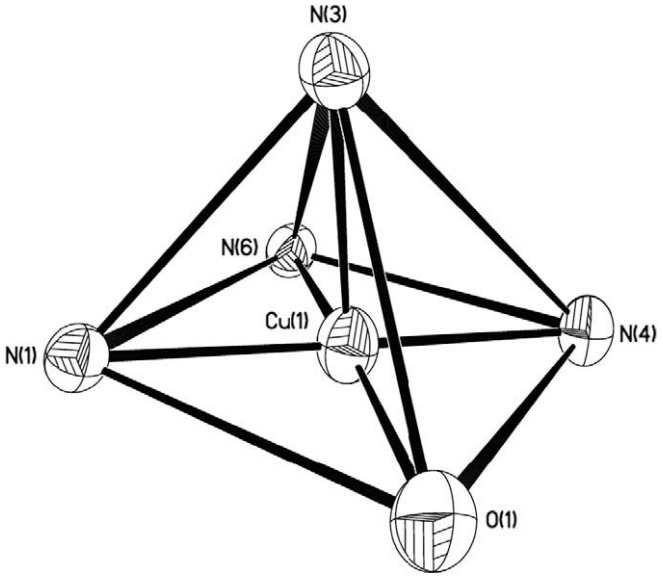
Table 3
The experimental and optimized bond lengths (Å) and angles (°) for $[Cu(pybzim)_2(NO_3)](NO_3)$.

Bond lengths	Experimental	Optimized	Bond angles	Experimental	Optimized
Cu(1)–N(1)	1.982(2)	2.030	N(1)–Cu(1)–N(4)	177.40(10)	174.79
Cu(1)–N(3)	2.223(2)	2.412	N(4)–Cu(1)–N(6)	81.23(10)	79.78
Cu(1)–N(4)	1.964(2)	2.021	N(1)–Cu(1)–N(6)	96.21(9)	96.49
Cu(1)–N(6)	2.045(2)	2.113	N(4)–Cu(1)–O(1)	94.65(9)	93.33
Cu(1)–O(1)	2.044(2)	1.993	N(1)–Cu(1)–O(1)	87.76(8)	91.24
			N(6)–Cu(1)–O(1)	167.83(9)	162.85
			N(4)–Cu(1)–N(3)	102.24(9)	101.68
			N(1)–Cu(1)–N(3)	78.70(10)	75.56
			N(6)–Cu(1)–N(3)	102.17(9)	103.74
			O(1)–Cu(1)–N(3)	89.87(9)	93.00

Table 4
Parameters used for assigning nitrate coordination modes [25] and parameters of the coordinated nitrate group in the $[Cu(pybzim)_2(NO_3)]^+$ cation.



	Monodentate	Anisobidentate	Bidentate	$[Cu(pybzim)_2(NO_3)]^+$
l_2–l_1 (Å)	>0.6	0.3–0.6	<0.3	0.5922
A_1–A_2 (°)	>28	14–28	<14	28.93
l_3–l_2	<0.1	0.1–0.2	>0.2	0.0466
A_3 (°)	<162	162–168	>168	160.54



Scheme 1.

the equatorial plane. This elongation of the fifth-ligand is typical of a square-based pyramidal stereochemistry [28].

To confirm five coordination, the bond valences were computed as $v_{ij} = \exp[(R_{ij} - d_{ij})/0.37]$ [29–32], where R_{ij} is the bond-valence parameter (in the formal sense R_{ij} is the single bond length between i and j atoms), d_{ij} – bond length between i and j atoms and b was taken as 0.37 [33].

The R_{Cu-O} and R_{Cu-N} were taken as 1.679 [34] and 1.713 [32], respectively. The computed bond valences of the copper are $v_{Cu(1)-O(1)} = 0.374$, $v_{Cu(1)-N(1)} = 0.486$, $v_{Cu(1)-N(3)} = 0.253$, $v_{Cu(1)-N(4)} = 0.507$ and $v_{Cu(1)-N(6)} = 0.410$ v.u. (valence units), thus the computed valence of the Cu(1) atom is 2.03 v.u. Because only deviation of valence sum rule larger than 0.5–0.1 v.u. can indicate omission or misinterpretation of coordination sphere [35], it can be stated that in considered compound the copper atom is five-coordinated and even weak interactions are not omitted. Noteworthy is the fact that the Cu(1)–O(1) bond is slightly stronger than Cu(1)–N(3) bond, but it is weaker than other Cu–N bonds. The pybzim molecule indicated by N(1) atom is weaker-bonded to the central atom (0.739 v.u.) than molecule containing N(3) atom (0.917 v.u.).

3.2. Geometry optimization and population analysis

The geometry of the $[Cu(pybzim)_2(NO_3)]^+$ cation was optimized in doublet state using the DFT method with the B3LYP functional. The optimized geometric parameters are gathered in Table 3. In general, the predicted bond lengths are somewhat longer in comparison with the values based upon the X-ray crystal structure data, and the general trends observed in the experimental data are well reproduced in the calculations.

None of the natural bond orbitals between central ion and nitrogen and oxygen atom donors were detected, indicating a conceivable predominant Coulomb-type Cu–ligand interaction in the $[Cu(pybzim)_2(NO_3)]^+$ cation.

The calculated charge on the copper atom in $[Cu(pybzim)_2(NO_3)]^+$ is equal to 0.964 and it is lower than the formal charge +2. It is a result of charge donation from the donor atoms of ligands. Table 5 presents electron population of the valence core of the central ion, nitrogen donors and oxygen atoms the $[Cu(pybzim)_2(NO_3)]^+$ cation.

3.3. Electronic spectrum

The nature of the transitions observed in the UV–Vis spectrum of the title complex has been studied by the time-dependent density functional (TDDFT) method. The calculated electronic spec-

Table 5
Electron population of the valence core of the central ion, nitrogen donors and oxygen atoms in the $[Cu(pybzim)_2(NO_3)]^+$ cation.

Cu(1)		N(1)		N(3)		N(4)		N(6)		O(1)		O(2)		O(3)	
4s	3d	2s	2p	2s	2p	2s	2p	2s	2p	2s	2p	2s	2p	2s	2p
0.31	9.31	1.32	4.20	1.34	4.12	1.32	4.18	1.32	4.15	1.75	4.76	1.75	4.70	1.75	4.59

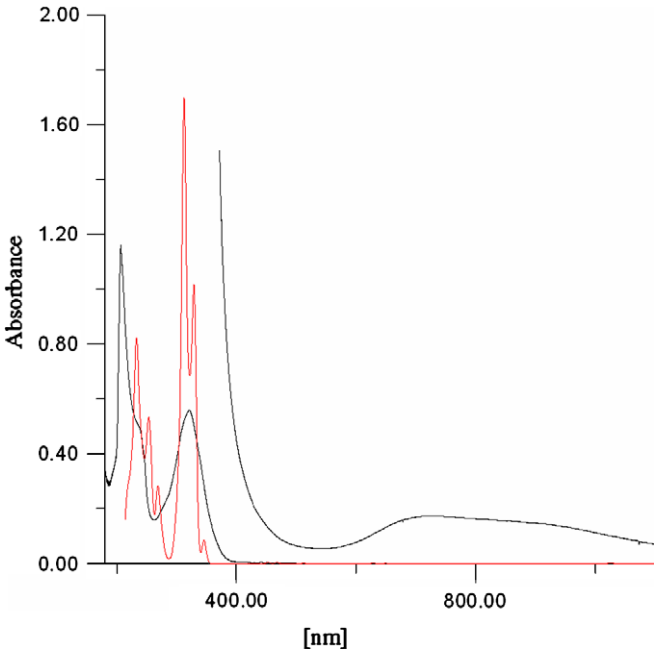


Fig. 3. The experimental (black) and calculated (red) electronic absorption spectra of methanolic solution of $[Cu(pybzim)_2(NO_3)](NO_3)$. (For interpretation of the references to colour in this figure legend, the reader is referred to the web version of this article.)

trum of $[Cu(pybzim)_2(NO_3)]^+$ in comparison with the experimental one is presented in Fig. 3. Each calculated transition is represented by a gaussian function $y = ce^{-bx^2}$ with the height (c) equal to the oscillator strength and b equal to 0.04 nm^{-2}.

Table 6 presents the most important electronic transitions calculated with the TDDFT method for $[Cu(pybzim)_2(NO_3)]^+$ and their assignments to the observed absorption bands of the complex. For the high energy part of the spectrum, only transitions with oscillator strengths larger than 0.0300 are listed in Table 6. The assignment of the calculated orbital excitations to the experimental bands was based on an overview of the contour plots and relative energy of occupied (HOMO) and unoccupied (LUMO) molecular orbitals involved in the electronic transitions (Fig. 4).

The TDDFT/PCM calculations show that the longest wavelength experimental band at 984.2 nm originates in the HOMO-4(β) → LUMO(β) transition. As can be seen from the Fig. 3, the LUMO orbital with β-spin is mainly $d_{x^2-y^2}$ copper orbital in character, the β-spin HOMO-4 orbital are composed of d_{z^2} copper orbital and the π-bonding orbitals of nitrate group and pybzim ligand. The experimental band at 678.6 nm originates predominately in the transitions between β-spin HOMO-13, HOMO-12, HOMO-11 and LUMO. The HOMO-13, HOMO-12 and HOMO-11 and HOMO-9 are composed of ligand (nitrate and 2-(2-pyridyl)benzimidazole) π-bonding orbitals and d_{Cu} orbitals. Accordingly, the transitions assigned to the two longest wavelength experimental bands (at 984.2 and 678.6 nm) can be seen as mixed nitrate/pybzim → Cu (*ligand–metal charge transfer*; *LMCT*) and d → d (*ligand field; LF*) transitions.

Table 6
The spin-allowed doublet–doublet electronic transitions calculated with the TDDFT method and the assignments of the calculated transitions to the experimental absorption bands of $[Cu(pybzim)_2(NO_3)](NO_3)$.

The most important orbital excitations	Character	λ (nm)	E (eV)	f	Experimental Λ (nm) (E (eV)) ε
H-4(β) → L(β)	π(NO_3)/d/π(pybzim) → d	1025.4	1.21	0.0014	984.2 (1.26) 60
H-13(β) → L(β) H-11(β) → L(β)	d/π(pybzim) → d π(NO_3)/d → d	649.7	1.91	0.0007	678.6 (1.83) 79
H-12(β) → L(β)	π(pybzim)/π(NO_3)/d → d	628.5	1.97	0.0009	
H-17(β) → L(β)	d/π(NO_3)/π(pybzim) → d	608.9	2.04	0.0002	
H-9(β) → L(β)	π(NO_3)/d/n(N) → d				
H-1(β) → L+1(β) H-1(α) → L(α)	π(pybzim) → π*(pybzim)	329.7	3.76	0.3224	321.6 (3.86) 34900
H-2(α) → L(α)	π(pybzim) → π*(pybzim)	322.3	3.85	0.0368	
H-3(α) → L(α) H-3(β) → L+1(β)	π(pybzim) → π*(pybzim)	321.6	3.86	0.1221	
H(α) → L+1(α) H(β) → L+2(β)	π(pybzim) → π*(pybzim)	313.0	3.96	0.5307	
H-2(α) → L+1(α) H-2(β) → L+2(β)	π(pybzim) → π*(pybzim)	305.3	4.06	0.0724	
H-1(α) → L+3(α) H-1(β) → L+4(β)	π(pybzim) → π*(pybzim)	268.9	4.61	0.0848	235.0 (5.28) 32010
H-12(β) → L(β)	π(pybzim)/π(NO_3)/d → d	255.6	4.85	0.0614	
H-13(β) → L(β) H-16(β) → L(β)	π(pybzim)/d → d π(NO_3)/π(pybzim) → d	252.5	4.91	0.0644	
H-2(α) → L+4(α) H-2(β) → L+5(β)	π(pybzim) → π*(pybzim)	246.0	5.04	0.0315	
H-16(β) → L(β)	π(NO_3)/π(pybzim) → d	241.3	5.14	0.0592	
H-8(α) → L(α)	π(pybzim)/π(NO_3)/d → π*(pybzim)	238.5	5.20	0.0381	
H-7(β) → L+1(β) H-8(α) → L(α)	π(pybzim)/π(NO_3) → π*(pybzim)	234.2	5.29	0.0906	
H-5(β) → L+2(β) H-6(α) → L+1(α)	π(pybzim) → π*(pybzim)	232.9	5.32	0.1140	
H(α) → L+6(α) H-2(α) → L+9(α)	π(pybzim) → π*(pybzim)	226.4	5.48	0.0508	207.2 (5.98) 72250
H-9(α) → L+1(α) H-8(β) → L+2(β)	π(pybzim)/π(NO_3)/d → π*(pybzim) π(pybzim)/d → π*(pybzim)	217.6	5.70	0.0349	

ε – molar absorption coefficient ($dm^3\ mol^{-1}\ cm^{-1}$).
f – oscillator strength.
H – highest occupied molecular orbital.
L – lowest unoccupied molecular orbital.

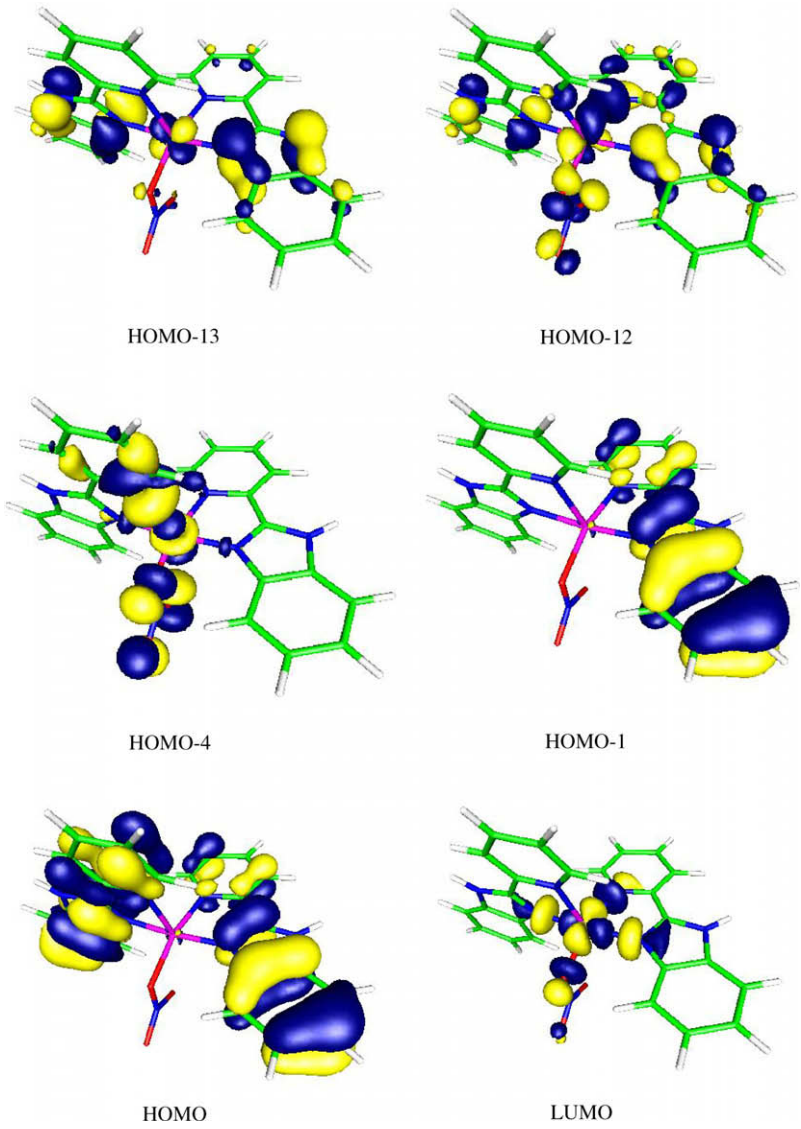


Fig. 4. Contour plots and energy of the selected β-spin HOMO and β-spin LUMO orbitals active in the electronic transitions. The orbitals were plotted with contour values −0.04 (yellow) and 0.04 au (blue). (For interpretation of the references to colour in this figure legend, the reader is referred to the web version of this article.)

The experimental bands at 322.1, 235.0 and 210.4 nm originates predominately in the *intraligand* (IL) and *ligand–ligand charge transfer* (*LLCT*) transitions. However some contribution of the *ligand–metal charge transfer* from the nitrate and 2-(2-pyridyl)benzimidazole orbitals to the d copper orbitals in the band at 235 nm is also confirmed by the calculations.

Acknowledgements

The GAUSSIAN-03 calculations were carried out in the Wrocław Centre for Networking and Supercomputing, WCSS, Wrocław, Poland under calculational Grant No. 51/96.

Appendix A. Supplementary data

Supplementary data for $C_{24}H_{18}N_8O_6Cu$ can be found, in the online version, at doi:10.1016/j.poly.2009.02.007.

References

[1] M. Tadokoro, K. Nakasuji, Coord. Chem. Rev. 198 (2000) 205.
[2] Y. Sunatsuki, Y. Motoda, N. Matsumoto, Coord. Chem. Rev. 226 (2002) 199.
[3] R. Rowan, T. Tallon, A.M. Sheahan, R. Curran, M. McCann, K. Kavanagh, M. Devereux, V. McKee, Polyhedron 25 (2006) 1771.
[4] Y.-M. Fu, Y.-H. Zhao, Y.-Q. Lan, Y. Wang, Y.-Q. Qiu, K.-Z. Shao, Z.-M. Su, Inorg. Chem. Commun. 10 (2007) 720.
[5] T. Higa, M. Moriya, Y. Shimazaki, T. Yajima, F. Tani, S. Karasawa, M. Nakano, Y. Naruta, O. Yamauchi, Inorg. Chim. Acta 360 (2007) 3304.
[6] P. Deschamps, P.P. Kulkarni, M. Gautam-Basak, B. Sarkar, Coord. Chem. Rev. 249 (2005) 895.
[7] O. Szilágyi, K. Ősz, K. Várnagy, D. Sanna, H. Süli-Vargha, I. Sóvágó, G. Micera, Polyhedron 25 (2006) 3173.
[8] K. Várnagy, I. Sóvágó, H. Süli-Vargha, D. Sanna, G. Micera, J. Inorg. Biochem. 81 (2000) 35.
[9] I. Török, P. Surdy, A. Rockenbauer, L. Korecz Jr., G.J.A.A. Koolhaas, T. Gajda, J. Inorg. Biochem. 71 (1998) 7.
[10] K. Ősz, K. Várnagy, H. Süli-Vargha, A. Csámpay, D. Sanna, G. Micera, I. Sóvágó, J. Inorg. Biochem. 98 (2004) 24.
[11] H. Chermette, Coord. Chem. Rev. 178–180 (1998) 699.
[12] STOE and Cie, X-RED, Version 1.18, STOE and Cie GmbH, Darmstadt, Germany, 1999.
[13] CRYSALIS RED, Oxford Diffraction Ltd., Version 1.171.29.2.
[14] G.M. Sheldrick, Acta Crystallogr. A46 (1990) 467.
[15] G.M. Sheldrick, SHELXL97, Program for the Refinement of Crystal Structures, University of Gottingen, Germany, 1997.
[16] G.M. Sheldrick, SHELXTL: Release 4.1 for Siemens Crystallographic Research Systems, 1990.
[17] M.J. Frisch, G.W. Trucks, H.B. Schlegel, G.E. Scuseria, M.A. Robb, J.R. Cheeseman, J.A. Montgomery Jr., T. Vreven, K.N. Kudin, J.C. Burant, J.M. Millam, S.S. Iyengar,

J. Tomasi, V. Barone, B. Mennucci, M. Cossi, G. Scalmani, N. Rega, G.A. Petersson, H. Nakatsuji, M. Hada, M. Ehara, K. Toyota, R. Fukuda, J. Hasegawa, M. Ishida, T. Nakajima, Y. Honda, O. Kitao, H. Nakai, M. Klene, X. Li, J.E. Knox, H.P. Hratchian, J.B. Cross, C. Adamo, J. Jaramillo, R. Gomperts, R.E. Stratmann, O. Yazyev, A.J. Austin, R. Cammi, C. Pomelli, J.W. Ochterski, P.Y. Ayala, K. Morokuma, G.A. Voth, P. Salvador, J.J. Dannenberg, V.G. Zakrzewski, S. Dapprich, A.D. Daniels, M.C. Strain, O. Farkas, D.K. Malick, A.D. Rabuck, K. Raghavachari, J.B. Foresman, J.V. Ortiz, Q. Cui, A.G. Baboul, S. Clifford, J. Cioslowski, B.B. Stefanov, G. Liu, A. Liashenko, P. Piskorz, I. Komaromi, R.L. Martin, D.J. Fox, T. Keith, M.A. Al-Laham, C.Y. Peng, A. Nanayakkara, M. Challacombe, P.M.W. Gill, B. Johnson, W. Chen, M.W. Wong, C. Gonzalez, J.A. Pople, GAUSSIAN-03, Revision B.03, Gaussian Inc., Pittsburgh, PA, 2003.
[18] A.D. Becke, J. Chem. Phys. 98 (1993) 5648.
[19] C. Lee, W. Yang, R.G. Parr, Phys. Rev. B 37 (1988) 785.
[20] M.E. Casida, in: J.M. Seminario (Ed.), Recent Developments and Applications in Modern Density Functional Theory, Theoretical and Computational Chemistry, vol. 4, Elsevier, Amsterdam, 1996.
[21] E. Reed, L.A. Curtiss, F. Weinhold, Chem. Rev. 88 (1988) 899.
[22] K. Nakamoto, Infrared and Raman Spectra of Inorganic and Coordination Compounds, 4th Ed., Wiley-Interscience, New York, 1986.
[23] G.R. Desiraju, T. Steiner, The Weak Hydrogen Bond in Structural Chemistry and Biology, Oxford University Press, 1999.
[24] G.A. Jeffrey, W. Saenger, Hydrogen Bonding in Biological Structures, Springer-Verlag, 1994.
[25] G.J. Kleywegt, W.G.R. Wiesmeijer, G.J. Van Driel, W.L. Driessen, J. Reedijk, J.H. Noordik, J. Chem. Soc., Dalton Trans. (1985) 2177.
[26] Hui Wang, M.-X. Li, M. Shao, X. He, Polyhedron 26 (2007) 5171.
[27] A.W. Addison, T.N. Rao, J. Reedijk, J. Rijn, G.C. Verschoor, J. Chem. Soc., Dalton Trans. (1984) 1349.
[28] G. Wilkinson, R.D. Gillard, J.A. MaCleverty, Comprehensive Coordination Chemistry, vol. 5, Pergamon, Oxford, UK, 1987.
[29] W.H. Zachariasen, J. Less-Common Metals 62 (1978) 1.
[30] I.D. Brown, Acta Crystallogr. B48 (1992) 553.
[31] I.D. Brown, Acta Crystallogr. B53 (1997) 381.
[32] M. O'Keeffe, N.E. Brese, J. Am. Chem. Soc. 113 (1991) 3226.
[33] L. Sieron, M. Bukowska-Strzyzewska, Acta Crystallogr. C55 (1999) 1230.
[34] M. O'Keeffe, N.E. Brese, Acta Crystallogr. B47 (1997) 192.
[35] G.J. Palenik, Inorg. Chem. 42 (2003) 2725.

complexes, as well as laying the foundation for the rational design of new photoprobes and photonucleases of DNA.

2. Experimental

2.1. Materials and chemicals

Solutions of DNA in 5 mM Tris–HCl buffer (pH 7.0), 50 mM NaCl gave a ratio of UV absorbance at 260 and 280 nm of 1.8–1.9:1, indicating that the DNA was sufficiently free of protein [16]. The concentration of calf thymus DNA (CT-DNA) was determined spectrophotometrically using the molar absorption 6600 M^{-1} cm^{-1} (260 nm) [17].

CT-DNA was purchased from the Sino-American Biotechnology Company and pBR322 DNA from the Sangon (Canada) Biotechnology Company. All reagents and solvents were purchased commercially and were used without further purification, unless specially noted. At the same time, doubly distilled water was used to prepare buffer solutions.

2.2. Synthesis

5-Nitro-1,10-phenanthroline, 5-nitro-6-amino-1,10-phenanthroline, *cis*-$[Ru(bpy)_2Cl_2]\cdot 2H_2O$, *cis*-$[Ru(phen)_2Cl_2]\cdot 2H_2O$, $[Ru(bpy)_2$(5-amino-6-nitro-1,10-phenanthroline)$]^{2+}$, $[Ru(phen)_2$-(5-amino-6-nitro-1,10-phenanthroline)$]^{2+}$, $[Ru(bpy)_2$(5,6-diamino-1,10-phenanthroline)$]^{2+}$ and $[Ru(phen)_2$(5,6-diamino-1,10-phenanthroline)$]^{2+}$ were prepared and characterized according to the literature references [18–22]. Pyrimidine-2-iminoacetate was obtained from the reaction of 2-cyanopyrimidine with sodium methoxide and a few drops of glacial acetic acid, refluxing the mixture for 2 h.

2.2.1. $[Ru(bpy)_2(pmip)](PF_6)_2\cdot 2H_2O$ (**1**)

$[Ru(bpy)_2$(5,6-diamino-1,10-phenanthroline)$]^{2+}$ (200 mg, 0.22 mmol) was dissolved in glacial acetic acid (10 mL) and pyrimidine-2-iminoacetate (82 mg, 0.6 mmol) was added. The mixture was refluxed for 4 h under an argon atmosphere. The cooled reaction mixture was diluted with water (40 mL) and filtered to remove solid impurities, neutralized with aqueous ammonia, and then ammonium hexafluorophosphate was added. The red solid was collected and washed with small amounts of H_2O, EtOH and Et_2O, dried under vacuum, and purified by chromatography over alumina, using MeCN–toluene (5:1, v/v) as an eluent, yield: 164 mg, 72%. The sample shows good solubility in solvents such as MeCN, DMSO and acetone. ^1H NMR [$(CD_3)_2SO$]: δ 9.22 (s (singlet), 1H), 9.07 (d (doublet), 2H), 8.85 (t (triplet), 4H), 8.21 (t, 2H), 8.10 (m (multiplet), 4H), 7.94 (t, 2H), 7.82 (d, 2H), 7.69 (t, 1H), 7.62 (d, 2H), 7.58 (t, 2H), 7.34 (t, 2H). *Anal.* Calc. for $C_{37}H_{30}F_{12}N_{10}O_2P_2Ru$: C, 42.83; H, 2.91; N, 13.50. Found: C, 42.85; H, 2.93; N, 13.51%. ESI-MS (electrospray ionisation mass spectrometry): *m/z* 711 (M-2PF_6-H), 356 (M-2PF_6/2). UV–VIS (UV–visible) (λ (nm), ε (M^{-1} cm^{-1})) (CH_3CN): 459 (17200), 286 (86550), 261 (27700).

2.2.2. $[Ru(phen)_2(pmip)](PF6)_2\cdot 2H_2O$ (**2**)

With 0.22 mmol, 221 mg $[Ru(phen)_2$(5,6-diamino-1,10-phenanthroline)$]^{2+}$ in place of $[Ru(bpy)_2$(5,6-diamino-1,10-phenanthroline)$]^{2+}$, this complex was obtained by a procedure similar to that described for **1**. Yield: 167 mg, 70%. ^1H NMR [$(CD_3)_2SO$]: δ 9.32 (s, 1H), 9.07 (d, 2H), 8.76 (d, 4H), 8.37 (s, 4H), 8.17 (d, 2H), 8.06 (d, 2H), 8.01 (d, 2H), 7.76–7.65 (m, 8H). *Anal.* Calc. for $C_{41}H_{30}F_{12}N_{10}O_2P_2Ru$: C, 45.36; H, 2.79; N, 12.90. Found: C, 45.34; H, 2.80; N, 12.89%. ESI-MS: *m/z* 759 (M-2PF_6-H), 380 (M-2PF_6/2). UV–VIS (λ (nm), ε (M^{-1} cm^{-1})) (CH_3CN): 455 (22200), 263 (103000), 241 (34000).

2.3. Physical measurements

Elemental analyses (C, H and N) were carried out with a Perkin–Elmer 240C elemental analyzer. ^1H NMR spectra were recorded on a Bruker DRX-500 NMR spectrometer with $(CD_3)_2SO$ as the solvent and $SiMe_4$ as an internal standard. Electrospray ionisation mass spectra (ESI-MS) were acquired on a Thermo Finnigan LCQ DECA XP ion trap mass spectrometer, equipped with an ESI source. Emission spectra were measured on a Shimadzu RF-5000 spectrofluorophotometer with excitation at 459 nm. Circular-dichroism (CD) spectra were measured on a JASCO J-810 spectropolarimeter and high-frequency noise was filtered out using JASCO J-600 software.

Electronic spectroscopic titrations were carried out at room temperature to determine the binding affinity between DNA and the complexes. Initially, 3000 L solutions of the blank buffer and the ruthenium complex sample (20 M) were placed in the reference and sample cuvettes (1 cm path length), respectively, and then the first spectrum was recorded in the range of 200–600 nm. During the titration, an aliquot (1–10 L) of buffered DNA solution (concentration of ~5–10 mM in base pairs) was added to each cuvette to eliminate the absorbance of DNA itself, and the solutions were mixed by repeated inversion. After the solutions were mixed for ~5 min, the absorption spectra were recorded. The titration processes were repeated until there was no change in the spectra for four titrations at least, indicating binding saturation had been achieved. The changes in the metal complex concentration due to dilution at the end of each titration were negligible.

Viscosity measurements were carried out using an Ubbelohde viscometer maintained at a constant temperature of 30.0 (±0.1) °C in a thermostatic bath. The DNA samples contained approximately 200 bp. Flow time was measured with a digital stopwatch and each sample was measured three times and an average flow time was calculated. Data are presented as $(\eta/\eta^0)^{1/3})$ versus binding ratio [23,24], where η is the viscosity of DNA in the presence of complex and η^0 is the viscosity of DNA in the absence of complex.

Thermal DNA denaturation experiments were carried out with a Perkin–Elmer Lambda 850 spectrophotometer equipped with a Peltier temperature-control programmer (±0.1) °C. The temperature of the solution was increased from 30 to 90 °C at a rate of 1 °C min^{-1}, and the absorbance at 260 nm was continuously monitored for solutions of CT-DNA (50 M) in the absence and presence of the Ru(II) complexes (5.0 M). The data are presented as $(A - A_0)/(A_f - A_0)$ versus temperature, where A_f, A_0 and A are the final, the initial, and the observed absorbance at 260 nm, respectively.

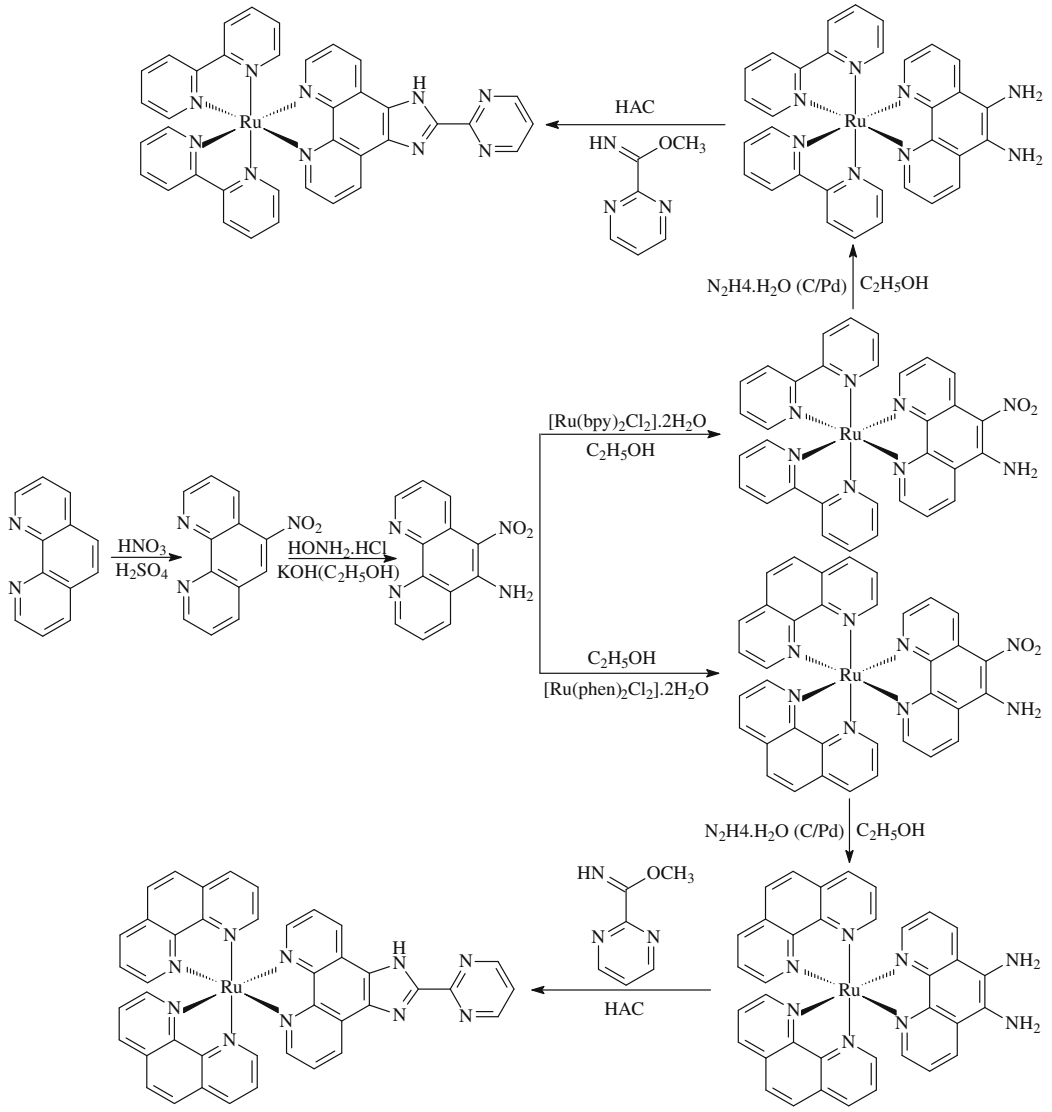
For the gel electrophotolysis experiments, supercoiled pBR322 DNA (10 μM) was treated with the enantiomers in 50 mM Tris–HCl (Tris = Tris(hydroxymethyl)methylamine) buffer (pH 8.3), 18 mM NaCl, and the solutions were then irradiated at room temperature with a UV lamp (365 nm, 10 W) for 60 min. The samples were analysed by electrophotolysis for about 2–3 h at 50 V on 1% agarose gel in Tris–boracic acid–EDTA (EDTA, ethylenediamine tetraacetate) buffer. The gel was stained with 0.5 μg ml^{-1} ethidium bromide (EB) and photographed with an Alpha Innotech IS-5500 fluorescence chemiluminescence and visible imaging system.

All the results obtained from the experiments were performed at least in triplicate.

3. Results and discussion

3.1. Synthesis and common spectral characteristics

The synthetic route to the complexes is summarized in Scheme 1. Both Ru(II) complexes were synthesized by treating $[Ru(L)_2$(5,6-diamino-1,10-phenanthroline)$]^{2+}$ (where L = 2,2′-bipyridine (bpy)



Scheme 1. Synthetic routes for the preparation of the complexes $[Ru(bpy)_2(pmip)]^{2+}$ (**1**) and $[Ru(phen)_2(pmip)]^{2+}$ (**2**).

or 1,10-phenanthroline (phen)) with pyrimidine-2-iminoacetate in glacial acetic acid. Each synthetic step involved here is straightforward and provides a good-to-moderate yield of the desired product in the pure form. These products were characterized by elemental analysis, ^{1}H NMR, electrospray ionisation mass spectra (ESI-MS) and UV/VIS spectroscopy.

The electronic spectra of these Ru(II) complexes in water (CH_3CN) are characterized by an intense ligand-centered transition (LC) in the UV region, at 286 and 263 nm, and a metal-to-ligand charge transfer (MLCT) in the visible region, at 459 and 455 nm for $[Ru(bpy)_2(pmip)]^{2+}$ and $[Ru(phen)_2(pmip)]^{2+}$, respectively, typical of any polypyridyl ruthenium(II) complex [25–28]. The visible bands around 455 nm are attributed to the overlap of Ru(dπ) → bpy/phen (π^*) and Ru(dπ) → pmip (π^*) transitions. Apart from these, ultraviolet bands around 284 and 238 nm for $[Ru(bpy)_2(pmip)]^{2+}$ can be attributed to (bpy) $\pi \rightarrow \pi^*$ transitions; the bands centered at 286 and 263 nm are attributed to (phen) $\pi \rightarrow \pi^*$ transitions for $[Ru(phen)_2(pmip)]^{2+}$.

3.2. UV/VIS spectroscopic studies

The application of electronic absorption spectroscopy is one of the most useful techniques in DNA-binding studies [29]. Complex binding with DNA through intercalation usually result in hypochromism and bathchromism, due to the intercalative mode involving a strong stacking interaction between an aromatic chromophore and the base pairs of DNA. The extent of the hypochromism commonly parallels the intercalative binding strength. Both **1** and **2** were titrated with CT-DNA. The changes in the spectral profiles during titration are shown in Fig. 1a and b. As the DNA concentration is increased, $[Ru(bpy)_2(pmip)]^{2+}$ and $[Ru(phen)_2(pmip)]^{2+}$ show hypochromicity (22.7% and 28.2%) and isosbestic points (478 and 475 nm), respectively. From the decay of the absorbance of complexes **1** and **2** monitored at 459 and 456 nm upon addition CT-DNA, an intrinsic binding constant K is obtained using Eq. (1), which was first developed by Bard [30]:

$$C_b = (b - (b^2 - 2K^2C_t[DNA]/s)^{1/2})/2K \quad (1a)$$

$$b = 1 + KC_t + K[DNA]/2s \quad (1b)$$

where C_b is the concentration of the bound complex, K is the microscopic binding constant for each site, [DNA] is the concentration of DNA in the nucleotide, C_t is the total metal complex concentration, and s is the site size in base pairs. This treatment is valid for cases of non-cooperative, non-specific binding to DNA [30]. The values of K and s for complexes **1** and **2** obtained from Marquart–Levichberg non-linear least-squares analysis are 5.13×10^5 M^{-1} (s = 2.41) and

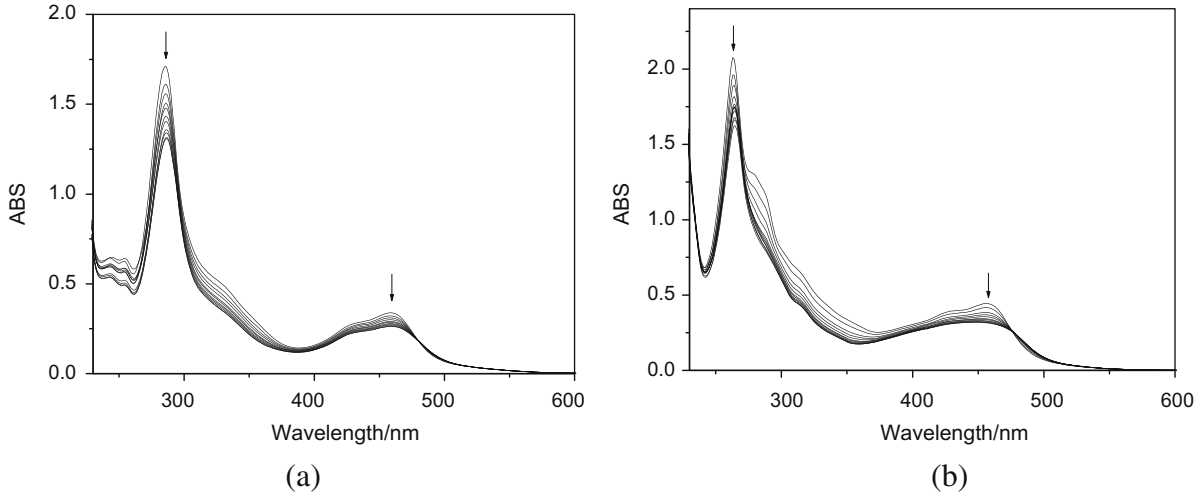


Fig. 1. Absorption spectra of **1** (a) and **2** (b) in 5 mM Tris buffer, pH 7.0, in the presence of calf thymus DNA ([Ru] = 20 μM, [DNA] = 0–200 μM). Arrow shows the absorbance changes upon increasing DNA concentration.

6.64×10^5 M^{-1} (s = 2.06), respectively, which are virtually identical to the values obtained for the ruthenium analogues [31,32]. Based on the measurement of the spectroscopic properties and binding constants, the DNA-binding affinity of complex **2** is greater than that of **1**. The results are due to the different ancillary ligands. On going from bpy to phen, the plane area and hydrophobicity increase, leading to a greater DNA-binding affinity for complex **2**.

3.3. Luminescence studies

In the absence of DNA, both complexes **1** and **2** can emit luminescence in Tris buffer at ambient temperature, with a maximum appearing at 599 and 598 nm, respectively. The results of the emission titrations for complexes **1** and **2** with DNA are illustrated in Fig. 2. Upon addition of CT-DNA, the emission intensities of complexes **1** and **2** increase to around 2.14 and 2.78 times larger than the original intensities, respectively (Fig. 3). This implies that both complexes can strongly interact with DNA and be protected by DNA efficiently, since the hydrophobic environment inside the DNA helix reduces the accessibility of solvent water molecules to the complex and the complex mobility is restricted at the binding site, leading to a decrease of the vibrational modes of relaxation.

3.4. Viscosity studies

To further clarify the nature of the interaction between the complexes and DNA, viscosity measurements were carried out. Optical photophysical probes provide necessary, but not sufficient, evidence to support the model of binding of the Ru(II) complexes with DNA. Hydrodynamic measurements that are sensitive to length change (i.e., viscosity and sedimentation) are regarded as the least ambiguous and the most critical tests of a binding model in solution in the absence of crystallographic structural data [33,34]. Intercalation is expected to lengthen the DNA helix as the base pairs are pushed apart to accommodate the bound ligand, leading to an increase in the DNA viscosity. In contrast, a partial, non-classical intercalation of the ligand could bend (or kink) the DNA helix, reduce its effective length and, concomitantly, its viscosity. The effects of complexes **1** and **2**, together with $[Ru(bpy)_3]^{2+}$ and EB on the viscosity of rod-like DNA are shown in Fig. 4. The well-known DNA intercalator EB increases the viscosity of DNA with increments of the concentration. On the other hand, for $[Ru(bpy)_3]^{2+}$, which has been well known to bind with DNA through the electrostatic mode, there is no effect on the relative viscosity of the DNA solution. Upon increasing the amount of **1** or **2**, the relative

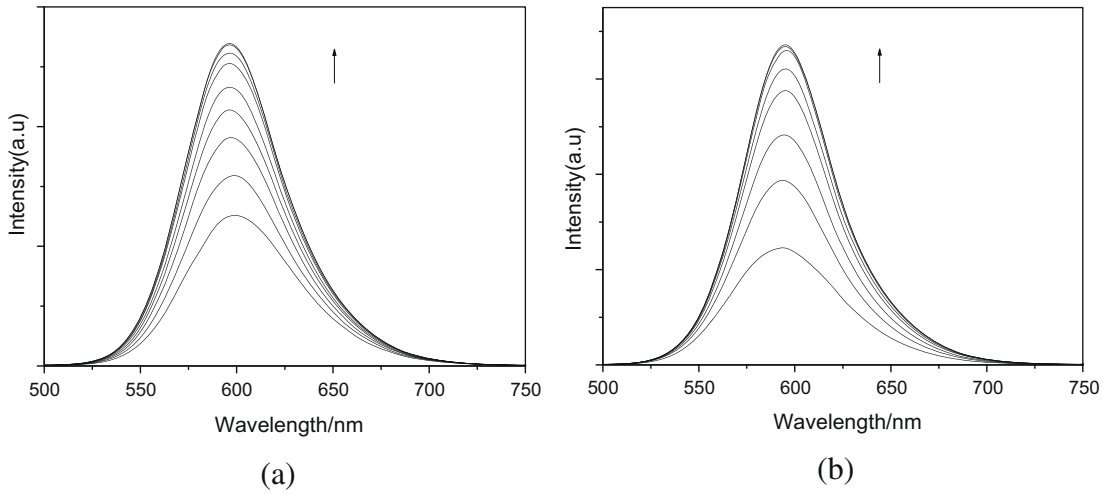


Fig. 2. Emission spectra of **1** (a) and **2** (b) in the presence of increasing amounts of CT-DNA, [Ru] = 20 μM, [DNA] = 0–500 μM. Arrow shows the emission intensity changes upon increasing DNA concentrations.

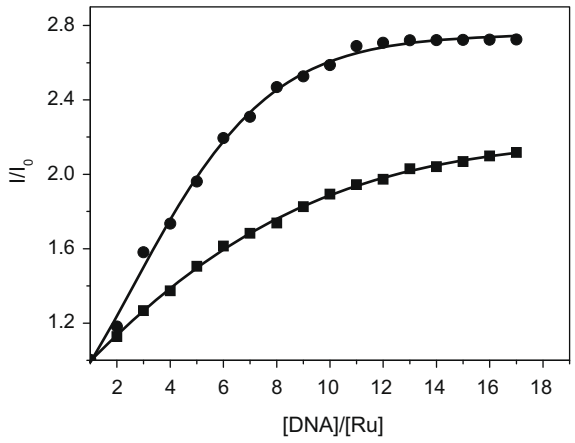


Fig. 3. Plots of relative emission intensity (I/I_0) vs. the [DNA]/[Ru] ratio for Ru(II) complexes **1** (■) and **2** (●) in 5 mM Tris–HCl buffer (pH 7.0), 50 mM NaCl, [Ru] = 20 μM.

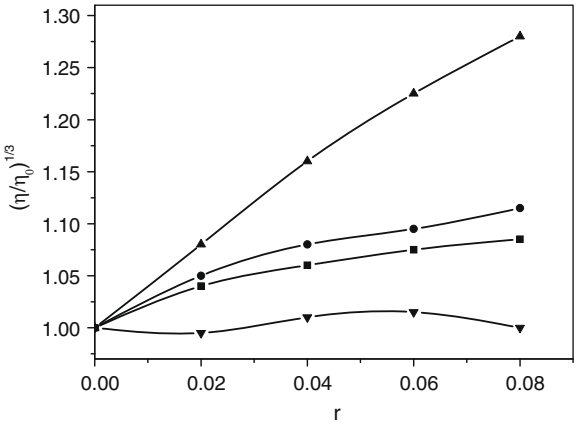


Fig. 4. Effects of increasing amounts of complexes **1** (■); **2** (●); EB (▲); $[Ru(bpy)_3][PF_6]_2$ (▼) on the relative viscosities of CT-DNA at 30 (±0.1) °C; [DNA] = 0.5 mM; r = [Ru]/[DNA].

viscosity of DNA increased steadily, similarly to the case of EB. The increase of the relative viscosity, expected to correlate with the DNA-intercalating potential of a compound, follows the order EB > **2** > **1** > $[Ru(bpy)_3]^{2+}$. These results suggest that the both title complexes intercalate between the base pairs of DNA, the difference in binding strength probably being caused by the different ancillary ligands.

3.5. Thermal denaturation studies

The thermal behavior of DNA in the presence of complexes can give insight into their conformational changes when the temperature is raised, and offer information about the interaction strength of the complexes with DNA. It is well known that when the temperature in the solution increases, the double stranded DNA gradually dissociates to single strands, generating a hyperchromic effect in the absorption spectra of the DNA bases (λ_{max}, 260 nm). To identify this transition process, the melting temperature T_m, which is defined as the temperature where half of the total base pairs are unbonded, is usually determined. According to the literature [35,36], the intercalation of metallo-intercalators generally results in a considerable increase of T_m. The melting curves of CT-DNA in the absence and presence of the complexes are presented in Fig. 5. Here, the thermal denaturation experiment carried out

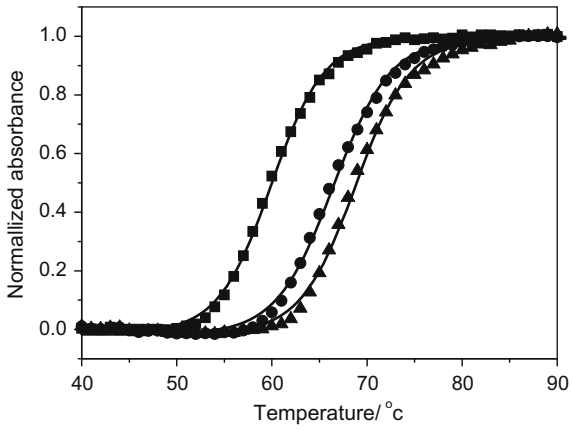


Fig. 5. Melting temperature curves of CT-DNA in the absence (■) and presence of complexes **1** (●) and **2** (▲). [Ru] = 5 μM, [DNA] = 50 μM.

for DNA in the absence of the Ru(II) complexes revealed a T_m of 60.0 °C under our experimental conditions. On addition of **1** or **2**, T_m of DNA increased to 66.5 and 68.8 °C, respectively, at a concentration ratio [DNA]/[Ru] of 10:1. The large increase (6.5 and 8.8) in T_m is comparable to that observed for classical intercalators [35,36].

The DNA intrinsic binding constant at T_m can be obtained from the McGhee equation (Eq. (3)) [37], where T_m^0 is the melting temperature of CT-DNA alone, T_m is the melting temperature in the presence of the Ru(II) complex, ΔH_m is the enthalpy of DNA (per base pair), R is the gas constant, K is the DNA-binding constant at T_m, L is the free complex concentration (approximated at T_m by the total complex concentration) and n is the size of the binding site

$$\frac{1}{T_m^0} - \frac{1}{T_m} = \left(\frac{R}{\Delta H_m}\right) \ln(1 + KL)^{1/n} \quad (2)$$

For the CT-DNA used in these studies, under identical solution conditions, a melting enthalpy of 6.9 kcal mol^{-1} was determined by differential scanning calorimetry [34]. On the basis of the absorption spectra titration experiment and the neighbor-exclusion principle, the value of n for both complexes was assumed to be 2.0 bp. K was determined to be 1.99×10^4 M^{-1} at 66.5 °C for **1** and 2.74×10^4 M^{-1} at 68.8 °C for **2** by substitution of the required parameters into Eq. (2). The standard enthalpy, standard entropy and standard free-energy change of the binding of **1** and **2** to CT-DNA were determined by the van't Hoff's equations (3)–(5), where K_1 and K_2 are the DNA-binding constants of the metal complex at temperatures T_1 and T_2, respectively, and ΔH^0, ΔG^0 and ΔS^0 are the standard enthalpy, standard free-energy and standard entropy changes of the metal-complex-binding to DNA, respectively:

$$\ln\left(\frac{K_1}{K_2}\right) = \frac{\Delta H^0}{R}\left(\frac{T_1 - T_2}{T_1 T_2}\right) \quad (3)$$

$$\Delta G^0 = -RT \ln K \quad (4)$$

$$\Delta G^0 = \Delta H^0 - T\Delta S^0 \quad (5)$$

The values of ΔH^0, ΔG^0 and ΔS^0 were found to be −65.9 kJ mol^{-1}, −32.6 kJ mol^{-1} and −111.7 J mol^{-1} K^{-1} for **1**, and −61.6.1 kJ mol^{-1}, −33.2 kJ mol^{-1} and −95.4 J mol^{-1} K^{-1} for **2**, respectively. The negative ΔG^0 values suggest that the energy of the complex–DNA adduct is lower than the sum of the energies of the free complex and DNA. The negative ΔH^0 values suggest that the binding of the complex to DNA at 25 °C is exothermic and is driven by enthalpy. The negative entropy values indicate that the degree of freedom of the Ru(II)

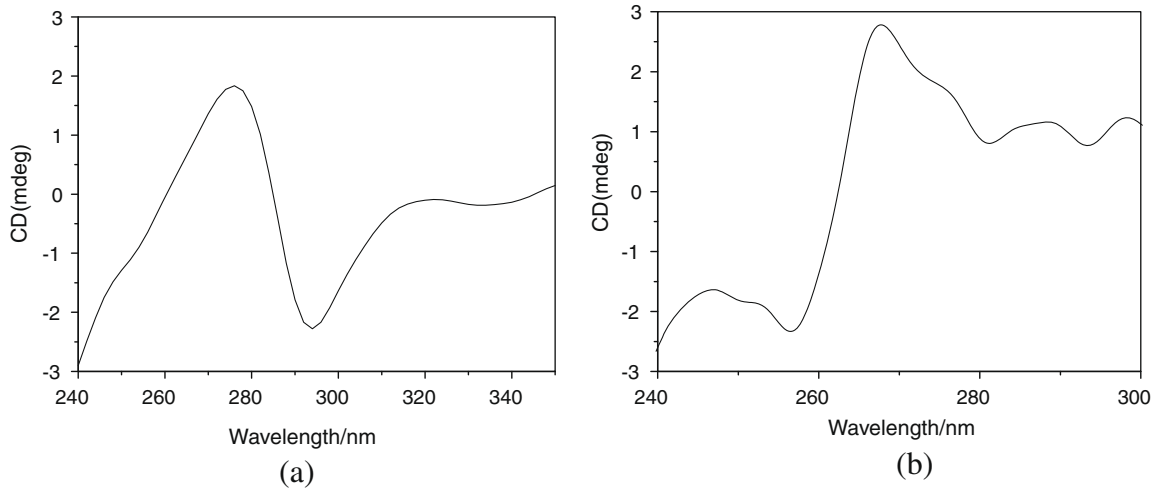


Fig. 6. CD spectra of dialysates of **1** (a) and **2** (b) against CT-DNA for 24 h with the solution stirred; [Ru] = 50 μM, [DNA] = 1.0 mM).

complexes is decreased after the binding, and that the DNA conformational freedom is also reduced upon complex–DNA binding.

3.6. Enantioselective DNA binding

Equilibrium dialysis experiments offer the opportunity to examine the enantioselectivity of complexes binding to DNA. According to the proposed binding mode [38], the Δ-enantiomer of the complex, a right-handed propeller-like structure, will display a greater affinity to the right-handed calf thymus DNA helix than the Λ-enantiomer, due to the appropriate steric matching. The enantiospecific binding of a complex to DNA can be observed clearly from circular-dichroism spectra. The presence of CD signals indicates enrichment of the enantiomer binding less favorably to DNA in the dialysate. Thus, racemic solutions of the two complexes were dialyzed against CT-DNA for 24 h and then subjected to circular-dichroism (CD) analysis. The CD spectra in the UV region of dialysates of **1** and **2** are shown in Fig. 6. The dialysate of complex **1** shows two strong CD signals with a positive peak at 276 nm and a negative peak at 294 nm, while complex **2** shows strong CD signals with a positive peak at 271 nm and a negative peak at 256 nm. Although neither of the complexes is resolved into the pure enantiomer, and we cannot determine which enantiomer binds preferentially to CT-DNA, it is evident that both **1** and **2** bind to CT-DNA enantioselectively.

3.7. DNA photocleavage

There is substantial and continuing interest in DNA endonucleolytic cleavage reactions that are activated by metal ions. The cleavage reaction on plasmid DNA can be monitored by agarose gel electrophoresis. When circular plasmid DNA is subjected to electrophoresis, relatively fast migration will be observed for the intact supercoil form (form I). If scission occurs on one strand (nicking), the supercoil will relax to generate a slower-moving open circular form (form II). If both strands are cleaved, a linear form (form III) that migrates between forms I and II will be generated [39]. The photocleavage of pBR 322 DNA in the absence and presence of the Ru(II) complexes was carried out in 50 mM Tris–HCl buffer (pH 8.3), 18 mM NaCl under UV-irradiation, as seen in Fig. 7. Almost no DNA cleavage was observed for the control, in which metal complex was absent (lane 0). With increasing concentrations of the Ru(II) complexes (lanes 1–4 and 5–8), the amount of form I of pBR322 DNA diminishes gradually, whereas form II increases. Under comparable experimental conditions, complex **2** exhibits more

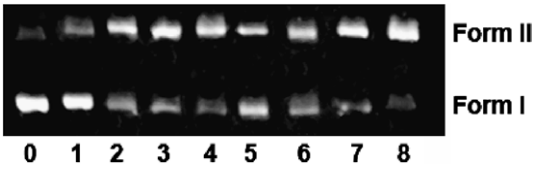


Fig. 7. Photoactivated cleavage of pBR 322 DNA in the absence (lane 0) and presence of **1** (lanes 1–4) or **2** (lanes 5–8) of 20, 40, 60, 80 μM, respectively; all lanes were irradiation at 365 nm for 60 min.

effective DNA cleavage activity than complex **1**. This may be related to the different binding affinity of **1** and **2** to DNA. Further detailed studies are currently underway to clarify the cleavage mechanism.

4. Conclusions

In summary, two new Ru(II) complexes, $[Ru(bpy)_2(pmip)]^{2+}$ and $[Ru(phen)_2(pmip)]^{2+}$, were synthesized and characterized. Their DNA-binding and photocleavage properties were also investigated. Spectroscopic studies, thermal denaturation study and viscosity experiments support that the two complexes can intercalate into DNA base pairs via the pmip ligand. When irradiated at 365 nm, the two Ru(II) complexes are efficient photocleavers of the plasmid pBR 322 DNA.

Acknowledgments

The authors thank the National Natural Science Foundation of China (20472065), the Research Fund for the Doctoral Program of Higher Education, the Program for Young Excellent Talents in Tongji University and Students Innovation Training Program (SITP) for their support of this research.

References

[1] B. Nordén, P. Lincoln, B. Akerman, E. Tuite, in: A. Sigel, H. Sigel (Eds.), Metal Ions in Biological Systems, vol. 33, Dekker, New York, 1996, p. 177.
[2] C. Metcalfea, J.A. Thomas, Chem. Soc. Rev. 32 (2003) 215.
[3] B. Elias, A.K.D. Mesmaeker, Coord. Chem. Rev. 250 (2006) 1627.
[4] K.E. Erkkila, D.T. Odom, J.K. Barton, Chem. Rev. 99 (1999) 2777.
[5] B.M. Zeglis, V.C. Pierre, J.K. Barton, Chem. Commun. (2007) 4565.
[6] L.N. Ji, X.H. Zou, J.G. Liu, Coord. Chem. Rev. 216–217 (2001) 513.
[7] Y. Xiong, L.N. Ji, Coord. Chem. Rev. 185–186 (1999) 711.
[8] M.S. Deshpande, A.A. Kumbhar, A.S. Kumbhar, Inorg. Chem. 46 (2007) 5450.
[9] D.S. Sigman, D.R. Graham, V. Daurora, A.M. Stern, J. Biol. Chem. 254 (1979) 12269.

[10] M. Oivanen, S. Kuusela, H. Lonnberg, Chem. Rev. 98 (1998) 961.
[11] G. Pratviel, J. Bernadou, B. Meunier, Angew. Chem., Int. Ed. Engl. 34 (1995) 746.
[12] W.K. Pogozelski, T.D. Tullius, Chem. Rev. 98 (1998) 1089.
[13] M.G. Alvarez, G. Alzuet, J. Borras, B. Macias, A. Castineiras, Inorg. Chem. 42 (2003) 2992.
[14] J.W. Chen, X.Y. Wang, Y. Shao, J.H. Zhu, Y.G. Zhu, Y.Z. Li, Q. Xu, Z.J. Guo, Inorg. Chem. 46 (2007) 3306.
[15] T.A. Shell, J.E. Glass, M.A. Mackey, K.A. Layman, D.L. Mohler, Inorg. Chem. 46 (2007) 8120.
[16] J. Marmur, J. Mol. Biol. 3 (1961) 208.
[17] M.E. Reichmann, S.A. Rice, C.A. Thomas, P. Doty, J. Am. Chem. Soc. 76 (1954) 3047.
[18] E. Amouyal, A. Homsi, J.C. Chambron, J.P. Sauvage, J. Chem. Soc., Dalton Trans. (1990) 1841.
[19] J. Bolger, A. Gourdon, E. Ishow, J.P. Launay, Inorg. Chem. 35 (1996) 2937.
[20] E. Ishow, A. Gourdon, J.P. Launay, Chem. Commun. (1998) 1909.
[21] E. Ishow, A. Gourdon, J.P. Launay, C. Chiorboli, F. Scandola, Inorg. Chem. 38 (1999) 1504.
[22] F.M. MacDonnell, S. Bodige, Inorg. Chem. 35 (1996) 5758.
[23] J.B. Chaires, N. Dattagupta, D.M. Crothers, Biochemistry 21 (1982) 3933.
[24] G. Cohen, H. Eisenberg, Biopolymers 8 (1969) 45.
[25] J.Z. Wu, B.H. Ye, L. Wang, L.N. Ji, J.Y. Zhou, R.H. Li, Z.Y. Zhou, J. Chem. Soc., Dalton Trans. (1997) 1395.
[26] L.F. Tan, H. Chao, Y.F. Zhou, L.N. Ji, Polyhedron 26 (2007) 3029.
[27] X.H. Zou, B.H. Ye, H. Li, J.G. Liu, Y. Xiong, L.N. Ji, J. Chem. Soc., Dalton Trans. (1999) 1423.
[28] H. Deng, J.W. Cai, H. Xu, H. Zhang, L.N. Ji, J. Chem. Soc., Dalton Trans. (2003) 325.
[29] J.K. Barton, A.T. Danishefsky, J.M. Goldberg, J. Am. Chem. Soc. 106 (1984) 2172.
[30] M.T. Carter, M. Rodriguez, A.J. Bard, J. Am. Chem. Soc. 111 (1989) 8901.
[31] R.B. Nair, E.S. Teng, S.L. Kirkland, C.J. Murphy, Inorg. Chem. 37 (1998) 139.
[32] S. Shi, J. Liu, J. Li, K.C. Zheng, C.P. Tan, L.M. Chen, L.N. Ji, J. Chem. Soc., Dalton Trans. (2005) 2038.
[33] S. Satyanarayana, J.C. Dabrowiak, J.B. Chaires, Biochemistry 31 (1992) 9319.
[34] S. Satyanarayana, J.C. Dabrowiak, J.B. Chaires, Biochemistry 32 (1993) 2573.
[35] M.J. Waring, J. Mol. Biol. 13 (1965) 269.
[36] G.A. Neyhart, N. Grover, S.R. Smith, W.A. Kalsbeck, T.A. Fairly, M. Cory, H.H. Thorp, J. Am. Chem. Soc. 115 (1993) 4423.
[37] J.D. McGhee, Biopolymers 15 (1976) 1345.
[38] J.K. Barton, Science 233 (1986) 727.
[39] J.K. Barton, A.L. Raphael, J. Am. Chem. Soc. 106 (1984) 2466.

1720 spectrophotometer, from KBr pellets in the 4000–370 cm^{-1} range and on a Perkin–Elmer FT-IR 1700X spectrophotometer, from polyethylene pellets in the 500–150 cm^{-1} range. Electronic spectrum in a solution of ATHAc was measured on a Shimadzu UV-3101 PC spectrophotometer using a 10 mm quartz cell. The UV–Vis–NIR reflectance spectra for nickel complexes in the 200–1200 nm range were registered from a pellet of the sample, using a Shimadzu UV-3101 PC spectrophotometer and $BaSO_4$ as a reference. Magnetic measurements were made in the temperature range 2–300 K with a magnetometer with a pendulum MANICS DSM8, equipped with a helium continuous-flow cryostat and an electromagnetometer DRUSCH EAF 16 UE. Data were corrected for diamagnetic contributions, which were estimated from the Pascal constants. ^1H and ^{13}C NMR spectra for ATHAc were obtained with a Bruker AM 400 instrument at 400 and 100 MHz, respectively, in $CDCl_3$ using Me_4Si as the internal standard.

2.2. Synthesis of 2-acetyl-2-thiazoline semicarbazone (ATsc)

The synthesis of ATsc was performed according to the procedure reported elsewhere [18].

2.3. Synthesis of 2-acetyl-2-thiazoline acetylhydrazone (ATHAc)

To a solution containing 2-acetyl-2-thiazoline (800 mg, 6.20 mmol) in 5 mL absolute ethanol were added a solution of acetylhydrazine 90% (510 mg, 6.43 mmol) in 15 mL absolute ethanol and 1 mL of glacial acetic acid, and the resulting solution was heated to reflux for 3 h. Then the solution was cooled and a white solid appeared (671 mg, 59%). This solid was recrystallized from dichloromethane, yielding prismatic crystals, of considerable size, suitable for X-ray diffraction.

^1H NMR ($CDCl_3$): δ 9.77 (s, 1H, NH), 4.43 (t, J = 8 Hz, 2H, CH_2–N), 3.27 (t, J = 8 Hz, 2H, CH_2–S), 2.35 (s, 3H, C(7)H_3), 2.24 (s, 3H, C(5)H_3); ^{13}C NMR ($CDCl_3$): δ 174.4 C(1), 169.6 C(6), 144.0 C(4), 65.2 C(2), 32.1 C(3), 20.4 C(7), 12.1 C(5). *Anal.* Calc. for $C_7H_{11}N_3SO$: C, 45.39; H, 5.98; N, 22.68; S, 17.31. Found: C, 45.47; H, 6.05; N, 22.81; S, 17.18%. IR(KBr): ν(NH) 3183, 3119, 3086; ν(C=O) 1677; ν(C=N) 1620; ring vibrations 1584, 1008, 921, 738, 722, 672, 601, 549, 442 cm^{-1}. UV–Vis (EtOH): λ_{max}, nm; (ε, L mol^{-1} cm^{-1}) 264 (35 720).

2.4. Preparation of [{Ni(ATsc)(MeOH)}$_2$(μ-Cl)$_2$]Cl$_2$ (**1**)

This complex was prepared by reacting a methanol solution (2 mL) of $NiCl_2 \cdot 6H_2O$ (121 mg, 0.51 mmol) with a methanol solution (40 mL) of ATsc (100 mg, 0.51 mmol). The resulting solution was surrounded with ether using a liquid–vapour diffusion method to obtain green crystals (103 mg, 55%). The crystals were filtrated, washed with cold ether and finally air dried. *Anal.* Calc. for $C_{14}H_{28}Cl_4N_8Ni_2O_4S_2$: C, 24.16; H, 4.05; N, 16.10; S, 9.21. Found: C, 23.94; H, 3.83; N, 16.17; S, 8.96%. IR(KBr): $\nu(NH_2)$ 3295; ν(NH) 3230, 3177; ν(C=O) 1679; ν(C=N) 1654; ring vibrations 1601, 1019, 856, 747, 690, 630, 574, 539, 446 cm^{-1}.

2.5. Preparation of [{Ni(ATHAc)(H_2O)}$_2$(μ-Cl)$_2$]Cl$_2$ (**2**)

$NiCl_2 \cdot 6H_2O$ (64 mg, 0.27 mmol) dissolved in ethanol (2 mL) was added to a ethanol solution (20 mL) of ATHAc (50 mg, 0.27 mmol). The resulting solution was allowed to evaporate slowly at room temperature. After a few days, green prismatic crystals of considerable size were isolated from the solution (77 mg, 86%). Crystals were separated by filtration, washed with cold ether and air dried. *Anal.* Calc. for $C_{14}H_{26}Cl_4Ni_2N_6O_4S_2$: C, 25.26; H, 3.94; N, 12.62; S, 9.63. Found: C, 25.29; H, 3.93; N, 12.22; S, 9.40%. IR(KBr): $\nu(H_2O)$ 3421; ν(NH) 3044; ν(C=O) 1643; ν(C=N) 1629; ring vibrations 1572, 1006, 956, 760, 715, 688, 602, 501, 443 cm^{-1}.

2.6. Crystal structure determinations

Experimental details of the crystal structure determinations, including crystal data, data collection, structure determination and refinement parameters for ATHAc, **1** and **2** are listed in Table 1. X-ray diffraction measurements were performed using a Bruker SMART CCD diffractometer with Mo Kα radiation (λ = 0.71073 Å, graphite monochromator). The first fifty frames were measured at the end of the data collection to monitor instrument and crystal stability. Absorption corrections were applied using the program SADABS [20]. The structures were solved by direct methods and subsequent Fourier differences using the SHELXS-97 [21] program and refined by full-matrix least-squares on F^2 with SHELXL-97 [22], included in WINGX [23] package assuming anisotropic displacement parameters for non-hydrogen atoms. The hydrogen atoms on ATHAc were obtained from a difference Fourier synthesis and refined without any constraints, excepting hydrogen atoms of methyl groups which were calculated in ideal positions. In complexes, all hydrogen atoms attached to carbon and nitrogen atoms were positioned geometrically, with U_{iso} values derived from U_{eq} values of the corresponding carbon and nitrogen atoms. The crystal structure of **1** presents a disorder affecting the methyl group of the methanol molecule. Due to the impossibility of modelizing the disorder, the EADP restraints were applied to the disordered atom C(7), remaining two Fourier peaks corresponding carbon disorder positions, Q1 (*0.1049, 0.8578, 0.9479*) and Q2 (*0.0059, 0.9334, 0.9247*), located approx. at 0.8 Å of C(7). Diagrams were generated using ORTEP3 for Windows [24].

3. Results and discussion

3.1. Description of the structures

An ORTEP diagram of the molecular structure of ATHAc is shown in Fig. 1. Selected bond lengths, angles and hydrogen-bond parameters are listed in Table 2.

In the S–C(1)–N(1)–C(2)–C(3) ring the short endocyclic C=N bond [C(1)–N(1) = 1.266(3) Å] is accompanied by a high N–C–S angle [N(1)–C(1)–S = 118.7(2)°] and a relatively long S^{II}–C(sp^2) bond [S–C(1) = 1.757(2) Å], which is characteristic of a thiazoline ring [25]. It is known that the imino tautomers can exist as two geometric isomers, *syn* (*Z*) and *anti* (*E*), but in this crystal, only the *E* isomers have been observed.

Both thiazoline ring and acetylhydrazone group are essentially planar with maximum least square plane deviations for C(3) [0.012 Å] and N(3) [0.026 Å], respectively.

The molecular units of ATHAc are linked by hydrogen bonds in which carbonyl oxygen atom acts as acceptor of hydrogen, whereas the nitrogen atom N(3) acts as donor. A diagram showing the hydrogen bonds is given in Fig. 1.

The X-ray study of **1** revealed that the crystals are made up of monoclinic unit cells, each containing two dimeric [{Ni(ATsc)(MeOH)}$_2$(μ-Cl)$_2$]$^{2+}$ cations and four Cl anions. The molecular structure of the dimeric cation with the atomic labelling is shown in Fig. 2. Selected bond lengths, angles and hydrogen-bond parameters are given in Table 3. In dimeric cations there are two six-coordinate nickel(II) centres, each of which is bonded to a tridentate NNO ATsc ligand. The remaining coordination sites on each metal are occupied by a methanol ligand and two bridging chloride ligands. The bridging Ni_2Cl_2 unit is strictly planar by the presence of the crystallographic inversion centre in the middle of the dimer.

The environment around each nickel(II) atom may be described as a distorted octahedral geometry with the ligand–metal–ligand

Table 1
Crystal data, data collection and refinement details for ATHAc, **1** and **2**.

	ATHAc	**1**	**2**
Crystal shape	prism	prism	prism
Colour	colourless	green	green
Size (mm)	0.39 × 0.35 × 0.27	0.30 × 0.15 × 0.09	0.32 × 0.19 × 0.10
Chemical formula	$C_7H_{11}N_3OS$	$C_{14}H_{28}Cl_4N_8Ni_2O_4S_2$	$C_{14}H_{26}Cl_4N_6Ni_2O_4S_2$
Formula weight	185.25	695.8	665.8
Crystal system	monoclinic	monoclinic	monoclinic
Space group	$P2_1/c$	$P2_1/c$	$P2_1/c$
Unit cell dimensions			
a (Å)	4.736(1)	8.694(2)	11.648(3)
b (Å)	17.076(4)	17.026(4)	8.560(2)
c (Å)	11.415(3)	9.793(2)	13.403(4)
β (°)	94.432(4)	101.440(4)	112.042(5)
Cell volume (Å^3)	920.4(4)	1420.8(5)	1238.7(6)
Z	4	2	2
T (K)	293	120	293
D_{calc} (g cm^{-3})	1.337	1.626	1.758
μ (mm^{-1})	0.309	1.884	2.154
$F(000)$	392	712	680
θ range	2.2–26.7	2.4–26.4	1.9–27.1
Index ranges	$-5 \leqslant h \leqslant 5$, $0 \leqslant k \leqslant 21$, $-0 \leqslant l \leqslant 14$	$-10 \leqslant h \leqslant 10$, $0 \leqslant k \leqslant 21$, $0 \leqslant l \leqslant 12$	$-14 \leqslant h \leqslant 13$, $0 \leqslant k \leqslant 10$, $0 \leqslant l \leqslant 17$
Independent reflections	1935	2921	2726
Observed reflections [$F > 4.0\sigma(F)$]	1933	2285	2104
Data completeness	1	0.999	0.999
Max./min. transmission	0.921/0.889	0.849/0.602	0.813/0.546
No. of reference parameters	131	154	153
R [$F > 4.0\sigma(F)$][a]	0.046	0.039	0.030
wR [$F > 4.0\sigma(F)$][b]	0.148	0.100	0.068
Goodness-of-fit [c]	0.874	1.100	1.060
ρ_{max}, ρ_{min} (e Å^{-3})	0.242/−0.172	1.000/−1.937	0.327/−0.306

[a] $R = \sum ||F_o| - |F_c|| / \sum |F_o|$.
[b] $R = \{\sum[w(F_o^2 - F_c^2)^2] / \sum[w(F_o^2)^2]\}^{1/2}$.
[c] The goodness-of-fit (GOF) equals $\{\sum[w(F_o^2 - F_c^2)^2]/(N_{rflns} - N_{params})\}^{1/2}$.

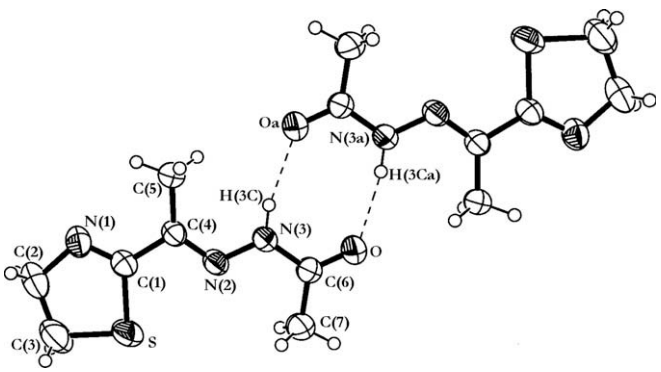


Fig. 1. Crystal structure of ATHAc, showing the atom-numbering scheme and the hydrogen-bond network. The thermal ellipsoids are plotted at the 50% probability level.

Table 2
Selected bond lengths (Å), angles (°) and hydrogen-bond parameters for ATHAc.

S–C(1)	1.757(2)	S–C(3)	1.791(3)
O–C(6)	1.227(3)	N(2)–C(4)	1.279(3)
N(2)–N(3)	1.360(3)	N(3)–C(6)	1.360(3)
C(1)–N(1)	1.266(3)	N(1)–C(2)	1.459(3)
C(1)–S–C(3)	89.7(1)	C(4)–N(2)–N(3)	119.2(2)
C(6)–N(3)–N(2)	119.2(2)	N(2)–C(4)–C(1)	113.5(2)
N(2)–C(4)–C(5)	127.3(2)	N(1)–C(1)–C(4)	122.6(2)
N(1)–C(1)–S	118.7(2)	C(4)–C(1)–S	118.8(2)
C(1)–N(1)–C(2)	112.1(2)	O–C(6)–N(3)	119.4(2)
O–C(6)–C(7)	123.2(2)	N(3)–C(6)–C(7)	117.4(2)
N(1)–C(2)–C(3)	111.8(2)	C(2)–C(3)–S	107.7(2)
Bond H–D ···A	Position of A	A···D (Å)	A···H–D (°)
N(3)–H(3C)···O	$-x-1, -y+1, -z$	2.941(2)	169(2)

bite angles varying between 76.8(1)° [N(2)–Ni–N(1)] and 103.2(1)° [N(1)–Ni–Cl(1)].

The {Ni(μ-Cl)$_2$Ni} motif is asymmetrical with Ni–Cl bond lengths of 2.348(1) and 2.396(1) Å. The Ni···Ni distance within dimer is 3.399(1) Å. The Ni–Cl and Ni···Ni bond lengths have been compared with the mean value calculated using the data of 49 dichloride-bridged six-coordinate nickel(II) dimers obtained from CSD [9]. The short Ni–Cl$_{bridging}$, the long Ni–Cl$_{bridging}$ and the Ni···Ni distances are shorter than the calculated average values 2.416(45), 2.471(56) and 3.60(11) Å, respectively. Likewise, the Ni–O$_{methanol}$ bond length is similar to the average value [2.115(44) Å] calculated using the data of 188 six-coordinated nickel(II) complexes containing this kind of union from CSD [9]. In the same way, the Ni–O$_{ketone}$

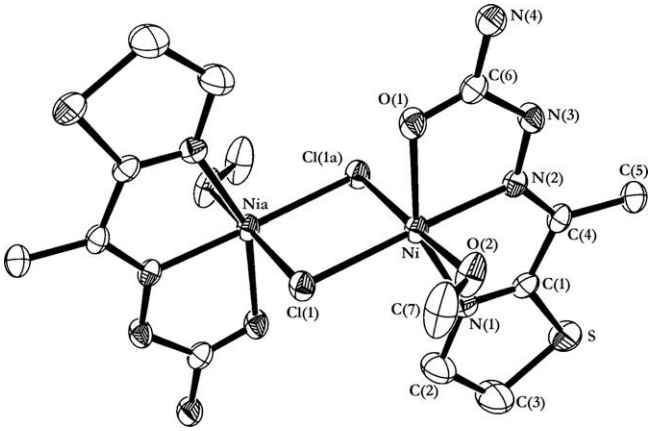


Fig. 2. Molecular structure of complex cation [{Ni(ATsc)(MeOH)}$_2$(μ-Cl)$_2$]$^{2+}$, showing the atom-numbering scheme. The thermal ellipsoids are drawn at the 40% probability level.

Table 3
Selected bond lengths (Å), angles (°) and hydrogen-bond parameters for **1** and **2**.

	1		**2**
Ni–Cl(1)	2.348(1)		2.327(1)
Ni–Cl(1a)	2.396(1)		2.471(1)
Ni–O(1)	2.133(2)		2.134(2)
Ni–O(2)	2.071(3)		
Ni–O(1W)			2.083(2)
Ni–N(1)	2.088(3)		2.053(2)
Ni–N(2)	2.025(3)		2.015(2)
N(2)–Ni–O(2)	85.7(1)		
N(2)–Ni–O(1W)			91.5(1)
N(2)–Ni–N(1)	76.8(1)		78.2(1)
O(2)–Ni–N(1)	92.0(1)		
O(1W)–Ni–N(1)			92.8(1)
N(2)–Ni–O(1)	77.0(1)		76.5(1)
O(1)–Ni–O(2)	86.8(1)		
O(1)–Ni–O(1W)			86.8(1)
N(1)–Ni–O(1)	153.8(1)		154.6(1)
N(2)–Ni–Cl(1)	177.4(1)		175.4(1)
O(2)–Ni–Cl(1)	91.7(1)		
O(1W)–Ni–Cl(1)			92.7(1)
N(1)–Ni–Cl(1)	103.2(1)		99.7(1)
O(1)–Ni–Cl(1)	103.00(1)		105.7(1)
Cl(1)–Ni–Cl(1a)	88.5(1)		87.3(3)
N(2)–Ni–Cl(1a)	94.2(1)		88.6(1)
O(2)–Ni–Cl(1a)	176.3(1)		
O(1W)–Ni–Cl(1a)			177.7(1)
N(1)–Ni–Cl(1a)	91.5(1)		99.7(1)
O(1)–Ni–Cl(1a)	89.6(1)		91.0(1)
Bond H–D ···A	Position of A	A···D (Å)	A···H–D (°)
1			
O(2)–H(2C)···Cl(2)	x,y,z	3.022(3)	169(5)
N(3)–H(3C)···Cl(2)	$-x,-y+2,-z+1$	3.086(3)	154(1)
N(4)–H(4B)···Cl(2)	$-x,-y+2,-z+1$	3.214(3)	152(1)
N(4)–H(4A)···Cl(2)	$-x,y+0.5,-z+1.5$	3.175(3)	149(1)
2			
N(3)–H(3C)···Cl(2)	x,y,z	3.129(3)	167.8(2)
O(1W)–H(1W)···Cl(2)	$-x+2,-y+1,-z$	3.163(2)	172.1(18)
O(1W)–H(2W)···Cl(2)	$-x,y+1.5,z+0.5$	3.136(2)	174.6(17)

and Ni–N_{imine} bond lengths have been compared with the mean value calculated with the data of eight nickel(II) complexes bonded to a semicarbazone moiety obtained from the CSD [9]. Thus, these bond lengths are in good agreement with the mean value of 2.105(29) Å for the Ni–O_{ketone} distance and 2.000(23) Å for the Ni–N_{imine} distance. Finally, the Ni–$N_{thiazoline}$ bond length is comparable to the calculated average value [2.049(53) Å] for eight nickel(II) complexes with the 2-thiazoline ligand collected in CSD [9].

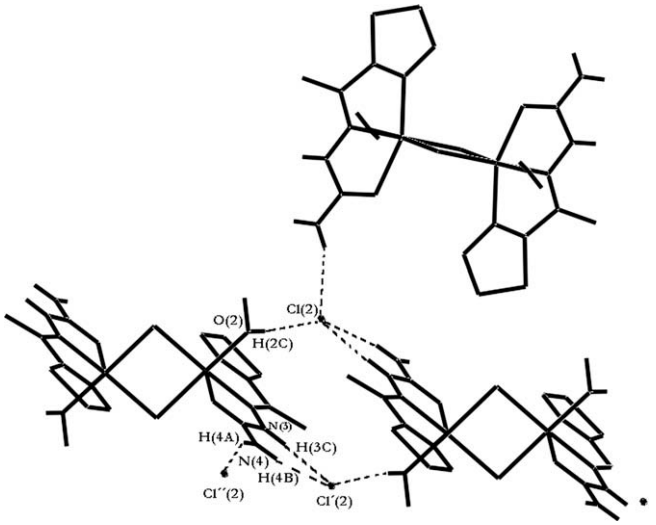


Fig. 3. View of the hydrogen bonds of **1**. Symmetry codes: $'-x,-y+2,-z+1$; $''-x,y+0.5,-z+1.5$.

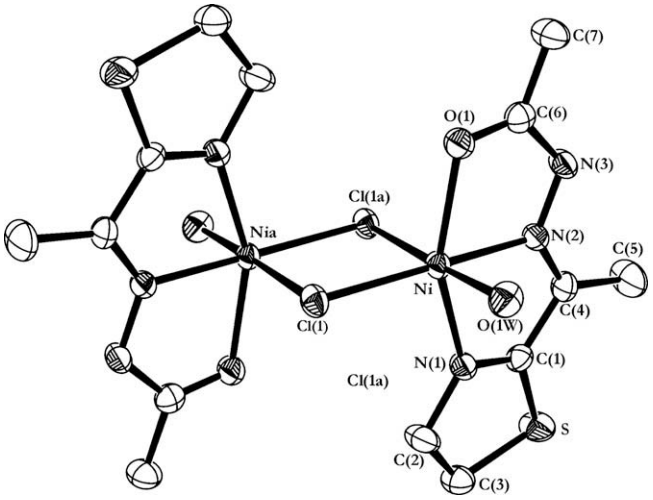


Fig. 4. Molecular structure of cation complex $[\{Ni(ATHAc)(H_2O)\}_2(\mu\text{-}Cl)_2]^{2+}$, showing the atom-numbering scheme. The thermal ellipsoids are drawn at the 40% probability level.

The five-membered chelate rings are essentially planar with maximum deviation in relation to the corresponding mean plane for C(4) (0.031 Å) [chelate ring Ni–N(1)–C(1)–C(4)–N(2)] and C(6) (0.039 Å) [chelate ring Ni–N(2)–N(3)–C(6)–O(1)].

Finally, the crystal structure is stabilized by a hydrogen-bond network in which chloride ions Cl(2) act as acceptors of hydrogen, whereas the OH group of the methanol ligand and nitrogen atoms N(3) and N(4) act as donors. A diagram showing this network is given in Fig. 3.

The crystal structure of **2** with the atomic labelling is shown in Fig. 4. Selected bond lengths, angles and hydrogen-bond parameters are given in Table 3.

The structure of **2** is very similar to that of **1**, which has been already described, being the methanol molecule substituted by a water molecule in the coordination sphere of **2**, and having the organic ligand ATHAc a terminal methyl group instead of an amine one as in ATsc. Thus, the structure of **2** shows a Ni(II)–Ni(II) dinuclear unit in which the chromophore group around each nickel atom is also $NiCl_2N_2O_2$. The distance between the two Ni(II) atoms [3.475(1) Å] is longer than that found in **1**. The octahedral coordination sphere of the Ni centres is distorted, as is indicated by the bond angles around the metal (Table 3).

The Ni–O_{water} bond distance is comparable to the mean value [2.105(70) Å] calculated with the data of six six-coordinated Ni(II) complexes containing the chromophore group $NiCl_2N_2O_2$ found in CSD [9]. The asymmetry of Ni–Cl_{bridge} distances [δ = 0.144 Å] is larger than that found in **1**. Likewise, the rest of the Ni–ligand distances are similar to those of **1**.

The five-membered chelate rings Ni–N(1)–C(1)–C(4)–N(2) and Ni–N(2)–N(3)–C(6)–O(1) are essentially planar with maximum mean plane deviation for C(1) (0.040 Å) and C(6) (0.014 Å), respectively.

The crystal structure presents a network of hydrogen bonds in which the amine group and the water molecule act as hydrogen donors and Cl ions act as acceptors, as it is shown in Fig. 5.

Finally, it should be pointed out that the main difference in both complexes with respect to the structure of free ligands ATsc and ATHAc is due to the different degree of rotation of the thiazoline rings around the C(1)–C(4) bond, which permits the coordination through thiazoline nitrogen atoms [torsion angle S–C(1)–C(4)–N(2) = −173.5° in **1**; 4.4° in ATsc [18]; S–C(1)–C(4)–

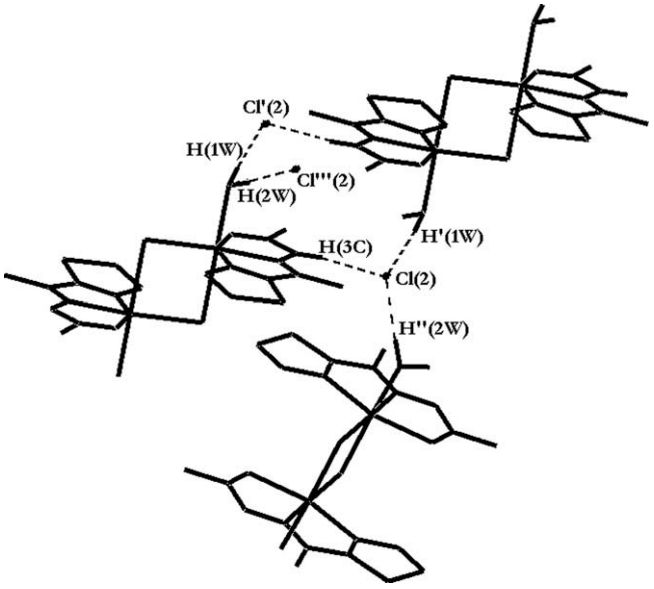


Fig. 5. View of the hydrogen bonds of **2**. Symmetry codes: $'-x+2,-y+1,-z$; $''-x,y+1.5,z+0.5$; $'''x,-y+1.5,z-0.5$.

N(2) = −172.4° in **2**; 3.2° in ATHAc]. The formation of the complexes requires also rotation around the C(6)–N(3) bond, which permits the coordination through the carbonyl oxygen atoms [N(2)–N(3)–C(6)–O(1) = 1.2° in **1**; 177.5° in ATsc [18]; N(2)–N(3)–C(6)–O(1) = 1.1° in **2**; −177.4° in ATHAc].

3.2. IR spectra

The IR spectrum of ATHAc in the 4000–370 cm^{-1} region shows the presence of bands registered at 1677 and 1620 cm^{-1} that can be assigned to ν[C=O] and ν[C=N] vibrations, respectively [26,27]. Moreover, in the IR spectra of the complexes **1** and **2** relevant bands are registered at 1679 [ν(C=O)] and 1654 cm^{-1} [ν(C=N)] for **1** and at 1643 [ν(C=O)] and 1629 cm^{-1} [ν(C=N)] for **2**.

The far IR spectra of these complexes show the appearance of bands due to metal–ligand stretching vibrations. Thus, the band that is registered at 244 cm^{-1} in the spectrum of **1** has been tentatively assigned to the $\nu(Ni–O_{methanol})$ vibration, while the band at 329 cm^{-1} for **2** corresponds to the $\nu(Ni–O_{water})$ vibration [28–30]. The bands that appear at 203 and 226 cm^{-1} for **1** and at 196 and 233 cm^{-1} for **2** can be assigned to ν(Ni–Cl) vibrations, in accord with the literature data for this type of bond [26,31,32]. The bands at 294 cm^{-1} for **1** and at 293 cm^{-1} for **2** are attributed to the $\nu(Ni–N_{thiazoline})$ vibration [28,33] and the bands registered at 309 cm^{-1} for **1** and at 311 cm^{-1} for **2** are assigned to the $\nu(Ni–N_{imino})$ vibration [33–36]. Finally, the $\nu(Ni–O_{ketone})$ vibration corresponds to the bands at 347 cm^{-1} for both complexes [26].

3.3. Electronic spectra

The reflectance spectra of complexes **1** and **2** (see Fig. 6) are very similar and show one intense band at 32 890 cm^{-1} (304 nm) for **1** and another one at 32 260 cm^{-1} (310 nm) for **2**, that are assigned to charge transfer bands. Moreover, the spectra exhibit bands at 8820, 12 740 (sh), 14 080 and 24 450 (sh) cm^{-1} for **1** and at 9210, 12 820 (sh), 14 580 and 25 000 (sh) cm^{-1} for **2**. These bands may be assigned for each spectrum as $\nu_1[^3A_{2g}(F) \rightarrow {}^3T_{2g}(F)]$, $[^3A_{2g}(F) \rightarrow {}^1E_g(D)]$, $\nu_2[^3A_{2g}(F) \rightarrow {}^3T_{1g}(F)]$ and $\nu_3[^3A_{2g}(F) \rightarrow {}^3T_{1g}(P)]$ transitions, respectively, in an idealized O_h symmetry. The ligand field parameters, 10Dq and B, has been calculated from the position of the observed d–d transitions, using the following known relationships [37]:

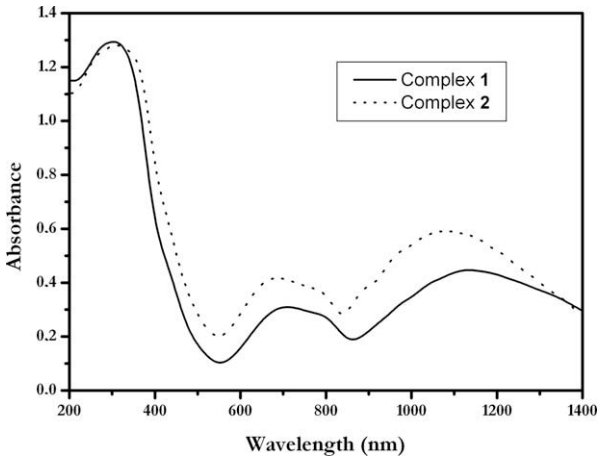


Fig. 6. Electronic spectra in the solid state for **1** and **2**.

$$\nu_1 = 10Dq \quad (1)$$

$$\nu_2 = (1/2)(15B + 30Dq) - (1/2)[(15B - 10Dq)^2 + 12B \cdot 10Dq]^{1/2} \quad (2)$$

$$\nu_3 = (1/2)(15B + 30Dq) - (1/2)[(15B - 10Dq)^2 + 12B \cdot 10Dq]^{1/2} \quad (3)$$

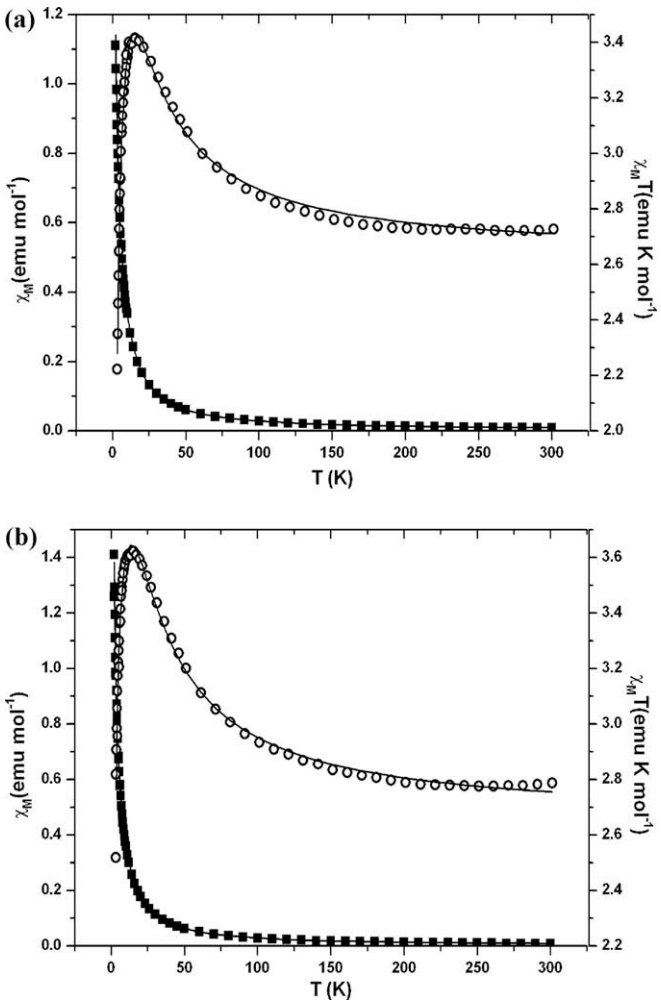


Fig. 7. χ_m vs. T (■) and χ_mT vs. T (○) plot for **1** (a) and **2** (b). Solid lines represent the best fit of the data with the model described in the text.

Table 4
Magnetostructural parameters for chloro-bridged nickel(II) dimers.

Compound[a]	J (cm^{-1})	Ni–Cl–Ni (°)	Ni–Cl_s (Å)	Ni–Cl_l (Å)	X (Å)	Reference
$[Ni_2Cl_2(TTF^{+})_2]$–$(I_3)_4(I_2)_3\cdot(H_2O)_2\cdot(C_4H_8O)_3$	5.0	90.5; 91.8	2.365	2.391	4.756	[46]
1	6.4	91.5	2.348	2.396	4.744	present paper
2	7.1	92.7	2.327	2.471	4.798	present paper
$[\{Ni(TPA)Cl\}_2]$–$(ClO_4)_2\cdot 2HNEt_3ClO_4$	7.6	92.63	2.365	2.507	4.872	[43,47]
$[\{Ni(TPA)Cl\}_2]$–$(ClO_4)(OH)\cdot H_2O$	6.72	92.9	2.365	2.497	4.862	[48]
$[Ni_2Cl_8(H_2O)_2](C_3H_6N_2H_6)_2$	8.13	95.05	2.430	2.459	4.889	[49]
$[\{Ni(eg)_2Cl\}_2]Cl_2$	9.0	93.03	2.383	2.383	4.766	[50,51]
$[\{Ni(en)_2Cl\}_2]Cl_2$	13.3	96.6	2.461	2.551	5.012	[52]
$[\{Ni(TPA)Cl\}_2]$–$(ClO_4)_2\cdot H_2O$	14.6	92.7	2.363	2.503	4.866	[53]
$[Ni_2(bipy)_2(\mu\text{-}Cl)_2Cl_2(H_2O)_2]$	16.8	91.56	2.396	2.405	4.801	[54]
$[\{Ni(en)_2Cl\}_2](ClO_4)_2$	17.8	95.4	2.461	2.512	4.973	[52]
$[\{Ni(en)_2Cl\}_2](Ph_4B)_2$	19.0	95.6	2.403	2.503	4.906	[45,52]
$[\{Ni(L)\}_2(\mu\text{-}Cl)_2](ClO_4)_2$	21.07; 19.90	93.52	2.381	2.535	4.916	[44,55]

[a] *Abbrevations for ligands:* TTF, 4,5-bis(2piridylmethylsulfanyl)-4′,5′-ethylenedithiotetrathiafulvene; TPA, tris-(2-pyridylmethyl)amine; eg, ethylene glycol; en, ethylendiamine; bipy, bipyridine; L, 3,11-dithia-7,17-diazabicyclo[11.3.1]heptadeca-1(17),13,15-triene. Ni–Cl_s is the shorter of the two Ni–Cl bonds, Ni–Cl_l is the longer of the two Ni–Cl bonds, and X is the sum of Ni–Cl_s and Ni–Cl_l.

The calculated values of the ligand field parameters $10Dq = 8675\ cm^{-1}$ and $B = 827\ cm^{-1}$ for **1** and $10Dq = 9040\ cm^{-1}$ and $B = 791\ cm^{-1}$ for **2** are similar to those found in other octahedral nickel(II) complexes [33,38].

3.4. Magnetic properties

The temperature dependence of the magnetic susceptibility of **1** and **2**, in the form of χ_m and $\chi_m T$, is shown in Fig. 7, being χ_m the magnetic susceptibility per dinuclear Ni(II) compound and T the temperature. The high-temperature data ($T > 140$ K) were fit to a Curie–Weiss relationship, yielding $C = 2.70\ cm^3\ mol^{-1}\ K$ and $\theta = 3.36$ K for **1** and $C = 2.73\ cm^3\ mol^{-1}\ K$ and $\theta = 4.60$ K for **2**, which clearly indicate that magnetic interaction between nickel(II) ions is ferromagnetic. The corrected magnetic moments measured were 3.30 BM for **1** and 3.34 BM for **2**, which can be related to an octahedral environment in nickel(II) complexes [39]. The room-temperature $\chi_m T$ product is $2.73\ cm^3\ K\ mol^{-1}$ for **1** and $2.79\ cm^3\ K\ mol^{-1}$ for **2**, which is slightly larger than that expected for two magnetically isolated ions ($2.0\ cm^3\ K\ mol^{-1}$) [40]. $\chi_m T$ increases with decreasing temperature to a maximum of $3.42\ emu\ K\ mol^{-1}$ for **1** and $3.62\ emu\ K\ mol^{-1}$ for **2** at 14.0 K due to a ferromagnetic exchange coupling and then $\chi_m T$ decreases sharply to 2.1 K, which could be due to intermolecular interactions and/or single-ion zero-field splitting [41]. Inclusion of zero-field splitting terms in the analysis of the magnetic susceptibility data means Ginsberg's equation [41] provided poor data fittings. Moreover, the decrease in magnetic moment below 5 K as well as structural data that indicate the presence of a hydrogen-bond network in the packing of the structure suggest antiferromagnetic interdimer interactions [42]. Therefore, the experimental data were fitted considering the molecular field approximation given by Khan (Eq. (4)) [1]:

$$\chi_m = \frac{\chi_{dimer}}{1 - (2zJ'/Ng^2\mu_B^2)\chi_{dimer}} \tag{4}$$

$$\chi_{dimer} = \frac{2Ng^2\mu_B^2}{kT}\left[\frac{\exp(2J/kT) + 5\exp(6J/kT)}{1 + 3\exp(2J/kT) + 5\exp(6J/kT)}\right]$$

Here J is the intradimer exchange interaction, zJ' is the interdimer coupling constant, and the other symbols have their usual meaning. The parameters for the best fit were $g = 2.291(3)$, $J = 5.7(2)\ cm^{-1}$ and $zJ' = -0.253(3)\ cm^{-1}$ for **1** and $g = 2.302(5)$, $J = 6.6(3)\ cm^{-1}$ and $zJ' = -0.153(4)\ cm^{-1}$ for **2**, respectively. The agreement factor R, defined as

$$R = \sum[(\chi T_{Mj}^{obs} - \chi T_{Mj}^{calc})/\chi T_{Mj}^{obs}]$$

is then equal to 1.71×10^{-4} for **1** and 5.52×10^{-4} for **2**. These results indicate ferromagnetic intradimer exchange behaviour and weak antiferromagnetic interdimer exchange behaviour. The ferromagnetic coupling is in good agreement with pseudo-octahedral geometry around nickel(II) ions where the degeneracy of e_g level is maintained [43]. Comparable J and zJ' values are obtained, in agreement with the similarities in structure.

To our knowledge, this is the first analysis of magnetic properties for dinuclear chloro-bridged Ni(II) compounds with tridentate ligands. More structural and magnetic data on related compounds will be necessary for rationalize the magnetic properties. In this way, we have collected all chloride-bridged nickel dimers found in CSD [9] with octahedral Ni(II) ions and magnetic properties which are indicated in Table 4. Although several authors as Tamayo et al. [44] or Bkouche-Waskman et al. [45] have established a correlation between J value and the length of the superexchange pathway for compounds with a close structural resemblance, from the analysis of some more examples can be deduced that Ni–Cl–Ni angle and Ni–Cl distances do not determine in a clear form the value of the exchange constant. In fact, in our compounds the major value of J appears in **2**, where this angle and these distances are larger, but this tendency is not clearly observed in Table 4.

4. Conclusion

We prepared and characterized a new ligand, 2-acetil-2-thiazoline acetylhydrazone (ATHAc), and two new chloride-bridged dinuclear nickel(II) complexes with tridentate NNO ligands, namely, $[\{Ni(ATsc)(MeOH)\}_2(\mu\text{-}Cl)_2]Cl_2$ (**1**) and $[\{Ni(ATHAc)(H_2O)\}_2(\mu\text{-}Cl)_2]Cl_2$ (**2**). The complexes have similar structures features with octahedral Ni(II) centres bridged by two chloride ligands. Variable temperature magnetic susceptibility measurements for the solid samples of **1** and **2** in the range 2–300 K show that ferromagnetic interactions occur in both complexes. To our knowledge, this is the first analysis of magnetic properties for dinuclear chloro-bridged Ni(II) compounds with tridentate ligands. We tried to relate the magnetic properties to the structure of nickel dimers with bridging chloride ligands, finding that no relation exists according to our results and bibliographic data. From the results of diffuse reflectance for **1** and **2** we could deduce that H_2O ligand have a higher d orbital splitting ability than MeOH ligand.

Acknowledgements

We would like to thank the Junta de Extremadura (III PRI+D+I) and the FEDER [Project PRI08A022] and University of Extremadura [Project A7-05] for financial support.

Appendix A. Supplementary data

CCDC 675726, 675727 and 675728 contain the supplementary crystallographic data for ATHAc, **1** and **2**, respectively. These data can be obtained free of charge via http://www.ccdc.cam.ac.uk/conts/retrieving.html, or from the Cambridge Crystallographic Data Centre, 12 Union Road, Cambridge CB2 1EZ, UK; fax: (+44) 1223-336-033; or e-mail: deposit@ccdc.cam.ac.uk. Supplementary data associated with this article can be found, in the online version, at doi:10.1016/j.poly.2009.02.030.

References

[1] O. Khan, Molecular Magnetism, VCH, New York, 1993.
[2] A.R. Paital, T.W. Wing, G. Aromí, D. Ray, Inorg. Chem. 46 (2007) 5727.
[3] D. Ghosh, S. Mukhopadhyay, S. Samanta, K.-Y. Choi, A. Endo, M. Chaudhury, Inorg. Chem. 42 (2003) 7189.
[4] J.R. Lancester Jr., Bioinorganic Chemistry of Nickel, VCH, New York, 1988.
[5] S. Sain, S. Bid, A. Usman, H.-K. Fun, G. Aromí, X. Solans, S.K. Chandra, Inorg. Chim. Acta 358 (2005) 3362.
[6] S. Ogo, R. Kabe, K. Uehara, B. Kure, T. Nishimura, S.C. Menon, R. Harada, S. Fukuzumi, Y. Higuchi, T. Ohhara, T. Tamada, R. Kuroki, Science 316 (2007) 585.
[7] H. Sakiyama, T. Suzuki, K. Ono, R. Ito, Y. Watanabe, M. Yamasaki, M. Mikuriya, Inorg. Chim. Acta 358 (2005) 1897.
[8] F.H. Allen, Acta Crystallogr. B 58 (2002) 380.
[9] I.J. Bruno, J.C. Cole, P.R. Edington, M. Kessler, C.F. Macrae, P. McCabe, J. Pearson, R. Taylor, Acta Crystallogr. B 58 (2002) 389.
[10] S.W. Golding, T.W. Hambley, G.A. Lawrance, S.M. Luther, M. Maeder, P. Turner, J. Chem. Soc., Dalton Trans. (1999) 1975.
[11] M.J. Goldcamp, S.E. Edison, L.N. Squires, D.T. Rosa, N.K. Vowels, N.L. Coker, J.A.K. Bauer, M.J. Baldwin, Inorg. Chem. 42 (2003) 717.
[12] E.C. Constable, D. Phillips, P.R. Raithby, Inorg. Chem. Commun. 5 (2002) 519.
[13] A.A. Korlyukov, M.Yu. Antipin, S.P. Knyazev, E.G. Gordeev, M.V. Pechersky, A.S. Frenkel, P.A. Storozhenko, Russ. J. Gen. Chem. 75 (2005) 1959.
[14] P.C. Junk, J.W. Steed, Inorg. Chim. Acta 360 (2007) 1661.
[15] W.-H. Sun, K. Wang, K. Wedeking, D. Zhang, S. Zhang, J. Cai, Y. Li, Organometallics 26 (2007) 4781.
[16] M. Zhang, S. Zhang, P. Hao, S. Jie, W.-H. Sun, P. Li, X. Lu, Eur. J. Inorg. Chem. (2007) 3816.
[17] W.-Z. Lee, H.-S. Tseng, T.-S. Kuo, Dalton Trans. (2007) 2563.
[18] F.J. Barros-García, F. Luna-Giles, M.A. Maldonado-Rogado, E. Viñuelas-Zahínos, Polyhedron 24 (2005) 2972.
[19] T. Doornbos, H.G. Peer, Recl. Trav. Chim. Pays-Bas. 91 (1972) 711.
[20] Bruker AXS Inc., SADABS, Version 2.03, Bruker AXS Inc., Madison, WI, 2001.
[21] M. Sheldrick, SHELXS-97, Program for Crystal Structures Solution, University of Göttingen, Germany, 1997.
[22] M. Sheldrick, SHELXL-97, Program for Crystal Structures Refinement, University of Göttingen, Germany, 1997.
[23] L.J. Farrugia, J. Appl. Crystallogr. 32 (1999) 837.
[24] L.J. Farrugia, J. Appl. Crystallogr. 30 (1997) 565.
[25] C. Cohen-Addad, Acta Crystallogr. B 38 (1982) 1753.
[26] G. Ibrahim, M.A. Khan, P. Richomme, O. Benali-Baitich, G. Bouet, Polyhedron 16 (1997) 3455.
[27] R.T. Conley, in: Espectroscopia Infrarroja, Alhambra, Madrid, 1979.
[28] A. Bernalte-García, F.J. García-Barros, F.J. Higes-Rolando, A.M. Pizarro-Galán, C. Valenzuela-Calahorro, Thermochim. Acta 95 (1999) 339.
[29] M.A. Ali-Beg, S. Ashfaq-Husain, Polyhedron 2 (1983) 881.
[30] F.J. Barros-García, A. Bernalte-García, F.J. Higes-Rolando, F. Luna-Giles, R. Pedrero-Marín, Polyhedron 23 (2004) 1453.
[31] K. Nakamoto, Infrared and Raman Spectra of Inorganic and Coordination Compounds, 5th Ed., Wiley, New York, 1997.
[32] J.R. Ferraro, Low-Frequency Vibrations of Inorganic and Coordination Compounds, Plenum Press, New York, 1971.
[33] E. Viñuelas-Zahínos, M.A. Maldonado-Rogado, F. Luna-Giles, F.J. Barros-García, Polyhedron 27 (2008) 879.
[34] B. Singh, R.N. Singh, R.C. Aggarwal, Polyhedron 4 (1985) 401.
[35] M. Shakir, S.P. Varkey, F. Firdaus, P.S. Hamed, Polyhedron 13 (1994) 2319.
[36] M.M. Mostafa, M.A. Khattab, K.M. Ibrahim, Polyhedron 2 (1983) 583.
[37] D.K. Rastogi, K.C. Sharma, S.K. Dua, M.P. Teotia, J. Inorg. Nucl. Chem. 37 (1975) 685.
[38] L. Sacconi, F. Mani, A. Bencini, in: G. Wilkinson (Ed.), Comprehensive Coordination Chemistry, Late Transitions Elements, vol. 5, Pergamon Press, Oxford, 1987, p. 51.
[39] J. Reedijk, P.W.N.M. van Leeuwen, W.L. Groeneveld, Rec. Trav. Chim. Pays-Bas. 87 (1968) 129.
[40] J.-H. Zhou, R.-M. Cheng, Y. Song, Y.-Z. Li, Z. Yu, X.-T. Chen, X.-Z. You, Polyhedron 25 (2006) 2426.
[41] A.P. Ginsberg, R.L. Martin, R.W. Brookes, R.C. Sherwood, Inorg. Chem. 11 (1972) 2884.
[42] A. Escuer, R. Vicente, M.S. El Fallah, X. Solans, M. Font-Bardia, Inorg. Chim. Acta 247 (1996) 85.
[43] B. Tong, S.-C. Chang, E.E. Carpenter, C.J. O'Connor, J.O. Lay Jr., R.E. Norman, Inorg. Chim. Acta 300–302 (2000) 855.
[44] A. Tamayo, L. Escriche, C. Lodeiro, J. Ribas-Ariño, J. Ribas, B. Covelo, J. Casabó, Inorg. Chem. 45 (2006) 7621.
[45] I. Bkouche-Waskman, Y. Journaux, O. Khan, Transition Met. Chem. 6 (1981) 176.
[46] S. Liu, C. Ambrus, S. Dolder, A. Neels, S. Decurtins, Inorg. Chem. 45 (2006) 9622.
[47] B. Tong, R.E. Norman, S. Chang, Acta Crystallogr. C 55 (1999) 1236.
[48] S. Yan, L. Zhang, H. Yan, D. Liao, Z. Jiang, G. Wang, H. Wang, X. Yao, Acta Chim. Sinica 57 (1999) 583.
[49] C.P. Landee, R.D. Willett, Inorg. Chem. 20 (1981) 2521.
[50] D. Knetsch, W.L. Groeneveld, Inorg. Nucl. Chem. Lett. 12 (1976) 24.
[51] B.-M. Antti, Acta Chem. Scand., Ser. A 29 (1975) 76.
[52] Y. Journaux, O. Kahn, J. Chem. Soc., Dalton Trans. (1979) 1575.
[53] Z.H. Zhang, X.H. Bu, Z.A. Zhu, Z.H. Jiang, Y.T. Chen, Transition Met. Chem. 21 (1996) 235.
[54] O.F. Ikotun, W. Ouellette, F. Lloret, M. Julve, R.P. Doyle, Eur. J. Inorg. Chem. (2007) 2083.
[55] A. Tamayo, J. Casabó, L. Escriche, C. Lodeiro, B. Covelo, C.D. Brondino, R. Kivekäs, R. Sillampää, Inorg. Chem. 45 (2006) 1140.

The reaction of **1a** with equimolar amounts of *cis*-[$PtCl_2(dmso)_2$] and $Na(CH_3CO_2)$ was also carried out in methanol at 65 °C for 72 h; under these conditions reduction of platinum was minimized and the yield was increased up to 45%. It is interesting to note that the use of a molar ratio amine:metal = 1:1 and of polar solvents such as methanol are among the key factors that have been reported to facilitate *ortho*-palladation of primary amines [2].

In an attempt to isolate the coordination compounds which are postulated as precursors of the cyclometallated derivatives, the reactions of *cis*-[$PtCl_2(dmso)_2$] with amines **1a** and **1b** were also carried out in methanol at room temperature with continuous stirring for 24 h. Under these conditions, compound **Ia** in which (*S*)-(−)-α-methylbenzylamine is coordinated to platinum was obtained while the corresponding reaction for (*R*)-(+)-1-(1-naphthyl)ethylamine produced cyclometallated compound **2b**.

As shown in the scheme, it was confirmed that compound **Ia** evolves to **2a** under adequate conditions. Although the *trans*-configured complexes [MX_2L_2] of palladium and platinum are considered intermediates in the cyclometallation [1b,5], **Ia** displays a *cis* arrangement. As reported for mixed ligand platinum(II) complexes containing sulfoxide and N-donor ligands [12], the *cis* compounds are more stable than the *trans* isomers.

On the other hand, the easy formation of compound **2b** is an interesting result indicating that this cycloplatinated derivative is produced in mild reaction conditions, at room temperature and without requiring the presence of an external base. Previously reported cycloplatination reactions of primary amines took place only in the presence of either sodium acetate [4] or an excess of the amine [5].

The reaction of compounds **2a** and **2b** with triphenylphosphine were carried out in acetone at room temperature to produce compounds **3a** and **3b** in which a triphenylphosphine ligand replaces the dimethylsulfoxide. In addition, the reaction of **2b** with 1,2-bis(diphenylphosphine) was also studied; both the dimethylsulfoxide and the chloro ligands are replaced by the chelated diphosphine leading to ionic cyclometallated compound **4b**. These results suggest that the metallacycles are stable and do not cleave upon reaction with phosphines.

All compounds were characterized by elemental analyses, electrospray mass spectrometry and nuclear magnetic resonance spectra. In the ^1H NMR spectra of **Ia**, **2a** and **2b** anisotropy was observed for both the dimethylsulfoxide and the amino protons. For the cyclometallated derivatives **2a** and **2b**, both the amino protons and the aromatic proton adjacent to the metallated position (H^1) are coupled to platinum with values in the range 59–69 Hz for the former and 44–48 Hz for the latter. 2D-COSY and NOESY spectra confirm the proposed assignments of the observed resonances while the presence of four (**2a**) or six (**2b**) cross-peaks in the aromatic region of the ^1H–^{13}C HSQC spectra confirm the activation of an aromatic C–H bond.

For the triphenylphosphine derivatives **3a** and **3b**, the amino protons are non-equivalent and in each case one of them is coupled to platinum with lower values (51–52 Hz) than those observed for **2a** and **2b**. Conversely, the values of the coupling of the aromatic proton H^1 to platinum (53–57 Hz) are higher than those obtained for the parent compound. The ^1H NMR spectra of **4b** is more complex and the resonances were assigned using 2D-COSY and NOESY spectra. Both amino resonances are strongly shielded when compared to those of **2b**, and one of them is coupled to platinum (^3J(Pt–H) = 43 Hz). In the ^{31}P NMR spectra, one resonance coupled to platinum (*J*(P–Pt) *ca.* 4320 Hz) is observed for compounds **3a** and **3b**, while two resonances with *J*(P–Pt) values of 3706 and 1691 Hz are observed for **4b**. In the latter case, the higher *J* value is assigned to the phosphorous atom *trans* to the amino and the lower to that *trans* to the metallated carbon in agreement with the expected values [13].

2.2. Crystal structure of [$PtCl_2\{NH_2CH(CH_3)C_6H_5\}\{SOMe_2\}$] (**Ia**)

Crystals of compound **Ia** were grown from dichloromethane-methanol. The crystal structure is composed of discrete molecules separated by van der Waals interactions. The structure is shown in Fig. 1 and selected molecular dimensions are listed in Table 1. The coordination sphere of platinum is square-planar with two mutually *cis* chloro ligands, the S-bound dimethylsulfoxide and the N-donor ligand completing the coordination sphere. The stereochemistry of the asymmetric carbon is *S*. The angles between adjacent atoms in the coordination sphere of platinum lie in the range 87.3(2)–91.11(9)° and Pt–Cl, Pt–N and Pt–S bond lengths are well within the range of values obtained for similar complexes of platinum [12,14]. As expected from the high *trans* influence of the dimethylsulfoxide, the Pt–Cl bond length *trans* to this ligand is slightly longer (2.322(2) Å) than that *trans* to a N-donor ligand (2.300(2) Å). When compared to the reported structure for *trans*-[$PtCl_2\{NH_2CH_2(4\text{-}ClC_6H_4)SOMe_2\}$] [14], the Pt–N bond length is shorter (2.034(7) versus 2.079(10) Å) which can be related to the presence of a chloro versus a dimethylsulfoxide ligand in a *trans* position. The amino hydrogen atoms are involved in intramolecular interactions, one with O(1) (d(N···O) = 2.933(10) Å) and the other with Cl(1) (d(N···Cl) = 3.364(8) Å).

The shortest distance between platinum and the *ortho* hydrogen atoms is 4.702 Å for Pt···H(5), a similar value to that obtained for *trans*-[$PtCl_2\{NH_2CH_2(4\text{-}ClC_6H_4)SOMe_2\}$] (4.668 Å) [14]. These values are significantly larger than those obtained for imines [13] or oximes [15] which are in the range 2.6–3.3 Å in agreement with the lower proclivity to cyclometallate observed for primary amines.

2.3. Conclusions

The results here obtained indicate that cycloplatination of primary amines can be achieved in high yield using *cis*-[$PtCl_2(dmso)_2$] when appropriate amines are used. While cycloplatination of 4-chlorobenzylamine gives poor yields [4], cycloplatination of α-methylbenzylamine was achieved with 45% yield, and a higher yield (95%) was obtained for the naphthylethylamine. Moreover, the latter amine could also be metallated at room temperature in the absence of sodium acetate. It is therefore evident that the ease to cyclometallate follows the sequence: 4-chlorobenzylamine < α-methylbenzylamine < naphthylethylamine. In agreement with the results reported for analogous reactions [5], electronic effects could account for the low reactivity of 4-chlorobenzylamine compared to the easier cyclometallation of **1a** and **1b** which contain an electron-donor methyl group. However, no significant differences are expected between **1a** and **1b** for which the basicity is in the same range [16]. Therefore, the results here reported suggest that the higher bulk of the amine arising from both the methyl group in the α-position (in **1a** and **1b**) and the presence of a naphthyl substituent (in **1b**) might be decisive in promoting the cyclometallation. Steric promotion has been reported for palladium analogues [2,9] and attributed to both an increase in the electrophilicity of the metallic centre in the coordination intermediate and to a less favoured coordination of a second amine leading to unreactive bis-amine coordination compounds. As a whole, cycloplatination of primary amines share common features with those reported for cyclopalladation; for instance the use of molar ratio amine: metal = 1:1, the use of polar solvents and the use of sterically hindered amines grant successful syntheses.

In addition, the easy displacement reactions of dimethylsulfoxide in **2a** and **2b** for mono or diphosphines without cleaving the metallacycle makes them promising candidates to be used as resolving agents for Lewis bases as reported for palladium analogues [10,11] and as chiral reagents in stoichiometric and catalytic processes.

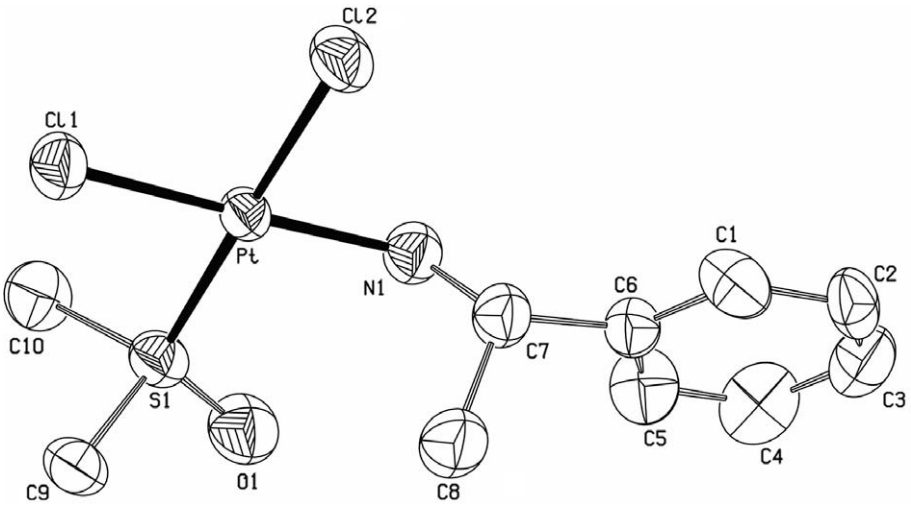


Fig. 1. Molecular structure of compound **Ia** with thermal ellipsoids at 50% probability.

Table 1
Bond lengths (Å) and angles (°) for **Ia**.

Pt–N(1)	2.034(7)	N(1)–Pt–S(1)	90.8(2)
Pt–S(1)	2.2010(19)	S(1)–Pt–Cl(1)	90.73(8)
Pt–Cl(1)	2.300(2)	N(1)–Pt–Cl(2)	87.3(2)
Pt–Cl(2)	2.322(2)	Cl(1)–Pt–Cl(2)	91.11(9)
N(1)–C(7)	1.489(11)		
C(6)–C(7)	1.552(12)		
C(7)–C(8)	1.549(15)		

3. Experimental

3.1. General

Microanalyses were performed by Serveis Cientifico-tècnics (Universitat de Barcelona) and by Servei de Recursos Científics i Tècnics de la Universitat Rovira i Virgili (Tarragona). Mass spectra were performed at Servei d'Espectrometria de Masses (Universitat de Barcelona). Electrospray mass spectra were carried out in a LC/MSD-TOF spectrometer using H_2O–CH_3CN 1:1 to introduce the sample. NMR spectra were performed at Unitat de RMN d'Alt Camp de la Universitat de Barcelona using Varian Unity 300 (^{1}H, 300 MHz; ^{31}P–{^{1}H}, 121.4 MHz) and Mercury-400 (^{1}H, 400 MHz; ^{1}H–^{1}H NOESY, ^{1}H–^{1}H COSY, ^{1}H–^{13}C gHSQC) spectrometers, and referenced to $SiMe_4$ (^{1}H, ^{13}C) and H_3PO_4 (^{31}P). δ values are given in ppm and J values in Hz. *Abbreviations used: s,* singlet; d, doublet; t, triplet; q, quadruplet; se, sextuplet; m, multiplet; br, broad; NMR labelling as shown in Scheme 1.

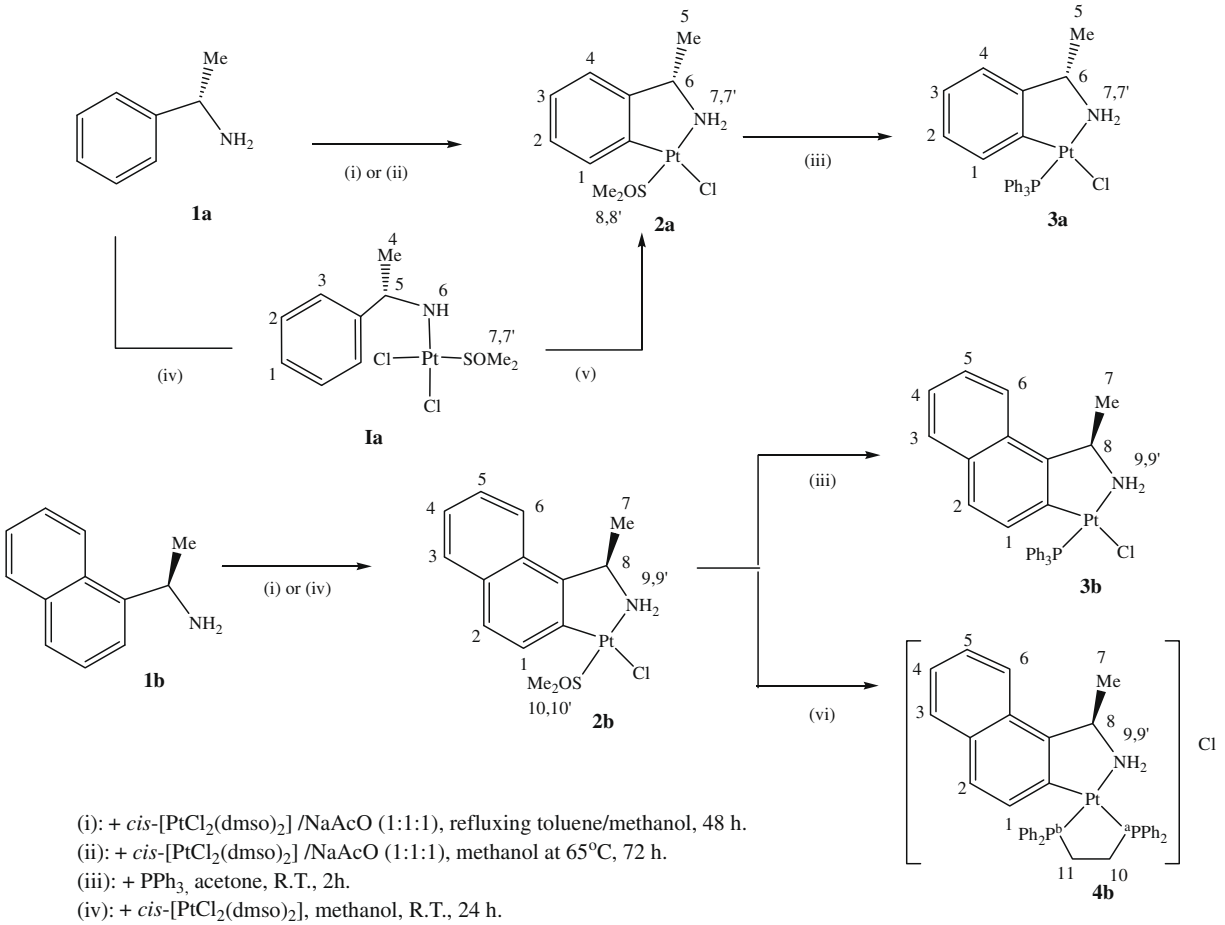
3.2. Preparation of the compounds

cis-[$PtCl_2$(dmso)$_2$] was prepared using a reported procedure [17]. Amines **1a** and **1b** were obtained from commercial sources and used as received.

cis-[$PtCl_2${$NH_2CH(CH_3)C_6H_5$}{$SOMe_2$}] (**Ia**) was obtained as colourless crystals from 100 mg (0.23 mmol) of *cis*-[$PtCl_2${$SOMe_2$}$_2$] and 29 mg (0.23 mmol) of (*S*)-(−)-α-methylbenzylamine which were stirred in methanol at room temperature for 24 h. The solvent was removed and the residue was allowed to crystallize in CH_2Cl_2:MeOH (1:1) at room temperature. Yield 77 mg (70%). ^{1}H NMR (400 MHz, $CDCl_3$): δ = 7.54 [dd, ^3J(H^3–H^2) = 8.0, ^4J(H^3–H^1) = 1.4, 2H, H^3]; 7.39–7.46 [m, 3H, H^{1,2}]; 4.65 [se, ^3J(H^5–H^4) = ^3J(H^5–H^6) = ^3J(H^5–H$^{6\prime}$) = 6.8, 1H, H^5]; 4.32 [br s, 1H, H^6]; 4.26 [br s, 1H, H$^{6\prime}$]; 3.39 [s, 3H, ^3J(H^7–Pt) = 21.2, H^7]; 2.90 [s, 3H, ^3J(H$^{7\prime}$–Pt) = 19.6, H$^{7\prime}$]; 1.74 [d, ^3J(H^4–H^5) = 6.8, 3H, H^4]. ESI-MS, *m*/*z*: 895.05 [2M−Cl]$^+$; 430.04 [M−Cl]$^+$. *Anal.* Calc. for $C_{10}H_{17}Cl_2NOPtS$: C, 25.81; H, 3.68; N, 3.01; S, 6.89. Found: C, 26.4; H, 3.7; N, 3.0; S, 6.9%.

[PtCl{$NH_2CH(CH_3)C_6H_4$}{$SOMe_2$}] (**2a**) was obtained from 153 mg (0.36 mmol) of *cis*-[$PtCl_2${$SOMe_2$}$_2$], 44 mg (0.36 mmol) of (*S*)-(−)-α-methylbenzylamine and 29 mg (0.36 mmol) of sodium acetate dissolved in methanol (2 mL). The mixture was refluxed in 25 mL of toluene under nitrogen atmosphere for 48 h, and a small amount of metallic platinum was filtered off. The solvent was removed in a rotary evaporator to yield an oily residue that was crystallized in CH_2Cl_2:MeOH (1:1) at low temperature, to produce a white solid. Yield: 51 mg (33%). Alternatively, the reaction between equimolar amounts of *cis*-[$PtCl_2${$SOMe_2$}$_2$], (*S*)-(−)-α-methylbenzylamine and sodium acetate was carried out in methanol at 65 °C for 72 h and compound **2a** was obtained with 45% yield. In addition, the reaction of 25 mg (0.05 mmol) of **Ia** and the equimolar amount of sodium acetate (4.5 mg) in methanol at 65 °C for 72 h produced compound **2a** with 46% yield. ^{1}H NMR (300 MHz, $CDCl_3$): δ = 7.95 [dd, ^3J(Pt–H^1) = 48.2, ^3J(H^1–H^2) = 7.2, ^4J(H^1–H^3) = 1.8, 1H, H^1]; 7.10–7.02 [m, 2H, H^{2,3}]; 6.92 [dd, ^3J(H^3–H^4) = 6.9, ^4J(H^2–H^4) = 2.0, 1H, H^4]; 4.85 [br s, ^2J(Pt–H^7) = 64.3, 1H, H^7]; 4.40 [q, ^3J(H^5–H^6) = 6.2, 1H, H^6]; 3.98 [br s, ^2J(Pt–H$^{7\prime}$) = 69.6, 1H, H$^{7\prime}$]; 3.41 [br s, 3H, H^8]; 3.39 [br s, 3H, H$^{8\prime}$]; 1.60 [d, ^3J(H^5–H^6) = 6.6, 3H, H^5]. gHSQC (400 MHz, $CDCl_3$): δ = 134.2 [C^1]; 126.7 [C^2]; 125.3 [C^3]; 122.9 [C^4]; 60.2 [C^6]; 46.6 [C$^{8\prime}$]; 46.2 [C^8]; 24.5 [C^5]. ESI-MS, *m*/*z*: 858.06 [2M+H]$^+$; 430.03 [M+H]$^+$; 393.06 [M−Cl]$^+$. *Anal.* Calc. for $C_{10}H_{16}ClNOPtS$: C, 28.01; H, 3.76; N, 3.27; S, 7.47. Found: C, 28.4; H, 3.7; N, 3.3; S, 7.3%.

[PtCl{$NH_2CH(CH_3)C_{10}H_6$}{$SOMe_2$}] (**2b**) was obtained from 150 mg (0.355 mmol) of *cis*-[$PtCl_2${$SOMe_2$}$_2$], 61 mg (0.356 mmol) of (*R*)-(+)-1-(1-naphthyl)ethylamine and 29 mg (0.36 mmol) of sodium acetate using the same procedure as for **2a**. A white solid was obtained. Yield: 162 mg (95%). Alternatively, the reaction of equimolar amounts of *cis*-[$PtCl_2${$SOMe_2$}$_2$] and (*R*)-(+)-1-(1-naphthyl)ethylamine was carried out in methanol at room temperature for 24 h and compound **2b** was crystallized with 75% yield within three days. ^{1}H NMR (400 MHz, $CDCl_3$): δ = 8.09 [d, ^3J(Pt–H^1) = 44.5, ^3J(H^1–H^2) = 8.6, 1H, H^1]; 7.71 [dd, ^3J(H^3–H^4) = 7.2, ^4J(H^3–H^5) = 2.2, 1H, H^3]; 7.48 [d, ^3J(H^1–H^2) = 8.8, 1H, H^2]; 7.35 [d, ^3J(H^5–H^6) = 8.3, 1H, H^6]; 7.33–7.28 [m, 2H, H^{4,5}]; 5.43 [br s, ^2J(Pt–H^9) = 63.9, 1H, H^9]; 4.90 [m, ^3J(Pt–H^8) = 69.7, ^3J(H^8–H^{7,9}) = 6.1, 1H, H^8]; 3.91 [d, ^2J(Pt–H$^{9\prime}$) = 59.6, ^3J(H^9–H$^{9\prime}$) = 10.3, 1H, H$^{9\prime}$]; 3.40 [br s, 3H, H^{10}]; 3.25 [br s, 3H, H$^{10\prime}$];



(i): + *cis*-[$PtCl_2(dmso)_2$] /NaAcO (1:1:1), refluxing toluene/methanol, 48 h.
(ii): + *cis*-[$PtCl_2(dmso)_2$] /NaAcO (1:1:1), methanol at 65°C, 72 h.
(iii): + PPh_3, acetone, R.T., 2h.
(iv): + *cis*-[$PtCl_2(dmso)_2$], methanol, R.T., 24 h.
(v): + NaAcO (1:1), methanol at 65°C, 72 h.
(vi): + dppe, acetone, R.T., 5h.

Scheme 1.

1.69 [d, $^3J(H^7–H^8) = 6.4$, 3H, H^7]. gHSQC (400 MHz, $CDCl_3$): $\delta = 132.2$ [C^1]; 128.7 [C^3]; 126.3 [C^2]; 126.2 [C^5]; 124.6 [C^4]; 123.6 [C^6]; 58.6 [C^8]; 46.8 [C^{10}]; 45.7 [$C^{10\prime}$]; 24.5 [C^7]. ESI-MS, *m*/*z*: 921.12 [2M−Cl]$^+$; 443.07 [M−Cl]$^+$. *Anal.* Calc. for $C_{14}H_{18}ClNOPtS \cdot H_2O$: C, 33.84; H, 4.06; N, 2.82; S, 6.45. Found: C, 34.1; H, 3.9; N, 2.9; S, 6.0%.

[$PtCl\{NH_2CH(CH_3)C_6H_4\}\{P(C_6H_5)_3\}$] (**3a**) was obtained from 34 mg (0.08 mmol) of compound **2a** and 21 mg (0.08 mmol) of triphenylphosphine which were allowed to react in acetone at room temperature for 2 h. The solvent was removed in a rotary evaporator and the residue was washed with ether and dried in vacuo. A white solid was obtained after re-crystallisation in CH_2Cl_2:MeOH. Yield 39 mg (79%). ^{1}H RMN (300 MHz, $CDCl_3$): $\delta = 7.77–7.70$ [m, 6H, $H^{o\text{-}PPh3}$]; 7.45–7.31 [m, 9H, $H^{m,p\text{-}PPh3}$]; 6.92 [dd, $^3J(H^3–H^4) = 7.3$, $^4J(H^2–H^4) = 1.7$, 1H, H^4]; 6.87 [td, $^3J(H^3–H^{2,4}) = 7.2$, $^4J(H^1–H^3) = 1.19$, 1H, H^3]; 6.51 [ddd, $^3J(Pt–H^1) = 56.9$, $^3J(H^1–H^2) = 8.0$, $^4J(H^1–H^3) = 2.8$, $^5J(H^1–H^4) = 1.1$, 1H, H^1]; 6.40 [td, $^3J(H^2–H^{1,3}) = 7.3$, $^4J(H^2–H^4) = 1.8$, 1H, H^2]; 4.66–4.45 [m, 2H, $H^{6,7}$]; 3.87 [br s, $^2J(Pt–H^{7\prime}) = 51.0$, 1H, $H^{7\prime}$]; 1.70 [d, $^3J(H^5–H^6) = 6.6$, 3H, H^5]. ^{31}P RMN (121 MHz, $CDCl_3$): $\delta = 23.84$ [s, $^1J(Pt–P) = 4326.8$]. ESI-MS, *m*/*z*: 577.14 [M−Cl]$^+$. *Anal.* Calc. for $C_{26}H_{25}ClNPPtS$: C, 50.94; H, 4.11; N, 2.28. Found: C, 51.0; H, 4.1; N, 2.4%.

[$PtCl\{NH_2CH(CH_3)C_{10}H_6\}\{P(C_6H_5)_3\}$] (**3b**) was obtained as a white solid from 44 mg (0.09 mmol) of compound **2b** and 24 mg (0.09 mmol) of triphenylphosphine using the same procedure than for **3a**. Yield 52 mg (87%). ^{1}H RMN (400 MHz, $CDCl_3$): $\delta = 7.77–7.71$ [m, 6H, $H^{o\text{-}PPh3}$]; 7.68 [d, J(H–H) = 8.4, 1H, H^{ar}]; 7.56 [d, $^3J(H^5–H^6) = 8.3$, 1H, H^6]; 7.42–7.23 [m, 11H, 2 H^{ar} + $H^{m,p\text{-}PPh3}$]; 6.88 [d, $^3J(H^1–H^2) = 8.6$, 1H, H^2]; 6.72 [dd, $^3J(Pt–H^1) = 52.7$, $^3J(H^1–H^2) = 8.6$, $^4J(P–H^1) = 2.8$, 1H, H^1]; 5.40 [q, $^3J(Pt–H^8) = 55.5$, $^3J(H^7–H^8) = 6.0$, 1H, H^8]; 4.70 [br s, 1H, H^9]; 4.13 [m, $^2J(Pt–H^{9\prime}) = 52.4$, 1H, $H^{9\prime}$]; 1.89 [d, $^3J(H^7–H^8) = 6.3$, 3H, H^7]. ^{31}P RMN (121 MHz, $CDCl_3$): $\delta = 24.32$ [s, $^1J(Pt–P) = 4318.5$]. ESI-MS, *m*/*z*: 627.15 [M−Cl]$^+$. *Anal.* Calc. for $C_{30}H_{27}ClNPPt \cdot 1/2CH_2Cl_2$: C, 51.92; H, 4.10; N, 1.99. Found: C, 52.0; H, 4.1; N, 1.9%.

[$Pt\{NH_2CH(CH_3)C_{10}H_6\}\{(C_6H_5)_2PCH_2CH_2P(C_6H_5)_2\}$]Cl (**4b**) was obtained as a white solid from 40 mg (0.08 mmol) of compound **2b** and 32 mg (0.08 mmol) of 1,2-bis(diphenylphosphine)ethane (dppe) using the same procedure than for **3a** and a reaction time of 5 h. Yield 63 mg (99%). ^{1}H RMN (400 MHz, $CDCl_3$): $\delta = 8.11–8.06$ [m, 2H, $H^{2,3}$]; 7.91–7.83 [m, 4H, H^{PPh2}]; 7.77 [d, $^3J(H^5–H^6) = 8.3$, 1H, H^6]; 7.67–7.43 [m, 16H, H^{PPh2}]; 7.38–7.28 [m, 2H, $H^{4,5}$]; 7.05 [m, 1H, H^1]; 5.98 [q, $^3J(Pt–H^8) = 59.4$, $^3J(H^7–H^8) = 6.2$, 1H, H^8]; 4.58 [d, $^2J(Pt–H^{9\prime}) = 43.0$, $^2J(H^9–H^{9\prime}) = 12.1$, 1H, $H^{9\prime}$]; {2.85–2.67 [m, 1H]; 2.61–2.44 [m, 1H]; 2.31–2.15 [m, 1H]; 2.18–2.03 [m, 1H]; $H^{10,11}$}; 1.80 [br s, 1H, H^9]; 1.59 [d, $^3J(H^7–H^8) = 6.3$, 3H, H^7]. ^{31}P RMN (121 MHz, $CDCl_3$): $\delta = 47.67$ [s, $^1J(Pt–P) = 1691.4$, 1P, P^a]; 43.75 [s, $^1J(Pt–P) = 3706.3$, 1P, P^b]. ESI-MS, *m*/*z*: 763.20 [M]$^+$. *Anal.* Calc. for $C_{38}H_{36}ClNP_2Pt \cdot CH_2Cl_2$: C, 52.9; H, 4.33; N, 1.58. Found: C, 52.63; H, 4.54; N, 1.7%.

3.3. X-ray structure analysis

A prismatic crystal was selected and mounted on a MAR345 diffractometer with an image plate detector. Unit cell parameters were determined from 4749 reflections ($3° < \theta < 31°$) and refined

Table 2
Crystal data and structure refinement for **Ia**.

Empirical formula	$C_{10}H_{17}Cl_2NOPtS$
Molecular weight	465.30
Temperature (K)	293(2)
Wavelength (Å)	0.71073
Crystal system, space group	monoclinic, $P2_1$
Unit cell dimensions (Å, °)	a = 8.492(4)
	b = 9.761(4)
	c = 9.501(3)
	β = 108.61(2)
Volume (Å^3)	746.4(5)
Z, D_{calc} (Mg m^{-3})	2, 2.070
Absorption coefficient (mm^{-1})	9.879
F(000)	440
Crystal size (mm)	0.2 × 0.2 × 0.2
Theta range for data collection (°)	2.81–32.19
Reflections collected/unique [R_{int}]	7088/3909 [0.0659]
Completeness to θ = 25.00	95.8%
Refinement method	full-matrix least-squares on F^2
Data/restraints/parameters	3909/7/145
Goodness-of-fit on F^2	1.136
Final R indices [$I > 2\sigma(I)$]	R_1 = 0.0356, wR_2 = 0.1021
R indices (all data)	R_1 = 0.0361, wR_2 = 0.1024
Absolute structure parameter	−0.010(12)
Largest difference in peak and hole (e Å^{-3})	0.639 and −0.532

by least-squares method. Intensities were collected with graphite monochromatized Mo Kα radiation. 7088 reflections were measured in the range $2.81° < \theta < 32.19°$; 3909 were non-equivalent by symmetry [R_{int} (on I) = 0.065] and 3800 were assumed as observed applying the condition $I > 2\sigma(I)$. Lorentz polarization and absorption corrections were made.

The structure was solved by direct methods, using SHELXS Computer Program [18] and refined by the full-matrix least-squares method, with the SHELX97 computer program using 7088 reflections (very negative intensities were not assumed). The function minimized was $\Sigma w||F_o|^2 - |F_c|^2|^2$, where $w = [\sigma^2(I) + (0.0667P)^2 + 0.5181P]^{-1}$, and $P = (|F_o|^2 + 2|F_c|^2)/3$. f, f' and f'' were taken from International Tables of X-ray Crystallography [19]. The chirality of the structure was defined from the Flack coefficient [20], which is equal to −0.010(12) for the given results. All hydrogen atoms were computed and refined using a riding model with an isotropic temperature factor equal to 1.2 times the equivalent temperature factor of the atom to which they are linked. Further details are given in Table 2.

Supplementary data

CCDC 713902 contains the supplementary crystallographic data for compound **Ia**. These data can be obtained free of charge via http://www.ccdc.cam.ac.uk/conts/retrieving.html, or from the Cambridge Crystallographic Data Centre, 12 Union Road, Cambridge CB2 1EZ, UK; fax: (+44) 1223-336-033; or e-mail: deposit@ccdc.cam.ac.uk.

Acknowledgment

This work was supported by the Ministerio de Ciencia y Tecnología (Project: CTQ2006-02007/BQU).

References

[1] (a) A.D. Ryabov, Synthesis (1985) 233;
(b) A.D. Ryabov, Chem. Rev. 90 (1990) 403;
(c) V.V. Dunina, O.A. Zalevskaya, V.M. Potapov, Russ. Chem. Rev. 57 (1988) 434;
(d) P. Espinet, M.A. Esteruelas, L.A. Oro, J.L. Serrano, E. Sola, Coord. Chem. Rev. 117 (1992) 215;
(e) C. Navarro-Ranninger, I. López-Solera, J.M. Pérez, J.R.MasaguerC. Alonso, Appl. Organomet. Chem. 7 (1993) 57;
(f) M. Albrecht, M. Lutz, A.L. Spek, G. van Koten, Nature 406 (2000) 970;
(g) J. Dupont, M. Pfeffer, J. Spencer, Eur. J. Inorg. Chem. (2001) 1917;
(h) M. Albrecht, G. van Koten, Angew. Chem., Int. Ed. 40 (2001) 3750;
(i) I. Omae, Coord. Chem. Rev. 248 (2004) 995;
(j) J. Dupont, C.S. Consorti, J. Spencer, Chem. Rev. 105 (2005) 2527.
[2] J. Vicente, I. Saura-Llamas, Comments on Inorg. Chem. 28 (2007) 39, and references therein.
[3] A. Avshu, R.D. O'Sullivan, A.W. Parkins, N.W. Alcock, R.M. Countryman, J. Chem. Soc., Dalton Trans. (1983) 1619.
[4] A. Capapé, M. Crespo, J. Granell, M. Font-Bardía, X. Solans, Dalton Trans. (2007) 2030.
[5] B. Calmuschi-Cula, U. Englert, Organometallics 27 (2008) 3124.
[6] (a) P.R.R. Ranatunge-Bandarage, B.H. Robinson, J. Simpson, Organometallics 13 (1994) 500;
(b) A.D. Ryabov, G.M. Kazankov, I.M. Panyashkina, O.V. Grozovsky, O.G. Dyachenko, V.A. Polyakov, L.G. Kuz'mina, J. Chem. Soc., Dalton Trans. (1997) 4385;
(c) Y.J. Wu, L. Ding, H.X. Wang, Y.H. Liu, H.Z. Yuan, X.A. Mao, J. Organomet. Chem. 535 (1997) 49;
(d) L. Ding, D.P. Zou, Y.J. Wu, Polyhedron 17 (1998) 2511;
(e) L. Alexandrova, O.G. D'yachenko, G.M. Kazankov, V.A. Polyakov, P.V. Samuleev, E. Sansores, A.D. Ryabov, J. Am. Chem. Soc. 122 (2000) 5189;
(f) A.D. Ryabov, S. Otto, P.V. Samuleev, V.A. Polyakov, L. Alexandrova, G.M. Kazankov, S. Shova, M. Revenco, J. Lipkowski, M.H. Johansson, Inorg. Chem. 41 (2002) 4286;
(g) A.D. Ryabov, I.M. Panyashkina, V.A. Polyakov, A. Fisher, Organometallics 21 (2002) 1633;
(h) S. Pérez, C. López, A. Caubet, X. Solans, M. Font-Bardía, New J. Chem. 27 (2003) 975.
[7] (a) C.R. Baar, H.A. Jenkins, J.J. Vittal, G.P.A. Yap, R.J. Puddephatt, Organometallics 17 (1998) 2805;
(b) C.R. Baar, G.S. Hill, J.J. Vittal, R.J. Puddephatt, Organometallics 17 (1998) 32;
(c) C.M. Anderson, M. Crespo, M.C. Jennings, A.J. Lough, G. Ferguson, R.J. Puddephatt, Organometallics 10 (1991) 2672.
[8] A. Capapé, M. Crespo, J. Granell, A. Vizcarro, J. Zafrilla, M. Font-Bardía, X. Solans, Chem. Commun. (2006) 4128.
[9] V.V. Dunina, L.G. Kuz'mina, M.Y. Kazakova, O. Gorunova, Y.K. Grishin, E.I. Kazakova, Eur. J. Inorg. Chem. (1999) 1029.
[10] (a) J. Vicente, I. Saura-Llamas, P.G. Jones, J. Chem. Soc., Dalton Trans. (1993) 3619;
(b) J. Albert, J. Granell, A. Luque, J. Minguez, R. Moragas, M. Font-Bardia, X. Solans, J. Organomet. Chem. 522 (1996) 87;
(c) Y. Fujita, K. Yoshinaga, Y. Ikeda, J. Kinoshita-Kawashima, J. Chem. Soc., Dalton Trans. (1997) 2495.
[11] J. Albert, J.M. Cadena, J. Granell, Tetrahedron: Asymmetry 8 (1997) 991.
[12] (a) F.D. Rochon, C. Tessier, Inorg. Chim. Acta 361 (2008) 2591;
(b) N. Nédélec, F.D. Rochon, Inorg. Chim. Acta 319 (2001) 95;
(c) F.D. Rochon, J.R.L. Priqueler, Can. J. Chem. 82 (2004) 649.
[13] P.S. Pregosin, R.W. Kunz, in: P. Diehl, E. Fluck, R. Kosfeld (Eds.), ^{31}P and ^{13}C NMR of Transition Metal Phosphine Complexes, Springer-Verlag, Berlin, 1979.
[14] M. Crespo, R. Martín, T. Calvet, M. Font-Bardia, X. Solans, Polyhedron 27 (2008) 2603.
[15] S. Otto, A. Chanda, P.V. Samuleev, A.D. Ryabov, Eur. J. Inorg. Chem. (2006) 2561.
[16] D.A. Spivak, J. Campbell, Analyst (2001) 793.
[17] (a) J.H. Price, A.N. Williamson, R.F. Schramm, B.B. Wayland, Inorg. Chem. 11 (1972) 1280;
(b) V.Y. Kukushkin, A.J.L. Pombeiro, C.M.P. Ferreira, L.I. Elding, Inorg. Synth. 33 (2002) 189.
[18] G.M. Sheldrick, SHELXS97, A Computer Program for Crystal Structure Determination, University of Göttingen, Germany, 1997.
[19] International Tables of X-ray Crystallography, vol. IV, Kynoch Press, Birmingham, UK, 1974, p. 99.
[20] H.D. Flack, Acta Crystallogr. A39 (1983) 876.

(EB), a phenanthridine drug, is a cationic molecule able to interact with polynucleotides. Ethidium bromide (EB) is a well-known intercalator, which is often used as a spectral probe to establish the mode of binding of small molecules to double-helical DNA. The present study deals with the interaction between DNA and colloidal TiO_2 nanoparticles, which is useful in the biomedical field.

2. Materials and methods

2.1. Materials

Calf thymus-deoxyribonucleic acid (DNA), titanium (IV) 2-propoxide and ethidium bromide (EB) were purchased from Aldrich (Bangalore, India). The DNA used in this work was double-stranded DNA (dsDNA). The stock solution of DNA was prepared by dissolving an appropriate amount of DNA in phosphate buffer overnight and storing at 4 °C in the dark. The concentration of the DNA stock solution (2.4×10^{-4} M) was determined from the UV absorption spectrum at 260 nm using the molar absorption coefficient $\varepsilon_{260} = 6600\ M^{-1}\ cm^{-1}$. The purity of the DNA was checked by monitoring the ratio of the absorbance at 260 nm to that at 280 nm. The resulting ratio, $A_{260}/A_{280} > 1.8$, indicated that the DNA was sufficiently free from protein [44,45]. All measurements were performed at ambient temperature.

2.2. Preparation of colloidal TiO_2 nanoparticles

The colloidal TiO_2 nanoparticles was prepared by the hydrolysis of titanium(IV) 2-propoxide, based on the literature procedure [46]. Typically, titanium(IV) 2-propoxide (153 μl) in 2-propanol (10 ml) was injected by using syringe into 40 ml of water with constant stirring under nitrogen atmosphere (for 8 h), resulting in a 1×10^{-2} M titania stock solution. No stabilizing agent was used during the hydrolysis process. The colloidal suspensions of TiO_2 prepared by this method were stable for 3–5 days. Fresh colloidal TiO_2 dispersed in water was prepared before each set of experiments. The stock suspension was diluted with water to obtain the desired concentrations of TiO_2. No attempts were made to exclude the traces of 2-propanol present in the colloidal TiO_2 nanoparticles and it was confirmed separately that the presence of 2-propanol did not affect the photochemical measurements, as earlier reported [47].

2.3. Steady-state measurements

The fluorescence quenching measurements were carried out using a JASCO FP-6500 spectrofluorimeter (Tokyo, Japan). The excitation wavelength of EB–DNA was 480 nm and the emission was monitored at 597 nm. The excitation and emission slit widths (each 5 nm) and scan rate (500 nm/min) were kept constant for all the measurements. The samples were deoxygenated by bubbling with pure nitrogen gas.

Absorption spectral measurements were recorded by using a Cary 300 UV–Vis spectrophotometer (USA). A 3 ml solution, containing the appropriate concentration of DNA (1×10^{-6} M), was titrated by successive addition of 30 μl stock solutions of colloidal TiO_2 nanoparticles (1×10^{-3} M). Titrations were manually done by using micro pipette for the addition of colloidal TiO_2. UV–Vis spectra of all the solutions were recorded in the range of 200–800 nm.

2.4. Time resolved fluorescence measurements

Fluorescence lifetime measurements were carried out in a picosecond time correlated single photon counting (TCSPC) spectrometer. The excitation source was a tunable Ti-sapphire laser (Tsunami, Spectra Physics, USA). The fluorescence decay was analyzed by using the software provided by IBH (DAS-6).

2.5. XRD measurements

X-ray powder diffraction patterns were recorded on a Bruker AXS B8 Discover model using Cu Kα radiation ($\lambda = 0.154$ nm) and a graphite monochromator in the diffracted beam. The TiO_2 sample was in the form of powder. A scan rate of $0.05^\circ\ min^{-1}$ was applied to record the XRD pattern in the 2θ range 20–80°.

2.6. Fourier transform infrared spectroscopy (FT-IR) measurements

FT-IR spectra were obtained using a Perkin–Elmer Spectrum RXI FT-IR Spectrometer (USA) at room temperature in the range 4000–400 cm^{-1}. The samples were placed in a liquid cell between two windows (CaF_2). The mirror velocity was 0.3 cm/s and the number of co-added scans was 4, and the total collection time was less than 2 min.

3. Results and discussion

3.1. XRD characterization of TiO_2 nanoparticles

Fig. 1 shows the XRD pattern of typical powdered TiO_2 nanoparticles obtained by rotary evaporation of colloidal TiO_2 at 30 °C. The XRD peaks are found to be broad, indicating the fine size of the sample grains. The pattern exhibits prominent broad peaks at 2θ values of 25.6°, 38.4°, 48.4°, 54.8° and 63.2°, which are similar to the reported [48] values for anatase TiO_2.

3.2. Determination of particle size of colloidal TiO_2 nanoparticles

For the anatase phase TiO_2, the absorption wavelength (λ) and the corresponding band gap energy (E_g) are well known, $\lambda = 385$ nm and $E_g = 3.2$ eV, respectively. The particle size of the prepared colloidal TiO_2 nanoparticles was determined from the relationship between the band gap shift (ΔE_g) and the radius (R) of the quantum size particles using the following Eq. (1) [49],

$$\Delta E_g = \frac{\pi^2 h^2}{2\mu R^2} - \frac{1.8e^2}{\varepsilon R} + \text{Polarization terms} \quad (1)$$

where h is Planck's constant, R is the radius of the particle, ε is the relative permittivity of the semiconductor, ΔE_g is the band gap shift. The calculated band gap shift for colloidal TiO_2 is 0.3 eV (extrapolating the spectral curve, the band gap energy of the colloidal TiO_2 was measured, $E_g = 3.5$ eV corresponding to $\lambda = 350$ nm, Fig. 2), as com-

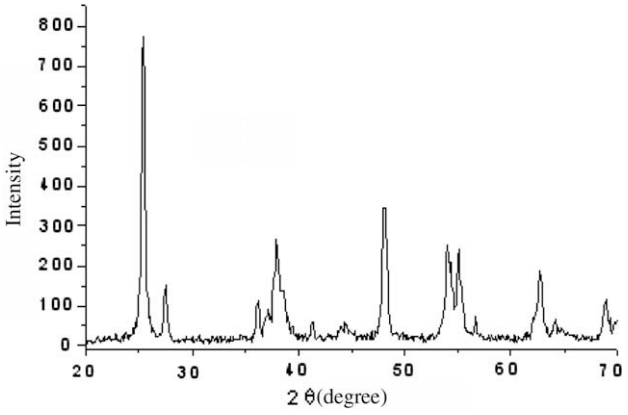


Fig. 1. X-ray diffraction (XRD) spectrum of the prepared TiO_2 nanoparticles.

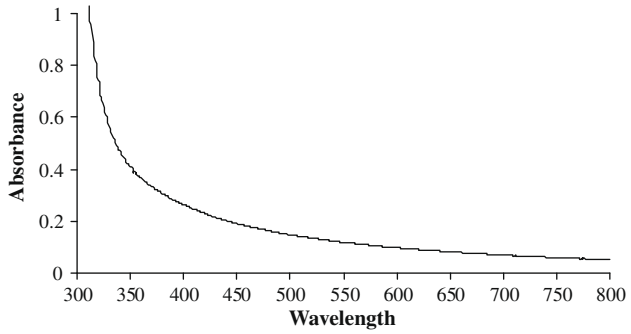


Fig. 2. Absorption spectrum of colloidal TiO_2 (1×10^{-3} M).

pared to bulk anatase. 'μ' is the reduced mass of the exciton, i.e., the reduced effective mass of the electron and the hole ($1/\mu = l/m_c^* + l/m_h^*$) in the semiconductor, '*e*' is the electronic charge, and '*c*' is the dielectric constant of the semiconductor. The value of $\mu = 1.63m_e$ (m_e is the electron rest mass) [50]. Since the optical dielectric constant of bulk titanium dioxide is very large ($\varepsilon = 170$), the columbic and polarization terms in Eq. (1) are neglected. The ΔE_g value of 0.3 eV for this blue shift compared to bulk anatase TiO_2 particles indicated a size of TiO_2 crystallites smaller than 10 nm, due to the so called quantum size effect [51]. The calculated size of the prepared colloidal TiO_2 is 1.1 nm.

3.3. Absorption characteristics of DNA–TiO_2

Fig. 3 shows the absorption spectra of DNA in the absence and presence of colloidal TiO_2 at various increasing concentrations. In the presence of colloidal TiO_2 nanoparticles, the absorbance of DNA increases markedly, without any change in the location of the peak (260 nm). This shows that while adding colloidal TiO_2 nanoparticles to the solution of DNA, the DNA gets adsorbed on the surface of the colloidal TiO_2 and is involved in the formation of a ground state complex of the type DNA···TiO_2. The formed complex also has an absorption at 260 nm. This may be the reason for the increase in absorbance of DNA with the addition of colloidal TiO_2, as supported by a similar observation made earlier [52]. The absorbance change that we observed in the spectrum of the complex was not due to the experimental error because baseline corrections were done for all measurements. These results indicate that there is an interaction between colloidal TiO_2 nanoparticles and DNA in the ground state via complex formation which is electrostatic in nature.

The equilibrium for the formation of the complex between DNA and colloidal TiO_2 nanoparticles is given by Eq. (2), where K_{app} represents the apparent association constant:

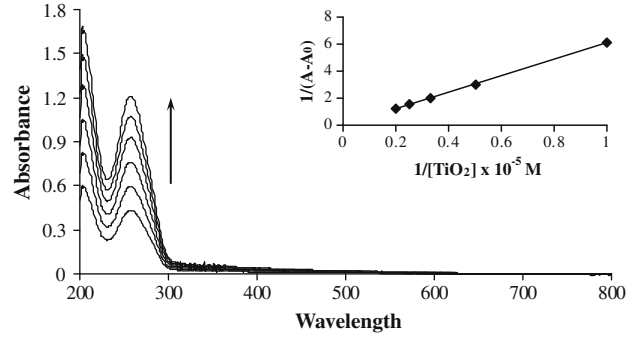


Fig. 3. Absorption spectra of DNA (1×10^{-6} M) in the presence of colloidal TiO_2 in the concentration range 0–5×10^{-5} M. The inset is the straight line dependence of $1/(A_{obs} - A_0)$ on the reciprocal concentration of colloidal TiO_2.

$$\mathrm{DNA} + \mathrm{TiO_2} \overset{K_{app}}{\rightleftharpoons} \mathrm{DNA}\cdots\mathrm{TiO_2} \tag{2}$$

$$K_{app} = \frac{[\mathrm{DNA}\cdots\mathrm{TiO_2}]}{[\mathrm{DNA}]\cdot[\mathrm{TiO_2}]}$$

K_{app} is obtained according to the method reported by Benesi and Hildebrand [53]:

$$A_{obs} = (1-\alpha)C_0\varepsilon_{DNA}l + \alpha C_0\varepsilon_c l \tag{3}$$

where A_{obs} is the observed absorbance of the solution containing different concentrations of colloidal TiO_2 nanoparticles at 260 nm, α is the degree of association between DNA and TiO_2, ε_{DNA} and ε_c are the molar extinction coefficients at the defined wavelength ($\lambda = 260$ nm) for DNA and the formed complex, respectively, C_0 is the initial concentration of DNA and '*l*' is the optical path length (always taken as unity). Eq. (3) can be expressed as Eq. (4), where A_0 and A_c are the absorbances of DNA and the complex at 260 nm, respectively, with a concentration of C_0:

$$A_{obs} = (1-\alpha)A_0 + \alpha A_c \tag{4}$$

At relatively high TiO_2 concentrations, α can be equated to $(K_{app}[TiO_2])/(1 + K_{app}[TiO_2])$. In this case, Eq. (4) can be changed to Eq. (5):

$$\frac{1}{A_{obs} - A_0} = \frac{1}{A_c - A_0} + \frac{1}{K_{app}(A_c - A_0)[TiO_2]} \tag{5}$$

Based on the enhancement of the absorbance at 260 nm due to absorption of the surface complex, we would expect a linear relationship between $1/(A_{obs} - A_0)$ and the reciprocal concentration of colloidal TiO_2, with a slope equal to $1/K_{app}(A_c - A_0)$ and an intercept equal to $1/(A_c - A_0)$ [Fig. 3, inset]. The value of the apparent association constant (K_{app}) determined from this linear plot is 2.85×10^3 M^{-1} ($R^2 = 0.9998$).

3.4. Fluorescence quenching of EB–DNA by colloidal TiO_2 nanoparticles

To study the interaction between DNA and TiO_2 nanoparticles in the excited state, we have chosen EB as a fluorescence probe for DNA. EB has a weak fluorescence, but in the presence of DNA it shows intense fluorescence at 597 nm on excitation at 480 nm, due to its strong intercalation with the adjacent DNA base pairs. It was previously reported that the enhanced fluorescence of EB–DNA can be quenched by the addition of a second molecule [54,55]. Based on the reports, in the present system we have studied the effect of colloidal TiO_2 nanoparticles on the fluorescence emission spectrum of EB bound DNA (Fig. 4). From the figure we observed that the addition of colloidal TiO_2 to a solution of EB bound DNA resulted in a decrease in fluorescence emission intensity of EB–DNA. This shows that quenching has occurred by the addition of colloidal TiO_2. The possible scattering due to the colloidal nature of TiO_2 has been omitted because of the fact that baseline correction was done for all the spectral measurements and also even after adding the highest concentration of colloidal TiO_2 nanoparticles the solution remains clear. So we inferred that the fluorescence quenching is only due to the interaction between DNA and colloidal TiO_2 and not due to scattering.

The fluorescence quenching is described by the Stern–Volmer relation:

$$I_0/I = 1 + K_{SV}[Q] = 1 + k_q\tau_0[Q] \tag{6}$$

where, I_0 and I are the emission intensities of the fluorophore in the absence and presence of quencher, respectively, K_{SV} is the Stern–Volmer constant related to the bimolecular quenching rate constant, k_q, by $K_{SV} = k_q \cdot \tau_0$, and τ_0 is the lifetime of the fluorophore in the excited state, which is 23 ns (EB bounded to double-stranded DNA has a maximum fluorescence lifetime) [56], [Q] is concentra-

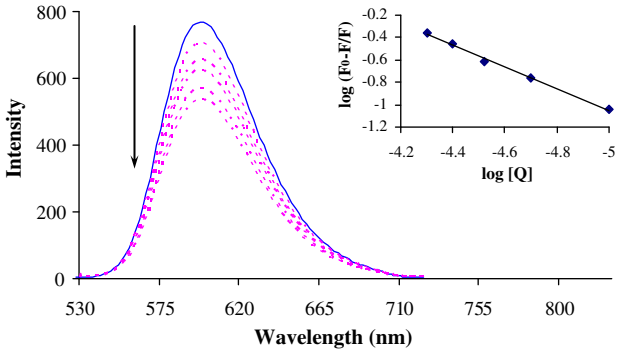


Fig. 4. Fluorescence quenching of EB–DNA (λ_{exi} = 480 nm; λ_{emi} = 597 nm) in the presence of various concentrations of colloidal TiO_2, [TiO_2] = 0–5 × 10^{-5} M. The inset shows the plot of log $[F^0 - F/F]/F$ vs. log[Q].

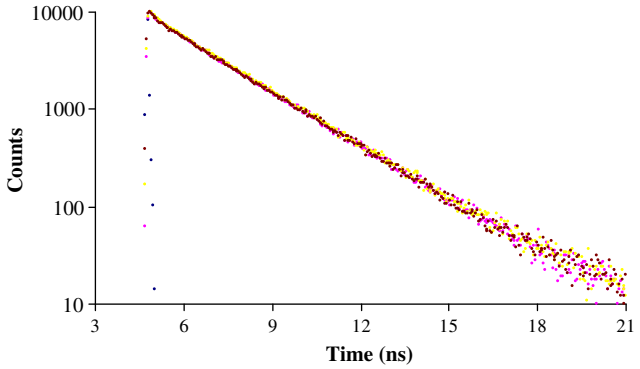


Fig. 6. Fluorescence decay profiles for EB–DNA in the absence and presence of colloidal TiO_2 (0–5 × 10^{-5} M).

tion of the quencher. According to Eq. (6) we obtained a linear plot [Fig. 5] for I_0/I against [TiO_2]. From the slope (K_{SV} = 8.61 × 10^3 M^{-1}) we have calculated the quenching rate constant (k_q) as 3.74 × 10^{11} M^{-1} s^{-1}. The obtained bimolecular quenching constant (k_q) is much larger than the limiting value of 1 × 10^{10} M^{-1} s^{-1} [57], which is considered the largest possible value in aqueous medium. Thus dynamic quenching may be ruled out for the quenching of EB–DNA fluorescence.

3.5. Fluorescence lifetime measurements

Fluorescence lifetime measurement is useful for understanding the interactions between donor and acceptor systems. The observation of a linear Stern–Volmer plot in the steady state measurement alone does not prove a dynamic nature of the quenching. Sometimes static quenching also results in a linear Stern–Volmer plot. In general, time resolved measurement is the most definitive method for differentiating static and dynamic quenching processes [57].

Fig. 6 shows the fluorescence decay curve of EB–DNA in the absence and presence of colloidal TiO_2 nanoparticles. EB–DNA exhibits its single exponential decay, not only in dilute solutions but also in the presence of colloidal TiO_2 nanoparticles. On increasing the concentration of colloidal TiO_2 there is no change in the fluorescence lifetime of EB–DNA. This observation shows that the quenching follows a static mechanism. It also supports the adsorption of DNA on the surface of colloidal TiO_2 and the formation of a ground state surface complex. In Fig. 6, though the decay traces of EB–DNA in the absence and presence of colloidal TiO_2 nanoparticles were plotted, the lifetime of EB–DNA remains the same under both conditions, hence the plot looks like a single decay curve due to the merging of the kinetic traces. This result proves that the quenching

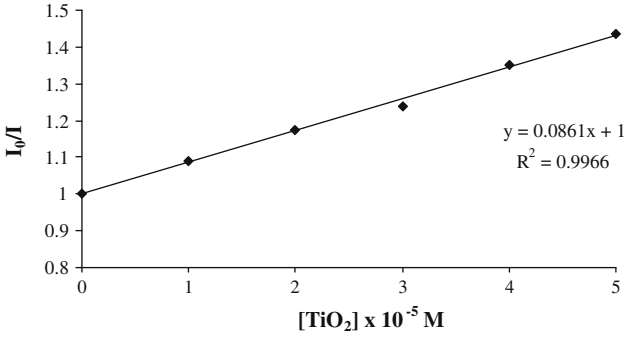


Fig. 5. Stern–Volmer plot for the steady state fluorescence quenching of EB–DNA by colloidal TiO_2 (0–5 × 10^{-5} M).

of EB–DNA by colloidal TiO_2 nanoparticles is static in nature. Static quenching arises from the formation of a complex between the fluorophore and the quencher. Hence the binding constant (K) was calculated by the method given in the following section.

3.6. Binding constant and number of binding sites

Fluorescence quenching data were used to determine the binding constant (K) and the binding sites (n) for the complex formation of TiO_2 with ct-DNA. Fig. 4 shows the fluorescence spectra of EB–DNA in the presence of different concentrations of colloidal TiO_2 nanoparticles. It can be seen that the fluorescence intensity at 597 nm decreases in the presence of colloidal TiO_2 nanoparticles. This change in fluorescence intensity at 597 nm was used to estimate K and n.

If it is assumed that there are similar and independent binding sites in EB–DNA, the relationship between the fluorescence intensity and the quencher medium can be deduced from the following Eq. (7):

$$nQ + B \rightarrow Q_n \cdots B \tag{7}$$

where B is the fluorophore, Q is the quencher, nQ + B is the postulated complex between the fluorophore and n molecules of the quencher. The constant K is given by

$$K = \frac{[Q_n \cdots B]}{[Q]^n [B]} \tag{8}$$

If the overall amount of biomolecules (bound or unbound with the quencher) is B_0, then $[B_0] = [Q_n \cdots B] + [B]$, where [B] is the concentration of unbound biomolecules, and then the relationship between the fluorescence intensity and the unbound biomolecule as $[B]/[B_0] = F/F_0$, that is:

$$\log\left[\frac{F_0 - F}{F}\right] = \log K + n \log[Q] \tag{9}$$

where K is the binding constant of colloidal TiO_2 with DNA, which can be determined from the intercept of $\log[(F_0 - F)/F]$ versus log[Q], as shown in the inset of Fig. 4. The calculated value of the binding constant (K) is 6.68 × 10^3 M^{-1} and the number of binding sites (n) is 0.97. The value of "n" approximately equals 1, and thus indicates the existence of just a single binding site in DNA for TiO_2.

3.7. FT-IR characterization

To verify the electrostatic type of interaction, FT-IR measurements were performed in the absence and presence of TiO_2 with DNA (shown only in the region of 1150–1400 cm^{-1} [Fig. 7]). Usually the phosphate peak position for DNA occurs in the region of

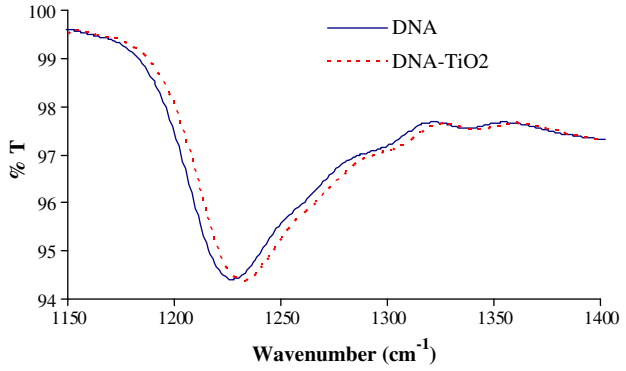


Fig. 7. The FT-IR spectra of DNA in the absence and presence of TiO_2 (shown only in the region of 1150–1400 cm^{-1}).

1222 cm^{-1}, but in the presence of TiO_2 the phosphate peak was shifted to 1226 cm^{-1}. From the shift in peak position we confirmed that the mode of interaction between DNA and TiO_2 is electrostatic in nature.

4. Summary

The interaction between colloidal TiO_2 nanoparticles and ct-DNA has been studied by using various spectroscopic measurements. The interaction between colloidal TiO_2 nanoparticles and DNA occurs through an electrostatic mode and the quenching follows a static mechanism. The quenching rate constant, binding constant and number of binding sites were calculated according to the relevant fluorescence data. The binding constants obtained from both absorbance and fluorescence methods are matched well. The present work is a viable model study to understand the conditions which can be optimized to carefully analyze the interaction of TiO_2 with DNA for later applications in photodynamic therapy.

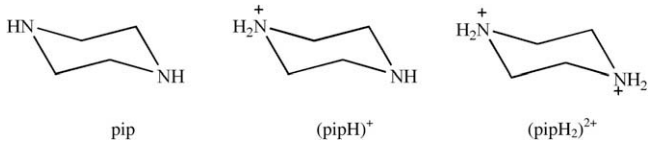
Acknowledgements

R.R. and A.K. thank CSIR, Government of India (Ref. No. 01(2217)/08/EMR-II, Date 06/05/2008), for the project and fellowship, respectively.

We are thankful to Prof. P. Ramamoorthy, NCUFP, University of Madras, Chennai, for lifetime measurements.

References

[1] S.Y. Lin, C.H. Chen, M.C. Lin, H.F. Hsu, Anal. Chem. 77 (2005) 4821.
[2] G. Raschke, S. Kowarik, T. Franzl, C. So1nnichsen, T.A. Klar, J. Feldmann, Nano Lett. 3 (2003) 935.
[3] Y. Nagasaki, T. Ishii, Y. Sunaga, Y. Watanabe, H. Otsuka, K. Kataoka, Langmuir 20 (2004) 6396.
[4] A. Verma, H. Nakade, J.M. Simard, V.M. Rotello, J. Am. Chem. Soc. 126 (2004) 10806.
[5] N. Nath, A. Chilkoti, Anal. Chem. 74 (2002) 504.
[6] T. You, O. Niwa, M. Tomita, S. Hirono, Anal. Chem. 75 (2003) 2080.
[7] X.X. He, K. Wang, W.H. Tan, B. Liu, X. Lin, C.M. He, D. Li, S.S. Huang, J. Li, J. Am. Chem. Soc. 125 (2003) 7168.
[8] T. Rajh, Z. Saponjic, J.Q. Liu, N.M. Dimitrijevic, N.F. Scherer, M. Vega-Arroyo, P. Zapol, L.A. Curtiss, M.C. Thurnauer, Nano Lett. 4 (2004) 1017.
[9] L.A. Ruiz-Taylor, T.L. Martin, P. Wagner, Langmuir 17 (2001) 7313.
[10] V.L. Colvin, M.C. Schlamp, A.P. Alivisators, Nature 370 (1994) 354.
[11] M.V. Artemyev, U. Woggon, R. Wannemacher, H. Jaschinski, W. Langbein, Nano Lett. 1 (2001) 309.
[12] A.P. Alivisatos, Science 271 (1996) 933.
[13] M. Bruchez, M. Moronne, P. Gin, S. Weiss, A.P. Alivisatos, Science 281 (1998) 2013.
[14] X. Wu, H. Liu, J. Liu, K. Haley, J. Treadway, J. Larson, N. Ge, F. Peals, M. Bruchez, Nat. Biotechnol. 21 (2003) 41.
[15] X. Gao, Y. Cui, R.M. Levenson, L. Chung, S. Nie, Nat. Biotechnol. 22 (2004) 969.
[16] B.K. Bernard, M.R. Osheroff, A. Hofman, J.H. Mennear, Environ. Health 28 (1989) 415.
[17] B. Miller, E. Pujads, E. Gocke, Environ. Mol. Mutagen. 26 (1995) 240.
[18] R.W. Tennant, B.H. Margolin, M.D. Shelby, E. Zeiger, J.K. Haseman, J. Spalding, W. Caspary, M. Resnick, S. Stasiewicz, B. Anderson, R. Minor, Science 236 (1987) 933.
[19] H. Sakai, E. Ito, R.X. Cai, T. Yoshioka, K. Hashimoto, A. Fujishima, Biochim. Biophys. Acta 1201 (1994) 260.
[20] A.C. Verdière, C. Dubernet, F. Nemati, M.F. Poupon, F. Puisieux, P. Couvreur, Cancer Chemother. Pharmacol. 33 (1994) 504.
[21] K. Sunada, Y. Kikuchi, K. Hashimoto, A. Fujishima, Environ. Sci. Technol. 32 (1998) 726.
[22] P.C. Maness, S. Smolinski, D.M. Blake, Z. Huang, E.J. Wolfrum, W.A. Jacoby, Appl. Environ. Microbiol. 65 (1999) 4094.
[23] R. Cai, Y. Kubota, T. Shiumi, H. Sakai, K. Hashimoto, A. Fujishima, Cancer Res. 52 (1992) 2346.
[24] A.P. Zhang, Y.P. Sun, World J. Gastroenterol. 10 (2004) 3191.
[25] A. Kathiravan, S. Anandan, R. Renganathan, Colloid Surf. A: Physicochem. Eng. Aspects 333 (2009) 91.
[26] A. Kathiravan, R. Renganathan, Colloid Surf. A: Physicochem. Eng. Aspects 324 (2008) 176.
[27] A. Kathiravan, R. Renganathan, S. Anandan, Polyhedron 28 (2009) 157.
[28] E.C. Miller, J.A. Miller, Cancer 47 (1981) 1055.
[29] S. Udenfriend, P. Zaltzman, Anal. Biochem. 3 (1962) 49.
[30] J.B. Lepecq, C. Paoletli, Anal. Biochem. 17 (1966) 100.
[31] J. Markovits, B.P. Roques, J.B. Lepecq, Anal. Biochem. 94 (1979) 260.
[32] W. Waner, J. Vinogard, J. Mol. Biol. 47 (1970) 419.
[33] C.G. Reinhardt, T.R. Krugh, Biochemistry 17 (1978) 4845.
[34] L. Vergani, G. Mascetti, P. Gavazzo, C. Nicolini, Thermochim. Acta 294 (1997) 193.
[35] J.C. Sutherla, B.M. Sutherla, Biopolymer 9 (1970) 639.
[36] Y. Cao, X.W. He, Z. Gao, L. Peng, Talanta 49 (1999) 377.
[37] T.R. Downs, W.W. Wilfinger, Anal. Biochem. 131 (1983) 538.
[38] H.S. Rye, J.M. Dabora, M.A. Quesada, R.A. Mathies, A.N. Glazer, Anal. Biochem. 208 (1993) 144.
[39] W.Y. Li, Z.H. Lu, Microchem. J. 60 (1998) 84.
[40] W.Y. Li, X.Q. Guo, J.G. Xu, Q.Z. Zhu, Y.B. Zhao, Anal. Chim. Acta 340 (1997) 291.
[41] Q.Z. Zhu, H.H. Yang, D.H. Li, J.G. Xu, Anal. Chim. Acta 394 (1999) 177.
[42] Q.Y. Chen, D.H. Li, Y. Zhao, H.H. Yang, Q.Z. Zhu, J.G. Xu, Analyst 124 (1999) 901.
[43] S. Wang, R. Gao, F. Zhou, M. Selke, J. Mater. Chem. 14 (2004) 487.
[44] J. Marmur, J. Mol. Biol. 3 (1961) 208.
[45] M.E. Reichmann, S.A. Rice, C.A. Thomas, P. Doty, J. Am. Chem. Soc. 76 (1954) 3047.
[46] D. Bahnemann, A. Henglein, J. Lilie, L. Spanhel, J. Phys. Chem. 88 (1984) 709.
[47] P.V. Kamat, J.P. Chauvet, R.W. Fessenden, J. Phys. Chem. 90 (1986) 1389.
[48] J.C. Tristao, F. Magalhaes, P. Corio, M.T.C. Sansiviero, J. Photochem. Photobiol. A: Chem. 181 (2006) 152.
[49] C. Kormann, D.W. Bahnemann, M.R. Hoffmann, J. Phys. Chem. 92 (1988) 5196.
[50] E. Joselevich, I. Willner, J. Phys. Chem. 98 (1994) 7628.
[51] A. Henglein, Ber. Bunsen-Ges. Phys. Chem. Chem. Phys. 86 (1982) 241.
[52] J. Wang, J. Wu, Z.H. Zhang, X.D. Zhang, L. Wang, L. Xu, B.D. Guo, H. Li, J. Tong, Chin. Chem. Lett. 16 (2005) 1105.
[53] H.A. Benesi, J.H. Hildebrand, J. Am. Chem. Soc. 71 (1949) 2703.
[54] B.C. Baguley, M. LeBret, Biochemistry 23 (1984) 937.
[55] J.R. Lakowicz, G. Webber, Biochemistry 12 (1973) 4161.
[56] D.P. Heller, C.L. Greenstock, Biophys. Chem. 50 (1994) 305.
[57] J.R. Lakowicz, Principles of Fluorescence Spectroscopy, Springer, New York, 2006.



Scheme 1.

$(pipH)^+$ on the metal–sulfur distances as well as the thermal decomposition products. It is interesting to note that the synthesis of such a $[MS_4]^{2-}$ compound containing the $(pipH)^+$ cation could be accomplished by a mechanical grinding of the reactants. The results of these investigations are described in this paper.

2. Experimental

2.1. Materials and methods

All the chemicals used in this study were of reagent grade and were used as received. The ammonium salts of the group VI tetrasulfidometalates were prepared by a published procedure [28]. Far-IR spectra (range 80–500 cm^{-1}) were recorded using a Bruker IFS 66 infrared spectrometer in pressed polyethylene disks. MIR spectra were recorded in a KBr matrix using a Shimadzu (IR Prestige-21) FT-IR spectrometer and a ATI Mattson Genesis infrared spectrometer in the range 4000–400 cm^{-1}. Raman spectra were recorded in the region 100–3500 cm^{-1} on a Bruker FRA 106 Fourier Transform Raman spectrometer. UV–Vis spectra were recorded on a Shimadzu UV-2450 double beam spectrophotometer using matched quartz cells. TG-DTA measurements were performed in nitrogen atmosphere, in Al_2O_3 crucibles on a STA-409CD simultaneous thermal analyzer from Netzsch. A heating rate of 4 K min^{-1} was employed for all measurements.

2.2. Preparation of $(pipH)_2[MS_4]$ (M = W **1**; M = Mo **2**)

Anhydrous piperazine (1.72 g, 10 mmol) was mixed with $(NH_4)_2[WS_4]$ (0.696 g, 2 mmol) and the solid mixture was mechanically ground in a mortar with a pestle for ~5 min. The resulting fine powder was dissolved in water (~10 mL) and briefly warmed on a water bath to expel traces of ammonia. The reaction mixture was filtered and the yellow filtrate was left aside for crystallization to obtain yellow needles. The crystalline product was isolated by filtration, washed with 2-propanol, followed by diethyl ether and air dried to yield 0.5 g of compound **1** in 51% yield. The use of freshly prepared $(NH_4)_2[MoS_4]$ (0.520 g, 2 mmol) instead of $(NH_4)_2[WS_4]$ in the above reaction afforded compound **2** as red needles in 60% yield. The needles of **1** and **2** thus obtained are suitable for X-ray structure determination.

Anal. Calc. for $(C_4H_{11}N_2)_2WS_4$ (**1**): C, 19.75; H, 4.56; N, 11.52; S, 26.37; WS_4, 64.17. Found: C, 19.79; H, 4.56; N, 11.55; S, 27.26; WS_4, 64.31%.

IR data (cm^{-1}): 3227 $\upsilon_{(N-H)free}$, 3022, 2972, $\upsilon_{(N-H)}$ 2800, 2708, 2582, 2528, 2420, 2388, 2183, 1597, 1462, 1391, 1365, 1323, 1307, 1217, 1165, 1107, 1078, 1051, 1001, 960, 891, 866, 841, 814, 613, 588, 481 (υ_1), 465 (υ_3), 445, 413, 397.

Raman data (cm^{-1}): 3229, 2997, 2964, 2948, 2907, 1437, 1330, 1018, 815, 481 (υ_1), 462 (υ_3), 442, 195, 178 (υ_2, υ_4).

UV–Vis data in nm (mol^{-1} L cm^{-1}): 393 (17360), 277 (25850).

Anal. Calc. for $(C_4H_{11}N_2)_2MoS_4$ (**2**): C, 24.11; H, 5.56; N, 14.06; S, 32.19; MoS_4, 56.26. Found: C, 23.95; H, 5.63; N, 14.02; S, 32.55; MoS_4, 56.12%.

IR data (cm^{-1}): 3223 $\upsilon_{(N-H)free}$, 3022, 2972 $\upsilon_{(N-H)}$, 2798, 2706, 2582, 2528, 2420, 2388, 2181, 1593, 1462, 1445, 1390, 1366, 1323, 1306, 1217, 1165, 1107, 1078, 1051, 1001, 961, 891, 864, 840, 814, 613, 590, 482, 472, 456, 450, 415, 396.

Table 1
Crystal data and structure refinement for compounds **1** and **2**.

Empirical formula	$(C_4H_{11}N_2)_2[WS_4]$ **1**	$(C_4H_{11}N_2)_2[MoS_4]$ **2**
Formula weight (g mol^{-1})	486.39	398.48
Temperature (K)	220(2)	293(2)
Wavelength (A)	0.71073	0.71073
Crystal system	triclinic	triclinic
Space group	$P\bar{1}$	$P\bar{1}$
Unit cell dimensions (Å, °)	a = 8.2524(7)	a = 8.2760(10)
	b = 9.7528(8)	b = 9.7570(10)
	c = 11.5897 (9)	c = 11.604 (2)
	α = 93.068(10)	α = 92.960(10)
	β = 101.772(10)	β = 101.860(10)
	γ = 115.111(9)	γ = 115.180(10)
Volume (Å^3)	816.47(12)	819.57(19)
Z	2	2
D_{calc} (mg/m^3)	1.978	1.615
Absorption coefficient (mm^{-1})	7.572	1.296
F(000)	472	408
Crystal size (mm^3)	0.2 × 0.18 × 0.17	0.15 × 0.14 × 0.14
θ range for data collection (°)	2.34–28.01	1.82–27.02
Index ranges	$-10 \leqslant h \leqslant 10$,	$0 \leqslant h \leqslant 10$,
	$-12 \leqslant k \leqslant 12$,	$-12 \leqslant k \leqslant 11$,
	$-15 \leqslant l \leqslant 15$	$-14 \leqslant l \leqslant 14$
Reflections collected	8498	3844
Independent reflections (R_{int})	3885 (0.0849)	3591 (0.0291)
Reflections with [$I > 2\sigma(I)$]	3588	2984
Completeness to θ (%)	98.6	99.8
Refinement method	full-matrix least-squares on F^2	full-matrix least-squares on F^2
Data/restraints/parameters	3885/0/155	3591/0/155
Goodness-of-fit on F^2	1.016	1.033
Final R indices [$I > 2\sigma(I)$]	R_1 = 0.0355,	R_1 = 0.0243,
	wR_2 = 0.0892	wR_2 = 0.0595
R indices (all data)	R_1 = 0.0383,	R_1 = 0.0394,
	wR_2 = 0.0905	wR_2 = 0.0626
Extinction coefficient	0.0143(10)	0.0169(12)
Largest difference in peak and hole (e Å^{-3})	2.614 and −3.500	0.349 and −0.527

Raman data (cm^{-1}): 3225, 2974, 2963, 2946, 2924, 2906, 1436, 1329, 1022, 815, 483, 471 (υ_3), 456, 448 (υ_1), 177 (υ_2, υ_4).

UV–Vis data in nm (mol^{-1} L cm^{-1}): 468 (8190), 316 (12320), 241 (19190).

2.3. X-ray crystal structure determination

Intensity data were collected on a STOE-Image Plate diffraction System (IPDS 1) for compound **1** and on an AED-2 four-circle diffractometer for compound **2** using graphite-monochromated Mo Kα radiation. The structures were solved with direct methods using SHELXS-97 [51] and refinement was done against F^2 using SHELXL-97 [51]. All non-hydrogen atoms were refined anisotropically. The C–H hydrogen atoms were positioned with idealized geometry and refined using a riding model. The N–H hydrogen atoms were located in the difference map, their bond lengths set to ideal values and afterwards they were refined isotropic using a riding model. The technical details of data acquisition and some selected refinement results are summarized in Table 1.

3. Results and discussion

3.1. Synthesis and spectroscopy

In earlier work we have shown that the reaction of an aqueous solution of $(NH_4)_2[MS_4]$ with piperazine (pip) in a 1:1 ratio results in the formation of $(pipH_2)[MS_4]$ compounds [26,27] containing the diprotonated cation of pip namely $(pipH_2)^{2+}$ (Eq. (1)). All our efforts to prepare $(pipH)_2[MS_4]$ compounds, which contain a monoprotonated cation of pip by the reaction of aqueous solutions

of $(NH_4)_2[MS_4]$ with pip in a 1:2 mole ratio, or use of an excess of pip or alternatively the aqueous reaction of $(pipH_2)[MS_4]$ with pip always resulted in the isolation of products containing either the known $(pipH_2)[MS_4]$ compound or a mixture of products containing $(pipH_2)[MS_4]$ as the major product. As different solution methods of synthesis did not result in the formation of a $[MS_4]^{2-}$ compound containing monoprotonated pip, the reaction of $(NH_4)_2[MS_4]$ with pip was investigated by mixing the reagents in the solid state. A mechanical grinding of solid $(NH_4)_2[MS_4]$ with pip (Eq. (2)) in a mortar and pestle afforded the new $(pipH)_2[MS_4]$ title compounds. The presence of a monoprotonated organic cation in the product can be readily evidenced by a comparison of the infrared spectra of the solid state reaction products with those of the previously reported $(pipH_2)[MS_4]$ compounds. The IR spectrum of $(pipH)_2[WS_4]$ exhibits two N–H vibrations for the free and protonated amine functionalities (Fig. 1). The sharp signal at 3227 cm^{-1} can be assigned to the N–H vibration of the free amine, while the doublet at around 3000 cm^{-1} can account for the vibration of the protonated amine $(N–H)^+$. In contrast, the IR spectrum of $(pipH_2)[WS_4]$ in which both amine N atoms are protonated, shows a single strong and broad signal centered around 3000 cm^{-1} assignable to the vibrations of the identical $(>N–H_2)^+$ groups. The presence of a free as well as a protonated amine group in the Mo compound **2** can be similarly inferred from its infrared spectrum (Supplementary Fig. 1). In order to prepare suitable crystals of **1** and **2** for structure determination, the reaction conditions were optimized which involves the use of excess pip during grinding followed by recrystallization from water. The products thus obtained, analyzed satisfactorily for new organic $[MS_4]^{2-}$ compounds containing $(pipH)^+$ and $[MS_4]^{2-}$ in a 2:1 mole ratio.

$$(NH_4)_2[MS_4] + pip \xrightarrow{H_2O} (pipH_2)[MS_4] + 2NH_4OH \quad (1)$$

$$(NH_4)_2[MS_4] + 2pip \xrightarrow{grinding} (pipH)_2[MS_4] + 2NH_3 \quad (2)$$

Compounds **1** and **2** which were crystallized from a strongly alkaline medium are not stable in acidic medium and are decomposed to insoluble metal sulfide products. However, on reaction with an aqueous solution of $[Ni(en)_3]Cl_2$ both compounds are converted quantitatively into the insoluble $[Ni(en)_3][MS_4]$ [25,36]. The electronic spectra of the colored compounds **1** and **2** exhibit signals which can be assigned to the intra-ligand charge transitions of the $[MS_4]^{2-}$ moiety and the observed values are in very good agreement with the reported data for $[MS_4]^{2-}$ chromophores [1,26,27].

The title compounds **1** and **2** exhibit several signals in their mid-infrared spectra above 500 cm^{-1} all of which originate from the organic cation, while the M–S vibrations of the $[MS_4]^{2-}$ moiety are observed at lower energies below 500 cm^{-1}. The isotypic $(pipH)_2[MS_4]$ compounds exhibit IR spectra which are identical in terms of their profile as well as number of signals. The only difference is in terms of the W–S vibrations which occur at slightly lower energies as compared to the corresponding isostructural Mo compounds. A comparison of the infrared spectra of both compounds **1** and **2** with those of $(pipH_2)[MS_4]$ reveals that all these spectra are very similar excepting for an additional band assignable for the N–H group of unprotonated N observed in **1** and **2**. The several signals observed above 500 cm^{-1} in the title compounds **1** and **2** can be assigned for the vibrations of the organic cations. For the free tetrahedral $[MS_4]^{2-}$ anion four characteristic vibrations $\upsilon_1(A_1)$, $\upsilon_2(E)$, $\upsilon_3(F_2)$ and $\upsilon_4(F_2)$ are expected. All four bands are Raman active while only υ_3 and υ_4 are IR active. When the tetrahedron is distorted the symmetry is reduced and as a result the symmetric vibration $\upsilon_1(A_1)$ appears in the infrared spectrum at 481 cm^{-1} as a signal of medium intensity and an intense signal for the triply degenerate $\upsilon_3(F_2)$ asymmetric stretching M–S vibration at 465 cm^{-1}. The assignments of these vibrations are in agreement with the literature reports (26, 27, 35–38). The distortion of the tetrahedron is also evident from the appearance of an additional signal at 445 cm^{-1}. The Raman spectra of both the compounds exhibit intense signals for the vibrations of the free and protonated N–H groups as well as the vibrations of the $[MS_4]^{2-}$ moiety (Supplementary Fig. 2). The observed Raman spectral data for the vibrations of the $[MS_4]^{2-}$ unit are in the expected range and add credence to the infrared data. The Mo compound **2** exhibits a similar behavior with the appearance of the $\upsilon_1(A_1)$ vibration in its infrared spectrum as well as additional signals and its IR and Raman spectra can be similarly explained [35–38].

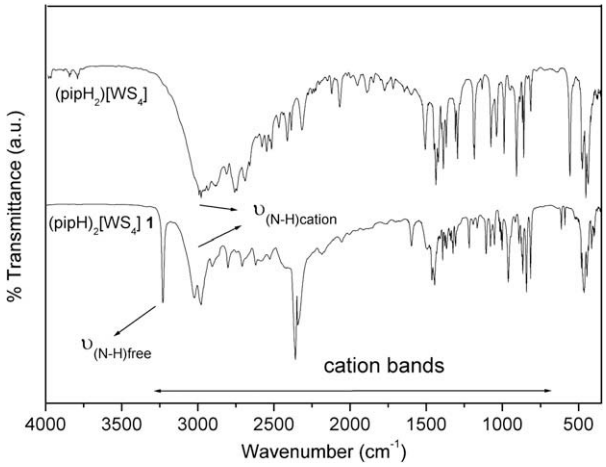


Fig. 1. Infrared spectra of $(pipH_2)[WS_4]$ (top) and $(pipH)_2[WS_4]$ **1** (bottom).

3.2. Description of crystal structures of $(pipH)_2[MS_4]$ (M = W **1**; M = Mo **2**)

The title compounds **1** and **2** are isostructural and crystallize in the centrosymmetric triclinic space group $P\bar{1}$. It is interesting to note that the related isostructural compounds $(pipH_2)[MS_4]$ containing the diprotonated $(pipH_2)^{2+}$ dication crystallize in the monoclinic space group $P2_1/c$ [26,27]. The crystal structures **1** and **2** consist of a tetrahedral $[MS_4]^{2-}$ dianion (M = W **1**; M = Mo **2**), two crystallographically independent piperazin-1-ium cations, all of which are located in general positions (Fig. 2). The monoprotonated cyclic organic ammonium cations adopt a chair confirma-

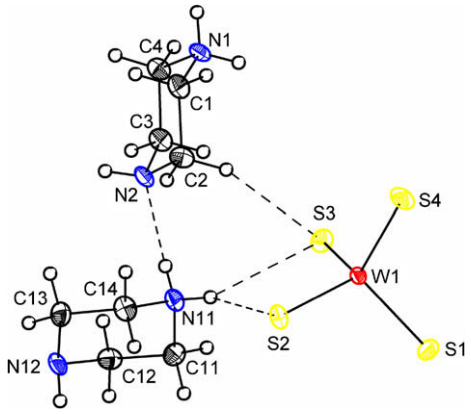


Fig. 2. The crystal structure of $(pipH)_2[WS_4]$ **1** showing the atom-labeling scheme. Displacement ellipsoids are drawn at the 50% probability level except for the H atoms, which are shown as circles of arbitrary radius. Intramolecular H-bonding is shown as broken lines. *Colour code:* C, black; N, blue; W, red; S, yellow. For the structure of the isostructural Mo compound **2**, see Supplementary data. (For interpretation of the references to colour in this figure legend, the reader is referred to the web version of this article.)

tion. In each cation, two of the C–N bond distances (Table 2) associated with the protonated N atoms (N1–C1 = 1.483(7) and N1–C4 = 1.499(6) Å in **1**) are elongated compared to the other two C–N distances made by the free N atom (N2–C2 = 1.466(6) and N2–C3 = 1.461(7) Å in **1**). A similar feature is observed for the C–N bond lengths of the cations in compound **2** (Table 3). This observation can explain the protonation of one of the amine groups of the cyclic diamine in both compounds. In compound **1** the WS_4 tetrahedron is slightly distorted as indicated by the S–W–S bond angles ranging between 108.82(5) and 110.41(5)° (Table 2). The W–S distances vary from 2.1789(7) to 2.2131(7) Å with a mean W–S bond length of 2.1915 Å. In the isostructural $[MoS_4]^{2-}$ compound the Mo–S bonds vary from 2.1734(12) to 2.2115(12) Å with a mean Mo–S bond length of 2.1908 Å (Table 3). The difference Δ between the longest and shortest M–S bond distances is 0.0342 and 0.0368 Å for compounds **1** and **2**, respectively. These Δ values are comparable with the reported Δ value of 0.0385 and 0.0431 Å, respectively, for $(pipH_2)[WS_4]$ and $(pipH_2)[MoS_4]$. Based on an analysis of such Δ values of several $[WS_4]^{2-}$ and $[MoS_4]^{2-}$ compounds, as a structural criterion, we demonstrated that for compounds with Δ larger than 0.033 Å the distortion induces a split M–S vibration in the infrared spectrum [35–38] as observed in the IR spectra of compounds **1** and **2**.

In compound **1**, three of the observed W–S distances (W1–S3, W1–S1 and W1–S4) are shorter than the mean W–S distance of 2.1915 Å indicating a distorted WS_4 tetrahedron. In compound **2** a similar distribution of one long and three short Mo–S bonds is observed. In the related $(pipH_2)[MS_4]$ compounds, a distribution of two short and two long M–S bonds were explained based on the strength and number of hydrogen bonding interactions between the cations and anions. Likewise, the distinct M–S bond lengths in **1** and **2** can be attributed to the several weak hydrogen bonding interactions observed among the $[MS_4]^{2-}$ anions, and the $[pipH]^+$ organic cations. A scrutiny of the structure of **1** reveals a total of 18 weak H-bonding interactions comprising of six N–H···S, two N–H···N and 10 C–H···S contacts the details of which are summarized in Table 4. Thus each $[WS_4]^{2-}$ ion is linked to 10 different piperazin-1-ium cations (Supplementary Fig. 3) with the aid of six N–H···S and 10 C–H···S interactions. One unique $(pipH)^+$ cation (N1, N2) is hydrogen bonded to four different tetrasulfidotungstate anions via three N–H···S and four C–H···S bonds and is further linked to two different cations with the aid of an intramolecular (N11–H5N···N2) and an intermolecular N–H···N interaction. Cation pairs are formed as a result of the intramolecular N–H···N interaction, and the pairs of cations thus formed are extended by the intermolecular N1–H2N···N12 bond into a one-dimensional chain of cations (Fig. 3). The second unique cation is hydrogen bonded to six $[WS_4]^{2-}$ anions and to two different cations with the aid of three varieties of interactions (Supplementary Fig. 4). As a result of H-bonding, a three-dimensional network of H-bonds is formed (see Fig. 4). A detailed analysis of the several H-bonds reveals that the S2 atom which makes the longest W–S distance is involved in two very short N–H···S bonds (N1–H1N···S2 and N11–H4N···S2) at 2.486 and 2.471 Å accounting for its elongation. The isotypic Mo compound **2** exhibits an identical H-bonding behavior (Supplementary Figs. 5–8) and the geometric parameters of its H-bonding interactions are listed in Supplementary Table 1.

Table 2
Selected bond lengths and bond angle (Å, °) for $(pipH)_2[WS_4]$ **1**.

W(1)–S(3)	2.1789(12)	W(1)–S(4)	2.1911(14)
W(1)–S(1)	2.1828(12)	W(1)–S(2)	2.2131(13)
S(3)–W(1)–S(1)	108.94(5)	S(3)–W(1)–S(2)	109.12(5)
S(3)–W(1)–S(4)	110.41(5)	S(1)–W(1)–S(2)	108.82(5)
S(1)–W(1)–S(4)	109.57(6)	S(4)–W(1)–S(2)	109.96(5)
N(1)–C(1)	1.483(7)	N(11)–C(11)	1.487(7)
N(1)–C(4)	1.499(6)	N(11)–C(14)	1.496(6)
C(1)–C(2)	1.522(7)	C(11)–C(12)	1.509(8)
C(2)–N(2)	1.466(6)	C(12)–N(12)	1.468(7)
N(2)–C(3)	1.461(7)	N(12)–C(13)	1.463(7)
C(3)–C(4)	1.514(7)	C(13)–C(14)	1.516(8)
C(1)–N(1)–C(4)	110.5(4)	C(11)–N(11)–C(14)	111.1(4)
N(1)–C(1)–C(2)	108.7(4)	N(11)–C(11)–C(12)	108.9(4)
N(2)–C(2)–C(1)	112.7(4)	N(12)–C(12)–C(11)	113.6(4)
C(3)–N(2)–C(2)	111.4(4)	C(13)–N(12)–C(12)	111.8(4)
N(2)–C(3)–C(4)	113.4(4)	N(12)–C(13)–C(14)	113.8(4)
N(1)–C(4)–C(3)	109.4(4)	N(11)–C(14)–C(13)	108.8(4)

Table 3
Selected bond lengths and bond angle (Å, °) for $(pipH)_2[MoS_4]$ **2**.

Mo(1)–S(3)	2.1734(7)	Mo(1)–S(4)	2.1825(7)
Mo(1)–S(1)	2.1786(7)	Mo(1)–S(2)	2.2115(7)
S(3)–Mo(1)–S(1)	108.84(3)	S(3)–Mo(1)–S(2)	109.12(3)
S(3)–Mo(1)–S(4)	110.39(3)	S(1)–Mo(1)–S(2)	108.86(3)
S(1)–Mo(1)–S(4)	109.61(3)	S(4)–Mo(1)–S(2)	110.00(3)
N(1)–C(1)	1.488(3)	N(11)–C(11)	1.489(3)
N(1)–C(4)	1.490(3)	N(11)–C(14)	1.493(3)
C(1)–C(2)	1.517(3)	C(11)–C(12)	1.512(3)
C(2)–N(2)	1.462(3)	C(12)–N(12)	1.474(3)
N(2)–C(3)	1.467(3)	N(12)–C(13)	1.471(3)
C(3)–C(4)	1.517(3)	C(13)–C(14)	1.504(4)
C(1)–N(1)–C(4)	111.19(19)	C(11)–N(11)–C(14)	111.03(19)
N(1)–C(1)–C(2)	109.01(19)	N(11)–C(11)–C(12)	108.80(19)
N(2)–C(2)–C(1)	113.2(2)	N(12)–C(12)–C(11)	114.2(2)
C(2)–N(2)–C(3)	111.32(19)	C(13)–N(12)–C(12)	111.03(19)
N(2)–C(3)–C(4)	113.8(2)	N(12)–C(13)–C(14)	114.0(2)
N(1)–C(4)–C(3)	109.1(2)	N(11)–C(14)–C(13)	109.38(19)

Table 4
Hydrogen bonding geometry (Å, °) for $(pipH)_2[WS_4]$ **1**.

D–H···A	D(H··A)	d(D··A)	<DHA	Symmetry code
N1–H1N···S1	2.828	3.373	123	$1+x,1+y,z$
N1–H1N···S2	2.486	3.275	153	$1+x,1+y,z$
N1–H2N···N12	2.012	2.859	168	$-1+x,y,z$
N2–H3N···S1	2.837	3.494	134	$x,1+y,z$
N11–H4N···S2	2.471	3.2523	151	x,y,z
N11–H4N···S3	2.861	3.4243	125	x,y,z
N11–H5N···N2	2.010	2.851	166	x,y,z
N12–H6N···S3	2.760	3.446	138	$-1+x,y,z$
C2–H2B···S3	2.825	3.724	153	x,y,z
C4–H4B···S2	2.812	3.629	141	$1-x,1-y,1-z$
C12–H12A···S1	2.779	3.6627	150	$x,1+y,z$
C14–H14A···S4	2.842	3.759	156	$1-x,1-y,1-z$
C3–H3B···S4	2.974	3.928	165	$1-x,1-y,1-z$
C4–H4A···S4	2.884	3.754	149	$x,1+y,z$
C11–H11B···S1	2.929	3.691	135	$1-x,1-y,-z$
C11–H11B···S3	2.942	3.748	140	$1-x,1-y,-z$
C13–H13A···S2	2.971	3.951	178.	$2-x,1-y,1-z$
C14–H14B···S4	2.910	3.803	152	$-1+x,y,z$

3.3. Thermal studies

All the observed thermal events for compounds **1** and **2** as well as the previously reported compounds $(pipH_2)[MS_4]$ containing the diprotonated piperazinediium cation are endothermic and occur below 350 °C. The W compound **1** is thermally more stable as compared to its Mo analogue **2**. An elemental analysis of the residue of all four compounds at 350 °C indicates the presence of considerable amounts of C and N (Table 5). Electron microscopic investigations reveal a porous morphology for the residues and for all the compounds the metal:sulfur ratio of the residue is very close to 1:2. It is well documented that the ammonium salts of the group VI tetrasulfidometalates decompose in two steps resulting in the formation of group VI metal disulfide [52]. The first endothermic

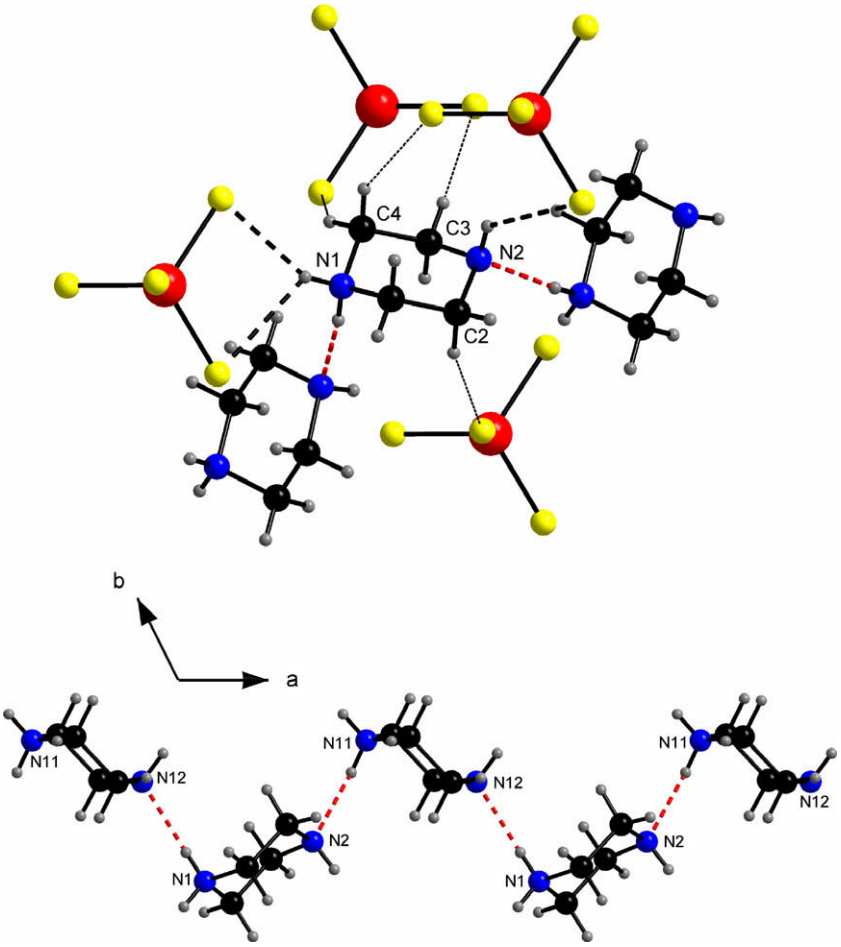


Fig. 3. H-bonding surroundings of one of the unique piperazin-1-ium (N1, N2) cation showing the three varieties of H-bonding interactions (top). The intra and intermolecular N–H···N interactions result in the formation of a one-dimensional H-bonded network of cations in the *ab* crystallographic plane. *Colour code:* C, black; H, medium grey; N, blue; W, red; S, yellow. (For interpretation of the references to colour in this figure legend, the reader is referred to the web version of this article.)

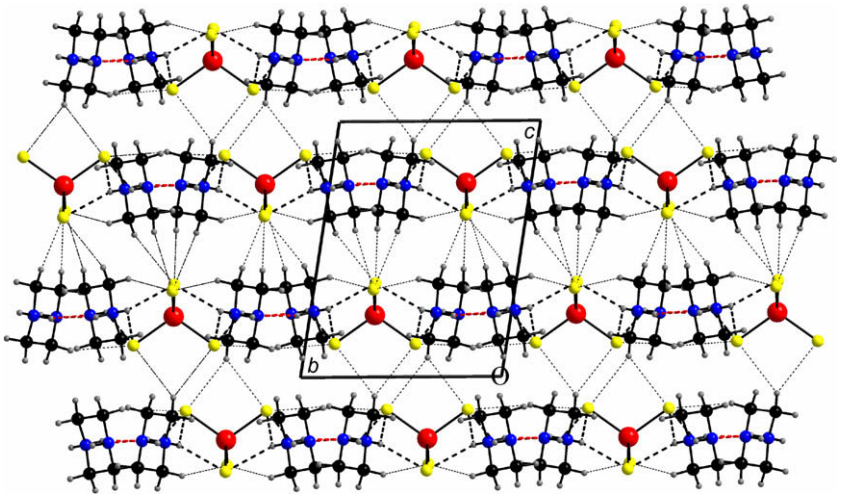


Fig. 4. A view along a axis of the crystallographic packing in compound **1** showing the intricate H-bonded network. H-bonds are shown as broken lines. *Colour code:* C, black; H, medium grey; N, blue; W, red; S, yellow. (For interpretation of the references to colour in this figure legend, the reader is referred to the web version of this article.)

step results in the formation of the amorphous trisulfide accompanied by loss of ammonia and H_2S. In the second step the MS_3 decomposes exothermically above 350 °C into MS_2 losing elemental S. In contrast, organic ammonium $[MS_4]^{2-}$ compounds decompose endothermically at lower temperatures and the decomposition processes are very complex involving structural phase transitions as well as emission of different organic fragments like disulfides and amines [53–55].

The thermal profile of compound **1** (Fig. 5) exhibits two closely related endothermic events centered at 227 and 245 °C as opposed

Table 5
Analytical data of residue at 350 °C.

Compound	C (wt%)	H (wt%)	N (wt%)	S (wt%)	M (wt%)	Composition
$(pipH)_2[WS_4]$ **1**	5.63	0.43	2.52	24.1	67.32	$WS_2C_{1.2}N_{0.5}H_{1.2}$
$(pipH)_2[MoS_4]$ **2**	9.22	0.55	4.18	33.57	52.48	$MoS_{1.9}C_{1.4}N_{0.5}H$
$(pipH_2)[WS_4]$	6.35	0.57	3.02	24.52	65.54	$WS_{2.1}C_{1.4}N_{0.6}H_{1.5}$
$(pipH_2)[MoS_4]$	9.64	0.65	4.32	35.285	50.08	$MoS_{2.1}C_{1.5}N_{0.5}H_{1.2}$

to a single endothermic event for $(pipH_2)[WS_4]$ which shows a single endothermic peak at 290 °C (Supplementary Fig. 9). The observed mass loss of 13.7% is almost twice that expected for the loss of only H_2S, indicating the complex nature of the process. Although the exact nature of thermal event cannot be commented upon in the absence of the mass spectral data of the emitted fragment, it is noted that the TG curve shows a steep drop indicating that the removal of the first fragment leads to further decomposition of **1**. The observed weight loss of 43.5% is lower than the calculated value of 49.4% for the loss of 2 m of pip, H_2S and S. In accordance with this, the observed residue of 56.5% is more than that expected for the formation of WS_2. The analytical data of the residue indicates the composition as $WS_2C_{1.2}N_{0.5}H_{1.2}$.

The DTA curve of $(pipH)_2[MoS_4]$ **2** (Fig. 6) exhibits endothermic events at 165 and 214 °C, respectively, and is very similar to that of $(pipH_2)[MoS_4]$ (see Supplementary Fig. 10). The observed first mass loss is 9.8% is more than the expected value for the removal of only H_2S. The total mass loss of 51.6% till 350 °C is also lower than the expected value of 59.83% for the loss of 2 mol of pip, H_2S and S leading to the formation of MoS_2 indicating incomplete removal of the volatile organic part. This is also evidenced by the presence of C and N in the residue. It is interesting to note that the composition of the residues obtained by the thermal decomposition of the carbon rich starting compounds $(pipH)_2[WS_4]$ **1** and $(pipH)_2[MoS_4]$

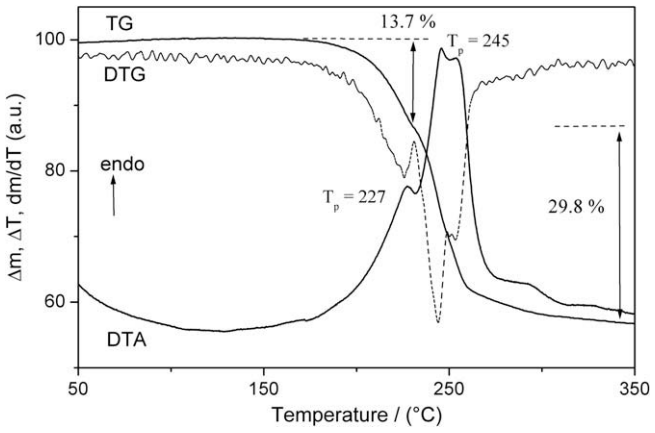


Fig. 5. TG-DTA thermogram of compound **1**.

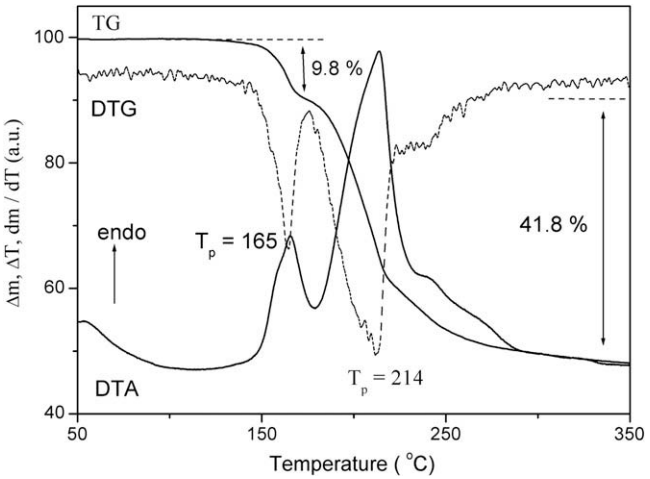


Fig. 6. TG-DTA thermogram of compound **2**.

2 as well as the $(pipH_2)[MS_4]$ compounds which contain the diprotonated piperazine cation are very nearly the same. The results clearly indicate that the carbon content of the precursor tetrasulfidometalates influences the starting decomposition temperature but it does not affect the final carbon content suggesting that the decomposition path for the tetrasulfidometalates containing piperazine cations is very similar and it does not proceed by the formation of MS_3. The formation of the trisulfide as an intermediate is a well documented thermal event for $(NH_4)_2MS_4$.

3.4. Comparative study of tetrasulfidometalates containing piperazine based cations

In addition to the title compounds **1** and **2** described in this work, three more compounds namely $(pipH_2)[WS_4]$, $(pipH_2)[MoS_4]$ and $(2\text{-pipH-1-EtNH}_3)[MoS_4]\cdot\frac{1}{2}H_2O$ (2-pipH-1-EtNH$_3$ = 4-(2-ammonioethyl)piperazin-1-ium) are known. A comparative study of these five compounds (Table 6) reveals certain interesting features. All the compounds which crystallize in centrosymmetric space groups exhibit a very long metal–sulfur bond distance above 2.2005 Å accompanied by Δ values greater than 3 pm and exhibit several weak hydrogen bonding interaction between the organic cation and the $[MS_4]^{2-}$ anion. All compounds including $(pipH_2)[MS_4]$ exhibit N–H···S and C–H···S interactions while the title compounds are additionally involved in N–H···N interactions resulting in the formation of a H-bonded chain of cations. The observed N–H···N interactions in **1** and **2** can be attributed as a possible explanation for the formation of these compounds in the solid state reaction. The hemihydrate $(2\text{-pipH-1-EtNH}_3)[MoS_4]\cdot\frac{1}{2}H_2O$ exhibits four varieties of H-bonding interactions. All compounds decompose endothermically resulting in the formation of residues which contain metal:sulfur in a 1:2 ratio with considerable amounts of C and N.

Table 6
Comparative study of the $[MS_4]^{2-}$ compounds containing organic cations based on piperazine.

Compound	Space group	M–S (long) (Å)	Δ (Å)	H-bonding	Composition of residue[a]	Reference
$(pipH)_2[WS_4]$ **1**	$P\bar{1}$	2.2131	0.0342	N–H···S, C–H···S, N–H···N	$WS_2C_{1.2}N_{0.5}H_{1.2}$	this work
$(pipH)_2[MoS_4]$ **2**	$P\bar{1}$	2.2115	0.0381	N–H···S, C–H···S, N–H···N	$MoS_{1.9}C_{1.4}N_{0.5}H$	this work
$(pipH_2)[WS_4]$	$P2_1/c$	2.2147	0.0385	N–H···S, C–H···S,	$WS_{2.1}C_{1.4}N_{0.6}H_{1.5}$	26
$(pipH_2)[MoS_4]$	$P2_1/c$	2.2114	0.0431	N–H···S, C–H···S,	$MoS_{2.1}C_{1.5}N_{0.5}H_{1.2}$	27
$(2\text{-pipH-1-EtNH}_3)[MoS_4]\cdot\frac{1}{2}H_2O$	$C2/c$	2.2005	0.0302	N–H···S, C–H···S, N–H···O, O–H···S	$MoS_{1.7}C_{2.4}N_{0.7}$[b]	38

Abbreviations: pipH, piperazin-1-ium; $pipH_2$, piperazinediium; 2-pipH-1-EtNH$_3$, 4-(2-ammonioethyl)piperazin-1-ium.
[a] Residue obtained at 350 °C.
[b] Residue obtained at 600 °C.

4. Conclusions

In the present report, we have described a solid state method for the preparation of two new organic tetrasulfidometalates **1** and **2** containing the monoprotonated piperazin-1-ium cation. The title compounds constitute two new examples to the growing list of structurally characterized organic tetrasulfidometalates. The isostructural compounds exhibit three varieties of weak H-bonding interactions between the organic cations and tetrasulfidometalate anion and decompose endothermically resulting in the formation of carbon containing metal sulfide residues.

Acknowledgements

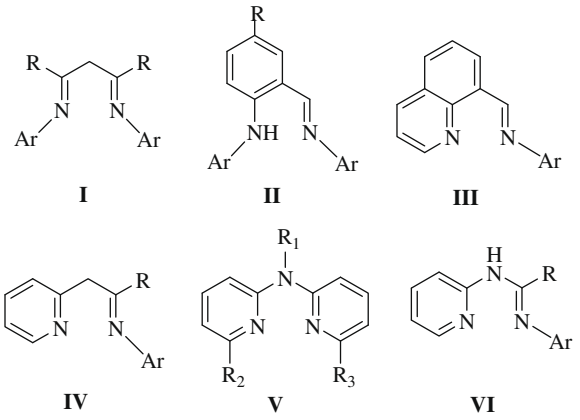
B.R.S. and W.B. acknowledge the financial support by the Indian National Science Academy (INSA), New Delhi, and the Deutsche Forschungsgemainschaft.

Appendix A. Supplementary data

CCDC 715142 and 715143 contain the supplementary crystallographic data for the structures of compounds **1** and **2**, respectively. These data can be obtained free of charge via http://www.ccdc.cam.ac.uk/conts/retrieving.html, or from the Cambridge Crystallographic Data Centre, 12 Union Road, Cambridge CB2 1EZ, UK; fax: (+44) 1223-336-033; or e-mail: deposit@ccdc.cam.ac.uk. Supplementary data associated with this article can be found, in the online version, at doi:10.1016/j.poly.2009.02.034.

References

[1] A. Müller, E. Diemann, R. Jostes, H. Bogge, Angew. Chem., Int. Ed. Engl. 20 (1981) 934. and references therein.
[2] T. Shibhahara, Coord. Chem. Rev. 123 (1993) 73.
[3] D. Coucouvanis, Adv. Inorg. Chem. 45 (1998) 1.
[4] S.H. Laurie, Eur. J. Inorg. Chem. (2000) 2443.
[5] G.J. Brewer, Drug Discovery Today 10 (2005) 1103.
[6] D.E. Schwarz, T.B. Rauchfuss, S.R. Wilson, Inorg. Chem. 42 (2003) 2410.
[7] T.B. Rauchfuss, Inorg. Chem. 43 (2004) 14.
[8] G. Alonso, J. Espino, G. Berhault, L. Alvarez, J.L. Rico, Appl. Catal. A 266 (2004) 29.
[9] M. Poisot, W. Bensch, S. Fuentes, C. Ornelas, G. Alonso, Catal. Lett. 117 (2007) 43.
[10] S.E. Skrabalak, K.E. Suslick, J. Am. Chem. Soc. 127 (2005) 9990.
[11] M. Polyakov, S. Indris, S. Schwamborn, A. Mazheika, M. Poisot, L. Kienle, W. Bensch, M. Muhler, W. Grünert, J. Catal. 260 (2008) 236.
[12] M. Polyakov, M.W.E. van den Berg, T. Hanft, M. Poisot, W. Bensch, M. Muhler, W. Grünert, J. Catal. 256 (2008) 126.
[13] M. Polyakov, M. Poisot, W. Bensch, M. Muhler, W. Grünert, J. Catal. 256 (2008) 137.
[14] H.J. Jakobsen, A.R. Hove, H. Bildsøe, J. Skibsted, M. Brorson, Chem. Commun. 1629 (2007).
[15] M.R. Hansen, M. Brorson, H. Bildsøe, J. Skibsted, H.J. Jakobsen, J. Magn. Reson. 190 (2008) 316.
[16] H.J. Jakobsen, H. Bildsoe, J. Skibsted, M.R. Hansen, M. Brorson, B.R. Srinivasan, W. Bensch, Inorg Chem 48 (2009), <http://dx.doi.org/10.1021/ic8023937>.
[17] C.J. Crossland, I.R. Evans, J.S.O. Evans, Dalton Trans. (2008) 1597.
[18] J. Ellermeier, W. Bensch, Z. Naturforsch. 56b (2001) 611.
[19] J. Ellermeier, W. Bensch, Monatsh. Chem. 133 (2002) 945.
[20] B.R. Srinivasan, S.N. Dhuri, A.R. Naik, Tetrahedron Lett. 45 (2004) 2247.
[21] B.R. Srinivasan, J. Chem. Sci. 116 (2004) 251.
[22] B.R. Srinivasan, B.K. Vernekar, K. Nagarajan, Indian J. Chem. 40A (2001) 563.
[23] B.R. Srinivasan, S.N. Dhuri, C. Näther, W. Bensch, Acta Crystallogr. E58 (2002) m622.
[24] B.R. Srinivasan, S.N. Dhuri, C. Näther, W. Bensch, Acta Crystallogr. C59 (2003) m124.
[25] B.R. Srinivasan, S.N. Dhuri, C. Näther, W. Bensch, Inorg. Chim. Acta 358 (2005) 279.
[26] B.R. Srinivasan, S.N. Dhuri, M. Poisot, C. Näther, W. Bensch, Z. Anorg. Allg. Chem. 631 (2005) 1087.
[27] B.R. Srinivasan, S.N. Dhuri, M. Poisot, C. Näther, W. Bensch, Z. Naturforsch. 59b (2004) 1083.
[28] J.W. McDonald, G.D. Friesen, L.D. Rosenhein, W.E. Newton, Inorg. Chim. Acta 72 (1983) 205.
[29] G. Alonso, G. Berhault, R.R. Chianelli, Inorg. Chim. Acta 316 (2001) 105.
[30] B.R. Srinivasan, S.N. Dhuri, C. Näther, W. Bensch, Acta Crystallogr. E59 (2003) m681.
[31] B.R. Srinivasan, M. Poisot, C. Näther, W. Bensch, Acta Crystallogr. E60 (2004) i136.
[32] B.R. Srinivasan, C. Näther, W. Bensch, Acta Crystallogr. E61 (2005) m2454.
[33] B.R. Srinivasan, C. Näther, A.R. Naik, W. Bensch, Acta Crystallogr. E62 (2006) m1635.
[34] B.R. Srinivasan, C. Näther, W. Bensch, Acta Crystallogr. C62 (2006) m98.
[35] B.R. Srinivasan, C. Näther, S.N. Dhuri, W. Bensch, Monatsh. Chem. 137 (2006) 397.
[36] B.R. Srinivasan, C. Näther, S.N. Dhuri, W. Bensch, Polyhedron 25 (2006) 3269.
[37] B.R. Srinivasan, A.R. Naik, C. Näther, W. Bensch, Z. Anorg. Allg. Chem. 633 (2007) 582.
[38] B.R. Srinivasan, S.N. Dhuri, A.R. Naik, C. Näther, W. Bensch, Polyhedron 27 (2008) 25.
[39] B.R. Srinivasan, A.R. Naik, C. Näther, W. Bensch, Acta Crystallogr. E62 (2006) m3491.
[40] B.R. Srinivasan, A.R. Naik, C. Näther, W. Bensch, Acta Crystallogr. C63 (2007) m81.
[41] B.R. Srinivasan, C. Näther, W. Bensch, Acta Crystallogr. E63 (2007) i167.
[42] B.R. Srinivasan, S.V. Girkar, P. Raghavaiah, Acta Crystallogr. E63 (2007) m2737.
[43] B.R. Srinivasan, S.V. Girkar, P. Raghavaiah, Acta Crystallogr. E63 (2007) m3100.
[44] B.R. Srinivasan, C. Näther, A.R. Naik, W. Bensch, Acta Crystallogr. E64 (2008) m66.
[45] B.R. Srinivasan, C. Näther, W. Bensch, Acta Crystallogr. E64 (2008) m296.
[46] M. Poisot, C. Näther, W. Bensch, Z. Naturforsch. 61b (2006) 1061.
[47] M. Poisot, C. Näther, W. Bensch, Z. Naturforsch. 62b (2007) 209.
[48] M. Poisot, C. Näther, W. Bensch, Acta Crystallogr. E62 (2006) m1326.
[49] U. Siemeling, F. Bretthauer, C. Bruhn, Z. Anorg. Allg. Chem. 632 (2006) 1027.
[50] M.G. Kanatzidis, D. Coucouvanis, Acta Crystallogr. C39 (1983) 835.
[51] G.M. Sheldrick, Acta Crystallogr. A64 (2008) 112.
[52] T.P. Prasad, E. Diemann, A. Müller, J. Inorg. Nucl. Chem. 35 (1973) 1895.
[53] B.R. Srinivasan, S.N. Dhuri, C. Näther, W. Bensch, Transition Met. Chem. 32 (2007) 64.
[54] M. Poisot, W. Bensch, S. Fuentus, G. Alonso, Theromochim. Acta 444 (2006) 35.
[55] M. Poisot, W. Bensch, Theromochim. Acta 453 (2007) 42.



Scheme 1. Types of [N,N] six-membered ring ligands.

chloride, *p*-anisoyl chloride, 2-amino-6-methylpyridine and 2-amino-5-nitropyridine were purchased from Aldrich Chemical Co. and used as received. Benzoyl chloride was purchased from Guangzhou Chemical Reagent Factory and used without further purification. 2-Aminopyridine was purchased from Shanghai Chemical Reagent Factory and used after recrystallization from ethanol. Methylaluminoxane (MAO) was prepared by partial hydrolysis of trimethylaluminum (TMA) in toluene at 0–60 °C with $Al_2(SO_4)_3 \cdot 18H_2O$ as the water source. The initial $[H_2O]/[Al]$ in molar ratio was 1.3.

2.3. Measurement

^1H and ^{13}C NMR spectra were recorded on a Varian Mercury-Plus 300 MHz NMR spectrometer and referenced versus TMS as standard. Elemental analyses were determined with a Vario EL Series Elemental Analyzer from Elementar. The GC–MS data were recorded with a Finnigan Voyager GC-8000 Top Series GC–MS System with DB-5MS GC column. The following temperature program of the oven was adopted: keeping 40 °C for 2 min, increasing the temperature by 5 °C/min heating to 110 °C, and then by a 15 °C/min heating until 250 °C which was kept constant for a further 2 min.

2.4. X-ray structure determination

The X-ray diffraction data of single crystals were obtained with the $\omega-2\theta$ scan mode on a Bruker SMART 1000 CCD diffractiometer with graphite-monochromated Mo Kα radiation (λ = 0.71073 Å) at 173 K. The structure was solved using direct methods, and further refinement with full-matrix least squares on F^2 was obtained with the SHELXTL program package. All non-hydrogen atoms were refined anisotropically. Hydrogen atoms were introduced in calculated positions with the displacement factors of the host carbon atoms.

2.5. Ethylene oligomerization

Ethylene oligomerization reactions were performed in a 50 mL glass flask equipped with a magnetic stirrer, and continuous feed of ethylene was used. A typical reaction was performed by adding proper amount of MAO solid and solvent (19 mL) into the reactor under ethylene atmosphere. The catalyst in dichloromethane solution (1 mL, Ni = 5 μmol) was injected into the reactor *via* syringe. Ethylene was continuously fed in order to maintain the ethylene pressure at 0.5 atm. After 30 min, the reaction was terminated by addition of cold acidic ethanol (ethanol–HCl, 95:5). The organic layer was analyzed quickly by gas chromatography (GC) for determining the composition and mass distribution of the oligomers.

2.5.1. Synthesis of 2,6-$iPr_2C_6H_3$–N=C(Ph)–NH–Py (**L1**)

Benzoyl chloride (1.1 mL, 10 mmol) and triethylamine (1.6 mL, 11 mmol) were added to a vigorously stirred solution of 2,6-diisopropylaniline (1.9 mL, 10 mmol) in CH_2Cl_2 (45 mL). After 3 h, the precipitate of $(C_2H_5)_3N \cdot HCl$ was filtrated, and white solid powder benzamide was obtained by evaporating the solvent. Then excess of thionyl chloride (2.0 mL, 28 mmol) was added to the benzamide and the reaction mixtures were stirred for 2 h at 80 °C. The remainder thionyl chloride was distilled off under reduced pressure, to give the imidoyl chloride as yellow and slowly solidifying oil. Successively, toluene (40 mL), triethylamine (1.6 mL, 11 mmol) and 2-aminopyridine (0.94 g, 10 mmol) were added to the reaction system. The mixtures were heated to reflux for 24 h under the protection of nitrogen atmosphere. $(C_2H_5)_3N \cdot HCl$ was removed by filtration, and toluene was evaporated from the filtrate. After recrystallization of the product from ethanol, **L1** was obtained as light yellow crystal in 48% yield (1.72 g, 4.83 mmol). Melting point: 156 °C. ^1H NMR (300 MHz, $CDCl_3$), δ (ppm) [an isomer (*E-syn* and *E-anti*) ratio of 1.2:1] major isomer: 13.31(s, 1H, N*H*), 8.25 (br, 1H, pyridyl α-H), 7.66–6.92 (m, 11H, pyridyl and phenyl protons), 3.26 (m, 2H, C*H*$(CH_3)_2$), 1.14 (d, 12H, CH(C*H*$_3)_2$). Minor isomer: 13.31 (s, 1H, N*H*), 8.25 (br, 1H, pyridyl α-H), 7.66–6.92 (m, 11H, pyridyl and phenyl protons), 3.04 (m, 2H, C*H*$(CH_3)_2$), 0.94 (d, 12H, CH(C*H*$_3)_2$). ^{13}C NMR (75 MHz, $CDCl_3$), δ (ppm) major isomer: 162.79, 144.99, 144.56, 137.27, 136.04, 134.41, 129.12, 128.80, 128.29, 127.47, 127.10, 123.30, 117.47, 113.26, 28.65, 25.19. Major isomer: 160.53, 144.99, 144.56, 137.27, 136.04, 134.41, 129.12, 128.80, 128.29, 127.47, 127.10, 123.30, 117.47, 113.26, 28.27, 21.83. EI-MS (*m*/*z*): 358 $[M]^+$; 264 $[M-C_5H_5N_2]^+$. Elemental *Anal.* Calc. for $C_{24}H_{27}N_3$: C, 80.63; H, 7.61; N, 11.75. Found: C, 80.47; H, 7.59; N, 11.64%.

2.5.2. Synthesis of 2,6-$iPr_2C_6H_3$–N=C(Ph)–NH–(5-NO_2–Py) (**L2**)

L2 was prepared according to the method described for **L1**, the mixtures were purified by column chromatography on silica gel using petroleum ether/ethyl acetate (10/1) as eluent, and then recrystallized from ethanol in 31% yield. Melting point: 140 °C. ^1H NMR (300 MHz, $CDCl_3$): δ (ppm) [an isomer ratio of 2.3:1] major isomer: 13.12 (s, 1H, N*H*), 9.13 (br, 1H, pyridyl α-H), 8.38 (br, 1H, pyridyl γ-H), 7.40–7.06 (m, 9H, pyridyl and phenyl protons), 3.13 (m, 2H, C*H*$(CH_3)_2$), 1.13 (d, 12H, CH(C*H*$_3)_2$). Minor isomer: 13.12 (s, 1H, N*H*), 9.13 (br, 1H, pyridyl α-H), 8.38 (br, 1H, pyridyl γ-H), 7.40–7.06 (m, 9H, pyridyl and phenyl protons), 2.94 (m, 2H, C*H*$(CH_3)_2$), 0.92 (d, 12H, CH(C*H*$_3)_2$). ^{13}C NMR (75 MHz, $CDCl_3$), δ (ppm) major isomer: 163.38, 144.08, 142.95, 138.56, 134.92, 132.01, 130.18, 129.04, 128.54, 128.50, 127.99, 122.70, 123.65, 122.35, 28.49, 25.12. Minor isomer: 163.05, 144.08, 142.95, 138.56, 134.92, 132.01, 130.18, 129.04, 128.54, 128.50, 127.99, 122.70, 123.65, 122.35, 28.39, 21.79. EI-MS (*m*/*z*): 403 $[M]^+$; 264 $[M-C_5H_4N_2O_2]^+$. Elemental *Anal.* Calc. for $C_{24}H_{26}N_4O_2$: C, 71.62; H, 6.51; N, 13.92. Found: C, 71.40; H, 6.61; N, 14.08%.

2.5.3. Synthesis of 2,6-$iPr_2C_6H_3$–N=C(4-$CH_3OC_6H_4$)–NH–Py (**L3**)

L3 was prepared according to the method described for **L1** in 46% yield. Melting point: 169 °C. ^1H NMR (300 MHz, $CDCl_3$): δ (ppm) [an isomer ratio of 1.3:1] major isomer: 13.25 (s, 1H, N*H*), 8.23 (br, 1H, pyridyl α-H), 7.64 (br, 1H, pyridyl γ-H), 7.38–6.68 (m, 9H, pyridyl and phenyl protons), 3.72 (s, 3H, OC*H*$_3$), 3.24 (m, 2H, C*H*$(CH_3)_2$), 1.13 (d, 12H, CH(C*H*$_3)_2$). Minor isomer: 13.25 (s, 1H, N*H*), 8.23 (br, 1H, pyridyl α-H), 7.64 (br, 1H, pyridyl γ-H), 7.38–6.68 (m, 9H, pyridyl and phenyl protons), 3.72 (s, 3H, OC*H*$_3$), 3.02 (m, 2H, C*H*$(CH_3)_2$), 0.94 (d, 12H, CH(C*H*$_3)_2$). ^{13}C NMR (75 MHz, $CDCl_3$), δ (ppm) major isomer: 162.82, 144.97, 144.47, 137.19, 134.72, 130.50, 128.56, 126.98, 123.56, 122.41, 117.20, 113.67, 113.21, 112.85, 55.15, 28.65, 25.12. Minor isomer:

160.25, 144.97, 144.47, 137.19, 134.72, 130.50, 128.56, 126.98, 123.56, 122.41, 117.20, 113.67, 113.21, 112.85, 55.15, 28.25, 21.94. EI-MS (*m*/*z*): 388 $[M]^+$; 294 $[M-C_5H_4N_2]^+$. Elemental *Anal.* Calc. for $C_{25}H_{29}N_3O$: C, 77.48; H, 7.54; N, 10.84. Found: C, 77.55; H, 7.64; N, 10.76%.

*2.5.4. Synthesis of 2,6-iPr$_2$C$_6$H$_3$–N=C(4-CH$_3$C$_6$H$_4$)–NH–(6-CH$_3$–Py) (**L4**)*

L4 was prepared according to the method described for **L1**. The mixtures were purified by column chromatography on silica gel using petroleum ether/ethyl acetate (10/1) as eluent, and then recrystallized from ethanol in 63% yield. Melting point: 119 °C. ^{1}H NMR (300 MHz, $CDCl_3$): δ (ppm) [an isomer ratio of 1.5:1] major isomer: 13.35 (s, 1H, N*H*), 7.56–6.80 (m, 10H, pyridyl and phenyl protons), 3.30 (m, 2H, C*H*$(CH_3)_2$), 2.45 (s, 3H, methyl protons on pyridyl), 2.50 (s, 3H, CH_3), 1.15 (d, 12H, CH(CH_3)$_2$). Minor isomer: 13.35 (s, 1H, N*H*), 7.56–6.80 (m, 10H, pyridyl and phenyl protons), 3.04 (m, 2H, C*H*$(CH_3)_2$), 2.45 (s, 3H, methyl protons on pyridyl), 2.50 (s, 3H, CH_3), 0.99 (d, 12H, CH(CH_3)$_2$). ^{13}C NMR (75 MHz, $CDCl_3$), δ (ppm) major isomer: 162.39, 153.65, 152.72, 144.70, 139.00, 137.50, 134.56, 133.31, 128.76, 128.08, 126.97, 123.20, 119.41, 116.62, 28.53, 25.43, 24.29, 21.81. Minor isomer: 160.50, 153.65, 152.72, 144.70, 139.00, 137.50, 134.56, 133.31, 128.76, 128.08, 126.97, 123.20, 119.41, 116.62, 28.23, 24.29, 21.81, 21.36. EI-MS (*m*/*z*): 386 $[M]^+$; 278 $[M-C_6H_7N_2]^+$. Elemental *Anal.* Calc. for $C_{26}H_{31}N_3$: C, 81.00; H, 8.10; N, 10.90. Found: C, 80.93; H, 8.05; N, 10.91%.

*2.5.5. Synthesis of [2,6-iPr$_2$C$_6$H$_3$–N=C(Ph)–NH–Py]NiBr$_2$ (**1**)*

L1 (358 mg, 1.0 mmol) was dissolved in 40 mL anhydrous dichloromethane under nitrogen atmosphere. (DME)$NiBr_2$ (308 mg, 1.0 mmol) was added under room temperature. The light yellow solution changed into purple quickly, and the solution was stirred for another 12 h. Then the reaction mixture was filtrated and 20 mL hexane was added. After being filtrated from Celite, the solid was washed by hexane (2 × 10 mL). Drying in vacuum, 532 mg of complex **1** was obtained in 92% yields. Decomposition temperature: 289 °C. FAB$^+$-MS: *m*/*z*: 575, 576, 577, 578 $[M]^+$; 495, 496, 497 $[M-Br]^+$; 415, 416, 417 $[M-2Br]^{2+}$; 264, 265 $[L1-C_5H_5N_2]^+$. Elemental *Anal.* Calc. for $C_{24}H_{27}Br_2N_3Ni$: C, 50.05; H, 4.72; N, 7.30. Found: C, 49.72; H, 4.83; N, 7.16%.

*2.5.6. Synthesis of [2,6-iPr$_2$C$_6$H$_3$–N=C(Ph)–NH–(5-NO$_2$–Py)]NiBr$_2$ (**2**)*

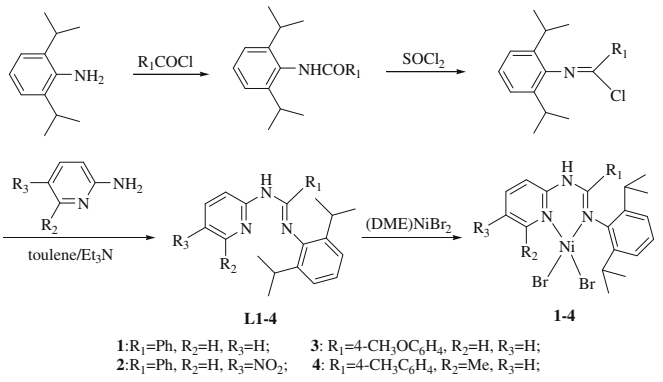
Complex **2** was prepared according to the method described for **1** in 77% yields as brown solid. Decomposition temperature: 277 °C. FAB$^+$-MS: *m*/*z*: 619, 620, 621, 622 $[M]^+$; 539, 541, 542 $[M-Br]^+$; 460, 461, 462 $[M-2Br]^{2+}$; 264, 265 $[L2-C_5H_4N_2O_2]^+$. Elemental *Anal.* Calc. for $C_{24}H_{26}Br_2N_4NiO_2$: C, 46.42; H, 4.22; N, 9.02. Found: C, 46.15; H, 4.13; N, 8.89%.

*2.5.7. Synthesis of [2,6-iPr$_2$C$_6$H$_3$–N=C(4-CH$_3$OC$_6$H$_4$)–NH–Py]NiBr$_2$ (**3**)*

Complex **3** was prepared according to the method described for **1** in 89% yields as purple solid. Decomposition temperature: 302 °C. FAB$^+$-MS: *m*/*z*: 605, 606, 607, 608 $[M]^+$; 525, 526, 527 $[M-Br]^+$; 445, 446, 447 $[M-2Br]^{2+}$; 294, 295 $[L3-C_5H_4N_2]^+$. Elemental *Anal.* Calc. for $C_{25}H_{29}Br_2N_3NiO$: C, 49.55; H, 4.82; N, 6.93. Found: C, 49.34; H, 4.91; N, 6.86%.

*2.5.8. Synthesis of [2,6-iPr$_2$C$_6$H$_3$–N=C(4-CH$_3$C$_6$H$_4$)–NH–(6-CH$_3$–Py)]NiBr$_2$ (**4**)*

Complex **4** was prepared according to the method described for **1** in 76% yields as purple solid. Decomposition temperature: 305 °C. FAB$^+$-MS: *m*/*z*: 603, 604, 605, 606, 607 $[M]^+$; 523, 524, 525, 526 $[M-Br]^+$; 443, 444, 445 $[M-2Br]^{2+}$; 278, 279 $[L4-C_6H_7N_2]^+$. Elemental *Anal.* Calc. for $C_{26}H_{31}Br_2N_3Ni$: C, 51.70; H, 5.17; N, 6.96. Found: C, 51.51; H, 5.34; N, 6.83%.



Scheme 2. Preparation of nickel complexes **1**–**4**.

3. Results and discussion

3.1. Ligand and nickel complex syntheses

Four new 2-pyridylbenzamidine ligands with various steric and electronic substituents were synthesized following a classical route for *N*,*N*-disubstituted amidines [49,50]. The synthetic procedures are outlined in Scheme 2, and the particulars of each step were detailed in the Section 2. Benzamide could be easily available from 2,6-diisopropylaniline and substituted benzoyl chloride in high yield with triethylamine as the precipitator. Imidoyl chloride could be produced by the dehydration reaction between benzamide and excess of thionyl chloride. After distilling the residue of thionyl chloride, the 2-pyridylbenzamidine ligands were obtained by the reaction between the quantitative 2-aminopyridine derivatives and imidoyl chlorides in refluxing toluene. Pure **L1** and **L3** were obtained as light yellow crystals by recrystallization in ethanol, while **L2** and **L4** were purified using silica chromatography and then recrystallized in ethanol. All of these ligands were proved by ^{1}H and ^{13}C NMR, MS and elemental analyses. A single crystal of **L2** grown from ethanol solution also assuredly confirmed the ligand structure.

The nickel complexes **1**–**4** were synthesized by mixing (DME)-$NiBr_2$ and corresponding ligand in anhydrous dichloromethane in high yield. Because of paramagnetism, nickel complexes **1**–**4** were

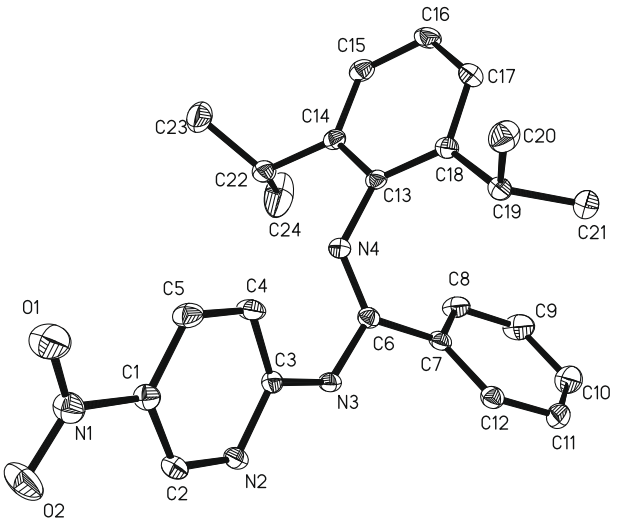


Fig. 1. Molecular structure of **L2** depicted with 30% thermal ellipsoids and with hydrogen atoms omitted. Selected bond lengths (Å): C(3)–N(3) 1.371(2), C(6)–N(3) 1.393(2), C(6)–N(4) 1.276(2), C(13)–N(4) 1.416(2).

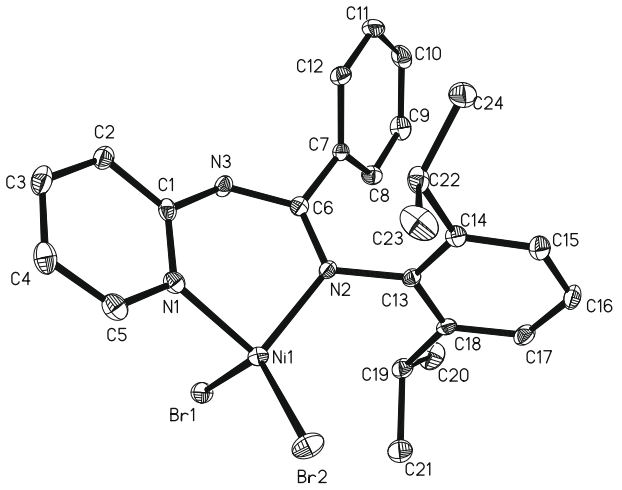


Fig. 2. Molecular structure of **1** depicted with 30% thermal ellipsoids and with hydrogen atoms omitted. Selected bond lengths (Å) and angles (°): C(1)–N(3) 1.402(5), C(6)–N(3) 1.375(4), C(6)–N(2) 1.291(4), C(13)–N(2) 1.449(4), Ni(1)–N(1) 1.985(3), Ni(1)–N(2) 1.974(3), Ni(1)–Br(1) 2.3911(7), Ni(1)–Br(2) 2.3263(7), N(1)–Ni(1)–N(2) 92.6(1), N(1)–Ni(1)–Br(1) 101.21(9), N(1)–Ni(1)–Br(2) 110.30(9), N(2)–Ni(1)–Br(1) 105.14(9), N(2)–Ni(1)–Br(2) 115.22(9), Br(1)–Ni(1)–Br(2) 126.38(3).

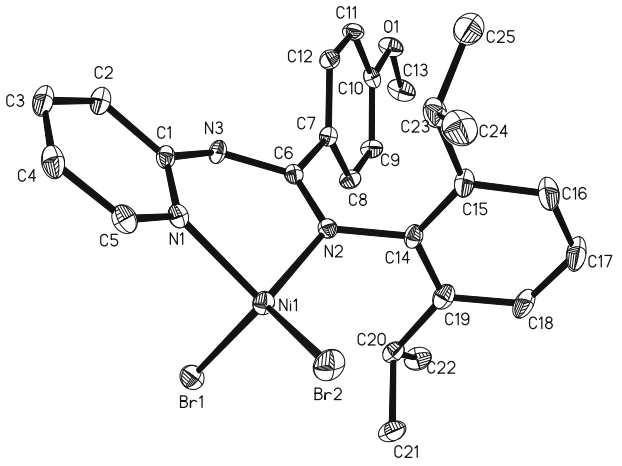


Fig. 3. Molecular structure of **3** depicted with 30% thermal ellipsoids and with hydrogen atoms omitted. Selected bond lengths (Å) and angles (°): C(1)–N(3) 1.397(4), C(6)–N(3) 1.370(4), C(6)–N(2) 1.298(4), C(14)–N(2) 1.453(5), Ni(1)–N(1) 1.984(3), Ni(1)–N(2) 1.968(3), Ni(1)–Br(1) 2.4006(7), Ni(1)–Br(2) 2.3342(7), N(1)–Ni(1)–N(2) 92.7(1), N(1)–Ni(1)–Br(1) 99.90(10), N(1)–Ni(1)–Br(2) 112.70(9), N(2)–Ni(1)–Br(1) 103.89(9), N(2)–Ni(1)–Br(2) 118.01(9), Br(1)–Ni(1)–Br(2) 123.94(3).

not characterized by ^{1}H NMR but were characterized by MS, elemental analysis, and X-ray crystallography.

3.2. Molecular structure

A previous reference [48] reported that the *N*,*N*-phenylpyridylbenzamidine forms a dimer in the solid state which results from the presence of weak inter-molecular hydrogen bond involving the hydrogen atom in the amidine nitrogen atom and the pyridyl groups. In contrast, the X-ray structure of ligand **L2** (Fig. 1) shows that the 2-pyridylbenzamidine ligand exhibits a monomer structure, and adopts *E-syn* rather than *E-anti* geometry. In addition, the bond lengths of N(4)–C(6) and N(3)–C(6) are 1.276(2) and 1.393(2) Å, indicative of double and single bonds, respectively.

Nickel complexes suitable for X-ray diffraction determination were grown from dichloromethane/hexane or tetrahydrofuran/hexane at ambient temperature under a nitrogen atmosphere. ORTEP diagrams are given in Figs. 2–4 along with selected bond

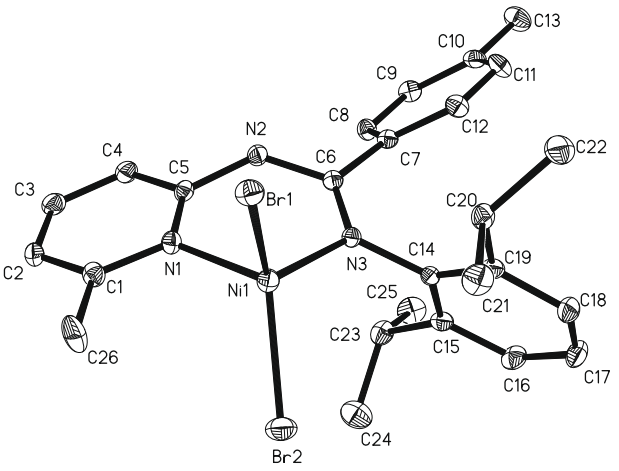


Fig. 4. Molecular structure of **4** depicted with 30% thermal ellipsoids and with hydrogen atoms omitted. Selected bond lengths (Å) and angles (°): C(5)–N(2) 1.399(4), C(6)–N(2) 1.368(3), C(6)–N(3) 1.299(3), C(14)–N(3) 1.458(3), Ni(1)–N(1) 1.997(2), Ni(1)–N(3) 1.989(2), Ni(1)–Br(1) 2.3997(5), Ni(1)–Br(2) 2.3483(5), N(1)–Ni(1)–N(3) 95.8(1), N(1)–Ni(1)–Br(1) 100.79(7), N(3)–Ni(1)–Br(2) 104.98(7), N(3)–Ni(1)–Br(1) 114.28(7), N(3)–Ni(1)–Br(2) 104.98(7), Br(1)–Ni(1)–Br(2) 126.25(1).

lengths and bond angles, respectively. The data collection and structure refinement parameters are summarized in Table 1.

Similar to the β-diimine nickel complexes [36], all of the nickel complexes reveal a distorted tetrahedral geometry around the nickel metal center and the [N,N] six-membered chelating rings exhibit a boat conformation with metal atom. The nickel atom is surrounded by a pyridyl nitrogen atom, an imine N atom, and two terminal Br atoms. In addition, there is no *intra-* or *inter*-molecular hydrogen bonding (Ni···H) between the hydrogen on the amidine nitrogen atom and nickel metal atom. Bearing the similar steric hindrance of ligand, the Ni–$N_{pyridine}$ and Ni–N_{imine} bond lengths of **1** and **3** are nearly the same. In contrast, the Ni–$N_{pyridine}$ and Ni–N_{imine} bond lengths of **4** are 1.997(2) and 1.989(2) Å, respectively, which are longer than those of **1** and **3**. The result indicates that the introduction of methyl on the *ortho* position of pyridyl decreases the bonding ability between pyridine, imine and nickel metal. Moreover, the N–Ni–N bite angles of **1** and **3** are 92.6(1)° and 92.7(1)°, respectively, which are smaller than that of **4** (95.8(1)°), well in accordance with those observed for nickel complexes bearing bulky substituents oriented in a more open environment [46–47,51].

3.3. Ethylene oligmerization

Ethylene oligomerizations were carried out with the nickel complexes in the presence of MAO in order to study their catalytic properties. Initially, toluene was used as the reaction media for ethylene oligomerization, and consumption of ethylene was observed. However, it was surprising that the obtained liquid mixtures were complicated and only small amount of ethylene oligomers was detected by GC–MS (Fig. 5). According to the GC–MS analysis, peak **A** and **B** can be assigned to butene and hexene, respectively, while peaks **C**–**G** can be attributed to alkylated toluene and the collected peaks **H** should be ascribed to ditolylmethanes. The existence of oligomers of ethylene, alkylated toluene and ditolylmethanes in the products means that there are multiple catalytic processes in the system, involving ethylene oligomerization and toluene alkylations by either ethylene or the oligomers by a Friedel–Crafts process [52–55] and disproportionation [56]. Very recently, nickel complexes bearing [N,P] five-membered chelating ring were reported to catalyze reactions with ethylene producing oligomers and alkylated toluene [57].

Table 1
Crystallographic data for **L2**, **1**, **3** and **4**.

Compound	**L2**	**1**	**3**	**4**
Formula	$C_{24}H_{25}N_4O_2$	$C_{24}H_{27}Br_2N_3Ni$	$C_{25}H_{29}Br_2N_3NiO$	$C_{26}H_{31}Br_2N_3Ni$
Formula weight	401.48	576.02	606.04	604.07
Crystal size (mm)	0.12 × 0.09 × 0.01	0.09 × 0.07 × 0.05	0.10 × 0.08 × 0.06	0.10 × 0.08 × 0.05
Crystal system	triclinic	monoclinic	monoclinic	monoclinic
Space group	$P\bar{1}$	$P2(1)/n$	$P2(1)/n$	$P2(1)/n$
a (Å)	8.2857(15)	9.4357(12)	9.3676(12)	9.7549(10)
b (Å)	11.834(2)	18.215(2)	19.349(2)	18.1652(18)
c (Å)	12.549(2)	14.0164(18)	13.9412(19)	14.5490(14)
α (°)	110.520(3)	90	90	90
β (°)	107.437(3)	101.021(3)	98.471(2)	91.968(2)
γ (°)	90.894(3)	90	90	90
Z	2	4	4	4
Volume (Å^3)	1089.4(3)	2364.6(5)	2499.3(6)	2576.6(4)
D_{calc} (g cm^{-3})	1.224	1.618	1.611	1.557
$F(000)$	426	1160	1224	1224
μ (mm^{-1})	0.080	4.216	3.996	3.873
No. of observed reflections	8533	11 162	12 445	12 028
No. of unique reflections	4230	5031	5357	5024
R_{int}	0.0263	0.0347	0.0472	0.0224
Data/parameters	4230/271	5031/271	5357/289	5024/289
Goodness of fit	1.038	1.099	0.986	1.029
R_1/wR_2 ($I > 2\sigma(I)$)	0.0449, 0.1166	0.0344, 0.0760	0.0398, 0.0824	0.0267, 0.0672
R_1/wR_2 (all data)	0.0732, 0.1348	0.0653, 0.0993	0.0805, 0.0975	0.0388, 0.0732

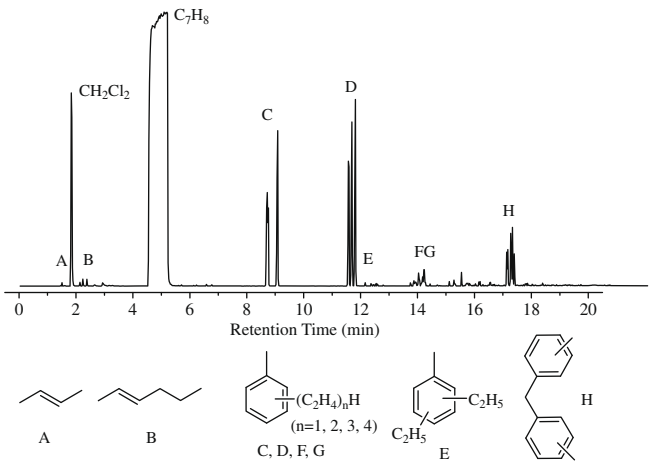


Fig. 5. GC–MS analysis of the products obtained from **2**/MAO in toluene at 0 °C.

In order to obtain the onefold oligomers, dichloromethane was used as solvent instead of toluene and the results of the catalytic reactions are summarized in Table 2. It was shown that four complexes exhibited moderate catalytic activities (TOF *ca.* 10^3–10^4 mol ethylene/mol Ni h). To evaluate the effect of the catalyst structure on TOF, **1**–**4** complexes were screened under the same conditions of T = 20 °C and Al/Ni = 600. In comparison to **1**, **4** with methyl on the *ortho* position of pyridine, and **3** containing electron-donating methoxy on the *para* position of the phenyl exhibited a lower TOF. Meanwhile, **2** containing electron-withdrawing nitro group on the *meso* position of pyridine showed the highest TOF up to 10.5 × 10^3 mol ethylene/(mol Ni h). A reasonable explanation for the TOF enhancement is that the introduction of an electron-withdrawing group would generate a more electrophilic nickel center, resulting in reduction of activation energy for ethylene insertion and favoring ethylene monomer coordination and insertion [9,58].

Furthermore, the structure of the complexes also affects the distribution of oligomers. GC–MS analyses confirmed that the oligomers obtained by **1**, **3** and **4**/MAO at 20 °C mainly contained butene and hexene. Besides butene and hexene, the products obtained by **2**/MAO also contained higher oligomers such as octene and decene (Fig. 6).

Compared with other nickel complexes with [N,N] six-membered chelating ring, it revealed that complexes **1**–**4** show higher

Table 2
The data of ethylene oligomerizations with **1**–**4**/MAO in CH_2Cl_2.

Run	Complex	Al/Ni	T (°C)	TOF[a]	Distribution of oligomers (mol%)			
					C4	C6	C8	C10
1	**1**	600	20	4.5	55.7	44.3	–[b]	–
2	**2**	600	20	10.5	31.8	38.7	25.4	4.1
3	**3**	600	20	2.3	76.2	23.8	–	–
4	**4**	600	20	3.6	69.6	20.4	–	–
5	**2**	600	−10	3.2	17.8	26.3	46.2	9.7
6	**2**	600	0	7.9	19.9	30.1	42.4	7.6
7	**2**	400	20	8.1	34.7	42.5	15.6	7.2
8	**2**	800	20	11.7	28.3	34.9	27.7	9.1
9	**2**	1200	20	9.8	35.6	49.2	12.0	3.2
10[c]	**1**–**4**	600	0	2.1–5.6	alkylated toluene and ditolylmethanes			

Reaction conditions: Ni complex, 5 μmol; t_p, 0.5 h; CH_2Cl_2, 20 mL; ethylene pressure, 0.5 atm.
[a] 10^3 mol ethylene/(mol Ni h).
[b] Not detected or in trace.
[c] Toluene was used instead of CH_2Cl_2 as solvent.

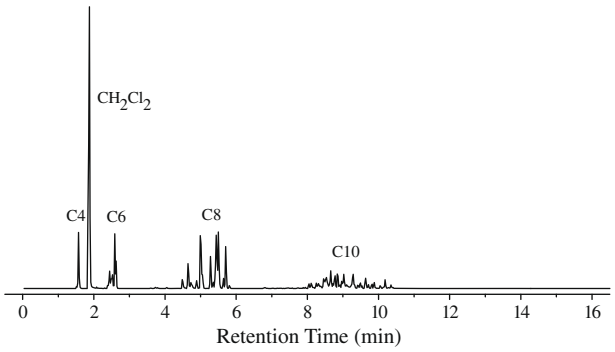


Fig. 6. GC–MS analysis of ethylene oligomers obtained by **2**/MAO in CH_2Cl_2 at 0 °C (run 6 in Table 2).

activity than that of quinolylimine nickel complex(III) [45]. It is supposed that the hydrogen atom on the amidine nitrogen may lose in the presence of MAO. In this case, the neutral amidine ligand transfers to anionic ligand, resulting in a stronger strength of the Ni–N_{imine} bond. As a result, it may stabilize the transition state for ethylene insertion, and increase the activity of the ethylene oliogmerization [26,19,40]. However, they are one or two orders of magnitude lower than those of β-pyridylimine(IV) [46] and dipyridylamine(V) nickel complexes [47]. Moreover, the carbon lengths of oligomers produced by **1**–**4**/MAO are shorter than those by dipyridylamine(V) nickel complexes. Considering the hydrogen atom on the amidine nitrogen atom is being replaced by one bulky alkyl substituent in dipyridylamine(V) nickel complexes, there is increased steric hindrance in the axial position in the dipyridylamine(V) nickel complexes, which could protect the active species, thus enhancing the catalytic activity and obtaining higher oligomers in the process of oligomerizaion.

To test the role of reaction parameters in catalytic properties, further studies were performed with **2**/MAO system as the representative. The reaction temperature greatly influenced the TOF. With an increase in the reaction temperature from −10 to 20 °C, the TOF increased consistently. Meanwhile, the distribution of oligomers changed with the increase of temperature. In general, increasing temperature led to a decrease in the proportions of higher oligomers, which suggested that the process of β-H elimination accelerates in ethylene oligomerization at high temperature.

Besides, the amount of cocatalyst also influenced the catalytic performances. The enhancement of Al/Ni molar ratio from 400 to 800 resulted in an increase of TOF up to 11.7×10^3 mol ethylene/(mol Ni h). However, a further increase of the Al/Ni molar ratio showed a slightly negative effect on TOF. The oligomers were confirmed as olefins, and no alkanes were observed, which indicated that the termination of propagation chain is via β-H elimination rather than transferring to MAO.

4. Conclusion

Four 2-pyridylbenzamidine nickel complexes with different steric and electronic substituents (**1**–**4**) have been synthesized and characterized. The solid state structures of **1**, **2** and **4** confirmed that the nickel complexes adopt distorted tetrahedral geometry, forming a six-membered chelating ring. All of these nickel complexes showed a moderate TOF for ethylene oligomerization after activated with MAO. The solvent had a great influence on products of the catalytic reactions. In toluene, ethylene oligomers, alkylated toluene and ditolylmethanes were detected. In contrast, only ethylene oligomers were obtained in dichloromethane. Moreover, the catalyst structure showed important effects on TOF and distribution of oligomers. Bearing an electron-withdrawing substituent, complex **2** exhibited the highest TOF and obtained higher order oligomers. Besides, the reaction temperature and Al/Ni molar ratio also proved to affect the catalytic properties.

Supplementary data

CCDC 713921, 713922, 713923 and 713924 contains the supplementary crystallographic data for **L2**, **1**, **3** and **4**, respectively. These data can be obtained free of charge via http://www.ccdc.cam.ac.uk/conts/retrieving.html, or from the Cambridge Crystallographic Data Centre, 12 Union Road, Cambridge CB2 1EZ, UK; fax: (+44) 1223-336-033; or e-mail: deposit@ccdc.cam.ac.uk.

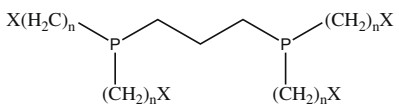
Acknowledgments

The financial Supports by NSFC (Projects 20604034, 20674097 and 20734004), the Science Foundation of Guangdong Province (Project 8251027501000018 and 06300069) and the Ministry of Education of China (Foundation for Ph.D. Training) are gratefully acknowledged.

References

[1] S.D. Ittel, L.K. Johnson, M. Brookhart, Chem. Rev. 100 (2000) 1169.
[2] V.C. Gibson, S.K. Spitzmesser, Chem. Rev. 103 (2003) 283.
[3] W. Keim, F.H. Kowaldt, R. Goddard, C. Krüger, Angew. Chem., Int. Ed. Engl. 17 (1978) 466.
[4] W. Keim, A. Behr, B. Limbäcker, C. Krüger, Angew. Chem., Int. Ed. Engl. 22 (1983) 503.
[5] W. Keim, Angew. Chem., Int. Ed. Engl. 29 (1990) 235.
[6] A. Kermagoret, P.J. Braunstein, Dalton Trans. (2008) 822.
[7] L.K. Johnson, C.M. Killian, M. Brookhart, J. Am. Chem. Soc. 117 (1995) 6414.
[8] C.M. Killian, L.K. Johnson, M. Brookhart, Organometallics 16 (1997) 2005.
[9] D.P. Gates, S.A. Svejda, E. Onate, C.M. Killian, L.K. Johnson, P.S. White, M. Brookhart, Macromolecules 33 (2000) 2320.
[10] D. Meinhard, M. Wegner, G. Kipiani, A. Hearley, P. Reuter, S. Fischer, O. Marti, B. Rieger, J. Am. Chem. Soc. 129 (2007) 9182.
[11] C. Bianchini, G. Giambastiani, I.G. Rios, G. Mantovani, A. Meli, A.M. Segrra, Coord. Chem. Rev. 250 (2006) 1391.
[12] V.C. Gibson, C. Redshaw, G.A. Solan, Chem. Rev. 107 (2007) 1745.
[13] E. Nelkenbaum, M. Kapon, M.S. Eisen, J. Organomet. Chem. 690 (2005) 2297.
[14] E. Nelkenbaum, M. Kapon, M.S. Eisen, J. Organomet. Chem. 690 (2005) 3154.
[15] E. Nelkenbaum, M. Kapon, M.S. Eisen, Organometallics 24 (2005) 2645.
[16] B.Y. Lee, X. Bu, G.C. Bazan, Organometallics 20 (2001) 5425.
[17] X. Tang, W-H. Sun, T. Gao, J. Hou, J. Chen, W. Chen, J. Organomet. Chem. 690 (2005) 1570.
[18] J.M. Benito, E. De Jesús, F.J. de la Mata, J.C. Flores, F. Gómez, P. Gómez-Sal, Organometallics 25 (2006) 3876.
[19] Z. Huang, K. Song, F. Liu, J. Long, H. Hu, H. Gao, Q. Wu, J. Polym. Sci., Part A: Polym. Chem. 46 (2008) 1618.
[20] T.R. Younkin, E.F. Connor, J.I. Henderson, S.K. Friedrich, R.H. Grubbs, D.A. Banselen, Science 287 (2000) 460.
[21] D. Zhang, G.X. Jin, L.H. Weng, F. Wang, Organometallics 23 (2004) 3270.
[22] J.C. Jenkins, M. Brookhart, Organometallics 22 (2003) 250.
[23] I. Göttker-Schnetmann, P. Wehrmann, C. Röhr, S. Mecking, Organometallics 26 (2007) 2348.
[24] S. Yu, A. Berkefeld, I. Göttker-Schnetmann, G. Mü1ller, S. Mecking, Macromolecules 40 (2007) 421.
[25] P. Wehrmann, S. Mecking, Organometallics 27 (2008) 1399.
[26] W-H. Sun, W. Zhang, T. Gao, X. Tang, L. Chen, Y. Li, X. Jin, J. Organomet. Chem. 689 (2004) 917.
[27] E.K. Beuken, W.J. Smeets, A.L. Spek, B.L. Feringa, Chem. Commun. (1998) 223.
[28] M.J. Rachita, R.L. Huff, J.L. Bennett, M. Brookhart, J. Polym. Sci., Part A: Polym. Chem. 43 (2004) 4627.
[29] O. Daugulis, M. Brookhart, Organometallics 21 (2002) 5926.
[30] F. Speiser, P. Braunstein, L. Saussine, Acc. Chem. Res. 38 (2005) 784.
[31] Z. Weng, S. Teo, T.S.A. Hor, Organometallics 25 (2006) 4878.
[32] N.A. Cooley, S.M. Green, D.F. Wass, Organometallics 20 (2001) 4769.
[33] J. Stephen, S.J. Dossett, A. Gillon, A.G. Orpen, J.S. Fleming, P.G. Pringle, D.F. Wass, M.D. Jones, Chem. Commun. (2001) 699.
[34] C. Bianchini, L. Gonsalvi, W. Oberhauser, D. Sémeril, P. Brüggeller, R. Gutmann, Dalton Trans. (2003) 3869.
[35] J.N.L. Dennett, A.L. Gillon, K. Heslop, D.J. Hyett, J.S. Fleming, C.E. Lloyd-Jones, A.G. Orpen, P.G. Pringle, D.F. Wass, Organometallics 23 (2004) 6077.
[36] J. Feldman, S.J. Mclain, A. Parthasarathy, W.J. Marshall, J.C. Calabrese, S.D. Arthur, Organometallics 16 (1997) 1514.
[37] H.L. Wiencko, E. Kogut, T.H. Warren, Inorg. Chim. Acta 345 (2003) 199.
[38] M.-S. Zhou, S.-P. Huang, L.-H. Weng, W.-H. Sun, D.-S. Liu, J. Organomet. Chem. 665 (2003) 237.

[39] E. Kogut, A. Zeller, T.H. Warren, T.J. Strassner, J. Am. Chem. Soc. 126 (2004) 11984.
[40] J. Zhang, Z. Ke, F. Bao, J. Long, H. Gao, F. Zhu, Q. Wu, J. Mol. Catal. A: Chem. 249 (2006) 31.
[41] Y. Li, L. Jiang, L. Wang, H. Gao, F. Zhu, Q. Wu, Appl. Organomet. Chem. 20 (2006) 181.
[42] Y. Li, L. Wang, H. Gao, F. Zhu, Q. Wu, Appl. Organomet. Chem. 20 (2006) 436.
[43] H. Gao, W. Guo, F. Bao, G. Gui, J. Zhang, F. Zhu, Q. Wu, Organometallics 23 (2004) 6273.
[44] H. Gao, Z. Ke, L. Pei, K. Song, Q. Wu, Polymer 48 (2007) 7249.
[45] G.J.P. Britovsek, S.P.D. Baugh, O. Hoarau, V.C. Gibson, D.F. Wass, A.J.P. White, D.J. Williams, Inorg. Chim. Acta 345 (2003) 279.
[46] L. Wang, C. Zhang, Z. Wang, Eur. J. Inorg. Chem. (2007) 2477.
[47] T. Schareina, G. Hillebrand, H. Fuhrmann, R. Kempe, Eur. J. Inorg. Chem. (2001) 2421.
[48] F.A. Cotton, P. Lei, C.A. Murillo, L.-S. Wang, Inorg. Chim. Acta 349 (2003) 165.
[49] R.T. Boeré, V. Klassen, G. Wolmershäuser, Dalton Trans. (1998) 4147.
[50] A. Xia, H.M. El-Kaderi, M.J. Heeg, C.H. Winter, J. Organomet. Chem. 682 (2003) 224.
[51] R.J. Butcher, E. Sinn, Inorg. Chem. 16 (1997) 2334.
[52] K.D. Black, F.D. Gunstone, Chem. Phys. Lipids 79 (1996) 79.
[53] C. Perego, P. Ingallina, Catal. Today 73 (2002) 3.
[54] R.J. Davis, J. Catal. 216 (2003) 396.
[55] L. Xiao, K.E. Johnson, R.G. Treble, J. Mol. Catal. A: Chem. 214 (2004) 121.
[56] S. Svelle, K. Lillerud, S. Kolboe, M. BjØrgen, J. Am. Chem. Soc. 128 (2006) 5618.
[57] P.W. Dyer, J. Fawcett, M.J. Hanton, Organometallics 27 (2008) 6273.
[58] C. Carlini, A. Macinai, F. Masi, A.M.R. Galletti, R. Santi, G. Sbrana, A. Sommazzi, J. Polym. Sci., Part A: Polym. Chem. 42 (2004) 2534.



n= 6 X=OH
n=2-6,8 X=P(O)(OEt)$_2$
n=3 X=NH$_3$

L

2. Experimental

2.1. Materials

All experiments were carried out under an atmosphere of argon, unless otherwise stated. Solvents were dried by standard methods and distilled under nitrogen prior to use. Palladium(II) acetate and allylamine were purchased from Across and Fluka, respectively. The diprimary phosphine $H_2P(CH_2)_3PH_2$ was prepared according to reported procedures [15]. The alkenyl phosphonates $CH_2{=}CH{-}(CH_2)_n{-}P(O)(OEt)_2$ were obtained either from commercial suppliers (n = 0, 1) or prepared by literature methods (n = 2–4, 6) [16,17]. The synthesis and the physical characterization of the ligand 1,3-bis[di(6-hydroxyhexyl)phosphino]propane (**a**) and the complex *cis*-[Pd(**a**)(OAc)$_2$] (**1**) have been described previously [12] and the X-ray structure of **1** is report herein for the first time.

2.2. Instrumentation

Elemental analyses were carried out with an Elementar Vario El analyzer. The NMR measurements were obtained using a Bruker DRX 250 at 20 °C using $CDCl_3$ as the solvent. ^{1}H (250.13 MHz) and $^{13}C\{^1H\}$ (62.9 MHz) NMR chemical shifts are reported in ppm downfield from the external standard TMS. $^{31}P\{^1H\}$ spectra were measured relative to 85% H_3PO_4. Mass spectra were acquired by a Finnigan MAT 711A instrument modified by AMD and reported as mass/charge (m/z). The IR spectra were recorded on a Bruker IFS 48 FTIR spectrometer.

2.3. General procedure for the preparation of the diphosphines (*L*)

In a quartz Schlenk tube 1,3-diphosphinopropane (600 mg, 5.55 mmol) and an excess amount of the corresponding olefin were magnetically stirred, and the resultant mixture was irradiated with the ultraviolet light of a mercury high pressure lamp at 20 °C. After 10 h, the excess olefin was removed under reduced pressure. Further purification was not necessary.

2.3.1. 1,3-Bis[bis(2-diethylphosphonatoethyl)phosphino]propane (*b*)

Yield: 4.0 g (95%). *Anal.* Calc. for $C_{27}H_{62}O_{12}P_6$: C, 42.41; H, 8.17. Found: C, 42.06; H, 8.51%. ^{1}H NMR ($CDCl_3$): δ 1.27 (t, $^3J_{HH}$ = 7.1 Hz, 24H, $PO(OCH_2CH_3)_2$), 1.45–1.90 (m, 22H, $(CH_2)_n$, H1, H2, H3), 4.01–4.07 (m, 16H, $PO(OCH_2CH_3)_2$). $^{13}C\{^1H\}$ NMR ($CDCl_3$): δ 16.8 (d, $^3J_{PC}$ = 6.1 Hz, CH_3CH_2O), 18.95 (dd, $^1J_{PC}$ = 16.2, $^2J_{PC}$ = 6.7 Hz, $O{=}PCH_2CH_2P$), 22.0 (dd, $^1J_{PC}$ = 140.5, $^2J_{PC}$ = 13.8 Hz, $O{=}PCH_2CH_2P$), 22.7 (s, CH_2CH_2P), 28.6 (*N* [18] = 26.3 Hz, CH_2P), 62.0 (d, $^2J_{PC}$ = 6.7 Hz, CH_3CH_2O). $^{31}P\{^1H\}$ NMR ($CDCl_3$): δ −22.0 (t, $^3J_{PP}$ = 51.2 Hz, 2P, *P*1), 32.3 (d, $^3J_{PP}$ = 51.2 Hz, 4P, $PO(OCH_2CH_3)_2$). IR (KBr, cm^{-1}): ν 2981, 2934, 2908 (CH_2), 1240 (P=O), 1028 (P–OEt). MS (FAB, 50 °C): m/z 765.3 $[M+H]^+$.

2.3.2. 1,3-Bis[bis(3-diethylphosphonatopropyl)phosphino]propane (*c*)

Yield: 4.3 g (95%). *Anal.* Calc. for $C_{31}H_{70}O_{12}P_6$: C, 45.37; H, 8.60. Found: C, 45.05; H, 8.86%. ^{1}H NMR ($CDCl_3$): δ 1.26 (t, $^3J_{HH}$ = 7.1 Hz, 24H, $PO(OCH_2CH_3)_2$), 1.4–1.8 (m, 30H, $(CH_2)_n$, H1, H2, H3), 3.96–4.05 (m, 16H, $PO(OCH_2CH_3)_2$). $^{13}C\{^1H\}$ NMR ($CDCl_3$): δ 16.8 (d, $^3J_{PC}$ = 6.1 Hz, CH_3–CH_2O), 19.52 (dd, $^1J_{PC}$ = 15.5, $^3J_{PC}$ = 4.7 Hz, $O{=}P(CH_2)_2CH_2P$), 27.5 (dd, $^1J_{PC}$ = 139.8, $^3J_{PC}$ = 11.8 Hz, $O{=}PCH_2(CH_2)_2P$), 28.0–28.6 (m, $CH_2CH_2PCH_2CH_2CH_2P{=}O$), 29.1 (*N* [18] = 21.6 Hz, CH_2P), 61.7 (d, $^2J_{PC}$ = 6.7 Hz, CH_3CH_2O). $^{31}P\{^1H\}$ NMR ($CDCl_3$): δ −32.0 (s, 2P, *P*1), 32.4 (s, 4P, $PO(OCH_2CH_3)_2$). IR (KBr, cm^{-1}): ν 2981, 2932, 2907 (CH_2), 1236 (P=O), 1029 (P–OEt). MS (FAB, 50 °C): m/z 821.2 $[M+H]^+$.

2.3.3. 1,3-Bis[bis(4-diethylphosphonatobutyl)phosphino]propane (*d*)

Yield: 4.7 g (97%). *Anal.* Calc. for $C_{31}H_{70}O_{12}P_6$: C, 47.94; H, 8.97. Found: C, 47.62; H, 9.40%. ^{1}H NMR (CD_3OD): δ 1.26 (t, $^3J_{HH}$ = 7.1 Hz, 24H, $PO(OCH_2CH_3)_2$), 1.4–1.8 (m, 38H, $(CH_2)_n$, H1, H2, H3), 3.96–4.09 (m, 16H, $PO(OCH_2CH_3)_2$). $^{13}C\{^1H\}$ NMR (CD_3OD): δ 17.0 (d, $^3J_{PC}$ = 6.1 Hz, CH_3CH_2O), 23.9 (s, CH_2CH_2P), 25.2 (dd, $^1J_{PC}$ = 11.8, $^4J_{PC}$ = 5.1 Hz, $O{=}P{-}(CH_2)_3CH_2P$), 26.8 (d, $^1J_{PC}$ = 140.1 Hz, $O{=}PCH_2(CH_2)_3P$), 27.6–27.8 (m, $O{=}PCH_2CH_2{-}(CH_2)_2P$), 27.9–28.0 (m, $O{=}P(CH_2)_2CH_2CH_2P$), 30.1 (*N* [18] = 22.9 Hz, CH_2P), 60.5 (d, $^2J_{PC}$ = 6.1 Hz, CH_3CH_2O). $^{31}P\{^1H\}$ NMR (CD_3OD): δ −33.2 (s, 2P, *P*1), 33.0 (s, 4P, $(PO(OCH_2CH_3)_2$). IR (KBr, cm^{-1}): 2981, 2934, 2907, 2872 (CH_2), 1246 (P=O), 1053 (P–OEt). MS (FAB, 50 °C): m/z 877.2 $[M+H]^+$.

2.3.4. 1,3-Bis[bis(5-diethylphosphonatopentyl)phosphino]propane (*e*)

Yield: 5.07 g (98%). *Anal.* Calc. for $C_{39}H_{86}O_{12}P_6$: C, 50.21; H, 9.29. Found: C, 49.80; H, 9.19%. ^{1}H NMR ($CDCl_3$): δ 1.03 (t, $^3J_{HH}$ = 7.1 Hz, 24H, $PO(OCH_2CH_3)_2$), 1.1–1.5 (m, 46H, $(CH_2)_n$, H1, H2, H3), 3.69–3.8 (m, 16H, $PO(OCH_2CH_3)_2$). $^{13}C\{^1H\}$ NMR ($CDCl_3$): δ 15.9 (d, $^3J_{PC}$ = 6.1 Hz, CH_3CH_2O), 21.5–21.6 (m, $CH_2CH_2P((CH_2)_3CH_2CH_2)_2$), 24.8 (dd, $^1J_{PC}$ = 13.5, $^5J_{PC}$ = 6.7 Hz; $O{=}P(CH_2)_4CH_2P$), 24.9 (d, $^1J_{PC}$ = 140.1 Hz, $O{=}PCH_2(CH_2)_4P$), 26.4 (d, $^2J_{PC}$ = 12.1, $O{=}P(CH_2)_3CH_2CH_2P$), 31.4–31.8 (m, $CH_2CH_2P((CH_2)_2CH_2(CH_2)_2)_2$), 60.8 (d, $^2J_{PC}$ = 6.1 Hz, CH_3CH_2O). $^{31}P\{^1H\}$ NMR ($CDCl_3$): δ *−30.7* (s, 2P, *P*1), 33.3 (s, 4P, $PO(OCH_2CH_3)_2$). IR (KBr, cm^{-1}): ν 2981, 2934, 2907, 2869 (CH_2), 1244 (P=O), 1053 (P–OEt). MS (FAB, 50 °C): m/z 933.2 $[M+H]^+$.

2.3.5. 1,3-Bis[bis(6-diethylphosphonatohexyl)phosphino]propane (*f*)

Yield: 5.4 g (99%). *Anal.* Calc. for $C_{31}H_{70}O_{12}P_6$: C, 52.22; H, 9.58. Found: C, 51.76; H, 9.69%. ^{1}H NMR ($CDCl_3$): δ 1.45–1.52 (m, 24H, $PO(OCH_2CH_3)_2$), 1.6–1.9 (m, 54H, $(CH_2)_n$, H1, H2, H3), 4.16–4.27 (m, 16H, $PO(OCH_2CH_3)_2$). $^{13}C\{^1H\}$ NMR ($CDCl_3$): δ 16.8 (d, $^3J_{PC}$ = 6.1 Hz, CH_3CH_2O), 22.49–22.91 (m, $CH_2CH_2P((CH_2)_4$-$CH_2CH_2)_2$), 25.9 (d, $^1J_{PC}$ = 140.1 Hz, $O{=}PCH_2(CH_2)_5P$), 26.03 (d, $^1J_{PC}$ = 12.1 Hz, $O{=}P(CH_2)_5CH_2P$), 27.4 (d, $^2J_{PC}$ = 10.8 Hz, $O{=}P(CH_2)_4CH_2CH_2P$), 30.7 (d, $^3J_{PC}$ = 16.8 Hz, $O{=}P(CH_2)_3CH_2$-$(CH_2)_2P$), 31.1–31.4 (m, $CH_2CH_2P((CH_2)_3CH_2(CH_2)_2)_2$), 61.7 (d, $^2J_{PC}$ = 6.1 Hz, CH_3CH_2O). $^{31}P\{^1H\}$ NMR ($CDCl_3$): δ *−30.3* (s, 2P, *P*1), 33.6 (s, 4P, $PO(OCH_2CH_3)_2$). IR (KBr, cm^{-1}): ν 2980, 2930, 2907, 2864 (CH_2), 1241 (P=O), 1024 (P–OEt). MS (FAB, 50 °C): m/z 989.5 $[M+H]^+$.

2.3.6. 1,3-Bis[bis(8-diethylphosphonatooctyl)phosphino]propane (*g*)

Yield: 5.9 g (97%). *Anal.* Calc. for $C_{31}H_{70}O_{12}P_6$: C, 55.62; H, 10.07. Found: C, 55.11; H, 9.59%. ^{1}H NMR ($CDCl_3$): δ 3.8–3.9 (m, 16H, $PO(OCH_2CH_3)_2$). $^{13}C\{^1H\}$ NMR ($CDCl_3$): δ 16.7 (d, $^3J_{PC}$ = 6.1 Hz, CH_3CH_2O), 22.4–22.6 (m, $CH_2CH_2P((CH_2)_6CH_2CH_2)_2$), 25.8 (d, $^1J_{PC}$ = 140.1 Hz, $O{=}PCH_2(CH_2)_7P$), 26.1 (d, $^1J_{PC}$ = 12.1 Hz, $O{=}P(CH_2)_7CH_2P$), 27.36 (d, $O{=}P(CH_2)_2CH_2(CH_2)_5P$), 28.69–29.6 (m, $O{=}P(CH_2)_5CH_2CH_2CH_2P$), 30.7 (d, $^4J_{PC}$ = 16.84 Hz, $O{=}P(CH_2)_3CH_2(CH_2)_4P$), 31.3–31.7 (m, $CH_2CH_2P((CH_2)_3CH_2$-$(CH_2)_4)_2$), 61.5 (d, $^2J_{PC}$ = 6.1 Hz, CH_3CH_2O). $^{31}P\{^1H\}$ NMR ($CDCl_3$): δ

−30.6 (s, 2P, *P*1), 33.6 (s, 4P, *P*O(OCH_2CH_3)$_2$). IR (KBr, cm^{-1}): *v* 2980, 2926, 2854 (CH_2), 1248 (P=O), 1030 (P–OEt). MS (FAB, 50 °C): *m*/*z* 1101.4 $[M+H]^+$.

*2.3.7. 1,3-Bis[bis(3-aminopropyl)phosphino]propane (**h**)*

Yield: 1.77 g (95%). *Anal.* Calc. for $C_{15}H_{38}N_4P_2$: C, 53.55; H, 11.38; N, 16.65. Found: C, 53.18; H, 11.69; N, 16.10%. ^1H NMR ($CDCl_3$): δ 0.85–1.13 (m, 22H, $(CH_2)_n$, H1, H2, H3), 2.25–2.32 (m, $CH_2CH_2P((CH_2)_2CH_2NH_2)_2$). $^{13}C\{^1H\}$ NMR ($CDCl_3$): δ 24.9 (t, $^2J_{PC}$ = 13,81 Hz, CH_2CH_2P), 26.7 (d, $^1J_{PC}$ = 12.1 Hz, $CH_2CH_2P(CH_2(CH_2)_2NH_2)_2$), 31.6 (*N* [18] = 23.6 Hz, CH_2CH_2P), 32.4 (d, $^2J_{PC}$ = 12.1 Hz, $CH_2CH_2P(CH_2CH_2CH_2NH_2)_2$), 46.02 (d, $^3J_{PC}$ = 11.45 Hz, $CH_2CH_2P((CH_2)_2CH_2NH_2)_2$). $^{31}P\{^1H\}$ NMR ($CDCl_3$): δ −30.2 (s). IR (KBr, cm^{-1}): *v* 3355, 3278 (NH), 2923, 2854 (CH_2), 1072 (C–N). MS (FAB, 50 °C): *m*/*z* 337.3 $[M+H]^+$.

2.4. General procedure for the preparation of the palladium(II) complexes **1**–**8**

Palladium(II) acetate (363 mg, 0.475 mmol) in 50 ml of acetonitrile was added to a solution of **L** (0.475 mmol) in 50 ml of dichloromethane at 25 °C. After stirring for 5 min, the solvents were removed under reduced pressure. Finally the orange oil complexes **1**–**8** were precipitated from dichloromethane with *n*-hexane and dried in vacuum.

*2.4.1. cis-[Pd(b)(OAc)$_2$] (**2**)*

Yield: 0.399 g (85%). *Anal.* Calc. for $C_{31}H_{68}O_{16}P_6Pd$: C, 37.64; H, 6.93. Found: C, 37.26; H, 6.81%. ^1H NMR ($CDCl_3$): δ 1.22–1.33 (m, 24H, PO(OCH_2CH_3)$_2$), 1.5–2.6 (m, 28H, $(CH_2)_n$, H1, H2, H3), 3.99–4.1 (m, 16H, PO(OCH_2CH_3)$_2$). $^{13}C\{^1H\}$ NMR ($CDCl_3$): δ 16.8 (d, $^3J_{PC}$ = 6.1 Hz, CH_3CH_2O), 19.9–20.1 (m, O=PCH$_2$–CH_2P), 20.7 (d, $^1J_{PC}$ = 140.8, O=PCH_2CH_2P), 21.1 (s, CH_2CH_2P), 23.8 (s, $CH_3CO_2^-$), 30.3 (*s*, CH_2P), 62.4–62.7 (m, CH_3CH_2O), 177.3 (s, $CH_3CO_2^-$). $^{31}P\{^1H\}$ NMR ($CDCl_3$): δ 22.1 (A – part of an $AX_2A'X'_2$ spin pattern, 2P, *P*1), 30.0 (X – part of an $AX_2A'X'_2$ spin pattern, 4P, *P*O(OCH_2CH_3)$_2$). IR (KBr, cm^{-1}): *v* 2982, 2931, 2908 (CH_2), 1238 (P=O), 1028 (P–OEt), v_s 1403 ($CH_3CO_2^-$), v_{as} 1576 ($CH_3CO_2^-$). MS (FAB, 50 °C): *m*/*z* 929.0 $[M-OAc]^+$.

*2.4.2. cis-[Pd(c)(OAc)$_2$] (**3**)*

Yield: 0.416 g (84%). *Anal.* Calc. for $C_{35}H_{76}O_{16}P_6Pd$: C, 40.22; H, 7.33. Found: C, 39.77; H, 7.76%. ^1H NMR ($CDCl_3$): δ 1.26 (m, 24H, PO(OCH_2CH_3)$_2$), 1.6–2.1 (m, 30H, $(CH_2)_n$, H1, H2, H3), 3.96–4.1 (m, 16H, PO(OCH_2CH_3)$_2$).$^{13}C\{^1H\}$ NMR ($CDCl_3$): δ 16.8 (d, $^3J_{PC}$ = 6.1 Hz, CH_3CH_2O), 18.1 (d, $^3J_{PC}$ = 5.4 Hz, O=P–$CH_2CH_2CH_2$P), 19.4 (s, CH_2CH_2P), 23.9 (s, $CH_3CO_2^-$), 25.4–26.2 (m, $CH_2CH_2PCH_2$–CH_2CH_2P=O), 26.7 (d, $^1J_{PC}$ = 139.8 Hz, O=P$CH_2CH_2CH_2$P), 27.6–27.8 (m, CH_2P), 62.0 (m, CH_3CH_2O), 177.3 (s, $CH_3CO_2^-$). $^{31}P\{^1H\}$ NMR ($CDCl_3$): δ 14.3 (s, 2P, *P*1), 31.7 (s, 4P, *P*O(OCH_2CH_3)$_2$). IR (KBr, cm^{-1}): *v* 2984, 2932, 2908 (CH_2), 1238 (P=O), 1028 (P–OEt), v_s 1403 ($CH_3CO_2^-$), v_{as} 1576 ($CH_3CO_2^-$). MS (FAB, 50 °C): *m*/*z* 985.2 $[M-OAc]^+$.

*2.4.3. cis-[Pd(d)(OAc)$_2$] (**4**)*

Yield: 0.454 g (87%). *Anal.* Calc. for $C_{39}H_{84}O_{16}P_6Pd$: C, 42.53; H, 7.69. Found: C, 42.15; H, 7.62%. ^1H NMR ($CDCl_3$): δ 1.26 (t, $^3J_{HH}$ = 7.1 Hz, 24H, PO(OCH_2CH_3)$_2$). 1.48–2.0 (m, 36H, $(CH_2)_n$, H1, H2, H3), 3.95–4.07 (m, 16H, PO(OCH_2CH_3)$_2$). $^{13}C\{^1H\}$ NMR ($CDCl_3$): δ 16.8 (d, $^3J_{PC}$ = 6.1 Hz, CH_3CH_2O), 19.7 (s, CH_2CH_2P), 23.8 (s, $CH_3CO_2^-$), 24.2–24.5 (m, O=PCH$_2$CH$_2$CH$_2$CH$_2$P), 25.2 (d, $^1J_{PC}$ = 140.8 Hz, O=P$CH_2(CH_2)_3$P), 25.4 (N [18] = 22.2 Hz, O=P$(CH_2)_3CH_2$P), 25.5 (s, O=PCH$_2$CH$_2$CH$_2$–CH$_2$P), 32.1 (*s*, CH_2P), 62.0 (m, CH_3CH_2O), 177.3 (s, $CH_3CO_2^-$). $^{31}P\{^1H\}$ NMR ($CDCl_3$): δ 15.3 (s, 2P, *P*1), 32.5 (s, 4P, *P*O(OCH_2CH_3)$_2$). IR (KBr, cm^{-1}): *v* 2983, 2931, 2908 (CH_2), 1252 (P=O), 1031 (P–OEt), v_s 1402 ($CH_3CO_2^-$), v_{as} 1577 ($CH_3CO_2^-$). MS (FAB, 50 °C): *m*/*z* 1041.2 $[M-OAc]^+$.

*2.4.4. cis-[Pd(e)(OAc)$_2$] (**5**)*

Yield: 0.45 g (82%). *Anal.* Calc. for $C_{43}H_{92}O_{16}P_6Pd$: C, 44.62; H, 8.01. Found: C, 44.23; H, 8.49%. ^1H NMR (CD_3CN): δ 1.45 (t, $^3J_{HH}$ = 7.1 Hz, 24H, PO(OCH_2CH_3)$_2$). 1.7–2.3 (m, 52H, $(CH_2)_n$, H1, H2, H3), 4.2–4.3 (m, 16H, PO(OCH_2CH_3)$_2$). $^{13}C\{^1H\}$ NMR (CD_3CN): δ 15.5 (d, $^3J_{PC}$ = 6.1 Hz, CH_3CH_2O), 19.2–19.8 (m, CH_2CH_2P), 22.1 (d, $^2J_{PC}$ = 4.7, O=PCH$_2$CH$_2$(CH$_2$)$_3$P), 23.3 (s, $CH_3CO_2^-$), 24.0 (s, O=P$(CH_2)_3CH_2CH_2$P), 24.2 (d, $^1J_{PC}$ = 139.5 Hz, O=P$CH_2(CH_2)_4$P), 24.6 (N [18] = 30.32 Hz, O=P$(CH_2)_4CH_2$P), 30.9–31.4 (m, CH_2CH_2P), 33.6 (d, $^3J_{PC}$ = 16.8 Hz, O=P$(CH_2)_2CH_2$–$(CH_2)_2$P), 60.7 (d, $^2J_{PC}$ = 6.1 Hz, CH_3CH_2O), 174.8 (s, $CH_3CO_2^-$). $^{31}P\{^1H\}$ NMR (CD_3CN): δ 17.3 (s, 2P, *P*1), 33.1 (s, 4P, *P*O(OCH_2CH_3)$_2$). IR (KBr, cm^{-1}): *v* 2981, 2932, 2908 (CH_2), 1244 (P=O), 1026 (P–OEt), v_s 1402 ($CH_3CO_2^-$), v_{as} 1577 ($CH_3CO_2^-$). MS (FAB, 50 °C): *m*/*z* 1097.5 $[M-OAc]^+$.

*2.4.5. cis-[Pd(f)(OAc)$_2$] (**6**)*

Yield: 0.50 g (87%). *Anal.* Calc. for $C_{47}H_{100}O_{16}P_6Pd$: C, 46.52; H, 8.31. Found: C, 46.44; H, 8.29%. ^1H NMR ($CDCl_3$): δ 1.1 (t, $^3J_{HH}$ = 7.1 Hz, 24H, PO(OCH_2CH_3)$_2$), 1.2–1.7 (m, 60H, $(CH_2)_n$, H_1, H_2, H_3), 3.8–3.9 (m, 16H, PO(OCH_2CH_3)$_2$). $^{13}C\{^1H\}$ NMR ($CDCl_3$): δ 22.2 (d, $^3J_{PC}$ = 6.1 Hz, CH_3CH_2O), 25.2–25.8 (m, CH_2CH_2P), 22.6 (d, $^2J_{PC}$ = 4.7, O=PCH$_2$CH$_2$(CH$_2$)$_4$P), 29.2 (s, $CH_3CO_2^-$), 29.9 (s, O=P$(CH_2)_4CH_2CH_2$P), 31.01 (N [18] = 30.32 Hz, O=P$(CH_2)_5CH_2$P), 31.1 (d, $^1J_{PC}$ = 140.8 Hz, O=P$CH_2(CH_2)_5$P), 35.8 (d, $^3J_{PC}$ = 16.8 Hz, O=P$(CH_2)_3CH_2(CH_2)_2$P), 36.3–36.5 (m, CH_2–CH_2P$((CH_2)_3$-$CH_2(CH_2)_2)_2$), 67.2 (d, $^2J_{PC}$ = 6.1 Hz, CH_3CH_2O), 182.0 (s, $CH_3CO_2^-$). $^{31}P\{^1H\}$ NMR ($CDCl_3$): δ 15.1 (s, 2P, *P*1), 33.2 (s, 4P, *P*O(OCH_2CH_3)$_2$). IR (KBr, cm^{-1}): *v* 2981, 2934, 2908 (CH_2), 1240 (P=O), 1028 (P–OEt), v_s 1402 ($CH_3CO_2^-$), v_{as} 1577 ($CH_3CO_2^-$). MS (FAB, 50 °C): *m*/*z* 1153.1 $[M-OAc]^+$.

*2.4.6. cis-[Pd(g)(OAc)$_2$] (**7**)*

Yield: 0.54 g (85%). *Anal.* Calc. for $C_{55}H_{116}O_{16}P_6Pd$: C, 49.83; H, 8.82. Found: C, 49.30; H, 8.72%. ^1H NMR ($CDCl_3$): δ 1.26 (t, $^3J_{HH}$ = 7.1 Hz, 24H, PO(OCH_2CH_3)$_2$), 1.5–1.9 (m, 76H, $(CH_2)_n$, H1, H2, H3), 3.98–4.1 (m, 16H, PO(OCH_2CH_3)$_2$). $^{13}C\{^1H\}$ NMR ($CDCl_3$): δ 16.8 (d, $^3J_{PC}$ = 6.1 Hz, CH_3CH_2O), 22.5–22.7 (m, CH_2CH_2P-$((CH_2)_6CH_2CH_2)_2$), 23.9 (s, $CH_3CO_2^-$), 24.6 (s, O=P$(CH_2)_2$-$CH_2(CH_2)_5$P), 25.6 (N [18] = 32.3 Hz, O=PCH$_2$(CH$_2$)$_6$CH$_2$P), 25.9 (d, $^1J_{PC}$ = 140.8 Hz, O=P$CH_2(CH_2)_7$P), 29.2–29.3 (m, O=P$(CH_2)_5$-$CH_2CH_2CH_2$P), 30.7 (d, $^4J_{PC}$ = 16.8 Hz, O=P$(CH_2)_3CH_2(CH_2)_4$P), 31.3–31.6 (m, $CH_2CH_2P((CH_2)_3CH_2(CH_2)_4)_2$), 61.7 (d, $^2J_{PC}$ = 6.1 Hz, CH_3CH_2O), 177.0 (s, $CH_3CO_2^-$). $^{31}P\{^1H\}$ NMR ($CDCl_3$): δ 14.4 (s, 2P, *P*1), 33.7 (s, 4P, *P*O(OCH_2CH_3)$_2$). IR (KBr, cm^{-1}): *v* 2980, 2928, 2855 (CH_2), 1243 (P=O), 1030 (P–OEt), v_s 1369 ($CH_3CO_2^-$), v_{as} 1620 ($CH_3CO_2^-$). MS (FAB, 50 °C): *m*/*z* 1265.0 $[M-OAc]^+$.

*2.4.7. cis-[Pd(h)(OAc)$_2$] (**8**)*

Yield: 0.23 g (85%). *Anal.* Calc. for $C_{19}H_{44}N_4O_4P_2Pd$: C, 40.68; H, 7.91; N, 9.99. Found: C, 40.55; H, 7.82; N, 9.51%. ^1H NMR ($CDCl_3$): δ 1.8–2.1 (m, 28H, $(CH_2)_n$, H1, H2, H3). 2.7–3.0 (m, $CH_2CH_2P(CH_2CH_2CH_2NH_2)_2$). $^{13}C\{^1H\}$ NMR ($CDCl_3$): δ 18.8 (s, CH_2CH_2P), 20.2–20.9 (m, $CH_2CH_2P(CH_2CH_2CH_2NH_2)_2$), 25.1 (s, $CH_3CO_2^-$), 25.8 (s, $CH_2CH_2P(CH_2CH_2CH_2NH_2)_2$), 41.9 (s, $CH_2CH_2P(CH_2CH_2CH_2NH_2)$, 177.8 (s, $CH_3CO_2^-$). $^{31}P\{^1H\}$ NMR ($CDCl_3$): δ 1.1 (s). IR (KBr, cm^{-1}): *v* 3355, 3278 (NH), 2927, (CH_2), 1078 (C–N), v_s 1398 ($CH_3CO_2^-$), v_{as} 1570 ($CH_3CO_2^-$). MS (FAB, 50 °C): *m*/*z* 501.2 $[M-OAc]^+$.

2.5. X-ray data collection and processing

Previously attempts to crystallize complex **1** and its family by different methods, such as slow evaporation of water or ethanol

Table 1
Crystal data and structure refinement for complex **1**.

Empirical formula	$C_{31}H_{64}O_8P_2Pd.H_2O$
Formula weight	751.18
Temperature (K)	173(2)
Crystal color	colorless
Wavelength	0.639
Crystal system	triclinic
Space group	$P\bar{1}$
Unit cell dimensions	
a (Å)	11.777(3)
b (Å)	12.423(10)
c (Å)	13.787(3)
α (°)	73.98(3)
β (°)	85.46(2)
γ (°)	71.29(4)
V (Å^3)	1836.3(16)
Z	2
D_{calc} (Mg m^{-3})	1.359
Crystal size (mm^3)	0.4 × 0.15 × 0.05
θ range for data collection	2.03–27.49
$F(000)$	800
Absorption coefficient	0.639
Index ranges	±10, ±15, ±17
Reflections collected	14306
Goodness-of-fit on F^2	0.954
R indices (all data)	R_1 = 0.0503, wR_2 = 0.0940

$R_1 = \sum||F_o| - |F_c||/\sum|F_o|$; $wR_2 = \{\sum[w(F_o^2 - F_c^2)^2]/\sum[w(F_o^2)^2]\}^{1/2}$.

solutions, have proven to be unsuccessful so far [12]. Here, we succeeded in crystallizing this complex by slow diffusion of ether into a concentrated solution of **1** in dichloromethane. The crystal data and the details of data collection for complex **1** are listed in Table 1. The crystal was mounted on a glass fiber and transferred to a P4 Siemens diffractometer, using graphite-monochromated Mo Kα radiation. The lattice constants were determined by 25 precisely centered high-angle reflections and refined by least-squares methods. The structure was solved by direct methods and refined by full-matrix least-squares on F^2 using SHELXTL-97 [19,20]. All non-hydrogen atoms were refined anisotropically (based on F^2). Hydrogen atoms were placed in calculated positions, except for hydrogen atoms of water that were located by a difference Fourier map and were then refined isotropically.

3. Result and discussion

3.1. Synthesis

The new water-soluble diphosphine ligands **a**–**h** have been prepared photochemically by hydrophosphination of the corresponding excess 1-alkene (CH_2=CH–$(CH_2)_n$–X (n = 4, X = OH; n = 2–6, 8, P(O)$(OEt)_2$; n = 3 X = NH_2) with $H_2P(CH_2)_3PH_2$, as shown in Scheme 1.

It is worth mentioning that this method of synthesis can be considered as a good way to prepare a wide spectrum of functionalized bis(phosphines) ligands. All the diphosphine ligands (**a**–**h**) are air-sensitive and the oily products are soluble in water and chlorinated hydrocarbons like dichloromethane and chloroform. All the new compounds were characterized by various spectroscopic techniques. Their chemical constitution was confirmed by ^{1}H and ^{31}P NMR spectroscopy. The ^{31}P NMR spectra for the ligands (**b**–**h**) may be explained in terms of an AX_2 spin pattern, where A correspond to the two phosphorus (P1) centers and X to the four phosphonate phosphorus (P2) centers. As a representative example, Fig. 1 shows the $^{31}P\{^1H\}$ NMR spectrum of the phosphonate ligand **b**. The two signals between δ −22 and 32, in a 1:2 ratio, represent an AX_2 spin system. The two singlets at higher field ($\delta \sim 32$) with a coupling constant of about 50 Hz are assigned to the phosphonate phosphorus (X_2), whereas the triplet at lower field ($\delta \sim -22$) is assigned to the phosphine phosphorous (A). This phenomenon of phosphorus coupling was not observed previously [14]. The $^{31}P\{^1H\}$ NMR spectra of the ligands **a** and **h** reveal only a singlet at $\delta \approx -31$.

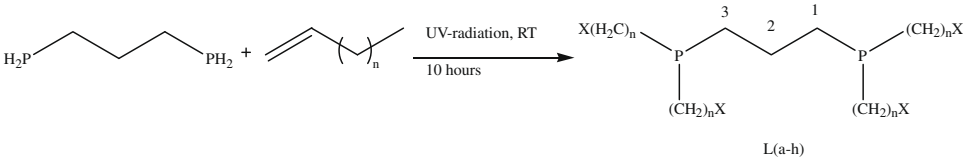
In addition, the chelating nature of the functionalized ligands **L** (**a**–**h**) provides useful avenues for the development of new classes of transition metal complexes **1**–**8**. The synthesis of *cis*-[Pd(**L**)$(OAc)_2$] was achieved by the reaction of palladium(II) acetate with the ligands **L** in a 1:1 mixture of dichloromethane and acetonitrile at room temperature (Scheme 2).

The hydrophilic nature of **1**–**8** has presented significant problems in getting the complexes as a solid. The complexes tend to be waxy solids even after drying in vacuum for 48 h. These neutral complexes **1**–**8** are air stable, diamagnetic and their structures were confirmed by ^{1}H, ^{31}P NMR spectra, and X-ray diffraction for complex **1**. The aliphatic region in the ^{1}H NMR spectra of complexes **1**–**8** consists of several coupled multiplets due to aliphatic protons of the alkyl group of **L**. There is a marked downfield shift and significant change of the multiplicity in the $^{31}P\{^1H\}$ NMR spectra for the phosphine group upon coordination of the ligands **b**–**g** to the Pd metal (Fig. 2). Similar chemical shift trends were also noted for the rhenium(V) and palladium complexes derived from water-soluble hydroxymethylphosphines [12,14].

The phosphine phosphorous (A) peaks are shifted from a triplet (δ = −22) to a multiplet (δ = 22) upon coordination. The $^{31}P\{^1H\}$ NMR spectra of the phosphine complexes **2**–**7** are characterized by two signals in a 1:2 ratio, representing an $AX_2A'X'_2$ spin system, which are assigned to the phosphonate ($X_2X'_2$) and phosphine (AA′) groups. As a representative spectrum, Fig. 2 shows the $^{31}P\{^1H\}$ NMR spectrum for complex **2**. The two singlet signals located at higher field (δ = 32) are assigned to the phosphonate function ($X_2X'_2$), whereas that at lower field (δ = 22) is traced back to the phosphines (AA′). Complexes **1** and **8** give rise to a singlet at δ = 19 and 15 ppm, respectively.

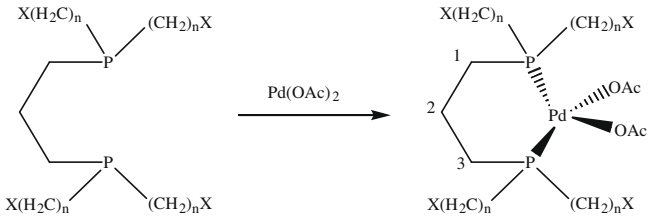
3.2. Crystal structure

The structure of complex **1** was further confirmed by X-ray crystallography and an ORTEP figure of complex **1** is shown in Fig. 3. Selected inner coordination sphere bond parameters of **1**



n	6	2	3	4	5	6	8	3
X	OH	$PO(OEt)_2$	$PO(OEt)_2$	$PO(OEt)_2$	$PO(OEt)_2$	$PO(OEt)_2$	$PO(OEt)_2$	NH_2
L	a	b	c	d	e	f	g	h

Scheme 1.



Scheme 2.

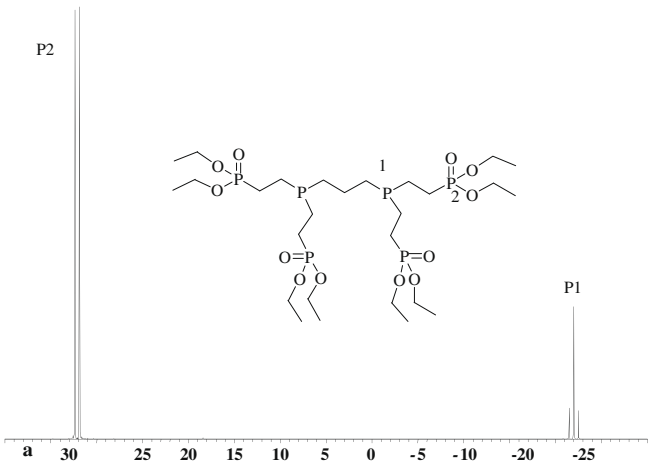


Fig. 1. $^{31}P\{^{1}H\}$ NMR spectrum of the ligand **b** showing an AX_2 pattern.

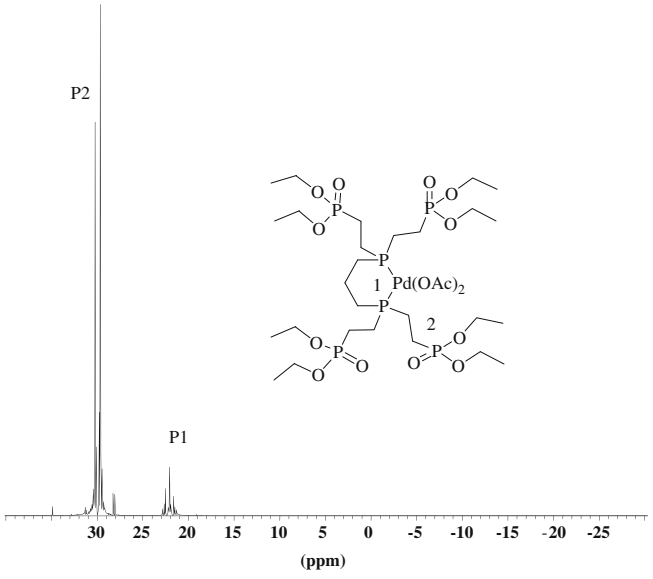


Fig. 2. $^{31}P\{^{1}H\}$ NMR spectrum of complex **2** showing an $AX_2A'X'_2$ spin pattern.

are listed in Table 2. Complex **1** crystallizes in the triclinic space group $P\bar{1}$ with two formula units per unit cell. The bond angles P1–Pd–P2 (95.29(6)°) and O5–Pd–O7 (92.47(14)°) differ slightly from an ideal square planar geometry. Pd, P1, P2, O5 and O7 deviate by less than 0.12 Å from a planar arrangement. Remarkably, the six-membered ring, formed by the diphosphine ligand and the metal atom, is flattened at the metal, and Pd1 and C2 deviate by −0.095(3) and 0.700(7) Å, respectively. The diphosphine unit is

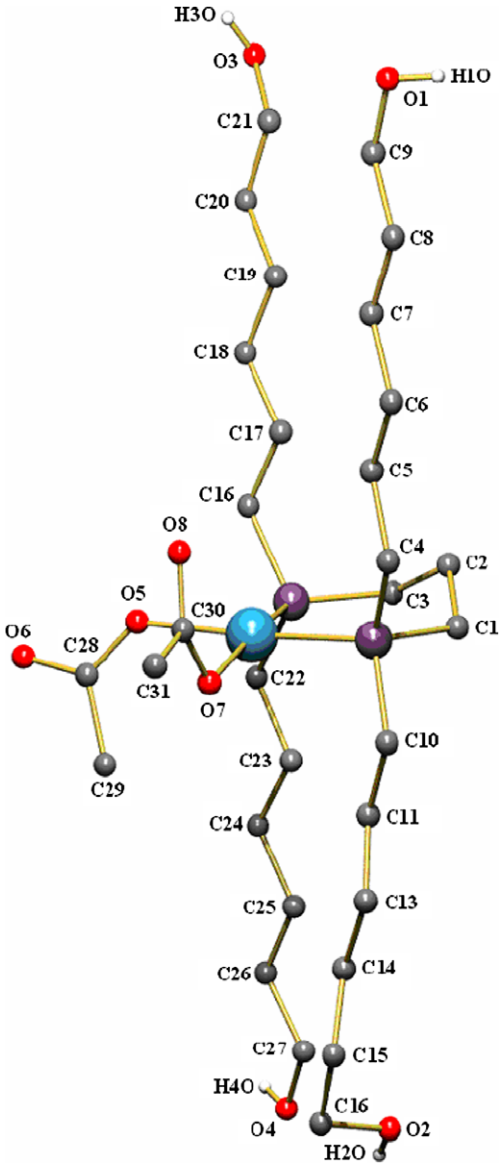


Fig. 3. Thermal ellipsoid plot (20%) of complex **1**. Solvent molecules are omitted for clarity.

coordinated to the metal in a chelating fashion. The Pd1–P1 and Pd–P distances are 2.2225(15) and 2.2276(15) Å, respectively. The Pd1–O5 and Pd1–O7 distances are 2.108(3) and 2.116(3) Å, respectively. The P1–Cl and P2–C3 distances are 1.806(5) and 1.815(5) Å. For complex **1**, The Pd–P distances (average, 2.2251 Å) are shorter than the Pd–P distances (average, 2.2504 Å) in similar reported dicationic palladium(II) complexes $([(R_2P(CH_2)_3PR_2)Pd(NCCH_3)_2][BF_4]_2$, R = $(CH_2)_2CH_3$) by 0.03 Å [12]. This shortening may be due to greater π-back donation from the electron rich Pd → d orbital to the empty d orbital of the phosphorous atom of the diphosphine ligand.

Extensive hydrogen bonding links the hydroxyl oxygens (O1, O2, O3 and O4) to the acetate oxygens (O5, O6 and O8) and to the water oxygen (O9). It is noted from Table 3 that the water molecule behaves as a H-donor and a H-acceptor. H20O of the O9 water molecule makes a bifurcated hydrogen bond with O6 and O5 of the acetate group, the later being a rather weak and acute bond, at symmetry positions $-x+2$, $y+1$, $z+1$. H21O of the O9 water molecule makes a single hydrogen bond with the hydroxyl O4. Further O9 of the water molecule, via its lone pairs, forms a

Table 2
Bond lengths (Å) and angles (°) for complex **1**.

Bond lengths (Å)		Bond angles (°)			
Pd1–O5	2.108(3)	O5–Pd1–O7	92.47(13)	C10–P1–Pd1	107.85(16)
Pd1–O7	2.116(3)	O5–Pd1–P1	175.52(10)	C16–P2–Pd1	110.29(19)
Pd1–P1	2.2225(15)	O7–Pd1–P1	86.97(10)	C3–P2–Pd1	121.48(17)
Pd1–P2	2.2276(15)	O5–Pd1–P2	85.80(	C22–P2–Pd1	108.91(17)
P2–C3	1.815(5)	O7–Pd1–P2	172.80(10)	C28–O5–Pd1	130.4(3)
P1–C1	1.806(5)	P1–Pd1–P2	95.30(6)	C30–O7–Pd1	116.3(3)
O1–H1O	0.8400	C1–P1–Pd1	119.60(17)	C2–C1–P1	117.4(3)
O2–H2O	0.8400	C4–P1–Pd1	111.97(17)	C3–C2–C1	114.0(4)
O3–H3O	0.8400	C9–O1–H1O	109.5	C15–O2–H2O	109.5
O4–H4O	0.8400	C21–O3–H3O	109.5	C27–O4–H4O	109.5

Table 3
Hydrogen bond lengths (Å) and angles (°) for complex **1**.

Bond lengths (Å)				Angles (°)
O1–H1O···O6#1	0.84	1.94	2.766(5)	167.0
O2–H2O···O8#2	0.84	1.96	2.798(6)	175.6
O3–H3O···O9#3	0.84	1.95	2.786(7)	170.7
O4–H4O···O9#4	0.84	2.23	2.806(7)	125.6
O9–H20O···O6#5	0.92(6)	2.02(6)	2.916(6)	165(5)
O9–H20O···O5#5	0.92(6)	2.96(6)	3.478(6)	117(4)
O9–H21O···O4#4	0.79(9)	2.08(9)	2.806(7)	153(10)

Symmetry transformations used to generate equivalent atoms: #1: $x-1, y+1, z$; #2: $x, y-1, z$; #3: $x, y+1, z+1$; #4: $-x+2, -y, -z+1$; #5: $-x+2, -y+1, -z+1$.

hydrogen bond with the hydroxyl groups (O3 and O4) from different asymmetric units.

4. Conclusion

New family of water-soluble functionalized bis(phosphine) ligands **L** (**a**–**h**) of the general formula $CH_2(CH_2PR_2)_2$, where for **a**: R = $(CH_2)_6OH$; **b**–**g**: R = $(CH_2)_nP(O)(OEt)_2$, $n = 2$–6 and $n = 8$; **h**: R = $(CH_2)_3NH_2$ (Scheme 1), have been prepared photochemically by hydrophosphination of the corresponding 1-alkenes with $H_2P(CH_2)_3PH_2$. The reactions of these ligands with $Pd(OAc)_2$ in dichloromethane–acetonitrile produced water-soluble palladium complexes of the general formula *cis*-[Pd(**L**)$(OAc)_2$] (**1**–**8**). The $^{31}P\{1H\}$ NMR spectra of **L** and its palladium(II) complexes display two signals in a 2:1 ratio, assigned to the phosphonate and phosphine substituents. A marked shift and a significant change of the multiplicity in the $^{31}P\{^1H\}$ NMR spectra for the phosphine group in this ligand from a triplet ($\delta = -22$) to a multiplet at $\delta = 22$ upon reaction of palladium(II) acetate with $R_2P(CH_2)_2PR_2$ have been observed. Crystallographic studies of **1** show that the diphosphine units are coordinated to the metal in a chelating fashion. The square planar geometry formed from the acetate ligands and the diphosphine ligand deviate by less than 0.12 Å from the ideal planar arrangement.

Acknowledgements

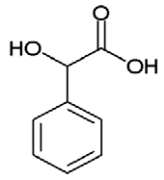
Authors would like to thank the Universitaet Tuebingen (Germany) and Hashemite University (Jordan) for their research support and Dr. Klaus Eichele, Universitaet Tuebingen (Germany), for fruitful discussions and for analyzing the X-ray experiments.

Appendix A. Supplementary data

CCDC 707138 contains the supplementary crystallographic data for compound **1**. These data can be obtained free of charge via http://www.ccdc.cam.ac.uk/conts/retrieving.html, or from the Cambridge Crystallographic Data Centre, 12 Union Road, Cambridge CB2 1EZ, UK; fax: (+44) 1223-336-033; or e-mail: deposit@ccdc.cam.ac.uk. Supplementary data associated with this article can be found, in the online version, at doi:10.1016/j.poly.2009.01.040.

References

[1] (a) E. Drent, P.H.M. Budzelaar, Chem. Rev. 96 (1996) 663;
(b) L.H. Pignolet, Homogeneous Catalysis with Metal Phosphine Complexes, Plenum Press, New York, 1983;
(c) G. Papadogiankis, R.A. Sheldon, New. J. Chem. 20 (1996) 175.
[2] (a) D. Morel, Rhone Poulenc Ind., French Patent 2,486,525, 1980;
(b) Rhone Poulenc Ind., French Patent 2,505,322, 1981;
(c) Rhone Poulenc Ind., French Patent 2,541,675, 1983.
[3] (a) J.W. Ellis, K.N. Harrison, P.A.T. Hoyle, A.G. Orpen, P.G. Pringle, M.B. Smith, Inorg. Chem. 31 (1992) 3026;
(b) P. Stobel, H.A. Mayer, F. Auer, Eur. J. Inorg. Chem. 37 (1998) 37;
(c) C.J. Smith, V.S. Reddy, K.V. Katti, J. Chem. Soc., Dalton Trans. (1998) 1365.
[4] (a) T. Okano, Y. Moriyama, H. Konishi, J. Kiji, Chem. Lett. (1986) 1463;
(b) Y. Amrani, D. Sinou, J. Mol. Catal. 36 (1986) 319.
[5] F. Janin, E.G. Kuntz, J.B. Tommasino, O.M. Vittori, J. Mol. Catal. A: Chem. 188 (2002) 71.
[6] (a) B. Mohr, D.M. Lynn, R.H. Grubbs, Organometallics 15 (1996) 4317;
(b) M.K. Markiewicz, M.C. Baird, Inorg. Chim. Acta 113 (1986) 95.
[7] A. Sen, Acc. Chem. Res. 16 (1993) 303.
[8] (a) A.S. Abu-Surrah, G. Eckert, W. Pechhold, W. Wilke, B. Rieger, Macromol. Rapid Commun. 17 (1996) 559;
(b) E.A. Klop, B.J. Lommerts, J. Veurink, J. Aerts, R.R. van Puijenbroek, J. Polym. Sci., Part B: Polym. Phys. 33 (1995) 315.
[9] (a) A. Sen, Z. Jiang, J.T. Chen, Macromolecules 22 (1989) 2012;
(b) S. Siddhart, Z. Jiang, A. Sen, Polym. Prep. 34 (1993) 378.
[10] (a) F.Y. Xu, C.W. Jame, Macromolecules 26 (1993) 3485;
(b) M.D.E. Forbes, Macromolecules 27 (1994) 1020.
[11] (a) A. Batistini, G. Consiglio, U. Suter, Angew. Chem., Int. Ed. Engl. 31 (1992) 303;
(b) M. Barsacchi, A. Batistini, G. Consiglio, U.W. Suter, Macromolecules 25 (1992) 3604.
[12] E. Lindner, M. Schmid, J. Wald, J. Queisser, M. Geprägs, P. Wegner, C. Nachtigal, J. Organomet. Chem. 602 (2000) 173.
[13] Z. Csákai, R. Skoda-Földes, L. Kollaŕ, Inorg. Chim. Acta 286 (1999) 93.
[14] V. Sreenivasa Reddy, K.V. Katti, W.A. Volkert, J. Chem. Soc., Dalton Trans. (1996) 4459.
[15] R.C. Taylor, D.B. Walters, Inorg. Synth. 14 (1966) 10.
[16] (a) W. Reppe, A. Magin, US Patent 2,577,208, 1951;
(b) W. Reppe, A. Magin, Chem. Abstr. 46 (1952) 6143.
[17] L.M. Beauchamp, J.V. Tuttle, M.E. Rodriguez, M.L. Sznaidman, J. Med. Chem. 39 (1996) 949.
[18] R.K. Harris, Can. J. Chem. 42 (1964) 2275.
[19] G.M. Sheldrick, Acta Crystallogr., Sect A 51 (1995) 33.
[20] G.M. Sheldrick, SHELXTL V5.03, Program for Crystal Structure Refinement, University of Göttingen, Germany, 1995.



Structure of mandelic acid

2. Experimental

Reagent grade mandelic acid and hafnium oxychloride were used for the present experiment. Humic acid (ACROSS) was used. Ten milligrams of hafnium oxychloride was irradiated in Dhruva reactor of Bhabha Atomic Research Centre, Trombay (flux $\sim 10^{14}$ n cm^{-2} s^{-1}) for a time period of 7 days to obtain high specific activity ^{181}Hf. For the preparation of mandelate complex, zirconium was used as a carrier for hafnium. Zirconyl chloride solution containing ^{181}Hf activity was mixed with a mandelic acid solution in 1 M HCl under hot condition. The complex was precipitated, filtered and washed with distilled water. In the case of Hf–humate complex, a small aliquot from the ^{181}Hf stock solution was evaporated to dryness and humic acid solution, having pH 2 (20 mg/l) was added to it. Hafnium concentration in the solution was around 10^{-7} M, which is small compared to the humic acid concentration (10^{-4} M). The solution, equilibrated for 48 h, was subsequently centrifuged. The solid residue was found to contain 99% of the Hf activity. Three BaF_2 detectors of a fast-slow coincidence setup, coupled to multi-parameter data acquisition system, were used for TDPAC counting. The time resolution for 133–482 keV cascade of ^{181}Hf was 0.8 ns.

3. Results and discussion

Fig. 1 shows the TDPAC spectrum of the Hf–mandelate complex calculated using the formula,

$$A_2G_2(t) = 2\frac{W(180^\circ,t) - W(90^\circ,t)}{W(180^\circ,t) + 2W(90^\circ,t)} \quad (1)$$

where $W(180^\circ,t)$ and $W(90^\circ,t)$ are the coincidence counts between 133 and 482 keV gamma rays at 180° and 90°, respectively. The attenuation factor ($G_{22}(t)$) contains the information about the interaction frequencies (ω_n) and the asymmetry parameter η:

$$G_{22}(t) = S_{k0} + \sum_{n=1}^{3} S_{kn}\cos\omega_n t \quad (2)$$

where S_{kn} are the amplitudes of the corresponding frequencies (ω_n). The data were analyzed using the software DEPAC to obtain the interaction frequency (ω_1) and asymmetry parameter (η) of the EFG [17]. The quadrupole interaction frequency (ω_q) was obtained from ω_1 using the following relation [18]:

$$\omega_Q = \frac{\omega_1}{4[7(3+\eta^2)]^{1/2}\sin\left[\frac{1}{3}(\cos^{-1}\beta)\right]} \quad (3)$$

The EFG can be deduced from quadrupole interaction frequency (ω_Q) by the equation

$$\omega_Q = eQV_{ZZ}/4I(2I-1)\hbar \quad (4)$$

where Q is the quadrupole moment of the intermediate level and I is its spin. The asymmetry parameter (η) is given by

$$\eta = (V_{XX} - V_{YY})/V_{ZZ} \quad (5)$$

where $|V_{ZZ}| > |V_{XX}| > |V_{YY}|$.

The Fourier transform of TDPAC spectrum (Fig. 1) of Hf–mandelate complex shows two ω_Q values. The data for quadrupole interaction frequencies for two sites are given in Table 1. The existence of two sites was also observed by Baussaha et al. [19] while Barbieri et al. [20] observed only one quadrupole frequency. The two ω_Q values indicate that in Hf–mandelate, Hf is complexed in two types of well defined environments. The IR spectroscopy of Hf–mandelate shows bands at 2600, 2300 and 1850 cm^{-1} which are typical of compounds with hydrogen bonds and these bonds link alcoholic oxygen of one bridging mandelate and carboxylic oxygen of second bridging mandelate [21]. These results show the possible existence of monomeric and dimeric species which could be present in Hf–mandelate. The existence of other complexes, like, $Hf(L)_3OH$ or $Hf(L)_2OH$ (L = mandelate) could also lead to different electronic environments around Hf nuclei and thus in different quadrupole frequencies.

Table 1
TDPAC experimental data for two Hf sites in Hf–mandelate complex.

Abundance (%)	ω_Q (Mrad/s)	η	δ	V_{ZZ} ($\times 10^{18}$) (V/cm^2)
26.9	77 ± 0.4	0.7	0.054 ± 0.005	0.80 ± 0.004
73.0	111 ± 3.1	0.3	0.57 ± 0.04	1.16 ± 0.03

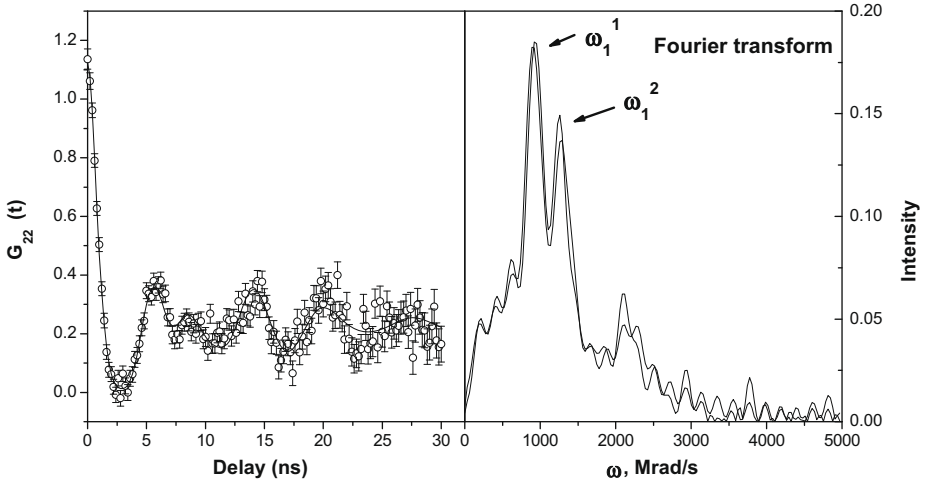


Fig. 1. TDPAC spectrum of Hf–mandelate complex at 300 K and its Fourier transform showing interactions frequencies $\omega_1{}^1$ and $\omega_1{}^2$ for the site 1 and 2, respectively.

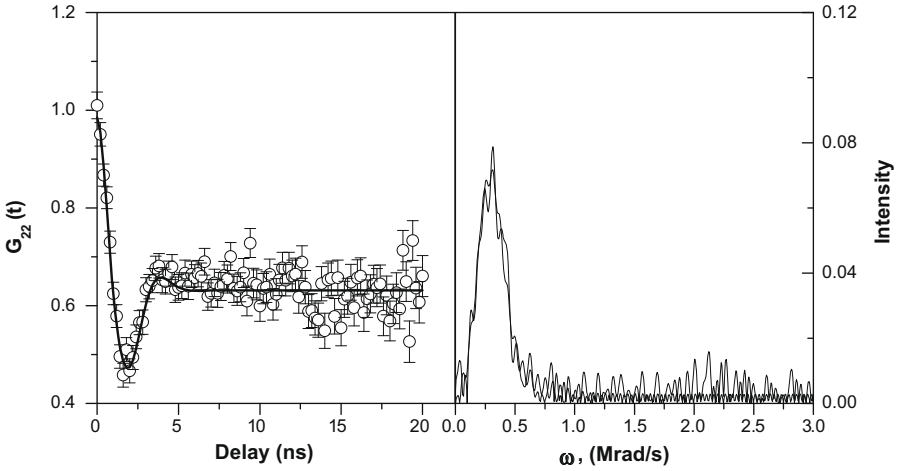


Fig. 2. TDPAC spectrum of Hf–humate complex and its Fourier transform.

In the case of humate complex, the Fourier transform of the TDPAC spectrum showed a broad distribution of quadrupole interaction frequencies (Fig. 2). This indicates absence of specific binding site in HA. Metal ions may be bound to the humic acid by direct association with the donor groups (specific site binding model) [22] or they may be associated with anionic macromolecule as a whole (polycondensate model) [23]. While in the case of specific site binding, we expect well defined quadrupole interaction frequencies, in the case of polycondensate model any such specific coordination site may be absent. The present observations point towards the polyconsendate model. Stability constants of metal–humate complexes are known to decrease with increasing metal ion concentration, indicating the presence of different binding sites with widely varying affinity for the metal ions [24]. The fraction of high affinity binding sites is expected to be small. These sites cannot selectively bind the metal ion at concentration levels of μg/ml, as in the present case (0.9 μg/ml). Similar results were obtained in the case of ^{111m}Cd–humate complex by Kupsch et al. [15]. Therefore, it would be interesting to carry out these studies at concentration level of ng/ml. It is possible with carrier free radioisotopes.

Table 2
Experimental and theoretical values of EFG (V_{ZZ}) and asymmetry parameter (η).

Species	Theoretical values		Experimental values	
	η	EFG (au)	η	EFG (au)
L_3 Hf (μ-L)$_2$Hf L_3	0.38	0.35	0.3	0.19 ± 0.01

4. Theoretical calculations

To find out the present species exactly, we independently calculated the EFG on the Hf nuclei using ab initio molecular orbital methods. Theoretical calculations were done using GAMESS. The Gaussian Orbital Valence basis sets were used for Hf. The 60 core electrons of Hf were described by the effective core potential of Hay et al. [25] which incorporates mass velocity and Darwin relativistic effects into the potential and the valence electrons by a (5s6p3d)/[3s3p2d] Gaussian function basis set. To reduce the number of atoms for ab initio calculation of Hf with large ligand, the phenyl groups were replaced by hydrogen. Table 2 gives the theoretically calculated EFG for dimeric species of Hf–mandelate and is compared with experimentally obtained EFG. The structure of dimeric species used for EFG calculation is given in Fig. 3. The reasonably good agreement between theoretical and experimental values confirms the presence of dimeric Hf–mandelate species.

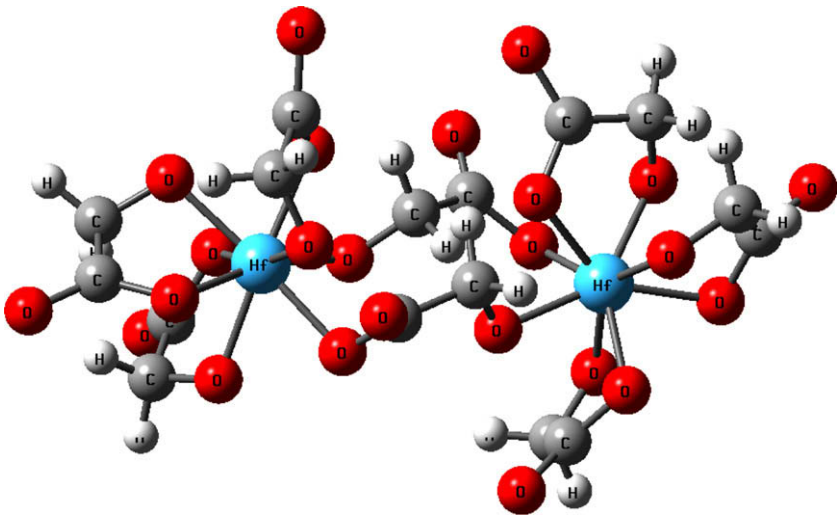


Fig. 3. Structure of L_3 Hf (μ-L)$_2$Hf L_3 used for EFG calculation.

5. Conclusion

The TDPAC spectrum of Hf–mandelate showed two well defined chemical environments around Hf nuclei. The experimentally obtained perturbation parameters show good agreement with the theoretically obtained parameters using GAMESS code. The TDPAC data confirm that Hf–mandelate exist predominantly as dimeric species while the minor species could be a mixed hydroxy mandelate complex of hafnium. The TDPAC of Hf–humate, on the other hand, indicates non specific site binding of metal ion.

Acknowledgement

Authors thank A. Bhattacharya for his help in the theoretical calculations of EFG.

References

[1] G.R. Choppin, in: G.R. Choppin, M.K. Khankhasayev (Eds.), Chemical Separation Technologies and Related Methods of Nuclear Waste Management, Kluwer Academic Publishers, 1999, p. 247.
[2] R. Artinger, B. Kienzler, W. Schubler, J.I. Kim, J. Contam. Hydrol. 35 (1998) 261.
[3] M. Samadfam, T. Jintoku, S. Sato, H. Ohashi, T. Mitsugashira, M. Hara, Y. Suzuki, Radiochim. Acta 88 (2000) 717.
[4] R. Artinger, B. Kienzler, W. Schubler, J.I. Kim, Radiochim. Acta 91 (2003) 743.
[5] F.J. Stevenson, Humus Chemistry, Genesis, Composition, Reactions, Wiley-Interscience Publication, 1982.
[6] A. Jain, M. Mohapatra, S.V. Godbole, B.S. Tomar, Spectrochim. Acta A: Mol. Biomol. Spectr. 71 (2008) 1007.
[7] J.I. Kim, H. Wimmer, R. Klenze, Radiochim. Acta 54 (1991) 35.
[8] M. Morgenstern, R. Klenze, J.I. Kim, Radiochim. Acta 88 (2000) 7.
[9] S. Sachs, V. Brendler, G. Geipel, Radiochim. Acta 95 (2007) 103.
[10] J.M. Monsallier, R. Artinger, M.A. Denecke, F.J. Scherbaum, G. Buckau, J.I. Kim, Radiochim. Acta 91 (2003) 567.
[11] K. Schmeide, T. Reich, S. Sachs, Inorg. Chim. Acta 359 (2006) 237.
[12] S. Sacha, K. Schmeide, T. Reich, V. Brendler, K.H. Heise, G. Bernhard, Radiochim. Acta 93 (2005) 17.
[13] D. Schild, C.M. Marquardt, Radiochim. Acta 88 (2000) 587.
[14] J.P. Adloff, Radiochim. Acta 25 (1978) 57.
[15] H. Kupsch, K. Franke, D. Degering, W. Troger, T. Butz, Radiochim. Acta 73 (1996) 145.
[16] M.W. Schmidt, K.K. Baldridge, J.A. Boatz, S.T. Elbert, M.S. Gordon, J.H. Jensen, K. Koseki, N. Matsunaga, K.A. Nguyen, S. Su, T.L. Windus, M. Dupuis, J.A. Montgomery, J. Comput. Chem. 14 (1993) 1347.
[17] DPAC – A Data Analysis Program for DEPAC by Bengt Lindgren. Available from: <http://material.fysik.uu.se>.
[18] J.A. Martinez, M.C. Caracoche, A.M. Rodriguez, P.C. Rivas, Chem. Phys. Lett. 102 (1983) 277.
[19] A. Baussaha, A. Marques Netto, J.Ch. Abbe, A. Haessler, Radiochem. Radioanal. Lett. 24 (1976) 43.
[20] R.S. Barbieri, S.I. Klein, A.M. Netto, Polyhedron 7 (1988) 2165.
[21] E.M. Larsaen, E.H. Homeier, Inorg. Chem. 11 (1972) 2687.
[22] E. Tipping, Comput. Geosci. 20 (1994) 973.
[23] R.D. Porasso, J.C. Benegas, M.A.G.T. van den Hoop, J. Phys. Chem. B 103 (1999) 2361.
[24] T. Kubota, O. Tochiyama, K. Tanska, Y. Niibori, Radiochim. Acta 90 (2002) 569.
[25] P.J. Hay, R. Willard, J. Wadt, Chem. Phys. 82 (1985) 299.

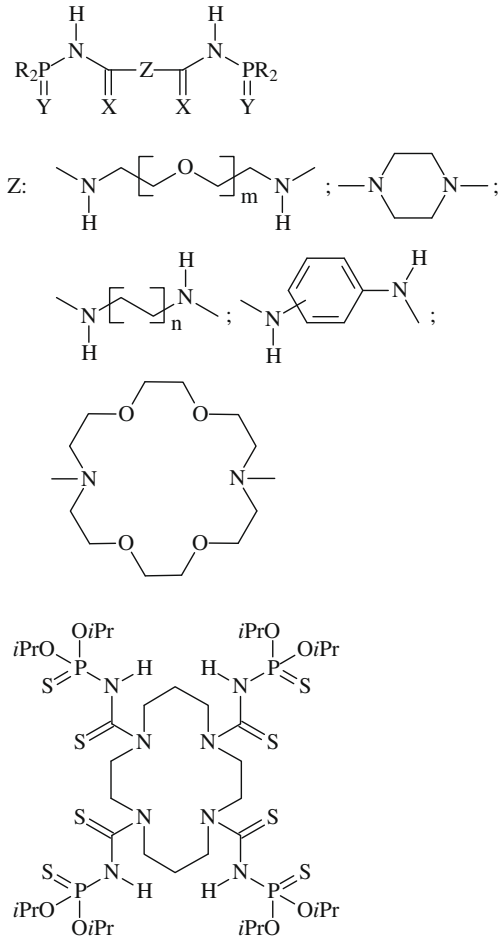
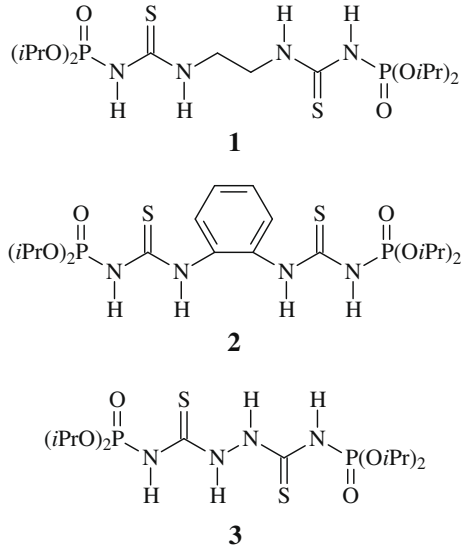


Chart 1.



Scheme 1.

3: Yield: 2.13 g (89%). Viscous oil. ^{1}H NMR ($CDCl_3$): δ = 1.28–1.43 (m, CH_3), 2.36–2.93 (m, NH_2), 4.49–4.92 (m, OCH), 8.40, 8.85 (br s, PNH), 11.30, 11.78 (br s, NH) ppm. ^{1}H NMR (DMSO-d_6): δ = 1.67, 2.09, 2.16, 2.27 (s, CH_3), 5.57–7.17 (m, OCH + PNH), 9.52 (br s, NH) ppm. ^{31}P NMR ($CDCl_3$): δ = −20.7 (br s, 1P, PNCS), −6.4 (q, $^3J_{POCH}$ = 6.3 Hz, $^2J_{PNH}$ = 7.5 Hz, 1P), −5.7 (d. t, $^3J_{POCH}$ = 6.2 Hz, $^2J_{PNH}$ = 11.2 Hz, 4.6P), −0.6 (t, $^3J_{POCH}$ = $^2J_{PNH}$ = 7.0 Hz, 1.9P) ppm. ^{31}P NMR (DMSO-d_6): δ = −5.4 (br s, 1P), −2.8 (br s, 2.4P) ppm. *Anal.* Calc. for $C_{14}H_{32}N_4O_6P_2S_2$ (478.50): C, 35.14; H, 6.74; N, 11.71. Found: C, 35.02; H, 6.81; N, 11.64%.

2.2. Physical measurements

NMR spectra were obtained on a Bruker Avance 300 MHz spectrometer at 25 °C. ^{1}H and ^{31}P NMR spectra were recorded at 299.948 and 121.420 MHz, respectively. Chemical shifts are reported with reference to $SiMe_4$ (^{1}H) and H_3PO_4 (^{31}P). Elemental analyzes were performed on a CHNS HEKAtech EuroEA 3000 analyzer.

2.3. Crystal structure determination and refinement

The X-ray data for both **1** and **2** were collected on a STOE IPDS-II diffractometer with graphite-monochromatized Mo Kα radiation generated by a fine-focus X-ray tube operated at 50 kV and 40 mA. The images were indexed, integrated and scaled using the X-area data reduction package [11]. Data were corrected for absorption using the PLATON program [12]. The structures were solved by direct methods using SHELXS-97 [13] and refined first isotropically and then anisotropically using SHELXL-97 [13]. Hydrogen atoms were revealed from $\Delta\rho$ maps and those bonded to C were refined using appropriate riding models. H-atoms bonded to N were freely refined. The isopropyl group in **2** shows signs of disorder, but no split model could be found.

3. Results and discussion

The compounds **1–3** were synthesized by treatment of 1,2-diaminoethylene, 1,2-diaminophenylene or hydrazine hydrate with the isothiocyanate $(i\text{PrO})_2\text{P(O)NCS}$ in high yields. Their composition was proved by microanalysis data.

The ^{31}P NMR spectra of **1** and **2** in $CDCl_3$ each contain a triplet signal at −6.5 and −6.6 ppm, respectively, which is typical for *N*-phosphoryl thioureas [1]. In the ^{1}H NMR spectra of **1** and **2**, the ethylene and phenylene proton signals are at 3.90–3.97 and 7.30–7.71 ppm, respectively. The spectra of both bis-thioureas contain a set of signals for the *i*PrO protons: a triplet or doublet for the

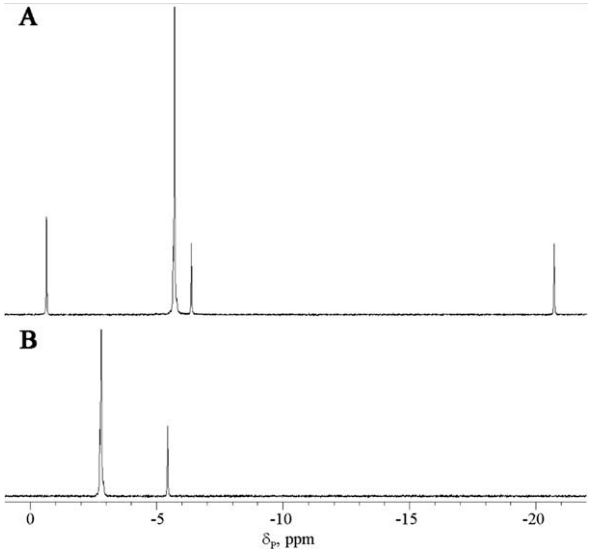
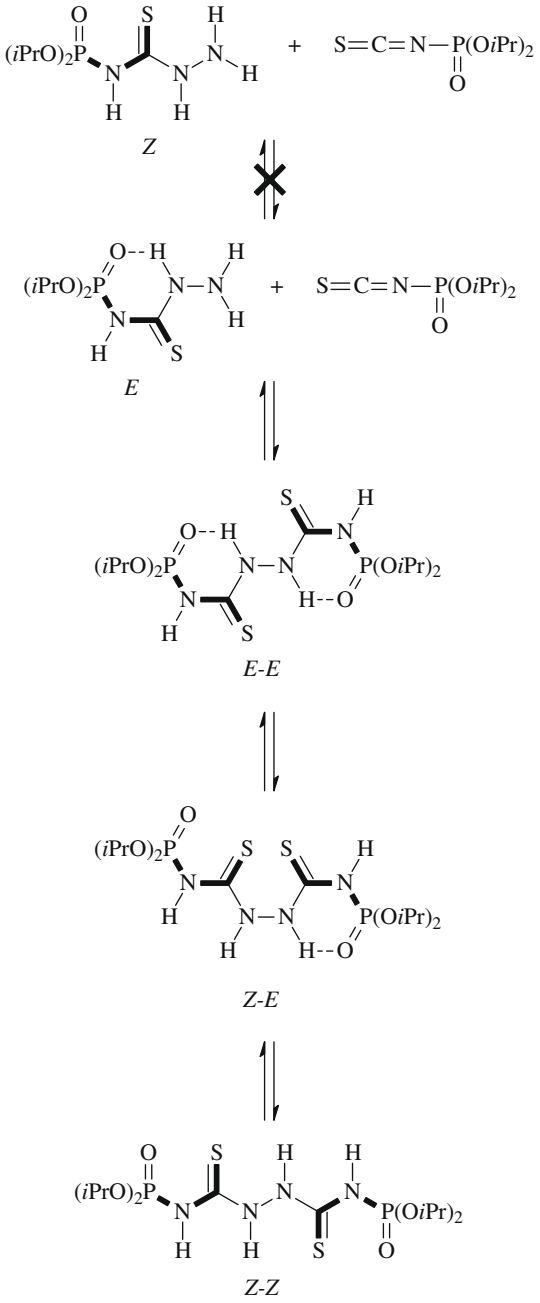


Fig. 1. ^{31}P NMR spectra of **3** in $CDCl_3$ (A) and DMSO-d_6 (B).



Scheme 2.

Table 1
Crystal data, data collection and refinement details for **1** and **2**.[a]

	1	**2**
Empirical formula	$C_{16}H_{36}N_4O_6P_2S_2$	$C_{20}H_{36}N_4O_6P_2S_2$
Formula weight	506.57	554.61
a (Å)	12.7077(8)	16.5175(5)
b (Å)	15.3048(7)	16.4421(6)
c (Å)	13.1930(8)	22.0451(6)
β (°)	98.802(5)	109.815(2)
V (Å^3)	2535.7(3)	5632.6(3)
$D_{calc.}$ (Mg m^{-3})	1.327	1.308
Absorption correction, μ (mm^{-1})	0.373	0.342
F(000)	1080	2352
Crystal size (mm)	0.26 × 0.27 × 0.29	0.28 × 0.32 × 0.34
Recording range, θ_{max} (°)	3.4-25.8	2.3–25.9
Number of recorded reflections	30330	77562
Number of recorded independent reflections	4763 [R_{int} = 0.065]	10962 [R_{int} = 0.082]
Final R indices [I > 2σ(I)]	R_1 = 0.0408, wR_2 = 0.0989	R_1 = 0.0398, wR_2 = 0.0890
R indices (all data)	R_1 = 0.0522, wR_2 = 0.1036	R_1 = 0.0703, wR_2 = 0.0958
S	1.11	0.88

[a] Measurements at 173(2) K using Mo Kα radiation with λ = 0.71073 (Å). Structure solution using direct methods in monoclinic $P2_1/n$ (Z = 4) and $P2_1/c$ (Z = 8) for **1** and **2**, respectively.

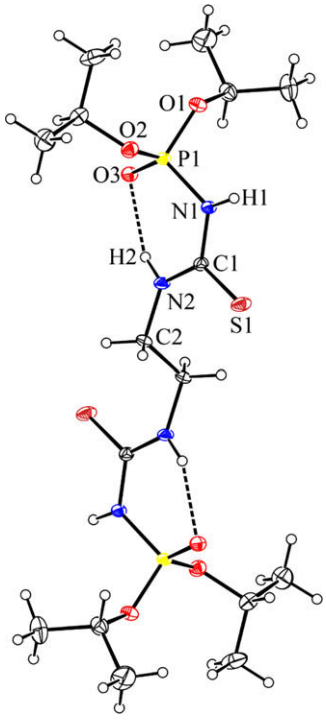


Fig. 2. Thermal ellipsoid representation of one of the two independent molecules of **1**. Ellipsoids are drawn at the 30% probability level.

CH_3 protons at 1.36–1.39 ppm and a doublet of septets for the CH proton in the area 4.70–4.81 ppm. The signals at 6.43 and 6.98 ppm correspond to the PNH protons in **1** and **2**, respectively. The main difference involves the signals at 9.17 ppm in the spectrum of **1** and at 10.36 ppm for **2**, corresponding to the NH hydrogen atoms. Thus, the ^{1}H NMR spectra of the thioureas **1** and **2** clearly show the presence of strong intramolecular N—H···O=P hydrogen bonds [1].

Surprisingly, there are four signals in the ^{31}P NMR spectrum of **3** in $CDCl_3$ solution: a major signal at −5.7 and minor peaks at −20.7, −6.4 and −0.6 ppm with integral intensities 4.6:1:1:1.9, respectively (Fig. 1). We suppose that the major signal corresponds to the *E*-*E*-isomer, which is stabilized by intramolecular hydrogen bonds, whereas the peak at −0.6 ppm shows the formation of *Z*–*Z*-form, as was previously observed for the *N*-thiophosphorylated analog $[NHC(S)NHP(S)(OiPr)_2]_2$ [14] (Scheme 2). The signal at −20.7 ppm corresponds to the phosphorus atom of $(iPrO)_2P(O)NCS$ (Scheme 2). This testifies that compound **3** partially decomposes in $CDCl_3$ solution, with elimination of an isothiocyanate molecule. The same behavior was observed for the tetrafunctional *N*-thiophosphorylated thiourea, based on a cyclam backbone [2]. The signal at −6.4 ppm is rather close to the value of the *E*-*E*-isomer of **3**. This peak corresponds to the monosubstituted *N*-phosphorylated hydrazine $NH_2NHC(S)NHP(O)(OiPr)_2$ (**4**), showing the *E*-isomeric form in $CDCl_3$ solution (Scheme 2). No $E \leftrightarrow Z$ equilibrium is observed for **4**. In the ^{1}H NMR spectrum of **3** in $CDCl_3$ solution, beside several sets of signals corresponding to the *i*PrO, PNH and NH

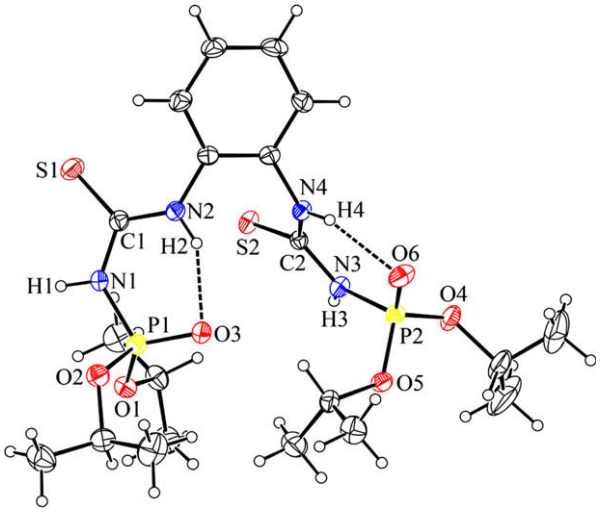


Fig. 3. Thermal ellipsoid representation of one of the two independent molecules of **2**. Ellipsoids are drawn at the 30% probability level.

protons, there is a multiplet signal for the NH_2 protons at 2.36–2.93 ppm. This testifies to the presence of the non-substituted NH_2 group of the parent hydrazine.

Only two signals were observed in DMSO-d_6 solution: the peaks appeared at −5.4 and −2.8 ppm (Fig. 1). The integral intensity ratio is 1:2.4 for the high- and low-field signals, respectively. Only doubling of the signals is observed in the ^{1}H NMR spectrum of **3** in DMSO-d_6 solution. There is no evidence for the dissociation reaction leading to the hydrazine **4**.

The chemical shifts of phosphorus are in the area which is characteristic for the *E*- and *Z*-isomers of *N*-phosphorylthioureas related by structure to the investigated compound **3** [1].

Crystals of **1** and **2** were obtained by recrystallization from a 1:5 (v/v) mixture of dichloromethane and *n*-hexane (Table 1). The molecular conformations of **1** and **2** are shown in Figs. 2 and 3, and geometric parameters are given in Tables 1 and 2. The NMR probes and the crystals for the X-ray determination were taken from the same samples. The parameters of the C═S, C—N, P—N and P═O bonds observed for both compounds (Tables 2 and 3) are in the typical range for *N*-phosphorylated thiourea derivatives [1].

The two N—C(S)—N—P(O) moieties in **1** and **2** are significantly flattened. The two chelate backbones, C(S)—N—P(O), in **1** are in

Table 2
Selected bond lengths (Å), and bond angles (°) for **1**.

Bond lengths			
S(1)–C(1)	1.672(2)	P(1)–N(1)	1.6564(18)
P(1)–O(1)	1.5684(17)	N(1)–C(1)	1.382(3)
P(1)–O(2)	1.5533(16)	N(2)–C(1)	1.336(3)
P(1)–O(3)	1.4733(16)	N(2)–C(2)	1.460(3)
Bond angles			
O(1)–P(1)–O(2)	103.59(9)	P(1)–N(1)–C(1)	127.74(15)
O(1)–P(1)–O(3)	115.30(9)	C(1)–N(2)–C(2)	123.58(19)
O(1)–P(1)–N(1)	103.60(9)	S(1)–C(1)–N(1)	119.36(16)
O(2)–P(1)–O(3)	115.99(9)	S(1)–C(1)–N(2)	123.81(17)
O(2)–P(1)–N(1)	105.38(9)	N(1)–C(1)–N(2)	116.81(19)
O(3)–P(1)–N(1)	111.72(9)		
Torsion angles			
O(1)–P(1)–N(1)–C(1)	–85.62(19)	P(1)–N(1)–C(1)–N(2)	–24.9(3)
O(2)–P(1)–N(1)–C(1)	165.88(18)	C(2)–N(2)–C(1)–S(1)	–9.1(3)
O(3)–P(1)–N(1)–C(1)	39.1(2)	C(2)–N(2)–C(1)–N(1)	172.62(19)
P(1)–N(1)–C(1)–S(1)	156.73(13)		

Table 3
Selected bond lengths (Å), and bond angles (°) for **2**.

Bond lengths			
P(1)–O(3)	1.4652(18)	P(1A)–O(3A)	1.4663(17)
P(1)–O(1)	1.5537(17)	P(1A)–O(1A)	1.5615(17)
P(1)–O(2)	1.5618(17)	P(1A)–O(2A)	1.5674(17)
P(1)–N(1)	1.660(2)	P(1A)–N(1A)	1.654(2)
P(2)–O(6)	1.4697(16)	P(2A)–O(6A)	1.4689(18)
P(2)–O(4)	1.5556(17)	P(2A)–O(4A)	1.5466(17)
P(2)–O(5)	1.5571(16)	P(2A)–O(5A)	1.5458(18)
P(2)–N(3)	1.656(2)	P(2A)–N(3A)	1.661(2)
S(1)–C(1)	1.658(2)	S(1A)–C(1A)	1.659(2)
S(2)–C(2)	1.670(2)	S(2A)–C(2A)	1.668(2)
N(1)–C(1)	1.391(3)	N(1A)–C(1A)	1.387(3)
N(2)–C(1)	1.346(3)	N(2A)–C(1A)	1.350(3)
N(3)–C(2)	1.373(3)	N(3A)–C(2A)	1.379(3)
N(4)–C(2)	1.334(3)	N(4A)–C(2A)	1.341(3)
Bond angles			
O(3)–P(1)–O(1)	118.32(11)	O(3A)–P(1A)–O(1A)	116.88(10)
O(3)–P(1)–O(2)	116.62(11)	O(3A)–P(1A)–O(2A)	115.85(10)
O(1)–P(1)–O(2)	96.89(9)	O(1A)–P(1A)–O(2A)	101.90(9)
O(3)–P(1)–N(1)	110.18(11)	O(3A)–P(1A)–N(1A)	111.21(10)
O(1)–P(1)–N(1)	106.46(11)	O(1A)–P(1A)–N(1A)	102.21(10)
O(2)–P(1)–N(1)	107.05(11)	O(2A)–P(1A)–N(1A)	107.42(10)
O(6)–P(2)–O(4)	114.76(10)	O(6A)–P(2A)–O(4A)	115.60(10)
O(6)–P(2)–O(5)	117.78(10)	O(6A)–P(2A)–O(5A)	117.64(12)
O(4)–P(2)–O(5)	103.84(9)	O(5A)–P(2A)–O(4A)	101.64(10)
O(6)–P(2)–N(3)	112.08(10)	O(6A)–P(2A)–N(3A)	109.68(11)
O(4)–P(2)–N(3)	108.01(10)	O(4A)–P(2A)–N(3A)	107.89(10)
O(5)–P(2)–N(3)	98.80(9)	O(5A)–P(2A)–N(3A)	103.28(10)
C(1)–N(1)–P(1)	132.28(19)	C(1A)–N(1A)–P(1A)	131.16(17)
C(2)–N(3)–P(2)	131.15(17)	C(2A)–N(3A)–P(2A)	131.53(17)
N(2)–C(1)–N(1)	114.5(2)	N(2A)–C(1A)–N(1A)	115.0(2)
N(2)–C(1)–S(1)	126.67(19)	N(2A)–C(1A)–S(1A)	126.65(19)
N(1)–C(1)–S(1)	118.81(18)	N(1A)–C(1A)–S(1A)	118.32(18)
N(4)–C(2)–N(3)	116.3(2)	N(4A)–C(2A)–N(3A)	116.8(2)
N(4)–C(2)–S(2)	123.02(18)	N(4A)–C(2A)–S(2A)	122.83(18)
N(3)–C(2)–S(2)	120.70(17)	N(3A)–C(2A)–S(2A)	120.37(17)
Torsion angles			
O(3)–P(1)–N(1)–C(1)	6.2(3)	O(3A)–P(1A)–N(1A)–C(1A)	4.3(3)
O(1)–P(1)–N(1)–C(1)	135.6(2)	O(1A)–P(1A)–N(1A)–C(1A)	129.8(2)
O(2)–P(1)–N(1)–C(1)	–121.6(2)	O(2A)–P(1A)–N(1A)–C(1A)	–123.4(2)
O(6)–P(2)–N(3)–C(2)	1.6(3)	O(6A)–P(2A)–N(3A)–C(2A)	–5.1(3)
O(4)–P(2)–N(3)–C(2)	–125.8(2)	O(4A)–P(2A)–N(3A)–C(2A)	121.6(2)
O(5)–P(2)–N(3)–C(2)	126.5(2)	O(5A)–P(2A)–N(3A)–C(2A)	–131.3(2)
P(1)–N(1)–C(1)–N(2)	–4.9(3)	P(1A)–N(1A)–C(1A)–N(2A)	–14.6(3)
P(1)–N(1)–C(1)–S(1)	175.44(15)	P(1A)–N(1A)–C(1A)–S(1A)	165.56(15)
P(2)–N(3)–C(2)–N(4)	5.6(3)	P(2A)–N(3A)–C(2A)–N(4A)	–1.6(3)
P(2)–N(3)–C(2)–S(2)	–174.82(14)	P(2A)–N(3A)–C(2A)–S(2A)	178.41(13)

Table 4
Hydrogen bond lengths (Å) and angles (°) for **1** and **2**.

	D–H···A*	*d*(D–H)	*d*(H···A)	*d*(D···A)	∠(DHA)
1[a]	N(1)–H(1)···O(3A)#3	0.900(10)	1.914(11)	2.802(2)	169(3)
	N(2)–H(2)···O(3)	0.904(10)	2.047(17)	2.838(2)	145(2)
	N(1A)–H(1A)···O(3)#4	0.896(10)	1.985(11)	2.811(2)	153(2)
	N(2A)–H(2A)···O(3A)	0.901(10)	2.010(18)	2.803(3)	146(2)
2[b]	N(1)–H(1)···O(6)#1	0.75(3)	2.24(3)	2.965(3)	165(3)
	N(2)–H(2)···O(3)	0.83(3)	1.96(3)	2.726(3)	153(2)
	N(3)–H(3)···S(2A)	0.81(3)	2.53(3)	3.313(2)	164(2)
	N(4)–H(4)···O(6)	0.81(3)	2.04(3)	2.761(3)	149(3)
	N(1A)–H(1A)···O(6A)#2	0.88(3)	1.98(3)	2.828(3)	159(3)
	N(2A)–H(2A)···O(3A)	0.86(3)	1.97(3)	2.739(3)	148(2)
	N(3A)–H(3A)···S(2)	0.75(2)	2.64(3)	3.359(2)	160(3)
	N(4A)–H(4A)···O(6A)	0.79(3)	2.03(3)	2.733(3)	148(3)

[a] Symmetry transformations used to generate equivalent atoms: #1 –x + 2, –y + 2, –z + 1; #2 –x + 1, –y, –z + 1; #3 –x + 1, –y + 1, –z + 1; #4 –x + 3/2, y–1/2, –z + 1/2.

[b] Symmetry transformations used to generate equivalent atoms: #1 –x, y + 1/2, –z + 1/2; #2 –x + 1, y–1/2, –z + 1/2.

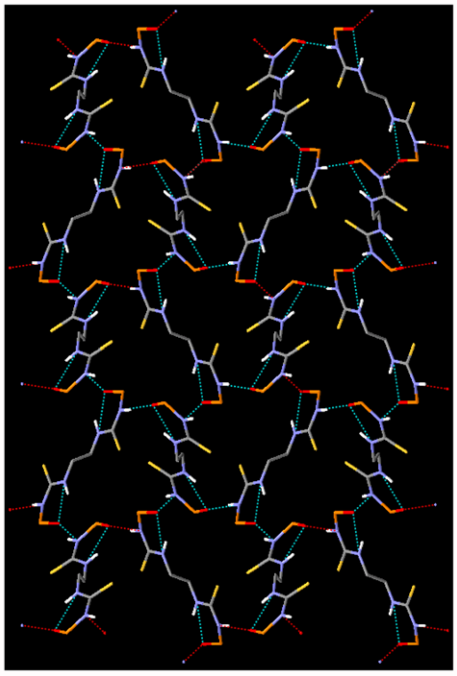


Fig. 4. Crystal packing of **1**. *i*PrO groups and H-atoms, not involved in hydrogen bonding, are omitted for clarity.

an *anti*-disposition relative to the ethylene spacer, whereas in **2** these fragments are on the same side of the phenylene fragment.

The bis-thioureas crystallize in the monoclinic space groups $P2_1/n$ and $P2_1/c$ for **1** and **2**, respectively. The asymmetric unit contains two independent molecules.

There are intra- and intermolecular hydrogen bonds of the type N—H···O=P in the crystal of **1** (Table 4), whereas intramolecular hydrogen bonds of the type N—H···O=P and intermolecular H-bonds of types N—H···O=P and N—H···S=C are observed in the crystal of **2** (Table 4). The intramolecular H-bonds are formed between the oxygen atoms of the P=O groups and the hydrogen atoms of the —$NHCH_2CH_2NH$— (**1**) or —NHC_6H_4-2-NH— (**2**) fragments, which in turn leads to the *E*-*E*-conformation of the S—C—N—P backbones. The intermolecular H-bonds in **1** are formed between the oxygen atoms of the P=O groups and the hydrogen atoms of the PNH groups. In **2**, these bonds are formed between the H-atom of one PNH group of a molecule, and the P=O oxygen atom of the neighboring molecule, while the H-atom of the other PNH group forms intermolecular hydrogen bonds with the C=S sulfur atom of a further neighboring molecule. As a result of the intermolecular H-bonds 3D structures are formed in the crystals of **1** and **2** (Figs. 4 and 5).

4. Conclusions

In summary, we have demonstrated the syntheses of two new *N*-phosphorylated bis-thioureas and a dithiobiurea by addition of phosphorylisothiocyanate to the corresponding bis-amine or hydrazine. An *E*-*E*-arrangement of the C=S and P—N bonds in the SCNPS backbones was found both in the crystal phase and in $CDCl_3$ solution for the bis-thioureas **1** and **2**. The 2,5-dithiobiurea **3** is present as a mixture of *E*- and *Z*-conformation isomers, stabilized by H-bonds in DMSO-d_6 and $CDCl_3$ solutions. Comparison of the ^{31}P NMR data indicates the superiority of the *E*-*E*-isomer. Moreover, according to the NMR data the dithiobiurea **3** partially decomposes in $CDCl_3$ solution, with the elimination of an isothiocyanate molecule. Single crystal X-ray diffraction studies showed the bis-thioureas **1** and **2** to form both intra- and intermolecular hydrogen bonds, which in turn lead to the formation of 3D structures.

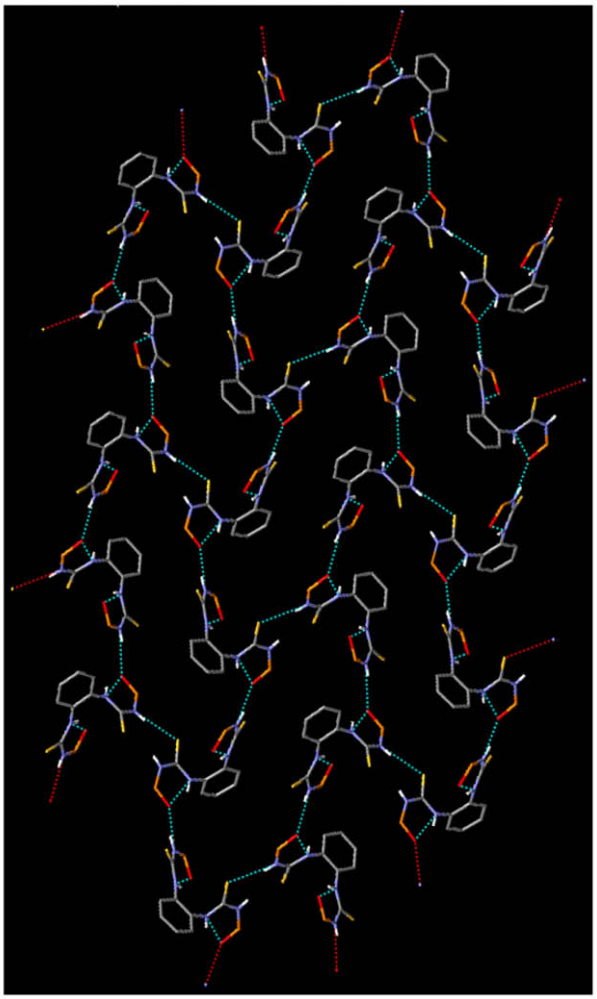


Fig. 5. Crystal packing of **2**. *i*PrO groups and H-atoms, not involved in hydrogen bonding, are omitted for clarity.

5. Supplementary data

CCDC 719775 and CCDC 719776 contain the supplementary crystallographic data for **1** and **2**. These data can be obtained free of charge via http://www.ccdc.cam.ac.uk/conts/retrieving.html, or from the Cambridge Crystallographic Data Centre, 12 Union Road, Cambridge CB2 1EZ, UK; fax: +44 1223 336 033; or e-mail: deposit@ccdc.cam.ac.uk.

Acknowledgments

This work was supported by the Russian Science Support Foundation. MGB and DAS thank DAAD for the scholarships (Forschungsstipendien 2008/2009).

References

[1] F.D. Sokolov, V.V. Brusko, N.G. Zabirov, R.A. Cherkasov, Curr. Org. Chem. 10 (2006) 27.
[2] D.A. Safin, M.G. Babashkina, F.D. Sokolov, N.G. Zabirov, J. Galezowska, H. Kozlowski, Polyhedron 26 (2007) 1113.

[3] N.G. Zabirov, V.V. Brusko, A.Y. Verat, D.B. Krivolapov, I.A. Litvinov, R.A. Cherkasov, Phosphorus, Sulfur and Silicon 177 (2002) 1869.
[4] A.Y. Verat, F.D. Sokolov, N.G. Zabirov, M.G. Babashkina, D.B. Krivolapov, V.V. Brusko, I.A. Litvinov, Inorg. Chim. Acta. 359 (2006) 475.
[5] N.G. Zabirov, V.V. Brusko, A.Y. Verat, D.B. Krivolapov, I.A. Litvinov, R.A. Cherkasov, Polyhedron 23 (2004) 2243.
[6] H. Tsukube, Talanta 40 (1993) 1313.
[7] F.C.J.M. van Vegel, W. Verboom, D.N. Reinhoudt, Chem. Rev. 94 (1994) 279.
[8] A.E.V. Gorden, J. Xu, K.N. Raymond, P. Durbin, Chem. Rev. 103 (2003) 4207.
[9] M. Ouchi, T. Hakushi, Coord. Chem. Rev. 148 (1996) 171.
[10] F.D. Sokolov, D.A. Safin, M.G. Babashkina, N.G. Zabirov, V.V. Brusko, N.A. Mironov, D.B. Krivolapov, I.A. Litvinov, R.A. Cherkasov, B.N. Solomonov, Polyhedron 26 (2007) 1550.
[11] Stoe & Cie. X-Area, Area-Detector Control and Integration Software, Stoe & Cie, Darmstadt, Germany, 2001.
[12] A.L. Spek, J. Appl. Cryst. A36 (2003) 7.
[13] G.M. Sheldrick, Acta Cryst. A64 (2008) 112.
[14] F.D. Sokolov, D.A. Safin, M. Bolte, E.R. Shakirova, M.G. Babashkina, Polyhedron 27 (2008) 3141.

upon the formation constant and the free energy of the complexes formed was studied.

2. Experimental

2.1. Reagents

The salicylaldehyde, 4-methoxysalicylaldehyde, 5-methoxysalicylaldehyde, 5-chlorosalicylaldehyde, 5-bromosalicylaldehyde, 5-nitrosalicylaldehyde, 5-sodium sulfitesalicylaldehyde, 2,4-dihydroxysalicylaldehyde, 2-hydroxyacetophenone, 2-hydroxybenzophenone, 1,2-ethylendiamine, 1,2-diaminopropane, ammonia solution, carbon disulfide, dimethylsulfate, cyclopentanone, methanol, ethanol, chloroform, hydrochloric acid and nickel acetate tetrahydrate were commercially obtained from Merck or Fluka and were used without further purification. Spectrograde solvents were used for spectral measurements.

2.2. Physical measurements

UV–Vis measurements were carried out in JASCO V-530 and Perkin–Elmer (LAMBDA 2) UV–Vis spectrophotometers. The NMR spectra were recorded on a Bruker Avance DPX 250 MHz spectrometer. IR spectra were recorded by a Shimadzu FT-IR 8300 infrared spectrophotometer. Elemental analyses were carried out by a Termo Sininngan-Flash-1200 and mass spectra were obtained on a Perkin–Elmer R MU-6E instrument.

2.3. Synthesis

Methyl-2-{N-(2′-aminoethane)}-amino-1-cyclopentenedithiocarboxylate (Hcden) and methyl-2-(1-methyl-2′-aminoethane)-amino-1-cyclopentenedithiocarboxylate (HcdMeen) were prepared by published methods [24–27]. The ligands were prepared by the addition of an equimolar amount of the appropriate salicylaldehyde derivatives and other diketones to a methanolic solution of Hcden and HcdMeen. The yellow products were recrystallized from methanol/chloroform 1:1 (V:V). To a solution of the appropriate ligand (0.1 mmol) in 10 mL of chloroform/methanol 2:1 (V:V), a solution of nickel(II) acetate (0.1 mmol) in 10 mL of methanol was added. The solution was stirred for 15 min and then allowed to stand at room temperature for 24 h. After filtering, the crude product was recrystallized from acetonitrile/methanol 1:1 (V:V), (see Scheme 1).

2.4. Thermodynamic studies

The formation constant measurements were carried out by spectrophotometric titration of the ligands H_2cdXsalen and H_2cdXsalMeen with a solution of nickel ions at constant ionic strength 0.1 M ($NaClO_4$) at 25 °C. In a typical measurement, 2.5 mL solution of the ligand (10^{-5} M) in DMF was titrated with various concentrations of the metal acetate (10^{-5}–10^{-4} M) in DMF. UV–Vis spectra were recorded in the range 290–700 nm about 5 min after each addition. The formed product showed a different absorption from the free ligand, while the metal ion solution showed no absorption at those wavelengths. As an example, the variation of the electronic spectra for [H_2cd5Clsalen] titrated with various concentrations of Ni(II) acetate at 25 °C in DMF is shown in Fig. 1. The same is valid for the other systems. Also the electronic spectra of the complexes formed during the titrations were the same as the electronic spectra of the separately synthesized complexes (Fig. 2).

2.5. Crystal structure determination

The data for the nickel(II) complex were collected on a Bruker SMART APEXII CCD area detector diffractometer with MoKα radiation (λ = 0.71073 Å) equipped with an Oxford cryosystem Cobra low temperature attachment. Cell parameters were retrieved using SMART [28] software and refined using SAINT [29] on all observed reflections. Data reduction and correction for Lp and decay were performed using SAINT PLUS software. Absorption corrections were applied using SADABS [30]. The structure was solved by direct methods and refined by the least squares method on F^2 using the SHELXTL program package [31]. All non-hydrogen atoms were refined anisotropically. A riding model was used in the refinement process of the geometrically calculated hydrogen positions of the [Ni(cdClsalen)] complex.

3. Results and discussion

The elemental analyses and the physical constants of the prepared ligands and their complexes are shown in Tables 1 and 2. All the ligands and their complexes gave satisfactory elemental analysis.

3.1. IR and ^{1}H NMR spectra

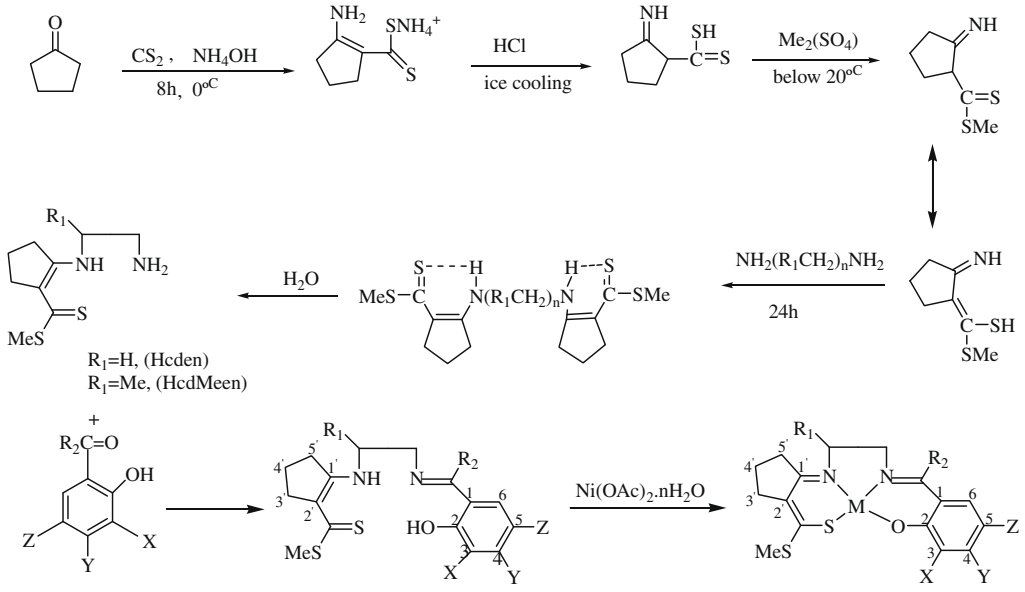
The IR and ^{1}H NMR spectra are in accord to the proposed structures. The ^{1}H NMR spectra of the ligands and the nickel Schiff base complexes are collected in Tables 3 and 4. The OH proton signals in the ^{1}H NMR spectra of the free ligands are observed at 12.45–15.58 ppm and NH or SH proton signals are observed around 12.18–12.52 ppm, and these disappear in the Ni(II) complexes, indicating that the OH and NH or SH groups have been deprotonated and bond to the metal ions [32]. The azomethine proton signals of the ligands (8.22–8.63 ppm), are shifted to higher fields in the Ni(II) complexes, confirming the coordination of the metal ion to those groups. On the other hands, the FT-IR spectra of all the complexes, compared with those of the corresponding ligands, indicate that the ν(C=N) band around 1600 cm^{-1} [33], ν(C—O) band at 1220–1286 cm^{-1} [34,35], ν(C=C) band in the region of 1456–1496 cm^{-1} [36], ν(C—S) band at 700–790 cm^{-1} and ν(C—S)+ν(C—N) cm^{-1} bands between 1099 and 1180 cm^{-1} are shifted to lower energies. These results show that the Ni(II) ion is coordinated through the nitrogen atoms of the amine group, oxygen atom of the phenolic group and sulfur of the C=S group for all the complexes [37–39] (see Tables 5 and 6).

The ^{1}H NMR spectra of the substituted phenyl ring of the Schiff bases show additional signals. A singlet signal at δ = 3.77–3.90 ppm is assigned to those Schiff bases and their complexes that have a OMe group. The Schiff base compound which has a methyl group in the azomethine position (C(CH_3)=N) shows a singlet signal at δ = 2.41 ppm. The signals due to OMe, CH_3 and aromatic protons are also affirmed, showing an upfield change in chemical shift for the Ni(II) complexes.

In IR spectra the appearance of two sharp peaks around 1300 and 1550 cm^{-1} in the ligands H_2L^7 and H_2L^{17} and two absorption bands around 650 and 1200 cm^{-1} in the ligands H_2L^8 and H_2L^{18} are assigned to nitro group and S=O stretching, which undergo minor changes in the corresponding complexes. It may therefore indicate that they are not coordinated to the metal ions [40].

3.2. The electronic spectra

The electronic spectra of the Schiff base ligands in the DMF solvent show a low intensity band in the 310–316 nm region, which is assigned to a π–π^* transition, and a relatively intense band in the 391–400 nm region, which is due to n–π^* excitation [41,42]. The electronic spectra of the Ni(II) complexes of the H_2cdXsalen and H_2cdXsalMeen ligands are very similar, where two or three intense bands in the region 320–476 nm are observed (see Tables 7 and 8).



No	Empirical formula	R_1	R_2	X	Y	Z	Abbreviation of compounds
H_2L^1	$C_{22}H_{24}N_2OS_2$	H	Ph	H	H	H	H_2cdPhsalen
H_2L^2	$C_{17}H_{22}N_2O_2S_2$	H	H	H	OMe	H	H_2cd4OMesalen
H_2L^3	$C_{17}H_{22}N_2O_2S_2$	H	H	H	H	OMe	H_2cd5OMesalen
H_2L^4	$C_{16}H_{20}N_2O_2S_2$	H	H	H	OH	H	H_2cd4OHesalen
H_2L^5	$C_{16}H_{19}N_2ClOS_2$	H	H	H	H	Cl	H_2cd5Clsalen
H_2L^6	$C_{16}H_{19}N_2BrOS_2$	H	H	H	H	Br	H_2cd5Brsalen
H_2L^7	$C_{16}H_{19}N_3O_3S_2$	H	H	H	H	NO_2	H_2cd5NO_2salen
H_2L^8	$C_{16}H_{19}N_2O_4S_3Na$	H	H	H	H	SO_3Na	H_2cd5SO_3Nasalen
H_2L^9	$C_{18}H_{24}N_2OS_2$	Me	Me	H	H	H	H_2cdMesalMeen
H_2L^{10}	$C_{23}H_{26}N_2OS_2$	Me	Ph	H	H	H	H_2cdPhsalMeen
H_2L^{11}	$C_{18}H_{24}N_2O_2S_2$	Me	H	OMe	H	H	H_2cd3MesalMeen
H_2L^{12}	$C_{18}H_{24}N_2O_2S_2$	Me	H	H	OMe	H	H_2cd4OMesalMeen
H_2L^{13}	$C_{18}H_{24}N_2O_2S_2$	Me	H	H	H	OMe	H_2cd5OMesalMeen
H_2L^{14}	$C_{17}H_{22}N_2O_2S_2$	Me	H	H	OH	H	H_2cd4OHsalMeen
H_2L^{15}	$C_{17}H_{21}N_2ClOS_2$	Me	H	H	H	Cl	H_2cd5ClsalMeen
H_2L^{16}	$C_{17}H_{21}N_2BrOS_2$	Me	H	H	H	Br	H_2cd5BrsalMeen
H_2L^{17}	$C_{17}H_{21}N_3O_3S_2$	Me	H	H	H	NO_2	H_2cd5NO_2salMeen
H_2L^{18}	$C_{17}H_{21}N_2O_4S_3Na$	Me	H	H	H	SO_3Na	H_2cd5SO_3NasalMeen

Scheme 1.

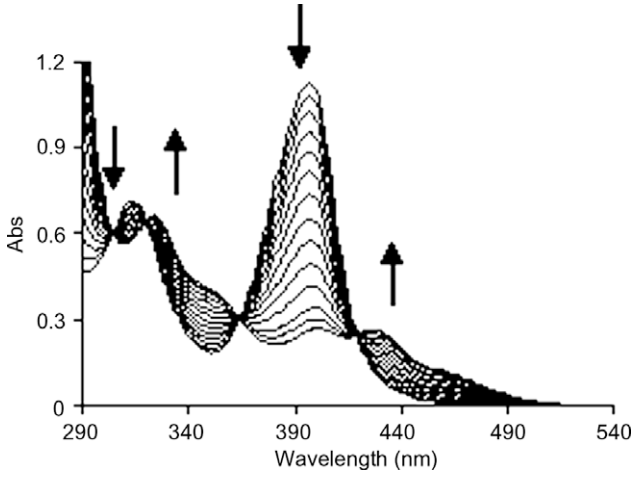


Fig. 1. The variation of the electronic spectra of H_2cd5Clsalen with Ni(II) acetate at 25 °C in DMF, $[H_2cd5Clsalen] = 5 \times 10^{-5}$ and $[Ni^{2+}] = 5 \times 10^{-6}$.

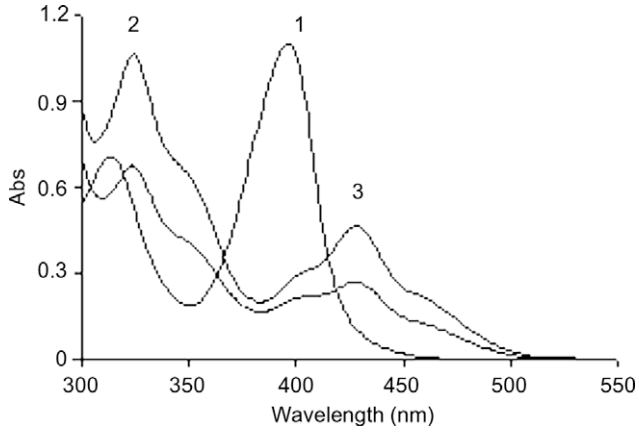


Fig. 2. UV–Vis spectra of the ligand [H_2cd5Clsalen] (1), the end point of the titration of the ligand with Ni^{+2} (2), and the synthesized [Ni(cd5Clsalen)] complex (3) in DMF.

Table 1
Analytical and physical data of the ligands.

Ligand	Formula weight	Yield (%)	m.p. (°C)	Anal. Found (*Anal.* Calc.)(%)			
				C	H	N	S
H_2L^1	396.56	67	186	66.33(66.63)	6.01(6.10)	7.02(7.06)	16.28(16.17)
H_2L^2	350.49	75	87	58.42(58.26)	6.45(6.33)	7.76(7.99)	17.98(18.29)
H_2L^3	350.49	85	137	58.49(58.26)	6.03(6.33)	7.89(7.99)	18.56(18.29)
H_2L^4	336.46	83	187	57.07(57.12)	6.05(5.99)	8.07(8.33)	19.26(19.06)
H_2L^5	354.91	70	121	54.33(54.15)	5.19(5.40)	7.77(7.89)	18.14(18.07)
H_2L^6	399.36	70	129	48.00(48.12)	5.01(4.80)	6.67(7.01)	15.78(16.06)
H_2L^7	365.46	93	191	52.68(52.58)	5.55(5.24)	11.73(11.50)	17.32(17.54)
H_2L^8	422.50	57	267	45.18(45.48)	4.65(4.53)	6.42(6.63)	22.48(22.76)
H_2L^9	348.52	63	146	61.95(62.03)	6.92(6.94)	8.32(8.04)	18.14(18.40)
H_2L^{10}	410.59	63	124	66.97(67.28)	6.47(6.38)	6.95(6.82)	15.31(15.62)
H_2L^{11}	364.52	78	113	59.03(59.31)	6.82(6.64)	7.93(7.69)	17.28(17.59)
H_2L^{12}	364.52	73	117	58.98(59.31)	6.65(6.64)	7.86(7.69)	17.64(17.59)
H_2L^{13}	364.52	83	152	59.07(59.31)	6.75(6.64)	7.84(7.69)	17.32(17.59)
H_2L^{14}	350.49	81	174	58.43(58.26)	6.27(6.33)	7.74(7.99)	18.40(18.29)
H_2L^{15}	368.93	72	89	55.63(55.34)	5.62(5.74)	7.34(7.59)	17.15(17.38)
H_2L^{16}	413.39	70	87	49.13(49.39)	5.09(5.12)	6.68(6.78)	15.70(15.51)
H_2L^{17}	379.49	93	152	53.98(53.81)	5.41(5.58)	11.03(11.07)	16.71(16.90)
H_2L^{18}	436.53	55	237	46.48(46.77)	5.06(4.85)	6.68(6.42)	21.79(22.03)

Table 2
Analytical and physical data of the nickel(II) complexes.

Complexes	Formula weight	Yield (%)	m.p. (°C)	Anal. Found (*Anal.* Calc.)(%)			
				C	H	N	S
NiL^1	453.24	76	>265	58.03(58.30)	4.94(4.89)	5.98(6.18)	14.35(14.15)
NiL^2	407.17	76	237	49.99(50.15)	4.94(4.95)	6.98(6.88)	15.84(15.75)
NiL^3	407.17	84	214	50.07(50.15)	4.86(4.95)	6.62(6.88)	15.80(15.75)
NiL^4	393.15	82	263	47.52(47.79)	4.89(4.76)	6.90(6.97)	15.63(15.94)
NiL^5	410.60	75	250	46.42(46.69)	4.21(4.31)	6.83(6.66)	15.43(15.24)
NiL^6	456.04	75	240	41.87(42.14)	4.02(3.76)	5.96(6.14)	13.88(14.06)
NiL^7	422.14	94	>265	44.82(44.57)	4.04(4.21)	9.98(9.75)	14.76(14.87)
NiL^8	479.19	57	>265	39.81(40.14)	3.74(3.58)	5.67(5.85)	19.95(20.07)
NiL^9	405.20	63	254	53.45(53.36)	5.64(5.47)	6.85(6.91)	15.64(15.82)
NiL^{10}	467.27	63	247	59.07(59.12)	5.48(5.18)	6.09(6.00)	13.56(13.72)
NiL^{11}	421.20	77	193	51.21(51.33)	5.38(5.26)	6.41(6.65)	14.91(15.22)
NiL^{12}	421.20	75	249	51.24(51.33)	5.42(5.26)	6.38(6.65)	15.07(15.22)
NiL^{13}	421.20	81	204	51.02(51.33)	5.55(5.26)	6.46(6.65)	14.99(15.22)
NiL^{14}	407.17	79	178	50.35(50.15)	4.98(4.95)	6.58(6.88)	15.83(15.75)
NiL^{15}	425.62	69	240	47.65(47.97)	4.53(4.50)	6.74(6.58)	15.21(15.06)
NiL^{16}	470.07	69	233	43.66(43.44)	4.22(4.07)	5.78(5.96)	13.78(13.64)
NiL^{17}	436.17	94	226	46.05(45.87)	4.26(4.53)	9.47(9.44)	14.37(14.40)
NiL^{18}	493.21	54	>265	41.24(41.40)	3.98(3.88)	5.38(5.68)	19.56(19.50)

Table 3
^{1}H NMR data (250 MHz, room temperature, TMS, ppm) of the ligands.

No	OH proton	NH or SH proton	Imine proton	Phenyl proton	Diamine proton	SCH_3	Substituted (*X,Y,Z*)
H_2L^{1a}	14.89	12.29	–	6.57–7.50	3.60–3.68	2.57	–
H_2L^{2a}	13.32	12.38	8.27	6.40–7.11	3.66–3.76	2.57	3.81
H_2L^{3a}	12.70	12.45	8.37	6.77–6.90	2.77–3.47	2.60	3.77
H_2L^{4b}	13.26	12.18	8.31	6.17–7.15	3.69–4.08	2.48	–
H_2L^{5a}	12.84	12.35	8.33	6.84–7.23	3.71–3.85	2.57	–
H_2L^{6a}	12.87	12.34	8.32	6.84–7.40	3.71–3.83	2.58	–
H_2L^{7a}	13.99	12.33	8.48	7.01–8.21	3.77–3.90	2.55	–
H_2L^{8b}	13.14	12.22	8.63	6.77–7.66	3.71–3.79	2.48	–
H_2L^{9a}	15.58	12.52	–	6.80–7.53	1.48 and 3.71–3.76	2.57	2.41
H_2L^{10a}	15.00	12.27	–	6.64–7.47	1.23 and 2.77–3.54	2.52	–
H_2L^{11a}	13.39	12.37	8.37	6.81–6.92	1.39 and 3.48–3.56	2.56	3.90
H_2L^{12a}	13.53	12.38	8.26	6.40–7.09	1.37 and 2.76–3.52	2.56	3.81
H_2L^{13a}	12.45	12.37	8.28	6.73–7.24	1.39 and 3.52–3.55	2.56	3.77
H_2L^{14a}	13.26	12.37	8.22	6.32–7.05	1.37 and 3.51–3.53	2.55	–
H_2L^{15a}	12.91	12.32	8.32	6.88–7.20	1.39 and 3.50–3.86	2.56	–
H_2L^{16a}	12.93	12.33	8.27	6.83–7.40	1.39 and 3.49–3.88	2.57	–
H_2L^{17a}	14.06	12.30	8.46	6.99–8.20	1.43 and 3.61–3.66	2.55	–
H_2L18^b	13.12	12.21	8.62	6.77–7.66	1.26 and 3.47–3.62	2.39	–

[a] Solvent is $CDCl_3$.
[b] Solvent is DMSO-d_6.

Table 4
^{1}H NMR data (250 MHz, room temperature, TMS, ppm) of the Ni(II) complexes.

No	OH proton	NH or SH proton	Imine proton	Phenyl proton	Diamine proton	SCH_3	Substituted (*X,Y,Z*)
NiL[1a]	–	–	–	6.27–7.49	3.06–3.16	2.70	–
NiL[2a]	–	–	7.62	6.16–6.95	3.22–3.46	2.68	3.72
NiL[3a]	–	–	7.70	6.52–6.83	3.20–3.49	2.67	3.70
NiL[4a]	–	–	7.64	6.13–6.98	3.21–3.43	2.67	–
NiL[5a]	–	–	7.70	6.72–7.07	3.23–3.53	2.67	–
NiL[6a]	–	–	7.69	6.67–7.18	3.21–3.50	2.67	–
NiL[7a]	–	–	8.19	6.75–7.96	3.28–3.59	2.69	–
NiL[8b]	–	–	8.13	6.41–7.49	3.13–3.50	2.48	–
NiL[9a]	–	–	–	6.48–7.42	1.33 and 3.16–3.44	2.67	2.33
NiL[10a]	–	–	–	6.28–7.52	1.37 and 3.20–3.42	2.70	–
NiL[11a]	–	–	7.72	6.41–6.73	1.47 and 3.38–3.57	2.68	3.75
NiL[12a]	–	–	7.57	6.13–6.96	1.43 and 2.86–3.50	2.65	3.72
NiL[13a]	–	–	7.66	6.54–6.83	1.46 and 2.86–3.57	2.67	3.71
NiL[14a]	–	–	7.58	6.10–6.98	1.41 and 2.85–3.76	2.67	–
NiL[15a]	–	–	7.65	6.72–7.25	1.45 and 2.87–3.58	2.67	–
NiL[16a]	–	–	7.62	6.67–7.16	1.47 and 2.87–3.55	2.67	–
NiL[17a]	–	–	8.18	6.75–8.00	1.41 and 2.68–3.65	2.63	–
NiL[18b]	–	–	8.10	6.39–7.51	1.33 and 2.87–3.65	2.49	–

[a] Solvent is $CDCl_3$.
[b] Solvent is DMSO-d_6.

Table 5
IR characterization of the Schiff base ligands (in cm^{-1} unit).

No	(C—S)	(C—S + C—N)	Phenolic (C—O)	(C=C)	(C=N)	Substituted (*Y,Z*)
H_2L^1	759	1150	1278	1481	1600	–
H_2L^2	794	1126	1280	1496	1629	–
H_2L^3	783	1161	1269	1485	1635	–
H_2L^4	786	1172	1234	1465	1625	3425
H_2L^5	792	1190	1263	1481	1639	–
H_2L^6	776	1150	1259	1477	1633	–
H_2L^7	725	1180	1265	1487	1653	1338, 1550
H_2L^8	720	1110	1265	1488	1651	650, 1200
H_2L^9	768	1151	1273	1475	1616	–
H_2L^{10}	763	1143	1272	1471	1605	–
H_2L^{11}	786	1156	1269	1456	1624	–
H_2L^{12}	786	1166	1265	1478	1629	–
H_2L^{13}	783	1157	1276	1481	1635	–
H_2L^{14}	786	1114	1272	1477	1629	3402
H_2L^{15}	750	1166	1274	1473	1622	–
H_2L^{16}	790	1151	1275	1475	1629	–
H_2L^{17}	752	1099	1266	1477	1649	1332, 1550
H_2L^{18}	729	1130	1275	1482	1630	650, 1200

Table 6
IR characterization of the Ni(II) complexes (in cm^{-1} unit).

No	(C—S)	(C—S + C—N)	Phenolic (C—O)	(C=C)	(C=N)	Substituted (*Y,Z*)
NiL[1]	746	1143	1266	1463	1598	
NiL[2]	770	1118	1265	1461	1620	
NiL[3]	771	1161	1228	1461	1627	
NiL[4]	740	1120	1215	1461	1621	3403
NiL[5]	712	1150	1260	1460	1629	
NiL[6]	727	1107	1250	1463	1625	
NiL[7]	719	1107	1255	1461	1635	1335, 1548
NiL[8]	718	1029	1260	1463	1627	648, 1198
NiL[9]	744	1141	1265	1447	1600	
NiL[10]	750	1130	1251	1444	1598	
NiL[11]	738	1061	1245	1470	1624	
NiL[12]	725	1122	1220	1462	1608	
NiL[13]	763	1145	1253	1461	1627	
NiL[14]	780	1072	1272	1461	1612	3259
NiL[15]	746	1122	1274	1460	1616	
NiL[16]	768	1135	1275	1458	1617	
NiL[17]	752	1094	1251	1461	1624	1332, 1546
NiL[18]	704	1112	1274	1468	1629	648, 1200

Table 7
UV–Vis bands λ_{max}(DMF/nm) of the Schiff bases ligands.

No	π–π^*	n–π^*
H_2L^1	310	396
H_2L^2	312	398
H_2L^3	316	398
H_2L^4	310	396
H_2L^5	314	396
H_2L^6	313	397
H_2L^7	316	396
H_2L^8	314	400
H_2L^9	315	392
H_2L^{10}	314	395
H_2L^{11}	316	393
H_2L^{12}	312	398
H_2L^{13}	314	398
H_2L^{14}	312	391
H_2L^{15}	314	395
H_2L^{16}	314	398
H_2L^{17}	313	398
H_2L^{18}	314	396

Table 8
UV–Vis bands λ_{max}(DMF/nm) of the Ni(II) complexes.

No	π–π^*	n–π^*	Charge transfer
NiL^1	322	420	464(sh)
NiL^2	325	414	476(sh)
NiL^3	330	428	472(sh)
NiL^4	322	410	474(sh)
NiL^5	324	428	466(sh)
NiL^6	325	430	468(sh)
NiL^7	320	410	475(sh)
NiL^8	326	426	464(sh)
NiL^9	324	426	468(sh)
NiL^{10}	324	430	464(sh)
NiL^{11}	325	428	466(sh)
NiL^{12}	322	416	474(sh)
NiL^{13}	330	426	470(sh)
NiL^{14}	324	414	472(sh)
NiL^{15}	326	430	475(sh)
NiL^{16}	324	428	464(sh)
NiL^{17}	320	416	468(sh)
NiL^{18}	326	428	464(sh)

sh: Shoulder.

Table 9
Mass spectral data of the Schiff base ligands.

No	m/z
H_2L^1	397, 396, 224, 198, 152, 135, 108, 83, 57
H_2L^2	351, 350, 303, 199, 152, 135, 111
H_2L^3	351, 350, 304, 196, 160, 140, 110, 87, 59
H_2L^4	337, 336, 186, 152, 135, 108, 71
H_2L^5	354, 257, 236, 211, 194, 171, 127, 111, 83
H_2L^6	400, 399, 352, 310, 256, 239, 212, 135
H_2L^7	366, 365, 318, 199, 169, 152, 138, 108
H_2L^8	423, 422, 212, 184, 152, 128, 92, 69
H_2L^9	349, 348, 301, 257, 213, 183, 166, 107, 91, 58
H_2L^{10}	411, 410, 363, 319, 238, 165, 149, 122, 105, 77, 55
H_2L^{11}	365, 364, 256, 213, 175, 151, 126
H_2L^{12}	365, 364, 317, 301, 279, 256, 235, 213, 183, 166, 97
H_2L^{13}	365, 364, 287, 186, 166, 150, 123, 97, 81, 57
H_2L^{14}	351, 350, 236, 213, 166, 149, 111, 83
H_2L^{15}	369, 368, 322, 278, 257, 214, 149, 69
H_2L^{16}	413, 412, 365, 254, 213, 186, 166, 149, 122, 97
H_2L^{17}	380, 379, 368, 257, 236, 121, 83, 58
H_2L^{18}	437, 436, 256, 236, 208, 185, 167, 111, 87, 45

Table 10
Mass spectral data of the Ni(II) complexes.

No	m/z
NiL^1	453, 375, 367, 314, 236, 208, 185, 165, 123, 97, 71, 55
NiL^2	407, 386, 350, 301, 278, 149, 111, 83
NiL^3	407, 376, 320, 256, 191, 152, 129, 57
NiL^4	392, 375, 318, 286, 264, 194, 151, 111
NiL^5	410, 373, 321, 305, 195, 137, 121, 97, 69
NiL^6	456, 412, 375, 349, 305, 285, 257, 236, 194
NiL^7	421, 375, 349, 315, 264, 236, 195, 168, 152, 137, 111, 55
NiL^8	479, 466, 398, 372, 262, 236, 152, 133, 83
NiL^9	405, 367, 236, 152, 137, 124, 111, 83, 56
NiL^{10}	467, 465, 416, 373, 235, 208, 152,83
NiL^{11}	421, 406, 389, 315, 231, 192, 162, 149, 57
NiL^{12}	422, 421, 405, 389, 325, 225, 185, 152, 134, 80
NiL^{13}	421, 408, 399, 338, 230, 191, 173, 150, 104
NiL^{14}	407, 369, 283, 255, 236, 207, 185, 149, 129, 111, 83
NiL^{15}	425, 369, 315, 231, 196, 165, 137, 55
NiL^{16}	470, 455, 380, 325, 236, 213, 167, 149, 133, 97
NiL^{17}	435, 420, 388, 372, 196, 171, 150, 129, 110, 85
NiL^{18}	493, 413, 387, 302, 286, 267, 134, 106

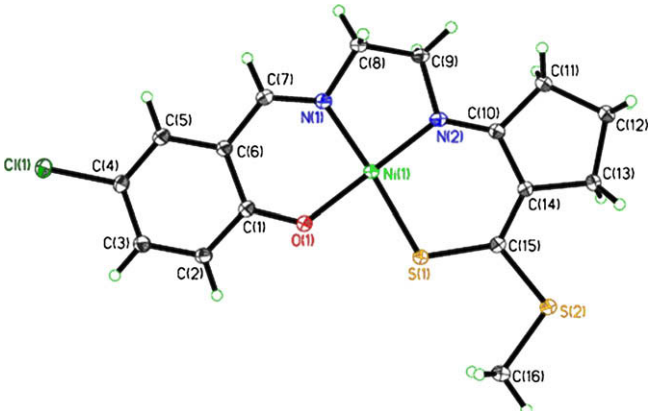


Fig. 3. Molecular structure of the complex [Ni(cd5Clsalen)] with the atom numbering scheme. Displacement ellipsoids are drawn at the 50% probability level.

Table 11
Crystal data, data collection and structure refinement parameters of Ni(cd5Clsalen)].

Crystal shape	prismatic needle
Chemical formula	$C_{16}H_{17}ClN_2NiOS_2$
Formula weight	411.60
Crystal system	triclinic
Space group	$P\bar{1}$
Unit cell dimensions	
a (Å)	8.261(2)
b (Å)	9.261(2)
c (Å)	10.802(2)
α (°)	93.636(10)
β(°)	98.111(10)
γ(°)	91.278(10)
Cell volume (Å^3)	816.15(3)
Z value	2
Calculated density (g/cm^3)	1.675
μ (mm^{-1})	1.612
F(0 0 0)	424
Crystal size (mm)	0.43 × 0.18 × 0.12
θ range for data collection (°)	2.2–40.0
Index range	h – 14 to 14, k – 16 to 15, l –19 to 19
Independent reflections	10,025 (R_{int} = 0.044)
Reflections with [$I > 2\sigma(I)$]	7727
Minimum and maximum transmission	0.542 and 0.833
Structure solution	direct method
Goodness of fit on F^2	1.07
Largest and mean shift/su	0.00 and 0.00
Largest diff, peak and hole (eÅ^3)	1.24 and −0.88
Final R indices [$F^2 > 2\sigma$]	R = 0.0373, wR_2 = 0.095
$(\Delta/\sigma)_{max}$	0.001

$w = 1/[\sigma 2(F_o)^2 + (0.0462P)^2 + 0.0079\ P]$ where $P = (F_o^2+2F_c^2)/3$.

Table 12
Selected bond lengths(Å) and angles (°) for the complex [Ni(cd5Clsalen)].

Ni1–O1	1.867(8)	N1–C8	1.463(15)
Ni1–N1	1.872(10)	N2–C9	1.478(15)
Ni1–N2	1.875(9)	N2–C10	1.314(14)
Ni1–S1	2.166(3)	C1–C6	1.420(15)
S1–C15	1.714(11)	C1–O1	1.307(14)
S2–C15	1.760(11)	C6–C7	1.436(16)
S2–C16	1.795(13)	C10–C14	1.425(15)
N1–C7	1.286(15)	C14–C15	1.371(16)
O1–Ni1–N1	93.53(4)	N1–Ni1–N2	86.43(4)
O1–Ni1–N2	176.64(4)	N1–Ni1–S1	173.68(3)
O1–Ni1–S1	82.28(3)	N2–Ni1–S1	98.04(3)

The observed bands in the region 460–476 nm are probably due to S–M and O–M, LMCT transitions, and occur at energies similar to those found for the corresponding symmetric metal complexes [M(salen)] [43] and [M(cd$_2$en)] [32]. The d–d bands are not ob-

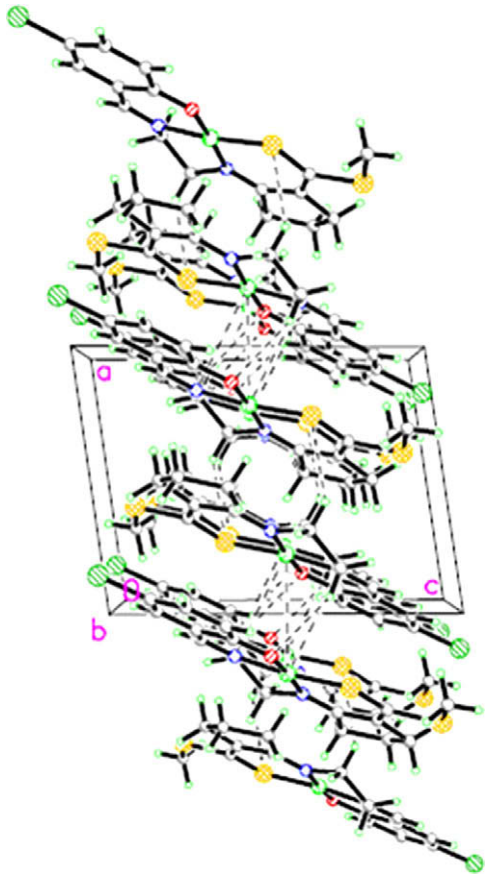


Fig. 4. The crystal packing in [Ni(cd5Clsalen)], showing the one-dimensional infinite chain along the *a*-axis. Intermolecular interactions are shown as dashed lines.

Table 13
Selected bond lengths (Å) and bond angles (°) for [Ni(cdsalen)], [Ni(cdClsalen)], [Ni(cd_2en)] and [Ni(salen)].

Complex	[Ni(cdClsalen)]	[Ni(cdsalen)]	[Ni(cd_2en)]	[Ni(salen)]
Ni1–N1	1.872(10)	1.872(5)	1.893(6)	1.853(2)
Ni1–N2	1.875(9)	1.867(5)	1.902(11)	1.843(2)
Ni1–O1	1.867(8)	1.860(4)	–	1.850(2)
Ni1–O2	–	–	–	1.855(2)
Ni1–S1	2.166(3)	2.163(3)	2.174(4)	–
Ni1–S2	–	–	2.170(2)	–

served due to the low concentration ($\sim 10^{-4}$ M) of the complexes in solution. These bands should be low in intensity in the region of 600–700 nm.

Analysis of the results shows that the positions of the *d*–*d* and LMCT bands are not very sensitive to the different substituents (R_1, R_2, *X*, *Y*, *Z*) of the ligand, and may not be directly related to the electron donor/acceptor ability of the substituent. This behavior has been observed for square planar Ni(II) complexes and was explained by the electronic and structural effects induced by the substituents which may have opposite effects [44].

Fig. 2 shows the electronic spectral change observed in DMF solution when the Ni^{2+} ion was added to the Schiff base ligand [H_2cd5Clsalen]. In the absence of the Ni^{2+} ion, the yellow [H_2cd5Clsalen] solution showed absorption bands at 314 and 396 nm. As the Ni^{2+} ion solution was added, the signals of [H_2cd5Clsalen] decreased and those of the complex [Ni(cd5Clsalen)], at 324, 428 and 466 (sh) nm increased in intensity with isosbestic points at 304, 319, 363, 418 and 512 nm. The last spectrum

Table 14
The formation constants, logK_f, and the free energy, $\Delta G°$, for the complexes of the unsymmetrical ligands with the Ni^{2+} ion at 25 °C, in DMF.

Ligand	Ni^{2+}	
	logK_f	$\Delta G°$ (kJ mol^{-1})
H_2cdsalen [26]	4.21(0.08)	−24.01(0.19)
H_2cdMesalen [26]	4.85(0.12)	−27.66(0.29)
H_2L^1	3.63(0.04)	−20.70(0.09)
H_2cd3OMesalen [26]	4.78(0.13)	−27.26(0.32)
H_2L^2	4.75(0.18)	−27.09(0.44)
H_2L^3	4.86(0.14)	−27.71(0.34)
H_2L^4	4.76(0.05)	−27.14(0.12)
H_2L^5	3.88(0.11)	−22.12(0.27)
H_2L^6	4.11(0.16)	−23.44(0.39)
H_2L^7	3.65(0.14)	−20.81(0.34)
H_2L^8	3.70(0.06)	−21.10(0.14)
H_2cdsalMeen [27]	4.23(0.22)	−24.12(0.54)
H_2L^9	4.87(0.14)	−27.77(0.34)
H_2L^{10}	3.63(0.13)	−20.70(0.32)
H_2L^{11}	4.83(0.17)	−27.54(0.42)
H_2L^{12}	4.80(0.15)	−24.37(0.37)
H_2L^{13}	4.89(0.08)	−27.88(0.19)
H_2L^{14}	4.79(0.02)	−27.31(0.04)
H_2L^{15}	3.93(0.18)	−22.41(0.44)
H_2L^{16}	4.17(0.14)	−23.78(0.34)
H_2L^{17}	3.68(0.02)	−20.98(0.04)
H_2L^{18}	3.73(0.16)	−21.27(0.39)

The numbers in parentheses are the standard deviations.

of the titration was similar to the spectrum of the [Ni(cd5Clsalen)] complex that has been synthesized by published methods [24–27] and characterized separately.

3.3. Mass spectra

The mass spectra of all the ligands show intense molecular ion peaks *m*/*z* $[M]^+$. The mass spectra of some compounds also show a prominent peak corresponding to *m*/*z* $[M+1]^+$ (see Tables 9 and 10).

3.4. Crystal structure of [Ni(cd5Clsalen)]

The molecular structure of the complex [Ni(cd5Clsalen)] is shown in Fig. 3, in conjunction with the numbering scheme used. Crystal data and details of structure refinement are summarized in Table 11. Relevant bond lengths, bond angles, deviations from best coordination plane are given in Table 12. Full lists of bond lengths, bond angles and anisotropic displacements are available as supplementary material (Fig. 4).

The complex has a N_2OS coordination sphere, with the two nitrogens coordinated in a *cis* configuration. The coordination around nickel is essentially square-planar with a small tetrahedral distortion (dihedral angle of 5.43(3)° between coordination planes NNiO and SNiN). The molecular structures of [Ni(salen)] [43], [Ni(cd_2en)] [32] and [Ni(cdsalen)] [26] have been determined previously and may be compared with the structure of [Ni(cd5Clsalen)]. All bond lengths and bond angles are similar to those reported for the [Ni(salen)] and [Ni(cd_2en)] complexes, and there are only minor differences in the metal-ligand bond lengths. The Ni—N and Ni—O bond lengths of the [Ni(cdClsalen)] complex are 0.019–0.029 Å and 0.012–0.017 Å larger than in [Ni(salen)], while the Ni—N and Ni—S bond lengths are 0.021–0.030 Å and 0.004–0.011 Å shorter than in [Ni(cd_2en)] (see Table 13). These differences indicate that the NO fragment behaves as a weaker ligand, the NS fragment seems to be more tightly bound to the metal ion than in the corresponding symmetric complexes, and may be related to the different steric requirements of the O and S donors.

In addition, bond lengths and bond angles within the ligand are indicative of a strong delocalization of π-electron density in both

Table 15
The formation constants and the free energy values for [(Ni(cdXsalen)] complexes at 25 °C, in DMF.

Ligand	Ni^{2+}	
	logK_f	$\Delta G°$ (kJ mol^{-1})
H_2cd5OMesalen	4.86(0.14)	−27.71(0.34)
H_2cdsalen [26]	4.21(0.08)	−24.01(0.19)
H_2cd5Brsalen	4.11(0.16)	−23.44(0.39)
H_2cd5Clsalen	3.88(0.11)	−22.12(0.27)
H_2cd5SO_3Nasalen	3.70(0.06)	−21.10(0.14)
H_2cd5NO_2salen	3.65(0.14)	−20.81(0.34)

The numbers in parentheses are the standard deviations.

Table 16
The formation constants and the free energy values for [(Ni(cdXsalMeen)] complexes at 25 °C, in DMF.

Ligand	Ni^{2+}	
	log K_f	$\Delta G°$ (kJ mol^{-1})
H_2cd5OMesalMeen	4.89(0.08)	−27.88(0.19)
H_2cdsalMeen [27]	4.23(0.22)	−24.12(0.54)
H_2cd5BrsalMeen	4.17(0.14)	−23.78(0.34)
H_2cd5ClsalMeen	3.93(0.18)	−22.41(0.44)
H_2cd5SO_3NasalMeen	3.73(0.16)	−21.27(0.39)
H_2cd5NO_2salMeen	3.68(0.02)	−20.98(0.04)

The numbers in parentheses are the standard deviations.

the NO and NS six-membered chelate rings, suggesting that the dithioester fragment behaves essentially as a Schiff base ligand, coordinating via an imine nitrogen and a thiolate sulfur.

The molecular structure of [Ni(cdsalen)] [26] has been determined and may be compared with the structure of [Ni(cdClsalen)]. Some selected structural parameters for the complexes are collected in Table 13. The most striking difference lies in the extent of tetrahedral distortion, which is more pronounced in the present complex than in the other one, which has an almost planar structure. The bond lengths are almost independent of the different NO fragments, although the Ni—S bond length is slightly shorter in [Ni(cdsalen)].

3.5. The formation constants and the thermodynamic free energy calculations for unsymmetrical Schiff bases with Ni^{+2} ion in DMF solvent

The formation constants have been determined by UV–Vis absorption spectroscopy through titration of the ligands with various concentrations of the metal ion at 25 °C. The complex formation constants, K_f, were calculated using the SQUAD computer program [45], designed to calculate the best values for the formation constants of the proposed equation model (Eq. (1)) by employing a non-linear, least-squares approach.

$$M(OAc)_2 \cdot nH_2O + H_2L^X \rightarrow ML^X + 2HOAc + (n-2)H_2O \quad (X = 1-18) \tag{1}$$

Also, the free energy change, $\Delta G°$, of the complexes were determined by $\Delta G° = -RT \ln K_f$, at 25 °C where K_f is the complex formation constant, R is the gas constant and T is the temperature in Kelvin. The formation constants and the free energy data are collected in Table 14.

The formation constants in DMF for the series H_2cdXsalMeen are larger than of the H_2cdXsalen series. It was observed that the addition of a methyl group to Schiff base ligands increases the formation constant of the complexes.

3.5.1. The electronic effect of para substituted Schiff base ligands

In this part of the work, we have studied the electronic effect of the *para* substitutional groups bonded to the Schiff base ligands complexed to the Ni(II) ion. The formation constants and the thermodynamic free energies are collected in Tables 15 and 16. On the bases of the thermodynamic results, the formation of the complexes follows the sequence below:

Ni(cd5OMsalen) > Ni(cdsalen) > Ni(cd5Brsalen) > Ni(cd5Clsalen) > Ni(cd5SO_3Nasalen) > Ni(cd5NO_2salen).
and
Ni(cd5OMsalMeen) > Ni(cdsalMeen) > Ni(cd5BrsalMeen) > Ni(cd5ClsalMeen) > Ni(cd5SO_3NasalMeen) > Ni(cd5NO_2salMeen).

This trend is in contrast to our previous work where the charge donation from M(II) (M = Ni, Cu) ion into Schiff base π^* molecular orbital is increased by electron withdrawing groups on the Schiff base ligands [22]. In the *para* substituted Schiff base ligands, the formation constants vary as can be expected according to the electronic effects of the substituents at position 5. Thus, the formation constants decrease according to the sequence OMe > H > Br > Cl > SO_3 > NO_2, i.e. in order of the increase in both electron-withdrawing and π-acceptor qualities of the substituents and the donor ability of the ligand groups (mainly the phenoxy groups). Similar results have been reported previously for the electrochemical properties of the analogous Cu(II), Ni(II) and Co(III) systems [46–48]. The withdrawing functional groups make the Schiff base a poorer donor ligand and decrease the formation constants, while the electron donor groups increase the formation constants because they lead to an increase of the donor ability of Schiff base ligands. Therefore ligands having NO_2 and SO_3 groups, i.e. (H_2cd5NO_2salen), (H_2cd5NO_2salMeen), (H_2cd5SO_3Nasalen) and (H_2cd5SO_3NasalMeen), have the smallest formation constants, while ligands with an OMe group have the highest formation constants because OMe is a donating group [22]. Therefore, in the stabilization of the tetra-coordinated complexes, the donation power of the Schiff base is important, and hence the formation constants, K_f, of Schiff bases with donor groups are higher.

3.5.2. The effect of the position of the methoxy substituents of the Schiff base

In continuation of our studies on the formation constants of the complexes, we have studied the effect of the position of substituents on the phenyl ring of the Schiff base on the formation constant of the complexes, using H_2cd3OMesalen, [26] H_2cd4OMesalen and H_2cd5OMesalen (H_2L^2 and H_2L^3), H_2cd3OMesalMeen, H_2cd4OMesalMeen and H_2cd5OMesalMeen (H_2L^{11}, H_2L^{12} and H_2L^{13}) with the Ni(II) ion. The results show the following trend of complex formation for a given cation towards the Schiff bases:

Ni(cd5OMesalen) > Ni(cd3OMesalen) > Ni(cd4OMesalen)
and
Ni(cd5OMesalMeen) > Ni(cd3OMesalMeen) > Ni(cd4OMesalMeen)

Table 17
The formation constants, logK_f, and the free energy, $\Delta G°$, data for [(Ni(cd3-, 4-, 5-OMesalen)] complexes at 25 °C, in DMF.

Ligand	Ni^{2+}	
	logK_f	$\Delta G°$ (kJ mol^{-1})
H_2cd5OMesalen	4.86(0.14)	−27.71(0.34)
H_2cd3OMesalen [26]	4.78(0.13)	−27.26(0.32)
H_2cd4OMesalen	4.75(0.18)	−27.09(0.44)

The numbers in parentheses are the standard deviations.

Table 18
The formation constants, log K_f, and the free energy, $\Delta G°$, data for [(Ni(cd3-, 4-, 5-OMesalMeen)] complexes at 25 °C, in DMF.

Ligand	Ni^{2+}	
	log K_f	$\Delta G°$ (kJmol^{-1})
H_2cd5OMesalMeen	4.89(0.08)	−27.88(0.19)
H_2cd3OMesaMeen	4.83(0.17)	−27.54(0.42)
H_2cd4OMesaMeen	4.80(0.15)	−24.37(0.37)

The numbers in parentheses are the standard deviations.

Table 19
The formation constants, logK_f, and the free energy, $\Delta G°$, data for [(Ni(cdMesalen)], [(Ni(cdsalen)] and [(Ni(cdPhsalen)] complexes at 25 °C, in DMF.

Ligand	Ni^{2+}	
	logK_f	$\Delta G°$ (kJmol^{-1})
H_2cdMesalen [26]	4.85(0.12)	−27.66(0.29)
H_2cdsalen [26]	4.21(0.08)	−24.01(0.19)
H_2cdPhsalen	3.63(0.04)	−20.70(0.09)

The numbers in parentheses are the standard deviations.

Table 20
The formation constants, logK_f, and the free energy, $\Delta G°$, data for [(Ni(cdMesalMeen)], [(Ni(cdsalMeen)] and [(Ni(cdPhsalMeen)]complexes at 25 °C, in DMF.

Ligand	Ni^{2+}	
	logK_f	$\Delta G°$ (kJmol^{-1})
H_2cdMesalMeen	4.87(0.14)	−27.77(0.34)
H_2cdsalMeen [27]	4.23(0.22)	−24.12(0.54)
H_2cdPhsalMeen	3.63(0.13)	−20.70(0.32)

The numbers in parentheses are the standard deviations.

In the case of H_2cd5OMesalen and H_2cd5OMesalMeen, the methoxy group situated in the *para* position to the phenolic oxygen of the NNOS backbone can release electron directly to the phenyl and is better than that of the *meta* position in H_2cd4OMesalen and H_2cd4OMesalMeen [46], and H_2cd3OMesalen, H_2cd3OMesalMeen, which show steric effects (see Tables 17 and 18).

3.5.3. The electronic effect of the equatorial Schiff base ligands

The substitutional effects on the imine bond were studied by determining the formation constants for [Ni(cdMesalen)][26] and [Ni(cdPhsalen)], and [Ni(cdMesalMeen)] and [Ni(cdPhsalMeen)]. The results show the following trend in complex formation between the ligand Schiff bases H_2(cdMesalen), (H_2L^1), (H_2L^9) and (H_2L^{10}) with the Ni(II) ion (see Tables 19 and 20):

Ni(cdMesalen) > Ni(cdsalen) > Ni(cdPhsalen)
and
Ni(cdMesalMeen) > Ni(cdsalMeen) > Ni(cdPhsalMeen)

The values for electron releasing methyl Schiff bases were more than those for electron withdrawing phenyl Schiff bases. The phenyl group makes the Schiff base a poor donor ligand (and a good acceptor ligand), and decreases the formation constant, while the methyl group is a donating group and increases the formation constant [49].

4. Conclusions

By considering the formation constants and free energy data of formation for the unsymmetrical Schiff base ligands as a donor and Ni^{2+} ion as an acceptor, the following conclusions have been drawn:

1. The formation constants for the nickel(II) Schiff base complexes follow the sequence: cdXsalMeen > cdXsalen
2. The complex formation of the *para* substitutional groups bonded to the Schiff base ligands complexed to the Ni(II) ion decrease as follows:cd5OMsalen > cdsalen > cd5Brsalen > cd5Clsalen > cd5SO_3Nasalen > cd5NO_2salen and cd5OMsalMeen > cdsalMeen > cd5BrsalMeen > cd5ClsalMeen > cd5SO_3NasalMeen > cd5NO_2salMeen
3. The formation constants for [Ni(cd3-, 4-, 5-OMsalen)] and [Ni(cd3-, 4-, 5-OMsalMeen)] complexes have the following trend:cd5OMesalen > cd3OMesalen > cd4OMesalen and cd5OMesalM een > cd3OMesalMeen > cd4OMesalMeen
4. The complex formation with substitution on the imine bond of the Schiff base ligands complexed to the Ni(II) ion decreases as follows:cdMesalen > cdsalen > cdPhsalen and cdMesalMeen > cdsalMeen > cdPhsalMeen
5. In the series [H_2cdXsalen] and [H_2cdXsalMeen], it seems that the combination of strain, strength of the ligand field, the electronic effect, the geometry of the ligand, the electron configuration and the ionic radii of the metal can affect the complex formation constants.

Supplementary data

CCDC 693382 contains the supplementary crystallographic data for this paper. These data can be obtained free of charge via http://www.ccdc.cam.ac.uk/conts/retrieving.html, or from the Cambridge Crystallographic Data Centre, 12 Union Road, Cambridge CB2 1EZ, UK; fax: (+44) 1223-336-033; or e-mail: deposit@ccdc.cam.ac.uk.

Acknowledgements

We are grateful to Shiraz University Research Council for their financial support. The authors express their sincere thanks to Dr. R. Kia (Universiti Sains Malaysia) for providing X-ray data preparation.

References

[1] M.H. Habibi, M. Montazerozohori, A. Lalegani, R.W. Harrington, W. Clegg, J. Fluorine Chem. 6 (2006) 7691.
[2] G.H. Hamor, D. Watson, J. Pharma. Sci. 60 (2006) 925.
[3] A. Gama, L.Z. Flores-lopez, G. Aguirre, M. ParraHake, R. Somanathan, P.J. Walsh, Tetrahedron 13 (2002) 149.
[4] M.K. Taylor, K.D. Trotter, J. Reglinski, L.E.A. Berlouis, A.R. Kennedy, C.M. Spickett, R.J. Sowden, Inorg. Chim. Acta 361 (2008) 2851.
[5] S. Rayati, N. Torabi, A. Chaemi, S. Mohebbi, A. Wojtczak, A. Kozakiewicz, Inorg. Chim. Acta 361 (2008) 1239.
[6] J. Dai, Y. Chai, R. Yuan, X. Zhong, Y. Liu, D. Tang, Anal. Sci. 20 (2006) 1661.
[7] L.A. Kovbasyuk, I.O. Fritzky, V.N. Kokozay, T.S. Iskenderov, Tetrahedron 16 (1997) 1723.
[8] K.C. Gupta, H.K. Abdulkadir, S. Chand, J. Macromol. Sci. 39 (2002) 1451.
[9] J. Bu, Z.M.A. Judeh, C.B. Ching, S. Kawi, Catal. Lett. 85 (2003) 183.
[10] S.K. Das, A. Kumar, S. Nandrajog, Tetrahedron 43 (1995) 7909.
[11] Z. Zhou, Z. Li, K. Li, Z. Yang, G. Zhao, L. Wang, Q. Zhou, C. Tang, Inorg. Chem. 178 (2003) 1771.
[12] B. Gigante, A. Corma, H. Garcia, M.J. Sabater, Catal. Lett. 68 (2000) 113.
[13] A.A. Aly, K.M. Elshaieb, Tetrahedron 60 (2004) 3797.
[14] J. IqBal, S.A. Tirmizi, F.H. Wattoo, M. Imran, M.H. Sarwarwattoo, Sh. Sharfuddin, Sh. Latf, Turk. J. Biol. 30 (2006) 1.
[15] J.Z. Li, J.Q. Xie, W. Weng, X. Wei, B. Zhou, X. Zeng, Sh.Y. Qin, Transition Met. Chem. 29 (2004) 488.
[16] U. Hassan, A. Scozzafava, Zh. Chohan, C.T. Supuran, J. Enzyme Inhib. 16 (2001) 499.
[17] Z.J. Dong, C.B. Allan, S.B. Choudhurg, R. Franco, J.J.G. Moura, J. Hegall, A.E. Przybyla, W. Roseboom, S.P.J. Albracht, M.J. Axley, R.A. Scott, M.J. Maroney, J. Am. Chem. Soc. 118 (1996) 11155.
[18] H. Frydendahl, H. Toftland, J.C. Dutton, K.S. Murray, L.F. Taylor, P. Anderson, E.R.T. Tiekink, Inorg. Chem. 34 (1995) 4467.

[19] M. Asadi, Kh. Mohammadi, A.H. Kianfar, J. Iran. Chem. Soc. 3 (2006) 247.
[20] M. Asadi, A.H. Sarvestani, Z. Asadi, M. Setoodehkhah, Synth. React. Inorg. Metal-Org. Nano-Met. Chem. 35 (2005) 639.
[21] M. Asadi, A.H. Kianfar, S. Torabi, Kh. Mohammadi, J. Chem. Thermodynamic 40 (2008) 523.
[22] M. Asadi, A.H. Saravestani, M. Abbasi, J. Chem. Res. (2007) 56.
[23] M. Asadi, Z. Asadi, J. Coord. Chem. 61 (2008) 640.
[24] B. Bordas, P. Sohar, G. Matolcsy, P. Berencsi, J. Org. Chem. 37 (1972) 1727.
[25] K. Nag, D.S. Joardar, Inorg. Chim. Acta 14 (1975) 133.
[26] B. Castro, E. Pereira, L. Gomes, Inorg. Chim. Acta 271 (1998) 83.
[27] K. Nag, S.K. Mondal, P. Paul, R. Roy, Transition Met. Chem. 9 (1984) 247.
[28] SMART: Bruker Molecular Analysis Research Tool, Bruker AXS Inc., Madison, Wisconsin, USA, 2005.
[29] SAINT (Version V7.12A), Data Reduction and Correction Program, Bruker AXS Inc., Madison, Wisconsin, USA, 2005.
[30] SADABS (Version 2004/1). An Emprical Absorption Correction Program, Bruker AXS Inc., Madison, Wisconsin, USA.
[31] G.M. Sheldrick, Acta Crystallogr., Sect. A 64 (2008) 112.
[32] E.M. Martin, R.D. Bereman, Inorg. Chim. Acta 188 (1991) 221.
[33] A. Khandar, B. Shaabani, F. Belaj, A. Bakhtiari, Polyhedron 25 (2006) 1893.
[34] A. Garnovskii, A.L. Nivorozhkin, V.I. Minkin, Coord. Chem. Rev. 126 (1993) 14.
[35] G.C. Percy, D.A. Thorton, J. Inorg. Nucl. Chem. 34 (1972) 3357.
[36] Y.L. Zhang, W.J. Ruan, X.J. Zhao, H.G. Wang, Z.A. Zhu, Polyhedron 20 (2003) 1535.
[37] S. Chandra, A. Rathi, J. Saudi. Chem. Soc. 5 (2001) 175.
[38] S.C. Cummings, P.R. Blum, R.M.C. Wei, J. Inorg. Chem. 13 (1974) 450.
[39] S. Chandra, U. Kumar, Spectrochim. Acta, Part A 61 (2005) 219.
[40] D. Nandan Kumar, B.S. Garg, Spectrochim. Acta, Part A 64 (2006) 141.
[41] S.M. Grawford, Spectrochim. Acta, Part A 19 (1963) 255.
[42] R.C. Felicio, E.T.G. Canalheiro, E.R. Dockal, Polyhedron 20 (2001) 61.
[43] R.H. Holm, J. Am. Chem. Soc. 82 (1960) 5632.
[44] (a) B.J. Hathaway, G. Wilkinson, R.D. Gillard, J.A. McCleverty, Comprehensive Coordination Chemistry. The Synthesis, Reactions, Properties and Applications of Coordination Compounds, vol. 5, Pergamon, Oxford, 1987;
(b) B.J. Hathaway, D.E. Billing, Coor. Chem. Rev. 5 (1970) 1420.
[45] D.L. Leggett, Computational Methods for the Determination of Formation Constant, Plenum Press, New York, 1985.
[46] A.H. Sarvestani, S. Mohebbi, J. Iran. Chem. Soc. 4 (2007) 215.
[47] M. Asadi, Kh. Aein Jamshid, A.H. Kianfar, Inorg. Chim. Acta 360 (2007) 1725.
[48] A.J. Gordon, R.A. Ford, The Chemist's Companion: A Handbook of Practical Data Techniques and References, vol. 145, Wiley, New York, 1972.
[49] M. Asadi, Z. Asadi, Transition Met. Chem. 32 (2007) 387.

C, H and N contents were determined using a GmbH VariuoEL V3.00 automatic elemental analyzer. Elemental analysis for Cu was detected by an IRIS ER/S · WP-1 ICP atomic emission spectrometer. IR spectra were recorded on a VERTEX70 FT-IR spectrophotometer, with samples prepared as KBr (500–4000 cm^{-1}) and CsI (100–500 cm^{-1}) pellets. UV–Vis absorption spectra in the 200–800 nm range were recorded on a Hitachi UV-3010 spectrophotometer in DMF solution. TG-DTA analyses were carried out on a ZRY-1P thermoanalyzer at a heating rate of 3 °C/min. ^1H NMR spectra were recorded on a Mercury-400BB spectrometer at room temperature using DMSO–d_6 as the solvent. X-ray single crystal structures were determined on a Bruker Smart 1000 APEX CCD area detector. Melting points were measured by the use of a microscopic melting point apparatus made by the Beijing Taike Instrument Limited Company, and the thermometer was uncorrected. Molar conductance value measurements were carried out on a model DDS-11D type conductivity bridge using a 1.0×10^{-3} mol dm^{-3} solution in DMF at 25 °C.

2.2. Synthesis and characterization of 6,6′-dihydroxy-2,2′-[ethylenediyldioxybis(nitrilomethylidyne)]diphenol (H_4L)

The major reaction steps involved in the synthesis of 6,6′-dihydroxy-2,2′-[ethylenediyldioxybis(nitrilomethylidyne)]diphenol (H_4L) are given in Scheme 1.

1,2-Bis(phthalimidoxy)ethane was prepared according to the literature [10]. Yield: 95.6%. m.p. 250 °C.

1,2-Bis(aminooxy)ethane was synthesized according to an analogous method reported earlier [10]. ^1H NMR (400 MHz, $CDCl_3$, δ, ppm): 3.79 (s, 4H), 5.52 (s, 4H).

2,3-Dihydroxybenzaldehyde was synthesized according to an analogous method reported earlier [11]. The Salen-type bisoxime ligand H_4L was synthesized according to an analogous method reported earlier in the literature [11,12]. The reaction of 1,2-bis(aminooxy)ethane (0.0924 g, 1.00 mmol) with two equivalents of 2,3-dihydroxybenzaldehyde (0.277 g, 2.00 mmol) in ethanol (7 ml) afforded the desired ligand as a colorless microcrystalline powder. Yield: 0.130 g (39.1%). m.p. 114–116 °C. ^1H NMR (400 MHz, $CDCl_3$, δ, ppm): 2.34 (s, 6H), 4.50 (t, J = 3.4 Hz, 4H), 6.89 (dd, J = 5.8 Hz, 2H), 6.95 (dd, J = 1.2 Hz, 2H), 7.25 (dd, J = 1.6 Hz, 2H), 7.41 (dd, J = 1.4 Hz, 2H), 11.10 (s, 2H). UV–Vis (DMF): λ_{max} (ε_{max}) 274 and 322 nm (2985.38 and 6.52 M^{-1} cm^{-1}). IR (KBr, cm^{-1}) 3410(s), 3175(b), 2949(w), 2880(w), 1610(s), 1580(m), 1475(s), 1265(s). *Anal.* Calc. for $C_{18}H_{20}N_2O_4$: C, 65.84; H, 6.14; N, 8.53. Found: C, 65.76; H, 6.24; N, 8.46%.

2.3. Synthesis of complexes **1**, **2**, **3** and **4**

The four solvent-induced Cu(II) complexes **1**, **2**, **3** and **4** are obtained by the reaction of the Salen-type bisoxime ligand H_4L with $Cu(OAc)_2 \cdot H_2O$ in a 1:1 (or 2:3 for complex **3**, because single crystals were not obtained from the reaction in a molar ratio of 1:1) molar ratio in absolute methanol, ethanol, n-propanol and n-butanol solvents, respectively. Single crystals of complexes **1**, **2**, **3** and **4** suitable for X-ray diffraction analysis were grown using the gaseous diffusion method.

2.3.1. [{Cu(HL)(CH_3OH)}$_2$Cu] · CH_3OH (**1**)

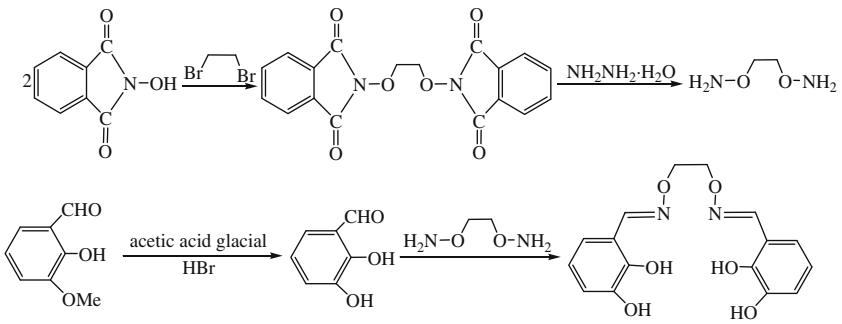
A pale-blue methanol solution (3 ml) of $Cu(OAc)_2 \cdot H_2O$ (0.0037 g, 0.019 mmol) was added dropwise to a colorless methanol solution (3 ml) of H_4L (0.0063 g, 0.019 mmol) at room temperature. The color of the mixed solution turned to dark-brown immediately. The solution obtained was placed in an n-hexane atmosphere and stored at room temperature for two weeks. With the diffusion of n-hexane into the mixed solution of the complex, dark-brown block-shaped single crystals suitable for X-ray crystallographic analysis were obtained. Yield: 0.0063 g (35.1%). UV–Vis (DMF): λ_{max} (ε_{max}) 294 and 379 nm (816.58 and 6.01 M^{-1} cm^{-1}). IR (KBr, cm^{-1}) 3576(w), 3384(b), 2945(w), 2876(w), 1616(s), 1591(s), 1549 (s), 1452(s), 1260(b), 534(w), 465(w), 401(w). *Anal.* Calc. for [{Cu(HL)(CH_3OH)}$_2$Cu] · CH_3OH ($C_{35}H_{38}Cu_3N_4O_{15}$): C, 44.47; H, 4.05; N, 5.93; Cu, 20.17. Found: C, 44.56; H, 4.21; N, 5.72; Cu, 20.21%.

2.3.2. [{(Cu(HL))$_2$(CH_3CH_2OH)$_2$}Cu] (**2**)

The single crystals of complex **2** were grown by a similar procedure to that aforementioned, taking $Cu(OAc)_2 \cdot H_2O$ (0.0050 g, 0.025 mmol) and H_4L (0.0078 g, 0.024 mmol) in 5 ml absolute ethanol solution. The obtained dark-brown mixture was placed in an n-hexane atmosphere and stored at room temperature for one month. With the diffusion of n-hexane into the mixed solution of the complex, dark-brown block-shaped single crystals suitable for X-ray crystallographic analysis were obtained. Yield: 0.0077 g (32.5%). UV–Vis (DMF): λ_{max} (ε_{max}) 294 and 379 nm (199.07 and 4.13 M^{-1} cm^{-1}). IR (KBr, cm^{-1}) 3420(b), 2945(w), 2879(w), 1612(s), 1591(s), 1551(s), 1452(s), 1263(s), 536(w), 463(w), 401(w). *Anal.* Calc. for [{(Cu(HL))$_2$(CH_3CH_2OH)$_2$}Cu] ($C_{36}H_{38}Cu_3N_4O_{14}$): C, 45.93; H, 4.07; N, 5.95; Cu, 20.25. Found: C, 45.80; H, 4.17; N, 5.81; Cu, 20.17%.

2.3.3. [{CuL(H_2O)}$_2$$Cu_2$] · 2$CH_3CH_2CH_2OH$ (**3**)

The single crystals of complex **3** were grown by a similar procedure to that aforementioned, taking $Cu(OAc)_2 \cdot H_2O$ (0.0052 g, 0.026 mmol) and H_4L (0.0058 g, 0.017 mmol) in 6 ml n-propanol solution. The obtained dark-brown mixture was placed in an n-hexane atmosphere and stored at room temperature for two months. With the diffusion of n-hexane into the mixed solution of the complex, dark-brown block-shaped single crystals suitable for X-ray crystallographic analysis were obtained. Yield: 0.0083 g (29.8%). UV–Vis (DMF): λ_{max} (ε_{max}) 294 and 379 nm (2187.76 and



Scheme 1. Major reaction steps involved in the synthesis of 6,6′-dihydroxy-2,2′-[ethylenediyldioxybis(nitrilomethylidyne)]diphenol (H_4L^1).

8.28 M^{-1} cm^{-1}). IR (KBr, cm^{-1}) 3427(b), 2958(w), 2872(w), 1614(s), 1593(s), 1551(s), 1452(s), 1261(s), 557(w), 536(w), 463(w), 405(w). *Anal.* Calc. for $[\{CuL(H_2O)\}_2Cu_2]\cdot 2CH_3CH_2CH_2OH$ ($C_{38}H_{44}Cu_4N_4O_{16}$): C, 48.37; H, 4.46; N, 5.63; Cu, 19.15. Found: C, 48.26; H, 4.48; N, 5.52; Cu, 19.28%.

2.3.4. [{(Cu(HL))$_2$(CH$_3$CH$_2$CH$_2$CH$_2$OH)$_2$}Cu] (**4**)

The single crystals of complex **4** were grown by a similar procedure to that aforementioned, taking $Cu(OAc)_2\cdot H_2O$ (0.0038 g, 0.019 mmol) and H_4L (0.0063 g, 0.019 mmol) in 6 ml n-butanol solution. The obtained dark-brown mixture was placed in an n-hexane atmosphere and stored at room temperature for three months. With the diffusion of n-hexane into the mixed solution of the complex, dark-brown block-shaped single crystals suitable for X-ray crystallographic analysis were obtained. Yield: 0.0056 g (28.9%). UV–Vis (DMF): λ_{max} (ε_{max}) 294 and 379 nm (413.85 and 5.33 M^{-1} cm^{-1}). IR (KBr, cm^{-1}) 3437(b), 2957(w), 2866(w), 1614(s), 1591(s), 1551(s), 1452(s), 1261(s), 536(w), 453(w), 417(w). *Anal.* Calc. for $[\{(Cu(HL))_2(CH_3CH_2CH_2CH_2OH)_2\}Cu]$ ($C_{40}H_{44}Cu_3N_4O_{14}$): C, 42.78; H, 4.16; N, 5.25; Cu, 23.82. Found: C, 42.92; H, 4.24; N, 5.09; Cu, 23.68%.

2.4. Crystal structure determination

Single crystal X-ray diffraction data were collected on a Bruker AXS single crystal X-ray diffractometer using a Bruker Smart 1000 CCD area detector. The X-ray generator was operated at 50 kV and 35 mA using Mo Ka radiation (λ = 0.71073 Å). The raw intensities were corrected for Lorentz and polarization effects, and a numerical absorption correction was applied for all complexes. The data were reduced by SAINT-PLUS [13] and an empirical absorption correction was applied using the package SADABS [13]. All the structures were solved by direct methods using SHELXS and refinement was done against F^2 using SHELXL [14]. Molecular and packing diagrams were generated by ORTEP-32 [15] and CAMERON [16] present in the WINGX (Version 1.64.03b) [17] program suite. The geometric calculations were done by PARST-95 [18] and PLATON [19]. All non-hydrogen atoms were refined using anisotropic displacement parameters. The hydrogen atoms were located in the difference map, but in most cases were positioned with an idealized geometry and refined isotropically using a riding model. The technical details of data acquisition and some selected refinement results for complexes **1**, **2**, **3** and **4** are summarized in Table 1.

3. Results and discussion

3.1. Molar conductances

The complexes **1**, **2**, **3** and **4** are soluble in DMF, DMSO, chloroform and dichloromethane, but not soluble in ethanol, methanol, acetonitrile, acetone, THF, ethyl acetate and n-hexane. Molar conductance values of complexes **1**, **2**, **3** and **4** at 25 °C of 10^{-3} mol dm^{-3} DMF solutions are 12.7, 13.5, 19.2 and 18.0 Ω^{-1} cm^2 mol^{-1}, respectively, indicating that these complexes are non-electrolytes.

3.2. Spectral investigation

3.2.1. IR spectra analyses

The IR spectra of H_4L and its corresponding Cu(II) complexes show a characteristic C=N stretching band. For the free ligand H_4L this band appears at 1610 cm^{-1}, while the C=N bands of the Cu(II) complexes **1**, **2**, **3** and **4** are observed at 1616, 1612, 1614 and 1614 cm^{-1}, respectively. The shifts toward higher wavenumbers of the C=N absorption of about 2–6 cm^{-1} on going from the

Table 1
X-ray crystallographic data collection, solution and refinement parameters for complexes **1**, **2**, **3** and **4**.

Compound code	**1**	**2**	**3**	**4**
Empirical formula	$C_{35}H_{38}Cu_3N_4O_{15}$	$C_{36}H_{38}Cu_3N_4O_{14}$	$C_{38}H_{44}Cu_4N_4O_{16}$	$C_{40}H_{46}Cu_3N_4O_{14}$
Formula weight	945.31	941.32	1066.93	995.41
Temperature (K)	298(2)	298(2)	298(2)	293(2)
Wavelength (Å)	0.71073	0.71073	0.71073	0.71073
Crystal system	monoclinic	monoclinic	monoclinic	monoclinic
Space group	*C*2/*c*	*C*2/*c*	*C*2/*c*	*C*2/*c*
Unit cell dimensions				
a (Å)	23.863(2)	21.466(2)	15.1342(18)	23.086(2)
b (Å)	12.8048(11)	12.9105(12)	10.8464(14)	12.9970(14)
c (Å)	15.2474(15)	15.0349(16)	24.916 (3)	15.1456(18)
α (°)	90	90	90	0
β (°)	121.283(2)	112.444(2)	92.403(2)	113.917(2)
γ (°)	90	90	90	0
V (Å^3)	3981.6(6)	3851.1(7)	4086.4(8)	4154.2(8)
Z	4	4	4	4
D_{calc} (Mg/m^3)	1.577	1.624	1.734	1.592
μ (mm^{-1})	1.661	1.715	2.132	1.595
F(000)	1932	1924	2176	2044
Crystal size (mm)	0.45 × 0.43 × 0.16	0.50 × 0.44 × 0.18	0.43 × 0.17 × 0.14	0.40 × 0.38 × 0.24
θ Range (°)	1.88–25.01	1.88–25.01	2.31–25.01	1.84–25.01
Index ranges	$-26 \leqslant h \leqslant 28$, $-15 \leqslant k \leqslant 15$, $-18 \leqslant l \leqslant 9$	$-25 \leqslant h \leqslant 16$, $-15 \leqslant k \leqslant 14$, $-17 \leqslant l \leqslant 17$	$-18 \leqslant h \leqslant 11$, $-12 \leqslant k \leqslant 12$, $-29 \leqslant l \leqslant 27$	$-27 \leqslant h \leqslant 27$, $-15 \leqslant k \leqslant 14$, $-14 \leqslant l \leqslant 18$
Reflections collected	10100	9285	9705	10216
Independent reflections	3509	3370	3352	3656
R_{int}	0.0345	0.0981	0.0626	0.0303
Completeness to θ = 25.00 (%)	99.9	99.3	98.8	99.7
Data/restraints/parameters	35.9/0/269	3370/0/258	3352/0/281	3656/0/276
Goodness of fit (GOF)	1.098	1.046	1.057	1.087
R_1	0.0455	0.0546	0.0741	0.0447
wR_2 [$I > 2\sigma(I)$]	0.1714	0.1504	0.2030	0.1428
$\Delta\rho_{max,min}$ (e Å^{-3})	0.967 and −0.308	0.885 and −0.535	1.032 and −1.686	0.727 and −0.701

free ligand H_4L to the complexes suggest a weak π-accepting ability of the coordinated ligand.

The Ar–O stretching frequencies appear as a strong band within the 1263–1213 cm^{-1} range, as reported for similar Salen-type ligands. These bands occur at 1265 cm^{-1} for H_4L, 1260 cm^{-1} for complex **1**, 1263 cm^{-1} for complex **2** and 1261 cm^{-1} for complexes **3** and **4**. The Ar–O stretching frequency is shifted to a lower value, indicating that Cu–O bonds are formed between the Cu(II) ions and the oxygen atoms of the phenolic groups [20].

The O–H stretching frequency of the free ligand H_4L appears at 3410 cm^{-1}. The bending vibration of the phenolic alcohols in H_4L appears at 1238 cm^{-1}, and this is observed at 1238–1242 cm^{-1} in complexes **1**, **2** and **4**, but disappears in complex **3**. This phenomenon indicates the oxygen atoms in the phenolic alcohols of complex **3** have been completely deprotoned and coordinated to Cu(II) ions, while the ligand is partially deprotoned in complexes **1**, **2** and **4**. In addition, the broad absorption centered on 3384, 3420, 3427 and 3437 cm^{-1} in complexes **1**, **2**, **3** and **4**, respectively, which may be assigned to the O–H stretching vibration of the solvent or water molecules.

The far-infrared spectra of complexes **1**, **2**, **3** and **4** were also obtained in the region 500–100 cm^{-1} in order to identify frequencies due to Cu–O and Cu–N bonds. The IR spectra of complexes **1**, **2**, **3** and **4** show ν(Cu–N) (or ν(Cu–O)) vibrational absorption frequencies at 465, 463, 463 and 453 (or 401, 401, 405 and 417) cm^{-1}, respectively, which are consistent with the literature frequency values [21]. These bands are observed as new peaks for complexes **1**, **2**, **3** and **4**, and are not present in the spectrum of the free ligand H_4L. As pointed out by Percy and Thornton [22], the metal–oxygen and metal–nitrogen frequency assignments are at times very difficult.

3.2.2. UV–Vis spectra analyses

The absorption spectra of H_4L and its corresponding Cu(II) complexes **1**, **2**, **3** and **4** in diluted DMF solution show that the spectra of the complexes **1**, **2**, **3** and **4** are similar to each other, but are different from the spectrum of the ligand (H_4L). The UV–Vis spectrum of the free ligand H_4L exhibits two absorption peaks at *ca.* 274 and 322 nm. The former absorption peak at 274 nm can be assigned to the π–π^* transition of the benzene rings and the latter one at 322 nm can be attributed to the intra-ligand π–π^* transition of the C=N bonds [23].

Compared with the absorption peak of the ligand, a corresponding absorption peak at 294 nm is observed in complexes **1**, **2**, **3** and **4**, which is bathochromically shifted by *ca.* 20 nm, indicating the coordination of Cu(II) ions with the ligand. Meanwhile, a new absorption peak is observed at 379 nm in complexes **1**, **2**, **3** and **4**, which is assigned to the n–π^* charge transfer transition from the filled pπ orbital of the bridging phenolic oxygen to the vacant d-orbital of the Cu(II) ions [24]. It is noteworthy that the same UV–Vis absorption spectra of complexes **1**, **2**, **3** and **4** clearly indicate that the structures of the four complexes are similar to each other.

3.3. Thermal properties

Thermal stability studies were performed for complexes **1**, **2**, **3** and **4**. The TG curve of complex **1** can be divided into three stages. The first stage is at 41–64 °C. The TG curve shows that the weight loss corresponding to this temperature range is 3.8%, which roughly coincides with the value of 3.4% calculated for the loss of one crystallizing methanol molecule from the outer coordination sphere of complex **1**. The second stage starts from 87 to 98 °C with a weight loss of 7.5%, which corresponds to the loss of two methanol molecules (theoretical mass loss, 6.8%) which takes part in coordination to the Cu(II) ions. The solid remains stable up to 216 °C and the third weight loss starts at around 223 °C, with decomposition of the compound. The TG curve shows around 77% total mass loss at 800 °C, indicating the complete removal of the $(HL)^{3-}$ units. The main residual product was CuO, with a value of 23% (theoretical residual value was 25.2%). TG curves of complexes **2** and **4** are similar to those of the second and third stages of complex **1**.

The thermal decomposition process of complex **3** appears in three stages. The initial weight loss occurs in the range 75–96 °C. The TG curve shows that the weight loss corresponding to this temperature range is 10.5%, consistent with the 11.3% calculated for the loss of two crystallizing n-propanol molecules. The second stage is from 114 to 126 °C, with a weight loss of 4.5%, which corresponds to the loss of two water molecules (theoretical mass loss, 3.4%) coordinated to Cu. The solid remains stable up to 217 °C and the third weight loss starts at around 224 °C, with further decomposition of the compound. Subsequently, a continuous mass loss was observed up to 800 °C. At this temperature, CuO is formed. The total mass loss found (73%) was approximately consistent with that calculated (70.2%).

3.4. Description of the crystal structures

Selected bond lengths and bond angles are presented in Table 2. A list of hydrogen bonds in complexes **1**, **2**, **3** and **4** is given in Table 3.

3.4.1. Structure of complex *1*

The X-ray crystal structure analysis of complex **1** shows the molecule consists of three Cu(II) ions, two partially deprotonated $(HL)^{3-}$ units, two coordinated and one crystallizing methanol molecules (Fig. 1). The terminal Cu(II) (Cu1) ion is five-coordinated by two oxime nitrogen (N1 and N2) and two phenolic oxygen (O3 and O5) atoms of the pentadentate Salen-type $(HL)^{3-}$ trianion in the basal plane, and by one oxygen (O7) atom from one coordinated methanol molecule in the apical position. The coordination geometry around the terminal Cu(II) (Cu1) ion is found to be slightly distorted square pyramidal. The two phenolic oxygen atoms and two oxime nitrogen atoms are in mutually *cis* positions. The primary distances of Cu–N and Cu–O are in the normal ranges (Cu1–N1 = 2.019(4), Cu1–N2 = 1.961(4), Cu1–O3 = 1.969(3) and Cu1–O5 = 1.885(3) Å) (Table 2) though, with the exception of Cu1-O5, all these lengths are slightly larger than the corresponding bond lengths found in the complexes Cu(salen), Cu(5-MeOsalen) and Cu(5-Clsalen), reported earlier [25]. The bond length (Cu1-O7) between the Cu(II) ion and the apical oxygen (O7) atom is 2.485(4) Å, which is obviously longer than the distances between the Cu(II) ion and the basal oxygen and nitrogen atoms. This significant elongation has been observed in the Cu(II) complex with the Salen ligand (in the complex Cu(salen), Cu-N1 = 1.953(4), Cu-N2 = 1.952(4), Cu–O1 = 1.905(3), Cu–O2 = 1.946(3) Å, with the apical bond Cu–O(2a) = 2.423(3) Å) [26].

The "Sal1" and "Sal2" planes are bent asymmetrically, making angles of 15.09(2)° and 49.37(1)°, respectively, with respect to the N_2O_2 plane. In addition, the ethylenedioxime carbon atoms (C1 and C2) in complex **1** are buckled asymmetrically from the Cu1N1N2 plane, with the displacement for C1 being 1.789(3) Å towards the plane and for C2 only 1.272(3) Å in the same direction. It is anticipated that the two oxime nitrogen atoms and its carbon chain form a seven-membered chelate ring with the Cu(II) ion (Cu1) in complex **1**; the chelating bite angle (∠N1Cu1N2) in the seven-membered ring is 95.34(2)°. The coordination sphere of the other terminal Cu(II) centre ($Cu1^{\#1}$) is the same as that of the Cu1 ion.

The central Cu(II) ion (Cu2) is tetra-coordinated by four phenoxo oxygen atoms from two $[Cu(HL)(CH_3OH)]^-$ anions, discussed above, and adopts a square planar geometry distorted tetrahedrally

Table 2
Selected bond lengths (Å) and bond angles (°) for complexes **1**, **2**, **3** and **4**.

Complex **1**		Complex **2**		Complex **4**		Complex **3**	
Bond	Distance	Bond	Distance	Bond	Distance	Bond	Distance
Cu(1)–O(5)	1.885(3)	Cu(1)–O(5)	1.886(3)	Cu(2)–O(5)	1.875(3)	Cu(1)–O(4)	1.915(6)
Cu(1)–N(2)	1.961(4)	Cu(1)–N(2)	1.958(4)	Cu(2)–N(2)	1.955(4)	Cu(1)–O(3)	1.933(6)
Cu(1)–O(3)	1.969(3)	Cu(1)–O(3)	1.969(3)	Cu(2)–O(3)	1.961(3)	Cu(2)–O(5)	1.963(6)
Cu(1)–N(1)	2.019(4)	Cu(1)–N(1)	2.021(4)	Cu(2)–N(1)	2.020(4)	Cu(2)–N(2)	1.970(7)
Cu(1)–O(7)	2.485(4)	Cu(1)–O(7)	2.444(4)	Cu(2)–O(7)	2.619(4)	Cu(2)–N(1)	2.023(7)
Cu(2)–O(4)	1.899(3)	Cu(2)–O(4)	1.887(3)	Cu(1)–O(4)	1.908(4)	Cu(2)–O(7)	2.050(6)
Cu(2)–O(3)	1.978(3)	Cu(2)–O(3)	1.980(3)	Cu(1)–O(3)	1.978(3)	Cu(2)–O(3)	2.067(5)
						Cu(3)–O(6)	1.857(6)
						Cu(3)–O(5)	2.015(5)
Bond	Angle	Bond	Angle	Bond	Angle	Bond	Angle
O(5)–Cu(1)–N(2)	90.98(2)	O(5)–Cu(1)–N(2)	91.45(2)	O(5)–Cu(2)–N(2)	91.21(2)	O(4)–Cu(1)–O(4)$^{\#4}$	159.5(4)
O(5)–Cu(1)–O(3)	85.70(1)	O(5)–Cu(1)–O(3)	85.96(1)	O(5)–Cu(2)–O(3)	86.47(1)	O(4)–Cu(1)–O(3)	85.80(2)
N(2)–Cu(1)–O(3)	165.3(2)	N(2)–Cu(1)–O(3)	166.2(2)	N(2)–Cu(2)–O(3)	166.2(2)	O(4)$^{\#4}$–Cu(1)–O(3)	96.80(2)
O(5)–Cu(1)–N(1)	172.0(2)	O(5)–Cu(1)–N(1)	169.8(2)	O(5)–Cu(2)–N(1)	172.5(2)	O(3)–Cu(1)–O(3)$^{\#4}$	165.7(4)
N(2)–Cu(1)–N(1)	95.34(2)	N(2)–Cu(1)–N(1)	94.81(2)	N(2)–Cu(2)–N(1)	94.78(2)	O(5)–Cu(2)–N(2)	90.00(3)
O(3)–Cu(1)–N(1)	86.97(1)	O(3)–Cu(1)–N(1)	86.06(2)	O(3)–Cu(2)–N(1)	86.64(2)	O(5)–Cu(2)–N(1)	172.4(3)
O(5)–Cu(1)–O(7)	84.25(1)	O(5)–Cu(1)–O(7)	85.20(1)	O(5)–Cu(2)–O(7)	84.41(1)	N(2)–Cu(2)–N(1)	97.60(3)
N(2)–Cu(1)–O(7)	106.7(2)	N(2)–Cu(1)–O(7)	104.5(2)	N(2)–Cu(2)–O(7)	107.5(2)	O(5)–Cu(2)–O(7)	88.60(2)
O(3)–Cu(1)–O(7)	86.33(1)	O(3)–Cu(1)–O(7)	88.83(1)	O(3)–Cu(2)–O(7)	85.82(1)	N(2)–Cu(2)–O(7)	132.8(3)
N(1)–Cu(1)–O(7)	98.43(2)	N(1)–Cu(1)–O(7)	100.9(1)	N(1)–Cu(2)–O(7)	98.06(2)	N(1)–Cu(2)–O(7)	85.70(3)
O(4)$^{\#1}$–Cu(1)–O(4)	175.6(2)	O(4)–Cu(2)–O(4)$^{\#2}$	176.6(3)	O(4)–Cu(1)–O(4)$^{\#3}$	173.8(2)	O(5)–Cu(2)–O(3)	89.40(2)
O(4)$^{\#1}$–Cu(2)–O(3)$^{\#1}$	84.54(1)	O(4)–Cu(2)–O(3)	84.75(2)	O(4)–Cu(1)–O(3)	84.46(1)	N(2)–Cu(2)–O(3)	119.5(3)
O(4)–Cu(2)–O(3)$^{\#1}$	96.17(1)	O(4)–Cu(2)–O(3)$^{\#2}$	95.69(2)	O(4)–Cu(1)–O(3)$^{\#3}$	96.65(1)	N(1)–Cu(2)–O(3)	87.50(3)
O(3)–Cu(2)–O(3)$^{\#1}$	161.4(2)	O(3)–Cu(2)–O(3)$^{\#2}$	165.0(2)	O(3)$^{\#3}$–Cu(1)–O(3)	159.6(2)	O(7)–Cu(2)–O(3)	107.7(3)
						O(6)$^{\#4}$–Cu(3)–O(6)	159.4(4)
						O(6)–Cu(3)–O(5)	84.60(2)
						O(5)$^{\#4}$–Cu(3)–O(5)	145.6(3)

Symmetry transformations used to generate equivalent atoms: $^{\#1}$: $-x+1, y, -z+3/2$, $^{\#2}$: $-x, y, -z+1/2$, $^{\#3}$: $-x+1, y, -z+1/2$ and $^{\#4}$: $-x+2, y, -z+1/2$ for complexes **1**, **2**, **3** and **4**, respectively.

by 19.58(3)° (defined by the angle between two sites of the coordination planes O3–Cu2–O4 and O3$^{\#1}$–Cu2–O4$^{\#1}$), indicating the four phenoxo oxygen donors are not rigidly co-planar. A similar distortion was also observed for the complexes Cu(Salen) [26] and Cu(Saltn) [27], although the analogues Cu(Salamo) and Cu(3-MeOSalamo), with a shorter carbon chain, showed more distortion [28]. In addition, the four phenoxo oxygen donors are distributed symmetrically with the displacement for O3 (or O3$^{\#1}$) and O4 (or O4$^{\#1}$) being 0.196 Å, in opposite directions from the O3–O3$^{\#1}$–O4–O4$^{\#1}$ plane. The Cu–O bond lengths show a significant difference (Cu2–O3 = 1.899(3) and Cu2–O4 = 1.978(3) Å), which can be explained by the large steric repulsion force mainly resulted from the pentadentate $(HL)^{3-}$ units. The Cu2 ion has a displacement of 0.123(2) Å above the mean plane. The central Cu(II) (Cu2) ion sits on a crystallographic inversion center in the crystal, therefore the whole Cu(II) complex is rigorously centrosymmetric.

The Cu1···Cu2 (or Cu1$^{\#1}$···Cu2) distance is 3.540(3) Å, which is not particularly short, implying a weak metal–metal bonding interaction. The Cu1–O3–Cu2 bridging angle (or Cu1$^{\#1}$–O3$^{\#1}$–Cu2) is 127.5(2)°, indicating non-collinear Cu–O–Cu fragments, not suitable for significant electronic exchange [29].

In complex **1**, the two coordinated methanol molecules attached to the terminal Cu(II) ions (Cu1 and Cu1$^{\#1}$) lie in trans positions toward the terminal Cu(II) ions. There are eight strong intramolecular hydrogen bonds (Table 3) providing strong stabilizing forces, the bond lengths of the hydrogen bonds are 2.186 (O6–H6···O5), 2.241 (O6–H6···O4), 1.887 (O7–H7···O4) and 2.568 Å (O7–H7···O5). The hydrogen bonds are formed between the undeprotonated hydroxyl (O6–H6 or O6$^{\#1}$–H6$^{\#1}$) groups at the 3-position of the salicylidene moieties or the coordinated methanol molecules (O7–H7 or O7$^{\#1}$–H7$^{\#1}$) and the deprotonated oxygen atoms (O5 and O4 or O5$^{\#1}$ and O4$^{\#1}$) in the pentadentate $(HL)^{3-}$ units.

Table 3
Intra- and intermolecular hydrogen geometries (Å, °) for complexes **1**, **2**, **3** and **4**.

Complex	D–H	d(D–H)	d(H...A)	d(D...A)	∠DHA	A
1	O6–H6	0.820	2.186	2.647	115.71	O5
	O6–H6	0.820	2.241	3.003	154.80	O4
	O7–H7	0.820	1.887	2.699	170.04	O4
	O7–H7	0.820	2.568	2.964	111.18	O5
2	O6–H6	0.820	2.194	2.645	114.81	O5
	O6–H6	0.820	2.415	3.138	147.52	O4
	O7–H7	0.820	1.869	2.681	170.44	O4
4	O6–H6	0.820	2.199	2.651	114.95	O5
	O6–H6	0.820	2.269	3.008	150.13	O4
	O7–H7	0.820	1.898	2.716	175.11	O4
3	O7–H7A	0.850	1.804	2.631	163.66	O6
	O7–H7B	0.850	1.881	2.726	171.99	O8
	O8–H8	0.820	1.856	2.650	162.74	O4

3.4.2. Structures of complexes *2* and *4*

X-ray crystal structure analyses of complexes **2** and **4** reveal that they have the same individual trinuclear neutral molecular unit [{(Cu(HL))$_2$(solvent)$_2$}Cu] (the solvents are ethanol and n-butanol in complexes **2** and **4**, respectively), as shown in Figs. 2 and 3, while the different solvents observed lead to the formation of the typical solvent-induced Cu(II) complexes [8].

The terminal Cu(II) ions lie in a penta-coordinated environment and adopt distorted square pyramidal geometries, where the inner N_2O_2 cavities of the pentadentate $(HL)^{3-}$ units comprise the basal planes, and one oxygen atom from the coordinated solvent molecules (ethanol or n-butanol) occupies the apical position. The primary Cu–O bond length (Cu1–O5 = 1.886(3) Å in complex **2** and Cu2–O5 = 1.875(3) Å in complex **4**) is close to the typical value of the Cu–O bonds found in the related Salen-type Cu(II) complexes Cu(Saltn), Cu(3-MeOSalamo) and Cu(PnSalen) [26,28], while the other Cu–O bond length (Cu1–O5 = 1.969(3) Å in complex **2** or Cu2–O3 = 1.961(3) Å in complex **4**) is not close to those found in the related complexes mentioned above. Although the primary

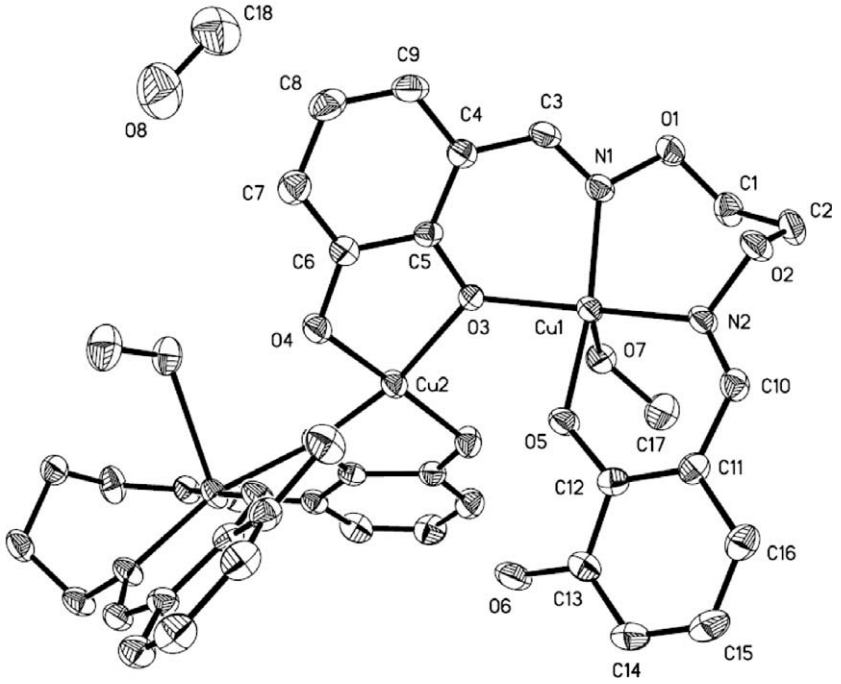


Fig. 1. Molecular structure of complex **1** with the atom numbering. The hydrogen atoms are omitted for clarity.

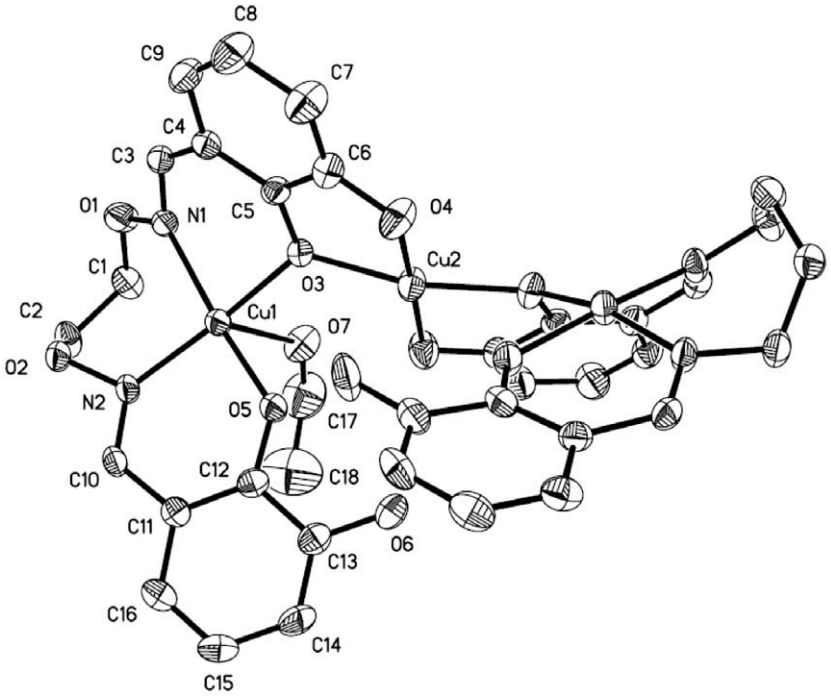


Fig. 2. Molecular structure of complex **2** with the atom numbering. The hydrogen atoms are omitted for clarity.

Cu–N bond length (Cu1–N1 = 2.021(4) Å in complex **2** and Cu2–N1 = 2.020(4) Å in complex **4**) is longer than those of the reported Cu(II) complexes, the other Cu–N bond length (Cu1–N2 = 1.958(4) Å in complex **2** or Cu2–N2 = 1.955(4) Å in complex **4**) approaches that observed in Cu(Salen) and $[Cu(Saltn)]_2$ [25,26]. The dihedral angle between the two coordinated planes of O3–Cu1–N1 and O5–Cu1–N2 (or O3–Cu2–N1 and O5–Cu2–N2) is 15.36° in complex **2** (or 14.01° in complex **4**). The four primary coordination atoms (two N and two O) give a mean plane with a slight tetrahedral distortion, with N2 and O3 below average by 0.0555 Å and with N1 and O5 above average by the same deviation as that mentioned above in complex **2** (or 0.0825 Å in complex **4**). The Cu(II) ion is situated above the mean plane with a deviation of 0.179(3) Å (or 0.148(3) Å in complex **4**).

The central Cu(II) ions are both tetra-coordinated, surrounded by four oxygen atoms from the two $[Cu(HL)(solvent)]^-$ anions,

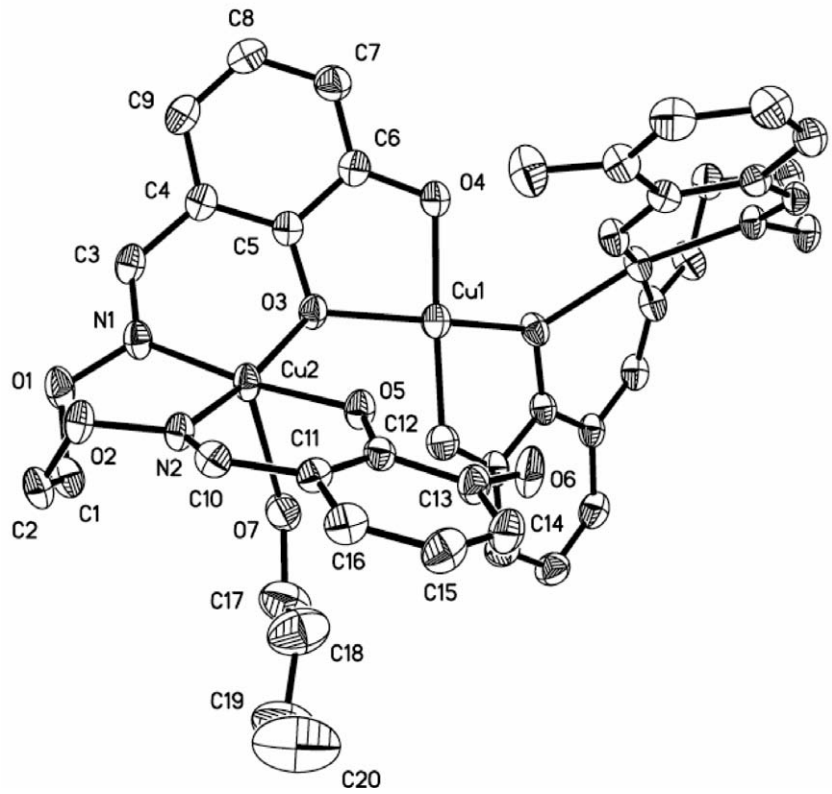


Fig. 3. Molecular structure of complex **4** with the atom numbering. The hydrogen atoms are omitted for clarity.

with the same coordination environment as that of the central Cu(II) ion in complex **1**. Two phenoxo oxygen donors (O3 and $O3^{\#2}$ or $O3^{\#3}$) bridge the terminal and central Cu(II) ions with a separation of 3.530(2) Å in complex **2** (or 3.525(5) Å in complex **4**), which is not sufficiently short to imply a strong metal–metal bonding interaction. The bridging angle of Cu1–O3–Cu2 is 126.7(2)° in complex **2** (Cu2–O3–Cu1 is 127.0(2)° in complex **4**), indicating non-collinear Cu–O–Cu fragments, not suitable for significant electronic exchange.

In complexes **2** and **4**, the two coordinated ethanol or n-butanol molecules attached to the terminal Cu(II) ions lie in trans positions toward the terminal Cu(II) ions, which are similar to what that observed in complex **1**. In these two complexes, there are six strong intramolecular hydrogen bonds (Table 3) providing strong stabilizing forces. Hydrogen bonds between the hydroxyl groups (O7–H7) and the oxygen atom (O5) are not formed in these two complexes, which is different from complex **1**.

*3.4.3. Structure of complex **3***

The crystal of this complex consists of four Cu(II) ions, two completely deprotonated L^{4-} ligand units, two coordinated water and two crystallizing n-propanol molecules. A perspective view of this is shown in Fig. 4, together with the atomic labelling of the coordinated polyhedrons. The two Cu(II) centres (Cu1 and Cu2) are linked by one phenoxo oxygen atom (O3) from one L^{4-} unit, forming an μ-phenoxo bridged Cu1–Cu2 motif. Another Cu(II) centre ($Cu2^{\#4}$) is again bonded with the Cu1–Cu2 motif via a similar bridging segment ($O3^{\#4}$) and generates the Cu2–Cu1–$Cu2^{\#4}$ core. The fourth Cu(II) centre (Cu3) is bonded to the terminal Cu(II) centres (Cu2 and $Cu2^{\#4}$) by two phenoxo oxygen atoms (O5 and $O5^{\#4}$), so there exists a Cu–O–Cu–O–Cu–O–Cu–O eight-membered ring.

The geometries of the terminal $\{CuO_2N_2O'\}$ coordination cores can be classified as trigonal bipyramidal, with an oxime nitrogen (N1) and an oxygen atom (O5) from the completely deprotonated L^{4-} ligand units being located in the axial positions; the N1–Cu2–O5 angle is 172.4(3)°. The phenoxo oxygen (O3) atom lies in the position just perpendicular to the nearly linear arrangement with N1–Cu2–O3 and O3–Cu2–O5 bond angles of 87.5(3)° and 89.4(2)°, respectively. The other oxime nitrogen atom (N2) and one oxygen atom (O7) from the coordinated water molecules are bound equatorially and form an N2–Cu2–O7 angle of 132.8(3)°, lying just in-between that of an ideal trional bipyramid (120°) and a square-planar arrangement (180°). Unexpectedly, the bond lengths of Cu2–O5 (1.963(6) Å) and Cu2–N2 (1.970(7) Å) are almost equal, while the bond lengths of Cu2–N1 (2.023(7) Å) and Cu2–O7 (2.050(6) Å) are correspondingly longer, within the $\{CuO_2N_2O'\}$ coordination units, which is distinct from those of [Co(^{t}Bu)(Me)(salmdptn)] and [Cu(^{t}Bu)(Me)(salmdptn)] [30]. The weakest bond in the $\{CuO_2N_2O'\}$ coordination unit is that to the equatorial oxygen atom (O3) from the deprotonated L^{4-} ligand units, with a Cu2–O3 bond distance of 2.067(5) Å, which is considerably shorter than those in the [Co(^{t}Bu)(Me)(salmdptn)] and [Cu(^{t}Bu)(Me)(salmdptn)]. The coordination polyhedron thus resembles a trigonal bipyramid (3 + 2 coordination) rather than the tetragonal pyramid (4 + 1 coordination) in the complex [Cu(^{t}Bu)(Me)(salmdptn)] [30]. The "sal" moieties in each L^{4-} ligand unit are twisted with respect to each other (twist angle 31.6°) and make angles of 20.56° and 30.15° with the best plane of the N_2O_2 donors.

The central Cu(II) ion (Cu1) is tetra-coordinated by four phenoxo oxygen atoms (O3, O4, $O3^{\#4}$ and $O4^{\#4}$) from the two completely deprotonated L^{4-} ligand units. The donors do not form a perfect plane but deviate by *ca.* ±0.291 Å from their best plane to form a tetrahedrally distorted square planar geometry around the Cu1 centre. The four Cu–O bonds (Cu1–O3, Cu1–O4, Cu1–$O3^{\#4}$ and Cu1–$O4^{\#4}$) are similar and compare well with the literature values [25]. These Cu–O distances are somewhat shorter than those in the terminal $\{CuO_2N_2O'\}$ coordination cores, perhaps due to the decrease in the coordination number of Cu from 5 to 4. In

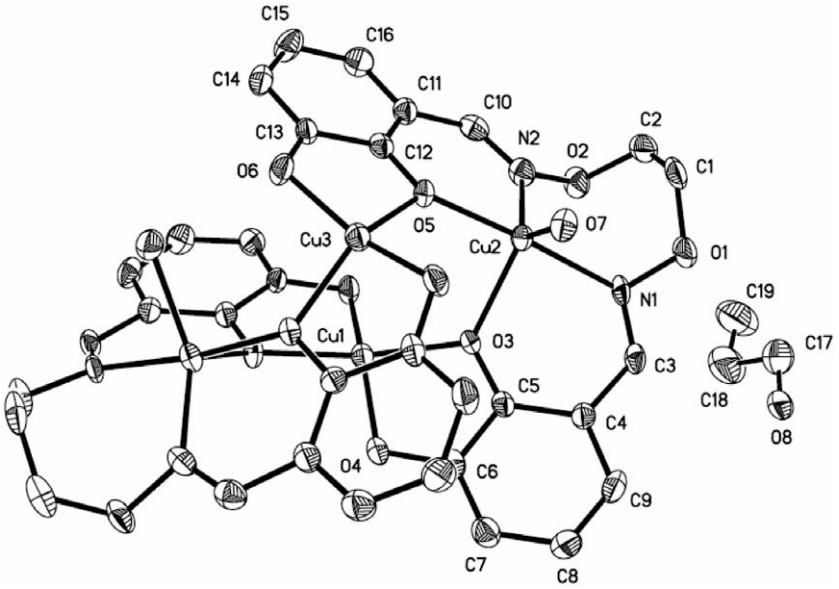


Fig. 4. Molecular structure of complex **3** with the atom numbering. The hydrogen atoms are omitted for clarity.

this complex, the other Cu(II) centre (Cu3) possesses the same coordination environment as that of the Cu1 atom. The only exception is the donors, which take part in coordination to Cu3, namely O5, O6, $O5^{\#4}$ and $O6^{\#4}$.

The structure of complex **3** contains a tetrametal eight-membered ring which sits on a crystallographic symmetric axis across the line of Cu1···Cu3. The intracomplex metal–metal separations are 3.527 Å (for Cu1···Cu2 or Cu1···$Cu2^{\#4}$) and 3.486 Å (for Cu3···Cu2 or Cu3···$Cu2^{\#4}$), which is not sufficiently short to imply strong metal–metal bonding interactions. The Cu1–O3–Cu2 (or Cu1–$O3^{\#4}$–$Cu2^{\#4}$) and Cu3–O5–Cu2 (or Cu3–$O5^{\#4}$–$Cu2^{\#4}$) bridging angles are 123.6(3)° and 122.4(3)°, respectively, indicating non-collinear Cu–O–Cu fragments, not suitable for significant electronic exchange.

Complex **3** is distinct from complexes **1**, **2** and **4** in that the two coordinated water molecules attached to the terminal Cu(II) ions lie on the same side of the terminal Cu(II) ions. There are four strong intramolecular and two strong intermolecular hydrogen bonds (Table 3) existing in the structure of complex **3**. The intramolecular hydrogen bonds are formed between the hydroxyl groups (O7–H7A and O7–H7AB) from the coordinated water molecules and the deprotonated oxygen atoms (O6 and $O6^{\#4}$) in the L^{4-} ligand units or the oxygen atom (O8) from the crystallizing n-propanol molecules. The intermolecular hydrogen bonds are found between the hydroxyl groups (O8–H8) from the crystallizing n-propanol molecules and the deprotonated oxygen atoms (O4 and $O4^{\#4}$) of the L^{4-} ligand units in the adjacent molecule. Meanwhile, the crystallizing n-propanol molecules link two other adjacent complex molecules into a self-assembling infinite 2D supramolecular structure via the intermolecular hydrogen bond O8–H8···O4 (Fig. 5).

3.4.4. Solvent effect

As shown in Fig. 6, because of the introduction of different solvent molecules, complexes **1**, **2**, **3** and **4** present two kinds of stoi-

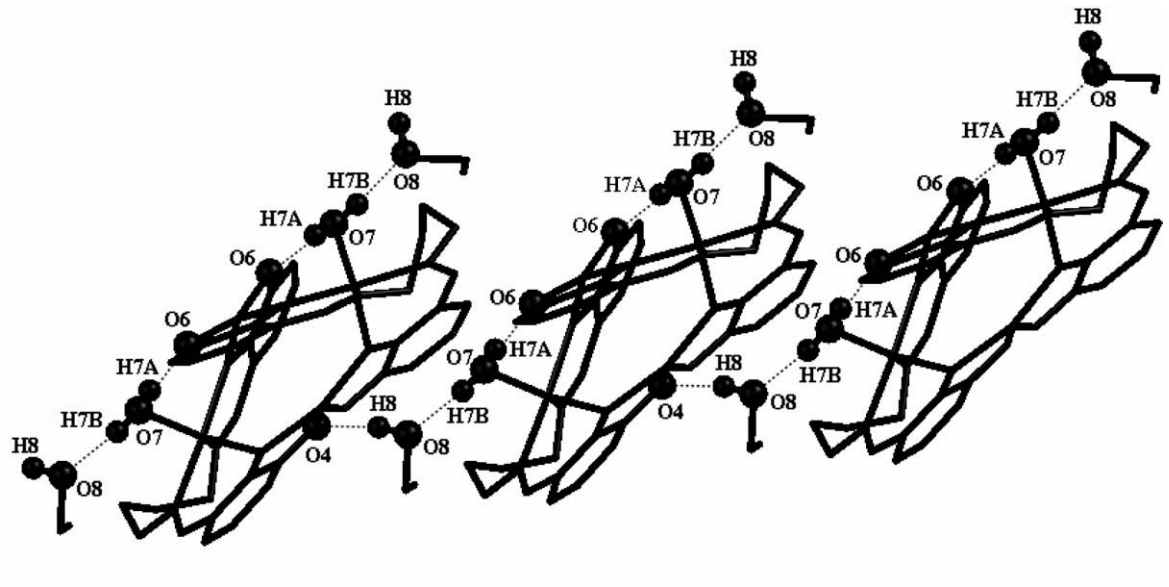


Fig. 5. Infinite 2D supramolecular structure of complex **3** showing intra- and intermolecular hydrogen bonds.

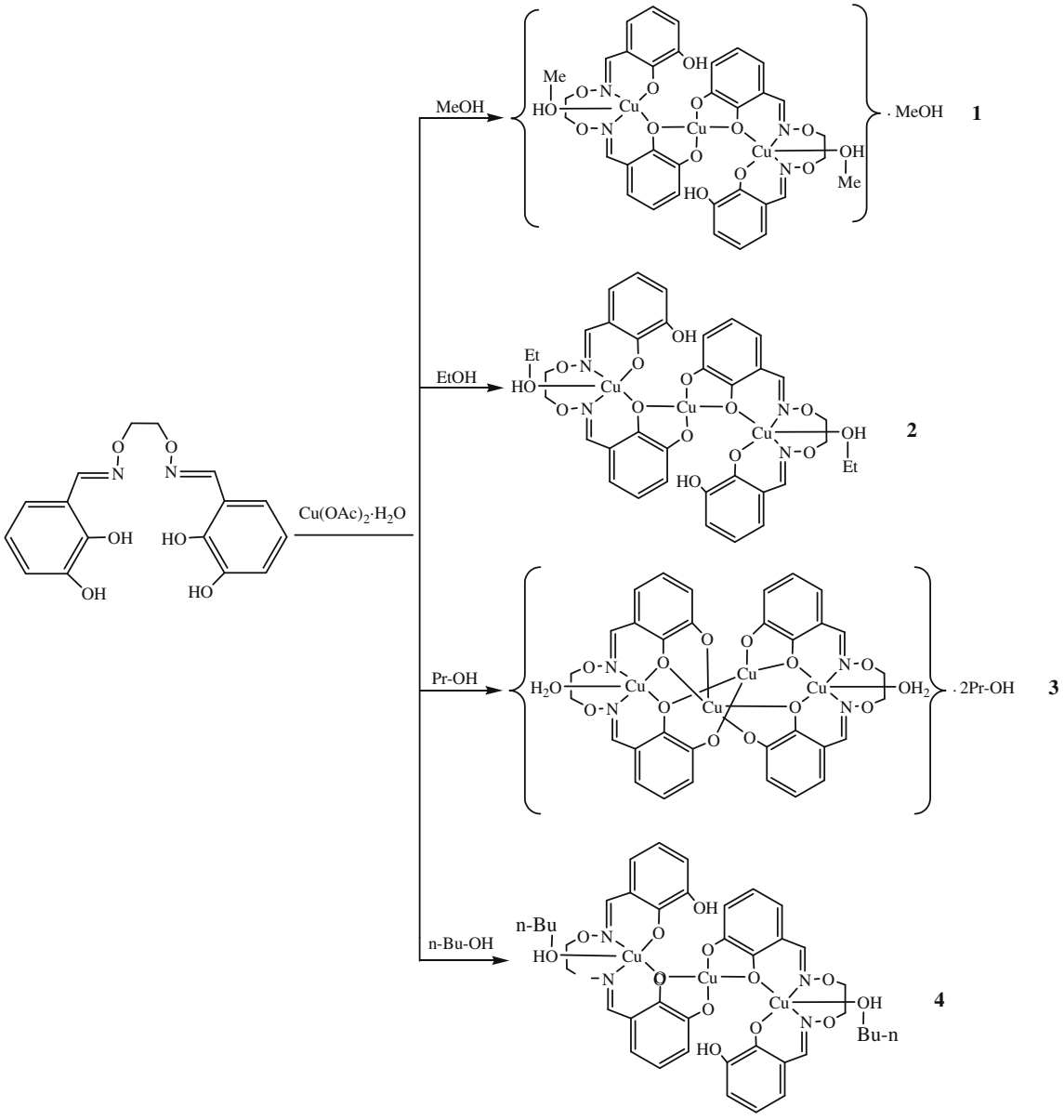


Fig. 6. Controlled design of solvent-induced Cu(II) complexes **1**, **2**, **3** and **4**.

chiometric ratio: the ratio of ligands and the Cu(II) ions are all 2:3 in complexes **1**, **2** and **4**, while it is 2:4 in complex **3**.

These complexes possess different structural features, mentioned above, with different performances of the ligand. In complexes **1**, **2** and **4**, the ligands are partially deprotonated as pentadentate $(HL)^{3-}$ trianions coordinating to three Cu(II) ions, and there are two solvent molecules coordinating to the two terminal Cu(II) ions, while in complex **3** the ligands are completely deprotonated as hexadentate L^{4-} tetraanions coordinating to four Cu(II) ions, and there are two water molecules coordinating to the two terminal Cu(II) ions.

The influence of solvent effect is clearly revealed in selected bond distances (Å) and bond angles (°) for complexes **1**, **2**, **3** and **4** (Table 2). It is noteworthy that the bond lengths from the oxygen atoms (O7) of coordinated solvent molecules (methanol, ethanol or n-butanol) to the terminal Cu(II) ions in complexes **1**, **2** and **4** are 2.485(4), 2.444(4) and 2.619(4) Å, respectively, which do not present a regular elongation when the steric hindrance successively becomes larger from methanol, ethanol to n-butanol.

4. Conclusion

As mentioned above, four solvent-induced Cu(II) complexes, $[\{Cu(HL)(CH_3OH)\}_2Cu]\cdot CH_3OH$ (**1**), $[\{(Cu(HL))_2(CH_3CH_2OH)_2\}Cu]$ (**2**), $[\{CuL(H_2O)\}_2Cu_2]\cdot 2CH_3CH_2CH_2OH$ (**3**) and $[\{(Cu(HL))_2(CH_3CH_2CH_2CH_2OH)_2\}Cu]$ (**4**), have been synthesized and structurally characterized. Because of the different performance of the ligand and the introduction of different solvent molecules, these complexes present two different structural features.

In complexes **1**, **2** and **4**, the ligands are partially deprotonated as pentadentate $(HL)^{3-}$ trianions coordinating to three Cu(II) ions and there are two solvent molecules coordinating to the two terminal Cu(II) ions. These complexes have elongated square-pyramidal coordination environments with an unusually long bond from the penta-coordinated Cu(II) centres to the oxygen atoms of the apical coordinated solvent molecules for the terminal Cu(II) ions, and square planar geometries distorted tetrahedrally for the central Cu(II) ions. While in complex **3**, the ligands are completely deprotonated as hexadentate L^{4-} tetraanions coordinating to four Cu(II)

ions, and there are two water molecules coordinating to the two terminal Cu(II) ions. In this complex the terminal Cu(II) ions lie in trigonal bipyramidal coordination geometries constituted by equatorial O_2N donor sites, with one oxygen atom from one of the coordinated water molecules and one nitrogen atom from a completely deprotonated L^{4-} ligand unit in the axial positions, and the central Cu(II) ions are in slightly tetrahedrally distorted square planar geometries constituted by four phenoxo oxygen donors from two completely deprotonated L^{4-} ligand units, and these form a tetrametal Cu–O–Cu–O–Cu–O–Cu–O eight-membered ring.

These complexes exhibit strong hydrogen bonding interactions in the solid state. In the case of complex **1**, the undeprotonated hydroxyl groups at the 3-position of the salicylidene moieties and the coordinated solvent molecules behave as hydrogen bond donors in contrast to the deprotonated oxygen atoms from the ligand $(HL)^{3-}$ units acting as receptors. Similar donor–acceptor modes are also witnessed in complexes **2** and **4**. In complex **3**, the hydroxyl groups of coordinated water molecules behave as hydrogen bond donors and the deprotonated oxygen atoms from the ligand $(HL)^{3-}$ units act as receptors in contrast to the crystallizing n-propanol molecules acting both as donors and acceptors. Moreover, the crystallizing n-propanol molecules link two other adjacent complex molecules into a self-assembling infinite 2D supramolecular structure via the intermolecular hydrogen bond O8–H8···O4.

Supplementary data

CCDC 670376, 696132, 712171 and 696144 contain the supplementary crystallographic data for **1**, **2**, **3** and **4**. These data can be obtained free of charge via http://www.ccdc.cam.ac.uk/conts/retrieving.html, or from the Cambridge Crystallographic Data Centre, 12 Union Road, Cambridge CB2 1EZ, UK; fax: (+44) 1223-336-033; or e-mail: deposit@ccdc.cam.ac.uk.

Acknowledgements

This work was supported by the Foundation of the Education Department of Gansu Province (No. 0604-01) and the 'Qing Lan' Talent Engineering Funds of Lanzhou Jiaotong University (QL-03-01A), which are gratefully acknowledged.

References

[1] J. Costamagna, J. Vargas, R. Latorre, A. Alvarado, G. Mena, Coor. Chem. Rev. 119 (1992) 67.
[2] L. Canali, D.C. Sherrington, Chem. Soc. Rev. 28 (1999) 85.
[3] S.S. Sun, C.L. Stern, S.T. Nguyen, J.T. Hupp, J. Am. Chem. Soc. 126 (2004) 6314.
[4] L. Xu, Y.P. Zhang, Y.X. Sun, J.Y. Shi, W.K. Dong, Chinese J. Inorg. Chem. 23 (2007) 1999.
[5] W.K. Dong, X. Chen, Y.X. Sun, X.N. He, Z.W. Lv, H.B. Yan, X.L. Tang, C.Y. Zhao, Chinese J. Inorg. Chem. 24 (2008) 1325.
[6] W.K. Dong, X.N. He, Y.H. Guan, L. Xu, Z.L. Ren, Acta Crystallogr. E64 (2008) o1810.
[7] W.K. Dong, Y.X. Sun, Y.P. Zhang, L. Li, X.N. He, X.L. Tang, Inorg. Chim. Acta 362 (2009) 117.
[8] W.Y. Bi, X.Q. Lv, W.L. Chai, W.J. Jin, J.R. Song, W.K. Wong, Inorg. Chem. Commun. 11 (2008) 1316.
[9] D.D. Perrin, W.L.F. Armarigo, D.R. Perrin, Purification of Laboratory Chemicals, 2nd ed., Pergamon Press, Oxford, 1980.
[10] D.W. Dixon, R.H. Weiss, J. Org. Chem. 49 (1984) 4487.
[11] S. Akine, T. Taniguchi, W.K. Dong, S. Masubuchi, T. Nabeshima, J. Org. Chem. 70 (2005) 1704.
[12] S. Akine, T. Taniguchi, W.K. Dong, T. Nabeshima, J. Inorg. Chem. 45 (2006) 4677.
[13] Bruker, SMART, SAINT, SADABS, XPREP, SHELXTL, Bruker AXS Inc., Madison, WI, USA, 1998.
[14] G.M. Sheldrick, Acta Crystallogr. A64 (2008) 112.
[15] L.J. Farrugia, J. Appl. Crystallogr. 30 (1997) 565.
[16] D.M. Watkin, L. Pearce, C.K. Prout, CAMERON: A Molecular Graphics Package, Chemical Crystallography Laboratory, University of Oxford, England, 1993.
[17] L.J. Farrugia, J. Appl. Crystallogr. 32 (1999) 837.
[18] M. Nardelli, J. Appl. Crystallogr. 28 (1995) 569.
[19] A.L. Spek, Acta Crystallogr., Sect A 46 (1990) C34.
[20] M. Asadi, K.A. Jamshid, A.H. Kyanfar, Inorg. Chim. Acta 360 (2007) 1725.
[21] H.F. Xu, S.H. Zhang, Y.M. Jiang, X.X. Zhong, F. Gao, Chinese J. Struct. Chem. 23 (2004) 808.
[22] G.C. Percy, J. Thornton, J. Inorg. Nucl. Chem. 35 (1973) 2319.
[23] T. Ghosh, B. Mondal, T. Ghosh, M. Sutradhar, G. Mukherjee, M.G.B. Drew, Inorg. Chim. Acta 360 (2007) 1753.
[24] Z.L. Chu, W. Huang, J. Mol. Struct. 837 (2007) 15.
[25] M.M. Bhadbhade, D. Srinivas, Inorg. Chem. 32 (1993) 6122.
[26] L.C. Nathan, J.E. Koehne, J.M. Gilmore, K.A. Hannibal, W.E. Dewhirst, T.D. Mai, Polyhedron 22 (2003) 887.
[27] R.G. Xiong, B.L. Song, J.L. Zuo, X.Z. You, X.Y. Huang, Polyhedron 15 (1996) 903.
[28] S. Akine, T. Taniguchi, T. Nabeshima, Chem. Lett. (2001) 682.
[29] A. Gerli, K.S. Hagen, L.G. Marzilli, Inorg. Chem. 30 (1991) 4673.
[30] R. Boca, H. Elias, W. Haase, M. Hüber, R. Klement, L. Müller, H. Paulus, I. Svoboda, M. Valko, Inorg. Chim. Acta 278 (1998) 127.

The positions of bands were found by Gaussian multi-peak fitting in ORIGINPRO 7.

All of the drawings of the structures in this paper were prepared in MERCURY program, version 1.4.2, or ORTEP-3 version 1.08 for Windows [20].

2.3. Synthesis of the complexes

Usually, either an appropriate metavanadate MVO_3 (M = Li, Na, K, Rb or Cs) or V_2O_5 are used as a starting substrate in the synthesis of the peroxo complexes of vanadium [21]. We applied both methods in order to test and compare them.

2.3.1. Method 1(metavanadate)

Ten millimole of the proper MVO_3 (M = alkali metal ion) was dissolved in 10% H_2O_2 (used in excess, with a molar ratio vanadium:H_2O_2 = 1:2.6). To the obtained transparent, yellow solution, which was cooled in an ice bath, 20 ml of an ethanol solution of 2,2′-bipyridine (1.56 g, 10 mmol) was added dropwise with constant stirring. The temperature of the reaction mixture should not exceed 10 °C (exothermic reaction) during the synthesis. Subsequently, 50 ml of ice-cooled ethanol was added to form a crystalline, yellow product. The solid phase was filtered off via a glass frit, washed with 10 ml of cold ethanol and dried in air, in a dark place, for 24 h, then was stored in a refrigerator (ca. −10 °C). Yield: 70–80%. *Anal.* Calc. for $C_{10}H_{18}LiN_2O_{10}V$, MW = 384.14, **Li[VO(O$_2$)$_2$(bpy)] · 5H$_2$O (LibpV)**: C, 31.3; H, 4.7; N, 7.3; O_2^{2-}, 16.7; V, 13.3. Found: C, 31.7; H, 4.5; N, 7.2, O_2^{2-} 16.6; V, 13.4%. *Anal.* Calc. for $C_{10}H_{24}N_2NaO_{13}V$, MW = 454.24, **Na[VO(O$_2$)$_2$(bpy)] · 8H$_2$O (NabpV)**: C, 26.4; H, 5.3; N, 6.2; O_2^{2-}, 14.1; V, 11.2. Found: C, 26.7; H, 5.1; N, 6.2; O_2^{2-}, 14.3; V, 11.1%. *Anal.* Calc. for $C_{10}H_{16}KN_2O_9V$, MW = 398.29, **K[VO(O$_2$)$_2$(bpy)] · 4H$_2$O (KbpV)**: C, 30.2; H, 4.1; N, 7.0. Found: C, 30.3; H, 4.1; N, 7.0%. *Anal.* Calc. for $C_{10}H_{10}CsN_2O_7V$, MW = 454.05, **Cs[VO(O$_2$)$_2$(bpy)]·H$_2$O$_2$ (CsbpV)**: C, 25.4; H, 2.6; N, 5.9; V, 10.8. Found: C, 25.8; H, 2.4; N, 6.0; V, 10.9%.

2.3.2. Method 2 (V_2O_5)

All of the complexes were also synthesised using V_2O_5 as starting: 5 mmol (0.91 g) V_2O_5 was dissolved in aqueous solution of alkali metal hydroxide with gentle heating, until complete dissolution. To this mixture, 30% H_2O_2 was added dropwise until the pH reached 4. The transparent, yellow solution was then treated as in Method 1.

Results of elemental analysis of the complexes prepared by Method 2 were the same within experimental uncertainties as for the complexes prepared according to Method 1.

The rubidium salt could only be obtained by the latter method. Yield: 70-80%. *Anal.* Calc. for $C_{10}H_{16}N_2O_9RbV$, MW = 444.65, **Rb[VO(O$_2$)$_2$(bpy)] · 4H$_2$O (RbbpV)**: C, 27.0; H, 3.6; N, 6.3. Found: C, 27.0; H, 3.7; N, 6.3%.

2.4. X-ray structure determination

Single crystals of LibpV, NabpV, KbpV and RbbpV were grown by slow precipitation from their water–ethanol reaction solutions at a temperature of ca. −10 °C. Diffraction data for the lithium and rubidium salts were collected on a Bruker Smart Apex CCD diffractometer with graphite monochromatized Mo Kα radiation (λ = 0.71073 Å), equipped with an Oxford Cryosystems cryostat, at 153(2) K, and processed using the SAINT and SADABS program systems. The space group was found using the XPREP program, and the structures were solved by the heavy-atom method with SHELXS-97 [22]. Diffraction data for the sodium and potassium salts were collected on a Nonius KappaCCD diffractometer with graphite monochromatized Mo Kα radiation at 100(1) K using Oxford Cryostream 700 low temperature device and processed using the DENZO/SCALEPACK program package [23]. The empirical absorption correction method implemented into this package was applied during data processing. Crystal data and a summary of data collection and structure refinement parameters are given in Table 1. The structure of NabpV was solved by the heavy-atom method with SHELXS-97, while the structure of KbpV was solved by direct methods using the SIR program [24]. All structures were refined on F^2 using all data by full matrix least-squares procedures with SHELXL-97 with anisotropic displacement parameters for all non-hydrogen atoms. Hydrogen atoms of the bpy molecule were included at calculated positions while those of the water molecules were localized on difference Fourier maps and refined with geometry constrains.

Attempts to obtain a good quality single crystals for the caesium salt, Cs[$VO(O_2)_2$bpy] · H_2O_2, were not successful probably because of the multiple twinning or high absorption. Therefore, powder diffraction data were collected using Philips X' Pert Pro diffractometer, and Cu Kα radiation (λ = 1.54177 Å), at 293(1) K. The XRD pattern was taken in the 2θ range from 5.0° to 60.0° with step size 0.02° and time per step 20 s. The lattice parameters were determined using the PROSZKI package [25].

Table 1
Crystallographic data for M[$VO(O_2)_2$bpy] · nH_2O.

	LibpV	NabpV	KbpV	RbbpV
Chemical formula	$C_{10}H_{18}LiN_2O_{10}V$	$C_{10}H_{24}N_2NaO_{13}V$	$C_{10}H_{16}KN_2O_9V$	$C_{10}H_{16}N_2O_9RbV$
Formula weight	384.14	454.24	398.29	444.65
Crystal system	orthorhombic	triclinic	monoclinic	monoclinic
Space group	*Pmna*	$P\bar{1}$	$P2_1/c$	$P2_1/c$
a (Å)	16.944(2)	7.2090(2)	6.9346(2)	6.9345(8)
b (Å)	7.3234(9)	11.2720(3)	12.6998(4)	12.7359(15)
c (Å)	13.2773(15)	13.7330(4)	17.9629(5)	18.129(2)
α (°)	90.00	68.326(1)	90.00	90.00
β (°)	90.00	89.157(1)	95.280(2)	94.228(2)
γ (°)	90.00	88.081(2)	90.00	90.00
V (Å^3)	1647.6(3)	1036.46(5)	1575.24(8)	1596.8(3)
Z	4	2	4	4
μ (mm^{-1})	0.654	0.561	0.941	3.697
Reflections collected	10522	4730	13757	18754
Unique reflections	2023	4730	3569	3638
Reflections [$I \geqslant 2\sigma(I)$]	1154	4024	2987	2516
R_1, wR_2 [$I \geqslant 2\sigma(I)$]	0.0373, 0.0564	0.0339, 0.0766	0.0328, 0.0645	0.0371, 0.0780
R_1, wR_2 [all data]	0.0764, 0.0613	0.0447, 0.0829	0.0445, 0.0683	0.0569, 0.0816
Goodness-of-fit on F^2	0.758	1.040	1.083	0.880
Largest peak and hole (e Å^{-3})	0.664, −0.398	0.294, −0.299	0.432, −0.0344	0.800, −0.563

Table 2
Crystallographic data for $Cs[VO(O_2)_2bpy] \cdot H_2O_2$.

	CsbpV
Chemical formula	$C_{10}H_{10}CsN_2O_7V$
Formula weight	454.05
Crystal system	triclinic
Space group	$P\bar{1}$
a (Å)	7.895(3)
b (Å)	7.971(3)
c (Å)	11.675(4)
α (°)	72.91(3)
β (°)	85.78(3)
γ (°)	74.60(3)
V (Å^3)	677.1(3)
Z	2
Number of observations	2462
Number of reflections	361
F_{30}	30.09
M_{30}	11.55
R_P (%)	14.30
R_B(%)	23.80

The structure model was built on the basis of a global optimization method, using the FOX program [26]. The obtained model was used for the Rietveld refinement performed using the XRS-82 program [27]. Weak geometric restraints on bond distances and angles were applied during the refinement procedure. The preferred orientation correction was applied according to the March–Dollase formula. The preferred orientation direction was chosen, by trial and error method, along the [1 1 0]. The crystal data, summary of data collection and structure refinement parameters are given in Table 2, while the Rietveld plot is presented in Fig. 1.

3. Results and discussion

The complexes were prepared either by reacting solutions of peroxovanadate, generated from metavanadate $M[VO_3]$ (M = Li, Na, K, Cs) and H_2O_2, with bipyridine, or by dissolving V_2O_5 in aqueous MOH (M = Li, Na, K, Rb and Cs), followed by treatment with H_2O_2 and bpy. Both synthetic methods provide products with similar purities and yields. However, Method 1 turned out to be more convenient one. In Method 2, some problems arise with dissolving V_2O_5 in hydroxide, moreover, the reaction can proceed violently when H_2O_2 is added too fast and/or the temperature of the reaction mixture is too high.

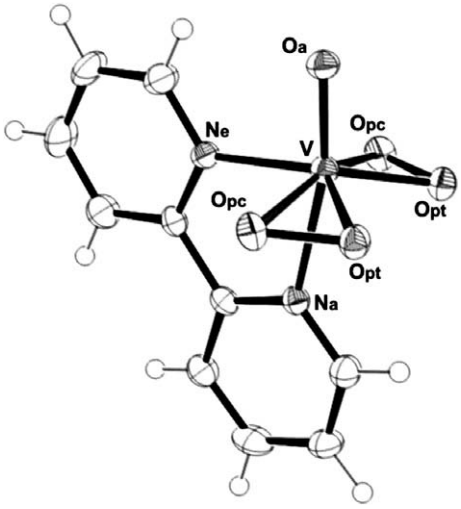


Fig. 2. General view of the coordination sphere of V with marked position of coordinating atoms: O_a – vanadyl oxygen atom, O_p – peroxo oxygen atoms in cis (O_{pc}) and trans (O_{pt}) positions, N_e and N_a – nitrogen atoms in equatorial and axial positions, respectively.

3.1. X-ray structures of $M[VO(O_2)_2bpy] \cdot nH_2O$ (M = Li^+, Na^+, K^+ and Rb^+) and $Cs[VO(O_2)_2bpy] \cdot H_2O_2$

The crystal structure of $Na[VO(O_2)_2(bpy)] \cdot 8H_2O$ has been reported previously by Fedorova et al. [28]. In the present paper, comparison of structure parameters of the sodium compound with those of the other alkali metal compounds is based on our own data reported below.

The coordination sphere of vanadium with the atom labeling scheme is shown in Fig. 2 and selected structural parameters are

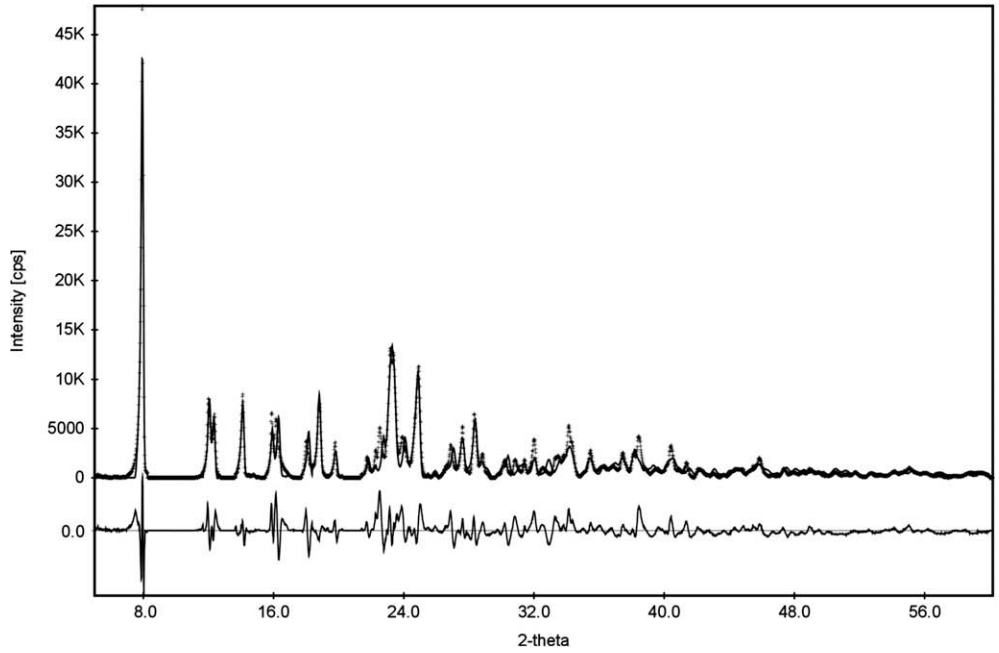


Fig. 1. The Rietveld refinement plots for $Cs[VO(O_2)_2bpy] \cdot H_2O_2$.

Table 3
Selected structural parameters for crystal structures of the complexes.

Distance [Å]	LibpV	NabpV	KbpV	RbbpV	CsbpV
V=Oa	1.616(2)	1.611(1)	1.624(1)	1.606(2)	1.62(18)
V–Opc	1.907(2)	1.915(1)	1.905(2)	1.890(2)	1.89(19)
	1.907(2)	1.916(1)	1.915(2)	1.894(2)	1.84(19)
V–Opt	1.882(2)	1.882(1)	1.891(1)	1.870(2)	1.9(2)
	1.882(2)	1.885(1)	1.891(2)	1.874(2)	1.84(19)
V–Ne	2.118(3)	2.151(2)	2.138(2)	2.128(3)	2.3(3)
V–Na	2.273(3)	2.306(1)	2.300(2)	2.283(3)	2.3(3)
Op–Op	1.463(2)	1.459(2)	1.471(2)	1.459(3)	1.5(2)
	1.463(2)	1.460(2)	1.471(2)	1.458(3)	1.5(2)
Oa···M^+	2.021(6)	2.473(1)	2.764(2)	2.855(2)	2.80(18)
			2.957(2)	3.101(2)	3.40(18)
α···V[a]	0.330	0.326	0.328	0.320	0.436
bpy···bpy[b]	3.662	3.618	3.435	3.452	2.868

[a] The distance between V atom and mean plane α formed from all O_p and N_e atoms in coordination sphere of V.

[b] The distance between two interacting bpy rings (π-stacking), calculated as mean distance between planes formed from all non-hydrogen atoms of two bpy rings.

given in Table 3. All complexes have the same inner coordination sphere, containing vanadium (coordination number 7) in the center of distorted pentagonal bipyramid. KbpV and RbbpV are isomorphous. Vanadium is coordinated to two peroxo groups, O_2^{2-}, in the side-on mode, and one of the nitrogen atoms of 2,2'-bipyridine, N_e, in the equatorial plane. The axial positions are occupied by the oxidovanadium(V) oxygen O_a, and the second nitrogen atom of bpy, N_a. The axial V–N_a bonds, on average, are 0.136 Å longer than the equatorial V–N_e bonds reflecting the *trans* influence of the oxidovanadium(V) oxygen (O_a). For the isomorphous potassium and rubidium salts, a weak influence of the alkali metal ion on the bond distance V=O_a is observed. For KbpV the distance equals 1.624 Å, while for RbbpV it is shorter (1.606 Å). This fact can be explained by the size of the cation M^+ which interacts with O_a possessing a partial negative charge. The $M^+ \cdots O_a$=V interactions are stronger, and the V=O_a bond increases for a cation with a smaller radius and thus a more pronounced polarizing power. The distance $d(\alpha \cdots V)$ of vanadium from a mean plane α (formed by all atoms in equatorial positions) ranges from 0.32 to 0.33 Å, showing a similar degree of deformation of the vanadium coordination polyhedra, except for the Cs salt, where $d(\alpha \cdots V)$ is 0.436 Å. This difference possibly reflects that the deformation is not simply driven by the nature of the alkaline metal cation. Rather, the nature of the molecules in the hydration sphere (H_2O_2 for CsbpV and H_2O for all other cations) also plays a role.

The lengths of the vanadium–peroxo oxygen bonds, V–O_p, differ (Table 3), as commonly observed for this type of compounds. The bond lengths V–O_{pc} (peroxo oxygen in *cis* position to the nitrogen atom in the equatorial plane (N_e)) are longer than the V–O_{pt} in (*trans* position). For the nomenclature (subscript "pc" and "pt") cf. ref.[29].

The crystal structures are stabilized by π-stacking of the 2,2'-bipyridine rings and by hydrogen bond networks. The interacting bpy rings form columns, where the vanadium atoms are placed alternately on the left and right sight of the column (see Fig. 3). The distances between two interacting bpy rings are ca. 3.4-3.7 Å for all compounds (for detailed data see Table 3). The hydrogen bond networks will be described in detail in Section 3.3.

The alkali metal ion is surrounded by oxygen atoms stemming from oxidovanadium(V) O_a, coordinated peroxide (except for M = Li) and water or (M = Cs) · H_2O_2. Coordination numbers differ, except for the isomorphous potassium and rubidium salts. In LibpV (Fig. 4) the lithium cation has the coordination number 4 (tetrahedral coordination mode: $[LiO_a(H_2O)_3]$). In the structure, separate units of $\{[Li(H_2O)_3]–\mu\text{-}O_a–[V(O_2)_2(bpy)]\}$ can be identified. Two remaining water molecules present in the structure link the units by hydrogen bonds formed between water molecules and also between water molecules and the O_p atoms of both peroxo ligands.

In NabpV, the sodium cation is in the octahedral coordination mode, surrounded by five water molecules and one O_a. The octahedra $[NaO_a(H_2O)_5]$ are linked together by bridging oxygen atoms O6,

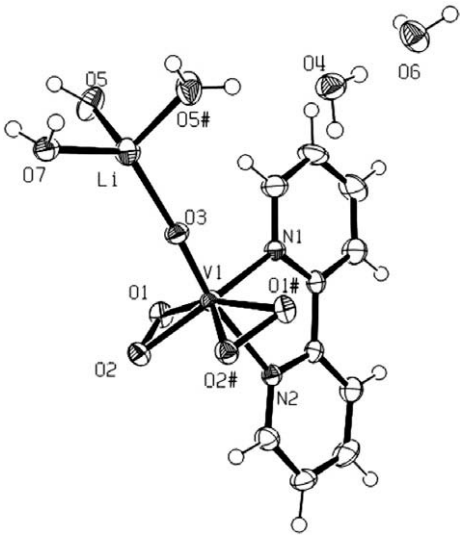


Fig. 4. Asymmetric unit of $Li[VO(O_2)_2(bpy)] \cdot 5H_2O$.

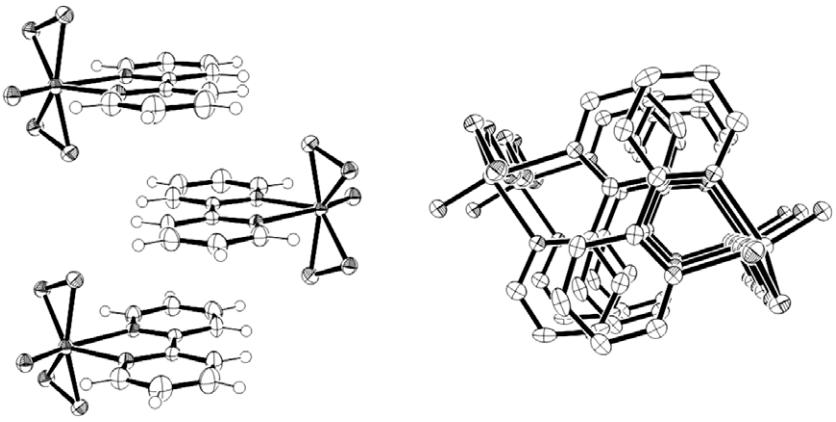


Fig. 3. π-stacking of bpy rings (view along (001) on the left and view along (010) on the right). Hydrogen atoms in the drawing on the right have been removed for clarity.

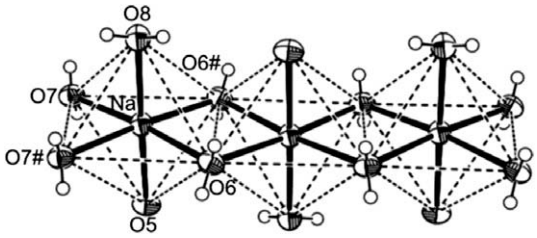


Fig. 5. Coordination sphere of Na^+ in NabpV.

O6#, O7, O7# coming from water molecules (Fig. 5) thus forming a pseudopolymeric chain. Atoms marked with # are related by symmetry and formally belong to an adjacent polyhedron. The remaining water molecules form water channels, where an extensive system of hydrogen bonds is linking the pseudopolymeric chains together. Such water channels are found only in the sodium salt, see Fig. 6.

In KbpV and RbbpV the coordination number for the alkaline metal cation is 8 (Fig. 7). The coordination geometry of M^+ resembles a distorted dodecahedron, which is shown in Fig. 8 for potassium. In the coordination sphere of M^+, 4 water molecules, 2 O_p and 2 O_a are present. The polyhedra $[M(O)_4(H_2O)_4]$, like in NabpV are linked together to form a pseudopolymeric chain. The bridging oxygen atoms O7 and O7# are coming from water molecules and the other two oxygens, O5 and O5# are oxidovanadium(V) O_a atoms. One water molecule (O9 in Fig. 7), which does not belong to the coordination sphere of M^+, connects two chains through hydrogen bonds.

The caesium salt (Fig. 9) is the only one containing a hydrogen peroxide molecule. The caesium cation attains coordination number 9 (Fig. 10).

In the coordination sphere of Cs^+, following oxygen atoms are present: two O_a atoms from two V=O groups (O1, $O1^{\#}$), six O_p atoms, and one H_2O_2. Each coordination polyhedron is sharing three edges (containing O_a and O_p oxygen bridging atoms) with neighboring polyhedra to form layers resembling a two-dimensional network.

The coordination number for alkali metal ions increases with increasing the ionic radius and adopts typical values for each alkali metal: Li (4), Na (6), K, Rb (8) and Cs (9).

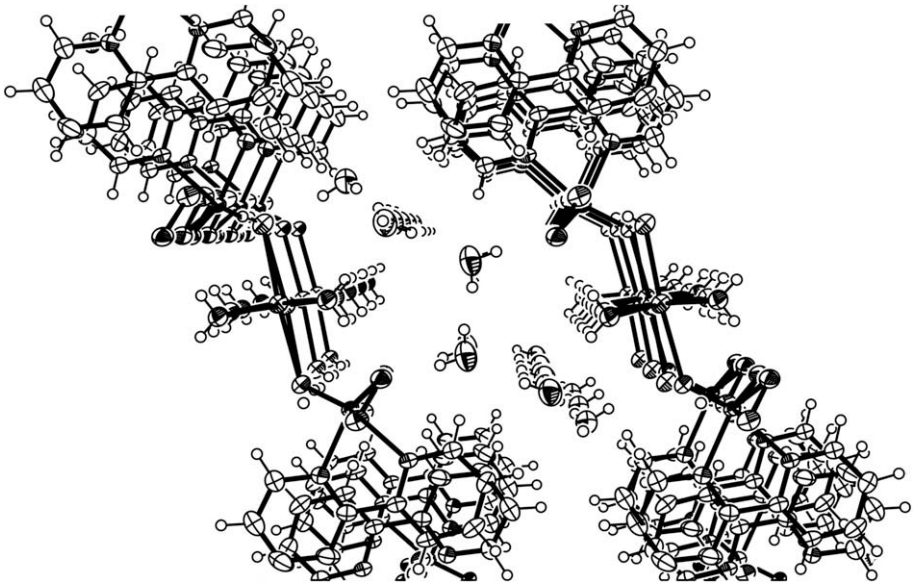


Fig. 6. Water channel in NabpV.

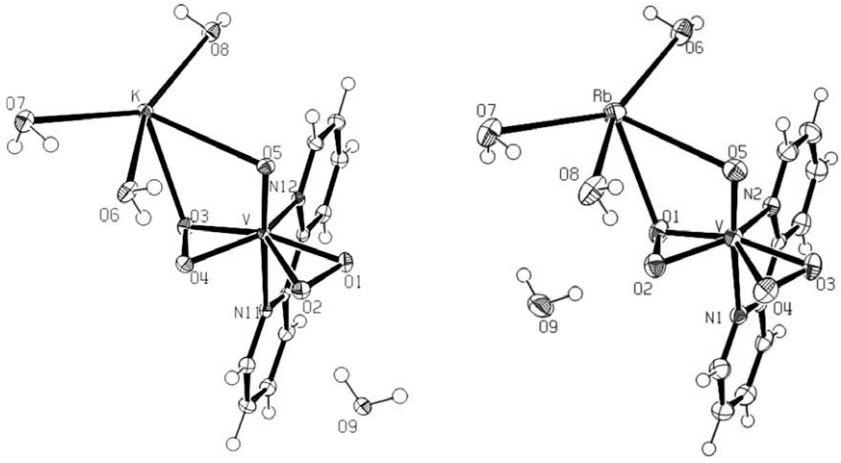


Fig. 7. Asymmetric units of isostructural salts: KbpV (on the left) and RbbpV (on the right).

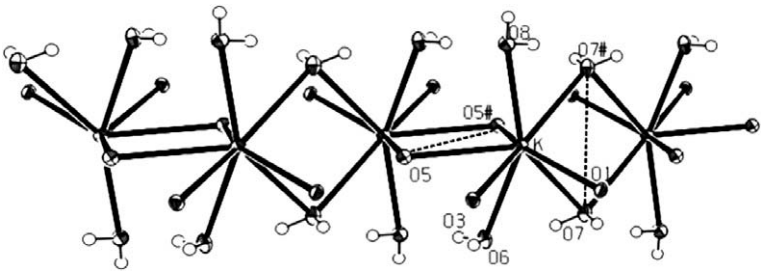


Fig. 8. Coordination sphere of K^+ in KbpV. Atoms marked with # are related by symmetry. Dashed lines show sharing edges in coordination polyhedra.

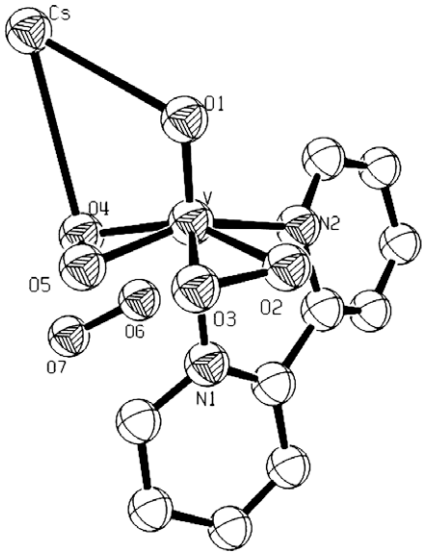


Fig. 9. Asymmetric unit of CsbpV.

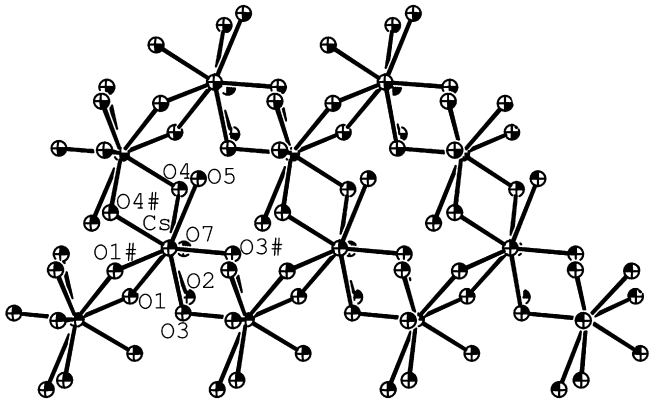


Fig. 10. Coordination sphere of Cs^+ in CsbpV.

The proximity between the M^+ cation and the peroxido ligands (O_p) suggests that an interaction exists which influences the tendency to shift electron density from the peroxido ligand to the vanadium cation which, in turn, has an impact on oxygen liberation by auto-decomposition of the complex. In the case of the K, Rb and Cs salts, this influence opposes the electron density shift, thus making the complex more stable. In the Na and Li complexes, where the cation is farther away from the peroxo ligands, this influence is minimized, and therefore the compounds are expected to be less stable. Similarly, distances between M^+ and the oxidovanadium(V) oxygen (O_a) can also, in principle, have impact on the complex stability. However, in this case the influence on electron density transfer between the peroxido ligand and the central cation is expected to be negligible. The effect by hydrogen bonds from the water molecules follows the same scheme: bonds to peroxo ligands stabilize the complex, while bonds to the oxidovanadium(V) ion have virtually no effect.

3.2. Hydrogen bond networks

Hydrogen bonds play a very important role in stabilizing crystal structures. Two types of hydrogen bonds can be found in the investigated compounds: (i) formed between water molecules (O–H···O) and (ii) formed between a water molecule and an oxygen atom of a peroxo group (O–H···O_p). Water molecules act both as donors and acceptors in type (i) hydrogen bonds and only as donors in type (ii).

There are many different ways to define the strength of a hydrogen bond given in the literature [30–32]. The geometric parameters of the hydrogen bonds and the hydrogen bond strengths according to the [32] for the Li, Na, K, Rb salts are given in Table 4 and hydrogen bond networks is shown in Fig. 11.

The hydrogen bonds formed between lattice water molecules are present in all salts and are most numerous in Na salt.

In Li and Na salts water molecules form hydrogen bonds to both oxygen atoms (O_{pt} and O_{pc}) of each peroxo ligand while in K and Rb salts only to O_{pt} atoms.

In the potassium and rubidium complexes some hydrogen bonds are replaced by interactions between the alkali metal ion and the oxygen atom from the peroxo ligand in *cis* position, $M^+\cdots O_{pc}$. This may be traced back to (i) the relatively large size of alkali metal ions and (ii) opposite charges on these interacting fragments of the structure – the cation is positively charged while the peroxo ligand has a partial negative charge. In CsbpV, almost all oxygen atoms forming the coordination sphere of vanadium belong also to a coordination sphere of caesium cations (from the same or an adjacent complex).

3.3. IR and UV–VIS characterisation

All of the complexes display typical spectral patterns in the infrared region, involving absorptions due to oxidovanadium(V) group, coordinated peroxido and 2,2'-bipyridine groups, lattice water and/or hydrogen peroxide. The positions of all bands are in good agreement with previously reported data [28,33]. Selected IR bands are given in Table 5.

Interestingly, the IR spectrum of NabpV in KBr pellet shows the ν(V=O) band shifted to 927 cm^{-1} with respect to 946 cm^{-1} in nujol, with other bands retaining their positions. This shift can be explained by cation exchange of Na^+ to K^+ (from KBr) under experimental conditions. The positions of ν(O–O) and $\nu(VO_2)$ are typical for a side-on coordination mode of O_2^{2-}.

In the Li–Cs series the positions of ν(V=O) band is passing through a maximum for NabpV and indicating complex effect of: (i) the V=O bond length (the correlation between ν(V=O) and

Table 4
Geometric parameters of the hydrogen bonds and the hydrogen bond strengths according to Gilli et al. [32].

D–H···A	LibpV		D–H···A	NabpV		D–H···A	KbpV		D–H···A	RbbpV	
	D···A (Å)	D–H···A (°)		D···A (Å)	D–H···A (°)		D···A (Å)	D–H···A (°)		D···A (Å)	D–H···A (°)
O4–H41···O6	2.674	172 (m)	O6–H061···O2	2.810	174 (w)	O6–H061···O4	2.772	168 (m)	O8–H081···O2	2.776	168 (m)
O4–H42···O7[1]	2.673	148 (vw)	O6–H062···O11	2.859	175 (w)	O6–H062···O8[1]	2.753	178 (m)	O8–H082···O6[4]	2.729	177 (m)
O5–H51···O2[2]	2.813	172 (w)	O7–H071···O4[1]	2.804	170 (w)	O7–H071···O6	2.726	164 (vw)	O7–H072···O8	2.711	155 (vw)
O5–H52···O4	2.760	175 (m)	O7–H072···O9	2.864	173 (w)	O7–H072···O2	2.705	167 (m)	O7–H071···O4[3]	2.715	174 (m)
O6–H61···O2[3]	2.867	171.5 (w)	O8–H081···O1[2]	2.743	167 (m)	O8–H081···O9[2]	2.662	176 (m)	O6–H062···O9[2]	2.625	177 (s)
O7–H71···O1[4]	2.681	165 (m)	O8–H082···O3[1]	2.760	159 (vw)	O8–H082···O7	2.688	161 (vw)	O6–H061···O7[1]	2.691	158 (vw)
			O9–H091···O13[3]	2.797	174 (m)	O9–H091···O4[3]	2.825	174 (w)	O9–H091···O2	2.793	176 (m)
			O9–H092···O10[1]	2.778	170 (m)	O9–H092···O2	2.779	169 (m)	O9–H092···O4[3]	2.746	170 (m)
			O10–H101···O8	2.773	170 (m)						
			O10–H102···O11	2.854	165 (w)						
			O11–H111···O12[4]	2.791	174 (m)						
			O11–H112···O9[2]	2.803	174 (w)						
			O12–H121···O12[4]	2.823	142 (vw)						
			O12–H122···O2	2.740	171 (m)						
			O13–H131···O12[5]	2.776	174 (m)						
			O13–H132···O4	2.730	174 (m)						
Equivalent positions: [1](−x, −½ + y, −z); [2](−x, 1 − y, −z); [3](½ + x, ½ − y, ½ − z); [4](−x, ½ + y, −z)			Equivalent positions: [1](−x + 1, −y + 1, −z + 1); [2](−x, −y + 1, −z + 1); [3](x, y + 1, z); [4](−x, −y, −z + 1); [5](x + 1, y, z)			Equivalent positions: [1](2 − x, 1 − y, 1 − z); [2](1 − x, ½ − y, ½ − z); [3](-1 + x, y, z)			Equivalent positions: [1](−x, 1 − y, −z); [2](x, ½−y, −½ + z); [3](−1 + x, y, z); [4](1 − x, 1 − y, −z)		

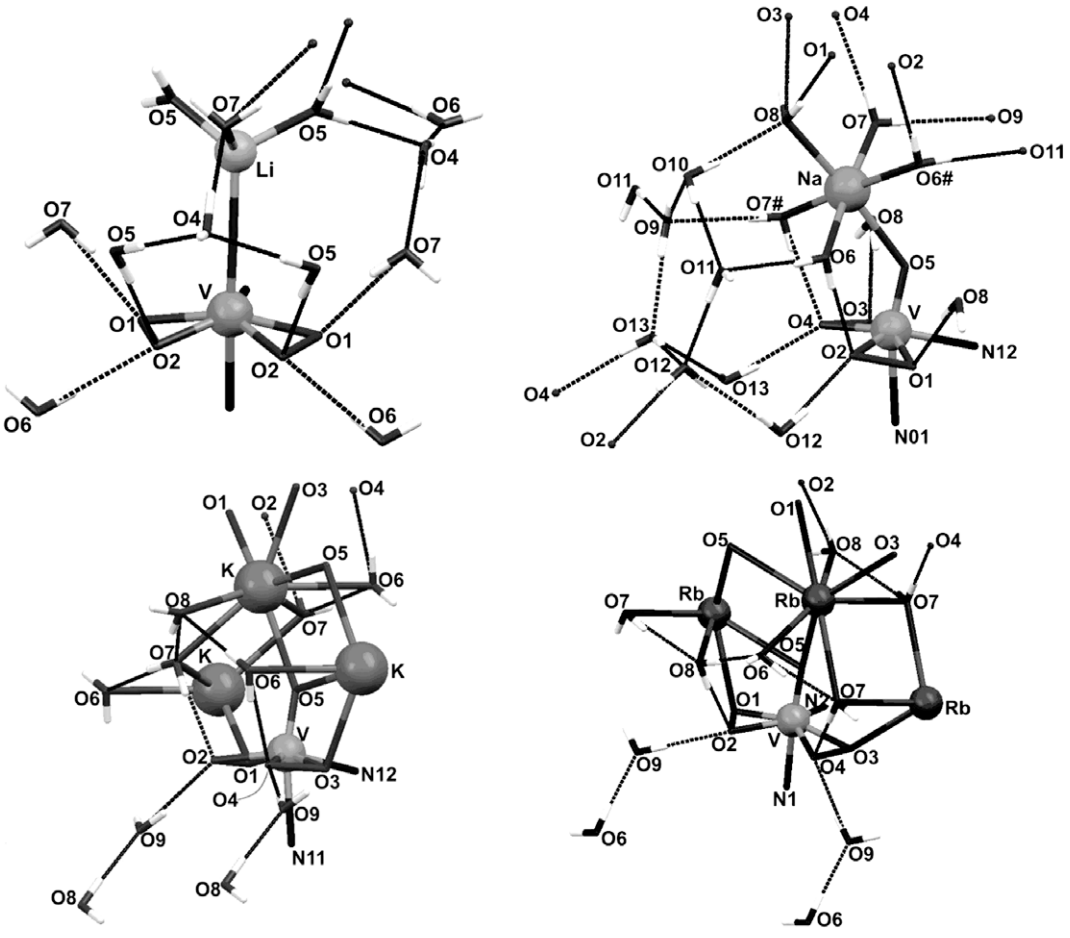


Fig. 11. Hydrogen bond networks in the complexes MbpV, M = Li, Na, K and Rb.

d(V=O) was observed only for Li, Na and K salts), (ii) polarizing power and/or polarizability of the M^+ ions [34] located close to the oxidovanadium(V) oxygen, on the V=O bond force constant.

UV–VIS reflectance spectra of all complexes show three peaks at 377, 300 and 245 nm. The first one can be assigned to the ligand-to-metal charge-transfer (LMCT) electron transition from the per-

Table 5
Relevant IR vibrations in cm^{-1} of $M[VO(O_2)_2bpy] \cdot nH_2O$ ($M = Li^+$, Na^+, K^+ and Rb^+) and $Cs[VO(O_2)_2bpy] \cdot H_2O_2$ measured in nujol.

Assignment	LibpV	NabpV	KbpV	RbbpV	CsbpV
$\nu(V{=}O)$	938	946	932	931	916
$\nu(O{-}O)_{asym}$	875	895	874	876	873
$\nu(O{-}O)_{sym}$	860	872	857	856	858
$\nu(VO_2)$	612	626	623	623	619
	589	589	586	584	585

oxido group to vanadium. The next two bands (in the UV region) can be assigned to π–π^* transitions within the bpy ligand.

4. Conclusions

The synthesis of oxido-bis(peroxido)vanadates(V) is more convenient when using metavanadate(V) as a starting substrate. The crystal structures of all complexes show a vanadium atom in the centre of a distorted pentagonal bipyramid. Except for LibpV, all complexes form pseudopolymeric chains, exploiting electrostatic interactions. Extensive hydrogen bonding networks are formed, which are interlinking the coordination polyhedra of vanadium through acceptor peroxo (O_p) atoms with water molecules. With increasing ionic radius of alkali metal cation, the degree of hydration decreases, causing an increase in the number of ionic-like ($M^{+\cdots}O_2^{2-}$ interactions. In the compounds containing water of hydration (i.e. all except CsbpV, which contains H_2O_2) the type of alkali metal cation influences the network of hydrogen bonds which in turn define the crystallographic structure.

It is interesting to compare the complexes K[VO(O2)2(bpy)]?8-H2O and $Rb[VO(O_2)_2(bpy)] \cdot 4H_2O$ which are isostructural and therefore only the alkali metal cation can be the source of differences in the physicochemical properties. Both salts have a similar hydrogen bond network. The structure of the complex KbpV (smaller cation) reveals a somewhat stronger hydrogen bond network than RbbpV.

All of these findings have a large impact on spectroscopic properties. We have observed shifts of certain bands in the IR spectra. The position of the band depends on two main factors: type of the crystal structure and the polarizing power of the alkali metal ion.

5. Supplementary data

CCDC 298937, 706501 and 298936 contain the supplementary crystallographic data for LibpV, KbpV and RbbpV. These data can be obtained free of charge via http://www.ccdc.cam.ac.uk/conts/retrieving.html, or from the Cambridge Crystallographic Data Centre, 12 Union Road, Cambridge CB2 1EZ, UK; fax: (+44) 1223-336-033; or e-mail: deposit@ccdc.cam.ac.uk.

Acknowledgments

Wojciech Przybylski wants to thank Prof. Alina Samotus' family for awarding a scholarship to Hamburg University. He is also grateful to Prof. Dr. Ulrich Behrens and Prof. Dr. Jürgen Kopf (from Hamburg University) for consultation and all the help in solving the crystal structures.

References

[1] A. Butler, M.J. Ciague, G.E. Meister, Chem. Rev. 94 (1994) 625.
[2] T. Hirao, Chem. Rev. 97 (1997) 2707.
[3] C. Slebodnick, B.J. Hamstra, V.L. Pecoraro, Struct. Bond. 89 (1997) 51.
[4] D. Rehder, Coord. Chem. Rev. 182 (1999) 297.
[5] A. Shaver, J.B. Ng, D.A. Hall, B.I. Posner, Mol. Cell. Biochem. 153 (1995) 5.
[6] A.P. Bevan, P.G. Drake, J.F. Yale, A. Shaver, B.I. Posner, Mol. Cell. Biochem. 153 (1995) 49.
[7] K.H. Thompson, J.H. McNeill, C. Orvig, Chem. Rev. 99 (1999) 2561.
[8] D. Rehder, Inorg. Chem. Commun. 6 (2003) 604.
[9] R.M. Brand, F.G. Hamel, Int. J. Pharm. 183 (1999) 117.
[10] L.A. Nolte, D. Han, P.A. Hansen, K.A. Hucker, J.O. Holloszy, Diabetes 52 (2003) 1918.
[11] B.I. Posner, R. Faure, J.W. Burgess, A.P. Bevan, D. Lachance, G. Zhang-Sun, I.G. Fantus, J.B. Ng, D.A. Hall, B.S. Lum, A. Shaver, J. Biol. Chem. 269 (1994) 4596.
[12] C.J. Doillon, R.L. Faure, B.I. Posner, P.E. Savard, Angiogenesis 3 (1999) 361.
[13] J. Ban, D. Maysinger, V. Kovač, I. Galetić, M. Matulić, M. Hadžija, B. Užarewić, Life Sci. 68 (2000) 165.
[14] N. Westergaard, C.L. Brand, R.H. Lewinsky, H.S. Andersen, R.D. Carr, A. Burchell, K. Lundgren, Arch. Biochem. Biophys. 366 (1999) 55.
[15] I. Castan, J. Wijkander, V. Manganiello, E. Degerman, Biochem. J. 339 (1999) 281.
[16] M. Audette, L. Larouche, I. Lussier, N. Fugere, Eur. J. Biochem. 268 (2001) 1828.
[17] H. Sakurai, H. Tamura, K. Okatani, Biochem. Biophys. Res. Commun. 206 (1995) 133.
[18] D. Caron, P.E. Savard, Ch.J. Doillon, M. Olivier, E. Shink, J.G. Lussier, R.L. Faure, Cancer Lett. 262 (2008) 265.
[19] (a) D.C. Crans, J.J. Smee, E. Gaidamauskas, L. Yang, Chem. Rev. 104 (2004) 849; (b) K.H. Thompson, C. Orvig, J. Inorg. Biochem. 100 (2006) 1925; (c) H. Sakurai, A. Katoh, Y. Yoshikawa, Bull. Chem. Soc. Jpn. 79 (2006) 1645; (d) D. Rehder, J. Inorg. Biochem. 102 (2008) 1152; (e) D. Rehder, Bioinorganic Vanadium Chemistry, Wiley & Sons, Chichester, 2008.
[20] L.J. Farrugia, J. Appl. Cryst. 30 (1997) 565.
[21] N. Vuletić, C. Djordjević, Dalton Trans. (1973) 1137.
[22] G.M. Sheldrick, Acta Crystallogr., Sect. A 64 (2008) 112–122.
[23] Z. Otwinowski, W. Minor, in: C.W. Carter Jr., R.M. Sweet (Eds.), Methods in Enzymology, vol. 276, Academic Press, New York, 1997, p. 307.
[24] M.C. Burla, M. Camalli, B. Carrozzini, G.L. Cascarano, C. Giacovazzo, G. Polidori, R. Spagna, J. Appl. Cryst. 36 (2003) 1103.
[25] W. Łasocha, K. Lewiński, J. Appl. Cryst. 27 (1994) 437.
[26] V. Favre-Nicolin, R. Cerny, J. Appl. Cryst. 35 (2002) 734.
[27] C. Baerlocher, The X-Ray Rietveld System (XRS-82), A Set of Computer Programs for the Rietveld Refinement of X-ray Powder Data, Institut für Kristallographie, ETH, Zürich, Switzerland, 1982.
[28] E.V. Fedorova, V.B. Rybakov, V.M. Senyavin, L.A. Aslanov, A.V. Anisimov, Russ. J. Coord. Chem. 28 (7) (2002) 483.
[29] P. Schwendt, K. Volka, M. Suchanek, Spectrochim. Acta Part A 44 (8) (1988) 839.
[30] P.A. Kollman, L.C. Allen, Chem. Rev. 72 (1972) 283.
[31] A. Novak, Struct. Bond. 18 (1974) 177.
[32] P. Gilli, V. Bertolasi, V. Ferretti, G. Gilli, J. Am. Chem. Soc. 116 (1994) 909.
[33] P. Schwendt, Collect. Czech. Chem. Commun. 48 (1983) 248.
[34] C. Le Borgne, B. Illien, M. Beignon, M. Chabanel, Phys. Chem. Phys. Chem. 1 (1999) 4701.

above 3 MΩ in-house. Thermogravimetric analysis was performed on a TA Instruments TGA 2050 Thermogravimetric Analyzer with a heating rate of 10 °C/min up to 900 °C. Elemental Analysis was carried out using a Perkin–Elmer 2400 Series II CHNS/O Analyzer. IR spectra were recorded on powdered samples on a Perkin–Elmer Spectrum One DRIFT-IR instrument. The luminescence spectrum for **3** was obtained with a Hitachi F-4500 Fluorescence Spectrometer on solid crystalline samples anchored to quartz microscope slides with Rexon Corporation RX-22P ultraviolet-transparent epoxy adhesive.

2.2. Preparation of $[Co(aze)(dpa)(H_2O)]_n$ (**1**)

$CoCl_2 \cdot 6H_2O$ (88 mg, 0.37 mmol), dpa (63 mg, 0.37 mmol) and azelaic acid (70 mg, 0.37 mmol) were added to 10 mL of distilled H_2O in a 23 mL Teflon lined Parr acid digestion bomb. The bomb was sealed, heated to 120 °C for 48 h, and then gradually cooled to ambient temperature. Magenta blocks of **1** (80 mg, 0.18 mmol, 50% yield based on Co) were obtained after filtration, washing with distilled water and acetone, and drying in air. Crystals of **1** were stable indefinitely in air. *Anal.* Calc. for $C_{19}H_{25}CoN_3O_5$ **1**: C, 52.54; H, 5.80; N, 9.67. Found: C, 52.72; H, 5.39; N, 9.75%. IR (cm^{-1}): 3156 w, 2927 w, 1588 s, 1538 m, 1507 s, 1483 m, 1455 m, 1434 m, 1403 m, 1331 s, 1309 m, 1203 m, 1100 w, 1060 w, 1017 m, 1008 m, 921 w, 900 w, 870 w, 842 m, 822 s, 740 m, 731 m, 673 w, 660 w.

2.3. Preparation of $[Ni(aze)(dpa)(H_2O)]_n$ (**2**)

The procedure for the synthesis of **1** was followed but with $NiCl_2 \cdot 6H_2O$ (88 mg, 0.37 mmol), as the metal source. Green blocks of **2** (76 mg, 0.17 mmol, 47% yield based on Ni) were obtained after filtration, washing with distilled water and acetone, and drying in air. Crystals of **2** were stable indefinitely in air. *Anal.* Calc. for $C_{19}H_{25}N_3NiO_5$ **2**: C, 52.57; H, 5.81; N, 9.68. Found: C, 52.67; H, 5.47; N, 9.82%. IR (cm^{-1}): 3271 w br, 1612 w, 1595 m, 1522 s, 1442 m, 1412 m, 1376 m, 1352 s, 1250 w, 1213 m, 1147 w, 1120 w, 1059 w, 1018 s, 1000 w, 977 w, 903 w, 848 w, 815 m, 783 s, 732 s, 677 w.

2.4. Preparation of $\{[Cd(aze)(dpa)] \cdot 2H_2O\}_n$ (**3**)

$Cd(ClO_4)_2 \cdot 6H_2O$ (100 mg, 0.30 mmol), dpa (110 mg, 0.64 mmol) and azelaic acid (60 mg, 0.32 mmol) were added to 10 mL of distilled H_2O in a 23 mL Teflon lined Parr acid digestion bomb. The bomb was sealed, heated to 120 °C for 48 h, and then gradually cooled to ambient temperature. Colorless blocks of **3** (45 mg, 0.045 mmol, 30% yield based on Cd) were obtained after filtration, washing with distilled water and acetone, and drying in air. Crystals of **3** were stable indefinitely in air. *Anal.* Calc. for $C_{38}H_{50}Cd_2N_6O_{12}$ **3**: C, 45.29; H, 5.00; N, 8.34. Found: C, 44.90; H, 5.36; N, 8.21%. IR (cm^{-1}): 3266 w, 2940 w, 2853 w, 1592 m, 1524 s, 1419 s, 1396 m, 1348 m, 1335 m, 1316 w, 1270 w, 1229 w, 1211 m, 1102 w, 1059 w, 1014 m, 929 w, 903 w, 839 w, 813 m, 786 w, 776 w, 709 m, 662 w, 624 w.

3. X-ray crystallography

Single crystals of **1**–**3** were subjected to X-ray diffraction using either a Bruker APEX2 (**3**) or a Bruker-AXS SMART 1000 (**1** and **2**) CCD instrument at 173(2) K. Reflection data were acquired using graphite-monochromated Mo Kα radiation ($\lambda = 0.71073$ Å). The data was integrated via SAINT [21]. Lorentz and polarization effect and empirical absorption corrections were applied with SADABS [22]. The structures were solved using direct methods and refined on F^2 using SHELXTL [23]. All non-hydrogen atoms were refined anisotropically. Hydrogen atoms bound to carbon atoms were placed in calculated positions and refined isotropically with a riding model. The hydrogen atoms bound to the central nitrogen of the dpa moieties and the ligated or unligated water molecules were found via Fourier difference maps, restrained at fixed positions, and then refined isotropically with thermal parameters 1.2 times the average U_{ij} values of the atoms to which they are bound. Hydrogen atoms could not be located for the disordered water molecules of crystallization in **3**. Disordered carbon atoms in **1** and **2** were modeled with partial occupancies and anisotropic thermal parameters; their occupancies were allowed to refine freely in early stages of the refinement and then were fixed. Pertinent crystallographic data is listed in Table 1.

4. Results and discussion

4.1. Synthesis and spectral characterization

The coordination polymers **1**–**3** were prepared under hydrothermal conditions via combination of 4,4′-dipyridylamine and azelaic acid with cobalt chloride, nickel chloride or cadmium perchlorate. Their infrared spectra were consistent with their crystal structures. Sharp, medium intensity bands in the range of ~1600 to ~1200 cm^{-1} were ascribed to stretching modes of the pyridyl rings of the dpa moieties [24]. Features corresponding to pyridyl ring puckering mechanisms were evident in the region between 820 and 600 cm^{-1}. Asymmetric and symmetric C–O stretching modes of the carboxylate groups were marked by very strong, slightly broadened bands at ~1590 and ~1340 cm^{-1}. Broad bands in the region of ~3400 to ~3200 cm^{-1} in all three cases represent N–H stretching modes within the dpa ligands and O–H stretching modes within the bound and/or unligated water molecules. The broadness of these spectral features is caused by hydrogen-bonding patterns within these materials.

4.2. Structural description of $[Co(aze)(dpa)(H_2O)]$ (**1**)

Compound **1** possesses an asymmetric unit consisting of a divalent cobalt atom, one azelate dianion, one dpa ligand and one aqua ligand. Although the carbon positions at each end of the α,ω-dicarboxylate aliphatic chain are fully occupied, its methylene carbons atoms are disordered over two sets of positions in an 80/20 ratio (*aze-A*, C11–C12–C13–C14–C15–C16–C17–C18–C19; *aze-B*, C11–C12A–C13A–C14A–C15A–C16A–C17A–C18A–C19). The coordination environment at cobalt is depicted in Fig. 1, showing both *aze-A* and *aze-B* disordered positions.

The coordination sphere about cobalt is a distorted $[MO_4N_2]$ octahedron, with *cis* disposed nitrogen donor atoms from two different dpa molecules. Two of the oxygen donors are part of a chelating carboxylate endcap of an aze ligand, and the aqua ligand is oriented in a *cis* fashion with respect to an oxygen donor atom from a monodentate aze carboxylate group. Bond lengths and angles (Table 2) at cobalt are standard for octahedral coordination complexes with one chelating ligand.

Extension of the cobalt coordination environments of **1** through their dpa ligands generates 1-D $[Co(H_2O)(dpa)]_n^{2n+}$ chains that course along the *b* crystal direction (Fig. 2), with Co···Co through-ligand distances of 11.679 Å. The inter-ring torsion within the dpa ligands measures 37.6°. These cationic chains are subsequently linked into two idealized $[M(aze)(dpa)(H_2O)]_n$ coordination polymer layer patterns by crystallographically disordered aze ligands in their *A* and *B* orientations, heretofore denoted *layer-A* and *layer-B*.

The *aze-A* ligands adopt a *gauche–anti–anti–anti–anti–gauche* conformation (four C-atom torsion angles = 60.6°, 178.0°, 175.8°,

Table 1
Crystal and structure refinement data.

Data	1	2	3
Empirical formula	$C_{19}H_{25}CoN_3O_5$	$C_{19}H_{25}N_3NiO_5$	$C_{38}H_{50}Cd_2N_6O_{12}$
Formula weight	434.35	434.13	1007.64
Collection T (K)	173(2)	173(2)	173(2)
Color and habit	pink block	green block	colorless block
Crystal size (mm)	0.24 × 0.16 × 0.12	0.20 × 0.16 × 0.10	0.40 × 0.22 × 0.20
λ (Å)	0.71073	0.71073	0.71073
Crystal system	monoclinic	monoclinic	triclinic
Space group	$P2_1/n$	$P2_1/c$	$P\bar{1}$
a (Å)	8.5773(1)	8.6092(19)	10.5277(2)
b (Å)	15.4864(3)	15.910(3)	11.3546(2)
c (Å)	14.8736(3)	14.569(3)	17.9779(3)
α (°)	90	90	89.436(1)
β (°)	104.921(1)	105.770(3)	84.930(1)
γ (°)	90	90	85.119(1)
V (Å^3)	1909.07(6)	1920.4(7)	2132.86(7)
Z	4	4	2
D_{calc} (g cm^{-3})	1.511	1.502	1.569
μ (mm^{-1})	0.936	1.047	1.063
Min./max. transition	0.6974/0.7452	0.6948/0.7457	0.6870/0.7452
hkl ranges	$-10 \le h \le 10$, $-18 \le k \le 18$, $-17 \le l \le 17$	$-11 \le h \le 11$, $-20 \le k \le 20$, $-18 \le l \le 18$	$-12 \le h \le 12$, $-13 \le k \le 13$, $-21 \le l \le 21$
Total reflections	37578	20870	49526
Unique reflections	3495	4397	7685
R_{int}	0.0656	0.0652	0.0416
Parameters/restraints	323/13	271/14	586/8
R_1 (all data)[a]	0.0556	0.0901	0.0532
R_1 ($I > 2\sigma(I)$)[a]	0.0347	0.0571	0.0347
wR_2 (all data)[b]	0.1048	0.1473	0.0886
wR_2 ($I > 2\sigma(I)$) [b]	0.0875	0.1313	0.0800
Max./min. residual (e$^-$/Å^3)	0.448/−0.386	1.796/−1.222	0.925/−0.946
Goodness-of-fit	1.102	1.045	1.047

[a] $R_1 = \Sigma||F_o| - |F_c||/\Sigma|F_o|$.
[b] $wR_2 = \{\Sigma[w(F_o^2 - F_c^2)^2]/\Sigma[wF_o^2]^2\}^{1/2}$.

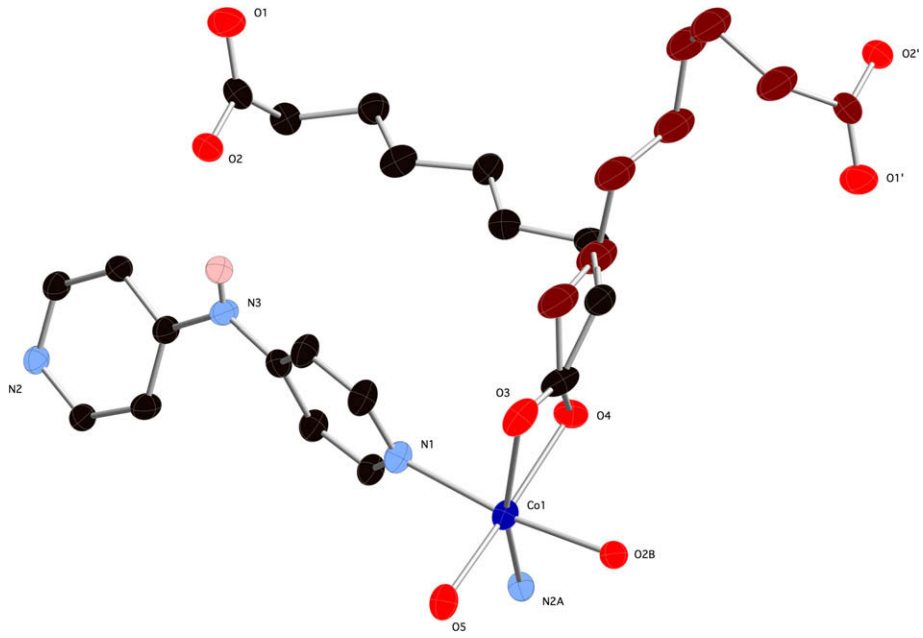


Fig. 1. Coordination environment of **1** with thermal ellipsoids shown at 50% probability and partial numbering scheme. The major and minor disordered azelate orientations are shown in black and brown, respectively. Most hydrogen atoms have been omitted. (For interpretation of the references to color in this figure legend, the reader is referred to the web version of this article.)

179.3°, 168.5°, 63.2°) and conjoin two cobalt atoms in a chelating/monodentate bridging mode. If all of the aze dianions in **1** were sited in position *A*, ruffled $[Co(aze\text{-}A)(dpa)(H_2O)]_n$ (4,4) grid-like layers are formed parallel to the *ab* crystal planes (*layer-A*, Fig. 3, shown in both face-on and side-on perspectives). The through-aze Co···Co distances in *layer-A* measure 9.067 Å; the through-space Co···Co distances across the rhomboid grid apertures are 8.577 and 15.486 Å. The apertures themselves are quite puckered, with Co···Co···Co angles subtending 46.78°, 46.78°, 83.06° and 117.29°. Hydrogen-bonding donation between the aqua ligands and the unligated oxygen atoms of the monodentate aze termini serve an ancillary stabilization role. It is also plausible that the

Table 2
Selected bond distance (Å) and angle (°) data for **1**.

Co1–O5	2.067(2)	$N2^{\#1}$–Co1–$O4^{\#2}$	99.55(8)
Co1–$N2^{\#1}$	2.115(2)	O2–Co1–$O4^{\#2}$	85.17(7)
Co1–O2	2.1287(18)	O5–Co1–$O3^{\#2}$	107.56(8)
Co1–$O4^{\#2}$	2.1404(18)	$N2^{\#1}$–Co1–$O3^{\#2}$	159.82(9)
Co1–$O3^{\#2}$	2.1786(19)	O2–Co1–$O3^{\#2}$	84.07(7)
Co1–N1	2.199(2)	$O4^{\#2}$–Co1–$O3^{\#2}$	60.61(8)
		O5–Co1–N1	93.51(8)
O5–Co1–$N2^{\#1}$	92.06(8)	$N2^{\#1}$–Co1–N1	95.32(8)
O5–Co1–O2	91.45(8)	O2–Co1–N1	171.86(7)
$N2^{\#1}$–Co1–O2	90.94(7)	$O4^{\#2}$–Co1–N1	88.67(8)
O5–Co1–$O4^{\#2}$	167.94(7)	$O3^{\#2}$–Co1–N1	88.27(8)

Symmetry related positions: #1 $-x+3/2$, $y+1/2$, $-z+3/2$; #2 $-x+1/2$, $y-1/2$, $-z+3/2$.

presence of this hydrogen-bonding interaction prevents the occurrence of a bis(chelating) dicarboxylate bridging mode, thereby providing a modicum of structure direction during self-assembly.

The *aze-B* ligands instead adopt a more spread out *anti–anti–anti–gauche–gauche–gauche* conformation (four C-atom torsion angles = 164.2°, 163.2°, 174.0°, 55.0°, 43.8° and 44.4°). Despite the conformational difference between *aze-A* and *aze-B*, they both connect cobalt atoms through the same chelating/monodentate bridging mode. If all the dicarboxylate ligands were considered to adopt the *aze-B* orientation, idealized $[Co(aze\text{-}B)(dpa)(H_2O)]_n$ (4,4) grid-like layers are constructed (*layer-B*, shown in Fig. 4 as face-on and edge-on perspectives); these align parallel to the (1 0 1) crystal plane.

The splayed-open conformation of *aze-B* ligands in layer-*B* promotes Co···Co through-ligand contact distances of 10.677 Å,

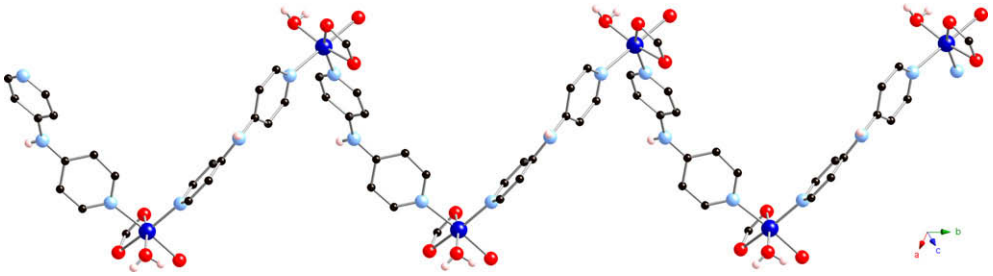


Fig. 2. A single $[Co(H_2O)(dpa)]_n^{2n+}$ chain motif in **1**.

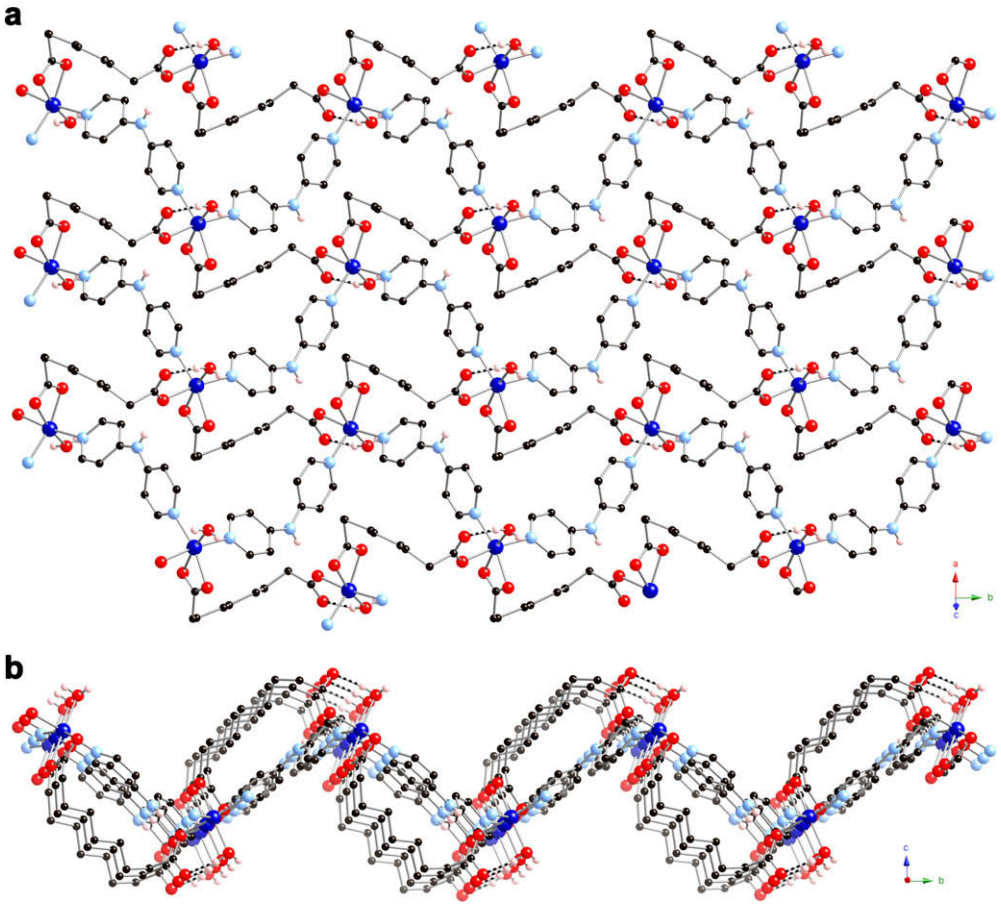


Fig. 3. Idealized layer-*A* motif in **1**. Hydrogen-bonding interactions are shown as dashed lines. (top) Face-on view; (bottom) edge-on view.

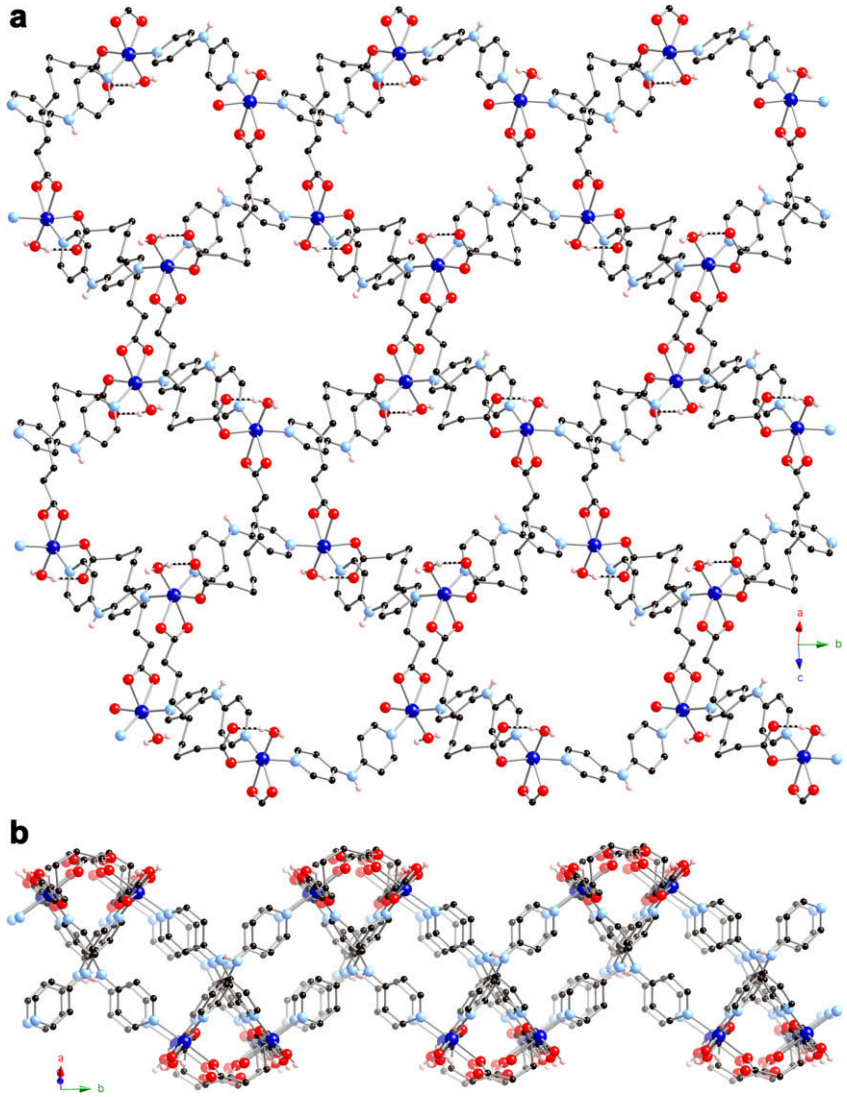


Fig. 4. Idealized layer-*B* motif in **2**. Hydrogen-bonding interactions are shown as dashed lines. (top) Face-on view; (bottom) edge-on view.

approximately 1.6 Å longer than those in layer-*A*. In contrast to *layer-A*, the ruffled *layer-B* pattern exhibits two distinct apertures, with Co···Co distances of 14.187 and 17.037 Å in one and 12.172 and 18.779 Å within the other. The Co···Co···Co angles around these apertures' respective perimeters are 78.6° and 101.4°, and 65.8° and 114.2°.

Crystallographic disorder among the aze ligands produces a three-dimensional structure for **1** that represents a weighted average of idealized *layer-A* and *layer-B* patterns in a 4:1 ratio. If the atomic positions within idealized layers were both fully occupied, the overarching coordination polymer network would be a six-connected α-Po primitive cubic lattice. Yet, each cobalt atom can only be 4-connected within the structure of **1**, with only two connections possible through aze ligands. Thus it is proper to view the covalent framework of **1** as a primitive cubic lattice with "ligand vacancies", wherein every fifth *aze-A* position is missing and every fifth *aze-B* position is occupied (Fig. 5). A similar topology was seen in the suberate analog of **1** [25]. Hydrogen-bonding interactions between the central amine groups of the dpa ligands and the ligated oxygen atoms of the monodentate aze termini, and between the aqua ligands and one of the chelating aze oxygen atoms, act in tandem to stabilize the three-dimensional structure of **1**. Geometric parameters for the hydrogen-bonding interactions in **1** are given in Table 3.

4.3. Structural description of [Ni(aze)(dpa)(H_2O)] (**2**)

The asymmetric unit of **2** (Fig. 6) is similar to that of **1**, with a very closely related $\{NiO_4N_2\}$ coordination environment and an identical geometrical arrangement of donor atoms and dicarboxylate binding modes. Here, the disordered *aze-A* and *aze-B* conformations refine best with a 70/30 ratio. Unlike **1**, the aze ligand conformations in **2** share the two carbon atoms at the ends of the aliphatic chain. Bond lengths are slightly contracted relative to **1**, consistent with well-established ionic radius trends (Table 4) [26]. These subtle variances propagate themselves in the shortened Ni···Ni contact distances within the 1-D $[Ni(H_2O)(dpa)]_n^{2n+}$ chains (11.554 Å), and lengthened Ni···Ni distances in the $[Ni(aze\text{-}A)(dpa)(H_2O)]_n$ and $[Ni(aze\text{-}B)(dpa)(H_2O)]_n$ idealized (4,4) grid-like layers (9.202 and 10.889 Å, respectively) present in the structure of **2**.

As in **1**, the structure of **2** is a three-dimensional "ligand vacancy" primitive cubic lattice consisting of a weighted average of $[Ni(aze\text{-}A)(dpa)(H_2O)]_n$ and $[Ni(aze\text{-}B)(dpa)(H_2O)]_n$ idealized layers, which are arranged parallel to the (0 0 1) and (1 0 −2) crystal planes, respectively. Similar hydrogen-bonding mechanisms to those in **1** are evident within the structure of **2**, serving an additional role in network generation and/or stabilization (Table 3).

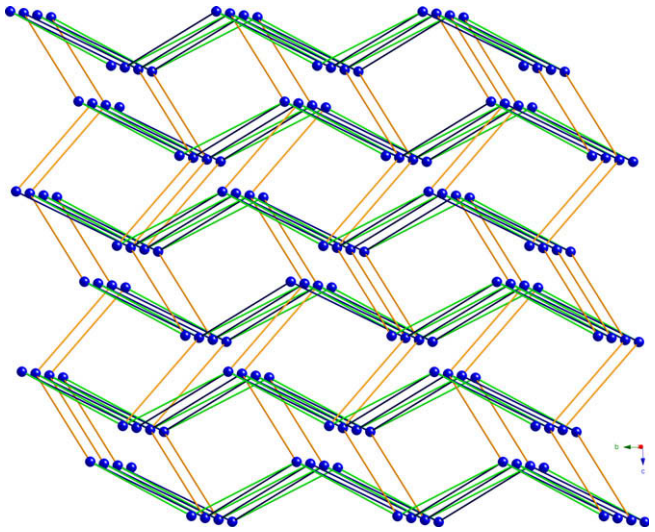


Fig. 5. Simplified perspective of the 3-D four-connected lattice of **1** and **2**, based on a primitive cubic network with "ligand vacancies". Metal atoms are shown as spheres. Linkages through-azelate dianions in orientations *A* and *B* are illustrated as green and red sticks, respectively. Linkages through dpa tethers are shown in blue. (For interpretation of the references to color in this figure legend, the reader is referred to the web version of this article.)

4.4. Structural description of $\{[Cd(aze)(dpa)] \cdot 2H_2O\}_n$ (**3**)

The asymmetric unit of compound **3** (Fig. 7) contains two crystallographically distinct divalent cadmium atoms, aze ligands (*aze-A*, C21–C29/O1–O4; *aze-B*, C31–C39/O5–O8), and dpa ligands (*dpa-A*, C1–C10/N1–N3; *dpa-B*, C11–C20/N4–N6), along with four water molecules of crystallization, two of which are distributed over multiple disordered positions. In contrast to **1** and **2** which exhibit octahedral coordination environments, the $\{CdO_5N_2\}$ environment about each crystallographically distinct cadmium atom is best described as a slightly distorted pentagonal bipyramid. In both environments the nitrogen donor atoms from two crystallographically distinct dpa ligands occupy the axial positions. The equatorial plane of each pentagonal bipyramid contains donor atoms from two chelating carboxylate aze termini along with a single oxygen donor atom from a third aze ligand. Bond lengths and angles are standard for a chelated seven-coordinated cadmium complex and are listed in Table 5.

Cd2 atoms are connected through *aze-A* ligands, which adopt a *gauche–anticlinal–anticlinal–anti–anti–gauche* conformation (four C-atom torsion angles = 75.7°, 140.3°, 123.2°, 169.2°, 167.8°, 24.3°). While both *aze-A* carboxylate termini bind to cadmium ions in a chelating fashion, one of the carboxylate oxygen atoms (O5) also binds to a second cadmium atom. Thus, the *aze-A* ligand is exotridentate, constructing a $[Cd(aze\text{-}A)]_n$ double chain motif (*chain-A*, Fig. 8a) containing $[Cd_2O_2]$ rhomboid dinuclear units. The Cd···Cd and O···O distances across the rhombs are 3.815 and 2.923 Å, respectively, with inscribed angles of 74.9° and 105.1°. The "staple" like conformation of *aze-A* results in bis(chelating) bridged Cd···Cd distance of 8.598 Å within *chain-A*.

Exotridentate *aze-B* ligands with a similar binding mode connect Cd1 atoms into a $[Cd(aze\text{-}B)]_n$ double chain motif (*chain-B*, Fig. 8b), which also contain $[Cd_2O_2]$ dinuclear units. The *aze-B* aliphatic chain rests in a *gauche–anti–anti–anti–gauche* conformation with torsion angles of 60.8°, 174.4°, 179.7°, 173.0°, 178.1° and 74.8°. This "S-shaped" conformation results in a significantly longer bis(chelating) bridged Cd···Cd distance of 11.355 Å. The Cd···Cd and O···O distances across the rhombic units in *chain-B* are slightly shorter than those in *chain-A*, measuring, respectively, 3.787 and 2.828 Å; the Cd–O–Cd and O–Cd–O angles within the $[Cd_2O_2]$ units are 106.5° and 73.5°, respectively.

Sets of *chain-A* and *chain-B* motifs are arranged parallel to the *a* and *b* crystal directions, respectively. These sets of chains are connected together into a three-dimensional coordination polymer network (Fig. 9) *via* tethering *dpa-A* and *dpa-B* ligands, which result in Cd1···Cd2 contact distances of 12.100 and 11.818 Å, respectively. The differences between these distances are likely causes by subtle variances in the inter-ring torsion angles within the dpa ligands (34.1° for *dpa-A*, 35.0° for *dpa-B*). If the centroids of the $[Cd_2O_2]$ rhombs are considered as nodes, and pairs of aze and dpa ligands as linkers, a 4-connected $6^5 8$-**cds** topology network ($CdSO_4$ lattice) can be invoked for **3**.

Entrained in the incipient voids within the 3-D framework of **3**, which occupy 11.2% of the unit cell volume according to a calculation with PLATON [27], are isolated water molecules of crystallization and water molecule trimers held in place by hydrogen-bonding donation by the central amine groups of the *dpa-B* ligands and hydrogen-bonding acceptance on the part of the *aze-A* and *aze-B* carboxylate oxygen atoms. Covalent connectivity within the coordination polymer framework is supplemented by hydrogen bonding between central amines of the *dpa-A* ligands and carboxylate oxygen atoms belonging to *aze-A* tethers. In addition, significant π–π stacking interactions between the pyridyl rings of *dpa-A* and *dpa-B* ligands (ring centroid-to-ring centroid distances = 3.622(2) and 3.837(2) Å) across the $[Cd_2O_2]$ rhombs serve an ancillary stabilization role. Metrical parameters for the identified hydrogen-bonding pathways in **3** are given in Table 3.

Table 3
Hydrogen-bonding distance (Å) and angle (°) data for **1**–**3**.

D–H	*d*(H···*A*)	∠*DHA*	*d*(*D*···*A*)	Symmetry transformation for *A*
1				
O5–H5A···O1	1.79(3)	165(3)	2.583(3)	
O5–H5B···O3	1.95(3)	167(3)	2.718(3)	$x-1/2,-y+3/2,z-1/2$
N3–H3N···O2	2.19(3)	173(3)	2.987(3)	$-x+1/2,y-1/2,-z+3/2$
2				
O5–H5A···O4	1.86(2)	164(4)	2.696(4)	$-x+2,-y+2,-z$
O5–H5B···O1	1.77(2)	168(5)	2.602(4)	$-x+2,y-1/2,-z+1/2$
N2–H2N···O2	2.13(2)	176(4)	3.008(4)	$-x+1,y-1/2,-z+1/2$
3				
O1W–H1WA···O8	1.89(2)	165(5)	2.733(4)	
O1W–H1WB···O1	1.98(2)	170(5)	2.821(4)	$x,y+1,z-1$
O2W–H2WA···O3WC	2.02(2)	176(5)	2.939(15)	$x,y,z-1$
O2W–H2WB···O6	2.03(3)	163(6)	2.866(5)	$-x+3,-y,-z$
N2–H2N···O3	2.02(2)	162(4)	2.879(4)	
N5–H5N···O1W	1.89(2)	164(4)	2.750(5)	

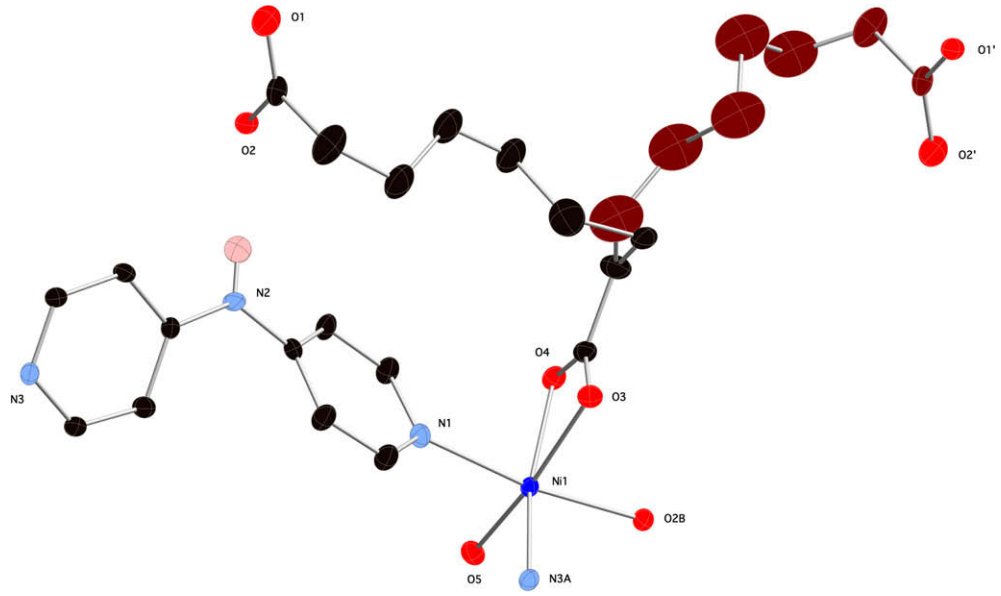


Fig. 6. Coordination environment of **2** with thermal ellipsoids shown at 50% probability and partial numbering scheme. The two disordered azelate orientations are shown in black and brown. Most hydrogen atoms have been omitted. (For interpretation of the references to color in this figure legend, the reader is referred to the web version of this article.)

Table 4
Selected bond distance (Å) and angle (°) data for **2**.

Ni1–O5	2.050(3)	N3–Ni–O4	163.08(12)
Ni1–N3	2.055(3)	$O2^{\#1}$–Ni–O4	84.77(10)
Ni1–$O2^{\#1}$	2.087(3)	O5–Ni–O3	165.75(10)
Ni1–O4	2.107(3)	N3–Ni–O3	101.55(12)
Ni1–O3	2.141(3)	$O2^{\#1}$–Ni–O3	85.24(10)
Ni1–N1	2.144(3)	O4–Ni–O3	61.93(10)
		O5–Ni–N1	92.77(12)
O5–Ni–N3	92.65(12)	N3–Ni–N1	95.08(12)
O5–Ni–$O2^{\#1}$	93.61(11)	$O2^{\#1}$–Ni–N1	171.37(11)
N3–Ni–$O2^{\#1}$	90.43(11)	O4–Ni–N1	88.06(11)
O5–Ni–O4	103.82(11)	O3–Ni–N1	87.14(11)

Symmetry related positions: #1 $-x+2, y-1/2, -z+1/2$.

4.5. Luminescence behavior of *3*

Upon irradiation with ultraviolet light (λ_{ex} = 300 nm), a solid polycrystalline sample of **3** exhibited blue-violet visible light emission (Fig. 10), although the maximum emission wavelength fell in the ultraviolet region (λ_{max} = 360 nm). Similar emissive behavior has been observed for several other cadmium coordination polymers containing aromatic ligands [6], including $[Cd(glu)(dpa)]_n$ [16]. Unligated dpa also photoluminesces [17], showing a weak broad emission with λ_{max} = 420 nm with (λ_{ex} = 300 nm). Thus, the most plausible origin for the photoluminescence of **3** is π–π^* or a π–n electronic transition behavior within the molecular orbital manifolds of the aromatic ligands of the dpa ligands.

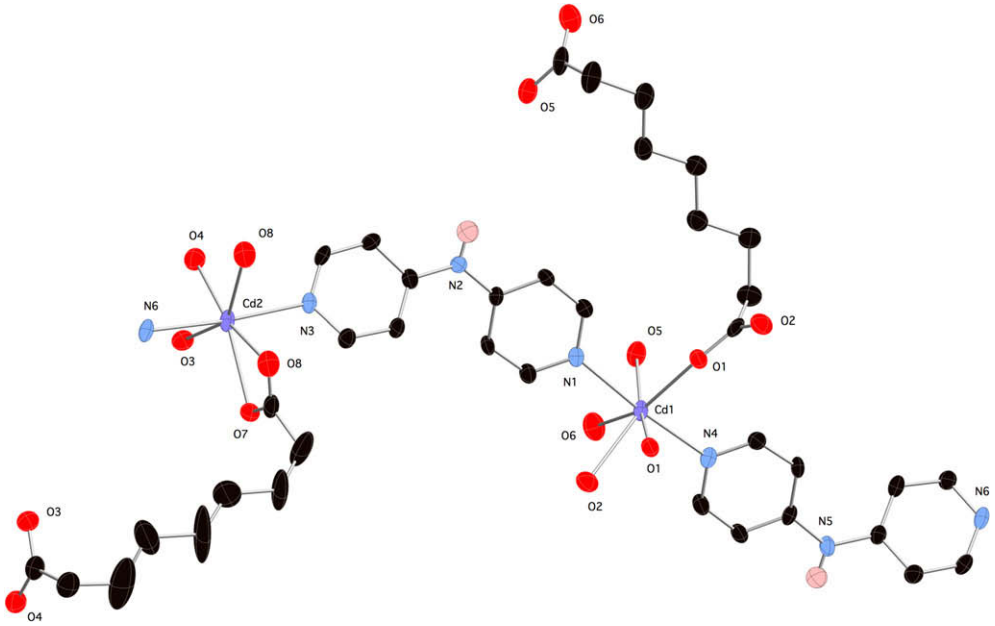


Fig. 7. Coordination environment of **3** with thermal ellipsoids shown at 50% probability and partial numbering scheme. Hydrogen atoms have been omitted.

Table 5
Selected bond distance (Å) and angle (°) data for **3**.

Cd1–N1	2.304(3)	N1–Cd1–O8$^{\#1}$	94.76(10)
Cd1–O7$^{\#1}$	2.319(3)	O7$^{\#1}$–Cd1–O8$^{\#1}$	55.04(11)
Cd1–N4	2.320(3)	N4–Cd1–O8$^{\#1}$	81.56(10)
Cd1–O5	2.335(3)	O5–Cd1–O8$^{\#1}$	94.02(10)
Cd1–O5$^{\#2}$	2.391(3)	O5$^{\#2}$–Cd1–O8$^{\#1}$	165.92(10)
Cd1–O8$^{\#1}$	2.438(3)	N1–Cd1–O6$^{\#2}$	100.03(10)
Cd1–O6$^{\#2}$	2.559(3)	O7$^{\#1}$–Cd1–O6$^{\#2}$	85.60(10)
Cd2–N6$^{\#3}$	2.307(3)	N4–Cd1–O6$^{\#2}$	84.89(10)
Cd2–N3	2.335(3)	O5–Cd1–O6$^{\#2}$	124.86(9)
Cd2–O2	2.370(3)	O5$^{\#2}$–Cd1–O6$^{\#2}$	52.24(9)
Cd2–O4$^{\#4}$	2.381(3)	O8$^{\#1}$–Cd1–O6$^{\#2}$	138.12(10)
Cd2–O1	2.410(3)	N6$^{\#3}$–Cd2–N3	172.67(11)
Cd2–O4$^{\#5}$	2.426(3)	N6$^{\#3}$–Cd2–O2	89.72(10)
Cd2–O3$^{\#5}$	2.462(3)	N3–Cd2–O2	90.66(11)
		N6$^{\#3}$–Cd2–O4$^{\#4}$	83.42(10)
N1–Cd1–O7$^{\#1}$	90.81(11)	N3–Cd2–O4$^{\#4}$	89.25(10)
N1–Cd1–N4	175.08(11)	O2–Cd2–O4$^{\#4}$	90.33(11)
O7$^{\#1}$–Cd1–N4	89.74(11)	N6$^{\#3}$–Cd2–O1	103.05(10)
N1–Cd1–O5	89.39(10)	N3–Cd2–O1	83.10(10)
O7$^{\#1}$–Cd1–O5	148.97(11)	O2–Cd2–O1	54.76(10)
N4–Cd1–O5	87.62(10)	O4$^{\#4}$–Cd2–O1	143.95(10)
N1–Cd1–O5$^{\#2}$	91.63(10)	N6$^{\#3}$–Cd2–O4$^{\#5}$	85.50(10)
O7$^{\#1}$–Cd1–O5$^{\#2}$	137.51(10)	N3–Cd2–O4$^{\#5}$	92.29(10)
N4–Cd1–O5$^{\#2}$	91.26(10)	O2–Cd2–O4$^{\#5}$	164.93(10)
O5–Cd1–O5$^{\#2}$	73.48(10)	O4$^{\#4}$–Cd2–O4$^{\#5}$	74.94(12)
		O1–Cd2–O4$^{\#5}$	140.28(10)

Symmetry related positions: #1 $-x+2,-y+1,-z$; #2 $-x+2,-y,-z$; #3 $x+1,y-1,z+1$; #4 $x+1,y,z$; #5 $-x+2,-y-1,-z+1$; #6 $x-1,y,z$.

4.6. Thermogravimetric analysis

Thermogravimetric analyses were performed in order to evaluate the thermal stability of the coordination polymers in this study. Dehydration of **1** began at ~130 °C, with a mass loss by ~200 °C of 4.5%, roughly consistent with loss of the ligated water molecules (4.1% calculated). Combustion of the organic components occurred at ~250 °C, with a mass remnant of 19% at 900 °C, matching reasonably well with production of CoO (17% calculated). According to the TGA trace of **3**, the sample had lost one equivalent of water molecules on long-term standing, as the mass loss of 3.6% by ~60 °C matches well with elimination of one equivalent of water (3.7% calculated). Ejection of the organic components from **3** commenced at ~200 °C. Mass elimination was virtually complete by ~450 °C, with the mass remnant of 21% corresponding well with a deposition of Cd metal (23% calculated). A slow mass decrease above 450 °C likely indicates some evaporation of Cd metal (bp 767 °C). TGA traces for **1** and **3** are depicted in Supplementary Figs. S1 and S2, respectively.

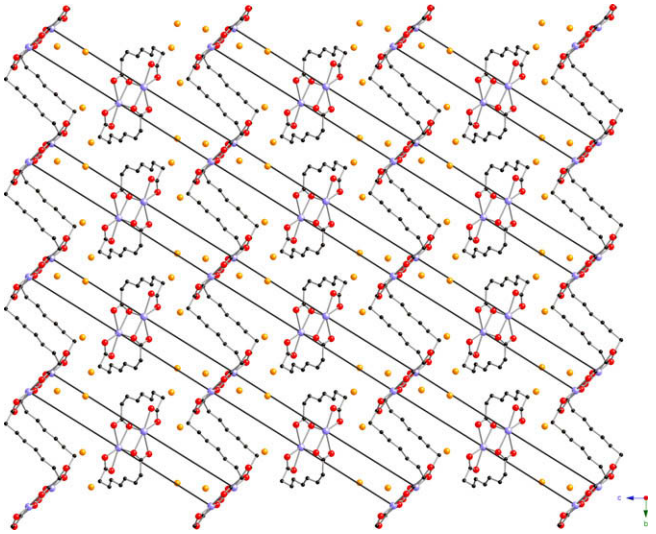


Fig. 9. The non-interpenetrated $6^5 8$ $CdSO_4$ topology 3-D structure of **3**. For clarity, dpa ligands are shown as green sticks. Water molecules of crystallization are indicated as isolated spheres. (For interpretation of the references to color in this figure legend, the reader is referred to the web version of this article.)

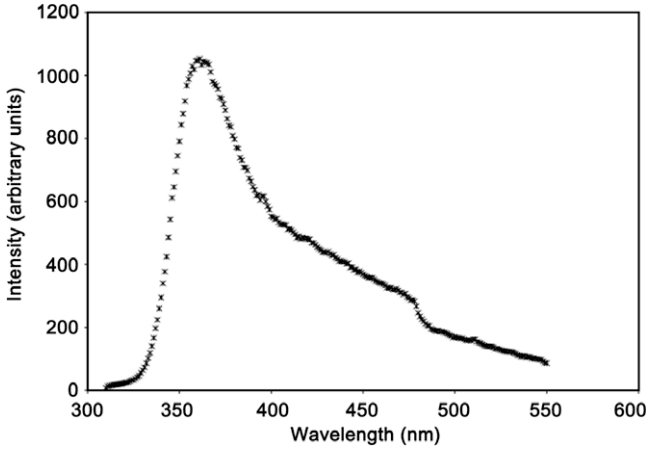


Fig. 10. Luminescence spectrum of **3**.

5. Conclusions

Self-assembly of divalent transition metal ions with a very long-spanning aliphatic α,ω-dicarboxylate ligand and the kinked

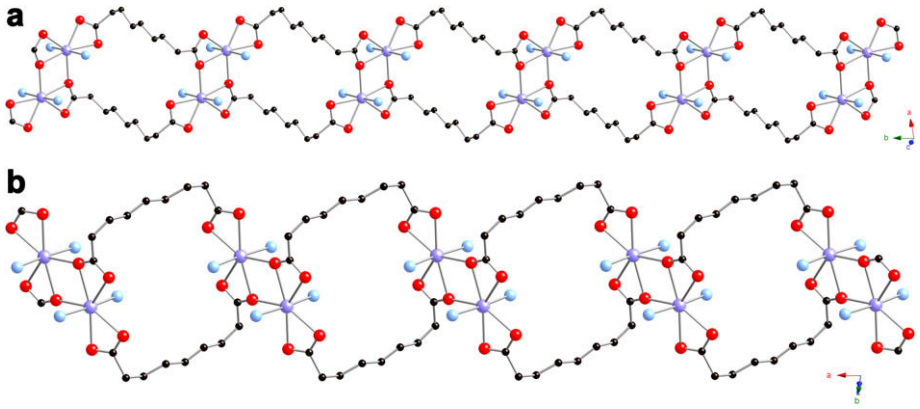


Fig. 8. The two crystallographically distinct $[Cd(aze)]_n$ ribbon patterns in **3** (top, *chain-A*; bottom, *chain-B*).

and hydrogen-bonding capable 4,4′-dipyridylamine ditopic tethering ligand has resulted in three-dimensional coordination polymers whose structural elements depend greatly on coordination geometry preferences at the metal and the conformations of the azelate ligands. The ability of the flexible dicarboxylate tethers to access energetically similar conformations during self-assembly promoted crystallographic disorder that resulted in an intriguing 4-connected "ligand vacancy" 3-D primitive cubic-type covalent network in the cobalt and nickel derivatives. The larger ionic radius of cadmium allowed an exotridentate binding mode for the azelate carboxylate termini, generating a relatively uncommon non-interpenetrated $6^5 8$ 3-D topology constructed from orthogonally disposed sets of $[Cd(aze)]_n$ 1-D double chain motifs. Hydrogen-bonding mechanisms instilled by the dpa ligands' central amine groups also play an important structure-directing role in these extended complexes, likely by influencing the conformational reorganizations of the flexible azelate ligands. Further efforts towards the synthesis and characterization of dual-ligand coordination polymers using underutilized long, conformationally flexible α,ω-dicarboxylates are underway in our laboratory.

Acknowledgements

The authors gratefully acknowledge Michigan State University and the donors of the American Chemical Society Petroleum Research Fund for financial support of this work. We thank Dr. Rui Huang for elemental analysis and Ms Lindsey Johnston for the acquisition of the infrared spectra. E. S. thanks the MSU High School Honors Science Program and Dr. Gail Richmond for his participation in this research.

Appendix A. Supplementary data

CCDC 702678–702680 contain the supplementary crystallographic data for **1**–**3**, respectively. These data can be obtained free of charge via http://www.ccdc.cam.ac.uk/conts/retrieving.html, or from the Cambridge Crystallographic Data Centre, 12 Union Road, Cambridge CB2 1EZ, UK; fax: (+44) 1223-336-033; or e-mail: deposit@ccdc.cam.ac.uk. Supplementary data associated with this article can be found, in the online version, at doi:10.1016/j.poly.2009.03.004.

References

[1] (a) B. Wang, A.P. Côté, H. Furukawa, M. O'Keeffe, O.M. Yaghi, Nature 453 (2008) 207;
(b) R. Matsuda, R. Kitaura, S. Kitagawa, Y. Kubota, R.U. Belosludov, T.C. Kobayashi, H. Sakamoto, T. Chiba, M. Takata, Y. Kawazoe, Y. Mita, Nature 436 (2005) 238;
(c) L. Pan, D. Holson, L.R. Ciemnolonski, R. Heddy, J. Li, Angew. Chem., Int. Ed. 46 (2006) 616;
(d) N. Rosi, J. Eckert, M. Eddaoudi, D.J. Vodak, J. Kim, M. O'Keeffe, O.M. Yaghi, Science 300 (2003) 1127;
(e) M. Dinca, A.F. Yu, J.R. Long, J. Am. Chem. Soc. 128 (2006) 8904;
(f) G. Férey, M. Latroche, C. Serre, F. Millange, T. Loiseau, A. Percheron-Guegan, Chem. Commun. (2003) 2976;
(g) X. Zhao, B. Xiao, A.J. Fletcher, K.M. Thomas, D. Bradshaw, M.J. Rosseinsky, Science 306 (2004) 1012;
(h) J.L.C. Roswell, O.M. Yaghi, Angew. Chem., Int. Ed. 44 (2005) 4670;
(i) M. Kondo, T. Okubo, A. Asami, S.I. Noro, T. Yoshitomi, S. Kitagawa, T. Ishii, H. Matsuzaka, Angew. Chem., Int. Ed. 38 (1999) 140;
(j) A.C. Sudik, A.R. Millward, N.W. Ockwig, A.P. Côté, O.M. Yaghi, J. Am. Chem. Soc. 127 (2005) 7110.
[2] (a) J.S. Seo, D. Whang, H. Lee, S.I. Jun, J. Oh, Y.J. Jeon, K. Kim, Nature 404 (2000) 982;
(b) A. Cingolani, S. Galli, N. Masciocchi, L. Pandolfo, C. Pettinari, A.J. Sironi, J. Am. Chem. Soc. 127 (2005) 6144.
[3] (a) Q.-R. Fang, G.-S. Zhu, M. Xue, J.-Y. Sun, S.-L. Qiu, Dalton Trans. (2006) 2399;
(b) X.-M. Zhang, M.-L. Tong, H.K. Lee, X.-M. Chen, J. Solid State Chem. 160 (2001) 118;
(c) O.M. Yaghi, H. Li, T.L. Groy, Inorg. Chem. 36 (1997) 4292.
[4] (a) N. Guillou, P.M. Forster, Q. Gao, J.S. Chang, M. Nogues, S.-E. Park, A.K. Cheetham, G. Férey, Angew. Chem., Int. Ed. 40 (2001) 2831;
(b) C.-D. Wu, A. Hu, L. Zhang, W. Lin, J. Am. Chem. Soc. 127 (2005) 8940;
(c) H. Han, S. Zhang, H. Hou, Y. Fan, Y. Zhu, Eur. J. Inorg. Chem. (2006) 1594;
(d) W. Mori, S. Takamizawa, C.N. Kato, T. Ohmura, T. Sato, Micropor. Mesopor. Mater. 73 (2004) 15;
(e) S.G. Baca, M.T. Reetz, R. Goddard, I.G. Filippova, Y.A. Simonov, M. Gdaniec, N. Gerbeleu, Polyhedron 25 (2006) 1215;
(f) J.-S. Kim, H. Kim, M. Ree, Chem. Mater. 16 (2004) 2981.
[5] (a) J. Tao, J.X. Shi, M.L. Tong, X.X. Zhang, X.M. Chen, Inorg. Chem. 40 (2001) 6328;
(b) J. Tao, M.L. Tong, J.X. Shi, X.M. Chen, S.W. Ng, Chem. Commun. (2000) 2043;
(c) J.C. Dai, X.T. Wu, Z.Y. Fu, C.P. Cui, S.M. Hu, W.X. Du, L.M. Wu, H.H. Zhang, R.Q. Sun, Inorg. Chem. 41 (2002) 1391;
(d) W. Chen, J.Y. Wang, C. Chen, Q. Yue, H.M. Yuan, J.S. Chen, S.N. Wang, Inorg. Chem. 42 (2003) 944;
(e) N. Hao, E. Shen, Y.B. Li, E.B. Wang, C.W. Hu, L. Xu, Eur. J. Inorg. Chem. (2004) 4102.
[6] (a) W.-G. Lu, C.-Y. Su, T.-B. Lu, L. Jiang, J.-M. Chen, J. Am. Chem. Soc. 128 (2006) 34;
(b) S. Horike, R. Matsuda, S. Kitagawa, Stud. Surf. Sci. Catal. 156 (2005) 725;
(c) C. Qin, X.-L. Wang, Y.-G. Li, E.-B. Wang, Z.-M. Su, L. Xu, R. Clerac, Dalton Trans. (2005) 2609;
(d) Y.-Q. Zheng, E.-R. Ying, Polyhedron 24 (2005) 397;
(e) S.K. Ghosh, J. Ribas, P.K. Bharadwaj, Cryst. Growth Des. 5 (2005) 623;
(f) X.-Z. Sun, Y.-F. Sun, B.-H. Ye, X.-M. Chen, Inorg. Chem. Commun. 6 (2003) 1412;
(g) Y.-M. Dai, E. Ma, E. Tang, J. Zhang, J.-Z. Li, X.-D. Huang, Y.-G. Yao, Cryst. Growth Des. 5 (2005) 1313;
(h) B. Chen, C. Liang, J. Yang, D.S. Contreras, Y.L. Clancy, E.B. Lobkovsky, O.M. Yaghi, S. Dai, Angew. Chem., Int. Ed. 45 (2006) 1390.
[7] (a) L.A. Borkowski, C.L. Cahill, Cryst. Growth Des. 6 (2006) 2248;
(b) J. Baier, U. Thewalt, Z. Anorg. Allgem. Chem. 628 (2002) 315.
[8] (a) Y. Rodriguez-Martin, M. Hernandez-Molina, F.S. Delgado, J. Pasan, C. Ruiz-Perez, J. Sanchiz, F. Lloret, M. Julve, CrystEngComm. 4 (2002) 440;
(b) S. Sain, T.K. Maji, G. Mostafa, T.-H. Lu, N.R. Chaudhuri, New J. Chem. 27 (2003) 185;
(c) T.-F. Liu, H.-L. Sun, S. Gao, S.-W. Zhang, T.-C. Lau, Inorg. Chem. 42 (2003) 4792.
[9] (a) R. Vaidhyanathan, S. Natarajan, C.N.R. Rao, Inorg. Chem. 41 (2002) 5226;
(b) C. Livage, C. Egger, G. Férey, Chem. Mater. 13 (2001) 410;
(c) C. Livage, C. Egger, M. Nogues, G. Férey, Chem. Mater. 11 (1999) 1546;
(d) C. Livage, C. Egger, M. Nogues, G. Férey, J. Mater. Chem. 8 (1998) 2743;
(e) P.M. Forster, A.K. Cheetham, Angew. Chem., Int. Ed. 41 (2002) 457;
(f) S.-M. Ying, J.-G. Mao, Y.-Q. Sun, H.-Y. Zen, Z.-C. Dong, Polyhedron 22 (2003) 3097;
(g) Y.Q. Zheng, Z.P. Kong, Z. Anorg. Allgem. Chem. 629 (2003) 1469.
[10] (a) D.P. Martin, R.M. Supkowski, R.L. LaDuca, Cryst. Growth Des. 8 (2008) 3518;
(b) A. Thirumurugan, C.N.R. Rao, J. Solid State Chem. 181 (2008) 1184;
(c) E.C. Yang, H.K. Zhao, B. Ding, X.G. Wang, X.J. Zhao, Cryst. Growth Des. 7 (2007) 2009.
[11] (a) L.-S. Long, Y.-R. Wu, R.-B. Huang, L.-S. Zheng, Inorg. Chem. 43 (2004) 3798;
(b) R.-F. Hu, Y. Kang, J. Zhang, Z.-J. Li, Y.-Y. Qin, Y.-G. Yao, Z. Anorg. Allgem. Chem. 631 (2005) 3053;
(c) Y.-Q. Zheng, J.-L. Lin, Z.-P. Kong, Inorg. Chem. 43 (2004) 2590.
[12] (a) J.L. Lin, Y.Y. Wang, Acta Crystallogr. E64 (2008) m527;
(b) S. Mallika Krishnan, M.R. Montney, R.L. LaDuca, Polyhedron 27 (2008) 821;
(c) N. Guillou, C. Livage, G. Férey, Eur. J. Inorg. Chem. (2006) 4963;
(d) H. Flemig, I. Pantenburg, G. Meyer, Z. Anorg. Allgem. Chem. 632 (2006) 2205.
[13] (a) Y.-Q. Zheng, J. Sun, Y.-F. Wang, J. Coord. Chem. 58 (2005) 1551;
(b) B. Benmerad, A. Guehria-Laidoudi, S. Dahaoui, C. Lecomte, Acta Crystallogr. C60 (2004) m407;
(c) J. Sun, Y.-Q. Zheng, Z. Anorg. Allgem. Chem. 629 (2003) 1001.
[14] (a) L.A. Borkowski, C.L. Cahill, Cryst. Growth Des. 6 (2006) 2241;
(b) Y.J. Kim, E.W. Lee, D.-Y. Jung, Chem. Mater. 13 (2001) 2684.
[15] M.R. Montney, S. Mallika Krishnan, N.M. Patel, R.M. Supkowski, R.L. LaDuca, Cryst. Growth Des. 7 (2007) 1145.
[16] M.R. Montney, D.P. Martin, R.L. LaDuca, Cryst. Growth Des. 8 (2008) 3091.
[17] M.R. Montney, S. Mallika Krishnan, N.M. Patel, R.M. Supkowski, R.L. LaDuca, Inorg. Chem. 46 (2007) 7362.
[18] S. Mallika Krishnan, N.M. Patel, W.R. Knapp, R.M. Supkowski, R.L. LaDuca, CrystEngComm. 9 (2007) 503.
[19] M.A. Braverman, R.M. Supkowski, R.L. LaDuca, J. Solid State Chem. 180 (2007) 1852.
[20] P.J. Zapf, R.L. LaDuca, R.S. Rarig, K.M. Johnson, J. Zubieta, Inorg. Chem. 37 (1998) 3411.
[21] SAINT, Software for Data Extraction and Reduction, Version 6.02, Bruker AXS Inc., Madison, WI, 2002.

[22] SADABS, Software for Empirical Absorption Correction, Version 2.03, Bruker AXS Inc., Madison, WI, 2002.
[23] G.M. Sheldrick, SHELXTL, Program for Crystal Structure Refinement, University of Gottingen, Gottingen, Germany, 1997.
[24] M. Kurmoo, C. Estournes, Y. Oka, H. Kumagai, K. Inoue, Inorg. Chem. 44 (2005) 217.
[25] S. Mallika Krishnan, R.M. Supkowski, R.L. LaDuca, Cryst. Growth Des. 9 (2009) 358.
[26] R.D. Shannon, Acta Crystallogr. A32 (1976) 751.
[27] A.L. Spek, PLATON, A Multipurpose Crystallographic Tool, Utrecht University, Utrecht, The Netherlands, 1998.

Complexes of fluorinated tpzb ligand often show very different physicochemical properties to their non-fluorinated analogs [17]. For example, the carbonyl stretching frequency of 2137 cm^{-1} in [Cu(Lf6)(CO)] is the highest value in the known copper(I) carbonyl complexes with tpzb ligands; this value is 71 cm^{-1} higher than that of 2066 cm^{-1} in [Cu(L0)(CO)] [19,20]. However, the Cu–CO bond length of 1.808(4) Å in [Cu(Lf6)(CO)] is experimentally equivalent to that of the corresponding distance in non-fluorinated analogs; 1.785(4) Å in [Cu(L0)(CO)] [19,21]. In addition, $^{31}P\{^{1}H\}$ NMR spectroscopy of the copper(I) triphenylphosphine complex [Cu(Lf6)(PPh_3)] showed distinctive behavior unlike that of [Cu(L0)(PPh_3)] [19b,22]. The partially trifluoromethylated L0f$^-$ ligand has also been demonstrated to be a useful ligand for systematic studies. For copper complexes with L0f$^-$, the structures of [Cu^{II}(L0f)(ONO)], [Cu^{II}(L0f)(O_2CMe)], [Cu^{II}(L0f){O_2CCH(OH)Me}], [Cu^{I}(L0f)(NCMe)], [Cu^{I}(L0f)]$_2$, and [{Cu(L0f)}$_2$(μ-O_2)] have been reported [23–27]. It is well known that the oxygen reactivity of copper(I) complexes with alkyl-substituted tpzb is carried out at low temperature [2,3]. Interestingly, when the copper(I) complex [Cu^{I}(L0f)]$_2$ was investigated by Gorun and co-workers, the resulting μ-η^2:η^2-peroxo binuclear copper(II) complex [{Cu(L0f)}$_2$(μ-O_2)] showed reversible binding property towards dioxygen even at room temperature [26,27].

Although the copper(I) complexes derived from L0f$^-$ display interesting behavior, there are only a few reports of their study [18,23–27]. In this paper, the full descriptions of the syntheses and structural characterization of new copper(I) complexes, i.e. [Cu^{I}(L0f)(CO)] (**1**) and [Cu^{I}(L0f)(PPh_3)] (**2**), derived from L0f$^-$ are described. Their structures were determined by an X-ray analysis. Further, all complexes were characterized by IR, far-IR, and NMR spectroscopy. Finally, the reactivity of copper(I) complexes toward CO/MeCN/PPh_3 was investigated.

2. Experimental

2.1. Materials

Preparation and handling of all the complexes was performed under an argon atmosphere using standard Schlenk tube techniques or in a VAC inert atmosphere glovebox containing an argon gas. Dichloromethane and toluene were carefully purified by refluxing and distilling under an argon atmosphere over phosphorous pentoxide and over sodium benzophenone kethyl, respectively [28]. Deuteriumed solvents and ^{13}C-enriched carbon monoxide were obtained from Cambridge Isotope Laboratories, Inc. Anhydrous solvent (acetone) was purchased from Aldrich Chemical Company, Inc. and stored in a glovebox. Copper(I) chloride and triphenylphosphine purchased from Wako Pure Chemical Ind. Ltd. This copper(I) chloride was purified according to a published method [29]. Other reagents are commercially available and were used without further purification. The copper(I) acetonitrile complex [Cu(L0f)(NCMe)] (**3**) was prepared by a literature procedure [23]. The synthesis of [Cu(L0f)(CO)] (**1**) and [Cu(L1)(PPh_3)] (**4**) have been reported before, however, their crystal structures have not been reported [23,29].

2.2. Measurements

IR and far-IR spectra were recorded on KBr pellets in the 4000–400 cm^{-1} region and on CsI pallets in the 650–150 cm^{-1} region, respectively, using a JASCO FT/IR-550 spectrophotometer. Abbreviations used in the description of vibration data are follows: vs, very strong; s, strong; m, medium; w, weak. For *in situ* solution IR, the sample solution was stirred in the Schlenk tube purged with carbon monoxide atmosphere for a few minutes and stirred for a day at room temperature. Then this solution was transferred to a Spectralys Specac KBr plate of solution-IR cell. ^{1}H NMR (600 MHz), ^{13}C NMR (150 MHz), and ^{31}P NMR (242 MHz) spectra were obtained on a Bruker AVANCE-600 NMR spectrometer at room temperature (296 K) in $CDCl_3$ or CD_2Cl_2. ^{19}F NMR (470 MHz) and ^{13}C NMR (125 MHz) spectra were obtained on a Bruker AVANCE-500 NMR spectrometer at room temperature (296 K) in $CDCl_3$ or CD_2Cl_2. ^{1}H and ^{13}C chemical shifts were reported as δ values downfield from the internal standard tetramethylsilane and the residual solvent peaks. ^{31}P and ^{19}F chemical shifts were referenced relative to an external standard of PPh_3 (δ 0.0 ppm) in CD_2Cl_2 and trifluorobenzene (δ 164.9 ppm) in $CDCl_3$, respectively. The elemental analysis (C, H, N) was performed by the Department of Chemistry at the University of Tsukuba.

2.3. Preparations of complexes

2.3.1. [Cu{HB(3-CF_3-5-Mepz)$_3$}(CO)], [Cu(L0f)(CO)] (*1*)

A solution of NaL0f (0.30 g, 0.62 mmol) in acetone (20 cm^3) was added to a solution of CuCl (0.066 g, 0.67 mmol) in acetone (10 cm^3) in a glovebox. After stirring for 1 h, the argon gas in the Schlenk tube was replaced by carbon monoxide. After stirring for 24 h, the solvent was evaporated under reduced pressure. The resulting solid was extracted with dichloromethane (20 cm^3). The filtrate was evaporated under reduced pressure and a white powder was obtained. Crystallization from dichloromethane/toluene at −50 °C afforded colorless crystals. Yield: 71% (0.25 g, 0.45 mmol). *Anal.* Calc. for $C_{16}H_{13}N_6BCuF_9O$: C, 34.90; H, 2.38; N, 15.26. Found: C, 34.62; H, 2.42; N, 14.90%. IR (KBr, cm^{-1}): 3140m, 2995w, 2575m, 2107vs (^{12}C≡O), 1495, 1471s, 1261s, 1173s, 1063s, 1002s, 842s, 643s. far-IR (CsI, cm^{-1}): 591w, 561w, 467s, 455m, 438m, 422s (Cu–^{12}C), 389m, 365w, 343w, 295s, 216m. ^{1}H NMR (CD_2Cl_2) (δ): 2.44 (s, 9H, *Me*), 6.26 (s, 3H, pz-4*H*). ^{13}C NMR (CD_2Cl_2) (δ): 12.5 (*C*H_3), 104.2 (pz-4*C*), 121.0 (*C*F_3, q, $J_{C,F}$ = 269 Hz), 142.2 (pz-3*C*, q, $J_{C,F}$ = 37 Hz), 145.1 (pz-5*C*). ^{19}F NMR ($CDCl_3$) (δ): −61.9 (C*F*$_3$).

A ^{13}CO labeled complex was prepared by the same method as the corresponding unlabeled complex, but using ^{13}CO gas. IR (KBr, cm^{-1}): 2058s (^{13}C≡O). far-IR (CsI, cm^{-1}): 419w (Cu–^{13}C). ^{1}H NMR (CD_2Cl_2) (δ): 172.9 (*^{13}CO*).

2.3.2. [Cu{HB(3-CF_3-5-Mepz)$_3$}(PPh_3)], [Cu(L0f)(PPh_3)] (*2*)

A solution of NaL0f (0.30 g, 0.62 mmol) in acetone (20 cm^3) was added to a solution of CuCl (0.061 g, 0.62 mmol) in acetone (10 cm^3) in a glovebox. After stirring for 1 h, a solution of PPh_3 (0.17 g, 0.66 mmol) in acetone (10 cm^3) was added to the solution. After stirring for 1 h, the solvent was evaporated under reduced pressure. The resulting solid was extracted with dichloromethane (20 cm^3). The filtrate was evaporated under reduced pressure and a white powder was obtained. Crystallization from dichloromethane/toluene at −50 °C afforded colorless crystals. Yield: 59% (0.28 g, 0.36 mmol). *Anal.* Calc. for $C_{33}H_{28}N_6BCuF_9P{\cdot}CH_2Cl_2$: C, 46.95; H, 3.48; N, 9.66. Found: C, 47.23; H, 3.43; N, 9.69%. IR (KBr, cm^{-1}): 3447w, 3138m, 3057m, 2564m, 1496m, 1467s, 1437s, 1257vs, 1197vs, 1165vs, 1134vs, 1065vs, 994s, 796s, 743s, 695s, 647m. far-IR (CsI, cm^{-1}): 619w, 561w, 528s, 502s, 468m, 439m, 426w, 390m, 346w, 299m, 252w, 225m, 193m. ^{1}H NMR (CD_2Cl_2) (δ): 2.49 (s, 9H, *Me*), 6.23 (s, 3H, pz-4*H*), 7.26–7.40 (m, 9H, P*Ph*$_3$(o,p)), 7.48–7.55 (m, 6H, P*Ph*$_3$(m)). ^{13}C NMR ($CDCl_3$) (δ): 13.5 (*C*H_3), 105.1 (pz-4*C*), 121.2 (*C*F_3, q, $J_{C,F}$ = 270 Hz)), 143.2 (pz-3*C*, q, $J_{C,F}$ = 37 Hz)), 145.3 (pz-5*C*). ^{19}F NMR ($CDCl_3$) (δ): −60.2 (C*F*$_3$). ^{31}P NMR (CD_2Cl_2) (δ): 10.60 (s, br, *P*Ph_3).

2.3.3. [Cu{HB(3,5-iPr_2pz)$_3$}(PPh_3)], [Cu(L1)(PPh_3)] (*4*)

The preparation was carried out by the same method as that for the complex **2** using CuCl (0.063 g, 0.64 mmol), KL1 (0.32 g, 0.63 mmol), and PPh_3 (0.16 g, 0.63 mmol) in acetone (50 cm^3) in

a glovebox [13]. Crystallization from dichloromethane/propionitrile (1/2) at −50 °C gave colorless crystals. Yield: 25% (0.16 g, 0.16 mmol).

*2.3.4. Reaction of [Cu(L0f)(CO)] (**1**) or [Cu(L0f)(PPh$_3$)] (**2**) with MeCN*

In a Schlenk tube, complex **1** or **2** was dissolved in acetonitrile and stirred at room temperature for 72 h under an argon gas. The resultant solution was evaporated to dryness under reduced pressure, and then the white solid obtained was characterized by IR and ^{1}H NMR spectroscopy, showing almost negligible formation of [Cu(L0f)(NCMe)] (**3**) from both reactions.

*2.3.5. Reaction of [Cu(L0f)(CO)] (**1**) or [Cu(L0f)(NCMe)] (**3**) with PPh$_3$*

In a Schlenk tube, complex **1** or **3** and PPh$_3$ (10 eq) was dissolved in dichloromethane and stirred at room temperature for 72 h under an argon gas. The resultant solution was evaporated to dryness under reduced pressure, and then the white solid obtained was characterized by IR and ^{1}H NMR spectroscopy, showing almost quantitative formation of [Cu(L0f)(PPh$_3$)] (**2**) from both reactions.

*2.3.6. Reaction of [Cu(L0f)(PPh$_3$)] (**2**) or [Cu(L0f)(NCMe)] (**3**) with CO*

In a Schlenk tube, complex **1** or **3** was dissolved in dichloromethane under an argon gas. The atmosphere was replaced by carbon monoxide, and the solution was stirred at room temperature for 72 h. The resultant solution was evaporated to dryness under reduced pressure, and the white solid obtained was characterized by IR and ^{1}H NMR spectroscopy, showing small quantity of [Cu(L0f)(CO)] (**1**) from complex **2** and almost quantitative formation of complex **1** from **3**.

2.4. Crystal structure determination

The diffraction data for complexes **1**, **2**, and **4** were measured on a Rigaku/MSC Mercury CCD system with graphite monochromated Mo Kα (λ = 0.71069 Å) radiation at −89 ± 1 °C. Each crystal was mounted on the tip of a glass fiber by highly viscous oil. The unit cell parameters of each crystal were determined from 6 image frames using Rigaku Daemon software and refined using CRYSTALCLEAR [30]. Data were collected in 0.5° intervals for 48 s/frame (**1**) and for 32 s/frame (**2** and **4**) in ϕ and ω to a maximum 2θ value of 55°. A total of 744 oscillation images were collected. The highly redundant data sets were reduced using CRYSTALCLEAR and corrected for Lorentz and polarization effects. An empirical absorption correction was applied [30–32]. The structures were solved by direct methods (SIR97 [33] or SHELX97 [34]). The position of the metal atoms and their first coordination sphere were located from the *E*-map; other non-hydrogen atoms were found in alternating difference Fourier syntheses (DIRDIF99 [35]). Least-squares refinement on *F* was conducted using CRYSTALSTRUCTURE with anisotropical displacement parameters for non-hydrogen atoms, and hydrogen atoms were placed in calculated positions [31,32]. One of CF_3 group of **1** was highly disordered, and each fluorine atoms was refined with a site occupancy factor of 0.50. Higher *R* and GOF values of **4** are due to the disordered dichloromethane molecules in the unit cell. Crystal data and refinement parameters for **1**, **2**, and **4** are as follows. For **1**: formula: $C_{16}H_{13}BCuF_9N_6O$, crystal system: monoclinic, space group: $P2_1/m$ (No. 11), lattice parameters: a = 8.1639(4), b = 13.7720(5), c = 9.8864(4) Å, β = 106.1026(5)°, V = 1067.95(8) Å^3, Z = 2, D_{calc} = 1.712 g cm^{-3}, μ = 11.222 cm^{-1}, reflections collected = 8677, unique reflections = 2531, R_{int} = 0.018, no. of observations = 2281 ($I > 3\sigma(I)$), R = 0.033, Rw = 0.047. For **2**·CH_2Cl_2: formula: $C_{34}H_{30}BCl_2CuF_9N_6P$, crystal system: triclinic, space group: $P\bar{1}$ (No. 2), lattice parameters: a = 11.445(7), b = 11.456(5), c = 18.471(4) Å, α = 72.05(13), β = 72.16(13), γ = 60.03(11)°, V = 1961.4(14) Å^3, Z = 2, D_{calc} = 1.473 g cm^{-3}, μ = 8.097 cm^{-1}, reflections collected = 15 479, unique reflections = 8587, R_{int} = 0.020, no. of observations = 6961 ($I > 3\sigma(I)$), R = 0.050, Rw = 0.060. For **4** · 3CH_2Cl_2: formula: $C_{48}H_{67}BCl_6CuN_6P$, crystal system: monoclinic, space group: $P2_1/n$ (No. 14), lattice parameters: a = 12.5017(2), b = 19.0580(5), c = 22.8008(5) Å, β = 95.7520(4)°, V = 5405.1(2) Å^3, Z = 4, D_{calc} = 1.285 g cm^{-3}, μ = 7.674 cm^{-1}, reflections collected = 42 294, unique reflections = 12 301, R_{int} = 0.034, no. of observations = 9327 ($I > 3\sigma(I)$), R = 0.066, Rw = 0.089.

3. Results and discussion

3.1. Synthesis

All copper(I) complexes were prepared in a glovebox to avoid reaction with atmospheric dioxygen and moisture. Copper(I) carbonyl complex **1** was obtained from the reaction of the unpurified reactive [Cu(L0f)]$_2$ with carbon monoxide [23,24]. Copper(I) triphenylphosphine complex **2** was obtained in the same manner as for complex **1** but using PPh$_3$. Finally, copper(I) triphenylphosphine complex **4** was obtained as crystals using the ligand L1$^-$ by the reported method similar to that used for complex **2** [29].

3.2. Crystal structures

The structures of complexes **1**, **2**, and **4** were determined by X-ray crystallography, indicating that all complexes are mononuclear. Molecular structures of these complexes with selected bond distances and angles in the respective figure captions are shown in Figs. 1–3. All the complexes feature a tetrahedral coordination geometry defined by the three nitrogen atoms of L0f$^-$ or L1$^-$ and the carbon atom of carbon monoxide in complex **1**, or the phosphorus atom of triphenylphosphine in complexes **2** and **4**.

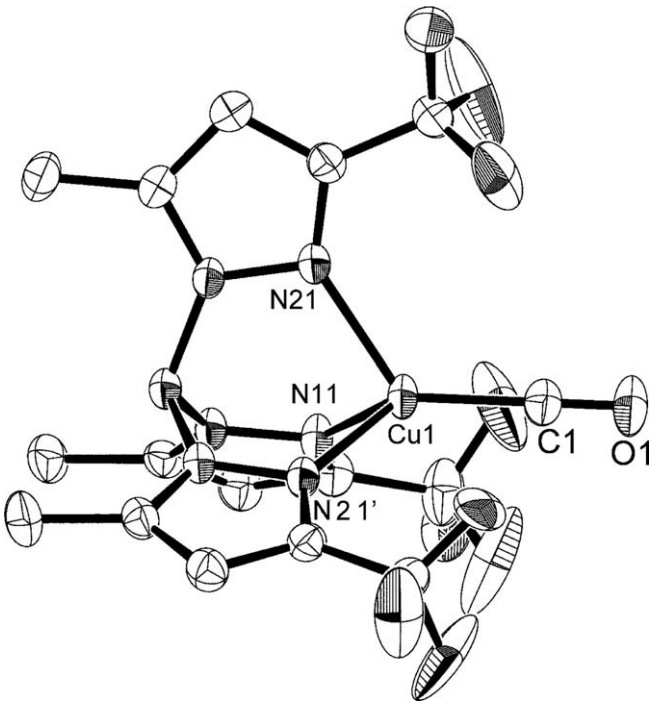


Fig. 1. Molecular structure of [Cu(L0f)(CO)] (**1**) showing 50% displacement ellipsoids and the atom labeling schemes. All hydrogen atoms are omitted for clarity. Selected bond distances (Å) and angles (°) are as follows: Cu1–C1, 1.799(3); Cu1–N11, 2.042(2); Cu1–N21, 2.062(2); C1–O1, 1.122(3); Cu1–C1–O1, 180.0(2); N11–Cu1–C1, 123.52(10); N21–Cu1–C1, 125.43(6), N11–Cu1–N21, 90.96(6); N21–Cu1–N21′, 90.09(6). Symmetry operators: $x, -y + 1/2, z$.

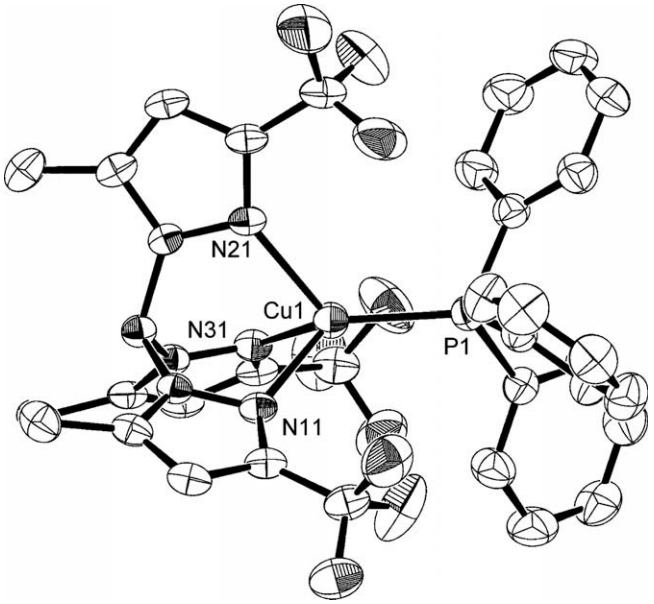


Fig. 2. Molecular structure of [Cu(L0f)(PPh_3)] (**2**) showing 50% displacement ellipsoids and the atom labeling schemes. All hydrogen atoms and CH_2Cl_2 molecules of crystallization are omitted for clarity. Selected bond distances (Å) and angles (°) are as follows: Cu1–P1, 2.2150(7); Cu1–N11, 2.170(2); Cu1–N21, 2.177(2); Cu–N31, 2.176(2); N11–Cu1–P1, 125.33(5); N21–Cu1–P1, 125.50(5), N31–Cu1–P1, 125.49(8); N11–Cu1–N21, 89.76(9); N11–Cu1–N31, 89.71(9); N21–Cu1–N31, 89.79(8).

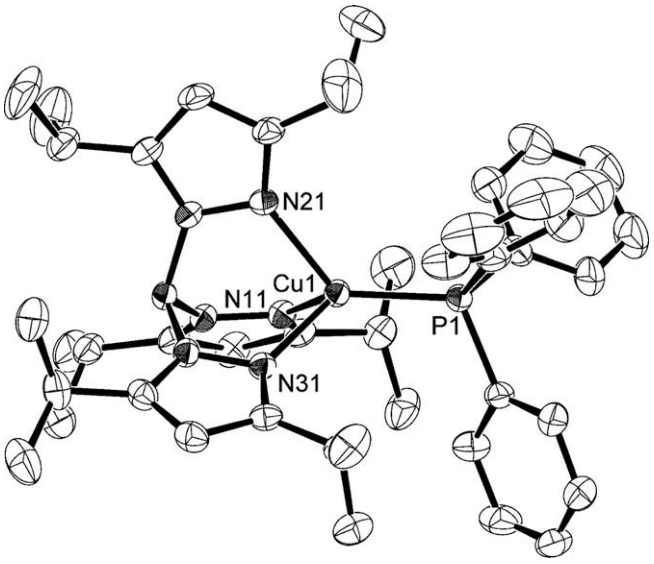


Fig. 3. Molecular structure of [Cu(L1)(PPh_3)] (**4**) showing 50% displacement ellipsoids and the atom labeling schemes. All hydrogen atoms and CH_2Cl_2 molecules of crystallization are omitted for clarity. Selected bond distances (Å) and angles (°) are as follows: Cu1–P1, 2.1635(10); Cu1–N11, 2.065(3); Cu1–N21, 2.093(3); Cu–N31, 2.088(3); N11–Cu1–P1, 125.01(9); N21–Cu1–P1, 127.69(9), N31–Cu1–P1, 121.90(8); N11–Cu1–N21, 90.82(12); N11–Cu1–N31, 90.89(12); N21–Cu1–N31, 89.82(11).

Complex **1** has a crystallographically imposed plane of symmetry containing one of the pyrazolyl rings, boron atom, copper atom, and the carbon and oxygen atoms of the carbon monoxide molecule. In complex **1** as in the previously described copper(I) carbonyl complexes with other tpzb ligands, the copper(I) ions are almost linearly ligated by carbon monoxide with Cu–C≡O angles in the range of 176–180° (Table 1). The Cu–C distance of 1.799(3) Å in complex **1** is experimentally equivalent to the Cu–C distances of 1.808(4) Å in [Cu(Lf6)(CO)], 1.785(4) Å in [Cu(L0)(CO)], 1.783(7) Å in [Cu(L1′)(CO)](PF_6) [8,19a,21], and 1.769(8) Å in [Cu(L1)(CO)] [29]. Thus, crystallography does not reliably differentiate between the structures. Differences were expected, as explained in the following. It is noted that carbon monoxide is weak σ-donor and strong π*-acceptor ligand. The Cu(I)–CO interaction is entirely dominated by π back-bonding between the two degenerate π* orbitals of CO and two t_2 type d orbitals of copper(I) ion [8]. The levels of electron densities around copper(I) center in the complexes with tpzb ligands are influenced by substituents at third and/or fifth position(s) of the pyrazolyl rings. As the number of the electron-withdrawing substituents increase, the levels of electron density around copper(I) center decrease. In addition, the electron densities of copper(I) center in the complexes with tpzm ligands are lower than those of copper(I) center in the complexes with alkyl group substituted tpzb ligands because of effect of the total charge of the N3 type ligands [8]. According to the above consideration, the C≡O distance is supposed to be shorter as the electron density around copper(I) ion is lower. However, this trend was not also observed from X-ray crystallography; 1.122(3) Å in **1**, 1.118(10) Å in [Cu(L0)(CO)], and 1.110(5) Å in [Cu(Lf6)(CO)] [19a,21]. This observation is consistent with no relationships between structural parameters and some properties for Cu–C, C≡O, and Cu–P bonds in other system [8,11–13].

The Cu–P bond distance of 2.2150(7) Å in complex **2** is experimentally equivalent to 2.219(1) Å found in [Cu(Lf6)(PPh_3)] and both are longer than the corresponding distances of 2.166(6) Å in [Cu(L0)(PPh_3)] and 2.1635(10) Å in complex **4**, as collated in Table 2. Both complexes **2** and **4** have crystallographic pseudo C_{3v} symmetry so that three pyrazolyl rings of ligand and the three phenyl rings of triphenylphosphine are alternately placed to avoid the steric repulsion. Triphenylphosphine is a strong σ-donor ligand, which is entirely different from carbon monoxide. As the electron density around copper(I) ion is lower, triphenylphosphine coordinates strongly to copper(I) ion. Therefore, the Cu–P distance in complex **2** with electron-withdrawing CF_3 group should be shorter than the Cu–P distances with other alkyl group substituted tpzb ligands. Again, this trend was not confirmed by X-ray crystallography. However, the spectroscopic results do follow the expected trends as detailed below.

3.3. IR spectra

The C≡O stretching frequencies of the copper(I) carbonyl complexes with tpzb and tpzm ligands are also listed in Table 1. The copper(I) carbonyl complexes exhibit intense C≡O stretching vibrations in 2050–2100 cm^{-1} middle-IR region [8,44]. The C≡O stretching frequency of 2107 cm^{-1} in complex **1** is 41 cm^{-1} higher than 2066 cm^{-1} observed for [Cu(L0)(CO)] and is 30 cm^{-1} lower than 2137 cm^{-1} in [Cu(Lf6)(CO)]. These C≡O stretching frequency shifts are consistent with expected trends in electron density around copper(I) ion in these carbonyl complexes. That is to say, as the electron density around copper(I) ion in the carbonyl complex is lower, the C≡O stretching frequency is shifted to higher energy side as explained in Section 3.2. The C≡O stretching frequencies in complex **1**, the other carbonyl complexes with tpzb ligands containing halogenated substituents, and the carbonyl complexes with tpzm ligands are shifted to higher energy side than those in the complexes with tpzb ligands containing alkyl side chains. In addition, the electron-donating substituents such as the *i*Pr or *t*Bu groups lead to the lower C≡O stretching frequencies compared to methyl or aryl substituents in both the tpzm and tpzb complexes. These comparisons lead to the following order in the C≡O stretching frequencies for the pyrazolyl substituents in the tpzb ligands:

Table 1
Selected structural parameters and C–O streching frequencies of copper(I) carbonyl complexes with coordinated tpzb and tpzm ligands.

Complex	Cu–C (Å)	C≡O (Å)	Cu–C≡O (°)	ν(C–O) (cm^{-1})	Reference
[Cu(L0f)(CO)] (**1**)	1.799(3)	1.122(3)	180.0(2)	2107	this work
[Cu{HB(3-CF_3pz)$_3$}(CO)]	1.790(4)	1.126(5)	179.0(4)	2100	[36]
[Cu{HB(3-C_2F_5pz)$_3$}(CO)]	1.804(4)	1.115(5)	178.1(4)	2110	[37]
[Cu{HB(3-C_3F_7pz)$_3$}(CO)]	1.799(10)	1.119(13)	178.7(6)	2102	[37]
[Cu(Lf6)(CO)]	1.808(4)	1.110(5)	179.8(4)	2137	[19a]
[Cu{HB(pz)$_3$}(CO)][a]	1.755(11)	1.120(13)	180.0	2083	[38,39]
	1.775(5)	1.120(6)	176.6(5)		
[Cu(L0)(CO)]	1.785(4)	1.125(4)	179.3(4)	2066	[20,21]
[Cu(L1)CO)]	1.769(8)	1.118(10)	178.6(9)	2056	[29,40]
[Cu{HB(3-*t*Bu-5-Mepz)$_3$}(CO)][a]	1.789(6)	1.113(6)	177.6(6)	2059	[41,42]
	1.805(6)	1.106(6)	177.6(6)		
[Cu{HB(3-*t*Bu-5-*i*Prpz)$_3$}(CO)]	1.76(1)	1.14(1)	178(1)	2057	[8]
[Cu{HB(3,5-Ph_2pz)$_3$}(CO)]	1.78(1)	1.08(1)	180.0(1)	2086	[29,40,41]
[Cu(L1′)(CO)][PF_6)	1.783(7)	1.118(9)	175.6(6)	2107	[8]
[Cu(L1′)(CO)][ClO_4)	1.777(5)	1.127(6)	176.7(5)	2107	[8]

[a] Two crystallographically independent molecules are presented, whose structural features are essentially identical.

Table 2
Selected structural parameters and ^{31}P chemical shifts of copper(I) triphenylphosphine complexes with coordinated tpzb.

Complex	Cu–P (Å)	δ (^{31}P) (ppm)	Half width (Hz)	Reference
[Cu(L0f)(PPh_3)] (**2**)	2.2150(7)	10.60	445.9	this work
[Cu(Lf6)(PPh_3)]	2.219(1)	13.2	broad[a]	[19b]
[Cu(L0)(PPh_3)]	2.166(6)	8.39	1885.9	[22], this work
[Cu(L1)(PPh_3)] (**4**)	2.1635(10)	10.73	1628.5	[29], this work
[Cu(L1′)(PPh_3)][ClO_4)	2.159(4)	12.11	323.5	[13], this work

[a] The half width value was not reported.

iPr_2 ≈ (*t*Bu, *i*Pr) < (*t*Bu, Me) < Me_2 < (*t*Bu, H) < H_2 < Ph_2 < (CF_3, H) < (CF_3, Me) < $(CF_3)_2$

In the middle-IR region, no characteristic bands were observed in copper(I) triphenylphosphine complexes.

3.4. Far-IR spectra

The copper(I) carbonyl complexes exhibit intense Cu–C stretching vibrations in 420–470 cm^{-1} far-IR region [8,44]. The Cu–C stretching frequency of 422 cm^{-1} in complex **1** is confirmed by the ^{13}CO labeling experiment (419 cm^{-1} (Cu–^{13}C)). This value is 20–40 cm^{-1} lower than the Cu–C stretching frequencies of 466 cm^{-1} in [Cu(L1)(CO)] and of 445 cm^{-1} in [Cu{HB(3-*t*Bu-5-*i*Prpz)$_3$}(CO)] [8]. These Cu–C stretching frequency shifts are consistent with the expected variations in electron density around copper(I) ion in these carbonyl complexes, demonstrating the anticipated electron-withdrawing effects.

The far-IR spectra of the copper(I) triphenylphosphine complex **2** show two strong bands at 528 and 502 cm^{-1}, which are assignable to Cu–P stretching vibration and C–P–C bending vibrations [13,44,45]. Unfortunately, the Cu–P stretching vibration could not be identified from the spectra. This observation is consistent with the bands in other alkyl group substituted tpzb and tpzm ligands due to these broad peaks [13].

3.5. NMR spectra

^{1}H, ^{13}C, and ^{19}F NMR spectra were measured for L0f$^-$ ligand and the copper(I) complexes **1**, **2**, and **3**. In all cases, the expected signals of the protons, carbon, and fluorine atoms are observed with the exception of the signal due to the BH proton which was not observed experimentally, in accord with expectation [8]. In addition, ^{31}P NMR spectra were measured for complexes **2** and **4**. The ^{31}P chemical shifts of copper(I) triphenylphosphine complexes are listed in Table 2.

In the carbonyl complex **1**, the signal of the carbonyl carbon atom can be detected by ^{13}C NMR spectroscopy. In general, ^{13}C NMR resonances for the terminal CO ligands in classical metal carbonyls appear in the range of 184–223 ppm [8,43]. Complex **1** prepared in this study using unlabeled CO showed no signal due to the carbonyl cabon atom owing to the low natural abundance of ^{13}CO. Therefore, complex **1** was also prepared using ^{13}C-enriched carbon monoxide. Using the labeled compound of **1**, a broad signal of the carbonyl carbon atom is observed at 172.9 ppm as shown in Fig. 4. The ^{13}C NMR signals of the carbonyl carbons in [Cu(L1′)(CO)][PF_6) (174.0 ppm) and [Cu(L1′)(CO)][ClO_4) (173.8 ppm) also appear as a broad resonance. It is noted that the ^{13}C NMR signals due to

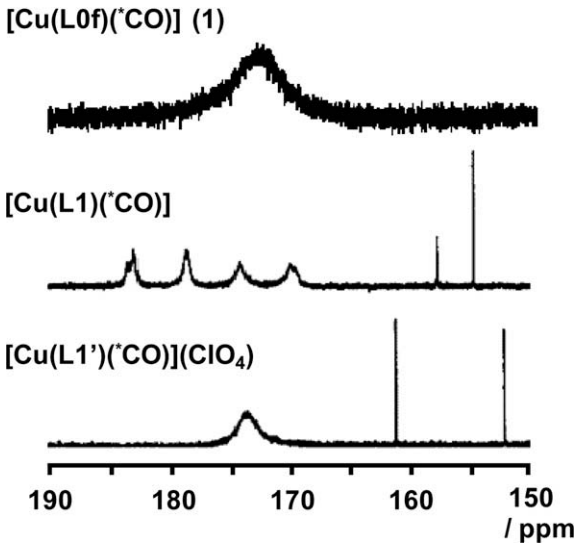


Fig. 4. ^{13}C NMR spectra of the ^{13}CO enriched copper(I) carbonyl complexes.

the carbonyl carbons are split into four broad resonances in [Cu(L1)(CO)] (centered at 176.4 ppm) and [Cu{HB(3-*t*Bu-5-*i*Prpz)$_3$}(CO)] (174.0 ppm) [8]. The splitting of each of these signals is effected by the bonding strength of Cu–C. As the bonding strength of Cu–C becomes stronger, the coupling between ^{13}C and ^{65}Cu ($I = 3/2$) is observed. Thus, the signals of the carbonyl carbon atoms with a strong Cu–C bond in the tpzb complexes are split into four broad resonances. Conversely, the signals in the carbonyl complexes with a weak Cu–C bond in tpzm ligands are not split and appear rather as a broad resonance. Interestingly, even although complex **1** is carbonyl complex with tpzb, the signal of the carbonyl carbon atom appear as a broad resonance. This result indicates that the electric differences of L0f$^-$ (including electron-withdrawing CF_3 group) are similar to tpzm ligands, whereby both ligands decrease the electron density around copper(I) ion.

In the triphenylphosphine complex **2**, the signal of the phosphorus atom in PPh_3 can be detected by ^{31}P NMR spectroscopy as shown in Fig. 5. The ^{31}P chemical shifts of PPh_3 in complex **2** and other triphenylphosphine complexes appear downfield from the free triphenylphosphine resonance ($\delta = 0.0$), indicating a decrease in shielding due to the presence of the metal, which is the expected for a σ-donor ligand like phosphine. Moreover, the ^{31}P NMR signals of the phosphorus atom in these complexes are broad. The half width of the signal of 445.9 Hz in complex **2** is narrower than the half widths of the signals, i.e. 1885.9 Hz in [Cu(L0)(PPh_3)] and 1628.5 Hz in [Cu(L1)(PPh_3)] (Table 2). On the other hand, the half width of the signal of 323.5 Hz in the tpzm triphenylphosphine complex [Cu(L1′)(PPh_3)](ClO_4) is also narrower than the half widths of these signals. According to the literature, the differences in broadness of these signals are due to the inherent instability of the complexes in solution [13] and therefore, correlate with the bonding strength of the Cu–P bond in solution. The bonding strength of each Cu–P bond is consistent with the differences in electron density around the copper(I) ion in each complexes. That is to say, as the electron density around copper(I) ion is lower, the bonding strength of Cu–P is stronger as explained in the Section 3.2. Therefore, the bonding strength of Cu–P bond in complex **2** with electron-withdrawing CF_3 group is stronger than the bonding strengthes of Cu–P in other complexes with alkyl-substituted tpzb ligands. Moreover, these differences of the broadness of the signals may be caused by differences of bulkiness of the substituents at the third position of the pyrazolyl rings. However, the broadness of the signal of complex **2** is narrower than that of [Cu(L0)(PPh_3)], whose bulkiness is much small than that of L0f$^-$. Thus, these differences are due to electron-withdrawing CF_3 group, not due to their gross structural differences.

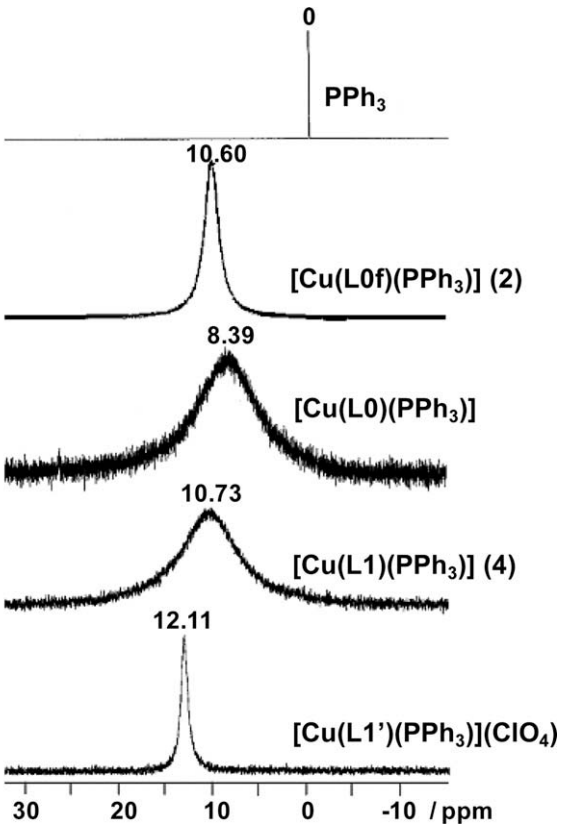


Fig. 5. ^{31}P NMR spectra of copper(I) triphenylphosphine complexes.

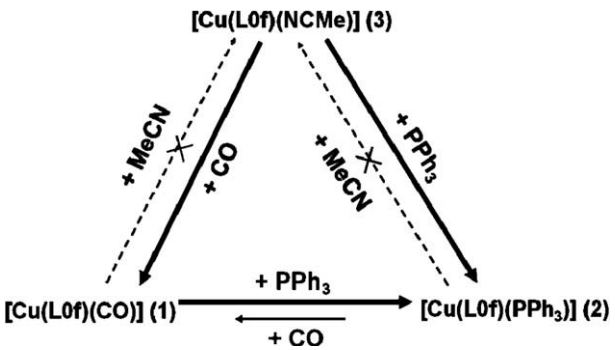
3.6. Reactivity of each complex

In this work, the reaction cycle of the copper(I) complexes between **1**, **2** and **3** was also studied. The reactivity of each complex is described in Scheme 1.

First, the reactivity between complexes **1** and **2** in Scheme 1 is discussed. The reaction of **1** with 1 equivalent of PPh_3 was performed in dichloromethane solution. The C≡O stretching frequency at 2107 cm^{-1} in complex **1** was not observed which indicates that this reaction proceeds to completion to generate the triphenylphosphine complex **2**; ^1H NMR spectrum supports this observation. The reverse reaction was also attempted. Thus, the reaction of complex **2** with CO was also performed in dichloromethane. After this reaction, a weak C≡O stretching frequency of 2107 cm^{-1} due to complex **1** was observed. This result indicates that the reaction of **2** with CO generates a small amount of carbonyl complex **1**; the ^1H NMR spectrum supports this indication. In addition, the solution-IR spectrum of the reaction mixture corresponds to the result obtained from the solid-state IR spectra. ^1H NMR spectra of reaction solution ($CDCl_3$) also corresponds the same result of the above ^1H NMR spectra. In summary, the stability experiments between **1** and **2** revealed that **2** is more stable than **1**.

Second, the reactivity between **1** and **3** in Scheme 1 was investigated. The reaction of complex **1** with MeCN and the reverse reaction of complex **3** with CO were performed. After reaction, the strong C≡O stretching frequency of 2107 cm^{-1} in complex **1** is observed in both reaction products indicating that the reaction of complex **1** with MeCN does not proceed and the reaction of complex **3** with CO proceeds to generate carbonyl complex **1**. ^1H NMR spectra confirm these indications. The stability experiments between **1** and **3** revealed that **1** is much more stable than **3**.

Finally, the reactivity between **2** and **3** in Scheme 1 was investigated. In this system, the reaction products were analyzed with only ^1H NMR spectra, since no characteristic bands such as



Scheme 1. Reaction cycle between **1**, **2**, and **3**.

carbonyl bands are observed in these copper(I) triphenylphosphine and acetonitrile complexes. After the reaction of complex **2** with MeCN, the resonances of complex **2** were observed in the NMR spectrum, indicating no discernable reaction. It is acknowledged that these results may be due to dissociation of the coordinated MeCN molecule under reduced pressure. However, the ^{1}H NMR spectrum of reaction solution (CD_3CN) corresponds the same result. Conversely, after reaction of complex **3** with PPh_3, only the resonances due to complex **2** were observed in ^{1}H NMR spectrum. The stability experiments of **2** and **3** revealed that **2** is much more stable than **3**. Concluding this investigation of the above reactivity tests, the descending order of the stability of the complexes **1**–**3** is **3** < **1** < **2**.

4. Conclusion

In this paper, two novel copper(I) complexes **1** and **2** with L0f$^-$ were reported. The electron density around copper(I) in the complexes with L0f$^-$ is lower than those in the other complexes with alkyl-substituted tpzb ligands. Therefore, the copper(I) complexes with L0f$^-$ may show very different physicochemical properties compared with the non-fluorinated analogs.

First, in copper(I) carbonyl complexes, as the electron density around copper(I) ion is lower, the strength of Cu–C is weaker and strength of C≡O is stronger. While not shown by X-ray crystallography, these results were confirmed by far-IR and ^{13}C NMR spectra. The Cu–C stretching frequency in complex **1** is by 20–40 cm^{-1} lower than the Cu–C stretching frequencies in [Cu(L1)(CO)] and [Cu{HB(3-*t*Bu-5-*i*Prpz)$_3$}(CO)]. The ^{13}C NMR signals of the carbonyl carbons in **1** and the complexes with tpzm ligands appear as a broad peak. On the other hand, the ^{13}C NMR signals of the carbonyl carbons appear to be split into four broad peaks in the complexes with alkyl group substituted tpzb ligands. Additionally, the C≡O distances were supposed to be shorter as the electron density around copper(I) ion is lower, but this trend was not observed by X-ray crystallography. However, the C≡O stretching frequency in complex **2** is 40 cm^{-1} higher than that in [Cu(L0)(CO)] and is 31 cm^{-1} lower than that in [Cu(Lf6)(CO)] in IR spectra.

Second, in copper(I) triphenylphosphine complexes, as the electron density around copper(I) ion is lower, triphenylphosphine coordinates strongly to copper(I) ion. In the ^{31}P NMR spectra, the broadness of the signal in complex **2** is different from the signals of the phosphorus atom in copper(I) triphenylphosphine complexes with tpzb ligands, in which the signals appear as a broader resonance. The half widths of the signals in complex **2** and the complexes with tpzm ligands are narrower than those in the complexes with alkyl group susbtituted tpzb ligands. This means that the electron density of complex **2** is very close to that of neutral tpzm due to electron-withdrawing CF_3 group.

Finally, the reaction cycle of the copper(I) complexes between the complexes **1**–**3** was studied by ^{1}H NMR, solid-state IR, and *in situ* solution IR spectroscopy. The descending order of the stability of the complexes **1**–**3** is **3** < **1** < **2**. These stabilities of the complexes with the electron-withdrawing CF_3 ligand are consistent with the complexes with alkyl group substituted tpzb ligands [29].

Supplementary data

CCDC 695036, 695037, and 695038 contain the supplementary crystallographic data for **1**, **2**, and **4**, respectively. These data can be obtained free of charge via http://www.ccdc.cam.ac.uk/conts/retrieving.html, or from the Cambridge Crystallographic Data Centre, 12 Union Road, Cambridge CB2 1EZ, UK; fax: (+44) 1223-336-033; or e-mail: deposit@ccdc.cam.ac.uk.

Acknowledgments

This research was supported by grants for Grant-in-Aid for Scientific Research (B) (17350043) from JSPS and for Scientific Research on Priority Areas "Advanced Molecular Transformations of Carbon Resources" (19020011) from MEXT.

References

[1] S. Trofimenko, Chem. Rev. 93 (1993) 943.
[2] N. Kitajima, W.B. Tolman, Prog. Inorg. Chem. 43 (1995) 419.
[3] (a) S. Trofimenko, Scorpionates—The Coordination Chemistry of Polypyrazolylborate Ligands, Imperial College Press, London, 1999; (b) C. Pettinari, Scorpionates II: Chelating Borate Ligands, Imperial College Press, London, 2008.
[4] G. Parkin, Chem. Commun. (2000) 1971.
[5] D.M. Tellers, S.J. Skoog, R.G. Bergman, T.B. Gunnoe, W.D. Harman, Organometallics 19 (2000) 2428.
[6] (a) J.C. Calabrese, S. Trofimenko, J.S. Thompson, J. Chem. Soc., Chem. Commun. (1986) 1122; (b) S. Trofimenko, J.C. Calabrese, J.S. Thompson, Inorg. Chem. 26 (1987) 1507.
[7] K. Fujisawa, T. Ono, H. Aoki, Y. Ishikawa, Y. Miyashita, K. Okamoto, H. Nakazawa, H. Higashimura, Inorg. Chem. Commun. 7 (2004) 330.
[8] K. Fujisawa, T. Ono, Y. Ishikawa, N. Amir, Y. Miyashita, K. Okamoto, N. Lehnert, Inorg. Chem. 45 (2006) 1698.
[9] M. Nabika, S. Kiuchi, T. Miyatake, K. Okamoto, K. Fujisawa, J. Mol. Catal. A: Chem. 269 (2007) 163.
[10] N. Lehnert, U. Cornelissen, F. Neese, T. Ono, Y. Noguchi, K. Okamoto, K. Fujisawa, Inorg. Chem. 46 (2007) 3916.
[11] K. Fujisawa, A. Tateda, Y. Miyashita, K. Okamoto, F. Paulat, V.K.K. Praneeth, A. Merkle, N. Lehnert, J. Am. Chem. Soc. 130 (2008) 1205.
[12] F. Paulat, N. Lehnert, Y. Ishikawa, K. Okamoto, K. Fujisawa, Inorg. Chem. Acta 361 (2008) 901.
[13] K. Fujisawa, Y. Noguchi, Y. Miyashita, K. Okamoto, N. Lehnert, Inorg. Chem. 46 (2007) 10607.
[14] N.M. Doherty, N.W. Hoffman, Chem. Rev. 91 (1991) 553.
[15] S.H. Strauss, Chem. Rev. 93 (1993) 927.
[16] (a) J.L. Kiplinger, T.G. Richmond, C.E. Osterberg, Chem. Rev. 94 (1994) 373; (b) R.J. Kulawiec, R.H. Crabtree, Coord. Chem. Rev. 99 (1990) 89.
[17] (a) H.V.R. Dias, M. Fianchini, Comments Inorg. Chem. 28 (2007) 73; (b) H.V.R. Dias, J. Wu, Eur. J. Inorg. Chem. (2008) 509; (c) H.V.R. Dias, C.J. Lovely, Chem. Rev. 108 (2008) 3223.
[18] C.K. Ghosh, J.K. Hoyano, R. Krentz, W.A.G. Graham, J. Am. Chem. Soc. 111 (1989) 5480.
[19] (a) H.V.R. Dias, H.-L. Lu, Inorg. Chem. 34 (1995) 5380; (b) H.V.R. Dias, W. Jin, H.-J. Kim, H.-L. Lu, Inorg. Chem. 35 (1996) 2317.
[20] C. Mealli, C.S. Arcus, J.L. Wilkinson, T.J. Marks, J.A. Ibers, J. Am. Chem. Soc. 98 (1976) 711.
[21] A.J. Blake, D.A. Carling, M.W. George, P. Hubberstey, R.L. Garcia, C. Wilson, Acta Crystallogr., Sect. E 58 (2002) m41.
[22] N. Kitajima, T. Koda, S. Hashimoto, T. Kitagawa, Y. Moro-oka, J. Am. Chem. Soc. 113 (1991) 5664.
[23] J.L. Schneider, S.M. Carrier, C.E. Ruggiero, V.G. Young Jr., W.B. Tolman, J. Am. Chem. Soc. 120 (1998) 11408.
[24] Z. Hu, S.M. Gorun, Inorg. Chem. 40 (2001) 667.
[25] D. Diaconu, Z. Hu, S.M. Gorun, J. Am. Chem. Soc. 124 (2002) 1564.
[26] Z. Hu, R.D. Williams, D. Tran, T.G. Spiro, S.M. Gorun, J. Am. Chem. Soc. 122 (2000) 3556.
[27] Z. Hu, G.N. George, S.M. Gorun, Inorg. Chem. 40 (2001) 4812.
[28] W.L.F. Armarego, D.D. Perrin, Purification of Laboratory Chemicals, 4th Ed., Butterworth-Heinemann, Oxford, UK, 1997.
[29] N. Kitajima, K. Fujisawa, C. Fujimoto, Y. Moro-oka, S. Hashimoto, T. Kitagawa, K. Toriumi, K. Tatsumi, A. Nakamura, J. Am. Chem. Soc. 114 (1992) 1277.
[30] J.W. Pflugrath, Acta Crystallogr., Sect. D 55 (1999) 1718.
[31] CRYSTALSTRUCTURE 3.8, Crystal Structure Analysis Package, Rigaku and Rigaku/MSC, 2006.
[32] D.J. Watkin, C.K. Prout, J.R. Carruthers, P.W. Betteridge, CRYSTAL ISSUE 10, Chemical Crystallography Laboratory: Oxford, UK, 1996.
[33] A. Altomare, M.C. Burla, M. Camalli, G.L. Cascarano, C. Giacovazzo, A. Guagliardi, A.G.G. Moliterni, G. Polidori, R. Spagna, J. Appl. Crystallogr. 32 (1999) 115.
[34] G.M. Sheldrick, Acta Crystallogr., Sect. A 64 (2008) 112.
[35] P.T. Beurskens, G. Admiraal, G. Beurskens, W.P. Bosman, R. Gelder, R. Israel, J.M.M. Smits, DIRDIF-99, Technical Report of the Crystallography Laboratory, University of Nijmegen, The Netherlands, 1999.
[36] H.V.R. Dias, H.-J. Kim, H.-L. Lu, K. Rajeshwar, N.R. de Tacconi, A. Derecskei-Kovacs, D.S. Marynick, Organometallics 15 (1996) 2994.
[37] H.V.R. Dias, H.-J. Kim, Organometallics 15 (1996) 5374.
[38] M.I. Bruce, A.P.P. Ostazewski, J. Chem. Soc., Dalton Trans. (1973) 2433.
[39] M.R. Churchill, B.G. DeBoer, F.J. Rotella, O.M.A. Salah, M.I. Bruce, Inorg. Chem. 14 (1975) 2051.
[40] N. Kitajima, K. Fujisawa, C. Fujimoto, Y. Moro-oka, Chem. Lett. 18 (1989) 421.

[41] S. Imai, K. Fujisawa, T. Kobayashi, N. Shirasawa, H. Fujii, T. Yoshimura, N. Kitajima, Y. Moro-oka, Inorg. Chem. 37 (1998) 3066.
[42] S. Kiani, J.R. Long, P. Stavropoulos, Inorg. Chim. Acta 263 (1997) 357.
[43] (a) F. Abuke, C. Wang, Coord. Chem. Rev. 137 (1994) 483;
(b) H. Willner, F. Abuke, Angew. Chem., Int. Ed. Engl. 36 (1997) 2402;
(c) S.H. Strauss, J. Chem. Soc., Dalton Trans. (2000) 1;
(d) A.J. Lupinetti, S.H. Strauss, G. Frenking, Prog. Inorg. Chem. 49 (2001) 1.
[44] K. Nakamoto, Infrared and Raman Spectra of Inorganic and Coordination Compounds, 5th Ed., John Wiley and Sons Inc., New York, 1997.
[45] (a) K. Shobatake, C. Postmus, J.R. Ferraro, K. Nakamoto, Appl. Spectr. 23 (1969) 12;
(b) C. Pettinari, F. Marchetti, R. Polimante, A. Cingolani, G. Portalone, M. Colapietro, Inorg. Chim. Acta 249 (1996) 215.

spectroscopy. The TEM images were obtained on a Philips EM208 transmission electron microscope with an accelerating voltage of 100 kV. Fourier transform infrared (FT-IR) spectra were recorded on Shimadzu Varian 4300 spectrophotometer in KBr pellets. The magnetic measurements were carried out in a vibrating sample magnetometer (VSM, BHV-55, Riken, Japan) at room temperature.

2.3. Synthesis of $NiFe_2O_4$ nanocrystals

In a typically synthesis, a 0.4 M (25 mL) solution of iron chloride ($FeCl_3 \cdot 6H_2O$) and a 0.2 M (25 mL) solution of nickel chloride ($NiCl_2 \cdot 6H_2O$) were mixed in double distilled deionized water. Deionized distilled water was used as the solvent in order to avoid the production of impurities in the final product. A specified amount of octanoic acid was added to the solution as a surfactant and coating material. A 1.5 M (25 mL) solution of sodium hydroxide (NaOH) was prepared and slowly added to the salt solution dropwise. The pH of the solution was constantly monitored as the NaOH solution was added. The reactants were constantly stirred using a magnetic stirrer until a pH level of 7–8 was reached. The liquid precipitate was then brought to a reaction temperature of 80 °C and stirred for 1 h. The product was then cooled to room temperature. To get particles free from sodium and chlorine compounds, the precipitate was washed twice with distilled water and then with ethanol to remove the excess surfactant from the solution. To isolate the supernatant liquid, the beaker contents were then centrifuged for 15 min at 3000 rpm. The supernatant liquid was then decanted, and then centrifuged until only thick black precipitate remained. The obtained products were dried at 100 °C for 8 h. The acquired substance was then ground into a fine powder. At this stage the product ($NiFe_2O_4$) contains some associated water (up to 10 wt%), which was then removed by heating at 600 °C for 4 h (Fig. 1). The final samples were then confirmed by different techniques, such as XRD, SEM, TEM, etc.

3. Results and discussion

Fig. 2 shows the XRD pattern of the $NiFe_2O_4$. XRD peaks for the nanometer sized nickel ferrite (n-$NiFe_2O_4$) sample are significantly broader than those for a micrometer sized sample, indicating a very small particle size [17]. The crystallinity and structure of the $NiFe_2O_4$ nanocrystals were also confirmed by powder X-ray diffraction (XRD). Fig. 2a shows the XRD diffractograms for the studied sample. All the characteristic peaks of $NiFe_2O_4$ are present: 30.29° (220), 35.7° (311), 37.31° (222), 43.36° (400), 53.80° (422), 57.36° (511), 62.92° (440) and 74.64° (533). The diffractogram exhibits sharp lines; this indicates that the sample has high crystallinity. From the XRD data, the crystallite size (D_c) of the as-prepared $NiFe_2O_4$ particles was calculated to be 22 nm, using the Debye–Scherrer equation [18],

$$D_c = \frac{K\lambda}{\beta \cos\theta}$$

where β is the breadth of the observed diffraction line at its half-intensity maximum, K is the so-called shape factor, which usually takes a value of about 0.9, and λ is the wavelength of the X-ray source used in the XRD. No characteristic peaks of impurities can be detected. The strong and sharp reflection peaks suggest that the as-prepared nanocrystals are well crystallized. Fig. 2b shows the XRD patterns of the standard $NiFe_2O_4$ from JCPDS No. 74–2081.

The morphology and particle sizes of the as-prepared sample were determined by SEM and TEM. The SEM images of $NiFe_2O_4$ are shown in Fig. 3. These indicate that sphere-like $NiFe_2O_4$ nanostructures obtained by this method are uniform in both morphology and particle size, but have agglomeration to some extent. Fig. 4 shows a typical TEM image of $NiFe_2O_4$. The average size was calculated to be 25 ± 5 nm from the measurements on the TEM micrographs.

The IR spectra of the $NiFe_2O_4$ samples show small differences in the range 4000–1000 cm^{-1}. In the range 1000–100 cm^{-1}, the IR bands of solids are usually assigned to vibration of ions in the crys-

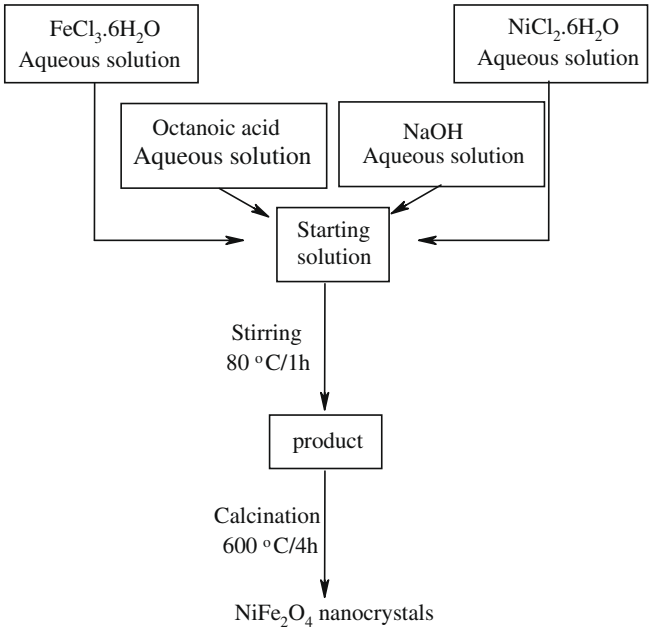


Fig. 1. Diagram of the chemical process for the formation of $NiFe_2O_4$ nanocrystals.

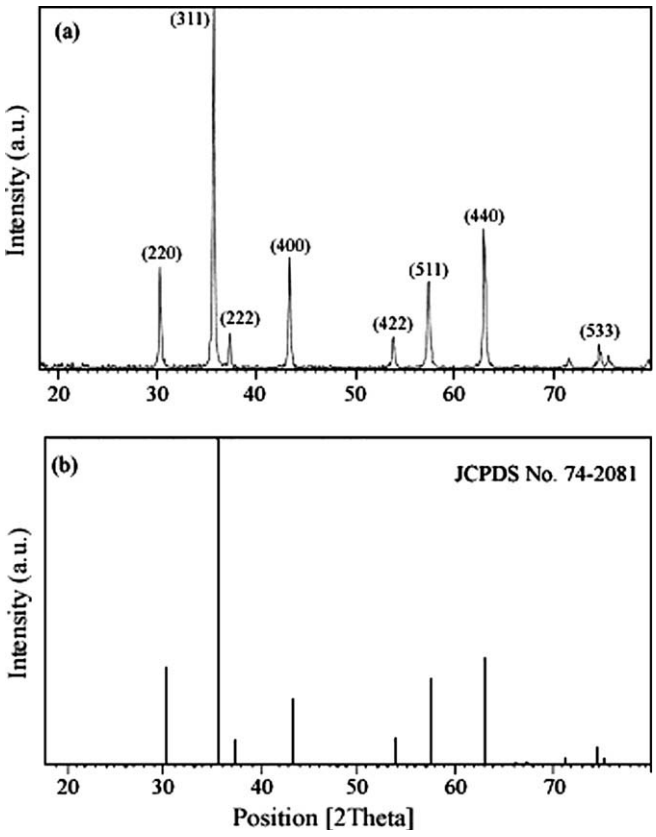


Fig. 2. (a) XRD pattern of the $NiFe_2O_4$ nanocrystals. (b) The standard $NiFe_2O_4$ from JCPDS No. 74–2081.

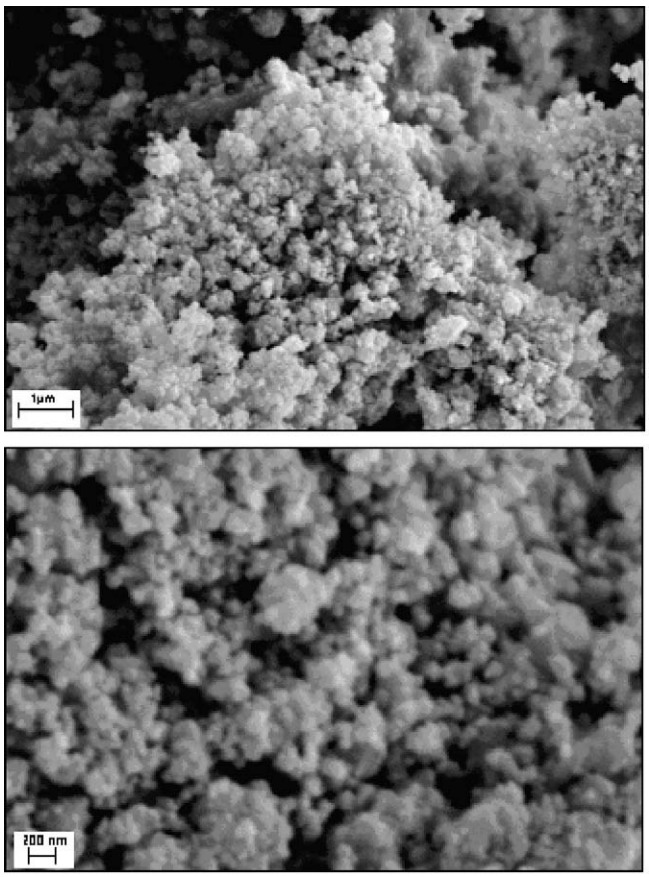


Fig. 3. SEM images of the $NiFe_2O_4$ nanocrystals.

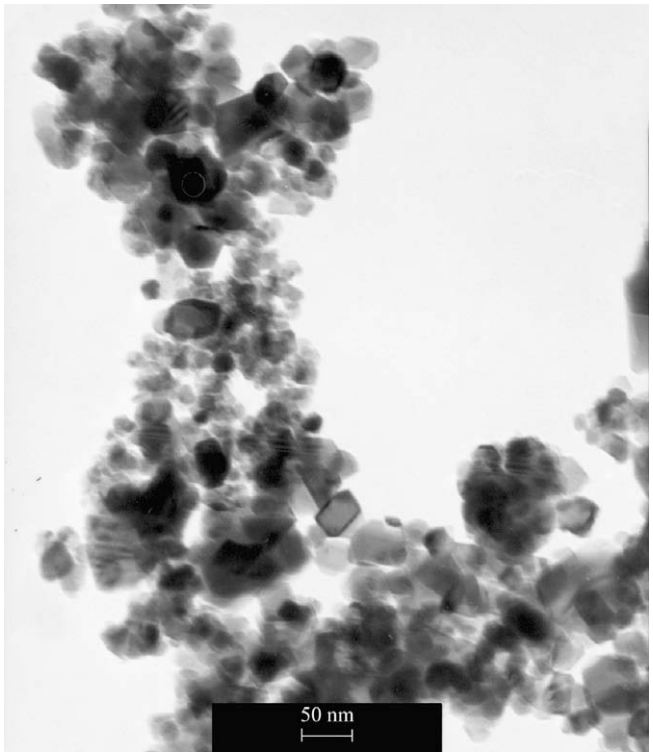


Fig. 4. TEM image of the $NiFe_2O_4$ nanocrystals prepared after calcination at 600 °C for 4 h.

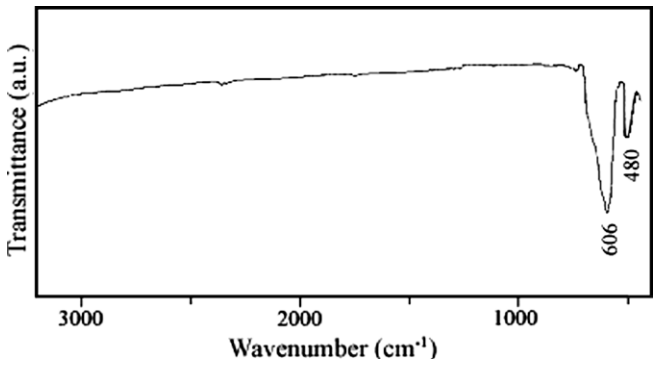


Fig. 5. IR spectrum of the $NiFe_2O_4$ nanocrystals calcined at 600 °C (4 h).

tal lattice [15]. Two main broad metal–oxygen bands are seen in the IR spectra of all spinels, and ferrites in particular. The highest one ν_1 (Fig. 5), observed at 606 cm^{-1}, corresponds to intrinsic stretching vibrations of the metal at the tetrahedral site, $M_{tetra} \leftrightarrow O$, whereas the ν_2-lowest band, usually observed at 480 cm^{-1}, is assigned to octahedral-metal stretching, $M_{octa} \leftrightarrow O$ [19,20]. However, no clear peak due to octahedrally coordinated metal ions was observed, which would be expected to be around 400 cm^{-1}. This may be due to the broadening of this peak attributed to very small particles of spinel ferrites [21].

The room temperature magnetization curve of the $NiFe_2O_4$ is shown in Fig. 6. The magnetic properties of the sample were measured by using a VSM, which showed that the sample exhibited typical ferromagnetic behavior at room temperature, while a finite coercivity of 245.5 Oe was present at 300 K (Fig. 6). The observed value of saturation magnetization of the sample (23.13 emu/g) is significantly lower than that for the reported multidomain bulk particles (55 emu/g). In the particle size range 10–100 nm, the decrease in the saturation magnetization has been explained in terms of its non-collinear spin arrangement at or near the surface of the particle. In addition, the magnetic hysteresis measured shows that the nanoparticles obtained display low ferromagnetic properties at room temperature. We found that for smaller crystals the saturation magnetization had a value that was significantly lower than the bulk value, while larger sized crystals have values approaching those of the bulk. In comparison with Fe_3O_4, these nanoparticles have low coercivity because of the non-magnetic Ni^{2+} ion presence in the lattice. The nickel ions are located between the grains and increase the affect of the grains on each other. The value of M_S in the crystals is attributed to the greater fraction of surface spins in these crystals that tend to be in a canted or a spin glass-like state with a smaller net moment.

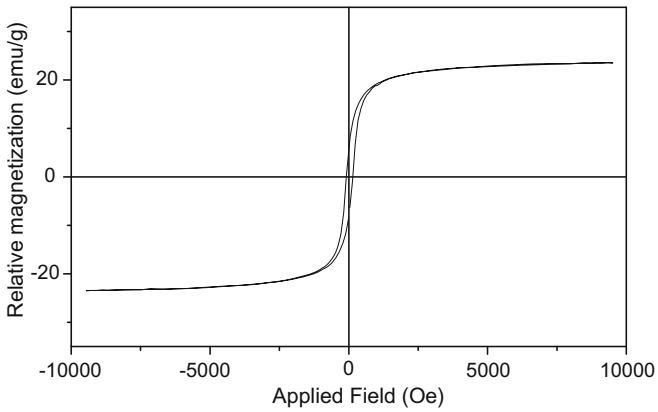


Fig. 6. Hysteresis loop for $NiFe_2O_4$ nanocrystals at room temperature.

4. Conclusion

In summary, nickel ferrite crystals with a normal spinel structure were obtained, with octanoic acid as a surfactant. Co-precipitation is a suitable method for the control of nanoparticle sizes with variation of the reaction conditions. The diameter of the nanocrystals is about 25 ± 5 nm. The size of the nanocrystals was measured both by XRD and TEM and the results were in very good agreement with each other. According to the TEM image there was some agglomeration of nanoparticles, but the size distribution of the prepared nanocrystals was small. The results of VSM indicate that the saturation magnetization of $NiFe_2O_4$ shows a maximum of 23.13 emu/g at room temperature.

Acknowledgement

Authors are grateful to the Council of the University of Kashan for providing financial support to undertake this work.

References

[1] M.P. Pileni, Adv. Funct. Mater. 5 (2001) 323.
[2] F.Y. Cheng, C.H. Su, Y.S. Yang, C.S. Yeh, C.Y. Tsai, C.L. Wu, M.T. Wu, D.B. Shieh, Biomaterials 26 (2005) 729.
[3] Q. Song, Z.J. Zhang, J. Am. Chem. Soc. 126 (2004) 6164.
[4] J. Sun, Sh. Zhou, P. Hou, Y. Yang, J. Weng, X. Li, M. Li, J. Biomedica. Mat. Res. A 83 (2006) 333.
[5] A. Chatterjee, D. Das, S.K. Pradhan, D. Chakravorty, J. Magn. Magn. Mater. 127 (1993) 214.
[6] S.G. Doh, E.B. Kim, B.H. Lee, J.H. Oh, J. Magn. Magn. Mater. 272–276 (2004) 2238.
[7] B. Baruwati, R.K. Rana, S.V. Manorama, J. Appl. Phys. 101 (2007) 014302.
[8] J. Wang, Y. Zhu, W. Li, Q. Chen, Mater. Lett. 59 (2005) 2101.
[9] S. Balaji, R.K. Selvan, L.J. Berchmans, S. Angappan, K. Subramanian, C.O. Augustin, Sci. Eng., B, Solid-State Mater. Adv. Technol. 119 (2005) 119.
[10] H. Yang, X. Zhang, W. Ao, G. Qiu, Mater. Res. Bull. 39 (2004) 833.
[11] J. Fang, N. Shama, L.D. Tung, E.Y. Shin, C.J. O'Connor, K.L. Stokes, J. Appl. Phys. 93 (2003) 7483.
[12] X.D. Li, W.S. Yang, F. Li, D.G. Evans, X. Duan, J. Phys. Chem. Solids 67 (2006) 1286.
[13] E.A. Souza, J.G.S. Duque, L. Kubota, C.T. Meneses, J. Phys. Chem. Solids 68 (2007) 594.
[14] H. Zhao, X. Sun, C. Mao, J. Du, Physica B 404 (2009) 69.
[15] A. Baykal, N. Kasapoğlu, Y. Köseoğlu, M.S. Toprak, H. Bayrakdar, J. Alloys Compd. 464 (2008) 514.
[16] M.R. Barati, S.A. Seyyed Ebrahimi, A. Badiei, J. Non-Cryst. Solids 354 (2008) 5184.
[17] S.K. Kurinec, N. Okeke, S.K. Gupta, H. Zhang, T.D. Xiao, J. Mater. Sci. 41 (2006) 8181.
[18] H.P. Klug, L.E. Alexander, X-ray Diffraction Procedures for Polycrystalline and Amorphous Materials, second ed., Wiley, New York, 1974.
[19] S. Hafner, Z. Krist. 115 (1961) 331.
[20] R.D. Waldron, Phys. Rev. 99 (1955) 1727.
[21] M. Mouallem-Bahout, S. Bertrand, O. Peña, J. Solid State Chem. 178 (2005) 1080.

2.2. Kinetic data

Rate data (25.0 °C, $[Co]_T = 2.5 \times 10^{-3}$ M, $I = 1.0$ M) for the acid hydrolysis of $[Co(uns\text{-}penp)(O_2CO)]^+$ and $[Co(dppa)(O_2CO)]^+$ were obtained using a Varian 500 Scan UV–Vis NIR spectrometer by observing the absorbance decrease at 493 and 494 nm, respectively. Data were fitted to a single exponential to obtain k_{obs} values.

2.3. X-ray structure determinations

X-ray data were collected at temperatures between 85 and 90 K on a Bruker Kappa APEX-II system using graphite-monochromated Mo Kα radiation with exposures over 0.5°, and were corrected for Lorentz and polarisation effects using SAINT [12]. All structures were solved using SIR-97 [13] running within the WINGX package [14] and weighted full-matrix refinement on F^2 was carried out using SHELXL-97 [15]. Hydrogen atoms attached to carbon and nitrogen were included in calculated positions, and were refined as riding atoms with individual (or group, where appropriate) isotropic displacement parameters. Only water hydrogen atoms which could be found in the difference map were included in the final cycles of refinement. Disorder was present in the three propyl chains of the complex $[Co(trpn)(O_2CO)]ClO_4 \cdot H_2O$ due to two different chelate ring conformations of similar energies. This was successfully modelled using a 70:30 distribution of the two conformations.

2.4. DFT calculations

Geometries of the complex cations were fully optimised using the gradient-corrected B3LYP density functional [16–18] with the 6-31G* basis set, in both gas and aqueous phase using the GAUSSIAN 03 program package [19]. In order to include solvent polarity effects, we have adopted the SCRF (self-consistent reaction field) [20–23] approach with a polarised continuum model (PCM) [24], using the dielectric constant of water. The nuclear magnetic shieldings σ were calculated at the optimised geometries using the B3LYP/6-31G* method. ^{59}Co chemical shifts (δ) were calculated from $\delta = |\sigma_{ref} - \sigma|$, where $[K_3Co(CN)_6]$ was used as the reference compound. The σ_{ref} value was calculated as −5825.8489 ppm. TD-DFT (time-dependent density functional theory) [25], as implemented in GAUSSIAN 03, [19] was used to calculate electronic transition energies. The vertical excitation energies and oscillator strengths were calculated using different combinations of functionals (B3LYP, MO5, PBE, BP86) and basis sets (6-31G*, 6-311G*, TZVP). From the data calculated using the B3LYP/6-31G* method, UV–Vis absorption spectra in the 800–335 nm wavelength range were simulated by convoluting each electronic transition with a Gaussian function having an area proportional to the oscillator strength and a full width at half maximum of 3000 cm^{-1} to match the experimental widths.

2.5. Synthesis

2.5.1. (3-Aminopropyl)bis(2-pyridylmethyl)amine · 3HCl · 0.5H$_2$O (dppa)

$NaBH(OAc)_3$ (6.00 g, 28.3 mmol) was added to a solution of *N*-acetylpropylenediamine (1.16 g, 10.0 mmol) and 2-pyridinecarbaldehyde (2.14 g, 20.0 mmol) in 1,2-dichloroethane (100 mL). The resulting suspension was stirred at room temperature for 3 h and the reaction was then quenched with 2 M NaOH(aq) (100 mL). The organic layer was separated and the aqueous layer extracted with CH_2Cl_2 (2 × 100 mL). The organic fractions were combined and washed with saturated NaCl(aq) (100 mL), then dried over anhydrous Na_2SO_4, filtered, and reduced to dryness (rotavap) to yield an orange oil. This was dissolved in 5 M HCl(aq) (100 mL) and heated at reflux for 20 h. Following cooling and removal of solvent (rotavap), the resulting oil was dissolved in the minimum volume of ethanol, added dropwise to ether (400 mL) and stirred for 3 days. The resulting brown solid was crystallised from hot ethanol to give dppa · 3HCl · 0.5H$_2$O (1.26 g, 31%). *Anal.* Calc. for $C_{15}H_{24}N_4O_{0.5}Cl_3$: C, 48.08; H, 6.46; N, 14.95; Cl, 28.38. Found: C, 48.24; H, 6.68; N, 14.72; Cl, 28.56%. ESI-MS. Calcd for $C_{15}H_{21}N_4^+$, 257. Found, 257. ^{1}H NMR (D_2O) δ 8.39 (2H, m), 8.19 (2H, m), 7.73 (2H, d), 7.62 (2H, m), 3.96 (4H, s), 2.60 (2H, t), 2.44 (2H, t), 1.60 (2H, m); ^{13}C NMR (D_2O) δ 152.86, 147.60, 141.66, 127.35, 126.62, 55.44, 51.76, 37.56, 23.96 ppm.

2.5.2. [Co(baep)(O$_2$CO)]ClO$_4$

Solid baep · 4HCl · 1.5H$_2$O (1.35 g, 4.05 mmol) was added to a suspension of $Na_3[Co(O_2CO)_3] \cdot 3H_2O$ (2.50 g, 7.00 mmol) in H_2O (30 mL). The mixture was heated at 65 °C for 5 min, evolving CO_2 and giving a dark red solution which was then filtered through celite, diluted to 800 mL with distilled water and loaded onto a Sephadex SP C-25 cation exchange column. The pink band which eluted with 0.1 M $NaClO_4$(aq) was reduced to near dryness (rotavap) and cooled on ice to give a pink solid. This was removed by filtration, washed with ethanol and ether, and dried under vacuum. The product was crystallised by dissolution in the minimum volume of warm water, addition of isopropanol dropwise until the solution just became cloudy, and subsequent cooling. The resulting pink solid was removed by filtration and washed with isopropanol. Dissolution of the product in the minimum volume of water and layering with isopropanol gave X-ray quality red crystals of [Co(baep)O$_2$CO]ClO$_4$ (0.29 g, 17%). *Anal.* Calc. for $CoC_8H_{20}N_4O_7Cl$: C, 25.36; H, 5.28; N, 14.80; Cl, 9.38. Found: C, 25.40; H, 5.40; N, 14.68; Cl, 9.59%. ESI-MS. Calcd for $CoC_8H_{20}N_4O_3^+$, 279. Found, 279. UV–Vis (H_2O) [λ_{max}, nm (ε, dm^3 mol cm^{-1})]: 508 (107), 352 (90). ^{1}H NMR (D_2O) δ 2.67 (6H, m), 2.49 (3H, m), 2.36 (2H, m), 2.22 (1H, m), 1.71 (2H, m); ^{13}C NMR (D_2O) δ 166.86, 65.93, 59.20, 57.89, 41.92, 41.10, 39.60, 24.14 ppm. ^{59}Co NMR (D_2O): δ 8728 ppm. X-ray crystallography showed the complex to exist as a hemihydrate with complete desolvation occurring upon drying.

2.5.3. [Co(abap)(O$_2$CO)]ClO$_4$

Solid abap · 4HCl · 3H$_2$O (0.45 g, 1.20 mmol) was added to a suspension of $Na_3[Co(O_2CO)_3] \cdot 3H_2O$ (0.50 g, 1.20 mmol) in H_2O (10 mL). The mixture was heated at 60 °C for 15 min, evolving CO_2 and giving a red solution which was filtered through celite, diluted with H_2O and loaded onto a Sephadex SP C-25 cation exchange column. A magenta band was eluted with 0.1 M $NaClO_4$. This was reduced in volume to ~5 mL, and then added dropwise to EtOH (100 mL) to give the product as a magenta solid, which was removed by filtration, washed with EtOH and Et_2O, and air-dried. (0.24 g, 50%). *Anal.* Calc. for $CoC_9H_{22}N_4O_7Cl$: C, 27.53; H, 5.65; N, 14.27; Cl, 9.03. Found: C, 27.24; H, 5.64; N, 14.03; Cl, 9.31%. UV–Vis (H_2O) [λ_{max}, nm (ε, dm^3 mol cm^{-1})]: 524 (125), 362 (136). ^{1}H NMR (D_2O) δ 3.18 (1H, m), 3.04 (4H, m), 2.88 (1H, m), 2.75 (1H, m), 2.59 (1H, m), 2.43 (3H, m), 2.23 (2H, m), 1.90 (3H, m). ^{13}C NMR (D_2O) δ 167.87, 66.18, 60.39, 56.00, 43.27, 39.77 and 39.65 (doublet), 38.63, 25.39, 24.33 ppm. ^{59}Co NMR (D_2O): δ 9117 ppm.

2.5.4. [Co(uns-penp)(O$_2$CO)]ClO$_4$

Solid uns-penp · 3HCl (2.67 g, 7.60 mmol) was added to a suspension of $Na_3[Co(O_2CO)_3] \cdot 3H_2O$ (2.75 g, 7.60 mmol) in H_2O (60 mL). The mixture was heated at 65 °C for 5 min, evolving CO_2 and giving an orange-red solution which was filtered through celite, diluted with H_2O and loaded onto a Sephadex SP C-25 cation-exchange column. An orange band was eluted with 0.1 mol L^{-1} $NaClO_4$, reduced to near dryness (rotavap) and refrigerated to give an orange solid which was removed by filtration (1.19 g, 34%). The crude product was crystallised by dissolution in the minimum vol-

ume of hot water, addition of $NaClO_4$(s) and subsequent cooling to give X-ray quality crystals of [Co(uns-penp)(O_2CO)]ClO_4 which were filtered off and washed with isopropanol (0.41 g, 12%). *Anal.* Calc. for $C_{15}H_{18}N_4O_7ClCo$: C, 39.10; H, 3.94; N, 12.16; Cl, 7.69. Found: C, 39.29; H, 4.08; N, 12.00; Cl, 7.95%. UV–Vis (H_2O) [λ_{max}, nm (ε, L mol^{-1} cm^{-1})]: 493 (180), 352 (173). ESI-MS: Calcd for $CoC_{15}H_{18}N_4O_3^+$ 361; Found 361. ^{1}H NMR (D_2O): δ 8.61 (2H, dd), 8.21 (2H, td), 7.76 (4H, m), 5.15 (2H, d), 4.71 (2H, d), 3.19 (2H, t), 2.23 (2H, t) ppm. ^{13}C (D_2O): δ 167.09, 163.40, 151.06, 142.45, 127.29, 123.85, 67.82, 64.17, 42.75 ppm. ^{59}Co NMR (D_2O): δ 8132 ppm. X-ray crystallography showed the complex to exist as a monohydrate with complete desolvation occurring upon drying.

2.5.5. [Co(dppa)(O_2CO)]ClO_4

Solid dppa · 3HCl · 0.5H_2O (1.00 g, 2.49 mmol) was added to a suspension of Na_3[Co($O_2CO)_3$] · 3H_2O (0.900 g, 2.49 mmol) in H_2O (20.0 mL). The mixture was heated at 65 °C for 5 min to give an orange-red solution which was then filtered through celite, diluted to 800 mL with distilled water and loaded onto a Sephadex SP C-25 cation exchange column. The red band eluted with 0.1 M $NaClO_4$(aq) was reduced to low volume (rotavap) and the crude product was obtained as an oil upon addition of isopropanol. Trituration with ether gave the solid the red/orange product, which was collected by filtration and dried under vacuum. Red crystals of [Co(dppa)O_2CO]ClO_4 suitable for X-ray structure determination were obtained on dissolution of the product in the minimum volume of water and layering with isopropanol (0.13 g, 10%). *Anal.* Calc. for $CoC_{16}H_{20}N_4O_7Cl$: C, 40.48; H, 4.25; N, 11.80; Cl, 7.47. Found: C, 40.49; H, 4.11; N, 11.82; Cl, 7.53%. ESI-MS. Calc. for $CoC_{16}H_{20}N_4O_3^+$, 375. Found, 375. UV–Vis (H_2O) [λ_{max}, nm (ε, dm^3 mol cm^{-1})]: 494 (134). ^{1}H NMR (D_2O) δ 8.41 (2H, dd), 7.94 (1H, td), 7.85 (1H, td), 7.60 (2H, dd), 7.52 (1H, t), 7.44 (1H, t), 7.28 (1H, dd), 4.80 (2H, dd), 4.68 (1H, d), 4.45 (1H, d), 3.20 (2H, m), 2.61 (1H, m), 2.41 (1H, q), 2.11 (1H, dd), 1.71 (1H, q); ^{13}C NMR (D_2O) δ 166.51, 163.00, 158.15, 149.40, 149.31, 141.46, 141.09, 126.90, 126.69, 122.86, 122.28, 73.16, 66.27, 61.61, 39.13, 24.79 ppm. ^{59}Co NMR (D_2O): δ 8365 ppm.

2.5.6. [Co(trpn)(O_2CO)]ClO_4

Trpn (1.82 g, 9.60 mmol) in H_2O/MeOH (1:1, 50 mL) was added to a solution of [Co($H_2O)_6$]($ClO_4)_2$ (3.51 g, 9.60 mmol) in H_2O (40 mL). To this were added $NaHCO_3$ (0.806 g, 9.60 mmol) and PbO_2 (0.344 g, 1.44 mmol) and the resulting suspension was stirred overnight at room temperature. After filtering through celite, the purple filtrate was diluted with H_2O and loaded onto a Sephadex SP C-25 cation exchange column. The purple band eluted with 0.1 mol L^{-1} $NaClO_4$ was reduced to near dryness (rotavap) to give crystalline purple [Co(trpn)O_2CO]ClO_4, which was removed by filtration, washed with isopropanol and dried *in vacuo* (1.32 g, 34%). *Anal.* Calc. for $C_{10}H_{24}N_4O_7ClCo$: C, 29.53; H, 5.95; N, 13.78; Cl, 8.72. Found: C, 29.36; H, 6.17; N, 13.49; Cl, 8.82%. ESI-MS: Calc. for $CoC_{10}H_{24}N_4O_3^+$ 307; Found 307 [M$^+$]. UV–Vis (H_2O) [λ_{max}, nm (ε, L mol^{-1} cm^{-1})]: 534 (120), 367 (147). ^{1}H NMR (D_2O): δ 2.87 (2H, m), 2.57 (10H, m), 2.05 (4H, m), 1.87 (2H, m) ppm. ^{13}C NMR (D_2O): δ 167.76, 58.21, 56.17, 38.47, 37.61, 23.93, 21.52 ppm. ^{59}Co NMR (D_2O): δ 9574 ppm. Crystallisation of the crude product from an aqueous solution layered with isopropanol gave X-ray quality purple crystals of the monohydrate of the complex.

3. Results and discussion

3.1. Synthesis and characterisation

Fig. 1 shows the structures of the ligands used in this work. The dppa ligand was prepared via an adaptation of a method used for the synthesis of the related ligand uns-penp [9]. Schiff base condensation of *N*-acetylpropylenediamine with 2 equiv. of 2-pyridinecarbaldehyde, reduction with $NaBH(OAc)_3$ and deacetylation with HCl, gave dppa as the trihydrochloride hemihydrate. This contrasts with previous syntheses of dppa which involve reaction of di(2-pyridylmethyl)amine with either acrylonitrile [26–28] or *N*-(3-bromopropyl)phthalimide [29,30] and subsequent reduction or deprotection, respectively. As the abap, dppa, uns-penp and baep ligands were all isolated as hydrochloride salts, the Co(III) complexes containing these ligands were most conveniently pre-

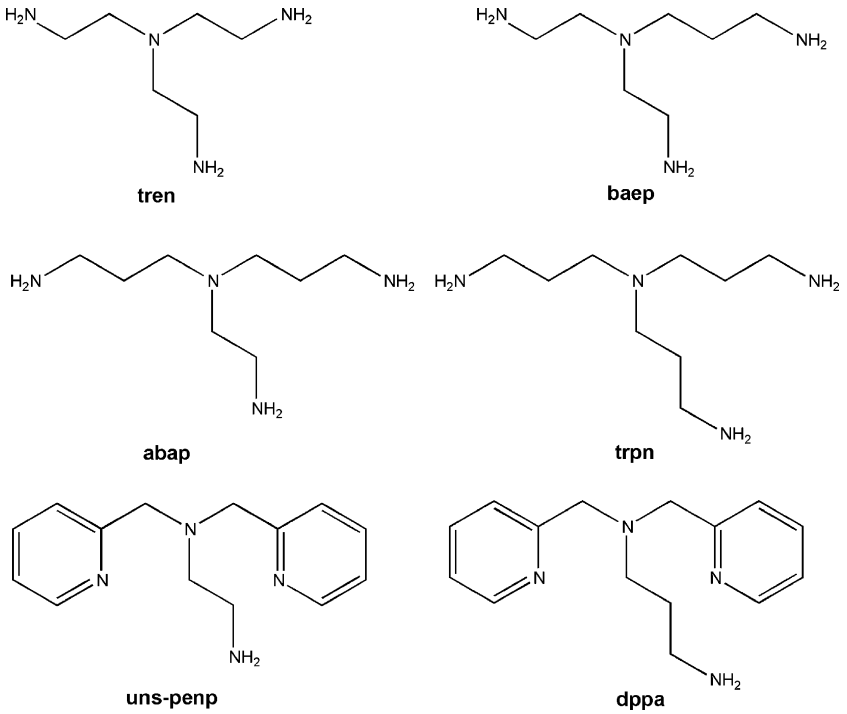


Fig. 1. Structures of the tripodal tetraamine ligands.

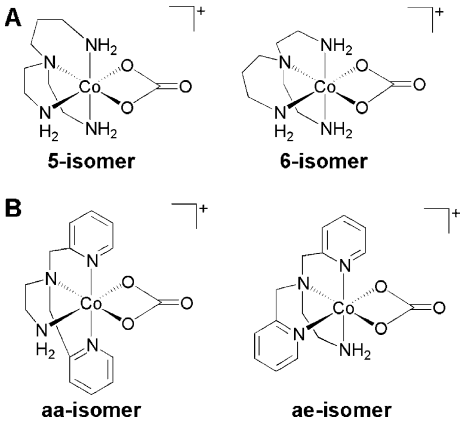


Fig. 2. Isomeric possibilities in $[Co(L)(O_2CO)]^+$ complexes. (A) 5- and 6-isomers of $[Co(baep)(O_2CO)]^+$. The five- and six-descriptors refer to the size of the chelate ring in the same plane as the carbonate ligand. Such isomers are possible for L = baep, abap and dppa. B) aa- and ae-isomers of $[Co(uns\text{-}penp)(O_2CO)]^+$. The aa- (axial, axial) and ae- (axial, equatorial) descriptors refer to the positioning of the pyridyl donors relative to the plane containing the Co ion and the coordinated O atoms of the carbonate ligand. Such isomers are possible for L = uns-penp and dppa.

pared by reaction with $Na_3[Co(O_2CO)_3] \cdot 3H_2O$. In aqueous solution at 60–65 °C, these reactions gave rapid evolution of CO_2 and colour changes to red or orange-red. $[Co(trpn)(O_2CO)]ClO_4$ was prepared by PbO_2 oxidation of a solution of Co(II), HCO_3^- and the free base ligand in aqueous solution. Purification of all complexes was effected by cation exchange chromatography on Sephadex SP-C25 resin and the complexes were crystallised as perchlorate salts. Elemental analysis and mass spectral data were consistent with the proposed formulae in all cases. All complexes except $[Co(trpn)(O_2CO)]^+$ can potentially form two geometric isomers, owing to the different possible relative positionings of either the five- and six-membered chelate rings (baep, abap, dppa) or the two pyridine rings (dppa, uns-penp) (Fig. 2), and NMR proved unequivocal both in showing that the syntheses of these complexes proceeded in a stereoselective manner and in characterising the single isomer formed. Central to the identification of the isomers is the $[Co(trpn)(O_2CO)]^+$ ion for which, somewhat ironically, there are no geometric isomeric possibilities. Although the solid state structure of this ion (Fig. 5) shows that all of the CH_2 carbon atoms are chemically inequivalent, the presence of disorder in each of the three chelate rings implies that there is a very low energy barrier to chelate ring inversion even in the solid state, and this is borne out by the observation of 6, rather than 9, CH_2 peaks in the ^{13}C NMR spectrum of $[Co(trpn)(O_2CO)]^+$ in D_2O, 3 of which are approximately twice the intensity of the other 3 [31]. Therefore, each pair of C atoms in the 'axial' chelate rings is rendered equivalent on the NMR timescale by chelate ring inversion processes, thereby giving the ion an apparent mirror plane through the cobalt ion and the four equatorial donor atoms. Such ring inversion processes are generally facile for all but the most rigid of chelate rings [4] and allow the definitive assignment of the possible geometric isomers formed when the tripodal ligand has only two of the three arms identical. For example the observation of 7 CH_2 peaks of approximately equal intensity in the ^{13}C NMR spectrum of $[Co(baep)(O_2CO)]^+$ shows all the CH_2 carbon atoms are chemically inequivalent, implying that the ion exists exclusively as the 5-isomer [32] in which a five-membered chelate rings lies in the same plane as the carbonate ligand. The 5-isomer was also observed in the two other crystallographically characterised 6-coordinate complexes containing baep [33] while the related complex $[Co(baep)(NO_2)_2]^+$ also displays 7 ^{13}C NMR peaks in solution, consistent with formation of the 5-isomer [7]. The presence of 8 peaks [34] in the ^{13}C NMR spectrum of $[Co(abap)(O_2CO)]^+$ shows that this complex is formed as the 6-isomer, and such a preference has been found in the three other structurally characterised 6-coordinate abap complexes in which the remaining coordination sites are occupied by a chelating ligand [8,33,35]. Interestingly, X-ray crystallographic data show that the 5-isomer appears to be preferred when two monodentate ligands, rather than a single chelating ligand, are present [33,36–38], although solution studies of 5-$[Co(abap)(OH_2)_2]^{3+}$ at varying pH have shown that isomerisation to the 6-isomer does occur [32]. The observation of only a single set of pyridine C resonances in the ^{13}C NMR spectrum of the $[Co(uns\text{-}penp)(O_2CO)]^+$ cation show this to be the aa isomer (Fig. 2), in which the aliphatic N atoms are situated in the same plane as the coordinated carbonate O atoms. This appears to be the preferred isomer in all but one of the structurally characterised 6-coordinate complexes containing uns-penp, regardless of whether the complex contains one bidentate or two monodentate ligands. The one exception is the bis(μ-oxo) manganese (III,IV) dimer $[(uns\text{-}penp)Mn(O)_2Mn(uns\text{-}penp)]^{3+}$ in which an uns-penp ligand coordinates to each Mn ion such that one pyridine ring is equatorial and one axial [39]. There are two observations concerning the ^{13}C NMR spectrum of the $[Co(dppa)(O_2CO)]^+$ ion that are consistent with its assignment as the ae-isomer in solution. Firstly, 10, rather than 5 peaks due to the pyridine C atoms are observed, and these appear as 5 closely spaced pairs of peaks. Secondly, the presence of five peaks in the aliphatic region of the spectrum shows that the two CH_2 carbon atoms adjacent to the pyridine rings are

Table 1
Crystal data and structure refinement for $[Co(L)O_2CO]ClO_4$ complexes.

	L = baep	L = abap	L = trpn	L = uns-penp	L = dppa
Empirical formula	$C_8H_{21}ClCoN_4O_{7.5}$	$C_9H_{22}ClCoN_4O_7$	$C_{10}H_{24}ClCoN_4O_8$	$C_{15}H_{18}ClCoN_4O_8$	$C_{16}H_{20}ClCoN_4O_7$
Formula weight	387.67	392.69	422.71	476.71	474.74
T (K)	158(2)	89(2)	85(2)	89(2)	163(2)
λ (Å)	0.71073	0.71073	0.71073	0.71073	0.71069
Space group	$P2_1$	$Pca2_1$	$P2_1/c$	$P\bar{1}$	$P\bar{1}$
a (Å)	11.4047(2)	15.8744(11)	11.9510(19)	6.7544(3)	8.594(5)
b (Å)	11.2059(2)	8.6200(6)	12.0740(19)	11.5523(5)	10.751(5)
c (Å)	11.9022(2)	21.8568(15)	12.917(2)	12.3201(6)	11.178(5)
α (°)	90	90	90	73.397(2)	73.982(5)
β (°)	103.243(1)	90	117.56(4)	89.749(2)	75.039(5)
γ (°)	90	90	90	84.551(2)	79.824(5)
V (Å^3)	1480.65(4)	2990.8(4)	1652.4(4)	916.82(7)	952.8(8)
Z	2	8	4	2	2
D_{calc} (Mg m^{-3})	1.739	1.744	1.635	1.720	1.655
μ (mm^{-1})	1.382	1.367	1.240	1.136	1.089
Final R indices [$I > 2\sigma(I)$]	$R_1 = 0.0498$, $wR_2 = 0.1283$	$R_1 = 0.0350$, $wR_2 = 0.0902$	$R_1 = 0.0476$, $wR_2 = 0.1188$	$R_1 = 0.0277$, $wR_2 = 0.0842$	$R_1 = 0.0295$, $wR_2 = 0.0781$
R indices (all data)	$R_1 = 0.0553$, $wR_2 = 0.1330$	$R_1 = 0.0370$, $wR_2 = 0.0917$	$R_1 = 0.0567$, $wR_2 = 0.1275$	$R_1 = 0.0317$, $wR_2 = 0.0980$	$R_1 = 0.0320$, $wR_2 = 0.0793$

inequivalent. The ae-isomer is also found in the other crystallographically characterised 6-coordinate complexes containing dppa [30,40].

3.2. X-ray crystal structures

Table 1 gives crystallographic data for the complexes studied, while ORTEP diagrams of the cations of 5-[Co(baep)(O_2CO)]$ClO_4 \cdot 0.5H_2O$, 6-[Co(abap)(O_2CO)]ClO_4, [Co(trpn)(O_2CO)]$ClO_4 \cdot H_2O$, aa-[Co(uns-penp)(O_2CO)]$ClO_4 \cdot H_2O$ and ae-[Co(dppa)(O_2CO)]ClO_4 and are given in Figs. 3–7 respectively. In all cases, the four N atoms of the tripodal ligand are coordinated to the central Co(III) ion, whose primary coordination sphere is completed by two O atoms from a chelating carbonate ligand. The geometry of the chelated carbonate ligand is similar across all five complexes; the two Co–O bonds in each complex are of different lengths, and this leads to a slight asymmetry in the chelate, while the O–Co–O angles range between 68.45° and 69.61°. The complexes $[Co(L)(O_2CO)]^+$ (L = tren [41–43], baep, abap, trpn) form an homologous series and a comparison of their geometries is instructive. The average Co–N distance increases across the series (L = tren, 1.943 Å; baep, 1.962 Å; abap, 1.964 Å; trpn, 1.976 Å), presumably as a result of the increasing number of six-membered chelate rings. Such lengthening has been seen before in related homologous series of complexes [4,5] and corresponds to a weakening in the ligand field strength of the tripodal ligand. The bond to the tertiary N atom increases in length significantly across the series (1.927–2.027 Å) but there are no consistent trends in the other Co–N distances. The N–Co–N bond angles involving six-membered chelate rings are consistently larger than those involving five-membered chelate rings, and this effect is most marked when the chelate ring lies in the equatorial plane. Thus while the N–Co–N bond angles of the axial six-membered chelate rings in the baep, abap and trpn complexes range from 90.98° to 93.85°, those in the equatorial plane range from 98.74° to 100.27°, and this presumably is a consequence of the presence of a rigid *trans* disposed four-membered chelate ring, thus allowing expansion of this angle. Some similar trends in bond

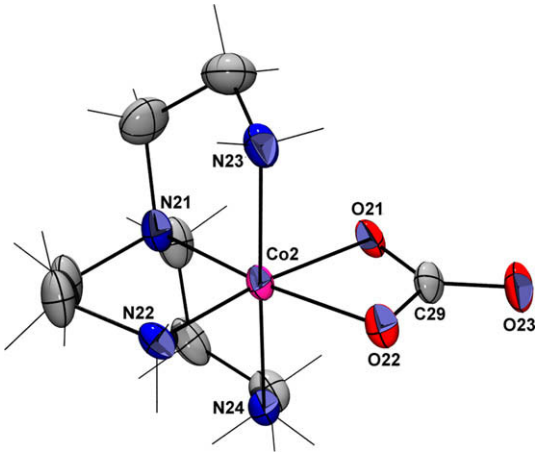


Fig. 3. Structure of the 5-[Co(baep)(O_2CO)]$^+$ cation with ellipsoids drawn at the 50% probability level. Selected bond distances (Å) and angles (°): Co(1)–O(12) 1.917(4); Co(1)–O(11) 1.931(4); Co(1)–N(13) 1.944(4); Co(1)–N(12) 1.958(5); Co(1)–N(14) 1.960(5); Co(1)–N(11) 1.984(5); Co(2)–O(21) 1.927(4); Co(2)–O(22) 1.939(4); Co(2)–N(23) 1.947(4); Co(2)–N(22) 1.948(5); Co(2)–N(24) 1.973(5); Co(2)–N(21) 1.978(5); O(11)–C(18) 1.335(7); O(12)–C(18) 1.313(7); O(13)–C(18) 1.232(7); O(22)–C(28) 1.319(7); O(21)–C(28) 1.306(7); O(23)–C(28) 1.248(7); O(12)–Co(1)–O(11) 68.75(16); O(12)–Co(1)–N(13) 170.43(18); O(11)–Co(1)–N(13) 101.68(18); O(12)–Co(1)–N(12) 87.43(19); O(11)–Co(1)–N(12) 91.3(2); N(13)–Co(1)–N(12) 92.8(2); O(12)–Co(1)–N(14) 89.68(19); O(11)–Co(1)–N(14) 90.13(19); N(13)–Co(1)–N(14) 90.5(2); N(12)–Co(1)–N(14) 176.1(2); O(12)–Co(1)–N(11) 102.31(18); O(11)–Co(1)–N(11) 170.92(19); N(13)–Co(1)–N(11) 87.2(2); N(12)–Co(1)–N(11) 86.6(2); N(14)–Co(1)–N(11) 91.5(2); O(21)–Co(2)–O(22) 68.45(16); O(21)–Co(2)–N(23) 101.95(18); O(22)–Co(2)–N(23) 170.40(18); O(21)–Co(2)–N(22) 91.6(2); O(22)–Co(2)–N(22) 87.90(19); N(23)–Co(2)–N(22) 92.6(2); O(21)–Co(2)–N(24) 88.43(19); O(22)–Co(2)–N(24) 88.81(19); N(23)–Co(2)–N(24) 90.8(2); N(22)–Co(2)–N(24) 176.4(2); O(21)–Co(2)–N(21) 171.45(18); O(22)–Co(2)–N(21) 103.03(18); N(23)–Co(2)–N(21) 86.6(2); N(22)–Co(2)–N(21) 87.3(2); N(24)–Co(2)–N(21) 92.2(2).

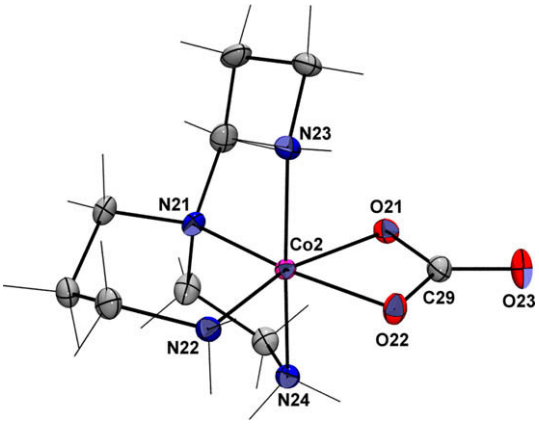


Fig. 4. Structure of the 6-[Co(abap)(O_2CO)]$^+$ cation with ellipsoids drawn at the 50% probability level. Selected bond distances (Å) and angles (°): Co(1)–O(12) 1.9055(16); Co(1)–O(11) 1.9149(16); Co(1)–N(14) 1.9426(19); Co(1)–N(12) 1.9622(19); Co(1)–N(13) 1.964(2); Co(1)–N(11) 1.9855(19); Co(2)–O(22) 1.9024(16); Co(2)–O(21) 1.9361(16); Co(2)–N(24) 1.9444(19); Co(2)–N(22) 1.9552(17); Co(2)–N(23) 1.9690(19); Co(2)–N(21) 1.9922(19); O(12)–C(19) 1.329(3); O(13)–C(19) 1.228(3); O(11)–C(19) 1.311(3); O(22)–C(29) 1.310(3); O(21)–C(29) 1.308(3); O(23)–C(29) 1.242(3); O(12)–Co(1)–O(11) 68.99(7); O(12)–Co(1)–N(14) 89.22(8); O(11)–Co(1)–N(14) 86.53(8); O(12)–Co(1)–N(12) 93.48(8); O(11)–Co(1)–N(12) 162.46(8); N(14)–Co(1)–N(12) 93.94(8); O(12)–Co(1)–N(13) 90.96(8); O(11)–Co(1)–N(13) 89.95(9); N(14)–Co(1)–N(13) 176.15(9); N(12)–Co(1)–N(13) 89.88(9); O(12)–Co(1)–N(11) 167.43(7); O(11)–Co(1)–N(11) 98.80(7); N(14)–Co(1)–N(11) 87.02(8); N(12)–Co(1)–N(11) 98.74(9); N(13)–Co(1)–N(11) 91.99(9); O(22)–Co(2)–O(21) 68.60(7); O(22)–Co(2)–N(24) 91.16(8); O(21)–Co(2)–N(24) 85.63(7); O(22)–Co(2)–N(22) 91.98(7); O(21)–Co(2)–N(22) 160.59(8); N(24)–Co(2)–N(22) 94.98(7); O(22)–Co(2)–N(23) 89.28(8); O(21)–Co(2)–N(23) 90.67(7); N(24)–Co(2)–N(23) 175.82(8); N(22)–Co(2)–N(23) 89.16(8); O(22)–Co(2)–N(21) 168.96(7); O(21)–Co(2)–N(21) 100.47(7); N(24)–Co(2)–N(21) 86.23(8); N(22)–Co(2)–N(21) 98.92(8); N(23)–Co(2)–N(21) 92.55(8).

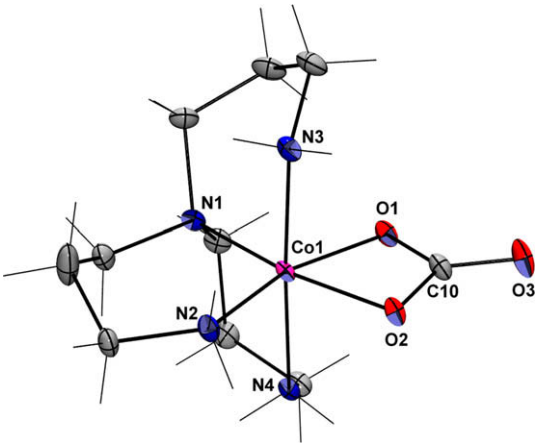


Fig. 5. Structure of the [Co(trpn)(O_2CO)]$^+$ cation with ellipsoids drawn at the 50% probability level. Selected bond distances (Å) and angles (°): Co(1)–O(2) 1.9154(11) Co(1)–O(1) 1.9191(11); Co(1)–N(2) 1.9506(13); Co(1)–N(4) 1.9606(13); Co(1)–N(3) 1.9638(14); Co(1)–N(1) 2.0271(13); O(2)–C(10) 1.3073(18); O(1)–C(10) 1.3251(19); O(3)–C(10) 1.2347(18); O(2)–Co(1)–O(1) 68.74(5); O(2)–Co(1)–N(2) 90.90(5); O(1)–Co(1)–N(2) 159.61(5); O(2)–Co(1)–N(4) 86.56(5); O(1)–Co(1)–N(4) 89.52(5); N(2)–Co(1)–N(4) 90.36(6); O(2)–Co(1)–N(3) 88.74(5); O(1)–Co(1)–N(3) 89.81(5); N(2)–Co(1)–N(3) 88.62(6); N(4)–Co(1)–N(3) 175.17(5); O(2)–Co(1)–N(1) 168.81(5); O(1)–Co(1)–N(1) 100.08(5); N(2)–Co(1)–N(1) 100.27(6); N(4)–Co(1)–N(1) 93.85(6); N(3)–Co(1)–N(1) 90.98(6).

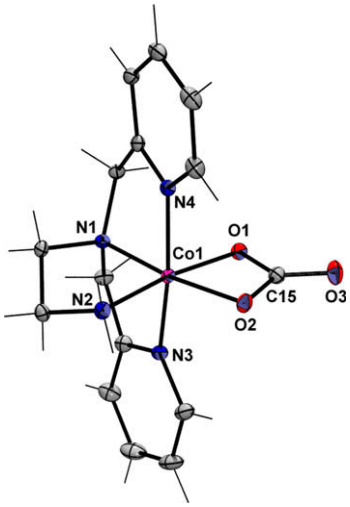


Fig. 6. Structure of the aa-[Co(uns-penp)(O_2CO)]$^+$ cation with ellipsoids drawn at the 50% probability level. Selected bond distances (Å) and angles (°): Co(1)–O(2) 1.9024(11); Co(1)–O(1) 1.9179(11); Co(1)–N(4) 1.9212(13); Co(1)–N(3) 1.9213(13); Co(1)–N(1) 1.9394(12); Co(1)–N(2) 1.9486(12); O(2)–C(15) 1.3204(18); O(3)–C(15) 1.2391(19); O(1)–C(15) 1.3165(19); O(2)–Co(1)–O(1) 69.21(5); O(2)–Co(1)–N(4) 93.36(5); O(1)–Co(1)–N(4) 89.26(5); O(2)–Co(1)–N(3) 96.16(5); O(1)–Co(1)–N(3) 90.20(5); N(4)–Co(1)–N(3) 169.60(5); O(2)–Co(1)–N(1) 170.97(5); O(1)–Co(1)–N(1) 102.00(5); N(4)–Co(1)–N(1) 84.22(5); N(3)–Co(1)–N(1) 85.73(5); O(2)–Co(1)–N(2) 101.05(5); O(1)–Co(1)–N(2) 170.19(5); N(4)–Co(1)–N(2) 92.62(5); N(3)–Co(1)–N(2) 89.66(5); N(1)–Co(1)–N(2) 87.78(5).

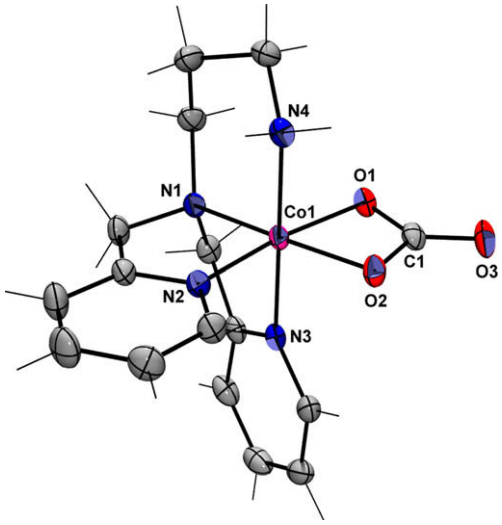


Fig. 7. Structure of the ae-[Co(dppa)(O_2CO)]$^+$ cation with ellipsoids drawn at the 50% probability level. Selected bond distances (Å) and angles (°): Co(1)–O(2) 1.9093(15); Co(1)–O(1) 1.9175(14); Co(1)–N(2) 1.9330(17); Co(1)–N(3) 1.9576(17); Co(1)–N(4) 1.9628(17); Co(1)–N(1) 2.0043(17); O(3)–C(1) 1.239(2); O(1)–C(1) 1.330(2); O(2)–C(1) 1.338(2); O(2)–Co(1)–O(1) 69.61(7); O(2)–Co(1)–N(2) 101.56(7); O(1)–Co(1)–N(2) 171.15(6); O(2)–Co(1)–N(3) 92.10(6); O(1)–Co(1)–N(3) 90.83(6); N(2)–Co(1)–N(3) 88.95(7); O(2)–Co(1)–N(4) 87.89(6); O(1)–Co(1)–N(4) 89.87(7); N(2)–Co(1)–N(4) 90.31(7); N(3)–Co(1)–N(4) 179.25(6); O(2)–Co(1)–N(1) 170.99(6); O(1)–Co(1)–N(1) 102.28(7); N(2)–Co(1)–N(1) 86.50(7); N(3)–Co(1)–N(1) 83.94(7); N(4)–Co(1)–N(1) 96.18(7);

lengths and angles are seen in the [Co(uns-penp)(O_2CO)]$^+$ and [Co(dppa)(O_2CO)]$^+$ cations. The average Co–N distance increases as the number of six-membered chelate rings increases and the N–Co–N bond angle involving the six-membered chelate ring in the dppa complex is larger than the other angles about Co in both complexes. In addition, Co–N bond lengths to pyridyl N atoms are shorter than those to aliphatic N atoms in both complexes. As discussed above, the complexes containing the baep, abap, uns-penp and dppa ligands can all potentially form two geometric isomers, and in all cases, the isomer obtained in the solid state is identical to that observed in solution via NMR (see Table 2).

3.3. Acid hydrolysis

The complexes described herein all undergo hydrolysis in aqueous acidic solution at various rates to give the corresponding diaqua species as the final product. Of particular interest are the hydrolysis rates for the [Co(uns-penp)(O_2CO)]$^+$ and [Co(dppa)(O_2CO)]$^+$ cations; in 1.0 M $HClO_4$(aq) at 25.0 °C, k_{obs} values for the hydrolysis reactions are 2.9×10^{-2} s^{-1} and 2.7×10^{-4} s^{-1}, respectively, a two order of magnitude difference for complexes containing very similar ancillary ligands. This surprising difference is probably attributable to the different isomeric preferences of the two cations. We [4,5,44] and others [45,46] have previously shown that the wide variety of acid hydrolysis reaction rates in complexes containing chelated carbonate is due to the ease with which the coordinated *endo* O atoms of the carbonate ligand can be protonated, and steric hindrance by the ancillary ligand is crucial in stabilising such complexes in aqueous acidic solution. As discussed above, the [Co(uns-penp)(O_2CO)]$^+$ cation exists in solution as the aa isomer, while the less reactive [Co(dppa)(O_2CO)]$^+$ cation exists as the ae isomer. As a result, the steric accessibility of the coordinated *endo* O atoms is quite different in the two cations, as shown in the space-filling diagrams (Fig. 8). One of the coordinated O atoms is hindered by the CH_2 protons from one arm of the tripodal ligand in [Co(uns-penp)(O_2CO)]$^+$ while access to the other coordinated O atom is relatively open. However, in [Co(dppa)(O_2CO)]$^+$, both coordinated O atoms undergo significant hindrance. As above, the CH_2 protons hinder approach to one O atom, while the 6-proton of the pyridyl ligand now lies in very close proximity to the other O atom; this latter interaction can only occur when the pyridyl group is situated in the same plane as the carbonate ligand.

3.4. ^{59}Co NMR

Despite its quadrupolar $I = 7/2$ spin, which leads to broad peaks, the 100% abundance of the NMR active ^{59}Co isotope usually allows facile detection of the ^{59}Co NMR signal, and ^{59}Co NMR data for a large number of complexes are available [47,48]. We have previously shown that the ^{59}Co chemical shift of [(L)Co(O_2CO)]$^+$ complexes is very dependent on the identity of the tripodal tetradentate ligand L, with a range of over 2000 ppm observed as L is varied from tpa to either tepa or Me_3tpa. [4,5] We have now recorded ^{59}Co NMR chemical shifts for the homologous series of complex cations [(L)Co(O_2CO)]$^+$ (L = tren, baep, abap, trpn) as well

Table 2
UV–Vis and ^{59}Co NMR data for [Co(L)(O_2CO)]$^+$ complexes. L = tripodal tetraamine ligand.

L	UV–Vis maxima (nm)	Δ (cm^{-1})	δ ^{59}Co (ppm)
tpa	487, 348	22172	7965
uns-penp	493, 352	21906	8132
dppa	494 [a]		8395
tren	504, 352	21542	8450
pmea	500, 357	21599	8509
Me-tpa	502, 355	21563	8606
baep	508, 352	21414	8728
pmap	515, 360	21077	9096
abap	524, 362	20775	9117
Me_2-tpa	516, 365	20976	9162
trpn	534, 367	20413	9574
tepa	526, 384	20425	10121
Me_3-tpa	544, 379	19970	10251

[a] The high energy *d*–*d* band appears as a shoulder on an intense charge-transfer band and cannot be resolved.

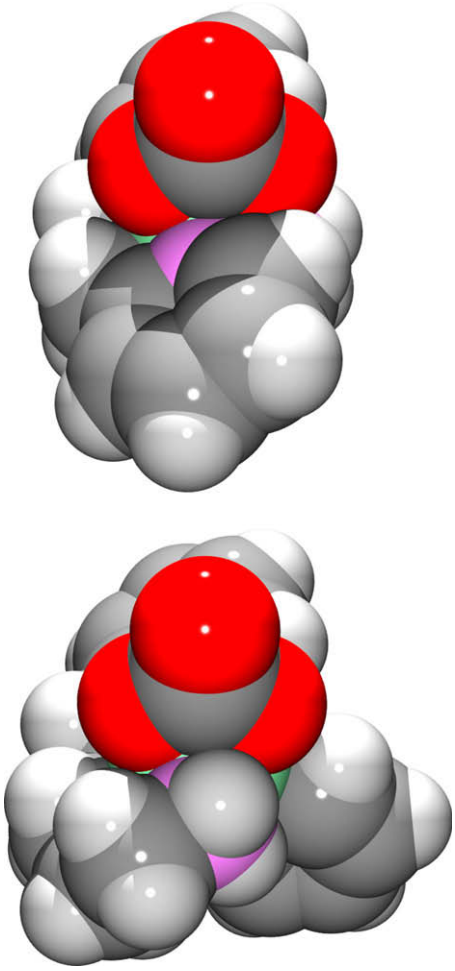


Fig. 8. Space filling diagrams of the aa-[Co(uns-penp)(O_2CO)]$^+$ (top) and ae-[Co(dppa)(O_2CO)]$^+$ (bottom) cations emphasising the hindrance of the *endo* O atoms of the chelated carbonate ligands by atoms of the ancillary tripodal ligand.

as the mixed donor complex cations [Co(dppa)(O_2CO)]$^+$ and [Co(uns-penp)(O_2CO)]$^+$, and again find a large range of chemical shifts. Values of 8450, 8728, 9117 and 9574 ppm, respectively, for the complex cations [(L)Co(O_2CO)]$^+$ (L = tren, baep, abap, trpn) show that the ligand field strength of the tripodal ligand decreases as the number of six-membered chelate rings increase, as was also found for complex cations containing the pyridyl analogues of these ligands. The increase in chemical shift is concomitant with an increase in the average Co–N bond distance across the series of complexes (1.949 Å, L = tren; 1.962 Å, L = baep; 1.965 Å, L = abap; 1.976 Å, L = trpn) and a corresponding decrease in Δ, the *d*-orbital splitting parameter (21 542 cm^{-1}, L = tren; 21 414 cm^{-1}, L = baep; 20 775 cm^{-1}, L = abap; 20 413 cm^{-1}, L = trpn). A similar dependence of the chemical shift on the size of the chelate rings has been previously observed in a series of complexes containing an N_4S_2 donor set [49], although the effect in the current case is somewhat more marked. The complex cations [(L)Co(O_2CO)]$^+$ (L = uns-penp, dppa) display smaller chemical shifts (δ = 8132 and 8395 ppm, respectively) than their aliphatic analogues (L = tren, δ = 8450 ppm; L = baep, δ = 8728 ppm), suggesting that the presence of two pyridyl donors leads to an increased ligand field compared to that exerted by solely aliphatic N atoms. This is borne out in the Δ value for the uns-penp complex of 21 906 cm^{-1} (Δ for the dppa complex could not be determined, owing to partial obscuring of the high energy *d*–*d* band by an intense charge transfer band). The predicted linear relationship (R^2 = 0.962) between the wavelength of the lowest energy *d*–*d* transition (λ_{max}) and γ, the magnetogyric ratio of the ^{59}Co nucleus,[50,51] is observed for the [(L)Co(O_2CO)]$^+$ complex cations (L = tren, baep, abap, trpn, uns-penp, dppa) (Fig. 9, top) and extrapolation gives γ_o = (10.03 ± 0.02) MHz T^{-1} for the bare ^{59}Co nucleus, a value comparable to that obtained previously from an extensive study of Co(III) complexes with O_6, N_6, S_6, Se_6, C_6 P_6 and As_6 donor sets [52].

We have also found an excellent correlation between Δ and δ(^{59}Co) for [(L)Co(O_2CO)]$^+$ complexes, as outlined in Fig. 9 (bottom, R^2 = 0.95). While the majority of these complexes contain a tripodal tetradentate N_4 ancillary ligand, those having L = $(en)_2$ (Δ = 21 199 cm^{-1}, δ = 9181 ppm) and L = $(NH_3)_4$ (Δ = 20 746 cm^{-1}, δ = 9620 ppm) [53] also show an acceptable fit. Thus it appears that this correlation exists regardless of the aliphatic or aromatic nature of the N donor atoms, and whether the N donor atoms are part of a chelating ligand. However, the correlation is not solely dependent on the identity of the donor atoms bound to the Co(III) ion; for example, inclusion of data for the [Co$(en)_2(OH_2)_2$]$^{3+}$ ion, which, like the above complexes, contains an N_4O_2 donor set, worsens the fit noticeably. It appears that the geometric constraint provided by the chelated carbonate ligand is necessary for this correlation, and a different ligand field obtains when such a constraint is not present. An analogous correlation, albeit using fewer data points, can be seen in the structurally similar [Co(RN_4S_2amp)]$^{3+}$ series of

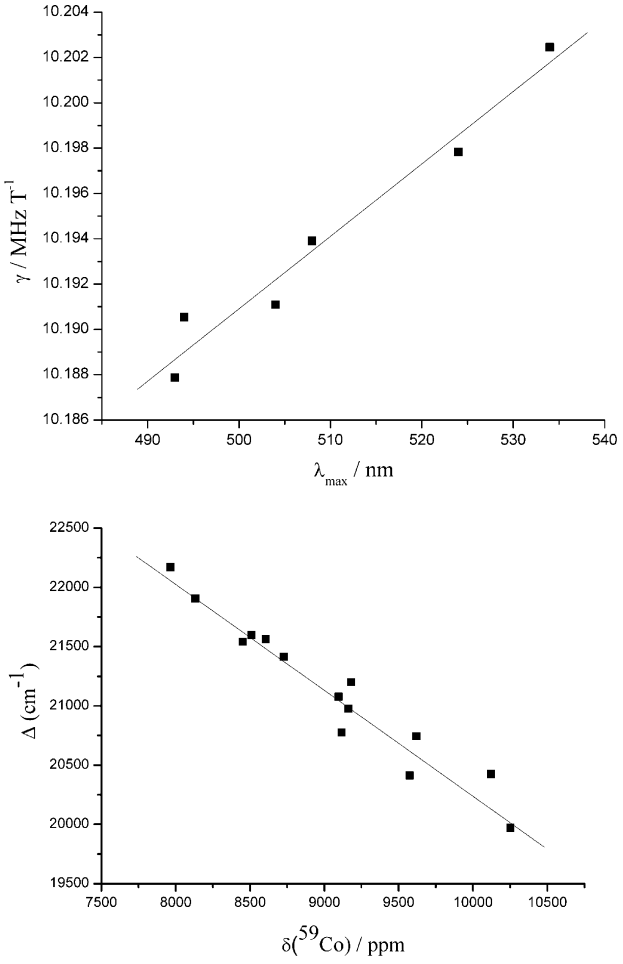


Fig. 9. Top: Plot of γ vs λ_{max} for [(L)Co(O_2CO)]$^+$ complex cations (L = tren, baep, abap, trpn, uns-penp, dppa). Bottom: Plot showing the correlation between Δ and δ(^{59}Co) for [(L)Co(O_2CO)]$^+$ complex cations (L = a tripodal tetraammine ligand, $(en)_2$, $(NH_3)_4$).

complexes (R = Et, Pr, Bu, Xy) [49]; however, again this does not extend to all complexes having an N_4S_2 donor set.

3.5. DFT calculations

As discussed above, geometric isomers are possible for the $[(L)Co(O_2CO)]^+$ (L = baep, abap, dppa, uns-penp) complex cations, and we were interested to see if the lower energy isomer predicted by DFT calculations corresponded to the isomer isolated experimentally. We also included the $[(L)Co(O_2CO)]^+$ (L = pmap, pmea) complex cations, for which geometric isomers are possible, from our previous work, both of which are isolated (ClO_4^- salts) as the 6-isomer [4]. Results of these calculations are given in Table 3. The energy differences between each pair of geometric isomers range span an order of magnitude, from 2.49 to 25.5 kJ mol^{-1}. As can be seen, the calculated lower energy isomer is the one isolated experimentally in all cases except for the $[Co(uns\text{-}penp)(O_2CO)]^+$ cation, where the ae-isomer is predicted, but the aa-isomer is isolated. It should be noted that the calculated energy difference between these, as well as the isomers of the abap and pmea complexes, is small, and some uncertainty as to the lowest energy isomer is to be expected. However, the same relative energy ordering of the isomers is found for the range of functionals and basis sets outlined in Section 2. NMR analysis of the crude reaction products, prior to crystallisation, show that the formation reactions of these complexes are remarkably stereoselective, and only the $[Co(pmea)(O_2CO)]^+$ complex shows any evidence of the presence of both isomers. The reasons for such stereoselectivity are unclear; given the small calculated energy differences between the isomers, particularly in the cases of the abap, pmea and uns-penp complexes, it might be expected that isomerisation between these would be relatively facile, especially at the elevated temperatures used in their syntheses. However, such a process would probably have a significant activation barrier; assuming a dissociative mechanism typical of ligand substitution reactions at Co(III) centres [54], isomerisation would require Co–O bond cleavage, followed by significant reorganisation within the resulting 5-coordinate intermediate, and subsequent rechelation of the carbonate ligand. The fact that there is no 'spontaneous' hydrolysis pathway for Co(III) carbonate complexes [46] implies that unassisted Co–O bond cleavage in such complexes would be expected to be extremely slow, thereby rendering isomerisation difficult. On the other hand, small amounts of Co(II) present in the reaction mixtures could serve to labilise the complexes, thus allowing formation of the thermodynamically preferred isomer.

Table 3
Energy differences between $[(L)Co(O_2CO)]^+$ isomers (ΔE), as calculated by DFT (B3LYP/6-31G*).

Experimentally isolated isomer	Calculated lowest energy isomer	ΔE (kJ mol^{-1})
6-$[Co(abap)(O_2CO)]^+$	6-$[Co(abap)(O_2CO)]^+$	2.50
5-$[Co(baep)(O_2CO)]^+$	5-$[Co(baep)(O_2CO)]^+$	15.5
6-$[Co(pmap)(O_2CO)]^+$	6-$[Co(pmap)(O_2CO)]^+$	25.5
6-$[Co(pmea)(O_2CO)]^+$	6-$[Co(pmea)(O_2CO)]^+$	3.05
ae-$[Co(dppa)(O_2CO)]^+$	ae-$[Co(dppa)(O_2CO)]^+$	6.59
aa-$[Co(uns\text{-}penp)(O_2CO)]^+$	ae-$[Co(uns\text{-}penp)(O_2CO)]^+$	2.49

Table 5
Calculated and observed λ_{max} values for $[(L)Co(O_2CO)]^+$ complexes.

Complex	Observed λ_{max} (nm)	Calculated λ_{max} (nm)
6-$[Co(abap)(O_2CO)]^+$	524, 362	493, 362
6-$[Co(pmap)(O_2CO)]^+$	515, 360	526, 373
5-$[Co(baep)(O_2CO)]^+$	508, 352	493, 352
6-$[Co(pmea)(O_2CO)]^+$	500, 357	497, 362
ae-$[Co(dppa)(O_2CO)]^+$	494[a]	487, 352
aa-$[Co(uns\text{-}penp)(O_2CO)]^+$	493, 352	496, 358

[a] The higher energy band appears as a shoulder on an intense charge-transfer band and cannot be resolved.

Table 4 shows observed and calculated ^{59}Co NMR chemical shifts for the experimentally isolated isomer of the $[(L)Co(O_2CO)]^+$ complexes (L = abap, pmap, baep, pmea, dppa, uns-penp) in aqueous solution. Although the calculated chemical shifts are less than the observed chemical shifts in each case, with differences in the order of 900–1400 ppm, the calculated data successfully reproduce the observed trends in the experimental values. Differences of this magnitude have been observed in previous similar studies [6,55]. Inclusion of solvent appears vital in obtaining acceptable agreement between observed and calculated chemical shifts, as the same calculations carried out in the gas phase lead to chemical shift differences in the range 2100–2600 ppm. The importance of including solvent effects parallels recent observations made by Hocking et al. with respect to geometry optimisations of Co and Pt complexes [56].

Similarly, it is necessary to include solvent in order to obtain good agreement between observed and calculated (TD-DFT) UV–Vis spectra of the complexes. Table 5 gives the observed and calculated λ_{max} values for the $^1A_{1g} \rightarrow {}^1T_{1g}$ and $^1A_{1g} \rightarrow {}^1T_{2g}$ d–d electronic transitions [57] of the complexes while Fig. 10 shows the measured and calculated UV–Vis spectra for two representative examples. When calculations were carried out in the absence of solvent, the resulting spectra generally displayed markedly poorer agreement with the observed spectra, with three, rather than two, bands often predicted. In a previous paper [6], we calculated the HOMO/LUMO gap (ΔE_{H-L}) as a measure of Δ, the d-orbital splitting parameter, for a number of $[(L)Co(O_2CO)]^+$ complexes using the PBE functional, and obtained good agreement with observed values. We carried out such calculations using the B3LYP functional for the complexes reported herein, but consistently obtained Δ values that were too large by a factor of ~2 compared to the experimental values. We therefore carried out TD-DFT excitation energy and HOMO/LUMO calculations on the 'model' complex $[Co(NH_3)_4(O_2CO)]^+$ using a variety of functionals and basis sets, and results of these are given in Table 6. From this it can be seen that, while the TD-DFT vertical excitation energies are essentially independent of the functional and basis set, and are consistent with previous calculations [6], the same is not true of the calculated values of the HOMO/LUMO gap. The ΔE_{H-L} values calculated using the hybrid functionals (B3LYP, M05) are approximately a factor of two larger than the values obtained from pure functionals (PBE, BP86).

Table 4
Calculated and observed ^{59}Co NMR chemical shifts for $[(L)Co(O_2CO)]^+$ complexes.

Cation	Observed chemical shift (ppm)	Calculated chemical shift (ppm)	Chemical shift difference (ppm)
6-$[Co(abap)(O_2CO)]^+$	9117	7784	1333
6-$[Co(pmap)(O_2CO)]^+$	9096	8189	907
5-$[Co(baep)(O_2CO)]^+$	8728	7309	1419
6-$[Co(pmea)(O_2CO)]^+$	8509	7341	1168
ae-$[Co(dppa)(O_2CO)]^+$	8395	7012	1383
aa-$[Co(uns\text{-}penp)(O_2CO)]^+$	8132	6839	1293

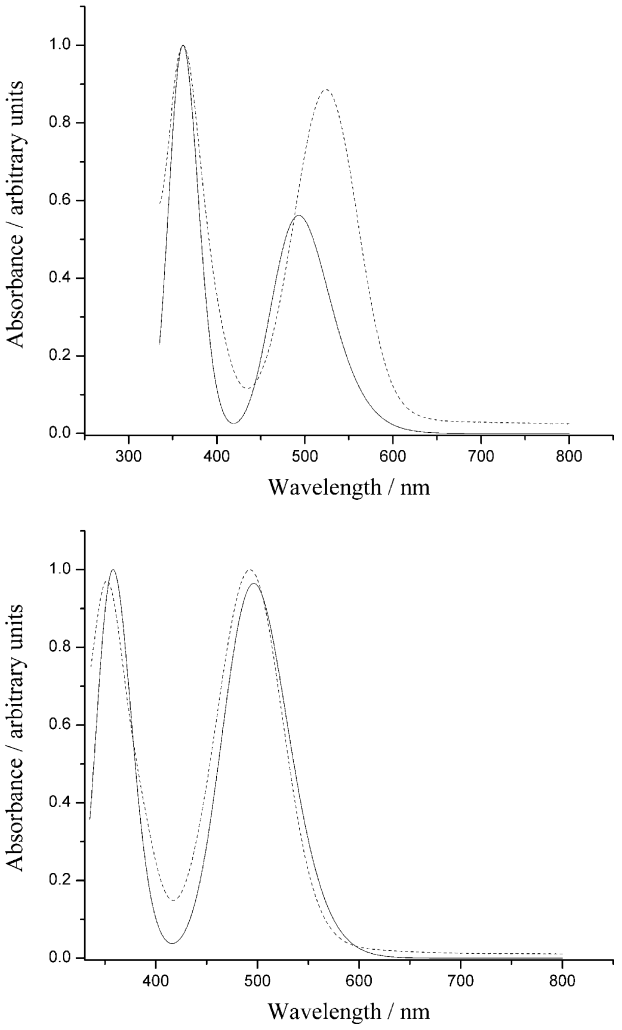


Fig. 10. Measured (dotted line) and calculated (solid line) UV–Vis spectra of 6-$[Co(abap)(O_2CO)]^+$ (top) and aa-$[Co(uns\text{-}penp)(O_2CO)]^+$ (bottom).

Table 6
The TD-DFT first vertical excitation energy (ΔE_{TDDFT}) and HOMO–LUMO energy gap (ΔE_{H-L}) of $[Co(NH_3)_4(O_2CO)]^+$ determined using different functionals and basis sets. Energies are in cm^{-1}.

Functional	Basis set	ΔE_{TDDFT}	ΔE_{H-L}
B3LYP	6-31G*	19438	45812
B3LYP	6-311G*	19357	44683
M05	6-311G*	19438	47506
PBE	6-31G*	20970	20164
PBE	TZVP	20325	19680
BP86	6-31G*	20890	20325

4. Conclusions

The results outlined above show that DFT can be used as a predicative tool to determine the geometric isomeric preference of Co(III) complexes, as well as their UV–Vis and ^{59}Co spectroscopic properties. The observed correlation between Δ and $\delta(^{59}Co)$ also allows determination of an approximate value of one of these when the other is known; such cases may occur when the higher energy UV–Vis transition of the complex is obscured by charge transfer transitions, or when the complex is of sufficiently low solubility to preclude collection of a ^{59}Co NMR spectrum. The kinetic data for the hydrolysis of the carbonate complexes further serve to emphasise the importance of steric effects in stabilising the chelated carbonate ligand under acidic conditions, and our investigations into the stabilisation of other oxyanion chelates are ongoing.

5. Supplementary data

CCDC 717930, 717931, 717932, 717933 and 717934 contain the supplementary crystallographic data for $[(L)Co(O_2CO)]ClO_4 \cdot xH_2O$ (L = abap, $x = 0$; L = trpn, $x = 1$; L = uns-penp, $x = 1$; L = dppa, $x = 0$; L = baep, $x = 0.5$). These data can be obtained free of charge via http://www.ccdc.cam.ac.uk/conts/retrieving.html, or from the Cambridge Crystallographic Data Centre, 12 Union Road, Cambridge CB2 1EZ, UK; fax: (+44) 1223-336-033; or e-mail: deposit@ccdc.cam.ac.uk.

Acknowledgements

We thank staff at the X-ray crystallographic facilities at the University of Auckland and the University of Canterbury for the collection of some X-ray data. We also thank the Department of Chemistry, University of Otago, for support of this research. L.F.M. thanks the Foundation of Research, Science and Technology for the award of a Bright Futures Ph.D scholarship.

References

[1] A.G. Blackman, Polyhedron 24 (2005) 1.
[2] A.G. Blackman, Eur. J. Inorg. Chem (2008) 2633.
[3] L.M. Berreau, Comments Inorg. Chem. 28 (2007) 123.
[4] P.M. Jaffray, L.F. McClintock, K.E. Baxter, A.G. Blackman, Inorg. Chem. 44 (2005) 4215.
[5] S.E. Cheyne, L.F. McClintock, A.G. Blackman, Inorg. Chem. 45 (2006) 2610.
[6] G. Cavigliasso, R. Stranger, L.F. McClintock, S.E. Cheyne, P.M. Jaffray, K.E. Baxter, A.G. Blackman, Dalton Trans. (2008) 2433.
[7] R.J. Geue, A.M. Sargeson, R. Wijesekera, Aust. J. Chem. 46 (1993) 1021.
[8] R.L. Fanshawe, A.G. Blackman, Inorg. Chem. 34 (1995) 421.
[9] M. Schatz, M. Leibold, S.P. Foxon, M. Weitzer, F.W. Heinemann, F. Hampel, O. Walter, S. Schindler, Dalton Trans. (2003) 1480.
[10] E. Kimura, S. Young, J.P. Collman, Inorg. Chem. 9 (1970) 1183.
[11] R. Bramley, M. Brorson, A.M. Sargeson, C.E. Schaeffer, J. Am. Chem. Soc. 107 (1985) 2780.
[12] SAINT, Bruker AXS Inc., Madison, WI, USA 2001.
[13] A. Altomare, M.C. Burla, M. Camalli, G.L. Cascarano, C. Giacovazzo, A. Guagliardi, A.G.G. Moliterni, G. Polidori, R. Spagna, J. Appl. Crystallogr. 32 (1999) 115.
[14] L.J. Farrugia, J. Appl. Crystallogr. 32 (1999) 837.
[15] G.M. Sheldrick, T.R. Schneider, Meth. Enzymol. 277 (1997) 319.
[16] A.D. Becke, J. Chem. Phys. 98 (1993) 5648.
[17] A.D. Becke, Phys, Rev. A: At., Mol., Opt. Phys. 38 (1988) 3098.
[18] C. Lee, W. Yang, R.G. Parr, Phys. Rev. B: Condens. Matter Mater. Phys. 37 (1988) 785.
[19] M.J. Frisch, G.W. Trucks, H.B. Schlegel, G.E. Scuseria, M.A. Robb, J.R. Cheeseman, J.J.A. Montgomery, T. Vreven, K.N. Kudin, J.C. Burant, J.M. Millam, S.S. Iyengar, J. Tomasi, V. Barone, B. Mennucci, M. Cossi, G. Scalmani, N. Rega, G.A. Petersson, H. Nakatsuji, M. Hada, M. Ehara, K. Toyota, R. Fukuda, J. Hasegawa, M. Ishida, T. Nakajima, Y. Honda, O. Kitao, H. Nakai, M. Klene, X. Li, J.E. Knox, H.P. Hratchian, J.B. Cross, V. Bakken, C. Adamo, J. Jaramillo, R. Gomperts, R.E. Stratmann, O. Yazyev, A.J. Austin, R. Cammi, C. Pomelli, J.W. Ochterski, P.Y. Ayala, K. Morokuma, G.A. Voth, P. Salvador, J.J. Dannenberg, V.G. Zakrzewski, S. Dapprich, A.D. Daniels, M.C. Strain, O. Farkas, D.K. Malick, A.D. Rabuck, K. Raghavachari, J.B. Foresman, J.V. Ortiz, Q. Cui, A.G. Baboul, S. Clifford, J. Cioslowski, B.B. Stefanov, G. Liu, A. Liashenko, P. Piskorz, I. Komaromi, R.L. Martin, D.J. Fox, T. Keith, M.A. Al-Laham, C.Y. Peng, A. Nanayakkara, M. Challacombe, P.M.W. Gill, B. Johnson, W. Chen, M.W. Wong, C. Gonzalez, J.A. Pople, GAUSSIAN 03, Gaussian Inc., Wallingford, CT, 2004.
[20] S. Miertus, E. Scrocco, J. Tomasi, Chem. Phys. 55 (1981) 117.
[21] O. Tapia, J. Math. Chem. 10 (1992) 139.
[22] J. Tomasi, M. Persico, Chem. Rev. 94 (1994) 2027.
[23] B.Y. Simkin, I.I. Sheikhet, Quantum Chemical and Statistical Theory of Solutions: A Computational Approach, Ellis Horwood Series in Physical Chemistry, Prentice Hall PTR, 1995.
[24] V. Barone, M. Cossi, J. Tomasi, J. Chem. Phys. 107 (1997) 3210.
[25] N.N. Matsuzawa, A. Ishitani, D.A. Dixon, T. Uda, J. Phys. Chem. A 105 (2001) 4953.
[26] F.A. Mautner, C.N. Landry, A.A. Gallo, S.S. Massoud, J. Mol. Struct. 837 (2007) 72.
[27] L.C.F. Pimentel, A.L.F. de Souza, T.L. Fernandez, J.L. Wardell, O.A.C. Antunes, Tetrahedron Lett. 48 (2007) 831.

[28] S. Yamanaka, H. Okawa, K.-i. Motoda, M. Yonemura, D.E. Fenton, M. Ebadi, A.B.P. Lever, Inorg. Chem. 38 (1999) 1825.
[29] S. James, K.P. Maresca, D.G. Allis, J.F. Valliant, W. Eckelman, J.W. Babich, J. Zubieta, Bioconjug. Chem. 17 (2006) 579.
[30] G.S. Matouzenko, A. Bousseksou, S. Lecocq, P.J. van Koningsbruggen, M. Perrin, O. Kahn, A. Collet, Inorg. Chem. 36 (1997) 5869.
[31] It should be noted that our observation of 6 CH_2 peaks differs from the 4 reported by Chin and coworkers in a previous synthesis of this ion. See: J.A. Connolly, M. Banaszczyk, R.C. Hynes, J. Chin, Inorg. Chem. 33 (1994) 665.
[32] R.L. Fanshawe, A.G. Blackman, C.R. Clark, Inorg. Chim. Acta 342 (2003) 114.
[33] C. Ochs, F.E. Hahn, T. Lugger, Eur. J. Inorg. Chem (2001) 1279.
[34] Note that the "two" peaks at 39.77 and 39.65 ppm are due to a single C atom adjacent to an NH_2 group. NHD and ND_2 isotopologues are possible owing to exchange with D_2O and C atoms adjacent to the N atoms exhibit slightly different chemical shifts for each isotopologue.
[35] H. Chen, X.-Y. Xu, J. Gao, X.-J. Yang, L.-D. Lu, X. Wang, Jiegou Huaxue 25 (2006) 247.
[36] S.S. Massoud, F.A. Mautner, R. Vicente, A.A. Gallo, E. Ducasse, Eur. J. Inorg. Chem. (2007) 1091.
[37] I. Bernal, X. Xia, F. Somoza, Fundamental principles of molecular modeling, in: Proceedings of an International Workshop on Fundamental Principles of Molecular Modeling, Skukuza, S. Afr., August 20–25, 1995, p. 223.
[38] R.L. Fanshawe, C.R. Clark, A.G. Blackman, Acta Crystallogr., Sect. E 57 (2001) m17.
[39] O. Horner, M.-F. Charlot, A. Boussac, E. Anxolabehere-Mallart, L. Tchertanov, J. Guilhelm, J.-J. Girerd, Eur. J. Inorg. Chem (1998) 721.
[40] C.A. Otter, R.M. Hartshorn, Dalton Trans. (2004) 150.
[41] E.O. Schlemper, P.K. Sen Gupta, T.P. Dasgupta, Acta Crystallogr., Sect. C 39 (1983) 1012.
[42] Y. Dupre, E. Bartscherer, O. Maas, J. Sander, K. Hegetschweiler, Z. Kristallogr. – New Cryst. Struct. 214 (1999) 405.
[43] R. Wen, I. Bernal, J. Coord. Chem. 52 (2000) 15.
[44] A.J. Clarkson, A.G. Blackman, Polyhedron 25 (2006) 373.
[45] D.A. Buckingham, C.R. Clark, Inorg. Chem. 32 (1993) 5405.
[46] D.A. Buckingham, C.R. Clark, Inorg. Chem. 33 (1994) 6171.
[47] J.C.C. Chan, S.C.F. Au-Yeung, Annu. Rep. NMR Spectrosc. 41 (2000) 1.
[48] A. Yamasaki, J. Coord. Chem. 24 (1991) 211.
[49] C.A. Sharrad, G.E. Cavigliasso, R. Stranger, L.R. Gahan, Dalton Trans. (2004) 767.
[50] J.S. Griffith, L.E. Orgel, Trans. Faraday Soc. 53 (1957) 601.
[51] R. Freeman, G.R. Murray, R.E. Richards, Proc. Roy. Soc. (Lond.) A242 (1957) 455.
[52] N. Juranic, Inorg. Chem. 22 (1983) 521.
[53] A. Yamasaki, F. Yajima, S. Fujiwara, Inorg. Chim. Acta 2 (1968) 39.
[54] D.T. Richens, Chem. Rev. 105 (2005) 1961.
[55] M. Buehl, S. Grigoleit, H. Kabrede, F.T. Mauschick, Chem. Eur. J. 12 (2006) 477.
[56] R.K. Hocking, R.J. Deeth, T.W. Hambley, Inorg. Chem. 46 (2007) 8238.
[57] Note that, although conventionally used for Co(III) complexes in general, these symmetry labels apply only to complexes having strictly octahedral geometry.

directional associative protocol of the naphthalimide group with the well-studied chemistry of the $[Ru(bipy)_3]^{2+}$ core [6], in order to determine the effect of the 1,8-naphthalimide moiety on the properties of the ruthenium complex.

2. Experimental

2.1. General considerations

Unless otherwise specified, all operations were carried out under a nitrogen atmosphere by using either standard Schlenk techniques or a Vacuum Atmospheres HE-493 inert atmosphere dry box. Solvents for synthetic procedures and spectroscopic studies were dried by conventional methods and distilled under a N_2 atmosphere immediately prior to use. All chemicals were purchased from Aldrich Chemicals. Mass spectrometric measurements recorded in ESI(±) mode were obtained on a Micromass Q-Tof spectrometer. NMR spectra were recorded by using a Varian Mercury/VX 300 or Unity Inova 500 (PGSE-NMR spectra). Chemical shifts were referenced to solvent resonances at δ_H 7.26 for $CDCl_3$ and δ_H 6.00 for $C_2D_2Cl_4$. 5-Methyl-2,2'-bipyridine was synthesized by modification of a literature preparation [7a] and 5-(bromomethyl)-2,2′-bipyridine was synthesized according to the literature [7b]. Fluorescence measurements were performed using an SLM-Aminco 8100 spectrofluorometer using degassed dichloromethane as solvent. The excitation wavelengths used are 333 and 450 nm with a slit width setting of 8. All spectral and NMR measurements for {ruthenium[bis(bipyridyl)][N-(5-methyl-2,2'-bipyridyl)-1,8-naphthalimide]}$(PF_6)_2$ (**1**) were performed using the powder form of the product. Voltammetric experiments were performed in a three-compartment cell with potentiometric control by an RDE4 bipotentiostat (Pine Instrument). Electrode potentials used in voltammetric experiments were measured and reported versus the saturated calomel electrode (SCE). The working and auxillary electrodes for all voltammetric experiments were platinum. Voltammetric data were collected using a personal computer equipped with a BNC-2110 data acquisition interface (National Instruments) and Labview data acquisition software (National Instruments). The electrolyte used in the voltammetric experiment was 0.1 M tetra-*n*-butyl ammonium hexafluorophosphate in acetonitrile.

2.2. N-(5-methyl-2,2'-bipyridyl)-1,8-naphthalimide (*L*)

A solution of 5-(bromomethyl)-2,2'-bipyridine (1.00 g, 4.01 mmol) and 1,8-naphthalimide (0.791 g, 4.01 mmol) in acetone (40 mL) was heated at reflux over potassium carbonate (3.00 g, 22.1 mmol) under ambient atmosphere for 18 h. The resulting transparent, golden brown mixture was filtered and the solvent removed via rotary evaporation resulting in 0.582 g (40% yield) of off-white solid. This compound was used without further purification. ^{1}H NMR (300 MHz, $CDCl_3$, 25 °C): δ 8.92 (s, 1H, *py*), 8.66 (br d, 2H, *py*), 8.62 (d, J = 8.4 Hz, 2H, *napht*), 8.39 (br t, 2H, *py*), 8.25 (d, J = 8.4 Hz, 2H, *napht*), 8.03 (br d, 1H, *py*), 7.78 (t, J = 7.6 Hz, 2H, *napht*), 7.30 (br t, 1H, *py*), 5.46 (s, 2H, $-CH_2-$). ES^+/MS for $\{C_{23}H_{15}N_3O_2 + H\}^+$: Calc. = 366.1242; Obs. = 366.1243.

2.3. {Ruthenium[bis(bipyridine)][N-(5-methyl-2,2′-bipyridine)-1,8-naphthalimide]}$(PF_6)_2$ (*1*)

An ethanol solution (30 mL) of N-(5-methyl-2,2′-bipyridine)-1,8-naphthalimide (0.236 g, 0.65 mmol) and *bis*(2,2′-bipyridine)ruthenium(II) dichloride · $2H_2O$ (0.336 g, 0.65 mmol) was heated at reflux for 12 h. The solution was condensed to a smaller volume (~5 mL) via rotary evaporation and saturated, aqueous ammonium hexafluorophosphate was added, resulting in a copious quantity of bright red powder. The powder was filtered and air dried giving a yield of 0.563 g (82%) of solid. ^{1}H NMR (500 MHz, $C_2D_2Cl_4$, 25 °C): δ 8.58–7.39 (m, 29H, all aromatics), 5.26, 5.13 (d, d; J = 14.5; 1H, 1H; CH_2). ES^+/MS for $[(C_{43}H_{31}N_7O_2Ru)(PF_6)]^+$: Calc. = 924.1237; Obs. = 924.1272.

2.4. X-ray crystallographic determination

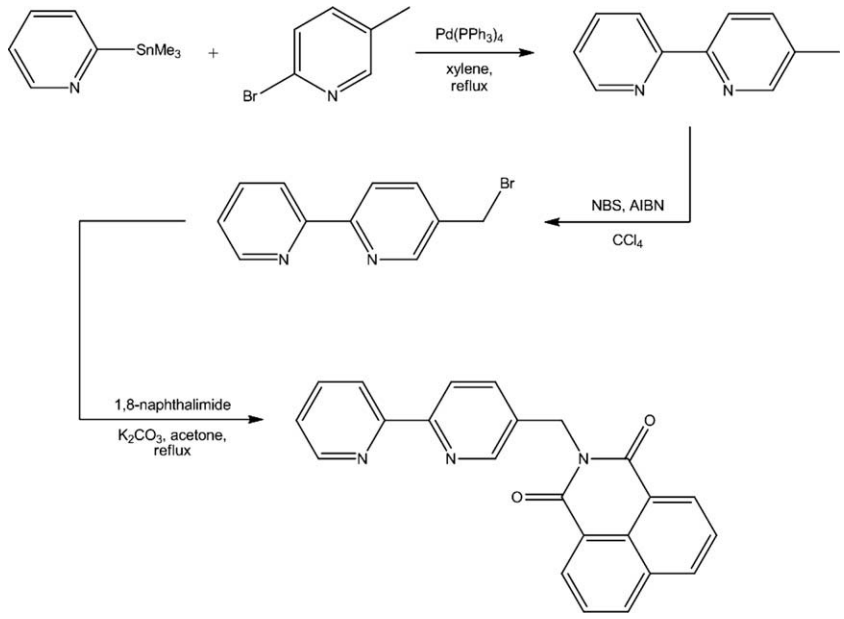
X-ray quality crystals of **1** · C_3H_6O were grown from acetonitrile via diethyl ether vapor-phase diffusion. X-ray diffraction intensity data from a flat red needle crystal were measured at 150(1) K on a Bruker SMART APEX diffractometer (Mo Kα radiation, λ = 0.71073 Å) [8]. Raw area detector data frame integration was performed with SAINT+ [8]. Final unit cell parameters were determined by least-squares refinement of 5112 strong reflections from the data set. Analysis of the data showed negligible crystal decay during collection. Direct methods structure solution, difference Fourier calculations and full-matrix least-squares refinement against F^2 were performed with SHELXTL [9].

The compound crystallizes in the triclinic system. The space group $P\bar{1}$ was assumed and confirmed by the successful solution and refinement of the data. The asymmetric unit consists of one Ru(II) complex, two independent PF_6^- ions, an acetone molecule of crystallization and another region of unidentified electron density. Disorder is prevalent in the crystal, not all of which could be modeled successfully. The displacement ellipsoids of the naphthalimide group atoms C47–C53 are severely elongated, indicating some disorder most noticeably affecting the extremity of this group. A satisfactory, stable disorder model could not be achieved however, and the elongated ellipsoids were allowed to account for the disorder. One PF_6^- anion (P2) is disordered and was modeled as occupying two orientations (P2A/P2B) in the ratio 60/40. A total of 63 distance restraints were used to assist in modeling the disorder. Unusual displacement ellipsoids and the presence of several residual electron density peaks in the vicinity of this anion indicate the disorder is not fully described by a two-component model. There is a region of unidentifiable residual electron density centered at (0,0,0), which was assumed to be disordered solvent molecules. No reasonable disorder model could be achieved for these species, and they were accounted for with the Squeeze routine in PLATON [10]. Squeeze calculated a solvent-accessible void volume of 290.0 Å^3, corresponding to 67 electrons per unit cell. The contribution of these diffusely scattering species was removed from subsequent structure factor calculations. The reported F(000), D_{calc} and FW reflect known unit cell contents only. All non-hydrogen atoms were refined with anisotropic displacement parameters except for the fluorine atoms of P2B (common isotropic displacement parameter). Hydrogen atoms were placed in geometrically idealized positions and included as riding atoms.

3. Results and discussion

3.1. Synthesis

The new ligand, *N*-(5-methyl-2,2′-bipyridyl)-1,8-naphthalimide, was synthesized by the reaction of commercially available 1,8-naphthalimide, 5-(bromomethyl)-2,2′-bipyridine and potassium carbonate in refluxing acetone (Scheme 1). Reaction of this ligand and bis(bipyridyl)ruthenium(II) dichloride in refluxing ethanol and subsequent exposure to saturated, aqueous ammonium hexafluorophosphate resulted in high yield of {ruthenium-[bis(bipyridyl)][N-(5-methyl-2,2′-bipyridyl)-1,8-naphthalimide]}-$(PF_6)_2$ (**1**) as a bright red powder.



Scheme 1. Synthesis of *N*-(5-methyl-2,2'-bipyridyl)-1,8-naphthalimide (**L**).

3.2. Solid-state and supramolecular structure

The ORTEP diagram, shown in Fig. 1, shows the cation of **1** · C_3H_6O. The naphthalimide-functionalized ligand chelates the ruthenium(II) in the standard fashion for a 2,2'-bipyridine ligand (for crystallographic information, see Table 1). The Ru–N bond lengths (see Table 2) match with other literature values and have an average value of 2.054 Å [11]. The ruthenium(II) cation is further organized by the 1,8-naphthalimide synthon [4a]. The naphthalimide moieties are stacked in a 180° antiparallel fashion accompanied by a naphthalimide centroid–centroid slip angle of 21° (Fig. 2a). The π–π stacking distance between the adjacent naphthalimide groups is 3.325 Å, a distance indicating a strong π–π stacking interaction (Fig. 2b) [3]. The crystal structure does not contain any additional explicit non-covalent interactions but is further organized by standard electrostatic and van der Waals interactions.

3.3. PGSE-NMR experiments

With the solid-state structure analysis showing the strong π–π stacking of the 1,8-naphthalimide moiety, we performed the

Table 1
Crystallographic data for {ruthenium[bis(bipyridyl)][N-(5-methyl-2,2'-bipyridyl)-1,8-naphthalimide]}$(PF_6)_2$ · (C_3H_6O) (**1** · C_3H_6O).

Formula	$C_{46}H_{37}F_{12}N_7O_3P_2Ru$
Formula weight (g/mol)	1126.84
Space group	$P\bar{1}$
Crystal system	triclinic
a (Å)	12.2041(6)
b (Å)	13.4566(7)
c (Å)	16.7531(8)
α (°)	89.6750(10)
β (°)	81.9440(10)
γ (°)	64.5570(10)
V (Å^3)	2455.4(2)
Z	2
Crystal color, habit	red, flat needle
D_{calc} (g cm^{-3})	1.524
T (K)	150(1)
Diffractometer	Bruker SMART APEX CCD
Radiation	Mo Kα (λ = 0.71073 Å)
$R(F)^a$	0.0721
$R(wF^2)^a$	0.1324

[a] Quantity minimized: $R(F) = \sum[F_o - F_c]/\sum[F_o]$; $R(wF^2) = \sum[w(F_o^2 - F_c^2)^2]/\sum[(wF_o^2)^2]^{1/2}$.

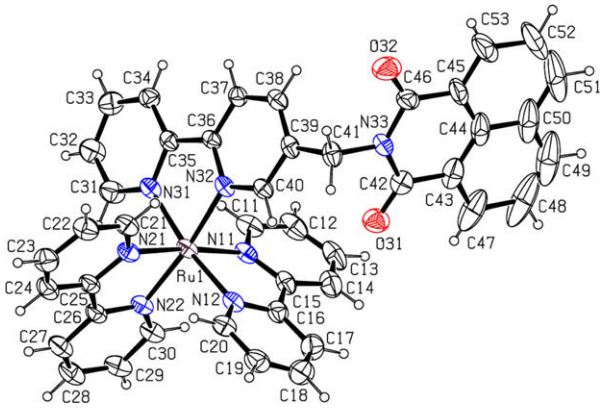


Fig. 1. ORTEP diagram of the cation in **1** · C_3H_6O.

Table 2
Selected bond lengths (Å) and bond angles (°) for **1** · C_3H_6O.

Atoms	Bond distances (Å)
Ru(1)–N(11)	2.056(5)
Ru(1)–N(12)	2.049(5)
Ru(1)–N(21)	2.062(5)
Ru(1)–N(22)	2.046(5)
Ru(1)–N(31)	2.069(5)
Ru(1)–N(32)	2.044(5)
Avg. bond dist. = 2.054	
Atoms	**Bond angles (°)**
N(11)–Ru(1)–N(12)	79.0(2)
N(21)–Ru(1)–N(22)	78.5(2)
N(31)–Ru(1)–N(32)	78.6(2)
Avg. bond angle = 78.7	

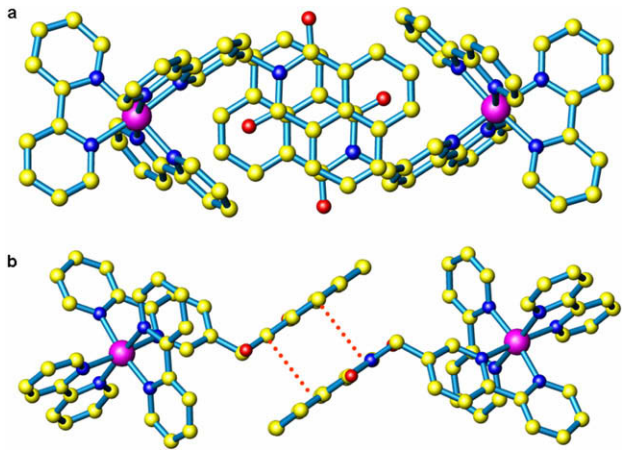


Fig. 2. (a) Top-view of two **1** · C_3H_6O cations demonstrating the 180° antiparallel character and 21° slip angle of the 1,8-naphthalimide synthon. (b) Side-view showing the π-stacking interaction.

pulsed-field gradient spin-echo NMR experiment (PGSE-NMR) to determine if this interaction persists in solution. Described in detail elsewhere [12], the PGSE-NMR technique provides an indirect measure of molecular size by allowing the determination of the diffusion coefficient of a given species in solution. Subsequent application of the Stokes–Einstein relation then yields the hydrodynamic radius, which typically falls within ca. 20% of the crystallographic radius. This technique has been successfully used in many different applications, including establishing the presence or absence of dimeric species in solution [13]. For the ruthenium(II) complex, the PGSE-NMR method radius (12.98 Å) is in accordance with that found from the X-ray data (13.44 Å) for the dimeric units, with a difference of only 3.4%, indicating that the 1,8-naphthalimide groups are associated in solution and that their dipole vectors are oriented at approximately 180°. Any significant deviation from linearity would produce smaller radii values in the PGSE-NMR experiment. For comparison, similar experiments with $Re(CO)_3Br[(3\text{-pyrenyl-pz})_2CH(^nPr)]$ (pz = pyrazolyl ring) that we have reported previously showed the complexes were monomeric in solution even though the solid state structure showed association by π–π stacking of the pyrene groups [13b]. While we had previously demonstrated that the π–π stacking interaction of metal complexes containing 1,8-naphthalimide persists in solution, this is the first demonstration that cationic species organized by the 1,8-naphthalimide synthon persist in solution.

3.4. UV–VIS and fluorescence spectral data

The UV–VIS and fluorescence spectra of **1** are shown in Figs. 3 and 4, respectively. The UV–VIS spectrum (Fig. 3), which shows that the absorbance intensity decreased linearly as concentration decreased, is characterized by a λ_{max} peak located at 452 nm for the MLCT (metal-to-ligand charge transfer) transition for the $[Ru(bipy)_3]^{2+}$ core. This $[Ru(bipy)_3]^{2+}$ core transition is red shifted by approximately 12 nm in relation to that of an unsubstituted $[Ru(bipy)_3]^{2+}$. The naphthalimide group shows a complicated set of transitions with an absorbance at 288 nm, a series of absorbances in the range of 315–350 nm, and a broad absorbance centered at 428 nm. While somewhat similar to those reported previously for naphthalimides substituted on the ring nitrogen [14], the substitution on the ring is influencing the behavior when compared to simple alkyl substituted naphthalimides.

The fluorescence spectrum (Fig. 4), which also had a linear decrease of intensity as concentration decreased, was obtained using samples of the same concentrations as those used for UV–VIS analysis. The excitation wavelength was 333 nm with a slit width setting of 8. The spectrum is characterized by a peak located a λ_{max} 595 nm that is very similar to the fluorescence associated with the $[Ru(bipy)_3]^{2+}$ core of other systems [15]. There are also peaks

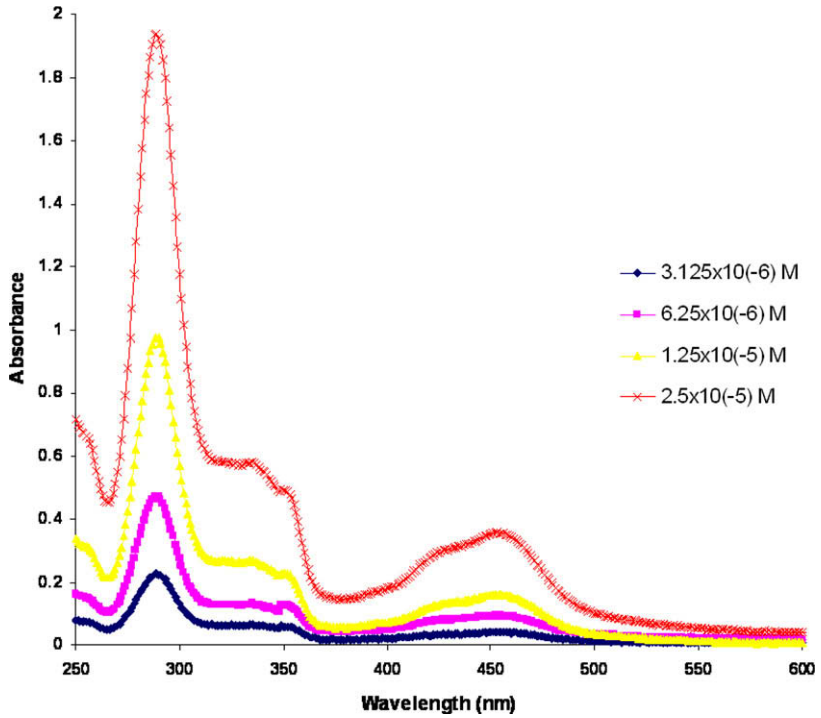


Fig. 3. UV–VIS spectra of **1** in degassed methylene chloride.

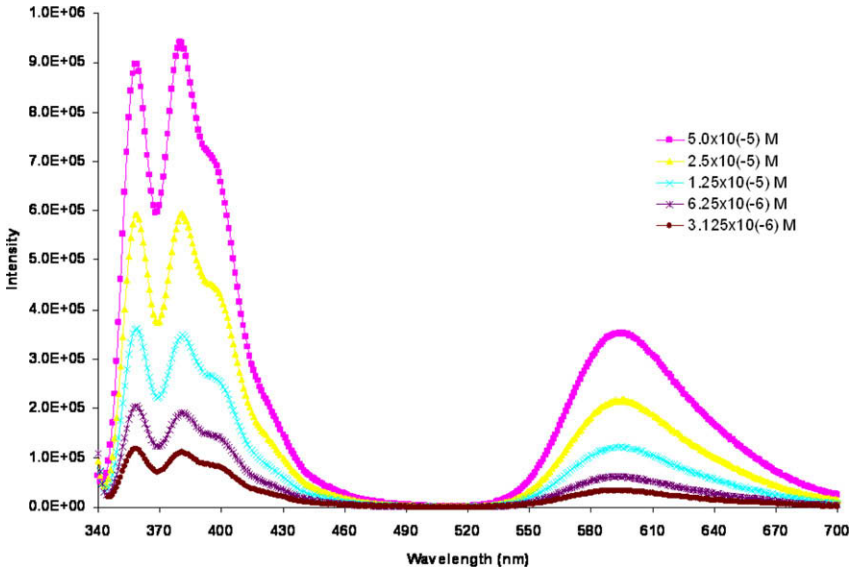


Fig. 4. Fluorescence spectra of **1** in degassed methylene chloride with an excitation wavelength of 333 nm.

at 360 (λ_{max} at concentrations 1.25×10^{-5} M and lower) and 382 (λ_{max} at concentrations 2.5×10^{-5} M and higher) with a shoulder at 398 nm, indicative of the fluorescence associated with the 1,8-naphthalimide moiety. The fluorescence efficiency of the 1,8-naphthalimide moiety was calculated relative to the $[Ru(bipy)_3]^{2+}$ core (fluorescence efficiency of 5.3×10^{-2}) and was found to have a value of 3.58×10^{-2}, an increase from 2.9×10^{-2} for unsubstituted 1,8-naphthalimide [14]. Increases of this magnitude are comparable to increases achieved by organic substitution of the naphthalimide system [14].

3.5. Electrochemical Measurements

The cyclic voltammogram of **1** (Fig. 5) shows two significant areas. A major reversible electrochemical process is centered on a potential of approximately 1.30 V, which suggests that this couple is due to the ruthenium (II) ion in the complex. This observed potential is in close agreement with the work conducted by De Cola et al. for other $[Ru(bipy)_3]^{2+}$ core molecules [15]. The other significant area is in the −1.00 V to −1.50 V range. Although not as distinct as the ruthenium (II) ion couple, there appears to be at least two elec-

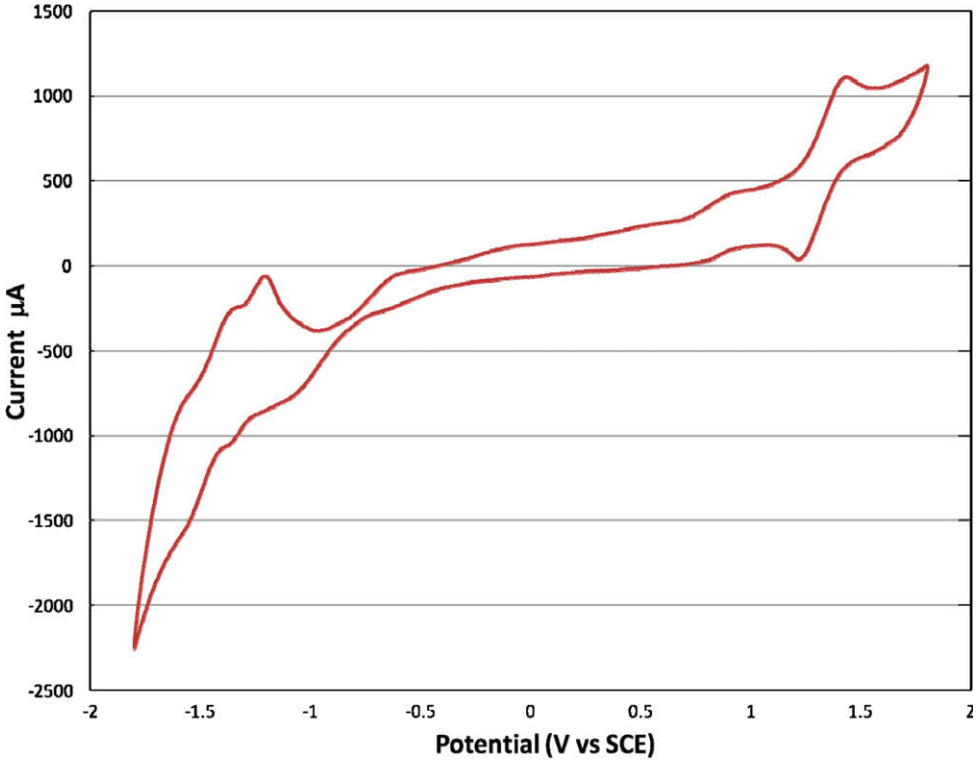


Fig. 5. Cyclic voltammogram of **1** in acetonitrile with 0.1 M tetra-*N*-butyl ammonium hexafluorophosphate as supporting electrolyte.

trochemical processes in this range. In comparison to the work by Martin et al. [5], the reversible process seen at approximately −1.35 V is due to the 1,8-naphthalimide portion of the ligand, although its appearance is more complex than a simple naphthalimide compound [5].

4. Conclusion

The synthesis of *N*-(5-methyl-2,2'-bipyridyl)-1,8-naphthalimide and {ruthenium[bis(bipyridyl)][N-(5-methyl-2,2'-bipyridyl)-1,8-naphthalimide]}$(PF_6)_2$ has been successfully carried out. In the solid state structure of **1**, the 1,8-naphthalimide groups are π–π stacked in a 180° antiparallel arrangement. This π–π stacking interaction was also shown to be present in solution by PGSE-NMR analysis, further demonstrating the utility of the 1,8-naphthalimide synthon to organize the structures in both the solid state and in solution of metal systems, either neutral [4a] or cationic, as shown here. Thus, we have now demonstrated that the strong, directionally oriented π–π stacking of the 1,8-naphthalimide synthon can be easily transferred to a variety of metal based systems. UV–VIS, fluorescence spectroscopy analysis and the electrochemical experiments show that the behavior of the $[Ru(bipy)_3]^{2+}$ group is only slightly changed by the presence of the naphthalimide group and its highly organized π–π stacking interactions.

5. Supplementary data

CCDC 715283 contains the supplementary crystallographic data for this paper. These data can be obtained free of charge via http://www.ccdc.cam.ac.uk/conts/retrieving.html, or from the Cambridge Crystallographic Data Centre, 12 Union Road, Cambridge CB2 1EZ, UK; fax: (+44) 1223-336-033; or e-mail: deposit@ccdc.cam.ac.uk.

Acknowledgment

The authors thank the National Science Foundation (CHE-0715559) for support of this research.

References

[1] (a) J.L. Atwood, L.J. Barbour, A. Jerga, Angew. Chem., Int. Ed. 43 (2004) 2948;
(b) C.K. Broder, M.G. Davidson, V.T. Forsyth, J.A.K. Howard, S. Lamb, S.A. Mason, Cryst. Growth Des. 2 (2002) 163;
(c) J.-P. Collin, V. Heitz, J.-P. Sauvage, Top. Curr. Chem. 262 (2005) 29;
(d) E. DeIonno, H.-R. Tseng, D.D. Harvey, J.F. Stoddart, J.R.J. Heath, Phys. Chem. B 110 (2006) 7609;
(e) Design of Organic Solids, in: E. Weber (Ed.), Topics in Current Chemistry, vol. 198, Springer, Berlin, 1998.;
(f) G.R. Desiraju, Chem. Commun. (2005) 2995;
(g) G.R. Desiraju, T. Steiner, The Weak Hydrogen Bond in Structural Chemistry and Biology, Oxford University Press, Oxford, 1999;
(h) M. Du, Z.H. Zhang, X. Zhao, J. Cryst. Growth Des. 5 (2005) 1199;
(i) K.T. Holman, A.M. Pivovar, J.A. Swift, M.D. Ward, Acc. Chem. Res. 34 (2001) 107;
(j) P. Metrangolo, H. Neukirch, T. Pilati, G. Resnati, Acc. Chem. Res. 38 (2005) 386;
(k) N.N.P. Moonen, A.H. Flood, J.M. Fernandez, J.F. Stoddart, Top. Curr. Chem. 262 (2005) 99;
(l) E. Pidcock, W.D.S. Motherwell, Cryst. Growth Des. 5 (2005) 2232;
(m) K. Sada, K. Inoue, T. Tanaka, A. Tanaka, A. Epergyes, S. Nagahama, A. Matsumoto, M. Miyata, J. Am. Chem. Soc. 126 (2004) 1764.
[2] N.A. Campbell, Photosynthesis. Biology, 4th ed., Benjamin/Cummings Publishing Company, Inc., Menlo Park, CA, 1996; pp. 182–200.
[3] C. Janiak, J. Chem. Soc., Dalton Trans. (2000) 3885. and references therein.
[4] (a) D.L. Reger, J.D. Elgin, R.F. Semeniuc, P.J. Pellechia, M.D. Smith, Chem. Commun. (2005) 4068;
(b) D.L. Reger, R.F. Semeniuc, J.D. Elgin, V. Rassolov, M.D. Smith, Cryst. Growth Des. 12 (2006) 2758.
[5] (a) E. Martin, R. Weigand, Chem. Phys. Lett. 288 (1998) 52;
(b) T.P. Le, J.E. Rogers, L.A. Kelly, J. Phys. Chem. A 104 (2000) 6778;
(c) J.E. Rogers, S.J. Weiss, L.A. Kelly, J. Am. Chem. Soc. 122 (2000) 427;
(d) M. Licchelli, A.O. Biroli, A. Poggi, D. Sacchi, C. Sangermani, M.J. Zema, J. Chem. Soc., Dalton Trans. (2003) 4537.
[6] (a) S. Anderson, K.R. Seddon, J. Chem. Res., Synopses 2 (1979) 74;
(b) T. Klumpp, M. Linsenmann, S.L. Larson, B.R. Limoges, D. Buerssner, E.B. Krissinel, C.M. Elliott, U.E. Steiner, J. Am. Chem. Soc. 121 (1999) 1076;
(c) J.K. Nagle, R.C. Young, T.J. Meyer, Inorg. Chem. 16 (1977) 3366;
(d) D.P. Rillema, W.J. Dressick, T.J. Meyer, Chem. Commun. (1980) 247;
(e) M. Seiler, H. Duerr, I. Willner, E. Joselevich, A. Doron, J.F. Stoddart, J. Am. Chem. Soc. 116 (1994) 3399.
[7] (a) P.F.H. Schwab, F. Fleisher, J. Michl, J. Org. Chem. 67 (2002) 443;
(b) M. Heller, U.S. Schubert, J. Org. Chem. 67 (2002) 8269.
[8] SMART Version 5.630, SAINT+ Version 6.45, Bruker Analytical X-ray Systems Inc., Madison, WI, USA, 2003.
[9] G.M. Sheldrick, SHELXTL Version 6.14; Bruker Analytical X-ray Systems Inc., Madison, WI, USA, 2000.
[10] A.L. Spek, PLATON, A Multipurpose Crystallographic Tool, Utrecht University, Utrecht, The Netherlands, 1998.
[11] D.P. Rillema, D.S. Jones, H.A. Levy, Chem. Commun. (1979) 849.
[12] (a) P. Stilbs, Prog. Nucl. Magn. Reson. Spectrosc. 19 (1987) 1;
(b) M. Valentni, P.S. Pregosin, H. Rüegger, Organometallics 19 (2000) 2551.
[13] (a) K. Moon, A.E. Kaifer, J. Am. Chem. Soc. 126 (2004) 15016;
(b) D.L. Reger, J.R. Gardinier, P.J. Pellechia, M.D. Smith, K.J. Brown, Inorg. Chem. 42 (2003) 7635.
[14] M.S. Alexiou, V. Tychopoulos, S. Ghorbanian, J.H.P. Tyman, R.G. Brown, P.I. Brittain, J. Chem. Soc., Perkin Trans. 2 (1990) 837.
[15] L. De Cola, V. Balzani, F. Barigelletti, L. Flamigni, P. Belser, A. von Zelewesky, M. Frank, F. Voegtle, Inorg. Chem. 32 (1993) 5228.

obtained commercially and dried before use. Potassium carbonate (K_2CO_3), urea, 1-chloronaphthalene (1-CNP), deuterated chloroform ($CDCl_3$), phenol, 1,8-diazabicyclo[5.4.0]undec-7-ene (DBU), lead acetate, 4-*tert*-butylphenol and 4-benzyloxyphenol were purchased from Aldrich and used as received. Dimethylsulfoxide (DMSO) was purchased from SAARCHEM, and dried over alumina before use. 4-Nitrophthalonitrile (**1**) [13] and 4,5-dichlorophthalonitrile (**2**) [14] were synthesized and purified according to literature procedures. Column chromatography was performed on silica gel 60 (0.04–0.063 mm).

2.2. Equipment

Ground state electronic absorption spectra were performed on a Varian Cary 500 UV–Vis–NIR spectrophotometer; infra-red spectra (KBr pellets) on Perkin Elmer Spectrum 2000 FT-IR Spectrometer and ^{1}H nuclear magnetic resonance (^{1}H NMR) spectra on a Bruker EMX 600 NMR spectrometer. Triplet lifetimes (τ_T) and yields were obtained using an Nd-YAG laser providing 400 mJ, 90 ns of laser light at 10 Hz, pumping a Lambda-Physik FL 3002 dye laser. A 300 W xenon arc lamp (Thermo Oriel) provided the analysing light. Kinetic curves were averaged over 256 laser pulses using a Tektronix TDS 360 digital oscilloscope. The τ_T values were obtained by fitting an exponential curve to the kinetic data using ORIGIN Pro 6.0. Elemental analyses were obtained using Elementar Vario Micro Cube CHNS Analyser). Microwave irradiations were carried out in a Defy DM206T microwave oven at a power of 1000 W.

2.3. Photophysical properties

Fluorescence quantum yields (Φ_F) were determined by the comparative method, using the following equation [15,16]:

$$\Phi_F = \Phi_F^{std}\frac{F\cdot A_{std}\cdot n^2}{F_{std}\cdot A\cdot n_{std}^2} \tag{1}$$

where F and F_{std} are the areas under the fluorescence curves of the MPc derivatives and the standard, respectively. A and A_{std} are the respective absorbances of the sample and standard at the excitation wavelengths (which was ~0.05 in all solvents used), and n and n_{std} are the refractive indices of the solvents used for sample and standard, respectively. ZnPc was employed as a standard in DMSO (Φ_F = 0.20) [15].

The triplet quantum yields were determined using the following equation:

$$\Phi_T = \Phi_T^{std}\frac{\Delta A_T\cdot \varepsilon_T^{std}}{\Delta A_T^{std}\cdot \varepsilon_T} \tag{2}$$

where ΔA_T and ΔA_T^{std} are the changes in triplet state absorbance of MPc derivatives and the standard, respectively. ε_T and ε_T^{std} are the triplet state molar extinction coefficients for the MPc derivatives and the standard, respectively. Φ_T^{std} is the triplet quantum yield for the standard, ZnPc (Φ_T = 0.65 in DMSO [17], 0.58 in DMF [18] and 0.65 in toluene [19]). Quantum yields of internal conversion were obtained from Eq. (3), which assumes that only three processes (fluorescence, intersystem crossing and internal conversion), jointly deactivate the excited singlet state of a Pc molecule

$$\Phi_{IC} = 1 - (\Phi_F + \Phi_T). \tag{3}$$

2.4. Nonlinear optical parameters

The important parameters in this section are (i) k: the ratio of the absorption cross-sections of the ground (σ_g) and excited (σ_{ex}) states, I_{lim} (the threshold limit intensity), $I_m[\chi^{(3)}]$ and γ, the third and second order susceptibilities, respectively.

k can be calculated using Eq. (4). A good optical limiter should have k of more than one

$$k = \frac{\sigma_{ex}}{\sigma_g} \tag{4}$$

The I_{lim} values were calculated using Eq. (5) [4,20]:

$$I_{lim} = \frac{h\omega^*}{2\pi\sigma_g\tau_T} \tag{5}$$

where ω^*, σ_g and τ_T are the frequency at which the system absorbs, singlet absorption cross-section and triplet lifetimes, respectively.It therefore makes sense in this regard to mention that an ideal optical limiter should have a low threshold limit value (I_{lim}), if it is too high, it becomes less reliable in terms of protection of light-sensitive elements.

2.4.1. Third order susceptibility $\chi^{(3)}$ and second hyperpolarizability, γ

The third order susceptibility, $I_m[\chi]^{(3)}$, is given by [20]

$$I_m[\chi^{(3)}] = \frac{2c^2n^2\beta}{\pi\omega^*}\times 10^{-22} \tag{6}$$

where n, c and ω^* are, respectively, the linear refractive index (n = 1.478 in DMSO), the speed of light and the frequency. β represents a nonlinear absorption term which averages the molar extinction coefficient ε_g and ε_{ex} according to the following equation [20]:

$$\beta = 5.3\varepsilon_g\varepsilon_{ex}[C]\Phi_{ISC} \tag{7}$$

where ε_g and ε_{ex} are extinction coefficients for the ground and excited state, respectively, $[C]$ is the concentration of active species in the triplet state and Φ_{ISC} is the intersystem crossing quantum yield.

At a molecular level, $I_m[\chi]^{(3)}$ is directly related to the second hyperpolarizability, γ, through the following equation [4,21,22]:

$$\gamma = \frac{I_m[\chi^{(3)}]}{f^4[C]N_a} \tag{8}$$

where N_a is Avogadro's constant, C is the concentration of the active species in the triplet state and f is Lorentz local field factor, $f = (\eta^2 + 2)/3$, where η is the viscosity.

These nonlinear parameters, $I_m[\chi^{(3)}]$ and γ, are used to quantify the nonlinear absorption.

2.5. Synthesis

4-(4-Benzyloxyphenoxy)phthalonitrile (**3a**) and 4,5-bis(4-benzyloxyphenoxy) phthalonitrile (**4a**) were synthesized and characterized according to reported procedures [23].

2.5.1. 2,(3)-Tetrakis(4-benzyloxyphenoxy)phthalocyaninato lead (**5a**)

A mixture of compound **3a** (0.10 g, 0.29 mmol), lead acetate (0.05 g, 0.14 mmol), DBU (0.2 ml) and 5 ml *n*-pentanol was irradiated at 1000 W in a microwave for 15 min. After cooling, the product was washed with methanol and chromatographed over silica gel with hexane as eluent to remove impurities. The column was then eluted with THF and then hexane and the solvents were evaporated off, thus affording **5a**. Yield: 80 mg (19%). UV–Vis (DMSO): λ_{max}, nm (log ε) 710 (4.98), 641 (4.32), 346 (4.46). IR [(KBr) ν_{max}/cm^{-1}]: 2948 (CH_2), 1605 (C=C), 1218(C–O–C), 941, 827, 734, 696 (Pc skeletal). ^{1}H NMR (DMSO-d_6): δ, ppm 7.52–7.58 (4H, m, Pc–H), 7.44–7.49 (8H, m, Pc–H), 7.35–7.42 (20H, m, phenyl–H), 7.22–7.28 (16H, m, phenyl–H), 5.20 (8H, s, CH_2). *Anal.* Calc. for $C_{84}H_{56}N_8O_8Pb$.hexane: C, 67.63; H, 4.38; N, 7.01. Found: C, 68.35; H, 4.70; N, 7.33%.

*2.5.2. 2,3-Octakis(4-benzyloxyphenoxy)phthalocyaninato lead (**6a**)*

Synthesis and purification was as outlined for **5a** except **4a** instead of **3a** was employed. The amounts of the reagents employed were as follows: **4a** (0.25 g, 0.36 mmol), lead acetate (0.06 g, 0.18 mmol), DBU (0.2 ml) and *n*-pentanol (5 ml). Irradiation was for 8 min. Yield: 0.75 g (46%). UV–Vis (DMSO): λ_{max}, nm ($\log\varepsilon$) 712 (5.01), 638 (4.34), 347 (4.45) IR [(KBr) ν_{max}/cm^{-1}]: 2925 (CH_2), 1504 (C=C), 1231 (C–O–C), 1000, 875, 839, 739, 694 (Pc skeletal). ^{1}H NMR (DMSO-d_6): δ, ppm 7.54–7.56 (8H, br, Pc–H), 7.44–7.48 (32H, br, phenyl–H), 7.22–7.38 (40H, br, phenyl–H), 5.09–5.26 (16H, s, CH_2). *Anal.* Calc. for $C_{136}H_{96}N_8O_{16}Pb$: C, 70.85; H, 4.20; N, 4.86. Found: C, 71.31; H, 4.30; N, 5.38%.

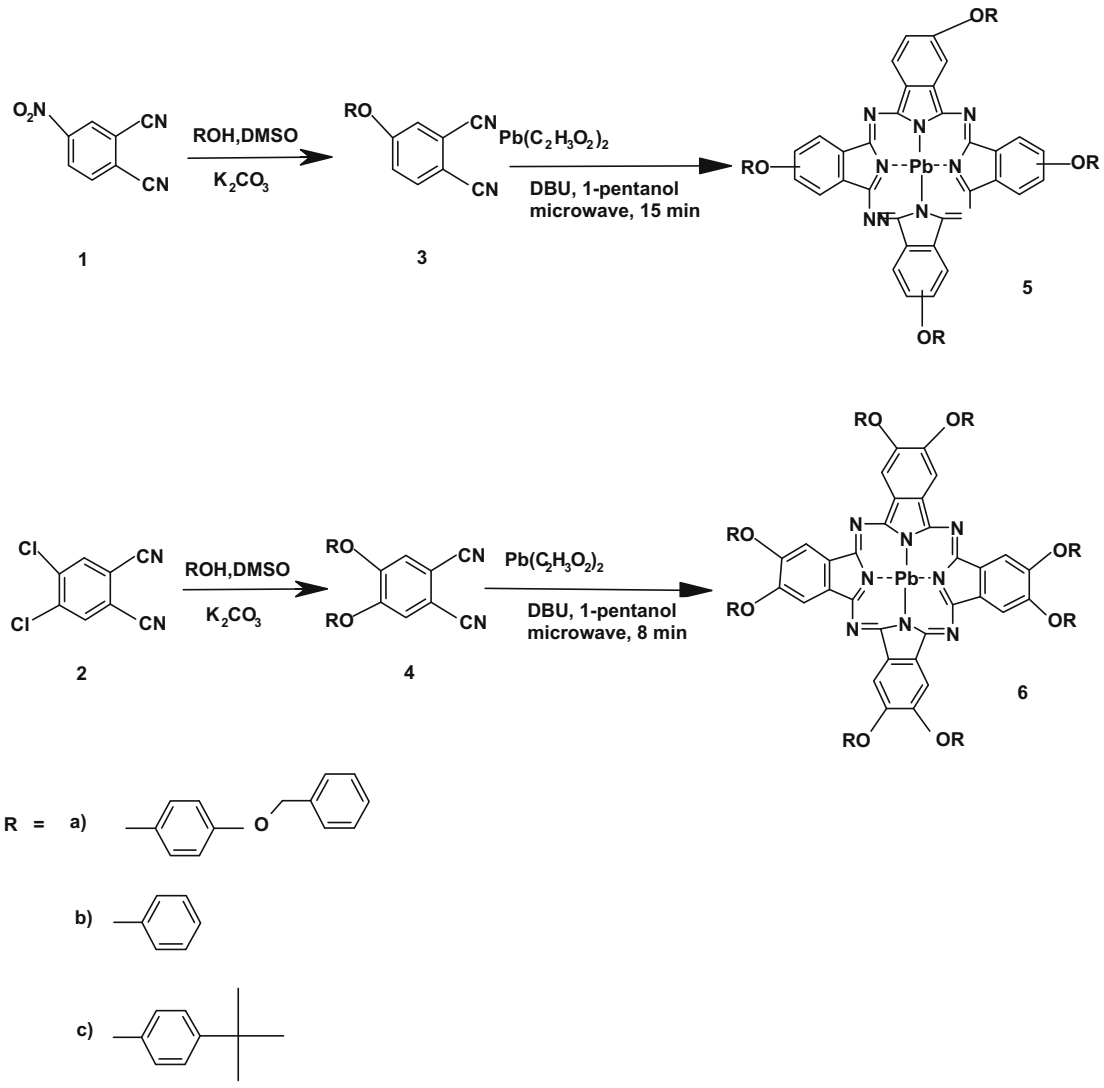
3. Results and discussion

3.1. Syntheses and characterization

Scheme 1 gives the synthetic pathways for the PbPc complexes discussed in this work. The general procedure for synthesis of substituted phthalonitrile derivatives has been well documented [24] and the preparation of the substituted 4-benzyloxyphenoxy derivatives was carried out as reported before [23]. PbPcs can be synthesized using many methods including treatment of phthalonitrile with lead acetate without solvent [25] or heating in the presence of high boiling solvent [12,26] or by addition of lead acetate to a solution of Li_2Pc or H_2Pc in alcohol [26,27] and can also be obtained by microwave method [28]. In this work, we employed microwave method to prepare the target PbPcs.

The complexes were characterized by UV–Vis, IR and ^{1}H NMR spectroscopies, and elemental analyses. The analyses were consistent with the predicted structures as shown in Section 2. The sharp peak for the C≡N vibrations in the IR spectra of phthalonitriles **3a** and **4a** at ~2230 cm^{-1} disappeared after conversion into PbPcs, indicative of metallophthalocyanine formation. All compounds showed vibrational peaks between 700 and 1000 cm^{-1} which may be assigned to phthalocyanines skeletal vibrations [29]. The characteristic vibrations corresponding to ether groups (C–O–C) at ca. 1200–1235 cm^{-1}, C=C at ca. 1500–1600 cm^{-1} and aliphatic CH stretching at ca. 2900–3000 cm^{-1} were observed for the substituted MPc derivatives.

The PbPc derivatives were found to be pure by ^{1}H NMR with all the substituents and ring protons observed in their respective regions. The CH_2 protons were observed at 5.20 ppm for compound **5a** integrating for 8 protons and 5.09–5.26 ppm for **6a** integrating for 16 protons. The resonances belonging to aromatic protons were observed between 7.22 and 7.58 ppm as multiplets for



Scheme 1. Synthesis of tetra- and octa-substituted lead phthalocyanines.

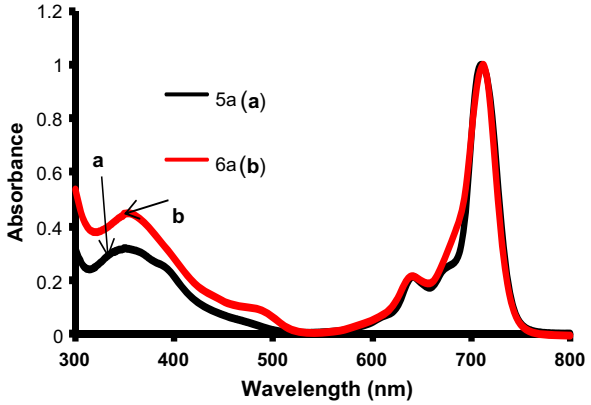


Fig. 1. UV–Vis spectra for (a) tetra- and (b) octakis(4-benzyloxyphenoxy) substituted PbPcs in DMSO (~2×10^{-6} M).

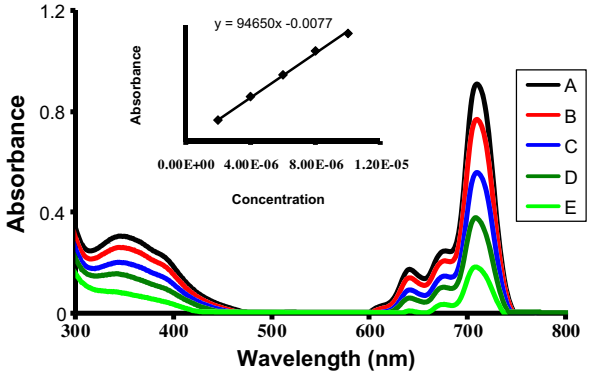


Fig. 2. Absorption spectra of compound **5a** in DMSO at different concentrations: (A) 1×10^{-5}, (B) 6×10^{-6}, (C) 4×10^{-6}, (D) 2×10^{-6}, (E) 2×10^{-6} M

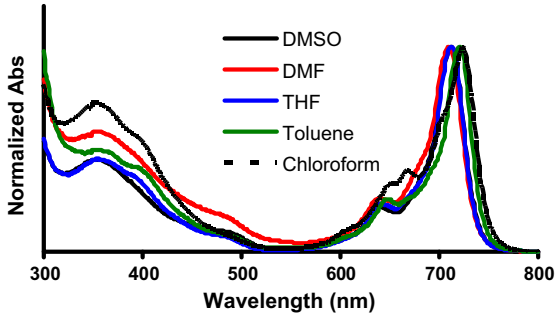


Fig. 3. Absorption spectra of complex **6a** in different solvents (~2×10^{-6} M).

tetra-substituted complex (**5a**) integrating for a total of 48 protons while for octa-substituted complex (**6a**), the aromatic protons were observed as broad peaks from 7.22 to 7.56 ppm, integrating for a total of 80 protons expected. Although the presence of isomers for tetra-substituted complex as well as phthalocyanine aggregation at the concentration used for the NMR measurements may lead to broadening of the aromatic signals [30–32], the NMR peaks were relatively well-resolved.

The ground state electronic absorption spectra of **5** and **6** show sharp Q-bands, Fig. 1. The Q-bands were observed at 710 and 712 nm in DMSO (Fig. 1) for complexes **5a** and **6a**, respectively. The Q-bands are slightly red shifted in the complexes when compared to unsubstituted PbPc [33], suggesting a small electron donating ability of the substituents, hence lowering HOMO–LUMO gap. The B-bands are broad due to the superimposition of the B_1 and B_2 bands in 300–400 nm region.

Aggregation is usually depicted as a coplanar association of rings progressing from monomer to dimer and higher order complexes. It is dependent on the concentration, nature of the solvent, nature of the substituents, complexed metal ions and temperature [34]. The aggregation behaviour of complexes **5a** and **6a** were investigated at different concentrations in DMSO (Fig. 2 for complex **5a**). The intensity of the Q- and B-bands increased with increase in concentration and there were no new bands observed due to aggregated species. Beer–Lambert's law was obeyed for both compounds at concentrations ranging from 2.0×10^{-6} to 1.0×10^{-5} mol dm^{-3}, even though **6a** shows some broadening in the Q-band area. The aggregation behaviour was also investigated in different solvents (Fig. 3 for complex **6a** in DMSO, DMF, Toluene, THF and $CHCl_3$). There was evidence of new bands in the 650 nm region (in some solvents) suggesting aggregation [35]. Fig. 3 and Table 1 show that the largest red-shift of the Q-band was observed in chloroform, which could partly be explained by considering the refractive indices of the solvents. It is known that red-shifting of absorption spectra is a function of the solvent's refractive index [36].

3.2. Photophysical properties

3.2.1. Fluorescence spectra and quantum yields

All complexes showed similar fluorescence behaviour. The fluorescence and absorption spectra are shown in Fig. 4. No emission was observed to the red of the Q-band absorption spectra. The excitation spectra were different from absorption spectra in all solvents due to demetallation upon excitation, as judged by the blue shifted and split Q-band. The excitation spectra were similar to the absorption spectra of the corresponding demetallated H_2Pc derivatives, confirming demetallation upon excitation. Emission spectra for all compounds were from the demetallated species. Metal free

Table 1
Spectral and photophysical parameters of PbPc complexes in different solvents.

MPc	Solvent	λ_{max} (nm)			Φ_F	Φ_T[a]	Φ_{IC}[a]	τ_T (μs)
		Absorption	Emission	Excitation				
5a	DMSO	710	706	699	<0.01	0.82	0.17	40
	DMF	707	705	702, 672	<0.01	0.80	0.19	5
	Toluene	718	707	702, 673	0.03	0.83	0.14	6
	$CHCl_3$	723	710	702, 671	0.07	[a]	[a]	5
	THF	708	702	698, 671	0.02	[a]	[a]	4
6a	DMSO	712	706	700	<0.01	0.84	0.15	30
	DMF	710	704	701, 672	<0.01	0.83	0.16	6
	Toluene	720	708	703, 674	0.01	0.86	0.13	7
	$CHCl_3$	725	710	703, 672	0.05	[a]	[a]	5
	THF	709	702	699, 671	0.02	[a]	[a]	8

[a] Values not obtained in THF and $CHCl_3$ due to lack of reference standards.

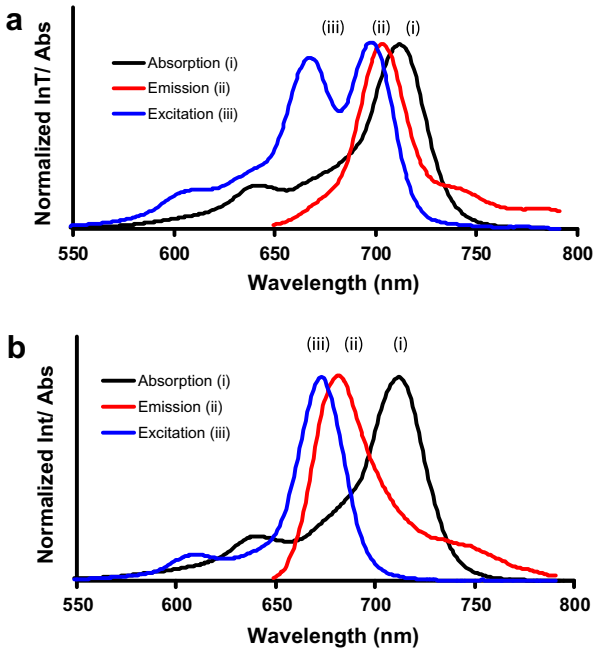


Fig. 4. (a) Absorption (i), emission (ii) and excitation (iii) spectra of compound **6a** in toluene ($\sim 2 \times 10^{-6}$ M). (b) Absorption (i), emission (ii) and excitation (iii) spectra of compound **6a** in DMSO ($\sim 2 \times 10^{-6}$ M).

Pcs are known to emit with only one main peak in non-aqueous media which has been assigned as the 0–0 transition [37]. Complete splitting of the Q-band in excitation spectra was observed in THF, $CHCl_3$, toluene and DMF. In DMSO (Fig. 4), the Q-band was not split. It has been documented that in basic solvents such as DMSO, the inner pyrrole hydrogens are acidic enough to dissociate resulting in an unsplit Q-band [35].

The fluorescence quantum yields (Φ_F) of complexes **5a** and **6a** are given in Table 1. The Φ_F values were found be less than 0.1, hence less than typical values for MPc [38]. The small Φ_F values (Table 1) were due to the presence of heavy atom (Pb), which enhances intersystem crossing to populate the triplet state, consequently reducing the number of fluorescing molecules. The fact that the PbPc complexes become demetallated on excitation suggests that the Φ_F values are for the fully or partially demetallated complexes in different solvents.

3.2.2. Triplet quantum yields and lifetimes

Table 1 lists the triplet state parameters, Φ_T, Φ_{IC} and τ_T for complexes **5a** and **6a** in different solvents. The triplet quantum yield (Φ_T) is a measure of the fraction of absorbing molecules that undergo intersystem crossing to the metastable triplet excited state. Since intersystem crossing and fluorescence are two competing deactivating processes for the excited singlet state, their values for a particular species are expected to be complementary. Thus Table 1 shows high Φ_T values (0.80–0.86) in DMSO, DMF and toluene, corresponding to low Φ_F values. These values are high due to the presence of lead. Since PbPc demetalates on excitation, the reported Φ_T values are of demetallated species, but since Pb is still in solution, the values are high due to the heavy atom effect. The Φ_T values in $CHCl_3$ and THF could not be determined due to the lack of standard Φ_T values in those solvents. The triplet lifetimes τ_T Table 1, were relatively short compared to, for example ZnPc with a triplet lifetime of 350 μs, in DMSO [38]. The short triplet lifetimes could be due to their large triplet state quantum yields. Quantum yields of internal conversion (Φ_{IC}) were calculated using Eq. (3).

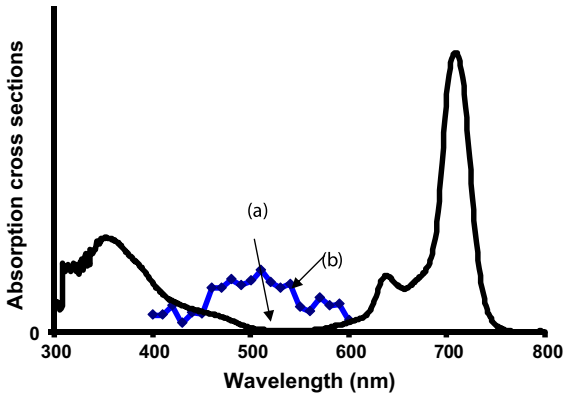


Fig. 5. Absorption cross-sections for the ground (a) and excited triplet (b) state for compound **5c** in DMSO ($\sim 1 \times 10^{-6}$ M).

Table 1 shows that the values of Φ_{IC} were similar and relatively low, Table 1.

3.3. Nonlinear optical properties

The nonlinear optical parameters were calculated for PbPc complexes (**5a–c**, **6a–c**) in DMSO. The absorption cross-sections were determined from Fig. 5 (for complex **5c**). $k(\sigma_{ex}/\sigma_g)$ values >1 were obtained, Table 2. As mentioned above, a good optical limiter should have a k of more than one. The higher the k, the better limiting power, thus octa-substituted PbPcs (**6**) are the better optical limiters than their corresponding tetra-substituted PbPc derivatives (**5**).

The limiting threshold intensity (I_{lim}) values (Table 2) were found to be small, compared to those reported in the literature for GaPcs and InPcs [39]. An optical limiter should possess a low threshold limit value in order to be reliable in terms of protection of optical elements. The smaller the liming intensity (I_{lim}), the better optical limiter. The value of 10^2 W/cm^2 is generally taken as the standard value for the minimum intensity using the human eye as the reference light-sensing element [4]. The I_{lim} values obtained in Table 2 showed that PbPc derivatives are good optical limiters.

Table 2 shows the values of third order susceptibility ($I_m[\chi^{(3)}]$) and second hyperpolarizability (γ) for PbPc complexes. For a good optical limiter, $I_m[\chi^{(3)}]$ should fall within the 10^{-15} to 10^{-9} esu range and γ within the 10^{-34} and 10^{-29} esu range [40–44]. These values were lower than those reported for InPc and GaPc [39]. This is most likely due to the heavy atom effect because it has been reported that the value of $I_m[\chi^{(3)}]$ decreased in MPcs with increasing atomic number of a metal [4], hence the low values for PbPc are not surprising. Except for complexes containing 4-benyloxyphenoxy substituent (**a**), the $I_m[\chi^{(3)}]$ values for octa-substituted PbPcs were marginally larger than tetra-substituted PbPc derivatives (compare **5b** with **6b** and **5c** with **6c**). The second hyperpolarizability (γ) values were well within the range of the values reported in the literature for Ga and InPc derivatives [39].

Table 2
Nonlinear optical parameters of PbPc derivatives in DMSO.

MPc in DMSO	τ_T (μs)	$I_m[\chi^{(3)}]$ (esu)	γ (esu)	(k) σ_{ex}/σ_g	I_{lim} (W cm^{-2})
5a	40	6.3×10^{-12}	1.6×10^{-34}	27	3.1
5b	20	3.3×10^{-12}	0.9×10^{-34}	23	6.6
5c	30	5.3×10^{-12}	1.3×10^{-34}	26	3.9
6a	30	4.8×10^{-12}	2.8×10^{-34}	35	2.1
6b	20	4.2×10^{-12}	2.2×10^{-34}	26	3.8
6c	50	5.6×10^{-12}	2.9×10^{-34}	33	2.3

4. Conclusion

From the results obtained in this work, it can be concluded that the fluorescence spectra were different from absorption spectra due to the loss of symmetry as a result of demetallation upon excitation. The high triplet quantum yields and low triplet lifetimes were observed as the result of heavy atom (Pb) effect. The optical limiting threshold intensity (I_{lim}) values for the PbPc derivatives confirm that they are good limiters. The I_{lim} values obtained were far less than of 10^2 W cm^{-2}, which is generally taken as the standard value for the minimum intensity using the human eye as the reference light-sensing element.

Acknowledgements

This work has been supported by the Department of Science and Technology (DST) and National Research Foundation (NRF), South Africa through DST/NRF South African Research Chairs Initiative for Professor of Medicinal Chemistry and Nanotechnology as well Rhodes University and Medical Research Council of South Africa and CSIR.

References

[1] T.H. Mainman, Nature 187 (1960) 493.
[2] D. Dini, M. Calvete, S. Vargin, M. Hanack, A. Eriksson, C. Lopes, J. Porphyr. Phthalocya. 10 (2006) 1165.
[3] N. Bloembergen, Nonlinear Optics, Benjamin, New York, 1965.
[4] D. Dini, M. Hanack, in: K.M. Kadish, K.M. Smith, R. Guilard (Eds.), The Porphyrin Handbook: Physical Properties of Phthalocyanine-based Materials, vol. 17, Academic press, USA, 2003, p. 22.
[5] M. Hanack, T. Schneider, M. Barthel, J.S. Shirk, S.R. Flom, R.G.S. Pong, Coord. Chem. Rev. 219 (2001) 235.
[6] Y. Chen, M. Hanack, Y. Araki, O. Ito, Chem. Soc. Rev. 34 (2005) 517.
[7] A. Beck, K.M. Mangold, M. Hanack, Chem. Ber. 124 (1991) 2315.
[8] H. Zhan, W. Chen, M. Wang, Mater. Lett. 59 (2005) 1395.
[9] W. Sun, C.C. Byeon, M.M. Mckerns, G.M. Gray, D. Wang, C.M. Lawson, SPIE 3472 (1998) 127.
[10] P. Buck, A. Dogariu, D.J. Hagan, E.W. Van Stryland, SPIE 2853 (1996) 12.
[11] P.M. Burnham, I. Chabrier, D.L. Hughes, B. Isare, R.J. Poynter, K.A. Powell, M.J. Cook, J. Porphyr. Phthalocya. 10 (2006) 1202.
[12] D.K. Modibane, T. Nyokong, Polyhedron 27 (2008) 1102.
[13] J.G. Young, W. Onyebuagu, J. Org. Chem. 55 (1990) 2155.
[14] D. Wöhrle, M. Eskes, K. Shigehara, A. Yamada, Synthesis (1993) 194.
[15] A. Ogunsipe, J.Y. Chen, T. Nyokong, New J. Chem. 28 (2004) 822.
[16] S. Fery-Forgues, D.j. Lavabre, Chem. Ed. 76 (1999) 1260.
[17] T.H. Tran-Thi, C. Desforge, C. Thiec, J. Phys. Chem. 93 (1989) 1226.
[18] J. Kossanyi, O. Chahraoui, Int. J. Photoenerg. 2 (2000) 9.
[19] S.M. Bishop, A. Beeby, A.W. Parker, M.S.C. Foley, D. Phillips, J. Photochem. Photobiol. A: Chem. 90 (1995) 29.
[20] D. Dini, M. Barthel, M. Hanack, Eur. J. Org. Chem. (2000) 3759.
[21] D. Dini, M. Hanack, M. Meneghetti, J. Phys. Chem. B 109 (2005) 12691.
[22] J. Simon, C. Sirlin, Pure Appl. Chem. 61 (1989) 1625.
[23] P. Tau, T. Nyokong, Electrochim. Acta 52 (2007) 3641.
[24] W.M. Sharman, J.E. van Lier, in: K.M. Kadish, K.M. Smith, R. Guilard (Eds.), The Porphyrin Handbook, vol. 15, Academic Press, New York, 2003, p. 22 (Chapter 97).
[25] A.W. Snow, N.L. Jarvis, J. Am. Chem. Soc. 106 (1984) 4706.
[26] Y. Bian, L. Li, J. Dou, D.Y.Y. Cheng, R. Li, C. Ma, D.K.P. Ng, N. Kobayashi, J. Jiang, Inorg. Chem. 43 (2004) 7539.
[27] C.C. Leznoff, in: C.C. Leznoff, A.B.P. Lever (Eds.), Phthalocyanines: Properties and Applications, vol. 1, VCH, New York, 1989, p. 1 (Chapter 1).
[28] B.N. Achar, T.M.M. Kumar, K.S. Lokesh, J. Porphyr. Phthalocya. 9 (2005) 872.
[29] M.M. El-Nahass, K.F. Abd-El-Rahman, A.A.A. Darwish, Mater. Chem. Phys. 92 (2005) 185.
[30] M. Durmus, T. Nyokong, Polyhedron 26 (2007) 3323.
[31] M. Durmus, T. Nyokong, Spectrochim. Acta Part A 69 (2008) 1170.
[32] S. Gaspard, P. Maillard, Tetrahedron 43 (1987) 1083.
[33] T.M.M. Kumar, B.N. Achar, J. Organomet. Chem. 691 (2006) 331.
[34] H. Enkelkamp, R.J.M. Nolte, J. Porphyr. Phthalocya. 4 (2000) 454.
[35] M.J. Stillman, T. Nyokong, in: C.C. Leznoff, A.B.P. Lever (Eds.), Phthalocyanines: Properties and Applications, vol. 1, VCH, New York, 1989, p. 133 (Chapter 3).
[36] A. Ogunsipe, D. Maree, T. Nyokong, J. Mol. Struct. 650 (2003) 131.
[37] W. Freyer, S. Mueller, K. Teuchner, J. Photochem. Photobiol. A: Chem. 163 (2004) 231.
[38] T. Nyokong, Coord. Chem. Rev. 251 (2007) 1707.
[39] V. Chauke, M. Durmuş, T. Nyokong, J. Photochem. Photobiol. A: Chem. 192 (2007) 179.
[40] Y. Liu, S.M. O'Flaherty, Y. Chen, Y. Araki, J. Bai, J. Doyle, W.J. Blau, O. Ito, Dyes Pigments 75 (2007) 88.
[41] E.M. Garćıa-Frutos, S.M. O'Flaherty, S.V. Hold, G. de la Torre, S. Maier, P.Vázquez, W. Blau, T. Torres, Synth. Met. 137 (2003) 1479.
[42] E.M. García-Frutos, S.M. O'Flaherty, E.M. Maya, G. de la Torre, W. Blau, P.Vázquez, T. Torres, J. Mater. Chem. 13 (2003) 749.
[43] A. Auger, W.J. Blau, P.M. Burnham, I. Chambrier, M.J. Cook, B. Isare, F. Nekelson, S.M. O'Flaherty, J. Mater. Chem. 13 (2003) 1042.
[44] S.M. O'Flaherty, S.V. Hold, M.J. Cook, T. Torres, Y. Chen, M. Hanack, W.J. Blau, Adv. Mater. 15 (2003) 19.

CCD detector and using graphite-monochromated Mo Kα radiation (λ = 0.71073 Å). The raw data were integrated with the CRYSALIS Data Reduction Program (version 1.172.32.6) [8] taking into account an absorption correction. The intensities of the reflections were corrected for Lorentz and polarization effects. The crystal structures were solved by direct methods [9] and refined by a full-matrix least-squares method using the SHELXL-97 program [9]. Non-hydrogen atoms were refined with anisotropic displacement parameters. H-atoms were located from the difference Fourier maps and refined assuming a 'ride-on' model.

2.3. Spectroscopic and magnetic measurements

IR spectra were recorded as KBr pellets or Nujoll mulls using Perkin–Elmer FTIR-2000 and Perkin–Elmer 1600 spectrophotometers in the range 4000–50 cm^{-1}. The NIR–Vis–UV solid state-reflectance and absorbance electronic spectra in DMSO solution for complexes **1** and **2** and the L-tyrosine disodium salt (L) were obtained on a Cary 500 Scan Spectrophotometer in the range 5000–50 000 cm^{-1} with a resolution of 10 cm^{-1} and concentration [L] = 1.78 × 10^{-3} M, [**1**] = 8.66 × 10^{-4} M, [**2**] = 1.00 × 10^{-3} M. The variable digital filter method and deconvolution of the spectral contour into Gaussian components were applied for analysis of DMSO solution spectra in the range 11 000–23 000 cm^{-1} for **2** [10].

EPR spectra were recorded at room temperature and 77 K on a Bruker ESP 300 spectrometer operating at the X-band equipped with an ER 035 M Bruker NMR gaussmeter and HP 5350B Hewlett–Packard microwave frequency counter. Magnetic measurements in the temperature range 1.8–300 K were performed using a Quantum Design SQUID-based MPMSXL-5-type magnetometer. The SQUID magnetometer was calibrated with a palladium rod sample (Materials Research Corporation, measured purity 99.9985%). The superconducting magnet was generally operated at a field strength ranging from 0 to 5 T. Measurements were made at a magnetic field of 0.5 T. Corrections are based on subtracting the sample holder signal and a contribution χ_D estimated from Pascal constants [11]. A temperature–independent paramagnetism of 60 × 10^{-6} cm^3 mol^{-1} K for each copper(II) ion was used for calculations. Magnetization measurements were carried out at 2 K in the magnetic field from 0 to 5 T.

3. Results and discussion

3.1. Crystal structure characterization of {[Zn(tyr)$_2$(H$_2$O)]H$_2$O}$_n$ (**1**) and [Cu(tyr)$_2$]$_n$ (**2**)

The crystal data and refinement details for {[Zn(tyr)$_2$(H$_2$O)]-H$_2$O}$_n$ (**1**) and [Cu(tyr)$_2$]$_n$ (**2**) are presented in Table 1. {[Zn(tyr)$_2$(H$_2$O)]H$_2$O}$_n$ (**1**) and [Cu(tyr)$_2$]$_n$ (**2**) [5,6] crystallize in the non-centrosymmetric space groups $P2_1$ and $P2_12_12_1$, respectively (Table 1).

The coordination spheres in {[Zn(tyr)$_2$(H$_2$O)]H$_2$O}$_n$ (**1**) and [Cu(tyr)$_2$]$_n$ (**2**) are created by two symmetrically independent anions of tyrosine in both studied compounds. Fig. 1 shows the coordination sphere for **1** and **2** with the atom numbering. One tyrosine anion (A) coordinates by the nitrogen atom from the amino group, N1A, and two oxygen atoms from the carboxylate group, O1A and O2A, whereas the second tyrosine anion (B) coordinates via the nitrogen atom, N1B, and only one oxygen atom from the carboxylate group (Fig. 1). Both tyrosinate anions act as chelating ligands to the Zn^{2+} and Cu^{2+} ions, and additionally L-Tyr(A) acts a bridging entity through the carboxylate group. This arrangement occurs in compounds **1** and **2**, also the *trans* coordination of the N1A and N1B

Table 1
Crystal data and structure refinement for complexes **1** and **2**.

	1	**2**
Chemical formula	$C_{18}H_{22}N_2O_7ZnH_2O$	$C_{18}H_{20}CuN_2O_6$
M_r	461.76	423.90
Cell setting, space group	monoclinic, $P2_1$	orthorhombic, $P2_12_12_1$
Temperature (K)	295(2)	295(2)
a (Å)	6.0255(8)	6.0439(6)
b (Å)	8.0326(9)	13.0291(9)
c (Å)	20.377(2)	22.1901(14)
α (°)	90.00	90.00
β (°)	95.532(9)	90.00
γ (°)	90.00	90.00
V (Å^3)	981.7(2)	1747.4(2)
Z	2	4
Dx (Mg m^{-3})	1.562	1.611
Radiation type	Mo Kα	Mo Kα
μ (mm^{-1})	1.30	1.29
Crystal form, colour	plate, colourless	plate, blue
Crystal size (mm)	0.60 × 0.48 × 0.01	0.52 × 0.39 × 0.03
Data collection method	ω-scan	ω-scan
Absorption correction	numerical	numerical
T_{min}, T_{max}	0.520, 0.989	0.662, 0.959
No. of measured, independent and observed reflections	11 743, 3695, 2711	22 791, 4153, 3333
Criterion for observed reflections	$I > 2\sigma(I)$	$I > 2\sigma(I)$
R_{int}	0.065	0.046
θ_{max} (°)	26.4	27.9
Refinement on	F^2	F^2
$R[F^2 > 2\sigma(F^2)]$, $wR(F^2)$, S	0.037, 0.066, 0.90	0.032, 0.059, 0.95
No. of reflections	3695	4153
No. of parameters	262	244
Weighting scheme	calculated $w = 1/[\sigma^2(F_o^2) + (0.0237P)^2]$ where $P = (F_o^2 + 2F_c^2)/3$	calculated $w = 1/[\sigma^2(F_o^2) + (0.0293P)^2]$ where $P = (F_o^2 + 2F_c^2)/3$
(Δ/σ)max	0.009	0.001
$\Delta\rho_{max}$, $\Delta\rho_{min}$ (e Å^{-3})	0.31, −0.37	0.47, −0.26
Absolute structure [35]	−0.030(12), 1539 Friedel pairs	−0.031(10), 1754 Friedel pairs
Flack parameter	−0.030(12)	−0.031(10)

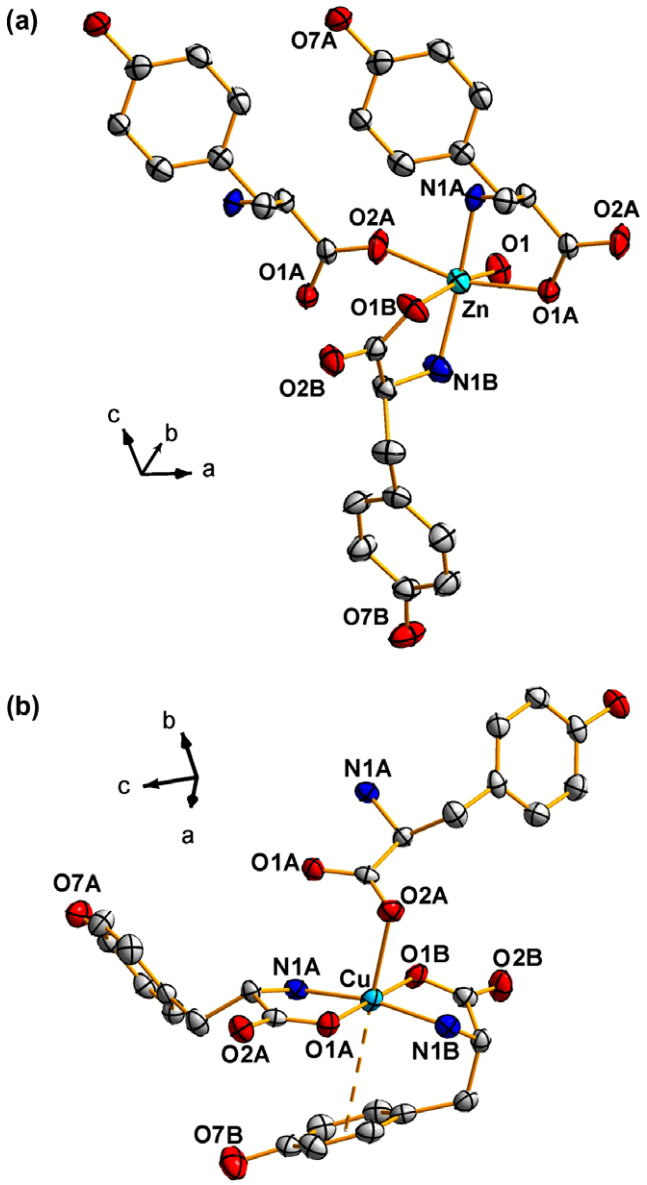


Fig. 1. Coordination sphere for $\{[Zn(tyr)_2(H_2O)]H_2O\}_n$ (**1**) and $[Cu(tyr)_2]_n$ (**2**). Hydrogen atoms are omitted for clarity.

atoms is maintained. A six-coordination sphere is created around the Zn^{2+} ion by the N and O atoms from two tyrosine anions and is completed by an O atom from a water molecule. The $Zn–O(1)_{water}$ bond distance is comparable with other six-coordinated zinc(II) complexes with aminoacids [12–14]. The coordination polyhedron around the Zn^{2+} ion is compressed along the Zn–N bonds (Table 2).

In the case of the compound $[Cu(tyr)_2]_n$ (**2**), a penta-coordinated geometry of the copper ion is well determined [5,6]. Three oxygen atoms and two nitrogen atoms form a square-pyramidal arrangement around the copper ion (Fig. 1b). A flexible chain of carbon atoms in tyrosine provide an aromatic ring which interacts with a copper ion ($Cu\cdots\pi_{centroid}$ = 3.409 Å) [4h,4i]. Thus, an extended six-coordination sphere occurs when the Cu···π interaction is taken into account. Two maximal angles, namely β = O(1A)–Cu(1)–O(1B) and α = N(1A)–Cu(1)–N(1B), result in an angular parameter $\tau = (\beta - \alpha)/60 = 0.19$ [15] which is associated with a distorted pyramidal geometry (Table 2). The Cu–N distances in compound (**2**) are comparable with the Cu–O distances, because O1A, O1B, N1A and N1B create a base of the square pyramid. The vertex of this pyramid is occupied by the O2A atom from the bridging tyrosine. The Cu–O2A bond length, 2.387(2) Å, is longer than the Cu–N and Cu–O distances in the base of the square pyramid. The respective O2A atom from the bridging tyrosine in $\{[Zn(tyr)_2(H_2O)]H_2O\}_n$ (**1**) lies in the base of the octahedron and the Zn–O2A bond length, 2.145(3) Å, is comparable with other Zn–O distances.

Table 2
Bond lengths (Å) and angles (°) for **1** and **2**.

1		**2**	
Zn–N(1A)^{i}	2.046(3)	Cu–O(1A)	1.9200(17)
Zn–N(1B)	2.086(3)	Cu–O(2A)^{ii}	2.3870(17)
Zn–O(1)	2.128(3)	Cu–O(1B)	1.9560(16)
Zn–O(1B)	2.131(3)	Cu–N(1A)	1.9907(18)
Zn–O(2A)	2.145(3)	Cu–N(1B)	2.004(2)
Zn–O(1A)^{i}	2.148(2)		
C(1A)–O(1A)	1.280(4)	C(1A)–O(1A)	1.269(3)
C(1A)–O(2A)	1.243(4)	C(1A)–O(2A)	1.238(3)
C(1B)–O(1B)	1.264(4)	C(1B)–O(1B)	1.260(3)
C(1B)–O(2B)	1.266(4)	C(1B)–O(2B)	1.247(3)
N(1A)^{i}–Zn–O(1A)^{i}	79.64(10)	O(1A)–Cu–N(1A)	84.75(7)
N(1A)^{i}–Zn–O(2A)	86.74(10)	O(1A)–Cu–O(2A)^{ii}	90.75(6)
N(1A)^{i}–Zn–N(1B)	172.27(14)	O(1A)–Cu–O(1B)	179.31(8)
N(1A)^{i}–Zn–O(1B)	94.08(11)	O(1A)–Cu–N(1B)	96.93(7)
N(1A)^{i}–Zn–O(1)	97.41(12)	O(1B)–Cu–O(2A)^{ii}	89.91(6)
N(1B)–Zn–O(1)	90.31(12)	O(1B)–Cu–N(1A)	95.25(7)
N(1B)–Zn–O(1A)^{i}	100.84(11)	O(1B)–Cu–N(1B)	82.92(7)
N(1B)–Zn–O(2A)	93.94(12)	N(1A)–Cu–O(2A)^{ii}	104.58(7)
N(1B)–Zn–O(1B)	78.22(12)	N(1A)–Cu–N(1B)	167.74(8)
O(1)–Zn–O(1B)	168.27(11)	N(1B)–Cu–O(2A)^{ii}	87.57(7)
O(1)–Zn–O(1A)^{i}	84.27(11)		
O(1)–Zn–O(2A)	88.17(10)		
O(1B)–Zn–O(1A)^{i}	100.18(11)		
O(1B)–Zn–O(2A)	90.14(11)		
O(2A)–Zn–O(1A)^{i}	163.41(10)		

Symmetry transformations used to generate equivalent atoms: (i) $x+1,y,z$; (ii) $x-1/2,-y+3/2,-z$.

One-dimensional coordination polymeric structures exist in $\{[Zn(tyr)_2(H_2O)]H_2O\}_n$ (**1**) and $[Cu(tyr)_2]_n$ (**2**) (Figs. 2 and 3), due to one tyrosine ligand acting as a bridging ligand. In the case of the compound (**1**), the coordination polymer is created as an unstranded chain (Fig. 2) with *trans* coordination of the carboxylate groups of L-Tyr(A). The distance between the Zn^{2+} ions in the chain is associated with the parameter a = 6.0255(8) Å. The distance between the Zn^{2+} ions in the neighbouring chains equals 10.951(1) Å. However, the chains are slightly shifted with respect to each other along the a-axis as a result of crystallization with

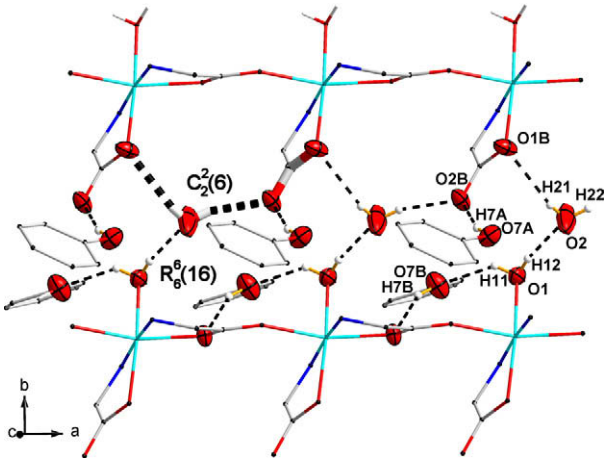


Fig. 2. Two chains of the 1D coordination polymer connected by a hydrogen bonding network in the structure of $\{[Zn(tyr)_2(H_2O)]H_2O\}_n$ (**1**). Some atoms were omitted for clarity.

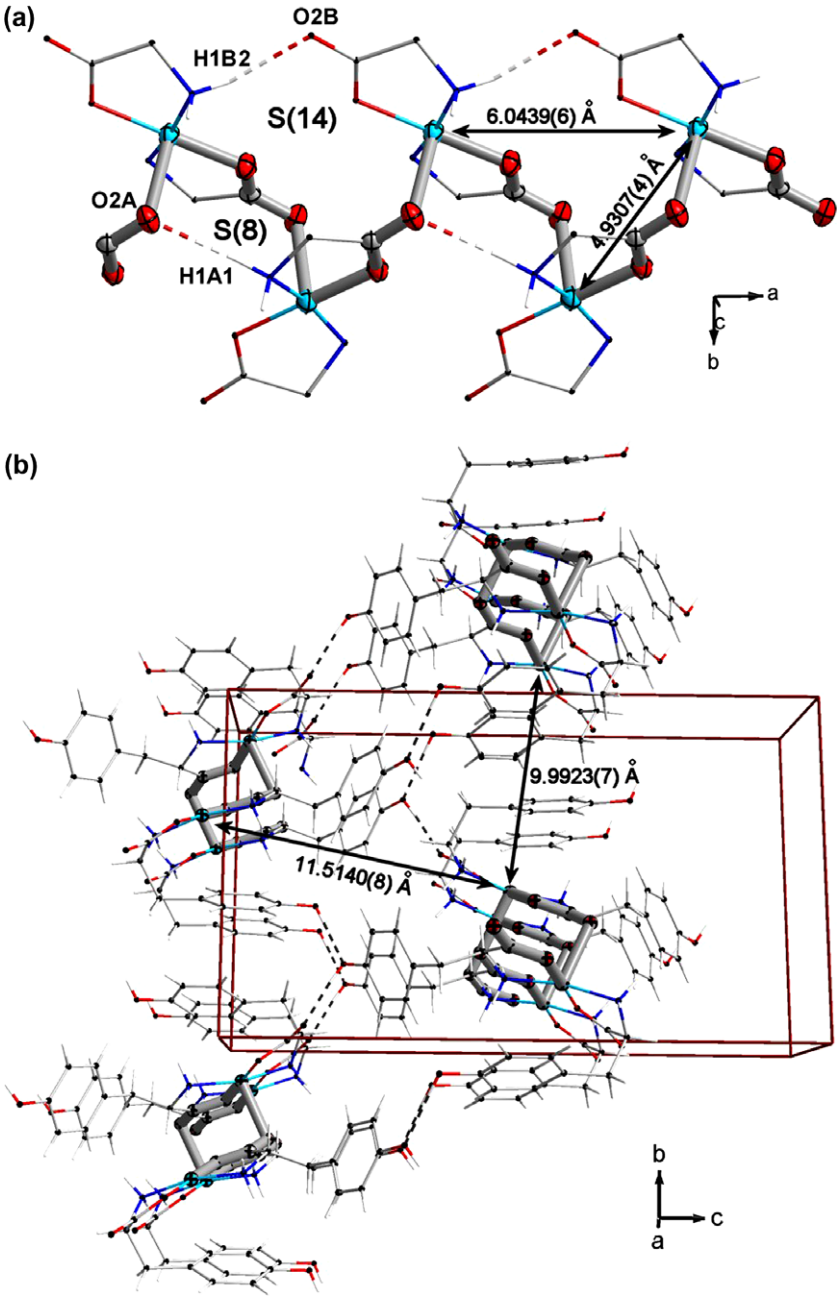


Fig. 3. (a) A helical chain of $[Cu(tyr)_2]_n$ (**2**) stabilized by two intramolecular hydrogen bonds. (b) Hydrogen bonding interactions between helixes viewed down [1 0 0].

the monoclinic space group with $\beta = 95.532(9)^\circ$. Contrary to the unstranded 1D polymeric structure of **1**, $[Cu(tyr)_2]_n$ (**2**) has a left-handed helical arrangement. The helix is extended along the *a*-axis and undergoes a complete turn every two copper ions, which are distanced from each other by 4.9307(4) Å (Fig. 3).

The most important reason for the unstranded structure formation of **1** and the helical structure of **2** is a different stereo geometry of the bridging carboxylate group in the coordination sphere of the Zn^{2+} and Cu^{2+} ions. A *trans* coordination results in the unstranded chain in **1**, whereas the *cis* coordination in **2** facilitates the helical structure which is also allowed by the symmetry element (2_1 axis). Overall, it appears that helical coordination polymers can be formed when the bridging ligands realize a *cis* coordination mode, as in the case of *catena*-(μ-CrO_4-O,O′)[$Ni(HIm)_3(H_2O)$] (HIm = 1H-imidazole) [16]. Additionally, if no enantiomeric molecule acts as a ligand, then left- and right-handed helixes exist simultaneously in the structure.

The polymeric structures of the compounds {$[Zn(tyr)_2(H_2O)]$-H_2O}$_n$ (**1**) and $[Cu(tyr)_2]_n$ (**2**) are stabilized by intra- and interchain hydrogen bonds (Figs. 2 and 3b; Table 3). However, intrachain hydrogen bonds exist only in the helical chain of compound (**2**). They are formed between the amino and carboxylate groups from L-Tyr(A), N(1A)–H(1A1)···O(2A), and this hydrogen bonding pattern is denoted by the S(8) graph set (Fig. 3a) [17]. The second intrachain hydrogen bond is created by the L-Tyr(B) anion, N(1B)–H(1B2)···O(2B), and the pattern is described by the S(14) graph set [17]. This arrangement resembles the hydrogen bond network in the α-helical structure of proteins. The helical structure of (**2**) is stabilized by two interchain hydrogen bonds created by the hydroxyl group from L-Tyr(A). This group is involved as a donor in the

Table 3
Hydrogen bonds for **1** and **2** (Å and °).

D–H···A	d(D–H)	d(H···A)	d(D···A)	<(DHA)
1				
N(1A)–H(1A1)···O(7A)^{i}	0.90	2.10	2.938(4)	154.7
N(1B)–H(1B1)···O(7B)^{iii}	0.90	2.44	3.243(5)	149.3
O(7A)–H(7A)···O(2B)^{ii}	0.82	1.89	2.690(3)	163.3
O(7B)–H(7B)···O(1A)^{iv}	0.82	1.96	2.721(3)	153.4
O(1)–H(11)···O(7B)^{iii}	0.80	2.34	2.961(4)	135.1
O(1)–H(12)···O(2)	0.80	1.90	2.675(4)	163.2
O(2)–H(21)···O(1B)^{v}	0.78	2.32	3.007(5)	147.4
O(2)–H(22)···O(2B)^{vi}	0.78	2.02	2.777(4)	162.5
2				
N(1A)–H(1A1)···O(2A)^{vii}	0.90	2.20	3.072(2)	162.7
N(1B)–H(1B2)···O(2B)^{ix}	0.90	2.23	3.080(3)	156.7
O(7A)–H(7A)···O(2B)^{viii}	0.82	1.81	2.631(2)	174.4
O(7B)–H(7B)···O(7A)^{x}	0.82	1.93	2.746(3)	178.7

Symmetry transformations used to generate equivalent atoms: (i) $-x,y+1/2,-z+2$; (ii) $-x+1,y+1/2,-z+2$; (iii) $-x+1,y+1/2,-z+1$; (iv) $-x+1,y-1/2,-z+1$; (v) $x,y+1,z$; (vi) $x+1,y+1,z$; (vii) $x-1,y,z$; (viii) $-x+1/2,-y+1,z+1/2$; (ix) $x+1,y,z$; (x) $-x+1,y-1/2,-z+1/2$.

O(7A)–H(7A)···O(2B) hydrogen bond as well as an acceptor in the O(7B)–H(7B)···O(7A) hydrogen bond.

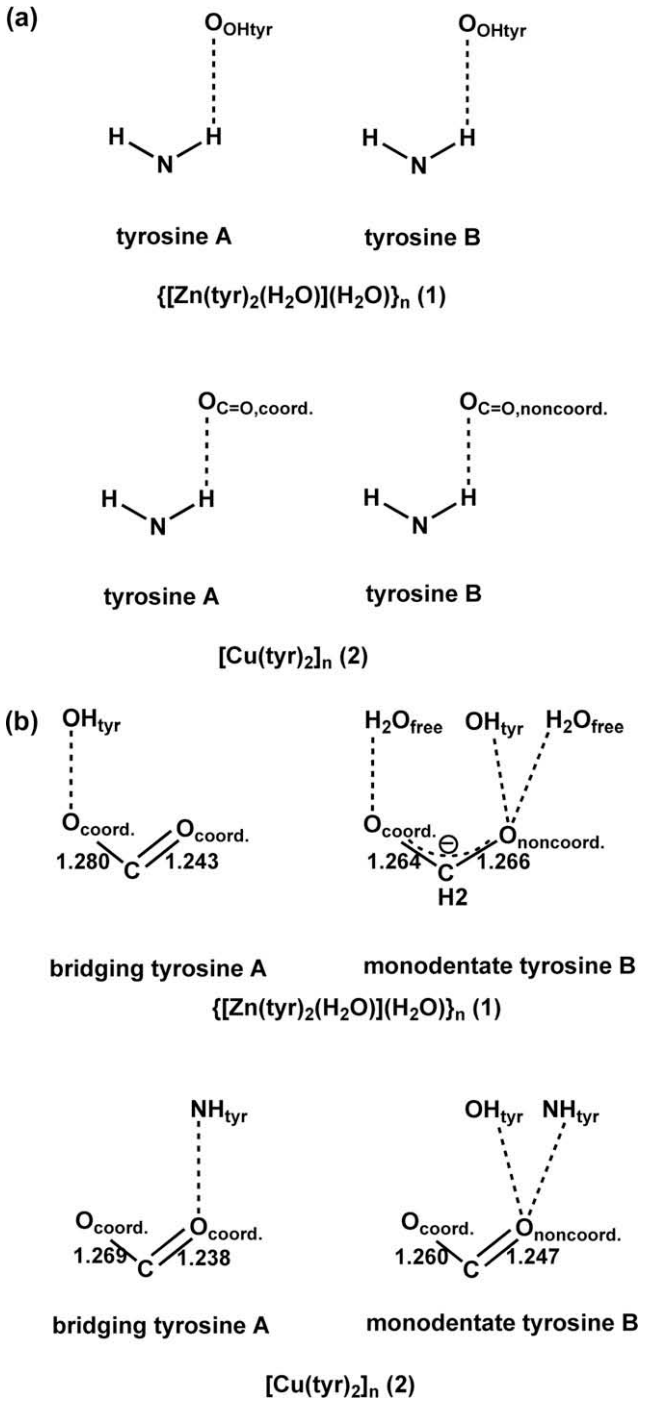
Contrary to the structure of (**2**), the amino groups create only interchain hydrogen bonds in the structure of $\{[Zn(tyr)_2(H_2O)]\text{-}H_2O\}_n$ (**1**) (Table 3). Each of the amino groups from two independent L-tyrosinate anions, L-Tyr(A) and L-Tyr(B), is involved in one hydrogen bond with the hydroxyl group as an acceptor. Besides, two molecules of water exist in the asymmetric unit of $\{[Zn(tyr)_2\text{-}(H_2O)]H_2O\}_n$ (**1**) (Table 3, Scheme 1). A non-coordinated molecule, H_2O_{free}, interacts with the carboxylate group from L-Tyr(B) resulting in a binary chain pattern, $C_2^2(6)$ (Fig. 2). A coordinated molecule of water interacts with H_2O_{free}, O(1)–H(12)···O(2), and the hydroxyl group of L-Tyr(B), O(1)–H(11)···O(7B), giving a large ring pattern designated as $R_6^6(16)$. Therefore, it appears that the presence of molecules of water is essential for the stabilisation of the Zn–COO–Zn backbone of the coordination polymer and additionally for stabilisation of the L-tyrosinate residue.

3.2. Vibrational IR–FIR spectroscopy

In the spectra of $\{[Zn(tyr)_2(H_2O)]H_2O\}_n$ (**1**) and $[Cu(tyr)_2]_n$ (**2**), a broad absorption presents a multiple structure in the frequency range 3310–2500 cm^{-1}, which is assigned to ν_{as} and ν_s of the N–H and C–H vibrations [18,19]. These bands are observed at the same frequencies as for the ligand spectrum. An additional band, which appears at 3552 cm^{-1} in the spectra of complex **1**, is correlated with the ν(O–H) vibration of water molecules.

The region 1610–1290 cm^{-1} is characteristic of ν_{as} and ν_s vibrations of the carboxylate groups [1,20–22]. The coordination mode of the carboxylate group can be determined according to the correlation reported in [1,20a], where the value of the relation $\Delta\nu(COO) = \nu_{as}(COO) - \nu_s(COO)$ follows the order: $\Delta\nu_{monodentate}$ (much longer than 50 cm^{-1}) > $\Delta\nu_{ionic} \approx \Delta\nu_{bridging} > \Delta\nu_{chelate}$ (less than 50 cm^{-1}). The band assigned to the ν_{as} COO group vibrations is found at 1600 cm^{-1} for tyrosine salt and at 1604 and 1602 cm^{-1} for **1** and **2**, respectively. The ν_s COO vibration frequency equals 1422 cm^{-1} for sodium L-tyrosinate, whereas for both complexes the ν_s vibration is found as a doublet with components centred at 1450, 1404 cm^{-1} (**1**) and 1458, 1402 cm^{-1} (**2**). The magnitudes of separation $\Delta\nu = \nu_{as} - \nu_s$ for the complexes (154 cm^{-1} (**1**) and 144 cm^{-1} (**2**)) are close to the value for L-tyrosine salt (the ionic value is 175 cm^{-1}) and imply a bridging coordination mode of the carboxylate, which is in good agreement with the structural data.

In the ligand spectrum an intensive absorption at 1559 cm^{-1} is correlated with the δ NH_2 vibration, whereas very strong bands at



Scheme 1. The hydrogen bonds created by amino and carboxylate groups.

1279 and 1265 cm^{-1} are assigned to ρ_r NH_2 [20a,b,18]. The δ NH_2 bands are centred at 1592 cm^{-1} (**1**) and 1581 cm^{-1} (**2**), whereas the respective ρ_r vibrations are correlated with very strong bands at 1255, 1243 cm^{-1} (**1**) and 1247, 1234 cm^{-1} (**2**). A single band at 1101 cm^{-1} found in the spectrum of the tyrosine salt is correlated with the ρ_t and ρ_w NH_2 vibrations [20a,b,18]. This band becomes more intensive and is split into two well resolved components at 1099 cm^{-1}, 1080 cm^{-1} for (**1**) and 1093 cm^{-1}, 1078 cm^{-1} for (**2**). In addition, these bands are shifted to lower energy and this effect can be connected with the weak hydrogen bond interaction of the NH_2 group (Scheme 1).

In the range 650–50 cm^{-1} the spectra of the $\{[Zn(tyr)_2(H_2O)]\text{-}H_2O\}_n$ (**1**) and $[Cu(tyr)_2]_n$ (**2**) show the bands located at 496(m)

(**1**) and 488(s) cm^{-1} (**2**), which are tentatively assigned to ν_{asym} M–N vibrations. The ν_{asym} M–$O_{carboxylate}$ vibrations are found at 349 and 333 cm^{-1} for **1** and **2**, respectively [1,20e,23,24]. Additionally, the spectrum of $\{[Zn(tyr)_2(H_2O)]H_2O\}_n$ (**1**) exhibits a broad and weak band at 589 cm^{-1} which is connected with H_2O librations.

3.3. Electronic NIR–Vis–UV spectroscopy

Fig. 4 presents the NIR–Vis–UV electronic spectra of $\{[Zn(tyr)_2(H_2O)]H_2O\}_n$ (**1**), $[Cu(tyr)_2]_n$ (**2**) and the L-tyrosine disodium salt (L). The reflectance spectra of the free ligand and the compounds show intense and slightly resolved bands in the region 27000–50000 cm^{-1}, related to the intraligand charge transfer π–π^* and n–π^* transitions in the L-tyrosine salt. The intraligand transition bands are blue-shifted upon coordination. These bands are observed for $\{[Zn(tyr)_2(H_2O)]H_2O\}_n$ (**1**) as a clearly marked maxima at *ca.* 36000 and 42370 cm^{-1} (Fig. 4a).

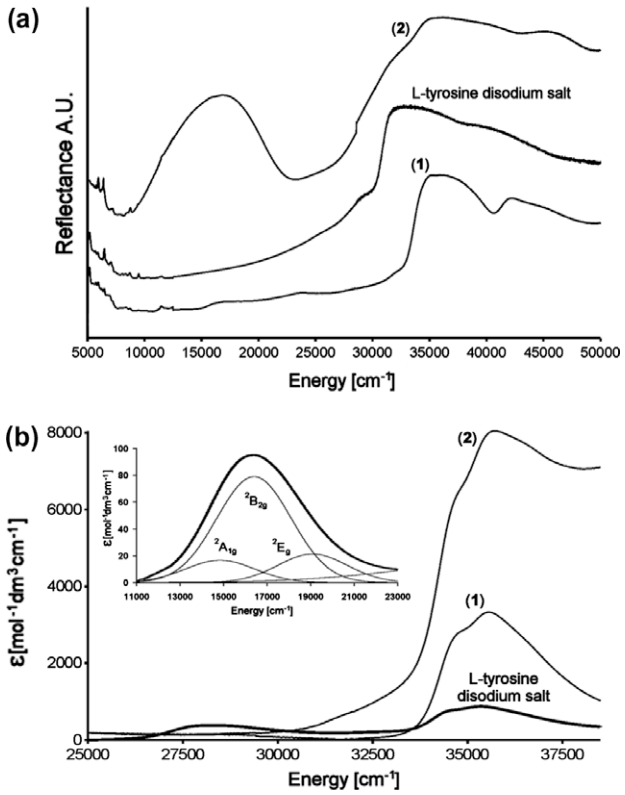


Fig. 4. (a) The reflectance spectra of $\{[Zn(tyr)_2(H_2O)]H_2O\}_n$ (**1**), $[Cu(tyr)_2]_n$ (**2**) and the L-tyrosine disodium salt. (b) The absorbance spectra for **1**, **2** and the L-tyrosine disodium salt in DMSO solution. The inset shows the gaussian analysis of the spectrum of $[Cu(tyr)_2]_n$ (**2**) in the 11000–23000 cm^{-1} region.

The spectrum of the free ligand dissolved in DMSO presents two broad absorption bands at 28300 cm^{-1} (ε = 400 mol^{-1} dm^3 cm^{-1}) and 35400 cm^{-1} (ε = 880 mol^{-1} dm^3 cm^{-1}) with a shoulder at 34580 cm^{-1} (ε = 780 mol^{-1} dm^3 cm^{-1}). For the solution spectra of both complexes slight blue-shifted bands appear at 35700 cm^{-1} (ε = 8000 mol^{-1} dm^3 cm^{-1}) and 35620 cm^{-1} (ε = 3300 mol^{-1} dm^3 cm^{-1}) for **1** and **2**, respectively, and they are related to the n–π^* charge transfer transition (Fig. 4b). Such an absorption at 35700 cm^{-1} (ε = 2940 mol^{-1} dm^3 cm^{-1}) was noticed for $[Zn(tyr)_2] \cdot 2H_2O$ in DMSO solution by Refat et al. [2]. Additionally, these authors have observed a broad band at 30770 cm^{-1} (ε = 500 mol^{-1} dm^3 cm^{-1}) and have assigned it to the charge transfer Zn(II) ← L transition for $[Zn(tyr)_2] \cdot 2H_2O$ [2]. For the spectra of $\{[Zn(tyr)_2(H_2O)]H_2O\}_n$ (**1**) dissolved in DMSO we expected an analogous intensive band at 30770 cm^{-1}, but it was not observed. The band at 30770 cm^{-1} observed for $[Zn(tyr)_2] \cdot 2H_2O$ by Refat et al. [2] probably is correlated with a n–π^* transition in pure L-tyrosine, but not with a Zn(II) ← L transition. However, a broad absorption without a distinct maximum for the $[Cu(tyr)_2]_n$ (**2**) solution and solid state spectra in the energy range 27000–33000 cm^{-1} can be tentatively related to a Cu(II) ← L-tyrosine charge transfer transition (Fig. 4).

3.3.1. d–d transitions in $[Cu(tyr)_2]_n$ (2)

It follows from the crystal structure of $[Cu(tyr)_2]_n$ (**2**) that the five-coordinate geometry around the Cu^{2+} ions results in a *trans*-CuN_2O_2O' chromophore (Fig. 1b). Such a chromophore involving the Cu^{2+} ion has been formed by other bidendate N,O-coordinated amino acids in $[Cu(L\text{-}Arg)_2(H_2O)]^{2+}$ [21], $[Cu(L\text{-}Arg)_2(H_2O)]_2^{4+}$ [25], $[Cu(DL\text{-}alaO)_2(H_2O)]^{2+}$ [26] and $[Cu(DL\text{-}pipe\text{-}3)_2(H_2O)]$ [22]. The reflectance spectrum of **2** exhibits an asymmetric single broad band with a maximum at 16790 cm^{-1} and a slightly marked shoulder at 12360 cm^{-1}, which is characteristic of a penta-coordinated geometry of the Cu^{2+} ion. A pseudo-octahedral geometry with $Cu\cdots\pi_{centroid}$ = 3.409 Å as a six-coordination place (see Section 3.1) should be rejected from a spectroscopic point of view.

The five-coordinated geometry can be described as an ideal square-pyramidal (SP) when the angular structure parameter $\tau = 0$, or an ideal trigonal-bipyramidal (TBP) with $\tau = 1$ [15]. For $[Cu(tyr)_2]_n$ (**2**), the value of the τ parameter is 0.19 which implies that the geometry can be described as a slightly distorted square pyramid. In addition, the value of the tetragonality parameter T (T = the average four-in-plane distance/the axial out-of plane distance) also displays a slight axial distortion, with T = 0.824.

Table 4 presents the values of τ, T and electronic energy transitions for a series of compounds with a distorted square-pyramidal geometry and the CuN_2O_2O' chromophore. The electronic spectra of $[Cu(L\text{-}Arg)_2(H_2O)]^{2+}$ [21], $[Cu_2(\mu\text{-}O_2CCH_3)_2(\mu\text{-}OCOCH_3)(dpyam)_2](BF_4)$ [28] and $[Cu(DL\text{-}pipe\text{-}3)_2(H_2O)]$ [22] exhibit a single band and the value of τ is almost 0. The reflectance electronic spectra of $[Cu(L\text{-}Arg)_2]_2(pma) \cdot 4H_2O$ [18], $[Cu_2(\mu\text{-}O_2CCH_3)(\mu\text{-}OH)(\mu\text{-}OH_2)(phen)_2](ClO_4)_2$, $[Cu_2(\mu\text{-}O_2CCH_2CH_3)(\mu\text{-}OH)(\mu\text{-}OH_2)(bpy)_2]$

Table 4
The spectroscopic data of compounds with a square-pyramidal geometry and the CuN_2O_2O' chromophore.

	Compound	T	τ	Energy band (in cm^{-1})	References
1	$[Cu(L\text{-}Arg)_2(H_2O)]CO_3 \cdot H_2O$	0.850	0.03	16130	[21]
2	$[Cu_2(\mu\text{-}OOCCH_3)_2(\mu\text{-}OOCCH_3)(dpyam)_2](BF_4)$	0.925	0.07	14100	[28]
3	$[Cu(DL\text{-}pipe\text{-}3)_2(H_2O)]$	0.883	0.085	16340	[22]
4	$[Cu(L\text{-}Arg)_2]_2(pma) \cdot 4H_2O$	0.788	0.16	$14280_{(sh)}$, 16670	[25]
5	$[Cu_2(\mu\text{-}O_2CCH_3)(\mu\text{-}OH)(\mu\text{-}OH_2)(phen)_2](ClO_4)_2$	0.835, 0.825	0.02, 0.14	$13070_{(sh)}$, 16310	[28]
6	$[Cu_2(\mu\text{-}O_2CCH_2CH_3)(\mu\text{-}OH)\ (\mu\text{-}OH_2)(bpy)_2](ClO_4)_2$	0.824, 0.825	0.16, 0.20	$14080_{(sh)}$, 16860	[28]
7	$[Cu(tyr)_2]_n$ (**2**)	0.824	0.19	$12360_{(sh)}$, 16790	[5], this work

τ, angular structure parameter (index of trigonality); T, tetragonality; L-Arg, L-arginine; dpyam, di-2pyridylamine; DL-pipe-3, DL-piperidine-3-carboxylic acid; pma, 1,2,4,5-tetracarboxylate (pyromellitate); Phen, phenantroline; bpy, 2,2′-bipyridine.

$(ClO_4)_2$ [28] and $[Cu(tyr)_2]_n$ (**2**) show a broad band at ~16500 cm^{-1} with a lower energy shoulder at ~13500 cm^{-1}. The τ parameters found for these compounds are in the range 0.14–0.20 and the Cu^{2+} environments can be more precisely analysed as a near square based pyramid (SBP), showing a slight distortion towards trigonal bipyramid. This distortion probably results in the shoulder at ~13500 cm^{-1}. The spectrum of $[Cu(phen)_2Cl](BPh_4)$ exhibits a high-energy peak at 14500 cm^{-1} with a clearly resolved shoulder at 11500 cm^{-1}, and the τ parameter is equal to 0.19, such as for $[Cu(tyr)_2]_n$ (**2**). However, a bathochromic effect is observed due to the chlorine anion coordinated to the Cu^{2+} in $[Cu(phen)_2Cl](BPh_4)$ [27].

The $[Cu(tyr)_2]_n$ (**2**) reflectance spectrum was analysed for the one-electron ground state configuration in square-pyramidal geometry, $d_{x^2-y^2} \gg d_{z^2} > d_{xy} > d_{xz} \approx d_{yz}$ [27–30]. The principal high-energy band at 16500 cm^{-1} results from $d_{xy}, d_{xz} \approx d_{yz} \rightarrow d_{x^2-y^2}$ transitions [27], whereas the shoulder band at 13500 cm^{-1} can be assigned to the $d_{z^2} \rightarrow d_{x^2-y^2}$ transition (Fig. 4a). In the tetragonal ligand field (D_{4h} or C_{4V} symmetry), the ground state term $^2E_g(O_h)$ is split into $^2B_{1g}(d_{x^2-y^2})$ and $^2A_{1g}$ (d_{z^2}) states, whereas the state term $^2T_{2g}(O_h)$ is also split into $^2B_{2g}$ (d_{xy}) and ^2E_g (d_{xz}, d_{yz}). Thus, for C_{4V} (sP) symmetry three spin allowed electronic transitions $^2B_1$ ($d_{x^2-y^2}$) → $^2A_1$ (d_{z^2}), $^2B_2$ (d_{xy}) and ^2E (d_{xz}, d_{yz}) are expected as single overlapped bands under the broad absorption shape [31,32]. The band analysis was performed with a maximum of three Gaussian curves centred at 14850 cm^{-1} (ε = 16.5 mol^{-1} dm^3 cm^{-1}), 16410 cm^{-1} (ε = 78.9 mol^{-1} dm^3 cm^{-1}) and 19100 cm^{-1} (ε = 21.1 mol^{-1} dm^3 cm^{-1}) corresponding to the transitions $^2B_1 \rightarrow {}^2A_1$, $^2B_1 \rightarrow {}^2B_2$ and $^2B_1 \rightarrow {}^2E$, respectively (Fig. 4b).

3.4. EPR and magnetic characterization of $[Cu(tyr)_2]_n$ (**2**)

A study of the magnetic susceptibility data for the examined complex has been performed within the temperature range 1.80–300 K. The experimental data, plotted as thermal variations of χ_M and $\chi_M T$, are shown in Fig. 5a. The χ_M values increase slowly with the decrease of temperature, but in the low-temperature region a rapid increase of the molar susceptibility occurred without showing a peak.

The value of $\chi_M T$ at room temperature is equal to 0.41 cm^3 mol^{-1} K (1.82 B.M.) as expected for an uncoupled copper(II) ion [33]. The $\chi_M T$ value decreases smoothly over a wide range of temperatures and decreases rapidly at the lowest temperatures to 0.34 cm^3 mol^{-1} K (1.65 B.M.). The slight decrease of $\chi_M T$ in the low-temperature range is caused by the occurrence of an antiferromagnetic interaction between the nearest Cu(II) ions.

To quantitatively interpret the susceptibility data, we have used a one-dimensional model [2] in which the magnetic chain is provided by an array of equally spaced copper(II) ions with S_{Cu} = ½ local spins. The relevant spin Hamiltonian in a zero-field adapted to describe the isotropic interaction between the nearest neighbour ions is defined by Eq. (1) [31,34]:

$$H = -J\sum_{i=1}^{n} S_{A_i} \cdot S_{A_{i+1}} \quad (1)$$

The magnetic susceptibility for $J < 0$ is defined by the Bonner and Fischer equation (2):

$$\chi_M = \frac{Ng^2\beta^2}{kT}\frac{0.25 + 0.074975x + 0.075235x^2}{1.0 + 0.9931x + 0.172135x^2 + 0.757825x^3} \quad (2)$$

with

$$x = |J|/kT$$

where N is Avogadro's number, g is the spectroscopic splitting factor, β is the Bohr magneton, k is the Boltzmann constant and J is the intramolecular exchange parameter.

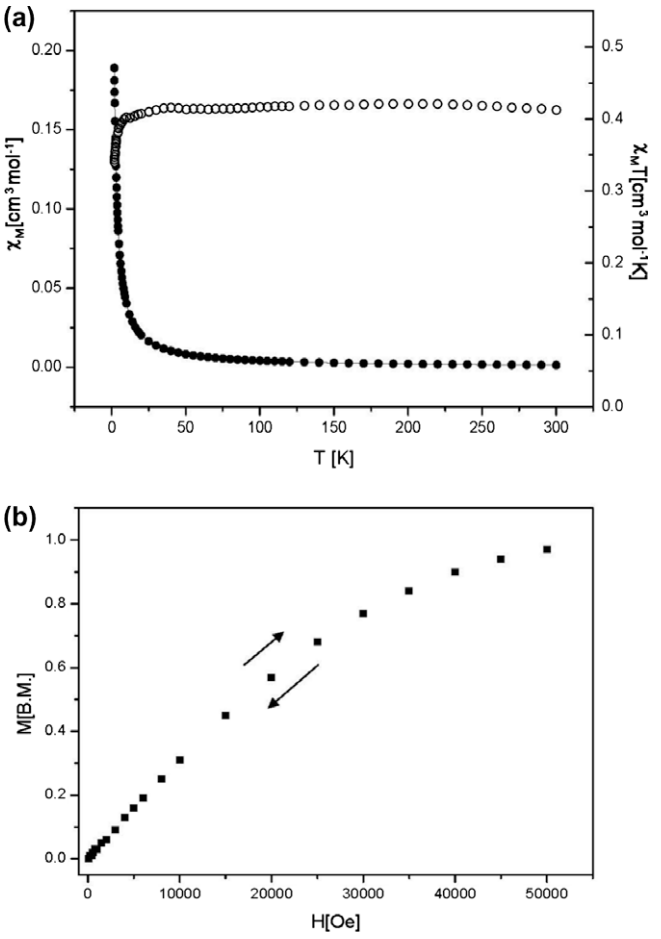


Fig. 5. (a) The thermal dependence of $\chi_M T$ (○) and χ_M (●) for $[Cu(tyr)_2]_n$ (**2**), the solid line is the calculated curve and (b) the field dependence of the magnetization for **2**.

The best fit parameters of g = 2.17 and J = −0.10 cm^{-1} were obtained with a good agreement factor for $R = 1.46 \times 10^{-6}$:

$$\left[R = \sum (M_{exp} - M_{calc})^2 \Big/ \sum (M_{exp})^2\right].$$

The values of the Curie and Weiss constants determined from the relation $1/\chi_M T = f(T)$ over the temperature range 50–300 K are equal to 0.42 cm^3 mol^{-1} and −0.47 K. A negative value of the Weiss constant and intramolecular exchange parameter obtained from the calculation confirm the occurrence of a weak antiferromagnetic interaction between the nearest copper centres.

The variation of the magnetization versus magnetic field at 2 K (Fig. 5b), clearly supports the occurrence of spontaneous magnetic moments in the examined compound with M_s = 0.97 B.M. at 5 T. The obtained value is typical of a $S = {}^1/_2$ ground state of the Cu(II) ion. Very weak antiferromagnetic interactions in the examined complex could be assigned to the intramolecular interactions between the copper centres inside the polymeric chain, which may be transmitted through the L-tyrosinate ligand. As mentioned in the structure discussion, this complex can be viewed as a one-dimensional chain, which is stabilized by the hydrogen bond network formed between the uncoordinated C=O oxygen atoms with tyrosine OH group. These features create further possibilities for the magnetic exchange pathway. Unfortunately the distances between the copper ions in the neighbouring chains are equal to 9.9923(7) or 11.5140(8) Å and are much longer than the intramolecular distances between the metallic centres in the same chain,

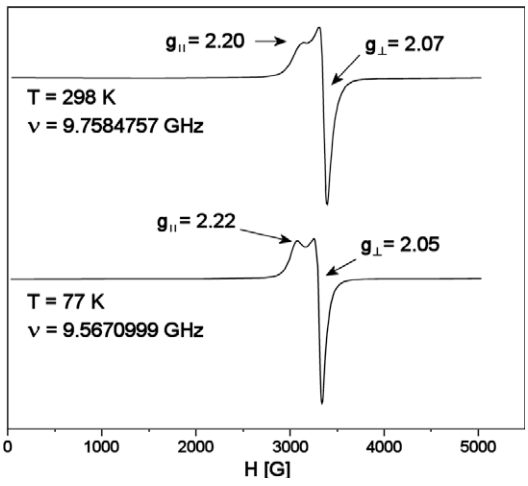


Fig. 6. EPR spectra for $[Cu(tyr)_2]_n$ at room temperature and 77 K.

4.9307(4) and 6.0439(7) Å. This fact suggests that an interchain interaction (J') can be ruled out.

The EPR spectrum of a polycrystalline sample of the examined compound measured at room temperature and 77 K presents an anisotropic signal composed of two line at $g_{II} = 2.20$ and $g_{\perp} = 2.07$ (298 K) and $g_{II} = 2.22$ and $g_{\perp} = 2.05$ (77 K) (Fig. 6). The structure is associated only with the electronic configuration ($S = {}^1/_2$) of the $d_{x^2-y^2}$ ground state for a distorted square based pyramidal ligand field.

Supplementary data

CCDC 707764 contains the supplementary crystallographic data for $\{[Zn(tyr)_2(H_2O)]H_2O\}_n$. These data can be obtained free of charge via http://www.ccdc.cam.ac.uk/conts/retrieving.html, or from the Cambridge Crystallographic Data Centre, 12 Union Road, Cambridge CB2 1EZ, UK; fax: (+44) 1223-336-033; or e-mail: deposit@ccdc.cam.ac.uk.

Acknowledgments

This work was supported by a grant from the Wroclaw University of Technology (No. 343-677/Z03-04). One of the authors (M.D.) is grateful to the Foundation for Polish Science for The Domestic Grant for Young Scientists.

References

[1] (a) F. Zhang, T. Yajlma, H. Masuda, A. Odani, O. Yamauchi, Inorg. Chem. 36 (1997) 5777;
(b) N. Nakamura, T. Kohzuma, H. Kuma, S. Suzuki, J. Am. Chem. Soc. 114 (1992) 6550;
(c) C. Redshaw, V.C. Gibson, W. Clegg, A.J. Edwards, B. Miles, J. Chem. Soc., Dalton Trans. (1997) 3343;
(d) P. Emseis, D.E. Hibbs, P. Leverett, N. Reddy, P.A. Wiliams, Inorg. Chim. Acta 357 (2004) 3251;
(e) R. Hamalainen, K. Lajunen, J. Valkonen, Finn. Chem. Lett. (1997) 108;
(f) K. Kobayashi, H. Takahashi, M. Nishio, Y. Umezawa, K. Tsuboyama, S. Tsuboyama, Anal. Sci. 16 (2000) 1103;
(g) Xue-Yi Le, Ming-Liang Tong, Yin-Lian Fu, Liang-Nian Ji, Acta Chim. Sinica 690 (2002) 367;
(h) F. Apfelbaum-Tibika, A. Bino, Inorg. Chem. 23 (1984) 2902;
(i) J.McB. Harrowfield, A.M. Sargeson, J. Springborg, M.R. Snow, D. Taylor, Inorg. Chem. 22 (1983) 186;
(j) C.A. McAuliffe, S.G. Murray, Inorg. Chim. Acta 7 (1973) 171.
[2] M.S. Refat, S.A. El-Korashy, A.S. Ahmed, J. Mol. Struct. 881 (2008) 28.
[3] Q. Xe, Y.-H. Li, Q. Wu, Y.-M. Song, J.-X. Wang, H. Zhao, R.-G. Xiong, Z. Xue, Chem. Eur. J. 11 (2005) 998.
[4] (a) Yamel Pel, Li Wang, Acta Crystallogr., Sect. E 62 (2006) m1668;
(b) P. Emseis, D.E. Hibbs, P. Leverett, N. Reddy, P.A. Williams, Inorg. Chim. Acta 357 (2004) 2669;
(c) D.U. Miodragovic, G.A. Bogdanovic, S.M. Milosavijevic, M.J. Malinar, M.B. Celap, A. Spasojevic-de Bire, S. Macura, N. Juranic, Enantiomer 6 (2001) 299;
(d) R. Dreos, G. Nardin, L. Randaccio, P. Siega, G. Tauzher, Inorg. Chem. 43 (2004) 3433;
(e) G.A. Bogdanovic, D.U. Miodragovic, M.J. Malinar, Acta Crystallogr., Sect. C 58 (2002) m338;
(f) P. Emseis, D.E. Hibbs, P. Leverett, N. Reddy, P.A. Williams, J. Coord. Chem. 56 (2003) 661;
(g) O. Yamauchi, A. Odani, T. Kohzuma, H. Masuda, K. Toriumi, K. Sato, Inorg. Chem. 28 (1989) 4066;
(h) X. Solans, L. Ruiz-Ramirez, A. Martinez, L. Gasque, R. Moreno-Esparza, Acta Crystallogr., Sect. C 48 (1992) 1785;
(i) T. Sugimori, H. Masuda, N. Ohata, K. Koiwai, A. Odani, O. Yamauchi, Inorg. Chem. 36 (1997) 576;
(j) R. Hamalainen, M. Ahlgren, U. Turpeinen, T. Raikas, Cryst. Struct. Commun. 7 (1978) 379;
(k) T.C. Jarzab, C.R. Hare, D.A. Langs, Cryst. Struct. Commun. 2 (1973) 399;
(l) O. Yamauchi, A. Odani, H. Masuda, Inorg. Chim. Acta 198 (1992) 749;
(m) K. Majumder, R.J. Butcher, S. Bhattacharya, Inorg. Chem. 41 (2002) 4605;
(n) P. Emseis, P. Leverett, P.A. Williams, R.J. Butcher, Inorg. Chim. Acta 357 (2004) 4614;
(o) R. Dreos, G. Nardin, L. Randaccio, P. Siega, G. Tauzher, Inorg. Chem. 24 (2004) 3433.
[5] Jiabao Weng, Maochun Hong, Qian Shi, Rong Cao, Albert S.C. Chan, Eur. J. Inorg. Chem. (2002) 2553.
[6] D. van der Helm, C.E. Tatsch, Acta Crystallogr., Sect. B 28 (1972) 2307.
[7] N. Okabe, M. Hokaze, Chem. Pharm. Bull. 41 (1993) 605.
[8] M. Mayer, CRYSALIS Data Reduction Program, Version 1.171.32.6, Oxford Diffraction Ltd., 2006.
[9] G.M. Sheldrick, SHELXS and SHELXL, University of Göttingen, Germany, 1997.
[10] (a) G. Bierman, H. Ziegler, Anal. Chem. 58 (1986) 536;
(b) J. Myrczek, Spectr. Lett. 23 (1990) 1027;
(c) A. Wojciechowska, Z. Staszak, A. Pietraszko, W. Bronowska, M. Cieślak-Golonka, Polyhedron 21 (2001) 2063;
(d) I.A. Slavić, Nucl. Instr. Meth. 134 (1976) 285;
(e) A. Bartecki, Z. Staszak, Comp. Enh. Spectr. 2 (1984) 129.
[11] E. König, Magnetic Properties of Coordination and Organometallic Transition Metal Compounds, Springer-Verlag, Berlin, 1966.
[12] M. Rombach, M. Gelinsky, H. Vahrenkamp, Inorg. Chim. Acta 334 (2002) 25.
[13] R. Hamalainen, Finn. Chem. Lett. (1977) 113.
[14] L. Kryger, S.E. Rasmussen, Acta Chem. Scand. 27 (1973) 2674.
[15] A.W. Addison, T.N. Rao, J. Reedijk, J. van Rijn, G.C. Verschoor, J. Chem. Soc., Dalton Trans. (1984) 1349.
[16] M. Daszkiewicz, W. Bronowska, A. Pietraszko, Z. Staszak, M. Cieślak-Golonka, J. Mol. Struct. 754 (2005) 124.
[17] For graph set analysis see for example J. Bernstein, R.E. Davis, L. Shimoni, N.-L. Chang, Angew. Chem., Int. Ed. Engl. 34 (1995) 1555.
[18] C. Batiu, C. Jelic, N. Leopold, O. Cozar, L. David, J. Mol. Struct. 744–747 (2005) 325.
[19] G.B. Deacon, R.J. Phillips, Coord. Chem. Rev. 33 (1980) 227.
[20] (a) A. Stanila, A. Marcu, D. Rusu, M. Rusu, L. David, J. Mol. Struct. 834–836 (2007) 364;
(b) S.A. Sadeek, M.S. Refat, S.M. Teleb, S.M. El-Megharbel, J. Mol. Struct. 737 (2005) 139;
(c) R.F. de Farias, C. Airoldi, J. Inorg. Biol. 76 (1999) 273;
(d) R.F. de Farias, H. Scantena Jr., C. Airoldi, J. Inorg. Biochem. 73 (1999) 253;
(e) M.S. Refat, I.M. El-Deen, H.K. Ibrahim, S. El-Ghool, Spectrochim. Acta A 65 (2006) 1208;
(f) S. Tanase, M. van Son, G.A. van Albada, R. de Gelder, E. Bouwman, J. Reedijk, Polyhedron 25 (2006) 2967;
(g) S.G. Baca, M.T. Reetz, R. Goddard, I.G. Filippova, Y.A. Simonov, M. Gdanic, N. Gerbeleu, Polyhedron 25 (2006) 1215;
(h) I. Chadjistamatis, A. Terzis, C.P. Raptopoulou, S.P. Perlepes, Inorg. Chem. Commun. 6 (2003) 1365;
(i) J. Gao, S-L. Ma, Ch-Y. Jin, D.-Z. Liao, Polyhedron 15 (1996) 2633;
(j) D. Dobrzyńska, T. Lis, L.B. Jerzykiewicz, Inorg. Chem. Commun. 8 (2005) 1090;
(k) S.T. Warzeska, F. Micciche, M. Chiara Mimmi, E. Bouwman, H. Kooijman, A.L. Spek, J. Reedijk, J. Chem. Soc., Dalton Trans. (2001) 3507;
(l) D. Dobrzyńska, L.B. Jerzykiewicz, M. Duczmal, Polyhedron 24 (2005) 407;
(m) G. Facchin, M.H. Torre, E. Kremer, O.E. Piro, E.E. Castellano, E.J. Baran, J. Inorg. Biochem. 89 (2002) 174;
(n) G. Christou, S.P. Perlepes, E. Libby, K. Folting, J.C. Huffman, R.J. Webb, D.N. Hendrickson, Inorg. Chem. 29 (1990) 3657;
(o) T. Głowiak, H. Kozłowski, L. Strinna Erre, G. Micera, Inorg. Chim. Acta 236 (1995) 149.
[21] I. Viera, M.H. Torre, O.E. Piro, E.E. Castellano, E.J. Baran, J. Inorg. Biochem. 99 (2005) 1250.
[22] Y. Inomata, M. Ando, F.S. Howell, J. Mol. Struct. 616 (2002) 201.
[23] S.M. Moussa, R.R. Fenton, B.J. Kennedy, R.O. Plitz, Inorg. Chim. Acta 288 (1999) 29.
[24] A.W. Herlinger, S.L. Wenhold, T.V. Long, J. Am. Chem. Soc. (1970) 6474.
[25] N. Ohata, H. Masuda, O. Yamauchi, Inorg. Chim. Acta. 286 (1999) 37.

[26] M.A. Hitchman, L. Kwan, L.M. Engelhardt, A.H. White, J. Chem. Soc., Dalton Trans. (1987) 457.
[27] G. Murphy, P. Nagle, B. Murphy, B. Hathaway, J. Chem. Soc., Dalton Trans. (1997) 2645.
[28] Ch. Chailuecha, S. Youngme, Ch. Pakawatchai, N. Chaichit, G.A. van Albada, J. Reedijk, Inorg. Chim. Acta 359 (2006) 4168.
[29] J. Stankowski, J. Mol. Struct. 597 (2001) 109.
[30] Chan-Cheng Su, Shin-Yi Chiu, Polyhedron 15 (1996) 2623.
[31] T. Murakami, T. Takei, Y. Ishikawa, Polyhedron 16 (1997) 89.
[32] Md. Fayazuddin, N.C. Gangi Reddy, G. Siva Reddy, S. Lakshmi Reddy, P. Sambasiva Rao, R.L. Frost, Spectrochim. Acta A 68 (2007) 807.
[33] O. Kahn (Ed.), Magnetism: A Supramolecular Function, NATO ASI Series C484, Kluwer Academic Publishers, Dordrecht, 1996.
[34] O. Kahn, Molecular Magnetism, VCH, New York, 1993.
[35] H.D. Flack, Acta Crystallogr., Sect. A 39 (1983) 876.

strategy in our study to obtain soluble polymer-substituted phthalocyanines, poly-THF-terminated side chains were initially introduced onto the Pc core. Poly-THF side chains, together with an aliphatic hexylthio moieties on the periphery of CoPcLC (**3**), provide both solubility and discotic mesogenic behaviour to rigid phthalocyanine core. To our knowledge, no other example of a liquid crystal polymeric MPc bearing poly-THF side chains has been published to date.

In the present work, we have described the design and the liquid crystal properties of a new discotic mesogen CoPcLC (**3**) derived from the flexible 6-(3,4-dicyanophenylthio)-hexyl-2-polytetrahydrofuranacetatephthalonitrile polymeric ligand.

2. Experimental

4-(6-Hydroxyhexylthio)-1,2-dicyanobenzene and 4-nitrophthalonitrile were prepared according to the literature procedures [17,24]. Chloroform ($CHCl_3$), 2-chloroethylchloride, triethylamine, tetrahydrofuran (THF), silvertetrafluoroborate ($AgBF_4$) and $CoCl_2$ were purchased from Merck and Alfa Aesar, and were used as received. All other reagents were obtained from Fluka, Aldrich and Alfa Aesar Chemical Co. and were used without purification. The purity of the products was tested in each step by TLC (SiO_2, $CHCl_3$, hexane and MeOH). FTIR (KBr) spectra were recorded on an ATI UNICOM-Mattson 1000 spectrophotometer. Chromatography was performed with silica gel (Merck grade 60 and sephadex) from Aldrich. Elemental analysis (C, H and N) was performed at the instrumental Analysis Laboratory of Marmara University. UV–Vis spectra were obtained in a quartz cuvette on an Agillent Model 8453 diode array spectrophotometer. ^{1}H NMR and ^{13}C NMR spectra were recorded on a Bruker 300 spectrometer instrument. The liquid crystal behaviour of CoPcLC (**3**) doped with 4-cyano-4′-n-pentylbiphenyl (5CB) was examined by temperature-controlled polarizing microscopy, differential scanning calorimetry (DSC) and capacitance–voltage measurements.

2.1. Synthesis of 6-(3,4-dicyanophenylthio)-hexyl-2-chloroacetate (*1*)

One gram of (3.84 mmol) of 4′-(6-hydroxyhexylthio)-1,2-dicyanobenzene and ca 0.32 mL (excess) of triethylamine were dissolved in 20 mL of THF at room temperature. The mixture was placed in an ice-bath. 0.45 mL (4.20 mmol, excess 10%) of 2-chloroethylchloride was added dropwise to the stirred solution at −5 °C. The mixture was stirred at 0 °C for 3 h and at room temperature for 12 h and finally heated for 1 h at 30 °C. The reaction mixture was poured into water and the resulting precipitate was filtered and washed with an excess amount of water. It was dried under vacuum for 12 h at room temperature, then chromatographed over a silica gel column using a mixture of $CHCl_3$:MeOH 100/5 as eluent, giving yellow 6-(3,4-dicyanophenylthio)-hexyl-2-chloroacetate. Finally the pure powder was dried in vacuum.

Yield: 1.04 g (80.47%), m.p.: 80 °C. *Anal.* Calc. for $C_{16}H_{17}ClN_2O_2S$ (336.5 g/mol) (%): C, 57.05; H, 5.09; N, 8.32; S, 9.52. Found: C, 56.77; H, 5.11; N, 8.08; S, 9.36%. FTIR (KBr) ν/cm^{-1}: 3020 (w), 2956, 2928 (aliph-CH_2), 2226 (CN, st), 1755, 1721 (–COOR, strong), 1476 (w), 1450, 1389, 1370, 1311, 1244 (Ar–S–CH_2), 1145 (st), 1048, 960, 873, 931, 879, 748, 699. ^{1}H NMR ([D6]−DMSO) δ: 7.68 (dd, 1H, ortho to Ar–S–), 7.64 (s, isomer, 1H, ortho to CN and Ar–H), 7.60 (dd, 1H, ortho to CN and Ar–H, phenyl H6), 4.35 (s, br, –CO*CH*$_2$Cl aliph., 4.10 (t, 2H, CH_2*CH*$_2$–OCO), 2.78 (t, 2H, –S–*CH*$_2$–CH_2–) 1.54–1.63 (m, superimposed 4H, –O–CH_2*CH*$_2$–CH_2–and –S–CH_2–*CH*$_2$–CH_2), 1.27–1.31 (m, 4H, –OCH_2 CH_2*CH*$_2$–CH_2– and –S–CH_2–CH_2–*CH*$_2$) ppm. ^{13}C NMR ([300 MHz, δ, D6]−DMSO): 167.2 (C=O), 143,2 (isomer, Ar–*C*–S), 132.6 (Bz), 132.1, 129.9, 116.8 112.7 (Bz), 64.7 (CH_2*O*CO), 40.9 (CO–CH_2Cl), 40.4 (DMSO), 36.8 (S–*C*H_2), 30.9 (SCH$_2$*CH*$_2$), 28.6 (OCH$_2$*CH*$_2$), 28.2 (SCH$_2$CH$_2$*CH*$_2$), 25.4 (CH_2*CH*$_2$ CH_2CH_2O) ppm. MS (ESI-MS): *m*/*z* (%): 370, 0 $[M]^+$ (27%).

2.2. Synthesis of 6-(3,4-dicyanophenylthio)-hexyl-2-polytetrahydrofuranacetate (*2*) (typical cationic polymerization of THF)

Experiments were carried out in a N_2 atmosphere. Freshly distilled THF (57.60 g, 0.80 mol) was put into a two-neck round bottom flask heated in vacuum with a heat gun and flushed with dry N_2. Stoichometric amounts of 6-(3,4-dicyanophenylthio)-hexyl-2-chloroacetate (0.61 g, 2.00 mmol) and $AgBF_4$ (0.78 g, 4.00 mmol) solution in THF were added under efficient stirring at room temperature. After 24 h, methanol was added to the reaction mixture to terminate the polymerization. After centrifuging, the polymer was poured into a methanol–water mixture (1/1 (V/V)) and cooled. The precipitated polymer was filtered off and dried in vacuum. Molecular weight (M_{an}) of the polymer was found to be 1500 from GPC measurements.

Yield: 2.05 g. FTIR (KBr) ν/cm^{-1}: 3088, 3061 (w), 2944, 2953, 298, 2855 (aliph-CH_2), 2226 (CN, st) 1755 (–COOR, strong), 1726 (–COOR, strong, sh), 1582, 1541, 1462, 1410, 1387, 1365, 1319, 1280 (Ar–S–CH_2), 1216, 1186 (st), 1166, 1127, 1068, 1024, 1068, 979, 929, 931, 838, 789, 747. ^{1}H NMR ([D6]−DMSO) δ: 8.03 (dd, 1H, ortho to Ar–S–), 7.90 (s, isomer, 1H, ortho to CN and Ar–H), 7.78 (dd, 1H, ortho to CN and Ar–H, phenyl H6), 4.40 (s, –CO*CH*$_2$O aliph.), 4.15 (t, 2H, CH_2*CH*$_2$–OCO), 3.40 (t, mH, poly-OCH_2CH_2–), 3.00 (t, 2H, –S–*CH*$_2$–CH_2–) 1.45–1.64 (m, superimposed 4H, –O–CH_2*CH*$_2$–CH_2–, –S–CH_2–*CH*$_2$–CH_2 and –OCH_2–*CH*$_2$–*CH*$_2$–CH_2), 1.40–1.27 (m, 6H, –OCH_2 CH_2*CH*$_2$–CH_2–, –S–CH_2–CH_2–*CH*$_2$ and terminal CH_2–CH_2–CH_2–CH_2) ppm. ^{13}C NMR ([300 MHz, δ, D6]−DMSO): 170.88 (C=O), 144,12 (isomer, Ar–*C*–S), 134.36 (Bz), 131.27, 130.42, 116.86, 115.80 (Bz), 110.22, 72.34 (–*CH*$_2$–O*CH*$_2$–), 71.80 (–CO–CH_2–O–*CH*$_2$), 66.08 (*CH*$_2$OCO, O*CO*CH_2), 40.4 (DMSO), 36.79 (S–*CH*$_2$), 30.55 (SCH$_2$*CH*$_2$), 28.30 (OCH$_2$*CH*$_2$), 28.26 (SCH$_2$CH$_2$*CH*$_2$), 26.45 (CH_2*CH*$_2$$CH_2$*CH*$_2$O), 25.33 ($CH_2$*CH*$_2$$CH_2$ CH_2O, CH_2*CH*$_2$$CH_2$*CH*$_2$S), 20.48 (terminal CH_2) ppm.

2.3. Synthesis of 2,9,16,23-Tetrakis-{6-(polytetrahydrofuran-2-carboxylate)-hexylthio-phthalocyaninatocobalt(II) (*3*)

6-(3,4-Dicyanophenylthio)-hexyl-2-polytetrahydrofuranacetate (0.150 g, 0.405 mmol) and $CoCl_2$ (0.014 g, 0.103 mmol; left one night in an oven at 110 °C) was heated in dry N,N′-(dimethylamino)-ethanol (0.5 mL) under stirring and refluxing for 8 h. After cooling, the dark-green-blue crude product formed during the reaction was treated with MeOH several times and filtered off. The dark-green-blue colored compound **3** was treated with CH_3CN several times and then filtered until the impurities were removed. The residue was then purified by column chromatography with silica gel (first with $CHCl_3$/MeOH 100/1 and then with THF/hexane 10/1). The desired compound is moderately soluble in $CHCl_3$, CH_2Cl_2 and acetone, and has good solubility in THF.

Yield: 0.020 g. FTIR (KBr) ν/cm^{-1}: 3307 (w, NH), 3084 (w), 2934, 2954, 2852 (aliph-CH_2), 1751 (–COOR, strong), 1713 (–COOR, strong, sh), 1587, 1535, 1442, 1357, 1327, 1266 (Ar–S–CH_2), 1167, 1159, 1088, 1002, 973, 858, 740, 722. UV–Vis (THF), λ_{max}/nm: 684 (Q; π–π^*), 650 (agg), 618 (n–π^*), 344 (B; deeper π–π^*).

3. Results and discussion

The novel amphiphilic disc-like polymeric cobalt phthalocyanine, CoPcLC (**3**), was synthesized according to the conventional method by heating a pulverized mixture of 6-(3,4-dicyanophenylthio)-hexyl-2-polytetrahydrofuranacetate (**2**) with anhydrous

$CoCl_2$ salts at ca. 150 °C under N_2 atmosphere in the presence of N,N-dimethylaminoethanol (Fig. 1) [18,19,21–22]. The presence of isomers of tetrasubstituted MPc (M = Co) could be verified by the slight broadening observed in the UV–Vis absorption bands when compared with those of octa substituted phthalocyanines composed of a single isomer [21,22,24]. The blue cyclotetramerization product, MPc (M = Co), was purified by column chromatography in moderate yield (ca 20 mg). The structure of **3** was verified by FTIR and UV–Vis spectrophotometry. All spectral data are consistent with the predicted structures.

The introduction of poly-THF chains into the disc-like molecules induced the assembly of the inorganic sources. The synthesized phthalocyanine derivative exhibited excellent solubility in THF and moderate solubility in $CHCl_3$. Fig. 2 shows the UV–Vis spectrum of CoPcLC in THF. Cyclotetramerization of **2** was confirmed by the disappearance of the sharp –C≡N vibration at 2226 cm^{-1} and two different strong COOR bands in compound **3** at around 1755 and 1726 cm^{-1} came out with a small shift compared to the starting compound. The IR spectra of phthalocyanines **1** and **2** are very similar, with the exception of small shifts. In the FTIR spectrum of **3**, the absence of characteristic bands for the N–H groups also confirms its formation. The ^1H NMR spectra of compound **1** and polymeric ligand **2** are somewhat similar, except for the poly-THF moiety in **2**. The resonances related to $OOCCH_2$, $COOCH_2$, CH_2, SCH_2 and Ar–H protons in the ^1H NMR spectrum of **2** are very similar to those of compound **1** and show the typical chemical shifts for protons of $-COCH_2O$ aliph. at 4.40, CH_2CH_2–OCO at 4.15, poly-OCH_2CH_2 at 3.40, –S–CH_2–CH_2– at 3.00, –O–CH_2CH_2–CH_2– –OCH_2 CH_2CH_2–CH_2–, –S–CH_2–CH_2–CH_2–CH_2 and terminal CH_2–CH_2–CH_2–CH_2 at 1.40–1.27 ppm. The UV–Vis spectrum of CoPcLC exhibits characteristic Q and B bands, one in the visible region at ca. 600–750 nm (Q-band) attributed to the π–π^* transition from the HOMO to the LUMO of the Pc^{2-} ring, and the other in the UV-region at ca. 300–400 nm (B-band) arising from deeper

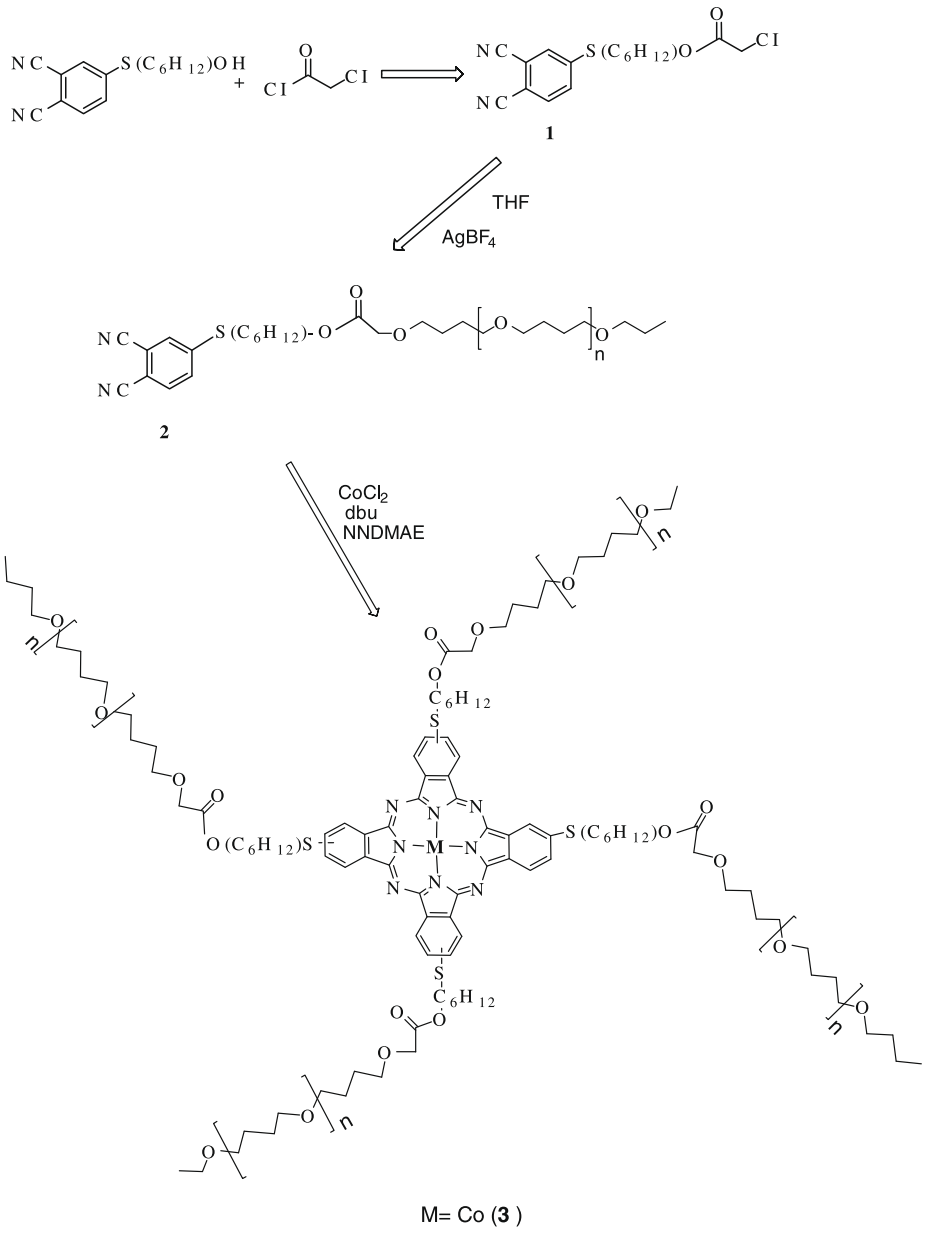


Fig. 1. Synthetic route to 6-(3,4-dicyanophenylthio)-hexyl-2-chloroacetate (**1**), 6-(3,4-dicyanophenylthio)-hexyl-2-polytetrahydrofuranacetate (**2**) and 2,9,16,23-tetrakis-{6-(polytetrahydrofuran-2-carboxylate)-hexylthio-phthalocyaninatocobalt(II) (**3**).

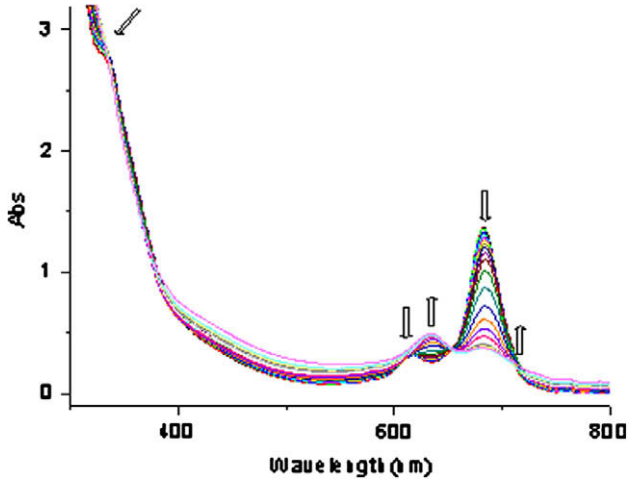


Fig. 2. UV–Vis spectra of **3** in THF during titration by Ag^{+} (in THF/MeOH (1:1)).

π–π^{*} transitions [25]. The divalent CoPcLC (**3**) gave a single Q-band of high intensity due to a single π–π^{*} transition, typical of a non-aggregated phthalocyanine, as expected from the result of the D_{4h} symmetry [18,26]. The Q-band absorption of **3** in THF was observed at 684 nm, with a shoulder at the slightly higher energy side of the Q-band. The B bands are broad due to the superimposition of the B1 and B2 bands in the 330–350 nm region in the case of compound **2** [26].

3.1. Spectroscopic metal ion binding titrations

The absorption spectrum of CoPcLC (**3**) in THF was evaluated in terms of monomer–dimer–trimer and oligomer formation. It is known that sulfur donor atoms on the periphery of the tetra or octa-substituted phthalocyanines act as low-valent transition metal ionophores (IB and IIB) and impart a preference for coordination especially with Ag^{I} and Pd^{II}, resulting in the formation of aggregates when the peripheral heteroatoms are able to interact with the same soft metals [18–23]. These interactions are readily monitored by UV–Vis spectroscopy. In the aggregated state, the electronic structure of the peripherally complexed phthalocyanine ring is perturbed resulting in alternation of the ground and excited state electronic structures [11,23,26].

In this study, titrations were carried out using a THF solution of the MPc's to ensure complete dissolution of $AgNO_3$ dissolved in THF/MeOH (1/1). Here, the concentration of the MPc and the metal salt were *ca.* 10^{-5} and 10^{-3} mol dm^{-3}, respectively. The reason for the higher concentration of the metal salt was to produce negligible changes by dilution after its addition to the phthalocyanine solution. A blank test was applied before the titration with heavy metal ions. No significant aggregation was observed in this mixture of solvents.

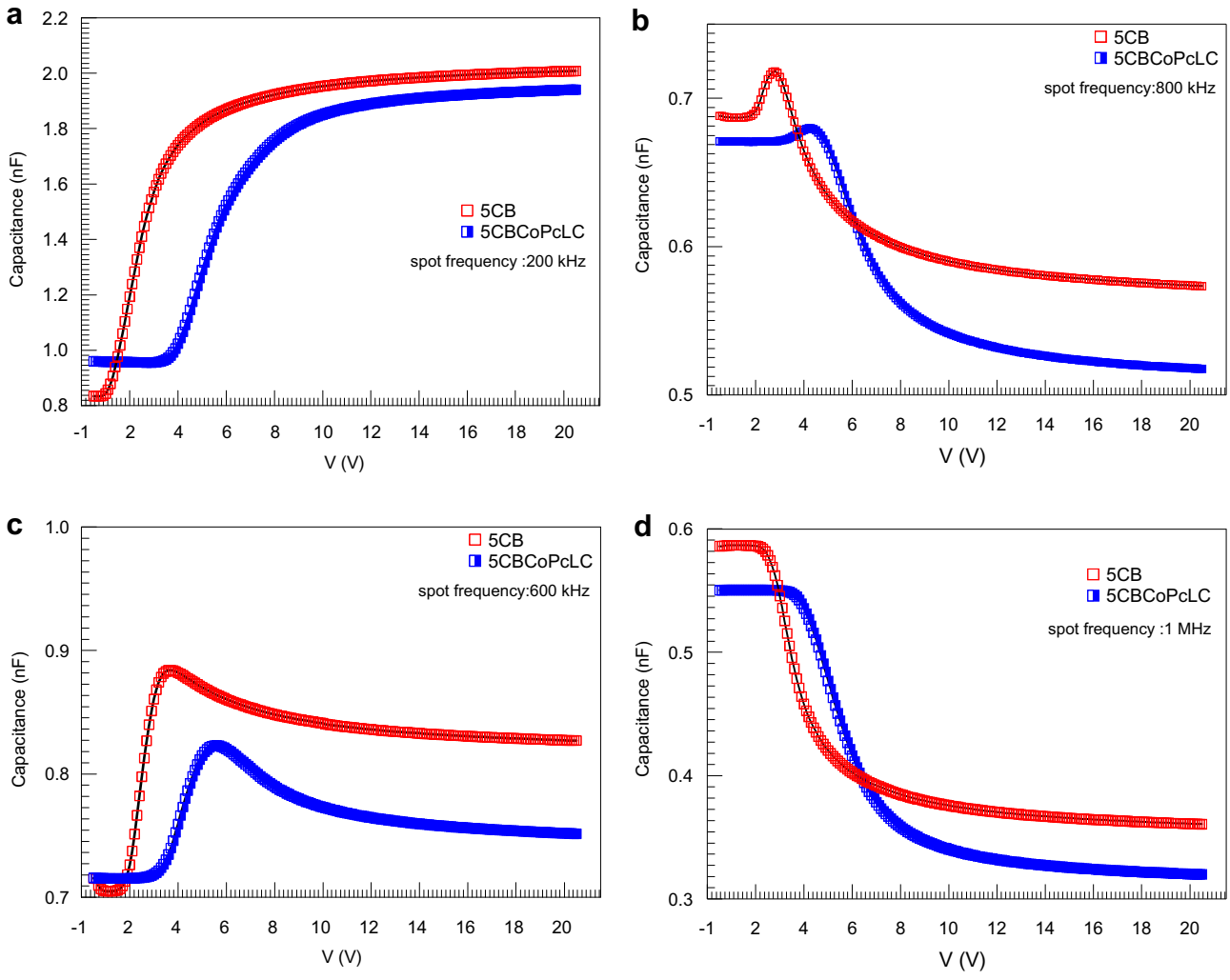


Fig. 3. *C–V* plots of the liquid crystals at different spot frequencies.

Table 1
Dielectric anisotropy and phase transition temperature of the 5CB and 5CBCoPcLC liquid crystals.

Liquid crystal	$\Delta\varepsilon$ at 200 kHz	$\Delta\varepsilon$ at 1 MHz	T_p (°C)
5CB	8.53	−1.71	34.8
5CBCoPcLC	7.17	−1.68	40.5

Gradual addition (μL) of Ag^I to the THF solution of CoPcLC caused a gradual color change from blue-green to an intractable less soluble dark-green aggregated CoPcLC. The binding of Ag^I to the donor atoms of CoPcLC results in pronounced effects in the Q and B bands (blue shift) (Fig. 2). This observation is in accord with previously reported studies [18–23]. As shown in Fig. 2, addition of small increments of Ag^I to CoPcLC leads to a gradual disappearance of the monomeric species, which show absorptions for CoPcLC at 684, 650, 618 and 344 nm, and an enhancement of the intensity of the oligomeric aggregated species around 635 nm. B bands of CoPcLC shift to the higher energy side, by about 5–10 nm, with a change in intensity. These spectroscopic changes indicate the coordination of Ag^I by the donor atoms of CoPcLC to form less soluble oligomeric aggregated species. As demonstrated in Fig. 2, the titrations show clear isobestic points at 713, 653, 615, 383 and 334 nm for CoPcLC.

3.2. Liquid crystal properties

We have evaluated that the mesomorphic properties of the CoPc can exhibit a columnar phase because it is well known that phthalocyanines form columnar liquid crystals [27–28] and mesomorphic properties of phthalocyanines depend on the number, position and character of the substituents, and the nature of the central metal atom. Fig. 3 shows the plots of capacitance–voltage (*C–V*) of 5CB and CoPcLC doped with 5CB liquid crystal at different spot frequencies. The capacitance values of the liquid crystals increase from the initial value to the final value. At lower voltages, the capacitance hardly changes with voltage, and then it increases with increasing voltage and reaches saturation. As seen in Fig. 3, the *C–V* plots of the liquid crystals show a threshold voltage. The CoPcLC doping increases the threshold voltage. This suggests that the ability of molecular reorientation decreases with CoPcLC doping. For liquid crystals, the dielectric anisotropy is expressed by the following relation [29],

$$\Delta\varepsilon = \varepsilon_{||} - \varepsilon_{\perp} \quad (1)$$

where $\varepsilon_{||}$ is the dielectric constant in the direction parallel to the director and $\varepsilon_{\perp}$ is the dielectric constant perpendicular to the director. Materials with $\Delta\varepsilon > 0$ are called p-type, in which their molecules are aligned with the director parallel to the electric field, whereas in n-type materials, with $\Delta\varepsilon < 0$, they align perpendicular to the electric field [30]. Fig. 3b shows *C–V* plots of the LC for $\Delta\varepsilon > 0$. As seen in Fig. 3b, the parallel capacitance decreases with increasing voltage. This indicates the reorientation of the molecules in parallel to the applied electrical field and this variation is completed for 1 MHz. The *C–V* curves of the LCS show that the structure changes from the positive to negative type. The dielectric anisotropy values of the LCs were calculated from the *C–V* curves of the liquid crystals and are given in Table 1. The $\Delta\varepsilon$ value of the 5CB li-

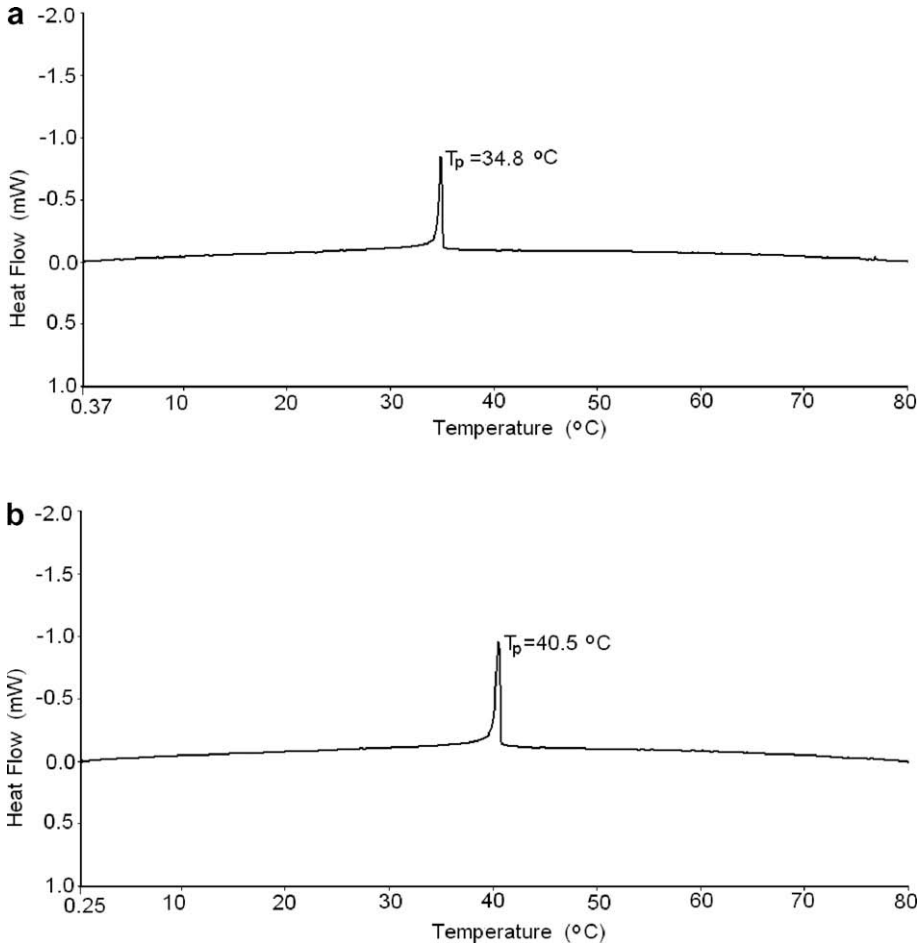


Fig. 4. DSC curves of the liquid crystals: (a) 5CB and (b) 5CBCoPcLC.

quid crystal is higher than that of 5CBCoPcLC liquid crystal. This suggests that the CoPcLC doping decreases the dielectrical anisotropy value of the 5CB liquid crystal.

The differential scanning calorimetry (DSC) curves of the 5CB and 5CBCoPcLC liquid crystals are shown in Fig. 4a and b. The curves indicate a peak, corresponding to the phase transition temperature. For 5CB liquid crystal, the phase transition temperature was found to be 34.8 °C, and this temperature is in agreement with the literature [31]. In this temperature, a phase transition from the nematic (N) to isotropic (ISO) phase is taking place. For the 5CBCoPcLC composite liquid crystal, the phase transition temperature was found to be 40.5 °C, as shown in Fig. 4b. This suggests that the CoPcLC dopant increases the phase transition temperature of the 5CB liquid crystal. Thus, we have evaluated that CoPCLc has liquid crystal properties. The DSC curves of the liquid crystals confirm the phase transition temperatures, detected under a microscope (Fig. 4). Fig. 5 shows the textures of the 5CB and 5CBCoPcLC liquid crystals at different temperatures. The nematic phase transition in 5CBCoPcLC liquid crystal takes place at 30 °C. The nematic phase of 5CBCoPcLC at 40 °C is shown in Fig. 5b. Fig. 5c shows a phase transition from nematic to isotropic and then at 50 °C, an isotropic phase occurs (Fig. 5d). Fig. 5e shows the texture of the nematic phase of 5CB liquid crystal at 30 °C.

Fig. 6a and b show the current–voltage (I–V) characteristics of the 5CB and 5CBCoPcLC liquid crystals. The current–voltage characteristics of the liquid crystals show non-linear behaviour. The current for 5CB liquid crystal does not increase with illumination, whereas at higher voltages illumination increases the electrical

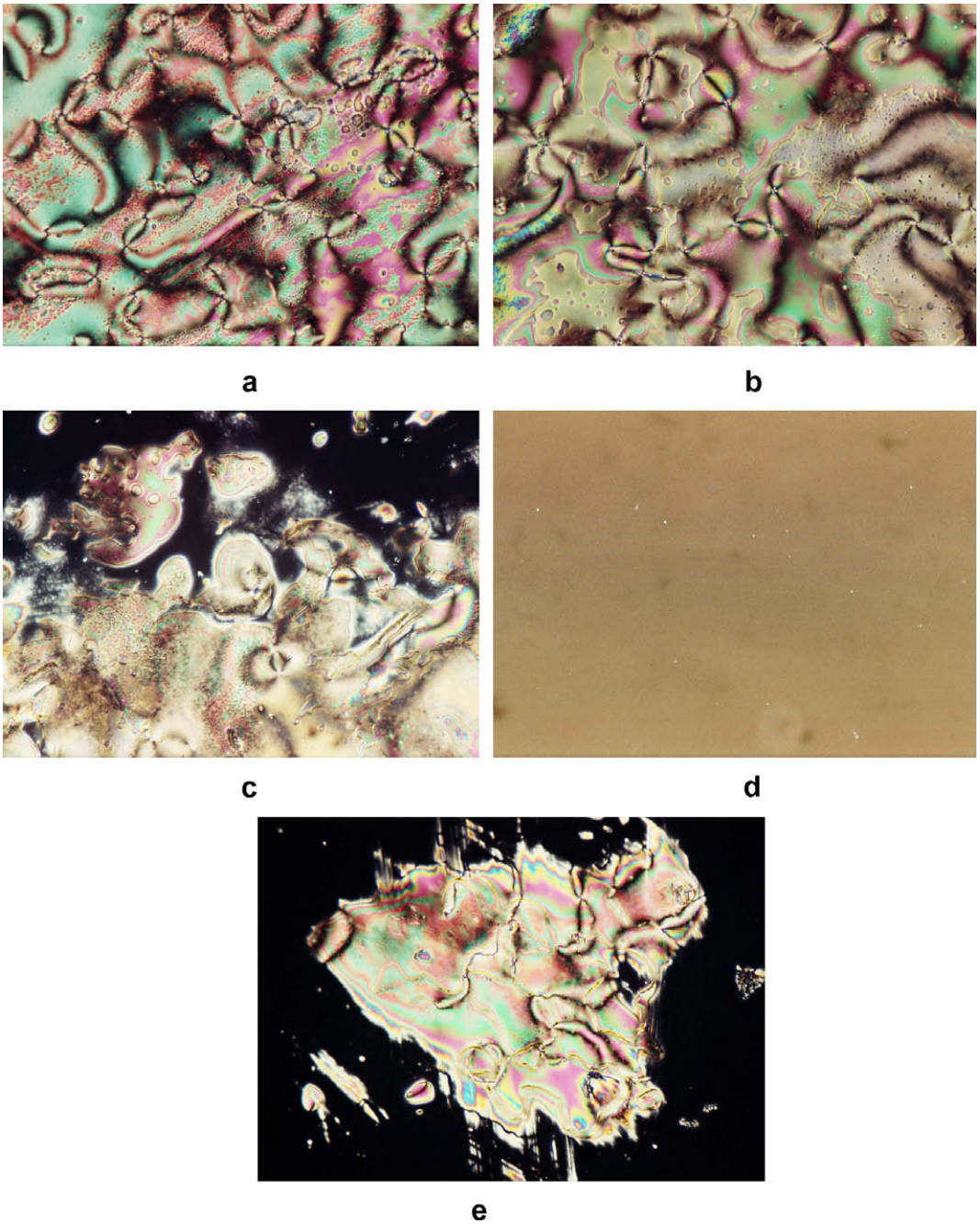


Fig. 5. Textures of the liquid crystals. (a) Nematic phase variation for 5CBCoPcLC at 30 °C. (b) Nematic phase for 5CBCoPcLC at 40 °C. (c) N-ISO phase for 5CBCoPcLC at 42 °C. (d) ISO phase for 5CBCoPcLC at 50 °C. (e) Nematic phase for 5CB at 30 °C.

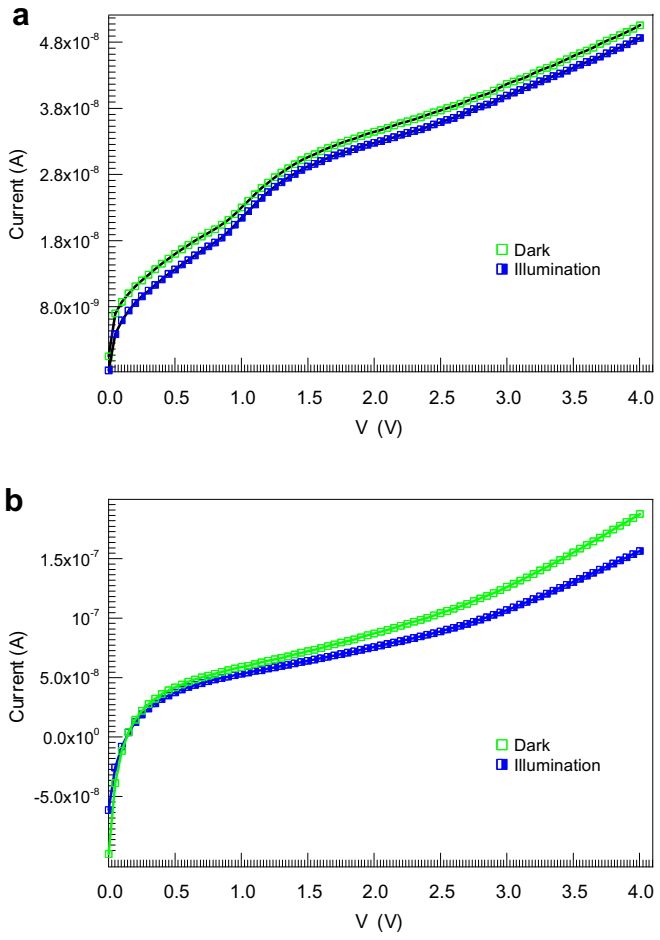


Fig. 6. The current–voltage characteristics of the liquid crystals under dark and illuminated conditions: (a) 5CB and (b) 5CBCoPcLC.

conductivity of the 5CBCoPcLC liquid crystal. The increase in the conductivity of 5CBCoPcLC is attributed to the optical properties of CoPcLC.

Acknowledgements

This work was supported by Research Funds of Sakarya University and TUBİTAK (Project No. TBAG: 108T094), the Management Unit of Scientific Research Projects of Firat University (FUBAP) under Project 1230 and Turkish Scientific and Technological Research Council of Turkey (TUBİTAK) (Project No. 106T406).

References

[1] J. Hoogboom, P.M.L. Garcia, M.B.J. Otten, J.A.A.W. Elemans, J. Sly, S.V. Lazarenko, T. Rasing, A.E. Rowan, R.J.M. Nolte, J. Am. Chem. Soc. 127 (31) (2005) 11047.
[2] J. Simon, J.J. Andre, Molecular Semiconductors, Springer, Berlin, 1985.
[3] B.A. Minch, W. Xia, C.L. Donley, R.M. Hernandez, C. Carter, M.D. Carducci, A. Dawson, D.F. O'Brien, N.R. Armstrong, Chem. Mater. 17 (2005) 1618.
[4] N.B. Mc Keown, J. Mater. Chem. 10 (9) (2000) 1979.
[5] A. Muranaka, K. Yoshida, T. Shoji, N. Moriichi, S. Masumoto, T. Kanda, Y. Ohtake, N. Kobayashi, Org. Lett. 8 (12) (2006) 2447.
[6] M. Kimura, K. Wada, K. Ohta, K. Hanabusa, H. Shirai, N. Kobayashi, Macromolecules 34 (14) (2001) 4706.
[7] P. Gattinger, H. Rengel, D. Neher, M. Gurka, M. Buck, A.M. van de Craats, J.M. Warman, J. Phys. Chem. B 103 (1999) 3179.
[8] L.R.H. High, S.J. Holder, H.V. Penfold, Macromolecules 40 (20) (2007) 7157.
[9] C. Piechocki, J. Simon, A. Skoulios, D. Guillon, P. Weber, J. Am. Chem. Soc. 104 (19) (1982) 5245.
[10] T. Nyokong, F. Furuya, N. Kobayashi, D.M. Du, W. Liu, J.Z. Jiang, Inorg. Chem. 39 (1) (2000) 128.
[11] M. Kimura, K. Wada, K. Ohta, K. Hanabusa, H. Shirai, N. Kobayashi, J. Am. Chem. Soc. 123 (10) (2001) 2438.
[12] D.M. Knawby, T.M. Swager, Chem. Mater. 9 (1997) 535.
[13] C.Y. Liu, A. Fechtenkotter, M.D. Watson, K. Mullen, A.J. Bard, Chem. Mater. 15 (2003) 124.
[14] F. Yılmaz, D. Atilla, V. Ahsen, Polyhedron 23 (2004) 1931.
[15] T. Kimura, T. Suzuki, Y. Takaguchi, A. Yomogita, T. Wakahara, T. Akasaka, Eur. J. Org. Chem. 5 (2006) 1262.
[16] G. de la Torre, T. Torres, F. Agulló-López, Adv. Mater. 9 (3) (1997) 265.
[17] M.N. Yaraşır, M. Kandaz, A. Koca, B. Salih, Polyhedron 26 (5) (2007) 1139.
[18] M.N. Yaraşır, M. Kandaz, B.F. Senkal, A. Koca, B. Salih, Polyhedron 26 (2007) 5235.
[19] S.J. Lange, J.W. Sibert, A.G.M. Barrett, B.M. Hoffman, Tetrahedron 56 (2000) 7371.
[20] M. Kandaz, S.L.J. Michel, B.M. Hoffman, J. Porphyr. Phthalocya. 7 (2003) 700.
[21] M.N. Yaraşır, M. Kandaz, A. Koca, B. Salih, J. Porphyr. Phthalocya. 10 (2006) 1022.
[22] S.L.J. Michel, A.G.M. Barrett, B.M. Hoffman, Inorg. Chem. 42 (2003) 814.
[23] M. Kandaz, Ö. Bekaroğlu, Chem. Ber. 130 (12) (1997) 1833.
[24] J.G. Young, W. Onyebuagu, J. Org. Chem. 55 (7) (1990) 2155.
[25] M. Gouterman, in: D. Dolphin (Ed.), The Porphyrins, vol. 3, Academic Press, New York, 1978, pp. 1–65.
[26] C.C. Leznoff, A.B.P. Lever, in: C.C. Leznoff, A.B.P. Lever (Eds.), Phthalocyanines: Properties and Applications, vols. 1–4, VCH, Weinheim, 1989–1996.
[27] José Antonio Duro, Gema de la Torre, Joaqúin Barbera, Jose Luis Serrano, Tomás Torres, Chem. Mater. 8 (1996) 1061.
[28] C. Piechocki, J. Simon, J. Am. Chem. Soc. 104 (1982) 5245.
[29] E. Lueder, Liquid Crystal Displays, John Wiley and Sons Ltd., England, 2001.
[30] F. Yakuphanoglu, M. Okutan, O. Köysal, S.-R. Keum, Dyes Pigments 76 (1) (2008) 202.
[31] M.A. Morsy, G.A. Oweimreen, J.S. Hwang, J. Phys. Chem. 100 (20) (1996) 8331.

Table 1
Crystal data and structure refinement for the complexes **1**–**5**.

Complex	**1**		**2**		**3**		**4**		**5**	
Empirical formula	C108 H90 Cl18 Fe3 La2 N6 O24 P6		C148 H124 Cl36 Eu3 Fe4 N9 O35 P8		C150 H126 Cl42 Fe4 Ho3 N9 O35 P8		C68 H56 Fe2Lu N2 O10 P4		C68 H56 Fe3 N2 O10 P4	
Formula weight	3125.16		4791.8		5069.45		1471.7		1352.58	
Temperature (K)	150(2)		150(2)		150(2)		150(2)		150(2)	
Wavelength (Å)	0.71073		0.71073		0.71073		0.71073		0.71073	
Crystal system	triclinic		monoclinic		monoclinic		triclinic		triclinic	
Space group	$P\bar{1}$		$C2/c$		$C2/c$		$P\bar{1}$		$P\bar{1}$	
Unit cell dimensions	a = 12.982(7) Å	α = 70.047(9)°	a = 31.509(3) Å	α = 90°	a = 31.356(3) Å	α = 90°	a = 12.682(2) Å	α = 64.028(2)°	a = 12.888(3) Å	α = 76.119(4)°
	b = 16.820(9) Å	β = 73.561(9)°	b = 28.599(3) Å	β = 110.530(3)°	b = 28.608(3) Å	β = 110.697(3)°	b = 18.445(3) Å	β = 73.205(3)°	b = 14.574(3) Å	β = 75.644(4)°
	c = 19.634(11) Å	γ = 70.107(7)°	c = 23.677(2) Å	γ = 90°	c = 23.647(2) Å	γ = 90°	c = 19.542(3) Å	γ = 76.209(3)°	c = 18.439(4) Å	γ = 80.810(4)°
Volume (Å^3)	3721(4)		19981(3)		19843(3)		3900.0(12)		3238.8(12)	
Z	1		4		4		2		2	
D_{calc} (Mg/m^3)	1.394		1.593		1.697		1.253		1.387	
Absorption coefficient (mm^{-1})	1.293		1.821		2.164		1.754		0.821	
F(000)	1560		9520		10032		1482		1392	
Crystal size (mm)	0.28 × 0.19 × 0.15		0.23 × 0.12 × 0.10		0.35 × 0.14 × 0.11		0.25 × 0.21 × 0.10		0.29 × 0.22 × 0.20	
θ range for data collection (°)	1.12–23.33		0.99–27.00		0.99–27.00		1.33–23.29		1.64–23.29	
Index ranges	$-14 \leqslant h \leqslant 14$, $-18 \leqslant k \leqslant 18$, $-21 \leqslant l \leqslant 21$		$-40 \leqslant h \leqslant 38$, $-36 \leqslant k \leqslant 36$, $-30 \leqslant l \leqslant 30$		$-39 \leqslant h \leqslant 39$, $-36 \leqslant k \leqslant 36$, $-29 \leqslant l \leqslant 30$		$-14 \leqslant h \leqslant 14$, $-20 \leqslant k \leqslant 20$, $-21 \leqslant l \leqslant 21$		$-14 \leqslant h \leqslant 14$, $-16 \leqslant k \leqslant 16$, $-20 \leqslant l \leqslant 20$	
Reflections collected	22911		83615		82304		24421		20229	
Independent reflections [R_{int}]	10688 [0.0535]		21769 [0.0996]		21618 [0.1364]		11201 [0.0228]		9296 [0.0225]	
Completeness to θ (%)	98.9		99.8		99.8		99.90		99.4	
Absorption correction	empirical		empirical		empirical		empirical		empirical	
Max. and min. transmission	0.86 and 0.66		0.862 and 0.724		0.862 and 0.652		0.745 and 0.652		0.93 and 0.81	
Refinement method	full-matrix least-squares on F^2		full-matrix least-squares on F^2		full-matrix least-squares on F^2		full-matrix least-squares on F^2		full-matrix least-squares on F^2	
Data/restraints/parameters	10688/0/754		21769/0/1096		21618/0/1096		11201/0/784		9296/0/784	
Goodness-of-fit on F^2	1.043		0.861		0.890		0.993		1.059	
Final R indices [$I > 2\sigma(I)$]	R_1 = 0.0672, wR_2 = 0.1685		R_1 = 0.0572, wR_2 = 0.1160		R_1 = 0.0613, wR_2 = 0.1181		R_1 = 0.0248, wR_2 = 0.0590		R_1 = 0.0345, wR_2 = 0.0955	
R indices (all data)	R_1 = 0.0836, wR_2 = 0.1760		R_1 = 0.1090, wR_2 = 0.1283		R_1 = 0.1265, wR_2 = 0.1377		R_1 = 0.0280, wR_2 = 0.0559		R_1 = 0.0412, wR_2 = 0.0987	
Largest difference in peak and hole (e Å^{-3})	1.883 and −1.513		1.683 and −0.842		1.457 and −1.126		0.940 and −0.646		0.366 and −0.267	
Solvent accessible void (Å^3)	858.2		1805.4		1795		1129.9		460	
Estimated solvent electron count	222e		476e		516e		290e		125e	

interaction of "ionic" nitrate with H-bonding molecules can lead to infrared spectra which are essentially the same as for a coordinated nitrate.

4. Structures

4.1. General points

Details of the data collection and refinement for the crystal structures are given in Table 1 and selected bond lengths in Table 2.

The Ln–O distances show the effect of the lanthanide contraction showing a linear decrease in both Ln–O(N) and Ln–O(P) with decreasing ionic radius of the lanthanide as shown in Fig. 1. The Ln–O(N) distances are consistently longer than the Ln–O(P) which is a general feature of PO complexes with lanthanide nitrates. The magnitude of the difference in Ln–O(N) – Ln–O(P) (=Δ) appears to reflect the degree of strain in the bonding region. Due to the strongly ionic nature of the interaction between the PO oxygen and the lanthanide ion a linear Ln^{3+}–O^{-}–P^{+} arrangement is favoured on electrostatic grounds. Values of Δ calculated from literature structures show that for non-chelated PO such as in $Ln(NO_3)_3(Ph_3PO)_n$ [17] and $Y(NO_3)_3(Ph_3PO)_n$ [18] values of Δ in the region of 0.21 Å are found. Constraining the PO in a six membered chelate ring in complexes such as $Ln(NO_3)_3[(^iPrO)_2P(O)C_5H_4N(O)]_2$ [19], $Ln(NO_3)_3[(EtO)_2P(O)CH_2P(O)(OEt)_2]_2$ [20] and $Ln(NO_3)_3[(MeO)_2P(O)CMe(OH)P(O)(OMe)_2]$ [21] lengthens the Ln–O(P) distance and hence reduces Δ to about 0.13–0.14 Å (interesting exceptions to this are complexes of $Ph_2P(O)CH_2P(O)Ph_2$ where a smaller Δ of 0.06 Å is observed [16]). Increasing the size of the chelate ring might be expected to increase the flexibility of the structure and allow Ln–O–P angles to approach linearity and thus values of Δ approaching those of an "unconstrained" ligand. Complexes with 10-membered chelate rings 1,3-$[Ph_2P(O)]_2C_6H_4$ [22] do indeed show this effect with Δ of 0.21 Å. In this study, a value of Δ = 0.22 Å is found, again implying relatively unconstrained coordination of the PO groups. This is further seen in the values of the Ln–O–P angles which average 161.8° (range 152.3–177.3°) over all the lanthanide complexes reported here.

It has been previously observed that small bite angle ligands such as nitrate should preferentially bind to larger metal ions [23]. Although it should be noted that all the metals here fall in to the category of large ions it is still interesting in this respect to examine the changes in Ln–O bond distances. When the Ln–O(N) distances are corrected for the lanthanide contraction, by subtracting the ionic radius of the lanthanide ion with the appropriate coordination number [24], the difference should be constant if no other effects are significant. Single factor Anova analysis of the data reveals that significant differences occur between the sets of distances. Post hoc analysis of the results was carried out by unpaired *t*-test assuming a null hypothesis of no difference between the means and unequal variance at a 95% confidence level. The results of such an analysis show that there are significant differences between the La–O(N) and other Ln–O distances, with La–O(N) being shorted than expected. The differences between the Eu–O(N), Ho–O(N) and Lu–O(N) are not significant once the effect of the lanthanide contraction is taken into account. The average Ln–O distances corrected for the lanthanide ion size are significantly larger for the Eu and Ho complexes. In the Eu and Ho complexes the larger residual differences with averages of 1.314(2) Å, compared with 1.256(2) Å for the La and Lu complexes, can be ascribed to the hydrogen bonding between chloroform and the coordinated nitrate ions. In the La complex this interaction is considerably weaker with a shortest (N)O···$HCCl_3$ of 2.547 Å compared with 2.246 and 2.232 Å, respectively, for the Eu and Ho complexes and this may in part account for the stronger La–O interaction. There are short contacts between one of the H atoms on the cyclopentadiene ring and one of the O(N) atoms in all the complexes. These distances, in the region of 2.3 Å, are shorter than the sum of van der Waals radii of O and H (2.60 Å), but, as such interactions occur in all complexes, they cannot account for the variations in distances observed.

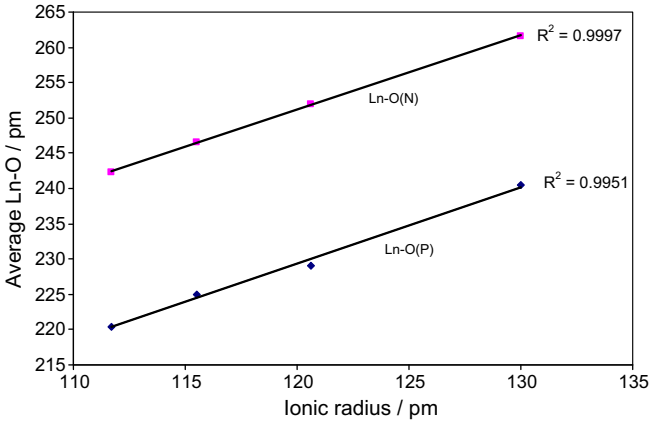


Fig. 1. The relationship between the Ln–O(P) and Ln–O(N) distances and the ionic radius of the lanthanide ion for complexes **1**–**4**.

A similar analysis for the Ln–O(P) distances for the chelate rings reveals significant differences between the La–O(P) distances and those for the other complexes. The values of Ln–O(P) corrected for the size of the lanthanide ion, again indicate a stronger La–O interaction with residual distances of 1.048 Å for La and 1.085, 1.094 and 1.087 Å for the Eu, Ho and Lu complexes respectively. It is difficult to see a reason for this. The non-bonded (P)O···O(P) distances within the chelate rings are larger for the Eu and Ho complexes (3.262 (Eu) and 3.212 Å (Ho) compared with 3.160 and

Table 2
Selected bond lengths for the lanthanide complexes.

	La		Eu	Ho	Lu	Fe
La(1)–O(2)	2.403(5)	Ln(1)–O(2)	2.276(4)	2.232(4)	2.2043(18)	1.9753(19)
La(1)–O(1)	2.406(5)	Ln(1)–O(1)	2.283(4)	2.240(4)	2.2152(19)	1.9713(19)
La(1)–O(3)	2.425(5)	Ln(1)–O(4)	2.303(4)	2.258(4)	2.2008(19)	1.9749(18)
La(1)–O(11)	2.591(5)	Ln(1)–O(3)	2.302(4)	2.266(4)	2.1962(19)	1.9814(19)
La(1)–O(8)	2.592(6)	Ln(1)–O(9)	2.490(4)	2.428(5)	2.4158(19)	
La(1)–O(5)	2.593(5)	Ln(1)–O(5)	2.523(4)	2.467(5)	2.4183(19)	2.0458(19)
La(1)–O(7)	2.632(6)	Ln(1)–O(6)	2.523(4)	2.468(4)	2.434(2)	
La(1)–O(4)	2.632(5)	Ln(1)–O(8)	2.542(4)	2.497(5)	2.423(2)	2.0120(19)
La(1)–O(10)	2.654(5)					
P(1)–O(1)	1.495(5)		1.504(4)	1.492(5)	1.496(2)	1.517(2)
P(2)–O(2)	1.496(5)		1.501(4)	1.501(5)	1.4935(19)	1.502(2)
P(3)–O(3)	1.503(5)		1.492(4)	1.488(4)	1.502(2)	1.500(2)
P(4)–O(4)			1.499(4)	1.493(5)	1.496(2)	1.4987(19)

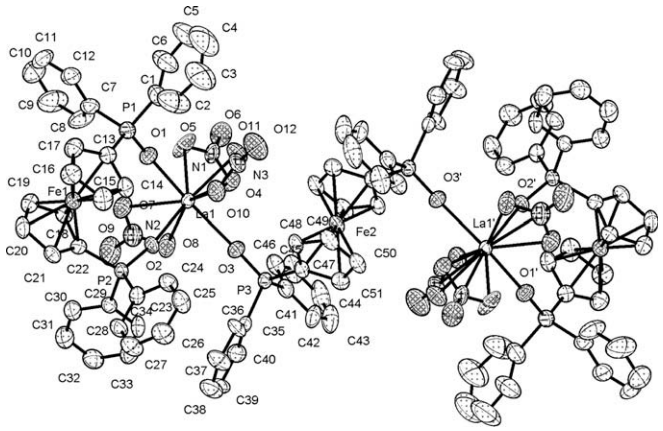


Fig. 2. The structure of $[LaL(NO_3)_3]_2\mu$-L. The Fe2 atom is located on a centre of symmetry. Symmetry related atoms generated by $1-x, 1-y, -z$.

3.175 Å for the La and Lu complexes, respectively) implying smaller electrostatic repulsions, which in turn suggests that stronger binding to the metal might be possible. The other obvious candidate for repulsive interactions which might lead to a weakening of the Ln–O(P) bonds are the non-bonded interactions between the (P)O and (N)O atoms. Significant differences are also indicated by single factor Anova analysis for the non-bonded P(O)···O(N) distances. A post hoc analysis of the non-bonded P(O)···O(N) distances by *t*-tests between the pairs of complexes shows a trend of increasing significance in the differences of the means. The differences between the La and Eu, complex is only significant at an 88.3% confidence level, whilst this increases to 98.9% and 99.9% for the differences between the La complex and the Ho and Lu complexes, respectively. For the La complex the shortest of these non-bonded interactions is over 3 Å whilst for all the others it is lower, showing a trend in values of 2.885 (Eu), 2.814 (Ho) and 2.768 Å (Lu). This trend mirrors the confidence levels at which the differences in the P(O)···O(N) means between the La complex and the respective sets of distances for the other complexes become significant.

The structures of the complexes have a number of features in common. The twist angles of the cyclopentadiene rings, measured from the torsional angles between the vectors from the ring centroid and ring carbon atoms on corresponding positions of the two rings, vary depending on whether the ligand is chelating or bridging. In the bridging mode observed in the lanthanum complex, the ligand is able to adopt a similar structure to that of the free ligand itself, namely with staggered rings and the diphenylphosphine oxide groups in a *trans* arrangement. Here the twist angle between the rings averages at 38.0 ± 0.7°, which is in good agreement with the average values of 37.7 ± 0.5° in the free ligand [25], 36.1 ± 1.5° found in the polymeric form of CoI_2L [2], and 26.6 ± 0.9° found for the bridging ligands in the zinc chloride complex of $[C_5H_4P(O)(OEt)_2]_2Fe$ [14]. The formation of chelate rings imposes a more eclipsed conformation on the ferrocenyl nucleus. The twist angles for the chelating ligands in the complexes are similar, with those in the lanthanum complex averaging at 8.6 ± 0.4° with averages of 12.8 ± 0.6° and 5.9 ± 0.5° (Eu), 12.1 ± 0.8° and 5.6 ± 0.3° (Ho) and 6.8 ± 0.3° and 4.5 ± 0.3° (Lu). These values are similar to that found in $PdCl_2L$ (7.3 ± 1.4°) but larger than observed in monomeric form of CoI_2L which has an average twist angle of 1.8 ± 0.6°.

4.2. The structure of $LLa(NO_3)_3$-μL–$La(NO_3)_3L$ (**1**)

The lanthanum nitrate complex (**1**) crystallised as a dimer, $LLa(NO_3)_3$-μL–$La(NO_3)_3L$ in which each La is nine coordinate. The structure is shown in Fig. 2. The coordination geometry does not conform to any simple polyhedron, but can be considered as a somewhat distorted octahedron if the nitrates are visualised as monodentate ligands bonded via the N-atoms. The octahedron thus conceptualised is a *mer*-isomer with "*cis*" angles at La averaging 92.4 ± 9.3° whilst the corresponding "*trans*" angles average 162.1 ± 9.4°. The La–O(P) distances for the chelating phosphine oxide are essentially identical (2.404(5) Å) and shorter than that from the bridging PO group (2.425(5) Å). These differences are not reflected in the PO distances themselves which are apparently equal at 1.4978(5) Å regardless of whether the PO groups are in the chelating or bridging mode. The nitrate groups bond asymmetrically to the lanthanum ion with one short and one long La–O distance, with averages of 2.592(8) and 2.639(10) Å, respectively. These differences are reflected in the bond distances within each nitrate ion itself, with a short O–N distance (1.254(6) Å)corresponding to the short La–O and the longer N–O associated with the longer La–O (1.276(9) Å). The P–O–La angles approach the idealised linear geometry for all the phosphoryl groups, as expected for predominantly ionic bonding where the structure imposes relatively few constraints on ligand architecture.

4.3. The structures of $[Eu(NO_3)_2L_2]_2[Eu(NO_3)_5]$ (**2**), $[Ho(NO_3)_2L_2]_2[Ho(NO_3)_5]$ (**3**) and $[Lu(NO_3)_2L_2][NO_3]$ (**4**)

In general, the reduction of the ionic radius tends to lower the coordination number of the metal. The cations in these complexes have eight-coordinate lanthanide ions and are rather similar in motif; the structure of the cation in **2** is shown as a representative example in Fig. 3. The coordination geometries can be visualised as distorted octahedra if the nitrate ions are considered as pseudomonodentate ligands attached via the N-atom. The *trans*-N–Ln–N angles are 176.21(15)° (Eu), 176.63(17)° (Ho) and 177.53(7)° (Lu) whilst the average corresponding *trans*-O–Ln–O angles are 163.6 ± 0.3°, 162.9 ± 0.4° and 164.9 ± 4.1°. The *cis*-N–Ln–O angles give averages close to 90°, at 90.1 ± 8.5° (Eu), 90.0 ± 8.7° (Ho) and 90.0 ± 10.1° (Lu) whilst the *cis*-O–Ln–O angles are rather more uniform with averages of 91.2 ± 1.0°, 91.3 ± 0.8° and 91.7 ± 0.8° for Eu, Ho and Lu, respectively. The $Ln(NO_3)_5^{2-}$ ions contain 10-coordinate lanthanide ions but are readily envisaged as trigonal bipyramids,

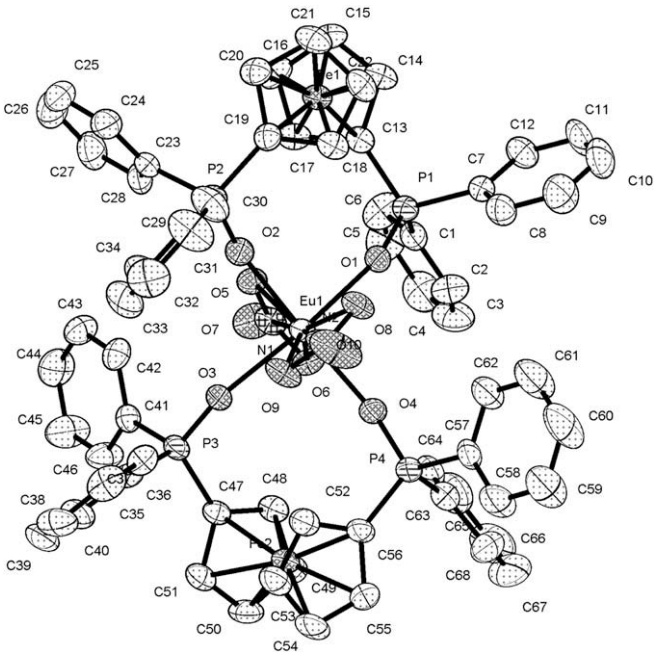


Fig. 3. The cation in $[EuL_2(NO_3)_2]_2^+$ $[Eu(NO_3)_5]^{2-}$.

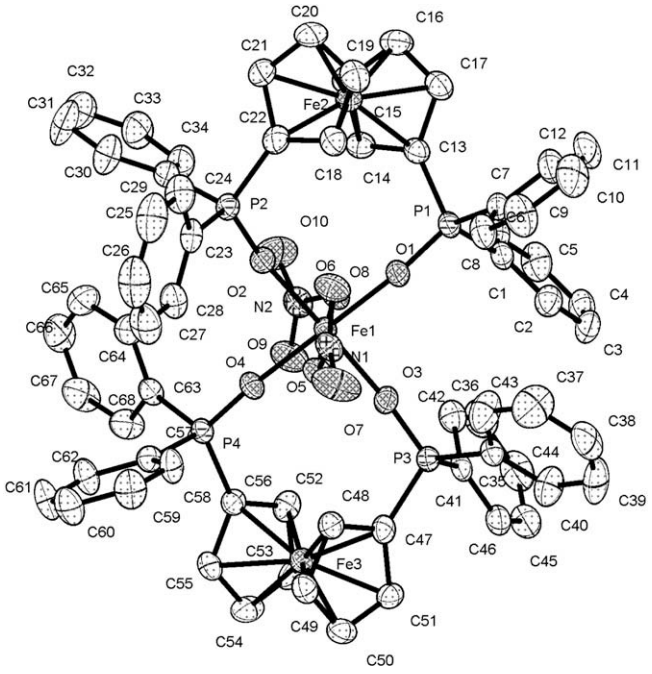


Fig. 4. The structure of $[FeL_2(NO_3)_2]NO_3$.

again taking the nitrate ions as pseudomonodentate ligands. The equatorial nitrogen atoms and the lanthanide ion are coplanar in both structures, the N_{ax}–Ln–N_{ax} angles are 177.9°, the N_{eq}–Ln–N_{eq} average to 120.0° (range 118.77–122.45°) whilst the N_{eq}–Ln–N_{ax} angles average at 91.7 ± 5.3° and 90.0 ± 6.2° for the Eu and Ho complexes, respectively. There are many examples of $Ln(NO_3)_5^{2-}$ counter-ions in the literature [26].

4.4. The structure of $[FeL_2(NO_3)_2]NO_3$

The structure of $[FeL_2(NO_3)_2]NO_3$ (**5**) is shown in Fig. 4 and shows interesting differences with the Lu complex with which it is superficially analogous. The iron is six-coordinate with the nitrate ions bound in a monodentate manner. The geometry about the metal is essentially octahedral with the *trans-O–Fe–O* angles averaging at 177.1 ± 1.1° and the *cis-O–Fe–O* at 90.0 ± 3.3°. The cyclopentadiene rings are eclipsed with twist angles of 2.6 ± 0.5° and 0.3 ± 0.1° for the two ligands. The P–O–Fe angles have a slightly larger range than the corresponding angles in the lanthanide complexes with one ligand having angles approaching linearity, whilst the other is significantly bent. This seems to have little effect on the Fe–O or P–O distances which are in essence independent of the angle at the oxygen atoms.

5. Mass spectrometry

Electrospray mass spectra were recorded for all the complexes in CH_2Cl_2. The base peak in all cases is $[L+H]^+$. The loss of a single nitrate to give $[LnL_2(NO_3)_2]^+$ is observed for all the complexes generally as a low intensity signal. The most notable feature of the mass spectra is the presence of ions formed as the result of ligand redistribution reactions. Thus signals of significant intensity are observed for ions such as $[LnL_4]^{3+}$ (5–10%), $[LnL_3]^{3+}$ (70–10%), $[LnL_3(NO_3)]^{2+}$ (40–5%) and $[LnL(NO_3)]^{2+}$ (10–30%). Some trends in the relative intensities of the signals from the ions are explicable by the lanthanide contraction. Thus the intensity of the peak assigned as $[LnL_3]^{3+}$ decreases from 70% for La to 10% for the Yb complex. Similarly the intensity of the peak due to $[LnL_3(NO_3)]^{2+}$ decreases from 40% (La) to below 5% (Yb) reflecting the increased steric interactions as the ionic radius decreases.

The negative ion spectra of the complexes showed a base peak at $m/z = 62.1$ assigned as NO_3^- and no other peaks of significant intensity. A much lower intensity signal (<1%) at $m/z = 648$ which is assigned as $[L+NO_3]^-$. There were no observed peaks which could be assigned to species such as $Ln(NO_3)_4^-$ or $Ln(NO_3)_5^{2-}$. Such species might have been anticipated given the solid state structures of the Ho and Eu complexes.

Table 3
Peak potentials[a] for selected complexes.

	1	**2**	$Dy(NO_3)_3L_2 \cdot 2H_2O$	**4**
$E_{½}$ (complex) (mV)[b]	628	661	681	683
ΔE (ferrocene) (mV)	70	77	70	78
ΔE (complex) (mV)	57	66	75	83

[a] Relative to ferrocene as internal reference.
[b] All peak potentials are measured with respect to ferrocene using a pseudoreference Ag wire.

6. Cyclic voltammetry

The oxidation behaviour of L, **1**, **2**, $Dy(NO_3)_3L_2 \cdot 2H_2O$ and **4** was studied by cyclic voltammetry in 0.1 M Bu_4NClO_4 solution in acetonitrile, with ferrocene as internal standard. Ligand L and each complex display a single reversible oxidation event corresponding to each {L} unit; in no case is any other wave evident, such as might suggest inequivalent L environments, or any degree of electronic communication between equivalent environments. Nevertheless, in the case of **1**, we clearly have a case of a complex which possesses inequivalent L environments in the solid state. We can offer no explanation for the single redox wave, other than a solution fluxionality or lability of the complex over the approximate 700 ms duration of the oxidation and re-reduction waves. All complexes, as written above, display a continuous shift toward more positive oxidation potentials with atomic number (Table 3). Ligand L itself is shifted some +458 mV with respect to ferrocene in good agreement with the literature value of +430 mV afforded by a previous determination in a different solvent system [10]. The Ln complexes follow a clear pattern which offers evidence for a closely associated molecular complex between Ln and L, albeit fluxional, being present in solution in each case. The trend is consistent with increasing polarising power of the smaller lanthanide metals drawing electron density onto the O atoms of the L ligand and away from the Fe centre. We attempted to reduce the Eu complex **2** in the same electrolyte solution after deoxygenation by nitrogen sparging, but no reduction peaks were observed in the potential window of the solvent/electrolyte system used.

7. Experimental

7.1. Crystallography

Crystals were transferred to and handled under a dried mineral oil to minimise the deterioration of the crystals prior to data collection. All X-ray data for the complexes were measured on a Bruker SMART diffractometer with a 2 K CCD area detector using graphite monochromated Mo Kα radiation ($\lambda = 0.71073$ Å). Absorption corrections, based on comparison of Laue equivalents, were applied to the data sets. The structures were solved by Patterson methods and refined by full-matrix least-squares cycles on F^2 for all data, using SHELXTL [27]. All non-hydrogen atoms of the metal complexes were refined with anisotropic displacement parameters and all

hydrogen atoms were included in refinement cycles riding on bonded atoms. For all structures the metal complex was unambiguous and refined satisfactorily. For **1**, **2** and **3** lattice $CHCl_3$ was located and refined. However, all the structures were found to have regions of unresolved disordered solvent, thought to be $CHCl_3$, that could not be modelled satisfactorily. The SQUEEZE option of the programme PLATON [28] was used to omit the data for the disordered regions for each of the structures. The solvent accessible void volume and estimated solvent electron count for each structure is given in Table 1.

7.2. Infrared spectroscopy

Infrared spectra were recorded on a Thermo Nicolet Avatar 370 FT-IR spectrometer operating in ATR mode. Samples were compressed onto the optical window and spectra recorded without further sample pre-treatment.

7.3. Electrospray mass spectrometry

Electrospray mass spectra were obtained by the EPSRC National Mass Spectrometry Service Centre at Swansea University as described previously [29]. The spectra were recorded on a VG Quattro II triple quadrupole mass spectrometer. Samples dissolved in CH_2Cl_2 were loop injected into a stream of MeOH passing through a steel capillary held at high voltage (+3.5 kV for positive mode and −3.0 kV for negative mode). Nebulisation of the resulting spray was pneumatically assisted by a flow of nitrogen bath gas and heated source (70 °C). Declustering and molecular fragmentation were promoted by increasing the cone voltage from 8 to 50 V.

7.4. Electrochemistry

The oxidation behaviour of L, **1**, **2**, $Dy(NO_3)_3L_2 \cdot 2H_2O$ and **4** was studied using a PC-driven Bioanalytical Systems BAS100B Electrochemical Analyzer/BAS PA1 Preamplifier combination operating in cyclic voltammetry mode with a sweep width of 1400 mV and sweep rate of 200 mV s^{-1}. The working electrode was polished Pt disc, the auxiliary electrode Pt wire and the pseudoreference electrode Ag wire. Approximately 1–5 mg samples were dissolved in approximately 20 ml of 0.1 M Bu_4NClO_4 in acetonitrile solution, with ferrocene as internal standard. Commercial white-spot nitrogen was used as spargent for reduction experiments.

7.5. Synthesis

$(C_5H_4P(O)Ph_2)_2$ Fe: $(C_5H_4PPh_2)_2Fe$ (5.17 g) was suspended in 50 ml acetone and H_2O_2 (3.00 g 30% aqueous solution) slowly added at such a rate as to maintain a gentle reflux. The suspension was stirred overnight, filtered and the resulting yellow solid washed with a little acetone and diethyl ether and dried at the pump to give 5.31 g (93% as the hydrate) yellow powder. Infrared/cm^{-1} (ATR) ν_{PO} 1165(s) ν_{OH} 3409(m).

$[La(NO_3)_3]_2L_3 1.5CHCl_3$: $La(NO_3)_3 6H_2O$ (0.38 g 0.87 mmol) in 3 ml EtOH was added in portions to a solution of L (0.25 g 0.42 mmol) in 5 ml hot EtOH. A yellow-brown precipitate was formed on each addition. On cooling, the yellow-brown solid formed, and was filtered, washed with a little EtOH and dried at the pump to yield 0.23 g. Crystals suitable for X-ray analysis were grown by slow diffusion of toluene into a $CHCl_3$ solution to give dark brown crystals.

Infrared (ATR) ν_{NO} 1436(s) 1295(s), ν_{PO} 1138(s). *Anal.* Calc.: C, 48.03; H, 3.33; N, 3.25. Found: C, 47.88; H, 3.39; N, 3.51%.

$[Eu(NO_3)_3L_2]_2[Eu(NO_3)_5]2.5CHCl_3$: $Eu(NO_3)_3 6H_2O$ (0.29 g, 0.65 mmol) in 2 ml EtOH was added in portions to a solution of L (0.32 g, 0.55 mmol) in 3 ml hot EtOH as for the La complex above and gave 0.41 g yellow-brown powder. Crystals for X-ray analysis grown by slow diffusion of toluene into a $CHCl_3$ solution rapidly lost solvent on exposure to air.

Infrared/cm^{-1} (ATR) ν_{NO} 1473(s) 1282(s), ν_{PO} 1142(s). *Anal.* Calc. for $[Eu(NO_3)_2L_2]_2[Eu(NO_3)_5]2.5CHCl_3$: C, 45.48; H, 3.16; N, 3.45. Found: C, 45.11; H, 3.66; N, 3.81%.

$[Ho(NO_3)_3L_2]_2[Ho(NO_3)_5]2CHCl_3$: $Ho(NO_3)_3 6H_2O$ (0.32 g, 0.70 mmol) in 2 ml EtOH was added in portions to a solution of L (0.30 g, 0.50 mmol) in 3 ml hot EtOH as for the La complex above gave 0.24 g yellow-brown powder. Crystals for X-ray analysis grown by slow diffusion of toluene into a $CHCl_3$ solution rapidly lost solvent on exposure to air.

Infrared/cm^{-1} (ATR) ν_{NO} 1473(s) 1287(s), ν_{PO} 1146(s). *Anal.* Calc. for $[Ho(NO_3)_2L_2]_2[Ho(NO_3)_5]2CHCl_3$: C, 45.57; H, 3.16; N, 3.47. Found: C, 45.37; H, 3.24; N, 3.63%.

$Dy(NO_3)_3L_2 \cdot 2H_2O$: A solution of $Dy(NO_3)_3 6H_2O$ (0.12 g) in 1.0 ml EtOH was added to a solution of L (0.36 g) in 2 ml EtOH. A yellow-brown precipitate formed on each addition. On complete addition the solid was filtered, washed with EtOH and dried at the pump (0.25 g).

Infrared (ATR) ν_{NO} 1477(s) 1283(s), ν_{PO} 1142(s). *Anal.* Calc.: C, 52.45; H, 3.88; N, 2.70. Found: C, 52.08; H, 3.79; N, 2.54%.

$Lu(NO_3)_3L_2 \cdot 2H_2O$: A solution of $Lu(NO_3)_3 6H_2O$ (0.10 g) in 1.5 ml EtOH was added to a solution of L (0.27 g) in 10 ml EtOH. On reduction of the volume of the solution to about 5 ml brown crystals were deposited which were filtered washed with EtOH and dried at the pump to give the product (0.25 g).

Infrared/cm^{-1} (ATR) ν_{OH} 3400(w) ν_{NO} 1499(s) 1482(s) 1359(m) 1337(m) 1307(m) 1288(s), ν_{PO} 1152(s). *Anal.* Calc.: C, 52.03; H, 3.85; N, 2.68. Found: C, 52.30; H, 3.81; N, 2.74%.

$Fe(NO_3)_2L_2NO_3 \cdot 3.5H_2O$: A solution of L (2.01 g) and silver nitrate (1.03 g) in 40 ml ethanol was heated under reflux for 8 h. The solution was cooled, filtered and allowed slowly to evaporate to 25 ml when dark brown crystals formed. These were filtered, washed with a small quantity of ethanol, and dried at the pump to give dark brown crystals (0.59 g).

Infrared/cm^{-1} ν_{OH} 3389(w) ν_{NO} 1489(m), 1488(m), 1481(m), 1280(s), ν_{PO} 1135(s), 1120(s). *Anal.* Calc.: C, 55.25; H, 4.30; N, 2.84. Found: C, 55.30; H, 4.50; N, 2.94%.

Supplementary data

CCDC 620324–620328 contains the supplementary crystallographic data for Fe, La, Eu, Ho and Lu structures, respectively. These data can be obtained free of charge via http://www.ccdc.cam.ac.uk/conts/retrieving.html, or from the Cambridge Crystallographic Data Centre, 12 Union Road, Cambridge CB2 1EZ, UK; fax: (+44) 1223-336-033; or e-mail: deposit@ccdc.cam.ac.uk.

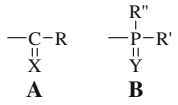
Acknowledgements

We are grateful to the Royal Society of Chemistry for support from the research fund and the EPSRC for use of the National Mass Spectrometry Service at Swansea University.

References

[1] J.S.L. Yeo, J.J. Vittal, T.S.A. Hor, J. Chem. Soc., Chem. Commun. (1999) 1477.
[2] T. Aviles, A. Dinis, J. Orlando GonÇalves, V. Felix, M.J. Calhorda, A. Prazeres, M.G.B. Drew, H. Alves, R.T. Henriques, V. da Gama, P. Zanello, M. Fontana, J. Chem. Soc., Dalton Trans. (2002) 4595.
[3] G. Pilloni, G. Valle, C. Corvaja, B. Longato, B. Corain, Inorg. Chem. 34 (1995) 5910.
[4] G. Pilloni, B. Corain, M. Degano, B. Longato, G. Zanotti, J. Chem. Soc., Dalton Trans. (1993) 1777.
[5] I.A. Razak, U. Usman, H.-K. Fun, B.M. Yamin, N.A.M. Kasim, Acta Crystallogr., Sect. C 58 (2002) 225.
[6] M. Emília, N.P.R.A. Silva, A.J.L. Pombeiro, J.J.R. Fraústo da Silva, R. Herrmann, N. Deus, T.J. Castilho, M. Fátima, C.G. Silva, J. Organomet. Chem. 421 (1991) 75.

[7] M. Emília, N.P.R.A. Silva, A.J.L. Pombeiro, J.J.R. Fraústo da Silva, R. Herrmann, N. Deus, R.E. Bozak, J. Organomet. Chem. 480 (1994) 81.
[8] W.L. Davis, R.F. Shago, E.H.G. Langner, J.C. Swart, Polyhedron 24 (2005) 1611.
[9] J. Podlaha, P. Stepnicka, J. Ludvik, I. Cisarova, Organometallics 15 (1996) 543.
[10] G. Pilloni, B. Longato, B. Corain, J. Organomet. Chem. 420 (1991) 57.
[11] P. Zanello, G. Opromolla, G. Giorgi, G. Sasso, A. Togni, J. Organomet. Chem. 506 (1996) 61.
[12] D.A. Durfey, R.U. Kirss, C. Frommen, W. Feighery, Inorg. Chem. 39 (2000) 3506.
[13] T.M. Miller, K.J. Ahmed, M.S. Wrightson, Inorg. Chem. 28 (1989) 2347.
[14] O. Oms, F. Maurel, F. Carré, J. le Bideau, A. Vioux, D. Leclercq, J. Organomet. Chem. 689 (2004) 2654.
[15] K. Nakamoto, Infrared and Raman Spectra of Inorganic and Coordination Compounds, 5th Ed., Wiley, 1997.
[16] A.M.J. Lees, A.W.G. Platt, Inorg. Chem. 42 (2003) 4673.
[17] W. Levason, E.H. Newman, M. Webster, Polyhedron 19 (2000) 2697.
[18] L. Deakin, W. Levason, M.C. Popham, G. Reid, M. Walker, J. Chem. Soc., Dalton Trans. (2000) 2439.
[19] G.S. Conary, A.A. Russell, R.T. Paine, J.H. Hall, R.R. Ryan, Inorg. Chem. 27 (1988) 3242.
[20] A.M.J. Lees, R.A. Kresinski, A.W.G. Platt, New J. Chem. 28 (2004) 1457.
[21] A.M.J. Lees, J.M. Charnock, R.A. Kresinski, A.W.G. Platt, Inorg. Chim. Acta 312 (2001) 170.
[22] Y.-C. Tan, X.-M. Gan, J.C. Stanchfield, E.N. Duesler, R.T. Paine, Inorg. Chem. 40 (2001) 2910.
[23] R.D. Hancock, A.E. Martell, Chem. Rev. 89 (1989) 1875.
[24] R.D. Shannon, Acta Crystallogr. A32 (1972) 751.
[25] Z.-G. Fang, T.S.A. Hor, Y.-S. Wen, L.-K. Liu, T.C.W. Mak, Polyhedron 14 (1995) 2403.
[26] F.H. Allen, Acta Crystallogr. B58 (2002) 380.
[27] SHELXTL, An Integrated System for Solving, Refining and Displaying Crystal Structures, Version 5.10, Bruker Analytical X-ray Systems, Madison, WI, USA, 1997.
[28] A.L. Spek, PLATON, Version 1.5, A Multi-Purpose Crystallographic Tool, Utrecht University, Utrecht, The Netherlands, 2002.
[29] J. Fawcett, A.W.G. Platt, D.R. Russell, Polyhedron 21 (2002) 287.



X, Y = O, S, Se
R, R', R'' = alkyl, aryl, O-alkyl, O-aryl, N-alkyl$_2$, N-aryl$_2$

Chart 1.

In this contribution we report the synthesis, structures, and chemical properties of complexes of *N*-(diisopropoxyphosphoryl)-*p*-bromothiobenzamide *p*-Br$C_6H_4C(S)NHP(O)(OiPr)_2$ (**HL**) [45] with Zn(II) ([Zn(L-*O*,*S*)$_2$], **1**) and Cd(II) ([Cd(*p*-Br$C_6H_4C(S)NH_2$-*S*)(L-*O*,*S*)$_2$], **2**; [Cd(HL-*O*)$_2$(L-*O*,*S*)$_2$], **3**) cations. In the ligand **HL** both –C(X)R and –P(Y)R′R″ functional groups are combined (X = S, Y = O, R = *p*-C_6H_4, R′ = R″ = O*i*Pr), and bonded by the NH fragment. The phosphorylated thiobenzamide **HL** is easily deprotonated in alkaline medium, leading to a thioamide with the negative charge delocalized in the O–P–*N*–C–S backbone [23].

The luminescence properties of the novel compounds and previously described [24] complexes of thiobenzamide $C_6H_5C(S)NHP(O)(OiPr)_2$ (**HQ**) with Zn(II) and Cd(II) cations: [Zn(Q-*O*,*S*)$_2$] (**4**), [Cd$_2$(Q-*O*,*S*)$_4$] (**5**), [Cd(HQ-*O*)$_2$(Q-*O*,*S*)$_2$] (**6**), were also measured.

2. Results and discussion

The ligand **HL** was prepared by the reaction of *p*-bromothiobenzamide *p*-Br$C_6H_4C(S)NH_2$ with diisopropyl chlorophosphate $(iPrO)_2P(O)Cl$ [45]. The product was carefully purified by extraction and recrystallization, and it definitely contains no traces of starting thioamide according to the spectral and microanalysis data.

Complexes **1**–**3** were prepared by the following procedure: the ligand was deprotonated *in situ* using KOH, followed by reaction with salts of the corresponding metals. The compounds obtained are crystalline solids, which are soluble in most polar solvents. The corresponding reaction using $ZnCl_2$ in aqueous EtOH leads exclusively to the formation of the complex [ZnL$_2$] (**1**), while the same reaction with $Cd(CH_3COO)_2$ leads to the formation of two complexes: [Cd(*p*-Br$C_6H_4C(S)NH_2$)L$_2$] (**2**) and [Cd(HL)$_2$L$_2$] (**3**) (Scheme 1). Complex **3** was separated from the mixture by extraction with *n*-hexane.

The properties of complexes of the "soft", easily polarizable Cd(II) cation differ considerably from those of Zn(II) derivatives with the same ligands. The coordination environment of CdO_2S_2 turns out to be considerably less stable than that of CdS_4 or ZnO_2S_2. As a result, the complexes are hydrolytically unstable and tend to increase the coordination number of the central atom even in dry solvents [24,25].

We assume that the reason for the propensity of Cd(II) complexes to hydrolysis is the formation of dimeric molecules [Cd$_2$L$_4$] in the aqueous ethanol medium:

$$2Cd(CH_3COO)_2 + 4KL \rightarrow [Cd_2L_4] + 4CH_3COOK$$
$$[Cd_2L_4] \leftrightarrows 2CdL_2 \quad (1)$$

The structure of a similar dimeric complex **5** was reported earlier [24]. In the dimeric molecule of composition [Cd$_2$Q$_4$] the complex units [CdQ$_2$] are connected by bridging Cd–S–Cd bonds (Scheme 2).

X-ray data have shown that the cyclic bonds in the bridging tridentate ligands **Q** are significantly elongated in comparison with terminal bidentate ones. Decrease of the electron density, introduced by the electron-withdrawing effect of the two Cd(II) cations might result in the facilitation of the nucleophilic attack of H_2O molecules and, thus, promote hydrolysis. An assumed reaction of that type is shown in the following equation:

$$[Cd_2L_4] + 3H_2O \rightarrow [CdL_2] + p\text{-}BrC_6H_4C(S)NH_2 + (iPrO)_2P(O)OH + Cd(OH)_2 + HL \quad (2)$$

Recently, we have established [24] that the complex **5** is unstable in solution and dissociates to the mononuclear complexes. However, even if the equilibrium is almost quantitatively shifted to the right (Eq. (1)), the small amount of easily hydrolyzing dimer molecules could provide the accumulation of the hydrolysis product in the reaction mixture. Interestingly, Zn(II) complexes exhibit no dimer formation under the same reaction conditions.

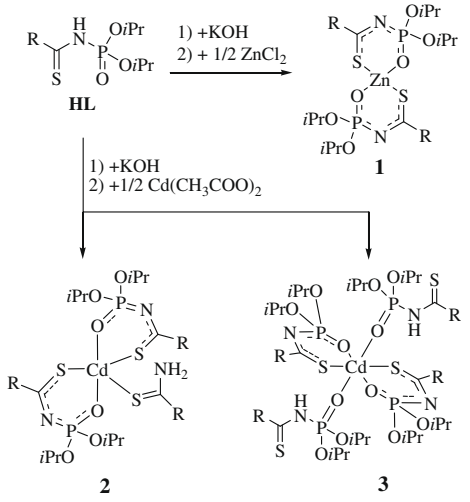
N-Phosphoryl-*p*-bromothiobenzamide **HL** and *p*-Br$C_6H_4C(S)NH_2$, which are formed as a result of hydrolysis (Eq. (2)), can serve as neutral ligands in the coordination sphere of [CdL$_2$] as in complexes **2** and **3**. In the $^{31}P\{^1H\}$ spectrum of the reaction mixture there is also a signal at −1.7 ppm, which might correspond to $(iPrO)_2P(O)OH$ (δ_P 2.98 ppm in THF-d_8 [46]).

The molecular structures of these compounds were investigated by MALDI, IR, ^1H, $^{31}P\{^1H\}$ NMR spectroscopy and by microanalysis.

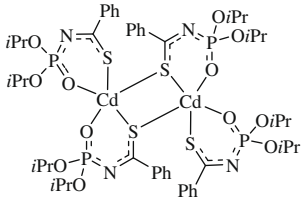
In the IR spectrum of **HL** there are bands of all characteristic groups. The P═O group is observed as an intense band at 1256 cm^{-1}. The band at 1504 cm^{-1} corresponds to the S═C–N fragment. The NH group shows a band at 3080 cm^{-1}.

The IR spectrum of **1** in Nujol is similar to the spectrum of **2**. The resonances of the P═O group of the anionic forms of **L** in complexes **1** and **2** are shifted by approximately 100 cm^{-1} to low frequencies relative to the band of the parent ligand **HL**. This confirms their participation in chelate formation. The spectra contain very intense bands corresponding to the conjugated SCN group at 1512–1544 cm^{-1}. This fact also confirms the formation of the anionic forms of **L** [23–25].

The main difference between the two complexes **1** and **2** involves the absorption bands of the NH_2 group in the IR spectrum of complex **2** while for complex **1** no signals are observed in the



Scheme 1. Preparation of complexes **1**–**3** (R = *p*-BrC_6H_4).



Scheme 2. Structure of **5** [24].

characteristic area of the NH group. There is an intense band at 1664 cm^{-1} and two bands of low intensity at 3104 and 3280 cm^{-1}.

The IR spectrum of **3** shows two bands for different phosphorus groups. Along with the above band corresponding to the **L** form at 1156 cm^{-1}, a strong P=O band is observed at 1248 cm^{-1} due to the bound neutral molecules of **HL**. Its frequency also decreases relative to that of the band of the free ligand; however, the shift is only 8 cm^{-1}. The band for the NH group at 3160 cm^{-1} also indicates the presence of **HL** molecules in complex **3**. The SCN group shows an intense band at 1528 cm^{-1} and indicates the presence of the anionic form of **L**.

The IR spectra of **HL** and complexes **1**–**3** exhibit a very intense band at 1000–1008 cm^{-1} corresponding to the POC group.

The $^{31}P\{^1H\}$ NMR signals of complexes **1** and **2** appear at $\delta = 6.9$ and 4.3 ppm, respectively, and a down-field shift, relative to that of the free ligand **HL** ($\delta = -5.9$ ppm), is observed.

The ^1H NMR spectra of complexes **1** and **2** contain a single set of signals for the $(i\text{PrO})_2P(O)$ and C_6H_4 protons of the anionic form **L**. The *o*-phenylene proton signals in **1** and **2** are shifted down-field relative to that of the free ligand ($\Delta\delta = 0.36$ ppm), while the *m*-C_6H_4 proton signals are practically not shifted ($\Delta\delta = 0.01$–0.04 ppm). The signal for the NHP(O) group proton is absent in the ^1H NMR spectra. This confirms the presence of the **HL** anionic form in the structures of complexes **1** and **2**.

The main difference involves the proton signals of the *p*-$BrC_6H_4C(S)NH_2$ group in the ^1H NMR spectrum of complex **2**. The signals for the C_6H_4 protons of the *p*-bromothiobenzamide are observed at $\delta = 7.55$ and 7.68 ppm. There are two singlets at $\delta = 7.35$ and 9.61 ppm corresponding to the NH_2 group protons due to the constrained rotation around the CN bond, typical for the thioamide group.

There are two singlets at $\delta = -5.3$ and 4.4 ppm, which have identical integrated intensities, in the $^{31}P\{^1H\}$ NMR spectrum of complex **3**. The signal at $\delta = -5.3$ ppm is in the region characteristic for neutral *N*-phosphorylated thioamides and thioureas, whereas the second signal corresponds to the amidophosphate environment in complexes of *N*-acylamidophosphate anions.

The ^1H NMR spectrum contains a double set of equal intensity signals for the $(i\text{PrO})_2P(O)$ and C_6H_4 protons. The assignment of the ^1H NMR spectrum of compound **3** is executed by comparing the spectrum of **3** with those of **HL** and complex **2**. For more exact reference of OCH and C_6H_4 proton signals of complex **3,** the spectrum of a mixture of **3** and **HL** was recorded at a molar ratio of 2:1. The increase in intensities of the low-field OCH group signal and the signals for the *m*- and *o*-C_6H_4 protons at $\delta = 7.47$ and 7.81 ppm, respectively, concerning the neutral **HL** form, confirms the reference made by comparison of the spectra. The ^1H NMR spectrum of complex **3** shows a signal for the NH group of the phosphorylamide fragment as a doublet ($^2J_{P,H} = 10.1$ Hz).

MALDI experiments on complexes **1** and **2** show peaks for the molecular ions $[M+H]^+$, $[M+Na]^+$ and $[M+K]^+$. These peaks are very intense in the mass spectrum of **1** but have low intensities (less than 8%) in the spectrum of complex **2**. In the MALDI mass spectrum of **2** there are molecular ion peaks corresponding to the additional *p*-bromothiobenzamide ligand.

The molecular ion peak of **3** is not observed under the same measurement conditions, only ions characteristic for the $[CdL_2]$ complex core, $[CdL_2 + H]^+$, $[CdL_2 + Na]^+$ and $[CdL_2 + K]^+$, are found in the MALDI spectrum.

The MALDI data of **1**–**3** show propensity to dimer formation. The intensity of the $[M_2L_3]^+$ peak in the spectra of complexes **1**–**3** is in the range of 12–19%. The peaks corresponding to the dimer formation were also observed in the ES (electrospray) mass spectra of complexes **4**–**6** [24].

The data of the emission spectra for complexes **1**–**6** in the solid state at room temperature are listed in Table 1 (note that neither parent ligands **HL** and **HQ** nor *p*-$BrC_6H_4C(S)NH_2$ show any emission under the same conditions). On first view, all compounds **1**–**6** exhibit practically the same fluorescence properties, respectively.

Table 1
Photophysical data for complexes **1**–**6**[a].

Complex	Emission max, nm	Complex	Emission max, nm
1	395	4	392
2	331, 397	5	322, 394
3	394	6	397

[a] Excitation at 249 nm.

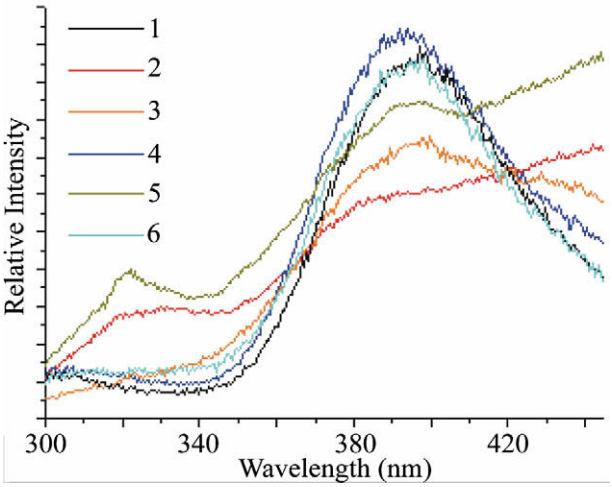


Fig. 1. Emission spectra of complexes **1**–**6** (the excitation wavelength was 249 nm).

Complexes **1**, **3**, **4** and **6** show a blue emission band with the maximum intensity at 392–397 nm upon excitation at 249 nm (Table 1, Fig. 1). Complexes **2** and **5** give a blue emission band at 394–397 nm and additionally exhibit bands of low intensity at 322–331 nm (Table 1, Fig. 1). The emissions of **1**–**6** are proposed to be the result of the coordination of **L**, **Q** and *p*-$BrC_6H_4C(S)NH_2$ to Zn(II) or Cd(II), and according to previous data [32,33], these emission bands can be assigned to the emission from a an excited ligand-to-metal charge transfer (LMCT) state.

In the solid state, the emission bands of complexes **1** and **6** have equal intensities. Replacing the *p*-bromosubstituted ligand to the nonsubstituted analog in the complexes with the same environment of the metal cation (compare complexes **1** to **4** and, **3** to **6** respectively), leads to an increase in intensity, which may be due to stronger σ-donation from **Q** and **HQ** than **L** and **HL**.

Emission spectra of **2** and **5** are practically isomorphic and the intensities of both bands in **2** are smaller than in **5**. The Cd(II) cation in complexes **2** and **5** is pentacoordinated with trigonal-bipyramidal O_2S_3 environment, which may lead to the appearance of the low-intensive band at 322–331 nm. There are two metal atoms in a molecule of **5** and only one central cation in **2**. Thus, this fact together with more electron donation from **Q** leads to an increase in intensity of both emission bands in complex **5** compared with **2**.

Crystals of **1**–**3** were obtained by slow evaporation of the solvent from dichloromethane/*n*-hexane solutions of the complexes. The crystals were measured and the structures were solved under the conditions and with the results outlined in Table 2.

According to the X-ray data, complex **1** in a crystal is a spirocyclic chelate with a distorted tetrahedral ZnO_2S_2 core (Fig. 2). S(1)–Zn–O(1) and O(1)–Zn–O(1)a ($1 - x$, $1 - y$, $-z$) angles are reduced whereas S(1)–Zn–O(1)a ($1 - x$, $1 - y$, $-z$) and S(1)–Zn–S(1)a ($1-x$, $+1$, $-y$, $-z$) are increased in comparison with an ideal tetrahedral

Table 2
Crystal data, data collection and refinement details for **1–3**.

	1	2	3
Empirical formula	$C_{26}H_{36}Br_2N_2O_6P_2S_2Zn$	$C_{33}H_{42}Br_3CdN_3O_6P_2S_3$	$C_{52}H_{74}Br_4Cd_1N_4O_{12}P_4S_4$
Formula weight	823.82	1086.97	1634.32
Crystal system	monoclinic	monoclinic	triclinic
Space group	*C*2/c	*P*2(1)	*P*–1
a (Å)	13.184(1)	15.144(3)	12.352(14)
b (Å)	21.878(2)	11.918(2)	12.763(15)
c (Å)	13.648(2)	23.868(5)	12.89(3)
α (°)	90	90	101.36(2)
β (°)	117.356(1)	96.41(3)	95.89(2)
γ (°)	90	90	114.90(1)
V (Å^3)	3496.2(7)	4281(2)	1767(5)
Z	4	4	1
D_{calc} (Mg m^{-3})	1.565	1.686	1.533
Absorption coefficient, μ (mm^{-1})	3.238	3.574	2.833
F(000)	1664	2160	822
Recording range, θ (°)	2.0–28.0	3.2–25.0	2.8–22.2
Number of recorded reflections	9753	14922	8306
Number of recorded independent reflections (R_{int})	4014 (0.028)	14922 (0.0000)	4006 (0.151)
R indices (all data)	R_1 = 0.0337, wR_2 = 0.0809	R_1 = 0.0579, wR_2 = 0.1521	R_1 = 0.0711, wR_2 = 0.1381
S	1.03	1.01	0.90

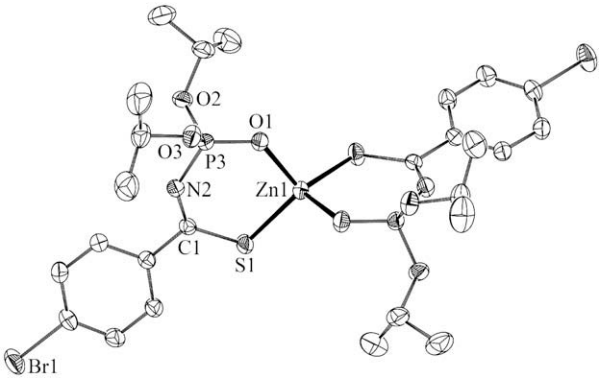


Fig. 2. Thermal ellipsoid representation of complex **1** (hydrogen atoms are omitted for clarity). Ellipsoids are drawn at the 30% probability level.

Table 3
Selected bond lengths (Å), and bond angles (°) for complex **1.**

Bond lengths			
Zn(1)–O(1)	1.960(2)	Zn(1)–S(1)	2.2980(7)
P(3)–O(1)	1.490(2)	N(2)–C(1)	1.286(3)
P(3)–O(2)	1.568(2)	O(2)–C(8)	1.466(3)
P(3)–O(3)	1.551(2)	O(3)–C(11)	1.481(3)
P(3)–N(2)	1.607(2)	S(1)–C(1)	1.734(2)
Bond angles			
O(1)–Zn(1)–O(1)a	107.6(1)	O(3)–P(3)–N(2)	101.8(1)
O(1)–Zn(1)–S(1)	103.31(5)	O(2)–P(3)–N(2)	107.1(2)
O(1)–Zn(1)–S(1)a	111.70(6)	N(2)–C(1)–C(2)	115.7(2)
S(1)–Zn(1)–S(1)a	118.98(4)	N(2)–C(1)–S(1)	129.0(2)
C(1)–S(1)–Zn(1)	107.45(9)	C(2)–C(1)–S(1)	115.3(2)
P(3)–O(1)–Zn(1)	124.8(1)	C(1)–N(2)–P(3)	133.6(2)
O(1)–P(3)–O(3)	113.2(1)	C(8)–O(2)–P(3)	122.8(2)
O(1)–P(3)–O(2)	104.7(1)	C(11)–O(3)–P(3)	121.9(2)
O(3)–P(3)–O(2)	108.8(1)	O(3)–C(11)–C(12)	106.7(3)
O(1)–P(3)–N(2)	120.9(1)	O(3)–C(11)–C(13)	106.7(3)
Torsion angles			
O(1)–Zn(1)–S(1)–C(1)	110.0(1)	O(2)–P(3)–O(1)–Zn(1)	129.5(1)
S(1)a–Zn(1)–S(1)–C(1)	−129.75(9)	O(3)–P(3)–O(1)–Zn(1)	−112.2(1)
O(1)a–Zn(1)–S(1)–C(1)	−5.3(1)	N(2)a–P(3)–O(1)–Zn(1)	8.8(2)
S(1)–Zn(1)–O(1)–P(3)	127.6(1)	O(2)–P(3)–N(2)a–C(1)a	−130.2(3)
S(1)a–Zn(1)–O(1)–P(3)	−1.4(1)	O(3)–P(3)–N(2)a–C(1)a	115.8(3)
O(1)a–Zn(1)–O(1)–P(3)	−119.7(1)	S(1)–C(1)–N(2)–P(3)a	1.5(4)
Zn(1)–S(1)–C(1)–N(2)	6.2(3)	C(1)–C(1)–N(2)–P(3)a	−177.9(2)
Zn(1)–S(1)–C(1)–C(2)	−174.4(2)		
(1 − *x*,1 − y, −*z*)			

angle of 109.5° (Table 3). Similarly to those of the [Co(II)Q_2] [28,29] and complex **4** [24], investigated by us earlier, the six-membered chelate rings are practically planar in the molecule of **1**. The maximum deviation from the best plane Zn–O–P–*N*–C–S is observed for P(1) phosphorus and O(1) oxygen atoms. The phenylene ring is rotated relative to the plane of the conjugated SCN moiety [torsion angles are N(2)–C(1)–C(2)–C(3) 16.1(3)° and S(1)–C(1)–C(2)–C(7) 17.8(3)°].

Complex **2** (Fig. 3) crystallizes in the chiral space group *P*2(1). The asymmetric unit contains two independent molecules.

There are intra- and intermolecular hydrogen bonds of the type N–H···O in the crystal of complex **2**. The intramolecular H-bond is formed between the oxygen atom of the P═O group of the anionic ligand **L** and one of the hydrogen atom of the NH_2 fragment of *p*-bromothiobenzamide. The intramolecular hydrogen bond parameters in Molecule 1 are as follows: N(3)–H(3 M)···O(4), *d*(H···O) 2.2(1) Å, *d*(N···O) 2.93(1) Å, ∠(N–H···O) 158(1)°. The hydrogen bond parameters in Molecule 2 are as follows: N(6)–H(6 M)···O(10), *d*(H···O) 2.1(1) Å, *d*(N···O) 2.86(1) Å, ∠(N–H···O) 157(1)°.

As a result of the intermolecular H-bonds chains along the *b* axis are formed. The intermolecular H-bonds are as follows: N(3)–H(3 N)···O(1) (−1 − *x*, 1/2 + *y*, 2 − *z*), *d*(H···O) 1.91(9) Å, *d*(N···O) 2.93(1) Å, ∠(N–H···O) 172.1(8)° N(6)–H(6 N)···O(7) (−1 − *x*, 1/2–*y*, 3–*z*), *d*(H···O) 2.3(1) Å, *d*(N···O) 3.0(1) Å, ∠(N–H···O) 169(1)°.

The Cd(II) cations are present in a distorted trigonal-bipyramidal environment (O_2S_3). The axial positions are occupied by the oxygen atoms of the phosphoryl groups. Three sulfur atoms, corresponding to the two anionic forms **L** and one *p*-bromothiobenzamide, lie in its base. The six-membered Cd–O–P–*N*–C–S cycles have a distorted boat conformation with the C═S sulfur atom and the P═O oxygen atom in apical positions (Table 4). The lengths of the Cd–S bonds in the chelate rings of the Molecule 1 are practically equivalent, but in the Molecule 2 the difference is about 0.014(1) Å. The third Cd–S bonds in both molecules are almost equal to each other ($\Delta \approx 0.003$ Å). The bonds with the oxygen atoms in the chelate rings of the Molecule 1 differ on 0.08 Å, but the Cd–O bonds difference in the Molecule 2 is only 0.03 Å. The Cd(1)–O(1) and Cd(2)–O(7) bonds in the Molecules 1 and 2, respectively, deviate from the normal to the CdS_3 plane [O(1)–Cd(1)–O(4) 169.3(2)° and O(7)–Cd(2)–O(10) 171.1(2)°], while the Cd(1)–O(4)

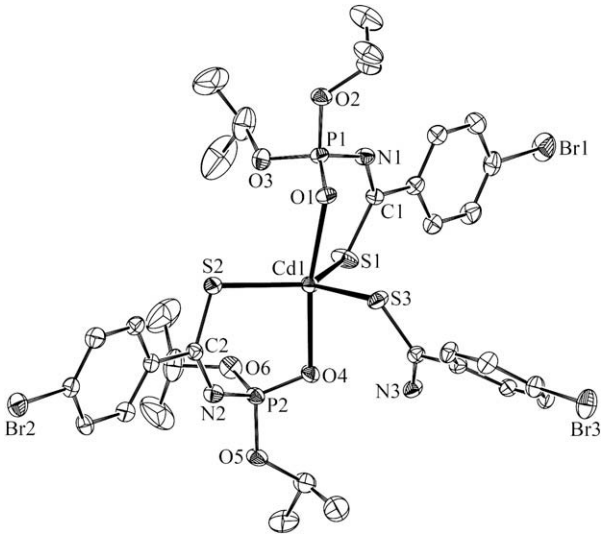


Fig. 3. Thermal ellipsoid representation of one of the two independent molecules of complex **2** (hydrogen atoms are omitted for clarity). Ellipsoids are drawn at the 30% probability level.

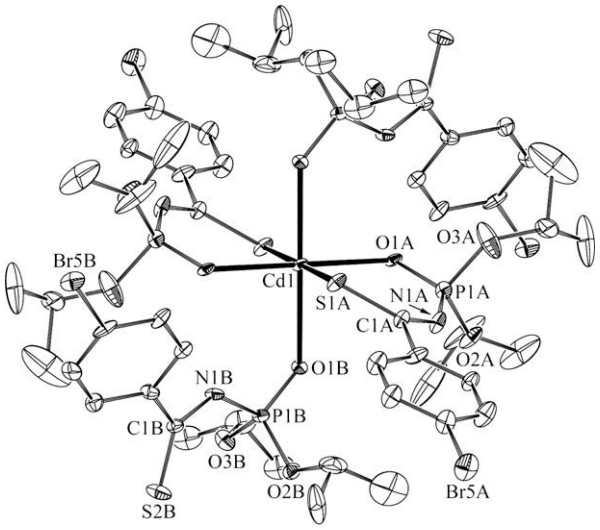


Fig. 4. Thermal ellipsoid representation of complex **3** (hydrogen atoms are omitted for clarity). Ellipsoids are drawn at the 30% probability level.

Table 4
Selected bond lengths (Å), and bond angles (°) for complex **2.**

Molecule 1		Molecule 2	
Bond lengths			
Cd(1)–O(1)	2.418(6)	Cd(2)–O(7)	2.355(6)
Cd(1)–O(4)	2.339(6)	Cd(2)–O(10)	2.323(6)
Cd(1)–S(1)	2.514(3)	Cd(2)–S(4)	2.516(3)
Cd(1)–S(2)	2.519(2)	Cd(2)–S(5)	2.530(2)
Cd(1)–S(3)	2.570(3)	Cd(2)–S(6)	2.567(2)
P(1)–O(1)	1.493(6)	P(3)–O(7)	1.467(6)
P(1)–O(2)	1.565(7)	P(3)–O(8)	1.587(9)
P(1)–O(3)	1.556(7)	P(3)–O(9)	1.524(8)
P(1)–N(1)	1.637(8)	P(3)–N(4)	1.620(8)
P(2)–O(4)	1.491(6)	P(4)–O(10)	1.494(6)
P(2)–O(5)	1.567(7)	P(4)–O(11)	1.579(7)
P(2)–O(6)	1.563(7)	P(4)–O(12)	1.558(7)
P(2)–N(2)	1.613(8)	P(4)–N(5)	1.623(8)
Bond angles			
O(4)–Cd(1)–O(1)	169.3(2)	O(4)–Cd(1)–S(1)	88.9(2)
O(1)–Cd(1)–S(1)	91.1(2)	O(4)–Cd(1)–S(2)	94.5(2)
O(1)–Cd(1)–S(2)	94.2(2)	S(1)–Cd(1)–S(2)	126.4(1)
O(4)–Cd(1)–S(3)	93.9(2)	O(1)–Cd(1)–S(3)	76.7(2)
S(1)–Cd(1)–S(3)	118.2(1)	S(2)–Cd(1)–S(3)	114.86(9)
O(10)–Cd(2)–O(7)	171.1(2)	O(10)–Cd(2)–S(4)	96.5(2)
O(7)–Cd(2)–S(4)	91.6(2)	O(10)–Cd(2)–S(5)	92.3(2)
O(7)–Cd(2)–S(5)	86.8(2)	S(4)–Cd(2)–S(5)	120.70(9)
O(10)–Cd(2)–S(6)	93.8(2)	O(7)–Cd(2)–S(6)	78.8(2)
S(4)–Cd(2)–S(6)	120.27(9)	S(5)–Cd(2)–S(6)	117.42(9)
C(1)–S(1)–Cd(1)	111.6(3)	C(51)–S(4)–Cd(2)	108.9(3)
C(8)–S(2)–Cd(1)	107.5(3)	C(58)–S(5)–Cd(2)	110.0(3)
C(15)–S(3)–Cd(1)	114.6(3)	C(65)–S(6)–Cd(2)	112.8(3)
P(1)–O(1)–Cd(1)	110.6(3)	P(3)–O(7)–Cd(2)	119.2(4)
P(2)–O(4)–Cd(1)	113.3(3)	P(4)–O(10)–Cd(2)	114.7(3)
Torsion angles			
S(2)–Cd(1)–S(1)–C(1)	105.6(4)	O(2)–P(1)–O(1)–Cd(1)	171.6(3)
S(3)–Cd(1)–S(1)–C(1)	−65.8(4)	O(3)–P(1)–O(1)–Cd(1)	58.5(4)
O(1)–Cd(1)–S(1)–C(1)	9.7(4)	N(1)–P(1)–O(1)–Cd(1)	−68.5(5)
O(4)–Cd(1)–S(1)–C(1)	−159.6(4)	O(1)–P(1)–N(1)–C(1)	61.3(9)
S(1)–Cd(1)–O(1)–P(1)	31.6(4)	O(2)–P(1)–N(1)–C(1)	−174.7(8)
S(2)–Cd(1)–O(1)–P(1)	−95.0(4)	O(3)–P(1)–N(1)–C(1)	−64.4(9)
S(3)–Cd(1)–O(1)–P(1)	150.4(4)	O(5)–P(2)–O(4)–Cd(1)	68.4(4)
S(1)–Cd(1)–O(4)–P(2)	−108.7(3)	O(6)–P(2)–O(4)–Cd(1)	−173.3(3)
S(2)–Cd(1)–O(4)–P(2)	17.7(3)	N(2)–P(2)–O(4)–Cd(1)	−56.6(5)
S(3)–Cd(1)–O(4)–P(2)	133.1(3)	P(1)–N(1)–C(1)–S(1)	−1.6(1)
Cd(1)–S(1)–C(1)–N(1)	−27.0(1)		

and Cd(2)–O(10) bonds stay practically perpendicular to the CdS_3 plane.

The molecule of complex **3** in the crystal is located in a special position at the symmetry centre. The coordination geometry of the Cd(II) atom is tetragonal bipyramidal ($D_{2\,h}$) (Fig. 4). Isostructural complexes of Co(II) [28,29], Ni(II) [35] with **HQ**, and Cd(II), Ni(II) with **HL** [24,45] have been synthesized and structurally characterized by us previously.

The equatorial positions of the bipyramid are occupied by two *N*-phosphoryl-*p*-bromothiobenzamide anions **L**, bonded through sulfur atoms and oxygen atoms of thiocarbonyl and phosphoryl groups, respectively. The six-membered Cd–O–P–*N*–C–S cycle lies between a boat and a chair conformations since the O–P–*N*–C–S backbone is flat (Table 5). The ligands show *trans* configuration. Neutral ligand molecules are coordinated in the axial positions through the oxygen atoms of the phosphoryl groups. The lengths of the Cd–O bonds in the chelate rings are 2.300(9) Å while the bonds with the axial oxygen atoms are 2.419(9) Å.

There are two intramolecular NH···O bonds between the oxygen atom of the P═O group of the anionic ligand **L** and the hydrogen atom of the NH fragment of the neutral ligand **HL** in the crystal of complex **3**. The hydrogen bond parameters are as follows: N(1B)–H(1B)···O(1A) $(1-x, -y, -z)$, d(H···O) 2.11 Å, d(N···O) 2.92(1) Å, ∠(N–H···O) 157°.

3. Experimental

Infrared spectra (Nujol) were recorded with a Specord M-80 spectrometer in the range 400–3600 cm^{-1}. NMR spectra were obtained on a Varian Unity-300 NMR spectrometer at 25 °C. ^1H and $^{31}P\{^1H\}$ NMR spectra ($CDCl_3$) were recorded at 299.948 and 121.420 MHz, respectively. Chemical shifts are reported with reference to $SiMe_4$ (^1H) and H_3PO_4 ($^{31}P\{^1H\}$). MALDI mass spectra of **1**–**3** were obtained using a Bruker Reflex IV spectrometer. Fluorescence measurements were made on a SLM Aminco 500 spectrofluorometer at room temperature. Elemental analyses were performed on a Perkin–Elmer 2400 CHN microanalyser.

3.1. Syntheses

p-$BrC_6H_4C(S)NHP(O)(OiPr)_2$ (***HL***). *N*-(diisopropoxyphosphoryl)-*p*-bromothiobenzamide was prepared according to previously described methods [45].

Table 5
Selected bond lengths (Å), and bond angles (°) for complex **3**.

Bond lengths			
Cd(1)–O(1A)	2.300(9)	P(1B)–O(1B)	1.475(8)
Cd(1)–O(1B)	2.419(9)	P(1B)–O(2B)	1.557(9)
Cd(1)–S(1A)	2.570(7)	P(1B)–O(3B)	1.57(1)
N(1A)–C(1A)	1.28(2)	P(1A)–N(1A)	1.61(1)
N(1B)–C(1B)	1.42(2)	P(1B)–N(1B)	1.66(1)
P(1A)–O(1A)	1.509(9)	S(1A)–C(1A)	1.74(1)
P(1A)–O(2A)	1.54(1)	S(2B)–C(1B)	1.61(1)
P(1A)–O(3A)	1.59(2)		
Bond angles			
O(1A)–Cd(1)–O(1B)	89.7(2)	O(1A)–P(1A)–O(3A)	103.8(6)
O(1A)–Cd(1)–O(1A_a)	180.00	O(1A)–P(1A)–N(1A)	122.2(5)
O(1A)–Cd(1)–O(1B_a)	90.3(2)	O(1B)–P(1B)–O(2B)	114.9(5)
S(1)–Cd(1)–O(1ª)	89.6(2)	O(1B)–P(1B)–O(3B)	116.0(5)
S(1)–Cd(1)–O(1ª_a)	90.4(2)	O(1B)–P(1B)–N(1B)	108.0(4)
S(1A)–Cd(1)–O(1B)	90.2(2)	O(2A)–P(1A)–O(3A)	110.2(7)
S(1A)–Cd(1)–O(1B_a)	89.8(2)	O(2A)–P(1A)–N(1A)	101.8(5)
S(1A)–Cd(1)–S(1ª_a)	180.00	O(3A)–P(1A)–N(1A)	104.7(6)
Cd(1)–S(1A)–C(1ª)	108.5(4)	O(2B)–P(1B)–O(3B)	101.2(5)
Cd(1)–O(1A)–P(1ª)	124.6(4)	O(2B)–P(1B)–N(1B)	108.7(4)
Cd(1)–O(1B)–P(1B)	136.1(4)	O(3B)–P(1B)–N(1B)	107.6(5)
O(1A)–P(1A)–O(2A)	113.7(5)		
Torsion angles			
O(1A)–Cd(1)–S(1ª)–C(1A)	−30.8(5)	Cd(1)–O(1A)–P(1A)–O(3A)	−126.2(6)
O(1B)–Cd(1)–S(1ª)–C(1A)	58.9(5)	Cd(1)–O(1A)–P(1A)–N(1A)	−8.7(8)
O(1A_a)–Cd(1)–S(1A)–C(1A)	149.2(5)	Cd(1)–O(1B)–P(1B)–O(2B)	−136.2(6)
O(1B_a)–Cd(1)–S(1A)–C(1A)	−121.1(5)	Cd(1)–O(1B)–P(1B)–O(3B)	106.2(6)
S(1A)–Cd(1)–O(1A)–P(1A)	27.7(5)	Cd(1)–O(1B)–P(1B)–N(1B)	−14.7(8)
O(1B)–Cd(1)–O(1A)–P(1A)	−62.5(5)	C(1A)–N(1A)–P(1A)–O(1A)	−19.9(2)
S(1ª_a)–Cd(1)–O(1A)–P(1A)	−152.3(5)	C(1A)–N(1A)–P(1A)–O(2A)	−148.0(1)
O(1B_a)–Cd(1)–O(1A)–P(1A)	117.5(5)	C(1A)–N(1A)–P(1A)–O(3A)	97.3(2)
S(1A)–Cd(1)–O(1B)–P(1B)	80.3(6)	C(1B)–N(1B)–P(1B)–O(1B)	−168.6(1)
O(1A)–Cd(1)–O(1B)–P(1B)	169.9(7)	C(1B)–N(1B)–P(1B)–O(2B)	−43.4(1)
S(1A_a)–Cd(1)–O(1B)–P(1B)	−99.7(6)	C(1B)–N(1B)–P(1B)–O(3B)	65.5(1)
O(1A_a)–Cd(1)–O(1B)–P(1B)	−10.1(7)	N(1A)–C(1A)–S(1A)–Cd(1)	21.6(1)
Cd(1)–O(1A)–P(1A)–O(2A)	114.1(5)	S(2B)–C(1B)–N(1B)–P(1B)	−11.9(2)

[ZnL_2] (***1***)**.** A suspension of **HL** (1.9 g, 5 mmol) in aqueous ethanol (20 mL) was mixed with an ethanol solution of potassium hydroxide (0.28 g, 5 mmol). An aqueous (20 mL) solution of $ZnCl_2$ (0.82 g, 2.8 mmol) was added dropwise under vigorous stirring to the resulting potassium salt. The mixture was stirred at room temperature for further 3 h and left overnight. The complex was obtained by extraction of the reaction mixture by dichloromethane, washed with water and dried using anhydrous $MgSO_4$. The solvent was then removed in vacuo. A colorless precipitate was recrystallized from a dichloromethane/*n*-hexane mixture. Yield 1.73 g (84%), m.p. 143 °C. (Found: C, 37.82; H, 4.47; N, 3.31%. $C_{26}H_{36}Br_2N_2O_6P_2S_2Zn$ requires C, 37.90; H, 4.40; N, 3.40%.). ν_{max}/cm^{-1} 1544 (SCN), 1152 (P═O), 1000 (POC). δ_H 8.14 (4H, m, ^3J 8.4, *o*-H, C_6H_4), 7.50 (4H, m, ^3J 8.4, *m*-H, C_6H_4), 4.71 (4H, d sept, ^3J 6.2, OCH), 1.36 (12H, d, ^3J 5.6, CH_3), 1.35 (12H, d, ^3J 5.6, CH_3). δ_P 6.9. *m*/*z* (MALDI) 826 (81) $[M+H]^+$, 849 (100) $[M+Na]^+$, 864 (52) $[M+K]^+$, 1271 (12) $[Zn_2L_3]^+$.

*[Cd(p-$BrC_6H_4C(S)NH_2$)L_2] (**2**) and [Cd(HL)$_2$$L_2$]* (***3***)**.** A suspension of **HL** (1.91 g, 5 mmol) in aqueous ethanol (20 mL) was mixed with an ethanol solution of potassium hydroxide (0.28 g, 5 mmol). An aqueous (20 mL) solution of $Cd(CH_3COO)_2 \cdot 2H_2O$ (0.82 g, 2.8 mmol) was added dropwise under vigorous stirring to the resulting potassium salt. The mixture was stirred at room temperature for a further 3 h and left overnight. The complex was obtained by extraction of the reaction mixture by dichloromethane, washed with water and dried with anhydrous $MgSO_4$. The solvent was then removed in vacuo. The residue was extracted using *n*-hexane. The hexane insoluble residue was recrystallized from a dichloromethane/*n*-hexane mixture, and complex **2** was isolated. Complex **2** was obtained as colorless crystals. Yield 0.44 g, mp 129 °C. (Found: C, 36.35; H, 3.96; N, 3.81%. $C_{33}H_{42}Br_3CdN_3O_6P_2S_3$ requires C, 36.46; H, 3.89; N, 3.87%.). ν_{max}/cm^{-1} 3280, 3104, 1664 (NH_2), 1512 (SCN), 1157 (P═O), 1000 (POC). δ_H 9.61 (1H, br. s, NH_2), 8.14 (4H, m, ^3J 8.5, *o*-H, C_6H_4, L), 7.68 (2H, m, ^3J 8.4, *o*-H, C_6H_4), 7.55 (2H, m, ^3J 8.4, *m*-H, C_6H_4), 7.47 (4H, m, ^3J 8.5, *m*-H, C_6H_4, L), 7.35 (1H, s, NH_2), 4.72 (4H, d sept, ^3J 6.3 Hz, OCH), 1.34 (24H, d, ^3J 6.1, CH_3). δ_P 4.3. *m*/*z* (MALDI) 217 (100) [*p*-$BrC_6H_4C(S)NH_2 + H]^+$, 240 (13) [*p*-$BrC_6H_4C(S)NH_2 + Na]^+$, 217 (5) [*p*-$BrC_6H_4C(S)NH_2 + K]^+$, 873 (34) $[CdL_2 + H]^+$, 896 (48) $[CdL_2 + Na]^+$, 1089 (6) $[M + H]^+$, 1112 (3) $[M + Na]^+$, 1128 (7) $[M + K]^+$, 1364 (19) $[Cd_2L_3]^+$. At the solvent-removal stage (hexane soluble), product **3** was isolated. Complex **3** was obtained as orange crystals. Yield 0.21 g, m.p. 114 °C. (Found: C, 38.37; H, 4.46; N, 3.50%. $C_{52}H_{74}Br_4CdN_4O_{12}P_4S_4$ requires C, 38.28; H, 4.57; N, 3.43%.). ν_{max}/cm^{-1} 3160 (NH), 1528 (SCN), 1248 (P═O, HL), 1156 (P═O, L), 1004 (POC). δ_H 9.00 (2H, d, ^3J 10.1, NH), 8.13 (4H, m, ^3J 7.9, *o*-H, C_6H_4, L), 7.81 (4H, m, ^3J 8.3, *o*-H, C_6H_4, HL), 7.53 (4H, m, ^3J 7.9, *m*-H, C_6H_4, L), 7.47 (4H, m, ^3J 7.9, *m*-H, C_6H_4, HL), 4.83 (4H, d sept, ^3J 6.3, OCH, HL), 4.65 (4H, d sept, ^3J 6.2, OCH, L), 1.36 (12H, d, ^3J 6.3, CH_3, L), 1.30 (36H, br s, CH_3, L + HL). δ_P 4.4 (2P, L), −5.3 (2P, HL). *m*/*z* (MALDI) 873 (67) $[CdL_2 + H]^+$, 896 (100) $[CdL_2 + Na]^+$, 912 (17) $[CdL_2 + K]^+$, 1364 (15) $[Cd_2L_3]^+$.

3.2. Structure determination

The data for **1** and **3** were collected at 20 °C using a Bruker Smart Apex2 diffractometer and graphite-monochromated Mo Kα radiation generated from Diffraction X-ray tube operated at 50 kV and 30 mA. The images were indexed, integrated and scaled using the APEX2 data reduction package [47]. All raw data were corrected for absorption using SADABS [48] The structure was solved by heavy atom and direct method using SIR [49] program and the

refinement was carried out with SHELXL [50] using anisotropic thermal parameters for all non-hydrogen atoms. Hydrogen atoms were added to the structure model on calculated positions and were refined as rigid atoms. All calculations were performed on PC computer using WINGX [51] program.

X-ray diffraction data for **2** were collected on a Enraf Nonius Kappa CCD diffractometer equipped with a rotating anode generator and with Mo $K\alpha$ radiation. The structure solutions were found with SHELXS [52], and the refinement was carried out with SHELXL [50] using anisotropic thermal parameters for all non-hydrogen atoms. Hydrogen atoms were added to the structure model on calculated positions and were refined as rigid atoms.

All figures were made using the program PLATON [53].

4. Conclusions

The data obtained testify that the structure of the chelate complexes of 12 Group metal cations with *N*-phosphorylated thioamides of general formula RC(S)NHP(O)R′R″ depends on the nature of the central ion, and unlike dithioanaloges RC(S)NHP(S)R′R″ which form only complexes with a MS_4 core. For the ligands containing different donor atoms, sulfur and oxygen simultaneously, the increase in the coordination number of the central atom by dimerization or interaction with nucleophilic species is observed for complexes of Cd(II), while only tetracoordinated [M{RC(S)NP(O)R′R″}-*O*,*S*)$_2$] complexes of Zn(II) have been obtained [24,25].

We assume, that dimerization of the Cd(II) compounds in aqueous ethanol media can promote their hydrolysis, while the mononuclear Zn(II) compounds are obtained in good yield and show no tendency to hydrolytic destruction.

The luminescent properties of the new complexes has shown that the observed emission bands can be assigned ligand-to-metal charge transfer (LMCT).

Acknowledgments

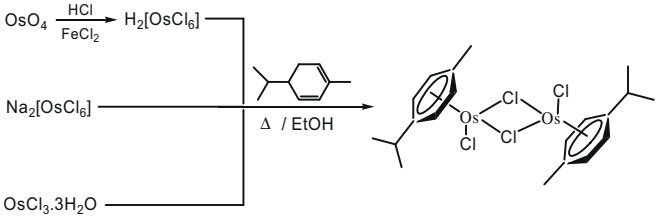
This work was supported by the Russian Science Support Foundation and partly by University of Wroclaw. M.G.B. and D.A.S. thank DAAD for the scholarships (Forschungsstipendien 2008/2009). We also thank Dr. P. Mayer for collecting the data sets for the crystal structure determination.

Appendix A. Supplementary data

CCDC 664765, 682366 and 664766 contain the supplementary crystallographic data for (**1**), (**2**) and (**3**). These data can be obtained free of charge via http://www.ccdc.cam.ac.uk/conts/retrieving.html, or from the Cambridge Crystallographic Data Centre, 12 Union Road, Cambridge CB2 1EZ, UK; fax: (+44) 1223-336-033; or e-mail: deposit@ccdc.cam.ac.uk.

References

[1] S. Blaurock, F.T. Edelman, I. Haiduc, P. Poremba, Inorg. Chim. Acta 361 (2008) 407.
[2] F.T. Edelman, A. Fischer, I. Haiduc, Inorg. Chem. Commun. 656 (2003) 225.
[3] I. Haiduc, J. Organomet. Chem. 623 (2001) 29.
[4] A. Silvestru, D. Bilc, R. Roesler, J.E. Drake, I. Haiduc, Inorg. Chim. Acta 305 (2000) 106.
[5] I. Szekely, C. Silvestru, J.E. Drake, G. Balazs, S.I. Farcas, I. Haiduc, Inorg. Chim. Acta 299 (2000) 247.
[6] J. Novosad, M. Necas, J. Marek, P. Veltsistas, C. Papadimitriou, I. Haiduc, M. Watanabe, J.D. Woollins, Inorg. Chim. Acta 290 (1999) 56.
[7] (a) J.E. Drake, A. Silvestru, J. Yang, I. Haiduc, Inorg. Chim. Acta 271 (1998) 75; (b) I. Haiduc, Coord. Chem. Rev. 158 (1997) 325.
[8] C. Silvestru, I. Haiduc, Coord. Chem. Rev. 147 (1996) 117.
[9] C. Silvestru, J.E. Drake, Coord. Chem. Rev. 223 (2001) 117.
[10] C.W. Liu, T.S. Lobana, B.K. Santra, C.-M. Hung, H.-Y. Liu, B.-J. Liaw, J.-C. Wang, Dalton Trans. (2006) 560.
[11] I. Haiduc, in: J. McCleverty, T.J. Mayer (Eds.), Comprehensive Coordination Chemistry II, vol. II, Pergamon, London, 2004, pp. 323–348.
[12] I.P. Gray, A.M.Z. Slawin, J.D. Woollins, Dalton Trans. (2005) 2188.
[13] A.A. Memon, M. Afzaal, M.A. Malik, C.Q. Nguyen, P. O'Brien, J. Raftery, Dalton Trans. (2006) 4499.
[14] M.C. Copsey, A. Panneerselvam, M. Afzaal, T. Chivers, P. O'Brien, Dalton Trans. (2007) 1528.
[15] M. Afzaal, D.J. Crouch, P. O'Brien, J. Raftery, P.J. Skabara, A.J.P. White, D.J. Williams, J. Mater. Chem. 14 (2004) 233.
[16] D. Fan, M. Afzaal, M.A. Mallik, C.Q. Nguyen, P. O'Brien, P.J. Thomas, Coord. Chem. Rev. 251 (2007) 1878.
[17] J.S. Ritch, T. Chivers, M. Afzaal, P. O'Brien, Chem. Soc. Rev. 10 (2007) 1622.
[18] J.C. Bruce, N. Revaprasadu, K.R. Koch, New J. Chem. 9 (2007) 1647.
[19] C.C. Landry, J. Lockwood, A.R. Barron, Chem. Mater. 7 (1995) 699.
[20] A.D. Garnovskii, D.A. Garnovskii, I.S. Vasilchenko, A.S. Burlov, A.P. Sadimenko, I.D. Sadekov, Russ. Chem. Rev. 66 (1997) 389.
[21] T.Q. Ly, J.D. Woollins, Coord. Chem. Rev. 176 (1998) 451.
[22] V.V. Skopenko, V.M. Amirkhanov, T.Yu. Sliva, I.S. Vasilchenko, E.L. Anpilova, A.D. Garnovskii, Russ. Chem. Rev. 73 (2004) 737.
[23] F.D. Sokolov, V.V. Brusko, N.G. Zabirov, R.A. Cherkasov, Curr. Org. Chem. 10 (2006) 27.
[24] F.D. Sokolov, D.A. Safin, N.G. Zabirov, V.V. Brusko, B.I. Khairutdinov, D.B. Krivolapov, I.A. Litvinov, Eur. J. Inorg. Chem. (2006) 2027.
[25] F.D. Sokolov, D.A. Safin, N.G. Zabirov, P.V. Zotov, R.A. Cherkasov, Russ. J. Gen. Chem. 75 (2005) 1919.
[26] N.G. Zabirov, V.V. Brusko, A.Yu. Verat, D.B. Krivolapov, I.A. Litvinov, R.A. Cherkasov, Phosphorus Sulfur Silicon 17 (2002) 1869.
[27] V.V. Brusko, A.I. Rakhmatullin, N.G. Zabirov, Russ. J. Gen. Chem. 70 (2000) 1603.
[28] F.D. Sokolov, D.A. Safin, N.G. Zabirov, L.N. Yamalieva, D.B. Krivolapov, I.A. Litvinov, Mendeleev Commun. 14 (2004) 51.
[29] D.A. Safin, P. Mlynarz, F.E. Hahn, M.G. Babashkina, F.D. Sokolov, N.G. Zabirov, J. Galezowska, H. Kozlowski, Z. Anorg. Allg. Chem. 633 (2007) 1472.
[30] D.A. Safin, M.G. Babashkina, F.D. Sokolov, N.G. Zabirov, Inorg. Chem. Commun. 9 (2006) 1133.
[31] D.A. Safin, F.D. Sokolov, N.G. Zabirov, V.V. Brusko, D.B. Krivolapov, I.A. Litvinov, R.A. Cherkasov, Polyhedron 25 (2006) 3330.
[32] D.A. Safin, F.D. Sokolov, H. Nöth, M.G. Babashkina, T.R. Gimadiev, J. Galezowska, H. Kozlowski, Polyhedron 27 (2008) 2022.
[33] D.A. Safin, H. Nöth, F.D. Sokolov, M.G. Babashkina, N.G. Zabirov, J. Galezowska, H. Kozlowski, in: Proceedings of the VII Science Conference on "Materials and technologies of XXI centuries", Kazan, Russia, 2007, p. 111.
[34] F.D. Sokolov, N.G. Zabirov, L.N. Yamalieva, V.G. Shtyrlin, Ruslan R. Garipov, V.V. Brusko, A.Yu. Verat, S.V. Baranov, P. Mlynarz, T. Glowiak, H. Kozlowski, Inorg. Chim. Acta 359 (2006) 2087.
[35] A.Yu. Verat, B.I. Khairutdinov, V.G. Shtyrlin, F.D. Sokolov, L.N. Yamalieva, D.B. Krivolapov, N.G. Zabirov, I.A. Litvinov, V.V. Klochkov, Mendeleev Commun. 18 (2008) 150.
[36] F.D. Sokolov, N.G. Zabirov, V.V. Brusko, D.B. Krivolapov, I.A. Litvinov, Mendeleev Commun. 13 (2003) 72.
[37] V.V. Brus'ko, F.D. Sokolov, N.G. Zabirov, R.A. Cherkasov, A.I. Rakhmatullin, A.Yu. Verat, Russ. J. Gen. Chem. 69 (1999) 664.
[38] N.G. Zabirov, I.A. Litvinov, O.N. Kataeva, S.V. Kashevarov, F.D. Sokolov, R.A. Cherkasov, Russ. J. Gen. Chem. 68 (1998) 1408.
[39] F.D. Sokolov, M.G. Babashkina, D.A. Safin, A.I. Rakhmatullin, F. Fayon, N.G. Zabirov, M. Bolte, V.V. Brusko, J. Galezowska, Henryk Kozlowski, Dalton Trans. (2007) 4693.
[40] D.A. Safin, M.G. Babashkina, F.D. Sokolov, N.G. Zabirov, J. Galezowska, H. Kozlowski, Polyhedron 26 (2007) 1113.
[41] A. Zazybin, O. Osipova, U. Khusnutdinova, I. Aristov, B. Solomonov, F. Sokolov, M. Babashkina, N. Zabirov, J. Mol. Catal. A: Chem. 253 (2006) 234.
[42] A.Y. Verat, F.D. Sokolov, N.G. Zabirov, M.G. Babashkina, D.B. Krivolapov, V.V. Brusko, I.A. Litvinov, Inorg. Chim. Acta 359 (2006) 475.
[43] N.G. Zabirov, A.Yu. Verat, F.D. Sokolov, M.G. Babashkina, D.B. Krivolapov, V.V. Brusko, Mendeleev Commun. 13 (2003) 163.
[44] V.N. Soloviev, A.N. Chechlov, N.G. Zabirov, I.V. Martynov, Dokl. Chem. 341 (1995) 502.
[45] D.A. Safin, F.D. Sokolov, S.V. Baranov, Ł. Szyrwiel, M.G. Babashkina, E.R. Shakirova, F.E. Hahn, H. Kozlowski, Z. Anorg. Allg. Chem. 634 (2008) 835.
[46] R.R. Abdreimova, D.N. Akbayeva, G.S. Polimbetova, A.-M. Caminade, J.-P. Majorals, Phosphorus Sulfur Silicon Relat. Elem. 156 (2000) 239.
[47] APEX2 (Version 2.1), SAINTPLUS. Data Reduction and Correction Program (Version 7.31A, Bruker Advanced X-ray Solutions, BrukerAXS Inc., Madison, WI, USA, 2006.
[48] G.M. Sheldrick, SADABS, Program for Empirical X-ray Absorption Correction, Bruker-Nonius, 1990–2004.
[49] A. Altomare, G. Cascarano, C. Giacovazzo, D. Viterbo, Acta Crystallogr., Sect. A. 47 (1991) 744.
[50] G.M. Sheldrick, SHELXL-97 – 2 Program for Crystal Structure Refinement, University of Goettingen, Germany, 1997.
[51] L.J. Farrugia, WINGX 1.64.05 An Integrated System of Windows Programs for the solution, Refinement and Analysis of Single Crystal X-ray Diffraction Data, J. Appl. Crystal. 32 (1999) 837.
[52] G.M. Sheldrick, SHELXS-97 Program for Crystal Structure Solution, University of Goettingen, Germany, 1997.
[53] A.L. Spek, Acta Crystallogr., Sect. A 46 (1990) 34.



Scheme 1. Reported synthetic methods for dimeric η^6-*p*-cymene osmium(II) complexes [1,2].

using Xenon gas and all matrices were made with 3-nba (3-nitrobenzyl alchohol). Microanalyses were conducted with a Thermo Flash 1112 Series CHNS-O Analyzer instrument. FT-IR spectra were recorded on a Perkin–Elmer Spectrum One FT-IR Spectrometer, using solution cells with NaCl windows.

Melting points were recorded with a Kofler hot stage microscope (Riechert Thermovar). GC analyses were carried out using a Varian 3900 gas chromatograph equipped with an FID and a 30 m × 0.32 mm CP-Wax 52 CB column (0.25 μm film thickness). The carrier gas was helium at 5.0 psi. The oven was programmed to hold at 32 °C for 4 min and then to ramp to 200 °C at 10 °C/min and hold 5 min.

2.3. Preparation of arene-osmium complexes

2.3.1. Synthesis of $[(\eta^6\text{-}p\text{-}MeC_6H_4Pr^i)OsBr_2]_2$ (**1**)

$K_2[OsO_2(OH)_4]$ (5.070 g, 13.760 mmol) was dissolved in HBr (50 ml, 48% aq) and EtOH (100 ml 96%) and refluxed for 18 h. To the solution was added α-phellandrene (10 ml) and refluxed for a further 18 h. The solvent was removed under vacuum to give a red oil. The product was extracted with CH_2Cl_2 (5 × 80 ml) and the solution concentrated to approximately 50 ml and diethyl ether added. The solution was cooled at −15°C overnight to give orange-red crystals. Yield (4.39 g, 66%); m.p. 246–249 °C. Elemental *Anal.* Calc. for $C_{20}H_{28}Br_4Os_2$: C, 24.78; H, 2.89. Found: C, 24.93; H, 2.87%. ^{1}H NMR (300 MHz, $CDCl_3$) δ ppm: 1.12–1.30 (m 6H) CH*Me*$_2$, 2.17 (s, 3H) C*Me*, 2.45–2.76 (m, 1H) C*H*Me$_2$, 6.02 (d, 2H J = 5.65 Hz) C$_6$*H*$_4$, 6.15 (d, 2H J = 5.64 Hz) C$_6$*H*$_4$.

2.3.2. Synthesis of $[(\eta^6\text{-}C_6Me_6)OsBr_2]_2$ (**2**)

$[(\eta^6\text{-}p\text{-}MeC_6H_4Pr^i)OsBr_2]_2$ (**1**) (500 mg, 0.516 mmol) and hexamethylbenzene (4.00 g 24.648 mmol) were transferred into a sealable tube. The tube was evacuated and heated at 175–180 °C. After 24 h the melt was allowed to reach room temperature and extracted with CH_2Cl_2 (25 ml). The solvent was removed using a rotary evaporator and a brown-orange solid was obtained and washed with (4 × 50 ml) of *n*-hexane to remove the excess hexamethylbenzene and dried under vacuum for 3 h. Yield (315 mg, 60%); decomposes without melting at 280 °C. Elemental *Anal.* Calc. for $C_{24}H_{36}Br_4Os_2$: C, 28.13; H, 3.54. Found: C, 28.49; H, 3.57%. ^{1}H NMR (300 MHz, $CDCl_3$) δ ppm: 2.25 (s 36H) 2{C$_6$*Me*$_6$}.

2.3.3. Synthesis of $[(\eta^6\text{-}p\text{-}MeC_6H_4Pr^i)Os(PPh_3)Br_2]$ (**3**)

To a suspension of $[(\eta^6\text{-}p\text{-}MeC_6H_4Pr^i)OsBr_2]_2$ (**1**) (1.070 g, 1.032 mmol) in *n*-hexane (80 ml) was added PPh_3 (560 mg, 2.064 mmol) and heated to reflux. After 4 h the solvent was removed using a rotary evaporator to give an orange solid residue. The solid was dissolved in a minimum of CH_2Cl_2 (15 ml), filtered and diethyl ether added to give an orange solid. Yield (1.424 g, 92%). Elemental *Anal.* Calc. for $C_{28}H_{29}Br_2OsP$: C, 45.03; H, 3.88. Found: C, 45.07; H, 3.86%; m.p. 223–225 °C; ^{1}H NMR (400 MHz, $CDCl_3$) δ ppm: 1.19 (d, 6H J = 6.93 Hz) CH*Me*$_2$, 1.97 (s, 3H) C*Me*, 2.99 (q, 1H J = 7.04, 7.23, 7.23 Hz) C*H*Me$_2$, 5.13 (d, 2H J = 5.82 Hz) C$_6$*H*$_4$, 5.47 (d, 2H J = 5.90 Hz) C$_6$*H*$_4$, 7.30–7.82 (m, 15H) P*Ph*$_3$; ^{31}P NMR (121 MHz, $CDCl_3$) δ ppm: −17.57 (s), $^1J(^{187}Os\text{–}^{31}P)$ = 283 Hz.

Complexes **4**–**8** were prepared using the same procedure as described for the preparation of complex **3**.

2.3.4. $[(\eta^6\text{-}p\text{-}MeC_6H_4Pr^i)Os(PEt_3)Br_2]$ (**4**)

Complex **4** was prepared using $[(\eta^6\text{-}p\text{-}MeC_6H_4Pr^i)OsBr_2]_2$ (**1**) (200 mg, 0.206 mmol) and PEt_3 (48 mg, 0.413 mmol). The product was obtained as an orange solid and dried under vacuum for 2 h. Yield (191 mg, 73%). Elemental *Anal.* Calc. for $C_{16}H_{29}Br_2OsP$: C, 31.90; H, 4.85. Found: C, 31.02; H, 4.99%; m.p. 119–122 °C; ^{1}H NMR (300 MHz, $CDCl_3$) δ ppm: 1.04–1.22 (m, 9H) P–(CH$_2$*Me*)$_3$, 1.27 (d, 6H J = 6.86 Hz) CH*Me*$_2$, 2.05–2.18 (m, 6H) P–(*CH*$_2$Me)$_3$, 2.28 (s, 3H) C*Me*, 2.88 (q, 1H J = 7.04, 7.23, 7.23 Hz) C*H*Me$_2$, 5.55 (d, 2H J = 4.98 Hz) C$_6$*H*$_4$, 5.61 (d, 2H J = 5.71 Hz) C$_6$*H*$_4$; ^{31}P NMR (121 MHz, $CDCl_3$) δ ppm: −28.35 (s) $^1J(^{187}Os\text{–}^{31}P)$ = 269 Hz.

2.3.5. $[(\eta^6\text{-}p\text{-}MeC_6H_4Pr^i)Os(PMePh_2)Br_2]$ (**5**)

Complex **5** was prepared using $[(\eta^6\text{-}p\text{-}MeC_6H_4Pr^i)OsBr_2]_2$ (**1**) (460 mg, 0.475 mmol) and $PMePh_2$ (190 mg, 0.950 mmol). The product was isolated as an orange-yellow solid. Yield (566 mg, 87%). Elemental *Anal.* Calc. for $C_{23}H_{27}Br_2OsP$: C, 40.36; H, 3.98. Found: C, 40.11; H, 3.52%; m.p. 196–198 °C; ^{1}H NMR (400 MHz, $CDCl_3$) δ ppm: 1.22 (d, 6H J = 6.97, Hz) CH*Me*$_2$, 2.02–2.15 (m, 3H) P–*Me*Ph$_2$, 2.18 (d, 3H J = 10.68 Hz) C*Me*, 2.89 (q, 1H J = 7.04, 7.23, 7.23 Hz) C*H*Me$_2$, 5.40 (d, 2H J = 5.75 Hz) C$_6$*H*$_4$, 5.49 (d, 2H J = 5.71 Hz) C$_6$*H*$_4$, 7.39–7.76 (m, 10H) P–Me*Ph*$_2$; ^{31}P NMR (121 MHz, $CDCl_3$) δ ppm: −26.68 (s) $^1J(^{187}Os\text{–}^{31}P)$ = 274 Hz.

2.3.6. $[(\eta^6\text{-}p\text{-}MeC_6H_4Pr^i)Os\{P(OMe)_3\}Br_2]$ (**6**)

Complex **6** was prepared using $[(\eta^6\text{-}p\text{-}MeC_6H_4Pr^i)OsBr_2]_2$ (**1**) (200 mg, 0.206 mmol) and $P(OMe)_3$ (51 mg, 0.413 mmol). The product was obtained as a red-orange crystalline solid. Yield (185 mg, 74%). Elemental *Anal.* Calc. for $C_{13}H_{23}O_3Br_2OsP$: C, 25.66; H, 3.78. Found: C, 25.29; H, 3.73%; m.p. 154–157 °C; ^{1}H NMR (400 MHz, $CDCl_3$) δ ppm: 1.25 (d, 6H J = 6.95 Hz) CH*Me*$_2$, 2.33 (d, 3H J = 1.71 Hz) C*Me*, 2.99 (q, 1H J = 7.04, 7.23, 7.23 Hz) C*H*Me$_2$, 3.58 (d, 9H J = 10.90 Hz) P–(O*Me*)$_3$, 5.49 (d, 2H J = 5.88 Hz) C$_6$*H*$_4$, 5.64 (d, 2H J = 5.93 Hz) C$_6$*H*$_4$; ^{31}P NMR (121 MHz, $CDCl_3$) δ ppm: 68.06 (s) $^1J(^{187}Os\text{–}^{31}P)$ = 455 Hz.

2.3.7. $[(\eta^6\text{-}p\text{-}MeC_6H_4Pr^i)Os\{P(OBu^n)_3\}Br_2]$ (**7**)

Complex **7** was prepared using $[(\eta^6\text{-}p\text{-}MeC_6H_4Pr^i)OsBr_2]_2$ (**1**) (1.000 g, 1.032 mmol) and $P(OBu^n)_3$ (516 mg, 2.065 mmol). The product was isolated as a bright orange solid. Yield (1.284 g, 85%). Elemental *Anal.* Calc. for $C_{22}H_{41}O_3Br_2OsP$: C, 35.97; H, 5.58. Found: C, 35.95; H, 5.39%; m.p. 57–60 °C; ^{1}H NMR (400 MHz, $CDCl_3$) δ ppm: 0.83–0.95 (m, 9H) P–{O(CH$_2$)$_3$*CH*$_3$}$_3$, 1.21 (d, 6H J = 6.95 Hz) CH*Me*$_2$, 1.36 (qd, 6H J = 14.38, 7.24, 7.24, 7.15 Hz) P–{O(CH$_2$)$_2$*CH*$_2$CH$_3$}$_3$, 1.52–1.69 (m, 6H) P–{OCH$_2$*CH*$_2$CH$_2$CH$_3$}$_3$, 2.28 (s, 3H) C*Me*, 2.87–2.92 (m, 1H) C*H*Me$_2$, 3.76 (dd, 6H J = 6.90, 13.90 Hz) P–{OC*H*$_2$(CH$_2$)$_2$CH$_3$}$_3$, 5.43 (d, 2H J = 5.76 Hz) C$_6$*H*$_4$, 5.57 (d, 2H J = 5.72 Hz) C$_6$*H*$_4$; ^{31}P NMR (121 MHz, $CDCl_3$) δ ppm: 62.43 (s) $^1J(^{187}Os\text{–}^{31}P)$ = 449 Hz.

2.3.8. $[(\eta^6\text{-}p\text{-}MeC_6H_4Pr^i)Os\{P(OPh)_3\}Br_2]$ (**8**)

Complex **8** was prepared using $[(\eta^6\text{-}p\text{-}MeC_6H_4Pr^i)OsBr_2]_2$ (**1**) (500 mg, 0.516 mmol) and $P(OPh)_3$ (320 mg, 1.033 mmol). The product was isolated as an orange solid. Yield (662 mg, 81%). Elemental *Anal.* Calc. for $C_{28}H_{29}Br_2O_3OsP$: C, 42.33; H, 3.68. Found: C, 42.45; H, 3.18%; m.p. 175–177 °C; ^{1}H NMR (300 MHz, $CDCl_3$) δ ppm: 1.20 (d, 6H J = 6.99 Hz) CH*Me*$_2$, 2.23 (s, 3H) C*Me*, 2.55–2.78 (m, 1H) C*H*Me$_2$, 5.16 (d, 2H J = 5.92 Hz) C$_6$*H*$_4$, 5.48 (d, 2H J = 5.92 Hz) C$_6$*H*$_4$, 7.09–7.36 (m, 15H) P(O*Ph*)$_3$; ^{31}P NMR (121 MHz, $CDCl_3$) δ ppm: 52.28 (s), $^1J(^{187}Os\text{–}^{31}P)$ = 476 Hz.

*2.3.9. Synthesis of [(η^6-p-MeC$_6$H$_4$Pr^i)Os(CO)Br$_2$] (**9**)*

CO gas was bubbled through a suspension of [(η^6-*p*-MeC$_6$H$_4$-Pr^i)OsBr$_2$]$_2$ (**1**) (500 mg, 0.195 mmol) in *n*-hexane (25 ml). After 45 min the solvent was removed using a rotary evaporator to give a red-orange solid which was dried under vacuum for 1 h. Yield (482 mg, 91%). Elemental *Anal.* Calc. for $C_{11}H_{14}Br_2OOs$: C, 25.79; H, 2.75. Found: C, 25.55; H, 2.66%; decomposes without melting above 200 °C; IR (CH_2Cl_2, cm^{-1}): ν(C≡O) 2022; ^{1}H NMR (300 MHz, $CDCl_3$) δ ppm: 1.20 (d, 6H J = 6.99 Hz) CH*Me*$_2$, 2.13 (s, 3H) C*Me*, 2.77 (q, 1H J = 7.04, 7.23, 7.23 Hz) C*H*Me$_2$, 5.14 (d, 2H J = 5.82 Hz) C$_6$*H*$_4$, 5.47 (d, 2H J = 5.90 Hz) C$_6$*H*$_4$.

*2.3.10. Synthesis of [(η^6-C$_6$Me$_6$)Os(CO)Br$_2$] (**10**)*

CO gas was bubbled through a solution of [Os(η^6-C$_6$Me$_6$)Br$_2$]$_2$ (**2**) (200 mg, 0.195 mmol) dissolved in dry chloroform (40 ml). After 45 min the solvent was removed using a rotary evaporator to give a dark orange solid which was dried under vacuum for 1 h. Yield (89 mg, 42%). Elemental *Anal.* Calc. for $C_{13}H_{18}Br_2OOs$: C, 28.90; H, 3.33. Found: C, 28.52; H, 3.85%; decomposes without melting above 280 °C; IR ($CHCl_3$, cm^{-1}): ν(C≡O) 2005; ^{1}H NMR (300 MHz, $CDCl_3$) δ ppm: 1.98 (s, 18H) {C$_6$*Me*$_6$}.

*2.3.11. Synthesis of [(η^6-p-MeC$_6$H$_4$Pr^i)(PPh$_3$)Os{(CH$_2$)$_3$CH=CH$_2$}$_2$] (**11**)*

[(η^6-*p*-MeC$_6$H$_4$Pr^i)Os(PPh$_3$)Br$_2$] (**3**) (1.000 g, 1.420 mmol) was transferred into a Schlenk tube and dissolved in freshly dried THF (30 ml). To this was added BrMg(CH$_2$)$_3$CH=CH$_2$ (0.54 M, 10.56 ml, 5.690 mmol) under N_2 at −78 °C. The solution was then allowed to reach room temperature and stirred for 18 h, during which time it had turned from orange to yellow. A saturated NH_4Cl solution (15 ml) was added drop wise to the solution at −78 °C in order to hydrolyze the excess Grignard reagent. After reaching room temperature dichloromethane (20 ml) was added and the organic layer was separated, dried over anhydrous $MgSO_4$ and filtered. The volatiles were removed using a rotary evaporator to give a yellow-brown oil which was dried under vacuum for 30 min. Yield (745 mg, 72%); ^{1}H NMR (300 MHz, C_6D_6) δ ppm: 0.82–0.91 (m, 4H) Os–C*H*$_2$, 1.21 (d, 6H J = 6.99 Hz) CH*Me*$_2$, 1.40–1.88 (m, 8H) C*H*$_2$, 1.99 (s, 3H) C*Me*, 2.98 (q, 1H J = 7.04, 7.23, 7.23 Hz) C*H*Me$_2$, 4.52–5.04 (m, 4H) =C*H*$_2$, 5.32 (d, 2H J = 5.90 Hz) C$_6$*H*$_4$, 5.53 (d, 2H J = 5.88 Hz) C$_6$*H*$_4$, 5.61–5.79 (m, 2H) C*H*=, 7.28–7.82 (m, 15H) P*Ph*$_3$; ^{31}P NMR (121 MHz, $CDCl_3$) δ ppm: 12.61 (s).

Complexes **12**–**14** were prepared using the same procedure as described for the preparation of complex **11**.

*2.3.12. [(η^6-p-MeC$_6$H$_4$Pr^i){P(OBu^n)$_3$}Os{(CH$_2$)$_3$CH=CH$_2$}$_2$] (**12**)*

Complex **12** was prepared using [(η^6-*p*-MeC$_6$H$_4$Pr^i)Os{P(OBu^n)$_3$}Br$_2$] (**7**) (190 mg, 0.259 mmol) in freshly dried THF (35 ml) and BrMg(CH$_2$)$_3$CH=CH$_2$ (2.0 M, 0.5 ml, 1.035 mmol). The product was obtained as a yellow oil. Yield (178 mg, 97%); ^{1}H NMR (300 MHz, C_6D_6) δ ppm: 0.78–0.89 (m, 13H) Os–C*H*$_2$ and P–{O(CH$_2$)$_3$C*H*$_3$}$_3$, 1.24 (d, 6H J = 6.93 Hz) CH*Me*$_2$, 1.40–1.70 (m, 16H) C*H*$_2$ and P–{OCH$_2$(C*H*$_2$)$_2$CH$_3$}$_3$, 1.87–2.03 (m, 4H) C*H*$_2$, 2.28 (s 3H) C*Me*, 2.92 (m, 1H) C*H*Me$_2$, 3.77 (dd, 6H J = 6.90, 13.90 Hz) P–{OC*H*$_2$(CH$_2$)$_2$CH$_3$}$_3$, 4.72–5.05 (m, 4H) =C*H*$_2$, 5.56 (d, 2H J = 5.76 Hz) C$_6$*H*$_4$, 5.62 (d, 2H J = 5.72 Hz) C$_6$*H*$_4$, 5.68–5.84 (m, 2H) C*H*=; ^{31}P NMR (121 MHz, $CDCl_3$) δ ppm: 79.41 (s), $^1J(^{187}Os–^{31}P)$ = 476 Hz.

*2.3.13. [(η^6-p-MeC$_6$H$_4$Pr^i)(CO)Os{(CH$_2$)$_3$CH=CH$_2$}$_2$] (**13**)*

Complex **13** was prepared using [(η^6-*p*-MeC$_6$H$_4$Pr^i)Os(CO)Br$_2$] (**9**) (150 mg, 0.291 mmol) in freshly dried THF (25 ml) and BrMg(CH$_2$)$_3$CH=CH$_2$ (0.32 M, 3.64 ml, 1.167 mmol). This compound was obtained as a dark brown oil after an aqueous work-up. Yield (96 mg, 68%); IR (CH_2Cl_2, cm^{-1}): ν(C≡O) 1965; ^{1}H NMR (300 MHz, C_6D_6) δ ppm: 0.77–0.91 (m, 4H) Os–C*H*$_2$, 1.18 (d, 6H J = 6.99 Hz) CH*Me*$_2$, 1.20–1.88 (m, 8H) C*H*$_2$, 1.96 (s, 3H) C*Me*, 2.68 (q, 1H J = 7.04, 7.23, 7.23 Hz) C*H*Me$_2$, 4.83–5.08 (m, 4H) =C*H*$_2$, 5.10 (d, 2H J = 5.67 Hz) C$_6$*H*$_4$, 5.35 (d, 2H J = 5.77 Hz) C$_6$*H*$_4$, 5.45–5.90 (m, 2H) C*H*=.

*2.3.14. [(η^6-C$_6$Me$_6$)(CO)Os{(CH$_2$)$_3$CH=CH$_2$}$_2$] (**14**)*

Complex **14** was prepared using [Os[(η^6-C$_6$Me$_6$)(CO)Br$_2$] (60 mg, 0.111 mmol) in dry benzene and BrMg(CH$_2$)$_3$CH=CH$_2$ (1.66 M, 0.26 ml, 0.444 mmol). The product was obtained as a brown oil. Yield (28 mg, 49%); IR ($CHCl_3$, cm^{-1}): ν(C≡O) 1897; LRMS (FAB) $C_{23}H_{26}OOs$: m/z = 519.3 [M]$^+$, 451.2 [M−(CH$_2$)$_3$CH=CH$_2$]$^+$, 383.1 [M−2((CH$_2$)$_3$CH=CH$_2$)]$^+$; ^{1}H NMR (300 MHz, C_6D_6) δ ppm: 0.82–0.89 (m, 4H) Os–C*H*$_2$, 1.02–1.80 (m, 8H) C*H*$_2$, 2.03 (s, 18H) {C$_6$*Me*$_6$}, 4.93–5.20 (m, 4H) =C*H*$_2$, 5.55 (d, 2H J = 5.18 Hz) C*H*=.

*2.3.15. [(η^6-p-MeC$_6$H$_4$Pr^i)(CO)Os(CH$_3$)$_2$] (**15**)*

A solution of [(η^6-*p*-MeC$_6$H$_4$Pr^i)Os(CO)Br$_2$] (**9**) (200 mg, 0.390 mmol) in dry THF (30 ml) was cooled to −78 °C. MeLi (0.66 M, 2.5 ml, 1.560 mmol) was then added drop wise to this solution. The solution was allowed to reach room temperature and stirred for 10 h, during which time it turned from orange to yellow. After 10 h the solvent was removed using a rotary evaporator to give a brown oil residue. The product was extracted with *n*-hexane (3 × 15 ml) and the solvent was removed to give a brown oil of [(η^6-*p*-MeC$_6$H$_4$Pr^i)(CO)Os(CH$_3$)$_2$] (**15**). Yield (106 mg, 71%); IR (CH_2Cl_2, cm^{-1}): ν(C≡O) 1923; ^{1}H NMR (400 MHz, C_6D_6) δ ppm: 0.95 (s, 6H) Os–C*H*$_3$, 0.99 (d, 6H J = 6.90 Hz) CH*Me*$_2$, 1.71 (s, 3H) C*Me*, 2.88 (q, 1H J = 7.04, 7.23, 7.23 Hz) C*H*Me$_2$, 5.47(d, 2H J = 5.80 Hz) C$_6$*H*$_4$, 5.81 (d, 2H J = 5.80 Hz) C$_6$*H*$_4$.

2.4. X-ray crystal structures

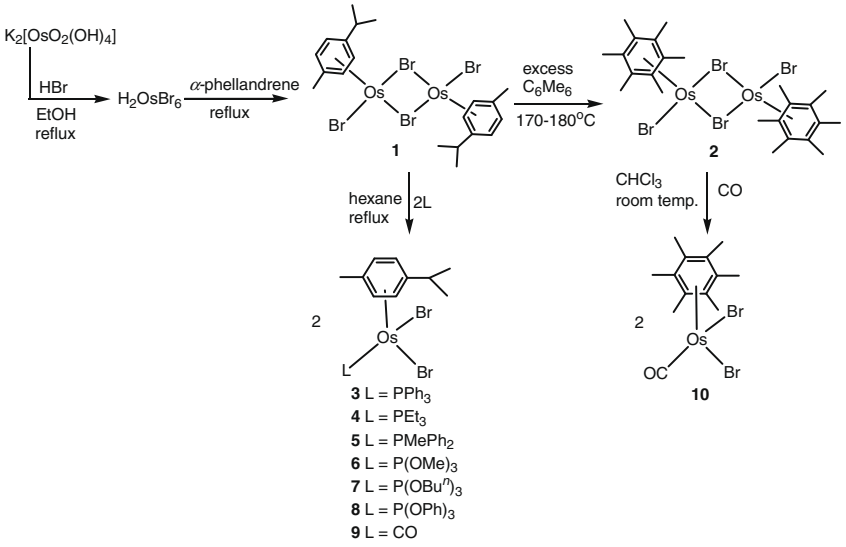
The data for **1** were collected at 293 K on a Siemens P4 diffractometer fitted with a Bruker 1 K CCD detector and SMART control software using graphite-monochromated, Mo Kα radiation by means of a combination of phi and omega scans. Data reduction was performed using SAINT+ and the intensities were corrected for absorption using SADABS [8]. The structure was solved by direct methods using SHELXTS [8] and refined by full-matrix least-squares using SHELXTL [8] and SHELXL-97 [9].

The data for **3** were collected at 293 K on a Nonius Kappa-CCD diffractometer using graphite-monochromated Mo Kα radiation. The strategy for the data collection was evaluated using the Bruker Nonius "COLLECT" program. Data were reduced and scaled using DENZO-SMN software [10]. Face indexed absorption corrections were made using the program XPREP. The structure was solved by direct methods and refined employing full-matrix least-squares with the program SHELXL-97 [9] refining on F^2, using the graphic interface X-seed [11]. All non-H atoms were first refined isotropically followed by anisotropic refinements. Hydrogen atoms were first located in the difference electron density maps then positioned geometrically and allowed to ride on their respective parent atoms.

3. Results and discussion

3.1. Syntheses and characterization of arene-osmium dimeric complexes

The dimer [(η^6-*p*-MeC$_6$H$_4$Pr^i)OsBr$_2$]$_2$ (**1**) was prepared by heating a solution of potassium osmate, $K_2[OsO_2(OH)_4]$, in concentrated HBr and aqueous ethanol at reflux for 18 h followed by addition of α-phellandrene and further heating for an additional 18 h (Scheme 2). The complex was isolated in a moderate yield of 66% as a red-brown stable solid which was also found to be stable in



Scheme 2. The syntheses of arene-osmium dimers **1** and **2** and osmium dibromide complexes **3**–**10**.

Table 1
Crystal data and structure refinement details.

	1	**3**
Empirical formula	$C_{20}H_{28}Br_4Os_2 \cdot \frac{1}{3}H_2O$	$C_{28}H_{29}Br_2OsP$
Formula weight	974.52	746.50
Crystal system	monoclinic	monoclinic
Space group	$C2/c$	$P2_1/n$
Crystal dimensions (mm)	0.46 × 0.40 × 0.36	0.09 × 0.07 × 0.06
a (Å)	42.739(5)	9.20140(10)
b (Å)	8.0787(9)	21.59420(10)
c (Å)	24.322(3)	13.54940(10)
α (°)	90	90
β (°)	119.162(2)	106.9670(10)
γ (°)	90	90
V (Å^3)	7333.5(14)	2575.04(4)
ρ (Mg/m^3)	2.648	1.926
Z	12	4
F(000)	5320	1432
Total reflections measured	18297	90817
Independent reflections [R_{int}]	6894 [0.0555]	4872 [0.0465]
Goodness-of-fit on F^2	1.024	1.076
Final R indices [$I > 2\sigma(I)$]	R_1 = 0.0629, wR_2 = 0.1706	R_1 = 0.0199, wR_2 = 0.0394
R indices (all data)	R_1 = 0.0711, wR_2 = 0.1795	R_1 = 0.0261, wR_2 = 0.0411
Extinction coefficient	0.00041(3)	0.00089(6)
Largest difference in peak and hole (e Å^{-3})	4.715 and −2.911	0.544 and −0.624

solution, including in chlorinated solvents. Syntheses of the chloride and iodide analogues of this complex have been reported before using OsO_4 and $OsCl_3 \cdot 3H_2O$ as starting materials, respectively [12]. The iodo complex $[(\eta^6\text{-}p\text{-}MeC_6H_4Pr^i)OsI_2]_2$ was prepared by halide metathesis of the analogous chloro complex with NaI [12d]. Synthesis of $[(\eta^6\text{-}C_6Me_6)OsBr_2]_2$ (**2**) was achieved by following a reported protocol for the chloride analogue [13]. Using this method, complex **2** and excess hexamethylbenzene were heated at 170–180 °C in a sealed and evacuated tube for 24 h (Scheme 2). After extraction with dichloromethane, the complex **2** was obtained as a stable brown solid which decomposes without melting at 280 °C.

The ^{1}H NMR spectrum of complex **1** displayed characteristic *p*-cymene ligand chemical shifts, while a singlet at 2.25 ppm corresponding to the methyl groups of the hexamethylbenzene ligands in complex **2** was observed in its ^{1}H NMR spectrum (Table 2). The signal for these methyl groups appeared at a slightly higher frequency when compared to the chloride analogue (1.92 ppm) [13]. This is evidence of less electronic interaction between the bromide ion and the metal centre as opposed to when the more electronegative chloride ion is present. Satisfactory elemental analyses were obtained for both complexes **1** and **2** (Table 2).

3.2. Syntheses and characterization of arene-osmium dibromide complexes

A series of arene-osmium dibromide complexes **3**–**8** of the type $[(\eta^6\text{-}p\text{-}MeC_6H_4Pr^i)OsLBr_2]$ (L = tertiary phosphine and phosphite ligands) were prepared by heating suspensions of the dimeric compound **1** in refluxing *n*-hexane with two equivalents of the appropriate ligand over 4 h (Scheme 2). These complexes were obtained as stable red-orange to orange solids in yields ranging from

Table 2
^{1}H NMR data, elemental analyses and melting points of complexes **1** and **2**.

Complex	δ (ppm)[a]	J (Hz) assignment	C[b] (%)	H[b] (%)	m.p. (°C)
1	1.12–1.30 (m)	$CH(CH_3)_2$	24.93(24.78)	2.87(2.89)	246–249
	2.17 (s)	$C(CH_3)$			
	2.78 (m)	$CH(CH_3)_2$			
	6.02 (d) J = 5.65	C_6H_4			
	6.15 (d) J = 5.64	C_6H_4			
2	2.25 (s)	$C_6(CH_3)_6$	28.49(28.13)	3.57(3.54)	Decomposes without melting at 280

[a] Spectra recorded in $CDCl_3$, internal standard was tetramethylsilane (TMS).
[b] Calculated values in parentheses.

73% to 92%. Furthermore, complexes **3**–**8** were found to be stable in solution including in chlorinated solvents, with compound **3** showing remarkable stability in chloroform on the bench top for 2 weeks and thereafter decomposing to a brown unidentified species.

Only one example was found in the literature of a similar dibromide complex, i.e. $[(\eta^6\text{-}p\text{-}MeC_6H_4Pr^i)Os(PMe_3)Br_2]$. This complex was prepared by a method involving metathesis of the chlorides in $[(\eta^6\text{-}p\text{-}MeC_6H_4Pr^i)Os(PMe_3)Cl_2]$ with NaBr [14]. All other reports found described dichloride and di-iodide complexes [5,12,14]. Thus, to the best of our knowledge complexes **3**–**8** and its precursor **1** are all new. Complexes **9** and **10** were formed by bubbling CO gas through a suspension of compound **1** in *n*-hexane or a solution of compound **2** in chloroform at room temperature over 45 min (Scheme 2). Red-orange, solids of complexes **9** and **10** were afforded in good yields of 91% and 62%, respectively.

The carbonyl complexes $[(\eta^6\text{-}p\text{-}MeC_6H_4Pr^i)Os(CO)Br_2]$ (**9**) and $[(\eta^6\text{-}C_6Me_6)Os(CO)Br_2]$ (**10**) were remarkably thermally stable, only decomposing to black unidentified species at and above 200 °C, respectively. The complexes with tertiary phosphine ligands **3**–**5** all had high melting points of between 196 and 225 °C while, phosphite containing complexes **6**–**8** showed melting points of between 85 and 177 °C.

The ^{1}H NMR spectra of complexes **3**–**9** all exhibited signals characteristic of *p*-cymene ligands. These signals are similar to those reported for the analogous dichloride and di-iodide compounds [14], with slight shifts as a result of the different halides present. In general, the aromatic proton signals for the bromide complexes appeared downfield relative to the chloride analogues and upfield relative to the iodo complexes. $[(\eta^6\text{-}C_6Me_6)Os(CO)Br_2]$ (**10**) displayed a singlet corresponding to the methyl groups of hexamethylbenzene at 1.98 ppm, slightly more downfield than that reported for the chloride derivative $[(\eta^6\text{-}C_6Me_6)Os(CO)Cl_2]$ (1.96 ppm) [13].

The phosphine containing complexes **3**–**5** showed low field ^{31}P NMR peaks together with satellites due to coupling with ^{187}Os (Table 3). Larger coupling constants were seen in the phosphite bearing complexes **6**–**8**, whose ^{31}P NMR signals appeared as singlets in the more deshielded region, when compared to their phosphine counterparts (Table 3). This clearly shows that the type of phosphorus donor ligand, affects the ^{31}P NMR chemical shifts in $(\eta^6\text{-}p\text{-}MeC_6H_4Pr^i)OsLBr_2]$ type complexes. Similar coupling of ^{187}Os and ^{31}P has been reported for related (η^6-arene)osmium(II) complexes [14].

Comparison of the ^{31}P NMR signals and $^1J(^{187}Os\text{–}^{31}P)$ coupling constants of complexes **3**–**8** with those of chloride and iodide analogues reveals that the complexes exhibit halide dependence, with deshielding of the ^{31}P NMR signal in the order of Cl > Br > I, thus replacement of the bromide ligands of complexes **3**–**8** with chlorides results in an upfield shift of the ^{31}P NMR signal. The opposite effect can be seen when the bromide ligands are replaced by iodide ligands (Table 3) [14]. A slight increase in $^1J(^{187}Os\text{–}^{31}P)$ coupling constants can also be seen from I^- to Br^- and Cl^- containing complexes.

Complexes **9** and **10** showed expected terminal ν(CO) bands at 2022 and 2005 cm^{-1}, respectively.

3.3. Crystal structures of $[(\eta^6\text{-}p\text{-}MeC_6H_4Pr^i)OsBr_2]_2$ and $(\eta^6\text{-}p\text{-}MeC_6H_4Pr^i)Os(PPh_3)Br_2$

Red crystals of **1** and **3** were obtained by slow evaporation of dichloromethane solutions at room temperature. The crystallographic details and selected bond distances and angles for both structures are given in Tables 1 and 4, respectively. The molecular structures and atomic numbering schemes for **1** and **3** are presented in Figs. 1 and 2, respectively.

The molecular structures are similar to those reported for the analogous chloride complexes $[(\eta^6\text{-}p\text{-}MeC_6H_4Pr^i)OsCl_2]_2$ [15] and $(\eta^6\text{-}p\text{-}MeC_6H_4Pr^i)Os(PPh_3)Cl_2$ [14]. The C_6 ring in both **1** and **3** is planar in contrast to the puckering of the aromatic ring observed in $(\eta^6\text{-}p\text{-}MeC_6H_4Pr^i)Os(PPh_3)Cl_2$. For **1** the asymmetric unit consists of one complete dimeric complex plus half of a second one as this molecule lies across a centre of inversion. Each asymmetric unit was found to contain half a water molecule and hence there is one water molecule per three molecules of the complex. As in the chloride complex, each Os of the dimer is bonded to two bridging Br ligands and one terminal Br ligand, with a slightly long bond measured for the bridging Br ligand. No direct interaction was observed between the osmium centres.

Complex **3** exhibits a three-legged piano-stool geometry at osmium and many of the corresponding distances and angles are

Table 3
^{31}P NMR data for complexes **3**–**8** and previously reported related complexes.

Complex[a]	δ^b (^{31}P)	$^1J^c$ (^{187}Os,^{31}P)	Reference
$[(\eta^6\text{-}p\text{-}MeC_6H_4Pr^i)Os(PPh_3)Br_2]$ (**3**)	−17.5	283	this work
$[(\eta^6\text{-}p\text{-}MeC_6H_4Pr^i)Os(PEt_3)Br_2]$ (**4**)	−28.3	269	this work
$[(\eta^6\text{-}p\text{-}MeC_6H_4Pr^i)Os(PMePh_2)Br_2]$ (**5**)	−26.6	274	this work
$[(\eta^6\text{-}p\text{-}MeC_6H_4Pr^i)Os\{P(OMe)_3\}Br_2]$ (**6**)	68.0	455	this work
$[(\eta^6\text{-}p\text{-}MeC_6H_4Pr^i)Os\{P(OBu^n)_3\}Br_2]$ (**7**)	62.4	449	this work
$[(\eta^6\text{-}p\text{-}MeC_6H_4Pr^i)Os\{P(OPh)_3\}Br_2]$ (**8**)	52.2	476	this work
$[(\eta^6\text{-}p\text{-}MeC_6H_4Pr^i)Os(PPh_3)Cl_2]$	−13.1	282	[14]
$[(\eta^6\text{-}p\text{-}MeC_6H_4Pr^i)Os(PMePh_2)Cl_2]$	−20.3	275	[14]
$[(\eta^6\text{-}p\text{-}MeC_6H_4Pr^i)Os\{P(OMe)_3\}Cl_2]$	73.6	453	[14]
$[(\eta^6\text{-}p\text{-}MeC_6H_4Pr^i)Os\{P(OBu^n)_3\}Cl_2]$	68.0	447	[14]
$[(\eta^6\text{-}p\text{-}MeC_6H_4Pr^i)Os\{P(OPh)_3\}Cl_2]$	58.4	477	[14]
$[(\eta^6\text{-}p\text{-}MeC_6H_4Pr^i)Os(PMePh_2)I_2]$	−37.6	275	[14]
$[(\eta^6\text{-}p\text{-}MeC_6H_4Pr^i)Os(PPh_3)I_2]$	−23.7	285	[14]

[a] Spectra recorded in $CDCl_3$ at room temperature with chemical shifts relative to H_3PO_4.
[b] δ in ppm.
[c] J in Hz.

Table 4
Selected bond lengths (Å), bond angles (°) and torsion angles (°) for **1** and **3**.

$[(\eta^6\text{-}p\text{-}MeC_6H_4Pr^i)OsBr_2]_2$ (**1**)		$(\eta^6\text{-}p\text{-}MeC_6H_4Pr^i)Os(PPh_3)Br_2$ (**3**)	
Bond lengths (Å)			
Os(1)–C(1)	2.220(15)	Os(1)–C(2)	2.248(3)
Os(1)–C(2)	2.132(14)	Os(1)–C(3)	2.199(3)
Os(1)–C(3)	2.169(14)	Os(1)–C(4)	2.173(3)
Os(1)–C(4)	2.175(14)	Os(1)–C(5)	2.263(3)
Os(1)–C(5)	2.167(13)	Os(1)–C(6)	2.235(3)
Os(1)–C(6)	2.164(14)	Os(1)–C(7)	2.185(3)
Os(1)–Br(1)	2.5353(14)	Os(1)–Br(1)	2.5548(3)
Os(1)–Br(2)	2.5811(13)	Os(1)–Br(2)	2.5505(4)
Os(2)–C(11)	2.205(15)	Os(1)–P(1)	2.3546(8)
Os(2)–C(12)	2.168(14)		
Os(2)–C(13)	2.126(16)		
Os(2)–C(14)	2.162(18)		
Os(2)–C(15)	2.141(17)		
Os(2)–C(16)	2.186(15)		
Os(3)–C(21)	2.198(13)		
Os(3)–C(22)	2.192(13)		
Os(3)–C(23)	2.168(17)		
Os(3)–C(24)	2.138(18)		
Os(3)–C(25)	2.109(17)		
Os(3)–C(26)	2.181(16)		
Bond angles (°)			
Br(1)–Os(1)–Br(2)	87.16(5)	Br(1)–Os(1)–Br(2)	86.672(13)
Br(4)–Os(2)–Br(5)	81.34(4)	P(1)–Os(1)–Br(1)	86.46(2)
		P(1)–Os(1)–Br(2)	88.99(2)
Torsion angles (°)			
C(3)–C(4)–C(8)–C(9)	27(2)	C(6)–C(5)–C(8)–C(9)	26.9(4)
C(3)–C(4)–C(8)–C(10)	−96.5(18)	C(6)–C(5)–C(8)–C(10)	−97.9(4)

similar to those found for the analogous chloride complex. As expected, slightly longer Os–X bond lengths were measured in the $(\eta^6\text{-}p\text{-}MeC_6H_4Pr^i)Os(PPh_3)Br_2$ complex (2.55 Å) when compared to the analogous Cl complex (2.42 Å) since the difference in covalent radii of Cl and Br is 0.15 Å. However, exchange of the chloride ligands for bromide ligands left the Os–P bond length unchanged at 2.35 Å.

3.4. Reactivity of arene-osmium dibromide complexes

In an attempt to prepare osmium bis(alkenyl) complexes, the dibromide complexes **3**, **7**, **9** and **10** were reacted with excess 5-pentenyl Grignard reagents in THF and yellow to brown oily products were isolated from these reactions. These oils proved to be very unstable, therefore difficult to characterize completely. However, ^{1}H and ^{31}P NMR data as well as IR data obtained for the products, were consistent with the formation of bis(1-pentenyl)osmium(II) complexes **11**–**14** (Scheme 3). In addition, the bis(1-pentenyl) complexes **11**–**14** all decomposed at room temperature to give black species and when the residues were extracted and analysed by GC, the results showed that the complexes decompose to yield 1,4-pentadiene and 1-pentene exclusively as the organic products. These are similar decomposition products to those reported in the thermal decomposition studies of platinum bis(1-alkenyl) complexes containing mono- and diphosphine ligands [16].

In addition to shifts corresponding to the protons of the respective tertiary phosphine or phosphite ligands, the ^{1}H NMR spectra of complexes **11**–**13** all displayed expected signals for the *p*-cymene ligand. Complex **14** showed a signal for the methyl groups of the hexamethylbenzene at 2.03 ppm.

The alkenyl chains of all the complexes showed similar ^{1}H NMR patterns. The Os–C*H*$_2$ protons appeared furthest downfield as broad multiplets integrating for four protons at *ca.* 0.78–0.91 ppm. Osmium has a shielding effect on the methylene protons adjacent to it. This shielding effect has also been observed in similar Pt and Pd bis(1-alkeny) [17]. Signals for the remaining methylenes of the pentenyl chains gave rise to broad multiplets in the region of *ca.* 1.02–2.03 ppm, while the pendant alkenyl functionality gave rise to distinct multiplets in the region of *ca.* 4.52 and 5.20 for the =C*H*$_2$ protons and *ca.* 5.45 and 5.90 for the C*H*= protons.

The PPh_3 derivative **11** exhibited deshielding of its ^{31}P NMR signal from −17.57 ppm in complex **3** to 12.61 ppm. The $P(OBu^n)_3$ containing complex **12** also exhibited deshielding of its ^{31}P NMR signal from 62.43 ppm in complex **7** to 79.41 ppm, together with an increase in $^1J(^{187}Os–^{31}P)$ coupling constant from 449 to 476 Hz.

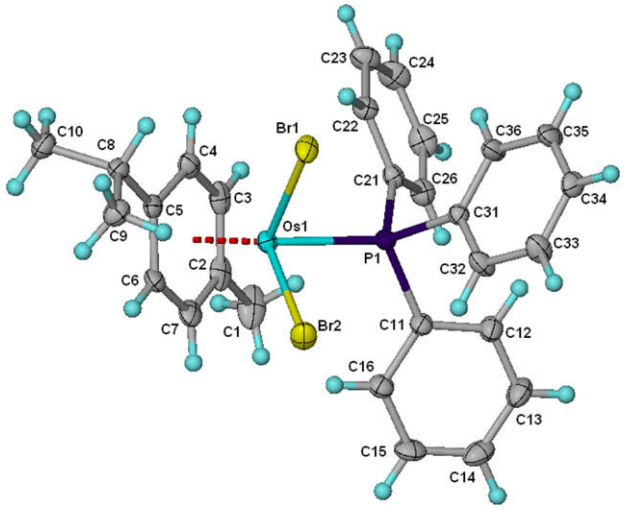


Fig. 2. Molecular structure of $[(\eta^6\text{-}p\text{-}MeC_6H_4Pr^i)Os(PPh_3)Br_2]$ (**3**) with ellipsoids shown at the 30% probability density level.

IR spectra of complexes **13** and **14** displayed strong ν(C≡O) bands at 1965 and 1897 cm^{-1}, respectively. These bands occurred at lower frequencies when compared to their starting materials **9** and **10**, and these shifts may be attributed to the change in basicity of the ligands on the osmium.

A satisfactory mass spectrum was obtained for complex **10**. The spectrum showed a peak corresponding to the parent ion (m/z = 519.3[M]$^+$) with a fragmentation pattern that corresponds to the sequential loss of the pentenyl moieties (m/z = 451.2[M−C_5H_9]$^+$) and (m/z = 383.1[M−$(C_5H_9)_2$]$^+$).

Reaction of $[(\eta^6\text{-}p\text{-}MeC_6H_4Pr^i)(CO)OsBr_2]$ (**9**) with excess MeLi resulted in the formation of the di-methyl complex **15** (Eq. (1)) as evidenced by ^{1}H NMR and IR spectral data. We expected this complex **15** to be more stable than the bis(1-pentenyl) analogue **13** since it has no β-hydrogens, however the compound was isolated as a brown oil and was also found to be very unstable and difficult to handle. Unlike complex **15**, the di-alkyl complex *cis*-$[Os(CO)_4Me_2]$ exists as a stable white crystalline solid [18]. The related complex $[(\eta^6\text{-}p\text{-}MeC_6H_4Pr^i)(PPh_3)OsMe_2]$ was isolated as a brownish yellow oil by Maitlis and co-workers [12c].

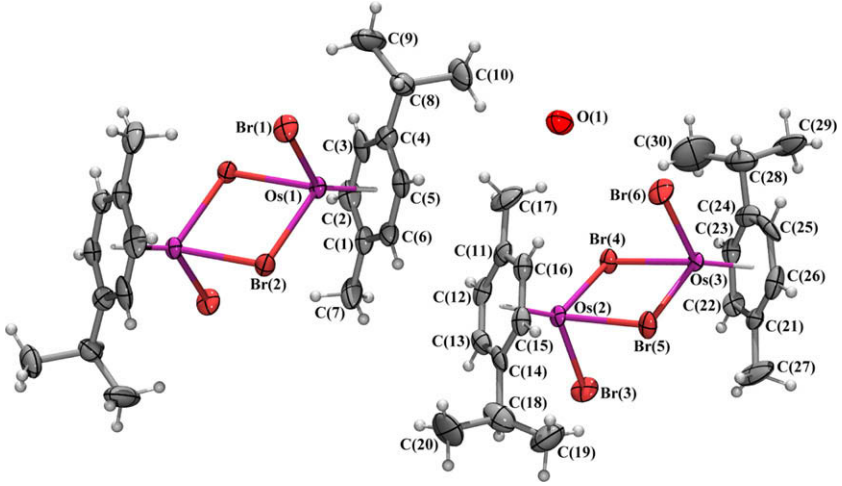
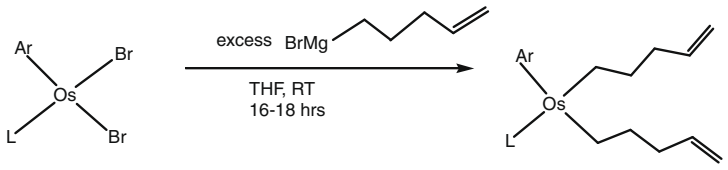
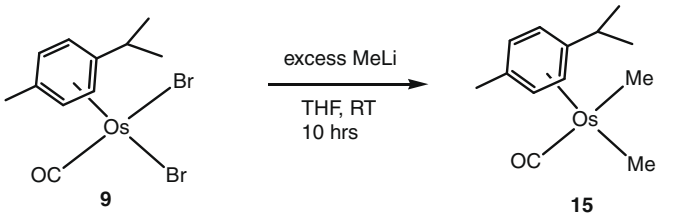


Fig. 1. Molecular structure of two crystallographically independent $[(\eta^6\text{-}p\text{-}MeC_6H_4Pr^i)OsBr_2]_2$ (**1**) molecules with ellipsoids shown at the 30% probability density level. A co-crystallised water molecule is included.



11 L = PPh_3, Ar = *p*-cymene
12 L = $P(OBu^n)_3$, Ar = *p*-cymene
13 L = CO, Ar = *p*-cymene
14 L = CO, Ar = C_6Me_6

Scheme 3. The synthesis of osmium bis(1-pentenyl) complexes **11**–**14**.



9 **15** (1)

4. Conclusions

The dimers $[(\eta^6\text{-}p\text{-}MeC_6H_4Pr^i)OsBr_2]_2$ and $[(\eta^6\text{-}C_6Me_6)OsBr_2]_2$ can be prepared from potassium osmate following the procedures reported herein. From these dimers a series of new arene-osmium dibromide complexes containing CO, tertiary phosphines and phosphites were obtained. The osmium dibromide complexes reacted with 5-pentenyl Grignard and MeLi to give the putative bis(1-pentenyl)osmium(II) complexes and $[(\eta^6\text{-}p\text{-}MeC_6H_4Pr^i)(CO)OsMe_2]$, respectively, which were isolated as unstable yellow to brown oils. The bis(1-pentenyl)osmium(II) complexes decomposed to yield 1,4-pentadiene and 1-pentene exclusively as the organic products. This is consistent with the formation of these compounds prior to their decomposition.

Supplementary data

CCDC 706183 and 707752 contain the supplementary crystallographic data for **1** and **3**. These data can be obtained free of charge via http://www.ccdc.cam.ac.uk/conts/retrieving.html, or from the Cambridge Crystallographic Data Centre, 12 Union Road, Cambridge CB2 1EZ, UK; fax: (+44) 1223-336-033; or e-mail: deposit@ccdc.cam.ac.uk.

Acknowledgements

We would like to thank the Anglo Platinum Corporation, University of Cape Town and University of South Africa. We also thank the National Research Foundation (NRF) of South Africa and NRF-DST Centre of Excellence in Catalysis (C^* Change) for financial support and David Liles at the University of Pretoria for solving the crystal structure of complex **1**.

References

[1] (a) R.G. Gastinger, K.J. Klabunde, Transition Met. Chem. 4 (1979) 1. and references therein;
(b) R.D. Adams, J.P. Selegue, in: G. Wilkinson, F.G.A. Stone, E.W. Abel (Eds.), Comprehensive Organometallic Chemistry, vol. 4, Pergamon, Oxford, 1982, p. 1020.
[2] (a) J. Huang, S. Serron, S.P. Nolan, Organometallics 17 (1998) 4004;
(b) U. Wecker, H. Werner, J. Organomet. Chem. 424 (1992) 199;
(c) S. Stahl, H. Werner, J. Am. Chem. Soc. 113 (1991) 2944;
(d) M.A. Bennett, T.W. Matheson, G.B. Robertson, A.K. Smith, P.A. Tucker, Inorg. Chem. 19 (1980) 1014;
(e) M.A. Bennett, M. Brown, L.Y. Goh, D.C.R. Hockless, T.R.B. Mitchell, Organometallics 14 (1995) 1000.
[3] R. Castarlenas, M.A. Esteruelas, E. Oñate, Organometallics 24 (2005) 4343.
[4] (a) M.A. Bennett, A.M.M. Weerasuria, J. Organomet. Chem. 394 (1990) 481;
(b) H. Werner, K. Zenkert, J. Chem. Soc., Chem. Commun. (1985) 1607;
(c) S.-A. Brough, C. Hall, A. McCamley, R.N. Perutz, S. Stahl, U. Wecker, H. Werner, J. Organomet. Chem. 504 (1995) 33.
[5] (a) T. Arthur, T.A. Stephenson, J. Organomet. Chem. 208 (1981) 369;
(b) A. Demonceau, C.A. Lemoine, A.F. Noels, Tetrahedron Lett. 37 (1996) 1025;
(c) A. Demonceau, A.W. Stumpf, E. Saive, A.F. Noels, Macromolecules 30 (1997) 3127;
(d) A. Hafner, A. Muhlebach, P.A. van der Schaaf, Angew. Chem., Int. Ed. 36 (1997) 2121.
[6] G.J. Perkins, M.I. Bruce, B.W. Skelton, A.H. White, Inorg. Chim. Acta 359 (2006) 2644.
[7] G.S. Silverman, P.E. Rakita (Eds.), Handbook of Grignard Reagents, Marcel Dekker Inc., New York, 1996.
[8] SMART (Version 5.054), SAINT (Version 6.45), SADABS (Version 2.10) and SHELXTS/SHELXTL (Version 6.12), Bruker AXS Inc., Madison, WI, USA, 2001.
[9] G.M. Sheldrick, SHELXS-97 and SHELXL-97, University of Gottingen, Germany, 1997.
[10] Z. Otwinowski, W. Minor, in: C.W. Carter Jr., R.M. Sweet (Eds.), Methods in Enzymology, Macromolecular Crystallography, Part A, vol. 276, Academic Press, 1997, p. 307.
[11] L.J. Barbour, J. Supramol. Chem. 1 (2001) 189.
[12] (a) Y. Hung, W.-J. Kung, H. Taube, Inorg. Chem. 20 (1981) 457;
(b) D.M. Heinekey, T.G.P. Harper, Organometallics 10 (1991) 2891;
(c) J.A. Cabeza, P.M. Maitlis, J. Chem. Soc., Dalton Trans. (1985) 573;
(d) H. Werner, K. Zenkert, J. Organomet. Chem. 345 (1988) 151;
(e) S. Stahl, H. Werner, Organometallics 9 (1990) 1876;
(f) H. Werner, R. Weinand, W. Knaup, K. Peters, H.G. von Schnering, Organometallics 10 (1991) 3967.
[13] W.A. Kiel, R.G. Ball, W.A.G. Graham, J. Organomet. Chem. 383 (1990) 481.
[14] A.G. Bell, W. Koźmiński, A. Linden, W. von Philipsborn, Organometallics 15 (1996) 3124.
[15] S.F. Watkins, F.R. Fronczek, Acta Crystallogr. B38 (1982) 270.
[16] F. Zheng, A. Sivaramakrishna, J.R. Moss, Inorg. Chim. Acta 361 (2008) 2871.
[17] (a) T. Mahamo, F. Zheng, A. Sivaramakrishna, G.S. Smith, J.R. Moss, J. Organomet. Chem. 693 (2008) 103;
(b) A. Sivaramakrishna, H. Su, J.R. Moss, Angew. Chem., Int. Ed. 46 (2007) 3541.
[18] (a) M.J. Overett, J.R. Moss, Inorg. Chim. Acta 358 (2005) 1715;
(b) R.D. George, S.A.R. Knox, F.G.A. Stone, J. Chem. Soc., Dalton Trans. (1973) 972.

Yield: 14.2 mg (0.018 mmol, 55.8% assuming the 0.10 mmol of Cu(II) in the starting solution).

The ^{63}Cu and ^{65}Cu labeled isotopologues were prepared exactly as the compound with natural copper. Yields: 11.0 mg (0.014 mmol, 42.2%) for ^{63}Cu and 11.8 mg (0.015 mmol, 45.4%) for ^{65}Cu. The copper isotopes were purchased from Trace Sciences International Corp., Canada.

2.2. Spectroscopy

The IR spectra were measured on Perkin–Elmer 2000 FT spectrometer with sample in KBr pellet or Nujol mull for middle and far-IR regions, respectively. The spectra were obtained as the average of 64 scans, collected with 2 cm^{-1} resolution.

The Raman spectrum was recorded on Bruker RFS-100 instrument equipped with Nd:YAG laser (1064 nm) operating at 300 mW. Final spectrum was computed from 32 scans measured with 2 cm^{-1} resolution at the back-scattering geometry.

2.3. DFT calculations

In order to support the interpretation of the recorded vibrational spectra, the quantum calculations based on the Density Functional Theory (DFT) approach have been performed using the GAUSSIAN 03 package [9]. The B3LYP functional [10] operating on the LanL2DZ basis set [11], expanded with d-polarization functions on C and N atoms, was applied. The structure optimization and subsequent computation of normal vibrations were carried out on the $[Cu(biz)_2]^{2+}$ cation and $[Cu_2Br_4]^{2-}$ anion, separately. For both ions, the optimization of molecular geometry started from the X-ray structural parameters, reported here. The optimized structure of the $[Cu(biz)_2]^{2+}$ ion very well corresponds to that measured. The RMS for skeletal bond distances is 0.02 Å and for skeletal angles 0.71°. The geometry optimization of the $[Cu_2Br_4]^{2-}$ ion resulted in the RMS deviations of 0.38 Å and 10.6° for bond lengths and angles, respectively. The higher RMS for angles is due to the elongation of the Cu–Cu distance (observed 2.6806(9) Å, calculated 3.3779 Å). The quasi-flat and centrosymmetric structures of both ions were preserved.

Based on the optimized structures, the wavenumbers, IR intensities, Raman activities and atom displacements for all normal vibrations were computed with harmonic approximation. The computed frequencies were not scaled. The visual animations of normal vibrations were generated using the MOLEKEL program [12], whereas the theoretical IR and Raman spectra were simulated employing the MOLDEN application [13].

2.4. Crystallography

Data collection was carried out on KUMA KM4CCD diffractometer with graphite-monochromatized Mo Kα radiation for a crystal cut out from a larger needle. Data reduction and analytical absorption correction were carried out using CRYSALIS software [14].

The structure was solved by direct methods in SHELXS97 [15] and refined in SHELXL97 [15]. All H atoms were found on the difference Fourier map. Subsequently, H atoms bonded to C atoms were constrained using AFIX 23 constraints. For H atoms bonded to N atoms DFIX restraints were used setting the N–H bond distances at 0.860(2) Å. Subsequently, H atoms bonded to N atoms were constrained using AFIX 3 constraints. All H atoms were refined with $U_{eq} = 1.2U_{eq}$ (parent atom). On the final difference Fourier map the highest peak of 1.77 e/Å^3 was located at 0.73 Å from the Br2 atom.

Pertinent data for the structure determination are listed in Table 1. All figures and packing diagrams were made using ORTEP program [16].

Table 1
Crystal data and structure refinement.

Empirical formula	$C_{12}H_{20}CuN_8{\cdot}Br_4Cu_2$
Formula weight	786.62
Temperature (K)	100(2)
Wavelength (Å)	0.71073
Crystal system	monoclinic
Space group	$P2_1/c$
Unit cell dimensions	
	a = 7.424 (3) Å
	b = 10.606(3) Å
	c = 13.569(4) Å
	β = 101.33(3)°
Volume (Å^3)	1047.6(6)
Z	2
D_{calc} (Mg/m^3)	2.494
Absorption coefficient (mm^{-1})	10.662
$F(000)$	750
Crystal size (mm)	0.11 × 0.06 × 0.03
θ range for data collection (°)	3.39–36.84
Index ranges	$-10 \leqslant h \leqslant 12$, $-16 \leqslant k \leqslant 17$, $-20 \leqslant l \leqslant 21$
Reflections collected/unique [R_{int}]	17265/4537 [0.0683]
Refinement method	full-matrix least-squares on F^2
Data/restrains/parameters	4537/0/124
Goodness-of-fit on F^2	0.996
Final R indices [$I > 2\sigma(I)$]	R_1 = 0.0472, wR_2 = 0.1044
R indices (all data)	R_1 = 0.0704, wR_2 = 0.1151
Largest difference in peak and hole (Å^{-3})	1.77 and −1.14

3. Results and discussion

3.1. Description of the structure

The investigated mixed-valence copper compound is build of discrete complex cations with Cu(II) as central atoms and well known $[Cu_2Br_4]^{2-}$ anions. Both ions, presented in Fig. 1, are centrosymmetric and roughly planar, their selected structural parameters are listed in Table 2.

In the $[Cu(biz)_2]^{2+}$ cation, the Cu1 atom lies on an inversion center and its coordination environment is perfectly planar and nearly square. The copper–nitrogen bond lengths are almost the same, equal 1.984(3), 1.987(3) Å and are very similar to those reported for $[Cu(biz)_2](ClO4)_2$ [8], being 1.982(4) and 1.965(4) Å. The deviation from the square shows the N1–Cu1–N4 angle, equal 82.2(1)° as it may be expected for the five-membered chelate ring. The inspection of contacts in the axial direction shows that the nearest are the Br1 atoms of two opposite $[Cu_2Br_4]^{2-}$ anions. The Cu1···Br1^{v} (v: $x, -y + 1/2, +z - 1/2$) distance, equal 3.323(1) Å, is much longer than typical Cu–Br bond length and it is beyond the semi-coordinate category (about 3.1 Å [17,18]). Thus, the metal coordination environment is a regular rectangle.

Fortunately, the X-ray data are available for similar cation formed by Cu(II) and 2,2′-biimidazole (bim) [19]. Comparison of the copper–nitrogen bond lengths shows that the partial saturation of the imidazole rings, giving the biimidazoline, does not change significantly the chelation abilities of these systems. The present Cu–N distances are only slightly shorter than in the $[Cu(bim)_2]^{2+}$ being 2.03(1) Å. Similar differences (<0.05 Å) were found in the remaining bond lengths of whole chelate ring.

Despite the high symmetry of the free ligand [20], in the present complex, the imidazoline rings show some differences in bond lengths, angles and deviation from planarity. As results from the data in Table 2, the differences between the lengths of corresponding bonds are small and not exceed 1%. Similar conclusion can be formulated about the skeletal angles. The largest differences are in the planarity of the imidazoline rings. The ring with N1 atom is close to planar (the maximum deviation from the best plane is

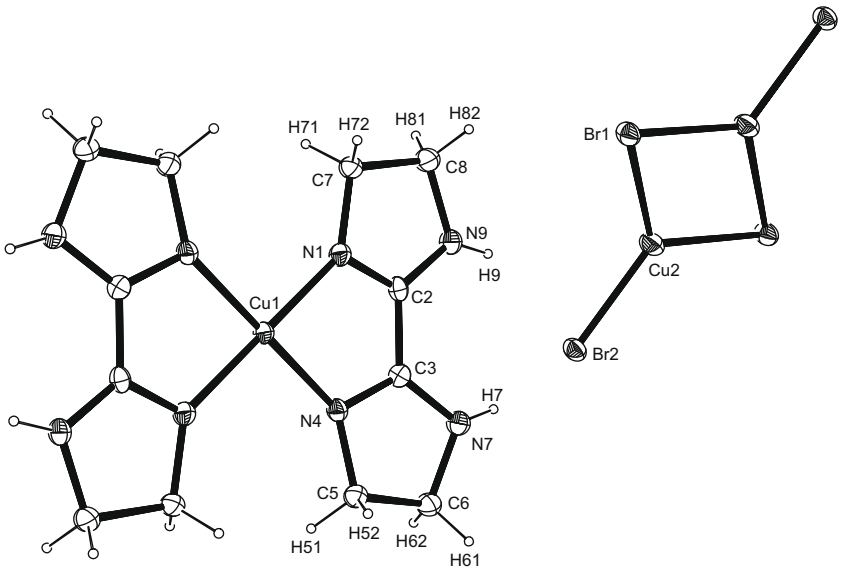


Fig. 1. Structure of $[Cu(biz)_2][Cu_2Br_4]$ showing the atomic numbering. The unlabeled atoms are generated by the symmetry operations. Thermal ellipsoids enclose the 50% probability.

Table 2
Structural parameters (Å, °) of $[Cu(biz)_2]^{2+}$ and $[Cu_2Br_4]^{2-}$ skeletons, compared with that of free 2,2′-bi-2-imidazoline [20].

Present compound				Biz [20]
Cu1–N1	1.987(3)	Cu1–N4	1.984(3)	
N1–C2	1.300(5)	N4–C3	1.310(5)	1.2847(19)
N1–C7	1.484(5)	N4–C5	1.478(5)	1.4820(19)
C7–C8	1.555(5)	C5–C6	1.541(5)	1.536(2)
C8–N9	1.474(5)	C6–N7	1.477(5)	1.450(2)
C2–N9	1.334(4)	C3–N7	1.341(5)	1.3436(19)
		C2–C3	1.471(5)	1.479(3)
N1–Cu1–N4	82.2(1)	N1–Cu1–N4^{i}	97.8(1)	
Cu1–N1–C2	113.0(2)	Cu1–N4–C3	112.6(2)	
N1–C2–C3	115.9(3)	N4–C3–C2	115.6(3)	
C2–N1–C7	107.9(3)	C3–N4–C5	106.9(3)	105.66(12)
N1–C7–C8	104.4(3)	N4–C5–C6	103.8(3)	106.44(12)
C7–C8–N9	102.4(3)	C5–C6–N7	101.7(3)	101.51(12)
C2–N9–C8	108.8(3)	C3–N7–C6	107.1(3)	109.04(13)
N1–C2–N9	116.5(3)	N4–C3–N7	116.1(3)	117.32(14)
Cu2–Br1	2.4314(9)	Cu2–Br1^{ii}	2.4108(9)	
Cu2–Br2	2.3346(8)	Cu2–Cu2	2.6806(9)	
Br2–Cu2–Br1	121.71(3)	Br2–Cu2–Br1^{ii}	125.08(3)	
Br1–Cu2–Br1^{ii}	112.77(3)	Cu2–Br1–Cu2^{ii}	67.23(3)	
Br2–Cu2–Cu2^{ii}	173.49(3)			

i: $-x, -y, -z$; ii: $-x+1, -y+1, -z+1$.

0.012(4) Å for C8 atom) and it is nearly parallel to the N1–Cu1–N4 plane (corresponding dihedral angle is 3.0(1). The second imidazoline ring is more distorted with the N4, C5, C6 and N7 atoms being +0.045(3), −0.127(4), +0.140(4) and −0.070(3) Å displaced from the best plane, respectively. The dihedral angle between this best plane and metal vicinity is 10.5(1)°. The chelate ring is also not planar, due to the N1, N4 and C3 atoms which are slightly displaced from the best plane by +0.060(3), 0.026(3) and −0.062(3) Å, respectively. This best plane forms the dihedral angles of 8.7(1) and 1.2(1)° with the best planes of both imidazoline rings which in turn form a dihedral angle of 7.5(1)°. All those relatively small dihedral angles support the final conclusion that the geometry of the $[Cu(biz)_2]^{2+}$ cation is close to planar.

It is interesting to trace how the metal chelation influences the imidazoline ring geometry. Comparison with the respective data of pure ligand [20] (Table 2) surprisingly shows that not all bonds between carbon and coordinated nitrogen atoms are markedly affected. The N1–C7 and N4–C5 bond lengths are almost the same as in the uncoordinated ligand. The neighbor N1–C2 and N4–C3 bonds are elongated by 0.015 and 0.025 Å, respectively. The bonds by the N9 and N7 atoms are also affected, but in different extent; these positioned closer to the center of the ligand are shortened whereas two others are elongated. However, in the explanation of this phenomenon, the involvement of the N–H groups into the hydrogen bonding must also be taken into account.

In the di-μ-bromo-dibromocuprate(I) anion, two copper(I) and two bridging bromide ligands form a perfect plane, whereas two terminal bromide ligands are positioned slightly above and below this plane, making the very-flat-chair structure of whole anion. The displacement of Br2 atoms from the central plane is well represented by the Br2–Cu2–Cu2^{ii} (ii: $-x+1, -y+1, -z+1$) angle being

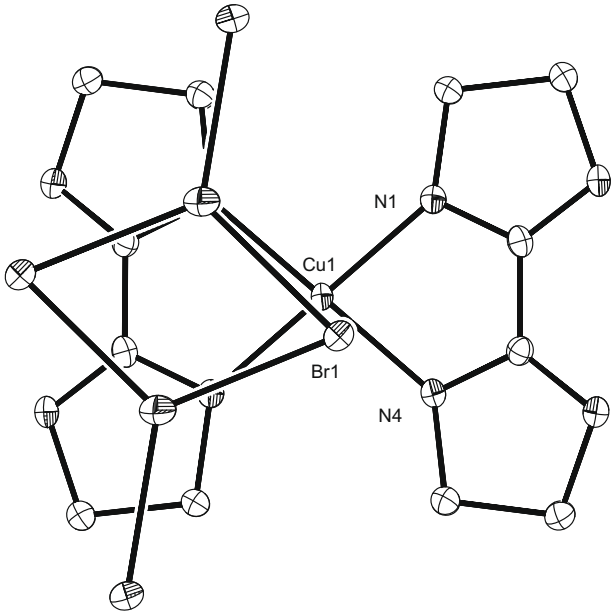


Fig. 2. Mutual orientation of $[Cu(biz)_2]^{2+}$ and $[Cu_2Br_4]^{2-}$ skeletons, viewed normal to the $[Cu1–N_4]$ plane. Only one $[Cu_2Br_4]^{2-}$ ion has been shown for clarity, the second anion is positioned as required by the inversion center, located at the Cu1 atom.

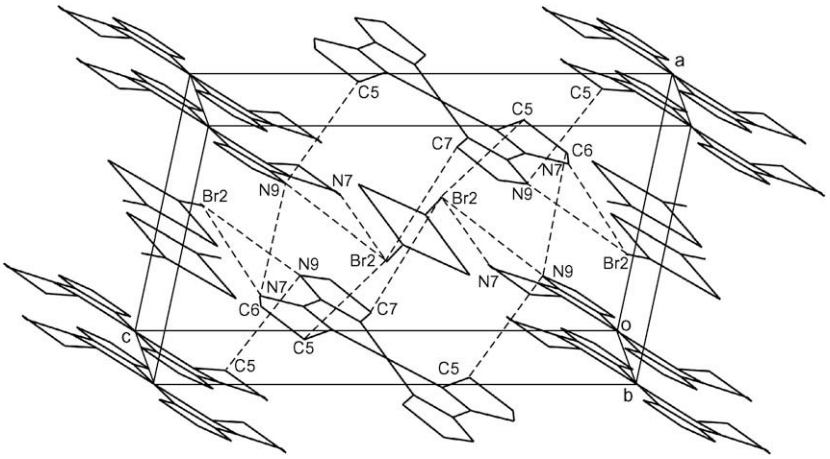


Fig. 3. Crystal packing described as the layers of cations and anions expanding parallel to the (1 0 0) plane, or two sets of ribbons expanding along (1 1 1) and (1 $\bar{1}$ 1) directions. Broken lines connect the donor and acceptor atoms of the formed the hydrogen bonds. Hydrogen atoms were omitted for clarity.

173.49(3)°. Other structural parameters, like bond lengths and angles are within the corresponding values observed for similar $[Cu_2Br_4]^{2-}$ anions, accompanied by different organic cations [21–23].

In the crystal lattice, the mutual orientation of complex cation and anion is close to parallel; the dihedral angle between [Cu1–N_4] plane and that formed by Cu(I) and Br1 atoms is 8.9(1)°. Both ions are such oriented, that the Br1 atom is almost above the Cu1 atom, as has been shown in Fig. 2, presenting the view normal to the [Cu1–N_4] plane.

The crystal packing may be presented as layers of cations and anions expanding parallel to the (1 0 0) plane, as has been demonstrated in Fig. 3. However, if strong hydrogen bonds between cations and anions will be taken into account, then two sets of ribbons expanding along (1 1 1) and (1 $\bar{1}$ 1) directions can be distinguished (Fig. 3).

For the strong hydrogen bonding, each ligand molecule offers only two centers, namely the N7–H7 and N9–H9 groups. Both these donors interact with the same Br2 atom of the $[Cu_2Br_4]^{2-}$ anion, but these H-bonds are not the same, as results from Table 3. The interaction between mentioned ribbons is mainly electrostatic, but it is enhanced by two C–H···Br and two C–H···N type hydrogen bonds, shown in Fig. 3. The hydrogen bonds are also partially responsible for mentioned differences in the geometry of two imidazoline rings present in the organic ligand. Each ring is involved in three hydrogen bonds, but all these bonds have different lengths and directions. The structural details of all hydrogen bonds have been given in Table 3.

3.2. Vibrational spectroscopy

The ionic structure of presented compound suggests that part of its IR and Raman spectra may be covered by bands resulting from the $[Cu(biz)_2]^{2+}$ cation and $[Cu_2Br_4]^{2-}$ anion. In order to recognize the wavenumber range of such overlap, the vibrations of both ions have been calculated and respective spectra computed. The resulted theoretical spectra are presented in Fig. 4, which demonstrates that the vibrations of heavy-atom $[Cu_2Br_4]^{2-}$ anion have very low frequencies, not exceeding the 220 cm^{-1} limit. Unfortunately, the IR spectrum is not well structured in this region, whereas the Raman spectrum is obscured by the strong Rayleigh scattering. Therefore, the vibrations of the $[Cu_2Br_4]^{2-}$ ion will not be further discussed, due to the lack of enough experimental data. The location of the $[Cu_2Br_4]^{2-}$ vibrations below 220 cm^{-1} simultaneously shows that the rests of the observed spectra are covered by the $[Cu(biz)_2]^{2+}$ bands, exclusively.

The $[Cu(biz)_2]^{2+}$ cation is built of 41 atoms which perform 117 normal vibrations, classified into $57A_g$ and $60A_u$ modes under the C_s symmetry. According to the mutual exclusion rule, the A_g vibrations are active in the Raman spectrum, whereas the A_u are observed as the IR absorptions. In contrast to the above numbers

Table 3
Hydrogen bond parameters (Å, °) with e.s.d.'s in parentheses.

Bond	D–H	D···A	H···A	D–H···A
N7–H7···Br2	0.861(3)	3.370(3)	2.521(1)	169.0(2)
N9–H9···Br2	0.859(3)	3.582(3)	2.784(1)	155.2(2)
C5–H51···Br2^{iii}	0.990(4)	3.616(4)	2.804(1)	139.7(2)
C5–H52···N9^{iv}	0.990(4)	3.527(5)	2.614(3)	153.3(2)
C6–H62···N9^{iii}	0.991(4)	3.779(5)	2.811(3)	165.8(2)
C7–H72···Br2^{v}	9.989(4)	3.773(4)	2.974(1)	138.6(2)

Equivalent positions: iii: $-x+1,+y-1/2,-z+1/2$; iv: $-x,+y-1/2,-z+1/2$; v: $x,-y+1/2,+z-1/2$.

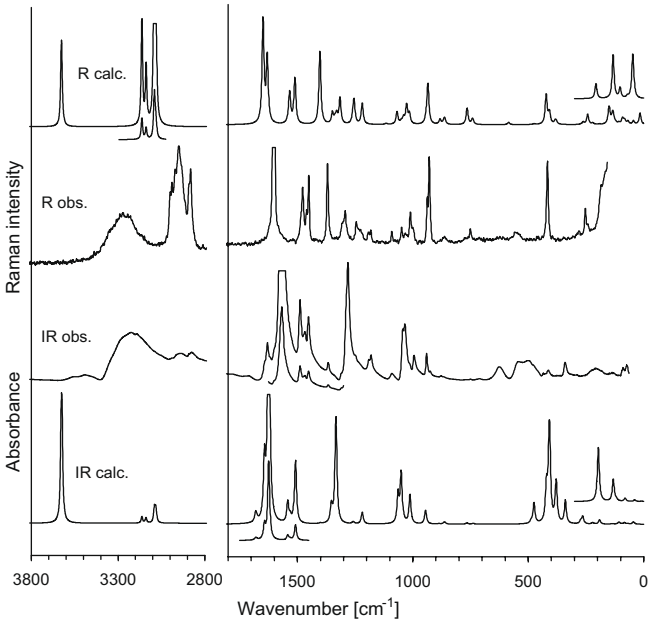


Fig. 4. Observed and calculated spectra of $[Cu(biz)_2][Cu_2Br_4]$. The computed spectra of $[Cu_2Br_4]^{2-}$ are presented as low frequency insets placed above the respective spectra of $[Cu(biz)_2]^{2+}$.

of expected bands, the collected spectra show about two times less bands. The explanation of that phenomenon is provided by performed calculations. First reason is the similarity of vibrational frequencies observed for normal vibrations of similar molecular fragments. In the $[Cu(biz)_2]^{2+}$ cation, there are four such fragments, namely the imidazoline rings. The rings are separated by the Cu–N or C–C bonds which cause that the vibrational coupling between some atomic motions, similar in all rings, is rather weak. As a consequence, the normal modes composed of similar internal vibrations have very close frequencies and contribute in the same IR or Raman band. Second reason is important when the wavenumbers computed for the symmetry related modes are more separated; then the large differences between their relative intensities may decide that only one, the strongest mode is observed. Finally, the analysis of the computed IR intensities and Raman activities shows that some transitions are so much weak that cannot be distinguished from the background noises.

The above conclusions are supported by the theoretical spectra, presented in Fig. 4, together with the observed ones. Visual comparison of the computed and observed Raman spectra shows a big similarity between their band positions and relative intensities. In the case of the IR spectra, such similarity is somewhat disturbed by hydrogen bonding effects, being intense in the IR absorption. The most visible difference is in the region above 3000 cm^{-1}, where the predicted stretching vibrations of the N–H groups are monitored by one sharp and strong band at about 3620 cm^{-1}, but its observed IR counterpart is a broad absorption with maximum at 3220 cm^{-1}, being typical for the H-bonded systems, as those of N–H···Br, found in the present compound. Except some computed frequency overestimations, typical for theoretical methods, the calculations performed here provided a very good overall reproduction of the observed spectra, which allows for the unambiguous transfer of the computed mode assignments to the observed bands.

The computer animation of calculated vibrations shows that the D_{2h} symmetry can be used for the approximate description of the atom displacements in all normal modes. Despite that the symmetry of $[Cu(biz)_2]^{2+}$ cation is lower (C_i), the classification of normal vibrations into irreducible representations of the D_{2h} group could be done basing only on the phases of atom displacements during given normal vibrations; the related amplitudes mostly do not follow the D_{2h} symmetry requirements. Such classification simplifies

Table 4
Observed IR and Raman band positions (cm^{-1}) and their attribution to computed normal vibrations classified in terms of approximate D_{2h} symmetry.

Observed		Calculated normal vibrations								
IR	R	A_g	B_{1g}	B_{2g}	B_{3g}	A_u	B_{1u}	B_{2u}	B_{3u}	Predominant mode
3220	**3265**	**3627**[a]	3620					3621	**3625**	ν(N–H)
	2990			3162	**3163**	3162	3163			$\nu_{a,s}(CH_2)$
	2970			**3138**	3139	3137	3140			$\nu_{a,a}(CH_2)$
2935	**2950**	3091	3091					3091	**3091**	$\nu_{s,s}(CH_2)$
2875	**2883**	**3084**	3080					**3084**	3080	$\nu_{s,a}(CH_2)$
1631			1675					**1681**		ν_a(N1–C2–N9)
1631	**1605**	**1649**							**1643**	ν(N1–C2) + $\nu\nu$(C2–C3)
1567	**1605**	**1631**							**1624**	ν(N2–N9) + ν(C2–C3)
1489	**1478**	**1534**	1540					**1542**	1531	$\delta_s(CH_2)$
	1451	1516	**1511**					1517	1509	$\delta_a(CH_2)$
1452			1506					**1508**		ν_s(N1–C2–N9)
1366	**1370**	**1403**	1348					**1353**	1400	$\omega_s(CH_2)$
1282	**1306**	1338	1330					1335	**1333**	$\omega_a(CH_2)$
	1293	**1316**							1314	δ_s(NH)
			1257					1262		δ_a(NH)
	1246			**1254**	1261	1256	1260			$\gamma_a(CH_2)$
1190	**1195**			1217	**1220**	1218	**1219**			$\gamma_s(CH_2)$
				1116	1115	1113	1118			$\rho_a(CH_2)$
1091	**1091**	**1069**	1041					**1051**	1064	ν(N1–C7)
1035	**1048**	**1050**							**1048**	δ1(im)
995	**1011**	1015	**1027**					1029	**1012**	ν(N9–C8)
940	**929**	**935**	942					**945**	931	ν(C7–C8)
880	**862**		**882**					**887**		δ1(im)
	862			859	**867**	863	**861**			$\rho_s(CH_2)$
750	**750**	**765**	738					742	**766**	δ2(im)
					743	741				τ1(ch) + τ2(im)
				584			585			τ2(im) + τ2(ch)
434			475					488		δ2(ch)
413	**417**	423							421	ν(C2–C3)
~**520**	**558**			**410**	379	384	**407**			π(NH)
342		**151**	132					273	**339**	ν(Cu–N)
(210)[b]					**264**	262				τ2(im)
	(254)	**243**							191	δ1(ch) + ν(Cu–N)
				92			221			τ2(ch)
				148			122			τ1(im) + τ2(ch)
(138)					141					τ1(im) + τ1(ch)
(90)				106			108			ω(im–im′)
					84	81				τ(im–im′)
(74)								68		δ(L–L′)
							45			ω(L–L′) "butterfly"
						16				τ(L–L′)

Abbreviations: ν, stretching; δ, bending; τ, torsion; γ, twisting; ω, wagging; ρ, rocking; π, out-of-plane bending; *s,a*, symmetric; asymmetric with respect to local plane symmetry of CH_2 group or imidazoline ring, respectively.

[a] Wavenumbers of normal modes most contributing into intensities of respective theoretical bands are boldfaced.

[b] IR band positions below 300 cm^{-1} are given in parentheses because they may also origin from $[Cu_2Br_4]^{2-}$ vibrations.

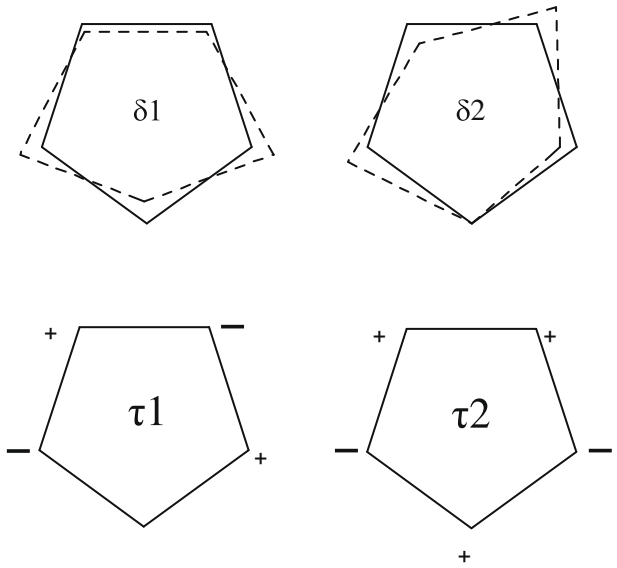


Fig. 5. In-plane and out-of-plane deformations of the five-membered chelate and imidazoline rings. The plus and minus signs represent the atom displacements out of the ring plane.

the description of normal vibrations and has been used in Table 4, listing the observed band positions and their attribution to the calculated normal vibrations.

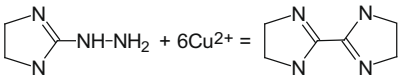
As results from Table 4, most of the symmetry related normal modes have very similar frequencies and have been attributed to the same observed band. The most outstanding exception is noted for the Cu–N stretching vibrations with wavenumbers calculated between 340 and 130 cm^{-1}. Such phenomenon is understandable because the Cu–N bonds are joined with common metal atom and mechanical coupling of their motions is very strong. Despite these frequency differences, only one observed ν(Cu–N) band is listed. This band was detected applying the metal isotope technique. The comparison of the far-IR spectra measured for complexes with ^{63}Cu and ^{65}Cu pure isotopes monitored only one, 3 cm^{-1} down-shift of 342 cm^{-1} band. The vibrational effects due to ^{63}Cu–^{65}Cu substitution have also been reproduced in performed DFT calculations, giving the 3.3 and 2.8 cm^{-1} frequency shifts of two asymmetric ν(Cu–N) normal vibrations calculated at 339 and 273 cm^{-1}. First vibration very well corresponds to the observed 342 cm^{-1} band; the second transition is predicted to be relatively weak, which explains why more isotope shifted bands were not detected. The remaining ν(Cu–N) normal vibrations at 151 and 132 cm^{-1} are symmetric with respect to the inversion center, which cause that the metal atom is not oscillating, than these vibrations are not sensitive to the different masses of applied copper isotopes.

Some modes listed in Table 4 were described as combinations of two internal coordinates, which represents their strong vibrational coupling. This coupling, especially between the deformation modes of the imidazoline and chelate rings is a consequence of molecular structure where mentioned rings have common carbon and nitrogen atoms. The same reason is for the coupling between stretching vibrations of the inter-ring C–C bond and neighbor C–N bonds. The abbreviations used for chelate and imidazoline ring deformation modes have been explained in Fig. 5.

3.3. Chemical reactions

The X-ray detection of the 2,2′-biimidazoline (biz) as the chelating agent, undoubtedly shows that the starting ligand, 2-hydrazino-2-imidazoline (hi) has undergone the chemical conversion to biz. Such transformation is very similar to that of phenylhydrazine which under oxidation with silver or mercuric oxides gives the diphenyl as one of the isolated products [24].

In the present case, the oxidizing agent is copper(II), because without these ions, the hi ligand is stable in the methanol/ethanol solution. Finally, we propose the following reaction of the hi oxidation leading to biz:



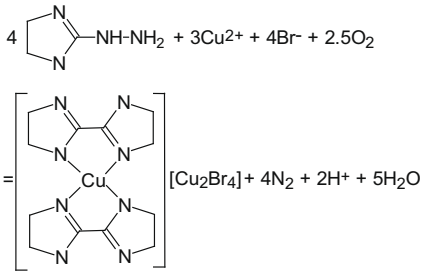
(1)

Since the mother solution was prepared by dissolving the $Cu(OH)_2$ precipitate in the hi·HBr solution, the Cu: hi ratio was 1:2. With such ratio, all Cu^{2+} ions should be converted into Cu^{+} in the reaction (1). However, the presence of copper(II) in the final complex suggests the partial reoxidation of Cu^{+} ions by the atmospheric oxygen.

$$4Cu^{+} + O_2 + 4H^{+} = 4Cu^{2+} + 2H_2O \quad (2)$$

In order to prove the necessity of the above process, the special experiment was carried out where the mother solution was kept in the fully filled capped vial, without contact with air oxygen. Under such conditions, the complex was not obtained.

Taking into account the reactions (1) and (2), the total complex formation process can be written as:



(3)

The yield of the above reaction is not high – between 20% and 50% with respect to the Cu^{2+} content in the mother solution and depends on the applied substrate concentrations. Such low yield may be due to the Cu^{2+} deficiency in relation to hi, and the self-acidification, which shifts the reaction equilibrium toward the substrates. An experiment with hi: $CuBr_2$ ratio required in reaction (3) was unsuccessful, which suggests that the relative concentrations of used reagents are important in this complicated process.

4. Conclusion

The reaction of copper(II) hydroxide and 2-hydrazino-2-imidazoline hydrobromide produced a coordination compound which, according to the X-ray analysis, appeared to be a complex salt with copper atoms at different oxidation states. The copper(I) is present in the $[CuBr_2]^{2-}$ anion, whereas the counter cation contains copper(II) chelated by two new biimidazoline ligands resulted from the oxidation of starting 2-hydrazino-2-imidazoline substrate. The analysis of the reaction conditions leads to the conclusion that copper(II) ions act partially as oxidizing reagent and partially as the catalyst of the 2-hydrazino-2-imidazoline oxidation by the atmospheric oxygen.

Supplementary data

CCDC 707358 contains the supplementary crystallographic data for this paper. These data can be obtained free of charge via http://

www.ccdc.cam.ac.uk/conts/retrieving.html, or from the Cambridge Crystallographic Data Centre, 12 Union Road, Cambridge CB2 1EZ, UK; fax: (+44) 1223-336-033; or e-mail: deposit@ccdc.cam.ac.uk.

Acknowledgements

The authors thank the Centers for Supercomputing and Networking in Poznań and Wrocław, and J. Hanuza for the Raman instrument facilities.

References

[1] J.C. Wang, J.E. Bauman, Inorg. Chem. 4 (1965) 1613.
[2] M.B. Burnett, V. McKee, S.M. Nelson, J. Chem. Soc., Dalton Trans. (1981) 1492.
[3] J.P. Roth, S. Lovell, J.M. Mayer, J. Am. Chem. Soc. 122 (2000) 5486.
[4] G.A. van Albada, A. Mohamadou, I. Mutikainen, U. Turpeinen, J. Reedijk, Acta Crystallogr. E60 (2004) m237.
[5] G.A. van Albada, A. Mohamadou, A.M. Manotti Lanfredi, I. Mutikainen, U. Turpeinen, F. Ugozzoli, J. Reedijk, J. Chem. Crystallogr. 35 (7) (2005) 541.
[6] J.C. Yoder, J.P. Roth, E.M. Gussenhoven, A.S. Larsen, J.M. Mayer, J. Am. Chem. Soc. 125 (2003) 2629.
[7] A. Mohamadou, G.A. van Albada, H. Kooijman, B. Wieczorek, A.L. Spek, J. Reedijk, New J. Chem. 27 (2003) 983.
[8] A. Mohamadou, G.A. van Albada, W.L. Driessen, R. de Gelder, J. Reedijk, Polyhedron 23 (2004) 1969.
[9] J. Frisch, G.W. Trucks, H.B. Schlegel, G.E. Scuseria, M.A. Robb, J.R. Cheeseman, J.A. Montgomery Jr., T. Vreven, K.N. Kudin, J.C. Burant, J.M. Millam, S.S. Iyengar, J. Tomasi, V. Barone, B. Mennucci, M. Cossi, G. Scalmani, N. Rega, G.A. Petersson, H. Nakatsuji, M. Hada, M. Ehara, K. Toyota, R. Fukuda, J. Hasegawa, M. Ishida, T. Nakajima, Y. Honda, O. Kitao, H. Nakai, M. Klene, X. Li, J.E. Knox, H.P. Hratchian, J.B. Cross, C. Adamo, J. Jaramillo, R. Gomperts, R.E. Stratmann, O. Yazyev, A.J. Austin, R. Cammi, C. Pomelli, J.W. Ochterski, P.Y. Ayala, K. Morokuma, G.A. Voth, P. Salvador, J.J. Dannenberg, V.G. Zakrzewski, S. Dapprich, A.D. Daniels, M.C. Strain, O. Farkas, D.K. Malick, A.D. Rabuck, K. Raghavachari, J.B. Foresman, J.V. Ortiz, Q. Cui, A.G. Baboul, S. Clifford, J. Cioslowski, B.B. Stefanov, G. Liu, A. Liashenko, P. Piskorz, I. Komaromi, R.L. Martin, D.J. Fox, T. Keith, M.A. Al-Laham, C.Y. Peng, A. Nanayakkara, M. Challacombe, P.M.W. Gill, B. Johnson, W. Chen, M.W. Wong, C. Gonzalez, J.A. Pople, GAUSSIAN 03, Revision C.02, Gaussian Inc., Wallingford, CT, 2004.
[10] A.D. Becke, J. Chem. Phys. 104 (1996) 1040.
[11] A.D. Hay, W.R. Wadt, J. Chem. Phys. 82 (1985) 270.
[12] S. Portmann, P.F. Fluekiger, MOLEKEL – Molecular Visualization Program, Swiss National Supercomputing Centre, 2007.
[13] G. Schaftenaar, J.H. Noordik, J. Comput. – Aided Mol. Design 14 (2000) 123.
[14] CRYSALIS RED, Version 1.171.31.5, Oxford Diffraction Ltd. (Release 28.08.2006 CrysAlis171.NET).
[15] G.M. Sheldrick, Acta Crystallogr. A46 (1990) 467.
[16] L.J. Farrugia, J. Appl. Crystallogr. 30 (1997) 565.
[17] R.D. Willett, G. Pon, C. Nagy, Inorg. Chem. 40 (2001) 4342.
[18] R.P. Hammond, D.J. Chesnut, J.A. Zubieta, J. Solid State Chem. 158 (2001) 55.
[19] A. Bencini, F. Mani, Inorg. Chim. Acta 154 (1988) 215.
[20] C.J. Brennan, V. McKee, Acta Crystallogr. C55 (1999) 1492.
[21] S. Andersson, S. Jagner, Acta Crystallogr. C43 (1987) 1089.
[22] S. Andersson, S. Jagner, Acta Chem. Scand. A39 (1985) 423.
[23] M. Asplund, S. Jagner, Acta Chem. Scand. A38 (1984) 135.
[24] R.L. Hardie, R.H. Thomson, J. Chem. Soc. (1957) 2512.

Polyhedron 28 (2009) 1595

Contents lists available at ScienceDirect

Polyhedron

journal homepage: www.elsevier.com/locate/poly

Preface

The International Conference of Molecule-based Magnets, ICMM, has a longstanding tradition of collaboration with *Polyhedron*, which is taking care of the publication of the papers presented in the 2008 edition held in Florence on September 21–24, 2008. In fact, it is by no means trivial the choice of the Journal hosting the proceedings of a largely interdisciplinary conference like ICMM. Anyway, good traditions must be conserved and I am glad to express my gratitude to George Christou for giving us the opportunity of exploiting the professional efficiency of this important Journal.

Molecule-based Magnets, or as anybody would say, Molecular Magnetism, is enjoying another period of expansion being more and more eager to export towards other disciplines its original approach to magnetism, and to learn from others how to find new challenging areas to develop. The organization of ICMM 2008 was based on these views of strong interactions with such diverse fields as spintronics and biomedicine. In fact the Plenary Lectures were delivered by George Whitesides, who showed how even diamagnetism can produce exciting effects; by Susumu Kitagawa who fascinated the audience with beautiful porous coordination polymers; and by Albert Fert who showed the relevance of carbon nanotubes in spintronics. The main area of Molecular Magnetism was firmly occupied by Joel Miller, who was the second Olivier Kahn Lecturer, and gave a brilliant resume of his achievements in a field which he largely contributed to develop.

The Olivier Kahn International Award, reserved by the European Network of Excellence MAGMANet, to a young researcher was assigned too Josè Ramon Galan Mascaros who delivered a brilliant lecture explaining his synthetic chemist's view of Molecular Magnetism.

There were on the whole 46 oral presentations, including 15 keynotes and two hot results. The decrease in the number of oral presentations compared to that of ICMM2006 (65) was more than compensated by the number of posters which jumped to 399. In fact the Conference was attended by ca. 500 people coming from 31 different countries.

The ICMM tradition of experimental demonstrations has been continued in a series of events organized by Michel Verdaguer and Françoise Villain in the campus of the University of Florence, first for the general public and then for the schools, from primary to college. The demonstrations were so entertaining that the children did not want to go home!

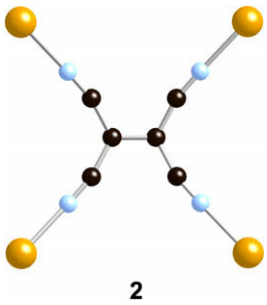
A Conference with 500 attendants is not easy to organize, but everything is fine if you have excellent collaborators. I must say that I was lucky enough. The International Advisory Board gave excellent suggestions for organizing the scientific content of the Conference and the format. The Local Organizing Committee found a great help in parallel organizations, like OIC, coordinated by Viviana Vitali and Annalisa Batistini, who were the clever interfaces with the participants, and INSTM coordinated by Claudia Bettaccini who gave the administrative help to the organization. I must express my gratitude to Anna Maria Papini who enthusiastically accepted the idea of the organization of conference on the magnetism for the general public and one week of demonstrations for primary and secondary schools at the OPENLab, at the University of Florence.

Finally let me thank the two Andreas who were the true motors of ICMM: Andrea Cornia who made an accurate work in the hectic phase when there was the storm of abstracts coming in all together, and Andrea Caneschi who coordinated in an efficient way all the activities.

Dante Gatteschi
Department of Chemistry,
University of Florence, INSTM,
UdR Florence, Via della Lastruccia 3,
50019 Sesto Fiorentino,
Italy
E-mail address: dante.gatteschi@unifi.it

0277-5387/$ - see front matter © 2009 Published by Elsevier Ltd.
doi:10.1016/j.poly.2009.05.046

four Fe^{II} ions in parallel, but undulating layers. These layers are connected in the former material via $S = 0$ μ_4-$[C_4(CN)_8]^{2-}$ bridging to four Fe^{II} ions, and capped by two $S = 0$ MeCN molecules in the latter material. Hence, both materials are layered magnets, and the presence $S = 1/2$ μ_4-$[TCNE]^{\cdot-}$ bridging to four V^{II} ions in parallel, but undulating layers were instantly thought to be present for $V[TCNE]_x$.



2

The lack of planarity of the $Fe^{II}_4[TCNE]^{\cdot-}$-based (**2**) magnetic layers that leads to the observed undulating layers is attributed to the competition between the octahedral environment about each Fe^{II} ion (i.e. preferred 90° *cis*-CN–Fe–NC linkages) and linear coordination of the nitriles to the Fe^{II} ions (i.e. preferred 180° sp-hybridized Fe–N–C linkages) that from simple geometrical considerations cannot coexist, as 165° Fe–N–C angles are needed (assuming 90° *cis*-CN–Fe–NC). Hence, to be more linear, i.e. Fe–N–C angle >165°, adjacent Fe^{II}-based octahedra cant with respect to each other and the layers buckle. This lack of planarity is also reported for some [11], but not all [11e,12], reduced μ_4-TCNQ-based materials.

The factor-of-four higher T_c for $V[TCNE]_x$ (400 K) with respect to these iron-containing magnets (~100 K) suggests that $V[TCNE]_x$ may have different structure that stabilizes the higher T_c. The Mean Field expression for T_c

$$T_c = \frac{2JzS(S+1)}{3k_B} \quad (1)$$

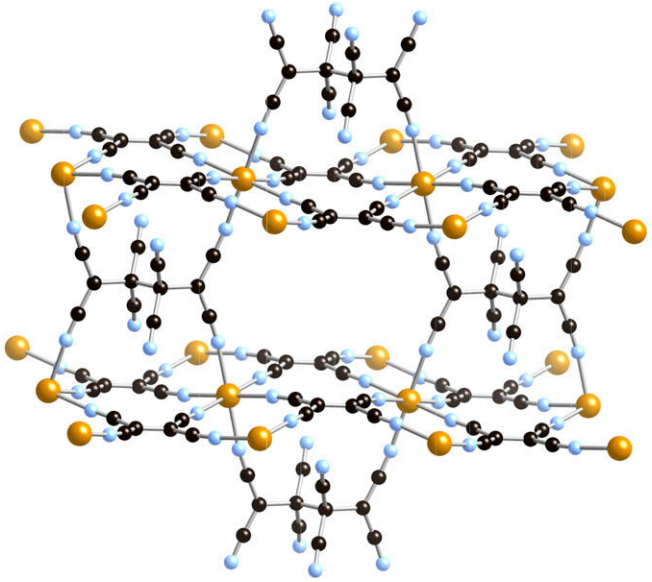


Fig. 1. Structure of $Fe^{II}[TCNE]_2 \cdot yCH_2Cl_2$ best formulated as $Fe^{II}[\mu_4\text{-}TCNE][\mu_4\text{-}C_4(CN)_8]_{1/2} \cdot yCH_2Cl_2$ (CH_2Cl_2 is disordered and resides in the channels within the porous framework structure) [9]. Each Fe^{II} is bonded to 6 nitrogens, and only some μ_4-$[C_4(CN)_8]^{2-}$ are shown for clarity.

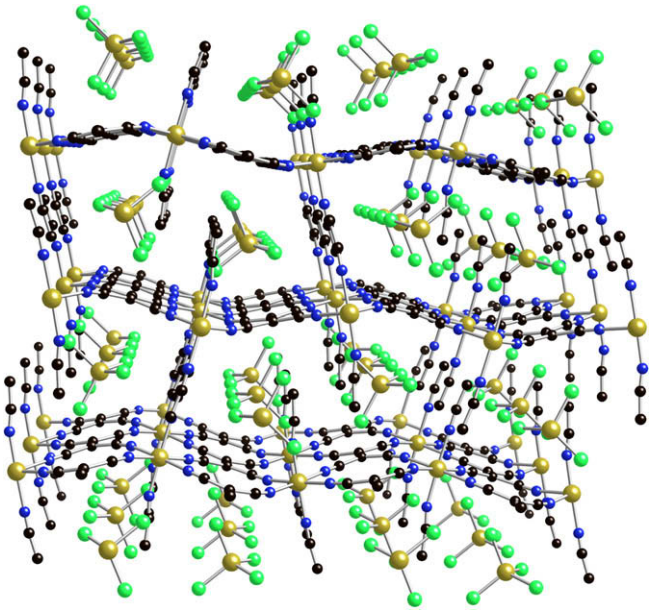


Fig. 2. Structure of $[Fe^{II}[TCNE](NCMe)_2][Fe^{III}Cl_4]$ [10].

(J is the nearest neighbor exchange coupling, z is the number of nearest neighbors, and k_B is Boltzmann's constant) reveals that by increasing the number of nearest neighbors (z) from 4 to 6, T_c increases by 50%. Hence, a 3-D structural motif should have a higher T_c, and it is appealing to consider that $V[TCNE]_x$ has a 3-D magnetic structure, as originally postulated [1a]. For a ferrimagnet with two different spin sites, i and j, with z_i and z_j nearest neighbors, respectively, the Mean Field expression is expanded to Eq. (2) [13,14]

$$T_c = \frac{2|J|[z_i z_j S_i(S_i+1)S_j(S_j+1)]^{1/2}}{3k_B} \quad (2)$$

Assuming a constant J, increasing z from 4 to 6 for each V site (3-D) [15], and reducing S from 2 (Fe^{II}) to 3/2 (V^{II}) should result in a small reduction in T_c by 3.2%, which is at variance to the observed factor-of-four increase. Hence, a 3-D structural motif is insufficient, and an enhanced J is needed to account for the factor-of-four increase in T_c.

1.1. Structural aspects

A 3-D magnetic structure can be envisaged via bridging $S = 1/2$ μ_4-$[TCNE]^{\cdot-}$ magnetic layers with μ-$[TCNE]^{\cdot-}$ (Fig. 3), among other possibilities [8a]. While this structural model is attractive, as it is consistent with the EXAFS and XANES data, it per se does not account for the enhanced T_c. Furthermore, this simplistic model is inconsistent with the diffraction data, as the structure would be ordered, and thus should diffract to some extent. Thus, the enhanced T_c must arise, at least in part, from a larger exchange coupling, J.

From an analysis of the saturation magnetization temperature dependence, $M_s(T)$, by the Block law for spin wave theory, J/k_B is estimated to be 100 K for $V[TCNE]_x$ [3]. Using Eq. (2) and $z_V = 4$ (and 6), a 447 K (and 548 K) T_c is expected. While both 2- and 3-D structural models predict a T_c above room temperature, the former is sufficient and closer to the observed value. While sufficient, magnetic anisotropy is needed for magnetic ordering in 2-D (Ising), which is not present for $V[TCNE]_x$.

Although the structure for $V[TCNE]_x$ is unknown, direct exchange coupling is expected to occur via V–NCCCN–V and V–NCCCCN–V spin-bearing linkages that are analogous to the Fe–NCCCN–Fe and Fe–NCCCCN–Fe linkages solely present for both layered (2-D) $Fe^{II}[TCNE][C_4(CN)_8]_{1/2}$ and $[Fe^{II}[TCNE](NCMe)_2][Fe^{III}Cl_4]$,

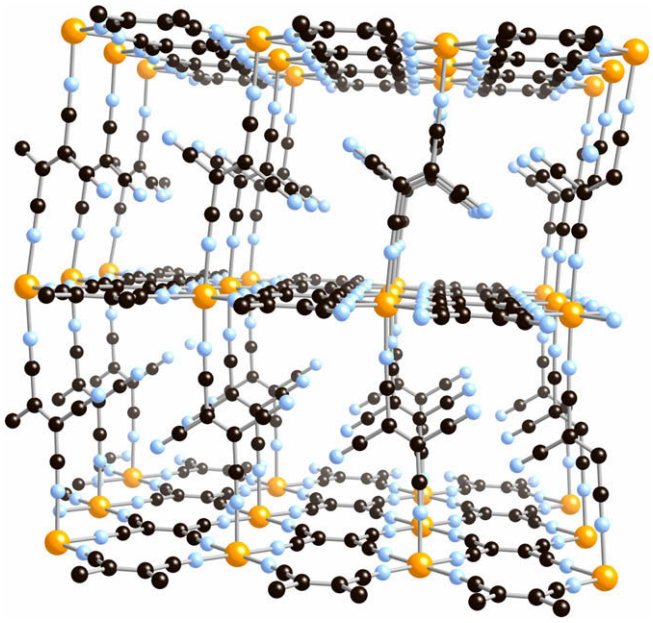


Fig. 3. An idealized proposed 3-D structure of $V^{II}[TCNE]_x$ ($x = 2$) possessing a 3-D magnetic motif with layers possessing μ_4-$[TCNE]^{\cdot-}$ being connected by μ-$[TCNE]^{\cdot-}$.

and more linkages, and as expected for a 3-D motif, would increase z and lead to a higher T_c, albeit offset due the reduced value of S for V.

For comparison, based on the 100-K T_c for $Fe[TCNE]_2$ a 12.5 K J is calculated via Eq. (2) [16]. The larger J for V^{II} with respect to Fe^{II} is expected due to greater mixing of the $[TCNE]^{\cdot-}$ π^* SOMO with the V^{II} d_π (t_{2g}-like) orbitals with respect to the Fe^{II} orbitals due to less nuclear shielding and thus being closer in energy, Fig. 4.

Note that a significantly enhanced J for V^{II} with respect to Fe^{II} ions, as reflected by a greater T_c, has also been noted for Prussian blue structured magnets. Prussian blue structured magnets with

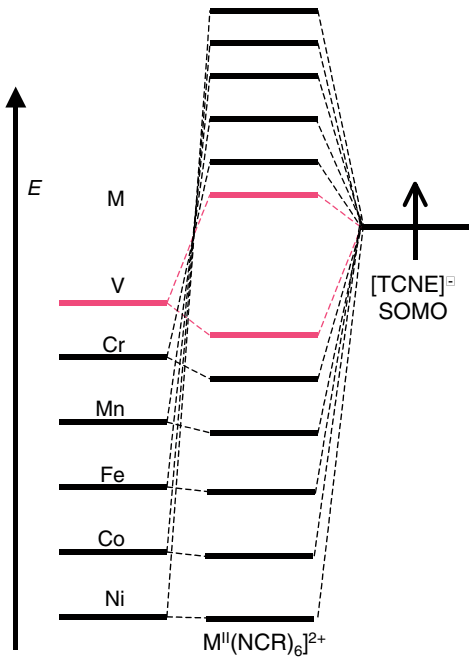


Fig. 4. Schematic illustration of the increasing M^{II} (M = V > Cr > Mn > Fe > Co > Ni) orbital interactions with the $[TCNE]^{\cdot-}$ π^* SOMO orbital with the M^{II} d_π (t_{2g}-like) orbitals.

V^{II}–NC–Cr^{III} linkages have T_c's exceeding room temperature [13,17], whereas those with Fe^{II}–NC–Cr^{III} linkages have substantially lower T_c's, by a factor of 15 {21 K for $Fe^{II}_3[Cr^{III}(CN)_6]_2 \cdot 15H_2O$ [18]}. This greater than an order of magnitude increase in T_c (and J) is also attributed to the better overlap of the orbitals on V^{II} with the CN^- π^* that leads to indirect coupling with the $S = 3/2$ Cr^{III} [19]. This overlap is likewise qualitatively valid for $M[TCNE]_x$. Hence, the higher T_c for $V[TCNE]_x$ with respect to $Fe[TCNE]_2$ is primarily attributed to stronger coupling. $[TCNE]^{\cdot-}$ is expected to provide strong coupling as it is directly coupled, not indirect as occurs for cyanide.

2. Composition of $V[TCNE]_x$

Since the discovery of $V[TCNE]_x$ in 1991 [1a], numerous characteristic properties have been established that reflect its composition and structure. Insight into the bulk composition can be obtained from the combustion analyses whereby the %C, H, N etc. is obtained, and fit to plausible formula by computational analysis [20]. The results of numerous elemental percentages have been garnered over the years, but the situation continues to be as it was when it was first reported. Namely "For $V[TCNE]_x{\cdot}yCH_2Cl_2$ a range of x and y is observed for preparations differing in solvents and mole ratios of the starting materials; oxygen and perhaps a benzene in small amounts are present in some cases. For the material discussed herein $x \sim 2$, and $y \sim 1/2$. Magnetic materials with $1.5 \leqslant x \leqslant 2$ and $0 \leqslant y \leqslant 1$ have also been prepared. Elemental analysis. Calc. (observed) for $C_{12.5}HClN_8V$: %C = 42.95 (42.81, 43.20, 43.00), and %H = 0.29 (0.14, 0.68, 0.35), %N = 32.05 (30.63, 30.00, 21.04), and %V = 14.57 (15.31), % chlorine was not reproducible." Additionally, strong ν_{CN} IR absorptions at 2188 ± 9 and 2099 ± 5 cm^{-1} were also reported [1]. The magnetization of ~6000 emuOe/mol was also reported to be in accord with the expectation of 5585 emuOe/mol for a ferrimagnet of $V[TCNE]_x{\cdot}yCH_2Cl_2$ ($x = 2$) composition.

Since the first report of this magnet, additional elemental percentages, IR spectra, as well as magnetic data etc. have obtained. The elemental analyses continue to be hampered by its oxygen sensitively, as well as solvent loss, but it is clear that $1.5 < x < 2$ and $0 \leqslant y \leqslant 1$ for materials made from solvent, and, of course, $y = 0$ for solvent-free films made via CVD [3,21]. It should be noted that co-formation of vanadium metal along with $V[TCNE]_2$ would give an effective composition of $V[TCNE]_x$ ($x < 2$); however, evidence for V^o was not identified from XPS [1c], EXAFS, and XANES [4] studies [21a]. As noted above, several IR absorptions assignable to ν_{CN} in the 2100 ± 100 cm^{-1} region exit for these magnetic materials, however, slight shifts, shoulders having different maxima, and differences in the relative intensities occur (Fig. 5a) [1–3].

The presence of $[TCNE]^{2-}$ is evident from the ν_{CN} IR absorptions. TCNE can be found in many forms in several oxidation states, i.e. $[TCNE]^n$ ($n = 0$, 1-, 2-) and its ν_{CN} absorptions are diagnostic of the oxidation states, and to a lesser extend the coordination environment [22]. ν_{CN} absorptions below 2150 cm^{-1} are indicative $[TCNE]^{2-}$, and are not present for either $[Fe^{II}\mu_4\text{-}[C_4(CN)_8](MeCN)_2]$ [23], $[Fe^{II}\mu_4\text{-}[TCNE](NCMe)_2][FeCl_4]$ [10], or $[Fe^{II}\mu_4\text{-}[TCNE]^{\cdot-}\{\mu_4\text{-}[C_4(CN)_8]^{2-}\}_{1/2}$ [9] (Fig. 5a). Absorptions below 2150 cm^{-1}, however, are present for $V^{II}[TCNE]_x$ prepared by several different routes [1–3] (Fig. 5b), and, thus, indicate that $[TCNE]^{2-}$ is present in some form. Recently $[VCp_2]_2[TCNE] \cdot 2B(C_6F_5)_3]$ and $\{[VCp_2][TCNE] \cdot 2B(C_6F_5)_3\}_2$ (Cp = cyclopentadienide) was characterized to possess μ_4-$[TCNE]^{2-}$ with ν_{CN} absorptions at 2200 and 2152 cm^{-1} [24], while absorptions at 2176 and 2097 cm^{-1} occur for *trans*-μ-$[TCNE]^{2-}$ that is present in $[Ir^I(CO)(PPh_3)_2]_2[TCNE]$ [25].

Monoreduced TCNE can occur in many forms, e.g. σ-$[TCNE]^{\cdot-}$, μ-$[TCNE]^{\cdot-}$, μ_4-$[TCNE]^{\cdot-}$, μ_4-$[C_4(CN)_8]^{2-}$, and π-$[TCNE]_2^{2-}$, and thus can coordinate to a metal ion in several modes, via the terminal

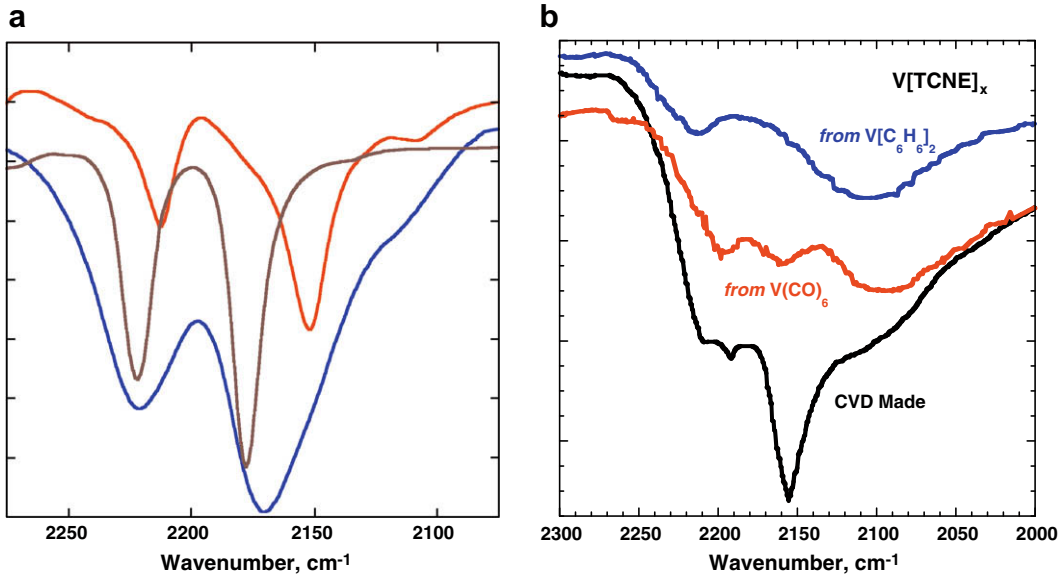


Fig. 5. ν_{CN} region for $[Fe^{II}\mu_4\text{-}[C_4(CN)_8](MeCN)_2$ (top), $[Fe^{II}\mu_4\text{-}[TCNE](NCMe)_2][FeCl_4]$ (middle), and $[Fe^{II}\mu_4\text{-}[TCNE]^{\cdot-}\{\mu_4\text{-}[C_4(CN)_8]^{2-}\}_{1/2}]$ (bottom) (a), $V[TCNE]_x \cdot yCH_2Cl_2$ prepared from $V(C_6H_6)_2$, $V(CO)_6$, [2], and a $V[TCNE]_x \cdot$ CVD-prepared thin film (b) [3a].

nitrogens [22]. Each of these forms have different ν_{CN} absorptions occurring above 2150 cm^{-1} [22], however, due to broadness and variability of the observed ν_{CN} absorptions (Fig. 5a) their presence cannot be conclusively identified for $V[TCNE]_x$, except to note that they arise from $[TCNE]^{\cdot-}$, and not from either $TCNE^o$ or $[TCNE]^{2-}$.

The magnetization also varies with sample, and values exceeding 10,000 emuOe/mol have been noted [2]. Hence, while magnetic materials ordering above room temperature are reproducibly made, the details of their physical properties differ. Thus, based on the lack of significant diffraction, and sample-to-sample as well as within-a-sample variability with respect to the elemental percentages, ν_{CN} absorptions, as well as magnetization, and as noted above this material was ascribed to being nonstoichiometric and inhomogeneous [1–3]. Hence, developing a structural model and theoretical insight for this material has been elusive.

The magnetization data is also consistent with the presence of $[TCNE]^{2-}$. The observed low field magnetization nominally ranges from 5000 to more than 10000 emuOe/mol [2], and its sample-to-sample variability has made the understanding of this material challenging. The limiting stoichiometry of $V^{II}[TCNE]_2$ with the $S = 3/2$ V^{II} antiferromagnetically coupled to two $S = 1/2$ $[TCNE]^{\cdot-}$ s, each with $g = 2$, leads to the expectation of a magnetization of 5585 emuOe/mol (or 27,925 emuOe/mol, if ferromagnetically coupled). Hence, values in the range ~5000 to ~6000 emuOe/mol are reasonable for antiferromagnetic coupling, especially due to the presence of solvent that is easily lost. Higher magnetization values, however, are expected if $S = 0$ $[TCNE]^{2-}$ or any diamagnetic form of $[TCNE]^{\cdot-}$ {e.g. $[C_4(CN)_8]^{2-}$ observed for $Fe[TCNE]_2$, or $[TCNE]_2{}^{2-}$} is present, as there would be only antiferromagnetic coupling with the single $S = 1/2$ $[TCNE]^{\cdot-}$ present. Thus, if $x = 1.5$, then $z = 0.5$, and V^{II} could only antiferromagnetically couple with one $[TCNE]^{\cdot-}$ s leading to an expected magnetization of 11,170 emuOe/mol. Hence, for $2 > x > 1.5$ the magnetization will be between 5585 and 11,170 emuOe/mol, as depicted in Fig. 6. These values would, however, be reduced if in actuality the composition (molecular weight) was assumed to be $V[TCNE]_2$, but would still be significantly larger than 5585 emuOe/mol (Fig. 6). The determination of the molar magnetization is further complicated due to the presence of solvent, which varies with sample, and some of it is easily lost. Nonetheless, $= V^{II}[TCNE]^{\cdot-}{}_z[TCNE]^{2-}{}_{1-z/2}$ will have higher magnetization than $V[TCNE]_x$.

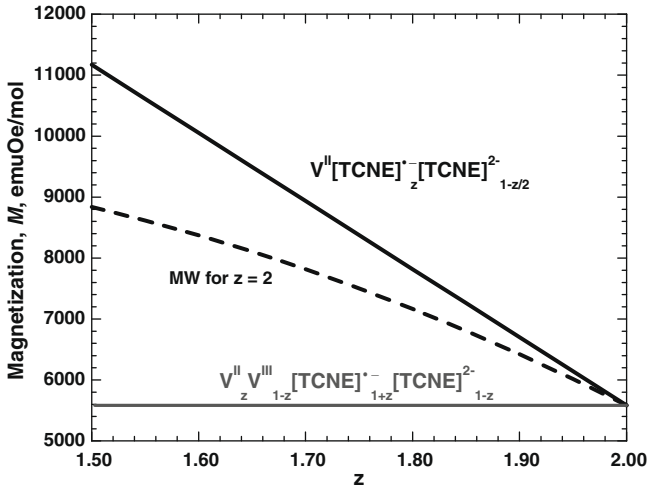


Fig. 6. Magnetization of the $V^{II}[TCNE]^{\cdot-}{}_z[TCNE]^{2-}{}_{1-z/2}$ formulation as a function of z assuming its molecular weight (top), and the molecular weight (MW) for $z = 2$ (dashed), and the constant magnetization for $V^{II}{}_zV^{III}{}_{1-z}[TCNE]^{\cdot-}{}_{1+z}[TCNE]^{2-}{}_{1-z}$ formulation.

Excluding the solvent from the solvated form, $V^{II}[TCNE]^{-}{}_z[TCNE]^{2-}{}_{1-z/2}$ is a good description for $V[TCNE]_x$. This is based upon full consideration of all of the data, although more complex formulations additionally possessing $\mu_4\text{-}[C_4(CN)_8]^{2-}$ [9,23] and/or $\pi\text{-}[TCNE]_2{}^{2-}$ [22,26,23c,27] etc. cannot be excluded. This formulation is predicated on the presence of $[TCNE]^{2-}$, and the TCNE:V ratio, x [$= z + 1 - z/2 = 1 + z/2 < 2$ ($z \neq 0$)], will vary with the amount of $[TCNE]^{2-}$ present, but will always be less than 2 when present, due to charge conservation.

While evidence for the presence of $[TCNE]^{2-}$ is presented, a mechanism for its formation is elusive. The reactions of TCNE with $V(C_6H_6)_2$ and $V(CO)_6$ to form $V[TCNE]_x$ appear to proceed by distinctly different mechanisms [28]. The reversible one-electron reduction potential for $V(C_6H_6)_2$ is −0.36 V (versus SCE), but its irreversible oxidation to V^{II} is +0.24 V [29a,b]; hence, it is insufficient to form $[TCNE]^{2-}$ {TCNE [$E^{-/o} = +0.25$; $E^{2-/-} = -0.83$ V (CH_2Cl_2) [30]}. Likewise, due to the irreversible, high oxidation potential of

$V(CO)_6$ (+0.88 V) [29c] its reaction with TCNE must not initially proceed by electron transfer [31]. Hence, in both mechanisms intermediates must form, at least transiently, that reduce the oxidation potential of the V species enabling the formation of $[TCNE]^{2-}$; but the details of this are not known.

Nonetheless, reduction of $[TCNE]^{\cdot-}$ to $[TCNE]^{2-}$ requires an oxidation, and oxidation of V^{II} to V^{III} seems reasonable, although based on the above discussion of oxidation potentials, it is not obvious. Thus, $V[TCNE]_x$ could be formulated as ${V^{II}}_z{V^{III}}_{1-z}[TCNE^-]_{1+z}-[TCNE]^{2-}{}_{1-z}$, and thus also possess the experimentally observed $[TCNE]^{2-}$. This formulation, however, is less likely due to requiring a TCNE:V ratio of 2 that is not observed. Also, the presence of V^{III} via XPS, EXAFS, or XANES studies has not been identified, but may be obscured or below the limits of measurements [3a,4,21]. Furthermore, V^{III} unlike V^{II}, and is not known to be stabilized by six nitrile-containing ligands, although coordinating halides stabilize V^{III}-acetonitrile complexes [32]. Finally, the expected magnetization for ${V^{II}}_z{V^{III}}_{1-z}\,[TCNE]^-_{1+z}[TCNE]^{2-}{}_{1-z}$ is inconsistent with the observed magnetization, as it is independent of z (Fig. 6) and values greater than 5585 emuOe/mol, as observed, should not occur.

Reduction of $[TCNE]^{\cdot-}$ to form $[TCNE]^{2-}$ might also be a consequence of oxidation of a second V^{I} (or V^{o}) site, and form V^{II}-$[TCNE]^-_z[TCNE]^{2-}{}_{1-z/2}$ This route requires that some of the oxidized V^{o} does not end up in the product, and while it might stay in solution for solution-made $V[TCNE]_x \cdot yCH_2Cl_2$, it cannot be reconciled for CVD-made $V[TCNE]_x$.

As models tend to be simplistic, the presence of TCNE:V < 2 could arise from the presence of V^{III}, such that ${V^{II}}_z{V^{III}}_{1-z}[TCNE]^-_a[TCNE]^{2-}_b$ ($b > 0$; $a + b = 2$; $a + 2b = 3 - z$; $a \neq 1 + z$; $b \neq 1 - z$) occurs with the same caveats as noted above.

The $V^{II}[TCNE]^-_z[TCNE]^{2-}{}_{1-z/2}$ formulation is in accord with the elemental analyses, ν_{CN} IR data, EXAFS, XANES, XPS, as well as magnetization data. Evaluation of elemental percentages, as noted earlier, show $1.5 < x < 2$ in accord with the $V^{II}[TCNE]^-_z[TCNE]^{2-}{}_{1-z/2}$ ($z < 2$) formulation. Note that this differs from $Fe[TCNE]_2$ where one of the $[TCNE]^{\cdot-}$ species is present as one-half of a $[C_4(CN)_8]^{2-}$. Diamagnetic $[C_4(CN)_8]^{2-}$ being the σ-dimer of $[TCNE]^{\cdot-}$ could as well as be replaced by its diamagnetic π-dimer, π-$[TCNE]_2{}^{2-}$ to maintain the charge and stoichiometry.

Thus, while $V^{II}[TCNE]^-_z[TCNE]^{2-}{}_{1-z/2}$ ($z < 2$) is formulated for $V[TCNE]_x$, the additional presence of these and/or other monoreduced forms of TCNE cannot be excluded, and likely are present to some extent. The presence of these and/or other monoreduced forms of TCNE, however, will maintain a 2:1 TCNE:V ratio, and only the presence of $[TCNE]^{2-}$, assuming no V^{III}, will reduce the ratio, as is observed [33].

3. Structural models for $V^{II}[TCNE]_x$

A limiting structure for the $V^{II}[TCNE]^-_z[TCNE]^{2-}{}_{1-z/2}$ formulation, i.e. $z = 1$ {$x = 1.5$: $V^{II}[TCNE]_{1.5}$}, is proposed to have $S = 1/2$ μ_4-$[TCNE]^{\cdot-}$ (**2**) layers bridged by $S = 0$ μ_4-$[TCNE]^{2-}$, Fig. 7. All V^{II} ions would be surrounded by six nitriles from six different reduced TCNEs in accord with the EXAFS and XANES data, and in this idealized structure there is 1.5 reduced TCNEs per V^{II}, of which one is $[TCNE]^{\cdot-}$ and one-half is $[TCNE]^{2-}$. This proposed structure portrays both μ_4-$[TCNE]^{\cdot-}$ and μ_4-$[TCNE]^{2-}$ as being planar ($\sim D_{2h}$). Planarity is expected for $[TCNE]^{\cdot-}$, but not necessarily for $[TCNE]^{2-}$. $[TCNE]^{2-}$ has a central C–C bond order of one; thus, free rotation is expected, and its structurally characterized examples are nonplanar [24,25,34]. Nonetheless, $[TCNE]^{2-}$ could be planar in this solid-state motif, as depicted in Fig. 7.

Planar $[TCNE]^{2-}$ should be ~0.1 Å wider than $[TCNE]^{\cdot-}$, i.e. the M1 Fe···Fe separation should be 7.32 Å versus an observed average of 7.22 Å (Table 1), due to the central C–C single bond [22], and while this should be kept in mind, this increase in length is sufficiently small that the structural parameters for the more extensively structurally characterized $[TCNE]^{\cdot-}$ can be used to model $[TCNE]^{2-}$.

The question arises as to the validity of $[TCNE]^{2-}$ being a structural replacement for $[C_4(CN)_8]^{2-}$ observed for $Fe[TCNE]_2$ [9] for $V[TCNE]_x$. The reported M···M separations for μ_4-$[TCNE]^{\cdot-}$ and μ_4-$[C_4(CN)_8]^{2-}$ are presented in Table 1. The *cis*-1,2-Fe–NCCCCN–Fe (M1), *cis*-1,1-Fe–NCCCN–Fe (M2), and *trans*-Fe–NCCCCN–Fe for μ_4-$[TCNE]^{\cdot-}$ distances, and thus for $[TCNE]^{2-}$, are 7.22 (M1), 7.29 (M2), and 10.26 Å (M3), respectively. The M1 distances lies within the range observed for $[C_4(CN)_8]^{2-}$; i.e. 7.17 to 9.37 Å for M1, but is ~0.3 Å less than the 7.56 to 8.70 Å range for M2, and 1.0 Å below the shortest reported M3 distance that ranges from 11.27 to 12.04 Å. From geometrical considerations, the M1–M3 distances can be estimated assuming a 90° rotation about the central C–C bond, i.e. D_{2d}, to be 8.32, 8.24, and 8.33 Å, respectively – almost cubic (Table 1). As a consequence, the M2 value falls within the observed range for μ_4-$[C_4(CN)_8]^{2-}$, but M3 is now ~3 Å below the observed range. This suggests that planar μ_4-$[TCNE]^{2-}$ is more compatible, but a small deviation from planarity may occur. The system is quite forgiving, as noted by the large range for the M1, M2, and M3 distances reported for the known μ_4-$[C_4(CN)_8]^{2-}$-containing structures (Table 1).

From a modeling perspective by increasing the relative canting of the adjacent Fe-based octahedra, such that, for example, M1 = 6.42, M2 = 7.73, and M3 = 10.05 Å, planar $[TCNE]^{2-}$ can fit the system, as illustrated in Fig. 7. Nonplanar, twisted $[TCNE]^{2-}$ likely can also be accommodated, and would alter the 3-D structural framework to some extent. The presence of both μ_4-$[TCNE]^{\cdot-}$ and μ_4-$[TCNE]^{2-}$ in the above discussion has magnetic layers possessing the μ_4-$[TCNE]^{\cdot-}$ separated by μ_4-$[TCNE]^{2-}$. In all cases channels exist within the structure to accommodate the solvent.

However, via movement of the electron among adjacent sites (hopping) both of μ_4-$[TCNE]^{\cdot-}$ and μ_4-$[TCNE]^{2-}$ species would be randomly located. This could explain the observed relatively high electrical conductivity that approaches 10^{-2} S/cm at room temperature that is attributed to electron hopping [35] between the structurally similar $[TCNE]^{\cdot-}$ and $[TCNE]^{2-}$ sites, i.e. μ_4-$[TCNE]^{\cdot-}$ + μ_4-$[TCNE]^{2-}$ = μ_4-$[TCNE]^{2-}$ + μ_4-$[TCNE]^{\cdot-}$, with a 0.5 V band gap.

Additionally, why does $[TCNE]^{2-}$ exist for V^{II}, while $[C_4(CN)_8]^{2-}$ {$= \sigma-[TCNE]_2{}^{2-}$} exists for Fe^{II}? The latter is physically twice the size as the latter, but the nominal space available for it, as well as charge, is the same. Perhaps V, being an earlier transition metal, has a sufficiently larger radii than Fe consistent with the expected trend [36] that it requires M1, M2, and M3 distances that are incompatible with stabilizing $[C_4(CN)_8]^{2-}$, as the central C–C bond is long and weak [10,23], but the observed V-NCMe distances, 2.11 ± 0.03 Å [5], are comparable and even less than that 2.16 ± 0.06 Å for $[Fe^{II}\mu_4$-$[TCNE](NCMe)_2][FeCl_4]$ [10] and $[Fe^{II}\mu_4$-$[TCNE]^{\cdot-}\{\mu_4$-$[C_4(CN)_8]^{2-}\}_{1/2}]$ [9]. Hence, this is an unlikely explanation. More likely is the stronger reducing ability (lower ionization potential) of V^{II} with respect to Fe^{II} that leads to the reduction of $[TCNE]^{\cdot-}$ to $[TCNE]^{2-}$, albeit by an unknown mechanism (vide supra).

The ideal $V^{II}[TCNE]_{1.5}$ and $V^{II}[TCNE]_2$ limiting compositions provide a basis to understand the material. The actual compositions lie between these extremes, i.e. $V^{II}[TCNE]^-_z[TCNE]^{2-}{}_{1-z/2}$ ($1 < z < 2$), and may possess a small amount of V^{III} [23c]. For intermediate values of z, μ_4-$[TCNE]^{2-}$ could be randomly replaced with μ-$[TCNE]^{\cdot-}$, but each V^{II} ion should maintain its octahedral coordination environment. This replacement should occur between the layers, but since electrons could hop between μ_4-$[TCNE]^{\cdot-}$ and μ_4-$[TCNE]^{2-}$ sites, i.e. μ-$[TCNE]^{\cdot-}$ + μ_4-$[TCNE]^{2-}$ = μ-$[TCNE]^{2-}$ + μ_4-$[TCNE]^{\cdot-}$, in addition to between the aforementioned μ_4-$[TCNE]^{\cdot-}$ and μ_4-

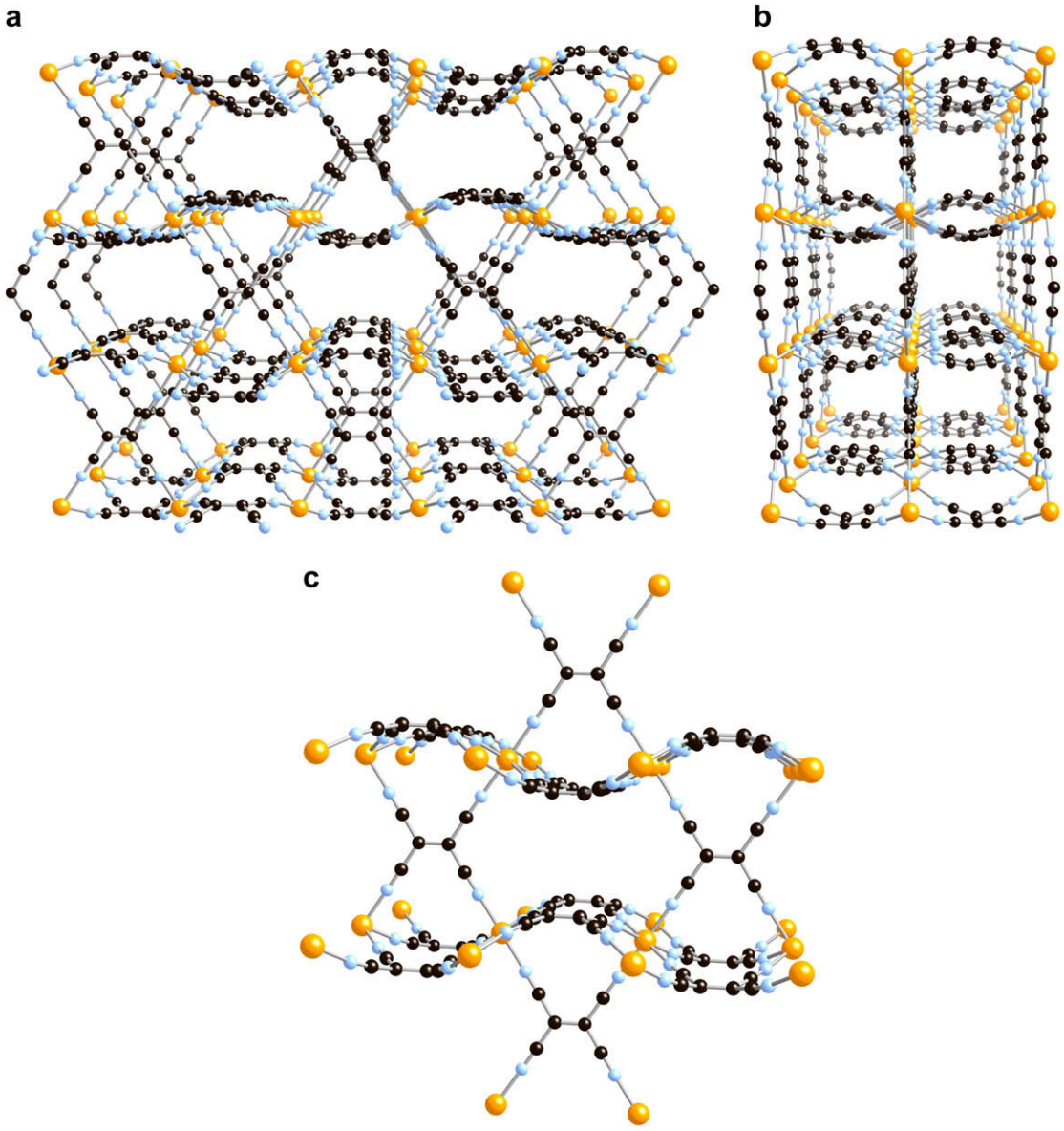


Fig. 7. A proposed limiting structure for $V^{II}[TCNE]^{\cdot-}{}_{z}[TCNE]^{2-}{}_{1-z/2}$ ($z = 1$) {$= V^{II}[TCNE]^{\cdot-}[TCNE]^{2-}{}_{1/2} = V^{II}[TCNE]_{1.5}$} possessing $S = 1/2$ μ_4-$[TCNE]^{\cdot-}$ layers bridged by $S = 0$ μ_4-$[TCNE]^{2-}$ through the hexacoordinate V^{II} ion; side view (a), end view (b). Note that the solvent would reside with the 2-D channels of this porous framework structure, and each V^{II} is bonded to 6 nitrogens, and only some μ_4-$[TCNE]^{2-}$ are shown for clarity.

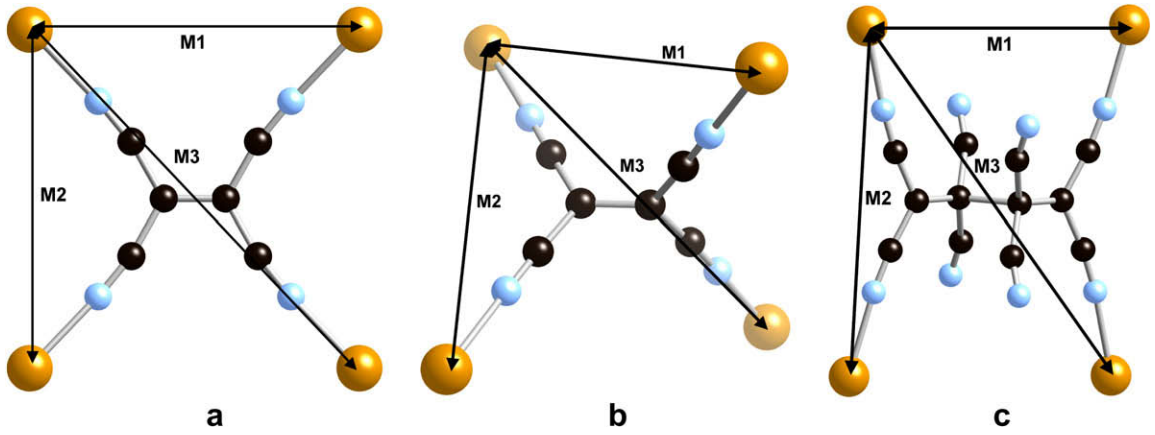
$[TCNE]^{2-}$ sites in accord with the observed high electrical conductivity. Furthermore, as the material immediately precipitates, the μ-$[TCNE]^{\cdot-}$ would be randomly located contributing to the structural disorder.

The intralayer replacement of μ_4-$[TCNE]^{2-}$ with *trans*-μ-$[TCNE]^{\cdot-}$ suggests a geometrical mismatch, as it should have a V···V separation comparable to the M3 Fe···Fe values in Table 1, which are significantly larger than the M2 distance noted for μ_4-$[TCNE]^{2-}$. The M2 Fe···Fe separation (Table 1) for μ_4-$[TCNE]^{\cdot-}$ (7.24–7.33 Å) and μ_4-$[C_4(CN)_8]^{2-}$ (7.56–8.70 Å) is ~3 Å shorter than the reported M3 distances for μ_4-$[TCNE]^{\cdot-}$ (~10.26 Å) and μ_4-$[C_4(CN)_8]^{2-}$ (11.27–12.04 Å). Nonetheless, the M3 distance for [MnTP*P][TCNE] · 2PhMe [H_2TP*P = *meso*-tetrakis(3,5-di-*t*-butyl-4-hydroxyphenyl)porphyrin], which like the large family of [MnTPP][TCNE] · *x*S (H_2TPP = *meso*-substituted tetraphenylporphyrins; S = solvent) magnetically order as ferrimagnets [1c], is 8.59 Å [37]. Hence, by reducing the M–N–C angle from the idealized 180° to a much lower values, such as 129° angle for [MnTP*P][TCNE] · 2PhMe, the μ-$[TCNE]^{\cdot-}$ moiety can replace either μ_4-$[TCNE]^{2-}$ or μ_4-$[C_4(CN)_8]^{2-}$ moieties.

Furthermore, the *trans*-μ-$[TCNE]^{\cdot-}$ intralayer replacement of μ_4-$[TCNE]^{2-}$ should enhance the magnetic coupling. In addition to the obvious existence of direct magnetic coupling available with $S = 1/2$ μ-$[TCNE]^{\cdot-}$ that is not present for $S = 0$ μ_4-$[TCNE]^{2-}$, the required reduced M–N–C angle should lead to stronger intralayer coupling, with respect to larger M–N–C angles approaching 180°. The inverse correlation between the M–N–C and the coupling has been established for the [MnTPP][TCNE]·*x*S family of ferrimagnets [1c,38]. Thus, the smaller M–N–C angle needed to accommodate μ-$[TCNE]^{\cdot-}$ should strengthen the coupling.

The aforementioned discussion refers to two limiting structures that should exhibit some degree crystalline order, and, thus, diffract to some extent, which does not occur. These two limiting structures could exit in different regions, inter-grow, or occur randomly. For example for a limiting structure for $V[TCNE]_{1.75}$ alternate layers of μ_4-$[TCNE]^{\cdot-}$ and μ-$[TCNE]^{2-}$, which via electron

Table 1
Summary of the reported M···M separations for compounds containing μ_4-[TCNE]$^{\cdot-}$ and μ_4-$[C_4(CN)_8]^{2-}$.



		M1, Å	M2, Å	M3, Å	Ref
μ_4-[TCNE]$^{\cdot-}$					
$Fe^{II}[\mu_4\text{-TCNE}][\mu_4\text{-}C_4(CN)_8]_{1/2}$	**a**	7.28	7.24	10.27	[9]
$Fe^{II}[TCNE](NCMe)_2][Fe^{III}Cl_4]$	**a**	7.16	7.33	10.25	[10]
D_{2h}-μ_4-[TCNE]$^{\cdot-}$	**a**	7.22	7.29	10.26	
D_{2d}-μ_4-[TCNE]$^{\cdot-}$	**b**	8.32	8.24	8.33	
Fig. 6 Model structure	**a**	6.43	7.73	10.05	
μ_4-$[C_4(CN)_8]^{2-}$					
$Fe^{II}[\mu_4\text{-TCNE}][\mu_4\text{-}C_4(CN)_8]_{1/2}$	**c**	7.16	8.70	11.27	[10]
$Fe[C_4(CN)_8]_2{\cdot}2MeCN$	**c**	9.37	7.56	11.96	[23b]
$Fe[C_4(CN)_8]_2{\cdot}2MeCN \cdot CH_2Cl_2$	**c**	9.37	7.56	12.12	[23a]
$Mn[C_4(CN)_8]_2{\cdot}3MeCN$	**c**	9.34	7.58	12.03	[23a]
$MnTPyA[C_4(CN)_8]_{1/2}$	**c**	8.07	8.33	11.59	[23c]

hopping will randomize the location of the unpaired spin, again accounting for the high electrical conductivity, and providing a means for 3-D Mean Field-like magnetic coupling.

The lack of diffraction for the V[TCNE]$_x$ can be attributed to either very small crystallites (<10 Å) or the material being an amorphous glass. The particle size radius, assuming uniform spherical particles, is estimated to be 250 Å based on its 100 m^2/g surface area [1b,39]. This is sufficiently large and diffraction, albeit broadened, is expected, and even if it were a magnitude smaller, i.e. 25 Å, diffraction albeit with enhanced broadening, would likewise be anticipated. The direct measurement of its particle size distribution has been thwarted due to the extreme oxygen and water sensitivity. Very small spatial domains may result from the instantaneous formation of V[TCNE]$_x$; however, TEM studies do not provide evidence for this. TEM photographs reveal a featureless morphology consistent with a glassy material, Fig. 8. Hence, the lack of diffraction is most likely due to V[TCNE]$_x$ being a glassy material, i.e. an inhomogeneous, nonstoichiometric material composed differing components and linkages, as exists for window glass or coal. Nonetheless, several attempt to grow a more crystalline form of the V[TCNE]$_x$ magnet was pursued.

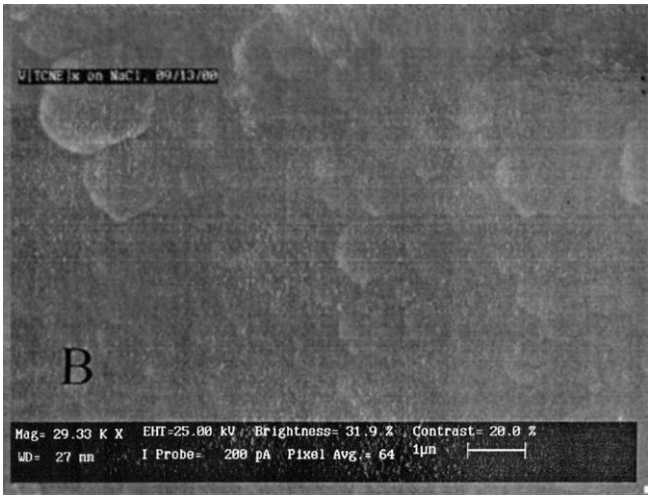


Fig. 8. Transmission electron micrograph (TEM) of a V[TCNE]$_x$ film on NaCl.

4. Attempts to grow crystalline V[TCNE]$_x$ by slow diffusion

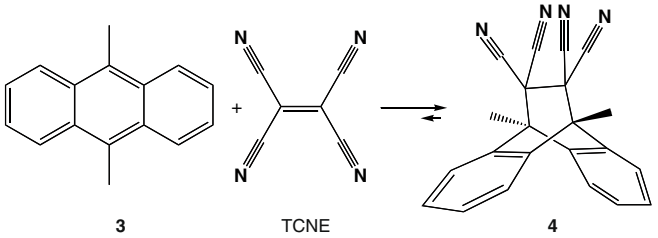
The growth of crystalline V[TCNE]$_x$ in any form has yet to be successful. Being a material, different preparative routes may form materials with different degrees of crystallinity and/or different structural modifications, and physical properties, if not differing variations of the composition for nonstoichiometric materials. Since its discovery, the V[TCNE]$_x$ magnet has been successfully prepared (i.e. T_c > room temperature) innumerable times via different vanadium sources {e.g. $V(C_6H_6)_2$, $V(PhMe)_2$, $V(CO)_6$, $[V(CO)_6]^-$, and $[V(NCMe)_6]^{2+}$}, and solvents (e.g. PhMe, CH_2Cl_2, THF, and n-C_6H_{14}), as well as by chemical vapor deposition [3a], and while powder X-ray diffraction (PXRD) analysis was not performed on every sample, it was obtained for many samples, especially those via new routes. Significant diffraction, except for that associated with the presence of an amorphous component, was not obtained.

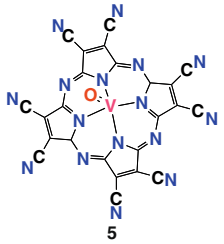
Specific attempts to grow crystals by traditional methods for growing crystals have been unsuccessful. Many strategies and tactics have been established through the decades to grow crystals,

and certainly not all have been tried (or are even suitable) for $V[TCNE]_x$. Generally for an insoluble, rapidly precipitating material such as $V[TCNE]_x$, which instantaneously forms when TCNE is reacted with a suitable vanadium source, as discussed above, reducing the rate of reaction may lead to its slow formation and greater crystallinity. Attenuation of the reaction rate, in practice, in complicated by the extreme air and water/protic solvent sensitivity of the $V[TCNE]_x$ product, not to mention of the vanadium source. Using slower and more dilute solutions enabled the increasingly slower dropwise addition of reactants in solution to form the product, but even using a syringe pump this was not successful.

Slowing a reaction down via diffusing the reactants through a sol–gel is a known method that has been quite successful for many materials, and has been used to grow crystals of the quite air-sensitive, but not water sensitive, $KV[Cr(CN)_6] \cdot 2H_2O$ room-temperature Prussian blue-structured magnet [17j]. The medium used for sol–gel crystal growth is typically aqueous/alcohol based, which is completely incompatible with the reactants as well as the $V[TCNE]_x$ product, even under achievable anaerobic conditions (<1 ppm O_2). Hence, $V(C_6H_6)_2$ and TCNE were reacted using polystyrene and polyvinyl chloride gels, as they were similar to the solvents (toluene and CH_2Cl_2) that were typically used to form the bulk magnetic material. This procedure led to formation of an expected black precipitate, but it neither diffracted nor magnetically ordered.

An alternate route for the slow formation of $V[TCNE]_x$ would be to react a vanadium source with slow release source of TCNE. The in situ slow generation of TCNE would limit the rate of the formation of $V[TCNE]_x$, due to it low availability. TCNE is a dienophile and forms Diels-Alder products with numerous dienes, and while these products are quite stable, in principle this reaction is reversible. Due to the stability of the Diels-Alder products, virtually no release of the TCNE was expected; hence, one with reduced stability was sought, and a sterically hindered diene was targeted. 9,10-Dimethylanthracene (**3**) was identified as a sterically hindered diene, and its Diels-Alder product with TCNE (**4**) forms [40]. The rate constant for the dissociation of **4** to **3** and TCNE is reported to be $2 \times 10^{-4}\ s^{-1}$ at 25 °C in 1,2-$C_2H_4Cl_2$, hence, it was suitable slow-release source for TCNE. The reaction of **4**, which slowly generates TCNE, slowly reacts with $V(C_6H_6)_2$ and $V(CO)_6$ to form an expected black precipitate over a several day period, but while paramagnetic, it neither diffracted nor magnetically ordered. Hence, these, and other attempts to slowly form a more crystalline form of the $V[TCNE]_x$ magnet were not only unsuccessful, but did not form a magnetically ordered material. The later may be due to the known thermal instability of the $V[TCNE]_x$ magnet whereby the magnetic ordering is lost upon thermal treatment [1–3]. The vanadyl-containing compound **5** has been identified as a thermal/oxidative product [41].





These results suggest that the $V[TCNE]_x$ room temperature magnet is a kinetic product, and the thermodynamic product does not magnetically order; hence, preparing a crystalline kinetic product will be challenging.

5. Current status of the structure of $V[TCNE]_x$

The formulation $V^{II}[TCNE]^-_z[TCNE]^{2-}_{1-z/2}$ $(1 < z < 2)$ for $V[TCNE]_x$ $(x = 1 + z/2)$ is sufficient to explain its observed ν_{CN} IR absorptions, elemental percentages, XANES, EXAFS, XPS, and magnetization data [42]. Foremost is the presence of ν_{CN} IR absorptions characteristic of $[TCNE]^{2-}$. This differs from $Fe^{II}[TCNE]_2$ and $[Fe^{II}[TCNE](NCMe)_2][Fe^{III}Cl_4]$ which lack both these absorptions and $[TCNE]^{2-}$. $Fe^{II}[TCNE]_2$, however, possesses $[C_4(CN)_8]^{2-}$, and like $[C_4(CN)_8]^{2-}$ $[TCNE]^{2-}$ is envisioned to bridge the Fe^{II}-[μ_4-$[TCNE]^{\cdot-}$ layers. $[TCNE]^{2-}$ may twist, due to the free rotation about the central C–C single bond, but it is likely close to planar, perhaps due to geometrical constraints from the lattice. This is a plausible description for the limiting $z = 1$ case. Thus, this limiting structure could possess a layered (2-D) structure, as observed for $Fe^{II}[TCNE]_2 \cdot yCH_2Cl_2$ and $[Fe^{II}[TCNE](NCMe)_2][Fe^{III}Cl_4]$, and while stronger magnetic coupling between $[TCNE]^{\cdot-}$ and V^{II} with respect to Fe^{II}, as discussed above, is expected, the isotropic nature of the $S = 1/2$ $[TCNE]^{\cdot-}$ and $S = 3/2$ V^{II} spin sites is inconsistent with 2-D Ising magnetic ordering.

The mechanism for the formation of $[TCNE]^{2-}$ {as well as $V[TCNE]_x$} and why $Fe^{II}[TCNE]_2$ possesses $[TCNE]^{2-}$ and not $[C_4(CN)_8]^{2-}$ are unknown, but lower ionization potential of vanadium with respect to iron likely is important.

The presence of both μ_4-$[TCNE]^{\cdot-}$ and μ_4-$[TCNE]^{2-}$, especially planar μ_4-$[TCNE]^{2-}$, about each V^{II} site should enable facile electron hopping among these sites randomizing the location of the reduced TCNE's and enabling the observed relatively high dc electrical conductivity, and forming an extended 3-D magnetic structure, and explain the observed T_c that exceeds room temperature.

For the limiting $z = 2$ case, planar $[TCNE]^{\cdot-}$ is envisioned to bridge the $Fe^{II} - [\mu_4 - TCNE]^{\cdot-}$ layers, as *trans*-μ-$[TCNE]^{\cdot-}$ forming an extended 3-D magnetic structure, and for the observed solid solution where $1 < z < 2$ an appropriate random distribution of $[TCNE]^{\cdot-}$ and $[TCNE]^{2-}$ would exist.

This intralayer replacement of μ_4-$[TCNE]^{2-}$ with *trans*-μ-$[TCNE]^{\cdot-}$ suggests a lattice mismatch; however, suitable distances can be accommodated by substantially reducing the idealized 180° M–N–C angle, as occurs for $[MnTP^*P][TCNE] \cdot 2PhMe$ [37]. Furthermore, in addition to the additional direct magnetic coupling, the attenuated M–N–C angle should lead to stronger intralayer coupling.

These to two limiting structures should exhibit some degree crystalline order, and, thus, diffract to some extent, which does not occur. These limiting structures, however, could exit in different regions, inter-grow, or occur randomly, with very small spatial domains such that diffraction is sufficiently broadened such that it is not evident. More likely, such very small spatial domains results for the instantaneous formation of $V[TCNE]_x$, and based on TEM data, which show a featureless morphology, it is a glassy material. Hence, the lack of diffraction is most likely due to $V[TCNE]_x$ being a glassy material, i.e. an inhomogeneous, nonstoichiometric material composed differing components and linkages, as exists for window glass or coal. Nonetheless, several attempt to grow a more crystalline form of the $V[TCNE]_x$ magnet was pursued.

This is in contrast the formation of $Fe[TCNE]_2$ that requires several days by either the reaction of $Fe(CO)_5$ or $FeI_2 \cdot x$MeCN with TCNE [43], and yields magnetic materials that diffract [9]. Retardation of the rate of $V[TCNE]_x$ formation; however, neither resulted in a form that diffracted, nor magnetically order. The later is attributed thermal instability of $V[TCNE]_x$ whereby the magnetic order-

ing is lost upon thermal treatment [1–3], and suggests that the $V[TCNE]_x$ room temperature magnet is a kinetic product, and the thermodynamic product does not magnetically order. Thus, formation a diffracting kinetic phase of the $V[TCNE]_x$ room temperature magnet will be demanding.

The $V^{II}[TCNE]^{-}{}_{z}[TCNE]^{2-}{}_{1-z/2}$ formulation is in accord with the observed physical and chemical properties. This is simplest formulation as some V^{III} as well as other reduced forms of TCNE than the $[TCNE]^{\cdot-}$ and $[TCNE]^{2-}$ species may be present, and vary in occurrence within and between samples. Additionally, structural defects such that terminal, *cis*-1,1-, *cis*-1,2-, *trans*-1,2-μ-$[TCNE]^{\cdot-}$, μ_3-$[TCNE]^{\cdot-}$ and $[TCNE]^{2-}$ etc. may be present to enhance the complexity of the material, and further contribute to its disordered and amorphous nature.

This description for $V[TCNE]_x$ room temperature magnet lacks many answers and begs a plethora of additional questions, but provides for a status report from the author's perspective. As such, future studies will provide additional data to enable greater clarity of the description of this material, and undoubtedly new perspectives will emerge.

Acknowledgments

We appreciate the helpful discussions with Prof. Arthur J. Epstein (The Ohio State University), Konstantin I. Pokhodnya (North Dakota State University), Prof. Fernando Palacio (Universidad de Zaragoza), and William W. Shum (University of Utah), and the continued partial support by the Department of Energy Division of Materials Science (Grant Nos. DE-FG03-93ER45504 and DE-FG02-01ER4593) and Army Research Office (Grant No. DAAD19-01-1-0562) is appreciated.

References

[1] (a) J.M. Manriquez, G.T. Yee, R.S. McLean, A.J. Epstein, J.S. Miller, Science 252 (1991) 1415;
(b) J.S. Miller, G.T. Yee, J.M. Manriquez, A.J. Epstein, in: The Proceedings of Nobel Symposium #NS-81 Conjugated Polymers and Related Materials: The Interconnection of Chemical and Electronic Structure, Oxford University Press, 1993, 461; La Chim. La Ind. 1992, 74, p. 845.;
(c) J.S. Miller, A.J. Epstein, J. Chem. Soc., Chem. Commun. (1998) 1319.
[2] J. Zhang, P. Zhou, W.B. Brinckerhoff, A.J. Epstein, C. Vazquez, R.S. McLean, J.S. Miller, A. C. S. Sym. Ser. 644 (1996) 311.
[3] (a) K.I. Pokhodnya, A.J. Epstein, J.S. Miller, Adv. Mater. 12 (2000) 410;
(b) K.I. Pokhodnya, D. Pejakovic, A.J. Epstein, J.S. Miller, Phys. Rev. B 63 (2001) 174408.
[4] D. Haskel, Z. Islam, J. Lang, C. Kmety, G. Stajer, K.I. Pokhodnya, A.J. Epstein, J.S. Miller, Phys. Rev. B 70 (2004) 054422.
[5] (a) P. Chandrasekhar, P.H. Bird, Inorg. Chim. Acta 97 (1985) L31;
(b) D.A. Clemente, Inorg. Chim. Acta 358 (2005) 1725;
(c) P.B. Hitchcock, D.L. Hughes, G.J. Leigh, J.R. Sanders, J. de Souza, C.J. McGarry, L.F. Larkworthy, J. Chem. Soc. Dalt. Trans. (1994) 3683;
(d) Z. Janas, L.B. Jerzykiewicz, S. Przybylak, R.L. Richards, P. Sobota, Organometallics 19 (2000) 4252.
[6] V.N. Prigodin, N.P. Raju, K.I. Pokhodnya, J.S. Miller, A.J. Epstein, Adv. Mater. 14 (2002) 1230.
[7] (a) S.A. Wolf, J. Supercond. 13 (2000) 195;
(b) G. Prinz, Science 282 (1998) 1660;
(c) H. Ohno, F. Matsukura, Solid State Commun. 117 (2001) 179.
[8] (a) A.L. Tchougéeff, R. Hoffmann, J. Phys. Chem. 97 (1993) 350;
(b) A.L. Tchougéeff, R. Dronskowski, J. Compd. Chem. 29 (2008) 2220. A computational study based on this geometry has recently been reported.
[9] (a) J.-H. Her, P.W. Stephens, K.I. Pokhodnya, M. Bonner, J.S. Miller, Angew. Chem. Int. Ed. 46 (2007) 1521;
(b) J.-H. Her, P.W. Stephens, K.I. Pokhodnya, M. Bonner, J.S. Miller, Angew. Chem. 119 (2007) 1543.
[10] K.I. Pokhodnya, M. Bonner, J.-H. Her, P.W. Stephens, J.S. Miller, J. Am. Chem. Soc. 126 (2006) 15592.
[11] (a) R.A. Heintz, H. Zhao, X. Ouyang, G. Grandinetti, J. Cowen, K.R. Dunbar, Inorg. Chem. 38 (1999) 144;
(b) H. Hartmann, W. Kaim, I. Hartenbach, T. Schleid, M. Wanner, J. Fiedler, Angew. Chem. Int. Ed. 40 (2001) 2842;
(c) L. Shields, J. Chem. Soc. Faraday Trans. 2 (1985) 81;
(d) S.A. O'Kane, R. Clerac, H. Zhao, X. Ouyang, J.R. Galan-Mascaros, R. Heintz, K.R. Dunbar, J. Solid State Chem. 152 (2000) 159;
(e) S. Shimomura, R. Matsuda, T. Tsujino, T. Kawamura, S. Kitagawa, J. Am. Chem. Soc. 128 (2006) 16416.
[12] H. Miyasaka, C.S. Campos-Fernandez, R. Clerac, K.R. Dunbar, Angew. Chem. Int. Ed. 39 (2000) 3831.
[13] M. Verdaguer, A. Bleuzen, V. Marvaud, J. Vaissermann, M. Seuleiman, C. Desplanches, A. Scuiller, C. Train, R. Garde, G. Gelly, C. Lomenech, I. Rosenman, P. Veillet, C. Cartier, F. Villain, Coord. Chem. Rev. 190–192 (1999) 1023.
[14] H. Tanaka, N. Okawa, T. Kawai, Solid State Commun. 110 (1999) 191;
J.E. Greedan, C.-L. Chien, R.G. Johnston, J. Solid State Chem. 19 (1976) 155;
J.E. Greedan, Phys. Chem. Solids 32 (1971) 819;
Y. Kimishima, Y. Ichiyanagi, K. Shimizu, T. Mizuno, J. Magn. Magn. Mater. 210 (2000) 244;
T.E. Vos, Y. Liao, W.W. Shum, J.-H. Her, P.W. Stephens, W.M. Reiff, J.S. Miller, J. Am. Chem. Soc. 126 (2004) 11630.
[15] Assumes 3-D system for which the Mean Field model was intended.
[16] Note that using Eq. (2), a 5.5-K J is calculated for $Mn[TCNE]_2$ based on its 75 K T_c, and being less than that for Fe is at variance with that observed for Prussian blue structured magnets.
[17] (a) T. Mallah, S. Thiébaut, M. Verdaguer, P. Veillet, Science 262 (1993) 1554;
(b) S. Ferlay, T. Mallah, R. Ouahes, P. Veillet, M. Verdaguer, Nature 378 (1995) 701;
(c) W.E. Buschmann, S.C. Paulson, C.M. Wynn, M. Girtu, A.J. Epstein, H.S. White, J.S. Miller, Adv. Mater. 9 (1997) 645;
(d) W.E. Buschmann, S.C. Paulson, C.M. Wynn, M. Girtu, A.J. Epstein, H.S. White, J.S. Miller, Chem. Mater. 10 (1998) 1386;
(e) E. Dujardin, S. Ferlay, X. Phan, C. Desplanches, C.C.D. Moulin, P. Sainctavit, F. Baudelet, E. Dartyge, P. Veillet, M.J. Verdaguer, Am. Chem. Soc. 120 (1998) 11347;
(f) S. Ferlay, T. Mallah, R. Ouahes, P. Veillet, M. Verdaguer, Inorg. Chem. 38 (1999) 229;
(g) M. Verdaguer, A. Bleuzen, C. Train, R. Garde, F. Fabrizi de Biani, C. Desplanches, Phil. Trans. R. Soc. Lond. A 357 (1999) 2959;
(h) K. Hashimoto, S. Ohkoshi, Phil. Trans. R. Soc. Lond. A 357 (1999) 2977;
(i) Ø. Hatlevik, W.E. Buschmann, J. Zhang, J.L. Manson, J.S. Miller, Adv. Mater. 11 (1999) 914;
(j) S.M. Holmes, G.S. Girolami, J. Am. Chem. Soc. 121 (1999) 5593;
(k) M. Verdaguer, G.S. Girolami, in: J.S. Miller, M. Drillon (Eds.), Magnetism Molecules to Materials, Wiley-VCH, Weinheim, 2005, p. 283.
[18] S.-i. Ohkoshi, K. Hashimoto, J. Am. Chem. Soc. 121 (1999) 10591.
[19] Since $S = 3/2$ for V(II) and 2 for Fe(II), the $S(S+1)$ contribution to T_c would suggest an higher T_c for Fe than V assuming constant J.
[20] J.S. Miller, A.O. Goedde, J. Chem. Ed. 50 (1973) 431.
[21] (a) e.g. obs: %C = 44.61; %N = 35.42; %H = 0.025; and %V = 19.77 (sum = 99.80%) was fit to $V[TCNE]_x$ film (x = 1.58: calculated: %C = 44.95; %N = 34.94; %H = 0.0; and %V = 20.11).;
(b) The best fit for $V^{o}_{x}[V[TCNE]_2$ is for $x = 0.23$ calculated: %C = 45.21 (+0.60%); %N = 35.14 (+0.28%); %H = 0.0; and %V = 19.65 (−0.12%), and is poorer than for (a). The detection limit for V^{o} or V^{III} are <5% from the XANES/EXAFS studies [4].
[22] J.S. Miller, Angew. Chem. Int. Ed. Engl. 45 (2006) 2508.
[23] (a) J. Zhang, L.M. Liable-Sands, A.L. Rheingold, R.E. Del Sesto, D.C. Gordon, B.M. Burkhart, J.S. Miller, J. Chem. Soc., Chem. Commun. (1998) 1385;
(b) K.I. Pokhodnya, M. Bonner, A.G. Dipasquale, A.L. Rheingold, J.S. Miller, Chem. Eur. J. 14 (2008) 714;
(c) G. Wang, C. Slebodnick, G.T. Yee, Inorg. Chem. 46 (2007) 9641.
[24] R. Choukroun, C. Lorber, D. de Caro, L. Vendier, Organometallics 25 (2006) 4243.
[25] G.T. Yee, J.C. Calabrese, C. Vazquez, J.S. Miller, Inorg. Chem. 32 (1993) 377.
[26] (a) R.E. Del Sesto, J.S. Miller, J.J. Novoa, P. Lafuente, Chem. Eur. J. 8 (2002) 4894;
(b) J.S. Miller, J.J. Novoa, Acc. Chem. Res. 40 (2007) 189.
[27] Recently reported examples of μ-$[TCNE]_2^{2-}$ bridging to M^{II} ions two are plausible, but more likely μ_4 or μ_8 -$[TCNE]_2^{2-}$ bridging would be needed. see: Wang, G.; Zhu, H.; Fan, J.; Slebodnick, C.; Yee, G. T. Inorg. Chem. 2006, 48, 1406;
G. Wang, C. Slebodnick, G.T. Yee, Inorg. Chim. Acta 361 (2008) 3593.
[28] (a) D.C. Gordon, L. Deakin, A.M. Arif, J.S. Miller, J. Am. Chem. Soc. 122 (2000) 290;
(b) E.B. Vickers, T.D. Selby, J.S. Miller, J. Am. Chem. Soc. 126 (2004) 3716.
[29] (a) C. Elschenbroich, J. Hurley, B. Metz, W. Massa, G. Baum, Organometallics 9 (1990) 889;
(b) C. Elschenbroich, R. Bar, E. Bilger, D. Mahrwald, M. Nowotny, B. Metz, Organometallics 12 (1993) 3373;
(c) A.M. Bond, F.A. Cotton, Inorg. Chem. 15 (1976) 2036.
[30] S.L. Schiavo, G. Bruno, P. Zanello, F. Laschi, P. Piraino, Inorg. Chem. 36 (1997) 1004.
[31] This is attributed to an associative reaction leading to disproportionation of $V(CO)_6$ as occurs for $V(CO)_6$ and MeCN T.G. Richmond, Q.-Z. Shi, W.C. Trogler, F. Basolo, J. Am. Chem. Soc. 106 (1984) 76;
Q.-Z. Shi, T.G. Richmond, W.C. Trogler, F. Basolo, J. Am. Chem. Soc. 106 (1984) 71.
[32] F.A. Cotton, G.E. Lewis, W. Schwotzer, Inorg. Chem. 25 (1986) 3528.
[33] Clearly the presence of both monoreduced forms of TCNE and $[TCNE]^{2-}$ will lead to a TCNE:V (x) ratio <2.

[34] (a) D.A. Dixon, J.S. Miller, J. Am. Chem. Soc. 109 (1987) 3656;
(b) R. Fox, B.M. Foxman, D. Guerrer, J.S. Miller, A.H. Reis Jr., J. Mater. Chem. 6 (1996) 1627.
[35] G. Du, J. Joo, A. J. Epstein, J. S. Miller, *J. Appl. Phys.* **1993**, 73, 6566. K. I. Pokhodnya, A. J. Epstein, J. S. Miller, in preparation.
[36] D.M.P. Mingos, Essential Trends in Inorganic Chemistry, Oxford University Press, Oxford, UK, 1998. p. 335.
[37] A. Böhm, C. Vazquez, R.S. McLean, J.C. Calabrese, S.E. Kalm, J.L. Manson, A.J. Epstein, J.S. Miller, Inorg. Chem. 35 (1996) 3083.
[38] E.J. Brandon, C. Kollmar, J.S. Miller, J. Am. Chem. Soc. 120 (1998) 1822;
J.-H. Her, P. W. Stephens, J. D. Bagnato, J. S. Miller, in preparation.
[39] $r_{ave} = 3/S_a\ \rho$, where S_a is the surface area and ρ is the density.
[40] V.D. Kislev, V.B. Malkov, A.I. Konovalov, Zh. Organ. Khim. 26 (1990) 229.
[41] L.G. Klapshima, I.S. Grigoryev, W.E. Douglas, A.I. Trifonov, I.D. Gudilenkov, V.V. Seminov, B.A. Buskuk, ChemComm. (2007) 1942.
[42] Note the caveats and possibility of other forms of $[TCNE]^{\cdot-}$, e.g. $[TCNE]_2^{2-}$ and $[C_4(CN)_8]^{2-}$, as well as V^{III}, being present.
[43] (a) J. Zhang, J. Ensling, V. Ksenofontov, P. Gütlich, A.J. Epstein, J.S. Miller, Angew. Chem. Int. Ed. 37 (1998) 657;
(b) K.I. Pokhodnya, N. Petersen, J.S. Miller, Inorg. Chem. 41 (2002) 1996.

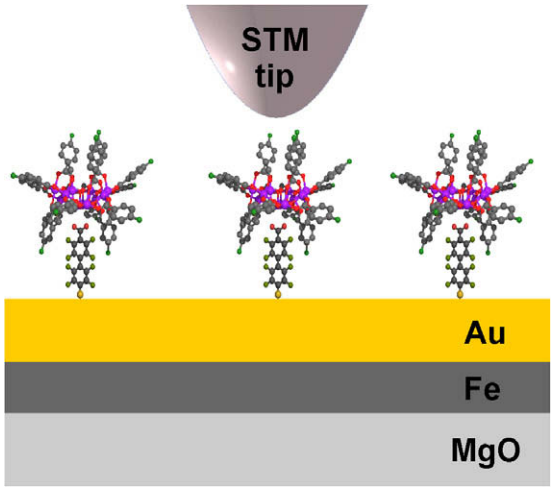


Fig. 1. Schematic representation of the STM investigation of Mn_{12}-pfb deposited on Au(100)/Fe(100)/MgO(100) via ligand exchange reaction with 4-MOBCA.

evaporated onto MgO from an electron beam evaporator at room temperature at a rate of 1.5 Å/min. (3) After the Fe deposition the sample was annealed at 870 K for 30 min. (4) Finally, Au was evaporated from a thermal evaporator (effusion cell) at a rate of 6.5 Å/min at a sample temperature of 600 K. After the preparation and investigation of Au(100)/Fe(100)/MgO(100), Mn_{12}-pfb was deposited on the surface via ligand exchange reaction with 4-MOBCA as described elsewhere [10e]. A sketch of the sample configuration is shown in Fig. 1. STM, STS and X-ray photoelectron spectroscopy (XPS) measurements were performed in an Omicron Multiprobe UHV system at room temperature. For the STM/STS measurements, electrochemically etched tungsten tips, flash-annealed by electron bombardment were used. XPS spectra were obtained with Al Kα radiation ($h\nu$ = 1486.6 eV) with the resolution of the EA 125 energy analyzer set to 0.65 eV.

3. Results and discussion

Fig. 2 shows two STM images obtained from Fe(100)/MgO(100) (a; 16 nm thick iron layer) and from Au(100)/Fe(100)/MgO(100) (b; 20 nm thick gold layer). In Fig. 2a, Fe terraces along with monoatomic steps with perpendicular edges are visible which is in agreement with previous studies [15a,b]. Fig. 2b shows terraces and monoatomic steps of the Au(100) surface. The inset of Fig. 2b shows the surface reconstruction of Au(100) which appears as a straight line pattern in contrast to the herringbone reconstruction of Au(111). The surface morphology is in agreement with previous studies [16]. In the present study, the preparation parameters were optimized to fabricate surfaces with low roughness and sufficiently large Au terraces facilitating the addressing of Mn_{12} monolayers deposited on the surface by means of STM.

Fig. 3 shows an STM image obtained after deposition of Mn_{12}-pfb on Au(100)/Fe(100)/MgO(100) via ligand exchange reaction with 4-MOBCA. A monolayer of clusters is visible which is in agreement with previous STM studies on Mn_{12} monolayers deposited on Au(111) single crystals [10e,12a]. The shape of the subjacent terraces and steps can be estimated due to slight differences of the apparent height that are visible in the image. The individual molecules have been further investigated by means of scanning tunneling spectroscopy (STS; see inset of Fig. 3) which revealed the presence of a large conductance gap in agreement with previous studies [17]. In addition, XPS confirmed the presence of the Mn 2p peaks also observed in previous works (see Fig. 4) [10e,12a]. The agreement with previous studies demonstrates that Mn_{12}-pfb was successfully deposited on Au(100)/Fe(100)/MgO(100). Furthermore, the results demonstrate that details of the gold surface morphology, like different surface reconstructions or terrace shapes in the case of Au(100) and Au(111) do not significantly influence the arrangement of the Mn_{12} molecules. This observation is in agreement with a previous study which suggested a statistical arrangement of Mn_{12} on 4-MOBCA/Au [10e].

To investigate a possible influence of the wet chemical deposition of Mn_{12} on the properties of the Au-covered iron layer, XPS measurements were performed in order to detect a possible oxidation of the iron. Fig. 5a shows a Fe 2p spectrum obtained from Fe(100)/MgO(100). The peak positions (Fe $2p_{1/2}$: 719.9 eV, Fe

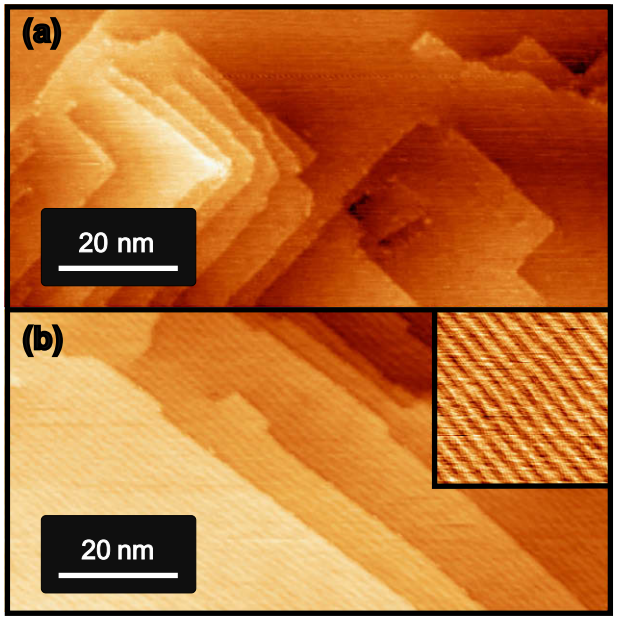


Fig. 2. STM images (100 × 50 nm^2) of (a) Fe(100)/MgO(100) and (b) Au(100)/Fe(100)/MgO(100). The inset of (b) shows a 20 × 20 nm^2 STM image of the surface reconstruction of Au(100).

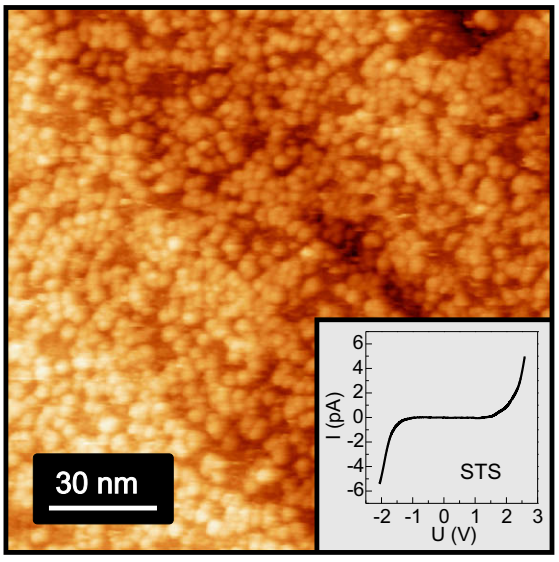


Fig. 3. STM image (150 × 150 nm^2) of Mn_{12}-pfb molecules (U_T = 2.5 V; I_T = 8.6 pA). The inset shows an STS spectrum of a single Mn_{12}-pfb molecule obtained at a set voltage of 2.7 V (set current 6.9 pA).

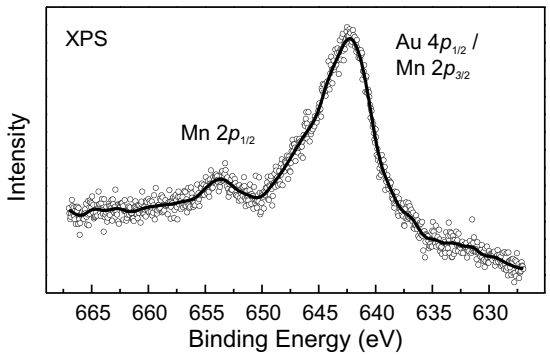


Fig. 4. XPS Mn 2*p*/Au 4$p_{1/2}$ spectrum obtained after deposition of Mn_{12}-pfb on Au(100)/Fe(100)/MgO(100).

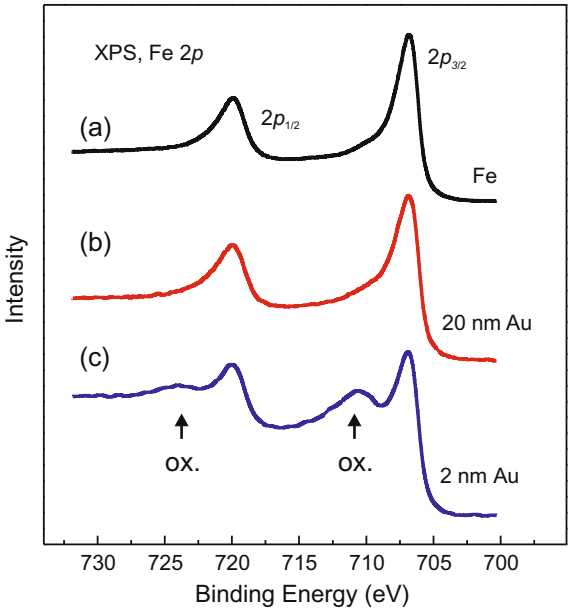


Fig. 5. XPS Fe 2*p* spectra of (a) Fe(100)/MgO(100) (after in situ Fe evaporation), (b) Mn_{12}-pfb on Au(100)[20 nm]/Fe(100)/MgO(100) after removal of Mn_{12}, 4-MOBCA, and Au via sputtering, (c) Mn_{12}-pfb on Au(100)[2 nm]/Fe(100)/MgO(100) after removal of Mn_{12}, 4-MOBCA, and Au via sputtering.

$2p_{3/2}$: 706.8 eV) as well as the shape of the spectrum are consistent with metallic iron [18]. This measurement was performed immediately after the deposition of Fe on MgO. It is well known that removing the unprotected iron layer from the UHV would result in an oxidation. Hence, sensitive samples are usually covered with protection layers like gold thin films prior to sample transfers or further processing. Nevertheless, it is important to carefully investigate the Mn_{12}/Au(100)/Fe(100)/MgO(100) system since the adopted preparation steps (immersion in solvents [19], possibly corrosive 4-MOBCA etc.) are significantly different from an ordinary sample transfer. To study a possible oxidation of the iron layer during the preparation ex situ, the Mn_{12}/4-MOBCA/Au(100) layers had to be removed from the sample because the information depth of XPS is limited to a few nm [20]. To this end, the sample was continually sputtered with Ar^+ ions at 800 eV for 10 min in each step. After each sputtering cycle, an XPS spectrum was recorded. Due to the XPS information depth of a few nm the transition from a pure Au to a mixed Au/Fe signal could be easily identified and the sputtering was terminated at this time to avoid an accidental removal of a possibly oxidized iron layer. Subsequently, a XPS Fe 2*p* spectrum was recorded. Fig. 5b shows the spectrum obtained from the sample previously covered with Mn_{12}. The spectrum coincides with those of metallic iron and thus provides evidence that the iron layer was not oxidized. In the next step, a control experiment was performed with an only 2 nm thick Au layer while all different parameters and preparation steps were identical to those of the previous sample. Fig. 5c shows an Fe 2*p* spectrum that reveals the occurrence of additional Fe 2*p* peaks after the exposure to ambient conditions. The comparison of the position of the additional Fe $2p_{3/2}$ peak (710.5 eV) with previous studies indicates a partial oxidation of the iron layer [18].

The comparison of the XPS spectra demonstrates that the iron layer underneath the 20 nm Au layer is not oxidized during the wet chemical deposition of Mn_{12} while in the case of a thin layer an oxidation cannot be ruled out. This observation suggests a trade-off between oxidation protection and spin polarization. Although the spin diffusion length in Au can be significantly larger than 20 nm [21], a thin buffer layer may be preferable to achieve a sufficient spin injection.

In conclusion, a possibility to fabricate samples for future spin-polarized transport studies on Mn_{12} single molecule magnets was investigated. The results demonstrate that Mn_{12} molecules can be deposited on Au(100)/Fe(100)/MgO(100) layer systems by means of wet chemical deposition methods without altering the metallic nature of the ferromagnetic iron which is required as a source for spin-polarized electrons. The insights will contribute to future transport studies on Mn_{12} and possibly different single molecule magnets.

Acknowledgement

This work was supported by the Deutsche Forschungsgemeinschaft (DFG) via the Collaborative Research Center (SFB) 767, project C5.

References

[1] D. Gatteschi, R. Sessoli, Angew. Chem., Int. Ed. 42 (2003) 268.
[2] G. Christou, D. Gatteschi, D.N. Hendrickson, R. Sessoli, MRS Bull. 25 (2000) 66.
[3] (a) J.R. Friedman, M.P. Sarachik, J. Tejada, R. Ziolo, Phys. Rev. Lett. 76 (1996) 3830;
(b) L. Thomas, F. Lionti, R. Ballou, D. Gatteschi, R. Sessoli, B. Barbara, Nature 383 (1996) 145;
(c) E. del Barco, A.D. Kent, S. Hill, J.M. North, N.S. Dalal, E.M. Rumberger, D.N. Hendrickson, N. Chakov, G. Christou, J. Low Temp. Phys. 140 (2005) 119;
(d) W. Wernsdorfer, N.E. Chakov, G. Christou, Phys. Rev. Lett. 95 (2005) 037203.
[4] (a) M. Misiorny, J. Barnas, Phys. Rev. B 75 (2007) 134425;
(b) F. Elste, C. Timm, Phys. Rev. B 73 (2006) 235305;
(c) M. Misiorny, J. Barnas, Phys. Rev. B 76 (2007) 054448.
[5] (a) P. Artus, C. Boskovic, J. Yoo, W.E. Streib, L.-C. Brunel, D.N. Hendrickson, G. Christou, Inorg. Chem. 40 (2001) 4199;
(b) R. Sessoli, H.-L. Tsai, A.R. Schake, S. Wang, J.B. Vincent, K. Folting, D. Gatteschi, G. Christou, D.N. Hendrickson, J. Am. Chem. Soc. 115 (1993) 1804.
[6] A. Cornia, A.C. Fabretti, M. Pacchioni, L. Zobbi, D. Bonacchi, A. Caneschi, D. Gatteschi, R. Biagi, U. del Pennino, V. de Renzi, L. Gurevich, H.S.J. van der Zant, Angew. Chem. 115 (2003) 1683.
[7] S.A. Wolf, D.D. Awschalom, R.A. Buhrman, J.M. Daughton, S. von Molnar, M.L. Roukes, A.Y. Chtchelkanova, D.M. Treger, Science 294 (2001) 1488.
[8] L. Bogani, W. Wernsdorfer, Nat. Mater. 7 (2008) 179.
[9] (a) R. Wiesendanger, H.-J. Güntherodt, G. Güntherodt, R.J. Gambino, R. Ruf, Phys. Rev. Lett. 65 (1990) 247;
(b) S. Krause, L. Berbil-Bautista, G. Herzog, M. Bode, R. Wiesendanger, Science 317 (2007) 1537.
[10] (a) L. Zobbi, M. Mannini, M. Pacchioni, G. Chastanet, D. Bonacchi, C. Zanardi, R. Biagi, U. del Pennino, D. Gatteschi, A. Cornia, R. Sessoli, Chem. Commun. (2005) 1640;
(b) A. Naitabdi, J.-P. Bucher, P. Gerbier, P. Rabu, M. Drillon, Adv. Mater. 17 (2005) 1612;
(c) M. Cavallini, M. Facchini, C. Albonetti, F. Biscarini, Phys. Chem. Chem. Phys. 10 (2008) 784;
(d) J. Gomez-Segura, J. Veciana, D. Ruiz-Molina, Chem. Commun. (2007) 3699;
(e) M. Burgert, S. Voss, S. Herr, M. Fonin, U. Groth, U. Rüdiger, J. Am. Chem. Soc. 129 (2007) 14362;

(f) S. Voss, O. Zander, M. Fonin, U. Rüdiger, M. Burgert, U. Groth, Phys. Rev. B 78 (2008) 155403.
[11] (a) M. Mannini, P. Sainctavit, R. Sessoli, C.C. dit Moulin, F. Pineider, M.-A. Arrio, A. Cornia, D. Gatteschi, Chem. Eur. J. 14 (2008) 7530;
(b) S. Voss, M. Fonin, U. Rüdiger, M. Burgert, U. Groth, Phys. Rev. B 75 (2007) 045102.
[12] (a) S. Voss, M. Burgert, M. Fonin, U. Groth, U. Rüdiger, Dalton Trans. (2008) 499;
(b) S. Voss, M. Fonin, L. Burova, M. Burgert, Y.S. Dedkov, A.B. Preobrajenski, E. Goering, U. Groth, A.R. Kaul, U. Ruediger, Appl. Phys. A. in press, doi: 10.1007/s00339-008-4911-6.
[13] L. Bogani, L. Cavigli, M. Gurioli, R.L. Novak, M. Mannini, A. Caneschi, F. Pineider, R. Sessoli, M. Clemente-Leon, E. Coronado, A. Cornia, D. Gatteschi, Adv. Mater. 19 (2007) 3906.
[14] (a) J.A. Stroscio, D.T. Pierce, A. Davies, R.J. Celotta, M. Weinert, Phys. Rev. Lett. 75 (1995) 2960;
(b) M. Getzlaff, J. Bansmann, G. Schönhense, Fresenius J. Anal. Chem. 353 (1995) 748;
(c) T. Ohkochi, K. Mibu, N. Hosoito, J. Phys. Soc. Jpn. 75 (2006) 104707.
[15] (a) A. Subagyo, H. Oka, G. Eilers, K. Sueoka, K. Mukasa, Jpn. J. Appl. Phys. 39 (2000) 3777;
(b) K. Thürmer, R. Koch, M. Weber, K.H. Rieder, Phys. Rev. Lett. 75 (1995) 1767.
[16] N. Spiridis, J. Korecki, Appl. Surf. Sci. 141 (1999) 313.
[17] S. Voss, M. Fonin, U. Rüdiger, M. Burgert, U. Groth, Appl. Phys. Lett. 90 (2007) 133104.
[18] V. Di Castro, S. Ciampi, Surf. Sci. 331–333 (1995) 294.
[19] W.R.T. Barden, S. Singh, P. Kruse, Langmuir 24 (2008) 2452.
[20] M.P. Seah, W.A. Dench, Surf. Interface Anal. 1 (1979) 2.
[21] J.-H. Ku, J. Chang, H. Kim, J. Eom, Appl. Phys. Lett. 88 (2006) 172510.

The "pump" and "probe" beams traversed the same optical path close to the sample, but the focusing lens was systematically removed from the way of the pump beam to obtain a large spot size of *ca.* 5 mm. Under these conditions the experiments could be repeated many times on the same sample without degrading it.

3. Results and discussion

3.1. Experimental observations

Vibrational spectroscopy is known to be a valuable tool to investigate spin crossover phenomena due to the strong electron-lattice coupling in these materials [7]. In particular, in the Fe(pyrazine)[$M(CN)_4$] (M = Pt, Pd, Ni) family of compounds the intensity ratio of various Raman modes have been identified as excellent markers to track the change of HS/LS fractions [8]. Notably, the mode characteristic of in-plane bending vibrations of the pyrazine ring is associated with two frequencies, around 647 and 677 cm^{-1} for HS and LS states, respectively [8,9], and these are selected to follow the light-induced spin state change (Fig. 1).

Fig. 1 reveals a typical photo-induced LS → HS spin transition observed in Fe(pyrazine)[$Pt(CN)_4$] by applying a single 20 mJ/cm^2 green pulse (532 nm) at 301 K. Such an excitation produces a marked colour change from deep red (LS state) to yellow-orange (HS state) of the irradiated sample area. This photoinduced state remains stable in ambient conditions for (at least) several weeks without particular storage precautions.

To investigate the efficiency of the spin conversion process as a function of the excitation power, we irradiated the same sample with single laser pulses of different energy and controlled the resulting spin state of the system by Raman spectroscopy (Fig. 2). After each measurement the sample was converted in the pure LS state (by cooling down to 240 K) and then slowly heated up to 298 K again. In this way we ensure that every experimental point in Fig. 2 corresponds to the spin transition from the pure LS state. Two observations deserve particular attention.

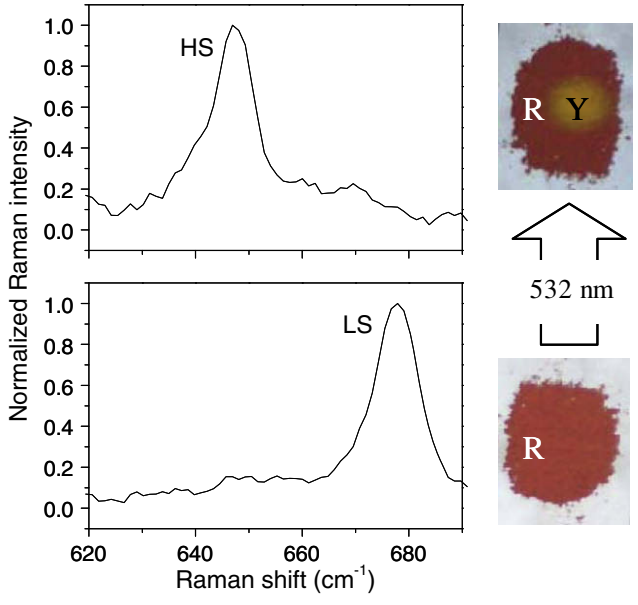


Fig. 1. Colour change (right) and Raman spectra (left) in the Fe(pyrazine)[$Pt(CN)_4$] powder sample before (bottom) and after (top) a single-shot irradiation of 20 mJ/cm^2 at 301 K. In the photographs, the powder sample is deep red (R) in the LS state and turns to yellow-orange (Y) in the HS state after the laser excitation. (For interpretation of the references to colour in this figure legend, the reader is referred to the web version of this article.)

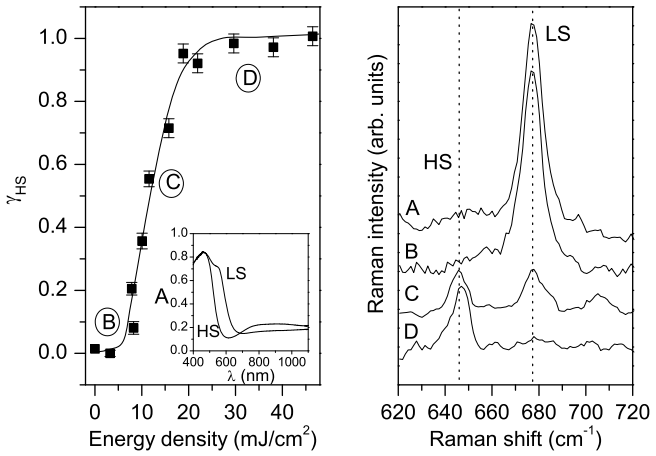


Fig. 2. Conversion efficiency as a function of the laser pulse energy density at 298 K (left panel) evaluated from the intensity ratio of spectral bands around 647 and 677 cm^{-1} (right panel). Typical spectra associated to the regions B, C and D are plotted in the right panel. The spectrum A was recorded before any pulsed excitation. A threshold energy density of *ca.* 5 mJ/cm^2 and a saturation value of *ca.* 20 mJ/cm^2 can be inferred. The inset shows absorption spectra in the HS and LS states extracted from diffuse reflectance measurements [4]. The solid line in the left panel is a guide for the eye.

First of all the observed 100% conversion efficiency (for high energy pulses) refers directly to the involvement of cooperative phenomena in this photo-induced phase transition. Indeed, as the absorption coefficient is significantly higher at 532 nm than at 633 nm in the LS state (inset of Fig. 2), the red probe beam penetrates necessarily deeper in the material than the green pump laser pulse. In the absence of interactions between the spin state changing iron ions, we should not observe a 100% spin conversion of the probed area since the thickness of the sample is much bigger than the laser penetration depth whatever the wavelength.

The occurrence of cooperative interactions is also confirmed by the existence of an energy density threshold (Fig. 2) in the conversion efficiency curve as has already been pointed out by several

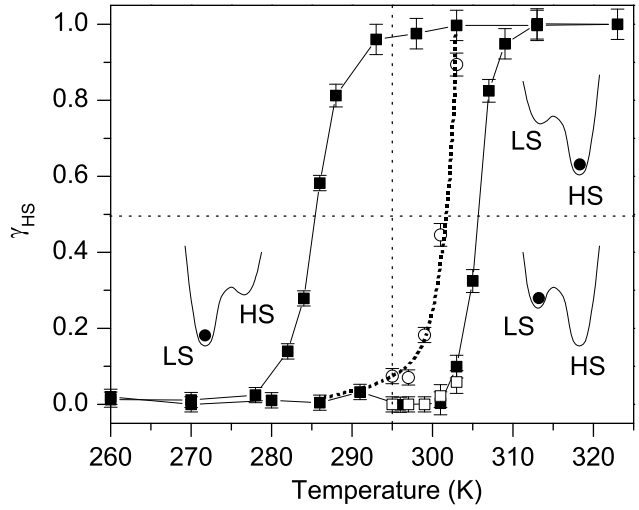


Fig. 3. Conversion efficiency as a function of the temperature for a fixed pulse energy density (11 mJ/cm^2) calculated from the intensity ratio of spectral bands around 645 and 675 cm^{-1}. Black squares describe the thermal hysteresis loop determined from Raman measurements, open squares the initial state of the material before excitation by the light pulse and open circles the final state after excitation. From 270 K up to T_c = 295 K, the system is in the stable LS state (see schematic free energy curves in inset). On heating from 295 K, the LS state becomes metastable and the stable HS state is progressively populated.

authors on various materials [3,10]. In our case three regions appear in the conversion efficiency versus energy density curve. Below the threshold value of *ca.* 5 mJ/cm^2, no conversion happens after a 532 nm laser shot (region B). The molecules remain in the LS state. It is important to note that the application of a large number of shots (typically 300 pulses at a rate of 1 Hz) weaker than 5 mJ/cm^2 did not affect the Raman spectra and thus the spin state of the system. Between 5 and 20 mJ/cm^2, the spin conversion efficiency increases rapidly with the energy density. The 677 cm^{-1} LS marker band sharply falls and the 647 cm^{-1} HS marker band grows (region C). Beyond 20 mJ/cm^2, a saturation corresponding to a pure HS state is reached (region D).

Fig. 3 shows the temperature dependence of the conversion on the ascending branch of the hysteresis loop induced by a fixed 11 mJ/cm^2 laser pulse energy. With increasing temperature the spin conversion efficiency rises significantly. It is noteworthy that conversion from both the metastable LS state to the stable HS state (above T_c) and from the stable LS state to the metastable HS state (below T_c) are possible, but the latter case is much less efficient at 11 mJ/cm^2 and requires a higher energy density to reach a full conversion (>27 mJ/cm^2).

3.2. Theoretical description

A qualitative explanation of the observed photo-induced spin state conversion can be proposed using the mean-field model of Slichter and Drickamer [11], as already suggested by Tokoro et al. for a Prussian blue analogue [12]. From this theoretical approach, the free energy (G) of a system whose thermal evolution of the HS fraction (γ_{HS}) exhibits an hysteresis loop is described by the equation

$$G = \gamma_{HS}\Delta H + \Gamma\gamma_{HS}(1-\gamma_{HS}) + T[R(\gamma_{HS}\ln\gamma_{HS} + (1-\gamma_{HS}) \times \ln(1-\gamma_{HS})) - \gamma_{HS}\Delta S], \quad (1)$$

where R is the gas constant, Γ is a phenomenological interaction parameter expressing the cooperative phenomena accompanying the spin crossover, ΔH (=$H_{HS} - H_{LS}$) is the transition enthalpy and ΔS (=$S_{HS} - S_{LS}$) the transition entropy.

Fig. 4 depicts the free energy of the system as a function of γ_{HS} in the temperature range of the hysteresis loop (286–310 K). The curves have been calculated using Eq. (1) with the parameters ΔH = 25 kJ mol^{-1}, ΔS = 84 J K^{-1} mol^{-1} and Γ = 7.11 kJ mol^{-1} in nice agreement with our previous investigations [5,13]. The larger parameter Γ compared to the value evaluated for single crystals allows for the wider hysteresis loop (24 K for the microcrystalline powder instead of 14 K for the single crystal [5]).

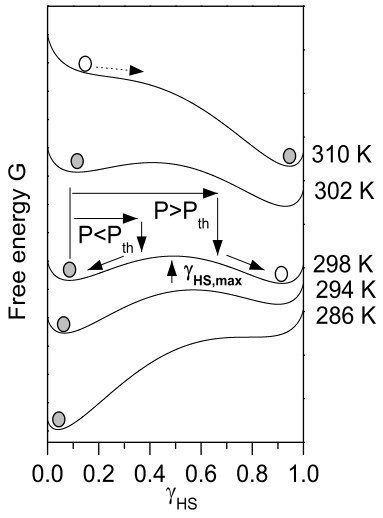


Fig. 4. Temperature dependence of the free energy as a function of the HS fraction calculated using Eq. (1) with the parameters ΔH = 25 kJ mol^{-1}, ΔS = 84 J K^{-1} mol^{-1} and Γ = 7.11 J mol^{-1}. Grey spheres indicate the thermal population and white spheres the photo-induced population with one laser shot at 532 nm.

The minimum of the potential energy curve increases from $\gamma_{HS} \approx 0$ to ≈ 1 with the temperature. At 298 K, an energy barrier stands at $\gamma_{HS} \approx 0.49$ (noted $\gamma_{HS,max}$). These potential energy curves provide information on the mechanism at the origin of the photo-excitation energy density threshold (P_{th}). Before irradiation the sample is in the LS state ($\gamma_{HS} \approx 0$). After a pulsed excitation is applied, the HS fraction rises instantaneously. When the converted HS fraction is lower than $\gamma_{HS,max}$, the system recovers its initial state. However, as soon as γ_{HS} exceeds $\gamma_{HS,max}$, the irradiated sample reaches a pure HS state. In the frame of our model, the material is considered homogeneous, that is as a single domain. Therefore the mixed states arising from either a distribution of complexes with different macroscopic energy barriers or the nucleation and growth of photo-induced spin domains [8,14] cannot be reproduced. The occurrence of such phenomena should be investigated by considering other models [15], which is far beyond the scope of this paper.

The decrease in the threshold value P_{th} under heating can be also understood with the potential energy curves of Fig. 4. Within the hysteresis loop, the value of $\gamma_{HS,max}$ depends on the temperature. For instance, $\gamma_{HS,max}$ is higher at 294 K ($\gamma_{HS,max}$ = 0.57) than at 298 K ($\gamma_{HS,max}$ = 0.49). To jump over the energy barrier located at $\gamma_{HS,max}$ at 298 K, a lower laser energy density is required, and consequently, for a given excitation energy density, the conversion efficiency will increase with temperature, which nicely matches our experimental results reported in Fig. 3. However we cannot exclude the possibility that some laser-induced heating is able to contribute more efficiently to the switching process at higher temperature.

4. Conclusions

The single-laser-pulse-induced LS to HS photo-conversion has been investigated on the polycrystalline SCO complex Fe(pyrazine)[Pt(CN)$_4$]. The main finding of this work is the clear observation of an energy density threshold of *ca.* 5 mJ/cm^2, below which no photo-induced phase transition occurs. On the other hand, above this value, a rapid increase in photoconversion occurs up to an energy density of *ca.* 20 mJ/cm^2. For higher values a complete phase transformation takes place. The experimental observation of the decrease of this threshold with increasing temperature is corroborated by a simple theoretical description which does not take nucleation and growth of spin domains into account.

Acknowledgements

This work was supported by the ANR project FASTSWITCH and a Grant-in-Aid for Creative Scientific Research. D.O. thanks JSPS (Japan) for financial support.

References

[1] (a) S. Decurtins, P. Gütlich, C.P. Köhler, H. Spiering, A. Hauser, Chem. Phys. Lett. 105 (1984) 1;
(b) A. Hauser, Chem. Phys. Lett. 124 (1986) 543.
[2] (a) E. Freysz, S. Montant, S. Létard, J.-F. Létard, Chem. Phys. Lett. 394 (2004) 318;
(b) J. Degert, N. Lascoux, S. Montant, S. Létard, E. Freysz, G. Chastanet, J.-F. Létard, Chem. Phys. Lett. 415 (2005) 206.
[3] H. Liu, A. Fujishima, O. Sato, Appl. Phys. Lett. 86 (2005) 122511.
[4] S. Bonhommeau, G. Molnár, A. Galet, A. Zwick, J.A. Real, J.J. McGarvey, A. Bousseksou, Angew. Chem., Int. Ed. 44 (2005) 4069.

[5] S. Cobo, D. Ostrovskii, S. Bonhommeau, L. Vendier, G. Molnár, L. Salmon, K. Tanaka, A. Bousseksou, J. Am. Chem. Soc. 130 (2008) 9019.
[6] V. Niel, M. Martínez-Agudo, M.C. Muñoz, A.B. Gaspar, J.A. Real, Inorg. Chem. 40 (2001) 3838.
[7] A. Bousseksou, J.J. McGarvey, F. Varret, J.A. Real, J.P. Tuchagues, A.C. Dennis, M.L. Boillot, Chem. Phys. Lett. 318 (2000) 409.
[8] G. Molnár, V. Niel, A.B. Gaspar, A. Zwick, J.A. Real, A. Bousseksou, J.J. McGarvey, J. Phys. Chem. B 106 (2002) 9701.
[9] G. Molnár, A. Bousseksou, A. Zwick, J.J. McGarvey, Chem. Phys. Lett. 367 (2003) 593.
[10] (a) S. Koshihara, Y. Tokura, K. Takeda, T. Koda, Phys. Rev. Lett. 68 (1992) 1148;
(b) S. Koshihara, Y. Tokura, K. Takeda, T. Koda, Phys. Rev. B 52 (1995) 6265;
(c) S. Koshihara, I. Takahashi, H. Sakai, Y. Tokura, T. Luty, J. Phys. Chem. B 103 (1999) 2592;
(d) N. Hosaka, H. Tachibana, N. Shiga, M. Matsumoto, Y. Tokura, Phys. Rev. Lett. 82 (1999) 1672;
(e) E. Collet, M.-H. Lemée-Cailleau, M. Buron-Le Cointe, H. Cailleau, M. Wulff, T. Luty, S.-Y. Koshihara, M. Meyer, L. Toupet, P. Rabiller, S. Techert, Science 300 (2003) 612;
(f) H. Matsuzaki, T. Matsuoka, H. Kishida, K. Takizawa, H. Miyasaka, K. Sugiura, M. Yamashita, H. Okamoto, Phys. Rev. Lett. 90 (2003) 046401;
(g) H.W. Liu, K. Matsuda, Z.Z. Gu, K. Takahashi, A.L. Cui, R. Nakajima, A. Fujishima, O. Sato, Phys. Rev. Lett. 90 (2003) 167403;
(h) M. Chollet, L. Guerin, N. Uchida, S. Fukaya, H. Shimoda, T. Ishikawa, K. Matsuda, T. Hasegawa, A. Ota, H. Yamochi, G. Saito, R. Tazaki, S. Adachi, S. Koshihara, Science 307 (2005) 86.
[11] C. Slichter, H. Drickamer, J. Chem. Phys. 56 (1972) 2142.
[12] H. Tokoro, T. Matsuda, K. Hashimoto, S. Ohkoshi, J. Appl. Phys. 97 (2005) 10M508.
[13] T. Tayagaki, A. Galet, G. Molnár, M. Muñoz, A. Zwick, K. Tanaka, J. Real, A. Bousseksou, J. Phys. Chem. B 109 (2005) 14859.
[14] (a) E. Collet, M.B.L. Cointe, H. Cailleau, J. Phys. Soc. Jpn. 75 (2006) 011002;
(b) Y. Ogawa, S. Koshihara, K. Koshino, T. Ogawa, C. Urano, H. Takagi, Phys. Rev. Lett. 84 (2000) 3181;
(c) S. Pillet, J. Hubsch, C. Lecomte, Eur. Phys. J. B 38 (2004) 541;
(d) Y. Moritomo, M. Kamiya, A. Nakamura, A. Nakamoto, N. Kojima, Phys. Rev. B 73 (2006) 012103;
(e) K. Ichiyanagi, J. Hebert, L. Toupet, H. Cailleau, P. Guionneau, J.F. Létard, E. Collet, Phys. Rev. B 73 (2006) 060408.
[15] (a) M. Nishino, S. Miyashita, K. Boukheddaden, J. Chem. Phys. 118 (2003) 4594;
(b) O. Sakai, M. Ishii, T. Ogawa, K. Koshino, J. Phys. Soc. Jpn. 71 (2002) 2052.

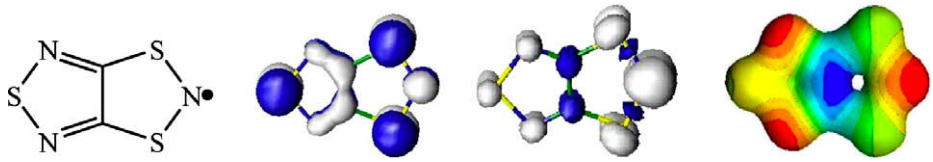


Fig. 1. Left to right: molecular structure, SOMO (white indicates positive values and blue negative ones), spin density (white indicates positive values and blue negative ones), and molecular electrostatic potential map (MEP map, red indicates regions of negative electron density, minimum −0.15259 atomic units, and blue regions of positive electron density, maximum +0.28326 a.u.) of **1**.

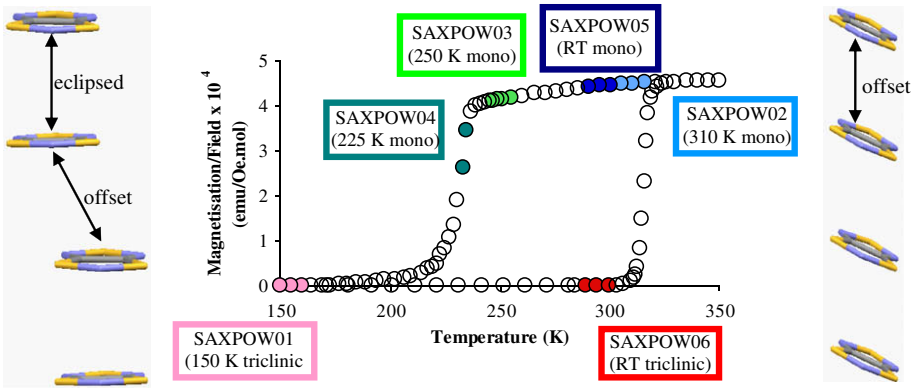


Fig. 2. *Centre*: Magnetization curve of **1** as a function of the temperature (two polymorphs are known, and their structures have been recorded at various temperatures, as identified in the figure); *Left*: structure of one of the stacks in the low temperature (triclinic) phase; *Right*: structure of one of the stacks in the high temperature (monoclinic) phase.

level provides values [2,3] of $J_{intra} = -220\ cm^{-1}$ and $J_{inter} = -42\ cm^{-1}$ (both J_{AB} values refer to the $\hat{H} = -2\Sigma_{A>B} J_{AB}\hat{S}_A\hat{S}_B$ Heisenberg Hamiltonian). In our studies, we began by investigating the mechanism of the magnetic interaction of both polymorphic forms using the first principles bottom-up methodology [7]. In this work we report the results for the high temperature phase as the first step in the study. The first principles bottom-up procedure is an advanced theoretical methodology that derives the macroscopic magnetic properties from the microscopic J_{AB} interactions in a rigorous way. In this manner, one can gain an insight into how the individual magnetic interactions are modified when the phase transition occurs, irrespective of the exact pathway followed during the transition. This is a preliminary step of the overall project, which is aimed at understanding the structural factors that result in the existence of these two minimum energy structures on the potential energy surface of the crystal. In other words, we are studying the way in which the phase transition takes place between the two polymorphs and why it follows a different pathway when going from the low towards the high temperature polymorph, compared to the reverse transition.

2. Computational details

The first principles bottom-up methodology computes the macroscopic magnetic properties using the crystal structure data as the only input, in other words without making any starting assumptions about the nature or strength of the magnetic interactions that couple the radicals of the crystal. The methodology is described in the following four steps [7]:

(1) Analysis of the crystal structure to find all unique radical–radical pairs present in the crystal, in this case the room temperature data set of **1** (see Fig. 2), whose refcode in the Cambridge Structural Database is SAXPOW05. All the other high temperature data sets (SAXPOW02, 03 and 04) give the same crystal analysis results;
(2) Computation of the radical–radical magnetic exchange coupling interactions (J_{AB}) for each unique radical–radical pair found in the crystal;
(3) Determination of the magnetic topology of the crystal and some possible magnetic models derived from the infinite magnetic topology;
(4) Calculation of the macroscopic magnetic properties of the crystal using the full energy spectrum obtained by diagonalisation of the matrix representation of the appropriate Heisenberg Hamiltonian (the matrix representation is computed in the space of the spin functions of the magnetic models). This matrix representation is a function of the J_{AB} pair interactions whose values were computed in step 2. The smallest model that leads to a magnetic susceptibility curve that most closely agrees with the experimental data is called the *minimal magnetic model*.

The procedure is called *bottom-up* because the macroscopic magnetic properties are obtained from the microscopic radical–radical magnetic interactions without making any assumptions of the type of mechanism acting between the radicals of the crystal. It is referred to as *first principles* because the J_{AB} for each pair is obtained from the energy difference between the appropriate states computed by first principles methods (accurate *ab initio* [8] or DFT methods [9]). Once the J_{AB} values have been computed, one can diagonalise the corresponding matrix representation of the Heisenberg Hamiltonian. We have used the following Heisenberg Hamiltonian, which allows the use of faster computer codes:

$$\hat{H} = -2\sum_{A,B} J_{AB}(\hat{S}_A \cdot \hat{S}_B + \frac{1}{4}\hat{I}_{AB}) \quad (1)$$

where $\hat{I}_{AB}$ is the identity operator while $\hat{S}_A$ and $\hat{S}_B$ are the spin operators acting on radicals A and B. The energy spectrum computed using this Hamiltonian results in the same energy differences between eigenvalues as those obtained using the more common expression (Eq. (2)) and thus in the same susceptibility curve:

$$\hat{H} = -2\sum_{A,B} J_{AB}\hat{S}_A \cdot \hat{S}_B \qquad (2)$$

The energy spectra for these Hamiltonians are obtained by diagonalisation of their matrix representation on the basis of the spin-eigenfunctions of a finite crystal model that mimics the magnetic properties of the infinite crystal (the so-called *minimal magnetic model space*). This allows the rigorous computation of the macroscopic magnetic properties using the appropriate statistical mechanical expressions.

The minimal magnetic model space is selected once the magnetic topology of the crystal is determined (step 3 in the first principles bottom-up procedure) in terms of the magnetic connectivity that the non-negligible $\boldsymbol{J}_{AB}$ pair interactions define between the radicals. It is formed by the smallest group of radicals whose propagation along the three crystallographic axes reproduces the topology and therefore the infinite crystal. This model must include all significant $\boldsymbol{J}_{AB}$ interactions in proportions as similar as possible to those found in the infinite crystal. Furthermore, the macroscopic properties computed using these finite spaces should converge towards the experimental data (which would theoretically correspond to the infinite crystal) as they are enlarged. Note that the index of the matrix representation of the Heisenberg Hamiltonian increases with the number N of doublet radical centres as $N!/[(N/2)!(N/2)!]$. In practice, this means that we are limited to a maximum of 16 different spin centres.

The only spin-carrying units in the crystals of **1** are the 1,3,5-trithia-2,4,6-triazapentalenyl (abbreviated to TTTA) radicals. Each molecular unit is a doublet radical, with the radical electron formally ascribed to the deprotonated N atom present in the dithiazolyl five-membered ring (see Fig. 1). However, as illustrated in Fig. 1, the unpaired electron is in fact delocalised over both heterocyclic rings due to spin polarization, although most of it remains located at the parent N atom. This delocalisation is potentially important in terms of magnetic exchange, and is consistent with results from EPR studies on dilute solutions [3,10,11] and with previous DFT calculations [3,11].

Only two states are therefore possible when two TTTA radicals interact in any of the radical–radical pairs found in crystals of **1**: a singlet state and a triplet state. The value of $\boldsymbol{J}_{AB}$ for each pair is thus obtained from the energy difference between the open-shell singlet and triplet states, computed at the crystal geometry of the pair. Both energies were calculated for the room temperature data set (SAXPOW05) using the B3LYP functional [12,13] and 6-31+G(d) basis set [14,15], and for the 250 K data set (SAXPOW03) using the same functional and the aug-c-pVTZ basis set [16]. All these calculations were done using the GAUSSIAN 03 package [17]. Note that the broken-symmetry approximation [18,19] was used to compute the open-shell singlet, thus allowing a proper description of the energy of this state. Within this approximation the value of $\boldsymbol{J}_{AB}$ for Hamiltonians (1) and (2) is obtained as $2\boldsymbol{J}_{AB} = 2(E^S_{BS} - E^T)$, where E^T is the energy of the triplet state and E^S_{BS} is the energy of the singlet state found using the broken-symmetry approach (the expression for $\boldsymbol{J}_{AB}$ derives from the original broken-symmetry equations when the SOMO orbitals of the two radicals do not overlap or their overlap is small, which is the usual situation in through-space magnetic interactions, such as those found in the TTTA crystal). Our experience indicates that this expression gives results closer to the experimental values than other approaches where projection is used [20,21]. The first principles bottom-up methodology has been successfully applied to a series of crystals representative of a variety of macroscopic behaviours [22–29].

3. Results and discussion

The first principles bottom-up procedure begins with the search for all unique radical pairs in the SAXPOW05 crystal. The selection was made by taking all pairs whose centroid–centroid (calculated centre of mass) separation was smaller than 8.0 Å (this includes all first nearest neighbours, and some second nearest neighbours). The 11 unique radical pairs resulting from this selection are those given in Fig. 3, where the shortest interatomic contacts between the two molecules of the pair are highlighted. The radical centres that are linked by these pairs and their relative positions within the SAXPOW05 crystal are indicated in Fig. 4. In some of these pairs (A, D, J, and K) the radicals of the pair approach each other in a π–π sense that allows a more efficient overlap of their π-type SOMO orbitals (dependent on distance), while in the remaining pairs the radicals are either placed such that the SOMO–SOMO overlap is restricted to being in a lateral sense, or the pair geometry is a compromise between these two extremes. Particularly relevant is Pair A, the intra-stack radical pair that was taken in previous studies as being responsible for the observable magnetic properties of this crystal (its propagation gives rise to the π-stacks perpendicular to the *ac* plane). The radicals in Pair A associate with a slipped π–π geometry with one radical slightly laterally offset relative to the other (see Fig. 2, right). It should be pointed out that Pair A does not in fact contain the shortest intermolecular atom-atom contact distance between two radicals.

The value of $\boldsymbol{J}_{AB}$ was computed (step 2 of the first principles bottom-up procedure) for each of the 11 unique pairs using the procedure indicated above from the values of the energy computed at the B3LYP/6-31+G(d) level for the triplet and the broken-symmetry singlet. The dependence on the basis set of the Pair A value was tested by doing B3LYP calculations on the $\boldsymbol{J}_{AB}$(A) value for the room temperature data set (SAXPOW05) using the 6-31+G(d), aug-cc-pVDZ and aug-cc-pVTZ basis sets. The results obtained with these basis sets, using the B3LYP functional, were −134.5, −149.0 and −155.6 cm^{-1}, respectively, thus confirming the convergence of the $\boldsymbol{J}_{AB}$(A) value as the basis set is increased. This convergence, coupled with the better agreement with the experimental data of the susceptibility curve calculated from the SAXPOW03 (250 K) data, led us to focus on the SAXPOW03 data set and the larger basis set (aug-cc-pVTZ). The 8 magnetically significant $\boldsymbol{J}_{AB}$ values (Pairs A–H) were therefore recalculated under these conditions. These 8 pairs include all 12 first nearest neighbours and are shown as a group in Fig. 5). The results thus obtained are collected in the last column of Table 1 (the $\boldsymbol{J}_{AB}$ values for the three disregarded dimers (I, J and K) are given for completeness although they were not recalculated under the new conditions). Three of these $\boldsymbol{J}_{AB}$ parameters have absolute values smaller than 0.5 cm^{-1}, seven absolute values in the range 0.5–10 cm^{-1}, and the remaining value is an order of magnitude larger, −183.8 cm^{-1}. The presence of a similar number of ferromagnetic and antiferromagnetic interactions among these values should also be noted, although the dominant magnetic interaction is antiferromagnetic.

Using the $\boldsymbol{J}_{AB}$ values the magnetic topology can be constructed and a proper minimal magnetic model space that represents the magnetic structure of the crystal can be extracted from the infinite topology. The magnetic topology that is constructed from $\boldsymbol{J}_{AB}$ pair interactions whose absolute value is larger than 0.5 cm^{-1} is shown in Fig. 6a. This is a 3D topology that can be qualitatively described as a set of weakly interacting antiferromagnetic 1D chains (the geometrical and magnetic details of each 1D chain are shown from a side-on perspective in Fig. 6b). From this topology, and from

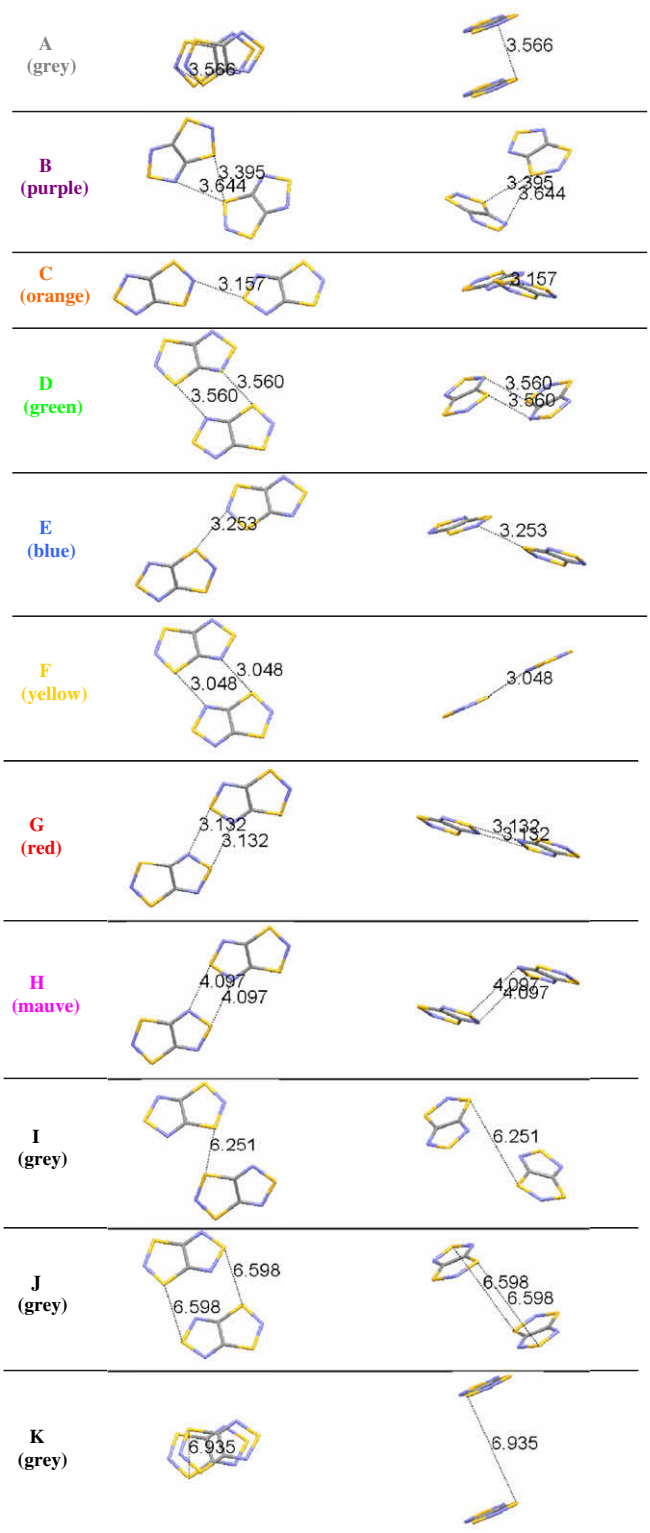


Fig. 3. Top and side views (left- and right-hand columns, respectively) of the geometry of the 11 unique pairs found in the high temperature (monoclinic) structure of **1**. Contact distances correspond to the room temperature data set, SAXPOW05. The shortest interatomic contacts found within each pair are indicated. Each pair is identified with the letters A to K, where the colour of each letter reflects the atomic colouring scheme used in Fig. 3 for letters A to H (its name is also given in parentheses). The molecules in this figure are coloured according to atom type, N: blue, S: yellow and C: grey. (For interpretation of the references to colour in this figure legend, the reader is referred to the web version of this article.)

testing the susceptibility that is calculated with a wide range of different finite magnetic models, we conclude that the most

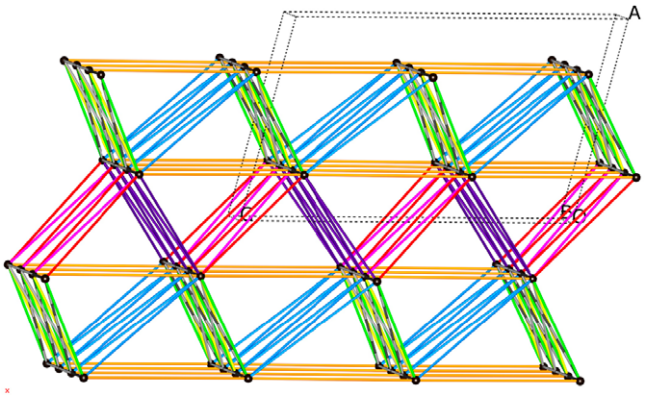


Fig. 4. Arrangement of the linkages in the 11 unique pairs in the high temperature structure of **1**. Each pair is identified by a coloured line that links the two radicals of the pair. Black dots denote the calculated centroids of the radicals. Some of the radical pairs are not clearly observed (I, J, K) because their exchange lines overlap with those for other pairs. (For interpretation of the references to colour in this figure legend, the reader is referred to the web version of this article.)

appropriate 3D minimal magnetic model space involving a maximum of 16 centres is that depicted in Fig. 7, which is a set of four 1D chains connected via their intra- and inter-chain interactions (and thus will be referred to hereafter as the 4-4s model). Note that when only the strongest J_{AB} interaction ($J_{AB}(A) = -183.8\ cm^{-1}$) is considered to be magnetically relevant this is equivalent to making all inter-stack interactions equal to zero, and in this case the minimal magnetic model space would be just a chain of four spin sites, as depicted in Fig. 6b (hereafter referred to as the 1-4s model).

Using the 4-4s magnetic model one can compute the energy spectra of the magnetic states in this finite space (this is done by diagonalising the matrix representation of the Heisenberg Hamiltonian that is based on the spin functions of the spin states of this finite space, corresponding to step 4 of the first principles bottom-up procedure). From there, one can compute the magnetic susceptibility curve for the high temperature polymorph of **1** at temperatures above 250 K (see Fig. 2). The calculation was also carried out using the 1-4s model to compare the results for the 3D magnetic model space with those where the inter-stack interactions have been omitted, and with the results from a chain of 16 nodes (hereafter identified as the 1-16s model). As shown in Fig. 8, the magnetic susceptibilities computed using the 4-4s and 1-4s models overlap with each other and also closely coincide with the experimental curve in the region above 250 K. It is also observed in Fig. 8 that when the 1-16s model is used the computed curve nearly matches the experimental one. The small differences that remain between the 1-16s and experimental curve are probably due to the thermal variation in the geometry of the radical pairs due to thermal expansion that leads to differences in the magnitude of J_{AB}. For instance, in the room temperature structure the shortest S...S distance in Pair A is 3.711 Å, which becomes 3.681 Å in the 250 K structure. Note that the magnetic susceptibility curve in Fig. 8 was computed using only the J_{AB} pair interactions computed from the 250 K structure. One can also expect that results computed using a 4-16s model should be identical to those obtained with the 1-16s model, but this model is to large to allow its calculation with our current resources.

We have also investigated why the 1-4s and 4-4s models give nearly identical magnetic susceptibility curves above 250 K. Fig. 9 shows the energy spectra computed with these two models. Obviously the number of spin states is a lot larger in the 4-4s space, a fact that explains the higher density of states of this model. However, the calculation of the magnetic susceptibility using statistical mechanical methods depends only on the energy difference

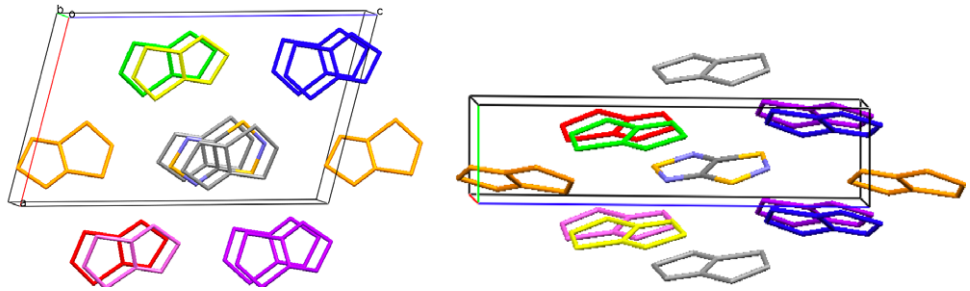


Fig. 5. Top (left) and side (right) views of the crystal structure of the high temperature phase of **1** at room temperature (SAXPOW05). The central molecule is the multicoloured one in the centre, and the neighbours are identified according to the colouring scheme employed in Figs. 3 and 4. (For interpretation of the references to colour in this figure legend, the reader is referred to the web version of this article.)

Table 1
Values of the J_{AB} parameters (in cm^{-1}) computed for the 11 unique radical pairs found in the SAXPOW03 crystal. The values have been computed by doing B3LYP/aug-cc-pVTZ calculations, except the smallest three, which were computed using the 6-31+G(d) basis and the room temperature structure (SAXPOW05) and given their small size were not recomputed. The centroid–centroid separation and the value and nature of the closest atom-atom contact are also described (as π–π, twisted or a lateral contact).

Pair	Centroid sepn. (Å)	Shortest atom–atom contact (Å)	Between atoms	J_{AB}
A	3.681	3.553	S···N (π–π)	−183.8
B	5.805	3.379	S···S (twist)	+9.9
C	7.536	3.146	S···N (twist)	−8.9
D	5.162	3.539	S···N (π-π)	+6.5
E	7.134	3.242	S···N (twist)	+2.7
F	5.501	3.038	S···N (lateral)	−0.9
G	6.720	3.119	S···N (lateral)	−1.4
H	6.984	4.071	S···N (lateral)	+0.8
I[a]	7.832	6.251	S···S (twist)	−0.2
J[a]	7.109	6.598	S···S (π–π)	−0.1
K[a]	7.422	6.935	S···S (π–π)	−0.1

[a] Structural parameters and J_{AB} for I, J and K correspond to the SAXPOW05 data set. J_{AB} are calculated using the 6-31+G(d) basis set. Thus only I, J and K correspond to the contacts given in Fig. 4 and contacts (and J_{AB}) given here for A–H correspond to the 250 K data set. Data for I, J and K was not re-calculated with the larger basis set due to their numerically small size.

between consecutive spin states. The energy difference between states that lie close together (i.e. are almost degenerate) is negligible, so the only differences expected to have an impact on the susceptibility are those between states that are far apart in energy. We can see from Fig. 9 that the lowest lying and therefore most easily thermally populated states are in fact well separated. Looking only at the lowest energy states of singlet and triplet multiplicity, the $[E_0(T) - E_0(S)]$ value for the lowest two states is 177.2 E_h in the 1-4s model and 166.0 E_h in the 4-4s model. A similar energy gap is observed when comparing the two lowest energy singlets ($[E_1(S) - E_0(S)]$, 465.8 and 337.8 E_h, respectively), or the two lowest energy triplets of groups of close-lying states ($[E_1(T) - E_0(T)]$, 190.2

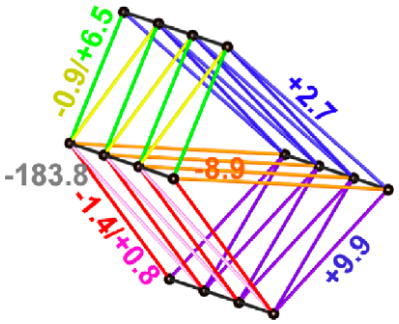


Fig. 7. Minimal 3D magnetic model space (4-4s) that reproduces the properties of the magnetic topology shown in Fig. 6.

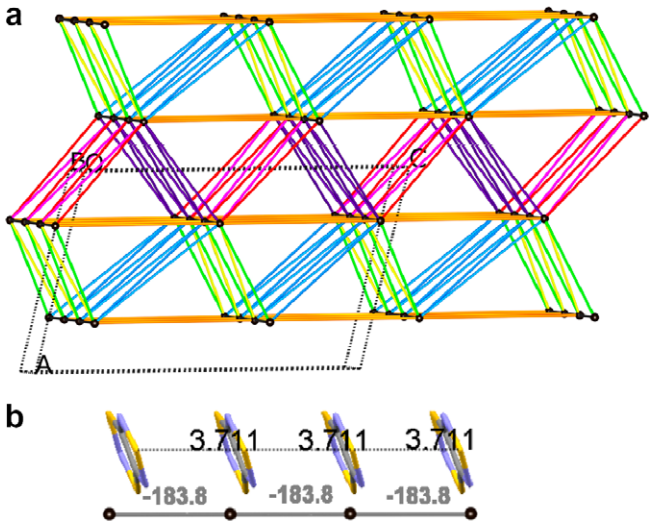


Fig. 6. (a) Magnetic topology generated within the room temperature structure of **1** by the 8 non-negligible radical pairs (A to H). The strongest-interacting J_{AB} pair is drawn in grey, connecting the stacks along the *b*-direction (note the 3D character of the magnetic topology); (b) lateral view of the π-stacks chains found along the *b* axis (showing the J_{AB} magnetic exchange interactions and the relative geometry and regular atomic spacing between neighbouring radicals in the chains).

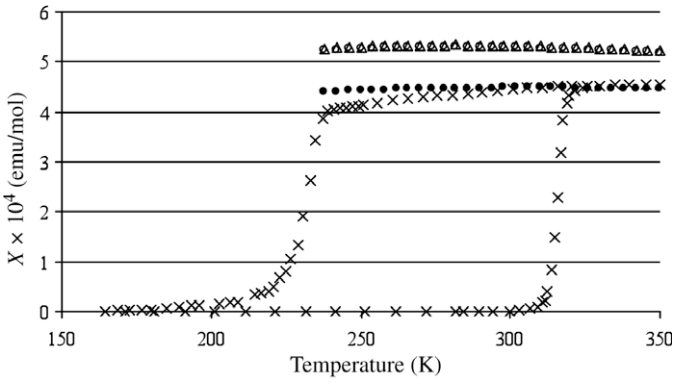


Fig. 8. Magnetic susceptibility curve computed for the 250 K data set of **1** (SAXPOW03) using the 4-4s (△), 1-4s (○), and 1-16s (●) models. The experimental results (×) are given for comparison. It is important to keep in mind here that the high temperature polymorph of **1** only exists above 250 K. Within this range the qualitative agreement between the computed and experimental values is good for the *x*-4s models and excellent for the 1-16s model.

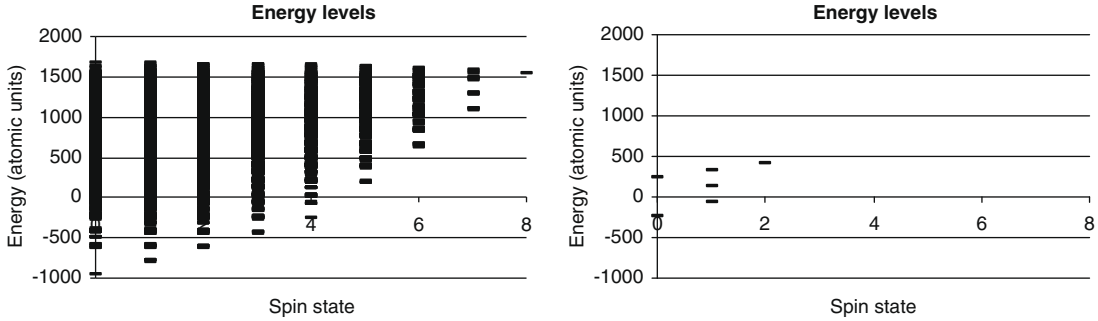


Fig. 9. Energy spectra for the 4-4s model (left) and 1-4s model (right).

E_h in the 1-4s model and $[E_5(T) - E_0(T)]$ 165.0 E_h in the 4-4s model). Similar trends are also observed in other cases. Therefore, as the dominant terms in the expression of the macroscopic magnetic susceptibility are those including a non-negligible ΔE, the reason behind the similarity in the magnetic susceptibility curves computed using the 1-4s and 4-4s models is a likeness in the non-negligible ΔE terms.

4. Conclusions

The first principles bottom-up study of the high temperature phase of the TTTA radical at room temperature indicates that there are 11 unique radical pairs. When the value of the $\boldsymbol{J}_{AB}$ pair interactions are computed for all these pairs at the B3LYP/aug-cc-pVTZ level one finds 8 that have absolute values larger than 1 cm^{-1}, some of them ferromagnetic and others antiferromagnetic, with one very large interaction (-183.8 cm^{-1}) and all other interactions having an absolute value smaller than 11 cm^{-1}. After making improvements based on basis set and the temperature at which the data set is recorded, a second set of 8 $\boldsymbol{J}_{AB}$ values is calculated for the 250 K data set using the aug-cc-pVTZ basis set. These values have been used to calculate the bulk magnetic susceptibility above 250 K and we obtain good agreement with the experimental curve and reveal a higher level of detail than that available from previous experimental fitting studies. The magnetic topology of these interactions is clearly 3D and is characterised by weakly interacting antiferromagnetic 1D chains. However, the magnetic susceptibility curves computed using the full 3D model or one comprising only isolated 1D chains are practically identical. This fact is explained by the fact that the magnetic susceptibility expression depends on energy differences, and that the energy differences in the smaller model are similar to those for the larger model. However, the 3D nature of the magnetic topology suggests that the origin of the bistability of this material must be fully investigated by considering not only at the changes within the stacks but also the interstack interactions. This is the aim of further studies that will compare this data with the magnetic properties of the low temperature phase of the TTTA radical, looking for the main microscopic differences between the polymorphs and how they are related to the intermolecular bonds being created and broken.

Acknowledgements

We thank the Spanish Science and Education Ministry for support (Projects BQU2002-04587-C02-02 and CTQ2005-02329), the Catalan DURSI (Grants 1999SGR-00046 and 2005SGR-00036), and the computer time allocated by CESCA and BSC. Furthermore, C.S.C. thanks B.S.C. and the European Community for the award of various grants by HPC-Europa (project RII3-CT-2003-506079 under the FP6 "Structuring the European Research Area" Programme and project 211437 under the FP7 "Coordination and support action" Programme).

References

[1] O. Kahn, Chem. Brit. 35 (1999) 24.
[2] W. Fujita, K. Awaga, Science 286 (1999) 261.
[3] G.D. McManus, J.M. Rawson, N. Feeder, J. van Dujin, E.J.L. McInnes, J.J. Novoa, R. Burriel, F. Palacio, P. Oliete, J. Mater. Chem. 11 (2001) 1992.
[4] F.H. Allen, Acta Crystallogr., Sect. B 58 (2002) 380.
[5] H. Matsuzaki, W. Fujita, K. Awaga, H. Okamoto, Phys. Rev. Lett. 91 (2003) 017403.
[6] W. Fujita, K. Awaga, H. Matsuzaki, H. Okamoto, Phys. Rev. B 65 (2002) 064434.
[7] M. Deumal, M.J. Bearpark, J.J. Novoa, M.A. Robb, J. Phys. Chem. A 106 (2002) 1299.
[8] A. Szabo, N.S. Ostlund, Modern Quantum Chemistry, Macmillan, New York, 1982.
[9] E.G. Parr, W. Yang, Density Functional Theory, Oxford University Press, New York, 1989.
[10] G. Wolmershäuser, R. Johann, Angew. Chem., Int. Ed. Engl. 28 (1989) 920.
[11] Y.-L. Chung, J.P.B. Sandall, L.H. Sutcliffe, H. Joly, K.F. Preston, R. Johann, G. Wolmershäuser, Magn. Reson. Chem. 29 (1991) 625.
[12] A.D. Becke, Phys. Rev. A 38 (1988) 3098.
[13] C. Lee, W. Yang, R.G. Parr, Phys. Rev. B 37 (1988) 785.
[14] P.C. Hariharan, J.A. Pople, Theor. Chim. Acta 28 (1973) 213.
[15] M.M. Francl, W.J. Pietro, W.J. Hehre, J.S. Binkley, M.S. Gordon, D.J. DeFrees, J.A. Pople, J. Chem. Phys. 77 (1982) 3654.
[16] D.E. Woon, T.H. Dunning, J. Chem. Phys. 98 (1993) 1358.
[17] M.J. Frisch, G.W. Trucks, H.B. Schlegel, G.E. Scuseria, M.A. Robb, J.R. Cheeseman, J.A. Montgomery Jr., T. Vreven, K.N. Kudin, J.C. Burant, J.M. Millam, S.S. Iyengar, J. Tomasi, V. Barone, B. Mennucci, M. Cossi, G. Scalmani, N. Rega, G.A. Petersson, H. Nakatsuji, M. Hada, M. Ehara, K. Toyota, R. Fukuda, J. Hasegawa, M. Ishida, T. Nakajima, Y. Honda, O. Kitao, H. Nakai, M. Klene, X. Li, J.E. Knox, H.P. Hratchian, J.B. Cross, V. Bakken, C. Adamo, J. Jaramillo, R. Gomperts, R.E. Stratmann, O. Yazyev, A.J. Austin, R. Cammi, C. Pomelli, J.W. Ochterski, P.Y. Ayala, K. Morokuma, G.A. Voth, P. Salvador, J.J. Dannenberg, V.G. Zakrzewski, S. Dapprich, A.D. Daniels, M.C. Strain, O. Farkas, D.K. Malick, A.D. Rabuck, K. Raghavachari, J.B. Foresman, J.V. Ortiz, Q. Cui, A.G. Baboul, S. Clifford, J. Cioslowski, B.B. Stefanov, G. Liu, A. Liashenko, P. Piskorz, I. Komaromi, R.L. Martin, D.J. Fox, T. Keith, M.A. Al-Laham, C.Y. Peng, A. Nanayakkara, M. Challacombe, P.M.W. Gill, B. Johnson, W. Chen, M.W. Wong, C. Gonzalez, J.A. Pople, GAUSSIAN 03, Revision C.02, Gaussian, Inc., Wallingford CT, 2004.
[18] L. Noodlemann, J. Chem. Phys. 74 (1981) 5737.
[19] L. Noodlemann, E.R. Davidson, Chem. Phys. 109 (1986) 131.
[20] It should be noted that there has been some controversy about the use of projection when computing the values of the J_{AB} pair interactions using the broken-symmetry approach within the DFT context. For two leading references, see: E. Ruiz, S. Alvarez, J. Cano, V. Polo, J. Chem. Phys. 123 (2005) 164110.
[21] C. Adamo, V. Barone, A. Bencini, R. Broer, M. Filatov, N.M. Harrison, F. Illas, J.P. Malrieu, I.P.R. Moreira, J. Chem. Phys. 124 (2006) 107101.
[22] M. Deumal, M.J. Bearpark, M.A. Robb, Y. Pontillon, J.J. Novoa, Chem. Eur. J. 10 (2004) 6422.
[23] M. Deumal, M.A. Robb, J.J. Novoa, Polyhedron 22 (2003) 1935.
[24] M. Deumal, M.J. Bearpark, M.A. Robb, Y. Pontillon, J.J. Novoa, Chem. Eur. J. 10 (2004) 6422.
[25] M. Deumal, F. Mota, M.J. Bearpark, M.A. Robb, J.J. Novoa, Mol. Phys. 104 (2006) 857.
[26] J. Jornet, M. Deumal, J. Ribas-Ariño, M.J. Bearpark, M.A. Robb, R.G. Hicks, J.J. Novoa, Chem. Eur. J. 12 (2006) 3995.
[27] M. Deumal, S. LeRoux, J.M. Rawson, M.A. Robb, J.J. Novoa, Polyhedron 26 (2007) 1949.
[28] L. Li, M.M. Turnbull, C.P. Landee, J. Jornet, M. Deumal, J.J. Novoa, J.L. Wikaira, Inorg. Chem. 46 (2007) 11254.
[29] J. Jornet, M.A. Robb, M. Deumal, J.J. Novoa, Inorg. Chim. Acta 361 (2008) 3586.

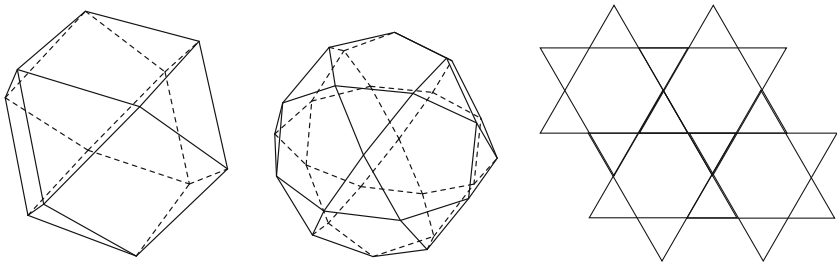


Fig. 1. Cuboctahedron, icosidodecahedron, and (part of the) kagome lattice.

3. The regular cuboctahedron

The regular cuboctahedron belongs to the class of geometrically frustrated antiferromagnets built of corner-sharing triangles. Such systems possess an extended magnetization plateau at 1/3 of the saturation magnetization $\mathscr{M}_{\rm sat}$ caused by dominant up–up–down contributions [23,24], an unusually high jump of the magnetization at the saturation field due to independent magnons [22,6] as well as low-lying singlets below the first triplet level [29,30,24]. These features are shared for instance by the icosidodecahedron and by the kagome lattice.

Fig. 2 shows the magnetization curves at $T = 0$ for the regular cuboctahedron with $s = 1/2$, $s = 1$, and $s = 3/2$. These curves show besides the plateau at $\mathscr{M}_{\rm sat}/3$ a jump to saturation of height $\Delta M = 2$. Both features are reflected by the differential susceptibility function which is displayed in Fig. 3. Each step in Fig. 2 corresponds to a peak in Fig. 3. One notices that the peaks are washed out for higher temperatures, but that the minimum that corresponds to the plateau at $\mathscr{M}_{\rm sat}/3$ persists up to temperatures of the order of the exchange coupling.

As a function of the intrinsic spin s the differential susceptibility $\mathrm{d}\mathscr{M}/\mathrm{d}B$ exhibits two properties. With increasing spin quantum number s the individual peaks oscillate more and more with smaller relative amplitude, but the minimum at 1/3 is actually sharpened. It is known that in the classical limit, i.e. for $s \to \infty$, the differential susceptibility is practically flat below the saturation field except for the dip at 1/3 [23].

For zero-field Fig. 4 shows the low-lying energy levels. In the case of $s = 1/2$ (l.h.s. of Fig. 4) one notices the low-lying singlets below the first triplet. These states are a cornerstone of geometric frustration and as well present in the kagome lattice and the icosidodecahedron with $s = 1/2$ [29]. It is interesting to note that with increasing s, i.e. towards a more classical behavior, the number of these states decreases. For $s = 1$ (middle of Fig. 4) the first excited singlet level is already (slightly) above the lowest triplet level. For $s = 3/2$ (r.h.s. of Fig. 4) a doubly degenerate excited singlet level remains below the lowest triplet, the others have disappeared. This behavior, i.e. no excited singlets below the lowest triplet for integer spins and a doubly degenerate excited singlet below the lowest triplet, does not change anymore for higher spin quantum numbers as can be checked e.g. by Lanczos methods.

The rather high symmetry of the cuboctahedron leads to many degenerate energy levels. As examples we label some low-lying energy levels in Fig. 4 by their multiplicity d_S, i.e. by the degeneracy of the whole multiplet. The full degeneracy including the multiplicity of the magnetic sublevels d_M is then $d = d_S \times d_M$. Clearly, such high multiplicities have an important impact on the magnetocaloric behavior since they increase the entropy for low temperatures [30,31]. In the following we would like to discuss the impact of low-lying singlets below the first triplet which in the case of extended lattices are supposed to condense in infinite number onto the ground state.

Fig. 5 compares the heat capacity (l.h.s.) and the zero-field susceptibility (r.h.s.) for the regular cuboctahedron with $s = 1/2$, $s = 1$, and $s = 3/2$. The heat capacity shows a pronounced double peak structure for $s = 1/2$ and $s = 1$ which dissolves into a broad peak with increasing spin quantum number. The broad peak also moves to higher temperatures with increasing s. The reason for the first sharp peak is twofold. Since there are several gaps between the low-lying levels the density of states has a very discontinuous structure which results in the double peak structure. For $s = 1/2$ the low-lying singlets provide a very low-lying non-magnetic density of states which is responsible for the fact that the first sharp peak is at such low temperatures. For $s = 1$ the first sharp peak results from both excited singlet as well as lowest triplet levels. For $s = 3/2$ a remnant of the first sharp peak is still visible; it is given by the low-lying singlets, but since they are so few, also influenced by the lowest triplet levels.

The behavior of the heat capacity is contrasted by the susceptibility on the r.h.s. of 5 which reflects mostly the density of states of magnetic levels and is only weakly influenced by low-lying singlets. Therefore, the first sharp peak, or any other structure at very low temperatures, is absent.

4. The irregular cuboctahedron

In this section we investigate how the magnetic properties of the cuboctahedron change if random variations of the exchange coupling parameters are introduced. This study is motivated by

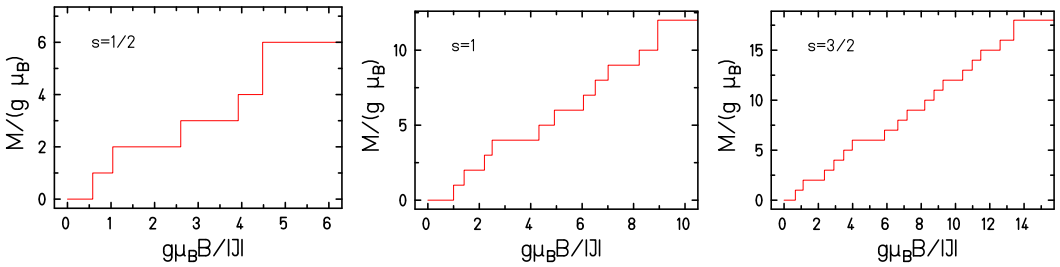


Fig. 2. Magnetization as a function of applied field at $T = 0$ for the regular cuboctahedron with $s = 1/2$, $s = 1$, and $s = 3/2$. The extended plateau at $\mathscr{M}_{\rm sat}/3$ is clearly visible.

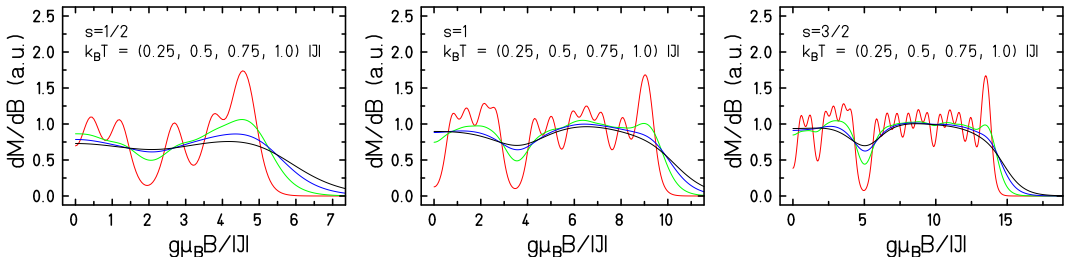


Fig. 3. Differential susceptibility as a function of applied field at $k_BT/|J| = 0.25, 0.5, 0.75, 1.0$ for the regular cuboctahedron with $s = 1/2$, $s = 1$, and $s = 3/2$. The smoother the curve, the higher the temperature.

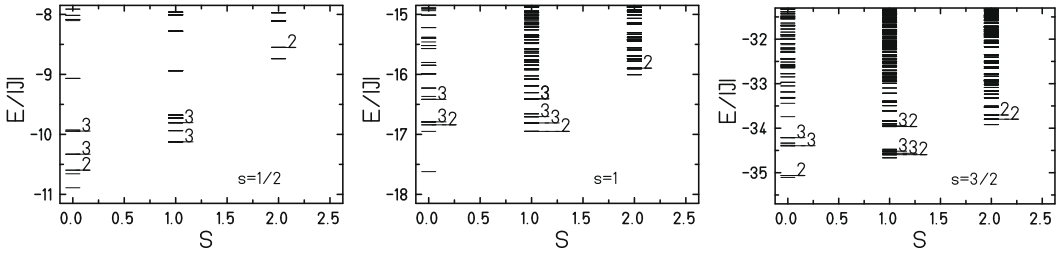


Fig. 4. Low-lying energy levels for the regular cuboctahedron with $s = 1/2$, $s = 1$, and $s = 3/2$. Numbers attached to selected levels denote their multiplicities d_S; unlabeled levels below the highest labeled level have $d_S = 1$.

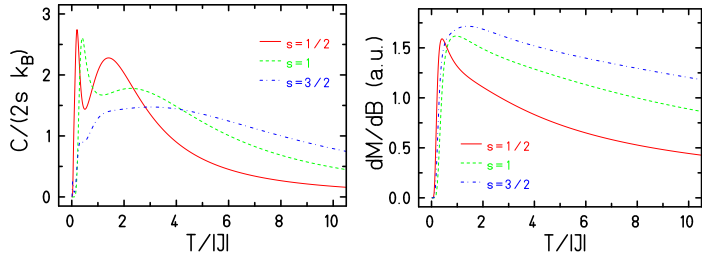


Fig. 5. Heat capacity (l.h.s.) and zero-field susceptibility (r.h.s.) for the regular cuboctahedron with $s = 1/2$, $s = 1$, and $s = 3/2$.

recent magnetization measurements of the icosidodecahedral molecules $\{Mo_{72}Fe_{30}\}$ [18] and $\{Mo_{72}Cr_{30}\}$ [20] published in Ref. [28], which were interpreted by assuming random distributions of exchange parameters in a classical Heisenberg model description.

We introduce variations of the exchange parameters of the Hamiltonian (1) by replacing the common nearest-neighbor exchange parameter $J_{uv} = J$ with values of a flat random distribution $J - 0.5\Delta \leqslant J_{uv} \leqslant J + 0.5\Delta$. Thus the mean exchange parameter is kept to be J. In order to gain sufficient statistical certainty we use ensembles of 10 000 spectra for realizations of the irregular cuboctahedron with $s = 1/2$; the results do not deviate from those for 1000 realizations. For larger s the production of sufficiently large ensembles is hindered by prohibitively many diagonalizations of larger matrices.

Fig. 6 shows the differential susceptibility that results from averages using distributions with various Δ. The figure on the l.h.s. compares $\mathrm{d}\mathscr{M}/\mathrm{d}B$ at the rather low temperature of $k_BT = 0.1|J|$ for $\Delta = 0$, i.e. the regular cuboctahedron, with $\Delta = 0.5|J|$, $\Delta = 1.0|J|$, and $\Delta = 2.0|J|$. One clearly sees that the pattern which mainly originates from ground state level crossings does not change much for $\Delta = 0.5|J|$ and $\Delta = 1.0|J|$. It needs a variation as large as $\Delta = 2.0|J|$, i.e. ferromagnetic interactions occur, to qualitatively change the differential susceptibility function. The reason is that smaller variations do no alter the structure of low-lying energy gaps. The

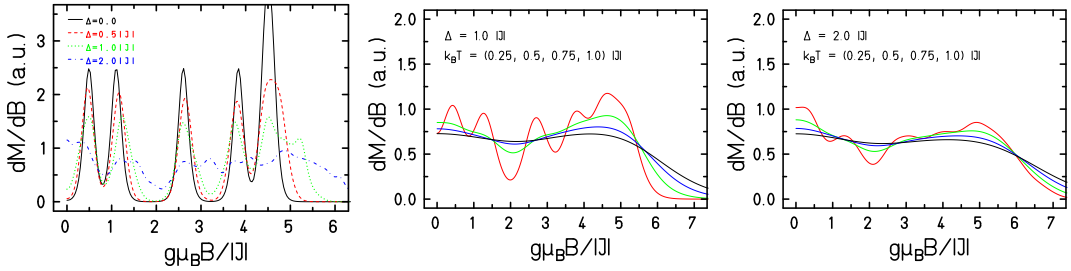


Fig. 6. Differential susceptibility as a function of applied field for the irregular cuboctahedron with $s = 1/2$. L.h.s.: dependence on the width Δ of the random distribution. Middle: dependence on the temperature $k_BT/|J| = 0.25, 0.5, 0.75, 1.0$ for $\Delta = 1.0|J|$. R.h.s.: same as middle for $\Delta = 2.0|J|$.

singlet–triplet gap, which is approximately 0.765 $|J|$, does not vary very much for the ensembles with smaller Δ, and so does the singlet–triplet crossing which is determined by the singlet–triplet gap. It needs an appreciable variance of the exchange parameter distribution in order to impose large variations of the level crossing fields.

The middle and the r.h.s. of 6 display $\mathrm{d}\mathscr{M}/\mathrm{d}B$ for temperatures $k_BT/|J| = 0.25, 0.5, 0.75, 1.0$ and $\Delta = 1.0|J|$ and $\Delta = 2.0|J|$, respectively. As already explained, there is only very little difference between the behavior of an irregular cuboctahedron with $\Delta = 1.0|J|$ (middle) and the regular one. For $\Delta = 2.0|J|$ (r.h.s.) the differential susceptibility is much more smeared out which includes an appreciable broadening at the saturation field. Considering the irregular cuboctahedron we can conclude that the magnetic properties are rather stable against random fluctuations of the exchange parameters. This means that the striking behavior especially of the experimental differential susceptibility of $\{M0_{72}Fe_{30}\}$ and $\{Mo_{72}Cr_{30}\}$ which shows no signs of level crossings at all [28] needs further theoretical exploration of the microscopic origin.

Acknowledgements

Computing time at the Leibniz Computer Center in Garching is greatly acknowledged as well as helpful openMP advices by Dieter an Mey and Christian Terboven of High Performance Computing, RWTH Aachen University. We thank Boris Tsukerblat for motivating discussions about the irreducible tensor operator technique.

References

[1] A.P. Ramirez, Annu. Rev. Mater. Sci. 24 (1994) 453.
[2] J. Greedan, J. Mater. Chem. 11 (2001) 37.
[3] H. Diep, editor, Magnetic Systems with Competing Interactions, World Scientific, Singapore, 1994.
[4] Y. Narumi, K. Katsumata, Z. Honda, J.-C. Domenge, P. Sindzingre, C. Lhuillier, Y. Shimaoka, T.C. Kobayashi, K. Kindo, Europhys. Lett. 65 (2004) 705.
[5] M.E. Zhitomirsky, Phys. Rev. Lett. 88 (2002) 057204.
[6] J. Schulenburg, A. Honecker, J. Schnack, J. Richter, H.-J. Schmidt, Phys. Rev. Lett. 88 (2002) 167207.
[7] J.L. Atwood, Nat. Mater. 1 (2002) 91.
[8] O. Tchernyshyov, R. Moessner, S.L. Sondhi, Phys. Rev. Lett. 88 (2002) 067203.
[9] R. Moessner, Can. J. Phys. 79 (2001) 1283.
[10] S.T. Bramwell, M.J.P. Gingras, Science 294 (2001) 1495.
[11] E. Berg, E. Altman, A. Auerbach, Phys. Rev. Lett. 90 (2003) 147204.
[12] K. Penc, N. Shannon, H. Shiba, Phys. Rev. Lett. 93 (2004) 197203.
[13] J.-H. Chung, M. Matsuda, S.-H. Lee, K. Kakurai, H. Ueda, T.J. Sato, H. Takagi, K.-P. Hong, S. Park, Phys. Rev. Lett. 95 (2005) 247204.
[14] C.L. Henley, Phys. Rev. Lett. 96 (2006) 047201.
[15] H.-J. Schmidt, J. Richter, R. Moessner, J. Phys. A: Math. Gen. 39 (2006) 10673.
[16] M.E. Zhitomirsky, H. Tsunetsugu, Phys. Rev. B 75 (2007) 224416.
[17] A.J. Blake, R.O. Gould, C.M. Grant, P.E.Y. Milne, S. Parsons, R.E.P. Winpenny, J. Chem. Soc., Dalton Trans. (1997) 485.
[18] A. Müller, S. Sarkar, S.Q.N. Shah, H. Bögge, M. Schmidtmann, S. Sarkar, P. Kögerler, B. Hauptfleisch, A. Trautwein, V. Schünemann, Angew. Chem., Int. Ed. 38 (1999) 3238.
[19] A. Müller, A.M. Todea, J. van Slageren, M. Dressel, H. Bögge, M. Schmidtmann, M. Luban, L. Engelhardt, M. Rusu, Angew. Chem., Int. Ed. 44 (2005) 3857.
[20] A.M. Todea, A. Merca, H. Bögge, J. van Slageren, M. Dressel, L. Engelhardt, M. Luban, T. Glaser, M. Henry, A. Müller, Angew. Chem., Int. Ed. 46 (2007) 6106.
[21] C.P. Pradeep, D.-L. Long, P. Kögerler, L. Cronin, Chem. Commun. (2007) 4254.
[22] J. Schnack, H.-J. Schmidt, J. Richter, J. Schulenburg, Eur. Phys. J. B 24 (2001) 475.
[23] C. Schröder, H. Nojiri, J. Schnack, P. Hage, M. Luban, P. Kögerler, Phys. Rev. Lett. 94 (2005) 017205.
[24] I. Rousochatzakis, A.M. Läuchli, F. Mila, Phys. Rev. B 77 (2008) 094420.
[25] D. Gatteschi, L. Pardi, Gazz. Chim. Ital. 123 (1993) 231.
[26] J.J. Borras-Almenar, J.M. Clemente-Juan, E. Coronado, B.S. Tsukerblat, Inorg. Chem. 38 (1999) 6081.
[27] O. Waldmann, Phys. Rev. B 61 (2000) 6138.
[28] C. Schröder, R. Prozorov, P. Kögerler, M.D. Vannette, X. Fang, M. Luban, A. Matsuo, K. Kindo, A. Müller, A.M. Todea, Phys. Rev. B 77 (2008) 224409.
[29] R. Schmidt, J. Schnack, J. Richter, J. Magn. Magn. Mater. 295 (2005) 164.
[30] J. Schnack, R. Schmidt, J. Richter, Phys. Rev. B 76 (2007) 054413.
[31] A. Honecker, M. Zhitomirsky, J. Phys. Conf. Ser. 145 (2009) 012082.

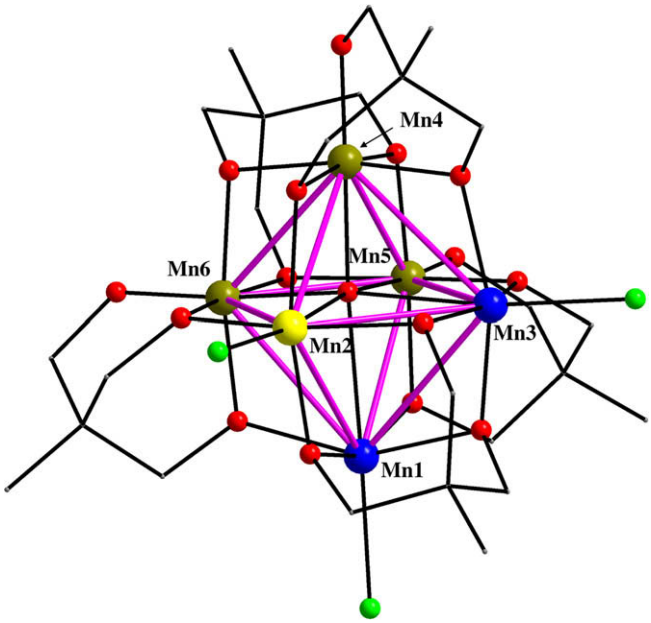


Fig. 1. Partially labeled representation of complex **1** with Mn–Mn vectors shown in purple to emphasize the Mn_6 octahedron. H atoms have been omitted for clarity. Colour scheme: Mn^{II} yellow; Mn^{III} blue; Mn^{IV} olive; O red; Cl green; C grey. (For interpretation of the references to colour in figure legends, the reader is referred to the web version of this article.)

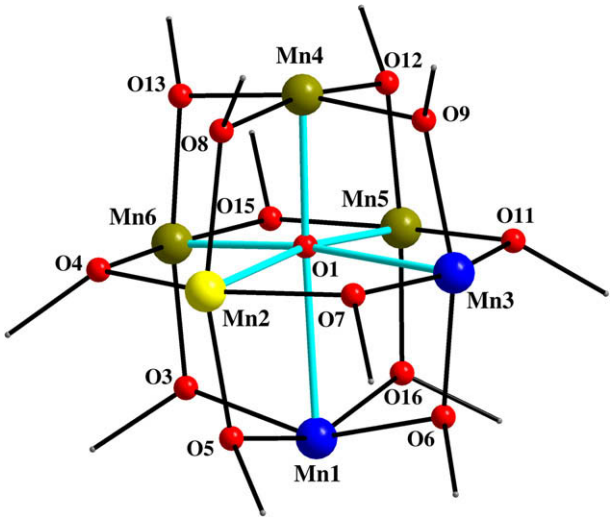


Fig. 2. Labeled PovRay representation of the complete $[Mn_6(\mu_6\text{-}O)(\mu\text{-}OR)_{12}]^{6+}$ core, emphasizing the central $[Mn_6(\mu_6\text{-}O)]^{18+}$ unit. Colour scheme as in Fig. 1.

Mn(1)–Mn(3), with the C_3 axis passing through central O1 and perpendicularly through the midpoint of the Mn(1)–Mn(3) triangular plane. Atoms Mn(1) and Mn(2) are thus related by a virtual mirror plane, and it is perhaps not unreasonable that they would be statically disordered about it. In fact, the virtual symmetry of the molecule is C_S if we distinguish Mn^{III} atom Mn(3) from the disordered pair Mn(1)/Mn(2), the mirror plane passing through Mn(3), Mn(6), O(1), O(5) and O(12) (Fig. 2).

All Mn atoms are six-coordinate with distorted octahedral geometry, and only Mn(3) atom shows clearly the Jahn-Teller (JT) distortion expected for a high-spin, Mn^{III} (d^4) ion in near-octahedral geometry, taking the form of an axial elongation of the two *trans* Mn(3)–Cl(2) (2.329(1) Å) and Mn(3)–O(1) bonds (2.398(3) Å). There are no strong intermolecular hydrogen-bonds, only weak

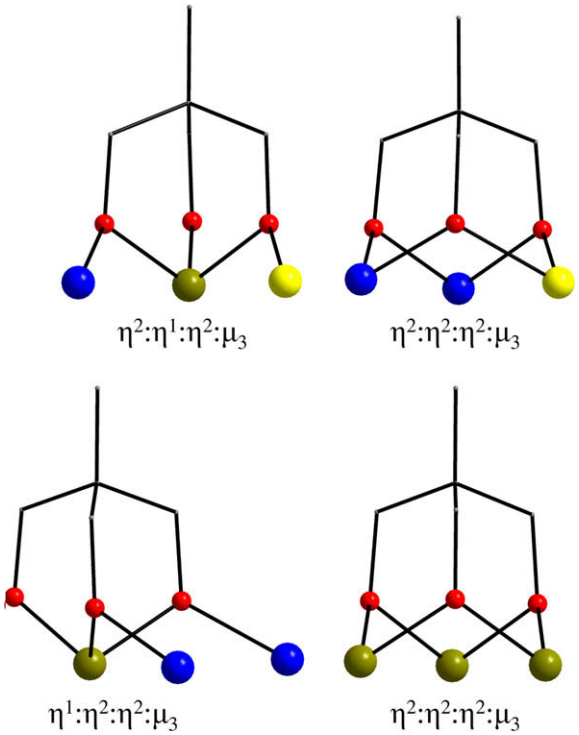


Fig. 3. The coordination modes of $thme^{3-}$ found in complex **1**. Colour scheme as in Fig. 1.

C–H···Cl contacts between C–H bonds of $thme^{3-}$ and lattice CH_2Cl_2 groups and the terminal Cl^- ions. Complex **1** is the first Mn_6 cluster at the Mn^{2+}, $2Mn^{3+}$, $3Mn^{4+}$ level, as well as a rare example of a hexanuclear molecular species with the $[M_6(\mu_6\text{-}O^{2-})]$ octahedral core [7], and the first in Mn coordination chemistry.

Solid-state DC (direct current) magnetic susceptibility (χ_M) data for complex **1** were collected in the temperature range 5.0–300 K in an applied field of 1 kOe (0.1 T). The $\chi_M T$ value steadily increases from 21.04 cm^3 K mol^{-1} at 300 K to a maximum of 54.48 cm^3 K mol^{-1} at 25 K, before dropping to 46.42 cm^3 K mol^{-1} at 5.0 K (Fig. 4). The spin-only ($g = 2$) value for a non-interacting $[Mn^{II}\text{-}Mn^{III}_2Mn^{IV}_3]$ unit is 16.0 cm^3 K mol^{-1}. This indicates ferromagnetic exchange interactions within **1**, and the 25 K data strongly suggest a very large ground-state spin (S) value for the complex, with the sharp decrease at the lowest temperatures assigned to Zeeman ef-

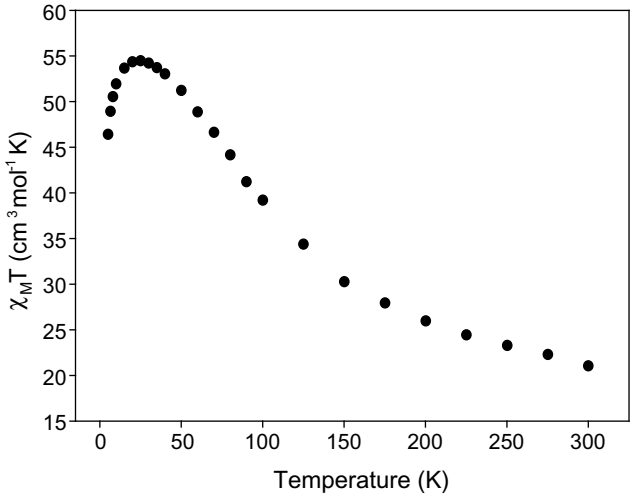


Fig. 4. $\chi_M T$ vs. T plot for **1** in a 1 kG field.

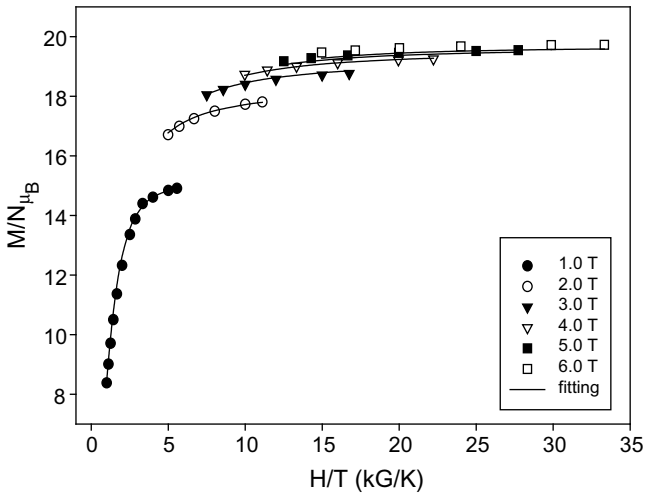


Fig. 5. Magnetization (M) vs. field (H) and temperature (T) data, plotted as reduced magnetization ($M/N\mu_B$) vs. H/T, for complex **1** at applied fields of 1.0–6.0 T and in the 1.8–10 K temperature range. The solid lines are the fit of the data; see the text for the fit parameters.

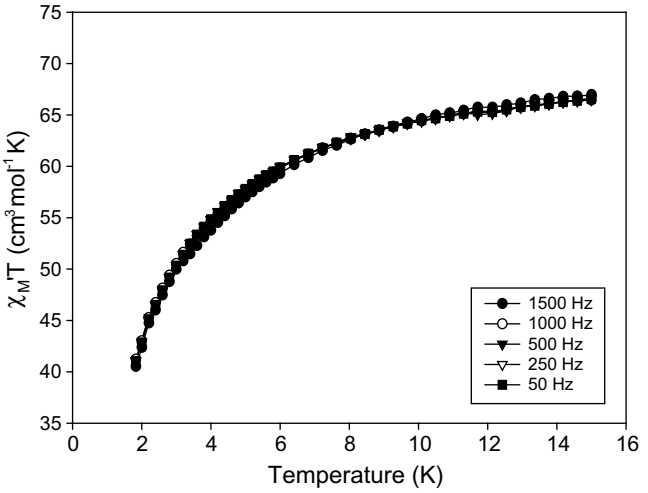


Fig. 6. Plot of the in-phase (χ'_M) as $\chi'_M T$ AC magnetic susceptibility vs. T in a 3.5 G field oscillating at the indicated frequencies for complex **1**.

fects, zero-field splitting and/or weak intermolecular interactions. The 25 K value is consistent with an $S = 10$ or 11 ground state, the latter being the maximum possible, and a g value of 2.0 or slightly below, as expected for a $Mn^{II}/Mn^{III}/Mn^{IV}$ system [5]; the spin-only ($g = 2$) values for $S = 10$ and 11 state are 55 and 66 $cm^3\,K\,mol^{-1}$.

In order to determine the ground state of **1**, magnetization (M) data were collected in the 1–6 T and 1.8–10.0 K ranges, and these are plotted as $M/N\mu_B$ versus H/T in Fig. 5. The data were fit by matrix-diagonalization to a model that assumes only the ground state is populated, includes axial zero-field splitting ($D\hat{S}_z^2$) and the Zeeman interaction, and carries out a full powder average. The best fit (solid lines in Fig. 5) gave $S = 11$, $g = 1.97(2)$ and $D = -0.07(3)\ cm^{-1}$, indicating a very high ground state spin with little magnetic anisotropy; an alternative fit with $S = 10$ is less favoured due to an unreasonable value for g of ~1.72. We conclude that **1** has ground state of $S = 11$ and the small D value is consistent with the small content of JT-distorted Mn^{III} atoms within the molecule.

The $S = 11$ ground state was further supported by AC (alternating current) magnetic susceptibility experiments, in which a weak field of 3.5 G oscillating at a particular frequency (ν) was applied to the sample. Ac susceptibility studies use no dc field and thus are an excellent complementary tool for determining S by avoiding potential complications from a large dc field and/or low-lying excited states. For **1**, the in-phase (χ'_M) AC signal, shown as $\chi'_M T$ in Fig. 6, is only slightly decreasing with decreasing temperature in the 8–15 K region; extrapolation of the data above 8 K (to avoid the effects of weak intermolecular interactions at lower temperatures, both dipolar and superexchange in nature) down to 0 K gives ~60 $cm^3\,K\,mol^{-1}$, indicating an $S = 11$ ground state with $g \sim 1.91$, in good agreement with the DC magnetization fits.

There is no out-of-phase (χ''_M) AC susceptibility signal down to 1.8 K, which indicates an insignificant barrier (versus kT) to magnetization relaxation. To explore whether slow relaxation might become apparent at even lower temperatures, magnetization versus dc field scans are required to be performed at low enough temperatures using the micro-SQUID apparatus [8]. Such studies are currently in progress and the corresponding results will be reported in due course.

In summary, the employment of the $thme^{3-}$ ligand in higher oxidation state Mn cluster chemistry has yielded a mixed-valence-(II/III/IV) molecule with a $[Mn_6(\mu_6\text{-}O)]^{18+}$ octahedral core and a high $S = 11$ ground state. Note that the $S = 11$ for **1** is the maximum for a Mn^{II}, $2Mn^{III}$, $3Mn^{IV}$ species, indicating all interactions to be ferromagnetic. This might at first glance seem strange for a complex that contains a Mn^{IV}_3 triangular subunit, since $Mn^{IV}Mn^{IV}$ interactions are almost always antiferromagnetic, but note that the Mn^{IV} atoms are within a $[Mn_3(\mu_3\text{-}O)(\mu\text{-}O)_3]$ defect-cubane subunit involving bis-monoatomically-bridged $[Mn(\mu\text{-}O)_2Mn]$ pairs, and this results in acute Mn^{IV}–O–Mn^{IV} angles (95–101°) that can reasonably yield ferromagnetic interactions [9]. In fact, this is in accord with the ferromagnetic interactions seen within the central $[Mn^{IV}_4(\mu_3\text{-}O)_4]$ cubane of $[Mn_{12}O_{12}(O_2CR)_{16}(H_2O)_4]$ complexes [9d], which have Mn–O–Mn angles in the 95.0–100.7° range. Similarly for the interactions in **1** between Mn^{IV} and Mn^{II} or Mn^{III} atoms, and interactions amongst the Mn^{II}/Mn^{III} atoms, which all again involve bis-monoatomically-bridged Mn_2 pairs and particularly acute Mn–O^{2-}–Mn angles in the 89.19–90.62° and 83.37–84.25° ranges, respectively. A completely ferromagnetically coupled Mn_6 complex **1** is thus reasonable. These points will be analyzed in greater detail in the full paper.

Acknowledgement

We thank the U.S. National Science Foundation (Grant CHE-0414555) for support of this work.

Appendix A. Supplementary data

CCDC 704395 contains the supplementary crystallographic data for $\mathbf{1} \cdot 3CH_2Cl_2$. These data can be obtained free of charge via http://www.ccdc.cam.ac.uk/conts/retrieving.html, or from the Cambridge Crystallographic Data Centre, 12 Union Road, Cambridge CB2 1EZ, UK; fax: (+44) 1223-336-033; or e-mail: deposit@ccdc.cam.ac.uk. Supplementary data associated with this article can be found, in the online version, at doi:10.1016/j.poly.2008.10.031.

References

[1] For reviews see: (a) G. Aromi, E.K. Brechin, Struct. Bond 122 (2006) 1; (b) D. Gatteschi, R. Sessoli, Angew. Chem., Int. Ed. 42 (2003) 268.
[2] For reviews see: (a) G. Christou, D. Gatteschi, D.N. Hendrickson, R. Sessoli, MRS Bull. 25 (2000) 66; (b) R. Bircher, G. Chaboussant, C. Dobe, H.U. Güdel, S.T. Oshsenbein, A. Sieber, O. Waldmann, Adv. Funct. Mater. 16 (2006) 209.
[3] G. Christou, Polyhedron 24 (2005) 2065, and references therein.
[4] (a) G. Rajaraman, E.C. Sanudo, M. Helliwell, S. Piligkos, W. Wernsdorfer, G. Christou, E.K. Brechin, Polyhedron 24 (2005) 2450;

(b) H. Miyasaka, R. Clérac, W. Wernsdorfer, L. Lecren, C. Bonhomme, K. Sugiura, M. Yamashita, Angew. Chem., Int. Ed. 43 (2004) 2801;
(c) C.J. Milios, A. Prescimone, A. Mishra, S. Parsons, W. Wernsdorfer, G. Christou, S.P. Perlepes, E.K. Brechin, Chem. Commun. (2007) 153;
(d) C.J. Milios, C.P. Raptopoulou, A. Terzis, F. Lloret, R. Vicente, S.P. Perlepes, A. Escuer, Angew. Chem., Int. Ed. 43 (2004) 210;
(e) L.F. Jones, G. Rajaraman, J. Brockman, M. Murugescu, E.C. Sanudo, J. Raftery, S.J. Teat, W. Wernsdorfer, G. Christou, E.K. Brechin, D. Collison, Chem. Eur. J. 10 (2004) 5180;
(f) A.J. Tasiopoulos, A. Vinslava, W. Wernsdorfer, K.A. Abboud, G. Christou, Angew. Chem., Int. Ed. 43 (2004) 2117;
(g) C.J. Milios, A. Vinslava, W. Wernsdorfer, S. Moggach, S. Parsons, S.P. Perlepes, G. Christou, E.K. Brechin, J. Am. Chem. Soc. 129 (2007) 2754;
(h) Th.C. Stamatatos, D. Foguet-Albiol, C.C. Stoumpos, C.P. Raptopoulou, A. Terzis, W. Wernsdorfer, S.P. Perlepes, G. Christou, J. Am. Chem. Soc. 127 (2005) 15380;
(i) Th.C. Stamatatos, D. Foguet-Albiol, S.-C. Lee, C.C. Stoumpos, C.P. Raptopoulou, A. Terzis, W. Wernsdorfer, S.O. Hill, S.P. Perlepes, G. Christou, J. Am. Chem. Soc. 129 (2007) 9484.

[5] (a) M. Soler, W. Wernsdorfer, K.A. Abboud, J.C. Huffman, E.R. Davidson, D.N. Hendrickson, G. Christou, J. Am. Chem. Soc. 135 (2003) 3576;
(b) S.M.J. Aubin, Z. Sun, L. Pardi, J. Krzystek, K. Folting, L.-C. Brunel, A.L. Rheingold, G. Christou, D.N. Hendrickson, Inorg. Chem. 38 (1999) 5329;
(c) E.K. Brechin, M. Soler, D. Davidson, S. Parsons, G. Christou, Chem. Commun. (2002) 2252;
(d) R. Bagai, G. Christou, Inorg. Chem. 46 (2007) 10810;
(e) M. Murugesu, M. Habrych, W. Wernsdorfer, K.A. Abboud, G. Christou, J. Am. Chem. Soc. 126 (2004) 4766;
(f) Th.C. Stamatatos, K.A. Abboud, W. Wernsdorfer, G. Christou, Angew. Chem., Int. Ed. 46 (2007) 884.

[6] (a) Bond-valence sum (BVS) calculations for the Mn ions of **1** gave values of: 2.86 for the only clearly Mn^{3+} ion (Mn3), 4.00-4.01 for Mn^{4+} ions (Mn(4,5,6)), and 2.35-2.64 for the intermediate oxidation state (average 2.5+) Mn ions, Mn(1,2);
(b) W. Liu, H.H. Thorp, Inorg. Chem. 32 (1993) 4102;
(c) I.D. Brown, D. Altermatt, Acta Crystallogr. Sect. B (1985) 244.

[7] (a) Y.-B. Jiang, H.-Z. Kou, R.-J. Wang, A.-L. Cui, J. Ribas, Inorg. Chem. 44 (2005) 709;
(b) M.I. Khan, Q. Chen, H. Hope, S. Parkin, C.J. O'Connor, J. Zubieta, Inorg. Chem. 32 (1993) 2929;
(c) K. Hegetschweiler, H. Schmalle, H.M. Streit, W. Schneider, Inorg. Chem. 29 (1990) 3625;
(d) M.I. Khan, Q. Chen, J. Zubieta, D.P. Goshom, Inorg. Chem. 31 (1992) 1556;
(e) K. Hegetschweiler, H. Schmalle, H.M. Streit, V. Gramlich, H.-U. Hund, Inorg. Chem. 31 (1992) 1299;
(f) A. Cornia, D. Gatteschi, K. Hegetschweiler, L. Hausherr-Primo, V. Gramlich, Inorg. Chem. 35 (1996) 4414;
(g) J. Spandl, M. Kusserow, I. Brudgam, Z. Anorg. Allg. Chem. 629 (2003) 968.

[8] W. Wernsdorfer, Adv. Chem. Phys. 118 (2001) 99.

[9] For example see: (a) Th.C. Stamatatos, K.A. Abboud, W. Wernsdorfer, G. Christou, Angew. Chem., Int. Ed. 45 (2006) 4134;
(b) Th.C. Stamatatos, K.M. Poole, D. Foguet-Albiol, K.A. Abboud, T.A. O'Brien, G. Christou, Inorg. Chem. 47 (2008) 6593;
(c) O. Kahn, Molecular Magnetism, VCH Publishers, New York, 1993;
(d) Th.C. Stamatatos, G. Christou, Philos. Trans. R. Soc. A 366 (2008) 113, and references therein.

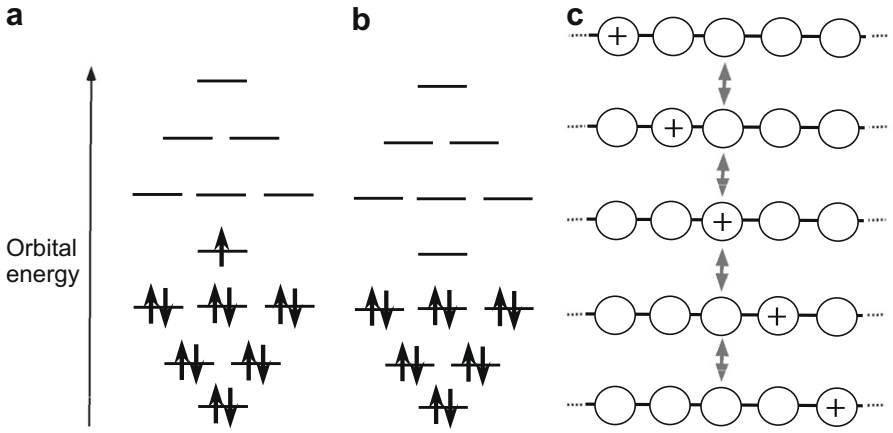


Fig. 1. (a) An orbital energy diagram of the phenalenyl radical. (b) An orbital energy diagram of the phenalenyl cation. (c) A schematic illustration of conductivity of a one-dimensional hole-doped system; the gray double-sided arrow indicates the in-phase superposition of configurations due to itinerancy of the hole.

states [27–44]. This is an example of a known fact that the KS-DFT with a semilocal approximation such as local density approximation (LDA) and generalized gradient approximation (GGA), does not work for the cation radical, in particular at the dissociated limit. The one-electron self-interaction error (SIE) is the spurious classical Coulomb of the excess electron with itself and inevitable in any semilocal approximation of the exchange-correlation functional [45]. Miehlich et al. pointed out that this spurious SIE leads to a spurious stability of a delocalized electronic structure for many ion–radical systems [27]. In fact, the B3LYP method [26], a de facto standard hybrid DFT method, fails to describe the potential surface of the cation radical as shown below. Furthermore, recent surveys on ion–radical systems using various types of HF and hybrid DFT reveal that the problem is more complicated: Gräfenstein, Kraka, and Cremer found that the exact correction for one-electron self-interaction error developed by Perdew and Zunger (PZ-SIC) also suffers from the 'size-inconsistency' error [28]. This result implies that the problem of the ion–radical systems is beyond the scope of the usual PZ-SIC method [45], by which almost all problems involved with the KS-DFT applications were resolved. Mori-Sanchez, Cohen, and Yang (MCY) have emphasized that it is needed for the energy functional to satisfy a relation proposed by Perdew, Parr, Levy, and Balduz (the PPLB relation) to treat correctly ion–radical systems as described in details below [33,36,39]. We suggested that combining exact exchange in KS-DFT with a resonating correction provides a possible answer for this problem [43]. In fact, it is shown that the double exchange interaction, which is an essential source of ferromagnetism for hole-doped magnetic systems, is correctly described by this method [44]. Thus, following the studies of Refs. [43,44], we employ the resonating (Res) broken-symmetry (BS) configuration interaction (CI) using spin unrestricted HF solutions as bases. At first, we examine the chemical bonding of a simplified model of $\mathbf{1}_2^+$ by B3LYP, UHF, and Res-BS CI methods. Furthermore, using Res-BS CI method, we investigate acetylene-bridged and methylene-bridged phenalenyl dimeric cations. The results are discussed from the viewpoint of the relation between the mediate unit (vacuum, acetylene, and methylene) in the phenalenyl dimeric compounds and fundamental characters of electronic structures.

2. Theoretical background

As described above, the electronic structure of the ion–radical systems now becomes an important issue in the field of computational physics-and-chemistry. In this section, we will briefly review this topic from the viewpoint of the 2-center 3-electron bond and the PPLB relation for our theoretical approaches examined in this study.

2.1. General discussion for the electronic structure of ion–radical systems

In order to consider importance of the description of the excess electron in ion–radical systems, we shall recall the Robin and Day's three types of mixed valence transition metal (MV-TM) systems in the field on inorganic chemistry [46,47]: according to the excess electron (hole) behavior, they classified the MV-TM compounds into three classes, the localized (Class I), the intermediate (Class II), and the fully delocalized (Class III) ones. These classes exhibit the class-specific magnetic, conductive, and optical properties [46,47]. If an ab initio method favors the specific one among them, it is difficult to determine the electronic properties correctly.

For simplicity, consider a two-atomic mono-cationic system A_2^+, of which two sites are equivalent each other. Roughly speaking, if the overlap between SOMO of the cationic site (A^+) and the HOMO of the neutral site (A) is not zero, the bond-order of A_2^+ is 0.5. So the dependency on the charge distribution of the energy is expected to be given by

$$E(A^{+0.5} + A^{+0.5}) < 0.5\,E(A + A^+) + 0.5\,E(A^+ + A). \quad (1)$$

Here, $E(A + A^+)$ and $E(A^+ + A)$are energies of the hypothetical electronic structures, in which the charges assume to localize at right and left sites respectively, while $E(A^{+0.5} + A^{+0.5})$ is the energy of the bonding state. As the intersite distance increases, the bond-order reduces to be 0. Then, the energy relation must be

$$E(A^{+0.5} + A^{+0.5}) = 0.5\,E(A + A^+) + 0.5\,E(A^+ + A). \quad (2)$$

This simplest example exemplifies the PPLB relation [40] for cation radical species. In the theoretical framework of an extended version of DFT at the zero temperature, PPLB state that the exact energy functional for fractional number of electrons, $N + \omega (0 \leqslant \omega \leqslant 1)$, depends linearly on the number of electrons as

$$E_{\mathrm{PPLB}}(N + \omega) = (1 - \omega)E_{\mathrm{PPLB}}(N) + \omega E_{\mathrm{PPLB}}(N + 1). \quad (3)$$

Obviously, this is a generalized version of Eq. (2).

2.2. KS-DFT description of ion–radical systems

Mori-Sanchez, Cohen, and Yang (MCY) have showed [33,36,39] that the dependency of electron numbers of various DFT-XC functionals is given by

$$E_{\text{KS-DFT}}(N+\omega) < (1-\omega)E_{\text{KS-DFT}}(N) + \omega E_{\text{KS-DFT}}(N+1). \quad (4)$$

This holds also for the usual hybrid XC functional such as B3LYP. Therefore, if we compute the phenalenyl (P) cationic dimer at the dissociation limit, the relation is given by

$$E_{\text{KS-DFT}}(P^{+0.5} + P^{+0.5}) < 0.5\, E_{\text{KS-DFT}}(P + P^{+}) + 0.5\, E_{\text{KS-DFT}}(P^{+} + P), \quad (5)$$

implying that the phenalenyl cationic dimer energy at the dissociation limit is lower than the sum of neutral and cationic phenalenyls: the potential surface of P_2^+ is expect to break down.

This indicates the usual DFT and hybrid-DFT favor the Class III in the context of the Robin and Day's classification. This discussion is consistent with a well-known result that the DFT and hybrid DFT methods favor delocalized electronic structure states for transition states of chemical reactions and metallic states of solids [39].

2.3. Hartree–Fock treatment of ion–radical systems

In contrast, the dependency of the UHF energy on the electron numbers is given by [33,36,39]

$$E_{\text{UHF}}(N+\omega) > (1-\omega)E_{\text{UHF}}(N) + \omega E_{\text{UHF}}(N+1). \quad (6)$$

As a result, the UHF calculation of the dissociation limit of the phenalenyl cationic dimer will be given by

$$E_{\text{UHF}}(P^{+0.5} + P^{+0.5}) > E_{\text{UHF}}(P + P^{+}) = E_{\text{UHF}}(P^{+} + P). \quad (7)$$

In other words, the UHF potential surface of P_2^+ is expected to reduce to the energy sum of P plus P^+. In energetic view of the potential surface of P_2^+, this is correct. However, note that the excess electron described by the UHF method prefers the localized state too much. Among the Robin and Day's three classes, the UHF method energetically favors the Class I. This feature causes known artifacts of the UHF method, i.e., the overestimation of band-gaps of some semiconductors and the over-stabilization of the spurious magnetic states for some cases [48]. This is because a localized solution obtained using the UHF method often corresponds to a hole-localized configuration, missing conductivity due to hole-delocalization effects illustrated in Fig. 1c. In principle, the resonating effect is essential for conductivity emerging from the hole-(or charge-) doping [23,41].

2.4. Resonating broken-symmetry CI treatment of ion–radical systems

A goal of this issue is to construct the exchange-correlation functional, by which the PPLB relation given by Eq. (3) holds for all atomic and molecular species. MCY have indeed designed two functionals called MCY3 and rCAM-B3LYP to satisfy Eq. (3) *approximately* [36]. On the other hand, we consider that this type of the problem is related to the resonating effects among several valence bond configurations [23,41]. In fact, the magnetic metal states of hole-doped bis-and-tris (methylene) amines were well described by MR plus perturbation treatment [23], by which we include all possible configurations in the variational (complete-active) space. Recently, we present that not only the variational space for wavefunctions, but also the linearity of the working equation are important to obtain the resonating state for ion–radical systems consisting of two equivalent sites (i.e., A_2^+) [43,44]. In these recent studies [43,44], we suggest an ab initio recipe in order to correctly treat ion–radical systems as follows:

(i) First, we obtain possible broken-symmetry solutions by implementing a mean-field theory, of which the electron-number dependency satisfies the Eq. (6). A simple choice is the UHF theory: UHF calculations of A_2^+ at dissociation limit are expected to yield two equivalent solutions, in which the charge localizes at left and right sites as denoted by $|L\rangle$ and $|R\rangle$, respectively.

(ii) Using $|L\rangle$ and $|R\rangle$ as bases, solve a non-orthogonal CI equation with employing ab initio Hamiltonian to yield the resonating CI solution given by

$$|\text{Res}\rangle = C_L|L\rangle + C_R|R\rangle. \quad (8)$$

In Refs. [43,44], we analyzed the dependence of the Res-HF CI energy on the Mulliken charge distribution by varying the set of CI coefficients, $\{C_L, C_R\}$ in Eq. (8). As a result, we presented that the relation,

$$E_{\text{Res-HF CI}}(A^{+0.5} + A^{+0.5}) < 0.5\, E_{\text{Res-HF CI}}(A + A^{+}) + 0.5\, E_{\text{Res-HF CI}}(A^{+} + A), \quad (9)$$

holds for finite intersite distances, and the relation,

$$E_{\text{Res-HF CI}}(A + A^{+}) = E_{\text{Res-HF CI}}(A^{+\omega} + A^{+(1-\omega)}) = E_{\text{Res-HF CI}}(A^{+} + A), \quad (10)$$

holds for the dissociation limits of various cationic dimmers [43,44]. This fact implies that the Res-HF CI satisfy the PPLB relation, which is the reason for that we employ this method for ion–radical systems.

3. Computational results

In the following calculations, we use Gaussian 03 [44] for UHF and DFT calculations, and a non-orthogonal CI code developed by S.N. for Res-CI calculations. The cc-pVDZ basis [49] is employed. In order to cut computational costs, we employed a simplified phenalenyl (P) unit, in which we replace all *tert*-butyl groups in the X-ray structure by hydrogen atoms. The molecular structure of this simplified monomer is shown in Fig. 2a. This is similar to that employed in the previous computational studies [13–16], and the authors of these studies confirmed that this simplification does not affect computational results significantly.

Now, we shall examine an antiparallel staggered cationic dimer (P_2^+), of which the geometry is illustrated in Fig. 2b. The potential surfaces computed by several methods are plotted in Fig. 3. We

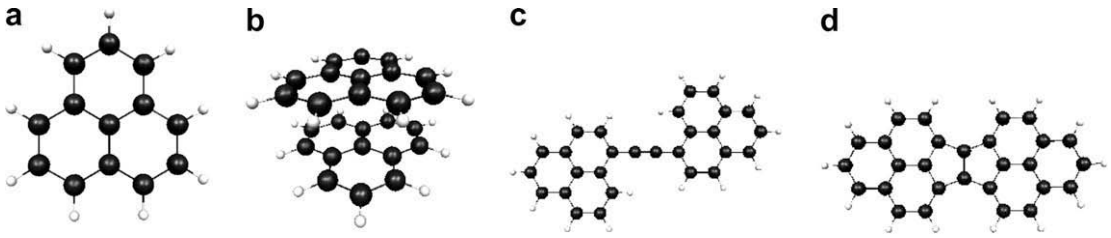


Fig. 2. Geometries of (a) the simplified phenalenyl (P) radical monomer, (b) the cationic dimer of Ps with the antiparallel stacking conformation, (c) an acetylene-bridged P cationic dimeric compound, and (d) an ethylene-bridged P cationic compound.

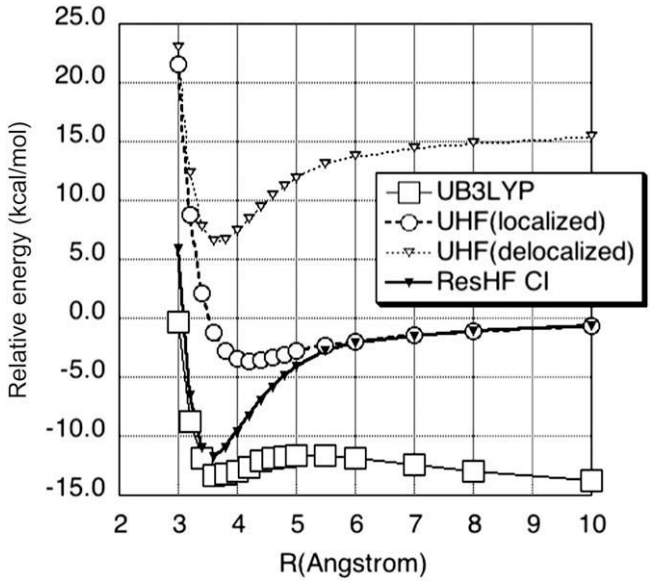


Fig. 3. The potential surfaces for cationic dimer of phenalenyls calculated by the UB3LYP, UHF, and Res-HF CI methods.

show the corresponding Mulliken charges on the relatively cationic site in Fig. 4. The UB3LYP curve in Fig. 3 obviously fails to converge the dissociation limit and all of the solutions along the surface, which are presented in Fig. 4, are delocalized ones, as in the results for other ion–radicals pointed out by DFT researchers [27–44]. On the other hand, there are two UHF solutions, of which the plus charge is localized and delocalized respectively. We can see from Fig. 3 that the delocalized UHF solution is unstable for all regions and the stable UHF solution is localized one, being consistent with the above discussion. Further, there are two equivalent localized UHF solutions, denoted as $|L\rangle$ and $|R\rangle$. Thus, our recipe to reach the resonating HF CI solution, of which the solution is given Eq. (8)

$$|\mathrm{Res}\rangle = C_L|L\rangle + C_R|R\rangle,$$

was implemented. The potential surface and charge distributions of these Res-HF CI solutions are also plotted in Figs. 3 and 4, respectively. Of course, the charge delocalization effect is recovered by the Res-HF CI treatment as shown in Fig. 4. The resonating energy that is the energy gap between the localized UHF solution and the corresponding Res-HF CI solution, however, reduces to zero as the intermolecular distance becomes large. This fact implies the relation,

$$E_{\mathrm{UHF}}(A + A^+) = E_{\text{Res-HF CI}}\,(A^{+0.5} + A^{+0.5}) = E_{\mathrm{UHF}}(A^+ + A) \qquad (11)$$

approximately holds for large intermolecular distances. Comparing Eq. (10) with Eq. (11), it can be concluded that the Res-HF CI method satisfies the PPLB condition for this system. This result is similar to the situation emphasized in the previous study for the small ion–radicals and double-exchange systems [43,44]. In addition, a point is that the resonating energy is considerably large for all region of potential surface: the binding energy of Res-HF CI solutions is approximately 12 kcal/mol, which is larger than that of UHF solution by 8 kcal/mol. The experimentally reported value (the enthalpy change upon formation of the cation radical) is 6.5 kcal/mol [16], which is smaller than our Res-HF CI value, but, as pointed out by Small et al. it is expected that the solvation effects considerably contribute (may reduce) to this experimental value.

Next, we proceed to the case that two phenalenyl units are bridged by acetylene and ethylene units as shown in Fig. 2c and d, respectively. The nonlinear optical properties of these compounds were examined previously for the neutral case [8,14] to utilize the phenalenyl unit as a constituent of supermolecules. Now, according to the recipe described in the Section 2.4, we shall examine the fundamental characters of these cationic dimeric compounds in compared with the through-space case described above. In the context of antiferromagnetic interactions, the through-bond (super-exchange) interactions are much larger than the through-space (direct exchange) interactions [50].

The optimized geometries of the bridged parts which are obtained in Ref. [14], are used, while that of phenalenyl unit is fixed to be experimental one. For the acetylene-bridged one, there is only the delocalized UHF (ROHF) solution, of which charge distribution is illustrated in Fig. 5. Comparing the through-space dimer case, the acetylene bridge is expected to play a enhancement factor for the conductivity of hole-doped phenalenyl compounds. In contrast, there are three low-lying spin-density wave (SDW) type of UHF solutions within 0.13 eV for the ethylene-bridged one, of which the charge distributions on phenalenyl units and the ethylene bridge, together with relative energies, are summarized in Table 1. We can see from this table that these solutions are similar each other. However, the spin distributions, which are summarized in Table 2, are different each other. Obviously, the bridged ethylene contributes to spin-density waves for all of SDW1, SDW2, and SDW3. Then using these solutions as bases,

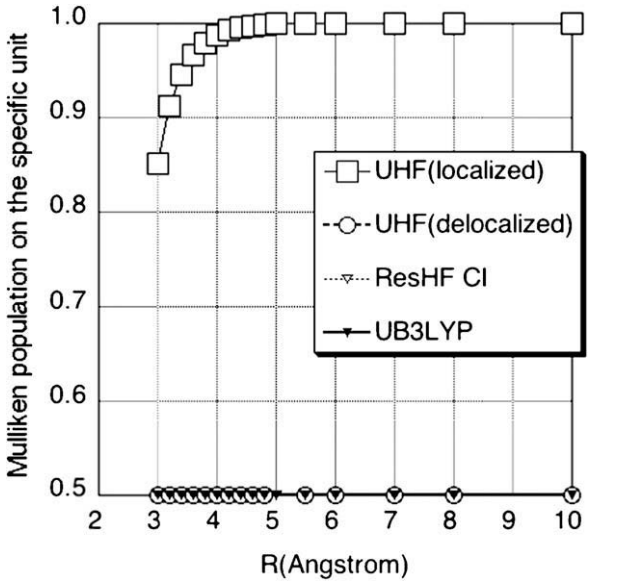


Fig. 4. Calculated Mulliken charge distributions on a relatively cationic site of cationic dimer of phenalenyls for various intersite distances.

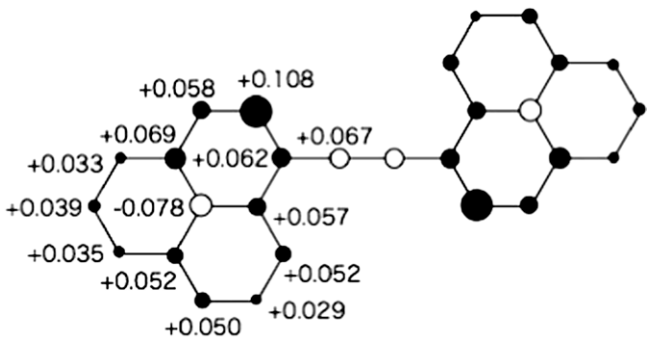


Fig. 5. Charge distributions of the acetylene-bridged phenalenyl cationic dimer calculated by the UHF method. The distribution at the right unit is symmetric to the left one.

Table 1
Charge distributions of low-lying UHF solutions for ethylene-bridged phenalenyl cationic dimer, together with the relative energies.

	Phenalenyl (right)	Ethylene (bridge)	Phenalenyl (left)	Relative energies to SDW3solution (eV)
SDW1	0.583461	−0.146494	0.563033	0.128
SDW2	0.563047	−0.146507	0.583458	0.128
SDW3	0.555383	−0.110767	0.555383	0

Table 2
Spin distributions of low-lying UHF solutions for ethylene-bridged phenalenyl cationic dimer.

	Phenalenyl (right)	Ethylene (bridge)	Phenalenyl (left)
SDW1	0.837411	0.950317	−0.787728
SDW2	−0.787708	0.950265	0.837444
SDW3	0.904001	−0.808006	0.904001

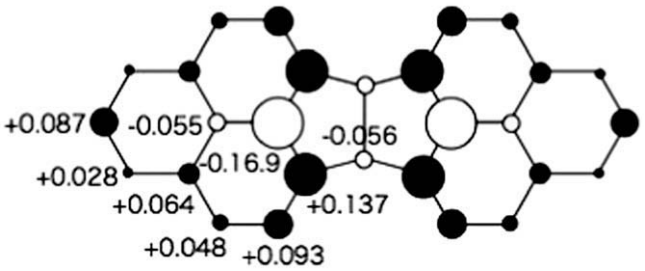


Fig. 6. Charge distributions of Res-HF CI solutions for the ethylene-bridged phenalenyl cationic dimer. The distribution at the right unit is symmetric to the left one.

we implemented Res-HF CI calculations. The resulting wavefunction is given by

$$|\mathrm{Res}\rangle = C_{\mathrm{SDW1}}|\mathrm{SDW1}\rangle + C_{\mathrm{SDW2}}|\mathrm{SDW2}\rangle + C_{\mathrm{SDW3}}|\mathrm{SDW3}\rangle, \quad (12)$$

with $C_{\mathrm{SDW1}} = C_{\mathrm{SDW2}} = 0.139$ and $C_{\mathrm{SDW3}} = 0.981$, indicating that the most stable UHF solution, the SDW3 type, is dominant for this Res-HF CI solution. The resulting charge distribution is shown in Fig. 6. This is similar to that of the SDW3 solution, due to the large CI coefficient in Eq. (12). When we see this solution as a charge-density wave from this figure, it is found that the ethylene plays a small amount of contribution. Thus the ethylene-bridge plays a role for the spin density wave, but little role for charge density wave.

4. Conclusions

We investigated phenalenyl cationic dimer systems using ab initio methods. First, the potential surface of the antiparallel staggered cationic dimer of the simplified phenalenyl molecules is examined with focusing our attention on the hole-behavior and the shapes of the potential surfaces by UB3LYP, UHF, and Res-HF CI methods. The results are similar to those of other ion–radical systems: the UB3LYP calculations always yield the delocalized state, and the UB3LYP energy at the dissociation limit is lower than the sum of neutral and phenalenyl cationic monomers. In contrast, the UHF method yields the correctly dissociated curve and the localized solutions for the long intermolecular distances. Then the Res CI computation based on the left-and-right localized UHF solutions is implemented. The results are that the charge delocalized effect for long inter units distances is recovered and that the resonating energies reach at approximately 8 kcal/mol at the equilibrium distance and reduce to zero at the dissociation limit, implying that these Res-HF CI solutions satisfy the PPLB condition of exact solutions for the ion–radical systems.

Then, we applied the Res-HF CI method for the acetylene-bridged and ethylene-bridged phenalenyl cationic dimers. However, we obtained only delocalized type of the UHF solutions for the former case. This result indicates that the acetylene-bridge works as a conductivity-enhanced-bridge for hole-doped phenalenyl compounds. On the other hand, there are three low-lying spin-density wave types of UHF solutions within 0.13 eV for the ethylene-bridged phenalenyl cationic compound. However, the Res-HF CI calculation shows that the most stable spin-density wave type of the UHF solution is dominant for the ground-state Res-HF CI wavefunction. For both acetylene-and-ethylene bridge cation dimmers, main distributions of holes are on both phenalenyl sites equivalently, but the small amount of holes is delocalized on the bridge part. Judging from our computational results in this study, different bridges-or-stacks lead to different hole behaviors, implying the possibility of various electronic functionalities of the hole-doped phenalenyl compounds.

A remaining, and important problem is that we omit the distortion of molecules in this study. Introducing this effect might change the situation drastically: a most possible situation is forming the (spin) polaron in which the distortion of the molecular geometry and the charge (spin) density distribution are coupled [51]. This effect is a disturbing factor if we intend to model organic magnetic metals, so the examination of this effect will be important issue. From the viewpoint of computational chemistry, the geometry optimization is needed. A noteworthy point here is that, as just presented also in this study, the potential surfaces of ion–radical species for various geometries strongly depend on the method we employed. In our recent studies of ion–radical systems [43,44], a many-electron self-interaction free method is needed to described the equivalent-sites limit of ion–radical species. There are two possible ways towards this line: one is to improve the hybrid-DFT as MCY suggested [36] and another is the resonating approach based on a wavefunction theory such as CASSCF (Res-CASSCF) and spin unrestricted coupled-cluster (Res-CC) [43]. Note that the latter way, which is never developed by the precursors in this field, is expected to provide precise information of ion–radical systems even at unstable geometries that are beyond the scope of experimental studies at present. On the basis of such information, the former way, i.e., construction of an accurate hybrid DFT functional will be refined. Because both the former and the later are not trivial extensions of the present work, these are theme in the future studies. We limited the Res-HF CI treatment in this study. However, it is noteworthy that most of results presented here are not affected by introducing electron correlations. In particular, the acetylene-bridged phenalenyl compounds are expected to exhibit strong conductivity by doping a hole, because the UHF method, which usually favors the localized state in general, leads to the delocalized hole. Even if the Res-CC will be implemented, this conclusion is expected to remain true because the CC method is expected to include the delocalization effects of ion–radical systems,[1] but not the localization effects, compared with the UHF method.

Acknowledgements

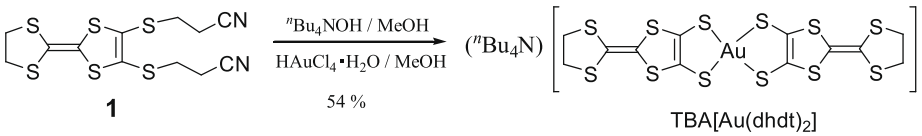
We acknowledge Dr. M. Shoji and Mr. T. Ukai for valuable discussions of the electronic structure of mixed-valence systems. This work is supported by both the CREST project by Japan Science and Technology Agency (JST). We are also grateful to the Ministry of Education, Culture, Sports, Science and Technology (MEXT) for a grant-in-aid for Research and Development of the Next-Generation

[1] For instance, see Fig. 6b in Ref. [43].

Integrated Simulation of Living Matter, a part of the Development and Use of the Next-Generation Supercomputer Project.

References

[1] K. Goto, T. Kubo, K. Yamamoto, K. Nakasuji, K. Sato, D. Shiomi, T. Takui, M. Kubota, T. Kobayashi, K. Yakusi, J. Ouyang, J. Am. Chem. Soc. 121 (1999) 1619.
[2] K. Fukui, K. Sato, D. Shiomi, T. Takui, K. Itoh, K. Goto, T. Kubo, K. Yamamoto, K. Nakasuji, A. Naito, Synth. Met. 103 (1999) 2257.
[3] K. Fukui, K. Sato, D. Shiomi, T. Takui, K. Itoh, T. Kubo, K. Goto, K. Yamamoto, K. Nakasuji, A. Naito, Mol. Cryst. Liq. Cryst. 334 (1999) 49.
[4] Y. Morita, S. Nishida, J. Kawai, K. Fukui, S. Nakazawa, K. Sato, D. Shiomi, T. Takui, K. Nakasuji, Org. Lett. 4 (2002) 1985.
[5] Y. Morita, T. Aoki, K. Fukui, S. Nakazawa, K. Tamaki, S. Suzuki, A. Fuyuhiro, K. Yamamoto, K. Sato, D. Shiomi, A. Naito, T. Takui, K. Nakasuji, Angew. Chem., Int. Ed. 41 (2002) 1793.
[6] Y. Morita, K. Fukui, S. Suzuki, T. Aoki, S. Nakazawa, K. Tamaki, A. Fuyuhiro, K. Yamamoto, K. Sato, D. Shiomi, A. Naito, T. Takui, K. Nakasuji, Polyhedron 22 (2003) 2199.
[7] Y. Morita, J. Kawai, K. Fukui, S. Nakazawa, K. Sato, D. Shiomi, T. Takui, K. Nakasuji, Org. Lett. 5 (2003) 3289.
[8] K. Nakasuji, T. Kubo, Bull. Chem. Soc. Jpn. 77 (2004) 1791.
[9] T. Kubo, M. Sakamoto, K. Nakasuji, Polyhedron 24 (2005) 2522.
[10] S. Suzuki, Y. Morita, K. Fukui, K. Sato, D. Shiomi, T. Takui, K. Nakasuji, Polyhedron 24 (2005) 2618.
[11] T. Kubo, A. Shimizu, M. Sakamoto, M. Uruichi, K. Yakushi, M. Nakano, D. Shiomi, K. Sato, T. Takui, Y. Morita, K. Nakasuji, Angew. Chem., Int. Ed. 44 (2005) 6564.
[12] S. Suzuki, Y. Morita, K. Fukui, K. Sato, D. Shiomi, T. Takui, K. Nakasuji, J. Am. Chem. Soc. 128 (2006) 2530.
[13] Y. Takano, T. Taniguchi, H. Isobe, T. Kubo, Y. Morita, K. Yamamoto, K. Nakasuji, T. Takui, K. Yamaguchi, J. Am. Chem. Soc. 124 (2002) 11122.
[14] M. Nakano, T. Kubo, K. Kamada, K. Ohta, R. Kishi, S. Ohta, N. Nakagawa, H. Takahashi, S. Furukawa, Y. Morita, K. Nakasuji, K. Yamaguchi, Chem. Phys. Lett. 418 (2006) 142.
[15] T. Ukai, K. Nakata, S. Yamanaka, T. Takada, T. Kubo, Y. Morita, Y. Kitagawa, K. Yamaguchi, Polyhedron 26 (2007) 2313.
[16] D. Small, V. Zaitsev, Y. Jung, S.V. Rosokha, M. Head-Gordon, J.K. Kochi, J. Am. Chem. Soc. 126 (2004) 13850.
[17] E. Cubero, F.J. Luque, M. Orozco, Proc. Natl. Acad. Sci. USA 95 (1998) 5976.
[18] B. Miehlich, H. Stoll, A. Savin, Mol. Phys. 91 (1997) 527.
[19] J. Gräfenstein, D. Cremer, Chem. Phys. Lett. 316 (2000) 569.
[20] S. Yamanaka, K. Nakata, T. Takada, K. Kusakabe, J.M. Ugalde, K. Yamaguchi, Chem. Lett. 35 (2006) 242.
[21] K. Nakata, T. Ukai, S. Yamanaka, T. Takada, K. Yamaguchi, Int. J. Quantum Chem. 106 (2006) 3325.
[22] T. Ukai, K. Nakata, S. Yamanaka, T. Takada, K. Yamaguchi, Mol. Phys. 105 (2007) 2667.
[23] S. Yamanaka, M. Okumura, H. Nagao, K. Yamaguchi, Chem. Phys. Lett. 233 (1995) 88.
[24] W. Kohn, L.J. Sham, Phys. Rev. 140 (1964) A1131.
[25] R.G. Parr, W. Yang, Density Functional Theory of Atoms and Molecules, Oxford University Press, 1989.
[26] A.D. Becke, J. Chem. Phys. 98 (1993) 5648.
[27] R. Merkle, A. Savin, H. Press, J. Chem. Phys. 97 (1992) 9216.
[28] J. Gräfenstein, E. Kraka, D. Cremer, J. Chem. Phys. 120 (2004) 524.
[29] M. Lundberg, P.E.M. Siegbahn, J. Chem. Phys. 122 (2005) 224103.
[30] S.M. Valone, S.R. Atlas, Phys. Rev. Lett. 97 (2006) 256402.
[31] A. Ruzsinszky, J.P. Perdew, S.I. Csonka, O.A. Vydrov, G.E. Scuseria, J. Chem. Phys. 125 (2006) 94112.
[32] O.A. Vydrov, G.E. Scuseria, J. Chem. Phys. 125 (2006) 234109.
[33] P. Mori-Sanchez, A.J. Cohen, W. Yang, J. Chem. Phys. 125 (2006) 201102.
[34] J.P. Perdew, A. Ruzsinszky, G.I. Csonka, O.A. Vydrov, G.E. Scuseria, V.N. Staroverov, J. Tao, Phys. Rev. A 76 (2007) R040501.
[35] A. Ruzsinszky, J.P. Perdew, S.I. Csonka, O.A. Vydrov, G.E. Scuseria, J. Chem. Phys. 126 (2007) 104102.
[36] A.J. Cohen, P. Mori-Sanchez, W. Yang, J. Chem. Phys. 126 (2007) 191109.
[37] O.A. Vydrov, G.E. Scuseria, J.P. Perdew, J. Chem. Phys. 126 (2007) 154109.
[38] Q. Wu, C.-L. Cheng, T.V. Voorhis, J. Chem. Phys. 127 (2007) 164119.
[39] A.J. Cohen, P. Mori-Sanchez, W. Yang, Science 321 (2008) 792.
[40] J.P. Perdew, R.G. Parr, M. Levy, J.L. Balduz Jr., Phys. Rev. Lett. 49 (1982) 1691.
[41] S. Yamanaka, K. Yamaguchi, Bull. Chem. Soc. Jpn. 77 (2004) 1269.
[42] R. Takeda, S. Yamanaka, K. Yamaguchi, Int. J. Quantum Chem. 106 (2006) 3303.
[43] S. Nishihara, S. Yamanaka, T. Ukai, K. Nakata, K. Kusakabe, Y. Yonezawa, H. Nakamura, T. Takada, K. Yamaguchi, Int. J. Quantum Chem. 108 (2008) 2966.
[44] S. Nishihara, S. Yamanaka, K. Kusakabe, K. Nakata, Y. Yonezawa, H. Nakamura, T. Takada, K. Yamaguchi, J. Phys.: Condens. Matter, in press.
[45] J.P. Perdew, A. Zunger, Phys. Rev. B 23 (1981) 5048.
[46] M.B. Robin, P. Day, Adv. Inorg. Chem. Radiochem. 10 (1967) 247.
[47] F. Shriver, P.W. Atkins, in: C.H. Langford (Ed.), Inorganic Chemistry, second ed., Oxford University Press, Oxford, 1994.
[48] For instance, the discussion in the context of LDA + U and dynamical mean-field theory can be seen in the following: G. Kotliar, S.Y. Savrasov, K. Haule, V.S. Oudovenko, O. Parcollet, C.A. Marianetti, Rev. Mod. Phys. 78 (2006) 865.
[49] D.E. Woon, T.H. Dunning Jr., J. Chem. Phys. 100 (1994) 2975.
[50] K. Itoh, M. Kinoshita (Eds.), Molecular Magnetism, Gordon and Breach Science Publishers, 2000.
[51] H. Mizouchi, A. Ikawa, H. Fukutome, Synth. Met. 15 (1997) 1769.



Scheme 1.

diethyl ether to the filtrate afforded (n-Bu$_4$N)[Au^{III}(dhdt)$_2$] as brown powder in 54% yield.

Tetraphenylphosphonium salt, (Ph$_4$P)[Au^{III}(dhdt)$_2$], was obtained by slow diffusion of THF–methanol solution of tetraphenylphosphonium bromide to THF–methanol solution of (n-Bu$_4$N)[Au^{III}(dhdt)$_2$] to give black needle crystals suitable for X-ray structural analysis.

2.3. Preparation of neutral complex [Au(dhdt)$_2$]

Neutral complex, [Au(dhdt)$_2$], was prepared by electrochemical oxidation of (n-Bu$_4$N)[Au^{III}(dhdt)$_2$] at a constant current of 0.2–0.5 μA in benzonitrile or benzonitrile with 5–20% methanol or ethanol containing n-Bu$_4$NBr as a supporting electrolyte at 25 °C. All the solvents were purified before use. Concentration of (n-Bu$_4$N)[Au^{III}(dhdt)$_2$] and n-Bu$_4$NBr were 0.3–3.0 and 25 mM, respectively. For all the reaction condition, only powder samples were obtained. *Anal.* Calc. for [Au(dhdt)$_2$] (C$_{12}$H$_8$AuS$_{12}$): C, 19.64; H, 1.10. Found: C, 19.77; H, 1.22%.

2.4. X-ray crystallography

Diffraction data were collected at 293 K on a Bruker SMART APEX diffractometer fitted with a CCD type area detector, and a full sphere of data were collected using graphite-monochromated Mo Kα radiation (λ = 0.71073 Å). The data frames were integrated using SAINT and merged to give a unique data set for structure determination. Total reflections collected were 18646 of which independent reflections were 5686 (R_{int} = 0.0531). The structure was solved by direct methods and refined by the full-matrix least-squares method on all F^2 data using the SHELEX 5.1 package (Bruker Analytical X-ray Systems). Non-hydrogen atoms were refined with anisotropic thermal parameters. Hydrogen atoms were included in calculated positions and refined with isotropic thermal parameters riding on those the parent atoms.

Crystal data for (Ph$_4$P)$_2$[Au^{III}(dhdt)$_2$]$_2$: C$_{72}$H$_{56}$Au$_2$P$_2$S$_{24}$, F.W. = 2146.48; black needle, monoclinic, space group $P2_1/c$, a = 8.304(1), b = 22.249(3), c = 21.571(3) Å, β = 95.738(2)°, V = 3965.5(8) Å^3, Z = 2, R = 0.0521, Rw = 0.1339.

2.5. Electrical conductivity and magnetic susceptibility

Temperature dependence of resistivity was measured on a compressed pellet of a powder sample of [Au(dhdt)$_2$] by the four-probe dc method using gold wire contacted to the pellet by carbon paste. Magnetic susceptibility was measured for a powder sample in the temperature range of 2–300 K using a superconducting quantum interference device magnetometer with 20000 Oe field application. The diamagnetic contribution of [Au(dhdt)$_2$] was calculated to be -305.46×10^{-6} emu mol^{-1} using Pascal's law. Magnetization data were collected as a function of the applied field up to 5 T at 1.8 K.

3. Results and discussion

3.1. Electrochemical property of Au complex

The redox potentials of (Ph$_4$P)[Au^{III}(dhdt)$_2$] were investigated by cyclic voltammetry at 25 °C in acetonitrile containing n-Bu$_4$NPF$_6$ as a supporting electrolyte at a scan rate of 50 mV s^{-1}, using glassy-carbon working and platinum counter electrodes and a saturated calomel electrode (SCE) as the reference electrode. The redox potentials of Au complex were summarized in Table 1 together with those of Ni complex, (Ph$_4$P)[Ni^{III}(dhdt)$_2$]. While the irreversible step corresponding to the oxidation from monovalent [Au(dhdt)$_2$]$^-$ to neutral Au complex was observed at −0.06 V, the reduction step from [Au(dhdt)$_2$]$^-$ to divalent [Au(dhdt)$_2$]$^{2-}$ at −0.85 V. Compared with the corresponding potentials of the Ni complex, oxidation to the neutral complexes occurs at almost same potentials, but the reduction potential to the divalent species of the Au complex is more negative than that of the Ni complex.

3.2. Crystal structure of (Ph$_4$P)[Au^{III}(dhdt)$_2$]

X-ray structural analysis for (Ph$_4$P)[Au^{III}(dhdt)$_2$] revealed that the complex crystallized in the monoclinic space group $P2_1/c$ consisting of two [Au^{III}(dhdt)$_2$]$^-$ anions and one tetraphenylphosphonium cation. The Au(III) ions are located on the center of inversion, so that the stoichiometry of tetraphenylphosphonium cation and [Au^{III}(dhdt)$_2$]$^-$ anion is 1: 1. Fig. 1a shows the molecular structure of the [Au^{III}(dhdt)$_2$]$^-$ anion. The Au(III) ions of both the crystallographically independent [Au^{III}(dhdt)$_2$]$^-$ anions adopt a square planar coordination surrounded by four sulfur atoms from dhdt^{2-} ligands. The Au–S bond lengths are 2.288(3)–2.308(3) Å, which are comparable to the mean Au–S bond length (2.296 Å) observed in [Au^{III}(tmdt)$_2$] [6], suggesting the Au ions in [Au(dhdt)$_2$]$^-$ anions are trivalent Au(III). The [Au(dhdt)$_2$]$^-$ anions are arranged in a windmill manner [7] in the bc plane and they stacked along the a-axis as shown in Fig. 1b. The cations are located in the hollow surrounded by four [Au(dhdt)$_2$]$^-$ anions. There is no sulfur–sulfur contacts shorter than the sum of van der Waals radii between the [Au(dhdt)$_2$]$^-$ anions.

3.3. Electrical conductivity and magnetic susceptibility of [Au(dhdt)$_2$]

Fig. 2 shows the temperature dependence of resistivity of the neutral complex [Au(dhdt)$_2$] measured on a compress pellet. The electrical conductivity at room temperature was σ_{rt} = 8.3 S cm^{-1}, which is higher than that of the corresponding Ni complex, [Ni(dhdt)$_2$], measured for a single crystal (σ_{rt} = 0.084 S cm^{-1}) [5]. As seen in Fig. 1, the conducting behavior was the activation-type, and the activation energy was calculated to be E_a = 23 meV from the Arrhenius plot, $\rho(T) = A\exp(\Delta E/k_BT)$, where A is a temperature-independent constant, k_B, the Boltzmann constant, and ΔE, the activation energy. The activation energy of the Au complex is smaller than that of the Ni complex (E_a = 40 meV).

Since the Au(III) ion has d^8 electronic configuration, the neutral Au dithiolato complex has one unpaired electron. Thus magnetic

Table 1
Redox potentials of (Ph$_4$P)[M^{III}(dhdt)$_2$] (M = Au and Ni) in acetonitrile (V vs. SCE, 25 °C).

Compound	E_1	E_2
(Ph$_4$P)[Au^{III}(dhdt)$_2$]	−0.06	−0.85
(Ph$_4$P)[Ni^{III}(dhdt)$_2$]	−0.12	−0.52

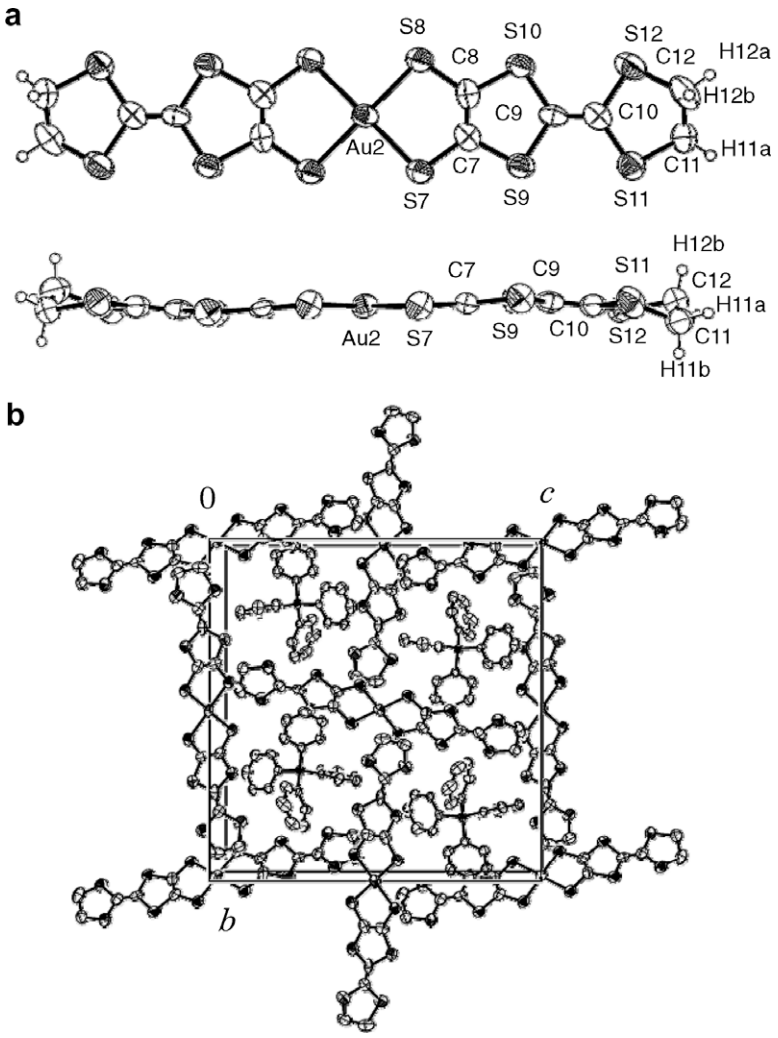


Fig. 1. Crystal structure of $(Ph_4P)[Au(dhdt)_2]$. (a) Molecular structure of $[Au(dhdt)_2]^-$ anion. (b) Crystal structure viewed along *a*-axis.

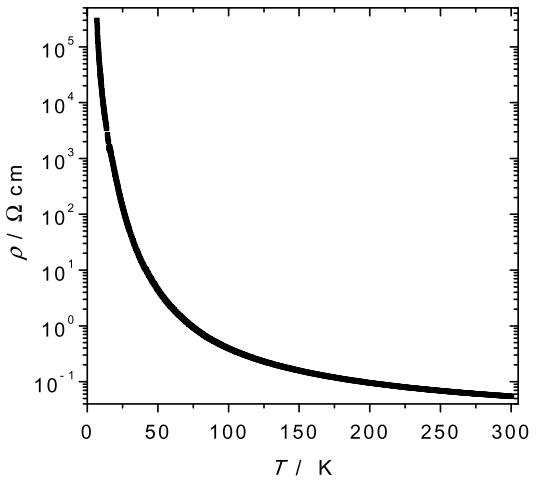


Fig. 2. Temperature dependence of resistivity of $[Au(dhdt)_2]$.

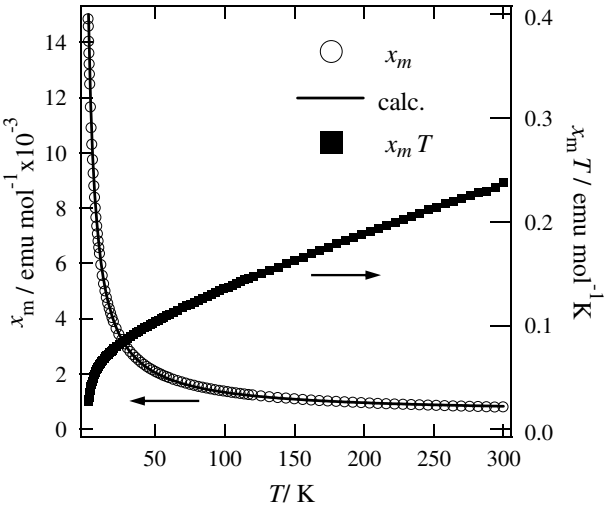


Fig. 3. Temperature dependence of magnetic susceptibility and $\chi_m T$ of $[Au(dhdt)_2]$. The solid line is a fit by the sum of the Curie–Weiss law and temperature independent component.

properties of the neutral Au complex should be very attractive [6]. In order to investigate magnetism of the neutral complex $[Au(dhdt)_2]$, temperature dependence of the magnetic susceptibility was measured by using a SQUID magnetometer at 20 000 Oe from 300 to 2 K (Fig. 3). The susceptibility at 300 K was 7.94×10^{-4} emu mol^{-1}. The $\chi_m T$ value was 0.238 emu mol^{-1} K at 300 K, which is smaller than the expected value of 0.375 emu mol^{-1} K for $S = 1/2$, and decreased gradually with

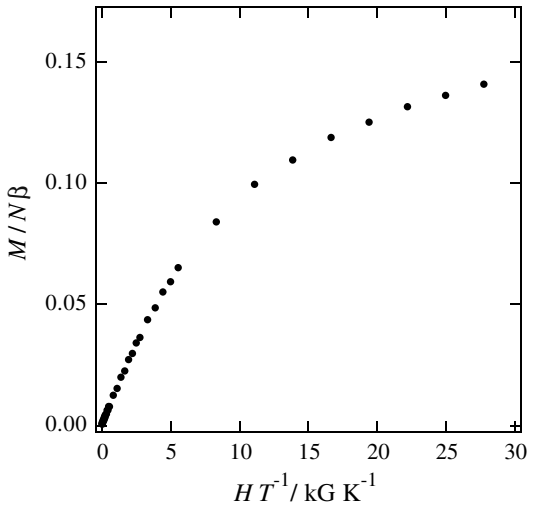


Fig. 4. Magnetization (M) vs. magnetic field strength (H/T) plot for [Au(dhdt)$_2$].

decrease of temperature, and then sudden drop was observed at 20 K. The magnetic susceptibility was well reproduced by the sum of the Curie–Weiss law and the temperature independent component attributable to the conduction π-electron over the whole temperature range as shown by the solid line in Fig. 3. The least-squares fit is found for the Curie constant $C = 7.98 \times 10^{-2}$ emu mol^{-1} K, Weiss temperature $\theta = -3.46$ K, and $\chi_\pi = 5.75 \times 10^{-4}$ emu mol^{-1}, respectively. The value of Curie term is about 20% of the $S = 1/2$ paramagnetic system, which is fairly large for impurity. Fig. 4 shows the magnetic field dependence of magnetization measured at 1.8 K up to 5 T with a SQUID magnetometer. The $M/N\beta$ values increased with increasing magnetic filed strength, and did not show saturation up to 5 T. Although the saturation was not complete, the magnetization under the applied field of 5 T was *ca.* 0.15 $N\beta$ which is much smaller than the value for $S = 1/2$ and comparable to the result obtained by the magnetic susceptibility measurement.

4. Conclusion

A gold dithiolato complex coordinated by the dihydro-TTF ligand of which π-electron system is reduced compared with those of TTF-dithiolato metal complexes was newly synthesized and isolated as tetra-*n*-butylammoium salt of [Au(dhdt)]$^-$ monoanion. Crystal structure of tetraphenylphosphonium salt, (Ph_4P)[Au(dhdt)], was revealed by X-ray crystallography. The Au(III) ions in the [Au(dhdt)]$^-$ anions have a square planar coordination and the mean Au–S bond length suggests the Au ions are in the trivalent Au(III) state. A neutral complex [Au(dhdt)$_2$] was obtained by the electrochemical oxidation of (n-Bu_4N)[Au(dhdt)$_2$] to give a dark brown powder sample. Conducting behavior of the neutral [Au(dhdt)$_2$] complex was semiconductive with room temperature conductivity of $\sigma_{rt} = 8.3$ S cm^{-1} and activation energy of $E_a = 23$ meV, indicating higher conductivity than those of the neutral Ni complex [Ni(dhdt)$_2$] ($\sigma_{rt} = 0.084$ S cm^{-1}, $E_a = 40$ meV). Magnetic susceptibility of [Au(dhdt)$_2$] was well explained by the sum of the Curie component and the constant value attributable to the conduction π-electron. The Curie term is about 20% of the $S = 1/2$ paramagnetic system. Details on the electronic and magnetic structure of this complex is continuously investigated as well as preparation of a single crystal of the neutral [Au(dhdt)$_2$] complex for X-ray structural analysis and further investigation on the physical properties.

5. Supplementary data

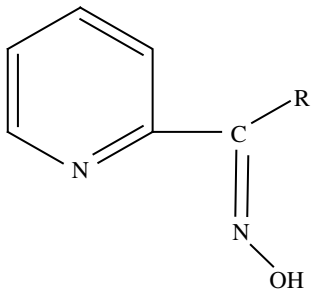
CCDC 702730 contains the supplementary crystallographic data for (Ph_4P)$_2$[Au^{III}(dhdt)$_2$]$_2$. These data can be obtained free of charge via http://www.ccdc.cam.ac.uk/conts/retrieving.html, or from the Cambridge Crystallographic Data Centre, 12 Union Road, Cambridge CB2 1EZ, UK; fax: (+44) 1223-336-033; or e-mail: deposit@ccdc.cam.ac.uk.

Acknowledgement

This work was partly supported by a Grant-in-Aid for Scientific Research (C) (20550118) from JSPS.

References

[1] (a) H. Inokuchi, G. Saito, P. Wu, K. Seki, T.B. Tang, T. Mori, K. Imaeda, T. Enoki, Y. Higuchi, K. Inaka, N. Yasuoka, Chem. Lett. (2001) 1263;
(b) Y. Yamashita, S. Tanaka, K. Imaeda, H. Inokuchi, M. Sano, J. Org. Chem. 57 (1992) 5517;
(c) N.L. Navor, N. Robertson, T. Weyland, J.D. Kilburn, A.E. Underhill, M. Webster, N. Svenstrup, J. Becker, J. Chem. Soc., Chem. Commun. (1996) 1363;
(d) M. Nakano, A. Kuroda, T. Maikawa, G. Matsubayashi, Mol. Cryst. Liq. Cryst. 284 (1996) 301;
(e) M. Kumasaki, H. Tanaka, A. Kobayashi, J. Mater. Chem. 8 (1998) 301;
(f) K. Ueda, Y. Kamata, M. Iwamatsu, T. Sugimoto, H. Fujita, J. Mater. Chem. 9 (1999) 2979;
(g) M.E. Itkis, X. Chi, A.W. Cordes, R.C. Haddon, Science 296 (2002) 1443.
[2] H. Tanaka, Y. Okano, H. Kobayashi, W. Suzuki, A. Kobayshi, Science 291 (2001) 285.
[3] A. Kobayshi, H. Tanaka, H. Kobayashi, J. Mater. Chem. 11 (2001) 2078.
[4] (a) H. Nishiakwa, T. Morimoto, T. Kodama, I. Ikemoto, K. Kikuchi, J. Yamada, H. Yoshino, K. Murata, J. Am. Chem. Soc. 124 (2002) 730;
(b) H. Nishikawa, A. Machida, T. Morimoto, K . Kikuchi, T. Kodama, I. Ikemoto, J. Yamada, H. Yoshino, K. Murata, Chem. Commun. (2003) 494.
[5] K. Yokoyama, H. Nishikawa, T. Kodama, I. Ikemoto, K. Kikuchi, J. Yamada, Synth. Met. 135–136 (2004) 297.
[6] W. Suzuki, E. Fujiwara, A. Kobayshi, Y. Fujishiro, E. Nishibori, M. Tanaka, M. Sakata, H. Fujiwara, H. Kobayashi, J. Am. Chem. Soc. 125 (2003) 1486.
[7] Y. Misaki, T. Kaibuki, M. Taniguchi, K. Tanaka, T. Kawamoto, T. Mori, T. Nakamura, Chem. Lett. (2000) 1274.



R=H; paoH

R=Me; mpkoH

R=Ph; ppkoH

Scheme 1. The 2-pyridyl oxime ligands used in this work.

100 instrument. Magnetic susceptibility measurements were performed at room temperature by the Faraday method using a Cahn-Ventron RM-2 balance standardized with $HgCo(NCS)_4$. Pascal's constants were used to estimate the diamagnetic corrections which were subtracted from the experimental susceptibilities to give the corrected molar magnetic susceptibilities. The variable-temperature magnetic susceptibility properties of complex **2** were investigated using a M600 SQUID magnetometer.

2.2. Compound preparation

2.2.1. $[Co(pao)_3]$ (**1**)

Method A. A pink suspension of $Co(O_2CMe)_2 \cdot 4H_2O$ (0.13 g, 0.50 mmol) in MeCN (25 ml) was treated with solid paoH (0.18 g, 1.50 mmol). The resulting orange slurry was refluxed for 2.5 h, during which time the solids dissolved and the colour of the solution turned to dark red. The solution obtained was stirred at ambient temperature for a further 1 h, during which time a dark orange microcrystalline solid rapidly precipitated. The solid product was isolated by filtration, washed with cold MeCN (2 × 3 mL) and Et_2O (2 × 5 mL), and dried in air for 1 h. Dissolution of the solid in MeOH (20 mL) and slow evaporation of the resulting filtrate at room temperature gave dark orange crystals of **1** after 8 days. The crystals were collected by filtration, washed with cold MeOH (1 × 2 mL) and Et_2O (2 × 5 mL), and dried in air. Yield 60% (based on the ligand). *Anal.* Calc. for $C_{18}H_{15}CoN_6O_3$: C, 51.19; H, 3.59; N, 19.91%. Found: C, 51.06; H, 3.52; N, 19.88%. Selected IR data (KBr pellet, cm^{-1}): 1602s, 1484vs, 1426s, 1348s, 1298w, 1224m, 1180m, 1148m, 1022w, 890w, 806m, 764m, 676m, 580w, 452w.

Method B. Solids $Co(O_2CMe)_2 \cdot 4H_2O$ (0.13 g, 0.50 mmol) and paoH (0.18 g, 1.50 mmol) were dissolved under refluxing conditions in a solvent mixture comprising MeCN/DMF (20 ml, 1:1 v/v) to give a dark red solution. The obtained solution was allowed to stand undisturbed at room temperature for 10 days, during which time well-formed, X-ray quality dark orange crystals of **1** appeared. The crystals were collected by filtration, washed with cold MeCN (1 × 3 mL) and Et_2O (2 × 5 mL), and dried in air. Yield 40% (based on the ligand). The identity of the product was confirmed by elemental analyses (C, H, N) and IR spectroscopic comparison with authentic material from Method A.

2.2.2. $[Co_3(pao)_6](ClO_4)_2$ (**2**)

Method A. An orange suspension of **1** (0.42 g, 1.00 mmol) in MeCN (30 ml) was treated with solid $Co(ClO_4)_2 \cdot 6H_2O$ (0.19 g, 0.50 mmol). The resulting orange-red slurry was refluxed for 12 h, during which time the solids dissolved and the colour of the solution turned to dark red. The solution was filtered, and the filtrate left undisturbed at room temperature to concentrate slowly by evaporation. After 5 days, dark red crystals of **2** were collected by filtration, washed with cold MeCN (2 × 2 mL) and Et_2O (2 × 5 mL), and dried in air. Yield 80%. *Anal.* Calc. for $C_{36}H_{30}Co_3N_{12}O_{14}Cl_2$: C, 39.22; H, 2.75; N, 15.25. Found: C, 39.26; H, 2.90; N, 15.28%. Selected IR data (KBr pellet, cm^{-1}): 1606s, 1564m, 1522s, 1476m, 1438m, 1350m, 1232s, 1205m, 1148vs, 1112m, 1086vs, 902m, 770m, 678m, 628m, 590m, 466m.

Method B. A pink solution of $Co(ClO_4)_2 \cdot 6H_2O$ (0.19 g, 0.50 mmol) in MeOH (20 mL) was added to a colourless solution of paoH (0.12 g, 1.00 mmol) and $Me_4NOH \cdot 5H_2O$ (0.18 g, 1.00 mmol) in the same solvent (10 mL). The resulting dark red solution was stirred for 20 min, filtered, and the filtrate left undisturbed at room temperature to concentrate slowly by evaporation. After 2 days, dark red crystals of **2** were collected by filtration, washed with cold MeOH (2 × 2 mL), and dried in air. Yield 50% (based on the ligand). The identity of the product was confirmed by elemental analyses (C, H, N) and IR spectroscopic comparison with authentic material from Method A.

2.2.3. $[Co(ppko)_3] \cdot 0.25H_2O$ (**3** · $0.25H_2O$)

A pink suspension of $Co(O_2CMe)_2 \cdot 4H_2O$ (0.13 g, 0.50 mmol) in MeCN (30 ml) was treated with solid ppkoH (0.30 g, 1.50 mmol). The resulting orange slurry was refluxed for 1.5 h, during which time the solids dissolved and the colour of the solution turned to dark red. The solution obtained was stirred at ambient temperature for a further 30 min, during which time a dark orange microcrystalline solid rapidly precipitated. The solid product was isolated by filtration, washed with cold MeCN (2 × 3 mL) and Et_2O (2 × 5 mL), and dried in air for 1 h. Dissolution of the solid in DMF (15 mL) and slow evaporation of the resulting filtrate at room temperature gave dark orange crystals of **3** · $0.25H_2O$ after 12 days. The crystals were collected by filtration, washed with cold DMF (1 × 2 mL) and Et_2O (2 × 5 mL), and dried under vacuum. Yield 40% (based on the ligand). The dried sample analyzed as solvent-free (**3**). *Anal.* Calc. for $C_{36}H_{27}CoN_6O_3$: C, 66.46; H, 4.19; N, 12.92. Found: C, 66.44; H, 4.12; N, 12.88%. Selected IR data (KBr pellet, cm^{-1}): 1598m, 1522m, 1464vs, 1438s, 1222m, 1146m, 1030w, 976w, 780m, 748m, 708s, 614m, 470m.

2.2.4. $[Co_3(ppko)_6](PF_6)_2 \cdot 6MeCN$ (**4** · 6MeCN)

Method A. An orange suspension of **3** (0.65 g, 1.00 mmol) in MeCN (30 ml) was treated with a pink aqueous solution (5 mL) of $CoCl_2 \cdot 6H_2O$ (0.12 g, 0.50 mmol) and $NaPF_6$ (0.17 g, 1.00 mmol). The resulting orange-red slurry was refluxed for 5 h, during which time the solids dissolved and the colour of the solution turned to dark red. The solution was filtered, and the filtrate left undisturbed at room temperature to concentrate slowly by evaporation. After 6 days, dark red crystals of **4** · 6MeCN were collected by filtration, washed with cold MeCN (2 × 2 mL), and dried under vacuum. Yield 65%. The dried sample analyzed as solvent-free (**4**). *Anal.* Calc. for $C_{72}H_{54}Co_3N_{12}O_6P_2F_{12}$: C, 46.61; H, 2.94; N, 9.06. Found: C, 46.54; H, 2.92; N, 9.18%. Selected IR data (KBr pellet, cm^{-1}): 1598m, 1524m, 1464vs, 1438m, 1358w, 1216m, 1146m, 1030w, 977w, 842vs, 776m, 746m, 706s, 658w, 612w, 558m, 466m.

Method B. Solids $Co(O_2CMe)_2 \cdot 4H_2O$ (0.13 g, 0.50 mmol), ppkoH (0.30 g, 1.50 mmol) and $NaPF_6$ (0.17 g, 1.00 mmol) were dissolved under refluxing conditions in MeCN (30 ml) to give a dark red solution. The obtained solution was stirred for a further 15 min, filtered, and the filtrate was layered with Et_2O (60 mL). After 4 days, dark red crystals of **4** · 6MeCN were collected by filtration, washed with cold MeCN (2 × 2 mL) and Et_2O (2 × 5 mL), and dried under vacuum. Yield 70% (based on the ligand). The identity of the product was confirmed by elemental analyses (C, H, N) and IR spectroscopic comparison with authentic material from Method A.

Method C. A pink solution of $CoCl_2 \cdot 6H_2O$ (0.12 g, 0.50 mmol) and $NaPF_6$ (0.17 g, 1.00 mmol) in MeOH (10 mL) was added to a pale yellow solution of ppkoH (0.20 g, 1.00 mmol) and $Me_4NOH{\cdot}5H_2O$ (0.18 g, 1.00 mmol) in MeCN (20 mL). The resulting dark red solution was stirred for 30 min, filtered, and the filtrate left undisturbed at room temperature to concentrate slowly by evaporation. After 3 days, dark red crystals of **4** · 6MeCN were collected by filtration, washed with cold MeCN (2 × 2 mL), and dried under vacuum. Yield 55% (based on the ligand). The identity of the product was confirmed by elemental analyses (C, H, N) and IR spectroscopic comparison with authentic material from Method A.

2.2.5. $[Co(mpko)_3] \cdot 3MeNO_2$ (**5** · $3MeNO_2$)

Method A. A pink suspension of $Co(O_2CMe)_2 \cdot 4H_2O$ (0.13 g, 0.50 mmol) in $MeNO_2$ (30 ml) was treated with solid mpkoH (0.20 g, 1.50 mmol). The resulting orange slurry was refluxed for 3 h, during which time the solids dissolved and the colour of the solution turned to dark red. The obtained solution was stirred for a further 30 min, filtered, and the filtrate was layered with a solvent mixture comprising Et_2O/*n*-hexane (60 mL, 1:1 v/v). After 5 days, dark orange crystals of **5** · $3MeNO_2$ were collected by filtration, washed with cold $MeNO_2$ (1 × 3 mL) and Et_2O (2 × 5 mL), and dried under vacuum. Yield 50% (based on the ligand). The dried sample analyzed satisfactorily as **5** · $3MeNO_2$. *Anal.* Calc. for $C_{24}H_{30}CoN_9O_9$: C, 44.51; H, 4.68; N, 19.47. Found: C, 44.42; H, 4.62; N, 19.58%. Selected IR data (KBr pellet, cm^{-1}): 3056w, 2964w, 1636w, 1600s, 1472vs, 1430s, 1302m, 1228vs, 1156m, 1118m, 1084w, 986w, 768s, 692m, 504w, 454w.

Method B. A pink solution of $CoCl_2{\cdot}6H_2O$ (0.12 g, 0.50 mmol) in MeOH (5 mL) was added to a colourless solution of mpkoH (0.20 g, 1.50 mmol) and $Me_4NOH \cdot 5H_2O$ (0.27 g, 1.50 mmol) in $MeNO_2$ (20 mL). The resulting dark red solution was stirred for 45 min, filtered, and the filtrate left undisturbed at room temperature to concentrate slowly by evaporation. After 10 days, dark orange crystals of **5** · $3MeNO_2$ were collected by filtration, washed with cold $MeNO_2$ (1 × 3 mL) and Et_2O (2 × 5 mL), and dried under vacuum. Yield 35% (based on the ligand). The identity of the product was confirmed by elemental analyses (C, H, N) and IR spectroscopic comparison with authentic material from Method A.

2.2.6. $[Co_3(mpko)_6](PF_6)_2$ (**6a**)

An orange suspension of **5** · $3MeNO_2$ (0.65 g, 1.00 mmol) in MeCN (30 ml) was treated with a pink aqueous solution (5 mL) of $CoCl_2{\cdot}6H_2O$ (0.12 g, 0.50 mmol) and $NaPF_6$ (0.17 g, 1.00 mmol). The resulting orange-red slurry was refluxed for 7 h, during which time the solids dissolved and the colour of the solution turned to dark red. The solution was filtered, and the filtrate left undisturbed at room temperature to concentrate slowly by evaporation. After 4 days, a dark red microcrystalline solid appeared, which was collected by filtration, washed with cold MeCN (2 × 2 mL) and Et_2O (2 × 3 mL), and dried under vacuum. Yield 55%. The dried sample analyzed as solvent-free (**6a**). *Anal.* Calc. for $C_{42}H_{44}Co_3N_{12}O_6P_2F_{12}$: C, 39.48; H, 3.32; N, 13.16. Found: C, 39.44; H, 3.42; N, 13.18%. Selected IR data (KBr pellet, cm^{-1}): 1601m, 15548w, 1495s, 1434m, 1417w, 1223w, 1088vs, 948s, 843vs, 782m, 695w, 629s, 559m, 461m.

2.2.7. $[Co_3(mpko)_6](ClO_4)_2$ (**6b**)

An orange suspension of **5** · $3MeNO_2$ (0.65 g, 1.00 mmol) in MeCN (30 ml) was treated with solid $Co(ClO_4)_2 \cdot 6H_2O$ (0.19 g, 0.50 mmol). The resulting orange-red slurry was refluxed for 10 h, during which time the solids dissolved and the colour of the solution turned to dark red. The solution was filtered, and the filtrate left undisturbed at room temperature to concentrate slowly by evaporation. After 6 days, a dark red microcrystalline solid appeared, which was collected by filtration, washed with cold MeCN (2 × 2 mL) and Et_2O (2 × 3 mL), and dried under vacuum. Yield 60%. The dried sample analyzed as solvent-free (**6b**). *Anal.* Calc. for $C_{42}H_{44}Co_3N_{12}O_{14}Cl_2$: C, 42.50; H, 3.57; N, 14.17. Found: C, 42.54; H, 3.62; N, 14.38%. Selected IR data (KBr pellet, cm^{-1}): 1602m, 1554w, 1490s, 1438m, 1414w, 1222w, 1088vs, 948s, 782m, 696w, 624s, 460m.

2.3. Single-crystal X-ray crystallography

The crystallographic data and structure refinement details for the five, structurally characterized complexes are summarized in Table 1. Selected crystals of **1** (0.12 × 0.16 × 0.22 mm), **2** (0.15 × 0.16 × 0.20 mm), **4** · 6MeCN (0.05 × 0.10 × 0.55 mm) and **5** · $3MeNO_2$ (0.30 × 0.40 × 0.50 mm) were mounted in capillary,

Table 1
Crystallographic data for complexes **1**, **2**, **3** · $0.25H_2O$, **4** · 6MeCN and **5** · $3MeNO_2$.

Parameter	**1**	**2**	**3**·$0.25H_2O$	**4**·6MeCN	**5**·$3MeNO_2$
Formula	$C_{18}H_{15}CoN_6O_3$	$C_{36}H_{30}Co_3N_{12}O_{14}Cl_2$	$C_{36}H_{27.5}N_6CoO_{3.25}$	$C_{84}H_{72}Co_3N_{18}O_6P_2F_{12}$	$C_{24}H_{30}CoN_9O_9$
Formula weight	422.29	1102.44	655.07	1896.32	647.50
Crystal system	orthorhombic	hexagonal	monoclinic	triclinic	hexagonal
Space group	*Pbca*	*R*$\bar{3}$	$P2_1/c$	$P\bar{1}$	*R*$\bar{3}$
a (Å)	15.8383(8)	14.213(5)	9.980(10)	13.909(8)	15.415(6)
b (Å)	12.5001(7)	14.213(5)	10.810(10)	15.61(1)	15.415(6)
c (Å)	17.2242(8)	19.992(8)	27.98(3)	10.793(7)	21.249(8)
α (°)	90	90	90	89.98(2)	90
β (°)	90	90	94.98(4)	82.71(2)	90
γ (°)	90	120	90	73.31(2)	120
V ($Å^3$)	3410.1(3)	3497(2)	3007(5)	2225(2)	4373(3)
Z	8	3	4	1	6
ρ_{calc} (g cm^{-3})	1.645	1.570	1.447	1.415	1.475
Radiation, λ (Å)	Mo Kα, 0.71073	Mo Kα, 0.71073	Mo Kα, 0.71073	Mo Kα, 0.71073	Mo Kα, 0.71073
Temperature (K)	100	298	298	298	298
μ (mm^{-1})	1.042	1.245	0.620	0.675	0.655
Data collected/unique	33131/5658	2906/1368	3086/3009	8284/7832	3645/1723
(R_{int})	(0.0641)	(0.0274)	(0.0291)	(0.0155)	(0.0259)
Data with $I > 2\sigma(I)$	3896	1214	2283	5537	1559
R_1 ($I > 2\sigma(I)$)[a]	0.0439	0.0353	0.0529	0.0620	0.0425
wR_2 ($I > 2\sigma(I)$)[b]	0.1303	0.0957	0.1311	0.1650	0.1164

[a] $R_1 = \Sigma(|F_o| - |F_c|)/\Sigma(|F_o|)$.
[b] $wR_2 = \sum[w(F_o^2 - F_c^2)^2]/\sum[w(F_o^2)^2]^1/2$.

whereas a selected crystal of **3** · 0.25H_2O (0.08 × 0.15 × 0.40 mm) was mounted in air. Diffraction measurements were made on a Crystal Logic Dual Goniometer diffractometer using graphite-monochromated Mo radiation. Unit cell dimensions were determined and refined by using the angular settings of 25 automatically centered reflections in the range $11 < 2\theta < 23°$. Intensity data were recorded using a $\theta - 2\theta$ scan to a maximum 2θ value of 50°. Three standard reflections monitored every 97 reflections showed less than 3% variation and no decay. Lorentz, polarization corrections were applied using Crystal Logic software. All five structures were solved by direct methods using SHELXS-86 [11a] and refined on F^2 by full-matrix least squares techniques with SHELXL-97 [11b]. All H atoms were located by Fourier difference maps and refined isotropically, except those on the solvent molecules (**3** · 0.25H_2O, **4** · 6MeCN and **5** · 3$MeNO_2$) which were introduced at calculated positions as riding on bonded atoms. All non-H atoms were refined anisotropically.

3. Results and discussion

3.1. Brief synthetic comments and IR spectra

Aerobic reactions of $Co(O_2CMe)_2 \cdot 4H_2O$ with the appropriate 2-pyridyl oximes in an 1:3 ratio in various solvents under reflux gave dark red solutions, from which were subsequently isolated the orange mononuclear Co^{III} complexes **1**, **3** and **5**, upon conventional workup. The formation of the representative compound **1** can be represented by Eq. (1)

$$2Co^{II}(O_2CMe)_2 \cdot 4H_2O + 6paoH + 1/2O_2 \rightarrow 2[\underset{\mathbf{1}}{Co^{III}(pao)_3}] + 4MeCO_2H + 9H_2O \quad (1)$$

The $MeCO_2^-$ ions act as a base deprotonating the two-thirds (2/3) of the amount of the organic ligand. Note that **1** and **3** have the *trans* (or *mer*) configuration, whereas complex **5** is the *cis* (or *fac*) isomer (vide infra). The three complexes can be also prepared by the 1:3 aerobic reactions between $CoCl_2 \cdot 6H_2O$ and the oximes in various solvents *in the presence of a base*, see Eq. (2). A typical such preparation is reported in Section 2.2.5 (Method B)

$$2Co^{II}Cl_2 \cdot 6H_2O + 6mpkoH + 4Me_4NOH + 1/2O_2 \rightarrow 2[\underset{\mathbf{5}}{Co^{III}(mpko)_3}] + 4Me_4NCl + 17H_2O \quad (2)$$

Since **1**, **3** and **5** each possesses three free, i.e. uncoordinated, oximate oxygen atoms, we suspected that these mononuclear Co^{III} complexes could act as "ligands" (the so-named "metal complexes as ligands strategy" [5]) and would further react with Co^{II} sources leading to mixed-valent Co^{II}/Co^{III} clusters; such clusters are of great current magnetochemical interest [12]. This, indeed, turned out to be the case and led to the trinuclear $Co_2^{III}Co^{II}$ clusters **2**, **4**, **6a** and **6b**; typical preparations are illustrated by Eqs. (3) and (4). The three oximate oxygen atoms that had been free in the

$$2[\underset{\mathbf{1}}{Co^{III}(pao)_3}] + Co^{II}(ClO_4)_2 \cdot 6H_2O \rightarrow [\underset{\mathbf{2}}{Co^{III}_2Co^{II}(pao)_6}](ClO_4)_2 + 6H_2O \quad (3)$$

$$2[\underset{\mathbf{3}}{Co^{III}(ppko)_3}] + Co^{II}Cl_2 \cdot 6H_2O + 2NaPF_6 \rightarrow [\underset{\mathbf{4}}{Co^{III}_2Co^{II}(ppko)_6}](PF_6)_2 + 2NaCl + 6H_2O \quad (4)$$

mononuclear precursors **1**, **3** and **5** were indeed coordinated to the Co^{II} center in **2**, **4**, **6a** and **6b**. Two Co centers are in the oxidation state III and the products are thus cationic. Therefore, an appropriate counteranion should be present in the reaction mixture, either as the inorganic anion of the Co^{II} source (ClO_4^-) or added externally (PF_6^-). The trinuclear clusters have the three oximate groups of each corresponding Co^{III} metalloligand in a *fac* configuration around the Co^{II} center (vide infra). Since the oximate disposition is different in **1**, **3** and **5** (*mer* versus *fac*), we anticipated different products from the reactions of the metalloligands **1** and **3** with the Co^{II} source compared with the product from the reaction of **5** with Co^{II}. In a sense, complexes **1** and **3** can be considered as bidentate-monodentate bridging "ligands" (due to the *mer* geometry of the three, free oximate oxygens), whereas complex **5** can be viewed as a tridentate chelating "ligand" (due to the *fac* geometry of the three, free oximate oxygens). Somewhat to our surprise, however, the molecular structures of the trinuclear cations seem to be very similar. This means that the geometry of **5** only is preserved in the trinuclear cluster cation (**6a** and **6b**). The *mer* isomers **1** and **3** are also converted to mixed-valent, trinuclear cations (**2** and **4**) that contain the *fac*-$[Co^{III}(pao)_3]$ and *fac*-$[Co^{III}(ppko)_3]$ metalloligand units, respectively. This may suggest the occurrence of an equilibrium between *mer* and *fac* mononuclear, 1:3 Co^{III} species in solution (at least for **1** and **3**), which shifts to the *fac* isomer upon addition of external Co^{II}.

Complexes **2**, **4**, **6a** and **6b** can be also prepared under aerobic conditions by "one-pot" procedures involving the appropriate reaction mixture of a Co^{II} starting material, counteranion and 2-pyridyl oxime, in the presence (when the inorganic anions present are ClO_4^-, Cl^-/ClO_4^- or Cl^-/PF_6^-) or absence (when $MeCO_2^-$ ions are present) of external OH^- ions. Typical preparations are reported in Sections 2.2.2 (Method B) and 2.2.4 (Methods B and C) and illustrated by Eqs. (5) and (6)

$$3Co^{II}(ClO_4)_2 \cdot 6H_2O + 6paoH + 4Me_4NOH + 1/2O_2 \rightarrow [\underset{\mathbf{2}}{Co^{III}_2Co^{II}(pao)_6}](ClO_4)_2 + 4Me_4NClO_4 + 23H_2O \quad (5)$$

$$3Co^{II}(O_2CMe)_2 \cdot 4H_2O + 6ppkoH + 2NaPF_6 + 1/2O_2 \rightarrow [\underset{\mathbf{4}}{Co^{III}_2Co^{II}(ppko)_6}](PF_6)_2 + 2NaCO_2CMe + 4MeCO_2H + 13H_2O \quad (6)$$

The IR spectra of complexes **2** and **6a** exhibit bands near 1090 and 625 cm^{-1}, due to the $\nu_3(F_2)[\nu_d(ClO)]$ and $\nu_4(F_2)[\delta_d(OClO)]$ modes of the uncoordinated T_d ClO_4^- ions, respectively [13]. A strong band at ~840 cm^{-1} and a medium-intensity band at ~560 cm^{-1} in the spectra of **4** and **6b** are assigned [13] to the $\nu_3(F_{1u})[\nu(PF)]$ and $\nu_4(F_{1u})[\delta(FPF)]$ vibrations of the O_h PF_6^- ion, confirming its ionic nature. Two bands, one of variable intensity at 1228–1205 cm^{-1} assigned to ν(N–O) and one of medium to strong intensity at 1606–1598 cm^{-1} assigned to $\nu(C{=}N)_{oximate}$, are common in the spectra of all the prepared complexes [14]; the higher-wavenumber band most probably overlaps with a 2-pyridyl stretch. The ν(N–O) band is located at a slightly lower wavenumber in **2**, **4**, **6a** and **6b** than for their corresponding metalloligand Co^{III} complexes **1**, **3** and **5**, respectively, consistent with the oximate O-coordination in the trinuclear clusters. The in-plane deformation bands of the 2-pyridyl ring of the free paoH, ppkoH and mpkoH ligands at 620–650 cm^{-1} shift upwards (708–676 cm^{-1}) in the spectra of the mononuclear and trinuclear compounds, confirming the involvement of the ring-N atom in coordination [15]. The similar spectral behaviour of **6a** and **6b** (we could not grow single crystals of these complexes suitable for their X-ray structural characterization) in the regions of the $\nu(C{=}N)_{oximate}$, ν(N–O) and δ(Py) vibrations, compared with that of the structurally characterized trinuclear complexes **2** and **4**, is a strong evidence that the cations of the former are structurally analogous to the cations of **2** and **4**.

3.2. Description of structures

The molecular structures of the mononuclear complexes **1**, **3** and **5** are depicted in Figs. 1–3, respectively. Selected interatomic

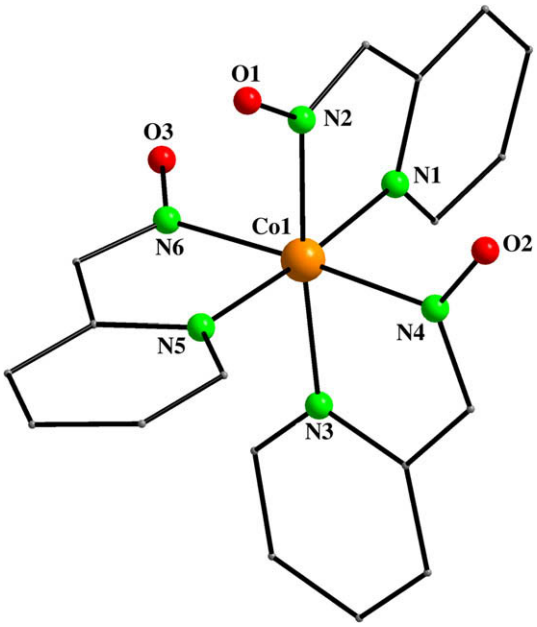


Fig. 1. Molecular structure of complex **1** with selected atom labelling. H atoms have been omitted for clarity. Colour scheme: Co^{III}, orange; O, red; N, green; C, gray.

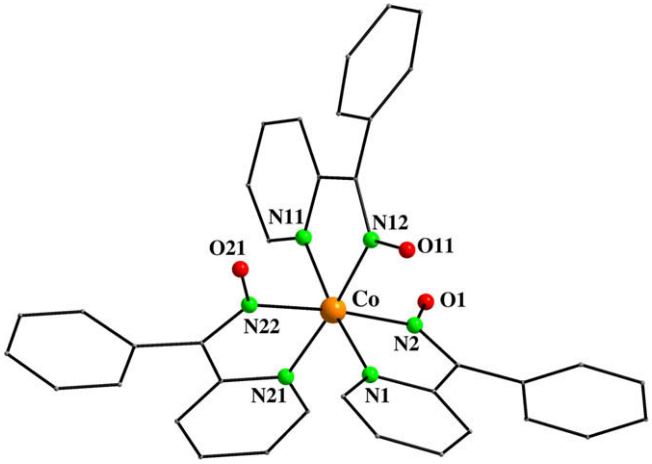


Fig. 2. Partially labelled plot of complex **3**; colour scheme as in Fig. 1. H atoms have been omitted for clarity.

distances and angles for the same compounds are listed in Table 2. Partially labelled representations of the cations of complexes **2** and **4** are shown in Figs. 4 and 5, respectively, while their selected interatomic distances and angles are listed in Table 3.

Complex **1** crystallizes in the orthorhombic space group *Pbca*. Its structure consists of well-separated [Co(pao)$_3$] molecules. The Co^{III} ion is coordinated by three N,N′-bidentate chelating (or 1.011 [16]) pao$^-$ ligands. The pao$^-$ donor atoms are the nitrogen atoms of the deprotonated oxime and the 2-pyridyl groups. The six-coordinate molecule is the *mer* (or *trans*) isomer. Complex **3** · 0.25H_2O crystallizes in the monoclinic space group $P2_1/c$ and its structure comprises mononuclear [Co(ppko)$_3$] units and solvate H_2O molecules; the latter will not be further discussed. The six-coordinate Co^{III} ion possesses a distorted octahedral geometry and is (similarly to **1**) the *mer* isomer. The coordination sphere of the Co^{III} atom in **3** · 0.25H_2O consists of three N,N′-bidentate chelating (or 1.011 [16]) ppko$^-$ ligands. The molecular structures of **1** and **3** are very similar, and the replacement of the H atom by the

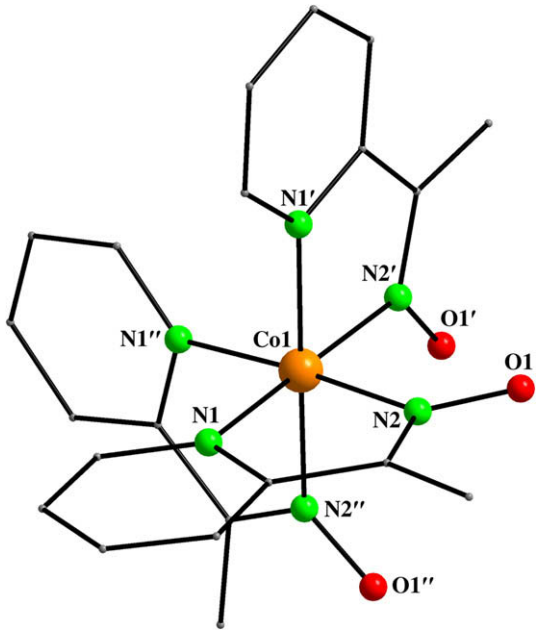


Fig. 3. Partially labelled plot of complex **5**; colour scheme as in Fig. 1. H atoms have been omitted for clarity.

Table 2
Selected bond lengths (Å) and angles (°) for complexes **1**, **3**·0.25H_2O and **5**·3$MeNO_2$.

Parameter[a]		Parameter	
1			
Co(1)–N(1)	1.921(2)	N(1)–Co(1)–N(3)	94.2(7)
Co(1)–N(2)	1.909(2)	N(1)–Co(1)–N(5)	175.3(7)
Co(1)–N(3)	1.958(2)	N(2)–Co(1)–N(3)	174.6(7)
Co(1)–N(4)	1.943(2)	N(2)–Co(1)–N(4)	92.4(7)
Co(1)–N(5)	1.931(2)	N(2)–Co(1)–N(6)	90.0(7)
Co(1)–N(6)	1.941(2)	N(3)–Co(1)–N(5)	88.7(7)
		N(4)–Co(1)–N(6)	176.5(7)
***3** · 0.25H_2O*			
Co–N(1)	1.927(5)	N(1)–Co–N(11)	172.7(2)
Co–N(2)	1.920(5)	N(1)–Co–N(21)	93.6(2)
Co–N(11)	1.931(5)	N(2)–Co–N(12)	92.2(2)
Co–N(12)	1.907(5)	N(2)–Co–N(22)	174.0(2)
Co–N(21)	1.949(5)	N(11)–Co–N(21)	93.6(2)
Co–N(22)	1.934(5)	N(12)–Co–N(21)	174.3(2)
		N(12)–Co–N(22)	92.7(2)
***5** · 3$MeNO_2$*			
Co(1)–N(1)	1.946(2)	N(1)-Co(1)–N(2′)	176.1(8)
Co(1)–N(1′)	1.946(2)	N(1′)-Co(1)–N(2″)	176.1(8)
Co(1)–N(1″)	1.946(2)	N(1″)-Co(1)–N(2)	176.1(8)
Co(1)–N(2)	1.905(2)	N(1)-Co(1)–N(1′)	95.2(9)
Co(1)–N(2′)	1.905(2)	N(2)–Co(1)–N(2′)	93.9(9)
Co(1)–N(2″)	1.905(2)		

[a] Unprimed, primed and doubly-primed atoms have the symmetry operators (−1 + *x* − *y*, 1 − *y*, *z*), (*x*, *y*, *z*) and (1 − *x*, 2 − *x* + *y*, *z*), respectively.

Ph group has thus little structural effect. Complex **5** · 3$MeNO_2$ crystallizes in the hexagonal space group $R\bar{3}$, with mononuclear [Co(mpko)$_3$] units and solvate $MeNO_2$ molecules in general positions. The Co^{III} ion, which sits on a 3-fold axis of symmetry, is coordinated by three N,N′-bidentate chelating (or 1.011 [16]) mpko$^-$ ligands. Surprisingly, and by contrast with **1** and **3**, the six-coordinate complex **5** · 3$MeNO_2$ is the *fac* (or *cis*) isomer. The Co-N bond lengths agree well with values expected for low-spin Co^{III} in octahedral environments [4]. The observed, similar coordination modes of the oximate ligands in complexes **1**, **3** and **5** are interesting because the deprotonated oxygen atom remains uncoordinated.

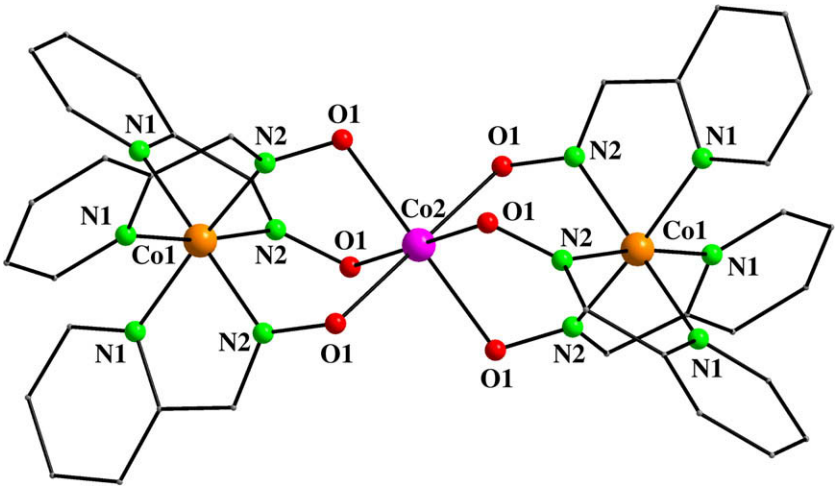


Fig. 4. Partially labelled representation of the mixed-valence(III/II/III) cation $[Co_3(pao)_6]^{2+}$ present in complex **2**. Identical numbers are used for atoms generated by symmetry. H atoms have been omitted for clarity. Colour scheme: Co^{II}, pink; Co^{III}, orange; O, red; N, green; C, gray.

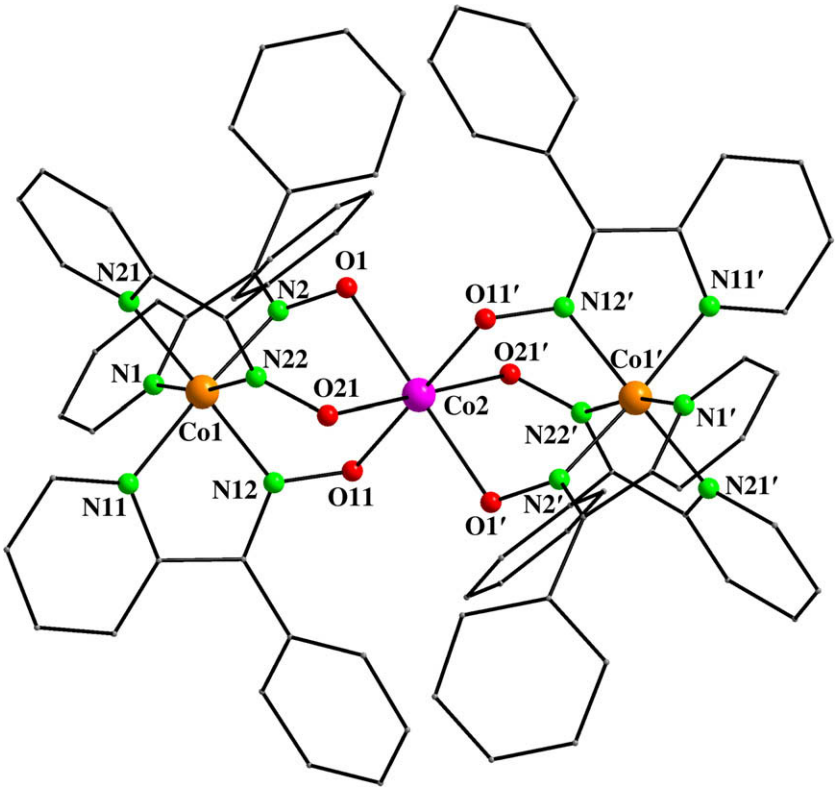


Fig. 5. Molecular structure of the mixed-valence (III/II/III) cation $[Co_3(ppko)_6]^{2+}$ present in complex **4**·6MeCN with selected atom labelling; colour scheme as in Fig. 4. Primes are used for symmetry-related $(-x,-y,-z)$ atoms. H atoms have been omitted for clarity.

The cations of **2** (Fig. 4) and **4** (Fig. 5) are structurally similar in many aspects, except the nature of the coordinated 2-pyridyl oximate group (pao^- versus $ppko^-$) and the counteranion (ClO_4^- versus PF_6^-), and thus only the structure of complex **2** will be described in detail. The crystal structure of **2** reveals the formation of a linear trinuclear cation. The central metal ion, Co(2), sits on a 3-fold inverse axis of symmetry, while the terminal metal ion, Co(1), sits on a 3-fold symmetry axis. The central metal ion is octahedrally coordinated by six oxygen atoms [O(1), and its symmetry-related partners] belonging to six pao^- ligands. The six coordination sites on each of the distorted octahedral, terminal Co ions are occupied by the nitrogen atoms [N(1), N(2), and their symmetry-related partners] that belong to the "chelating" part of three pao^- ligands, with the three oximate N atoms in the facial (or *cis*) configuration. The core for **2** (and **4**) appears to be $[Co^{II}Co_2^{III}(\mu\text{-}ONR')_6]^{2+}$. Charge considerations require a formal $2Co^{III}$,Co^{II} description of **2** (and **4**), and the terminal metal ions are clearly low-spin Co^{III} ions based on their Co–N bond lengths (all <1.96 Å), which have lengths similar to Co^{III}–N bond lengths in other structurally characterized cobalt(III) complexes with

Table 3
Selected bond lengths (Å) and angles (°) for complexes **2** and **4**·6MeCN.

Parameter[a]		Parameter	
2			
Co(1)–N(1)	1.961(2)	N(1)–Co(1)–N(1)	93.6(8)
Co(1)–N(2)	1.899(2)	N(1)–Co(1)–N(2)	172.0(8)
Co(2)–O(1)	2.102(2)	N(2)–Co(1)–N(2)	91.2(7)
		O(1)–Co(2)–O(1)	180.0(9)
4·*6MeCN*			
Co(1)–N(1)	1.945(4)	Co(2)–O(1)	2.127(3)
Co(1)–N(2)	1.901(4)	Co(2)–O(1′)	2.127(3)
Co(1)–N(11)	1.955(4)	Co(2)–O(11)	2.077(3)
Co(1)–N(12)	1.881(4)	Co(2)–O(11′)	2.077(3)
Co(1)–N(21)	1.955(4)	Co(2)–O(21)	2.110(3)
Co(1)–N(22)	1.905(4)	Co(2)–O(21′)	2.110(3)
N(1)–Co(1)–N(22)	169.1(2)	N(2)–Co(1)–N(22)	88.4(2)
N(2)–Co(1)–N(11)	173.8(2)	N(12)–Co(1)–N(22)	92.0(2)
N(12)–Co(1)–N(21)	173.8(2)	O(1)–Co(2)–O(1′)	180.0(3)
N(1)–Co(1)–N(11)	94.8(2)	O(11)–Co(2)–O(11′)	180.0(3)
N(1)–Co(1)–N(21)	92.1(2)	O(21)–Co(2)–O(21′)	180.0(3)
N(11)–Co(1)–N(21)	94.7(2)	O(1)–Co(2)–O(11)	90.6(1)
N(2)–Co(1)–N(12)	92.5(2)	O(1)–Co(2)–O(21)	87.3(1)
		O(11)–Co(2)–O(21)	91.2(1)

[a] Primes are used for symmetry-related ($-x$, $-y$, $-z$) atoms.

N-ligation [4]. The central cobalt center [Co(2)] has all six Co–O distances 2.102(2) Å indicating that this is a Co^{II} ion [4]. The pao^- ions in **2** (and the $ppko^-$ groups in **4**) function as $\eta^1{:}\eta^1{:}\eta^1{:}\mu$ ligands (or as $2.1_1 1_2 1_2$ ligands using Harris notation [16]); each ligand chelates one Co^{III} ion through the 2-pyridyl and the oximate nitrogen atoms forming a five-membered chelating ring, and bridges this metal center with the central Co^{II} ion through the terminally ligated, deprotonated oxygen atom. Complexes **2** and **4** join a handful of structurally characterized linear, valence-trapped $Co^{III}Co^{II}Co^{III}$ clusters [17].

3.3. Magnetochemistry and ligand-field spectra

Complexes **1**, **3** · $0.25H_2O$ and **5** · $3MeNO_2$ are diamagnetic, as expected. The room-temperature, effective magnetic moment (μ_{eff}) values of **2**, **4**, **6a** and **6b** are 4.81, 5.13, 4.99 and 5.07 B.M. per trimer, respectively; these values are consistent with the presence of one high-spin Co^{II} ion with octahedral stereochemistry [18].

The μ_{eff} value of the representative trinuclear cluster **2** decreases gradually to 4.01 B.M. per trimer at 25 K and then drops to 3.53 B.M. at 2.0 K. This behaviour may be understood as arising from the combined effects of orbital degeneracy and zero-field splitting [17h].

The solid-state (diffuse reflectance) UV–Vis spectra of **1**, **3** · $0.25H_2O$ and **5** · $3MeNO_2$ are typical for low-spin $Co^{III}N_6$ chromophores [19]. The low-spin octahedral ground term is $^1A_{1g}$ and there are two relatively low lying spin allowed transitions, with lower lying spin triplet partners, all derived from $(t_{2g})^5(e_g)$. Under this scheme, the bands in the spectrum of **5**, for example, at 29.13, 21.35, 17.10 and 13.36 kK are assigned [19] to the $^1A_{1g} \rightarrow {}^1T_{2g}, {}^1T_{1g}, {}^3T_{2g}$ and $^3T_{1g}$ transitions, respectively. The spectra of the trinuclear $Co^{III}Co^{II}Co^{III}$ clusters exhibit bands at approximately the same energies with those of their corresponding mononuclear Co^{III} complexes, and maxima characteristic of octahedral $Co^{II}O_6$ chromophores [19]. For instance, the spectrum of **6a** shows bands/shoulders at 29.27, 21.55, 17.50 and 13.00 kK due to its *fac*-$[Co^{III}(mpko)_3]$ units (and assigned as above), and additional bands at 19.23 and 15.80 kK due to its high-spin octahedral $Co^{II}(O_{oximato})_6$ unit and assigned (under O_h symmetry) to the $^4T_{1g} \rightarrow {}^4T_{1g}(P), {}^4A_{2g}$ transitions, respectively [19]. The electronic spectra of **2**, **4** and **6b** are very similar supporting similar structures.

4. Conclusions

This work extends the body of results that emphasize the ability of the anionic 2-pyridyl oximate ligands to form interesting structural types in 3d-metal chemistry. The initial use of pao^-, $ppko^-$ and $mpko^-$ in Co non-carboxylate chemistry has provided access to diamagnetic mononuclear Co^{III} complexes and to paramagnetic mixed-valence $Co_2{}^{III}Co^{II}$ clusters. The incorporation of only one Co^{II} center in the trinuclear clusters precludes the observation of interesting magnetic properties as these complexes behave as mononuclear Co^{II} species. The flexibility of the 2-pyridyl oximate ligands and some very recent results in our group let us believe that we have only seen the tip of the iceberg in Co/2-pyridyl oximate chemistry and that some new clusters with interesting magnetic properties await discovery. From the synthetic inorganic chemistry viewpoint, this work demonstrates the utility of the "metal complexes as ligands" approach in transition metal cluster chemistry. Preliminary experiments show that the reactions of **1**–**3** with sources of other divalent 3d metals lead to a variety of mixed-metal Co^{III}/M^{II} complexes (M = Fe, Mn, Ni, Cu).

5. Supplementary data

CCDC 264168, 264167, 264166, 264165 and 264169 contains the supplementary crystallographic data for **1**, **2**, (**3** · $0.25H_2O$), (**4** · 6MeCN), and (**5** · $3MeNO_2$). These data can be obtained free of charge via http://www.ccdc.cam.ac.uk/conts/retrieving.html, or from the Cambridge Crystallographic Data Centre, 12 Union Road, Cambridge CB2 1EZ, UK; fax: (+44) 1223-336-033; or e-mail: deposit@ccdc.cam.ac.uk.

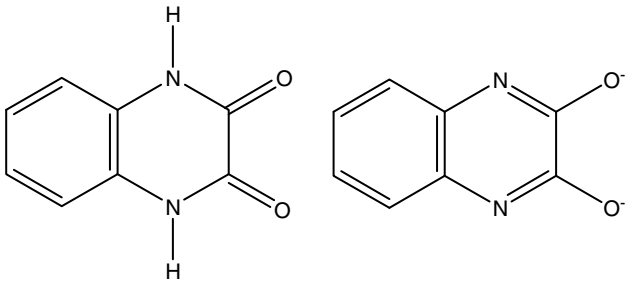
Acknowledgements

This work was supported by EPEAEK II (Program PYTHAGORAS I, Grant b.365.037 to S.P.P) and by The British Council and the Greek General Secretariat for Research and Technology (to R.E.P.W and S.P.P).

References

[1] R.E.P. Winpenny, in: J.P. Sauvage (Ed.), Transition Metals in Supramolecular Chemistry, vol. 5, Wiley, Chichester, 1999, pp. 193–223.
[2] (a) For reviews, see: G. Christou, D. Gatteschi, D.N. Hendrickson, R. Sessoli, MRS Bull. 25 (2000) 66;
(b) D. Gatteschi, R. Sessoli, Angew. Chem., Int. Ed. 42 (2003) 268;
(c) R. Birchner, G. Chaboussant, C. Dobe, H.U. Güdel, S.T. Ochsenbein, A. Sieber, O. Waldman, Adv. Funct. Mater. 16 (2006) 209;
(d) G. Aromi, E.K. Brechin, Struct. Bonding 122 (2006) 1.
[3] (a) E.-C. Yang, D.N. Hendrickson, W. Wernsdorfer, M. Nakano, L.N. Zakharov, R.D. Sommer, A.L. Rheingold, M. Ledezma-Gairraud, G. Christou, J. Appl. Phys. 91 (2002) 7382;
(b) M. Murrie, S.J. Teat, H. Stoeckli-Evans, H.U. Güdel, Angew. Chem., Int. Ed. 42 (2003) 4653;
(c) S.J. Langley, M. Helliwell, R. Sessoli, P. Rosa, W. Wernsdorfer, R.E.P. Winpenny, Chem. Commun. (2005) 5029;
(d) A.K. Boudalis, C.P. Raptopoulou, B. Abarca, R. Ballesteros, M. Chadlaoui, J.-P. Tuchagues, A. Terzis, Angew. Chem., Int. Ed 45 (2006) 432;
(e) Y.-Z. Zhang, W. Wernsdorfer, F. Pan, Z.-H. Wang, S. Gao, Chem. Commun. (2006) 3302;
(f) M.-H. Zeng, M.-X. Yao, H. Liang, W.-X. Zhang, M.-X. Chen, Angew. Chem., Int. Ed. 46 (2007) 1832;
(g) A. Ferguson, A. Parkin, J. Sanchez-Benitez, K. Kamenev, W. Wernsdorfer, M. Murrie, Chem. Commun. (2007) 3473.
[4] (a) For example, see: Th.C. Stamatatos, A.K. Boudalis, K.V. Pringouri, C.P. Raptopoulou, A. Terzis, J. Wolowska, E.J.L. McInnes, S.P. Perlepes, Eur. J. Inorg. Chem. (2007) 5098;
(b) Th.C. Stamatatos, S. Dionyssopoulou, G. Efthymiou, P. Kyritsis, C.P. Raptopoulou, A. Terzis, R. Vicente, A. Escuer, S.P. Perlepes, Inorg. Chem. 44 (2005) 3374.
[5] G. Denti, S. Serroni, S. Campagna, A. Juris, M. Ciano, V. Balzani, in: A.F. Williams, C. Floriani, A.E. Merbach (Eds.), Perspectives in Coordination Chemistry, VCH, Weinheim, 1992, pp. 153–164.

[6] For a comprehensive review, see: C.J. Milios, Th.C. Stamatatos, S.P. Perlepes, Polyhedron 25 (2006) 134 (Polyhedron Report).
[7] For example, see: Th.C. Stamatatos, D. Foguet-Albiol, S.-C. Lee, C.C. Stoumpos, C.P. Raptopoulou, A. Terzis, W. Wernsdorfer, S.O. Hill, S.P. Perlepes, G. Christou, J. Am. Chem. Soc. 129 (2007) 9484.
[8] For example, see: H. Miyasaka, R. Clérac, K. Mizushima, K. Sugiura, M. Yamashita, W. Wernsdorfer, C. Coulon, Inorg. Chem. 42 (2003) 8203.
[9] Th.C. Stamatatos, A. Bell, P. Cooper, A. Terzis, C.P. Raptopoulou, S.L. Heath, R.E.P. Winpenny, S.P. Perlepes, Inorg. Chem. Commun. 8 (2005) 533.
[10] M. Orama, H. Saarinen, J. Korvenranta, J. Coord. Chem. 22 (1990) 183.
[11] (a) G.M. Sheldrick, SHELXS-86, Structure Solving Program, University of Göttingen, Germany, 1986;
(b) G.M. Sheldrick, SHELXS-97, Program for the Refinement of Crystal Structures from Diffraction Data, University of Göttingén, Germany, 1997.
[12] For Example, see: L.F. Chibotaur, L. Ungur, C. Aronica, H. Elmoll, G. Pilet, D. Luneau, J. Am. Chem. Soc. 130 (2008) 12445.
[13] K. Nakamoto, Infrared and Raman Spectra of Inorganic and Coordination Compounds, 4th ed., Wiley, New York, 1986. pp. 147–155, 251.
[14] D. Burdinski, F. Birkelbach, T. Weyhermüller, U. Flörke, H.-J. Haupt, M. Lengen, A.X. Trautwein, E. Bill, K. Wieghardt, P. Chaudhuri, Inorg. Chem. 37 (1998) 1009.
[15] C. Papatriantafyllopoulou, C.G. Efthymiou, C.P. Raptopoulou, A. Terzis, E. Manessi-Zoupa, S.P. Perlepes, Spectrochim. Acta Part A 70 (2008) 718.
[16] R.A. Coxall, S.G. Harris, D.K. Henderson, S. Parsons, P.A. Tasker, R.E.P. Winpenny, J. Chem. Soc., Dalton Trans. (2000) 2349.
[17] (a) For example, see: J.A. Bertrand, J.A. Kelley, E.G. Vassian, J. Am. Chem. Soc. 91 (1969) 2394;
(b) D.A. House, V. McKee, P.J. Steel, Inorg. Chem. 25 (1986) 4884;
(c) V.M. Novorortsev, O.G. Ellert, T.S. Kapanadze, A.Y. Buslaev, Koord. Khim. 14 (1986) 856;
(d) C. Fukuhara, E. Asato, T. Shimoji, K. Katsura, M. Mori, K. Matsumoto, S. Ooi, J. Chem. Soc., Dalton Trans. (1987) 1305;
(e) B. Ballet, A. Bino, S. Cohen, H. Rubin, T. Zor, Inorg. Chim. Acta 188 (1991) 91;
(f) A. Golobic, B. Stefane, S. Polance, Polyhedron 18 (1999) 3661;
(g) T.S. Billson, J.D. Crane, O.D. Fox, S.L. Heath, Inorg. Chem. Commum. 3 (2000) 718;
(h) M. Rat, R.A. de Sousa, A. Tomas, Y. Frapart, J.-P. Tuchagues, I. Artaud, Eur. J. Inorg. Chem. (2003) 759;
(i) S. Pal, A.K. Barik, S. Gupta, S. Roy, T.N. Mandal, A. Hazra, M.S. El Fallah, R.J. Butcher, S.-M. Peng, G.-H. Lee, S.K. Kar, Polyhedron 27 (2008) 357.
[18] F.A. Cotton, G. Wilkinson, C.A. Murillo, M. Bochmann, Advanced Inorganic Chemistry, 6th ed., Wiley, New York, 1999. pp. 820–824.
[19] A.B.P. Lever, Inorganic Electronic Spectroscopy, 2nd ed., Elsevier, Amsterdam, 1984. pp. 463, 464, 473–478, 480–489.



Scheme 1. The structural formulae of the ligands discussed in the text. The neutral ligand is written in the amide (ketoamine) tautomeric form, while the dianionic ligand in the hydroxylamine (or iminol) tautomeric form; these forms have been established by single-crystal X-ray crystallography (see text for details). Due to the different tautomeric forms involved, different abbreviations are used for the free neutral molecule and the dianionic ligand (H_2L' vs L^{2-}).

2. Experimental

2.1. General and spectroscopic measurements

All manipulations were performed under aerobic conditions using materials (reagent grade) and solvents as received. Microanalyses (C, H, N) were performed by the University of Ioannina (Greece) Microanalytical Laboratory using an EA 1108 Carlo Erba analyzer. IR spectra (4000–450 cm^{-1}) were recorded on a Perkin-Elmer 16 PC FT-spectrometer with samples prepared as KBr pellets. Magnetic susceptibility measurements in the range 2–300 K were carried out on a polycrystalline sample of **1** using a Quantum Design SQUID magnetometer, under a magnetic field of 0.1 T, at the Magnetochemistry Service of the University of Barcelona. Diamagnetic corrections were estimated from Pascal tables.

2.2. Compound preparation

2.2.1. $[Cu_3L_2Cl_2(DMF)_4]_n$ (**1**)

Method A: A solution of $[Cu_2(O_2CMe)_4(H_2O)_2]$ (0.12 g, 0.30 mmol), $CuCl_2$ (0.013 g, 0.10 mmol) and H_2L' (0.049 g, 0.30 mmol) in DMF (8 ml) was heated at 130 °C in a sealed tube for 6 h, followed by slow cooling down to ambient temperature over a period of 2 days. X-ray quality dark green crystals of $[Cu_3L_2Cl_2(DMF)_4]_n$ (**1**) were obtained directly from the reaction solution. The crystals were collected by filtration under vacuum, washed with cold DMF (2 ml) and Et_2O (5 ml) and dried in air. Typical yields (based on the ligand) were in the 50–55% range. FT-IR (KBr pellet, cm^{-1}): 3421wb, 2924w, 1640vs, 1586m, 1560s, 1545vs, 1492s, 1473sh, 1419w, 1389m, 1375m, 1276m, 1156vw, 1118vw, 1104w, 1060vw, 955w, 754m, 693w, 642m. *Anal.* Calc. for $C_{28}H_{36}N_8O_8Cl_2Cu_3$ (874.26): C, 38.46; H, 4.16; N, 12.82. Found: C, 38.27; H, 4.18; N, 12.88%.

Method B: DMF (25 ml) was added to a mixture of $CuCl_2$ (0.061 g, 0.45 mmol), H_2L' (0.049 g, 0.30 mmol) and $LiOH \cdot H_2O$ (0.025 g, 0.60 mmol). The solids soon dissolved upon stirring. The resulting pale green solution was refluxed for 4 h and then layered with Et_2O (20 ml). Slow mixing gave a dark green microcrystalline solid which was isolated by filtration, washed with DMF (1 ml) and Et_2O (2 × 5 ml), and dried in air. Yield: 70%. The identity of the product was confirmed by elemental analyses and IR comparison with the authentic material prepared by Method A.

2.3. Single-crystal X-ray crystallography

The data were collected using a Bruker APEXII CCD diffractometer on station 16.2 of the Synchrotron Radiation Source at Daresbury Laboratory UK. Crystal data and selected parameters for data collection and processing are listed in Table 1. The data were integrated using SAINT v7.23a and the absorption correction was applied by SADABS. The SHELXTL suite of programs was used to solve the structure using direct methods and perform the least squares refinement. All non-hydrogen atoms were refined anisotropically, with displacement parameter restrains being used in the modeling of the ligands. Hydrogen atoms were placed geometrically where possible, the methyl hydrogen atoms were found in a rotational Fourier map; all were constrained and refined with a riding model.

Table 1
Crystallographic data for complex **1**.

Parameter	**1**
Chemical formula	$C_{28}H_{36}N_8Cu_3O_8Cl_2$
Formula weight	874.17
Crystal system, space group	tetragonal, $I4_1/a$
a (Å)	24.616(2)
b (Å)	24.616(2)
c (Å)	11.6525(10)
V (Å^3)	7060.8(10)
Z	4
T (K)	150(2)
Radiation, wavelength (Å)	synchrotron, 0.7848
ρ_{calc} (g cm^{-3})	1.645
μ (mm^{-1})	2.619
R_1[a]	0.0453[b]
wR_2[a]	0.1255[b]

[a] $w = 1/[\sigma^2(F_o^2) + (\alpha P)^2 + bP]$ and $P = (\max\ F_o^2, 0) + 2F_c^2/3$, $R_1 = \sum(|F_o| - |F_c|)/\sum(|F_o|)$ and $wR_2 = \{\sum[w(F_o^2 - F_c^2)^2]/\sum[w(F_o^2)^2]\}^{1/2}$.
[b] For 4234 reflections with $F^2 > 2\sigma(I)$.

3. Results and discussion

3.1. Brief synthetic comments and IR spectra

Complex **1** was initially obtained by solvothermal synthesis. Heating a solution of $[Cu_2(O_2CMe)_4(H_2O)_2]$, $CuCl_2$ and H_2L' in a 3:1:3 ratio in DMF at 130 °C in a sealed tube under autogenous pressure for 6 h, followed by slow cooling at room temperature, gave dark green crystals of the product. The $MeCO_2^-$ ions act as a base helping the deprotonation of the ligand. The usefulness of superheated fluids, i.e. solvothermal conditions, for preparing extended frameworks based on metal–ligand interactions has been demonstrated by several groups [7]. The temperature regime available in solvothermal techniques, intermediate between low-temperature solution chemistry and high-temperature solid-state chemistry, can favour the formation of metastable kinetic products rather than the thermodynamic products favoured at high temperature.

With the identity of **1** established by single-crystal, X-ray crystallography, we sought a convenient synthesis of the pure material under alternative, mild reaction conditions. It was logical to impose upon the knowledge of the chemical composition of **1** to select the starting materials and their ratios. Thus, the reaction of three equivalents of $CuCl_2$ with 2 equiv. of H_2L' and 4 equiv. of $LiOH \cdot H_2O$ in DMF gave, after convenient workup, the product in ~70% yield. The formation of the complex can be summarized by Eq. (1):

$$3n\mathrm{CuCl_2} + 2n\mathrm{H_2L'} + 4n\mathrm{LiOH{\cdot}H_2O} + 4n\mathrm{DMF} \xrightarrow{\mathrm{DMF}} \underset{1}{[\mathrm{Cu_3L_2Cl_2(DMF)_4}]_n} + 4n\mathrm{LiCl} + 8n\mathrm{H_2O} \quad (1)$$

Note that the ligand in the product is not the doubly deprotonated amide, i.e., L'^{2-}, but instead the di-iminolate (-2) [or diolate (-2)], i.e., L^{2-} (vide infra), see Scheme 1.

The IR spectrum of free H_2L' shows the characteristic bands of the *cis* secondary amide groups with the bands at ~3100, 1682, 1472 and 1392 cm^{-1} assigned to ν(NH), ν(C=O), $\nu(CN)_{amide}$ and δ(NH), respectively [8,9]. This spectral behaviour is consistent with the solid-state structure of the ligand (vide infra). The spectrum of **1** does not exhibit a band in the region for the amide carbonyl stretching, as expected from the absence of L'^{2-} in the product. The ν(C=O) and δ(OCN) vibrational modes of the coordinated DMF molecules appear at 1640 and 693 cm^{-1}, respectively [10]. Due to coordination, the ν(C=O) and δ(OCN) bands are shifted to lower and higher wavenumbers, respectively, when compared with the corresponding bands in the spectrum of free DMF [11].

3.2. Description of structure

Various structural features of **1** are shown in Figs. 1–3. Selected interatomic distances and angles are listed in Table 2.

Complex **1** is a 3D coordination polymer built from centrosymmetric trinuclear $[Cu_3L_2Cl_2(DMF)_4]$ units containing 2,3-dioxyquinoxalinate(-2) (L^{2-} in Scheme 1, vide infra) ligands that are responsible for the polymer formation. A perspective view of the trinuclear unit is shown in Fig. 1. Within the crystallographic asymmetric unit there are two, structurally different Cu^{II} sites, Cu(1) and Cu(2). The central Cu(1) ion sits on a crystallographically imposed inversion centre exhibiting *trans* coordination to two terminal chlorides and to two symmetry related L^{2-} ligands *via* the one of nitrogen atoms [N(1)] in each ligand. Each of the two "terminal" Cu^{II} ions [Cu(2), Cu(2′)] is bonded to two oxygen atoms of two terminal DMF molecules, both oxygen atoms from one L^{2-} ligand and to one nitrogen atom [N(2)] from an equivalent ligand in a different asymmetric unit.

The coordination geometry around Cu(1) is square planar. The Cu(1)–Cl(1) bond length of 2.277(1) Å is typical for square planar copper(II) complexes involving chloro ligands [12]. The Cu(2) coordination geometry is well described as square pyramidal with the DMF oxygen O(3) occupying the apical position. Analysis of the shape-determining angles using the approach of Reedijk and Addison [13] yields a value for the trigonality indet τ of 0.26 for Cu(2)

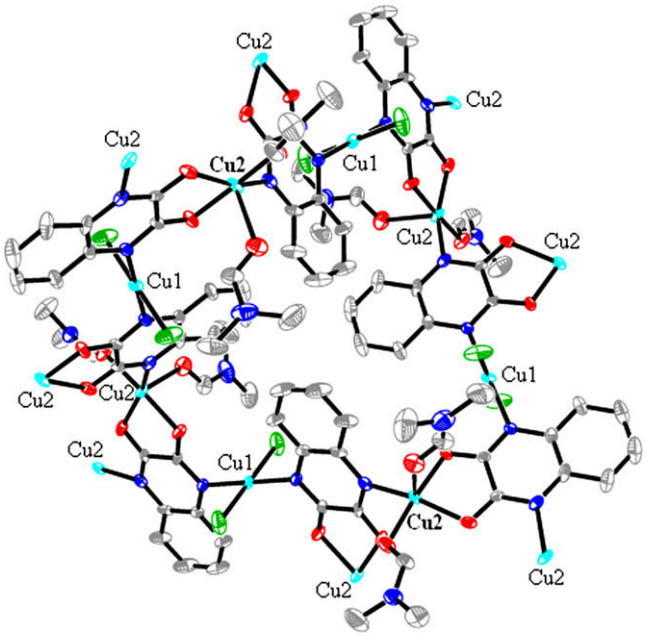


Fig. 2. The half folded square ring which makes up the substructure of **1**, with the fold along the Cu^{II} ions labeled in bold and the rest of the molecule being further away from the viewer. Displacement parameters are plotted at the 50% probability level.

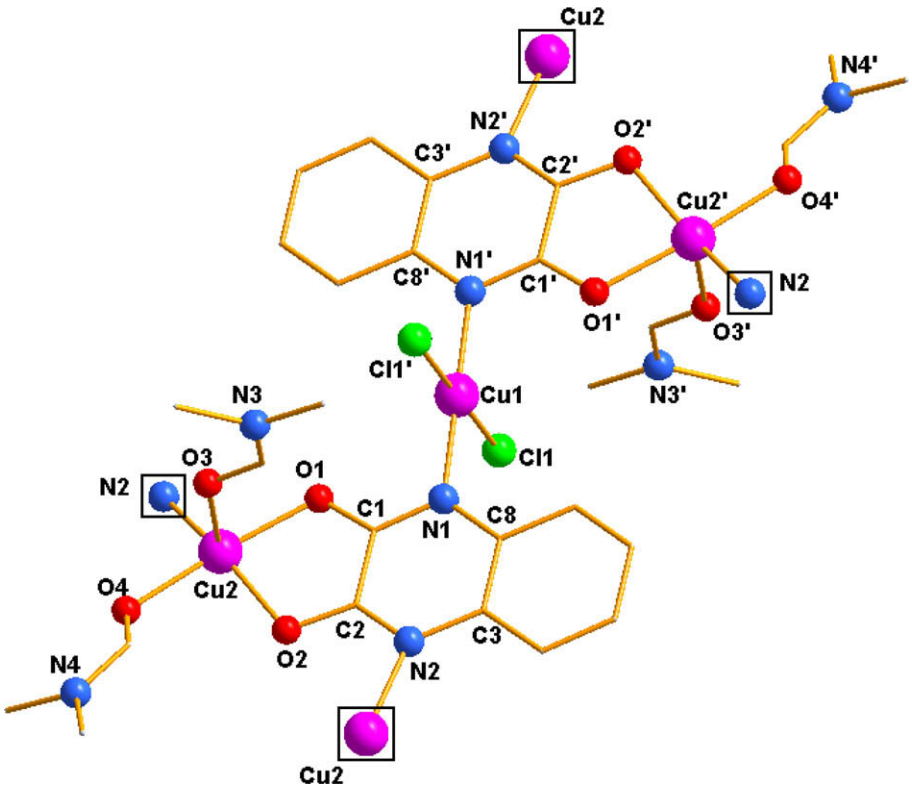


Fig. 1. The molecular structure of the repeat, centrosymmetric trinuclear unit present in the 3D network of **1**. The squared atoms belong to neighbouring units. The primed and unprimed atoms within the trinuclear unit are related by the symmetry operation $-x+2$, $-y+1$, $-z$.

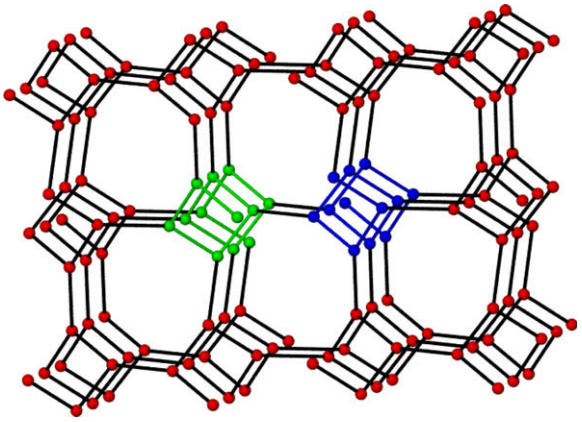


Fig. 3. Schematic representation of the (8^2.10)-a net of **1,** viewed along the *c* axis, containing 4-fold helices with opposite handedness (blue and green). (For interpretation of the references to colour in this figure legend, the reader is referred to the web version of this article.)

Table 2
Selected interatomic distances (Å) and angles (°).

Distances			
Cu(1)···Cu(2)	4.898(1)	Cu(2)–O(2)	1.972(2)
Cu(1)–Cl(1)	2.277(1)	Cu(2)–O(3)	2.336(2)
Cu(1)–N(1)	1.973(2)	Cu(2)–O(4)	1.988(2)
Cu(2)–O(1)	1.965(2)	Cu(2)–N(2″)	1.987(2)
Bond Angles			
Cl(1)–Cu(1)–Cl(1′)	180.0	O(1)–Cu(2)–N(2″)	93.8(1)
N(1)–Cu(1)–N(1′)	180.0	O(2)–Cu(2)–O(3)	91.1(1)
Cl(1)–Cu(1)–N(1)	89.8(1)	O(2)–Cu(2)–O(4)	89.9(1)
Cl(1)–Cu(1)–N(1′)	90.2(1)	O(2)–Cu(2)–N(2″)	158.9(1)
O(1)–Cu(2)–O(2)	89.5(1)	O(3)–Cu(2)–O(4)	87.0(1)
O(1)–Cu(2)–O(3)	90.5(1)	O(3)–Cu(2)–N(2″)	110.0(1)
O(1)–Cu(2)–O(4)	173.8(1)	O(4)–Cu(2)–N(2″)	92.4(1)

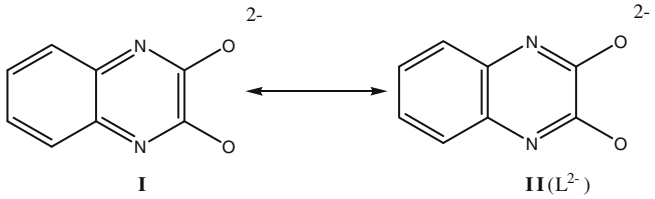
Symmetry operations used to generate equivalent atoms:
(′) $-x+2, -y+1, -z$; (″) $x-1/4, -y+5/4, z-1/4$.

(τ = 0 and 1 for perfect square pyramidal and trigonal bipyramidal geometries, respectively) suggesting a distorted stereochemistry. As expected, the axial Cu(2)–O(3) bond is the longest [2.336(2) Å].

In solution, 1,4-dihydro-2,3-quinoxalinedione (H_2L', Scheme 1) is in equilibrium with the tautomers with one and two hydroxyl groups [14]. The question of which tautomer is predominant in the solid state was answered with the help of single-crystal X-ray crystallography some 30 years ago [14]; this technique revealed that the molecule is a dione (H_2L' in Scheme 1). A comparison of the structural data for the dianionic ligand in complex **1** with those of the free ligand H_2L' [14] shows that the excess electron density of the deprotonated nitrogen atom is partially delocalized over the oxygen atoms of the amido groups; this permits the formulation of the resonance structures **I** and **II** [15], see Scheme 2. In the case of **1**, the C–O bonds appear to be weaker than in H_2L' (1.278 and 1.284 versus 1.232 and 1.225 Å), whereas the C(1)–C(2) bond is stronger (1.484 versus 1.552 Å). This indicates less double-bond character in the CO bonds and more double-bond character in the CC bond for L^{2-}; this may suggest at first glance the dominance of the resonance form **I** (Scheme 2) in the real structure of the coordinated dianionic ligand. On the other hand, the CN bond lengths between the carbon atoms of the phenyl ring and nitrogen atoms in the heterocyclic ring for **1** (1.384 and 1.390 Å) are typical of those of a single C–N bond, as in the case of the free ligand (1.392 and 1.398 Å) [14]. Moreover, the C–$N_{\text{"amide"}}$ bond distances in **1** [(C(1)–N(1) = 1.316 Å, C(2)–N(2) = 1.318 Å)], which are less than the corresponding distances in the free ligand (1.337 and 1.345 Å), indicate the existence of double bonds. Thus, the CN bond distances of **1** are consistent with the dominance of the resonance form **II** (see Scheme 2) in the real structure of the coordinated dianionic ligand [15]; for this reason, the dianionic ligand is represented using the form **II** in Scheme 1 and Fig. 4 (vide infra).

The structural elements that are present in the repeat trinuclear unit of **1** arrange into a half folded square ring consisting of four Cu(1) and four Cu(2) ions and eight L^{2-} ligands (Fig. 2); each of these ligands is then coordinated through a square pyramidal copper [Cu(2)] *via* either nitrogen or both oxygens alternately to form a 3D coordination polymer. In this arrangement, the L^{2-} ligands serve as "T" shaped three-connected nodes while the Cu^{II} centres serve as linear bridges creating a rather uncommon three-connected (8^2.10)-a network, known also as **lig** (LiGe) (Fig. 3) [16,17]. This contains 4-fold helices with opposite handedness (Fig. 3). Although the (8^2.10)-a net has been predicted by Wells [18], it remains rare in coordination polymer chemistry. To the best of our knowledge, there are only five examples of coordination polymers adopting the **lig** topology [19], two of which are 2-fold interpenetrating [20]. Therefore, **1** represents the fourth example of a non-interpenatrating (8^2.10)-a topology and the sixth example of a (8^2.10)-a network. Given the relative roles of the ligands which serve as nodes and metal centres which serve as bridges within the (8^2.10)-a network, **1** can be characterized as an Inverted Metal–Organic Framework (IMOF) [21].

The ligand L^{2-} adopts the 3.1111 (using Harris notation [22]) coordination mode in **1** (Fig. 4). This is a novel coordination mode for this ligand. Complex **1** joins a handful of structurally character-



Scheme 2. Two resonance structures for the 2,3-dihydroxyquinoxalinate(-2) ion.

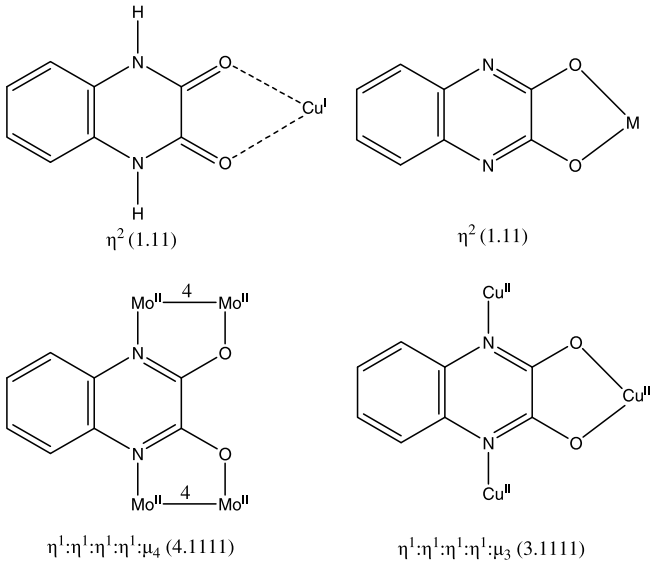


Fig. 4. The up-to-date crystallographically established coordination modes of 1,4-dihydro-2,3-quinoxalinedione (H_2L') and its 2,3-dioxyquinoxalinate(-2) dianionic ligand; the description of the modes by using the Harris notation [17] is shown in parentheses. The dashed lines represent weak interactions. M = Fe^{III}, Ru^{III}.

ized metal complexes containing H_2L' or L^{2-} as ligands [5,15,23,24]. The previously reported complexes are $[Mo^{II}_4(DAniF)_6(L)]$ [5], $[Fe^{III}(L)_3]^{2-}$ [15], $[Cu^{I}(CN)(H_2L')]_n$ [23] and the organometallic compound $[(Cp^*)Ru(NO)(L)]$ [24], where $DAniF^-$ is the *N*,*N*′-di-*p*-anisylformamidinate(-1) ligand. The ligands H_2L' and L^{2-} have been observed in four ligation modes in these complexes (including **1**). The observed coordination modes are shown in Fig. 4. The metric parameters of L^{2-} in all the previous complexes support its formulation as shown in Scheme 1, i.e. the dominance of the resonance form **II** (see Scheme 2). Thus compound **1** is the first crystallographically characterized metal complex in which 2,3-dioxyquinoxalinate(-2) coordinates in the ene-1,2-diolate mode as a bridging ligand.

3.3. Magnetochemistry

Solid-state dc magnetic susceptibility data (Fig. 5) were collected on dried **1** under a constant field of 0.1 T in the temperature range 2.0-300 K. The product $\chi_M T$ at room temperature is 1.17 $cm^3\ mol^{-1}\ K$ per trinuclear unit, close to the value of 1.24 $cm^3\ mol^{-1}\ K$ expected for three non-interacting Cu^{II} ions with a *g* value of 2.1. The value of the $\chi_M T$ product decreases gradually upon cooling until ca. 60 K, and below this temperature it decreases rapidly down to a value of 0.62 $cm^3\ K\ mol^{-1}$ at 6 K, before increasing sharply at lower temperatures; the $\chi_M T$ value is 0.81 $cm^3\ K\ mol^{-1}$ at 2.0 K. Magnetization experiments performed at 2.0 K in the field range 0–5 T indicate a saturation value close to one electron per Cu^{II}_3 unit exhibiting a Brillouin shape for $S = 1/2$ and $g = 2.06(4)$, see inset of Fig. 5.

For a 3D compound in which all the superexchange pathways were operative and antiferromagnetic in nature, an $S = 0$ "ground state" would be expected in the absence of competitive interactions. The non-zero "ground" state of **1** can be explained by considering carefully the structural details of the complex. There are two different superexchange pathways, both provided by the ligand L^{2-}, and thus two different kinds of *J* values (Fig. 6; from now onwards the numbering scheme that will be used is the same with that used in the real structure of **1**, see Fig. 1). J_1 is associated with the *inter*trimer Cu(1)···Cu(2) interaction through the "pyrazine" portion of L^{2-} and J_2 is associated with two equivalent [one *intra*trimer Cu(1)···Cu(2) and one *inter*trimer Cu(2)···Cu(2)] interactions through the NCO^- and $NCCO^-$ moieties of L^{2-}. The magnetic data, which are indicative of the presence of one unpaired electron

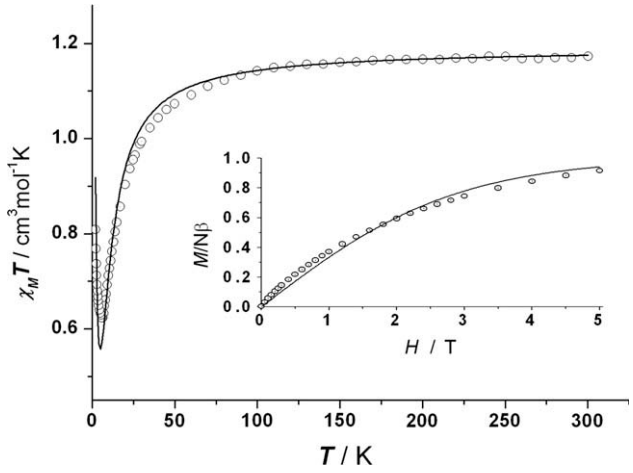


Fig. 5. $\chi_M T$ vs *T* for **1**; the solid line represents the best fit of the experimental data (see the text for the fit parameters). The inset shows magnetization data for the Cu^{II}_3 subunit; the solid line represents the Brillouin curve for the $S = 1/2$ state.

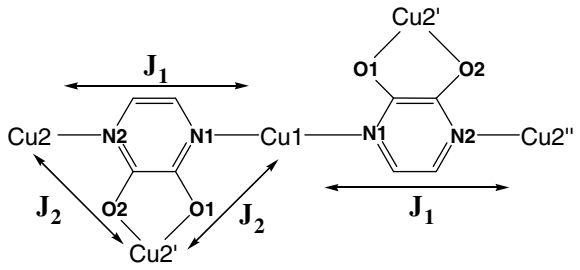


Fig. 6. The 2-*J* magnetic model initially considered for complex **1**; see the text for details. The benzene 'part' of the ligand L^{2-} has been omitted for clarity.

for each Cu^{II} triad, suggest that one of the pathways is not magnetically operative. Taking into account that (i) J_2 propagates the antiferromagnetic interaction in the three dimensions, and (ii) the quinoxaline bridge is a weak to moderate, but effective mediator of magnetic exchange interactions [25], we decided to fit the data assuming a negligible value of J_2. Since the J_1 interaction creates *pseudo*isolated Cu(2)···Cu(1)···Cu(2) subunits of the type shown in Fig. 6 (see also Fig. 1), we used the Hamiltonian of Eq. (2), including a Θ term in an attempt to adjust the low temperature data. Best-fit parameters are $J_1 = -10.4(3)\ cm^{-1}$, $g = 2.057(6)$ and $\Theta = +1.1(1)$ K.

$$H = -J_1(S_2 \cdot S_1 + S_1 \cdot S_{2''}) \quad (2)$$

The obtained *J* value is in good agreement with reported values involving the exchange interaction between Cu^{II} ions through the quinoxaline bridging ligand, which is always weakly to moderately antiferromagnetic [25]. The minimum in the $\chi_M T$ versus T plot at 6 K (Fig. 5) indicates that J_2 (see Fig. 6) is not strictly zero. It is not possible to calculate accurately the value of this coupling constant for a 3D system with the observed topology, but the positive sign and low value of the Θ term clearly indicate that a very weak ferromagnetic interaction is mediated by the $NCO^-/NCCO^-$ moieties of L^{2-}.

4. Concluding comments and perspectives

The commercially available compound 1,4-dihydro-2,3-quinoxalinedione (H_2L') has fulfilled its promise as a good ligand for the preparation of coordination polymers with interesting structures and properties. The ligand has been transformed to the 2,3-dioxyquinoxalinate (L^{2-}) form upon complexation with copper(II). The obtained 3D coordination polymer **1** is novel in multiple ways, as described, but it also provides a rare example of a complicated structural type where the main magnetic exchange interaction is propagated through only one pathway. We also believe that the 'catecholate'-type deprotonated oxygen atoms of L^{2-} can each bridge two Cu^{II} ions, thus increasing its coordination potential to μ_4 or μ_5, a fact that may favour new structural types. Complexes of L^{2-} with Mn^{II}, Fe^{II}, Co^{II} and Ni^{II} are not known to date, and it is currently not evident whether the chemical identity and structure of such compounds are dependent on the particular nature of the metal ion; based on the unique nature of Cu^{II} among the divalent 3d-metals, we predict that the Mn^{II}, Fe^{II}, Co^{II} and Ni^{II}/L^{2-} polymers will have different structures and magnetic properties. Efforts to test the above expectations are currently in progress.

Supplementary data

CCDC 663054 contains the supplementary crystallographic data for **1**. These data can be obtained free of charge from The Cambridge Crystallographic Data Centre via www.ccdc.cam.ac.uk/data_request/cif.

Acknowledgements

S.P.P., K.F.K. and E.M.-Z thank the European Social Fund (ESF), the Operational Program for Educational and Vocational Training II (EPEAEK II) and particularly the Program PYTHAGORAS (Grant b. 365.037), for funding this work. The Advanced Light Source is supported by the Director, Office of Science, Office of Basic Energy Sciences, of the US Department of Energy under Contract No. DE-AC02-05CH11231. G.A. thanks the Spanish Government for a "Ramon y Cajal" contract. A.E. is grateful to Ministerio de Ciencia y Technologia of Spain (Project CTQ2006/01759) for financial support.

References

[1] (a) For selected reviews see: A.Y. Robin, K.M. Fromm, Coord. Chem. Rev. 250 (2006) 2127;
(b) A. Erxleben, Coord. Chem. Rev. 246 (2003) 203;
(c) S.R. Batten, Curr. Opin. Solid State Mater. Sci. 5 (2001) 107;
(d) D.-K. Bučar, G.S. Papaefstathiou, T.D. Hamilton, Q.L. Chu, I.G. Georgiev, L.R. MacGillivray, Eur. J. Inorg. Chem. (2007) 4559;
(e) C. Coulon, H. Miyasaka, R. Clérac, Struct. Bond. 122 (2006) 163;
(f) Y. Zhou, M. Hong, X. Wu, Chem. Commun. (2006) 135;
(g) M.L. Rosseinsky, Micropor. Mesopor. Mater. 73 (2004) 15.
[2] For an excellent review, see: S.R. Batten, R. Robson, Angew. Chem., Int. Ed. 37 (1998) 1460.
[3] For a review, see: C. Janiak, Dalton Trans. (2003) 2781.
[4] For example, see R.H. Cayton, M.H. Chisholm, J.C. Huffman, E.B. Lobkovsky, J. Am. Chem. Soc. 113 (1991) 8709.
[5] For example see F.A. Cotton, J.P. Donahue, C.A. Murillo, L.M. Perez, R. Yu, J. Am. Chem. Soc. 125 (2003) 8900.
[6] K.F. Konidaris, S.P. Perlepes, G. Aromi, S.J. Teat, A. Escuer, E. Manessi-Zoupa, Inorg. Chem. Commun. 11 (2008) 186.
[7] (a) For example, see L. Cheng, W.-X. Zhang, B.H. Ye, J.B. Lin, X.–M. Chen, Eur. J. Inorg. Chem. (2007) 2668;
(b) M.B. Doran, A.J. Norquist, D. O' Hare, Inorg. Chem. 42 (2003) 6968;
(c) S.O.H. Gutschke, D.J. Price, A.K. Powell, P.T. Wood, Angew. Chem., Int. Ed. 40 (2001) 1920.
[8] H.O. Desseyn, in: S. Patai (Ed.), The Chemistry of Acid Derivatives, vol. 2, Wiley, New York, pp. 291–293
[9] A.T.H. Lenstra, B. Bracke, B. Van Dijk, S. Maes, C. Van Alsenoy, H.O. Desseyen, S.P. Perlepes, Acta Crystallogr., Sect. B 54 (1998) 859.
[10] Th.C. Stamatatos, G.S. Papaefstathiou, L.R. MacGillivray, A. Escuer, R. Vicente, E. Ruiz, S.P. Perlepes, Inorg. Chem. 46 (2007) 8843.
[11] C. Airoldi, Inorg. Chem. 20 (1981) 998.
[12] K. Skorda, Th.C. Stamatatos, A.P. Vafiadis, A.T. Lithoxoidou, A. Terzis, S.P. Perlepes, J. Mrozinski, C.P. Raptopoulou, J.C. Plakatouras, E.G. Bakalbassis, Inorg. Chim. Acta 358 (2005) 565.
[13] A.W. Addison, T.N. Rao, J. Reedijk, T. Rijn, G.C. Verschoor, J. Chem. Soc., Dalton Trans. (1984) 1349.
[14] C. Svensson, Acta Chem. Scand. B 30 (1976) 581.
[15] M.C. Muñoz, R. Ruiz, M. Traianidis, A. Aukauloo, J. Cano, Y. Journaux, I. Fernández, J.R. Pedro, Angew. Chem., Int. Ed. 37 (1998) 1833.
[16] V.A. Blatov, L. Carlucci, G. Ciani, D.M. Proserpio, CrystEngCommun 6 (2004) 377.
[17] N.L. Rosi, J. Kim, M. Eddaoudi, B. Chen, M. O'Keeffe, O.M. Yaghi, J. Am. Chem. Soc. 127 (2005) 1504.
[18] A.F. Wells, Three-dimensional Nets and Polyhedra, Wiley, New York, 1977.
[19] (a) J.-P. Zhang, Y.-Y. Lin, X.-C. Huang, X.-M. Chen, Dalton Trans. (2005) 3681;
(b) T. Wu, B.-H. Yi, D. Li, Inorg. Chem. 44 (2005) 4130;
(c) K. Li, Z. Xu, H. Xu, P.J. Carroll, J.C. Fettinger, Inorg. Chem. 45 (2006) 1032.
[20] (a) J.-C. Dai, X.-T. Wu, Z.-Y. Fu, S.-M. Hu, W.-X. Du, C.-P. Cui, L.-M. Wu, H.-H. Zhang, R.-Q. Sun, Chem. Commun. (2002) 12;
(b) J.-C. Dai, X.-T. Wu, Z.-Y. Fu, S.-M. Hu, W.-X. Du, C.-P. Cui, L.-M. Wu, H.-H. Zhang, R.-Q. Sun, Chem. Commun. (2008) 1296.
[21] (a) G.S. Papaefstathiou, L.R. MacGillivray, Angew. Chem., Int. Ed. 41 (2002) 2070;
(b) G.S. Papaefstathiou, L.R. MacGillivray, Coord. Chem. Rev. 246 (2003) 169.
[22] R.A. Coxall, S.G. Harris, D.K. Henderson, S. Parsons, P.A. Tasker, R.E.P. Winpenny, J. Chem. Soc., Dalton Trans. (2000) 2349.
[23] M. Heller, W.S. Sheldrick, Z. Anorg. Allg. Chem. 627 (2001) 569.
[24] K. Yang, S.G. Bott, M.G. Richmond, J. Chem. Crystallogr. 25 (1995) 283.
[25] (a) W.W. Richardson, W.E. Hatfield, J. Am. Chem. Soc. 98 (1976) 835;
(b) C.P. Landee, A. Delcheva, C. Galerium, G. Pena, M.M. Turnbull, R.D. Willett, Polyhedron 22 (2003) 2235.

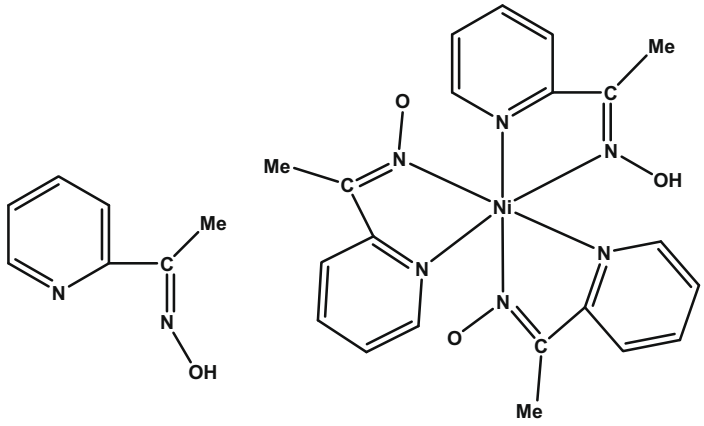


Fig. 1. The organic ligand (left) and the metalloligand (right) used in our efforts.

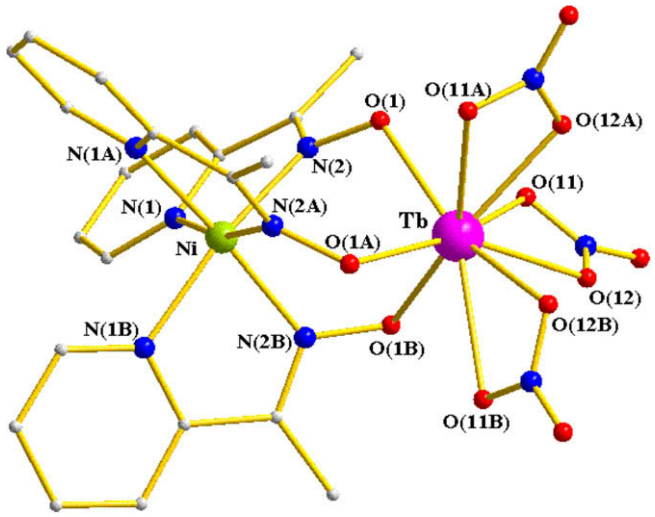


Fig. 2. The molecular structure of **2**.

crystallographic axis. The Ni^{II} center has an octahedral $Ni^{II}N_6$ chromophore. The three oximate/oxime O atoms that were free in the precursor complex **1** are coordinated to the Tb^{III} center in **2**; three chelating NO_3^- groups complete 9-coordination at Tb^{III}. The *cis–cis–cis* disposition of the oxime/oximate groups is preserved in the product. It is very likely that the C_3 symmetry axis is masking the presence of a proton statically disordered among the three ligand groups. Note that the O(1)···O(1A), O(1A)···O(1B), and O(1)···O(1B) distances [3.208(11) Å] are consistent with a (33%) hydrogen bond. It should also be mentioned that a vacuum-dried sample of **2** exhibits an IR band (KBr, hexachlorobutadiene) at ~3400 cm^{-1} assignable to the $\nu(OH)_{oxime}$ mode.

$$[\underset{\mathbf{1}}{Ni\{(py)C(Me)NO\}_2\{(py)C(Me)NOH\}} + Tb(NO_3)_3 \cdot 6H_2O \rightarrow [\underset{\mathbf{2}}{NiTb\{(py)C(Me)NO\}_2(NO_3)_3\{(py)C(Me)NOH\}} + 6H_2O \quad (1)$$

In the starting metalloligand **1** and the dinuclear product **2**, one of the three organic ligands is formally neutral. We suspected that the presence of a base could affect the product identity and this has, indeed, turned out to be the case. *Keeping all the other synthetic parameters constant*, the presence of one (or more) equivalents of base, e.g., Et_3N, per metalloligand **1** gave the nitrate-free clusters $[Ni_2Dy_2\{(py)C(Me)NO\}_6(NO_3)_4]$ (**3**) and $[Ni_2Tb_2\{(py)C(Me)NO\}_6(NO_3)_4]$ (**4**)[1] depending on the lanthanide used in good yield, see Eq. (2). The molecular structure[2] of **3** is shown in Fig. 3. The molecule lies on a crystallographic inversion center and consists of two dimeric $NiDy\{(py)C(Me)NO\}_2(NO_3)_2$ units which have a structural resemblance to the dinuclear molecules of **2**. The formerly neutral oxime group is now deprotonated and bridging providing the interdimer linkage. Thus, four $(py)C(Me)NO^-$ anions behave as $\eta^1{:}\eta^1{:}\eta^1{:}\mu$ ligands and two as $\eta^1{:}\eta^1{:}\eta^2{:}\mu_3$ ligands. As expected, treatment of **2** with base leads to **4**.

$$2[\underset{\mathbf{1}}{Ni\{(py)C(Me)NO\}_2\{(py)C(Me)NOH\}} + 2Ln(NO_3)_3 \cdot 6H_2O + 2Et_3N \xrightarrow{MeOH} [\underset{\mathbf{3,4}}{Ni_2Ln_2\{(py)C(Me)NO\}_6(NO_3)_4}] + 2Et_3NH(NO_3) + 12H_2O \quad (2)$$

In the above described dinuclear and tetranuclear clusters, the molar ratio of the metal ions is 1:1. Since the coordination sphere of the Tb^{III} ion in **2** is completed by three terminal NO_3^- groups, we suspected that using a 2:1 metalloligand to Tb^{III} reaction ratio would lead to trinuclear clusters. The reaction of $Tb(NO_3)_3 \cdot 6H_2O$ with 2 equiv. of **1** and 2 equiv. of base in MeOH gave complex $[Ni_2Tb\{(py)C(Me)NO\}_6](NO_3)$ (**5**)[2] in moderate yield, see Eq. (3). The molecular structure of the centrosymmetric cation of **5** is

$$2[\underset{\mathbf{1}}{Ni\{(py)C(Me)NO\}_2\{(py)C(Me)NOH\}} + Tb(NO_3)_3 \cdot 6H_2O + 2Et_3N \xrightarrow{MeOH} [\underset{\mathbf{5}}{Ni_2Tb\{(py)C(Me)NO\}_6}](NO_3) + 2Et_3NH(NO_3) + 6H_2O \quad (3)$$

shown in Fig. 4. The $(py)C(Me)NO^-$ anions behave as $\eta^1{:}\eta^1{:}\eta^1{:}\mu$ ligands. The cation can be viewed as a six-coordinate Tb^{III} complex featuring two deprotonated, tridentate chelating metalloligands. Complex **5** can also be prepared by the reaction of **2** with 1 equiv. of **1** in MeOH in the presence of a base, see Eq. (4).

$$[\underset{\mathbf{2}}{NiTb\{(py)C(Me)NO\}_2(NO_3)_3\{(py)C(Me)NOH\}}] + [\underset{\mathbf{1}}{Ni\{(py)C(Me)NO\}_2\{(py)C(Me)NOH\}}] + 2Et_3N \xrightarrow{MeOH} [\underset{\mathbf{5}}{Ni_2Tb\{(py)C(Me)NO\}_6}](NO_3) + 2Et_3NH(NO_3) \quad (4)$$

Complexes **2**–**5** were also prepared by the 'one-pot' approach, i.e., by the direct reactions between $Ni(ClO_4)_2 \cdot 6H_2O$, $Ln(NO_3)_3 \cdot 6H_2O$ and (py)C(Me)NOH using the appropriate reactants ratios (those imposed on by the stoichiometric formulae of the compounds) and base equivalents.

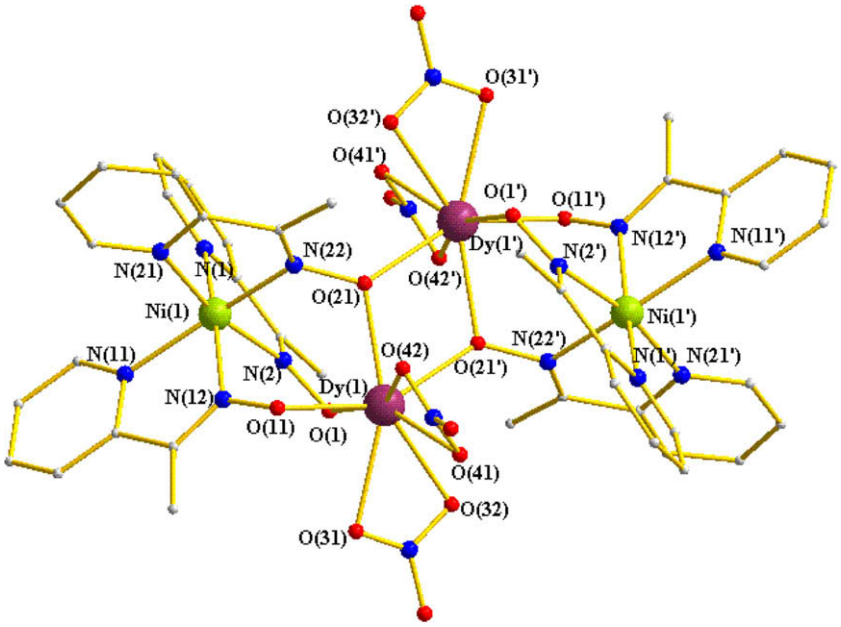


Fig. 3. The molecular structure of **3**.

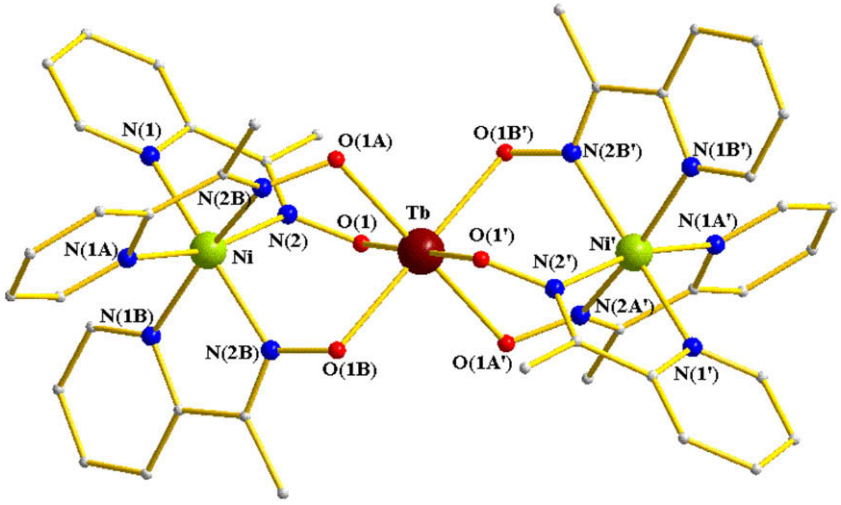


Fig. 4. The molecular structure of the cation present in complex **5**.

Solid-state dc magnetic susceptibility data (χ_M) data for the representative complexes **2** and **5** were collected in the 2.0–300 K range in a 5 KG (0.5 T) field. Data in the form of $\chi_M T$ versus T plots are shown in Fig. 5. The room temperature $\chi_M T$ value of 13.34 $cm^3\ mol^{-1}\ K$ for **2** (Ni^{2+}, $S = 1$; Tb^{3+}, $^7F_6$, $S = 3$, $L = 3$, $J = 6$) decreases slightly upon cooling to ~75 K, where it begins to drop sharply to a value of 4.16 $cm^3\ mol^{-1}\ K$ at 2.0 K. An analogous behavior is observed for **5** with the $\chi_M T$ values at 300 and 2.0 K being 13.54 and 2.80 $cm^3\ mol^{-1}\ K$, respectively. The field dependence of the magnetization (M) was also measured at 2.0 K. Data are shown in Fig. 6. The experimental M value of **2** and **5** reaches a value of 6.71 and 6.41 $N\mu_B$ at 5 T, respectively.

The observed decrease of the $\chi_M T$ product as T decreases is mainly governed by the thermal depopulation of the ground-state sublevels (Stark sublevels) that result from the spin–orbit coupling and a low symmetry crystal field [9]. Moreover, the 4f electrons are little involved in chemical bonding due to the inner nature of the 4f orbitals, thus inducing very weak superexchange and magnetic

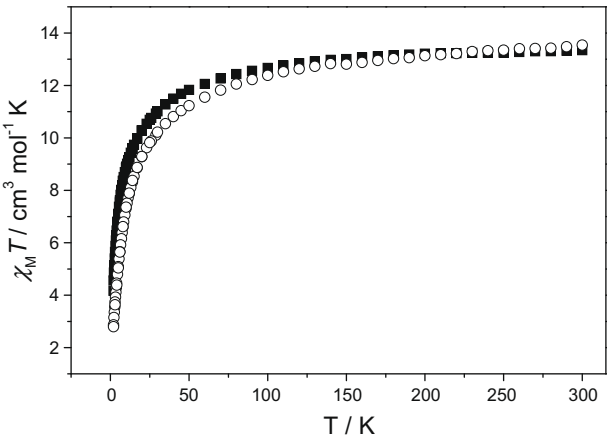


Fig. 5. Plot of $\chi_M T$ as a function of T for **2** (black squares) and **3** (open circles).

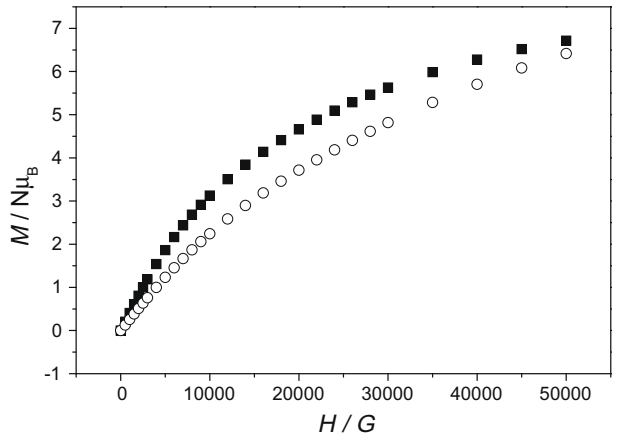


Fig. 6. Magnetic field (H) dependence of the magnetization (M) at 2 K for **2** (black squares) and **5** (open circles).

couplings with the 3d-metal electrons [9]. Hence, it is very difficult to determine the relative contributions of the thermal depopulation of the Stark sublevels versus the intramolecular magnetic interactions [9]. To extract some information on the absence/presence and the nature of the Ni^{II}–Tb^{III} interaction in the two complexes, the approach of Kahn et al. [10] should be applied. The approach requires the preparation and magnetic study of the corresponding dinuclear and trinuclear Ni^{II}/La^{III}, Lu^{III} or Y^{III}, Ni^{II}/Gd^{III} and Zn^{II}/Tb^{III} complexes, and this effort is currently in progress.

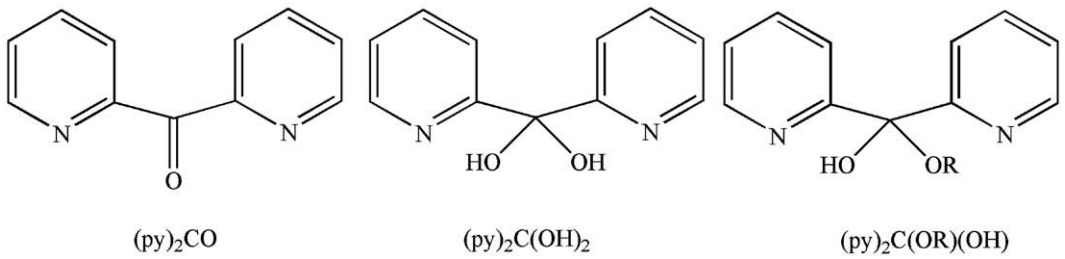
In summary, complexes **2**–**5** are new valuable additions in the relatively small family of mixed Ni^{II}/Ln^{III} clusters. The magnetic properties of these clusters are complicated by the large spin–orbit coupling effects of Tb^{III} and Dy^{III}, making difficult the quantitative study of the magnitude of the exchange parameters and their resulting ground state description. This preliminary work also demonstrates the utility of the 'metal complexes as ligands' approach based on the use of 2-pyridyloximates for the preparation of mixed 3d/4f-metal complexes. We do believe that the use of Ln^{III} ions to modulate the magnetic properties of transition-metal clusters, high-spin molecules and SMMs is still an interesting area that promises new science as it matures.

Acknowledgements

We thank European Social Fund (ESF), Operational Program for Educational and Vocational Training II (EPEAEK II), and particularly the Program PYTHAGORAS (Grant b. 365.037 to SPP) for funding the above work. C. D. thanks Spanish and Catalan Governments (Projects CTQ2006/03949/BQU and 2005SGR 00593, respectively) for the financial support.

References

[1] (a) For reviews see: G. Christou, D. Gatteschi, D.N. Hendrickson, R. Sessoli, MRS Bull. 25 (2000) 66;
(b) D. Gatteschi, R. Sessoli, Angew. Chem., Int. Ed. 42 (2003) 268;
(c) G. Aromi, E.K. Brechin, Struct. Bond. 122 (2006) 1.
[2] (a) For example see: A. Mishra, W. Wernsdorfer, K.A. Abboud, G. Christou, J. Am. Chem. Soc. 126 (2004) 15648;
(b) S. Osa, T. Kido, N. Matsumoto, N. Re, A. Pochaba, J. Mrozinski, J. Am. Chem. Soc. 126 (2004) 420;
(c) A. Mishra, W. Wernsdorfer, S. Parsons, G. Christou, E.K. Brechin, Chem. Commun. (2005) 2086;
(d) J.-P. Costes, F. Dahan, W. Wernsdorfer, Inorg. Chem. 45 (2006) 5;
(e) V.M. Mereacre, A.M. Aco, R. Clérac, W. Wernsdorfer, G. Filoti, J. Bartolomé, C.E. Anson, A.K. Powell, J. Am. Chem. Soc. 129 (2007) 9248.
[3] (a) F. Mori, T. Ishida, T. Nogami, Polyhedron 24 (2005) 2588;
(b) V. Chandrasekhar, B.M. Pandian, R. Boomishankar, A. Steiner, J.J. Vittal, A. Houri, R. Clérac, Inorg. Chem. 47 (2008) 4918.
[4] G. Denti, S. Serroni, S. Campagna, A. Juris, M. Ciano, V. Balzani, in: A.F. Williams, C. Floriani, A.E. Merbach (Eds.), Perspectives in Coordination Chemistry, VCH, Weinheim, 1992, p. 153.
[5] C. Papatriantafyllopoulou, A. Terzis, S.P. Perlepes, manuscript in preparation.
[6] For a comprehensive review, see: C.J. Milios, Th.C. Stamatatos, S.P. Perlepes, Polyhedron 25 (2006) 134. Polyhedron Report.
[7] (a) For example, see: Th.C. Stamatatos, D. Foguet-Albiol, S.-C. Lee, C.C. Stoumpos, C.P. Raptopoulou, A. Terzis, W. Wernsdorfer, S.O. Hill, S.P. Perlepes, G. Christou, J. Am. Chem. Soc. 129 (2007) 9484;
(b) F. Mori, T. Nyui, T. Ishida, T. Nogami, K.-Y. Choi, H. Nojiri, J. Am. Chem. Soc. 128 (2006) 1440.
[8] For example, see: R. Clérac, H. Miyasaka, M. Yamashita, C. Coulon, J. Am. Chem. Soc. 124 (2002) 12837.
[9] C. Benelli, D. Gatteschi, Chem. Rev. 102 (2002) 2369.
[10] M.L. Kahn, P. Lecante, M. Verelst, C. Mathonière, O. Kahn, Chem. Mater. 12 (2000) 3073.



Scheme 1. The $(py)_2CO$-based ligands discussed in the text; note that $(py)_2C(OH)_2$ and $(py)_2C(OR)(OH)$ and their anions exist *only* in their respective metal complexes (R = Me, Et, etc.).

give an extraordinary structural flexibility in the $(py)_2CO/R'CO_2^-/N_3^-$ mixed ligand system. This has, indeed, turned out to be the case. Preliminary results of this work have been communicated [13].

2. Experimental

2.1. General and physical measurements

All manipulations were performed under aerobic conditions using materials (reagent grade) and solvents as received. $Cu(O_2CPh)_2 \cdot 2H_2O$ was prepared as described elsewhere [14]. *Caution*! Although no such behavior was observed during the present work, azide salts are potentially explosive; such compounds should be synthesized and used in small quantities, and treated with utmost care at all times.

Microanalyses (C, H, N) were performed by the University of Ioannina (Greece) Microanalytical Laboratory using an EA 1108 Carlo Erba analyzer. IR spectra (4000–450 cm^{-1}) were recorded on Perkin–Elmer 16 PC and Nicolet 520 FTIR spectrometers with samples prepared as KBr pellets. Magnetic susceptibilities were measured on polycrystalline powders with a Cryogenic S600 SQUID magnetometer. Powders were pressed in a pellet to prevent preferential crystallite orientation with the magnetic field.

2.2. Compound preparation

2.2.1. $[Cu_6(O_2CPh)_4(N_3)_2\{(py)_2CO_2\}_2\{(py)_2C(OH)O\}_2] \cdot 2H_2O \cdot 4.5MeCN$ (**1** $\cdot 2H_2O \cdot 4.5MeCN$)

Method A: To a stirred solution of $(py)_2CO$ (0.06 g, 0.30 mmol) and $LiOH \cdot H_2O$ (0.01 g, 0.30 mmol) in MeCN (20 ml) was added solid NaN_3 (0.02 g, 0.30 mmol). The mixture was stirred for 15 min and then solid $Cu(O_2CPh)_2 \cdot 2H_2O$ (0.21 g, 0.60 mmol) was added under vigorous stirring, which caused a rapid color change from blue to dark green. The resulting solution was stirred for a further 1 h, filtered, and the filtrate was layered with Et_2O (40 ml). After 10 days, X-ray quality dark-green prismatic crystals of **1** $\cdot 2H_2O \cdot 4.5MeCN$ were collected by filtration, washed with MeCN (2×5 ml) and Et_2O (2×5 ml), and dried in air. Yield 55%. The dried sample analyzed as **1** $\cdot 2H_2O$. *Anal.* Calc. for $C_{72}H_{58}Cu_6N_{14}O_{18}$: C, 48.35; H, 3.27; N, 10.96. Found: C, 48.51; H, 3.14; N, 10.91%. Selected IR data (KBr pellet, cm^{-1}): 3428m, 2058vs, 1602s, 1562s, 1474m, 1442m, 1382vs, 1298w, 1224w, 1158w, 1126w, 1078s, 980w, 776w, 722m, 684w, 652w, 462w, 424w.

Method B: To a stirred solution of $(py)_2CO$ (0.06 g, 0.30 mmol) in MeCN (20 ml) was added solid NaN_3 (0.02 g, 0.30 mmol). The mixture was stirred for 35 min and then solid $Cu(O_2CPh)_2 \cdot 2H_2O$ (0.21 g, 0.60 mmol) was added under vigorous stirring, which caused a rapid color change from blue to dark green. The resulting solution was stirred for a further 1 h, filtered, and the filtrate was layered with Et_2O (40 ml). After 13 days, X-ray quality dark-green prismatic crystals of **1** $\cdot 2H_2O \cdot 4.5MeCN$ were collected by filtration, washed with MeCN (2×5 ml) and Et_2O (2×5 ml), and dried in air. Yield 13%. The identity of the product was confirmed by elemental analysis (C, H, N) and IR spectroscopic comparison with authentic material from Method A.

2.2.2. $[Cu_4(O_2CPh)_2(N_3)_4\{(py)_2C(OMe)O\}_2]_n$ (**2**) and $[Cu_2(O_2CPh)(N_3)_2\{(py)_2C(OMe)O\}]_n$ (**3**) in a mixture

To a stirred solution of $(py)_2CO$ (0.06 g, 0.30 mmol) in MeOH (20 ml) was added solid NaN_3 (0.02 g, 0.30 mmol). The mixture was stirred for 15 min and then solid $Cu(O_2CPh)_2 \cdot 2H_2O$ (0.21 g, 0.60 mmol) was added under vigorous stirring, which caused a rapid color change from blue to dark green. The solution was stirred for a further 30 min, filtered, and the filtrate was layered with Et_2O (40 ml). After 20 days, X-ray quality dark-green plate-like crystals of **2** *and* dark-green needles of **3** were collected by filtration, washed with cold MeOH (2×5 ml) and Et_2O (2×5 ml), and dried in air. The two products were separated manually and individually identified as complexes **2** and **3** (both by single-crystal X-ray crystallography), respectively. Typical yields were ~20% (**2**) and ~10% (**3**).

2.3. Single-crystal X-ray crystallography

The crystallographic data and structure refinement details for the three complexes are summarized in Table 1. Selected crystals of **1** $\cdot 2H_2O \cdot 4.5MeCN$ ($0.30 \times 0.40 \times 0.65$ mm) and **3** ($0.05 \times 0.10 \times 0.55$ mm) were mounted in capillary, whereas a selected

Table 1
Crystallographic data for complexes **1** $\cdot 2H_2O \cdot 4.5MeCN$, **2** and **3**.

Parameter	**1** $\cdot 2H_2O \cdot 4.5MeCN$	**2**	**3**
Formula	$C_{81}H_{71.50}Cu_6N_{18.50}O_{18}$	$C_{38}H_{32}Cu_4N_{16}O_8$	$C_{19}H_{16}Cu_2N_8O_4$
Formula weight	1973.31	1094.96	547.48
Crystal system	triclinic	monoclinic	monoclinic
Space group	$P\bar{1}$	$P2_1/c$	$P2_1/n$
a (Å)	16.289(8)	21.690(10)	12.994(6)
b (Å)	17.295(8)	12.867(9)	8.630(4)
c (Å)	18.125(8)	16.810(10)	19.302(9)
α (°)	69.870(10)	90	90
β (°)	69.18(2)	114.46(2)	102.13(3)
γ (°)	73.48(2)	90	90
V (Å^3)	4404(4)	4270(4)	2116.2(17)
Z	2	4	4
ρ_{calc} (g cm^{-3})	1.488	1.703	1.718
Radiation	Mo Kα	Cu Kα	Cu Kα
λ (Å)	0.71073	1.54180	1.54180
Temperature (K)	298	298	298
μ (mm^{-1})	1.499	2.859	2.884
Data collected/ unique (R_{int})	16118/15406 (0.0205)	6410/6174 (0.0373)	3152/3044 (0.0270)
Data with $I > 2\sigma(I)$	11619	5448	2310
R_1 ($I > 2\sigma(I)$)[a]	0.0478	0.0389	0.0485
wR_2 ($I > 2\sigma(I)$)[b]	0.1253	0.1025	0.1189

[a] $R_1 = \sum(|F_o| - |F_c|)/\sum(|F_o|)$.
[b] $wR_2 = \{\sum[w(F_o^2 - F_c^2)^2]/\sum[w(F_o^2)^2]\}^{1/2}$.

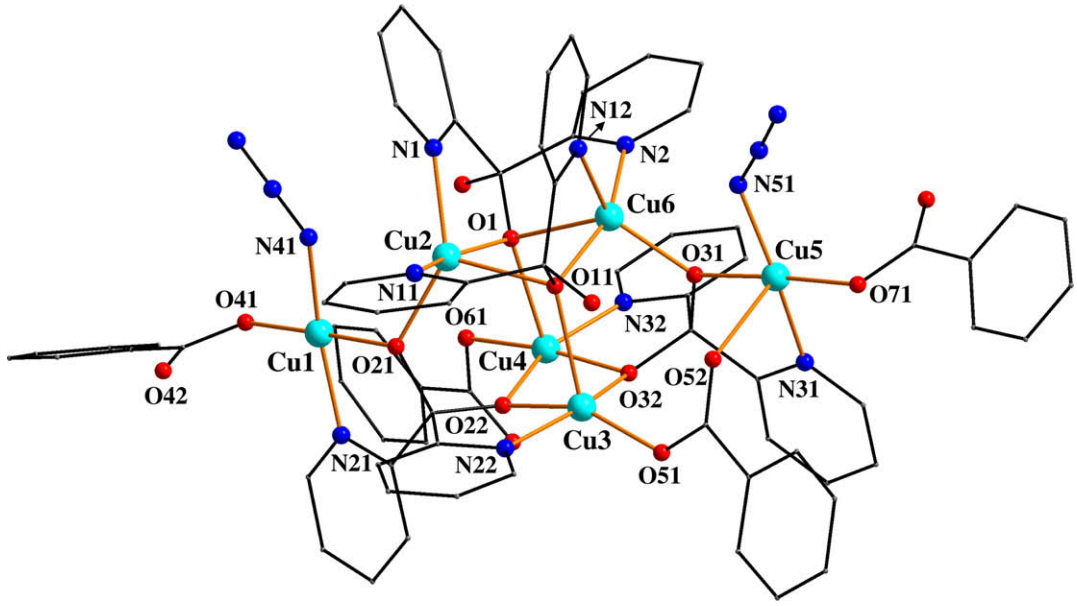


Fig. 1. Molecular structure of **1**. Color scheme: Cu^{II}, sky blue; O, red; N, dark blue; C, gray. (For interpretation of the references to color in this figure legend, the reader is referred to the web version of this article.)

crystal of **2** (0.05 × 0.15 × 0.25 mm) was mounted in air. Diffraction measurements for **1** · $2H_2O$ · 4.5MeCN were made on a Crystal Logic Dual Goniometer diffractometer using graphite-monochromated Mo radiation. Crystallographic data for complexes **2** and **3** were collected on a $P2_1$ Nicolet diffractometer upgraded by Crystal Logic using graphite-monochromated Cu radiation. Unit cell dimensions were determined and refined by using the angular settings of 25 automatically centered reflections in the range $11° < 2\theta < 23°$ (for **1** · $2H_2O$ · .5MeCN) and $22° < 2\theta < 54°$ (for **2** and **3**). Intensity data were recorded using a θ–2θ scan to a maximum 2θ value of 50° (for **1** · $2H_2O$ · 4.5MeCN) and 118° (for **2** and **3**). Three standard reflections monitored every 97 reflections showed less than 3% variation and no decay. Lorentz, polarization corrections were applied using CRYSTAL LOGIC software. All three structures were solved by direct methods using SHELXS-97 [15a] and refined on F^2 by full-matrix least squares techniques with SHELXL-97 [15b]. All H atoms were located by Fourier difference maps and refined isotropically, except those on the solvent molecules (**1** · $2H_2O$ · 4.5MeCN) which were introduced at calculated positions as riding on bonded atoms. All non-H atoms were refined anisotropically.

3. Results and discussion

3.1. Syntheses and IR spectroscopy

The reaction of $Cu(O_2CPh)_2 \cdot 2H_2O$, $(py)_2CO$, LiOH and NaN_3 in a 2:1:1:1 molar ratio in MeCN gave a dark green solution which upon conventional workup gave cluster **1** (as the **1** · $2H_2O$ · 4.5MeCN solvate) in good yield, see the balanced equation (1). The Cu^{II}-mediated nucleophilic attack of H_2O (from the solvent and/or the starting material) is responsible for the formation of the *gem*-diolate(-1) ligand $(py)_2C(OH)O^-$ (Scheme 1) [10]. Complex **1** was also obtained in the absence of

$$6Cu(O_2CPh)_2 \cdot 2H_2O + 4(py)_2CO + 2NaN_3 + 2LiOH \xrightarrow{MeCN} [Cu_6(O_2CPh)_4(N_3)_2\{(py)_2CO_2\}_2\{(py)_2C(OH)O\}_2] + 2NaO_2CPh + 2LiO_2CPh + 4PhCO_2H + 10H_2O \quad (1)$$

external OH^-s, but the yields were appreciably lower. In this case, the deprotonation of '$(py)_2C(OH)_2$' is achieved solely by the $PhCO_2^-$ groups and the formation of the cluster can be summarized by the balanced equation (2):

$$6Cu(O_2CPh)_2 \cdot 2H_2O + 4(py)_2Co + 2NaN_3 \xrightarrow{MeCN} [Cu_6(O_2CPh)_4(N_3)_2\{(py)_2CO_2\}_2\{(py)_2C(OH)O\}_2] + 2NaO_2CPh + 6PhCO_2H + 8H_2O \quad (2)$$

with the identity of **1** established, we also tried several other $Cu(O_2CPh)_2/(py)_2CO/OH^-/N_3^-$ ratios, and particularly with a large excess of N_3^- ions, to see if azido-bridged products could be obtained, but in all cases **1** was the isolated product, in varying yields.

The chemical and structural identity of the products from the $Cu(O_2CPh)_2/(py)_2CO/N_3^-$ reactions systems depends on the solvent used. Exactly the same preparative and crystallization

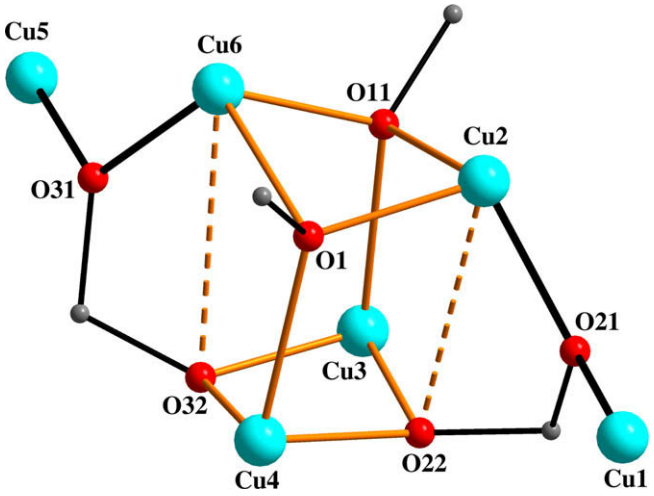


Fig. 2. The $[Cu_6^{II}(\mu_3\text{-}OR'')_2(\mu\text{-}OR'')_4]^{6+}$ core of **1**, emphasizing the central defective cubane subcore (orange thick lines). The orange dashed lines represent the two missing edges of the cubane unit. Color scheme: Cu^{II}, sky blue; O, red; C, gray. (For interpretation of the references to color in this figure legend, the reader is referred to the web version of this article.).

procedures as those of **1** but employing MeOH instead of MeCN, gave a mixture of dark-green plate- and needle- like crystals, crystallographically characterized as the 1D and 2D coordination polymers $[Cu_4(O_2CPh)_2(N_3)_4\{(py)_2C(OMe)O\}_2]_n$ (**2**) and $[Cu_2(O_2CPh)(N_3)_2\{(py)_2C(OMe)O\}]_n$ (**3**), respectively. Although polymeric in nature, the non-optimized yields were rather low (~20% and ~10% for **2** and **3**, respectively). The formation of the complexes can be summarized by the balanced equations (3) and (4):

$$4n\mathrm{Cu(O_2CPh)_2\cdot 2H_2O} + 2n\mathrm{(py)_2CO} + 4n\mathrm{NaN_3} + 2n\mathrm{MeOH} + 2n\mathrm{LiOH} \overset{\mathrm{MeOH}}{\rightarrow} \underset{\mathbf{2}}{[\mathrm{Cu_4(O_2CPh)_2(N_3)_4\{(py)_2C(OMe)O\}_2]_n}} + 4n\mathrm{NaO_2CPh} + 2n\mathrm{LiO_2CPh} + 10n\mathrm{H_2O} \quad (3)$$

$$2n\mathrm{Cu(O_2CPh)_2\cdot 2H_2O} + n\mathrm{(py)_2CO} + 2n\mathrm{NaN_3} + n\mathrm{MeOH} + n\mathrm{LiOH} \overset{\mathrm{MeOH}}{\rightarrow} \underset{\mathbf{3}}{[\mathrm{Cu_2(O_2CPh)(N_3)_2\{(py)_2C(OMe)O\}]_n}} + 2n\mathrm{NaO_2CPh} + n\mathrm{LiO_2CPh} + 5n\mathrm{H_2O} \quad (4)$$

Mainly due to the identical $Cu^{II} : PhCO_2^- : N_3^- : (py)_2C(OMe)O^-$ (2:1:2:1) ratio present in the two complexes, the two polymeric compounds could not be isolated separately. Changes in the crystallization procedures also failed to lead to the separate isolation of the two materials.

The IR spectra of **1**–**3** do not exhibit a band in the region of the carbonyl stretching vibration [ν(CO)] as expected, with the nearest bands at ~1600 cm^{-1} assigned as a 2-pyridyl stretching vibration [this band also has a $\nu_{as}(CO_2)$ character] raised from 1582 cm^{-1} on coordination as observed earlier [16] upon complex formation involving hydration of $(py)_2CO$. In the spectrum of **1**, the strong band at 1562 cm^{-1} is also assigned [17] to $\nu_{as}(CO_2)$; the $\nu_s(CO_2)$ modes appear at 1442 and 1382 cm^{-1}. The appearance of two distinct bands for each mode reflects the presence of two different types of $PhCO_2^-$ ligands in the complex. The 1602 and 1382 cm^{-1} pair [$\Delta = \nu_{as}(CO_2) - \nu_s(CO_2) = 220\ cm^{-1}$] are assigned [17] to the monodentate $PhCO_2^-$ groups, while the 1562 and 1442 cm^{-1} pair ($\Delta = 120\ cm^{-1}$) to the bidentate bridging $PhCO_2^-$ group. The differ-

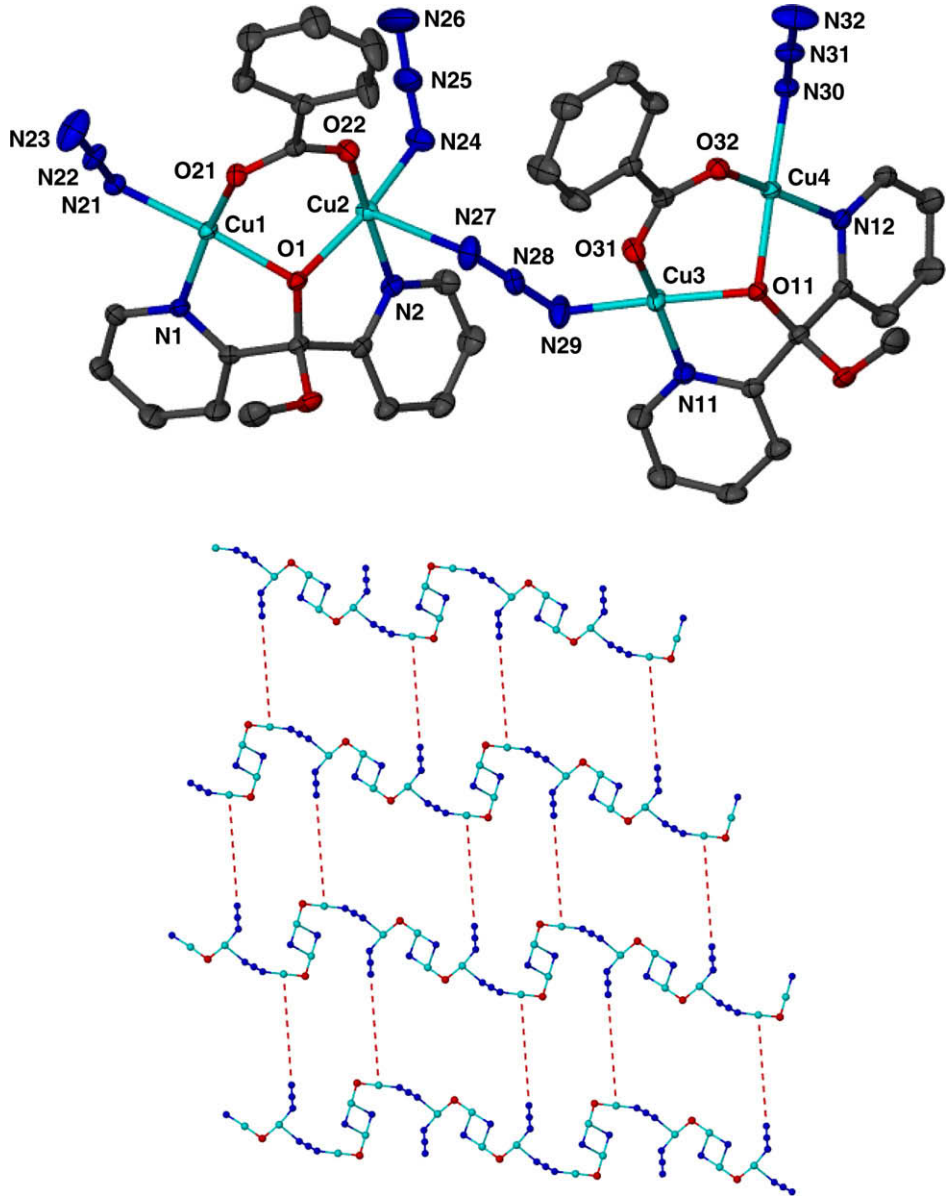


Fig. 3. ORTEP view of the asymmetric unit of **2** at the 30% probability level (top) and a view (with many atoms omitted) of the zig-zag chains and the herringbone layer (bottom) formed by artificially connecting (red dashed lines) the terminal azide (on Cu2) to Cu3. Color scheme as in Fig. 1. (For interpretation of the references to color in this figure legend, the reader is referred to the web version of this article.)

ences are more (220 cm^{-1}) and less (120 cm^{-1}) than the Δ value for NaO_2CPh (184 cm^{-1}), as expected for the monodentate and bidentate modes, respectively, of carboxylate ligation. The Δ values for **2** and **3** are ~140 cm^{-1} in accordance with the crystallographically established bidentate bridging ligation mode of the $PhCO_2^-$ groups [17]. The strong band at 2045–2065 cm^{-1} in the spectra of **1**–**3** is assigned to the asymmetric stretching mode of the azido ligands [18].

3.2. Description of structures

The molecular structure of complex **1** is depicted in Fig. 1, whereas ORTEP representations of the asymmetric units of **2** and **3** are shown in Figs. 3 and 4, respectively. Selected interatomic distances and angles for compounds **1**–**3** are listed in Tables 2 and 3.

Complex **1** crystallizes in the triclinic space group $P\bar{1}$. The hexanuclear molecule (Fig. 1) is held together by two 4.2211 (Harris notation [19]) $(py)_2CO_2^{2-}$ ligands, two 3.3011 $(py)_2C(OH)O^-$ groups and a single *syn,anti*-2.11 $PhCO_2^-$ group. Peripheral ligation is provided by three monodentate (1.10) $PhCO_2^-$ groups and two terminal (1.100) N_3^- ligands. The new core (Fig. 2) consists of four, 5-coordinate Cu^{II} atoms [Cu(2,3,4,6)] located at four alternate vertices of a central defective cubane unit (a cubane missing two opposite edges), two μ_3 O atoms (O1, O11) from the 3.3011 $(py)_2C(OH)O^-$ groups and two μ O atoms (O22, O32) from two different 4.2211 $(py)_2CO_2^{2-}$ ligands (these four O atoms occupy the remaining vertices of the cube), two additional satellite Cu^{II} atoms (Cu1 is square planar; Cu5 is 5-coordinate) across the missing edges, and two μ O atoms (O21, O31) that belong to the two different $(py)_2CO_2^{2-}$ groups and each links the cubane unit with a satellite metal ion.

Analysis of the shape-determining angles using the approach of Reedijk, Addison and co-workers [20] yields trigonality index, τ, values of 0.35, 0.08, 0.22, 0.18 and 0.28 for Cu2, Cu3, Cu4, Cu5 and Cu6, respectively (τ = 0 and 1 for perfect *spy* and *tbp* geometries, respectively). This suggests that the coordination geometry of Cu(3,4,5,6) is slightly to moderately distorted square pyramidal; the coordination polyhedron of Cu2 is very distorted and can be considered either as a square pyramid or as a trigonal bipyramid.

Complex **1** joins a very small family of hexanuclear Cu_6^{II}/N_3^- clusters; however, in the three previous examples the azido ligands were bridging [21]. This nuclearity is the second highest in copper(II) azide chemistry [12] after the impressive $(Cu_7^{II})_2/N_3^-$ cluster synthesized by Thompson's group [22].

The asymmetric unit of **2** (Fig. 3, top) consists of two similar $Cu_2^{II,II}$ subunits A (Cu1, Cu2) and B (Cu3, Cu4) bridged by a single end-to-end (EE or $\mu_{1,3}$) N_3^- ligand through the square pyramidal Cu2 (τ = 0.07) and the square planar Cu3 ions. The two Cu^{II} centers within each dinuclear unit are bridged by one 2.2011 $(py)_2C(OMe)O^-$ ligand and one *syn,syn*-2.11 $PhCO_2^-$ group. Two end-on (EO or $\mu_{1,1}$) N_3^- ligands bridge two Cu1 atoms from two dinuclear units A. Similarly two dinuclear units B are bridged through two EO N_3^- ligands via two Cu4 centers. Both Cu1 (τ = 0.21) and Cu4 (τ = 0.19) are in distorted square pyramidal environments with azido nitrogens at the apical positions. Thus, tetranuclear units A = A and B = B form, while one EE azido ligand bridges the tetranuclear units A═A and B═B, giving rise to a an octanuclear repeating unit of –A═A–B═B–, where "═" and "–" denote double EO and single EE azide bridges, respectively. The AABB repeating unit forms an infinite zigzag chain running along the *ac* diagonal (Fig. 3, bottom). Therefore, chemically **2** is best formulated as $[Cu_8(O_2CPh)_4(N_3)_8\{(py)_2C(OMe)O\}_4]_n$.

The asymmetric unit of **3** (Fig. 4, top) consists of dinuclear $[Cu_2(O_2CPh)(N_3)_2\{(py)_2C(OMe)O\}]$ moieties, where the two square pyramidal Cu^{II} centers (Cu1, τ = 0.13; Cu2, τ = 0.25) are bridged (as in **2**) by one 2.2011 $(py)_2C(OMe)O^-$ ligand and one *syn,syn*-2.11 $PhCO_2^-$ group. The dinuclear units assemble with two EO azido ligands that bridge the Cu2 atoms to form a tetranuclear unit (Fig. 4, middle). The latter are linked through the Cu1 centers via four EE azido ligands to form a 2D layer along the (1 0 −1) plane (Fig. 4,

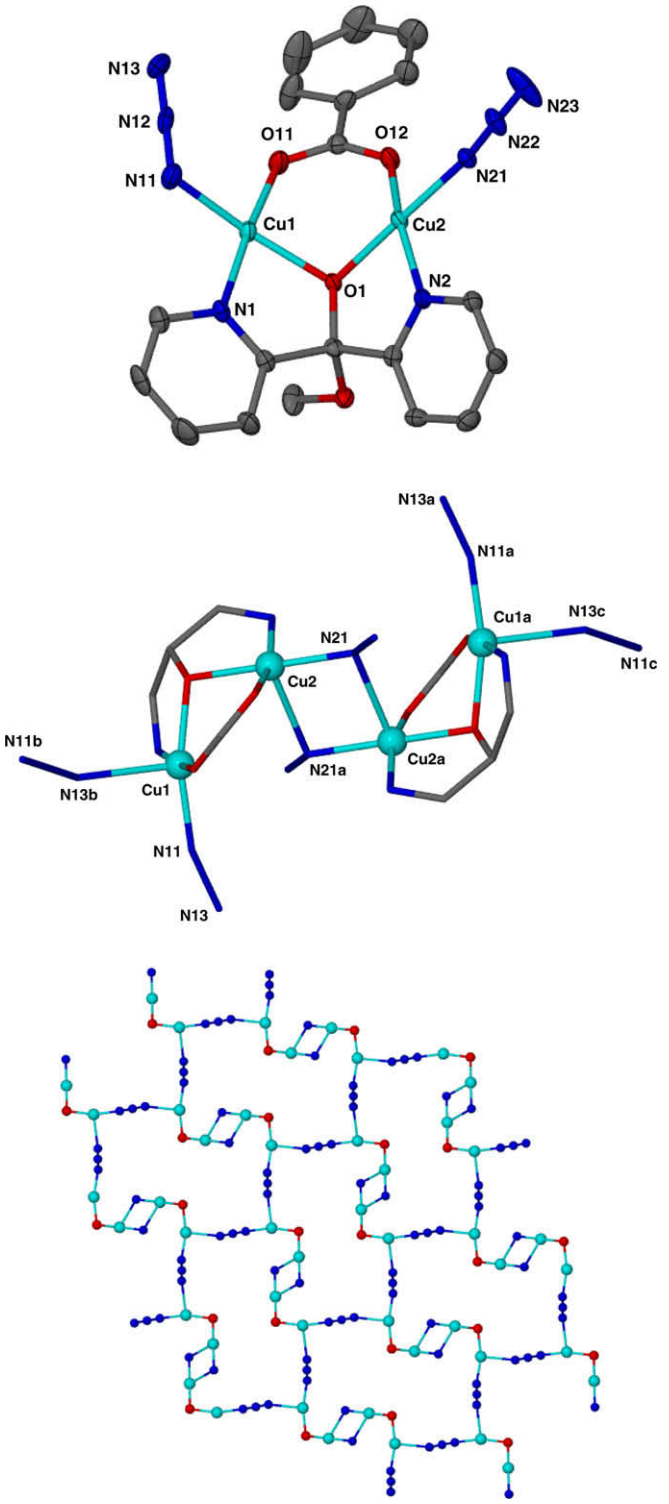


Fig. 4. ORTEP view of the asymmetric unit of **3** at the 30% probability level (top), the assembly of two dinuclear units (middle) of **3** and the 2D layer running along the (1 0 −1) plane (bottom). Symmetry code: a: 2 − *x*, −*y*, −*z*; b: 1.5 − *x*, 0.5 + *y*, 1.5 − *z*; c: 0.5 + *x*, −0.5 − *y*, 0.5 + *z*. Color scheme as in Fig. 1. (For interpretation of the references to color in this figure legend, the reader is referred to the web version of this article.)

Table 2
Selected bond lengths (Å) and angles (°) for complex **1** · $2H_2O$ · 4.5MeCN.

Parameter		Parameter	
Cu(1)···Cu(2)	3.317(3)	Cu(2)···Cu(6)	3.085(7)
Cu(1)···Cu(3)	5.431(7)	Cu(3)···Cu(4)	3.003(2)
Cu(1)···Cu(4)	4.238(3)	Cu(3)···Cu(5)	4.327(2)
Cu(1)···Cu(5)	8.833(7)	Cu(3)···Cu(6)	3.557(1)
Cu(1)···Cu(6)	6.031(4)	Cu(4)···Cu(5)	5.452(5)
Cu(2)···Cu(3)	3.729(5)	Cu(4)···Cu(6)	3.659(1)
Cu(2)···Cu(4)	3.561(5)	Cu(5)···Cu(6)	3.335(4)
Cu(2)···Cu(5)	6.103(5)	Cu(4)–O(1)	2.379(3)
Cu(1)–O(21)	1.929(3)	Cu(4)–O(22)	1.950(3)
Cu(1)–O(41)	1.928(3)	Cu(4)–O(32)	1.945(3)
Cu(1)–N(21)	1.979(4)	Cu(4)–O(61)	1.956(3)
Cu(1)–N(41)	1.938(5)	Cu(4)–N(32)	1.993(4)
Cu(2)–O(1)	1.941(3)	Cu(5)–O(31)	1.947(3)
Cu(2)–O(11)	2.299(3)	Cu(5)–O(71)	1.930(3)
Cu(2)–O(21)	1.989(3)	Cu(5)–N(31)	2.003(4)
Cu(2)–N(1)	2.030(4)	Cu(5)–N(51)	1.949(4)
Cu(2)–N(11)	1.974(3)	Cu(6)–O(1)	2.338(3)
Cu(3)–O(11)	2.437(3)	Cu(6)–O(11)	1.950(3)
Cu(3)–O(22)	1.937(3)	Cu(6)–O(31)	1.979(3)
Cu(3)–O(32)	1.931(3)	Cu(6)–N(2)	1.993(3)
Cu(3)–O(51)	1.933(3)	Cu(6)–N(12)	2.024(4)
Cu(3)–N(22)	1.970(4)		
Cu(1)–O(21)–Cu(2)	115.7(2)	Cu(3)–O(11)–Cu(6)	107.9(1)
Cu(2)–O(1)–Cu(4)	110.7(1)	Cu(3)–O(22)–Cu(4)	101.1(1)
Cu(2)–O(1)–Cu(6)	91.8(1)	Cu(3)–O(32)–Cu(4)	101.6(1)
Cu(2)–O(11)–Cu(3)	103.8(1)	Cu(3)–O(32)–Cu(6)	83.8(1)
Cu(2)–O(11)–Cu(6)	92.8(1)	Cu(4)–O(1)–Cu(6)	101.7(1)
Cu(2)–O(22)–Cu(3)	91.8(1)	Cu(4)–O(32)–Cu(6)	86.9(1)
Cu(2)–O(22)–Cu(4)	85.8(1)	Cu(5)–O(31)–Cu(6)	116.3(2)
O(21)–Cu(1)–O(41)	176.9(2)	O(32)–Cu(4)–O(61)	171.3(1)
N(21)–Cu(1)–N(41)	168.1(2)	O(22)–Cu(4)–N(32)	158.0(1)
O(1)–Cu(2)–N(11)	159.5(1)	O(31)–Cu(5)–O(71)	176.5(1)
O(21)–Cu(2)–N(1)	138.8(1)	N(31)–Cu(5)–N(51)	165.6(2)
O(51)–Cu(3)–O(22)	153.7(1)	O(11)–Cu(6)–N(2)	156.7(1)
O(32)–Cu(3)–N(22)	158.5(1)	O(31)–Cu(6)–N(12)	139.7(1)

Table 3
Selected bond lengths (Å) and angles (°) for complexes **2** and **3**.

Parameter[a]		Parameter	
Complex ***2***			
Cu(1)···Cu(1a)	3.302(2)	Cu(2)···Cu(3)	5.829(4)
Cu(1)···Cu(2)	3.112(4)	Cu(2)···Cu(4)	6.703(5)
Cu(1)···Cu(3)	8.676(1)	Cu(3)···Cu(4)	3.026(7)
Cu(1)···Cu(4)	9.741(1)	Cu(4)···Cu(4b)	3.255(1)
Cu(1)–O(1)	1.956(2)	Cu(3)–O(11)	1.952(2)
Cu(1)–O(21)	1.932(2)	Cu(3)–O(31)	1.919(3)
Cu(1)–N(1)	1.966(3)	Cu(3)–N(11)	1.966(3)
Cu(1)–N(21)	1.986(3)	Cu(3)–N(29)	1.920(4)
Cu(2)–O(1)	1.958(2)	Cu(4)–O(11)	1.949(2)
Cu(2)–O(22)	1.950(3)	Cu(4)–O(32)	1.941(3)
Cu(2)–N(2)	2.006(3)	Cu(4)–N(12)	1.962(3)
Cu(2)–N(24)	1.934(3)	Cu(4)–N(30)	1.989(3)
Cu(2)–N(27)	2.496(3)		
Cu(1)–O(1)–Cu(2)	105.3(1)	O(22)–Cu(2)–N(2)	169.2(1)
Cu(3)–O(11)–Cu(4)	101.7(1)	O(11)–Cu(3)–N(29)	173.6(1)
O(1)–Cu(1)–N(21)	176.5(1)	O(31)–Cu(3)–N(11)	163.0(1)
O(21)–Cu(1)–N(1)	164.0(1)	O(11)–Cu(4)–N(30)	177.5(1)
O(1)–Cu(2)–N(24)	164.9(1)	O(32)–Cu(4)–N(12)	165.9(1)
Complex ***3***			
Cu(1)···Cu(1a)	6.058(1)	Cu(1)–N(13b)	2.425(5)
Cu(1)···Cu(2)	3.070(1)	Cu(2)–O(1)	1.954(3)
Cu(2)···Cu(2a)	3.328(1)	Cu(2)–O(12)	1.930(4)
Cu(1)–O(1)	1.971(3)	Cu(2)–N(2)	1.976(4)
Cu(1)–O(11)	1.925(4)	Cu(2)–N(21)	1.991(4)
Cu(1)–N(1)	1.981(4)	Cu(2)–N(21a)	2.495(4)
Cu(1)–N(11)	1.964(5)		
Cu(1)–O(1)–Cu(2)	102.9(2)	O(11)–Cu(1)–N(1)	172.3(2)
Cu(2)–N(21)–Cu(2a)	95.1(2)	O(1)–Cu(2)–N(21)	178.1(1)
O(1)–Cu(1)–N(11)	164.7(2)	O(12)–Cu(2)–N(2)	163.3 (2)

[a] Atoms designated by a and b are related by symmetry operators.

bottom). The 2D layer of **3** adopts the "herringbone" or "parquet floor" architecture. The familiar herringbone network is based on T-shaped 3-connected nodes bridged by linear spacers (Fig. 5, left), while in **3** each tetranuclear unit serves as two fused 3-connected nodes that self-assemble to create the herringbone architecture (Fig. 5, right). Alternatively, **3** can be described as the assembly of tetranuclear clusters bridged by four EE azido ligands that serve as linear spacers. To the best of our knowledge, **3** joins only a handful of extended 2D networks that adopt the herringbone architecture which is *not* based on T-shaped nodes [23].

A detailed examination of the crystal structures of **2** and **3** reveals that the 2D structure of the latter "contains" the 1D chains of the former. Complex **3** could have derived from **2** if the terminal azide ligand on Cu2 in **2** (Fig. 3) had bridged the Cu3 atom in an EE fashion (Fig. 6). Complexes **2** and **3** are the first copper(II) coordination polymers with any $(py)_2CO$-based ligand/N_3^- combination; this combination has been found in the recently reported tetranuclear structure $[Cu^{II}_4(N_3)_2\{(py)_2C(OMe)O\}_4][Cu^{I}Cl_2]$ [24].

3.3. Magnetochemistry

Solid-state direct current magnetic susceptibility (χ_M) data on dried **1** · $2H_2O$ were collected in an 0.1 T field in the 2.0–300 K range and are plotted as $\chi_M T$ versus T, and χ_M versus T in Fig. 7. χ_M increases from 48×10^{-4} emu mol^{-1} at room temperature to a maximum value of 56×10^{-4} emu mol^{-1} at 170 K and then decreases drastically to a minimum of 3×10^{-4} emu mol^{-1} at 20 K, before increasing again to the value of 21×10^{-4} emu mol^{-1} at 6 K. Based on the room-temperature $\chi_M T$ value of 1.43 emu mol^{-1} K, which is lower than the value expected for six $S = 1/2$ uncoupled spins (2.25 emu mol^{-1} K with $g = 2.0$) and the maximum in the χ_M versus T plot at 170 K, we conclude that strong antiferromagnetic exchange interactions between the Cu^{II} atoms are operative within the cluster. The Curie tail in the low temperature susceptibility data reveals the existence of a paramagnetic, possibly monomeric, impurity. According to the core (Fig. 2) a simplified spin Hamiltonian that describes the exchange interactions in **1** is

$$H = -2J_1(S_1 \cdot S_2 + S_5 \cdot S_6) - 2J_2 S_2 \cdot S_6 - 2J_3 S_3 \cdot S_4 \quad (5)$$

Magnetic susceptibility data were fitted using the MAGPACK [25] program (based on the Irreducible Tensor Operator method for diagonalization of the energy matrix) employed with the non-linear, least-squares curve-fitting program, DSTEPIT [26]. Best-fit (solid lines in Fig. 7) parameters are $J_1 = -94(5)$ cm^{-1}, $J_2 = -110(5)$ cm^{-1}, $J_3 = -116(5)$ cm^{-1}, $g = 2.05$, and $\rho = 0.15\%$, leading to an overall $S = 0$ ground state. Antiferromagnetic exchange interactions are often found in copper(II) complexes with $(py)_2CO$-based bridging ligands [27]. A fourth exchange parameter (J_4) incorporating the

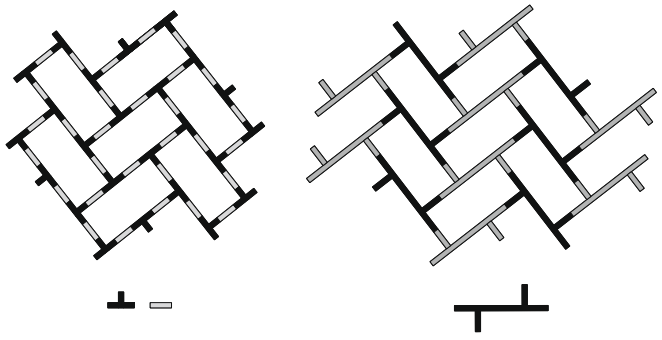


Fig. 5. The familiar herringbone motif based on T-shaped 3-connected nodes and spacers (left), and the herringbone architecture of **3** based on the tetranuclear units which serve as two fused 3-connected nodes (right).

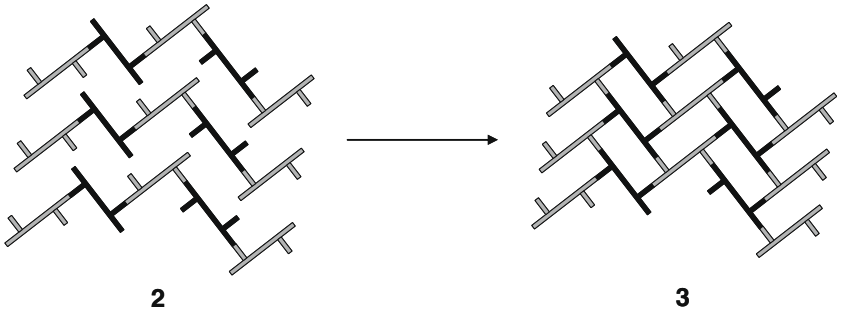


Fig. 6. The transformation of the one-dimensional polymer **2** to the two-dimensional polymer **3**.

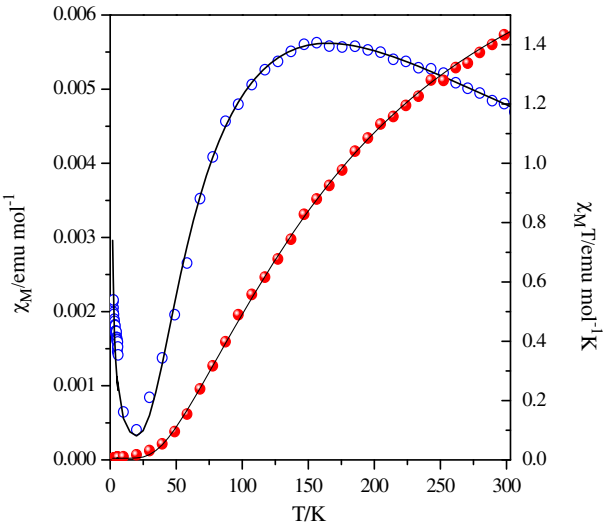


Fig. 7. χ_M vs. T (open blue cycles) and $\chi_M T$ vs. T (solid red cycles) plots for **1** · $2H_2O$ in a 1 kG field. The solid lines are the fit of the data; see the text for the fit parameters.

S_2S_3, S_2S_4, S_3S_6 and S_4S_6 magnetic interactions was not considered because the relevant Cu···Cu distances are rather long (3.56–3.73 Å, see Table 1); incorporation of J_4 leads to significant correlations between the fitted parameters. Efforts to employ a 2-J model, assuming $J_2 = J_3$, did not give a satisfactory fit.

4. Conclusions

An important chemical message from this work is that the $(py)_2CO/PhCO_2^-/N_3^-$ ligand combination looks like a promising candidate system for the generation of interesting copper(II) clusters and coordination polymers. The hexanuclear cluster **1** has a novel core, while the coordination polymers **2** and **3** exhibit interesting structural features. The products provide an example of the dependence of the structural type (cluster versus polymers) on the reaction solvent. The three complexes augur well that they are merely the first member of a new family of $Cu^{II}/(py)_2CO$-based ligands/$R'CO_2^-/N_3^-$ compounds. Preliminary results reveal that the nature of the carboxylate ligand, i.e. the nature of R′, affects the identity of the products.

5. Supplementary data

CCDC 702630, 702631 and 702629 contain the supplementary crystallographic data for **1** · $2H_2O$ · 4.5MeCN, **2** and **3**. These data can be obtained free of charge via http://www.ccdc.cam.ac.uk/conts/retrieving.html, or from the Cambridge Crystallographic Data Centre, 12 Union Road, Cambridge CB2 1EZ, UK; fax: (+44) 1223-336-033; or e-mail: deposit@ccdc.cam.ac.uk.

Acknowledgements

This work was supported by the program PYTHAGORAS I (Grant b.365.037) and the Special Account for Research Grants (SARG) of the University of Athens.

References

[1] (a) R.E.P. Winpenny, in: J.A. McCleverty, T.J. Meyer (Eds.), Comprehensive Coordination Chemistry III, vol. 7, Elsevier, Amsterdam, 2004, p. 125;
(b) Th.C. Stamatatos, G. Christou, Philos. Trans. Roy. Soc. London A 366 (2008) 113.
[2] (a) For reviews, see: A.Y. Robin, K.M. Fromm, Coord. Chem. Rev. 250 (2006) 2127;
(b) Y. Zhou, M. Hong, X. Wu, Chem. Commun. (2006) 135 (Feature Article);
(c) S.R. Batten, Curr. Opin. Solid State Mater. Sci. 5 (2001) 107;
(d) M. Munakata, L.P. Wu, T. Kuroda-Sowa, Adv. Inorg. Chem. 46 (1999) 173.
[3] (a) For reviews see: G. Christou, D. Gatteschi, D.N. Hendrickson, R. Sessoli, MRS Bull. 25 (2000) 66;
(b) D. Gatteschi, R. Sessoli, Angew. Chem., Int. Ed. 42 (2003) 268;
(c) G. Aromi, E.K. Brechin, Struct. Bond. 122 (2006) 1.
[4] C. Janiak, Dalton Trans. (2003) 2781 (Dalton Perspective).
[5] R.E.P. Winpenny, J. Chem. Soc., Dalton Trans. (2002) 1.
[6] Th.C. Stamatatos, K.A. Abboud, W. Wernsdorfer, G. Christou, Angew. Chem., Int. Ed. 47 (2008) 6694.
[7] A.K. Boudalis, Y. Sanakis, J.M. Clemente-Juan, B. Donnadieu, V. Nastopoulos, A. Mari, Y. Coppel, J.-P. Tuchagues, S.P. Perlepes, Chem. Eur. J. 14 (2008) 2514.
[8] G.S. Papaefstathiou, S.P. Perlepes, A. Escuer, R. Vicente, M. Font-Bardia, X. Solans, Angew. Chem., Int. Ed. 40 (2001) 884.
[9] G.S. Papaefstathiou, A. Escuer, R. Vicente, M. Font-Bardia, X. Solans, S.P. Perlepes, Chem. Commun. (2001) 2414.
[10] For a review, see: G.S. Papaefstathiou, S.P. Perlepes, Commun. Inorg. Chem. 23 (2002) 249.
[11] (a) For example, see: Y. Li, S. Xiang, T. Sheng, J. Zhang, S. Hu, R. Fu, X. Huang, X. Wu, Inorg. Chem. 45 (2006) 6577;
(b) B.F. Abrahams, T.A. Hudson, R. Robson, Chem. Eur. J. 12 (2006) 7095.
[12] For a microreview, see: A. Escuer, G. Aromi, Eur. J. Inorg. Chem. (2006) 4721.
[13] Th.C. Stamatatos, V. Tangoulis, C.P. Raptopoulou, A. Terzis, G.S. Papaefstathiou, S.P. Perlepes, Inorg. Chem. 47 (2008) 7969.
[14] M. Inoue, M. Kishita, M. Kubo, Inorg. Chem. 3 (1964) 239.
[15] (a) G.M. Sheldrick, SHELXS-97, Structure Solving Program, University of Göttingén, Germany, 1997;
(b) G.M. Sheldrick, SHELXS-97, Program for the Refinement of Crystal Structures from Diffraction Data, University of Göttingén, Germany, 1997.
[16] G.S. Papaefstathiou, A. Escuer, F.A. Mautner, C. Raptopoulou, A. Terzis, S.P. Perlepes, R. Vicente, Eur. J. Inorg. Chem. (2005) 879.
[17] G.B. Deacon, R.J. Phillips, Coord. Chem. Rev. 33 (1980) 227.
[18] Th.C. Stamatatos, G.S. Papaefstathiou, L.R. MacGillivray, A. Escuer, R. Vicente, E. Ruiz, S.P. Perlepes, Inorg. Chem. 46 (2007) 8843.
[19] R.A. Coxall, S.G. Harris, D.K. Henderson, S. Parsons, P.A. Tasker, R.E.P. Winpenny, J. Chem. Soc., Dalton Trans. (2000) 2349.
[20] A.W. Addison, T.N. Rao, J. Reedijk, J. Rijn, G.C. Verschoor, J. Chem. Soc., Dalton Trans. (1984) 1349.
[21] (a) K.D. Karlin, Q.F. Gan, A. Farooq, S. Liu, J. Zubieta, Inorg. Chem. 29 (1990) 2549;
(b) M.A.S. Goher, F.A. Mautner, Cryst. Res. Technol. 27 (1992) 817;
(c) R. Vicente, A. Escuer, X. Solans, M. Font-Bardia, J. Chem. Soc., Dalton Trans. (1996) 1835.

[22] S.S. Tandon, S.D. Bunge, L.K. Thompson, Chem. Commun. (2007) 798.
[23] (a) Two representative examples: K. Edda, Y. Iriki, K. Kawamura, T. Ikuki, M. Hayashi, J. Solid State Chem. 180 (2007) 3588;
(b) S. Zang, Y. Su, Y. Li, Z. Ni, Q. Meng, Inorg. Chem. 45 (2006) 45.
[24] D.-Y. Wu, W. Huang, W.-J. Hua, Y. Song, C.-Y. Duan, S.-H. Li, Q.J. Meng, Dalton Trans. (2007) 1838.
[25] J.J. Borràs-Almenar, J.M. Clemente-Juan, E. Coronado, B.S. Tsukerblat, J. Comput. Chem. 22 (2001) 985.
[26] PROGRAM 66, Quantum Chemistry Program Exchange, Indiana University, Bloomington, IN, USA, 1986.
[27] V. Tangoulis, C.P. Raptopoulou, A. Terzis, S. Paschalidou, S.P. Perlepes, E.G. Bakalbassis, Inorg. Chem. 36 (1997) 3996.

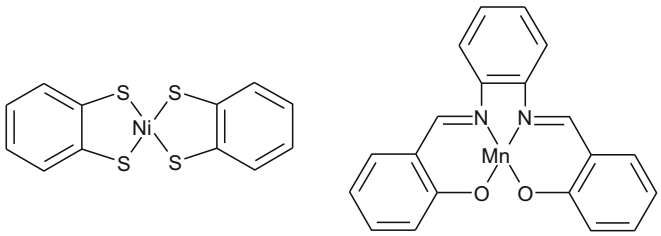


Fig. 1. The molecular structures of $[Ni(bdt)_2]^-$ (left) and $[Mn(Saloph)]^+$ (right).

respectively. A unit cell of the crystal contains a half crystallographically independent $[Mn_2(Saloph)_2(\mu\text{-}OH)]^+$ and $[Ni(bdt)_2]^-$. The bridging $[OH]^-$ groups should be originated from the proton dissociation of H_2O molecules contained in the raw material $[Mn(Saloph)(H_2O)(ClO_4)]$. The dimerization of $[Mn(Saloph)]^+$ units mediated by a $[OH]^-$ group occurs in some cases depending on the crystallization conditions [15]. The bond lengths of Mn–O (1.882(3) and 1.905(2) Å) and Mn–N (1.986(3) and 1.991(3) Å) in the [Mn(Saloph)] unit are in agreement with those of [Mn(III)(Saloph)] complexes reported [11,15,16], suggesting the trivalent state of manganese cation. Mn–OH bond length of 2.046(1) Å is identical with the literature value of $[Mn(III)_2(Saloph)_2(\mu\text{-}OH)]^+$ [15], and clearly shorter than Mn(III)–OH_2 bond lengths ranging from 2.2 to 2.3 Å [11,16]. The Mn–OH–Mn bond angle of 153.2(2)° is roughly the same as that of the literature value, while the torsion angle of ca. 55.6° between two $[Mn(Saloph)]^+$ units is approximately twice that of the literature value of 30.7° [15]. In the crystal, $[Mn_2(Saloph)_2(\mu\text{-}OH)]^+$ cations are stacked one dimensional elongated parallel to the *c*-axis.

$[Ni(bdt)_2]^-$ anions form square lattice in the *bc*-plane as shown in Fig. 2b. In the anion sheet, terminal carbon atoms of benzenedithiolate ligands are placed over the sulfur atoms of adjacent anions with the short CH–S contacts of 3.63 and 3.92 Å. There is no other short contact between anion molecules, therefore magnetic interaction between anions is owing to these CH–S contacts. It is noted that this T-shaped stacking of $[Ni(bdt)_2]^-$ is uncommon. The anion prefers to stack in the side-by-side manner in ordinary cases [8–10] where the size of intermolecular cavities are minimized. In the present case, a cavity surrounded by four $[Ni(bdt)_2]^-$ anions is filled up with a phenyl ring protruding from a cation, resulting in the stabilization of the T-shaped stacking of anions. Though the intra-molecular bond lengths of $[Ni(bdt)_2]^{n-}$ ($n = 0$–2) are approximately independent of the valence *n* [17], we can conclude that the valence state is $[Ni(III)(bdt)_2]^-$ based on the charge neutrality of a unit cell. The anion layers and cation layers are stacked alternately, resulting in the 2D character of the magnetic interaction as shown later.

Table 1
Crystallographic data.

	$[Mn_2(Saloph)_2(\mu\text{-}OH)][Ni(bdt)_2](CH_3CN)_2$
Chemical formula	$C_{56}H_{43}Mn_2N_6NiO_5S_4$
Formula weight	1176.83
Temperature (K)	293(2)
Crystal system	monoclinic
Space group	*C*2/*c*
a (Å)	30.101(6)
b (Å)	12.566(2)
c (Å)	14.443(3)
α (°)	90
β (°)	105.668(4)
γ (°)	90
V (Å^3)	5260.1(17)
Z	4
Measured reflections	25686
Unique reflections	5991
$I > 2\sigma$ reflections	5085
R_1 for $I > 2\sigma$	0.0740
wR_2 for $I > 2\sigma$	0.1457

$R_1 = \sum(||F_o| - |F_c||)/\sum|F_o|$, $wR_2 = [\sum w(|F_o|^2 - |F_c|^2)^2/\sum w(|F_o|^2)^2]^{1/2}$.

3.2. Magnetic property

Fig. 3 shows the temperature and field dependence of the χT value and the magnetization, respectively. The χT value of 3.23 emu K mol^{-1} at 300 K is obviously smaller than that expected

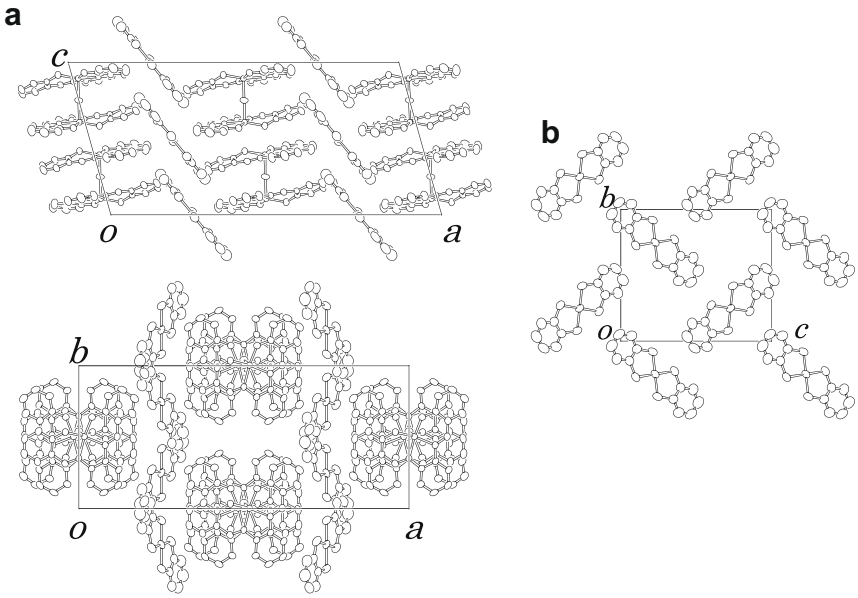


Fig. 2. Thermal ellipsoid plot (50% probability) of (a) the crystal structure and (b) an anion layer of $[Mn_2(Saloph)_2(\mu\text{-}OH)][Ni(bdt)_2](CH_3CN)_2$ drawn by ORTEP-3 for Windows [18]. Acetonitrile molecules and hydrogen atoms are omitted for clarity.

from the sum of the spin only value of $[Mn(III)_2(Saloph)_2(\mu\text{-}OH)]^+$ (two $S = 2$ units) and $[Ni(III)(bdt)_2]^-$ ($S = 1/2$), suggesting the strong antiferromagnetic interaction between the oxygen-bridged two $[Mn(Saloph)]^+$ fragments. The value gradually decreases as the temperature decreases, and reaches a minimum of 0.622 emu K mol^{-1} at around 20 K, followed by a rapid rise indicating the existence of a ferromagnetic interaction. No magnetic transition was observed down to 1.8 K. The χT value coincides with the sum of the theoretical values as follows. The susceptibility of $[Mn_2(Saloph)_2(\mu\text{-}OH)]^+$ and $[Ni(bdt)_2]^-$ were calculated based on the $S = 2$ Van Vleck dimer model [19]:

$$\chi_{Mn} = \frac{Ng_{Mn}^2\mu_B^2}{k_BT}\left[\frac{30 + 14x^8 + 5x^{14} + x^{18}}{9 + 7x^8 + 5x^{14} + 3x^{18} + x^{20}}\right],$$

$$x = \exp\left(-\frac{J_{Mn}}{k_BT}\right)$$

and the $S = 1/2$ Heisenberg square lattice model with constant coupling approximation [20]:

$$\chi_{Ni} = \frac{Ng_{Ni}^2\mu_B^2}{4k_BT}\exp\left(\frac{2J_{Ni}}{k_BT}\right)$$

where χ_{Mn}, χ_{Ni}, N, g_{Mn}, g_{Ni}, μ_B and k_B are the susceptibilities of $[Mn(Saloph)]^+$ units and $[Ni(bdt)_2]^-$ anions, the Avogadro constant, the g-values for $[Mn(Saloph)]^+$ units and $[Ni(bdt)_2]^-$ anions, the Bohr magneton and the Boltzmann constant, respectively. The typical g-values of $[Mn(Salen)]^+$ type complexes ($g = 2.0$) [21] and $[Ni(bdt)_2]^-$ ($g = 2.1$) [9] are employed for the calculation. The exchange interactions J between Mn–Mn (J_{Mn}) and Ni–Ni (J_{Ni}) are defined in the following Hamiltonian:

$$H = -2J\sum\nolimits_{\{ij\}} S_i \cdot S_j$$

The best fit with the parameters of $2J_{Mn} = -92.4$ and $2J_{Ni} = +4.5$ K is nearly indistinguishable from the experimental data as shown in Fig. 3a. The origin of the ferromagnetic interaction between $[Ni(bdt)_2]^-$ anions is discussed later.

The strong antiferromagnetic interaction between $[Mn(Saloph)]^+$ units and ferromagnetic interaction between $[Ni(bdt)_2]^-$ are also evidenced by the magnetization curve measured at 1.8 K. Below $H < 2$ T, the magnetization exhibits a rapid rise reaching a value of ca. 1 μ_B followed by a slight rise. This field dependency of the magnetization is in consistent with the model that the material is consists of strongly antiferromagnetically coupled $[Mn_2(Saloph)_2(\mu\text{-}OH)]^+$ binuclear cations which bring the slight rise of the magnetization, and ferromagnetically coupled $S = 1/2$ $[Ni(bdt)_2]^-$ anions which cause the rapid rise in the low field region. The absence of hysteresis indicates that the magnetic ordering temperature is lower than 1.8 K, which is consistent with the temperature dependence of the χT value as mentioned above.

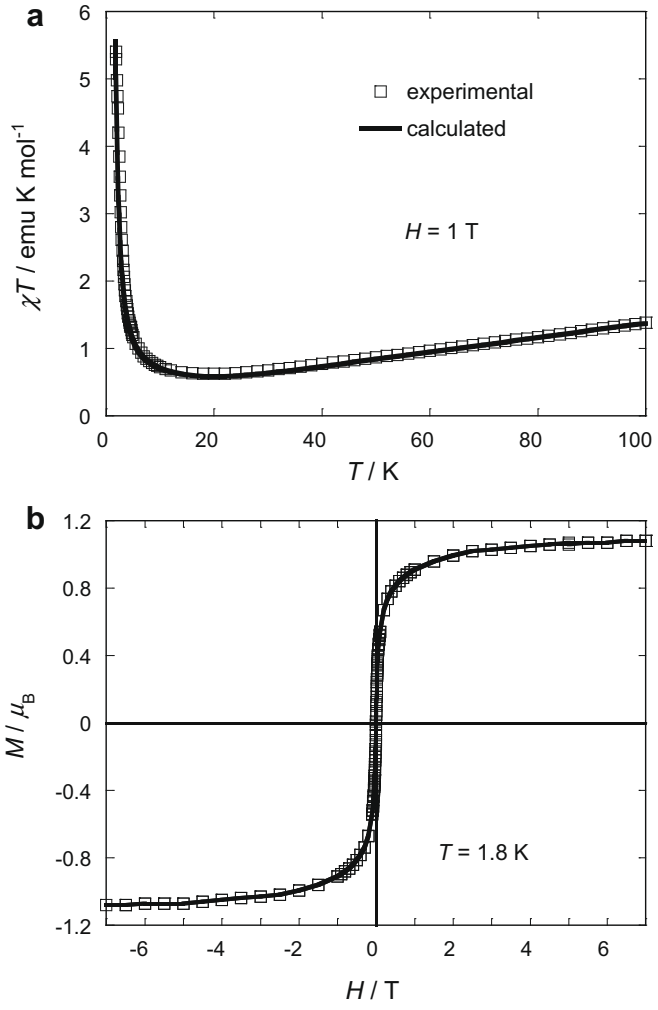


Fig. 3. (a) Temperature dependence of the χT value of $[Mn_2(Saloph)_2(\mu\text{-}OH)][Ni(bdt)_2](CH_3CN)_2$ measured under a field of $H = 1$ T. The solid line indicates the best fit to the experimental data (see text). (b) The magnetization curve of $[Mn_2(Saloph)_2(\mu\text{-}OH)][Ni(bdt)_2](CH_3CN)_2$ at 1.8 K.

3.3. Origin of ferromagnetic interaction

The origin of the ferromagnetic interaction between $[Ni(bdt)_2]^-$ anions can be explained by the modified McConnell-II model [22,23]. Fig. 4 shows the T-shaped intermolecular orbital overlap modes between adjacent $[Ni(bdt)_2]^-$ anions. As mentioned before, the spins on neighboring two anions can interact through the intermolecular contact between the sulfur atoms and the carbon atoms at the edge of the benzene ring. The molecular orbital has the same sign on these two carbon atoms in both cases of the SOMO and the NHOMO. On the other hand, the SOMO has different signs on the neighboring two sulfur atoms, while the NHOMO has the same sign as shown in Fig. 4, resulting in the small intermolecular overlap between the SOMOs and the large overlap between the SOMO and the NHOMO.

In the case of the charge transfer between the SOMOs, antiferromagnetic arrangement of radical spins is required to transfer the electron from one side to another. In other words, the SOMO–SOMO overlap stabilizes an antiferromagnetic arrangement of adjacent radicals, and the small SOMO–SOMO overlap of $[Ni(bdt)_2]^-$ anions weakens the intermolecular antiferromagnetic interaction. On the other hand, the charge transfer from the NHOMO to the SOMO of adjacent $[Ni(bdt)_2]^-$ brings a ferromagnetic interaction. When a radial molecule (named "R_A") has an up spin electron in the SOMO, only a down spin electron can be transferred from the NHOMO of an adjacent radial ("R_B") to the SOMO of R_A. Consequently, the spin of the residual electron in the NHOMO of R_B is up, which ferromagnetically interacts with the electron in the SOMO of R_B because of the intra-molecular electron–electron repulsion like as Hund's rule. As a result, the NHOMO–SOMO overlap brings a ferromagnetic interaction between adjacent $[Ni(bdt)_2]^-$ anions like as the galvinoxyl radical [24].

4. Conclusion

A new molecule-based magnetic material $[Mn_2(Saloph)_2(\mu\text{-}OH)][Ni(bdt)_2](CH_3CN)_2$ is reported. The material consists of one dimensional chains of $[Mn_2(Saloph)_2(\mu\text{-}OH)]^+$ and square lattices of $[Ni(bdt)_2]^-$. Its magnetism is well described by the sum of the

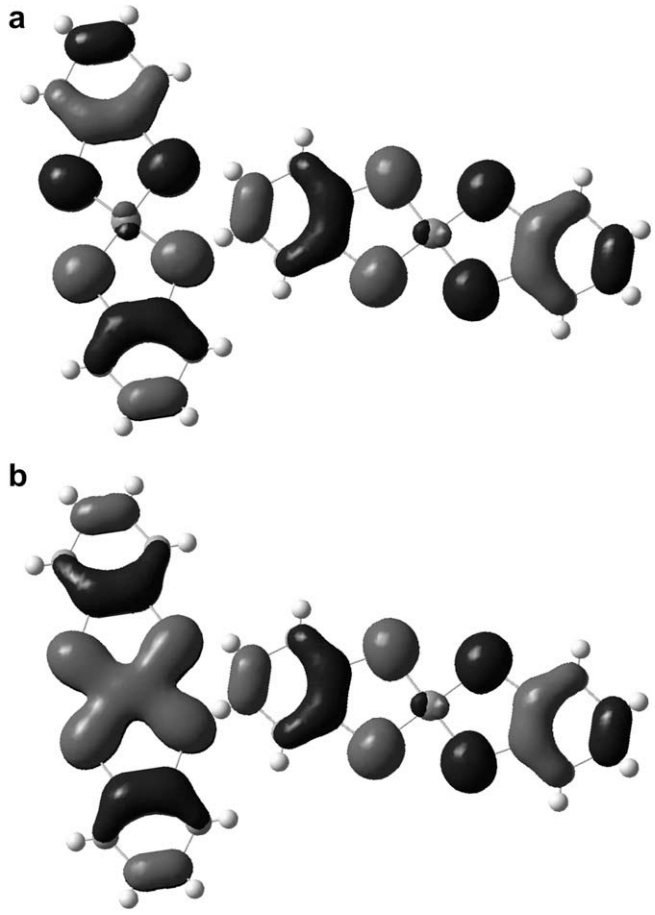


Fig. 4. Orbital overlap modes of adjacent $[Ni(bdt)_2]^-$ anions. (a) SOMO–SOMO and (b) NHOMO–SOMO.

antiferromagnetically coupled two $[Mn(Saloph)]^+$ units with $2J = -92.4$ K and ferromagnetically coupled square lattice of $[Ni(bdt)_2]^-$ anions with $2J = +4.5$ K. The origin of the ferromagnetic interaction is attributed to the small SOMO–SOMO overlap which diminishes the antiferromagnetic interaction, and the large NHOMO–SOMO overlap which brings the ferromagnetic interaction. This result evidences the usefulness of the $[Ni(bdt)_2]^-$ anion for constructing strong intermolecular interaction due to its large coefficient of molecular orbitals on the benzene ring.

5. Supplementary data

CCDC 702069 contains the supplementary crystallographic data for this paper. These data can be obtained free of charge via http://www.ccdc.cam.ac.uk/conts/retrieving.html, or from the Cambridge Crystallographic Data Centre, 12 Union Road, Cambridge CB2 1EZ, UK; fax: (+44) 1223-336-033; or e-mail: deposit@ccdc.cam.ac.uk.

Acknowledgment

This work was supported by a Grant-in-Aid for Scientific Research No. 20750119 from the Ministry of Education, Culture, Sports, Science and Technology, Japan.

References

[1] A.T. Coomber, D. Beljonne, R.H. Friend, J.L. Brédas, A. Charlton, N. Robertson, A.E. Underbill, M. Kurmoo, P. Day, Nature 380 (1996) 144.
[2] M. Kinoshita, P. Turek, M. Tamura, K. Nozawa, D. Shiomi, M. Ishikawa, M. Takahashi, K. Awaga, T. Inabe, Y. Maruyama, Chem. Lett. (1991) 1225.
[3] E. Coronado, J.R. Galán-Mascarós, C.J. Gómez-García, V. Laukhin, Nature 408 (2000) 447.
[4] J. Nishijo, E. Ogura, J. Yamaura, A. Miyazaki, T. Enoki, T. Takano, Y. Kuwatani, M. Iyoda, Solid State Commun. 116 (2000) 661.
[5] P.-M. Allemand, G. Srdanov, F. Wudl, J. Am. Chem. Soc. 112 (1990) 9391.
[6] K. Awaga, A. Yamaguchi, T. Okuno, T. Inabe, T. Nakamura, M. Mutsuyoshi, M. Maruyama, J. Mater. Chem. 4 (1994) 1377.
[7] J. Nishijo, A. Miyazaki, T. Enoki, Bull. Chem. Soc. Jpn. 77 (2004) 715.
[8] N. Robertson, S. Parsons, K. Awaga, W. Fujita, CrystEngCommun 2 (2000) 121.
[9] J.-L. Xie, X.-M. Ren, C. He, Y. Song, C.-Y. Duan, S. Gao, Q.-J. Meng, Polyhedron 22 (2003) 299.
[10] G.-X. Liu, L.-F. Huang, X.-M. Ren, Appl. Organomet. Chem. 21 (2007) 1054.
[11] S. Biswas, K. Mitra, C.H. Schwalbe, C.R. Lucas, S.K. Chattopadhyay, B. Adhikary, Inorg. Chim. Acta 358 (2005) 2473.
[12] M.J. Baker-Hawkes, E. Billing, H.B. Gray, J. Am. Chem. Soc. 88 (1966) 4870.
[13] M.C. Burla, R. Caliandro, M. Camalli, B. Carrozzini, G.L. Cascarano, L. De Caro, C. Giacovazzo, G. Polidori, R. Spagna, J. Appl. Crystallogr. 38 (2005) 381.
[14] G.M. Sheldrick, Acta Crystallogr., Sect. A 64 (2008) 112.
[15] S. Biswas, K. Mitra, B. Adhikary, C.R. Lucas, Transition Met. Chem. 30 (2005) 586.
[16] T. Fukuda, F. Sakamoto, M. Sato, Y. Nakano, X.-S. Tan, Y. Fujii, Chem. Commun. 182 (1998) 1391.
[17] K. Ray, T. Weyhermüller, F. Neese, K. Wieghardt, Inorg. Chem. 44 (2005) 5345.
[18] ORTEP-3 for Windows: L.J. Farrugia, J. Appl. Crystallogr. 30 (1997) 565.
[19] J.H. Van Vleck, Theory of Electric and Magnetic Susceptibilities, Oxford University Press, 1932.
[20] P.W. Kasteleijn, J. von Kranendonk, Physica 22 (1956) 317.
[21] H. Miyasaka, R. Clérac, T. Ishii, H.-C. Chang, S. Kitagawa, M. Yamashita, J. Chem. Soc., Dalton Trans. (2002) 1528.
[22] H.M. McConnell, Proc. R. A. Welch Found Conf. Chem. Res. 11 (1967) 144.
[23] J.B. Torrance, S. Oostra, A. Nazzal, Synth. Met. 19 (1987) 709.
[24] K. Awaga, T. Sugano, M. Kinoshita, Chem. Phys. Lett. 141 (1987) 540.

CDW and the CP structures. Next, the intra-chain and the inter-chain exchange interactions between spins on Pt_2 units in the CP structure are calculated by using those model structures.

2. Calculated models

In order to carry out DFT calculations, we constructed two model structures for $K_4[Pt_2(pop)_4X] \cdot 2H_2O$ (X = Cl and Br) complexes *i.e.* the single chain and the double chain models as illustrated in Fig. 1A and B, respectively. The models approximate an infinite chain as a cluster model. The whole geometry was taken from data of X-ray crystal structure analyses by Yamashita and Toriumi [7], although all water molecules in the crystal were removed. There are two positions for one halogen ion in the X-ray data as illustrated in Fig. 1C. If we consider a total symmetry of the crystal, this disorder makes two combinations of the position of halogen ions as illustrated in Fig. 1D and E. The former reproduces the CDW structure and the latter is the CP structure. Pt–Pt and Pt–X distances in Cl and Br complexes are summarized in Table S1 in Supplementary data. The positions of hydrogen atoms of pop ligands were determined by partial optimization that was carried out only for hydrogen atoms. Terminals of the chains were capped by point charges of +1.7*e* and +1.6*e* reproducing Pt ions. A slight difference between left and right charges expresses a charge imbalance caused by the difference in Pt–X distance. In order to examine the effect of potassium ions around the MMX chains, we examined two models *i.e.* the real potassium and point charge (Pc) models. In case of the real potassium model (K^+ model), potassium ions are included in the UB3LYP calculations however they are replaced by point charges (+1.0*e*) in case of the Pc model.

3. Computational details

All calculations were performed by use of LANL2DZ [16] basis set for Pt atoms and 4-31G basis set for pop ligands. 6-31+G and 6-31G basis sets were used for axial halogen atoms and K atoms, respectively. The unrestricted hybrid DFT method (UB3LYP [17]) was applied for all calculations on GAUSSIAN98 [18].

4. Calculated results and discussion

4.1. Difference in stability between CDW and CP structures

First, we calculated total energies of the CDW and the CP structures by using the single chain model. Calculated total energies are summarized in Table S2 in Supplementary data. The calculated results indicate that the CDW structure is stable in comparison with CP structure in both Cl and Br complexes. And those results are consistent with the experiment of iodine complex [12]. The differences in total energies between the two structures ($\Delta^{CP-CDW} = E(CP) - E(CDW)$) are summarized in Table 1. The values of Cl complex are about 0.3 eV, which is larger than that of Br complex (ca. 0.2 eV). Matsuzaki et al. reported a relation between the Pt–I–Pt distance (d(Pt–I–Pt)) and the optical gap energy (E_{CT}) [13]. The values of d(Pt–I–Pt) of Cl and Br complexes are 5.768 Å and 5.756 Å, respectively. Calculated Δ^{CP-CDW} values are smaller than an estimated value (ca. 0.5 eV) from "E_{CT} versus d(Pt–I–Pt) plot" in the paper [13] but are reproducing the value, qualitatively. The results also indicate that charge transfer from one Pt_2 unit to adjoining one occurs easily in the Br complex than the Cl complex.

Differences in the Δ^{CP-CDW} values between the K^+ and the Pc models are 0.02 eV and 0.01 eV for Cl and Br complexes, respectively. These very small differences indicate that orbitals of K^+ ions do not affect to the stability of CDW and CP structures, however the results do not deny the importance of ion sizes and positive charges of K^+ ions.

4.2. Intra-chain magnetic interaction in CP structure

In the CP structure, one spin ($S = 1/2$) is supposed to be on one Pt_2 unit, while there is no local spins in the CDW structure as illustrated in Fig. 2. Calculated spin densities of Cl and Br complexes summarized in Tables S3 and S4 in Supplementary data also support the predicted spin structures. The intensity of spin densities of the Br complex is slightly smaller than that of the Cl complex, suggesting a larger SOMO–SOMO ($d\sigma^*$–$d\sigma^*$) overlap between Pt_2 units in the Br complex than the Cl complex.

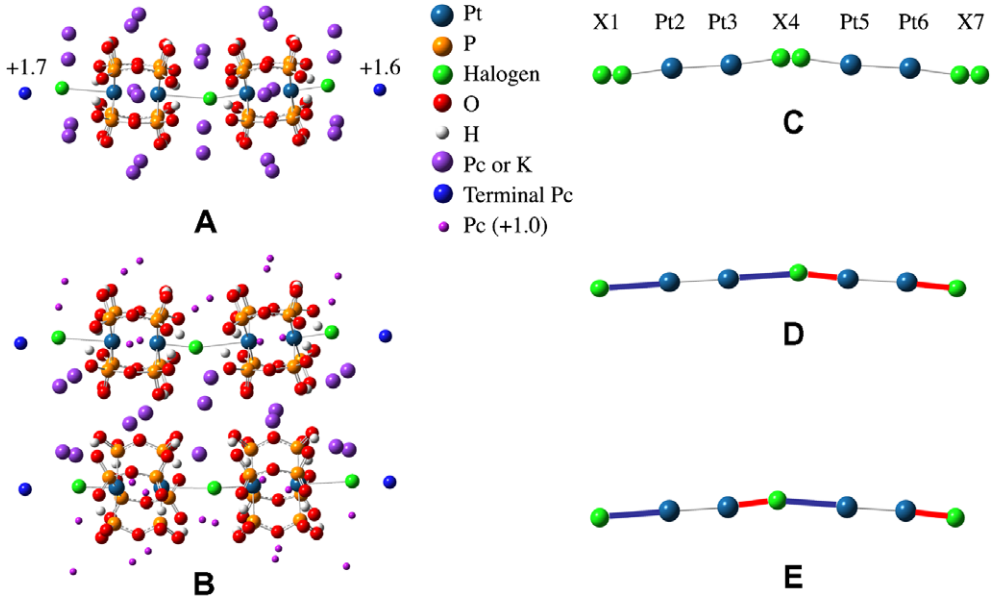


Fig. 1. Structure of (A) the single chain model and (B) the double chain model. Pc denotes a point charge. (C) Illustration of two positions for one halogen ion in X-ray data. (D) Combinations of positions of halogen ions for (D) CDW structure and (E) CP structure. Bold blue and red lines indicate longer and shorter distances, respectively. (For interpretation of the references to colour in this figure legend, the reader is referred to the web version of this article.)

Table 1
Calculated energy gaps between the CP structure and the CDW structure (Δ^{CP-CDW}).

X	Δ^{CP-CDW} (eV)	
	Pc model	K^+ model
Cl	0.32	0.34
Br	0.24	0.23

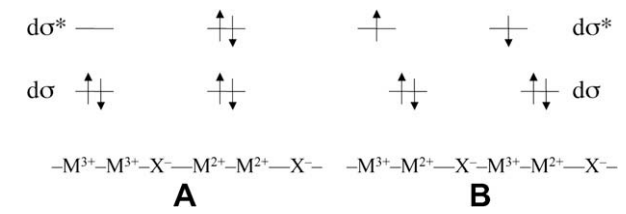


Fig. 2. Illustration of spin structures of (A) the CDW structure and (B) the CP structure.

The spins on the Pt_2 units in the CP structure cause intra- and inter-chain magnetic interactions as illustrated in Fig. 3A and C. The magnetic properties of transition metal complexes are usually investigated by the use of Heisenberg Hamiltonian [19–21],

$$\hat{H}^{H} = -2\sum J^{H}_{ab}\hat{S}_a \cdot \hat{S}_b, \quad (1)$$

where J^{H}_{ab} is the orbital-averaged effective exchange integrals between the spin site a and b with total spin operators $\hat{S}_a$ and $\hat{S}_b$, respectively. Yamaguchi et al. has proposed that J^{H}_{ab} value can be calculated from the energy splitting between a broken-symmetry (BS) low spin (LS) and a high spin (HS) states by using an equation,

$$J^{H}_{ab} = \frac{E^{LS} - E^{HS}}{\langle \hat{S}^2 \rangle^{HS} - \langle \hat{S}^2 \rangle^{LS}}, \quad (2)$$

where E^X and $\langle \hat{S}^2 \rangle^X$ denote the total energy and total spin angular momentum for the spin state X (X = LS and HS), respectively [22,23]. The definition of LS and HS states in the single chain model is explained in Fig. 3B. We note that the Eq. (2) can eliminate a spin contamination error, which is a problem of the BS method, from calculated J^{H}_{ab} values [24]. On the other hand, Ising Hamiltonian is also often used for a consideration of the magnetic interaction between fully localized spins,

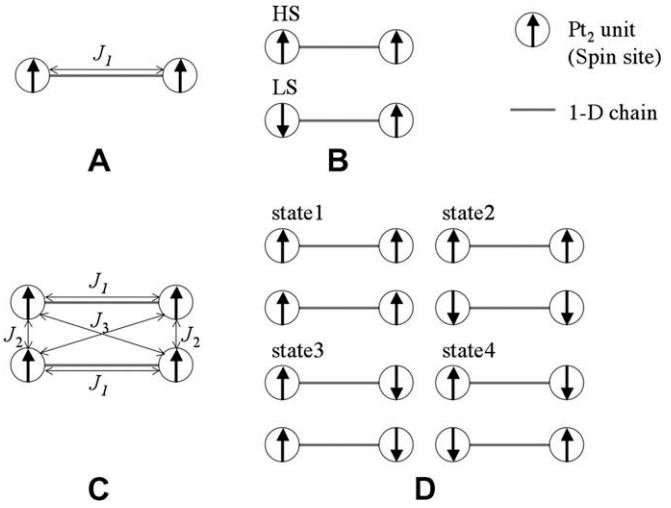


Fig. 3. Illustration of spin–spin interactions in each model and of spin states required for the calculation of J values. (A) Spin–spin interactions in the single chain model and (B) two spin states required for the calculation of J_1. (C) Spin–spin interactions in the double chain model and (D) four spin states required for the calculation of J_1, J_2 and J_3.

$$\hat{H}^{I} = -2\sum J^{I}_{ab}\hat{S}^{z}_a \cdot \hat{S}^{z}_b, \quad (3)$$

where J^{I}_{ab} is the exchange integrals of Ising Hamiltonian with total spin operators for z-axis; $\hat{S}^{z}_a$ and $\hat{S}^{z}_b$, respectively [14]. And J^{I}_{ab} between two Pt_2 units in the single chain model can be calculated by

$$J^{I}_{ab} = E^{LS} - E^{HS}. \quad (4)$$

By using those Eqs. (2) and (4), the intra-chain magnetic interactions are examined. Calculated results are summarized in Table 2. Those J values indicate the strong anti-ferromagnetic (AF) interaction between Pt_2 units and are consistent with our previous result for $Pt_2(dta)_4I$ complex ($-1274\ cm^{-1}$) [15]. Such a strong AF interaction means a large SOMO–SOMO overlap between adjoining Pt_2 units. It is also expected that the Br complex, which shows a stronger AF interaction, has the larger SOMO–SOMO overlap than the Cl complex.

In order to examine the overlap between two Pt_2 units, natural orbital (NO) analysis is carried out for both complexes. The SOMO–SOMO overlap (T_{SOMO}) can be calculated by using occupation number (n_{occ}) of NO [14],

$$T_{SOMO} = n_{occ} - 1. \quad (5)$$

Calculated NOs and n_{occ} numbers are illustrated in Figs. S1 and S2 in Supplementary data. The calculated T_{SOMO} values of the Cl and the Br complexes that are 0.45 and 0.67, respectively, indicate that the Br complex has a larger SOMO–SOMO overlap. Kumoo and Clark pointed out that a mixing of halogen pσ orbitals in the dσ Pt–Pt wave functions was in the order Cl < Br < I [10]. The order of T_{SOMO} (Cl < Br) strongly suggests the contribution of halogen pσ orbitals to the orbital overlap.

On the other hand, we find that K^+ ions slightly decrease $|J|$ values for both Cl and Br complexes. A decrease of the AF coupling means a decrease of SOMO–SOMO overlap. However they do not change qualitative properties.

4.3. Inter-chain magnetic interaction in CP structure

In previous section, we indicated that the intra-chain spin–spin interaction is a strong AF coupling. Therefore a spin density wave (SDW)-like order is expected in the single chain of CP phase. However it is important to know the inter-chain magnetic interaction to consider a spin order in a bulk system. In order to calculate the inter-chain interaction, we apply Ising Hamiltonian to the double chain model because Eq. (2) is not applicable to multi-J systems. The schematic view of spin–spin interactions in the double chain model is illustrated in Fig. 3C. In this model, there are two types of inter-chain spin–spin interactions *i.e.* J_2 and J_3. For the calculation of J_1, J_2 and J_3, we have to calculate total energies of four spin states (state1 ~ state4) illustrated in Fig. 3 and have to solve simultaneous equations below,

$$J_1 = \frac{1}{4}\left[\left(E^{state3} + E^{state4}\right) - \left(E^{state1} + E^{state2}\right)\right], \quad (6)$$

$$J_2 = \frac{1}{4}\left[\left(E^{state2} + E^{state4}\right) - \left(E^{state1} + E^{state3}\right)\right], \quad (7)$$

$$J_3 = \frac{1}{4}\left[\left(E^{state2} + E^{state3}\right) - \left(E^{state1} + E^{state4}\right)\right], \quad (8)$$

Table 2
Intra-chain J values for the CP structures of the Cl and the Br model structures calculated by Heisenberg model (J^{H}_{ab}) and Ising model (J^{I}_{ab}).

X	J^{H}_{ab} (cm^{-1})		J^{I}_{ab} (cm^{-1})	
	Pc model	K^+ model	Pc model	K^+ model
Cl	−912	−889	−1104	−1072
Br	−1573	−1537	−2290	−2230

Table 3
Intra- and inter-chain J values calculated by double chain models. Definitions of J_1, J_2 and J_3 are illustrated in Fig. 3C.

J (cm^{-1})	Cl complex		Br complex	
	Pc model	K^+ model	Pc model	K^+ model
J_1	−1029.8	−1011.2	−2208.1	−2172.4
J_2	−0.1	0.0	−0.1	0.0
J_3	0.0	0.0	0.1	0.0

where $E^{\text{state}X}$ is a total energy of state X [14]. Calculated J values are summarized in Table 3. The intra-chain exchange (J_1) is consistent with the values of the previous single chain models. In contrast to the large AF exchange coupling in the chain, the inter-chain interactions are negligible within the calculated models here. As explained above, water molecules in the crystal are removed from the original X-ray data, therefore magnetic interaction paths through hydrogen bonds were not included in these models. Because the hydrogen bonds may increase spin–spin interaction, it is desirable to include those water molecules for a further study about the inter-chain magnetic interaction. On the other hand, we can not find significant efficiency of K^+ ions however they also seem to decrease the absolute values of J values.

5. Conclusion

In this study, electronic structures, CDW/CP stability and magnetic properties of $K_4[Pt_2(pop)_4X]\cdot 2H_2O$ (X = Cl, Br) complexes are examined. Calculated total energies support that the CDW state is the ground state and the CP state is the excited state for both complexes. Calculated J values indicated the strong AF intra-chain interaction but suggest the negligible inter-chain interaction. In addition, it is also elucidated that orbitals of potassium ions scarcely affect to $\Delta^{\text{CP–CDW}}$ and J values. Therefore, the experimental result, which the ordering structures depend on the counter ion, seems to originate from only the ion size but not from orbitals of counter ions [8]. Recent experimental result, which E_{CT} depends on d(Pt–I–Pt) [13] also consistent with our result.

Acknowledgements

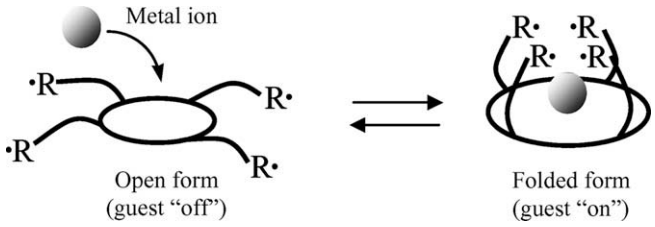
This work has been supported by Grants-in-Aid for Scientific Research (KAKENHI) (Nos. 19750046, 19350070, 18350008) from Japan Society for the Promotion of Science (JSPS) and that on Priority Areas (No. 19029028) from the Ministry of Education, Culture, Sports, Science and Technology (MEXT).

Appendix A. Supplementary data

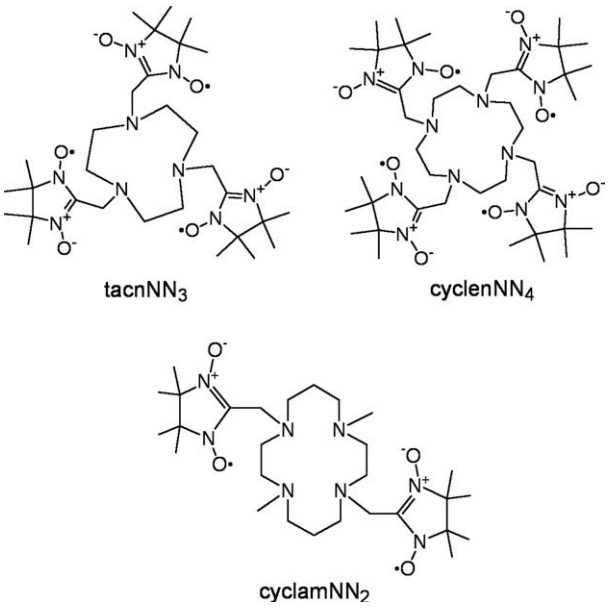
Supplementary data associated with this article can be found, in the online version, at doi:10.1016/j.poly.2008.10.037.

References

[1] J.K. Bera, K.R. Dunbar, Angew. Chem., Int. Ed. 41 (2002) 23.
[2] C. Bellitto, G. Dessy, U. Fares, Inorg. Chem. 24 (1985) 2815.
[3] C. Bellitto, A. Flamini, L. Gastaldi, L. Scaramuzza, Inorg. Chem. 24 (1983) 444.
[4] M. Yamashita, Y. Wada, K. Toriumi, T. Mitani, Mol. Cryst. Liq. Cryst. 216 (1992) 207.
[5] M. Mitsumi, T. Murase, H. Kishida, T. Yoshinari, Y. Ozawa, K. Toriumi, T. Sonoyama, H. Kitagawa, T. Mitani, J. Am. Chem. Soc. 123 (2001) 11179.
[6] A. Kobayashi, H. Kitagawa, R. Ikeda, S. Kitao, M. Seto, M. Mitsumi, K. Toriumi, Synth. Met. 135–136 (2003) 405.
[7] M. Yamashita, T. Toriumi, Inorg. Chem. Acta 178 (1990) 143.
[8] M. Yamashita, S. Miya, T. Kawashima, T. Manabe, T. Sonoyama, H. Kitagawa, T. Mitani, H. Okamoto, R. Ikeda, J. Am. Chem. Soc. 121 (1999) 2321.
[9] H. Kitagawa, N. Onodera, T. Sonoyama, M. Yamamoto, M. Fukawa, T. Mitani, M. Seto, Y. Maeda, J. Am. Chem. Soc. 121 (1999) 10068.
[10] M. Kumoo, R. Clark, Inorg. Chem. 24 (1985) 4420.
[11] N. Kimura et al., Chem. Phys. Lett. 220 (1994) 40.
[12] H. Matsuzaki, H. Kishida, K. Takizawa, M. Yamashita, H. Okamoto, Synth. Met. 135–136 (2003) 607.
[13] H. Matsuzaki, T. Matsumoto, H. Kishida, K. Takizawa, H. Miyasaka, K. Sugiura, M. Yamashita, H. Okamoto, Phys. Rev. Lett. 90 (2003) 046401.
[14] S. Nakano, Y. Kitagawa, T. Kawakami, K. Yamaguchi, Polyhedron 22 (2003) 2027.
[15] Y. Kitagawa, M. Shoji, K. Koizumi, T. Kawakami, M. Okumura, K. Yamaguchi, Polyhedron 26 (2007) 2154.
[16] W.R. Wadt, P.J. Hay, J. Chem. Phys. 82 (1985) 299.
[17] A.D. Becke, J. Chem. Phys. 98 (1993) 5648.
[18] M.J. Frisch, G.W. Trucks, H.B. Schlegel, G.E. Scuseria, M.A. Robb, J.R. Cheeseman, V.G. Zakrzewski, J.A. Montgomery, Jr., R.E. Stratmann, J.C. Burant, S. Dapprich, J.M. Millam, A.D. Daniels, K.N. Kudin, M.C. Strain, O. Farkas, J. Tomasi, V. Barone, M. Cossi, R. Cammi, B. Mennucci, C. Pomelli, C. Adamo, S. Clifford, J. Ochterski, G.A. Petersson, P.Y. Ayala, Q. Cui, K. Morokuma, N. Rega, P. Salvador, J.J. Dannenberg, D.K. Malick, A.D. Rabuck, K. Raghavachari, J.B. Foresman, J. Cioslowski, J.V. Ortiz, A.G. Baboul, B.B. Stefanov, G. Liu, A. Liashenko, P. Piskorz, I. Komaromi, R. Gomperts, R.L. Martin, D.J. Fox, T. Keith, M.A. Al-Laham, C.Y. Peng, A. Nanayakkara, M. Challacombe, P.M.W. Gill, B. Johnson, W. Chen, M.W. Wong, J.L. Andres, C. Gonzalez, M. Head-Gordon, E.S. Replogle, J.A. Pople, GAUSSIAN 98, Gaussian, Inc., Pittsburgh, PA, 2002.
[19] D. Gatteschi, O. Kahn, J.S. Miller, F. Palacio (Eds.), Magnetic Molecular Materials, Kluwer Academic Publishers, Dordrecht, 1991.
[20] O. Kahn (Ed.), Magnetism: A Supermolecular Function, NATO ASI Series C, vol. 484, Kluwer Academic Publishers, Dordrecht, 1996.
[21] E. Coronado, P. Dekhais, D. Gatteschi, J.S. Miller (Eds.), Molecular Magnetism: From Molecular Assemblies to the Devices, NATO ASI Series E, vol. 321, Kluwer Academic Publishers, Dordrecht, 1996.
[22] T. Kawakami, S. Yamanaka, S. Yamada, W. Mori, K. Yamaguchi, in: M.M. Turnbull, T. Sugimoto, L.K. Thompson (Eds.), Molecular-Based Magnetic Materials, Theory, Technique and Applications, ACS Symposium Series 644, American Chemical Society, Washington, DC, 1996, p. 30.
[23] K. Yamaguchi, in: R. Carbeó, M. Klobukowski (Eds.), Self-Consistent Field Theory and Applications, Studies in Physical and Theoretical Chemistry 70, Elsevier, Amsterdam–Oxford–New Tork–Tokyo, 1990, p. 727.
[24] Y. Kitagawa, T. Saito, M. Ito, M. Shoji, K. Koizumi, S. Yamanaka, T. Kawakami, M. Okumura, K. Yamaguchi, Chem. Phys. Lett. 442 (2007) 445.



Scheme 1. Open and folded forms of poly(radical-armed) azacrowns.



Scheme 2. Structural formulas of the paramagnetic host compounds.

$$\chi_{mol} = C/(T - \theta_{cw}) \quad (1)$$

2.2. Complex of cyclamNN$_2$ with copper(II) ion

We planned host–guest complexation using cyclamNN$_2$ and transition metal ions, giving a three-centered radical–metal–radical system as depicted in Scheme 3. We utilized copper(II) and nickel(II) perchlorates as a metal source. In case of copper(II) compounds, coordination structures such as a square planar or square pyramid are also possible.

Complexation reaction of cyclamNN$_2$ with $Cu(ClO_4)_2$ in dichloromethane–ethanol gave dark purple crystals of $[Cu(cyclamNN_2)] \cdot (ClO_4)_2 \cdot 0.5(CH_2Cl_2)$ (**1**). The formula was determined from the elemental analysis and X-ray crystallographic analysis. The crystallographic analysis was successfully performed, but the thermal displacement factors remained somewhat large (Fig. 2), especially for terminal methyl groups probably owing to conformational disorder. The geometry around Cu1 seems sufficiently reliable. We found a semi-folded structure (Scheme 3) in the $[Cu(cyclamNN_2)]^{2+}$, giving a five-coordination sphere at Cu1.

The copper ion is located at the center of the cyclam cavity as indicated with the Cu–N bonds (2.121(6), 2.057(9), 2.131(7), and 1.975(8) Å for Cu1–N1, Cu1–N2, Cu1–N3, and Cu1–N4, respectively). One radical arm is coordinated at an axial position with the Cu1–O1 distance of 2.196(7) Å. These structural features imply that the copper ion in **1** is regarded to possess an intermediate structure between a square-pyramid and a trigonal-bipyramid. However, the relatively long Cu1–O1 bond suggests that the former is more likely. The other radical group does not participate in coordination.

The magnetic susceptibility of a polycrystalline sample of **1** was measured on a SQUID magnetometer (Fig. 3). On cooling from 300 K, the $\chi_{mol}T$ value once increased, reached a maximum around 15 K, and finally decreased. The increase of the $\chi_{mol}T$ value down to 15 K indicates the presence of ferromagnetic interaction in **1**.

The ferromagnetic coupling can be attributed to the copper-radical direct coordination, and accordingly the magnetic susceptibility is formulated as the sum of a singlet–triplet model [19] and a doublet. The final $\chi_{mol}T$ drop below 10 K indicates the presence of antiferromagnetic interaction among the singlet–triplet and doublet species. The Weiss mean field parameter θ is introduced. We utilized Eq. (2) for the analysis of the magnetic data on **1**, giving the best fit parameters as follows: $2J/k_B = +44(3)$ K, $g_{avg} = 2.091(6)$ and $\theta = -0.67(5)$ K. The calculated curve reproduced well the experimental data. The small θ implies small intermolecular exchange coupling.

$$\chi_{mol} = \frac{Ng_{avg}^2\mu_B^2}{k_B(T-\theta)}\left[\frac{1}{4} + \frac{2}{3+\exp(-2J/k_BT)}\right] \quad (2)$$

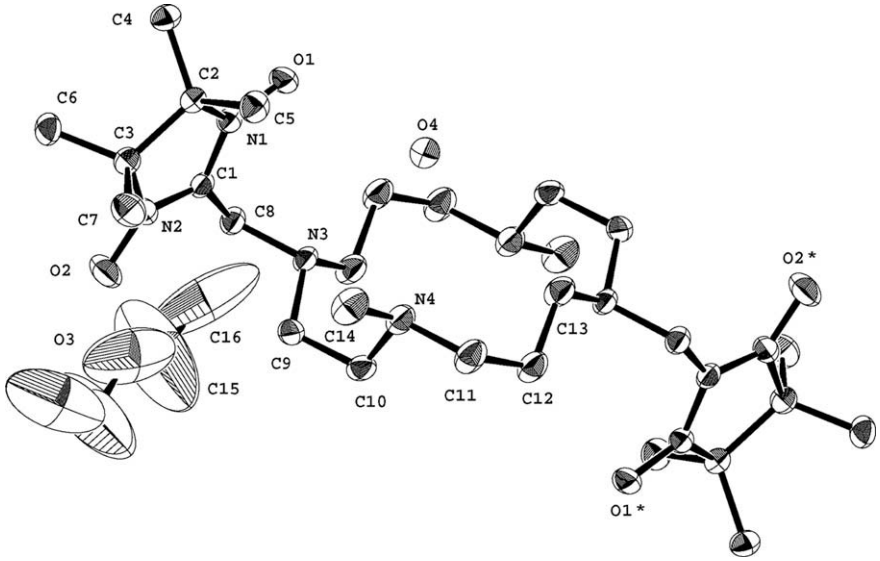
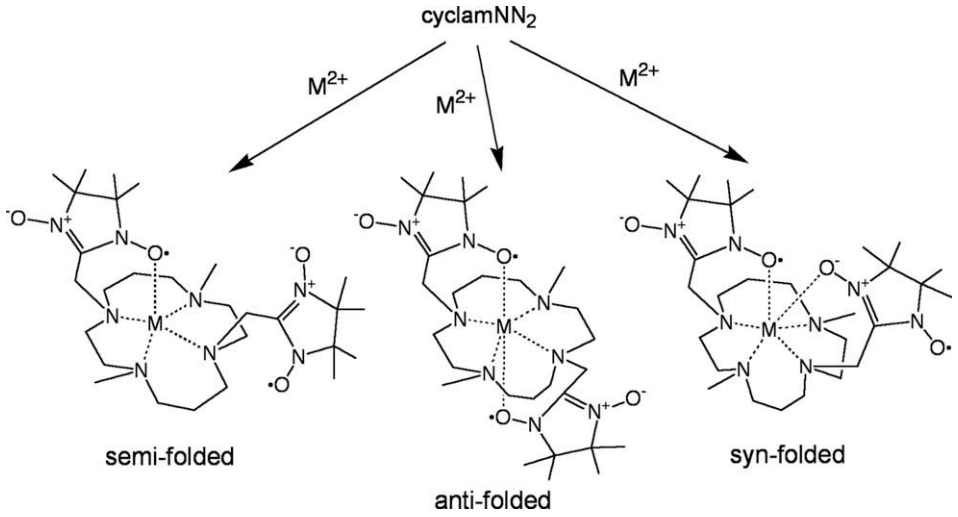


Fig. 1. Molecular structure of cyclamNN$_2$ with thermal ellipsoids at the 50% probability level. Hydrogen atoms are omitted for clarity.



Scheme 3. Possible structures from complexation of cyclamNN$_2$ and metal ions.

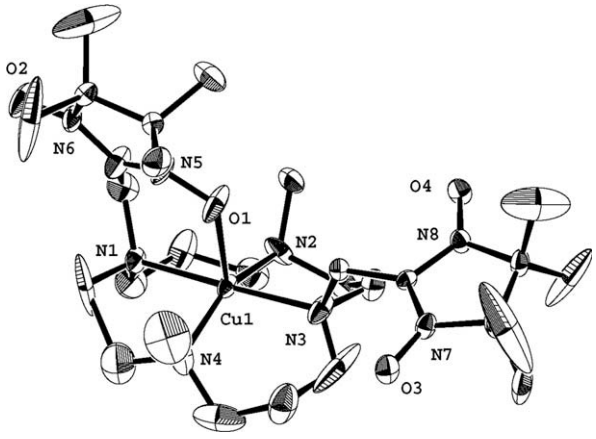


Fig. 2. Molecular structure of $[Cu \cdot cyclamNN_2]^{2+}$ in **1**. Thermal ellipsoids are drawn at the 50% probability level. Counterions, solvent molecules, and hydrogen atoms are omitted for clarity.

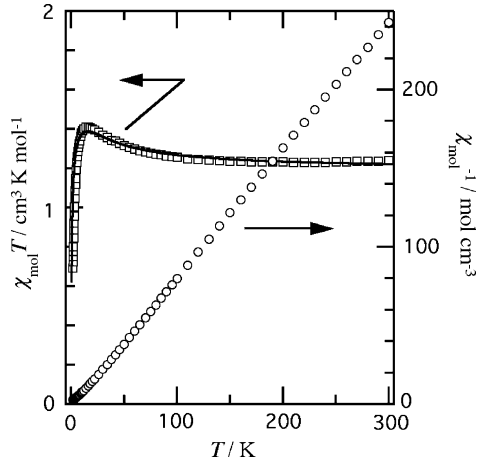


Fig. 3. Temperature dependence of $\chi_{mol}T$ and χ_{mol}^{-1} for **1**. A solid line represents a calculated curve. For the equation and parameters, see the text.

2.3. Complex of cyclamNN$_2$ with nickel(II) ion

Similarly to the case of the copper(II) complex, reaction of cyclamNN$_2$ with $Ni(ClO_4)_2$ gave red powder of $[Ni(cyclamNN_2)] \cdot (ClO_4)_2 \cdot (CH_2Cl_2)$ (**2**). Unfortunately, no single crystal suitable for X-ray crystallographic analysis could be obtained. The formula was determined from the elemental analysis.

The magnetic susceptibility of a polycrystalline sample of **2** was measured and the result is displayed in Fig. 4. On cooling from 300 K, the $\chi_{mol}T$ value drastically increased and reached to a maximum of 5.5 cm^3 K mol^{-1} around 16 K. The increase of the $\chi_{mol}T$ value indicates the presence of ferromagnetic interaction in **2**. Furthermore the Ni ion has a $S = 1$ spin state and possibly possesses an octahedral sphere as a folded structure.

The magnetic data above 20 K were analyzed according to Eq. (1), to give $C = 1.270(6)$ cm^3 K mol^{-1} and $\theta_{CW} = +13.5(6)$ K. The largely positive θ_{CW} value implies the presence of appreciable ferromagnetic coupling. The maximum $\chi_{mol}T$ value is larger than the theoretical spin-only value (3.0 cm^3 K mol^{-1} for the maximum high-spin $S_{total} = 2$ state in a molecule), indicating that the ferromagnetic coupling is operative beyond a formula unit; namely the complex would have a polymeric or polynuclear structure. A final drop of the $\chi_{mol}T$ value may be attributed to the interchain or intercluster antiferromagnetic interaction.

The Curie constant is smaller than the theoretical paramagnetic limit (1.75 cm^3 K mol^{-1}) for **2**. The reason is not clear at present, but a possible explanation is that the specimen would contain $[H_2cyclamNN_2] \cdot (ClO_4)_2$ (**3**) as an impurity. In fact, this salt was

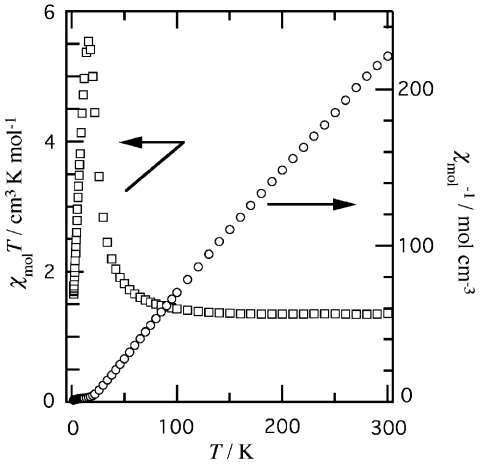


Fig. 4. Temperature dependence of $\chi_{mol}T$ and χ_{mol}^{-1} for **2**.

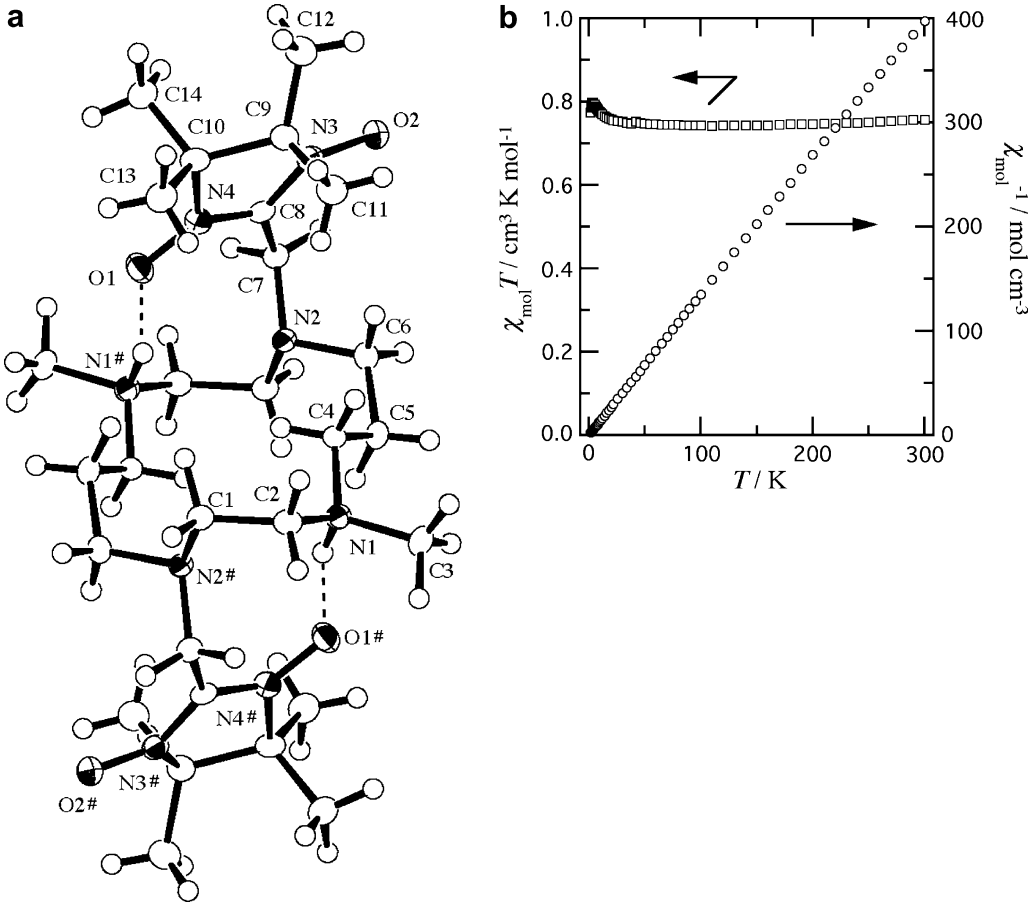


Fig. 5. (a) Molecular structure of $[H_2cyclamNN_2]^{2+}$ in **3**. Thermal ellipsoids are drawn at the 50% probability level for non-hydrogen atoms. Counterions are omitted for clarity. Hydrogen bonds are indicated with dotted lines. Symmetry operation code of # is $1-x, -y, 2-z$. (b) Temperature dependence of $\chi_{mol}T$ and χ_{mol}^{-1} for **3**.

isolated from a second crop of the reaction mixture and characterized by means of X-ray crystallographic analysis (Fig. 5a). Note that **3** possesses an anti-folded form with the aid of hydrogen bonds. The O1–O1# distance is 7.018(2) Å. Compound **3** exhibited negligible ferromagnetic coupling (θ_{CW} = +0.23(2) K with C = 0.756(1) $cm^3\,K\,mol^{-1}$ from Eq. (1)) (Fig. 5b). The steep $\chi_{mol}T$ upsurge in Fig. 4 is attributed to the magnetic properties of **2**.

3. Discussion

The ferromagnetic coupling in metal–radical hybrid solids originates from the orthogonal arrangement between the magnetic orbitals (metal dσ and radical π*) [8,13–15]. In the present work, the ferromagnetic coupling was successfully achieved, and the magnitude of the magnetic coupling in **1** was determined as $2J/k_B$ = +44(3) K. Similar axial NN–Cu geometries have been reported on the one-dimensional polymer $[Cu(hfac)_2 \cdot (CH_3\text{–}NN)]_n$ [20] for example, where Hhfac and CH_3–NN stand for 1,1,1,5,5,5-hexafluoropentane-2,4-dione and 2,4,4,5,5-pentamethylimidazolin-1-oxyl 3-oxide, respectively. The NN oxygen atoms are located at the axial positions of the Cu center, and the exchange couplings are reported to be 37 K, which is comparable to that of **1**, though the magnitude of the couplings largely depends on many geometrical parameters such as O–Cu lengths and N–O–Cu angles. There have been many reports regarding this argument [8,21,22]. The ferromagnetic exchange was operative in the axial coordination of the NN radical to the square-pyramidal copper(II) ion in **1**.

In the complexation reactions with copper(II) ions, we obtained only the singly NN-coordinated compound (**1**) so far. There have been several reports on the six-coordinated copper(II) complexes from bis(2-pyridylmethyl)-substituted cyclam derivatives and related host compounds [23]. In that case the chelate rings at the arms are five-membered, whereas **1** has a six-membered chelate ring. Doubly NN-coordinated (fully folded) compounds may hardly be formed for such a steric reason.

The crystal structure of **2** is unknown. The poor crystallinity suggests that **2** would consist of polymeric coordination compounds. In the literature, however, the ferromagnetic coupling in radical-nickel coordination compounds seems rare. The mononuclear compound $[Ni(hfac)_2 \cdot (proxyl)_2]$ exhibited antiferromagnetic coupling to give a singlet ground state [24], where proxyl stands for 2,2,5,5-tetramethylpyrrolidin-1-oxyl. Furthermore, polymeric $[Ni(hfac)_2 \cdot (CH_3\text{–}NN)]_n$ also exhibited antiferromagnetic coupling ($2J/k_B < -500$ K) [25]. Some paramagnetic ligands involving a 2-pyridyl group are reported to favor strictly planar chelate rings and accordingly to exhibit ferromagnetic couplings between the nickel(II) and nitroxide spins [15,26–28].

In the case of **2**, the ferromagnetic coupling is operative but the magnitude is moderate. Assuming that the curvature of the increase of the $\chi_{mol}T$ on cooling is ascribable to the coupling between Ni S = 1 spin and the radical S = 1/2 spin, we can preliminarily estimate $2J/k_B$ as ca. +18 K. The moderate exchange coupling may be caused by partial violation from the strict orthogonal arrangement of the nickel dσ and radical π* orbitals.

Table 1
Selected crystallographic data for cyclamNN$_2$, **1**, and **3**.

Compounds	cyclamNN$_2$	**1**	**3**
Formula	$C_{32}H_{68}N_8O_7$	$C_{30}H_{58}Cl_6CuN_8O_{12}$	$C_{28}H_{56}Cl_2N_8O_{12}$
Formula weight	676.94	999.10	767.70
Habit	red block	deep purple block	red block
Dimension (mm^3)	0.8 × 0.6 × 0.6	0.4 × 0.3 × 0.2	0.40 × 0.35 × 0.35
T (K)	124	120	100
Crystal system	monoclinic	triclinic	monoclinic
Space group	$C2/c$	$P\bar{1}$	$P2_1/c$
a (Å)	17.0417(9)	12.54530(10)	10.5909(5)
b (Å)	17.4841(8)	14.0263(2)	14.9188(7)
c (Å)	12.8640(8)	14.2066(3)	12.0189(7)
α (°)	90	74.1747(16)	90
β (°)	97.1500(10)	64.2976(15)	92.121(3)
γ (°)	90	77.7444(11)	90
V (Å^3)	3803.1(4)	2154.36(6)	1897.73(17)
Z	4	2	2
D_{calc} (g cm^{-3})	1.182	1.540	1.343
Unique data	4298	9732	4331
μ (Mo Kα) (mm^{-1})	0.084	0.944	0.238
R (F)[a] ($I > 2\sigma$ (I))	0.0669	0.1353	0.0658
$R_w(F^2)$[b] (all data)	0.0977	0.1586	0.0811

[a] $R = \Sigma\ ||F_o| - |F_c||/\Sigma\ |F_o|$.
[b] $R_w = [\Sigma w(F_o^2 - F_c^2)^2/\Sigma\ w(F_o^2)^2]^{1/2}$.

4. Conclusions

We prepared [M(cyclamNN$_2$)](ClO$_4$)$_2$ (M = Cu (**1**), Ni (**2**)). The molecular structures of cyclamNN$_2$ and **1** were determined by means of X-ray crystal structure analysis. The copper ion is located at the center of the cyclam cavity and one radical arm is coordinated at an axial position. They showed ferromagnetic coupling as indicated by an increase of the $\chi_m T$ value on cooling. As for **2**, intermolecular ferromagnetic coupling is suggested as well as intramolecular one. These paramagnetic hosts (tacnNN$_3$, cyclenNN$_4$, and cyclamNN$_2$) seem to be promising building blocks for the development of supramolecular-switchable magnetic materials as well as metal–radical hybrid magnets.

5. Experimental

5.1. Materials

CyclamNN$_2$: an acetonitrile solution (8 mL) containing 2-chloromethyl-4,4,5,5-tetramethylimidazolin-1-oxyl 3-oxide [18] (NN–CH$_2$Cl; 400 mg; 1.9 mmol) was added to a mixture of acetonitrile (8 mL), 1,8-dimethyl-1,4,8,11-tetraazacyclotetradecane (1,8-dimethylcyclam, Aldrich) (200 mg; 0.88 mmol), and K_2CO_3 (740 mg; 5.4 mmol). The resultant mixture was stirred at 45 °C for 4 h. After addition of chloroform (ca. 100 mL), the organic layer was washed with water, dried over Na_2CO_3, and filtered, to give a deep violet solution. The solvent was removed under reduced pressure, and a solidified product was obtained by adding ether (ca. 100 mL). The crude product of cyclamNN$_2$ was collected on a filter and dried (267 mg; 0.47 mmol) in 54% yield. M.p. 89–91 °C. IR (KBr disc): 541, 1137, 1375, 1411, 1457, 2798, 2991 cm^{-1}. MS (ESI): m/z 567.3 (100%, M+H$^+$) (calc. 567.3 for $C_{28}H_{54}N_8O_4$+H), 589.3 (33%, M+Na$^+$) (calc. 589.4 for $C_{28}H_{54}N_8O_4$+Na). ESR (X-band, toluene, room temperature) five lines with an intensity ratio of 1/2/3/2/1. a_N = 7.18 G, g = 2.0066. *Anal.* Calc. for $C_{32}H_{68}N_8O_7$: C, 56.78; H, 10.13; N, 16.54. Found: C, 56.06; H, 9.07; N, 16.85%. The crystals tend to incorporate solvent molecules.

[Cu(cyclamNN$_2$)] · (ClO$_4$)$_2$ · 0.5(CH$_2$Cl$_2$) (**1**): after gently adding an ethanol solution (2 mL) of Cu(ClO$_4$)$_2$ · 6H$_2$O (35 mg; 0.094 mmol) over a dichloromethane solution (2 mL) of cyclamNN$_2$ (47 mg; 0.083 mmol), the two solutions were slowly diffused each other in a refrigerator. Dark violet crystals were formed. *Anal.* Calc. for [Cu(cyclamNN$_2$)] · (ClO$_4$)$_2$ · 0.5(CH$_2$Cl$_2$): C, 39.27; H, 6.36; N, 12.85. Found: C, 39.01; H, 6.79; N, 12.74%.

[Ni(cyclamNN$_2$)] · (ClO$_4$)$_2$ · (CH$_2$Cl$_2$) (**2**): after adding an ethanol solution (3 mL) of Ni(ClO$_4$)$_2$ · 6H$_2$O (43 mg; 0.12 mmol) over a dichloromethane solution (5 mL) of cyclamNN$_2$ (65 mg; 0.12 mmol), a red powdery product was precipitated immediately. The product was separated on a filter. *Anal.* Calc. for [Ni(cyclamNN$_2$)] · (ClO$_4$)$_2$ · (CH$_2$Cl$_2$): C, 39.49; H, 6.40; N, 12.63. Found: C, 39.48; H, 6.78; N, 12.53%. Red crystals were precipitated from the above filtrate as an undesired product, [H$_2$cyclamNN$_2$] · (ClO$_4$)$_2$ · (CH$_2$Cl$_2$) (**3**). *Anal.* Calc. for [H$_2$cyclamNN$_2$] · (ClO$_4$)$_2$ · (CH$_2$Cl$_2$): C, 40.85; H, 6.86; N, 13.14. Found: C, 40.40; H, 6.96; N, 13.38%. The latter formula was also determined by the X-ray crystallographic analysis and magnetic measurements.

5.2. X-ray crystallographic analysis

X-Ray diffraction data of cyclamNN$_2$, **1**, and **3** were collected on a Rigaku *R*-axis RAPID diffractometer with graphite monochromated Mo Kα radiation (λ = 0.71069 Å). The structures were directly solved by a heavy-atom method and expanded using Fourier techniques in the CRYSTALSTRUCTURE 3.8.2 program package [29]. Numerical absorption correction was used. All of the hydrogen atoms were experimentally found and the parameters were refined isotropically for cyclamNN$_2$ and **3**. On the other hand, all of the hydrogen atoms were located at calculated positions and the parameters were refined as "riding" for **1**. The thermal displacement parameters of non-hydrogen atoms were refined anisotropically for both compounds. Full-matrix least-squares methods were applied using all of the unique reflection data. Selected crystallographic data are listed in Table 1.

5.3. Magnetic measurements

Magnetic properties of polycrystalline specimens of cyclamNN$_2$, **1**, **2**, and **3** were measured at 5000 Oe in a temperature range 1.8–300 K on a Quantum Design MPMS SQUID magnetometer. The magnetic responses were corrected with diamagnetic blank data of the sample holder measured separately. The diamagnetic contribution of the sample itself was estimated from Pascal's constants.

6. Supplementary data

CCDC 702736, 702737, and 702738 contain the supplementary crystallographic data for cyclamNN$_2$, **1**, and **3**. These data can be obtained free of charge via http://www.ccdc.cam.ac.uk/conts/retrieving.html, or from the Cambridge Crystallographic Data Centre, 12 Union Road, Cambridge CB2 1EZ, UK; fax: (+44) 1223-336-033; or e-mail: deposit@ccdc.cam.ac.uk.

Acknowledgement

This work was supported by Grants-in-Aid for Scientific Research (Nos. 16550121 and 19550135) from the Ministry of Education, Culture, Sports, Science and Technology, Japan.

References

[1] (a) K. Awaga, E. Coronado, M. Drillon, MRS Bull. 25 (2000) 52;
(b) J. Larionova, S.A. Chavan, J.V. Yakhmi, A.G. Froystein, J. Sletten, C. Sourisseau, O. Kahn, Inorg. Chem. 36 (1997) 6374;
(c) A. Rujiwatra, C.J. Kepert, J.B. Claridge, M.J. Rosseinsky, H. Kumagai, M. Kurmoo, J. Am. Chem. Soc. 123 (2001) 10584;
(d) M. Kurmoo, H. Kumagai, K.W. Chapman, C.J. Kepert, Chem. Commun. (2005) 3012.

[2] D. Maspoch, D. Ruiz-Molina, K. Wurst, N. Domingo, M. Cavallini, F. Biscarini, J. Tejada, C. Rovira, J. Veciana, Nat. Mater. 2 (2003) 190.
[3] (a) G.J. Halder, C.J. Kepert, B. Moubaraki, K.S. Murray, J.D. Cashion, Science 298 (2002) 1762;
(b) V. Niel, A.L. Thompson, M.C. Munoz, A. Galet, A.E. Goeta, J.A. Real, Angew. Chem., Int. Ed. 42 (2003) 3760.
[4] (a) J. Omata, T. Ishida, D. Hashizume, F. Iwasaki, T. Nogami, Polyhedron 20 (2001) 1557;
(b) T. Ishida, J. Omata, T. Nogami, Polyhedron 22 (2003) 2133.
[5] (a) T. Kusaka, T. Ishida, T. Nogami, Mol. Cryst. Liq. Cryst. 379 (2002) 259;
(b) N. Takagami, T. Ishida, T. Nogami, Bull. Chem. Soc. Jpn. 77 (2004) 1125;
(c) K. Yuza, T. Ishida, T. Nogami, Chem. Lett. 34 (2005) 974.
[6] T. Nakabayashi, T. Ishida, T. Nogami, Inorg. Chem. Commun. 7 (2004) 1221.
[7] E.F. Ullman, J.H. Osiecki, D.G.B. Boocock, R. Darcy, J. Am. Chem. Soc. 94 (1972) 7049.
[8] A. Caneschi, D. Gatteschi, P. Rey, R. Sessoli, Acc. Chem. Res. 22 (1989) 392.
[9] K. Igarashi, T. Nogami, T. Ishida, Chem. Commun. (2007) 501.
[10] P.D. Beer, P.A. Gale, D.K. Smith, Supramolecular Chemistry, Oxford University Press Inc., New York, 1999.
[11] J.-M. Lehn, Supramolecular Chemistry: Concepts and Perspective, VCH, Weinheim, 1995.
[12] KS. Buøen, J. Dale, P. Groth, J. Krane, J. Chem. Soc., Chem. Commun. (1982) 1172.
[13] O. Kahn, R. Prins, J. Reedijk, J.S. Thompson, Inorg. Chem. 26 (1987) 3557.
[14] D. Luneau, F.M. Romero, R. Ziessel, Inorg. Chem. 37 (1998) 5078.
[15] A. Okazawa, Y. Nagaichi, T. Nogami, T. Ishida, Inorg. Chem. 47 (2008) 8859.
[16] G. Ulrich, P. Turek, R. Ziessel, A. De Cian, J. Fischer, Chem. Commun. (1996) 2461.
[17] K.E. Vostrikova, E. Belorizky, J. Pécaut, P. Rey, Eur. J. Inorg. Chem. (1999) 1187.
[18] G. Ulrich, P. Turek, R. Ziessel, Tetrahedron Lett. 37 (1996) 8755.
[19] B. Bleaney, K.D. Bowers, Proc. R. Soc. London, Ser. A 214 (1952) 451.
[20] A. Caneschi, D. Gatteschi, J. Laugier, P. Rey, J. Am. Chem. Soc. 109 (1987) 2191.
[21] A. Caneschi, D. Gatteschi, A. Grand, J. Laugier, L. Pardi, P. Rey, Inorg. Chem. 27 (1988) 1031.
[22] (a) A. Grand, P. Rey, R. Subra, Inorg. Chem. 22 (1983) 391;
(b) D. Gatteschi, J. Laugier, P. Rey, C. Zanchini, Inorg. Chem. 26 (1987) 938;
(c) A. Bencini, C. Benelli, D. Gatteschi, C. Zanchini, J. Am. Chem. Soc. 106 (1984) 5813.
[23] (a) A.E. Goeta, J.A.K. Howard, D. Maffeo, H. Puschmann, J.A.G. Williams, D.S. Yufit, J. Chem. Soc., Dalton Trans. (2000) 1873;
(b) H. Tsukube, Y. Mizutani, S. Shinoda, T. Okazaki, M. Tadokoro, K. Hori, Inorg. Chem. 38 (1999) 3506.
[24] L.C. Porter, M.H. Dickman, R.J. Doedens, Inorg. Chem. 27 (1988) 1548.
[25] A. Caneschi, D. Gatteschi, J.P. Renard, P. Rey, R. Sessoli, Inorg. Chem. 28 (1989) 2940.
[26] C. Aoki, T. Ishida, T. Nogami, Inorg. Chem. 42 (2003) 7616.
[27] K. Osanai, A. Okazawa, T. Nogami, T. Ishida, J. Am. Chem. Soc. 128 (2006) 14008.
[28] D. Luneau, G. Risoan, P. Rey, A. Grand, A. Caneschi, D. Gatteschi, J. Laugier, Inorg. Chem. 32 (1993) 5616.
[29] CRYSTALSTRUCTURE, version 3.8.2, Rigaku/MSC, The Woodlands, TX 77381, 2003.

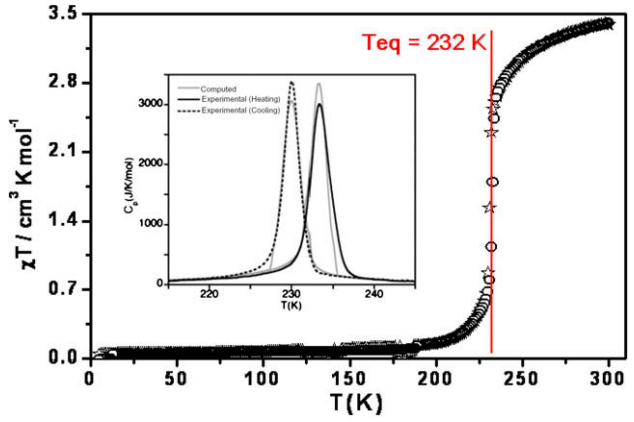


Fig. 1. The steep thermal transition with narrow hysteresis ~2 K wide, showing the presence of elastic interactions. Inset: calorimetric data (after [2]).

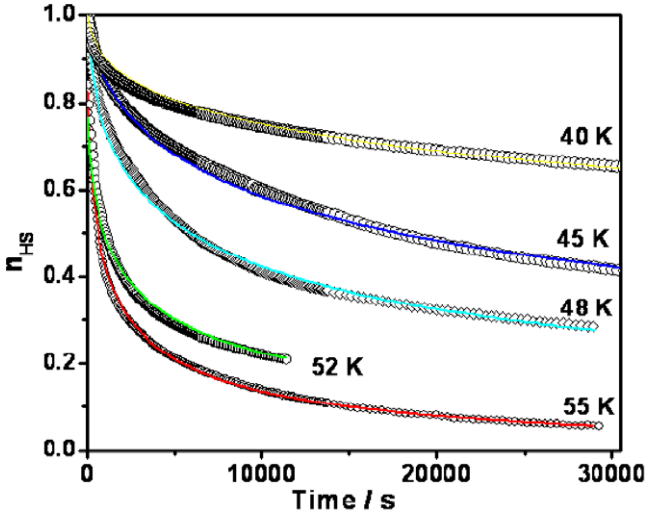


Fig. 2. Isothermal relaxation curves independently fitted by macroscopic Gaussian distributions of barrier energies, in absence of elastic interactions (after [2]).

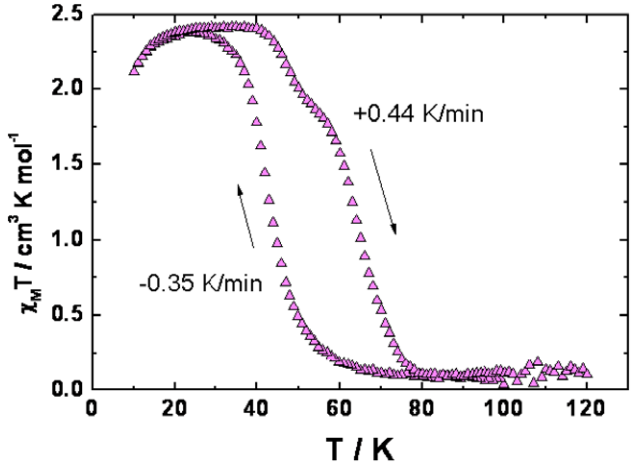


Fig. 3. The light-induced thermal hysteresis (LITH) loop of the compound under permanent laser irradiation (514.5 nm, 25 mW) (present work).

("macroscopic") distributions. We focus on the static hysteresis loop and the set of isothermal relaxation curves with the goal of elucidating the problem of the correlations between the parameters of opposite or identical effects. By the way, we found the present results poorly consistent with the LITH and T(LIESST) experimental data of the present compound, and we suggest here possible underlying mechanisms for explaining the observed discrepancies.

1.1. Mean-field model with short- and long-range distributions of parameters

At variance from the first macroscopic model developed by Hauser [10], we take advantage of the Master Equation formalism which provides a straightforward solution for both the dynamic and static case (the latter is obtained at the limit of vanishing temperature scan rate). Simple analytical considerations showing how the static case can be derived from the master equation can be found in [11]. The master equation writes (after [11])

$$dn/dt = [1 - n(t)][I_{LH}\eta_{LH}\sigma_{LH} + k_{LH}(T,n)] - n(t)[I_{HL}\eta_{HL}\sigma_{HL} + k_{HL}(T,n)], \quad (1)$$

where, $n = n_{HS}$ is the population of the metastable state and $I_{LH}\eta_{LH}\sigma_{LH}$, $I_{HL}\eta_{HL}\sigma_{HL}$ are the photo-excitation terms accounting for light intensities, quantum yields and absorption cross sections; k_{HL} and k_{LH} are the $HS \rightarrow LS$ and $LS \rightarrow HS$ relaxation rate constants, respectively.

The assumption of a linear dependence of the barrier energy on the population of the metastable state leads to simple mean-field expressions of the $HS \rightarrow LS$ cooperative relaxation rate [12]. The present expressions refer to the properties of isolated molecules, obtained when the effects of *HS* and *LS* neighboring molecules cancel each other (that is, when $n = 1/2$)

$$k_{HL}(T,n) = k_{HL}(T,1/2)\exp[-\alpha(n-1/2)], \quad (2)$$

$$k_{LH}(T,n) = k_{LH}(T,1/2)\exp[+\alpha(n-1/2)] \quad (3)$$

where, the ± signs in the exponential factors result from opposite variations of the E_{HL} and E_{LH} barrier energies driven by the internal pressure effect. The self-acceleration parameter α is associated with elastic interactions in the solid. In the thermal activation regime, according to both experiments [13], mean-field [12,14] and microscopic [15] models, it is written

$$\alpha = 2zJ/k_B T \quad (4)$$

with z the number of interacting neighbors, and J the intermolecular interaction parameter. Accordingly, the relaxation rate constants are written

$$k_{HL}(T,n) = k_\infty \exp(-E_{HL}/k_B T)\exp[-\alpha(n-1/2)] \quad (5)$$

$$k_{LH}(T,n) = g k_\infty \exp(-E_{LH}/k_B T)\exp[+\alpha(n-1/2)] \quad (6)$$

with $g = g_{HS}/g_{LS}$ the "effective" degeneracy ratio of the states, accounting for both electronic and vibrational effects [16].

In addition to the thermal contribution to the relaxation process, we also considered a tunneling contribution, phenomenologically written

$$k_{HL}(\text{tunnel}) = k_0 \exp(-\alpha_0 n) \quad (7)$$

where, the values given to the constants $k_0 = 5 \cdot 10^{-6}\ s^{-1}$, $\alpha_0 = 19$ mainly arises from the analysis of the 20 K relaxation curve (see below).

The numerical resolution of the master equation is straightforward. Time is incremented by suited values $dt \sim 0.01'$ or longer, according to the evolution rate of the system. At time t, dn/dt is computed using $n(t)$ values so as to obtain $n(t + dt)$.

In the present work, the system is considered to be made up of independent domains possessing similar spreading of their param-

eters around different central values. Intra-domain parameter spreading will be denoted "short-range distribution", and the inter-domain one, "long-range distribution", corresponding to the "microscopic" and "macroscopic" variants of the model, respectively. As in Ref. [2] we considered Gaussian distributions of the barrier energy E_{HL} for the low temperature kinetic properties, and of the energy gap Δ_{el} for the thermal transition. These distributions are characterized by their standard deviations denoted σ_{SR}, σ_{LR}. The possible relationship between the E_{HL} and Δ_{el} distributions was discussed in [2], and will not be addressed here.

Models including short-range distributions basically differ from the usual macroscopic models which are based on long-range distributions. The latter describe independent domains in the sample and lead to a set of independent macroscopic equations which can be solved straightforwardly in both the static and the dynamic cases. On the contrary, the "short-range" models lead to a set of coupled equations because the self-acceleration factor $\alpha\ (n - 1/2)$ is calculated in average over the different spin-crossover units (according to the mean-field approximation). The set of coupled equations is not tractable in the static case. But, we easily solve the problem numerically in the dynamic case thanks to the Master Equation formalism, and the (quasi) static case is obtained at the limit of vanishing temperature scan rates. It is worth noting that in absence of interactions the difference vanishes between macroscopic and microscopic models, as long as the thermal activation process is considered alone. Indeed, when the tunnel contribution is introduced, as tiny difference appears due to the separate treatment of the tunneling terms in the independent domains.

In practice, the total system is divided into 40 domains, each of them being divided into 40 different spin-crossover sites representing the microscopic (short-range) distribution. For convenience, the distributions are introduced using a Gaussian histogram which gives equal weights to all fractions. For each domain, the set of coupled equations is treated numerically at each time step of the simulation. The different domains are treated separately, and finally the average value of the HS fraction over all domains is expressed.

2. Results and discussion

We show in Figs. 4 and 5 the transition curve of the compound, modeled with the microscopic variant of the model (Fig. 4, after [2]), taking into account both short-range and long-range distributions (Fig. 5). Obviously, the short- and long-range distributions have different impacts. The short-range distribution merely competes against the long-range interaction but does not impede the abrupt character of the transition. In other words, the short-range distribution effect is averaged by the long-range character of the interaction, and only tends to decrease the final cooperativity of the transition. The parameters associated with interactions (zJ) and short-range distribution ($\sigma_{SR}(\Delta_{el})$) cannot be measured separately. They are strongly correlated. On the other hand, the long-range distribution does not reduce the cooperativity of the transition, it trivially gives the hysteresis loop a bent character and can be determined separately.

The experimental data were fitted at best by combining short- and long-range distributions with various values of the interaction parameter zJ, see Fig. 5. There is no sizable correlation between $\sigma_{LR}(\Delta_{el})$ and the set of strongly correlated parameters zJ, $\sigma_{SR}(\Delta_{el})$. Only $\sigma_{LR}(\Delta_{el}) \approx 5$ K was unambiguously determined.

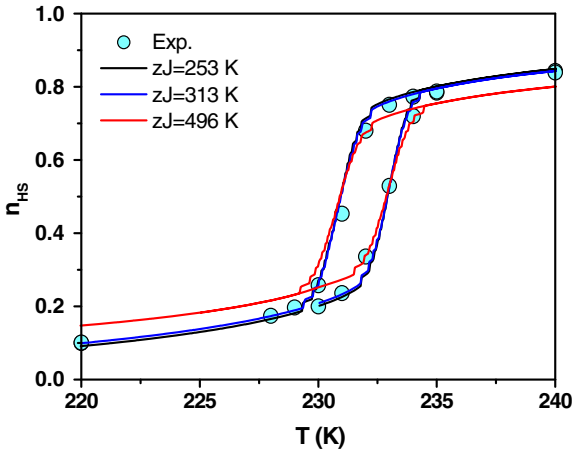


Fig. 5. The hysteresis loop of the spin transition, modeled using the present model, with $\sigma_{LR}(\Delta_{el}) = 5$ K and the sets of parameters: $zJ = 253$ K, $\sigma_{SR}(\Delta_{el}) = 0$ K (black curve); $zJ = 313$ K, $\sigma_{SR}(\Delta_{el}) = 260$ K (blue curve); $zJ = 496$ K, $\sigma_{LR}(\Delta_{el}) = 640$ K (red curve). The stepped character of the curves is due to the discretization of the "macroscopic" Gaussian distribution. (For interpretation of the references to colour in this figure legend, the reader is referred to the web version of this article.)

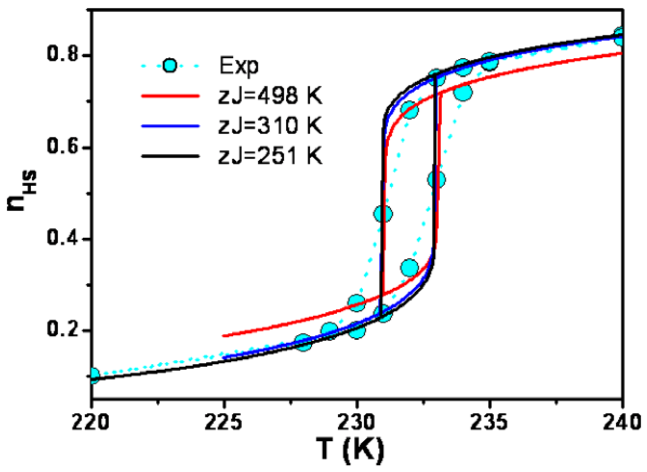


Fig. 4. The hysteresis loop of the spin transition, modeled using the microscopic variant of the model, with the sets of parameters: $zJ = 251$ K, $\sigma_{SR}(\Delta_{el}) = 0$ K (black curve); $zJ = 310$ K, $\sigma_{SR}(\Delta_{el}) = 260$ K (blue curve); $zJ = 498$ K, $\sigma_{SR}(\Delta_{el}) = 640$ K (red curve) (after [2]). (For interpretation of the references to colour in this figure legend, the reader is referred to the web version of this article.)

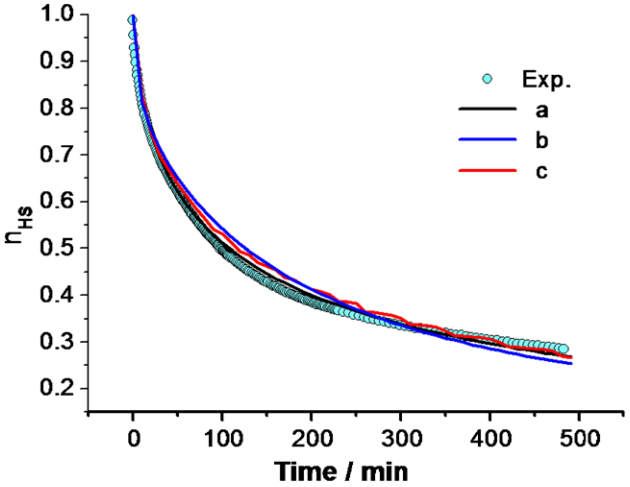


Fig. 6. A typical relaxation curve, in shape of stretched exponential, with fitted curves using the present model. The parameter values are given in Table 1. *(a) non-cooperative, (b) microscopic distribution, (c) macroscopic distribution.* The stepped character of the last curve reflects the discretization of the Gaussian distribution: the computed curve is an envelop of sigmoidal curves.

Table 1
Fitted parameters for the relaxation curve at 48 K (Fig. 6), with model including the tunnel contribution. The χ^2 (variance) parameter refers to a small number of data, corresponding to n_{HS} values in arithmetic progression (0.9, 0.8, 0.7,...).[a]

zJ (K)	σ_{SR} (E_{HL}) (K)	σ_{LR} (E_{HL}) (K)	k_{HL} (48 K, n = 1/2) (s^{-1})	$\chi 2$ (arb.units)	Fig.
0	102	0	$9.1 \cdot 10^{-5}$	54	Fig. 6a
	0	102	$8.9 \cdot 10^{-5}$	56	(black)[b]
125	185	0	$1.5 \cdot 10^{-4}$	181	
250	272	0	$2.0 \cdot 10^{-4}$	409	Fig. 6b
					(blue)[b]
125	0	118	$3.14 \cdot 10^{-4}$	62	
250	0	127	$1.95 \cdot 10^{-3}$	63	Fig. 6c (red)[b]

[a] Underlined values were fixed.
[b] For interpretation to color in Fig. 6, the reader is referred to the web version of this article.

A typical relaxation curve is shown in Fig. 6, with computed curves according to various assumptions, which are summarized in Table 1. It is observed that the relaxation curve does not allow to discriminate the short-range or long-range character of the E_{HL} distributions, which remain tightly correlated to the zJ value. The presence of interactions is hidden by the distribution effects. In other words, the sigmoidal character of cooperative relaxation is blurred out by the stretchening effect of the distributions. For example the non-cooperative solution (top row) and the cooperative solution with zJ = 250 K (bottom row) can be accepted as well due to their similar χ^2 values. In Table 1 it can be observed that the relationships between zJ and $\sigma_{SR}(E_{HL})$ or $\sigma_{LR}(E_{HL})$ are somewhat different.

The strong impact of the present indetermination upon k_{HL} makes it extremely unsafe for any further determination of E_{HL} and k_∞ using the familiar Arrhenius plot. Instead, the global fitting of the whole set of relaxation curves is needed. Several attempts have been made which are shown in Fig. 7, with the fitted parameter values listed in Table 2. It can be observed that a rough agreement is obtained is all cases (cooperative, non-cooperative, short-range or long-range disorder). However the agreement is sizably better when interactions are not taken into account. This is indeed a puzzling result with respect to the existence of the LITH loop. In addition, the "best-fit" value of the limiting frequency, $k_\infty \sim 20\ s^{-1}$,

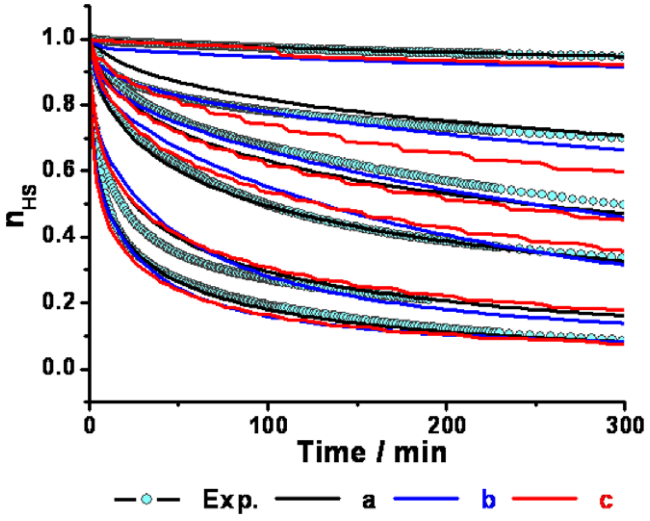


Fig. 7. Global fitting of the set of isothermal curves, for selected set of parameters listed in Table 2. *(a) non-cooperative, (b) microscopic distribution, (c) macroscopic distribution.* The difference with the previous fitting of the 48 K curve originates from the choice of a logarithmic time scale for fine-tuning the parameters, which puts the emphasis on the short-time data.

Table 2
Fitted parameters for complete set of relaxation curves (Fig. 7). χ^2 here is the sum of variances at all temperatures, for time values in the same geometric progression (t = 1, 3, 9, 27,... min.).[a]

zJ (K)	σ_{SR} (E_{HL}) (K)	σ_{LR} (E_{HL}) (K)	$\langle E_{HL} \rangle$ (K)	k_∞ (s^{-1})	χ^2 (arb.units)	Fig.
0	144	0	1126	$8.\ 10^5$	263	
0	124	0	899	$1.\ 10^4$	124	
0	110	0	734	400	81	
0	105	0	664	100	74 ~ min	Fig. 7a
						(black)[b]
	0	103	665	100	76 ~ min	
0	99	0	584	20	87	
250	268	0	562	20	139	
250	260	0	480	4	117	
250	252	0	410	1	113 ~ min	Fig. 7b (blue)[b]
250	244	0	330	0.2	135	
250	0	155	476	20	179	
250	0	148	389	4	146	
250	0	140	319	1	125	
250	0	126	231	0.2	122 ~ min	Fig. 7c (red)[b]
250	0	118	166	0.05	135	

[a] Underlined values were fixed.
[b] For interpretation to color in Fig. 7, the reader is referred to the web version of this article.

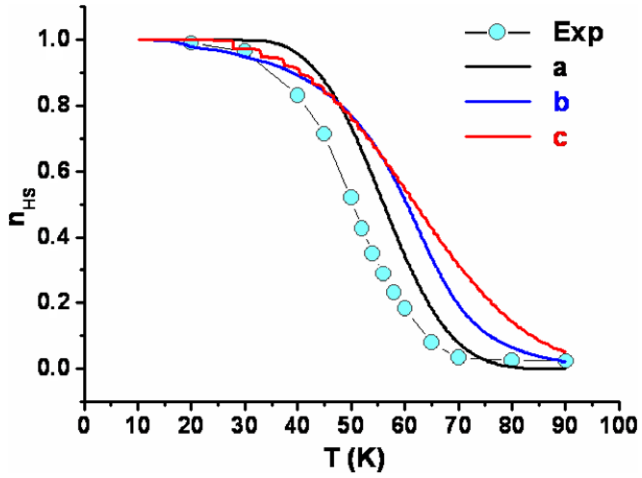


Fig. 8. The experimental T(LIESST) curve recorded in the dark at scan rate 0.3 K/min (after [2]), and simulations using the sets of parameters selected in Table 2. *(a) non-cooperative, (b) microscopic distribution, (c) macroscopic distribution.*

is incredibly low with respect to the molecular vibration frequencies which are usually relevant to the relaxation process [17]. This low value cannot be ascribed, as in previous works, to the vicinity of the tunneling regime, since the tunneling contribution has been explicitly accounted for. A possible explanation might be the presence of a strong "tail effect", resulting from the onset of correlations [18] due to short-range interactions, which mainly develop at long times [19] and may contribute to the stretched shape of the relaxation curves. Further experiments following the strategy defined in [18], are needed for establishing this crucial point.

3. Discussion

We were intrigued by the unusually low value of the frequency factor (k_∞) and because of that we tried to simulate experimental data further, see Figs. 8 and 9. The T(LIESST) procedure [20] provides a convenient fingerprint of the thermal activation of relaxation, and the LITH loop was previously shown as a solid cue for the presence of interactions in the system. A glance at Figs. 8 and

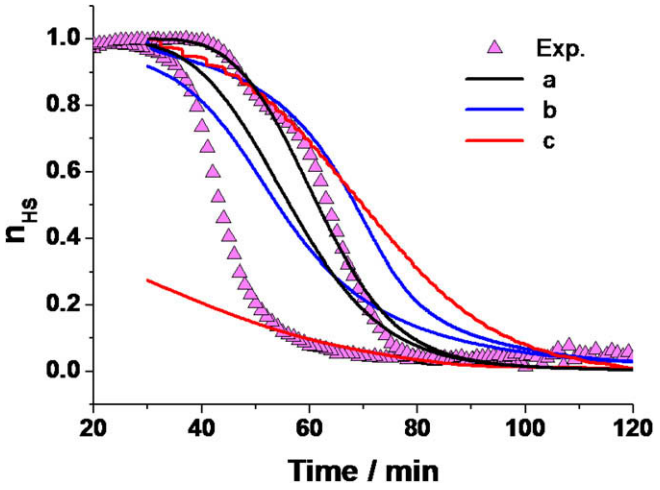


Fig. 9. The experimental LITH loop and simulations using the sets of parameters selected in Table 2. *(a) non-cooperative, (b) microscopic distribution, (c) macroscopic distribution.*

9 show strong discrepancies. Fig. 8 shows that the timescale is not convenient and explains why a lower barrier energy had to be assigned to the T(LIESST) process in Ref. [2]. Fig. 9 confirms the unconvenience of the timescale and suggests that strong interactions and distributions of short- and long-range character are both present.

We have also performed independent analyses of the T(LIESST) curve and LITH loop, and obtained conclusions somewhat similar to those obtained in the previous section: the T(LIESST) does not lift the correlations between the interaction and distribution parameters. The LITH loop is more informative and disentangles the short-range distribution effect from the correlated set of parameters: mean-field interaction and short-range distribution parameter. We present the LITH data in Fig. 10, along with the T(LIESST) curves simulated using the same sets of parameters, which are listed in Table 3. The figure shows the T(LIESST) and LITH data are rather coherent with each other, from the viewpoint of the timescale. It also suggests that the LITH process is slightly more cooperative than the T(LIESST) one.

The discrepancies evident in Figs. 8 and 9 might be attributed to the tail effect (short-range interactions) already quoted, which

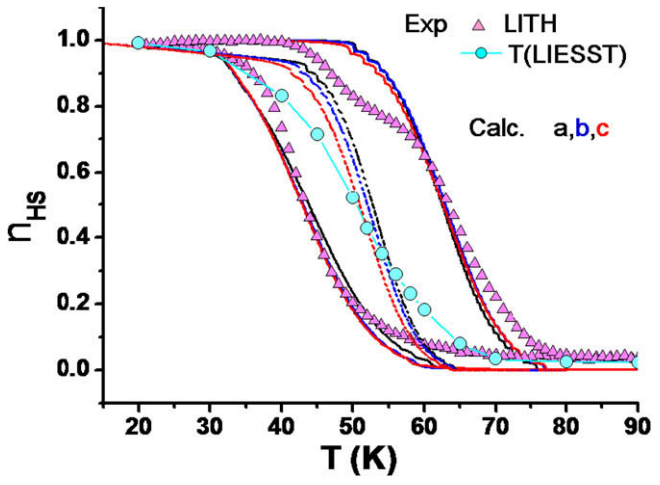


Fig. 10. The experimental LITH loop fitted by independent simulations (full lines), and the resulting simulated T(LIESST) curves (dotted lines). The sets of parameters are listed in Table 3.

Table 3
Selected sets of parameters for the best overlap of the LITH loop (Fig. 10).[a]

zJ (K)	σ_{SR} (E_{HL}) (K)	σ_{LR} (E_{HL}) (K)	$\langle E_{HL} \rangle$ (K)	k_∞ (s^{-1})	Fig.
310	0	80	805	40000	
285	0	80	720	8000	
260	0	80	635	1600	Fig. 10a (black)[b]
350	110	80	630	1600	Fig. 10b (blue)[b]
450	190	80	625	1600	Fig. 10c (red)[b]

[a] Underlined values were fixed.
[b] For interpretation to color in Fig. 10, the reader is referred to the web version of this article.

only occurs at long times, and tend to slowdown the relaxation process. Theoretical work on the grounds of Ref. [19] is needed for investigating the possible impact of short-range interactions on the T(LIESST) curve and LITH loop. It is speculated that such correlations should not occur to a large extent in both experiments, because of the random effect of light [21] on the LITH loop and relatively shorter time needed for recording the T(LIESST) curve at usual scan rate (0.3 K/min). An alternative or complementary origin of the discrepancies might be the coupling between the spin equilibrium and the structural effects associated with the temperature-dependent orientational disorder of the solvent molecules and anions, observed in [2]. The presence of a structural reorganisation might contribute to the slow but strongly cooperative character of the relaxation process, in addition to the relaxation tail effect. Unfortunately the crystallographic structure of the photoexcited state could be not determined, due to the loss of quality induced by the thermal transition on cooling the crystal [2].

4. Conclusion and prospects

We have shown that a square-shaped hysteretic transition can hide short-range disorder which is "averaged" by the mean-field treatment of the long-range elastic interaction. Conversely, stretched relaxation curves can hide disorder, at both the long and short ranges. Disorder and interactions have opposite effects, which can hardly be disentangled. In other words, the fitting of relaxation curves is an over-parameterised problem when interactions and disorder coexist. The effect of short-range interactions which enhance the stretched character of the relaxation curves remains to be investigated and increases the complexity of the problem.

For the present compound, we have found sizable discrepancies between the refined data of the relaxation curves, the T(LIESST) curve, and LITH loop. Further experiments are planned for evidencing the eventual presence of short-range interactions, and for investigating the possible influence of a structural transformation coupled with the spin state switching.

Acknowledgements

CNRS, Université de Versailles Saint Quentin, Indo-French Center for Advanced Research, European Network of Excellence MAGMANet, and Prof. K. Boukheddaden for useful discussions.

References

[1] P. Gütlich, in: P. Gütlich, H. Goodwin (Eds.), Topics in Current Chemistry: Spin Crossover in Transition Metal Compounds, 2004, 233, p. 1.
[2] V. Mishra, R. Mukherjee, J. Linares, C. Balde, C. Desplanches, J.-F. Létard, E. Collet, L. Toupet, M. Castro, F. Varret, Inorg. Chem. 47 (2008) 7577.
[3] (a) J. Wanjflasz, R. Pick, J. Phys. Colloid 32 (1971) C1;
(b) A. Bousseksou, J. Nasser, J. Linares, K. Boukheddaden, F. Varret, J. Phys. I 2 (1992) 1381.
[4] S. Singh, V. Mishra, J. Mukherjee, N. Seethalekshmi, R. Mukherjee, Dalton Trans. (2003) 3392.

[5] B. A Leita, S.M. Neville, G.J. Halder, B. Moubaraki, C.J. Kepert, J.-F. Létard, K.S. Murray, Inorg. Chem. 46 (2007) 8784.
[6] J.-F. Létard, P. Guionneau, L. Rabardel, J.A.K. Howard, A.E. Goeta, D. Chasseau, O. Kahn, Inorg. Chem. 37 (1998) 4432.
[7] (a) A. Desaix, O. Roubeau, J. Jeftic, J.G. Haasnoot, K. Boukheddaden, E. Codjovi, J. Linarès, M. Noguès, F. Varret, Eur. Phys. J. B 6 (1998) 183;
(b) F. Varret, K. Boukheddaden, J. Jeftic, O. Roubeau, J. Mol. Cryst. Liq. Cryst. 335 (1999) 1273.
[8] (a) S. Gawali-Salunke, F. Varret, I. Maurin, M. Malarova, C. Enachescu, K. Boukheddaden, E. Codjovi, H. Tokoro, S. Ohkoshi, K. Hashimoto, J. Phys. Chem. B 109 (2005) 8251;
(b) M. Castro, J.M. Rodríguez-Velamazán, K. Boukheddaden, F. Varret, H. Tokoro, S. Ohkoshi, Eur. Phys. Lett. 79 (2007) 27007.
[9] (a) H. Spiering, in: P. Gütlich, H. Goodwin (Eds.), Topics in Current Chemistry: Spin Crossover in Transition Metal Compounds, 2004, 234, p. 129.;
(b) K.S. Murray, C.J. Kepert, in: P. Gütlich, H. Goodwin (Eds.), Topics in Current Chemistry: Spin Crossover in Transition Metal Compounds, 2004, 233, p. 195.
[10] A. Hauser, J. Adler, P. Gütlich, Chem. Phys. Lett. 152 (1988) 468.
[11] F. Varret, K. Boukheddaden, E. Codjovi, I. Maurin, H. Tokoro, S. Ohkoshi, K. Hashimoto, Polyhedron 24 (2005) 2857.
[12] A. Hauser, P. Gutlich, H. Spiering, Inorg. Chem. 25 (1986) 4245.
[13] C. Enachescu, J. Linares, F. Varret, J. Phys.: Condens. Matter 13 (2001) 2481.
[14] F. Varret, S. Arun Salunke, K. Boukheddaden, A. Bousseksou, E. Codjovi, C. Enachescu, J. Linares, C.R. Chim. 6 (2003) 395.
[15] K. Boukheddaden, I. Shteto, B. Hôo, F. Varret, Phys. Rev. B 62 (2000) 14796.
[16] A. Bousseksou, H. Constant-Machado, F. Varret, J. Phys. I 5 (1995) 747.
[17] A. Hauser, Coord. Chem. Rev. 111 (1991) 275.
[18] H. Romstedt, H. Spiering, P. Gütlich, J. Phys. Chem. Solids 59 (1998) 1353.
[19] B. Hôo, K. Boukheddaden, F. Varret, Eur. Phys. J. B 17 (2000) 449.
[20] J-F Létard, P. Guionneau, L. Rabardel, J.A.K. Howard, A.E. Goeta, D. Chasseau, O. Kahn, Inorg. Chem. 37 (1998) 4432.
[21] A. Hauser, J. Phys. Chem. Solids 59 (1998) 1353.



Fig. 1. The three elastic constants in function of the two neighbor atoms spin state.

$$H_{phon} = E_c + E_p, \tag{2}$$

is the phonon Hamiltonian.

The chain potential energy:

$$E_P = \sum_{i=1}^{N} \frac{1}{2} e_{i,i+1} q_i^2, \tag{3}$$

where $q_i = u_{i+1} - u_i$ is the displacement of the ith atom from its equilibrium position which we assume to be independent of the electronic states of the atoms. Due to the periodic condition, $q_{p+N} = q_p$ for $p = 1, 2, \ldots, N$; and $e_{i,i+1}$ is elastic force constant which is given by

$$e_{i,i+1} = \frac{\lambda + 2\mu + \nu}{4} + \frac{\nu - \lambda}{4}(\hat{\sigma}_i + \hat{\sigma}_{i+1}) + \frac{\lambda - 2\mu + \nu}{4}\hat{\sigma}_i\hat{\sigma}_{i+1}. \tag{4}$$

The potential energy can be decomposed as

$$V_o = \sum_{i=1}^{N} \frac{\lambda + 2\mu + \nu}{8} q_i^2, \tag{5}$$

$$V_1 = \sum_{i=1}^{N} \frac{\nu - \lambda}{8}(q_1^2 + q_{i+1}^2)\hat{\sigma}_i, \tag{6}$$

$$V_2 = \sum_{i=1}^{N} \frac{\lambda - 2\mu + \nu}{8} q_i^2 \hat{\sigma}_i\hat{\sigma}_{i+1}, \tag{7}$$

V_1 has a Zeeman-like energy form; each spin $\hat{\sigma}_i$ is submitted to an effective field h_i given by:

$$h_i = \frac{\nu - \lambda}{8}(q_i^2 + q_{i+1}^2) = h_0(q_i^2 + q_{i+1}^2), \tag{8}$$

and V_2 has an exchange-like energy form. In the V_2 expression,

$$J_{i,i+1} = \frac{\lambda - 2\mu + \nu}{8} q_{i+1}^2 = J_0 q_{i+1}^2, \tag{9}$$

can be seen like a exchange parameter.

In the following we take $\hbar\omega_M(\lambda)$ as the unit energy, where $\omega_M(\lambda)$ is the maximum phonon frequency when the chain is periodic with an elastic force λ is given by $\omega_M(\lambda) = 2\sqrt{\frac{\lambda}{M}}$, where M is the atom mass.

In this contribution we introduce the same reduced parameters as in [6]:

- Reduced temperature: $t_r = \frac{k_B T}{\hbar\omega_M(\lambda)}$;
- The dimensionless electronic excitation energy: $\delta = \frac{\Delta}{\hbar\omega_M(\lambda)}$;
- The elastic force constant ratio: $x = \frac{\nu}{\lambda}$;
- The dimensionless parameter y defined by: $\mu = \frac{\lambda+\nu}{2} + \frac{\lambda-\nu}{2}y$.

3. Monte Carlo–Metropolis simulation for 1D spin crossover

The Metropolis algorithm provides most representative configurations of the thermodynamical system through a Markov chain of elementary transformations yielding a limit which corresponds to the canonical equilibrium distribution.

For finding all configurations, Metropolis et al. [10] proposed the using of a Markov configurations chain where ith configuration is obtained from $(i-1)$th configuration due to the near $W(i-1 \to j)$ transition probability. A sufficient condition for that, the states distributions generated to strive to the equilibrium one, when the number of configurations $N \to \infty$, is to satisfied the detailed balance equation.

$$P(i,T)W(i \to j,T) = P(j,T)W(j \to i,T) \tag{10}$$

From Eq. (16) one may observe that, the transition probabilities ratio for a $i \to j$ step and the inverse step $j \to i$ depends only on the ratio:

$$W(i \to j) = \begin{cases} 1 & \text{if } P(j) \geqslant P(i) \\ \frac{P(j)}{P(i)} & \text{if } P(j) < P(i) \end{cases}. \tag{11}$$

The probability $P(\alpha)$ of a configuration (α) is given by $P(\alpha) = \frac{e^{-\frac{E_\alpha}{k_B T}}}{Z}$, where E_α, the energy of the configuration, is the sum of the electronic and phonon energies.To obtain the phonon frequency of a chain, first we consider the dynamical equation for each atom's displacement u_i:

$$\begin{cases} M\ddot{u}_1 = e_{1,2}(u_2 - u_1) + e_{1,N}(u_N - u_1) \\ M\ddot{u}_2 = e_{2,3}(u_3 - u_2) + e_{2,1}(u_1 - u_2) \\ \vdots \\ M\ddot{u}_N = e_{1,N}(u_1 - u_N) + e_{N-1,N}(u_{N-1} - u_N) \end{cases}. \tag{12}$$

Then we construct the dynamical matrix of the system. The eigenvalues of this matrix are the phonon frequencies.

For each phonon frequency we obtain

$$\sum_{n=0}^{\infty} e^{-\beta\hbar w_i\left(n+\frac{1}{2}\right)} = \frac{1}{2\sinh\left(\frac{\beta\hbar w_i^\alpha}{2}\right)}, \tag{13}$$

and then for a chain of N atoms:

$$P(\alpha) = \frac{1}{Z} e^{-\beta\left(\frac{\Delta - k_B T \ln r}{2} m_\alpha\right)} \prod_{i=1}^{N} \left(\frac{1}{2\sinh\frac{\beta\hbar w_i^\alpha}{2}}\right), \tag{14}$$

where $m = <\hat{\sigma}>$.

Fig. 2 shows some typical results obtained for 1D spin crossover: no thermal hysteresis is obtained. In this "atom–phonon coupling" model, $x = \frac{\nu}{\lambda}$ affects at the same time the "short" and "long" range interactions but this last contribution is not enough to produce phase transition at 1D (see also [11]).

In order to reproduce thermal hysteresis for 1D systems, as has been obtained experimentally [12] we propose, as in [13,14] to introduce a long-range interaction $-G\langle\hat{\sigma}\rangle$.

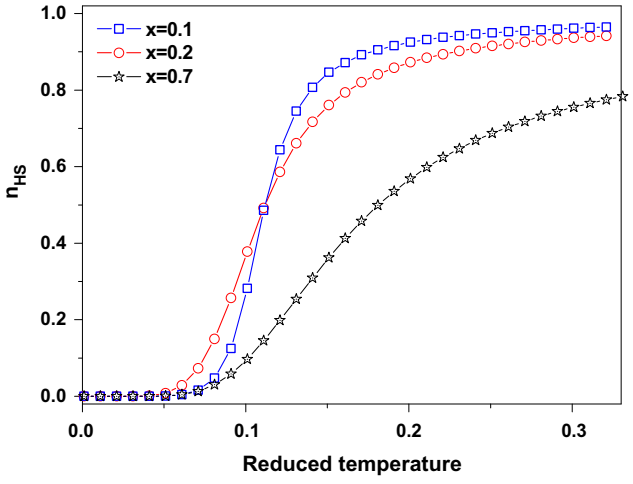


Fig. 2. The high spin fraction evolution in function of the reduced temperature, obtained for 1D system for different x values, using: $N = 100$ molecules, $y = 0$, $r = 15$, $\delta = 0.55$, $G = 0.0$.

This means that we consider that the molecular chains interact with each other. This long-range interaction is due to elastic coupling mediated by the lattice. The Hamiltonian for one chain of N atoms may be written in this case as

$$H = \sum_{i=1}^{N} \left(\frac{\Delta}{2} - G\langle\hat{\sigma}\rangle \right) \hat{\sigma}_i, \tag{15}$$

which means that Δ in the Eq. (1) must be replaced by $\Delta - 2 * G * \langle\hat{\sigma}\rangle$.

With this new long-range interaction parameter a thermal hysteresis is now obtained (see Fig. 3): it means, as has been noted in [13,14] a first-order phase transition accompanied by a hysteresis loop is obtained.

For a fixed G, y, r and Δ values, the width of the hysteresis loop is controlled by the x value as it is shown in Fig. 4. If we compare this result with what is reported in [13] we can conclude that $x = \frac{v}{\lambda}$ is essentially a "short-range" interaction type.

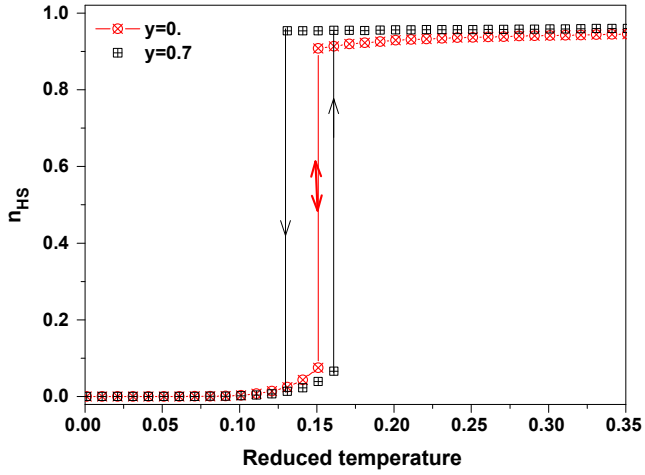


Fig. 3. The high spin fraction evolution in function of the reduced temperature, obtained for 1D system, for different y values, using: $N = 100$, $x = 0.4$, $r = 15$, $\delta = 0.55$, $G = 0.41$.

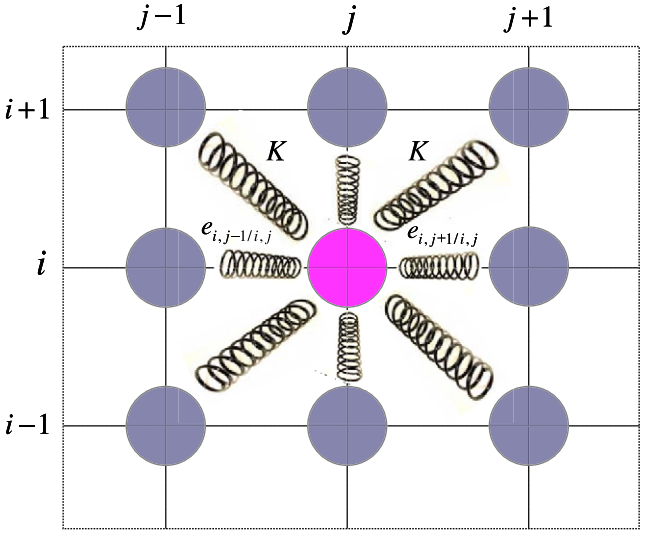


Fig. 4. The 2D network with the elastic constants corresponding to the nearest and the next-nearest neighbors.

4. Monte Carlo–Metropolis simulations for 2D spin crossover systems

The next step in our simulation is to consider a 2D square lattice of spin crossover compounds; nearest as well as next-nearest interactions have been taken into account. As we have assumed in the 1D case the elastic constant between nearest atoms is func-

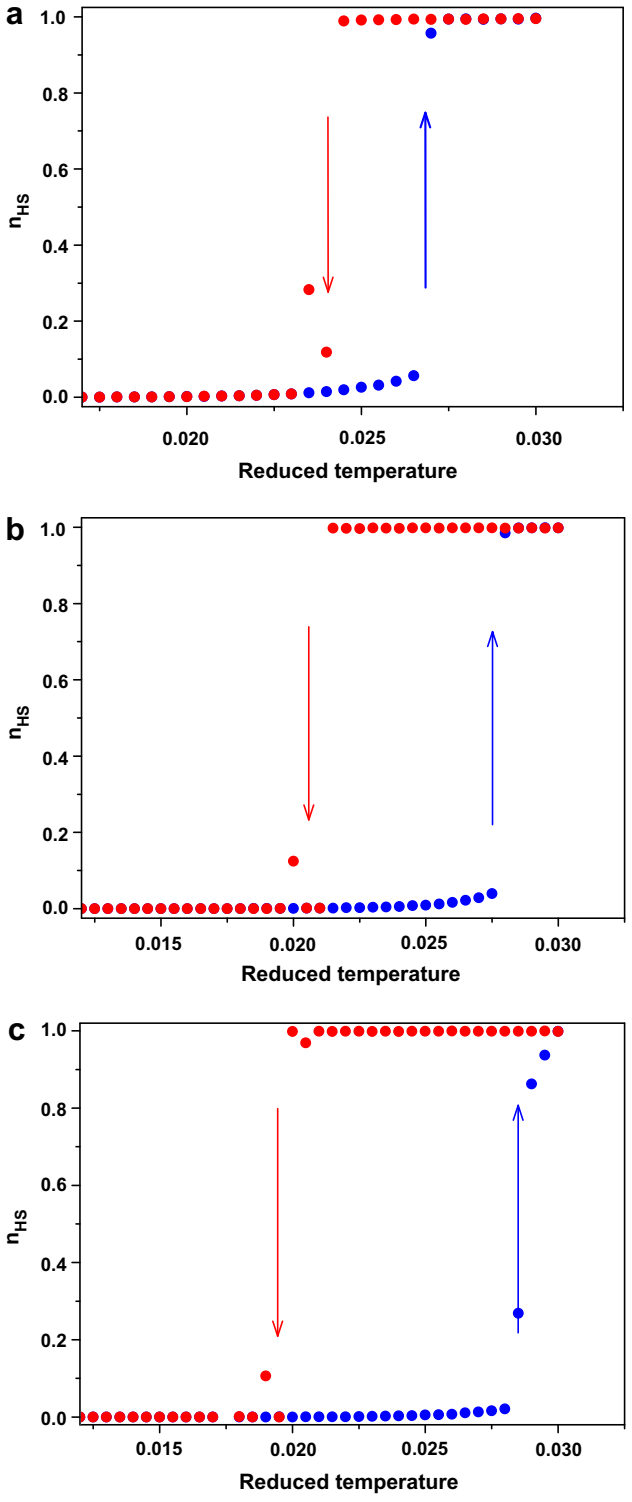


Fig. 5. The high spin fraction evolution in function of the reduced temperature, obtained for 2D system using: $N = 10 \times 10$, $x = 0.1$, $r = 15$, $\delta = 0.55$, K = 0.01 for (a) $y = 0.02$, (b) $y = 0.10$, (c) $y = 0.15$.

tion of the spin states of these atoms. The elastic constant for the next-nearest atoms are smaller than the previous one and in order to simplify the calculations we have taken this elastic constant as a constant K (see Fig. 4).

The dynamical equation for each displacement's atom and for a perpendicular wave is given by

$$m\ddot{\mathbf{u}}_{i,j} = \mathbf{I}_1 + \mathbf{I}_2, \tag{16}$$

with

$$\mathbf{I}_1 = e_{i-1,j/i,j}(\mathbf{u}_{i-1,j} - \mathbf{u}_{i,j}) + \mathbf{e}_{i,j+1/i,j}(\mathbf{u}_{i,j+1} - \mathbf{u}_{i,j}) + \mathbf{e}_{i+1,j/i,j}(\mathbf{u}_{i+1,j} - \mathbf{u}_{i,j}) + \mathbf{e}_{i,j-1/i,j}(\mathbf{u}_{i,j-1} - \mathbf{u}_{i,j}), \tag{17}$$

and

$$\mathbf{I}_2 = K(\mathbf{u}_{i-1,j} + \mathbf{u}_{i,j+1} + \mathbf{u}_{i+1,j} + \mathbf{u}_{i,j-1} - 4\mathbf{u}_{i,j}) \tag{18}$$

As for a one dimensional case, the eigenvalues of the dynamical matrix give the phonon frequencies. Fig. 5 shows a thermal hysteresis obtained for a square lattice with periodic conditions.

5. Conclusion

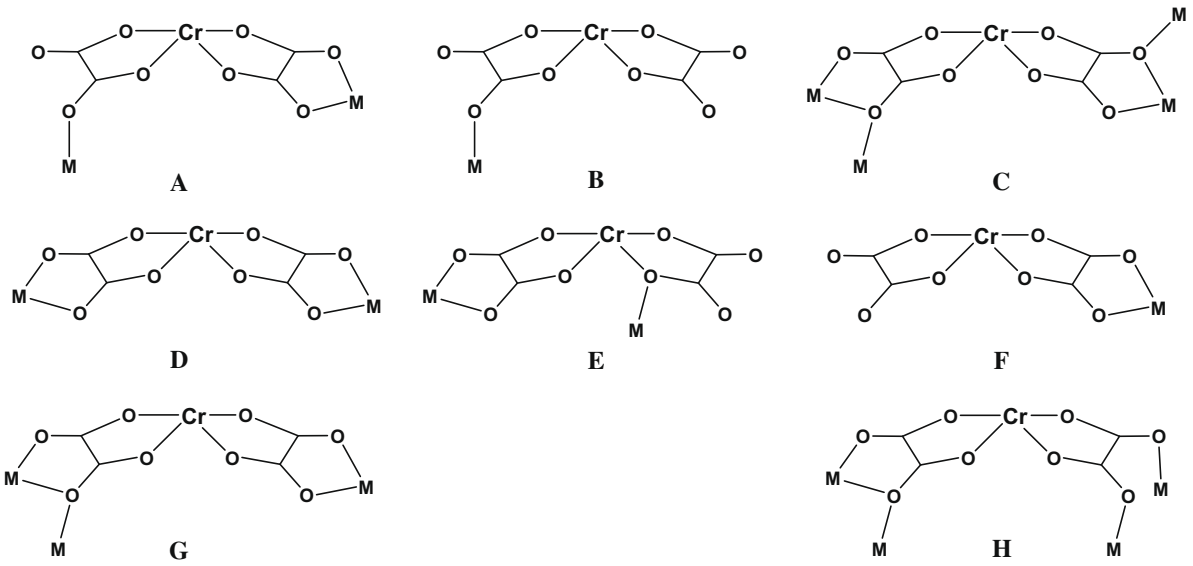
In the framework of the "atom–phonon coupling" model the thermal hysteresis is not obtained for a single chain. If we introduce a long-range interaction, which means to introduce interactions between the molecular chains, the hysteresis is reproduced. The rate of the ν and λ elastic constants parameters plays a crucial role in the hysteresis' width. For 2D spin crossover systems, the hysteresis is obtained without this G "long-range" interaction. In this case the $x = \frac{\nu}{\lambda}$ controls also the width of the hysteresis.

Acknowledgements

This work was partially supported by European Union FP6-Network of Excellence MAGMANET (Contract NMP3-CT-2005-515767-2), the program PHC/BRANCUSI (14737QG), and CNCSIS-IDEI FASTSWITCH grant.

References

[1] P. Gütlich, A. Hauser, H. Spiering, Angew. Chem. 106 (1994) 2109.
[2] A. Hauser, J. Jeftic, H. Romstedt, R. Hinek, H. Spiering, Coord. Chem. Rev. 190 (1999) 471.
[3] C. Enachescu, J. Linares, F. Varret, J. Phys.: Condens. Mat. 13 (2001) 2481.
[4] C.P. Slichter, H.G. Drickamer, J. Chem. Phys. 86 (1972) 2142.
[5] J. Wajnflasz, Phys. Status Solidi 40 (1970) 537.
[6] A. Bousseksou, J. Nasser, J. Linares, K. Boukheddaden, F. Varret, J. Phys. I2 (1992) 1381.
[7] S. Klokishner, J. Linares, J. Phys. Chem. C111 (2007) 10644.
[8] J. Nasser, Eur. Phys. J. B23 (2001) 3.
[9] J. Nasser, K. Boukheddaden, J. Linares, Eur. Phys. J. B39 (2004) 219.
[10] N. Metropolis, A.W. Rosenbluth, M.N. Rosenbluth, A.H. Teller, E. Teller, J. Chem. Phys. 21 (1953) 1087.
[11] K. Boukheddaden, S. Miyashita, M. Nishino, Phys. Rev. 75 (2007) 094112.
[12] Y. Garcia, V. Ksenofontov, G. Levchenko, P. Gütlich, J. Mater. Chem. 10 (2000) 2274.
[13] J. Linares, H. Spiering, F. Varret, Eur. Phys. J. B10 (1999) 271.
[14] K. Boukheddaden, J. Linares, H. Spiering, F. Varret, Eur. Phys. J. B15 (2000) 317.



Scheme 1.

well as other diamines, such as dipyridylamine, 2,2′-bipyrimidine), are extremely versatile tectons for the synthesis of heteropolynuclear complexes [7]. They exhibit various coordination modes toward the second metal ion. Those already observed experimentally are depicted in Scheme 1. We also have shown that the auxiliary ligands attached to the assembling cations play a crucial role in the self-assembly process [7].

Manganese(III) complexes with salen type ligands are valuable starting materials for obtaining heterometallic Mn(III)–M(II/III) complexes [9]. The related ligands obtained from *o*-vanillin (H_2valen being the simplest case) are largely used to obtain heterometal complexes, especially 3d–4f [10]. Others and we have shown that the second compartment, O_2O_2', when it is not occupied by a second metal ions, can act as a hydrogen bond acceptor, directing the packing of the molecules in the crystal [11].

Here we present the first oxalato-bridged Mn(III)–Cr(III) complexes, which are obtained by employing $[Cr(AA)(C_2O_4)_2]^-$ building-blocks. As assembling cation we employ a manganese(III) complex, $[Mn(valen)(H_2O)(CH_3CN)]^+$ (H_2valen is a bicompartmental Schiff-base proligand, resulting from the 2:1 condensation of 3-methoxysalicyladehyde with ethylenediamine).

2. Experimental

2.1. Synthesis

The manganese precursor, $[Mn(valen)(H_2O)(CH_3CN)](ClO_4)\cdot CH_3CN$, has been obtained as already reported [11c] The two chromium precursors were synthesized as described in previous papers[7c,d].

The two Mn(III)–Cr(III) compounds, $[\{Mn(H_2O)(valen)\}\{Cr(bipy)(C_2O_4)_2\}]\cdot 3H_2O$ **1** and $[\{Mn(H_2O)(valen)\}\{Cr(phen)(C_2O_4)_2\}]\cdot 3H_2O$ **2,** have been synthesized by the same procedure to a solution of $[Mn(valen)(H_2O)(CH_3CN)](ClO_4)\cdot CH_3CN$ (0.05 mmol) in 20 mL 1:1 CH_3CN/H_2O mixture, were added 20 mL solution of $AsPh_4[Cr(ox)_2(AA)]$ (0.05 mmol in 1:1 CH_3CN/H_2O mixture). The resulting brown solution was stirred for about 1.5 h and then filtered. The slow evaporation of the filtrate, at room temperature, yielded black crystals, suitable for X-ray diffraction. IR data (KBr, cm^{-1}): Compound **1**: 3413, 2926, 2854, 1719, 1680, 1620, 1551, 1468, 1439, 1398,1358, 1302, 1254, 1220, 850, 807, 739, 723, 550. Compound **2**: 3415, 2927, 2853, 1711, 1684, 1645, 1620, 1552, 1468, 1439, 1398, 1358, 1302, 1254, 1220, 850, 807, 739, 723, 550.

2.2. Physical measurements

The IR spectra were recorded on KBr pellets with a Bio-Rad FTS 135 spectrophotometer in the 4000–400 cm^{-1} range. Magnetic data were obtained with a Quantum Design MPMS SQUID susceptometer. Magnetic susceptibility measurements were performed in the 1.95–300 K temperature range in a 1000 Gauss applied magnetic field, and diamagnetic corrections were applied by using Pascal's constants.

2.3. X-ray crystallography

X-ray diffraction measurements were performed on Oxford Diffraction XCALIBUR diffractometer for **1,** and on a STOE IPDS II diffractometer for **2**, both operating with a Mo Kα (λ = 0.71073 Å) X-ray tube with a graphite monochromator. The structures were solved by direct methods and refined by full-matrix least squares techniques based on F^2. The non-H atoms were refined with anisotropic displacement parameters. Calculations were performed using SHELX-97 crystallographic software package.

3. Results and discussion

3.1. Crystal structures

The two new Mn(III)–Cr(III) complexes, $[\{Mn(H_2O)(valen)\}\{Cr(AA)(C_2O_4)_2\}]\cdot 3H_2O$, have been obtained by reacting $[Mn(valen)(H_2O)(CH_3CN)](ClO_4)\cdot CH_3CN$ with $AsPh_4[Cr(AA)(C_2O_4)_2]$ (AA = 2,2′bipyridine (bipy) **1**; 1,10-phenahroline (phen) **2**). During the assembling process, the anionic chromium complex replaces the acetonitrile molecule coordinated into the apical position of the Mn(III) ion. Since their molecular structures are quite similar, they will be discussed together Table 1.

The crystallographic investigation of the two compounds reveals neutral binuclear $[\{Mn(H_2O)(valen)\}\{Cr(AA)(C_2O_4)_2\}]\cdot$ species along with crystallization water molecules. The $[Cr(AA)(C_2O_4)_2]^-$ ion acts as a monodentate ligand through an oxalato oxygen atom toward the $\{Mn(valen)(H_2O)\}$ moiety (Scheme 1 **A**, Fig. 1). The intramolecular Cr···Mn distances are as follows 5.329

Table 1
Crystallographic data, details of data collection and structure refinement parameters for compounds **1** and **2**.

Compound	**1**	**2**
Chemical formula	$C_{32}H_{33}CrMnN_4O_{15.50}$	$C_{34}H_{26}CrMnN_4O_{16}$
M (g mol^{-1})	828.56	853.53
Temperature (K)	180	293
Wavelength (Å)	0.71073	0.71073
Crystal system	monoclinic	triclinic
Space group	$C2/c$	$P\bar{1}$
a (Å)	36.1488(10)	8.6265(10)
b (Å)	11.5215(3)	11.5294(13)
c (Å)	16.5434(5)	18.8783(19)
α (°)	90	87.203(9)
β (°)	105.682(3)	84.008(9)
γ (°)	90	70.425(9)
V (Å^3)	6633.7(3)	1759.2(3)
Z	8	2
D_{calc} (g cm^{-3})	1.659	1.611
μ (mm^{-1})	0.792	0.751
$F(000)$	3408	870
Goodness-of-fit on F^2	1.1136	0.867
Final R_1, wR_2 [$I > 2\sigma(I)$]	0.0275, 0.0300	0.0711, 0.1001
R_1, wR_2 (all data)	0.0608, 0.0497	0.1814, 0.1260
Largest difference in peak and hole (e Å^{-3})	0.32 and −0.40	0.438 and −0.408

(**1**); 5.442 Å (**2**). The manganese ions exhibit the characteristic elongated octahedral geometry, with two nitrogen and two oxygen atoms from the inner compartment of the Schiff-base ligand describing the basal plane, and one oxalato oxygen and one aqua ligand into the apical positions. The apical Mn–O(oxalato) distances for the two compounds are 2.2681(15) (**1**) and 2.289(3) Å (**2**), and the Mn–O(aqua) ones are 2.2767(15) (**1**) and 2.314(3) Å (**2**). The basal Mn–N and Mn–O distances are in the range 1.9697(18)–1.9820(17) Å, and, respectively, 1.8627(15)–1.8804(14) Å. The chromium atoms are coordinated by two nitrogen atoms arising from the chelating diamine, and by four oxalato oxygen atoms, adopting a distorted octahedral geometry. The short bites of the heterocyclic diamines and oxalato ligands are the main factors responsible for the distortion of the [CrN_2O_4] chromophore. The Cr–N bond distances (ave 2.045 for **1** and 2.066 Å for **2**] are somewhat longer than the Cr–O(ox) ones. The Cr–O bond distances are slightly shorter for the terminal oxalato ligand [ave 1.949 Å for **1**, and 1.946 Å for **2**] than for the bridging ones [ave 1.961 for **1**, and 1.968 Å for **2**]. Selected bond distances and angles are gathered in Table 2.

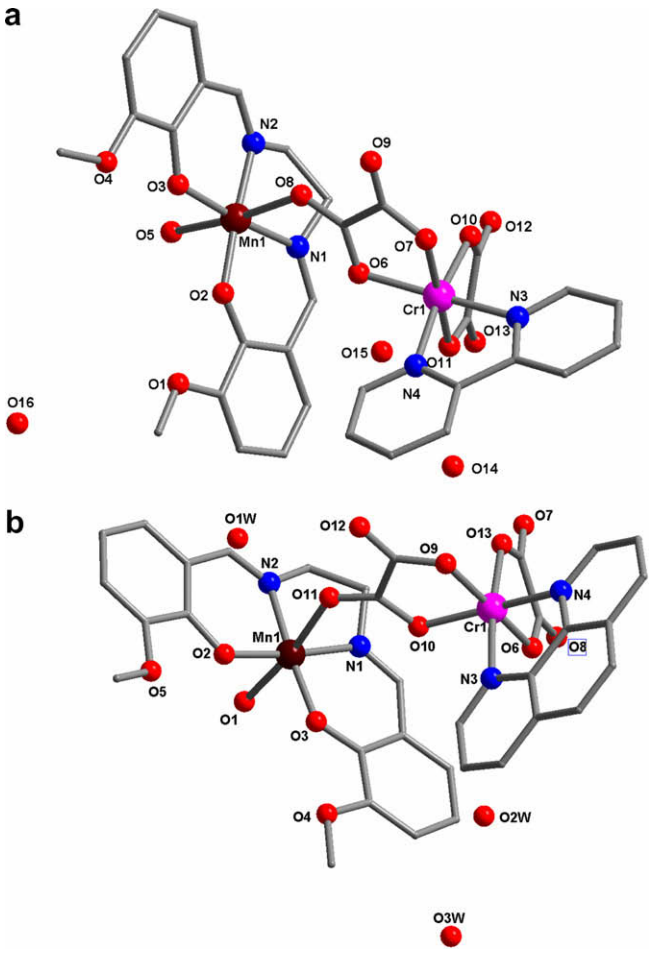
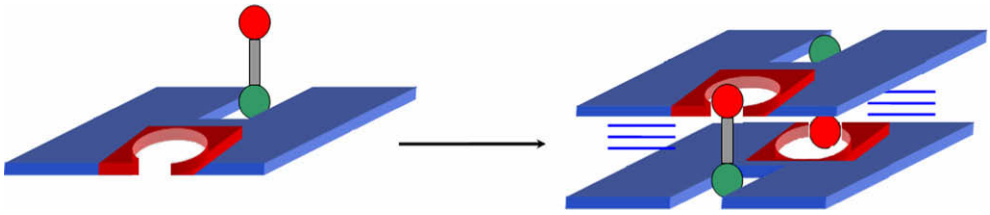


Fig. 1. Perspective view of the binuclear complexes (a) [{Mn(H_2O)(valen)}{Cr(bipy)(C_2O_4)$_2$}] **1**; (b) [{Mn(H_2O)(valen)}{Cr(phen)(C_2O_4)$_2$}] **2**.

The central problem in crystal engineering concerns the control over the intermolecular forces, especially the strongly directional ones, that allows the construction of crystals with desired structures and properties. For compounds **1** and **2**, the packing of the molecules in the crystal, up to certain level, can be easily predicted. There are two organizing forces intervening here: hydrogen bond and $\pi-\pi$ stacking interactions. In a preceding paper [11c], we have shown that the {Mn(valen)(H_2O)} moieties are self-complementary, that is, the aqua ligand from one moiety is hydrogen bonded to the oxygen atoms from the free O_2O_2' compartment of another one (Scheme 2). Moreover, the stability of the resulting dimer of complexes is reinforced by $\pi-\pi$ stacking interactions established between the aromatic rings of the Schiff-base ligands. Let us take the case of compound **1**. The {Mn(valen)(H_2O)} moieties from two [MnCr] units are hydrogen bonded, as expected, resulting in a tetranuclear supercomplex (Fig. 2a). These dimers are then interconnected through aromatic interactions occurring between the bipy ligands coordinated to the chromium ions (3.38–3.91 Å). Supramolecular chains are thus formed (Fig. 2a). This structural

Table 2
Selected bond distances and angles for compounds **1** and **2**.

1		**2**	
Mn1–O8	2.2681(15)	Mn1–O11	2.289(3)
Mn1–O5	2.2767(15)	Mn1–O1	2.314(3)
Mn1–N2	1.9697(18)	Mn1–N1	1.976(4)
Mn1–N1	1.9820(17)	Mn1–N2	1.982(4)
Mn1–O3	1.8804(14)	Mn1–O2	1.877(3)
Mn1–O2	1.8627(15)	Mn1–O3	1.873(3)
Cr1–O6	1.9638(15)	Cr1–N3	2.070(5)
Cr1–O7	1.9595(14)	Cr1–N4	2.063(5)
Cr1–O10	1.9463(16)	Cr1–O13	1.950(4)
Cr1–O11	1.9532(15)	Cr1–O6	1.943(4)
Cr1–N3	2.0408(17)	Cr1–O9	1.976(4)
Cr1–N4	2.0499(18)	Cr1–O10	1.960(4)
O3–Mn1–O5	91.96(6)	O1–Mn1–O2	90.19(14)
O5–Mn1–O2	92.82(6)	O2–Mn1–N2	91.51(15)
O2– Mn1–N1	92.00(7)	N2–Mn1–O11	84.51(14)
N1– Mn1–O8	92.63(6)	O11–Mn1–N1	89.02(15)
O8– Mn1–N2	87.87(6)	N1–Mn1–O3	91.78(15)
N2– Mn1–O3	91.28(7)	O3–Mn1–O2	93.35(14)
N2– Mn1–O2	174.83(7)	O1–Mn 1–O11	172.49(12)
O5–Mn1–O8	173.71(6)	N2–Mn1–O3	175.13(18)
O3–Mn1–N1	174.22(7)	O2–Mn1–N1	174.23(15)
N4–Cr1–N3	79.05(7)	O9–Cr1–O10	82.53(16)
O6–Cr1–O7	82.04(6)	O10–Cr1–N3	92.49(18)
O11–Cr1–O10	83.12(6)	N3–Cr1–O6	92.16(17)
O7–Cr1–O10	91.99(6)	O6–Cr1–O13	83.10(18)
O10–Cr1–N3	95.35(7)	O6–Cr1–N4	97.23(19)
N4–Cr1–O11	91.66(7)	N4–Cr1–O13	96.1(2)
O11–Cr1–O6	94.19(6)	O13–Cr1–O9	91.88(17)
O6–Cr1–N4	97.23(19)	N3–Cr1–N4	80.0(2)



Scheme 2.

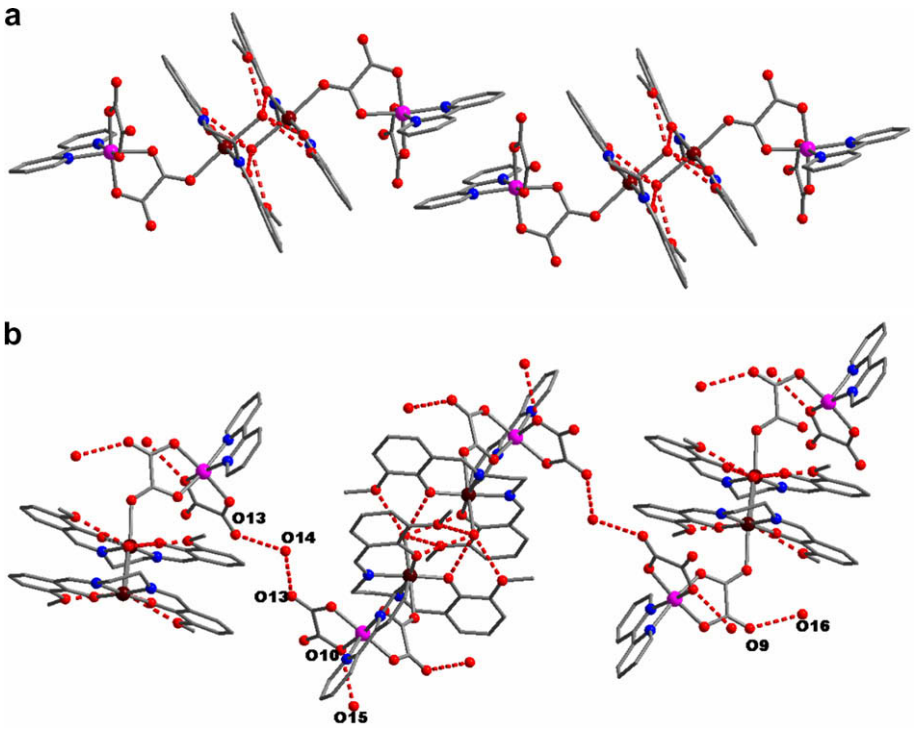


Fig. 2. Packing diagram for crystal **1**: (a) formation of the tetranuclear supercomplex and of the supramolecular chains through aromatic interactions; (b) hydrogen bonds established between the supramolecular tetramers and the water molecules.

motif has already been observed with other heterometallic systems constructed from $[Cr(AA)(C_2O_4)_2]^-$ building-blocks [7]. The structure is expanded into the second direction through hydrogen bonds involving one water molecule (O14) and two oxygen atoms from two terminal oxalato ligands (O13 and $O13^i$, i = 1 – *x*, *y*, 1.5 – *z*) as illustrated in Fig. 2b. The two other water molecules (O15 and O16) are hydrogen bonded to oxalato oxygen atoms ($O15\cdots O10^{ii}$ = 2.867 Å, ii = *x*, –*y*, –0.5 + *z*; $O16\cdots O9^{iii}$ = 2.854 Å, iii = 0.5 – *x*, 0.5 – *y*, 1 – *z*). Surprisingly, although the binuclear complexes in two compounds are similar and they crystallize with the same number of water molecules, the hydrogen bond pattern involving the crystallization water molecules is different for the two compounds. The formation of the tetranuclear supercomplexes, which are interconnected through aromatic interactions, occurs for compounds **2** as well. For compound **2**, the supramolecular chains are connected by all the crystallization water molecules, which form hydrogen bonds with the oxalato oxygen atoms as well as with the aqua ligand (O1) coordinated to the manganese ion (Fig. 3).

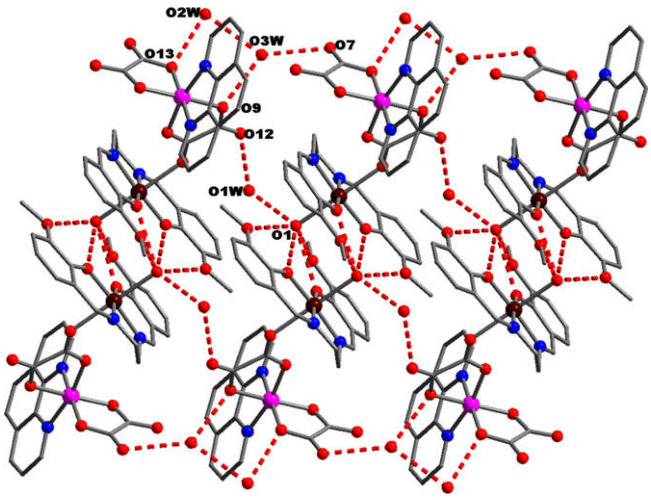


Fig. 3. Packing diagram for crystal **2**.

3.2. Magnetic properties

The magnetic behavior of the two compounds has been investigated from 1.9 to 300 K. The $\chi_M T$ versus *T* curves are represented in Fig. 4 (χ_M is the molar paramagnetic susceptibility). At room temperature, the values of the $\chi_M T$ products for compounds **1** and **2** are, respectively: 4.77 and 5.07 $cm^3\ mol^{-1}$ K, which correspond to

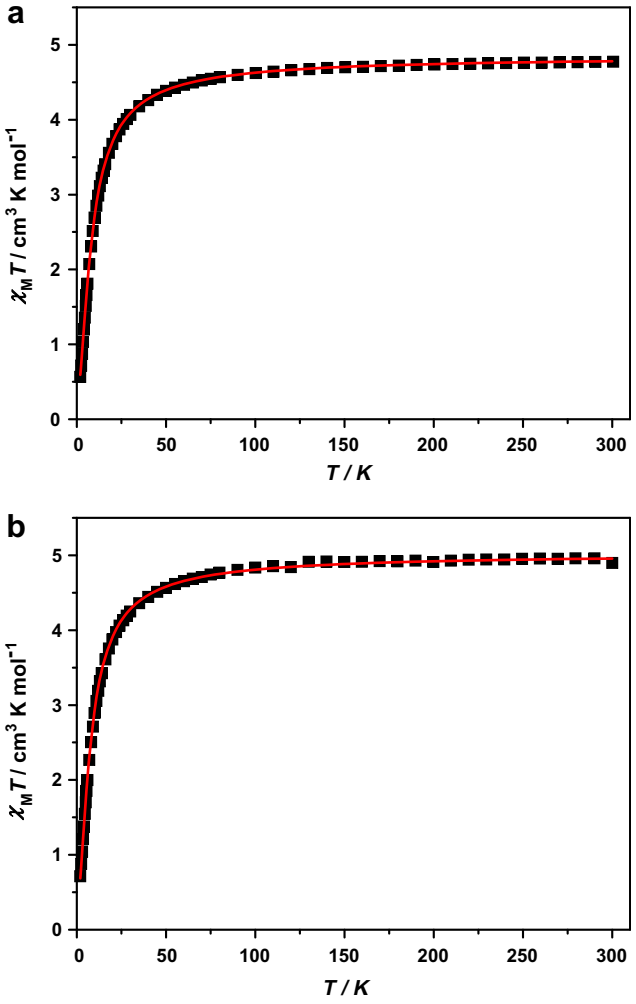


Fig. 4. Thermal variation of the $\chi_M T$ product for compound **1** (a), and **2** (b).

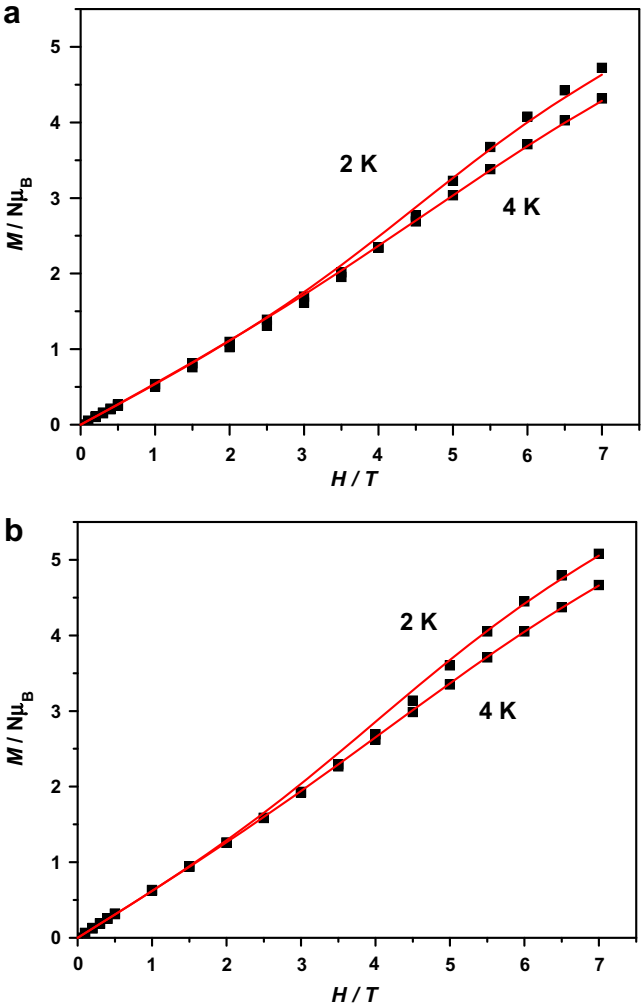


Fig. 5. Magnetization vs. field curves for compound **1** (a), and compound **2** (b).

the expected values for uncoupled Cr(III) and Mn(III) ions (4.88 cm^3 mol^{-1} K, assuming $g_{Cr} = g_{Mn} = 2$).

For both compounds, by decreasing the temperature, the $\chi_M T$ product remains constant down to 100 K, then it decreases more and more rapidly reaching 0.56 cm^3 mol^{-1} K (for **1**) and 0.65 cm^3 mol^{-1} K (for **2**). This behavior is ascribed to the antiferromagnetic exchange interaction between the Mn(III) and Cr(III) ions, mediated by the oxalato group, and/or to the zero-field-splitting effects associated to the axially elongated Mn(III) ion.

The magnetization *versus* field curves are illustrated in Fig. 5. The slow saturation of the magnetization is due to the antiferromagnetic interaction between Mn(III) and Cr(III), as well as to the large zero-field-splitting of the Mn(III) ion.

Both magnetization and susceptibility data were simultaneously fitted by full-matrix diagonalization of the following spin Hamiltonian:

$$H = -2JS_{Mn}S_{Cr} + D_{Mn}[S^2_{Mnz} - 1/3S_{Mn}(S_{Mn}+1)] + D_{Cr}[S^2_{Crz} - 1/3S_{Cr}(S_{Cr}+1)]$$

The first term refers to the exchange interaction between the manganese(III) and chromium(III) ions within the binuclear species. The second and the third ones take into account the zero-field-splitting (ZFS) effects for the two manganese and the chromium ions. In view of the axially elongated structure around Mn(III), a negative sign is expected for D_{Mn} [12], thus D was constrained to negative values in our calculations. In order to avoid oveparametrization, we used fixed values for the g parameters: $g_{Mn} = 2.04$; $g_{Cr} = 1.98$. The best set of parameters which match the experimental data were found to be: $J = -1.06$ cm^{-1}, $D_{Mn} = -2.4$ cm^{-1}, $|D_{Cr}| = 0.16$ cm^{-1}, (for **1**); $J = -1.01$ cm^{-1}, $D_{Mn} = -2.1$ cm^{-1}, $|D_{Cr}| = 0.11$ cm^{-1}, (for **2**). The solid lines in Figs. 4 and 5 correspond to the calculated curves. As expected, according to the crystal structures, the values of the J parameters are very close. The D values are in the usual range (-1 to -4 cm^{-1}) observed for manganese(III) complexes with Schiff-base ligands [12,13].

4. Supplementary data

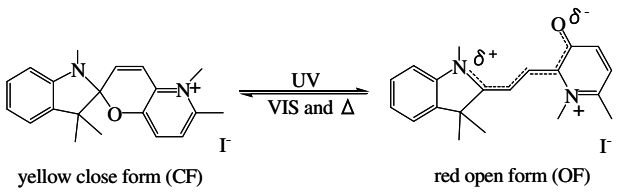
CCDC 704112 and 704113 contain the supplementary crystallographic data for 1 and **2**. These data can be obtained free of charge via http://www.ccdc.cam.ac.uk/conts/retrieving.html, or from the Cambridge Crystallographic Data Centre, 12 Union Road, Cambridge CB2 1EZ, UK; fax: (+44) 1223-336-033; or e-mail: deposit@ccdc.cam.ac.uk.

Acknowledgements

Financial support from the CEEX Program (Project D11-17) and EC "MAGMANet" NMP3-CT-2005-515767 is gratefully acknowledged.

References

[1] (a) O. Kahn, Struct. Bond. (Berlin) 68 (1987) 89;
(b) O. Kahn, Adv. Inorg. Chem. 43 (1995) 179.
[2] (a) R. Ruiz, J. Faus, F. Lloret, M. Julve, Y. Journaux, Coord. Chem. Rev. 193–195 (1999) 1069;
(b) O. Kahn, Acc. Chem. Res. 33 (2000) 647.
[3] R. Clément, S. Decurtins, M. Gruselle, C. Train, in: W. Linert, M. Verdaguer (Eds.), Molecular Magnets. Recent Highlights, Springer, Wien, 2003, p. 1.
[4] (a) K.R. Dunbar, R.A. Heintz, Prog. Inorg. Chem. 45 (1997) 283;
(b) M. Verdaguer, A. Bleuzen, V. Marvaud, J. Vaissermann, M. Seuleiman, C. Desplanches, A. Scuiller, C. Train, R. Garde, G. Gelly, C. Lomenech, I. Rosenman, P. Veillet, C. Cartier, F. Villain, Coord. Chem. Rev. 190–192 (1999) 1023;
(c) M. Ohba, H. Okawa, Coord. Chem. Rev. 198 (2000) 313;
(d) J. Černák, M. Orendáč, I. Potočňák, J. Chomič, A. Orendáčová, J. Skoršepa, A. Feher, Coord. Chem. Rev. 224 (2002) 51.
[5] (a) M. Ohba, H. Tamaki, N. Matsumoto, H. Okawa, S. Kida, Chem. Lett. (1991) 1157;
(b) M. Ohba, H. Tamaki, N. Matsumoto, H. Okawa, Inorg. Chem. 32 (1993) 5385.
[6] T. Sanada, T. Suzuki, T. Yoshida, S. Kaizaki, Inorg. Chem. 37 (1998) 4712.
[7] (a) M. Andruh, R. Melanson, C.V. Stager, F.D. Rochon, Inorg. Chim. Acta 251 (1996) 309;
(b) F.D. Rochon, R. Melanson, M. Andruh, Inorg. Chem. 35 (1996) 6086;
(c) M.C. Muñoz, M. Julve, F. Lloret, J. Faus, M. Andruh, J. Chem. Soc., Dalton Trans. (1998) 3125;
(d) G. Marinescu, M. Andruh, R. Lescouëzec, M.C. Muñoz, J. Cano, F. Lloret, M. Julve, New J. Chem. 24 (2000) 527;
(e) G. Marinescu, D. Visinescu, A. Cucos, M. Andruh, Y. Journaux, V. Kravtsov, Yu.A. Simonov, J. Lipkowski, Eur. J. Inorg. Chem. (2004) 2914.
[8] (a) See for example: Z.J. Zhong, N. Matsumoto, H. Okawa, S. Kida, Chem. Lett. (1990) 87;
(b) S. Decurtins, H.W. Schmalle, H.R. Oswald, A. Linden, J. Ensling, P. Gütlich, A. Hauser, Inorg. Chim. Acta 216 (1994) 65;
(c) S. Decurtins, H.W. Schmalle, P. Schneuwly, J. Ensling, P. Gütlich, J. Am. Chem. Soc. 116 (1994) 9521;
(d) S. Decurtins, M. Gross, H.W. Schmalle, S. Ferlay, Inorg. Chem. 37 (1998) 2443;
(d) M. Pilkington, S. Decurtins, in: J.S. Miller, M. Drillon (Eds.), Magnetism: Molecules to Materials II, VCH, Weinheim, 2001, p. 339.
[9] H. Miyasaka, A. Saitoh, S. Abe, Coord. Chem. Rev. 251 (2007) 2622.
[10] J.-P. Costes, F. Dahan, A. Dupuis, J.-P. Laurent, Inorg. Chem. 35 (1996) 2400.
[11] (a) A.M. Madalan, N. Avarvari, M. Andruh, New J. Chem. 30 (2006) 521;
(b) M. Nayak, R. Koner, H.-H. Lin, U. Flörke, H.-H. Wei, S. Mohanta, Inorg. Chem. 45 (2006) 10764;
(c) S. Nastase, F. Tuna, C. Maxim, C.A. Muryn, N. Avarvari, R.E.P. Winpenny, M. Andruh, Cryst. Growth Des. 7 (2007) 1825.
[12] B.J. Kennedy, K.S. Murray, Inorg. Chem. 24 (1985) 1552.
[13] D. Visinescu, L.M. Toma, F. Lloret, O. Fabelo, C. Ruiz-Pérez, M. Julve, Dalton Trans. (2008) 4103.



Scheme 1. Molecule structure of cationic pyrido-spiropyran.

and the photo-isomerization of spiropyran (photo-isomerization-induced charge transfer phase transition).

In this paper, we present the detailed ^{57}Fe Mössbauer study comparing unirradiated sample of (SP-Me)[$Fe^{II}Fe^{III}$(dto)$_3$] with irradiated one. Although ^{57}Fe Mössbauer spectroscopy is a microscopic probe for iron including oxidation and spin state, the ^{57}Fe Mössbauer spectra of this system are hard to analyze because of the complicated shape. In this case, it is helpful to use ^{57}Fe isotope enriched material. Therefore, we describe here the ^{57}Fe Mössbauer spectra of (SP-Me)[$^{57}Fe^{II}Fe^{III}$(dto)$_3$] with isotope enrichment in Fe^{II} starting from ^{57}Fe metal.

2. Results and discussions

Fig. 1 shows the ^{57}Fe Mössbauer spectra of (SP-Me)[$^{57}Fe^{II}Fe^{III}$-(dto)$_3$] at 200, 70, 10 and 6 K. The Mössbauer parameters are summarized in Table 1 in Supplementary data. At 200 K, the spectrum clearly indicates the presence of two quadrupole doublets similar to (n-C_nH_{2n+1})[$Fe^{II}Fe^{III}$(dto)$_3$] (n = 3–6) [7], which are assigned to Fe^{II} (S = 2) and Fe^{III} (S = 1/2) as described in Fig. 1. Although only ferrous iron was enriched with ^{57}Fe isotope, the observed spectra show a considerable amount of ferric ^{57}Fe ion (ca. 40% at 200 K). This result indicates that both reorientation of the dto ligand and redox reaction between $^{57}Fe^{II}$ and Fe^{III} occurs, and as a result Fe^{II}–$O_2C_2S_2$–$^{57}Fe^{III}$ linkage isomer appears in the precipitation process. According to Hard and Soft Acids and Bases principle (HSAB), a hard acid, Fe^{III} tends to prefer the hard base sites (O_2) in dto ligand and a soft acid, Fe^{II} tends to prefer the soft base sites (S_2) in dto ligand [10], which induces the linkage-isomerization. Moreover, the linkage-isomerization associates the charge transfer from Fe^{II} to Fe^{III} because the HTP is more stable than the LTP in (SP-Me)[$Fe^{II}Fe^{III}$(dto)$_3$] around room temperature. At 70 K, the peak at 2.0 mm s^{-1} corresponding to Fe^{II} (S = 2) decreases and new peaks between 0.1 and 0.9 mm s^{-1} corresponding to the superposition of Fe^{II} (S = 0) and Fe^{III} (S = 5/2) appear. The spectrum at 70 K is assignable using four quadrupole doublets, Fe^{II} (S = 2), Fe^{III} (S = 1/2), Fe^{II} (S = 0), and Fe^{III} (S = 5/2), as shown in Fig. 1. This feature is quite similar to the ^{57}Fe Mössbauer spectra of (n-C_3H_7)$_4$N[$Fe^{II}Fe^{III}$(dto)$_3$] and (n-C_4H_9)$_4$N[$Fe^{II}Fe^{III}$(dto)$_3$] at 77 K [7], which indicates that the LTP appears in (SP-Me)[$^{57}Fe^{II}Fe^{III}$(dto)$_3$] between 200 and 70 K due to the CTPT. The hyperfine parameters of the LTP in (SP-Me)[$^{57}Fe^{II}Fe^{III}$(dto)$_3$] are consistent with those of (n-C_3H_7)$_4$N[$Fe^{II}Fe^{III}$(dto)$_3$] and (n-C_4H_9)$_4$N[$Fe^{II}Fe^{III}$(dto)$_3$], including relatively larger value of the quadrupole splitting of Fe^{III} (S = 5/2). The same trend has been observed in A[$Fe^{II}Fe^{III}$(ox)$_3$] (ox = oxalato) complexes where the high-spin Fe^{III} is expected to be in the highly distorted octahedral environment [11]. The coordination environment of ^{57}Fe ion in (SP-Me)[$^{57}Fe^{II}Fe^{III}$(dto)$_3$] at 200 and 70 K is displayed in Fig. 2. From the relative area of the ^{57}Fe Mössbauer spectrum, almost the half of ^{57}Fe ion undergoes the CTPT in Fe^{III}–$S_2C_2O_2$–$^{57}Fe^{II}$ site (normal coordination site) and Fe^{II}–$O_2C_2S_2$–$^{57}Fe^{III}$ site (linkage-isomer site), respectively. The one component with the charge transfer phase transition is named A phase and the other without the charge transfer phase transition is named B phase [9].

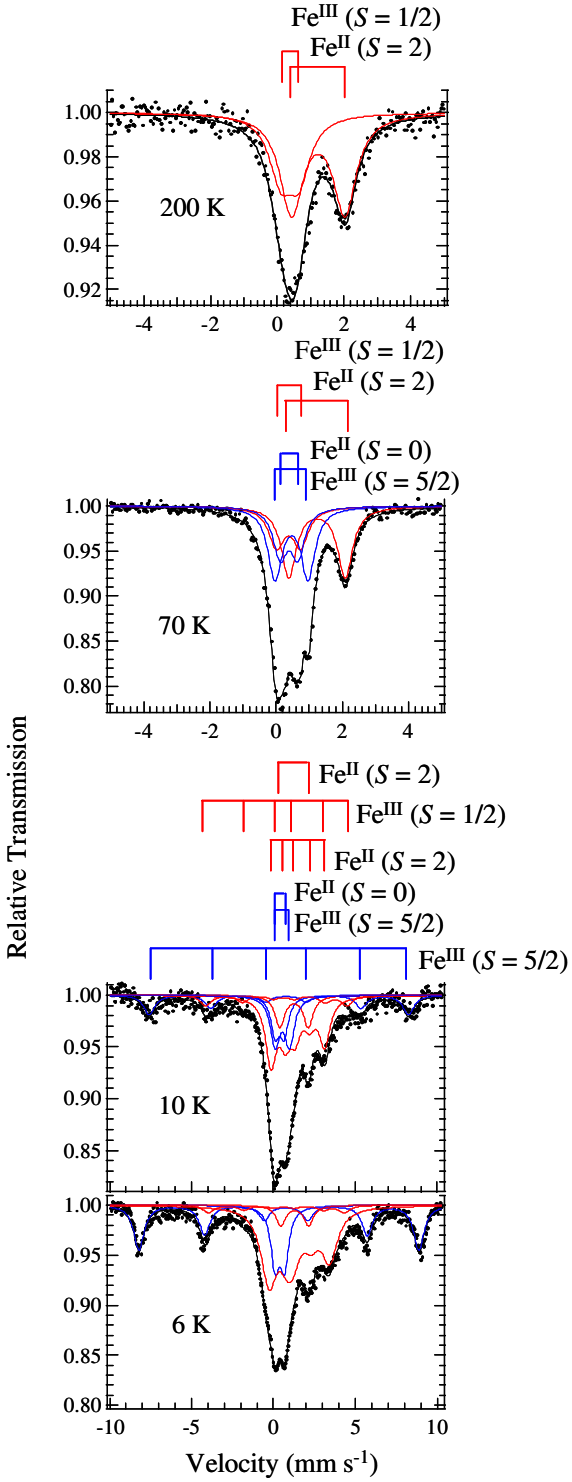


Fig. 1. ^{57}Fe Mössbauer spectra of (SP-Me)[$^{57}Fe^{II}Fe^{III}$(dto)$_3$] before UV-irradiation at 200, 70, 10 and 6 K.

At 10 and 6 K, the ^{57}Fe Mössbauer spectra show an obvious change in shape and reveal some broad sextets, exhibiting the magnetically ordered spectra. The sextet with a large hyperfine field from −8 to 8 mm s^{-1} is typical of the magnetically ordered spectrum of Fe^{III} (S = 5/2) and the quadrupole doublet around 0.3 mm s^{-1} can be assigned to non-magnetic Fe^{II} (S = 0), which is the clear evidence of the presence of the LTP corresponding to the A phase. The magnetic sextets of Fe^{II} (S = 2) and Fe^{III} (S = 1/2) and the quadrupole doublet of Fe^{II} (S = 2) are also required to fit

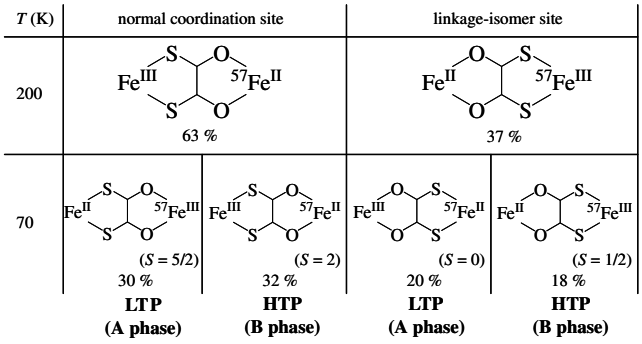


Fig. 2. Coordination environments of ^{57}Fe ion and their fractions calculated from the ^{57}Fe Mössbauer spectra in (SP-Me)[^{57}Fe^{II}Fe^{III}(dto)$_3$] before UV-irradiation at 200 and 70 K. A and B phases are explained in the text.

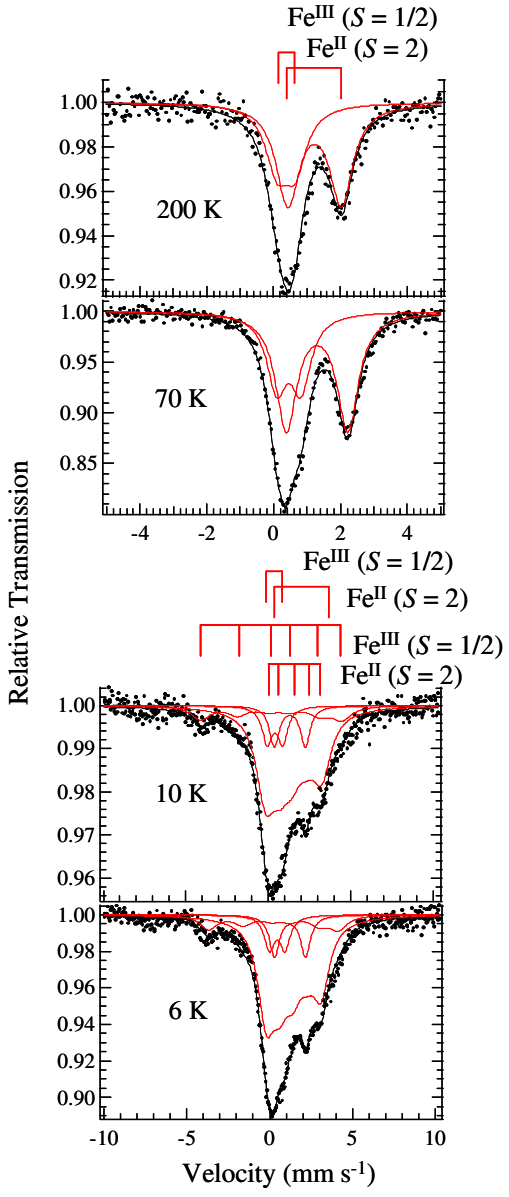


Fig. 3. ^{57}Fe Mössbauer spectra of (SP-Me)[^{57}Fe^{II}Fe^{III}(dto)$_3$] after UV-irradiation at 200, 70, 10 and 6 K.

the spectra, corresponding to the B phase. The angle (θ) between the internal magnetic field (H) and the principal axis of V_{zz} as the Mössbauer nucleus in (SP-Me)[^{57}Fe^{II}Fe^{III}(dto)$_3$] was estimated by applying the following approximate equation for axial symmetry; $\Delta\varepsilon_1 - \Delta\varepsilon_2 = -1/2eV_{zz}(3\cos^2\theta - 1)$, where $\Delta\varepsilon_1$ and $\Delta\varepsilon_2$ represent the interval between the lowest-energy and the second lowest-energy peaks, and that between the highest-energy and the second highest-energy peaks, respectively. The θ values could not be determined uniquely, because the $\Delta\varepsilon_1 - \Delta\varepsilon_2$ value is not informative about the sign of V_{zz} for this case. On the assumption of positive V_{zz}, θ is estimated at 90°, while θ is estimated at 40° on the assumption of negative V_{zz}. Here, it is reasonable to take the principal axis of V_{zz} along the D_3 axis which goes through the iron atom in [Fe^{II}Fe^{III}(dto)$_3$] layer and consider θ to be 90°, because the internal magnetic field (H) appears to be parallel to the basal layers according to the anisotropic magnetization measurement of (n-C$_3$H$_7$)$_4$N[Fe^{II}Fe^{III}(dto)$_3$] [12]. Note that (SP-Me)[Fe^{II}Fe^{III}(dto)$_3$] has two ferromagnetic transition temperatures, 22 and 5 K. The spectrum at 10 K is a superposition of the paramagnetic quadrupole doublet and the magnetic sextet of Fe^{III} (S = 5/2) in the ratio of 1:1. This behavior results from the dynamic behavior of the short-range magnetic exchange correlations and the short-range magnetic ordering gives the sextet despite of the temperature above ferromagnetic transition temperature of 5 K. As temperature is decreased to 6 K, the doublet disappears and the sextet grows. On the other hand, the sextets of Fe^{II} (S = 2) and Fe^{III} (S = 1/2) almost shows no change between 10 and 6 K. This result supports that the ferromagnetic transition temperatures of the HTP and LTP in (SP-Me)[Fe^{II}Fe^{III}(dto)$_3$] are 22 and 5 K, respectively.

Fig. 3 shows the ^{57}Fe Mössbauer spectra of (SP-Me)[^{57}Fe^{II}Fe^{III}(dto)$_3$] at 200, 70, 10 and 6 K after UV-irradiation of 350 nm for 3 h at room temperature. The Mössbauer parameters are also summarized in Table 1 in Supplementary data. In this case, the spectrum at 200 K shows the same line profile as that of unirradiated sample at 200 K, but remains unchanged with decreasing temperature to 70 K, unlike the unirradiated one. At 10 K, the spectrum exhibits a superposition of broadened sextets and paramagnetic doublets and it is also unchanged with decreasing temperature to 6 K. The magnetically ordered spectra are assignable to Fe^{II} (S = 2) and Fe^{III} (S = 1/2), indicating that the charge transfer phase transition is suppressed and the HTP is more stable than LTP between 200 and 6 K in the UV-irradiated sample. The spectral change derived from the UV-irradiation proves that the photo-isomerization of spiropyran in (SP-Me)[Fe^{II}Fe^{III}(dto)$_3$] induces the transformation from the A to B phase, as described in the literature [9].

3. Conclusion

^{57}Fe Mössbauer measurement have been performed between 200 and 6 K to probe the microscopic state of iron ions in (SP-Me)[^{57}Fe^{II}Fe^{III}(dto)$_3$] before and after UV-irradiation. The ^{57}Fe Mössbauer spectra of the sample without UV-irradiation below 70 K clearly show the appearance of the LTP arising from the charge transfer phase transition. In the case of the UV-irradiated sample, on the contrary, the charge transfer phase transition is not observed and only the HTP exists between 200 and 6 K. The ^{57}Fe Mössbauer spectra at 10 and 6 K show the broad sextets corresponding to the magnetically ordered state and support that the ferromagnetic transition temperatures of the HTP and LTP in (SP-Me)[Fe^{II}Fe^{III}(dto)$_3$] are 22 and 5 K, respectively.

4. Experimental

4.1. Materials

4.1.1. Preparation of (SP-Me)[^{57}Fe^{II}Fe^{III}(dto)$_3$]

(SP-Me)[^{57}Fe^{II}Fe^{III}(dto)$_3$] was prepared in a similar way to that reported in the literature [9]. In this process, ^{57}FeCl$_2 \cdot 4$H$_2$O used

as Fe^{II} source was prepared by dropping hydrochloric acid to powdered ^{57}Fe under N_2. Elemental *Anal.* Calc. for $C_{26}H_{23}N_2O_7S_6Fe_2$: C, 40.06; H, 2.97; N, 3.59. Found: C, 40.11; H, 5.00; N, 3.76%.

4.2. Physical measurements

For ^{57}Fe Mössbauer spectroscopic measurement, ^{57}Co in Rh was used as a Mössbauer source. The spectra were calibrated by using the six lines of a body-centered cubic iron foil (α-Fe), the center of which was taken as zero isomer shift. Mössbauer spectra were fitted with a MOSSWINN 3.0 program [13]. In the fit of the magnetically ordered state, the adjustable hyperfine parameters for a given component in the spectral fits are the isomer shift δ, the amplitude of the relaxing magnetic field H, the quadrupole interaction ΔE_Q, the component of the electric field gradient (EFG) V_{zz}, the asymmetry parameter of the EFG η, the angle θ between the principle axis of the electric field gradient and the magnetization direction, and the line-width Γ. The V_{zz} parameter has the unit: 10^{21} [V/m^2]. The model is calculated by solving the exact Hamiltonian for mixed magnetic and quadrupole interaction with arbitrary relative orientation [14]. In all fits reported herein, $\eta = 0$. In addition, at a given temperature, the δ, ΔE_Q, and Γ values associated with a given iron oxidation and spin states have been constrained to be equal. The sample irradiation was performed under N_2 with a Xe lamp Asahi Spectra Co. LAX-101 (350 nm, 40 mW/cm^2) as UV source using band pass filters.

Acknowledgments

The authors thank Dr. Ono for valuable discussions on the Mössbauer measurement. This work was supported by a Grant-in-aid for Scientific Research, a Grant-in-aid of the 21st century COE (Center of Excellence) Program, and a Grant-in-Aid for Scientific Research on Priority Areas from the Ministry of Education, Culture, Sports, Science and Technology, Japan.

Appendix A. Supplementary data

Supplementary data associated with this article can be found, in the online version, at doi:10.1016/j.poly.2008.10.060.

References

[1] For recent examples see: Y. Einaga, J. Photochem. Photobiol. C. 7 (2006) 69 and references cited therein.
[2] N. Kojima, W. Aoki, M. Itoi, Y. Ono, M. Seto, Y. Kobayashi, Yu. Maeda, Solid State Commun. 120 (2001) 165.
[3] T. Nakamoto, T. Miyazaki, M. Itoi, Y. Ono, N. Kojima, M. Sorai, Angew. Chem., Int. Ed. 40 (2001) 4716.
[4] N. Kojima, W. Aoki, M. Seto, Y. Kobayashi, Yu. Maeda, Synth. Met. 121 (2001) 1796.
[5] Y. Ono, M. Okubo, N. Kojima, Solid State Commun. 126 (2003) 291.
[6] M. Itoi, A. Taira, M. Enomoto, N. Matsushita, N. Kojima, Y. Kobayashi, K. Asai, K. Koyama, T. Nakamoto, Y. Uwatoko, J. Yamaura, Solid State Commun. 130 (2004) 415.
[7] N. Kojima, Y. Ono, K. Kobayashi, M. Seto, Hyperfine Interact. 156–157 (2004) 175.
[8] M. Itoi, Y. Ono, N. Kojima, K. Kato, K. Osaka, M. Takata, Eur. J. Inorg. Chem. 2006 (2006) 1198.
[9] N. Kida, M. Hikita, I. Kashima, M. Okubo, M. Itoi, M. Enomoto, K. Kato, M. Takata, N. Kojima, J. Am. Chem. Soc., in press.
[10] D. Coucouvanis, D. Piltingsrud, J. Am. Chem. Soc. 95 (1973) 5556.
[11] S.G. Carling, D. Visser, D. Hautot, I.D. Watts, P. Day, J. Ensling, P. Gütlich, G.J. Long, F. Grandjean, Phys. Rev. B 95 (2002) 104407.
[12] M. Itoi, M. Enomoto, N. Kojima, J. Magn. Magn. Mater. 272–276 (2004) 1093.
[13] MOSSWIN 3.0 Dr. Zoltan Klencsar. <http://www.netx.hu/mosswinn/index.html>.
[14] R.W. Grant, U. Gonser (Eds.), Mössbauer Spectroscopy, vol. 5, Springer-Verlag, 1975, p. 97.

2.2. Preparations

2.2.1. $[Mn^{III}_2La_2(bdea)_2(bdeaH)_2(piv)_6]\cdot 2MeCN$(**1**)

A solution of N-bdea (0.64 g, 4.0 mmol) in 10 ml of MeCN and $La(NO_3)_3\cdot 6H_2O$ (0.22 g, 0.5 mmol) as a solid were added to a stirred solution of $Mn(OAc.)_2\cdot 4H_2O$ (0.12 g, 0.5 mmol) and pivalic acid (0.20 g, 2.0 mmol) in 10 ml of MeCN resutling in a dark brown solution. After 48 h, brown crystals were collected by filtration and washed with acetonitrile. Yield 57% (based on Mn). Elemental *Anal.* Calc. for **1**: $C_{63.2}H_{125.8}Mn_2La_2N_{4.6}O_{20}$ (corresponds to loss of 1.4 MeCN): C, 45.76; H, 7.65; N, 3.89. Found: C, 45.60; H, 7.53, N, 3.90. IR (KBr disk, cm^{-1}): 3434 (b), 2957 (vs), 2932 (s), 2865 (m), 1606 (vs), 1539 (vs), 1481 (vs), 1457 (w), 1423(s), 1397 (s), 1344 (vs), 1222 (s), 1088 (s), 1072 (w), 1042 (w), 911 (w), 891 (m), 804 (w), 786 (w), 761 (w), 655 (w),622 (s), 596 (s), 543 (w), 474 (m).

2.2.2. $[Mn^{III}_2Ce_2(bdea)_2(bdeaH)_2(piv)_6]\cdot 2MeCN$(**2**)

This was prepared in a similar way as **1** but using $Ce(NO_3)_3\cdot 6H_2O$. Yield 30% (based on Mn). Elemental *Anal.* Calc. for **2**: $C_{63.2}H_{125.8}Mn_2Ce_2N_{4.6}O_{20}$ (corresponds to loss of 1.4 MeCN): C, 45.71; H, 7.64; N, 3.88. Found: C, 45.44; H, 7.38, N, 4.07. IR data (KBr disk, cm^{-1}): 3421 (b), 2956 (vs), 2932 (s), 2864 (m), 1606 (vs), 1542 (vs), 1481 (vs), 1458 (w), 1424 (s), 1397 (s), 1357 (s), 1343 (vs), 1223 (s), 1089 (s), 1070 (w), 1042 (w), 912 (w), 892 (m), 805 (w), 787 (w), 760 (w), 656 (w), 623 (s), 598 (s), 544 (w), 475 (m).

2.2.3. $[Mn^{III}_2Pr_2(bdea)_2(bdeaH)_2(piv)_6]\cdot 2MeCN$(**3**)

This was prepared in a similar way as **1** but using $Pr(NO_3)_3\cdot 6H_2O$ Yield 36% (based on Mn). Elemental *Anal.* Calc. for **3**: $C_{63.2}H_{125.8}Mn_2Pr_2N_{4.6}O_{20}$ (corresponds to loss of 1.4 MeCN): C, 45.65; H, 7.63; N, 3.88. Found: C, 45.22; H, 7.38, N, IR data (KBr disk, cm^{-1}): 3414 (b), 2956 (vs), 2931 (s) , 2865 (m), 1608 (vs), 1542 (vs), 1482 (vs), 1456 (w), 1425 (s), 1406 (s), 1397 (s), 1357 (s), 1342 (vs), 1223 (s), 1090 (s), 1071 (w), 1042 (w), 912 (w), 893 (m), 805 (w), 790 (w), 760 (w), 657 (w), 623 (s), 599 (s), 545 (w), 475 (m).

2.2.4. $[Mn^{III}_2Nd_2(bdea)_2(bdeaH)_2(piv)_6]\cdot 2MeCN$(**4**)

This was prepared in a similar way as **1** but using $Nd(NO_3)_3\cdot 6H_2O$). Yield 60% (based on Mn). Elemental *Anal.* Calc. for **4**: $C_{63}H_{125.5}Mn_2Nd_2N_{4.5}O_{20}$ (corresponds to loss of 1.5 MeCN): C, 45.57; H, 7.62; N, 3.80. Found: C, 45.61; H, 7.42, N, 3.74. IR data (KBr disk, cm^{-1}): 3418 (b), 2957 (vs), 2930 (s) , 2866 (m), 1609 (vs), 1542 (vs), 1482 (vs), 1456 (w), 1426 (s), 1407 (m), 1397 (s), 1357 (s), 1343 (vs), 1223 (s), 1092 (s), 1071 (w), 1042 (w), 912 (w), 893 (m), 806 (w), 790 (w), 761 (w), 657 (w), 624 (s), 599 (s), 544 (w), 476 (m).

2.3. Physical measurements

IR spectra were measured on Perkin Elmer Spectrum One spectrometer with samples prepared as KBr discs.

The magnetic susceptibility measurements on compounds **1**–**4** were obtained with the use of a Quantum Design SQUID magnetometer MPMS-XL. This magnetometer works between 1.8 and 400 K for dc applied fields ranging from −7 to 7 T. Measurements were performed on polycrystalline samples of 15.0, 9.1, 10.1 and 9.5 mg for complexes **1**, **2**, **3** and **4**, respectively. ac susceptibility measurements have been measured with an oscillating ac field of 3 Oe and ac frequencies ranging from 1 to 1500 Hz. *M* versus *H* measurements were performed at 100 K to check for the presence of ferromagnetic impurities; none were found. The magnetic data were corrected for the sample holder and the diamagnetic contribution.

2.4. Powder diffraction/crystal structure determination

The X-ray powder diffraction pattern for **4** was measured at room temperature using a Stoe STADI-P diffractometer with a Cu Kα radiation.

X-ray data for **1**–**3** were collected at 100 K on a Bruker SMART Apex CCD diffractometer using graphite-monochromated Mo Kα radiation. Crystallographic details and detail of data collection and refinement are summarized in Table 1. Semi-empirical absorption corrections were made using SADABS[14a]. The structures were solved using direct methods, followed by full matrix least-squares refinement against F^2 (all data) using SHELXTL[14b]. Anisotropic refinement for all ordered non-H atoms; organic H atoms were placed in calculated positions, while coordinates of the hydroxo H atom H(3) were refined with the O–H distance re-

Table 1
Crystallographic data and structural refinement parameters for complexes **1**–**3**.

	1	**2**	**3**
Formula	$C_{66}H_{130}La_2Mn_2N_6O_{20}$	$C_{66}H_{130}Ce_2Mn_2N_6O_{20}$	$C_{66}H_{130}Pr_2Mn_2N_6O_{20}$
Mr	1715.46	1717.88	1719.46
Crystal size (mm)	0.21 × 0.17 × 0.05	0.21 × 0.04 × 0.01	0.21 × 0.08 × 0.06
Crystal system	Triclinic	Triclinic	Triclinic
Space group	$P\bar{1}$	$P\bar{1}$	$P\bar{1}$
T (K)	100	100	100
a (Å)	11.1359(7)	11.1152(8)	11.1094(7)
b (Å)	14.4764(9)	14.4348(10)	14.4256(9)
c (Å)	14.6769(9)	14.6271(10)	14.6102(9)
α (°)	60.641(1)	60.740(1)	60.787(1)
β (°)	87.896(1)	87.864(1)	87.894(1)
γ (°)	74.368(1)	74.460(1)	74.608(1)
V (Å^3)	1973.0(2)	1960.3(2)	1958.3(2)
Z	1	1	1
ρ_{calc} (g/cm^{-3})	1.444	1.455	1.458
μ (Mo $K\alpha$) (mm^{-1})	1.442	1.523	1.606
$F(000)$	892	894	896
Reflections collected	13683	8729	13469
Unique data	8511	7068	8403
R_{int}	0.0146	0.0323	0.0243
data with $I > 2\sigma(I)$	7785	5829	7173
Parameters/restraints	437/1	449/44	437/1
wR_2 (all data)	0.0739	0.1049	0.0750
S on F^2 (all data)	1.055	1.072	1.039
R_1 [$I > 2\sigma(I)$]	0.0290	0.0474	0.0319
Largest residuals (e Å^{-3})	1.717/−0.971	1.752/−0.843	2.072/−1.149

strained. In **2** the lattice MeCN molecule was disordered, the atoms of the major component were refined anisotropically with similarity restraints on the thermal parameters and geometries of the two part molecules.

3. Results and discussion

3.1. Synthesis

Various strategies have been utilized in the synthesis of Mn-4f complexes. Many complexes have been prepared by self- or serendipitous assembly using small nuclearity preformed carboxylate species of $[Mn_3O]^{6+/7+}$ [6d,7], $[Mn_4O_2]^{8+}$ [7b] or $[Mn_6O_2]^{10+}$ [8,9,15] cores. However, our aim of this work is to use simple manganese salts to see the nuclearity of the final products. Small changes have been made in terms of the ratio of N-bdea: Ln:Mn: pivalic acid and/or the use of $Mn(NO_3)_2 \cdot 4H_2O$ in place of $Mn(OAc)_2 \cdot 4H_2O$ leading to compounds $[Mn^{III}_2Ln_2(bdea)_2(bdeaH)_2(piv)_6] \cdot 2MeCN$ discussed in this work. The synthetic procedures presented herein resulted in four isomorphous tetranuclear Mn–Ln (Ln = La, Ce, Pr and Nd) complexes, however, it should be noted that they were not reproducible for lanthanides such as Sm, Eu and Gd. With heavier lanthanides situated on the right side of Gd pentanuclear Mn_2Ln_3 compounds have been obtained which will be reported elsewhere. One of the explanations could be the ionic radius of the employed lanthanides.

3.2. Structural analysis

X-ray crystallographic studies reveal that complexes **1**–**3** crystallize isomorphously in the triclinic space group $P\bar{1}$ with $Z = 1$ (Table 1); showing $[Mn^{III}_2Ln^{III}_2]$ butterfly cores with centrosymmetric site symmetry. The crystal structure and its polyhedral representation (along the *a*-axis) of the Pr analogue (**3**) are representatively shown in Fig. 1. Compound **4** gave rather poor quality crystals, but was shown to be isomorphous (Fig. 2) with the other three complexes by comparison of its X-ray powder diffraction pattern with those simulated from the single-crystal structures of **1**–**3**.

The "butterfly" core comprises two outer "wingtip" nonacoordinate Ln^{III} ions and two inner hexacoordinate Mn^{III} ions, and these four cations are strictly coplanar. The oxidation states of Mn(1) and Ce(1) were determined by consideration of its coordination geometry (bond lengths, coordination numbers and the presence of Jahn–Teller elongation axes for Mn(1)) and by bond valence sum analysis [16]. Selected bond lengths and angles for complexes **1**–**3** are listed in Table 2.

The Mn centre Mn(1) is chelated by a doubly-deprotonated $(bdea)^{2-}$ ligand, of which one alkoxo oxygen O(1) forms a μ_3-bridge between the two manganese and one of the lanthanide cations, and the other, O(2) is edge bridging between Mn(1) and the inversion-related lanthanide centre Ln(1′). The singly deprotonated (bdeaH) ligands each chelate a lanthanide centre, Ln(1). The deprotonated alkoxide oxygens O(3) bridge between Ln(1) and Mn(1′), while the protonated oxygen, O(4), coordinates terminally to Ln(1). The three independent pivalate ligands in the asymmetric unit exhibit three different coordination modes. One forms a *syn–syn* bidentate bridge between Mn(1) and Ln(1′), one chelates Ln(1), and the third coordinates in a unidentate mode to Ln(1), with the non-coordinated oxygen accepting a hydrogen bond from O(4). Overall, Mn(1) shows the expected Jahn–Teller elongated octahedral geometry, with the Jahn–Teller axis defined by O(1′) and N(1), while the coordination geometry of the nonacoordinate Ln^{III} ions approximates to a tricapped trigonal prism.

The lanthanide cations in **1**, **3** and **4** are trivalent. However, although the four complexes are isomorphous, one must consider the possibility that the cerium cation Ce(1) in **2** might be Ce^{IV} rather than Ce^{III}, or that the crystal contains a mixture of the

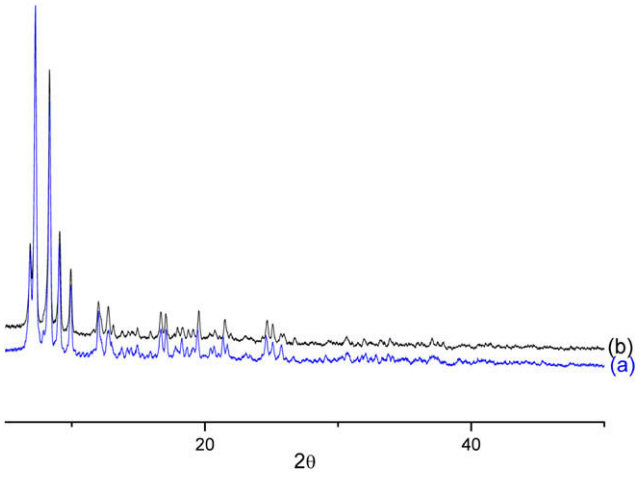


Fig. 2. X-ray powder diffraction: measured for complex **1** (a) and **4** (b).

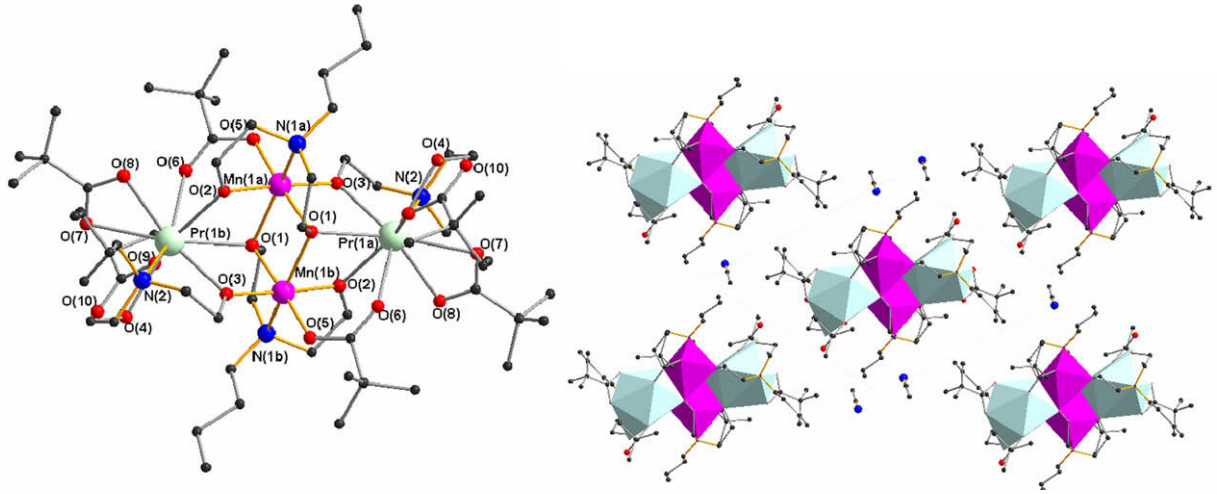


Fig. 1. $[Mn^{III}_2Pr_2(Bu\text{-}dea)_2(Bu\text{-}deaH)_2(piv)_6] \cdot 2MeCN$ (**3**) in the crystal (left). Polyhedral representation of **3** along the *a*-axis (right). The dimensions of the nitrogen atoms of MeCN solvent molecules are inflated for better view. Hydrogen atoms have been omitted for clarity.

Table 2
Selected bond lengths (Å) and angles (°) for **1**, **2** and **3** (primed atoms generated by $\{-x+1, -y+1, -z+1\}$).

1		**2**		**3**	
Bond lengths					
La1–O9	2.4089(18)	Ce1–O9	2.391(4)	Pr1–O9	2.375(2)
La1–O2′	2.5234(16)	Ce1–O2′	2.497(3)	Pr1–O2′	2.4696(19)
La1–O3	2.5498(16)	Ce1–O3	2.531(3)	Pr1–O3	2.5069(19)
La1–O8	2.5517(18)	Ce1–O8	2.535(4)	Pr1–O8	2.512(2)
La1–O6′	2.5718(17)	Ce1–O6′	2.553(3)	Pr1–O7	2.530(2)
La1–O7	2.5729(18)	Ce1–O7	2.544(4)	Pr1–O6′	2.5399(19)
La1–O1	2.6095(16)	Ce1–O1	2.588(3)	Pr1–O1	2.5745(19)
La1–O4	2.6211(18)	Ce1–O4	2.593(4)	Pr1–O4	2.579(2)
La1–N2	2.867(2)	Ce1–N2	2.853(4)	Pr1–N2	2.850(2)
Mn1–O3	1.8966(16)	Mn1–O3	1.898(3)	Mn1–O3	1.8995(19)
Mn1–O2	1.9112(16)	Mn1–O2	1.917(3)	Mn1–O2	1.9163(19)
Mn1–O5	1.9431(17)	Mn1–O5	1.933(3)	Mn1–O5	1.9405(19)
Mn1–O1	1.9664(16)	Mn1–O1	1.966(3)	Mn1–O1	1.9636(19)
Mn1–O1′	2.2595(17)	Mn1–O1′	2.256(3)	Mn1–O1′	2.2524(19)
Mn1–N1	2.301(2)	Mn1–N1	2.300(4)	Mn1–N1	2.296(2)
Mn1 ··· Mn1′	3.1656(7)	Mn1 ··· Mn1′	3.1544(14)	Mn1 ··· Mn1′	3.1452(8)
La1 ··· Mn1′	3.6647(4)	Ce1 ··· Mn1′	3.6464(8)	Pr1 ··· Mn1′	3.6284(5)
La1 ··· Mn1	3.6941(4)	Ce1 ··· Mn1	3.6731(8)	Pr1 ··· Mn1	3.6592(5)
Angles					
Mn1–O1–Mn1′	96.78(7)	Mn1–O1–Mn1′	96.45(14)	Mn1–O1–Mn1′	96.25(8)
Mn1–O1–La1	106.83(7)	Mn1–O1–Ce1	106.75(14)	Mn1–O1–Pr1	106.70(8)
Mn1′–O1–La1	97.39(6)	Mn1′–O1–Ce1	97.42(12)	Mn1′–O1–Pr1	97.25(7)
Mn1–O2–La1′	110.70(7)	Mn1–O2–Ce1′	110.72(15)	Mn1–O2–Pr1′	111.01(8)
Mn1–O3–La1	111.52(7)	Mn1–O3–Ce1	111.28(15)	Mn1–O3–Pr1	111.54(8)

Table 3
Magnetic data extracted from the χT products for compounds **1**–**4**.

Compounds	*Curie constant* for each Ln ion [5] at 300 K (cm^3 K/mol)	χT (cm^3 K/mol) predicted for Mn_2Ln_2 at 300 K	χT (cm^3 K/mol) measured for Mn_2Ln_2 at 300 K	Temperature (K) of the maximum of χT	Maximum value of χT (cm^3 K/mol)
Mn_2La_2 (**1**)	0	6.0	6.7	10	11.0
Mn_2Ce_2 (**2**)	0.80	7.6	7.7	3	13.8
Mn_2Pr_2 (**3**)	1.60	9.2	10.0	15	12.8
Mn_2Nd_2 (**4**)	1.64	9.3	10.1	3.7	21.1

two valences. However, the oxidation state calculated from bond valence sum analysis [16b] is 2.96, indicating that Ce(1) is in fact "pure" Ce^{III}.

Similar "butterfly" complexes $[Mn_2Ln_2O_2(piv)_8(pivH)_2(MeOH)_2]$ (Ln = Dy and Gd) have been published by Winpenny [15], while Brechin and co-workers have also reported a $[Mn^{III}_2Dy^{III}_2]$ complex [7]. Complexes **1**–**4** are the first examples of this type of Mn_2Ln_2 complex with the lighter lanthanides.

3.3. Magnetic properties of *1*–*4*

Dc magnetic susceptibility (χ) data for compounds **1–4** were collected in the 1.8–300 K temperature range under a field of 0.1 T. All these compounds show a similar thermal evolution of the susceptibility, with results summarized in Table 3. For all four compounds, the χT product at 300 K is close to the expected value for two Mn^{III} ($g = 2$, $S = 2$, $C = 3$ cm^3 K/mol) and two respective Ln^{III} ions [5]. On lowering the temperature, χT increases continuously to reach a maximum value, and then rapidly drops with further cooling to 1.8 K, indicating dominant ferromagnetic interactions within the complexes (Fig. 3 and ESI 1–4). The final decrease of χT suggests the presence of weak antiferromagnetic intermolecular interactions and/or a significant magnetic anisotropy.

As well as the two diamagnetic La^{III} ions, compound **1** contains two Mn^{III} ions linked directly *via* two single-O bridges, and these are likely to mediate ferromagnetic interactions between the Mn^{III} ions as observed in related Mn_4 compounds [17]. This would lead to a total spin ground state of $S_T = 4$, and the expected χT value at low temperature would be 10 cm^3 K/mol (taking $g_{av} = 2$), which is in good agreement with the experimental $(\chi T)_{max}$ (11.0 cm^3 K/mol) at 10 K. The $S_T = 4$ ground state is also qualitatively supported by the field dependence of the magnetization at low temperatures, which approaches 8 μ_B without saturating, reaching 7.4 μ_B at 7 T and 1.8 K (Fig. ESI 1).

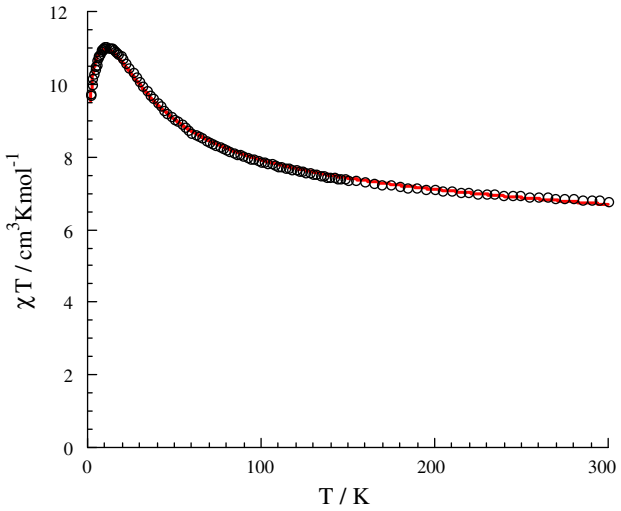


Fig. 3. Temperature dependence of magnetic susceptibility at 1000 Oe for Mn_2La_2 (**1**). Experimental data (open circles); fitting (red solid line), see the discussion in the text. (For interpretation of the references to colour in this figure legend, the reader is referred to the web version of this article.)

Given the difficulty of modeling complexes such as **2**–**4** containing Ce^{III}, Pr^{III} and Nd^{III}, in consequence of the spin–orbit coupling found for these lanthanide ions and the low symmetry of their crystal field, the only compound that can be easily modeled is **1** with diamagnetic La^{III} ions. The temperature behaviour of the magnetic susceptibility of this compound can be modeled using a simple isotropic Heisenberg dimer model of $S = 2$ spins with the following spin Hamiltonian $H_d = -2JS_1S_2$, where J is the exchange interaction between Mn^{III} ions. Application of the van Vleck equation [18,19] allows a determination of the low field analytical expression of the magnetic susceptibility:

$$\chi_{Mn2La2} = \frac{g_{av}^2 N\mu_B^2}{k_B T}\frac{2e^{\frac{2J}{k_BT}} + 10e^{\frac{6J}{k_BT}} + 28e^{\frac{12J}{k_BT}} + 60e^{\frac{20J}{k_BT}}}{1 + 3e^{\frac{2J}{k_BT}} + 5e^{\frac{6J}{k_BT}} + 7e^{\frac{12J}{k_BT}} + 9e^{\frac{20J}{k_BT}}}$$

This model was able to reproduce very well the experimental data from 300 K to 15 K. The best set of parameters found is: J/k_B = 5.0(1) K and g = 2.12(1). In order to fit the low temperature χT product below 15 K, inter-complex interactions have been introduced in the frame of the mean field theory [20]. The following definition of the susceptibility has been used:

$$\chi = \frac{\chi_{Mn2La2}}{1 - \frac{2zJ'}{Ng^2\mu_B^2}\chi_{Mn2La2}}$$

where χ_{Mn2La2} is the susceptibility of the non-interacting Mn_2La_2 complexes, z is the number of nearest neighbours and J' is the intermolecular magnetic interaction. The best set of parameters found is now: J/k_B = 4.9(1) K, g = 2.14(1) and zJ'/k_B = −0.014(1) K (Fig. 3). The value of the Mn^{III}–Mn^{III} interaction J is indeed comparable to those observed in related compounds [17]. It should be noticed that the inter-complex interactions, zJ', also include phenomenologically the magnetic anisotropy of the system, and therefore this value should be taken with caution and certainly not as a direct accurate measure of the magnitude of the inter-complex interactions but more as a higher limit value. The sign of the magnetic interaction confirms the $S_T = 4$ ground state of this compound and also indicates that in the other compounds of this family the Mn^{III}–Mn^{III} interactions are probably similarly ferromagnetic. However, the Mn^{III}–Ln^{III} magnetic interactions are likely of smaller magnitude and are difficult to evaluate due to the complicated intrinsic magnetic properties of the Pr^{III}, Ce^{III} and Nd^{III} metal ions (spin–orbit coupling and low symmetry of the crystal field).

The field dependence of the magnetization at 1.8 K for each of the compounds **1**–**4** shows a relative rapid increase of the magnetization at low fields, followed by an almost linear increase without clear saturation up to 7 T, when it reaches 7.3, 8.7, 9.6 and 12.7 μ_B for **1**, **2**, **3** and **4**, respectively (Fig. ESI 1-4). The high-field linear variation of M suggests the presence of low-lying excited states that can be populated under applied field in agreement with weak intra-molecular magnetic interactions (vide supra), and/or a significant magnetic anisotropy in those compounds. Indeed, when plotting M versus H/T at different fields, the curves are not all superposed on a single master-curve, further indicating the presence of these two effects.

Due to the likely presence of magnetic anisotropy in those compounds, ac susceptibility measurements were made under zero dc field. No out-of-phase signals could be measured above 1.8 K for **1** and **3**. However, frequency-dependent out-of-phase signals were

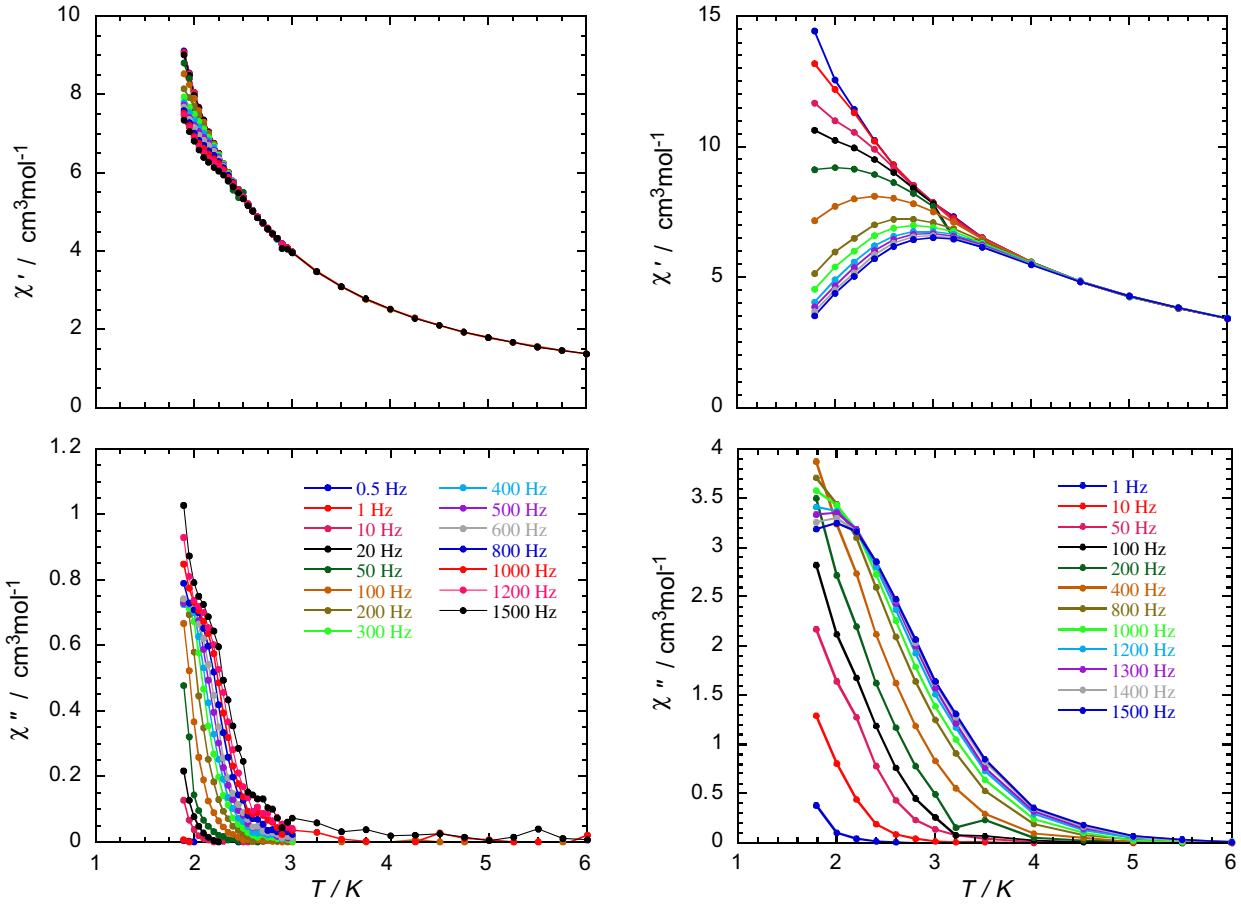


Fig. 4. Temperature dependence of the in-phase (top) and out-of-phase (bottom) component of the ac magnetic susceptibility in zero dc field; compound **2** (left) and **4** (right).

detected for compounds **2** and **4** (Fig. 4). In the case of **2**, the out-of-phase signal is clearly observed up to 4 K (for a frequency of 1500 Hz). This out-of-phase signal suggests that this compound exhibits slow relaxation of its magnetization, but with a blocking temperature still below 1.8 K, even at 1500 Hz. However, compound **4** clearly exhibits slow relaxation of its magnetization above 1.8 K and both in-phase and out-of-phase signals are frequency-dependent up to 5 K in the same frequency range. The out-of-phase signal showed a maximum at 2.0 K at a frequency of 1500 Hz. This feature (shape and frequency dependence) strongly suggests it might be a SMM. Fitting the frequency-dependent ac susceptibility data (Fig. ESI 5) of **4** by an Arrhenius law (Fig. ESI 6) leads to the characteristic SMM energy gap (Δ) of 10.0 K and the relaxation time (τ_0) at 1.4×10^{-6} s.

In order to study further this relaxation and check for any quantum tunnelling effect above 1.8 K, the frequency dependence of the ac susceptibility measurements at 1.8 K was measured with the application of a small dc field for compound **4** (Fig. ESI 7). In zero field, the characteristic frequency is 500 Hz at 1.8 K. With an increasing field, this frequency decreases to reach 18 Hz at 1500 Oe. Therefore a small dc field is indeed slowing down the relaxation time by suppressing quantum tunnelling of the magnetization, as has been observed previously for other SMMs [13,21].

4. Conclusions

A convenient one-step route for the synthesis of Mn–Ln polynuclear complexes is demonstrated, based on a simple reaction between manganese acetate, the corresponding lanthanide nitrate, pivalic acid and *N*-butyldiethanolamine. We have reported the structural and magnetic properties of four isostructural Mn_2Ln_2 tetranuclear compounds with Ln = La, Ce, Pr and Nd. The magnetic susceptibility of the Mn_2Ce_2 complexe **2** showed strong frequency-dependent out-of-phase signals (without maxima) which could be the tails of peaks lying at a temperature below 1.8 K. However, that of the Mn_2Nd_2 complex **4** showed out-of-phase signals with a clear maximum at 2.0 K, and the data could be fitted to the Arrhenius law to give an energy gap Δ of 10.0 K. Although much of the published research on SMMs based on combinations of manganese and lanthanides has concentrated on the heavier lanthanides (typically Dy), the work presented here shows that incorporation of lighter lanthanides can also lead to SMM behavior. Further experiments are underway to modify the structures reported here, using other lanthanides and tridentate ligands, with the aim of enhancing the SMM properties.

Acknowledgements

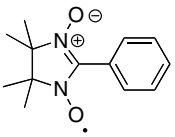
We thank the DFG (CFN and SPP 1137), QuEMolNa (MRTN-CT2003-504880), MAGMANet (NMP3-CT-2005-515767)), the Conseil Régional d'Aquitaine, the Université de Bordeaux, and the CNRS for financial support.

Appendix A. Supplementary data

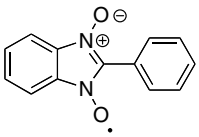
CCDC-701786, 701787 and 701788 contain the supplementary crystallographic data for **1, 2** and **3**. These data can be obtained free of charge via http://www.ccdc.cam.ac.uk/conts/retrieving.html, or from the Cambridge Crystallographic Data Centre, 12 Union Road, Cambridge CB2 1EZ, UK; fax: (+44) 1223-336-033; or e-mail: deposit@ccdc.cam.ac.uk. Supplementary data associated with this article can be found, in the online version, at doi:10.1016/j.poly.2008.10.062.

References

[1] (a) C. Edder, C. Piguet, J.-C.G. Bünzli, G. Hopfgartner, Chem. Eur. J. 7 (2001) 3014;
(b) W.-K. Wong, H. Liang, W.-Y. Wong, Z. Cai, K.-F. Li, K.-W. Cheah, New J. Chem. 26 (2002) 275.
[2] M.A. Subhan, T. Suzuki, S. Kaizaki, J. Chem. Soc., Dalton Trans. (2002) 1416.
[3] (a) B. Zhao, P. Cheng, Y. Dai, C. Cheng, D.Z. Liao, S.P. Yan, Z.H. Jiang, G.L. Wang, Angew. Chem., Int. Ed. 42 (2003) 934;
(b) B. Zhao, P. Cheng, X.Y. Chen, C. Cheng, W. Shi, D.Z. Liao, S.P. Yan, Z.H. Jiang, J. Am. Chem. Soc. 126 (2004) 3012.
[4] O. Margeat, P.G. Lacroix, J.P. Costes, B. Donnadieu, C. Lepetit, K. Nakatani, Inorg. Chem. 43 (2004) 4743.
[5] C. Benelli, D. Gatteschi, Chem. Rev. 102 (2002) 2369.
[6] (a) J.-P. Costes, F. Dahan, W. Wernsdorfer, Inorg. Chem. 45 (2006) 5;
(b) C. Aronica, G. Pilet, G. Chastanet, W. Wernsdorfer, F. Jacquot, D. Luneau, Angew. Chem. 118 (2006) 4775. Angew. Chem., Int. Ed. 45 (2006);
(c) M. Ferbinteanu, T. Kajiwara, K.-Y. Choi, H. Nojiri, A. Nakamoto, N . Kojima, F. Cimpoesu, Y. Fujimura, S. Takaishi, M. Yamashita, J. Am. Chem. Soc. 128 (2006) 9008;
(d) A. Mishra, W. Wernsdorfer, K.A. Abboud, G . Christou, J. Am. Chem. Soc. 126 (2004) 15648;
(e) S. Osa, T . Kido, N. Matsumoto, N. Re, A. Pochaba, J. Mrozinski, J. Am. Chem. Soc. 126 (2004) 420;
(f) C.M. Zaleski, E.C. Deppermann, E.C. Kampf, J.W. Kampf, M.L. Kirk, V.L. Pecoraro, Angew. Chem. 116 (2004) 4002. Angew. Chem., Int. Ed. 43 (2004) 3912.
[7] (a) A. Mishra, W. Wernsdorfer, S. Parsons, G. Christou, E.K. Brechin, Chem. Commun. (2005) 2080;
(b) M. Murugesu, A. Mishra, W. Wernsdorfer, K. Abboud, G. Christou, Polyhedron (2006) 613.
[8] V.M. Mereacre, A.M. Ako, R. Clérac, W. Wernsdorfer, G. Filoti, J. Bartolomé, C.E. Anson, A.K. Powell, J. Am. Chem. Soc. 129 (2007) 9248.
[9] V. Mereacre, A.M. Ako, R. Clérac, W. Wernsdorfer, I.J. Hewitt, C. E Anson, A.K. Powell, Chem. Eur. J. 14 (2008) 3577.
[10] (a) A. Caneschi, A. Cornia, S.J. Lippard, Angew. Chem., Int. Ed. Engl. 34 (1995) 467;
(b) S.P. Watton, P. Fuhrmann, L.E. Pence, A. Caneschi, A. Cornia, G.L. Abbati, S.J. Lippard, Angew. Chem., Int. Ed. Engl. 36 (1997) 2774;
(c) G.L. Abbati, A. Cornia, A.C. Fabretti, A. Caneschi, D. Gatteschi, Inorg. Chem. 37 (1998) 3759;
(d) A.L. Dearden, S. Parsons, R.E.P. Winpenny, Angew. Chem., Int. Ed. 40 (2001) 151.
[11] R.W. Saalfrank, C. Deutscher, S. Sperner, T. Nakajima, A.M. Ako, E. Uller, F. Hampel, F.W. Heinemann, Inorg. Chem. 43 (2004) 4372.
[12] A.M. Ako, O. Waldmann, V. Mereacre, F. Klöwer, I.J. Hewitt, C.E. Anson, H.U. Güdel, A.K. Powell, Inorg. Chem. 46 (2007) 756.
[13] A.M. Ako, V.M. Mereacre, I.J. Hewitt, R. Clérac, L. Lecren, C.E. Anson, A.K. Powell, J. Mater. Chem. 15 (2006) 2579.
[14] (a) G.M. Sheldrick, SADABS (the siemens Area Detector Absorption Correction), University of Göttingen, 1996;
(b) G.M. Sheldrick, SHEXTL 5.1, Bruker AXS. Inc., 6300 Enterprise Lane, Madison, WI 53719-1173, USA, 1997.
[15] C. Benelli, M. Murrie, S. Parsons, Richard E.P. Winpenny, J. Chem. Soc., Dalton Trans. (1999) 4125.
[16] (a) W. Liu, H.H. Thorp, Inorg. Chem. 32 (1993) 4102;
(b) P.L. Roulhac, G.J. Palenik, Inorg. Chem. 42 (2003) 118.
[17] (a) J. Yoo, A. Yamaguchi, M. Nakano, J. Krystek, W.E. Streib, L.C. Brunel, H. Hishimoto, G. Christou, D.N. Hendrickson, Inorg. Chem. 40 (2001) 4604;
(b) E.C. Yang, N. Harden, W. Wernsdorfer, L. Zakhrov, E.K. Brechin, A.L. Rheingold, G. Christou, D.N. Hendrickson, Polyhedron 22 (2003) 1857;
(c) D.N. Hendrickson, G. Christou, H. Ishimoto, J. Yoo, E.K. Brechin, A. Yamaguchi, E.M. Rumberger, S.M.J. Aubin, Z. Sun, G. Aromí, Polyhedron 20 (2001) 1479;
(d) L. Lecren, Y.-G. Li, W. Wernsdorfer, O. Roubeau, H. Miyasaka, R. Clérac, Inorg. Chem. Commun. 8 (2005) 626;
(e) L. Lecren, W. Wernsdorfer, Y.-G. Li, O. Roubeau, H. Miyasaka, R. Clérac, J. Am. Chem. Soc. 127 (2005) 11311.
[18] J.H. van Vleck, The Theory of Electric and Magnetic Susceptibility, Oxford University Press, 1932.
[19] K. Kambe, J. Phys. Soc. Jpn. 5 (1950) 48.
[20] (a) B.E. Myers, L. Berger, S. Friedberg, J. Appl. Phys. 40 (1969) 1149;
(b) C.J. O'Connor, Prog. Inorg. Chem. 29 (1982) 203.
[21] (a) D. Li, R. Clérac, S. Parkin, G. Wang, G.T. Yee, S.M. Holmes, Inorg. Chem. 45 (2006) 5251;
(b) F. Pointillart, K. Bernot, R. Sessoli, D. Gatteschi, Chem. Eur. J. 13 (2007) 1602;
(c) J. Martínez-Lillo, D. Armentano, G.D. Munno, W. Werndorfer, M. Julve, F. Lloret, J. Faus, J. Am. Chem. Soc. 128 (2006) 14218;
(d) G. Poneti, K. Bernot, L. Bogani, A. Caneschi, R. Sessoli, W. Wernsdorfer, D. Gatteschi, Chem. Commun. (2007) 1807;
(e) C. Kachi-Terajima, H. Miyasaka, A. Saitoh, N. Shirakawa, M. Yamashita, R. Clérac, Inorg. Chem. 46 (2007) 5861.

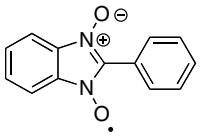


1

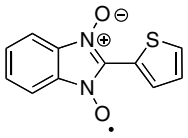


2

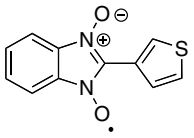
Earlier work on the effect of heterocyclic substitution on the structure of benzonitronyl nitroxides revealed that the benzonitronyl nitroxides are excellent electron acceptors, with reduction potentials on the order of 0.0 V vs. SCE [35]. Herein we present the magnetic behavior, spin density distribution, and electronic structure of acceptor–donor benzannelated nitronyl nitroxides in which the C-2 phenyl substituent of the parent radical (**2a**) has been replaced by an electron-rich thiophene (**2b**, **2c**). The SOMO–LUMO gap, spin density distribution, and solid-state magnetic behavior were found to be dependent on both the nature and position of substitution.



2a



2b



2c

2. Experimental

2.1. General methods

The synthesis of radicals **2b–c** are reported elsewhere [35]. Absorption spectra were recorded on an Agilent 8453 UV–Vis spectrometer with photodiode array and Peltier temperature controller, and a Carey 5 UV–Vis-NIR Spectrophotometer.

2.2. Computations

Quantum mechanical calculations were carried out at the B3LYP/6-31G(d,p) level of theory using the Gaussian 03 package [40]. Geometry optimizations were performed without symmetry constraints (starting from C_1) and tight convergence limits. Vibrational frequencies were used to characterize the nature of stationary points. Electronic excitation energies for the radical **2a** were obtained at the UB3LYP/6-31G(d,p) level using Time Dependent DFT calculations [41] supplied in the Gaussian 03 package.

2.3. Magnetic measurements

Magnetic measurements were performed on a Quantum Design MPMS 5.0 system, with fields in the range of 1–5 T, and temperature ranges between 2 and 300 K. The polycrystalline samples of radicals **2b** and **2c** were prepared by the macroscale evaporation of a saturated radical *n*-pentane solution over several days, followed by triturating the crystals with *n*-pentane and methanol, and drying under vacuum. Measurements were made on 6 independently synthesized and prepared samples in order to assure that the magnetic behavior observed was not due to the presence of impurities, which are expected to vary from sample to sample. The diamagnetic corrections for radical **2b** and **2c** were performed by using the experimentally measured diamagnetic susceptibility of the radical precursors (3.03E−04 emu K/mol).

2.4. X-ray crystallography

Crystals suitable for X-ray diffraction studies were obtained by slow evaporation of radical–pentane solutions. The diffraction intensity measurements were carried out on a Nonius KappaCCD (1997) diffractometer.

2.5. 2,2′-Thienylbenzimidazole N,N′-dioxide (**2b**)

A maroon crystal plate 0.48 × 0.12 × 0.02 mm was mounted on a glass capillary with oil. Data was collected at −143 °C with one set of exposure as follows: Type: φ, Scanlength 183.0°, with start v 3.70, φ −1.5, $\Omega = 160$, and $\kappa = 0$. Crystal-to-detector distance was 30 mm and exposure time was 90 s per degree for all sets. The scan width was 1.3°. Data collection was 87.5% complete to 25.00° in v. A total of 5877 partial and complete reflections were collected covering the indices, $h = -9$ to 9, $k = -6$ to 6, $l = -19$ to 19. 1662 reflections were symmetry independent and the $R_{int} = 0.1030$ indicated that the data was of average quality (0.07) consistent with the difficulties in obtaining suitable crystals for X-ray diffraction in these systems. Indexing and unit cell refinement indicated a monoclinic *P* lattice. The space group was found to be $P2_1/c$ (No. 14). The data was integrated and scaled using *hkl*-SCALEPACK [42]. This program applies a multiplicative correction factor (S) to the observed intensities (I) and has the following form: $S = \exp(2B(\sin q/\lambda)^2)/\text{scale}$. S is calculated from the scale and the B factor is determined for each frame and is then applied to I to give the corrected intensity (I_{corr}). Solution by direct methods (SIR92/7) [43] produced a complete heavy atom phasing model consistent with the proposed structure. All hydrogen atoms were located using a riding model. All of the non-hydrogen atoms were refined anisotropically by full-matrix least-squares. Due to the disorder of the system constraints were placed upon the thermal parameters of several atoms to ensure positive definite matrix elements. The model used to resolve the disorder of the system was the superposition of two molecules on top of one another. The asymmetric unit consists of the one unique half of the dimer pair. The full dimer is generated by a C_2 rotation perpendicular to the molecular plane. The oxygen atom positions are shared by both molecules and thus have full site occupancy. All other atoms were refined with 50% site occupancy.

2.6. 2,3′-Thienylbenzimidazole N,N′-dioxide (**2c**)

A dark red plate 0.41 × 0.05 × 0.02 mm was mounted on a glass capillary with epoxy. Data was collected at −143 °C with one set of exposure as follows: Type: φ, Scanlength 128.6°, with start v 3.70, φ −9.27, $\Omega = 160$, and $\kappa = 0$. Crystal-to-detector distance was 30 mm and exposure time was 120 s per degree for all sets. The scan width was 1.0°. Data collection was 59.2% complete to 23.77° in v. A total of 13828 partial and complete reflections were collected covering the indices, $h = -4$ to 4, $k = -14$ to 19, $l = -14$ to 13. 865 reflections were symmetry independent and the $R_{int} = 0.3254$ indicated that the data was of average quality (0.07) consistent with the difficulties in obtaining suitable crystals for X-ray diffraction in these systems. Indexing and unit cell refinement indicated a monoclinic *P* lattice. The space group was found to be $P2_1/c$ (No. 14). The data was integrated and scaled using *hkl*-SCALEPACK [42]. This program applies a multiplicative correction factor (S) to the observed intensities (I) and has the following form: $S = \exp(2B(\sin q/\lambda)^2)/\text{scale}$. S is calculated from the scale and the B factor is determined for each frame and is then applied to I to give the corrected intensity (I_{corr}). Solution by direct methods (SIR92/7) [43] produced a complete heavy atom phasing model consistent with the proposed structure. All hydrogen atoms were located using a riding model. All non-hydrogen atoms were refined aniso-

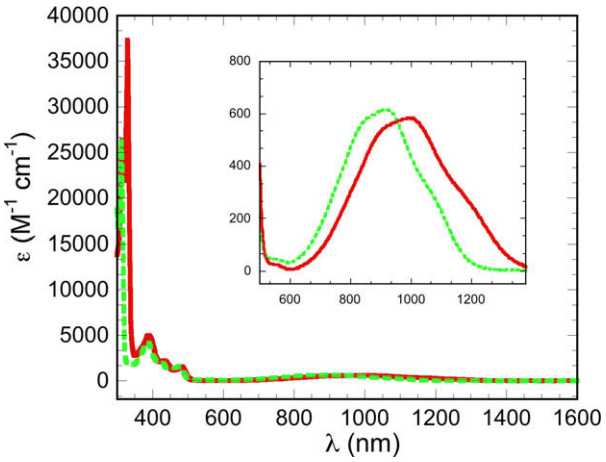


Fig. 1. Electronic absorption spectra of 10^{-6} M acetonitrile solutions of **2b** (---) and **2c** (—) at 300 K (inset: expansion of the long wavelength region).

tropically by full-matrix least-squares. The structure was refined as a structure containing disorder in the C_1 and S_1 positions. The positions were refined as both atoms having a site occupancy of 50% in both sites.

3. Results and discussion

3.1. Optical spectroscopy of acceptor–donor radicals

The electronic absorption spectra of the benzonitronyl nitroxides **2a–c** were measured in solution in order to investigate the effect of acceptor–donor interactions on the electronic structure of nitronyl nitroxides (Fig. 1). Solutions of radicals **2a**-**c** were bright green/yellow in color and exhibited absorption spectra with strong absorptions in the UV region (λ_{max} 240–480 nm) and a weak absorption in the near-IR (one broad transition at 1000 nm, $\varepsilon \sim 600\ M^{-1}\ cm^{-1}$) which was red-shifted relative to the parent radical **2a**. The absorption spectrum of the imidazolidinyl nitroxide **1** exhibits similar absorption bands in the UV region with an absorption band in the visible region at 600 nm assigned to a n–π^* transition [24].

The low energy transition was found to vary dramatically with substitution, and exhibit significant solvatochromism [35], consistent with a charge transfer band. Given the strong acceptor strength found for the benzonitronyl moiety (0.0 vs. SCE), the CT band can be rationalized as a benzonitronyl nitroxide (A)–thiophene (D) interaction. Using the theory of Mulliken and Hush [44–47] the strength of the electronic donor–acceptor coupling parameter (V_{ab}) was determined. The magnitude of the A–D interaction can be calculated using band shape analysis of the optical charge transfer transition using Eq. (1) in which v_{max} is the band energy (in cm^{-1}), $\Delta v_{1/2}$ is the bandwidth at half-height (in cm^{-1}), ε is the molar extinction coefficient (in $M^{-1}\ cm^{-1}$), and r_{DA} is the distance between the opposite charges in the charge separated $D^{\cdot+}A^{-}$ excited state (in Å).

$$V_{ab} = (2.05 \times 10^{-2}) \frac{[\varepsilon_{max} \Delta \upsilon_{1/2} \upsilon_{max}]^{1/2}}{r_{DA}} \quad (1)$$

When applying Hush theory, determination of the diabatic electron transfer distance (r_{DA}) in organic compounds suffers from the typically delocalized nature of the acceptor and donor, distinct from traditional inorganic systems in which the redox centers are localized and the metal–metal distance can be explicitly determined. Here r_{DA} has been estimated to be the length of the benzonitronyl nitroxide–thiophene carbon–carbon bond (1.43 Å) as determined from the X-ray crystallography, an appropriate estimation for these systems as the charge on the benzonitronyl nitroxide moiety is highly delocalized over the ONCNO atoms and thiophene is aromatic.

The electronic coupling energy V_{ab} for **2b** and **2c** was found to be the same within experimental error, that is, a coupling energy of 1900 cm^{-1} was calculated for both systems. The similarity in coupling energy is not unexpected as the magnitude of V_{ab} depends strongly on bridge length and differences in redox potential between the donor and acceptor. Since neither of these variables differs dramatically between **2b** and **2c**, the donor–acceptor electronic coupling is comparable. The magnitude of the donor–acceptor coupling is moderate to strong suggesting that radicals **2b–c** fall on the borderline between Robin-Day class II and class III A–D systems, consistent with the symmetrical band shape observed.

In order to better understand the nature of the low energy transition, vertical excitation energies and oscillator strengths for the parent radical **2a** were computed by TDDFT using the UB3LYP functional with 6-31G(d,p)+ basis set (Fig. 2). TDDFT is known to predict vertical excitation energies of open-shell PAHs to within 0.3 eV of the experimental data and oscillator strengths that are consistent with the measured absorption spectra [48]. For the first excited state, the largest coefficients in the CI expansion were found to be for the HOMO–LUMO (β) 0.96 (77%) and the HOMO–LUMO (α) transition (23%) for the unrestricted model with an excitation energy of 1.6 eV (775 nm) and oscillator strength of 0.0158. This corresponds well with the energy of the lowest energy band at 885 nm in pentane (825 in acetonitrile) and suggests that the transition is due primarily to a HOMO–SOMO transition (restricted model), with a 30% component due to the SOMO–LUMO transition. This transition into the half-filled orbital is consistent with the triphenylmethyl [49] and benzothiazinyl radicals [50], both of which have weak low energy transitions assigned to a HOMO–SOMO transition.

Substitution of the phenyl ring in **2a** with 2-pyridyl or 4-pyridyl leads to shifts in the low energy band by 6 nm (bathochromic) and 60 nm (hypsochromic), respectively, [35] while 2-thienyl (**2b**), and 3-thienyl (**2c**) substitution leads to bathochromic shifts of 150, and 105 nm, respectively. As the SOMO is primarily localized on the benzonitronyl nitroxide moiety, the changes in transition energy are consistent with localization of both the HOMO and LUMO on the C-2 aryl ring, leading to significant changes in the SOMO–HOMO and SOMO–LUMO gaps with substitution. Analysis of the charge distribution in the SOMO and HOMO suggests that the charge transfer transition occurs from the HOMO localized on the thienyl to the BNN moiety (SOMO). The extent of population overlap between the two states is consistent with the moderate couplings derived from a Mulliken–Hush analysis.

3.2. Structural analyses by X-ray crystallography

Maroon crystal plates of **2b** and dark red plates of **2c** were grown by slow evaporation of saturated *n*-pentane solutions, and their structures determined by X-ray diffraction. The 2-thienyl derivative **2b** crystals were twinned and severely disordered. Refinement of the structure led to monoclinic packing in the $P2_1/c$ space group. The crystal structure is disordered with respect to rotation about a C_2 axis perpendicular to the plane of the molecule, leading to superposition of two orientations each with 50% occupancy, as shown in Fig. 3. The molecule adopts an essentially planar geometry with a torsion angle between the benzimidazole and thiophene moieties of 1.7°. The 3-thienyl derivative **2c** exhibits monoclinic packing in the space group $P2_1/c$ with disorder with respect to rotation about a C_2 axis parallel to the long axis of the molecule, with 50% occupancy in each orientation, as shown in Fig. 3.

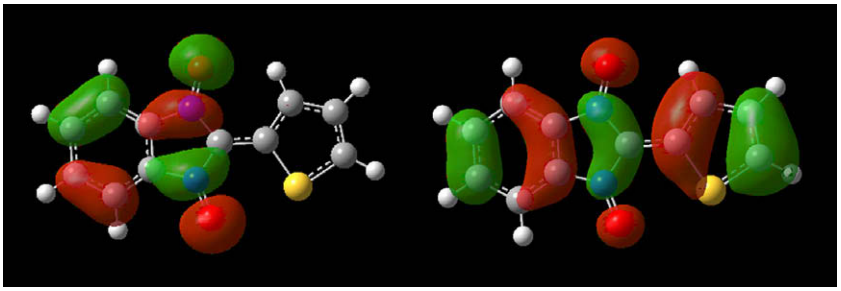


Fig. 2. Computational (DFT UB3LYP/6-31G(d,p)+) SOMO (left) and HOMO (right) of **2b** generated with GAUSSVIEW 03 (isovalue 0.02).

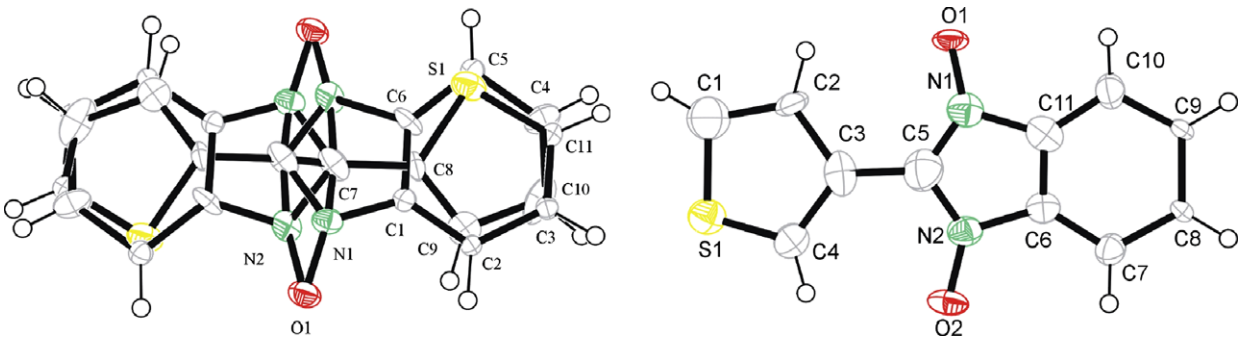


Fig. 3. ORTEP representations of radical **2b** (left) and **2c** (right) with 50% probability thermal ellipsoids. The packing disorder in **2b** arises from rotation about an axis perpendicular to the long axis of the molecule, while the disorder in **2c** arises form rotation about a C_2 axis parallel to the long axis of the molecule.

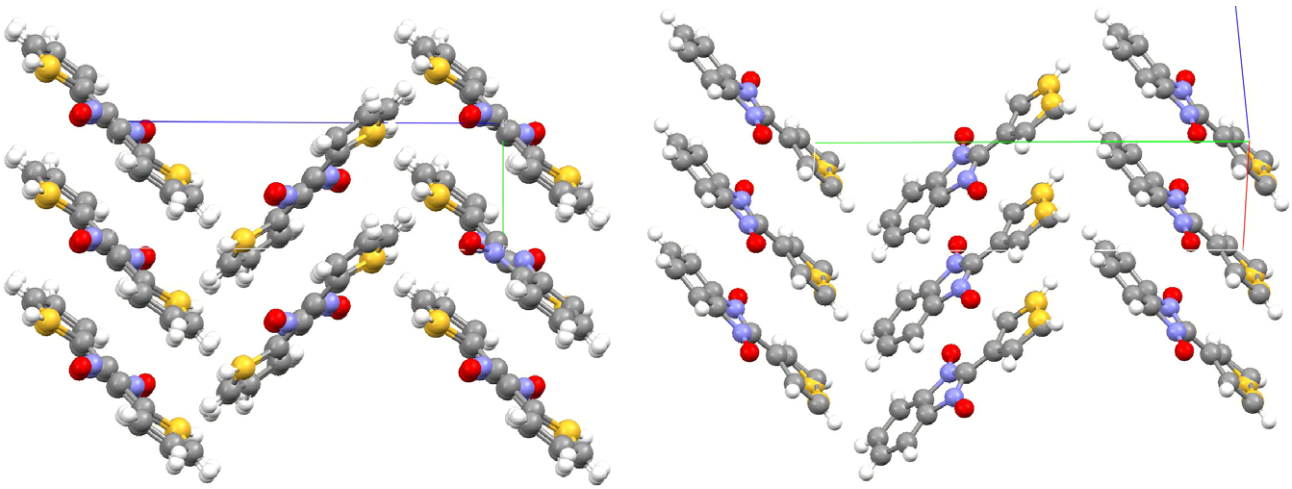


Fig. 4. Packing diagram of radical **2b** viewed along the *a*-axis, and **2c** viewed along [1 1 0]′.

The degree of planarity is slightly less than that of **2b**, with a torsion angle of 4.6°. The parent radical, **2a**, exhibits a larger torsional angle of 10° [37], and phenyl substituents containing *ortho* subtitution (Cl, F) exhibit much larger torsional angles of 54–76° [38].

The structural features of radicals **2b** and **2c** involve edge-to-face and π-stacking interactions leading to herringbone motifs (Fig. 4). The packing modes can be discussed within the context of structural types for aromatic hydrocarbons which depend on the relative importance of C···C, C···H, and H···H interactions [51,52]. The parent radical **2a** [37] packs in a sandwich herringbone motif which straddles the structural gap between γ and herringbone modes. The sandwich herringbone packing motif for aromatics is one in which both C···C and C···H interactions are important, leading to effective glide and stack stabilization [51]. In both radicals **2b** and **2c**, both the surface area available for stacking C···C interactions and the edge surface area available for C···H interactions is nearly equal, leading to packing in which both stacking and edge-to-face interactions are efficient. Analysis of the interplanar angle between molecules creating an edge-to-face interaction (84.86° (**2b**) and 89.23° (**2c**)) and shortest crystallographic axes for **2b** (*a*-axis) and **2c** (*b*-axis), is consistent with a γ phase herringbone motif. Both C···C stacking and C···H edge-to-face interactions are energetically favored in the γ phase herringbone motif, consistent with prediction of packing based solely on topology [51].

The nature of the edge-to-face interactions in **2c** arises from thiophenyl S···benzimidazole face interactions, with a closest dis-

tance 3.50 Å for the benzimidazole plane-to-sulfur distance. The interplanar distance between stacked molecules is 3.42 Å for **2b**, and 3.41 Å for **2c**, giving rise to short radical–radical contacts through π-stacking interactions. Unlike the parent radical **2a**, and electron deficient derivatives, no closest radical–radical O···O contacts exist below 6.0 Å in **2d**, and **2e**, thus, the magnetic interactions in these systems arise from through-space π-stacking and C···H interactions rather than radical–radical contacts.

3.3. Magnetic behavior of stable radicals *2b*, *2c*

The molar magnetic susceptibilities ($\chi_{m,p}$) were measured for polycrystalline samples of radicals **2b**/**2c** using a Quantum Design SQUID magnetometer in the temperature range of 2–300 K at DC fields of 0.1–5 T (Figs. 5 and 6). Diamagnetic corrections of the susceptibilities were made using experimental measurement of the diamagnetic susceptibilities of the radical precursors. The 2-thienyl (**2b**) and 3-thienyl (**2c**) derivatives exhibit magnetic moments close to the expected spin only value for a spin = 1/2 system (0.375 emu K/mol), with temperature independent magnetic moments above 100 K. In both systems, the magnetic moments (χT) decrease with decreasing temperature, consistent with antiferromagnetic exchange interactions.

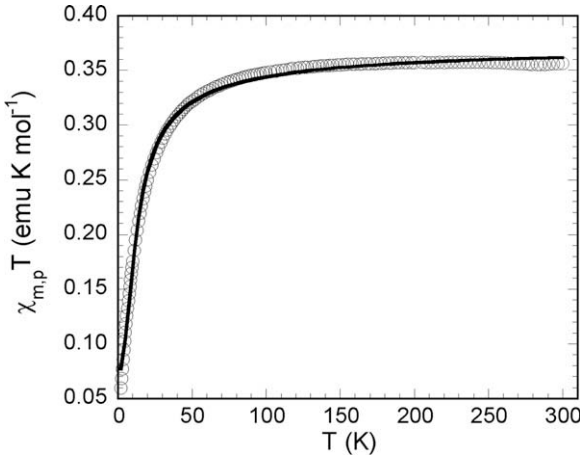


Fig. 5. Temperature dependence of the magnetic moment (χT) for radical **2b** (2–300 K) at 0.1 T with the fit to a Bonner–Fisher model: experimental (○) and fit (–).

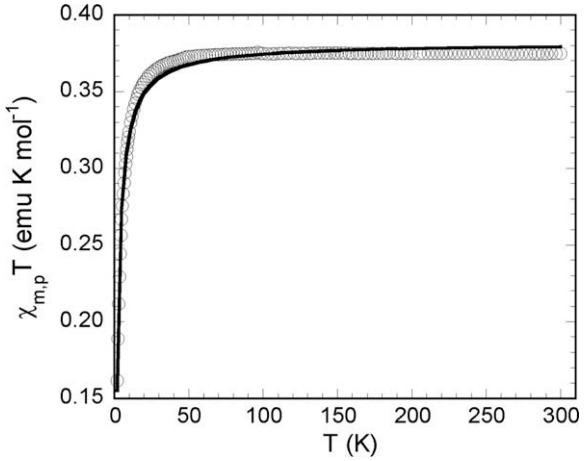


Fig. 6. Temperature dependence of the magnetic moment (χT) for radical **2c** (2–300 K) at 0.1 T with the fit to a Bonner–Fisher model: experimental (○) and fit (–).

Analysis of the crystal structure suggests that the dominant pathway for magnetic exchange interactions is through the slipped π-stack, with weak interchain interactions contributing to a minor extent. A fit of the magnetic moment (χT) as a function of temperature was obtained using the numerical solution for a Bonner–Fisher model [53]with the inclusion of a mean-field parameter according to equation:

$$\chi T = \rho \frac{\chi T'}{1 - \left(\frac{2zJ'}{Ng^2\beta^2}\right)\chi T'} + (1-\rho)\frac{C}{T}$$

$$\chi T' = \frac{Ng^2\beta^2}{k_B} \cdot \frac{0.25 + 0.074975x + 0.075235x^2}{1.0 + 0.9931x + 0.172135x^2 + 0.757825x^3}$$

$$x = \frac{|J|}{k_B T}$$

$$J \leqslant 0$$

The *g*-value was fixed to the experimentally derived value of 2.007, to give $J = -9.4\ \mathrm{cm}^{-1}$, $2zJ' = -0.7\ \mathrm{cm}^{-1}$, and a purity factor of 0.99822 (SI) for radical **2b**. Weaker exchange was found in radical **2c**, in which the exchange coupling was found to be $-2.0\ \mathrm{cm}^{-1}$ with $2zJ' = -0.4\ \mathrm{cm}^{-1}$, and a purity factor of 0.99725. Inclusion of the mean-field parameter did not alter the fit substantially, consistent with chain interactions dominating the magnetic exchange. The surprisingly weak exchange relative to other benzannelated nitronyl nitroxides is attributed to the disorder observed in the crystal packing.

Difficulties in fitting the temperature dependent magnetic susceptibilities to reasonable magnetic models for both the parent radical **2a** [37] and a class of electron deficient benzannelated nitronyl nitroxides radicals [38] have been previously noted. Such effects have been attributed to "a mysterious diamagnetic impurity invisible by MS and IR spectroscopy" [38], or the formation of high-spin spin clusters at low temperatures [39]. Polymorphism has also been observed in several of the known derivatives of **2a** [37,38]. This class of radicals is unique in that they are fully delocalized planar radicals that are stable toward dimerization in the solid state, unlike the phenalenyl or thiazyl classes of radicals. Directional non-covalent interactions are expected to be extremely weak or entirely absent, leading to little preference for molecular orientation in the crystalline state. The resulting disorder can cause complication of the dominant through-space pathways for magnetic exchange. Structural analysis of our systems indicates significant structural disorder in the solid state, leading to little preference for head-to-head (HH) versus head-to-tail (HT) π-stacking, or inversion about the molecular axis within chains. The distinction

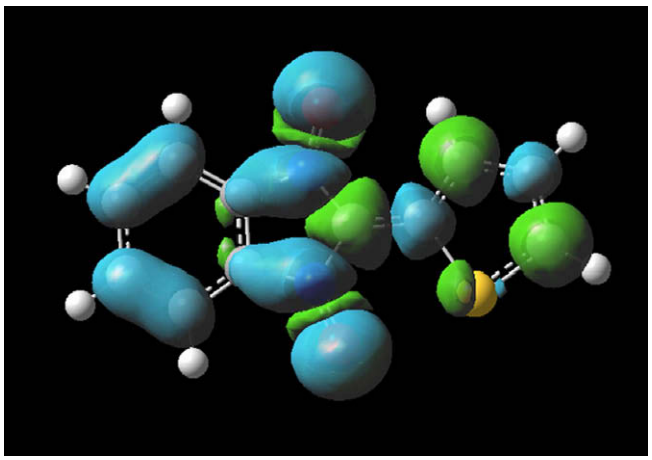


Fig. 7. Computational (DFT UB3LYP/6-31G**) spin density distribution of **2b** generated with GAUSSVIEW 03 (isovalue 0.002).

between HT and HH interactions discriminates between radical–radical contacts versus radical–aromatic contacts, providing two distinct pathways for magnetic exchange. As the spin density is highly delocalized (Fig. 7), this may give rise to different exchange parameters as a function of topology (HH vs. HT). This effect is expected to be present in the 2-thienyl derivative, giving rise to competing exchange interactions and a weak overall exchange parameter.

4. Conclusions

The magnetic behavior and structural characterization of acceptor–donor spin-delocalized radicals **2b** and **2c** are reported. Electronic absorption spectroscopy accompanied by computation reveals that the near-IR band can be assigned to a HOMO → SOMO charge transfer transition with electronic coupling of 1900 cm^{-1} between the benzimidazole and thiophene moiety. Structural analysis of the thienyl radicals in the crystalline state reveals disorder due to the high symmetry of the planar delocalized radicals, and the dominance of slipped π-stacks. Magnetic susceptibility measurements reveal weak antiferromagnetic interactions that are consistent with a linear chain Bonner–Fisher model. The magnetic properties are therefore dictated by the topology of the radical and not by perturbations in the spin density induced by substitution at C-2, which are minimal. The low reduction potentials and strength of the through-space magnetic exchange interactions demonstrated in the solid state make these extremely interesting systems for the development of multifunctional magnetic materials.

Acknowledgments

The authors thank the STC Program of the National Science Foundation No. DMR 0120967, NSERC (DG 311740-05), CFI (202373), BCKDF (803974), the Canada Research Chair Program, the University of Victoria, and the University of Washington for funding. BMD thanks NSERC for a PGS D3 Fellowship.

References

[1] I. Zutic, J. Fabian, S. Das Sarma, Rev. Mod. Phys. 76 (2004) 323.
[2] M. Fiebig, T. Lottermoser, D. Frohlich, A.V. Goitsev, R.V. Pisarev, Nature 419 (6909) (2002) 818.
[3] S.A. Wolf, D.D. Awschalom, R.A. Buhrman, J.M. Daughton, S. von Molnar, M.L. Roukes, A.Y. Chtchelkanova, D.M. Treger, Science 294 (5546) (2001) 1488.
[4] I. Malajovich, J.J. Berry, N. Samarth, D.D. Awschalom, Nature 411 (6839) (2001) 770.
[5] F.J. Jedema, A.T. Filip, B.J. van Wees, Nature 410 (6826) (2001) 345.
[6] H. Ohno, Physica E 6 (2000) 702.
[7] Y. Ohno, D.K. Young, B. Beschoten, F. Matsukura, H. Ohno, D.D. Awschalom, Nature 402 (1999) 790.
[8] I. Zutic, M. Fuhrer, Nat. Phys. 1 (2) (2005) 85.
[9] H.J. Choi, H.K. Seong, J. Chang, K.I. Lee, Y.J. Park, J.J. Kim, S.K. Lee, R.R. He, T. Kuykendall, P.D. Yang, Adv. Mater. 17 (11) (2005) 1351.
[10] M.P. de Jong, V.A. Dediu, C. Taliani, W.R. Salaneck, J. Appl. Phys. 94 (11) (2003) 7292.
[11] T. Hozumi, K. Hashimoto, S. Ohkoshi, J. Am. Chem Soc. 127 (11) (2005) 3864.
[12] M. Ruben, E. Breuning, J.M. Lehn, V. Ksenofontov, F. Renz, P. Gutlich, G.B.M. Vaughan, Chem. Eur. J. 9 (18) (2003) 4422.
[13] J.G. Moore, E.J. Lochner, C. Ramsey, N.S. Dalal, A.E. Stiegman, Angew. Chem., Int. Ed. Engl. 42 (24) (2003) 2741.
[14] P. Gutlich, Y. Garcia, T. Woike, Coord. Chem. Rev. 219–221 (2001) 839.
[15] R.C. Haddon, Nature 256 (1975) 394.
[16] C.D. Bryan, A.W. Cordes, R.M. Fleming, N.A. George, S.H. Glarum, R.C. Haddon, R.T. Oakley, T.T.M. Palstra, A.S. Perel, L.F. Schneemeyer, J.V. Waszczak, Nature 365 (1993) 821.
[17] T.M. Barclay, A.W. Cordes, R.C. Haddon, M.E. Itkis, R.T. Oakley, R.W. Reed, H. Zhang, J. Am. Chem Soc. 121 (5) (1999) 969.
[18] X. Chi, M.E. Itkis, B.O. Patrick, T.M. Barclay, R.W. Reed, R.T. Oakley, A.W. Cordes, R.C. Haddon, J. Am. Chem Soc. 121 (44) (1999) 10395.
[19] X. Chi, M.E. Itkis, K. Kirschbaum, A.A. Pinkerton, R.T. Oakley, A.W. Cordes, R.C. Haddon, J. Am. Chem. Soc. 123 (17) (2001) 4041.
[20] M.E. Itkis, X. Chi, A.W. Cordes, R.C. Haddon, Science 296 (5572) (2002) 1443.
[21] L. Beer, R.C. Haddon, M.E. Itki, A.A. Leitch, R.T. Oakley, R.W. Reed, J.F. Richardso, D.G. VanderVeer, Chem. Commun. 9 (2005) 1218.
[22] H.O. Stumpf, L. Ouahab, Y. Pei, D. Grandjean, O. Kahn, Science 261 (5120) (1993) 447.
[23] H.O. Stumpf, L. Ouahab, Y. Pei, D. Grandjean, O. Kahn, Adv. Mater. 6 (9) (1994) 635.
[24] E.F. Ullman, J.H. Siecki, D.G.B. Boocock, R. Darcy, J. Am. Chem. Soc. 94 (20) (1972) 7049.
[25] W. Fujita, K. Awaga, Science 286 (5438) (1999) 261.
[26] A. Alberola, R.J. Less, C.M. Pask, J.M. Rawson, F. Palacio, P. Oliete, C. Paulsen, A. Yamaguchi, R.D. Farley, D.M. Murphy, Angew. Chem., Int. Ed. Engl. 42 (39) (2003) 4782.
[27] R.G. Hicks, M.T. Lemaire, L.K. Thompson, B. TM, J. Am. Chem. Soc. 122 (33) (2000) 8077.
[28] F.A. Neugebauer, H. Fischer, C. Krieger, J. Chem. Soc., Perkin Trans. 2 (3) (1993) 535.
[29] F. Alies, D. Luneau, J. Laugier, P. Rey, J. Phys. Chem. 97 (1993) 2922.
[30] N.L. Frank, R. Clérac, M.T. Green, N. Daro, J.P. Sutter, O. Kahn, C. Coulon, S. Golhen, S. Ouahab, J. Am. Chem. Soc. 122 (2000) 2053.
[31] C. Adamo, A. di Matteo, P. Rey, V. Barone, J. Phys. Chem. A 103 (18) (1999) 3481.
[32] A. Caneschi, D. Gatteschi, The Chemistry and Magnetic Properties of Metal Nitronyl Nitroxide Complexes, vol. 39, John Wiley and Sons, Inc., New York, 1991. p. 332.
[33] M. Deumal, J. Cirujeda, J. Veciana, J.J. Novoa, Chem. Eur. J. 5 (5) (1999) 1631.
[34] L. Ohrstrom, C. R. Chim. 8 (9–10) (2005) 1374.
[35] B.M. Dooley, S.E. Bowles, T. Storr, N.L. Frank, Org. Lett. 9 (23) (2007) 4781.
[36] T.E. Gough, R. Puzic, J. Magn. Res. 23 (1976) 31.
[37] Y. Kusaba, M. Tamura, Y. Hosokoshi, M. Kinoshita, H. Sawa, R. Kato, H. Kobayashi, J. Mater. Chem. 7 (8) (1997) 1997.
[38] A. Zakrassov, V. Shteiman, Y. Sheynin, B. Tumanskii, M. Botoshansky, M. Kapon, A. Keren, M. Kaftory, T.E. Vos, J.S. Miller, J. Mater. Chem. 14 (12) (2004) 1827.
[39] D. Shiomi, K. Sato, T. Takui, K. Itoh, M. Tamura, Y. Nishio, K. Kajita, M. Nakagawa, T. Ishida, T. Nogami, Mol. Cryst. Liq. Cryst. 334 (1999) 1071.
[40] M.J. Frisch, G.W. Trucks, H.B. Schlegel, G.E. Scuseria, M.A. Robb, J.R. Cheeseman, J.A. Montgomery, J.T. Vreven, K.N. Kudin, J.C. Burant, J.M. Millam, S.S. Iyengar, J. Tomasi, V. Barone, B. Mennucci, M. Cossi, G. Scalmani, N. Rega, G.A. Petersson, H. Nakatsuji, M. Hada, M. Ehara, K. Toyota, R. Fukuda, J. Hasegawa, M. Ishida, T. Nakajima, Y. Honda, O. Kitao, H. Nakai, M. Klene, X.L. Li, J.E. Knox, H.P. Hratchian, J.B. Cross, C. Adamo, J. Jaramillo, R. Gomperts, R.E. Stratmann, O.Y. Yazyev, A.J. Austin, R. Cammi, C. Pomelli, J.W. Ochterski, P.Y. Ayala, K. Morokuma, G.A. Voth, P. Salvador, J.J. Dannenberg, V.G. Zakrzewski, S. Dapprich, A.D. Daniels, M.C. Strain, O. Farkas, D.K. Malick, A.D. Rabuck, K. Raghavachari, J.B. Foresman, J.V. Ortiz, Q. Cui, A.G. Baboul, S. Clifford, J. Cioslowski, B.B. Stefanov, G. Liu, A. Liashenko, P. Piskorz, I. Komaromi, R.L. Martin, D.J. Fox, T. Keith, M.A. Al-Laham, C.Y. Peng, A. Nanayakkara, M. Challacombe, P.M.W. Gill, B. Johnson, W. Chen, M.W. Wong, C. Gonzalez, J.A. Pople, GAUSSIAN 03, Revision B.04, Gaussian, Inc., Pittsburgh, PA, 2003.
[41] M.E. Casida, K.C.C. Christine Jamorski, Dennis R. Salahub, J. Chem. Phys. 108 (11) (1998) 4439.
[42] Z. Otwinowski, W. Minor, Meth. Enzymol. 276 (1996) 307.
[43] A. Altomare, G. Cascarano, C. Giacovazzo, M.C. Burla, G. Polidori, M. Camalli, J. Appl. Crystallogr. 27 (1994) 435.
[44] N.S. Hush, Electrochim. Acta 13 (5) (1968) 1005.
[45] N.S. Hush, Prog. Inorg. Chem. 8 (1967) 391.
[46] N.S. Hush, Coord. Chem. Rev. 64 (1985) 135.
[47] R.S. Mulliken, J. Am. Chem. Soc. 64 (1952) 811.
[48] S. Hirata, M. Head-Gordon, J. Szczepanski, M. Vala, J. Phys. Chem. A 107 (24) (2003) 4940.
[49] L. Anderson, J. Am. Chem Soc. 57 (1935) 1673.
[50] J. Zienkiewicz, P. Kaszynski, V.G.J. Young, J. Org. Chem. 69 (22) (2004) 7525.
[51] G.R. Desiraju, A. Gavezzotti, Acta. Crystallogr., Sect. B 45 (1989) 473.
[52] G.R. Desiraju, Crystal Engineering, vol. 54, Elsevier, Amsterdam, 1989.
[53] J.C. Bonner, M.E. Fisher, Phys. Rev. A 135 (1964) 640.

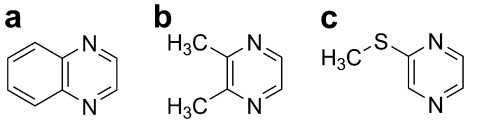


Fig. 1. (a) Quinoxaline (b) 2,3dmpz, and (c) meSpz.

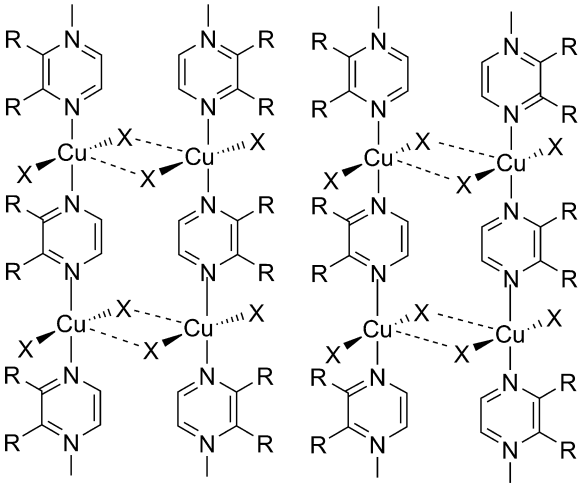


Fig. 2. A Cu(II) ladder complex resulting from a 2,3 di-substituted pyrazine ligand.

the monoclinic space group $C2/m$. The molecular unit of $[Cu(meSpz)Br_2]_n$ is shown in Fig. 3. A crystallographic mirror plane bisects the meSpz ring with the methylthio group disordered across the plane. The sulfur atom occupies each site (S1,S1A) to the extent of 50%. The C1–S1 bond length (1.735(5) Å) is in the normal range for a C–S bond, such as is seen in $Ru(meSpz)(CO)_3Cl_2$ (1.757 Å) [15]. The initial solution placed the methyl carbon on the mirror, but this resulted in a very long S1–C3 bond (1.947(6) Å) in comparison to the terminal S–CH_3 bond in $Ru(meSpz)(CO)_3Cl_2$[17] (1.806 Å) and relative to typical aryl-S-methyl bonds [1.777–1.858 Å] [16], suggesting that the carbon was also disordered and actually displaced toward the sulfur relative to the mirror plane.

Disordered sulfur atoms and methyl carbons are shown as dotted ellipses. Hydrogen atoms are shown as spheres of arbitrary size. Selected bond lengths [Å] and angles [°] for **1**: Cu1–Br1 = 2.4218(14), Cu1–Br1A = 2.8944(16), Cu1–Br2 = 2.3900(13), Cu1–N1 = 2.028(4), C3–S1 = 1.783(12); N1–Cu1–N1B = 175.3(2), N1–Cu1–Br2 = 89.36(10), N1–Cu1–Br1 = 90.19(10), Br1–Cu1–Br2 = 168.70(5), N1–Cu1–Br1A = 92.32(11), Br2–Cu1–Br1A = 101.26(4), Br1–Cu1–Br1A = 90.04(4), Cu1–Br1–Cu1A = 89.96(4), C(1)–S(1)–C(3) = 106.8(4). Symmetry transformations used to generate equivalent atoms: $A = -x + 1, -y, -z + 1$, $B = x, 1 - y, z$.

Placement of the methyl carbon off the mirror led to a stable refinement with the methyl hydrogen atoms placed in fixed positions. The new C3–S1 bond length (1.783(12) Å) is in much better agreement with expected values. Bond lengths and angles within the meSpz ring are otherwise unremarkable; the mean deviation of the constituent atoms from the ring is 0.016 Å with the sulfur and methyl carbon atoms displaced ~0.33 Å toward the Br2 face of the ring.

The copper coordination sphere is 5-coordinate and composed of two nitrogen atoms from two meSpz ligands and three bromide ions (see Fig. 4). The Cu–N bond length (2.023 Å) is in the normal range in comparison to other 5-coordinate compounds, such as Cu(quinoxaline)Br_2 [13] (2.068 Å) and Cu(((4-pyridylcarbonyl)-oxy)$_2$-1,3,4-oxadiazole)Br_2 [17] (2.002 Å). The Cu–Br bonds are somewhat shorter than seen in related five-coordinate bibridged dimer systems [18], but comparable to those seen in the isostructural quinoxaline complex [13].

As determined by the continuous symmetry measure (CSM) approach [19,20], the Cu polyhedron is very nearly square pyramidal [$S_{C4v} = 0.801$, $S_{D3h} = 5.487$] as is typical of Cu(II) halide coordination compounds with trans amine ligands. A symmetry related pair of Br1 ions form an unsymmetrical bihalide bridge between two copper ions ($d_{Br1-Cu1} = 2.4218(14)$ Å, $d_{Br1-Cu1A} = 2.8944(16)$ Å, Cu1–Br1–Cu1A = 89.96(4)°) forming the rungs of the ladder, while the bridging meSpz ligands form the rails.

The ladders pack parallel to the b-axis (Fig. 5). Short S···S contacts (3.169(5) Å) and S···Br contacts (3.564(4) Å) exist between adjacent ladders parallel to the c-axis. However, these are unlikely to propagate magnetic exchange due to the very large number of bonds in the pathways between Cu ions, and the closest interladder Cu···Br contact is 5.741(6) Å, suggesting that the ladders are magnetically well isolated along the c-direction.

However, close Br···Br contacts exist between adjacent ladders parallel to the a-axis. The resulting two-halide exchange pathway along the a-axis has the parameters $d_{Br\cdots Br} = 4.226$ Å, $\angle_1$ $_{Cu-Br\cdots Br} = 118.94°$, $\angle_2$ $_{Br\cdots Br-Cu} = 144.06°$, and $\tau_{Cu-Br\cdots Br-Cu} = 11.5°$. This

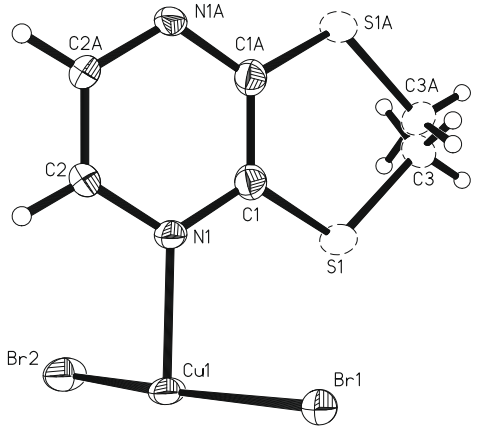


Fig. 3. The molecular unit of $[Cu(meSpz)Br_2]_n$ showing 50% probability thermal ellipsoids.

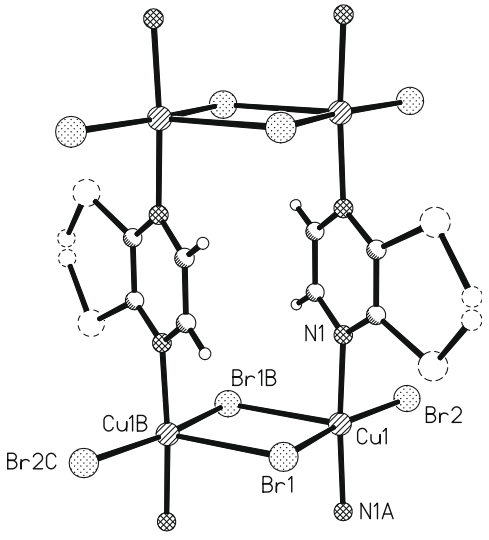


Fig. 4. A rung unit and copper coordination sphere of $[Cu(meSpz)Br_2]_n$ (**1**). Disordered sulfur atoms are shown as dotted circles. Hydrogen atoms on the disordered methyl groups have been excluded for clarity.

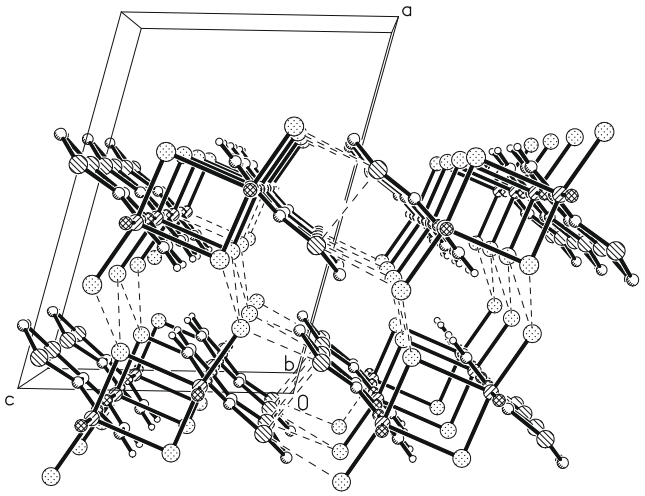


Fig. 5. The crystal structure of **1** viewed parallel to the *b*-axis. Hydrogen atoms on the disordered methyl groups have been excluded for clarity.

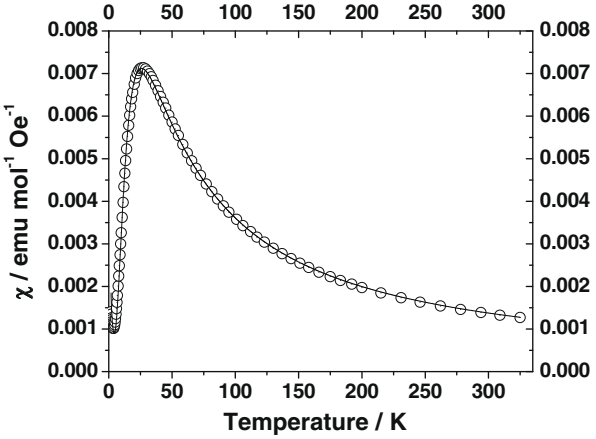


Fig. 6. Left: Magnetic susceptibility data (circles) for $[Cu(meSpz)Br_2]_n$ (**1**) and the fit (solid line) to a strong-rung ladder model.

opens the potential for magnetic exchange between the structural ladders.

All magnetic data have been interpreted in terms of the single *J* form of the Heisenberg Hamiltonian where a negative value of *J* corresponds to antiferromagnetic interactions.

$$H = -J\sum S_i \cdot S_{i+1}$$

Magnetic susceptibility data for $Cu(meSpz)Br_2$ show a rounded maximum at 26 K, followed by a rapid decrease in χ with decreasing temperature (Fig. 6)[3] The value of χT decreases with temperature over the range studied as expected for an antiferromagnetic material and the Curie–Weiss constant is negative ($\theta_{CW} = -27.5$ K) also indicating antiferromagnetic interactions. The susceptibility data show excellent agreement with the model for a strong-rung magnetic ladder [21] yielding the parameters $C = 0.440(12)$ emu K mol^{-1}, $J_{rung}/k_B = -39.8(2)$ K, $J_{rail}/k_B = -18.0(4)$ K, and a paramagnetic impurity of 0.75(3)%, which can be seen as a very small tail below 3.2 K in Fig. 5.

[3] Magnetic studies were performed on a Quantum Designs MPMS-XL SQUID magnetometer. External field dependent magnetic measurements at 1.8 K were measured in fields up to 5 T. Temperature dependent magnetic susceptibility data were collected in the range 1.8–325 K. Corrections were made for diamagnetic contributions (DIA) of the samples according to Pascal's constants and for temperature independent paramagnetism (TIP).

Table 1
Exchange values J_{rung} and J_{rail} for $Cu(2,3dmpz)Br_2$, $Cu(quinoxaline)Br_2$, and $Cu(meSpz)Br_2$.

	J_{rung}/k_B (K)	J_{rail}/k_B (K)	Ref.
$Cu(2,3\text{-}dmpz)Br_2$	−28.4(3)	−21.4(4)	[14]
$Cu(quinoxaline)Br_2$	−37	−27	[13]
$Cu(meSpz)Br_2$	−39.8(2)	−18.0(4)	this work

The values for J_{rung} and J_{rail} are reasonable in comparison to other neutral $CuBr_2$ ladder complexes bridged by diamine ligands, as shown in Table 1. The Cu–Br···Cu angle along the rungs of the ladder is 89.96(4)° in $[Cu(meSpz)Br_2]_n$. The value for J_{rung} in **1** is close to that observed in the dimeric complex $Cu(3,5dmpy)_2Br_2$ [22], which also has a Cu–Br···Cu angle of 89.96° and an exchange constant $J/k_B = -42$ K assigned to the bibridged halide exchange pathway.

Although there are close Br···Br contacts between ladders along the *a*-axis, giving the possibility of magnetic exchange between ladders, the strong-rung model fits the data well. This may result from the poor interladder Cu–Br···Br contact angles (118.9°, 114.06°) when angles approaching 180° have been shown to be optimum for providing a superexchange pathway [23]. The absence of a deviation from the isolated strong-rung ladder model may also be an effect of the reduced moment of the system due to the stronger antiferromagnetic interactions within the ladder.

Structurally, $[Cu(meSpz)Br_2]_n$ exhibits dibromide bridges forming the rungs and bridging meSpz ligands form the rails of a ladder motif parallel to the crystallographic *b*-axis. Moreover, $[Cu(meSpz)Br_2]_n$ is isostructural with the $[Cu(2,3dmpz)Br_2]_n$ and $[Cu(quinox)Br_2]_n$ coordination polymers. Magnetic data also suggest that the material behaves as a strong-rung ladder and that interactions between ladders are negligible. Theoretical calculations are in progress to verify the assignment of exchange strengths from the susceptibility experiments. Additionally, initial powder X-ray data indicate that the chloride analogue of **1** is isostructural to it. Work is in progress to obtain single crystals of $[Cu(meSpz)Cl_2]_n$.

Supplementary data

Atomic coordinates and isotropic thermal parameters, a full listing of bond lengths and angles, observed and calculated structure factors and anisotropic thermal parameters are available through the CCDC (**1**, 700680).

Acknowledgments

The MPMS-XL SQUID magnetometer was purchased with the assistance of funds from the National Science Foundation (IMR-0314773) and the Kresge Foundation.

References

[1] D.N. Hendrickson, in: R.D. Willett, D. Gatteschi, O. Kahn (Eds.), Magneto-Structural Correlations in Exchange Coupled Systems, Reidel Publishers, Dordrecht, 1985, p. 555.
[2] A. Santoro, A.D. Mighell, C.W. Reimann, Acta Crystallogr., B 26 (1970) 979.
[3] (a) J.F. Villa, W.E. Hatfield, J. Am. Chem. Soc. 93 (1971) 4081; (b) D.B. Losee, H.W. Richardson, W.E. Hatfield, J. Chem. Phys. 59 (1973) 3600.
[4] G. Mennenga, L.J. De Jongh, W.J. Huiskamp, J. Reedjik, J. Magn. Magn. Mater. 44 (1984) 89.
[5] T. Lancaster, S.J. Blundell, M.L. Brooks, P.J. Baker, F.L. Pratt, J.L. Manson, C.P. Landee, C. Baines, Phys. Rev. B 73 (2006) 020410.
[6] W.W. Richardson, W.E. Hatfield, J. Am. Chem. Soc. 98 (1976) 835.
[7] S. Amaral, W.E. Jensen, C.P. Landee, M.M. Turnbull, F.M. Woodward, Polyhedron 20 (2001) 1317.
[8] R.T. Schneider, C.P. Landee, M.M. Turnbull, F.F. Awwadi, B. Twamley, Polyhedron 26 (2007) 1849.
[9] G. Beobide, O. Castillo, U. Garcia-Couceiro, J.P. Garcia-Teran, A. Luque, M. Martinez-Ripoll, P. Roman, Eur. J. Inorg. Chem. (2005) 2586.

[10] L.-G. Zhu, S. Kitagawa, Inorg. Chem. Commun. 6 (2003) 1051.
[11] M.M. Turnbull, A.S. Albrecht, G.B. Jameson, C.P. Landee, Mol. Cryst. Liq. Cryst. Sec. A 335 (1999) 957.
[12] J.L. Manson, M.M. Conner, J.A. Schlueter, T. Lancaster, S.J. Blundell, M.L. Brooks, F.L. Pratt, T. Papageorgiou, A.D. Bianchi, J. Wosnitza, M.-H. Whangbo, Chem. Commun. (2006) 4894.
[13] (a) C.P. Landee, A. Delcheva, C. Galeriu, G. Pena, M.M. Turnbull, R.D. Willett, Polyhedron 22 (2003) 2325;
(b) S. Lindroos, P. Lumme, Acta Crystallogr., Sect. C C46 (1990) 2039.
[14] B.M. Wells, C.P. Landee, M.M. Turnbull, F.F. Awwadi, B. Twamley, J. Mol. Catal. A 228 (2005) 117.
[15] M.A. Moreno, M. Haukka, A. Turunen, T.A. Pakkanen, J. Mol. Catal. A: Chem. 240 (2005) 7.
[16] (a) C. Dai, Z. Yuan, J.C. Collings, T.M. Tafina, R.Ll. Thomas, K.P. Roscoe, L.M. Stimson, D.S. Yufit, A.S. Batsanov, J.A.K. Howard, T.B. Marder, CrystEngCommun 6 (2004) 184;
(b) A. Parfonry, B. Tinant, J.P. Declercq, M. van Meerssche, J. Klein, R. Merenyi, H.G. Viehe, Bull. Soc. Chim. Belg. 96 (1987) 89;
(c) A.C. Benniston, A. Harriman, J.P. Rostron, Phys. Chem. Chem. Phys. 7 (2005) 3041;
(d) A. Caneschi, F. Ferraro, D. Gatteschi, A. le Lirzin, M.A. Novak, E. Rentschler, R. Sessoli, Adv. Mater. 7 (1995) 476;
(e) M. Deumal, M.J. Bearpark, M.A. Robb, Y. Pontillon, J.J. Novoa, Chem. -Eur. J. 10 (2004) 6422.
[17] Yu-Bin Dong, Ting Sun, Jian-Ping Ma, Xia-Xia Zhao, Ru-Qi Huang, Inorg. Chem. 45 (2006) 10613.
[18] (a) M.A. Romero, J.M. Salas, M. Quiros, M.P. Sanchez, J. Romero, D. Martin, Inorg. Chem. 33 (1994) 5477;
(b) W.E. Marsh, T.L. Bowman, C.S. Harris, W.E. Hatfield, D.J. Hodgson, Inorg. Chem. 20 (1981) 3864;
(c) W.E. Marsh, T.L. Bowman, W.E. Hatfield, D.J. Hodgson, Inorg. Chim. Acta 19 (1982) 19.
[19] M. Pinsky, D. Avnir, Inorg. Chem. 37 (1998) 5575.
[20] B.R. Landry, M.M. Turnbull, B. Twamley, J. Chem. Crystallogr. 37 (2007) 81.
[21] D.C. Johnston, M. Troyer, S. Miyahara, D. Lidsky, K. Ueda, M. Azuma, Z. Hiroi, M. Takano, M. Isobe, Y. Ueda, M. A. Korotin, V. I. Anisimov, A. V. Mahajan, L.L. Miller, 65 (2000) arxiv:/arXiv:cond-mat/0001147.
[22] J.A.C. van Ooijen, J. Reedijk, E.J. Sonneveld, J.W. Visser, Transition Met. Chem. 4 (1979) 305.
[23] M.M. Turnbull, C.P. Landee, B.M. Wells, Coord. Chem. Rev. 249 (2005) 2567.

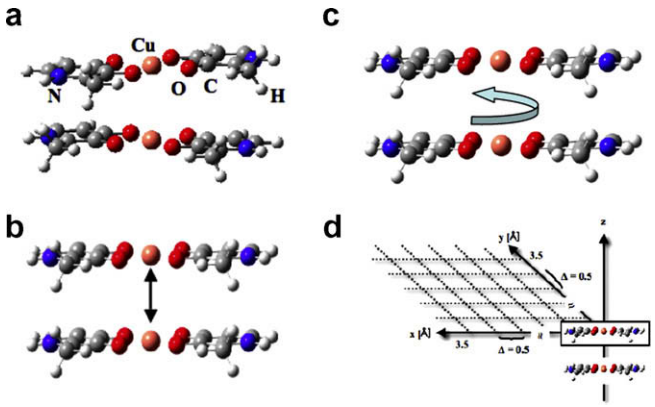


Fig. 1. The Calculated dimer models of Cu^{2+} mediated base pairs of hydroxypyridone nucleobases. Sugar-phosphate backbone is replaced by H atoms in the models. The structure (a) is the undistorted and (b)–(d) are distorted ones. Changed parameters are (b) the distance, (c) the rotation angle and (d) the slip in *X*–*Y* plane between two monomers.

$$\hat{H} = -2\sum_{a>b} J_{ab}\hat{S}_a\hat{S}_a, \tag{1}$$

where the parameter J_{ab} is a coupling parameter between localized spins *S* on metal ions a and b. The J_{ab} can be calculated by

$$J_{ab} = \frac{E^{LS} - E^{HS}}{\langle\hat{S}^2\rangle^{HS} - \langle\hat{S}^2\rangle^{LS}}, \tag{2}$$

where E^X and $\langle\hat{S}^2\rangle^X$ are total energy and total spin angular momentum of spin state X (X = low-spin (LS) and high spin (HS) states), respectively [8,9]. The positive (negative) J_{ab} value means ferromagnetic (anti-ferromagnetic) interaction. The total energies and $\langle\hat{S}^2\rangle$ values are calculated by UB3LYP [10] method with the use of 6-31+G* basis set for ligand, and Huzinaga MIDI+p basis set [11] for Cu^{2+} atoms on GAUSSIAN 03 program [12].

All J_{ab} values between Cu^{2+} ions in Cu^{2+}–DNA systems are calculated by two-unit dimer model as illustrated in Fig. 1a–d. Previous to the calculation of J_{ab} values with the dimer model, a structure of the monomer unit is optimized because there is no available information about the complex except for the inter-plane distance. The optimized structural parameters of the monomer unit are summarized in Table S1 in Supplementary material. A spin state of the monomer is doublet and one spin exists on $d_{x^2-y^2}$ orbital of Cu^{2+} as illustrated in Fig. S1 in Supplementary material. The dimer models are constructed by using the optimized monomers as described in later sections.

3. Results and discussion

3.1. J_{ab} values between Cu^{2+} ions with the reported structure

First, the J_{ab} value between two Cu^{2+} ions is calculated for the reported structure [4]. As described above, we are only able to use the structural information of the complex that the system is a right-handed DNA helix and the distance of adjacent planes are 3.7 Å [4]. Therefore it is assumed that the Cu–Cu axis is perpendicular to monomer plane and the rotational angle of the dimer is 36° based on B-DNA [3,4,13] which is the right-handed DNA. By using those information and assumptions, we constructed the model system as illustrated in Fig. 1a. Calculated total energies and $\langle\hat{S}^2\rangle$ values for a broken-symmetry (BS) LS and the HS states and J_{ab} value are summarized in Table S2 in Supplementary material.

The calculated energy splitting between the BS LS and the HS states is small. However the BS LS state is slightly stable and the calculated J_{ab} value is negative indicating an anti-ferromagnetic interaction. This result agrees with a metal–DNA (M-DNA) based on a natural B-DNA ($J = -0.0483\ cm^{-1}$) [5].

Also we consider solvent (water) effect for this system by PCM method because ESR measurement carried out under condition of aqueous solution. The calculation result of the J_{ab} value is $-1.4\ cm^{-1}$ and it is equal to non-solvent model. In other word, the J_{ab} value does not depend on the solvent effect in our model.

3.2. Change in J_{ab} values with deformations

It is well known that the DNA is flickered and changed its form such as A-, B- and Z-forms by solvent [13]. In this sense, a structural disorder of the DNA strand must be examined for the consideration of the origin of high spin species. Therefore we, next, consider three possibilities of deformations i.e. the distance, the rotation angle and the slip in *X*–*Y* plane between two monomers as illustrated in Fig. 1b–d, and examine a change in J_{ab} values with those deformations.

Calculated results for the distance and the rotation angle are summarized in Fig. 2. The range of Cu–Cu distance, and rotation angle are 3.0–5.0 Å and 0–180°, respectively. The experimental distance between two base pairs is 3.7 Å in B-form DNA. The calculated J_{ab} values are small in all range of distances and angles. The J_{ab} values simply depend on Cu–Cu distance and the anti-ferromagnetic interaction becomes stronger as the distance between two Cu ions becomes shorter, such as it was expected [14]. On the other hand, J_{ab} values show a periodic dependency on the rotation angle. For example, there are minima around 0°, 90° and 180°. The reason of this phenomenon stems from the symmetry of $d_{x^2-y^2}$ orbitals of Cu^{2+} ions of adjacent planes because the J_{ab} values depend on overlap between two spin orbitals on Cu^{2+} ions.

In order to explain the detail, the natural orbitals (NOs) of the system are examined for several angles. The NOs are obtained by diagonalization of a first order density matrix as

$$\rho(r, r') = \sum n_i\{\phi_i(r)\}^*\phi_i(r'), \tag{3}$$

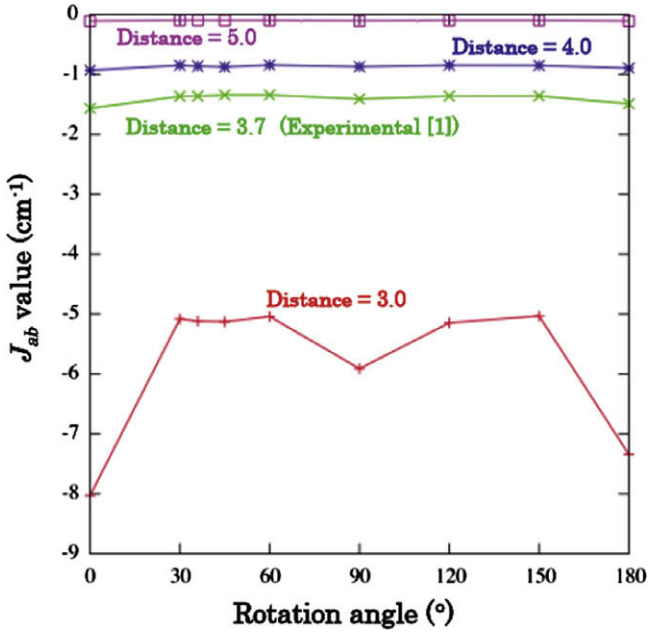


Fig. 2. J_{ab} values when the distance and the rotation angle between two base pairs are changed.

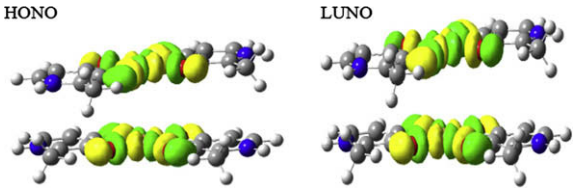


Fig. 3. Depicted HONO and LUNO of $[H–Cu^{2+}–H]_2$ for the BS LS state. The distance and angle between two base pairs are 3.7 Å and 36°, respectively.

where n_i denotes the occupation number of NO (ϕ_i) [8]. The occupation number is in proportion to the overlap between α and β orbitals, so that one can estimate SOMO–SOMO overlap from the number. The overlap is calculated by $n_i - 1$. Therefore, if an occupation number of a magnetic orbital is close to 1.0, then two electrons in the orbital are almost localized on each spin site. On the other hand, n_i should be equal to 2.0 if the two spins are delocalized on two spin sites. The NOs and their occupation numbers for the BS LS state are depicted in Fig. 3 and Table S3 in Supplementary material, respectively. The highest occupied natural orbital (HONO) and the lowest unoccupied natural orbital (LUNO) mainly consist of $d_{x^2-y^2}$ orbitals of Cu^{2+} ions, and their occupation numbers are almost 1.0 indicating overlap between two spins on Cu^{2+} ions are very small, allowing us to understand the weak magnetic interaction. Around 36° which is the angle of the B-DNA, overlap shows minimum but it is not completely orthogonal, while overlap shows maxima around 0°, 90° and 180°. The difference between 0° and 180° seems to originate from asymmetric methyl groups.

In case of 36°, the overlap estimated by the occupation number is 0.0001. In these systems, a slight structural change easily makes a change in overlap. If two orbitals are perpendicular each other, there is a possibility of the ferromagnetic interaction. As explained above, it is expected that the DNA backbone is always flickered by outer environment. So, we also investigate the slipping of two monomers in *X*–*Y* plane as illustrated in Fig. 1d. In this model, rotation angle is fixed to 36°. As summarized in Fig. 4, the J_{ab} values become smaller and close to zero but they show anti-ferromagnetic interaction in whole region.

3.3. Dependence on the J_{ab} values for various calculation methods

It has been reported calculated J_{ab} values sometimes depend on the DFT functional sets quantitatively, but not qualitatively. Therefore, we next investigated the dependency of the J_{ab} values on calculation methods such as BHandHLYP, PW91PW91, MPW91PW91, HF and MP2. Calculated results are shown in Table 1. Although the double helix of DNA is stabilized by π–π interaction, the DFT methods which cannot include π–π interaction give systematic J_{ab} values. MP2 can evaluate a dispersion interaction accurately. MP2 method shows an unreasonable weak ferromagnetic interaction at longer distance. On the other hand, the J_{ab} values calculated by DFT methods are almost equal each other. Tsuzuki et al. reported that the MP2 calculation overestimate π–π interaction such as benzene or naphthalene [15,16]. Our results also suggest the method may not be applicable to the long-distance $[H–Cu^{2+}–H]$ dimer.

Table 1
The J_{ab} values[a] of the dimer model calculated by several methods.

Distance[b]	BHandHLYP	PW91PW91	MPW1PW91	HF	MP2
3	−5.1	−3.5	−4.5	−2.4	−4.6
3.7	−1.2	−0.8	−0.9	−0.4	−0.4
4	−0.7	−0.6	−0.6	0.0	0.4
5	−0.1	−0.1	−0.1	0.0	2.1

[a] In cm^{-1}.
[b] In Å.

Table 2
Total energies, $\langle \hat{S}^2 \rangle$ values and J_{ab} values of trimer ($n = 3$), tetramer ($n = 4$) and pentamer ($n = 5$) models calculated by UB3LYP method.

n	HS state		LS state		J_{ab}[b]
	Total energy[a]	$\langle \hat{S}^2 \rangle$	Total energy[a]	$\langle \hat{S}^2 \rangle$	
3	−7545.34013157	3.7570	−7545.34014415	1.7572	−1.4
4	−10060.4546255	6.0093	−10060.4546442	2.0096	−1.4
5	−12575.5689211	8.7617	−12575.5689460	2.7620	−1.4

[a] In a.u.
[b] In cm^{-1}.

3.4. The J_{ab} values of trimer, tetramer and pentamer

In order to examine the dependency of the J_{ab} values on a chain length, we calculated the J_{ab} values of trimer, tetramer and pentamer models. In these methods, the distance between adjacent planes are 3.7 Å and rotation angle are 36°. Eq. (2) is rewrite like Eq. (4) when spin sites are more than three [17]:

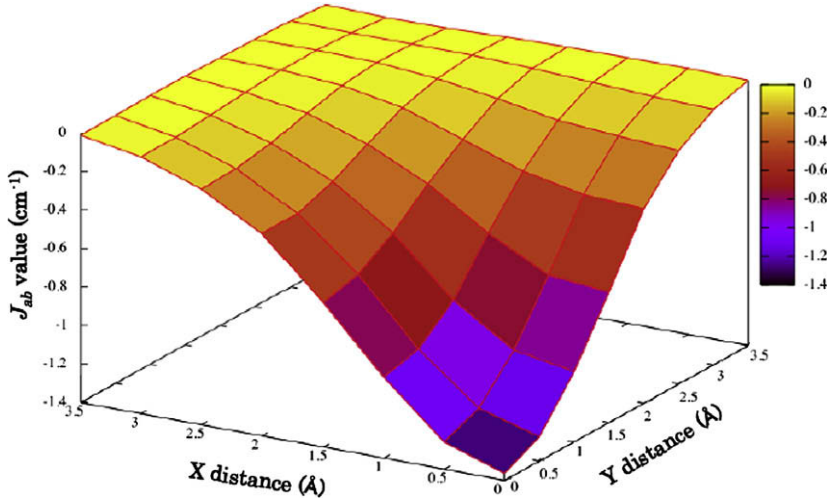


Fig. 4. The change in J_{ab} values when two monomers are slipped in *X*–*Y* plane. The distance and angle between two base pairs are 3.7 Å and 36°, respectively.

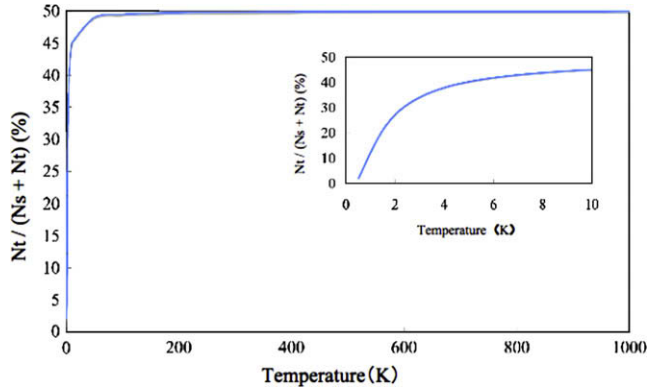


Fig. 5. The ratio of the population on triplet states by Boltzmann distribution simulation. The distance and angle between two base pairs are 3.7 Å and 36°, respectively. Ns and Nt means the population of singlet and triplet states, respectively. The enlarged picture shows the range of low temperature.

$$J_{ab} = \frac{E^{LS} - E^{HS}}{\langle \hat{S}^2 \rangle^{HS} - \langle \hat{S}^2 \rangle^{LS} + c}, \tag{4}$$

where

$$C = -S_a g(N)[\langle S^2 \rangle^{LS} - S_r(S_r + 1)]$$

and S_r denotes the exact spin angular momentum for molecules under discussion

$$S_r = n(S_a - S_b) \quad (N = 2n),$$
$$S_r = n(S_a - S_b) + S_a \quad (N = 2n + 1),$$

where the S_a and S_b are the sizes of spin at sites a and b. The results are shown in Table 2.

Their total energies of HS and BS LS states are energetically degenerate but the BS LS is slightly stable. Interestingly, the calculated J_{ab} values are equal to dimer model. In other words, we cannot find a dependency of J_{ab} values on the chain length.

3.5. Possibility of thermal excitation

From the calculated results, we cannot find the structure in which the HS state is more stable than the BS LS state, although EPR spectra show the existence of the HS species. On the other hand, the HS and the BS LS states are energetically degenerate. So, we examine a possibility of the thermal excitation from the LS state to the HS state. The ratio of population in the HS (triplet) and in the LS (singlet) is estimated by the Boltzmann distribution:

$$\frac{N(\text{triplet})}{N(\text{singlet})} = \exp\left(-\frac{E^{\text{triplet}} - E^{\text{singlet}}}{KT}\right), \tag{5}$$

at the various temperature (T) [18] in case that the distance and the rotation angle between two monomers are 3.7 Å and 36°. As illustrated in Fig. 5, a percentage of the triplet state $\left(\frac{N(\text{triplet})}{N(\text{singlet})+N(\text{triplet})} \times 100\right)$ is estimated to be about 21% at 1.5 K (ESR measurement temperature) and about 50% at 300 K. The result suggests that the HS species exist by the thermal excitation even at 1.5 K.

4. Conclusion

We theoretically investigated an origin of HS species of Cu^{2+} bridged hydroxypyridone pairs observed by EPR spectra. To our knowledge, this is the first report of a quantitative calculation for J_{ab} value between Cu^{2+} ions in metal–DNA systems. In all calculated results, the total energies of the HS and the BS LS states are degenerate but J_{ab} values show weak anti-ferromagnetic couplings within the examined model structures. These results agree with metal–DNA based on natural B-DNA [5]. Also J_{ab} value for dimer model is equal to more than trimer models that the distance and the angel are 3.7 Å and 36°. Together with the result of the Boltzmann distribution simulation, it is expected that the thermal excitation from the LS state to the HS state occurs in the system and the HS species are observed by the EPR spectroscopy.

Acknowledgements

This work has been supported by Grants-in-Aid for Scientific Research (KAKENHI) (Nos. 19750046, 19350070, 18350008) from Japan Society for the Promotion of Science (JSPS) and that on Priority Areas (No. 19029028) from the Ministry of Education, Culture, Sports, Science and Technology (MEXT).

Appendix A. Supplementary data

Supplementary data associated with this article can be found, in the online version, at doi:10.1016/j.poly.2008.10.052.

References

[1] E. Coronado, J.R. Galan-Mascaros, C.J. Gomez-Garcia, V. Laukhin, Nature 408 (2000) 447.
[2] M. Matsushita, H. Kawakami, Y. Kawada, T. Sugawara, Chem. Lett. 36 (2007) 110.
[3] K. Tanaka, A. Tengeiji, T. Kato, N. Toyama, M. Shiro, M. Shionoya, J. Am. Chem. Soc. 124 (2002) 12494.
[4] K. Tanaka, A. Tengeiji, T. Kato, N. Toyama, M. Shionoya, Science 299 (2003) 1212.
[5] K. Mizoguchi, S. Tanaka, T. Ogawa, N. Shiobara, H. Sakamoto, Phys. Rev. B 72 (2005) 033106.
[6] S.S. Mallajosyula, S.K. Pati, Phys. Rev. Lett. 98 (2007) 136601.
[7] H.Y. Zhang, A. Calzolari, R.D. Felice, J. Phys. Chem. B 109 (2005) 15345.
[8] K. Yamaguchi, in: R. Carbo, M. Klobukowski (Eds.), Self-Consistent Field Theory and Applications, Elsevier, Amsterdam, 1990, p. 727.
[9] T. Kawakami, S. Yamanaka, S. Yamada, W. Mori, K. Yamaguchi, in: M.M. Turnbull, T. Sugimoto, L.K. Thompson (Eds.), Molecular-based Magnetic Materials, Theory, Technique and Applications, ACS Symposium Series, vol. 644, American Chemical Society, Washington, DC, 1996, p. 30.
[10] A.D. Becke, J. Chem. Phys. 98 (1993) 5648.
[11] H. Tatewaki, S. Huzinaga, J. Chem. Phys. 72 (1980) 339.
[12] M.J. Frisch et al., GAUSSIAN 03, Revision D.02, Gaussian, Inc., Wallingford, CT, 2004.
[13] W. Saenger, Principles of Nucleic Acid Structure, Springer, New York, NY, 1984.
[14] Y. Kitagawa, T. Kawakami, Y. Yoshioka, K. Yamaguchi, Polyhedron 20 (2001) 1189.
[15] S. Tsuzuki, T. Uchimaru, K. Matsumura, M. Mikami, K. Tanabe, Chem. Phys. Lett. 319 (2000) 547.
[16] S. Tsuzuki, K. Honda, T. Uchimaru, M. Mikami, K. Tanabe, J. Am. Chem. Soc. 124 (2001) 104.
[17] Y. Kitagawa, T. Soda, Y. Shigeta, S. Yamanaka, Y. Yoshioka, K. Yamaguchi, Int. J. Quant. Chem. 84 (2001) 592.
[18] S. Nakano, Y. Kitagawa, T. Kawakami, M. Okumura, H. Nagao, K. Yamaguchi, Molecules 9 (2004) 792.

Mo Kα (λ = 0.71073 Å) radiation). The structures were solved by a direct method and expanded by using Fourier techniques using SHELXTL program. Empirical absorption corrections by SADABS (G.M. Sheldrick, 1994) were carried out. In the structure analyses, non-hydrogen atoms were refined with anisotropic thermal parameters. Hydrogen atoms were included in calculated positions and refined with isotropic thermal parameters riding on those of the parent atoms. Crystal data of **1** at −73 °C: $C_{67}H_{84}B_2Fe_3N_{26}O$, M = 1458.77, monoclinic space group $P2_1/c$, a = 14.2844(19), b = 14.844(2), c = 34.938(5) Å, β = 93.485(3)°, V = 7394.5(17) Å^3, Z = 4. A total of 43614 was collected ($3° < 2\theta < 56°$) of which 16202 unique reflections (R_{int} = 0.0575) were measured. Residual R and wR were 0.0629 and 0.1503, respectively, from the refinement on F^2 with $I > 2\sigma(I)$. Crystal data of **2** at −73 °C: $C_{82}H_{88}F_{24}Fe_4N_{28}O_{10}P_4$, M = 2429.08, triclinic space group $P\bar{1}$, a = 13.104(4), b = 13.935(4), c = 16.130(4) Å, α = 68.671(4)°, β = 88.352(4)°, γ = 74.264(4)°, V = 2632.9(12) Å^3, Z = 1. A total of 10724 was collected ($4° < 2\theta < 47°$) of which 7364 unique reflections (R_{int} = 0.0252) were measured. Residual R and wR were 0.0627 and 0.1733, respectively, from the refinement on F^2 with $I > 2\sigma(I)$.

2.3. Mössbauer spectral measurements

Mössbauer spectra of **1** and **2** were measured using a ^{57}Co/Rh source in a constant-acceleration transmission spectrometer. The spectra were recorded at 20 K, and Mössbauer parameters were calibrated relative to α-Fe foil.

2.4. Magnetic measurements

DC magnetic susceptibility data of **1** and **2** were collected by using a Quantum Design MPMS-XL SQUID magnetometer at temperatures ranging from 5 to 365 K for **1** and from 5 to 400 K for **2**, respectively.

3. Results and discussion

3.1. Descriptions of crystal structures

3.1.1. $[Fe^{III}_2Fe^{II}(CN)_6(tp^*)_2(tpa)] \cdot 4MeCN \cdot t\text{-}BuMeO$ (**1**)

X-ray crystal structure analysis for **1** was performed at 200 K, and ORTEP diagram of the complex molecule was depicted in Fig. 1. Compound **1** crystallized in monoclinic space group $P2_1/c$, and has a right angled trinuclear core composed of two $[Fe(CN)_3(tp^*)]^-$ and one $[Fe(tpa)]^{2+}$ units. Two $[Fe(CN)_3(tp^*)]^-$ units are bridged by $[Fe(tpa)]^{2+}$ via bridging cyanide ions with a bridging angle (N1–Fe2–N2) of 92.2(1)°. In $[Fe(CN)_3(tp^*)]^-$ units, Fe ions have FeC_3N_3 octahedral coordination geometry. Coordination bond lengths of Fe1–C are in the range of 1.926(4)–1.933(4) Å, while those of Fe1–N are 2.007(4)–2.009(4) Å, respectively. A coordination structure of Fe3 ion is very similar to that of Fe1 ion, and coordination bond lengths are 1.914(5)–1.923(5) Å and 1.990(4)–2.014(4) Å for Fe3–C and Fe3–N, respectively. The coordination structure of Fe2 ion in $[Fe(tpa)]^{2+}$ is six-coordinated octahedron with an FeN_6 chromophore, and Fe2 ion is coordinated by four nitrogen atoms from the tetradentate tpa ligand and two nitrogen atoms from the bridging cyanide ions. An average coordination bond length of Fe2 ion is 1.963 Å, which is very similar to those in Fe1 (1.969 Å) and Fe3 (1.960 Å) ions, and the structural feature of Fe1–Fe3 ions are characteristic of LS Fe(II) or Fe(III) ions. The coordination bond lengths in LS Fe(II) and Fe(III) ions are known to be very similar, and the assignment of oxidation states for each Fe ions is, therefore, difficult only by considering their structural parameters.

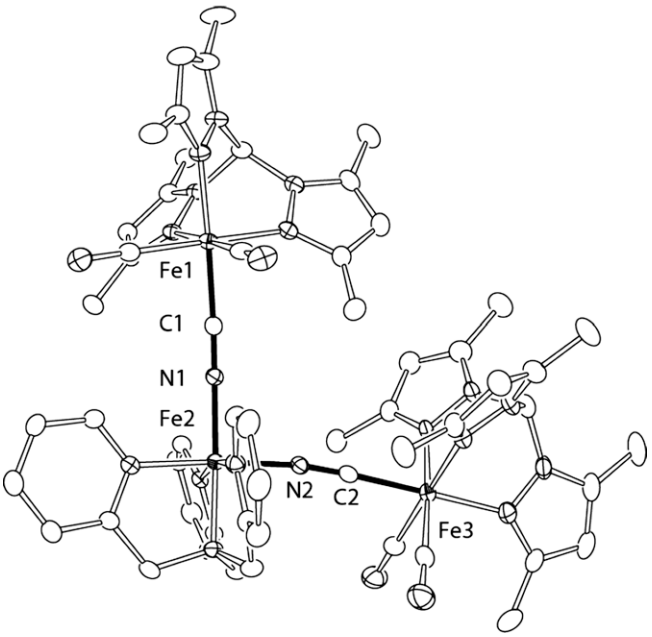


Fig. 1. ORTEP diagram of **1**.

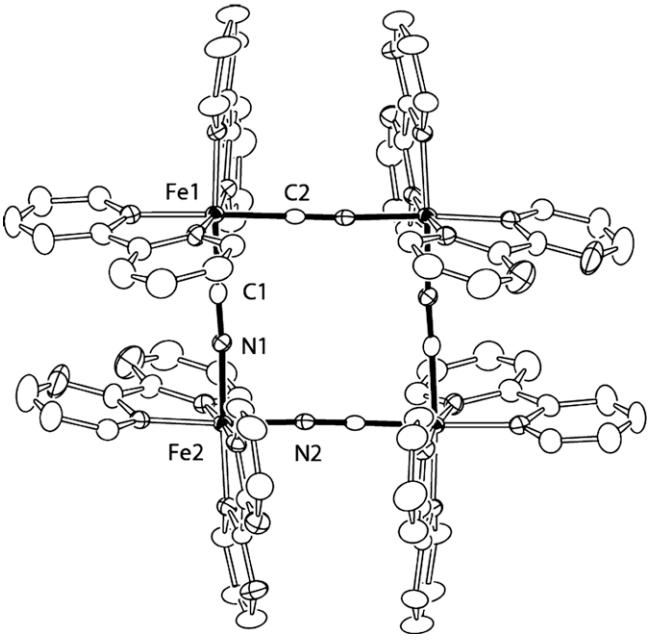


Fig. 2. ORTEP diagram of the cation in **2**.

3.1.2. $[Fe^{II}_4(CN)_4(bpy)_4(bpym)_4](PF_6)_4 \cdot 6MeOH \cdot 4H_2O$ (**2**)

2 crystallized in triclinic space group $P\bar{1}$ and a tetranuclear core locates on the centre of symmetry. The tetranuclear core in **2** is composed of four cyanide-bridged Fe(II) ions, and the overall core geometry is almost square (Fig. 2). Bridging angles of C1–Fe1–C2 and N1–Fe2–N2 are 87.3(2)° and 90.9(2)°, respectively. In the square, two $[Fe(bpy)_2]^{2+}$ centres and two $[Fe(bpym)]^{2+}$ centres are alternately bridged by four CN groups with the carbon atoms coordinated to the Fe(II) ions in $[Fe(bpy)_2]^{2+}$. The Fe(II) ions have

octahedral coordination geometry, and four of the coordination sites are occupied by nitrogen atoms from two bpy or bpym ligands. The two remaining *cis* positions are coordinated by either carbon or nitrogen atoms from the cyanide groups. The Fe1–N_{bpy} coordination bond lengths are ranging from 1.955(5) to 1.986(5) Å, and Fe1–C are 1.885(6) and 1.890(6) Å, respectively, while coordination bond lengths about Fe2 ions are 1.927(5)–1.966(5) Å. The average coordination bond lengths are 1.946 Å and 1.948 Å for Fe1 and Fe2 ions, respectively, which are characteristic of LS Fe(II) ions.

3.2. Mössbauer spectra of **1** and **2**

^{57}Fe Mössbauer spectra of **1** and **2** were recorded at 20 K and depicted in Fig. 3a and b, respectively. The spectrum of **1** is composed of two doublets (Fig. 3a), and their Mössbauer parameters were $\delta = 0.11$ and $\Delta E_Q = 1.28$ mm s^{-1} and $\delta = 0.45$ and $\Delta E_Q = 0.28$ mm s^{-1} at 20 K, characteristic of LS Fe(III) and LS Fe(II) species, respectively. The peak area ratio of the two peaks suggest that LS Fe(III) and Fe(II) ions correspond to two $[Fe(CN)_3(tp^*)]^-$ and one $[Fe(tpa)]^{2+}$ units, respectively.

A Mössbauer spectrum of **2** consists two doublets corresponding to LS Fe(II) ions with the Mössbauer parameters of $\delta = 0.22$ and $\Delta E_Q = 0.69$ mm s^{-1} (LS1) and $\delta = 0.40$ and $\Delta E_Q = 0.36$ mm s^{-1} (LS2) (Fig. 3b). The peak area ratio of LS1 and LS2 doublets was 0.52/0.48, suggesting different LS Fe(II) species in 1:1 ratio. The deviation of the area ratio is caused by the different Lamb–Mössbauer factors for each species. The LS Fe(II) ion (Fe1) in the $[Fe(CN)_2(bpy)_2]$ moiety has smaller isomer shifts than the Fe2 ions in $[Fe(NC)_2(bpym)]$ moieties, which is due to strong π back donation to cyanide ions. Therefore, the LS1 and LS2 doublets were assigned to the Fe1 and Fe2 ions, respectively.

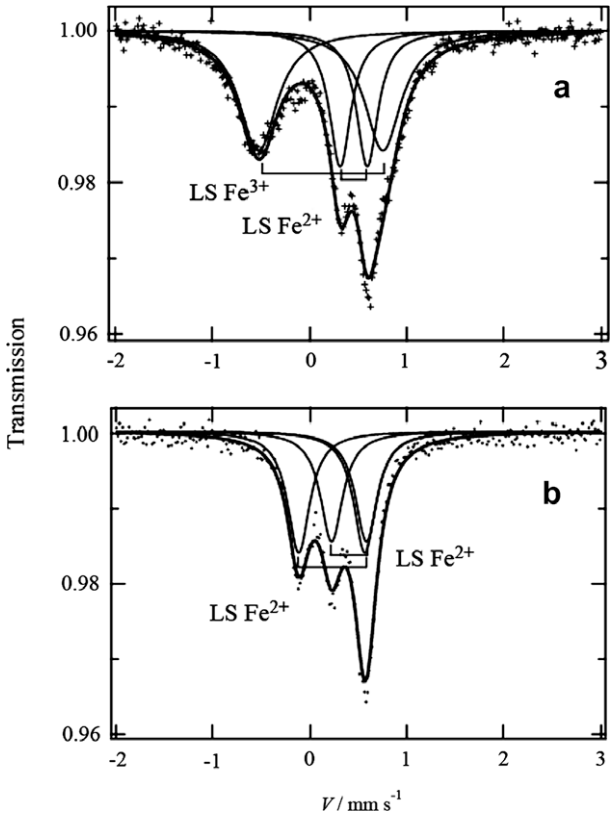


Fig. 3. Mössbauer spectra of (a) **1** and (b) **2** at 20 K.

3.3. Magnetic susceptibility measurements of **1** and **2**

Magnetic susceptibility measurements were carried out in the temperature range of 5–365 K and 5–400 K for **1** and **2** (Fig. 4). In **1**, the $\chi_m T$ values below 250 K are almost constant (1.34 emu mol^{-1} K at 250 K), which corresponds to the theoretical value (1.36 emu mol^{-1} K with $g = 2.7$) [11] for the uncorrelated two LS Fe(III) ions (Fig. 4a). As the temperature was increased, the gradual increase of $\chi_m T$ values was observed and the $\chi_m T$ value reached a maximum value of 2.86 emu mol^{-1} K at 340 K. It should be noted that this increase was recovered in the cooling process, suggesting an occurrence of a reversible thermal spin-crossover phenomenon. The Curie constant for HS Fe(II) ions is 3.00 emu mol^{-1} K ($g = 2.0$), and the $\chi_m T$ value (2.86 emu mol^{-1} K) at 340 K corresponds to ca. 50% of the Fe(II) ion being in the high-spin state.

The $\chi_m T$–T plot for **2** revealed that **2** is diamagnetic below 250 K (Fig. 4b), which agree with the X-ray and Mössbauer data suggesting the existence of the four diamagnetic LS Fe(II) ions in this temperature range. Upon heating, the $\chi_m T$ values increased gradually, and reached a maximum value of 3.42 emu mol^{-1} K at 400 K, suggesting the occurrence of spin transition from LS to HS state on Fe(II) ions. The $\chi_m T$–T curve in the cooling process is iden-

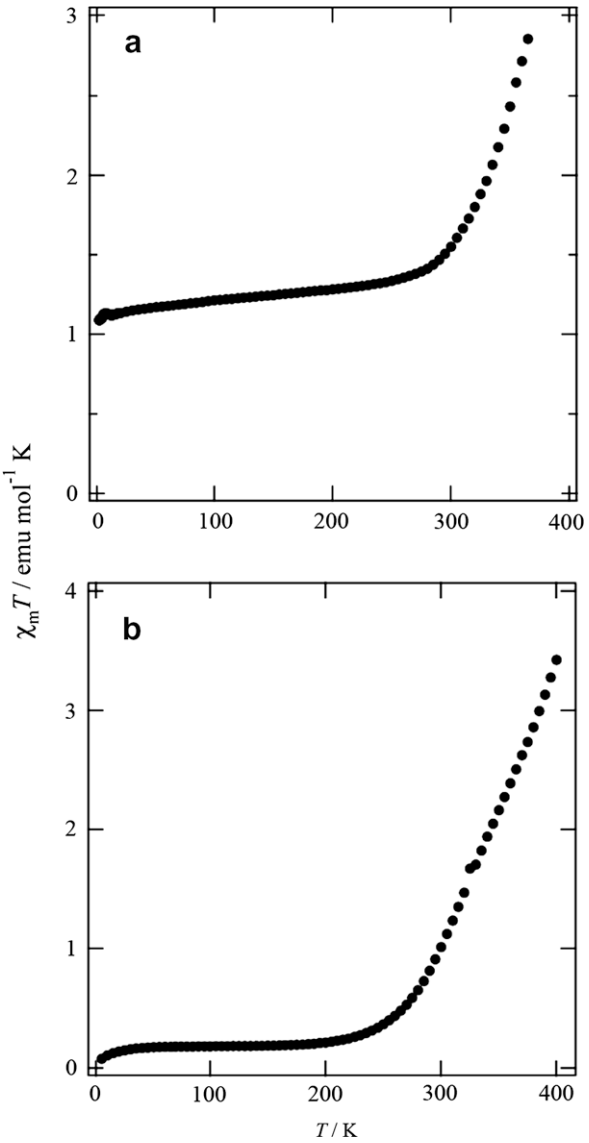


Fig. 4. $\chi_m T$–T plots for (a) **1** and (b) **2**.

tical with that in the heating process, suggesting that the spin transition in **2** was reversible. Compound **2** has crystallographically independent two Fe(II) ions (Fe1 and Fe2) in $[Fe(CN)_2(bpy)_2]$ and $[Fe(NC)_2(bpym)]$ centres. Fe1 is in the stronger ligand field than Fe2, because the bpy ligand is a strong π acid and the cyanide carbon atoms act as π acceptors [12]. Therefore, spin crossover sites in **2** must be two Fe2 ions in $[Fe(NC)_2(bpym)]$ units. Two Fe2 ions, which are related by the inversion centre, have the same coordination environment, and underwent one-step spin crossover.

4. Conclusion

We prepared novel cyanide-bridged tri- and tetra-nuclear complexes, and their structures and magnetic properties were studied. Magnetic susceptibility measurements revealed that introduction of medium ligand-field strength to the cyanide-bridged multi-nuclear cores leads to thermally induced spin crossover for both materials.

5. Supplementary data

CCDC 702339 and 702340 contain the supplementary crystallographic data for this paper. These data can be obtained free of charge via http://www.ccdc.cam.ac.uk/conts/retrieving.html, or from the Cambridge Crystallographic Data Centre, 12 Union Road, Cambridge CB2 1EZ, UK; fax: (+44) 1223-336-033; or e-mail: deposit@ccdc.cam.ac.uk.

Acknowledgement

This work was partially supported by a Grant-in-aid for Scientific Researches from the Ministry of Education, Culture, Sports, Science and Technology, Japan.

References

[1] (a) A.N. Holden, B.T. Matthias, P.W. Anderson, H.W. Lewis, Phys. Rev. 102 (1956) 1463;
(b) S. Ferlay, T. Mallah, R. Ohahès, P. Veillet, M. Verdaguer, Nature 378 (1995) 701;
(c) O. Sato, T. Iyoda, A. Fujishima, K. Hashimoto, Science 271 (1996) 49;
(d) J.S. Miller, MRS Bull. 25 (2000) 60.
[2] W. Kosaka, K. Nomura, K. Hashimoto, S. Ohkoshi, J. Am. Chem. Soc. 127 (2005) 8590.
[3] (a) J.J. Sokol, A .G. Hee, J.R. Long, J. Am. Chem. Soc. 124 (2002) 7656;
(b) H.J. Choi, J.J. Sokol, J.R. Long, Inorg. Chem. 43 (2004) 1606;
(c) E.J. Schelter, F. Karadas, C. Avendano, A.V. Prosvirin, W. Wernsdorfer, K.R. Dunbar, J. Am. Chem. Soc. 129 (2007) 8139.
[4] M. Nihei, M. Ui, N. Hoshino, H. Oshio, Inorg. Chem. 47 (2008) 6106.
[5] (a) C.P. Berlinguette, A. Dragulescu-Andrasi, A. Sieber, J.R. Galan-Mascarós, H.-U. Güdel, C. Achim, K.R. Dunbar, J. Am. Chem. Soc. 126 (2004) 6222;
(b) R. Herchel, R. Boča, M. Gembicky, J. Kožísek, F. Renz, Inorg. Chem. 43 (2004) 4103.
[6] (a) P. Gütlich, H.A. Goodwin (Eds.), Springer, Top. Curr. Chem. 233–235 (2004);
(b) J.A. Real, A.B. Gaspar, V. Niel, M.C. Muñoz, Coord. Chem. Rev. 236 (2003) 121;
(c) J.A. Real, A.B. Gaspar, M.C. Muñoz, Dalton Trans. (2005) 2062;
(d) P. Gütlich, A. Hauser, H. Spiering, Angew. Chem., Int. Ed. Engl. 33 (1994) 2024.
[7] (a) A. Bousseksou, G. Molnàr, J.A. Real, K. Tanaka, Coord. Chem. Rev. 251 (2007) 1822;
(b) O. Sato, J. Tao, Y.-Z. Zhang, Angew. Chem., Int. Ed. 46 (2007) 2152.
[8] M. Nihei, M. Ui, M. Yokota, L. Han, A. Maeda, H. Kishida, H. Okamoto, H. Oshio, Angew. Chem., Int. Ed. 44 (2005) 6484.
[9] A.A. Shilt, Inorg. Synth. XII (1970) 249.
[10] J. Kim, S. Han, I.-K. Cho, K.Y. Choi, M. Heu, S. Yoon, B.J. Suh, Polyhedron 23 (2004) 1333.
[11] D. Li, R. Clérac, O. Roubeau, E. Harté, C. Mathoniére, R.L. Bris, S.M. Holmes, J. Am. Chem. Soc. 130 (2008) 252.
[12] H. Vahrenkamp, A. Geiβ, G.N. Richardson, J. Chem. Soc., Dalton Trans. (1997) 3643.

and ~8 times (Co^{II}, $S = 3/2$) for Ni^{II} complex ($S = 0$), respectively [7]. Létard et al. have investigated a series of octahedral high-spin metal complexes, and showed that β value is corresponds to number of unpaired electrons [8]. These important suggestions may show that the spin-crossover compounds which exhibit interconversion of electronic configurations are able to switch the NLO response.

The goal of this study is to develop novel materials with switchable NLO response by using of the spin-crossover (SCO) phenomenon and photo-induced spin transition (LIESST) phenomena. It should be noted that no macroscopic non-linearities for the relationship between NLO properties and nature of metal have been investigated in solid so far. However, the macroscopic NLO response is essential for application, which is difficult to realize owing to request of non-centrosymmetry. To achieve macroscopic NLO response, we have attempted two methods; (i) chiral SCO complexes, (ii) Langmuir–Blodgett (LB) film. The LB film can be obtained a SHG-active non-centrosymmetric structure by transfer oriented single molecular layer from gas–water surface to the substrate, and the LB film is generally made of amphiphilic molecules. Therefore we introduced long alkyl chains into complexes in order to make the LB film. Here, we will report the evaluation of the second-order NLO response for these complexes in the LB film.

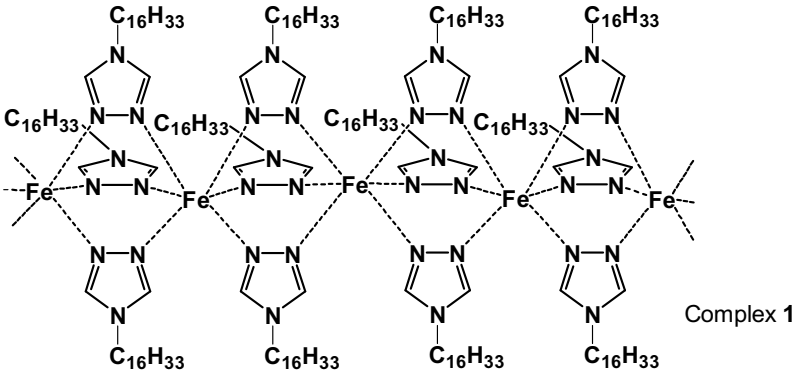
2. Experimental

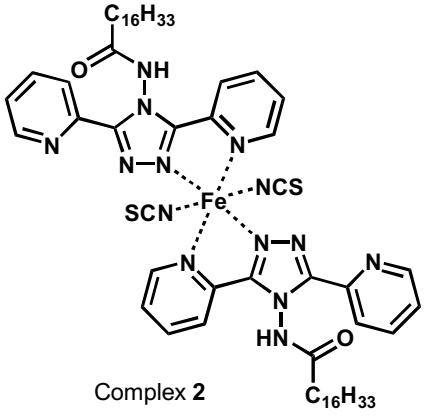
2.1. Synthesis

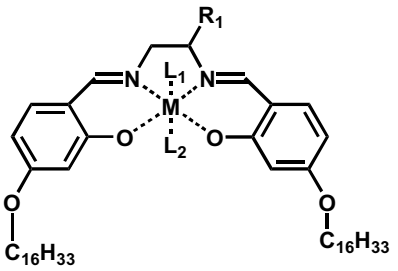
4-Hexadecyl-1,2,4-triazole (C_{16}-trz): formic hydrazine (1.20 g, 20 mmol) and triethyl orthoformate (3.56 g, 24 mmol) were refluxed in methanol (30 ml) for 24 h in inert atmosphere. After cooling, *n*-hexadecacyl amine (4.83 g, 20 mmol) were added and refluxed further 24 h was obtained by removing the solvent under reduced pressure and recrystallizing from methanol.

2.1.1. $\{[Fe(C_{16}\text{-}trz)_3](ClO_4)_2\}_n$ (**1**)

This compound was reported by Roubeau et al. already [9]. $Fe(ClO_4)_2 \cdot 4H_2O$ (0.18 g, 0.5 mmol) in methanol was added to the







3: M = Fe, R_1 = H, L_1 = Cl
4: M = Fe, R_1 = CH_3, L_1 = Cl
5: M = Fe, R_1 = H, L_1 = CN, L_2 = CN (**5** has K^+ as a counter ion)
6: M = Fe, R_1 = CH_3, L_1 = CN, L_2 =CN (**6** has K^+ as a counter ion)
7: M = Fe, R_1 = CH_3, L_1 = CN, L_2 =CN (**7** has Na^+ as a counter ion)
8: M = Mn, R_1 = H, L_1 = Cl
9: M = Ni, R_1 = H
10: M = Cu, R_1 = H

Scheme 1. Structures of complexes **1**–**10**.

solution of C_{16}-trz (0.59 g, 2 mmol) in methanol, and then precipitate was appeared. The solid was collected, washed methanol, and dried under the reduced pressure.

2.1.2. 3,5-Di(2-pyridyl)-4-amino-1,2,4-triazole (ABPT)

A mixture of 2-cyanopyridine (25 g, 0.24 mol) and an excess of hydrazine hydride (25 ml, 0.53 mol) was heated for 3 h at 100 °C. The collected solid was suspended in 2 N HCl (200 ml) and the mixture was boiled for 10 min. The mixture was cooled and made alkaline with ammonia solution. The thick precipitate was collected and crystallized aqueous ethanol in colorless needle. The yield was 4.90 g (8.6%). ^{1}H NMR ($CDCl_3$): 7.35 (dd, 2H), 7.76 (td, 2H), 8.06 (d, 2H), 8.56–8.60 (m, 3H).

2.1.3. N-(3,5-Di-2-pyridinyl-4H-1,2,4-triazol-4-yl)-hexadecanecarboxamide (C_{15}-BPT)

Palmitoyl chloride (0.55 g, 2 mmol) in chloroform was added dropwise to ABPT (0.47 g, 2 mmol) and triethylamine (0.20 g, 2 mmol) in chloroform at 0 °C and stirred overnight at room temperature. The mixture was filtered and the solvent removed under reduced pressure. The residue was recrystallized from methanol/water (1:1 v/v) and then recrystallized from acetone. ^{1}H NMR ($CDCl_3$): 0.88 (t, 3H), 1.1–1.4 (m), 2.32 (t, 2H), 7.38 (dd, 2H), 7.87 (td, 2H), 8.29 (d, 2H), 8.63 (d, 2H), 10.14 (s, 1H).

*2.1.4. [Fe(NCS)$_2$(C_{15}-BPT)$_2$] (**2**)*

$FeCl_2 \cdot 4H_2O$ (0.10 g, 0.5 mmol) and small amount of ascorbic acid in methanol (5 ml) and KNCS (0.10 g, 0.5 mmol) in methanol (5 ml) were mixed and stirred for 15 min. Then, 2,2′-dimethoxypropane (0.5 ml) was added and stirred further 5 min. The solution was filtrated, and dropwise to C_{15}-BPT (0.48 g, 1 mmol) in $CHCl_3$/CH_3OH (1:1 v/v, 10 ml). After few days, the compound crystallized upon slow evaporation of the solvent at room temperature. Red solid were collected and dried under reduced pressure.

2.1.5. 4-(Hexadecyloxy)-2-hydroxy-benzaldehyde (C_{16}-aldehyde)

2,4-Dihydroxybenzaldehyde (10.0 g, 72.4 mmol) and $KHCO_3$ (21.4 g, 70.1 mmol) and KI (catalytic amount) were suspended in acetone (200 ml) and refluxed for 24 h under argon. The reaction mixture was filtered while the solution was hot. The filtrate was acidified to ca. pH 6 by addition of 1 N HCl. The solution was concentrated, extracted by chloroform, and dried over $MgSO_4$. The solvent was removed under reduced pressure and purified by column chromatography on a silica gel (chloroform/hexane 1:1, Rf = 0.4). The yield was 6.64 g (26%). ^{1}H NMR ($CDCl_3$): 0.88 (t, 3H), 1.2–1.5 (m), 1.79 (m, 2H), 4.00 (t, 2H), 6.41 (d, 1H), 6.52 (dd, 1H), 7.40 (d, 1H), 9.71 (s, 1H), 11.49 (s, 1H).

2.1.6. N,N-Bis[4-(hexadecyloxy)salicylidene]ethylenediamine (C_{16}-salen)

C_{16}-aldehyde (1.45 g, 4 mmol) and ethylenediamine (0.12 g, 2 mmol) in chloroform (50 ml) were refluxed for 6 h. The solvent was removed under reduced pressure. The recrystallization from chloroform/methanol (1:1 v/v) gave yellow needle. The yield was 1.35 g (90.1%). ^{1}H NMR ($CDCl_3$): 0.87 (t, 6H), 1.3–1.5 (m), 3.84 (s, 4H), 3.94 (t, 4H), 6.36 (dd, 2H), 6.40 (d, 2H), 7.06 (d, 2H), 8.19 (s, 2H). C_{16}-salmmen was prepared using 1,2-diaminopropane instead of ethylenediamine.

*2.1.7. [FeCl(C_{16}-salen)] (**3**)*

$FeCl_3$ (0.29 g, 1.80 mmol) in chloroform/methanol (1:1 v/v, 10 ml) was added to C16-salen (1.35 g, 1.80 mmol) in chloroform/methanol (1:1 v/v, 30 ml) and refluxed for 3 h. The solvent was removed under reduced pressure and residue was recrystallized from acetone. The red brown solid was obtained (1.21 g, 80.1%). [FeCl(C_{16}-salmmen)] (**4**) was also synthesized the same preparation procedure.

*2.1.8. Na[Fe(C_{16}-salen)(CN)$_2$] (**5**)*

[FeCl(C_{16}-salen)] was dissolved in chloroform. To this solution, NaCN dissolved small amount of methanol/water (1:1 v/v) was added. The precipitated green solid was collected and dried under reduced pressure. *Anal.* Calc. for $C_{50}H_{78}Fe_1N_6K_1N_4O_4$: C, 67.17; H, 8.79; N, 6.27. Found: C, 67.00; H, 8.77; N, 6.04%. Na[Fe(C16-salmmen)(CN)$_2$] (**6**) was synthesized the same preparation procedure, and K[Fe(C16-salmmen)(CN)$_2$] (**7**) was prepared using KCN instead of NaCN.

*2.1.9. [Mn(C_{16}-salen)Cl] (**8**), [Ni(C_{16}-salen)] (**9**), and [Cu(C_{16}-salen)] (**10**)*

M(CH_3COO)$_2$ (M = Mn, Ni, Cu) in methanol was added to the equivalent C_{16}-salen in chloroform/methanol (1:1 v/v). The precipitate was appeared for Ni and Cu. In the case of Mn, the precipitate was obtained by addition of equivalent NaCl. The solid was filtered off and recrystallized from chloroform/methanol (1:1 v/v).

2.2. Film preparation

Complexes **1**–**10** dissolved in chloroform were spread onto the surface of the water. The floating film of complexes was compressed up to the surface pressure of 20 mN m^{-1}. The floating films of complexes were transferred onto the gas–water surface of glass substrates by vertical dipping.

2.3. Physical experiments

All elemental analyses date were obtained at the Service Center of the Elemental Analysis of Organic compounds, Department of Chemistry, Kyushu University. Metal analyses were done on a Shimadzu AA-625-11 Atomic Absorption/Flame Emission Spectrometer. Infrared spectra were recorded using KBr disk with a JASCO FT-IR-410. All NMR measurements were performed on a Bruker AVANCE SERIES DPX 400 instrument operating at 400 MHz. The magnetic susceptibilities $\chi(T)$ were measured between 5 K and 400 K with a superconducting quantum interference device magnetometer (Quantum Design MPMS-5S) in an external field of 0.5 T. Illumination experiment was done with using an Ar^+ laser (λ = 532 nm, continuous wave) as a light source. The measurements of SHG were carried out to detect at 532 nm upon irradiation with a 1064 nm laser.

3. Results and discussion

3.1. Materials

The prepared compounds can be expected to possess some advantage for second-order NLO materials. The analogue for compound **1** has been reported that the LB film for the analogue can make on the glass substrate [10], and it is able to expect for the formation of the LB film for **1**. Furthermore, compound **1** in the HS state is transparent in the visible region, and then the sample of **1** is an advantage example for SHG experiment. Because the SHG responses was enhanced when the light of the SHG is resonated with absorption band for compounds [2b], and the resonance effects make it difficult to estimate the intensity of the essential non-linearity of the materials.

For compound **2**, the C_{15}-BPT ligand is expected to coordinate to the metal asymmetrically by one of nitrogen atom of pyridine and triazole moiety. Because it has been reported that the compound [Fe(ABPT)$_2$(NCS)$_2$] with ABPT ligands forms asymmetric conforma-

tion in the ligand [11]. The asymmetrical conformations generate anisotropic charge transfer and large molecular hyperpolarizability. If two thiocyanato ions coordinated to metal center in *cis*-form, complex **2** is non-centrosymmetry in the single molecule. However, it is suggested that the thiocyanato ions for **2** are in *trans*-form because of the observation of the singlet peak in 2091 cm^{-1} by the IR measurement. Therefore the observation of NLO-active cannot be expected for **2**.

Compounds **5**–**7** have two axial ligands (CN^-). It is expected that the molecular array in the LB film affects the ligand field strengths for the compounds. The adequate ligand field strength closed to the SCO point can be controlled by changing axial ligands easily for the compounds.

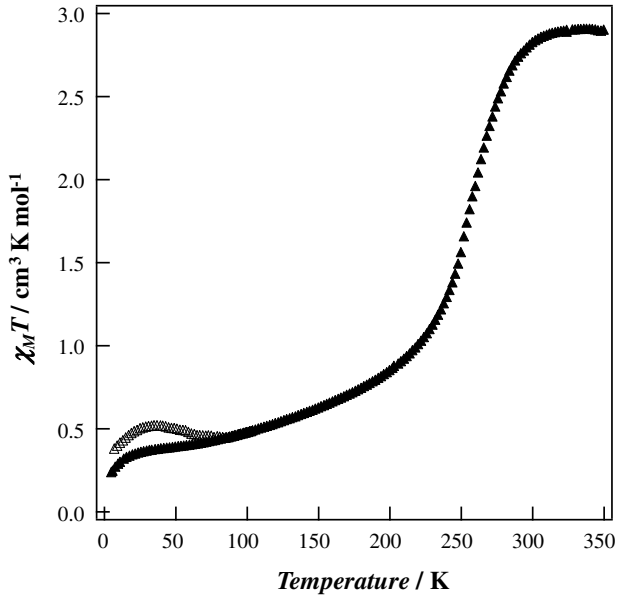


Fig. 1. Temperature dependence of $\chi_M T$ for complex **1**: (▲) data recorded in the warming mode without irradiation; (△) data recorded in the warming mode after the light irradiation, then turned off.

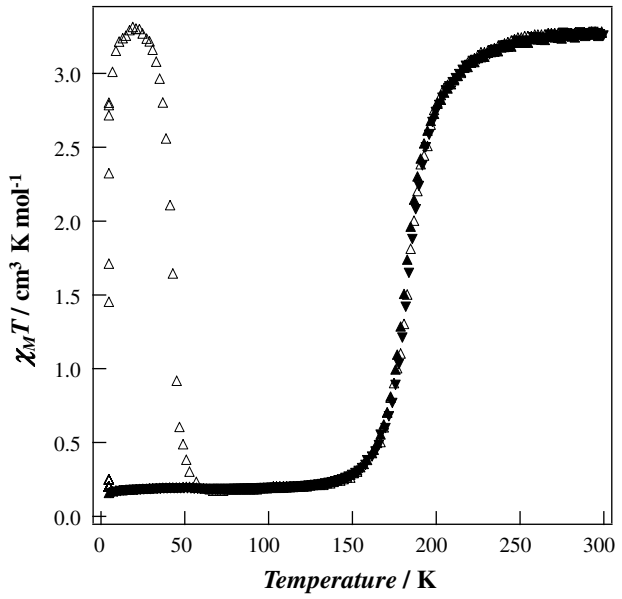


Fig. 2. Temperature dependence of $\chi_M T$ for complex **2**: (▲) and (▼) data recorded in the warming mode and cooling mode without irradiation, respectively; (Δ) data recorded in the warming mode (2 K min^{-1}) after the light irradiation, then turned off.

3.2. Magnetic properties

Temperature dependence of $\chi_M T$ for compound **1** is shown in Fig. 1. Compound **1** exhibited the SCO behavior. The $\chi_M T$ value is 2.92 cm^3 K mol^{-1} at 350 K and 0.39 cm^3 K mol^{-1} at 50 K. The residual high-spin (HS) fraction at 50 K is 13%, regarded the $\chi_M T$ value of 2.92 cm^3 K mol^{-1} at 350 K as in the HS state of 100% and the $\chi_M T$ value of low-spin (LS) state as zero. The LIESST effect was observed in a part of **1** by light irradiation at 5 K.

Temperature dependence of the $\chi_M T$ for compound **2** is shown in Fig. 2. The SCO behavior of compound **2** is abruptly transition. The $\chi_M T$ value is ca. 3.08 cm^3 K mol^{-1} above 250 K and ca. 0.16 cm^3 K mol^{-1} below 150 K and $T_{1/2}$ = 183 K. The hysteresis was not observed. The LIESST phenomenon was observed for compound **2**. The increase of the $\chi_M T$ value to 2.62 cm^3 K mol^{-1} was observed by light irradiation at 5 K. After the light irradiation stopped, the $\chi_M T$ value was increased according to warming in the temperature range <20 K. This increase of the $\chi_M T$ value corresponds to zero-field splitting. In the temperature range 20–50 K, the $\chi_M T$ value was decreased as a result of HS → LS thermal relaxation. It was estimated that the T(LIESST) was 43 K. This behavior is similar to that of $[Fe(ABPT)_2(NCS)_2]$ [11]. The substitutions of long alkyl chains are not influenced cooperative effect.

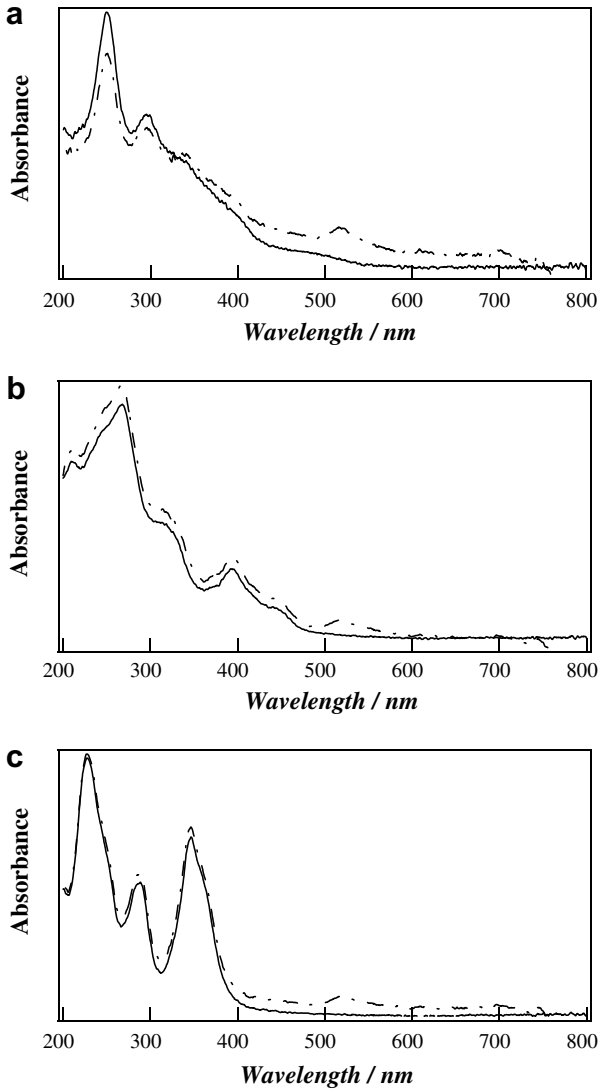


Fig. 3. UV–Vis spectra for **8** (a), **9** (b) **10** (c) in LB film. The solid line is 90° of incident angle, and dashed line is 45° of incident angle.

Compounds **3** and **4** were in the HS state ($t^3_{2g}e^2_g$; $S = 5/2$) in the temperature range of 5–300 K. In contrast, compounds **5**–**7** were in the LS state ($t^5_{2g}e^0_g$; $S = 1/2$) because of the axial coordination of the CN^- ligands between 5 and 300 K. Mn(III) compound **8** was in the HS state ($t^3_{2g}e^1_g$; $S = 2$), and compounds **9** and **10** were in $S = 0$ ($t^6_{2g}e^2_g$) and $S = 1/2$ ($t^6_{2g}e^3_g$), respectively.

3.3. UV–Vis spectra in the LB film

It was confirmed by UV–Vis spectra that compounds **3**–**10** on the water were transferred onto the glass substrates. All complexes showed absorption bands in the region $\lambda > 400$ nm originated from intraligand charge transfer and anisotropic bands in the region 500–600 nm assigned to d–d transition (Fig. 3). It is expected that the anisotropic d–d transitions are able to act favorably to the non-linearities. It should note that compounds **5**, **6** and **7** were in the LS state, and the d–d bands must red-shift compared with that for the HS compounds. Compounds **5**, **6** and **7** are unstable in solution, and the compounds were decomposed and transformed to the oxygen bridged complexes. UV–Vis spectra show that compounds **5**, **6**, and **7** in LB film are contained impurities.

3.4. Second-harmonic-generation (SHG) measurements

The powder samples were put onto surface of glass plates for **1**–**10**, and this glass plates were irradiated 1064 nm laser. However, no SHG signal was observed. The reason of this SHG-inactivity was caused by their crystal structures. The directions of the dipole moments are almost perpendicular for the screw axes, and the dipole moments are cancelled out each other. Furthermore, dipole moments remaining along the screw axes were also cancelled out by alternate arrangement of screw axes. The observation of the SHG responses in LB films was attempted because of no responses in solid. However, SHG signal could not be observed for compounds **1** and **2** in LB film. It is assumed that the compounds have inversion center in the molecules.

On the other hand, SHG signals could be observed for compounds **3**–**10**. The maker fringe patterns for the complexes are shown in Figs. 4–6. For compounds **3** and **4**, the SHG responses are relatively large value in the systems measured in this study. In complex **4**, the SH intensity is smaller than that of complex **3**, which is analogue of complex **4**. This difference of SHG response could not explain except for experimental factors. In spite of the similar structures, compounds **5**, **6** and **7** exhibit considerably difference SHG responses. The difference of the SHG responses between complex **6** and **7** could be explained by difference of cation sizes. It is suggested that compound **7** with small cation Na^+ forms more tight orientation on the glass substrate, and compound **7** exhibited larger non-linearity. The decompositions from compounds **5**, **6** and **7** to μ-oxo species can be shown in the UV–Vis spectra for LB film, and the SHG responses were different from the original ones. The differences of SHG intensities between complex **3** and complexes **8**–**10** which have different metal centers was also revealed. The clear Maker fringe patterns were obtained for complexes **3** and **8**, whereas the Maker fringe patterns for complexes **9** and **10** were poor S/N. The SH intensities are dependent

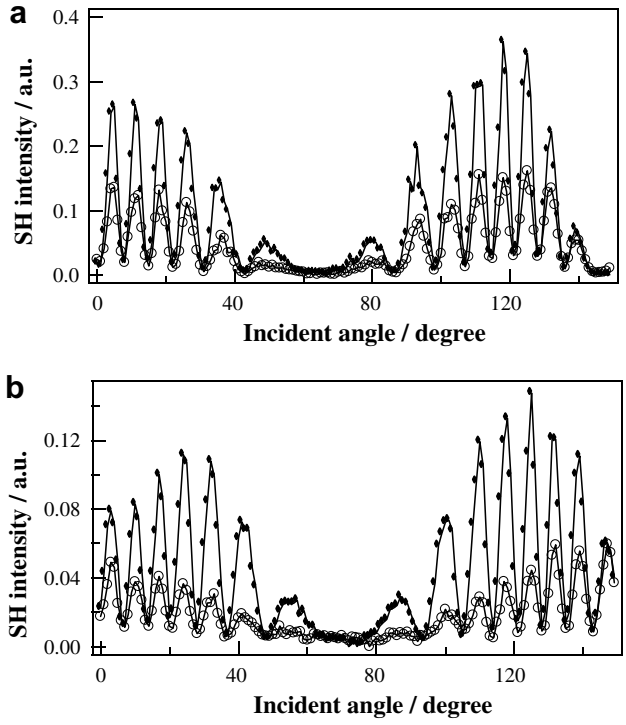


Fig. 4. Maker fringe pattern for **3** (a) and **4** (b). (♦) is irradiate laser polarized p (parallel) and (○) is irradiate lase polarized s (perpendicular).

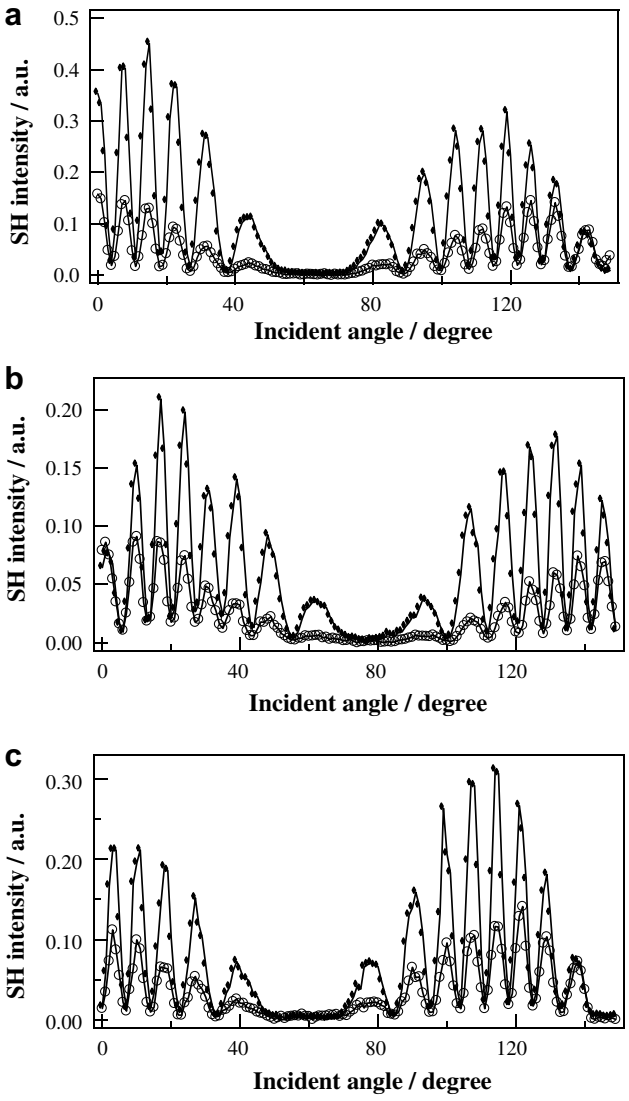


Fig. 5. Maker fringe pattern for **5** (a), **6** (b) and **7** (c). (♦) is irradiate laser polarized p (parallel) and (○) is irradiate lase polarized s (perpendicular).

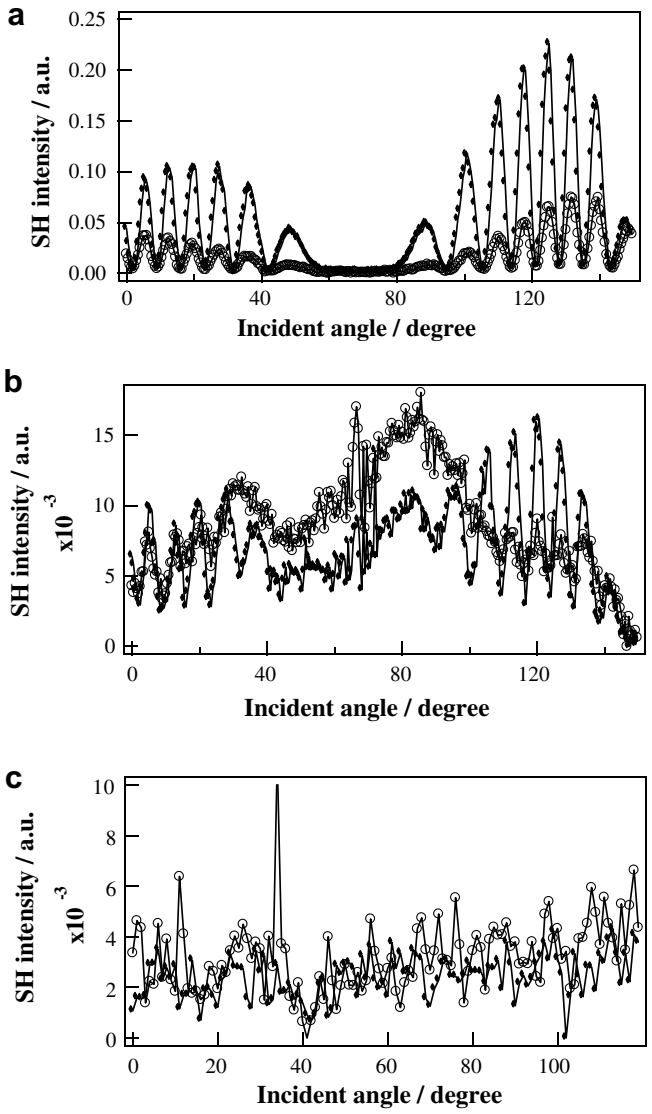


Fig. 6. Maker fringe pattern for **8** (a), **9** (b) and **10** (c). (♦) is irradiate laser polarized p (parallel) and (○) is irradiate lase polarized s (perpendicular).

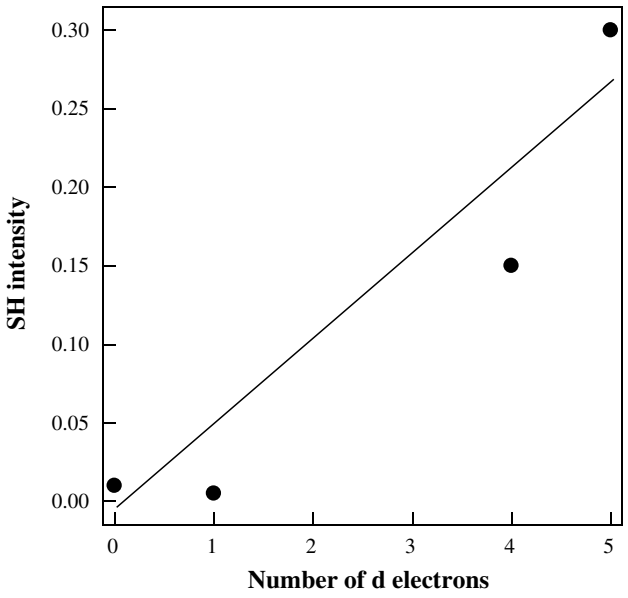


Fig. 7. The relation of number of d electrons and SH intensities.

on the kind of the metal ions, and the order of the intensities are **3** (Fe^{III}; $S = 5/2$) > **8** (Mn^{III}; $S = 2$) > **9** (Ni^{II}; $S = 0$) > **10** (Cu^{II}; $S = 1/2$) (Fig. 7). This order does not correspond to number of d electrons at the order of compounds **9** and **10**. However, this result is reasonable by taking the magnitude of SHG response for **9** and **10** into account.

4. Conclusions

Complexes **1**–**10** which have long alkyl chains to form LB films easily synthesized for the purpose of observing macroscopic second-order non-linearities. The preparation of LB films were succeed for complexes **1**–**10**. The SHG responses were investigated for the complexes in LB films, and the response was observed for the LB film form by some metal complexes. Especially, relatively large SHG signals were observed for compounds with salen or salmmen ligand. In complexes **3** and **8**–**10**, relationship between d electron and SHG intensities is similar to that of microscopic non-linearity. The goal of this study is switching of NLO response by using of SCO and LIESST effect. LB film formed by complex which can easy to change axis ligands is expected to good approach to achieve the purpose. However, complex **5**–**7** using in this study have a problem of stability in solution. Therefore, other complexes suitable for LB film (i.e. complex with stable orientation in LB film) are required. Furthermore, the evaluation of quality of LB film and the estimation method of SHG response are also needed.

Acknowledgements

This work was supported by "Development of Molecular Devices in Ferroelectric Metallomesogens" in 2006 from the New Energy and Industrial Technology Development Organization (NEDO) of Japan, and Grant-in-Aids for Science Research (No. 20350028) from the Ministry of Education, Culture, Sports, Science and Technology of the Japanese Government.

References

[1] M. Barzoukas, M. Blanchard-Desce, D. Josse, J.-M. Lehn, J. Zyss, Chem. Phys. 133 (1989) 323.
[2] (a) B.F. Levine, Chem. Phys. Lett. 37 (1976) 516;
(b) J.L. Ouder, D.S. Chemla, J. Chem. Phys. 66 (1977) 2664.
[3] J. Zyss, I. Ledoux, Chem. Rev. 94 (1994) 77.
[4] (a) B.F. Levine, C.G. Bethea, C.D. Thurmond, R.T. Lynch, J.L. Bernstein, J. Appl. Phys. 50 (1979) 2523;
(b) H. Yamamoto, S. Katogi, T. Watanabe, H. Sato, S. Miyata, T. Hosomi, Appl. Phys. Lett. 60 (1992) 935.
[5] J.L. Ouder, R. Hierle, J. Appl. Phys. 48 (1997) 2699.
[6] P.G. Lacroix, I. Malfant, R. Andreu, P. Cassoux, Synth. Met. 103 (1999) 2168.
[7] S. Di Bella, I. Fragalà, I. Ledoux, T.J. Marks, J. Am. Chem. Soc. 117 (1995) 9481.
[8] J.-B. Gaudry, L. Capes, P. Langot, S. Marcén, M. Kollmannsberger, O. Lavastre, E. Freysz, J.-F. Létard, O. Kahn, Chem. Phys. Lett. 324 (2000) 321.
[9] O. Roubeau, J.M.A. Gomez, E. Balskus, J.J.A. Kolnaar, J.G. Haasnoot, J. Reedijk, New J. Chem. 25 (2001) 144.
[10] F. Armand, C. Badoux, P. Bonville, A.R. Teixier, O. Kahn, Langmuir (1995) 113467.
[11] (a) N. Moliner, M.C. Muñoz, S. Létard, J.-F. Létard, X. Solans, R. Burriel, M. Castro, O. Kahn, J.A. Real, Inorg. Chim. Acta 291 (1999) 279;
(b) N. Moliner, M.C. Muñoz, P.J. van Koningsbruggen, J.A. Real, Inorg. Chim. Acta 274 (1998) 1.

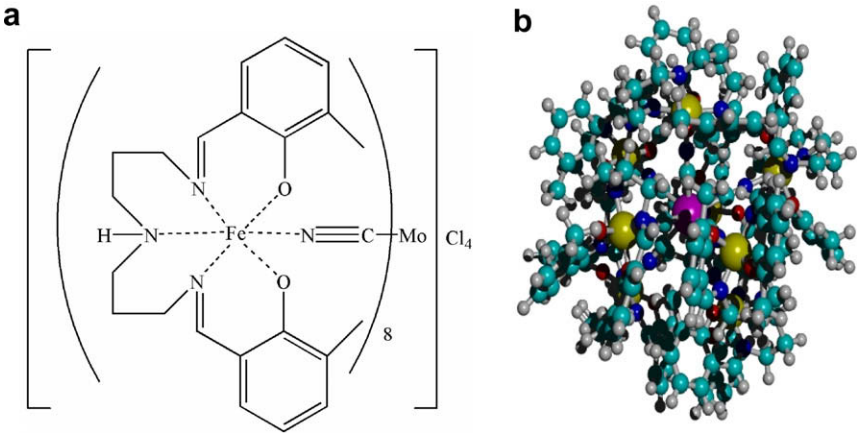
docking to the central Mo atom. The resulting dendrimer-type $[(LFe^{III}NC)_8Mo^{IV}]Cl_4$ clusters may display a maximum of eight multiple spin-crossovers, e.g. it may contain between 8 and 40 unpaired electrons and it exhibits a thermally induced spin crossover between the low-spin (LS; ^2T; $S = 1/2$) and the high-spin (HS; ^6A; $S = 5/2$) states.

Any practical application of molecular magnets as functional units for information storage requires the addressing of individual molecules, which is, imaging, probing, and eventually manipulating individual molecules [32,33]. This goal can be realized most easily by depositing target molecules on a suitable substrate with monolayer or submonolayer coverage [34–39] and by addressing those individually using scanning probe microscopy techniques [40]. While gold surfaces are important substrates for the examination of possible molecular transistor behaviour, other surfaces such as oxides might provide some advantages because interactions between molecule and substrate will be quite different [37]. In this contribution we describe the immobilization of $[(LFe^{III}NC)_8Mo^{IV}]^{4+}$ cation complexes onto the surface of TiO_2 nanowires using electrostatic interactions.

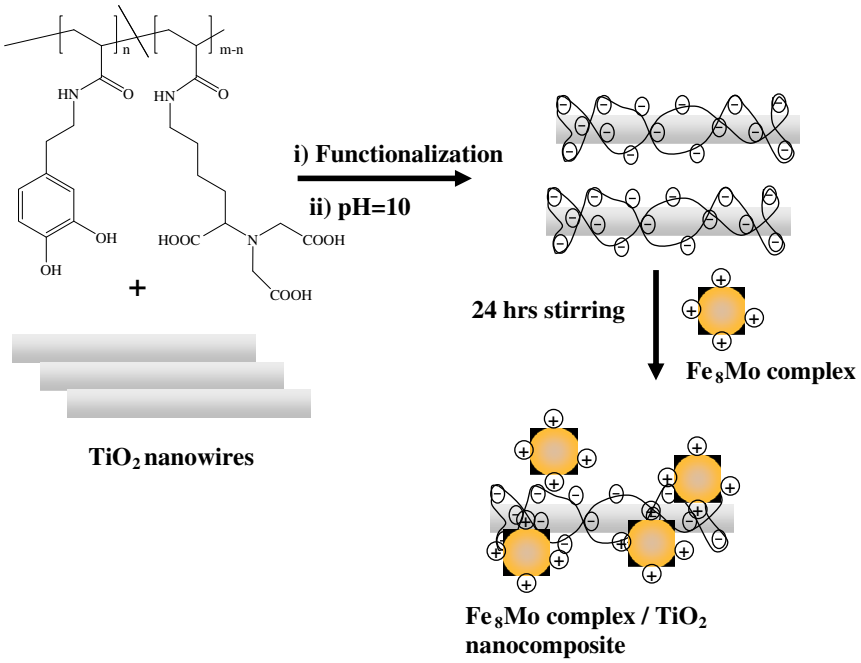
2. Results and discussion

We have used a multifunctional polymeric ligand to functionalize TiO_2 nanowires [41,42]. The high reactivity of pentafluorophenylacrylate active ester polymers with amines allows the formation of the corresponding poly (acrylamides) and opens the possibility to obtain multifunctional polymeric materials [43,44]. We have demonstrated the versatile use of these multifunctional polymers by covalent immobilization of functional molecules onto nanomaterials to build hierarchically organized nanoarchitectures [41,42,45]. As a step further, we exploit here the importance of these polymeric ligands to construct nanoarchitectures based on electrostatic interactions.

The synthesis of the multifunctional polymeric ligand starting from the precursor polymer was carried following the strategy outline in Refs. [41–44]. The resulting polymer exhibits two different properties: (i) 3-hydroxytyramine as an anchor group for the attachment onto the TiO_2 nanowires surface and (ii) multi-carboxylic groups in the back bone of polymeric ligand to create negatively charged surfaces. The multifunctional polymers were



Scheme 1. (a) Structural formula of the $[Mo^{IV}\{(CN)Fe^{III}(L)\}_8]Cl_4$ (Fe_8Mo) molecular switch. (b) Hyperchem7 calculated structure Mo and Fe atoms are enhanced.



Scheme 2. General scheme of the functionalization of TiO_2 nanowires followed by immobilization of Fe_8Mo single-molecular switch.

analyzed by ^{1}H NMR, FT-IR and GPC in order to determine the composition of the polymers. Within the polymeric ligand the respective NTA content was determined to 80 mol%, while the remaining 20 mol% of the functional groups was 3-hydroxytyramine.

Functionalization of TiO_2 nanowires was achieved by sealing a mixture of TiO_2 nanowires (synthesized from concentrated NaOH and titanium isopropoxide) [41,42] and 10 ml of polymeric ligand in benzyl alcohol under inert conditions and stirring at 60 °C for 4 h. The product was repeatedly washed with CH_2Cl_2 to remove unreacted ligand. The functionalized TiO_2 nanowires were characterized by IR and UV–Vis spectroscopy.

The immobilization of multistable molecular switches onto TiO_2 nanowires was carried out by stirring a suspension of functionalized TiO_2 nanowires in an ethanolic solution of as synthesized Fe_8Mo clusters. The structural formula of the molecular switch is shown in Scheme 1a. Scheme 1b shows the structure of the multistable Fe_8Mo complex as obtained by a molecular simulation. The approximate size of the cluster complex is about 2 nm. The fabrication of the TiO_2 nanowires decorated with spin switching iron clusters is illustrated in Scheme 2. In the first step the TiO_2 nanowires (grey) are functionalized with the multifunctional polymer ligand (black) by complexation through the catecholate groups thereby tailoring the surface of the TiO_2 nanowires with NTA groups. In the second step, the carboxylic groups were deprotonated by increasing the pH of the mixture to 10. The Fe_8Mo molecular switches were immobilized by the electrostatic interaction resulting from the net +4 charge of each Fe_8Mo cluster cation and the negatively charged functionalized TiO_2 nanowires.

Fig. 1 shows FTIR spectra of the synthesized molecular switches before and after immobilization onto TiO_2 nanowires. The absorption bands at 2847 cm^{-1} and 2920 cm^{-1}, observed in the infrared spectra show the presence of the non-aromatic C–H stretching vibrations. The aromatic C–H stretching bands seen in the free molecular switches are superimposed in the composite material. The band at 2117 cm^{-1} is assigned to the stretching vibrations of the cyano groups which indicate the presence of Fe_8Mo cluster onto TiO_2 nanowires. The absorption at 1738 cm^{-1} in the IR spectra of Fe_8Mo clusters on the TiO_2 nanowires corresponds to the C=O stretching vibrations of the polymeric ligand used for the functionalization and immobilization of the Fe_8Mo clusters on the TiO_2 nanowires.

As a comparison, the UV–Vis spectra of the as synthesized TiO_2 nanowires (black line), as synthesized Fe_8Mo molecular switches (red line), and the immobilized complexes (green line) were measured. The absorptions at 265, 236, 222 nm of the Fe_8Mo clusters (black line) in the composite material indicative the binding of Fe_8Mo clusters onto the TiO_2 nanowires (Fig. 2).

The immobilization of the Fe_8Mo clusters onto the TiO_2 nanowires was confirmed by high resolution transmission electron microscopy (HRTEM). Representative HRTEM images of iron clusters immobilized on functionalized TiO_2 nanowires are shown in Fig. 3b and c. These images show a nearly uniform dense coverage of the TiO_2 nanowires with isolated Fe_8Mo clusters over the entire length of the nanostructure. The local HRTEM image in Fig. 3c indicates that the iron clusters are spherical with approximate diameters of 2 nm. This is in good agreement with the values obtained from molecular modelling as shown in Scheme 1a. The EDX spectrum in Fig. 3d confirms the presence of Fe, Mo, along with Ti, O, and other expected elements.

Table 1 shows the results of a temperature-dependent Mössbauer study of the as-synthesized and surface bound nonanuclear Fe_8Mo cluster; Fig. 4 shows the Mössbauer spectrum of the as-synthesized cluster at room temperature and 20 K the unbound cluster undergoes a partial thermally induced spin-crossover from the high-spin (HS) to the low-spin (LS) state. The Mössbauer spectrum at room temperature exhibits a single doublet with an isomer shift IS = 0.35(1) mm s^{-1} and a quadrupole splitting ΔE_Q = 0.82(2) mm s^{-1}. These values are characteristic for Fe^{III} in the HS state. When the temperature is decreased a second quadrupole doublet appears, i.e. the transition is gradual and a low-spin fraction appears smoothly down to low-temperatures. At 20 K about 25% of the sample is present in the low-spin state. The situation changes only slightly when the Fe_8Mo cluster is immobilized on the TiO_2 nanowire surface. Similar as for the unbound cluster the spectrum at 300 K contains a single quadrupole doublet. While the IS value of 0.13(1) mm s^{-1} still is in the accepted range for Fe^{III}, its shift to lower values reflects a reduced shielding of the Fe nucleus due to the influence of the surface charge of the functionalized TiO_2 nanowire. Upon decreasing the temperature a second doublet appears whose Mössbauer parameters (IS = 0.15(1) mm s^{-1}, ΔE_Q = 2.50(2) mm s^{-1}) indicate the presence of $Fe^{(III)}$ in the LS state [46]. At 20 K the area fraction of the respective doublets A(HS-Fe^{III}):A(LS-Fe^{III}) is 83:17. These findings

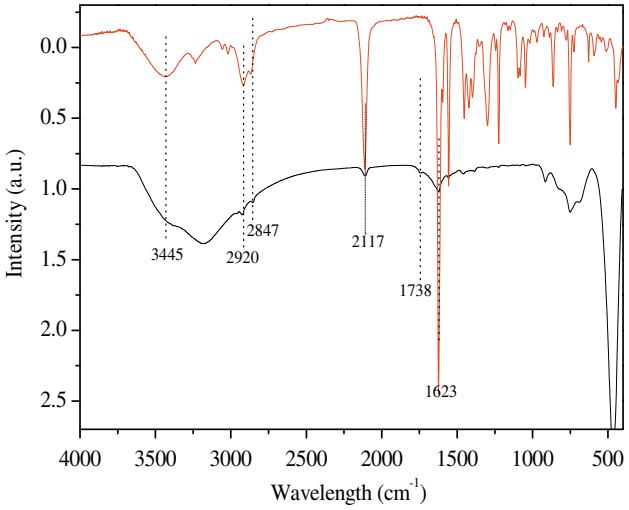


Fig. 1. IR spectra of the Fe_8Mo cluster cation (red, top curve) and the TiO_2 nanowires at Fe_8Mo composites (black, bottom curve). (For interpretation of the references to colour in this figure legend, the reader is referred to the web version of this article.)

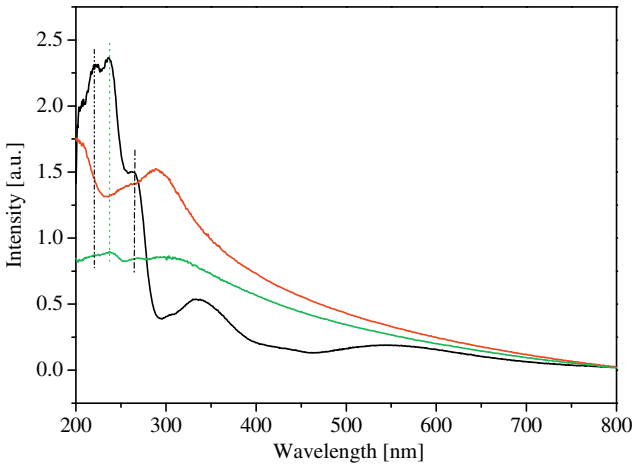


Fig. 2. UV data of the free Fe_8Mo cluster (black, lowest at 400), TiO_2 nanowires (red, highest at 400), and TiO_2 nanowires/Fe_8Mo composites (green, middle at 400). (For interpretation of the references to colour in this figure legend, the reader is referred to the web version of this article.)

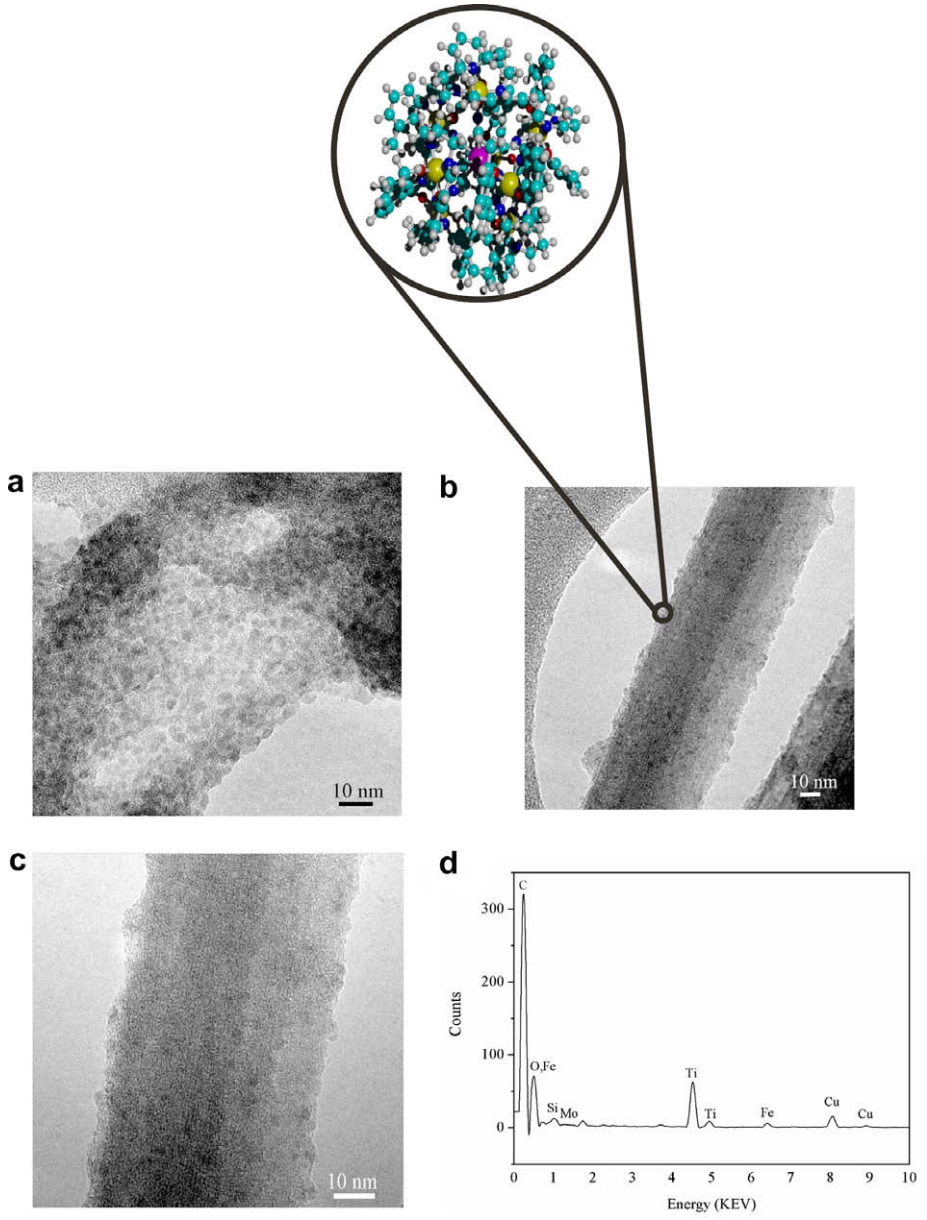


Fig. 3. HRTEM data of Fe_8Mo clusters (a) as synthesized, (b,c) immobilized onto TiO_2 nanowires, (d) EDX of Fe_8Mo clusters/ TiO_2 nanowires composites.

Table 1
Mössbauer data of immobilized and unbound Fe_8Mo clusters.

T(K)	Site 1 (HS)				Site 2 (LS)			
	IS (mm s^{-1})	QS (mm s^{-1})	Area (%)	HWHM (mm s^{-1})	IS (mm s^{-1})	QS (mm s^{-1})	Area(%)	HWHM (mm s^{-1})
Fe_8Mo clusters immobilized on TiO_2 nanowire								
300	0.13(1)	0.55(2)	100	0.47(2)				
20	0.36(1)	0.79(2)	83.0	0.23(2)	0.15(1)	2.50(2)	17	0.25(2)
Unbound Fe_8Mo clusters								
300	0.35(1)	0.82(2)	100	0.38(2)				
20	0.37(1)	0.80(2)	83	0.39(2)	0.15(1)	2.50(2)	17	0.25(2)

indicate (i) that in the unbound state the nona-nuclear Fe_8Mo cluster undergo a thermally induced transition from the HS and to the LS state. (ii) The surface charge has some influence on the shielding of the Fe nucleus, and (iii) the spin HS → LS transition occurs for both, unbound and immobilized clusters. This important finding indicates that an isolated surface bound molecular switch still acts as a switch and remains addressable in a potential information storage step. As several $Fe^{(III)}$ centres are present in the Fe_8Mo clusters, multiple electronic transitions of surface bound molecules can be envisaged.

In summary, a Fe_8Mo molecular switch was deposited onto functionalized TiO_2 nanowires by electrostatic interactions

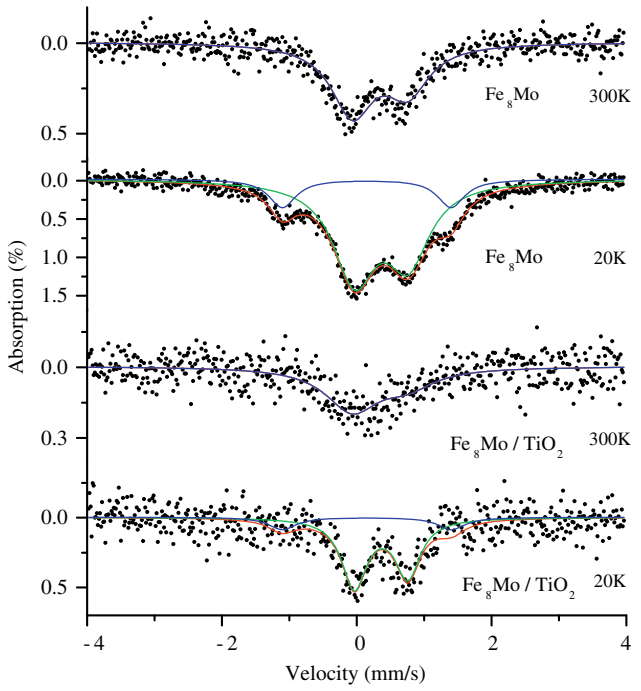


Fig. 4. Mössbauer spectra of Fe_8Mo cluster and Fe_8Mo onto TiO_2 at 300 K and 20 K.

between the cluster cations and the polymer functionalized titanium dioxide nanowire. The surface binding of the cluster molecule was demonstrated using IR and UV–Vis spectroscopy. (HR)TEM images indicate a homogeneous coverage of the TiO_2 nanowires by discrete and individual Fe_8Mo clusters. Given the small quantities of available material, a magnetic proof of the existence of SMMs on the surface cannot be obtained from bulk measurements. However, temperature-dependent Mössbauer spectroscopic studies show that the HS → LS transition observed in the free cluster molecules is preserved upon surface binding. Our results emphasize the possibility of fabricating molecule-based low-dimensional structures by using traditional bottom-up approaches based on the electrostatic interaction between the cluster cations and polymer functionalized nanowires (or oxide surfaces in general). These results can be generalized for the application to both charged and non-charged molecules.

3. Experimental

Precursor complex [Fe^{III}(L)Cl]: 12.5 mmol of the 3-methyl-salicylaldehyde were dissolved in approx. 8 mL of MeOH. 6.25 mmol of the corresponding di(aminopropyl)amine were added dropwise. This solution was boiled for 10 min. Subsequently, 6.25 mmol of $FeCl_3$ dissolved in approx. 80 mL of MeOH were added and stirred for 10 min at 50 °C. 12.5 mmol of triethylamine were added dropwise and stirred for 1 h at 50 °C. After cooling to room temperature some solvent was evaporated and the solution cooled until some precipitate appeared. This precipitate was filtered using a frit IV filter, cleaned with cold MeOH and diethylether and dried under vacuum for 24 h. Yield: 92% MS [EIMS, $C_{22}N_3H_{24}FeCl$] 421 *m/z*. C, H, N-analysis: (calc./exp.) 57.3/57.8, 6.7/5.9,9.3/9.2.

[Mo^{IV}{(CN)Fe^{III}(L)}$_8$]Cl_4 (Fe_8Mo): 10 ml of an aqueous methanol (1:1) solution of $K_4[Mo(CN)_8] \cdot 2H_2O$ (0.1 mmol) was added dropwise to 100 mL of a solution of [Fe^{III}(L)Cl] (0.8 mmol) in methanol. This mixture was stirred at room temperature for 30 min. The dark-blue solution was filtered and reduced under pressure to 50 mL at a temperature below 35 °C. For precipitation 50 mL of distilled cooled water were added. This product was filtered slowly through a frit IV funnel. The dark-blue-black molecular switch was washed with distilled water and diethyl ether and finally dried under vacuum for 24 h. Yield: 48% MS [EIMS, $(C_{22}N_3H_{24}Fe)_5$ Mo^+] 2411.8 *m/z*. MS [EIMS, C_{22} $N_3H_{24}FeCl$] 421 *m/z*. The molecular ion peak 3816.5 was not visible in EIS-MS.

The synthesis of the polymeric ligand and of the TiO_2 nanowires was carried out at as reported in Refs. [41,42].

Functionalization of TiO_2 nanowires: TiO_2 nanowires (5 mg) were dispersed in 10 mL of benzyl alcohol and sonicated for 15 min. In a separate vial 10 mg of the polymer ligand were dissolved in 10 mL of benzyl alcohol. Both suspension and solution were mixed under inert conditions and stirred at 60 °C for 4 h. Then the polymer functionalized nanowires were isolated and purified by repeated washing with CH_2Cl_2 using centrifugation. Subsequently they were dried under vacuum at room temperature.

Dried TiO_2 nanowires (3 mg) were suspended in an aqueous NaOH (0.001 M) solution and stirred at 25 °C for 1 h. The mixture was separated by filtration and washed with deionized water. Subsequently, it was dried in vacuo at 25 °C for 6 h to give the carboxylate-functionalized TiO_2 nanowires sodium salt. The functionalized TiO_2 nanowires were charged in 30 mL of ethanol, and 50 mg of Fe_8Mo, dissolved in 5 mL of ethanol were added followed by stirring for 48 h. The solid was then separated from the mixture by centrifugation and washed several times with excess ethanol. The black brown solid was collected and dried overnight in vacuo at 25 °C.

Mössbauer spectroscopy: Mössbauer measurements were performed in transmission geometry using a constant-acceleration spectrometer and a helium bath cryostat. ^{57}Fe Mössbauer spectra were recorded between room temperature and 4.2 K using the 50 mCi source ^{57}Co(Rh). The RECOIL 1.03 Mössbauer Analysis Software was used to fit the experimental spectra [47]. Isomer shift values are quoted relative α-Fe at 293 K.

Acknowledgements

This work was partly funded by the DFG (Re-1627/1-3), the "Fonds der chemischen Industrie", the University of Mainz ("Forschungsfond"; "Material-Wissenschaftliches Forschungs-Zentrum" = MWFZ), and the Leibniz University of Hannover.

References

[1] C. Joachim, J.K. Gimzewski, A. Aviram, Nature 408 (2000) 541.
[2] M.R. Metzger, Acc. Chem. Res. 32 (1999) 950.
[3] J. Park, A.N. Pasupathy, J.I. Goldsmith, C. Chang, Y. Yaish, J.R. Petta, M. Rinkoski, J.P. Sethna, H.D. Abrupa, P.L. McEuen, D.C. Ralph, Nature 417 (2002) 722.
[4] A.M. Ako, O. Waldmann, V. Mereacre, F. Klöwer, I.J. Hewitt, C.E. Anson, H.U. Güdel, A.K. Powell, Inorg. Chem. 46 (2007) 756.
[5] Z.G. Gu, W. Liu, O.F. Yang, Z.H. Zhou, J.Z. Zuo, X.Z. You, Inorg. Chem. 46 (2007) 3236.
[6] M. Bhattacharya, A.G. Samuelson, P.K. Das, J. Phys. Chem. B 111 (2007) 7122.
[7] H. Wendei, M. Bernien, J. Luo, C. Sorg, N. Ponpandian, J. Kurde, J. Miguel, M. Piantek, X. Xu, P. Eckhold, W. Kuch, K. Baberschke, P.M. Panchmatla, B. Sanyal, P.M. Oppeneer, O. Eriksson, Nat. Mater. 6 (2007) 516.
[8] J.K. McCusker, E.A. Schmitt, D.N. Hendrickson, D. Gatteschi, O. Kahn, J.S. Miller, F. Palacio (Eds.), Magnetic Molecular Materials, NATO ASI Series, vol. 198, Kluwer, Dordrecht, 1991, p. 297.
[9] O. Kahn, Molecular Magnetism, VCH, New York, 1993.
[10] D. Gatteschi, E. Coronado, P. Delhaes, D. Gatteschi, J.S. Miller, in: Molecular Magnetism: From Molecular Assemblies to the Devices, NATO ASI Series, vol. 321, Kluwer, Dordrecht, 1996, p. 141. 289.
[11] P.R. Ashton, S. Iqbal, J.F. Stoddart, N.D. Tinkerb, Chem. Commun. (1996) 479.
[12] M.C.T. Fyfe, P.T. Glink, S. Menzer, J.F. Stoddart, A.J.P. White, D.J. Williams, Angew. Chem., Int. Ed. Engl. 36 (1997) 2068.
[13] J.-M. Lehn, A. Rigault, Angew. Chem., Int. Ed. Engl. 27 (1998) 1095.
[14] R. Krher, J.-M. Lehn, A.D. Cian, J. Fischer, Angew. Chem., Int. Ed. Engl. 32 (1993) 703.
[15] P.N.W. Baxter, J.-M. Lehn, J. Fischer, M.T. Youniou, Angew. Chem., Int. Ed. Engl. 33 (1994) 2284.

[16] E. Breuning, M. Ruben, J.-M. Lehn, F. Renz, Y. Garcia, V. Ksenofontov, P. Gütlich, E. Wegelius, K. Rissanen, Angew. Chem., Int. Ed. 39 (2000) 2504.
[17] E. Breuning, U. Ziener, J.-M. Lehn, E. Wegelius, K. Rissanen, Eur. J. Inorg. Chem. (2001) 1515.
[18] A.M. Garcia, F.J. Romero-Salguero, D.M. Bassani, J.-M. Lehn, G. Baum, D. Fenske, Chem. Eur. J. 6 (1999) 1803.
[19] F. Renz, J. Hefner, D. Hill, M. Klein, Polyhedron 26 (2007) 2325.
[20] F. Renz, J. Hefner, D. Hill, M. Klein, Polyhedron 26 (2007) 2330.
[21] R.G. Hicks, M.T. Lemaire, L.K. Thompson, T.M. Barclay, J. Am. Chem. Soc. 122 (2000) 8077.
[22] T.B. Chaston, D.R. Richardson, Am. J. Hematol. 73 (2003) 200.
[23] C.J. Milios, A. Vinslava, W. Wernsdorfer, A. Prescimone, P.A. Wood, S. Parsons, S.P. Perlepes, G. Christou, E.K. Brechin, J. Am. Chem. Soc. 129 (2007) 6547.
[24] S.K. Dey, T.S.M. Abedin, L.N. Dawe, S.S. Tandon, J.L. Collins, L.K. Thompson, A.V. Postnikov, M.S. Alam, P. Müller, Inorg. Chem. 46 (2007) 7767.
[25] J.H. Yoon, J.H. Lim, H.C. Kim, C.S. Hong, Inorg. Chem. 45 (2006) 9613.
[26] M.N. Tahir, N. Zink, M. Eberhardt, H.A. Therese, U. Kolb, P. Theato, W. Tremel, Angew. Chem., Int. Ed. 45 (2006) 4809.
[27] M.N. Tahir, P. Theato, W.E.G. Müller, H.C. Schröder, A. Borejko, S. Faiß, A. Janshoff, J. Huth, W. Tremel, Chem. Commun. (2005) 5533.
[28] R. Alsfasser, S. Trofimenko, A. Looney, G. Parkin, H. Vahrenkamp, Inorg. Chem. 30 (1991) 4098.
[29] R. Alsfasser, M. Ruf, S. Trofimenko, H. Vahrenkamp, Chem. Ber. 126 (1993) 703.
[30] M.A. Halcrow, B. Chaudret, S. Trofimenko, J. Chem. Soc., Chem. Commun. (1993) 465.
[31] S. Trofimenko, Chem. Rev. 93 (1993) 943.
[32] B. Cage, S.E. Russek, R. Shoemaker, A.J. Barker, C. Stoldt, V. Ramachandaran, N.S. Dalal, Polyhedron 26 (2007) 2413.
[33] M.C. Leön, E. Coronado, A.F. Aliaga, P. Amorös, J.R. Castellanosc, J.M.G. Calbet, J. Mater. Chem. 13 (2003) 3089.
[34] M. Bartz, R. Seshadri, J. Küther, W. Knoll, W. Tremel, Angew. Chem. 110 (1998) 2646.
[35] S.A. Levi, P. Guatteri, F.C.J.M.G.J. van Veggel, V.D. Dalcanale, D.N. Reinhoudt, Angew. Chem. 113 (2001) 1945.
[36] S.A. Levi, P. Guatteri, F.C.J.M.G.J. van Veggel, V.D. Dalcanale, D.N. Reinhoudt, Angew. Chem., Int. Ed. 40 (2001) 1892.
[37] A. Cornia, A.C. Fabretti, M. Pacchioni, L. Zobbi, D. Bonacchi, A. Caneschi, D. Gatteschi, R. Biagi, U.D. Pennino, V.D. Renzi, L. Gurevich, H.S.J. van der Zant, Angew. Chem., Int. Ed. 42 (2003) 1645.
[38] M.N. Tahir, P. Theato, W.E.G. Müller, H.C. Schröder, A. Janshoff, J. Zhang, J. Huth, W. Tremel, Chem. Commun. (2004) 2848.
[39] G.G. Condorelli, A. Motta, I.L. Fragal, F. Giannazzo, V. Raineri, A. Caneschi, D. Matteschi, Angew. Chem., Int. Ed. 43 (2004) 4081.
[40] R.V. Martinez, G. Garcia, R. Garcia, E. Coronado, A.F. Aliaga, F.M. Romero, S. Tatay, Adv. Mater. 19 (2007) 291.
[41] M.N. Tahir, M. Eberhardt, P. Theato, S. Faiß, A. Janshoff, T. Gorelik, U. Kolb, W. Tremel, Angew. Chem., Int. Ed. 45 (2006) 908.
[42] M.N. Tahir, M. Eberhardt, H.A. Therese, U. Kolb, P. Theato, W.E.G. Müller, H.C. Schröder, W. Tremel, Angew. Chem., Int. Ed. 45 (2006) 4803.
[43] I. Potavova, R. Mruk, S. Prehl, R. Zentel, T. Basche, A. Mews, J. Am. Chem. Soc. 125 (2003) 320.
[44] M. Eberhardt, R. Mruk, P. Theato, R. Zentel, Eur. Polym. J. 41 (2005) 1569.
[45] M.N. Tahir, N. Zink, M. Eberhardt, H.A. Therese, S. Faiss, A. Janshoff, U. Kolb, P. Theato, W. Tremel, Small 3 (2007) 829.
[46] P. Gütlich, J. Ensling, in: R.I. Solomon, A.B.P. Lever (Eds.), Inorganic Electronic Structure and Spectroscopy, Wiley, New York, 1999, p. 161.
[47] K. Lagarec, D.G. Rancourt, Nucl. Instrum. Meth. B 129 (1997) 266.

Table 1
Crystallographic data for **1**, **2** and **3**.

	1	2	3
Formula	$C_{68}H_{52}Fe_2N_6O_6$	$C_{22}H_{17}FeN_2O_3$	$C_{21}H_{16}Cl_2FeN_2O_3$
M_w	1160.89	413.23	471.12
Crystal system	monoclinic	orthorhombic	triclinic
Space group	*C2/c*	*Pnma*	$P\bar{1}$
T (K)	110 ± 1	150 ± 1	106 ± 1
a (Å)	25.393(4)	19.562(4)	8.184 (4)
b (Å)	6.0376(7)	17.775(3)	10.218(5)
c (Å)	35.301(6)	5.1681(9)	11.371(6)
α (°)	90	90	93.348(6)
β (°)	108.635(6)	90	96.642(3)
γ (°)	90	90	98.844(7)
V (Å^3)	5128 (1)	1797.0(5)	930.5(8)
Z	4	4	2
D_{calc} (g cm^{-3})	1.503	1.527	1.681
$F(000)$	2408.0	852.0	480.0
μ (Mo Kα) (cm^{-1})	0.63	8.65	1.12
Measured reflections	30107 (total)	12902 (total)	10827 (total)
Observed reflections ($I > 2\sigma(I)$)	5846	2122	4237
Residual electron density (Å^{-3})	0.62 (max); −0.56 (min)	0.59 (max); −0.49 (min)	0.66 (max); −0.79 (min)
R_1	0.097	0.077	0.033
R_w	0.195	0.139	0. 082
Goodness-of-fit	1.33	1.28	1.07

Table 2
Selected bond lengths (Å) and angles (°) for complexes **1**, **2** and **3**.

Complex **1**			
Fe1–O1	1.978(3)	Fe1–O2	1.957(3)
Fe1–N1	2.102(4)	Fe1–N2	
Fe1–N3	2.148(3)		2.080(4)
O1–Fe1–O2	104.0(1)	O1–Fe1–N1	85.1(1)
O1–Fe1–N2	158.1(1)	O1–Fe1–N3	99.7(1)
O2–Fe1–N1	159.4(1)	O2–Fe1–N2	86.9(1)
O2–Fe1–N3	94.7(1)	N1–Fe1–N2	78.9(1)
Complex **2**			
Fe1–O1	1.953(3)	Fe1–O2	2.082(15)
Fe1–O3	2.105(8)		
O1–Fe1–O1[a]	98.17(13)	O1–Fe1–O2	106.3(2)
O1–Fe1–O3	115.6(2)	O1–Fe1–N1	88.42(12)
O1–Fe1–N1[a]	157.13(12)		
Complex **3**			
Fe1–O1	1.9527(14)	Fe1–O2	1.9696(12)
Fe1–O3	2.1378(14)	Fe1–N1	2.0965(13)
Fe1–N2	2.0954(16)		
O1–Fe1–O2	100.84(5)	O1–Fe1–O3	99.97(5)
O1–Fe1–N1	88.67(5)	O1–Fe1–N2	160.43(5)
O2–Fe1–O3	95.71(5)	O2–Fe1–N1	165.71(6)
O2–Fe1–N2	88.74(5)	O3–Fe1–N2	93.09(5)
O3–Fe1–N2	95.95(5)	N1–Fe1–N2	79.15(5)

[a] Symmetry codes: **2**: (1) x, $-y + 1/2$, z.

$C_{21}H_{16}Cl_2FeN_2O_3$: C, 53.54; H, 3.42; N, 5.95. Found: C, 52.59; H, 3.41; N, 5.94%.

2.4. X-ray crystal structure determination

A suitable crystal of **1**, **2** or **3** was mounted on a glass fiber. The X-ray measurements were made on a Rigaku/MSC Mercury CCD diffractometer with graphite-monochromated Mo Kα radiation (λ = 0.71069 Å). The diffraction data were collected at 110 K for complex **1**, 150 K for complex **2** and 106 K for complex **3** using the multi scan technique and totals of the 30107, 12902 and 10827 reflections were collected for **1**, **2** and **3**, respectively. The linear absorption coefficients μ were 0.632, 0.865 and 1.124 for **1**, **2** and **3**, respectively. Data were collected and processed using the CRYSTALCLEAR program (Rigaku). The structures were solved by direct methods (SIR-92 for **1** and SIR-97 for **2** and **3**) [3] and expanded using Fourier techniques [4]. All the non-hydrogen atoms of complexes **1** and **3** were refined anisotropically, while in complex **2**, disordered EtOH oxygen atoms O2 and O3 were refined isotropically with site occupation factors of 0.15 and 0.35, respectively, and the other non-hydrogen atoms were refined anisotropically. Hydrogen atoms were included but not refined. The final cycle of full-matrix least squares refinements [5] were based on 5846 reflections ($I > 2\sigma(I)$) and 370 variable parameters for **1**, 2122 reflections ($I > 2\sigma(I)$) and 135 variable parameters for **2**, and 4237 reflections ($I > 2\sigma(I)$) and 263 variable parameters for **3**. The unweighted and weighted agreement factor of $R_1 = \sum||F_o| - |F_c||/\sum|F_o|$ and $R_w = [\sum[w(F^2_o - F^2_c)^2]/\sum w(F^2_o)^2]^{1/2}$ are used. The R_1 and R_w values were (0.097 and 0.1953), (0.076 and

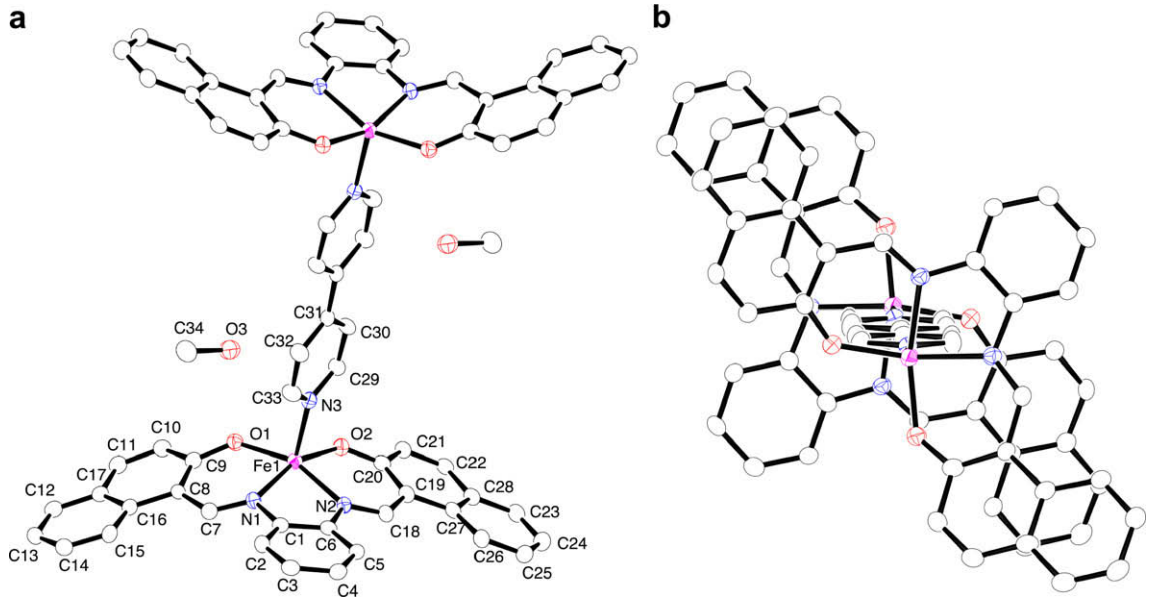


Fig. 1. (a) ORTEP drawing of **1** showing the 50% probability ellipsoids and (b) the same as (a) without crystalline solvent viewed from Fe–bpy–Fe′ direction. Hydrogen atoms have been omitted for clarity.

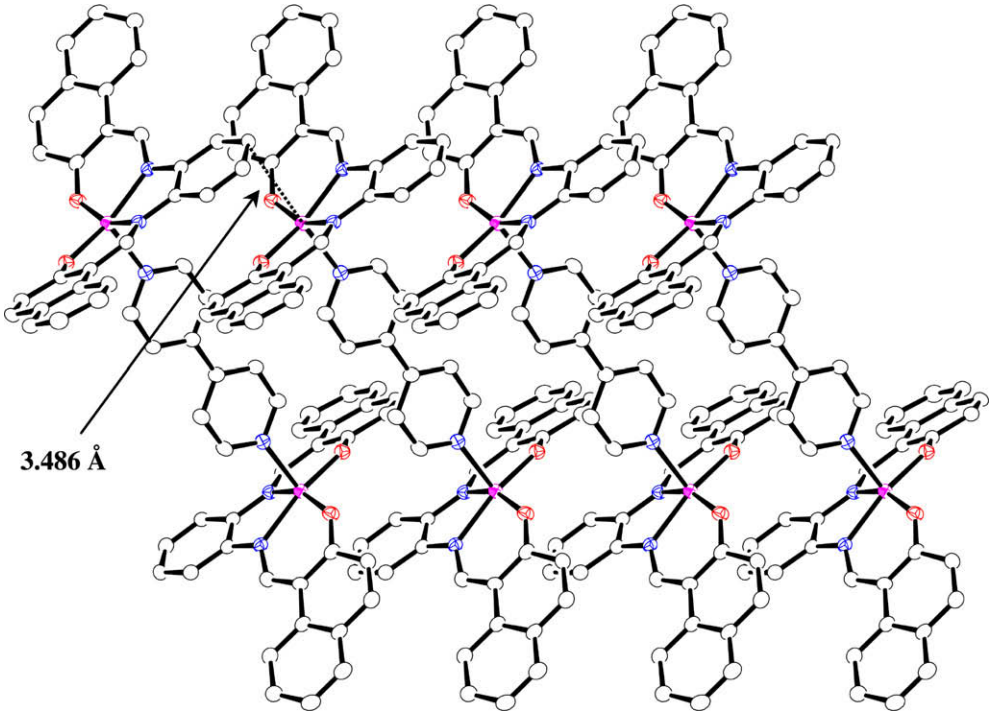


Fig. 2. The molecular packing of **1** showing Fe···π interaction.

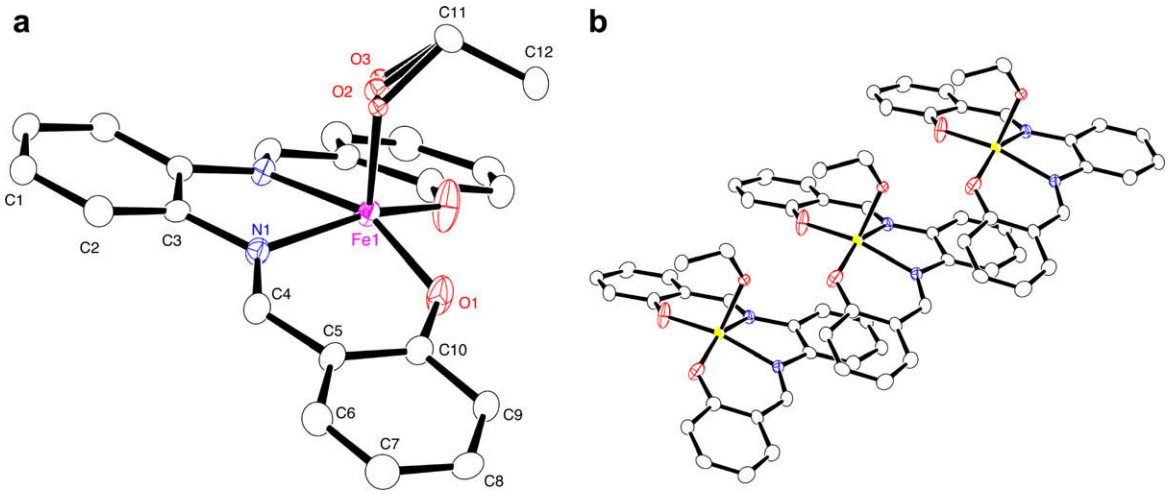


Fig. 3. (a) ORTEP drawing of **2**, showing the 50% probability ellipsoids. O2 and O3 are disordered oxygen atoms of EtOH. (b) A molecular packing of **2**. Hydrogen atoms have been omitted for clarity.

0.1392) and (0.0328 and 0.0820) for complexes **1**, **2** and **3**, respectively. All calculations were performed using the TEXSAN crystallographic software package of Molecular Structure Corporation.[2] Crystal data and details of the structure determination are summarized in Table 1.

2.5. Magnetic susceptibility measurements

Magnetic susceptibility data were collected on fresh microcrystalline samples on a Quantum Design MPMS2 SQUID magnetometer equipped with a 1 T magnet and capable of achieving temperatures of 1.7–400 K. A diamagnetic correction to the observed susceptibilities was applied using Pascal's constants.

3. Results and discussion

3.1. Sample preparation

Although the preparation of **1** and **2** were conducted with the excess bridging ligands, the dimer or monomer complexes were obtained. Possible reason is the low solubility of this type of complex, especially having extended p system such as naphthalene moiety. The low solubility of dimers prevents further coordination of bridging ligand to form one-dimensional chain in solution. Changing solvents may induce different results.

[2] TEXSAN: Crystal structure analysis package, Molecular Structure Corporation 1985 and 2004.

3.2. Crystal structure of $[Fe_2(L1)_2(4,4'\text{-bpy})] \cdot 2MeOH$ (**1**)

The molecular structure of **1** together with the atom numbering scheme is shown in Fig. 1a. Selected bond lengths and angles are summarized in Table 2. Two Fe(II)–L1 moieties are connected through 4,4′-bpy bridge and the molecule has an inversion center at the center of the 4,4′-bpy ligand. Each Fe(II) ions has a penta-coordinate square pyramidal geometry with a 0.296 Å lift of Fe(II) ion from the basal N_2O_2 plane. Bond lengths around the Fe(II) ion are shown in Table 2. The average Fe–O and Fe–N bond lengths are 1.97 and 2.11 Å, respectively, which are clearly longer than those reported for low-spin complexes (1.952 and 1.946 Å) [2c], indicating that the Fe(II) ion has a high-spin state. The dihedral angle of two naphthalene planes in each Fe(II)–L1 moiety is 41.6°. This is clear difference in one-dimensional chain complex bridged by pyz, [Fe(3-MeO–salophen)pyz] · CH_2Cl_2 [2c], where the corresponding dihedral angle is almost 0°. A molecular structure viewed from Fe–bpy–Fe′ direction is shown in Fig. 1b. Two pyridine planes in 4,4′-bpy are completely parallel. They are also parallel to the plane defined by N1–O2–N1′–O2′. This implies a possibility of interaction between two Fe(II) ions through p-orbitals of 4,4′-bpy, although Fe···Fe′ distances through 4,4′-bpy bridge is 11.431 Å and the magnetic interaction through 4,4′-bpy bridge is thought to be negligibly small [6,7]. Another interesting feature of this compound is the possibility of Fe···π interaction. As can be seen from the molecular packing view shown in Fig. 2, a phenyl ring of L1 belonging to the neighboring molecule is near the vacant site of Fe(II) ion with Fe···C3 distance of 3.486 Å, which leads to the Fe···Fe distance of 6.038 Å for the neighboring molecule. Since there are rich π–π interaction between the phenyl ring and naphthalene moieties, the Fe···π interaction may be induced by these π–π interactions. From the bond valence sum (BVS) analysis [8] of the Fe center, the oxidation state was estimated to be +2.37, which is, although slightly larger than expected, consistent with the valence of +2 for the Fe(II) ion.

3.3. Crystal structures of [Fe(L2)(EtOH)] (**2**) and [Fe(L3)(MeOH)] (**3**)

The ORTEP drawings of molecular structures of **2** and **3** including their molecular packing views are shown in Figs. 3 and 4, respectively. Both complexes show mononuclear structures with penta-coordinate square pyramidal geometries. The Fe(II) ions are surrounded by bis-Schiff base N_2O_2 donors from the equatorial position and an alcohol oxygen from the apical position. Bond

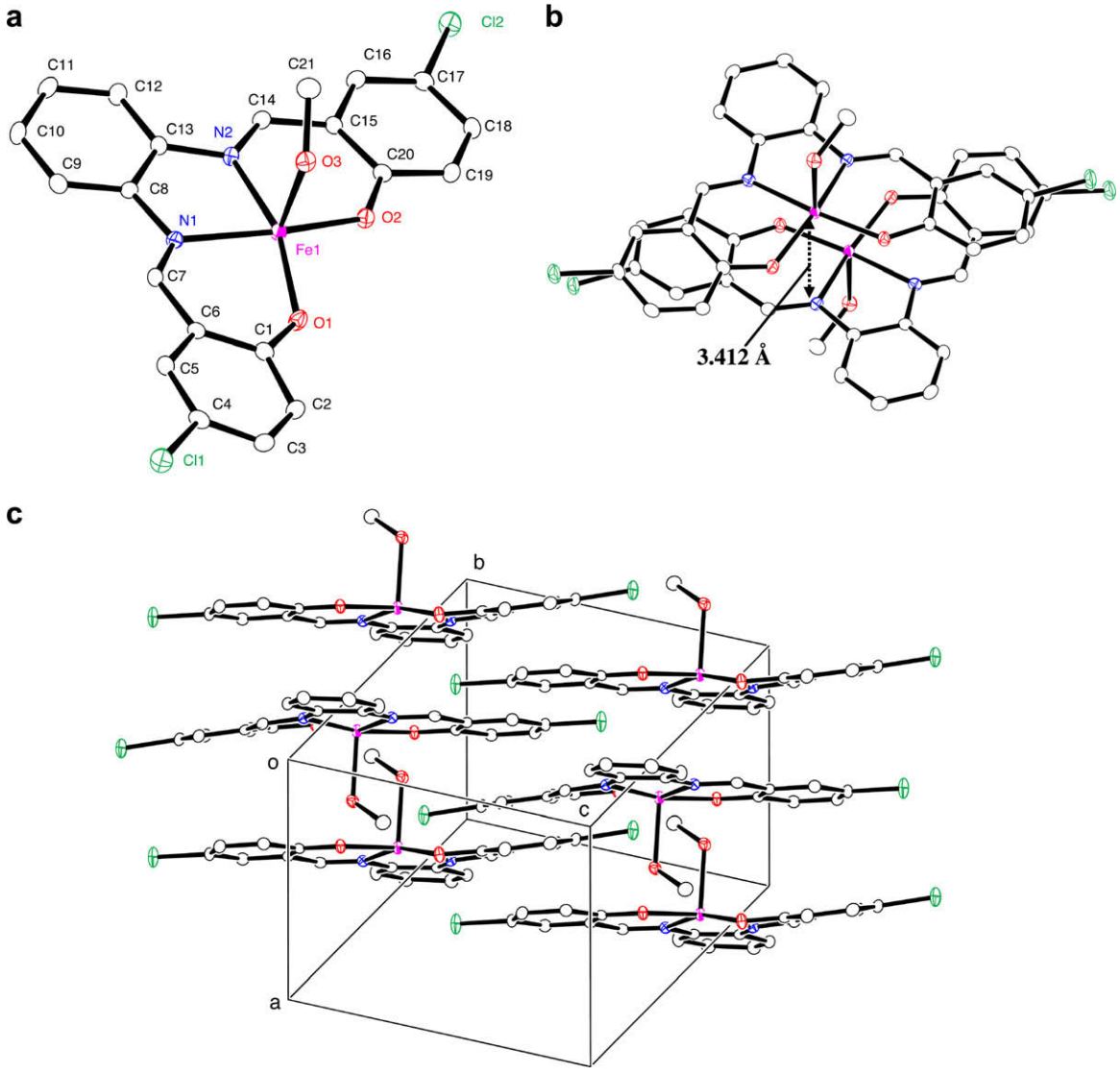


Fig. 4. (a) ORTEP drawing of **3**, showing the 50% probability ellipsoids. Hydrogen atoms have been omitted for clarity. (b) Dimeric structure of **3** through π–π interaction. (c) A molecular packing view of **3**.

lengths and angles around Fe(II) ions are tabulated in Table 2, which clearly indicates both Fe(II) ions are HS states. BVS analyses of Fe(II) ions gave the oxidation states of the iron ions to be +2.31 and +2.01 for complexes **2** and **3**, respectively. These values are again consistent to the valences of these iron ions. The dihedral angles of wing phenyl rings for **2** and **3** are 32.34° and 11.37°, respectively. The larger dihedral angle is corresponds to the larger displacement of the Fe(II) ion in **2** (0.356 Å) from the basal plane compared to that of **3** (0.223 Å). As can be seen from the molecular packing of **2** shown in Fig. 3b, each mononuclear complex is connected through π–π interaction (C4···C9′: 3.316 Å) and hydrogen bonds (O1···O2′: 2.9 Å) to form one-dimensional structure. Intrachain Fe···Fe′ distance is 5.168 Å. On the other hand, the molecular packing of **3** shown in Fig. 4b indicates a formation of a dimer structure through π–π interaction (C6···C16′:3.30 Å, O1···C14′: 3.106 Å) or Fe···π interaction (Fe1···N2′: 3.412 Å). The neighboring dimers are further connected through hydrogen bonds between coordinated alcohol oxygen and L3 (O1···O3′: 2.657 Å) as shown in Fig. 4c. Intra-dimer Fe···Fe′ distance is 4.021 Å while inter-dimer Fe···Fe′ distance is 4.721 Å. These rather short Fe···Fe′ separations indicate this structure can be seen as a dimer chain or an alternating one-dimensional chain.

3.4. Magnetic properties of *1*–*3*

Thermal variations of the $\chi_M T$ products for **1**–**3** are shown in Fig. 5. The $\chi_M T$ product of complex **1** at room temperature is 6.1 $cm^3\,K\,mol^{-1}$, being close to what is expected for two HS Fe(II) ions with $S = 2$. As the temperature is lowered, it increases below 50 K and reaches to 6.9 $cm^3\,K\,mol^{-1}$ at 14 K. The ferromagnetic interactions are also observed in complexes **2** and **3**. The $\chi_M T$ products of them at room temperature are around 3 $cm^3\,K\,mol^{-1}$ and again consistent to the existence of one HS Fe(II) ions with $S = 2$. As decreasing temperature, they are almost constant until 50 K and then gradually increase to show peak maxima of 4.14 $cm^3\,K\,mol^{-1}$ at 15 K for **2** and of 3.3 $cm^3\,K\,mol^{-1}$ at 10 K for **3**, then both decrease at lower temperatures. Since Fe(II) ion can be treated as Heisenberg-like in its behavior [9], except at very low temperature where some anisotropy may be important, we carried out data-fitting for the observed data above 15 K by using a simple spin Hamiltonian (1) for a dimer model.

$$\hat{H} = -2J_1 S_1 S_2 + g\mu_B(S_1 + S_2)B \quad (1)$$

The best fits are shown in Fig. 5 as solid lines and the obtained parameters are appeared in Table 3 together with those of related

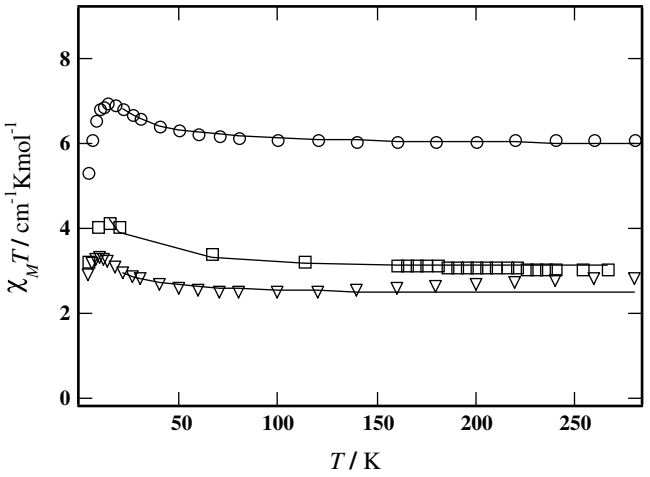


Fig. 5. $\chi_M T$ vs. T plots of **1** (○), **2** (□), and **3** (▽). Lines are least square fittings using equation stated in the text.

Table 3
The best fit parameters for magnetic data of **1**–**3** and those of related complexes.

Complex	g	J (cm^{-1})
1	1.99	+0.56
2	2.00	+1.1
3	1.80	+0.83
$[Fe_2(salen)_2(4,4'\text{-bpy})(NCS)_2]$[a]	2.03	−0.38
$[Fe_2(salpn)_2(\mu\text{-}N_3)_2]$[b]	1.964	1.054

[a] From Ref. [10].
[b] From Ref. [11].

complexes. Although these ferromagnetic interactions observed in **1**–**3** are small, some explanations are needed. As for the ferromagnetic interaction in complex **1**, there are two possible interaction pathways: through bpy ligand and through Fe···π interaction. As mentioned in the structure section, the perfect planarity of the bpy ligand together with the coincidence of the bpy plane and the coordinating plane (N1–O2–N1′–O2′) implies effective Fe···Fe′ interaction through bpy π-orbital, although antiferromagnetic interaction was reported for the bpy-bridged Fe(III) dimer with similar bis-Schiff base ligand [10]. However, we should abandon this idea because the complex **2** with uniform one-dimensional structure exhibits ferromagnetic behavior. The possible explanation for this phenomenon is the dimerization through Fe···π interaction occurred at lower temperature than X-ray measurement (150 K). If this type of dimerization can be occurred in complex **2**, the reason for the appearance of ferromagnetic behavior in **1** is also ascribed to the dimerization through Fe···π interaction at low temperature, not through bpy-bridge. The ferromagnetic interaction observed in **3** is reasonably understood by the dimer structure through π–π interaction together with relatively short Fe···Fe′ distance of 4.021 Å.

4. Concluding remarks

The Schiff base complexes are so famous but still many things remain unclear especially in solid state properties. Tetradentate bis-Schiff base macrocyclic ligands studied here forms unprecedented structures together with ferromagnetic behaviors. The origin of ferromagnetic interaction in complexes **1** and **2** are still unclear. They show significant Fe···π interaction, indicating dimerizations induced by this interaction maybe occurred at low temperature.

Supplementary data

CCDC 702693, 702694, 702695 contains the supplementary crystallographic data for **1**, **2** and **3**. These data can be obtained free of charge via http://www.ccdc.cam.ac.uk/conts/retrieving.html, or from the Cambridge Crystallographic Data Centre, 12 Union Road, Cambridge CB2 1EZ, UK; fax: (+44) 1223-336-033; or e-mail: deposit@ccdc.cam.ac.uk.

Acknowledgements

This work was supported in part by a Grant-in-Aid for Science Research from the Ministry of Education, Science and Culture, Japan. The authors are grateful to Kinki University for the financial support.

References

[1] (a) R.G. Wollman, D.N. Hendrickson, Inorg. Chem. 17 (1978) 926;
(b) J.C. Fanning, J.L. Resce, G.C. Lickfield, M.E. Kotun, Inorg. Chem. 24 (1985) 2884.
[2] (a) B. Weber, R. Tandon, D.Z. Himsl, Anorg. Allg. Chem. 633 (2007) 1159;
(b) B. Weber, E. Kaps, J. Weigand, C. Carbonera, J.-F. Létard, K. Achterhold, F.G. Parak, Inorg. Chem. 47 (2008) 487;

(c) A. Nabei, T. Kuroda-Sowa, T. Okubo, M. Maekawa, M. Munakata, Inorg. Chim. Acta 361 (2008) 3489.
[3] (a) SIR-92: A. Altomara, M.C. Burla, M. Camalli, M. Cascarano, C. Giacovazzo, A. Guagliardi, G. Polidori, J. Appl. Cryst. 27 (1994) 435;
(b) SIR-97: A. Altomara, M.C. Burla, M. Camalli, M. Cascarano, C. Giacovazzo, A. Guagliardi, A.G.G. Moliterni, G. Polidori, R.J. Spagna, Appl. Cryst. 32 (1999) 115.
[4] P.T. Beurskens, G. Admiraal, G. Beurskens, W.P. Bosman, R. de Gelder, R. Israel, J.M.M. Smits, DIRDIF-94: The DIRDIF-94 Program System, Technical Report of the Crystallography Laboratory, University of Nijmegen, 1994.
[5] G.M. Sheldrick, SHELXL-97: Program for the Solution of Crystal Structures, University of Goettingen, Germany, 1997.
[6] M. Julve, M. Verdaguer, J. Faus, F. Tinti, J. Mortal, A. Monge, E. Gutiérrez-Puebla, Inorg. Chem. 26 (1987) 3520.
[7] H.W. Park, S.M. Sung, K.S. Min, H. Bang, M.P. Suh, Eur. J. Inorg. Chem. (2001) 2857.
[8] I.D. Brown, D. Altermat, Acta Crystallogr., Sect. B 41 (1985) 244.
[9] B.J. Kennedy, K.S. Murray, Inorg. Chem. 24 (1985) 1552.
[10] X. Feng, J.-G. Wang, C.-Z. Xie, N.Z. Ma, Anorg. Allg. Chem. 633 (2007) 2085.
[11] K.R. Reddy, M.V. Rajasekharan, J.-P. Tuchagues, Inorg. Chem. 37 (1998) 5978.

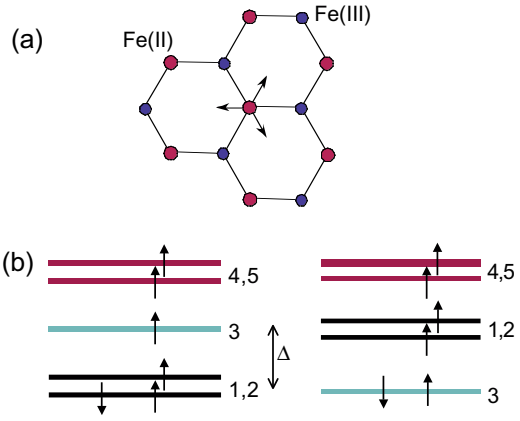


Fig. 1. (a) A portion of the open honeycomb lattice, displaying three equivalent displacements of the Fe(II) ion into the adjacent hexagons. (b) Two possible level-splitting schemes of the $3d^6$ Fe(II) orbitals in a C_3-symmetric crystal-field, with either the doublet $\psi_{1,2}$ or the singlet ψ_3 lowest in energy.

that bracket T_c [9]. Both the inverse, low-temperature transition $T_{JT}^{(l)}$ and the normal, high-temperature transition $T_{JT}^{(u)}$ are first order or discontinuous when the elastic parameters are appropriately chosen. A comparison with recent experiments [10] allows us to estimate the normal JT transition temperature $T_{JT}^{(u)}$ for Fe(II)Fe(III) bimetallic oxalates that exhibit MC. For normal Fe(II)Fe(III) compounds, the JT distortion either persists down to $T = 0$ if the doublet lies below the singlet or is absent altogether if the singlet lies below the doublets.

This paper contains an extended description of the JT transition first discussed in Ref. [9]. Section 2 develops the phenomenological model for MC and the JT distortion, with results discussed in Section 3. First-principles calculations are described in Section 4 and a summary is presented in Section 5.

2. Model

Bimetallic oxalates are characterized by three energy scales. The dominant energy is the Hund's coupling that determines the spins $S = 2$ and $S' = 5/2$ on the Fe(II) ($3d^6$) and Fe(III) ($3d^5$) sites. Next in importance is the C_3-symmetric crystal field V generated by the 6 oxygen atoms around each of the Fe sites. These 6 oxygen atoms form two triangles of slightly different sizes rotated by about 48° with respect to each other, one above and the other below the plane of Fe atoms. Because the two triangles have different sizes, the six oxygen atoms do not span a trigonally-compressed octahedron [11] and C_3 symmetry is the only point-group symmetry obeyed by the crystal-field potential. The weakest energies are the antiferromagnetic exchange coupling $J_c\mathbf{S}_i \cdot \mathbf{S}'_j$ between the Fe(II) and Fe(III) moments within each bimetallic layer, the spin–orbit coupling $\lambda\mathbf{L}_i \cdot \mathbf{S}_i$ on the Fe(II) sites ($\lambda \approx -12.65$ meV [12]), and any non-C_3-symmetric contributions of the crystal potential.

As shown in Fig. 1b, the C_3-symmetric potential V splits the $L = 2$ multiplet of the Fe(II) sites into two doublets $\psi_{1,2}$ and $\psi_{4,5}$, and a singlet ψ_3. We demonstrated in Ref. [8b] that the low-energy doublet $\psi_{1,2}$ carries an average orbital angular momentum $L_z^{cf} = |\langle\psi_{1,2}|L_{iz}|\psi_{1,2}\rangle|$ between 0 and 2, depending on the crystal-field parameters. Of course, the singlet state ψ_3 does not carry any orbital angular momentum.

Keep in mind that the orbital angular momenta L_z^{cf} of the low-energy doublet is modified by the crystal fields. It is not the same as the total angular momenta L of the Fe(II) multiplet before the crystal field is taken into account. Because $\langle\psi_{1,2}|\mathbf{L}_i|\psi_{1,2}\rangle = \pm L_z^{cf}\mathbf{z}$, the average orbital angular momentum of the doublet is an Ising-like degree of freedom.

So the effective Hamiltonian of the Fe(II)Fe(III) bimetallic oxalates is given by

$$H = J_c \sum_{\langle i,j\rangle} \mathbf{S}_i \cdot \mathbf{S}'_j - |\lambda| \sum_i S_i^z L_i^z, \tag{1}$$

where the $\langle i,j\rangle$ sum runs over all nearest-neighbors and the i sum runs over all Fe(II) sites. The antiferromagnetic exchange J_c is positive. As discussed above, $L_i^z = \pm L_z^{cf}$. This model has recently been generalized [13] to treat any bimetallic oxalate, with possible spin–orbit coupling on both the M(II) and M′(III) sites.

Including its orbital contribution, the Fe(II) magnetic moment can be written $M(T) = M_S(T) + M_L(T) \leqslant 0$, where $M_S = 2\langle S_i^z\rangle$ and $M_L = \langle L_i^z\rangle$. The Fe(III) magnetic moment $M'(T) = M_{S'}(T) = 2\langle S_j^{z'}\rangle \geqslant 0$ contains no orbital contribution. Mean-field (MF) theory is used to treat the nearest-neighbor exchange

$$J_c\mathbf{S}_i \cdot \mathbf{S}'_j \approx J_c\left\{\left(M_S S_j^{z'} + S_i^z M_{S'}\right)/2 - M_S M_{S'}/4\right\} \tag{2}$$

between neighboring Fe(II) and Fe(III) spins. The MF eigenvalues of $\psi_{1,2;\sigma}$ and $\psi_{3\sigma}$ with z spin component $\sigma = 0, \pm 1$ or ± 2 are

$$\epsilon_{1\sigma} = (-|\lambda|L_z^{cf} + 3J_c M_{S'}/2)\sigma, \tag{3}$$

$$\epsilon_{2\sigma} = (|\lambda|L_z^{cf} + 3J_c M_{S'}/2)\sigma, \tag{4}$$

$$\epsilon_{3\sigma} = (3J_c M_{S'}/2)\sigma + \Delta, \tag{5}$$

so that the doublet $\psi_{1,2;\sigma}$ is split by the spin–orbit coupling with $|\epsilon_{2\sigma} - \epsilon_{1\sigma}| = 2|\lambda\sigma|L_z^{cf}$. Because the crystal-field potential is assumed much larger than the spin–orbit and exchange energies, $|\Delta| \gg J_c$ or $|\lambda|$.

Using Eqs. (3) and (4) for the eigenvalues $\epsilon_{1,2;\sigma}$, it is straightforward to evaluate $M(T), M'(T)$, and the average magnetization $M^{avg}(T) = (M(T) + M'(T))/2 = (|M'(T)| - |M(T)|)/2$. When $l_c \approx 0.238 < L_z^{cf} < 1, M^{avg}(T)$ passes through 0 at the compensation temperature $T_{comp} < T_c$. Just below $T_c, M^{avg}(T) < 0$ because the parallel spin–orbit coupling between $\mathbf{L}_i$ and $\mathbf{S}_i$ causes the Fe(II) moment $M(T)$ to increase in amplitude more rapidly than the Fe(III) moment $M'(T)$. But at $T = 0$, the Fe(III) moment saturates at the larger value $|M'(0)| = 2S' > |M(0)| = 2S + L_z^{cf}$ so that $M^{avg}(0) > 0$.

After comparing the observed values of $T_{comp}/T_c \approx 0.62$ and $T_c \approx 45$ K with the theoretical predictions, we estimated [8] that $J_c \approx 0.46$ meV and $L_z^{cf} \approx 0.28$ in MC compounds. Normal compounds can fall into two categories. Either the doublet remains lower than the singlet ($\Delta > 0$) but with $L_z^{cf} < l'_c \approx 0.234$ or the singlet lies lowest in energy ($\Delta < 0$). Our model also predicted that two compensation points were possible in the narrow window $l'_c < L_z^{cf} < l_c$. The recent observation by Tang et al. [10] of two compensation points in the compound $N(n\text{-}C_4H_9)_4[Fe(II)Fe(III)ox_3]$ (data shown in the inset to Fig. 2a) would seem to confirm that prediction.

In the absence of spin–orbit coupling, a doubly-degenerate level occupied by a single electron is always split by a local displacement of the ion, which linearly lowers the electronic energy while incurring a quadratic cost in the elastic energy. The mixing of the Fe(II) eigenstates $\psi_{1\sigma}$ and $\psi_{2\sigma}$ due to the JT distortion is described by the Hamiltonian[1]

$$\underline{H}_\sigma^{mix} = \begin{pmatrix} \epsilon_{1\sigma} & \xi \\ \xi & \epsilon_{2\sigma} \end{pmatrix}, \tag{6}$$

where ξ is independent of σ. If $\epsilon_{1\sigma} = \epsilon_{2\sigma}$ are given by the MF result $\epsilon_{0\sigma} \equiv 3J_c M'\sigma/2$, then the eigenstates of $\underline{H}_\sigma^{mix}$ are

[1] Diagonal terms in $\underline{H}_\sigma^{mix}$ involving ξ can be neglected because the doublet states are related by the time-reversal operations $\psi_{1\sigma} = -K\psi_{2,-\sigma}$ and $\psi_{2\sigma} = -K\psi_{1,-\sigma}$, where K is the time-reversal operator. So for any spin-independent electrostatic potential $V = K^{-1}VK, \langle\psi_{1\sigma}|V|\psi_{1\sigma}\rangle = \langle\psi_{2,-\sigma}|K^{-1}VK|\psi_{2,-\sigma}\rangle = \langle\psi_{2\sigma}|V|\psi_{2\sigma}\rangle$, leading only to a shift of the doublet with respect to the singlet.

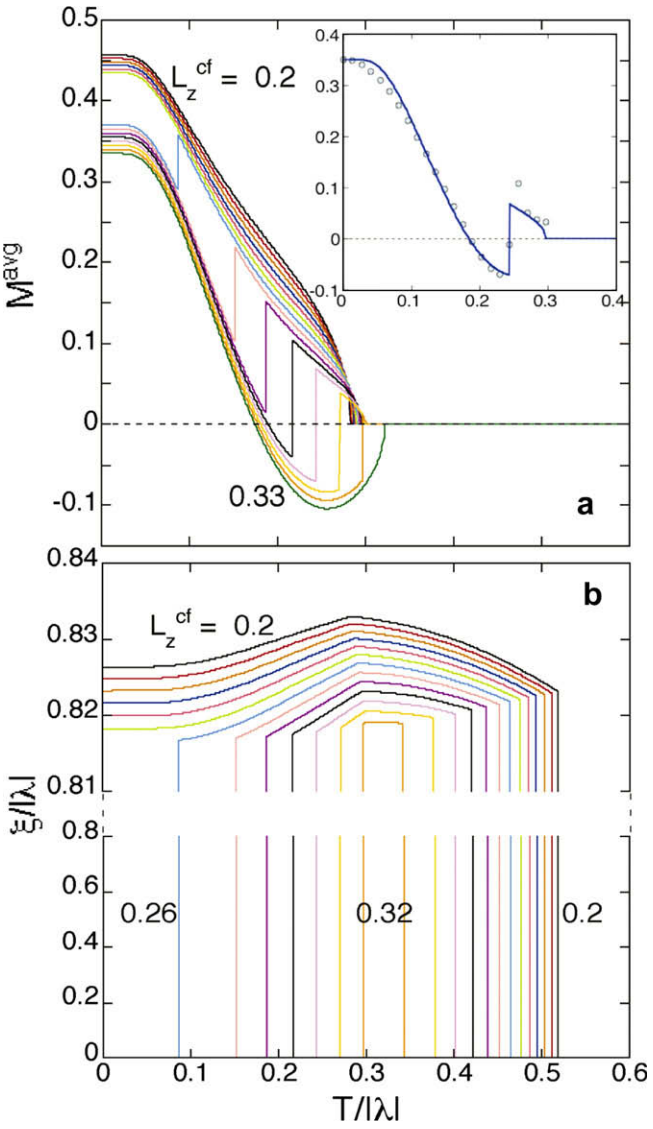


Fig. 2. (a) The average magnetization and (b) the JT energy ξ normalized by $|\lambda|$ versus temperature $T/|\lambda|$ for a range of L_z^{cf} in increments of 0.01 using $J_c/|\lambda| = 0.037$ and the elastic constants given in the text. Inset in (a) is the average magnetization for $L_z^{cf} = 0.3$ together with the experimental data of Ref. [10] rescaled so that $M^{avg}(0) = 0.35$.

$\psi_{a\sigma} = (1/\sqrt{2})(\psi_{1\sigma} + \psi_{2\sigma})$ and $\psi_{b\sigma} = (1/\sqrt{2})(\psi_{1\sigma} - \psi_{2\sigma})$, with $L_{a,b;\sigma} = \langle\psi_{a,b;\sigma}|L_i^z|\psi_{a,b;\sigma}\rangle = 0$ and eigenvalues $\epsilon_{a,b;\sigma} = \epsilon_{0\sigma} \pm \xi$. So in the absence of spin-orbit coupling, the average orbital angular momentum is quenched by the JT distortion and the doublet $\psi_{a,b;\sigma}$ is split by $2|\xi|$. The $T = 0$ energy is then given by

$$\frac{E}{N} = -3J_cSS' - \xi + \alpha\frac{\xi^2}{|\lambda|}, \tag{7}$$

where the final term is an elastic restoring potential and N is the number of Fe(II) or Fe(III) sites in each bimetallic layer. Since $\alpha > 0$, the $T = 0$ equilibrium value for ξ is $\xi(0) = |\lambda|/2\alpha > 0$.

Including the spin–orbit interaction $-|\lambda|\mathbf{L}_i \cdot \mathbf{S}_i$ and using the MF values $\epsilon_{1\sigma}$ and $\epsilon_{2\sigma}$ given by Eqs. (3) and (4), the eigenvalues of $\underline{H}_\sigma^{mix}$ are

$$\epsilon_{a\sigma} = \epsilon_{0\sigma} + t_\sigma, \tag{8}$$
$$\epsilon_{b\sigma} = \epsilon_{0\sigma} - t_\sigma, \tag{9}$$

where

$$t_\sigma = -\mathrm{sgn}(\sigma)\sqrt{(\lambda L_z^{cf}\sigma)^2 + \xi^2}. \tag{10}$$

Hence, the doublet splitting $\delta \equiv 2|t_\sigma|$ is enhanced by the JT effect (strictly speaking, the pseudo-JT effect when $\epsilon_{1\sigma} \neq \epsilon_{2\sigma}$). Because there is no spin-orbit coupling when $\sigma = 0, t_0 = \xi$ and $L_{a0} = L_{b0} = 0$. Since $t_{-2} > 0$ and $\epsilon_{0,-2} < 0$, the lowest eigenvalue of $\underline{H}_\sigma^{mix}$ is $\epsilon_{b,-2}$.

For $\sigma \neq 0$, the spin-orbit coupling maintains a nonzero average orbital angular momentum $L_{a\sigma} = -L_{b\sigma}$ even in the presence of a JT distortion:

$$L_{a\sigma} = (L_z^{cf})^2|\lambda|\sigma\frac{|\lambda|L_z^{cf}\sigma - t_\sigma}{(\lambda L_z^{cf}\sigma)^2 - |\lambda|L_z^{cf}\sigma t_\sigma + \xi^2}, \tag{11}$$

so that $L_{a\sigma} = L_{a,-\sigma}$. Since $\sigma t_\sigma < 0$, we see that $L_{a\sigma} \geqslant 0$. When $\xi \neq 0$, the JT distortion suppresses the average orbital angular momenta $L_{a\sigma} < L_z^{cf}$ for $\sigma = \pm 1$ and ± 2, as described in Ref. [8b].

With a correction to avoid double counting, the MF free energy can be written

$$\frac{F}{N} = -T\log\{Z_{II}Z_{III}e^{3J_cM_SM_{S'}/4T}\} + \alpha|\lambda|\left\{\left(\frac{\xi}{|\lambda|}\right)^2 + \gamma_3\left(\frac{\xi}{|\lambda|}\right)^3 + \gamma_4\left(\frac{\xi}{|\lambda|}\right)^4\right\}, \tag{12}$$

where

$$Z_{II} = 2\sum_\sigma e^{-3J_cM_{S'}\sigma/2T}\cosh(t_\sigma/T), \tag{13}$$

$$Z_{III} = 2\sum_{\sigma'} e^{-3J_cM_S\sigma'/2T}. \tag{14}$$

The sums in the partition functions Z_{II} and Z_{III} are over $\sigma = 0, \pm 1, \pm 2$ and $\sigma' = \pm 1/2, \pm 3/2, \pm 5/2$. The second line in Eq. (12) corresponds to the elastic energy.

Breaking C_3 symmetry, a local JT distortion with $\pm\xi$ involves the displacement of an Fe(II) atom either into one of the three open hexagons or towards one of the three neighboring Fe(III) atoms. The former distortions are sketched in Fig. 1a. The $\gamma_3(\xi/|\lambda|)^3$ term in Eq. (12) reflects the different energy costs for those two types of distortions. Thus, an anharmonic restoring potential arises quite naturally on the open honeycomb lattice. The sign of γ_3 does not affect any physical results and is chosen to be negative only for convenience so that the free energy is minimized when $\xi \geqslant 0$. Any fluctuations between the distorted atomic configurations are assumed slow compared to the electronic time scales.

It is simple to obtain the equilibrium values for M_S and $M_{S'}$ from the extremal conditions $\partial F/\partial M_S = \partial F/\partial M_{S'} = 0$:

$$M_S = \frac{4}{Z_{II}}\sum_\sigma \sigma e^{-3J_cM_{S'}\sigma/2T}\cosh(t_\sigma/T), \tag{15}$$

$$M_{S'} = 2S'B_{S'}(-3J_cM_SS'/2T), \tag{16}$$

where $B_{S'}(x)$ is the spin S' Brillouin function. Because the spin-orbit energy $-|\lambda|\mathbf{L}_i \cdot \mathbf{S}_i$ is treated exactly, M_L is not a variational parameter in the MF free energy and must be determined separately from the condition

$$M_L = -\frac{2}{Z_{II}}\sum_\sigma L_{a\sigma}e^{-3J_cM_{S'}\sigma/2T}\sinh(t_\sigma/T). \tag{17}$$

At $T = 0$, the $\sigma = -2$ term dominates in both the numerator and denominator of Eq. (17) and $M_L(0) = -L_{a2} = L_{b,-2} < 0$. Of course, the equilibrium value for the JT energy is obtained from the extremal condition $\partial F/\partial\xi = 0$.

3. Model results

The average magnetization and JT energy ξ are plotted versus temperature in Fig. 2a and b for $\alpha = 3.7, \gamma_3 = -1.9$, and $\gamma_4 = 1.1$.

As expected, the MC threshold $l_c \approx 0.282$ is enhanced by the JT distortion. When $L_z^{cf} < 0.260$, the JT distortion $\xi(T)$ persists down to $T = 0$. For $L_z^{cf} = 0$ (but still taking $\Delta > 0$), $\xi(0) \approx 0.842|\lambda| \approx 10.5$ meV and $T_{JT}^{(u)} \approx 0.578|\lambda|$. For $L_z^{cf} = 0.2$, the JT distortion would increase the splitting of the $\sigma = 2$ doublet from $4|\lambda|L_z^{cf} = 10$ meV to $2\sqrt{(2\lambda L_z^{cf})^2 + \xi^2} \approx 23$ meV.

When $L_z^{cf} \geqslant 0.260$, the JT distortion is quenched at $T = 0$ due to the strong orbital ordering. For $0.324 \geqslant L_z^{cf} \geqslant 0.260$, we obtain both lower and upper JT transitions, $T_{JT}^{(l)}$ and $T_{JT}^{(u)}$. Notice that ξ vanishes below $T_{JT}^{(l)}$ and is nonzero above $T_{JT}^{(l)}$. The temperature range $T_{JT}^{(u)} - T_{JT}^{(l)}$ decreases as L_z^{cf} increases and vanishes when $L_z^{cf} > 0.324$. We find that the JT transitions at $T_{JT}^{(u)}$ and $T_{JT}^{(l)}$ always bracket T_c. The first-order or discontinuous nature of the JT transitions at $T_{JT}^{(u)}$ and $T_{JT}^{(l)}$ is caused by the anharmonic term $\gamma_3(\xi/|\lambda|)^3$ in the free energy of Eq. (12).

Because the orbital contribution $M_L(T)$ to the Fe(II) moment drops as ξ jumps at the inverse JT transition, $T_{JT}^{(l)}$ is marked by a discontinuous increase in $M^{avg}(T)$. With decreasing L_z^{cf}, both the orbital contribution $M_L(T)$ and the magnitude of the change in $M^{avg}(T)$ become smaller. For $l_c < L_z^{cf} \leqslant 0.324$, the inverse JT transition is associated with a change in sign of $M^{avg}(T)$, as shown in the inset to Fig. 2a for $L_z^{cf} = 0.30$.

This inset shows the striking agreement between the theoretical prediction for $L_z^{cf} = 0.30$ and the measurements of Ref. [10] for A = N(n-C_4H_9)$_4$. So rather than indicating two compensation points, Ref. [10] provides compelling evidence for an inverse JT transition at $T_{JT}^{(l)} \approx 42$ K. According to Fig. 2b, a normal JT transition will be found at $T_{JT}^{(u)} \approx 70$ K. Indeed, recent X-ray measurements [14] on the same compound confirm that the hexagonal symmetry present at room temperature is absent in the monoclinic lattice below 60 K.

Measurements on several Fe(II)Fe(III) compounds [14,7] suggest that most MC compounds exhibit a small jump in the magnetization between T_c and T_{comp}. The predicted jumps in Fig. 2a are much too large to explain those measurements. X-ray diffraction studies [15] reveal that stacking faults in several compounds promote the coexistence of two phases: one with a six-layer repeat and the other with a two-layer repeat. The small magnetization jumps observed [14,7] in most MC compounds are likely caused by a mixture of those two stacking types. Indeed, a mixture of two phases, type 1 with $L_z^{cf} = 0.30$ (5% of the sample) and type 2 with $L_z^{cf} = 0.33$ (95% of the sample),[2] produces a small jump that is quite similar to the ones observed. The much larger jump found by Tang et al. [10] may be caused by the greater fraction of type 1 ($L_z^{cf} \approx 0.30$) stacking in their sample.

While there is no JT distortion ($\xi = 0$) when $\Delta < 0$, $\xi(T)$ remains nonzero down to $T = 0$ when $\Delta > 0$ and $L_z^{cf} < 0.260$. So our model predicts that normal bimetallic oxalates with $L_z^{cf} < 0.260$ will not exhibit a discontinuity in the magnetization, which may explain why such a jump has never been observed in a normal compound [7]. Nevertheless, normal Fe(II)Fe(III) compounds with $\Delta > 0$ (so that the doublet remains lowest in energy) should manifest a normal JT transition at $T_{JT}^{(u)} \approx 0.58|\lambda|$ or about 85 K.

But any non-C_3-symmetric cation like N(n-C_4H_9)$_4$ will also induce a permanent distortion of the hexagonal lattice. Depending on the size and shape of the cation, this distortion can be weakly-correlated or long-ranged. A non-C_3-symmetric potential can be included within our model by changing the off-diagonal terms in $\underline{H}_\sigma^{mix}$ from ξ to $\xi + \xi_0$. In the absence of spin–orbit coupling and a spontaneous JT distortion ξ, the doublet splitting δ is then $2\xi_0$. Since the anharmonic elastic potential proportional to ξ^3 favors $\xi > 0$, it acts to enhance the total distortion $|\xi + \xi_0|$when $\xi_0 > 0$ and to suppress the total distortion when $\xi_0 < 0$. For any nonzero ξ_0, there is a spontaneous JT distortion $\xi(T) \neq 0$ at all temperatures due to the linear term of order $-\xi\xi_0/|\lambda|$ in the free energy.

As shown in Fig. 3 for $L_z^{cf} = 0.3$ and the elastic parameters given earlier, increasing ξ_0 for a fixed L_z^{cf} decreases $T_{JT}^{(l)}$ while keeping T_{comp} almost unchanged until $T_{JT}^{(l)} < T_{comp}$. When $\xi_0 > 0.047|\lambda| \approx 0.6$ meV, the spontaneous JT distortion ξ at $T = 0$ jumps to a value near $0.81|\lambda| \approx 10$ meV and the lower JT transition disappears. When $\xi_0 < -0.019|\lambda| \approx -0.2$ meV, the spontaneous JT distortion is eliminated but MC survives until $\xi_0 < -0.43|\lambda| \approx -5.4$ meV, as seen in the inset to Fig. 3a. Except in the narrow window $0 > \xi_0 > -0.019|\lambda|$, the permanent distortion ξ_0 and the electronic distortion ξ have the same sign. For either sign of ξ_0, MC is eliminated when the violation of C_3 symmetry and $|\xi_0|$ become sufficiently large.

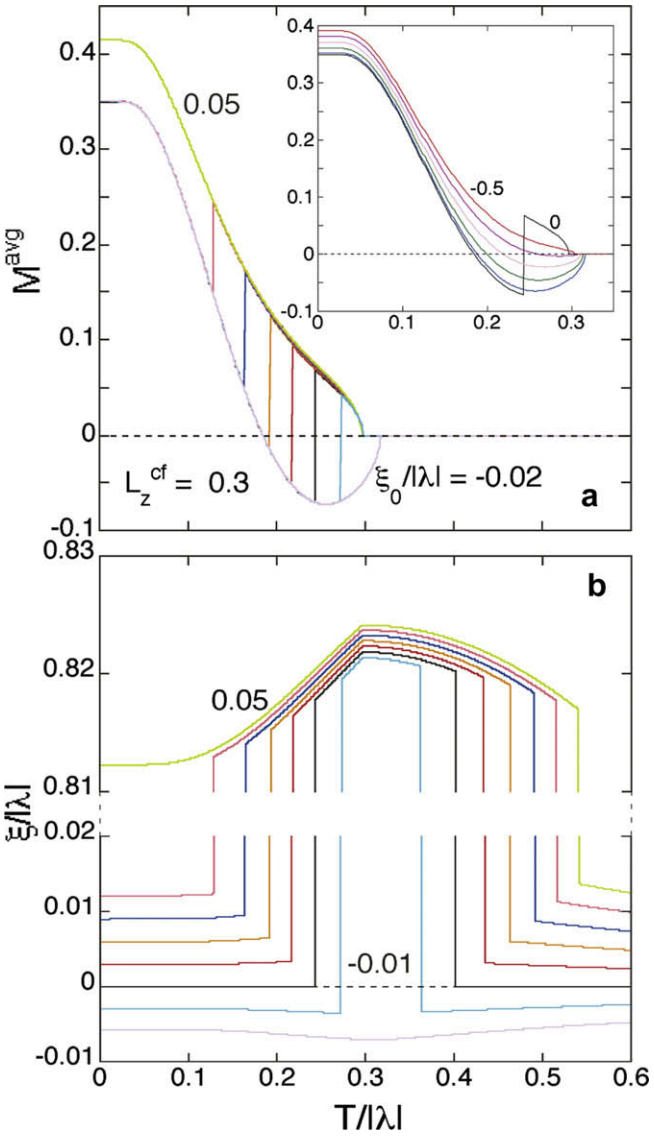


Fig. 3. (a) The average magnetization and (b) the JT mixing energy ξ normalized by $|\lambda|$ versus temperature $T/|\lambda|$ for several values of the permanent distortion $\xi_0/|\lambda|$ from -0.02 to 0.05 in increments of 0.01. Inset in (a) is the magnetization versus $T/|\lambda|$ for $\xi_0/|\lambda|$ between -0.5 and 0 in increments of 0.1. These plots use $L_z^{cf} = 0.3$, $J_c/|\lambda| = 0.037$ and the elastic constants given in the text.

[2] In a Mn(II)Fe(III) compound, Ref. [15a] reported a mixture of two stacking types with a faulting probability between 20% and 30%. In the Fe(II)Fe(III) family, MC compounds were found to be more monophasic.

Clearly, the electronic JT distortion ξ vanishes if the Fe(II) singlet lies below the doublet with $\Delta < 0$. So two conditions are required for C_3 symmetry to remain unbroken at $T = 0$. First, the cation itself must preserve C_3 symmetry so that there is no permanent distortion ξ_0. Second, either $\Delta < 0$ or if $\Delta > 0$, the average orbital angular momentum L_z^{cf} of the doublet must be sufficiently large to quench the spontaneous JT distortion ξ ($L_z^{cf} \geqslant 0.260$ in Fig. 2). Specific examples of symmetry breaking will be discussed in the next section.

4. First-principles calculations

In order to estimate the orders of magnitude of the spontaneous JT distortion ξ and the permanent distortion ξ_0, a series of first-principles calculations within the framework of density-functional theory (DFT) were performed. We employed the local spin-density approximation (SDA) in the plane-wave-pseudopotential approach with the PBE [16] exchange correlation functional as implemented in the Quantum-ESPRESSO package [17]. These calculations used Vanderbilt ultrasoft pseudopotentials [17–19] including, for the case of Fe [17,19], d electrons in the valence and non-linear core corrections. An energy cut-off of 600 eV was applied. Since the orbitals at the Fermi level are very localized in this ionic solid, we used a single **k**-point. Spin orbit coupling was not included. In order to stabilize the electronic density, the calculations were performed at an electronic temperature of 270 meV.

Predictions of the experimental electronic and magnetic structure in highly localized systems pose significant challenges for most approximations of DFT. Indeed, we find that the energy difference between ferromagnetic and antiferromagnetic configurations is below the resolution of our theory. Moreover, the charge-density wave observed experimentally (which results in inter-penetrated Fe(II) and Fe(III) networks) is not predicted to be the ground state. This discrepancy possibly signals the presence of strong self-interaction errors for the localized d orbitals [20]. The observed ferrimagnetic Fe(II)/Fe(III) ordering is stabilized by enforcing the net spin within each unit cell to equal 1/2.

Calculations were performed for several possible stackings (*ab*, *aab*, *abc*) of the bimetallic Fe(II)-Fe(III) layers with A = N(n-C_3H_7)$_4$ cations. As expected from the high degree of polymorphism and the low energy cost for stacking faults [15], the total energy differences between these three stackings were below the accuracy of our theory. Since the relative energy difference Δ between the doublet and singlet is quite sensitive to the stacking of the bimetallic planes, the angular momentum L_z^{cf} of the ground state may also depend on the stacking of the bimetallic planes.

The doublet splittings and the order of magnitude of the JT distortions were estimated by focusing on a single bimetallic layer with different cations A. Within hexagonal supercells, we studied the cations A = NH_4 (1) and N(n-C_3H_7)$_4$ (2). We also considered A = N(n-C_3H_7)$_4$ (3) in a non-hexagonal supercell.

(1) Because it is too small to stabilize the stacking of open honeycomb lattices, no oxalates actually contain the cation NH_4. However, calculations using this cation allow us to estimate the JT distortion in a C_3-symmetric environment. First, we relaxed the forces on all atoms while enforcing C_3 symmetry. The Fermi level for the majority band then lies at a doublet localized at the Fe(II) sites and occupied by a single electron. This configuration is consistent with our model, which requires the partial occupation of a doublet to explain the MC and the JT distortion. Second, the Fe(II) ion was displaced from the symmetric position on a grid of points **r**. From the *ab-initio* calculations, we extracted the total energy $E(\mathbf{r})$ of the configuration and the energy splitting $\delta(\mathbf{r})$ induced in the partially-occupied doublet. Because calculations where performed at an electronic temperature much larger than the splittings, both electronic levels of the doublet have an equal occupation of 1/2. At this large electronic temperature, no JT electronic energy was gained and the symmetric point $\mathbf{r} = 0$ remained the position with minimum energy, as expected.

Nevertheless, the energy gain at $T = 0$ can be estimated as $E(\mathbf{r}) - \delta(\mathbf{r})/2$. This expression assumes that the total energy difference is given by the sum of the occupied eigenvalues at zero temperature and neglects a small change in the electronic density [21]. Within this approximation, we can estimate the Fe(II) position and doublet splitting at zero temperature. In the absence of the spin-orbit coupling, we find that the Fe(II) moves 0.03 Å (the nearest-neighbor Fe(II)–Fe(III) distance is about 5.4 Å) with an energy gain of 2 meV and a doublet spitting of 8 meV. This JT splitting is quite close to the spin–orbit coupling $|\lambda| L_z^{cf} S \approx 7.5$ meV with $L_z^{cf} = 0.3$.

(2) Because moderately-sized cations such as N(n-C_3H_7)$_4$ are themselves non-C_3-symmetric, they will break the C_3 symmetry of the crystal-field potential at the Fe(II) sites. While a N(n-C_3H_7)$_4$ isomer with three C_3H_7 radicals below the oxalate plane would preserve C_3 symmetry, the remaining propyl chain oriented towards the hexagonal hole in the oxalates plane must then break C_3 symmetry. This symmetry violation produces a crystal-field splitting $2\xi_0$ of the doublet and a permanent distortion of the open honeycomb lattice.

Calculations were performed in a hexagonal unit-cell containing a single A = N(n-C_3H_7)$_4$ cation with periodic boundary conditions, corresponding to to an ordered configuration where every N(n-C_3H_7)$_4$ cation is oriented in the same way. After relaxing the positions of the atoms, we obtained an intrinsic doublet splitting $2\xi_0$ of about 10 meV at an electronic temperature of 270 meV.

These calculations also indicate that the intrinsic distortion introduced by the cation will be increased at low temperature by the electronic energy gain of the Fe(II) JT distortion. So in the absence of spin-orbit coupling, the parameters ξ and ξ_0 of our model have the same sign for this cation.

(3) The molecule N(n-C_3H_7)$_4$ is just small enough to allow individual cations to rotate independently of each other. Hence, a uniform distortion of the crystal is possible. Such a uniform distortion of the open honeycomb structure has been observed in bimetallic oxalates with radical cations [22]. For an ordered arrangement of A = N(n-C_3H_7)$_4$ cations and allowing the supercell to break hexagonal symmetry, we obtain a doublet splitting $\delta \sim 20$ meV, which should increase to about 30 meV when the electronic temperature approaches zero.

By contrast, larger cations such as A = N(n-C_4H_9)$_4$ studied in Ref. [10] are unable to independently rotate within each unit cell. Locked into a highly-disordered configuration during synthesis, such cations will break the local C_3 symmetry around each Fe(II) ion but not the overall C_3 symmetry of the bimetallic planes. Since the spin–orbit coupling competes with the small, local lattice distortions, MC is still possible when the cations are large and disordered. This leads to an interesting conjecture: due to their ability to spatially order, smaller cations like N(n-C_3H_7)$_4$ may be more effective at enhancing the departure from C_3 symmetry and suppressing MC than larger cations like N(n-C_4H_9)$_4$.

5. Conclusion

The simple Hamiltonian introduced in Eq. (1) explains all of the important properties of Fe(II)Fe(III) bimetallic oxalates. It provides a natural explanation for the origin of the magnetic anisotropy on the Fe(II) sites due to the splitting of the $L = 2$ multiplet by the crystal-field potential. Unlike models [23,24] that rely on the interlayer coupling, Eq. (1) explains the appearance of MC in compounds with large layer separations [6,7]. Because flipping the orbital angular momentum L_i^z requires an energy $2|\lambda| L_z^{cf} S \approx 175$ K

$\gg T_{comp}$, Eq. (1) explains the persistence of negative magnetization below T_{comp} in small fields. Due to the enhanced magnetic anisotropy and orbital moment, this model also explains why MC compounds have higher transition temperatures and Curie constants than normal compounds [6,7]. Finally, Eq. (1) explains the recently-observed jump [10] in the magnetization between T_{comp} and T_c, which is produced by an inverse JT transition.

Although these conclusions were based on a MF treatment of Eq. (1), Monte-Carlo calculations [25] have recently confirmed almost all of our earlier results [8], including the development of MC above a threshold value of L_z^{cf}. So we are confident that a more sophisticated analysis would also confirm our predictions for the lower and upper JT transitions.

Indeed, the robustness of the predicted inverse JT transition is easy to demonstrate. At high temperatures, fluctuations of the neighboring magnetic moments that are neglected within MF theory will also break the local C_3 symmetry and compete with the spin–orbit interaction. At low temperatures, however, magnetic fluctuations are suppressed and the spin-orbit interaction will act to restore C_3 symmetry. Therefore, the predicted inverse JT transition cannot be eliminated by magnetic fluctuations.

Our first-principles allow us to make more specific conclusions than are possible based on a phenomenological model alone. The calculations discussed in the previous section imply that large cations like N(n-C_4H_9)$_4$ induce a significant local distortion ξ_0 of the hexagonal lattice but are unable to reach an ordered ground state. On the other hand, smaller cations like N(n-C_3H_7)$_4$ can order at low temperatures. For an ordered configuration of N(n-C_3H_7)$_4$ cations with $|\xi_0| \approx 5$ meV (the value suggested by our first-principles results), the model results in Fig. 3 imply that an inverse JT transition will be absent and that, if present at all, MC will be rather weak with a high T_{comp}/T_c. Indeed, N(n-C_3H_7)$_4$[Fe(II)Fe(III)ox$_3$] bimetallic oxalates [6] show no signs of a JT transition below T_c and a rather high compensation temperature of about $0.75T_c$.

With the spin–orbit coupling set to zero ($L_z^{cf} = 0$), the doublet splitting $\delta = 2\xi(0) \approx 21$ meV obtained using the model parameters of Fig. 2 is more than twice as large as that obtained from first-principles calculations in a C_3-symmetric environment. So it is likely that the organic cation N(n-C_4H_9)$_4$ plays a significant role in breaking the local C_3 symmetry and enhancing the doublet splitting. A more sophisticated description of the experimental measurements may be possible once additional information about the atomic structure becomes available.

Observation of the JT distortion between $T_{JT}^{(l)} \approx 42$ K and $T_{JT}^{(u)} \approx 70$ K in MC compounds would provide unambiguous support for the model of Eq. (1). We hope that this work will inspire systematic X-ray scattering measurements that will verify the predictions made in this paper, including the long-range ordering of small, non-C_3-symmetric cations in this important class of layered, molecule-based magnets.

Acknowledgements

We would like to acknowledge conversations with Dr. Murilo Tiago. This research was sponsored by the Laboratory Directed Research and Development Program of Oak Ridge National Laboratory, managed by UT-Battelle, LLC for the US Department of Energy under Contract No. DE-AC05-00OR22725 and by the Division of Materials Science and Engineering of the US DOE.

References

[1] See for example: I.B. Bersuker, The Jahn–Teller Effect, Cambridge University Press, Cambridge, 2006. and references therein.
[2] J.B. Goodenough, Magnetism and the Chemical Bond, Interscience, New York, 1963.
[3] (a) M. Sorai, M. Nakano, Y. Miyazaki, Chem. Rev. 106 (2006) 976;
(b) C. Beghidja, G. Rogez, J. Kortus, M. Wesolek, R. Welter, J. Am. Chem. Soc. 128 (2006) 3140;
(c) J.A. Hatnean, R. Raturi, J. Lefebvre, D.B. Leznoff, G. Lawes, S.A. Johnson, J. Am. Chem. Soc. 128 (2006) 14992;
(d) C.J. Milios, A. Vinslava, W. Wernsdorfer, A. Prescimone, P.A. Wood, S. Parsons, S.P. Perlepes, G. Christou, E.K. Brechin, J. Am. Chem. Soc. 129 (2007) 6547.
[4] H. Tamaki, Z.J. Zhong, N. Matsumoto, S. Kida, M. Koikawa, N. Achiwa, Y. Hashimoto, H. Õkawa, J. Am. Chem. Soc. 114 (1992) 6974.
[5] See the review: R. Clément, S. Decurtins, M. Gruselle, C. Train, Mon. für Chem. 117 (2003) 117.
[6] (a) C. Mathoniére, S.G. Carling, P. Day, J. Chem. Soc., Chem. Commun. (1994) 1551;
(b) C. Mathonière, C.J. Nuttall, S.G. Carling, P. Day, Inorg. Chem. 35 (1996) 1201.
[7] C.J. Nuttall, P. Day, Chem. Mater. 10 (1998) 3050.
[8] (a) R.S. Fishman, F.A. Reboredo, Phys. Rev. Lett. 99 (2007) 217203;
(b) R.S. Fishman, F.A. Reboredo, Phys. Rev. B 77 (2008) 144421.
[9] R.S. Fishman, S. Okamoto, F.A. Reboredo, Phys. Rev. Lett. 101 (2008) 116402.
[10] G. Tang, Y. He, F. Liang, S. Li, Y. Huang, Physica B 392 (2007) 337.
[11] E.I. Stiefel, G.F. Brown, Inorg. Chem. 11 (1972) 436.
[12] B. Bleaney, K.W.H. Stevens, Rep. Prog. Phys. 16 (1953) 108.
[13] P. Reis, R.S. Fishman, F.A. Reboredo, J. Moreno, Phys. Rev. B 77 (2008) 174433.
[14] I.D. Watts, S.G. Carling, P. Day, D. Visser, J. Phys. Chem. Solids 66 (2005) 932.
[15] (a) C.J. Nuttall, P. Day, J. Solid State Chem. 147 (1999) 3;
(b) N.S. Ovanesyan, V.D. Makhaev, S.M. Aldoshin, P. Gredin, K. Boubekeur, C. Train, M. Gruselle, Dalton Trans. 18 (2005) 3101.
[16] J.P. Perdew, K. Burke, M. Ernzerhof, Phys. Rev. Lett. 77 (1996) 3865.
[17] S. Baroni, A. Dal Corso, S. deGironocli, P. Giannozzi, <http://www.pwscf.org>.
[18] D. Vanderbilt, Phys. Rev. B 41 (1990) 7892.
[19] A.M. Rappe, K.M. Rabe, E. Kaxiras, J.D. Joannopoulos, Phys. Rev. B 41 (1990) 1227.
[20] J.P. Perdew, A. Zunger, Phys. Rev. B 23 (1981) 5048.
[21] See Eq. (17) in: J. Ihm, A. Zunger, M. Cohen, J. Phys. C 12 (1979) 4409.
[22] (a) M. Clemente-León, E. Coronado, J.R. Galán-Mascarós, C.J. Gómez-García, Chem. Commun. (1997) 1727;
(b) E. Coronado, J.R. Galán-Mascarós, C.J. Gómez-García, J. Ensling, P. Gütlich, Chem. Eur. J. 6 (2000) 552.
[23] Y. Nakamura, J. Phys.: Condens. Matter 12 (2000) 4067.
[24] Y. Nakamura, Phys. Rev. B 62 (2000) 11742.
[25] P. Henelius, R.S. Fishman, Phys. Rev. B 78 (2008) 214405.

and this type of materials are expected to exhibit interesting magnetic properties, i.e. the photo-induced magnetization [18]. The SQUID chip on which the microcrystal was mounted by using an optical microscope manipulator were set in the dipstick unit, including a 3D magnetic coil system for the measurement. Our measurement procedure consisted of measuring the critical current of the SQUID while sweeping the external magnetic field. Because the critical current exhibited a modulation with a period of $1\Phi_0$ as a function of magnetic flux as it passed through the SQUID loop, the magnetization curve could be deduced by counting the number of detected fluxes in the SQUID loop.

3. Results and discussion

According to previous work using a large single crystal, this material exhibits a long range magnetic ordering below 40 K and a saturation magnetization of 9 $\mu_B N$ where μ_B is Bohr magneton and N is the Avogadro's number [17]. As shown in Fig. 1, we cut a section of the large crystal into a microcrystal, and mounted it on the SQUID. Fig. 2 represents the magnetization curves of the microcrystal at 35 K [16]. The microcrystal exhibited hysteresis with a coercive field of 7 Oe, and reached a saturated value of $40\Phi_0$ around 300 Oe.

However, to understand obtained data, the relative arrangement of the sample and the SQUID loop must be considered. We roughly calculated the flux passing through the SQUID loop, which was produced by the sample with a saturation magnetic moment in $\mathbf{H_{ex}}$. We assumed that the sample shape was a rhombic prism and that the line joining the median points of the sample bottom face and the SQUID loop paralleled $\mathbf{H_{ex}}$. According to previous work, the effective area of the SQUID loop is $7 \times 11\ \mu m^2$ [16]. Because the crystal sample of **1** was uniformly magnetized below 40 K, the intensity of magnetization $I = I_{sat} = 9\mu_0\mu_B N D_{crystal}/M_A$ where I_{sat} is the saturation magnetization, $D_{crystal}$ is the crystal density of 2.198 g cm^{-1}, and M_A is the molar weight of 632.97 g mol^{-1}. We equally partitioned the sample into volume elements with an equal edge length of dr_m, and also partitioned the flux detection area of the SQUID into area elements with an equal side length of dr_s (Fig. 3). The volume element of the sample possesses a magnetic moment, $\mathbf{m} = I_{sat}\ \Delta V_m\ \mathbf{n}$, where $\Delta V_m = \sin\theta\ (dr_m)^3$ is the volume of the element, $\theta = 72°$ is the angle between the edges of the bottom face rhombus, $\mathbf{n}$ is the unit vector of the magnetic moment and in the present case the magnetic moment is in the same direction as $\mathbf{H_{ex}}$. We defined the coordinates of the volume elements in the sample as the center of the element and expressed as $\mathbf{r_m} = \mathbf{r_{m0}} + A_m\mathbf{e_a} + B_m\mathbf{e_b} + C_m\mathbf{e_c}$, where $\mathbf{r_{m0}}$ is the coordinate of one of the vertices of the sample bottom face, $\mathbf{e_a}$, $\mathbf{e_b}$, $\mathbf{e_c}$ are the unit vectors parallel to the prism edges from $\mathbf{r_{m0}}$, and A_m, B_m, C_m are the coefficients. We also defined the coordinates of the area elements in the SQUID as the center of the element and expressed as $\mathbf{r_s} = X_s\mathbf{e_x} + Y_s\mathbf{e_y}$, where $\mathbf{e_x}$, $\mathbf{e_y}$ are the unit vectors and X_s, Y_s are the coefficients. Here $\mathbf{e_a} = -\cos(\theta/2)\mathbf{e_x} + \sin(\theta/2)\mathbf{e_y}$, $\mathbf{e_b} = -\cos(\theta/2)\mathbf{e_x} - \sin(\theta/2)\mathbf{e_y}$, and $\mathbf{e_c} = \mathbf{e_z}$. By applying the point-dipole approximation to this volume element, the magnetic flux density $\mathbf{b(r_s)}$ at $\mathbf{r_s}$ produced by $\mathbf{m(r_m)}$ is given by the following equation

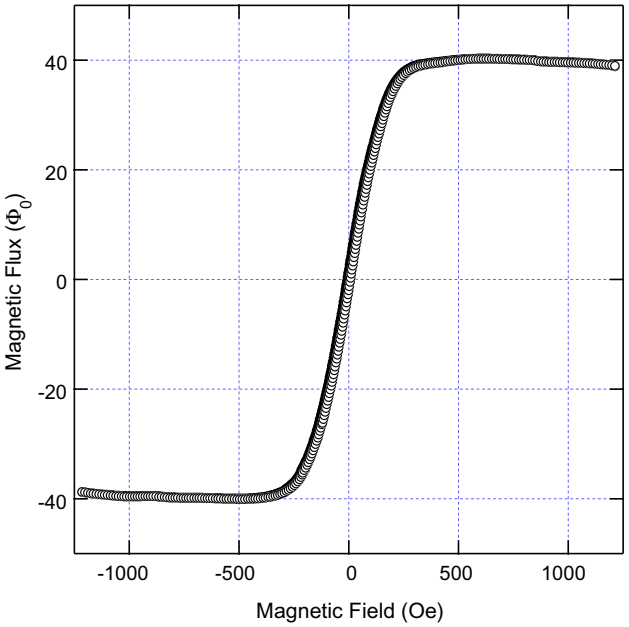


Fig. 2. Magnetization curves for microcrystal sample in a magnetic field of $\mathbf{H_{ex}}$. Filled and open markers indicate the plots in the field-reducing and -increasing processes, respectively.

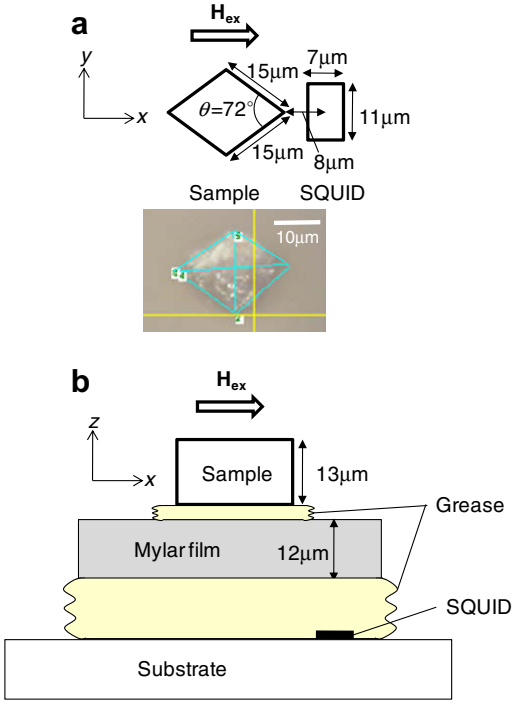


Fig. 1. Schematic illustration of the relative arrangement of microcrystal sample and the SQUID loop. Sample is fixed with grease on a 12 μm thick Mylar sheet covering the SQUID. (a) Top view of the illustration and the photo by the laser microscope and (b) horizontal sectional view of the illustration.

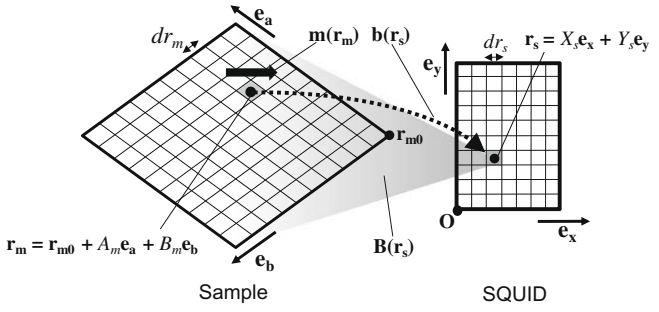


Fig. 3. Illustration of an equally partitioned sample and the SQUID loop. Parameters in the figure are explained in the text.

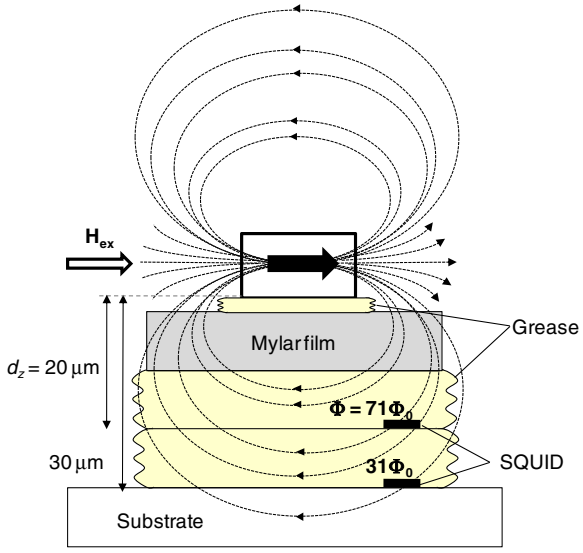


Fig. 4. Schematic illustration of the sample flux.

$$\mathbf{b}(\mathbf{r_s}) = \frac{1}{4\pi}\left(-\frac{\mathbf{m}}{r^3}+\frac{3(\mathbf{m}\cdot\mathbf{r})\mathbf{r}}{r^5}\right) = \frac{I_{sat}\Delta V_m}{4\pi}\left(-\frac{\mathbf{n}}{r^3}+\frac{3(\mathbf{n}\cdot\mathbf{r})\mathbf{r}}{r^5}\right). \quad (1)$$

Here $\mathbf{r} = \mathbf{r_s}-\mathbf{r_m}$ and $r = |\mathbf{r}|$. Then the magnetic flux density from the entire sample at $\mathbf{r_s}$ is

$$\mathbf{B}(\mathbf{r_s}) = \sum_{A_m}\sum_{B_m}\sum_{C_m}\frac{I_{sat}\Delta V_m}{4\pi}\left(-\frac{\mathbf{n}}{r^3}+\frac{3(\mathbf{n}\cdot\mathbf{r})\mathbf{r}}{r^5}\right). \quad (2)$$

The flux $\phi(\mathbf{r_s})$ from $\mathbf{m}$, which is detected by the square element with an area of $\Delta S = (dr_s)^2$ at $\mathbf{r_s}$ within the SQUID loop, is

$$\phi(\mathbf{r_s}) = (\mathbf{B}(\mathbf{r_s})\cdot\mathbf{e_x})\Delta S. \quad (3)$$

The total flux from the sample through the SQUID loop is obtained as

$$\Phi = \sum_{X_m}\sum_{Y_m}(\mathbf{B}(\mathbf{r_s})\cdot\mathbf{e}_z)\Delta S. \quad (4)$$

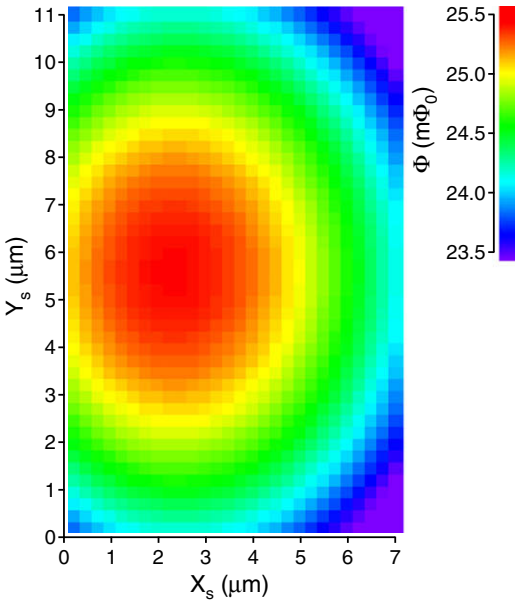


Fig. 5. The calculation result of the distribution of the intensity of the flux detected by the SQUID loop with $dr_m = dr_s = 0.25$ and $d_z = 30$ μm. The inset indicates the relationship between the intensity of the flux detected in the area element and the color gradation.

In the present case, the SQUID substrate was covered with a 12 μm thick Mylar sheet, and grease was used to mount the crystal sample onto the film. From our experience, the grease penetrates the substrate and the film. Thus, the distance between the bottom face of the sample and the SQUID plane d_z becomes ~10 μm longer than the thickness of the film (Fig. 4). Hence, grease thickness was considered when calculating the flux with $d_z = 20$ and 30 μm. We found that the flux value almost converged with $dr_m = dr_s < 0.2$ μm. With $dr_m = dr_s = 0.2$ μm, we obtained flux values $\Phi = 71\Phi_0$ and $31\Phi_0$ at $d_z = 20$ and 30 μm, respectively. These values are reasonable compared to the experimental value of $40\Phi_0$. We also show the calculation result of the distribution of the intensity of the flux detected by the area elements in the SQUID loop with $dr_m = dr_s = 0.25$ and $d_z = 30$ μm (Fig. 5). We can guess where to mount the sample on the SQUID loop in order to detect the flux most effectively.

4. Conclusion

Using the dipole approximation, we verified the flux value of $40\Phi_0$ from the saturation magnetic moment of a ferrimagnetic microcrystal of $[Mn_2(H_2O)_2(CH_3COO)][W(CN)_8]\cdot 2H_2O$. This flux value was obtained by the magnetization measurement using the HTS micro SQUID magnetometer. Upon considering the thickness of the film and the grease between the sample as well as the SQUID plane d_z, we obtained flux values of $\Phi = 71\Phi_0$ and $31\Phi_0$ at $d_z = 20$ and 30 μm, respectively. The obtained values are consistent with the experimentally measured one. We are now planning to measure the magnetic flux reversal with Prussian blue analogs, which exhibit a compensation temperature [19] or an inverted magnetic hysteresis loop [20] using the present HTS micro SQUID.

Acknowledgments

The authors are grateful to Professor Mizushi Matsuda from the Muroran Institute of Technology for his assistance fabricating the micro SQUID chips. The present research was supported in part by a GCOE Program for Chemistry Innovation, a Grant-in-Aid for Young Scientists (S) and (B) from Japan Society for the Promotion of Science, Inamori Foundation, and the Kurata Memorial Hitachi Science and Technology Foundation.

References

[1] A.D. Kent, S. von Molnár, S. Gider, D.D. Awschalom, J. Appl. Phys. 76 (1994) 6656.
[2] A.K. Geim, I.V. Grigorieva, S.V. Dubonos, J.G.S. Lok, J.C. Maan, A.E. Filippov, F.M. Peeters, Nature 390 (1997) 259.
[3] K.S. Novoselov, A.K. Geim, S.V. Dubonos, E.W. Hill, I.V. Grigorieva, Nature 426 (2003) 812.
[4] Y. Li, P. Xiong, S. von Molnár, S. Wirth, Y. Ohno, H. Ohno, Appl. Phys. Lett. 80 (2002) 4644.
[5] Y. Li, Ph.D Thesis, Florida State University, 2003.
[6] Y. Li, C. Ren, P. Xiong, S. von Molnár, Y. Ohno, H. Ohno, Phys. Rev. Lett. 93 (2004) 246602.
[7] M. Bode, E.Y. Vedmedenko, K. von Bergmann, A. Kubetzka, P. Ferriani, S. Heinze, R. Wiesendanger, Nat. Mater. 5 (2006) 477.
[8] Y. Yayon, V.W. Brar, L. Senapati, S.C. Erwin, M.F. Crommie, Phys. Rev. Lett. 99 (2007) 067202.
[9] MPMS®-XL Brochure from Quantum Design.
[10] W. Wernsdorfer, K. Hasselbach, A. Benoit, B. Barbara, D. Mailly, J. Tuaillon, J.P. Perez, V. Dupuis, J.P. Dupin, G. Guiraud, A. Perex, J. Appl. Phys. 78 (1995) 7192.
[11] W. Wernsdorfer, Ph.D. Thesis, Joseph Fourier University, Grenoble, 1996.
[12] W. Wernsdorfer, E. Bonet Orozco, K. Hasselbach, A. Benoit, D. Mailly, O. Kubo, H. Nakano, B. Barbara, Phys. Rev. Lett. 79 (1997) 4014.
[13] W. Wernsdorfer, R. Sessoli, Science 284 (1999) 133.
[14] M. Jamet, W. Wernsdorfer, C. Thirion, D. Mailly, V. Dupuis, P. Mélinon, A. Pérez, Phys. Rev. Lett. 86 (2001) 4676.
[15] K. Takeda, H. Mori, A. Yamaguchi, H. Ishimoto, T. Nakamura, S. Kuriki, T. Hozumi, S. Ohkoshi, J. Appl. Phys. 103 (2008) 07E911.
[16] K. Takeda, H. Mori, A. Yamaguchi, H. Ishimoto, T. Nakamura, S. Kuriki, T. Hozumi, S. Ohkoshi, Rev. Sci. Instrum. 79 (2008) 033909.

[17] Y. Song, S. Ohkoshi, Y. Arimoto, H. Seino, Y. Mizobe, K. Hashimoto, Inorg. Chem. 42 (2003) 1848.
[18] (a) R. Garde, C. Desplanches, A. Bleuzen, P. Veillet, M. Verdaguer, Mol. Cryst. Liquid Cryst. 334 (1999) 587;
(b) P. Przychodzeń, T. Korzeniak, R. Podgajny, B. Sieklucka, Coord. Chem. Rev. 250 (2006) 2234;
(c) Z.J. Zhong, H. Seino, Y. Mizobe, M. Hidai, A. Fujishima, S. Ohkoshi, K. Hashimoto, J. Am. Chem. Soc. 122 (2000) 2952;
(d) J. Larionova, M. Gross, M. Pilkington, H. Andres, H. Stoeckli-Evans, H.U. Güdel, S. Decurtins, Angew. Chem. Int. Ed. 39 (2000) 1605;
(e) D. Li, L. Zheng, Y. Zhang, J. Huang, S. Gao, W. Tang, Inorg. Chem. 42 (2003) 6123;
(f) Z.J. Zhong, H. Seino, Y. Mizobe, M. Hidai, M. Verdaguer, S. Ohkoshi, K. Hashimoto, Inorg. Chem. 39 (2000) 5095;
(g) S. Ohkoshi, H. Tokoro, T. Hozumi, Y. Zhang, K. Hashimoto, C. Mathonière, I. Bord, G. Rombaut, M. Verelst, C. Cartier dit Moulin, F. Villain, J. Am. Chem. Soc. 128 (2006) 270;
(h) T.S. Venkatakrishnan, R. Rajamani, S. Ramasesha, J.-P. Sutter, Inorg. Chem. 46 (2007) 9569;
(i) R. Podgajny, D. Pinkowicz, T. Korzeniak, W. Nitek, M. Rams, B. Sieklucka, Inorg. Chem. 46 (2007) 10416;
(j) S. Ohkoshi, Y. Hamada, T. Matsuda, Y. Tsunobuchi, H. Tokoro, Chem. Mater. 20 (2008) 3048.
[19] (a) S. Ohkoshi, T. Iyoda, A. Fujishima, K. Hashimoto, Phys. Rev. B 56 (1997) 11642;
(b) S. Ohkoshi, S. Yorozu, O. Sato, T. Iyoda, A. Fujishima, K. Hashimoto, Appl. Phys. Lett. 70 (1997) 1040;
(c) S. Ohkoshi, A. Fujishima, K. Hashimoto, J. Am. Chem. Soc. 120 (1998) 5349;
(d) S. Ohkoshi, K. Hashimoto, Phys. Rev. B 60 (1999) 12820;
(e) S. Ohkoshi, K. Hashimoto, J. Am. Chem. Soc. 121 (1999) 10591;
(f) S. Ohkoshi, Y. Abe, A. Fujishima, K. Hashimoto, Phys. Rev. Lett. 82 (1999) 1285;
(g) S. Ohkoshi, K. Arai, Y. Sato, K. Hashimoto, Nat. Mater. 3 (2004) 857.
[20] S. Ohkoshi, T. Hozumi, K. Hashimoto, Phys. Rev. B 64 (2001) 132404.

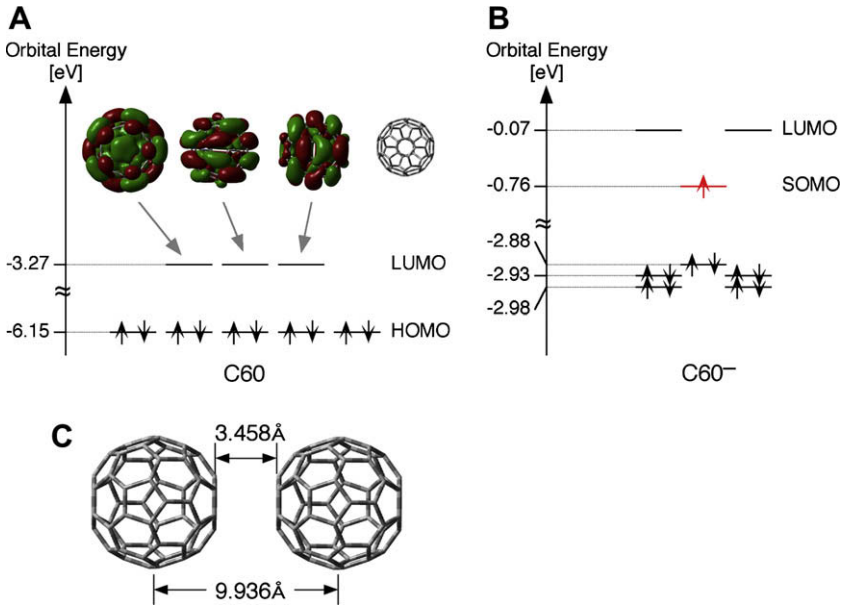


Fig. 1. (A) Calculated HOMOs and LUMOs of C_{60}, (B) calculated SOMO, HOMOs and LUMOs of C_{60}^-, and (C) calculated model structure of C_{60}^- dimer.

3. Calculated results

3.1. C_{60} and C_{60}^-

First we examined the electronic structures of C_{60} and C_{60}^-. Calculated total energies and $\langle S^2 \rangle$ values were summarized in Table 1. The calculated HOMOs and LUMOs of C_{60} molecule were depicted in Fig. 1A. HOMOs were five-fold degenerated and LUMOs were three-fold degenerated reflecting its I_h symmetry. The orbital energies of HOMOs and LUMOs were −6.15 and −3.27 eV, respectively. Calculated C_{60}^- orbital energies around SOMO were also depicted in Fig. 1B. The orbital energy of SOMO was −0.76 eV. By one electron doping, the five-fold degenerated HOMOs of neutral C_{60} were divided into two doubly degenerated and one non-degenerated orbitals although LUMOs were still remaining the degeneracy. An energy difference between C_{60} and C_{60} anion that corresponds to adiabatic electron affinity (EA), was 2.0 eV as mentioned in Table 1. The calculated EA was smaller than experimental value (2.65 eV [16]) because the experimental structure of neutral C_{60} was substitutionally used for the calculation of C_{60} anion. However the value is consistent with the experiment qualitatively.

3.2. Effective exchange integrals (J_{ab}) between two C_{60}^-s

One of the characteristic of three LUMOs depicted in Fig. 1A has a major node in their equatorial planes. In terms of the equatorial nodes, it is considered that those three LUMOs are very similar to p-type orbitals in a coarse view as illustrated in Fig. 2A. Because the SOMO of C_{60} anion is constructed by LUMOs of neutral C_{60}, there are four types of interactions between two SOMOs of two

Table 1
Calculated total energies[a], $\langle S^2 \rangle$ values of C_{60} and C_{60}^-. Electron affinity of C_{60} was calculated by the energy difference between C_{60} and C_{60}^-.

Molecule	Total energy (a.u.)	$\langle S^2 \rangle$	EA (eV)
C_{60}	−2283.138544	0.0000	2.00 (2.65)[b]
C_{60}^-	−2283.212188	0.7543	

[a] Convergence threshold is 10^{-6} (a.u.) in densities.
[b] Experimental value by Yang et al. [16] is in parenthesis.

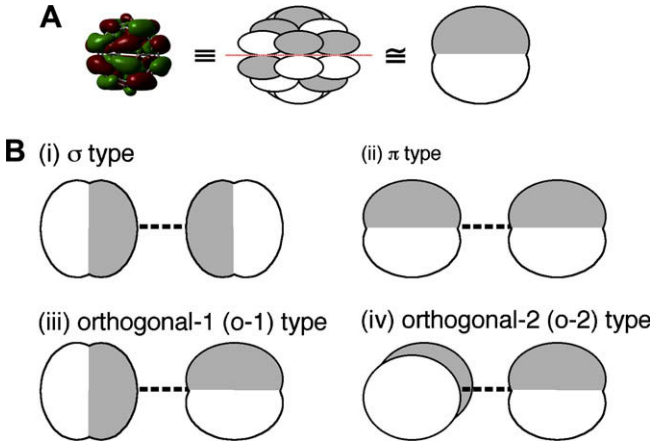


Fig. 2. (A) Illustrations of LUMOs of C_{60} as a conceptual view and (B) four types of interactions between two C_{60}^-s.

C_{60}^-s if we regard those LUMOs as p-type orbitals, i.e. **σ**–, **π**– and **o-1**, **o-2** type interactions as illustrated in Fig. 2B. Among the four type interactions, the **σ**- and **π**-type interactions have SOMO–SOMO overlap. Therefore anti-ferromagnetic interaction is easily expected. While other interactions (**o-1**, **o-2**) seems to be orthogonal. If the SOMO–SOMO overlap is zero, a ferromagnetic interaction is expected by analogy with Kanamori-Goodenough rule [17].

The magnetic properties are usually investigated by the use of the Heisenberg Hamiltonian,

$$\hat{\mathbf{H}} = -2\sum J_{ab}\hat{\mathbf{S}}_a \cdot \hat{\mathbf{S}}_b, \tag{1}$$

where J_{ab} is the orbital-averaged effective exchange integral between the spin sites a and b (or C_{60} anions a and b) with total spin operators $\hat{\mathbf{S}}_\mathbf{a}$ and $\hat{\mathbf{S}}_\mathbf{b}$, respectively [18–20]. Our group has proposed a calculation method for J_{ab} values based on broken-symmetry methods as follows:

$$J_{ab} = \frac{E^{LS} - E^{HS}}{\langle \hat{\mathbf{S}}^2 \rangle^{HS} - \langle \hat{\mathbf{S}}^2 \rangle^{LS}}, \tag{2}$$

Table 2
Total energies[a] and $\langle S^2 \rangle$ values for the LS (singlet) and the HS (triplet) states, respectively. Effective exchange integrals (J_{ab}) and the energy differences (ΔE) were calculated by using Eqs. (2) and (3), respectively.

Type	LS (singlet)		HS (triplet)		J_{ab} (cm^{-1})	ΔE (eV)
	Total energy (a.u.)	$<S^2>$	Total energy (a.u.)	$<S^2>$		
σ	−4566.373044	1.0067	−4566.373028	2.0087	−3.5	0.000
o-1	−4566.372846	1.0086	−4566.372844	2.0086	−0.4	0.005
o-2	−4566.372560	1.0086	−4566.372581	2.0086	4.6	0.013
π	−4566.372539	1.0003	−4566.372497	2.0087	−9.1	0.014

[a] Convergence threshold is 10^{-7} (a.u.) in densities.

where E^X and $\langle \hat{\mathbf{S}}^2 \rangle^X$ denote the total energy and the total spin angular momentum for the spin state X (X = low spin (LS) and high spin (HS)), respectively [21–23].

The calculated results are summarized in Table 2. First, we focus on the energy difference among **σ**–, **π**–, **o-1** and **o-2** type models. Because the most stable model is the **σ**-type one, we assessed the energy difference as follows:

$$\Delta E(X) = \text{Total energy}(\sigma\text{-}type) - \text{Total energy}(X) \quad (3)$$

where *X denotes* **π**-, **o-1** and **o-2** interactions. As summarized in Table 2, ΔE values are quite small. The results suggest that interactions between each spin site (C_{60}^-) are very weak.

The calculated J_{ab} values by using Eq. (2) are summarized in Table 2. Small absolute values of those J_{ab} values are also indicating weak spin–spin interactions. Among the four interactions, **σ**- and **π**-type interaction show a weak anti-ferromagnetic interaction, while **o-2** interaction shows a weak ferromagnetic interactions as expected. J_{ab} value of **o-1** model is almost zero, meaning that an energy gap between singlet and triplet is negligible. Interestingly, J_{ab} values suggested that **π**-type interaction is stronger than **σ**-type one. In case of interactions between usual p type atomic orbitals (AOs) e.g. 2p AOs in carbon atom, **σ**-type interaction is stronger than **π**-type one because an overlap between two AOs in **σ**-type is larger than that of **π**-type. Therefore it suggests that overlap of **π**-type interaction is larger than **σ**-type one. The reason is understandable from a distribution of the SOMO of C_{60}^- on the axial axis as depicted in Fig. 1A. An insufficient distribution of the SOMO on the axial axis seems to lead the small SOMO–SOMO overlap in **σ**-type interaction.

In order to clarify the relations between the effective exchange interactions and the overlaps, we introduced natural orbitals (NOs), which were determined by diagonalizing their first order density matrices as

$$\rho(r, r') = \sum n_i \{\phi_i(r)\}^* \phi_i(r'), \quad (4)$$

where n_i denoted the occupation number of NO ϕ_i [24,25]. In the case of C_{60}^- dimer, ϕ_i and ϕ_i^* means bonding and anti-bonding orbitals constructed by singly occupied natural orbitals (SONOs) of each C_{60}^-, namely magnetic orbitals. If an occupation number (n_i) is close to 1.0, then two electrons in the orbital are almost localized on each C_{60}^-. On the other hand, n_i should be equal to 2.0 if two spins on C_{60}^-s are completely delocalized and stable chemical bond is constructed between them. To assess a degree of spin localization, instability value (y_i) for an orbital *i* is sometimes introduced,

$$y_i = 2W_D^2 = \frac{n_i^2 - 4n_i + 4}{n_i^2 - 2n_i + 2}, \quad (5)$$

where W_D denotes the weight of double excitation for orbital *i* [26]. y_i value is usually expressed by using a percentage. If two spins are localized as a radical at each C_{60}^- sites, y_i is close to 100%. On the other hand, y_i value close to zero if two spins are fully delocalized on both C_{60}^- sites.

Table 3
Occupation numbers (NOs) of HONO and LUNO for each models. Instability value (y_i) was calculated by Eq. (5).

NOs	**σ**	**π**	**o-1**	**o-2**
LUNO	0.956	0.909	0.994	1.000
HONO	1.044	1.091	1.006	1.000
y_i (%)	91	82	99	100

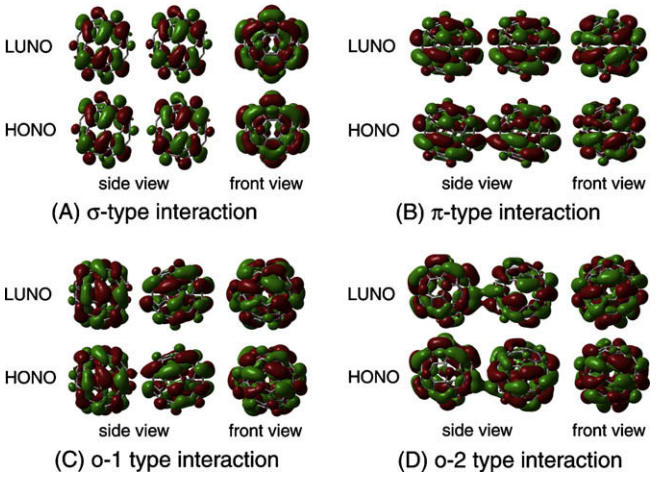


Fig. 3. Highest occupied natural orbitals (HONO) and lowest unoccupied natural orbitals (LUNO) of calculated four types C_{60}^- dimer.

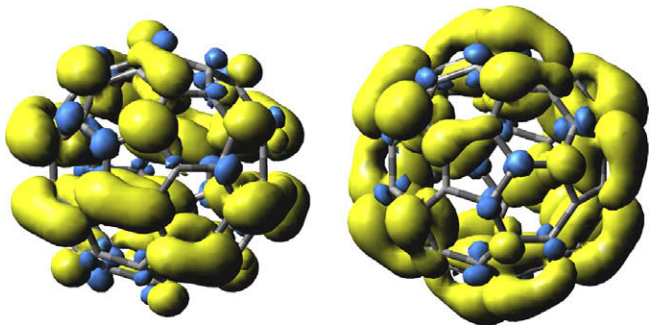


Fig. 4. Calculated spin densities of **o-2** model. Yellow and blue are indicating high spin density and low spin density, respectively. (For interpretation of the references to colour in this figure legend, the reader is referred to the web version of this article.)

Calculated occupation numbers of the highest occupied natural orbitals (HONOs), the lowest unoccupied natural orbitals (LUNOs) and their y_i values are summarized in Table 3. All occupation numbers of HONOs are closed to 1.0 and y_i values are closed to 100%,

indicating that spins are considerably localized on each C_{60}^- site as radicals. Among them, **o-2** type interaction indicates a fully localizing spin structure. In other words, two SONOs are orthogonal in the **o-2** model. The results also shows that overlap in π-type model is larger than that of σ-type one as we expected above. Those NOs depicted in Fig. 3 significantly support them.

Finally we depicted the spin density of the HS state of **o-2** type C_{60}^- dimer to examine whether the DSP occurs or not. In case of the DSP mechanism, the down spin and up spin densities appear alternately on their connecting face as described in Ref. [10]. However, the up spin density is distributed to all carbon atoms as depicted in Fig. 4. Therefore, the result supports the orbital orthogonality as the mechanism for the ferromagnetic interaction rather than the DSP.

4. Conclusions

Four types of magnetic interactions between C_{60}^- anions were examined by using UB3LYP calculations. Although all of calculated J_{ab} values were small, the results indicated that three of four interactions were anti-ferromagnetic but **o-2** type was only the ferromagnetic interaction. The mechanism of such exchange coupling was explained orbital orthogonality. In this study, we assumed that a structure of C_{60}^- is consistent with that of C_{60}. Bond alternation, however, will be occurred on C_{60} molecule by one electron doping into LUMO. For the further discussion, structural optimization should be carried out for C_{60}^- molecule.

By using the Langevin–Weiss mean field approximation, T_c can be estimated as follows [27]:

$$k_B T_c = \frac{2}{3} \sum_{a<b} S(S+1) J_{ab} \tag{6}$$

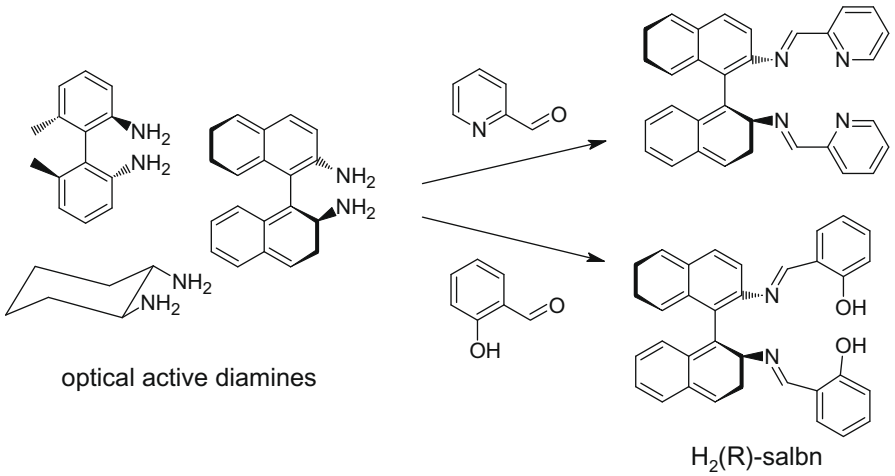
By substituting the obtained J_{ab} value of **o-2** type model (4.6 cm^{-1}) into Eq. (6), we obtain T_c = 8.7 K. The lower T_c than that of C_{60}-TDAE indicates the necessity of stronger ferromagnetic interaction. There are some candidates to promote the ferromagnetic interaction. One is the double exchange interaction between C_{60}^- and C_{60}^{2-}. If we can synthesize mixed valence like state of C_{60}^- and C_{60}^{2-}, much stronger ferromagnetic interaction will be realized. The second is the distance between C_{60}^-s. The distance seems to be important because SOMO–SOMO overlap is not negligible in spite of 9.936 Å interval from neighboring C_{60}^- (face to face distance is 3.458 Å as illustrated in Fig. 1C). In case of C_{60}-TDAE complex, an interval of nearest neighboring C_{60}^-s is 9.859 Å [28], closer in comparison with *fcc* C_{60}'s one. The shorter C_{60}^-–C_{60}^- distance may bring strong interactions. In addition, there is a possibility that C_{60}^-–TDAE– C_{60}^- interaction increases the ferromagnetic interaction. In those points of view, an appropriate design of counter cation is required to control the SOMO–SOMO overlap between C_{60} anions for the ferromagnetic interaction.

Acknowledgments

This work has been supported by Grants-in-Aid for Scientific Research (KAKENHI) (Nos. 19750046, 19350070, 18350008) from Japan Society for the Promotion of Science (JSPS) and that on Priority Areas (No. 19029028) from the Ministry of Education, Culture, Sports, Science and Technology (MEXT).

References

[1] H.W. Kroto, J.R. Heath, S.C. O'Brien, R.F. Curl, R.E. Smalley, Nature 318 (1985) 162.
[2] W. Kräschmer, L.D. Lamb, K. Fostiropoulos, D.R. Huffman, Nature 347 (1990) 354.
[3] O. Gunnarsson, Rev. Mod. Phys. 69 (1997) 575.
[4] K. Tanigaki, T.W. Ebbesen, S. Saito, J. Mizuki, J.S. Tsai, Y. Kubo, S. Kuroshima, Nature 352 (1991) 222.
[5] T.T.M. Palstra, O. Zhou, Y. Iwasa, P.E. Sulewski, R.M. Fleming, B.R. Zegarski, Solid State Commun. 93 (1995) 327.
[6] R.D. Johnson, M.S. Vries, J. Salem, D.S. Bethune, C.S. Yannoni, Nature 355 (1992) 239.
[7] H. Tou, Y. Maniwa, Y. Iwasa, H. Shimoda, T. Mitani, Phys. Rev. B62 (2000) R775.
[8] H. Kitano, R. Matsuo, K. Miwa, A. Maeda, T. Takenobu, Y. Iwasa, T. Mitani, Phys. Rev. Lett. 88 (2002) 096401.
[9] P.-M. Allemand, K.C. Khemani, A. Koch, F. Wudl, K. Holczer, S. Donovan, G. Grüner, J.D. Thompson, Science 253 (1991) 301.
[10] K. Yamaguchi, S. Hayashi, M. Okumura, M. Nakano, W. Mori, Chem. Phys. Lett. 226 (1994) 372.
[11] K. Tanaka, Y. Asai, T. Sato, T. Kuga, T. Yamabe, M. Tokumoto, Chem. Phys. Lett. 259 (1996) 574.
[12] K. Tanaka, A.A. Zakhidov, K. Yoshizawa, K. Okahara, T. Yamabe, Phys. Rev. B47 (1993) 7554.
[13] B. Narymbetov, A. Omerizu, V.V. Kabanov, M. Tokumoto, H. Kobayashi, D. Mihailovic, Nature 407 (2000) 883.
[14] H.-B. Burgi, E. Blanc, D. Schwarzenbach, Shengzhong Liu, Ying-jie Lu, M.M. Kappes, J.A. Ibers, Angew. Chem., Int. Ed. Engl. 31 (1992) 640.
[15] M.J. Frisch, G.W. Trucks, H.B. Schlegel, G.E. Scuseria, M.A. Robb, J.R. Cheeseman, V.G. Zakrzewski, J.A. Montgomery Jr., R.E. Stratmann, J.C. Burant, S. Dapprich, J.M. Millam, A.D. Daniels, K.N. Kudin, M.C. Strain, O. Farkas, J. Tomasi, V. Barone, M. Cossi, R. Cammi, B. Mennucci, C. Pomelli, C. Adamo, S. Clifford, J. Ochterski, G.A. Petersson, P.Y. Ayala, Q. Cui, K. Morokuma, N. Rega, P. Salvador, J.J. Dannenberg, D.K. Malick, A.D. Rabuck, K. Raghavachari, J.B. Foresman, J. Cioslowski, J.V. Ortiz, A.G. Baboul, B.B. Stefanov, G. Liu, A. Liashenko, P. Piskorz, I. Komaromi, R. Gomperts, R.L. Martin, D.J. Fox, T. Keith, M.A. Al-Laham, C.Y. Peng, A. Nanayakkara, M. Challacombe, P.M.W. Gill, B. Johnson, W. Chen, M.W. Wong, J.L. Andres, C. Gonzalez, M. Head-Gordon, E.S. Replogle, J.A. Pople, GAUSSIAN 98, Gaussian, Inc., Pittsburgh PA, 2002.
[16] S.H. Yang, Cl.L. Pettiette, J. Conceicao, O. Cheshnovsky, R.E. Smalley, Chem. Phys. Lett. 139 (1987) 233.
[17] J. Kanamori, J. Phys. Chem. Solids 10 (1959) 87.
[18] D. Gatteschi, O. Kahn, J.S. Miller, F. Palacio (Eds.), Magnetic Molecular Materials, Kluwer Academic Publishers, Dordrecht, 1991.
[19] O. Kahn (Ed.), Magnetism: A Supermolecular Function, NATO ASI Series C, vol 484, Kluwer Academic Publishers, Dordrecht, 1996.
[20] E. Coronado, P. Dekhais, D. Gatteschi, J.S. Miller (Eds.), Molecular Magnetism: From Molecular Assemblies to the Devices; NATO ASI Series E, vol. 321, Kluwer Academic Publishers, Dordrecht, 1996.
[21] K. Yamaguchi, In Self-Consistent Field, Theory and Applications, in: R. Carbeó, M. Klobukowski (Eds.), Studies in Physical and Theoretical Chemistry 70, Elsevier, Amsterdam-Oxford-New York-Tokyo, 1990, p. 727.
[22] T. Kawakami, S. Yamanaka, S. Yamada, W. Mori, K. Yamaguchi, K. In Molecular-based magnetic materials, theory, technique and applications, in: M.M. Turnbull, T. Sugimoto, L.K. Thompson (Eds.), ACS Symposium Series 644, American Chemical Society, Washington, DC, 1996, p. 30.
[23] Y. Kitagawa, T. Soda, Y. Shigeta, S. Yamanaka, Y. Yoshioka, K. Yamaguchi, Int. J. Quantum Chem. 84 (2001) 592.
[24] K. Takatsuka, T. Fueno, K. Yamaguchi, Theor. Chem. Acta 48 (1978) 175.
[25] Y. Takano, Y. Kitagawa, T. Onishi, Y. Yoshioka, K. Yamaguchi, N. Koga, H. Iwamura, J. Am. Chem. Soc. 124 (2002) 450.
[26] K. Yamaguchi, T. Kawakami, Y. Takano, Y. Kitagawa, Y. Yamashita, H. Fujita, Int. J. Quantum Chem. 90 (2002) 370.
[27] M. Okumura, K. Yamaguchi, M. Nakano, W. Mori, Chem. Phys. Lett. 207 (1993) 1.
[28] P.W. Stephenes, D. Cox, J.W. Lauher, L. Mihaly, J.B. Wiley, P.M. Allemand, A. Hirsch, K. Holczer, Q. Li, J.D. Thompson, F. Wudl, Nature 3555 (1992) 331.



Scheme 1. Syntheses of tetradentate chiral ligands.

resultant solution was added $FeCl_3 \cdot 6H_2O$ (27 mg, 0.1 mmol) in methanol (2 ml). Brown prismatic crystals of **2** were obtained by slow diffusion of Et_2O vapor into the methanol solutions in a sealed tube. *Anal. Calc.* for $C_{70}H_{54}Fe_2N_4O_8$: C, 70.60; H, 4.57; N, 4.70. Found: C, 70.98; H, 4.76; N, 4.83%.

2.3. X-ray crystal structure analyses

Each single crystal was mounted on the tip of a glass fiber with epoxy resin. Diffraction data were collected at −73 °C on a Bruker SMART APEX diffractometer fitted with a CCD-type area detector using monochromated Mo Kα radiation (λ = 0.71073 Å). The data frames were integrated using SAINT (Bruker Analytical X-ray Systems). Empirical absorption corrections were applied to the data for **1** by SADABS (G.M. Sheldrick, 1994) and Gaussian face-indexed corrections were applied to the data for **2** by XPREP (Bruker, 2001). The structures were solved by direct methods and refined by the full-matrix least-squares method on all F^2 data using the SHELXTL program package (Bruker Analytical X-ray Systems). Non-hydrogen atoms were refined with anisotropic thermal parameters. Hydrogen atoms were included in calculated positions and refined with isotropic thermal parameters riding on those of the parent atoms.

Crystal data for **1**: $C_{76}H_{57}ClN_8Ni_2O_8$, formula weight = 1363.17, orthorhombic, space group $P2_12_12_1$, a = 12.0058(16), b = 16.646(2), c = 32.682(4) Å, V = 6531.4(15) Å^3, Z = 4, ρ_{calcd} = 1.386 g cm^{-3}, T = 200(2) K, 26 191 reflections collected, 11 961 unique, (R_{int} = 0.0794), R_1 = 0.0745, wR_2 = 0.1378, Flack x = 0.019(17) using 11 961 reflections with $I > 2\sigma(I)$.

Crystal data for **2**: $C_{78}H_{74}Fe_2N_4O_{10}$, formula weight = 1339.11, tetragonal, space group $P4_12_12$, a = 13.597(4), c = 37.891(15) Å, V = 7005(4) Å^3, Z = 4, ρ_{calcd} = 1.270 g cm^{-3}, T = 200(2) K, 33 563 reflections collected, 6662 unique, (R_{int} = 0.0812), R_1 = 0.0592, wR_2 = 0.1562, Flack x = 0.02(2) using 6662 reflections with $I > 2\sigma(I)$.

2.4. Magnetic susceptibility measurements

Magnetic susceptibility measurements in temperature range of 1.8–300 K were carried out on powdered samples of complex **1** and **2** with applying magnetic field of 500 Oe, using a Quantum Design MPMS XL-5 type magnetometer. Corrections were based on subtracting the sample-holder signal and the diamagnetic contribution was estimated from the Pascal constants [10].

3. Results and discussion

3.1. Crystal structure of *1*

Complex **1** crystallized in the chiral space group $P2_12_12_1$, and an ORTEP diagram of complex molecule in **1** is given in Fig. 1. Complex **1** is a dinuclear Ni(II) complexes in which two Ni(II) ions are doubly linked by μ_2-phenoxo groups, each having NiN_3O_3 core. Bridging bond angles of Ni–O–Ni are 98.79(18) and 100.98(18)°, and the interatomic separation of Ni1···Ni2 is 3.1317(11) Å. A mono-cationic complex molecule of **1** contains two Ni(II) ions and two tetradentate ligands. Charge consideration suggests that three of four protons in the ligands are deprotonated. Note that the difference Fourier map showed an extra-peak between O1 and O3 atoms, which can be assigned to the hydrogen bonded proton. Each Ni(II) ion has six coordination geometry with Δ configuration. (*R*)-salbn^{2-} occupied four coordination sites of the Ni(II) ions with coordination of two imino nitrogen and two phenoxo oxygen atoms, and the asymmetric structure of (*R*)-salbn^{2-} results in Δ configuration on the Ni(II) ions. The remaining two coordination sites of Ni(II) ions are occupied by the acetonitrile molecule and the μ_2-phenoxo group of (*R*)-salbn of the other side of the Ni(II) unit. Coordination bond lengths of Ni1–O are 2.038(4), 2.047(4) and 2.104(5) Å, while those of Ni1–N_{amine} are 2.042(5) and 2.047(4) Å. Coordination bond length with nitrogen atom from acetonitrile (2.122(6) Å) is slightly longer than those of Ni1–N_{amine}

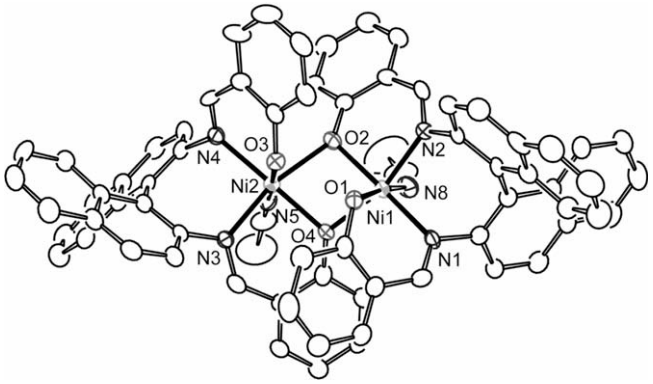


Fig. 1. ORTEP diagram of **1**.

bonds. The structural feature around the Ni2 ion is similar to those for the Ni1 ion. The Ni2 ion with Δ configuration was coordinated to similar manner to the Ni1 ion, and the coordination bond lengths in the Ni2 ion are in the range of 2.021(4)–2.095(4) Å.

3.2. Crystal structure of **2**

An ORTEP diagram of a complex molecule in **2** is shown in Fig. 2. Complex **2** crystallized in the chiral space group $P4_12_12$, and a crystallographic twofold axis passes through Fe1 and Fe2 ions. The complex molecule contains two Fe(III) ions, two (*R*)-salbn^{2-}, and two methoxy ions. The (*R*)-salbn^{2-} acts as a bis-bidentate ligand, and each N/O donor set coordinates to the iron(III) ion to form six-membered chelate rings. Each Fe(III) ion is coordinated by two (*R*)-salbn^{2-} ligands, leading to a Fe(III) dinuclear core which is supported by two μ_2-methoxo bridges. A bridging angle of Fe1–O3–Fe2 is 106.54(12)° with the intermetallic distance of Fe1···Fe2 being 3.1947(15) Å. The Fe(III) ions has an octahedral FeN_2O_4 chromophore with Λ configuration, and the six coordination sites are occupied by two imino nitrogen and two phenoxo oxygen atoms from two chelating salicylideneamino moieties and two μ_2-methoxo oxygen atoms. Coordination bond lengths with the axial ligands are 2.191(3) Å for Fe1 and 2.181(3) Å for Fe2. The equatorial coordination bond lengths are in the ranges of 1.917(3)–1.997(3) Å for Fe1 and 1.942(3)–1.989(3) Å for Fe2.

3.3. Magnetic properties

Magnetic susceptibility measurements for **1** and **2** were performed in the temperature range of 1.8–300 K (Fig. 3). The χ_mT value of **1** is 2.19 emu mol^{-1} K at 300 K, which is slightly larger than the value expected for the uncorrelated two Ni(II) ions (2.0 emu mol^{-1} K with $g = 2.0$). The χ_mT values gradually decreased as the temperature was lowered, suggesting the occurrence of the antiferromagnetic interaction between Ni(II) ions. The magnetic susceptibility data above 20 K were analyzed using the isotropic spin Hamiltonian $H = -2J\mathbf{S}_1 \cdot \mathbf{S}_2$, and the J value was estimated to be −18.6(1) cm^{-1} with $g = 2.21(1)$ for **1**.

The χ_mT value of **2** at 300 K is 4.79 emu mol^{-1} K, which is almost half of the value expected for the uncorrelated two Fe(III) ions (8.75 emu mol^{-1} K with $g = 2.0$), and this suggests the existence of the relatively strong antiferromagnetic interaction. The χ_mT values monotonically decreased as the temperature was lowered. The magnetic susceptibility data above 20 K were analyzed by using the isotropic spin Hamiltonian $H = -2J\mathbf{S}_1 \cdot \mathbf{S}_2$ and the J value was estimated to be −18.0(1) cm^{-1} for **2**.

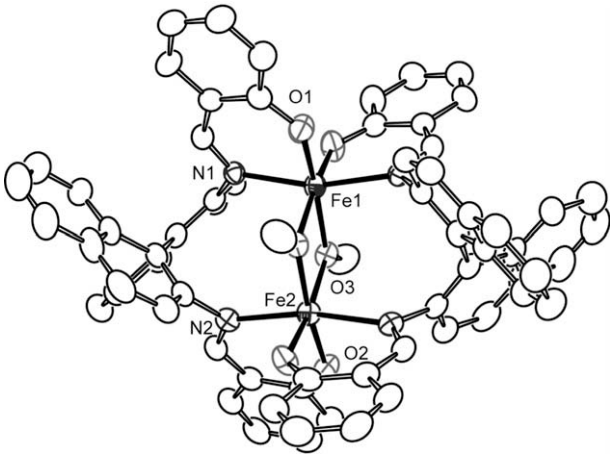


Fig. 2. ORTEP diagram of **2**.

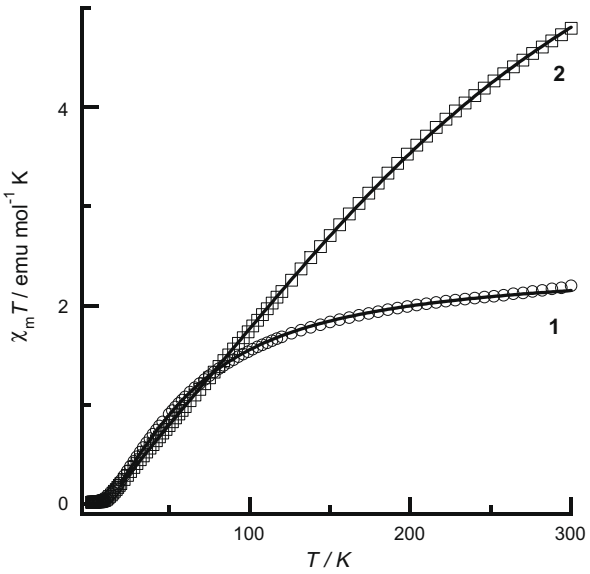


Fig. 3. Plots of χ_mT versus temperature for **1** and **2**.

4. Conclusion

Novel chiral dimer complexes of **1** and **2** were prepared. X-ray structure analyses revealed that the Δ and Λ configurations are selectively formed around metal centers in **1** and **2**, respectively, by using chiral tetradentate ligand of H_2(*R*)-salbn. Dc magnetic susceptibility measurements showed the occurrence of antiferromagnetic interactions between metal centers both in **1** and **2**.

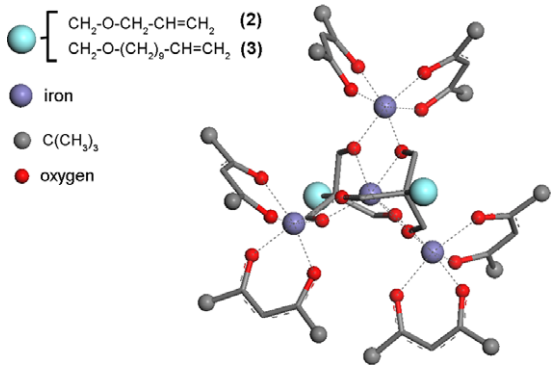
Supplementary data

CCDC 705073 and 705074 contains the supplementary crystallographic data for **1** and **2**. These data can be obtained free of charge via http://www.ccdc.cam.ac.uk/conts/retrieving.html, or from the Cambridge Crystallographic Data Centre, 12 Union Road, Cambridge CB2 1EZ, UK; fax: (+44) 1223-336-033; or e-mail: deposit@ccdc.cam.ac.uk.

References

[1] (a) T. Kimura, T. Goto, H. Shintani, K. Ishizaka, T. Arima, Y. Tokura, Nature 426 (2003) 55;
(b) Y. Tokura, Science 312 (2006) 1481.
[2] H. Katsura, N. Nagaosa, A.V. Balatsky, Phys. Rev. Lett. 95 (2005) 057205.
[3] I.A. Sergienko, E. Dagotto, Phys. Rev. B 73 (2006) 094434.
[4] J. Kishine, K. Inoue, Y. Yoshida, PTP Suppl. 159 (2005) 82.
[5] (a) G. Wagniere, A. Mejer, Chem. Phys. Lett. 93 (1982) 78;
(b) L.D. Barron, J. Vrbancich, J. Mol. Phys. 110 (1984) 546;
(c) G.L.J.A. Rikken, E. Raupach, Nature 390 (1997) 493.
[6] (a) K. Inoue, H. Imai, P.S. Ghalsasi, K. Kikuchi, M. Ohba, H. Okawa, J.V. Yakhmi, Angew. Chem., Int. Ed. 40 (2001) 4242;
(b) K. Inoue, K. Kikuchi, M. Ohba, H. Okawa, Angew. Chem., Int. Ed. 42 (2003) 4810;
(c) H. Imai, K. Inoue, K. Kikuchi, Y. Yoshida, M. Ito, T. Sunahara, S. Onaka, Angew. Chem., Int. Ed. 43 (2004) 5618;
(d) H. Higashikawa, K. Okuda, J. Kishine, N. Masuhara, K. Inoue, Chem. Lett. 36 (2007) 1022.
[7] (a) G.J. Britovsek, J. England, A.J.P. White, Daltan Trans. (2006) 1399;
(b) C. Vedder, F. Schaper, H.-H. Brintzinger, M. Kettunen, S. Babik, G. Fink, Eur. J. Inorg. Chem. (2005) 1071;
(c) H. Huang, T. Okuno, K. Tsuda, M. Yoshimura, M. Kitamura, J. Am. Chem. Soc. 128 (2006) 8716;
(d) K. Bernardo, S. Leppard, A. Robert, G. Commenges, F. Dahan, B. Meunier, Inorg. Chem. 35 (1996) 387;
(e) J. Glerup, K. Michelsen, N. Arulsamy, D.J. Hodgson, Inorg. Chim. Acta 274 (1998) 155;
(f) R.R. Fenton, F.S. Stephens, R.S. Vagg, P.A. Williams, Inorg. Chim. Acta 231 (1995) 73;

(g) S. Schoumacker, O. Hamelin, J. Pécaut, M. Fantecave, Inorg. Chem. 42 (2003) 8110;
(h) M. Kettunen, C. Vedder, F. Schaper, M. Leskelä, I. Mutikainen, H.-H. Brintzinger, Organometallics 23 (2004) 3800.
[8] P.D. Knight, P. Scott, Coord. Chem. Rev. 242 (2003) 125.
[9] S.G. Telfer, T. Sato, T. Harada, R. Kuroda, J. Lefebvre, D.B. Leznoff, Inorg. Chem. 43 (2004) 6168.
[10] O. Kahn, Molecular Magnetism, Wiley-VCH, Weinheim, Germany, 1993.



Scheme 1. Schematic structures of single molecule magnets **2** and **3**.

diethyl ether (6 × 50 ml). The combined organic extracts were dried over $MgSO_4$ and the solvent was evaporated at reduced pressure to give (according to ^1H NMR analysis) 1-methyl-4-undec-10-enyloxymethyl-2,6,7-trioxa-bicyclo[2.2.2]octane *plus* the elimination product undeca-1,10-diene (2.25 g). The mixture was dissolved in methanol (4 ml) and treated overnight with HCl 0.01 M (16 ml, 0.16 mmol) to accomplish acid deprotection. Solid $NaHCO_3$ (0.60 g, 7.0 mmol) was added and the solution was stirred over a 6-h period until complete liberation of the trimethylol function (TLC, SiO_2, toluene:EtOAc 2:1). The solvent was removed under vacuum with moderate heating (40–45 °C) and the solid was purified by column chromatography on silica gel (CH_2Cl_2:MeOH 97.5:2.5) to give pure H_3L^2 (0.90 g, 50% vs. 4-(hydroxymethyl)-1-methyl-2,6,7-trioxabicyclo[2.2.2]octane over two reaction steps). ^1H NMR (200 MHz, $CDCl_3$, 25 °C): δ (ppm) = 5.81 [m, 1H, $-HC{=}CH_2$], 5.04–4.88 [m, 2H, $-HC{=}CH_2$], 3.70 [s, 6H, $-CH_2OH$], 3.45 [s, 2H, $-OCH_2C(-CH_2OH)_3$], 3.41 (t, J = 6.5 Hz, 2H, $-OCH_2CH_2-$), 2.89 [s, br, 3H, OH], 2.03 [m, 2H, $-CH_2-HC{=}CH_2$], 1.55 [m, 2H, $-OCH_2CH_2-$], 1.44–1.21 (m, 12 H, Aliph).

*$[Fe_4(L^2)_2(tmhd)_6]$ (**3**):* Compound **1** (0.0607 g, 0.0402 mmol) was dissolved in dry Et_2O (25 ml) to give a yellow solution. Then the triol H_3L^2 (0.0554 g, 0.192 mmol) was added with stirring. Vapor diffusion of dry methanol (40 ml) in the clear yellow solution afforded yellow-orange prisms, which were washed with the external diffusion mixture, with dry methanol and then vacuum dried (0.0687 g, 90% assuming no crystallization solvent). *Anal.* Calc. for $C_{98}H_{172}Fe_4O_{20}$: C, 62.15; H, 9.15. Found: C, 62.48; H, 9.18%.

2.1. Monolayer preparation

Direct anchoring: Solutions of Fe_4 complexes (**2** or **3**) in mesitylene (10^{-3} M) were placed in a chamber with a quartz window and were deoxygenated by stirring in a dry box for at least 1 h. A Czochralski grown boron doped Si(100) substrate was treated in a piranha solution for 12 min, rinsed in water for 2 min, etched in 1.0% hydrofluoric acid for 90 s, quickly rinsed in water, dried under N_2 and immediately placed in the cluster solution. The chamber remained under UV irradiation (254 nm) for 90 min. The sample was then removed from the solution, rinsed with mesitylene and dichloromethane and sonicated in dichloromethane for 5 min.

*Ligand exchange reaction with **4**:* After the 90-min photochemical grafting of **3** at 254 nm, the silicon sample was taken away from the solution, rinsed in mesitylene and diethyl ether and finally introduced in a solution of **4** in diethyl ether for 6 h at room temperature. Subsequently, the sample was removed from the solution, copiously rinsed with diethyl ether, sonicated in the same solvent and analyzed.

One pot anchoring: Similarly to the direct anchoring procedure, a solution of **2** or **3** in mesitylene was placed in a photochemical reactor and was deoxygenated by stirring in a dry box for at least 1 h. Subsequently, a Czochralski grown boron doped Si(100) substrate, treated as described above, was placed in the solution and was submitted to the photochemical hydrosilylation at 254 nm for 90 min. After the photochemical treatment, the sample was left undisturbed in the solution for 6 h. The sample was then removed from the solution, washed many times with mesitylene and sonicated in dichloromethane for 10 min in order to remove any physisorbed clusters.

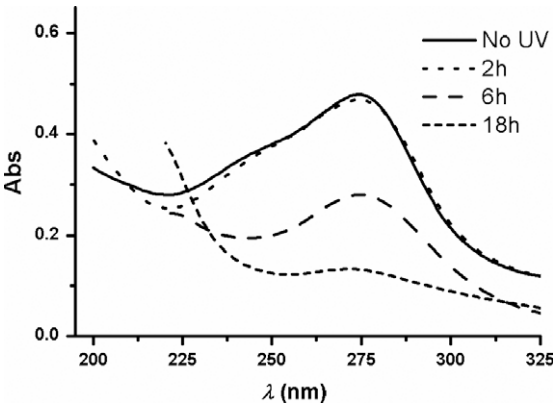


Fig. 1. Spectral changes upon irradiating cluster **2** in cyclohexane solution at 254 nm at various times.

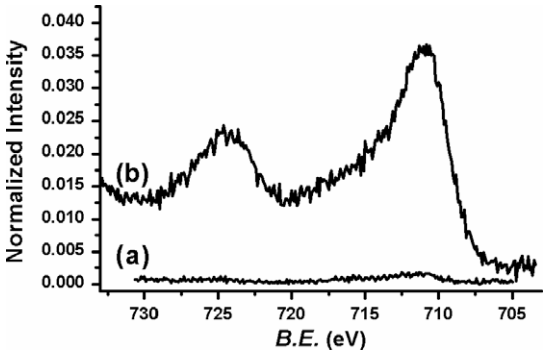


Fig. 2. High resolution Fe 2p XPS region of samples (a) exposed to direct photochemical grafting of **3** and (b) exposed to direct photochemical grafting of **3** followed by the ligand exchange reaction with **4**. The intensities are normalized to the total Si 2p intensity. Take off photoelectron angle was 45° relative to the surface.

2.2. Surface characterization techniques

The XPS spectra were recorded with a PHI ESCA/SAM 5600 Multy technique spectrometer equipped with a monochromatized Al Kα X-ray source. The analyses were carried out at 45° photoelectron take off angle relative to the sample surface with an acceptance angle of ±7°. Binding Energy (BE) scale was calibrated by centering the adventitious/hydrocarbon carbon C1s at 285.0 eV [8].

ATR-IR spectra of the monolayers were recorded on JASCO FT-IR 430 equipped with a Harrick GATR germanium single reflection accessory, collecting the spectra with 80 scans at 2 cm^{-1} resolution from 4000 to 400 cm^{-1}.

AFM images were obtained in high amplitude mode (tapping mode) by a NT-MDT instrument. The noise level before and after each measurement was 0.01 nm.

3. Results and discussion

Direct photochemical grafting: The photochemical stability of Fe_4 derivatives was tested by UV–Vis spectroscopy on a solution of **2** in cyclohexane.

Table 1
XPS quantitative data (%) relative to the functionalized silicon surfaces. Take off photoelectron angle was 45° relative to the surface.

	Fe	C	O	Si	Cl
HF-etched Si(100)	/	7.2	1.5	91.3	/
2, no irradiation	0.2	9.8	18.9	72.3	/
2, direct grafting	0.2	24.2	19.6	56.2	/
3, direct grafting	0.3	26.3	19.5	53.8	/
3, direct grafting and exchange with **4**	1.6	41.2	24.9	31.9	0.4
2, *one pot* route	1.4	36.3	26.3	36.0	/
3, *one pot* route	1.5	37.4	21.5	39.6	/

The room temperature UV–Vis spectrum registered in the range between 200 and 325 nm is shown in Fig. 1 as a function of irradiation time at 254 nm, the wavelength to be used for the photochemical hydrosilylation [5].

The UV–Vis spectrum before irradiation is dominated by an absorption around 274 nm, which is assigned to the $\pi \rightarrow \pi^*$ transition of the β-diketonate ligand [9]. After 2 h of exposure at 254 nm the spectrum does not change significantly. After 6-h irradiation the intensity of the band centered at 274 nm decreases and a shift of absorbance to higher frequency is noted. After 18-h irradiation, the characteristic bands of the Fe_4 complex become negligible thus indicating that Fe_4 clusters undergo extensive decomposition upon prolonged irradiation.

To perform the photochemical hydrosilylation while avoiding significant complex decomposition, the irradiation time for the SMM grafting was set lower than 2 h. Therefore, direct photochemical Si-anchoring of **2** and **3** was attempted by exposing H-terminated silicon surfaces to the respective complex solutions under 90 min of UV irradiation [5].

After the photochemical reaction, XPS spectra of the silicon substrates show the presence of carbon, silicon and oxygen. The intensity of the Fe 2p doublet is very low (Fig. 2a), suggesting a negligible presence of iron on the surface.

The elemental compositions of the samples after the direct grafting process are reported in Table 1. Moreover, XPS data of two reference samples, a freshly etched Si(100) and the same sample after 18 h immersion in a solution of **2** with no irradiation are also reported for comparison.

The iron concentration of the grafted samples is similar to that detected in the reference sample exposed to a solution of **2** with no UV irradiation and, hence, comparable to the contribution of physisorbed clusters. Therefore, the direct photochemical grafting appears to have sever drawbacks presumably due to the scarce reactivity of the functionalized tetrairon(III) complexes with the H-terminated surface.

However, the amount of carbon after direct photochemical grafting is much higher than in the two reference samples (see Table 1), indicating the presence of a carbonaceous overlayer on the substrates.

The carbonaceous overlayer can be due to the hydrosilylation reaction between the Si surface and the free tripodal ligands in equilibrium with **2** and **3**.

AFM lithography has been used to determine if the thickness of the organic overlayers is consistent with monolayers of H_3L^1 and

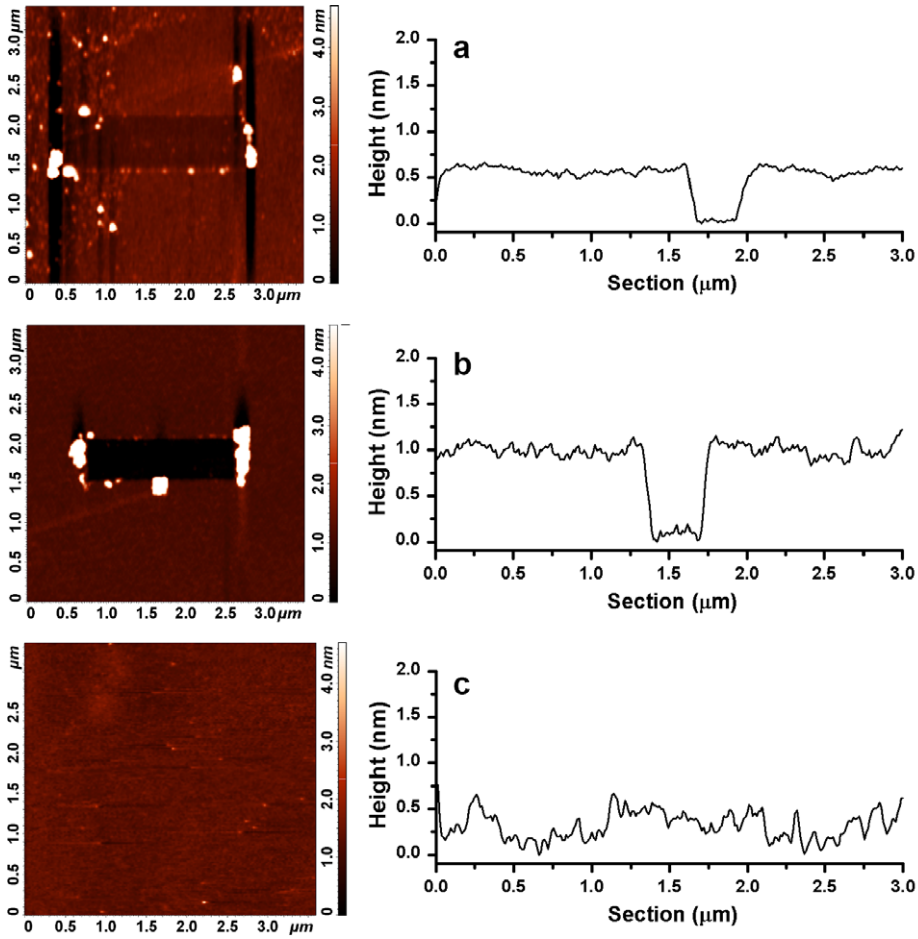


Fig. 3. The semi-contact AFM topography images and the relative height profiles after the lithography procedure, recorded on (a) a H-terminated silicon surface after 90-min photochemical grafting in a solution of **2**, (b) in a solution of **3** and (c) a H-terminated silicon surface after immersion of 18 h in a solution of **2** with no irradiation.

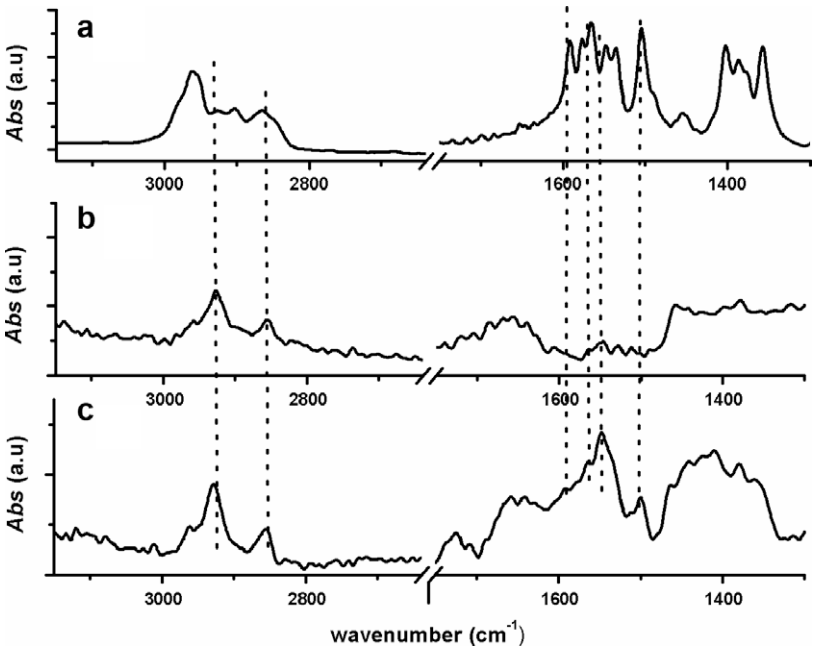
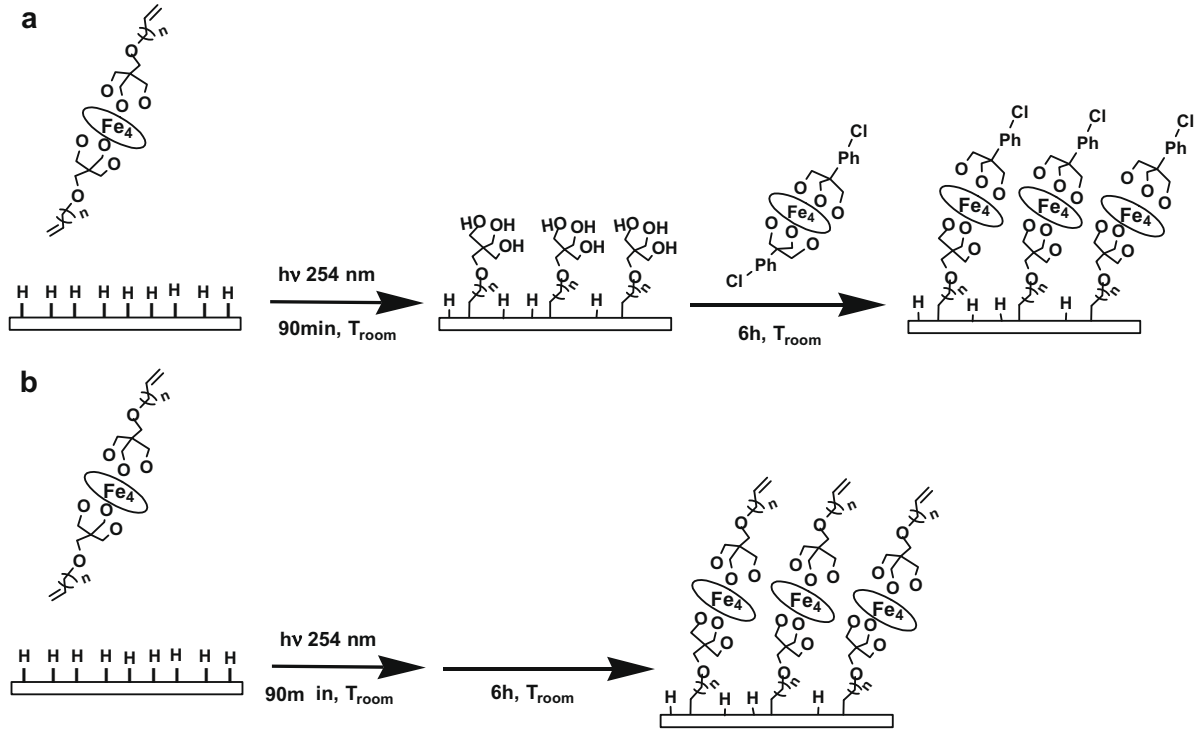


Fig. 4. (a) FT-IR spectrum of a microcrystalline sample of **2**, (b) ATR-IR spectrum of an H-terminated silicon surface after 90 min photochemical grafting in a solution of **2** and (c) of the H-terminated silicon surface after *one pot* procedure using **2**.

H_3L^2 grafted on the Si surface. The technique consists in removing the molecular film by applying a significant force on the layer with the AFM tip. The AFM lithography was used to scratch an area of 2 μm × 0.5 μm, by rastering the AFM tip (30 nm of curvature radius) in contact mode and applying a force of ~180–200 nN [10,11]. A larger area 3.5 μm × 3.5 μm containing the rastered zone was scanned for a second time in semi-contact regime to acquire a topographic image (Fig. 3).

It was observed that the organic material on the surface is displaced as a consequence of the high pressure applied on the sample: regular scratches were produced on samples obtained by photochemical grafting with solutions of both **2** and **3**, thus indicating the presence of monolayers on the silicon surface (Fig. 3a and b).

The depth of these scratches, evaluated in the cross sections, is considered equal to the layer thickness and amounts to ~0.6 nm



Scheme 2. (a) Photochemical grafting followed by ligand exchange with chlorine-marked cluster **4** and (b) Fe_4 cluster anchoring with *one pot* route.

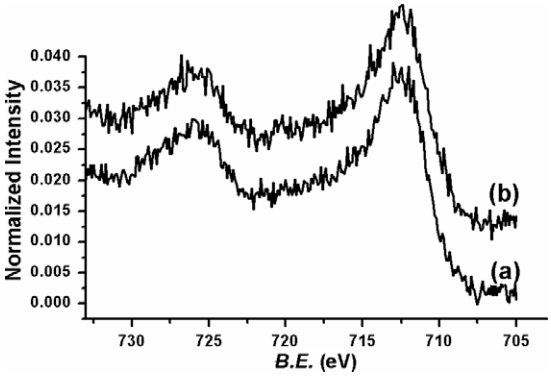


Fig. 5. High resolution Fe 2p XPS region relative to the silicon surface after the *one pot* procedure with **2** (a) and **3** (b). The intensities are normalized to the total Si 2p intensity. For clarity, the spectrum of **3** is reported with a 0.01 *y*-axis shift. Take off photoelectron angle was 45° relative to the surface.

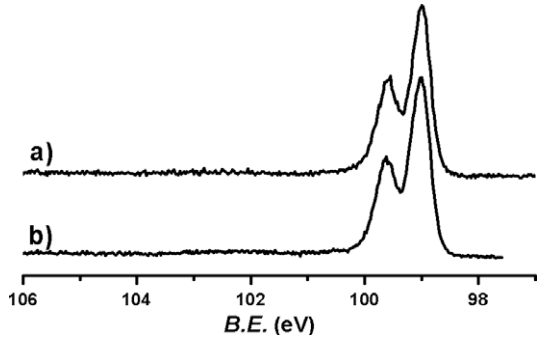


Fig. 6. High resolution XPS Si 2p region of (a) **2** and (b) **3** grafted silicon via *one pot* process.

and ~0.9 nm for **2** and **3**, respectively. These values are lower than the lengths of the respective tripodal ligands (H_3L^1 = ~0.8 nm and H_3L^2 = ~1.6 nm) optimized with a QM-DFT modeling package. This is consistent with the presence of H_3L^1 and H_3L^2 monolayers with a bent configuration of the alkyl chains.

To prove that the applied lithography conditions cannot scratch the substrate but only the organic overlayer, the same lithography process was applied to the reference sample obtained after 18 h immersion in a solution of **2** with no irradiation. In this case, no scratch was created by the AFM tip in the same operative conditions (Fig. 3c).

ATR-IR measurements have been used to determine the nature of the carbon overlayer. Fig. 4b shows the ATR-IR spectrum of the grafted silicon sample immersed in the solution of complex **2** for 90 min under UV irradiation.

The stretching modes of CH_x moieties in the range 2800–3000 cm^{-1} are easily detectable indicating the presence of the ligand alkyl chain, however, no significant further information can be obtained. The analysis does not allow to identify the diagnostic signals of species at the surface like hydroxyl functionalities of the tripodal receptors ($\nu \sim 3450$ cm^{-1}), since they are hidden beneath the broad band of H_2O adsorbed on the surface whose bending vibration is also visible at ca. 1650 cm^{-1}. The hydrophilic behavior of the surface can be due to the presence of terminal –OH functionalities of the tripodal receptors H_3L^1 and H_3L^2 at the surface. At lower wave numbers, no signal from β-diketonate C–O stretching is observed around 1560 cm^{-1}.

To confirm the nature of the H_3L^1 and H_3L^2 monolayers formed after the photochemical grafting from **2** and **3**, respectively, we attempted a ligand exchange reaction using a previously-described chlorine-marked Fe_4 cluster $[Fe_4(L^3)_2(tmhd)_6]$ (**4**), where H_3L^3 = 2-(4-chloro-phenyl)-2-hydroxymethyl-propane-1,3-diol [5].

The XPS spectrum of the sample after photochemical grafting using a solution of **3** and after the ligand exchange reaction shows the presence of all the elements expected: O, C, Si, Fe and Cl.

Both XPS quantitative analysis (Table 1) and the intensity of the Fe 2p XPS bands (Fig. 2b) indicate the presence of the anchored Fe_4 cluster on the tripodal ligands. Moreover, the Cl/Fe intensity ratio is halved as compared with that observed on a microcrystalline sample of **4**, as expected for the exchange of one L^{3-} ligand with one surface-bound tripodal receptor (Scheme 2a).

One pot procedure: The formation of ligand monolayers as result of the direct photochemical grafting of **2** and **3** suggested to extend the immersion time after UV irradiation so as to allow subsequent ligand exchange. The new approach thus consists in a 90-min UV irradiation of the Fe_4 solution (**2** or **3**), followed by a 6-h waiting time in which the Si substrate is left undisturbed in the solution with no irradiation. This novel procedure will be named *one pot* reaction, since it requires just one reaction environment.

The XPS spectra of samples obtained by *one pot* process present all the expected elements: O, C, Si and Fe. The high resolution XPS region of Fe 2p shows the presence of the doublet 3/2 and 1/2 with the $2p_{3/2}$ peak centered at 711.0 eV as expected (Fig. 5). The position and the shape of Fe 2p band are similar to those detected on microcrystalline samples of **1** and **4** and are in good agreement with the presence of Fe^{+3} species. XPS atomic concentrations for samples obtained by *one pot* route are reported in Table 1.

The intensity of the Fe 2p peaks (Fig. 5 and Table 1) for both **2** and **3** is notably higher as compared to the signal observed in the case of the direct photochemical grafting (Fig. 2 and Table 1) and indicates the successful anchoring of the iron cluster.

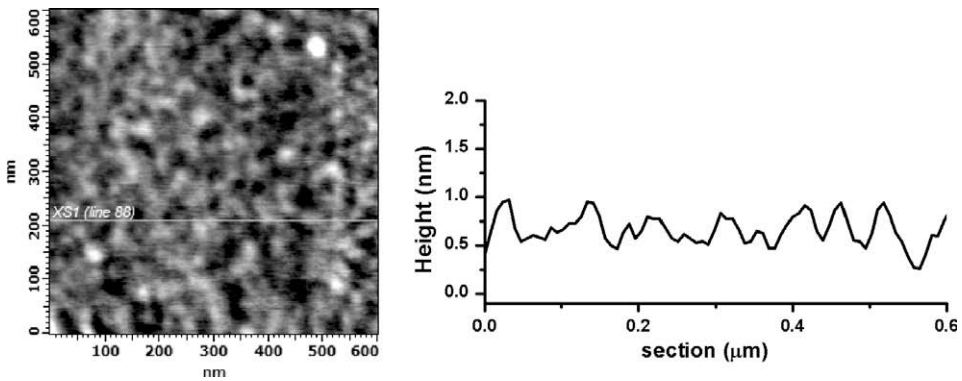


Fig. 7. (a) The semi-contact AFM morphology image and (b) height profile of a Si (100) surface after the "one pot" process using **3**.

As compared with previously-reported [5] multistep procedures, the herein proposed one-step approach is faster and has lesser manipulation requirements. Indeed, while the Si 2p XPS regions observed after the three-step Fe_4 anchoring shows a component centered at ~102.5 eV [5] indicating the presence of surface oxidation, nearly no detectable oxide component is observable after the *one pot* procedure with both **2** and **3** (Fig. 6).

The morphology of the surfaces was evaluated by AFM (Fig. 7): as seen previously for the three-step procedure [5], the presence of iron clusters slightly modifies the morphology of the surface that appears more structured (R.M.S. = 0.21) if compared with the monolayer of ligands (R.M.S. = 0.11) shown in Fig. 3.

The profile in the cross section shows that the average size of the structures is ~0.7 nm consistent with the expected height of the magnetic complex.

ATR-IR spectra were also recorded after *one pot* procedure using **2**. Fig. 4c shows new bands around 1550–1600 cm^{-1}, which compare well with those observed in microcrystalline **2** (Fig. 4a) and are attributed to the β-diketonate ligands [5,12].

4. Conclusions

A novel route for the *one pot* grafting of Fe_4-type SMM on H-terminated Si using photochemical hydrosilylation has been developed. Two Fe_4 complexes have been used which contain tripodal ligands featuring alkene-terminated hydrocarbon chains of different length. Direct photochemical hydrosilylation reaction from cluster solutions leads to the formation of ligand layers. Further contact of the substrate with the cluster solutions without UV irradiation leads to cluster anchoring via ligand exchange.

This one-step anchoring procedure is simpler and faster than the previously reported [5] three-step approach. Furthermore, it requires lesser surface manipulation and thus affords cleaner and less oxidized surfaces.

Acknowledgements

This work was supported by MIUR through FIRB 2003 (RBNE033KMA) project and by ISTM-CNR and INSTM within the PROMO "Nanostrutture organiche, organometalliche polimeriche ed ibride: ingegnerizzazione supramolecolare delle proprietà fotoniche e dispositivistica innovativa per optoelettronica" project.

References

[1] A.-L. Barra, A. Caneschi, A. Cornia, F. Fabrizi de Biani, D. Gatteschi, C. Sangregorio, R. Sessoli, L. Sorace, J. Am. Chem. Soc. 121 (1999) 5302.
[2] A. Cornia, A.C. Fabretti, P. Garrisi, C. Mortalò, D. Bonacchi, D. Gatteschi, R. Sessoli, L. Sorace, W. Wernsdorfer, A.-L. Barra, Angew. Chem., Int. Ed. 43 (2004) 1136.
[3] S. Accorsi, A.-L. Barra, A. Caneschi, G. Chastanet, A. Cornia, A.C. Fabretti, D. Gatteschi, C. Mortalò, E. Olivieri, F. Parenti, P. Rosa, R. Sessoli, L. Sorace, W. Wernsdorfer, L. Zobbi, J. Am. Chem. Soc. 128 (2006) 4742.
[4] A.-L. Barra, F. Bianchi, A. Caneschi, A. Cornia, D. Gatteschi, L. Gorini, L. Gregoli, M. Maffini, F. Parenti, R. Sessoli, L. Sorace, A.M. Talarico, Eur. J. Inorg. Chem. 26 (2007) 4145.
[5] G.G. Condorelli, A. Motta, G. Pellegrino, A. Cornia, L. Gorini, I.L. Fragala, C. Sangregorio, L. Sorace, Chem. Mater. 20 (2008) 2405.
[6] A. Cornia, L. Gregoli, C. Danieli, A-L. Barra, G. Pellegrino, R. Sessoli, in preparation.
[7] T.J. Dunn, W.L. Neumann, M.M. Rogic, S.R. Woulfe, J. Org. Chem. 55 (1990) 6368.
[8] P. Swift, Surf. Interface Anal. 4 (1982) 47.
[9] R.L. Lintvedt, L.K. Kernitsky, Inorg. Chem. 9 (1970) 491.
[10] X.N. Xie, H.J. Chung, C.H. Sow, A.T.S. Wee, Mater. Sci. Eng. R 54 (2006) 1.
[11] A. Gulino, F. Lupo, G.G. Condorelli, M.E. Fragalà, M.E. Amato, G. Scarlata, J. Mater. Chem. 18 (2008) 5011.
[12] K. Nakamoto, Infrared and Raman Spectra of Inorganic and Coordination Compounds, John Wiley and Sons Inc., New York, 1978. p. 249.

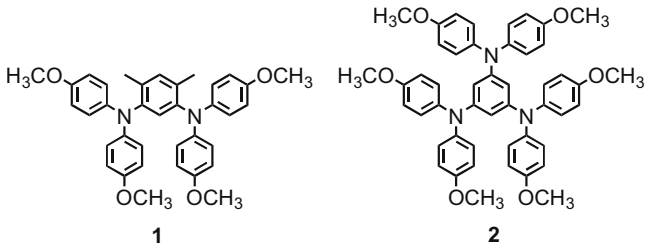


Fig. 1. Structures of *N,N,N′,N′*-tetrakis(4-anisyl)-4,6-dimethyl-1,3-phenylenediamine (**1**) and *N,N,N′,N′,N″,N″*-hexakis(4-anisyl)-1,3,5-phenylenetriamine (**2**).

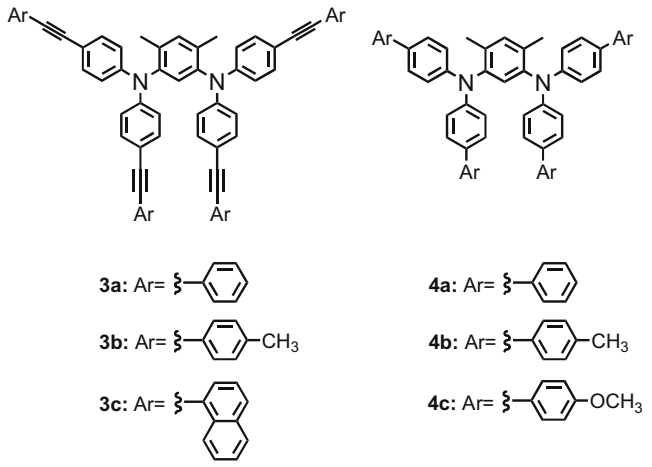


Fig. 2. Structures of **3** and **4**.

In this paper, we will report on a novel family of highly π-extended tetraaryl-*m*-phenylenediamines (**4a–c**), where aryl groups are directly attached to the peripheral aromatic rings of the diamine framework (Fig. 2). We also describe molecular design rules to stabilize the oligocationic state.

2. Results and discussion

2.1. Molecular design and synthesis of the diamines by Suzuki coupling

During the last two decades, much efforts have been paid to design, generation and detection of triarylamine-based positively charged high-spin molecules. The stability of the corresponding mono- and dicationic states is a key issue to realize them. Generally, introduction of electrodonating groups raises the HOMO energy level, leading to the thermodynamically more stable oxidized states. Thus, one may consider that the more electron donating groups are introduced, the more stable the corresponding oligocationic states are. This strategy worked well enough for the generation and characterization of triarylamine-based high-spin molecules as exemplified by **1**. However, taking into account their applications to molecular devices and supramolecular systems, more sophisticated molecular design rules should be established. In concrete terms, both (i) facile π-extension of molecular structures and (ii) high stability of the corresponding oxidized states should be satisfied.

Generally, aryl halides are widely used as convenient compounds in conventional and modern organometallic syntheses. Until now, numerous organic syntheses using aryl halides have been reported. Among them, Suzuki coupling [4] is an attractive and powerful method for syntheses of biaryls in excellent yields. In fact, the coupling has been utilized in many laboratories for syntheses of natural and artificial molecules. *N,N,N′,N′-tetrakis(4-iodophenyl)-4,6-dimethyl-1,3-phenylenediamine* (**5**) was prepared by the method reported by us [2m]. A series of π-extended tetraaryl-*m*-phenylenediamines were prepared by Suzuki coupling as shown in Fig. 3. The synthetic procedure of **4a** is described below.

The mixture of compound **5**, catalytic amount of Pd $(PPh_3)_4$, excess amount of K_3PO_4 and 5 equivalents of phenyl boronic acid in *n*-butanol, was refluxed for 18 h under argon atmosphere. The obtained crude powder was repeatedly washed with ethanol to give **4a** as pale yellow crystals in 72% yield. Compounds **4b–c** were also prepared in the similar manner. The NMR spectra and HRMS data for these molecules are consistent with their assigned structures as shown below:

4a: ^{1}H NMR($CDCl_3$); δ 2.08 (s, 6H), 7.08 (d, 8H, *J* = 8.8 Hz),7.11 (s, 1H), 7.20 (s, 1H), 7.28 (t, 4H, *J* = 7.3 Hz), 7.39 (t, 8H, *J* = 7.3 Hz) 7.45 (m, 5H, *J* = 8.8 Hz) 7.54 (d, 8H, *J* = 7.3 Hz).

HRMS(FAB): *m*/*z*: calc. for $C_{56}H_{44}N_2$ $[M]^+$: 744.3505. Found: 744.3506%.

4b: ^{1}H NMR($CDCl_3$); δ 2.08 (s, 6H), 2.38 (s, 12H) 7.07 (d, 8H, *J* = 8.8 Hz), 7.11 (s, 1H), 7.19 (m, 9H), 7.43 (d, 16H, *J* = 8.8 Hz).

HRMS(FAB): *m*/*z*: calc. for $C_{60}H_{52}N_2$ $[M]^+$: 800.4131. Found: 800.4131%.

4c: ^{1}H NMR($CDCl_3$); δ 2.07 (s, 6H), 3.84 (s, 12H), 6.92 (d, 8H, *J* = 8.8 Hz), 7.05 (d, 8H, *J* = 8.8 Hz), 7.08 (s, 1H), 7.17 (s, 1H), 7.39 (d, 8H, *J* = 8.8 Hz), 7.46 (d, 8H, *J* = 8.8 Hz).

HRMS(FAB): *m*/*z*: calc. for $C_{60}H_{52}N_2O_4$ $[M]^+$: 864.3927. Found: 864.3924%.

2.2. UV/Vis and emission spectra

We previously reported the UV/Vis and emission spectra of **3a–c**. Compound **3a** exhibited a broad absorption band around 360 nm in THF. Upon excitation at 360 nm, **3a** exhibited blue emission at 410 nm. This was the first report of fluorescent tetraaryl-1,3-phenylenediamines. On the other hand, Compounds **4a** exhibited a broad absorption band around 330 nm in THF, which is remarkably red-shifted in comparison with that of **1** (λ_{max} = 295 nm). Compound **4b-c** exhibited similar absorption peaks around 330–350 nm, respectively. Upon excitation at 330 nm, **4a** exhibited a strong emission at 400 nm. Compound **4b-c** exhibited similar strong emission peaks around 400–420 nm upon excitation at the absorption peak wavelength around 330–350 nm, respectively. The absorption and emission spectra of **4a** are shown in Fig. 4 as representative cases. These compounds can also be regarded as fluorescent high-spin molecule precursors.

2.3. Cyclic voltammetry

Redox potentials of tetraaryl-1,3-phenylenediamines are important factor to predict the stability of the corresponding mono- and dicationic states. For example, compound **1** [2b,c,j], which gives very stable mono- and dicationic states, has the lowest oxidation potentials in a series of tetraaryl-1,3-phenylenediamines we have examined ($E_1^0 = 0.21$ V, $E_2^0 = 0.37$ V versus Fc/Fc^+). Upon cyclic voltammetry in *n*-butyronitrile with 0.1 M Bu_4NPF_6 as a

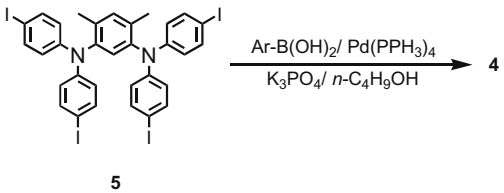


Fig. 3. Synthetic route of **4**.

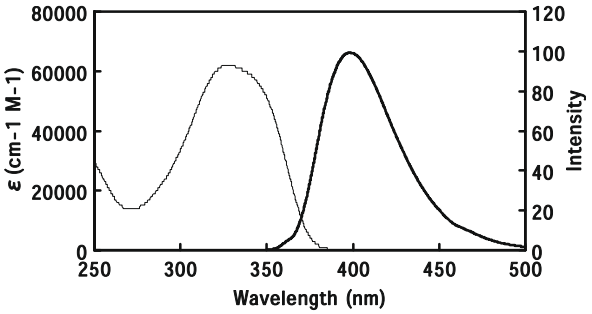


Fig. 4. Absorption (plain) and emission (bold) spectra of **4a** in THF.

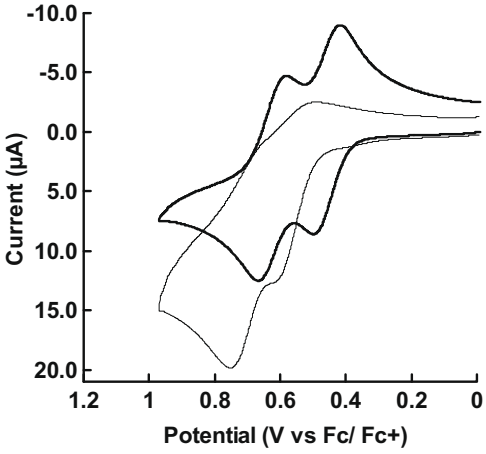


Fig. 5. Cyclic voltammograms of **3a** (plain) and **4a** (bold) in *n*-butyronitrile at ambient temperature.

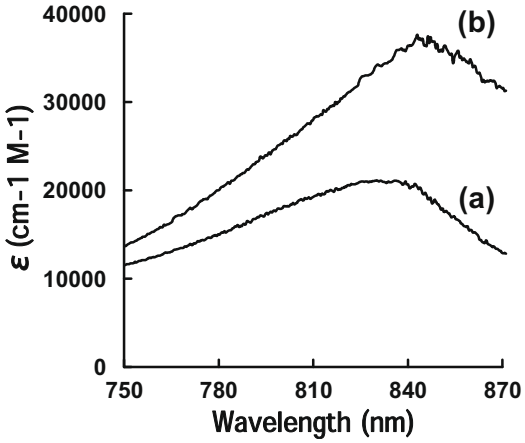


Fig. 6. Absorption spectra observed after mixing of an AN solution of 0.10 mM $TDBPA^{+\cdot}$ with an AN solution of (a) 0.10 mM and (b) 0.050 mM of **4a**.

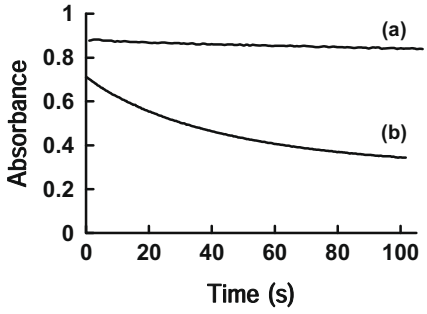


Fig. 7. Time profiles in the absorbance maximum observed after mixing of an AN solution of 0.10 mM $TDBPA^{+\bullet}$ with an AN solution of (a) 0.10 mM and (b) 0.050 mM of **4a**.

supporting electrolyte, compound **4a** showed two sets of reversible redox couples ($E_1^0 = 0.45$ V, $E_2^0 = 0.60$ V versus Fc/Fc^+), indicating stable mono- and dicationic states. The cyclic voltammograms of **3a** and **4a** are shown in Fig. 5 as representative cases. Similarly, compounds **4b** and **4c** exhibited similar reversible redox couples, respectively (**4b**: $E_1^0 = 0.42$ V, $E_2^0 = 0.59$ V versus Fc/Fc^+, **4c**: $E_1^0 = 0.37$ V, $E_2^0 = 0.52$ V versus Fc/Fc^+). Previously, we reported that compounds **3a–c** with acetylene moieties, give very unstable monocationic states, respectively. As we have expected, compounds **4a–c** without acetylene moieties, give stable mono- and dicationic states in the time scale of CV measurements. Direct introduction of four aryl groups endowed tetraaryl-1,3-phenylenediamine with high stability of the mono- and dicationic states.

2.4. Electron transfer stopped-flow (ETSF) measurements

In order to examine the absorption spectra of oxidized species of **4a–c**, ETSF measurements were conducted. The detail of the ETSF method was described previously [5,6]. The ETSF measurements were carried out in dehydrated acetonitrile (AN) as solvent at ambient temperature. In this study, tris (2,4-dibromophenyl) amine cation radical ($TDBPA^{+\cdot}$) [7] was employed. Compound **4a**, upon mixing with one equivalent of $TDBPA^{+\cdot}$, exhibited a broad absorption peak at 830 nm (Fig. 6), which is remarkably red-shifted in comparison with that of $\mathbf{1}^{+\cdot}$ (λ_{max} = 685 nm), and no decrease in the peak intensity was observed over 100 s, indicating the generation of the stable monocation $\mathbf{4a}^{+\cdot}$ (Fig. 7). The molar absorptivity (ε) of $\mathbf{4a}^{+\cdot}$ was determined to be $2.11 \times 10^4\ M^{-1}\ cm^{-1}$ at 830 nm.

Upon mixing with two equivalents of $TDBPA^{+\cdot}$, **4a** exhibited an absorption peak of the dication $\mathbf{4a}^{2+}$ at 846 nm. The ε value for $\mathbf{4a}^{2+}$ was $3.75 \times 10^4\ M^{-1}\ cm^{-1}$ at 846 nm (Fig. 6). The ratio of ε for the monocation:dication of **4a** was nearly 1:2 as expected. The peak gradually decreased over 40 s, indicating unstable dication $\mathbf{4a}^{2+}$ (Fig. 7). Compared to **3a** with phenylacetylene units, the stability

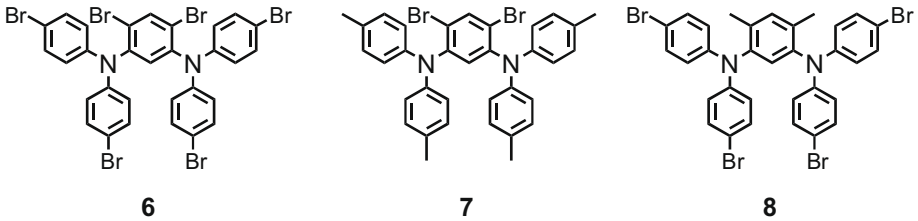


Fig. 8. Structures of **6–8**.

of the monocation $\mathbf{4a}^{+\cdot}$ was remarkably increased, whereas the dication $\mathbf{4a}^{2+}$ was still unstable. Cyclic voltammetry measurements showed **4b** and **4c** are easily oxidized than **4a**, thus, monocations, $\mathbf{4b}^{+\cdot}$ and $\mathbf{4c}^{+\cdot}$, are expected to be thermodynamically more stable than **4a**.

Surprisingly, similar ETSF measurements for **4b** and **4c** revealed that the monocations, $\mathbf{4b}^{+\cdot}$ and $\mathbf{4c}^{+\cdot}$, were less stable than $\mathbf{4a}^{+\cdot}$ ($\mathbf{4b}^{+\cdot}$; λ_{max} = 869 nm, $\mathbf{4c}^{+\cdot}$; λ_{max} = 876 nm). These monocations slowly decomposed over 30 s, respectively. Introduction of electrodonating groups is an effective strategy to stabilize the oxidized states as described above; however that is not the sole one. For example, we have systematically designed and synthesized three types of brominated tetraaryl-*m*-phenylenediamine (**6–8**) (Fig. 8). Cyclic voltammetry and ETSF measurements have revealed that only **6** and **7** give very stable dicationic states, i.e., the bromo groups on the central aromatic ring stabilize the dicationic states effectively. We are currently exploring effective substitution groups that can stabilize the mono- and dicationic states.

3. Conclusion

In conclusion, we have designed and successfully synthesized highly π-extended tetraaryl-1,3-phenylenediamines in excellent yields by Suzuki coupling. Direct introduction of four aryl groups endowed tetraaryl-1,3-phenylenediamine with fluorescent property. The ETSF measurements showed that **4a** gives the very stable monocation and fairly stable dication. The fluorescent property of $\mathbf{4a}^{+\cdot}$ is now under study. Unfortunately, **4b–c** gave less stable monocation radicals. Molecular designs and syntheses of novel photochemically or electrochemically active diamines derived from **5** by organometallic methods are also in progress.

References

[1] K. Itoh, M. Kinoshita (Eds.), Molecular Magnetism, New Magnetic Materials, Gordon & Breach, Inc., Amsterdam, 2000 (Kodansha as copublisher, Tokyo).
[2] (a) P.M. Lahti (Ed.), Magnetic Properties of Organic Materials, Marcel Dekker Inc., New York, 1999 (Chapter 9) and references therein;
(b) K. Sato, M. Yano, M. Furuichi, D. Shiomi, K. Abe, T. Takui, K. Itoh, A. Higuchi, K. Katuma, Y. Shirota, J. Am. Chem. Soc. 119 (1997) 6607;
(c) M. Yano, K. Sato, D. Shiomi, A. Ichimura, K. Abe, T. Takui, K. Itoh, Tetrahedron Lett. 37 (1996) 9207;
(d) K.R. Stickley, S.C. Blackstock, J. Am. Chem. Soc. 116 (1994) 11576;
(e) K.R. Stickley, S.C. Blackstock, Tetrahedron Lett. 36 (1995) 1585;
(f) K.R. Stickley, T.D. Selby, S.C. Blackstock, J. Org. Chem. 62 (1994) 448;
(g) T.D. Selby, S.C. Blackstock, J. Am. Chem Soc. 62 (1997) 448;
(h) A. Ito, H. Ino, K. Tanaka, K. Kanemoto, T. Kato, J. Org. Chem. 67 (2002) 491;
(i) M. Yano, Y. Ishida, K. Aoyama, M. Tatsumi, K. Sato, D. Shiomi, A. Ichimura, T. Takui, Synth. Met. 137 (2003) 1275;
(j) M. Yano, Y. Ishida, M. Tatsumi, K. Sato, D. Shiomi, M. Oyama, T. Takui, J. Phys. Chem. Solids 65 (2004) 733–736;
(k) M. Yano, Y. Nakanishi, K. Matsushita, M. Tatsumi, M. Oyama, K. Sato, T. Takui, Polyhedron 24 (2005) 2116;
(l) M. Yano, A. Fujiwara, M. Tatsumi, M. Oyama, K. Sato, T. Takui, Polyhedron 26 (2007) 2008;
(m) M. Yano, T. Furuya, M. Yonezawa, M. Tatsumi, M. Oyama, K. Sato, T. Takui, Polyhedron 24 (2005) 2121.
[3] (a) E.T. Seo, R.F. Nelson, J.M. Fritsch, L.S. Marcoux, D.W. Leedy, R.N. Adams, J. Am. Chem. Soc. 88 (1966) 3498;
(b) R.F. Nelson, R.N. Adams, J. Am. Chem. Soc. 90 (1968) 3925.
[4] N. Miyaura, A. Suzuki, Chem. Rev. 95 (1995) 2457.
[5] M. Oyama, T. Higuchi, S. Okazaki, J. Chem. Soc. Perkin Trans. 2 (2001) 1287.
[6] M. Oyama, J. Matsui, H. Park, Chem. Commun. (2002) 604.
[7] TDBPA was synthesized by WAKO Pure Chemicals Ltd. after receiving our special order. See also Ref. [6].

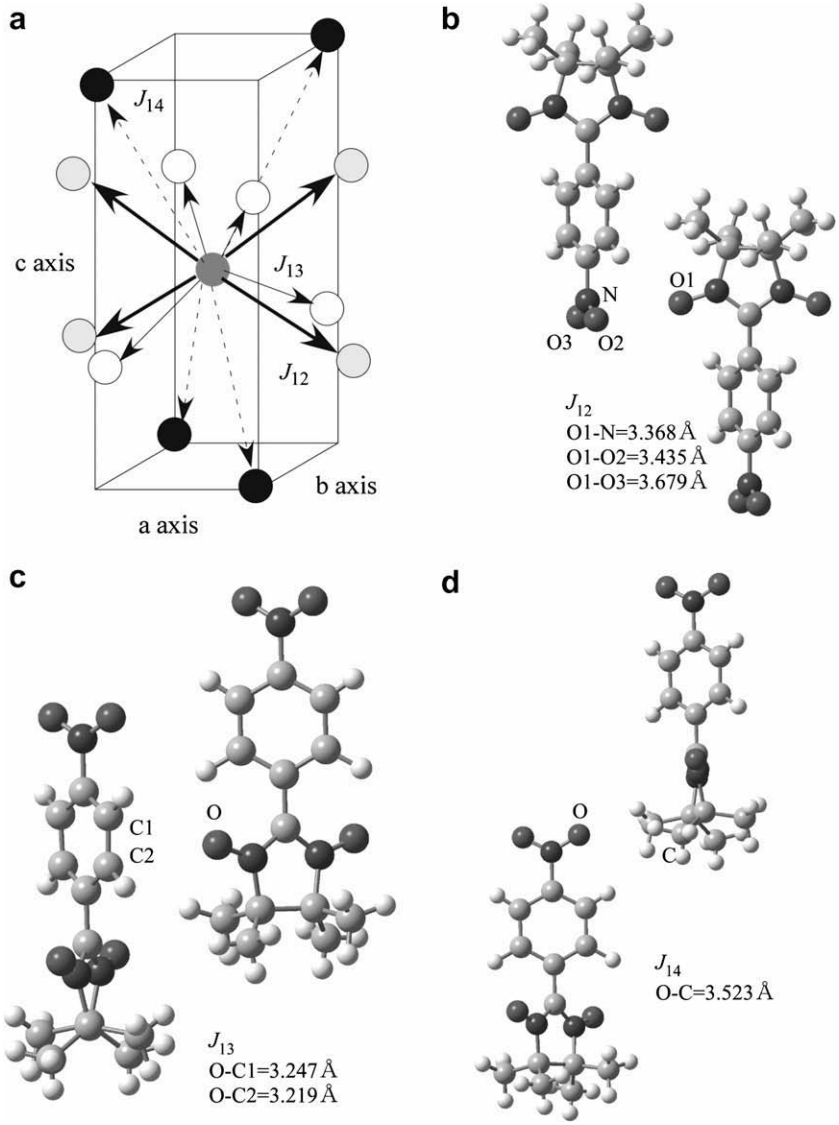


Fig. 1. (a) The crystal structure of the β-phase *p*-NPNN with the Fdd2 space symmetry. J_{1n} (n = 2–4) denotes the effective exchange interactions of (b) J_{12} type intermolecular interaction in the *ac* plane, (c) J_{13} type intermolecular interaction and (d) J_{14} type intermolecular interaction.

The ferromagnetic phase transition temperature is calculated by the Langevin–Weiss mean-field theory in combination with the calculated J values as shown [13–15]:

$$k_B T_c = \frac{2}{3} S(S+1) \sum J_{ij} \quad (3)$$

Moreover, in order to detail analysis of the magnetic transition temperatures of β- and γ-phase *p*-NPNN crystals, Monte Carlo ising spin simulation was also carried out. In these simulations, $12 \times 12 \times 12$ lattice with a periodic boundary condition was used. Especially, Wolff type cluster flipping method was applied for γ-phase *p*-NPNN model system [16].

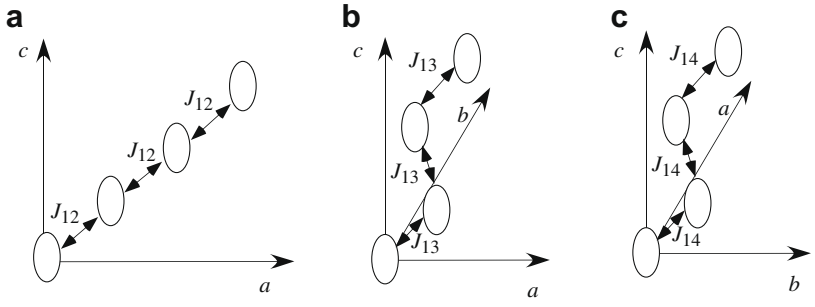


Fig. 2. The oligomers in the β-phase *p*-NPNN of (a) J_{12} type interaction, (b) J_{13} type interaction and (c) J_{14} type interaction.

Table 1
Total energies (a.u.) and effective exchange integrals J_{1n} (cm^{-1}) of the cluster of β-phase *p*-NPNN.

Type	Cluster	Spin state	Energy[a], a.u.	$\langle S^2\rangle$[a]	J_{ab}, cm^{-1}
J_{12}	dimer	singlet	−1939.41160932	1.1126	
		triplet	−1939.41161045	2.1126	0.248
	trimer	doublet	−2909.11754918	1.9168	
		quartet	−2909.11755151	3.9180	0.256
	tetramer	singlet	−3878.82351329	2.2234	
		quintet	−3878.82351663	6.2234	0.254
J_{13}	dimer	singlet	−1939.41265716	1.1120	
		triplet	−1939.41266013	2.1119	0.652
	trimer	doublet	−2909.12012582	1.9168	
		quartet	−2909.12013082	3.9167	0.549
	tetramer	singlet	−3878.82754989	2.2217	
		quintet	−3878.82755672	6.2215	0.519
J_{14}	dimer	singlet	−1939.41134569	1.1151	
		triplet	−1939.41134569	2.1151	0.000
	trimer	doublet	−2909.11815251	1.9231	
		quartet	−2909.11815251	3.9231	0.000
	tetramer	singlet	−3878.82505972	2.2311	
		quintet	−3878.82505971	6.2311	−0.001

[a] UB3LYP/6-31G**.

3. Results and discussion

3.1. β-Phase p-NPNN

Fig. 1a illustrates the crystal structure of the β-phase *p*-NPNN with the Fdd2 space symmetry. Fig. 1a shows 12 nearest-neighbor p-NPNN molecules exist around the central *p*-NPNN. They are classified into three groups, which are denoted by the white, shaded and black circles. The effective exchange integrals between the central *p*-NPNN and the nearest neighbors in each group are equivalent and therefore one of them is explicitly defined as J_{1n} (n = 2–4) without loss of generality as shown in Fig. 1. Additionally, we have also examined the exchange interactions in the extended oligomers as illustrated in Fig. 2 in order to clarify the reliability of the nearest-neighbor approximation. The effective exchange integrals in the oligomers illustrated in Fig. 2a–c named J_{12}, J_{13}, and J_{14}, respectively. The Table 1 summarizes the total energies, $\langle S^2\rangle$ and J_{1n} values for clusters of β-phase *p*-NPNN by UB3LYP method. The $\langle S^2\rangle$ values of the dimers should be about 1.0 and 2.0, respectively, for the singlet and triplet broken symmetry solutions of the pure diradicals without spin polarizations of nonradical orbital

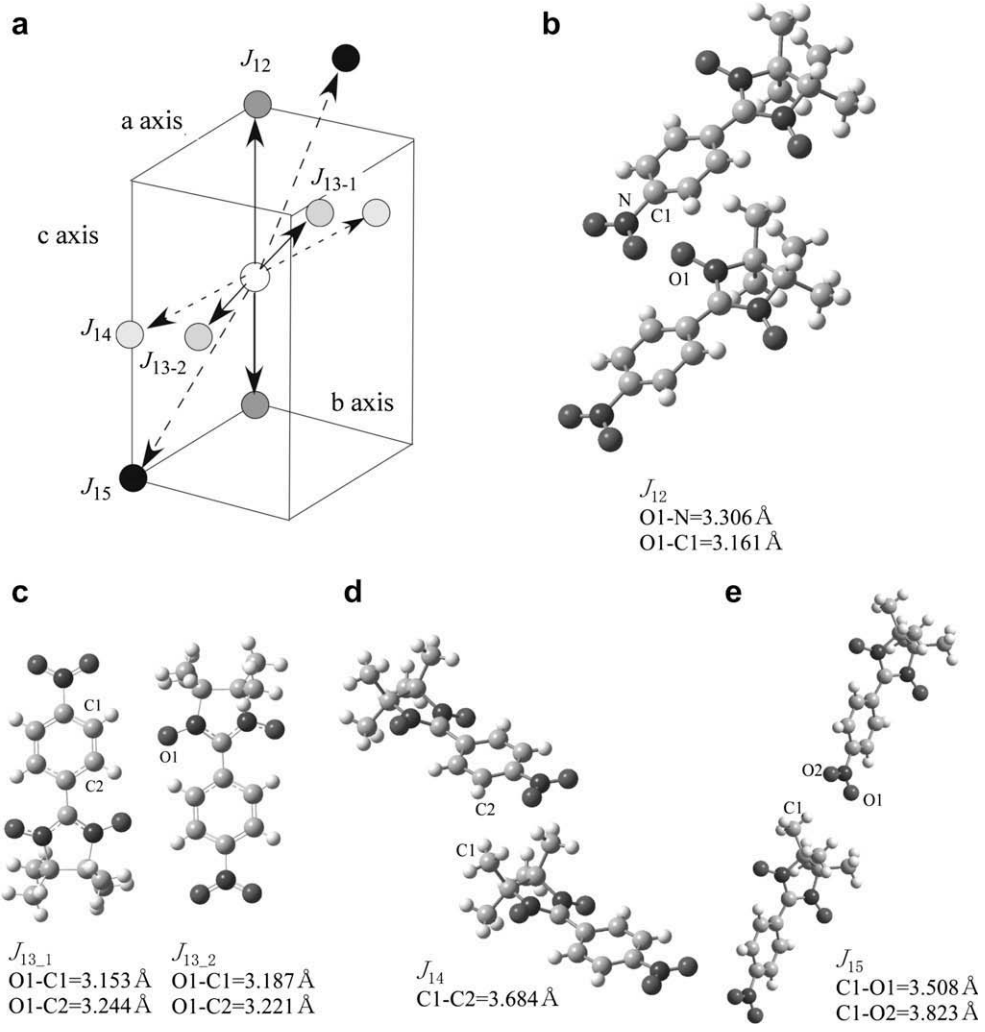


Fig. 3. (a) The crystal structure of the γ-phase *p*-NPNN with the $P\bar{1}$ space symmetry. J_{1n} (n = 2, 3_1, 3_2, 4, 5) denotes the effective exchange interactions, of (b) J_{12} type intermolecular interaction in the *c* direction of the γ-phase, (c) J_{13_1} and J_{13_2} type intermolecular interactions in the *bc* plane, (d) J_{14} type intermolecular interaction and (e) J_{15} type intermolecular interaction.

Table 2
Total energies (a.u.) and effective exchange integrals J_{1n} (cm^{-1}) of the cluster of γ-phase *p*-NPNN.

Type	Cluster	Spin state	Energy[a], a.u.	$\langle S^2\rangle$[a]	J_{ab}, cm^{-1}
J_{12}	dimer	singlet	−1939.38978705	1.1200	
		triplet	−1939.38980188	2.1202	3.254
J_{13_1}	dimer	singlet	−1939.47722688	1.1234	
		triplet	−1939.47722817	2.1234	0.283
J_{13_2}	dimer	singlet	−1939.47604225	1.1250	
		triplet	−1939.47604727	2.1251	1.102
J_{14}	dimer	singlet	−1939.38581447	1.1262	
		triplet	−1939.38581436	2.1262	−0.024
J_{15}	dimer	singlet	−1939.41300526	1.1293	
		triplet	−1939.41300530	2.1293	0.009

[a] UB3LYP/6-31G**.

pairs. The deviations of $\langle S^2\rangle$ values from the normal $\langle S^2\rangle$ values of the singlet and triplet broken symmetry solutions are about 0.1 for both states of the *p*-NPNN dimer, indicating the spin polarization effect. From Table 1, the J_{12} values for the clusters in Fig. 1b were calculated to be in the range 0.248–0.254 cm^{-1} at the experimental geometry. From the crystal structure in Fig. 1a, it is concluded that the ferromagnetic interaction is operative within the *ac* plane in accord with the experiment. The effective exchange integral (J_{13}) for the clusters in Fig. 1c is ferromagnetic in the range 0.652–0.519 cm^{-1}. From the spin density population analysis, it was found that the so-called McConnell-type spin density-product term between O–C1 and O–C2 atomic pairs are positive and negative, respectively. The net interaction after the mutual cancellation remains ferromagnetic in this stacking mode. The J_{14} values for clusters in Fig. 1d are almost zero. Therefore, the net interplane magnetic interaction is ferromagnetic. These results indicate the adequacy of the quasi three-dimensional Heisenberg-type model. In the next, UB2LYP (0.35) method was also applied to the β-phase *p*-NPNN dimmers. The obtained J_{1n} values were summarized in Table 6. The calculated J_{12} and J_{13} values also show the same signs with those using UB3LYP while the calculated J_{13} value by UB2LYP (0.35) is much smaller than that by UB3LYP. On the other hand, the J_{14} value by UB2LYP (0.35) has negative while that by UB3LYP is zero. However, the three-dimensional magnetic order in the β-phase *p*-NPNN crystal was ferromagnetic as the absolute values of J_{12} and J_{13} are larger than that of J_{14}. Therefore, it could be concluded that the calculation results by both hybrid-DFT methods predict the long-range three-dimensional ferromagnetic ordering in the β-phase *p*-NPNN crystal.

Then the ferromagnetic transition temperatures (T_c) calculated by Langevin–Weiss model and Monte Carlo simulation using the *J* values calculate by UB3LYP are 2.2 and 1.7 K, respectively. These values are slightly larger than the experimental value (T_c = 0.60 K). On the other hand, the ferromagnetic transition temperatures (T_c) calculated by Monte Carlo simulation using the *J* values calculate by UB2LYP (0.35) are 0.7 K. The obtained ferromagnetic transition temperature is much closer to the experimental result. Therefore, it could be concluded that the obtained results are in qualitatively agreement with the experimental results.

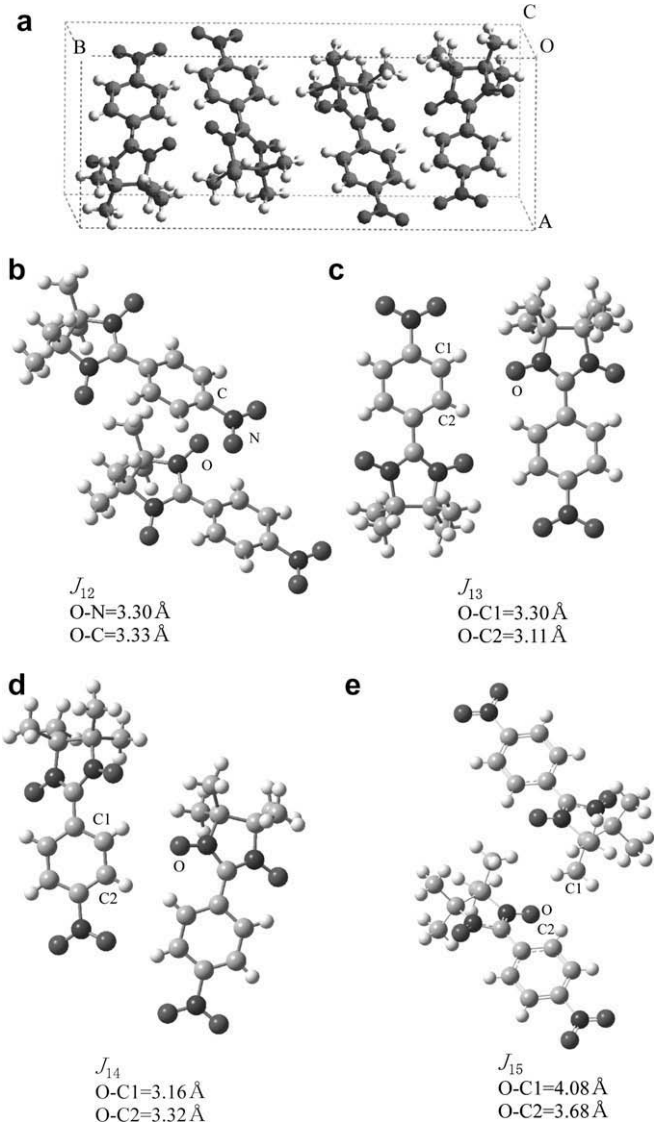


Fig. 4. (a) The crystal structure of the δ-phase *p*-NPNN with the $P2_1/c$ space symmetry. J_{1n} (n = 2–5) denotes the effective exchange interactions, of (b) J_{12} type intermolecular interaction, (c) J_{13} type intermolecular interaction, (d) J_{14} type intermolecular interaction and (e) J_{15} type intermolecular interaction.

3.2. γ-Phase p-NPNN crystal

Fig. 3a shows the schematic diagram of the crystal structure of the γ-phase *p*-NPNN with $P\bar{1}$ space symmetry. From Fig. 3a, there are eight nearest-neighbor *p*-NPNN molecules in this monoclinic crystal. According to this space symmetry, the effective exchange interactions among these molecules are classified into five different types which are defined by J_{12}, J_{13_1}, J_{13_2}, J_{14} and J_{15} as shown in Fig. 3b–e illustrate intermolecular interactions which are responsible for the above mentioned *J* values. UB3LYP calculations of the dimmers were carried out to examine the *J* values. Table 2 summarizes the total energies, $\langle S^2\rangle$, and *J* values. The deviations of the $\langle S^2\rangle$ values form the normal values are about 0.1 for both states of the *p*-NPNN dimer. This tendency is similar to the results of β-phase *p*-NPNN model clusters. The effective exchange integral

Table 3
The calculated magnetic phase transition temperatures for β- and γ-phase *p*-NPNN.

Crystal	Phase transition	Method		
		LW[a]/K	MC[b]/K	Exp./K
β-Phase	ferromagnetic	2.2	1.7 (0.7)[c]	0.60
γ-Phase	antiferromagnetic	5.7	2.0 (2.2)[c]	0.65

[a] Langevin–Weiss model.
[b] Monte Carlo simulation.
[c] The phase transition temperatures estimated by *J* values calculated by UB2LYP (0.35) are in parentheses.

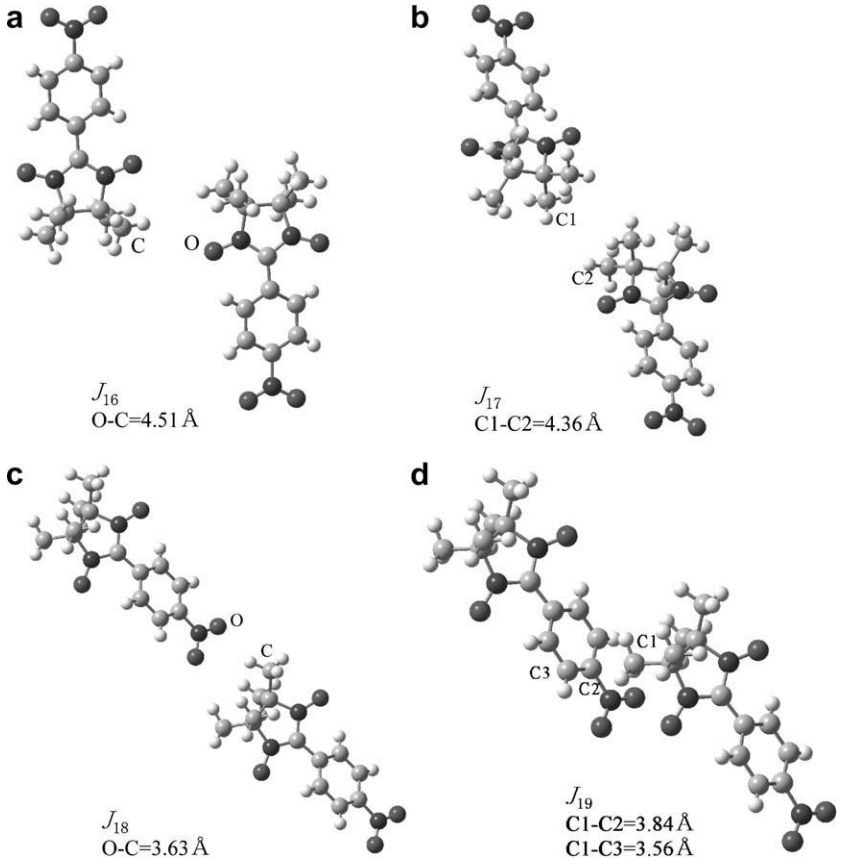


Fig. 5. (a) J_{1n} (n = 6–9) denotes the effective exchange interactions, of (b) J_{16} type intermolecular interaction, (c) J_{17} type intermolecular interactions, (d) J_{18} type intermolecular interaction and (e) J_{19} type intermolecular interaction.

(J_{12}) between the spins on *p*-NPNN molecules shown in Fig. 3b is positive (ferromagnetic) and is the largest in magnitude among the calculated J values in Table 2. The oxygen atom (O1) of the nitronyl nitroxide group of *p*-NPNN interacts with the C1 of its nearest-neighbor *p*-NPNN in the *bc* plane, as illustrated in Fig. 3b. Judging from the spin density analysis, the McConnell-type spin-density-product term between the O1–C4 pair should be negative and the resulting effective exchange integral is positive (ferromagnetic). Consequently, the through-space interaction gives rise to a parallel spin alignment of the SOMO spins via the spin polarization mechanism.

Fig. 3c illustrates the neighboring dimer of γ-phase *p*-NPNN depicted as the J_{13} type interaction in Fig. 3a. As the geometries of these dimers in Fig. 3a are slightly different, they named J_{13_1} and J_{13_2} type interactions, respectively. The sign of J_{13_1} and J_{13_2} are also positive. The oxygen atom (O1) of the nitronyl nitroxide group of *p*-NPNN interacts with C1 and C2 of its nearest neighbor in the *bc* plane. From the populations of the spin densities on these atoms, the McConnell-type spin-density-product terms between the O1–C2 pair and between the O1–C3 pair should be ferromagnetic and antiferromagnetic, respectively. The net through-space interaction is positive (ferromagnetic), giving rise to the parallel spin alignment of the SOMO spins via the spin polarization mechanism. Consequently, the two-dimensional ferromagnetic magnetic interactions would be presented by the J_{12} and J_{13} type stacking modes as shown in Fig. 7a.

Fig. 3d and e shows the J_{14} and J_{15} type interactions. The sign of J_{14} is calculated to be negative by the UB3LYP method, whereas that of J_{15} is positive. The magnitude of the former is a little larger than the latter, giving rise to the net antiferromagnetic interplane interaction the γ-phase. Therefore, the γ-phase crystal should exhibit an antiferromagnetic long-range order at a low temperature as the magnetic interaction between the neighboring two-dimensional ferromagnetic layers is antiferromagnetic.

In the next, UB2LYP (0.35) method was also applied to the γ-phase *p*-NPNN dimmers. The obtained J_{1n} values were summarized in Table 6. The calculated J values by UB2LYP (0.35) show the same signs and the similar absolute values with those using UB3LYP. Consequently, the calculation results by both HDFT methods suggest that the γ-phase crystal would exhibit an antiferromagnetic long-range order at a low temperature.

The Néel temperature of the γ-phase of *p*-NPNN can be estimated by using the J values calculated by the UB3LYP method:

$$k_B T_N = \frac{2}{3} S(S+1)(2J_{12} + J_{13_1} + J_{13_2} + 2|J_{14} + J_{15}|)$$

The calculated T_N is 5.7 K which is about 5 K larger than the experimental value (0.65 K). This is due to the low-dimensional antiferromagnetic interactions in the γ-phase *p*-NPNN crystal. Therefore, Wolff type Monte Carlo ising spin simulation was carried out in order to consider the effect of the low-dimensional magnetic interactions in the γ-phase *p*-NPNN. The Néel temperature is estimated to be 2.0 K by Monte Carlo simulation using the J values calculated by the UB3LYP method. The deviation from the experimental value was greatly reduced as the calculated T_N is about 1.3 K higher than the experimental value. The Néel temperature estimated by Monte Carlo simulation using the J values calculated by UB2LYP (0.35) method is almost same as the obtained J values are not so different from those by UB3LYP method. From the calculation results of the Néel temperature, it could be

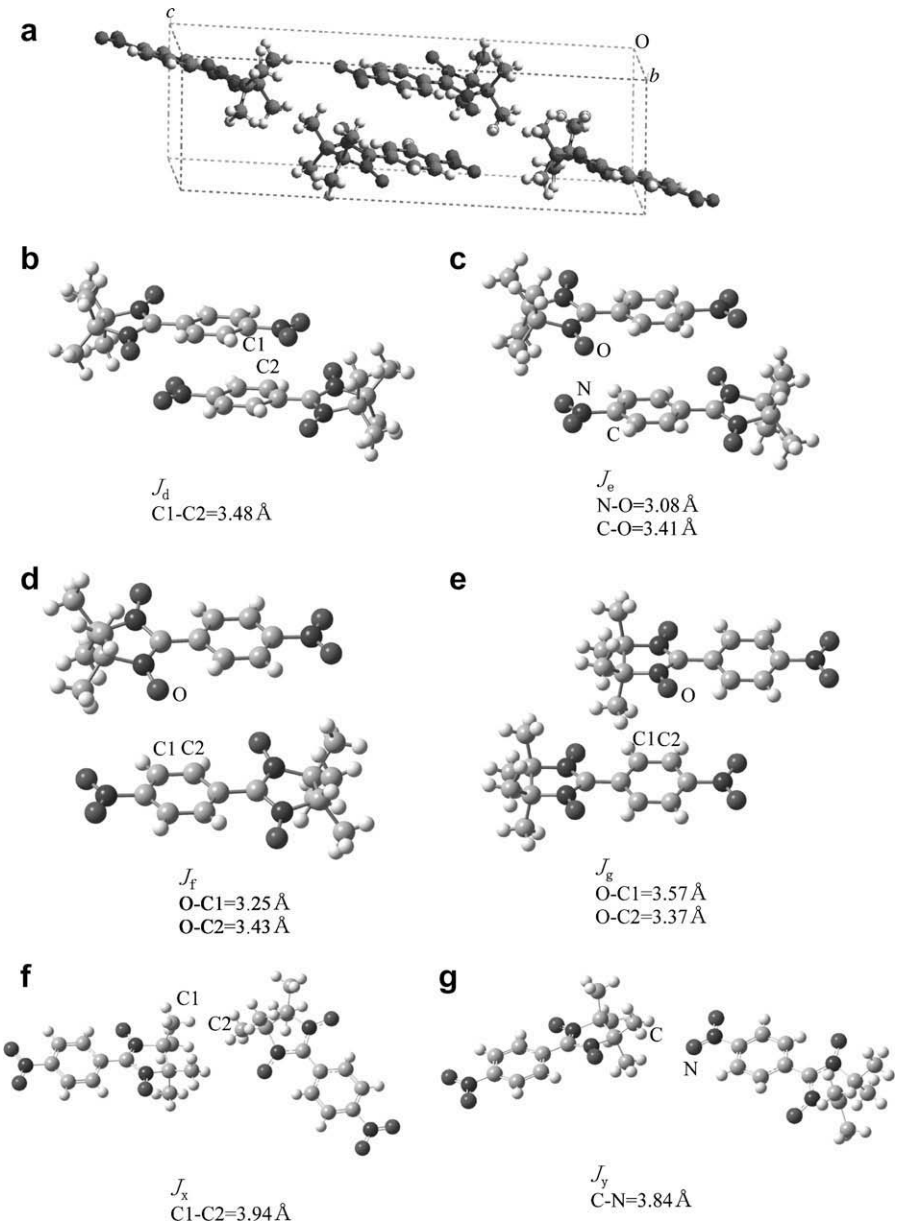


Fig. 6. (a) The crystal structure of the α-phase *p*-NPNN with the $P2_1/c$ space symmetry. J_{1n} (n = 2–7) denotes the effective exchange interactions, of (b) J_{12} type intermolecular interaction, (c) J_{13} type intermolecular interaction, (d) J_{14} type intermolecular interaction, (e) J_{15} type intermolecular interaction, (f) J_{16} type intermolecular interaction and (g) J_{17} type intermolecular interaction.

presumed that the magnetic interaction of J_{12} and J_{13} type model clusters were overestimated. This is due to the overestimation of the spin polarization on the phenyl group in *p*-NPNN molecule as the inclusion of Hartree Fock exchange integral into the hybrid E_{ec} functional enhances this effect.

3.3. δ- and α-phase p-NPNN crystals

The space symmetry of the δ-phase *p*-NPNN crystal is $P2_1/c$. The crystal structure of δ-phase *p*-NPNN was displayed in Fig. 4a. In this phase, there is a head-to-tail NO···NO_2 stacking mode running along the *c*-axis with the translational symmetry as shown in Fig. 4b. Other stacking modes are the side-by-side intermolecular interactions between the NO···phenyl groups illustrated in Fig. 4c and e. In the δ-phase *p*-NPNN, another kind of NO···phenyl interaction is found as a result of the *c*-glide symmetry of the δ-phase. This stacking mode is also depicted in Fig. 4d. Therefore, these structures suggest that there is a relatively strong 2D intermolecular network in the δ-phase and these 2D networks are connected with weak methyl···methyl interactions.

The calculations of the magnetic interactions between the neighboring *p*-NPNN dimers in the δ-phase depicted in Fig. 4 were carried out by UB3LYP method. The obtained results are summarized in Table 3. The J_{12} and J_{14} type interactions depicted in Fig. 4a and c have relatively large positive values (ferromagnetic) while J_{13} and J_{15} have smaller positive values than J_{12} and J_{13} values. Consequently, the through-space interaction in this 2D layer gives rise to parallel spin alignment of the SOMO spin as shown in Fig. 7b. These calculation results are in qualitative agreement with the experimental results for the mean-field Curie–Weiss behavior of the χ_p^{-1} versus T plot of δ-phase *p*-NPNN. In the next, magnetic interaction between the ferromagnetic 2D layers were examined. The magnetic interactions between the neighboring *p*-NPNN molecules are classified into four models. These models depicted in Fig. 5

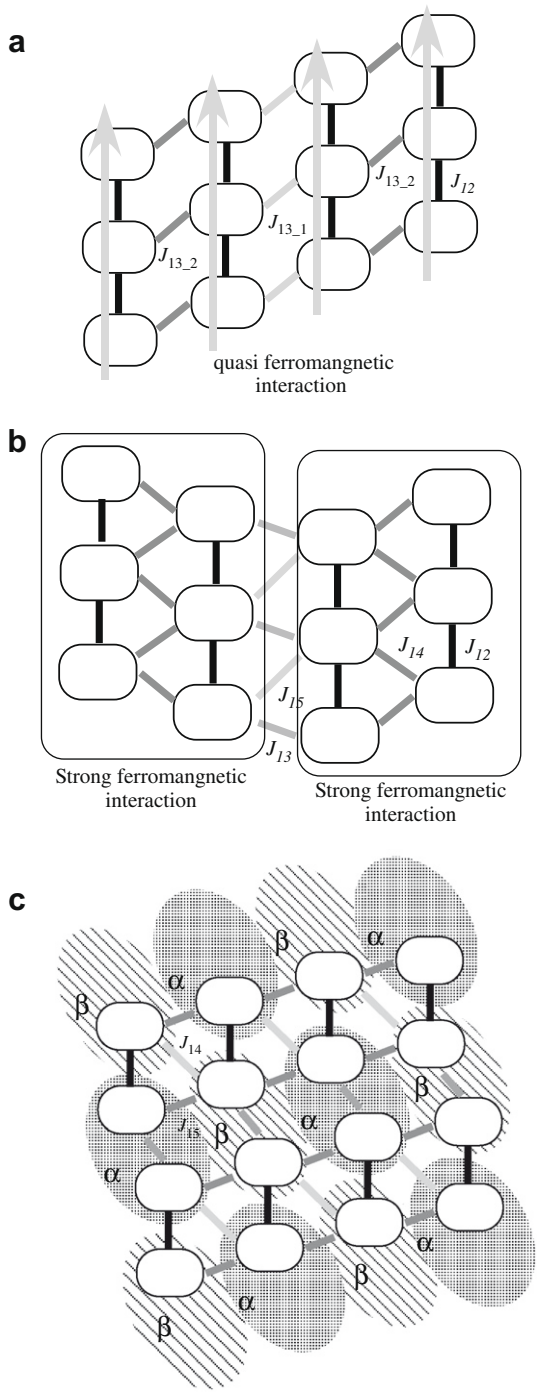


Fig. 7. The two-dimensional magnetic interactions in (a) γ-phase *p*-NPNN, (b) δ-phase *p*-NPNN and (c) α-phase *p*-NPNN.

were also examined by UB3LYP method. The obtained *J* values are also summarized in Table 3. As these dimers are connected with weak methyl. . .methyl interactions, the absolute values of the obtained *J* values are much smaller than those of the intralayer *J* values in the δ-phase. From the calculation results, it was found that there are three negative *J* values and one positive *J* value between the neighboring 2D layers. As the summation of these four *J* values is negative, it seems that the magnetic interaction between the 2D layers is negative (antiferromagnetic).

In the next, α-phase *p*-NPNN was investigated. The space symmetry of the α-phase *p*-NPNN crystals is also $P2_1/c$. The crystal structure is depicted in Fig. 6a. The figures depicted in Fig. 6

Table 4
Total energies (a.u.) and effective exchange integrals J_{1n} (cm^{-1}) of the cluster of δ-phase *p*-NPNN.

Type	Cluster	Spin state	Energy[a], a.u.	$\langle S^2\rangle$[a]	J_{ab}, cm^{-1}
J_{12}	dimer	singlet	−1939.53286598	1.1224	
		triplet	−1939.53286990	2.1224	0.860
J_{13}	dimer	singlet	−1939.54180269	1.1218	
		triplet	−1939.54180362	2.1218	0.204
J_{14}	dimer	singlet	−1939.53231528	1.1239	
		triplet	−1939.53231941	2.1239	0.906
J_{15}	dimer	singlet	−1939.53037057	1.1266	
		triplet	−1939.53037165	2.1267	0.237
J_{16}	dimer	singlet	−1939.53128992	1.1263	
		triplet	−1939.53128991	2.1263	−0.002
J_{17}	dimer	singlet	−1939.52882462	1.1263	
		triplet	−1939.52882456	2.1263	−0.013
J_{18}	dimer	singlet	−1939.53725029	1.1289	
		triplet	−1939.53725034	2.1289	0.011
J_{19}	dimer	singlet	−1939.52929229	1.1275	
		triplet	−1939.52929203	2.1275	−0.057

[a] UB3LYP/6-31G**.

Table 5
Total energies (a.u.) and effective exchange integrals J_{1n} (cm^{-1}) of the cluster of α-phase *p*-NPNN.

Type	Cluster	Spin state	Energy[a], a.u.	$\langle S^2\rangle$[a]	J_{ab}, cm^{-1}
J_{12}	dimer	singlet	−1938.96274661	1.1393	
		triplet	−1938.96273659	2.1390	−2.200
J_{13}	dimer	singlet	−1938.96959515	1.1323	
		triplet	−1938.96962221	2.1326	5.937
J_{14}	dimer	singlet	−1938.96402157	1.1305	
		triplet	−1938.96402116	2.1304	−0.090
J_{15}	dimer	singlet	−1938.96140361	1.1282	
		triplet	−1938.96140317	2.1282	−0.097
J_{16}	dimer	singlet	−1938.95558309	1.1326	
		triplet	−1938.95558302	2.1326	−0.015

[a] UB3LYP/6-31G**.

Table 6
Effective exchange integrals *J* (cm^{-1}) of the model dimers of β- and γ-phase *p*-NPNN.

β-Phase		γ-Phase	
Type	J_{ab}[a], cm^{-1}	Type	J_{ab}[a], cm^{-1}
J_{12}	0.266	J_{12}	3.559
J_{13}	0.050	J_{13-n}	0.202
J_{14}	−0.007	J_{13-f}	1.099
		J_{14}	−0.072
		J_{15}	0.002

[a] UB2LYP (0.35)/6-31G**.

suggest that the NO···NO_2 and NO···phenyl interactions are the important stacking modes in the α-phase as the distance between two molecules are relatively close. The crystal structure of the α-phase *p*-NPNN by X-ray analysis shows that two molecular layers, which are crystallographically equivalent but have different orientations due to the *c*-glide or to the twofold screw symmetry [6]. The layer consists of the twofold stacking along the *a*-axis. The stack comprises two types of intermolecular stacking modes. The one is face-to-face phenyl–phenyl staking depicted in Fig. 6b. The other one is NO···NO_2 stacking mode depicted in Fig. 4c. There are also two different types of intermolecular contact between the above mentioned stack. They are depicted in Fig. 4d and e. The schematic view of the molecular layer which consists of these

intermolecular contacts is illustrated in Fig. 7c. This molecular layer also interacts with the neighboring molecular layers with the intermolecular contacts. They are depicted in Fig. 6e and f.

As shown in Fig. 6, the magnetic interactions between the neighboring *p*-NPNN molecules are classified into six models. For these model dimers, the UB3LYP calculations were also carried out. The obtained results are summarized in Table 4. The calculation results indicate that there are two large effective exchange integrals with different signs (J_{12} and J_{13}) and two relatively small negative exchange integrals (J_{14} and J_{15}: ~ -0.1 cm^{-1}). The two-dimensional layer consist of the above mentioned four J values are antiferromagnetically ordered as shown in Fig. 7c. These calculation results are in qualitative agreement with the experimental results for the mean-field Curie–Weiss behavior of the χ_p^{-1} versus T plot of α-phase *p*-NPNN. Additionally, it seems that the magnetic interaction between the neighboring two-dimensional layers in the crystal is antiferromagnetic as all the J values (J_{16} and J_{17}) for the interactions between the neighboring layers are negative. Therefore, the calculation results suggest that the three-dimensional antiferromagnetic ordering would be achieved (Table 5).

The computations of *p*-NPNN clusters with their α- and δ-phase crystal geometries suggest three-dimensional antiferromagnetic interactions, which are crucial for the occurrence of the long-range magnetic order in the Heisenberg model. However, such a long-range magnetic order was not observed in the real α- and δ-phases of *p*-NPNN. There are two possibilities to explain this discrepancy. One is the nonuniformity of their crystal structures due to the experimental conditions and the other is a lack of the computational accuracy. Especially, there is a tendency that the absolute values of the J values calculated by HDFT method, such as B3LYP, are relatively overestimated those of the experimental J values in the view point of the computational accuracy as the calculated magnetic phase transition temperature for β- and γ-phases *p*-NPNN are larger than those of the experimental values. Therefore, further investigation using much more accurate post-Hartree Fock calculations for the small J values ($|J| < 0.1$ cm^{-1}) that are closely related to the occurrence of the three-dimensional long-range magnetic order in the *p*-NPNN crystals must be needed. The elucidation of the weak magnetic interactions in the *p*-NPNN crystals would be the next task as it is currently impossible to examine the weak magnetic interactions in the *p*-NPNN crystals by using much more accurate post-Hartree Fock methods.

4. Conclusions

The present theoretical calculations have revealed theoretical explanations of the organic ferromagnetism observed for the β-phase of *p*-NPNN and the organic antiferromangnetism observed for the γ-phase of *p*-NPNN. For the α- and δ-phases of *p*-NPNN, our calculation results are in qualitative agreement with the experimental results for the mean-field Curie–Weiss behavior of the χ_p^{-1} versus T plots of their crystals. However, there is a discrepancy between the obtained calculation results and the experimental results for the α- and δ-phases of *p*-NPNN in the view point of the occurrence of the three-dimensional long-range magnetic orders. These results suggest the necessity of the much more accurate post-Hartree Fock calculations for the investigation of the weak magnetic interactions ($|J| < 0.1$ cm^{-1}).

Acknowledgment

This work has been supported by a Grant-in-Aid for Scientific Research on Priority Areas from the Ministry of Education, Culture, Sports, Science and Technology, Japan.

References

[1] M. Kinoshita, Philos. Trans. R. Soc. London, Ser. A 357 (1999) 2855.
[2] M. Kinosita, Molecular magnetism: new magnetic materials, in: K. Itoh, M. Kinosita (Eds.), Gordon and Breach Science Publishers and Kodansha Ltd., Tokyo, 2000 (Chapter 1 and Sections 4.2 and 4.3).
[3] M. Kinoshita, Jpn. J. Appl. Phys. 33 (1994) 5718.
[4] M. Tamura, Y. Nakazawa, D. Shiomi, K. Nozawa, Y. Hosokoshi, M. Ishikawa, M. Takahashi, M. Kinoshita, Chem. Phys. Lett. 186 (1991) 401.
[5] Y. Nakazawa, M. Tamura, N. Shirakawa, D. Shiomi, M. Ishikawa, M. Takahashi, M. Kinoshita, Phys. Rev. B 46 (1992) 8906.
[6] M. Tamura, Y. Hosokoshi, D. Shiomi, M. Kinoshita, Y. Nakazawa, M. Ishikawa, H. Sawa, T. Kitazawa, A. Eguchi, Y. Nishio, K. Kajita, J. Phys. Soc. Jpn. 72 (2003) 1735.
[7] K. Yamaguchi, H. Fukui, T. Fueno, Chem. Lett. (1986) 625.
[8] K. Yamaguchi, T. Fueno, Chem. Phys. Lett. 159 (1989) 465.
[9] K. Yamaguchi, H. Namimoto, T. Fueno, Mol. Cryst. Liq. Cryst. 176 (1989) 151.
[10] M. Okumura, K. Yamauchi, M. Nakano, W. Mori, Chem. Phys. Lett. 207 (1993) 1.
[11] M. Okumura, K. Takada, J. Maki, T. Noro, W. Mori, K. Yamaguchi, Mol. Cryst. Liq. Cryst. 233 (1993) 41.
[12] M. Okumura, W. Mori, K. Yamguchi, Chem. Phys. Lett. 219 (1994) 36.
[13] M.P. Langevin, J. Phys. 4 (1905) 678.
[14] P. Weiss, J. Phys. Radium 4 (1907) 661.
[15] L. Néel, Ann. Phys. 17 (8) (1932) 5.
[16] U. Wolff, Phys. Rev. Lett. 62 (1989) 759.

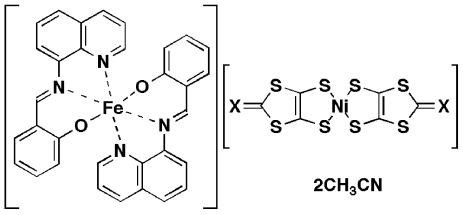


Fig. 1. Molecular structures of $[Fe(qsal)_2][Ni(dmise)_2] \cdot 2CH_3CN$ **1** (X = Se) and $[Fe(qsal)_2][Ni(dmit)_2] \cdot 2CH_3CN$ **2** (X = S).

droxy-1-naphtaldimine], demonstrated an almost complete spin transition between the low-spin (LS) and high-spin (HS) states, which is coupled with not only an electrical conducting modulation but also a uniaxial crystal lattice deformation [13]. The crystal structures before and after a spin conversion revealed that the anisotropic intermolecular $\pi-\pi$ interactions between the SCO cations as well as the change in volume of an SCO cation play an key role in the electrical conducting modulation. These results clearly indicate the importance of supramolecular interactions and their dimensionality.

It is well-known for large elastic contribution of lattice and molecular vibration for an SCO behavior. The modulation of the molecular size and electronic state by substitution gives an opportunity to clarify the mechanism of a spin transition of an SCO complex. In the further efforts to develop a new SCO materials, we have focused on $[Fe(qsal)_2][Ni(dmit)_2]\cdot 2CH_3CN$ **2**, which was the precursor of an SCO molecular conductor and showed a cooperative but irreversible spin transition [11]. In this paper we will disclose the magnetic properties and the crystal structures of the selenium analogue of **2**, namely, $[Fe(qsal)_2][Ni(dmise)_2]\cdot 2CH_3CN$ **1** (Fig. 1) and discuss the importance of intermolecular interactions for a cooperative spin transition.

2. Experimental

All chemicals were purchased and used without further purification. $[Fe(qsal)_2]Cl \cdot 1.5H_2O$ [14] and $TBA[Ni(dmise)_2]$ [15] were prepared according to the procedure of the previous literatures.

2.1. Synthesis of $[Fe(qsal)_2][Ni(dmise)_2] \cdot 2CH_3CN$ 1

The complex **1** was prepared by slow diffusion methods. An H-type glass cell where one arm placed $[Fe(qsal)_2]Cl \cdot 1.5H_2O$ (20 mg) and the other arm placed $TBA[Ni(dmise)_2]$ (25 mg) was slowly filled with acetonitrile (40 ml). Black prism crystals were grown within two weeks. The composition of **1** was determined by microanalysis.

Anal. Calc. for $C_{42}H_{28}N_6O_2FeNiS_8Se_2$: C, 42.83; H, 2.40; N, 7.14. Found: C, 42.70; H, 2.66; N, 6.96%.

2.2. Magnetic data collections

Variable temperature DC magnetic susceptibilities of polycrystalline samples (20 mg) were measured on a Quantum Design MPMS XL magnetometer with a field of 0.5 T and a scan speed of 2 K min^{-1} in the temperature range of 2–300 K.

2.3. X-ray data collections and refinement

A black prism crystal of **1** having approximate dimensions of $0.15 \times 0.10 \times 0.08$ mm was mounted in a nylon loop. All measurements were made on a Rigaku Mercury CCD area detector with graphite monochromated Mo Kα radiation generated by Rigaku CMF007 optics. The data were collected to a maximum 2θ value of 55.0°. A total of 720 oscillation images were collected. Data were collected and processed using CrystalClear (Rigaku). A numerical absorption correction was applied which resulted in transmission factors ranging from 0.617 to 0.799. The data were corrected for Lorentz and polarization effects. The structure was solved by direct methods and expanded using Fourier techniques. The non-hydrogen atoms were refined anisotropically. Hydrogen atoms were refined using the riding model. All calculations were performed using the CrystalStructure crystallographic software package (Rigaku).

2.4. Calculations of transfer integrals

The transfer integrals (t) were calculated by the extended Hückel molecular orbital calculation method by using lowest unoccupied molecular orbital (LUMO) of $Ni(dmise)_2$ and $Ni(dmit)_2$ for **1** and **2** as the basis functions within the tight-binding approximation [16]. The semiemperical parameters of Ni and Se for Slater-type atomic orbitals were taken from Refs. [17] and [18], respectively. The t between each pair of molecules is assumed to be proportional to the overlap integral (S), $t = ES$, where E is a constant value of -10.0 eV.

3. Results and discussion

3.1. Synthesis of $[Fe(qsal)_2][Ni(dmise)_2] \cdot 2CH_3CN$ 1

The $[Fe(qsal)_2][Ni(dmise)_2] \cdot xCH_3CN$ complexes were prepared by metathesis of $[Fe(qsal)_2]Cl \cdot 1.5H_2O$ and $TBA[Ni(dmise)_2]$ according to the previous report [11]. Slow addition of a filtered acetonitrile solution of $[Fe(qsal)_2]Cl \cdot 1.5H_2O$ to a filtered acetonitrile solution of $TBA[Ni(dmise)_2]$ gave black microcrystals, whose compositions were $[Fe(qsal)_2][Ni(dmise)_2] \cdot xCH_3CN$ (x = 1–1.5) by microanalysis. The $\chi_M T$ versus T products of these complexes showed sample dependence on the width and reproducibility of a thermal hysteresis loop. On the other hand, single crystals of $[Fe(qsal)_2][Ni(dmise)_2] \cdot 2CH_3CN$ **1** were obtained by a slow diffusion method. The composition of the complex **1** was confirmed by both microanalysis and crystal structural analysis (*vide infra*). Since the complex **1** showed reproducible magnetic properties, we will hereafter describe the magnetic properties and crystal structures of by using single crystalline samples.

3.2. Magnetic susceptibilities of 1

The temperature dependence of magnetic susceptibilities for **1** is shown in Fig. 2. The $\chi_M T$ value of **1** at 300 K is 4.22 cm^3 K mol^{-1}, suggesting that the Fe(III) ion is almost in the HS state.

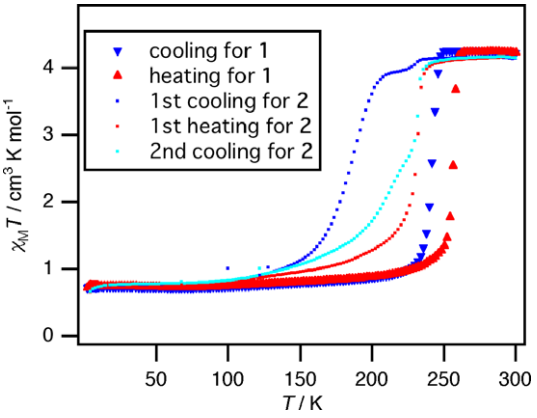


Fig. 2. $\chi_M T$ vs. T products for **1** and **2**.

On lowering the temperature, the $\chi_M T$ value decreased abruptly at 250 K. The spin conversion from the HS to LS states finished within 20 K ($T_{1/2}\downarrow$ = 241 K). The 87.5% Fe(III) ion of **1** is in the LS state at 200 K. On heating, the gradual spin conversion from the LS to HS states occurred at around 240 K and the $\chi_M T$ value recovered the original HS value at 260 K ($T_{1/2}\uparrow$ = 256 K). The reproducibility of the $\chi_M T$ versus T products of **1** on repeating the cooling and heating cycles reveals that the complex **1** exhibits a reversible spin transition with a thermal hysteresis loop of 15 K. The $\chi_M T$ values of **1** in both the low and high temperature phases are quite similar to those of the parent isostructural complex **2** [11] (*vide infra*), suggesting that the spins on the Ni(dmise)$_2$ molecules are antiferromagnetically coupled. The spin transition temperature of **2** in the first cooling process ($T_{1/2}\downarrow$ = 185 K) was different from that of **1** ($T_{1/2}\downarrow$ = 241 K). The similar increase in the spin transition temperatures induced by displacement with a heavy atom was reported for well-known Fe(II) SCO complexes, $Fe^{II}(phen)_2(NCX)_2$ [X = S and Se] [19]. On the other hand, the thermal hysteresis loop for the parent complex **2** in the first cooling and heating cycle disappeared in the second cycle, suggesting an irreversible structural change in **2** may occur after the first spin transition from the HS to the LS states.

3.3. Crystal structures for **1** at 273 and 200 K

The crystal analyses of **1** were performed at 273 and 200 K by using a Rigaku CMF007 Mercury CCD system. The molecular structures and the numbering schemes for Fe(qsal)$_2$ and Ni(dmise)$_2$ molecules of **1** are shown in Figs. 3 and 4, respectively. The crystallographic data are summarized in Table 1. The crystal of **1** at 273 K belongs to triclinic space group $P\bar{1}$ and is isostructural to that of the parent complex **2** [11]. As compared with the parent complex **2**, displacement of sulfur atoms with selenium atoms on the Ni(dmit)$_2$ molecule afforded about 0.7% expansion of the unit cell volume. The crystal structure viewed along the *b* axis at 273 K is shown in Fig. 5. One Fe(qsal)$_2$, one Ni(dmise)$_2$, and two acetonitrile molecules are crystallographically independent in an unsymmetrical unit. The crystal system and space group of **1** at 200 K does not change despite the spin transition from the HS to the LS states. The unit cell volume at 200 K is reduced by 1.5%.

3.3.1. Molecular structure and arrangement for Fe(qsal)$_2$ cation

Two qsal anion molecules as tridentate π-ligands were coordinated to the central iron (III) atom in an almost perpendicular manner, giving the distorted octahedral FeN_4O_2 coordination environments. Selected bond lengths and the sums of deviations (Σ) of

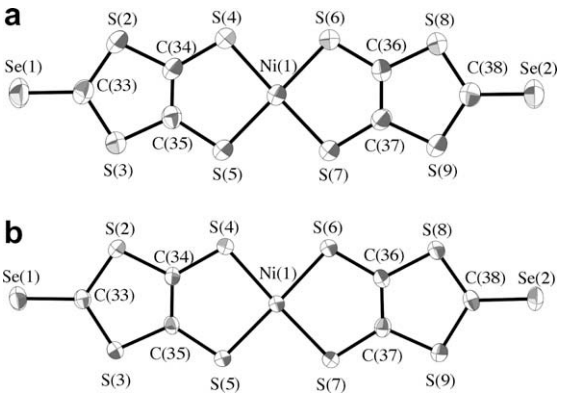


Fig. 4. ORTEP drawings (50% probability) of the molecular structures and numbering schemes for Ni(dmise)$_2$ cations in **1** at (a) 273 K and (b) 200 K .

the bite angle from 90° are given in Table 2. The coordination bond lengths and the distortion of the coordination sphere around the Fe(III) ion of **1** at 273 K are very similar to those of the parent complex **2**, suggesting that the Fe(qsal)$_2$ cation of **1** at 273 K is in the HS state. This is consistent with the similar $\chi_M T$ values in the high temperature phases of **1** and **2**. On the other hand, the coordination bond lengths are remarkably shortened (Δ_{Fe-O} = 0.032 Å, Δ_{Fe-N} = 0.17 Å) and the Σ value is also much smaller at 200 K. The coordination bond lengths and angles at 200 K are in good agreement with those in the LS state for [Fe(qsal)$_2$]NCSe · CH_2Cl_2 **3** reported previously [20], indicating that the Fe(III) ion of **1** at 200 K is almost in the LS state.

The intermolecular arrangements at 200 and 273 K are shown in Fig. 6. Each π-ligand in an Fe(qsal)$_2$ cation overlaps that in the neighboring cations, forming one-dimensional molecular arrays along the *b* axis. The mean distances between π-planes [C(6)–C(7)–N(1)–C(8) and C(22)–C(23)–N(3)–C(24)] along the one-dimensional array are 3.351 and 3.345 Å at 273 K, and 3.179 and 3.214 Å at 200 K, respectively. Those for the parent complex **2** are 3.367 and 3.340 Å at 273 K. This observation indicates that the molecular arrangements of the Fe(qsal)$_2$ for **1** and **2** are similar to each other. No short π–π contacts between these one-dimensional arrays of Fe(qsal)$_2$ molecules for the *a* direction are not observed due to the existence of acetonitrile molecule inbetween one-dimensional molecular arrays.

3.3.2. Molecular structure and arrangement for Ni(dmise)$_2$ molecule

Ni(dmise)$_2$ molecules are almost planar and dimerized in a face-to-face manner (Fig. 7). The mean distances between π-dimer

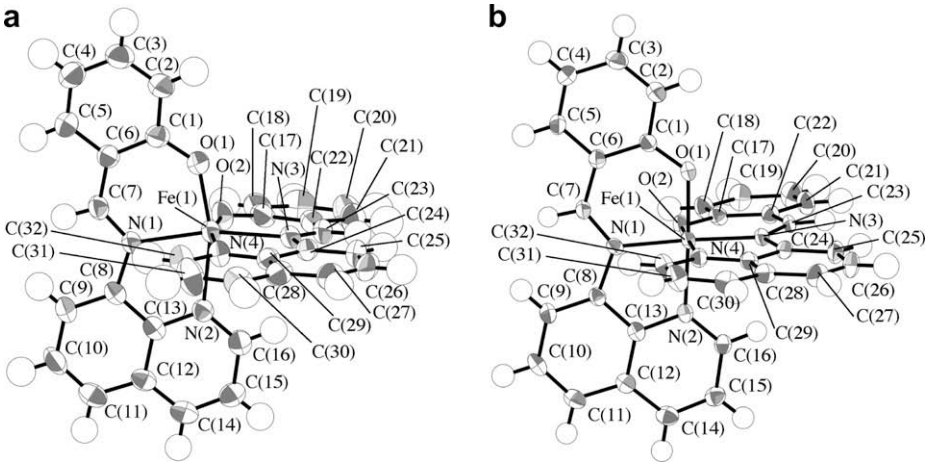


Fig. 3. ORTEP drawings (50% probability) of the molecular structures and numbering schemes for Fe(qsal)$_2$ cations in **1** at (a) 273 K and (b) 200 K .

Table 1
Summary of crystallographic data and refinement details for **1** and **2**.

Compound	**2**	**1**	**1**
Cation	$Fe(qsal)_2$	$Fe(qsal)_2$	$Fe(qsal)_2$
Anion	$Ni(dmit)_2$	$Ni(dmise)_2$	$Ni(dmise)_2$
Formula	$C_{42}H_{28}FeN_6NiO_2S_{10}$	$C_{42}H_{28}FeN_6NiO_2S_8Se_2$	$C_{42}H_{28}FeN_6NiO_2S_8Se_2$
T/K	273	273	200
Crystal system	Triclinic	Triclinic	Triclinic
Space group	$P\bar{1}$	$P\bar{1}$	$P\bar{1}$
a (Å)	11.409(2)	11.562(6)	11.2781(5)
b (Å)	12.435(2)	12.394(7)	12.2015(5)
c (Å)	17.875(3)	17.852(12)	18.6855(8)
α (°)	105.749(3)	105.360(11)	113.308(7)
β (°)	99.422(3)	98.914(10)	94.024(7)
γ (°)	109.537(3)	110.468(11)	108.091(8)
V (Å^3)	2207.7(7)	2223(2)	2189.16(16)
Z	2	2	2
D_{calc} (g cm^{-3})	1.630	1.760	1.786
μ/cm^{-1}	12.74	28.093	28.521
Reflections collected (R_{int})	23704 (0.037)	24432 (0.032)	24061 (0.032)
Data/parameters	9871/587	9992/587	9826/587
Observed data [$I > 2\sigma(I)$]	6714 [$I > 3\sigma(I)$]	7359	7280
R [$I > 2\sigma I$)]	0.0390 [$I > 3\sigma(I)$]	0.0412	0.0373
R_w [$I > 2\sigma(I)$]	0.1030 [$I > 3\sigma(I)$]	0.1116	0.0956
Goodness-of-fit (GOF) on F^2	1.013	1.003	1.009
	Ref. [11]	this work	this wok

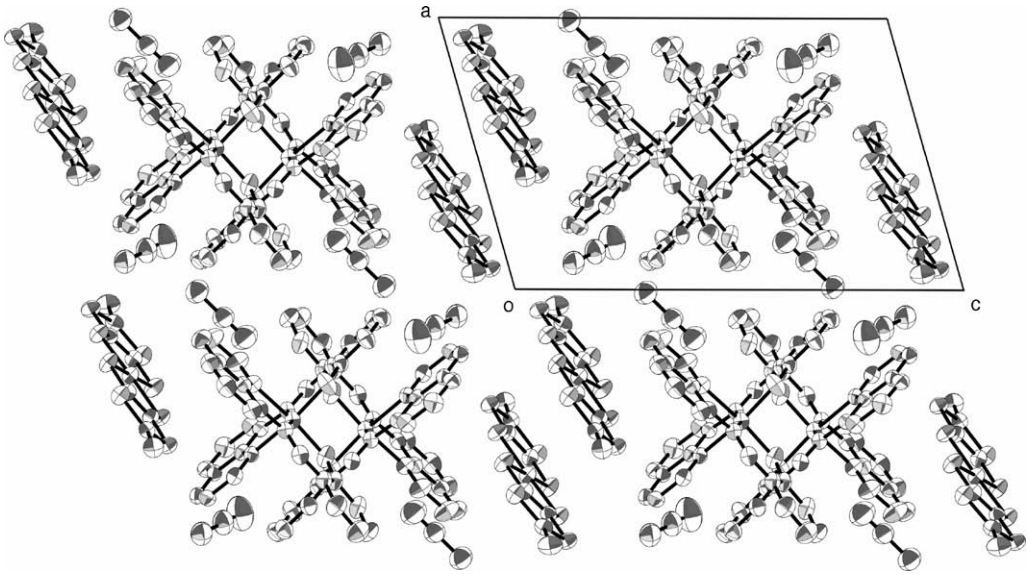


Fig. 5. Crystal structures of **1** viewed along the *b* axis at 273 K. Hydrogen atoms are omitted to clarify.

are 3.659 Å and 3.608 Å at 273 and 200 K, respectively. The short interdimer contacts within the sum of van der Waals radii are observed, affording two-leg ladder-like arrangement along the *b* axis [Se(2)–S(9): 3.4473(13), S(2)–S(9), 3.5563(13) Å at 273 K; Se(1)–S(9): 3.5748(9), Se(2)–S(2): 3.6596(9), S(2)–S(9): 3.4809(12) Å at 200 K]. No short contacts between these ladder chains for the *a* direction are observed due to the existence of acetonitrile molecule, either. It should be noted that remarkable slipping along the molecular long axis for π-dimer of $Ni(dmise)_2$ is observed before and after spin transition (Fig. 7, upper). This large structural modification results in reconstruction of the interdimer short contacts.

3.3.3. Intermolecular contacts between $Fe(qsal)_2$ and $Ni(dmise)_2$ molecules

The π−π stacking between dmise and quinolyl moieties is observed. Although the π-plane between dmise and quinolyl rings is not parallel, the distances between the π-plane of quinolyl ring and the atoms of dmise are in the range of 3.30−3.57 Å and 3.27–3.59 Å at 273 and 200 K, respectively. Furthermore, van der Waals contacts between qsal and dmise moieties in a face-to-edge molecular arrangement are also observed [273 K: S(3)–C(14∗): 3.504(3), S(3)–C(15∗), 3.586(3), S(6)–C(12): 3.535(3), S(6)–C(14): 3.478(3), S(6)–C(15): 3.579(4), S(8)–C(15): 3.578(4), S(8)–C(16): 3.520(4) Å; 200 K: Se(2)–C(10): 3.602(3), Se(2)–C(11): 3.629(3), S(3)–C(14∗): 3.394(3), S(3)–C(15∗): 3.586(2), S(6)–C(14): 3.483 (3), S(6)–C(15): 3.424(3), S(6)–C(16): 3.507(3) Å, ∗ indicates the atoms on the molecule translated by one-unit along the *a* axis]. It should be noted that the short intermolecular contacts between S(3) and C(14∗) or C(15∗) exist between two-dimensional layers composed of one-dimensional arrays of $Fe(qsal)_2$ molecules and two-leg ladder arrangements of $Ni(dmise)_2$ dimers. As mentioned above, intermolecular interactions between $Fe(qsal)_2$ molecules or between $Ni(dmise)_2$ molecules afford only one-dimensional

Table 2
Selected bond lengths, angles, and the sum of deviations of the bite angles from 90° of **1**, **2**, and related complex **3**.

Compound	**2**	**1**	**1**	**3**
T/K	273	273	200	rt
Spin state	HS			LS
Bond lengths (Å)				
Fe(1)–O(1)	1.913(2)	1.918(2)	1.8806(19)	1.879(2)
Fe(1)–O(2)	1.914(3)	1.909(3)	1.882(2)	1.875(3)
Fe(1)–N(1)	2.125(3)	2.114(3)	1.950(3)	1.944(3)
Fe(1)–N(2)	2.150(2)	2.151(2)	1.979(2)	1.985(3)
Fe(1)–N(3)	2.138(3)	2.126(3)	1.948(3)	1.953(3)
Fe(1)–N(4)	2.151(3)	2.133(3)	1.972(3)	1.991(3)
Angles (°)				
O(1)–Fe(1)–O(2)	95.1(1)	94.91(12)	94.06(10)	94.2(1)
O(1)–Fe(1)–N(1)	87.6(1)	87.73(11)	94.38(11)	94.6(1)
O(1)–Fe(1)–N(2)	163.7(1)	163.97(13)	175.48(12)	176.4(1)
O(1)–Fe(1)–N(3)	102.30(9)	101.99(11)	88.08(11)	85.4(1)
O(1)–Fe(1)–N(4)	90.5(1)	90.63(11)	88.73(10)	90.7(1)
O(2)–Fe(1)–N(1)	101.2(1)	101.30(12)	87.62(13)	87.7(1)
O(2)–Fe(1)–N(2)	91.75(9)	91.76(10)	89.48(10)	88.8(1)
O(2)–Fe(1)–N(3)	87.6(1)	87.54(13)	94.58(13)	94.0(1)
O(2)–Fe(1)–N(4)	163.9(1)	164.25(14)	176.20(13)	174.2(1)
N(1)–Fe(1)–N(2)	76.57(9)	76.66(11)	82.96(12)	83.6(1)
N(1)–Fe(1)–N(3)	166.21(9)	166.35(11)	176.59(11)	178.3(1)
N(1)–Fe(1)–N(4)	94.2(1)	93.63(12)	94.75(13)	95.1(1)
N(2)–Fe(1)–N(3)	92.71(9)	92.83(10)	94.44(12)	96.4(1)
N(2)–Fe(1)–N(4)	86.92(9)	86.78(10)	87.86(10)	86.4(1)
N(3)–Fe(1)–N(4)	76.4(1)	76.88(13)	82.93(13)	83.2(1)
Σ (°)	72.67	71.46	44.55	49.9
	Ref. [11]	this work	this work	Ref. [20]

interactions. However, our previous reports [12,13] suggest a cooperative spin transition should originate from two- or three-dimensional intermolecular interactions. Therefore, not only intermolecular interactions between SCO cations or between $Ni(dmise)_2$ anions but also intermolecular interactions between SCO cation and $Ni(dmise)_2$ anion play a key role in the cooperative spin transition of **1**.

3.4. Transfer integrals and magnetic interactions between $Ni(dmise)_2$ and $Ni(dmit)_2$ molecules in **1** and **2**

Since the magnetic exchange interaction energy (J) between the localized spins is given by

$$|J| = 2t^2/U_{\mathrm{eff}}$$

where t is transfer integral between the adjacent molecules and U_{eff} is effective onsite Coulombic interaction, the magnitude of magnetic interactions can be estimated by transfer integrals between $Ni(dmit)_2$ molecules. Nakamura and co-workers reported systematic investigations on magnetic behaviors of $Ni(dmit)_2$-based magnetic materials [21]. First of all, we have calculated transfer integrals for the parent $Ni(dmit)_2$ complex **2** by using the same parameters in order to compare with the reported transfer integrals for $Ni(dmit)_2$-based magnetic materials. The intradimer transfer integral for **2** at 273 K was 14.51×10^{-2} eV, which is the largest value among those reported in Ref. [21]. This value suggests that π-dimer of $Ni(dmit)_2$ is in the spin singlet state. This is in good agreement with the spin state of $Ni(dmit)_2$ supposed by magnetic susceptibilities and Mössbauer spectra [11]. The other transfer integrals for **2** were less than -1.27×10^{-2} eV within two-leg ladder arrangement, but the largest transfer integral between two-leg ladders for the a direction was found to be 0.73×10^{-2} eV. For **1**, the intradimer transfer integrals were 13.00×10^{-2} and -13.02×10^{-2} eV at 273 and 200 K, respectively. These values also suggest that π-dimer of $Ni(dmise)_2$ is in the spin singlet state in the temperature of 2–300 K. Interestingly, the transfer integrals are almost the same values despite a large molecular slipping of π-dimer of

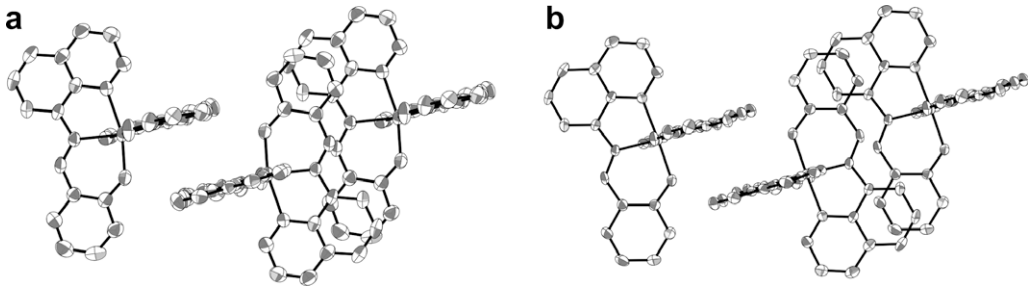


Fig. 6. Molecular arrangements of $Fe(qsal)_2$ molecules along the b axis at (a) 273 K and (b) 200 K. Hydrogen atoms are omitted to clarify.

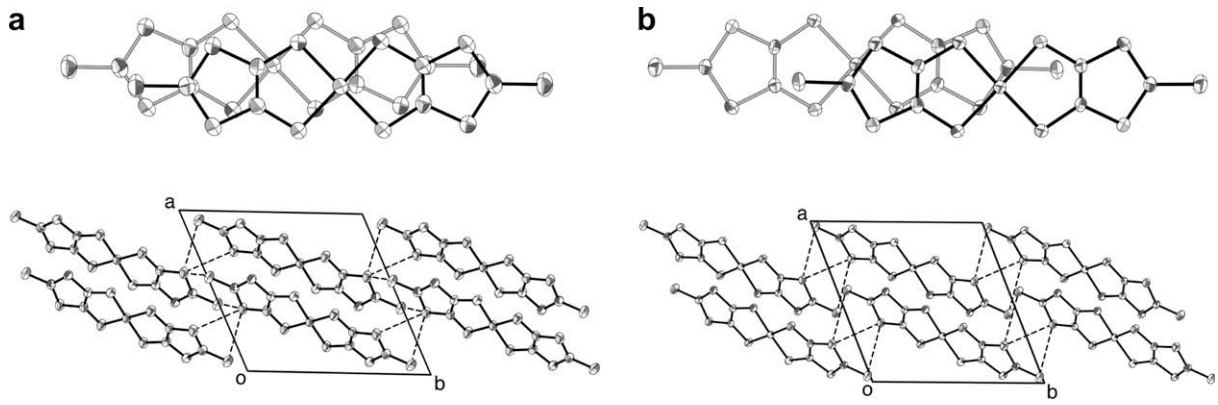


Fig. 7. Top views of the overlapping modes of $Ni(dmise)_2$ molecules and two-leg ladder-like molecular arrangements along the b axis at (a) 273 K and (b) 200 K. Dot lines indicate intermolecular short contacts.

$Ni(dmise)_2$ along the molecular long axis. This suggests that the overlapping positions of $Ni(dmise)_2$ molecules has bistability. The other transfer integrals for **1** were less than -2.57×10^{-2} and -1.04×10^{-2} eV within two-leg ladder arrangement at 273 and 200 K, respectively. On the other hand, the transfer integrals of 1.42×10^{-2} and -1.63×10^{-2} eV between two-leg ladders for the *a* direction were larger than those for **2**.

3.5. Consideration for spin-crossover mechanism of $[Fe(qsal)_2][Ni(dmise)_2] \cdot 2CH_3CN$ **1**

Detail investigations on the crystal structures of **1** in both the high and low temperature phases revealed a variety of $\pi-\pi$ interactions between $Fe(qsal)_2$ and $Ni(dmise)_2$ molecules throughout a crystal, which will result in strong cooperativity of the spin transition behavior of **1**. One of the important findings of structural investigation is a reversible molecular slipping of $Ni(dmise)_2$ involved in a remarkable structural change in size and geometry of Fe(III) SCO cation. This reversible structural change in $Ni(dmise)_2$ molecules is important to persist a thermal hysteresis loop, because preliminary temperature dependent crystal structural analyses for the parent complex **2** suggested that similar molecular slipping of $Ni(dmit)_2$ molecules occurred from the HS to the LS states in the first cooling process (see supplementary data: Nidmit_90K_cif), whereas the reverse molecular slipping was not observed after the heating process (see supplementary data: Nidmit_aged_cif).

4. Conclusion

We have prepared a novel Fe(III) SCO complex with $Ni(dmise)_2$ anion **1**. The magnetic susceptibility measurements revealed that **1** exhibited a cooperative spin transition with a thermal hysteresis loop of 15 K. The high and the low temperature structures of **1** indicated three-dimensional intermolecular $\pi-\pi$ interactions play a key role in the cooperative spin transition, accompanying a reversible molecular slipping of $Ni(dmise)_2$ molecules along the molecular long axis. The transfer integral calculations for **1** and **2** suggested π-dimer of $Ni(dmise)_2$ or $Ni(dmit)_2$ is in the spin singlet state, which is consistent with the previous supposed magnetic data of the parent complex **2**.

Acknowledgements

K.T. is grateful to Ms. Y. Isono for her experimental support and to Mr. Y. Okano for the use of his programs of molecular orbital calculations in this work. This work was partly supported by a Grant-in-Aid for Scientific Research on the Priority Area of Molecular Conductors (No. 18028024) and a Grant-in-Aid for Young Scientists (B) (No. 19750107) from the Ministry of Education, Culture, Sports, Science, and Technology of Japan.

Appendix A. Supplementary data

CCDC 706962 and 706963 contain the supplementary crystallographic data for **1** and **2**. These data can be obtained free of charge via http://www.ccdc.cam.ac.uk/conts/retrieving.html, or from the Cambridge Crystallographic Data Centre, 12 Union Road, Cambridge CB2 1EZ, UK; fax: (+44) 1223-336-033; or e-mail: deposit@ccdc.cam.ac.uk. Supplementary data associated with this article can be found, in the online version, at doi:10.1016/j.poly.2008.11.047.

References

[1] P. Gütlich, H.A. Goodwin (Eds.), Spin Crossover in Transition Metal Compounds I–III, Topics in Current Chemistry, 233–235, Springer, Berlin, 2004.
[2] P. Gütlich, A. Hauser, H. Spiering, Angew. Chem., Int. Ed. Engl. 33 (1994) 2024.
[3] S. Hayami, Z.-Z. Gu, M. Shiro, Y. Einaga, A. Fujishima, O. Sato, J. Am. Chem. Soc. 122 (2000) 7126.
[4] M. Nakano, N. Fujita, G. Matsubayashi, W. Mori, Mol. Cryst. Liquid Cryst. 379 (2002) 365.
[5] S. Dorbes, L. Valade, J.A. Real, C. Faulmann, Chem. Commun. (2005) 69.
[6] C. Faulmann, S. Dorbes, B.G. Bonneval, G. Molnár, A. Bousseksou, C. Gomez-Garcia, E. Coronado, L. Valade, Eur. J. Inorg. Chem. (2005) 3261.
[7] C. Faulmann, K. Jacob, S. Dorbes, S. Lampert, I. Malfant, M.-L. Doublet, L. Valade, J.A. Real, Inorg. Chem. 46 (2007) 8548.
[8] C. Faulmann, S. Dorbes, S. Lampert, K. Jacob, B.G. Bonneval, G. Molnár, A. Bousseksou, J.A. Real, L. Valade, Inorg. Chim. Acta 360 (2007) 3870.
[9] L.C.J. Pereira, A.M. Gulamhussen, J.C. Dias, I.C. Santos, M. Almeida, Inorg. Chim. Acta 360 (2007) 3887.
[10] K. Takahashi, T. Kawakami, Z.-Z. Gu, Y. Einaga, A. Fujishima, O. Sato, Chem. Commun. (2003) 2374.
[11] K. Takahashi, H.-B. Cui, H. Kobayashi, Y. Einaga, O. Sato, Chem. Lett. 34 (2005) 1240.
[12] K. Takahashi, H.-B. Cui, Y. Okano, H. Kobayashi, Y. Einaga, O. Sato, Inorg. Chem. 45 (2006) 5739.
[13] K. Takahashi, H.-B. Cui, Y. Okano, H. Kobayashi, H. Mori, H. Tajima, Y. Einaga, O. Sato, J. Am. Chem. Soc. 130 (2008) 6688.
[14] R.C. Dickinson, W.A. Baker, R.L. Collins, J. Inorg. Nucl. Chem. 39 (1977) 1531.
[15] J.P. Cornelissen, B. Pomarède, A.L. Spek, D. Reefman, J.G. Haasnoot, J. Reedijk, Inorg. Chem. 32 (1993) 3720.
[16] T. Mori, A. Kobayashi, Y. Sasaki, H. Kobayashi, G. Saito, H. Inokuchi, Bull. Chem. Soc. Jpn. 57 (1984) 627.
[17] R.H. Summerville, R. Hoffmann, J. Am. Chem. Soc. 98 (1976) 7240.
[18] H. Kobayashi, H. Tomita, T. Naito, A. Kobayashi, F. Sakai, T. Watanabe, P. Cassoux, J. Am. Chem. Soc. 118 (1996) 368.
[19] E. König, K. Madeja, Inorg. Chem. 6 (1967) 48.
[20] S. Hayami, Z.-Z. Gu, H. Yoshiki, A. Fujishima, O. Sato, J. Am. Chem. Soc. 123 (2001) 11644.
[21] (a) T. Akutagawa, T. Nakamura, T. Inabe, A.E. Underhill, Thin Solid Films 331 (1998) 264;
(b) T. Akutagawa, T. Nakamura, Coord. Chem. Rev. 226 (2001) 3.

Table 1
Crystallographic data and structure refinement for complexes **1** and **2**.

	1	**2**
Formula	$C_{54}H_{63}Fe_2N_5O_{24.5}Pr$	$C_{52}H_{60}Cl_{0.5}Fe_2GdN_{4.5}O_{23.5}$
Mr	1426.70	1410.72
Crystal size (mm)	0.12 × 0.05 × 0.03	0.21 × 0.15 × 0.05
Colour	purple	purple
Crystal system	monoclinic	monoclinic
Space group	$P2_1/c$	$P2_1/c$
T (K)	150	100
a (Å)	14.4546 (14)	14.7924(5)
b (Å)	19.8462 (17)	19.4629(6)
c (Å)	21.938 (2)	22.0420(7)
β (°)	105.852(7)	99.995(1)
V (Å^3)	6054.0(10)	6249.6(3)
Z	4	4
ρ_{calc} (g cm^{-3})	1.565	1.499
μ (Mo Kα) (mm^{-1})	1.350	1.607
F(000)	2916	2864
Reflections collected	36449	40580
Unique reflections	11136	12755
R_{int}	0.1138	0.0327
Reflections observed [$I > 2\sigma(I)$]	6300	10006
Parameters/restraints	810/19	792/49
wR_2 (all data)	0.2132	0.1284
S (all data)	0.973	1.024
R_1 [$I > 2\sigma(I)$]	0.0805	0.0470
Residuals (e Å^{-3})	+0.85/−1.89	+2.48/−0.67

Table 2
Bond lengths (Å) for **1** and **2**.

	1 (Ln=Pr)	**2** (Ln=Gd)
Ln(1)–O(3′)	2.445(7)	2.344(3)
Ln(1)–O(6)	2.432(7)	2.369(3)
Ln(1)–O(9)	2.465(6)	2.290(3)
Ln(1)–O(13)	2.527(7)	2.355(4)
Ln(1)–O(14)	2.567(6)	2.446(3)
Ln(1)–O(15)	2.632(6)	2.447(3)
Ln(1)–O(16)	2.553(7)	2.399(3)
Ln(1)–O(17)	2.489(8)	2.491(4)
Ln(1)–O(18)	2.515(6)	–
Fe(1)–O(1)	1.928(7)	1.927(3)
Fe(1)–O(2)	1.980(6)	1.983(3)
Fe(1)–O(4)	1.916(7)	1.925(3)
Fe(1)–O(5)	1.960(6)	1.978(3)
Fe(1)–N(1), (N(1A) and N(1B) for **2**)	2.176(9)	2.223(10), 2.118(10)
Fe(1)–N(2), (N(2A) and N(2B) for **2**)	2.173(9)	2.115(9), 2.246(9)
Fe(2)–O(7)	1.934(7)	1.934(3)
Fe(2)–O(8)	1.989(6)	2.000(3)
Fe(2)–O(10)	1.906(7)	1.920(3)
Fe(2)–O(11)	1.977(7)	1.973(3)
Fe(2)–N(3)	2.187(8)	2.203(4)
Fe(2)–N(4)	2.184(8)	2.168(4)

2.2. Synthesis of the complexes

2.2.1. Synthesis of $[Fe_2Pr(4\text{-Me-sal})_4(2,2'\text{-bipy})_2(H_2O)_6](NO_3)\cdot 2MeOH\cdot 1½H_2O$ (**1**)

A solution of $Pr(NO_3)_3\cdot 6H_2O$ (0.086 g, 0.2 mmol) in 5 ml of H_2O was added to a methanolic solution (10 ml) of 4-Me-salH_2 (0.122 g, 0.8 mmol) giving a pale yellow solution. To this was added a methanolic solution (10 ml) of $FeCl_3\cdot 4H_2O$ (0.054 g, 0.2 mmol) and 2,2′-bipy (0.031 g, 0.2 mmol), whereupon the colour of the solution changed to purple. After 1 h, Et_3N (0.052 ml, 0.4 mmol) was added slowly giving a pinkish purple solution. The solution was filtered and layered with ether. The next day small purple crystals were obtained. Yield: 55%. *Anal.* Calc. for $C_{55}H_{64}Fe_2PrN_5O_{24}$: C, 46.04; H, 4.24; N, 4.81. Found: C, 46.12; H, 4.47; N, 4.89%. Selected IR data (KBr disc, cm^{-1}): 3446 (br), 2919 (m), 1608 (s), 1558 (s), 1523 (m), 1443 (s), 1423 (s), 1320 (m), 1327 (s), 1249 (s), 1170 (m), 1024 (m), 959 (m), 764 (m), 635 (m), 612 (m), 416 (w).

2.2.2. Synthesis of $[Fe_2Gd(4\text{-Me-sal})_4(2,2'\text{-bipy})_2(H_2O)_5]Cl_{1/2}(NO_3)_{1/2}\cdot 5H_2O$ (**2**)

The synthesis of **2** was analogous to that of **1** using $Gd(NO_3)_3\cdot 6H_2O$ and by the same layering method purple crystals were isolated. Yield: 62%. *Anal.* Calc. for $C_{52}H_{60}Cl_{0.5}GdFe_2N_{4.5}O_{23.5}$: C, 44.27; H, 4.27; N, 4.47. Found: C, 44.24; H, 4.26; N, 4.47%. Selected IR data (KBr disc, cm^{-1}): 3382 (b), 2919 (m), 1607 (s), 1558 (s), 1520 (s), 1444 (s), 1425 (s), 1384 (s), 1249 (s), 1172 (s), 1025 (m), 959 (m), 767 (m), 635 (m), 613 (m), 416 (w).

2.2.3. Synthesis of $[Fe_2Dy(4\text{-Me-sal})_4(2,2'\text{-bipy})_2(H_2O)_5]Cl_{1/2}(NO_3)_{1/2}\cdot 5H_2O$ (**3**)

The synthesis of **3** was carried out as for **1** and **2** but using Dy$(NO_3)_3\cdot 6H_2O$, giving purple crystals in 84% yield. *Anal.* Calc. for $C_{52}H_{60}Cl_{0.5}DyFe_2N_{4.5}O_{23.5}$: C, 44.11; H, 4.27; N, 4.45. Found: C,

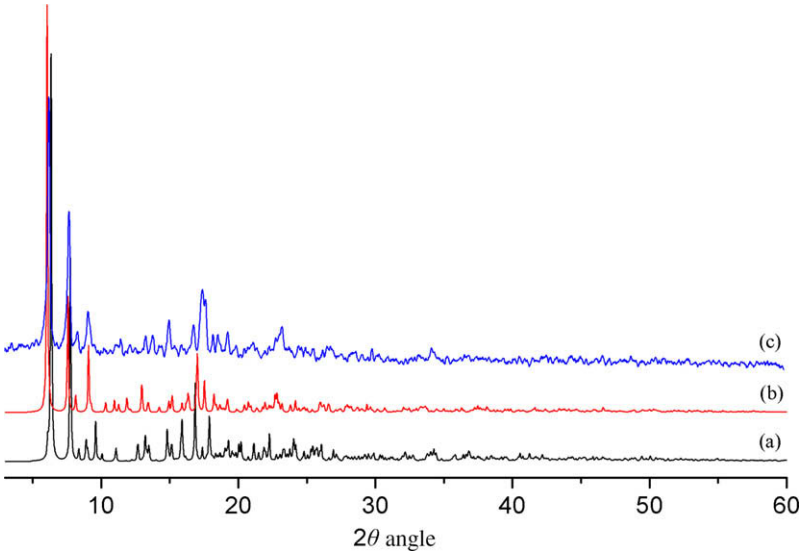


Fig. 1. X-ray powder diffraction: calculated for **1** (a) and **2** (b), measured for compound **3** (c). (For interpretation of the references to colour in this figure legend, the reader is referred to the web version of this article.)

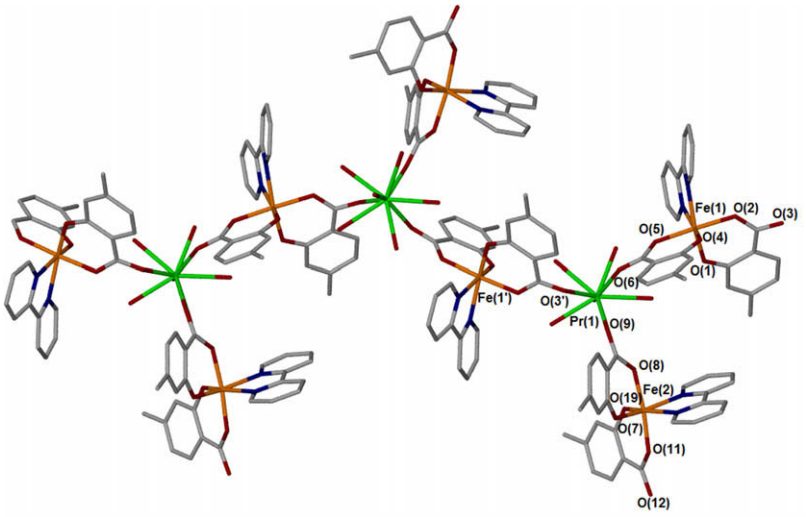


Fig. 2. The repeating unit, $[Fe_2Pr(4\text{-Me-sal})_4(2,2'\text{-bipy})_2(H_2O)_6](NO_3)\cdot 3MeOH$, of the 1D chain in **1**. Hydrogen atoms are omitted for clarity. Colour code: Fe(III), orange; Pr(III), light green; C, grey; O, red and N, blue. (For interpretation of the references to colour in this figure legend, the reader is referred to the web version of this article.)

Table 3
Stacking and H-aryl interactions in **1**.

Centroids distance (Å)	Least square planes distance (Å)		Offset (Å)
4.441	3.771		2.34
4.357	3.710		2.29
3.9672	3.505		1.87
4.015	3.512		1.95
3.660	3.589		0.72
C–H ··ring centroid[a]	H–π distance	γ [b] (°)	C–H–π angle (°)
C(16)–H(16B)···π_A	2.67	8.06	159
C(42)–H(42A)···π_B	2.99	15.89	174

[a] The centroids are of the following atoms with symmetry operators in brackets applied: π_A N(4)–C(48)–C(49)–C(50)–C(51)–C(52) [1 − x, 1 − y, 1 − z]; π_B C(9)–C(10)–C(11)–C(12)–C(13)–C(14) [1 + x, 1/2 − y, 1/2 + z].
[b] γ is defined as the angle between the normal to the plane of the π ring and the vector of the H-centroid interaction.

43.69; H, 4.07; N, 4.24%. IR (KBr disc, cm^{-1}): 3422 (b), 1607 (s), 1557 (s), 1514 (s), 1443 (s), 1423 (s), 1320 (m), 1250 (s), 1170 (s), 1024 (m), 959 (m), 765 (m), 636 (m), 613 (m), 416 (w).

2.3. Magnetic measurements

Magnetic susceptibility measurements were obtained using a Quantum Design SQUID magnetometer (MPMS-XL). Measurements were performed on polycrystalline samples of 11.8 mg (**1**), 14.7 mg (**2**) and 11.2 mg (**3**), respectively. *ac* susceptibility measurements were measured with an oscillating *ac* field of 3 Oe and a frequency of 1000 Hz. The magnetic data were corrected for the sample holder and the diamagnetic contribution. The samples were checked for the presence of ferromagnetic impurities by measuring the magnetization as a function of the field at 100 K; perfect straight lines were observed indicating the absence of such impurities.

Table 4
Stacking and H-aryl interactions in **2**.

Centroids distance (Å)	Least square planes distance (Å)		Offset (Å)
3.983	3.681		1.52
4.223	3.652		2.12
4.392	3.543		2.60
4.359	3.891		1.97
3.835	3.729		0.90
C–H ··ring centroid[a]	H–π distance	γ[b] (°)	C–H–π angle (°)
C(16)–H(16B)···π_A	2.73	9.18	139

[a] The centroids are of the following aotms with symmetry operators in brackets applied: π_A N(4)–C(48)–C(49)–C(50)–C(51)–C(52) [1 − x, −y, −z].
[b] γ is defined as the angle between the normal to the plane of the π ring and the vector of the H-centroid interaction.

2.4. X-ray crystallography

Single-crystal X-ray crystallographic data were collected at 100 K on a Bruker SMART Apex CCD diffractometer (**1**) or at 150 K on a Stoe IPDS II diffractometer (**2**) using graphite-monochromated Mo Kα radiation and semi-empirical absorption corrections were applied [16a,b]. Crystallographic data and details of the measurements and refinements are summarized in Table 1. The structures were solved using direct methods followed by full-matrix least-squares refinement against F^2 (all data) using SHELXTL [16b]. Anisotropic refinement was used for all non-H atoms; organic H atoms were placed in calculated positions while coordinates of hydroxo H atoms were refined.

3. Results and discussion

From the X-ray powder diffraction patterns it was clear that compounds **2** and **3** are isomorphous (Fig. 1). Therefore, the structures of **1** and **2** were determined using single-crystal X-ray diffraction (Tables 1 and 2). Both compounds crystallize in the monoclinic space group $P2_1/c$ with $Z = 4$. The asymmetric unit contains two Fe^{III} and one Ln^{III} cations, four 4-Me-sal ligands and two 2,2′-bipyridine ligands forming monocationic heterometallic zigzag $[Fe_2Ln(4\text{-Me-sal})_4(2,2'\text{-bipy})_2(H_2O)_x]^+$ chains, where $x = 6$ for Pr (**1**) and $x = 5$ for Gd (**2**) and Dy (**3**), running parallel to the *b*-axis while lattice methanol and water molecules for **1** and water molecules for **2** and **3** are held with H-bonds (Fig. 1). Charge balance considerations require a single counteranion per $\{Fe_2Ln\}$ formula unit; a nitrate anion was found in the asymmetric unit of **1,** with a disordered chloride and nitrate (ratio 1:1) for **2** and presumably also **3**, the latter will not be further discussed (see Fig. 2).

The two Fe^{III} centres Fe1 and Fe2 are each hexacoordinated in a distorted octahedral environment. Each is chelated, through phenoxo and carboxylate oxygens, by two different 4-Me-sal ligands, with further chelation by the two nitrogen atoms of a 2,2′-bipyri-

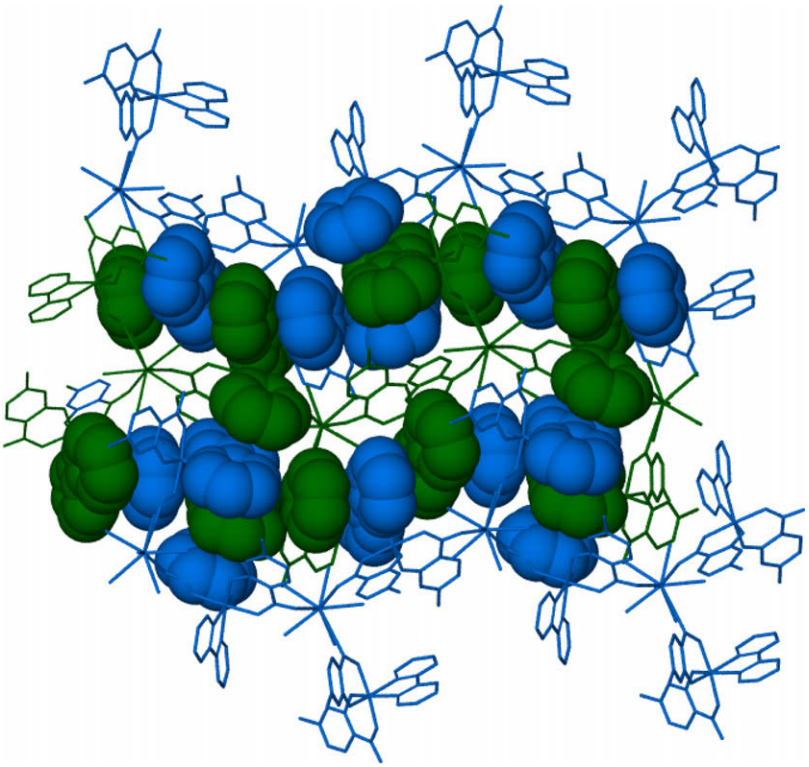


Fig. 3. A packing diagram of **1**, along the *b*-axis. The 1D chains are drawn in blue and green to emphasize the stacking interactions between the aryl rings that lead to a 2D robust layer in the plane of the paper. Organic hydrogen atoms have been omitted for clarity.

dyl ligand. This latter ligand is twofold disordered in the structure of **2**. The Fe–O bond lengths vary between 1.907 and 1.994 Å, with the mutually-*trans* Fe–O bonds systematically longer and the Fe–O bonds *trans* to nitrogen shorter. The Fe–N bond lengths were, as expected, longer, in the range 2.115–2.203 Å. In this way, two crystallographically independent anionic spacers, $[Fe1(2,2'\text{-bipy})(4\text{-Me-sal})_2]^-$ and $[Fe2(2,2'\text{-bipy})(4\text{-Me-sal})_2]^-$, can be defined. Each $[Fe2(2,2'\text{-bipy})(4\text{-Me-sal})_2]^-$ unit is linked to only one Ln^{III} by a *syn-anti* carboxylate bridge from one 4-Me-sal^{2-} ligand, whereas each $[Fe1(2,2'\text{-bipy})(4\text{-Me-sal})_2]^-$ is linked to two Pr1 by *syn-anti* carboxylate bridges from two 4-Me-sal^{2-} ligands.

Pr1 is nine-coordinate in **1**, while Gd1 is eight-coordinate in **2**, consistent with the expected smaller ionic radius for Gd^{III}. The coordination environment of each Pr^{III} consists of six water molecules (O13, O14, O15, O16, O17, O18) and three carboxylate oxygen atoms (O3, O6, O9) from three different bridging $\{Fe(2,2'\text{-bipy})(4\text{-Me-sal})_2\}^-$ units. For the Gd^{III} compound the lanthanide is coordinated by five water molecules (O13, O14, O15, O16, O17) and three carboxylate oxygen atoms (O3, O6, O9) from three different bridging $[Fe(2,2'\text{-bipy})(4\text{-Me-sal})_2]^-$ units. In **1**, the distances between Pr1 and three carboxylate oxygens are 2.451(4) Å (Pr1–O3), 2.430(6) Å (Pr1–O6) and 2.472(5) Å (Pr1–O9), whereas Pr1–Fe2 is 5.877(1) Å and Pr1–Fe1 is 5.698(1) Å. In **2**, the distances between Gd1 and three carboxylate oxygen atoms are 2.345(1) Å (Gd1–O3), 2.369(1) Å (Gd1–O6) and 2.290(1) Å (Gd1–O9). The Gd1–Fe2 distance is 6.221(2) Å and Gd1–Fe1 distance is 5.495(2) Å. The coordination environment around Pr in **1** can be described as tricapped trigonal prismatic, while for Gd in **2** it is square antiprismatic.

In this way, a trinuclear Fe_2Ln unit is formed and extended along the *b-axis* through the zigzag 1D polymeric chain. Adjacent 1D polymeric chains are connected through a combination of strong and medium π–π stacking interactions (Tables 3 and 4) between the aromatic rings of 2,2′-bipyridyl and 4-Me-sal^{2-} ligand forming robust 2D layers (Fig. 3) [17]. Furthermore, two such 2D layers are further linked though C–H···aryl interactions (Table 3), resulting in the formation of a metallosupramolecular structure.

4. Magnetic properties of compounds 1–3

Dc magnetic susceptibility measurements were performed on polycrystalline powder samples of **1**–**3** in the temperature range 1.8–300 K at 1000 Oe. Overall, the temperature dependences of magnetic susceptibilities of these three compounds show the same thermal evolution (Fig. 4). The experimental χT products at room

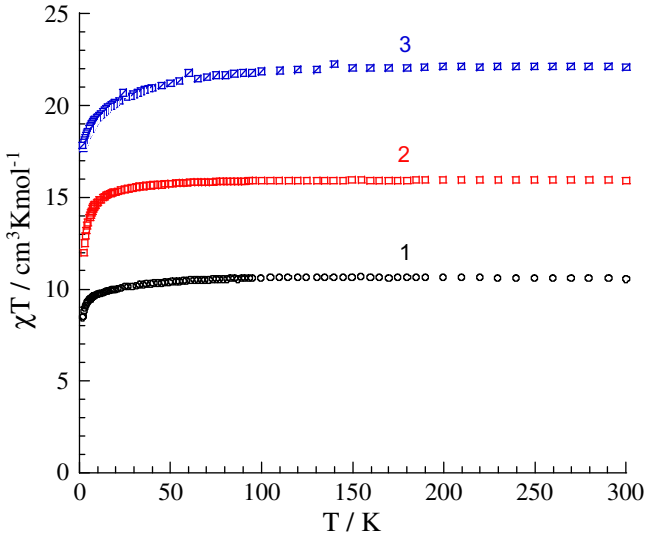


Fig. 4. χT vs. T plots for compounds **1**–**3**.

Table 5
Comparison of the χT products at room temperature between the expected and the experimental values for compounds **1**–**3**.

Compounds	χT ($cm^3\ K\ mol^{-1}$) theoretical value [18] for each Ln ion at RT	χT ($cm^3\ K\ mol^{-1}$) expected value for [Fe_2Ln] at RT	χT ($cm^3\ K\ mol^{-1}$) experimental value for [Fe_2Ln] at RT
[Fe_2Pr] (**1**)	1.60	10.35	10.5
[Fe_2Gd] (**2**)	7.875	16.63	15.9
[Fe_2Dy] (**3**)	14.17	22.92	22.2

temperature are in good agreement with the expected values for two Fe(III) ions ($S = 5/2$, $g = 2$) and one Ln(III) ion (Table 5). On decreasing the temperature, the χT product at 1000 Oe stays almost constant to about 30 K and then rapidly decreases to reach a minimum value at 1.8 K. This type of magnetic behavior indicates dominant antiferromagnetic interactions between the spin carriers. Since the Gd(III) has no orbital contribution and Fe(III) is a weakly anisotropic ion, the monotonic decrease of the susceptibility in **2** indicates the presence of antiferromagnetic interactions between Fe^{III} and Gd^{III}. A fit of the experimental data to a Curie–Weiss law above 2 K leads to a Curie constant of 16.0 $cm^3\ K\ mol^{-1}$ and Weiss constant of −0.85 K (Fig. S1). The small but negative Weiss constant also suggests the presence of very small interactions between Fe–Gd with a dominating antiferromagnetic contribution. The Fe^{III}–Ln^{III} magnetic interactions in **1** and **3** are hence probably antiferromagnetic, however, the depopulation of the Stark sublevels of the anisotropic Pr and Dy ions might be also partially responsible for the decrease of the χT product [19]. Therefore, the thermal decrease of the χT products might be due to a combination of those effects mentioned above.

For all three compounds, at low temperatures the magnetization smoothly increases with the applied dc field (Figs. S2–S4). In all cases, there is no clear saturation even at 7 T at which it reaches the value of 12.0, 15.9 and 15.1μ_B for compounds **1**, **2** and **3**, respectively, suggesting the presence of magnetic anisotropy and/or the population of low-lying excited states. This is also confirmed in the plots of the M versus H/T at low temperatures, in which the curves are not all superposed on a single master-curve as expected for isotropic systems. In the case of compound **2**, the magnitude of M at 15.9μ_B is fairly close to the value of 17μ_B expected for two Fe(III) ions ($S = 5/2$) and one Gd(III) ion ($S = 7/2$) if the spins are uncoupled. This observation indicates that the antiferromagnetic interactions are weak in this complex, as suggested by the χT versus T data and the small Weiss constant. In fact, at high field where the antiferromagnetic interactions are overcome, a saturation of the magnetization can be expected to occur at 17μ_B corresponding to all the spins being aligned parallel. Likewise, as can be seen from the M versus H plot of compound **3**, the magnetization is 15.1μ_B, which is in good agreement with the expected value (15.23μ_B) for all the spins aligned parallel arising from 10μ_B for two $S = 5/2$ Fe(III) ions and 5.23μ_B for one Dy(III) ion. This observation also indicates that very weak intramolecular antiferromagnetic interactions are present in this complex. However, despite the presence of anisotropy in these compounds, the ac susceptibility of compounds **1**–**3** in zero dc field shows a complete absence of out-of-phase components above 1.8 K, and no slow relaxation is observed in this series of compounds at this temperature.

5. Conclusion

The metal/methylsalicylate/co-ligand strategy towards heterometallic systems has successfully produced three new heterometallic 1D coordination polymers [Fe_2Pr(4-Me-sal)$_4$(2,2′-bipy)$_2$(H_2O)$_6$](NO_3) · 2MeOH · 1.5H_2O, (**1**) [Fe_2Gd(4-Me-sal)$_4$(2,2′-bipy)$_2$(H_2O)$_5$]$Cl_{1/2}$(NO_3)$_{1/2}$ · 5H_2O, (**2**) and [Fe_2Dy(4-Me-sal)$_4$(2,2′-bipy)$_2$(H_2O)$_5$]$Cl_{1/2}$(NO_3)$_{1/2}$ · 5H_2O (**3**). Efforts to increase the dimensionality of the final products are in progress. Magnetic studies show that the observed decrease of the χT value with decreasing temperature might be due to antiferromagnetic interactions between Fe–Ln centres and/or the depopulation of the Stark sublevels of the anisotropic Ln ions.

Acknowledgements

The authors are grateful to the European network MAGMANet (NMP3-CT-2005-515767), the EC-TMR Network QuEMolNa (MRTN-CT-2003-504880), the DFG (CFN and SPP-1137) and Gh.N. thanks the AvH Foundation for financial support.

Appendix A. Supplementary data

CCDC 707404 and 707405 contain the supplementary crystallographic data for **1** and **2**. These data can be obtained free of charge via http://www.ccdc.cam.ac.uk/conts/retrieving.html, or from the Cambridge Crystallographic Data Centre, 12 Union Road, Cambridge CB2 1EZ, UK; fax: (+44) 1223-336-033; or e-mail: deposit@ccdc.cam.ac.uk. Supplementary data associated with this article can be found, in the online version, at doi:10.1016/j.poly.2008.12.003.

References

[1] (a) J.M. Lehn, Angew. Chem., Int. Ed. 29 (1990) 1304;
(b) S.R. Batten, R. Robson, Angew. Chem., Int. Ed. 37 (1998) 1460;
(c) M. Eddaoudi, D.B. Moler, H. Li, B. Chen, T.M. Reineke, M. O'Keeffe, O.M. Yaghi, Acc. Chem. Res. 34 (2001) 319;
(d) B. Moulton, M.J. Zaworotko, Chem. Rev. 101 (2001) 1629;
(e) R. García-Zarracino, H. Höpfl, Angew. Chem., Int. Ed. 43 (2004) 1507;
(f) A.J. Blake, N.R. Champness, P. Hubberstey, W.–S. Li, A. Withersby, M. Schröder, Coord. Chem. Rev. 183 (1999) 117.
[2] (a) P. Horcajada, S. Surblé, C. Serre, D.Y. Hong, Y.K. Seo, J.S. Chang, J.M. Grenèche, I. Margiolaki, G. Férey, Chem. Commun. (2007) 2820;
(b) S.H. Cho, B.Q. Ma, S.T. Nguyen, J.T. Hupp, T.E. Albrecht-Schmitt, Chem. Commun. (2006) 2563.
[3] (a) J.W. Yoon, S.H. Jhung, Y.K. Hwang, S.M. Humphrey, P.T. Wood, J.S. Chang, Adv. Mater. 19 (2007) 1830;
(b) B.L. Chen, S.Q. Ma, F. Zapata, F.R. Fronczek, E.B. Lobkovsky, H.C. Zhou, Inorg. Chem. 46 (2007) 1233.
[4] (a) D. Maspoch, D.-R. Molina, K. Wurst, N. Domingo, M. Cavallini, F. Biscarini, J. Tejada, C. Rovira, J. Veciana, Nature Mater. 2 (2003) 190;
(b) S. Xiang, X. Wu, J. Zhang, R. Fu, S. Hu, X. Zhang, J. Am. Chem. Soc. 127 (2005) 16352.
[5] (a) L.G. Beauvais, M.P. Shores, J.R. Long, J. Am. Chem. Soc. 122 (2000) 2763;
(b) H. Jianghua, Y. Jihong, Z. Yuetao, P. Qinhe, X. Ruren, Inorg. Chem. 44 (2005) 9279.
[6] (a) B.F. Hoskins, R. Robson, J. Am. Chem. Soc. 112 (1990) 1546;
(b) L. Carlucci, G. Ciani, D.M. Proserpio, A. Sironi, J. Chem. Soc., Chem. Commun. (1994) 2755;
(c) Z. Wang, B. Zhang, M. Kurmoo, M.A. Green, H. Fujiwara, T. Otsuka, H. Kobayashi, Inorg. Chem. 44 (2005) 1230.
[7] (a) D. Sun, Y. Ke, T.M. Mattox, B.A. Ooro, H.-C. Zhou, Chem. Commun. (2005) 5447;
(b) M. Eddaoudi, J. Kim, M. O'Keefe, O.M. Yaghi, J. Am. Chem. Soc. 124 (2002) 376.
[8] (a) R. Natarajan, G. Savitha, P. Dominiak, K. Wozniak, J.N. Moorthy, Angew. Chem., Int. Ed. 44 (2005) 2115;
(b) K.I. Nättinen, K. Rissanen, Inorg. Chem. 42 (2003) 5126;
(c) P. Grosshans, A. Jouaiti, M.W. Hosseini, P. Kyritsakas, New J. Chem. 27 (2003) 793.
[9] (a) M. Sarkar, K. Biradha, CrysEngComm 6 (2004) 310;
(b) G.E. Kostakis, L. Casella, N. Hadjiliadis, E. Monzani, N. Kourkoumelis, J.C. Plakatouras, Chem. Commun. (2005) 3859.
[10] C. Janiak, Dalton Trans. (2003) 2781.
[11] (a) P. Lemoine, B. Viossat, G. Morgant, F.T. Greenaway, A. Tomas, N.H. Dung, J.R.J. Sorenson, J. Inorg. Biochem. 9 (2002) 18;
(b) A.L. Abuhijleh, C. Woods, Inorg. Chem. Commun. 5 (2002) 269;
(c) L.G. Zhu, S. Kitagawa, M. Kondo, H. Miyasaka, Chem. Lett. (2000) 536;
(d) L.-G. Zhu, S. Kitagawa, H. Miyasaka, H.-C. Chang, Inorg. Chim. Acta 355 (2003) 121.
[12] Z. Pučeková-Repická, J. Moncol, D. Valigura, T. Lis, M. Korabik, M. Melniík, J. Mroziński, M. Mazur, J. Coord. Chem. 60 (2007) 2449.

[13] S. Mukherjee, Y. Lan, G.E. Kostakis, R. Clérac, C.E. Anson, A.K. Powell, Crys. Growth Des., in press, doi:10.1021/cg800879c.
[14] (a) X.S. Tan, J. Chen, Z.N. Chen, P.J. Zheng, W.X. Tang, Inorg. Chim. Acta 234 (1995) 27;
(b) X.S. Tan, J. Sun, C.H. Hu, D.G. Fu, D.F. Xiang, P.J. Zheng, W.X. Tang, Inorg. Chim. Acta 257 (1997) 203;
(c) J.-R. Li, W.-T. Chen, M.-L. Tong, G.-C. Guo, Y. Tao, Q. Yu, W.-C. Song, X.-H. Bu, Crys. Growth Des. 8 (2008) 2780;
(d) L. Li, J. Li, H. Hou, Y. Fan, Y. Zhu, Inorg. Chim. Acta 359 (2006) 3139.
[15] (a) G.E. Kostakis, G. Abbas, C.E. Anson, A.K. Powell, CrystEngComm 10 (2008) 1117;
(b) G.E. Kostakis, G. Abbas, C.E. Anson, A.K. Powell, CrystEngComm 11 (2009) 82;
(c) D.J. Price, A.K. Powell, P.T. Wood, J. Chem. Soc., Dalton Trans. (2000) 3566;
(d) S.O.H. Gutschke, D.J. Price, A.K. Powell, P.T. Wood, Angew. Chem., Int. Ed. 40 (2001) 1920;
(e) S.O.H. Gutschke, D.J. Price, A.K. Powell, P.T. Wood, Eur. J. Inorg. Chem. (2001) 2739;
(f) M. Viertelhaus, P. Adler, R. Clérac, C.E. Anson, A.K. Powell, Eur. J. Inorg. Chem. (2005) 692.
[16] (a) G.M. Sheldrick, SADABS (the Siemens Area Detector Absorption Correction), University of Göttingen, 1996.;
(b) G.M. Cook, Acta Crystallogr., Sect. A 64 (2008) 112.
[17] (a) C. Janiak, J. Chem. Soc., Dalton Trans. (2000) 3885;
(b) V. Russell, M. Scudder, I. Dance, J. Chem. Soc., Dalton Trans. (2001) 789;
(c) G.E. Kostakis, E. Nordlander, N. Hadjiliadis, M. Haukka, J.C. Plakatouras, Inorg. Chem. Commun. 9 (2006) 915.
[18] C. Benelli, D. Gatteschi, Chem. Rev. 102 (2002) 2369.
[19] M.L. Kahn, J.-P. Sutter, S. Golhen, P. Guionneau, L. Ouahab, O. Kahn, D. Chasseau, J. Am. Chem. Soc. 122 (2000) 3413.

antiferromagnetic case, and must be taken into consideration when developing strategies for designing optimal SMMs. Indeed, it has recently been suggested that the barrier height may go as S^0 [12,13] as the spin value increases, thus implying that U does not change in the process. In this paper, we show experimentally that U does increase, and that it goes roughly as S^1 rather that S^2 or S^0.

2. Experiment details

Multi-high-frequency electron paramagnetic resonance (EPR) measurements were performed on single-crystals of $Mn_6^{III}O_2$(Me-sao)$_6$(O_2CCPh$_3$)$_2$(EtOH)$_4$ (**1**) and $Mn_6^{III}O_2$(Et-sao)$_6$(O_2CPh(Me)$_2$)$_2$(EtOH)$_6$ (**2**) at various frequencies from 50 to 350 GHz, and with dc fields applied along different crystallographic directions. Both complexes have monoclinic structures. However, magnetic data suggests complex **1** has a low spin ground state of $S = 4$, whereas complex **2** has a $S = 12$ ground state with a uniaxial molecular anisotropy $D = -0.43\ cm^{-1}$ [11]. Incidentally, it has been shown that **2** holds the record for the highest barrier for a SMM (U = 86.4 K [10]). EPR signals from single-crystals were detected using a sensitive cavity-perturbation technique in combination with a Millimeter-wave Vector Network Analyzer (described elsewhere [14,15]).

3. Data and discussion

The magnetic axial directions of **1** and **2** were determined using the one- and two-axis rotation techniques, respectively (described elsewhere [9,16,17]). Extensive measurements at various temperatures and frequencies were then performed with the dc field applied parallel to the easy-axis to determine the zero-field splitting (ZFS) in the ground state, i.e. the parameters in the simple spin Hamiltonian, $H = DS_z^2 + B_4^0\hat{O}_4^0 + g\mu_B\vec{B}\cdot\hat{S}$ (see [16] for an explanation of the operators/parameters).

Fig. 1 shows temperature-dependence spectra obtained at 331 GHz for complex **2** with the field applied approximately parallel to its easy-axis. A series of more-or-less evenly spaced resonances are seen (dips in transmission). As the temperature is reduced, intensity shifts from the higher field resonances to the lowest field transition. Based upon this observation, we can assign the peaks A1, A2, A3, A4, and A5 to the following EPR transitions: $m_S = -12 \rightarrow -11$, $-11 \rightarrow -10$, $-10 \rightarrow -9$, $-9 \rightarrow -8$, $-8 \rightarrow -7$, respectively, where m_S represents the spin projection along the easy (z-) axis of the crystal. Each of the peaks exhibits several fine structures on the high-field shoulders. This is quite a common observation

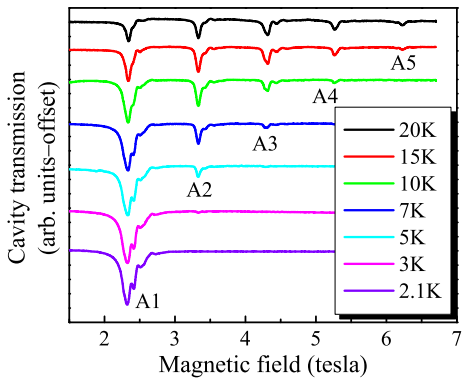


Fig. 1. Temperature dependence spectra obtained at 331 GHz for the easy-axis orientation for complex **2** ($S = 12$). See text for explanation.

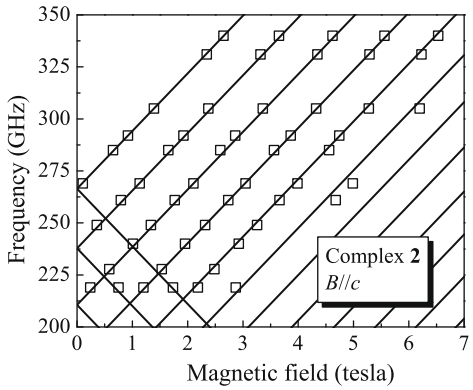


Fig. 2. Energy difference diagram constructed from frequency-dependent measurements for the easy-axis orientation for complex **2** at a temperature of 20 K. The solid lines are the simulations using the parameters given in the main text.

and likely signifies weak disorder in the crystal resulting in a distribution of microenvironments, i.e. a distribution in D [18].

Precise determination of the spin Hamiltonian parameters D, B_4^0 and g is made possible by recording EPR spectra at several high frequencies, as shown in Fig. 2 for this $S = 12$ complex (**2**). Simulations for the easy-axis direction suggest that the system is best described with $D = -0.360(5)\ cm^{-1}$, $B_4^0 = -5.7(5) \times 10^{-6}\ cm^{-1}$ and $g = 1.98(1)$. One can obtain a fairly reliable estimate of the barrier from these parameters, U = 75 K. This value is significantly lower than the one obtained from ac susceptibility measurements, though it remains the highest recorded value for any SMM. Similar discrepancies have been noted for many other SMMs, with ac susceptibility measurements consistently giving larger values for the 'effective' barrier in comparison to spectroscopic measurements [19].

Measurements performed on the $S = 4$ complex (**1**) give the following spin Hamiltonian parameters: $D = -1.272\ cm^{-1}$ and $B_4^0 = +1.3(3) \times 10^{-4}\ cm^{-1}$; g was not well determined because the field was only approximately aligned with the easy axis (within 15°). Fig. 3 shows the best simulation of the frequency dependent data for complex **1**. In addition to the main peaks corresponding to the $S = 4$ state (black squares), a weaker series of peaks is observed, as indicated in the figure by black circles and the dashed line. We note that it is not possible to simulate both sets of peaks simultaneously, even for spin values different from $S = 4$. We thus conclude that the extra peaks result from a low-lying excited state,

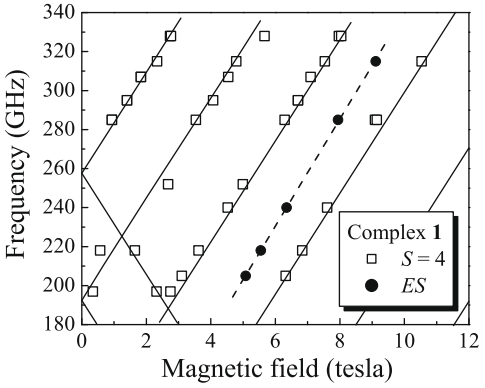


Fig. 3. Energy difference diagram constructed from frequency-dependent measurements for the field close to the easy-axis direction for complex **1**. The solid lines are the simulations using the parameters given in the main text for $S = 4$. The round data points and the dashed line correspond to excitations within a presumed low-lying excited state.

which is not surprising given the frustrated antiferromagnetic interactions within the Mn^{III} triangles. The sizeable positive B_4^0 value is also consistent with this observation. As we have shown previously, higher order terms (4th, 6th, etc.) are caused by ad-mixing of excited spin states to the ground state [20]. What is more, as a rule of thumb, the sign of the axial 4th order term usually reflects the sign of the exchange within the cluster [21]. Reliable evaluation of the spin and ZFS parameters on the basis of magnetic (thermodynamic) measurements for complexes with low-lying states can be problematic. Therefore, these EPR measurements provide an independent spectroscopic confirmation that the ground state of **1** really does correspond to $S = 4$.

An important conclusion from these experiments is that the factor $|D|S$ remains more-or-less unchanged as S increases for these two Mn_6 complexes, i.e. $|D|S = 4.3\ cm^{-1}$ for **2** and $5.1\ cm^{-1}$ for **1**—a 15% variation. Interestingly, the ZFSs between the ground and first excited states (Δ) are almost identical for the two complexes, i.e. $8.9\ cm^{-1}$ for **2** and $8.6\ cm^{-1}$ for **1**—a 3% variation. We note that, in the absence of 4th order anisotropy, $\Delta = D(2S - 1) \approx 2\,|D|S$ is roughly constant for large S. We emphasize that these are purely experimental observations that do not depend on any model or theory. Importantly, this suggests that as S increases, D decreases correspondingly, so that the barrier increases only as S^1, i.e. by a factor of 3 upon increasing S from 4 to 12. This prediction is in good agreement with ac susceptibility measurements which suggest an increase of ~2.7 [11].

4. Theoretical calculations

We next compare the experimental findings with calculations using: (i) projection operator techniques; and (ii) exact matrix diagonalization methods, where the total anisotropy of the molecule is determined in terms of the single-ion anisotropies, D_S, of the individual Mn^{III} atoms. The general expression for the spin Hamiltonian can be written as

$$H = \sum_{i<j}[J_{ij}\hat{S}_i \cdot \hat{S}_j + \hat{S}_i \cdot \vec{\vec{D}}_{ij} \cdot \hat{S}_j] + \sum_i[\hat{S}_i \cdot \vec{\vec{D}}_i \cdot \hat{S}_i + \mu_B \vec{B} \cdot \vec{\vec{g}}_i \cdot \hat{S}_i]. \quad (1)$$

The first summation parameterizes the isotropic (Heisenberg exchange) and anisotropic (dipolar) pairwise interactions between spins i and j in the cluster; the J_{ij} represent the pairwise scalar exchange constants, and the $\vec{\vec{D}}_{ij}$ dipolar tensors. The second sum accounts for the single-ion ZFS (spin–orbit) and Zeeman interactions for the ith spin in the cluster; $\vec{\vec{D}}_{ij}$ and $\vec{\vec{g}}_{ij}$ are the single-ion ZFS and Landé tensors.

We now make a number of approximations in order to simplify the calculations. We stress that it is not our goal to achieve precise agreement between experiment and theory, but rather to provide a general understanding of the factors that contribute to the raising of the anisotropy barrier in these Mn_6 complexes. The approximations are as follows:

(1) We neglect the dipolar contributions to the anisotropy, since these are at least an order of magnitude weaker than the Mn^{III} single-ion anisotropies.
(2) We consider only axial single-ion ZFS of the form $D_i\hat{S}_{zi}^2$. Furthermore, we assume that the ZFS tensors for all six Mn^{III} atoms are the same and aligned with the magnetic easy-axis. This reduces the problem to a single anisotropy parameter, D_S, representing the axial ZFS associated with a single Mn^{III} atom.
(3) We assume that D_S is the same for the ferromagnetic and antiferromagnetic cases, i.e. we assume that the structural modification that switches the sign of the exchange couplings (J_{ij}) does not significantly affect the spin-orbit coupling associated with the individual Mn^{III} centers.

Approximations (2) and (3) undoubtedly represent an oversimplification of the problem. However, our goal here is to obtain a simple correspondence between the molecular D value and the single-ion anisotropy D_S, which would not be possible without these simplifications.

In the strong exchange coupling limit ($J_{ij} \gg D_i$), one can project the anisotropies associated with individual spins onto the total spin state of the coupled system following the techniques described by Bencini and Gatteschi [22]. For a dinuclear system, the total anisotropy, D, is given by

$$D = d_1D_1 + d_2D_2 \quad (2)$$

where d_1 and d_2 are projection coefficients, and D_1 and D_2 are the anisotropies associated with the individual magnetic ions. This can be extended to the six particle case simply by adding spins one at a time to get a trimer, tetramer, etc., then re-computing the total anisotropy each time. Details of our calculations will be published in a longer paper [23].

A schematic of the model for the Mn_6 system, showing both the ferromagnetic and antiferromagnetic cases, is shown in Fig. 4. The calculation for the ferromagnetic case ($S = 12$) is trivial, and one obtains $D_{s=12} = 3D_s/23 = 0.13D_s$. The antiferromagnetic case ($S = 4$) is not as trivial, with the results depending on the coupling scheme: for scheme 1, $(((((S_1 + S_2) + S_4) + S_5) - S_3) - S_6)$, one obtains $D_{s=4} = 0.84D_s$, i.e. $D_{S=12}/D_{S=4} = 0.155$; and for scheme 2, $(((((S_1 + S_2) - S_3) + S_4) + S_5) - S_6)$, one obtains $D_{s=4} = 0.7D_s$, i.e. $D_{S=12}/D_{S=4} = 0.186$.

As an independent check, we set out to solve the problem numerically using a matrix diagonalization approach. For Mn_6, one has to deal with a Hilbert space of size $[(2S+1)^6]^2 = 15\,625\times$

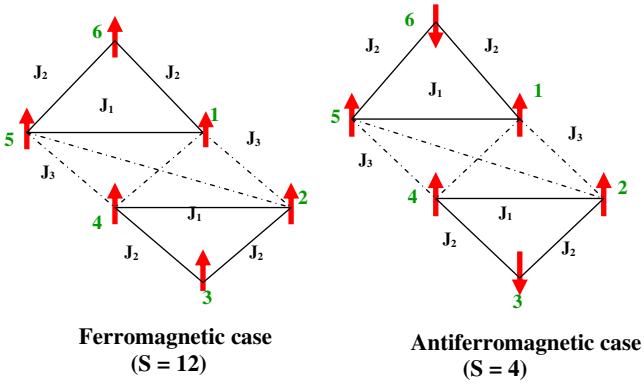


Fig. 4. Schematics of the two models used for the projection operator calculations.

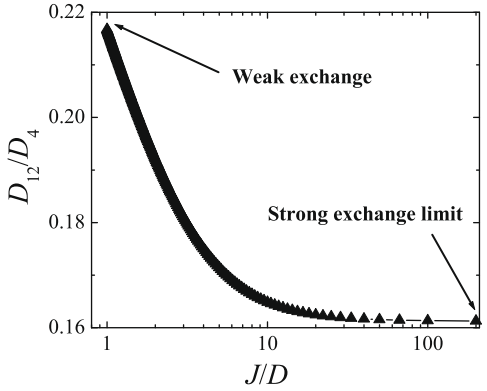


Fig. 5. Plot of the ratio $D_{S=12}/D_{S=4}$ versus J/D obtained from the matrix diagonalization calculations.

Table 1
Comparison between various theoretical and experimental ratios of the anisotropy associated with the $S = 12$ and $S = 4$ Mn_6 complexes (see also Fig. 4): D is the total molecular anisotropy; U is the magnetization reversal barrier; and Δ is the ZFS between the ground and first excited state. We note the somewhat artificial nature of this comparison given that the EPR measurements consider 4th order anisotropy, whereas the calculations do not.

Ratio	Projection operator[a]		Matrix diagonalization[b]		Experimental	
	Scheme 1	Scheme 2	$J \gg D_S$	$J = D_S$	EPR	ac χ''
$D_{S=12}/D_{S=4}$	0.155	0.186	0.160	0.216	0.283	
$U_{S=12}/U_{S=4}$	1.395	1.674	1.440	1.944	2.56	2.70
$\Delta_{S=12}/\Delta_{S=4}$	0.509	0.611	0.525	0.709	1.03	

[a] For the projector operator method the D values were computed exactly, then the other numbers in the table were obtained from these values via the following expressions: $U = DS^2$ and $\Delta = (2S - 1)D$.
[b] For the matrix diagonalization method, the ZFS (Δ) between the lowest two levels was calculated exactly. The other numbers in the table were then deduced by inverting the following expressions: $U = DS^2$ and $\Delta = (2S - 1)D$.

15 625. However, using the sparse matrix algorithm one can obtain the eigenvalues easily and, in the strong exchange limit, the ratio of anisotropies turns out to be $D_{S=12}/D_{S=4} = 0.160$, which differs by 3% and 16% from the ratios obtained using schemes 1 and 2, respectively. An advantage of the 'brute force' diagonalization approach is that one can relax the strong exchange condition and examine the more realistic situation in which $J_{ij} \sim D_S$ [11]. Results obtained assuming a single exchange constant ($J_{ij} = J$, for all i and j) are displayed in Fig. 5, where one sees that the $D_{S=12}/D_{S=4}$ ratio increases/diverges as J decreases. A summary of all experimental and theoretical results is presented in Table 1.

From inspection of Table 1, one can see that the numerical studies seem to suggest a much smaller increase in the barrier, U, than is found experimentally, i.e. a roughly 50% increase, rather than a threefold increase. This finding lends some weight to Waldmann's dire prediction that the barrier should increase as S^0 [12]. Naturally, it is quite likely that the differences between theory and experiment are due to the many approximations that were made in the present study. However, the weak exchange matrix diagonalization calculations ($J = D_S$) provide grounds for some optimism, where one notes that the numerical results start to approach the experimental numbers. We suspect that this may be due to an additional suppression of the barrier for the antiferromagnetic case caused by strong mixing of the $S = 4$ state with low-lying excited states. In other words, the barrier for the $S = 4$ Mn_6 complexes is far from optimized. Therefore, these findings do suggest that the idea of maximizing S by switching the sign of the exchange coupling in polynuclear transition metal complexes is a reasonable strategy for obtaining better SMMs.

5. Conclusion

Detailed high-frequency EPR studies on two Mn_6 complexes have enabled us to better understand how and why the barrier increases as the total molecular spin increases. The experimental results are compared with calculations which demonstrate that a significant increase of the barrier is possible in cases where the exchange and single-ion anisotropy within the cluster are comparable. Overall, our findings support this strategy of increasing S by switching as many exchange pathways in a molecule as possible from antiferromagnetic to ferromagnetic. However, one should not ignore other routes to obtaining better SMMs, particularly methods which maximize single-ion anisotropy and its projection onto the molecular spin ground state.

Acknowledgements

This work was supported by US National Science Foundation (Grant Nos. DMR0239481 and DMR0414809).

References

[1] R. Sessoli, H.L. Tsai, A.R. Schake, S. Wang, J.B. Vincent, K. Folting, D. Gatteschi, G. Christou, D.N. Hendrickson, J. Am. Chem. Soc. 115 (1993) 1804.
[2] A.M. Ako, I.J. Hewitt, V. Mereacre, R. Clérac, W. Wernsdorfer, C.E. Anson, A. Powell, Angew. Chem., Int. Ed. 45 (2006) 4926.
[3] M. Murugesu, S. Takahashi, A. Wilson, K.A. Abboud, W. Wernsdorfer, S. Hill, G. Christou, Inorg. Chem. 47 (2008) 9459.
[4] D.N. Hendrickson, G. Christou, H. Ishimoto, E.K. Brechin, A. Yamaguchi, E.M. Rumberger, S.M.J. Aubin, Z. Sun, G. Aromi, Mol. Cryst. Liq. Cryst. 376 (2002) 301.
[5] J.B. Vincent, H.R. Chang, K. Folting, J.C. Huffman, G. Christou, D.N. Hendrickson, J. Am. Chem. Soc. 109 (1987) 5703. and references therein.
[6] L.F. Jones, G. Rajaraman, J. Brockman, M. Murugesu, E. Carolina Sanudo, J. Raftery, S. Teat, W. Wernsdorfer, G. Christou, E.K. Brechin, D. Collison, Chem. Eur. J. 10 (2004) 5180.
[7] S.G. Seerama, S. Pal, Inorg. Chem. 41 (2002) 4843.
[8] T.C. Stamatatos, D. Foguet-Albiol, C.C. Stoumpos, C.P. Raptopoulou, A. Terzis, W. Wernsdorfer, S.P. Perlepes, G. Christou, J. Am. Chem. Soc. 127 (2005) 15380.
[9] T.C. Stamatatos, D. Foguet-Albiol, S.-C. Lee, C.C. Stoumpos, C.P. Raptopoulou, A. Terzis, W. Wernsdorfer, S.O. Hill, S.P. Perlepes, G. Christou, J. Am. Chem. Soc. 129 (2007) 9484.
[10] C.J. Milios, A. Vinslava, W. Wernsdorfer, S. Moggach, S. Parsons, S.P. Perlepes, G. Christou, E.K. Brechin, J. Am. Chem. Soc. 129 (2007) 2754.
[11] C.J. Milios, R. Inglis, A. Vinslava, R. Bagai, W. Wernsdorfer, S. Parsons, S.P. Perlepes, G. Christou, E.K. Brechin, J. Am. Chem. Soc. 129 (2007) 12505.
[12] O. Waldmann, Inorg. Chem. 46 (2007) 10035.
[13] E. Ruiz et al., Chem. Commun. 52 (2008).
[14] M. Mola, S. Hill, P. Goy, M. Gross, Rev. Sci. Instrum. 71 (2000) 186.
[15] S. Takahashi, S. Hill, Rev. Sci. Instrum. 76 (2005) 023114.
[16] S. Takahashi, R.S. Edwards, J.M. North, S. Hill, N.S. Dalal, Phys. Rev. B 70 (2004) 094429.
[17] E. del Barco, A.D. Kent, S. Hill, J.M. North, N.S. Dalal, E.M. Rumberger, D.N. Hendrickson, N. Chakov, G. Christou, J. Low Temp. Phys. 140 (2005) 119.
[18] J. Lawrence, E.-C. Yang, R. Edwards, M.M. Olmstead, C. Ramsey, N.S. Dalal, P.K. Gantzel, S. Hill, D.N. Hendrickson, Inorg. Chem. 47 (2008) 1965–1974.
[19] S. Hill et al., submitted for publication.
[20] A. Wilson, J. Lawrence, E-C. Yang, M. Nakano, D.N. Hendrickson, S. Hill, Phys. Rev. B 74 (2006) R140403.
[21] S. Datta, O. Waldmann, A.D. Kent, V.A. Milway, L.K. Thompson, S. Hill, Phys. Rev. B 76 (2007) 052407.
[22] A. Bencini, D. Gatteschi, EPR of Exchanged Coupled Systems, Springer-Verlag, 1990.
[23] S. Datta et al., in preparation.

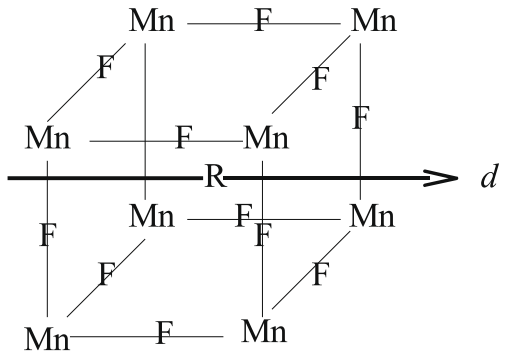


Fig. 1. The RMn_8F_{12} calculation models (R = K, Rb and Li) for the cubic perovskite-type fluorides of $KMnF_3$, $RbMnF_3$ and $K_{1-x}Li_xMnF_3$: (**1**) KMn_8F_{12} model (R = K), (**2**) $RbMn_8F_{12}$ model (R = Rb) and (**3**) $LiMn_8F_{12}$ model (R = Li). *d* is the displacement distance from the cubic center toward <100> direction.

manganese, potassium and rubidium, and 6-31G* for fluorine. All-electron calculations were performed by GAMESS program package [12].

2.2. Effective exchange integrals

The applicability of the approximate spin-projected (AP) effective exchange integral (J_{ab}) scheme by the use of the Heisenberg Hamiltonian was shown in our previous work [1,2]. The AP method resolves the spin contamination problem in the total energy of LS state. The AP J_{ab} value can be obtained by the energy difference between the highest spin (HS) and lowest spin (LS) states. Especially, the AP J_{ab} scheme for the three-dimensional (3D) eight nuclear cube is given by

$$J_{ab} = \{{}^{LS}E - {}^{HS}E\}/\{{}^{HS}\langle \mathbf{S}^2\rangle - {}^{LS}\langle \mathbf{S}^2\rangle + 8\{\langle\downarrow\uparrow\rangle - \langle\uparrow\uparrow\rangle\}\} \quad (2)$$

where ${}^{X}E$ and ${}^{X}\langle \mathbf{S}^2\rangle$ denote the total energy and spin angular momentum for the spin state *X* (*HS* or *LS*), respectively, and $\langle\uparrow\downarrow\rangle$ and $\langle\uparrow\uparrow\rangle$ mean the expectation values for antiferromagnetic and ferromagnetic spin couplings, respectively, which are given by

$$\langle\uparrow\downarrow\rangle = -S_aS_b \quad (3a)$$

$$\langle\uparrow\uparrow\rangle = S_aS_b \quad (3b)$$

where S_c ($c = a, b$) denotes the size of the spin angular momentum at the site. The detailed derivation of these equations is shown in Ref. [2].

3. Results and discussion

3.1. Effective exchange integral

It is known that $KMnF_3$ and $RbMnF_3$ exhibit the antiferromagnetic G-type ordering [13]. In order to discuss the magnetic interactions quantitatively in $KMnF_3$ and $RbMnF_3$, AP J_{ab} values were obtained for **1** and **2**. The Mulliken spin density population, which is the double size of the total spin angular momentum, is used to obtain the expectation values for the ferromagnetic and antiferromagnetic spin couplings between manganeses. Table 1 shows J_{ab} values for **1** and **2** by UHF, UBHHLYP and UB3LYP. J_{ab} values by UBHHLYP are roughly consistent with the experimental ones, while UHF and UB3LYP underestimates and overestimates $|J_{ab}|$ values, respectively. As the experimental J_{ab} values in the perovskte-type fluorides often provide 20–30% error, UBHHLYP can be treated as one of the proper calculations for these species.

3.2. Spin density and charge density populations

The Mulliken spin and charge density populations are useful indices to estimate the magnitudes of electron and spin correlations in the perovstite-type manganese fluorides. Table 2 shows the spin density and charge density populations of **1** and **2** in LS state, by UBHHLYP. There is no atomic spin density population in potassium and rubidium. Namely, there exists no direct magnetic interaction between manganese and counter cation, as expected from no magnetic moment in counter cation. On the other hand, the atomic charge density populations in potassium and rubidium are 0.814 and 0.836, respectively. In spite of no direct magnetic interaction between manganese and counter cation, the charge transfer from counter cation to fluorines occurs.

3.3. Electron density population

The shapes of the electron density population were displayed by MOLEKEL 4.3 [14]. Fig. 2 depicts the shapes of the electron density populations of **1** and **2** in LS state, by UBHHLYP. The overlap between manganeses via bridge-fluorine causes the antiferromagnetic superexchange (SE) interaction. Rubidium is more overlapped with fluorines than potassium. Our calculation result shows that the cavity in $RbMnF_3$ is excessively filled in comparison with $KMnF_3$. It is empirically predicted from the *t* values in $KMnF_3$ (0.96) and $RbMnF_3$ (1.03). It is considered that no phase transition from cubic structure in $RbMnF_3$ comes from the perfect fitting, while $KMnF_3$ displays cubic to tetragonal phase transition.

3.4. Intrinsic roles of counter cation

Here, we consider only the cubic phase in $KMnF_3$ and $RbMnF_3$, and counter cation is displaced from the cubic center, in order to investigate the intrinsic size and ionic effects of counter cation on the magnetic interaction. Here, the variations of the total energy and J_{ab} value were examined, changing the displacement distance (*d*) from the cubic center toward <100> direction. In relation to the lithium ion conduction, the intrinsic roles of lithium on the magnetic interaction were also investigated in $K_{1-x}Li_xMnF_3$.

Table 1
The total energy[a], spin angular momentum[b] and effective exchange integral (J_{ab}) value[c] for (**1**) KMn_8F_{12} and (**2**) $RbMn_8F_{12}$ models (UBHHLYP method).

Method	**1**			**2**		
	${}^{LS}E$	${}^{HS}E$	J_{ab}	${}^{LS}E$	${}^{HS}E$	J_{ab}
UHF	−10987.1885006532 (19.994)	−10987.1869634561 (420.004)	−1.125	−13324.3702970161 (19.995)	−13324.3689485813 (420.004)	−0.986
UBHHLYP	−11001.1218859766 (19.963)	−11001.1160825407 (420.004)	−4.245	−13339.3239838087 (19.966)	−13339.3186895278 (420.004)	−3.873
UB3LYP	−11001.7020687602 (19.874)	−11001.6903573365 (420.007)	−8.564	−13339.9182406185 (19.882)	−13339.9074488484 (420.007)	−7.892
Experiment			−5.050[d]			−4.700[d]

[a] The total energy is shown in a.u.
[b] The spin angular momentum is given in parenthesis.
[c] J_{ab} value is shown in cm^{-1}.
[d] The experimental J_{ab} values are shown in Ref. [13].

Table 2
The Mulliken spin density and charge density[a] populations of (**1**) KMn_8F_{12} and (**2**) $RbMn_8F_{12}$ models in LS state (UBHHLYP method).

	K (Rb)	Mn (up)	Mn (down)	*F*
1	0.000 (0.814)	4.915 (1.749)	−4.915 (1.749)	0.000 (−0.814)
2	0.000 (0.836)	4.917 (1.746)	−4.917 (1.746)	0.000 (−0.817)

[a] The charge density population is given in parenthesis.

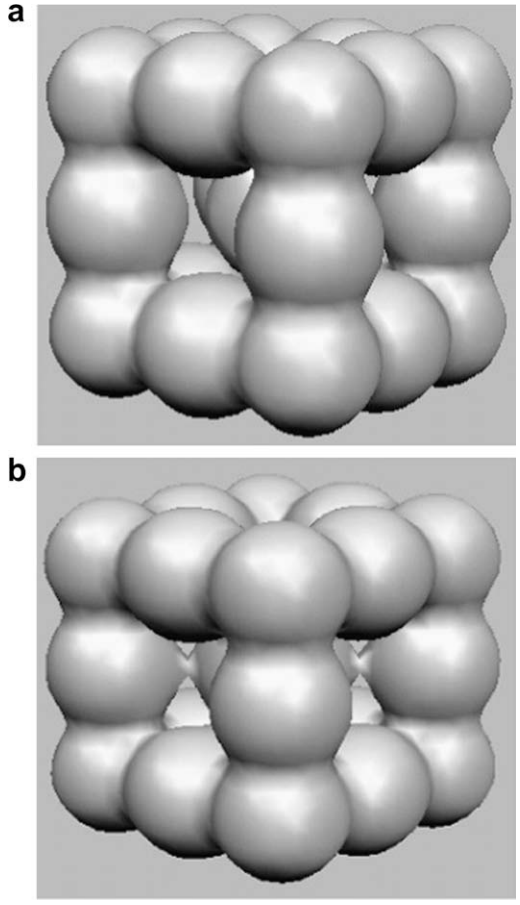


Fig. 2. The shapes of the electron density populations of (a) (**1**) KMn_8F_{12} model and (b) (**2**) $RbMn_8F_{12}$ model in LS state (UBHHLYP method, at the same threshold).

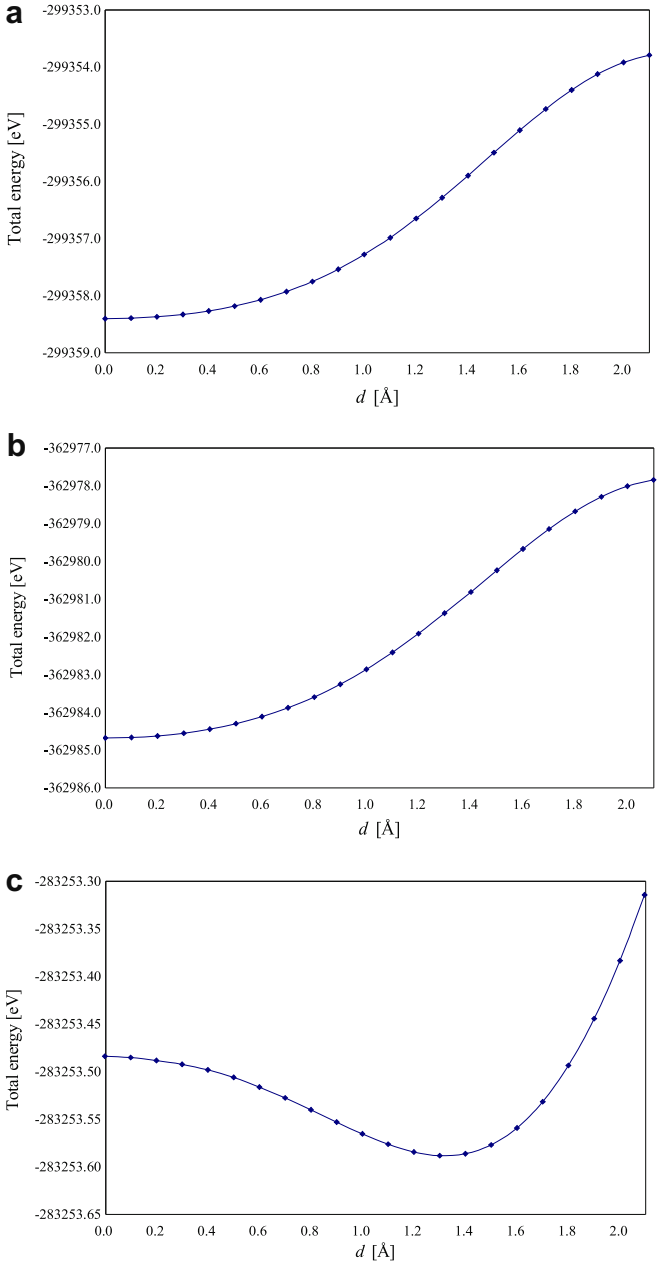


Fig. 3. The potential energy curves for (a) (**1**) KMn_8F_{12} model (b) (**2**) $RbMn_8F_{12}$ model and (c) (**3**) $LiMn_8F_{12}$ model, changing the displacement distance (*d*) from the cubic center toward <100> direction (UBHHLYP method).

Fig. 3 shows the potential energy curves for **1**, **2** and **3**, changing *d*, respectively. The potential energy curves for **1** and **2** increase monotonously. The energy differences between 0.0 Å and bottleneck, which is the Mn_4F_4 square part, in **1** and **2** are 4.612 and 6.837 eV, respectively. It shows that the steric repulsion between counter cation and bottleneck is large. In addition, the counter cation displacement makes the total energy in $RbMnF_3$ higher than that in $KMnF_3$. It comes from the perfect fitting of rubidium in the cubic center.

The potential energy curve for **3** has the minimum point at about 1.3 Å. It shows that lithium can move off the cubic center easily. The energy difference between the minimum point and cubic center (bottleneck) is 0.105 eV (0.274 eV). It is known that the activation energy of the lithium ion conduction in the perovskite-type titanium oxide of $La_{2/3-x}Li_{3x}TiO_3$ (LLT) is between 0.15 and 0.40 eV [15–17]. It is concluded that the lithium ion conduction in the perovskite-type manganese fluoride of $RMnF_3$ is possible, if the vacancy at R site exists as same as LLT. In addition, it shows that the steric repulsion between lithium and bottleneck is negligible, and the ionic bonds between lithium and other atoms are dominant.

Fig. 4 shows the J_{ab} curves for **1**, **2** and **3**, changing *d*, respectively. Eq. (2) is assumed even for the unsymmetrical configuration (*d* is not 0), under the approximation of the expectation values for ferromagnetic (25/4) and antiferromagnetic (−25/4) spin couplings. $|J_{ab}|$ values for **1** and **2** become larger by the increase of *d*. Because the orbital overlap between manganese and fluorine near the opposite bottleneck is more strengthened by the increase of *d*, due to the cavity of the electron density population of counter cation. It shows that potassium and rubidium in the cubic center control the strength of the magnetic interaction. On the other hand, $|J_{ab}|$ value variation for **3** by the increase of *d* is smaller in comparison with **1** and **2**. The orbital overlap between manganese and fluorine is little changed by the displacement of lithium. Hence,

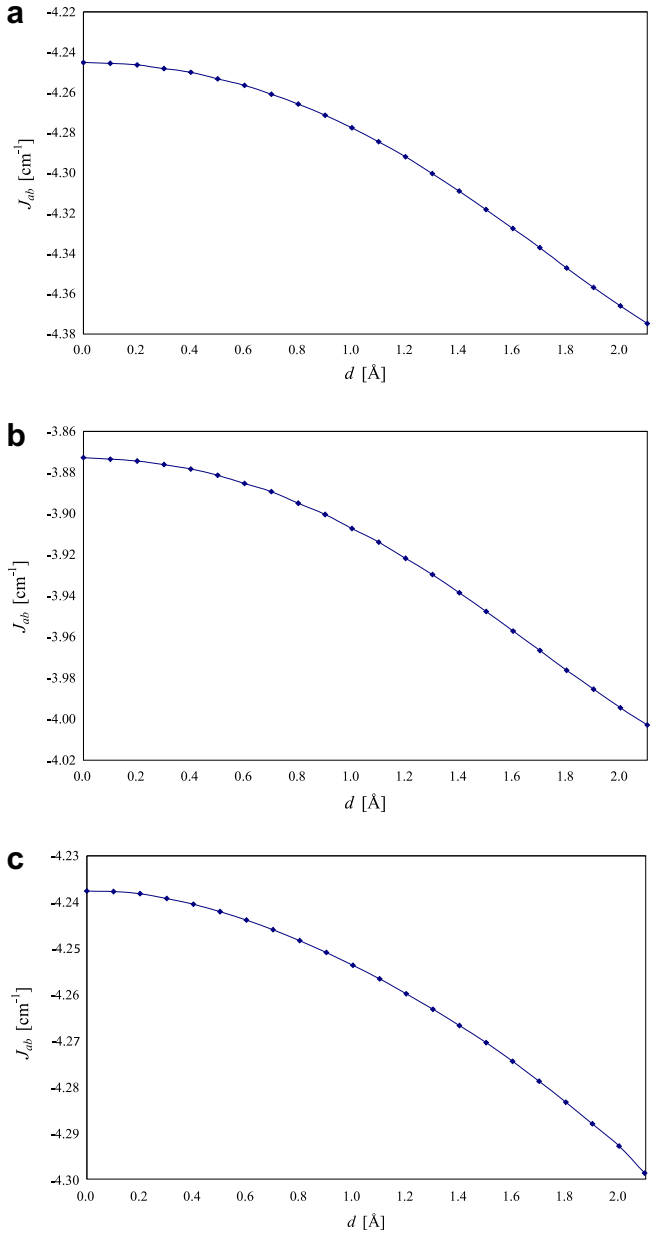


Fig. 4. The effective exchange integral (J_{ab}) curves for (a) (**1**) KMn_8F_{12} model, (b) (**2**) $RbMn_8F_{12}$ model, and (c) (**3**) $LiMn_8F_{12}$ model, changing the displacement distance (d) from the cubic center toward <100> direction (UBHHLYP method).

it is considered that the magnetic change is negligible, when the lithium ion conduction appears in $K_{1-x}Li_xMnF_3$.

4. Conclusion

We performed hybrid-DFT calculations for the perovskite-type manganese fluorides of $KMnF_3$, $RbMnF_3$ and $K_{1-x}Li_xMnF_3$. The J_{ab} value, spin density and charge density populations, electron density population and total energy were obtained. We concluded as follows:

1. UBHHLYP provided the reasonable J_{ab} value.
2. In $KMnF_3$ and $RbMnF_3$, there exists no direct magnetic interaction between manganese and counter cation. However, potassium (rubidium) has the role of controlling the strength of the magnetic interaction
3. No phase transition in $RbMnF_3$ comes from the perfect fitting.
4. The lithium ion conduction in $RMnF_3$ is possible, if the vacancy at R site exists. The magnetic change is negligible when the lithium ion conduction appears.

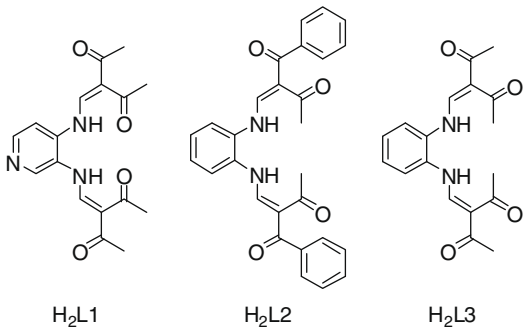
Our calculation results show that the antiferromagnetic perovskite-type fluorides are able to have the lithium ion conductivity. In comparison with the existing LLT, the degree of the structural distortion is small. In addition, the delocalization effect between manganese and fluorine is also small. Hence, the larger bottleneck of Mn_4F_4 square could be provided in spite of the existence of d-electron in manganese. It is considered that doping of the divalent counter cations such as Mg^{2+}, Ca^{2+}, Sr^{2+} and Ba^{2+} causes the vacancy at R site. In the near future, the vacancy doping technique would enable us to realize the new perovskite-type antiferromagnet with the lithium ion conductivity. From the viewpoint of the material science, $RMnF_3$ would be useful for the solid state electrolyte and positive electrode materials in the secondary lithium ion battery. For other perovskite-type transition metal fluorides such as $RNiF_3$, $RCoF_3$ and $RFeF_3$, our work is also in progress.

Acknowledgments

T. Onishi has been supported by "Iketani Science and Technology Foundation" and "Murata Science Foundation".

References

[1] T. Onishi, D. Yamaki, K. Yamaguchi, Y. Takano, J. Chem. Phys. 118 (2003) 9747.
[2] T. Onishi, K. Yamaguchi, J. Chem. Phys. 121 (2004) 2199.
[3] T. Onishi, Y. Yoshioka, e-J. Surf. Sci. Nanotech. 5 (2007) 17.
[4] T. Onishi, Y. Yoshioka, e-J. Surf. Sci. Nanotech. 5 (2007) 20.
[5] F. Borsa, D.J. Benard, W.C. Walker, A. Baviera, Phys. Rev. B. 15 (1977) 84.
[6] A. Waśkowska, A. Ratuszna, J. Solid State Chem. 137 (1998) 71.
[7] J.P. Toennies, R. Vollmer, Phys. Rev. B 44 (1991) 9833.
[8] D.T. Teaney, V.L. Moruzzi, B.E. Argyle, J. Appl. Phys. 37 (1966) 1122.
[9] R.D. Shannon, Acta Crystallogr. A32 (1976) 751.
[10] K. Terakura, T. Oguchi, A.R. Williams, J. Kübler, Phys. Rev. B 30 (1984) 4734.
[11] H. Tatewaki, S. Huzinaga, J. Chem. Phys. 71 (1980) 4339.
[12] M.W. Schmidt, K.K. Baldridge, J.A. Boatz, S.T. Elbert, M.S. Gordon, J.H. Jensen, S. Koseki, N. Matsunaga, K.A. Nguyen, S. Su, T.L. Windus, M. Dupuis, J.A. Montgomery, J. Comput. Chem. 14 (1993) 1347.
[13] J.B. Parkinson, J. Phys. C 2 (1969) 2003.
[14] P. Flükiger, H.P. Lüthi, S. Portmann, J. Weber, Swiss Center for Scientific Computing, Manno (Switzerland), 2000–2002, MOLEKEL 4.3, Stefan Portmann and Hans Peter Lüthi, MOLEKEL: An Interactive Molecular Graphics Tool, CHIMIA 54 (2000) 766.
[15] Y. Inaguma, J. Yu, Y.-J. Shan, M. Itoh, T. Nakamura, J. Electrochem. Soc. 142 (1995) L8.
[16] M. Yashima, T. Katsumata, M. Itoh, Y. Morii, T. Tsurui, Solid State Ionics 177 (2006) 3037.
[17] Y. Inaguma, J. Ceram. Soc. Jpn. 114 (2006) 1103.



Scheme 1. General scheme of Schiff-base like ligands H_2L1, H_2L2 and H_2L3 discussed in this work.

(%) = 329 (14) [M^+]. ^{1}H NMR (270 MHz, $CDCl_3$): δ/ppm = 2.35 (s, 3H, $COCH_3$), 2.41 (s, 3H, $COCH_3$), 2.55 (s, 3H, $COCH_3$), 2.60 (s, 3H, $COCH_3$), 7.21 (d, ^3J(HC–CH) = 5.56 Hz, 1H, CH), 8.05 (d, ^3J(HN–CH) = 11.56 Hz, 1H, NCH), 8.20 (d, ^{9U}J(HN–CH) = 11.58 Hz, 1H, NCH), 8.50 (d, ^3J(HC–CH) = 5.48 Hz, 1H, CH), 8.50 (s, 1H, CH), 12.89 (d, ^3J(HN–CH) = 11.48 Hz, 1H, CNH), 13.02 (d, ^3J(HN–CH) = 11.58 Hz, 1H, CNH).

[FeL1(MeOH)](MeOH) (**1**(MeOH)): A suspension of iron(II)acetate (3.75 g, 21.6 mmol) and H_2L1 (4.18 g, 12.7 mmol) was heated to reflux for one hour in 200 ml methanol. After cooling to room temperature a dark violet powder of **1**(MeOH) was obtained which was collected, washed twice with 10 ml methanol and dried in vacuum. The mother liquid was kept at 5 °C over a week to obtain single crystals of **1**(MeOH). Yield: 5.36 g, 12.0 mmol (94%). *Anal.* Calc. $C_{19}H_{25}FeN_3O_6$ (447.26): C, 51.02; H, 5.63; N, 9.39. Found: C, 50.77; H, 5.09; N, 9.78%. IR (PE): $\tilde{\nu}$ [cm^{-1}]: 1638 (CO), 1562 (CO). MS (DEI+): *m/z* (%) = 383 (73) [M^+], 44 (100) [$COCH_3$+H^+].

[FeL1(bipy)] (**2**): A suspension of **1**(MeOH) (0.46 g, 1.0 mmol) and bipy (1.73 g, 11.1 mmol) was heated to reflux for one hour in 30 ml methanol. After cooling to room temperature a red powder of **2** was obtained which was collected, washed twice with 5 ml methanol and dried in vacuum. Yield: 0.49 g, 0.91 mmol (91%). *Anal.* Calc. $C_{27}H_{25}FeN_5O_4$ (539.36): C, 60.12; H, 4.67; N, 12.98. Found: C, 59.87; H, 4.57; N, 12.95%. IR (PE): *v* [cm^{-1}]: 1647 (CO), 1560 (CO). MS (DEP/EI): *m/z* (%) = 383 (37) [M^+], 43 (100) [$COCH_3^+$], 156 (7) [bipy]. Single crystals of **2**$(MeOH)_{0.5}$ were slowly formed by diffusion techniques in methanol solution after several weeks.

[FeL2$(MeOH)_2$](MeOH) (**3**(MeOH)): A suspension of iron(II)acetate (2.04 g, 11.7 mmol) and H_2L2 (3.12 g, 6.9 mmol) was heated to reflux for one hour in 150 ml methanol. After cooling to room temperature a dark violet powder of [FeL2$(MeOH)_2$] (**3**) was obtained which was collected, washed twice with 10 ml methanol and dried

Table 1
Crystallographic data of the iron(II) complexes discussed in this work.

Compound	**1**(MeOH) [FeL1(MeOH)](MeOH)	**2**$(MeOH)_{0.5}$ [FeL1(bipy)]$(MeOH)_{0.5}$	**3**(MeOH) [FeL2$(MeOH)_2$](MeOH)
Empirical formula	$C_{19}H_{25}FeN_3O_6$	$C_{27}H_{25}FeN_5O_4$·0.5 MeOH	$C_{31}H_{34}FeN_2O_7$
Formula weight	447.27	555.39	602.46
Temperature (K)	200(3)	200	200(3)
Crystal size (mm)	0.24 × 0.07 × 0.07	0.166 × 0.090 × 0.026	0.45 × 0.24 × 0.14
Crystal system	orthorhombic	triclinic	triclinic
Space group	$Pca2_1$	$P\bar{1}$	$P\bar{1}$
λ (Å)	0.71069	0.71073	0.70930
a (Å)	8.862(3)	11.5630(3)	9.167(2)
b (Å)	20.877(5)	11.6015(3)	10.4630(17)
c (Å)	11.706(6)	19.6310(5)	16.712(4)
α (°)	90.0	81.352(2)	80.837(16)
β (°)	90.0	79.596(1)	89.089(19)
γ (°)	90.0	89.359(1)	67.905(10)
V (Å^3)	2165.8(14)	2560.37(12)	1464.6(5)
Z	4	2	2
ρ_{calc} (g/cm^3)	1.372	1.441	1.366
μ (mm^{-1})	0.735	0.635	0.565
F(000)	936	1156	632
θ range (°)	3.7–21.0	3.2–27.5	3.8–25.3
Index ranges	$-8 \leqslant h \leqslant 8$	$-15 \leqslant h \leqslant 15$	$-11 \leqslant h \leqslant 10$
	$-20 \leqslant k \leqslant 21$	$-15 \leqslant k \leqslant 12$	$-12 \leqslant k \leqslant 12$
	$-11 \leqslant l \leqslant 11$	$-25 \leqslant l \leqslant 25$	$-20 \leqslant l \leqslant 19$
Reflections collected	13928	20868	19519
Reflections unique [R_{int}]	2318 = 0.1210	11697 = 0.0487	5321 = 0.0500
R_1 (all)	0.0381 (0.0800)	0.0497 (0.1041)	0.0359 (0.0578)
wR_2	0.0828	0.1270	0.1020
Goodness-of-fit	0.985	1.028	1.012

Table 2
Selected bond lengths (Å) and angles (°) within the first coordination sphere of the iron(II) complexes discussed in this work.

Complex	Fe1–N1/2	Fe1–O1/2	Fe1–L_{ax}	O1–Fe1–O2	L_{ax}–Fe1–L_{ax}
1(MeOH)	2.100(6)	2.008(4)	2.232(5) (O)	112.3(2)	168.7(2)
[FeL1$(MeOH)_2$]	2.099(6)	2.037(6)	2.239(6) (N)		
	2.120(2)	2.019(2)	2.244(2) (N)		
2$(MeOH)_{0.5}$	2.110(2)	2.036(2)	2.251(2) (N)	114.48(8)	173.34(9)
[FeL1(bipy)]$(MeOH)_{0.5}$	2.116(2)	2.021(2)	2.232(2) (N)	113.06(8)	173.30(8)
	2101(2)	2.028(2)	2.279(2) (N)		
3(MeOH)	2.098(2)	2.034(2)	2.192(2) (O)	111.76(7)	165.53(7)

Table 3
Bond lengths (Å) and angles (°) of the classical and non-classical hydrogen bonds of the iron(II) complexes discussed in this work.

Complex		D···A	D–H···A	D–H	H···A
1(MeOH) [FeL1(MeOH)](MeOH)	O(5)–H(5A)···O(6)	2.721(8)	136	0.84	2.05
	O(6)–H(6A)···O(3)	2.697(9)	171	0.84	1.86
	C(6)–H(6)···O(4)	3.177(9)	125	0.95	2.45
	C(7)–H(7)···O(4)	3.181(10)	123	0.95	2.57
	C(18)–H(18A)···O(2)	3.189(14)	119	0.98	2.59
$2(MeOH)_{0.5}$ [FeL1(bipy)]$(MeOH)_{0.5}$	O(90B)–H(90H)···O(24)	2.750(6)	171	0.84	1.92
	C(20)–H(20)···O(24)	3.160(4)	138	0.95	2.39
	C(27)–H(27)···O(23)	3.147(4)	130	0.95	2.45
	C(49)–H(49)···O(13)	3.248(4)	137	0.95	2.49
3(MeOH) [FeL2$(MeOH)_2$](MeOH)	O(5)–H(51)···O(4)	2.749(3)	136	0.84	2.08
	O(6)–H(61)···O(7)	2.634(3)	158	0.84	1.84
	O(6)–H(71)···(1)	2.761(2)	177	0.84	1.92
	C(24)–H(24)···O(3)	3.449(3)	150	0.95	2.59
	C(28)–H(28)···N(1)	3.530(3)	170	0.95	2.59

in vacuum. Yield: 2.85 g, 5.00 mmol (72%). *Anal.* Calc. $C_{30}H_{30}FeN_2O_6$ (570.41): C, 63.17; H, 5.30; N 4.91. Found: C, 63.05; H, 5.18; N, 4.93%. IR (PE): ν [cm^{-1}]: 1556 (CO). MS (DEI+): *m/z* (%) = 506 (100) [M^+], 77 (38) [C_6H_5].

The mother liquid was kept at 5 °C for 18 d. The obtained dark violet, glistening crystals of **3**(MeOH) with the shape of long slices were collected and dried in vacuum. Yield: 0.40 g, 0.66 mmol (10%). *Anal.* Calc. $C_{31}H_{34}FeN_2O_7$ (602.46): C, 61.80; H, 5.69; N, 4.65. Found: C, 61.95; H, 5.82; N, 4.80%. IR (PE): ν [cm^{-1}]: 1561 (CO). MS (DEI+): *m/z* (%) = 506 (100) [M^+].

2.2. Magnetic measurements

Magnetic measurements of the samples were performed on a Quantum-Design-MPMSR2-SQUID-Magnetometer in a temperature range from 2 to 295 K. The measurements were carried out at a field strength of 0.05 T in the settle mode. The data were corrected for the magnetization of the sample holder and diamagnetic corrections were made using tabulated Pascal's constants.

2.3. X-ray crystallography

The intensity data of **1**(MeOH) and **3**(MeOH) were collected on an Oxford XCalibur diffractometer using graphite-monochromated Mo Kα radiation, the intensity data of **2**$(MeOH)_{0.5}$ were collected on a Nonius Kappa CCD diffractometer using graphite-monochromated Mo Kα radiation. Data were corrected for Lorentz and polarization effects. The structure was solved by direct methods (Sir 97) and refined by full-matrix least-square techniques against F_0^2 (SHELXL-97). The hydrogen atoms were included at calculated positions with fixed thermal parameters. ORTEP-III was used for structure representation. The crystallographic data are summarized in Table 1. Selected distances and angles are presented in Tables 2 and 3.

3. Results and discussion

3.1. Description of the X-ray structures

Crystals suitable for X-ray structure analysis were obtained for all complexes. The crystallographic data are summarized in Table 1. Fig. 1 displays an ORTEP drawing of the asymmetric unit of **1**(MeOH), **2**$(MeOH)_{0.5}$ and **3**(MeOH). Selected bond length and angles are summarized in Table 2.

In all complexes the iron centre is situated in an octahedral coordination sphere and the obtained bond lengths around the iron(II) centres of **1**(MeOH), **2**$(MeOH)_{0.5}$ and **3**(MeOH) are within the region reported for other octahedral iron(II) complexes of the same ligand type in the high-spin (HS) state [6–9]. The average values are 2.11 Å ($Fe–N_{eq}$), 2.03 Å ($Fe–O_{eq}$) and 2.23 Å ($Fe–L_{ax}$). The average $O_{eq}–Fe–O_{eq}$ angle with a value of 113° also indicates that all

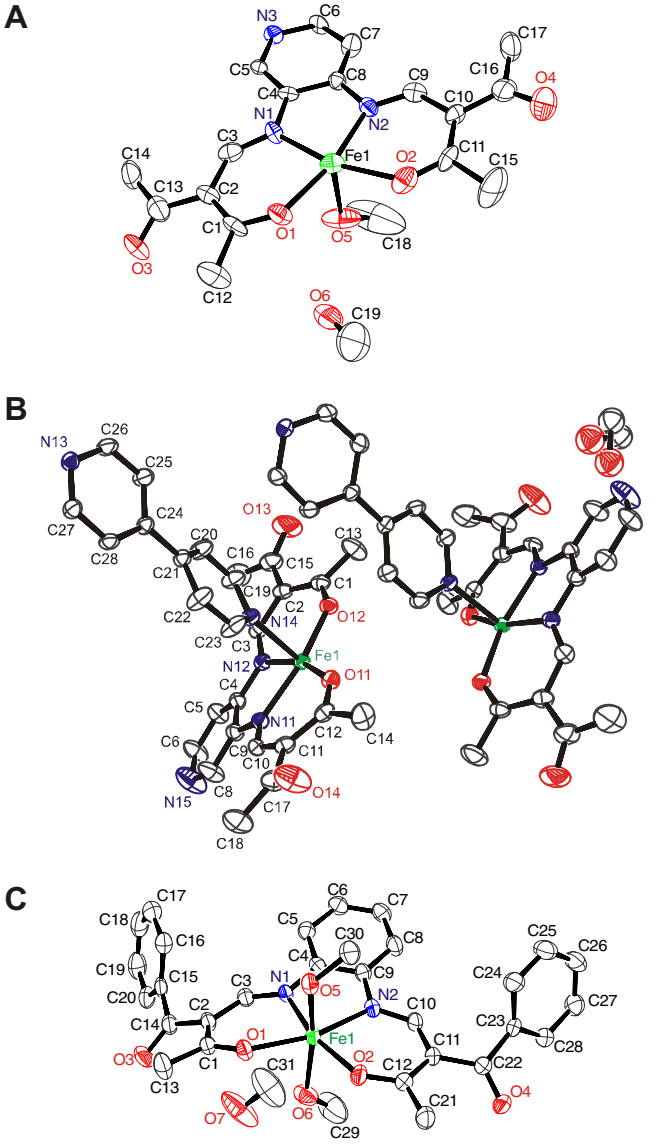


Fig. 1. ORTEP-drawing of the asymmetric unit of **1**(MeOH) (A), **2**$(MeOH)_{0.5}$ (B) and **3**(MeOH) (C). Hydrogen atoms were omitted for clarity. Thermal ellipsoids are shown at the 50% probability level.

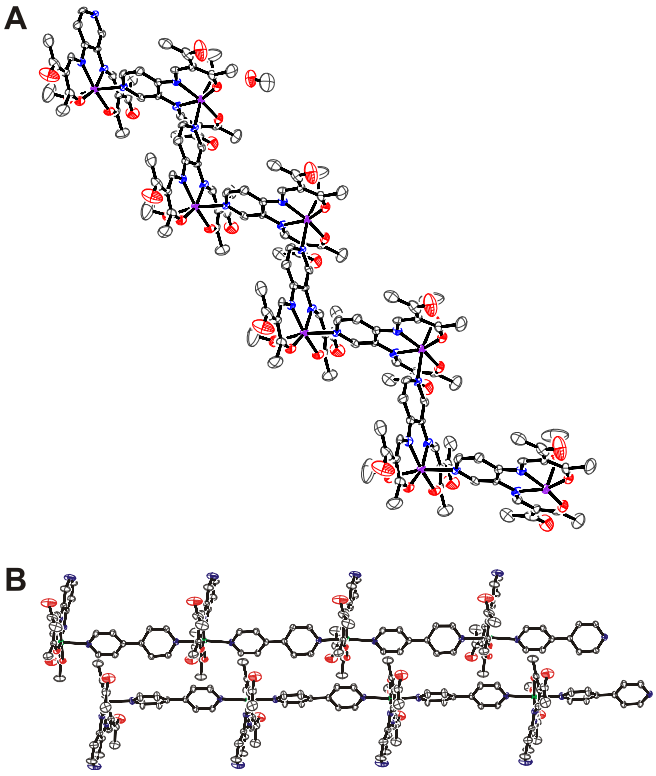


Fig. 2. ORTEP-drawing of the zigzag chain structure of **1**(MeOH) (A) and the linear chain structure of **2**$(MeOH)_{0.5}$ (B).

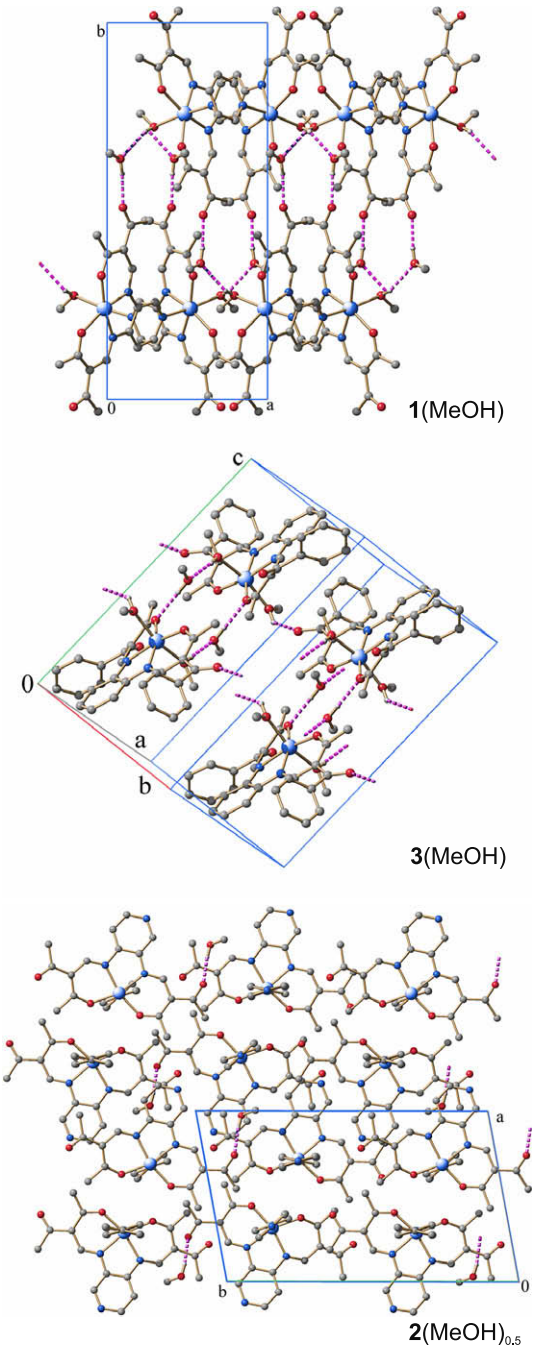


Fig. 3. A plot of the crystal packing of the molecules of **1**(MeOH) along [0 0 1] (top), **2**$(MeOH)_{0.5}$ (bottom) and **3**(MeOH) along [0 0 1] (middle).

complexes are clearly in the HS state. This angle typically changes from about 110° in the HS state to about 90° in the low-spin (LS) state for this type of complexes [6–9].

As expected, the pyridine nitrogen of the ligand H_2L1 in complex **1**(MeOH) acts as axial ligand at the neighbouring complex molecule. This result in the formation of 1D zigzag chain with an angle of 84° between two neighbouring equatorial ligands and an intermolecular Fe–Fe distance of 7.35 Å as shown in Fig. 2A. The second axial coordination side is occupied by a methanol molecule leading to a N_3O_3 coordination sphere at the iron centre. A similar motive was recently reported for a mononuclear complex of this ligand type with 3-aminopyridine and methanol as axial ligands [13]. If 4,4′-bipyridine is used as axial ligand instead of methanol (complex **2**$(MeOH)_{0.5}$) the bipy replaces the pyridine nitrogen of the equatorial ligand and a linear 1D chain with parallel equatorial ligands is obtained (Fig. 2B). The 4,4′-bipyridine occupies both coordination sides and an N_4O_2 coordination sphere is obtained. The inter-chain Fe–Fe distances in this example is with 11.60 Å in the same order of magnitude as reported for similar 4,4′-bipyridine bridged iron(II) complexes [8a]. Between two neighbouring chains the shortest Fe–Fe distances are 7.16 Å/6.03 Å for **1**(MeOH)/**2**$(MeOH)_{0.5}$. In complex **3**(MeOH) both axial coordination sides are occupied by a methanol molecule resulting in a N_2O_4 coordination sphere around the iron centre. For this example no chain formation is observed. The shortest Fe–Fe distance in the molecule packing of this complex is 7.12 Å.

Hydrogen bonding and π-stacking are always considered to play a central role for the mediation of cooperative interactions [5,6,9], independent of the discussed magnetic phenomena (spin crossover or long-range magnetic ordering). A plot of the crystal packing of the molecules of the three complexes is given in Fig. 3. The idea to used the phenyl group in H_2L2 to introduce π–π-interactions did not work for the complex **3**(MeOH) as no indication for this kind of interactions are observed. For the two methanol adducts **1**(MeOH) and **3**(MeOH) hydrogen bond interactions are found between the single molecules (**3**(MeOH)) or the 1D chains (**1**(MeOH)). The hydroxyl group of the axially coordinated methanol acts in both cases as hydrogen bond donor connecting two complex-molecules using the carbonyl oxygen of the neighbouring equatorial ligand as accepter. In both cases a 1D chain of hydrogen bond linked molecules is formed along [1 0 0]. For the monomer complex **3**(MeOH), half of the connections are communicated over the hydroxyl groups of the non-coordinating methanol molecules resulting in a 1D double-chain of linked molecules. For

the 1D chain compound **1**(MeOH), all connections include a non-coordinating methanol molecule that links two polymer chains together resulting in a 1D double-chain of linked molecules (Fig. 3, top).

For complex **2**$(MeOH)_{0.5}$ there are hydrogen bonds between carbonyl group of the equatorial ligand and hydroxyl group of non-coordinating methanol molecules without the formation of any additional network.

3.2. Magnetic properties

Magnetic susceptibility measurements for all compounds were performed in a temperature range from 295 to 2 K. The plots for $\chi_M T$ and $1/\chi_M$ versus T are given in Fig. 4. With decreasing temperature the $\chi_M T$ product decreases from a value of 3.86/3.29/3.60 $cm^3\ K\ mol^{-1}$ at 295 K to a value of 3.29/3.02/3.22 $cm^3\ K\ mol^{-1}$ at 25 K for the complexes **1**(MeOH), **2**$(MeOH)_{0.5}$ and **3**(MeOH), respectively. These susceptibility data can be fitted well with the Curie–Weiss law: $1/\chi_M = C/(T - \Theta)$. The parameters for complex **1**(MeOH) are $\Theta = -5.23$ K and $C = 3.91$ $cm^3\ K\ mol^{-1}$, for complex **2**$(MeOH)_{0.5}$ $\Theta = -3.22$ K and $C = 3.31$ $cm^3\ K\ mol^{-1}$ and for complex **3**(MeOH) $\Theta = -5.38$ K and $C = 3.64$ $cm^3\ K\ mol^{-1}$. The Curie constant is for all three complexes in a region expected for iron(II) HS complexes. The negative Weiss constant Θ and the decrease of the $\chi_M T$ product with decreasing temperature, both indicate weak antiferromagnetic interactions between the spin centres which are stronger for the methanol adducts **1**(MeOH) and **3**(MeOH). This is most likeably due to the missing hydrogen bond network in **2**$(MeOH)_{0.5}$. Below a temperature of 25 K the $\chi_M T$ product decreases further for **2**$(MeOH)_{0.5}$ and **3**(MeOH). This is due to weak antiferromagnetic exchange interactions (**3**(MeOH)) or zero-field splitting (**2**$(MeOH)_{0.5}$) or probably a combination of the two. For **1**(MeOH) the $\chi_M T$ product significantly increases below 10 K. Consequently field-cooled magnetization and zero-field-cooled magnetization (FCM/ZFCM) measurements were performed in a temperature range from 20 to 2 K for the complex **1**(MeOH) with $H = 30$ G. The results are shown in Fig. 5. The clear increase of the magnetization of complex **1**(MeOH) below 5 K shows the onset of long-range magnetic ordering with a critical temperature of $T_C = 3.5$ K. The high-temperature antiferromagnetic interactions in combination with the spontaneous magnetization at low temperatures are an indication for spin canting mechanism as the reason for the observed properties. The decrease of the magnetization below 3.5 K is most likely caused by antiferromagnetic interactions between the neighbouring 1D chains. These results are in good agreement with the results from X-ray structure analysis. The zigzag structure observed for **1**(MeOH) provides almost ideal foundations for spin canting with an optimal canting angle close to 90°. The obtained magnetization is significantly higher than that of analogue monomer complexes of this ligand type (e.g. [FeL3-$(MeOH)_2$], [5]). The destruction of the zigzag structure that can be equalized with going from the methanol adduct **1**(MeOH) to the corresponding 4,4′-bipyridine adduct **2**$(MeOH)_{0.5}$, results in a loss of spin canting and only weak antiferromagnetic interactions are observed. A similar observation is made for **3**(MeOH) where no canting angle between neighbouring molecules is observed and consequently no indication of a spontaneous magnetization below a critical temperature is obtained.

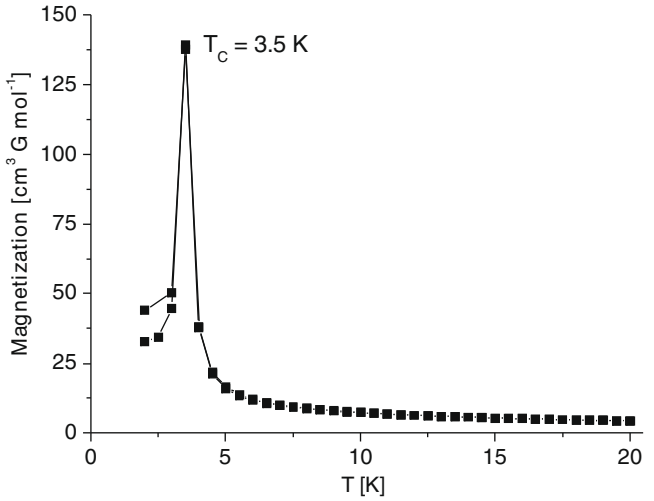


Fig. 5. Field-cooled magnetization and zero-field-cooled magnetization (FCM/ZFCM) measurements versus T plots under a week magnetic field of $H = 30$ G for complex **1**(MeOH).

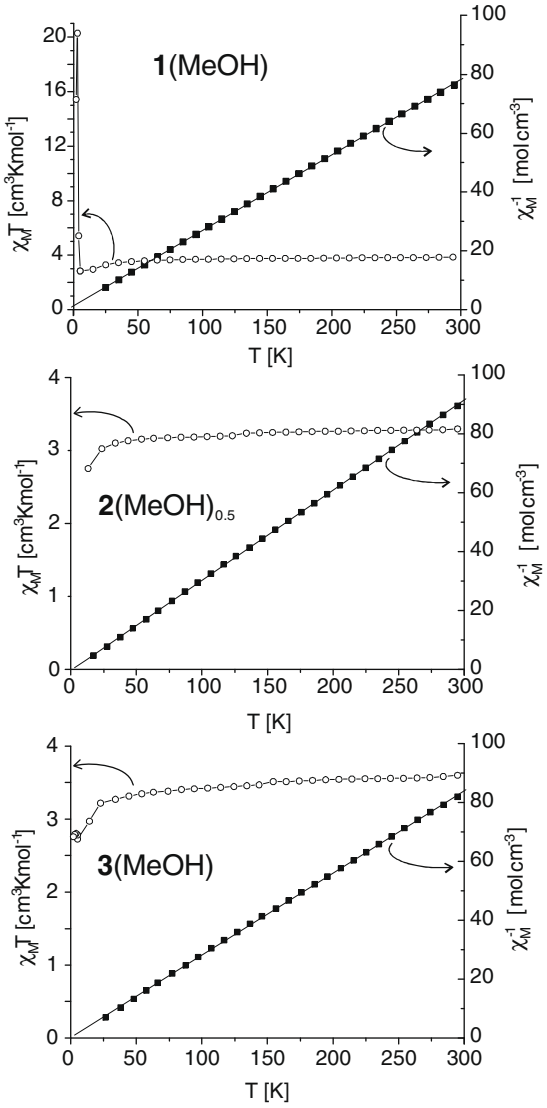


Fig. 4. Thermal variation of $\chi_M T$ (open circles), reciprocal molar susceptibility, $\chi_M{}^{-1}$ as function of temperature T (full squares) and the fits according to the Curie–Weiss law, $1/\chi_M = C/(T - \Theta)$, with the parameters $\Theta = -5.23$ K/$C = 3.91$ $cm^3\ K\ mol^{-1}$ for complex **1**(MeOH), $\Theta = -3.22$ K/$C = 3.31$ $cm^3\ K\ mol^{-1}$ for complex **2**$(MeOH)_{0.5}$ and $\Theta = -5.38$ K/$C = 3.64$ $cm^3\ K\ mol^{-1}$ for complex **3**(MeOH).

4. Conclusion

The introduction of the pyridine nitrogen in the tetradentate ligand H_2L1 provides an interesting possibility to control the magnetic exchange interactions. The nearly orthogonal arrangement of the neighbouring molecules results in ferromagnetic interactions due to spin canting. The only setback is the very low critical temperature. We will now try to further modify the ligand system in order to obtain shorter and by this more effective exchange pathways. This will be to topic of a subsequent paper.

Supporting Information

can be obtained free of charge on application to the Cambridge Crystallographic Data Centre, 12 Union Road, Cambridge CB2 1EZ, UK (Fax: int.code+(1223)336-033; e-mail www.fileserv@ccdc.cam.ac.uk).

Acknowledgements

This work has been supported financially by the Deutsche Forschungsgemeinschaft (SPP 1137) the Fonds der Chemischen Industrie and the Center for Integrated Protein Science Munich (CIPSM). The authors would like to thank S. Albrecht and P. Mayer for help with the acquisition of the crystallographic data.

Appendix A. Supplementary data

CCDC 706497, 706498 and 706496 contains the supplementary crystallographic data for **1**(MeOH), **2**$(MeOH)_{0.5}$ and **3**(MeOH), respectively. These data can be obtained free of charge via http://www.ccdc.cam.ac.uk/conts/retrieving.html, or from the Cambridge Crystallographic Data Centre, 12 Union Road, Cambridge CB2 1EZ, UK; fax: (+44) 1223-336-033; or e-mail: deposit@ccdc.cam.ac.uk. Supplementary data associated with this article can be found, in the online version, at doi:10.1016/j.poly.2008.12.010.

References

[1] O. Kahn, Molecular Magnetism, VCH, Wiley, 1993.
[2] O. Kahn, Inorg. Chim. Acta 62 (1982) 3–14.
[3] (a) P.W. Anderson, H. Hasegawa, Phys. Rev. 100 (1955) 675–681;
(b) G. Blondin, J.-J. Girerd, Chem. Rev. 90 (1990) 1359–1376;
(c) T. Glaser, T. Beissel, E. Bill, T. Weyhermüller, V. Schünemann, W. Meyer-Klaucke, A.X. Trautwein, K. Wieghardt, J. Am. Chem. Soc. 121 (1999) 2193–2208.
[4] (a) H.C. Longuet-Higgins, J. Chem. Phys. 18 (1950) 265–274;
(b) H. Iwamura, Adv. Phys. Org. Chem. 26 (1990) 179–253.
[5] (a) B.R. Müller, G. Leibeling, E.-G. Jäger, Chem. Phys. Lett. 319 (2000) 368–374;
(b) G. Leibeling, Ph.D. Thesis, University of Jena/Germany, 2003;
(c) B. Weber, E.-G. Jäger, Z. Anorg. Allg. Chem. 635 (2009) 130–133.
[6] (a) B. Weber, E. Kaps, J. Weigand, C. Carbonera, J.-F. Letard, K. Achterhold, F.-G. Parak, Inorg. Chem. 47 (2008) 487–496;
(b) B. Weber, E.S. Kaps, J. Obel, W. Bauer, Z. Anorg. Allg. Chem. (2008) 1421–1426;
(c) B. Weber, C. Carbonera, C. Desplanches, J.-F. Létard, Eur. J. Inorg. Chem. (2008) 1589–1598;
(d) B. Weber, E.S. Kaps, C. Desplanches, J.-F. Létard, K. Achterhold, F.G. Parak, Eur. J. Inorg. Chem. (2008) 4891–4898;
(e) B. Weber, W. Bauer, J. Obel, Angew. Chem. 120 (2008) 10252–10255;
(f) B. Weber, W. Bauer, Angew. Chem., Int. Ed. 47 (2008) 10098–10101;
(g) W. Bauer, B. Weber, Inorg. Chim. Acta (2008), doi:10.1016/j.ica.2008.10.018.
[7] (a) B. Weber, E. Kaps, Heteroatom Chem. 16 (2005) 391–397;
(b) B. Weber, F.-A. Walker, Inorg. Chem. 46 (2007) 6794–6803;
(c) B. Weber, E.S. Kaps, J. Obel, K. Achterhold, F.G. Parak, Inorg. Chem. 47 (2008) 10779–10787.
[8] (a) B. Weber, R. Tandon, D. Himsl, Z. Anorg. Allg. Chem. 633 (2007) 1159–1162;
(b) B. Weber, E.S. Kaps, C. Desplanches, J.-F. Létard, Eur. J. Inorg. Chem. (2008) 2963–2966.
[9] (a) B. Weber, Coord. Chem. Rev. (2008), doi:10.1016/j.ccr.2008.10.002;
(b) B. Weber, E.-G. Jäger, Eur. J. Inorg. Chem., doi:10.1002/ejic.200800891.
[10] Autorenkollektiv, Organikum, Johann Ambrosius Barth Gesellschaft mbH, 1993.
[11] E.-G. Jäger, B. Kirchhof, E. Schmidt, B. Remde, A. Kipke, R. Müller, Z. Anorg. Allg. Chem. 485 (1982) 141–172.
[12] B. Heyn, B. Hipler, G. Kreisler, D. Schreer, D. Walter, Anorganische Synthesechemie, Springer Verlag, Heidelberg, 1982, p. 2 (Auflage).
[13] W. Bauer, B. Weber, Acta Crystallogr. C64 (2008) m237–m239.

units or clusters in order to fill the empty voids or channels generated in the crystal packing [8].

Our previous work on malonate-containing copper(II) complexes has been expanded toward the synthesis, structural and magnetic characterization of two new mixed-ligand polymers of copper(II) in which one component is the methylmalonate ligand and the other a blocking unidentate N-donor molecule, 3-Iodopyridine (3-Ipy) (**1**) and 2,4′-bipyridine (2,4′-bpy) (**2**).

2. Experimental

2.1. Material and methods

Copper(II)-methylmalonate has been prepared according to the synthesis previously reported [7]. The other reagents and solvents used in the syntheses were purchased from commercial sources and used without further purification. Elemental analyses (C, H, N) were performed on an EA 1108 CHNS-O microanalytical analyzer.

2.2. Preparation of the complexes

2.2.1. Synthesis of [Cu(3-Ipy)(Memal)(H_2O)] (**1**)

A methanolic solution (5 cm^3) of 3-Iodopyridine (1 mmol, 102 mg) was added dropwise to an aqueous solution (10 cm^3) of copper(II)-methylmalonate (1 mmol) under stirring. The resulting blue solution was allowed to evaporate at room temperature. Prismatic deep blue single crystals appeared in the beaker after a few weeks, when almost all the solution has been evaporated. Yield *ca.* 60%. *Anal.* Calc. for $C_9H_{10}CuINO_5$ (**1**): C, 26.85; H, 2.50; N, 3.48. Found: C, 26.97; H, 2.71; N, 3.56%.

2.2.2. Synthesis of [Cu(2,4′-bpy)(Memal)(H_2O)] · 3H_2O (**2**)

An aqueous solution (5 cm^3) of copper(II)-methylmalonate (0.5 mmol) was set in one arm of a water filled H-shape tube, while the other arm was filled with a methanolic solution (5 cm^3) of 2,4′-bipyridine (0.5 mmol, 156 mg). Deep blue needle crystals were grown after one month at room temperature. Yield *ca.* 40%. *Anal.* Calc. for $C_{14}H_{20}CuN_2O_8$ (**2**): C, 41.23; H, 4.94; N, 6.87. Found: C, 41.33; H, 5.09; N, 6.98%.

Table 1
Crystallographic data for complexes **1** and **2**.

	1	**2**
Formula	$C_9H_{10}O_5NICu$	$C_{14}H_{20}O_8N_2Cu$
Formula weight	402.61	407.86
Crystal system	monoclinic	monoclinic
Space group	$P2_1/n$	$P2_1/n$
a (Å)	8.5874(13)	17.375(4)
b (Å)	7.1738(14)	7.3305(14)
c (Å)	19.093(5)	14.247(3)
β (°)	99.509(15)	111.409(15)
V (Å^3)	1160.0(4)	1689.4(6)
Z	4	4
μ(Mo Kα) (cm^{-1})	45.52	13.38
T (K)	293(2)	293(2)
ρ_{calc} (g cm^{-3})	2.294	1.604
λ (Å)	0.71073	0.71073
Index ranges	$-8 \leqslant h \leqslant 9$, $-7 \leqslant k \leqslant 7$, $-20 \leqslant l \leqslant 17$	$-22 \leqslant h \leqslant 22$, $-9 \leqslant k \leqslant 9$, $-15 \leqslant l \leqslant 18$
Independent reflection (R_{int})	1346 (0.0566)	3234 (0.0803)
Observed reflection [$I > 2\sigma(I)$]	1069	1879
Parameters	149	306
Goodness-of-fit	1.086	1.026
R [$I > 2\sigma(I)$]	0.0364	0.0663
R_w [$I > 2\sigma(I)$]	0.0585	0.0839
R (all data)	0.0573	0.1420
R_w (all data)	0.0635	0.1009

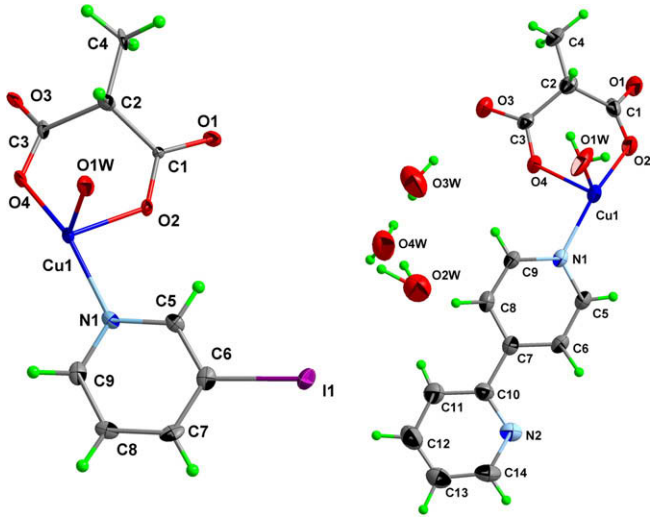


Fig. 1. An ORTEP view with the 50% probability of the asymmetric unit for the complexes **1** (left) and **2** (right) along with the numbering scheme.

2.3. Physical techniques

Magnetic susceptibility measurements on polycrystalline samples of **1** and **2** were performed in a Quantum Design SQUID magnetometer in the temperature range 2–300 K operating at 1 T (over the whole temperature range) and 0.1 T ($T < 15$ K) for compound **1** and operating at 1 T (over the whole temperature range), 0.1 T ($T < 20$ K) and 0.05 T ($T < 15$ K) for **2**. Diamagnetic corrections of the constituent atoms were estimated from Pascal's constants [9]. Experimental susceptibility values were also corrected for the temperature independent paramagnetism [60×10^{-6} cm^3 mol^{-1} per copper(II) ion] and the magnetization of the sample holder.

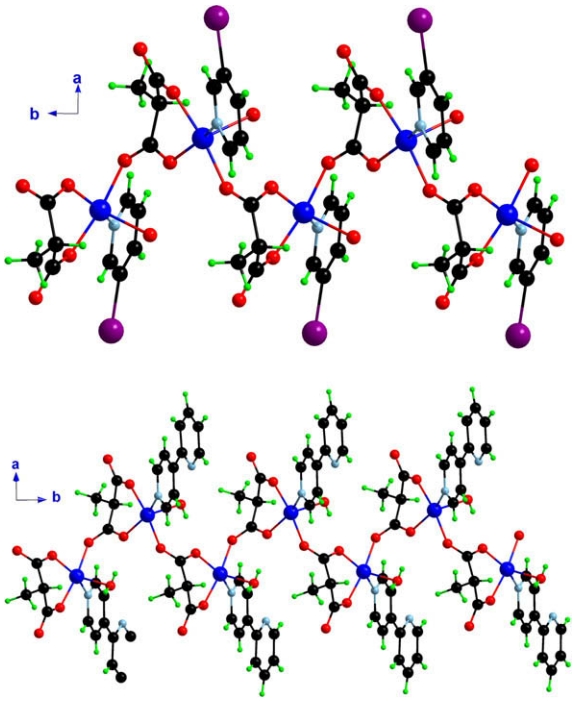


Fig. 2. A view of the carboxylate bridged copper(II) chains of **1** (up) and **2** (bottom) along the *c*-axis. Despite the different coligands, structurally the chains of both compounds are very similar.

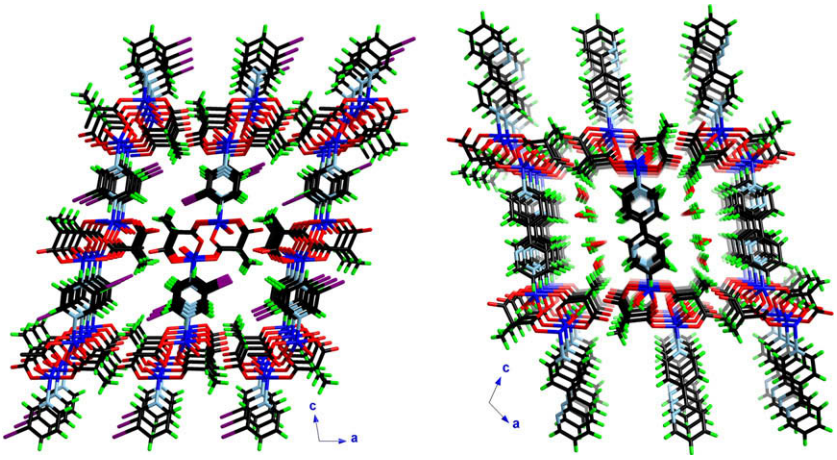


Fig. 3. Central projection of the crystal packing for **1** (left) and **2** (right) along the *b*-axis. The figures show the π–π stacking among the coligands and the crystallization water molecules which fill the channels of **2**.

2.4. X-ray crystallography

Single crystals of **1** and **2** were mounted on a Bruker-Nonius KappaCCD diffractometer and the crystallographic data were collected at 293(2) K using graphite-monochromated Mo Kα radiation (λ = 0.71073 Å). The data collection was carried out with φ–ω scans in the 6.41–21.99° (**1**) and 4.23–27.52° (**2**) θ ranges. The crystal structures were solved by direct methods and refined with the full-matrix least-squares technique on F^2 using the SHELXS-97 and SHEXL-97 programs [10] included in the WINGX software package [11]. All non-hydrogen atoms were refined anisotropically. The hydrogen atoms of **1** were geometrically positioned and refined using a riding model and those of **2** were located from difference Fourier maps and refined with isotropic temperature factors. The final geometrical calculations and the graphical manipulations were carried out with PARST95 [12] and DIAMOND [13] programs. A summary of the crystallographic data and structure refinement is given in the Table 1.

3. Results and discussion

3.1. Description of the crystal structures of *1* and *2*

The structures of the compounds **1** and **2** (Fig. 1) consist of *zig-zag* chains of *anti-syn* carboxylate-bridged copper(II) ions running along the *b* direction (Fig. 2). The pyridine-like ligands occupy one equatorial position of the copper environment avoiding the formation of the sheet-like arrangement observed in previously reported Memal complexes [7]. The chains are grouped together in hydrophilic layers [which grow in the (001) (**1**) and (101) (**2**) planes] through hydrogen bonds involving the coordinated water molecule and coordinated and uncoordinated methylmalonate oxygen atoms [O···O distances ranging from 2.677(7) to 2.729(7) Å]. The layers are pillared through the 3-Ipy (**1**) and 2,4′-bpy (**2**) ligands (Fig. 3) which are stacked through π–π interactions (Fig. 4) involving alternatively aromatic ligands from two adjacent chains. The two different separations between centroids of the 3-iodopyridine rings in **1** are 3.5371(7) and 3.6610(7) Å, whereas the off-set angles are 20.39(15)° and 23.23(15)°. These values are in agreement with those observed in pyridine-like ligands [14]. This is also true for the centroid–centroid distances [3.5689(7) and 3.8702(7) Å] and off-set angles [values ranging from 16.64(11)° to 28.66(11)°] between the 2,4′-bipyridine ligands in **2**. The pillared 2D sheets create interlayer 1D channels which are very small in **1** due to the small 3-iodopyridine ligand and the presence of the halogen atom, but large enough in **2** to include crystallization water molecules. These water molecules build a T5(2) pattern (following the nomenclature by Infantes et al.) [8] which is one of the most frequent tape motifs (Fig. 5) [8a]. The water pentagons exhibit a half-chair conformation with an axial length of the tape [distance between lower and upper atoms] of

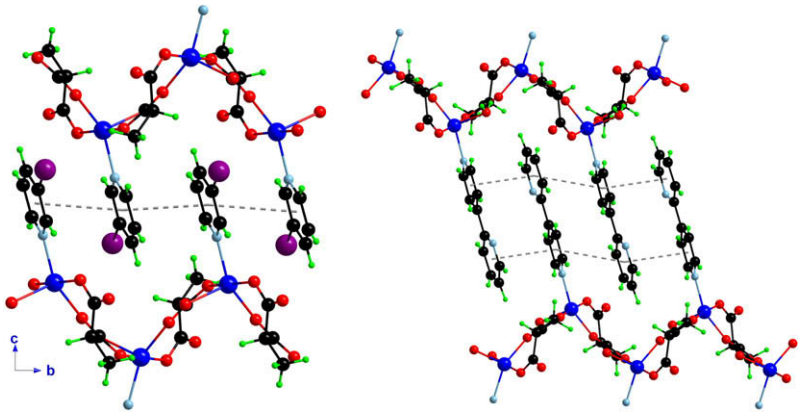


Fig. 4. Detail of the π–π stacking among the 3-iodopyridine groups in **1** (left) and among the 2,4′-bipyridine molecules in **2** (right). The dashed lines correspond to the centroid–centroid vectors.

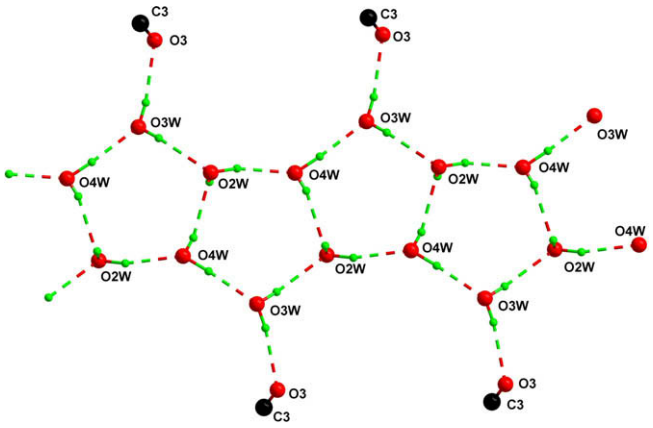


Fig. 5. T5(2) pattern formed by the crystallization water molecules in **2** with the numbering scheme.

6.939(9) Å. The water tape is anchored to the host through hydrogen bonds between a water molecule [O(3w)] from the tape acting as donor and an uncoordinated methylmalonate oxygen atom [O(3)] as acceptor. Selected H-bond distances and angles are listed in Table 2.

Each copper atom in **1** and **2** exhibits a distorted square pyramidal environment [the τ value [15] being 0.31 (**1**) and 0.32 (**2**)]. This feature is mainly due to steric effects of the 3-Ipy and 2,4′-bpy groups which are located in equatorial positions. Three oxygen atoms from two different methylmalonate ligands [O(2), O(3) and O(4)] and a nitrogen atom from a N-donor ligand [N(1)] build the basal plane. The average values of the Cu(1)–O(eq) bond are 1.952(5) for **1** and 1.950(3) Å for **2**, whereas those of Cu(1)–N are 2.040(6) Å (**1**) and 2.030(4) Å for (**2**). The apical position is filled by a water molecule [O(1w)], the Cu(1)–O(1w) bond distances being 2.205(5) (**1**) and 2.233(5) Å (**2**). The methylmalonate ligands act simultaneously as bidentate [through O(2) and O(4) with the angles subtended at the copper atom being 89.6(2)° (**1**) and 89.47(13)° (**2**)] and monodentate ligands [through O(3) in **1** and O(1) in **2**]. Selected bond lengths and bond angles are listed in Table 3.

The intrachain copper–copper separation in **1** through the *anti-syn* carboxylate bridge [5.1638(16) Å] is shorter than the interchain ones [the shortest separations being 6.671(2) Å between chains separated by the 3-iodopyridine ligand and 8.0206(16) Å between H-bonded chains]. A similar situation is observed in **2** where the intrachain separation between the copper atoms through the *anti-syn* carboxylate bridge is 5.0432(12) Å while the shortest interchain separations are 7.490(2) (between H-bonded chains) and 10.067(2) Å (between chains separated by the 2,4′-bipyridine ligand).

Table 2
Hydrogen bond distances and angles in **2**.

D–H···A	O–H (Å)	H···O (Å)	O–H···O (°)	O···O (Å)
T5(2) tape				
O(2w)–H···O(4w)	1.00(6)	1.90(6)	156(5)	2.850(7)
O(3w)–H···O(2w)	0.85(8)	2.09(9)	166(7)	2.922(8)
O(4w)–H···O(2w)	0.68(7)	2.18(7)	160(6)	2.841(8)
O(4w)–H···O(3w)	0.95(7)	1.88(7)	176(6)	2.837(8)
Anchorage of the tape				
O(3w)–H···O(3)	0.82(8)	2.04(8)	171(7)	2.854(8)
Other H-bonds				
O(1w)–H···O(2)	0.69(10)	2.18(8)	136(9)	2.730(6)
O(1w)–H···O(3)	0.78(9)	2.01(8)	158(9)	2.748(6)

Table 3
Selected bond angles (°) and lengths (Å) for **1** and **2**.

1			
Cu(1)–O(2)	1.931(5)	O(2)–Cu(1)–O(1w)	94.77(19)
Cu(1)–O(3a)[a]	1.966(5)	O(3a)–Cu(1)–O(4)	86.1(2)
Cu(1)–O(4)	1.959(5)	O(3a)–Cu(1)–N(1)	91.2(2)
Cu(1)–N(1)	2.040(6)	O(3a)–Cu(1)–O(1w)	93.14(19)
Cu(1)–O(1w)	2.205(5)	O(4)–Cu(1)–N(1)	153.1(2)
O(2)–Cu(1)–O(3a)	171.9(2)	O(4)–Cu(1)–O(1w)	109.3(2)
O(2)–Cu(1)–O(4)	89.6(2)	N(1)–Cu(1)–O(1w)	97.6(2)
O(2)–Cu(1)–N(1)	89.5(2)		
2			
Cu(1)–O(1b)	1.973(3)	O(1b)–Cu(1)–O(1w)	99.79(19)
Cu(1)–O(2)	1.949(3)	O(2)–Cu(1)–O(4)	89.47(13)
Cu(1)–O(4)	1.927(3)	O(2)–Cu(1)–N(1)	152.76(16)
Cu(1)–N(1)	2.030(4)	O(2)–Cu(1)–O(1w)	107.20(19)
Cu(1)–O(1w)	2.233(5)	O(4)–Cu(1)–N(1)	90.36(15)
O(1b)–Cu(1)–O(2)	85.37(14)	O(4)–Cu(1)–O(1w)	87.90(19)
O(1b)–Cu(1)–O(4)	171.73(14)	N(1)–Cu(1)–O(1w)	100.01(19)
O(1b)–Cu(1)–N(1)	91.27(15)		

[a] Symmetry operations: (a) = $-x+1/2$, $y+1/2$, $-z+1/2$; (b) = $-x+1/2$, $y+1/2$, $-z+3/2$.

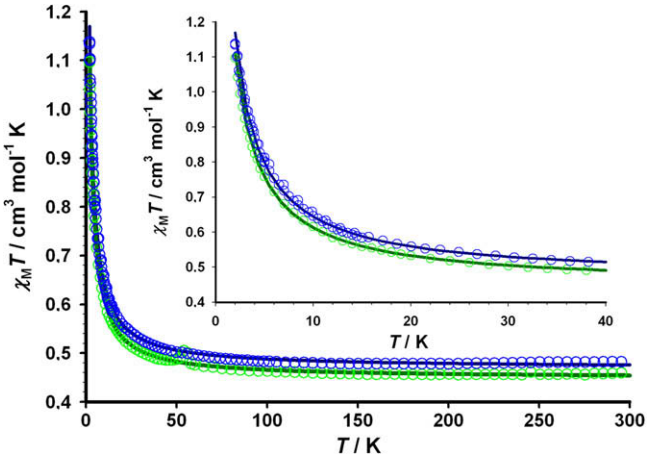


Fig. 6. $\chi_M T$ vs. T plot for **1** (blue) under applied fields of 1 T ($T > 15$ K) and 0.1 T ($T < 15$ K) and **2** (green) under applied fields of 1 T ($T > 20$ K), 0.1 T (20 K > $T > 15$ K) and 0.05 T ($T < 15$ K): (o) experimental data, (––) best fit curve. The inset shows a detail of the low temperature region.

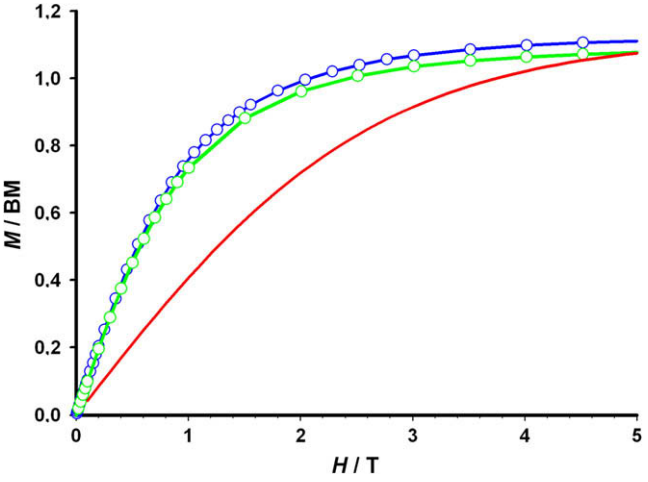


Fig. 7. M vs. H curve for **1** (blue) and **2** (green) together with the Brillouin function for a magnetically isolated spin doublet with the g value obtained from the fitting of the $\chi_M T$ curve of **1** [($g = 2.238(2)$] (red line). The blue and green lines are eye-guide lines.

Let us finish this structural description with a comparison of these structures with those synthesized with malonato or phenylmalonato-carboxylate ligands. The location of the 2,4′-bipyridine ligand in the equatorial position at the copper(II) environment is also observed in the Phmal-containing complex $[Cu(2,4'\text{-bpy})(Phmal)(H_2O)]_n$ [6c], in this case, however, a layered complex is formed. The static Jahn-Teller disorder of the copper(II) environment in that complex could be at the origin of the formation of the layers, a feature which is not observed in **2**. In the case of the malonic acid, to our knowledge, there are no complexes with the 3-Ipy ligand, but several compounds with the 2,4′-bpy ligand were reported [5e,5i]. A manganese(II) complex [5i] with similar layers as those formed in the Phmal compound [6c] and a copper(II) compound [5e] exhibiting a copper environment similar to that of **2**, where the 2,4′-bpy ligand occupies an equatorial position and a water molecule fills the apical one. However, in the malonate-containing complex the copper(II) chains are bent to form isolated tetranuclear entities with the copper atoms in the corners, the malonate ligands in the edges and the 2,4′-bpy ligands like paddles pointing outwards the unit.

3.2. Magnetic properties

The magnetic properties of the compounds **1** and **2** under the form of $\chi_M T$ versus T plot (χ_M being the molar susceptibility per copper(II) ion) are shown in Fig. 6. The $\chi_M T$ values at room temperature are 0.48 and 0.46 $cm^3\ mol^{-1}\ K$ for **1** and **2**, respectively. These values are as expected for a magnetically isolated spin doublet. Upon cooling, $\chi_M T$ increases smoothly until $T < 20$ K and then, it sharply increases to reach values of 1.13 (**1**) and 1.10 $cm^3\ mol^{-1}\ K$ (**2**) at 2.0 K. The magnetization (M) versus the applied magnetic field (H) plots for both compounds, which are depicted in Fig. 7, are clearly above the theoretical Brillouin curve for an isolated spin $S = 1/2$. The saturation of the magnetization is achieved for both compounds at *ca.* 3.0 T. All these features are indicative of the presence of ferromagnetic interactions between the copper(II) ions of **1** and **2**.

Given that the structures of these compounds consists of chains of copper(II) ions bridged by carboxylate-methylmalonate groups in the *anti-syn* conformation, their magnetic data were analysed by means of the numerical expression for an $S = 1/2$ ferromagnetic uniform chain [16]:

$$\chi_M = (N\beta^2 g^2/4kT)(A/B)^{2/3}$$
$$A = 1.0 + 5.7979916y + 16.902653y^2 + 29.376885y^3 + 29.832959y^4 + 14.036918y^5$$
$$B = 1.0 + 2.7979916y + 7.0086780y^2 + 8.6538644y^3 + 4.5743114y^4$$
$$\hat{H} = -J\sum\nolimits_i \hat{S}_i \cdot \hat{S}_{i+1}$$

with $y = J/2kT$, J is the intrachain magnetic coupling, and the other symbols have their usual meanings. Best least-squares fit parameters are: $J = +2.66(2)\ cm^{-1}$, $g = 2.238(2)$ and $R = 1.6 \times 10^{-5}$ for **1** and $J = +2.62(2)\ cm^{-1}$, $g = 2.188(2)$ and $R = 1.1 \times 10^{-5}$ for **2**, where R is the agreement factor defined as $\sum[(\chi_M T)_{obs} - (\chi_M T)_{calc}]^2 / \sum[(\chi_M T)_{obs}]^2$. The calculated curves match very well the experimental data in the whole temperature range (Fig. 6). At the same time, the values of J are practically identical for the two compounds, in agreement with their structural similarity.

The ferromagnetic nature of the magnetic interactions in **1** and **2** is in agreement with the data reported in the literature for the *anti-syn* equatorial–equatorial carboxylate bridge (see Table 4).

Table 4
Selected magneto-structural data for *anti-syn* equatorial–equatorial carboxylate-bridged R-malonate–copper(II) complexes.

Compound[a]	Cu···Cu[b] (Å)	β[c] (°)	τ[d]	J[e] (cm^{-1})	Ref.
$\{[Cu(H_2O)_3][Cu(mal)_2(H_2O)]\}_n$[f]	4.854(1)	85.6	0.24 0.28	+3.0 regular chain	[5a]
$[Cu_4(mal)_4(2,4'\text{-bpy})_4(H_2O)_4] \cdot 8H_2O$	4.670(1)	70.99(1)	0.15	+12.3 tetranuclear	[5f]
$[Cu_2(mal)_2(H_2O)_2(4,4'\text{-bpy})]$[g]	4.644(1)	72.72(1)	0.14	+12.4 tetranuclear	[5c]
$[\{Cu_3(mal)_2(bpa)_3(H_2O)_2\}(NO_3)_2]_n$[f]	4.7542(5)	89.05(8)	0.20 O_h	+22 trinuclear	[17]
$[Cu_4(mal)_4(bpe)_3]_n \cdot 6nH_2O$[f]	5.0082(10)	36.30(5)	0.009 O_h	+23 tetranuclear	[5h]
$\{[Cu(H_2O)_3][Cu(Phmal)_2]\}_n$[g]	4.6511(5) 5.0736(7)	87.62(7)	0.02 0.06	+4.44 regular chain	[6a]
$[Cu(pym)(Phmal)]_n$	5.100(8) 5.143(7)	63.2(2)	0.02	+5.6 square grid	[6d]
$[Cu(cbdca)(H_2O)]_n$	4.842(5)	82.3(8)	0	+4.76 square grid	[18]
$[Cu(Memal)(H_2O)]_n$	4.9653(12)	84.44(9)	0	+1.61 square grid	[7]
$[Cu(mal)(azpy)_{1/2}(H_2O)]_n \cdot nH_2O$[g]	5.0845(5)	61.29(4)	0.20	+8.73(3) regular chain	[19]
1	5.1638(16)	84.76(12)	0.31	+2.66(2) regular chain	this work
2	5.0432(12)	75.28(8)	0.32	+2.62(2) regular chain	this work

[a] Abbreviations used: H_2mal = malonic acid; 2,2′-bpy = 2,2′-bipyridine; 2,4′-bpy = 2,4′-bipyridine; 4,4′-bpy = 4,4′-bipyridine; bpe = 1,2-bis(4-pyridyl)ethylene; bpa = 1,2-bis(4-pyridyl)ethane; H_2Phmal = phenylmalonic acid; H_2cbdca = 1,1-cyclobutanedicarboxylic acid; H_2Memal = methylmalonic acid; azpy = 4,4′-azobispyridine.
[b] Separation between copper(II) ions through the operative carboxylate bridge.
[c] Dihedral angle between the mean equatorial planes of adjacent copper(II) ions.
[d] Value of the distortion of the five-coordinated environment ($\tau = 0$ being a perfect square pyramid and $\tau = 1$, a trigonal bipyramid). O_h refers to octahedral environments. When more than one value is listed, more than one crystallographically independent copper atom is present in the structure.
[e] Magnetic exchange coupling parameter. The type of system used to fit the experimental data is also indicated.
[f] More than one magnetic exchange pathway is considered in the fitting.
[g] A mean-field term was added to take into account other interactions.

According to the Kahn's model, the magnetic coupling for two interacting copper(II) ions can be decomposed in two different contributions of opposite nature, the *anti*-ferromagnetic one being dependent on square of the overlap of the magnetic orbitals (the smaller the overlap is, the lower the *anti*-ferromagnetic term) [20]. The magnetic orbitals at the copper atoms are of the $d(x^2 - y^2)$ type [the *x*- and *y*-axes roughly corresponding with the equatorial bonds of the copper environment] with some admixture of the dz^2 character [the *z*-axis being defined by the axial bond]. The angle between the basal planes of the magnetically coupled copper atoms are nearly orthogonal [84.76(12)° and 75.28(8)° for **1** and **2**, respectively], then the overlap is reduced to a minimum and the ferromagnetic contribution becomes predominant.

The magnitude of the interaction can be explained having in mind some structural considerations. The carboxylate exchange pathways link two equatorial positions at the adjacent copper(II) ions. This conformation is more favourable to the magnetic coupling (*J* values ranging from +3.0 to +23 cm^{-1}) (Table 4) than the equatorial–apical one. From the results listed in Table 4, the greater values for *J* are observed in the discrete polynuclear entities, despite other parameters. Within the complexes with a magnetic behaviour described by regular chains, complexes **1** and **2** lay in the lower limit of the *J* range. The large distortion of the square pyramidal environment in both compounds would be responsible for this situation.

4. Conclusion

In the present contribution, we show how the use of the methylmalonate as ligand toward the copper(II) ions affords other structures than the square grids previously reported. Complexes **1** and **2** consist of carboxylate-bridged chains of copper(II) atoms which build a pillared two-dimensional (2D) supramolecular network by means of weak $\pi\cdots\pi$ interactions and hydrogen bonds. The 3D network in **2** exhibits channels where water molecules are hosted, with a T5(2) pattern. Both compounds exhibit ferromagnetic interactions trough the carboxylate exchange pathway.

The preference of the pyridine-like ligands for the equatorial position at the copper atom has been observed previously in the $[Cu_2(4,4'\text{-bpy})(Memal)_2(H_2O)_2]_n$ [7] and $[Cu(2,4'\text{-bpy})(Memal)(H_2O)$ [6c] complexes. Thus, it is not surprising, although unexpected, that the two-dimensional (4,4) network of carboxylate-bridged copper ions has turned into carboxylate-bridged copper(II) chains due to the introduction of a terminal ligand in the basal plane of the copper atom environment.

Acknowledgements

Funding for this work was provided by the Spanish Ministerio de Ciencia e Innovación through projects MAT2007-60660, CTQ2007-61690, and "Factoría de Cristalización" (Consolider-Ingenio2010, CSD2006-00015). J.P. thanks the CSD2006-00015 for a postdoctoral contract.

Appendix A. Supplementary data

CCDC 705220 and 705221 contain the supplementary crystallographic data for **1** and **2**. These data can be obtained free of charge via http://www.ccdc.cam.ac.uk/conts/retrieving.html, or from the Cambridge Crystallographic Data Centre, 12 Union Road, Cambridge CB2 1EZ, UK; fax: (+44) 1223 336 033; or e-mail: deposit@ccdc.cam.ac.uk

Supplementary data associated with this article can be found, in the online version, at doi:10.1016/j.poly.2008.12.011.

References

[1] (a) O.M. Yaghi, H. Li, C. Davis, D. Richardson, T.L. Groy, Acc. Chem. Res. 31 (1998) 474;
(b) S. Kitagawa, M. Kondo, Bull. Chem. Soc. Jpn. 71 (1998) 1739;
(c) S.R. Batten, R. Robson, Angew. Chem., Int. Ed. 37 (1998) 1460;
(d) P.J. Hagram, D. Hagram, J. Zubieta, Angew. Chem., Int. Ed. 38 (1999) 2638;
(e) A.J. Blake, N.R. Champness, P. Hubberstey, W.-S. Li, M.A. Withersby, M. Schröder, Coord. Chem. Rev. 183 (1999) 117;
(f) M.J. Zaworotko, Chem. Commun. (2001) 1;
(g) R.J. Robson, Chem. Soc., Dalton Trans. (2000) 3735;
(h) B. Moulton, M. Zaworotko, J. Chem. Rev. 101 (2001) 1629;
(i) A. Erxleben, Coord. Chem. Rev. 246 (2003) 303;
(j) C. Janiak, Dalton Trans. (2003) 2781;
(k) S. Kitagawa, R. Kitaura, S. Noro, Angew. Chem., Int. Ed. 43 (2004) 2334;
(l) R. Robson, in: J.L. Atwood, J.E.D. Davies, D.D. MacNicol, F. Vögtle (Eds.), Comprehensive Supramolecular Chemistry, vol. 6, Pergamon, Oxford, UK, 1996, p. 733;
(m) D. Braga, F. Grepioni, Coord. Chem. Rev. 183 (1999) 19.
[2] H. Li, M. Eddaoudi, M. O'Keeffe, O. Yaghi, Nature 402 (1999) 276.
[3] S.S.-Y. Chui, S.M.-F. Lo, J.P.H. Charmant, A.G. Orpen, I.D. William, Science 283 (1999) 1148.
[4] C. Serre, F. Millange, C. Thouvenot, M. Noguès, G. Marsolier, D. Louër, G. Férey, J. Am. Chem. Soc. 124 (2002) 13519.
[5] (a) C. Ruiz-Pérez, J. Sanchiz, M. Hernández Molina, F. Lloret, M. Julve1, Inorg. Chem. 39 (2000) 1363;
[b] C. Ruiz-Pérez, M. Hernández-Molina, P. Lorenzo-Luis, F. Lloret, J. Cano, M. Julve, Inorg. Chem. 39 (2000) 3845;
(c) Y. Rodríguez-Martín, C. Ruiz-Pérez, J. Sanchiz, F. Lloret, M. Julve, Inorg. Chim. Acta 318 (2001) 159;
(d) Y. Rodríguez-Martín, C. Ruiz-Pérez, J. Sanchiz, F. Lloret, M. Julve, Inorg. Chim. Acta 326 (2001) 20;
(e) Y. Rodríguez-Martín, M. Hernández-Molina, F.S. Delgado, J. Pasán, C. Ruiz-Pérez, J. Sanchiz, F. Lloret, M. Julve, Crys. Eng. Commun. 4 (2002) 440;
(f) Y. Rodríguez-Martín, M. Hernández-Molina, F.S. Delgado, J. Pasán, C. Ruiz-Pérez, J. Sanchiz, F. Lloret, M. Julve, Crys. Eng. Commun. 4 (2002) 522;
(g) J. Sanchiz, Y. Rodríguez-Martín, C. Ruiz-Pérez, A. Mederos, F. Lloret, M. Julve, New J. Chem. 26 (2002) 1624;
(h) F.S. Delgado, J. Sanchiz, C. Ruiz-Pérez, F. Lloret, M. Julve, Inorg. Chem. 42 (2003) 5938;
(i) Y. Rodríguez-Martín, M. Hernández-Molina, J. Sanchiz, C. Ruiz-Pérez, F. Lloret, M. Julve, Dalton Trans. (2003) 2359;
(j) C. Ruiz-Pérez, Y. Rodríguez-Martín, M. Hernández-Molina, F.S. Delgado, J. Pasán, J. Sanchiz, F. Lloret, M. Julve, Polyhedron 22 (2003) 2111;
(k) J. Pasán, F.S. Delgado, Y. Rodríguez-Martín, M. Hernández-Molina, C. Ruiz-Pérez, J. Sanchiz, F. Lloret, M. Julve, Polyhedron 22 (2003) 2143;
(l) F.S. Delgado, N. Kerbellec, C. Ruiz-Pérez, J. Cano, F. Lloret, M. Julve, Inorg. Chem. 452 (2006) 1012.
[6] (a) J. Pasán, J. Sanchiz, C. Ruiz-Pérez, F. Lloret, M. Julve, New J. Chem. 27 (2003) 1557;
(b) J. Pasán, J. Sanchiz, C. Ruiz-Pérez, F. Lloret, M. Julve, Eur. J. Inorg. Chem. (2004) 4081;
(c) J. Pasán, J. Sanchiz, C. Ruiz-Pérez, F. Lloret, M. Julve, Inorg. Chem. 44 (2005) 7794;
(d) J. Pasán, J. Sanchiz, C. Ruiz-Pérez, J. Campo, F. Lloret, M. Julve, Chem. Commun. (2006) 2857.
[7] J. Pasán, J. Sanchiz, F. Lloret, M. Julve, C. Ruiz-Pérez, Crys. Eng. Commun. 9 (2007) 478.
[8] (a) L. Infantes, S. Motherwell, Cryst. Eng. Commun. 4 (2002) 454;
(b) L. Infantes, J. Chisholm, S. Motherwell, Crys. Eng. Commun. 5 (2003) 480;
(c) M. Mascal, L. Infantes, J. Chisholm, Angew. Chem., Int. Ed. 45 (2006) 32;
(d) O. Fabelo, J. Pasán, L. Cañadillas-Delgado, F.S. Delgado, A. Labrador, F. Lloret, M. Julve, C. Ruiz-Pérez, Cryst. Eng. Commun. 10 (2008) 1743. and references herein.
[9] R.L. Carlin, Magnetochemistry, Springer-Verlag, Berlin, Heidelberg, Germany, 1986.
[10] G.M. Sheldrick, SHELX97, Programs for Crystal Structure Analysis (Release 97-2), Institüt für Anorganische Chemie der Universität, Tammanstrasse 4, D-3400 Göttingen, Germany, 1998.
[11] L.J. Farrugia, J. Appl. Cryst. 32 (1999) 837 (WINGX).
[12] M. Nardelli, J. Appl. Cryst. 28 (1995) 659.
[13] DIAMOND 2.1d, Crystal Impact GbR, CRYSTAL IMPACT, K. Brandenburg and H. Putz GbR, Postfach 1251, D-53002 Bonn, Germany, 2000.
[14] C. Janiak, Dalton Trans. (2000) 3885.
[15] A.W. Addison, T.N. Rao, J. Reedijk, J. van Rijn, G.C. Verschoor, Dalton Trans. (1984) 1349.
[16] G.A. Baker, G.S. Rushbrooke, H.E. Gilbert, Phys. Rev. 135 (1964) A1272.
[17] S. Sain, T.K. Maji, G. Mostafa, T.-H. Lu, N.R. Chaudhuri, New J. Chem. 27 (2003) 185.
[18] R. Baldomá, M. Monfort, J. Ribas, X. Solans, M.A. Maestro, Inorg. Chem. 45 (2006) 8144.
[19] B. Li, X. Wang, Y. Zhang, S. Gao, Y. Zhang, Inorg. Chim. Acta 358 (2005) 3519.
[20] O. Kahn, Molecular Magnetism, VCH, New York, 1993.

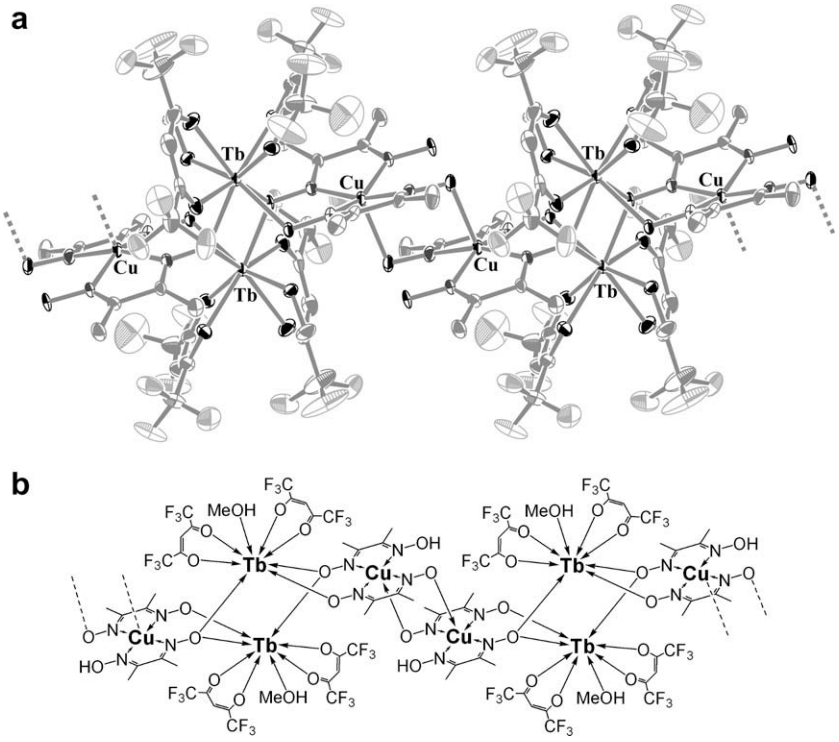


Fig. 1. (a) Crystal structure of $[Tb_2Cu_2]_n$ with the thermal ellipsoids at the 50% probability level. Two repeating units are shown. Hydrogen atoms are omitted for clarity. (b) Structural formula of $[Tb_2Cu_2]_n$. Note that the Gd, Dy, Ho, and Er derivatives exhibited an isomorphous structure.

Table 1
Selected crystallographic data for $[Ln_2Cu_2]_n$ (Ln = Tb, Ho, and Er).

Compounds	$[Tb_2Cu_2]_n$	$[Ho_2Cu_2]_n$	$[Er_2Cu_2]_n$
Formula	$C_{19}H_{19}CuF_{12}N_4O_9Tb$	$C_{19}H_{19}CuF_{12}HoN_4O_9$	$C_{19}H_{19}CuErF_{12}N_4O_9$
Formula weight	897.83	903.83	906.17
Habit	brown platelet	brown prism	brown prism
Dimension (mm^3)	$0.08 \times 0.07 \times 0.03$	$0.05 \times 0.04 \times 0.03$	$0.04 \times 0.04 \times 0.03$
T (K)	110	100	90
Crystal system	triclinic	triclinic	triclinic
Space group	$P\bar{1}$	$P\bar{1}$	$P\bar{1}$
a (Å)	10.573(5)	10.528(13)	10.517(12)
b (Å)	11.087(3)	11.048(8)	11.059(6)
c (Å)	14.151(10)	14.161(14)	14.130(4)
α (°)	71.65(5)	71.57(9)	71.55(7)
β (°)	75.87(5)	75.57(10)	75.47(7)
γ (°)	85.20(6)	84.85(11)	84.75(8)
V ($Å^3$)	1521.7(14)	1513(3)	1509(2)
Z	2	2	2
D_{calc} ($g\,cm^{-3}$)	1.959	1.984	1.994
Unique data	6900	6855	6845
μ (Mo Kα) (mm^{-1})	3.123	3.426	3.857
$R(F)$[a] ($I > 2\sigma(I)$)	0.0414	0.0513	0.0602
$R_w(F^2)$[b] (all data)	0.0613	0.0844	0.0802

[a] $R = \sum||F_o| - |F_c||/\sum|F_o|$.
[b] $R_w = [\sum w(F_o^2 - F_c^2)^2/\sum w(F_o^2)^2]^{1/2}$.

therefore further research work requires temperatures below 2 K to investigate SMM behavior. On the other hand, research on J_{4f-3d} can afford fruitful results at the present stage without observation of SMM behavior. We focus our attention on determination of J_{4f-3d}'s and their comparison among the analogs. Magnetic study below 2 K is not necessarily required, but we measured the pulsed-field $M-H$ curves at 0.5 K, because the experiments at lower temperatures could exhibit better step-shaped magnetization curves.

The pulse-field magnetization measurements on a polycrystalline specimen of $[Tb_2Cu_2]_n$ were collected at 0.5 K (Fig. 2a). The saturation magnetization (M_s) of 15.7 μ_B at 10 T was close to the calculated value 17 μ_B with $|J^z| = 5$ and $g_J = 3/2$, and did not reach the calculated one with maximal $|J^z| = 6$. A parallel study on the same specimen using a SQUID magnetometer supported this result. This finding indicates that a ground state of the Tb ions may be given by the value of $|J^z| = 5$. The field-oriented data were usually obtained in these measurements (see Section 5), but the M_s value may not be a full-saturation value because of incomplete orientation.

The differentiated magnetization curve on $[Tb_2Cu_2]_n$ is shown in the bottom of Fig. 2a, clarifying that the magnetic field at the dM/dB peak is 5.6 T. The gap of the jump corresponds to 4 μ_B from two

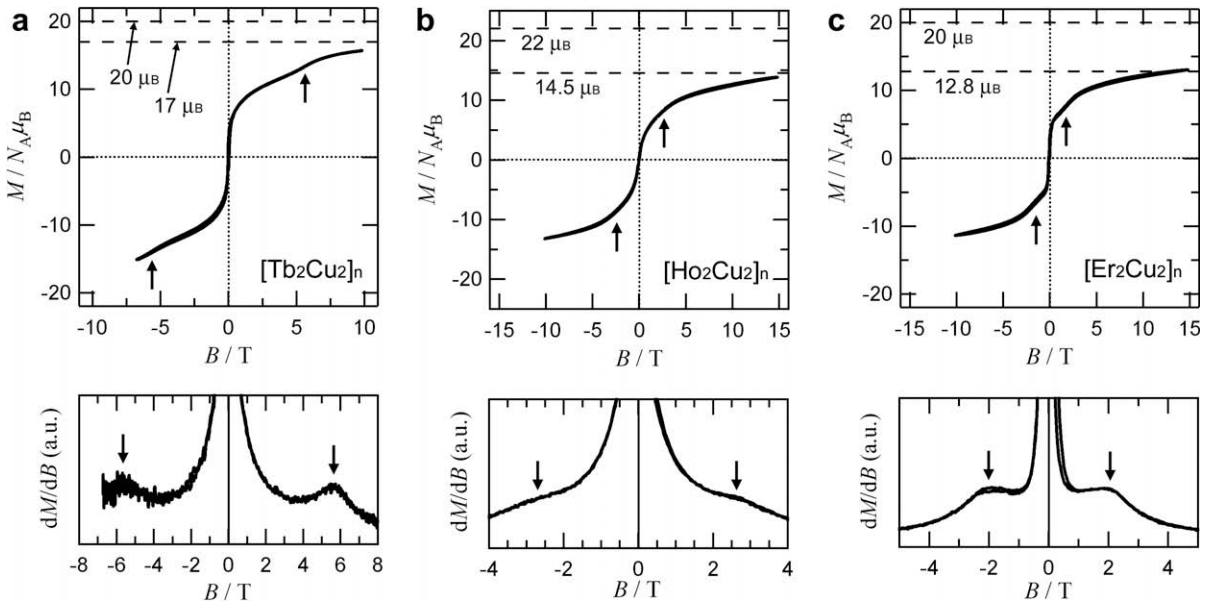


Fig. 2. Magnetization curves for $[Ln_2Cu_2]_n$ measured at 0.5 K, where Ln = Tb (a), Ho (b), and Er (c). Derivative curves are also shown in the bottom figures. The arrows show the positions of the magnetization jumps.

copper spins. Consequently, the jump is ascribable to the transition from the ground ferrimagnetic state ($[Tb(\uparrow)_2Cu(\downarrow)_2]_n$) to the ferromagnetic one ($[Tb(\uparrow)_2Cu(\uparrow)_2]_n$). In other words, the energy-level crossing takes place around 5.6 T in a Zeeman picture.

Similarly, the pulsed-field magnetization measurements on a polycrystalline specimen of $[Ho_2Cu_2]_n$ were collected at 0.5 K (Fig. 2b). The M_s value 13.8 μ_B at 15 T did not reach the calculated value with maximal $|J^z| = 8$ and $g_J = 5/4$. Assuming that the observed M_s is intrinsic, the ground state of the Ho ions would have a smaller moment such as $|J^z| = 6$ (the calculated M_s value 17 μ_B) or 5 (14.5 μ_B). The magnetic field at the dM/dB peak is 2.5 T (the bottom of Fig. 2b). The energy-level crossing between the ferrimagnetic ($[Ho(\uparrow)_2Cu(\downarrow)_2]_n$) and ferromagnetic ($[Ho(\uparrow)_2Cu(\uparrow)_2]_n$) states occurs around 2.5 T.

In the case of $[Er_2Cu_2]_n$ (Fig. 2c), the M_s value was 13.0 μ_B at 15 T, which did not reach the calculated value with maximal

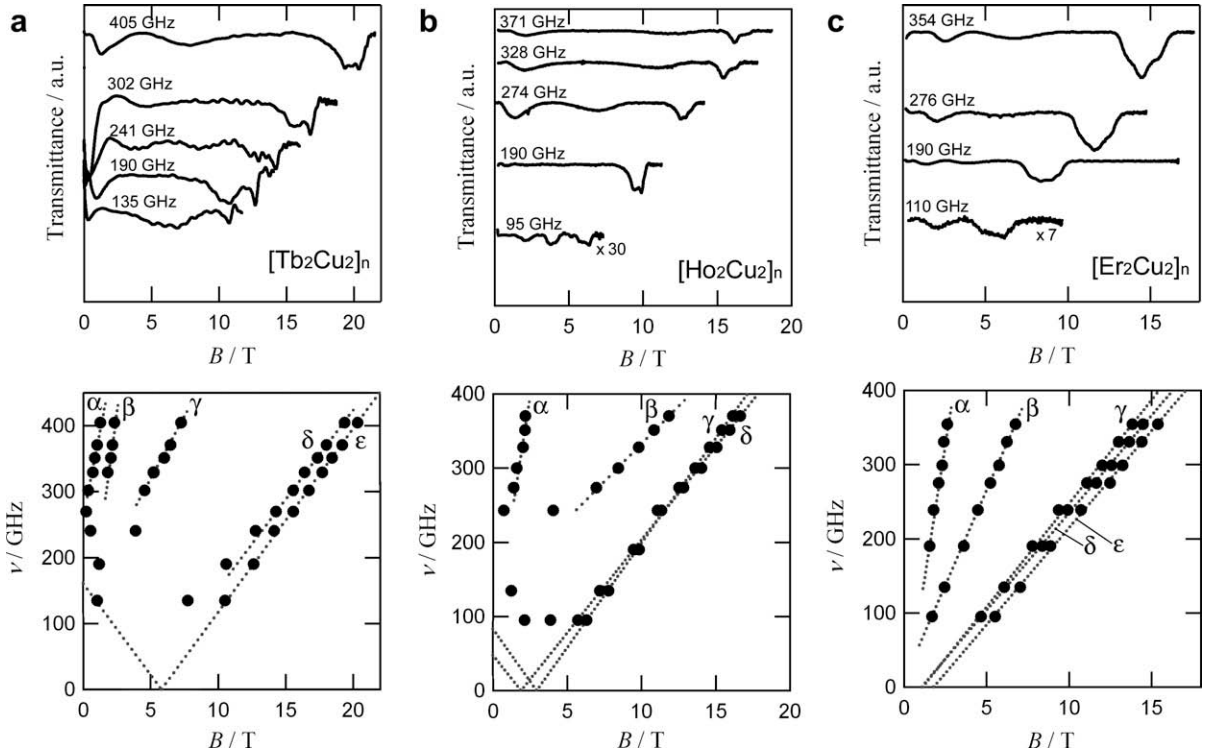


Fig. 3. (Top) Selected EPR spectra measured at 4.2 K as a function of frequency for (a) $[Tb_2Cu_2]_n$, (b) $[Ho_2Cu_2]_n$ and (c) $[Er_2Cu_2]_n$. The spectra are offset in a linear scale of the frequency. (Bottom) Frequency-field diagrams for (a) $[Tb_2Cu_2]_n$, (b) $[Ho_2Cu_2]_n$, and (c) $[Er_2Cu_2]_n$. Dotted lines are shown for a guide to the eye.

$|J^z| = 15/2$ and $g_J = 6/5$. The ground state of the Er ions may have a smaller moment such as $|J^z| = 11/2$ (the calculated M_s value 15.2 μ_B) or 9/2 (12.8 μ_B). The energy-level crossing between the ferrimagnetic and ferromagnetic states occurs around 2.5 T (the bottom of Fig. 2c). We have previously reported that the $M-H$ curves for $[Gd_2Cu_2]_n$ and $[Dy_2Cu_2]_n$, which exhibited a similar copper(II) spin-flip transition at ca. 7.0 and 5.56 T, respectively [5,11]. Therefore, the series of $[Ln_2Cu_2]_n$ involve 4f–3d antiferromagnetic couplings for all heavier-lanthanide ions investigated (Ln = Gd, Tb, Dy, Ho, and Er).

The precise level-crossing field is finally determined from the HF-EPR experiments. HF-EPR spectra of powder $[Tb_2Cu_2]_n$ were collected in a wide frequency range 95–405 GHz at 4.2 K (Fig. 3a). We found several series of signals shifted to a higher field with an increasing frequency ($\alpha-\varepsilon$ in Fig. 3b). The g value of the signals (ε) was 1.99(2) from the slope of the frequency-field plot. It is consistent with the Cu signal satisfying a conventional EPR selection rule of $\Delta m_s = \pm 1$. The g value slightly smaller than 2 was previously reported and discussed on $[Dy_2Cu_2]_n$ [5]. Extrapolation gives a critical field of 5.80(8) T, which implies the level-crossing of two states with respect to the Cu spin-flip. It is identical to the position of the magnetization jump in the $M-H$ curve, and the value from the HF-EPR is more precise than that of the $M-H$ measurements.

The g values of the other signals ($\alpha-\delta$) were ca. 10, ca. 15, 2.65(11) and 1.92(5), respectively. Some of them seem to be caused by transitions among $2J + 1$ multiplets of the Tb ions. For example, a transition of $\Delta m_J = \pm 10$ with $g_J = 3/2$ gives an apparent g value of 15; namely, the transition with g = ca. 15 (β) may be attributed to a forbidden transition with $\Delta m_J = \pm 10$ (e.g., $J^z = -5 \leftrightarrow +5$).

HF-EPR spectra of powder $[Ho_2Cu_2]_n$ were collected in a frequency range 95–371 GHz at 4.2 K. We found several series of signals shifted to a higher field with an increasing frequency ($\alpha-\delta$ in Fig. 3b). The g values of the γ and δ series were 2.01(2) and 1.79(4), respectively, from the slope of the frequency-field plot. They are assigned to the Cu signals, similarly to the $[Tb_2Cu_2]_n$ case. Extrapolations of their peaks give different critical fields of 1.9(2) T and 2.96(11) T. They may originate from different transitions. The Ho ions affect the internal field at the adjacent Cu ions in terms of exchange-bias fields. Accordingly, the position of the critical fields is in proportion to J^z. If the stronger peaks (γ) on a higher field are attributed to Er ions with maximal $J^z = \pm 8$, the weaker peaks (δ) might be to Er ions with $J^z = \pm 5$. The peaks of the δ series were stronger than those of the γ series in a small field region, indicating that a state with $J^z = \pm 5$ for Ho ions is the ground state among $2J + 1$ multiplets of the Ho ions while the first excited state has $J^z = \pm 8$ for Ho ions. This finding is consistent with the small M_s value of the magnetization measurements. The resonance-field positions of the α and β series were bent in a small field region, and their g values could not be calculated accurately. The g value of α is roughly estimated to be 8 or larger, and that of β to be 1.5 or larger. The origin of the α signals is ascribable to a forbidden transition among $2J + 1$ multiplets of the Ho ions. The β signals may be attributed to a transition with a smaller Δm_J value.

HF-EPR spectra of powder $[Er_2Cu_2]_n$ were collected in a frequency range 95–354 GHz at 4.2 K. We found several series of signals shifted to a higher field with an increasing frequency ($\alpha-\varepsilon$ in Fig. 3c). The g values of the γ, δ and ε series were 1.99(4), 1.88(6), and 1.87(3), respectively, which are ascribed to the Cu signals. Extrapolations of their peaks give different critical fields of 1.10(10) T, 1.35(15) T and 1.79(15) T. The presence of the various critical fields may be caused by different J^z values at Er ions ($J^z = \pm 15/2$, $\pm 13/2$, $\pm 11/2$, etc.). If the highest-field series (ε) is attributed to a species having Er ions with $J^z = \pm 15/2$, the other peaks (γ and δ) might be to molecules having Er ions with $J^z = \pm 11/2$ and $\pm 9/2$, respectively. The g values of the α and β series were 10.8(7) and 3.66(4), respectively. The former seems to be caused by transitions of the Er ion itself with a somewhat large J^z and possibly be assigned to a forbidden transition with $\Delta m_J = \pm 9$, because $\Delta m_J = \pm 9$ ($J^z = -9/2 \leftrightarrow +9/2$) with $g_J = 6/5$ gives an apparent g value of 10.8. The latter seems to be caused by transition between $J^z = -15/2 \leftrightarrow -9/2$, because $\Delta m_J = \pm 6$ with $g_J = 6/5$ gives an apparent g value of 3.6.

3. Discussion

For all compounds investigated here, 4f–3d couplings were antiferromagnetic, giving the ferrimagnetic ground state. The $M-H$ and HF-EPR measurements consistently indicate the critical field, ascribable to an energy-level crossing from the ferri- to ferromagnetic states. The present exchange-coupling model holds for $[Ln_2Cu_2]_n$ as well as $[Ln_4Cu]$ [4] and $[Ln_2M]$ [3]. Assuming the Ising character of Ln ions, the following general spin Hamiltonian is available for the repeating unit $[Ln_2Cu_2]$:

$$\hat{H} = -J_A(\hat{J}_2^z \cdot \hat{S}_1 + \hat{J}_3^z \cdot \hat{S}_4) - J_B(\hat{J}_3^z \cdot \hat{S}_1 + \hat{J}_2^z \cdot \hat{S}_4) + \mu_B H^z(g_1 S_1 + g_2 J_2^z + g_3 J_3^z + g_4 S_4)$$

Symbols J_2 and J_3 represent the total moments of Ln ions, while S_1 and S_4 the spins of Cu ions. The first and second terms stand for the Ising-type exchange interactions between Ln and Cu ions, where the coupling parameters are defined as $-J_A$ and $-J_B$, and the third term represents the Zeeman interaction (Fig. 4).

The EPR signals due to Ln ions were observed for the Tb, Ho, and Er analogs. These signals are originally "forbidden", but possible admixture of the states might violate the EPR selection rule and their signals become observable. In addition, in some case, the J^z value does not have a maximal value of $J = L + S$. Along this context, the Ising character is somewhat weakened, in contrast to the typical Ising character found in the Dy analog [5]. However, the anisotropic character of lanthanide ions is usually strong, and the moments are still large. The effective Ising-spin model seems to be valid in the analysis on J_{4f-3d}.

The parameter J_{4f-3d} was estimated using the above Hamiltonian; namely the energy gap between the ground ferrimagnetic state and first excited ferromagnetic state was derived directly from the magnitude of the level-crossing field. Since the level-crossing field found in the HF-EPR data has more accuracy than that of the $M-H$ data, we utilized the HF-EPR data. The results are summarized in Table 2. In the present analysis, we can estimate an average value on J_A and J_B. Separation of J_A and J_B requires more detailed analysis, according to the method already published elsewhere [5].

We obtained antiferromagnetic 4f–3d couplings in all compounds investigated here. A possible reason is stated as follows. Kahn et al. explained the magnetic couplings in 4f–3d compounds as follows [13]. When the number of 4f electrons is more than seven, the orbital and spin momenta of Ln ions are parallel, and the ferromagnetic spin coupling gives rise to an overall ferromagnetic interaction. There are ample reports on ferromagnetic J_{Dy-Cu} as well as J_{Gd-Cu} [13–15]. Antiferromagnetic couplings are explained

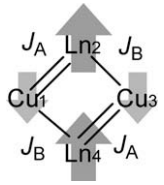


Fig. 4. Exchange coupling scheme for $[Ln_2Cu_2]$. The ground ferrimagnetic spin structure is drawn with arrows.

Table 2
Exchange parameter J_{4f-3d} for $[Ln_2Cu_2]_n$ determined from the HF-EPR study.

Ln	Gd[a]	Tb	Dy	Ho	Er
$J_{4f-3d}\ k_B^{-1}$ (K)	−1.3(2)[b]	−0.77(2)	−0.478(8)[c]	−0.250(12)	−0.149(15)
Reference	[11]	this work	[5]	this work	this work

[a] The Gd moments are treated as Heisenberg spins.
[b] Estimated from the dc magnetic susceptibility as a function of temperature.
[c] Averaged from the reported values J_A and J_B for two crystallographically independent exchange couplings.

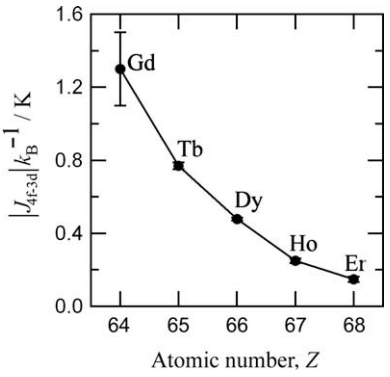


Fig. 5. Plot of the absolute values of the 4f–3d exchange coupling parameters in $[Ln_2Cu_2]_n$ as a function of the atomic number of the Ln ions. Solid line is shown for a guide to the eye.

in terms of the violation of the ferromagnetic interaction between the 4f spin portion and 3d spins [11,16]. In the present compounds, the severe torsion along the Ln–O–N–M linkage was found in common, and such out-of-plane geometry favors antiferromagnetic coupling, as previously discussed in $[Gd_2Cu_2]_n$ [11].

Furthermore, the absolute value of the exchange coupling parameter monotonically decreases with the atomic number from $_{64}$Gd to $_{68}$Er, as depicted in Fig. 5. The present simple relation is different from the typical trend of magnetic anisotropy as Dy > Tb > Ho > Er ≫ Gd [17]. On the other hand, the nominal number of 4f-electrons increases from $4f^7$ to $4f^{11}$, and accordingly the number of the 4f-spins decreases from seven to three, in the order from Gd^{3+} to Er^{3+}. This finding indicates that the exchange coupling takes place between the copper $3d_{x^2-y^2}$-spin and the lanthanide 4f-spin portion, regardless of the angular contribution or magnetic anisotropy from Ln ions. The observed antiferromagnetic coupling is approximately proportion to the overlap between the 4f and 3d magnetic orbitals, and the combination for the orbital overlap would increase with an increase of the number of magnetic 4f orbitals.

4. Concluding remarks

The advantages of HF-EPR are the extremely high resolution and the ability to identify quantum numbers of energy-levels by the EPR selection rule. The bias field at the copper(II) ions was detected, affording the information of exchange couplings. We have precisely evaluated J_{4f-3d} for $[Ln_2Cu_2]_n$, (Ln = Tb, Ho, and Er). These J_{4f-3d} values are comparable to those for Ln = Gd [11] and Dy [5], and the magnetic couplings in all compounds investigated here were antiferromagnetic. Furthermore, the $|J_{4f-3d}|$ value monotonically decreases in the order of Gd, Tb, Dy, Ho, and Er. The present methodology would be applicable to other 4f–3d heterometallic compounds. We are now investigating J_{4f-3d} in the $[Ln_2Cu_2]_n$ derivatives involving lighter-lanthanide ions.

5. Experimental

5.1. Materials

Complexes $[Ln_2Cu_2]_n$ ($[\{Ln(hfac)_2(CH_3OH)\}_2\{Cu(dmg)(Hdmg)\}_2]_n$; Ln = Tb, Ho, and Er) were synthesized by the complexation of $[Ln(hfac)_3(H_2O)_2]$ [18] and partially deprotonated $[Cu(Hdmg)_2]$ [19] in methanol (hfac stands for 1,1,1,5,5,5-hexafluoropentane-2,4-dionate; H_2dmg = dimethylglyoxime). $[Cu(Hdmg)_2]$ (15 mg, 0.050 mmol) was dissolved in 1.5 mL of MeOH containing 0.1 mmol of KOH. A methanol solution (1 mL) of $[Tb(hfac)_3(H_2O)_2]$ (82 mg, 0.050 mmol) was slowly added to the above solution. The resultant dark brown solution was allowed to stand at room temperature for a day, to give dark brown platelet crystals that were collected on a filter, washed with a small amount of MeOH, and dried in air. The yield of $[Tb_2Cu_2]_n$ was 23 mg (0.025 mmol; 50% on the repeating unit basis). Similarly, $[Ho_2Cu_2]_n$ and $[Er_2Cu_2]_n$ were prepared as brown prismatic crystals in 70% and 65% yield. The elemental analysis (C, H, N) of their complexes on a Fisons EA-1108 by a usual combustion method supported the chemical composition. $[Tb_2Cu_2]_n$: *Anal.* Calc. for $C_{19}H_{19}CuF_{12}N_4O_9Tb$: C, 25.42; H, 2.13; N, 6.24. Found: C, 22.60; H, 2.52; N, 5.65%. $[Ho_2Cu_2]_n$: *Anal.* Calc. for $C_{19}H_{19}CuF_{12}HoN_4O_9$: C, 25.25; H, 2.12; N, 6.20. Found: C, 23.35; H, 2.46; N, 5.78%. $[Er_2Cu_2]_n$: *Anal.* Calc. for $C_{19}H_{19}CuErF_{12}N_4O_9$: C, 25.18; H, 2.11; N, 6.18. Found: C, 24.94; H, 2.24; N, 5.81%.

5.2. X-ray crystallographic analysis

X-ray diffraction data of $[Ln_2Cu_2]_n$ (Ln = Tb, Ho, and Er) were collected on a Saturn70 CCD diffractometer with graphite monochromated Mo Kα radiation (λ = 0.71070 Å). The structures were directly solved by a heavy-atom method and expanded using Fourier techniques in the CRYSTALSTRUCTURE 3.8.2 program package [20]. Numerical absorption correction was used. All of the hydrogen atoms were located at calculated positions and the parameters were refined as "riding". The thermal displacement parameters of non-hydrogen atoms were refined anisotropically. Full-matrix least-squares methods were applied using all of the unique reflection data. Selected crystallographic data are listed in Table 1.

5.3. Magnetic measurements

The dc magnetic susceptibilities of $[Ln_2Cu_2]_n$ in a range of 1.8–300 K were measured on a Quantum Design SQUID magnetometer (MPMS-7). Typical sample masses were 20–50 mg. The magnetization curves were recorded from −7 to +7 T.

Low-temperature magnetization was measured by a conventional inductive probe in pulsed-magnetic fields, and the temperature was reached as low as 0.5 K using a ^{3}He cryostat [9]. Polycrystalline specimens (typically 20 mg) were mounted in a capillary made of polyimide Kapton (duPont). The sample was not fixed within the sample tube and then it aligned along the magnetic field direction. After we applied the magnetic field several times, the orientation effect was saturated, and the magnetization curves obtained in further shots were found to be identical.

5.4. HF-EPR measurements

HF-EPR spectrum for polycrystalline samples were obtained on the same pulsed-field generator [10]. The sample was packed in a case made of polyethylene. The radiation was produced by Gunn oscillators and backward traveling wave oscillators.

Acknowledgements

This work was partly supported by Grants-in-Aid for Scientific Research from the Ministry of Education, Culture, Sports, Science and Technology, Japan (Nos. 17550166, 18654058, and 19550135), the CASIO Science Promotion Foundation, and the Inter-University Cooperative Research Program of the Institute for Materials Research, Tohoku University. A part of this work was performed at CINTS, Tohoku University.

Appendix A. Supplementary data

CCDC 702758, 702759, and 702760 contain the supplementary crystallographic data for $[Ln_2Cu_2]_n$ (Ln = Tb, Ho, and Er, respectively). These data can be obtained free of charge via http://www.ccdc.cam.ac.uk/conts/retrieving.html, or from the Cambridge Crystallographic Data Centre, 12 Union Road, Cambridge CB2 1EZ, UK; fax: (+44) 1223-336-033; or e-mail: deposit@ccdc.cam.ac.uk. Supplementary data associated with this article can be found, in the online version, at doi:10.1016/j.poly.2008.12.035.

References

[1] (a) D. Gatteschi, R. Sessoli, J. Villain, Molecular Nanomagnets, Oxford University Press, New York, 2006;
(b) D. Gatteschi, R. Sessoli, Angew. Chem., Int. Ed. 42 (2003) 268.
[2] (a) N. Ishikawa, M. Sugita, T. Ishikawa, S.-y. Koshihara, Y. Kaizu, J. Am. Chem. Soc. 125 (2003) 8694;
(b) N. Ishikawa, M. Sugita, W. Wernsdorfer, J. Am. Chem. Soc. 127 (2005) 3650.
[3] (a) F. Mori, T. Nyui, T. Ishida, T. Nogami, K.-Y. Choi, H. Nojiri, J. Am. Chem. Soc. 128 (2006) 1440;
(b) F. Mori, T. Ishida, T. Nogami, Polyhedron 24 (2005) 2588;
(c) A. Okazawa, T. Nogami, H. Nojiri, T. Ishida, Inorg. Chem. 47 (2008) 9763.
[4] S. Ueki, T. Ishida, T. Nogami, K.-Y. Choi, H. Nojiri, Chem. Phys. Lett. 440 (2007) 263.
[5] (a) S. Ueki, A. Okazawa, T. Ishida, T. Nogami, H. Nojiri, Polyhedron 26 (2007) 1970;
(b) A. Okazawa, T. Nogami, H. Nojiri, T. Ishida, Chem. Mater. 20 (2008) 3110.
[6] S. Osa, T. Kido, N. Matsumoto, N. Re, A. Pochaba, J. Mrozinski, J. Am. Chem. Soc. 126 (2004) 420.
[7] C. Aronica, G. Pilet, G. Chastanet, W. Wernsdorfer, J.F. Jacquot, D. Luneau, Angew. Chem., Int. Ed. 45 (2006) 4659.
[8] J.P. Costes, S. Shova, W. Wernsdorfer, Dalton Trans. (2008) 1843.
[9] H. Nojiri, K.-Y. Choi, N. Kitamura, J. Magn. Magn. Mater. 310 (2007) 1468.
[10] H. Nojiri, Y. Ajiro, T. Asano, J.-P. Boucher, New J. Phys. 8 (2006) 218.
[11] S. Ueki, Y. Kobayashi, T. Ishida, T. Nogami, Chem. Commun. (2005) 5223.
[12] J. Krzystek, S.A. Zvyagin, A. Ozarowski, S. Trofimenko, J. Telser, J. Magn. Res. 178 (2006) 174.
[13] M. Andruh, I. Ramade, E. Codjovi, O. Guillou, O. Kahn, J.C. Trombe, J. Am. Chem. Soc. 115 (1993) 1822.
[14] (a) J.-P. Costes, F. Dahan, A. Dupuis, Inorg. Chem. 39 (2000) 5994;
(b) J.-P. Costes, F. Dahan, A. Dupuis, J.-P. Laurent, Inorg. Chem. 39 (2000) 169;
(c) J.-P. Costes, F. Dahan, A. Dupuis, J.-P. Laurent, Chem. Eur. J. 4 (1998) 1616.
[15] (a) T. Kido, Y. Ikuta, Y. Sunatsuki, Y. Ogawa, M. Matsumoto, N. Re, Inorg. Chem. 42 (2003) 398;
(b) M. Evangelisti, M.L. Kahn, J. Bartolome, L.J. de Jongh, C. Meyers, J. Leandri, Y. Leroyer, C. Mathoniere, Phys. Rev. B 68 (2003) 184405.
[16] Y. Kobayashi, S. Ueki, T. Ishida, T. Nogami, Chem. Phys. Lett. 378 (2003) 337.
[17] K. Bernot, L. Bogani, A. Caneschi, D. Gatteschi, R. Sessoli, J. Am. Chem. Soc. 128 (2006) 7974.
[18] M.F. Richardson, W.F. Wagner, D.E. Sands, J. Inorg. Nucl. Chem. 30 (1968) 1275.
[19] J.F. Villa, W.E. Hatfield, J. Chem. Phys. 55 (1971) 4758.
[20] CRYSTALSTRUCTURE, version 3.8.2, Rigaku/MSC, The Woodlands, TX 77381, USA, 2003.

$(\mathbf{1}\cdot 2H_2O\cdot 2MeCN)_\infty$). When the same reaction was repeated with $mpdH_2$ instead of pdH_2, $\{[Mn_{17}(\mu_4\text{-}O)_8(N_3)_5(O_2CMe)_4(mpd)_{10}(py)_8]\}_\infty$ $(\mathbf{2}\cdot 2H_2O)_\infty$[1] was isolated in 35% yield (single crystals could be obtained as $(\mathbf{2}\cdot 2.2H_2O\cdot 2MeCN)_\infty$).

The crystal structures of $(\mathbf{1}\cdot 2H_2O\cdot 2MeCN)_\infty$[2] (Fig. 1a) and $(\mathbf{2}\cdot 2.2H_2O\cdot 2MeCN)_\infty$),[3] both having crystallized in the triclinic space group $P\bar{1}$, consist of a $[Mn_{17}(\mu_4\text{-}O)_8(\mu_3\text{-}N_3)_4(O_2CMe)_2(L)_{10}]^{3+}$ (L = pd^{2-} (**1**); mpd^{2-} (**2**)) unit with a flattened octahedral topology. Bond-valence sum calculations [9], charge considerations, and inspection of metric parameters revealed a mixed-valent complex containing six Mn^{II} and eleven Mn^{III} ions. The 15 Mn ions of the core (Fig. 1b) are disposed in three nearly planar rectangles stacked one above the other, and the remaining two Mn ions occupy the top and bottom capping positions. The central plane consists of seven Mn ions, four at the vertices, two on opposite edges, and the seventh near its center, whereas each of the other two planes contains four Mn ions all of which lie on the edges. All the Mn^{II} ions are located at the vertices of the octahedron whereas the Mn^{III} ions are placed on the edges and near the center of the octahedron. The Mn ions of the core are held together by eight $\mu_4\text{-}O^{2-}$ and four μ_3-1,1,1-N_3^- ligands. The structures also contain ten bridging pd^{2-} (or mpd^{2-}), two bridging and two chelating acetate ligands and one μ-1,3-N_3^- group. The peripheral ligation of compounds **1** and **2** is completed by six and eight terminal pyridine groups, respectively. The μ-1,3-N_3^- ligands bridge Mn7 ion of the Mn_{17} unit to its symmetry-related Mn ion of the neighboring Mn_{17} unit resulting in the formation of the 1-D coordination polymer (Fig. 2). The shortest Mn···Mn separation between different Mn_{17} units is ~6.24 Å in $(\mathbf{1}\cdot 2H_2O\cdot 2MeCN)_\infty$ and slightly longer (6.421 Å) in $(\mathbf{2}\cdot 2.2H_2O\cdot 2MeCN)_\infty$. The chains run parallel in the crystal, and although there are H_2O and MeCN molecules of crystallization there are no significant interchain interactions.

Variable-temperature, solid state magnetic susceptibility measurements were performed on powdered polycrystalline samples of $(\mathbf{1}\cdot 2H_2O)_\infty$ and $(\mathbf{2}\cdot 2H_2O)_\infty$ in a 1 kG (0.1 T) field in the 5.0–300 K range. The obtained data for both compounds are shown as $\chi_M T$ versus T plots in Fig. 3. The $\chi_M T$ for $(\mathbf{1}\cdot 2H_2O)_\infty$ and $(\mathbf{2}\cdot 2H_2O)_\infty$ increases from 82.5 and 88.4 $cm^3\ mol^{-1}$ K at 300 K to a maximum of 375.4 and 428.1 $cm^3\ mol^{-1}$ K at 40.0 and 35 K, respectively, before dropping rapidly to 67.9 and 156.4 $cm^3\ mol^{-1}$ K at 5.00 K. The 300 K $\chi_M T$ values are significantly larger than the value expected if the constituent $Mn_6^{II}Mn_{11}^{III}$ atoms were non-interacting (59.25 $cm^3\ mol^{-1}$ K for $g = 2$) suggesting the presence of predominant ferromagnetic exchange interactions within the Mn_{17} units. The maximum $\chi_M T$ values indicate a very large ground state spin [for example, the $\chi_M T$ value of 428.1 $cm^3\ mol^{-1}$ K for $(\mathbf{2}\cdot 2H_2O)_\infty$ is consistent with an $S = 29$ spin ground state, for which the spin-only ($g = 2$) value is 435.0 $cm^3\ mol^{-1}$ K].

The low temperature steep decrease is undoubtedly due to intermolecular antiferromagnetic exchange interactions mediated by the end-to-end N_3^- ligands, resulting in a diamagnetic ground state for both polymeric species. This was confirmed by the in-phase ac susceptibility (χ'_M), plotted as $\chi'_M T$ versus T in Fig. 4, for the two polymers, which are clearly heading for zero at 0 K. This shows that the steep decrease of $\chi_M T$ in Fig. 3 is not due to an artefact of the applied dc field but indeed due to intermolecular interactions within the 1-D polymers.

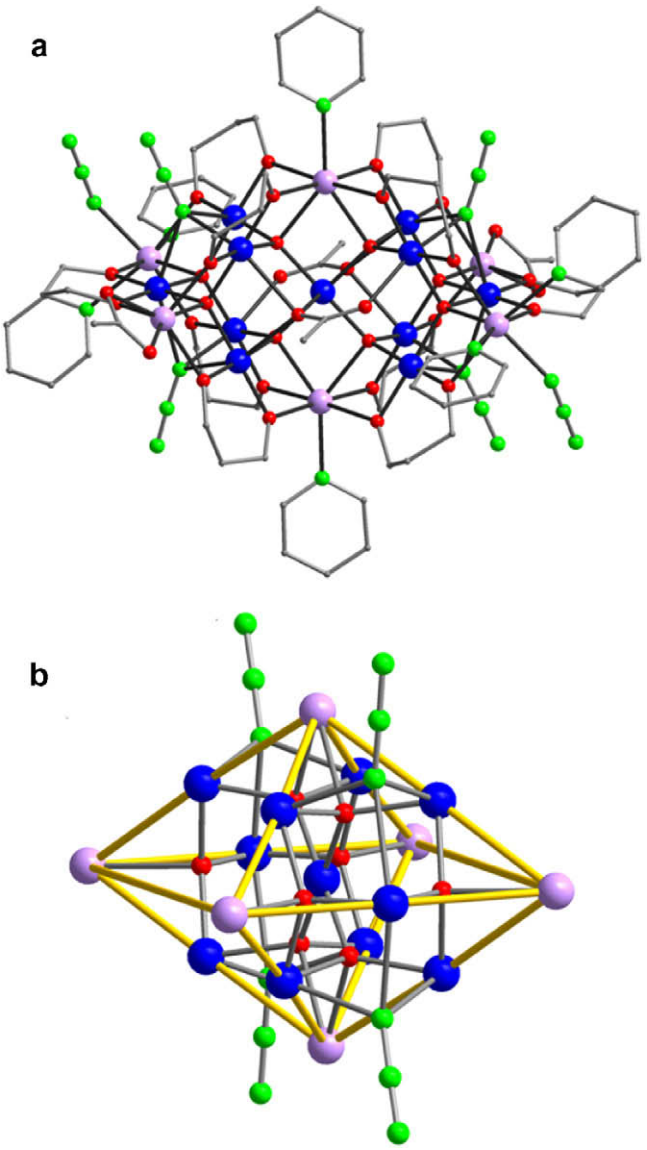


Fig. 1. (a) The molecular structure of **1**. (b) The $[Mn_{11}^{III}Mn_6^{II}(\mu_4\text{-}O)_8(\mu_3\text{-}N_3)_4]^{25+}$ octahedral core of **1** and **2**. Color code: Mn^{III}, blue; Mn^{II}, purple; O, red; N, green; C, grey. Hydrogen atoms have been omitted for clarity. (For interpretation of the references to color in this figure legend, the reader is referred to the web version of this article.)

In summary, the use of N_3^- ligands in Mn-propanediol chemistry has resulted in the isolation of two new one-dimensional coordination polymers based on a Mn_{17} repeating unit. Each Mn_{17} unit has an aesthetically-pleasing structure, in which the manganese ions have an octahedral topology. Furthermore, the repeating unit seems to have a giant ground spin state, but the connection of the clusters through the μ-1,3-N_3^- bridges results in antiferromagnetic intermolecular interactions between the neighboring Mn_{17} units and thus each polymer has an effective $S = 0$ spin ground state. The high-spin ground state for each Mn_{17} cluster is consistent with the presence of μ_3-1,1,1-N_3^- ligands, which are known to mediate ferromagnetic interactions [7]. Substitution of the μ-1,3-N_3^- ions with terminal ligands could lead to magnetically discrete Mn_{17} aggregates with interesting magnetic properties, instead of the present one-dimensional polymers, and such studies are in progress. Finally, the existence of a number of labile terminal ligands

[2] Crystallographic data for $(\mathbf{1}\cdot 2H_2O\cdot 2MeCN)_\infty$: $C_{72}H_{112}N_{23}O_{38}Mn_{17}$, M_r = 2841.80 g mol^{-1}, triclinic, space group $P\bar{1}$, a = 14.051(2) Å, b = 14.700(2) Å, c = 15.200(2) Å, α = 81.60(1)°, β = 66.66(2)°, γ = 78.31(1)°, V = 2815.2(6) $Å^3$, T = 100(2) K, Z = 1, ρ_{calc} = 1.676 g cm^{-3}, 43934 reflections collected, 12176 unique (R_{int} = 0.0424), R_1 = 0.0379, wR_2 = 0.0938, using 6131 reflections with $I > 2\sigma(I)$.

[3] Crystallographic data for $(\mathbf{2}\cdot 2.2H_2O\cdot 2MeCN)_\infty$: $C_{92}H_{142.4}N_{25}O_{38.2}Mn_{17}$, M_r = 3143.85 g mol^{-1}, triclinic, space group $P\bar{1}$, a = 14.8717(7) Å, b = 16.3561(6) Å, c = 16.9541(9) Å, α = 65.231(4)°, β = 65.975(5)°, γ = 67.563(4)°, V = 3307.5(3) $Å^3$, T = 100(2) K, Z = 1, ρ_{calc} = 1.578 g cm^{-3}, 43279 reflections collected, 11518 unique (R_{int} = 0.0323), R_1 = 0.0492, wR_2 = 0.1442, using 6772 reflections with $I > 2\sigma(I)$.

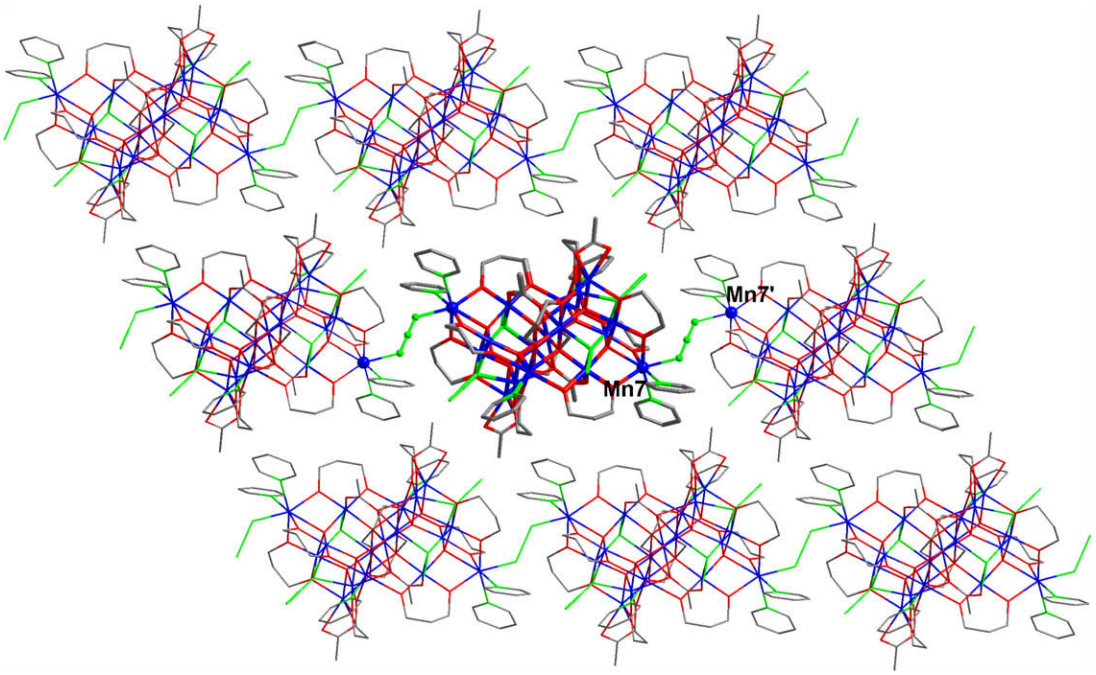


Fig. 2. Wire-frame representation of small sections of $(\mathbf{1})_\infty$ emphasizing the connection of the Mn_{17} units to form the overall 1-D polymeric networks. Color code: Mn, blue; O, red; N, green; C, grey. Hydrogen atoms have been omitted for clarity. (For interpretation of the references to color in this figure legend, the reader is referred to the web version of this article.)

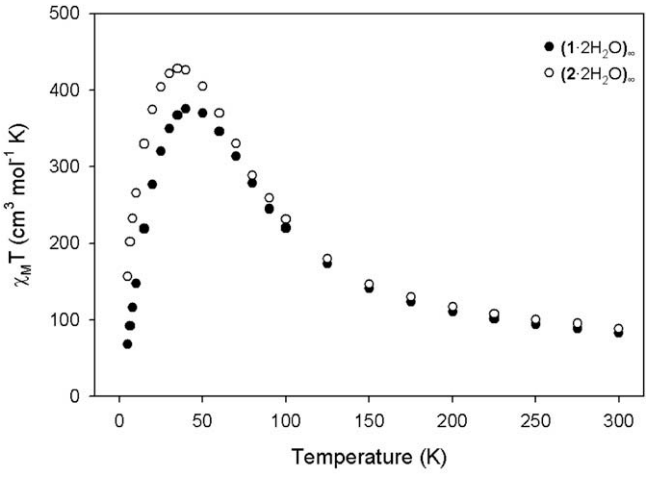


Fig. 3. Plots of $\chi_M T$ vs. T for $(\mathbf{1}\cdot 2H_2O)_\infty$ and $(\mathbf{2}\cdot 2H_2O)_\infty$.

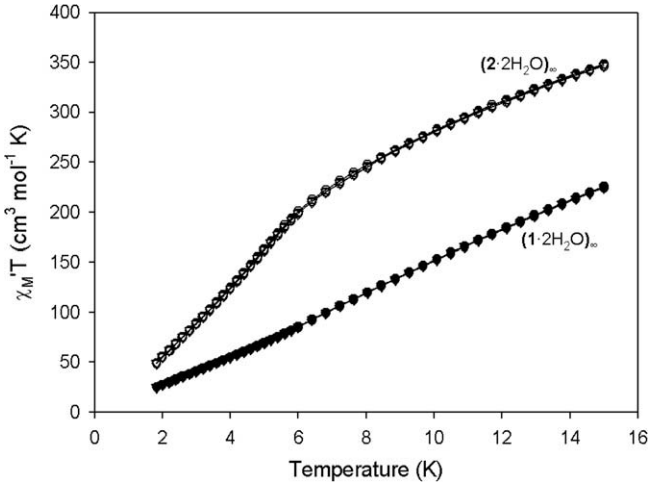


Fig. 4. Temperature-dependence of the in-phace (χ'_M) ac magnetic susceptibility of $(\mathbf{1}\cdot 2H_2O)_\infty$ and $(\mathbf{2}\cdot 2H_2O)_\infty$ at frequencies 50, 250, and 1000 Hz.

in each Mn_{17} units, offers a variety of possibilities for using them as building-blocks for the construction of multidimensional coordination polymers with interesting magnetic and/or structural properties.

Acknowledgements

This work was supported by the Cyprus Research Promotion Foundation (Grant PENEK-ENISX/0505/18), and the USA National Science Foundation (CHE-0414555).

Appendix A. Supplementary data

CCDC 699771 and 708857 contain the supplementary crystallographic data for this article. These data can be obtained free of charge via http://www.ccdc.cam.ac.uk/conts/retrieving.html, or from the Cambridge Crystallographic Data Centre, 12 Union Road, Cambridge CB2 1EZ, UK; fax: +44 1223 336 033; or e-mail: deposit@ccdc.cam.ac.uk.

Supplementary data associated with this article can be found, in the online version, at doi:10.1016/j.poly.2008.12.023.

References

[1] (a) A.M. Ako, I.J. Hewitt, V. Mereacre, R. Clérac, W. Wernsdorfer, C.E. Anson, A.K. Powell, Angew. Chem., Int. Ed. 45 (2006) 4926;
(b) O. Waldmann, A.M. Ako, H.U. Güdel, A.K. Powell, Inorg. Chem. 47 (2008) 3486.
[2] (a) R. Sessoli, H.-L. Tsai, A.R. Schake, S. Wang, J.B. Vincent, K. Folting, D. Gatteschi, G. Christou, D.N. Hendrickson, J. Am. Chem. Soc. 115 (1993) 1804;

(b) G. Christou, D. Gatteschi, D.N. Hendrickson, R. Sessoli, Mrs Bull. 25 (2000) 66.
[3] C.-H. Ge, Z.-H. Ni, C.-M. Liu, A.-L. Cui, D.-Q. Zhang, H.-Z. Kou, Inorg. Chem. Commun. 11 (2008) 675.
[4] M. Murugesu, M. Habrych, W. Wernsdorfer, K.A. Abboud, G. Christou, J. Am. Chem. Soc. 126 (2004) 4766.
[5] T.C. Stamatatos, K.A. Abboud, W. Wernsdorfer, G. Christou, Angew. Chem., Int. Ed. 46 (2007) 884.
[6] (a) M. Murugesu, W. Wernsdorfer, K.A. Abboud, G. Christou, Angew. Chem., Int. Ed. 44 (2005) 892;
(b) D. Foguet-Albiol, T.A. O'Brien, W. Wernsdorfer, B. Moulton, M.J. Zaworotko, K.A. Abboud, G. Christou, Angew. Chem., Int. Ed. 44 (2005) 897;
(c) T.C. Stamatatos, K.A. Abboud, W. Wernsdorfer, G. Christou, Angew. Chem., Int. Ed. 47 (2008) 6694.
[7] (a) A. Escuer, G. Aromí, Eur. J. Inorg. Chem. (2006) 4721;
(b) E. Ruiz, J. Cano, S. Alvarez, P. Alemany, J. Am. Chem. Soc. 120 (1998) 11122;
(c) T.C. Stamatatos, G. Christou, Inorg. Chem., in press.
[8] (a) E.E. Moushi, T.C. Stamatatos, W. Wernsdorfer, V. Nastopoulos, G. Christou, A.J. Tasiopoulos, Angew. Chem., Int. Ed. 45 (2006) 7722;
(b) E.E. Moushi, C. Lampropoulos, W. Wernsdorfer, V. Nastopoulos, G. Christou, A.J. Tasiopoulos, Inorg. Chem. 46 (2007) 3795.
[9] Bond valence sum calculations gave oxidation states of 2.90–3.07 (Mn^{III}) and 1.88–1.96 (Mn^{II}) for the Mn atoms of **1**, 2.84–3.06 (Mn^{III}) and 1.85–1.86 (Mn^{II}) for the Mn atoms of **2**; W. Liu, H.H. Thorp, Inorg. Chem. 32 (1993) 4102.

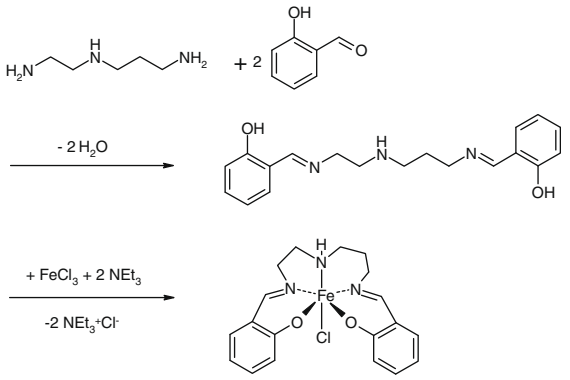


Fig. 1. Synthesis of the [Fe(L)Cl] precursor.

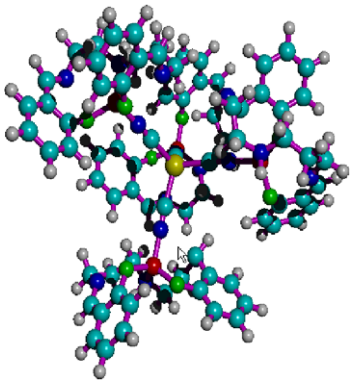


Fig. 3. MM+ structure of the molecular complex of $[(LFe^{III}–NC)_4Sn^{IV}]Cl_4$ optimized based on standard X-ray data.

2.3.2. ESI-MS

For this work an "LCQ" mass spectrometer from Thermo-Finnigan GmbH, Bremen, Germany was used.

2.3.3. Mössbauer spectroscopy

The Mössbauer spectra were recorded using constant acceleration Mössbauer spectrometers from WissEl Electronics Starnberg (Germany) (295 and 78 K) and from the Institute for Analytical Instrumentation St. Petersburg (Russia) (CM-2201, for 295 K). The used Mössbauer source of ^{57}Co in chromium matrix had an average activity of about 0.4 GBq. The ^{119m}Sn source in $CaSnO_3$ matrix had an average activity of 0.35 GBq. Proportional counters (LND Inc., Ocean Side, New York, USA) were used with a voltage between 1800 and 1950 V to detect the spectra. The sample of 33.5 mg was placed into a sealable cylindrical polyethylene sample compartment with an inner diameter of 19 mm. The ^{57}Fe Mössbauer spectra were recorded with a maximum velocity of ±3.20 mm/s (T = 295 K) and ±3.6 mm/s (T = 78 K) because no magnetic splitting could be observed. In the case of the ^{119m}Sn the Mössbauer spectra were recorded with a maximum velocity of ±7.95 mm/s (T = 295 K) and ±6.15 mm/s (T = 78 K). All ^{57}Fe spectra were referred to a standard α-Fe foil (Goodfellow). The ^{119m}Sn spectra were referred to SnO_2 and a Sn foil.

3. Results and discussion

The structure of the $[(LFe^{III}–NC)_4Sn^{IV}]$ complex is shown in Fig. 2. This was confirmed by observation of the molecular peak (M^+) in the ESI-MS. The MM+ force field structure of the $[(LFe^{III}–NC)_4Sn^{IV}]Cl_4$ cluster is shown as POV-ray in Fig. 3. The complex is characterized by IR-spectroscopy. On bridging the typical CN-bond stretching vibration switched from 2080 cm^{-1} to higher wave numbers which are above 2100 cm^{-1}.

Figs. 4 and 5 show the ^{119m}Sn and ^{57}Fe Mössbauer spectra for the compound $[(LFe^{III}–NC)_4Sn^{IV}]$. The spectra show that the oxidation state of tin is +4 at room temperature. On cooling to 78 K beside the tin(IV) an additional minor doublet is present which is characteristic for tin(II). This indicates a valence tautomeric switching in the molecule at the tin-core. For iron(III) the situation is quite different. At 295 and 78 K two doublets are present indicative for iron(III) in the low-spin and high-spin state. On cooling the molar ratio shifts from the dominant high-spin state at room temperature towards the low-spin state at 78 K. This indicates, that some iron(III)-molecules can reversibly be converted between high-spin and low-spin state. This proves that $[(LFe^{III}–NC)_4Sn^{IV}]$ is a multistable, i.e. multiple spin transition, and valence delocalised system on the Sn side.

The compound $[(LFe^{III}–NCS)_4Sn^{IV}]$ is an example for a non-switching molecule. This complex has the same topology as the $[(LFe^{III}–NC)_4Sn^{IV}]$ complex. Just the bridging units change from cyanide to thiocyanate. This complex was prepared like its analogous described above and get measured at the same way. IR-spectroscopy shows that on bridging the typical SCN-bond stretching vibration switched from 2050 cm^{-1} to higher wave numbers which are above 2060 cm^{-1}.

Figs. 6 and 7 show the ^{119m}Sn and ^{57}Fe Mössbauer spectra for the compound $[(LFe^{III}–NCS)_4Sn^{IV}]$. The spectra show that the oxidation state of tin is +4 at room temperature and 78 K. In the iron Mössbauer spectra a doublet is observed. This is characteristic for iron(III) in the high-spin state at 295 and 78 K (Tables 1 and 2). This proves that $[(LFe^{III}–NCS)_4Sn^{IV}]$ shows no indication of molecular switching neither spin transition nor valence tautomerism.

4. Conclusion

The ^{57}Fe-Mössbauer data indicate that the $[(LFe^{III}–NC)_4Sn^{IV}]$ show multiple spin transition between iron(III) in the high-spin and low-spin state. The ^{119m}Sn-Mössbauer data indicate a valence tautomerism between Sn(IV) at room temperature and a partial

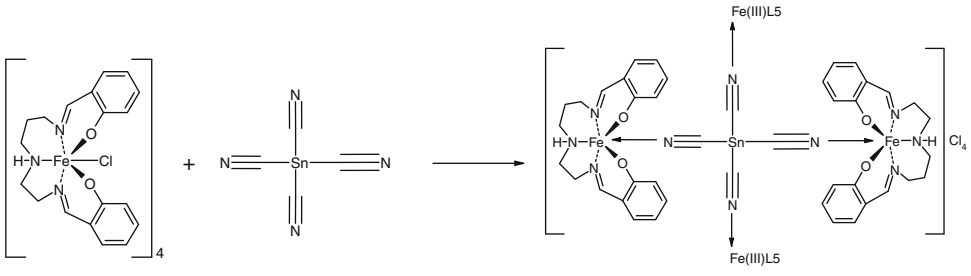


Fig. 2. Synthesis of the $[(LFe^{III}–NC)_4Sn^{IV}]Cl_4$ cluster.

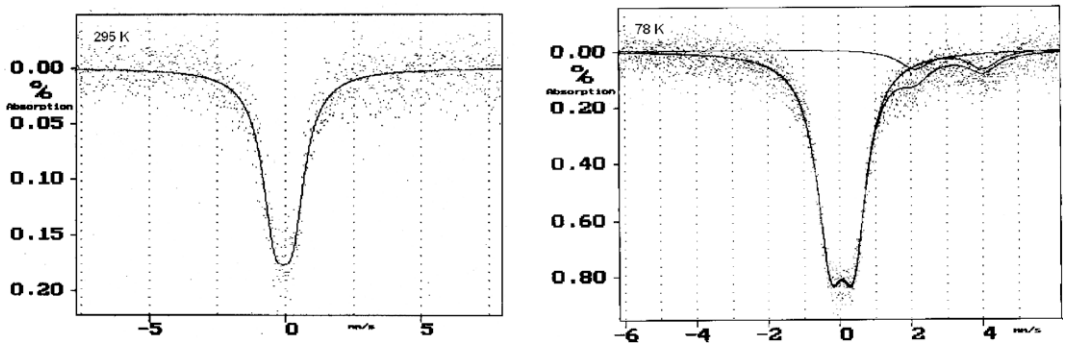


Fig. 4. ^{119m}Sn-Mössbauer spectra of [(LFe^{III}–NC)$_4$Sn^{IV}] at 295 K (left) and 78 K (right).

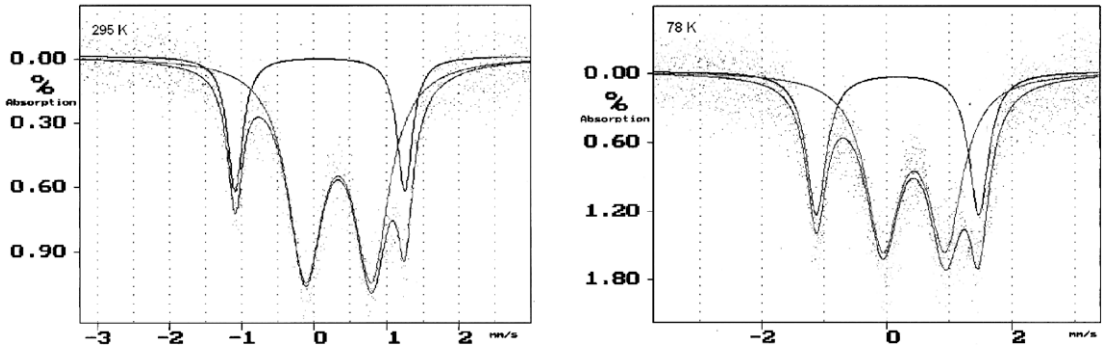


Fig. 5. ^{57}Fe-Mössbauer spectra of [(LFe^{III}–NC)$_4$Sn^{IV}] at 295 K (left) and 78 K (right).

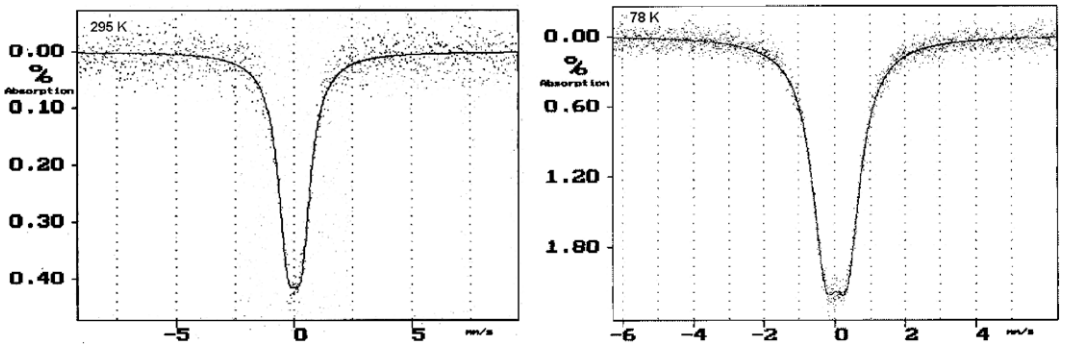


Fig. 6. ^{119m}Sn-Mössbauer spectra of [(LFe^{III}–NCS)$_4$Sn^{IV}] at 295 K (left) and 78 K (right).

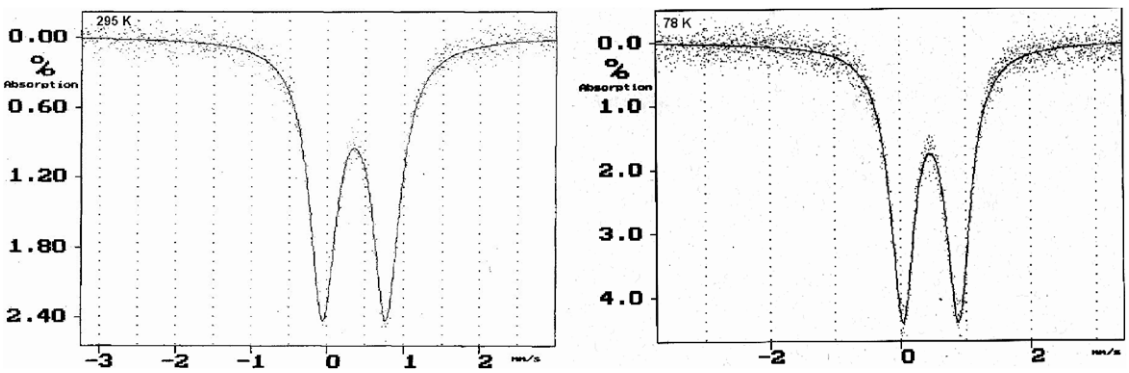


Fig. 7. ^{57}Fe-Mössbauer spectra of [(LFe^{III}–NCS)$_4$Sn^{IV}] at 295 K (left) and 78 K (right).

Table 1
^{119m}Sn-Mössbauer parameter of [(LFe^{III}–NC)$_4$Sn^{IV}] at 295 and 78 K.

	Sn (295 K)	Sn (78 K)	Comparison
	one doublet symmetric	two doublets symmetric	
δ (mm/s)	−0.1	**1. D** 0.085	−0.185
Δ (mm/s)	0.662	0.650	0.012
Fraction (%)	100	88.8	
δ (mm/s)		**2. D** 3.10	
Δ (mm/s)		1.912	
Fraction (%)		11.1	

Table 2
^{57}Fe-Mössbauer parameter of [(LFe^{III}–NC)$_4$Sn^{IV}] at 295 and 78 K.

	Fe (295 K)	Fe (78 K)	Comparison
	two doublets symmetric	two doublets symmetric	
δ (mm/s)	**1. D** 0.095	**1. D** 0.180	−0.085
Δ (mm/s)	2.345	2.601	−0.252
Fraction (%)	22.1	33.5	11.4
δ (mm/s)	**2. D** 0.348	**2. D** 0.443	−0.095
Δ (mm/s)	0.916	1.002	−0.086
Fraction (%)	77.9	66.5	−11.4

conversion to Sn(II) at 78 K. Changing the bridging unit from CN to NCS the [(LFe^{III}–NCS)$_4$Sn^{IV}] is in the Fe(III)-high-spin state and Sn(IV) between 295 and 78 K.

The results show that the compound [(LFe^{III}–NC)$_4$Sn^{IV}] is a switching molecular complex. We suggest that the electrons move between tin and iron, Sn(II) becomes Sn(IV) and two Fe(III) become Fe(II). An effect of 11.1% of switching tin causes 5.55% of Fe(II). Unfortunately this Fe(II)-signal is buried under the huge Fe(III)-absorption in the Mössbauer spectra. Further studies are in progress. Modification of the bridging unit from cyanide to thiocyanate turns the switchability off. This proves the usage of main group elements such as tin as central atoms in switching molecules.

References

[1] (a) P. Gütlich, P. van Koningsbruggen, F. Renz, In Optical Spectra and Chemical Bonding in Transition Metal Complexes, Structure and Bonding vol. 107, Springer-Verlag, 2004;
(b) P. Gütlich, H.A.Goodwin (Eds.). Spin Crossover in Transition Metal Compounds I–III, in: Topics in Current chemistry, Springer-Verlag, 2004, pp. 233–235;
(c) Real et al., J. Am. Chem. Soc. 114 (1992) 4650;
(d) Psomas et al., Inorg. Chem. 43 (2004) 590;
(e) Min et al., Chem. Commun. (2008) 317;
(f) Grunert et al., Angew. Chem., Int. Ed. 47 (2008) 2997;
(g) Ruben et al., Chem. Eur. J. 9 (2003) 4422.
[2] F. Renz, P. Kerep, Hyperfine Interact. 156/157 (2004) 371.
[3] F. Renz, P. Kerep, Polyhedron 24 (2005) 2849.
[4] R. Herchel, R. Boča, M. Gembickŷ, J. Kožiŝek, F. Renz, Inorg. Chem. 43 (2004) 4103.
[5] M. Gembicky, R. Boca, F. Renz, Inorg. Chem. Commun. 3 (2000) 662.
[6] F. Renz, J. Hefner, D. Hill, M. Klein, Polyhedron 26 (2007) 2330.
[7] F. Renz, D. Hill, P. Kerep, M. Klein, R. Müller-Seipel, F. Werner, Hyperfine Interact. 168 (2006) 1051.
[8] F. Renz, P. Kerep, D. Hill, M. Klein, Hyperfine Interact. 168 (2006) 981.
[9] M. Klein, F. Renz, Hyperfine Interact. 168 (2006) 1001.
[10] F. Renz, D. Hill, M. Klein, J. Hefner, Polyhedron 26 (2007) 2325.
[11] R. Boca, Y. Fukuda, M. Gembicky, R. Herchel, R. Jarosciak, W. Linert, F. Renz, J. Yuzurihara, Chem. Phys. Lett. 325 (2000) 411.
[12] M. Glockle, W. Kaim, A. Klein, E. Roduner, G. Hubner, S. Zalis, J. van Slageren, F. Renz, P. Gütlich, Inorg. Chem. 40 (2001) 2256.
[13] M. Boca, P. Baran, R. Boca, H. Fuess, G. Kickelbick, W. Linert, F. Renz, I. Svoboda, Inorg. Chem. 39 (2000) 3205.

allowed to stir for an additional 15 min while a milky suspension developed. After cooling the solution at 0 °C (ice bath), K_2(mto) was isolated by suction filtration and washed several times with ether.

*2.1.2. Preparation of (n-C_4H_9)$_4$N[$Fe^{II}Fe^{III}$(mto)$_3$] (**1**)*

In the formation process of **1**, according to HSAB principle (Hard and Soft Acids and Bases principle), the flipping of mto by 180° would take place here and there, which induces a linkage-isomerization from –Fe^{III}–SOC_2O_2–Fe^{II}– to –Fe^{III}–O_2C_2OS–Fe^{II}– [10]. In order to restrain the linkage-isomerization, **1** was synthesized at −20 °C. A methanol solution of iron(III) nitrate (0.14 g, 0.35 mmol) was added to a methanol solution of K_2(mto) (0.19 g, 1.05 mmol). After stirring for 5 min, $[Fe^{III}(mto)_3]^{3-}$ solution was given. This solution was filtered once to remove solid impurities. The filtrate was cooled at −20 °C, and was added a methanol solution (20 ml) of iron(II) chloride (68.9 mg, 0.35 mmol), (n-C_4H_9)$_4$NBr(112.8 mg, 0.35 mmol) and ascorbic acid (17.6 mg, 0.1 mmol). The mixture was stirred for 3 h. The dark-brown product was collected by suction filtration and dried in vacuo. Elemental *Anal.* Calc. for $C_{22}H_{36}NO_9S_3Fe_2$: C, 39.65; H, 5.45; N, 2.1. Found: C, 38.79; H, 5.50; N, 2.01%.

*2.1.3. Preparation of (n-C_4H_9)$_4$N[$^{57}Fe^{II}Fe^{III}$(mto)$_3$] (**2**)*

(n-C_4H_9)$_4$N[$^{57}Fe^{II}Fe^{III}$(mto)$_3$] was prepared in a similar way to Section 2.1.2. In this process, $^{57}FeCl_2 \cdot 4H_2O$ used as Fe^{II} source was prepared by dropping hydrochloric acid to powdered ^{57}Fe under N_2. Elemental *Anal.* Calc. for $C_{22}H_{36}NO_9S_3Fe_2$: C, 39.65; H, 5.45; N, 2.1. Found: C, 39.49; H, 5.65; N, 2.03%.

*2.1.4. Preparation of (n-C_4H_9)$_4$N[$Fe^{II}{}^{57}Fe^{III}$(mto)$_3$] (**3**)*

(n-C_4H_9)$_4$N[$Fe^{II}{}^{57}Fe^{III}$(mto)$_3$] was prepared in a similar way to Section 2.1.2. In this process, $^{57}Fe(NO_3)_3 \cdot 9H_2O$ used as Fe^{III} source was prepared by dropping nitric acid to powdered ^{57}Fe under N_2. Elemental *Anal.* Calc. for $C_{22}H_{36}NO_9S_3Fe_2$: C, 39.65; H, 5.45; N, 2.1. Found: C, 38.71; H, 5.51; N, 2.11%.

2.2. Measurements

The static magnetic susceptibility was measured by a Quantum Design, MPMS5 SQUID susceptometer under 5000 Oe between 2 and 300 K. The zero field cooled magnetization (ZFCM) and field cooled magnetization (FCM) were also measured for investigating the ferrimagnetic phase in the temperature range of 2–45 K under 30 Oe. The remnant magnetization (RM) was measured in the same temperature region under zero field. A sample was wrapped in polyethylene film and mounted inside the straw. The magnetic susceptibility obtained was corrected for the background and the core diamagnetism estimated from Pascal's constants.

The ^{57}Fe Mössbauer spectra were measured for **2** and **3**. The spectra were calibrated by using the six lines of a body-centered cubic iron foil (α-Fe), the center of which was taken as zero isomer shift. The ^{57}Fe Mössbauer spectra at low temperature were performed with a closed-cycle helium refrigerator cryostat (Iwatani Co., Ltd.).

The dielectric constant measurements were carried out between 4.2 and 300 K by an Agilent, 4284A LCR Meter with alternating electric fields of 1, 10 and 100 kHz. Polar plates were formed by carbon pastes and gold wires were fixed on the both faces of the pellet sample.

3. Results and discussion

Fig. 1 shows the molar magnetic susceptibility as a function of temperature, $\chi_M T$, for **1**. The effective magnetic moment, μ_{eff},

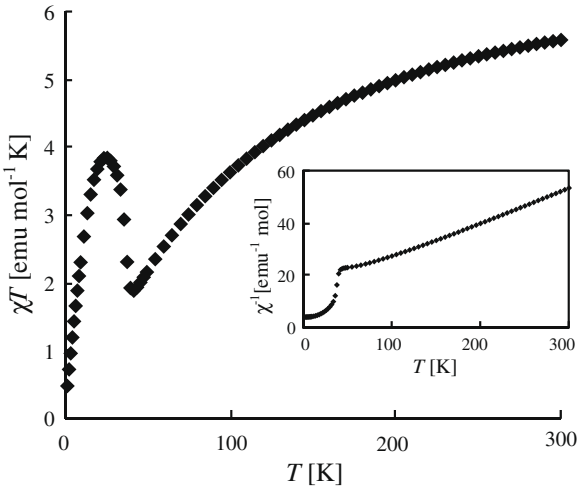


Fig. 1. Temperature dependence of the effective magnetic moment for **1**. Inset is temperature dependence of the inverse magnetic susceptibility for **1**.

decreases with decreasing temperature down to the minimum of 1.87 μ_B at 42 K, and it increases abruptly up to the maximum of 3.85 μ_B at 26 K, then decreases again. This behavior is typical of ferrimagnetism. The effective moment at room temperature is 5.60 μ_B. The spin-only magnetic moment is 7.68 μ_B for the combination of Fe^{III} ($S = 5/2$) and Fe^{II} ($S = 2$). On the other hand, that is 5.19 μ_B for the combination of Fe^{III} ($S = 1/2$) and Fe^{II} ($S = 2$). Therefore, the effective magnetic moment of **1** is situated in the middle value between the magnetic moment for the high-spin and the low-spin states of Fe^{III}. This implies the possibility that the spin state of Fe^{III} is the spin equilibrium of the high-spin ($S = 5/2$) and the low-spin ($S = 1/2$) states. The inverse magnetic susceptibility as a function of temperature is shown in the inset of Fig. 1. From the fitting of inverse magnetic susceptibility with the Curie–Weiss low, $\chi = C/(T-\theta)$, Weiss temperature, θ, is estimated at −93 K. In order to confirm the ferrimagnetic phase-transition, FCM, ZFCM and RM were investigated. This result is shown in Fig. 2. From the analysis of magnetization curves, the ferrimagnetic transition temperature is estimated at 38 K. The magnetic property of **1** is similar to that of (n-C_4H_9)$_4$N[$Fe^{II}Fe^{III}$(ox)$_3$] which shows the ferrimagnetic phase-transition at T_N = 43 K [11].

Fig. 3 shows the ^{57}Fe Mössbauer spectra of **2** and **3** at 200 and 77 K, respectively. The Mössbauer parameters are summarized in Table 1. In both of the ^{57}Fe Mössbauer spectra of **2** and **3**, the spectra clearly indicates the presence of two quadrupole doublets,

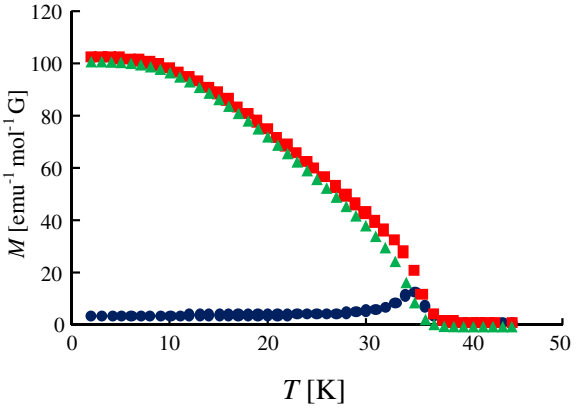


Fig. 2. Temperature dependence of magnetization for **1**. ■: Field cooled magnetization, ▲: remnant magnetization, ●: zero field cooled magnetization.

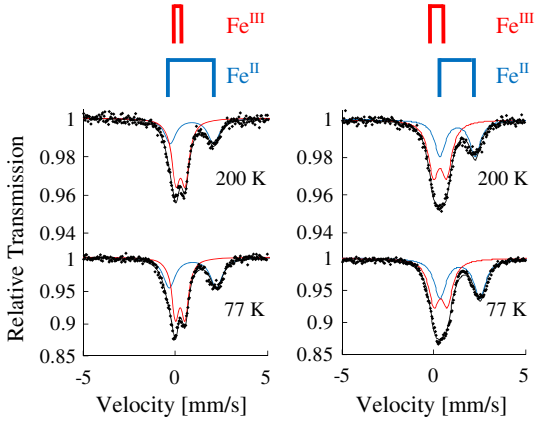


Fig. 3. ^{57}Fe Mössbauer spectra of **2** (left) and **3** (right) at 200 and 77 K.

Table 1
^{57}Fe Mössbauer parameters for **2** and **3**. δ: Isomer shift, ΔE_Q: quadrupole splitting, Γ: line width.

	T (K)	δ (mms^{-1})	ΔE_Q (mms^{-1})	Γ (mms^{-1})	Area (%)
$(n\text{-}C_4H_9)_4N[^{57}Fe^{II}Fe^{III}(mto)_3]$					
Fe^{II} ($S = 2$)	200	0.84	2.34	0.75	38.4
	77	0.92	2.55	0.80	47.6
Fe^{III} ($S = 5/2$)	200	0.22	0.50	0.54	61.6
	77	0.24	0.51	0.48	52.4
$(n\text{-}C_4H_9)_4N[Fe^{II}{}^{57}Fe^{III}(mto)_3]$					
Fe^{II} ($S = 2$)	200	1.30	1.93	0.70	42.0
	77	1.43	2.16	0.77	50.8
Fe^{III} ($S = 5/2$, 1/2)	200	0.35	0.71	0.70	58.0
	77	0.37	0.73	0.70	49.2

which are assigned to Fe^{II} ($S = 2$) and Fe^{III} ($S = 5/2$). The spectra of ^{57}Fe coordinated by O_6 is observed in **2**, while that coordinated by S_3O_3 is observed in **3**. The value of the quadrupole splitting (ΔE_Q) of the Fe^{III} coordinated by S_3O_3 is larger than the Fe^{III} coordinated by O_6. Therefore, this implies that the Fe^{III} coordinated by S_3O_3 is in the highly distorted octahedral environment. Although only one of the two Fe sites was enriched with ^{57}Fe isotope in preparation, the observed spectra show a considerable amount of the other Fe site. This result suggests that the charge transfer occurs between Fe^{II} and Fe^{III}. If the time scale of the charge transfer between Fe^{II} and Fe^{III} is slower than the time window of the ^{57}Fe Mössbauer spectra (10^{-7} s), the charge transfer seems to be static in the ^{57}Fe Mössbauer spectra.

The dielectric constant measurements were carried out to investigate the dynamics of the charge transfer between Fe^{II} and Fe^{III}. Fig. 4 shows the results of the dielectric constant measurements. As shown in Fig. 4, an anomalous enhancement in the real and imaginary parts of the dielectric constant appears above T_N. The anomalous enhancement depends on the frequency of the alternating electric fields. In the imaginary part of the dielectric constant, the peak position of the anomalous enhancement shifts to the higher temperature side with increasing the frequency of alternating electric field. In the dielectric measurements of $(n\text{-}C_3H_7)_4N[Fe^{II}Fe^{III}(dto)_3]$, the anomalous enhancement attributed to the charge transfer phase transition are observed at 120 K with thermal hysteresis and it is independent on the frequency of alternating electric fields [12]. As mentioned above, it should be considered that the anomalous enhancement in the dielectric constant of **1** corresponds to the valence fluctuation between Fe^{II} and Fe^{III} whose time scale depends on temperature. From the analysis of the ^{57}Fe Mössbauer spectra and the dielectric constant, the time scale of the charge transfer between Fe^{II} and Fe^{III} is slower than 10^{-7} s.

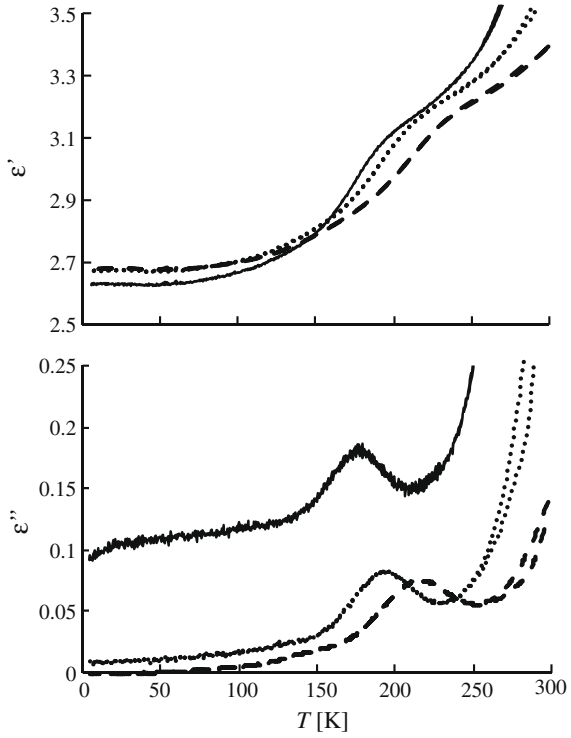


Fig. 4. Temperature dependence of the dielectric constants for **1**. Solid lines: 1 kHz, dotted lines: 10 kHz, dashed lines: 100 kHz.

From the fact that the anomalous enhancement in the dielectric constant of $(n\text{-}C_3H_7)_4N[Fe^{II}Fe^{III}(dto)_3]$ appears only at the charge transfer phase transition, while that of **1** appears in a wide temperature range, it should be considered that the charge transfer of **1** is the valence fluctuation without phase transition.

4. Conclusion

$(n\text{-}C_4H_9)_4N[Fe^{II}Fe^{III}(mto)_3]$ behaves as a ferrimagnet with $T_N = 38$ K and $\theta = -93$ K. The effective magnetic moment of **1** at room temperature is the middle value between those of Fe^{III} ($S = 5/2$)–Fe^{II} ($S = 2$) and Fe^{III} ($S = 1/2$)–Fe^{II} ($S = 2$), which implies the possibility of the spin equilibrium between $S = 5/2$ and $S = 1/2$ in the $Fe^{III}O_3S_3$ site. In fact, the EPR signal of **1** suggests the coexistence of the Fe^{III} ($S = 5/2$) and Fe^{III} ($S = 1/2$) states in a wide temperature range [6]. In connection with this, the following should be mentioned. In the case of tris(monothio carbamato)iron(III) complexes, the effective magnetic moments at room temperature are the middle value between those of Fe^{III} ($S = 5/2$) and Fe^{III} ($S = 1/2$), and the ^{57}Fe Mössbauer spectra corresponding to the $Fe^{III}O_3S_3$ sites have only one doublet, reflecting the rapid spin equilibrium between $S = 5/2$ and $S = 1/2$ [7].

From the analysis of ^{57}Fe Mössbauer spectra for ^{57}Fe enriched complexes, **2** and **3**, the charge transfer between Fe^{II} and Fe^{III} exists in the paramagnetic phase. The dielectric constant measurements were performed to confirm the valence fluctuation between Fe^{II} and Fe^{III}. The anomalous enhancement in the dielectric constant, which depends on the frequency of alternating electric field, was found between 170 and 250 K. This anomalous enhancement in the dielectric constant is presumably attributed to the valence fluctuation between Fe^{II} and Fe^{III}. In order to investigate the detailed dynamics of the valence fluctuation between Fe^{II} and Fe^{III}, the dielectric constant measurement in more wide frequency range is indispensable and in progress.

References

[1] N. Tajima, J. Fujisawa, N. Naka, T. Ishihara, R. Kato, Y. Nishio, K. Kajita, J. Phys. Soc. Jpn. 74 (2005) 511.
[2] S. Uji, H. Shinagawa, T. Terashima, T. Yakabe, Y. Terai, M. Tokumoto, A. Kobayashi, H. Tanaka, H. Kobayashi, Nature 410 (2001) 908.
[3] O. Sato, T. Iyoda, A. Fujishima, K. Hashimoto, Science 272 (1996) 704.
[4] N. Kojima, W. Aoki, M. Itoi, Y. Ono, M. Seto, Y. Kobayashi, Yu. Maeda, Solid State Commun. 120 (2001) 165.
[5] M. Itoi, A. Taira, M. Enomoto, N. Matsushita, N. Kojima, Y. Kobayashi, K. Asai, K. Koyama, T. Nakamoto, Y. Uwatoko, J. Yamamura, Solid State Commun. 130 (2004) 415.
[6] Y. Ono, Doctor Thesis, University of Tokyo, 2005.
[7] K.R. Kunze, D.L. Perry, L.J. Wilson, Inorg. Chem. 16 (1977) 594.
[8] M. Leitheiser, D. Coucouvanis, J. Inorg. Nucl. Chem. 39 (1977) 811.
[9] Z. Chen, Y. Zhang, Y. Gung, Y. Wu, Polyhedron 14 (1995) 3611.
[10] R.G. Pearson, J. Am. Chem. Soc. 85 (1963) 3533.
[11] H. Ōkawa, N. Matsumoto, H. Tamaki, M. Ohba, Mol. Cryst. Liq. Cryst. 233 (1993) 257.
[12] N. Kida, M. Enomoto, T. Suzuki, N. Kojima, Phys. Rev. B 77 (2008) 144427.

previous paper [4], except for using appropriate amount of $ZnCl_2$ in place of $FeCl_2 \cdot 4H_2O$. Diluted complexes were characterized by chemical analysis. The Fe^{II}/Zn^{II} ratios of all the complexes were determined by a JEOL EX-23000BU energy-dispersive X-ray spectroscopy (EDS) with a JEOL JSM-6700F field emission scanning electron microscopy (SEM). We obtained five compositions, that is, $x = 0.00$, 0.26, 0.48, 0.96 and 1.00 in $(n\text{-}C_3H_7)_4N[Fe^{II}_{1-x}Zn^{II}_xFe^{III}(dto)_3]$, using atomic ratio of $ZnCl_2$ is equal to 0.00, 0.05, 0.10, 0.53 and 1.00 in the starting solutions, respectively. Hereafter, x denotes the complex with each concentration of Zn atom in $(n\text{-}C_3H_7)_4N[Fe^{II}_{1-x}Zn^{II}_xFe^{III}\text{-}(dto)_3]$. The powder X-ray diffraction patterns for all the samples were measured with Rigaku multiflex diffractometer with Cu Kα radiation at room temperature. The temperature dependence of the zero-field cooled magnetization (ZFC) and the field cooled magnetization (FC) were measured in the temperature range between 2 and 30 K under external field of 30 Oe for all the complexes using a Quantum-Design MPMS-5 SQUID susceptometer. The remnant magnetization (RM) was also measured under 0 Oe. The temperature dependence of the magnetic susceptibility for them was also measured in the temperature range between 2 and 300 K under field of 5000 Oe by same apparatus. For ^{57}Fe Mössbauer spectroscopic measurement, ^{57}Co in Rh was used as a Mössbauer source. The spectra were calibrated by using the six lines of a body-centered cubic iron foil (α-Fe), the center of which was taken as zero isomer shift.

3. Results and discussions

Fig. 1 shows the powder X-ray diffraction patterns of $x = 0.00$, 0.26, 0.48, 0.96 and 1.00. The complex with $x = 0.00$, whose composition is equal to that of $(n\text{-}C_3H_7)_4N[Fe^{II}Fe^{III}(dto)_3]$, shows the same diffraction pattern with previous report [10]. Moreover, the others show similar diffraction pattern with $x = 0.00$, although their peaks become broad due to the highly disordered structure by substitution between Fe^{II} and Zn^{II}. This result means that $(n\text{-}C_3H_7)_4N[Fe^{II}_{1-x}Zn^{II}_xFe^{III}(dto)_3]$ are forming isomorphous structure in the whole range of zinc concentrations. Therefore, the two-dimensional honeycomb network structure with an alternating array of M^{II} (M = Fe or Zn) and Fe^{III} atoms through dto bridges is kept by the substitution of metal atoms.

Fig. 2a indicates the $\chi T - T$ plots for all the complexes. High temperature tails of these plots decrease with increasing of zinc ratio. Moreover, the magnetic interaction changes from the ferromagnetic interaction to the antiferromagnetic one between $x = 0.48$ and 0.96. These concentration dependencies are quantitatively analyzed by fitting of the temperature dependence of the magnetic susceptibility with the Curie–Weiss low, $\chi = C/(T - \theta)$, where C and θ denote the Curie constant and the Weiss temperature, respectively. The spin moment, s, is calculated from the Curie constant. As shown in Fig. 3, the concentration of spin is proportional to the Fe^{II}/Zn^{II} ratio. The spin moment is consistent with the sum of $Fe^{III}(S = 1/2)$ site and the concentration of $Fe^{II}(S = 2)$. On the other hand, as shown in Fig. 3, the Weiss temperature decreases and changes from ferromagnetic interaction to antiferromagnetic one between $x = 0.48$ and 0.96. This threshold-type change is typical behavior for low dimensional magnet. In Fig. 2b, the thermal hysteresis in the magnetic susceptibility for $x = 0.26$ disappears, unlike $x = 0.00$ in the inset of Fig. 2b. This fact shows that the substitution from Fe^{II} to Zn^{II} prevent the cooperative effect on the CTPT. Judging from Fig. 4, the Curie temperature shifts from $T_C = 7$ to 10 K with substitution from $x = 0.00$ to 0.26. Then, it becomes $T_C = 6$ K for $x = 0.48$. Moreover, the ferromagnetic transition almost disappears above $x = 0.96$. In general, a ferromagnetic transition temperature monotonically decreases with increasing the diluted ratio. However, in this system, the Curie

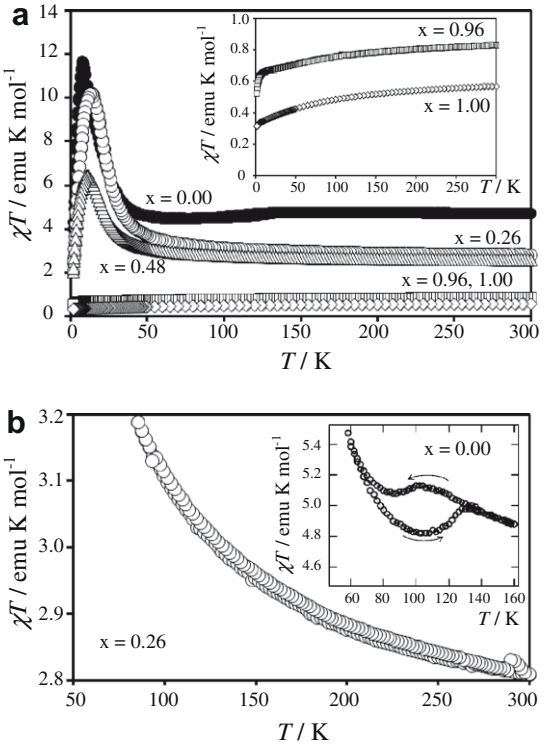


Fig. 2. (a) The $\chi T - T$ plots for $x = 0.00$, 0.26, 0.48, 0.96 and 1.00. Inset is the magnified figure for $x = 0.96$ and 1.00. (b) Absence of hysteresis loop for $x = 0.26$. Inset shows the thermal hysteresis for $x = 0.00$ for Ref. [4].

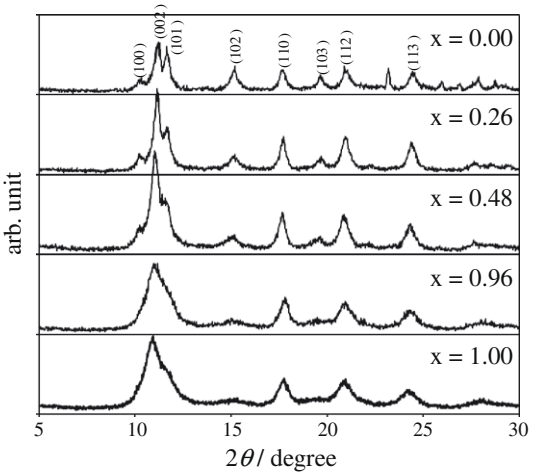


Fig. 1. The powder X-ray diffraction patterns for $x = 0.00$, 0.26, 0.48, 0.96 and 1.00 by Cu Kα radiation.

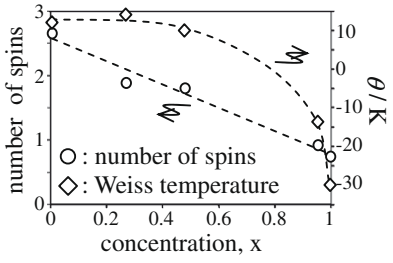


Fig. 3. The concentration dependence of the number of spins and Weiss temperature, θ. Dotted lines are guide for eyes.

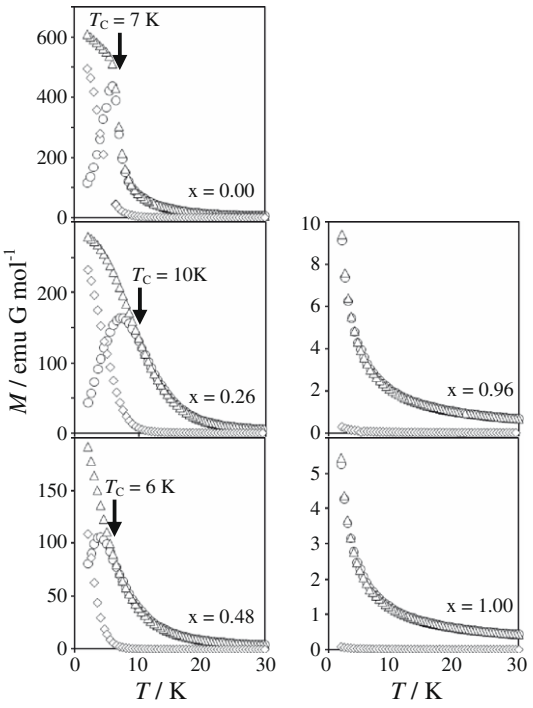


Fig. 4. ZFC (○), FC (△) and RM (◇) for x = 0.00, 0.26, 0.48, 0.96 and 1.00. Arrows show the ferromagnetic transition temperature.

temperature is once enhanced between x = 0.00 and 0.26, and then, it decreases with increasing x (see Fig. 5). This behavior can be explained as follows. For $(n\text{-}C_3H_7)_4N[Fe^{II}Fe^{III}(dto)_3]$, which is the same complex as x = 0.00, the ferromagnetic state is in the LTP with transition temperature of 7 K, while $(n\text{-}C_5H_{11})_4N[Fe^{II}Fe^{III}(dto)_3]$ shows T_C = 19.5 K with the HTP state in the ordering phase [4]. Therefore, HTP states are expected to give comparatively high transition temperature. It is noteworthy that x = 0.00 shows the two step ferromagnetic phase transition for a single crystal measurement with the LTP and the HTP. One transition temperature is 7 K in the LTP, while the other is 15 K in the HTP [3]. Judging from these facts, the Curie temperature monotonically decreases in the only HTP states. This anomalous enhancement of T_C between x = 0.00 and 0.26 is due to the conversion from the ferromagnetic transition in the LTP to that in the HTP.

To confirm the disappearance of the CTPT between x = 0.00 and 0.26 and the explanation for the shift of the Curie temperature, ^{57}Fe Mössbauer spectroscopy was carried out. Fig. 6 shows the ^{57}Fe Mössbauer spectra at 200 and 10 K for all the complexes. The magnetic state of x = 0.00 clearly changes from HTP to LTP, which is shown in Fig. 6a [4]. On the other hand, in Fig. 6d, x = 1.00 only indicates the Fe^{III}(S = 1/2) signal at 200 and 10 K. Its isomer shift, δ, and

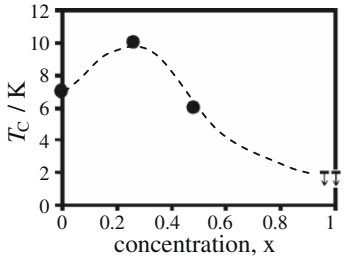


Fig. 5. The concentration dependence of the Curie temperature, T_C. T_C for x = 0.96 and 1.00 are below 2 K. Dotted line is guide for eyes.

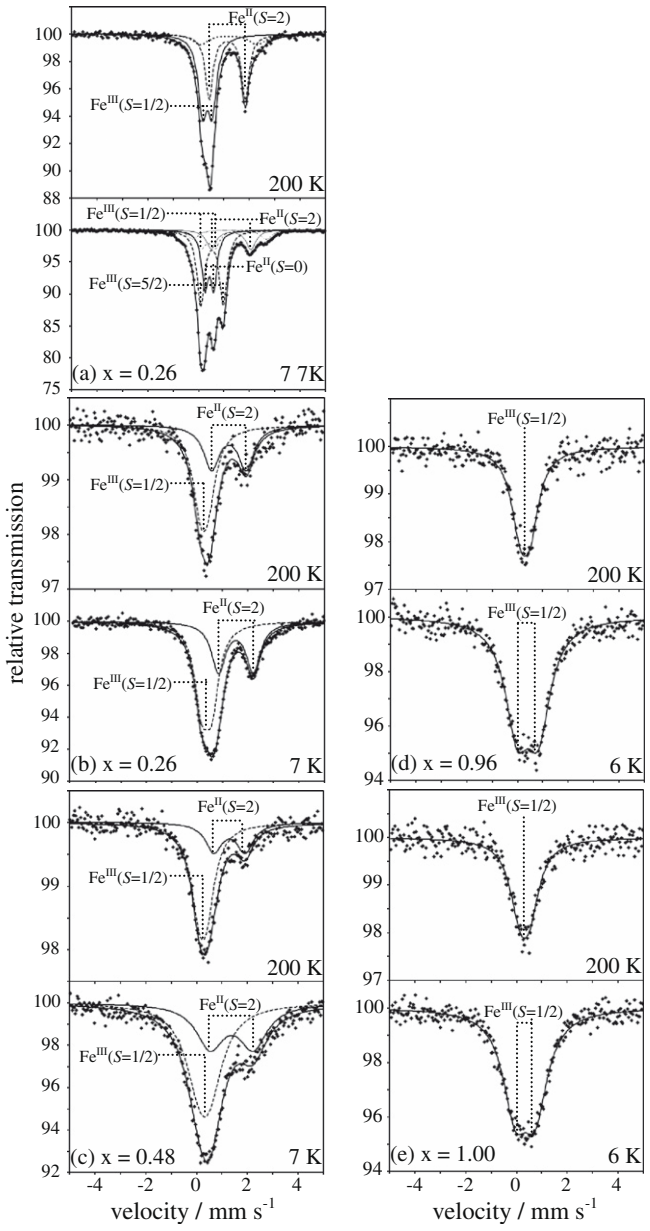


Fig. 6. The 57Fe Mössbauer spectra for x = 0.00, 0.26, 0.48, 0.96 and 1.00.

Table 1
Mössbauer parameters of $(n\text{-}C_3H_7)_4N[Fe^{III}_{1-x}Zn^{II}_xFe^{III}(dto)^3]$.

X	T (K)	Fe^{III}(LS) δ (mm/s)	ΔEQ (mm/s)	Fe^{II}(HS) δ (mm/s)	ΔEQ (mm/s)
0.00 [4b]	200	0.35	0.38	1.14	1.43
	200	0.26	0.30	1.24	1.36
0.26	10	0.37	0.40	1.52	1.37
	200	0.26	0.34	1.31	1.23
0.48	10	0.22	0.42	1.48	1.38
	200	0.31	0.40		
0.96	10	0.40	0.83		
	200	0.33	0.39		
1.0	10	0.30	0.79		

quadrupole splitting, ΔE_Q, are listed in Table 1. x = 0.96 complex shows almost the same spectra with x = 0.00 at 200 and 10 K (Fig. 6c and Table 1). For x = 0.96, small amount of Fe^{II}(S = 2) signal is too small to find in the Mössbauer spectra due to the low S/N ratio

caused by the γ-ray absorption by Zn atoms. These Mössbauer parameters are quite similar to that for the $Fe^{III}(S = 1/2)$ in HTP of $x = 0.00$ except for ΔE_Q in low temperature. This increasing of ΔE_Q is due to the distortion caused by the substitution of M^{II} site to smaller Zn ion. As shown in Fig. 6b and c, x = 0.26 and 0.48 gives a corresponding spectra with HTP of $x = 0.00$ at 200 and 10 K except for Fe^{III}/Fe^{II} ratio. Mössbauer parameters for them are also listed in Table 1. These values are also similar to the value for HTP of $x = 0.00$. The ordering component of $Fe^{II}(S = 2)$ is not clear in Fig. 6b, because the measuring temperature is very close to T_C. Although it is hard to separate between the ordering component of $Fe^{II}(S = 2)$ and the other iron components in $x = 0.26$ and 0.48, HTP remains in low temperature region. The disappearance of the CTPT above $x = 0.26$ is consistent with the result of magnetic susceptibility measurements.

4. Conclusion

Magnetic dilution effect of $(n\text{-}C_3H_7)_4N[Fe^{II}_{1-x}Zn^{II}_xFe^{III}(dto)_3]$ is investigated. The structure of this compound is isostructural in whole x range. The magnetic susceptibility measurements and the ^{57}Fe Mössbauer spectra show that the CTPT in $(n\text{-}C_3H_7)_4N[Fe^{II}Fe^{III}(dto)_3]$ disappears by Fe^{II} substitution of 26%. To investigate the expected value of critical concentration for the ferromagnetic transition temperature, we have to prepare middle concentration complex and measure the detailed concentration dependence of magnetic properties in further experiment.

Acknowledgements

This work was supported by a Grant-in-Aid for Scientific Research from the Ministry of Education, Science, Sports and Culture, Japan. Masaya Enomoto was also supported by a Grant-in-Aid for Young Scientists (B).

References

[1] N. Kojima et al., Solid State Commun. 120 (2001) 165.
[2] N. Kojima et al., Synth. Metals 121 (2001) 1796.
[3] M. Itoi et al., J. Mag. Mag. Mater. 272–276 (2004) 1093.
[4] (a) M. Itoi et al., Eur. J. Inorg. Chem. 6 (2006) 1198;
(b) N. Kojima et al., Hyperfine Interactions 156–157 (2004) 175.
[5] N. Kida, The University of Tokyo, Doctor thesis, 2009.
[6] (a) I. Kashima et al., Synth. Metals 153 (2005) 473;
(b) N. Kida et al., J. Am. Chem. Soc. 131 (2009) 212.
[7] Y. Ono, The University of Tokyo, Doctor thesis, 2005.
[8] M. Enomoto et al., Synth. Metals 152 (2005) 457.
[9] M. Pilkington et al., in: J.S. Miller, M. Drillon (Eds.), Magnetism: Molecules to Materials II, Wiley-VCH, Weinheim, 2001, p. 339. and references there in.
[10] M. Itoi et al., Solid State Commun. 130 (2004) 415.

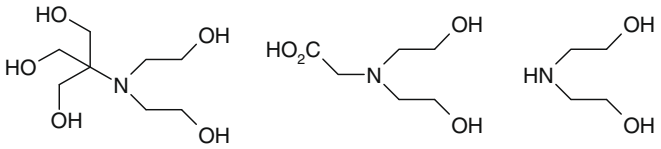


Chart 1. Ligands bis–tris, bicine and diethanolamine.

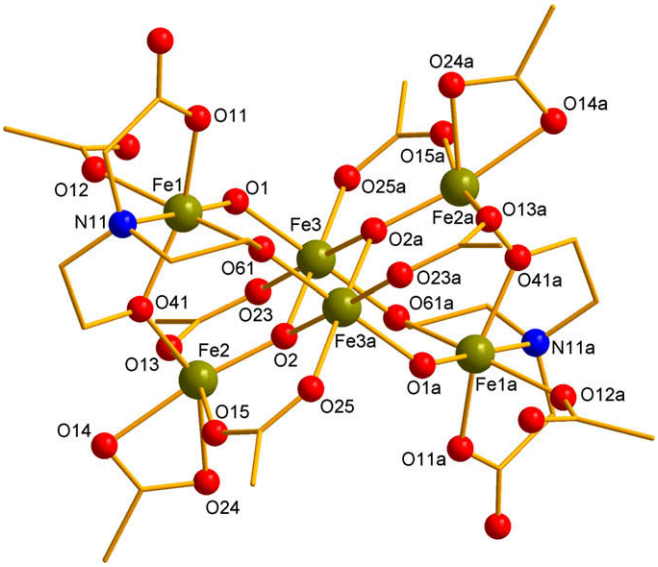


Fig. 1. Structure of the anion of **1** (ball and stick representation with Fe(III) gold; O, red; N, blue; C, brown; H atoms and Me groups of pivalate ligands omitted for clarity) [atom suffix a signifies the symmetry equivalent atom: $a = 1 - x, 1 - y, 1 - z$]. (For interpretation of the references to colour in this figure legend, the reader is referred to the web version of this article.)

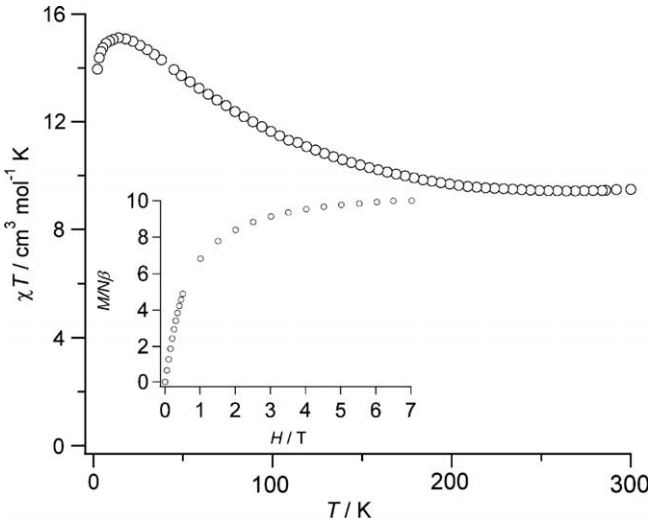


Fig. 2. Temperature dependence of χT for **1** from 300 to 1.8 K measured in a field of 1 kOe (inset, magnetisation versus field at 2 K).

of the Fe_4 butterfly core. This binding mode has been observed for the $[Fe_6(Bic)_6]$ wheel [12]. The hydroxide ligand (O1) also bridges Fe1 to a body iron(III) center (Fe1–O1–Fe3). Four of the eight pivalate ligands span the butterfly body-wing vectors in the typical 1,3-bridging mode. In addition, two are capping Fe2 and Fe2a in the 1,1′ mode and the remaining two are monodentate bound to Fe1 and Fe1a and hydrogen-bonding to the two hydroxide groups (O1 and O1a). All Fe(III) centers are six-coordinate although the 1,1′ bridging pivalate results in a rather distorted geometry at Fe2 (and s.e.). The $Et_2NH_2^+$ cations are located above and below the Fe6 cluster, hydrogen-bonded to the bicine carboxylates (O11 and O11a) and the 1,1-bridging carboxylates (O24a and O24).[3] We note that in this Fe_6 cluster, one Fe_4 butterfly unit is capped by two {Fe(Bic)} units. It is interesting to compare this Fe_6 cluster to our Fe_{10} clusters with bis–tris [7] where two Fe_4 butterfly units are bridged together by two {Fe(bis–tris)} units. Hence, we can show that clusters of different nuclearity and topology can be prepared by

[3] One of the crystallographically independent $Et_2NH_2^+$ cations is disordered over two positions.

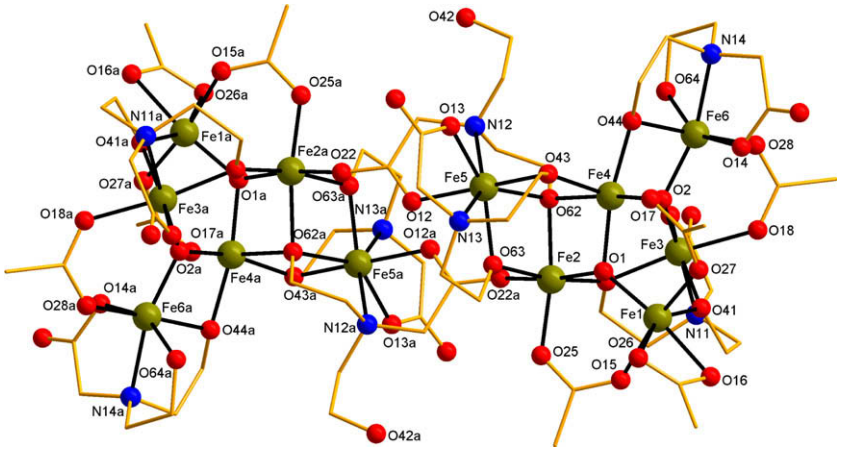


Fig. 3. Structure of **2** (ball and stick representation with Fe(III) gold; O, red; N, blue; C, brown; H atoms and Me groups of pivalate ligands omitted for clarity) [atom suffix a signifies the symmetry equivalent atom: $a = 0.5 - x, 2.5 - y, -z$]. (For interpretation of the references to colour in this figure legend, the reader is referred to the web version of this article.)

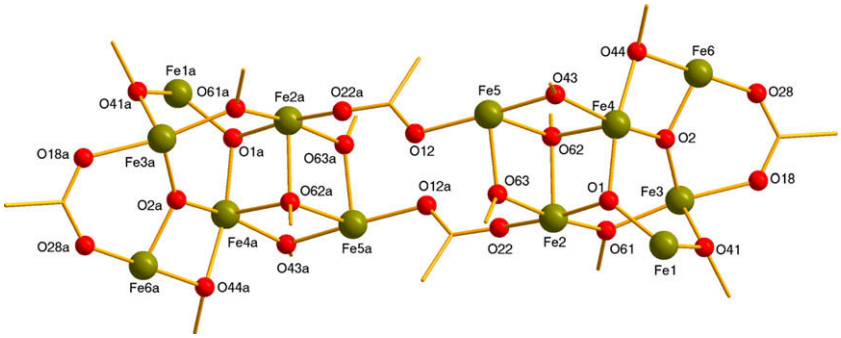


Fig. 4. Core structure of **2**.

adjusting carefully the nature of the polydentate ligand, to build upon the Fe_4 butterfly unit.

For **1** the value of χT at 300 K is 9.87 $cm^3\ mol^{-1}$ K, significantly lower than for six uncoupled Fe(III) ions (26.25 $cm^3\ mol^{-1}$ K for $g = 2$), indicating strong antiferromagnetic interactions between the Fe(III) centers (see Fig. 2). The value of χT increases steadily to a maximum of 15.0 $cm^3\ mol^{-1}$ K at 14.0 K, then drops sharply to 13.6 $cm^3\ mol^{-1}$ K at 1.8 K. This drop can be attributed to either zero-field splitting or intermolecular antiferromagnetic interactions. The magnetisation was measured as a function of applied field at 2 K, rising to a maximum value of $M/N\beta = 10.0$ at 7 T. Both the low temperature maximum in χT and the magnetisation data are consistent with a spin ground state of $S = 5$ for **1**. However, further measurements including EPR are required to determine the magnitude and size of any anisotropy. Further Fe_6 clusters have been reported recently, with broadly similar topologies and $S = 5$ ground states [19].

The change of base from Et_2NH to NaOMe produces a dodeca-nuclear complex $[Fe_{12}O_4(Bic)_4(HBic)_4(O_2CCMe_3)_8] \cdot 5MeCN$ (**2** · 5MeCN), in 12% yield, which crystallizes in the monoclinic space group C2/c (Fig. 3).[4] Compound **2** can be described as a dimer of Fe_6 units, which have a different topology to the Fe_6 cluster found in **1**. The two Fe_6 units are separated by 6 Å, bridged by the carboxylate arms from the bicine ligands (Fig. 4). Unlike **1**, compound **2** is not composed of Fe_4 butterfly units: for **2**, more bicine is incorporated into the structure. The structure of each Fe_6 unit is unusual and is formed from two corner-sharing Fe_3O triangles (Fe3, Fe6, Fe4 and Fe1, Fe2, Fe4). In addition, Fe5 bridges to Fe2 and Fe4 through three $CH_2CH_2O^-$ arms (O62, O43, O63) from two bicine ligands, such that Fe2, Fe4 and Fe5 form an incomplete $\{Fe_3O_4\}$ cubane.

The triply deprotonated bicine ligands (with N11 bound to Fe3 or N13 bound to Fe5) bind in the same $\eta^2{:}\eta^2{:}\eta^1{:}\eta^1{:}\mu_3$ mode as that found in **1**. One of the doubly deprotonated ligands (with N14 bound to Fe6) caps Fe6, with one $CH_2CH_2O^-$ arm bridging Fe6 to Fe4 and the second CH_2CH_2OH arm protonated (O64). The remaining Hbic ligand (with N12 bound to Fe5) displays a new binding mode, bridging the two halves of the cluster through the carboxylate arm. The deprotonated $CH_2CH_2O^-$ arm (O62) is μ_3-bridging (Fe2, Fe4, Fe5) with the second CH_2CH_2OH arm protonated and unbound (O42). Fig. 5 illustrates the different binging modes of bicine present in compounds **1** and **2**. Six of the pivalate ligands are 1,3-bridging with the remaining two 1,1′-bridging (to Fe1, Fe1a) as found in **1**. All Fe centers are six-coordinate except Fe5 (and s.e.),

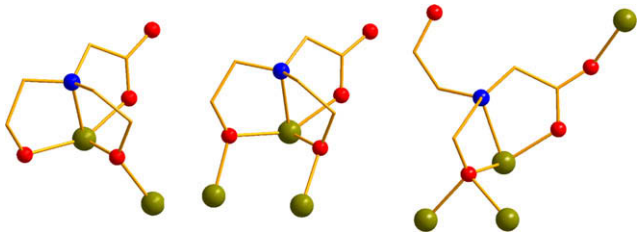


Fig. 5. Binding modes of $BicH^{2-}$ and Bic^{3-} found in **1** and **2**.

[4] Air-dried crystals analyze as **2** · 2MeCN · $4H_2O$, analysis (%) calc. (found): C, 37.05 (36.77); H, 5.75 (5.67); N, 4.70 (4.95), selected IR data: ν = 3397 (broad); 2962, 1624, 1533, 1484, 1422, 1358, 1227, 1080, 1040, 889, 795, 690 cm^{-1}. Crystal data for **2** · 5MeCN: monoclinic, C2/c, $a = 29.795(5)$, $b = 20.638(4)$, $c = 27.218(8)$ Å, $\beta = 120.749(7)°$, $U = 14384(6)$ Å^3, $M = 3033.64$, $Z = 8$, μ(Mo Kα) = 1.247, $T = 100$ K; R1 = 0.0575. CCDC 707009.

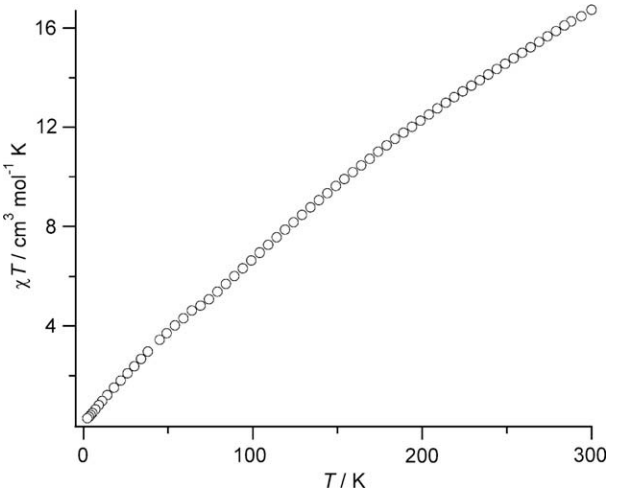


Fig. 6. Temperature dependence of χT for **2** from 300 to 1.8 K measured in a field of 1 kOe.

which are 7-coordinate showing a pentagonal bipyramidal geometry.

The value of χT for **2** at 300 K is 16.7 $cm^3\ mol^{-1}$ K, significantly lower than the expected value for 12 uncoupled Fe(III) ions (52.5 $cm^3\ mol^{-1}$ K for $g = 2$), indicating strong antiferromagnetic interactions between the Fe(III) centers (Fig. 6). The value of χT decreases steadily reaching a value of 0.09 $cm^3\ mol^{-1}$ K at 1.8 K consistent with an $S = 0$ ground state.

In conclusion, we have reported two new Fe(III) complexes that incorporate the bicine ligand together with pivalate ligands. We have shown the versatility of the ligand, which can exist in different binding modes and can act as a bridging unit within the structure. The nature of the base used in the reaction has an effect on the cluster produced and this warrants further investigation. Magnetic characterisation reveals $S = 5$ and $S = 0$ ground states for the hexa- and dodeca-nuclear complexes, respectively.

Acknowledgements

Financial support from The University of Glasgow and EPSRC is gratefully acknowledged. We thank Dr Javier Sanchez-Benitez, University of Edinburgh for collection of the magnetic data.

References

[1] G. Aromi, E.K. Brechin, Struct. Bonding (Berlin) 122 (2006) 1.
[2] M. Murrie, D.J. Price, Annu. Rep. Prog. Chem. Sect. A 103 (2007) 20.
[3] A. Ardavan, O. Rival, J.J.L. Morton, S.J. Blundell, A.M. Tyryshkin, G.A. Timco, R.E.P. Winpenny, Phys. Rev. Lett. 98 (2007) 057201/1.
[4] B. Cage, S.E. Russek, R. Shoemaker, A.J. Barker, C. Stoldt, V. Ramachandaran, N.S. Dalal, Polyhedron 26 (2007) 2413.
[5] M. Manoli, R.D.L. Johnstone, S. Parsons, M. Murrie, M. Affronte, M. Evangelisti, E.K. Brechin, Angew. Chem., Int. Ed. 46 (2007) 4456.
[6] L. Bogani, W. Wernsdorfer, Nature Mat. 7 (2008) 179.
[7] A. Ferguson, J. McGregor, A. Parkin, M. Murrie, Dalton Trans. (2008) 731.
[8] R.W. Saalfrank, I. Bernt, E. Uller, F. Hampel, Angew. Chem., Int. Ed. 36 (1997) 2482.
[9] R.W. Saalfrank, C. Deutscher, S. Sperner, T. Nakajima, A.M. Ako, E. Uller, F. Hampel, F.W. Heinemann, Inorg. Chem. 43 (2004) 4372.
[10] A.M. Ako, O. Waldmann, V. Mereacre, F. Klower, I.J. Hewitt, C.E. Anson, H.U. Güdel, A.K. Powell, Inorg. Chem. 46 (2007) 756.
[11] D. Foguet-Albiol, K.A. Abboud, G. Christou, Chem. Commun. (2005) 4282.
[12] M. Murugesu, K.A. Abboud, G. Christou, Dalton Trans. (2003) 4552.
[13] A. Messimeri, C.P. Raptopoulou, V. Nastopoulos, A. Terzis, S.P. Perlepes, C. Papadimitriou, Inorg. Chim. Acta 336 (2002) 8.
[14] (a) H. Yamaguchi, Y. Inomata, T. Takeuchi, Inorg. Chim. Acta 172 (1990) 105; (b) X.-F. He, L.-S. Long, X.-Y. Le, X.-M. Chen, L.-N. Ji, Z.-Y. Zhou, Inorg. Chim.Acta 285 (1999) 326; (c) H. Thakuria, G. Das, Polyhedron 26 (2007) 149.
[15] Z. Sun, P.K. Gantzel, D.N. Hendrickson, Polyhedron 16 (1997) 3267.
[16] A.S. Batsanov, Yu.T. Struchkov, G.A. Timko, Koord. Khim. 14 (1988) 266.
[17] (a) J.K. McCusker, J.B. Vincent, E.A. Schmitt, M.L. Mino, K. Shin, D.K. Coggin, P.M. Hagen, J.C. Huffman, G. Christou, D.N. Hendrickson, J. Am. Chem. Soc. 113 (1991) 3012; (b) P. Ammala, J.D. Cashion, C.M. Kepert, B. Moubaraki, K.S. Murray, L. Spiccia, B.O. West, Angew. Chem., Int. Ed. 39 (2000) 1688.
[18] (a) W. Liu, H.H. Thorp, Inorg. Chem. 32 (1993) 4102; (b) BVS analysis of **1**: Fe1, 2.96; Fe2, 3.04; Fe3, 3.10; O1, 1.12; O2, 1.86. BVS analysis of **2**: Fe1, 2.90; Fe2, 3.03; Fe3, 2.90; Fe4, 2.97; Fe5, 2.43; Fe6, 2.96; O1, 1.77; O2, 1.85.
[19] (a) I.A. Gass, C.J. Milios, A. Collins, F.J. White, L. Budd, S. Parsons, M. Murrie, S.P. Perlepes, E.K. Brechin, Dalton Trans. (2008) 2043; (b) R. Bagai, M.R. Daniels, K.A. Abboud, George Christou, Inorg. Chem. 47 (2008) 3318.

2.3. Susceptibility measurements

DC and AC magnetic susceptibility data were obtained on a Quantum Design MPMS-XL7 SQUID magnetometer. DC data were recorded from 1.8 K up to room temperature in a 0.1 T magnetic field, and the magnetic data were corrected for the diamagnetic contribution calculated from Pascal's constants. AC data were obtained for 1.8 K $\leqslant T \leqslant$ 4.2 K in an AC field of 5 Oe. Powder samples were wrapped in teflon tape. For measurements in frozen solution powder was dissolved in toluene, filled into gel capsules and sealed with cyanacrylate. Directly after preparation the solution was inserted into the magnetometer and thermally quenched to 4.2 K. For **2** a concentration of 0.5 mg/ml was used, whereas for **1** 5 mg/ml was chosen to obtain a better signal-to-noise ratio.

3. Results and discussion

3.1. Structure

The structures of **1** and **2** are analogous and can be described as centered Fe^{III} triangles consisting of a central Fe^{III} ion connected to three peripheral Fe^{III} ions through two fully deprotonated tripod^{3-} ligands that occupy the apical positions of the Fe_4 skeleton (Fig. 1). The tripod^{3-} ligands thus bridge in an η^2, η^2, η^2, μ^4-fashion. Six chelating acac$^-$ ligands complete the coordination sphere of the peripheral Fe ions. All metals are in distorted octahedral geometries with [FeO_6] coordination spheres. The molecules have principal C_3 symmetry axes perpendicular to the Fe_4 planes; with the peripheral Fe^{III} ions having a 2-fold axis perpendicular to the principal axis.

3.2. DC susceptibility

Fig. 2 shows the product of magnetic susceptibility and temperature ($\chi_{mol}T$) as a function of temperature. For **1** $\chi_{mol}T$ steadily decreases from 12.0 cm^3 mol^{-1} K at 300 K to a minimum of 10.3 cm^3 mol^{-1} K at 110 K, before strongly increasing to 14.3 cm^3 mol^{-1} K at 14 K, followed by a drop to 6.4 cm^3 mol^{-1} K at 1.8 K. For **2** $\chi_{mol}T$ steadily decreases from 11.1 cm^3 mol^{-1} K at 300 K to a minimum of 9.7 cm^3 mol^{-1} K at 120 K, before strongly increasing to 15.3 cm^3 mol^{-1} K at 16 K, followed by a drop to 6.2 cm^3 mol^{-1} K at 1.8 K. In both cases, the decrease of χT followed by an increase is indicative of antiferromagnetic exchange with a non-zero spin ground state. The susceptibility of **1** was fitted using the Kambe model. This model is applicable when the interacting spins can be divided into two groups where all members of one group have the same exchange interactions with all members of the other group [6]. In this case, group one is the central iron spin, and group two the three peripheral spins. The spin Hamiltonian and corresponding energies are:

$$\mathscr{H} = -2J(\hat{S}_1 + \hat{S}_2 + \hat{S}_3)\cdot\hat{S}_4 = J(\hat{S}_{123} - \hat{S}_T + \hat{S}_4)$$

$$E = J[S_{123}(S_{123}+1) - S_T(S_T+1) + S_4(S_4+1)].$$

For **1** the fit gives $J = -8.2 \pm 0.2$ cm^{-1}, with $g = 1.96 \pm 0.02$. The decrease in χT at the lowest measurement temperatures is due to zero-field splitting and is not reproduced, because it is not taken into account in the Kambe model. The resulting energy spectrum is shown in Fig. 3. The Kambe procedure did not result in an acceptable fit for **2**, presumably due to the presence of more than one exchange interaction.

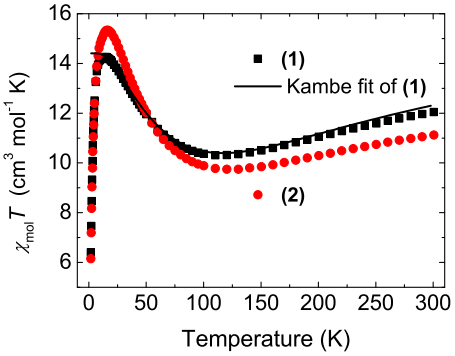


Fig. 2. Plot of measured DC susceptibility and Kambe fit (for 1) $\chi_{mol}T$ versus Temperature of powder samples of **1** and **2**.

3.3. AC susceptibility

AC susceptibility data on a powder of **1** show a slight decrease of χ' at low temperatures going from lower to higher frequencies (Fig. 4). The value of χ' at 1.8 K for 100 Hz is approximately 1.4% higher than at 997 Hz. AC susceptibility measurements on a powder sample of **2** also show a decrease of χ' for high frequencies at low temperatures, which is more pronounced than for **1** (Fig. 5). The value of χ' at 1.8 K for 100 Hz is ~7.7% higher than that seen for 997 Hz. For both **1** (Fig. 4) and **2** (Fig. 5) χ'' increases to low temperatures, but no peak can be observed in the experimental

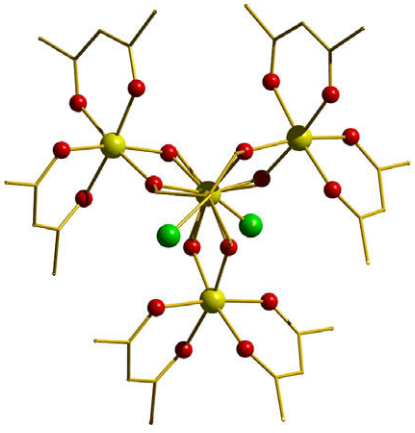


Fig. 1. Molecular structure of **1**. Fe: yellow, Br: green, O: red. (For interpretation of the references to colour in this figure legend, the reader is referred to the web version of this article.)

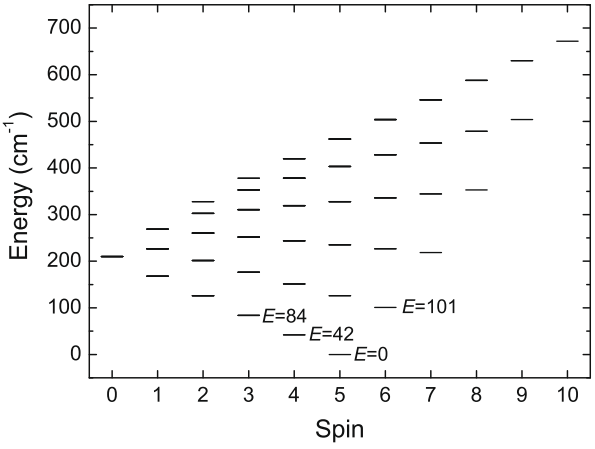


Fig. 3. The energy level spectrum resulting from the Kambe fit of the experimental magnetic susceptibility showing the $S = 5$ ground state for **1**.

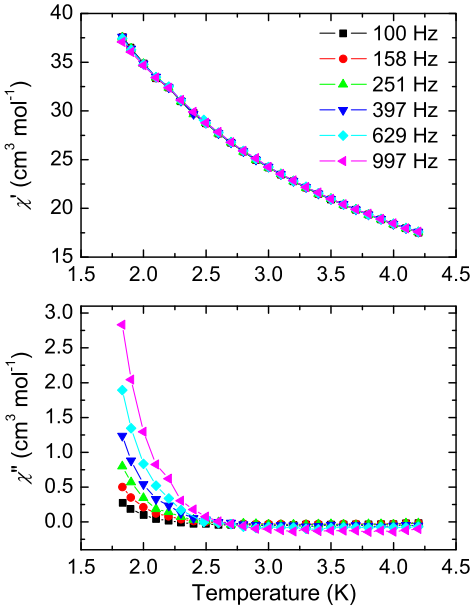


Fig. 4. Plot of the AC susceptibility χ' and χ'' versus T of a powder sample of **1**.

temperature range down to 1.8 K. The out-of-phase component χ'' is frequency dependent. This shows that the magnetization relaxation at these temperatures is slow compared to the timescale of the experiments. Slow magnetization dynamics can be due to SMM behaviour, but can also originate from long-range ordering [7], or spin glass behaviour [8]. The absence of a maximum in χ'' in the investigated temperature range precludes the unequivocal assignment of the origin of the observed slow dynamics.

To shed light on the slow magnetization dynamics, AC susceptibility measurements were performed on samples of **1** and **2** in solution. Both long-range ordering and spin glass behaviour will not be observed in solution, whereas SMM behaviour will most likely be preserved. For **1** in frozen solution, the decrease of χ' at higher frequencies is much more pronounced than in the powder

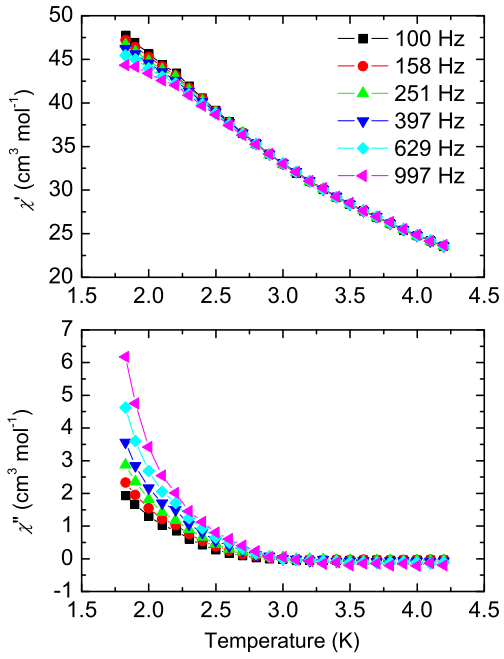


Fig. 5. Plot of the AC susceptibility χ' and χ'' versus T of a powder sample of **2**.

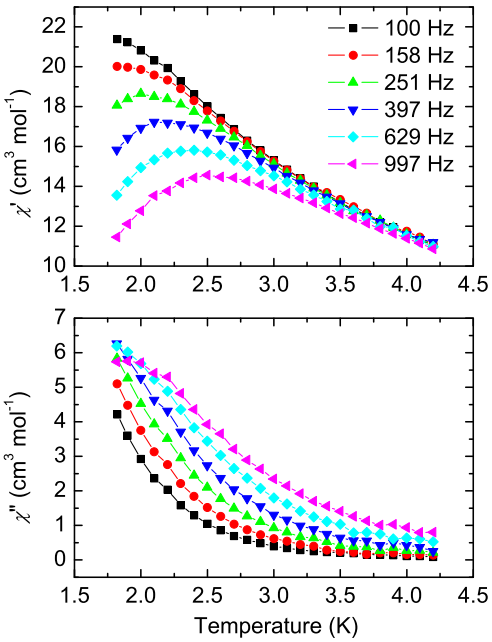


Fig. 6. Plot of the AC susceptibility χ' and χ'' versus T of a 5 mg/ml diluted frozen solution of **1** in toluene.

sample (Fig. 6). Thus, for 251–997 Hz a drop in χ' for low temperatures is observable. The strongly frequency dependent out-of-phase component χ'' is significantly larger in solution and has shifted to higher temperatures.

AC susceptibility measurements on **2** in frozen solution (Fig. 7) show that the frequency dependence of χ' is also much more pronounced than in the powder sample. The values of χ'' are higher than in the powder measurement. The signal-to-noise ratio for this measurement is worse than that for **1**, due to the lower concentration.

The clear observation of an out-of-phase signal in the AC susceptibility in frozen solution shows that both **1** and **2** are SMMs

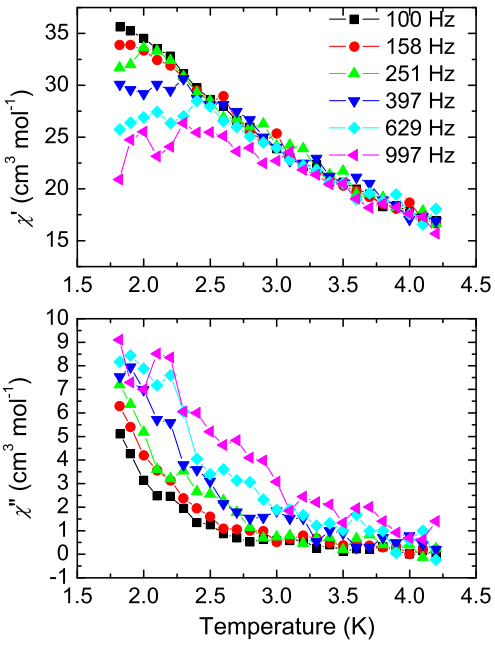


Fig. 7. Plot of the AC susceptibility χ' and χ'' versus T of a 0.5 mg/ml diluted frozen solution of **2** in toluene.

in solution. Interestingly, the shift of the peaks in χ'' to higher temperatures for **1** and **2** in solution compared to the powder sample evidence a higher activation energy of the magnetization of **1** and **2** in solution. This can be either due to an increased negative D value or to the decrease of tunnelling because intermolecular magnetic dipolar interactions have decreased.

4. Conclusion

To our knowledge this is the first study in which an increase of the energy barrier of a SMM in solution compared to the solid state has been observed.

Acknowledgements

We acknowledge the DFG, the EPSRC, the Royal Society and the Leverhulme Trust for funding.

Appendix A. Supplementary data

CCDC 717578 and 717579 contain the supplementary crystallographic data for $[Fe^{III}_4(acac)_6(Br\text{-}mp)_2]$ and $[Fe^{III}_4(acac)_6(tmp)_2]$. These data can be obtained free of charge via http://www.ccdc.cam.ac.uk/conts/retrieving.html, or from the Cambridge Crystallographic Data Centre, 12 Union Road, Cambridge CB2 1EZ, UK; fax: (+44) 1223 336 033; or e-mail: deposit@ccdc.cam.ac.uk. Supplementary data associated with this article can be found, in the online version, at doi:10.1016/j.poly.2009.01.030.

References

[1] R. Sessoli, D. Gatteschi, A. Caneschi, M.A. Novak, Nature 365 (1993) 141.
[2] R. Sessoli, Mol. Cryst. Liq. Cryst. (1995) 145.
[3] F. El Hallak, J. van Slageren, J. Gomez-Segura, D. Ruiz-Molina, M. Dressel, Phys. Rev. B 10 (2007) 104403.
[4] J. van Slageren, S. Dengler, J. Gómez-Segura, D. Ruiz-Molina, M. Dressel, Inorg. Chim. Acta (2008).
[5] R.L. Novak, F. Pineider, C. de Julián Fernández, L. Gorini, L. Bogani, C. Danieli, L. Cavigli, A. Cornia, R. Sessoli, Inorg. Chim. Acta 14–15 (2008) 3970.
[6] K. Kambe, J. Phys. Soc. Jpn. (1950) 48.
[7] E.C. Yang, W. Wernsdorfer, L.N. Zakharov, Y. Karaki, A. Yamaguchi, R.M. Isidro, G.D. Lu, S.A. Wilson, A.L. Rheingold, H. Ishimoto, D.N. Hendrickson, Inorg. Chem. 2 (2006) 529.
[8] J.A. Mydosh, Spin Glasses: An Experimental Introduction, Taylor and Francis, London, 1993.

compound $\{CuL_1[Co(NCS)_4]\}$ we used a stereoisomer of the macrocyclic complex $[CuL_1](ClO_4)_2$ and followed the procedure presented in the previous paper [2].

2.2. Magnetic measurements

Magnetic measurements in the temperature range 1.8–300 K were performed using a Quantum Design SQUID-based MPMSXL-5-type magnetometer. The SQUID magnetometer was calibrated with the palladium rod sample (Materials Research Corporation, measured purity 99.9985%). The superconducting magnet was generally operated at a field strength ranging from 0 to 5 T. Measurements were made at a magnetic field of 0.5 T. Corrections are based on subtracting the sample – holder signal and contribution χ_D estimated from the Pascal constants [4].

3. Results

3.1. Structural description

Crystallographic data for the structure of the complex were reported in the paper [2]. The compound creates infinite polymeric *zig-zag* chain in the crystal lattice (Fig. 1), which is assembled from repeating units of the CuL_1 cations and $[Co(NCS)_4]$ complex anions. The Co(II) ions have tetrahedral coordination symmetry and are connected with the Cu(II) ions in the octahedral environment *via* thiocyanate bridges (Fig. 2). Hereafter we abbreviate the system $\{CuL_1[Co(NCS)_4]\}$ as CuCo sample or simply CuCo chain.

As far as the molecular structure of the complex is concerned it crystallizes in the orthorhombic group $P2_12_12_1$. In the presented compound the cobalt atom is adopting a slightly distorted tetrahedral coordination and coordinated to four nitrogen atoms of the thiocyanate groups. The coordination polyhedral of the copper atoms can be described as distorted tetragonal bipyramid with the sulfured atoms in axial positions. The shortest intramolecular M–M distances are 6.4152(9) Å (Cu–Co) and the nearest M–M interchain distances are 6.8609(9) Å (Cu–Co).

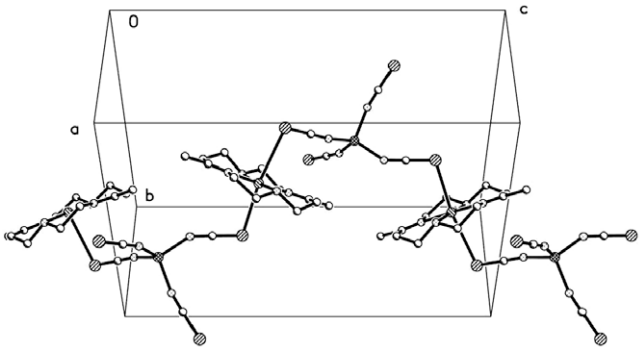


Fig. 1. Polymeric chains created by moieties of the complex $\{(CuL_1)[Co(NCS)_4]\}$.

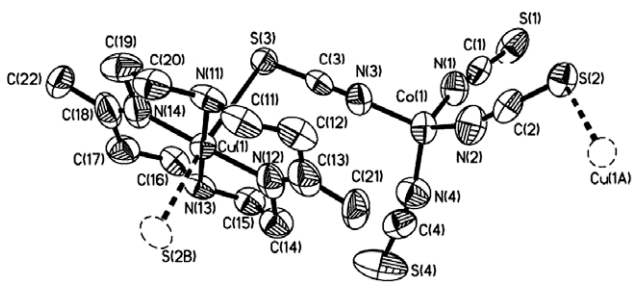


Fig. 2. Molecular structures of the complex $\{(CuL_1)[Co(NCS)_4]\}$ with atom labels.

3.2. Magnetic properties

For our analysis of the magnetic properties of the system $\{CuL_1[Co(NCS)_4]\}$, a quantum Heisenberg model with single-ion anisotropy in the Co(II) sites is applied:

$$H = \sum_{i=1}^{L/2}[J(s^x_{2i-1}S^x_{2i} + s^y_{2i-1}S^y_{2i} + s^z_{2i-1}S^z_{2i}) + [J(S^x_{2i}s^x_{2i+1} + S^y_{2i}s^y_{2i+1} + S^z_{2i}s^z_{2i+1}) + D(S^z_{2i})^2 - \mu_B H^x(g_{Cu}s^x_{2i-1} + g_{Co}S^x_{2i}) - \mu_B H^z(g_{Cu}s^z_{2i-1} + g_{Co}S^z_{2i})] \quad (1)$$

where spins $s = 1/2$ and $S = 3/2$ are located on the odd and even sites and refer to copper(II) and cobalt(II) ions, respectively, and L stands for the length of the chain. In our model the magnetic interactions are isotropic and the Co(II) ions are subject to the single-ion anisotropy. We assume that $g^x = g^y$ for both ions and the thermodynamic properties are isotropic in the xy plane. The Zeeman terms depend on the field directions but it is enough to consider the x and z orientations.

The thermodynamic quantities, as the free energy or magnetization, can be calculated by means of the partition function $Z = \mathrm{Tr}\exp(-H/k_BT)$ and exact diagonalization of the model (1) for a small size L only. In the exponential defining Z, k_B is the Boltzmann constant. To consider macroscopic CuCo chains, the quantum transfer matrix approach (QTM) is referred here [5,6]. Under the Suzuki-Trotter formula the partition function of the quantum chain can be converted into a series of approximants Z_M of the equivalent two-dimensional classical system [5], where M is called the Trotter number. In the limit $M \to \infty$ the partition function Z of the quantum system can be recovered. The computation of Z_M is possible for relatively small values of M so that the reliable estimates of the thermodynamic functions can be achieved by extrapolations only in a certain limited temperature region [5,6]. For M large enough, the linear dependence on $1/M^2$ is expected [5].

In order to overcome this restriction and cover the entire experimental 1.8–300 K temperature range, the density-matrix renormalization group approach (DMRG) [7–9] is applied. The DMRG method is a type of variational method, where the main idea is to find a representation of the Hilbert space of states in a restricted space which is much smaller than the original one. Both the QTM and DMRG methods are free from statistical errors and the negative sign problem which hampers convergence of physical quantities at low temperatures. For one-dimensional quantum systems DMRG approach offers a very efficient iterative truncation algorithm for constructing the effective transfer matrices with large Trotter numbers M.

For a given model, the convergence of the DMRG approximants depends on temperature and deteriorates with decreasing temperature. Before having analysed the experimental results, we have tested the M dependence of the approximants of the magnetic susceptibility in the region of low temperatures. In Fig. 3, the behaviour of the approximants as a function $1/M^2$ is plotted for two selected temperatures $T = 2$ K and $T = 10$ K and the model parameters $J/k_B = -1.0$ K, $D/k_B = 4.8$ K, $g_{Cu} = 2.08$ and $g_{Co} = 2.26$. The approximants correspond to relatively small values $3 \leqslant M \leqslant 6$, nevertheless the variation of the approximants is very weak and the linear scaling with respect to $1/M^2$ has been achieved. As can be estimated from Fig. 3, the uncertainty of the extrapolations is on the fourth decimal place for $T = 2$ K and on the sixth decimal place for $T = 10$ K. With increasing temperature the accuracy is still improving. We emphasize that the same variation of the finite-size data occurs in our calculations for other values of parameters

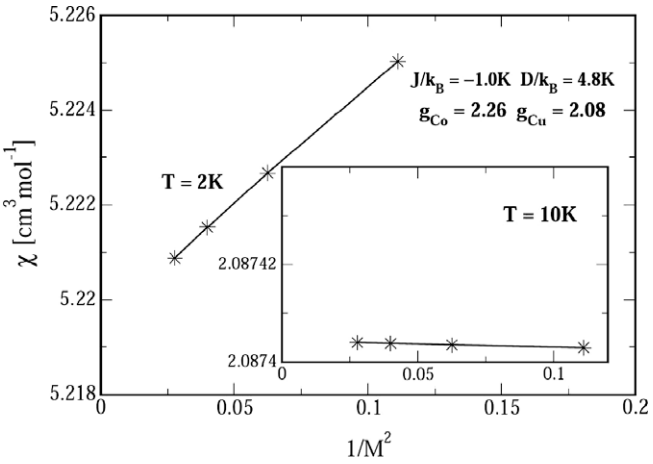


Fig. 3. Variation of the numerical finite-size data for the magnetic susceptibility along the z-axis against $1/M^2$ for two temperatures.

entering the Hamiltonian (1). The data shown in Fig. 3 demonstrate that the relative error bars of our simulation results are negligible (do not exceed 0.02%) and the DMRG technique is suitable for our analysis. The convergence is intensified by the presence of the 3/2 spins in the model (1). Hereafter the DMRG extrapolated data are reported.

In our analysis we have fitted simultaneously the magnetization and magnetic susceptibility data measured and calculated in the field $H = 0.5$ T. The typical results are shown in Figs. 4–6. Although the previous results [2] suggested ferromagnetic interactions through the thiocyanate bridge for the chain compound CuCo, we have scanned the positive and negative values of J. We have confirmed the conclusion about the ferromagnetic interactions, although our estimate $J/k_B = -1.0$ (±0.1) K is somewhat lower than that found before [2] and is justified by the large Cu(II)–Co(II) distance. In parentheses the uncertainty of a given value is defined.

Our simulations have revealed the importance of the Co(II) single-ion anisotropy which is crucial for the temperature behaviour of the χT susceptibility below the maximum (Figs. 4 and 5) and the low temperature magnetization profile (Fig. 6). However, using the experimental data available, only the absolute value $|D/k_B| = 4.6$ K (±0.6 K) can be determined. As to the g factors, we have

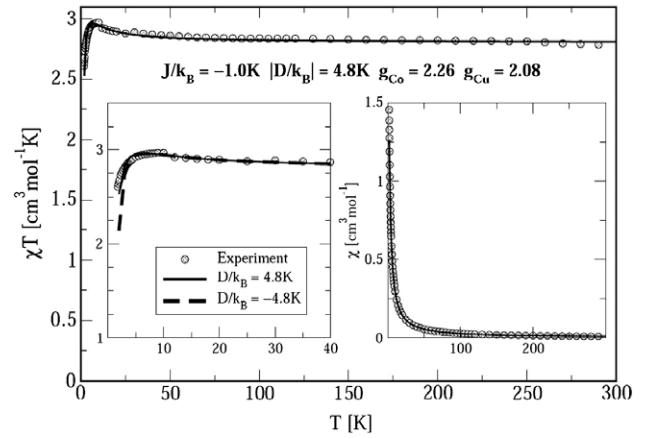


Fig. 4. Temperature dependence of the magnetic susceptibility for the CuCo sample plotted by the symbols and for the model with $|D/k_B| = 4.8$ K and the isotropic g factors. The results for the positive D are drawn by the solid lines and those for the negative D, by the dashed line. The left inset presents a comparison between experiment and our results for $D/k_B = \pm 4.8$ K in the low temperature regime. The right inset presents the average magnetic susceptibility vs. temperature.

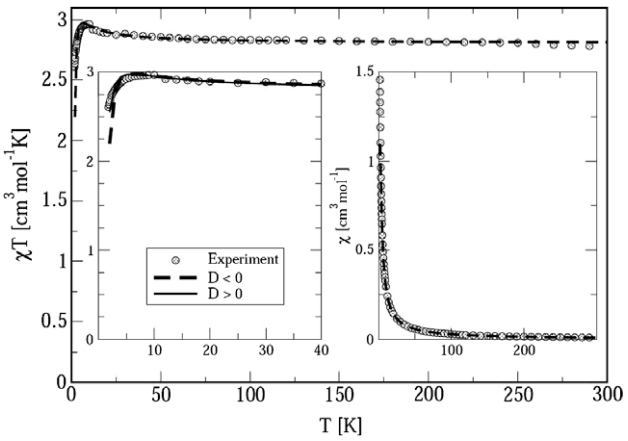


Fig. 5. Temperature dependence of the magnetic susceptibility for the CuCo sample and the models with anisotropic g factors. The dashed line corresponds to $J/k_B = -1$ K, $D/k_B = -4.8$ K, $g_{Co}^x = 2.27$, $g_{Co}^z = 2.22$ and $g_{Cu} = 2.14$ and the solid line to $J/k_B = -1$ K, $D/k_B = 4.5$ K, $g_{Co}^x = 2.25$, $g_{Co}^z = 2.27$ and $g_{Cu} = 2.14$. The left inset presents a comparison of experiment with the model χT curves in the low temperature regime. The right inset shows the magnetic susceptibility vs. temperature for the negative D.

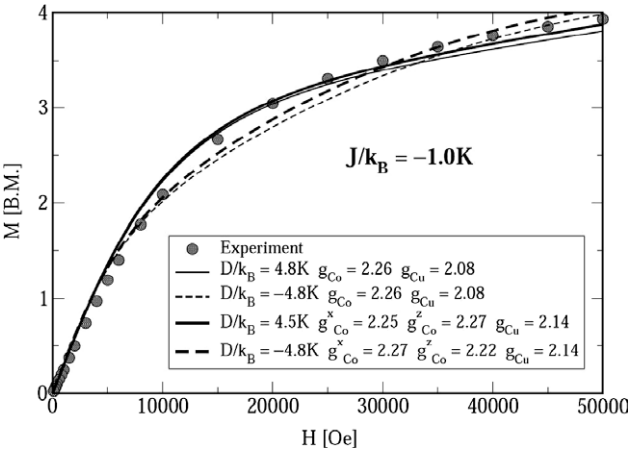


Fig. 6. Comparison of the field-dependent magnetization profiles for the experimental sample and theoretical models at $T = 2$ K. The values of the parameters are listed in the legend.

estimated the values: $g_{Cu}^{x,z} = 2.12$ (±0.04) and $g_{Co}^{x,z} = 2.25$ (±0.04). The condition [10] that the reliable determination of the single-ion parameter requires a low temperature (below $|D/k_B|$) data set is fulfilled here.

4. Discussion

In Fig. 4 we present a comparison between experiment and our simulation results for the anisotropy parameter $|D/k_B| = 4.8$ K and isotropic values $g_{Cu} = 2.08$ and $g_{Co} = 2.26$. The continuous lines refer to $D > 0$ and the dashed line to $D < 0$. The dashed line occurs if it can be distinguished from the continuous line. In the main panel, the χT product is plotted in the experimental temperature region, whereas in the left inset, in the low temperature region. Similar results for two sets of the anisotropic g_{Co} factors and a single g_{Cu} value are drawn in Fig. 5. In this case, the continuous line corresponding to the positive value D and $g_{Co}^x < g_{Co}^z$ is plotted if it can be distinguished from the dashed line for negative D and $g_{Co}^x > g_{Co}^z$. The magnetization profiles for the parameters selected from the domain found here are shown in Fig. 6. The symbols and curves are described in the legend.

The sign of D is difficult to fix for our CuCo sample. From the powder magnetic measurements only the average $\chi_{av} = 2/3\ \chi^x + 1/3\ \ \chi^z$ can be measured. The theoretical complication for the Co(II) with $S = 3/2$ in the tetrahedral environment follows from the existence of two Kramers doublets which differ only by the value of the spin component m. If D is negative then the lowest Kramers doublet corresponds to $m = \pm 3/2$, whereas for the positive D, it corresponds to $m = \pm 1/2$. This difference is not strong enough to be manifested clearly in the average thermodynamic functions. The independence of powder susceptibility data of the sign of the D parameter for some complexes, in particular those with $S = 3/2$, was noted in Ref. [10] and encountered in Ref. [11]. In the χT behaviour shown in the insets in Figs. 4 and 5 and in the magnetization profiles presented in Fig. 6, there is a signature that the results for $D > 0$ are somewhat superior to those for $D < 0$. However, this observation is not convincing enough. The sign of the Co(II) single-ion anisotropy could be determined, however, from the single-crystal magnetometry. This can be demonstrated from the results of our calculations of the longitudinal and perpendicular susceptibility (not presented here) and is also expected in literature [10].

There are cases [11,12] that Co(II) metal ions have a strong Ising-like anisotropy, so one could expect a negative D (an easy-axis) as a proper choice for our system. However, recently the systems have been found with Co(II) ions displaying the easy-plane anisotropy [10,13–15]. This conclusion is particularly strong in Ref. [13], where the high-field EPR experiments were performed and the transitions within the ground state Kramers doublet $m = \pm 1/2$ were identified.

Anticipating the presence of the Co(II) single-ion anisotropy in the CuCo compound, we have modelled the system using the anisotropic g_{Co} factors as their anisotropy has got the same origin [10]. *In such circumstances, there was no reason to neglect the g_{Co} anisotropy in the model (1).* We could afford an increase of the number of parameters, as we have exploited the accurate simulation technique. We have checked that the anisotropic g values which are theoretically expected, can model our system but the quality of the fits achieved using the powder data was not superior to those for the isotropic g values. The g values are estimated within 2% uncertainty and are consistent with the previous [2] isotropic estimates and the data published for the Cu(II) [10] and Co(II) [10,12] complexes. According to our findings, the difference in the magnitude $g_{Co}{}^x - g_{Co}{}^z$ can reach the value 0.08 which compares well with the differences reported in Ref. [12] for the Co(II) compounds.

The role of interchain interactions increases in low temperatures and may bring on the spontaneous magnetization. However, there is no experimental evidence of the long-range order down to 1.8 K so that an absence of such interactions in our Hamiltonian (1) and in our analysis is justified. It is worth adding that quite often they are accounted for within the molecular field approximation [10]. However, the molecular field corrections are meaningful only in the ordered phase, where an average value of magnetization is non-zero.

We emphasize that the lack of the molecular field term does not make our modeling task less demanding. In fact, it is challenging within the model (10) to find a maximum in the temperature behaviour of χT in the presence of the ferromagnetic coupling. We have accomplished the task due to the accurate simulations and taking into account the anisotropy term.

5. Conclusion

The modeling of the thiocyanate bridge compound $\{(CuL_1)[Co(NCS)_4]\}$ based on the anisotropic quantum spin-chain Hamiltonian has been carried out and the reliable DMRG technique has been exploited for the first time. The excellent convergence of the DMRG approximants has been demonstrated for relatively small values of the Trotter numbers $3 \leqslant M \leqslant 6$ and the high accuracy of the extrapolated data (not lower than 0.02%) has been reached for the estimates of susceptibility and magnetization.

The experimental susceptibility and field-dependent magnetization data have been fitted using the linear Heisenberg model with the single-ion anisotropy for the Co(II) ions and without the molecular field corrections, leading to the new set of the model parameters. The theoretical results for the thermodynamic functions agree quantitatively with experiment and the new parameters found are consistent with the literature data for the Cu(II) and Co(II) metal ions.

Our analysis has confirmed the weak ferromagnetic coupling between the Cu(II) and Co(II) ions, has revealed the importance of the anisotropy term for the Co(II) ions and has determined the absolute value of the parameter D, which was not resolved before.

Acknowledgements

We thank Prof. J. Krzystek and Prof. D. Gatteschi for some helpful and clarifying discussions. This work was supported by the EC 6th NoE Programme "MAGMANet" and by the Polish Ministry of Science and Higher Education through Grants No. N N202 309835 and 1 T09A12430. The numerical calculations were performed in PSNC Poznan, (Poland), TASK Gdansk (Poland) and the NIC Center in Juelich (Germany).

References

[1] R. Winpenny (Ed.), Single-Molecule Magnets and Related Phenomena Series: Structure and Bonding, vol. 122, Springer, New York, 2006.
[2] J. Kłak, J. Mroziński, R. Kruszyński, Polyhedron 27 (2008) 1401.
[3] O. Kahn, Molecular Magnetism, VCH, New York, 1993.
[4] E. König, Magnetic Properties of Coordination and Organometallic Transition Metal Compounds, Springer-Verlag, Berlin, 1966.
[5] T. Delica, H. Leschke, Physica A 176 (1990) 736.
[6] A. Caramico D'Auria, U. Esposito, F. Esposito, D. Gatteschi, G. Kamieniarz, S. Wałcerz, J. Chem. Phys. 109 (1998) 1613.
[7] U. Schollwoeck, Rev. Mod. Phys. 77 (2005) 259.
[8] X.Q. Wang, T. Xiang, Phys. Rev. B 56 (1997) 5061.
[9] N. Shibata, J. Phys. Soc. Jpn. 66 (1997) 2221.
[10] R. Boča, Coord. Chem. Rev. 248 (2004) 757.
[11] M. Nayak, S. Hazra, P. Lemoine, R. Koner, C.R. Lucas, S. Mohanta, Polyhedron 27 (2008) 1201.
[12] J. Krzystek, Andrew Ozarowski, Joshua Telser, Coord. Chem. Rev. 250 (2006) 2308.
[13] J. Krzystek, S.A. Zvyagin, Andrew Ozarowski, S. Trofimenko, Joshua Telser, J. Magn. Reson. 178 (2006) 174.
[14] R. Chiozzone, R. Gonzales, C. Kremer, G. de Munno, D. Armentano, F. Lloret, M. Julve, J. Faus, Inorg. Chem. 42 (2003) 1064.
[15] A. Rodriguez, H. Sakiyama, N. Masciocchi, S. Galli, N. Galvez, F. Lloret, E. Colacio, Inorg. Chem. 44 (2005) 8399.

*2.1.1. $[Mn_6O_2(salox)_6(MeOH)_6(NCNCONH_2)_2]$ (**1**)*

$Mn(ClO_4)_2 \cdot 6H_2O$ (0.623 g, 1.72 mmol) was dissolved in MeOH (50 ml). To this was added H_2salox (0.240 g, 1.710 mmol), sodium dicyanamide (0.155 g, 1.74 mmol) and Et_3N (0.176 g, 1.74 mmol) resulting in a deep green solution, which was stirred for 10 min. Vapor diffusion of Et_2O into the solution slowly produced crystals, after one week dark-green crystals were obtained. Crystals were collected by filtration, washed with MeOH, Et_2O and dried in vacuo. The yield was 48% (based on Mn). *Anal.* Calc. for $C_{52}H_{58}Mn_6N_{12}O_{22}$ (1532.74): C, 40.75; H, 3.81; N, 10.97. Found: C, 40.44; H, 3.80; N, 10.95%. IR data (KBr disk, cm^{-1}): 3413 (m), 3330 (m), 3228 (m), 2201 (m), 2169 (s), 1627 (m), 1597 (s), 1543 (m), 1473 (m), 1438 (s), 1417 (m), 1323 (w), 1277 (s), 1245 (w), 1202 (m), 1146 (w), 1121 (w), 1024 (s), 944 (w), 914 (s), 756 (s), 680 (vs), 506 (w), 483 (w), 466 (w).

*2.1.2. $[Mn_6O_2(salox)_6(EtOH)_4(H_2O)_2Cl_2]$ (**2**)*

$MnCl_2 \cdot 4H_2O$ (0.405 g, 2.05 mmol) and H_2salox (0.276, 2.00 mmol) were dissolved in EtOH (20 ml). To this was added 10 wt% water solution of NEt_4OH (1.472 g, 1.00 mmol) resulting in a deep green solution, which was stirred for 1 h. The solution was filtered to eliminate any remaining solid and the filtrate was layered with two volumes of Et_2O to slowly give well-formed dark-green crystals. After one week, crystals were collected by filtration, washed with Et_2O and dried in vacuo. The yield was 34% (based on Mn). *Anal.* Calc. for $C_{50}H_{58}Cl_2Mn_6N_6O_{21}$ (1479.55): C, 39.72; H, 3.99; N, 5.74. Found: C, 40.05; H, 4.17; N, 5.60%. IR data (KBr disk, cm^{-1}): 1597 (s), 1542 (m), 1470 (w), 1439 (m), 1327 (w), 1283 (s), 1203 (m), 1153 (w), 1119 (w), 1045 (s), 1026 (s), 918 (m), 758 (m), 677 (vs), 649 (m), 534 (w), 480 (w), 463 (w).

2.2. X-ray crystallography

Data collection parameters for complexes **1** and **2** are listed in Table 1. Diffraction measurements for complexes **1** and **2** were carried out using a Brucker Smart ApexCCD diffractometer with graphite-monochromated Mo Kα radiation ($\lambda = 0.7107$ Å). Structures were solved by direct methods and refined using the SHELXL-97 program [26] by full-matrix least-squares on F^2 values. All non-hydrogen atoms were refined anisotropically, whereas the hydrogen atoms were placed in ideal, calculated positions, with isotropic thermal parameters riding on their respective carbon atoms. Complexes **1** and **2** crystallize in the triclinic space group $P\bar{1}$ and monoclinic space group $P2_1/n$, respectively, with a Mn_6 cluster in the asymmetric unit.

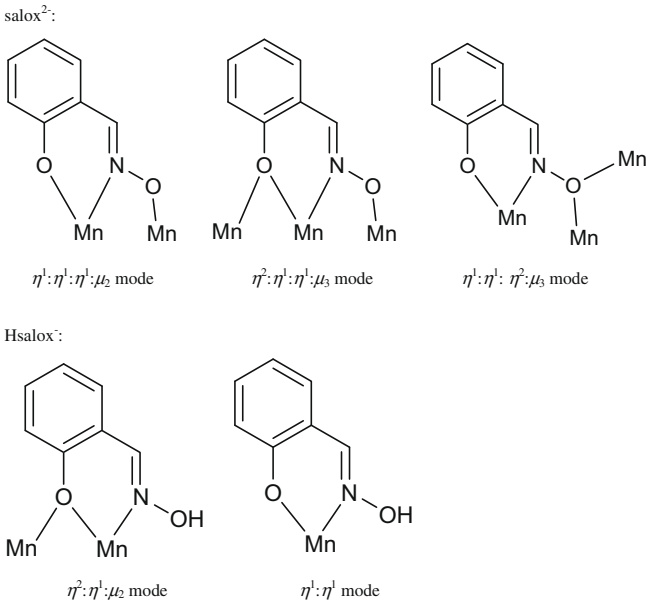
Table 1
Crystallographic data for **1** and **2**.

	1	**2**
Formula	$C_{52}H_{58}Mn_6N_{12}O_{22}$	$C_{50}H_{56}Cl_2Mn_6N_6O_{20}$
Formula weight	1532.74	1461.55
Crystal system	triclinic	monoclinic
Space group	$P\bar{1}$	$P2_1/c$
a (Å)	10.2280(5)	13.3510(6)
b (Å)	12.4245(7)	18.8326(8)
c (Å)	13.1243(7)	12.9116(6)
α (°)	83.418(1)	90
β (°)	68.907(1)	115.569(1)
γ (°)	72.037(1)	90
V (Å^3)	1480.20(14)	2928.5(2)
Z	1	2
T (K)	150(2)	150 (2)
Wavelength (Å)	0.71073	0.71073
ρ_{calc} (g cm^{-3})	1.719	1.657
μ (mm^{-1})	1.331	1.424
$(\Delta\rho)_{max}$, $(\Delta\rho)_{min}$ (e Å^{-3})	0.705, −0.860	0.590, −0.419
R_1[a], wR_2[b] (all data)	0.1036, 0.1628	0.0555, 0.0989
R_1[a], wR_2[b] ($I > 2\sigma(I)$)	0.0803, 0.1540	0.0413, 0.0922

[a] $R_1 = (\sum||F_o| - |F_c||)/\sum|F_o|$.
[b] $wR = [\sum[w(F_o^2 - F_c^2)^2]/\sum[w(F_o^2)^2]]^{1/2}$.

Table 2
Selected bond distances (Å) and angles (°) for complex **1**.

1			
Mn1–O1	1.885(3)	Mn2–N2	1.998(5)
Mn1–O2	1.908(4)	Mn2–O9	2.264(5)
Mn1–O7	1.944(4)	Mn2–O8	2.282(4)
Mn1–N1	1.999(4)	Mn3–O6	1.872(4)
Mn1–N4	2.165(5)	Mn3–O1	1.887(3)
Mn1–O7	2.334(4)	Mn3–O5	1.904(4)
Mn2–O1	1.874(3)	Mn3–N3	1.994(4)
Mn2–O4	1.878(4)	Mn3–O10	2.249(4)
Mn2–O3	1.915(4)	Mn3–O2	2.523(4)
O1–Mn1–O2	169.68(16)	O1–Mn2–O8	92.79(15)
O1–Mn1–O7	90.46(15)	O4–Mn2–O8	85.35(16)
O2–Mn1–O7	90.74(15)	O3–Mn2–O8	87.16(16)
O1–Mn1–N1	89.50(16)	N2–Mn2–O8	94.51(17)
O2–Mn1–N1	88.49(17)	O9–Mn2–O8	169.07(17)
O7–Mn1–N1	175.46(17)	O1–Mn2–Mn1	30.69(10)
O1–Mn1–N4	94.42(17)	O4–Mn2–Mn1	148.85(12)
O2–Mn1–N4	95.66(17)	O3–Mn2–Mn1	63.11(11)
O7–Mn1–N4	95.88(17)	N2–Mn2–Mn1	119.38(13)
N1–Mn1–N4	88.65(18)	O9–Mn2–Mn1	95.62(13)
O1–Mn1–O7	84.36(14)	O8–Mn2–Mn1	91.85(11)
O2–Mn1–O7	85.72(14)	O6–Mn3–O1	175.80(16)
O7–Mn1–O7	80.70(15)	O6–Mn3–O5	90.19(16)
N1–Mn1–O7	94.78(15)	O1–Mn3–O5	91.46(15)
N4–Mn1–O7	176.34(16)	O6–Mn3–N3	89.31(17)
O1–Mn1–Mn2	30.49(10)	O1–Mn3–N3	88.70(16)
O2–Mn1–Mn2	144.91(12)	O5–Mn3–N3	174.89(18)
O7–Mn1–Mn2	120.19(11)	O6–Mn3–O10	86.50(16)
N1–Mn1–Mn2	59.31(13)	O1–Mn3–O10	97.20(16)
N4–Mn1–Mn2	97.00(12)	O5–Mn3–O10	94.76(17)
O7–Mn1–Mn2	83.70(9)	N3–Mn3–O10	90.28(17)
O1–Mn2–O4	178.10(17)	O6–Mn3–O2	88.85(14)
O1–Mn2–O3	93.79(15)	O1–Mn3–O2	87.05(13)
O4–Mn2–O3	85.75(16)	O5–Mn3–O2	100.58(15)
O1–Mn2–N2	88.75(16)	N3–Mn3–O2	74.33(15)
O4–Mn2–N2	91.77(17)	O10–Mn3–O2	163.98(14)
O3–Mn2–N2	176.90(17)	Mn2–O1–Mn1	118.81(18)
O1–Mn2–O9	97.70(17)	Mn2–O1–Mn3	121.19(18)
O4–Mn2–O9	84.14(17)	Mn1–O1–Mn3	119.99(18)
O3–Mn2–O9	89.11(17)	Mn1–O2–Mn3	116.28(16)
N2–Mn2–O9	88.78(18)	Mn1–O7–Mn1	99.30(15)



Scheme 1. Coordination types of salicylaldoxime.

Table 3
Selected bond distances (Å) and angles (°) for complex **2**.

2			
Mn1–O2	Mn1–O2	Mn1–O2	Mn1–O2
Mn1–O1	Mn1–O1	Mn1–O1	Mn1–O1
Mn1–O7	Mn1–O7	Mn1–O7	Mn1–O7
Mn1–N1	Mn1–N1	Mn1–N1	Mn1–N1
Mn1–O8	Mn1–O8	Mn1–O8	Mn1–O8
Mn1–O7	Mn1–O7	Mn1–O7	Mn1–O7
Mn2–O4	Mn2–O4	Mn2–O4	Mn2–O4
Mn2–O1	Mn2–O1	Mn2–O1	Mn2–O1
O2–Mn1–O1	172.90(8)	O1–Mn2–O3	91.86(8)
O2–Mn1–O7	89.36(8)	O4–Mn2–N2	91.48(9)
O1–Mn1–O7	89.74(8)	O1–Mn2–N2	87.69(8)
O2–Mn1–N1	90.25(9)	O3–Mn2–N2	174.60(9)
O1–Mn1–N1	89.75(8)	O4–Mn2–O10	92.37(9)
O7–Mn1–N1	172.61(9)	O1–Mn2–O10	89.52(8)
O2–Mn1–O8	94.20(8)	O3–Mn2–O10	95.83(9)
O1–Mn1–O8	92.87(8)	N2–Mn2–O10	89.55(9)
O7–Mn1–O8	92.21(8)	O4–Mn2–O9	88.62(9)
N1–Mn1–O8	95.18(9)	O1–Mn2–O9	89.39(8)
O2–Mn1–O7	86.17(8)	O3–Mn2–O9	92.49(10)
O1–Mn1–O7	86.73(7)	N2–Mn2–O9	82.12(10)
O7–Mn1–O7	81.61(7)	O10–Mn2–O9	171.63(10)
N1–Mn1–O7	91.01(8)	O6–Mn3–O1	172.98(8)
O8–Mn1–O7	173.80(7)	O6–Mn3–O5	87.73(8)
O2–Mn1–Mn1	86.87(6)	O1–Mn3–O5	92.28(8)
O1–Mn1–Mn1	87.50(6)	O6–Mn3–N3	89.11(8)
O7–Mn1–Mn1	45.20(5)	O1–Mn3–N3	88.82(8)
N1–Mn1–Mn1	127.42(7)	O5–Mn3–N3	162.69(9)
O8–Mn1–Mn1	137.40(6)	Mn3–O1–Mn1	120.39(9)
O7–Mn1–Mn1	36.41(4)	Mn3–O1–Mn2	120.76(9)
O4–Mn2–O1	177.92(9)	Mn1–O1–Mn2	118.84(9)
O4–Mn2–O3	88.80(8)		

2.3. Physical measurements

Infrared spectra were recorded in the solid state (KBr pellets) on a Nicolet Magna 550 FTIR spectrometer in the 400–4000 cm^{-1} range. Elemental analyses have been carried out by using an Elementar vario EL III analyzer. Variable temperature dc and ac magnetic susceptibility measurements were collected on a microcrystalline sample, restrained in eicosane to prevent torquing, on a Quantum Design MPMS-XL SQUID magnetometer equipped with a 7.0 Tesla magnet and operating in the range of 1.8–300.0 K. Diamagnetic corrections were estimated from Pascal's constants [27] and subtracted from the experimental susceptibility data to obtain the molar paramagnetic susceptibility of the compound.

3. Results and discussion

3.1. Synthesis

The salicylaldoxime group (H_2salox) has been explored as a chelating ligand in the metal cluster chemistry. It has been observed in its singly-deprotonated (Hsalox$^-$) form as bidentate chelate with the protonated N–OH not bound [28], but it more commonly occurs in its doubly-deprotonated (salox^{2-}) form as a tridentate chelate [29,30]. These chelating forms can have a variety of possible binding modes, shown in Scheme 1 for Hsalox$^-$ and salox^{2-}. Based on this variety of possible binding modes of H_2salox, it may give rise to synthesize new nuclearities and topologies of complexes. Treatment of a methanolic solution of $Mn(ClO_4)_2$, NEt_3, $NaN(CN)_2$ and H_2salox in a 1:1:1:1 ratio leads to a reaction mixture comprising a dark-green solution. The residue was slowly diffused with Et_2O, to yield dark-green-brown triangle crystals of $[Mn_6O_2(salox)_6(MeOH)_6(NCNCONH_2)_2]$ (**1**) in a 48% yield. The IR spectra of complex **1** shows a simple ν_{as} absorption at 2201 cm^{-1} and a new moderately intense band at 1627 cm^{-1} in the carbonyl stretching region, together with enhanced intensity and complexity in the NH stretching region. X-ray crystallographic examination of this product readily explains the origin of the spectroscopic modifications. The dicyanamide $NCNCN^-$ has been changed to the corresponding amido $NCNCONH_2^-$, presumably through catalytic hydrolysis of the uncoordinated –CN link following attack by H_2O, activated by coordination to the Lewis acidic Mn^{III} ion. Consequently the IR spectrum demonstrates the presence of new CO and NH_2 absorptions, as well as simplification of the 2300–2100 cm^{-1} cyanamido region deriving from substitution of a single coupled NCN oscillator for the more complex NCNCN system. Catalytic hydration of nitriles is not unknown; indeed the dinickel salt of the pseudocryptand dipodand has been reported as a protein catalyst in the cooperative hydration of nitriles [31]. The activation of the β-carbon atom of the dicyanamido ligand by coordination to Cu^{II} against the reaction with methanol has been reported [32].

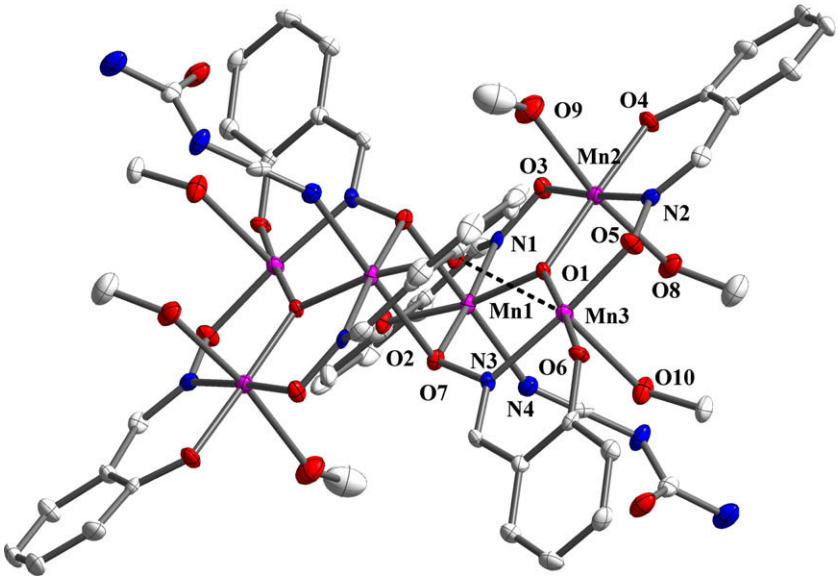


Fig. 1. ORTEP drawing of **1** with thermal ellipsoids set at 30% probability. H atoms have been omitted for clarity. The bond distance between O2′–Mn3 (dashed line) is 2.523 Å.

When the reaction process of complex **1** was carry out without $NaN(CN)_2$, complex **2** was obtained. Treatment of ethanolic solution of $MnCl_2$, with NEt_4OH and H_2salox in a 1:1:1 ratio produces a deep green solution. Layering of this solution with Et_2O leads dark-green crystals of $[Mn_6O_2(salox)_6(EtOH)_4(H_2O)_2Cl_2]$ (**2**) in 34% yield.

3.2. Description of structures

Selected interatomic distances and angles of complexes **1** and **2** are listed in Tables 2 and 3, respectively.

3.2.1. $[Mn_6O_2(salox)_6(MeOH)_6(NCNCONH_2)_2]$ (**1**)

Labeled ORTEP plot of $[Mn_6O_2(salox)_6(MeOH)_6(NCNCONH_2)_2]$ (**1**) is shown in Fig. 1. Complex **1** crystallizes in the triclinic space group $P\bar{1}$ with the molecule lying on an inversion center. The core of the complex **1** contains a nonplanar $[Mn^{III}_6(\mu_3\text{-}O^{2-})_2(\mu_3\text{-}OR)_2]^{12+}$ unit, whose topology consists of six Mn ions arranged as two $[Mn^{III}_3(\mu_3\text{-}O^{2-})]^{7+}$ triangular subunits bridged by two oximato O atoms (O7, O7′). Four of the $salox^{2-}$ ligands show the common $\eta^1{:}\eta^1{:}\eta^1{:}\mu_2$ coordination mode, while the other two adopt the $\eta^1{:}\eta^1{:}\eta^2{:}\mu_3$ mode. The three crystallographically independent MeOH ligands complete the six-coordination at Mn2 and five coordination at Mn3, while one crystallographically independent $NCN\text{-}CONH_2^-$ ligand completes the six-coordination at Mn1. Ions Mn1 and Mn2 display the Jahn–Teller elongation, as expected for high-spin $3d^4$ ions in near-octahedral geometry; the Jahn–Teller axes are O7–Mn1–N4 and O8–Mn2–O9. Mn3 has a distorted square-pyramidal geometry, with the MeOH oxygen O10 at the apical position. In addition, there is a shortening of the phenolato oxygen O2–

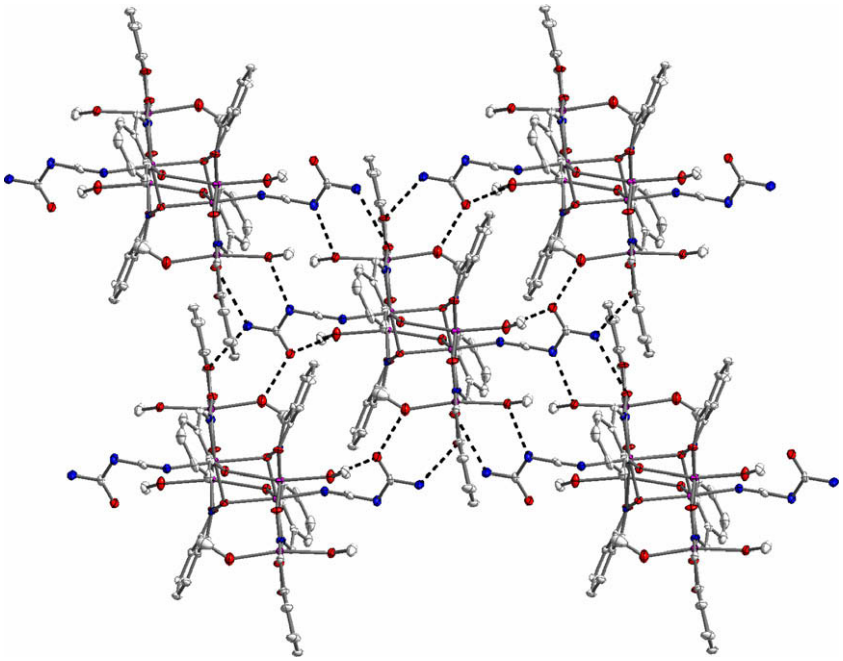


Fig. 2. The hydrogen bonding interactions (dashed line) between adjacent clusters forming a 2D network for complex **1**.

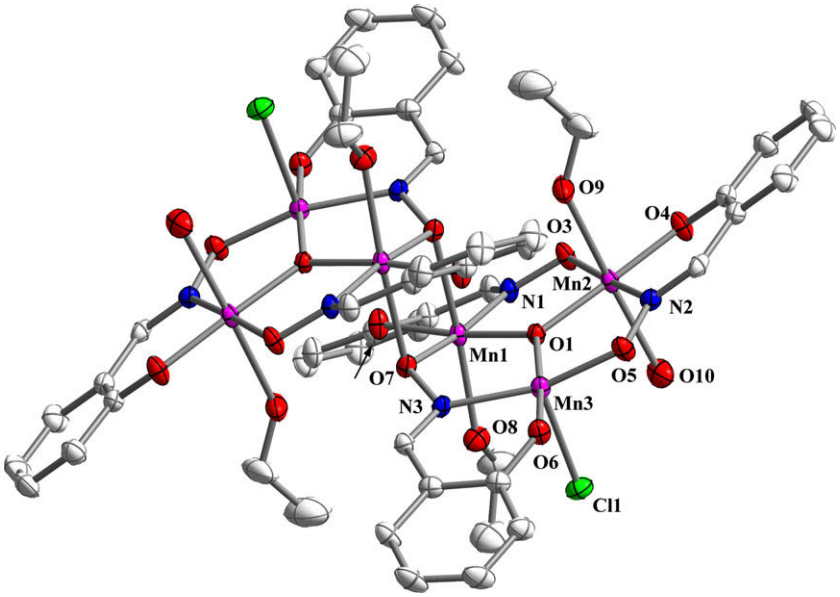


Fig. 3. ORTEP drawing of **2** with thermal ellipsoids set at 30% probability. H atoms have been omitted for clarity.

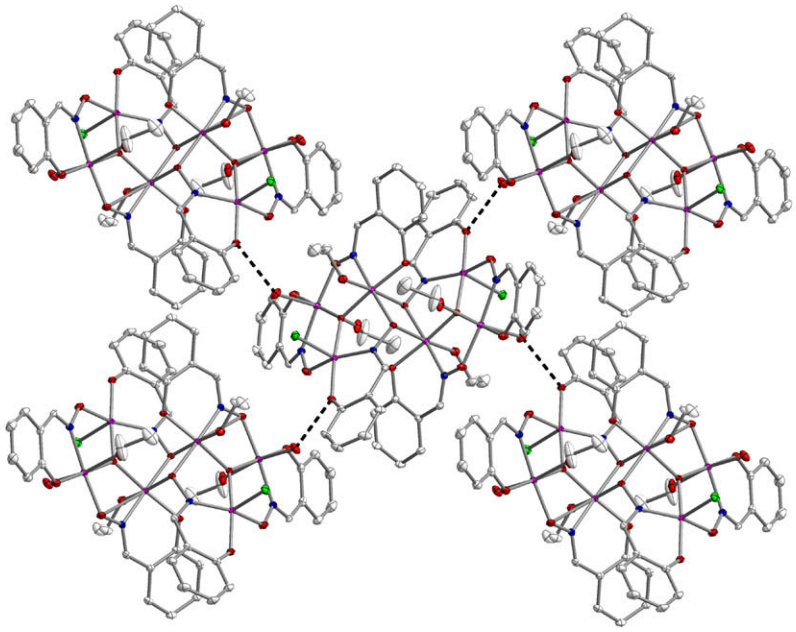


Fig. 4. The hydrogen bonding interactions (dashed line) between adjacent clusters forming a 2D network for complex **2**.

square-pyramidal Mn, Mn3, distance (~2.5 Å) within each Mn_3 subunit. Four intermolecular hydrogen bonding interactions in complex **1**, O1···O9 (2.688 Å), N5···O7 (2.779 Å), N6···O4 (2.972 Å) and N6···O6 (3.006 Å) link the clusters forming a 2D network (Fig. 2).

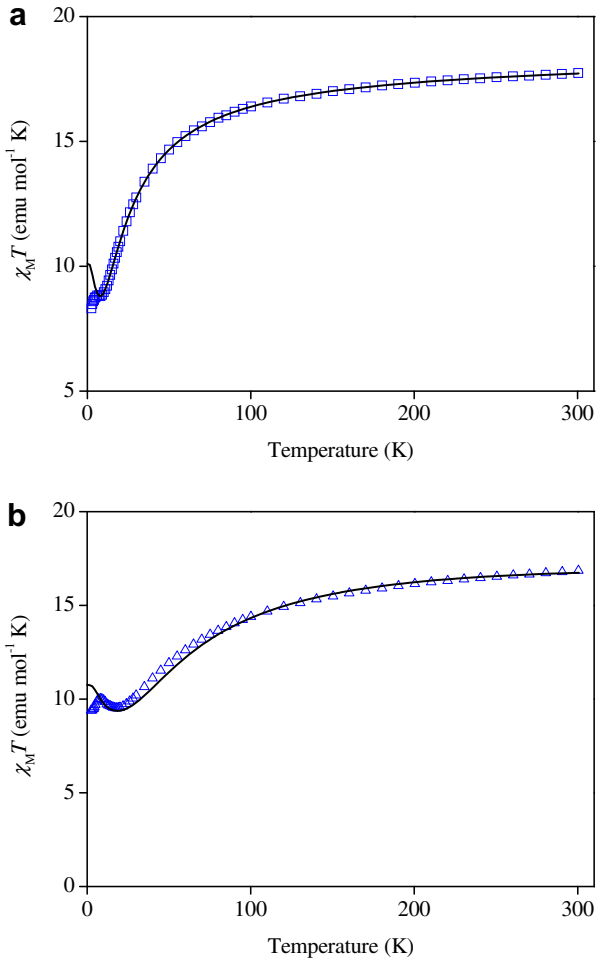


Fig. 5. Plots of $\chi_M T$ vs. temperature for a microcrystalline sample of complexes (a) **1** and (b) **2**. The solid line represents a least-squares fit of the data.

*3.2.2. $[Mn_6O_2(salox)_6(EtOH)_4(H_2O)_2Cl_2]$ (**2**)*

Labeled ORTEP plot of $[Mn_6O_2(salox)_6(EtOH)_4(H_2O)_2Cl_2]$ (**2**) is shown in Fig. 3. Complex **2** crystallizes in the monoclinic space group $P2_1/c$ with the molecule lying on an inversion center. The structure of complex **2** is quite similar to that of complex **1** with only difference of the terminal ligands. For complex **2**, there are two crystallographically independent EtOH and one water ligands complete the six-coordination at Mn1 and Mn2, while one crystallographically independent Cl^- ligand completes the five coordination at Mn3. Mn1 and Mn2 are bound to an O_5N set of donor atoms and display Jahn–Teller elongation and the Jahn–Teller axes are O7′–Mn1–O8 and O9–Mn2–O10. Mn3 has a distorted square-pyramidal geometry, with the terminal Cl^-, Cl1, at the apical position. The hydrogen bonding involved the O atom of phenol ring and

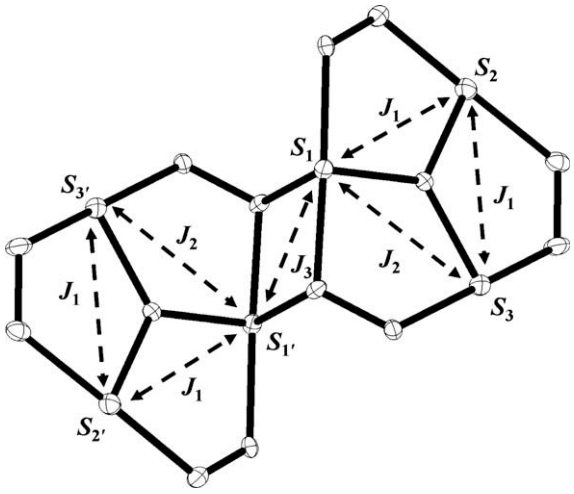


Fig. 6. Interaction path topology and magnetic exchange parameters for the complexes **1** and **2**.

the O atom from the terminal water ligand (O6···O10, 3.003 Å). These interactions link the clusters forming a 2D network (Fig. 4).

3.3. Direct current magnetic susceptibilities and magnetization

The variable temperature dc magnetic susceptibilities were collected for microcrystalline samples of complexes **1** and **2** in the temperature range of 2–300 K at a magnetic field of 1000 G. The experimental $\chi_M T$ versus temperature plots are depicted in Fig. 5a and b for complexes **1** and **2**, respectively. The value of $\chi_M T$ decreases from 17.74 emu K mol^{-1} for **1** and 16.85 emu K mol^{-1} for **2** at 300 K to reach a minimum of 8.80 emu K mol^{-1} at 8 K, and 9.52 emu K mol^{-1} at 18 K for **1** and **2**, respectively. Upon cooling the $\chi_M T$ increases slightly to 8.83 emu K mol^{-1} at 6 K, and 10.01 emu K mol^{-1} at 8 K for **1** and **2**, respectively, and then decrease to 8.45 emu K mol^{-1} at 2 K, and 9.74 emu K mol^{-1} at 2 K for **1** and **2**, respectively. The value of $\chi_M T$ at 300 K is slightly lower than the calculated spin-only value of 18.00 emu K mol^{-1} for a Mn_6^{III} complex with noninteracting metal centers with $g = 2.0$, suggesting that antiferromagnetic couplings dominate the overall intramolecular exchange interactions within the complexes. The maximum $\chi_M T$ values of 8.83 emu K mol^{-1} at 6 K and 10.01 emu K mol^{-1} at 8 K are consistent with the ground state $S = 4$ with $g = 1.90$ and 2.0 for **1** and **2**, respectively. The decreasing $\chi_M T$ at low temperature is likely due to the zero-field splitting and Zeeman effects of the high-spin ground state. The exchange interactions between manganese ions of complexes **1** and **2** were modelled taking into account the discussion by Brechin and co-workers for the hexanuclear analogue [33,34]. The topologies of the complexes afford the coupling scheme depicted in Fig. 6. Three inequivalent coupling constants are required and the spin Hamiltonian is given in Eq. (1):

$$H = -2J_1(S_1S_2 + S_2S_3 + S_{1'}S_{2'} + S_{2'}S_{3'}) - 2J_2(S_1S_3 + S_{1'}S_{3'}) - 2J_3(S_1S_{1'}) \quad (1)$$

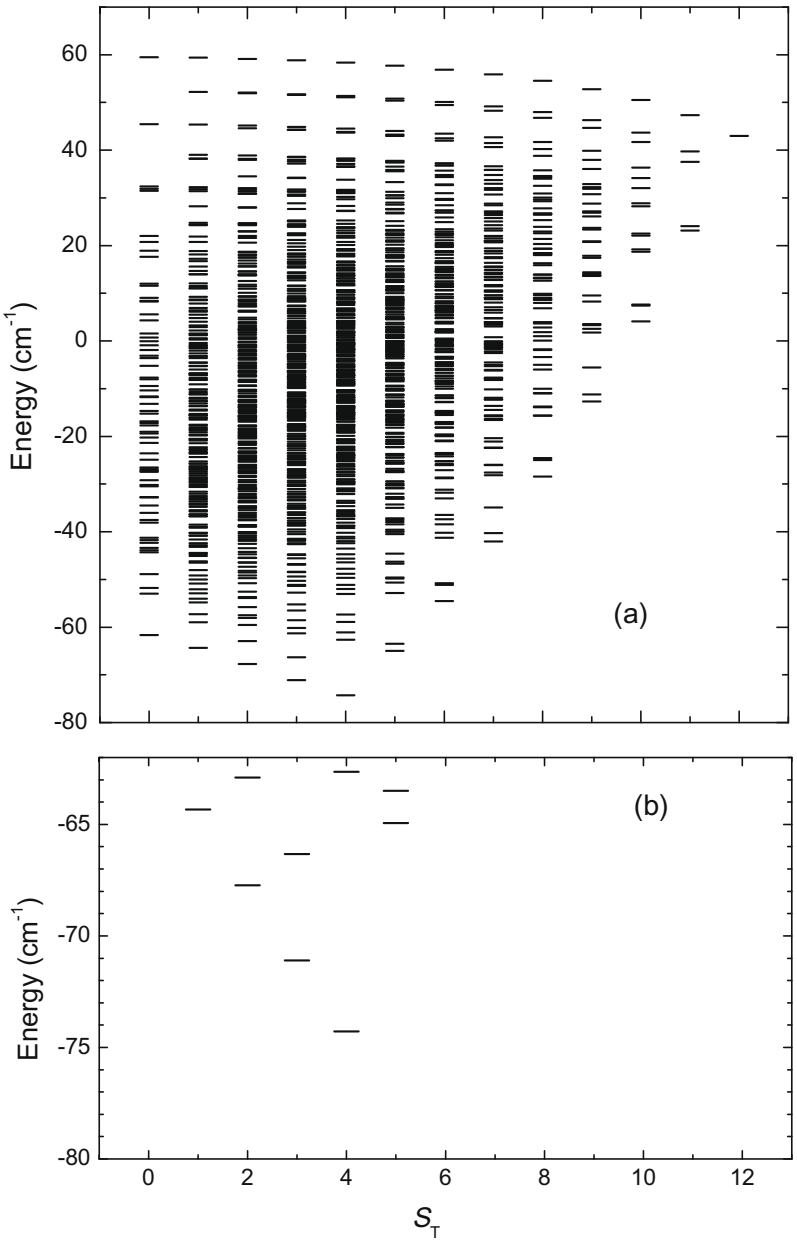


Fig. 7. (a) Diagram of all energy values for all S_T spin values of complex **1**. The ground-state spin corresponds to $S_T = 4$ with energy = −78 cm^{-1}. (b) Energy diagram of only and low-lying exciting states.

The Kambe approach for isotropic exchange-coupled systems [35] is very useful and facile method to yield energy eigenvalues and eigenvectors, however, is not applicable to the present systems because of entangled exchange paths which forbid to split a whole system into some interacting partial spin sums. An alternative approach, block diagonalization, is available for general isotropic spin systems [36–38]. It is based on the nature that the HDVV (Heisenberg–Dirac–Van Vleck) Hamiltonian preserves the z-component of total spin S, $S_Z = \sum_i S_Z(i)$, where $S_Z(i)$ stands for the z-component of spin on the ith metal ion in a molecule, owing to the commutation relation $[\hat{H}_{\mathrm{HDVV}}, S_Z] = 0$. In the $Mn(III)_6$ complexes, the full-matrix dimension is $(2S+1)^N = 15625$, which is not easily solved even by using a modern computer. However, the commutation relation allows us to solve each block matrix with different S_Z value separately and we can confine ourselves to an $S_Z = 0$ block matrix with its dimension of only 1751, much smaller than the full-matrix size.

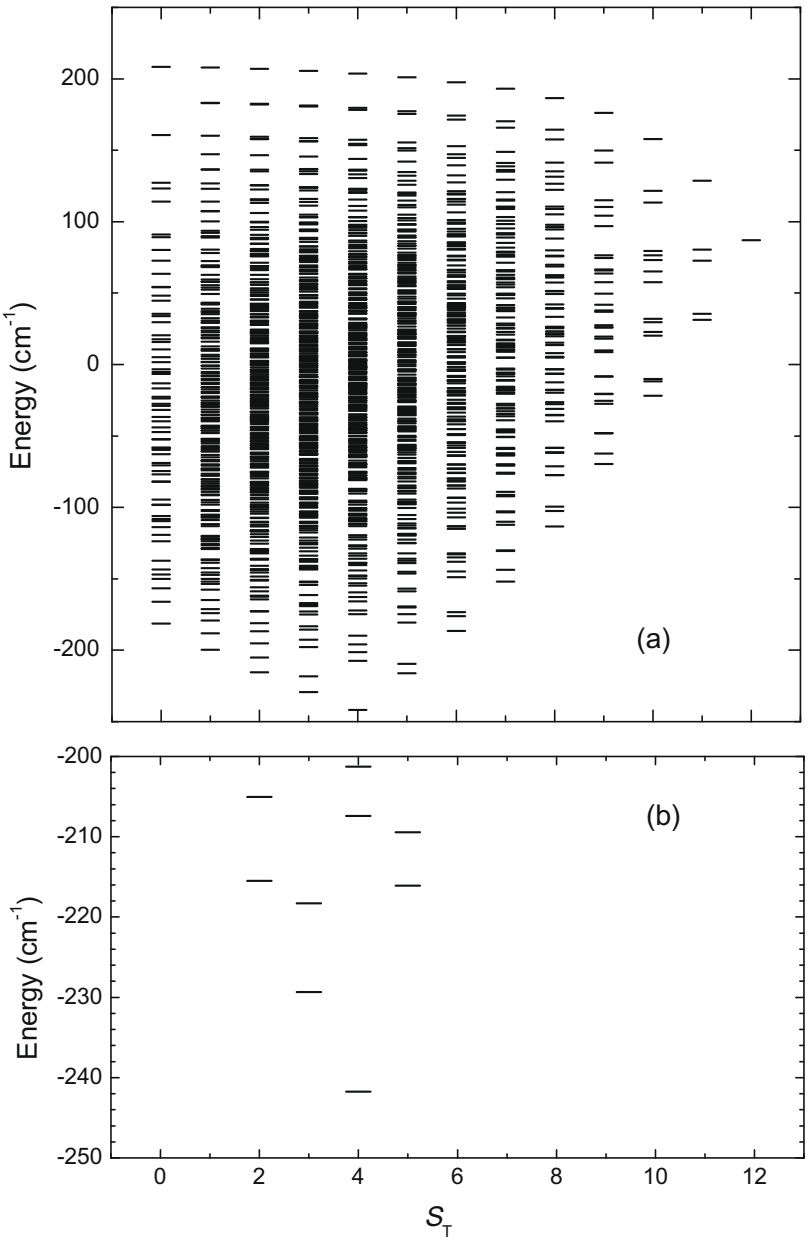


Fig. 8. (a) Diagram of all energy values for all S_T spin values of complex **2**. The ground-state spin corresponds to $S_T = 4$ with energy = -242 cm^{-1}. (b) Energy diagram of only and low-lying exciting states.

Table 4
Comparison of the exchange couplings and relative torsion angles of complexes **1** and **2** with Mn_6 analogous of $[Mn_6O_2(salox)_6(O_2CR)_2(S)_4]$.

Complex	Mn1–Mn2 (cm^{-1})	Mn2–Mn3 (cm^{-1})	Mn1–N1–O3–Mn2 (°)	Mn1–O7–N3–Mn3 (°)	Ref.
$[Mn_6O_2(salox)(O_2CMe)_2(EtOH)_4]$	−12.6	−3.5	10.70	22.83	[33]
$[Mn_6O_2(sao)(O_2CH)_2(MeOH)_4]$	−4.6	−1.8	25.57	18.01	[34]
$[Mn_6O_2(salox)_6(MeOH)_6(NCNCONH_2)_2]$ (**1**)	−1.65	0.29	19.89	37.45	this work
$[Mn_6O_2(salox)_6(EtOH)_4(H_2O)_2Cl_2]$ (**2**)	−4.66	0.53	22.97	31.24	this work

Although more aggressive reduction of matrix size can be sometimes attempted aided by topological symmetry of the molecule, S_Z block matrix diagonalization works without any symmetry restrictions and is applicable to general isotropic systems. Starting with decoupled basis vectors, $|S_Z(1), S_Z(2), S_Z(3), S_Z(4), S_Z(5), S_Z(6)\rangle$, the largest block matrix is constructed in the $S_Z = 0$ subspace for integer spin systems ($S_Z = -1/2$ subspace should be used for half-odd spin systems). The block matrix, being much easier to be solved than the full matrix is, is diagonalized to provide energy eigenvalues and eigenvectors expressed in terms of decoupled basis vectors. Invoking another commutation relation $[\hat{H}_{HDVV}, S_Z] = 0$, the square of total spin S^2 should be another good quantum number, which we require for labeling an eigenstate along with S_Z. In order to obtain S, the total-spin raising operator ($\hat{S}^+ = \sum_i \hat{S}^+(i)$) is evaluated for each eigenvector by $\rangle S_Z + 1|\hat{S}^+|S_Z\langle = \sqrt{(S - S_Z)(S + S_Z + 1)}$, yielding $S = \frac{1}{2}\left(\sqrt{1 + 4\rangle 1|\hat{S}^+|0\langle^2} - 1\right)$. For half-odd integer spin systems, $S = |\rangle + 1/2|\hat{S}^+|-1/2\langle| - \frac{1}{2}$ should be used instead.

Once the energy eigenvalues $E(S,S_Z)$ are obtained, the Van Vleck formula can be used to calculate magnetic susceptibilities as a function of temperature:

$$\chi_m = \frac{Ng^2\mu_B^2}{3k_BT}\frac{\sum_{\text{all } S} S(S+1)(2S+1)e^{[-E(S,S_Z)/k_BT]}}{\sum_{\text{all } S}(2S+1)e^{[-E(S,S_Z)/k_BT]}}$$

All the procedures were coded on IGOR PRO graphics software package [39], which is capable of performing non-linear least-squares optimization of a model Hamiltonian. In both cases, the data below 7 K were omitted in the fitting, because zero-field splitting and Zeeman effects are likely to have an effect on the susceptibilities in this temperature range. The simulation curves based on the fitting results are shown as solid lines in Fig. 5, with optimized parameters being $g = 2.00$, $J_1 = -1.65$ cm^{-1}, $J_2 = 0.29$ cm^{-1} and $J_3 = 0.81$ cm^{-1} for complex **1**; $g = 2.00$, $J_1 = -4.66$ cm^{-1}, $J_2 = 0.53$ cm^{-1} and $J_3 = 6.69$ cm^{-1} for complex **2**. In both cases, the temperature independent paramagnetism (TIP) was kept constant at 1200×10^{-6} emu mol^{-1}. Each set of parameters results in a ground state of $S = 4$ indicating that the Mn_6 complexes **1** and **2** have $S_T = 4$ ground states and the energy diagrams are given in Figs. 7 and 8, respectively. The first excited state is $S = 3$ expected at 3.1 and 12.4 cm^{-1} above the ground state for **1** and **2**, respectively.

The values obtained for exchange parameters of the two complexes are very similar. The comparison of the exchange couplings for complexes **1** and **2** with the analogous Mn_6 complexes are listed in Table 4. Exchange couplings for J_1, Mn^{III}–Mn^{III} bridged by one $\eta^1{:}\eta^1{:}\eta^1{:}\mu_2$ salox^{2-}, in these compounds are antiferromagnetic with values of -1.80 and -3.5 cm^{-1}, which close the values of -1.65 and -4.66 cm^{-1} for these interactions in **1** and **2**, respectively. The interactions of J_2, Mn^{III}–Mn^{III} bridged by one $\eta^1{:}\eta^1{:}\eta^2{:}\mu_3$ salox^{2-}, in complexes **1** and **2** are ferromagnetic with the values of 0.29 and 0.53 cm^{-1}, respectively, which show sharp difference to antiferromagnetic interaction observed in the Mn_6 analogue. These interactions may depend on the larger torsion angles of Mn1–O7–N3–Mn2 (37.45° and 31.24° for **1** and **2**, respectively). In the previous studies, it was reported that the larger torsion angle (usually >30°) causes ferromagnetic exchange interaction, and the exchange coupling of complexes **1** and **2** consistent with this results [40,41]. The exchange interactions of J_3, Mn^{III}–Mn^{III} bridged by two $\eta^1{:}\eta^1{:}\eta^2{:}\mu_3$ salox^{2-}, in the complexes **1** and **2** are consistent with the previously recognized fact that the exchange interaction is known to be ferromagnetic in complexes with the $[Mn^{III}_2(OR)_2]$ dimeric core [42].

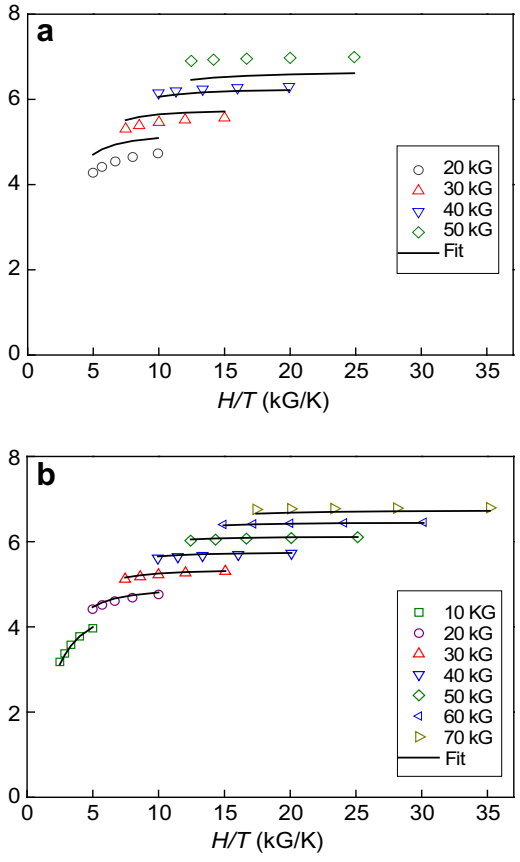


Fig. 9. The reduced magnetization of (a) **1** and (b) **2** plotted as $M/N\beta$ vs. H/T at indicated fields.

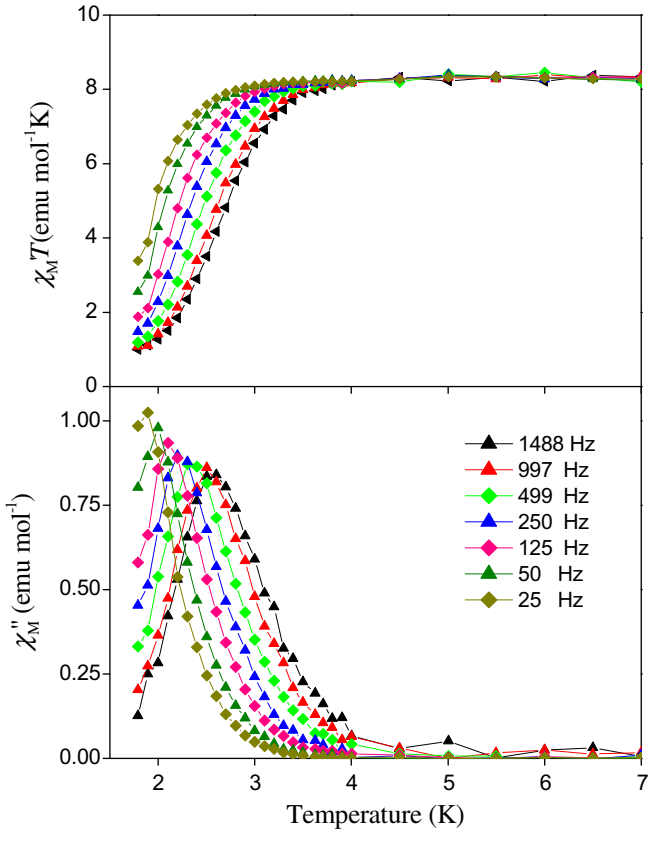


Fig. 10. Plots of $\chi'_M T$ (top) and χ''_M (bottom) vs. temperature for a microcrystalline sample of complex **1** in a 3.5 G ac field. The data were collected in an ac field oscillating at the indicated frequencies.

To determine the spin of the ground state, magnetization (M) measurements were also performed in the 2.0–4.0 K temperature range and the 1.0–70 kG dc magnetic field range. The data of complexes **1** and **2** are plotted as the magnetization ($M/N\beta$) versus H/T in Fig. 9a and b, respectively, where N is the Avogadro's number, β is the Bohr magneton, and H is the applied magnetic field. For a system characterized by a single S value and experiencing no zero-field splitting (ZFS), the various isofield curves of $M/N\beta$ would be superimposed on a Brillouin curve, saturating at a value of gS. The deviation of the isofield curves apart from a universal curve in Fig. 9 is indicative of the presence of significant ZFS. The data were fit using ANISOFIT software package [43] that assumes only the spin ground state of the molecule is populated. The best fit for complex **1** was given by $S = 4$, $g = 1.92$, $D = -0.82\ cm^{-1}$ and $E = 0.0015\ cm^{-1}$; $S = 4$, $g = 1.95$, $D = -1.18\ cm^{-1}$ and $E = -0.00005\ cm^{-1}$ for complex **2** (where D is the axial ZFS parameter and E is the rhombic ZFS parameter). The fitting for complex **1** is rather poor, which is likely due to significant populations of low-lying excited states even at low temperature, and it may introduce some ambiguity in the above ZFS values. The contrastive goodness of fitting reduced magnetization for those complexes is also consistent with the energy level scheme obtained from fitting of dc magnetic susceptibility (Figs. 7 and 8), with the lowest excited-level at $\sim 3.5\ cm^{-1}$ for complex **1** and at $13\ cm^{-1}$ for complex **2**. The ZFS parameters provide the upper bounds of spin-reversal energy barriers ($U = |D|S^2$) of 13 and 19 cm^{-1} (18.5 and 27 K) for complexes **1** and **2**, respectively.

3.4. Alternating current magnetic susceptibilities

The measurements of the ac magnetic susceptibility were performed on microcrystalline samples of complexes **1** and **2** in the temperature range 1.8–10 K in a zero dc field and a 3.5 G ac field oscillating at frequencies in the 25–1488 Hz range. The results for representative of complexes **1** and **2** are shown in Figs. 10 and 11, respectively. The observed frequency-dependent χ''_M signal is suggestive of the slow relaxation characteristic of the superparamagnetic-like properties of an SMM. Extrapolation of the plot of $\chi'_M T$ versus T to 0 K gives a value of ca. 8.15 and 9.84 emu K mol^{-1} for complexes **1** and **2**, respectively, indicative of an $S = 4$ ground state and these results are consistent with the dc magnetic susceptibility data and fitting of magnetization data. In addition, the temperature ranges of maximum position ac out-of-phase signals are slightly different for **1** and **2** in 1.9–2.6 and 2.1–3.2 K, respectively. The Arrhenius equation was applied to fit the data, and the rate of reversal of magnetization and the effective energy barrier of this molecule were obtained. The plot of the relaxation time as a function of inverse of temperature for complexes **1** and **2** are shown in Fig. 12. Good fits of the ac data were obtained, and the slope of the Arrhenius plot gave U_{eff} of 27.0(1) K and $\tau_0 = 3.8(2) \times 10^{-9}$ s for complex **1**, and U_{eff} of 25.1(6) K and $\tau_0 = 4.3(1) \times 10^{-8}$ s for complex **2**, which are consistent with the similar complexes reported in the literature [40].

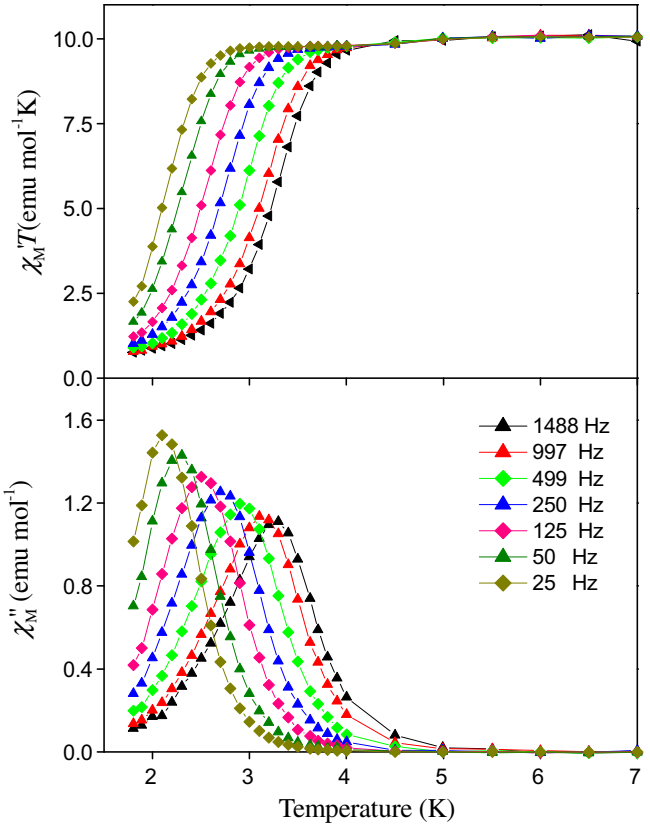


Fig. 11. Plots of $\chi'_M T$ (top) and χ''_M (bottom) vs. temperature for a microcrystalline sample of complex **2** in a 3.5 G ac field. The data were collected in an ac field oscillating at the indicated frequencies.

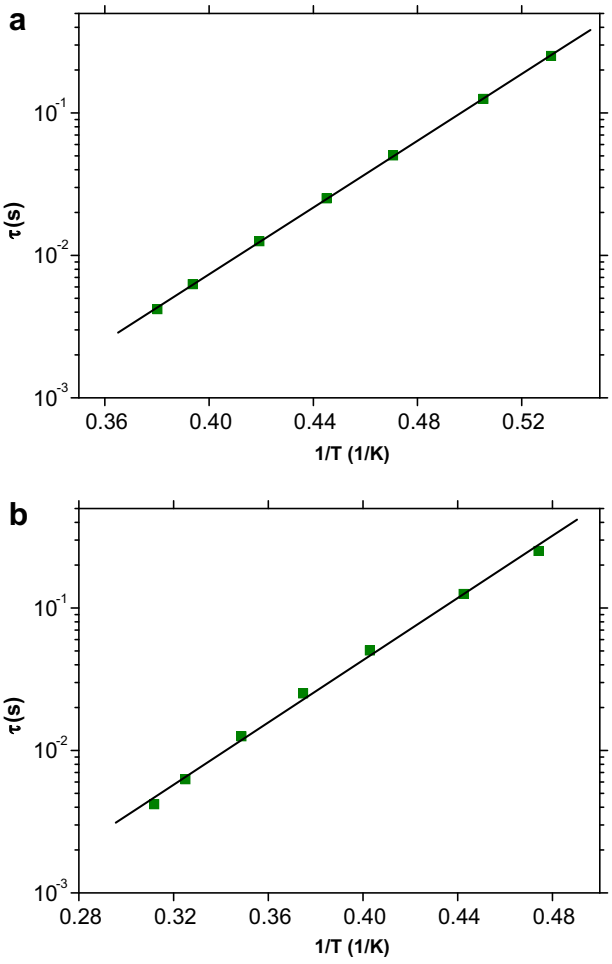


Fig. 12. Plots of τ vs. $1/T$ for (a) **1** and (b) **2** using ac χ''_M peak data. The solid lines correspond to a fit to the Arrhenius equation.

4. Conclusion

The use of H_2salox as a chelating ligand combined with $N(CN)_2^-$ or Cl^- with Mn^{II} sources afforded two Mn_6 complexes. Both Mn_6 complexes display SMM properties with $S = 4$ ground states from

dc and ac magnetic susceptibility measurements. Complexes **1** and **2** have slight variations of their magnetic properties due to the twisting of the structures. These difference of structural distortions in complexes **1** and **2** results in different magnetic interactions between the metal centers. With these two SMMs established, we have since managed to synthesize additional members of this Mn_6 family of SMMs using other linking groups.

Acknowledgements

The magnetic measurements were obtained from the SQUID magnetometer (MPMS XL-7) in NSYSU, and we thank the National Science Council of Taiwan (NSC-96-2113-M-006-010-MY3) for financial support.

Appendix A. Supplementary data

CCDC 693042 and 693043 contains the supplementary crystallographic data for this article. These data can be obtained free of charge via http://www.ccdc.cam.ac.uk/conts/retrieving.html, or from the Cambridge Crystallographic Data Centre, 12 Union Road, Cambridge CB2 1EZ, UK; fax: (+44) 1223-336-033; or e-mail: deposit@ccdc.cam.ac.uk. Supplementary data associated with this article can be found, in the online version, at doi:10.1016/j.poly.2009.02.001.

References

[1] D. Gatteschi, R. Sessoli, Angew. Chem., Int. Ed. 42 (2003) 268. and references therein.
[2] A.J. Tasiopoulos, A. Vinslava, W. Wernsdorfer, K.A. Abboud, G. Christou, Angew. Chem., Int. Ed. 43 (2004) 2117.
[3] R. Sessoli, H.-L. Tsai, A.R. Schake, S.Y. Wang, J.B. Vincent, K. Folting, D. Gatteschi, G. Christou, D.N. Hendrickson, J. Am. Chem. Soc. 115 (1993) 1804.
[4] R. Sessoli, D. Gatteschi, A. Caneschi, M.A. Novak, Nature 365 (1993) 141.
[5] D. Gatteschi, A. Caneschi, L. Pardi, R. Sessoli, Science 265 (1994) 1054.
[6] F.A. Cotton, G. Wilkinson, Advanced Inorganic Chemistry, 4th Ed., John Wiley and Sons, New York, 1980.
[7] M. Soler, W. Wernsdorfer, Z.M. Sun, J.C. Huffman, D.N. Hendrickson, G. Christou, Chem. Commun. (2003) 2672.
[8] C. Boskovic, W. Wernsdorfer, K. Folting, J.C. Huffman, D.N. Hendrickson, G. Christou, Inorg. Chem. 41 (2002) 5107.
[9] E.K. Brechin, M. Soler, J. Davidson, D.N. Hendrickson, S. Parsons, G. Christou, Chem. Commun. (2002) 2252.
[10] T.C. Stamatatos, D. Foguet-Albiol, C.C. Stoumpos, C.P. Raptopoulou, A. Terzis, W. Wernsdorfer, S.P. Perlepes, G. Christou, J. Am. Chem. Soc. 127 (2005) 15380.
[11] C.J. Milios, R. Inglis, A. Vinslava, A. Prescimone, S. Parsons, S.P. Perlepes, G. Christou, E.K. Brechin, Chem. Commun. (2007) 2738.
[12] C.J. Milios, I.A. Gass, A. Vinslava, L. Budd, S. Parsons, W. Wernsdorfer, S.P. Perlepes, G. Christou, E.K. Brechin, Inorg. Chem. 46 (2007) 6215.
[13] C.J. Milios, A. Prescimone, A. Mishra, S. Parsons, W. Wernsdorfer, G. Christou, S.P. Perlepes, E.K. Brechin, Chem. Commun. (2007) 153.
[14] T.C. Stamatatos, D. Foguet-Albiol, S.-C. Lee, C.C. Stoumpos, C.P. Raptopoulou, A. Terzis, W. Wernsdorfer, S.O. Hill, S.P. Perlepes, G. Christou, J. Am. Chem. Soc. 129 (2007) 9484.
[15] L.F. Jones, G. Rajaraman, J. Brockman, M. Murugesu, E.C. Sanudo, J. Raftery, S.J. Teat, W. Wernsdorfer, G. Christou, E.K. Brechin, D. Collison, Chem. Eur. J. 10 (2004) 5180.
[16] C.P. Raptopoulou, A.K. Boudalis, K.N. Lazarou, V. Psycharis, N. Panopoulos, M. Fardis, G. Diamantopoulos, J.-P. Tuchagues, A. Mari, G. Papavassiliou, Polyhedron 27 (2008) 3575.
[17] C.-I. Yang, W. Wernsdorfer, K.-H. Cheng, M. Nakano, G.-H. Lee, H.-L. Tsai, Inorg. Chem. 47 (2008) 10184.
[18] C.-I. Yang, W. Wernsdorfer, G.-H. Lee, H.-L. Tsai, J. Am. Chem. Soc. 129 (2007) 456.
[19] M. Murugesu, M. Habrych, W. Wernsdorfer, K.A. Abboud, G. Christou, J. Am. Chem. Soc. 126 (2004) 4766.
[20] G. Aromi, S. Parsons, W. Wernsdorfer, E.K. Brechin, E.J.L. McInnes, Chem. Commun. (2005) 5038.
[21] T.C. Stamatatos, K.A. Abboud, W. Wernsdorfer, G. Christou, Angew. Chem., Int. Ed. 45 (2006) 4134.
[22] E.E. Moushi, T.C. Stamatatos, W. Wernsdorfer, V. Nastopoulos, G. Christou, A.J. Tasiopoulos, Angew. Chem., Int. Ed. 45 (2006) 7722.
[23] A.M. Ako, I.J. Hewitt, V. Mereacre, R. Clérac, W. Wernsdorfer, C.E. Anson, A.K. Powell, Angew. Chem., Int. Ed. 45 (2006) 4926.
[24] T.C. Stamatatos, K.A. Abboud, W. Wernsdorfer, G. Christou, Angew. Chem., Int. Ed. 47 (2008) 6694.
[25] T.C. Stamatatos, K.A. Abboud, W. Wernsdorfer, G. Christou, Angew. Chem., Int. Ed. 46 (2007) 884.
[26] G.M. Sheldrick, SHELXL-97, University of Gottingen, Gottingen, Germany, 1997.
[27] E.A. Boudreaux, L.N. Mulay, in: Theory and Application of Molecular Paramagnetism, John Wiley and Sons, New York, 1976, p. 491.
[28] M. Lalia-Kantouri, A. Hatzidimitriou, M. Uddin, Polyhedron 18 (1999) 3441.
[29] J.M. Thorpe, R.L. Beddoes, D. Collison, C.D. Garner, M. Helliwell, J.M. Holmes, P.A. Tasker, Angew. Chem., Int. Ed. 39 (1999) 1119.
[30] C.P. Raptopoulou, A.K. Boudalis, Y. Sanakis, V. Psycharis, J.M. Clemente-Juan, M. Fardis, G. Diamantopoulos, G. Papavassiliou, Inorg. Chem. 45 (2006) 2317.
[31] A. Escuer, V.C. Kee, J. Nelson, E. Ruiz, N. Sanz, R. Vicente, Chem. Eur. J. 11 (2005) 398.
[32] R. Boča, M. Hvastijová, J. Kožíšek, M. Valko, Inorg. Chem. 35 (1996) 4794.
[33] G.J. Milios, C.P. Raptopoulou, A. Terzis, F. Lloret, R. Vicente, S.P. Perlepes, A. Escuer, Angew. Chem., Int. Ed. 43 (2004) 210.
[34] C.J. Milios, A. Vinslava, A.G. Whittaker, S. Parsons, W. Wernsdorfer, G. Christou, S.P. Perlepes, E.K. Brechin, Inorg. Chem. 45 (2006) 5272.
[35] K. Kambe, J. Phys. Soc. Jpn. 5 (1950) 48.
[36] C. Raghu, I. Rudra, D. Sen, S. Ramasesha, Phys. Rev. B 64 (2001) 064419.
[37] N. Regnault, Th. Jolicoeur, R. Sessoli, D. Gatteschi, M. Verdaguer, Phys. Rev. B 66 (2002) 054409.
[38] G. Chaboussant, A. Sieber, S. Ochsenbein, H.-U. Güdel, M. Murrie, A. Honecker, N. Fukushima, B. Normand, Phys. Rev. B 70 (2004) 104422.
[39] IGOR PRO 6, WaveMetrics Inc.
[40] C.J. Milios, A. Vinslava, W. Wernsdorfer, A. Prescimone, P.A. Wood, S. Parsons, S.P. Perlepes, G. Christou, E.K. Brechin, J. Am. Chem. Soc. 129 (2007) 6547.
[41] L.F. Jones, R. Inglis, M.E. Cochrane, K. Mason, A. Collins, S. Parsons, S.P. Perlepes, E.K. Brechin, Dalton Trans. (2008) 6205.
[42] R. Clèrac, H. Miyasaka, M. Yamashita, C. Coulon, J. Am. Chem. Soc. 124 (2002) 12837.
[43] M.P. Shores, J.J. Sokol, J.R. Long, J. Am. Chem. Soc. 124 (2002) 2279.

Since our sample is polycrystalline we have to average theoretical results over three directions. Thus, a total susceptibility is calculated as an arithmetic average:

$$\chi = -\left(\frac{\partial^2 F}{\partial B^2}\right)_T = \frac{1}{3}\left(\chi_x + \chi_y + \chi_z\right), \tag{3}$$

$$\chi_{x,y,z} = -\frac{\partial^2 F}{\partial B_{x,y,z}^2} \tag{4}$$

where $B_{x,y,z}$ stand for x, y or z component of the magnetic field B. The same average is calculated for the magnetization $\langle S\rangle$:

$$\langle S\rangle = \frac{1}{3}\left(\langle S^x\rangle + \langle S^y\rangle + \langle S^z\rangle\right), \quad S^{x,y,z} = \sum_{j=1}^{7} s_j^{x,y,z} \tag{5}$$

In order to facilitate our QTM calculations we compute $\chi_{x,y}$ by numerical differentiation of F and χ_z using the formula:

$$\chi_z = \beta(g\mu_B)^2\left(\langle (S^z)^2\rangle - \langle S^z\rangle^2\right). \tag{6}$$

We exploit the symmetry of the model imposing that χ_y for the magnetic field B in the plane $y-z$ is equal to χ_x with B in the plane $x-z$ (see Eq. (1)). For the sake of theoretical discussion we also calculate magnetic torque τ which for the field in $x-z$ plane has only yth component:

$$\tau_y = -g\mu_B B\left(\langle S^x\rangle\cos\theta - \langle S^z\rangle\sin\theta\right) \tag{7}$$

The thermodynamic quantities are calculated directly by means of QTM. Using ED we determine the energy structure of Hamiltonian (1) and confirm the results obtained by the QTM technique. The details of the QTM and ED techniques can be found in [9], where we also discuss parallelization of our algorithms.

3. Results and discussion

Magnetic measurements presented in this paper were performed on polycrystalline samples, by using a Quantum Design MPMS XL SQUID magnetometer equipped with a 7 T magnet. The samples were prepared by the method described in [5] and restrained in eicosane. Magnetic susceptibility data were recorded in the 2–300 K temperature range in applied magnetic fields of 0.1, 0.5 and 1 T (perpendicular to the direction of the measurement). Data were corrected for the diamagnetism of the sample by using Pascal's constants. The sample holder diamagnetism was also measured and subtracted from the raw data.

There are already two sets of microscopic parameters for Cr_7Cd found by fitting the specific heat (C-fit: $J_\perp = J_\parallel = 15.3$ K, $D_\perp = 0, D_\parallel = -0.31$ K) [2] and EPR (EPR-fit: $J_\perp = 16.83$ K, $J_\parallel = 16.54$ K, $D_\perp = 0.069$ K, $D_\parallel = -0.14$ K) [3] data. The C-fit assumes only single ion anisotropy, whereas the EPR-fit assumes both single and exchange ion anisotropies [3]. We calculated the susceptibility for these two sets of parameters and found that they agree quite well with the experiment below $T = 5$ K (the deviation from the experiment is smaller then 2%). For higher temperatures they differ systematically from each other and from the experiment up to about 6%. This discrepancy together with a good agreement below $T = 5$ K suggests that the mean values of the exchange integrals should be tuned. Thus we keep the values of the anisotropies in both sets of parameters and change the mean values of the exchange integrals to fit the experimental data.

We obtained a very good fit (see Figs. 1 and 2) for the following sets of parameters: *a-fit* – $J_\perp = J_\parallel = 16.01$ K, $D_\perp = 0, D_\parallel = -0.31$ K and *b-fit* – $J_\perp = 15.92, J_\parallel = 15.63$ K, $D_\perp = 0.069$ K, $D_\parallel = -0.14$ K. In all cases we keep $g = 1.98$. We added to the theoretical results for χ a diamagnetic correction equal to 0.001, which includes also any temperature independent paramagnetism.

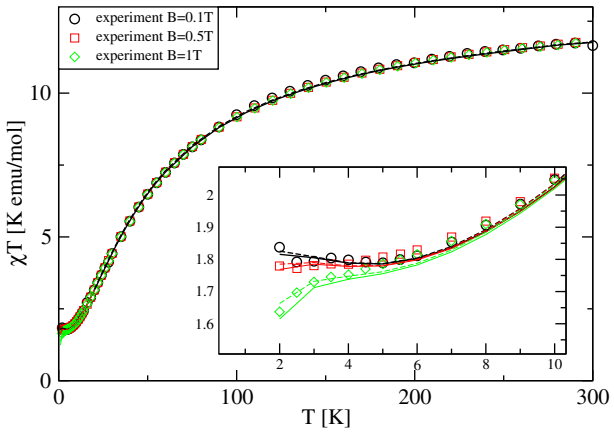


Fig. 1. Susceptibility χ of Cr_7Cd fitted with two theoretical curves. The a- and b-fits are depicted by full and broken lines, respectively.

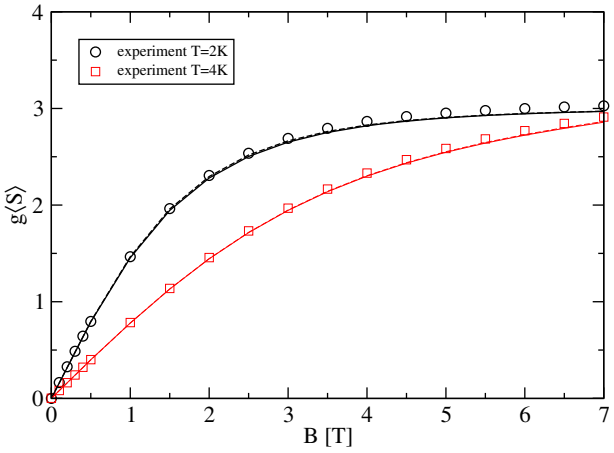


Fig. 2. Magnetization $\langle S\rangle$ of Cr_7Cd for $T = 2$ K and $T = 4$ K fitted by two theoretical curves. The a- and b-fits are depicted by full and broken lines, respectively.

The maximal difference between theory and experiment for both fits is smaller than 2% in whole temperature range. Thus, on the basis of these results we cannot decide whether there is only single ion anisotropy (a-fit), or also exchange anisotropy (b-fit) We notice that a good agreement of our two fits with each other is due to the fact that we calculate susceptibility and magnetization for a powder sample, i.e. we take the arithmetic average (3). The values of $\chi_{x,y,z}$ in low temperatures differ for a- and b-fits quite considerably (see Fig. 3).

Thus, in order to decide which anisotropy is present in Cr_7Cd one should perform measurements on a mono crystalline sample. As can be seen in Fig. 3 the susceptibility could be a good test quantity. However the magnetic torque seems to be much more suitable because it is very sensitive to anisotropy.

We have calculated the torque for various sets of parameters and found that the curves representing the torque as a function of the magnetic field B fall into two general categories determined by the anisotropy. With only one type of anisotropy (single ion or exchange) the τ curves exhibit sharp minima at the crossing fields. Depending on the sign of the anisotropy parameter (D or $J_\perp - J_\parallel$) the τ curves are ascending or descending with growing field B (see full and broken curves in Fig. 4).

However when we take into account both types of anisotropy (second category) the calculated curves have a quite different character (see dot-broken curves in Fig. 4. There are also descending

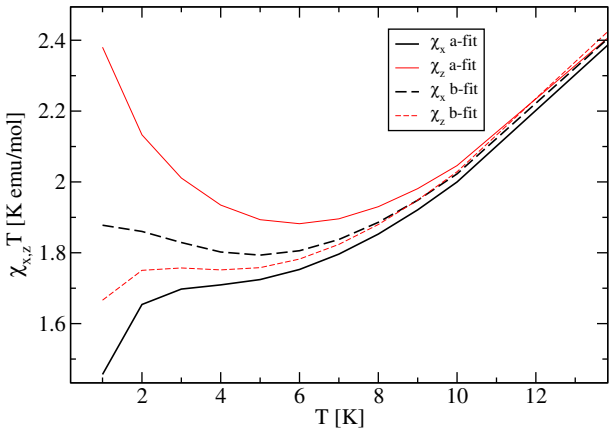


Fig. 3. Susceptibility χ of Cr_7Cd along x and z axes calculated for two sets of parameters.

curves for opposite sings of D and $J_\perp - J_\parallel$, not shown here for the sake of clarity.) They do not have characteristic peaks present in the first category of curves and ascribed to the anti-crossing (AC) gap [8]. We notice that a- and b-fits belong to two different categories.

The exact conditions for which this effect can be observed are currently under investigation. The preliminary results allow us to state, that to obtain a curve falling into the second category both exchange and single ion anisotropies should be of the same order and should have opposite character, i.e. one should be of an easy axis type and the other of an easy plane type. In the interesting for us case (b- and EPR-fits) a single ion anisotropy is of an easy axis type and the exchange one is of an easy plane type.

To understand better how these two kinds of behavior depend on the energy structure of the models we diagonalized Hamiltonian (1). We found that when two anisotropies (single ion and exchange) are present in the system the first AC gap between the ground state (from 3/2 multiplet) and the first excited state (from 5/2 multiplet) is considerably diminished. This effect does not appear if only one sort of anisotropy is taken into account (see Fig. 5). For some parameters the AC gap practically disappears for all values of angle θ (see diamonds in Fig. 5), or at least looses its strong θ dependence. This is why the peaks in the τ curves are swept out.

Furthermore we find that for the b-fit (EPR-fit) the ground (3/2) multiplet has an easy plane splitting and the lowest (5/2) multiplet has an easy axis splitting, i.e. precisely opposite to the situation in the a-fit (C-fit) [2].

As there are no experimental results of torque for Cr_7Cd we cannot directly verify our theoretical predictions. The most similar compound which, as concerns magnetic properties, should differ from our ring only in the quantitative way is the already mentioned Cr_7Zn. For this molecule there are results of the torque experiment available [8]. None of the shapes of τ curves presented in [8] resembles the one obtained by us for the mixed anisotropies. This would suggest that Cr_7Cd has only one type of anisotropy.

It is worth mentioning that the microscopic model used by us in this paper is not identical with the models employed in [2] and [3]. In the work of Affronte et al. [2] also the dipole–dipole intracluster interactions are taken into account, though only using the point-dipole approximation. Piligkos et al. [3] introduce rotational matrices into the Heisenberg like Hamiltonian with the site-dependent angles. Nevertheless a fact that the susceptibility in low temperature calculated by us using the parameters obtained from the C-fit agrees very well with that calculated with the EPR-fit parameters proves that the real differences between the models (at least for the quantities calculated) are very small. Though one cannot entirely exclude that it is a combined effect of approximations used here.

We neglected the small dipolar interactions and the changes in the directions of the local anisotropy axes. These effects could be incorporated in our scheme but the corresponding parameters were not available for us.

It has been already pointed out in [10] that though usually treated as equivalent single ion and exchange anisotropies may have qualitatively different influence on the properties of a system. Our calculations demonstrate that in case of Cr_7Cd both kinds of anisotropy have the same effect if they exist in separation. Their

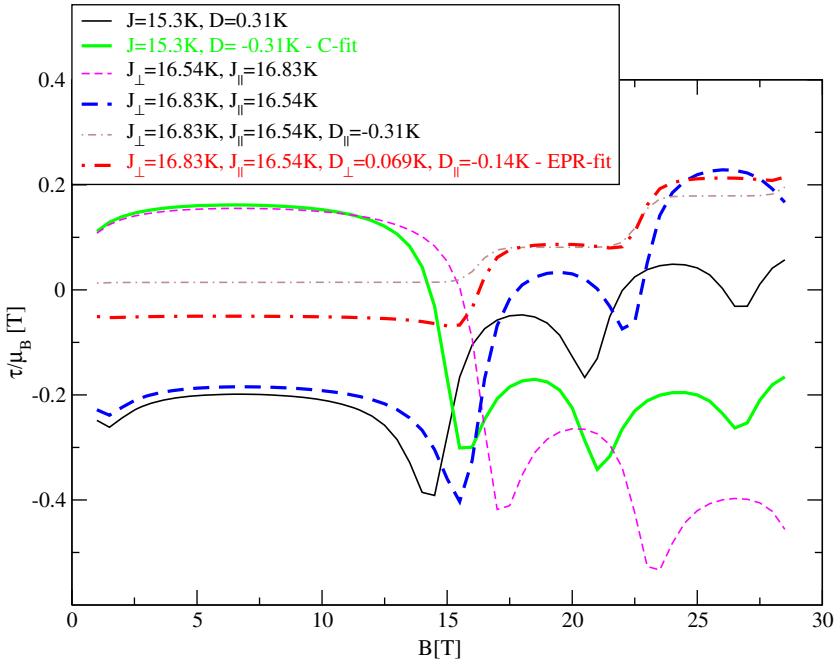


Fig. 4. Magnetic torque τ of Cr_7Cd calculated for pure and mixed anisotropies. $\theta = 5.5^\circ$ and $T = 0.4$ K.

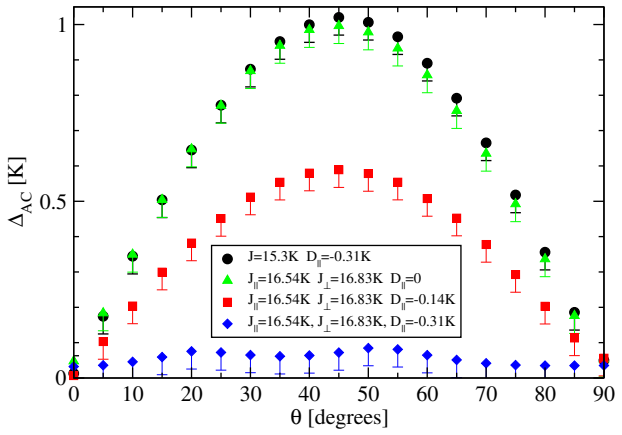


Fig. 5. Angular dependence of the first AC gap Δ_{AC} in Cr_7Cd calculated for few sets of parameters.

mixture however gives rise to qualitatively new behavior. It can be seen both on the level of measurable macroscopic quantities and on the level of the microscopic energy structure.

There remain many questions which are beyond the scope of this short communication. First of all it would be interesting to check whether this sort of quality change induced by mixing of two anisotropies can also be observed in models with different geometry/symmetry, e.g. in even membered or odd membered, but frustrated antiferromagnetic rings.

4. Conclusions

Starting from previously obtained theoretical results based on specific heat and EPR experiments we found two fits (a and b) to the measured by us magnetic susceptibility of polycrystalline Cr_7Cd. The a-fit assumes only single ion anisotropy, whereas the b-fit comprises a mixture of single ion and exchange anisotropy. Both fits are very good (the maximal deviation from the experiment is smaller than 2%) and none of them can be favored on the basis of a powder magnetic measurement. Therefore we calculated the magnetic torque for a mono crystal. We found that when only pure anisotropy (single ion or exchange) is present in the system the torque curves (torque versus magnetic field) have similar character. However if two types of anisotropy are taken into account and they are approximately of the same magnitude and different orientation (e.g. easy plane and easy axis) the properties of the system change significantly. The torque curves do not have characteristic peaks any more. On the microscopic level mixing of anisotropies corresponds to the vanishing of the AC gap between the ground and the lowest excited states and to a different splitting of first 3/2 and 5/2 multiplets.

Thus, in Cr_7Cd single ion and exchange anisotropy can lead to similar effects when existing in separation, but their mixture gives rise to qualitatively new behavior, both on the macroscopic and microscopic levels. On the basis of the torque experiment for a very similar compound (Cr_7Zn) we predict that there is no mixture of anisotropy in the Cr_7Cd, so the a-fit should be preferred to b. The definite answer to this question can be given by the torque experiment performed on a Cr_7Cd mono crystal.

Definitely more work on the interplay between single ion and exchange anisotropy in molecular magnets is needed. We hope to contribute to these efforts in the next paper where we are going to treat in more detail the problems discussed here and extend the discussion to other chromium-based rings, especially those with different geometry than Cr_7Cd.

Acknowledgements

The authors thank Prof. J. Schnack and J. van Slageren for helpful discussions. This work was supported in part by the European Commission within the Project NMP3-CT-2005-515767 MAGMA-Net. Numerical calculations were mainly carried out on the platforms of the Supercomputing and Networking Center in Poznań and the Academic Computer Center in Gdańsk, Poland, with some contribution from the NIC supercomputers in Juelich, Germany.

References

[1] A. Wilson, J. Lawrance, E-C. Yang, M. Nakabo, D.N. Hendrickson, S. Hill, Phys. Rev. B 74 (2006) 140403(R).
[2] M. Affronte, A. Ghiri, S. Carretta, G. Amoretti, S. Piligkos, G.A. Timco, R.E.P. Winpenny, Appl. Phys. Lett. 84 (2004) 3468.
[3] S. Piligkos, E. Bill, D. Collison, E.J.L. McInnes, G.A. Timco, H. Weihe, R.E.P. Winpenny, F. Neese, J. Am. Chem. Soc. 129 (2007) 760.
[4] E.J.L. McInnes, S. Piligkos, G.A. Timco, R.E.P. Winpenny, Coord. Chem. Rev. 249 (2005) 2577.
[5] F.K. Larsen, E.J.L. McInnes, H. El Mkami, J. Overgaard, S. Piligkos, G. Rajaraman, E. Rentschler, A.A. Smith, G.M. Smith, V. Boote, M. Jennings, G.A. Timco, R.E.P. Winpenny, Angew. Chem., Int. Ed. 42 (2003) 101.
[6] E. Micotti, Y. Furukawa, K. Kumagai, S. Carretta, A. Lascialfari, F. Borsa, G.A. Timco, R.E.P. Winpenny, Phys. Rev. Lett. 97 (2006) 267204.
[7] R. Caciuffo, T. Guidi, G. Amoretti, S. Carretta, E. Liviotti, P. Santini, C. Mondelli, G. Timco, C.A. Muryn, R.E.P. Winpenny, Phys. Rev. B 71 (2005) 174407.
[8] S. Carretta, P. Santini, G. Amoretti, M. Affronte, A. Ghirri, I. Sheikin, S. Piligkos, G. Timco, R.E.P. Winpenny, Phys. Rev. B 72 (2005) 060403(R).
[9] P. Kozłowski, G. Musiał, M. Antkowiak, G. Kamieniarz, D. Gatteschi, LNCS, accepted for publication.
[10] S.A. Leonel, A. Castro Oliveira, B.V. Costa, P. Zimmermann Coura, J. Magn. Magn. Mater. 305 (2006) 157.

colored/black precipitate was observed. It was then recrystallized from dimethyl sulfoxide (DMSO) over 2–3 week's period in the form of long black needles, suitable for single crystal X-ray diffraction. The small single crystalline product was directly obtained by slowly treating dilute solutions of TMPD and TCNB in benzene, giving yield over 90%. The precipitation from other solvents, like dichloromethane, chloroform, toluene, acetone, gave product indistinguishable with spectroscopic techniques.

3. Results and discussion

The crystal structure of the 1:1 complex formed between TMPD and TCNB has been determined by using single crystal X-ray diffraction at room temperature.[1] The complex crystallizes in the triclinic space group $P\bar{1}$ with cell dimensions: $a = 7.6772$ Å, $b = 8.0764$ Å, $c = 7.4986$ Å, $\alpha = 78.822°$, $\beta = 83.377°$, $\gamma = 86.289°$, volume 452.65 cm^3. The black color of these crystals ($1.0 \times 0.18 \times 0.1$ mm^3) suggests that there is a certain amount of charge transfer. The crystal structure of TMPD:TCNB reveals stacking of TMPD and TCNB molecules in infinite columns along the crystallographic *a*-axis, see Fig. 1.

Closer look at the crystal structure shows that along with this charge-transfer interaction, a prominent CN···HAr hydrogen bonded ribbon-like network is also present in a direction perpendicular CT interaction, see for detail Fig. 2. There are scarce of reports on the occurrence of CN···HAr hydrogen bonded network [12,14]. TCNB in the solid state exists as a dimer and its association is due to weak CN···HAr hydrogen bonding. I think, observed ribbon-like pattern is driven by charge-transfer interaction and its understanding is presently underway. On the other hand, presence of hydrogen bonded molecular tapes are common in literature, but they are normally observed through stronger synthon/synthons, and are rarely in electron donor–acceptor systems. In the present case, of CN···HAr hydrogen bonded ribbon network, distance observed between nitrogen of cyanide and hydrogen of neighboring aromatic carbon is 2.610 Å with angle of 147.19°. This is in agreement with the literature values for considering it as a weak hydrogen bonded interaction [12,14]. There is also a short distance interaction observed (as shown using dotted yellow line (see Fig. 2) amongst inter-ribboned TCNB molecules, which is at a distance of 2.935 Å with angle of 157.53°.

TCNB molecule is nearly planar with negligible deviation observed for the associated atoms from the mean plane. The TMPD molecule as a whole is not planar, but apart from the N-methyl groups, the rest of the atoms are nearly coplanar; the methyl groups are twisted away from the plane, as shown in Fig. 3a. The two molecules overlap each other with an interplanar spacing of 3.4 Å, though the molecular plane of the TCNB makes an angle of 7° with the mean plane passing through the phenylene ring and the two amine nitrogen atoms of TMPD. The two rings of TCNB and TMPD overlap only to a small extent contrary to Mulliken's prediction of large overlap of benzene rings in π-stacked complexes [15]. This is in accordance with the electronic orbital of the amine nitrogen atom, N(1), exhibiting tetrahedral character, and that the lone pair electrons of the nitrogen atom are not perfectly delocalized with π-electrons of the benzene ring. Thus, the structure does not show the usual π-π interaction between the two aromatic rings, but indicates n–π interaction localized between the nitrogen atoms of the donor and the cyano groups of the acceptor.

[1] The crystal analysis of the compound was carried out on a $1.0 \times 0.18 \times 0.10$ mm plate grown crystal. The data were collected with Mo Kα radiation with wavelength = 0.71073 Å, $T = 298$ K. Crystallographic coordinates and analysis summary in CIF format have been deposited with the Cambridge Crystallographic Database center (CCDC). Its reference number is CCDC 237161.

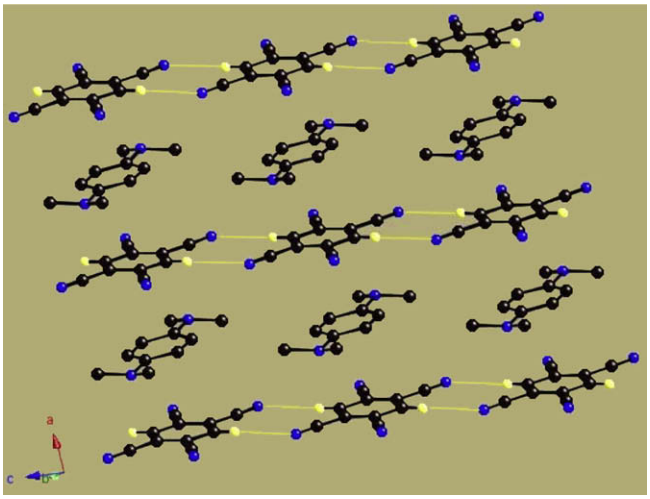


Fig. 1. Crystal packing of TMPD and TCNB molecules in TMPD:TCNB (C in black, H in off white, N in blue color; for clarity hydrogen atoms of TMPD are omitted). (For interpretation of the references to color in this figure legend, the reader is referred to the web version of this article.)

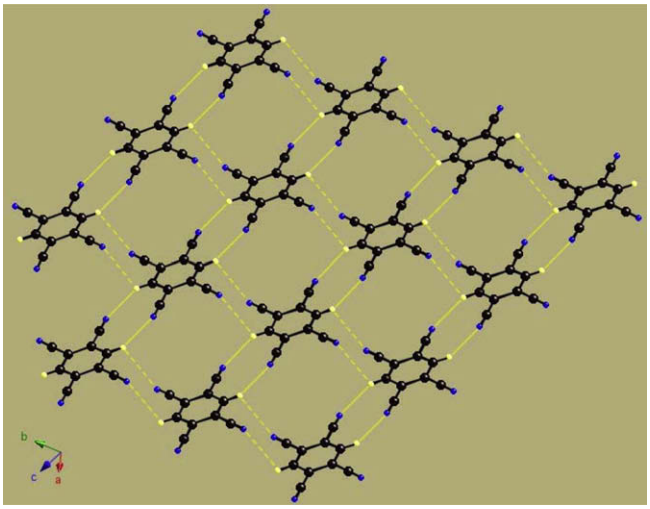


Fig. 2. Formation of ribbon-like network amongst TCNB molecules due to CN···HAr hydrogen bonding motif (shown in solid yellow line; dotted yellow line shows other close contacts amongst TCNB molecules). (For interpretation of the references to color in this figure legend, the reader is referred to the web version of this article.)

As shown in the Fig. 3b, the component molecules are tightly packed: the methyl groups of TMPD lie between the two cyano groups of TCNB, thus the TCNB molecule appears to be held together by the methyl groups. Consequently, the two N-methyl groups are closer to the ring carbon atoms of the TCNB molecule with the associated C–C distances of 3.502 and 3.620 Å. In the structure of TMPD–TCNQ complex [16,17] (TCNQ = 7,7,8,8-tetracyanoquinodimethane) however, the methyl groups do not affect the relative orientation, because of the geometry of TCNQ molecule. Also, the electron affinity of TCNQ is much larger than that of TCNB (0.17 eV; reversible in acetonitrile at room temperature versus SCE) which facilitates stronger π–π interaction for TCNQ than in the present complex. These facts indicate that the relative orientation of the two component molecules in the present complex is mainly determined by the packing of the molecules. On the basis of the observed short intermolecular distances, one can say that the lone pair electrons of the amine nitrogen atoms are partially

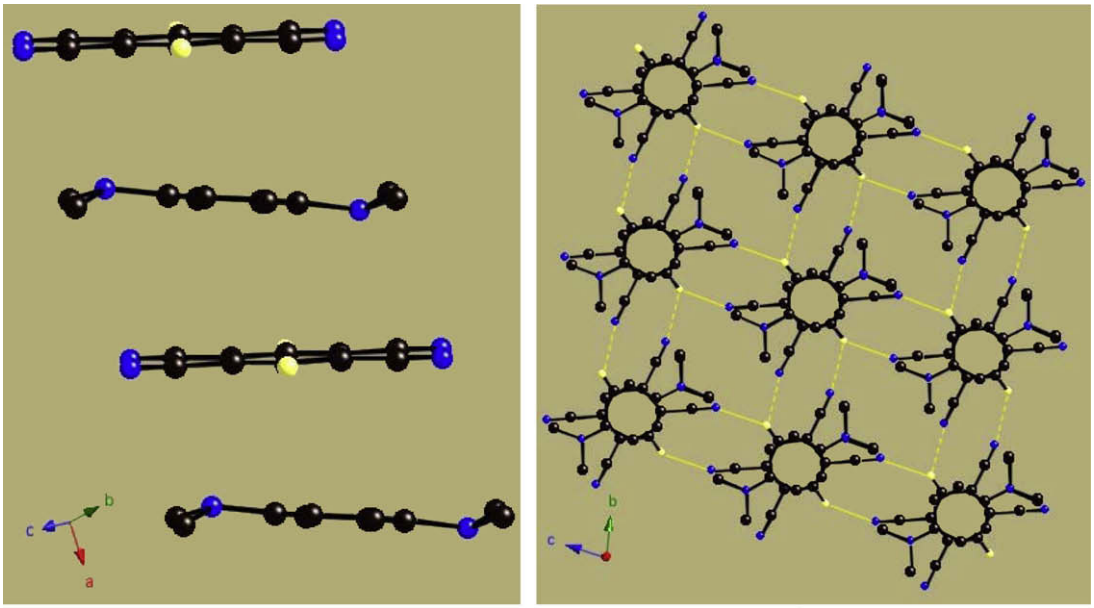


Fig. 3. The stacking of TMPD and TCNB molecules (a) showing tetrahedral nature of nitrogen and bending of dimethyl groups attached to phenylene nitrogen in TMPD and (b) showing tight packing of the N,N-dimethyl groups of TMPD and cyanide groups of TCNB.

transferred to the cyano groups through n–π interaction. The presence of n–π charge transfer is also supported by molecular orbital calculation showing the carbon atom of the cyano groups in a free molecule of TCNB is deficient in electron density [17].

Temperature dependent magnetic susceptibility χ measurements were carried out using a SQUID magnetometer on a powdered TMPD:TCNB. Fig. 4 shows a plot of product of χ (with the temperature independent diamagnetic contribution subtracted) and temperature versus temperature. Since $\chi = H\mu_{\text{eff}}^2/3kT$ where N is Avogadro's number, μ_{eff} is the effective magnetic moment ($\mu_{\text{eff}}^2 = g^2\mu_B^2 S(S+1)$) in Bohr magnetons, and k is the Boltzman constant, then, for a simple Curie law paramagnet, χT is constant. However, I observed an increase of χT as a function of temperature. This behavior indicates that short range antiferromagnetic interactions at higher temperatures between the stacked TMPD and TCNB radical ions, as has been observed in other charge-transfer complexes [18]. Thus, this data shows that in contrast to the diamagnetic precursors, the complex is magnetic, indicating substantial charge transfer.

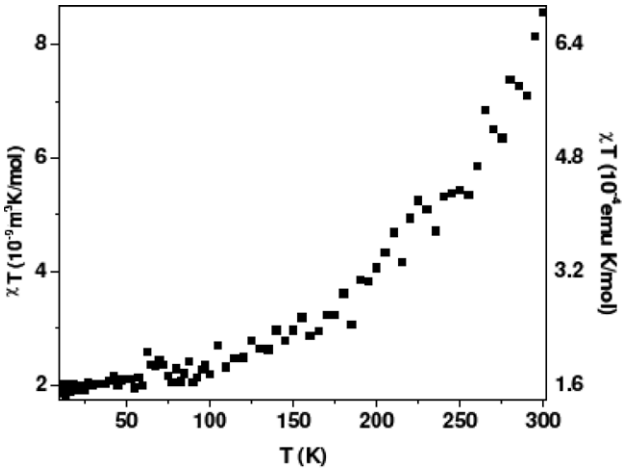


Fig. 4. Temperature dependent magnetic behavior of solid TMPD:TCNB.

Also, room temperature EPR data on powdered TMPD:TCNB shows two peaks, $g_\perp = 2.0009$ and $g_{||} = 2.0022$: the peak to peak linewidth, ΔH_{pp}, is 0.06 mT for $g_\perp$ and the width at half height, $\Delta H_{1/2}$, is 0.09mT for $g_{||}$ [13]. This result conforms TMPD:TCNB is magnetic and compares well to the literature g-values for the radical anions of ~2.002 for the similar acceptors like TCNQ and TCNE [19].

4. Conclusion

TMPD:TCNB complex showed presence of two distinct non-covalent interactions: (i) charge-transfer interaction and (ii) ribbon-like CN···HAr hydrogen bonding motif amongst electron acceptor molecules, which show interesting magnetic behavior. This latter type of hydrogen bonding interaction amongst electron acceptor molecules is a crucial element for engineering useful electron donor–acceptor type compounds without changing drastically electron donor or acceptor molecules. Although hydrogen bonding is a useful means to organize crystal scaffolding, its electronic effect on bulk magnetic and exchange behavior is not always straightforward to predict. Presently, I am expanding research to build new types of crystalline materials using non-covalent interactions amongst electron acceptor molecules, in the form of flexible host assemblies, and their possible magnetostructural relationship.

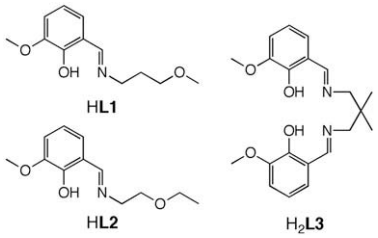
Acknowledgements

Author acknowledges support by the grants from Department of Science and Technology, India, under FAST Track proposals for Young Scientist, SR/FTP/CS/25/2006. Dr. Navamoney Arulsamy, for single crystal X-ray diffraction. Author also thanks, Dr. Brant Cage (National Institute of Standards and Technology, Boulder, CO, USA) for help in SQUID measurement; Prof. Jeff Yarger (Arizona State University, USA) and Dr. Pallavi Ghalsasi for encouragement and helpful discussions.

References

[1] J.-M. Lehn, Supramolecular Chemistry, VCH, Weinheim, 1996.
[2] K.T. Homan, M.D. Pivovar, M.D. Ward, Science 294 (2001) 1907.

[3] Y. Morita, T. Murata, K. Fukui, Y. Satoru, K. Sato, D. Shiomi, T. Takui, H. Kitagawa, H. Yamouchi, G. Saito, K. Nakatsuji, J. Org. Chem. 70 (2005) 2739.
[4] P. Taylor, P.M. Lahti, Chem. Commun. (2004) 2686.
[5] B. Moulton, J. Lu, R. Hajndl, S. Hariharan, M.J. Zaworotko, Angew. Chem., Int. Ed. Engl. 41 (2001) 2821.
[6] F.J. Disalvo, Science 247 (1990) 608.
[7] G.A. Jeffrey, An Introduction to Hydrogen Bonding, Oxford University Press, NY, 1999.
[8] E. Coronado, J.R. Galan-Mascaros, G.J. Gomez-Garcia, V. Laukhin, Nature 408 (2000) 447.
[9] P.M. Lahti, Magnetic Properties of Organic Materials, Marcel Dekker, NY, 1999.
[10] M.L. Taliaferro, M.S. Thorum, J.S. Miller, Angew. Chem., Int. Ed. Engl. 45 (2006) 5326.
[11] R. Foster, in: A.T. Blomquist (Ed.), Organic Charge Transfer Complexes, Academic Press, London, 1969.
[12] D.S. Reddy, K. Panneerselvam, T. Pilati, G.R. Desiraju, Chem. Commun. (1993) 661.
[13] P.S. Ghalsasi, B. Cage, J.L. Yarger, Molecules 9 (2004) 808. and reference therein.
[14] A.N.M.M. Rahman, R. Bishop, D.C. Craig, M.L. Scudder, Eur. J. Org. Chem. 72 (2003).
[15] R.S. Mulliken, J. Am. Chem. Soc. 72 (1950) 600.
[16] A.W. Hanson, Acta Crystallogr. 19 (1965) 610.
[17] S. Iwata, J. Tanaka, S. Nagakura, J. Am. Chem. Soc. 88 (1966) 894.
[18] Z.G. Soos, H.J. Keller, K. Ludolf, J. Queckboner, D. Wehe, S. Flandrois, J. Chem. Phys. 74 (1981) 5287.
[19] S.E. Bell, J.S. Field, R.J. Haines, M. Moscherosch, W. Matheis, W. Kaim, Inorg. Chem. 31 (1992) 3269.



Scheme 1. Structures of Schiff base ligands described in the main text.

Figs. 1 and 2 show crystal structures of two complexes. Both complexes crystallized in triclinic crystal system with space group $P\bar{1}$, and each unit cell involves two molecules related by the inversion center. In each complex, the Schiff base ligand $\mathbf{L3}^{2-}$ behaves as tetradentate O_2N_2 ligand for Cu(II) ion and tetradentate O_4 ligand for Tb(III) ion, and Tb and Cu are doubly bridged by two phenoxo oxygens (O2 and O4). O_2N_2 donor atoms are almost coplanar (maximum deviations from ideal planes are 0.0030(19) and 0.104(3) Å, respectively), and each Cu atom is located on the plane with deviations of 0.1385(19) and 0.103(3) Å, respectively. Coordination distances are in a range of 1.957(3)–1.989(4) Å for **3** and 1.954(4)–1.975(6) Å for **4**, and each apical position of the Cu atom is occupied by water oxygen atom (O14) or nitrate oxygen atom (O12) with the distances of 2.299(4) and 2.405(5) Å, respectively. Both Cu atoms in **3** and **4** are in an axially elongated pyramidal coordination, and the magnetic orbital ($d_{x^2-y^2}$) of Cu(II) ion with d^9 electronic configuration is located on the equatorial plane directing toward four donating atoms. The Schiff-base ligands are slightly bending from the O_2N_2 plane, with the dihedral angles of two phenyl rings being 21.5(2)° and 43.1(3)°. In the O_4 site of the ligand, four donor atoms are also arranged in a quite flat manner (maximum deviations from the ideal planes are 0.009(2) Å (**3**) and 0.065(3) Å (**4**)), and the Tb(III) are located 0.711(3) Å (**3**) and 0.6262(19) Å (**4**) above the planes, with the bonding distances ranging in 2.331(3)–2.495(3) Å for **3** and 2.333(4)–2.589(5) Å for **4**, respectively. The bridging angles of Tb–O–Cu were found to be 107.48(13)° and 108.35(13)° for **3** and 106.94(19)° and 107.06(19)° for **4**, and as a result, the core structures of $\{TbCu(\mathbf{L3})\}^{3+}$ moieties are quite similar in both complexes. Tb in **3** were further coordinated by three nitrate anions in a bidentate manner to complete the deca-coordination. The coordination modes are unsymmetrical among three nitrate anions; one is parallel to the Tb–Cu axis whereas two are skew to the axis. Consequently, the coordination geometry of Tb(III) ion can be assumed as a square-antiprism capped by two methoxo oxygen atoms (O1 and O3) with quite large distortion, which would be advantageous to realize an SMM character. In **4**, the nona-coordination of Tb(III) ion was completed by three additional ligands, a nitrate anion (O5 and O6) and an *o*-vanilate anion (O9 and O10) both in a chelating fashion, and a methanol molecule (O11) in a monodentate fashion. The phenoxo oxygen of the *o*-vanilate anion (O9) is collinear with Tb(III) and Cu(II) ions, and located on the opposite side of the two phenoxo oxygens of $\mathbf{L3}^{2-}$. As was described in the previous paper, the negative charge distribution of phenoxo oxygen atom is larger than other oxygen donors such as oxygen atom(s) in a nitrate anion, a methoxo group, and also a methanol molecule. Consequently, the axial positions of Tb(III) is occupied with more negative phenoxo oxygen atoms (O2, O4, and O9) and the equatorial positions were occupied by less negative oxygen donors (O1, O3, O5, O6, O10, and O11). The uni-axial crystal filed found in **4** might be advantageous for the enhancement of the easy-axial magnetic anisotropy of Tb(III) ion.

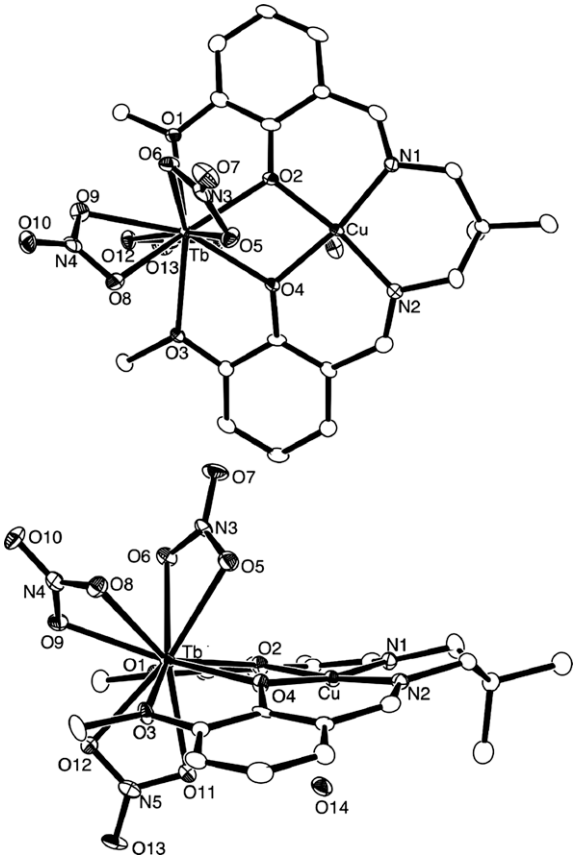


Fig. 1. Top view (upper) and side view (bottom) of ORTEP drawings of the complex **3** at 50% probability. Hydrogen atoms are omitted.

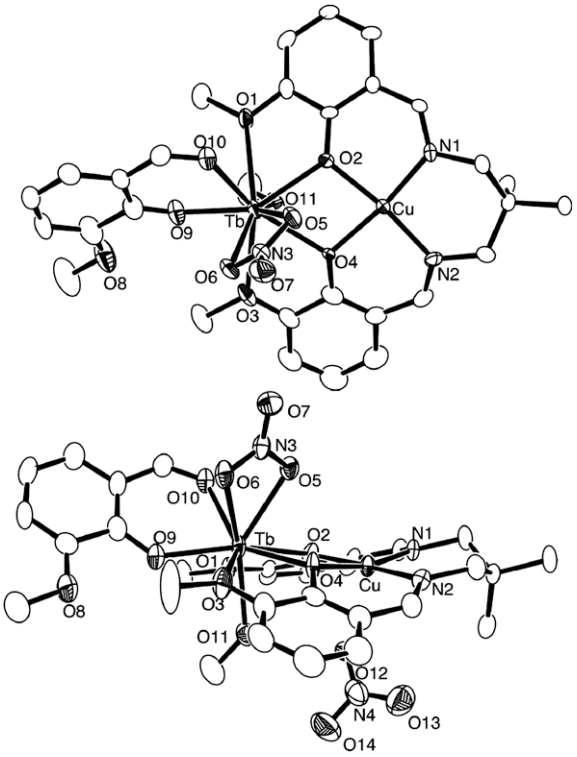


Fig. 2. Top view (upper) and side view (bottom) of ORTEP drawings of the complex **4** at 50% probability. Hydrogen atoms are omitted.

Dc susceptibility data were collected for poly crystalline samples of **3** and **4** (Fig. 3). The $\chi_M T$ values at room temperature, 13.06 (**3**) and 13.50 emu K mol^{-1} (**4**), were slightly larger than the expected value of 12.19 emu K mol^{-1} for magnetically independent Tb(III) ($J = 6$ and $g_{Tb} = 3/2$) and Cu(II) ($S = 1/2$ and $g_{Cu} = 2.0$) ions. The $\chi_M T$ gradually increased on lowering the temperature, which indicates the presence of weak ferromagnetic interactions between Tb(III) and Cu(II), as well as the presence of strong anisotropy of Tb(III) ions.

Ac magnetic susceptibility measurements were performed to observe the frequency dependence of χ'_M and χ''_M (Figs. 4 and 5). Both complexes showed a typical SMM behavior below 5 and 6 K. As the frequency was swept from 997 to 5 Hz, the temperature of maximum χ''_M shifted from 3.3 (997 Hz) to 2.0 K (5 Hz) for **3** and

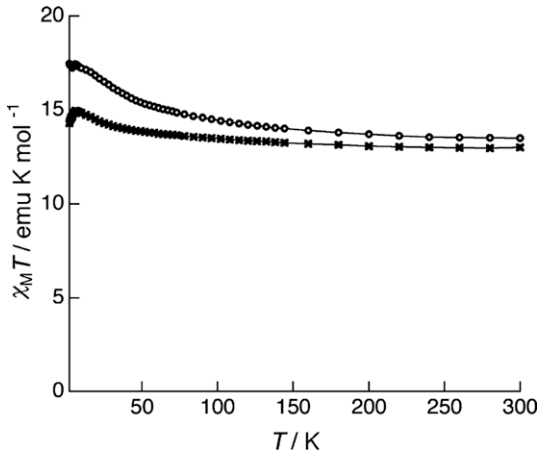


Fig. 3. $\chi_M T$–T plots for poly crystalline samples of **3** (×) and **4** (o).

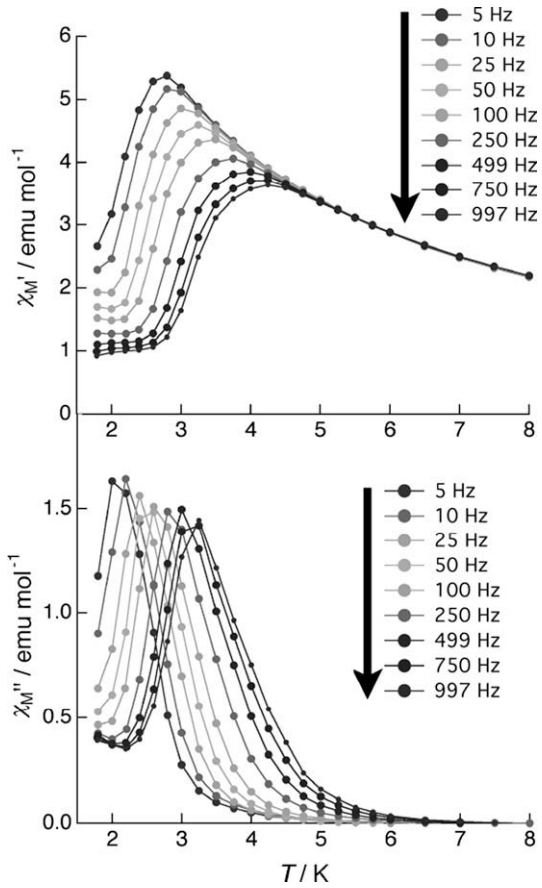


Fig. 4. Temperature dependences of χ'_M (top) and χ''_M (bottom) of **3** measured in 1000 Oe external dc field.

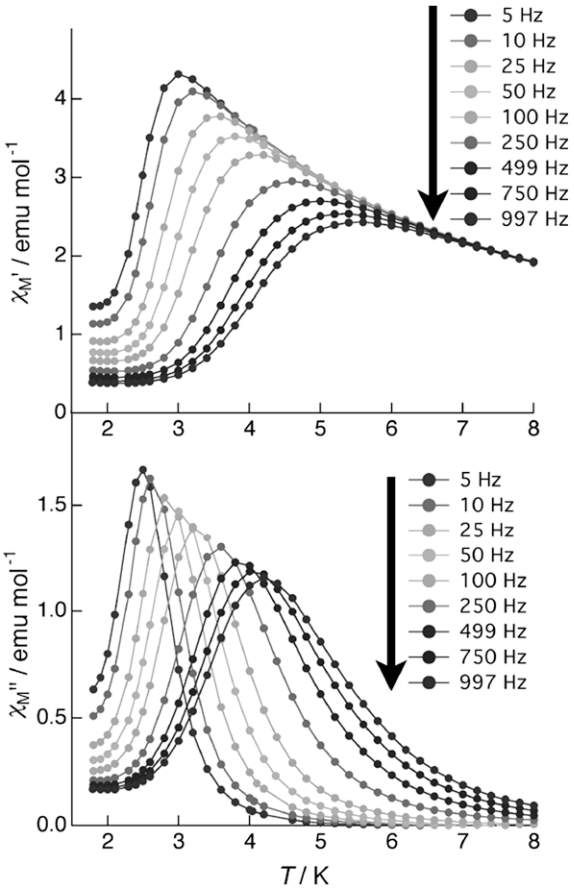


Fig. 5. Temperature dependences χ'_M (top) and χ''_M (bottom) of **4** measured in 1000 Oe external dc field.

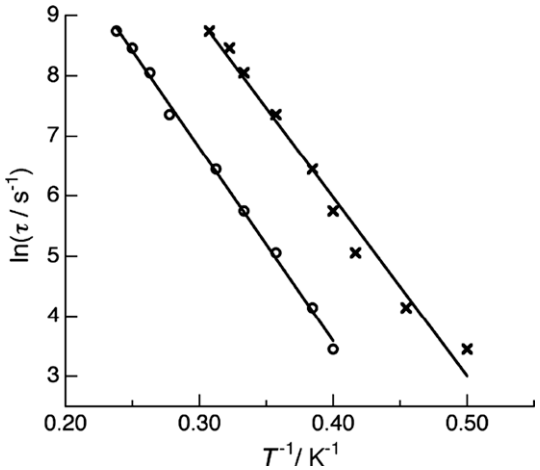


Fig. 6. Arrhenius plots of **3** (×) and **4** (o).

from 4.2 (997 Hz) to 2.5 K (5 Hz) for **4**, respectively. These observations indicate the presence of slow magnetic relaxations at low temperatures. Cole–Cole plots for **3** at the temperature range of 2.8–4.0 K showed semi-circle shapes with α parameters in the ranges of 0.27–0.41. Complex **4** showed smaller α parameters of 0.11–0.32 at the temperature range of 2.8–5.2 K. Complex **4**, having the smaller α-*values* in the wider temperature range, could be assumed as a better SMM compared with **3**. The energy barrier Δ/k_B, for the spin flipping in **3** and **4**, were estimated from the Arrhenius plot to be 29(2) and 32.2(6) K, respectively (Fig. 6). These values were larger than the previous complex **1**, which indicates the presence of larger magnetic anisotropy of Tb(III) in **3** and **4**. In **3**, the χ'_M below 3.0 K were reaching constant values and χ''_M below 2.5 K are increasing again, which is indicative for the presence of inter molecular interactions, reflecting on the larger α-*values* of 0.41 at 2.8 K. In fact, hydrogen bonding between terminal oxygen atom of nitrato anion and apical water molecule (O14 and O10$*$, 2.83 Å) was found in **3**, which could propagate a weak interaction between the adjoining molecules. In **4**, the balky *o*-vanilate anion prevents inter-molecular interaction which resulted into smaller α -*values* in wider temperature range (0.32 at 2.8 K).

From DFT calculations carried out for **1** and **2**, the negative charge distributions of the donor oxygen atoms were estimated that the Mulliken charge of phenoxo oxygen was larger than those of nitrate and methoxo oxygen atoms about twice in magnitude. The introduction of the phenoxo ligand on the Tb(III) ion at the opposite position from bridging phenoxo oxygens, which was found in **4**, would be effective to realize the uni-axial arrangement of negative charges, which also might enhance the easy-axis anisotropy of Tb(III) ion.

In conclusion, we have synthesized two Tb–Cu di-nuclear complexes both behaving as SMMs, to discuss the relationship between coordination morphology and the magnetic anisotropy. Tb(III) in **3** is in a more unsymmetrical crystal field compared with **1**, and as a result, **3** possesses higher barrier Δ/k_B compared with **1**. Tb(III) ion in **4** is located in an axial crystal field formed by two phenoxo oxygen atoms from $\mathbf{L3}^{2-}$ and one *o*-vanilate oxygen atom located on opposite sites around Tb(III) ion, and **4** showed large Δ/k_B. The larger Δ/k_B values can be explained by the enhancement of the easy-axis anisotropy of Tb(III) in a less symmetrical coordination (**3**) or uni-axial crystal field (**4**). The results here provide a useful guideline for designing the magnetic anisotropy of lanthanide ions, yielding novel SMM and single-chain magnet (SCM) families.

Supplementary data

CCDC 702761 and 702762 contains the supplementary crystallographic data for this paper. These data can be obtained free of charge via http://www.ccdc.cam.ac.uk/conts/retrieving.html, or from the Cambridge Crystallographic Data Centre, 12 Union Road, Cambridge CB2 1EZ, UK; fax: (+44) 1223-336-033; or e-mail: deposit@ccdc.cam.ac.uk.

Acknowledgment

This work was supported by a Grant-in-Aid for Scientific Research of Priority Areas (Area No. 440) from the Ministry of Education, Culture, Science, Sports, and Technology, Japan.

References

[1] (a) D. Gatteschi, R. Sessoli, Angew. Chem., Int. Ed. 42 (2003) 268;
(b) W. Wernsdorfer, R. Sessoli, Science 284 (1999) 133;
(c) S.M.J. Aubin, Z. Sun, L. Pardi, J. Krzystek, K. Folting, L.-C. Brunel, A.L. Rheingold, G. Christou, D.N. Hendrickson, Inorg. Chem. 38 (1999) 5329;
(d) L. Thomas, F. Lionti, R. Ballou, D. Gatteschi, R. Sessoli, B. Barbara, Nature 383 (1996) 145.
[2] S.J. Blundell, F.L. Pratt, T. Lancaster, I.M. Marshall, C.A. Steer, W. Hayes, T. Sugano, J.-F. Letard, A. Caneschi, D. Gatteschi, S.L. Heath, Physica B 326 (2003) 556.
[3] (a) K. Takeda, K. Awaga, S. Ohira, I. Watanabe, Synth. Met. 133–134 (2003) 609;
(b) A. Lascialfari, D. Gatteschi, F. Borsa, A. Shastri, Z.H. Jang, P. Carretta, Phys. Rev. B 57 (1998) 514.
[4] (a) S. Osa, T. Kido, N. Matsumoto, N. Re, A. Pochaba, J. Mronzinski, J. Am. Chem. Soc. 126 (2004) 420;
(b) C.M. Zaleski, E.C. Depperman, J.W. Kampf, M.L. Kirk, V. Pecoraro, Angew. Chem., Int. Ed. 43 (2004) 3912;
(c) A. Mishra, W. Wernsdorfer, K.A. Abboud, G. Christou, J. Am. Chem. Soc. 126 (2004) 15648;
(d) C. Aronica, G. Pilet, G. Chastanet, W. Wernsdorfer, J. -F. Jacquot, D. Luneau, Angew. Chem., Int. Ed. 45 (2006) 4659;
(e) F. Mori, T. Nyui, T. Ishida, T. Nogami, K.-Y. Choi, H. Nojiri, J. Am. Chem. Soc. 128 (2006) 1440;
(f) J.-P. Costes, F. Dahan, W. Wernsdorfer, Inorg. Chem. 45 (2006) 5;
(g) J.-P. Costes, M. Auchel, F. Dahan, V. Peyrou, S. Shova, W. Wernsdorfer, Inorg. Chem. 45 (2006) 1924;
(h) S. Ueki, T. Ishida, T. Nogami, K.-Y. Choi, H. Nojiri, Chem. Phys. Lett. 440 (2007) 263.
[5] (a) N. Ishikawa, M. Sugita, T. Ishikawa, S. Koshihara, Y. Kaizu, J. Am. Chem. Soc. 125 (2003) 8694;
(b) J. Tang, I. Hewitt, N.T. Madhu, G. Chastanet, W. Wernsdorfer, C.E. Anson, C. Benelli, R. Sessoli, A.K. Powell, Angew. Chem., Int. Ed. 45 (2006) 1729.
[6] V. Chandrasekhar, B.M. Pandian, R. Azhakar, J.J. Vittal, R. Clérac, Inorg. Chem. 46 (2007) 5140.
[7] D. Schmitt, J. Phys. 47 (1986) 677.
[8] T. Kajiwara, M. Nakano, S. Takaishi, M. Yamashita, Inorg. Chem. 47 (2008) 8604.
[9] J.-P. Costes, F. Dahan, A. Dupuis, J.-P. Laurent, Inorg. Chem. 36 (1997) 3429.

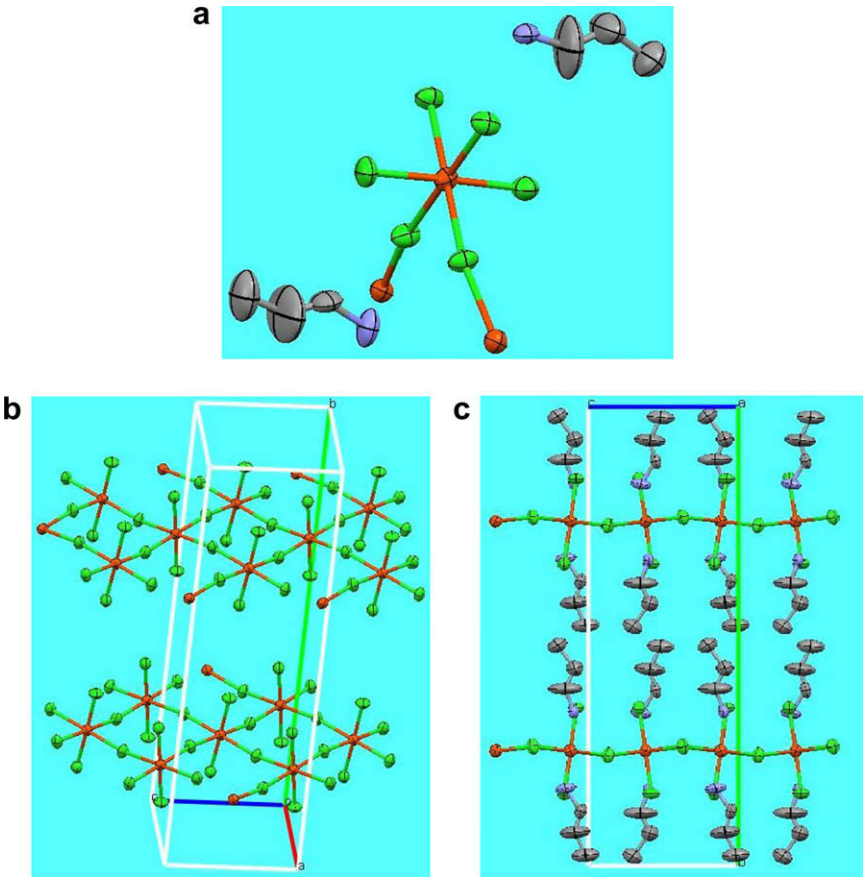


Fig. 1. Crystal structure of $(C_3)_2$–$FeCl_4$ showing, (a) asymmetric unit; (b) inorganic 2D network of $FeCl_4$ octahedra along *ac*-plane and (c) intercalation of organic ammonium salt in inorganic layers.

$b = 7.439(9)$ Å, $c = 25.303(8)$ Å with unit cell volume of 1359.95 cm^3, at room temperature. The structure parameters were refined with least square process to $R_1 = 0.067$. The overall structure consists of two-dimensional Fe(II)–chloride network, parallel to the *ac*-plane, interlayered by the ammonium ions with mirror plane perpendicular to the *a*-axis. The principal feature of interest in these structures is the Fe(II)–chloride layer as illustrated in Fig. 1b. In the layer, Fe–Cl distances (the four bridging chlorine atoms) are longer (2.587, 2.618 Å) than the two terminal Fe–Cl (2.364 Å) distances making compressed octahedral geometry around metal ions. Each octahedron shares four corners with neighboring octahedron in the layer to form a square 2D sheet. The Fe(II) ions occupy $2/m$ symmetry. The Fe–Cl–Fe bridges are symmetrical, but, as it is readily seen in Fig. 1, the bridging Fe–Cl–Fe angle (169.74°) is not linear. Therefore, the octahedra are alternately tipped forward and backward to produce the familiar puckering of the layer.

Each ammonium hydrogen atom participates in hydrogen bond to the chlorine atom in Fe–Cl layer. This not only ties down the NH_3^+ groups, for smaller liberational motion than the rest of ions, but possibly helps in puckering, that means altering Fe–Cl–Fe angle. Though, the latter effect looks smaller, it may have significant effect upon the interlayer exchange coupling since superexchange arguments predict the strength of the magnetic interaction should be dependent on the Fe–Cl–Fe bond angle. Thus, because of presence of stronger hydrogen bonding network N–H···Cl, there is virtually no contact between adjacent cations in the structure and it can be viewed as organic–inorganic hybrid layered structure.

The magnetic susceptibilities for both the compounds (both in single crystal and bulk form) were measured using SQUID magnetometer, in the 5–300 K range. Fig. 2a shows, representative temperature dependence of χT {zero-field cooled (ZFC) and field cooled (FC)} versus temperature measured at 10 and 1000 Oe for $(C_4)_2$–$FeCl_4$. The $\chi_{mol}T$ value, at 300 K was found out to be 2.5 emu K mol^{-1} (less than expected 3.0 emu K mol^{-1}, for high spin Fe^{2+} ions) decreases with decreasing temperature down to a minimum value of 1.1 emu K mol^{-1} at around 90 K. Upon further cooling $\chi_{mol}T$ value increases to a rounded maximum at about 90 K and then decreases on further cooling. Both compounds show similar behavior, where these features indicate a global antiferromagntic interaction. While, in the ZFC–FC magnetization measurements carried out with an applied field of 500 Oe as shown in Fig. 2b, we observed the onset of long range magnetic ordering below ~90 K.

Fig. 2c represents $M(H)$ curve taken at 85 K, on increasing the field from zero, we observed initial steep increase in the magnetization in a low field region, to a value much smaller than full Fe(II) moment. Subsequently, linear field dependence is found till 50 kOe. This behavior is of typical weak ferromagnet, where the steep increase at low H reflects spontaneous magnetization and the linear high-field behavior is due to the dominant antiferromagntic interactions. Large coercive field (3 kOe) classifies this compound as a hard magnet. Along with this, high remnant magnetization, $0.56\mu_B$ (corresponds to 11.53% canting) makes it among largest canted weak ferromagnets, which might be due to the competition between the local anisotropy vis-a-vis the antiferromagntic interaction [15].

We carried out some preliminary experiments on temperature dependence of AC-dielectric property using AG 4311B, Ando instrument, in the range 150–450 K. Fig. 3 shows permittivity

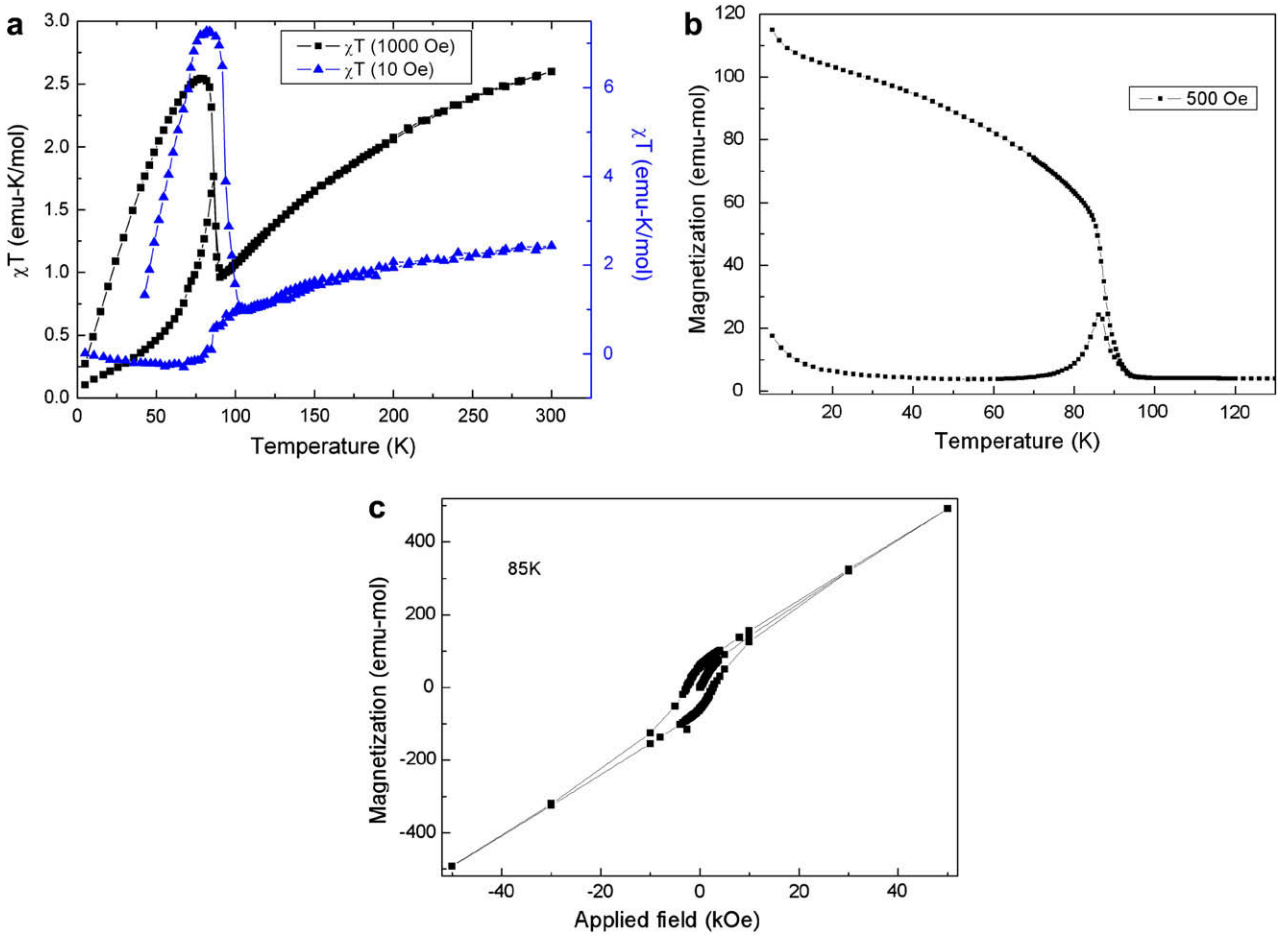


Fig. 2. Temperature dependent magnetic measurements on $(C_4)_2$–$FeCl_4$ (a) field dependent χT, (b) zero-field cooled–field cooled magnetization carried out at 500 Oe and (c) hysteresis taken at 85 K.

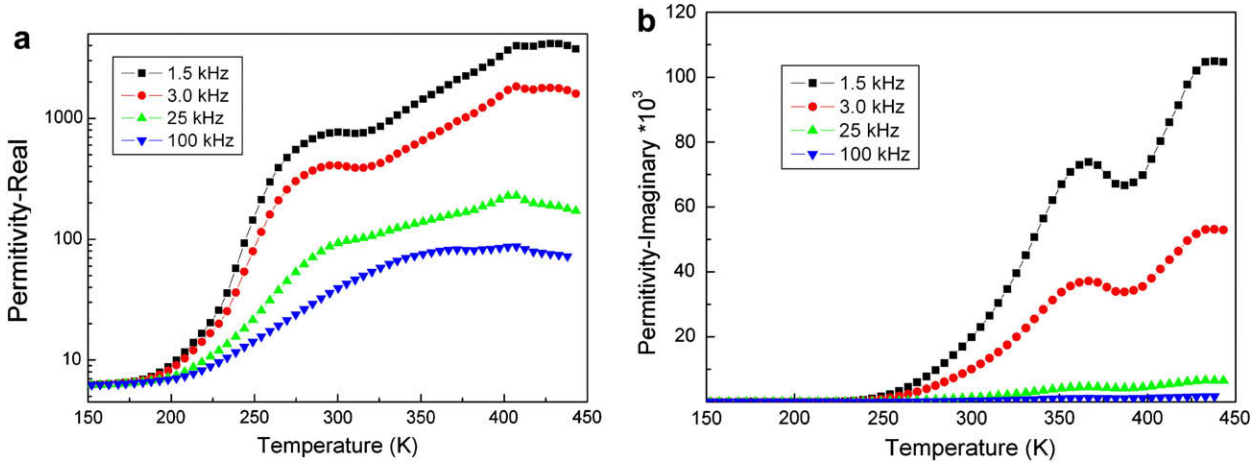


Fig. 3. Temperature dependent (a) real and (b) imaginary parts of the complex electric permittivity measured on polycrystalline $(C_4)_2FeCl_4$ at different frequencies.

versus temperature plot, for selected frequencies 1.5, 3.0, 25, 100 KHz, for $(C_4)_2FeCl_4$ compound. Both, imaginary as well as real permittivity show continuous increase of permittivity with increase in temperature, with a big hump around 300 K and a broad peak around 430 K. It is also clear that at higher temperature permittivity is frequency dependent. More detailed analysis is under investigation to understand the origin of the peak due to water absorption–desorption process, because of the moisture/water sensitive nature of the compounds [4,16]. DSC measurements carried out on $(C_4)_2FeCl_4$ have shown presence of reversible peak,

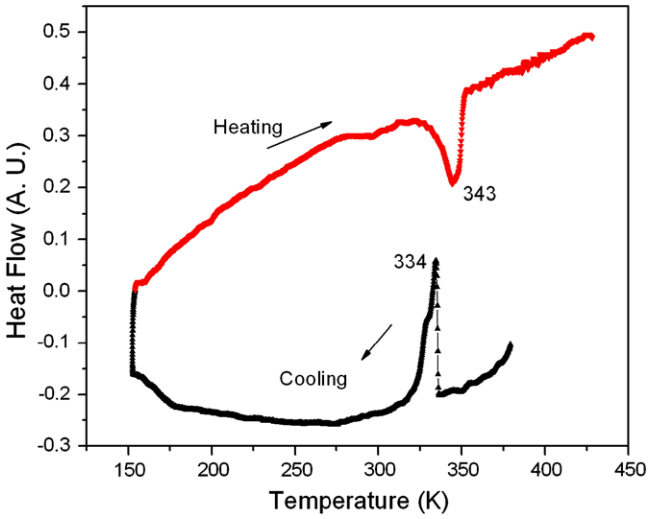


Fig. 4. DSC measurements on $(C_4)_2FeCl_4$.

indicating phase transition around 350 K, with a small hysteretic behavior (see Fig. 4). To confirm our findings, we carried out conductivity and DSC measurements on $(C_2)_2FeCl_4$, which is studied in literature [13] for, its ferroelastic behavior below 320 K and, they have been predicted ferro or antiferroelectric behavior below 200 K. $(C_2)_2FeCl_4$ showed a phase transition at 200 K, similar to observed for $(C_4)_2FeCl_4$ at 350 K using DSC. Single crystal study at various temperatures were carried out, but due to the very thin plate like nature of crystals, structure determinations became difficult, but no apparent phase transition is observed at lower temperature as is for $(C_2)_2FeCl_4$. In short, the obtained relative permittivity and DSC data can be explained by proposing a ferro or antiferroelectric state below 350 K, triggered due to electronic, ionic and/or deformational polarization. There is also possibility that these compounds are ferroelastic above RT. More detailed studies are going on to understand this behavior.

In summary, we have succeeded in synthesizing a new family of layered organic–inorganic hybrid weak ferromagnets with a ferro or antiferroelectric behavior. All of these compounds form plate like transparent, yellow-orange colored single crystalline products, and have thus imparting added advantage for magneto-optical behavior [17,18]. More studies using single crystals are in progress to understand role played by the alkyl ammonium compounds, especially in the driving asymmetric structure by the use of non-covalent interactions. For this reason we are also working on chiral ammonium salts [19,20]. Thus, a new route is opened to synthesize novel multiferroic materials in the form of layered structure.

Supplementary data

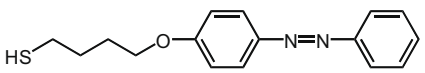
Crystal structure of $C_6H_{20}Cl_4N_2Fe$, $M = 316$, orthorhombic, space group $Cmc2_1$, $a = 7.223(9)$ Å, $b = 7.439(9)$ Å, $c = 25.303(8)$ Å, $V = 1359.95$ cm^3, $\lambda = 0.71609$ Å, a total of 6321 reflections were collected, and 2080 were unique. R_1 and wR are 0.067, and 0.1829, respectively. Crystallographic coordinates and analysis summary in CIF format have been deposited with the Cambridge Crystallographic Database center (CCDC). Its reference number is CCDC 721801. These data can be obtained free of charge via http://www.ccdc.cam.ac.uk/conts/retrieving.html, or from the Cambridge Crystallographic Data Centre, 12 Union Road, Cambridge CB2 1EZ, UK; fax: (+44) 1223-336-033; or e-mail: deposit@ccdc.cam.ac.uk.

Acknowledgements

PSG acknowledges the funding for research from SERC-DST, FAST TRACK proposals for young Scientist, India (SR/FTP/CS/25/2006). Authors acknowledge Grant-in-Aid for Scientific Research (B) (No. 15340124) from the Ministry of Education, Science, Sports and Culture. Single crystal structure is solved with the help of Dr. Motoko Akita and Mr. Yusuke Yoshida. Authors also thank Prof. T. Suzuki for helpful discussions.

References

[1] N.A. Spaldin, M. Fiebig, Science 309 (2005) 391.
[2] A.A. Belik, S. Iikubo, K. Kodama, N. Igawa, S. Shamoto, M. Maie, T. Nagai, Y. Matsui, J. Am. Chem. Soc. 128 (2006) 706.
[3] N.A. Hill, A. Filippetti, J. Phys. Chem. B 104 (2000) 6694.
[4] P. Jain, N.S. Dalal, B.H. Toby, H.W. Kroto, A.K. Cheetham, J. Am. Chem. Soc. 130 (2008) 10450.
[5] D.B. Mitzi, Prog. Inorg. Chem. 48 (1999) 1.
[6] R.D. Willet, C.J. Gomez-Garcia, B. Twamley, Polyhedron 24 (2005) 2293.
[7] H. Manaka, I. Yamada, M. Nishi, T. Goto, J. Phys. Soc. Jpn. 70 (2001) 241.7.
[8] M. Kurmoo, Chem. Mater. 11 (1999) 3370.
[9] V. Laget, C. Hornick, P. Rabu, M. Drillon, R. Ziessel, Coord. Chem. Rev. 178–180 (Pt. 2) (1988) 1533.
[10] J. Hemberger, P. Lunkenheimer, R. Fichtl, H.-A. Krug von Nidda, V. Tsurkan, A. Loidl, Nature 434 (2005) 364.
[11] T. Suzuki, M. Yoshizawa, T. Goto, T. Yamakami, M. Takahashi, T. Fujimura, J. Phys. Soc. Jpn. 52 (1983) 1669.
[12] M. Yoshizawa, T. Suzuki, T. Goto, T. Yamakami, T. Fujimura, T. Nakajima, H. Yamauchi, J. Phys. Soc. Jpn. 53 (1984) 261.
[13] A. Yoshihara, T. Suzuki, T. Yamakami, T. Fujimura, J. Phys. Soc. Jpn. 54 (1985) 3376.
[14] R.D. Willet, E.F. Riedel, Phys. Rev. B 4 (1971) 2213.
[15] R. Feyerherm, A. Loose, T. Ishida, T. Nogami, J. Kreitlow, D. Baabe, F.J. Litterst, S. Sullow, H.-H. Klauss, K. Doll, Phys. Rev. B 69 (2004) 134427.
[16] Y. Yoshida, K. Inoue, M. Kurmoo, Inorg. Chem. 48 (2009) 267.
[17] P. Day, Acc. Chem. Res. 12 (1979) 236.
[18] K. Sawada, N. Nagaosa, Phys. Rev. Lett. 95 (2005) 237402.
[19] J. Kishine, K. Inoue, Y. Yoshida, Prog. Theor. Phys. 159 (2005) 82.
[20] K. Inoue, H. Imai, P. Ghalsasi, K. Kikuchi, M. Ohba, H. Okawa, J.V. Yakhmi, Angew. Chem., Int. Ed. Engl. 40 (2001) 4242.



AZ

2.2. Synthesis of AZ–Au NPs (AZ-passivated gold nanoparticles)

AZ–Au NPs were synthesized by a process based on the Brust method [13] with two different Au/S ratios. An Au/S ratio of 1:2 was used to synthesize relatively smaller AZ–Au NPs while an Au/S ratio of 2:1 was used for relatively larger AZ–Au NPs. The detailed procedure is as follows. An aqueous solution of hydrogentetrachloroaurate(III)hydrate (9 mg, 0.00228 mmol) was added dropwise to a stirred solution of tetraoctylammonium bromide (0.056 g, 0.102 mmol) in 5 mL toluene. AZ (7.1 mg, 0.0228 mmol or 1.5 mg, 0.0057 mmol) in 2 mL toluene was added to the above solution. After 1 h, an aqueous solution of sodium borohydride (9 mg, 0.23 mmol) was added dropwise and stirred for a further 3 h. The toluene phase was collected and suspended in methanol (100 mL). It was kept in a refrigerator overnight. This was centrifuged at 8000 rpm for 30 min at ambient temperature and the supernatant liquid was discarded. The precipitate that was obtained was again dispersed in methanol and the process was repeated three times to remove any unbound AZ.

2.3. Physical methods

The UV–Vis absorption spectra were recorded on a V-560 spectrometer (JASCO). UV illumination (filtered light, λ_{max} = 360 nm, 1.0 mW cm^{-2}) was applied with an ultra-high pressure mercury lamp (HYPERCURE 200, Yamashita Denso). Visible light (400–700 nm, 1.0 mW cm^{-2}) was provided by a xenon lamp (XFL-300, Yamashita Denso). The XPS spectra were obtained on a JPS-9000MC (JEOL) using an Al Kα line source. The X-ray diffraction patterns were recorded on a RAD-C (RIGAKU) using Ni-filtered Cu Kα radiation. The XANES were recorded using a spectrometer installed in BL39XU at the SPring-8 Synchrotron Radiation Facilities. The magnetic properties were investigated with a SQUID magnetometer (model MPMS-XL Quantum Design). The lamps were guided into the SQUID magnetometer by an optical fiber to study the photo-magnetic effects. Measurements of the work function were performed in KFM mode with a SPM-9600 (Shimadzu).

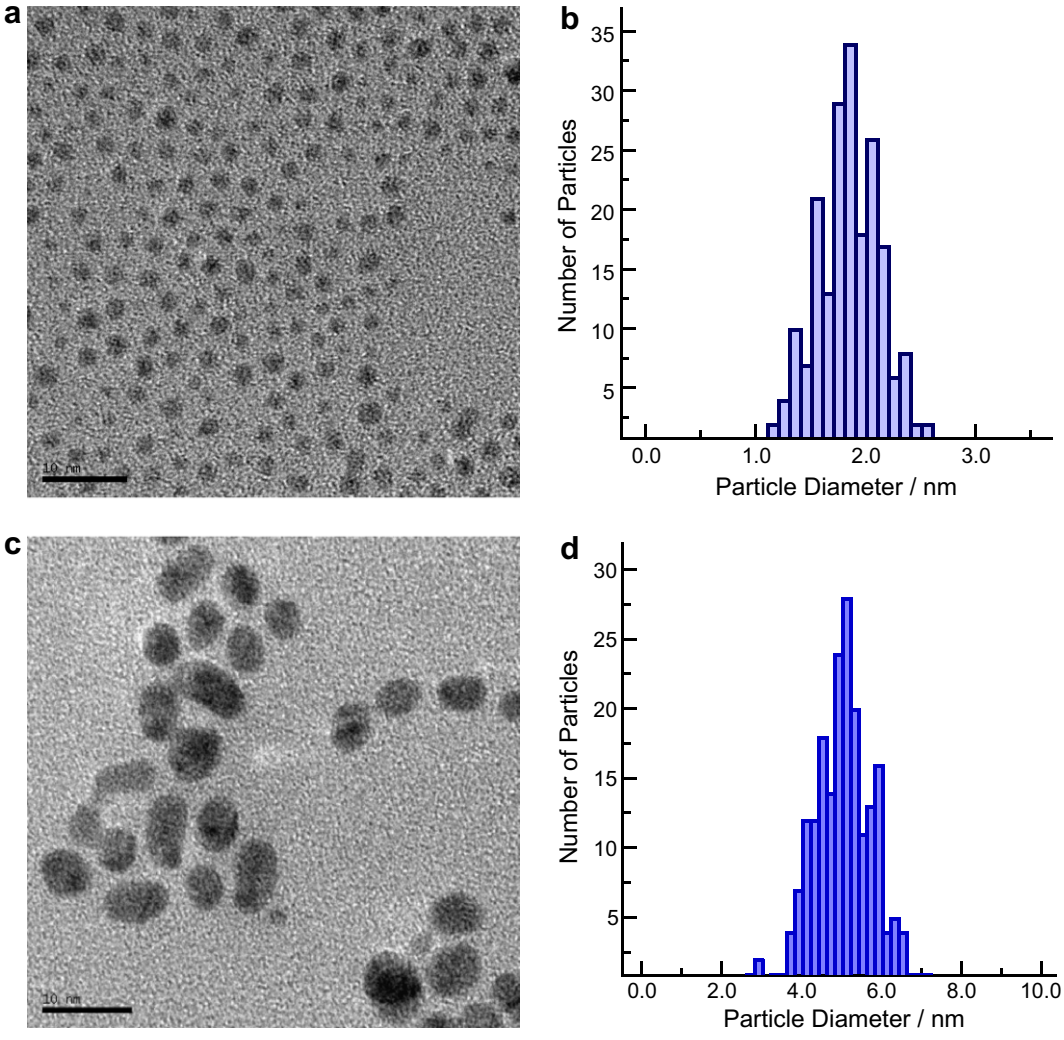


Fig. 1. (a) TEM micrograph and (b) size distribution histogram of AZ–Au NPs synthesized with an Au/S ratio of 1:2. (c) TEM micrograph and (d) size distribution histogram of AZ–Au NPs synthesized with an Au/S ratio of 2:1; scale bar = 10 nm.

3. Results and discussion

3.1. Basic characterization of AZ–Au NPs

Fig. 1 shows TEM images and size distribution histograms for the AZ-passivated gold nanoparticles (AZ–Au NPs) synthesized with Au/S ratio of 1:2 and with Au/S ratio of 2:1 deposited from a toluene dispersion onto a collodion coated copper grid. The AZ–Au NPs synthesized with Au/S ratio of 1:2 present a narrow size distribution with an average size of 1.7 nm ± 0.3 nm while the AZ–Au NPs synthesized with Au/S ratio of 2:1 present a relatively larger average size of 5.0 nm ± 0.8 nm. Here after each average size of AZ–Au NPs is denoted as AZ–Au NPs 1.7 and AZ–Au NPs 5.0, respectively. The reason of anisotropic shapes of AZ–Au NPs 5.0 is not clear at present. However, the percentage of the "odd" shapes nanoparticles is not substantial. Hence, the presence of anisotropic shapes particles would not be a big problem for following discussion.

The powder X-ray diffraction pattern of each AZ–Au NPs (Fig. 2) is consistent with a face-centered cubic crystal structure for the Au, with lattice constant $a = 2.33$ Å. The average particle size determined from the instrument corrected width β using the Scherrer relation: $D = K\lambda/\beta\cos\theta$ is 1.8 nm for AZ–Au NPs 1.7 and 5.2 nm for AZ–Au NPs 5.0 nm, which were in good agreement with the results from the TEM studies.

Fig. 3 shows the XANES spectra of the Au L_3-edge for the AZ–Au NPs 1.7 nm, AZ–Au NPs 5.0 nm and bulk-Au (foil). Typical XANES spectra of an fcc gold structure exhibit patterns with three peaks within the first 40 eV above the edge. The first resonance at the threshold associated with $2p_{3/2}$ to $5d_{5/2}$, $_{3/2}$ dipole transitions probes the density of the unoccupied d states (d-hole counts) at the Fermi level [14]. Although the 5d orbitals of bulk-Au are nominally full, a small concentration of itinerant holes at the d band can be detected in the XANES spectra of bulk-Au due to s–p–d level hybridization. In the case of the AZ–Au NPs 5.0, a small increase in the threshold resonance was detected when compared to the bulk-Au, indicating a little loss in 5d electron density due to d-charge transfer from the gold to the sulfur atoms. Furthermore, in the case of the AZ–Au NPs, the threshold resonance was significantly increased even when compared to the AZ–Au NPs 5.0, indicating the increase in specific surface area due to the size reduction that introduced a noticeable loss in 5d electron density.

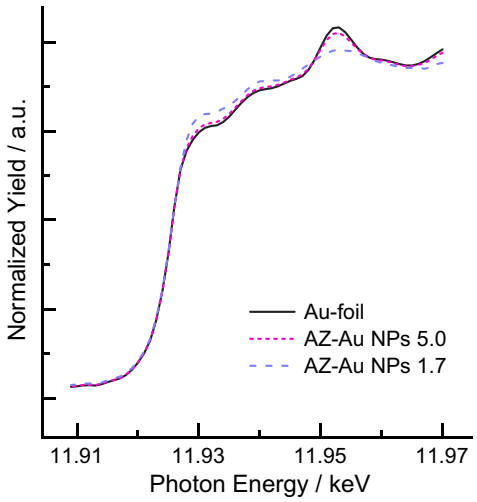


Fig. 3. Au L_3-edge XANES spectra for the AZ–Au NPs 1.7 (dashed line), the AZ–Au NPs 5.0 (dotted line) and gold foil (solid line).

3.2. Magnetic properties of AZ–Au NPs

The magnetization curves (M–H plots) measured at 300 K for AZ–Au NPs 5.0 and AZ–Au NPs 1.7 are shown in Fig. 4. The AZ–Au NPs 5.0 exhibit a diamagnetic behavior, similar to that of bulk gold (not shown here). On the other hand, typical hysteresis loops with coercivity (H_c) and remanent magnetization (M_r) were observed for AZ–Au NPs. The values of H_c and M_r were 100 G and 0.031 emu g_{Au}^{-1} at 300 K.

3.3. Optical absorption spectra of AZ–Au NPs

The photoisomerization of the AZ–Au NPs 5.0 and the AZ–Au NPs 1.7 in the solid state at room temperature were monitored by UV–Vis absorption spectroscopy (Fig. 5). Each spectrum of the initial state gave an intense absorption peak at 360 nm, which is ascribed to the π–π^* transition in the trans-isomer of the AZ ligands. After UV illumination of the AZ–Au NPs 5.0 for 1 min, the absorption at 360 nm decreased, suggesting the trans-to-cis photoisomerization of AZ occurred. Following subsequent illumi-

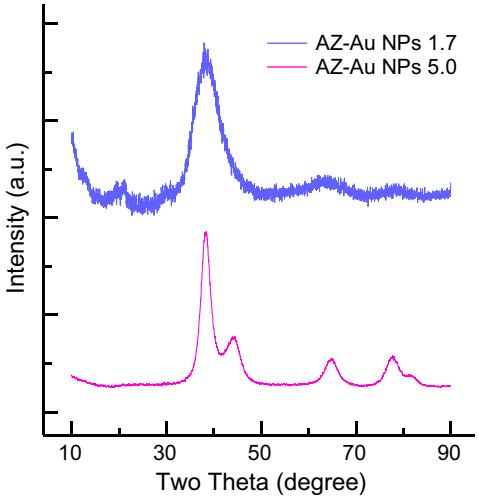


Fig. 2. XRD pattern for the AZ–Au NPs 1.7 (top line) and for the AZ–Au NPs 5.0 (bottom line).

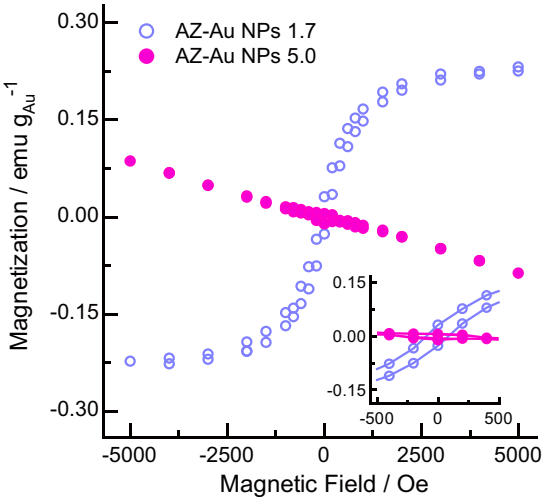


Fig. 4. Plot of magnetization M vs. applied magnetic field H at 300 K for the AZ–Au NPs 1.7 (open circles) and the AZ–Au NPs 5.0 (closed circles).

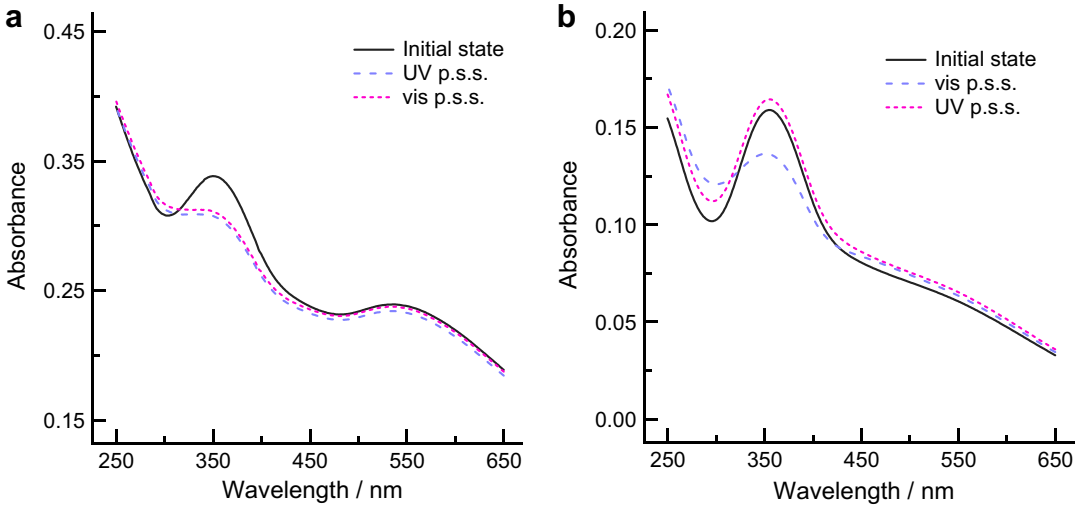


Fig. 5. Changes in the optical absorption spectra for the AZ–Au NPs 5.0 (a) and the AZ–Au NPs 1.7 (b) due to photoisomerization. The initial trans-state (solid line) was first illuminated with UV light for 1 min (dashed line). It was then illuminated with visible light for 1 min (solid line).

nation with visible light, the absorption at 360 nm showed almost no spectral changes, suggesting the cis-to-trans photoisomerization did not occur.

In the case of the AZ–Au NPs 1.7, the absorption at 360 nm also decreased after UV illumination of the trans-isomer for 1 min. Following subsequent illumination with visible light, the absorption at 360 nm increased again. After the second cycle, the cis-trans photoisomerization was repeated without any attenuation of the area between the curves. These reversible spectral changes indicate high-efficiency reversible photoisomerization, even in the solid state.

Normally, photoisomerization of azobenzene-containing compounds does not occur in the solid state because of the large volume changes that are involved [15]. In fact, reversible photoisomerization also does not occur in the absence of spacers when azobenzene-containing ligands are self-assembled on two-dimensional gold films [16]. The same tendency was also reported for azobenzen-passivated gold nanoparticles with average particle size of ca. 5.0 nm [17], that is consistent with observed phenomena for AZ–Au NPs 5.0. However, in the current system with its average particles diameter of 1.7 nm, reversible photoisomerization was observed in the solid state with high efficiency.

From the above observations, it is proposed that the decrease in particle size provided free volume between each of the AZ ligands because the adjacent angles between two neighboring AZ ligands would be increased with decreasing particle size. The average distance between two neighboring nitrogen double bonds on the AZ ligands could be estimated as 7.7 Å for the AZ–Au NPs 5.0, while it was 13.0 Å for the AZ–Au NPs 1.7. Fig. 6 shows a schematic illustration (not to scale) of geometric framework for the AZ–Au NPs 5.0 and the AZ–Au NPs 1.7.

Another important remark concerning the optical absorption spectra of AZ–Au NPs 1.7 (Fig. 5b) is almost no surface plasmon resonance around 550 nm despite the observation of significant surface plasmon resonance for the AZ–Au NPs 5.0, indicating the strong Au–S interactions make the 5d electrons of the core gold nanoparticles behave as partially-localized holes that have lost itinerancy [7a,14], because of the high-specific surface area for AZ–Au NPs 1.7.

The above observations are consistent with the observed d-charge transfer derived from the results of the XANES measurements and the observed ferromagnetism from the SQUID measurements. After all, reducing the particle size to 1.7 nm enhances not only the magnetic properties, but also the photo-responsibilities of the AZ–Au NPs.

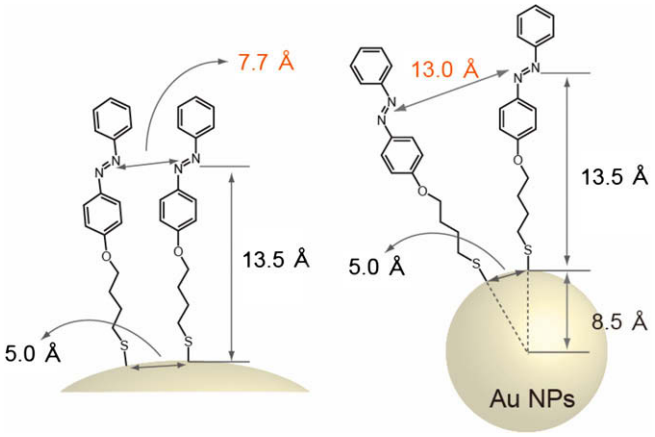


Fig. 6. Schematic illustrations (not to scale) of geometric framework for the AZ–Au NPs 5.0 (left) and the AZ–Au NPs 1.7 (right).

3.4. Photo-magnetic effects

Subsequently, we investigated the influence of photo-illumination on the magnetic properties of AZ–Au NPs 1.7 at 300 K (Fig. 7). During the UV illumination, the initial magnetization value under an applied field of 5 T decreased from 0.24 to 0.18 emu g_{Au}^{-1}. Even after the illumination was stopped, the decreased magnetization value was maintained for several hours at room temperature. The very slow recovery of the magnetization could be due to the cis-to-trans thermal back-isomerization of the AZ. We then illuminated AZ–Au NPs 1.7 with visible light, and the magnetization value increased from 0.18 to 0.24 emu g_{Au}^{-1}. After this process, the UV light-induced decrease and the visible light-induced increase in magnetization were repeated without any attenuation. The photo-induced changes in the magnetization values were estimated to be ca. 27%. We also observed such photo-induced magnetic transitions in field cooled magnetization curves for AZ–Au NPs 1.7 with external magnetic field of 5 T.

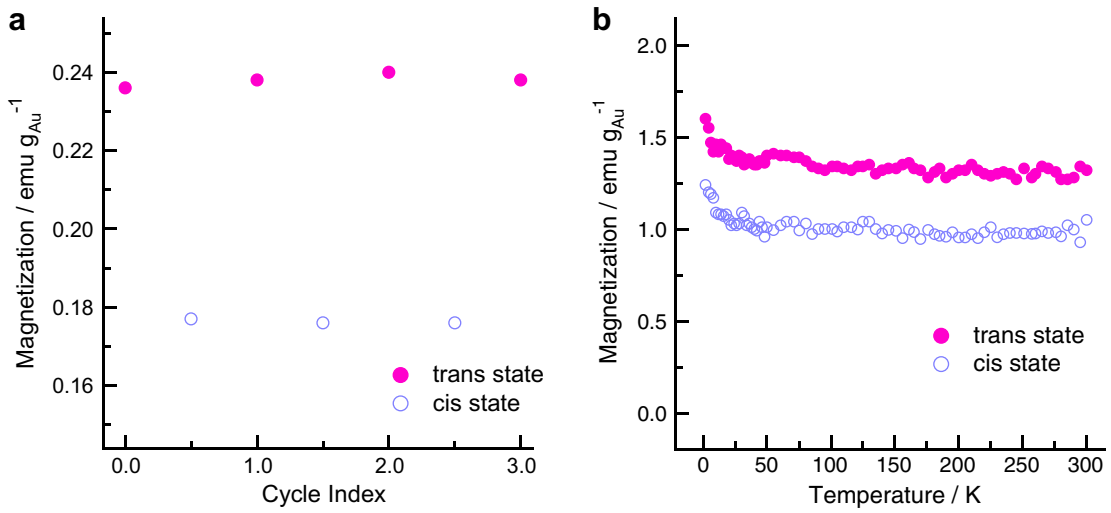


Fig. 7. (a) Changes in magnetization by photo-illumination at 300 K; AZ–Au NPs 1.7 were alternately illuminated with UV and visible light for 1 min each at 300 K under an external magnetic field of 5 T. (b) Changes in the field cooled magnetization curves by photo-illumination under the external magnetic field of 5 T; Plot of magnetization M vs. applied temperature T for trans-state (closed circles) and for cis-state (open circles).

We must mention that the observed photo-induced magnetic transition undoubtedly originated from the reversible photoisomerization of AZ. It might be argued that the observed behavior could be due to physical effects during photo-illumination, such as thermal effects or structural changes of the core-particles. Our comparative experiments show that gold nanoparticles coated with dodecanethiol (non-azo-ligands) did not show any photo-induced magnetic transitions, despite showing almost the same magnetic properties. Hence, the reversible photoisomerization of AZ was the origin of the observed phenomena.

3.5. Origin of photo-magnetic effects

As mentioned above, in AZ–Au NPs, the apparent ferromagnetism is associated with 5d localized holes in the 5d shell generated through Au–S bonding. The magnetic ordering is not due to the large exchange interaction, but rather is due to extremely high local magnetic anisotropy (estimated to be as high as 1×10^8 ergs cm^{-3}) which blocks the moments from switching, resulting in very high T_B in Au NPs [7a]. Hence, the observed photo-magnetic effects are not due to the changes in magnetic exchange interaction, but rather are due to the changes in absolute quantity of the magnetic moments. From the saturated magnetization value of the AZ–Au NPs under applied field of 5 T, the values of the magnetic moment per Au atom bound to sulfur in the trans-state and the cis-state are estimated to be 0.033 μ_B and 0.024 μ_B, respectively, where μ_B represents the Bohr magnetron. In a recent report concerning an XMCD (X-ray magnetic circular dichroism) study of thilated gold clusters, a considerable orbital magnetic moment of the Au 5d electrons was indicated, and the ratio of the orbital to the spin magnetic moment was estimated to be 12% [7b]. Therefore, the lower limit value of the d-hole counts per Au atom bound to sulfur in the trans-state and the cis-state are estimated as to be ca. 0.0039 e atom^{-1} and ca. 0.0027 e atom^{-1}, respectively. This result clearly suggests that the d-charge loss of ca. 0.0012 e atom^{-1} was decreased in the case of the cis-state. That is, the charge transfer from Au to S could be reversed with trans-to-cis photoisomerization.

These phenomena are also consistent with the reported cooperative effect of organic molecules in the electron transfer between a metal substrate and organic layers. In such organic–inorganic interfaces, charge transfer acts to reduce the dipole–dipole interaction between molecules but may either decrease or increase the molecules-to-surface dipole moment. The change in the work function is related to the dipole moment density perpendicular to the surface through the following relationship [11]:

$$\Delta\Phi = \frac{\mu N \cos\theta}{\varepsilon\varepsilon_0}$$

where N is the surface density of dipoles, μ is the effective dipole moment of the molecule, ε_0 is the permittivity of a vacuum, ε is the dielectric constant of the layer, and θ is the tilt angle of the molecule with respect to the surface normal.

In other words, the magnitude of the electron transfer to the organic layer becomes smaller for adsorbates with electro-negative end groups, while it becomes larger for adsorbates with electro-positive end groups. In fact, experimental evidence for such changes in the magnitude of the electron transfer from gold to the adsorbates has been reported previously [18].

In the current system, the values of $\mu\cos\theta$ for the AZ were calculated as −0.24 D (D = Debye) for the trans-state and 2.74 D for

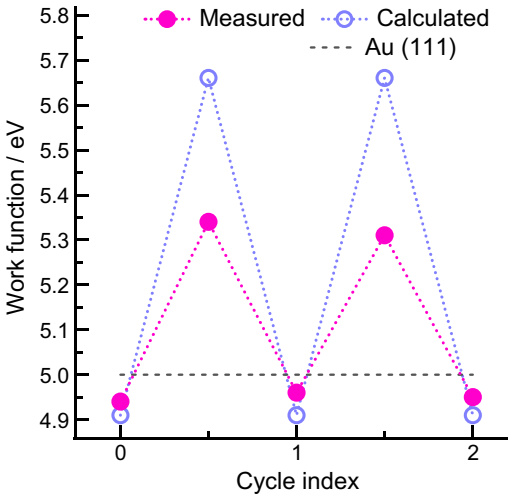


Fig. 8. Changes in work function values of the AZ–Au NPs 1.7 due to photoisomerization for the measured values (closed circles), the calculated values (open circles) and the known values for Au (1 1 1) (dashed line).

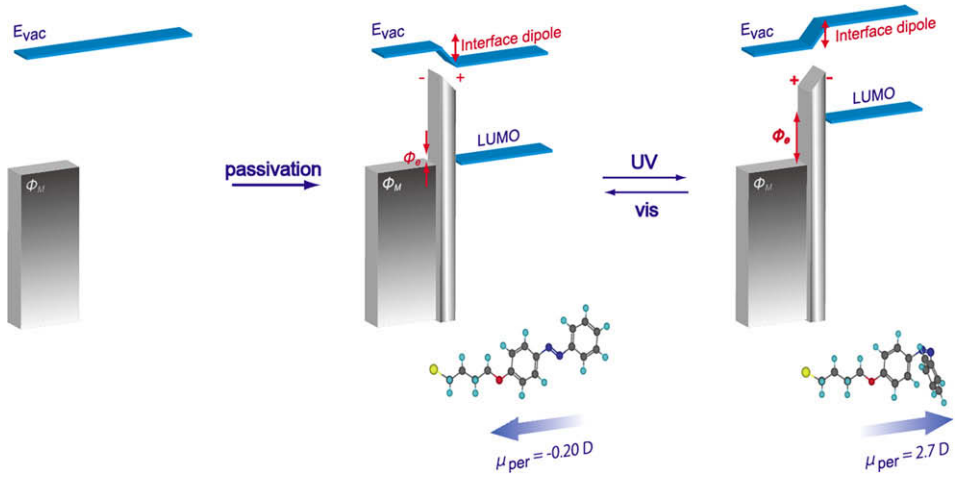


Fig. 9. Schematic illustrations of changes in the work function due to the photoisomerization. Left: schematic energy level diagrams for an untreated interface (without surface passivation). Middle: passivation of trans-AZ imposes an interface dipole that decreases local vacuum energy level (E_{vac}). Right: photoisomerization to cis-AZ imposes an interface dipole that increases local vacuum energy level (E_{vac}).

the cis-state, meaning that the sign of the work function change would be negative for the trans-state and positive for the cis-state (The $\mu\cos\theta$ values of AZ for the trans-state and cis-state were calculated with MOPAC/PM3 geometry. The tilt angles were taken to be 30° for both trans-state and cis-state according to the reported value [19,20]). Hence, the magnitude of electron transfer in the initial trans-state becomes smaller in the cis-state under UV light illumination, and it recovers to its initial value under visible light illumination. To elucidate this, we investigated the influence of photo-illumination on the work function value of the AZ–Au NPs 1.7 by means of Kervin probe analysis (Fig. 8). During the UV illumination, the initial work function value 4.94 eV of the AZ–Au NPs 1.7 increased to 5.34 eV, which were qualitatively in good agreement with the work function values calculated from the surface dipole value. The differences between the measured values and the calculated values observed especially in cis-state might be originated from the relatively disordered orientation of cis-AZ because of their larger volume. We then illuminated the AZ–Au NPs 1.7 with visible light, and the work function value decreased to near the value with initial state. After this process, the UV light-induced decrease and the visible light-induced increase in work function were repeated without any attenuation. These observations have provided clear evidence that the work function value of the AZ–Au NPs 1.7 can be effectively controlled with photoisomerization by employing alternating photo-illumination with UV and visible light. Schematic illustrations of the changes in the work function due to the photoisomerization of AZ are shown in Fig. 9. As a consequence, the magnetization value at Au–S interface could be controlled by employing alternating photo-illumination with UV and visible light, and are caused by changes in the d-charge loss due to the work function change with photoisomerization.

4. Conclusions

In conclusion, we have designed azobenzene-thiol-passivated gold nanoparticles with different sizes. In these systems, we have observed that size-reduction to 1.7 nm induced ferromagnetism even at room temperature, while diamagnetism was dominating with the particle size of 5.0 nm. The ferromagnetism could be controlled by alternating photo-illumination with UV and visible light in the solid state even at room temperature. The changes in the magnetization values were significant, and were estimated to be around 27%. This photo-magnetic effect could be attributed to photo-induced changes in the values of d-charge losses due to the photoisomerization of azo-ligands, which were accompanied by the inversion of surface dipole values to the opposite sign.

Acknowledgements

This work was supported by a Grant-in-Aid for Scientific Research (A) and Scientific Research in Priority Areas "Photochromism (No. 471)" from the Ministry of Education, Culture, Sports, Science and Technology (MEXT) of the Japanese Government.

References

[1] M.C. Daniel, D. Astruc, Chem. Rev. 104 (2004) 293.
[2] M.J. Hostetler, J.E. Wingate, C.J. Zhong, J.E. Harris, R.W. Vachet, M.R. Clark, J.D. Londono, S.J. Green, J.J. Stokes, G.D. Wignall, G.L. Glish, M.D. Porter, N.D. Evans, R.W. Murray, Langmuir 14 (1998) 17.
[3] R. Elghanian, J.J. Storhoff, R.C. Mucic, R.L. Letsinger, C.A. Mirkin, Science 277 (1997) 1078.
[4] W.L. Barnes, A. Dereux, T.W. Ebbesen, Nature 424 (2003) 824.
[5] R. Narayanan, M.A. El-sayed, J. Phys. Chem. B 109 (2001) 631.
[6] (a) I. Carmeli, G. Leitus, R. Naaman, S. Reich, Z. Vager, J. Chem. Phys. 118 (2003) 10372;
(b) A. Hernando, P. Crespo, M.A. García, E.F. Pinel, J. Venta, A. Fernández, S. Penadés, Phys. Rev. B 74 (2006) 052403.
[7] (a) P. Crespo, R. Litrán, T.C. Rojas, M. Multigner, J.M. Fuente, J.C. Sánchez-López, M.A. García, A. Hernando, S. Penadés, A. Fernández, Phys. Rev. Lett. 93 (2004) 087204;
(b) Y. Negishi, H. Tsunoyama, M. Suzuki, N. Kawamura, M.M. Matsushita, K. Maruyama, T. Sugawara, T. Yokoyama, T. Tsukuda, J. Am. Chem. Soc. 128 (2006) 12034;
(c) P. Dutta, S. Pal, M.S. Seehra, M. Anand, C.B. Roberts, Appl. Phys. Lett. 90 (2007) 213102;
(d) J.S. Garitaonandia, M. Insausti, E. Goikolea, M. Suzuki, J.D. Cashion, N. Kawamura, H. Ohsawa, I.G. Muro, K. Suzuki, F. Plazaola, T. Rojo, Nano Lett. 8 (2008) 661.
[8] M. Suda, N. Kameyama, M. Suzuki, N. Kawamura, Y. Einaga, Angew. Chem., Int. Ed. 47 (2008) 160.
[9] (a) Y. Einaga, O. Sato, T. Iyoda, A. Fujishima, K. Hashimoto, J. Am. Chem. Soc. 121 (1999) 3745;
(b) T. Yamamoto, Y. Umemura, O. Sato, Y. Einaga, Chem. Mater. 16 (2004) 1195;
(c) M. Taguchi, K. Yamada, S. Suzuki, O. Sato, Y. Einaga, Chem. Mater. 17 (2005) 4554.
[10] (a) R. Mikami, M. Taguchi, K. Yamada, K. Suzuki, O. Sato, Y. Einaga, Angew. Chem., Int. Ed. 43 (2004) 6135;
(b) M. Suda, Y. Miyazaki, Y. Hagiwara, O. Sato, S. Shiratori, Y. Einaga, Chem. Lett. 34 (7) (2005) 1028;
(c) M. Suda, M. Nakagawa, T. Iyoda, Y. Einaga, J. Am. Chem. Soc. 129 (2007) 5538.
[11] H. Ishii, K. Sugiyama, E. Ito, K. Seki, Adv. Mater. 11 (1999) 605.
[12] J. Hu, M.A. Fox, J. Org. Chem. 64 (1999) 4959.

[13] M. Brust, M. Walker, D. Bethell, D.J. Schiffrin, R. Whyman, J. Chem. Soc., Chem. Commun. (1994) 801.
[14] P. Zhang, T.K. Sham, Phys. Rev. Lett. 90 (2003) 244502.
[15] H. Nakahara, K. Fukuda, M. Shimomura, T. Kunitake, Nippon Kagaku Kaishi 7 (1988) 1001.
[16] S.D. Evans, S.R. Johnson, H. Ringsdorf, L.M. Williams, H. Wolf, Langmuir 14 (1998) 6436.
[17] A. Manna, P.L. Chen, H. Akiyama, T.X. Wei, K. Tamada, W. Knoll, Chem. Mater. 15 (2003) 20.
[18] S.G. Ray, H. Cohen, R. Naaman, H. Liu, D.H. Waldeck, J. Phys. Chem. B 109 (2005) 14064.
[19] A. Ulman, Chem. Rev. 96 (1996) 1533.
[20] K. Tamada, J. Nagasawa, F. Nakanishi, K. Abe, Langmuir 48 (1998) 3264.

[39]. The molecular orbitals and the spin densities for these complexes were visualized by Gauss View 3.0 [40].

The geometries of **1** were directly taken from X-ray crystallography analysis. For the purpose of accumulating the knowledge on the magnetic property of Cu(II) complexes with axially coordinated nitronyl nitroxide radicals, the electronic structures of a simplified model were analyzed. Simplified complex **2** is extracted from the geometries of **1**. The bond lengths and the bond angles of hydrogen in these complexes are optimized at UB3LYP/6-31G* (Fig. 1) [41–43].

2.2. Evaluation of spin density and effective exchange integral

The spin densities of these complexes were performed at UB3LYP/6-311G** for the Cu atoms and UB3LYP/6-31G* for the ligands. In order to analyze the magnetic properties in detail, the spin population for **1** was performed at UB3LYP/LANL2MB [44–46] with minimum basis set for the Cu atoms using Hay–Wadt effective core potential and STO-3G for the ligands.

The effective exchange integrals J for these complexes were estimated by the following Eq. (1), where E and S^2 denoted, respectively, the total energy and the total spin angular momentum for the spin state, that is, singlet state (*LS*) and triplet state (*HS*) [47]. J values were also calculated at UB3LYP/6-311G** for the Cu atoms and at UB3LYP/6-31G* for the ligands. Tight convergence was used to discuss small energy differences (10^{-8} au). Highest occupied molecular orbital – lowest unoccupied molecular orbital (HOMO–LUMO) mixed initial guesses were created to estimate broken-symmetry singlet-state energies [48,49]. This method follows the proposal of Perdew et al. [50], who suggest that the broken symmetry single determinant should be the correct solution of the Kohn–Sham equations for single state.

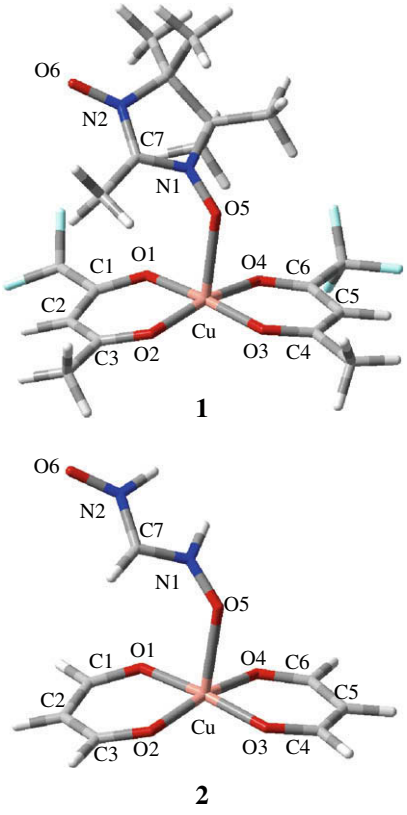


Fig. 1. Structures of **1** and **2**.

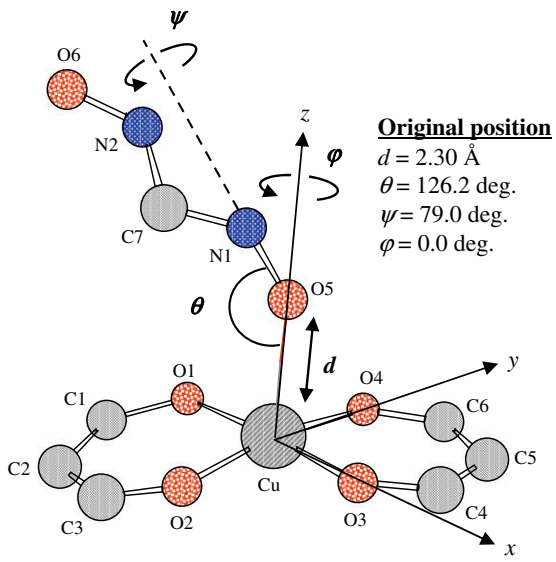


Fig. 2. Geometrical parameters of simplified complex **2** to examine the effect of overlap between magnetic orbitals.

$$J = \frac{E^{LS} - E^{HS}}{\langle S^2 \rangle^{HS} - \langle S^2 \rangle^{LS}} \tag{1}$$

2.3. Analysis of electronic structures for simplified complexes

The influence of the patterns of approach of the magnetic orbitals upon the magnetic interactions with **2** is described by using the values of the geometrical parameters d, θ, ψ and ϕ, which were the Cu–O5 distance, the Cu–O5–N1 angle, the Cu–O5–N1–C7 dihedral angle (being equal to the dihedral angle between the Cu–O5–N1 plane and the middle plane of the nitronyl nitroxide radical) and the O1–Cu–O5–N1 dihedral angle (being equal to the angle between the projection of the N1–O5 bond on the xy plane and the Cu–O1 (chelate ring) bond), respectively (Fig. 2). The coordinate of each moiety of bischelating Cu(II) and nitronyl nitroxide is fixed to the original position.

3. Results and discussion

The bonding pattern of the Cu(II) ion of **1** closely approximates a square pyramid, with the four oxygen atom of trifluoroacetylacetonate ligands in the basal plane and the nitronyl oxygen atom axially coordinated. There are two SOMO orbitals in **1** (Fig. 3). As the elongation axis is through Cu–O5, The SOMO_1 is an antibonding Cu–O orbital mainly localized onto the $3d_{x^2-y^2}$ atomic orbital, which is directed toward the equatorial oxygen atoms. On the other hand, the SOMO_2 is essentially formed by the N–O π^* orbital almost equally delocalized onto the N and O atoms of nitronyl nitroxide moiety. It is considered that the exchange interaction between the magnetic orbitals is attributed to the orthogonality of the Cu(II) $3d_{x^2-y^2}$ orbital with N–O π^* orbital [51].

DFT calculations often give good results for both signs and magnitudes of spin densities of open-shell molecules. It is found that the spin densities are mainly localized on the Cu(II) ion and the nitronyl nitroxide groups in both of the singlet and triplet states of **1** (Fig. 4). On the other hand, the sign of the spin density on the Cu(II) ion in the singlet state of **1** is opposite to that in the triplet state, despite the fact that the magnitudes of the spin densities on the Cu(II) ion and the nitronyl nitroxide groups remain unchanged (Table 1). This indicates that an antiferromagnetic spin

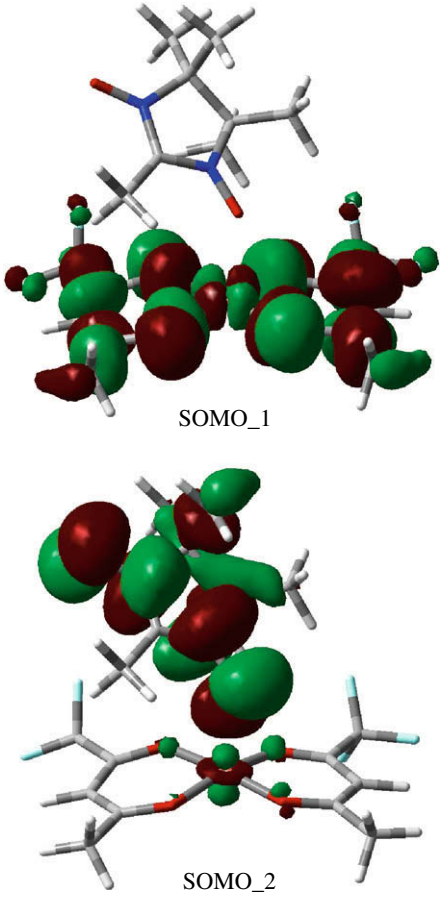


Fig. 3. SOMO distribution of **1** at UB3LYP/6-311G** for the Cu atoms and UB3LYP/6-31G* for the ligands.

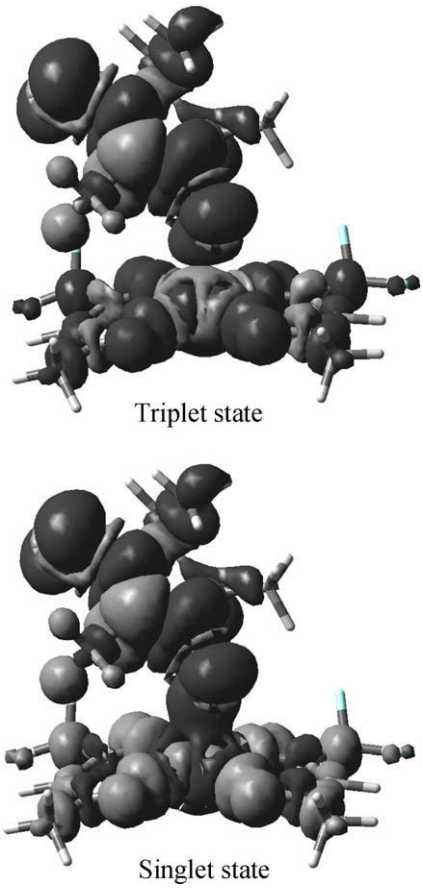


Fig. 4. Spin density for the triplet state of **1** at UB3LYP/6-311G** for the Cu atoms and UB3LYP/6-31G* for the ligands. The positive spin densities are shown in dark gray and the negative ones are in pale gray.

arrangement occurs in the singlet state of **1**, while a ferromagnetic spin arrangement occurs in the triplet state of **1**. The total spin population on the local nitronyl nitroxide (O5–N1–C7–N2–O6, see Fig. 1 for atom numbering.) group is close to integer 1 at triplet state. However, the net spin population on the Cu(II) ion is below integral 1 because of the spin polarization on the equatorial oxygen atoms of trifluoroacetylacetonate ligands coordinated to the Cu(II) ion. Moreover, the spin polarization on $3d_{z^2}$ orbital which contributes to the formation of Cu–O5 bond is observed at UB3LYP/LANL2MB (Table 2). SOMO_2 also indicates a non-negligible contribution of the $3d_{z^2}$ orbital which is perpendicular to the CuO_4 plane.

The result of the calculation for **2** reflects the electronic structure for **1**, because the SOMO distribution and spin density of **2** are similar to that of **1**. The orbital energies and the kinetic energies of **2** are also close to those of **1**. The *J* values of **1** and **2** estimated by the Eq. (1) are 47.5 cm^{-1} and 88.8 cm^{-1}, respectively. In contrast with the experimental value, it is considered that these values are within a permissible range of discussing the relationship between the geometrical parameters and the magnetic interaction of Cu(II) complexes with axially coordinated nitronyl nitroxide radicals [21].

Complex **2** is used for the purpose of describing the influence of the patterns of approach of the magnetic orbitals upon the magnetic interactions. In the case of shifting *d* under the fixed geometries of original θ, ψ and ϕ, *J* increases with decreasing in *d* (Fig. 5). Shorter Cu–O5 distance is better to form ferromagnetic coupling, and this result supports the tendency of the previous reports [37]. The behavior of the spin population on the Cu(II) ion in the triplet state of **2** shows the similar tendency of *J*, while the total spin population on the local nitronyl nitroxide (O5–N1–C7–N2–O6) group in the triplet state of **2** gradually decreases according to the decrease of *d* (Fig. 6). These results suggest the slight delo-

Table 1
Mulliken atomic spin population analysis for **1** at UB3LYP/6-311G** for the Cu atoms and UB3LYP/6-31G* for the ligands.

Atom	Spin population	
	Triplet state	Singlet state
Cu	0.705214	−0.693087
O1	0.067428	−0.066212
O2	0.068916	−0.067735
O3	0.078255	−0.076752
O4	0.070834	−0.068351
O5	0.239644	0.239027
O6	0.391005	0.392395
N1	0.267045	0.268324
N2	0.269494	0.270021
C7	−0.200226	−0.19904

Table 2
3d atomic orbital spin population for the triplet state of **1** at UB3LYP/LANL2MB.

Metal orbital	Population ratio (%)
$3d_{z^2}$	1.92
$3d_{zx}$	0.63
$3d_{yz}$	0.31
$3d_{x^2-y^2}$	96.72
$3d_{xy}$	0.42

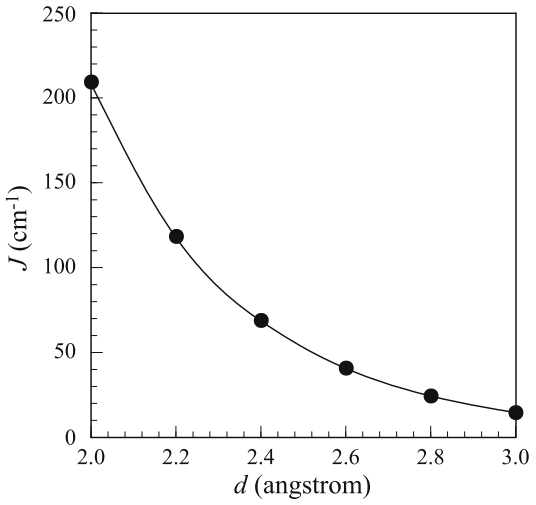


Fig. 5. Dependence of J on d for **2** under the fixed geometries of $\theta = 126.2°$, $\psi = 79.0°$ and $\phi = 0.0°$. Calculation is carried out at UB3LYP/6-311G** for the Cu atoms and UB3LYP/6-31G* for the ligands.

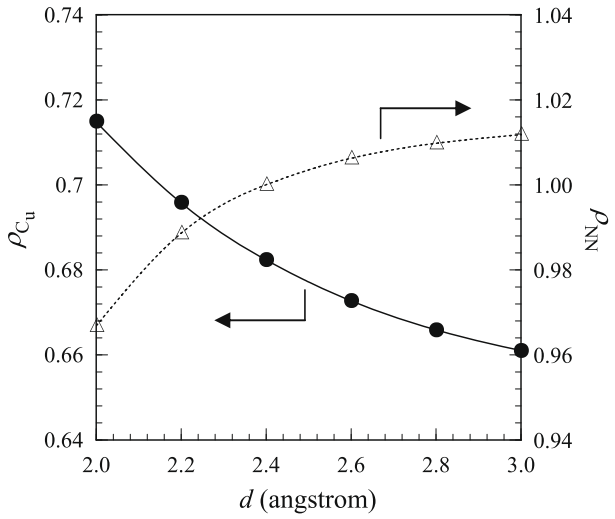


Fig. 6. Dependence of the spin densities of the Cu(II) ion (ρ_{Cu}) and the local nitronyl nitroxide (O5–N1–C7–N2–O6) group (ρ_{NN}) on d for **2** under the fixed geometries of $\theta = 126.2°$, $\psi = 79.0°$ and $\phi = 0.0°$.

calization of the unpaired electron from the π^*orbital of the nitronyl nitroxide group to the $3d_{z^2}$ atomic orbital of the Cu(II) ion. Therefore, the exchange parameter contains two main contributions, $J \cong J_{dir} + J_{del}$, where J_{dir} indicates the direct exchange mechanism and J_{del} indicates the delocalization mechanism [36]. On the other hand, there is only a low correlation between J and ϕ because the overlap integral between the $3d_{x^2-y^2}$ atomic orbital of the Cu(II) ion and N–O π^* orbital of the nitronyl nitroxide group is too small to lead to the change of J_{dir}. It is also suggested that the spin population on $3d_{z^2}$ atomic orbital of the Cu(II) ion should be approximately constant in the case of shifting ϕ under the fixed geometries of θ, d and ψ.

The values of the geometrical parameters θ and ψ play a key role in tuning the magnitude of the magnetic interaction in Cu(II) complexes with axially coordinated nitronyl nitroxide radicals as well as those of the geometrical parameter d (Fig. 7) [52]. When the value of θ is 180°, the $3d_{x^2-y^2}$ atomic orbital of the Cu(II) ion and N–O π^* orbital of the nitronyl nitroxide group are orthogonal to each other irrespective of ψ and ϕ. In this case the antiferromagnetic contribution vanishes, and a moderate ferromagnetic coupling can be developed. On the contrary, the decrease of θ considerably increases J_{del} except for the cases below θ = ca. 120° in which the ferromagnetic coupling may be prevented by the steric effect. This is due to the fact that the increase of θ leads to a more efficient overlap between the $3d_{z^2}$ atomic orbital of the Cu(II) ion and N–O π^* orbital of the nitronyl nitroxide group. The increase of ψ also contributes to the increase of J_{del}. When the value of ψ is 90°, the axes of N–O π^* orbital of the nitronyl nitroxide group are directed toward the Cu(II) ion. Such an orientation is especially favorable for the delocalization of an unpaired electron onto the $3d_{z^2}$ atomic orbital of the Cu(II) ion and, consequently, corresponds to the largest J_{del} value (Fig. 8).

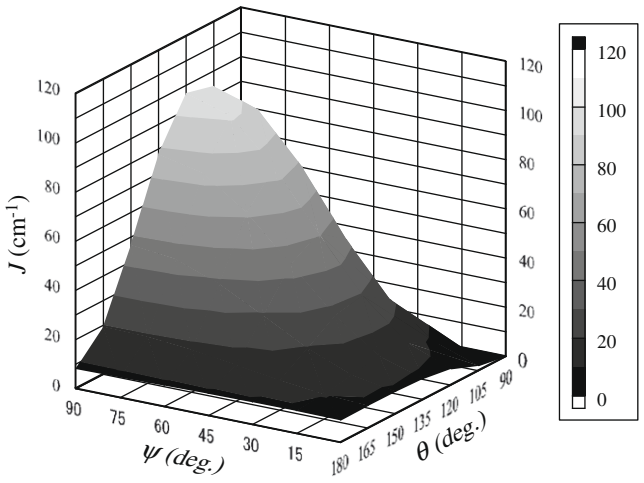


Fig. 7. Dependence of J on θ and ψ for **2** under the fixed geometries of d = 2.30 Å and $\phi = 0.0°$.

The calculated J values of other Cu(II) nitronyl nitroxide systems whose experimental results have been reported before are estimated by applying the values of their geometrical parameters to **2** (Fig. 9) [8,24,25]. Here the O1–Cu–O5 angles (see Fig. 2 for atom numbering.) are taken into account respectively [31,36], while these angular dependences are small in the range from 78° to 102° as a result of the computational analysis. The order of the experimental J values reported before is well reproduced by the calculated results for simplified complexes. It is indicated that the method described in this paper can be applied various Cu(II) complexes with axially coordinated nitronyl nitroxide radicals.

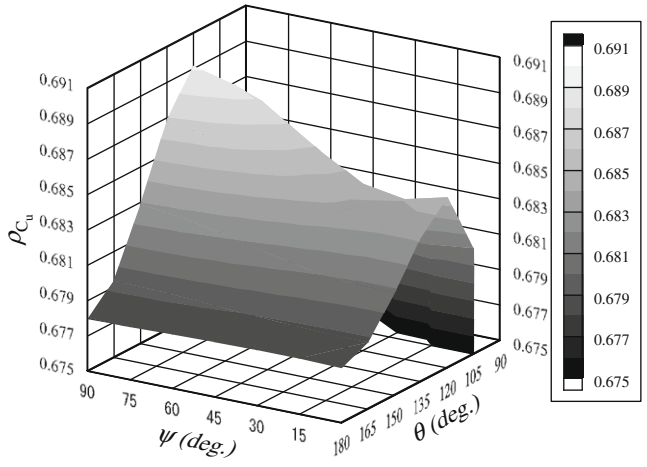


Fig. 8. Dependence of the spin density of the Cu(II) ion (ρ_{Cu}) on θ and ψ for **2** under the fixed geometries of d = 2.30 Å and $\phi = 0.0°$.

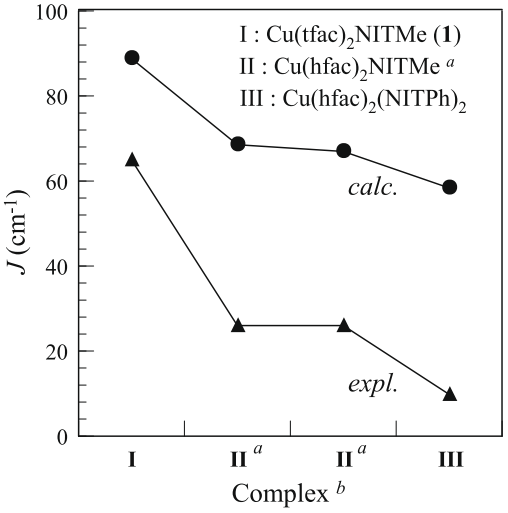


Fig. 9. Comparison between experimental *J* and calculated *J* for Cu(II) nitronyl nitroxide systems. The calculated *J* values are estimated by applying the values of their geometrical parameters to **2** respectively ([a]Two different Cu–O5 distances are observed in the cell. The experimental *J* for II is the averaged value. [b]tfac = trifluoroacetylacetonato, hfac = hexafluoroacetylacetonato, NITMe = 2,4,4,5,5-pentamethyl-4,5-dihydro-1*H*-imidazolyl-1-oxy-3-oxide, NITPh = 2-phenyl-4,4,5,5-tetramethyl-4,5-dihydro-1*H*-imidazolyl-1-oxy-3-oxide.).

4. Conclusion

It is important to investigate the primary structure of molecule-baesd magnets in order to encourage spin arrangement. The magnetic properties for Cu(II) complexes with axially coordinated nitronyl nitroxide radicals which exhibit ferromagnetic interaction are well reproduced by the results of DFT calculations. The electronic structures for these complexes are examined for the purpose of clarifying the mechanism of the ferromagnetic interaction. In summary, it is considered that the delocalization of the unpaired electron takes place from the π^* orbital of the nitronyl nitroxide group to the $3d_{z^2}$ atomic orbital of the Cu(II) ion. The delocalization mechanism is important for the ferromagnetic properties in Cu(II) complexes with axially coordinated nitronyl nitroxide radicals.

Acknowledgements

This work was supported in part by a Grant-in-Aid for Scientific Research (B) 20310060 from the Ministry of Education, Culture, Sports, Science, and Technology, Japan. Financial support from the Keio Gijuku Academic Development Funds is also acknowledged.

References

[1] P. Day, A.E. Underhill, Metal-Organic and Organic Molecular Magnets, The Royal Society of Chemistry, Cambridge, 1999.
[2] D. Gatteschi, O. Kahn, J.S. Miller, F. Palacio, Magnetic Molecular Materials, Kluwer Academic Publishers., Dordrecht, 1991.
[3] K. Inoue, Struct. Bond. 100 (2001) 61.
[4] A. Caneschi, D. Gatteschi, R. Sessoli, Acc. Chem. Res. 22 (1989) 392.
[5] A. Caneschi, D. Gatteschi, P. Rey, Prog. Inorg. Chem. 39 (1991) 331.
[6] D. Gatteschi, Adv. Mater. 6 (1994) 635.
[7] J. Laugier, P. Rey, C. Benelli, D. Gatteschi, C. Zanchini, J. Am. Chem. Soc. 108 (1986) 6931.
[8] A. Caneschi, D. Gatteschi, P. Rey, J. Chem. Soc., Faraday Trans. I 83 (1987) 3603.
[9] C.G. Pierpont, C.G. Lange, Prog. Inorg. Chem. 41 (1994) 331.
[10] M. Jenings, K.E. Preuss, J. Wu, Chem. Commun. (2006) 341.
[11] A. Bencini, C. Benelli, D. Gatteschi, C. Zanchini, J. Am. Chem. Soc. 106 (1984) 5813.
[12] C. Benelli, D. Gatteschi, D.W. Carnegie Jr., R.L. Carlin, J. Am. Chem. Soc. 107 (1985) 2560.
[13] E.F. Ullman, J.H. Osieckly, D.G.B. Boocock, R. Darcy, J. Am. Chem. Soc. 94 (1972) 49.
[14] A. Caneschi, D. Catteschi, P. Rey, R. Sessoli, Inorg. Chem. 27 (1988) 1756.
[15] U. Schatzschneider, T. Weyhermüller, E. Rentschler, Eur. J. Inorg. Chem. (2001) 2569.
[16] R.E. Del Sesto, A.M. Arif, J.S. Miller, Inorg. Chem. 39 (2000) 4894.
[17] K. Okada, O. Nagao, H. Mori, M. Kozaki, D. Shiomi, K. Sato, T. Takui, Y. Kitagawa, K. Yamaguchi, Inorg. Chem. 42 (2003) 3221.
[18] L.C. Porter, M.H. Dickman, R.J. Doedens, Inorg. Chem. 25 (1986) 678.
[19] D. Luneau, F.M. Romero, R. Ziessel, Inorg. Chem. 37 (1998) 5078.
[20] O.P. Anderson, T.C. Kuechler, Inorg. Chem. 19 (1980) 1417.
[21] A. Caneschi, D. Gatteschi, A. Grand, J. Laugier, L. Pardi, P. Rey, Inorg. Chem. 27 (1988) 1031.
[22] A. Grand, P. Rey, R. Subra, Inorg. Chem. 22 (1983) 391.
[23] J. Laugier, R. Ramasseul, P. Rey, J.C. Espie, A. Rassat, Neuv. J. Chim. 7 (1983) 11.
[24] A. Caneschi, D. Gatteschi, J. Laugier, P. Rey, J. Am. Chem. Soc. 109 (1987) 2191.
[25] D. Gatteschi, J. Laugier, P. Rey, C. Zanchini, Inorg. Chem. 26 (1987) 938.
[26] A. Caneschi, P. Chiesi, L. David, F. Ferraro, D. Gatteschi, R. Sessoli, Inorg. Chem. 32 (1993) 1445.
[27] C.I. Cabello, A. Caneschi, R.L. Carlin, D. Gatteschi, P. Rey, Inorg. Chem. 29 (1990) 2582.
[28] H. Oshio, T. Yaginuma, T. Ito, Bull. Chem. Soc. Jpn. 73 (2000) 1365.
[29] C. Benelli, D. Gatteschi, C. Zanchini, J.M. Latour, P. Rey, Inorg. Chem. 25 (1986) 4242.
[30] C. Sporer, H. Heise, K. Wurst, D. Ruiz-Molina, H. Kopacka, P. Jaitner, F. Koehler, J.J. Novoa, J. Veciana, Chem.-A Eur. J. 10 (2004) 1355.
[31] A. Ito, Y. Nakano, M. Urabe, K. Tanaka, M. Shiro, Eur. J. Inorg. Chem. (2006) 3359.
[32] W. Heisenberg, Z. Phys. 38 (1926) 411.
[33] P.J. Hay, J.C. Thibeault, R. Hoffmann, J. Am. Chem. Soc. 97 (1975) 4884.
[34] O. Kahn, B. Briat, J. Chem. Soc., Faraday Trans. II 72 (1976) 268.
[35] O. Kahn, Inorg. Chim. Acta 62 (1982) 3.
[36] R.N. Musin, P.V. Schastnev, S.A. Malinovskaya, Inorg. Chem. 31 (1992) 4118.
[37] C.-B. Liu, Y.-M. Sun, B. Zheng, R.-X. Wang, Chem. Phys. Lett. 411 (2005) 416.
[38] T. Kawakami, Y. Kitagawa, F. Matsuoka, Y. Yamashita, K. Yamaguchi, Polyhedron 20 (2001) 1235.
[39] M.J. Frisch et al., GAUSSIAN 03, Revision B.04, Gaussian, Inc., Pittsburgh, PA, 2003.
[40] R. Dennington II, et al., GaussView, Version 3.07, Semichem, Inc., Shawnee Mission, KS, 2003.
[41] A.D. Becke, J. Chem. Phys. 98 (1993) 5648.
[42] C. Lee, W. Yang, R.G. Parr, Phys. Rev. B 37 (1988) 785.
[43] B. Miehlich, A. Savin, H. Stoll, H. Preuss, Chem. Phys. Lett. 157 (1989) 200.
[44] P.J. Hay, W.R. Wadt, J. Chem. Phys. 82 (1985) 270.
[45] W.R. Wadt, P.J. Hay, J. Chem. Phys. 82 (1985) 284.
[46] P.J. Hay, W.R. Wadt, J. Chem. Phys. 82 (1985) 299.
[47] S. Yamanaka, T. Kawakami, H. Nagao, K. Yamaguchi, Chem. Phys. Lett. 231 (1994) 25.
[48] L. Noodleman, J. Chem. Phys. 74 (1981) 5737.
[49] E. Ruiz, J. Cano, S. Alvarez, P. Alemany, J. Comput. Chem. 20 (1999) 1391.
[50] J.P. Perdew, A. Savin, K. Burke, Phys. Rev. A 51 (1995) 4531.
[51] A. Bencini, F. Totti, C.A. Daul, K. Doclo, P. Fantucci, V. Barone, Inorg. Chem. 36 (1997) 5022.
[52] A. di Matteo, V. Barone, J. Phys. Chem. A 103 (1999) 7676.

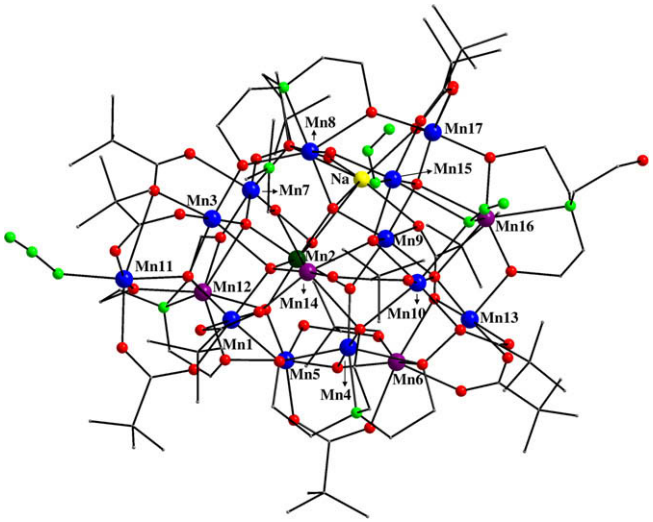


Fig. 1. Molecular structure of complex **1**. H atoms have been omitted for clarity. Color scheme: Mn^{II} purple; Mn^{III} blue; Mn^{IV} olive; Na yellow; O red; N green; C grey. (For interpretation of the references to color in this figure legend, the reader is referred to the web version of this article.)

$[Mn_4(\mu_3\text{-}O^{2-})_3(\mu_3\text{-}N_3)]$ cubane subunits at common atoms Mn2 and Mn9, respectively. All μ_3-O^{2-} ions in each cubane subunits convert to a μ_4 mode and bridge seven adjacent Mn atoms, three of which (Mn2,5,7) are fused to the corresponding triangular subunits. The three tea^{3-} groups are bound to up to six Mn atoms, acting as $\eta^3{:}\eta^1{:}\eta^2{:}\eta^3{:}\mu_6$, $\eta^2{:}\eta^1{:}\eta^3{:}\eta^2{:}\mu_5$ and $\eta^2{:}\eta^1{:}\eta^2{:}\eta^2{:}\mu_3$ ligands, the μ_6 mode being seen for a first time in the coordination chemistry of this group, while the only $teaH^{2-}$ group is bridging under the $\eta^2{:}\eta^1{:}\eta^2{:}\mu_3$ mode. Peripheral ligation about the core is provided by ten $\eta^1{:}\eta^1{:}\mu$, two $\eta^1{:}\eta^2{:}\mu$ and an $\eta^2{:}\eta^2{:}\mu_4$ $Me_3CCO_2^-$ groups, as well as two terminal N_3^- ions and a terminal DMF molecule. All Mn and Na atoms are near-octahedral, except five-coordinate Mn5 and seven-coordinate Mn12, which are square pyramidal ($\tau = 0.01$ [8]) and distorted pentagonal bipyramidal, respectively. The Mn^{II}/Mn^{III}/Mn^{IV}/Na^{I} oxidation states were established from the metric parameters, BVS calculations[3] [9], and the presence of Jahn–Teller (JT) distortions at octahedral Mn^{3+}. The protonation level of O^{2-}, OH^-, and OR^- groups was also confirmed by BVS calculations [9]. There are no significant intermolecular interactions of any kind, only strong intramolecular H-bonds between bridging OH^- and DMF and $Me_3CCO_2^-$ groups, respectively.

While the number of polynuclear complexes of 3d metals at intermediate oxidation states continues to grow rapidly, some nuclearities remain rare. Heptadecanuclear 3d metal complexes are particularly rare [10]; **1** is only the second Mn_{17} cluster ever reported [10a], and the first with such a closed-like structural topology.

Solid-state DC (direct current) magnetic susceptibility (χ_M) data for complex **1** were collected in the temperature range 5.0–300 K in an applied field of 1 kG (0.1 T). The data are plotted as $\chi_M T$ versus T in Fig. 2, and clearly indicate a relatively large ground-state spin (S) value. $\chi_M T$ for **1** steadily decreases from 44.74 cm^3 K mol^{-1} at 300 K to reach a plateau of ~35.50 cm^3 K mol^{-1} at 20–40 K, before further dropping to 33.49 cm^3 K mol^{-1} at 5.0 K; the latter decrease at the lowest temperatures is assigned to Zeeman effects, zero-field splitting and/or weak intermolecular interactions. The overall shape of the $\chi_M T$ versus T curve and the existence of the

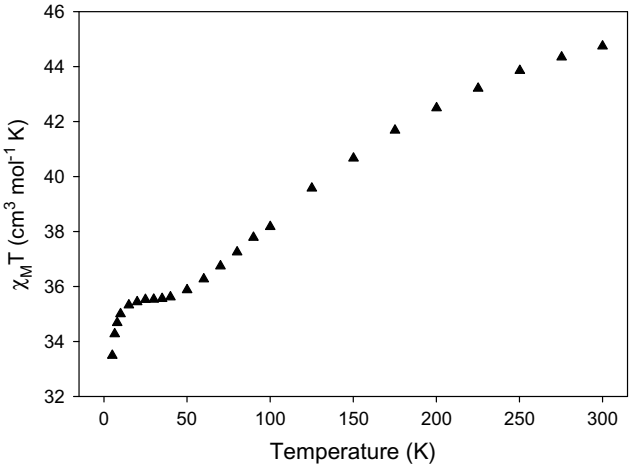


Fig. 2. $\chi_M T$ vs. T plot for **1** in a 1 kG field.

20–40 K plateau region are indicative of predominant antiferromagnetic exchange interactions within **1** and a well-isolated ground state S, respectively. The 20–40 K value is consistent with an $S = 17/2$ ground state and a g value slightly less than 2.0, as expected for a $Mn^{II,III,IV}$ complex; the spin-only ($g = 2$) value for an $S = 17/2$ state is 40.38 cm^3 K mol^{-1}.

In order to confirm the ground state of **1**, magnetization (M) data were collected in the 0.1–1.0 T and 1.8–10.0 K ranges, and these are plotted as $M/N\mu_B$ versus H/T in Fig. 3. We used only low field data ($\leqslant$1.0 T) to preclude problems from low-lying excited states, which are expected for high-nuclearity clusters with a high density of spin states and/or when Mn^{II} ions are present, which give weak exchange interactions. The data were fit by matrix-diagonalization to a model that assumes only the ground state is populated, includes axial zero-field splitting ($D\hat{S}_z^2$) and the Zeeman interaction, and carries out a full powder average. The best fit (solid lines in Fig. 3) gave $S = 17/2$, $g = 1.85$ and $D = -0.22$ cm^{-1}; alternative fits with $S = 15/2$ or 19/2 were rejected because they gave unreasonable values of g and D. We conclude that **1** has ground state of $S = 17/2$, respectively. This was further confirmed by AC (alternating current) susceptibility experiments.

As we have described before on multiple occasions [11], AC susceptibility studies in the 1.8–15 K range with a 3.5 G AC field oscil-

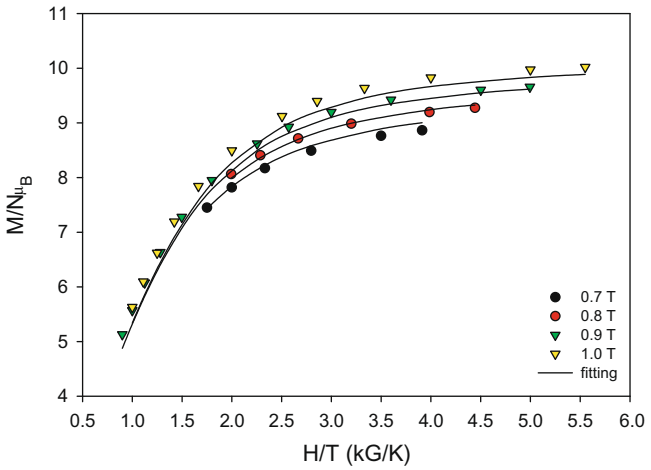


Fig. 3. Magnetization (M) vs. field (H) and temperature (T) data, plotted as reduced magnetization ($M/N\mu_B$) vs. H/T, for complex **1** at applied fields of 0.7–1.0 T and in the 1.8–10 K temperature range. The solid lines are the fit of the data; see the text for the fit parameters.

[3] Bond-valence sum (BVS) calculations for the Mn ions of **1** gave values of 1.77–1.94 for Mn^{2+} ions, 2.77–3.06 for Mn^{3+} ions, 4.03 for Mn^{4+} ion and 1.20 for Na^+ ion. BVS calculations for selected oxygen atoms in **1** gave values of 1.72–2.07 for O^{2-}, 0.90–1.01 for OH^-, 1.75–1.93 for RO^-, and 1.05–1.23 for ROH.

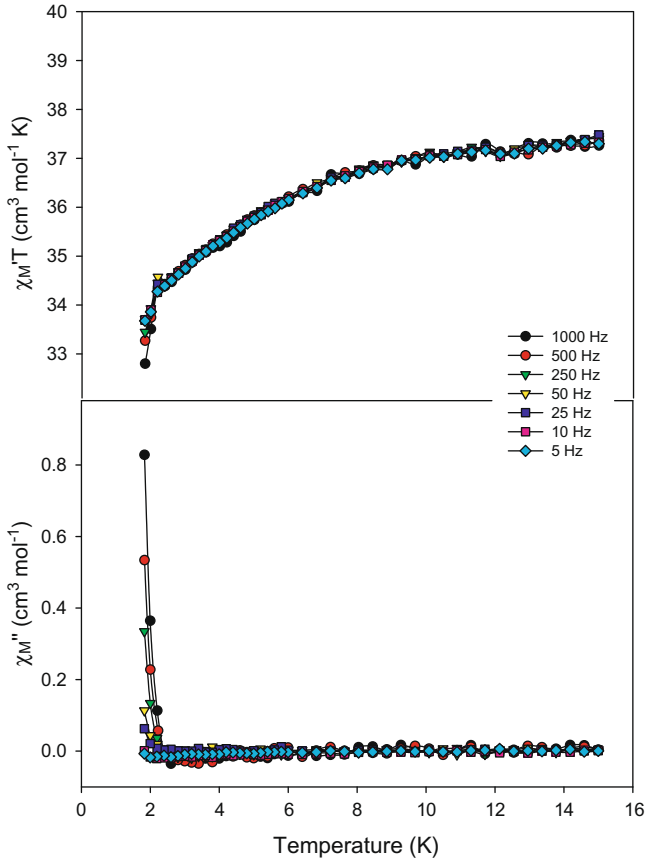


Fig. 4. Plots of the in-phase (χ'_M) as $\chi'_M T$ (top), and out-of-phase (χ''_M) (bottom) AC magnetic susceptibilities vs. T in a 3.5 G field oscillating at the indicated frequencies for complex **1**.

lating at 5–1000 Hz are a powerful complement to DC studies for determining the ground state of a system, because they preclude any complications arising from the presence of a DC field and/or low-lying excited states. For **1**, the in-phase (χ'_M) AC signal, shown as $\chi'_M T$ in Fig. 4 (top), is only slightly decreasing with decreasing temperature in the 8–15 K region; extrapolation of the data above 8 K (to avoid the effects of intermolecular interactions at lower temperatures) down to 0 K gives $\sim$36.5 $cm^3\,K\,mol^{-1}$, indicating an $S = 17/2$ ground state with $g \sim 1.95$, in good agreement with the DC magnetization fits.

The $S = 17/2$ ground state and the negative D value suggested that **1** might be SMM. The upper limit to the barrier is $U = (S^2\text{-}1/4)|D| = 15.70\ cm^{-1} = 22.59$ K, but the true, effective barrier (U_{eff}) will be significantly less due to QTM. At temperatures <3.0 K, frequency-dependent tails of out-of-phase (χ''_M) AC susceptibility signals for **1** were observed (Fig. 4, bottom) whose maxima lie below the operating minimum temperature of our SQUID instrument. Such signals are an indication of the superparamagnetic-like slow relaxation of an SMM. To confirm whether **1** is a SMM and shows hysteresis loops, the diagnostic property of a magnet, single-crystal magnetic studies are required to be performed at low enough temperatures using the micro-SQUID apparatus [12]. Such studies are currently in progress and the corresponding results will be reported in due course.

In summary, the combination of azide, carboxylate and $teaH_3$ ligands in Mn cluster chemistry has yielded an unprecedented heptadecanuclear, mixed-valence (II, III, IV) cage-like molecule with a fairly large $S = 17/2$ ground state and an appreciably large and negative D value. As a result, out-of-phase (χ''_M) AC tails of signals have been observed, indicative of the superparamagnetic-like slow relaxation of an SMM. Finally, the combined structural and magnetic results reported herein continue to emphasize how extensive is the ability of Mn chemistry to satisfy a variety of different tastes.

Acknowledgement

The authors thank the U.S. National Science Foundation (Grant CHE-0414555).

Appendix A. Supplementary data

CCDC 700136 contains the supplementary crystallographic data for **1** · 5MeCN. These data can be obtained free of charge via http://www.ccdc.cam.ac.uk/conts/retrieving.html, or from the Cambridge Crystallographic Data Centre, 12 Union Road, Cambridge CB2 1EZ, UK; fax: (+44) 1223-336-033; or e-mail: deposit@ccdc.cam.ac.uk. Supplementary data associated with this article can be found, in the online version, at doi:10.1016/j.poly.2008.10.032.

References

[1] (a) For reviews, see: G. Christou, D. Gatteschi, D.N. Hendrickson, R. Sessoli, MRS Bull. 25 (2000) 66;
(b) G. Aromi, E.K. Brechin, Struct. Bond. 122 (2006) 1;
(c) R. Bircher, G. Chaboussant, C. Dobe, H.U. Güdel, S.T. Oshsenbein, A. Sieber, O. Waldmann, Adv. Funct. Mater. 16 (2006) 209;
(d) D. Gatteschi, R. Sessoli, Angew. Chem., Int. Ed. 42 (2003) 268.
[2] J.R. Friedman, M.P. Sarachik, J. Tejada, R. Ziolo, Phys. Rev. Lett. 76 (1996) 3830.
[3] (a) W. Wernsdorfer, R. Sessoli, Science 284 (1999) 133;
(b) W. Wernsdorfer, M. Soler, G. Christou, D.N. Hendrickson, J. Appl. Phys. 91 (2002) 7164.
[4] G. Christou, Polyhedron 24 (2005) 2065.
[5] (a) L. Bogani, W. Wernsdorfer, Nat. Mater. 7 (2008) 179;
(b) M.N. Leuenberger, D. Loss, Nature 410 (2001) 789.
[6] A.J. Tasiopoulos, A. Vinslava, W. Wernsdorfer, K.A. Abboud, G. Christou, Angew. Chem., Int. Ed. 43 (2004) 2117.
[7] For a mini-review of azide groups in higher oxidation state manganese cluster chemistry, see: Th.C. Stamatatos, G. Christou, Inorg. Chem., in press and references cited therein.
[8] A.W. Addison, T.N. Rao, J. Reedijk, J. Rijn, G.C. Verschoor, J. Chem. Soc., Dalton Trans. (1984) 1349.
[9] (a) W. Liu, H.H. Thorp, Inorg. Chem. 32 (1993) 4102;
(b) I.D. Brown, D. Altermatt, Acta Crystallogr., Sect. B (1985) 244.
[10] (a) E.E. Moushi, Th.C. Stamatatos, W. Wernsdorfer, V. Nastopoulos, G. Christou, A.J. Tasiopoulos, Inorg. Chem., in press;
(b) G.W. Powell, H.N. Lancashire, E.K. Brechin, D. Collison, S.L. Heath, T. Mallah, W. Wernsdorfer, Angew. Chem., Int. Ed. 43 (2004) 5772;
(c) W. Micklitz, V. McKee, R.L. Rardin, L.E. Pence, G.C. Papaefthymiou, S.G. Bott, S.J. Lippard, J. Am. Chem. Soc. 116 (1994) 8061;
(d) S. Parsons, G.A. Solan, R.E.P. Winpenny, Chem. Commun. (1995) 1987;
(e) Y. Hayashi, K. Fukuyama, T. Takatera, A. Uehara, Chem. Lett. (2000) 770;
(f) N. Steunou, G. Kickelbick, K. Boubekeur, C. Sanchez, J. Chem. Soc., Dalton Trans. (1999) 3653.
[11] (a) For example, see: Th.C. Stamatatos, K.A. Abboud, W. Wernsdorfer, G. Christou, Angew. Chem., Int. Ed. 45 (2006) 4134;
(b) R.T.W. Scott, C.J. Milios, A. Vinslava, D. Lifford, S. Parsons, W. Wernsdorfer, G. Christou, E.K. Brechin, Dalton Trans. (2006) 3161;
(c) E. Moushi, C. Lampropoulos, W. Wernsdorfer, V. Nastopoulos, G. Christou, A.J. Tasiopoulos, Inorg. Chem. 46 (2007) 3795;
(d) M. Soler, W. Wernsdorfer, K. Folting, M. Pink, G. Christou, J. Am. Chem. Soc. 126 (2004) 2156.
[12] W. Wernsdorfer, Adv. Chem. Phys. 118 (2001) 99.

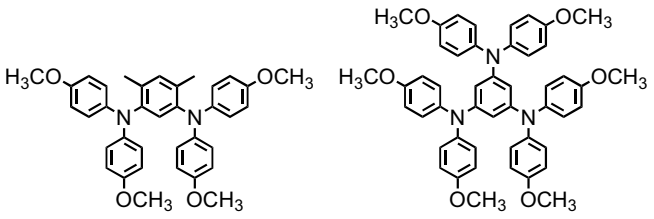


Fig. 1. Structures of *N,N,N′,N′*-tetrakis(4-anisyl)-4,6-dimethyl-1,3-phenylene-diamine (**1**) and *N,N,N′,N′, N″,N″*-hexakis(4-anisyl)-1,3,5-phenylenetriamine (**2**).

temperature. The electron transfer stopped-flow (ETSF) method allowed us to study the spectroscopic properties of the mono-, di- and tricationic states of **4**. These results are the first report on the detection of a one-dimensional oligoarylamine-based tricationic state [2j]. The enhancement of the thermodynamic and kinetic stability for oligo-cations of **4** is ascribed to the steric as well as electronic effects of the electrodonating methyl groups, which raise the HOMO energy level. The ESR study of the dication $\mathbf{4}^{2+}$ showed that the ground state is spin-triplet. The trication $\mathbf{4}^{3+}$ was not stable enough in a time scale for the conventional ESR sampling, indicating that chemical modification was not sufficient enough to stabilize the tricationic states in solution. We have also examined a highly alkylated triamine (**5**) with nine methyl groups at the peripheral aromatic rings, which gave stable mono- and dicationic state [2k]. Surprisingly, the peak of the trication $\mathbf{5}^{3+}$ completely disappeared in less than 0.2 s, indicating very unstable nature of the trication. The observations suggested that the introduction of extra methyl groups into the *meta* positions of the peripheral rings results in an unexpectedly large destabilizing effect on the tricationic states. An ESR study of the chemically oxidized **5** showed that the dication $\mathbf{5}^{2+}$ is spin-triplet in the ground state.

In this study, we have re-designed and synthesized a new alkylated triamine (**6**) with six methyl groups. The stabilities of the corresponding oligo-cationic states have been examined by using the cyclic voltammetry and ETSF method. The electronic states of the oligo-cationic states have been identified by cw-ESR measurements in rigid glass at low temperature.

2. Results and discussion

*2.2. Synthesis of 2,2′,4,4′-tetrabromo-3″,4″-dimethyl-5,5′-bis(di(4-methylphenyl)-amino)-triphenylamine (**6**)*

Compound **6** was synthesized and isolated as colorless powder by the similar method reported by Ito et al. [2g]. Dinitrotriarylamine (**7**) was reduced with $SnCl_2$/HCl to give diaminotriarylamine (**8**), which was reacted with 4-iodotoluene under Ullmann coupling condition to give a triamine (**9**). Compound **8** was brominated with benzyltrimethylammonium tribromide to give **6** in moderate yield (Fig. 3). All new compounds were fully characterized by spectroscopic methods. Data only for **6** and **9** are given below. Compound **9**: ^{1}H NMR ($CDCl_3$): δ 2.13 (s, 3H), 2.15 (s, 3H), 2.26 (s, 12H), 6.48–6.63 (m, 4H), 6.80 (t, 2H, J = 3.2 Hz), 6.87–7.05 (m, 21H), ^{13}C NMR ($CDCl_3$): 19.1, 19.9, 20.7, 116.9, 117.2, 118.4, 121.9, 123.8, 125.6, 129.3, 129.5, 130.2, 130.8, 131.7, 137.2, 145.0, 145.5, 148.3, 149.0. IR (KBr): 3019, 2916, 1570, 1508, 1292 cm^{-1}. M.p.: 84–85 °C.Compound **6**: ^{1}H NMR($CDCl_3$): δ 2.08 (s, 3H), 2.15 (s, 3H), 2.26 (s, 12H), 6.46 (dd, 1H, J = 8.0, 2.2 Hz), 6.52 (d, 1H, J = 2.2 Hz), 6.62 (s, 2H), 6.72 (d, 8H, J = 8.6 Hz), 6.87 (d, 1H, J = 8.6 Hz), 6.97 (d, 8H, J = 8.6 Hz), 7.72 (s, 2H), ^{13}C

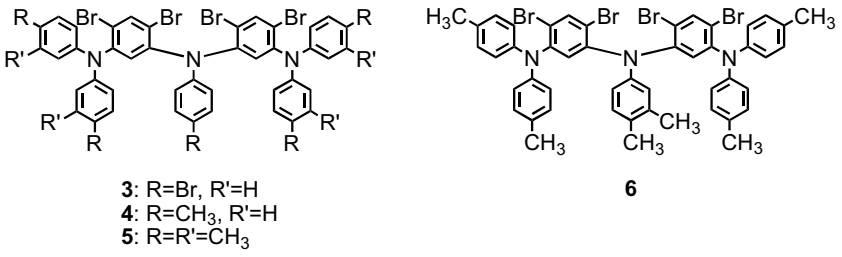


Fig. 2. Structures of 3,3′-bis(diarylamino)triphenylamines (**3**–**6**).

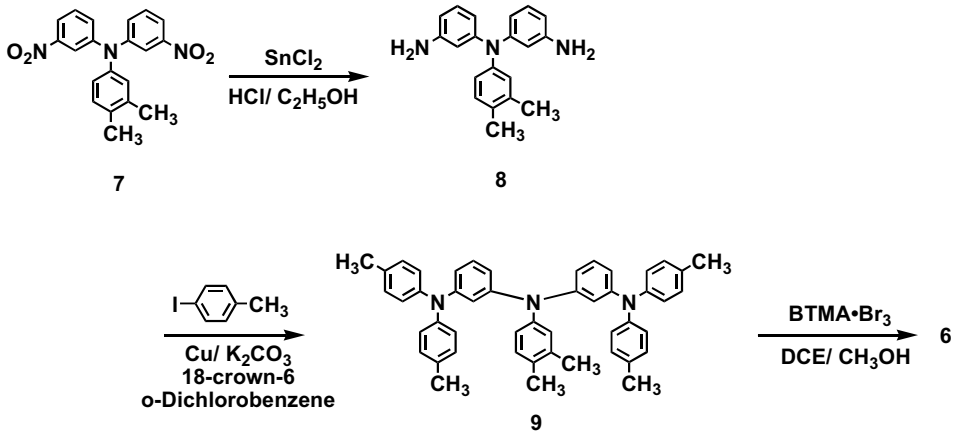


Fig. 3. Synthetic route of **6**.

NMR($CDCl_3$): δ 19.1, 19.8, 20.8, 117.1, 117.6, 119.0, 122.2, 123.1, 129.6, 129.8, 129.9, 131.2, 131.8, 137.2, 138.9, 143.5, 144.2, 145.8, 146.0. IR (KBr): 3024, 2917, 1570, 1506, 1463 cm^{-1}. M.p.: 109–110 °C. HRMS: Calc. for $C_{48}H_{41}N_3Br_4$, 975.0034; Obsd: 975.0031.

2.3. UV–Vis spectrum measurements

In order to examine the spectroscopic properties of **6**, UV–Vis spectroscopic measurements were carried out (Fig. 4). In chloroform solution, **6** exhibited a strong absorption around 300 nm, which is characteristic of triarylamine chromophores.

2.4. Cyclic voltammetry measurements

For the compound **6**, cyclic voltammetry in *n*-butyronitrile at ambient temperature revealed two couples of chemically reversible one-electron transfers (Fig. 5), indicating the generation of the corresponding stable mono-, di-, and trications in solution (E^0_1 = 0.60 V (2e transfer), E^0_2 = 1.00 V (1e transfer) versus Fc/Fc^+). No oxidation peak was observed upon further oxidation. Previously, we reported compound **4** gives stable mono-, di- and tricationic states. Comparing the first redox potentials of **6** and **4** (E^0_1 = 0.605 V versus Fc/Fc^+ (2e transfer)) [2j], **6** can be oxidized more easily, suggesting the occurrence of the elevated HOMO level. AM1 calculation also indicated that the HOMO energy level of **6** is slightly higher than that of **4**. Very recently, Bushby et al. have reported electrochemical and spectroscopic properties of a series of *meta*-connected oligoarylamines, where several methoxy groups

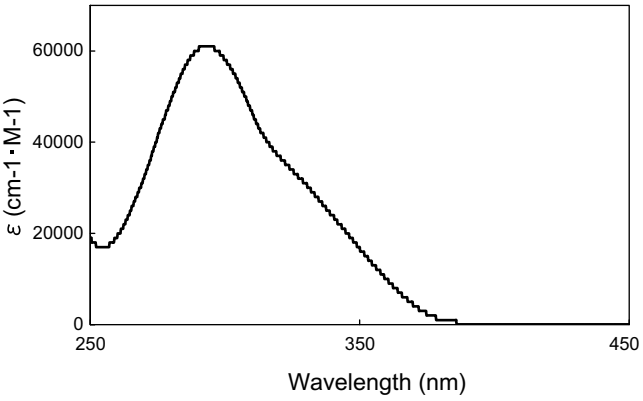


Fig. 4. Absorption spectra of **6** in acetonitrile.

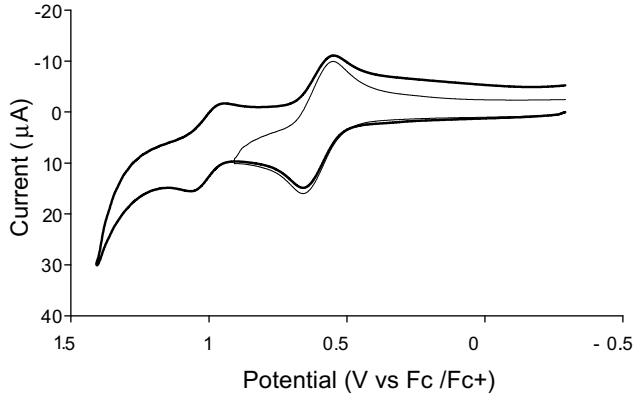


Fig. 5. Cyclic voltammogram of **6** in *n*-butyronitrile at ambient temperature.

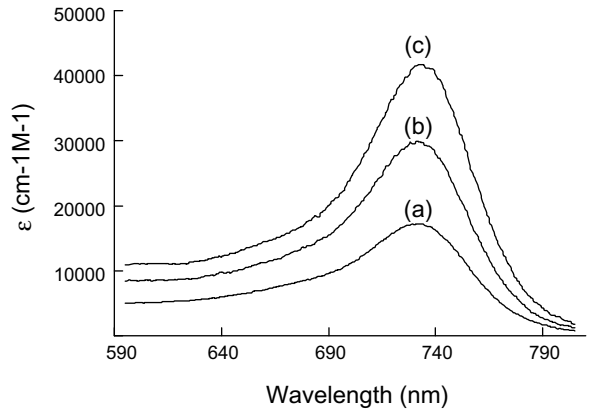


Fig. 6. Absorption spectra observed after mixing of an AN solution of 0.10 mM $TDBPA^{+\cdot}$ with an AN solution of (a) 0.10 mM, (b) 0.050 mM, (c) 0.033 mM of **6**.

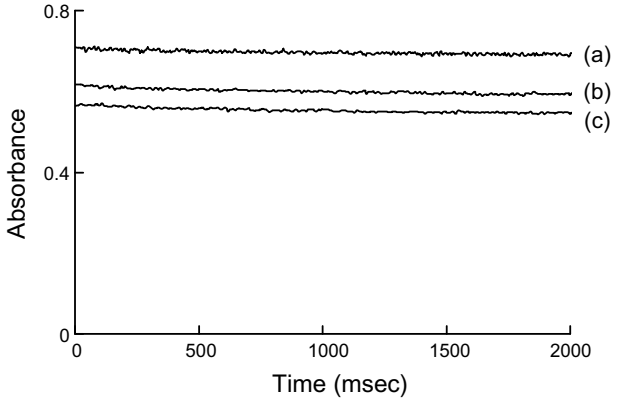


Fig. 7. Time profiles in the absorbance maximum observed after mixing of an AN solution of 0.10 mM $TDBPA^{+\cdot}$ with an AN solution of (a) 0.10 mM, (b) 0.050 mM, (c) 0.033 mM of **6**.

are introduced into the *ortho* positions of the triarylamine units [2l]. Compared with their systems, our diamines (**1**, **4**, **6**), where methyl or methoxy groups are introduced into the *para* positions, can be oxidized more easily [2c,j]. Thus, introduction of substituents into the *para* positions would be better strategy to obtain kinetically and thermodynamically stable *meta*-connected oligoarylamine-based high-spin systems.

2.5. Electron transfer stopped-flow (ETSF) method

The detail of the ETSF method was described previously [4,5]. The ETSF measurements were carried out in dehydrated acetonitrile (AN) as a solvent at ambient temperature. In this study, tris(2,4-dibromophenyl)amine cation radical ($TDBPA^{+\cdot}$)[1] was employed. Compound **6**, upon mixing with 1 equiv. of $TDBPA^{+\cdot}$, exhibited a broad absorption peak at 732 nm (Fig. 6), and no decrease in the peak intensity was observed for over 1 min, indicating the generation of the very stable monocation (Fig. 7). The molar absorptivity (ε) of $\mathbf{6}^{+\cdot}$ was determined to be 1.72×10^4 M^{-1} cm^{-1} at 732 nm.

Upon mixing with 2 equiv. of $TDBPA^{+\cdot}$, **6** exhibited an absorption peak of the dication $\mathbf{6}^{2+}$ at 732 nm. The ε value for $\mathbf{6}^{2+}$ was 3.00×10^4 M^{-1} cm^{-1} at 732 nm. No decrease in the peak intensity

[1] TDBPA was synthesized by WAKO Pure Chemicals Ltd. after receiving our special order. See also Ref. [5].

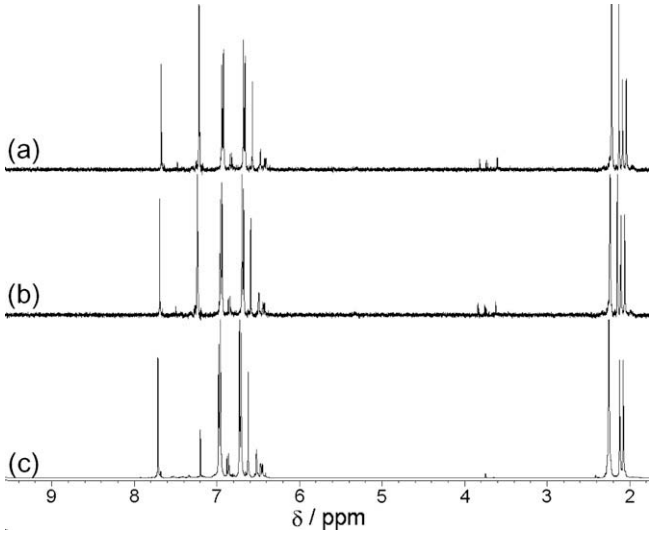


Fig. 8. ^{1}H NMR spectra of (a) product obtained by oxidation (4.5 equiv of $SbCl_5$) and following reduction of **6**, (b) product obtained by oxidation (10 equiv of $SbCl_5$) and following reduction of **6**, (c) **6**.

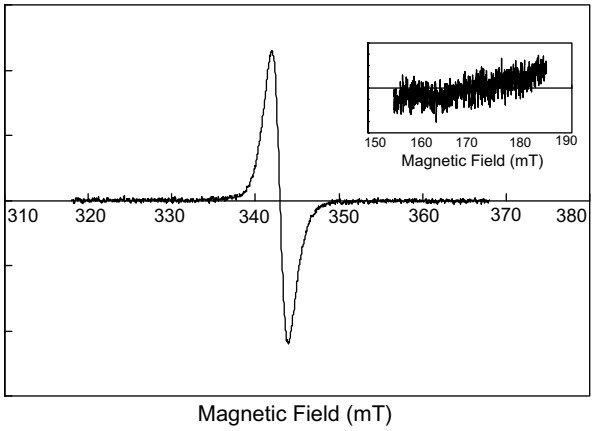


Fig. 9. ESR spectrum observed at 5 K for compound **6** after the oxidation by 10 equiv. of $SbCl_5$, in the allowed ESR transition region (inset: in the $\Delta Ms = \pm 2$ region).

was observed for over 1 min, indicating also that the very stable dication was generated.

Upon mixing with 3 equiv. of $TDBPA^{+\cdot}$, **6** exhibited an absorption peak of the trication $\mathbf{6}^{3+}$ at 734 nm ($\varepsilon = 4.18 \times 10^4\ M^{-1}\ cm^{-1}$). Similar to **4** and **5**, the ratio of ε for monocation:dication:trication of **6** was nearly 1:2:3, as expected. Previously we reported that compound **5** gives the very unstable trication with the lifetime of 0.2 s [2k]. Generally, introduction of electrodonating groups is effective to stabilize mono- and oligo-cationic states. The more electrodonating groups are attached, the more stable cationic states are expected to be generated. In the case of *meta*-connected one-dimensional triamines, introduction of the electrodonating group into the central phenyl ring would be effective to stabilize the corresponding tricationic states.

2.6. Stability of the trication generated by chemical oxidation

In order to examine the stability of the chemically generated trication, 4.5 equiv. of $SbCl_5$, minimum required amount to obtain the trication, was dropped to **6** in dichloromethane under nitrogen atmosphere at 15 °C. The color of the solution immediately turned purple, indicating the generation of oxidized species. The solution was stirred for 15 min at 15 °C and no change in color was observed. Upon addition of aqueous ascorbic acid, the color of the solution turned colorless. The obtained solution was extracted with chloroform, dried over sodium sulfate, and evaporated under reduced pressure to give white powder. The NMR spectrum of the product showed the quantitative recovery of **6**. Similar result was obtained using 10 equiv. of $SbCl_5$. Fig. 8 shows ^{1}H NMR spectra of the triamine and products obtained by reduction of the trication. Comparing the spectra, no significant difference was observed between before and after the $SbCl_5$/ascorbic acid treatment, indicating the generation of a room-temperature-stable trication. To our knowledge, this is the most stable *meta*-connected triamine-based tricationic state.

2.7. ESR measurements

In order to examine the electronic structures of the oligo-cationic states, cw-ESR measurements of chemically oxidized **6** were carried out at liquid-helium temperature. Upon addition of 10 equiv. of $SbCl_5$ into a CH_2Cl_2 solution of **6**, the color of the solution immediately turned blue, indicating the generation of oxidized species. The cw-ESR spectrum observed at 5 K for the oxidized species in the rigid glass is shown in Fig. 9. There appeared a broad line in the allowed ESR transition region and no forbidden transition $\Delta Ms = \pm 2$ of the appreciable intensity was observed in the $g = 4$ region. Judging from the result described in the previous section, one can rule out the possibility of the decomposition of the trication. Although we have successfully detected the quartet ground state for the two-dimensional triamine-based tricationic state, the ground state for the one-dimensional triamine-based tricationic state may not be quartet but doublet. Pulse-ESR based more sophisticated ESTN spectroscopy to identify the spin multiplicities of the ground- and thermally accessible excited states of the one-dimensional trication is underway.

3. Conclusions

Hexamethyl substituted triamine, 2,2′,4,4′-tetrabromo-3″,4″-dimethyl-5,5′- Bis(di(4-methylphenyl)amino)triphenylamine (**6**) has been designed and successfully synthesized. Cyclic voltammetry and ETSF measurements have revealed that **6** gives very stable mono-, di- and tricationic states at ambient temperature. The triamine was quantitatively recovered after chemical oxidation and following reduction at room temperature. ESR measurements of the trication suggested that the ground state is spin-doublet, contrasting to the high spin preference for the two-dimensional triamine-based trication.

References

[1] K. Itoh, M. Kinoshita (Eds.), Molecular Magnetism, New Magnetic Materials, Gordon & Breach, Inc. (Kodansha as copublisher), Amsterdam, Tokyo, 2000.
[2] (a) P.M. Lahti (Ed.), Magnetic Properties of Organic Materials, Marcel Dekker, Inc., New York, 1999 (Chapter 9 and references therein);
(b) K. Sato, M. Yano, M. Furuichi, D. Shiomi, K. Abe, T. Takui, K. Itoh, A. Higuchi, K. Katuma, Y. Shirota, J. Am. Chem. Soc. 119 (1997) 6607;
(c) M. Yano, K. Sato, D. Shiomi, A. Ichimura, K. Abe, T. Takui, K. Itoh, Tetrahedron Lett. 37 (1996) 9207;
(d) K.R. Stickley, S.C. Blackstock, J. Am. Chem. Soc. 116 (1994) 11576;
(e) K.R. Stickley, S.C. Blackstock, Tetrahedron Lett. 36 (1995) 1585;
(f) K.R. Stickley, T.D. Selby, S.C. Blackstock, J. Org. Chem. 62 (1997) 448;
(g) A. Ito, H. Ino, K. Tanaka, K. Kanemoto, T. Kato, J. Org. Chem. 67 (2002) 491;
(h) M. Yano, Y. Ishida, K. Aoyama, M. Tatsumi, K. Sato, D. Shiomi, A. Ichimura, T. Takui, Synth. Met. 137 (2003) 1275;
(i) M. Yano, Y. Ishida, M. Tatsumi, K. Sato, D. Shiomi, M. Oyama, T. Takui, J. Phys. Chem. Solids 65 (2004) 733;
(j) M. Yano, Y. Nakanishi, K. Matsushita, M. Tatsumi, M. Oyama, K. Sato, T. Takui, Polyhedron 24 (2005) 2116;

(k) M. Yano, A. Fujiwara, M. Tatsumi, M. Oyama, K. Sato, T. Takui, Polyhedron 26 (2007) 2008;
(l) R.J. Bushby, C.A. Kilner, N. Taylor, M.E. Vale, Tetrahedron 63 (2007) 11458.
[3] (a) E.T. Seo, R.F. Nelson, J.M. Fritsch, L.S. Marcoux, D.W. Leedy, R.N. Adams, J. Am. Chem. Soc. 88 (1966) 3498;
(b) R.F. Nelson, R.N. Adams, J. Am. Chem. Soc. 90 (1968) 3925.
[4] M. Oyama, T. Higuchi, S. Okazaki, J. Chem. Soc., Perkin Trans. 2 (2001) 1287.
[5] M. Oyama, J. Matsui, H. Park, Chem. Commun. (2002) 604.

22 spectrophotometer (KBr disc). Magnetic susceptibility data on polycrystalline sample were collected over the temperature range of 2–300 K using a MPMS-5S magnetometer (Quantum Design) in an external field of 0.2 T, the diamagnetism was corrected by Pascal constants [41].

2.3. Preparation of $Zn(TCNQ)_2 \cdot 2H_2O \cdot 2DMF$ (**1**)

To a solution of pyridine (348 mg, 4.4 mmol) in acetone (20 mL) was added $ZnCl_2$ (136.3 mg, 1.0 mmol) solid, the mixture was stirred at room temperature for 2 h. The white precipitate formed was filtered off, washed with acetone, and then dissolved in 25 mL water. To the stirred water solution was added Li(TCNQ) (426 mg, 2.0 mmol) in water (10 mL) at room temperature, and the green product immediately precipitated was filtered off and wished by methanol, then dissolved in 15 mL DMF. Dark-green plate crystals of **1** were obtained by dispersing Et_2O into the above DMF solution for *ca.* 6 days (Yield: ~50%). Elemental *Anal.* Calc. for $C_{30}H_{26}N_{10}O_4Zn$: C, 54.9; H, 3.99; N, 21.4. Found: C, 54.6; H, 4.01; N, 21.6%. IR(cm^{-1}): the bands at 2160 (sh), 2173 (sh) and 2195 (vs) are attributed to ν(CN) of $(TCNQ)^-$.

2.4. X-ray crystallography

Diffraction data of **1** were collected at 293 K on a SMART CCD diffractometer equipped with graphite-monochromated Mo Kα radiation. All computations were carried out using SHELXTL-PC program package [42]. Structure was solved by direct method and refined on F^2 by full-matrix least-squares method. All non-hydrogen atoms were anisotropically refined, and hydrogen atoms were placed in their calculated positions and refined following the riding model. Crystallographic details for **1** are summarized in Table 1.

2.5. DFT calculations

All density functional theory (DFT) calculations were carried out utilizing the GAUSSIAN 98 program [43]. The whole non-modelized molecular structure of the real complex **1**, was taken directly from X-ray crystallography complete structure, and calculations for magnetic exchange constants *J* are performed at ub3lyp level with the basis sets of Lanl2dz, the convergence criterion of SCF is 10^{-8}.

Table 1
Crystal and structure refinement data for **1**.

Empirical formula	$C_{30}H_{26}N_{10}O_4Zn$
Formula weight	656.00
Temperature (K)	293
Wavelength (Å)	0.71073
Space group	$P\bar{1}$
a (Å)	6.503(4)
b (Å)	8.054(5)
c (Å)	14.868(9)
α (°)	85.343(8)
β (°)	82.894(8)
γ (°)	76.785(8)
V (Å^3), *Z*	751.2(8), 1
θ Range for data collection (°)	1.38–28.00
Index ranges	$-8 \leqslant h \leqslant 8$, $-5 \leqslant k \leqslant 10$, $-18 \leqslant l \leqslant 19$
Reflections collected	4550
Independent reflections (R_{int})	3292 (0.0462)
Refinement method on F^2	full-matrix least-squares
Data/restraints/parameters	3292/0/207
Goodness-of-fit on F^2	1.075
Final *R* indices [$I > 2\sigma(I)$]	$R_1 = 0.0993$, $wR_2 = 0.3024$
Largest difference in peak and hole (e Å^{-3})	1.217 and −0.794

3. Results and discussion

3.1. Crystal structure

Crystal of **1** crystallizes in the triclinic space group $P\bar{1}$. As shown in Fig. 1, the Zn^{2+} ion occupies at an inversion centre and it is surrounded by two N atoms from two TCNQ molecules and four O atoms which belong respectively to two H_2O and two DMF molecules to form an almost perfectly octahedral coordination geometry with the bond lengths Zn1–N1 = 2.113(5) Å, Zn1–O1 = 2.047(7) Å and Zn1–O1W = 2.185(5) Å as well as the bond angles ∠N1–Zn1–O1W = 89.6(2)°, ∠N1–Zn1–O1 = 91.3(3)° and ∠O1–Zn1–O1W = 91.6(3)°, respectively. For the TCNQ molecule, the averaged lengths of chemically similar bonds are listed in Table 2, and the values are in agreement with those in other reported compounds of $TCNQ^-$ [44,45,20,46], and the mean-molecule-plane with the eight heavy atoms of the quinodimethane group is tilted with respect to the equatorial plane of the coordination octahedron (formed by $N1/O1/N1^{\#1}/O1^{\#1}$, and the symmetric code #1 = $-x$, $2-y$, $2-z$) with the dihedral angle of 19.6°.

The noticeable structural feature in **1** is the strong H-bonding and π···π stacking interactions (cf. Fig. 2). Two types of H-bonding interactions are respectively observed along the crystallographic *a*-axis and *c*-axis directions, the N···O distance for the H-bonding of NC- group of TCNQ molecule and O atom of H_2O molecule is 2.910 Å; the O···O distance for the H-bonding of the neighboring H_2O molecules is 2.869 Å. Along the crystallographic *a*-axis direction, the neighboring TCNQ molecules adopt a cofacial arrangement, in which the centers are offset along the long molecular axis of TCNQ, and the dihedral angles between the mean-molecule-planes with the eight heavy atoms of the quinodimethane group are exactly equal to 0° due to they are related to each other by the inversion centre. In such a TCNQ stack, the distances of the mean-molecule-planes alternate as 3.1957 Å and 3.2908 Å, and the shorter atomic contacts are observed in the neighboring TCNQ molecules with $d_{C4-C11A} = 3.272$, $d_{C7-C7A} = 3.305$, $d_{C6-C8A} = 3.253$, $d_{C4-C11B} = 3.336$, $d_{C7-C7B} = 3.421$ and $d_{C6-C8A} = 3.368$ Å (the symmetric code A = $1-x$, $2-y$, $-z$; B = $-x$, $2-y$, $-z$). The intermolecular H-bonding and π···π stacking interactions lead to a supramolecular network sheet forming on the crystallographic *ac*-plane, as illustrated in Fig. 3.

3.2. Magnetic susceptibility and DFT calculations

Temperature dependences of magnetic susceptibility for **1** in the forms of χ_m versus *T* and $\chi_m T$ versus *T* are presented in Fig. 4, and the variation of magnetic susceptibility with temperature does not follow Curie–Weiss law, the $\chi_m T$ value is *ca.* 0.18 emu K mol^{-1} at 300 K, which is much smaller than the spin-only value for two $S = ½$ spin system with *g*-factor = 2

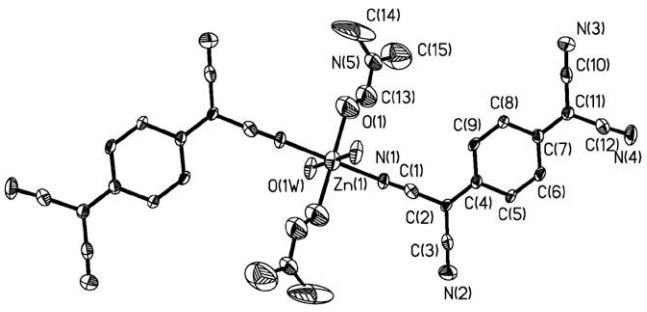
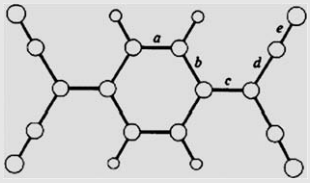


Fig. 1. ORTEP view of **1** with the displacement ellipsoids at 50% probability level (H-atoms omitted for clarity).

Table 2
Mean bond lengths (Å) of the TCNQ molecules in **1**.



	a	*b*	*c*	*d*	*e*
TCNQ in **1**	1.362	1.423	1.404	1.423	1.145
$TCNQ^0$ [47]	1.346	1.448	1.374	1.440	1.138
$TCNQ^{-1/2}$ [46]	1.355	1.433	1.396	1.424	1.145
$TCNQ^{-1}$ [45]	1.362	1.424	1.413	1.417	1.149

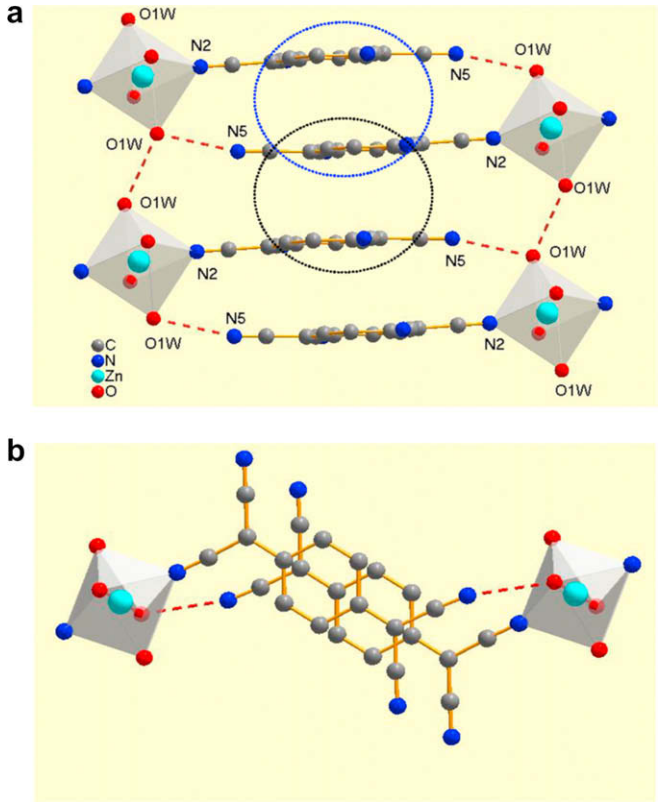


Fig. 2. H-bonding interactions between the coordinated water molecules and the CN groups of TCNQ species and $\pi\cdots\pi$ stacks between TCNQ species (a) the side view in which the blue and black circles represent two types of $[(TCNQ)_2]^{2-}$ dimers that are labeled as the dimer 1 (TCNQ and TCNQ($1-x$, $2-y$, $-z$)) and dimer 2 (TCNQ and TCNQ ($-x$, $2-y$, $-z$)), respectively and (b) the top view.

(0.75 emu K mol^{-1}). Upon cooling, the $\chi_m T$ value decreases linearly in the temperature range of 300–100 K, an inflect point occurs at around 100 K and after that the $\chi_m T$ value decreases linearly again.

In order to gain a deeper understanding of the magnetic behavior for **1**, the broken-symmetry DFT approach, which has being applied as a practical tool for investigating magnetic interactions on rather large systems with reasonable accuracy with partial consideration of electron correlation effects, was employed to evaluate the magnetic exchange constants [47–49]. The interaction between two spins $\vec{S}_1$ and $\vec{S}_2$ can be described with the Heisenberg–Dirac–van Vleck Hamiltonian [50–52]:

$$\hat{H} = -2J\vec{S}_1\vec{S}_2 \tag{1}$$

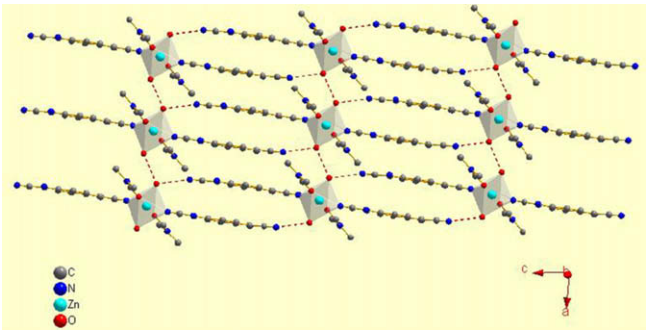


Fig. 3. Two-dimensional molecular sheet formed on the crystallographic *ac*-plane through intermolecular H-bonding interactions and $\pi\cdots\pi$ stacks in crystal of **1**.

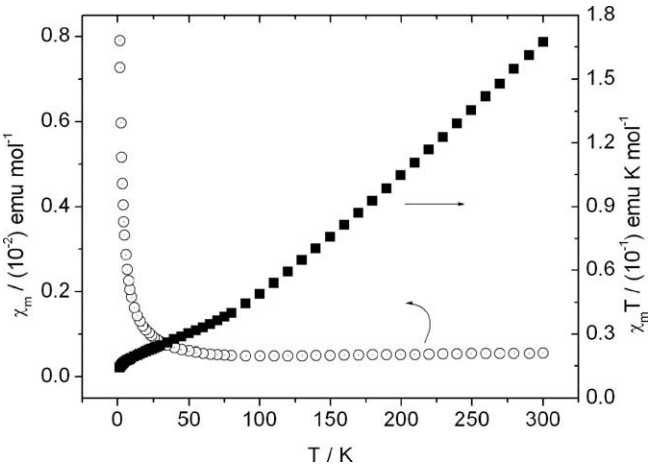


Fig. 4. Plots of $\chi_m - T$ and $\chi_m T - T$ for **1**.

where J is the magnetic exchange constant between $\vec{S}_1$ and $\vec{S}_2$. Assuming the so-called "weak bonding" regime, Noodleman et al. [53–55] evaluated J values within broken symmetry framework by

$$J^{(1)} = \frac{E_{BS} - E_T}{S^2_{max}} \tag{2}$$

where E_{BS} and E_T denote the total energies in the broken symmetry (BS) singlet state and triplet state, respectively, and S_{max} corresponds to the total spin of the high-spin state. It has been suggested that the following expression might give more reasonable solutions in the strong overlap region [56,57]:

$$J^{(2)} = \frac{E_{BS} - E_T}{S_{max}(S_{max}+1)} \tag{3}$$

However, Yamaguchi et al. claimed that J obtained by the approximate spin projection procedure reproduces the characteristic feature of J in the whole region [48,58,59]:

$$J^{(3)} = \frac{E_{BS} - E_T}{\langle S^2\rangle_T - \langle S^2\rangle_{BS}} \tag{4}$$

where $\langle S^2\rangle_T$ and $\langle S^2\rangle_{BS}$ denote the total spin angular momentum of triplet state and broken-symmetry singlet state, respectively. Thus the $J^{(3)}$ values obtained from Eq. (4) are employed in the following discussion.

In cases of both triplet and broken-symmetric states, the single point calculations for complex **1** have been performed on the non-modelized molecular geometry at the ub3lyp level with lanl2dz basis sets, and the molecular symmetry of **1** was restrained in the point group C_i owing to the feature of crystal structure. The cal-

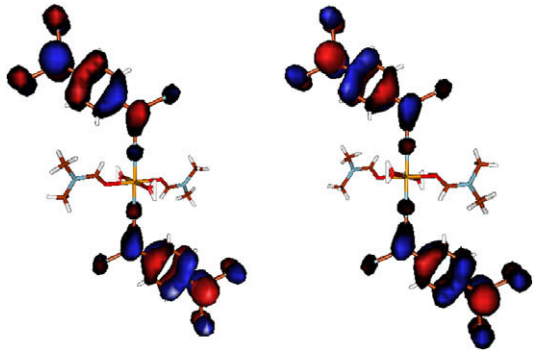


Fig. 5. Two SOMOs for the triplet state with E_{au} = −5.1277 eV and E_{ag} = −5.1201 eV.

culations indicated the singlet state is more stable than the triplet state, however, their energy gap is only 1.25×10^{-5} eV, and the estimated *J* value between two $TCNQ^-$ radicals is 0.145 K (the corresponding spin expected values for the triplet and broken-symmetric states are guesstimated as 2.0294 and 1.0294, respectively). Such small energy difference between the ground state and excited triplet state means the presence of partial population of excited triplet state (the two singly occupied molecular orbitals (SOMOs) with energy difference of 0.00762 eV is displayed in Fig. 5), and this prediction, is agreement with the paramagnetic character of this complex.

4. Conclusion

In summary, we synthesized and characterized structurally a new coordination compound consisting of Zn^{2+} with $TCNQ^-$ radical ligands. The crystal data indicates that the Zn^{2+} ion occupied at an inversion centre is bonded to two $TCNQ^-$ radical anions, two H_2O and two DMF molecules to form almost perfectly octahedral coordination geometry. The strong H-bonding (between the neighboring H_2O molecules as well as between H_2O molecule and $TCNQ^-$ radical anion) and $\pi\cdots\pi$ stack (between $TCNQ^-$ radical anions) interactions lead to a supramolecular network sheet forming on the crystallographic *ac*-plane, and the neighboring supramolecular network sheets further develop into three-dimensional supramolecular structure via weak van der Waals forces. Symmetry-broken approach in the theoretical formwork of DFT further disclosed that the ground state of **1** is singlet state, the excited triplet state is very closed to the nonmagnetic ground state with a small energy gap of 1.25×10^{-5} eV, and this prediction is in agreement with the paramagnetism of **1** observed in magnetic susceptibility. Within the TCNQ π-stacks, there exist antiferromagnetic (AFM) coupling interaction.

Acknowledgments

Authors thank the National Natural Science Foundation of China (Grant No. 20771006) and the Natural Science Foundation of the Education Committee, Anhui Province of China (Grant No. 2006kj042a) for financial support.

Appendix A. Supplementary data

CCDC 705240 contains the supplementary crystallographic data for **1**. These data can be obtained free of charge via http://www.ccdc.cam.ac.uk/conts/retrieving.html, or from the Cambridge Crystallographic Data Centre, 12 Union Road, Cambridge CB2 1EZ, UK; fax: (+44) 1223-336-033; or e-mail: deposit@ccdc.cam.ac.uk. Supplementary data associated with this article can be found, in the online version, at doi:10.1016/j.poly.2008.10.020.

References

[1] M. Mikuriya, D. Yoshioka, M. Handa, Coord. Chem. Rev. 250 (2006) 2194.
[2] W. Kaim, M. Moscherosch, Coord. Chem. Rev. 129 (1994) 157.
[3] H. Alves, A.S. Molinari, H. Xie, A.F. Morpurgo, Nat. Mater. 7 (2008) 574.
[4] N. Gonzalez-Lakunza, I. Fernández-Torrente, K.J. Franke, N. Lorente, A. Arnau, J.I. Pascual, Phys. Rev. Lett. 100 (2008) 156805.
[5] H. Okamoto, H. Matsuzaki, T. Wakabayashi, Y. Takahashi, T. Hasegawa, Phys. Rev. Lett. 98 (2007) 037401.
[6] A. Nafady, A.M. Bond, A. Bilyk, A.R. Harris, A.I. Bhatt, A.P. O'Mullane, R. DeMarco, J. Am. Chem. Soc. 129 (2007) 2369.
[7] M.B. Inoue, M. Inoue, Q. Fernando, K.W. Nebesny, J. Phys. Chem. 91 (1987) 527.
[8] O.H. LeBlanc Jr., J. Chem. Phys. 42 (1965) 4307.
[9] R. Jain, K. Kabir, J.B. Gilroy, K.A.R. Mitchell, K.-C. Wong, R.G. Hicks, Nature 445 (2007) 291.
[10] J.-H. Her, P.W. Stephens, K.I. Pokhodnya, M. Bonner, J.S. Miller, Angew. Chem. 119 (2007) 1543.
[11] H. Miyasaka, T. Izawa, N. Takahashi, M. Yamashita, K.R. Dunbar, J. Am. Chem. Soc. 128 (2006) 11358.
[12] M.L. Taliaferro, F. Palacio, J.S. Miller, J. Mater. Chem. 16 (2006) 2677.
[13] E.B. Vickers, T.D. Selby, M.S. Thorum, M.L. Taliaferro, J.S. Miller, Inorg. Chem. 43 (2004) 6414.
[14] J.M. Manriquez, G.T. Yee, R.S. McLean, A.J. Epstein, J.S. Miller, Science 252 (1991) 1415.
[15] J.S. Miller, J.C. Calabrese, R.L. Harlow, D.A. Dixon, J.H. Zhang, W.M. Reiff, S. Chittipeddi, M.A. Selover, A.J. Epstein, J. Am. Chem. Soc. 112 (1990) 5496.
[16] J.S. Miller, J.C. Calabrese, H. Rommelmann, S. Chittipeddi, J.H. Zhang, W.M. Reiff, A.J. Epstein, J. Am. Chem. Soc. 109 (1987) 769.
[17] J.S. Miller, J.C. Calabrese, A.J. Epstein, R.W. Bigelow, J.H. Zhang, W.M. Reiff, J. Chem. Soc., Chem. Commun. (1986) 1026.
[18] M.T. Azcondo, L. Ballester, S. Golhen, A. Gutierrez, L. Ouahab, S. Yartsev, P. Delhaes, J. Mater. Chem. 9 (1999) 1237.
[19] J.B. Torrance, B.A. Scott, F.B. Kaufman, Solid State Commun. 17 (1975) 1369.
[20] M. Konno, Y. Saito, Acta Crystallogr., Sect. B 30 (1974) 1294.
[21] J.G. Vegter, T. Hmma, J. Kommandetm, Chem. Phys. Lett. 3 (1969) 427.
[22] T. Erlbacher, M.P.M. Jank, H. Ryssel, L. Frey, R. Engl, A. Walter, R. Sezi, C. Dehmf, J. Electrochem. Soc. 155 (2008) H893.
[23] T. Kever, U. Böttger, C. Schindler, R. Wasser, Appl. Phys. Lett. 91 (2007) 083506.
[24] R. Muller, J. Genoe, P. Heremans, Appl. Phys. Lett. 88 (2006) 242105.
[25] C.A. Di, G. Yu, Y.Q. Liu, X.J. Xu, D.C. Wei, Y.B. Song, Y.M. Sun, Y. Wang, D.B. Zhu, J. Liu, X.Y. Liu, D.X. Wu, J. Am. Chem. Soc. 128 (2006) 16418.
[26] T. Oyamada, H. Tanaka, K. Matsushige, H. Sasabe, C. Adachi, Appl. Phys. Lett. 83 (2003) 1252.
[27] X.G. Wan, J. Li, D.Y. Chen, Y.M. Jiang, Z.Y. Hua, Phys. Stat. Sol. (a) 181 (2000) R13.
[28] R.S. Potember, T.O. Poehler, D.O. Cowan, Appl. Phys. Lett. 34 (1979) 405.
[29] J.J. Hoagland, X.D. Wang, K.W. Hipps, Chem. Mater. 5 (1993) 54.
[30] R.S. Potember, T.O. Poehler, R.C. Benson, Appl. Phys. Lett. 41 (1982) 548.
[31] X.L. Mo, G.R. Chen, Q.J. Cai, Z.Y. Fan, H.H. Xu, Y. Yao, J. Yang, H.H. Gu, Z.Y. Hua, Thin Solid Films 436 (2003) 259.
[32] H.L. Peng, Z. Chen, L.M. Tong, X.C. Yu, C.B. Ran, Z.F. Liu, J. Phys. Chem. B 109 (2005) 3526.
[33] C.B. Ran, H.L. Peng, W. Zhou, X.C. Yu, Z.F. Liu, J. Phys. Chem. B 109 (2005) 22486.
[34] D.F. Perepichka, M.R. Bryce, C. Pearson, M.C. Petty, E.J.L. McInnes, J.P. Zhao, Angew. Chem., Int. Ed. 42 (2003) 4636.
[35] J. Lu, S. Nagase, X.W. Zhang, D. Wang, M. Ni, Y. Maeda, T. Wakahara, T. Nakahodo, T. Tsuchiya, T. Akasaka, Z.X. Gao, D.P. Yu, H.Q. Ye, W.N. Mei, Y.S. Zhou, J. Am. Chem. Soc. 128 (2006) 5114.
[36] Y. Morita, E. Miyazaki, Y. Umemoto, K. Fukui, K. Nakasuji, J. Org. Chem. 71 (2006) 5631.
[37] E. Tsiperman, J.Y. Becker, V. Khodorkovsky, A. Shames, L. Shapiro, Angew. Chem., Int. Ed. 44 (2005) 4015.
[38] K.I. Pokhodnya, N. Petersen, J.S. Miller, Inorg. Chem. 41 (2002) 1996.
[39] H. Miyasaka, C.S. Campos-Fernandez, R. Clerac, K.R. Dunbar, Angew. Chem., Int. Ed. 39 (2000) 3831.
[40] L.R. Melby, R.J. Harder, W.R. Hertler, W. Mahler, R.E. Benson, W.E. Mochel, J. Am. Chem. Soc. 84 (1962) 3374.
[41] R.L. Carlin, Magnetochemistry, Springer-Verlag Publisher, Berlin, Heidelberg, 1986. p. 3.
[42] G.M. Sheldrick, SHELXTL, Structure Determination Software Programs, Version 5.10. Bruker Analytical X-ray Systems Inc., Madison, Wisconsin, USA, 1997.
[43] M.J. Frisch, G.W. Trucks, H.B. Schlegel, G.E. Scuseria, M.A. Robb, J.R. Cheeseman, V.G. Zakrzewski, J.A. Montgomery Jr., R.E. Stratmann, J.C. Burant, S. Dapprich, J.M. Millam, A.D. Daniels, K.N. Kudin, M.C. Strain, O. Farkas, J. Tomasi, V. Barone, M. Cossi, R. Cammi, B. Mennucci, C. Pomelli, C. Adamo, S. Clifford, J. Ochterski, G.A. Petersson, P.Y. Ayala, Q. Cui, K. Morokuma, P. Salvador, J.J. Dannenberg, D.K. Malick, A.D. Rabuck, K. Raghavachari, J.B. Foresman, J. Cioslowski, J.V. Ortiz, A.G. Baboul, B.B. Stefanov, G. Liu, A. Liashenko, P. Piskorz, I. Komaromi, R. Gomperts, R.L. Martin, D.J. Fox, T. Keith, M.A. Al-Laham, C.Y. Peng, A. Nanayakkara, M. Challacombe, P.M.W. Gill, B. Johnson, W. Chen, M.W. Wong, J.L. Andres, C. Gonzalez, M. Head-Gordon, E.S. Replogle, J.A. Pople, GAUSSIAN 98, Revision A.11, Gaussian, Inc., Pittsburgh, PA, 2001.

[44] G.J. Ashwell, D.D. Eley, A. Harper, A.C. Torrance, S.C. Wallwork, M.R. Willis, Acta Crystallogr., Sect. B 33 (1977) 2258.
[45] P.P. Richard, J.-C. Zanghi, J.-F. Guédon, N. Hota, Acta Crystallogr., Sect. B 34 (1978) 788.
[46] A. Hoekstra, T. Spoelder, A. Vos, Acta Crystallogr., Sect. B 28 (1972) 14.
[47] L. Noodleman, J.G. Norman Jr., J. Chem. Phys. 70 (1979) 4903.
[48] H. Nagao, M. Nishino, Y. Shigeta, T. Soda, Y. Kitagawa, T. Onishi, Y. Yoshioka, K. Yamaguchi, Coord. Chem. Rev. 198 (2000) 265.
[49] I. Ciofini, C.A. Daul, Coord. Chem. Rev. 238–239 (2003) 187.
[50] W. Heisenberg, Z. Phys. 49 (1928) 619.
[51] P.A.M. Dirac, The Principles of Quantum Mechanics, Clarendon Press, Oxford, UK, 1947.
[52] J.H. Van Vleck, The Theory of Electric and Magnetic Susceptibilities, Oxford University Press, Oxford, UK, 1932.
[53] A.P. Ginsberg, J. Am. Chem. Soc. 102 (1980) 111.
[54] L. Noodleman, J. Chem. Phys. 74 (1981) 5737.
[55] L. Noodleman, E.R. Davidson, Chem. Phys. 109 (1986) 131.
[56] A. Bencini, F. Totti, C.A. Daul, K. Doclo, P. Fantucci, V. Barone, Inorg. Chem. 36 (1997) 5022.
[57] E. Ruiz, J. Cano, S. Alvarez, P. Alemany, J. Comput. Chem. 20 (1999) 1391.
[58] T. Soda, Y. Kitagawa, T. Onishi, Y. Takano, Y. Shigeta, H. Nagao, Y. Yoshioka, K. Yamaguchi, Chem. Phys. Lett. 319 (2000) 223.
[59] Y. Takano, Y. Kitagawa, T. Onishi, Y. Yoshioka, K. Yamaguchi, N. Koga, H. Iwamura, J. Am. Chem. Soc. 124 (2002) 450.

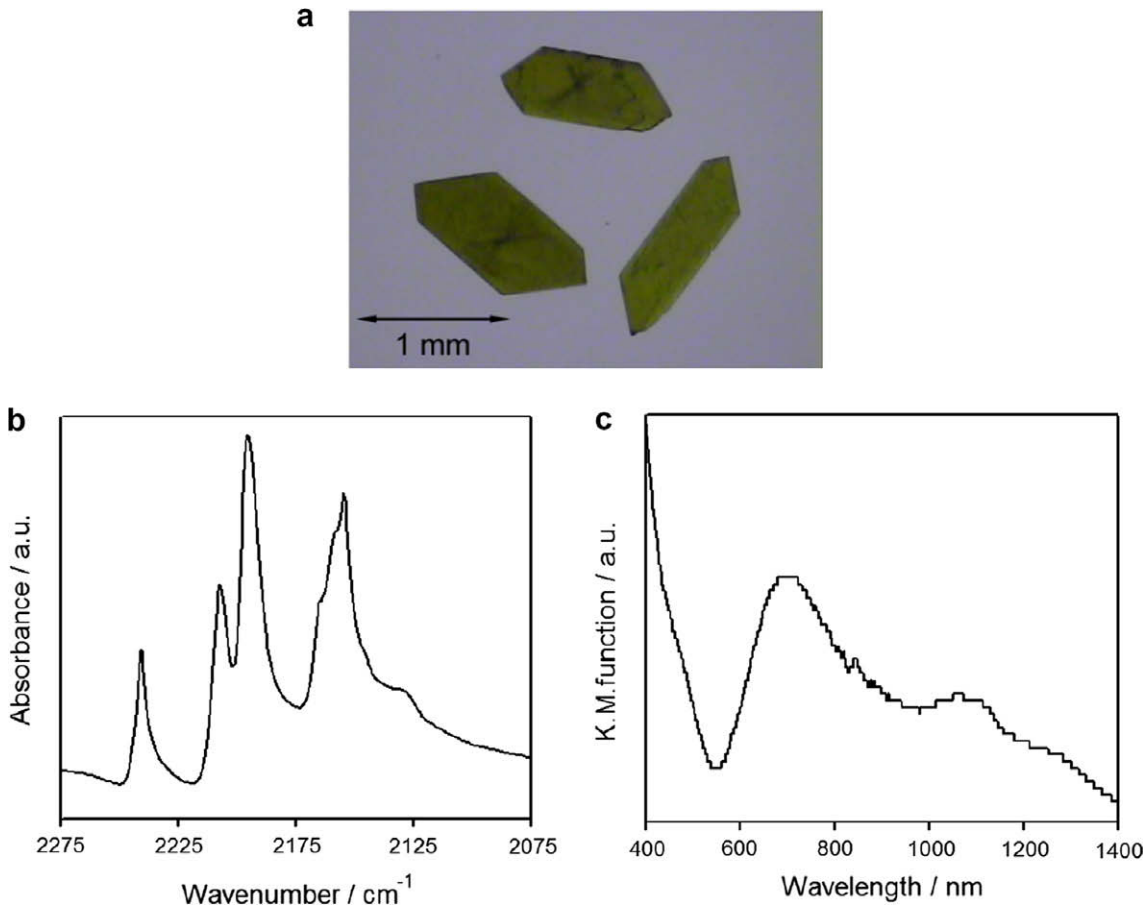


Fig. 1. (a) Photograph of green plate-type crystals, (b) IR spectrum, and (c) UV–Vis reflectance spectrum of $Cu_3[W(CN)_8]_2(pyrimidine)_2(3\text{-cyanopyridine})_2 \cdot 4H_2O$. (For interpretation of the references to colour in this figure legends, the reader is referred to the web version of this article.)

3. Results and discussion

3.1. Crystal structure

The prepared compound precipitated as green, plate-like crystals (Fig. 1a). In the Infrared (IR) spectra, CN stretching peaks were observed at 2155, 2159, 2165, 2195, 2207, and 2241 cm^{-1} (Fig. 1b). The peaks are attributed to the stretching vibrations of $[W(CN)_8]^{3-}$ ($\nu_{C\equiv N}$ = 2155, 2159, 2165, 2195, and 2207 cm^{-1}) and 3-cyanopyridine ($\nu_{C\equiv N}$ = 2241 cm^{-1}). The UV–Vis reflectance spectra showed absorption bands around 700 and 1100 nm due to the d–d transition on Cu^{II} (Fig. 1c). X-ray crystallographic analysis indicated that the asymmetric unit consists of a $[W(CN)_8]^{3-}$ anion, one-half of a $[Cu1(H_2O)_2]^{2+}$ cation, one-half of a $[Cu2(pyrimidine)_2]^{2+}$ cation, one-half of a $[Cu3(3\text{-cyanopyridine})]^{2+}$ cation, and a water molecule. Cu1 is coordinated to two nitrogen atoms from the CN ligands, two nitrogen atoms from the pyrimidine molecules, and two oxygen atoms from the H_2O molecules (Fig. 2a). Cu2 is coordinated to four nitrogen atoms from the CN ligands and two nitrogen atoms from the pyrimidine molecules, while Cu3 is coordinated to four nitrogen atoms from the CN ligands and two nitrogen atoms from the 3-cyanopyridine molecules.Fig. 2b and c shows the crystal structure for the *ac*-plane and *ab*-plane, respectively. The cyano-bridged-Cu2–W–Cu3-layer (Fig. 2b) is linked by a Cu1 pillar unit (Fig. 2c). In addition, a cavity exists along the *a* axis, which is occupied by 3-cyanopyridine molecules and zeolitic water molecules (Fig. 2d).

3.2. Magnetic properties

Fig. 3a and b shows the magnetic properties of the present compound. The field-cooled magnetization (FCM) curve at 10 Oe showed a spontaneous magnetization with a Curie temperature (T_c) of 7 K (Fig. 3a). The zero-field-cooled magnetization (ZFCM) and remnant magnetization (RM) curves also supported this T_c value. The magnetization versus external magnetic field curve at 2 K showed a coercive field (H_c) of 7 Oe and a saturation magnetization (M_s) value of 2.9 μ_B for the given formula (Fig. 3b). This M_s value indicates that this compound is a ferrimagnet where the W^{5+} ions ($S = 1/2$) and Cu^{2+} ions (Cu2 and Cu3) in the layer are ferromagnetically coupled, and W^{5+} ions and the bridged Cu^{2+} ions (Cu1) are antiferromagnetically coupled (Fig. 3c), i.e., $M_s = 2(S_{Cu} + S_{Cu} + 2S_W - S_{Cu}) = 3\ \mu_B$, assuming the *g*-factors of Cu^{II} and W^{V} are 2.0.

4. Conclusion

We prepared a new type of cyano-bridged Cu–W bimetallic assembly, $Cu_3[W(CN)_8]_2(pyrimidine)_2(3\text{-cyanopyridine})_2 \cdot 4H_2O$. This compound contains two types of organic ligands, and shows a ferrimagnetism with T_C of 7 K, M_s of 2.9 μ_B, and H_c of 7 Oe at 2 K. The framework of the present compound is analogous with $Co_3[W(CN)_8]_2(pyrimidine)_4 \cdot 6H_2O$, which shows thermally and optically charge-transfer phase transition [10]. Because one route to prepare nanoporous magnets with sophisticated geometrical

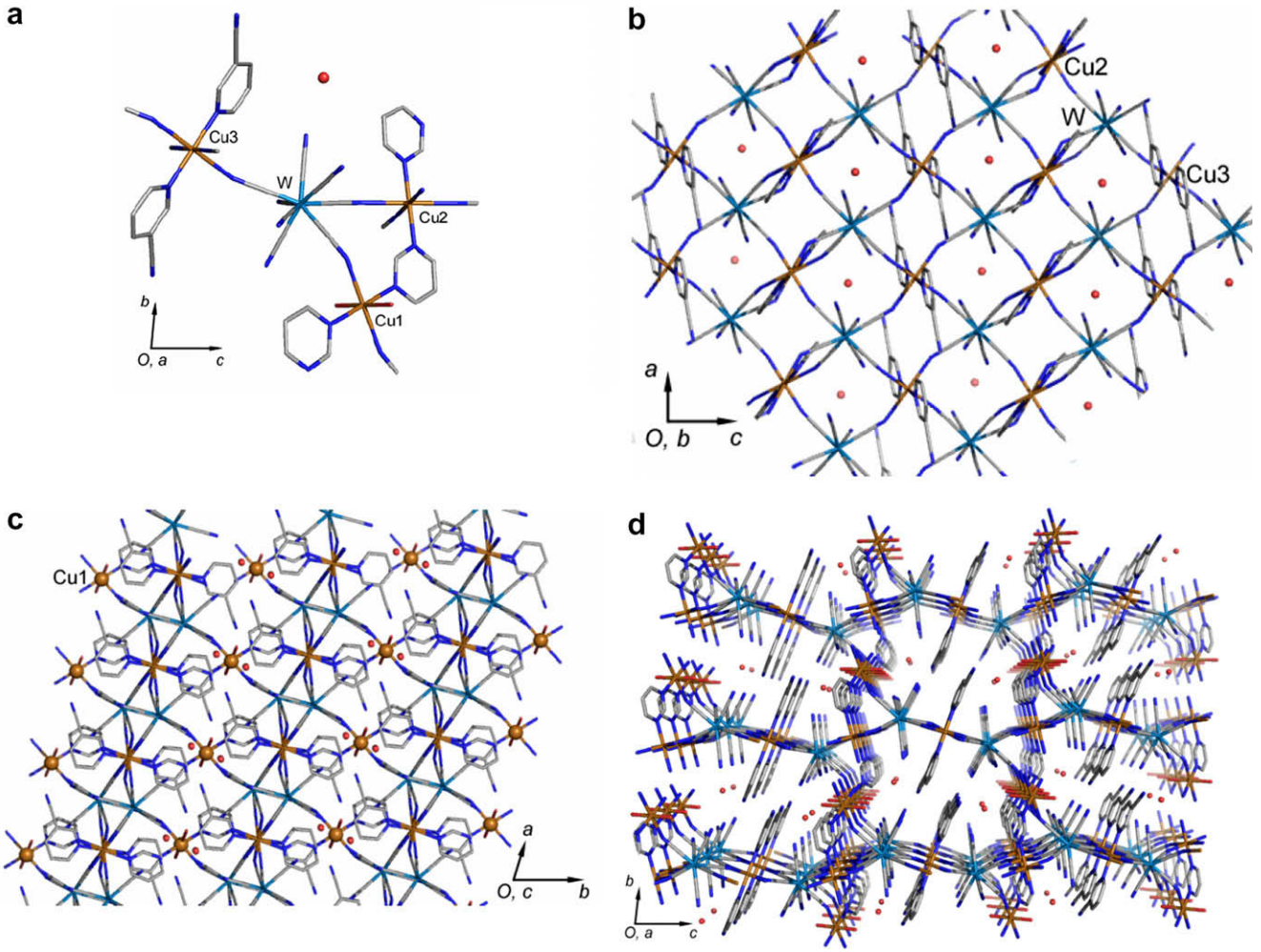


Fig. 2. X-ray crystal structure of $Cu_3[W(CN)_8]_2(pyrimidine)_2(3\text{-cyanopyridine})_2 \cdot 4H_2O$. Light blue, orange, gray, blue, and red represent W, Cu, C, N, and O atoms, respectively (in print, right gray and dark gray except for Cu and W in the frame work represent C and N, respectively). Hydrogen atoms are omitted for clarity. (a) Coordination environment around W and Cu atoms. (b) Cyano-bridged-Cu2–W–Cu3-layer in the *a*–*c* plane. (c) View along the *c* axis. Cu1 ions are represented by orange spheres. (d) View along the pore direction, the *a* axis. (For interpretation of the references to colour in this figure legends, the reader is referred to the web version of this article.)

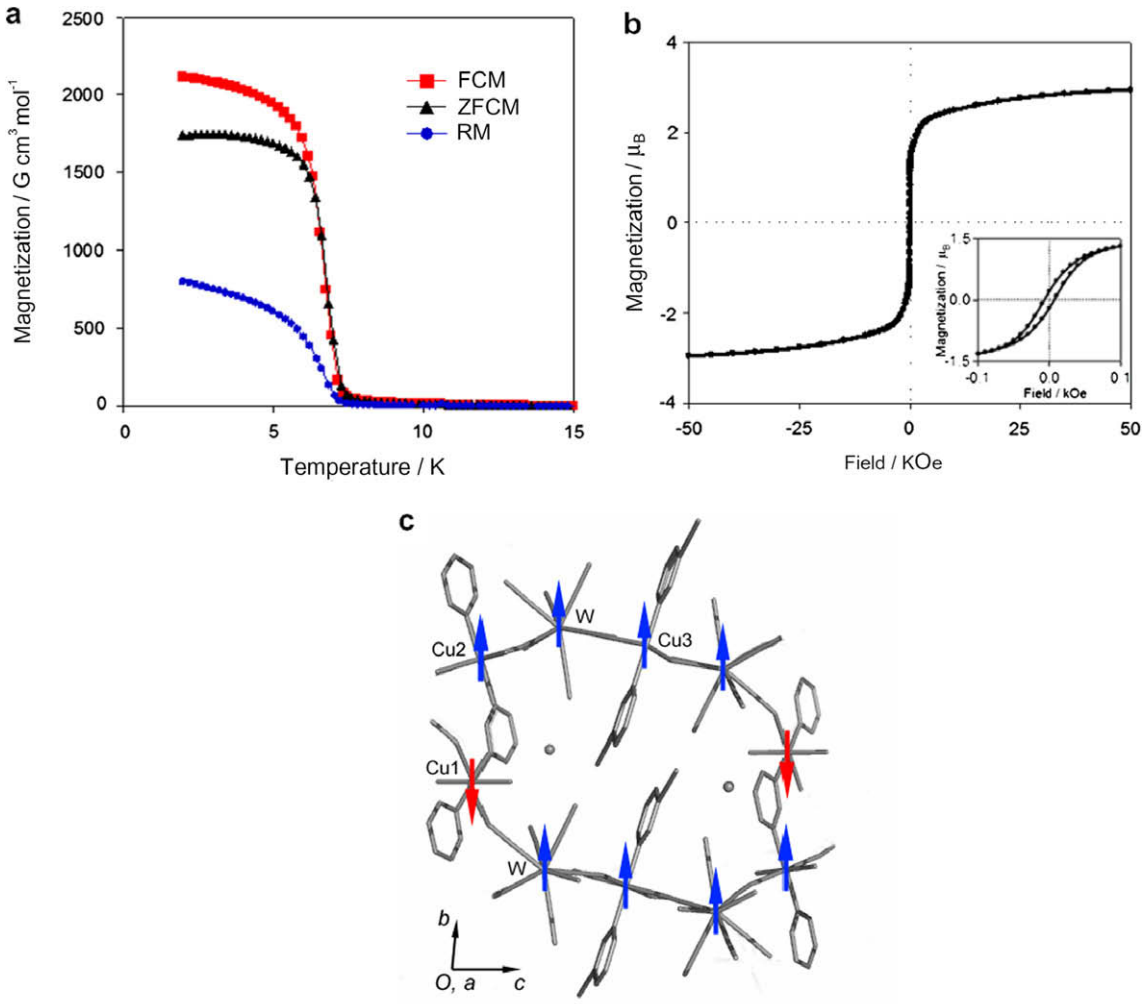


Fig. 3. Magnetic properties of $Cu_3[W(CN)_8]_2(pyrimidine)_2(3\text{-cyanopyridine})_2 \cdot 4H_2O$. (a) (■) Field-cooled magnetization (FCM) obtained with decreasing temperature (15 K → 2 K) in an applied field of 10 Oe; (▲) zero-field-cooled magnetization (ZFCM) with increasing temperature (2 K → 15 K) in an applied field of 10 Oe after the temperature was initially lowered in a zero field; (●) remnant magnetization (RM) obtained with increasing temperature (2 K → 15 K) after the temperature was initially lowered in an applied magnetic field of 10 Oe. (b) Magnetic field dependence of magnetization at 2 K. (c) Schematic illustration of the ferrimagnetic spin alignment. As denoted by the up arrows (blue), W, Cu2, and Cu3 ions in the layer are ferromagnetically coupled. As noted by the down arrows (red), Cu1 ions between the layers are antiferromagnetically coupled to the W ions. (For interpretation of the references to colour in this figure legends, the reader is referred to the web version of this article.)

structures is to combine multiple organic ligands, we are considering that the results presented herein may realize nanoporous magnets with unique functionalities.

Acknowledgments

The present research was supported in part by a Grant for the Global COE Program, "Chemistry Innovation through Cooperation of Science and Engineering", a Grant-in-Aid for Young Scientists (S) from Japan Society for the Promotion of Science (JSPS), The Inamori Foundation, The Kurata Memorial Hitachi Science and Technology Foundation.

Appendix A. Supplementary data

CCDC 702174 contains the supplementary crystallographic data for this paper. These data can be obtained free of charge via http://www.ccdc.cam.ac.uk/conts/retrieving.html, or from the Cambridge Crystallographic Data Centre, 12 Union Road, Cambridge CB2 1EZ, UK; fax: (+44) 1223-336-033; or e-mail: deposit@ccdc.cam.ac.uk. Supplementary data associated with this article can be found, in the online version, at doi:10.1016/j.poly.2008.10.065.

References

[1] R. Garde, C. Desplanches, A. Bleuzen, P. Veillet, M. Verdaguer, Mol. Cryst. Liq. Cryst. 334 (1999) 587.
[2] Z.J. Zhong, H. Seino, Y. Mizobe, M. Hidai, M. Verdaguer, S. Ohkoshi, K. Hashimoto, Inorg. Chem. 39 (2000) 5095.
[3] M. Pilkington, S. Decurtins, Chimica 54 (2000) 539.
[4] Y. Arimoto, S. Ohkoshi, Z.J. Zhong, H. Seino, Y. Mizobe, K. Hashimoto, J. Am. Chem. Soc. 125 (2003) 9240.
[5] L. Catala, C. Mathonière, A. Gloter, O. Stephan, T. Gacoin, J.-P. Boilot, T. Mallah, Chem. Commun. (2005) 746.
[6] S. Ohkoshi, S. Ikeda, T. Hozumi, T. Kashiwagi, K. Hashimoto, J. Am. Chem. Soc. 128 (2006) 5320.
[7] S. Ohkoshi, Y. Tsunobuchi, H. Takahashi, T. Hozumi, M. Shiro, K. Hashimoto, J. Am. Chem. Soc. 129 (2007) 3084.
[8] S. Ohkoshi, Y. Arimoto, T. Hozumi, H. Seino, Y. Mizobe, K. Hashimoto, Chem. Commun. (2003) 2772.
[9] M. Arai, W. Kosaka, T. Matsuda, S. Ohkoshi, Angew. Chem., Int. Ed. 47 (2008) 6885.
[10] S. Ohkoshi, Y. Hamada, T. Matsuda, Y. Tsunobuchi, H. Tokoro, Chem. Mater. 20 (2008) 3048.
[11] W. Kosaka, K. Hashimoto, S. Ohkoshi, Bull. Chem. Soc. Jpn. 81 (2008) 992.

[12] (a) Z.J. Zhong, H. Seino, Y. Mizobe, M. Hidai, A. Fujishima, S. Ohkoshi, K. Hashimoto, J. Am. Chem. Soc. 122 (2000) 2952;
(b) J. Larionova, M. Gross, M. Pilkington, H. Andres, H. Stoeckli-Evans, H.U. Güdel, S. Decurtins, Angew. Chem., Int. Ed. 39 (2000) 1605;
(c) B. Sieklucka, J. Szklarzewicz, Inorg. Chem. 39 (2000) 5156;
(d) F. Bonadio, M. Gross, H. Stoeckli-Evans, S. Decurtins, Inorg. Chem. 41 (2002) 5891;
(e) J.M. Herrera, V. Marvaud, M. Verdaguer, J. Marrot, M. Kalisz, C. Mathonière, Angew. Chem., Int. Ed. 43 (2004) 2;
(f) Y. Song, P. Zhang, X.-M. Ren, X.-F. Shen, Y.-Z. Li, X.-Z. You, J. Am. Chem. Soc. 127 (2005) 3708;
(g) D.E. Freedman, M.V. Bennett, J.R. Long, Dalton Trans. 23 (2006) 2829;
(h) J.H. Lim, J.H. Yoon, H.C. Kim, C.S. Hong, Angew. Chem., Int. Ed. 45 (2006) 7424.

[13] (a) G. Rombaut, S. Golhen, L. Ouahab, C. Mathonière, O. Kahn, J. Chem. Soc., Dalton Trans. (2000) 3609;
(b) R. Podgajny, T. Korzeniak, K. Stadnicka, Y. Dromzée, N.W. Alcock, W. Errington, K. Kruczała, M. Balanda, T.J. Kemp, M. Verdaguer, B. Sieklucka, Dalton Trans. (2003) 3458;
(c) R. Pradhan, C. Desplanches, P. Guionneau, J.-P. Sutter, Inorg. Chem. 42 (2003) 6607;
(d) D. Li, L. Zheng, Y. Zhang, J. Huang, S. Gao, W. Tang, Inorg. Chem. 42 (2003) 6123;
(e) Y.S. You, D. Kim, Y. Do, S.J. Oh, C.S. Hong, Inorg. Chem. 43 (2004) 6899;
(f) S. Ikeda, T. Hozumi, K. Hashimoto, S. Ohkoshi, Dalton Trans. (2005) 2120;
(g) D. Matoga, M. Mikuriya, M. Handa, J. Szklarzewicz, Chem. Lett. 34 (2005) 1550;
(h) P. Przychodzeń, K. Lewiński, R. Pelka, M. Balanda, K. Tomala, B. Sieklucka, Dalton Trans. (2006) 625;
(i) F. Prins, E. Pasca, L.J. Jongh, H. Kooijman, A.L. Spek, S. Tanase, Angew. Chem., Int. Ed. 46 (2007) 6081.

[14] (a) R. Podgajny, T. Korzeniak, M. Balanda, T. Wasiutynski, W. Errington, T.J. Kemp, N.W. Alcock, B. Sieklucka, Chem. Commun. (2002) 1138;
(b) J. Larionova, R. Clérac, B. Donnadieu, S. Willemin, C. Guérin, Cryst. Growth Des. 3 (2003) 267;
(c) T. Korzeniak, K. Stadnicka, M. Rams, B. Sieklucka, Inorg. Chem. 43 (2004) 4811;
(d) S. Kaneko, Y. Tsunobuchi, S. Sakurai, S. Ohkoshi, Chem. Phys. Lett. 446 (2007) 292.

[15] (a) Y. Song, S. Ohkoshi, Y. Arimoto, H. Seino, Y. Mizobe, K. Hashimoto, Inorg. Chem. 42 (2003) 1848;
(b) J.M. Herrera, A. Bleuzen, Y. Dromzée, M. Julve, F. Lloret, M. Verdaguer, Inorg. Chem. 42 (2003) 7052;
(c) T. Hozumi, S. Ohkoshi, Y. Arimoto, H. Seino, Y. Mizobe, K. Hashimoto, J. Phys. Chem. B 107 (2003) 74;
(d) T. Kashiwagi, S. Ohkoshi, H. Seino, Y. Mizobe, K. Hashimoto, J. Am. Chem. Soc. 126 (2004) 5024;
(e) T. Hozumi, K. Hashimoto, S. Ohkoshi, J. Am. Chem. Soc. 127 (2005) 3864;
(f) Z.-X. Wang, X.-F. Shen, J. Wang, P. Zhang, Y.-Z. Li, E.N. Nfor, Y. Song, S. Ohkoshi, K. Hashimoto, X.-Z. You, Angew. Chem., Int. Ed. 45 (2006) 3287;
(g) J.R. Withers, D. Li, J. Triplet, C. Ruschman, S. Parkin, G. Wang, G.T. Yee, S.M. Holmes, Inorg. Chem. 45 (2006) 4307;
(h) S. Ohkoshi, H. Tokoro, T. Hozumi, Y. Zhang, K. Hashimoto, C. Mathonière, I. Bord, G. Rombaut, M. Verelst, C. Cartier dit Moulin, F. Villain, J. Am. Chem. Soc. 128 (2006) 270.

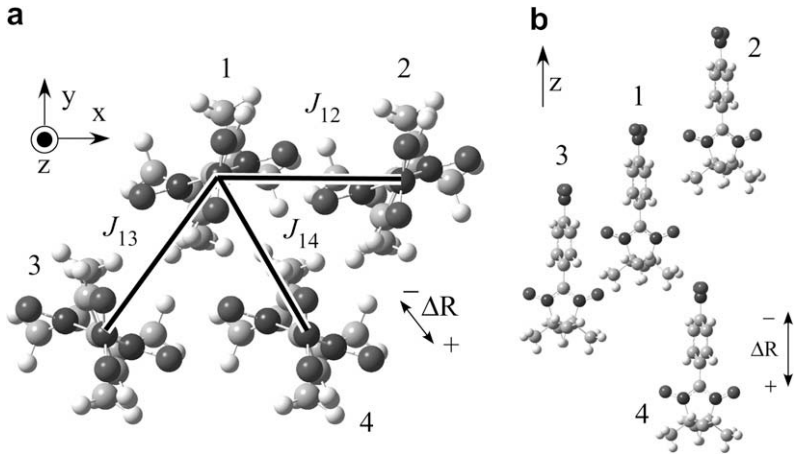


Fig. 1. (a) The crystal structure of the β-phase of *p*-NPNN with the *fdd*2 space symmetry where 1–4 denote the nearest neighbor *p*-NPNN molecules. J_{ab} (a,b = 1–4) denote the effective exchange integrals between them, (b) sliding dimer models of *p*-NPNN along the lattice axes which include variations of the J_{12} and J_{13} interactions.

Table 1
Effective exchange integral J_{ab}[a] (cm^{-1}) of the shifted tacking models of β-phase *p*-NPNN.

Δ*R* (Å)	J_{12}		J_{13}		J_{14}	
	x-axis	*z*-Axis	*xy*-plane	*z*-Axis	*xy*-plane	*z*-Axis
−1.0	2.993	0.612	1.700	1.172	0.007	−0.026
−0.8	1.839	0.628	2.721	1.332	0.007	−0.020
−0.6	1.111	0.573	2.367	1.356	0.004	−0.015
−0.4	0.669	0.474	1.688	1.236	0.002	−-0.007
−0.2	0.406	0.358	1.078	0.988	0.002	−0.002
0.0	0.248	0.248	0.652	0.652	0.000	0.000
0.2	0.149	0.162	0.382	0.292	0.000	0.002
0.4	0.097	0.094	0.226	−0.046	0.000	0.004
0.6	0.050	0.048	0.121	−0.305	0.000	0.007
0.8	0.026	0.015	0.068	−0.485	−0.002	0.007
1.0	0.015	0.002	0.035	−0.564	0.000	0.007

[a] UB3LYP/6-31G**.

the largest J_{ab} values calculated by INDO method was J_{12}. Therefore, the pressure effect for the β-phase *p*-NPNN crystal must be reinvestigated by UB3LYP that is more accurate than INDO method.

Since the X-ray structure of the β-phase *p*-NPNN under the high-pressure at low temperature is not known in detail, we have to consider the appropriate models for structure deformation which would be essential for qualitative understanding of the pressure effect. Takeda and co-workers reported relations between induced pressures and cell parameters. However, the geometry changes of *p*-NPNN molecules in the β-phase and the changes of the three dimensional stacking modes of the neighboring molecules were not known. Therefore, several sliding models of *p*-NPNN along the several lines were examined in order to elucidate variations of three J_{ab} values shown in Fig. 1a and b. In Table 1 the calculation results were summarized. The magnitude of the J_{12} value was variable with the sliding along the *x*- or *z*-axis, but its sign was invariant by this type of deformations. It could be concluded that the two dimensional ferromagnetic spin alignments in the *ac* plane remains intact after the sliding deformation of *p*-NPNN along the *x*- or *z*-axis.

As the J_{13} value is responsible for the effective exchange interaction between the *ac*-planes, the variation of J_{13} value is important for the creation of the three dimensional magnetic ordering. As a model for the pressure effects for the interplane interaction, *p*-NPNN (**3**) shown in Fig. 1 was shifted to the central *p*-NPNN (**1**) on the *xy*-plane. This means that the interplane distance between the *ac* planes is retained to be constant. The intermolecular distance (R) was expressed by the interatomic distance between the central carbon atoms of the nitronyl nitroxide groups, and the negative Δ*R* means the decrease of the intermolecular distance. From Table 1, it was found that the sign of J_{13} was changed in the case of *z*-axis sliding model. These results suggest that the J_{13} value is determined by the delicate balance of the two terms that are the ferromagnetic O–C1 interaction and the antiferro-magnetic O–C2 interaction in the normal condition as shown in Fig. 3. Therefore, this indicates that the radical spins in the neighboring *p*-NPNN molecules are aligned in parallel as the ferromagnetic O–C1 interaction overcome the antiferro-magnetic O–C2 interaction in the normal condition. However, the latter became predominant if Δ*R* was elongated, namely in the case of Δ*R* = 0.4–1.0 A.

The sign and magnitude of J_{14} were almost constant and small by the sliding deformations along the 1–4 line on the *xy*-plane and *z*-axis as shown in Table 1. Therefore, it was found that the J_{14} term is not essential for variations of the magnetism.

The rotations of substituents provide another possibility for modeling conformational changes under the high pressure conditions. We here examined variations of the interplane angle between nitronyl nitroxide and nitroxide groups. The side view of the rotational process was illustrated in Fig. 2a. The deformations were restricted to retain the crystal symmetry by assuming the concerted rotations of both components in Fig. 2. Fig. 4 shows variations of J_{12} with the rotational angles. The J_{12} value became negative by the rotation of nitroxide group at the ranges of the rotational angle from 25° to 45° and from 75° to 90°. Thus the ferromagnetic interaction within the *ac* plane can be destroyed by the rotation of nitroxide group of *p*-NPNN.

The rotation of nitrophenyl group was also examined as illustrated in Fig. 2b. Fig. 5 shows variations of J_{13} with the rotational angle. The calculated J_{13} values which exhibited antiferro-magnetic behavior at the ranges of the rotational angle from 15° to 25° and from −70° to −90°. Therefore, the ferro- to antiferro-magnetic transition for the interplane interaction was caused by the rotation which would be reasonable from the view point of the lattice compression by the high pressure.

Since the X-ray structure of β-phase under the high-pressure at low temperature is not known, we here consider plausible models for structure changes which would be essential for qualitative understanding of the effect. Takeda and co-workers reported relations between induced pressures (kPa) and cell parameters (a, b, c). Therefore, we examined the lattice compression dimer models with the internal rotation of nitronyl nitroxide group in *p*-NPNN

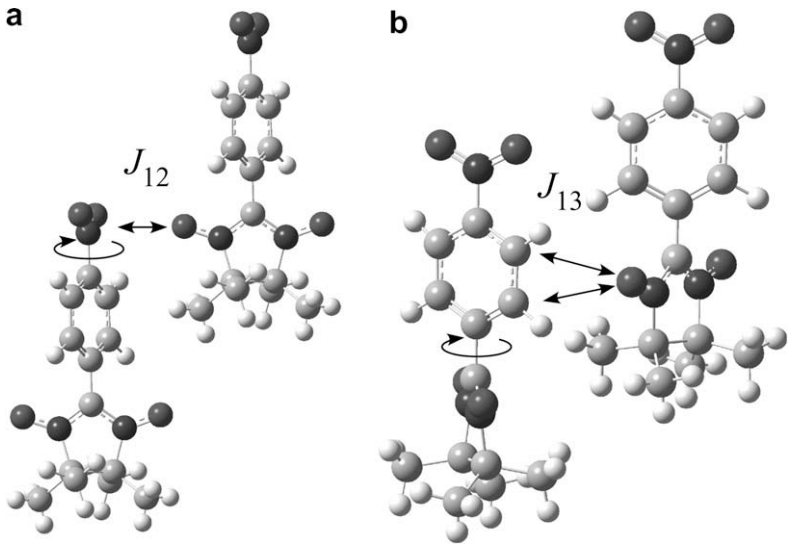


Fig. 2. The schematic diagrams of (a) rotational deformation of nitroxide group of *p*-NPNN which is responsible for variation of J_{12} and (b) rotational deformation of nitrophenyl group of *p*-NPNN which is responsible for variation of J_{13}.

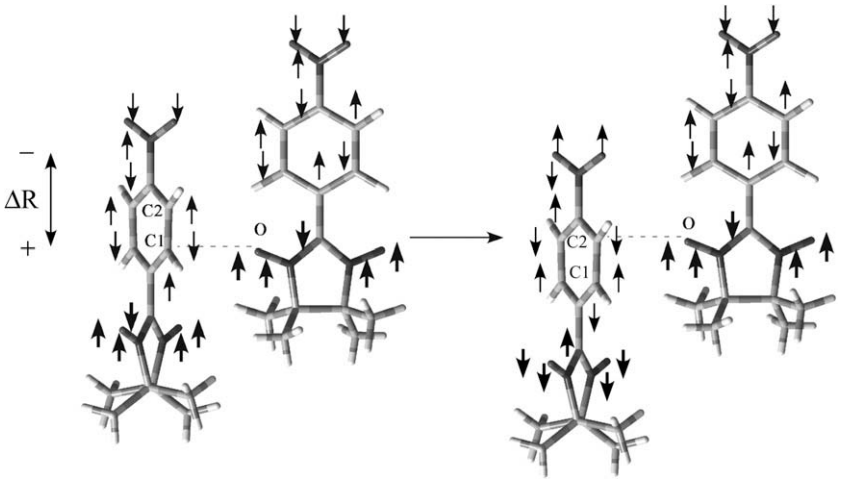


Fig. 3. The schematic illustrations of the magnetic interaction between the neighboring *p*-NPNN clusters in the case of sliding models along the *z*-axis.

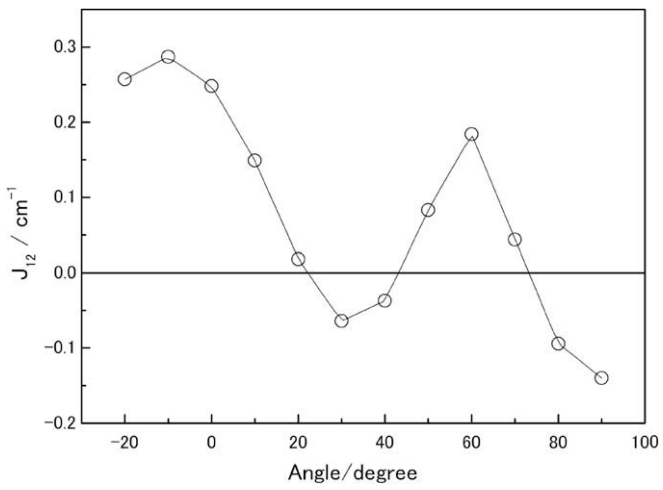


Fig. 4. Variations of the J_{12} values with the rotational process of nitroxide group of *p*-NPNN molecules.

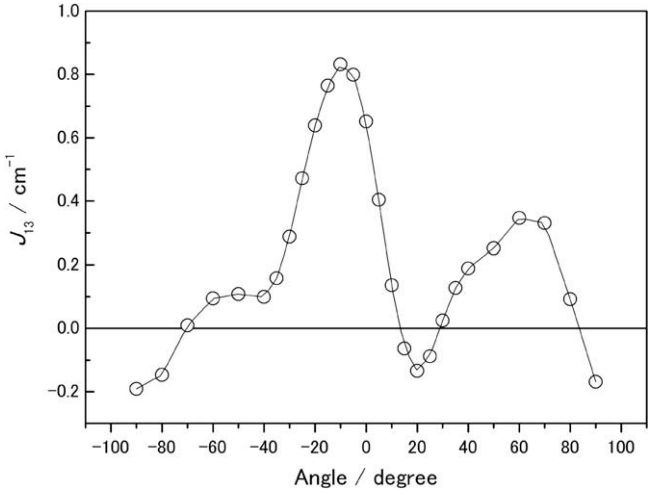


Fig. 5. Variations of the J_{13} values with the rotational process of nitrophenyl group of *p*-NPNN molecules.

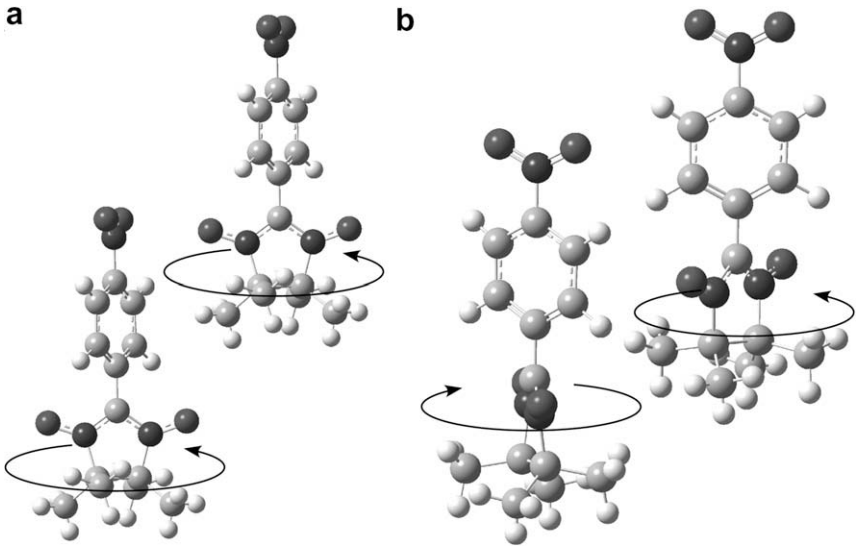


Fig. 6. The lattice compression models with the internal rotations of nitronyl nitroxide groups of *p*-NPNN molecules (a) J_{12} type and (b) J_{13} type dimer models.

Table 2
Variations of the J_{ab}[a] for the lattice compression dimer models with the internal rotations of nitronyl nitroxide group of *p*-NPNN molecules.

Angle (°)	J_{12} (cm^{-1})	J_{13} (cm^{-1})
−20.0	−0.176	0.845
−10.0	−0.070	0.209
0.00	0.651	1.488
10.0	0.691	5.849
20.0	0.235	5.655
30.0	−0.015	−0.386

[a] UB3LYP/6-31G**.

that lattice constants were varied so as to account for the decrease of intermolecular distances between the neighboring molecules. The cell parameters used in these calculations were those in the highest pressure condition (12.6 kPa). The cluster models examined were displayed in Fig. 6. The obtained J_{12} and J_{13} values were summarized in Table 2. The signs of J_{12} and J_{13} values were changed when the large internal rotations occurred in these models. Thus, these results indicate that the ferro- to antiferro-magnetic transition is also presented in these model systems. From these calculations, it could be presumed that the complex structure changes for the β-phase *p*-NPNN crystal were essential to present the ferro- to antiferro-magnetic transition in the high pressure conditions.

4. Conclusions

Consequently, we found three characteristic modes to understand the observed pressure-induced ferromagnetic to antiferromagnetic transition in the β-phase

(1) The sliding of *p*-NPNN along the z-axis to alter the sign of the interplane exchange integral (J_{13}).
(2) The rotation of nitrophenyl group to provide the negative J_{13}.
(3) The rotation of nitro group to inverse the sign of the intraplane exchange integral (J_{12}).
(4) The combination of the modification of the intermolecular distances between the neighboring *p*-NPNN molecules and the internal rotations of the nitronyl nitroxide group in *p*-NPNN also changes the sign of the exchange integrals.

However, the first makes the lattice constant larger, so it is hardly acceptable unless other conformational changes are coupled together. The second induces the antiferro-magnetic interaction between the *ac*-planes, while the third destroys the two-dimensional ferromagnetic interaction in the *ac*-plane. Since the heat capacity data exhibit the two dimensional magnetic ordering under the high pressure, the second model is conceivable as the simplest model for possible theoretical explanation of the pressure effect in the β-phase of *p*-NPNN. Although the real conformational changes in the β-phase under the high pressure are much more complex, the third and forth model calculations demonstrated that the signs of effective exchange integrals are variable by conformational changes of *p*-NPNN molecules in the β-phase crystal under the high pressure condition.

The present calculations suggest that the pressure-induced ferro- to antiferro-magnetic (vice versa) transitions would be the typical characteristics for many other organic ferromagnets which have flexible structures.

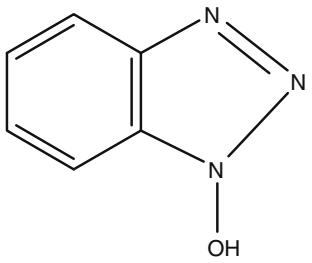
Acknowledgments

This work has been supported by a Grant-in-Aid for Scientific Research on Priority Areas from the Ministry of Education, Culture, Sports, Science and Technology, Japan.

References

[1] D. Gatteschi, K. Yamaguchi, in: E. Coronado (Ed.), From Molecular Assembles to the Devices, Kluwer Pub., 1996, p. 561.
[2] K. Yamaguchi, M. Okumura, J. Maki, T. Noro, H. Namimoto, M. Nakano, T. Fueno, K. Nakasuji, Chem. Phys. Lett. 190 (1992) 353.
[3] M. Okumura, K. Yamaguchi, K. Awaga, Chem. Phys. Lett. 228 (1994) 575.
[4] K. Takeda, K. Konishi, M. Tamura, M. Kinoshita, Phys. Rev. B 53 (1996) 3374.
[5] M. Mito, T. Kawae, M. Takumi, K. Nagata, M. Tamura, M. Kinoshita, K. Takeda, Phys. Rev. B 56 (1997) R14255.
[6] M. Okumura, T. Kawakami, A. Oda, K. yamaguchi, M. Mito, K. Takeda, Mol. Cryst. Liq. Cryst. 335 (1999) 623.
[7] M.J. Frisch, G.W. Trucks, H.B. Schlegel, G.E. Scuseria, M.A. Robb, J.R. Cheeseman, J.A. Montgomery Jr., T. Vreven, K.N. Kudin, J.C. Burant, J.M. Millam, S.S. Iyengar, J. Tomasi, V. Barone, B. Mennucci, M. Cossi, G. Scalmani, N. Rega, G.A. Petersson, H. Nakatsuji, M. Hada, M. Ehara, K. Toyota, R. Fukuda, J. Hasegawa, M. Ishida, T. Nakajima, Y. Honda, O. Kitao, H. Nakai, M. Klene, X. Li, J.E. Knox, H.P. Hratchian, J.B. Cross, V. Bakken, C. Adamo, J. Jaramillo, R. Gomperts, R.E. Stratmann, O. Yazyev, A.J. Austin, R. Cammi, C. Pomelli, J.W. Ochterski, P.Y. Ayala, K. Morokuma, G.A. Voth, P. Salvador, J.J. Dannenberg, V.G. Zakrzewski, S. Dapprich, A.D. Daniels, M.C. Strain, O. Farkas, D.K. Malick, A.D. Rabuck, K. Raghavachari, J.B. Foresman, J.V. Ortiz, Q. Cui, A.G. Baboul, S. Clifford, J. Cioslowski, B.B. Stefanov, G. Liu, A. Liashenko, P. Piskorz, I. Komaromi, R.L.

Martin, D.J. Fox, T. Keith, M.A. Al-Laham, C.Y. Peng, A. Nanayakkara, M. Challacombe, P.M.W. Gill, B. Johnson, W. Chen, M.W. Wong, C. Gonzalez, J.A. Pople, GAUSSIAN 03, Revision D.02, Gaussian, Inc., Wallingford, CT, 2004.
[8] A.D. Becke, Phys. Rev. A 38 (1988) 3098.
[9] C. Lee, W. Yang, R.G. Parr, Phys. Rev. B 37 (1988) 785.
[10] H.M. CcConnell, J. Chem. Phys. 39 (1963) 1930.
[11] K. Yamaguchi, T. Fueno, K. Nakasuji, I. Maruta, Chem. Lett. (1986) 629.
[12] K. Yamaguchi, T. Fueno, Chem. Phys. Lett. 159 (1989) 465.
[13] K. Yamaguchi, M. Okumura, M. Nakano, Chem. Phys. Lett. 191 (1992) 237.
[14] Y. Nakazawa, M. Tamura, N. Shirakawa, D. Shiomi, M. Takahashi, M. Kinoshita, M. Ishikawa, Phys. Rev. B 46 (1992) 8906.



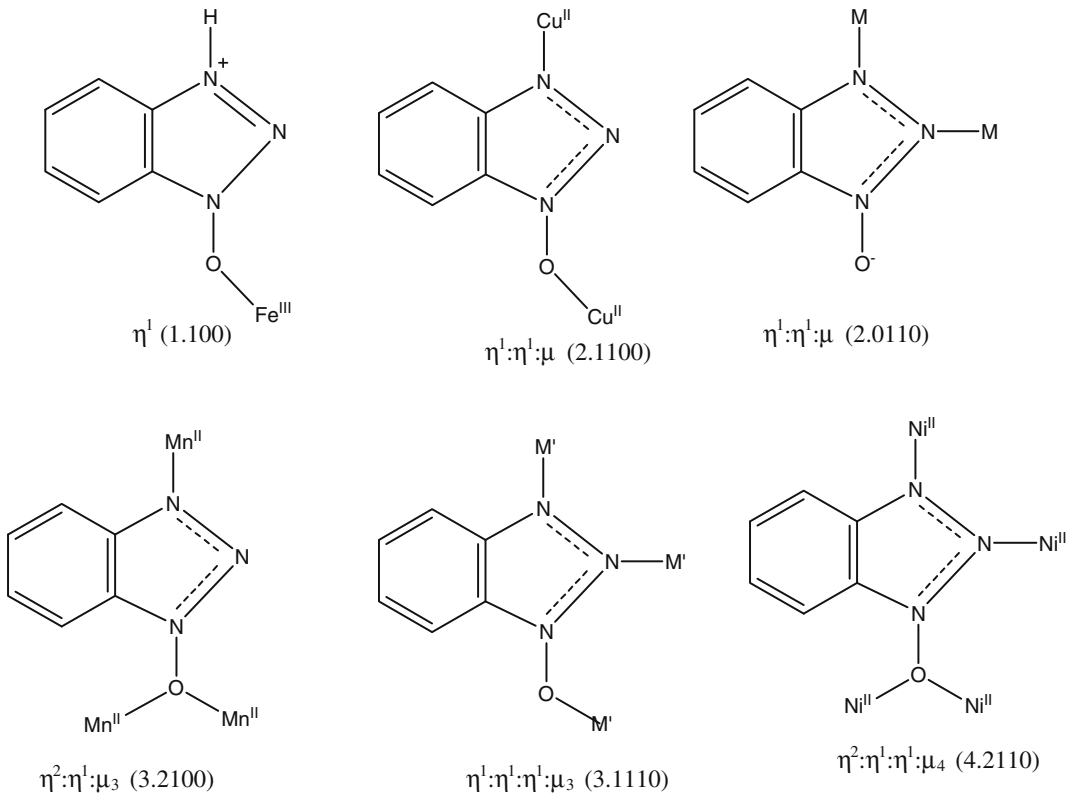
btaOH

Scheme 1. Structural formula of 1-hydroxybenzotriazole (btaOH).

type of coordination sites available on a single metal site and the donor set supplied by the ligand. It is clear, however, that we cannot simply trust to luck in preparing 3d-metal clusters; there thus has to be considerable forethought in the ligands, metals and conditions (reaction ratio, 'pH', solvent, etc.) used for any significant progress to be made. As the field develops, the boundary between 'designed' and 'serendipitous' assembly is becoming blurred [1].

In the context of the several variations of 'serendipitous assembly', we have been exploring 'ligand blend' reactions involving carboxylates and the various anionic forms of di-2-pyridyl ketone [11] and 2-pyridyl oximates [12] as a means to high-nuclearity species; the latter two families of ligands have the ability to bridge two or more metal ions with the *simultaneous* formation of chelating rings. We relatively recently decided to extend the exploration of ligand combinations by employing ligands that cannot chelate. One such ligand is 1-hydroxybenzotriazole (btaOH, Scheme 1), a well-known peptide-coupling additive [13] which exhibits corrosion inhibitive properties towards Cu [14,15] and Fe [16]. The coordination chemistry of btaOH has not attracted the interest of inorganic chemists and only few metal complexes have been prepared and studied. The synthetic investigation of the $[Cu_2(O_2CMe)_4(H_2O)_2]$–btaOH reaction system in MeOH resulted in the isolation of the three-dimensional (3D), diamond-like coordination polymer $[Cu(btaO)_2(MeOH)]_n$ [17], which is a soft magnet exhibiting two critical temperatures at 6.4 and 4.4 K. The anion $btaO^-$ is the 1-hydroxybenzotriazolate ligand (since the –OH group of 1-hydroxybenzotriazole is deprotonated, an alternative name of $btaO^-$ would be 1-oxidobenzotriazolate). Later [18], the reaction of $Ni(NO_3)\cdot 6H_2O$ with btaOH in aqueous NH_3–DMF yielded the trinuclear complex $[Ni_3(btaO)_6(NH_3)_6]$. Reaction of zerovalent Mn with btaOH and NH_4SCN in DMF has allowed the isolation of the one-dimensional (1D) polymer $[Mn_3(btaO)_2(SCN)_4(DMF)_8]_n$ [19a]. The use of the $btaO^-/MeCO_2^-$ combination in manganese(II) chemistry has recently yielded the 2D coordination polymer $[Mn^{II}_3(O_2CMe)_2(btaO)_4(MeOH)_2]_n$; the intra- and inter-magnetic exchange coupling constants for this complex were obtained from Monte Carlo calculations [19b]. The investigation of the $[Ni(acac)_2(H_2O)_2]$–btaOH reaction mixture in MeCN yielded the novel heptanuclear cluster $[Ni_7(OH)_2(acac)_8(btaO)_4(H_2O)_2]$ [20a]. It should be mentioned at this point that complex $[Fe(btaOH)_6](ClO_4)_3$ has also been structurally characterized by Zhang [20b]. The octahedral cation contains formally neutral btaOH ligands; however, the ligands exist as zwitterions exhibiting the 1.100 ligation mode, see Scheme 2.

The coordinative flexibility and versatility of the carboxylate ion and the μ_2, μ_3 or μ_4 potential of the deprotonated ligand (Scheme 2), $btaO^-$, prompted us to combine the two ligands to aim for new types of clusters. The loss of some degree of synthetic control may be more than compensated for by the vast diversity of structures expected using the combination of the two potentially *bridging* ligands. We describe herein the preparation and characterization of the complexes $[Ni_{13}(OH)_6(O_2CMe)_8(btaO)_{12}(H_2O)_6(n\text{PrOH})_4]$



Scheme 2. The up-to-date crystallographically established coordination modes of btaOH (up left) and $btaO^-$ in metal complexes; M = Ni^{II}, Os and M′ = Mn^{II}, Ni^{II}. The Harris notation [21] for the description of the modes is given in parentheses.

· $6.6H_2O$ · 4(*n*PrOH) (**1** · $6.6H_2O$ · 4(*n*PrOH)) and $[Ni_{13}(N_3)_6(O_2CMe)_8(btaO)_{12}(MeOH)_{10}]$ (**2**), which are the first tridecanuclear nickel(II) clusters reported to date. The last 5 years have witnessed a remarkable growth in interest in nickel(II) clusters because few of them have proven to be SMMs [22]. This work can be considered as a continuation of our interest in the chemistry of clusters of the middle and late 3d-metal ions with O,N-ligation [23]. Portions of this work have been previously communicated [23h].

2. Experimental

2.1. General and physical measurements

All manipulations were performed under aerobic conditions using materials (reagent grade) and solvents as received. Microanalyses (C, H, N) were performed by the University of Ioannina (Greece) Microanalytical Laboratory using an EA 1108 Carlo Erba analyzer. IR spectra (4000–400 cm^{-1}) were recorded on a Perkin–Elmer 16 PC FT-spectrometer with samples prepared as KBr pellets. Variable-temperature magnetic susceptibility measurements were carried out on powdered samples in the 2–300 K temperature range, using a Quantum Design MPMS SQUID susceptometer in a 1 kG applied magnetic field. Magnetization measurements were carried out at 2 K in the field range 0–6.5 T. All samples were packed into gelatine capsules and placed in a drinking straw sample holder. All magnetic susceptibility values were corrected with Pascal's constants and corrections were applied for the sample holder (eicosane, gel capsule and drinking straw).

Safety note! Benzotriazoles, azides and their metal complexes are potentially explosive; such compounds should be synthesized and used in small quantities, and treated with utmost care at all times.

2.2. Compound preparation

2.2.1. $[Ni_{13}(OH)_6(O_2CMe)_8(btaO)_{12}(H_2O)_6(nPrOH)_4] \cdot 6.6H_2O \cdot 4(nPrOH)$ (**1** · $6.6H_2O$ · 4(*n*PrOH))

A colourless solution (15 ml) of btaOH (0.081 g, 0.60 mmol) in *n*PrOH was added to a green solution of $Ni(O_2CMe)_2 \cdot 4H_2O$ (0.149 g, 0.60 mmol) in *n*PrOH (10 ml). The obtained pale green solution was filtered and allowed to stand undisturbed in a closed flask at room temperature. Green prismatic crystals of **1** · $6.6H_2O$ · 4(*n*PrOH) formed within 24–36 h and these were collected by filtration, washed with Et_2O (2 × 3 ml) and dried in vacuo. Typical yields were in the 50–60% range. Selected IR (KBr pellet) data: ν = 3422mb, 3320sb, 1592s, 1579s, 1439s, 1405m, 1200m, 1170m, 1125m. The dried solid analyzed satisfactorily as **1** · $5H_2O$ · 3(*n*PrOH). *Anal.* Calc. for $C_{109}H_{156}O_{52}N_{36}Ni_{13}$ (3654.85): C, 36.72; H, 4.41; N, 14.14. Found: C, 37.08; H, 4.63; N, 13.88%.

2.2.2. $[Ni_{13}(N_3)_6(O_2CMe)_8(btaO)_{12}(MeOH)_{10}]$ (**2**)

A suspension of compound $[Ni_{13}(OH)_6(O_2CMe)_8(btaO)_{12}H_2O)_6(nPrOH)_4] \cdot 6.6H_2O \cdot 4(nPrOH)$(**1** · $6.6H_2O$ · 4(*n*PrOH)) (1.097 g, 0.30 mmol) in MeOH (20 ml) was treated with solid NaN_3 (0.156 g, 2.40 mmol). The mixture was refluxed overnight, filtered to remove a few quantity of undissolved material, and the resulting dark green solution was allowed to stand undisturbed in a closed flask at room temperature. Green microcrystalline solid of **2** was precipitated within 4 days and this was collected by filtration, washed with Et_2O (2 × 3 mL) and dried in vacuo. Typical yields were in the 30–40% range. Selected IR (KBr pellet) data: ν = 3310sb, 2077s, 1592s, 1578s, 1440m, 1403m, 1199m, 1173m, 1124m. The dried solid analyzed as **2** · $2H_2O$. *Anal.* Calc. for $C_{98}H_{116}O_{40}N_{54}Ni_{13}$ (3453.36): C, 34.09; H, 3.39; N, 21.90. Found: C, 34.37; H, 3.72; N, 22.06%.

2.3. Single-crystal X-ray crystallography

A crystal of **1** · $6.6H_2O$ · 4(*n*PrOH) with approximate dimensions 0.15 × 0.20 × 0.40 mm was mounted in capillary. Diffraction measurements were made on a Crystal Logic Dual Goniometer diffractometer using graphite-monochromated Mo radiation. Complete crystal data and parameters for data collection and processing are listed in Table 1. Unit cell dimensions were determined and refined by using the angular settings of 25 automatically centred reflections in the range $11° < 2\theta < 23°$. Intensity data were recorded using the θ–2θ scan method. Three standard reflections monitored every 97 reflections showed less than 3% variation and no decay. Lorentz, polarization and Ψ-scan absorption were applied using the Crystal Logic software package.

The structure was solved by direct methods using SHELXS-86 [24] and refined by full-matrix least-squares techniques on F^2 with SHELXL-97 [25]. Hydrogen atoms of the $btaO^-$ and $MeCO_2^-$ ligands were introduced at calculated positions as riding on bonded atoms. Those of the hydroxo ligands, and coordinated H_2O and *n*PrOH molecules were located by difference maps and were refined isotropically. All non-hydrogen atoms were refined anisotropically, except those of the solvate molecules and the carbon atoms C94, C95 and C96 of a coordinated *n*PrOH which were refined isotropically. The monodentate $MeCO_2^-$ ligand and Ow3 coordinated on Ni7 were found disordered, switching positions in the coordination sphere, thus the $MeCO_2^-$ ligand was refined in two orientations with sum of occupation factors equal to one.

3. Results and discussion

3.1. Brief synthetic comments

Reaction of $Ni(O_2CMe)_2 \cdot 4H_2O$ with one equivalent of btaOH in propanol and storage of the obtained pale green solution at room temperature led to the precipitation of green prismatic crystals

Table 1
Summary of crystal data, data collection and structure refinement for the X-ray diffraction study of complex **1** · $6.6H_2O$ · 4(*n*PrOH).

Complex	**1** · $6.6H_2O$ · 4(*n*PrOH)
Empirical formula	$C_{112}H_{167.2}N_{36}Ni_{13}O_{54.6}$
Formula weight	3654.85
Colour, habit	green prisms
Crystal system	monoclinic
Space group	$P2_1/a$
a (Å)	16.807(10)
b (Å)	23.815(13)
c (Å)	22.884(13)
β (°)	93.106(18)
V (Å^3)	9146(9)
Z	2
ρ_{calc} (g cm^{-3})	1.327
Radiation, λ (Å)	Mo Kα, 0.71073
μ (mm^{-1})	1.384
$F(000)$	3784
Temperature (K)	298
$2\theta_{max}$ (°)	41.5
Ranges h, k, l	−16 → 16
	−23 → 0
	−22 → 0
Measured reflections	9639
Unique reflections (R_{int})	9345 (0.0427)
Reflections used ($I > 2\sigma(I)$)	5796
Parameters refined	968
Goodness-of-fit (on F^2)	1.091
R_1[a] ($I > 2\sigma(I)$)	0.0737
wR_2[b] ($I > 2\sigma(I)$)	0.1479
$(\Delta\rho)_{max}/(\Delta\rho)_{min}$ (e Å^{-3})	0.629/−0.620

[a] $R_1 = \sum(|F_o| - |F_c|)/\sum(|F_o|)$.
[b] $wR_2 = \{\Sigma[w(F_o^2 - F_c^2)^2]/\sum[w(F_o^2)^2]\}^{1/2}$.

of $[Ni_{13}(OH)_6(O_2CMe)_8(btaO)_{12}(H_2O)_6(n\text{PrOH})_4]\cdot 6.6H_2O\cdot 4Pr^nOH$ ($\mathbf{1}\cdot 6.6H_2O\cdot 4(n\text{PrOH})$) in ~55% yield (Eq. (1)). Obviously, btaOH is deprotonated by the basic $MeCO_2^-$ groups:

$$13Ni(O_2CMe)_2 4H_2O + 12btaOH + 4(n\text{PrOH}) \xrightarrow{n\text{PrOH}} \times [Ni_{13}(OH)_6(O_2CMe)_8(\underset{\mathbf{1}}{btaO})_{12}(H_2O)_6(n\text{PrOH})_4] + 18MeCO_2H + 40H_2O \quad (1)$$

Complex **1** seems to be the only product from the $Ni(O_2CMe)_2\cdot 4H_2O$/btaOH reaction mixture irrespective of the Ni^{II} to ligand reaction ratio. The addition of counterions such as ClO_4^- and PF_6^- (for the isolation of potentially existing cationic complexes) and the crystallization method have no influence on the identity of the product.

Following our well developed strategy [26], we tried to replace some or all the OH^- bridges in **1** with end-on N_3^- bridges in order to introduce ferromagnetic interactions (the end-on azido ligand is a ferromagnetic coupler [26]) in the superexchange scheme (vide infra) Thus, reaction of pre-isolated **1** with an excess (8–10 equivalents) of NaN_3 in MeOH under reflux gave a green solution from which microcrystalline $[Ni_{13}(N_3)_6(O_2CMe)_8(btaO)_{12}(MeOH)_{10}]$ (**2**) was precipitated in 30% yield upon storage at room temperature (Eq. (2)). Despite hundreds of experiments, we have failed to grow single crystals of the azido product suitable for crystallography due to poor diffraction and/or twinning problems (more than fifty crystals were examined). Thus, the characterization of complex **2** is based on the analytical and IR data (vide infra):

$$[Ni_{13}(OH)_6(O_2CMe)_8(\underset{\mathbf{1}}{btaO})_{12}(H_2O)_6(n\text{PrOH})_4] + 6NaN_3 + 10MeOH \xrightarrow[T]{MeOH} [Ni_{13}(N_3)_6(O_2CMe)_{\underset{\mathbf{2}}{8}}(btaO)_{12}(MeOH)_{10}] + 6H_2O + 4(n\text{PrOH}) \quad (2)$$

3.2. Description of structure

Partially labelled plots of the tridecanuclear molecule present in $\mathbf{1}\cdot 6.6H_2O\cdot 4(n\text{PrOH})$ is shown in Fig. 1. Selected interatomic distances and angles are listed in Table 2. Table 3 summarizes important hydrogen-bonding data.

Table 2
Selected interatomic distances (Å) and angles (°) for $\mathbf{1}\cdot 6.6H_2O\cdot 4(n\text{PrOH})$.

Bond distances			
Ni(7)···Ni(7′)	21.252(2)	Ni(4)–O(81)	2.080(9)
Ni(1)–N(3)	2.106(9)	Ni(4)–N(33)	2.073(10)
Ni(1)–N(23)	2.105(9)	Ni(5)–O(41)	2.094(8)
Ni(1)–N(43)	2.115(9)	Ni(5)–O(61)	2.000(8)
Ni(2)–O(61)	2.090(7)	Ni(5)–O(75)	2.109(9)
Ni(2)–O(62)	2.072(7)	Ni(5)–O(76)	2.092(8)
Ni(2)–O(63)	2.065(9)	Ni(5)–OW(1)	2.121(9)
Ni(2)–N(12)	2.122(10)	Ni(5)–N(53)	2.048(10)
Ni(2)–N(32)	2.097(10)	Ni(6)–O(1)	2.095(9)
Ni(2)–N(52)	2.082(9)	Ni(6)–O(63)	2.003(9)
Ni(3)–O(61)	2.074(8)	Ni(6)–O(73)	2.144(9)
Ni(3)–O(62)	2.077(6)	Ni(6)–O(74)	2.091(8)
Ni(3)–O(63)	2.052(9)	Ni(6)–O(82)	2.071(10)
Ni(3)–N(2)	2.102(9)	Ni(6)–N(13)	2.033(11)
Ni(3)–N(22)	2.080(9)	Ni(7)–O(11)	2.053(9)
Ni(3)–N(42)	2.083(10)	Ni(7)–O(31)	2.062(9)
Ni(4)–O(21)	2.075(7)	Ni(7)–O(51)	2.036(9)
Ni(4)–O(62)	1.992(7)	Ni(7)–O(77)	2.060(11)
Ni(4)–O(71)	2.207(8)	Ni(7)–OW(2)	2.100(14)
Ni(4)–O(72)	2.084(8)	Ni(7)–OW(3)	2.051(12)
Bond angles			
N(3)–Ni(1)–N(3′)	180.0(2)	O(1)–Ni(6)–O(82)	175.4(4)
N(23)–Ni(1)–N(23′)	180.0(4)	O(63)–Ni(6)–O(73)	166.2(4)
N(43)–Ni(1)–N(43′)	180.0(5)	O(74)–Ni(6)–N(13)	164.8(4)
O(61)–Ni(2)–N(32)	168.0(4)	O(11)–Ni(7)–OW(2)	174.8(5)
O(62)–Ni(2)–N(12)	166.6(3)	O(31)–Ni(7)–OW(3)	175.1(5)
O(63)–Ni(2)–N(52)	168.3(4)	O(51)–Ni(7)–O(77)	174.0(4)
O(61)–Ni(3)–N(22)	174.1(3)	Ni(2)–O(61)–Ni(3)	83.0(3)
O(62)–Ni(3)–N(2)	173.8(3)	Ni(2)–O(61)–Ni(5)	116.1(3)
O(63)–Ni(3)–N(42)	173.2(4)	Ni(3)–O(61)–Ni(5)	124.8(4)
O(21)–Ni(4)–O(81)	176.9(3)	Ni(2)–O(62)–Ni(3)	83.4(3)
O(62)–Ni(4)–O(71)	164.2(3)	Ni(2)–O(62)–Ni(4)	118.1(3)
O(72)–Ni(4)–N(33)	166.5(4)	Ni(3)–O(62)–Ni(4)	123.4(3)
O(41)–Ni(5)–OW(1)	179.2(3)	Ni(2)–O(63)–Ni(3)	84.2(3)
O(75)–Ni(5)–OW(1)	136.2(5)	Ni(2)–O(63)–Ni(6)	118.1(5)
O(76)–Ni(4)–N(53)	164.2(4)	Ni(3)–O(63)–Ni(6)	124.1(4)

Symmetry operation used to generate equivalent atoms: $-x+1, -y, -z+1$.

The structure of $\mathbf{1}\cdot 6.6H_2O\cdot 4(n\text{PrOH})$ consists of the tridecanuclear molecule $[Ni_{13}(OH)_6(O_2CMe)_8(btaO)_{12}(H_2O)_6(n\text{PrOH})_4]$ (Fig. 1), and solvate H_2O and nPrOH molecules; the solvate molecules will not be further discussed. The centrosymmetric [Ni(1) is a crystallographic inversion center] tridecanuclear molecular assembly is held together by six μ_3 (or 3.1 using Harris notation

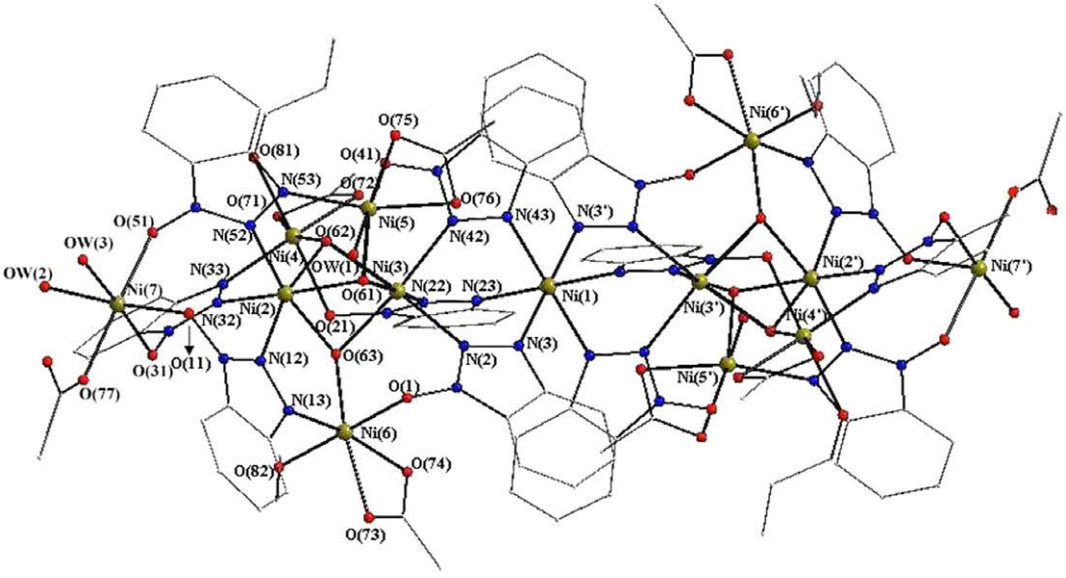


Fig. 1. The structure of **1** in the crystal. Primed and unprimed atoms are related by the crystallographic inversion center.

Table 3
Selected hydrogen-bonding interactions for complex **1** · 6.6H_2O · 4(*n*PrOH).[a]

D–H···A	D···A (Å)	H···A (Å)	D–H···A (°)	Symmetry operator of A
O(61)–H(O61)···O(1)	2.911	2.035	142.0	*x*, *y*, *z*
O(62)–H(O62)···O(41)	2.828	1.788	160.0	*x*, *y*, *z*
O(63)–H(O63)···O(21)	2.846	2.275	137.0	*x*, *y*, *z*
O(81)–H(O81)···O(71)	2.90	2.093	164.8	−*x*, −*y*, 1 − *z*
O(82)–H(O82)···O(1)[b]	2.645	2.091	122.1	0.5 − *x*, −0.5 + *y*, 1 − *z*
OW(1)–HW(O1A)···OP(1)[c]	2.664	1.492	149.3	0.5 − *x*, −0.5 + *y*, 1 − *z*
OW(1)–HW(O1B)···OP(2)[c]	2.691	1.503	158.1	0.5 − *x*, −0.5 + *y*, 1 − *z*
OW(2)–HW(O2A)···W(2)[b]	2.761	2.249	135.2	0.5 − *x*, −0.5 + *y*, 1 − *z*

[a] A = acceptor atom, D = donor atom.
[b] Atoms W(1) and W(2) belong to coordinated water molecules.
[c] Atoms OP(1) and OP(2) (not shown in Fig. 1) belong to lattice propanol.

[21]) hydroxo ligands [O(61), O(62), O(63) and their symmetry equivalents] and twelve $\eta^1{:}\eta^1{:}\eta^1{:}\mu_3$ (or 3.1110 [21], see Scheme 2) btaO$^-$ groups [the deprotonated O atoms of the btaO$^-$ groups are O(1), O(11), O(21), O(31), O(41), O(51) and their symmetry counterparts]. Peripheral ligation is provided by six chelating (η^2 or 1.11) $MeCO_2^-$ ligands, two monodentate (η^1 or 1.10) $MeCO_2^-$ groups, six terminal aqua ligands [OW(1), OW(2), OW(3) and their symmetry equivalents] and four terminal *n*PrOH molecules [O(81), O(82) and their symmetry equivalents]. Thus, the core is $\{Ni_{13}(\mu_3\text{-}OH)_6(\mu_3\text{-}ONNNR)_{12}\}^{8+}$ (Fig. 2), where R– = C_6H_4–. As a result of the above described ligation, the distorted octahedral chromophores of the seven, crystallographically independent metal ions are $Ni(1)N_6$, $Ni(2)(O_{hydroxo})_3N_3$, $Ni(3)(O_{hydroxo})_3N_3$, $Ni(4)(O_{hydroxo})(O_{acetate})_2(O_{btaO^-})(O_{propanol})N$, $Ni(5)(O_{hydroxo})(O_{acetate})_2(O_{btaO^-})(O_{aquo})N$, $Ni(6)(O_{hydroxo})(O_{acetate})_2(O_{btaO^-})(O_{propanol})N$ and $Ni(7)(O_{acetate})(O_{btaO^-})_3(O_{aquo})_2$.

The Ni–O(μ_3-hydroxo), Ni–$O_{acetate}$, Ni–O_{btaO^-}, Ni–O_{aquo}, Ni–$O_{propanol}$ and Ni–N bond lengths are typical for high-spin, six coordinate Ni(II) complexes [23a,b,27]. Each μ_3-OH^- group forms one short and two longer bonds to the metal ions. The Ni–O bond to the monodentate acetate ligand [Ni(7)–O(77) 2.060(11) Å] is slightly shorter, as expected, than the Ni–O bonds to the bidentate acetate groups [average value: 2.115(8) Å].

There is an amount of hydrogen bonding in **1** · 6.6H_2O · 4 (*n*PrOH) (see Table 3). The cluster molecules are directly connected forming "chains" through an intermolecular hydrogen bond involving the *n*PrOH oxygen atom O(81) (and its symmetry partner) as donor and the acetate oxygen atom O(71) (−*x*, −*y*, −*z* + 1), and its symmetry partner, as acceptor. The six μ_3 hydroxo ligands [O(61), O(62), O(63) and their symmetry equivalents] are intramolecularly hydrogen bonded with O atoms from six different btaO$^-$ ligands [O(1), O(41), O(21) and their symmetry equivalents, respectively]. The crystal structure is also stabilized by a variety of hydrogen bonds between the cluster molecule and/or the lattice solvent molecule resulting in a 3D network.

The metal ions Ni(7), Ni(2), Ni(3), Ni(1), Ni(3′), Ni(2′) and Ni(7′) are coplanar and almost colinear; this view is emphasized in Fig. 3. Using the perspective view of this figure, Ni(5) is 3.130 Å above the Ni_7 plane, while Ni(4) and Ni(6) are 2.318 and 0.812 Å, respectively, below the Ni_7 plane. The shortest $Ni^{II}\cdots Ni^{II}$ distance within the molecule is Ni(2)···Ni(3) [2.759(2) Å]; this short distance is a consequence of the presence of three monoatomic hydroxo bridges. The Ni(7)···Ni(7′) distance is the longest one [21.252(2) Å].

In addition to the various triangular topologies that are present in **1**, several other subunits are clearly visible within the core of **1**: (i) The $\{Ni(2)(OH)_3Ni(3)\}^+$ (and its symmetry equivalent) subcore has never been identified in Ni(II) cluster or polymer chemistry; (ii) the metal ions Ni(1), Ni(4), Ni(5), Ni(6), Ni(4′), Ni(5′) and Ni(6′) adopt the topology of two tetrahedra sharing a common apex at Ni(1) (Fig. 4); this topology is extremely rare in Ni(II)

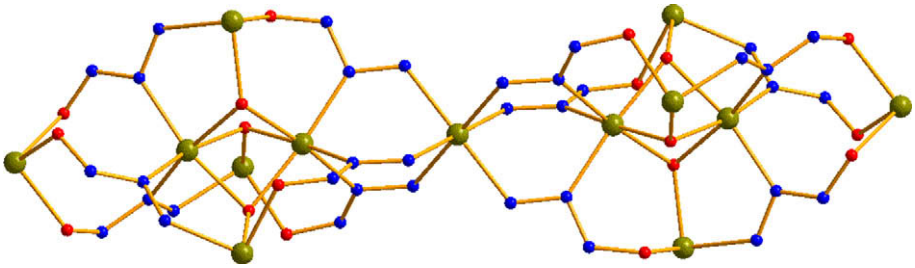


Fig. 2. The $\{Ni_{13}(\mu_3\text{-}OH)_6(\mu_3\text{-}ONNNR)_{12}\}^{8+}$ core of complex **1**, where R– = C_6H_4–. Colour code: Ni, green; O, red; N, blue. (For interpretation of the references to colour in this figure legend, the reader is referred to the web version of this article.)

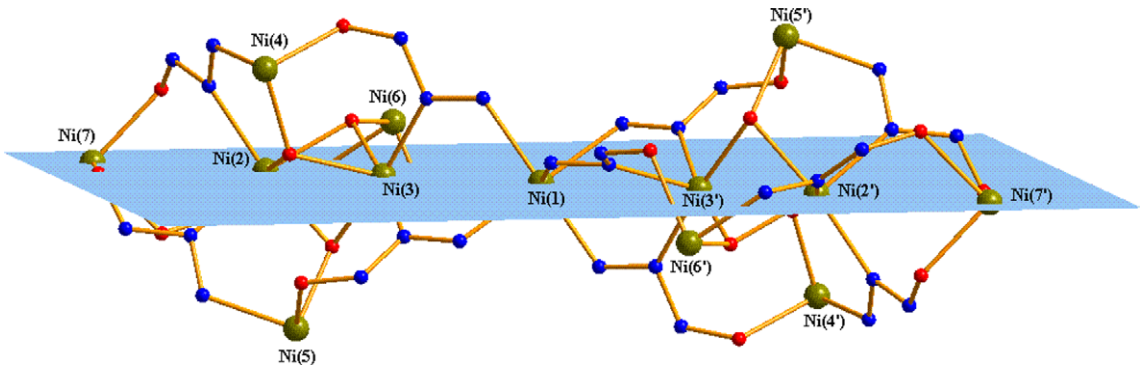


Fig. 3. A view of the core of complex **1** emphasizing the planarity and almost linearity of seven (out of 13) Ni^{II} ions.

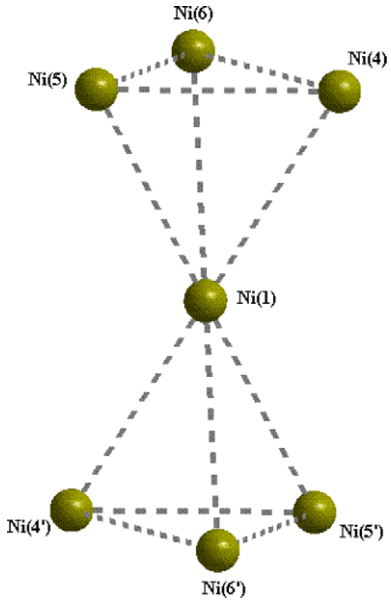


Fig. 4. The vertex-sharing, double tetrahedral topology of seven Ni^{II} ions.

chemistry and has been observed only in the chiral complex $[Ni_7(OH)_2L_3]$, where L is the tetra-anion of (2*R*,3*R*)-1,4-bis(3,5-di-*tert*-butylsalicylideneamino)-2,3-butanediol [28]; (iii) the {Ni(2)-Ni(3)Ni(4)Ni(5)Ni(6)(O(61)H)(O62)H)(O(63)H}$^{7+}$ subcore can be described as a 'mutant' butterfly, with Ni(2) and Ni(3) ions at the central ('body') and Ni(4), Ni(5), Ni(6) on its three end ('wingtip') positions (Fig. 5); tetranuclear Ni(II) clusters with a normal $\{Ni_4(\mu_3\text{-}OH)_2\}^{6+}$ topology have been structurally characterized [17]; and (iv) the central $\{Ni_3(\mu\text{-}NNR')_6\}$ subcore (R′– = C_6H_4NO–), which is present in **1** (Fig. 6), has been observed in the linear trinuclear cluster $[Ni_3(btaO)_6(NH_3)_6]$ [18]; in the latter the deprotonated oxygen atoms of the $btaO^-$ ligands are hydrogen bonded to the ammine ligands, whereas in the former the $btaO^-$ oxygen atoms are each coordinated to a Ni^{II} ion resulting in a higher nuclearity complex.

Compound **1** is the nineth structurally characterized complex of any metal containing $btaO^-$ ligands. Except the Werner-type complexes that are discussed in the Introduction [17–20], the other three compounds are the organometallic complexes $[Os_3H(CO)_{10}(btaO)]$, $[Os_3(C{=}NHPr^n)(CO)_{10}(btaO)]$ and $[Os_3(C{=}NHCH_2Ph)(CO)_{10}(btaO)]$ [29]. The 3.1110 coordination mode found in **1** has been observed only in $[Mn^{II}_3(O_2CMe)_2(btaO)_4(MeOH)_2]_n$ [19b]. Only the 2.0110 mode has been found in more than two complexes, i.e. in $[Ni_3(btaO)_6(NH_3)_6]$ [18], $[Ni_7(OH)_2(acac)_8(btaO)_4(H_2O)_2]$ [20] and in the Os organometallic compounds [29].

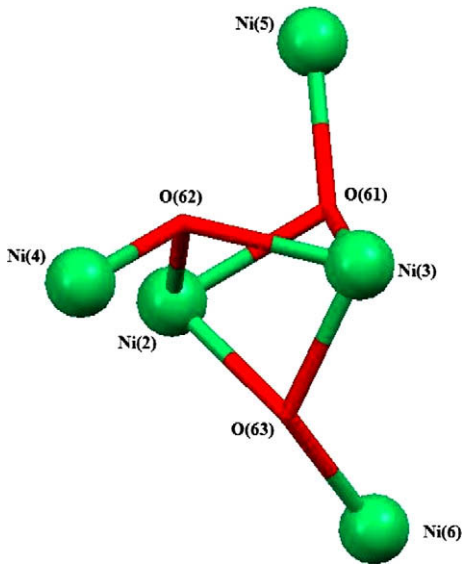


Fig. 5. The 'mutant' butterfly $\{Ni_5(\mu_3\text{-}OH)_3\}^{7+}$ subunit present in **1**.

Complex **1** joins a small but growing family of tridecanuclear metal complexes; these complexes have various metal topologies. Since most of these complexes have been reported only recently, we felt it timely to collect them in Table 4, together with their spin ground-state values, where there are available. Inspection of Table 4 shows that complex **1** is the first structurally characterized tridecanuclear Ni(II) cluster. While the number of polynuclear transition metal complexes reported continues to grow rapidly, some nuclearities remain extremely rare. Tridecanuclear complexes are particularly uncommon.

3.3. IR spectra

A characteristic feature in the IR spectrum of complex **1** is the appearance of a strong broad band at ~3320 cm^{-1} assignable to $\nu(OH)H_2O/n$PrOH. The presence of hydroxo ligands in the complex is manifested by a medium band at ~3420 cm^{-1} [34]. The broadness and relatively low frequency of these bands are both indicative of hydrogen bonding. The spectra of the sodium and potassium salts of 1-hydroxybenzotriazole (btaONa, btaOK) exhibit bands at 1180 and ca. 1105 cm^{-1}, associated with the ν(N=N) and ν(N–N) modes of vibration, respectively. These bands are shifted to 1200 and 1125 cm^{-1}, respectively, in the spectrum of the complex. The medium intensity band at 1170 cm^{-1} is assigned to ν(N–O) [20a]. This band has been shifted to lower wavenumber in **1** compared with its frequency (1224 cm^{-1}) in the IR spectrum of the potassium salt of 1-hydroxybenzotriazole, btaOK. Such a large shift to lower frequencies has also been observed [17,19,20a] in the spectra of other metal complexes where the deprotonated oxygen atom of $btaO^-$ is coordinated. The strong bands at 1592 and 1579 cm^{-1} are assigned [35] to the $\nu_{as}(CO_2)$ vibration; the $\nu_s(CO_2)$ vibrations appear [35] at 1439 and 1405 cm^{-1}. The presence of two distinct bands for each mode reflects the presence of two types of acetate ligands in the complex. The 1592 and 1405 cm^{-1} [$\Delta = \nu_{as}(CO_2) - \nu_s(CO_2) = 187\ cm^{-1}$] pair are assigned to the monodentate acetates, while the 1579 and 1439 cm^{-1} one ($\Delta = 140\ cm^{-1}$) to the chelating acetates [35]. The differences Δ are more (187 cm^{-1}) and less (140 cm^{-1}) than the Δ value for NaO_2CMe (164 cm^{-1}), as expected for the monodentate and bidentate of carboxylate ligation, respectively [35].

The IR spectrum of **2** is very similar to that of **1**, the main differences being the presence of one strong band at 2077 cm^{-1} and the absence of the band at ~3420 cm^{-1} in the former. This similarity supports analogous structures for **1** and **2**. The band at 2077 cm^{-1} is assigned to the asymmetric stretching mode of the azido ligand [36] and is situated at almost the same wavenumber observed in clusters containing end-on azido ligands [26d].

3.4. Magnetic properties

Variable-temperature dc magnetic susceptibility studies were performed on powdered samples of compounds **1** and **2** in an applied magnetic field of 0.1 T (1.0 KG) and in the 2.0–300 K range. The data are plotted as $\chi_M T$ versus T in Fig. 7. $\chi_M T$ at 300 K is 16.24 emu mol^{-1} K, lower than the 17.19 emu mol^{-1} K value (for $g = 2.3$) expected for a cluster of 13 non-interacting Ni^{II} ions. As T is lowered, the $\chi_M T$ product gradually decreases to 9.88 emu mol^{-1} K at 16 K where a plateau appears; the product

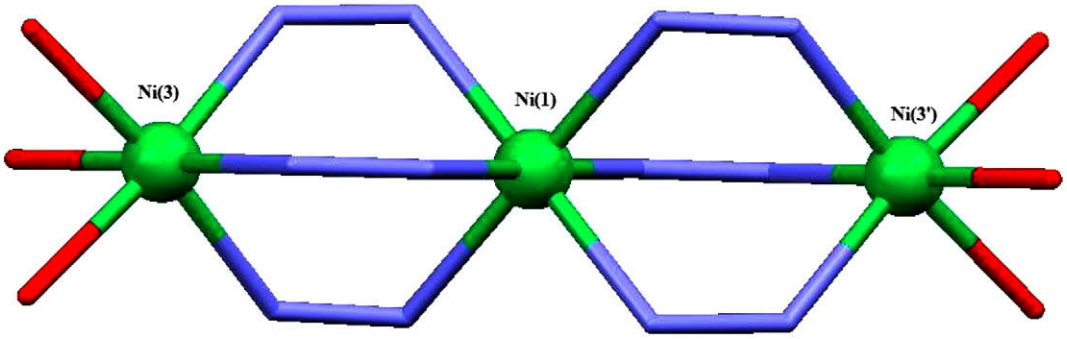


Fig. 6. The central $\{Ni_3(\mu\text{-}NNR')_6\}$ subcore (R′– = C_6H_4NO–) in **1**.

increases from this value at 9 K to 10.21 emu mol^{-1} K at 3.3 K before finally decreasing to 9.52 emu mol^{-1} K at 2.0 K. The low temperature behaviour is consistent with a frustrated magnetic system, where there are competitive antiferromagnetic exchange interactions, mainly within the pentanuclear Ni(2)Ni(3)Ni(4)Ni(5)-Ni(6)/Ni(2′)Ni(3′)Ni(4′)Ni(5′)Ni(6′) subunits (triangular spin topologies). From now onwards, the numbering scheme that will be used for the magnetic discussion of **1** is the same with that used in the real structure, see Figs. 1 and 3–5. We define spin frustration here in its more common, general sense of competing exchange interactions of similar magnitude that prevent the preferred spin alignments, rather than the original, most specific sense that competing interactions of the same magnitude lead to a degenerate ground state.

In an attempt to try to quantify the magnetic behaviour of the system, and since a phenomenological Hamiltonian of 13 $S = 1$ spins is a quite large system to be treated even with the ITO methods, some approximations were used. A simplified Hamiltonian of the system is given by Eq. (3):

$$H = -J_1(S_2S_3 + S_{2'}S_{3'}) - J_2[(S_2 + S_3)(S_4 + S_5 + S_6) + (S_{2'} + S_{3'}) \times (S_{4'} + S_{5'} + S_{6'})] - J_3[S_1(S_3 + S_{3'})] - J_4(S_2S_7 + S_{2'}S_{7'}) \quad (3)$$

To avoid parametrization, we decided to attempt to fit the susceptibility data considering that the main exchange interactions come from the pentanuclear subunits mentioned above, i.e. to use a 2-J model assuming that $J_3 = J_4 = 0$. These pentanuclear subunits contain monoatomic bridges (Fig. 5), derived from the μ_3-OH^- ligands, which give more effective coupling than the diatomic or triatomic bridges. Thus, in a simple approximation, the system can be considered as consisting of two pentanuclear subunits and three mononuclear Ni^{II} sites. Best-fit parameters are $J_1 = -24.5$ cm^{-1}, $J_2 = -12.6$ cm^{-1} and $g = 2.31$. The model used to fit the data does not take into account the decline of $\chi_M T$ below 3.3 K. This steep decrease, often occurring in polynuclear nickel(II) complexes, is associated [37] with the characteristic zero-field splitting of the Ni^{II} ion and probably with the intermolecular interactions present in the crystal structure of the complex. The fitting results are in accordance with the behaviour of the system, in which the existence of antiferromagnetic interactions within the triangular Ni(2)Ni(3)Ni(4,5,6) subunits leads to frustration (Scheme 3). It should be mentioned that despite the small Ni(2)–O(H)–Ni(3) angles [20a], the interaction J_1 is antiferromagnetic. We attribute this partly to the μ_3 character of the hydroxo ligands and partly to the frustrating behaviour of the system. Further investigation of the magnetic behaviour of **1** using Monte Carlo methodology [19b] is in progress in order to investigate the system without approximations; preliminary results indicate that our model is valid.

The $\chi_M T$ product for **2** at 300 K is 16.87 emu mol^{-1} K and remains practically constant in the 300–54 K range, below which it decreases drastically to a value of 5.93 emu mol^{-1} K at 2.2 K. *Assuming* a structural similarity between **1** and **2**, and employing

Table 4
Formulae and spin ground-state value for structurally characterized non-organometallic tridecanuclear metal complexes.

Complex	Spin ground state	Reference
$[V_{13}(\mu_6\text{-}O)_3(\mu_3\text{-}O)_6(\mu\text{-}O)_2O_9(\mu_3\text{-}OH)_3(\mu_2\text{-}OH)_3]^{3-}$		[30]
$[Co_{13}(OH)_3(chp)_{19}(O_3PPh)_2(H_2O)_2(Hchp)_2]$[a]		[31a]
$[Co_{13}(OH)_3(chp)_{19}(O_3PPh)_2(H_2O)_2(EtOAc)_2]$[a]		[31a]
$[Co_{13}(OH)_2(phth)(chp)_{20}]$[a,b]		[31b]
$[Mn_{13}(\mu_5\text{-}O)_6(\mu_3\text{-}O)_2(\mu_3\text{-}OEt)_6(O_2CPh)_{12}]$	15/2	[32a]
$[Mn_{13}O_{12}(Me_2Bta)_{12}F_6(MeOH)_{10}(H_2O)_2]$[c]		[32b]
$[Mn_{13}O_8(OEt)_6(O_2CC_6H_4OPh)_{12}]$	11/2	[32c]
$[Mn_{13}(\mu_3\text{-}O)(OMe)_8(O_3CCPh)_4(O_2CCMe_3)_{10}]$	5	[32d]
$[Mn_{13}O_8(OH)_6(ndc)_6]$[d]	9/2	[32e]
$[Mn_{13}O_8(OEt)_{5.5}(OH)_{0.5}(ndc)_6]$[d]	11/2	[32e]
$[Mn_{13}O_8(OEt)_6(O_2CPh)_{12}]$	11/2	[32e]
$[Fe_{13}O_4F_{24}(OMe)_{12}]^{5-}$		[33]
$[Ni_{13}(OH)_6(O_2CMe)_8(btaO)_{12}(H_2O)_6(n\text{PrOH})_4]$		this work

[a] Hchp = 6-chloro-2-hydroxypyridine.
[b] phth = phthalate.
[c] Me_2BtaH = dimethylbenzotriazole.
[d] ndc^{2-} = 1,8-naphthalenedicarboxylate.

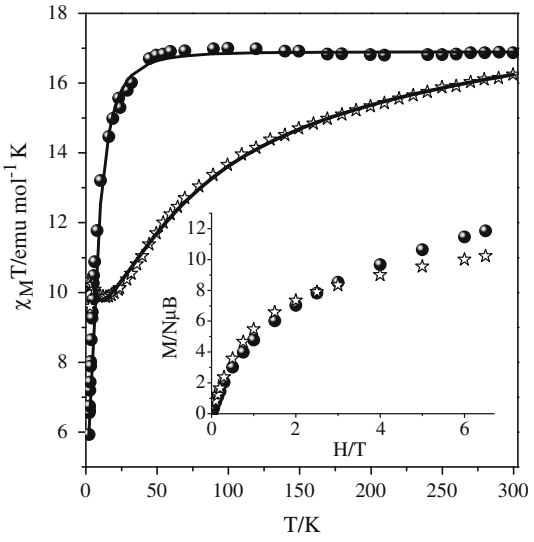
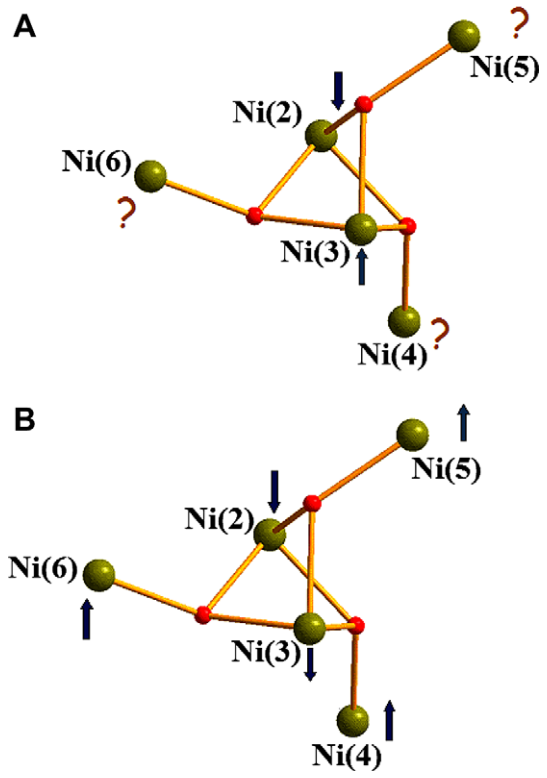


Fig. 7. Plot of $\chi_M T$ vs. T for powdered samples of **1** (open stars) and **2** (black circles); the solid lines represent the fit to the theoretical models (see text for the fit parameters). Plots of reduced magnetization ($M/N\mu_B$) vs. H at 2 K in the field range 0–6.5 T are shown in the inset.



Scheme 3. Spin topologies of the pentanuclear subunits present in complex **1** (A) and assumed to be present in complex **2** (B). The monoatomic bridges in A derive from the crystallographically established μ_3-OH$^-$ groups, while in B come from the nitrogen atoms of the μ_3 end-on N_3^- ligands which are proposed to be present in the azido product.

the same model and approximations used for **1**, best-fit parameters for **2** are $J_1 = 12.8\ cm^{-1}$, $J_2 = -1.93\ cm^{-1}$ and $g = 2.27$. Thus, the spin frustration observed in **1** seems to disappear in **2**, due to the existence of a ferromagnetic exchange interaction in the pentanuclear subunits of the latter (Scheme 3) [28].

According to Fig. 7, the ground-state spin of compound **2** is smaller than that of **1**. The most probable reason for this is the spin frustration in the latter which results in a larger S value compared with that in the former; it seems that the frustrated Ni^{II}_5 units have a larger spin value in the ground state than the non-frustrated ones. Thus the conversion of **1** into **2** represents an extremely rare case in which substitution of bridging hydroxo ligands by end-on bridging azide groups has led to a decrease in the ground-state S value; usually the addition of the latter is sought as a means of raising the value of S [26].

The magnetization curves of **1** and **2** are shown in the inset of Fig. 7; no saturation is observed indicating that many energy states are populated even at very low temperatures

4. Conclusions

The present work extends the body of results that emphasize the ability of the anionic ligand btaO$^-$ to form interesting structural types in 3d-metal chemistry. The initial use of the btaO$^-$/MeCO$_2^-$ combination in Ni(II) chemistry has provided access to cluster **1** with interesting structural and magnetic properties. This cluster is the highest nuclearity metal btaOH or btaO$^-$ to date and the first Ni_{13} complex, showing that btaO$^-$ can indeed support high nuclearity chemistry when coupled with appropriate ancillary ligands. Complex **1** is only the second complex of any metal in which btaO$^-$ and MeCO$_2^-$ groups coexist; the first one, namely $[Mn^{II}_3(O_2CMe)_2(btaO)_4(MeOH)_2]_n$, is a 2D coordination polymer [19b]. Another interesting point of this work is the rational reactivity of **1** with N_3^- ions which gave the – most probably – structurally analogous azido-bridged cluster **2** with different magnetic properties.

Complexes of 3d-metal ions other than Ni^{II} (this work) and Mn^{II} [19b] with the btaO$^-$/RCO$_2^-$ (R = H, Me, Ph, etc.) ligand combination are not known to date, and it is currently not evident whether the structural types (clusters versus polymers) of such compounds are dependent on the nature of the metal and the R group of the carboxylate ligand. Such matters are under intense investigation in our group.

Acknowledgements

We thank the European Social Fund (ESF), the Operational Program for Educational and Vocational Training II (EPEAEK II) and particularly the Program PYTHAGORAS (Grant b.365.037), for funding this work.

Appendix A. Supplementary data

CCDC 668367 contains the supplementary crystallographic data for **1** · 6.6H$_2$O · 4Pr^{n}OH. These data can be obtained free of charge via http://www.ccdc.cam.ac.uk/conts/retrieving.html, or from the Cambridge Crystallographic Data Centre, 12 Union Road, Cambridge CB2 1EZ, UK; fax: (+44)1223-336033; or e-mail: deposit@ccdc.cam.ac.uk.

References

[1] R.E.P. Winpenny, in: J.P. Sauvage (Ed.), Perspectives in Supramolecular Chemistry, vol. 5, Wiley, New York, 1999, p. 193 (Chapter 5).
[2] (a) For excellent reviews concerning SMMs, see: G. Christou, D. Gatteschi, D.N. Hendrickson, R. Sessoli, MRS Bull. 25 (2000) 66;
(b) D. Gatteschi, R. Sessoli, Angew. Chem., Int. Ed. 42 (2003) 268;
(c) R. Birchner, G. Chaboussant, C. Dobe, H. Güdel, S.T. Ochsenbein, A. Sieber, O. Waldman, Adv. Funct. Mater. 16 (2006) 209;
(d) G. Aromi, E.K. Brechin, Struct. Bond. 122 (2006) 1.
[3] (a) J.R. Friedman, M.P. Sarachik, J. Tejada, R. Ziolo, Phys. Rev. Lett. 76 (1996) 3380;
(b) L. Thomas, F. Lionti, R. Ballou, D. Gattechi, R. Sessoli, B. Barbara, Nature 383 (1996) 145.
[4] W. Wernsdorfer, R. Sessoli, Science 284 (1999) 133.
[5] (a) M.N. Leuenberger, D. Loss, Nature 410 (2001) 789;
(b) W. Wernsdorfer, N. Aliaga-Acalde, D.N. Hendrickon, G. Christou, Nature 416 (2002) 406;
(c) S. Hill, R.S. Edwards, N. Aliaga-Acalde, G. Christou, Science 302 (2003) 1015;
(d) J. Tehada, E.M. Chudnovsky, E. del Barco, J.M. Hernandez, T.P. Spiller, Nanotechnology 12 (2001) 181;
(e) R.E.P. Winpenny, Angew. Chem., Int. Ed. 47 (2008) 7992.
[6] R.E.P. Winpenny, in: J.A. McCleverty, T.J. Meyer (Eds.), Comprehensive Coordination Chemistry II, vol. 7, Elsevier, Amsterdam, 2004, p. 125 (Chapter 7.3).
[7] E. Breuning, U. Ziener, J.-M. Lehn, E. Wegelius, K. Rissanen, Eur. J. Inorg. Chem. (2001) 1515.
[8] R.W. Saalfrank, U. Reimann, M. Goritz, F. Hampel, A. Scheurer, F.W. Heinemann, M. Buschel, J. Daub, V. Schunemann, A.X. Trautwein, Chem. Eur. J. 8 (2002) 3614.
[9] M. Fujita, K. Umemoto, M. Yoshizawa, N. Fujita, T. Kusukawa, K. Biradha, Chem. Commun. (2001) 509 (Feature article).
[10] For a provocative perspective, see: R.E.P. Winpenny, J. Chem. Soc., Dalton Trans. (Dalton Perspective) (2001) 1.
[11] For a review, see: G.S. Papaefstathiou, S.P. Perlepes, Comm. Inorg. Chem. 23 (2002) 249.
[12] For a review, see: C.J. Milios, Th.C. Stamatatos, S.P. Perlepes, Polyhedron 25 (2006) 134 (Polyhedron Report).
[13] W. Konig, R. Geiger, Ber. Dtsch. Chem. Ges. 103 (788) (1970) 2024.
[14] W. Qafsaoui, C. Blanc, J. Roques, N. Pebere, A. Srhiri, C. Mijoule, G. Mankowski, J. Appl. Electrochem. 31 (2001) 223.
[15] R. Youda, H. Nishihara, K. Aramaki, Corros. Sci. 28 (1988) 87.
[16] M.J. Collie (Ed.), Corrosion Inhibitors: Developments Since 1980, Noyes Data Corporation, NJ, USA, 1983, p. 227.
[17] V. Tangoulis, C.P. Raptopoulou, V. Psycharis, A. Terzis, K. Skorda, S.P. Perlepes, O. Cador, O. Kahn, E.G. Bakalbassis, Inorg. Chem. 39 (2000) 2522.

[18] E. Diamantopoulou, S.P. Perlepes, D. Raptis, C.P. Raptopoulou, Transition Met. Chem. 27 (2002) 377.
[19] (a) G.S. Papaefstathiou, R. Vicente, C.P. Raptopoulou, A. Terzis, A. Escuer, S.P. Perlepes, Eur. J. Inorg. Chem. (2002) 2488;
(b) C.C. Stoumpos, E. Diamantopoulou, C.P. Raptopoulou, A. Terzis, S.P. Perlepes, N. Lalioti, Inorg. Chim. Acta 361 (2008) 3638.
[20] (a) E. Diamantopoulou, C.P. Raptopoulou, A. Terzis, V. Tangoulis, S.P. Perlepes, Polyhedron 21 (2002) 2117;
(b) X.-M. Zhang, Acta Crystallogr., Sect. E 61 (2005) m1799.
[21] R.A. Coxall, S.G. Harris, D.K. Henderson, S. Parsons, P.A. Tasker, R.E.P. Winpenny, J. Chem. Soc., Dalton Trans. (2000) 2349.
[22] (a) H. Andres, R. Basler, A.J. Blake, C. Cadiou, G. Chaboussant, C.M. Grant, H.-U. Güdel, M. Murrie, S. Parsons, C. Paulsen, F. Semadini, V. Villar, W. Wernsdorfer, R.E.P. Winpenny, Chem. Eur. J. 8 (2002) 867;
(b) S.T. Ochsenbein, M. Murrie, E. Rusanov, H. Stoeckli-Evans, C. Sekine, H.-U. Güdel, Inorg. Chem. 41 (2002) 5133;
(c) E.-C. Yang, W. Wernsdorfer, S. Hill, R.S. Edwards, M. Nakano, S. Maccagnano, L.N. Zakharov, A.L. Rheingold, G. Christou, D.N. Hendrickson, Polyhedron 22 (2003) 1727;
(d) M. Moragues-Cánovas, M. Helliwell, L. Ricard, E. Riviere, W. Wernsdorfer, E. Brechin, T. Mallah, Eur. J. Inorg. Chem. (2004) 2219;
(e) A. Bell, G. Aromi, S.J. Teat, W. Wernsdorfer, R.E.P. Winpenny, Chem. Commun. (2005) 2808;
(f) E.-C. Yang, W. Wernsdorfer, L.N. Zakharov, Y. Karaki, A. Yamaguchi, R.M. Isidro, G.-D. Lu, S.A. Wilson, A.L. Rheingold, H. Ishimoto, D.N. Hendrickson, Inorg. Chem. 45 (2006) 529;
(g) G. Aromi, S. Parsons, W. Wernsdorfer, E.K. Brechin, E.J.L. McInnes, Chem. Commun. (2005) 5038;
(h) D. Venegas-Yazigi, E. Ruiz, J. Cano, S. Alvarez, Dalton Trans. (2006) 2643.
[23] (a) For representative very recent papers, see: C. Papatriantafyllopoulou, G. Aromi, A.J. Tasiopoulos, V. Nastopoulos, C.P. Raptopoulou, S.J. Teat, A. Escuer, S.P. Perlepes, Eur. J. Inorg. Chem. (2007) 2761;
(b) Th.C. Stamatatos, E. Diamantopoulou, C.P. Raptopoulou, V. Psycharis, A. Escuer, S.P. Perlepes, Inorg. Chem. 46 (2007) 2350;
(c) Th.C. Stamatatos, D. Foguet-Albiol, S.-C. Lee, C.C. Stoumpos, C.P. Raptopoulou, A. Terzis, W. Wernsdorfer, S.O. Hill, S.P. Perlepes, G. Christou, J. Am. Chem. Soc. 129 (2007) 9484;
(d) Th.C. Stamatatos, C. Papatriantafyllopoulou, E. Katsoulakou, C.P. Raptopoulou, S.P. Perlepes, Polyhedron 26 (2007) 1830;
(e) C.J. Milios, R. Inglis, A. Vinslava, R. Bagai, W. Wernsdorfer, S. Parsons, S.P. Perlepes, G. Christou, E.K. Brechin, J. Am. Chem. Soc. 129 (2007) 12505;
(f) C.J. Milios, A. Prescimone, A. Mishra, S. Parsons, W. Wernsdorfer, G. Christou, S.P. Perlepes, E.K. Brechin, Chem. Commun. (2007) 153;
(g) C.J. Milios, P.A. Wood, S. Parsons, D. Foguet-Albiol, C. Lampropoulos, G. Christou, S.P. Perlepes, E.K. Brechin, Inorg. Chim. Acta 360 (2007) 3932;
(h) C. Papatriantafyllopoulou, E. Diamantopoulou, A. Terzis, N. Lalioti, V. Tangoulis, S.P. Perlepes, Inorg. Chem. Commun. 11 (2008) 454.
[24] G.M. Sheldrick, SHELXS-86, Structure Solving Program, University of Göttingen, Germany, 1986.
[25] G.M. Sheldrick, SHELXL-97, Program for the Refinement of Crystal Structures from Diffraction Data, University of Göttingen, Germany, 1997.
[26] (a) G.S. Papaefstathiou, A. Escuer, R. Vicente, M. Font-Bardia, X. Solans, S.P. Perlepes, Angew. Chem., Int. Ed. 40 (2001) 884;
(b) G.S. Papaefstathiou, A. Escuer, R. Vicente, M. Font-Bardia, X. Solans, S.P. Perlepes, Chem. Commun. (2001) 2414;
(c) A.K. Boudalis, B. Donnadieu, V. Nastopoulos, J.M. Clemente-Juan, A. Mari, Y. Sanakis, J.-P. Tuchages, S.P. Perlepes, Angew. Chem., Int. Ed. 43 (2004) 2266;
(d) G.S. Papaefstathiou, A.K. Boudalis, Th.C. Stamatatos, C.J. Milios, C.G. Efthymiou, C.P. Raptopoulou, A. Terzis, V. Psycharis, Y. Sanakis, R. Vicente, A. Escuer, J.-P. Tuchages, S.P. Perlepes, Polyhedron 26 (2007) 2089;
(e) A.K. Boudalis, Y. Sanakis, J.M. Clemente-Juan, B. Donnadieu, V. Nastopoulos, A. Mari, Y. Coppel, J.-P. Tuchagues, S.P. Perlepes, Chem. Eur. J. 14 (2008) 2514.
[27] Th.C. Stamatatos, E. Diamantopoulou, A. Tasiopoulos, V. Psycharis, R. Vicente, C.P. Raptopoulou, V. Nastopoulos, A. Escuer, S.P. Perlepes, Inorg. Chim. Acta 359 (2006) 4149.
[28] X. Xu, S. Gou, W. Huang, Y. Ma, Y. Li, Eur. J. Inorg. Chem. (2003) 2054.
[29] K.-L. Lu, S. Kumaresan, Y.-S. Wen, J.R. Hwu, Organometallics 13 (1994) 3170.
[30] T. Kurata, Y. Hayashi, A. Uehara, K. Isobe, Chem. Lett. 32 (2003) 1040.
[31] (a) E.K. Brechin, A. Graham, A. Parkin, S. Parsons, A.M. Seddon, R.E.P. Winpenny, J. Chem. Soc., Dalton Trans. (2000) 3242;
(b) E.K. Brechin, R.A. Coxall, A. Parkin, S. Parsons, P.A. Tasker, R.E.P. Winpenny, Angew. Chem., Int. Ed. 40 (2001) 2700.
[32] (a) Z. Sun, P.K. Gantzel, D.N. Hendrickson, Inorg. Chem. 35 (1996) 6640;
(b) L.F. Jones, E.K. Brechin, D. Collison, J. Raftery, S.J. Teat, Inorg. Chem. 42 (2003) 6971;
(c) A. Ferguson, K. Thompson, A. Parkin, P. Cooper, C.J. Milios, E.K. Brechin, M. Murie, Dalton Trans. (2007) 728;
(d) M. Shanmugam, G. Chastanet, T. Mallah, R. Sessoli, S.J. Teat, G.A. Timco, R.E.P. Winpenny, Chem. Eur. J. 12 (2006) 8777;
(e) C. Lampropoulos, M. Murugesu, K.A. Abboud, G. Christou, Polyhedron 26 (2007) 2129.
[33] A. Bino, M. Ardon, D. Lee, B. Spingler, S.J. Lippard, J. Am. Chem. Soc. 124 (2002) 4578.
[34] C.J. Milios, Th.C. Stamatatos, P. Kyritsis, A. Terzis, C.P. Raptopoulou, R. Vicente, A. Escuer, S.P. Perlepes, Eur. J. Inorg. Chem. (2004) 2885.
[35] G.B. Deacon, R.J. Phillips, Coord. Chem. Rev. 33 (1980) 227.
[36] Th.C. Stamatatos, G.S. Papaefstathiou, L.R. MacGillivray, A. Escuer, R. Vicente, E. Ruiz, S.P. Perlepes, Inorg. Chem. 46 (2007) 8843.
[37] Z.E. Serna, L. Lezama, M.K. Urtiaga, M.I. Arriortua, M.G. Barandika, R. Cortés, T. Rojo, Angew. Chem., Int. Ed. 39 (2000) 344.

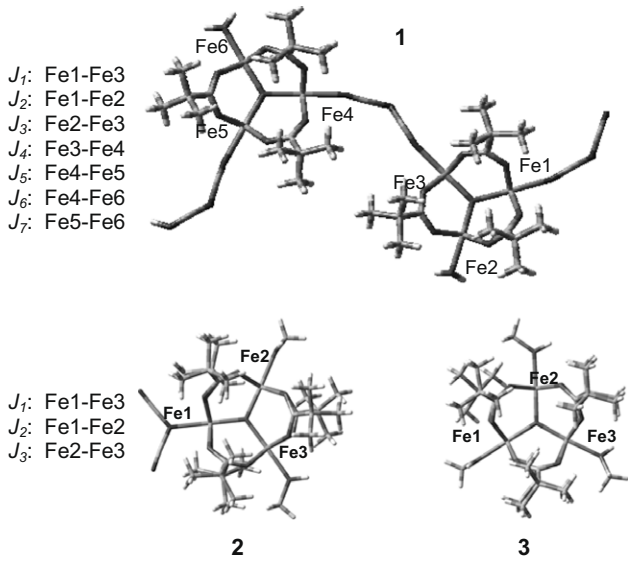


Fig. 1. Structures **1**, **2** and **3** employed in all calculations with the corresponding exchange coupling patterns adopted.

Table 1
Spin topologies describing all calculated broken symmetry states. + and – signs mean spin up and spin down, respectively.

Complex	BS	Fe_1	Fe_2	Fe_3	Fe_4	Fe_5	Fe_6
1	1	–	+	+	+	+	+
	2	+	–	+	+	+	+
	3	+	+	–	+	+	+
	4	+	+	+	–	+	+
	5	+	+	+	+	–	+
	6	+	+	+	+	+	–
	7	+	+	–	–	+	+
	8	+	+	+	–	–	–
2	1	–	+	+			
	2	+	–	+			
	3	+	+	–			
3	1	–	+	+			
	2	+	–	+			
	3	+	+	–			

of the real 1D chain, a proton was added to one terminal dca ligand. This hydrogen atom was placed at an ideal position and optimized with a simple molecular mechanics force field. In the case of the non-bridged Fe_3O complexes, the X-ray geometry was employed, running separately calculations for the two species co-crystallized in the structure [25], $[Fe_3O(Piv)_6(CH_3OH)_2dca]$ (**2**) and $[Fe_3O(Piv)_6(CH_3OH)_3]^+$ (**3**) (Fig. 1).

2.2. DFT calculations

Density functional theory (DFT) spin-unrestricted calculations were performed using the GAUSSIAN03 program [27] (revision D.01) at the B3LYP level employing the *LanL2DZ* basis set and in the case of the smaller complexes **2** and **3** the triple ζ valence split basis set from Ahlrichs with polarization functions (*TZVP*) was also used. Both basis sets were used as implemented in the Gaussian package. Tightly converged (10^{-8} Eh in energy) single point calculations were performed in order to analyze the exchange coupling between the iron centers. The methodology applied here relies on the broken symmetry formalism, originally developed by Noodleman for SCF methods [7], which involves a variational treatment within the restrictions of a single spin-unrestricted Slater determinant built upon using different orbitals for different spin. This approach has been later applied within the frame of DFT [8]. The HS (high spin) and BS (broken-symmetry) energies were then combined to estimate the exchange coupling parameter *J* involved in the widespread used Heisenberg–Dirac–van Vleck Hamiltonian:

$$\hat{H}_{\mathrm{HDvV}} = -2J\hat{S}_A\hat{S}_B \tag{1}$$

In the case of complexes **2** and **3**, we have calculated the three possible spin topologies of broken symmetry nature while in the case of the model complex **1** we have calculated seven broken-symmetry states (Table 1). The exchange coupling constants J_i can be obtained after considering the individual pair-like components spin interactions involved in the description of the different broken symmetry states. Three main reported methodologies can be followed: the Ising approach [28], where the broken symmetry states are directly considered as eigenstates of the HDvV Hamiltonian (Eq. (1)) with the corresponding equation:

$$E_{BS} - E_{HS} = 2J_{12}(2S_1S_2) \tag{2}$$

the non-projected method proposed by Ruiz and co-workers [19], where the following equation is applied:

$$E_{BS} - E_{HS} = 2J_{12}(2S_1S_2 + S_2), \quad \text{with } S_2 < S_1 \tag{3}$$

and finally the generalized multi-spin Yamaguchi method [21], based in the equation:

$$E_{BS} - E_{HS} = 2J_{12}(\langle S_1S_2\rangle_F - \langle S_1S_2\rangle_{AF}) \tag{4}$$

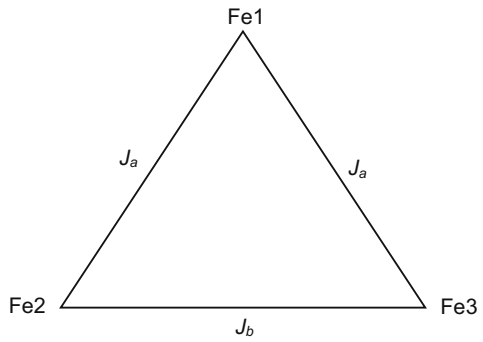
where $\langle S_1S_2\rangle$ ($_F$ = ferromagnetic, $_{AF}$ = anti-ferromagnetic) are the spin correlation functions between the interacting spins.

In all cases a set of linear equations must be solved to obtain the *J* parameters.

Table 2
Calculated exchange coupling constants for complexes **1**, **2** and **3**. All values in cm^{-1}.

Complex	Method	*J*1	*J*2	*J*3	*J*4	*J*5	*J*6	*J*7	Exp.[a]
1[b]	Ruiz	−21.5	−36.2	−38.0	−0.07	−24.4	−35.7	−37.4	$J_a = -35.3$ $J_b = -28.3$ $J' = -0.6$
	Yamaguchi	−25.8	−43.4	−45.4	-0.08	−29.2	−42.7	−44.8	
	Ising	−25.8	−43.5	−45.6	-0.08	−29.3	−42.8	−44.9	
		LanL2DZ				*TZVP*			
		J1	J2	J3		J1	J2	J3	
2	Ruiz	−32.7	−37.4	−32.8		−35.3	−38.3	−35.3	
	Yamaguchi	−39.1	−44.7	−39.3		−42.3	−45.8	−42.3	$J_a = -30.7$ $J_b = -25.5$ or $J_a = -27.0$ $J_b = -33.6$
	Ising	−39.2	−44.8	−39.4		−42.4	−46.0	−42.4	
3	Ruiz	−36.5	−31.2	−35.4		−38.3	−33.7	−37.4	
	Yamaguchi	−43.7	−38.2	−42.3		−45.9	−40.4	−44.7	
	Ising	−43.8	−38.3	−42.5		−46.0	−40.5	−44.9	

[a] From Ref. [25]
[b] All with *LanL2DZ* basis set.



Scheme 1. Exchange coupling pattern in the triangular core Fe_3O.

Further details about these methodologies can be found in Ref. [28,19,21].

Additionally, we have also employed the BS-type spin unrestricted solutions after a corresponding orbital transformation (COT) to visualize the interacting non-orthogonal magnetic orbitals [29]. These orbitals do not have a well-defined orbital energy, for this reason, orbital energies are not given explicitly but just their overlapping magnitudes as well as the spin-coupling exchange pathways.

Table 3
Crystallographic Fe-μ_3-O distances in the Fe_3O cores studied.

Complex	Distance/Å[a]	
1	Fe_2–O, Fe_6–O	1.875
	Fe_1–O, Fe_5–O	1.918
	Fe_3–O, Fe_4–O	1.922
2	Fe_1–O	1.895
	Fe_2–O	1.899
	Fe_3–O	1.914
3	Fe_1–O	1.907
	Fe_2–O	1.909
	Fe_3–O	1.890

[a] From Ref. [25].

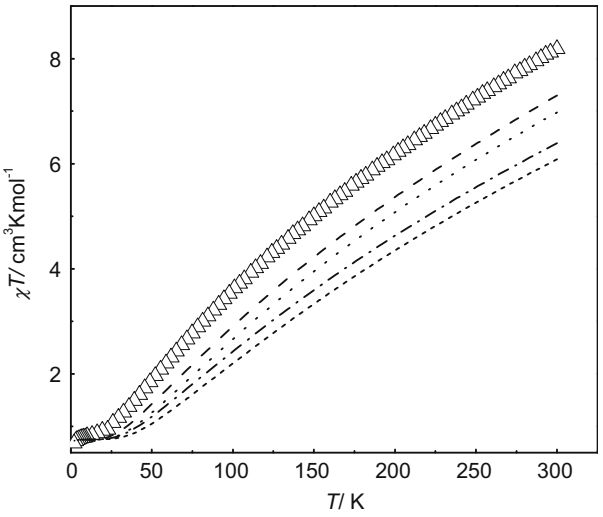


Fig. 2. χT vs. T plot for the complex $[Fe_3O(Piv)_6(CH_3OH)_2dca].[Fe_3O(Piv)_6(CH_3OH)_3]dca$. (Δ) Experimental data (Ref. [25]); (- -) Ruiz method (*LanL2DZ*); (. . .) Ruiz method (*TZVP*); (-·-) Yamaguchi method (*LanL2DZ*);(-···-) Yamaguchi method (*TZVP*).

3. Results and discussion

3.1. Trinuclear Fe_3O complexes **2** and **3**

The calculated J values for the Fe_3O units in complexes **2** and **3** (Table 2) are in good agreement with the experimental ones [25]. As expected, two J values are essentially identical reproducing the usual 2J behavior experimentally observed for this type of triangular Fe_3O cores with three high spin ($S = 5/2$) Fe(III) ions, and ruled by the following HDvV Hamiltonian (Scheme 1):

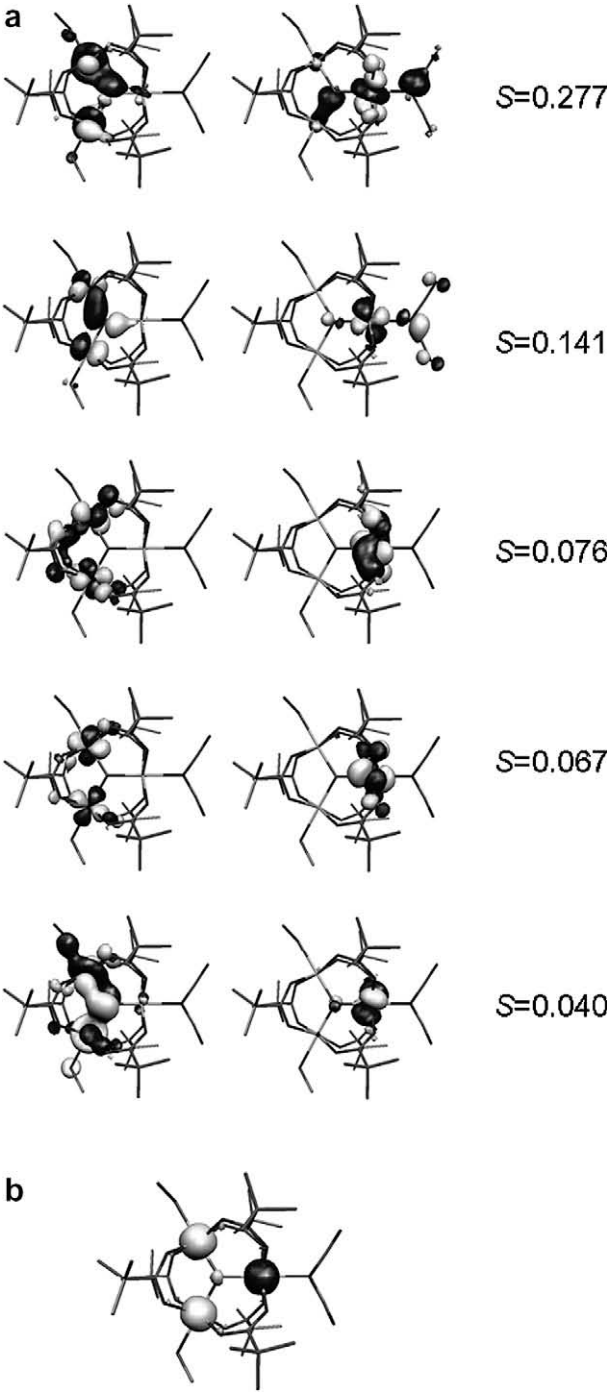


Fig. 3. (a) Magnetic orbitals arising from BS1 after a COT of complex **2** with their corresponding overlaps (S). Left: alpha orbitals, right: beta orbitals. (b) Spin density of BS1 of complex **2**, clear and dark regions corresponds to positive and negative spin densities.

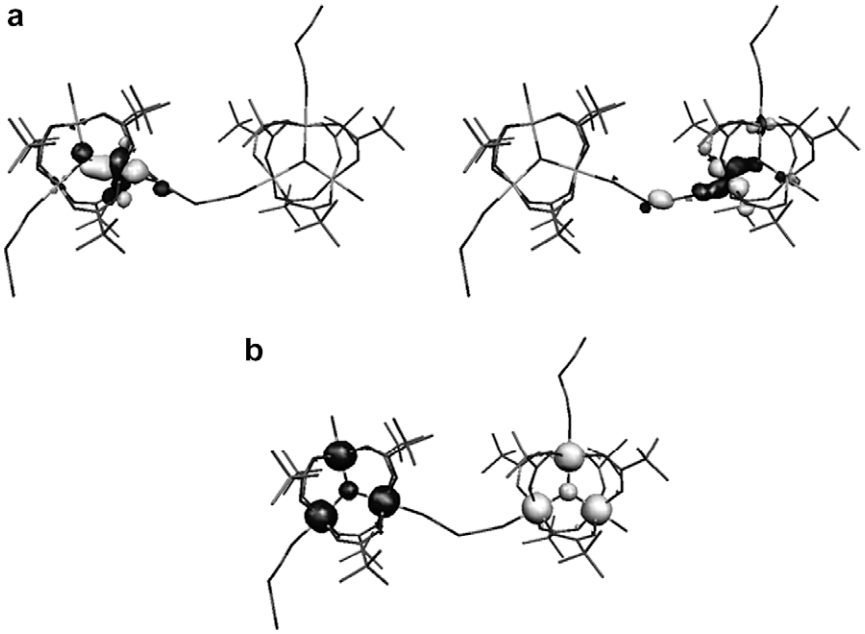


Fig. 4. (a) Magnetic orbitals of complex **1** arising from BS8 after a COT, with a non-negligible overlap trough the dca bridge. Left: alpha orbital, right: beta orbital. (b) Spin density of BS8 of complex **1**, clear and dark regions corresponds to positive and negative spin densities.

$$\hat{H} = -2J_a(\hat{S}_1 \cdot \hat{S}_2 + \hat{S}_1 \cdot \hat{S}_3) - 2J_b(\hat{S}_2 \cdot \hat{S}_3) \quad (5)$$

In the case of complex **2**, the lower obtained $|J|$ value corresponds to J_a, while in complex **3** it corresponds to J_b. This is compatible with experimental data as one short and two long Fe–O–Fe pathways are observed for **2** while the inverse pattern applies in the case of complex **3** (Table 3). It can be noticed that the use of a bigger basis set as *TZVP* instead of the core effective potential type *LanL2DZ* basis sets does not show an improvement in the final calculated values. It appears also that Ruiz methodology gives the more accurate results while the multi-spin Yamaguchi approach does not represent an improvement with respect to the Ising approximation. The $J_>/J_<$ ratio is well reproduced with the three methodologies, most noticeably in the case of the *LanL2DZ* basis set, with values of 1.14/1.16, in comparison to the experimental observed of $J_>/J_< = 1.2$. Hence, the $S = 1/2$ ground state experimentally observed is also reproduced by the calculations. Calculated χT versus T plots,[1] as the 1:1 contribution from complex **2** and **3**, are shown in Fig. 2. It is stressed that an almost identical plot is obtained when using averaged J values for both complexes and a factor of two is applied to the χT plot. This seems to be the most appropriate method as the former cannot be contrasted with experimental values because of severe over-parameterization. From the magnetic orbitals obtained after a COT, it can be observed that the exchange interactions occurred mainly through the central oxo bridging ligand, with two strongly σ-type overlapped magnetic orbitals, while the remaining ones, exhibit a considerably lower overlap, mediated by acetate ligands (Fig. 3). This characteristic is also found when analyzing the magnetic orbitals from the remaining BS states, but in these cases with three oxo mediated strongly overlapped set ($S = 0.258$, 0.243 and 0.153) instead of two. This difference between two or three strongly overlapped magnetic orbitals observed, depending on the spin topology of the BS state, reveals the existence of two different strength exchange interactions within the Fe_3O core, which nicely agrees with the 2J model employed.

[1] For details about calculation of simulated χ values refer to Ref. [25].

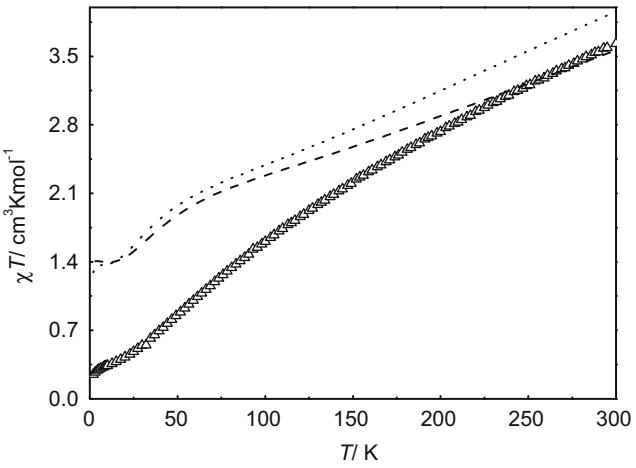


Fig. 5. χT vs. T plot for the model complex **1**. (Δ) Experimental data of the real 1D chain (Ref. [25]); (…) Ruiz method (*LanL2DZ*); (- -) Yamaguchi method (*LanL2DZ*).

3.2. Fe_3O-dca-Fe_3O dimer complex ***1*** model

The main task in the calculation with the complex **1** model was to evaluate its ability to reproduce the weak anti-ferromagnetic coupling (of the order of 1 cm^{-1}) between the Fe_3O units along the chain. Relying on the results obtained for the Fe_3O isolated complexes we used only the less computing demanding *LanL2DZ* basis set, as the bigger *TZVP* basis set did not show a real improvement in the calculated J values of the related complexes **2** and **3**. The calculated value around -0.1 cm^{-1} (Table 2) is far away in terms of the relative error (% Rel. error = $[|J_{calc} - J_{exp}|]/[(|J_{calc} + J_{exp}|)/2]$) with respect to -0.6 cm^{-1}, experimentally observed [25] (extracted employing a mean-field approximation correction, zJ', $z = 2$), however, it should be considered quite reasonable as it is in the limit of the computation precision. Noteworthy, direct

calculation of this J constant value from the BS8 energy,[2] afforded a positive value close to 1 cm^{-1}, clearly contradicting the experimental result. Only if all the other, much stronger J values are included by means of the remaining BS states, the right sign for this weak interaction is predicted. In spite of the ferromagnetic interaction obtained by the direct calculation, inspection of the involved magnetic orbitals after a COT shows that there is at least one small ($S = 0.032$) but non-negligible overlap of σ-nature between the Fe centers through the dca bridge (Fig. 4) providing a path for the anti-ferromagnetic coupling. As in the case of the Fe_3O complexes **2** and **3**, the calculated intra-Fe_3O core exchange interactions constants are in good agreement with the experimental values (Table 2). The almost identical values obtained for the pairs $J_1 - J_5$, $J_2 - J_6$ and $J_3 - J_7$ with the additional matching between the two latter pairs corroborates that the inclusion of the extra proton in our model system does not modify substantially the observed exchange coupling pattern in the real 1D complex. Concerning the method employed, a more accurate value for the $J_1 - J_5$ pair is obtained with the Yamaguchi methodology, while for the remaining J pair values Ruiz method appears more accurate. The bigger ratio $J_>/J_<$, due to an increased asymmetry in the Fe–μ_3O bonds length (Table 3), in comparison with the Fe_3O complexes **2** and **3** is also well reproduced. When the mean value between the calculated J constants in both Fe_3O moieties of complex **1** is considered, the $S = 1/2$ ground state of the weakly coupled Fe_3O cores in the 1D chain is correctly reproduced with all methods and basis sets. The simulated χT versus T plots are shown in Fig. 5.

4. Conclusions

We have employed a DFT broken-symmetry approach to calculate the different exchange coupling constants in two basic carboxylate iron complexes, $[Fe_3O(Piv)_6(CH_3OH)_2dca]$ and $[Fe_3O(Piv)_6(CH_3OH)_3]^+$, respectively, as well as in a 1D chain of dca linked Fe_3O units of formula $[Fe_3O(Piv)_6(H_2O)1,5\text{-}\mu\text{-}dca]_n$. The obtained values are in good agreement with experimental quantities and the weak anti-ferromagnetic exchange coupling constant between Fe_3O cores mediated by the dicyanamide ligand is reasonably well reproduced. Also the total ground state spin values are well reproduced by the theory. In order to tackle the problem of an infinite chain calculation we adopted a simplified model consisting of only a pair of Fe_3O units but preserving all the ingredients of the repetitive unit in the polymeric structure including the overall neutral charge. The successful results obtained suggest that this tool could be a promising methodology for calculating exchange coupling constants in 1D infinite systems at a lower computational cost.

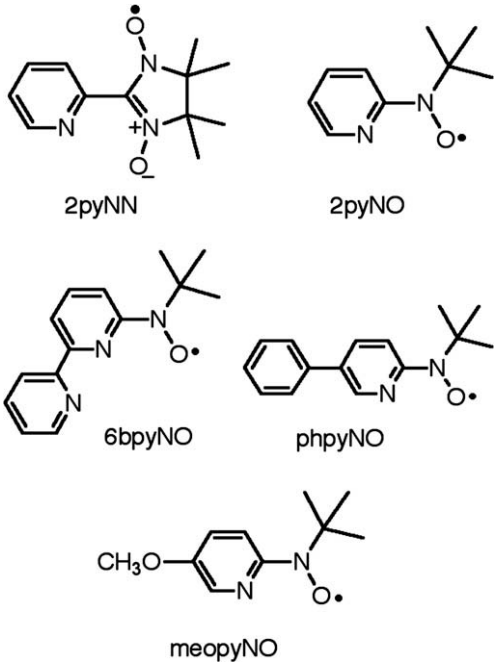
Acknowledgements

We gratefully acknowledge the Alexander von Humboldt Foundation for granting a post-doctoral fellowship. This work was partially supported by the National Center for Supercomputing Applications under grant TG-MCA05S010.

References

[1] H. Miyasaka, M. Yamashita, Dalton Trans. (2007) 399.
[2] J.S. Miller, Dalton Trans. (2006) 2742.
[3] D. Gatteschi, R. Sessoli, J. Magn. Magn. Mater. 272–276 (2004) 1030.
[4] D. Gatteschi, R. Sessoli, Angew. Chem., Int. Ed. 42 (2003) 268.
[5] G. Christou, D. Gatteschi, D.N. Hendrickson, R. Sessoli, MRS Bull. 25 (2000) 66.
[6] D. Gatteschi, R. Sessoli, J. Villain, Molecular Nanomagnets, Oxford University Press, 2006.
[7] L. Noodleman, J. Chem. Phys. 74 (1981) 5737.
[8] L. Noodleman, E.J. Baerends, J. Am. Chem. Soc. 106 (1984) 2316.
[9] E. Ruiz, J. Cano, S. Alvarez, P. Alemany, J. Comput. Chem. 20 (1999) 1391.
[10] T. Soda, Y. Kitagawa, T. Onishi, Y. Takano, Y. Shigeta, H. Nagao, Y. Yoshioka, K. Yamaguchi, Chem. Phys. Lett. 319 (2000) 223.
[11] A. Rodriguez-Fortea, P. Alemany, S. Alvarez, E. Ruiz, A. Scuiller, C. Decroix, V. Marvaud, J. Vaissermann, M. Verdaguer, I. Rosenman, M. Julve, Inorg. Chem. 40 (2001) 5868.
[12] W.G. Han, T. Lovell, T.Q. Liu, L. Noodleman, Inorg. Chem. 42 (2003) 2751.
[13] O. Loboda, I. Tunell, B. Minaev, H. Agren, Chem. Phys. 312 (2005) 299.
[14] K. Chlopek, E. Bothe, F. Neese, T. Weyhermuller, K. Wieghardt, Inorg. Chem. 45 (2006) 6298.
[15] S. Sinnecker, F. Neese, J. Phys. Chem. A 110 (2006) 12267.
[16] K. Chlopek, N. Muresan, F. Neese, K. Wieghardt, Chem. Eur. J. 13 (2007) 8391.
[17] K. Ray, T. Petrenko, K. Wieghardt, F. Neese, Dalton Trans. (2007) 1552.
[18] Y. Takano, T. Taniguchi, H. Isobe, T. Kubo, Y. Morita, K. Yamamoto, K. Nakasuji, T. Takui, K. Yamaguchi, J. Am. Chem. Soc. 124 (2002) 11122.
[19] E. Ruiz, A. Rodriguez-Fortea, J. Cano, S. Alvarez, P. Alemany, J. Comput. Chem. 24 (2003) 982.
[20] A. Bencini, F. Totti, Int. J. Quantum Chem. 101 (2005) 819.
[21] M. Shoji, K. Koizumi, Y. Kitagawa, T. Kawakami, S. Yamanaka, M. Okumura, K. Yamaguchi, Chem. Phys. Lett. 432 (2006) 343.
[22] L.M. Toma, F.S. Delgado, C. Ruiz-Perez, R. Carrasco, J. Cano, F. Lloret, M. Julve, Dalton Trans. (2004) 2836.
[23] S. Triki, C.J. Gomez-Garcia, E. Ruiz, J. Sala-Pala, Inorg. Chem. 44 (2005) 5501.
[24] B. Gillon, A. Goujon, S. Willemin, J. Larionova, C. Desplanches, E. Ruiz, G. Andre, J.A. Stride, C. Guerin, Inorg. Chem. 46 (2007) 1090.
[25] P. Alborés, E. Rentschler, Inorg. Chem. 47 (2008) 7960.
[26] P. Alborés, E. Rentschler, Eur. J. Inorg. Chem. (2008) 4004.
[27] M.J. Frisch et al., GAUSSIAN03, Revision D.1, Gaussian Inc., Pittsburgh PA, 2003.
[28] D.D. Dai, M.H. Whangbo, J. Chem. Phys. 118 (2003) 29.
[29] F. Neese, J. Phys. Chem. Solids 65 (2004) 781.

[2] It can be easily realized that the only contribution to this broken symmetry state comes from J_4.



Scheme 1. Structural formulas.

prepared some chelated compounds with meopyNO according to the reported procedure [5,7,8]. Simply mixing of meopyNO with metal(II) perchlorates in appropriate organic solvents gave ML_2-type compounds of **1** and **2**. They were characterized by means of elemental analysis and IR spectroscopy, and finally their molecular structures were determined by means of X-ray crystallographic analysis. Table 1 summarizes selected crystallographic data of **1** and **2**, and their molecular structures are shown in Fig. 1.

We can find five-membered chelate rings involving a metal center and nitroxide group. Water molecules occupy the axial positions. Compounds **1** and **2** are isomorphous in the space group $P\bar{1}$, except for the following: the coordination structure of the nickel(II) ion in **1** is an almost octahedron (the Ni1–O1, Ni1–N1, and Ni1–O3 distances are 2.020(2), 2.011(2), and 2.091(2) Å, respectively). The octahedral structure of nickel(II) coordination sphere implies $S_{Ni} = 1$. On the other hand, copper(II) ion in **2** shows the Jahn–Teller distortion as indicated with the somewhat longer Cu1–O3 distance of 2.4292(17) Å than those of the Cu1–O1 and Cu1–N1 distances (1.9688(13) and 1.9404(15), respectively). The five-membered chelate rings are very planar for both; the M1–O1–N1–C1 torsion angles are 4.2(3)° and 6.87(19)° for **1** and **2**, respectively. Such structures guarantee the orthogonal arrangement between the metal dσ orbitals (i.e., $3d_{x^2-y^2}$ and $3d_{z^2}$) and nitroxide π^* orbitals. We have proposed that the torsion angle along M–O–N–C_{2py} is convenient for an indicator of the orthogonality [3,8]. The small size of water seems responsible for such a planar geometry. On the other hand, perchlorate anions are relatively bulky in $[Cu(phpyNO)_2(ClO_4)_2]$ [8] and $[Cu(2pyNO)_2(ClO_4)_2]$ [5]. The perchlorate oxygen atom has a considerably bent angle of M–O–Cl, giving rise to the large M–O–N–C_{2py} torsion angles.

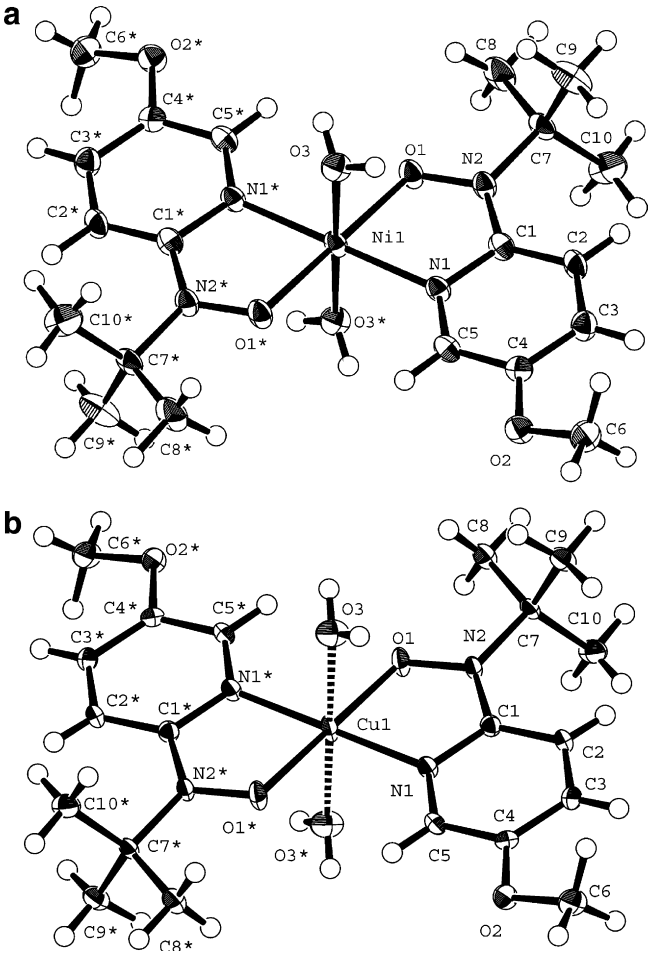


Fig. 1. Molecular structures of (a) **1** and (b) **2** with the thermal ellipsoids at the 50% probability level for non-hydrogen atoms. Atom numbering schemes are also shown. Counter anions are not shown for the sake of clarity.

Table 1
Selected crystallographic data for **1** and **2**.

Compounds	**1**	**2**[c]
Formula	$C_{20}H_{34}Cl_2N_4NiO_{14}$	$C_{20}H_{34}Cl_2CuN_4O_{14}$
Crystal system	triclinic	triclinic
Space group	$P\bar{1}$	$P\bar{1}$
a (Å)	8.3898(11)	8.8930(9)
b (Å)	8.5392(15)	8.7447(8)
c (Å)	10.1289(13)	9.2046(11)
α (°)	84.661(4)	84.640(4)
β (°)	85.308(3)	85.986(6)
γ (°)	89.921(7)	90.420(4)
V (Å^3)	720.07(18)	710.86(13)
Z	1	1
D_{calc} (g cm^{-3})	1.577	1.609
μ(Mo Kα) (mm^{-1})	0.932	1.029
R_{int}	0.065	0.030
$R(F)$[a] ($I > 2\sigma(I)$)	0.0476	0.0300
$R_w(F^2)$[b] (all data)	0.0731	0.0343
Goodness-of-fit	0.867	1.010
Unique reflections	3250	3193
T (K)	108	108

[a] $R = \Sigma||F_o| - |F_c||/\Sigma|F_o|$.
[b] $R_w = [\Sigma w(F_o^2 - F_c^2)^2/\Sigma w(F_o^2)^2]^{1/2}$.
[c] The cell parameters are modified for convenience of the comparison with those of **1**.

2.3. Intramolecular magnetic coupling in the copper(II) and nickel(II) complexes

Magnetic susceptibilities of **1** and **2** were measured on a SQUID magnetometer. Upon cooling from 300 to 2 K, the $\chi_{mol}T$ values of them once increased, indicating the presence of intramolecular ferromagnetic interactions, and then decreased (Fig. 2). The spin-only values are 3.0 and 1.88 cm^3 K mol^{-1} for **1** ($S_{total} = 2$) and for **2** ($S_{total} = 3/2$), respectively. The experimental $\chi_{mol}T$ values at their maximum clearly indicate that they have high-spin states. Final

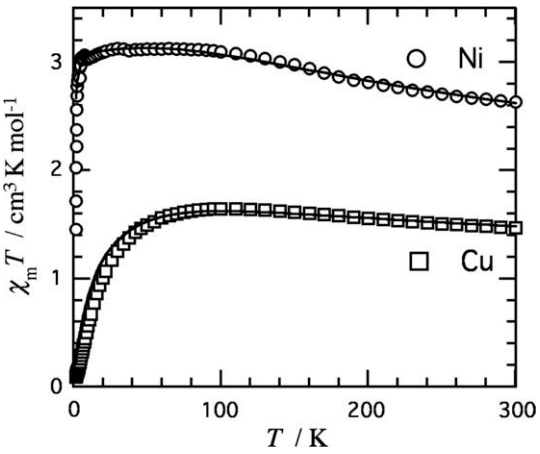


Fig. 2. Temperature dependence of $\chi_{mol}T$ for **1** (circles) and **2** (squares). Applied magnetic fields were 500 Oe for **1** and 1000 Oe for **2**. The solid lines represent calculated curves. See the text for the equations and optimized parameters.

drops of the $\chi_{mol}T$ values are assigned to intermolecular antiferromagnetic couplings, as well as zero-field splitting for the nickel(II) ions in **1**.

For all the complexes investigated here, the metal–radical geometry is unique due to the inversion symmetry, and accordingly the spin-Hamiltonian was defined as $H = -2J(S_1 \cdot S_2 + S_2 \cdot S_3)$ for the three-centered system, in which coupling between the terminal ions was disregarded. Thus, we applied the van Vleck equation to our systems, giving the following expressions, Eqs. (1 and 2) for the nickel(II) and copper(II) complexes, respectively [12].

$$\chi_{mol} = \frac{2Ng_{avg}^2\mu_B^2}{k_B(T-\theta)} \frac{\exp(-2J/k_BT) + 1 + 5\exp(2J/k_BT)}{\exp(-4J/k_BT) + 3\exp(-2J/k_BT + 3 + 5\exp(2J/k_BT)} \quad (1)$$

$$\chi_{mol} = \frac{Ng_{avg}^2\mu_B^2}{4k_B(T-\theta)} \frac{\exp(-2J/k_BT) + 1 + 10\exp(J/k_BT)}{\exp(-2J/k_BT) + 1 + 2\exp(J/k_BT)} \quad (2)$$

The experimental data were fitted to these equations and the optimized parameters are obtained as $g_{avg} = 2.050(2)$, $2J/k_B = +288(5)$ K, and $\theta = -0.32(2)$ K for **1**. On the other hand, we found that the accuracy of J and g_{avg} in **2** was somewhat unsatisfactory with an unrealistic statistical error, though the positive sign of J is meaningful. The J and g parameters interfere each other in this simulation, possibly leading to the considerable errors. The larger J value would give rise to the larger $\chi_{mol}T$ product in a high temperature region, but this bias can be compensated with an upward deviation of g, and vice versa. Thus, we fixed g_{avg} as a typical value of 2.05 [8], and analyzed the data again. The parameters were optimized as $2J/k_B = +178(3)$ K and $\theta = -13.7(3)$ K for **2**.

3. Discussion

As we mentioned above and discussed previously [8], the most important parameter is the M–O–N–C_{2py} torsion angle (ϕ), which indicates the out-of-plane dislocation from the chelate ring with respect to the N–O–M moiety. The ferromagnetic couplings observed here and for the related compounds are well explained in terms of the orbital orthogonality between radical π^* and nickel(II) or copper(II) $3d_{x^2-y^2}$ singly-occupied molecular orbitals (SOMOs) [13]. Now we have to check quantitatively the magnitude of J according to the magneto-structure relationship previously proposed [8].

We have already drawn a plot of J versus ϕ for the hexacoordinated copper(II) and nickel(II) complexes. It should be noted that the argument holds also for the chelates of nitronyl nitroxide (NN) radicals [3,4,14]. Here we superposed two points from **1** and **2** onto this plot (Fig. 3). The present results totally obey this relation. It is instructive to test the following equation, $2J/k_B = a + b|\phi|$ with $a = 440(50)$ K and $b = -35(3)$ K deg^{-1} previously proposed [8]. We calculated $2J/k_B = +293$ and +200 K from $\phi = 4.2°$ and 6.87°, respectively, which satisfactorily agree with the experimental values of $2J/k_B = +288(5)$ and +178(3) K. The expression is refined using all the data including those of **1** and **2**; $2J/k_B = a + b|\phi|$ with $a = 440(40)$ K and $b = -35(3)$ K deg^{-1}.

The present system has an advantage of strong exchange coupling because the spin density of the ligating oxygen atom is relatively high. The magnetic exchange coupling is proportional to the spin densities at the interacting atoms [11]. The spins on Ar–NN [3,4,14] (Scheme 1), Ar–iminonitroxide [4], Ar–verdazyl [15], and Ar–dithiazolyl radicals [16] (Scheme 2) are delocalized mainly onto conjugated N_2O_2, N_2O, N_4, and N_2S_2 systems, respectively, as clarified by the ESR hyperfine data, while the spin in the NO group is highly localized in two atoms. Thus, strong exchange couplings were realized in the present Ar–NO system.

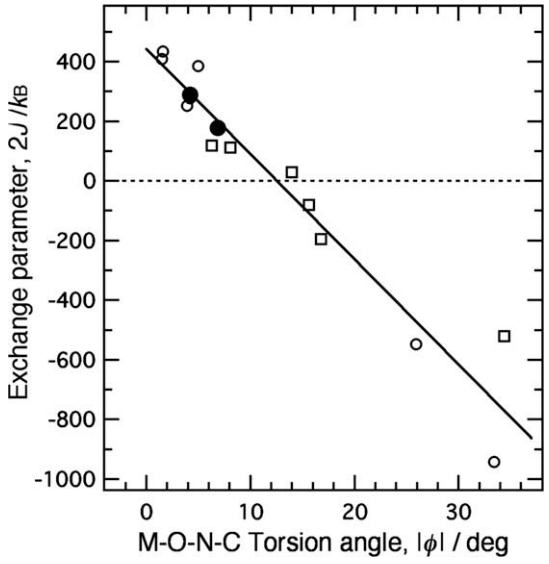
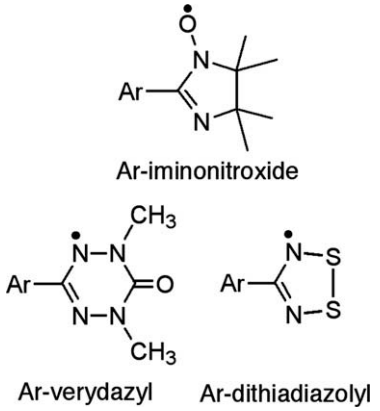


Fig. 3. A plot of the observed exchange coupling parameter ($2J$) vs. M–O–N–C_{2Ar} torsion angle (ϕ) as a magneto-structure relationship in the hexacoordinated nickel(II) or copper(II) complexes. Filled circles stand for the data points on **1** and **2**. Open circles and squares denote the data on known ArNO and ArNN complexes, respectively. The data of ArNO compounds were collected from Refs. [5,7,8], and those of ArNN complexes were from Refs. [3,14]. The line stands for a linear fit.



Scheme 2. Structural formulas.

4. Conclusion

We successfully utilized the new isolable synthetic intermediacy meopyNO, and complexation of nickel(II) and copper(II) perchlorates gave **1** and **2**, where the torsion angles (ϕ) around M–O–N–C_{2py} were as small as 4.2(3)° and 6.87(19)°, respectively. Both of them exhibit the considerably ferromagnetic metal–radical coupling. The 5-membered chelation in the 2-pyridyl–NO systems has an advantage over the 6-membered chelation in the 2-pyridyl–NN systems, with respect to the planarity and accordingly the $d\sigma$–π^* orbital orthogonality. 2-Pyridyl–NO system has another advantage; strong magnetic coupling owing to the high spin density on the ligating oxygen atoms.

5. Experimental

5.1. Materials

5.1.1. N-tert-Butyl N-(5-methoxy-2-pyridyl) hydroxylamine (meopyNOH)

The precursor 2-bromo-5-methoxypyridine [17] was prepared from 2-amino-5-methoxypyridine [18] by the Sandmeyer bromination. To the toluene solution (125 mL) containing 2-bromo-5-methoxypyridine (1.89 g; 10.0 mmol) was added a hexane solution (1.61 mol/L) of butyl lithium (6.8 mL; 11 mmol) at −78 °C under nitrogen atmosphere. After the mixture was stirred at −78 °C for 0.5 h, a toluene solution (25 mL) containing 2-methyl-2-nitrosopropane (1.23 g; 14.1 mmol) was added to the above mixture at −78 °C. The mixture was stirred, being allowed to warm gradually up to room temperature. The reaction mixture was quenched by aqueous NH_4Cl and neutralized with aqueous $NaHCO_3$ at room temperature. The organic layer was separated, dried over anhydrous Na_2SO_4, filtered, and concentrated under reduced pressure. A main product was purified by passing through a short column (silica gel) with 1/1 dichloromethane–ether as an eluent. Recrystallization from dichloromethane/hexane gave 0.238 g of a colorless solid of meopyNOH (1.30 mmol; 66%). M.p. 75–76 °C. ^{1}H NMR (270 MHz, $CDCl_3$) δ 1.19 (s, 9H), 3.85 (s, 3H), 7.06 (d, 1H, J = 8.9 Hz), 7.15 (br s, 1H), 7.19 (dd, 1H, J = 3.0 and 8.9 Hz), 8.04 (d, 1H, J = 3.0 Hz). ^{13}C NMR (68 MHz, $CDCl_3$) δ 25.4, 55.8, 62.1, 121.6, 125.2, 127.7, 149.2, 150.3.

5.1.2. tert-Butyl (5-methoxy-2-pyridyl) nitroxide (meopyNO)

Freshly prepared Ag_2O (695 mg) was added to a dichloromethane solution (10 mL) containing 196 mg (1.00 mmol) of meopyNOH and the mixture was stirred at room temperature for 0.5 h. The supernatant immediately turned red. The solution phase was filtered and concentrated under reduced pressure. A main product was purified by passing a short column (silica gel; dichloromethane as an eluent). Red viscous oil of meopyNO was obtained after the removal of the solvent. We obtained 194 mg (0.99 mmol) of meopyNO in 99% yield. M.p. Ca. 10 °C. ESR (X-band, room temperature, in toluene; Bruker ESP300E X-band (9.7 GHz)) g = 2.0059, a_N = 1.076 mT. MS (ESI+) m/z 218.1 $(M + Na)^+$, 162.0 $(M–t\text{-}Bu + Na)^+$.

5.1.3. Coordination compounds

A dichloromethane solution (0.5 mL) containing 78 mg (0.40 mmol) of meopyNO was combined to an ethanol solution (1 mL) containing 73 mg (0.20 mmol) of $Ni(ClO_4)_2 \cdot 6H_2O$. A slow diffusion with ether gave dark red crystals of **1** after being kept in a refrigerator for a few days. The crystals were separated on a filter and washed with water. The yield was 108 mg (0.158 mmol; 79%). Single crystals suitable for the X-ray diffraction study were obtained by slow diffusion of ether into an acetone solution of **1**. M.p. 170–172 °C (decomp.). *Anal.* Calc. for $C_{20}H_{34}Cl_2N_4NiO_{14}$: C, 35.11; H, 5.01; N, 8.19. Found: C, 35.03; H, 5.18; N, 8.18%. Similarly, **2** was prepared in 58% yield. M.p. 168–170 °C (decomp.). *Anal.* Calc. for $C_{20}H_{34}Cl_2CuN_4O_{14}$: C, 34.87; H, 4.97; N, 8.13. Found: C, 34.83; H, 4.82; N, 8.13%.

5.2. Instruments

5.2.1. X-ray crystal structure analysis

X-ray diffraction data of single crystals of **1** and **2** were collected on a Rigaku R-axis RAPID diffractometer with graphite monochromated Mo Kα (λ = 0.71069 Å) radiation. The structures were directly solved and the parameters were refined in the CRYSTAL STRUCTURE program package [19]. Numerical absorption correction was used. All of the hydrogen atoms were found experimentally for **1** and **2**. Thermal displacement parameters were refined anisotropically for non-hydrogen atoms and those of hydrogen atoms were treated isotropically. Selected crystallographic data are summarized in Table 1.

5.2.2. Magnetic measurements

Magnetic susceptibilities of the polycrystalline samples of **1** and **2** were measured on a Quantum Design MPMS SQUID magnetometer at an applied magnetic field of 500 or 5000 Oe in a temperature range down to 1.8 K. The magnetic response was corrected with diamagnetic blank data of the sample holder obtained separately. The diamagnetic contribution of the sample itself was estimated from Pascal's constant.

Supplementary data

CCDC 700744 and 700745 contain the supplementary crystallographic data for **1** and **2**, respectively. These data can be obtained free of charge via http://www.ccdc.cam.ac.uk/conts/retrieving.html, or from the Cambridge Crystallographic Data Centre, 12 Union Road, Cambridge CB2 1EZ, UK; fax: (+44) 1223-336-033; or e-mail: deposit@ccdc.cam.ac.uk

Acknowledgements

This work was supported by Grants-in-Aid for Scientific Research (Nos. 17550166 and 19550135) from the Ministry of Education, Culture, Sports, Science and Technology, Japan.

References

[1] (a) A. Caneschi, D. Gatteschi, R. Sessoli, P. Rey, Acc. Chem. Res. 22 (1989) 392;
(b) J.M. Manriquez, G.T. Yee, R.S. McLean, A.J. Epstein, J.S. Miller, Science 252 (1991) 1415;
(c) K. Inoue, T. Hayamizu, H. Iwamura, D. Hashizume, Y. Ohashi, J. Am. Chem. Soc. 118 (1996) 1803;
(d) M.T. Lamaire, Pure Appl. Chem. 76 (2004) 277.
[2] F.M. Romero, D. Luneau, R. Ziessel, Chem. Commun. (1998) 551.
[3] C. Aoki, T. Ishida, T. Nogami, Inorg. Chem. 42 (2003) 7616.
[4] (a) D. Luneau, P. Rey, J. Laugier, P. Fries, A. Caneschi, D. Gatteschi, R. Sessoli, J. Am. Chem. Soc. 113 (1991) 1245;
(b) D. Luneau, P. Rey, J. Laugier, E. Belorizky, A. Conge, Inorg. Chem. 31 (1992) 3578.
[5] A. Okazawa, T. Nogami, T. Ishida, Chem. Mater. 19 (2007) 2733.
[6] J.F.W. Keana, Chem. Rev. 78 (1978) 37.
[7] K. Osanai, A. Okazawa, T. Nogami, T. Ishida, J. Am. Chem. Soc. 128 (2006) 14008.
[8] A. Okazawa, Y. Nagaichi, T. Nogami, T. Ishida, Inorg. Chem. 47 (2008) 8859.
[9] (a) A. Calder, A.R. Forrester, J. Chem. Soc. (C) (1969) 1459;
(b) A.R. Forrester, S.P. Hepburn, J. Chem. Soc., Perkin I (1974) 2208.
[10] S. Kanegawa, S. Karasawa, M. Maeyama, M. Nakano, N. Koga, J. Am. Chem. Soc. 130 (2008) 3079.
[11] H.M. McConnell, J. Chem. Phys. 39 (1963) 1910.
[12] S.J. Gruber, C.M. Harris, E.J. Sinn, Chem. Phys. 49 (1968) 2183.
[13] O. Kahn, R. Prins, J. Reedijk, J.S. Thompson, Inorg. Chem. 26 (1987) 3557.

[14] (a) D. Luneau, G. Risoan, P. Rey, A. Grand, A. Caneschi, D. Gatteschi, J. Laugier, Inorg. Chem. 32 (1993) 5616;
(b) I.D. Luneau, F.M. Romero, R. Ziessel, Inorg. Chem. 37 (1998) 5078.
[15] (a) R.G. Hicks, M.T. Lemaire, L.K. Thompson, T.M. Barclay, J. Am. Chem. Soc. 122 (2000) 8077;
(b) T.M. Barclay, R.G. Hicks, M.T. Lemaire, L.K. Thompson, Chem. Commun. (2000) 2141;
(c) I.J.B. Gilroy, B.D. Koivisto, R. McDonald, M.J. Ferguson, R.G. Hicks, J. Mater. Chem. 16 (2006) 2618.
[16] (a) N.G.R. Hearns, K.E. Preuss, J.F. Richardson, S. Bin-Salamon, J. Am. Chem. Soc. 126 (2004) 9942;
(b) M. Jennings, K.E. Preuss, J. Wu, J. Chem. Commun. (2006) 341;
(c) I.K.E. Preuss, Dalton Trans. 23 (2007) 2357.
[17] A. Lützen, M. Hapke, H. Staats, J. Bunzen, Eur. J. Org. Chem. (2003) 3948.
[18] (a) P.D. Leeson, J.C. Emmett, J. Chem. Soc., Perkin Trans. I (1988) 3085;
(b) F. Effenberer, A. Krebs, P. Willrett, Chem. Ber. 125 (1992) 1131.
[19] Crystal Structure version 3.8, Rigaku/MSC, The Woodlands, TX 77381, USA, 2000–2006.

2-hydroxymethylpyridine, R is an alkyl substituent and X^- is either Cl^- or Br^- [4]. A key finding of this work was the fact that crystals of the high (S_4) symmetry $[Ni(hmp)(dmb)Cl]_4$ complex contained no solvate molecules, resulting in exceptionally high quality high-frequency electron paramagnetic resonance (HFEPR) spectra [17]. Furthermore, HFEPR measurements for a Zn analog doped with small quantities of Ni^{II} enabled evaluation of the single-ion ZFS tensors [18]. The combined studies provided important insights concerning the physics of SMMs [19]. The success of these investigations thus provided motivation for investigating two isostructural compounds: $[Co(hmp)(dmb)Cl]_4$ (**1**) and $[Zn_{1-x}Co_x(hmp)(dmb)Cl]_4$ (**2**).

Single-crystal HFEPR studies of $[Zn_{1-x}Co_x(hmp)(dmb)Cl]_4$ were reported previously [20], demonstrating that the ground state of the Co^{II} ions can be modeled as an effective spin $S' = 1/2$ Kramers doublet. Such a model ignores the upper Kramers levels associated with the $S = 3/2$ Co^{II} ions. The strong anisotropy is instead parameterized via an anisotropic g-tensor associated with the effective $S' = 1/2$ ground state Kramers doublet. The HFEPR studies of **2** established a huge g-anisotropy ($g_z = 7.8$ and $g_{x,y} \approx 2.0$) of the easy-axis type. It was also found that the individual easy-axis directions are tilted away from the crystallographic c direction by 58°. The huge g-anisotropy is close to the maximum expected for an octahedral Co^{II} complex [21], suggesting a very significant ZFS separating the two Kramers doublets. However, it was not possible to determine the magnitude of this ZFS on the basis of the HFEPR studies of **2**.

The clear success in modeling the HFEPR spectrum of the Co^{II} ions in crystals of complex **2** as effective spin-1/2 particles begs the obvious question as to whether such a simple approach may be extended to the polynuclear complex **1**. First and foremost, we note that a rigorous treatment of the spin–orbit coupling is computationally challenging (the Hamiltonian matrix has dimensions of 20736×20736), and also requires far more information concerning the Co^{II} ZFS than obtained from HFEPR studies of **2**. Thus, in some sense, the coupled $S' = 1/2$ description offers the only realistic starting point. However, at first sight, it is not obvious how one could couple four $S' = 1/2$ particles, giving rise to SMM behavior. One associates the magnetic bistability of a SMM with the ZFS within its spin ground state. At a very basic level, this ZFS (or zero-field anisotropy) arises from the projection (or addition) of the ZFS associated with the individual ions onto the spin ground state of the molecule [9,22]. Herein lies the problem: a spin-1/2 object displays no anisotropy in the absence of a magnetic field, i.e. it exhibits no ZFS. Thus, such a projection by itself cannot give rise to ZFS for the coupled system. Viewed slightly differently – by ignoring the ZFS splitting associated with the Co^{II} ions, one is throwing away all details of their zero-field anisotropy.

The arguments given above ignore one crucial detail: in the case of the coupled Co_4 system, each Co^{II} ion experiences an exchange field due to its neighboring ions in the cluster. However, the projection method completely ignores this exchange coupling. The solution to this problem turns out to be relatively simple, and involves a multispin Hamiltonian consisting of just the pairwise interactions between the Co^{II} ions together with the individual Zeeman interactions. The anisotropic spin–spin interactions are then parameterized in terms of an exchange tensor, $\overleftrightarrow{J}_{ij}$, and the Hamiltonian may be expressed as:

$$H = \sum_{i<j} \hat{S}_i \cdot \overleftrightarrow{J}_{ij} \cdot \hat{S}_j + \sum_i \mu_B \vec{B} \cdot \overleftrightarrow{g}_i \cdot \hat{S}_i. \quad (1)$$

For the case of four coupled spin-1/2 particles, the full Hamiltonian matrix has dimensions $2^4 \times 2^4$, i.e. 16×16. The problem is thus easily tractable, and involves just a handful of parameters, many of which are already known from the HFEPR studies of complex **2** [20].

In this paper, we attempt to qualitatively account for the main features observed in the HFEPR spectra obtained for the Co_4 complex **1** on the basis of Eq. (1), and we additionally consider the possibility that anisotropic exchange could give rise to magnetic bistability and SMM behavior. Naturally, the exchange anisotropy is merely a manifestation of the strong single-ion anisotropy associated with the individual Co^{II} ions. Nevertheless, this offers a new way of thinking about magnetic anisotropy in polynuclear clusters, and complex **1** appears to represent a model compound for exploring these ideas in detail.

2. Experimental

Crystals of complex **1** were prepared according to a similar procedure to the previously reported $[Co(hmp)(MeOH)Cl]_4$ complex [11]; a detailed account of the synthesis will be published elsewhere [23]. Good sized, dark red crystals form in the shape of a square-based pyramid, reflecting the S_4 symmetry of the structure. One can easily identify the principal crystallographic directions on the basis of the crystal morphology, the c-axis being oriented perpendicular to the square base of the pyramid, i.e. in the direction defined by the apex of the pyramid. All of the data presented in this paper were obtained with the magnetic field applied parallel to the crystal c-axis, which also corresponds to the S_4 axis; angle-dependent studies will be published in a longer paper. The sample was mounted with its square base attached with vacuum grease to a flat copper disk at the end of the HFEPR probe/cavity.

Experiments were performed in a 9 T superconducting magnet, and temperature control achieved using a ^{4}He flow cryostat equipped with a calibrated temperature sensor. As a spectrometer, we utilized a Millimeter-wave Vector Network Analyzer (MVNA, described elsewhere [24,25]), enabling measurements from 8 to 715 GHz at the University of Florida. At the higher frequencies (>200 GHz), a pair of external Gunn diodes were associated with the MVNA on both source and detection sides, enabling phase sensitive measurements up to 715 GHz. A quasioptical spectrometer was used for frequencies above ~200 GHz. This spectrometer, which has been described previously [26], employs a tapered corrugated HE_{11} waveguide tube, enabling single-pass reflectivity measurements with good coupling to relatively small crystals (<1 mm^3). For frequencies below 200 GHz, a cavity perturbation technique was employed (see [24,25]).

3. Data and discussion

Fig. 1 shows low-temperature ($T = 2$ K) HFEPR spectra obtained at several frequencies in the range from 258 to 715 GHz. Multiple peaks are observed at all frequencies. The signal-to-noise diminishes at the higher frequencies due to the reduced dynamic range of the high-frequency spectrometer. Nevertheless, clear resonances are observable at all of the frequencies shown, and each spectrum is highly reproducible. Given that the temperature is rather low (much less than the microwave quantum, which ranges from 12 to 34 K), one may assume that all of the observed HFEPR intensity involves excitations from the ground state of the Co_4 complex. Several obvious resonance branches become apparent upon close inspection of Fig. 1; this point has been emphasized by means of the colored arrows in the figure.

A 2D frequency versus field plot for resonances observed at many different frequencies, spanning a wider range from 50 to 715 GHz, is displayed in Fig. 2. This figure emphasizes only the stronger resonances, particularly those observed at the lowest temperatures (though data points are included for a range of temperatures). The solid curves superimposed on the various resonance branches are simply guides to the eye. The first point to

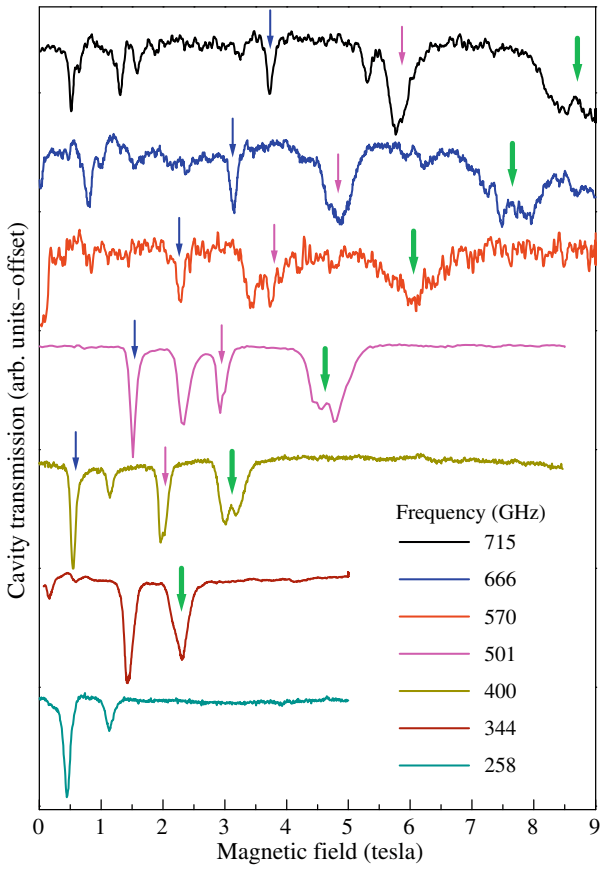


Fig. 1. Frequency dependence spectra obtained at $T = 2$ K with the magnetic field parallel to the *c*-axis of the crystal. The frequencies are given in the figure, and the colored arrows are included in order to differentiate between various resonance branches.

note from this figure is the fact that the different branches intersect the vertical zero-field axis at many different frequencies, suggesting that the Co_4 spectrum possesses many ZFS values ranging all the way from 50 GHz up to almost 700 GHz (and maybe higher?). It is also notable that the slopes of the branches correspond to *g*-values ranging from 2.0 (low-frequency branches) all the way up to ~7.4 (high-frequency branches). We note that this spread is comparable to the range of values found for the Co^{II} ions from HFEPR studies of complex **2** [20].

Representative temperature dependence measurements are shown for three different frequencies in Fig. 3. From this figure, one can conclude that the resonances observed at the highest frequencies (above ~250 GHz) correspond to excitations from the ground state. In contrast, at 99 GHz, all transitions except for the lowest field peak appear to originate from excited states, due to vanishing intensity as $T \rightarrow 0$. The corresponding data points in Fig. 2 have, therefore, been colored red so as to distinguish them from the strong ground state transitions. A particularly interesting observation is the fact that this Co_4 complex is almost EPR silent at fields above ~1 T for intermediate frequencies ranging from ~250 to 400 GHz. This frequency gap appears to separate the low- and high-*g* resonance branches.

The key finding from these experiments is the clear observation of significant ZFS associated with the low-lying spin states of complex **1**. Another important observation is the fact that it is completely impossible to fit the data in Fig. 2 using a giant-spin approximation. Based on such a model, one expects the 2D plot for the easy-axis (Fig. 2) to consist of more-or-less evenly spaced parallel branches of resonances, with only a single branch surviving to the lowest temperatures. As a check, we confirmed that the field was aligned with the easy-axis on the basis of detailed angle-dependent measurements (not shown [23]).

Many aspects of the data hint strongly at competing interactions/symmetries, such that neither the total spin, *S*, nor its projection, m_S, are good quantum numbers. First of all, the observation of multiple ground state resonances suggests an absence of simple selection rules. This contrasts the giant-spin case, where *S* and m_S are good quantum numbers and the $\Delta m_S = \pm 1$ EPR selection rule permits only one possible transition from the ground state. In addition, the non-linear character of some of the resonance branches, including obvious evidence for the repulsion between levels (e.g. red and black data in the 100–200 GHz range in Fig. 2), suggests a strong mixing of spin states. Finally, the observation of a wide range of *g*-values would again seem to suggest a complete absence of selection rules. Furthermore, the gap between low- and high-*g* resonance branches suggests a fundamentally different nature to the low- and high-frequency excitations, with the former perhaps occurring within a multiplet of low-energy states and the latter involving excitations from this multiplet to excited multiplets.

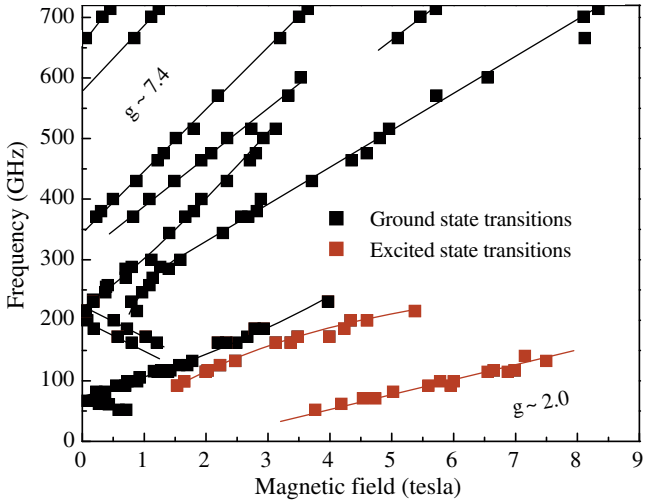


Fig. 2. A 2D frequency verses field plot representing the positions of the stronger resonances observed from the frequency dependence measurements with the field parallel to the *c*-axis. The solid curves are purely guides to the eye.

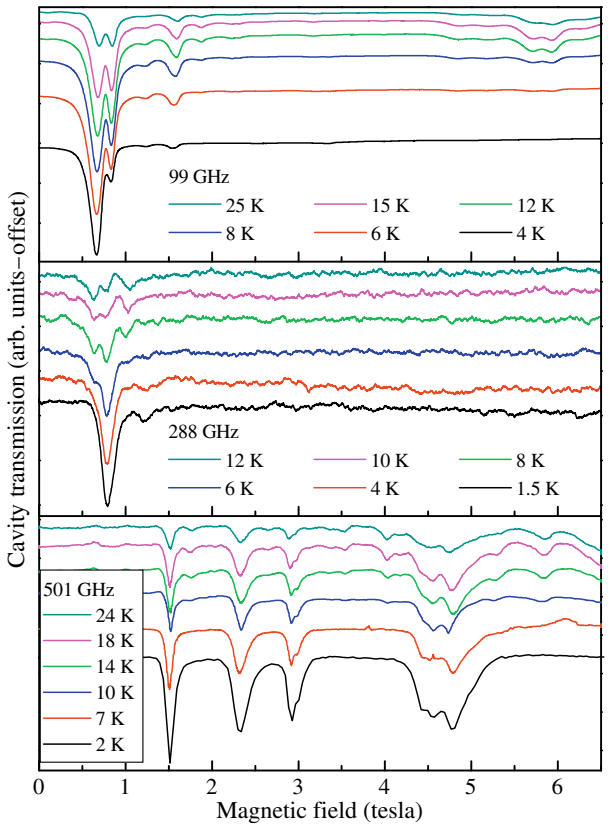


Fig. 3. Temperature dependence measurements ($B//c$) for three different frequencies; the temperatures and frequencies are given in the figures.

The idea of a 'spin multiplet' loses its meaning to some degree if there is strong mixing of spin states. Nevertheless, we use this concept as a basis for the discussion in the following section.

4. Numerical calculations

In this section, we attempt to account qualitatively for the experimental observations on the basis of Eq. (1). The results are summarized in Fig. 4. In the absence of exchange anisotropy, both S and m_S are exact quantum numbers. The zero-field solution to Eq. (1) is relatively straightforward in the case where one considers a single isotropic exchange coupling parameter, J: namely, the energy $E(S_T) = 1/2[S_T(S_T + 1) - 3]J$, where S_T (=0, 1 or 2) is the total spin of a given state. Application of a magnetic field simply lifts the degeneracy within each spin-multiplet, resulting in a set of $2S_T + 1$ levels whose energies shift according to the Zeeman interaction. This situation is illustrated in Fig. 4a, with $J = -200$ GHz, where we assumed that the axial single-ion g-tensors were all aligned parallel to the z-axis of the molecule. Likewise, the magnetic field was applied in this direction such that $\Delta E(B) = \mu_B g_z B m_S$, where B is the magnetic field strength; a value of $g_z = 6.0$ was used in this simulation.

It should be noted that each spin multiplet exhibits no ZFS in this simple isotropic case. Furthermore, the EPR selection rule forbids $\Delta S = \pm 1$ transitions. Thus, all resonance branches should depend linearly on the field, and intersect the 2D frequency/field plot (Fig. 2) at the origin. In fact, just a single EPR peak would be observed (see red arrows), since the energy spacing between successive levels is independent of m_S.

Fig. 4b considers an axial exchange anisotropy, also aligned with the molecular z-axis. We assume the same exchange between all ions (see below) and parameterize the interaction as follows:

$$H = J\sum_{i<j}\left[\hat{S}_{iz}\hat{S}_{jz} + \alpha\left(\hat{S}_{ix}\hat{S}_{jx} + \hat{S}_{iy}\hat{S}_{jy}\right)\right] + \sum_i \mu_B \vec{B}\cdot\overleftrightarrow{g}_i\cdot\hat{S}_i. \qquad (2)$$

Here, J characterizes the strength of the Ising component of the exchange, while the parameter α $(\leqslant 1)$ is a measure of the anisotropy. Obviously $\alpha = 1$ represents the isotropic limit; values of $\alpha = 2^{-1/2}$ and $J = -200$ GHz were used for the simulations in

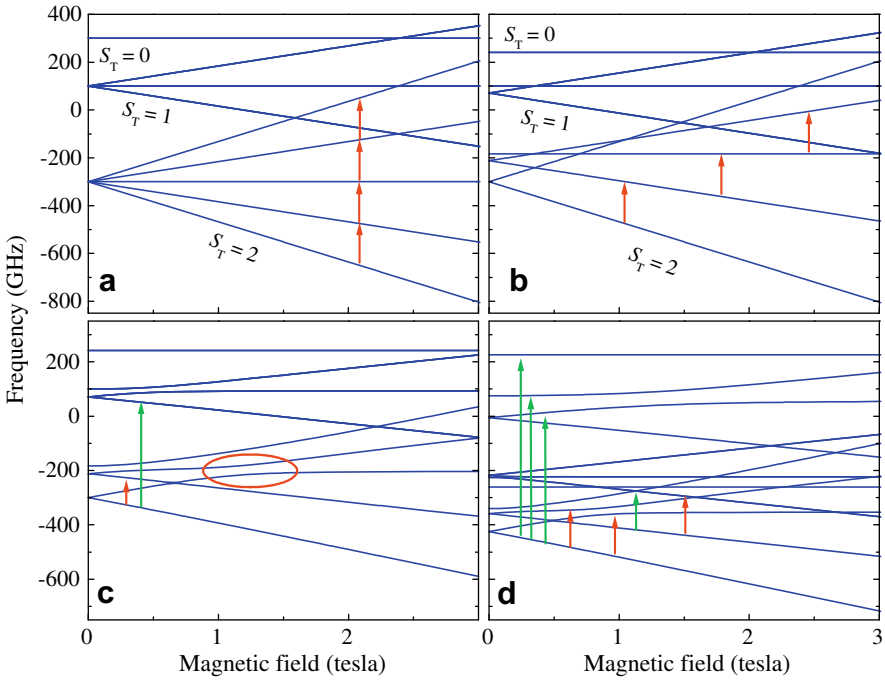


Fig. 4. Simulated Zeeman diagrams obtained for complex **1** on the basis of Eq. (1) (also Eq. (2)), using various different parameter sets: (a) represents the isotropic case; (b) adds an axial exchange anisotropy; (c) includes the effect of a tilting (58°) of the single-ion g-tensors away from the axial direction; and (d) considers two inequivalent exchange parameters within the cluster. See main text for details of the calculations (including values for the various parameters), and an in-depth discussion of these diagrams. The arrows represent possible HFEPR transitions.

Fig. 4b. Interestingly, S and m_S remain good quantum numbers for the situation in which the magnetic field is applied along z (Fig. 4b), due to the preservation of the axial symmetry. The effect of the exchange anisotropy is to lift the zero-field degeneracy within each spin multiplet. In fact, this is precisely the result we were looking for. The EPR spectrum would now be expected to exhibit multiple, albeit evenly spaced peaks (see red arrows) due to the ZFS within each spin multiplet. In fact, the ZFS within each multiplet could equally be parameterized using a giant-spin Hamiltonian.

It should be noted at this juncture that the spectrum displayed in Fig. 4b displays all of the hallmarks of a SMM, i.e. a relatively well isolated spin ground state possessing an axial anisotropy/ZFS. Any molecule possessing these characteristics should exhibit magnetization hysteresis below some characteristic blocking temperature. Thus, we have demonstrated that Eq. (1) can indeed give rise to SMM behavior. Nevertheless, we extend these calculations further, because the spectrum in Fig. 4b cannot yet account for many of the HFEPR observations.

It was noted from HFEPR studies of complex **2**, that the Co^{II} single-ion g-tensors are tilted considerably with respect to the molecular z-axis. For Fig. 4c, the g-tensors were tilted 58° away from z, and the field was again applied parallel to z; J and α remained the same as before. Solutions to Eq. (2) were obtained via exact matrix diagonalization. A number of things become immediately apparent upon including such tilting. First of all, the molecular g-value decreases significantly, as seen from the slope of the line corresponding to the ground state. This is due to the reduced projection of the (larger) g_z component of the single-ion tensors onto the molecular axis; a value of $g_{x,y} = 2.0$ was used for these simulations. In addition, one can now observe level repulsions (circled) for the first time, i.e. m_S is no longer an exact quantum number. Indeed, due to competing interactions (Zeeman and anisotropic exchange), one would also expect S-mixing. Thus, one should in principle start to observe a breaking of the simple EPR selection rules.

Given the presence of exchange anisotropy, one would also expect antisymmetric exchange for this molecule, which does not possess a center of inversion. Inclusion of such an interaction would immediately result in additional S-mixing and further relaxation of the $\Delta S = 0$ EPR selection rule to the extent that one could expect to observe strong inter-spin multiplet transitions, i.e. multiple ground state resonances spanning a wide frequency range (see red and green arrows in Fig. 4c).[1] Inclusion of an antisymmetric term in Eq. (1) adds very little in terms of computation. Nevertheless, for the sake of simplifying the discussion, we do not include such an interaction in the present work. However, we note that, with the consideration of S-mixing, Fig. 4c begins to embody many of the characteristics that would account qualitatively for the experimental observations. Nevertheless, inspection of Fig. 2 reveals many different ZFSs spanning the range from about 65 GHz up to 650 GHz. However, there remain significant zero-field gaps in Fig. 4c. These gaps can be filled to some extent if one relaxes the assumption of a single exchange parameter. In doing so, one finally arrives at Fig. 4d, which considers two exchange constants, consistent with the S_4 symmetry of the Co_4 cluster, i.e. $J_1 = -250$ GHz(4 bonds) and $J_2 = +50$ GHz(2 bonds), with the same anisotropy constant, α, for both.

Fig. 4d represents a crude attempt to account qualitatively and semi-quantitatively for many of the features observed in the HFEPR experiments of complex **1**. However, the exact numbers used for the simulations should not be taken too seriously. Our intent is to show that Eq. (1) contains essentially all of the physics needed to account for the EPR data and, possibly, the hysteresis measurements. The parameters were chosen so that (a) the ZFS between the ground and first excited state roughly matches the smallest ZFS in the experiment, i.e. 67 GHz, and (b) the full spectrum spans around 650 GHz, which was the largest ZFS observed in the experiment. We have not yet reached the stage where we are able to fit the data exactly to Eq. (1). However, further refinements in the experiments are under way in order to provide further constraints, particularly detailed angle-dependent studies [23]. It remains to be seen whether the spectrum in Fig. 4c could give rise to magnetization hysteresis.

[1] For interpretation to color in Fig. 4, the reader is referred to the web version of this article.

5. Conclusions

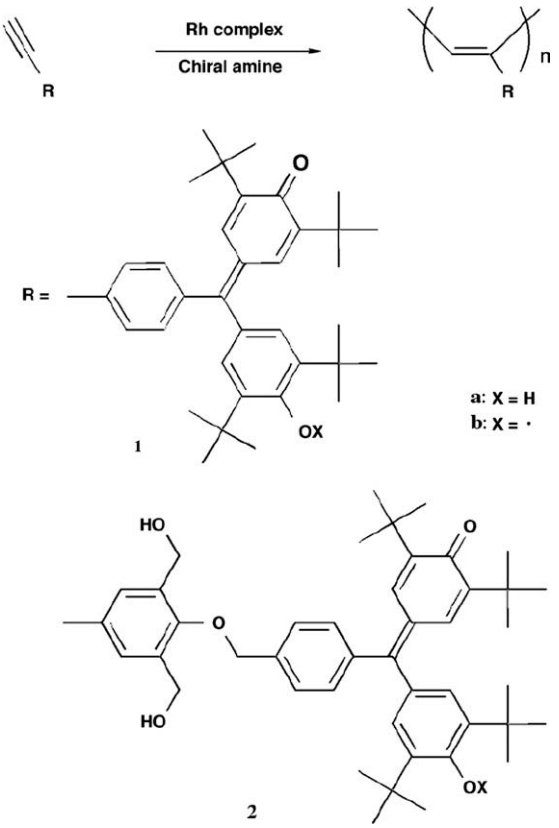
We consider the effects of anisotropic exchange interactions between the effective spin $S' = 1/2$ Kramers ions within the tetranuclear Co complex. Our model can account qualitatively and semi-quantitatively for many features observed in HFEPR experiments. We also demonstrate that this model can give rise to SMM behavior, even for spin-1/2 particles that themselves do not possess any zero-field anisotropy, i.e. the molecular anisotropy (ZFS) arises purely via anisotropic spin–spin interactions.

Acknowledgements

This work was supported by US National Science Foundation (Grant Nos. DMR0239481 and DMR0414809).

References

[1] D. Gatteschi, R. Sessoli, J. Villain, Molecular Nanomagnets, Oxford University Press, 2006.
[2] R. Sessoli, H.L. Tsai, A.R. Schake, S. Wang, J.B. Vincent, K. Folting, D. Gatteschi, G. Christou, D.N. Hendrickson, J. Am. Chem. Soc. 115 (1993) 1804.
[3] A.K. Boudalis, C.P. Raptopoulou, B. Abarca, R. Ballesteros, M. Chadlaoui, J.-P. Tuchagues, A. Terzis, Angew. Chem., Int. Ed. 45 (2006) 432.
[4] P.L. Feng, C.C. Beedle, C. Koo, J. Lawrence, S. Hill, D.N. Hendrickson, Inorg. Chim. Acta 361 (2008) 3465.
[5] P.L. Feng, C.C. Beedle, W. Wernsdorfer, C. Koo, M. Nakano, S. Hill, D.N. Hendrickson, Inorg. Chem. (Communication) 46 (2007) 8126.
[6] P.L. Feng, C.C. Beedle, C. Koo, W. Wernsdorfer, M. Nakano, S. Hill, D.N. Hendrickson, Inorg. Chem. 47 (2008) 3188.
[7] A. Mishra, W. Wernsdorfer, K.A. Abboud, G. Christou, J. Am. Chem. Soc. 126 (2004) 15648.
[8] C.J. Milios, A. Vinslava, W. Wernsdorfer, S. Moggach, S. Parsons, S.P. Perlepes, G. Christou, E.K. Brechin, J. Am. Chem. Soc. 129 (2007) 2754.
[9] S. Datta, E. Bolin, C.J. Milios, E.K. Brechin, S. Hill, Polyhedron 28 (2009) 1788.
[10] O. Kahn, Molecular Magnetism, Wiley, 1993.
[11] E.-C. Yang, D.N. Hendrickson, W. Wernsdorfer, M. Nakano, L.N. Zakharov, R.D. Sommer, A.L. Rheingold, M. Ledezma-Gairaud, G. Christou, J. Appl. Phys. 91 (2002) 7382.
[12] Y. Zhang, W. Wernsdorfer, F. Pan, Z. Wanga, S. Gao, Chem. Commun. (2006) 3302.
[13] M.D. Godbole, O. Roubeau, R. Clerac, H. Kooijman, A.L. Spek, E. Bouwman, Chem. Commun. (2005) 3715.
[14] B. Moubaraki, K.S. Murray, T.A. Hudson, R. Robson, Eur. J. Inorg. Chem. (2008) 4525.
[15] S.J. Langley, M. Helliwell, R. Sessoli, P. Rosa, W. Wernsdorfer, R.E.P. Winpenny, Chem. Commun. (2005) 5029.
[16] K.W. Galloway, A.M. Whyte, W. Wernsdorfer, J. Sanchez-Benitez, K.V. Kamenev, A. Parkin, R.D. Peacock, M. Murrie, Inorg. Chem. 47 (2008) 7438.
[17] J. Lawrence, E.-C. Yang, R. Edwards, M.M. Olmstead, C. Ramsey, N.S. Dalal, P.K. Gantzel, S. Hill, D.N. Hendrickson, Inorg. Chem. 47 (2008) 1965.
[18] E.-C. Yang, C. Kirman, J. Lawrence, L.N. Zakharov, A.L. Rheingold, S. Hill, D.N. Hendrickson, Inorg. Chem. 44 (2005) 3827.
[19] A. Wilson, J. Lawrence, E.-C. Yang, M. Nakano, D.N. Hendrickson, S. Hill, Phys. Rev. B 74 (2006) R140403.
[20] J. Lawrence, C. Beedle, J. Ma, S. Hill, D.N. Hendrickson, Polyhedron 26 (2007) 2299.
[21] L.L. Lohr, J.C. Miller, R.R. Sharp, J. Chem. Phys. 111 (1999) 10148.
[22] A. Bencini, D. Gatteschi, EPR of Exchanged Coupled Systems, Springer-Verlag, 1990.
[23] J. Liu, S. Datta, E. Bolin, J. Lawrence, C.C. Beedle, E.-C. Yang, D.N. Hendrickson, S. Hill, unpublished.
[24] M. Mola, S. Hill, P. Goy, M. Gross, Rev. Sci. Instrum. 71 (2000) 186.
[25] S. Takahashi, S. Hill, Rev. Sci. Instrum. 76 (2005) 023114.
[26] R.S. Edwards, S. Hill, P. Goy, R. Wylde, S. Takahashi, Physica B 346–347 (2004) 211.



Scheme 1.

were obtained by precipitation from the polymerization mixtures into methanol.

In the CD spectra of poly(**1a**) in chloroform, not only were negative Cotton effects observed in the absorption region (450–550 nm) of the backbone chromophore, but split-type induced CD signals also appeared in the absorption region (420 nm) of the hydrogalvinoxyl chromophore. CD and UV–Vis absorption spectra of poly(**1a**) exhibited the thermo- and solvatochromism [15]. The chiroptical thermo- or solvatochromism is novel for the one-handed helical polymers possessing no chiral moieties in the polymer chains, because they have two conformational enantiomers whose states are thermo-dynamically equivalent to one another, and the conformational rotations of polymers thermodynamically lead to the full racemization of polymers on the intra- and/or interchain. However, no Cotton effect was observed for the polyradical poly(**1b**) solution which was obtained by oxidizing poly(**1a**) by treatment of the polymer solution with fresh lead dioxide or potassium ferricyanide, while there was not significant change in the GPC elution curves of the polymer before and after the radical generation. But we succeeded in observing weak Cotton effects in the absorption region of the galvinoxyl radical chromophore through the chemical oxidation of the cast film of poly(**1a**) on a quartz plate. On the other hand, the split-type induced CD signals were observed for the chloroform solution of poly(**2a**) at 300 nm, and the CD intensities were nearly constant even when the solution was heated to 60 °C (Fig. 1). But the CD signals decreased and disappeared in CD spectra of poly(**2a**) by addition of DMF to the THF solution, which supported that the rigid and one-handed helical conformation was stabilized by intramolecular hydrogen bonds. The polyradical poly(**2b**) was obtained by oxidizing the polymer poly(**2a**) by treatment of the polymer solution in degassed THF with fresh lead dioxide under an oxygen-free atmosphere. The absorption maximum at 420 nm due to the hydrogalvinoxyl chromophore decreased, and a new absorption peak due to the galvinoxyl radical chromophore appeared at 470 nm. In the CD spectra of the polyradicals obtained by polymerization using (*R*)-PEA and (*S*)-PEA (abbreviated as poly(**2b**)$_R$ and poly(**2b**)$_S$, respectively), the split-type-induced CD signals at 300 nm, which are mirror images of each other, are still observed (Fig. 2), while no Cotton effect was observed for the polyradical which was obtained by polymerization using racemic PEA (abbreviated as poly(**2b**)$_{rac}$). It is clear that maintenance of the enantiomeric helical structure was achieved even after the oxidation reaction. In the MCD spectra of poly(**2b**) in THF, positive and negative Faraday effects were observed in the absorption region of the galvinoxyl chromophore (470 nm) corresponding to the negative and positive magnetic fields, respectively, which was independent of the conformation of poly(**2b**).

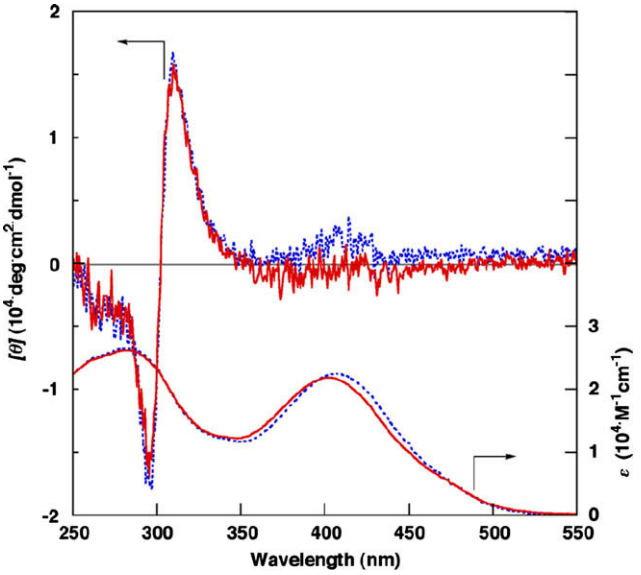


Fig. 1. CD and UV–Vis absorption spectra of poly(**2a**) at 20 (dashed line) and 60 (solid line) °C in chloroform (0.6 mM).

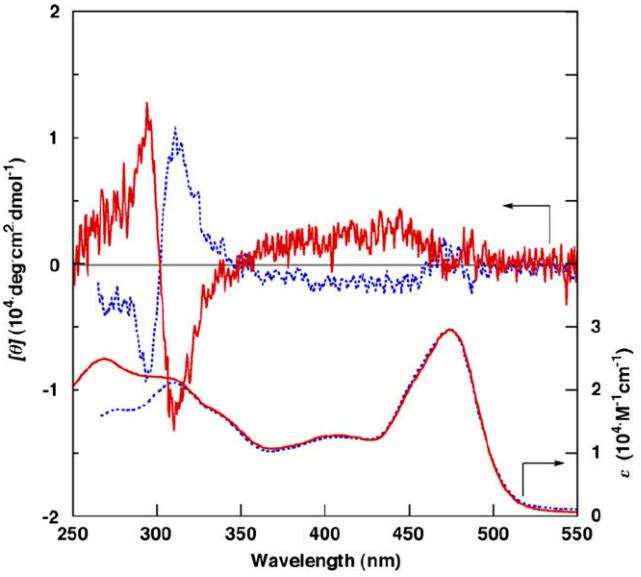


Fig. 2. CD and UV–Vis absorption spectra of poly(**2b**)$_R$ (solid line) and poly(**2b**)$_S$ (dashed line) at 20 °C in THF (0.5 mM).

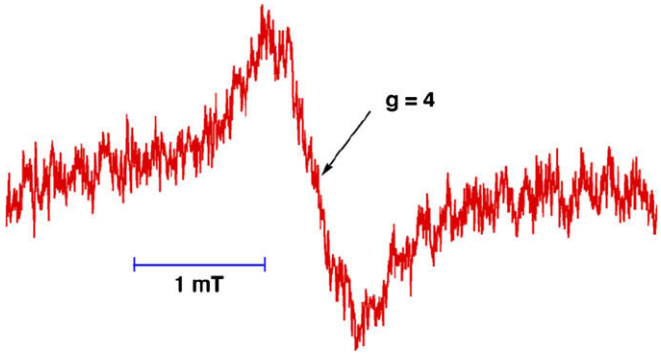


Fig. 3. ESR spectra of poly(**2b**)$_R$ in frozen 2-methyltetrahydrofuran glass at 77 K at $g = 4$.

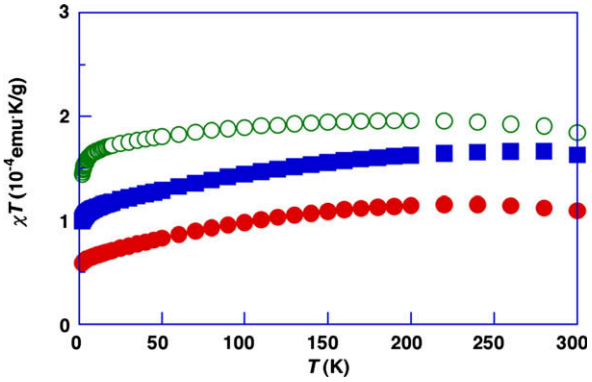


Fig. 4. χT vs. T plots of the powder samples of poly(**2b**)$_R$ (●), poly(**2b**)$_{rac}$ (○) and poly(**2b**)$_{RS}$ (■).

The polyradicals were appropriately stable for maintaining the initial spin concentration under the ESR and SQUID measurement conditions. The ESR spectrum of poly(**2b**) showed a broad signal at $g = 2.0047$, indicating formation of the phenoxyl radical. The $\Delta m_s = \pm 2$ forbidden transition was clearly observed at $g = 4$ in frozen 2-methyltetrahydrofuran glass at 77 K for poly(**2b**)$_R$, although no fine structure that gave zero-field splitting parameters D or E was detected at $g = 2$ (Fig. 3). This result suggests the magnetic interaction along the polymer chain because the sample was diluted in diamagnetic 2-methyltetrahydrofuran to minimize intermolecular interactions.

The static magnetic susceptibility (2–300 K at 0.5 T) of poly(**2b**) was measured using a SQUID magnetometer. The powder samples were prepared by evaporating solvent from the THF solution of poly(**2b**)$_R$, poly(**2b**)$_{rac}$ and the equivalent mixture of poly(**2b**)$_R$ and poly(**2b**)$_S$ (abbreviated as poly(**2b**)$_{RS}$), and by drying in vacuum. The χT *versus* T plots of poly(**2b**)$_R$, poly(**2b**)$_{rac}$ and poly(**2b**)$_{RS}$ are shown in Fig. 4. Downward deviation of the χT value of the polyradicals at lower temperatures indicates the antiferromagnetic interaction. The stronger antiferromagnetic interaction was observed for poly(**2b**)$_R$ synthesized by HSSP in comparison with poly(**2b**)$_{rac}$ whose helical conformation could racemize on the intrachain to be random conformation. The antiferromagnetic interaction of poly(**2b**)$_{RS}$ whose helical conformation racemized on the interchain was also stronger than that of poly(**2b**)$_{rac}$. These results and the above-mentioned ESR result of poly(**2b**)$_R$ suggest that the strong antiferromagnetic interaction of poly(**2b**)$_R$ was significantly affected by its helical conformation.

Acknowledgments

This work was partially supported by a Grant-in-Aid for Science Research on a Priority Area "Super-Hierarchical Structures" (Nos. 19022009 and 19022010) from MEXT, and by a Grant-in-Aid for Scientific Research (B) (Nos. 19350054 and 20310052) from JSPS.

References

[1] T. Aoki, T. Kaneko, M. Teraguchi, Polymer 47 (2006) 4867.
[2] T. Kaneko, T. Makino, H. Miyaji, M. Teraguchi, T. Aoki, M. Miyasaka, H. Nishide, J. Am. Chem. Soc. 125 (2003) 3554.
[3] T. Aoki, M. Kokai, K. Shinohara, E. Oikawa, Chem. Lett. (1993) 2009.
[4] K. Shinohara, T. Aoki, E. Oikawa, Polymer 36 (1995) 2403.
[5] T. Aoki, K. Shinohara, T. Kaneko, E. Oikawa, Macromolecules 29 (1996) 4192.
[6] T. Aoki, Y. Kobayashi, T. Kaneko, E. Oikawa, Y. Yamamura, Y. Fujita, M. Teraguchi, R. Nomura, T. Masuda, Macromolecules 32 (1999) 79.
[7] T. Kaneko, T. Yamamoto, T. Aoki, E. Oikawa, Chem. Lett. 28 (1999) 623.
[8] K. Shinohara, T. Aoki, T. Kaneko, J. Polym. Sci. Polym. Chem. Ed. 40 (2002) 1689.
[9] M. Teraguchi, J. Suzuki, T. Kaneko, T. Aoki, T. Masuda, Macromolecules 36 (2003) 9694.
[10] T. Aoki, T. Fukuda, K. Shinohara, T. Kaneko, M. Teraguchi, M. Yagi, J. Polym. Sci. Polym. Chem. Ed. 42 (2004) 4502.
[11] M. Teraguchi, K. Mottate, S.-Y. Kim, T. Aoki, T. Kaneko, S. Hadano, T. Masuda, Macromolecules 38 (2005) 6367.
[12] T. Aoki, T. Kaneko, N. Maruyama, A. Sumi, M. Takahashi, T. Sato, M. Teraguchi, J. Am. Chem. Soc. 125 (2003) 6346.
[13] T. Sato, T. Aoki, M. Teraguchi, T. Kaneko, S.-Y. Kim, Polymer 45 (2004) 8109.
[14] Y. Umeda, T. Kaneko, M. Teraguchi, T. Aoki, Chem. Lett. 34 (2005) 854.
[15] T. Kaneko, Y. Umeda, T. Yamamoto, M. Teraguchi, T. Aoki, Macromolecules 38 (2005) 9420.
[16] T. Kaneko, Y. Umeda, H. Jia, S. Hadano, M. Teraguchi, T. Aoki, Macromolecules 40 (2007) 7098.
[17] H. Katagiri, T. Kaneko, M. Teraguchi, T. Aoki, Chem. Lett. 37 (2008) 390.

Table 1
Crystal data for **1** and **2**.

Crystal data	**1** (123 K)	**1** (80 K)	**2**
Empirical formula	$C_{14}H_8Au_2FeN_6F_2$	$C_{14}H_8Au_2FeN_6F_2$	$C_{14}H_8Au_2MnN_6F_2$
FW	748.05	748.05	747.14
Temperature (K)	123	80	293
Crystal system	triclinic	monoclinic	monoclinic
Space group	$P\bar{1}$	$P2_1/c$	$P2_1/c$
a (Å)	8.877(2)	8.853(3)	9.0514(7)
b (Å)	13.530(3)	13.264(4)	14.0773(10)
c (Å)	15.202(4)	15.064(5)	15.5941(13)
α (°)	89.848(5)		
β (°)	83.494(5)	97.272(6)	95.5770(10)
γ (°)	88.049(5)		
V (Å^3)	1813.0(7)	1754.7(10)	1977.6(3)
Z	4	4	4
Dcalc (Mg/m^3)	2.741	2.832	2.509
F(000)	1344	1344	1340
Crystal size (mm^{-3})	0.20 × 0.18 × 0.15	0.20 × 0.17 × 0.16	0.23 × 0.21 × 0.20
Reflections collected	11541	8658	13410
Independent reflections	7683	4238	5021
R_1[a], wR_2[b]	0.0854, 0.1972	0.0864, 0.1881	0.0409, 0.0972

[a] $R_1 = (\sum||F_o| - |F_c||)/\sum|F_o|$.
[b] $wR_2 = \{\sum w(|F_o| - |F_c|)^2/\sum w|F_o|^2\}^{1/2}$.

2.2. Preparation of the complexes

2.2.1. Preparation of {Fe^{II}(3-fluoropyridine)$_2$[Au^{I}(CN)$_2$]$_2$}$_n$ (**1**)

Complex **1** was prepared according to a procedure described in the literature Ref. [10c].

2.2.2. Preparation of {Mn^{II}(3-fluoropyridine)$_2$[Au^{I}(CN)$_2$]$_2$}$_n$ (**2**)

In 10 mL of water, $MnCl_2 \cdot 4H_2O$ (0.02 g, 0.1 mmol) and K[Au(CN)$_2$] (0.04 g, 0.2 mmol) were solved. The vapor diffusion method using 3-fluoropyridine as a source of ligand molecules provided colorless polycrystalline crystals suitable for X-ray diffraction of **2** over a period of two days. **2**: Elemental *Anal.* Calc. for $C_{14}H_8Au_2MnN_6F_2$: C, 22.51; H, 1.08; N, 11.25. Found: C, 22.24; H, 1.09; N, 11.27%. IR (Nujol method, cm^{-1}): 2156 (ν_{CN} (CN)).

2.3. X-ray crystal structural determinations

Crystal structures of **1** at 80 K and 123 K and **2** at 293 K were determined using a BRUKER APEX SMART CCD area-detector diffractometer with monochrometed Mo Kα radiation (λ = 0.71073 Å). The diffraction data was treated using SMART and SAINT, and absorption correction was performed using SADABS [18]. The structures were solved by using direct methods with SHELXTL [19]. All non-hydrogen atoms were refined anisotropically, and the hydrogen atoms were generated geometrically. Pertinent crystallographic parameters are displayed in Table 1 and selected metric parameters for the complexes are presented in Table 2.

2.4. Magnetic measurement of **2**

Measurements of the temperature dependence of the magnetic susceptibility of **2** in the temperature range of 2–300 K with a cooling and heating rate of 1 K min^{-1} in a fixed field strength of 1 kOe field was measured on a MPMS-XL Quantum Design SQUID magnetometer. The molar susceptibility was corrected from the sample holder and diamagnetic contributions of all constituent atoms by using Pascal's constants.

Table 2
Selected bond lengths and angles for **1** and **2**.

1 (123 K)	**1** (123 K)	**1** (80 K)	**2** (293 K)
Bond lengths (Å)			
Fe(1)–N(1):2.24(3)	Fe(2)–N(3):2.02(2)	Fe(1)–N(1):2.05(2)	Mn(1)–N(1):2.318(6)
Fe(1)–N(2):2.19(2)	Fe(2)–N(4):2.03(2)	Fe(1)–N(2):2.04(2)	Mn(1)–N(2):2.293(6)
Fe(1)–N(5):2.10(3)	Fe(2)–N(9):1.96(2)	Fe(1)–N(3):1.94(2)	Mn(1)–N(3):2.209(6)
Fe(1)–N(6):2.13(2)	Fe(2)–N(10):1.91(2)	Fe(1)–N(4):1.98(2)	Mn(1)–N(4):2.198(7)
Fe(1)–N(7):2.10(3)	Fe(2)–N(11):1.92(3)	Fe(1)–N(5):1.95(2)	Mn(1)–N(5):2.223(6)
Fe(1)–N(8):2.14(2)	Fe(2)–N(12):1.93(2)	Fe(1)–N(6):1.94(2)	Mn(1)–N(6):2.212(6)
Au(1)–C(21)′:1.92(4)	Au(3)–C(22)′:1.99(3)	Au(1)–C(13):1.96(3)	Au(1)–C(13):1.984(8)
Au(1)–C(25):1.97(3)	Au(3)–C(26):1.98(3)	Au(1)–C(14)′:1.90(5)	Au(1)–C(14)′:1.967(7)
Au(2)–C(24)′:1.97(3)	Au(4)–C(23):2.06(4)	Au(2)–C(11)′:1.97(3)	Au(2)–C(11)′:1.975(8)
Au(2)–C(28):1.98(3)	Au(4)–C(27):2.00(4)	Au(2)–C(12):1.99(2)	Au(2)–C(12):1.974(7)
Bond angles (°)			
N(1)–Fe(1)–N(2):178.1(10)	N(3)–Fe(2)–N(4):177.6(10)	N(1)–Fe(1)–N(2):179.1(11)	N(1)–Mn(1)–N(2):178.8(2)
N(5)–Fe(1)–N(7):179.0(10)	N(9)–Fe(2)–N(11):179.1(11)	N(3)–Fe(1)–N(5):179.2(11)	N(3)–Mn(1)–N(5):178.6(2)
N(6)–Fe(1)–N(8):179.1(11)	N(10)–Fe(2)–N(12):178.2(10)	N(4)–Fe(1)–N(6):177.8(10)	N(4)–Mn(1)–N(6):178.2(2)
N(1)–Fe(1)–N(5):89.6(10)	N(3)–Fe(2)–N(9):88.3(10)	N(1)–Fe(1)–N(3):90.6(10)	N(1)–Mn(1)–N(3):87.8(2)
N(1)–Fe(1)–N(6):93.9(9)	N(3)–Fe(2)–N(10):89.1(10)	N(1)–Fe(1)–N(4):90.3(10)	N(1)–Mn(1)–N(4):90.7(3)
N(1)–Fe(1)–N(7):90.8(10)	N(3)–Fe(2)–N(11):90.8(11)	N(1)–Fe(1)–N(5):90.1(10)	N(1)–Mn(1)–N(5):93.6(2)
N(1)–Fe(1)–N(8):86.2(8)	N(3)–Fe(2)–N(12):89.3(10)	N(1)–Fe(1)–N(6):90.9(10)	N(1)–Mn(1)–N(6):90.3(2)
N(2)–Fe(1)–N(5):88.7(10)	N(4)–Fe(2)–N(9):94.1(9)	N(2)–Fe(1)–N(3):90.3(9)	N(2)–Mn(1)–N(3):91.6(2)
N(2)–Fe(1)–N(6):86.9(9)	N(4)–Fe(2)–N(10):91.2(10)	N(2)–Fe(1)–N(4):89.6(9)	N(2)–Mn(1)–N(4):90.4(3)
N(2)–Fe(1)–N(7):91.0(10)	N(4)–Fe(2)–N(11):86.8(10)	N(2)–Fe(1)–N(5):89.0(9)	N(2)–Mn(1)–N(5):87.0(2)
N(2)–Fe(1)–N(8):93.0(9)	N(4)–Fe(2)–N(12):90.4(10)	N(2)–Fe(1)–N(6):88.2(9)	N(2)–Mn(1)–N(6):88.6(2)
N(5)–Fe(1)–N(6):91.8(10)	N(9)–Fe(2)–N(10):91.3(11)	N(3)–Fe(1)–N(4):89.2(10)	N(3)–Mn(1)–N(4):87.9(3)
N(6)–Fe(1)–N(7):89.1(10)	N(10)–Fe(2)–N(11):89.0(10)	N(4)–Fe(1)–N(5):91.2(9)	N(4)–Mn(1)–N(5):92.0(3)
N(7)–Fe(1)–N(8):91.8(10)	N(11)–Fe(2)–N(12):90.1(10)	N(5)–Fe(1)–N(6):88.3(9)	N(5)–Mn(1)–N(6):89.4(3)
N(8)–Fe(1)–N(5):87.3(10)	N(12)–Fe(2)–−N(9):89.6(10)	N(3)–Fe(1)–N(6):91.3(10)	N(3)–Mn(1)–N(6):90.6(3)
C(21)–N(5)–Fe(1):171(2)	C(25)–N(9)–Fe(2):172(2)	C(11)–N(4)–Fe(1):171(2)	C(11)–N(4)–Fe(1):173.0(7)
C(22)–N(6)–Fe(1):168(2)	C(26)–N(10)–Fe(2):175(2)	C(12)–N(5)–Fe(1):175(2)	C(12)–N(5)–Fe(1):164.5(6)
C(23)–N(7)–Fe(1):170(3)	C(27)–N(11)–Fe(2):177(2)	C(13)–N(6)–Fe(1):172(2)	C(13)–N(6)–Fe(1):170.6(6)
C(24)–N(8)–Fe(1):169(2)	C(28)–N(12)–Fe(2):176(2)	C(14)–N(3)–Fe(1):171(2)	C(14)–N(3)–Fe(1):164.9(6)
C(21)′–Au(1)–C(25):176.1(11)	C(22)′–Au(3)–C(26):178.1(10)	C(11)′–Au(2)–C(12):175.4(10)	C(11)–Au(2)–C(12)′:177.5(3)
C(24)′–Au(2)–C(28):176.8(11)	C(23)–Au(4)–C(27):176.2(11)	C(13)–Au(1)–C(14)′:176.0(11)	C(13)–Au(1)–C(14)′:179.2(3)

3. Results and discussion

3.1. Synthesis and IR spectra

The reaction of an aqueous solutions of $FeSO_4 \cdot (NH_4)_2SO_4 \cdot 6H_2O$ or $MnCl_2 \cdot 4H_2O$ containing two equivalents of $K[Au(CN)_2]$ with a vapor diffusion method using pyridine-derivative ligand, 3-fluoropyridine, afforded colorless block single crystals of the coordination compounds $\{Fe^{II}(3\text{-fluoropyridine})_2[Au^{I}(CN)_2]_2\}_n$ (**1**) and $\{Mn^{II}(3\text{-fluoropyridine})_2[Au^{I}(CN)_2]_2\}_n$ (**2**).

The solid state IR spectra of **1** and **2** had C≡N bands at 2156 cm^{-1} for **1** and 2152 cm^{-1} for **2**, which are both at higher wavenumbers than that of free $[Au(CN)_2]^-$ (2135 cm^{-1}), at room temperature. This suggests that both of the CN groups of $[Au(CN)_2]^-$ act as bidentate bridging ligands.

3.2. Description of the crystal structures

3.2.1. Crystal structures of **1** (T = 80 K) and **2** (T = 293 K)

Coordination compounds **1** at 80 K and **2** at 293 K crystallized in the centrosymmetric space groups $P2_1/c$, respectively. The X-ray crystallographic analysis reveals that the asymmetric unit of **1** (80 K) and **2** (293 K) contains two 3-fluoropyridine ligands, one type of M^{2+} ion (M = Fe, Mn) and two types of crystallographically distinct $[Au(CN)_2]^-$ units. As shown in Fig. 1, the Fe^{II} and Mn^{II} centers have a slightly distorted octahedral geometry with a N_6 coordination sphere, which are tightly related to that of **1** at 293 K Refs. [10c,15c]. In the equatorial positions, four N atoms from bidentate CN^- moiety are coordinated to Fe(1) and Mn(1) centers. The pyridyl N ligation site at the two 3-fluoropyridine ligands occupy in the axial sites of octahedral metal centers. While the F(1) and F(2) in the 3-fluoropyridine ligand are disordered with each other, F(3) in the other 3-fluoropyridine ligand is not disordered. Thus the two 3-fluoropyridine ligands in $[Fe^{II}(3\text{-fluoropyridine})_2][Au^{I}(CN)_2]_2$ are not equivalent and coexist in *transoid* and *cisoid* conformations for Fe(1). The angles for **1** defined by C(13)–Au(1)–C(14) and C(11)–Au(2)–C(12) are 176.0(11) and 174.5(10) and for **2** defined by C(13)–Au(1)–C(14) and C(11)–Au(2)–C(12) are 179.2(3) and 177.5(3), respectively, which are close to a linear geometry. As depicted in Fig. 2, four M^{II} atoms and four $[Au(CN)_2]^-$ units form a rectangular ring $[M^{II}Au^{I}(CN)_2]_4$ and the rings are further connected by $[Au(CN)_2]^-$ units to generate a corrugated two-dimensional frameworks of **1** and **2** (shown in Fig. 2). In the macrometallacycle, the neighboring and diagonal distances are 15.064, 13.264 Å (Fe···Fe) and 15.594, 14.077 Å (Mn···Mn), respectively.

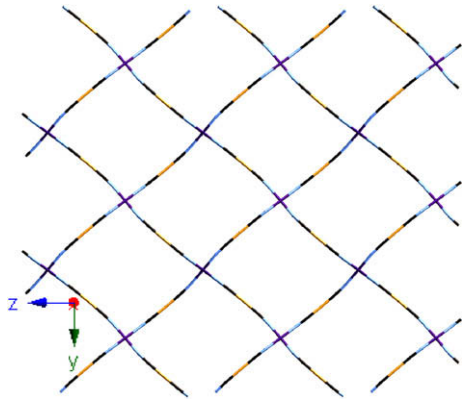


Fig. 2. The cylinder drawing, wave 2-D networks of **1** at 80 K. The 2-D frameworks of **1** at 123 K and **2** at 293 K are almost identical to that of **1** at 80 K. Consequently, we have used the same representation for these compounds. Atom code: Fe (purple), Au (yellow), N (blue), C (black). In this picture, hydrogen atoms and 3-fluoropyridine are omitted for clarity. (For interpretation of the references to colour in this figure legend, the reader is referred to the web version of this article.)

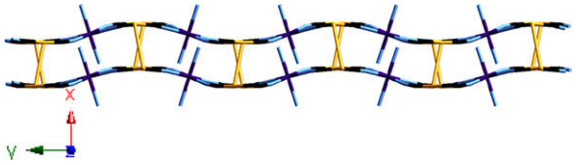


Fig. 3. Bilayer structure of **1** at 80 K with strong aurophilic interactions. The structure of **1** at 293 K is almost identical to that of **1** at 80 K. Consequently, we have used the same representation for both compounds. In this picture, H atoms and C atoms in the 3-fluoropyridine ligands are omitted for clarity.

It is worthy of note that the Au···Au interaction in the bilayer networks for **1** and **2** are very strong and the distance are 3.081 and 3.170 Å, which is well outside the range for a Au–Au bond (2.8–3.0 Å), even though these distances are less than the sum of the van der Waals radii of Au (3.60 Å) (shown in Fig. 3).

These Fe–N bond lengths for **1** at 80 K correspond quite well to those expected for LS state of Fe^{II} ion, which results agree completely with the magnetic behavior observed for **1** (see S1) Ref. [10c].

3.2.2. Crystal structures of **1** (T = 123 K)

Compound **1** at 123 K crystallizes in the space group $P\bar{1}$, in contrast to the **1** at 80 K ($P2_1/c$). The structure of **1** in this spin phase

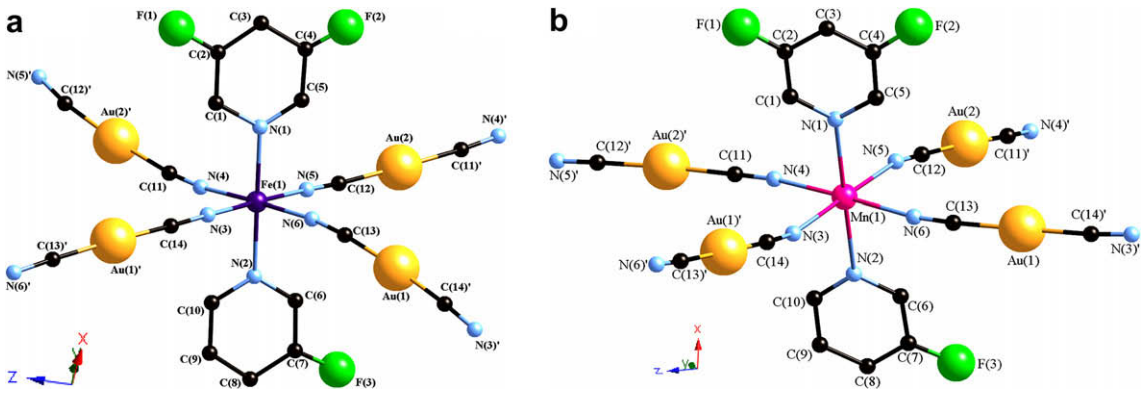


Fig. 1. Coordination structures of the Fe^{II} and Au^{I} ions in **1** at 80 K (a) and Mn^{II} and Au^{I} ions in **2** at 293 K (b). In this picture, hydrogen atoms are omitted for clarity. Atom code: Fe (purple), Mn (pink), Au (yellow), N (blue), C (black), F (green). (For interpretation of the references to colour in this figure legend, the reader is referred to the web version of this article.)

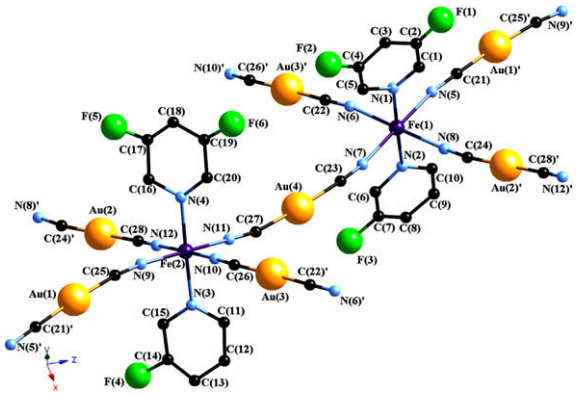


Fig. 4. Coordination structure of the Fe^{II} and Au^{I} ions in **1** at 123 K. In this picture, hydrogen atoms are omitted for clarity.

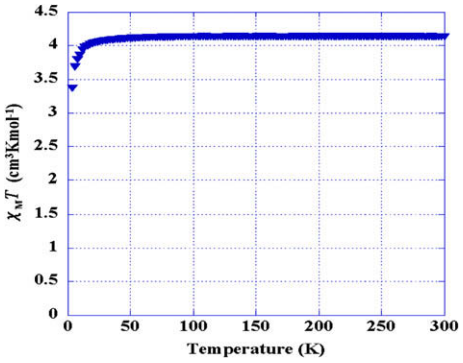


Fig. 5. Magnetic properties of **2**. $\chi_M T$ vs. T from 2 to 300 K.

has been already reported by Real et al. Ref. [15c], but its data were not good enough (R_1 [$I > 2\sigma(I)$] = 0.1649). Therefore, we have reexamined its structure (R_1 [$I > 2\sigma(I)$] = 0.0854).

The 2D grid frameworks of **1** at 123 K is almost identical to **1** at 80 K and **2** at 293 K (shown in Fig. 2). However, there are crystallographically different two Fe^{II} atoms defining distorted octahedral geometries, four 3-fluoropyridine ligands and four types of $[Au(CN)_2]^-$ units (shown in Fig. 4). The crystal packing of **1** at 123 K is also made up of a stacking of double layers interacted via strong aurophilic interactions [Au(1)···Au(2) = 3.128 and Au(3)···Au(4) = 3.072···Å]. These Fe–N bond lengths for **1** at 123 K correspond quite well to those expected for HS state of Fe(1) and LS state of Fe(2).

3.3. Magnetic properties of *2*

$\chi_M T$ versus T plots, with χ_M being the molar magnetic susceptibility and T the temperature, for **2** is shown in Fig. 5. At room temperature, the magnetic behaviors of the complexes **2** is characteristic of Mn(II) compounds in the high-spin state, $\chi_M T = 4.13\ cm^3\ K\ mol^{-1}$ the values of μ_{eff} are ($\mu_{eff} = 2.828\sqrt{(\chi_M T)}$) of **2** per one Mn^{II} ion at 300 K was 5.75. The value for **2** are slightly smaller than 5.92 ($=g\sqrt{(S(S+1))}$, $g = 2$, $S = 5/2$) that of a pure spin only system, whereas the values are similar to the μ_{eff} value at 300 K of other Mn^{II} compounds [20]. The $\chi_M T$ value was nearly constant in the range of 15–300 K; however, it decreased rapidly as the temperature was lowered less than 17 K. The profile is characteristic of HS state of the metallic Mn^{II} centers with zero-field splitting (ZFS) [21–23]. While the complex **1** shows spin-crossover behavior (see S1) Ref. [10c], the susceptibility data of **2** indicate the existence of HS Mn^{II} throughout the temperature range.

3.4. Photoluminescent properties of *1* and *2*

Coordination compounds containing Au atoms with aurophilic interactions usually exhibit photoluminescent properties [24], so we investigated the photoluminescent properties. The photoluminescent properties of **1** and **2** have been investigated in the solid state at room temperature. As shown in Fig. 6, the maximum emission peaks of complexes **1** and **2** are located at 452 and 435 nm upon excitation at 373 and 375 nm, respectively.

4. Conclusions

In conclusion, we have illustrated bimetallic coordination polymer with the formula $\{Fe^{II}(3\text{-fluoropyridine})_2[Au^{I}(CN)_2]_2\}_n$ (**1**), $\{Mn^{II}(3\text{-fluoropyridine})_2[Au^{I}(CN)_2]_2\}_n$ (**2**). In complexes **1** and **2**, M^{II} (M = Fe, Mn) and Au^{I} atoms constitute the building blocks of these structures. The quasi-linear bidentate $[Au(CN)_2]^-$ bridges octahedral M^{II} atoms, assemble to form a $\{M^{II}_4[Au^{I}(CN)_2]_4\}$ rectangular mesh 2D network. By the aurophilic interactions, compounds of **1** and **2** produces a bilayer structure.

The Fe–N bond lengths for **1** at 293 K, 123 K and 80 K correspond quite well to those expected for each spin state of Fe^{II} ion (Fe(1) at 293 K is the HS state, Fe(1) and Fe(2) at 123 K are the

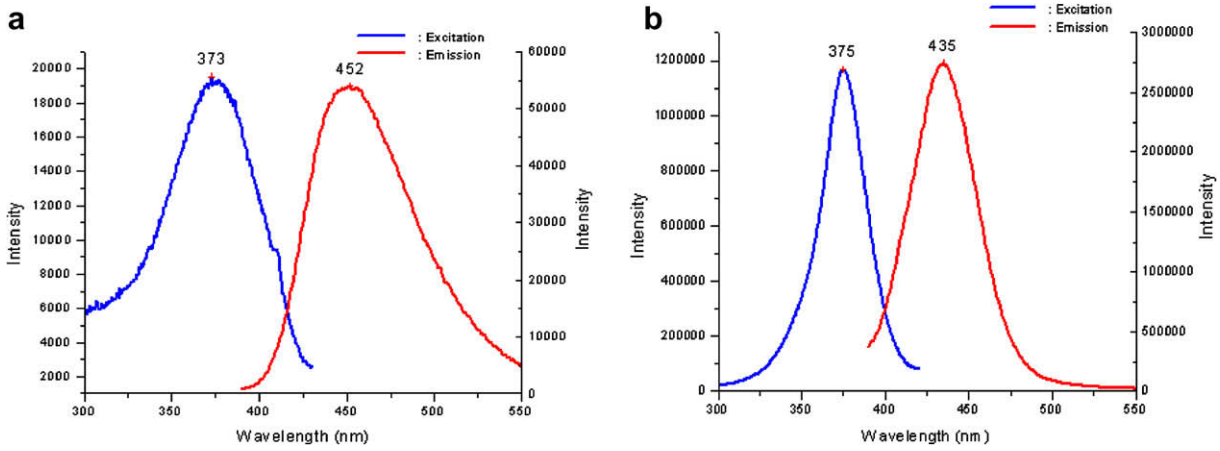


Fig. 6. Solid-state excitation (blue line) and emission (red line) spectra of **1** and **2** at room temperature. (For interpretation of the references to colour in this figure legend, the reader is referred to the web version of this article.)

HS and the LS states, respectively, Fe(1) at 80 K is the LS state), which results agree completely with the magnetic behavior observed for **1** (see S1) Ref. [10c]. Moreover, single-crystal X-ray analysis also reveals that the spin transition is accompanied by a crystallographic phase transition from monoclinic $P2_1/c$ at 293 K to the triclinic $P\bar{1}$ at 123 K to monoclinic $P2_1/c$ at 80 K.

From the measurements of the temperature dependence of the magnetic susceptibility, the profile of the magnetic behaviors of the complex **2** is not occurrence of spin transition.

The solids of complexes **1** and **2** are occurrence of photoluminescence at room temperature, which can be attributed to the presence of aurophilic interactions.

In these result, complex **1** shows multifunctional material, spin-crossover phenomena and photoluminescence. Multifunctional properties are presently the subject of intensive studies by chemists and physicists, aiming at the eventual use of their multi applications.

Acknowledgements

This work was supported by the "High Tech Research Center" Project 2005–2009 from MEXT (Ministry of Education, Culture, Sports, Science and Technology), and the Research Center for Materials with Integrated Properties, Toho University. We thank Dr. Suguru Inoue at Technical Plaza, Application Center of Horiba, LTD. for measurements of photoluminescent properties.

Appendix A. Supplementary data

CCDC 695475, 695476 and 696868 contain the supplementary crystallographic data for **1** (123 K), **1** (80 K) and **2** (293 K). These data can be obtained free of charge from The Cambridge Crystallographic Data Centre via www.ccdc.cam.ac.uk/data_request/cif. Supplementary data associated with this article can be found, in the online version, at doi:10.1016/j.poly.2008.11.006.

References

[1] R. Matsuda, R. Kitaura, S. Kitagawa, Y. Kubota, R.V. Belosludov, T.C. Kobayashi, H. Sakamoto, T. Chiba, M. Takata, Y. Kawazoe, Y. Mita, Nature 436 (2005) 238.
[2] R. Matsuda, R. Kitaura, S. Kitagawa, Y. Kubota, T.C. Kobayashi, S. Horike, M. Takata, J. Am. Chem. Soc. 126 (2004) 14063.
[3] S. Kitagawa, R. Kitaura, S. Noro, Angew. Chem., Int. Ed. 43 (2004) 2334.
[4] O.M. Yaghi, M. O'Keeffe, N.W. Ockwing, H.K. Chae, M. Eddaoudi, J. Kim, Nature 423 (2003) 705.
[5] C. Janiak, J. Chem. Soc., Dalton Trans. (2003) 2781.
[6] O.R. Evans, W. Lin, Acc. Chem. Res. 35 (2002) 511.
[7] M. Eddaoudi, D.B. Moler, H. Li, B. Chen, T. Reineke, M. O'Keeffe, O.M. Yaghi, Acc. Chem. Res. 34 (2001) 319.
[8] (a) T. Soma, T. Iwamoto, J. Inclus. Phenom. Mol. 26 (1996) 161;
(b) T. Soma, T. Iwamoto, Chem. Lett. (1994) 821.
[9] T. Kitazawa, Y. Gomi, M. Takahashi, M. Takeda, M. Enomoto, A. Miyazaki, T. Enoki, J. Mater. Chem. 6 (1) (1996) 119.
[10] (a) T. Kitazawa, T. Kawasaki, M. Takahashi, M. Takeda, KURRI-KR (KURRI-KR-106, Hoshasen to Genshikaku o Purobu to shita Bussei Kenkyu no Shintenkai) (2004) 1;
(b) J.A. Rodríguez-Velamazán, M. Castro, E. Palacios, R. Burriel, T. Kitazawa, T. Kawasaki, J. Phys. Chem. B 111 (6) (2007) 1256;
(c) T. Kosone, C. Kachi-Terajima, C. Kanadani, T. Saito, T. Kitazawa, Chem. Lett. 37 (2008) 422;
(d) T. Kitazawa, A. Suzuki, T. Kosone, KURRI-KR-136 (2008) 50;
(e) T. Kosone, C. Kachi-Terajima, C. Kanadani, T. Saito, T. Kitazawa, Chem. Lett. 37 (2008) 754.
[11] V. Niel, M.C. Muñoz, A.B. Gasper, A. Galet, G. Levchenko, J.A. Real, Chem. Eur. J. 8 (2002) 2446.
[12] (a) D.B. Leznoff, B.-Y. Xue, C.L. Stevens, A. Storr, R.C. Thompson, B.O. Patrick, Polyhedron 20 (2001) 1247;
(b) D.B. Leznoff, J. Lefebvre, Gold Bull. 38 (2005) 47.
[13] A. Galet, V. Niel, M.C. Muñoz, J.A. Real, J. Am. Chem. Soc. 125 (2003) 14224.
[14] V. Niel, A.L. Thompson, M.C. Muñoz, A. Galet, A.E. Goeta, J.A. Real, Angew. Chem., Int. Ed. 42 (2003) 3760.
[15] (a) A. Galet, M.C. Muñoz, V. Martínez, J.A. Real, Chem. Commun. (2004) 2268;
(b) M.C. Muñoz, A.B. Gaspar, A. Galet, J.A. Real, Inorg. Chem. 46 (2007) 8182;
(c) A. Agustí, M.C. Muñoz, A. Galet, J.A. Real, Inorg. Chem. 47 (2008) 2552.
[16] (a) Z.J. Zhong, H. Seino, Y. Mizobe, M. Hidai, A. Fujishima, S. Ohkoshi, K. Hashimoto, J. Am. Chem. Soc. 122 (2000) 2952;
(b) J.J. Sokol, A.G. Hee, J.R. Long, J. Am. Chem. Soc. 124 (2002).
[17] (a) P. Gütlich, A. Hauser, H. Spiering, Angew. Chem., Int. Ed. Engl. 33 (1994) 2024;
(b) P. Gütlich, H.A. Goodwin, Spin Crossover in Transition Metal Compounds, Top. Curr. Chem., vols. 233–235, Springer, Berlin–Heidelberg–New York, 2004.
[18] G.M. Sheldrick, SADABS, Program for Empirical Absorption Correction for Area Detector Data, University of Göttingen, Göttingen, Germany, 1996.
[19] G.M. Sheldrick, SHELXL, Program for the Solution of Crystal Structures, University of Göttingen, Göttingen, Germany, 1997.
[20] T. Kawasaki, C. Kachi, T. Saito, T. Kitazawa, Bull. Chem. Soc. Jpn. 81 (2008) 268.
[21] D.M.L. Goodgame, H. El Mkami, G.H. Smith, J.P. Zhao, E.J.L. McInnes, Dalton Trans. (2003) 34.
[22] S. Naskar, D. Mishra, S.K. Chattopadhyay, M. Corbella, A.J. Blake, Dalton Trans. (2005) 2428.
[23] C. Duboc, T. Phoeung, S. Zein, J. Pécaut, M.-N. Collomb, F. Neese, Inorg. Chem. 46 (2007) 4905.
[24] (a) M.A. Rawashdeh-Omary, M.A. Omary, G.E. Shankle, H.H. Patterson, J. Phys. Chem. B 104 (2000) 6143;
(b) H.B. Zhou, W. Dong, Z.Q. Liu, D.Z. Liao, Z.H. Jiang, S.P. Yan, P. Cheng, Inorg. Chim. Acta 358 (2005) 3287.

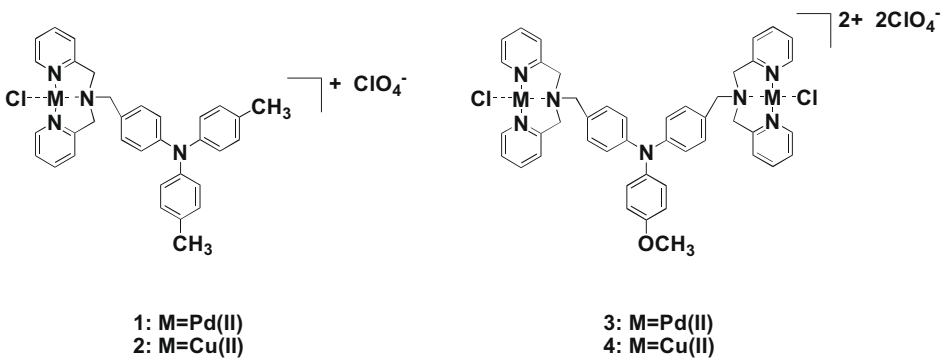


Fig. 1. Structures of complexes **1**–**4**.

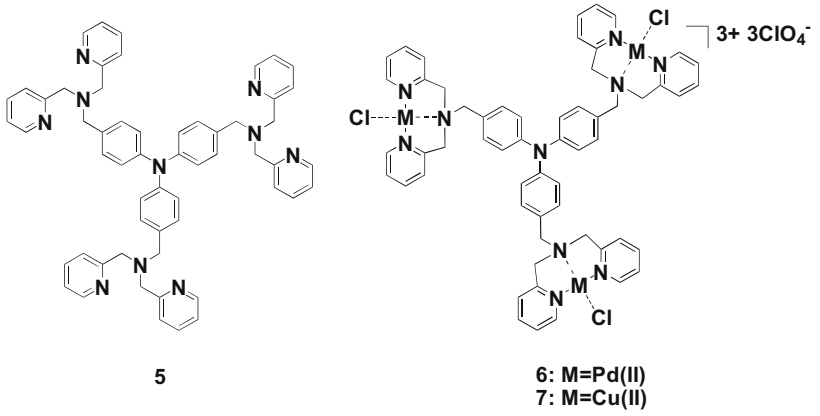


Fig. 2. Structures of a ligand **5** and its trinuclear complexes **6** and **7**.

redox active building unit to construct two-dimensional coordination polymer networks.

2. Experimental

2.1. Synthesis of 4,4′4″-[*N*-(2-picoryl) aminomethyl] triphenylamine

To the solution of 4,4′,4″-triformyltriphenylamine (1.151 g) [8] in methanol (150 ml) 2-picorylamine (2.268 g) was added. Then the color of the solution changed to yellow. Acetic acid was slowly added until the color of the solution changed to orange. Sodium tetrahydroborate (6 g) was carefully added at 0 °C and stirred at ambient temperature for 3 days. The solution was neutralized with conc.-hydrochloric acid and evaporated under reduced pressure. The residue was dissolved into chloroform and dried over sodium sulfate. The obtained crude oil was purified by silica gel column chromatography (chloroform: methanol = 10:1) to give pale yellow oil (yield 1.02 g, 48.3%).

^{1}H NMR($CDCl_3$): δ 3.79 (s, 6H), 3.95 (s, 6H), 7.02 (d, 6H, J = 8.6 Hz), 7.16 (m, 3H), 7.21 (d, 6H, J = 8.6 Hz), 7.34 (d, 3H, J = 7.8 Hz), 7.64 (dt, 3H, J = 7.8 Hz, 1.7 Hz), 8.56 (d, 3H, J = 4.9 Hz).

2.2. Synthesis of 4,4′,4″-tris[N,N-bis(2-pyridylmethyl)aminomethyl]triphenylamine (*5*)

To the solution of 4,4′-dimethoxy-4-(2-picorylaminomethyl) triphenylamine (1.02 g) in dry THF (50 ml) was added 2-(bromomethyl) pyridimium hydrobromide (2.54 g) in dry THF (50 ml), triethylamine (1.48 g) and stirred at ambient temperature for 5 days. The solution was filtered and evaporated under reduced pressure. The residue was dissolved into chloroform and dried over sodium sulfate and evaporated under reduced pressure to give crude oil, which was purified by silica gel column chromatography (chloroform: methanol = 10:1) to give orange oil (yield 0.74 g, 50%).

^{1}H NMR($CDCl_3$): δ 3.63 (s, 6H), 3.82 (s, 12H), 6.97 (d, 6H, J = 8.6 Hz), 7.14 (t, 6H, J = 6.3 Hz), 7.23 (d, 6H, J = 8.6 Hz), 7.64 (d, 12H, J = 8.6 Hz), 8.52 (d, 6H, J = 4.62 Hz).

HRMS: Calc.: 878.4533 for $C_{57}H_{54}N_{10}$, Obsd: 878.4506.

2.3. Synthesis of palladium(II) dichloro(4,4′,4″-tris[N,N-bis-(2-pyridylmethyl)aminomethyl]- triphenylamine) triperchrorate (*6*)

4,4′4″-Tris[*N*,*N*-bis(2-pyridylmethyl)aminomethyl]triphenylamine (0.2 g), palladium(II) dichloride (0.13 g) and sodium perchlorate (0.48 g) were dissolved into a small amount of acetonitrile and refluxed for 3 h, which was concentrated to 5 ml and allowed to stand overnight at 5 °C to give pale yellow powders (yield 0.34 g, 93%).

^{1}H NMR(DMSO-d_6): δ 4.15 (s, 6H), 4.68 (d, 6H, J = 16.0 Hz), 5.58 (d, 6H, J = 16.0 Hz), 7.64 (m, 12H, 7.84(d, 6H, J = 8.0 Hz), 8.20 (t, 6H, J = 8.0 Hz), 8.51 (d, 6H, J = 5.6 Hz).

ESI-MS: m/z 434.2 $[M-3ClO_4^-]^{3+}$; 701.4 $[M-2ClO_4^-]^{2+}$.

2.4. Synthesis of copper(II) dichloro(4,4′,4″-tris[N,N-bis-(2-pyridylmethyl)aminomethyl]- triphenylamine) triperchrorate (*7*)

The copper complex (**7**) was prepared by the similar method for **6** (yield 0.33 g, 99%).

ESI-MS: m/z 391.9 $[M-3ClO_4^-]^{3+}$.

CAUTION: Although no problem was encountered in the preparation of the perchlorate salts, suitable care should be taken when handling such potentially hazardous compounds.

3. Results and discussion

3.1. Synthesis of the ligand, and the trinuclear complex

The ligand, 4,4′,4″-tris[*N*,*N*-bis(2-pyridylmethyl)aminomethyl]-triphenylamine, was synthesized as shown in Fig. 3. Treatment of 4,4′,4″-triformyltriphenylamine [8] with three equivalents of 2-picolylamine and sodium borohydride gave the secondary amine, 4,4′,4″-tris[*N*, *N*-bis(2-pyridylmethyl) aminomethyl] triphenylamine. This compound then was reacted with 2-(bromomethyl)pyridine hydrobromide under a basic condition to give the target compound **5**, in excellent isolated yield (50%). The complex **6** and **7** were prepared by reacting **5** with palladium(II) chloride and copper(II) chloride in the presence of sodium perchlorate, respectively.

3.2. UV–Vis spectrum and cyclic voltammetry measurements

In order to examine the spectroscopic properties of the ligand and the metal complexes, UV–Vis absorption spectroscopic measurements were examined in DMF. The ligand **5** exhibited a strong absorption around 300 nm. **6** and **7** also exhibited a strong absorption around 300 nm, which is characteristic of triarylamine chromophores [9]. In addition, **7** exhibited a weak absorption at 680 nm ($\varepsilon = 180\ M^{-1}\ cm^{-1}$). This peak can be assigned to the d–d transition of the copper(II) ion (Fig. 4).

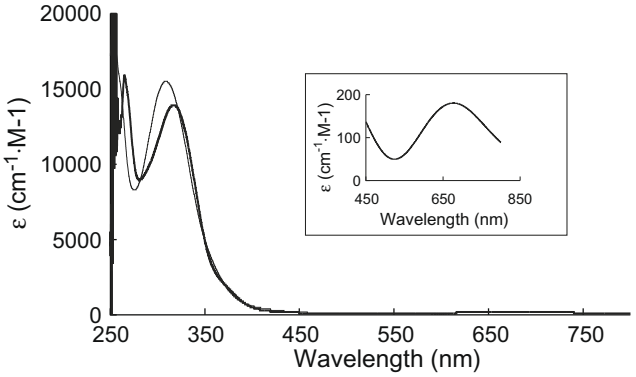


Fig. 4. UV–Vis spectra of **6** (plain) and **7** (bold) in DMF. Inset: UV–Vis spectrum of **7** in DMF.

3.3. Cyclic voltammetry measurements

Electrochemical behavior of the ligand **5** and the palladium complex **6** were studied by cyclic voltammetry in *n*-butyronitrile at ambient temperature. Upon sweeping anodically, **5** showed one set of reversible redox waves ($E^0 = 0.680$ V versus Fc/Fc^+), which can be assigned to the one electron oxidation process ($TAA/TAA^{+\cdot}$). Besides the oxidation peak, an irreversible shoulder oxidation peak ($Eox = 0.582$ V versus Fc/Fc^+) was also observed, which can be assigned to the one electron oxidation of the bis(2-picolylamino)aminomethylbenzene site. Similar electrochemical behavior was observed in our previous study for the ligand employed for the complex **1** [7a]. On the bother hand, **6** exhibited reversible redox waves ($E^0 = 0.782$ V versus Fc/Fc^+) as shown in Fig. 5, which can be assigned to the one electron oxidation process of the triarylamine unit. Compared to the redox potential of **1** ($E^0 = 0.464$ V versus Fc/Fc^+) and **3** ($E^0 = 0.473$ V versus Fc/Fc^+), the redox potential of **6** shifted more anodically, probably due to the tricationic structure. On the other hand, **7** showed a complicated

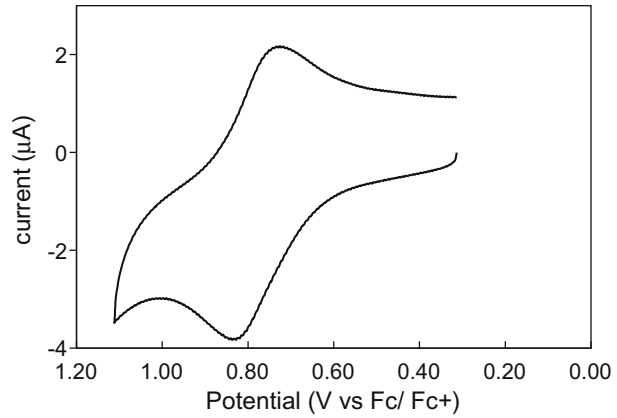


Fig. 5. Cyclic voltammogram of **6** in *n*-butyronitrile.

voltammogram upon sweeping anodically, indicating the decomposition of the oxidized species.

3.4. Two-dimensional NMR measurements

COSY (Correlated Spectroscopy) and ROESY (Rotating frame Overhauser Effect SpectroscopY) have been widely employed as powerful NMR techniques in organic chemistry. COSY and ROESY enable us to observe through-bond and through-space dipolar H–H interactions, respectively. ROESY cross peaks can be

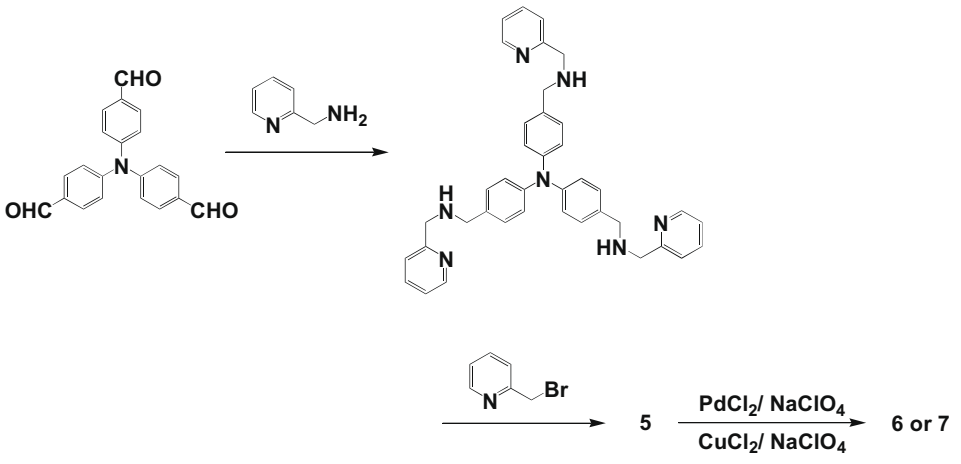


Fig. 3. Synthetic route of **5**, **6** and **7**.

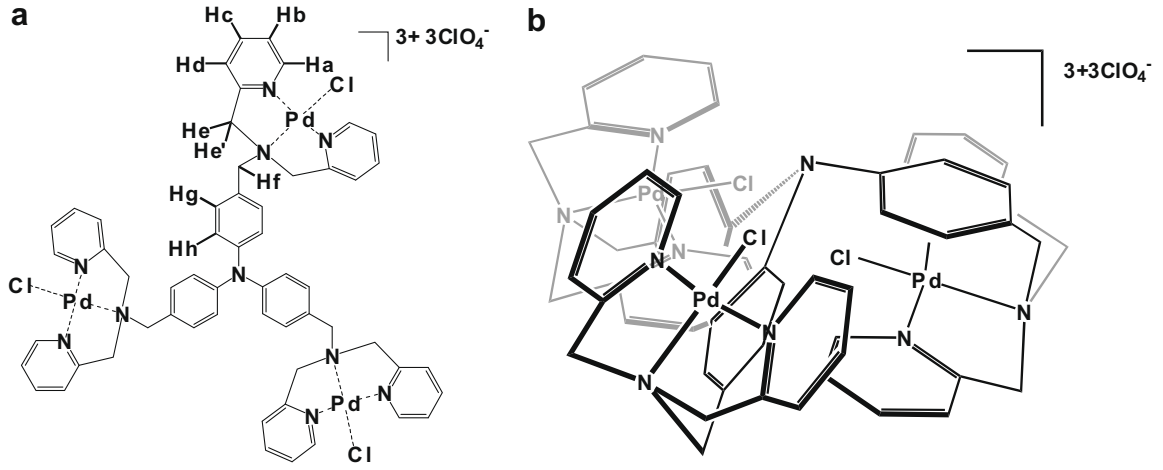


Fig. 6. An estimated conformation of **6** in DMSO-d_6 solution.

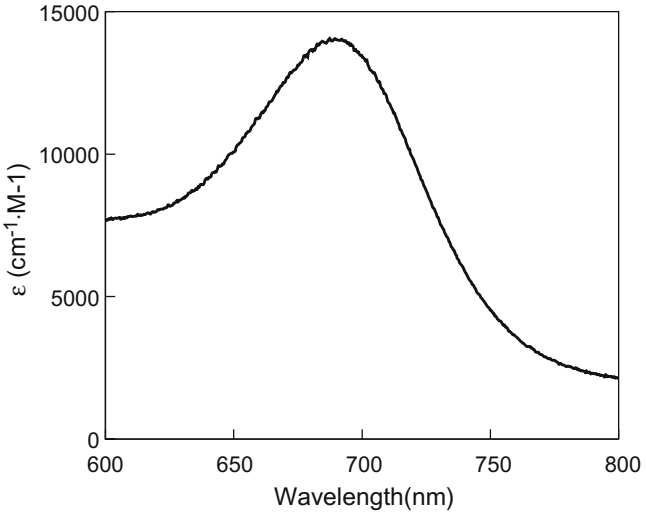


Fig. 7. Absorption spectra observed after mixing of an AN solution of 0.10 mM $TDBPA^{+\cdot}$ with an AN solution of 0.10 mM of **6**.

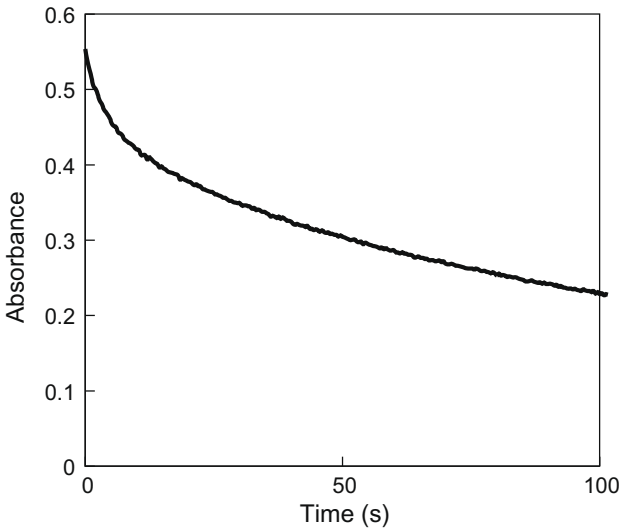
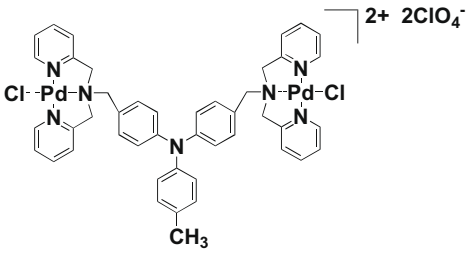


Fig. 8. Time profiles in the absorbance maximum observed after mixing of an AN solution of 0.10 mM $TDBPA^{+\cdot}$ with an AN solution of 0.10 mM of **6**.

observed only for nuclei that are proximate in space (<3.5 Å), which serve for the determination of the geometrical structure of molecules in solution. Previously, we have revealed that the dinuclear palladium complex **3** prefers a "folded conformation" at ambient temperature. COSY and ROESY measurements were applied to **6** to examine its conformation in DMSO-d_6 solution. In the ROESY spectrum of **6** at 25 °C, correlations were seen between the four hydrogen nuclei on the pyridine ring (Ha, Hb, Hc and Hd) and Hg peak. Similar correlations were also seen between the pyridine ring and He peak. These results indicate that the pyridine rings are proximate to the triarylamine unit in space. The findings clearly show that **6** prefers a "folded conformation" (Fig. 6) due to intramolecular stacking interactions. Even upon heating to 75 °C, the cross peaks did not disappear at all, indicating the occurrence of strong intramolecular stacking interactions.

3.5. Electron transfer stopped-flow (ETSF) method

The detail of the ETSF method was described previously [10]. The ETSF measurements were carried out in dehydrated acetonitrile as solvent at ambient temperature. In this study, tris(2,4-dibromophenyl)amine cation radical ($TDBPA^{+\cdot}$) [11] was employed. Complex **6**, upon mixing with one equivalent of $TDBPA^{+\cdot}$, exhibited a broad absorption peak at 687 nm ($\varepsilon = 1.40 \times 10^4$ cm $^{-1}$ M^{-1}), as shown in Fig. 7, which was gradually reduced for over 100 s (Fig. 8). Previously, we have reported the radical pen-



8

Fig. 9. Structure of complex **8**.

dant dinuclear palladium complex generated by one electron oxidation of **3**. The species showed no significant decrease in the peak intensity for 100 s. We have examined a similar complex **8** (Fig. 9), where the methyl group is attached instead of the methoxy group [12]. The radical pendant complex derived from **8** rapidly decomposed within 30 s. These result shows that a strong electrodonating group at least should be attached to the triarylamine unit to achieve persistent spin bearing ligands. The instability of the radical pendant complex derived from **6** would be attributed to its highly positively charged tetracationic structure.

4. Conclusion

A novel ligand having a redox active triarylamine group and two coordinating groups was designed and synthesized. The corresponding palladium and copper complex were also successfully prepared. The COSY and ROESY studies revealed that the palladium complex prefers the ‘‘folded conformation” in solution at ambient temperature. The cyclic voltammetry and ETSF study revealed that the palladium complexes gave novel complexes with a pendent radical upon one electron oxidation, which gradually decomposed at ambient temperature. These complexes can be regarded as prototypes for exploring redox active supramolecular metal clusters. A strong electrodonating group, such as the methoxy group, is essential to stabilize the corresponding oxidized states. Studies of self-assembled π-conjugated systems with intriguing magnetic properties are now underway.

References

[1] (a) K. Inoue, H. Iwamura, J. Chem. Soc., Chem. Commun. (1994) 2273;
(b) K. Inoue, T. Hayamizu, H. Iwamura, D. Hashizume, Y. Ohashi, J. Am. Chem. Soc. 118 (1996) 1803.

[2] (a) A. Caneschi, D. Gatteschi, R. Sessoli, P. Rey, Acc. Chem. Res. 22 (1982) 392;
(b) K. Fegy, D. Luneau, E. Belorizky, M. Novac, J.L. Tholence, C. Paulsen, T. Ohm, P. Rey, Inorg. Chem. 37 (1998) 4524;
(c) K. Fegy, D. Luneau, C. Paulsen, T. Ohm, P. Rey, Angew. Chem., Int. Ed. 37 (1998) 1270;
(d) A. Caneschi, D. Gatteschi, N. Lalioti, C. Sangregorio, R. Sessoli, G. Venturi, A. Vindigni, A. Rettori, M.G. Pini, M.A. Novak, Angew. Chem., Int. Ed. 40 (2001) 1760;
(e) M. Minguet, D. Luneau, C. Paulson, E. Lhotel, A. Gorski, J. Waluk, D.B. Amabilino, J. Veciana, Polyhedron 22 (2003) 2349.

[3] (a) E.T. Seo, R.F. Nelson, J.M. Fritsch, L.S. Marcoux, D.W. Leedy, R.N. Adams, J. Am. Chem. Soc. 88 (1966) 3498;
(b) R.F. Nelson, R.N. Adams, J. Am. Chem. Soc. 90 (1968) 3925.

[4] (a) K. Itoh, M. Kinoshita (Eds.), Molecular Magnetism, New Magnetic Materials, Gordon & Breach, Inc., Amsterdam (Kodansha as copublisher, Tokyo), 2000.;
(b) P.M. Lahti (Ed.), Magnetic Properties of Organic Materials, Marcel Dekker Inc., New York, 1999 (Chapter 9 and references therein);
(c) K. Sato, M. Yano, M. Furuichi, D. Shiomi, K. Abe, T. Takui, K. Itoh, A. Higuchi, K. Katuma, Y. Shirota, J. Am. Chem. Soc. 119 (1997) 6607;
(d) M. Yano, K. Sato, D. Shiomi, A. Ichimura, K. Abe, T. Takui, K. Itoh, Tetrahedron Lett. 37 (1996) 9207;
(e) K.R. Stickley, S.C. Blackstock, J. Am. Chem. Soc. 116 (1994) 11576;
(f) K.R. Stickley, S.C. Blackstock, Tetrahedron Lett. 36 (1995) 1585;
(g) K.R. Stickley, T.D. Selby, S.C. Blackstock, J. Org. Chem. 62 (1994) 448;
(h) T.D. Selby, S.C. Blackstock, J. Am. Chem. Soc. 62 (1997) 448;
(i) A. Ito, H. Ino, K. Tanaka, K. Kanemoto, T. Kato, J. Org. Chem. 67 (2002) 491;
(j) M. Yano, Y. Ishida, K. Aoyama, M. Tatsumi, K. Sato, D. Shiomi, A. Ichimura, T. Takui, Synth. Met. 137 (2003) 1275;
(k) M. Yano, Y. Ishida, M. Tatsumi, K. Sato, D. Shiomi, M. Oyama, T. Takui, J. Phys. Chem. Solids 65 (2004) 733;
(l) M. Yano, Y. Nakanishi, K. Matsushita, M. Tatsumi, M. Oyama, K. Sato, T. Takui, Polyhedron 24 (2005) 2116.

[5] (a) J. Bonvoisin, J.P. Launay, M.V. Auweraer, F.C.D. Schryver, J. Phys. Chem. 98 (1994) 5052;
(b) J. Bonvoisin, J.P. Launay, W. Verbouwe, M.V. Auweraer, F.C.D. Schryver, J. Phys. Chem. 100 (1996) 17079;
(c) C. Lambert, G. Nöll, J. Am. Chem. Soc. 121 (1999) 8434;
(d) C. Lambert, G. Nöll, Angew. Chem., Int. Ed. Engl. 37 (1998) 2107.

[6] R.J. Bushby, C. Kilner, N. Taylor, R.A. Williams, Polyhedron 27 (2008) 383.

[7] (a) M. Yano, K. Inoue, T. Motoyama, Y. Azuma, M. Tatsumi, O. Yamauchi, M. Oyama, K. Sato, T. Takui, Polyhedron 24 (2005) 2112;
(b) M. Yano, M. Fujita, M. Miyake, M. Tatsumi, T. Yajima, O. Yamauchi, M. Oyama, K. Sato, T. Takui, Polyhedron 26 (2007) 2174.

[8] Y. Nakano, T. Yagyu, T. Hirayama, A. Ito, K. Tanaka, Polyhedron 24 (2005) 2141.

[9] (a) F.A. Neugebauer, S. Bamberger, W.R. Groh, Chem. Ber. 108 (1975) 2406;
(b) W. Schmidt, E. Steckhan, Chem. Ber. 113 (1980) 577.

[10] (a) M. Oyama, T. Higuchi, S. Okazaki, J. Chem. Soc., Perkin Trans. 2 (2001) 1287;
(b) M. Oyama, J. Matsui, H. Park, Chem. Commun. (2002) 604.

[11] TDBPA was synthesized by WAKO Pure Chemicals Ltd. after receiving our special order. See also Ref. 10.

[12] Unpublished results.

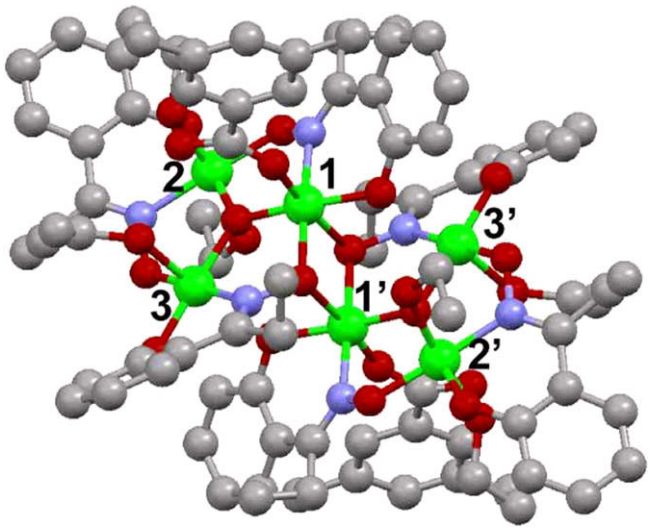


Fig. 1. Structure of the high-barrier Mn_6 molecule (H omitted for clarity). Green: Mn, red: O, blue: N, dark grey: C. (For interpretation of the references to colour in this figure legend, the reader is referred to the web version of this article.)

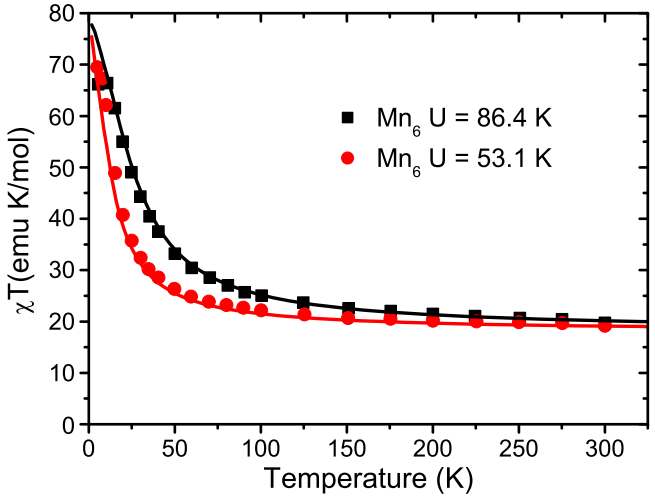


Fig. 2. Measured (points) and calculated (lines) T-dependence of the susceptibility for the two Mn_6 molecules. Calculations are made by including exchange interactions only, with the parameters determined by INS. $g = 2$ has been assumed.

Each Mn_6 molecule can be described by the following spin Hamiltonian [11]:

$$H = \sum_{i<j} J_{ij}\mathbf{s}(i)\cdot\mathbf{s}(j) + \sum_i d_i s_z^2(i) + \sum_i c_i(35s_z^4(i) + (25 - 30s(s+1))s_z^2(i)) + g\mu_B\mathbf{B}\cdot\mathbf{S} + H', \quad (1)$$

where $\mathbf{s}(i)$ are spin operators of the *ith* Mn ion and $\mathbf{S} = \sum_i \mathbf{s}(i)$ is the molecule's total spin. The first term is the isotropic exchange, while the second and third terms describe axial local crystal-fields (a z axis perpendicular to the triangles plane is assumed), and $\mathbf{B}$ is the external field [1]. H' (neglected in the following) represents additional small anisotropic terms. The minimal set of free parameters is given by three different exchange constants $J_{11'} \equiv J_1$, $J_{12} = J_{23} = J_{13} = J_{1'2'} = J_{2'3'} = J_{1'3'} \equiv J_2$, and $J_{13'} = J_{1'3} \equiv J_3$ (Fig. 1) and two sets of crystal-field (CF) parameters $d_1 = d_{1'}$, $c_1 = c_{1'}$, and $d_2 = d_{2'}$, $c_2 = c_{2'}$. The ligand cages of sites 1 and 3 are rather similar and we assumed the corresponding CF parameters to be equal. Since experimental information is insufficient to fix independently the two small c parameters,we have chosen to constrain the ratio c_1/c_2 to the ratio d_1/d_2. The anisotropic terms break rotational invariance and here lead to a large amount of mixing of different S multiplets (S mixing [12]). In the following we label the states by their leading S-component.

To determine the parameters appearing in (1), we have used the time-of-flight neutron spectrometers NEAT at the Helmholtz-Zentrum Berlin and IN5 at the Institute Laue Langevin (Grenoble). In addition, we have performed FDMRS measurements at the University of Stuttgart. Since FDMRS is sensitive to intra-multiplet transitions only, its use in conjunction with INS makes it easier to assess the character of the different observed excitations. Figs. 3 and 4 show examples of INS spectra together with theoretical simulations. The analysis of INS and FDMRS data leads to the following parameters for the higher (lower) barrier compounds: $J_1 = -0.84$

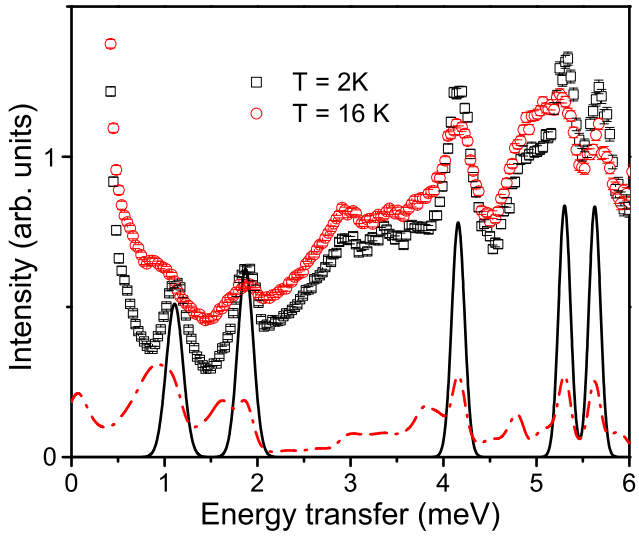


Fig. 3. INS spectra for the higher barrier molecule collected on IN5 with incident wavelength of 3.4 Å for $T = 2$ K (black) and $T = 16$ K (red). Lines are theoretical calculations with model (1). (For interpretation of the references to colour in this figure legend, the reader is referred to the web version of this article.)

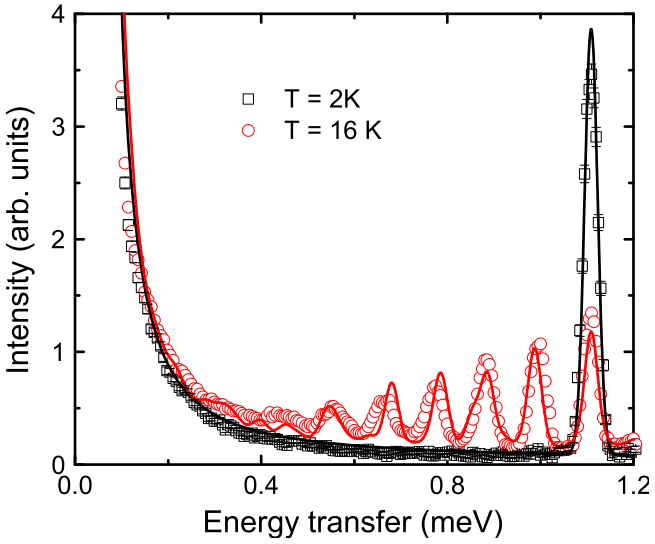


Fig. 4. INS spectra for the higher barrier molecule collected on IN5 with incident wavelength of 6.7 Å for $T = 2$ K (black) and $T = 16$ K (red). Lines are theoretical calculations with model (1). (For interpretation of the references to colour in this figure legend, the reader is referred to the web version of this article.)

(−0.61) meV, $J_2 = -0.59$ (−0.31) meV, $J_3 = 0.01$ (0.07) meV, $d_1 = -0.20$ (−0.23) meV, $d_2 = -0.76$ (−0.97) meV and $c_1 = -0.001$ (−0.0008) meV [11]. The agreement between simulations and data in Figs. 3 and 4 is very satisfactory considering that only three independent crystal-field parameters have been assumed. The parameters are also consistent with susceptibility measurements (see Fig. 2). Hence, anisotropy is similar in the two variants whereas the dominant ferromagnetic exchange is substantially larger in the higher-barrier compound. Figs. 5 and 6 show the energies of the S-multiplets resulting from the exchange part of (1). It is evident from these figures that the exchange splitting between the ground $S = 12$ manifold and many excited multiplets, including low-S ones, is smaller than the energy scale of anisotropic terms in (1). In particular, Fig. 6 shows that in the lower-barrier compound the energy of the lowest-lying $S = 0$ multiplet is only about 4 meV larger than that of the ground one. Thus, the giant spin mapping completely breaks down in these two molecules, not only for the large S-mixing in the wavefunctions, but even for failing to account for the number of states located below the barrier. The presence of a center of inversion (characterizing the structure determined at 150 K) implies that exchange multiplets can be classified according to their parity with respect to the associated spin-permutation operation. For instance, the ground $S = 12$ states are even, whereas the lowest-lying $S = 11$ states are odd.

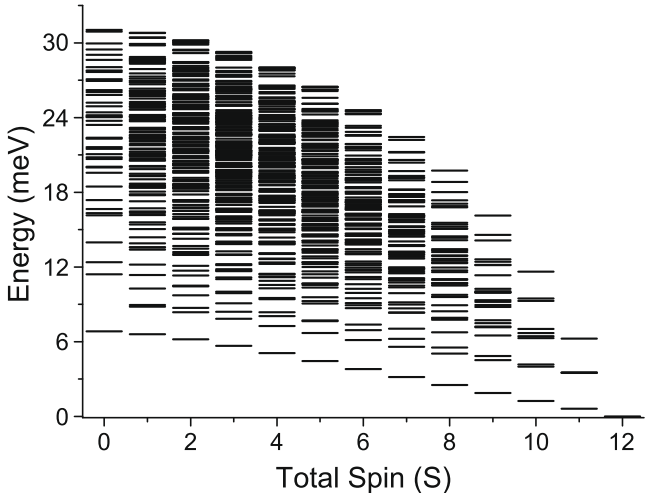


Fig. 5. Energy of all S-multiplets for the higher barrier compound, resulting from the exchange part of (1) with the parameters given in the text.

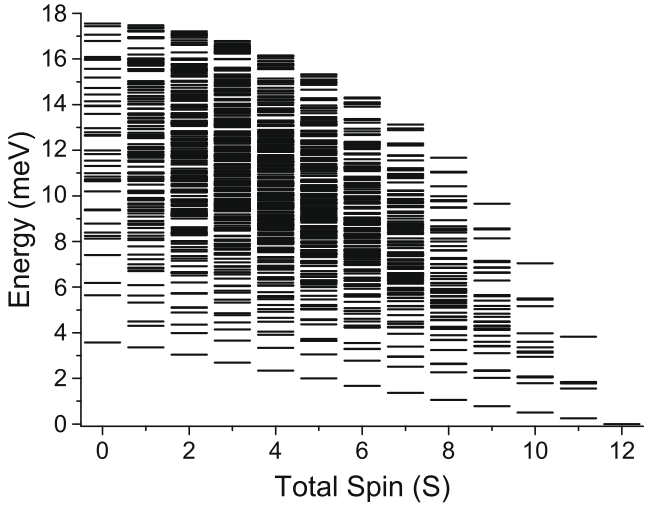


Fig. 6. Energy of all S-multiplets for the lower barrier compound, resulting from the exchange part of (1) with the parameters given in the text.

3. Relaxation of the magnetization

The main difference between the two Mn_6 variants is the position of the excited S manifolds, therefore the comparison between the relaxation behavior of these systems offers the opportunity to study the role played by low-lying excited multiplets. To address this issue, we adopt the well established framework presented in [13,14] for the irreversible evolution of the density matrix $\rho(t)$. By focusing on time scales much longer than the typical periods of free evolution of the system, the so-called "secular approximation" enables the time evolution of the diagonal matrix elements of the density matrix to be decoupled from that of the off-diagonal ones. In particular, the populations of the molecular eigenstates, $p_l(t)$, evolve through master equations:

$$\dot{p}_l(t) = \sum_m W_{lm} p_m(t), \tag{2}$$

where W_{lm} is the lm element of the rate matrix, i.e., the probability per unit time that a transition between levels $|m\rangle$ and $|l\rangle$ is induced by the interaction with the phonon heat bath. The latter can be calculated by perturbation theory once magnetoelastic (ME) interactions have been modelled. Experimental information is totally insufficient to fix all the many possible parameters appearing in the ME coupling potential. By assuming that the main contribution to this coupling arises from the modulation of the local rank-2 crystal fields and that quadrupole moments of each individual Mn ion are isotropically coupled to Debye acoustic phonons, we obtain [15]

$$W_{lm} = \gamma^2 \Delta_{lm}^3 n(\Delta_{lm}) \sum_{i,j,q_1,q_2} \langle l \mid O_{q_1,q_2}(\mathbf{s}_i) \mid m \rangle \times \langle m \mid O_{q_1,q_2}(\mathbf{s}_j) \mid l \rangle, \tag{3}$$

where i and j run over Mn ions, $O_{q_1,q_2}(\mathbf{s}_i)$ are the components of the cartesian quadrupole tensor operator, $n(x) = (e^{\hbar x/k_B T} - 1)^{-1}$ and $\Delta_{lm} = (E_l - E_m)/\hbar$. The single free parameter γ is proportional to the ME coupling strength. In spite of the complexity of their energy spectrum, for both variants the resulting relaxation spectrum at low T is dominated by a *single* relaxation time displaying a nearly Arrhenius behavior $\tau(T) = \tau_0 \exp(U/K_B T)$, in agreement with experiments [11]. In particular, the effective energy barrier for the magnetization reversal is crucially dependent on the position of low-lying excited S multiplets. Indeed, the large difference between the barriers of the two molecules mainly results from the variation of the ferromagnetic exchange constants and not from a variation in anisotropy. It is also worth to note that in the present case U is not set by the energy of the lowest-lying $M_S = 0$ state as one could naively expect.

The existence of several total-spin multiplets partially overlapping with the ground one implies that a magnetic field applied along the molecule's easy axis induces crossings involving states which are absent in a giant spin description. These can be turned into anticrossings (ACs) by the small transverse terms contained in H'. Fig. 7 shows that besides the "traditional" intra-$S = 12$ crossings at about 0, 0.4 (e.g., the square) and 0.8 T, many more occur for intermediate values of B. In particular, there are three different kinds of "non-traditional" field-induced crossings, i.e., absent in the giant spin description of the molecule. First of all there are crossings involving a pair of states belonging to a single low-energy S multiplet different from the ground one (for instance the higher-lying ellipsis at 0.3 T in Fig. 7). These crossing may lead to relaxation shortcuts if the dominant relaxation path passes

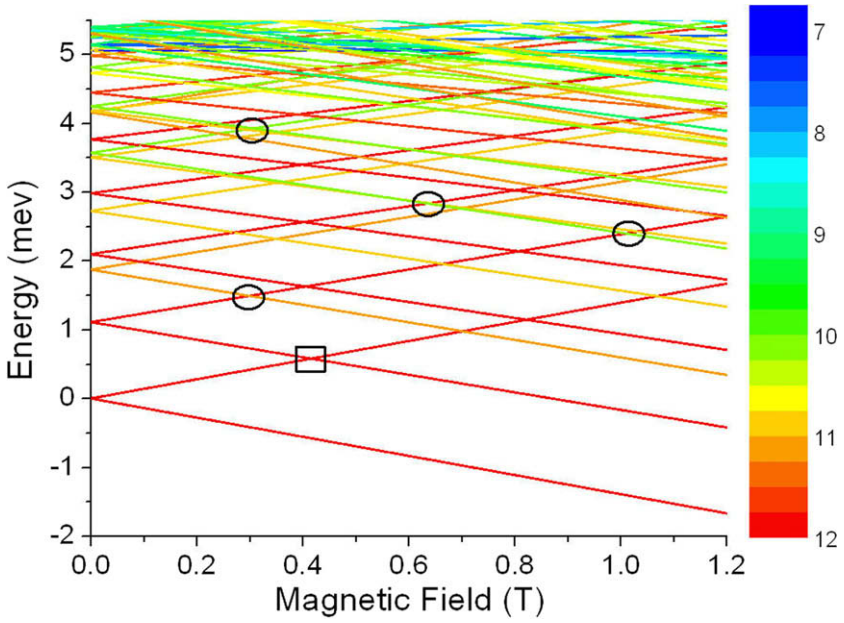


Fig. 7. Energy levels of the higher-barrier compound as a function of B, applied along the z axis. The color maps for each state the value of S_{eff}, where $\langle S^2 \rangle := S_{\text{eff}}(S_{\text{eff}}+1)$. Ellipses and the square indicate representative examples of level crossings.

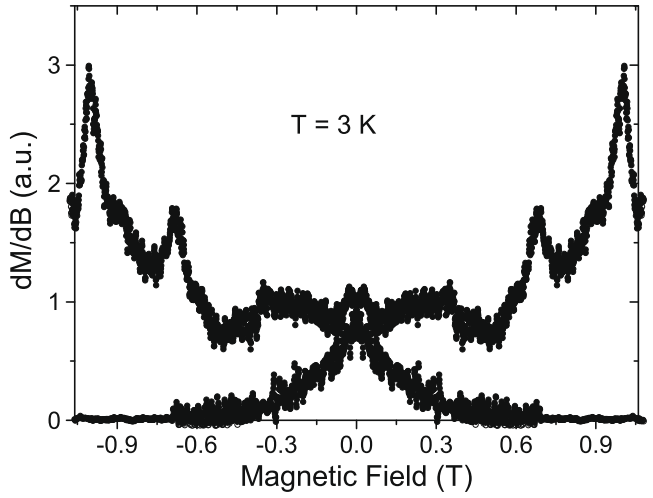


Fig. 8. Example of derivative of the hysteresis curves measured for the higher-barrier molecule in [6]. For each value of B, there are two points corresponding to increasing or decreasing B in the hysteresis cycle.

through them. The other two kinds of crossings (e.g. the other ellipses in Fig. 7) involve pairs of states belonging to different S-manifolds. The distinction arises from the symmetry properties of the two crossing states, i.e., they may have the same parity or not. In the first case (e.g., the crossings between red and green curves in the two ellipses at about 0.6 and 1 T) H' usually leads to an AC, whereas in the second case (e.g., the ellipse at about 0.3 T) an AC may occur to the extent that at low T the inversion center is removed by a distortion, leading to terms with low-enough symmetry in H'. Even if there are no structural data below 150 K, it is not unlikely for magnetic molecules to undergo a symmetry lowering at low T (see, e.g., [16,17]). "Non-traditional" ACs with the associated resonant incoherent tunneling, may result in relaxation shortcuts leading to additional steps in hysteresis cycles, absent in a giant-spin picture. For instance, Fig. 8 shows an example of derivative of the hysteresis curves measured at $T = 3$ K for the higher-barrier molecule [6]. The "traditional" ACs produce minor features in these curves, and the two main peaks are associated with "non-traditional" ACs. The effect of low-field ACs is more evident at higher T [11]. For instance, there are features at 0.3 T which may a priori originate from both crossings marked in Fig. 7.

4. Conclusions

By exploiting INS and FDMRS we have determined the microscopic Hamiltonian of two different high-spin variants of the Mn_6 nanomagnet. We have found that excited S multiplets overlapping with the ground one strongly affect the magnetic relaxation process. Moreover, we have demonstrated the existence of tunnelling pathways involving pairs of states belonging to different total spin manifolds. Hence, the energy separation between the ground and excited multiplets may be a key ingredient in determining the relaxation and tunnelling dynamics of molecular nanomagnets.

References

[1] D. Gatteschi, R. Sessoli, J. Villain, Molecular Nanomagnets, Oxford University Press, 2006.
[2] J. Villain, F. Hartmann-Boutron, R. Sessoli, A. Rettori, Europhys. Lett. 27 (1994) 159.
[3] A. Würger, J. Phys.: Condens. Matter 10 (1998) 10075.
[4] M.N. Leuenberger, D. Loss, Phys. Rev. B 61 (2000) 1286.
[5] D. Zueco, J.L. Garcia-Palacios, Phys. Rev. B 73 (2006) 104448.
[6] C.J. Milios, A. Vinslava, W. Wernsdorfer, S. Moggach, S. Parsons, S.P. Perlepes, G. Christou, E.K. Brechin, J. Am. Chem. Soc. 129 (2007) 2754.
[7] C.J. Milios, A. Vinslava, P.A. Wood, S. Parsons, W. Wernsdorfer, G. Christou, S.P. Perlepes, E.K. Brechin, J. Am. Chem. Soc. 129 (2007) 8.
[8] M. Soler, W. Wernsdorfer, Z. Sun, J.C. Huffman, D.N. Hendrickson, G. Christou, Chem. Commun. (2003) 2672.
[9] C.I. Yang, W. Wernsdorfer, G.H. Lee, H.L. Tsai, J. Am. Chem. Soc. 129 (2007) 456.
[10] C.M. Ramsey, E. del Barco, S. Hill, S.J. Shah, C.C. Beedle, D.N. Hendrickson, Nature Phys. 4 (2008) 277.
[11] S. Carretta, T. Guidi, P. Santini, G. Amoretti, O. Pieper, B. Lake, J. van Slageren, F. El Hallak, W. Wernsdorfer, H. Mutka, M. Russina, C.J. Milios, E.K. Brechin, Phys. Rev. Lett. 100 (2008) 157203.
[12] S. Carretta, E. Liviotti, N. Magnani, P. Santini, G. Amoretti, Phys. Rev. Lett. 92 (2004) 207205.

[13] K. Blum, Density Matrix Theory and Applications, Plenum Press, NY, 1996.
[14] P. Santini, S. Carretta, E. Liviotti, G. Amoretti, P. Carretta, M. Filibian, A. Lascialfari, E. Micotti, Phys. Rev. Lett. 94 (2005) 077203.
[15] S. Carretta, P. Santini, G. Amoretti, M. Affronte, A. Candini, A. Ghirri, I.S. Tidmarsh, R.H. Laye, R. Shaw, E.J. McInnes, Phys. Rev. Lett. 97 (2006) 207201.
[16] S. Carretta, J. van Slageren, T. Guidi, E. Liviotti, C. Mondelli, D. Rovai, A. Cornia, A.L. Dearden, F. Carsughi, M. Affronte, C.D. Frost, R.E. Winpenny, D. Gatteschi, G. Amoretti, R. Caciuffo, Phys. Rev. B 67 (2003) 094405.
[17] S. Carretta, P. Santini, G. Amoretti, T. Guidi, R. Caciuffo, A. Candini, A. Cornia, D. Gatteschi, M. Plazanet, J.A. Stride, Phys. Rev. B 70 (2004) 214403.

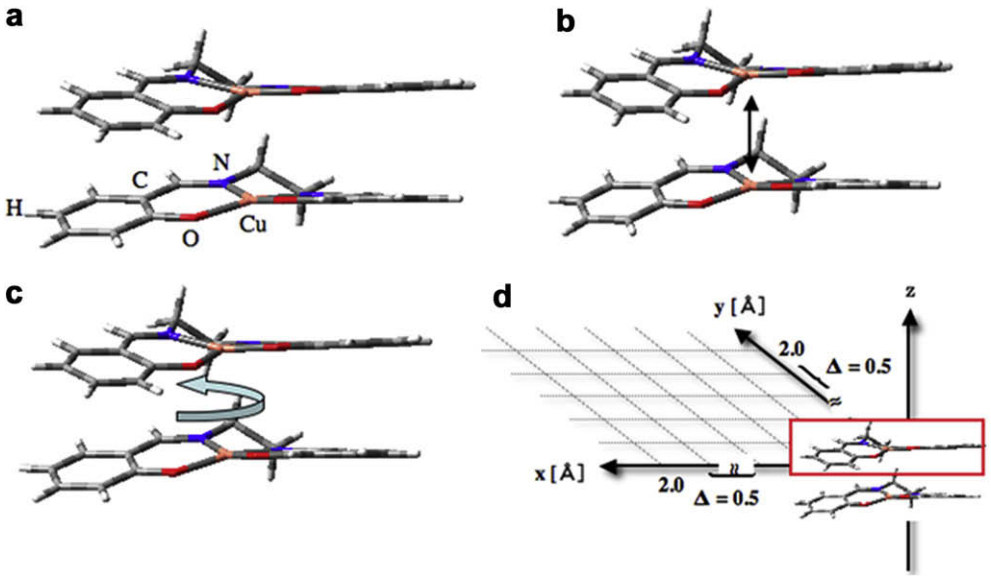


Fig. 1. The calculation dimer models of Cu^{2+} mediated base pairs of salen nucleobases. Sugar-phosphate backbone is replaced by H atoms in the models. The structure (a) is the undistorted and (b)–(d) are distorted ones. Changed parameters are (b) the distance, (c) the rotation angle and (d) the slip in *X*–*Y* plane between two monomers.

rotation angle and discrepancy in *XY*-plane, are changed in the model dimer structure as illustrated in Fig. 1b–d.

2. Theoretical background

An interaction between localized spins can be expressed by using Heisenberg Hamiltonian,

$$\hat{H} = -2\sum_{a,b} J_{ab}\hat{S}_a \cdot \hat{S}_b, \tag{1}$$

where the parameter J_{ab} is a coupling parameter between localized spins *S* on metal ions *a* and *b*.

A broken-symmetry (BS) method such as UHDFT and unrestricted Hartree–Fock (UHF) approximately involves the static correlation correction by splitting α and β electrons into two different orbitals, namely different orbitals for different spins (DODS) approach [9–12]. The low-spin species of BS method, however, suffer from a spin contamination of higher spin states, which influence total energy, optimized geometry, excited energy, and so on. Yamaguchi et al. have proposed approximate spin projection (AP) procedure by using Heisenberg Hamiltonian to eliminate the spin contamination [10,13]. Hence, we discuss J_{ab} values with the AP procedure.

$$J_{ab} = \frac{E_{BS}^{LS} - E_{BS}^{HS}}{\langle \hat{S}^2 \rangle_{BS}^{HS} - \langle \hat{S}^2 \rangle_{BS}^{LS}}. \tag{2}$$

Eq. (2) is the equation for the calculation of J_{ab} values with AP procedure [10,13]. The positive (negative) J_{ab} value means ferromagnetic (anti-ferromagnetic) interaction.

3. Computational details

In this study, we mainly use Becke's three parameter exchanges with Lee–Yang–Parr correlation functionals (E_c^{LYP}) known as B3LYP [14]. The equation of the exchange-correlation energy is as follow:

$$E_{xc} = c_1 E_x^{HF} + c_2 E_x^{Slater} + c_3 E_x^{Becke88} + c_4 E_c^{VWN} + c_5 E_c^{LYP}, \tag{3}$$

where E_x^{HF}, E_x^{Slater}, $E_x^{Becke88}$ and E_c^{VWN} are the HF exchange energy, Slater exchange functional, the Becke88 exchange functional, the Vosko–Wilk–Nusair (VWN) correlation functional, respectively. These parameters are $c_1 = 0.2$, $c_2 = 0.8$, $c_3 = 0.72$, $c_4 = 0.19$ and $c_5 = 0.81$. Besides B3LYP, we used various exchange-correlation functionals, BHandHLYP [15], PW91PW91 [16], MPW1PW91[17]. And we also examined by HF and MP2 [18], in order to elucidate dependency of J_{ab} values on computational methods.

All calculations were carried out with the use of 6-31G* basis set for ligands, and Huzinaga MIDI+pd basis set [19] for Cu^{2+} atoms using the GAUSSIAN 03 program package [20]. To confirm the effects of the diffuse function for ligands, the J_{ab} values were estimated with and without the diffuse function. As summarized in Table 1, the 6-31G* basis set gave J_{ab} values of −0.7, −0.9, −0.6 and −0.1 eV for the various separation distance of the metal–salen dimer ([**S**–Cu^{2+}–**S**]$_2$, where **S** means salen ligand), respectively, while the 6-31+G* basis set gave −0.6, −0.9, −0.6 and −0.1, respectively. The diffuse functions do not affect J_{ab} values of the [**S**–Cu^{2+}–**S**]$_2$ quantitatively, so that the 6-31G* basis set is used for estimating J_{ab} values, here.

We constructed model structures based on the X-ray structure of the metal–salen–base pair complex [8]. The structure of the metal–base pair in DNA, however, is difficult to decide whether it is the right handed or not, on the basis of experimental data, so that we assume that this structure is the right handed one. A distance between adjacent planes and rotation angle of the original

Table 1
Total energies, $\langle \hat{S}^2 \rangle$ of the HS and the BS LS states and J_{ab} values of [**S**–Cu^{2+}–**S**]$_2$ for the various distance between adjacent planes at the UB3LYP/6-31G* level.

Distance[a]	HS state		BS LS state		J_{ab}[c]
	Total energy[b]	$\langle \hat{S}^2 \rangle$	Total energy[b]	$\langle \hat{S}^2 \rangle$	
3	−5035.92722253	2.0063	−5035.92722550	1.0064	−0.7 (−0.6)[d]
3.375	−5036.06572735	2.0062	−5036.06573139	1.0063	−0.9 (−0.9)[d]
4	−5036.12941566	2.0062	−5036.12941832	1.0063	−0.6 (−0.6)[d]
5	−5036.13858055	2.0062	−5036.13858117	1.0062	−0.1 (−0.1)[d]

[a] In Å.
[b] In a.u.
[c] In cm^{-1}.
[d] J_{ab} values calculated by UB3LYP/6-31+G* are in parentheses.

structure are decided to be 3.375 Å and 36° on B–DNA form, respectively, as illustrated in Fig. 1a. Here we call this structure "original structure".

4. Results and discussion

4.1. J_{ab} values between Cu^{2+} ions for the original structure with and without-backbones

First, the J_{ab} values between two Cu^{2+} ions are calculated for the original structure with and without-backbones (sugar–phosphate). By using those assumptions, we constructed the model system as illustrated in Figs. 1a and 2. Calculated total energies, $\langle \hat{S}^2 \rangle$ values and the J_{ab} values of models without-backbone are summarized in Table 1. Results with backbones are also summarized in Table 2.

Within the both models, the calculated energy splitting between the BS LS and the HS states is small. However the BS LS state is slightly stable and the calculated J_{ab} values are negative, indicating an anti-ferromagnetic interaction. This result agrees with experimental J_{ab} values of a Metal–DNA (M–DNA) based on a natural B–DNA ($J = -0.0483\ cm^{-1}$) [4]. The J_{ab} values of with- and without-backbone models are same. These results can be easily understood by the natural orbitals (NOs) analysis. The NOs are obtained by diagonalization of a first order density matrix as

$$\rho(r, r') = \sum n_i \{\phi_i(r)\}^* \phi_i(r'), \quad (4)$$

where n_i denotes the occupation number of NO (φ_i). The occupation number is in proportion to the overlap between α and β orbitals, so that one can estimate SOMO–SOMO overlap from the number. The overlap is calculated by $n_i - 1$ [10]. Therefore, if an occupation number of a magnetic orbital is close to 1.0, then two electrons in the orbital are almost localized on each spin site. On the other hand, n_i should be equal to 2.0 if the two spins are delocalized on two spin sites. The NOs for the BS LS state are depicted in Fig. 3. The highest occupied natural orbital (HONO) and the lowest unoccupied natural orbital (LUNO) mainly consist of $d_{x^2-y^2}$ orbitals of Cu^{2+} ions, and their occupation numbers are almost 1.0, indicating that overlap between two spins on Cu^{2+} ions are very small. In "with-backbone" model, we cannot find population on backbone atoms, and occupation number of HONO is same to that of "without-backbone" model. These results indicate that backbone does not affect SOMO–SOMO overlap. Therefore the J_{ab} values of two models are same. Also we consider solvent (water) effect by using PCM method on the original structure. The calculated J_{ab} value is $-0.8\ cm^{-1}$ and it is almost equal to non-solvent model. These results suggested that the J_{ab} value does not depend on a chemical environment by solvent.

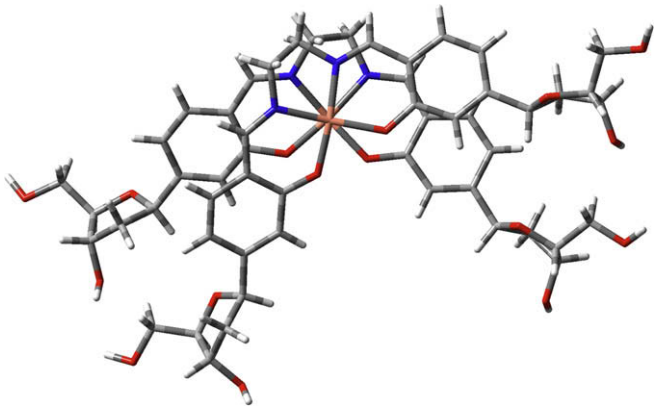


Fig. 2. Top view structure of [**S**–Cu^{2+}–**S**]$_2$ with backbones.

Table 2
Total energies, $\langle \hat{S}^2 \rangle$ of the HS and the BS LS states and J_{ab} values of [**S**–Cu^{2+}–**S**]$_2$ with backbones. The distance and angle between adjacent planes are 3.375 Å and 36°, respectively.

HS state		BS LS state		J_{ab}[b]
Total energy[a]	$\langle \hat{S}^2 \rangle$	Total energy[a]	$\langle \hat{S}^2 \rangle$	
−6719.75910069	2.0061	−6719.75910490	1.0063	−0.9

[a] In a.u.
[b] In cm^{-1}.

4.2. Change in J_{ab} values with deformations

It is well known that the DNA is flickered and changed their forms such as A-, B-and Z-forms by solvent [21]. In this sense, a structural disorder of the DNA strand must be examined for the consideration of the magnetic interaction. Therefore we, next, consider three possibilities of deformations i.e. the distance, the rotation angle and the slip in *X*–*Y* plane between two monomers as illustrated in Fig. 1b–d, and examine a change in J_{ab} values with those deformations. Calculated results for each distance and rotation angle are summarized in Table 1 and 3, respectively. The range of the separated distance and rotation angle are 3.0–5.0 Å and 0–180°, respectively. The calculated J_{ab} values are small in all range of distances and angles. Interestingly, the J_{ab} values are not in proportion to the separated distance. These is a minimum around 3.375 Å. In addition, J_{ab} values do not show a periodic dependency on the rotation angle. For example, there are minima around 120° and 150°. Usually, it should be minima around 0°, 90° and 180° when the symmetry of $d_{x^2-y^2}$ orbitals of Cu^{2+} ions of adjacent planes are considered, because the J_{ab} values depends on overlap between two spin orbitals on Cu^{2+} ions. The reason of this phenomenon is originated from the twisted salen structure as explained in Section 4.4.

In order to explain the detail, the NO analyses are carried out for several angles. The occupation numbers of the BS LS state are depicted in Table 4. All of their occupation numbers for HONO and LUNO are almost 1.0 indicating overlap between two spins on Cu^{2+} ions are very small.

As explained above, it is expected that the DNA backbone is always flickered by outer environment. So, we also estimate the slipping of two monomer in *X*–*Y* plane as illustrated in Fig. 1d. In this model, separated distance and rotation angle are fixed to 3.375 Å and 36°, respectively. As summarized in Fig. 4, the J_{ab} values do not show a simple behavior because of the twisted structure of salen, but anti-ferromagnetic interaction is observed in whole region.

4.3. Dependency of the J_{ab} values on various calculation methods

It has been reported calculated J_{ab} values sometimes depend on the DFT functional sets quantitatively, but not qualitatively. Therefore, we next investigated the dependency of the J_{ab} values on calculation methods such as BHandHLYP, PW91PW91, MPW91PW91, HF and MP2. Calculated results are shown in Table 5. Although the double helix of DNA is stabilized by π–π interaction, the DFT method which does not include π–π interaction gives systematic J_{ab} values. B3LYP, BHandHLYP and MPW1PW91 functional contain 20%, 50% and 25% HF exchange, respectively. From the results, it can be seen that the J_{ab} values depend on a ratio of HF exchange, but not depend on a correlation functional. In PW91PW91 (0% HF exchange), the J_{ab} value is a weak ferromagnetic interaction for the original structure. In MP2, the absolute values of the J_{ab} are larger at a long distance as compared others methods. This result of MP2 is unreasonable because magnetic interaction should be

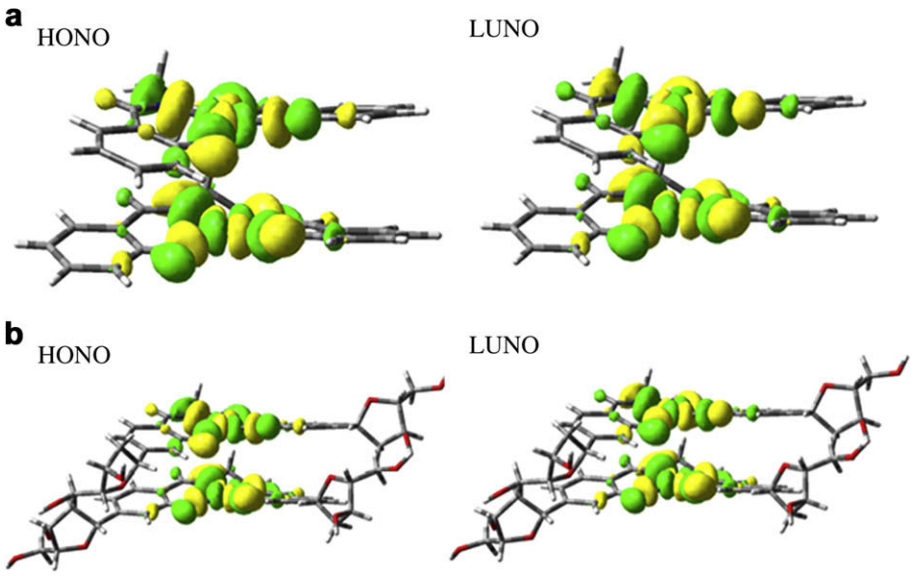


Fig. 3. Depicted HONO and LUNO of $[\mathbf{S}–Cu^{2+}–\mathbf{S}]_2$ (a) without and (b) with backbones for the BS LS state. The distance and angle between adjacent planes are 3.375 Å and 36°, respectively.

Table 3
Total energies, $\langle \hat{S}^2 \rangle$ of the HS and the BS LS states and J_{ab} values of $[\mathbf{S}–Cu^{2+}–\mathbf{S}]_2$ for the various rotation angle between adjacent planes.

Angle[a]	HS state		LS state		J_{ab}[c]
	Total energy[b]	$\langle \hat{S}^2 \rangle$	Total energy[b]	$\langle \hat{S}^2 \rangle$	
0	−5036.06325559	2.0062	−5036.06326300	1.0063	−1.6
30	−5036.04180731	2.0062	−5036.04181182	1.0063	−1.0
36	−5036.06573036	2.0062	−5036.06573441	1.0063	−0.9
60	−5036.06792164	2.0064	−5036.06793467	1.0063	−2.9
90	−5036.06982908	2.0063	−5036.06984002	1.0063	−2.4
120	−5036.06288079	2.0063	−5036.06289423	1.0063	−3.0
150	−5036.09932651	2.0063	−5036.09933549	1.0063	−2.0
180	−5036.13505917	2.0062	−5036.13506459	1.0063	−1.2

[a] In degree.
[b] In a.u.
[c] In cm^{-1}.

Table 4
The occupation number of HONO and LUNO of the BS LS state for $[\mathbf{S}–Cu^{2+}–\mathbf{S}]_2$. The separated distance is 3.375 Å.

Angle[a]	HONO	LUNO
0	1.0022	0.9978
30	1.0004	0.9996
36	1.0003	0.9997
60	1.0117	0.9883
90	1.0108	0.9892
120	1.0104	0.9896
150	1.0084	0.9916
180	1.0040	0.9960

[a] In degree.

close to zero at a long distance. Tsuzuki et al. reported that the MP2 calculation overestimate π–π interaction such as benzene or naphthalene [22,23]. Our results also suggest the method may not be applicable to the long distance $[\mathbf{S}–Cu^{2+}–\mathbf{S}]$ dimer.

4.4. Change in the J_{ab} values for planer $[\mathbf{S}–Cu^{2+}–\mathbf{S}]$ without ethylenediamine

As described above, on the metal–salen complex structure, the dihedral angle between the planes defined by the aromatic rings

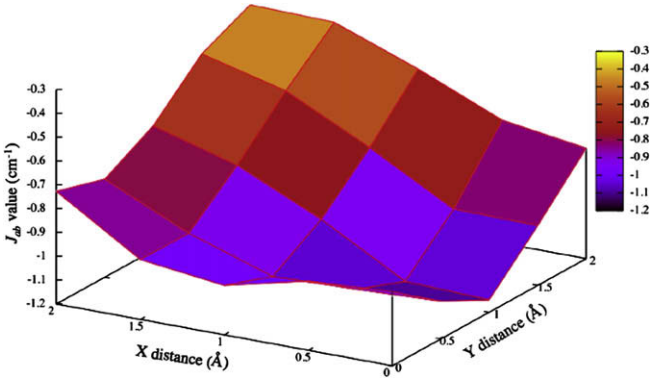


Fig. 4. The change in J_{ab} values when two monomer are slipped in X–Y plane. The distance and angle between adjacent planes are 3.375 Å and 36°, respectively.

Table 5
The J_{ab} values[a] for various calculation methods.

Distance[b]	BH and HLYP	PW91PW91	MPW1PW91	HF	MP2
3	−2.6	3.4	−0.5	−1.1	−2.8
3.375	−1.5	0.5	−0.6	−0.2	−0.4
4	−0.6	−0.3	−0.4	1.2	92.2
5	−0.1	−0.2	−0.1	3.2	−24.4

[a] In cm^{-1}.
[b] In Å.

was +22° because of crosslink by ethylenediamine. If the metal–salen monomer does not have the linking en, it will be planer complex. Therefore, we examined the J_{ab} values of planer $[\mathbf{S}–Cu^{2+}–\mathbf{S}]_2$ dimer without en to elucidate the effect of the twist structure of ligand. We changed the dihedral angel into 0° by removing en from $[\mathbf{S}–Cu^{2+}–\mathbf{S}]_2$ as shown in Fig. 5. The calculated results are shown Table 6. The calculated J_{ab} values are small in all range of distances. The J_{ab} values depend on the separated distance and the anti-ferromagnetic interaction becomes stronger as the distance between two Cu ions becomes shorter. From the result, the reason that, J_{ab} values of $[\mathbf{S}–Cu^{2+}–\mathbf{S}]_2$ dimer is not in proportion to the dimer distance seems to come from the twisted structure of the ligand.



Fig. 5. Structure of $[\mathbf{S}–Cu^{2+}–\mathbf{S}]_2$ without ethylenediamine.

Table 6
Total energies, $\langle \hat{S}^2 \rangle$ of the HS and the BS LS states and J_{ab} values of $[\mathbf{S}–Cu^{2+}–\mathbf{S}]_2$ without en. The angle between adjacent planes is 36°.

Distance[a]	HS state		LS state		J_{ab}[c]
	Total energy[b]	$\langle \hat{S}^2 \rangle$	Total energy[b]	$\langle \hat{S}^2 \rangle$	
3	−4881.31998146	2.0060	−4881.32000090	1.0062	−4.3
3.375	−4881.34174735	2.0060	−4881.34175742	1.0062	−2.2
4	−4881.34778912	2.0060	−4881.34779305	1.0061	−0.9
5	−4881.34706453	2.0061	−4881.34706519	1.0061	−0.1

[a] In Å.
[b] In a.u.
[c] In cm^{-1}.

5. Conclusion

We theoretically investigated magnetism of Cu^{2+} bridged salen–base pairs. To our knowledge, this is the first report on the magnetism for this system. In all calculated results using B3LYP, the total energies of the HS and the BSLS states are degenerated but J_{ab} values show weak anti-ferromagnetic couplings within the examined model structures. These results agree with Metal–DNA based on natural B-DNA [4]. So, we can conclude that artificial Metal–DNA (especially this system) shows anti-ferromagnetic interaction, which is consistent with the experimental result. The J_{ab} values strongly depend on the ligand structure caused by en but not backbones. Seeman et al. reported pioneering studies of DNA nanoarchitectures. They made, for example, the self-assembly of branched DNA molecules into a two-dimensional crystal and ligated DNA molecules form interconnected rings to create a cube-like structure [24]. Using these structures, it is possible to create a new material by arranging molecules in space precisely. Assimilating Seeman's structures and the metal-base pair in DNA, it is also possible to create a new magnetic material by arranging metals with spins. From our results, it seems to be effective to design the angle of aromatic ring to control the magnetic properties.

Acknowledgments

This work has been supported by Grants-in-Aid for Scientific Research (KAKENHI) (Nos. 19750046, 19350070, 18350008) from Japan Society for the Promotion of Science (JSPS) and that on Priority Areas (No. 19029028) from the Ministry of Education, Culture, Sports, Science and Technology (MEXT).

References

[1] J.W. Steed, J.L. Atwood, Supermolecular Chemistry, John Wiley & Sons Ltd, Chichester, 2000.
[2] K. Tanaka, A. Tengeiji, T. Kato, N. Toyama, M. Shionoya, Science 299 (2003) 1212.
[3] K. Tanaka, A. Tengeiji, T. Kato, N. Toyama, M. Shiro, M. Shionoya, J. Am. Chem. Soc. 124 (2002) 12494.
[4] K. Mizoguchi, S. Tanaka, T. Ogawa, N. Shiobara, H. Sakamoto, Phys. Rev. B 72 (2005) 033106.
[5] H.Y. Zhang, A. Calzolari, R.D. Felice, J. Phys. Chem. B 109 (2005) 15345.
[6] G.H. Clever, K. Polborn, T. Carell, Angew. Chem., Int. Ed. 44 (2005) 7204.
[7] G.H. Clever, T. Carell, Angew. Chem., Int. Ed. 46 (2007) 250.
[8] G.H. Clever, Y. Söltl, H. Burks, W. Spahl, T. Carell, Chem. Eur. J. 12 (2006) 8708.
[9] P.O. Luöwdin, Rev. Mod. Phys. 35 (1963) 496.
[10] K. Yamaguchi, in: R. Carbo, M. Klobukowski (Eds.), Self-Consistent Field Theory and Applications, Elsevier, Amsterdam, 1990, p. 727.
[11] K. Yamaguchi, T. Kawakami, Y. Takano, Y. Kitagawa, Y. Yamashita, H. Fujita, Int. J. Quantum Chem. 90 (2006) 370.
[12] Y. Kitagawa, T. Saito, M. Ito, Y. Nakanishi, M. Shoji, K. Koizumi, S. Yamanaka, T. Kawakami, M. Okumura, K. Yamaguchi, Int. J. Quantum Chem. 107 (2007) 3094.
[13] T. Kawakami, S. Yamanaka, S. Yamada, W. Mori, K. Yamaguchi, in: M.M. Turnbull, T. Sugimoto, L.K. Thompson (Eds.), Molecular-based Magnetic Materials Theory Technique and Applications, ACS Symposium Series, vol. 644, American Chemical Society, Washington, DC, 1996, p. 30.
[14] A.D. Becke, J. Chem. Phys. 98 (1993) 5648.
[15] A.D. Becke, J. Chem. Phys. 98 (1993) 1372.
[16] J.P. Perdew, J.A. Chevary, S.H. Vosko, K.A. Jackson, M.R. Pederson, D.J. Singh, C. Fiolhais, Phys. Rev. B 46 (1992) 6671.
[17] C. Adamo, V. Barone, J. Chem. Phys. 116 (2002) 5933.
[18] M. Head-Gordon, J.A. Pople, M.J. Frisch, Chem. Phys. Lett. 153 (1988) 503.
[19] H. Tatewaki, S. Huzinaga, J. Chem. Phys. 72 (1980) 339.
[20] M.J. Frisch et al., GAUSSIAN 03, Revision D.02, Gaussian Inc., Wallingford CT, 2004.
[21] W. Saenger, Principles of Nucleic Acid Structure, Springer, New York, NY, 1984.
[22] S. Tsuzuki, T. Uchimaru, K. Matsumura, M. Mikami, K. Tanabe, Chem. Phys. Lett. 319 (2000) 547.
[23] S. Tsuzuki, K. Honda, T. Uchimaru, M. Mikami, K. Tanabe, J. Am. Chem. Soc. 124 (2001) 104.
[24] N.C. Seeman, Nature 421 (2003) 427.

were obtained using a JEOL JMS-AX500 mass spectrometer. The infrared spectra were measured using a Shimadzu FT-IR-8700 C. The EPR spectra were recorded by a Brucker ELEXSYS E500. The X-ray data were collected by a Rigaku MSC Mercury CCD area detector with graphite monochrometer Mo Kα radiation. The magnetic susceptibility measurements were performed using a Quantum Design SQUID magnetometer MPMS-XL.

2.2. Synthesis of 2,4-diphenylcarbonohydrazide **3**

A Schlenk tube was charged with carbonohydrazide (1.0 g, 11 mmol), finely ground K_3PO_4 (4.6 g, 22 mmol), CuI (420 mg, 2.2 mmol), *N,N′*-dimethylethylenediamine (0.47 mL, 4.4 mmol), iodobenzene (6.1 mL, 55 mmol), and dry DMF (10 mL). The mixture was stirred under argon at 60–70 °C for 24 h. The resulting brownish suspension was filtered through a Celite pad and washed with 50 mL of ethyl acetate. The combined filtrate was concentrated and the residue was purified by flash chromatography on silica gel eluting with ethyl acetate to give **3** as a yellow oil (0.571 g, 21% yield), which was crystallized from a mixture of ethyl acetate-*n*-hexane in a freezer to give beautiful pale yellow prisms. Compound **3**: m.p. 60 °C; MS (FAB^+); *m*/*z* 242 (M^+); ^1H NMR (400 MHz, $CDCl_3$): δ 7.72 (td, *J* = 7.2, 1.2 Hz, 4H), 7.14 (dd, *J* = 7.8, 1.4 Hz, 4H), 7.03 (td, *J* = 7.2, 1.2 Hz, 2H), 4.47 (s, 4H); ^{13}C NMR (75 MHz, $CDCl_3$) δ 161.79, 144.63, 128.72, 125.23, 123.36; IR (KBr, cm^{-1}): 3342 (m), 3284 (m), 3062 (w), 1652 (s), 1585 (s), 1495 (s), 1361 (s), 1305 (s), 920 (m), 692 (s); *Anal.* Calc. for $C_{13}H_{14}N_4O$: C, 64.45; H, 5.82; N, 23.13. Found: C, 64.18; H, 5.83; N, 23.28%.

2.3. Synthesis of 2-(2,4-diphenyl-3-oxoverdazyl)-5,10-diphenyl-5,10-dihydrophenazine (**VzDPP**·)

A mixture of 5,10-diphenyl-5,10-dihydrophenazine-2-carbaldehyde (100 mg, 0.27 mmol) [10], pyridinium tosylate (21 mg, 0.08 mmol), and **3** (72 mg, 0.30 mmol) in methanol (5 mL) was refluxed for 30 min. The resulting precipitates were collected by filtration to give the expected condensation product, dihydro-**VzDPP** (162 mg, 96% yield). Thus obtained dihydro-**VzDPP** (50 mg, 0.16 mmol) was dissolved in CH_2Cl_2 (5 mL). The CH_2Cl_2 solution was treated with an excess amount of PbO_2 (203 mg, 0.85 mmol) and stirred for 1 h at room temperature. The mixture was filtered and concentrated. The residue was purified by chromatography on silica gel eluting with CH_2Cl_2–*n*-hexane (1:2), to give **VzDPP**· as a red powder (41 mg, 80% yield). **VzDPP**·: m.p. 254 °C; HRMS (FAB^+); *m*/*z* Calc. for $C_{38}H_{27}N_6O$+H: 584.2325; found 584.2303 (M+H); IR (KBr, cm^{-1}): 3057 (w), 1689 (s), 1591 (s), 1489 (s); EPR; *g* = 2.0037 (a_N = 6.49, 4.41 G, a_H = 0.68, 0.36 G) in toluene at room temperature.

2.4. Synthesis of 2-(2,4-diphenyl-3-oxoverdazyl)-5,10-diphenyl-5,10-dihydrophenazine radical cation $GaCl_4^-$ salt (**VzDPP**$^{\cdot+}\cdot GaCl_4^-$)

The following procedure was carried out in a glove box. To a solution of **VzDPP**· (30 mg, 0.05 mmol) in CH_2Cl_2 (5 mL), was added a solution of thianthrene$^{\cdot+}\cdot GaCl_4^-$ [11] (22 mg, 0.05 mmol) in CH_3CN (15 mL). The reaction mixture was stirred for 30 min at room temperature, filtered to remove insoluble materials, and concentrated under reduced pressure. The residue was dissolved in a minimum amount of CH_2Cl_2 (ca. 5 mL). Then, diethyl ether (20 mL) was added into the CH_2Cl_2 solution. **VzDPP**$^{\cdot+}\cdot GaCl_4^-$ was obtained as a dark red precipitate and was recrystallized from CH_2Cl_2–diethyl ether as follows: **VzDPP**$^{\cdot+}\cdot GaCl_4^-$ was dissolved in a minimum amount of CH_2Cl_2 in an uncapped small bottle. The bottle was placed in a larger capped bottle containing diethyl ether and kept at room temperature for two days. **VzDPP**$^{\cdot+}\cdot GaCl_4^-$ was obtained as dark red prisms (21 mg, 51% yield). **VzDPP**$^{\cdot+}\cdot GaCl_4^-$: m.p. 256 °C; MS (FAB^+); *m*/*z* 584 (**VzDPP**$^{\cdot+}$); MS (FAB^-); *m*/*z* 211 ($GaCl_4^-$); IR (KBr, cm^{-1}): 3076 (w), 1705 (s), 1589 (m), 1548 (m), 1485 (m); *Anal.* Calc. for $C_{38}H_{27}Cl_4GaN_6O$: C, 57.40; H, 3.42; N, 10.57. Found: C, 57.13; H, 3.67; N, 10.36%; EPR; *g* = 2.0030 in a powder form at room temperature, see Fig. 3 for the fine structures in butyronitrile at 123 K.

2.5. Synthesis of 2-(2,4-diphenyl-3-oxoverdazyl)-5,10-diphenyl-5,10-dihydrophenazine radical cation $FeCl_4^-$ salt (**VzDPP**$^{\cdot+}\cdot FeCl_4^-$)

The $FeCl_4^-$ salt was similarly prepared using thianthrene$^{\cdot+}\cdot FeCl_4^-$ [11]. **VzDPP**$^{\cdot+}\cdot FeCl_4^-$ was obtained as dark red prisms (54% yield). **VzDPP**$^{\cdot+}\cdot FeCl_4^-$: m.p. 250 °C; MS (FAB^+); *m*/*z* 584 (**VzDPP**$^{\cdot+}$); MS (FAB^-); *m*/*z* 198 ($FeCl_4^-$); IR (KBr, cm^{-1}): 3076 (w), 1703 (s), 1589 (m), 1545 (m), 1485 (m); *Anal.* Calc. for $C_{38}H_{27}Cl_4FeN_6O$: C, 58.41; H, 3.48; N, 10.76. Found: C, 58.33; H, 3.42; N, 10.64%; EPR; *g* = 2.0288 in a powder form at room temperature, see text for the fine structures in butyronitrile at 123 K.

3. Results and discussion

3.1. Syntheses of **VzDPP**· and **VzDPP**$^+\cdot MCl_4^-$ (M = Fe and Ga)

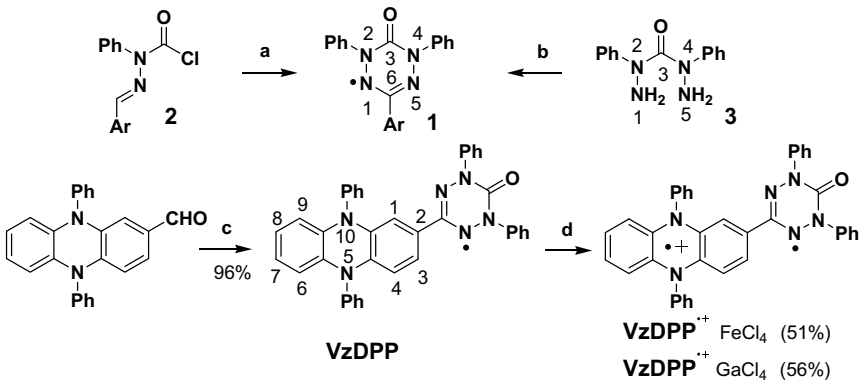
6-Aryl-2,4-diphenyl-3-oxoverdazyl derivatives **1** have generally been synthesized via 2-arylmethylidene-1-phenylhydrazinecarbonyl chloride **2** [12] (Scheme 1). Obviously, the condensation method of arylaldehyde with hitherto unknown 2,4-diphenylcarbonohydrazide **3** is much more convenient. We have therefore developed a synthetic route to **3** by applying the method of copper catalyzed amidation of aryl halides [13]. The synthesis of **3** was carried out in one step although the yield was moderate (~20%, see Section 2). Thus, neutral **VzDPP**· was synthesized through the condensation of 5,10-diphenyl-5,10-dihydrophenazine-2-carbaldehyde with **3**, followed by the oxidation with PbO_2 in CH_2Cl_2 in good yield (Scheme 1). **VzDPP**· exhibited two oxidation peaks at $E_{ox}(1)$ = +0.35 V (reversible) and $E_{ox}(2)$ = +0.90 V (irreversible) versus SCE in DMF in the presence of 0.1 M *n*-$Bu_4N^+\cdot ClO_4^-$. They can be assigned as oxidation potentials of **DPP**– and **Vz**·-moieties, respectively, by comparison with suitable model compounds (**DPP**: +0.30 V (reversible), **1** (Ar = Ph): +1.00 V (irreversible) versus SCE in DMF in the presence of 0.1 M *n*-$Bu_4N^+\cdot ClO_4^-$).

VzDPP$^{\cdot+}\cdot MCl_4^-$ (M = Fe and Ga) were obtained by the chemical oxidation of the neutral compound with thianthrene$^{\cdot+}\cdot MCl_4^-$ [11] salts as dark red prisms in moderate yields (Scheme 1).

3.2. Structures of **VzDPP**$^{\cdot+}\cdot MCl_4^-$ (M = Fe and Ga)

The molecular and packing structures of the $FeCl_4^-$ and $GaCl_4^-$ salts are very similar (see Table 1 for their crystallographic parameters). Fig. 1 shows a crystal packing structure of **VzDPP**$^{\cdot+}\cdot FeCl_4^-$ salt. There are several intermolecular short contacts within or close to the van der Waals contacts between magnetically important atoms. The **VzDPP**$^{\cdot+}$ moieties are combined by $FeCl_4^-$ in the b–c^* plane (green dotted lines (C–Cl contacts: 3.39–3.58 Å, Fig. 1I)). They are also aligned in the a^*–b plane through the intermolecular C–N contact (red dotted lines: 3.26 Å) and the C–C contact (black dotted lines: 3.29–3.50 Å), giving a ladder-type chain structure $[(\mathbf{VzDPP}^{\cdot+})_2]_n$ along the a^*-axis (Fig. 1II). The combination of these contacts makes a 3D network structure.

Quite similar contacts with similar contact-lengths were observed for **VzDPP**$^{\cdot+}\cdot GaCl_4^-$ salt (C–Cl contact: 3.39–3.59 Å, C–N contact: 3.25 Å, C–C contact: 3.28–3.49 Å).



Scheme 1. Reaction conditions: (a) $PhNHNH_2$, Et_3N in ethanol; (b) (i) ArCHO, (ii) oxidation; (c) (i) **3**, pyridinium tosylate (cat.) in methanol, (ii) PbO_2 in CH_2Cl_2; (d) thianthrene radical cation MCl_4^- (M = Fe and Ga) salts [11].

Table 1
Crystallographic data for **VzDPP**$^{\bullet+} \cdot MCl_4^-$ (M = Ga and Fe).

	VzDPP$^{\bullet+}\cdot GaCl_4^-$	**VzDPP**$^{\bullet+} \cdot FeCl_4^-$
Formula	$C_{38}H_{27}Cl_4GaN_6O$	$C_{38}H_{27}Cl_4FeN_6O$
Formula weight	795.20	781.33
Crystal system	monoclinic	monoclinic
Space group	$P2_1/n$ (#14)	$P2_1/n$ (#14)
a (Å)	10.1691(14)	10.1572(14)
b (Å)	20.163(3)	20.175(3)
c (Å)	17.465(2)	17.467(3)
β (°)	102.341(3)	102.447(3)
V (Å^3)	3498.3(8)	3495.2(8)
Z value	4	4
Crystal size (mm^3)	0.50 × 0.20 × 0.20	0.20 × 0.20 × 0.20
T (K)	123	123
D_{calc} (g cm^{-3})	1.510	1.485
F(000)	1616.00	1596.00
μ (cm^{-1})	11.331 (Mo Kα)	7.780 (Mo Kα)
Reflections measured	32989	33817
Unique reflections	7847	7922
Observation	6915 ($I > 2.00\sigma(I)$)	6018 ($I > 2.00\sigma(I)$)
Variables	478	478
Reflection/parameter	14.47	12.59
R_1 [$I > 2.00\sigma(I)$][a]	0.0309	0.0427
R_w[b]	0.0426	0.0479
Goodness-of-fit	0.823	0.815

[a] $R_1 = \sum||F_o| - |F_c||/\sum|F_o|$.
[b] $R_w = [\sum w(|F_o| - |F_c|)^2/\sum wF_o]^{1/2}$.

The magnetic interaction between **VzDPP**$^{\bullet+}$ ($S = 1$, *vide infra*) and Fe(III) ($S = 5/2$) in the above chain structure are most likely to be antiferromagnetic from the analogy of similar π–d type magnetic systems [14]. Thus, ferrimagnetic spin alignment may be expected in these π–d chain structures. However, the $[(\mathbf{VzDPP}^{\bullet+})_2]_n$ ladder chain includes several π–π type contacts, which are likely to be also antiferromagnetic. Especially, the short contacts between the carbon atom (C8, see Fig. 2 for numbering) and the nitrogen spin-center (N12 in the verdazyl moiety, see Fig. 2) would cause a sizable antiferromagnetic interaction as judged from the spin densities of **VzDPP**$^{\bullet+}$ (Fig. 2).

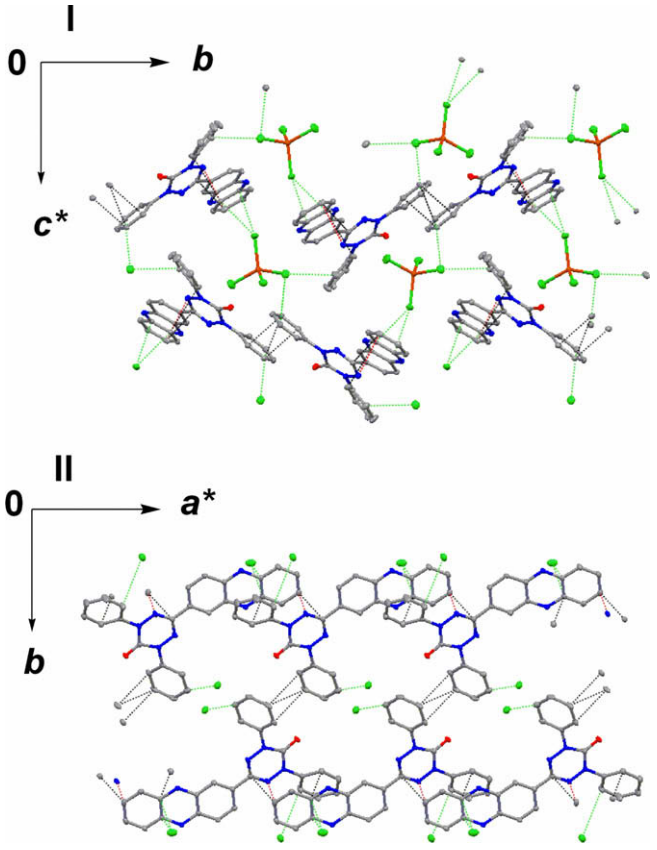


Fig. 1. Crystal packing structure of **VzDPP**$^{\bullet+} \cdot FeCl_4^-$, where intermolecular short contacts are shown by dotted lines; black: C–C contact, red: C–N contact, green: C–Cl ($FeCl_4$) contact. (I) A view projected along the a-axis. (II) Projected along the c-axis. In both views, the phenyl groups on **DPP** and all the hydrogen atoms were omitted for clarity. (For interpretation of the references to colour in this figure legend, the reader is referred to the web version of this article.)

3.3. EPR study and intramolecular magnetic interaction of *VzDPP*$^{\bullet+} \cdot MCl_4^-$ (M = Fe and Ga)

VzDPP$^{\bullet+} \cdot MCl_4^-$ (M = Fe and Ga) showed very similar EPR spectra in a frozen butyronitrile matrix at 123 K. Fig. 3 shows the spectrum of **VzDPP**$^{\bullet+} \cdot GaCl_4^-$. The spectrum has a characteristic feature of randomly oriented triplet pattern with the zero field parameters of $|D/hc| = 0.0112$ cm^{-1} and $|E/hc| = 0.0013$ cm^{-1} from the spectrum simulation. The weak signal due to $\Delta m_s = \pm 2$ forbidden transition was also observed in the half field region. The intensity of the weak $\Delta m_s = \pm 2$ signal linearly increased to the reciprocal temperature, which indicates either a triplet ground state or a singlet ground state with a small S–T gap. A small signal observed in the center field is due to a doublet impurity.

VzDPP$^{\bullet+} \cdot FeCl_4^-$ has similar zero field parameters of $|D/hc| = 0.0112$ cm^{-1} and $|E/hc| = 0.0015$ cm^{-1}. The signal due to Fe(III) was not observed under the conditions.

It is interesting to note that these $|D/hc|$ values are considerably larger than the nitronyl nitroxide substituted **DPP**$^{\bullet+}$ ($|D/hc| = 0.00725$ cm^{-1} in frozen butyronitrile at 123 K [9]). The larger

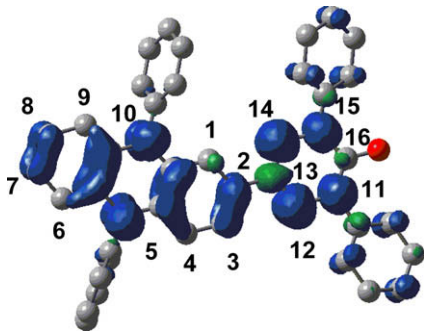


Fig. 2. Spin density map (blue: positive spin, green: negative spin) calculated at UB3LYP/6-31G* level and numbering of the atoms for **VzDPP**$^{\cdot+}$. (For interpretation of the references to colour in this figure legend, the reader is referred to the web version of this article.)

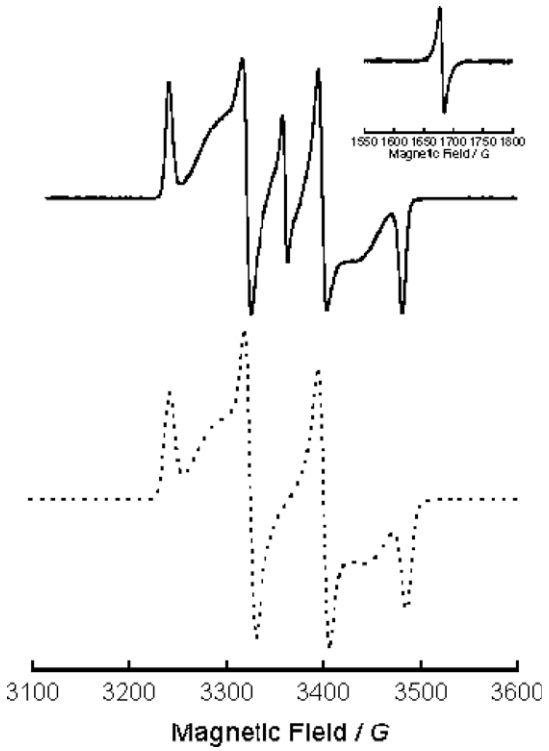


Fig. 3. EPR spectrum of **VzDPP**$^{\cdot+} \cdot GaCl_4^-$ in frozen butyronitrile matrix at 123 K (solid line: observed spectrum with $\nu_0 = 9.4277$ GHz, dotted line: simulation spectrum with parameters of $g_{xx} = 2.0034$, $g_{yy} = 2.0007$, $g_{zz} = 2.0032$, $|D/hc| = 0.0112\ cm^{-1}$, and $|E/hc| = 0.0013\ cm^{-1}$).

values for **VzDPP**$^{\cdot+} \cdot MCl_4^-$ are probably related to the higher delocalization nature of the spin densities in the verdazyl radicals (see also Fig. 2).

In order to obtain a theoretical insight into the intramolecular exchange interaction between **Vz**$^{\cdot}$ and **DPP**$^{\cdot+}$, DFT calculations were carried out using Gaussian 03 program (UB3LYP/6-31G*) [15]. The geometry of **VzDPP**$^{\cdot+}$ was taken from the X-ray structure analysis for the $GaCl_4^-$ salt. For the calculation of low-spin open-shell singlet state, the broken symmetry (BS) approach was employed [16]. The triplet state was more stable than the BS-singlet state by 0.512 kcal/mol. The exchange interaction after correction of the spin-contamination in both high- and low-spin states was estimated to be $J/k_B \sim +246$ K.

3.4. Magnetic properties of **VzDPP**$^{\cdot+} \cdot MCl_4^-$ (M = Fe and Ga)

The measurement of magnetic susceptibilities provides a clearer insight into the overall magnetic property including the intramolecular magnetic interaction between **Vz**$^{\cdot}$ and **DPP**$^{\cdot+}$. Fig. 4I shows $\chi_pT - T$ plots for **VzDPP**$^{\cdot+} \cdot GaCl_4^-$. The χ_pT values at room temperature is about 0.98 emu K mol^{-1} and almost constant in a temperature range of 200–300 K. This value is close to the theoretical value ($\chi_pT = 1.00$ emu K mol^{-1}) for the $S = 1$ state ($g = 2.0030$ from the powder EPR), indicating the intramolecular magnetic interaction between **Vz**$^{\cdot}$ and **DPP**$^{\cdot+}$ is strongly ferromagnetic ($J/k_B \geqslant +250$ K, $H = -2J\mathbf{S}_{Vz\cdot}\cdot\mathbf{S}_{DPP\cdot+}$) in accordance with the theoretical calculations for **VzDPP**$^{\cdot+}$ (*vide supra*) and the experimental result for the nitronyl nitroxide-substituted analoge [9]. The χ_pT value gradually decreased as the temperature was lowered. In the $GaCl_4$ salt, the intermolecular contacts between **VzDPP**$^{\cdot+}$ moiety and the chlorine atom ($GaCl_4^-$) would make minor contributions in the magnetic interactions because of the diamagnetic nature of Ga(III). Taking the crystal structure in consideration, the observed temperature change would be ascribed to the antiferromagnetic interaction within the $[(\mathbf{VzDPP}^{\cdot+})_2]_n$ ladder chain. The simulation based on a linear chain of $S = 1$ gave a poor result, which

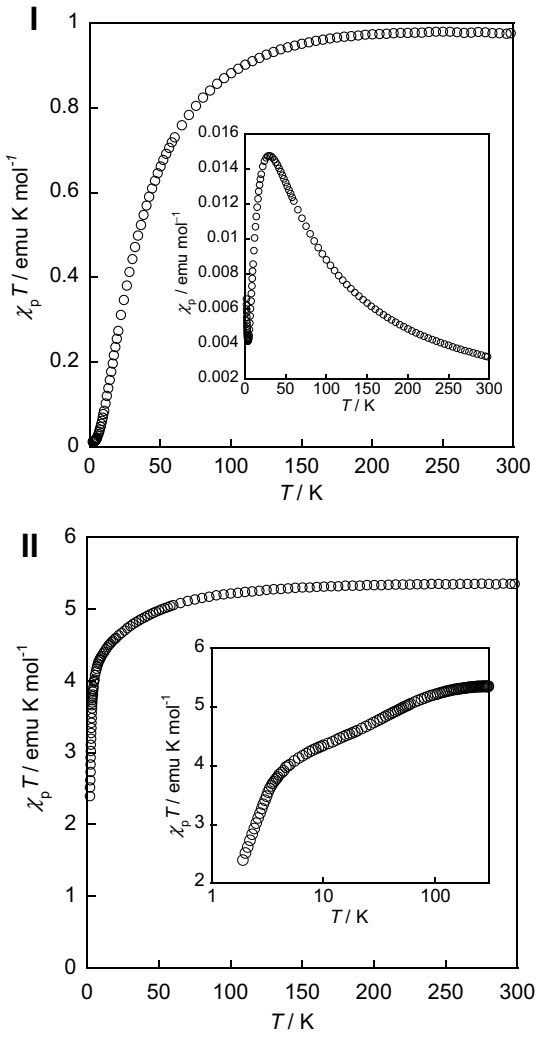


Fig. 4. Magnetic properties of **VzDPP**$^{\cdot+} \cdot MCl_4^-$ (M = Ga and Fe). (I) $\chi_pT - T$ plots for the Ga salt, inset: $\chi_p - T$ plots, (II) $\chi_pT - T$ plots for the Fe salt, inset: $\chi_pT - T$ (log scale) plots.

suggests the importance of the ladder type spin structure. The antiferromagnetic interaction was roughly estimated to be in the order of −30 K from the maximum temperature of χ_p.

The temperature dependence of χ_pT for **VzDPP**$^{\bullet+}\cdot FeCl_4^-$ is shown Fig. 4II. The χ_pT value at room temperature (χ_pT = 5.35 emu K mol^{-1}) is close to the theoretical summation of χ_pTs: 1.00 emu K mol^{-1} for **VzDPP**$^{\bullet+}$ (S = 1, g = 2.0030 from the powder EPR of **VzDPP**$^{\bullet+}\cdot GaCl_4^-$) plus 4.50 emu K mol^{-1} for Fe(III) (S = 5/2, g = 2.0288 from the powder EPR of **VzDPP**$^{\bullet+}\cdot FeCl_4^-$), indicating the presence of magnetically independent S = 1 (**VzDPP**$^{\bullet+}$) and S = 5/2 (Fe(III)) states at room temperature. χ_pT decreased and slowly approached an inflection point of ca. 4.5 emu K mol^{-1} by lowering the temperature (300 K → 10 K) and further decreased below 10 K. The value of 4.5 emu K mol^{-1} is close to that expected from only the S = 5/2 state. The decrease of χ_pT below 10 K may be attributed to the antiferromagnetic interaction between Fe(III) spins. The nearest intermolecular Fe–Fe distance is 9.14 Å. The through-space magnetic interaction with such a long distance seems to be almost impossible even at low temperature. Then, the antiferromagnetic interactions between Fe(III) spins would occur through the spin-vanishing ladder chain structures.

4. Conclusion

In order to develop a new molecular magnet based on the radical-substituted radical cation strategy, we prepared verdazyl-substituted dihydrophenazine radical cations, **VzDPP**$^{\bullet+}\cdot FeCl_4^-$ and **VzDPP**$^{\bullet+}\cdot GaCl_4^-$. The structure of **VzDPP**$^{\bullet+}$ was shown to have a large ferromagnetic interaction between **Vz**$^{\bullet}$ and **DPP**$^{\bullet+}$ ($J/k_B \sim$ ca. + 250 K). These salts had similar molecular and packing structures. Distinct features of the packing structures is (1) there are 2D type intermolecular contacts between the carbon atoms of **DPP**$^{\bullet+}$ and the chlorine atom of MCl_4^- moiety in the b–c^* plane, (2) **DPP**$^{\bullet+}$ moieties form a ladder chain structure, $[(\mathbf{VzDPP}^{\bullet+})_2]_n$ along the a^*-direction, thus the overall intermolecular contacts were shown to be in a 3D manner. The magnetic properties for these salts were clarified in the temperature range of 2–300 K. In both cases, χ_pT decreased as lowering of the temperature (300 K → 10 K), indicating an antiferromagnetic interaction. The antiferromagnetic interaction is assigned to be due to the ladder chain structure, $[(\mathbf{VzDPP}^{\bullet+})_2]_n$, and estimated to be ca. −30 K for the $GaCl_4^-$ salt. The same order of values is expected for the $FeCl_4^-$ salt from analogy of structures. For **VzDPP**$^{\bullet+}\cdot FeCl_4^-$, χ_pT decreased through the inflection point of ca. 4.5 emu K mol^{-1} around 10 K and further decreased below 10 K. No evidence of magnetic phase transition with long-range order was obtained.

Appendix A. Supplementary data

CCDC 707540 and 707541 contain the supplementary crystallographic data for $FeCl_4^-$ and $GaCl_4^-$. These data can be obtained free of charge via http://www.ccdc.cam.ac.uk/conts/retrieving.html, or from the Cambridge Crystallographic Data Centre, 12 Union Road, Cambridge CB2 1EZ, UK; fax: (+44) 1223-336-033; or e-mail: deposit@ccdc.cam.ac.uk. Supplementary data associated with this article can be found, in the online version, at doi:10.1016/j.poly.2008.11.002.

References

[1] (a) P.M. Lahti (Ed.), Magnetic Properties of Organic Materials, Marcel Dekker, New York, 1999;
(b) G. Antorrena, F. Palacio, J.M. Rawson, N.B. Smith, in: J. Veciana, C. Rovira, D.B. Amabillino (Eds.), Supramolecular Engineering of Synthetic Metallic Materials, Kluwer, Boston, 1998.
[2] (a) J.S. Miller, M. Drillon (Eds.), Magnetism: Molecules to Materials II–V, Wiley-VCH, New York, 2001;
(b) D. Gatteschi, R. Sessoli, J. Villain, Molecular Nanomagnets, Oxford, New York, 2006.
[3] K. Yamaguchi, H. Namimoto, T. Fueno, T. Nogami, Y. Shirota, Chem. Phys. Lett. 166 (1990) 408.
[4] T. Sugano, T. Fukasawa, M. Kinoshita, Synth. Met. 41–43 (1991) 3281.
[5] Y. Nakamura, N. Koga, H. Iwamura, Chem. Lett. (1991) 69.
[6] (a) H. Sakurai, A. Izuoka, T. Sugawara, J. Am. Chem. Soc. 122 (2000) 9723;
(b) M.M. Matsushita, H. Kawakami, T. Sugawara, Phys. Rev. B 77 (2008) 195208.
[7] (a) T. Sugimoto, S. Yamaga, M. Nakai, K. Ohmori, M. Tsuji, H. Nakatsuji, H. Fujita, J. Yamauchi, Chem. Lett. (1993) 1361;
(b) T. Sugimoto, S. Yamaga, M. Nakai, M. Tsuji, H. Nakatsuji, N. Hosoito, Chem. Lett. (1993) 1817.
[8] P.L. Nordio, Z.G. Soos, H.M. McConnell, Ann. Rev. Phys. Chem. 17 (1966) 237.
[9] S. Hiraoka, T. Okamoto, M. Kozaki, D. Shiomi, K. Sato, T. Takui, K. Okada, J. Am. Chem. Soc. 126 (2004) 58.
[10] V.D. Pokhodenko, V.G. Koshechko, A.N. Inozemtsev, J. Chem. Soc., Chem. Commun. (1985) 72.
[11] M. Kuratsu, S. Suzuki, M. Kozaki, D. Shiomi, K. Sato, T. Takui, K. Okada, Inorg. Chem. 46 (2007) 10153.
[12] F.A. Neugebauer, H. Fisher, C. Krieger, J. Chem. Soc., Perkin Trans. 2 (1993) 535.
[13] A. Klapars, X. Huang, S.L. Buchwald, J. Am. Chem. Soc. 124 (2002) 7421.
[14] A. Miyazaki, M. Enomoto, M. Enomoto, T. Enoki, G. Saito, Mol. Cryst. Liq. Cryst. 305 (1997) 425.
[15] M.J. Frisch, G.W. Trucks, H.B. Schlegel, G.E. Scuseria, M.A. Robb, J.R. Cheeseman, J.A. Montgomery Jr., T. Vreven, K.N. Kudin, J.C. Burant, J.M. Millam, S.S. Iyengar, J. Tomasi, V. Barone, B. Mennucci, M. Cossi, G. Scalmani, N. Rega, G.A. Petersson, H. Nakatsuji, M. Hada, M. Ehara, K. Toyota, R. Fukuda, J. Hasegawa, M. Ishida, T. Nakajima, Y. Honda, O. Kitao, H. Nakai, M. Klene, X. Li, J.E. Knox, H.P. Hratchian, J.B. Cross, V. Bakken, C. Adamo, J. Jaramillo, R. Gomperts, R.E. Stratmann, O. Yazyev, A.J. Austin, R. Cammi, C. Pomelli, J.W. Ochterski, P.Y. Ayala, K. Morokuma, G.A. Voth, P. Salvador, J.J. Dannenberg, V.G. Zakrzewski, S. Dapprich, A.D. Daniels, M.C. Strain, O. Farkas, D.K. Malick, A.D. Rabuck, K. Raghavachari, J.B. Foresman, J.V. Ortiz, Q. Cui, A.G. Baboul, S. Clifford, J. Cioslowski, B.B. Stefanov, G. Liu, A. Liashenko, P. Piskorz, I. Komaromi, R.L. Martin, D.J. Fox, T. Keith, M.A. Al-Laham, C.Y. Peng, A. Nanayakkara, M. Challacombe, P.M.W. Gill, B. Johnson, W. Chen, M.W. Wong, C. Gonzalez, J.A. Pople, GAUSSIAN 03, Revision C.02, Gaussian, Inc., Wallingford CT, 2004.
[16] K. Yamaguchi, T. Kawakami, Y. Takano, Y. Kitagawa, Y. Yamashita, H. Fujita, Int. J. Quantum Chem. 90 (2002) 370.

organization of zigzag chains in the crystal seems to be very important for the generation of the cooperative interaction network.

2. Results and discussion

Four types of calculations have been performed for the $[Fe(pyim)_2(bpy)](ClO_4)_2 \cdot 2C_2H_5OH$ system in both LS and HS states. Firstly, the calculations have been done using the X-ray defined structures (at 293 K for the HS, and at 173 K for the LS, respectively) [22]. The energy gap between two states $\Delta E = E_{HS} - E_{LS}$ has been found equal to 293 kJ/mol (per iron center). Although the calculations correctly predict the ground state, the energy gap is evidently too large, as for spin transition systems usually a value less than 100 kJ/mol is expected. Several reasons of such discrepancy can be suggested. Besides the deficiency of the method itself due to the choice of the exchange-correlation potential, several features of the experimentally studied system are neglected. In particular, the magnetic measurements show that some residual amount of the HS centers is present at 173 K. The calculations also neglect the disorder observed at both temperatures for the counter ion and solvent molecules, only the position with a maximal occupancy is used in calculations. The next step was to calculate just one polymeric chain with two counter ions and solvent molecules attached as it shown in Fig. 1, keeping interatomic distances found in the crystallographic experiment. This led to the energy gap equal to 172.3 kJ/mol demonstrating the effect of interchain interaction on this parameter essentially determining the transition temperature.

Two other calculations involved the total optimization of the crystal structure, or a partial optimization with parameters of the elementary cell fixed to their experimental values. The total optimization correctly reproduces the LS ground state with the energy gap ΔE equal to 79.3 kJ/mol. Although this value seems more reasonable than those given by single point calculations it remains still rather large. However, it has still to be corrected by the zero-energy-vibrations contribution, which diminishes the effective energy gap. The partial optimization with the elementary cell

Table 1
Comparison of some characteristic intrachain and intermolecular distances (in Å) for experimental and optimized structures.

	293 K (Exp)	HS full opt.	HS opt. fix. cell	173 K (Exp)	LS full opt.	LS opt. fix. cell
Fe–N(bpy)	2.202	2.169	2.202	2.026	1.962	1.986
Fe–N(im)	2.175	2.182	2.193	2.007	2.008	1.966
Fe–N(py)	2.217	2.173	2.205	2.033	1.991	2.005
Fe–Cl	6.507	6.333	6.477	6.340	6.282	6.325
Fe–O(Et)	8.653	8.393	8.476	8.354	8.365	8.522

Table 2
Experimental and calculated elementary cell parameters.

	293 K (Exp)	HS full opt.	173 K (Exp)	LS full opt.
a (Å)	23.625	22.799	23.188	22.983
b (Å)	11.892	11.378	11.559	11.515
c (Å)	16.51	16.543	16.256	15.927
β (°)	130.09	130.17	130.35	128.78
V (Å^3)	3548.58	3279.16	3320.56	3285.98

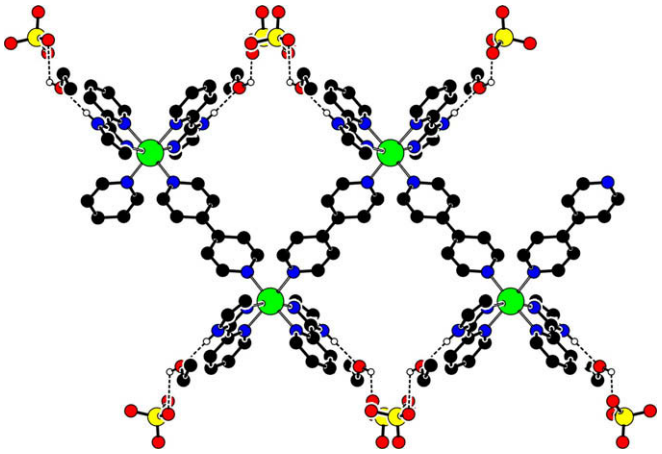


Fig. 1. One-dimensional zigzag chain structure of $[Fe(pyim)_2(bpy)](ClO_4)_2 \cdot 2C_2H_5OH$.

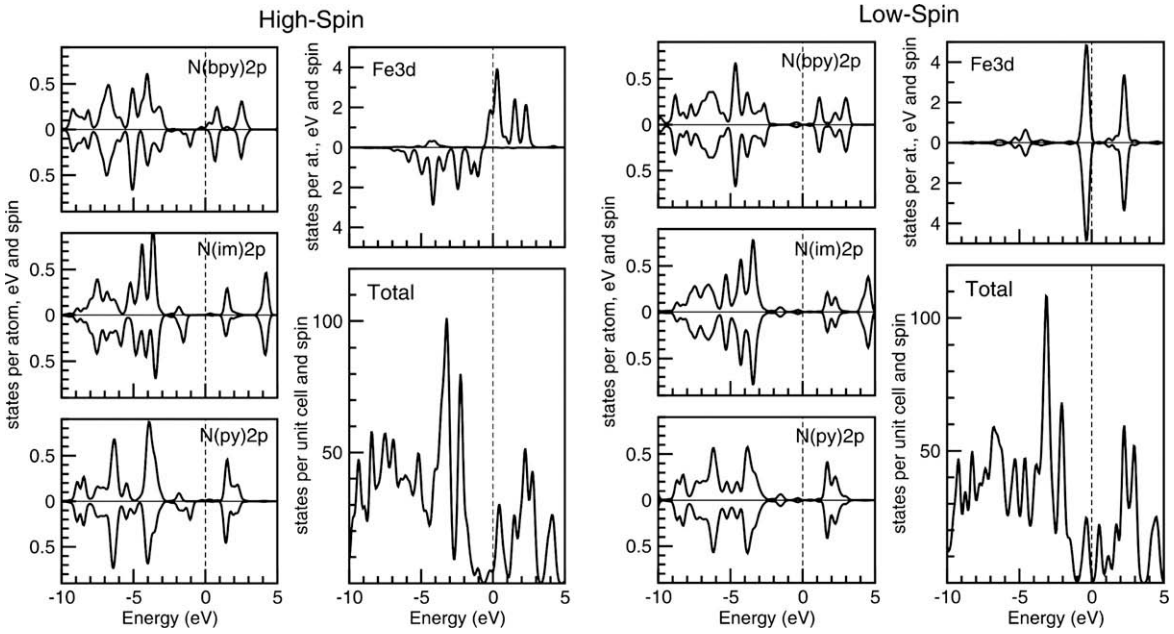


Fig. 2. Local (per Fe and N atoms) and total (per unit cell) DOS for the HS and LS states.

parameters fixed at their HS values results in ΔE equal to 155.2 kJ/mol. This value, intermediate between those obtained by the total optimization and by single chain calculations, shows the importance of lattice relaxation in the definition of the energy gap between two spin states. The total optimization leads to the geometry of the [FeN_6] coordination core close to the experimental one in both spin states (Table 1). The calculations reproduce the increase of metal–ligand bond lengths of about 0.2 Å in the HS state. However, the agreement for the intermolecular distances and elementary cell parameters is less satisfactory (Table 2). The calculations do not reproduce the increase of the *a* and *b* parameters upon the LS→HS transition and, consequently, the increase of the elementary cell volume. It is interesting to note the behavior of the calculated *c* parameter agrees with the X-ray data. As the polymer chains in the structure run parallel to *z*-axis, it means that the calculations correctly describe the structure along the chains, resulting in important errors in the description of the interchain space.

Fig. 2 shows partial and total densities of states (DOS) calculated for the structures with optimized chain parameters and fixed lattice vectors. In fact, the DOS for the fully optimized structures cannot be visually resolved from the present ones. The nominal electron configurations of the Fe ion can be easily read from the occupation of narrow bands, which can be identified as t_{2g} and e_g states. It is seen that the magnetization induced on nitrogen atoms of the first coordination sphere is not negligible; the hybridization of Fe3d–N2p states, very different in two spin channels, is especially well seen within 2 eV below the band gap. The structure of corresponding molecular orbitals will be discussed elsewhere.

3. Computational details

The periodic DFT calculations have been carried out using the SIESTA program [28] with only valence electrons described by basis sets of numerical localized atomic orbitals included in calculations. The generalized gradient approximation with the Perdew–Burke–Ernzerhof scheme [29] was employed for the exchange-correlation functional. Core electrons were replaced by norm-conserving pseudopotentials using the scalar-relativistic Troullier–Martins scheme [30] in the Kleinman-Bylander factorised form [31] with nonlinear core corrections. In the present work we used the molecular-dynamics technique with variable cell shape and coordinate optimization by conjugate gradients as provided within SIESTA.

4. Conclusions

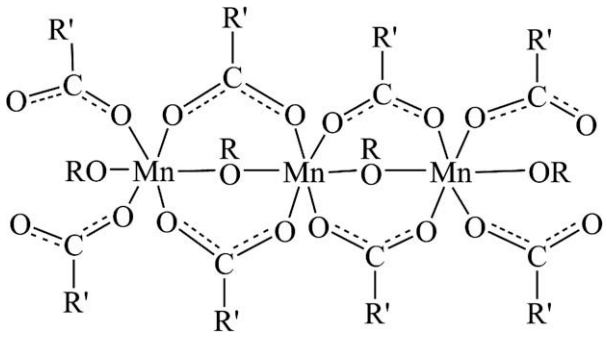
In this paper we attempted to apply periodic quantum chemical DFT approaches for the description of spin crossover coordination polymers. The calculations included full geometry optimization for both spin states. We have found that computational methods are able to describe correctly the energetic order of spin multiplets and the intrachain geometry. It appears that the calculations can be used to predict polymer structures for the cases when the X-ray structures are not available. However, the possibilities of calculations are somehow limited to describe the interchain geometry. It may be due to the well-known shortcomings of DFT methods in application to weak intermolecular interactions. From this point of view, the search of new exchange-correlation functionals adapted for the description of the spin states energetics of transition metal complexes as well as weak intermolecular interactions seems highly desirable. Also, an interesting perspective can appear with calculations based on the constrained geometry optimization, when the interchain geometry is fixed. One can hope that some reliable results can be obtained even with existing functionals for a series of parent compounds. Studies of the whole family of zigzag chain spin crossover polymers [25] are currently underway.

Acknowledgements

Y.C. acknowledges the financial support of the Marie Curie Incoming International Fellowships through the European Community's Sixth Framework Program. The Grant from EU NOE MAGMANET (515767-2) is also acknowledged. The computing resources were generously made available by IDRIS.

References

[1] P. Gütlich, H.A. Goodwin (Eds.), Topics in Current Chemistry, vols. 233-235, Springer, Berlin, 2004.
[2] A. Bousseksou, G. Molnàr, G.S. Matouzenko, Eur. J. Inorg. Chem. (2004) 4353.
[3] P. Gütlich, P.J. van Koningsbruggen, F. Renz, Struct. Bond. 107 (2004) 27.
[4] J.A. Real, A.B. Gaspar, M.C. Muñoz, Dalton Trans. (2005) 2062.
[5] M. Sorai, M. Nakano, Y. Miyazaki, Chem. Rev. 106 (2006) 976.
[6] M.A. Halcrow, Polyhedron 26 (2007) 3523.
[7] K.S. Murray, Eur. J. Inorg. Chem. (2008) 3101.
[8] H. Paulsen, A.X. Trautwein, J. Phys. Chem. Solids 65 (2004) 793.
[9] G. Baranovic, Chem. Phys. Lett. 369 (2003) 668.
[10] M. Reiher, Inorg. Chem. 41 (2002) 6928.
[11] S. Bonhommeau, T. Guillon, L.M. Lawson Daku, P. Demont, J.S. Costa, J.-F. Létard, G. Molnár, A. Bousseksou, Angew. Chem., Int. Ed. 45 (2006) 1625.
[12] S. Zein, G.S. Matouzenko, S.A. Borshch, Chem. Phys. Lett. 397 (4–6) (2004) 475.
[13] S. Zein, G.S. Matouzenko, S.A. Borshch, J. Phys. Chem. A 109 (2005) 8568.
[14] S. Zein, S.A. Borshch, J. Am. Chem. Soc. 127 (2005) 16197.
[15] T. Guillon, L. Salmon, G. Molnar, S. Zein, S.A. Borshch, A. Bousseksou, J. Phys. Chem. A 111 (2007) 8223.
[16] S. Zein, S.A. Borshch, P. Fleurat-Lessard, M.E. Casida, H. Chermette, J. Chem. Phys. 126 (2007) 014105.
[17] G. Lemercier, N. Bréfuel, S. Shova, J.A. Wolny, F. Dahan, M. Verelst, H. Paulsen, J.P. Tuchagues, Chem. Eur. J. 12 (2006) 7421.
[18] H.O. Jeschke, A. Salguero, B. Rahaman, C. Buchsbaum, V. Pashchenko, M.U. Schmidt, T. Saha-Dasgupta, R. Valenti, New J. Phys. 9 (2007) 448.
[19] L. Kabalan, S.F. Matar, M. Zakhour, J.F. Létard, Z. Naturforsch. B 63 (2008) 154.
[20] S. Lebègue, S. Pillet, J.G. Angyan, Phys. Rev. B 78 (2008) 024433.
[21] K. Yoshizawa, H. Miyajima, T. Yamabe, J. Phys. Chem. B 101 (1997) 4383.
[22] G.S. Matouzenko, G. Molnar, N. Bréfuel, M. Perrin, A. Bousseksou, S.A. Borshch, Chem. Mater. 15 (2003) 550.
[23] O. Kahn, E. Codjovi, Philos. Trans. Roy. Soc. London, Ser. A 354 (1996) 359.
[24] O. Kahn, Y. Garcia, J.F. Létard, C. Mathonière, NATO ASI Ser. C 518 (1998) 127.
[25] G.S. Matouzenko, M. Perrin, B. Le Guennic, C. Genre, G. Molnar, A. Bousseksou, S.A. Borshch, Dalton Trans. (2007) 934.
[26] C. Genre, G.S. Matouzenko, E. Jeanneau, D. Luneau, New J. Chem. 30 (2006) 1669.
[27] C. Genre, E. Jeanneau, A. Bousseksou, D. Luneau, S.A. Borshch, G.S. Matouzenko, Chem. Eur. J. 14 (2008) 697.
[28] J.M. Soler, E. Artacho, J.D. Gale, A. Garcıa, J. Junquera, P. Ordejon, D. Sanchez-Portal, J. Phys.: Condens. Matter 14 (2002) 2745.
[29] J.P. Perdew, K. Burke, M. Ernzerhof, Phys. Rev. Lett. 77 (1996) 3865.
[30] N. Troullier, J.L. Martins, Phys. Rev. B 43 (1991) 1993.
[31] L. Kleinman, D.M. Bylander, Phys. Rev. Lett. 48 (1982) 1425.



Scheme 1. A portion of the chain structure of the $[Mn^{III}(OR)(O_2CR')_2]_n$ family of polymers.

$\{[Mn(OH)(O_2CMe)_2] \cdot 2MeCO_2H \cdot H_2O\}_n$ (**1**) was prepared as described elsewhere [9d].

Microanalyses (C, H, N) were performed by the in-house facilities of the Chemistry Department at the University of Florida. IR spectra (4000–450 cm^{-1}) were recorded on a Nicolet Nexus 670 spectrometer with samples prepared as KBr pellets. Variable-temperature dc and ac magnetic susceptibility data were collected at the University of Florida using a Quantum Design MPMS-XL SQUID susceptometer equipped with a 7 T magnet and operating in the 1.8–300 K range. Samples were embedded in solid eicosane to prevent torquing. Pascal's constants were used to estimate the diamagnetic corrections, which were subtracted from the experimental susceptibilities to give the molar paramagnetic susceptibilities (χ_M).

Table 1
Crystallographic data for complexes **3** · toluene, and **4.**

Parameter	**3** · toluene	**4**
Formula[a]	$C_{76}H_{131}Mn_9N_2O_{33}$	$C_{40}H_{90}Fe_5Mn_5O_{40}$
Formula weight (g mol^{-1})	2095.29	1765.07
Crystal system	Monoclinic	Monoclinic
Space group	*C*2/*c*	$P2_1/c$
a (Å)	45.371(6)	25.747(2)
b (Å)	16.005(2)	15.882(1)
c (Å)	28.249(4)	29.232(2)
α (°)	90	90
β (°)	92.165(3)	114.240(2)
γ (°)	90	90
V (Å^3)	20499(5)	10899(2)
Z	8	6
ρ_{calc} (g cm^{-3})	1.358	1.614
Radiation, λ (Å)[b]	0.71073	0.71073
Temperature (K)	173(2)	173(2)
μ (mm^{-1})	1.141	1.892
R_1[c,d]	0.0484	0.0589
wR_2[e]	0.0964	0.1467

[a] Including solvate molecules.
[b] Graphite monochromator.
[c] $I > 2\sigma(I)$.
[d] $R_1 = 100\Sigma(||F_o|-|F_c||)/\Sigma|F_o|$.
[e] $wR_2 = 100[\Sigma \quad [w(F_o^2-F_c^2)^2]/\Sigma[w(F_o^2)^2]]^{1/2}$, $w = 1/[\sigma^2(F_o^2) + [(ap)^2 + bp]$, where $p = [\max(F_o^2, O) + 2F_c^2]/3$.

2.2. Compound preparation

2.2.1. $[Mn(OMe)(O_2CBu^t)_2]_n$ (**2**)

Compound **2** was synthesized following the same procedure as **1**, except that a solvent mixture of MeOH/Bu^tCO_2H was used in

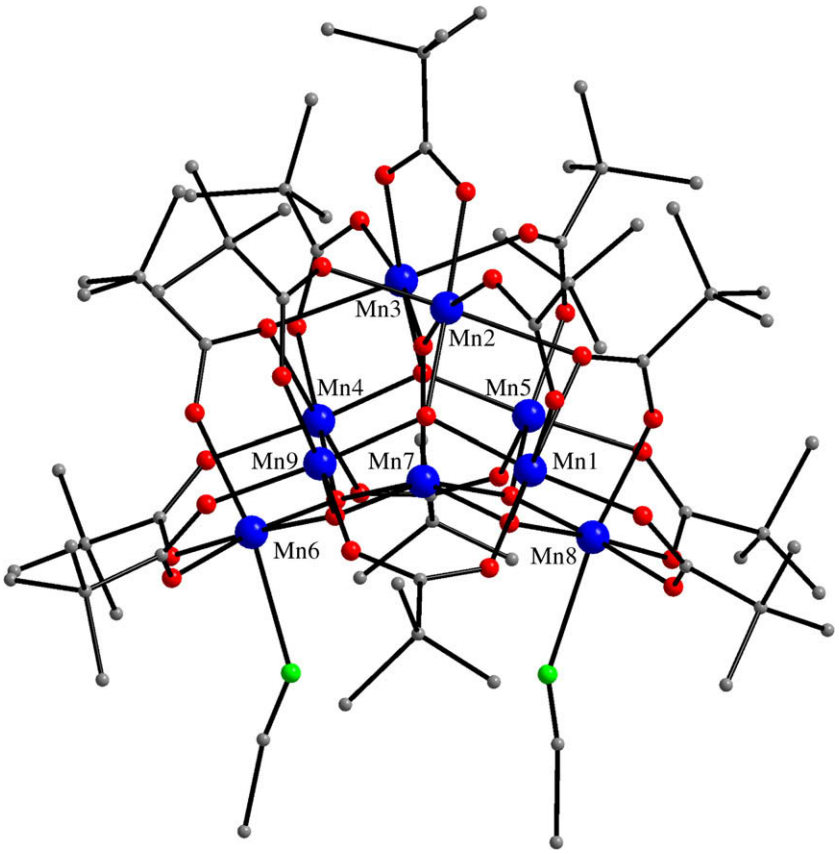


Fig. 1. Partially labeled PovRay representation of the structure of **3**, with the hydrogen atoms omitted for clarity. Color code: Mn^{III} blue, O red, N green, C grey. (For interpretation of the references to color in this figure legend, the reader is referred to the web version of this article.)

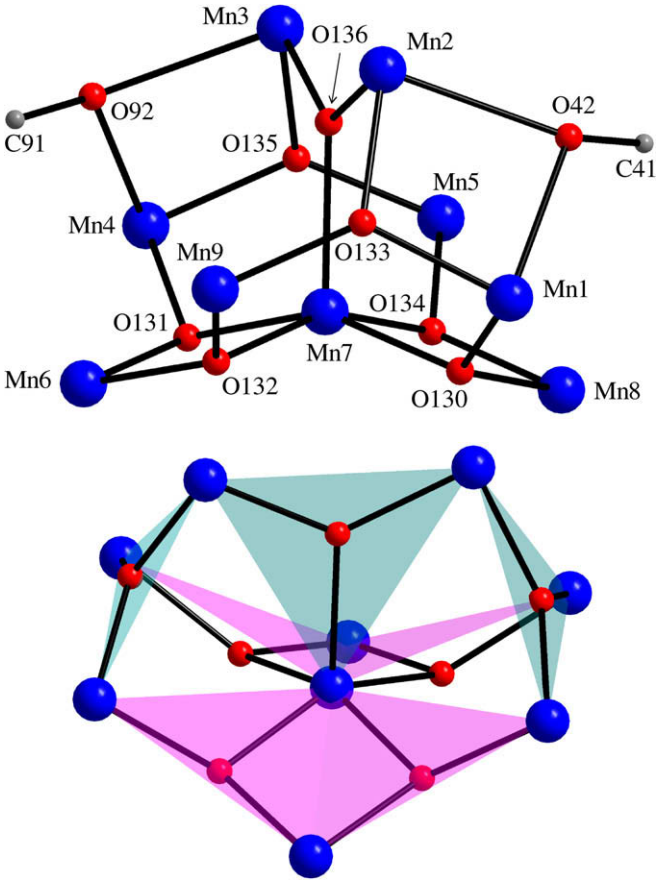


Fig. 2. (Top) PovRay representation of the labeled core of **3**; (bottom) The Mn_9 topology, emphasizing the butterfly $[Mn_4(\mu_3\text{-}O)_2]^{8+}$ and triangular $[Mn_3(\mu_3\text{-}O)]^{7+}$ subcores. Color code: Mn^{III} blue, O red, C grey.

place of H_2O/$MeCO_2H$. The identity of **2** was established by means of IR spectroscopic comparison with authentic material of **1**, and elemental analysis (C, H, N). Yield: 70 % (based on Mn). The dried sample analyzed as solvent-free. *Anal.* Calc. for $C_{11}H_{21}O_5Mn$: C, 45.84; H, 7.34; N, 0.00. Found: C, 45.84; H, 7.42; N, 0.01%. Selected IR data (KBr pellet, cm^{-1}): 2974s, 1705w, 1576s, 1549s, 1482s, 1406s, 1358s, 1226s, 1003m, 939w, 896w, 785w, 630s, 553s, 459m.

2.2.2. $[Mn_9O_7(O_2CBu^t)_{13}(MeCN)_2]$ · toluene (**3** · toluene)

Freshly prepared solid complex **2** (0.20 g, 0.70 mmol) was added to a solution composed of MeCN (25 mL) and toluene (15 mL). The resulting reddish-brown slurry was stirred overnight, during which time most of the solid dissolved, and the color of the solution changed to dark brown. A small quantity of undissolved material was removed by filtration, and the filtrate was allowed to stand undisturbed at room temperature. After 24 h, X-ray quality dark brown crystals of **3** · toluene were collected by filtration, washed with Et_2O (2×5 ml), and dried under vacuum. Yield: 60% (based on Mn). Material that had been dried under vacuum for 10–12 h and then stored in air was found to have lost the bound MeCN groups, which were replaced with H_2O molecules; thus, vacuum-dried solid analyzed as $[Mn_9O_7(O_2CBu^t)_{13}(H_2O)_2]$. *Anal.* Calc. for $C_{52}H_{121}O_{35}Mn_9$: C, 39.89; H, 6.23; N, 0.00. Found: C, 40.28; H, 6.08; N, 0.02%. IR (KBr pellet, cm^{-1}): 3853w, 3748w, 3433mb, 2969s, 2921s, 2355m, 1637m, 1558s, 1487s, 1421s, 1370s, 1229s, 1164m, 1114m, 1067mb, 903w, 788w, 692m, 625m.

Table 2
Selected interatomic distances (Å) and bond angles (°) for complex **3** · toluene.

Mn1–O133	1.874(3)
Mn1–O130	1.881(3)
Mn1–O12	1.948(3)
Mn1–O31	1.962(3)
Mn1–O2	2.124(3)
Mn1–O42	2.259(3)
Mn2–O136	1.854(3)
Mn2–O133	1.881(3)
Mn2–O62	1.934(3)
Mn2–O32	1.993(3)
Mn2–O52	2.234(3)
Mn2–O42	2.309(3)
Mn3–O136	1.851(3)
Mn3–O135	1.885(3)
Mn3–O61	1.936(3)
Mn3–O81	1.993(3)
Mn3–O71	2.225(3)
Mn3–O92	2.276(3)
Mn4–O135	1.872(3)
Mn4–O131	1.888(3)
Mn4–O112	1.939(3)
Mn4–O82	1.963(3)
Mn4–O102	2.106(4)
Mn4–O92	2.254(3)
Mn5–O135	1.855(3)
Mn5–O134	1.880(3)
Mn5–O22	1.922(3)
Mn5–O72	1.930(3)
Mn5–O101	2.052(4)
Mn6–O131	1.861(3)
Mn6–O132	1.876(3)
Mn6–O122	1.947(3)
Mn6–O111	1.958(3)
Mn6–O91	2.123(4)
Mn6–N2	2.354(5)
Mn7–O134	1.899(3)
Mn7–O132	1.907(3)
Mn7–O130	1.928(3)
Mn7–O131	1.934(3)
Mn7–O136	2.173(3)
Mn8–O130	1.865(3)
Mn8–O134	1.870(3)
Mn8–O21	1.946(3)
Mn8–O11	1.954(3)
Mn8–O41	2.132(3)
Mn8–N1	2.325(4)
Mn9–O133	1.859(3)
Mn9–O132	1.874(3)
Mn9–O51	1.919(3)
Mn9–O121	1.935(3)
Mn9–O1	2.055(3)
O2–Mn1–O42	170.77(12)
O52–Mn2–O42	166.66(12)
O71–Mn3–O92	165.89(12)
O102–Mn4–O92	170.51(13)
O91–Mn6–N2	170.13(15)
O41–Mn8–N1	171.23(16)
Mn8–O130–Mn1	121.99(15)
Mn8–O130–Mn7	97.80(13)
Mn1–O130–Mn7	120.38(15)
Mn6–O131–Mn4	122.57(15)
Mn6–O131–Mn7	97.84(13)
Mn4–O131–Mn7	119.76(14)
Mn9–O132–Mn6	125.54(16)
Mn9–O132–Mn7	120.41(15)
Mn6–O132–Mn7	98.28(13)
Mn9–O133–Mn1	128.45(16)
Mn9–O133–Mn2	123.65(16)
Mn1–O133–Mn2	106.73(13)
Mn8–O134–Mn5	124.94(15)
Mn8–O134–Mn7	98.68(13)
Mn5–O134–Mn7	120.58(15)
Mn5–O135–Mn4	128.81(17)
Mn5–O135–Mn3	123.83(15)
Mn4–O135–Mn3	106.38(14)
Mn3–O136–Mn2	126.60(16)
Mn3–O136–Mn7	116.47(14)

Table 2 (*continued*)

Mn2–O136–Mn7	116.91(14)
Mn4–O92–Mn3	83.21(10)
Mn1–O42–Mn2	82.55(10)
Mn1···Mn2	3.0133(11)
Mn3···Mn4	3.0079(11)
Mn6···Mn7	2.8614(9)
Mn7···Mn8	2.8591(10)

Table 3
Bond valence sum (BVS) calculations for the Mn atoms in **3**.[a]

Atom	MnII	Mn^{III}	Mn^{IV}
Mn(1)	3.15	3.03	3.18
Mn(2)	3.20	2.93	3.07
Mn(3)	3.22	2.95	3.10
Mn(4)	3.34	3.06	3.21
Mn(5)	3.27	2.99	3.14
Mn(6)	3.35	3.08	3.16
Mn(7)	2.99	2.73	2.87
Mn(8)	3.38	3.10	3.23
Mn(9)	3.27	2.99	3.14

[a] The underlined value is the one closest to the charge for which it was calculated. The oxidation state of a particular atom can be taken as the nearest whole number to the underlined value.

2.2.3. $[Mn_{10-x}Fe_x(OMe)_{20}(O_2CMe)_{10}]$ (**4**)

To a slurry of freshly prepared complex **1** (0.50 g, 2.00 mmol) in MeCN (25 mL)/MeOH (1 mL) was added solid $Fe(NO_3)_3 \cdot 9H_2O$ (0.10 g, 0.25 mmol). The resulting reddish-brown slurry was stirred overnight, during which time most of the solid dissolved and the color of the solution changed to dark brown. A small quantity of undissolved material was removed by filtration, and the filtrate was allowed to stand undisturbed at room temperature. After several days, only a handful of dark brown prismatic crystals of **4** had appeared, and these were devoted solely to single-crystal X-ray diffraction studies.

2.3. Single-crystal X-ray crystallography

Data for complexes **3** · toluene and **4** were collected at 173 K on a Siemens SMART PLATFORM equipped with a CCD area detector and a graphite monochromator utilizing MoKα radiation (λ = 0.71073 Å). Cell parameters were refined using up to 8192 reflections. A full sphere of data (1850 frames) was collected using the ω-scan method (0.3° frame width). The first 50 frames were remeasured at the end of data collection to monitor instrument and crystal stability (maximum correction on I was <1%). Absorption corrections by integration were applied based on measured indexed crystal faces. The structures were solved by direct methods in SHELXTL6 [10], and refined on F^2 using full-matrix least squares. The non-H atoms were treated anisotropically, whereas the H atoms were placed in ideal positions and refined as riding on their C atoms. Unit cell parameters and structure solution and refinement data are listed in Table 1.

For **3** · toluene, the asymmetric unit contains one Mn_9 cluster and one toluene molecule of crystallization. There are five disordered Bu^t groups, and each was refined in two parts with their site occupation factors dependently refined. A total of 1071 parameters were refined in the final cycle of refinement using 9621 reflections with $I > 2\sigma(I)$ to yield R_1 and wR_2 of 4.84 and 9.64%, respectively.

For **4**, the asymmetric unit consists of one and a half M_{10} ring located on an inversion center. All metal positions are disordered between Fe and Mn. Each position of the metal on the ring was refined with one Fe and one Mn with their site occupation factors dependently refined in the early refinement stages. All of the site occupation free variables refined to 50%, and thus they were all fixed at 50%. Each position of Fe/Mn metal atoms was constrained to maintain equivalent coordinates and displacement parameters. There are also several disordered methoxy groups where the methyl group was refined in two parts. Several electron density peaks of 2.5 electrons or less were observed around the rings and did not make chemical sense. Most likely, those are a result of ring disorder in the plane of the wheel. A total of 1266 parameters were refined in the final cycle of refinement using 13 806 reflections with $I > 2\sigma(I)$ to yield R_1 and wR_2 of 5.89 and 14.67%, respectively.

3. Results and discussion

3.1. Syntheses

Slow dissolution with stirring of $[Mn(OMe)(O_2CBu^t)_2]_n$ (**2**) in MeCN/toluene gave a dark brown solution from which was obtained $[Mn_9O_7(O_2CBu^t)_{13}(MeCN)_2]$ (**3**) as **3** · toluene in good yields (~60%). The reaction is clearly a hydrolysis involving adventitious water, causing an undoubtedly complicated structural rearrange-

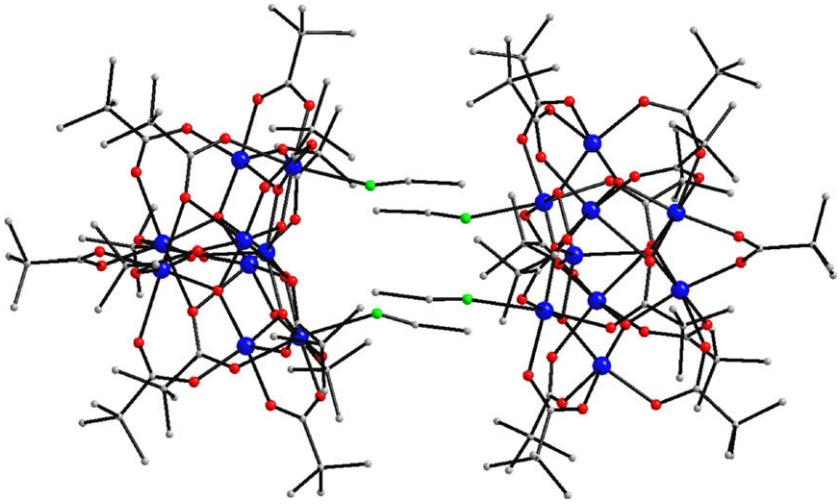


Fig. 3. PovRay representation of a pair of Mn_9 cages. Color code: Mn^{III} blue, O red, N green, C grey.

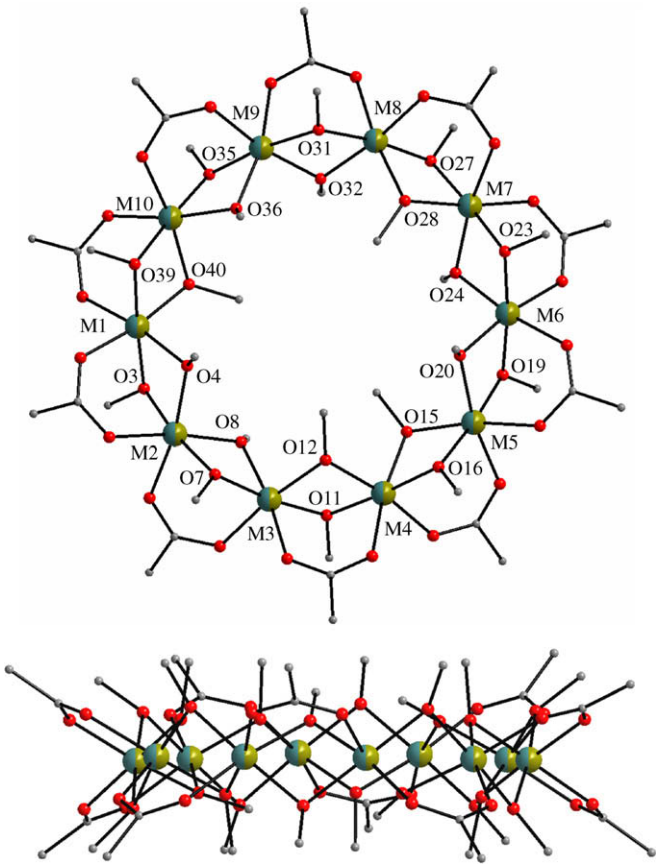


Fig. 4. (Top) Labeled PovRay representation of the structure of **4**, with the hydrogen atoms omitted for clarity; (bottom) side-view emphasizing the wheel planarity and O/M/O layered structure. Color code: M (Mn/Fe) blue/green, O red, C grey.

ment but no redox changes since the product contains only Mn^{III} atoms like the starting material **2**. The MeCN is essential for a high-yield transformation; reactions in neat toluene gave only a very low yield (~10%) of a product whose IR spectrum is almost identical with that of **3** and is assumed to be the form with two bound water molecules instead of MeCN. Changes to the exact MeCN:toluene ratio had no effect on the identity of the product, only small changes to the yield. With the identity of **3** established, we also tried similar reactions with $[Mn(OH)(O_2CMe)_2]_n$ (**1**) and, on the basis of IR spectroscopy and elemental analysis data, concluded that the product was the acetate version of **3** and thus did not study this product further. The reaction of **2** in MeCN/MeOH under various conditions yielded the known Mn_{84} complex [11], and/or non-crystalline materials difficult to characterize.

We have in the past used complex **1** as the starting material for the preparation of the heterometallic compound $[CeMn_8O_8(O_2CMe)_{12}(H_2O)_4]$ [12], and so we now also investigated the use of **1** and **2** in reactions with another 3d metal, namely iron. Thus, the reaction of **1** with $Fe(NO_3)_3 \cdot 9H_2O$ in a 8:1 ratio in MeCN/MeOH was explored. It was difficult to isolate pure products from this reaction system, and finally obtained some dark brown crystals in extremely low yields of what proved to be the decanuclear mixed-metal complex $[Mn_{10-x}Fe_x(OMe)_{20}(O_2CMe)_{10}]$ ($x < 10$) (**4**). The color of the crystalline material **4** clearly precludes assignment of all the metal ions as Fe^{III} ($x \neq 10$) since $[Fe_{10}(OMe)_{20}(O_2CMe)_{10}]$ is a known compound that has a light yellow color. On the other hand, it was also clear that this was not the completely Mn^{III} version $[Mn_{10}(OMe)_{20}(O_2CMe)_{10}]$ ($x \neq 0$). The product thus had to be mixed-metal, but the relative metal content was not possible to be accurately obtained from the refinement of the crystal structure

Table 4
Selected interatomic distances (Å) and bond angles (°) for **4.**

M1–O40	1.969(3)
M1–O3	1.974(2)
M1–O39	1.985(2)
M1–O4	2.007(2)
M1–O1	2.033(3)
M1–O38	2.063(2)
M2–O7	1.984(2)
M2–O3	1.986(2)
M2–O4	1.999(2)
M2–O8	2.001(3)
M2–O2	2.040(3)
M2–O5	2.043(2)
M3–O8	1.977(2)
M3–O7	1.984(3)
M3–O12	1.989(2)
M3–O11	1.991(3)
M3–O9	2.032(2)
M3–O6	2.064(2)
M4–O12	1.968(3)
M4–O11	1.979(2)
M4–O16	1.985(2)
M4–O15	2.002(3)
M4–O13	2.038(3)
M4–O10	2.071(3)
M5–O15	1.963(2)
M5–O19	1.988(2)
M5–O16	1.993(3)
M5–O20	2.002(2)
M5–O17	2.024(2)
M5–O14	2.047(3)
M6–O19	1.975(2)
M6–O23	1.978(2)
M6–O20	1.993(3)
M6–O24	2.002(2)
M6–O21	2.040(3)
M6–O18	2.066(2)
M7–O28	1.966(3)
M7–O24	1.991(2)
M7–O23	1.991(2)
M7–O27	1.996(2)
M7–O22	2.040(3)
M7–O25	2.045(3)
M8–O32	1.971(2)
M8–O31	1.976(3)
M8–O28	1.997(2)
M8–O27	2.000(3)
M8–O26	2.023(2)
M8–O29	2.081(2)
M9–O31	1.976(2)
M9–O35	1.980(2)
M9–O36	1.984(3)
M9–O32	2.002(3)
M9–O30	2.038(3)
M9–O33	2.039(3)
M10–O40	1.968(2)
M10–O35	1.976(3)
M10–O39	1.989(3)
M10–O36	1.999(2)
M10–O34	2.039(3)
M10–O37	2.043(2)
M1–O3–M2	99.70(10)
M2–O4–M1	98.15(10)
M3–O7–M2	99.68(11)
M3–O8–M2	99.37(11)
M4–O11–M3	99.24(11)
M4–O12–M3	99.65(11)
M5–O15–M4	99.75(10)
M4–O16–M5	99.30(10)
M6–O19–M5	99.79(11)
M6–O20–M5	98.69(11)
M6–O23–M7	99.43(10)
M7–O24–M6	98.63(10)
M7–O27–M8	98.48(11)
M7–O28–M8	99.58(12)
M8–O31–M9	99.83(11)
M8–O32–M9	99.12(11)
M10–O35–M9	100.07(10)

Table 4 (*continued*)

M9–O36–M10	99.17(10)
M1–O39–M10	98.36(11)
M10–O40–M1	99.63(11)

(vide infra). Reasons such as the similar Mn and Fe electronic densities and the complicated overall structure of **4** with a relatively large molecular weight preclude safe conclusions about the exact identity of the metal ions present. Unfortunately, not enough crystals were obtained to allow a metal analysis, and we were unable to increase the yield by varying the solvent ratio. With the identity of **4** established, we also tried to obtain the homometallic $[Mn_{10}(OMe)_{20}(O_2CMe)_{10}]$ wheel, but were unsuccessful. Reactions of **1** in pure MeOH, for example, gave only uncharacterized Mn^{II} products.

3.2. Description of structures

The molecular structure and the core of complex **3** are depicted in Figs. 1 and 2, respectively. Selected interatomic distances and angles are listed in Table 2. Complex **3** contains a $[Mn_9O_7]^{13+}$ core that can be described as two fused $[Mn_4O_2]$ butterflies (Mn1, Mn5, Mn7, Mn8, and Mn4, Mn6, Mn7, Mn9) sharing one Mn atom (Mn7). The remaining two Mn ions (Mn2 and Mn3) are connected to the fused butterfly unit through an O^{2-} ion (O136) forming a $[Mn_3O]$ triangle with Mn7. The $[Mn_3O_4]$ base of this unit (Mn6, Mn7 and Mn8) is non-planar, the Mn6–Mn7–Mn8 angle being ~145°. The metal ions are all Mn^{III}, as deduced by consideration of structural parameters and by bond valence sum (BVS) calculations (Table 3) [13]. Atoms Mn5, Mn7, and Mn9 are five-coordinate with distorted square pyramidal geometry (τ = 0.28, 0.09, and 0.35, where τ is 0 and 1 for ideal square pyramidal and trigonal bipyramidal geometries, respectively [14]), and their axial bonds [2.052(4)–2.173(3)] are significantly longer than the basal ones [1.855(3)–1.935(3)]. The remaining Mn atoms are all six-coordinate with distorted octahedral geometries, and display Jahn–Teller axial elongations. Eleven $Bu^tCO_2^-$ groups bind in the common μ-bridging mode and two in the rarer μ_3-mode, with one O atom bridging two metals. The two MeCN molecules are terminally bound to Mn6 and Mn8.

Complex **3** · toluene crystallizes in pairs, as shown in Fig. 3, in a head-to-head arrangement with the MeCN ligands interlocked and the two molecules rotated by ~90° with respect to each other to give an S_4 symmetry dimer. Compounds with a similar core to that in **3** have been previously reported [15], some containing Na^+ or K^+ ions, namely $[Mn_9Na_2O_7(O_2CPh)_{15}(MeCN)_2]$ [15c] and $[Mn_9K_2O_7(O_2CBu^t)_{15}(HO_2CBu^t)_2]$ clusters [15d], respectively; **3** is the third structurally characterized Mn_9 complex with the general formula $[Mn_9O_7(O_2CR)_{13}(L)_2]$ (R = Ph, L = terminal ligands, such as pyridine or 2,4-dimethyl-6-hydroxypyrimidine) [15a,8a].

The structure of complex **4** is shown in Fig. 4. Selected interatomic distances and angles are listed in Table 4. The structure is essentially identical to previously characterized Fe_{10} 'ferric wheels' [16] except that it is clearly a mixed-metal species. Several refinement cycles of the Mn/Fe content led to the conclusion that the compound contains both metals statically disordered about all 10 sites; thus, a general Mn_{10-x}–Fe_x (x < 10) metal content description was clearly the best fit to the observed electron density. The complex has virtual D_{5d} symmetry and comprises a near-planar (±0.003–0.040 Å) wheel of 10 octahedral metal atoms with each M_2 pair bridged by one $MeCO_2^-$ and two MeO^- groups, giving layers of O atoms above and below the M_{10} wheel (Fig. 4, bottom). The wheel has a central hole of ~3 Å diameter unoccupied by any guest molecule. The M_{10} molecules pack in the crystal on top of each other forming supramolecular nanotubular stacks parallel to the a axis, but with each molecule slightly tilted relative to this axis.

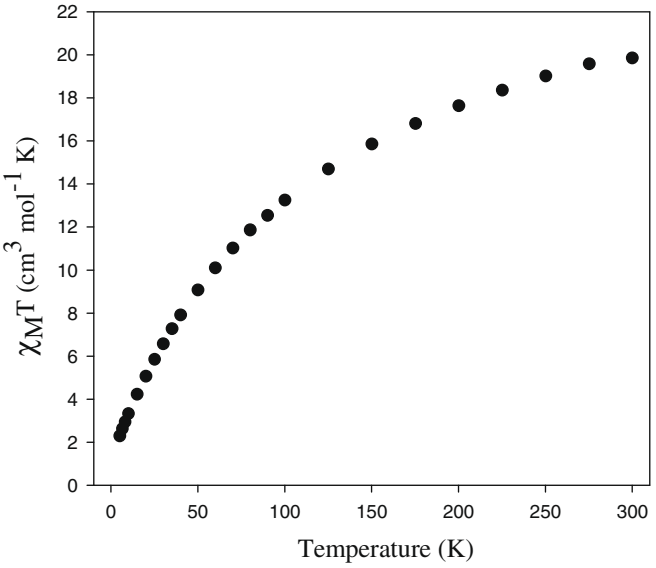


Fig. 5. $\chi_M T$ vs. T plot for complex **3**.

3.3. Magnetochemistry

Variable-temperature dc magnetic susceptibility data were collected on a powdered polycrystalline sample of **3**, restrained in eicosane, in a 1 kG (0.1 T) field and in the 5.0–300 K range. $\chi_M T$ for **3** steadily decreases from 19.86 cm^3 $Kmol^{-1}$ at 300 K to 2.29 cm^3 $Kmol^{-1}$ at 5.00 K (Fig. 5). The rate of decrease increases below ~50 K. The room temperature $\chi_M T$ value is much less than the spin-only value (g = 2.0) of 27 cm^3 $Kmol^{-1}$ for nine non-interacting Mn^{III} ions, indicating predominantly strong antiferromagnetic interactions within the molecule and a low, but possibly non-zero, ground state S value. To determine the ground state of the complex, magnetization data were collected in the magnetic field and temperature ranges 1–60 kG and 1.8–10.0 K. However, we could not get an acceptable fit using data collected over the whole field range, which is a common problem caused by low-lying excited states, especially if some have an S value greater than that of the ground state. A common solution is to only use data col-

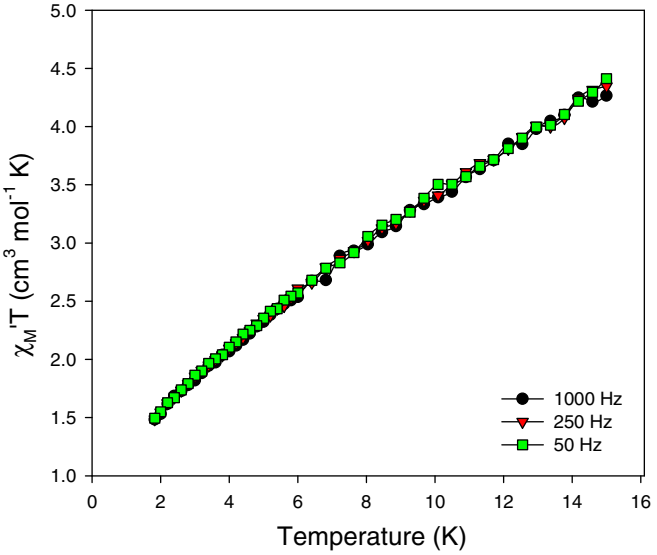


Fig. 6. Plot of the in-phase (χ'_M) ac magnetic susceptibility, as $\chi'_M T$ vs. T, in a 3.5 Oe field oscillating at the indicated frequencies for complex **3**.

lected with low fields ($\leqslant$1.0 T) [5a,5b]. However, it was still not possible to obtain a satisfactory fit assuming that only the ground state is populated in this temperature range. This suggests that the complex possesses particularly low-lying excited states that are populated, even at these relatively low temperatures.

Thus, we turned to ac susceptibility measurements in a 3.5 G ac field oscillating at frequencies in the 50–1000 Hz range. The in-phase $\chi'_M T$ vs. T data are shown in Fig. 6 and reveal several pertinent features: (i) $\chi'_M T$ for **3** decreases linearly with decreasing temperature in the whole temperature range, indicating depopulation of a high-density of low-lying excited states with spin S greater than that of the ground state, in agreement with the conclusion from the dc studies; (ii) extrapolation of the $\chi'_M T$ data to 0 K gives a value of $\sim$1 $cm^3\,Kmol^{-1}$ for **3**, indicative of an $S = 1$ ground state with $g \sim 2$. It does appear that the complex does indeed have a non-zero ground state spin, although it could be possible that there are extremely close $S = 0$, 1 and even 2 states. In any event, complex **3** clearly has a very small ground state spin. As expected, there were no out-of-phase ac signals down to 1.8 K.

4. Conclusions

The use of the carboxylate-bridged Mn^{III} polymeric compound of general formula $[Mn(OR)(O_2CR')_2]_n$ (R = H, Me; R′ = Me, Bu^t) has provided access to two new homo- and heterometallic Mn^{III}-based clusters. The homometallic Mn_9 complex **3** has a rare metal core topology, comprising adjacent $[Mn_4O_2]$ butterfly and $[Mn_3O]$ triangular subunits. The heterometallic M_{10} (M = Mn/Fe) wheel complex **4** is analogous to the known family of Fe_{10} ferric wheels, and clearly contains both Mn and Fe with a varying Mn:Fe ratio. Unfortunately, we have yet to develop a high-yield route to such mixed Mn/Fe wheels to allow us to study this point further, as well as to characterize the magnetic properties, and attempts along this direction are continuing.

Acknowledgments

The authors thank the US National Science Foundation (Grant CHE-0414555).

Appendix A. Supplementary data

CCDC 704819 and 704818 contain the supplementary crystallographic data for (**3**·toluene) and (**4**). These data can be obtained free of charge via http://www.ccdc.cam.ac.uk/conts/retrieving.html, or from the Cambridge Crystallographic Data Centre, 12 Union Road, Cambridge CB2 1EZ, UK; fax: (+44) 1223 336 033; or e-mail: deposit@ccdc.cam.ac.uk. Supplementary data associated with this article can be found, in the online version, at doi:10.1016/j.poly.2008.11.026.

References

[1] Sci. Am. (2001) 285, Special issue on Nanotechnology.
[2] (a) For reviews, see: G. Christou, D. Gatteschi, D.N. Hendrickson, MRS Bull. 25 (2000) 66;
(b) G. Christou, Polyhedron 24 (2005) 2065.
[3] (a) For some representative references, see: W. Wernsdorfer, N. Aliaga-Alcade, D.N. Hendrickson, G. Christou, Nature 416 (2002) 406;
(b) S. Hill, R.S. Edwards, N. Aliaga-Alcade, G. Christou, Science 302 (2003) 1015;
(c) R. Sessoli, D. Gatteschi, A. Caneschi, M.A. Novak, Nature 365 (1993) 141;
(d) Th.C. Stamatatos, K.A. Abboud, W. Wernsdorfer, G. Christou, Angew. Chem. Int. Ed. 45 (2006) 4134;
(e) Th.C. Stamatatos, D. Foguet-Albiol, C.C. Stoumpos, C.P. Raptopoulou, A. Terzis, W. Wernsdorfer, S.P. Perlepes, G. Christou, J. Am. Chem. Soc. 127 (2005) 15380;
(f) C.J. Milios, A. Vinslava, W. Wernsdorfer, S. Moggach, S. Parsons, S.P. Perlepes, G. Christou, E.K. Brechin, J. Am. Chem. Soc. 129 (2007) 2754;
(g) P.L. Feng, C. Koo, J.J. Henderson, M. Nakano, S. Hill, E. del Barco, D.N. Hendrickson, Inorg. Chem. 47 (2008) 8610;
(h) V. Mereacre, A.M. Ako, R. Clerac, W. Wernsdorfer, I.J. Hewitt, C.E. Anson, A.K. Powell, Chem. Eur. J. 14 (2008) 3577.
[4] (a) For recent reviews, see: D. Gatteschi, R. Sessoli, Angew. Chem. Int. Ed. 42 (2003) 268;
(b) G. Aromi, E.K. Brechin, Struct. Bond. 122 (2006) 1.
[5] (a) R. Bagai, K.A. Abboud, G. Christou, Inorg. Chem. 47 (2008) 621;
(b) C.J. Milios, A. Vinslava, P.A. Wood, S. Parsons, W. Wernsdorfer, G. Christou, S.P. Perlepes, E.K. Brechin, J. Am. Chem. Soc. 129 (2007) 8;
(c) M. Murugesu, W. Wernsdorfer, K.A. Abboud, G. Christou, Polyhedron 24 (2005) 2894;
(d) C. Lampropoulos, M. Murugesu, K.A. Abboud, G. Christou, Polyhedron 26 (2007) 2129.
[6] (a) J.B. Vincent, H.R. Chang, K. Folting, J.C. Huffman, G. Christou, D.N. Hendrickson, J. Am. Chem. Soc. 109 (1987) 5703;
(b) T. Lis, Acta Cryst. B36 (1980) 2042.
[7] (a) A.J. Tasiopoulos, W. Wernsdorfer, K.A. Abboud, G. Christou, Angew. Chem. Int. Ed. 43 (2004) 6338;
(b) A.J. Tasiopoulos, W. Wernsdorfer, K.A. Abboud, G. Christou, Inorg. Chem. 44 (2005) 6324;
(c) P. King, W. Wernsdorfer, K.A. Abboud, G. Christou, Inorg. Chem. 44 (2005) 8659.
[8] (a) N.E. Chakov, L.N. Zakharov, A.L. Rheingold, K.A. Abboud, G. Christou, Inorg. Chem. 44 (2005) 4555;
(b) T.C. Stamatatos, B.S. Luisi, B. Moulton, G. Christou, Inorg. Chem. 47 (2008) 1134;
(c) M. Manoli, A. Prescimone, R. Bagai, A. Mishra, M. Murugesu, S. Parsons, W. Wernsdorfer, G. Christou, E.K. Brechin, Inorg. Chem. 46 (2007) 6968;
(d) T.C. Stamatatos, D. Foguet-Albiol, S.-C. Lee, C.C. Stoumpos, C.P. Raptopoulou, A. Terzis, W. Wernsdorfer, S.O. Hill, S.P. Perlepes, G. Christou, J. Am. Chem. Soc. 129 (2007) 9484.
[9] (a) D.J. Price, S.R. Batten, B. Moubaraki, K.S. Murray, J. Chem. Soc. Chem. Commun. (2002) 762;
(b) D.J. Price, S.R. Batten, B. Moubaraki, K.S. Murray, Polyhedron 22 (2003) 2161;
(c) D.J. Price, S.R. Batten, B. Moubaraki, K.S. Murray, Polyhedron 26 (2007) 305;
(d) A.J. Tasiopoulos, N.C. Harden, K.A. Abboud, G. Christou, Polyhedron 22 (2003) 133.
[10] SHELXTL6; Bruker-AXS, Madison, WI, (2000).
[11] A.J. Tasiopoulos, A. Vinslava, W. Wernsdorfer, K.A. Abboud, G. Christou, Angew. Chem. Int. Ed. 43 (2004) 2117.
[12] (a) A.J. Tasiopoulos, W. Wernsdorfer, B. Moulton, M.J. Zaworotko, G. Christou, J. Am. Chem. Soc. 125 (2003) 15274;
(b) A. Mishra, A.J. Tasiopoulos, W. Wernsdorfer, E.E. Moushi, B. Moulton, M.J. Zaworotko, K.A. Abboud, G. Christou, Inorg. Chem. 47 (2008) 4832.
[13] W. Liu, H.H. Thorp, Inorg. Chem. 32 (1993) 4102.
[14] A.W. Addison, T.N. Rao, J. Reedijk, J. Rijn, G.C. Verschoor, J. Chem. Soc. Dalton Trans. (1984) 1349.
[15] (a) D.W. Low, D.M. Eichhorn, A. Draganescu, W.H. Armstrong, Inorg. Chem. 30 (1991) 877;
(b) E.K. Brechin, G. Christou, M. Soler, M. Helliwell, S.J. Teat, Dalton Trans. (2003) 513;
(c) H.L. Tsai, S. Wang, K. Folting, W.E. Streib, D.N. Hendrickson, G. Christou, J. Am. Chem. Soc. 117 (1995) 2503;
(d) M. Murrie, S. Parsons, R.E.P. Winpenny, Dalton Trans. (1998) 1423.
[16] (a) K.L. Taft, S.J. Lippard, J. Am. Chem. Soc. 112 (1990) 9629;
(b) K.L. Taft, C.D. Delfs, G.C. Papaefthymiou, S. Foner, D. Gatteschi, S.J. Lippard, J. Am. Chem. Soc. 116 (1994) 823;
(c) T.C. Stamatatos, A.G. Christou, C.M. Jones, B.J. O'Callaghan, K.A. Abboud, T.A. O'Brien, G. Christou, J. Am. Chem. Soc. 129 (2007) 9840;
(d) T.C. Stamatatos, A.G. Christou, S. Mukherjee, K.M. Poole, C. Lampropoulos, K.A. Abboud, T.A. O'Brien, G. Christou, Inorg. Chem. 47 (2008) 9021.

2. Computational details

The theoretical study of the magnetism of the $[(2,3\text{-dmpyH})_2CuBr_4]$ crystal was performed using the First-Principles *Bottom–Up* methodology [3], which consists in the sequential application of the following four steps:

(1) Analysis of the crystal packing to locate all unique radical–radical pairs:

This analysis was done looking at the distances between spin-carrying units. The only spin-carrying units in the $[(2,3\text{-dmpyH})_2CuBr_4]$ crystal are the $CuBr_4^{2-}$ anions. All pairs of radicals having a Cu···Cu distance shorter than 10.0 Å were considered as possible candidates. Among them, only those different by symmetry were selected as the candidate pairs for the next steps.

(2) Computation of the exchange magnetic interaction (J_{AB}) for each unique radical pairs:

The J_{AB} values are obtained from the energy difference between the appropriate states computed by First-Principles methods (either ab initio [4] or DFT [5] methods). The spin-carrying units, the $CuBr_4^{2-}$ anions, are doublet radicals (the spin density is not only located on the Cu(II) atoms, which have an unpaired electron, but also on the Br atoms [6]). Therefore, only two states are possible in any AB radical pairs: one singlet and one triplet state. The value of J_{AB} for each pair is obtained as $J_{AB} = (E^S_{BS} - E_T)$, where E^T is the energy of the triplet state and E^S_{BS} the energy of the singlet state computed using the broken-symmetry approach [7,8] for a proper description of the open-shell singlet state. The values of E^S_{BS} and E^T are calculated using a neutral model which consists of two $CuBr_4^{2-}$ anions and four $(2,3\text{-dmpyH})^+$ counterions, hereafter referred as the anion$_2$cation$_4$ model. The nearest four $(2,3\text{-dmpyH})^+$ counterions to each radical pair are thus included to model the most relevant effects that the electrostatic field induces on the radical pair wavefunctions (previous studies [3] have shown that the J_{AB} computed using this model is nearly identical to that obtained using much larger subsets of point charges). The geometry of these anion$_2$cation$_4$ models is that found in the crystal for the full molecules, without geometry optimization. The previous J_{AB} expression derives from the original broken-symmetry equations when the SOMO orbitals of the two radicals show a very small overlap, which is the usual situation in through-space magnetic interactions, such as those found in the $[(2,3\text{-dmpyH})_2CuBr_4]$ crystal. Our experience indicates that in through-space magnetic interactions this expression gives results closer to the experimental values than alternative ones [9,10] where projection is used. The following form of Heisenberg Hamiltonian was used:

$$\hat{H} = -2\sum_{A,B} J_{AB}\hat{S}_A \cdot \hat{S}_B \qquad (1)$$

The E^T and E^S_{BS} energies were computed using the B3LYP functional [11,12], as it has been shown to provide J_{AB} values close to the experimental results [3,13–15]. The Ahlrich-pVDZ [16] basis set for Cu, and a 6-31+G(d) [17] basis set for the remaining atoms were used. All calculations were done using the GAUSSIAN 03 code [18].

(3) Determination of the magnetic topology of the crystal and its minimal magnetic model space:

Once the J_{AB} values are known for all unique radical pairs, one can define the magnetic topology as the network of non-negligible magnetic interactions present among the radicals of the crystal. Then, one has to look for an appropriate minimal magnetic model space, a finite set of radical centers where all J_{AB} interactions are present in a ratio as close as possible to that found in the infinite

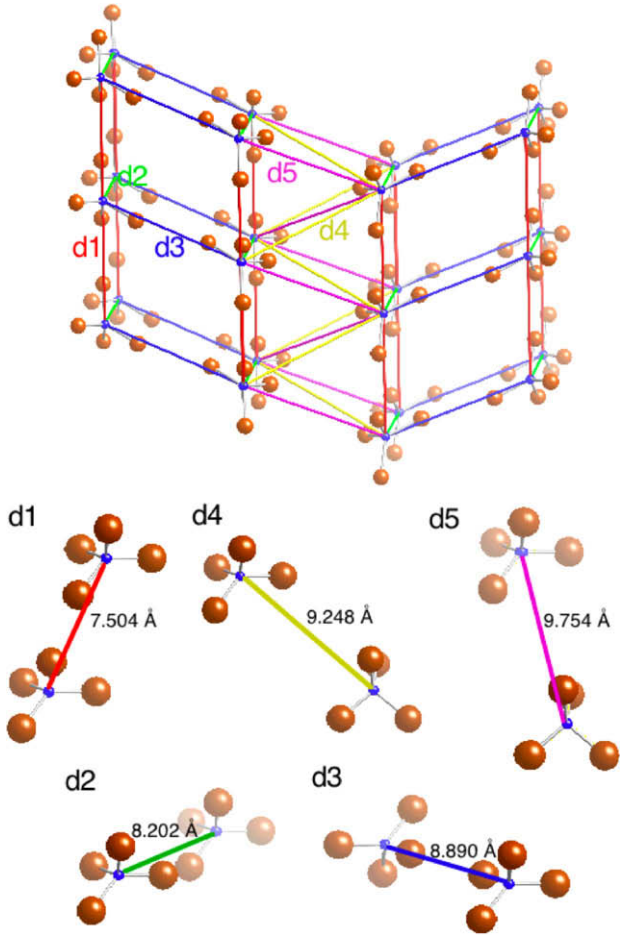


Fig. 1. Geometry of all unique $CuBr_4^{2-}$···$CuBr_4^{2-}$ radical pairs found in the 88 K crystal (only the anions are shown for an easier visualization of the crystal packing). The Cu···Cu distance (in Å) is also given for each pair. The unique pairs found in the 273 K structure are the same, although the Cu···Cu distances vary slightly (see Table 4).

Table 1
Crystal data and structure refinement for the 273 K structure of the $[(2,3dmpyH)_2CuBr_4]$ crystal.

Empirical formula	$C_{14}H_6D_{14}N_2CuBr_4$
Formula weight	613.50
Temperature (K)	273
Crystal system	monoclinic
Space group	$P2(1)/n$
Unit cell dimensions	
a (Å)	7.6402(6)
b (Å)	31.938(3)
c (Å)	8.3246(6)
β (°)	98.688(4)
V (Å^3)	2008.0(3)
Z	4
D_{calc} (Mg/m^3)	2.050
Absorption coefficient (mm^{-1})	9.042
Crystal size (mm^3)	0.50 × 0.46 × 0.04
Theta range for data collection (°)	2.55–28.59
Index ranges	$-10 \geqslant h \geqslant 10$, $-42 \geqslant k \geqslant 43$, $-11 \geqslant l \geqslant 11$
Reflections collected	37687
Independent reflections (R_{int})	5152 (0.0591)
Completeness to theta = 28.70° (%)	99.2
Absorption correction	empirical
Maximum and minimum transmission	0.782 and 0.211
Refinement method	full-matrix least-squares on F^2
Data/restraints/parameters	5152/0/212
Goodness-of-fit on F^2	1.054
Final R indices [$I > 2\sigma(I)$]	$R_1 = 0.0649$, $wR_2 = 0.1793$
R indices (all data)	$R_1 = 0.0996$, $wR_2 = 0.2075$

Table 2
Values of the unit cell parameters for the 88 and 273 K structures of the $[(2,3\text{-dmpyH})_2CuBr_4]$ crystal. The increment between the 273 and 88 K values is also indicated under each parameter in parenthesis.

Structure	*a* (Å)	*b* (Å)	*c* (Å)	*β* (°)
88 K	7.5037(6)	31.613(3)	8.2016(7)	98.972(2)
120(2) K	7.5039(4)(0.0002)	31.581(2)(−0.032)	8.1993(4)(−0.0023)	98.962(2)(−0.010)
273 K	7.6402(6)(0.1365)	31.938(3)(0.325)	8.3246(6)(0.1230)	98.688(4)(−0.284)

Table 3
Change in the four intramolecular Cu–Br distances and some representative Br–Cu–Br angles found in the 88 and 273 K structures of the $[(2,3\text{-dmpyH})_2CuBr_4]$ crystal. The increment between the 273 and 88 K values is also indicated in the last column.

Structure	88 K (red)	273 K (blue)	Difference
d_{Cu-Br1} (Å)	2.412	2.422	0.010
d_{Cu-Br2} (Å)	2.384	2.404	0.020
d_{Cu-Br3} (Å)	2.384	2.389	0.005
d_{Cu-Br4} (Å)	2.352	2.358	0.006
$a_{Br1-Cu-Br2}$ (°)	98.610	99.177	0.567
$a_{Br1-Cu-Br3}$ (°)	126.236	126.002	−0.234
$a_{Br1-Cu-Br4}$ (°)	102.252	102.630	0.478
$a_{Br2-Cu-Br3}$ (°)	101.122	101.153	0.031
$a_{Br2-Cu-Br4}$ (°)	130.604	129.223	−1.381
$a_{Br3-Cu-Br4}$ (°)	101.540	101.900	0.360

Table 4
Value of J_{AB} computed for each unique radical–radical pairs found in the 88 K (first row) and 273 K (second row) crystal structures. The shortest Cu···Cu and Br···Br distances between the radicals of the pair are also given in the second and third columns (the increment in these values when going from the 88 to 273 K structure is given in the third row, in italics).

Pairs *di*	*d*(Cu···Cu) (Å)	$d(Br\cdots Br)_{min}$ (Å)	$J(di)$ (cm^{-1})anion$_2$cation$_4$
d1	7.504	3.905	−7.79
	7.640	3.999	−1.82
	0.136	*0.084*	
d2	8.202	4.748	<|0.05|
	8.325	4.891	+1.20
	0.123	*0.143*	
d3	8.890	4.328	−3.49
	8.938	4.360	+0.25
	0.048	*0.032*	
d4	9.248	6.428	<|0.05|
	9.384	6.494	<|0.05|
	0.136	*0.066*	
d5	9.754	6.494	<|0.05|
	9.883	6.585	+0.06
	0.129	*0.089*	

crystal. When the minimal model space is extended along the three crystallographic axes it must reproduce the topology of the infinite crystal. The minimal model space will be used to compute the matrix representation of the Heisenberg Hamiltonian in Step 4 [3].

4) Calculation of the macroscopic magnetic properties of the crystal:

Once an appropriate minimal magnetic space has been found for the crystal, one can compute the matrix representation of the Heisenberg Hamiltonian Eq. (1), and then the full energy spectrum of the selected minimal magnetic model space by diagonalization of that matrix representation. For efficiency of the computer code, rather than using the Hamiltonian Eq. (1) we used the Hamiltonian:

$$\hat{H} = -2\sum_{A,B} J_{AB}\left(\hat{S}_A \cdot \hat{S}_B + \frac{1}{4}\hat{I}_{AB}\right) \qquad (2)$$

where $\hat{I}_{AB}$ is the identity operator, and $\hat{S}_A$ and $\hat{S}_B$ are the spin operators acting on radical A and B. The energy spectrum computed using the Hamiltonian in Eq. (2) presents the same differences between consecutive states than those obtained using the Hamiltonian of Eq. (1). As the macroscopic magnetic properties only depend on the energy differences between states, when using the same J_{AB} exchange values, the macroscopic properties predicted by the two Hamiltonians are the same. Since the size of the matrix representation the size of the matrix representation of the Heisenberg Hamiltonian increases with the number of doublet radical (N) centers as $N!/[(N/2)!(N/2)!]$, in practice the full diagonalization can reach up to 16 different doublet centers.

The rigorous computation of the macroscopic magnetic properties is done using the adequate Statistical Mechanics expressions [3]. When the proper minimal magnetic model space is selected, the macroscopic properties should converge as the size of the

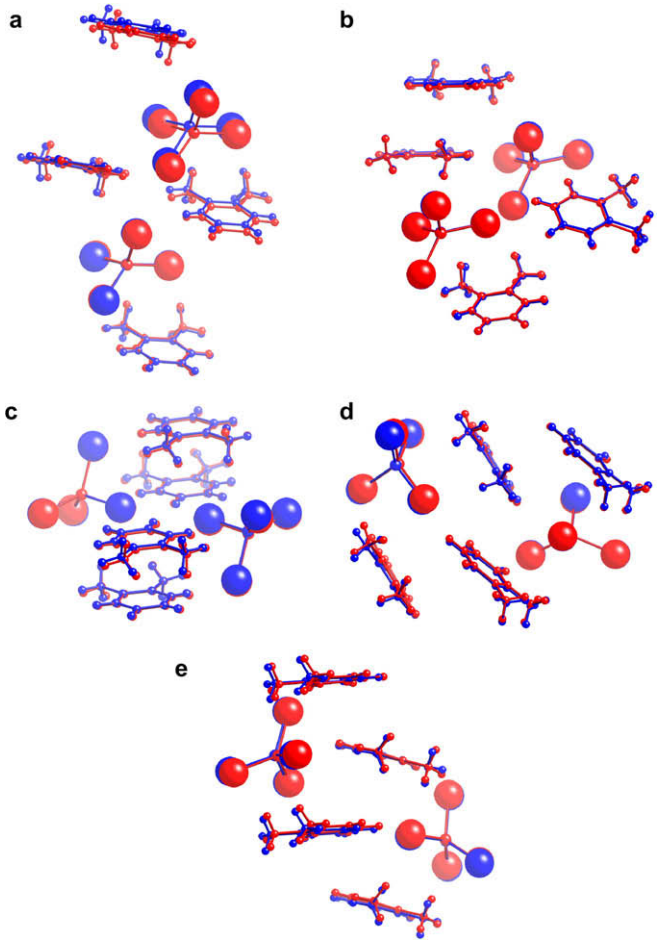


Fig. 2. Geometry of the anion$_2$cation$_4$ models employed to compute the $J(di)$ exchange interactions, for all unique pairs found in the 88 and 273 K structures of the $[(2,3\text{-dmpyH})_2CuBr_4]$ crystal (red corresponds to the 88 K structure, and blue to the 273 K structure). The pairs are identified as follows: (a) *d1*, (b) *d2*, (c) *d3*, (d) *d4* and (e) *d5*. The geometry of the pairs for the 88 K crystal are overlapped on top of the pairs for the 273 K crystal. (For interpretation of the references to colour in this figure legend, the reader is referred to the web version of this article.)

minimal magnetic model space is increased, and the converged value is very close to the experimental value of the property.

The First-Principles *Bottom–Up* procedure is general and unbiased (no previous assumptions are required, as it only requires the knowledge of the crystal structure). The results obtained when using this procedure reproduce very well the available experimental data in all cases studied to date [19–25]. It is also a very powerful analytical tool, as it allows one to connect the macroscopic magnetic properties with the microscopic magnetic interactions. We also would like to mention that the First-Principles *Bottom–Up* methodology is an improvement in comparison to the usual theoretical studies of molecule-based magnets, which usually perform only the first two steps of the First-Principles *Bottom–Up* procedure.

3. Results and discussion

The 88 K crystal structure of $[(2,3\text{-dmpyH})_2CuBr_4]$ has been previously reported (see Fig. 1) [2]. The structure determined at 273 K is reported in Table 1 [1]. At both temperatures, the crystal packs in the *P2(1)/n* space group. Furthermore, experimental observation showed no evidence of a first-order crystallographic phase transition while lowering the temperature from 273 to 120 K (we are also confident that there is no change from 120 to 88 K, based on the small changes in the crystallographic parameters between these two structures). This is further demonstrated by looking at the data in Table 2, which presents the crystallographic parameters for 88, 120 and 273 K. The lattice parameters (*a, b, c* and β) show small changes between the 88 and 273 K structures while negligible changes are seen between 88 and 120 K, completely consistent with the expected thermal expansion. All unit cell axes increase their values as the temperature increases, but the change in the *b* parameter is more than twice that for the *a* and *c* parameters, whose variation is very similar.

The changes in the cell parameters do not significantly affect the intramolecular geometry of the $CuBr_4^{2-}$ radicals (these are the only spin-carrying units in these crystals). As shown in Table 4, the differences in bond lengths is less than 1%, and that in bond angles is generally smaller than 1°. The anisotropic thermal expansion of the cell parameters predominantly affects the intermolecular distance (changes up to 0.14 Å, see Table 3) and relative orientation of the molecules in the crystal, particularly the $CuBr_4^{2-}$ radicals. These changes modify the magnetic properties of the 273 K crystal relative to the 88 K crystal, as we demonstrate hereafter by doing the First-Principles *Bottom–Up* study of the 273 K structure, and comparing these results with those already published for the 88 K structure [2].

In the first step of the First-Principles *Bottom–Up* study of the 88 K crystal [2], it was concluded that only five unique $CuBr_4^{2-}\cdots CuBr_4^{2-}$ radical pairs could be magnetically relevant in this structure (hereafter identified as the *d1–d5* pairs). Only the $CuBr_4^{2-}\cdots CuBr_4^{2-}$ radical pairs were searched because they are the only spin-carrying units. A view of these radical pairs and also of their position within the crystal is shown in Fig. 1, while Table 4 collects its two most significant intermolecular distances. It is worth pointing that the five unique pairs selected in step 1 for the 273 K crystal are the same found in the 88 K crystal. Furthermore, their geometrical arrangement is similar (see Fig. 2, where the geometry of these pairs and their nearest four counterions is overlapped). However, as shown in Table 4, the intermolecular Cu···Cu and Br···Br distances between the two crystals change in a non-isotropic pattern: as the temperature is raised the intermolecular distances within all radical pairs increase, although the variation is different from pair to pair.

Only two of the five pairs found in the 88 K structure presented non-negligible $J_{AB}(di)$ values: *d1* and *d3* (this calculation is the second step of the First-Principles *Bottom–Up* study of the 88 K crystal). The situation is different for the 273 K crystal. The

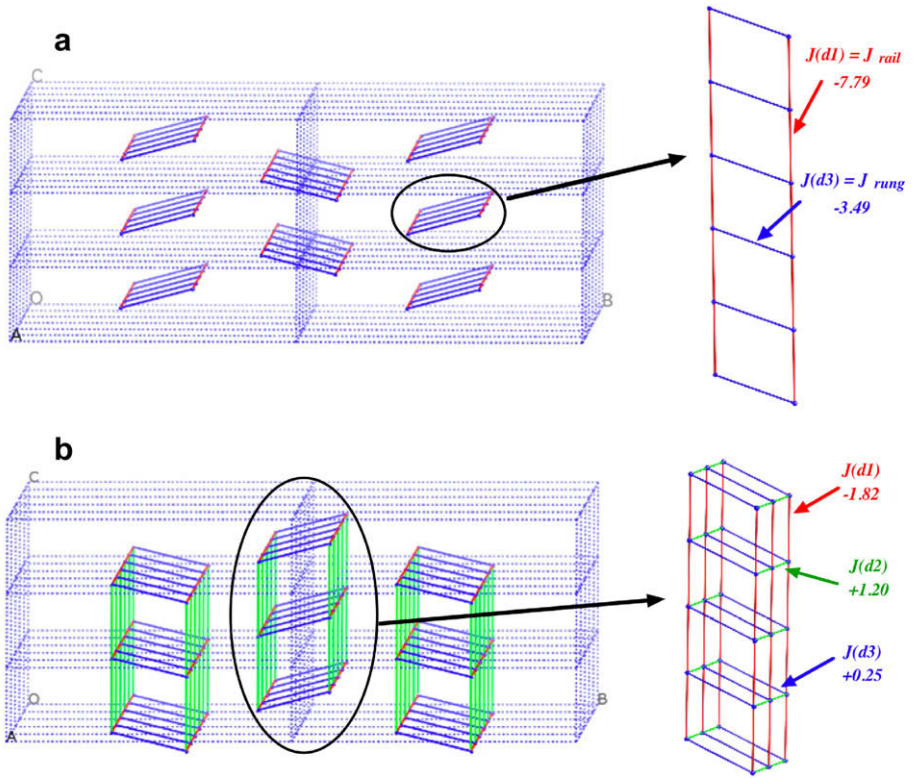


Fig. 3. Magnetic topology for the 88 K (a) and 273 K (b) structures of the $[(2,3\text{dmpyH})_2CuBr_4]$ crystal. Each spin-carrying unit has been replaced by a point site for a better visualization of the magnetic topology. The $J(di)$ values are given in wavenumber units.

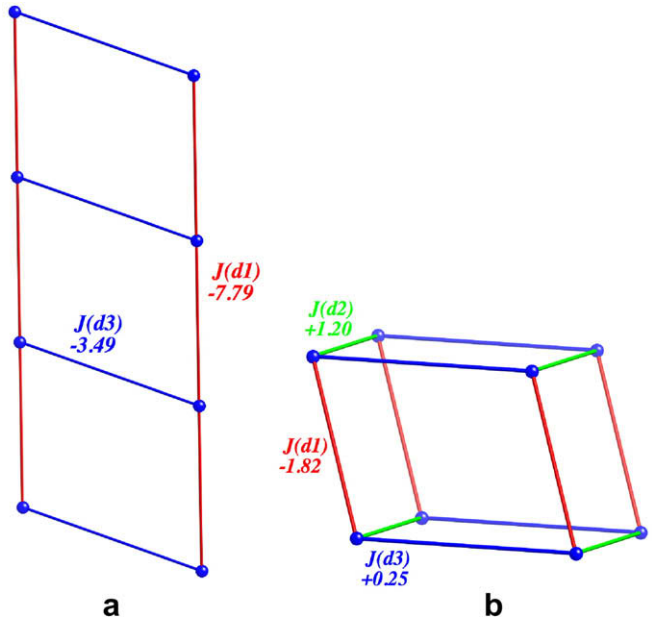


Fig. 4. Minimal magnetic model space for the (a) 88 K (8s) and (b) 273 K (4s–4s) structures of the $[(2,3\text{-dmpyH})_2CuBr_4]$ crystal.

non-isotropic thermal expansion of the crystal induces important changes when one compares the $J_{AB}(di)$ results computed on the 273 and 88 K crystals (see Table 4): (a) while only two non-negligible interactions are present in the 88 K structure, there are three non-negligible interactions in the 273 K structure ($J(d4) = 0.04\ cm^{-1}$ and $J(d5) = 0.06\ cm^{-1}$ are so small that, as will be shown below, they do not affect the computed macroscopic magnetic susceptibility curve), (b) $J_{AB}(d3)$ pair interaction changes from antiferromagnetic to ferromagnetic, and (c) the relative strength of the other $J_{AB}(di)$ pair interactions also changes.

One can now compare the magnetic topology for the 88 and 273 K structures of the $[(2,3\text{-dmpyH})_2CuBr_4]$ crystal (step 3 of the First-Principles *Bottom–Up* procedure). As shown in Fig. 3, the modifications in the $J(di)$ values give rise to a change in the magnetic topology of these crystals. At 88 K the magnetic topology is a strong-rail two-leg spin ladder ($J_{rail} = J(d1) = -7.79\ cm^{-1}$ and $J_{rung} = J(d3) = -3.49\ cm^{-1}$). At 273 K the magnetic topology can be described as planes of non-interacting bilayers, where the dominant $J(d1) = -1.82\ cm^{-1}$ and $J(d2) = +1.20\ cm^{-1}$ form a two alternating (antiferromagnetic and ferromagnetic) *ac*-planes connected by $J(d3) = -0.25\ cm^{-1}$. Only the 88 K magnetic topology is consistent with the experimental two-leg spin-ladder properties observed in the $[(2,3\text{-dmpyH})_2CuBr_4]$ crystal.

Using these two topologies one can compute the macroscopic magnetic properties for the 88 and 273 K structures (step 4 of the First-Principles *Bottom–Up* procedure). First, one has to select the proper minimal magnetic model space for both topologies. It is needed to compute the matrix representation of the Heisenberg Hamiltonian Eq. (2) and its energy spectrum. The minimal magnetic model for the two-leg spin ladder topology (88 K structure) is the 8s model shown in Fig. 4a, while for the isolated bilayer topology it is the 4s–4s model shown in Fig. 4b. Fig. 5 shows two commonly used representations of the magnetic susceptibility curve, $\chi(T)$ and $\chi T(T)$ computed using these models. The curves for the 88 and 273 K structures are very different. Only these computed using the 88 K structure reproduce the shape of the experimental curves at low temperatures. Notice also at high temperature the 88 and 273 K curves predict similar paramagnetic properties. This clearly demonstrates the importance of using the proper crystal structures in the analysis of the magnetic properties of molecule-based magnetic crystals.

Test calculations were also done on the 273 K structure using larger magnetic models. First, the effect of extending the

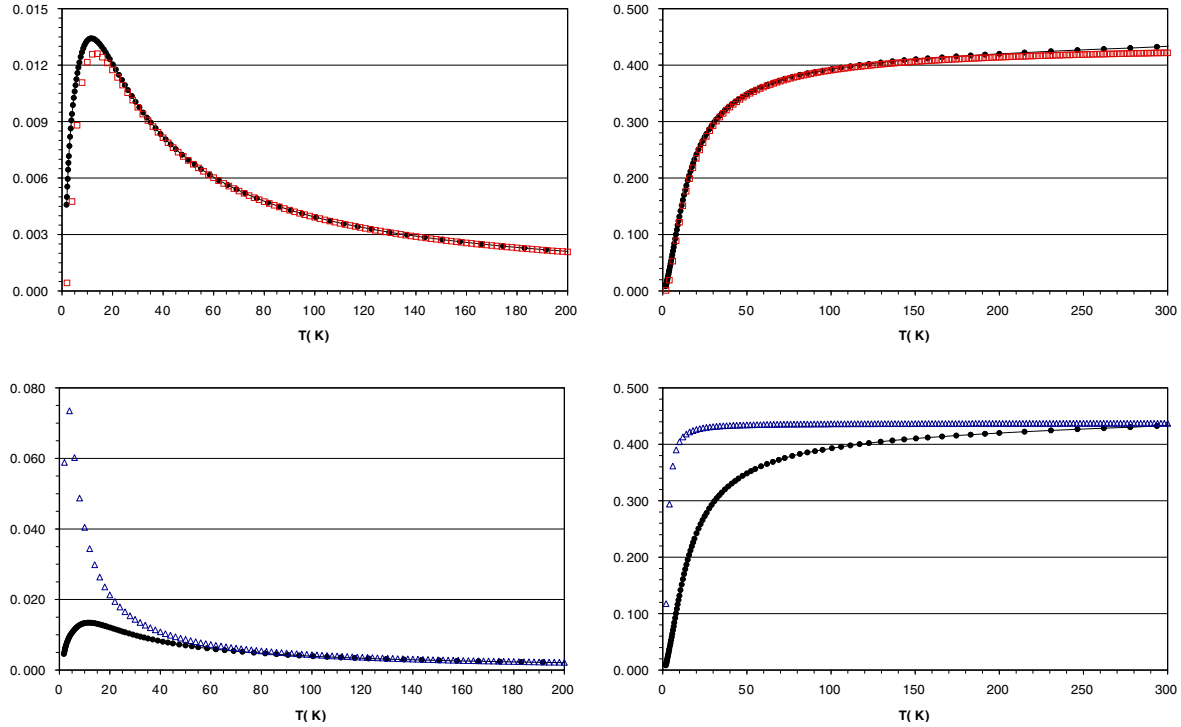


Fig. 5. *Top*: Computed $\chi(T)$ and $\chi T(T)$ curves for the 88 K structure (red) using the 8s minimal magnetic model and its comparison with the experimental curve (black); *Bottom*: Computed $\chi(T)$ and $\chi T(T)$ curves for the 273 K structure (blue) using the 4s–4s minimal magnetic model and the comparison with the experimental curve (black). Both minimal magnetic models are shown in Fig. 4. (For interpretation of the references to colour in this figure legend, the reader is referred to the web version of this article.)

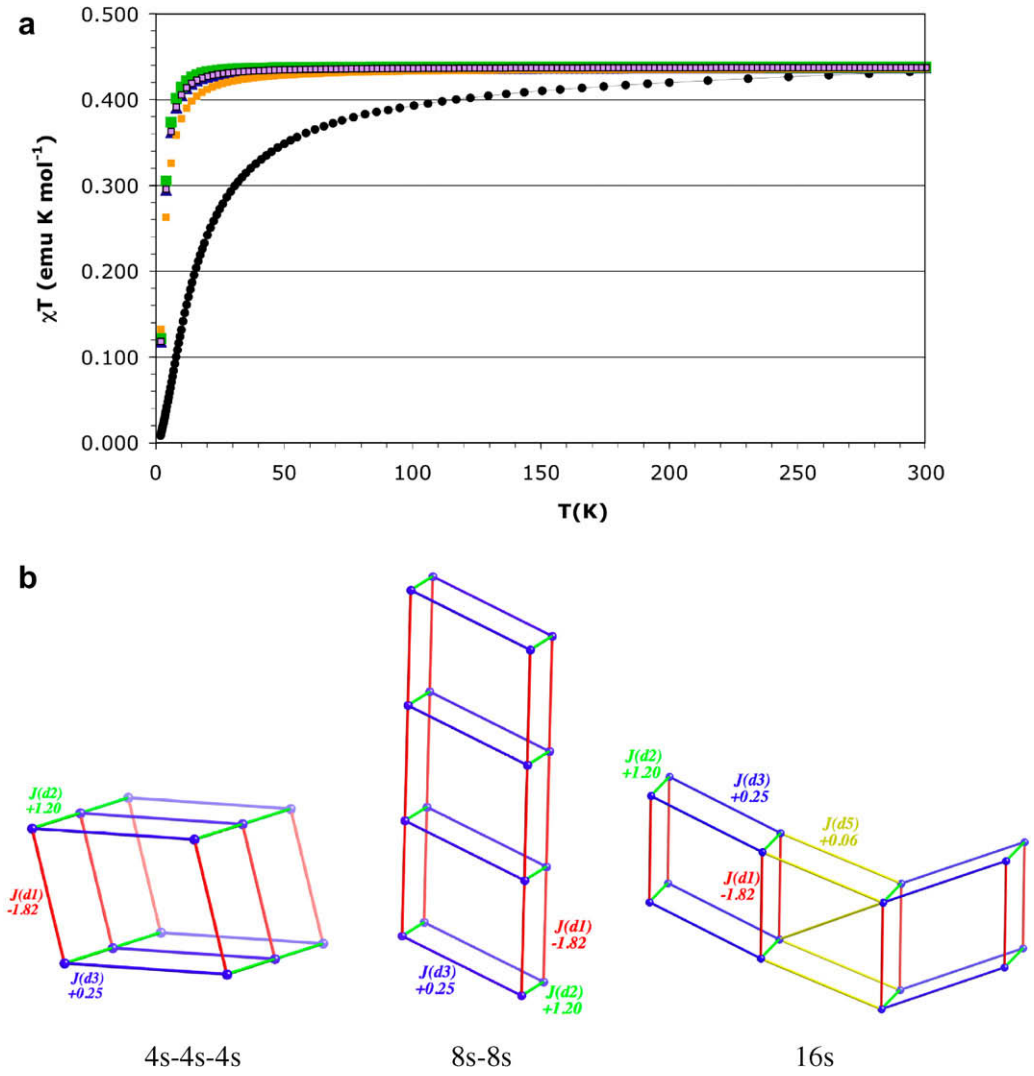


Fig. 6. (a) Magnetic susceptibility curve computed using the 4s–4s–4s (green squares), 8s–8s (orange squares) and 16s (violet squares) magnetic models. The curve obtained using the 4s–4s minimal magnetic model space is also shown for comparison (blue triangles), together with the experimental curve (black circles). (b) Magnetic models used in the calculations of the magnetic susceptibility. (For interpretation of the references to colour in this figure legend, the reader is referred to the web version of this article.)

minimal magnetic model along the crystallographic axes was evaluated (see magnetic models 4s–4s–4s and 8s–8s in Fig. 6). Then, it was tested the effect of including $J(d5) = 0.06\ cm^{-1}$ in the minimal magnetic model (see 16s magnetic model in Fig. 6). In none of these cases the shape of the computed $\chi(T)$ and $\chi T(T)$ curves changed with respect to those computed using the 4s–4s minimal magnetic model space (Fig. 6). Therefore, neither the extension of the minimal magnetic model nor the inclusion of the $J(d5)$ pair interactions have any effect in the computed macroscopic properties, as expected from previous studies. In summary, the 4s–4s model of Fig. 4 is a proper minimal magnetic model space for the study of the macroscopic properties of the 273 K structure of the $[(2,3dmpyH)_2CuBr_4]$ crystal. The fact that the low temperature macroscopic properties computed using a room temperature structure differ from the experimental results at that temperature demonstrates the relevance of using low temperature crystal structures in the study of the magnetic properties at this range of temperatures.

4. Conclusions

The results of the First-Principles Bottom–Up study of the 88 and 273 K structures of the $[(2,3\text{-}dmpyH)_2CuBr_4]$ crystal (range of temperatures where no first order phase transition is observed) shows that low temperature structures have to be used in order to perform theoretical studies and analysis of the magnetic properties of this crystal at these temperatures. Small variations in the intermolecular geometrical arrangement of the $CuBr_4^{2-}$ radicals caused by the anisotropic thermal expansion induce physically relevant changes in the nature and relative importance of the microscopic J_{AB} magnetic interactions. These modifications in the J_{AB} values do not correlate directly with the distance between the bromide ions or copper ions, therefore emphasizing that intermolecular angles are also significant in the magnetic exchange between the radicals of the crystals studied here [26]. As a result of these geometrical changes, the magnetic topology of the low and room temperature structures differ. The 88 K structure is found to be a two-leg spin-ladder [$J_{rail} = J(d1) = -7.79\ cm^{-1}$ and $J_{rung} = J(d3) = -3.49\ cm^{-1}$], i.e. a 1D magnetic topology. However, the 273 K structure presents a magnetic topology consisting of non-interacting bilayers [each layer formed by $J_{intra}(d1) = -1.82\ cm^{-1}$ and $J_{intra}(d2) = +1.20\ cm^{-1}$, which are then connected by $J_{inter}(d3) = -0.25\ cm^{-1}$], i.e. a 2D magnetic topology. The macroscopic magnetic susceptibility curves computed from these two magnetic topologies are strikingly different, and only that originating from the 88 K structure reproduces the experimental curve.

All these structural and magnetic changes are a consequence of the non-isotropy of the thermal expansion. Therefore, these anisotropic changes can be a problem when studying magnetic interactions, if they are not properly accounted for. This problem does not exist when using crystal structures determined at temperatures close enough to the temperature range to be studied.

Supplementary data

CCDC 699270 contains the supplementary crystallographic data for $C_{14}H_6D_{14}N_2CuBr_4$. These data can be obtained free of charge via http://www.ccdc.cam.ac.uk/conts/retrieving.html, or from the Cambridge Crystallographic Data Centre, 12 Union Road, Cambridge CB2 1EZ, UK; fax: (+44) 1223-336-033; or e-mail: deposit@ccdc.cam.ac.uk

Acknowledgments

M.M.T. is grateful for grants from the NSF (IMR-0314773) toward the purchase of the MPMS SQUID, from PCISynthesis Inc. toward the purchase of the D8 Powder X-ray Diffractometer, and the Kresge Foundation toward the purchase of both. The Spanish team also thanks the Spanish Science and Education Ministry for support (Projects BQU2002-04587-C02-02 and CTQ2005-02329), the Catalan DURSI (Grants 1999SGR-00046 and 2005SGR-00036), and the computer time allocated by CESCA and BSC. Furthermore, J.J. thanks the Spanish Science and Education Ministry for the award of his Ph. D. grant.

References

[1] A.S. Albrecht, C.P. Landee, M.M. Turnbull, J. Chem. Crystallogr. 33 (2003) 269.
[2] A. Shapiro, C.P. Landee, M.A. Turnbull, J. Jornet, M. Deumal, J.J. Novoa, M.A. Robb, W. Lewis, J. Am. Chem. Soc. 129 (2007) 952.
[3] M. Deumal, M.J. Bearpark, J.J. Novoa, M.A. Robb, J. Phys. Chem. A 106 (2002) 1299.
[4] A. Szabo, N.S. Ostlund, Modern Quantum Chemistry, Macmillan, New York, 1982.
[5] E.G. Parr, W. Yang, Density Functional Theory, Oxford University Press, New York, 1989.
[6] M. Deumal, G. Giorgi, M.A. Robb, M.M. Turnbull, C.P. Landee, J.J. Novoa, Eur. J. Inorg. Chem. (2005) 4697.
[7] L. Noodlemann, J. Chem. Phys. 74 (1981) 5737.
[8] L. Noodlemann, E.R. Davidson, Chem. Phys. 109 (1986) 131.
[9] E. Ruiz, S. Alvarez, J. Cano, V. Polo, J. Chem. Phys. 123 (2005) 164110.
[10] C. Adamo, V. Barone, A. Bencini, R. Broer, M. Filatov, N.M. Harrison, F. Illas, J.P. Malrieu, I.P.R. Moreira, J. Chem. Phys. 124 (2006) 107101.
[11] A.D. Becke, Phys. Rev. A 38 (1988) 3098.
[12] C. Lee, W. Yang, R.G. Parr, Phys. Rev. B 37 (1988) 785.
[13] J.J. Novoa, M. Deumal, Struct. Bond. 100 (2001) 34.
[14] J.J. Novoa, P. Lafuente, M. Deumal, F. Mota, in: J.S. Miller, M. Drillon (Eds.), Magnetism Molecules to Materials, vol. IV, Wiley-VCH, Weinheim, 2003.
[15] E. Ruiz, P. Alemany, S. Alvarez, J. Cano, J. Am. Chem. Soc. 119 (1997) 1297.
[16] A. Schafer, H. Horn, R. Ahlrichs, J. Chem. Phys. 97 (1992) 2751.
[17] P.C. Hariharan, J.A. Pople, Theor. Chim. Acta 28 (1973) 213.
[18] M. J. Frisch, G.W. Trucks, H.B. Schlegel, G.E. Scuseria, M.A. Robb, J.R. Cheeseman, J.A. Montgomery, Jr., T. Vreven, K.N. Kudin, J.C. Burant, J.M. Millam, S.S. Iyengar, J. Tomasi, V. Barone, B. Mennucci, M. Cossi, G. Scalmani, N. Rega, G.A. Petersson, H. Nakatsuji, M. Hada, M. Ehara, K. Toyota, R. Fukuda, J. Hasegawa, M. Ishida, T. Nakajima, Y. Honda, O. Kitao, H. Nakai, M. Klene, X. Li, J.E. Knox, H.P. Hratchian, J.B. Cross, V. Bakken, C. Adamo, J. Jaramillo, R. Gomperts, R.E. Stratmann, O. Yazyev, A.J. Austin, R. Cammi, C. Pomelli, J.W. Ochterski, P.Y. Ayala, K. Morokuma, G.A. Voth, P. Salvador, J.J. Dannenberg, V.G. Zakrzewski, S. Dapprich, A.D. Daniels, M.C. Strain, O. Farkas, D.K. Malick, A.D. Rabuck, K. Raghavachari, J.B. Foresman, J.V. Ortiz, Q. Cui, A.G. Baboul, S. Clifford, J. Cioslowski, B.B. Stefanov, G. Liu, A. Liashenko, P. Piskorz, I. Komaromi, R.L. Martin, D.J. Fox, T. Keith, M.A. Al-Laham, C.Y. Peng, A. Nanayakkara, M. Challacombe, P.M.W. Gill, B. Johnson, W. Chen, M.W. Wong, C. Gonzalez, J.A. Pople, GAUSSIAN 03, Revision C.02, Gaussian, Inc., Wallingford CT, 2004.
[19] M. Deumal, M.J. Bearpark, M.A. Robb, Y. Pontillon, J.J. Novoa, Chem. Eur. J. 10 (2004) 6422.
[20] M. Deumal, M.A. Robb, J.J. Novoa, Polyhedron 22 (2003) 1935.
[21] M. Deumal, F. Mota, M.J. Bearpark, M.A. Robb, J.J. Novoa, Mol. Phys. 104 (2006) 857.
[22] J. Jornet, M. Deumal, J. Ribas-Arino, M.J. Bearpark, M.A. Robb, R.G. Hicks, J.J. Novoa, Chem. Eur. J. 12 (2006) 3995.
[23] M. Deumal, S. LeRoux, J.M. Rawson, M.A. Robb, J.J. Novoa, Polyhedron 26 (2007) 1949.
[24] L. Li, M.M. Turnbull, C.P. Landee, J. Jornet, M. Deumal, J.J. Novoa, J.L. Wikaira, Inorg. Chem. 46 (2007) 11254.
[25] J. Jornet, M.A. Robb, M. Deumal, J.J. Novoa, Inorg. Chim. Acta 361 (2008) 3586.
[26] M. Deumal, C.P. Landee, J.J. Novoa, M.A. Robb, M.M. Turnbull, Polyhedron 22 (2003) 2235.

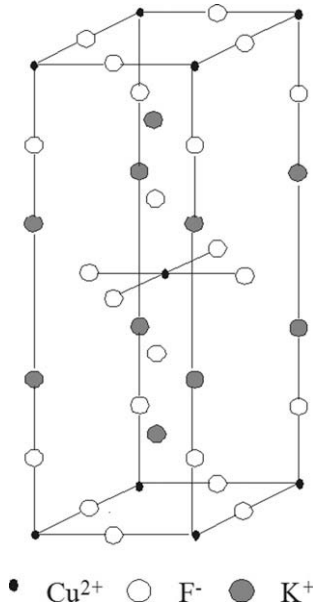


Fig. 1. The crystal structure of the perovskite-type copper fluoride of K_2CuF_4.

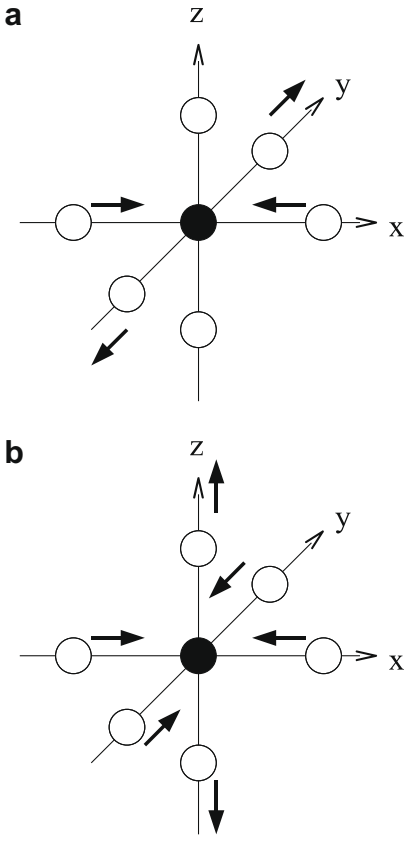


Fig. 2. The two types of normal vibration modes of octahedral fluorine anions around copper cation: (a) Q_2 mode, (b) Q_3 mode.

magnetism. The natural orbital analysis was also performed to examine the alternate $d_{z^2-x^2}$ type orbital ordering. The calculated potential energy curves were discussed, from the viewpoint of the theoretical total energy in the Jahn–Teller distorted structure.

2. Theoretical background

2.1. Computational methods

The computational method employed here is UB2LYP, which is one of the hybrid-density functional theory (DFT) methods, because we concluded that B2LYP is the reliable method for the perovskite-type transition metal solids [19–21]. In hybrid-DFT method, the exchange and correlation potentials are generally defined by

$$E_{XC} = C_1E_X^{HF} + C_2E_X^{Slater} + C_3E_X^{Becke88} + C_4E_C^{VWN} + C_5E_C^{LYP} \quad (3)$$

where E_X^{HF}, E_X^{slater}, and E_X^{Becke} denote HF, Slater [22,23], and Becke [24] exchange functionals, respectively, and E_C^{VWN} and E_C^{LYP} denote the Vosko, Wilk, and Nusair (VWN) [25], and Lee, Yang, and Parr (LYP) [26] correlation functionals, respectively. The mixing coefficients (C1, C2, C3, C4 and C5) in UB2LYP is (0.5, 0.5, 0.5, 1.0 and 1,0), respectively. Tatewaki–Huzinaga MIDI [27] basis sets plus Hay's diffuse function [28] were used for copper cation and 6-31G* basis set was used for fluorine anion. All calculations were performed by GAUSSIAN 94 program package [29].

2.2. Effective exchange integrals (J_{ab})

The magnetic property in the strongly correlated perovskite-type fluorides can be investigated by Heisenberg-type spin coupling Hamiltonian [30], which is expressed as

$$\hat{H}(HB) = -2J_{ab}\mathbf{S_a}\cdot\mathbf{S_b} \quad (4)$$

where J_{ab} is the orbital-averaged effective exchange integral between the a-th and b-th spin sites with total spin operators ($\mathbf{S_a}$ and $\mathbf{S_b}$). Previously, [20,21] we concluded that the approximate spin projected scheme is one of the best method to obtain J_{ab} values for the species. The J_{ab} value under the spin projected scheme $J_{ab}^{(1)}$ can be calculated by the difference of the total energies between the highest-spin (HS) state and the lowest-spin (LS) state

$$J_{ab}^{(1)} = \frac{^{LS}E(X) - {}^{HS}E(X)}{^{HS}\langle S^2\rangle - {}^{LS}\langle S^2\rangle} \quad (5)$$

where $^{Y}E(X)$ and $^{Y}\langle s^2\rangle$ the total energy and total spin angular momentum for the spin state Y (LS and HS) by the calculation method X (X = UB2LYP), respectively. Eq. (5) can be applied not only for linear chains of dimer and trimer but also for tetranuclear ring [20,21]. On the other hand, the J_{ab} value under the spin unprojected scheme for tetranuclear ring is given by $J_{ab}^{(2)}$ (*ring*) [20,21]

$$J_{ab}^{(2)}(ring) = \frac{^{LS}E(X) - {}^{HS}E(X)}{4NS_aS_b} \quad (6)$$

where N is total number of spin sites and S_c is spin size (S_c (c = a, b)). In the tetranuclear ring (N = 4), the denominator in Eq. (6) becomes 4, where S_a and S_b are also equal to 1/2, because of spin quantum numbers of copper cation.

2.3. Natural orbital analysis

The natural orbital is determined by diagonalizing their first-order density matrices as

$$\rho(r,r') = \sum n_i\phi_i(r)\phi_i(r')^* \quad (7)$$

where n_i and ϕ_i denote the occupation number and natural orbital, respectively. On the other hand, the magnetic orbitals are expressed by the different natural orbitals,

$$\chi_i = \cos\omega\phi_i + \sin\omega\phi_i^+ \quad (8a)$$
$$\eta_i = \cos\omega\phi_i - \sin\omega\phi_i^+ \quad (8b)$$

where ω is the orbital mixing parameter, and ϕ_i and ϕ_i^+ denote the i-th bonding and corresponding antibonding natural orbitals, respectively. The natural orbital mixing, in turn, provides the magnetic broken-symmetry orbitals (χ_i and η_i) localized on different sites. The orbital overlap (T_i) between magnetic orbitals is defined to elucidate their localizability

$$T_i = \langle \chi_i | \eta_i \rangle = \cos^2 \omega - \sin^2 \omega = \cos 2\omega \quad (9)$$

The occupation numbers of the occupied bonding and antibonding natural orbitals are close to 2.0 and 0.0, respectively. On the other hand, those of the magnetic singly occupied natural orbitals (SONOs), which are close to 1.0, are given by orbital overlap as

$$n_i = 1 + T_i,\ n_i = 1 - T_i. \quad (10)$$

3. Geometric structures

Both the smaller apical Cu–F distances, and the shortened and elongated equatorial Cu–F distances are responsible for the alternate $d_{z^2-x^2}$ type orbital ordering. The two dimensional cluster models surrounded by apical and equatorial fluorine anions were constructed as shown in Figs. 3a–3d. The sites numbers are shown in Fig. 3e. The apical and equatorial Cu–F distances in K_2CuF_4 are 1.950 Å and 2.080 Å, respectively [7,11,12]. In **1** and **2**, only equatorial fluorine anions on CuF_2 layer and apical fluorine anions are taken into account, respectively. On the other hand, in **3** and **4**, both the apical and equatorial fluorine anions are taken into account. **4** has the all apical and equatorial fluorine anions, while **3** has only the equatorial fluorine anions approaching to copper cations.

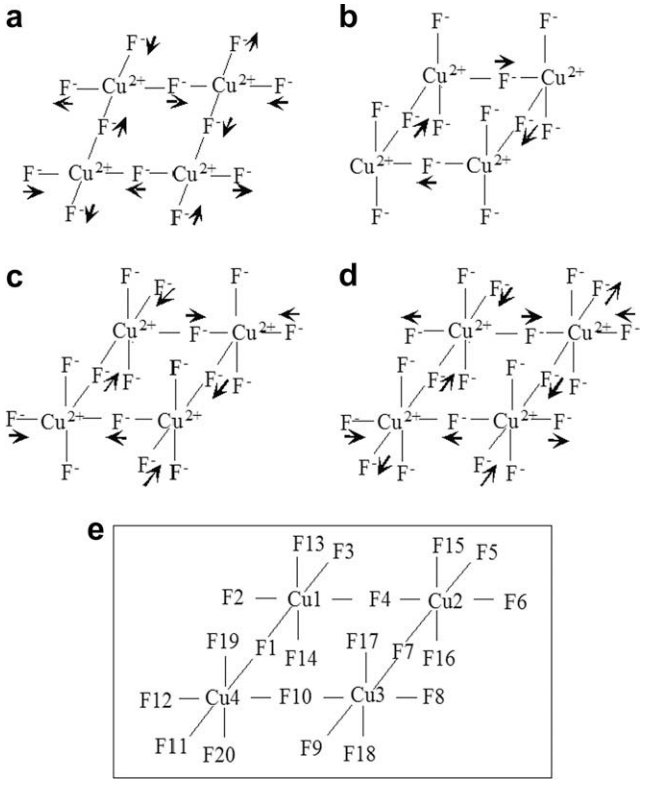


Fig. 3. The two dimensional cluster models of K_2CuF_4 and the site numbers: (a) **1**, (b) **2**, (c) **3**, (d) **4**, and (e) site numbers.

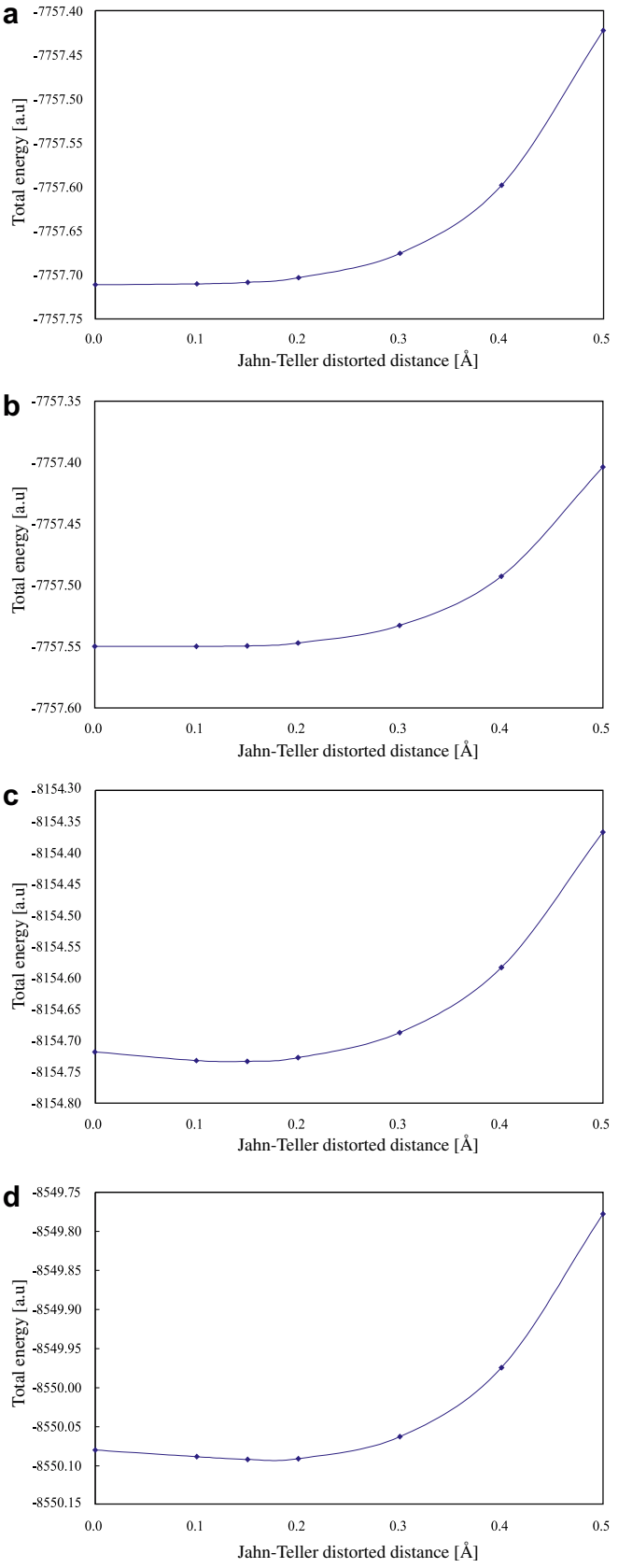


Fig. 4. The potential energy curves, changing the amplitude of Jahn–Teller distortion the equatorial fluorine anions from the initial position (q) in Q_2 mode: (a) **1**, (b) **2**, (c) **3**, and (d) **4**. (HS state, UB2LYP method).

4. Results and discussion

4.1. Potential energy curves

As shown in Fig. 4, we obtained the potential energy curves of HS state for **1**, **2**, **3**, and **4** by UB2LYP, changing the amplitude of Jahn–Teller distortion of the equatorial fluorine anions (q), while the apical fluorine anions are all fixed. Jahn–Teller distortion occurs in **3** and **4**, since the potential energy curves have the minimum points. On the other hand, no Jahn-Teller distortion occurs in **1** and **2**, since the potential energy curves are monotonous increasing.

4.2. Effective exchange integrals (J_{ab})

Table 1 shows J_{ab} values for **1**, **2**, **3**, and **4** by UB2LYP, changing the amplitude of Jahn–Teller distortion of the equatorial fluorine anions (q). As $J_{ab}^{(1)}$ values are almost equivalent with $J_{ab}^{(2)}(ring)$ values, the effect of the spin projection is small in K_2CuF_4. At q = 0.00 Å, **1**, **2** and **4** provide negative J_{ab} values, showing the antiferromagnetic interaction. On the other hand, the positive J_{ab} value for **3** at q = 0.00 Å indicates the ferromagnetic interaction. At the experimental amplitude of Jahn–Teller distortion (q = 0.15 Å) [31], J_{ab} values for **3** and **4** are 6.784 cm^{-1} and 6.162 cm^{-1}, respectively, while **1** and **2** provides negative J_{ab} values. They are well consistent with the experimental ones (5.212 $cm^{-1} \sim 7.739\ cm^{-1}$) [9–12]. Between 0.30 Å and 0.50 Å, J_{ab} values for **2** become positive. It is because the bridge-fluorine anions (F1, F4, F7 and F10) cause the alternate $d_{z^2-x^2}$ type orbital ordering without the other equatorial fluorine anions. However, the equatorial Cu–F distances are too large.

4.3. Natural orbital analysis

Fig. 5 shows the singly occupied natural orbital (SONO+1s) and their occupation numbers of HS state for **1**, **2**, **3**, and **4** by UB2LYP, at the experimental amplitude of Jahn–Teller distortion (q = 0.15 Å). J_{ab} values at q are approximately given by

$$J_{ab} \cong K_{ab} - c(T_i^q)^2 \tag{11}$$

where K_{ab}, c and T_i denote the Coulomb exchange integral, positive constant and orbital overlap between copper cations at q, respectively. J_{ab} values are negative if T_i^q values are non-negligible.

In **1** and **2**, $\mathbf{d}_z^2$ and $d_{x^2-y^2}$ orbitals exist in copper cations, respectively. However, in **3**, the alternate $d_{z^2-x^2}$ type orbital ordering occurs, where $d_{z^2-y^2}$ orbital of Cu1 (Cu3) interacts with equatorial F1 and F3, and apical F13 and F14 (equatorial F7 and F9, and apical F17 and F18), and $d_{z^2-x^2}$ orbital of Cu2 (Cu4) interacts with equatorial F4 and F6, and apical F15 and F16 (equatorial F10 and F12, and apical F19 and F20). Smaller $T_i^{0.15}$ value between $\chi_{SONO\pm1}$ and $\eta_{SONO\pm1}$ (0.002) shows the scarce orbital overlap between $d_{z^2-x^2}$ and $d_{z^2-y^2}$ orbitals. The proper ferromagnetic interactions between copper cations appear in **3**, resulting in the reasonable J_{ab} value (6.784cm^{-1}). Similarly, in **4**, $d_{z^2-y^2}$ ($d_{z^2-x^2}$) orbitals in Cu1 and Cu3 (Cu2 and Cu4) are formed. Smaller $T_i^{0.15}$ value between $\chi_{SONO\pm1}$ and $\eta_{SONO\pm1}$ (0.005) shows the scarce orbital overlap between $d_{z^2-x^2}$ and $d_{z^2-y^2}$ orbitals. The proper ferromagnetic interactions between copper cations also appear in 4, providing the reasonable J_{ab} value (6.162 cm^{-1}).

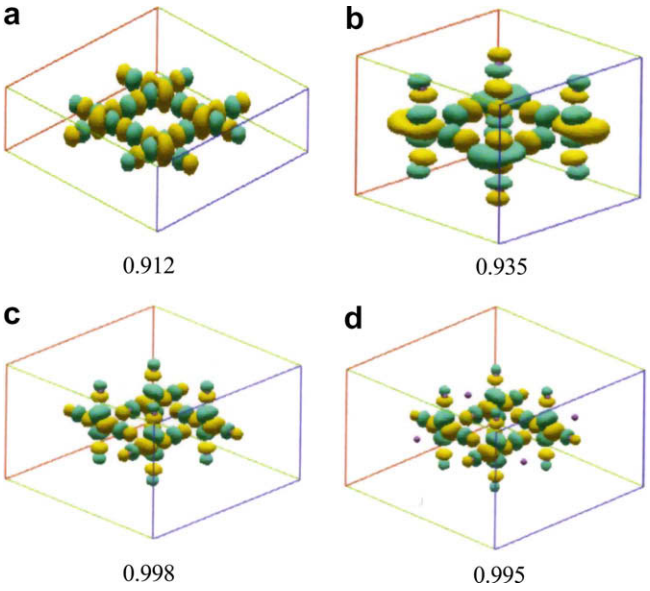


Fig. 5. The singly occupied natural orbital (SONO+1s) and the occupation numbers at the experimental amplitude of Jahn–Teller distortion: (a) **1**, (b) **2**, (c) **3**, and (d) **4** (HS state, UB2LYP method). The site numbers of back, right, front and left copper cations are Cu1, Cu2, Cu3 and Cu4, respectively.

4.4. Cooperative Jahn–Teller effect

From the viewpoint of the theoretical total energy in the Jahn–Teller distorted structure, we discuss the calculated potential energy curves. We considered only **3** and **4**, since no alternate $d_{z^2-x^2}$ type orbital ordering occurs in **1** and **2**. It is considered that the calculated potential energy curves may be expressed as the second-order polynomial by regarding q as the parameter in Eq. (2). In fact, as shown in Figs. 4c and 4d, the calculated potential energy curves of **3** and **4** are well fitted by Eq. (2), near the minimum point (0.10 Å $\sim$ 0.20 Å). Table 2 shows the calculated coefficients and amplitude of Jahn–Teller distortion (q_{calc}) in Eq. (2). The total energy is smaller by the Jahn–Teller distortion, due to the positive

Table 1
The spin projected and unprojected effective exchange integrals (J_{ab})[a] of **1**, **2**, **3**, and **4** by UB2LYP, changing the amplitude of Jahn–Teller distortion of the equatorial fluorine anions from the initial position (q)[b] in Q_2 mode.

q	**1**		**2**		**3**		**4**	
	$J_{ab}^{(1)}$	$J_{ab}^{(2)}$ (*ring*)	$J_{ab}^{(1)}$	$J_{ab}^{(2)}$ (*ring*)	$J_{ab}^{(1)}$	$J_{ab}^{(2)}$ (*ring*)	$J_{ab}^{(1)}$	$J_{ab}^{(2)}$ (*ring*)
0.00	−60.13	−60.26	−26.40	−26.45	4.920	4.921	−5.381	−5.383
0.10	−59.10	−59.23	−18.26	−18.29	7.236	7.236	5.762	5.762
0.15	−57.99	−58.11	−11.10	−11.11	6.784	6.784	6.162	6.162
0.20	−56.39	−56.50	−2.614	−2.617	5.535	5.535	4.605	4.606
0.30	−53.46	−53.56	8.935	8.940	2.007	2.007	0.0713	0.0713
0.40	−51.27	−51.37	14.07	14.07	−2.232	−2.232	−5.267	−5.268
0.50	−50.46	−50.56	14.83	14.83	−6.275	−6.276	−11.38	−11.38

The spin projected and unprojected J_{ab} values are denoted as $J_{ab}^{(1)}$ and $J_{ab}^{(2)}$ (*ring*), respectively.
[a] J_{ab} values are shown in cm^{-1}.
[b] q is shown in Å.

Table 2
The calculated coefficients and amplitude of Jahn–Teller distortion (q_{calc})[a] in $E = E_0 - Aq + (1/2)kq^2$.

	A	$(1/2)kq$	q_{calc}
3	0.351	1.326	0.132
4	0.305	0.930	0.164

[a] q_{calc} is shown in Å.

Table 3
The spin projected exchange integrals ($J_{ab}^{(2)}$)[a] of **3** and **4** with point charges by UB2LYP, changing the amplitude of Jahn–Teller distortion of the equatorial fluorine anions from the initial position (q)[b] in Q_2 mode.

q	**3**	**4**
0.00	3.512	−4.388
0.10	6.419	5.596
0.15	5.377	3.402
0.20	3.676	1.481
0.30	−0.658	−3.291
0.40	−5.595	−8.337
0.50	−11.08	−14.04

[a] $J_{ab}^{(1)}$ values are shown in cm^{-1}.
[b] q is shown in Å.

A values. On the other hand, the elastic energy becomes larger as the amplitude of Jahn–Teller distortion is larger, due to the positive k values. These facts explain that the minimum points are given in the calculated potential energy curves. The q_{calc} values in **3** and **4** are 0.132 Å and 0.164 Å, respectively. They are well consistent with the experimental value (q=0.15 Å) [31]. On the other hand, the potential energy curves are not fitted at the smaller and larger q values. It is because the degree of the contamination of e_g orbitals ($d_{x^2-y^2}$ and d_z^2 orbitals) differs. The third-order anharmonic term [14] describes them, which is given by

$$A'(\cos 3\theta)q^3 \tag{12}$$

where A' is the proportionality constant. This term includes the parameter of θ in Eq. (1).

In K_2CuF_4, the cooperative Jahn–Teller effect is dominative. The spin-orbit coupling is negligible, as spin angular momentum vanishes in ($d^9 t_{2g}^6 e_g^3$) configuration of copper cation. For example, when the spin angular momentum remains in the degenerated t_{2g} orbital, the quantum nature appears in the degree of freedom in orbital [32,33]. The dynamical effect, in which both the electronic and vibrational states make transitions simultaneously, is also negligible.

4.5. Effect of point charges

The cluster models adapted here are parts of K_2CuF_4. It is desirable for the cluster models to consider the effect on the rest of the crystal. Here, we estimated the J_{ab} values for the cluster models of **3** and **4** embedded in point charges. Table 3 shows $J_{ab}^{(1)}$ values for **3** and **4** with point charges by UB2LYP, changing the amplitude of Jahn–Teller distortion of the equatorial fluorine anions (q). At the experimental amplitude of Jahn–Teller distortion (q = 0.15 Å), $J_{ab}^{(1)}$ values of **3** and **4** with point charges become 5.374 cm^{-1} and 3.402 cm^{-1}, respectively. Though they are underestimated in comparison with $J_{ab}^{(1)}$ values of **3** and **4** without point charges, the difference of about 1 $cm^{-1} \sim 2$ cm^{-1} is negligible under hybrid-DFT level calculation. It is concluded that embedding of **3** and **4** in point charges has no effect on estimating the changes of the total energies and J_{ab} values. Hence, the bare cluster models of **3** and **4** can be adapted for calculation.

5. Conclusion

In this study, we examined the cooperative Jahn–Teller effect in K_2CuF_4, from the viewpoints of the potential energy curves, effective exchange integrals (J_{ab}) and the natural orbital analysis. We have concluded as follows:

1. The two dimensional cluster models under consideration of octahedral fluorine anions around copper cation reproduced the alternate $d_{z^2-x^2}$ type orbital ordering.
2. The calculated J_{ab} values showed the ferromagnetic interaction between $d_{z^2-x^2}$ and $d_{z^2-y^2}$ orbitals, and were well consistent with the experimental ones.
3. The calculated potential energy curves were well fitted with the theoretical total energy near the calculated amplitude of Jahn–Teller distortion.
4. The calculated amplitudes of Jahn–Teller distortion are also well consistent with the experimental ones.

Namely, the cluster calculation based on hybrid-DFT method provides the reasonable potential energy curves. It means that the first principle calculation enables us to estimate the amplitude of Jahn–Teller distortion theoretically. This method could be applicable for the other Jahn–Teller distorted systems.

Acknowledgments

T. Onishi has been supported by "IKETANI SCIENCE AND TECHNOLOGY FOUNDATION" and "MURATA SCIENCE FOUNDATION". The author would like to thank for Dr. Yu Takano for helpful discussion.

References

[1] S. Ishihara, S. Maekawa, Rep. Prog. Phys. 65 (2002) 561.
[2] Y. Tokura, N. Nagaosa, Science. 288 (2000) 462.
[3] Y. Motome, Bussei. Kenkyu. 89 (2008) 863.
[4] D.I. Khomskii, K.I. Kugel, Solid. State. Commun. 13 (1973) 763.
[5] K.I. Kugel, D.I. Khomskii, Sov. Phys. –JEPT. 64 (1973) 1429.
[6] A.E. Nikiforov, S.Y. Shashkin, M.L. Levitan, T.H. Agamalan, Phys. Status Solidi B 118 (1983) 419.
[7] K. Knox, J. Chem. Phys. 30 (1959) 991.
[8] I. Yamada, J. Phys. Soc. Jpn. 28 (1970) 1585.
[9] I. Yamada, H. Kubo, K. Shimohigashi, J. Phys. Soc. Jpn. 30 (1971) 896.
[10] I. Yamada, M. Ikebe, J. Phys. Soc. Jpn. 33 (1972) 1334.
[11] I. Yamada, J. Phys. Soc. Jpn. 33 (1972) 979.
[12] K. Hikakawa, H. Ikebe, J. Phys. Soc. Jpn. 35 (1973) 1328.
[13] Y. Ito, J. Akimitsu, J. Phys. Soc. Jpn. 40 (1976) 1333.
[14] J. Kanamori, J. Appl. Phys. 31 (1960) 14S.
[15] R. Englman, B. Halperin, Phys. Rev. B 2 (1970) 75.
[16] B. Halperin, R. Englman, Phys. Rev. B 3 (1971) 1698.
[17] J.B. Goodenough, Magnetism Chemical Bond, Interscience (1963).
[18] J. Kanamori, Kotai. Butsuri. 34 (1999) 225.
[19] T. Onishi, Int. J. Quantum. Chem. 107 (2007) 3089.
[20] T. Onishi, D. Yamaki, K. Yamaguchi, Y. Takano, J. Chem. Phys. 118 (2003) 9747.
[21] T. Onishi, Y. Takano, Y. Kitagawa, T. Kawakami, Y. Yoshioka, K. Yamaguchi, Polyhedron 20 (2000) 1177.
[22] P. Hohenberg, W. Kohn, Phys. Rev. 136 (1964) B864.
[23] W. Kohn, L. Sham, Phys. Rev. 140 (1965) A1133.
[24] A.D. Becke, Phys. Rev. A 38 (1998) 3098.
[25] S.H. Vosko, L. Wilk, M. Nusair, Can. J. Phys. 58 (1980) 1200.
[26] C. Lee, W. Wang, R.G. Parr, Phys. Rev. B 37 (1988) 785.
[27] H. Tatewaki, S. Huzinaga, J. Chem. Phys. 72 (1980) 4339.
[28] P.J. Hay, J. Chem. Phys. 66 (1977) 4377.
[29] M.J. Frich, G.W. Trucks, H.B. Schlegel et al., GAUSSIAN 94, Gaussian. Inc., 1995.
[30] W. Heisenberg, Z. Phys. 38 (1926) 411.
[31] M. Hidaka, K. Inoue, I. Yamada, P.J. Walker, Physica B 121 (1983) 343.
[32] Y. Motome, H. Seo, Z. Fang, N. Nagaosa, Phys. Rev. Lett. 90 (2003) 146602.
[33] S. Miyasaka, S. Onoda, Y. Okimoto, J. Fujioka, M. Iwama, N. Nagaosa, Y. Tokura, Phys. Rev. Lett. 94 (2005) 076405.

2. Experimental

2.1. Compound preparation

All chemicals and solvents were used as received. The complex $[Mn_{12}O_{12}(O_2CCH_3)_{16}(H_2O)_4]$ (Mn_{12}-ac) was prepared as described elsewhere [14]. Mn_{12}-phn was prepared as described below. A solution of diphenylphosphinic acid (0.79 g, 3.2 mmol) in CH_2Cl_2 (80 ml) was dropped into a solution of Mn_{12}-ac (0.50 g, 0.24 mmol) in acetonitrile (50 ml) within 1 h. The solvent was evaporated under reduced pressure to complete dryness. The remaining solid was redissolved in CH_2Cl_2 (70 ml) and filtered through kieselguhr. Hexane was added and the solution was allowed to stand undisturbed at 4 °C for 12 h. The resulting black crystals were collected by filtration, washed with hexane and dried in vacuo. A crystallography sample was grown slowly from CH_2Cl_2/hexane at 4 °C and maintained in mother liquor to avoid solvent loss. Selected IR bands (ATR, cm^{-1}): 3053 (w), 1570 (m), 1541 (m), 1485 (w), 1437 (m), 1384 (m), 1332 (m), 1124 (vs), 1046 (vs), 1014 (vs), 994 (vs), 751 (m), 723 (vs), 701 (vs). MALDI-TOF-MS (m/z): 3693.2 $[Mn_{12}O_{12}(O_2PC_{12}H_{10})_{12}(O_2CCH_3)_4]^+$; 3633.8 $[Mn_{12}O_{12}(O_2PC_{12}H_{10})_{12}(O_2CCH_3)_3]^+$; 3475.7 $[Mn_{12}O_{12}(O_2PC_{12}H_{10})_{11}(O_2CCH_3)_4]^+$. Details of the synthesis and the characterization of 4-MOBCA can be found elsewhere [12].

2.2. X-ray crystallography

Crystal data of Mn_{12}-phn: $C_{314.87}H_{264}Cl_{21.55}Mn_{24}O_{92}P_{24}$, $M_r = 8345.58$, tetragonal, $I41/a$, $a = 34.7178(9)$ Å, $b = 34.7178(9)$ Å, $c = 28.8662(10)$ Å, $V = 34793.2(18)$ Å^3, $Z = 4$, brown block, ρ_{calcd} (g/cm^3) = 1.593, μ(Mo K$_\alpha$) (cm^{-1}) = 1.192, $T = 100$, empirical absorption correction, $T_{max}/T_{min} = 0.650/0.699$, 124.917 reflections collected, 18.049 unique ($R_{int} = 0.133$), $R_1 = 0.0639$, $wR_2 = 0.1610$, using 17.930 reflections with $I > 2\sigma(I)$ to refine 1067 parameters. The crystallography data collection was performed at a STOE IPDS-II diffractometer equipped with a graphite monochromated radiation source ($\lambda = 0.71073$ Å) and an image plate detection system. The selection, integration and averaging procedure of the measured reflex intensities, the determination of the unit cell by a least-squares fit of the 2Θ values, data reduction, LP correction, and the space group determination were performed using the X-Area software package delivered with the diffractometer. An empirical absorption correction method was implemented after indexing of the crystal faces. The structure was solved by direct methods (SHELXS-97) [15] and standard Fourier techniques against F^2 with a full-matrix least-squares algorithm using SHELXL-97 [15] and the WinGX (1.70) [16] software package. All non-hydrogen atoms were refined anisotropically. Hydrogen atoms were placed in calculated positions and refined with a riding model.

2.3. Physical measurements

The magnetic measurements were performed by using a micro-Hall effect magnetometer to detect the magnetic dipolar field of a Mn_{12}-phn single crystal placed on top of the sensor. The field was aligned with the easy axis of magnetization using the transverse field method.

Mn_{12}-phn was deposited on the functionalized Au(1 1 1) surface via ligand exchange reaction with 4-MOBCA as described elsewhere [12]. STM and STS measurements were performed in an Omicron Multiprobe UHV system at room temperature. For the STM/STS measurements, electrochemically etched tungsten tips, flash-annealed by electron bombardment were used. The ± sign of the bias voltage denotes the voltage applied to the sample.

3. Results and discussion

Mn_{12}-phn crystallizes in the space group $I41/a$ with the two different complexes $[Mn_{12}O_{12}(O_2PC_{12}H_{10})_{12}(O_2CCH_3)_4]$ (complex **1a**) and $[Mn_{12}O_{12}(O_2PC_{12}H_{10})_{12}(O_2CCH_3)_4(H_2O)_4]$ (complex **1b**) per asymmetric unit. The structure of the $[Mn_{12}O_{12}]^{16+}$ core is similar to other Mn_{12} complexes (see Fig. 1). The central $[Mn^{IV}_4O_4]^{8+}$ cubane is surrounded by a ring of eight Mn^{III} ions that are held together via eight μ_3-O^{2-} ions. The residual free sites of the Mn^{III} ions are occupied with eight axial and four equatorial μ_2-bridging diphenylphosphinate molecules.

The axial Mn^{III}/Mn^{IV}-bridging molecules are four acetate molecules. The last four free sites of the Mn^{III} ions are occupied by four water molecules in the case of complex **1b**, in case of complex **1a** the free sites keep unoccupied. The ligand exchange reaction remains incomplete as only 12 of the 16 acetate molecules were exchanged. The first four of the equatorial acetate ligands and four of the axial acetate ligands are exchanged [17] as well as four of the equatorial acetate ligands afterwards. In this state the direct coordination sphere around the $[Mn_{12}O_{12}]^{16+}$ core is packed tightly and no further ligands can be exchanged. Only the acetate molecules are small enough to fill the free axial sites bridging the Mn^{III}/Mn^{IV} ions.

Magnetization hysteresis measurements were carried out on a well-shaped Mn_{12}-phn single crystal in the temperature range from 0.4 to 3.2 K, at a sweep rate of 1 T/min. Fig. 2a represents the temperature dependence of the hysteresis loops showing a series of steps, separated by plateaus. As the temperature is lowered, the hysteresis increases because there is a decrease in the transition rate of thermally assisted tunneling. The hysteresis loops become temperature independent below 0.6 K, demonstrating quantum tunneling at the lowest energy levels. The steps in the hysteresis loops are very sharp due to low solvent/ligand disorder in the crystals [18–20]. The field between two resonances allows an estimation of the anisotropy constant D, yielding for the difference between two steps at high fields a value of $D = 0.49$ K (assuming $g = 2$). Additional measurements were performed in the presence of a constant transverse field. The results of these measurements are presented in Fig. 2b showing oscillations of the tunneling probability at zero field as a function of the magnetic field applied approximately along the hard magnetization axis.

Fig. 3 shows STM images of Mn_{12}-phn clusters on the 4-MOBCA/Au(1 1 1) surface obtained at +2.8 V (a) and +0.4 V (b), respectively.

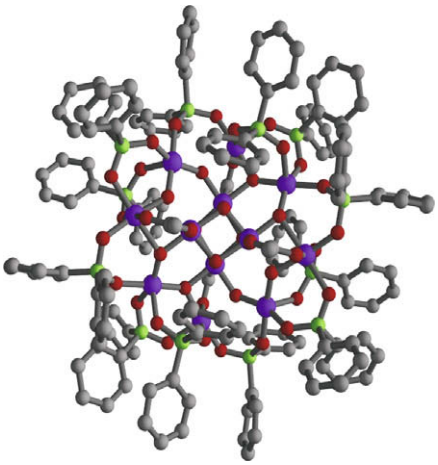


Fig. 1. The structure of Mn_{12}-phn viewed along the c-axis: Mn – violet, O – red, P – green, C – gray. (For interpretation of the references to colour in this figure legend, the reader is referred to the web version of this article.)

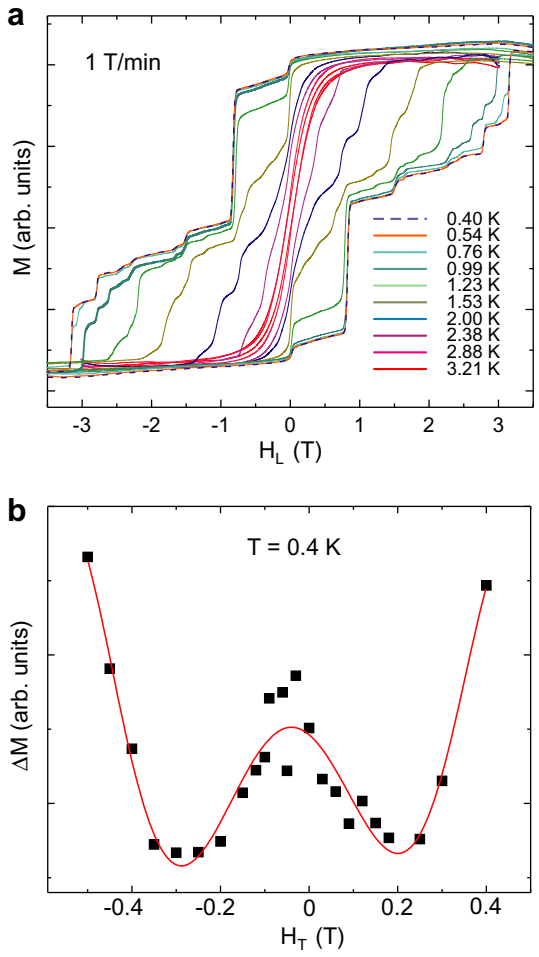


Fig. 2. (a) Hysteresis loops of a Mn_{12}-phn single crystal measured at different temperatures and a constant field sweep rate indicated in the figure. The loops display a series of steps, separated by plateaus. As the temperature is lowered, there is a decrease in the transition rate due to reduced thermally assisted tunneling. The hysteresis loops become temperature independent below 0.6 K. (b) ΔM at zero field as a function of transverse field measured at 0.4 K.

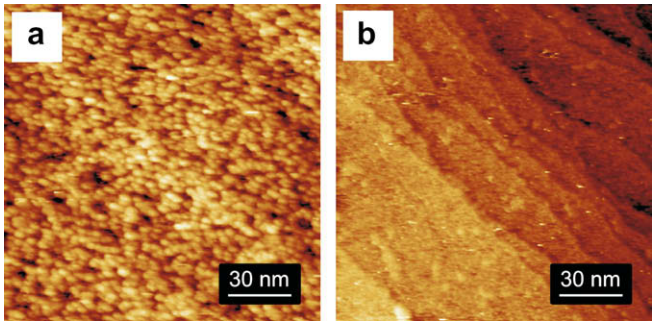


Fig. 3. 150 × 150 nm^2 STM images of Mn_{12}-phn clusters measured at +2.8 V (a) and +0.4 V (b) bias voltage. Mn_{12}-phn molecules are "invisible" for the STM tip at +0.4 V (within the conductance gap) and thus the characteristic steps of the 4-MOBCA covered Au(1 1 1) surface are visible. The two STM pictures were obtained from the same sample area.

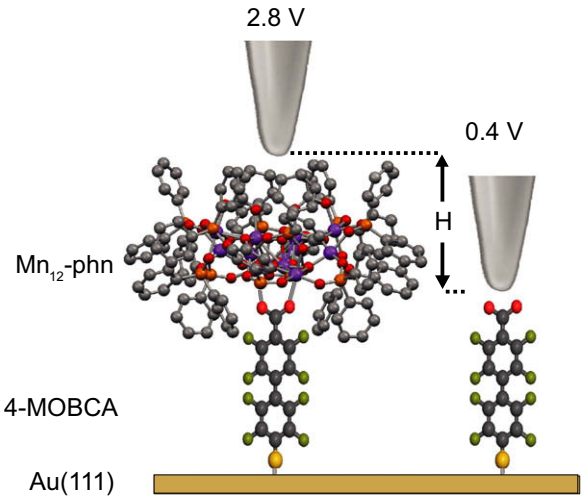


Fig. 4. Schematic representation of the *z*–*U* spectroscopy measurements on Mn_{12}-phn.

The higher bias voltage corresponds to the region of high conductance, whereas the lower value corresponds to the conductance gap region. The molecules are invisible for the STM operated at +0.4 V bias voltage, and thus the characteristic monoatomic steps of the 4-MOBCA covered Au(1 1 1) surface can be observed. At +2.8 V bias voltage the Mn_{12}-phn molecules are visible.

For the determination of molecular heights we utilized the *z*–*U* spectroscopy method described elsewhere [21,22]. The principle of *z*–*U* spectroscopy implemented in this study is shown in an idealized sketch in Fig. 4. An STM tip is brought into tunneling contact with a Mn_{12} molecule. This corresponds to a tip-molecule distance of about 0.5 nm. *z*–*U* characteristics of Mn_{12}-phn are obtained by varying the bias voltage and measuring the *z*-position of the tip. The feedback loop of the STM remains operating and a fixed set current is selected so that the tip position is altered whenever a variation of the tunneling current is detected. Since Mn_{12} molecules reveal a broad conductance gap in STS I-U measurements [12,13] no molecular states can be occupied by electrons at low bias voltage, thus the tunneling current rapidly decreases around the onset of the conductance gap. As a result, the tip is extended until the fixed set current is restored. STM images and STS spectra [22] show that this is the case for a tunneling contact with the 4-MOBCA functionalized substrate. In a previous work, [12] STS I-U spectra of 4-MOBCA also showed that the conductance is relatively low at low bias voltage. Consequently, the STM tip approaches the 4-MOBCA layer very closely and the difference *H* between the positions of (tunneling) contact with the Mn_{12} molecule and the substrate is a good estimation of the real height of the molecular layer.

Fig. 5a shows *z*–*U* spectra obtained from different Mn_{12}-phn clusters. The set current was 6.9 pA. In the *z*–*U* spectra, a distinct step is visible around 1 V, corresponding to −0.5 nm with respect to the 0 nm position for 2.8 V. The step separates two distance ranges which correspond to a tunneling contact with the Mn_{12}-phn molecule (high bias voltage) and with the 4-MOBCA functionalization layer (low bias voltage). To demonstrate that the step is not a measurement artifact, a *z*–*U* spectrum obtained from bare Au(1 1 1) in the bias voltage range between 0.4 V and 1.4 V is shown for comparison. The absolute *z* position is not directly comparable to the measurement on Mn_{12}-phn due to the different starting positions. Nonetheless, no hint of any step is visible in the *z*–*U* spectrum obtained from Au(1 1 1), clearly showing that the signatures obtained from Mn_{12}-phn are due to the molecule.

The evaluation of 40 *z*–*U* spectra obtained from Mn_{12}-phn yields an average step height of 1.4 nm with the individual step heights ranging from 1.1 to 1.7 nm. These values are in very good agreement with the diameter of the Mn_{12}-phn molecules derived from the X-ray structure, assuming random orientation and ligand exchange with 4-MOBCA. A broad spread of the measured molec-

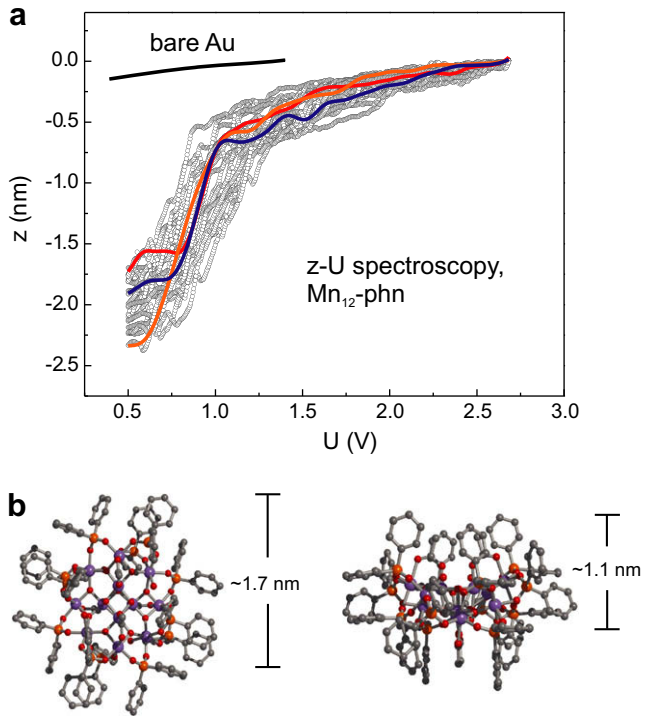


Fig. 5. (a) Representative distance–voltage characteristics obtained from different individual Mn_{12}-phn molecules (open circles) and from bare Au(111) (black line, upper corner, same scale). Three curves marked with different colors (red, orange, blue) are presented to demonstrate the different step heights. (b) Sketches of two orientations of Mn_{12}-phn molecules resulting in the minimum and maximum height values of 1.1 nm and 1.7 nm (measured with respect to the 4-MOBCA layer due to the exchange of ligands). (For interpretation of the references to colour in this figure legend, the reader is referred to the web version of this article.)

ular heights can be attributed to a random orientation of different molecules which can be explained by the equally high acidity of the diphenylphosphinic acid and of 4-MOBCA with no site-specific ligand exchange reaction being expected. The bulky diphenylphosphinate ligands effectively suppress the ligand exchange of the axial acetate ligands thus leading to the higher ligand exchange probability of the diphenylphosphinate ligands. Contrary to that, in the case of Mn_{12}-thiophenecarboxylate (Mn_{12}-th) a smaller spread of the measured molecular heights was observed. [22] Moreover, the comparison of the measured molecular heights with the structural X-ray data obtained from Mn_{12}-th single crystals indicated that the Mn_{12}-th molecules are oriented with the easy axis perpendicular to the surface. A preferred orientation was explained by a higher probability for exchange of axial ligands due to the higher acidity of 4-MOBCA compared to thiophenecarboxylate ligands. [23] Thus, we show that the substitution of the Mn_{12} ligand shell may have a major impact on the surface orientation of the Mn_{12} clusters deposited on Au, i.e. on the orientation of the easy magnetization axis. Moreover, the possibility to determine the orientation of individual Mn_{12} molecules is an important prerequisite for future well-defined magnetic field dependent cryogenic STS measurements. For such measurements, the orientation of the molecular easy magnetization axis with respect to an external magnetic field has to be known. According to the results of the *z–U* spectroscopy, the orientation can be identified by means of STS. Beyond the estimation of the real height, the *z–U* spectra also demonstrate the presence of a single Mn_{12}-phn monolayer on 4-MOBCA, thus confirming the success of the ligand exchange reaction.

4. Conclusion

The synthesis, investigation as well as surface deposition of a truly axial symmetry Mn_{12}-diphenylphosphinate (Mn_{12}-phn) single molecule magnet has been reported. Out of 16 acetate ligands encapsulating the $Mn_{12}O_{12}$ core, 12 ligands were exchanged by diphenylphosphinate in this compound. Mn_{12}-phn shows well-defined steps in the magnetic hysteresis loops indicating that the crystals possess a very high quality. A monolayer of Mn_{12}-phn was chemically grafted on a functionalized Au(111) substrate and studied by means of STM/STS. The presence of a conductance gap in Mn_{12} molecules was used for distance–voltage (*z–U*) spectroscopy that, in the present case, allows the determination of the real-space height of the molecules with high accuracy. A large spread in the measured molecular heights obtained from the *z–U* spectra indicates the absence of a preferential orientation of the Mn_{12}-phn molecular easy axis with respect to the surface which we attribute to the equally high acidity of the diphenylphosphinic acid and of 4-MOBCA. These results are compared with the data obtained from another Mn_{12} derivative containing 16 thiophenecarboxylate ligands which shows a preferential orientation of the clusters on the Au surface with the easy magnetic axis perpendicular to the surface plane. In general, we show that the substitution of the ligand shell may have a major impact on the surface orientation of Mn_{12} clusters deposited on Au, i.e. on the orientation of the easy magnetization axis. This represents a crucial step towards addressing the magnetic properties of individual Mn_{12} molecules in the future. The possibility to identify the orientation of individual molecules will allow measurements with a well-defined orientation of the easy magnetization axes with respect to an external magnetic field.

Acknowledgement

This work was supported by the Deutsche Forschungsgemeinschaft (DFG) via the Collaborative Research Center (SFB) 767, Project C5.

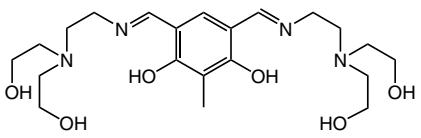
Appendix A. Supplementary data

Supplementary data associated with this article can be found, in the online version, at doi:10.1016/j.poly.2008.11.028.

References

[1] D. Gatteschi, R. Sessoli, Angew. Chem. Int. Ed. 42 (2003) 268.
[2] G. Christou, D. Gatteschi, D.N. Hendrickson, R. Sessoli, MRS Bull. 25 (2000) 66.
[3] M.N. Leuenberger, D. Loss, Nature 410 (2001) 789.
[4] L. Bogani, W. Wernsdorfer, Nature Mater. 7 (2008) 179.
[5] A. Cornia, A.C. Fabretti, M. Pacchioni, L. Zobbi, D. Bonacchi, A. Caneschi, D. Gatteschi, R. Biagi, U. del Pennino, V. De Renzi, L. Gurevich, H.S.J. van der Zant, Angew. Chem. 115 (2003) 1683.
[6] G.G. Condorelli, A. Motta, I.L. Fragal, F. Giannazzo, V. Raineri, A. Caneschi, D. Gatteschi, Angew. Chem. Int. Ed. 43 (2004) 4081.
[7] A. Naitabdi, J.-P. Bucher, P. Gerbier, P. Rabu, M. Drillon, Adv. Mater. 17 (2005) 1612.
[8] B. Fleury, L. Catala, V. Huc, C. David, W.Z. Zhong, P. Jegou, L. Baraton, S. Palacin, P.-A. Albouy, T. Mallah, Chem. Commun. (2005) 2020.
[9] E. Coronado, A. Forment-Aliaga, F.M. Romero, V. Corradini, R. Biagi, V. De Renzi, A. Gambardella, U. del Pennino, Inorg. Chem. 44 (2005) 7693.
[10] L. Bogani, L. Cavigli, M. Gurioli, R.L. Novak, M. Mannini, A. Caneschi, F. Pineider, R. Sessoli, M. Clemente-León, E. Coronado, A. Cornia, D. Gatteschi, Adv. Mater. 19 (2007) 3906.
[11] M. Mannini, P. Sainctavit, R. Sessoli, C. Cartier dit Moulin, F. Pineider, M.-A. Arrio, A. Cornia, D. Gatteschi, Chem. Eur. J. 14 (2008) 7530.
[12] M. Burgert, S. Voss, S. Herr, M. Fonin, U. Groth, U. Rüdiger, J. Am. Chem. Soc. 129 (2007) 14362.
[13] S. Voss, M. Fonin, U. Rüdiger, M. Burgert, U. Groth, Appl. Phys. Lett. 90 (2007) 133104.
[14] T. Lis, Acta Crystallogr., Sect. B: Struct. Crystallogr. Cryst. Chem. 36 (1980) 2042.

[15] G.M. Sheldrick, SHELX-97, An Integrated System for Solving and Refining Crystal Structures From Diffraction Data, University of Göttingen, Germany, 1997.
[16] L.J. Farrugia, J. Appl. Crystallogr. 32 (1999) 837.
[17] C. Boskovic, M. Pink, J.C. Huffman, D.N. Hendrickson, G. Christou, J. Am. Chem. Soc. 123 (2001) 9914.
[18] L. Bokacheva, A.D. Kent, M.A. Walters, Phys. Rev. Lett. 85 (2000) 4803.
[19] E. del Barco, A.D. Kent, S. Hill, J.M. North, N.S. Dalal, E.M. Rumberger, D.N. Hendrickson, N. Chakov, G. Christou, J. Low Temp. Phys. 140 (2005) 119.
[20] W. Wernsdorfer, M. Murugesu, G. Christou, Phys. Rev. Lett. 96 (2006) 057208.
[21] M. Kemerink, S.F. Alvarado, P. Müller, P.M. Koenraad, H.W.M. Salemink, J.H. Wolter, R.A.J. Janssen, Phys. Rev. B 70 (2004) 045202.
[22] S. Voss, O. Zander, M. Fonin, U. Rüdiger, M. Burgert, U. Groth, Phys. Rev. B 78 (2008) 155403.
[23] P. Artus, C. Boskovic, J. Yoo, W.E. Streib, L.-C. Brunel, D.N. Hendrickson, G. Christou, Inorg. Chem. 40 (2001) 4199.



Scheme 1. The ligand H_6ipa-bhea.

documented. In this paper we report the synthesis and chemical characterization of mono- and dinuclear copper(II) complexes based on the H_6ipa-bhea ligand. The magnetic properties of the dinuclear complex will be presented and discussed on the basis of density functional theory (DFT) calculations utilizing the broken symmetry (BS) approach.

2. Experimental

2.1. Materials

N,*N*-*bis*-(pyridin-2-ylmethyl)ethylenediamine (unspenp) [18], *N*,*N*-*bis*-(2-hydroxyethyl)ethylenediamine (bhea) [15], and 2-methyl-4,6-diformylresorcinol (ipa) [11] were synthesized according to literature procedures. All other starting materials are commercially available and were used without further purification. Further abbreviations used throughout the text: H_6ipa-bhea = 4,6-*bis*-(2-(*bis*-(2-hydroxyethyl)amino)ethylimino-methyl)-2-methyl-1,3-di hydroxybenzene, H_4hyforsa-bhea = 6-(2-(*bis*-(2-hydroxyethyl) amino)ethylimino-methyl)-4-formyl-2-methyl-1, 3-dihydroxybenzene, H_2hyforsa-unspenp = 6-(2-(*bis*-(pyridin-2-ylmethyl)amino) ethylimino-methyl)-4-formyl-2- methyl-1,3-dihydroxybenzene.

2.2. Physical measurement

Melting points are given uncorrected and were determined with a VEB Analytik Dresden HMK 72/41555. NMR spectra were recorded on Bruker Avance 200 and 400 MHz spectrometers at ambient temperatures. The chemical shifts were referenced to tetramethylsilane and are reported in ppm. The infrared spectra were recorded on a Bruker IFS55/EQUINOX spectrometer. Elemental analyses were determined on a Leco CHNS/932 and a VARIO EL III elemental analyzer. Magnetic susceptibilities were obtained from a polycrystalline sample using a Quantum-Design MPMSR-5S SQUID magnetometer, measurements were conducted with an applied magnetic field of 2000 and 5000 Oe in the temperature range from 300 to 2 K (for details see Ref. [19]). The measured values of χ_M were corrected for their diamagnetic contribution.

2.3. Synthesis of the ligand

2.3.1. H_6ipa-bhea

2-Methylresorcinol (0.75 g, 4 mmol) was added to a solution of bhea (1.24 g, 8 mmol) in ethanol (50 ml) leading to a yellow solution. The reaction mixture was stirred for additional 2 h at ambient temperature. After removing the volatile components *in vacuo* at ambient temperature the ligand was obtained as a yellow solid in quantitative yield (Yield: 1.80 g). M.p. 99 °C. *Anal.* Calc. for $C_{21}H_{36}N_4O_6$: C, 57.25; H, 8.24; N, 12.72. Found: C, 57.21; H, 8.39; N, 12.59%. ^{1}H NMR (200 MHz, DMSO–d_6): δ = 1.87 (s, 3H, CH_3); 2.59 (t, 8H, ^3J = 6.2 Hz, NCH_2CH$_2$OH); 2.75 (t, 4H, ^3J = 6.2 Hz, C=NCH$_2$CH_2N); 3.41 (t, 8H, ^3J = 6.2 Hz, CH_2OH); 3.56 (t, 4H, ^3J = 6.2 Hz, C=NCH_2CH$_2$N); 4.50 (s br, 4H, CH$_2$OH); 7.21 (s, 1H, arom. CH); 8.32 (s, 2H, CH=N); 14.30 ppm (s br, 2H, arom. OH). ^{13}C NMR (50 MHz, DMSO–d_6): δ = 7.5 (CH_3); 53.0 and 55.1 (NCH$_2$CH_2N); 56.0 (NCH_2CH$_2$OH); 59.3 (CH_2OH); 110.0 and 111.1 (arom. C^2; $C^{4,6}$); 136.8 (arom. C^5); 165.3 (CH=N); 168.6 ppm (arom. $C^{1,3}$). IR (KBr, cm^{-1}): 3376 s br, 2940 m, 2906 m, 2869 m, 2837 m, 1638 s, 1588 vs, 1444 m, 1348 w, 1295 w, 1196 s, 1044 m.

2.4. Synthesis of the complexes

2.4.1. [$Cu_2(H_4$ipa-bhea)](ClO$_4$)$_2$ (**1**)

Aqueous ammonia (2 equiv.) was added to a solution of H_6ipa-bhea (96 mg, 0.2 mmol) in methanol (3 ml). Subsequent dropwise addition of Cu(ClO$_4$)$_2$ · 6H$_2$O (162 mg, 0.4 mmol), dissolved in methanol (5 ml), initially resulted in the formation of a green precipitate, which upon complete addition fully redissolved. The resulting dark green solution was stirred for further 20 min. Slow diffusion of diethylether into this solution afforded green prisms of **1** · MeOH suitable for X-ray diffraction within two days. The crystals were filtered off and dried *in vacuo*, which leads to the loss of the solvent of crystallization (Yield: 132 mg, 79%). M.p. >280 °C. *Anal.* Calc. for $C_{21}H_{34}Cl_2Cu_2N_4O_{14}$: C, 32.99; H, 4.48; N, 7.33. Found: C, 31.95; H, 4.37; N, 6.92%. IR (KBr, cm^{-1}): 3400 s br, 2925 m, 1621 s, 1590 vs, 1447 m, 1398 m, 1272 m, 1201 s, 1142 m, 1108 vs, 1090 vs, 1060 m 715 w, 626 m.

2.4.2. [Cu(H_3hyforsa-bhea)]ClO$_4$ · 2H_2O (**2**)

H_6ipa-bhea (244 mg, 0.5 mmol), dissolved in water (5 ml), was added to a solution of Cu(ClO$_4$)$_2$ · 6 H$_2$O (410 mg, 1.1 mmol) in water (5 ml). The resulting turquoise solution was stirred for 10 min and kept undisturbed in a closed vessel. Overnight blue prisms of **2** suitable for X-ray diffraction were obtained. The bulk material was obtained by slow evaporation of the solvent at ambient temperature for additional three days. The crystals were separated by filtration, washed with a small amount of water and dried *in air* (Yield: 208 mg, 74%). M.p. >280 °C. *Anal.* Calc. for $C_{15}H_{25}ClCuN_2O_{11}$: C, 35.44; H, 4.96; N, 5.51. Found: C, 35.63; H, 4.57; N, 5.39%. IR (KBr, cm^{-1}): 3245 s br, 2926 m, 1633 vs, 1601 vs, 1559 vs, 1450 s, 1372 m, 1302 s, 1188 vs, 1121 vs, 1090 vs, 1060 s, 771 m, 730 m, 626 m.

2.4.3. [Cu(Hhyforsa-unspenp)]ClO$_4$ (**3**)

Complex **2** (145 mg, 0.3 mmol) was dissolved in methanol (10 ml) by stirring for about 30 min, resulting in a clear deep blue colored solution. Subsequently a solution of unspenp (69 mg, 0.3 mmol) in methanol (1 ml) was added accompanied by a color change to dark green. The reaction mixture was stirred for additional 5 min leading to a green precipitate and the mixture was kept overnight at ambient temperature. During this period a green microcrystalline solid was formed, which was filtered off, washed with methanol and finally redissolved in acetonitrile. Slow diffusion of diethylether into this solution afforded, within two days, green prisms of **3** suitable for X-ray diffraction. The crystals were separated by filtration and dried *in vacuo* (Yield: 129 mg, 80%). M.p. >280 °C. *Anal.* Calc. for $C_{23}H_{23}ClCuN_4O_7$: C, 48.77; H, 4.09; N, 9.89. Found: C, 48.63; H, 4.12; N, 9.85%. IR (KBr, cm^{-1}): 3357 s br, 3284 m, 2985 w, 2939 w, 2901 w, 1632 s, 1602 vs, 1542 vs, 1450 s, 1391 m, 1357 m, 1332 s, 1260 s, 1122 vs, 1108 vs, 1073 s, 1050 m, 901 w, 625 m.

2.5. X-ray crystallographic studies

X-ray measurements were carried out on a Nonius Kappa CCD diffractometer using graphite monochromated Mo Kα radiation (λ = 71.073 pm) at 183(2) K. The crystallographic data are summarized in Table 1. Data were corrected for Lorentz and polarization effects, but not for absorption effects [20]. The structures were solved by direct methods with SHELXS97 and refined by full-matrix least-squares techniques against F_o^2 using SHELXL97 [21]. For **1** · MeOH the observed systematic absences suggest either of the tetragonal space groups *Pca*2$_1$ and *Pcca*. Attempts to solve the

Table 1
Crystallographic and structure-refinement data for complexes **1**, **2**, and **3**.

Compound	**1** · MeOH	**2**	**3**
Empirical formula	$C_{22}H_{38}Cl_2Cu_2N_4O_{15}$	$C_{15}H_{25}ClCuN_2O_{11}$	$C_{23}H_{23}ClCuN_4O_7$
Formula weight	796.54	508.36	566.44
Crystal size (mm)	1.2 × 1.0 × 0.8	1.2 × 1.2 × 1.0	0.5 × 0.5 × 0.4
Crystal system	orthorhombic	monoclinic	monoclinic
Space group	$Pca2_1$	$P2_1/c$	$C2/c$
a (pm)	1300.67(5)	730.11(2)	1854.79(7)
b (pm)	1332.10(5)	1718.15(7)	1919.64(8)
c (pm)	1841.37(7)	1616.82(6)	1364.46(4)
α (°)	90	90	90
β (°)	90	98.663(2)	104.656(2)
γ (°)	90	90	90
V (nm^3)	3.1904(2)	2.00506(12)	4.7001(3)
Z	4	4	8
$D_{calcd.}$ (Mg m^{-3})	1.658	1.684	1.601
μ (mm^{-1})	1.575	1.285	1.097
θ range of data collection (°)	2.21, 27.49	2.37, 27.47	2.38, 27.47
Measured reflections	18417	4570	16484
Unique reflections (R_{int})	7037 (0.038)	3776 (0.030)	5377 (0.037)
Goodness-of-fit on F^2	1.063	1.014	1.031
R_1 ($I > 2\sigma(I)$)[a]	0.0657	0.0339	0.0471
wR_2 indices (all data)[b]	0.1849	0.0885	0.1369

[a] $R_1 = \sum ||F_o| - |F_c|| / \sum |F_o|$.
[b] $wR_2 = \left[\sum w(F_o^2 - F_c^2)^2 / \sum w(F_o^2)^2\right]^{\frac{1}{2}}$.

structure in the centrosymmetric space group were unsuccessful. This led in agreement with intensity statistics to the non-centrosymmetric orthorhombic space group $Pca2_1$ as the final choice. The refinement afforded a Flack parameter [22] of about 0.3, which changed to about 0.7 upon inversion of the parameter set. Therefore, the final structure refinement was performed by assuming racemic twinning and refining a free variable for the ratio of the two racemic components. All non-hydrogen atoms were refined anisotropically. The hydrogen atoms in structures of **1** · MeOH and **3** were included at calculated positions with fixed thermal parameters. For the structure of **2** the carbon-bounded hydrogen atoms were placed at calculated positions with fixed thermal parameters. All protic hydrogen atoms on oxygen atoms (water, phenol, and hydroxy) were found during structure solution and refined isotropically.

2.6. Computational details

The density functional theory (DFT) according to the Kohn–Sham scheme was employed to study the magnetic properties of the complex. All-electron DFT calculations and geometry optimizations were performed with the quantum chemical program package TURBOMOLE [23]. As implemented in this program, the gradient corrected (GGA) functional BP86 [24] in combination with the resolution-of-the-identity (RI) density-fitting technique [25] and the hybrid functional B3LYP [26] were used together with the def2-TZVP basis set which is of split-valence triple-ζ quality with additional polarization functions on all atoms [27]. For structure optimization a geometry gradient norm of 3×10^{-4} hartree/bohr was used as convergence criterion.

The magnetic properties of the dinuclear complex **1** are analyzed according the phenomenological Heisenberg Hamiltonian $\hat{H} = -J\hat{S}_1\hat{S}_2$, where the coupling constant J is given by the energy difference between the relevant singlet and singlet states ($J = E_S - E_T$). Therefore, a negative value of J indicates antiferromagnetic coupling with a triplet ground state. The BS approach originally proposed by Noodleman was used to cope with the DFT inherent problem that the singlet state cannot be expressed by a single determinant [28]. In this formalism, the energy of the singlet state is computed on the basis of a single determinate of broken spin and space symmetry built up by localizing spin up and spin down electrons onto the two copper centers, which is not a spin eigenstate. Although the original formalism was based on spin projection to extract the singlet energy, it has been shown that this energy can be directly estimated from the energy of the BS solution (E_{BS}) without performing any spin projection according to [29]:

$$J = E_{BS} - E_T \quad (1)$$

This procedure is in accordance with the proposal of Perdew et al. [30], who suggested that the BS determinant is the correct solution of the Kohn–Sham equations for the singlet state. Consequently, the inclusion of Hartree–Fock (HF) type contributions, which are known to usually overestimate the relative stability of the triplet state, can improve the accuracy of the calculated values [29]. Therefore, we used the gradient corrected (GGA) functional BP86 and the hybrid functional B3LYP for comparison.

3. Results and discussion

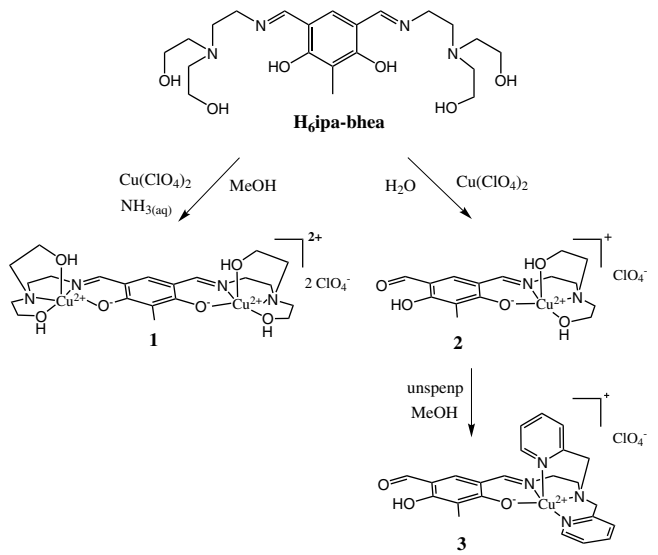
3.1. Synthesis and characterization

The ligand H_6ipa-bhea was prepared by Schiff-base condensation of 2-methyl-4,6-diformylresorcinol (ipa) with two equivalents of *N,N-bis*-(2-hydroxyethyl)ethylenediamine (bhea). The H_6ipa-bhea ligand provides two equal pentadentate [N_2O_3] binding pockets, with a phenolate oxygen, an imine and amine nitrogen, and two oxygen atoms of the hydroxy ethyl groups as potential donors. The reaction with two equivalents of $Cu(ClO_4)_2 \cdot 6H_2O$ leads to either the expected dinuclear or a mononuclear copper(II) complex depending on the reaction conditions as illustrated in Scheme 2.

If the reaction is carried out in methanol in the presence of two equivalents aqueous ammonia the desired dinuclear copper(II) complex $[Cu_2(H_4ipa\text{-}bhea)](ClO_4)_2$ (**1**) is obtained. The compound can be isolated as green crystals of the corresponding solvent containing compound **1** · MeOH. As both phenolate groups are deprotonated, the bridging ligand coordinates the two copper(II) ions in its dianionic form.

On the other hand, the complexation reaction in water results in the partial hydrolysis of the ligand H_6ipa-bhea. Such a copper assisted ligand hydrolysis is not uncommon and reported in literature for different Schiff-base ligands during complexation reaction [31]. One of the imine side chains is hydrolyzed under addition of two equivalents of $Cu(ClO_4)_2 \cdot 6H_2O$ regenerating a free formyl group. Whereas the second binding pocket remains intact and is coordinating a copper(II) ion resulting in the formation of the mononuclear complex $[Cu(H_3hyforsa\text{-}bhea)]ClO_4 \cdot 2H_2O$ (**2**). Here the hydrolyzed ligand H_4hyforsa-bhea coordinates in its monoanionic form. Because of the excellent solubility of the byproduct, the copper(II) complex formed by the in situ generated primary tetradentate amine *N,N-bis*-(2-hydroxyethyl)ethylenediamine (bhea) and the second equivalent copper(II) perchlorate, compound **2** can be easily isolated analytical pure and in high yield. As no analytic evidence for the formation of the corresponding dinuclear complex **1** could be detected, the mononuclear complex **2** is the sole resorcinol containing product of this reaction.

As complex **2** contains a free formyl group, it should be accessible for an additional Schiff-base condensation potentially forming an unsymmetric double-Schiff-base ligand. Besides the well-known synthetic multistep and protecting group approaches to unsymmetric ligands [32], we have recently established a straightforward general synthesis of unsymmetric compartmental end-off



Scheme 2. Synthesis of copper(II) complexes with H_6ipa-bhea.

double-Schiff-base ligands based on a stepwise Schiff-base condensation of the free ligand system [33].

Following this line we reacted the mononuclear complex **2** with the tetradentate amine *N*,*N*-*bis*-(pyridin-2-ylmethyl)ethylenediamine (unspenp) in methanol. From this reaction the mononuclear complex [Cu(Hhyforsa-unspenp)]ClO_4 (**3**) could be isolated, which unexpectedly contained an altered coordination pocket for the copper(II) ion. Most likely the intended reaction takes place, but the newly generated nitrogen-rich coordination pocket has a higher affinity to coordinate the copper(II) ion and in turn the initial Schiff-base group is hydrolytically cleaved. The resulting mono-Schiff-base ligand H_2hyforsa-unspenp formed from ipa and unspenp, again contains a free formyl group and coordinates as a mono anionic ligand. Nevertheless, under appropriate conditions and/or with a suitable amine component both mononuclear complexes **2** and **3** seem to be likely candidates as metal containing building blocks for the directed synthesis towards unsymmetric homo- and heterodinuclear transition metal complexes.

All complexes were characterized by X-ray structural analysis, elemental analysis, and IR spectroscopy. The crystals of **1** · MeOH lose the co-crystallized methanol molecules upon drying whereas crystals of **2** remained intact with two water molecules per complex moiety. The IR spectrum of the ligand exhibits two strong characteristic bands at 1638 and 1588 cm^{-1}, which can be attributed to the stretching vibration of the imine moieties ($\nu_{C=N}$) and the bridging phenylene ring ($\nu_{C=C}$). Upon coordination to copper(II) ions in the dinuclear complex **1**, these bands are slightly shifted to 1621 and 1590 cm^{-1}. In both mononuclear complexes **2** and **3** the IR spectra contain an additional band in this region as a result of the $\nu_{C=O}$ stretching vibration of the formyl group. The corresponding bands are observed at 1633, 1601, and 1559 cm^{-1} in **2** and 1632, 1602, and 1542 cm^{-1} in **3**. These bands are shifted to somewhat lower frequencies due to a formation of intramolecular hydrogen bonds with the *ortho*-positioned phenol, typical for salicylaldehyde derivatives. Due to the coordination of the copper(II) ion through the second phenolate oxygen atom affecting the relevant resonances an unambiguous assignment is not possible. Moreover, for all three complexes further strong bands, broad and structured, are observed in the region at around 1100 cm^{-1} characteristic for stretching vibrations of unbound perchlorate counterions in the crystal lattice.

3.2. Description of the structures

3.2.1. [Cu_2(H_4ipa-bhea)](ClO_4)$_2$ · MeOH (**1** · MeOH)

The homodinuclear complex [Cu_2(H_4ipa-bhea)](ClO_4)$_2$ · MeOH (**1** · MeOH) crystallizes in the orthorhombic space group $Pca2_1$. The molecular structure and labeling scheme of the complex cation of **1** · MeOH is depicted in Fig. 1. Selected bond lengths and angles are listed in Table 2.

The coordination sites at both copper ions are occupied by the N_2O_3 donor sets of the doubly deprotonated [H_4ipa-bhea]$^{2-}$ ligand system. The metal centers are coordinated through the phenolate oxygen atoms O1/O4, the Schiff-base nitrogen atoms N1/N3, the amine nitrogen atoms N2/N4 as well as both hydroxy oxygen atoms O2/O5 and O3/O6. The coordination polyhedra around Cu1 can best be described as slightly distorted square pyramid with a τ value of 0.21 (τ = 0 for an ideal tetragonal pyramid, τ = 1 for an ideal trigonal bipyramid [34]). The tetragonal plane is formed by the oxygen atoms O1 and O2 as well as the nitrogen atoms N1 and N2 with bond lengths ranging from 186 to 203 pm. The copper ion is displaced from this plane by 18 pm towards the apical position, which is occupied by the oxygen atom O3 with a Cu–O distance of 226 pm. As compared to the bond lengths of the relevant equatorial donor atoms, the Cu–O3 bond length is significantly elongated, due to the typical Jahn–Teller distortion of the copper(II) ion. In contrast, the Cu2 center exhibits a distorted trigonal–pyramidal coordination environment with τ = 0.77. The trigonal plane is formed by the Schiff-base nitrogen atom N3 at a distance of 192 pm and the two weak oxygen donors O5 and O6 of the hydroxy ethyl groups at a distance of about 212 pm. The apical positions with a *trans* angle of 178° are occupied by the phenolate oxygen atom O4 and the amine nitrogen atom N4 at distances of 188 and 203 pm, respectively.

The dinuclear cation [Cu_2(H_4ipa-bhea)]$^{2+}$ of complex **1** crystallizes together with two perchlorate counterions and one methanol

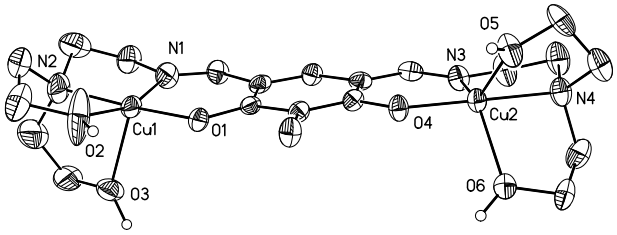


Fig. 1. Molecular structure of the complex cation of [Cu_2(H_4ipa-bhea)](ClO_4)$_2$ · MeOH (**1** · MeOH). Carbon-bound hydrogen atoms are omitted for clarity. Thermal ellipsoids are drawn at the 30% probability level.

Table 2
Selected bond lengths (pm) and angles (°) for [Cu_2(H_4ipa-bhea)](ClO_4)$_2$ · MeOH (**1** · MeOH).

Cu1–O1	186.2(4)	Cu2–O4	188.0(5)
Cu1–O2	202.5(9)	Cu2–O5	210.7(6)
Cu1–O3	226.4(6)	Cu2–O6	214.2(5)
Cu1–N1	192.2(8)	Cu2–N3	191.5(5)
Cu1–N2	202.8(7)	Cu2–N4	203.0(6)
O1–Cu1–O3	104.8(2)	O4–Cu2–O5	97.0(2)
O1–Cu1–O2	92.8(3)	O4–Cu2–O6	95.4(2)
O1–Cu1–N1	95.2(3)	O4–Cu2–N3	95.8(2)
O1–Cu1–N2	174.0(3)	O4–Cu2–N4	178.2(2)
O2–Cu1–O3	94.4(4)	O5–Cu2–O6	97.7(3)
O2–Cu1–N1	162.3(4)	O5–Cu2–N3	132.0(3)
O2–Cu1–N2	83.8(3)	O5–Cu2–N4	81.7(2)
O3–Cu1–N1	98.9(3)	O6–Cu2–N3	126.8(3)
O3–Cu1–N2	80.4(3)	O6–Cu2–N4	83.6(3)
N1–Cu1–N2	86.8(3)	N3–Cu2–N4	86.0(3)

molecule. The resulting hydrogen bonding for the cationic complex is depicted in Fig. 2. As the oxygen donors of the hydroxy ethyl groups are only weakly bound to the copper(II) ions, their actual coordination geometries seem to be influenced by the hydrogen bonding interactions with the methanol molecule. The relevant hydrogen bonding distances are well within the usually observed range [17,35,36]. Both perchlorate ions show a disorder of all oxygen atoms which is typical for unbounded and non-interacting tetrahedral counterions, and even not unexpected for cases with a terminal hydrogen bonding interaction like the perchlorate ion Cl1 (cf. Fig. 2) [37].

3.2.2. $[Cu(H_3hyforsa\text{-}bhea)]ClO_4 \cdot 2H_2O$ (**2**)

The molecular structure and atom labeling scheme of the complex cation $[Cu(H_3hyforsa\text{-}bhea)]^+$ is depicted in Fig. 3. The complex cation crystallizes together with one perchlorate counterion and two water molecules in the space group $P2_1/c$. One imine group of the initial double-Schiff-base ligand is hydrolyzed during complexation reaction while the second binding pocket remains intact and coordinates a copper(II) ion. The coordination geometry of the copper(II) ion is similar to the Cu1 center of complex **1**. The basal plane of the distorted square-pyramidal environment ($\tau = 0.28$) is formed by the donor atoms O1, O2, N1, and N2. The copper center is displaced from the basal plane by 15 pm towards the apical position occupied by the hydroxy oxygen atom O3. Selected bond lengths and angles are summarized in Table 3.

The phenol oxygen atom O4 remains protonated and is involved in an intramolecular hydrogen bonding interaction with the oxygen atom O5 of the free formyl group. Additional intermolecular hydrogen bonding of O5 with the oxygen atom O3 of the apical hydroxy ethyl side chain of an adjacent $[Cu(H_3hyforsa\text{-}bhea)]^+$ moiety leads to the formation of dimeric $[\{Cu(H_3hyforsa\text{-}bhea)\}_2]^{2+}$ units, as illustrated in Fig. 4. Moreover, within the dimeric units the phenylene rings are involved in π–π interactions at a distance of about

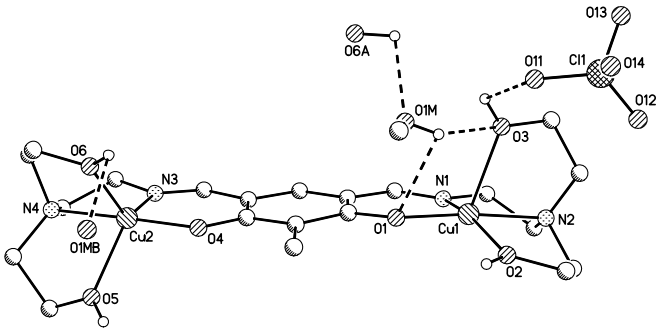


Fig. 2. Representation of the supramolecular structure of complex $[Cu_2(H_4ipa\text{-}bhea)](ClO_4)_2 \cdot MeOH$ (**1** · MeOH). Dashed lines indicate hydrogen bonds. Symmetry equivalent atoms are labeled with the suffixes A and B. Pertinent distances: O1···O1M 275, O3···O1M 289, O3···O11 289, O1M···O6A 265 pm.

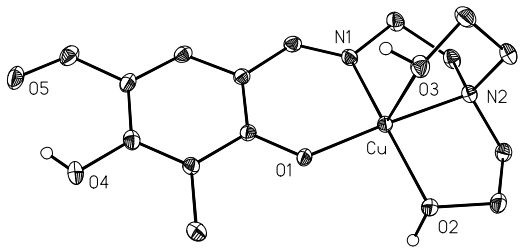


Fig. 3. Molecular structure of the complex cation of $[Cu(H_3hyforsa\text{-}bhea)]\text{-}ClO_4 \cdot 2H_2O$ (**2**). The carbon-bound hydrogen atoms are omitted for clarity. Thermal ellipsoids are drawn at the 30% probability level.

Table 3
Selected bond lengths (pm) and angles (°) for complexes $[Cu(H_3hyforsa\text{-}bhea)]\text{-}ClO_4 \cdot 2H_2O$ (**2**) and $[Cu(Hhyforsa\text{-}unspenp)]ClO_4$ (**3**).

2		**3**	
Cu1–O1	189.5(1)	Cu1–O1	188.5(2)
Cu1–O2	197.9(2)	Cu1–N1	195.5(3)
Cu1–O3	228.2(2)	Cu1–N2	203.8(3)
Cu1–N1	192.0(2)	Cu1–N3	207.3(2)
Cu1–N2	201.5(2)	Cu1–N4	214.8(2)
O1–Cu1–O2	91.32(06)	O1–Cu1–N1	94.39(10)
O1–Cu1–O3	98.96(06)	O1–Cu1–N2	178.40(10)
O1–Cu1–N1	95.58(07)	O1–Cu1–N3	97.00(09)
O1–Cu1–N2	177.51(07)	O1–Cu1–N4	101.72(10)
O2–Cu1–O3	96.77(07)	N1–Cu1–N2	84.85(11)
O2–Cu1–N1	160.94(07)	N1–Cu1–N3	128.11(09)
O2–Cu1–N2	86.19(07)	N1–Cu1–N4	122.13(09)
O3–Cu1–N1	99.66(07)	N2–Cu1–N3	82.39(10)
O3–Cu1–N2	81.36(07)	N2–Cu1–N4	79.87(11)
N1–Cu1–N2	86.79(07)	N3–Cu1–N4	104.67(09)

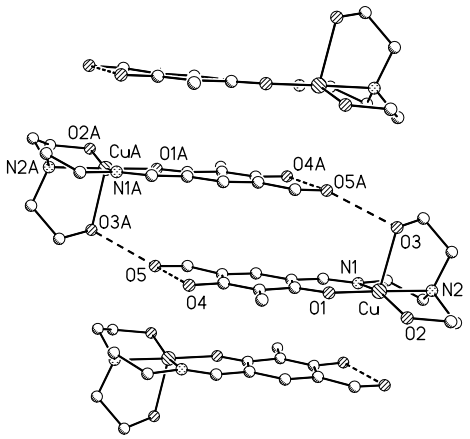


Fig. 4. Representation of the π–π stacking interactions of the complex cation $[Cu(H_3hyforsa\text{-}bhea)]^+$ of **2**. Dashed lines indicate hydrogen bonding interactions. Symmetry equivalent atoms are labeled with suffix A. Hydrogen atoms are omitted for clarity.

340 pm which is in the expected range [36,38]. Additional π–π stacking interactions with neighboring dimeric units lead to the formation of 1D chains running along the [1 0 0] direction.

These chains are further cross-linked through hydrogen bonding including both water molecules and the perchlorate counterion resulting in a 3D network depicted in Fig. 5. The water molecule O1W is involved in a hydrogen bonding network with the hydroxy group O2, the perchlorate counterion O11 and the second water molecule O2W. Furthermore, O2W is linked with the phenolate oxygen atom O1, the hydroxy group O3 and the perchlorate counterion O13. All hydrogen bonding interactions (see Fig. 5) are in the usually observed range [17,35,36]. It should be noted that the perchlorate counterion of **2** does not show any disorder, presumably due to the bridging connectivity within the hydrogen bonding network.

3.2.3. $[Cu(Hhyforsa\text{-}unspenp)]ClO_4$ (**3**)

The complex cation $[Cu(Hhyforsa\text{-}unspenp)]^+$ of complex **3** is depicted in Fig. 6. Selected bond lengths and angles are listed in Table 3. The copper center is penta-coordinated through the phenolate oxygen atom O1, the Schiff-base nitrogen atom N1, the amine nitrogen atom N2 and the two pyridine nitrogen atoms N3 and N4 of the ligand side chains. According to a distortion index of $\tau = 0.84$ the coordination environment at the copper center is best described as slightly distorted trigonal bipyramid. The trigonal plane is given by the nitrogen donor atoms N1, N3, and N4 with

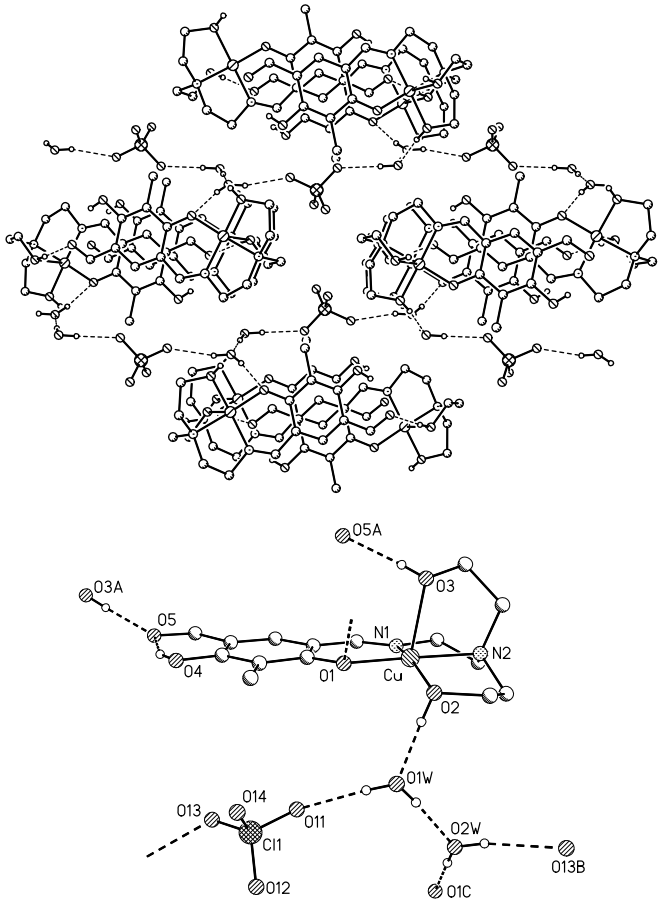


Fig. 5. Representation of the supramolecular structure of complex [Cu(H_3hyforsa-bhea)]$ClO_4 \cdot 2H_2O$ (**2**). Dashed lines indicate hydrogen bonding interactions. Symmetry equivalent atoms are labeled with the suffixes A to C. Pertinent distances (pm): O2···O1W 263, O3···O5 275, O4···O5 265, O1W···O11 288, O1W···O2W 270, O2W···O1C 295, O2W···O13B 301 pm.

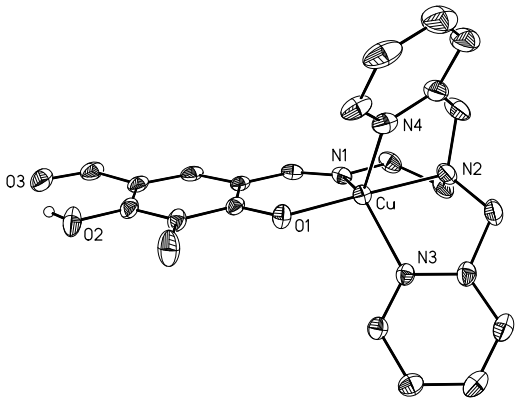


Fig. 6. Molecular structure of the complex cation of [Cu(Hhyforsa-unspenp)]ClO_4 (**3**). The carbon-bound hydrogen atoms are omitted for clarity. Thermal ellipsoids are drawn at the 30% probability level.

bond lengths ranging from 196 to 215 pm. With a *trans* angle of 178° the apical positions are occupied by the phenolate oxygen atom O1 and the amine nitrogen atom N3 at distances of 189 and 204 pm, respectively. As in the case of complex **2**, the oxygen atom O3 of the free formyl group is involved in an intermolecular hydrogen bonding with the phenolic group O2.

In the crystal structure the complex cations assemble coplanar and built 1D chains via π–π stacking interactions along the [001] direction as depicted in Fig. 7. Two alternating π–π interactions are present leading to face-to-face pairs at a distance of about 360 pm which are in turn stacked with an offset along the pseudo C_2 axis at a π–π interaction distance of about 330 pm.

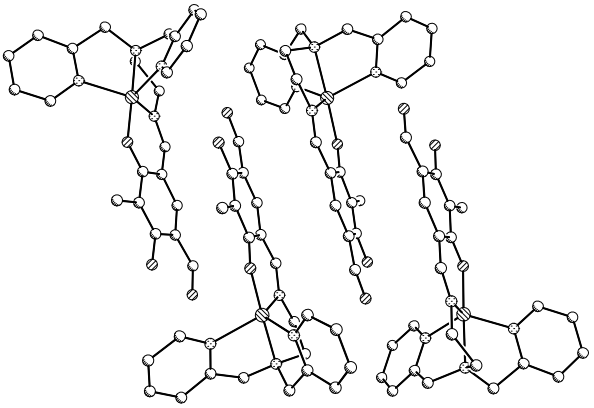


Fig. 7. Representation of the π–π stacking interactions of the complex cation $[Cu(Hhyforsa\text{-}unspenp)]^+$ of **3**. Hydrogen atoms are omitted for clarity.

4. Magnetochemistry

Variable temperature (2–300 K) magnetic susceptibility data collected on a polycrystalline sample of the dinuclear complex **1** are depicted in Fig. 8 as $\chi_M = f(T)$ and $\chi_M T = f(T)$. The experimental $\chi_M T$ value of 0.85 $cm^3\ K\ mol^{-1}$ at 300 K is in good agreement with the theoretical spin-only value expected for two independent copper(II) ions. Upon lowering the temperature $\chi_M T$ slightly decreases down to 0.74 $cm^3\ K\ mol^{-1}$ at about 50 K. Further lowering the temperature leads to a rapid decrease of $\chi_M T$ approaching values close to zero. This behavior is indicative for an antiferromagnetic exchange interaction between the two copper(II) centers with an $S = 0$ ground state mediated by the *meta*-dihydroxyphenylene bridge.

In order to interpret the magnetic properties the experimental $\chi_M T$ data has been analyzed using the Bleaney–Bowers equation for isolated dinuclear copper(II) complexes ($\hat{H} = -J\hat{S}_1\hat{S}_2$ with $S_1 = S_2 = 1/2$) [39]. The contribution of paramagnetic impurities (ρ) with $S = 1/2$ as well as the temperature independent paramagnetism (χ_{tip}) were also taken into account according to

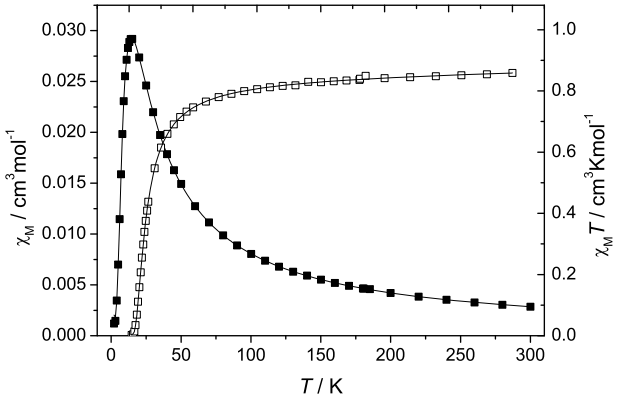


Fig. 8. Plot of the thermal dependence of χ_M (black filled squares, ■) and $\chi_M T$ (empty squares, □) for complex **1** with an applied magnetic field of 2000 Oe. The corresponding fit functions according to Eq. (2) are drawn as solid lines (for parameters see text).

$$\chi_M T = \frac{2N_A, g_{eff}^2, \beta^2}{k}\left[\frac{(1-\rho)}{[3+\exp(-J/kT)]}+\frac{\rho}{4}\right]+\chi_{tip}T \quad (2)$$

The best fit for complex **1** was obtained for the parameters $J = -16.38(4)\ cm^{-1}$, $g = 2.131(1)$, $\rho = 0.004(1)$, and $\chi_{tip} = 8.0(6)\cdot 10^{-5}\ cm^3\ mol^{-1}$ with a coefficient of determination of $r^2 = 0.99995$.

The obtained coupling constant for **1** is somewhat smaller than those observed for dinuclear copper(II) complexes with a double-Schiff-base ligands containing the same *meta*-dihydroxyphenylene-bridging unit but different carbonic acid hydrazides as amine components with J values ranging from -26 to $-28\ cm^{-1}$ [11]. There is another report describing magnetic properties of similarly bridged dinuclear copper(II) complexes with double-Schiff-base ligands of 4,6-diacetylresorcinol [12]. These complexes also show antiferromagnetic exchange interactions with reported Weiss constants θ ranging from -10 to -34 K depending on the amine component utilized. Regression of the Curie plot of **1** leads to a θ value of about -10 K, which is at the lower end of this reported range.

5. DFT calculations

In order to further elucidate the magnetic properties of the dinuclear copper(II) complex **1**, which contains a *meta*-phenylene linkage, we carried out DFT calculations, including the ligand explicitly, employing two density functionals (BP86 and B3LYP) in combination with the def2-TZVP basis set (see the Section 2 for details). The two density functionals particularly differ with respect to a special term in the functional and thus in the resulting potential, which is the so-called exact exchange admixture that has a systematic influence on the energy splittings between different spin states. While BP86 is a pure density functional with no exact exchange, 20% exact (Hartree–Fock type) exchange are introduced in the B3LYP density functional. The pure density functional BP86 was employed for structure optimization, as it can be combined with the computer-time-saving RI density-fitting technique. The structure optimization was carried out in the triplet state using the X-ray crystallographic molecular structure as a starting point.

The optimized structure is in reasonable agreement with the X-ray crystallographic structure, except for the relative orientation of the hydroxy ethyl groups of the two ligand compartments leading to a variation of the coordination geometry at the two copper centers. Therefore, the most difference with respect to the crystal structure is observed for the corresponding O–Cu–N angles and find its expression in converging τ values for the two copper centers Cu1 and Cu2 of 0.43 and 0.60, respectively (as compared to 0.21 and 0.77 for the crystal structure). This is in line with the interpretation, that the hydrogen bonding interactions in the crystal structure (cf. Fig. 2) influence the actually observed coordination geometry of the copper centers in the solid state structure.

The BS approach was utilized to calculate the singlet–triplet gap of the exchange-coupled dinuclear copper(II) complex (see Section 2). The calculations have been performed on the crystallographic structure of **1**. As expected, the exchange coupling constant $J = -90\ cm^{-1}$ calculated with the pure density functional BP86 is too large as compared to the experimental value. This is consistent with the generally observed overestimation of the stabilization of the singlet state relative to the triplet state by DFT methods. The inclusion of an appropriate amount of exact exchange is known to considerably improve the accuracy of the calculated values, with the hybrid functional B3LYP being a good choice [40]. Indeed, the calculation with the hybrid functional B3LYP yields an exchange coupling constants of $J = -19\ cm^{-1}$, which is in excellent agreement with the experimental value determined for **1**.

The magnetic orbitals as derived from the calculation of the BS state are depicted in Fig. 9. They have basically $d_{x^2-y^2}$ character with relevant contributions from the three donor atoms at each copper center which are approximately in the plane of the bridging *meta*-phenylene unit, namely the phenolate oxygen (O1/O4), the imine nitrogen (N1/N3), and the amine nitrogen atoms (N2/N4) of the H_6ipa-bhea ligand. This is somewhat surprising, as the two copper centers reveal large differences with respect to their coordination geometry (Cu1: distorted square pyramid $\tau = 0.21$; Cu2: distorted trigonal bipyramid $\tau = 0.77$). Together with the observed low contributions of the oxygen atoms of the hydroxy ethyl groups to the magnetic orbitals, this is indicative for a rather small influence of the latter on the electronic structure of the exchange-coupled dinuclear system. This is corroborated by the fact that the exchange coupling constant calculated for the optimized structure (Cu1: $\tau = 0.43$; Cu2: $\tau = 0.60$) is virtually unchanged with values of

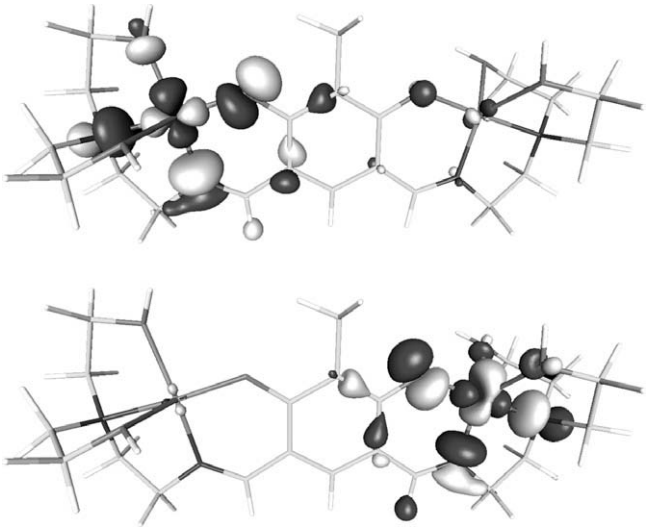


Fig. 9. Isodensity surfaces (0.05 au) of the magnetic orbitals for the Cu1 (top) and Cu2 (bottom) centers of complex **1** derived from BS calculation for the crystallographic geometry.

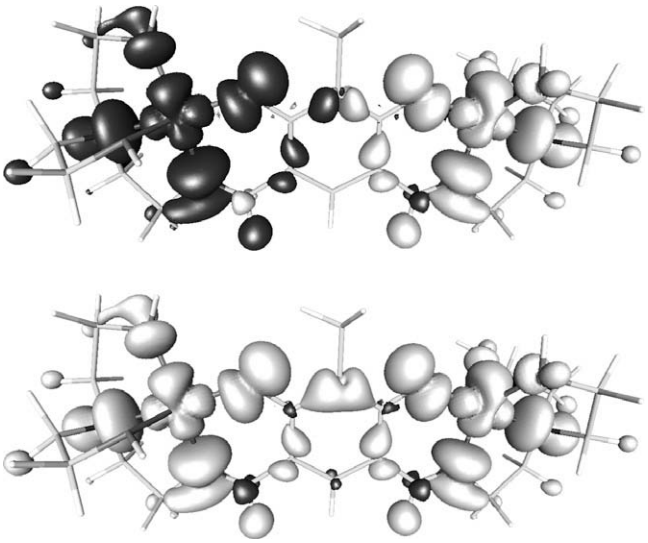


Fig. 10. Representation of the spin-density isosurfaces (0.001 au) of the BS (top) and triplet (bottom) state of complex **1** derived from DFT calculations for the crystallographic geometry (α: light gray, β: black).

−96 and −21 cm^{-1} for the BP86 and B3LYP functionals, respectively.

Although the simple picture of a spin-polarization mechanism would predict a ferromagnetic ground state for a *meta*-phenylene bridged system, it has been shown by Bencini et al. that both spin-polarization and superexchange effects contribute to the overall coupling behavior in such systems [10]. In fact, for systems with the magnetic orbitals almost orthogonal to the bridging π system usually leads to an indirect spin-polarization pathway which is less effective than relevant superexchange contribution. This is consistent with the spin-density maps of the BS and triplet state depicted in Fig. 10. The spin-density population calculated for the triplet state is alternating along the bridging π system as a fingerprint of the indirect spin-polarization. Whereas for the BS state a considerable spin-delocalization into the bridging ligand is observed, which is indicative of an efficient superexchange through the *meta*-phenylene unit.

6. Conclusions

The new double-Schiff-base ligand H_6ipa-bhea was synthesized providing two *meta*-phenylene bridged pentadentate [N_2O_3] binding pockets. The reaction with copper(II) perchlorate depending on the reaction conditions leads to either the dinuclear complex [Cu_2(H_4ipa-bhea)](ClO_4)$_2$ (**1**) or the mononuclear copper(II) complex [Cu(H_3hyforsa-bhea)]$ClO_4 \cdot 2H_2O$ (**2**). In the case of **2** partial hydrolysis of the ligand is observed, leading to a complex with available salicylaldehyde like moiety providing a free formyl group for further condensation reactions. The reaction of **2** with *N,N-bis*-(pyridin-2-ylmethyl)ethylenediamine leads to the new mononuclear complex [Cu(Hhyforsa-unspenp)]ClO_4 (**3**) with a pentadentate [N_4O] binding pocket and again a salicylaldehyde moiety with free formyl group. The newly introduced nitrogen-rich binding pocket has a higher affinity towards the coordination of copper(II) ions. Under appropriate conditions together with suitable amine components both mononuclear complexes **2** and **3** seem to be likely candidates for metal containing building blocks in the directed synthesis of unsymmetric homo- and heterodinuclear transition metal complexes with gradually adjustable properties of the binding pockets. Further studies utilizing this concept for the synthesis of unsymmetric Schiff-base ligands and their homo- and heterodinuclear transition metal complexes are under investigation. Temperature-dependent magnetic measurements for complex **1** reveal antiferromagnetic exchange interactions between the two copper(II) ions through the central resorcinol bridge with an isotropic coupling constant of −16 cm^{-1}. The electronic structure of the *meta*-phenylene bridged dinuclear complex **1** has been investigated by broken symmetry DFT calculations. Due to the orthogonal orientation of the magnetic orbitals with respect to the bridging π system, which in this case by the way is independent of the actual coordination geometry of the copper centers, only an indirect spin-polarization pathway is present. Consequently, the more effective superexchange pathway through the *meta*-dihydroxyphenylene-bridging unit dominates and lead to the overall antiferromagnetic exchange coupling between the copper centers.

7. Supplementary data

CCDC 707275, 707276, and 707277 contain the supplementary crystallographic data for **1** · MeOH, **2**, and **3**. These data can be obtained free of charge via http://www.ccdc.cam.ac.uk/conts/retrieving.html, or from the Cambridge Crystallographic Data Centre, 12 Union Road, Cambridge CB2 1EZ, UK; fax: (+44) 1223-336-033; or e-mail: deposit@ccdc.cam.ac.uk.

Acknowledgements

We thank the Deutsche Forschungsgemeinschaft (SPP 1137 Molecular Magnetism) for financial support and the John von Neumann Institute for Computing (Magnetic Interactions in Transition Metal Clusters) for the generous grant of computational time on the JUMP supercomputer. D.P. gratefully acknowledges the support by a Graduiertenstipendium of the Freistaat Thüringen.

References

[1] R.H. Holm, P. Kennepohl, E.I. Solomon, Chem. Rev. 96 (1996) 2239.
[2] E.I. Solomon, U.M. Sundaram, T.E. Machonkin, Chem. Rev. 96 (1996) 2563.
[3] (a) O. Kahn, Acc. Chem. Res. 33 (2000) 647;
(b) W. Plass, Chem. Unserer Zeit 32 (1998) 323;
(c) D. Gatteschi, R. Sessoli, J. Villain, Molecular Nanomagnets, Oxford University Press, Oxford, 2006.
[4] (a) A. Cornia, A.F. Costantino, L. Zobbi, A. Caneschi, D. Gatteschi, M. Mannini, R. Sessoli, Struct. Bonding 122 (2006) 133;
(b) S.J. Blundell, Contemp. Phys. 48 (2007) 275.
[5] (a) A. Rajca, Chem. Eur. J. 8 (2002) 4834;
(b) H. Iwamura, N. Koga, Acc. Chem. Res. 26 (1993) 346.
[6] (a) M. Ruben, J. Rojo, F.J. Romero-Salguero, L.H. Uppadine, J.-M. Lehn, Angew. Chem., Int. Ed. 43 (2004) 3644;
(b) T. Ishida, S.-i. Mitsubori, T. Nogami, N. Takeda, M. Ishikawa, H. Iwamura, Inorg. Chem. 40 (2001) 7059;
(c) K. Nakayama, T. Ishida, R. Takayama, D. Hashizume, M. Yasui, F. Iwasaki, T. Nogami, Chem. Lett. (1998) 497;
(d) F. Lloret, G. De Munno, M. Julve, J. Cano, R. Ruiz, A. Caneschi, Angew. Chem., Int. Ed. 37 (1998) 135.
[7] (a) J.A. McCleverty, M.D. Ward, Acc. Chem. Res. 31 (1998) 842;
(b) H. Oshio, H. Ichida, J. Phys. Chem. 99 (1995) 3294;
(c) S.R. Bayly, E.R. Humphrey, H. de Chair, C.G. Paredes, Z.R. Bell, J.C. Jeffery, J.A. McCleverty, M.D. Ward, F. Totti, D. Gatteschi, S. Courric, B.R. Steele, C.G. Screttas, J. Chem. Soc., Dalton Trans. (2001) 1401;
(d) V.A. Ung, S.M. Couchman, J.C. Jeffery, J.A. McCleverty, M.D. Ward, F. Totti, D. Gatteschi, Inorg. Chem. 38 (1999) 365;
(e) H. Theil, C.-G. Freiherr von Richthofen, A. Stammler, H. Bögge, T. Glaser, Inorg. Chim. Acta 361 (2008) 916.
[8] E. Pardo, R. Ruiz-García, J. Cano, X. Ottenwaelder, R. Lescouëzec, Y. Journaux, F. Lloret, M. Julve, Dalton Trans. (2008) 2780.
[9] (a) T. Ishida, T. Kawakami, S.-i. Mitsubori, T. Nogami, K. Yamaguchi, H. Iwamura, J. Chem. Soc., Dalton Trans. (2002) 3177;
(b) Y. Takano, T. Onishi, Y. Kitagawa, T. Soda, Y. Yoshioka, K. Yamaguchi, Int. J. Quantum Chem. 80 (2000) 681;
(c) J. Cano, E. Ruiz, S. Alvarez, M. Verdaguer, Comments Inorg. Chem. 20 (1998) 27.
[10] A. Bencini, D. Gatteschi, F. Totti, D.N. Sanz, J.A. McCleverty, M.D. Ward, J. Phys. Chem. A 102 (1998) 10545.
[11] D. Plaul, A. Buchholz, H. Görls, W. Plass, Polyhedron 26 (2007) 4581.
[12] N. Manada, H. Ōkawa, S. Kida, Bull. Chem. Soc. Japan 48 (1975) 64.
[13] (a) A. Taha, Spectrochim. Acta, Part A 59 (2003) 1611;
(b) H.S. Seleem, B.A. El-Shetary, S.M.E. Khalil, M. Mostafa, M. Shebl, J. Coord. Chem. (2005) 479;
(c) A.A.A. Emara, A.A.A. Abou-Hussen, Spectrochim. Acta, Part A 64 (2006) 1010;
(d) A.A.A. Abu-Hussen, J. Coord. Chem. 59 (2006) 157;
(e) A.A.A. Emara, A.A. Saleh, O.M.I. Adly, Spectrochim. Acta, Part A 68 (2007) 592.
[14] (a) W.-H. Gu, X.-Y. Chen, L.-H. Yin, A. Yu, X.-Q. Fu, P. Cheng, Inorg. Chim. Acta 357 (2004) 4085;
(b) M. Koikawa, H. Yamashita, T. Tokii, Inorg. Chim. Acta 357 (2004) 2635;
(c) A. Roth, J. Becher, C. Herrmann, H. Görls, G. Vaughan, M. Reiher, D. Klemm, W. Plass, Inorg. Chem. 45 (2006) 10066;
(d) S. Nica, M. Rudolph, H. Görls, W. Plass, Inorg. Chim. Acta 360 (2007) 1743;
(e) A. Burkhardt, E.T. Spielberg, H. Görls, W. Plass, Inorg. Chem. 47 (2008) 2485.
[15] W. Plass, Z. Anorg. Allg. Chem. 620 (1994) 1635.
[16] (a) W. Plass, Angew. Chem., Int. Ed. Engl. 35 (1996) 627;
(b) W. Plass, Inorg. Chim. Acta 244 (1996) 221;
(c) W. Plass, Z. Anorg. Allg. Chem. 623 (1997) 997;
(d) W. Plass, G. Fries, Z. Anorg. Allg. Chem. 623 (1997) 1205;
(e) W. Plass, Z. Anorg. Allg. Chem. 623 (1997) 461;
(f) W. Plass, Z. Anorg. Allg. Chem. 623 (1997) 1290;
(g) W. Plass, Eur. J. Inorg. Chem. (1998) 799.
[17] W. Plass, A. Pohlmann, J. Rautengarten, Angew. Chem., Int. Ed. 40 (2001) 4207.
[18] M. Schatz, M. Leibold, S.P. Foxon, M. Weitzer, F.W. Heinemann, F. Hampel, O. Walter, S. Schindler, Dalton Trans. 8 (2003) 1480.
[19] W. Plass, Inorg. Chem. 36 (1997) 2200.
[20] (a) SMART COLLECT, Data Collection Software, Nonius B.V., Netherlands.;
(b) SMART, Software for the CCD Detektor System, version 5.05, Bruker AXS, Madison, WI.
[21] G.M. Sheldrick, SHELXS97 and SHELXL97, University of Göttingen, Germany.

[22] H.D. Flack, Acta Crystallogr., Sect. A 39 (1983) 876.
[23] R. Ahlrichs, M. Bär, M. Häser, H. Horn, C. Kölmel, Chem. Phys. Lett. 162 (1989) 165.
[24] (a) A.D. Becke, Phys. Rev. A 38 (1988) 3098;
(b) J.P. Perdew, Phys. Rev. B 33 (1986) 8822.
[25] (a) E.J. Baerends, D.E. Ellis, P. Ros, Chem. Phys. 2 (1973) 41;
(b) B.I. Dunlap, J.W.D. Connolly, J.R. Sabin, J. Chem. Phys. 71 (1979) 3396.
[26] (a) A.D. Becke, J. Chem. Phys. 98 (1993) 5648;
(b) C. Lee, W. Yang, R.G. Parr, Phys. Rev. B 37 (1988) 785.
[27] (a) F. Weigend, Phys. Chem. Chem. Phys. 8 (2006) 1057;
(b) <ftp://ftp.chemie.uni-karlsruhe.de/pub/jbasen>.
[28] L. Noodleman, J. Chem. Phys. 74 (1981) 5737.
[29] E. Ruiz, S. Alvarez, J. Cano, V. Polo, J. Chem. Phys. 123 (2005) 164110.
[30] (a) J.P. Perdew, A. Savin, K. Burke, Phys. Rev. A 51 (1995) 4531;
(b) J.P. Perdew, M. Ernzerhof, K. Burke, A. Savin, Int. J. Quantum Chem. 61 (1997) 197.
[31] (a) D.E. Fenton, G.P. Westwood, A. Bashall, M. McPartlin, I.J. Scowen, J. Chem. Soc., Dalton Trans. 14 (1994) 2213;
(b) R.M. Kirchner, C. Mealli, M. Bailey, N. Howe, L.P. Torre, L.J. Wilson, L.C. Andrews, N.J. Rose, E.C. Lingafelter, Coord. Chem. Rev. 77 (1987) 89;
(c) P. Bhattacharyya, J. Parr, A.M.Z. Slawin, J. Chem. Soc., Dalton Trans. (1998) 3263;
(d) C.V. McDonnell, M.S. Michailidis, R.B. Martin, J. Phys. Chem. 74 (1970) 26;
(e) C. Biswas, S. Chattopadhyay, M.G.B. Drew, A. Ghosh, Polyhedron 26 (2007) 4411.
[32] (a) D.E. Fenton, Chem. Soc. Rev. 28 (1999) 159;
(b) A.L. Gavrilova, B. Bosnich, Chem. Rev. 104 (2004) 349;
(c) P.A. Vigato, S. Tamburini, Coord. Chem. Rev. 248 (2004) 1717;
(d) J.D. Crane, D.E. Fenton, J.M. Latour, A.J. Smith, J. Chem. Soc., Dalton Trans. (1991) 2979;
(e) E. Bernard, W. Moneta, J. Laugier, S. Chardon-Noblat, A. Deronzier, J.-P. Tuchagues, J.-M. Latour, Angew. Chem., Int. Ed. 33 (1994) 887;
(f) M. Suzuki, S. Fujinami, T. Hibino, H. Hori, Y. Maeda, A. Uehara, M. Suzuki, Inorg. Chim. Acta 283 (1998) 124;
(g) S. Uozumi, H. Furutachi, M. Ohba, H. Ōkawa, D.E. Fenton, K. Shindo, S. Murata, D.J. Kitko, Inorg. Chem. 37 (1998) 6281;
(h) P. Karsten, A. Neves, A.J. Bortoluzzi, M. Lanznaster, V. Drago, Inorg. Chem. 41 (2002) 4624;
(i) M. Andruh, O. Kahn, J. Sainton, Y. Dromzee, S. Jeannin, Inorg. Chem. 32 (1993) 1623.
[33] (a) A. Roth, A. Buchholz, M. Rudolph, E. Schütze, E. Kothe, W. Plass, Chem. Eur. J. 14 (2008) 1571;
(b) A. Roth, E.T. Spielberg, W. Plass, Inorg. Chem. 46 (2007) 4362.
[34] A.W. Addison, T.N. Rao, J. Reedijk, J. van Rijn, J.C. Verschoor, J. Chem. Soc., Dalton Trans. (1984) 1349.
[35] A. Roth, A. Buchholz, W. Plass, Z. Anorg. Allg. Chem. 633 (2007) 383.
[36] A. Roth, A. Buchholz, M. Gärtner, A. Malassa, H. Görls, G. Vaughan, W. Plass, Z. Anorg. Allg. Chem. 633 (2007) 2009.
[37] A. Burkhardt, E.T. Spielberg, S. Simon, H. Görls, A. Buchholz, W. Plass, Chem. Eur. J., doi:10.1002/chem.200800670.
[38] (a) C. Janiak, J. Chem. Soc., Dalton Trans. (2000) 3885;
(b) A.E. Ion, E.T. Spielberg, H. Görls, W. Plass, Inorg. Chim. Acta 360 (2007) 3925.
[39] (a) B. Bleaney, K.D. Bowers, Proc. Roy. Soc. (Lon.), Ser. A 214 (1952) 451;
(b) O. Kahn, Molecular Magnetism, VCH, Wiley, Weinheim, 1993.
[40] E. Ruiz, Chem. Phys. Lett. 460 (2008) 336.

silver(I) and gold(I) compounds is the metallophilic interactions [1,5–8,11–14]. Metallophilicity is a closed-shell intermolecular interaction between silver(I) or gold(I) atoms [15]. The metallophilic interactions are comparable to hydrogen bond interactions [14,15]. In the case of gold(I) compounds, such attraction has been called an aurophilic interaction.

We report here that synthesis, crystal structures, and magnetic properties of a new bimetallic spin crossover coordination polymers with the formula $\{Fe^{II}(3\text{-bromo-4-picoline})_2[Au^{I}(CN)_2]_2\}_n$ (**1**). The new compound **1** has more complicated interactions as compared with the traditional Hofmann-like structures and interesting spin crossover behaviors.

2. Experimental

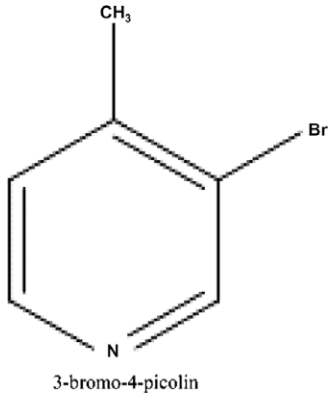
2.1. Materials

All the chemicals were purchased from commercial sources and used without any further purification.

2.2. Synthesis of the compound

2.2.1. $\{Fe^{II}(3\text{-bromo-4-picoline})_2[Au^{I}(CN)_2]_2\}_n$ (**1**)

In 10 mL of water, $FeSO_4 \cdot (NH_4)_2SO_4 \cdot 6H_2O$ (0.25 mmol, 98 mg) and $K[Au(CN)_2]$ (0.25 mmol, 72 mg) were dissolved. The vapor diffusion method using 3-bromo-4-picoline (Scheme 1) as a source of ligand molecules provided colorless polycrystalline crystals suitable for X-ray diffraction of **1** over a period of two days. **1**: Elemental *Anal.* Calc. for $C_{16}H_{12}Au_2FeN_6Br_2$: C, 21.40; H, 1.35; N, 9.36. Found: C, 21.54; H, 1.39; N, 9.27%. IR (nujol method, cm^{-1}):2156 (ν_{CN}).



3-bromo-4-picolin

Scheme 1. Molecular structure of the ligand.

2.3. X-ray crystal structural determinations

The crystal structure of **1** was determined using a BRUKER APEX SMART CCD area-detector diffractometer with monochromated Mo Kα radiation (λ = 0.71073 Å). The diffraction data was treated using SMART and SAINT, and absorption correction was performed using SADABS [16]. The structure was solved by using direct methods with SHELXTL [17]. All non-hydrogen atoms were refined anisotropically, and the hydrogen atoms were generated geometrically. The low quality of crystal data of **1** at 90 K is due to the occurrence of a sharp phase transition that provokes a notable increase of the mosaicity of the crystals in the low temperature phase. Pertinent crystallographic parameters are displayed in Table 1 and selected metric parameters for the complex are presented in Table 2.

2.4. Magnetic measurements

The temperature dependence of the magnetic susceptibility of the complex in the temperature range of 2–300 K with a cooling and heating rate of 1 $Kmin^{-1}$ in a 1 kOe field was measured on a MPMS-XL Quantum Design SQUID magnetometer.

3. Results and discussion

3.1. Preparation and IR spectra

The reaction of an aqueous solution of $FeSO_4 \cdot (NH_4)_2SO_4 \cdot 6H_2O$ containing two equivalents of $K[Au(CN)_2]$ with a vapor diffusion method using pyridine-derivative ligand, 3-bromo-4-picoline, afforded crystals of the 2D CN-bridged coordination compound $\{Fe^{II}(3\text{-bromo-4-picoline})_2[Au^{I}(CN)_2]_2\}_n$ (**1**).

The solid state IR spectra of **1** had C≡N bands at 2156 cm^{-1}, which is at a higher wavenumber than that of free $[Au(CN)_2]^-$ (2135 cm^{-1}), at room temperature. This suggests that the CN groups of $[Au(CN)2]^-$ act as bidentate bridging ligands.

Table 1
Crystal data and details of refinements for **1** at 293 K and 90 K.

Crystal data	**1** (293 K)	**1** (90 K)
Empirical formula	$C_{16}H_{12}Au_2FeN_6Br_2$	$C_{16}H_{12}Au_2FeN_6Br_2$
Formula weight	897.92	897.92
Temperature (K)	293	90
Crystal system	Monoclinic	Monoclinic
Space group	$P2_1/c$	$P2_1/c$
a (Å)	10.1421(6)	10.094(2)
b (Å)	14.5960(9)	14.310(9)
c (Å)	14.8945(9)	14.708(3)
β (°)	91.1080(10)	91.037(3)
V (Å^3)	2204.5(2)	2124.1(7)
Z	4	4
D_{calc} (Mg/m^3)	2.705	2.808
Absorption coefficient (mm^{-1})	17.564	18.229
F(000)	1616	1616
Crystal size (mm^{-3})	0.22 × 0.21 × 0.18	0.22 × 0.21 × 0.18
Reflections collected	13806	13019
Independent reflections [R_{int}]	5027 [0.0554]	4860 [0.1208]
Goodness of fit (GOF) on F^2	1.014	1.054
R_1[a], wR_2[b]	0.0684, 0.1803	0.1046, 0.2292
Largest difference peak and hole (e Å^{-3})	9.707 and −2.653	12.865 and −4.791

[a] $R_1 = (\Sigma||F_o|-|F_c||)/\Sigma|F_o|$.
[b] $R_2 = \{\Sigma_w(|F_o|-|F_c|)^2/\Sigma_w|F_o|^2\}1/2$.

Table 2
Selected bond lengths and angles.

1 (293 K)	**1** (90 K)
Bond lengths (Å)	
Fe(1)–N(1):2.191(13)	Fe(1)–N(1):2.137(18)
Fe(1)–N(2):2.218(16)	Fe(1)–N(2):2.11(3)
Fe(1)–N(3):2.145(16)	Fe(1)–N(3):2.05(3)
Fe(1)–N(4):2.180(17)	Fe(1)–N(4):2.05(4)
Fe(1)–N(5):2.163(19)	Fe(1)–N(5):2.04(3)
Fe(1)–N(6):2.176(16)	Fe(1)–N(6):2.08(3)
Au(1)–C(13):1.988(18)	Au(1)–C(13):2.01(4)
Au(1)–C(14):1.978(19)	Au(1)–C(14):2.04(4)
Au(2)–C(15):2.01(2)	Au(2)–C(15):2.05(3)
Au(2)–C(16):2.018(19)	Au(2)–C(16):2.02(3)
Bond angles (°)	
N(1)–Fe(1)–N(2):178.7(6)	N(1)–Fe(1)–N(2):177.1(12)
N(3)–Fe(1)–N(5):177.0(7)	N(3)–Fe(1)–N(5):177.2(12)
N(4)–Fe(1)–N(6):178.3(7)	N(4)–Fe(1)–N(6):178.1(13)
N(1)–Fe(1)–N(3):92.2(7)	N(1)–Fe(1)–N(3):90.6(11)
N(1)–Fe(1)–N(4):92.3(7)	N(1)–Fe(1)–N(4):93.2(11)
N(1)–Fe(1)–N(5):90.6(7)	N(1)–Fe(1)–N(5):92.0(11)
N(1)–Fe(1)–N(6):89.1(7)	N(1)–Fe(1)–N(6):87.2(11)
N(2)–Fe(1)–N(3):88.1(6)	N(2)–Fe(1)–N(3):89.3(11)
N(2)–Fe(1)–N(4):88.9(6)	N(2)–Fe(1)–N(4):89.7(12)
N(2)–Fe(1)–N(5):89.0(6)	N(2)–Fe(1)–N(5):88.0(10)
N(2)–Fe(1)–N(6):89.6(6)	N(2)–Fe(1)–N(6):89.9(13)
N(3)–Fe(1)–N(4):90.6(7)	N(3)–Fe(1)–N(4):91.6(11)
N(4)–Fe(1)–N(5):90.0(7)	N(4)–Fe(1)–N(5):89.2(11)
N(5)–Fe(1)–N(6):90.9(6)	N(5)–Fe(1)–N(6):88.9(11)
N(3)–Fe(1)–N(6):88.4(6)	N(3)–Fe(1)–N(6):90.3(12)
C(13)–N(6)–Fe(1):168.2(17)	C(13)–N(6)–Fe(1):170(3)
C(14)–N(5)–Fe(1):174.4(18)	C(14)–N(3)–Fe(1):175(3)
C(15)–N(4)–Fe(1):164.7(18)	C(15)–N(4)–Fe(1):168(3)
C(16)–N(3)–Fe(1):177.4(18)	C(16)–N(5)–Fe(1):176(3)
C(13)–Au(1)–C(14):179.1(9)	C(13)–Au(1)–C(14):178.7(13)
C(15)–Au(2)–C(16):177.1(8)	C(15)–Au(2)–C(16):176.5(14)

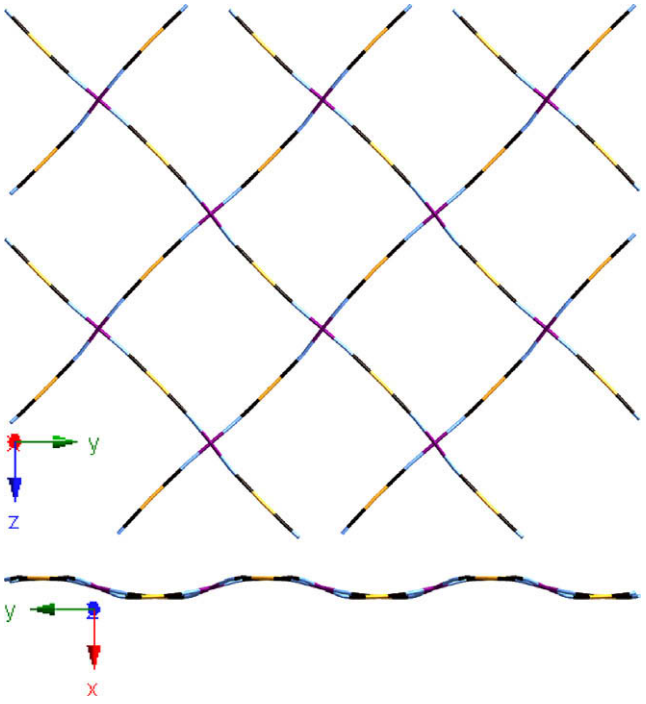


Fig. 1. The cylinder drawing, wave-shaped 2-D structure of **1** (90 K). The 2-D framework of **1** at 293 K is almost identical to that of **1** at 90 K. Consequently, we have used the same representation for these compounds. Atom code: Fe(purple), Au(yellow), N(blue), C(black). In this picture, hydrogen atoms and 3-bromo-4-picoline ligands are omitted for clarity. (For interpretation of the references to color in this figure legend, the reader is referred to the web version of this article.)

3.2. Crystal structure of **1** (293 K and 90 K)

Coordination compound **1** crystallized in the centrosymmetric space group $P2_1/c$ at 293 K and 90 K. Crystal structures of **1** (293 K) and **1** (90 K) are almost identical. Two-dimensional cyano-bridged corrugated framework of **1** is shown in Fig. 1. The two-dimensional frameworks are built-up in a stacked parallel arrangement. There is crystallographically one type of Fe^{II} ion which coordinates four N atoms from bidentate cyano substituents moiety in the equatorial positions. The complex has crystallographically two types of distinct almost linear $[Au(CN)_2]^-$ units (Fig. 2). The angles for **1** (293 K) and [**1** (90 K)] defined by C(13)–Au(1)–C(14) and C(15)–Au(2)–C(16) are 179.1(9) [178.7(13)] and 177.1(8) [176.5(14)], respectively. The pyridyl nitrogen ligation site at the two 3-bromo-4-picoline monodentated ligands coordinates in the axial positions of Fe(1) (Fig. 2). The two 3-bromo-4-picoline ligands in $[Fe^{II}(3\text{-bromo-4-picoline})_2][Au^{I}(CN)_2]$ are *transoid* conformations for Fe(1). The Fe···Fe distances in the Fe(1)–NC–Au(1)–CN–Fe(1) and Fe(1)–NC–Au(2)–CN–Fe(1) one-dimensional wave chain edges for **1** at 293 K [at 90 K] are 10.438 [10.254] and 10.450 [10.266] Å, respectively. Fe–N(1), Fe–N(2), Fe–N(3), Fe–N(4), Fe–N(5) and Fe–N(6) bond distances for **1** (293 K) and [**1** (90 K)] are 2.191(13) [2.137(18)], 2.218(16) [2.11(3)], 2.145(16) [2.05(3)], 2.180(17) [2.05(4)], 2.163(19) [2.04(3)] and 2.176(16) [2.08(3)] Å, respectively. These bond distances for **1** at 293 K and 90 K correspond to the excepted values for Fe^{II} 100% HS state and 50% HS 50% LS state respectively.

The interesting structural feature of **1** is that bilayer networks are formed by strong aurophilic interactions (Fig. 3). The Au···Au intermetallic short distances in the bilayers for **1** (293 K) and [**1** (90 K)] are 3.0455(11) [3.0098(19)] Å, less than the sum of the van der Waals radii of Au (3.32 Å). The Au···Au distance between two adjacent noninteracting layers is 7.205 Å for **1** (293 K) and

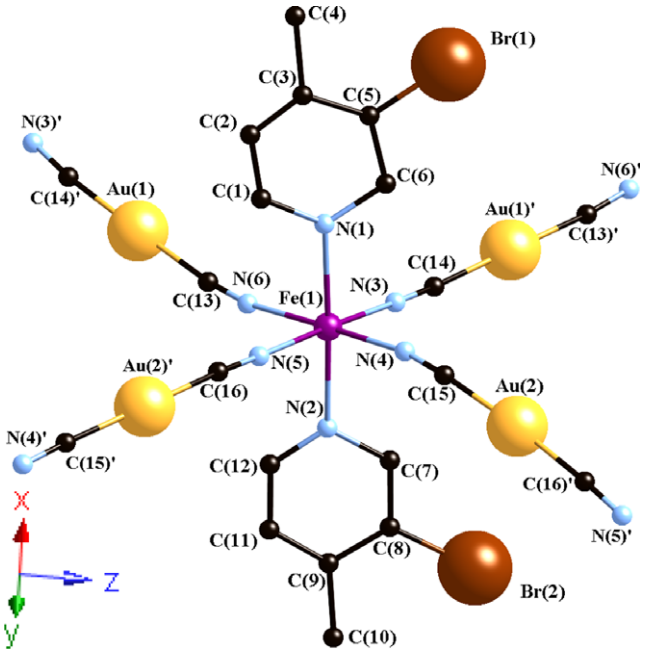


Fig. 2. Coordination structure of the Fe and Au ions in **1** (90 K) containing its asymmetric unit and atom numbering. The structure of **1** at 293 K is almost identical to that of **1** at 90 K. Consequently, we have used the same representation for these compounds. In this picture, hydrogen atoms are omitted for clarity. Atom code: Fe(purple), Au(yellow), N(blue), C(black), Br (brown). (For interpretation of the references to color in this figure legend, the reader is referred to the web version of this article.)

7.185 Å for **1** (90 K), respectively. Furthermore, intermolecular Au···Br and Br···Br distances in the complex are also significantly smaller than the sum of the van der Waals radii (3.61 and 3.90 Å) (Fig. 4). In particular, the Au(1)···Br(1) distance (3.51 Å (293 K) and 3.70 (90 K) Å) shows a strong interaction. The corresponding significant distances are gathered in Table 3.

3.3. Magnetic properties

$\chi_M T$ versus T plots, with χ_M being the molar magnetic susceptibility and T the temperature, for **1** are shown in Fig. 5. At room temperature, the magnetic behavior of the complexes **1** is characteristic of Fe(II) compounds in the high-spin state, $\chi_M T = 3.58$ and

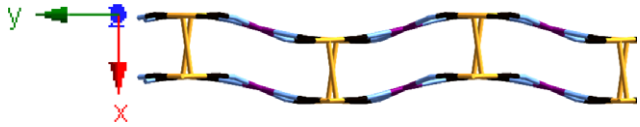


Fig. 3. Bilayer structure of **1** at 90 K with strong aurophilic interactions. In this picture, hydrogen atoms and 3-bromo-4-picoline are omitted for clarity. The structure of **1** at 293 K is almost identical to that of **1** at 90 K. Consequently, we have used the same representation for these compounds.

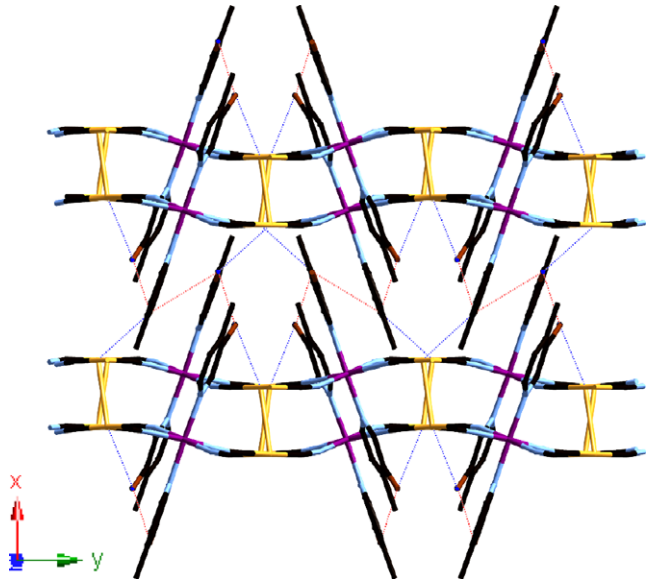


Fig. 4. Crystal packing showing the formation of a 3D supramolecular architecture by intermolecular Au···Br (blue dotted line) and Br···Br (red dotted line) interactions for **1** (90 K). In this picture, hydrogen atoms are omitted for clarity. The structure of **1** at 293 K is almost identical to that of **1** at 90 K. Consequently, we have used the same representation for these compounds. (For interpretation of the references to color in this figure legend, the reader is referred to the web version of this article.)

Table 3
Selected intermolecular Au···Br and Br···Br distances for **1** (293 K and 90 K).

1 (293 K)	**1** (90 K)
Lengths (Å)	
Au(1)–Br(2):3.338	Au(1)–Br(2):3.291
Au(2)–Br(1):3.688	Au(2)–Br(1):3.590
Br(1)–Br(2):3.710	Br(1)–Br(2):3.561
Br(2)–Br(2):3.810	Br(2)–Br(2):3.757

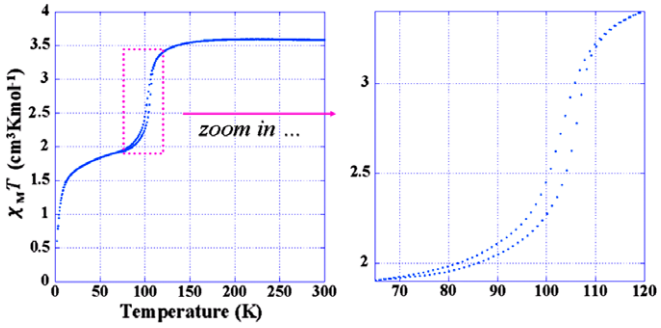


Fig. 5. Magnetic properties of **1**. $\chi_M T$ vs. T from 2 to 300 K.

the value of μ_{eff} is ($\mu_{eff} = 2.828\sqrt{(\chi_M T)}$) per one Fe^{II} ion at 300 K is 5.35 μ_B. The value for **1** is slightly higher than 4.90 ($=g\sqrt{(S(S+1))}$, $g = 2$, $S = 4/2$) that of a pure spin only system, whereas the values are similar to the μ_{eff} value at 300 K of other Hofmann-like spin crossover Fe^{II} compounds [3,4b,18b,18c]. Upon cooling, $\chi_M T$ remains almost constant down to 135 K; below this temperature, $\chi_M T$ undergoes a sharp decrease to around 50% conversion and the warming mode reveals the occurrence of a narrow hysteresis loop. The spin crossover behavior for this complex causes a reversible change of color from colorless to purple. The critical temperature for the cooling (T_c^{down}) and warming (T_c^{up}) modes are 107.3 and 110.9 K, giving an approximately 3.6 K hysteresis loop. The decrease in the value of $\chi_M T$ at lower temperatures is due to a typical behavior of zero-field splitting (ZFS) effects of the metallic Fe^{II} centers in the residual HS ($S = 2$) species.

4. Conclusions

In summary, we have prepared and characterized a new bimetallic spin crossover coordination polymer with the formula $\{Fe^{II}(3\text{-bromo-4-picoline})_2[Au^{I}(CN)_2]_2\}_n$ (**1**). The quasi-linear bidentate $[Au(CN)_2]^-$ unit connects octahedral Fe^{II} ions. As a result, these units assemble to construct huge $\{Fe^{II}_2[Au^{I}(CN)_2]_4\}$ rectangular mesh 2D network arrays which are slightly wave-shaped. The spaces between the 2D $Fe(-NCAuCN-Fe_{1/4})_4$ host frameworks are filled with the 3-bromo-4-picoline ligands. Intriguingly, these 2D layers are organized by pairs, in which strong binuclear aurophilic interactions hold the layers together. The Au···Au distance in the adjacent double layer is 3.0455(11) (293 K) and 3.0098(19) (90 K) Å. Moreover, Au···Br and Br···Br interactions would give rise to a three-dimensional supramolecular network. Similar Hofmann-like compounds $\{Fe(3\text{-Xpy})_2[M(CN)_2]_2\}$ (X = CN, F, Cl, Br, I) (M = Ag, Au) have already been reported [4c,7,18]. However, new complicated networks in **1** are unprecedented for Hofmann-like cyano-bridged coordination polymers.

From the measurements of the temperature dependence of the magnetic susceptibility, the profile of the magnetic behaviors of the complexes **1** includes a rapid 50 % spin transition with a narrow hysteresis loop. The spin crossover behavior of **1** is associated with the new complicated networks caused by Au···Au, Au···Br and Br···Br interactions.

This work shows that this new **1** may be a key material to develop Hofmann-like Fe(II) compounds, which have interesting magnetic properties such as spin-crossover phase transition and molecular magnetism.

Acknowledgements

This work was supported by the "High Tech Research Center" Project 2005–2009 from MEXT (Ministry of Education, Culture,

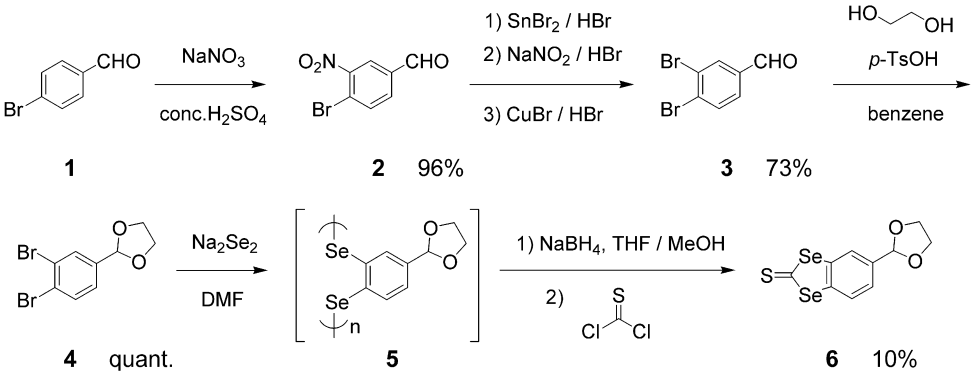
Sports, Science and Technology), and the Research Center for Materials with Integrated Properties, Toho University.

Appendix A. Supplementary data

CCDC 696866 and 696867 contain the supplementary crystallographic data for **1** (293 K) and **1** (90 K). These data can be obtained free of charge via http://www.ccdc.cam.ac.uk/conts/retrieving.html, or from the Cambridge Crystallographic Data Centre, 12 Union Road, Cambridge CB2 1EZ, UK; fax: (+44) 1223-336-033; or e-mail: deposit@ccdc.cam.ac.uk. Supplementary data associated with this article can be found, in the online version, at doi:10.1016/j.poly.2008.11.042.

References

[1] (a) T. Soma, T. Iwamoto, J. Inclusion, Phenom. Mol. Recogn. 26 (1996) 161;
(b) T. Soma, T. Iwamoto, Chem. Lett. (1994) 821.
[2] (a) Z.J. Zhong, H. Seino, Y. Mizobe, M. Hidai, A. Fujishima, S. Ohkoshi, K. Hashimoto, J. Am. Chem. Soc. 122 (2000) 2952;
(b) J.J. Sokol, A.G. Hee, J.R. Long, J. Am. Chem. Soc. 124 (2002) 7656.
[3] T. Kitazawa, Y. Gomi, M. Takahashi, M. Takeda, M. Enomoto, A. Miyazaki, T. Enoki, J. Mater. Chem. 6 (1) (1996) 119.
[4] (a) T. Kitazawa, T. Kawasaki, M. Takahashi, M. Takeda, KURRI-KR (KURRI-KR-106, Hoshasen to Genshikaku o Purobu to shita Bussei Kenkyu no Shintenkai) (2004) 1;
(b) J.A. Rodríguez-Velamazán, M. Castro, E. Palacios, R. Burriel, T. Kitazawa, T. Kawasaki, J. Phys. Chem. B 111 (6) (2007) 1256;
(c) T. Kosone, C. Kachi-Terajima, C. Kanadani, T. Saito, T. Kitazawa, Chem. Lett. 37 (2008) 422;
(d) T. Kitazawa, A. Suzuki, T. Kosone, KURRI-KR-136 (2008) 50;
(e) T. Kosone, C. Kachi-Terajima, C. Kanadani, T. Saito, T. Kitazawa, Chem. Lett. 37 (2008) 754.
[5] V. Niel, M.C. Muñoz, A.B. Gasper, A. Galet, G. Levchenko, J.A. Real, Chem. Eur. J 8 (2002) 2446.
[6] (a) D.B. Leznoff, B.-Y. Xue, C.L. Stevens, A. Storr, R.C. Thompson, B.O. Patrick, Polyhedron 20 (2001) 1247;
(b) D.B. Leznoff, J. Lefebvre, Gold Bull. 38 (2005) 47.
[7] A. Galet, V. Niel, M.C. Muñoz, J.A. Real, J. Am. Chem. Soc. 125 (2003) 14224.
[8] V. Niel, A.L. Thompson, M.C. Muñoz, A. Galet, A.E. Goeta, J.A. Real, Angew. Chem. Int. Ed. 42 (2003) 3760.
[9] (a) P. Gütlich, A. Hauser, H. Spiering, Angew. Chem. Int. Ed. Engl. 33 (1994) 2024;
(b) P. Gütlich, H.A. Goodwin, Top. Curr. Chem. 235 (2004).
[10] (a) O. Kahn, J. Kröber, C. Jay, Adv. Mater. 4 (1992) 718;
(b) S. Hayami, Z.-Z. Gu, M. Shiro, Y. Einaga, A. Fujishima, O. Sato, J. Am. Chem. Soc. 122 (2000) 7126;
(c) S. Hayami, Z.-Z. Gu, H. Yoshiki, A. Fujishima, O. Sato, J. Am. Chem. Soc. 123 (2001) 11644.
[11] T. Soma, H. Yuge, T. Iwamoto, Angew. Chem., Int. Ed. Engl. 33 (1994) 1665.
[12] I. Dasna, S. Golhen, L. Ouahab, N. Daro, J.-P. Sutter, Polyhedron 20 (2001) 1371.
[13] I.P.Y. Shek, W.-Y. Wang, T.-C. Lau, New J. Chem. 24 (2000) 733.
[14] E. Colacio, F. Lloret, R. Kivekäs, J. Ruiz, J. Suárez-Varela, M.R. Sundberg, Chem. Commun. (2002) 592.
[15] P. Pyykkö, Chem. Rev. 97 (1997) 597.
[16] G.M. Sheldrick, SADABS, Program for Empirical Absorption Correction for Area Detector Data, University of Göttingen, Göttingen, Germany, 1996.
[17] G.M. Sheldrick, SHELXL, Program for the Solution of Crystal Structures, University of Göttingen, Göttingen, Germany, 1997.
[18] (a) A. Galet, M.C. Muñoz, V. Martínez, J.A. Real, Chem. Commun. (2004) 2268;
(b) M.C. Muñoz, A.B. Gaspar, A. Galet, J.A. Real, Inorg. Chem. 46 (2007) 8182;
(c) A. Agustí, M. Muñoz, C.A. Galet, J.A. Real, Inorg. Chem. 47 (2008) 2552.



Scheme 1. Synthesis of benzo-1,3-diselenole-2-thione derivative **6**.

reaction afforded 3,4-dibromobenzaldehyde **3** [6]. The aldehyde **3** was transformed to 2-(3,4-dibromophenyl)-1,3-dioxolane **4** to protect the formyl group for the following reactions. Poly(diselenide) **5** was prepared by the reaction between dibromo compound **4** and sodium diselenide in DMF (*N*,*N*-dimethylformamide) [7]. Reduction of polymer **5** with sodium tetrahydroborate, followed by the treatment of thiophosgene, afforded the key thione **6**.

A cross-coupling reaction between thione **6** and 4,5-(ethylenedithio)-1,3-diselenole-2-one **7** was conducted in triethyl phosphite to obtain TSF-acetal derivative **8**. This acetal precursor **8** was hydrolyzed to give the formyl derivative **9**, which was reacted with 2,3-dimethyl-2,3-bis(hydroxyamino)butane in the presence of its sulfuric acid salt as a catalyst to afford cyclic bis(hydroxylamine) **10** as a radical precursor. The final product, **TSBN**, was obtained by the oxidation of precursor **10** with lead dioxide in a reasonable yield.

The ESR spectrum of **TSBN** in benzene solution showed quintet lines ($g = 2.0063$, $a_N = 0.73$ mT) which were assigned to the nitronyl nitroxide group. The magnetic susceptibility of **TSBN** was measured by a SQUID magnetometer. The temperature dependence of the χT value of sample was reproduced by the Curie–Weiss law; Curie constant and Weiss temperature were evaluated to be 0.372 emu K mol^{-1} and -0.21 K, respectively. These data supports that the radical unit is intact during the crystallization process.

2.2. Crystal structure of *TSBN*

Single crystals (black elongated plates) of **TSBN** · THF (tetrahydrofuran) were obtained by recrystallizaion from THF/hexane, and its crystal structure was determined by X-ray crystallography. The crystal data indicate that the crystal of **TSBN** · THF is isostructural to that of **ESBN** · THF. The molecular structure of neutral **TSBN** is shown in Fig. 1a. The nitronyl nitroxide plane is twisted from that of the benzoTSF with a small dihedral angle of 22.3(2)°, which suggests the presence of an effective intramolecular π–π interaction between the donor and radical sites. The crystal packing of **TSBN** is shown in Fig. 1b. The crystal of **TSBN** · THF belongs to an orthorhombic space group *Pbca*. The unit cell contains eight symmetrically related molecules, including THF. When the molecular arrangement in the crystal is viewed along the *b*-axis, short intermolecular chalcogen contacts between molecules A, B and C (related with A by the C_2 axis) are found to be 3.744(1), 3.653(1), 3.653(1) and 3.426(2) Å for Se3(A)···Se1(C), Se4(A)···Se2(B), S2(A)···Se4(B) and S2(A)···Se2(B), respectively (Fig. 2). Hence, the molecules form a sheet-like network within the *ac* plane through these intermolecular contacts, the network being separated from the adjacent ones by THF molecules and sterically-bulky radical moieties, as shown in Fig. 1b.

2.3. Electronic structure of *TSBN*

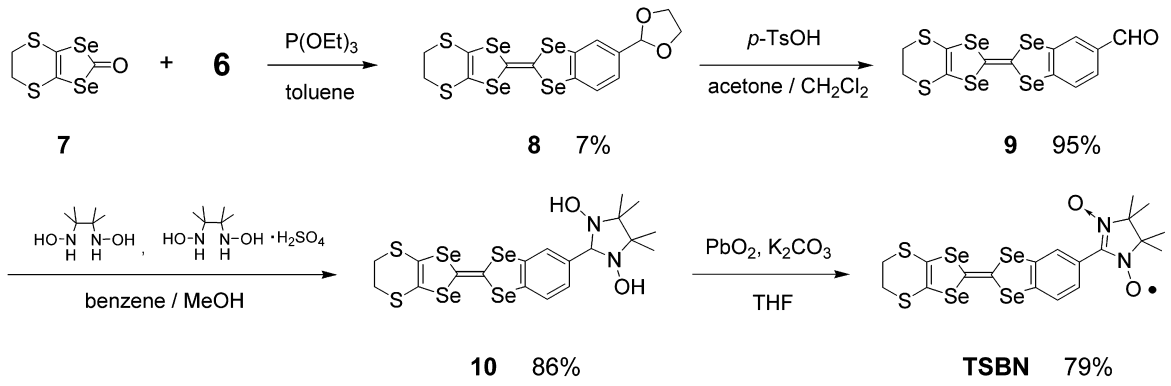
A cyclic voltammogram (CV) of **TSBN** was measured in a benzonitrile solution in the presence of 0.1 M tetrabutylammonium perchlorate as an electrolyte. Fig. 3a showed three reversible redox waves at 0.80, 0.93 and 1.13 V versus Ag/AgCl. In comparison with the redox potentials of acetal precursor **8** (0.79 and 1.05 V versus Ag/AgCl) and of phenyl nitronyl nitroxide (0.85 V versus Ag/AgCl), the first and third oxidation potentials of **TSBN** are assigned to the oxidation potentials of the TSF moiety, and the second oxidation potential of **TSBN** is assigned to the nitronyl nitroxide moiety, respectively. The one-electron oxidation of this donor radical is, therefore, considered to give rise to a reasonably stable cation diradical species.

Singly oxidized species of **TSBN** were generated by treatment with iodine in DMSO solution to show a set of ESR signals derived from a triplet species ($|D| = 2.5 \times 10^{-2}$ cm^{-1}, $|E| = 2.4 \times 10^{-3}$ cm^{-1}, $g_x = 2.0094$, $g_y = 2.0068$, $g_z = 2.0076$) at 4.2 K. The temperature dependence of signal intensity obeys the Curie law in the temperature range of 4.2–70 K, indicating that the triplet state is the ground state of **TSBN**$^{+\cdot}$.

The electronic structure of **TSBN** was calculated by DFT method (B3LYP/6-31G*), as shown in Fig. 3b. The orbital energy of SOMO(α) is lower than that of HOMO(α,β), supporting the CV data. In addition, the energy level of HOMO(α) is slightly lower than that of HOMO(β) because the β spin in HOMO is destabilized by the α spin in SOMO. The coefficients of SOMO are localized on the nitronyl nitroxide moiety, while those of HOMO are spread over the entire molecule. Due to this space-sharing nature of the relevant molecular orbitals, Hund rule in the MO level is expected to hold in the cation diradical (**TSBN**$^{+\cdot}$) which is formed by the removal of an electron from HOMO. Accordingly, **TSBN** is characterized by the spin-polarized electronic structure.

2.4. Magnetoresistance measurement of *TSBN*

Before preparing an ion-radical salt of **TSBN**, we examined a conducting property of the newly prepared **TSBN**. The conductivity of single crystal of neutral **TSBN,** measured by a four-probe method, was considerably low ($\sigma_{RT} < 10^{-9}$ S/cm). However, the neutral microcrystals of **TSBN,** which were mounted on interdigitated electrodes with a gap of 2 μm, exhibited a distinct nonlinear *I*–*V* characteristics ($I \propto V^m$,m = 11 ± 1) at 2 K, as shown in Fig. 4a. While the origin of the observed *I*–*V* characteristics is not clear at the present stage, the carrier injection into the sample from an electrode through a tunneling barrier at the boundary is conceivable as the reason for this nonlinear behavior. Such conduction behavior is known as a trapped-charge-limited conduction (TCLC), and it is frequently observed in *I*–*V* characteristics of organic EL devices [8].



Scheme 2. Synthesis of **TSBN**.

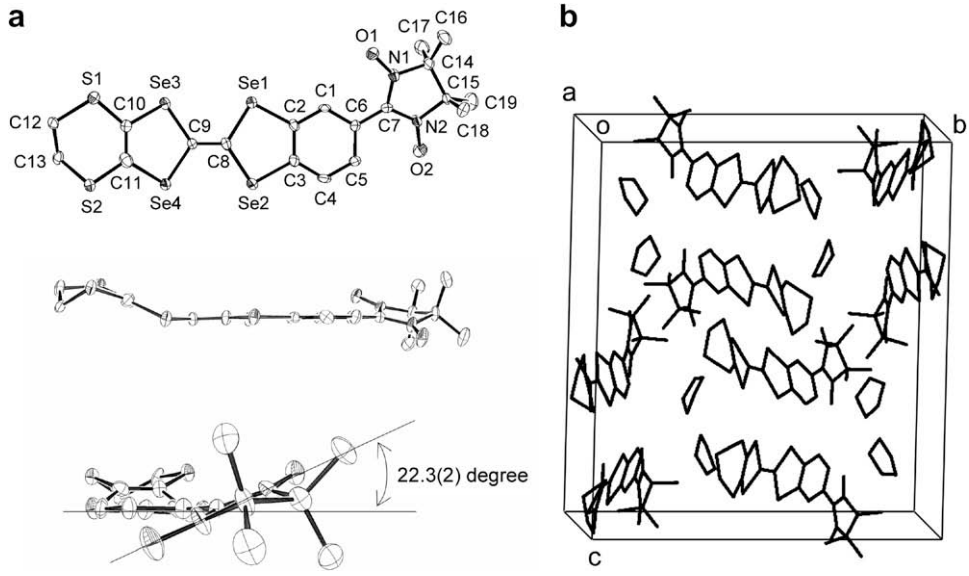


Fig. 1. (a) Ortep drawing of **TSBN** with thermal ellipsoids at the 50% probability level. Hydrogen atoms are omitted for clarity. (b) Molecular arrangement in the crystal of **TSBN**. Crystal structure of **TSBN** · THF: black elongated plate from THF/hexane, sized ca. 0.30 × 0.04 × 0.01 mm^3, $C_{23}H_{27}N_2O_3S_2Se_4$, MW = 759.43, orthorhombic, space group *Pbca* (No. 61), λ(Mo Kα) = 0.71070 Å, T = 113(2) K, a = 10.690(3), b = 21.044(5), c = 23.846(6) Å, V = 5365(2) Å^3, Z = 8, $D_{calc.}$ = 1.881 g cm^{-3}. Isotropic and anisotropic least-squares refinement (308 parameters) on 6102 merged reflections (R_{int} = 0.0648) converged at R_{all} = 0.0931 for all data; $R_1 > 2\sigma(I)$ = 0.0599 for 4370 observed data ($I > 2\sigma(I)$), GoF = 1.113.

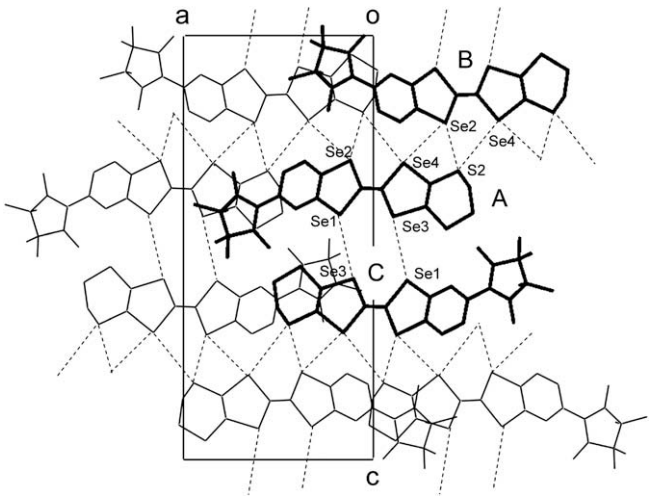


Fig. 2. The sheet-like network of **TSBN**. Molecular arrangement on the *ac* plane. THF molecules are omitted for clarity.

The magnetoresistance measurement of neutral microcrystals of **TSBN** using interdigitated electrodes was curried out with a constant bias voltage of 8 V, by applying a magnetic field between −5 and 5 T. As shown in Fig. 4b, the resistance of the sample decreased under 5 T at 2 K, exhibiting ca. −5% of the negative magnetoresistance, whereas the same sample showed ca. 1% of the positive magnetoresistance at 4 K. In contrast, acetal precursor **8** without carrying a localized spin did not exhibit the negative magnetoresistance effect in spite of showing a similar *I*-*V* characteristics. These results unequivocally suggest that the electron transportation is affected by localized spins of **TSBN** and the scattering by spins is suppressed by the application of an external magnetic field.

3. Conclusion

We have synthesized and characterized a novel TSF-based spin-polarized donor, **TSBN**. The neutral microcrystals of **TSBN** which were mounted on interdigitated electrodes showed distinct non-linear *I*–*V* characteristics at 2 K. Moreover, the sample exhibited the negative magnetoresistance (−5% at 2 K under 5 T). Therefore,

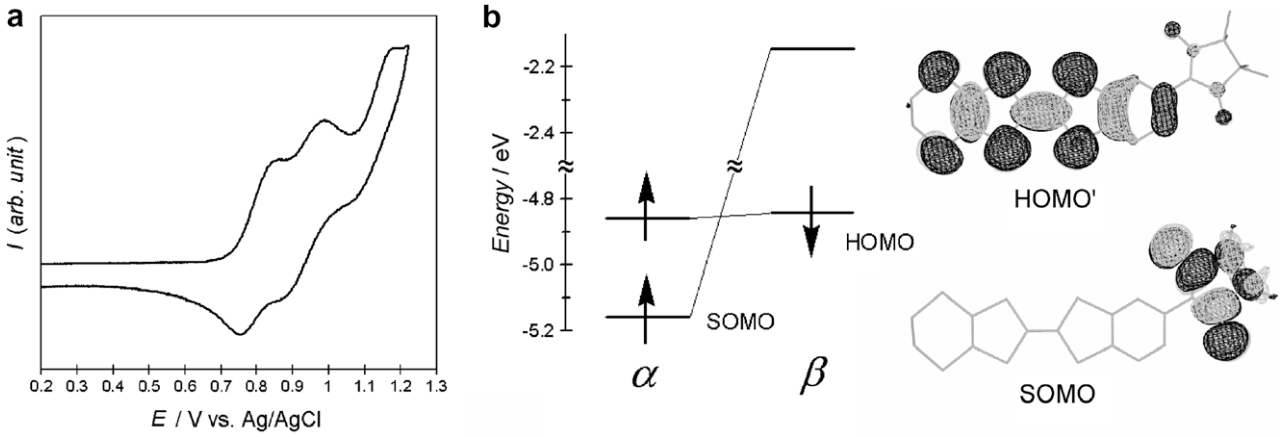


Fig. 3. (a) Cyclic voltammogram of **TSBN**. (b) Spin-polarized energy diagram of **TSBN** calculated by a DFT method (B3LYP/6-31G*). The space-sharing nature of HOMO′ and SOMO is also depicted; HOMO′ is derived from one-electron oxidation of HOMO.

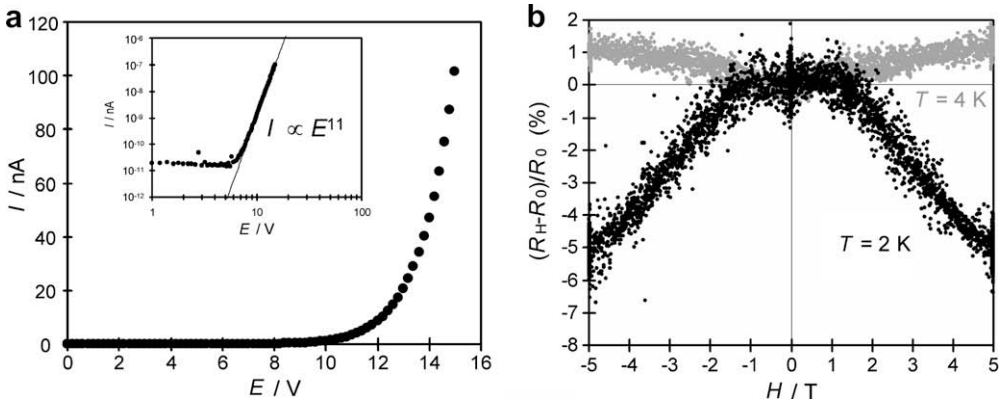


Fig. 4. (a) Nonlinear current–voltage characteristics of **TSBN** at 2 K. (b) Magnetic field dependence of magnetoresistance of **TSBN** at a bias voltage of 8 V.

TSBN would be expected to be an excellent component of an organic ferromagnetic metal, if the conductivity of an ion-radical salt is metallic.

4. Experimental

4.1. General

^{1}H NMR spectra and ^{13}C NMR spectra were recorded on a JEOL GSX-270 (270 MHz) spectrometer. The chemical shifts were reported in δ relative to tetramethylsilane (0.00 ppm). X-band ESR spectra were recorded on a JEOL JES-TE300 spectrometer. The microwave frequency was measured with an Advantest TR5212 counter, and the resonance magnetic field value was measured with the aid of a JEOL ES-FC5 NMR field meter. Elemental analyses were performed by the Center of Organic Elemental Analyses in the Department of Chemistry, Faculty of Science, The University of Tokyo. Cyclic voltammograms were recorded at room temperature with a platinum working electrode, using a BAS CV-50W Voltammetric analyzer. An Ag/AgCl electrode was used as the reference electrode. The temperature dependence of the magnetic susceptibility was measured using a Quantum Design MPMS-5XL SQUID magnetometer in a temperature range of 2–300 K. X-ray crystallographic analysis was carried out at 113 K on a Rigaku Mercury CCD X-ray diffractometer with graphite-monochromatized Mo Kα radiation (λ = 0.71070 Å; 50 kV, 250 mA). *I–V* characteristics and magnetoresistance measurement were carried out using a Quantum Design MPMS-5XL SQUID magnetometer and a Keithley 6487 picoammeter/voltage source. The geometry of the interdigitated Au electrodes with the area of 2×2 mm^2 is as follows: the thickness is 100 nm with 5 nm Ti as the adhesive layer, the gap is 2 μm, the electrode width is 2 μm. The electrodes are fabricated on a quartz substrate sized 5×10 mm^2.

Most of the reagents and solvents were purchased from Tokyo Chemicals Inc., Wako Chemicals Inc., Kanto Chemicals Inc. and Merck Inc. THF was distilled from sodium benzophenone ketyl under nitrogen atmosphere. All the other reagents were used as purchased without further purification. All reactions were monitored by thin-layer chromatography carried out on Merck 60F245 TCL plates. Column chromatography was performed on Merck Silicagel 60 with a mesh of 0.063–0.200 mm.

4.2. Synthesis

4.2.1. 5-(1,3-Dioxolan-2-yl)-1,3-benzodiselenole-2-thione (**6**)

To a suspension of selenium (5.21 g, 65.7 mmol) in 90 ml of DMF, sodium (1.85 g, 80.5 mmol) was added slowly at room temperature under nitrogen atmosphere, and the mixture was heated to 100 °C for 12 h. To the suspension, 2-(3,4-dibromophenyl)-1,3-dioxolane (**4**) (10.18 g, 33.1 mmol) in 10 ml of DMF was added, and the mixture was heated to 125 °C for 30 h. The mixture was cooled to room temperature, diluted with 100 ml of methanol, and poured into 500 ml of saturated aqueous sodium chloride.

The precipitates were filtered, washed with water and methanol, and dried *in vacuo* to afford 5.63 g of poly(diselenide) (**5**) as a orange-brown solid.

To a stirred suspension of poly(diselenide) (**5**) in 130 ml of THF and 100 ml of methanol, sodium tetrahydroborate (6.00 g, 0.159 mol) was added at 0 °C under nitrogen atmosphere. To the resultant homogeneous solution, thiophosgene (3.02 g, 26.3 mmol) was added at 0 °C under nitrogen atmosphere, and the mixture was stirred at 0 °C for 0.5 h. After the solvent was removed under reduced pressure, the residue was extracted with dichloromethane and the extract was washed with water. The separated organic layer was dried over sodium sulfate, filtered, and concentrated. The residue was purified by column chromatography (silica gel, eluent: dichloromethane-hexane (6:1)) to afford 1.21 g (10%) of **6** as a yellow solid.

^{1}H NMR (270 MHz, $CDCl_3$–TMS) δ 7.64 (d, J = 1.7 Hz, 1H), 7.52 (d, J = 8.2 Hz, 1H), 7.42 (dd, J = 1.7, 8.2 Hz, 1H), 5.82 (s, 1H), 4.15–4.01 (m, 4H). ^{13}C NMR (270 MHz, $CDCl_3$–TMS) δ 214.6, 146.4, 145.8, 137.6, 125.5, 125.0, 123.1, 102.5, 65.38. *Anal.* Calc. for $C_{10}H_8O_2SSe_2$: C, 34.30; H, 2.30. Found: C, 34.17; H, 2.38%.

*4.2.2. 2-[2-(5,6-Dihydro[1,3]diseleno[4,5-b][1,4]dithiin-2-ylidene)-1,3-benzodiselenol-5-yl]-1,3-dioxolane (**8**)*

A stirred mixture of thione-acetal **6** (0.95 g, 2.71 mmol), 4,5-(ethylenedithio)-1,3-diselenole-2-one (**7**) [9] (1.64 g, 5.43 mmol), 75 ml of triethyl phosphite and 75 ml of toluene was heated to 120 °C for 2 h under nitrogen atmosphere. After the solvent was removed under reduced pressure, the residue was suspended in 200 ml of chloroform and filtered. The solution was concentrated and subjected to column chromatography (silica gel, eluent: chloroform). The second red band gave 169 mg of red crude oil. The oil was purified by preparative GPC (eluent: chloroform) to afford 123 mg (7%) of **8** as an orange solid.

^{1}H NMR (270 MHz, $CDCl_3$–TMS) δ 7.42 (d, J = 1.7 Hz, 1H), 7.27 (d, J = 8.3 Hz, 1H), 7.23 (dd, J = 1.7, 8.3 Hz, 1H), 5.75 (s, 1H), 4.12–3.98 (m, 4H), 3.31 (s, 4H). *Anal.* Calc. for $C_{15}H_{12}O_2S_2Se_4$: C, 29.82; H, 2.00. Found: C, 29.76; H, 2.05%.

*4.2.3. 2-(5,6-Dihydro[1,3]diseleno[4,5-b][1,4]dithiin-2-ylidene)-1,3-benzodiselenol-5-carbaldehyde (**9**)*

To a solution of acetal **8** (95 mg, 0.16 mmol) in 10 ml of dichloromethane, 10 ml of acetone and small amount of *p*-toluenesulfonic acid monohydrate were added, and the mixture was stirred at room temperature for 2 h. The precipitates were filtered, washed with methanol and dried *in vacuo* to afford 84 mg (95%) of **9** as a golden brown solid.

^{1}H NMR (270 MHz, $CDCl_3$–TMS) δ 9.88 (s, 1H), 7.79 (d, J = 1.7 Hz, 1H), 7.60 (dd, J = 1.7, 8.0 Hz, 1H), 7.48 (d, J = 8.0 Hz, 1H), 3.33 (s, 4H). *Anal.* Calc. for $C_{13}H_8OS_2Se_4$: C, 27.87; H, 1.44. Found: C, 27.84; H, 1.54%.

*4.2.4. 2-[2-(5,6-Dihydro[1,3]diseleno[4,5-b][1,4]dithiin-2-ylidene)-1,3-benzodiselenol-5-yl]-4,4,5,5-tetramethylimidazolidine-1,3-diol (**10**)*

To a suspension of aldehyde **9** (70 mg, 0.13 mmol) in 42 ml of benzene-methanol (1:1), 2,3-dimethyl-2,3-bis(hydroxyamino)butane (93 mg, 0.63 mmol) and its sulfate (9 mg) were added, and the mixture was reflux for 3 days under nitrogen atmosphere. The precipitates were filtered, washed with methanol, and dried *in vacuo* to afford 74 mg (86%) of **10** as a pale orange solid.

^{1}H NMR (270 MHz, DMSO–d_6–TMS) δ 7.78 (s, 2H), 7.62 (s, 1H), 7.53 (d, J = 8.2 Hz, 1H), 7.29 (d, J = 8.2 Hz, 1H), 4.43 (s, 1H), 3.39 (s, 4H), 1.05 (s, 6H), 1.02 (s, 6H).

*4.2.5. 2-[2-(5,6-Dihydro[1,3]diseleno[4,5-b][1,4]dithiin-2-ylidene)-1,3-benzodiselenol-5-yl]-4,4,5,5-tetramethylimidazoline-3-oxide-1-oxyl (**TSBN**)*

To a stirred suspension of hydroxylamine **10** (80 mg, 0.11 mmol) in 25 ml of THF, potassium carbonate (0.7 g, 5.1 mmol) was added, and the mixture was stirred for 0.5 h. To the suspension, lead dioxide (0.7 g, 2.9 mmol) was added and vigorously stirred for 1.5 h. The reaction mixture was filtrated and the filtrate was concentrated. The residue was purified by column chromatography (silica gel, eluent: THF-hexane (1:1)) to afford 63 mg (79%) of **TSBN** as a dark green solid.

ESR (benzene) g = 2.0063, quintet, a_N = 0.728 mT (2 N). *Anal.* Calc. for $C_{19}H_{19}N_2O_2S_2Se_4 \cdot C_4H_8O$: C, 36.37; H, 3.58; N, 3.69. Found: C, 36.39; H, 3.67; N, 3.55%.

Acknowledgement

This work was supported by KAKENHI on Grant-in-Aid for Scientific Research (B) (Proposal No. 20350062) from Japan Society for the Promotion of Science (JSPS).

Appendix A. Supplementary data

CCDC 711160 contains the supplementary crystallographic data for **TSBN**. These data can be obtained free of charge via http://www.ccdc.cam.ac.uk/conts/retrieving.html, or from the Cambridge Crystallographic Data Centre, 12 Union Road, Cambridge CB2 1EZ, UK; fax: (+44) 1223-336-033; or e-mail: deposit@ccdc.cam.ac.uk. Supplementary data associated with this article can be found, in the online version, at doi:10.1016/j.poly.2008.12.005.

References

[1] (a) T. Mallah, C. Hollis, S. Bott, M. Kurmoo, P. Day, J. Chem. Soc., Dalton Trans. (1990) 859;
(b) E. Coronado, J.R. Galan-Mascaros, C.J. Gomez-Garcia, Nature 408 (2000) 447;
(c) T. Enoki, A. Miyazaki, Chem. Rev. 104 (2004) 5449;
(d) H. Fujiwara, K. Wada, T. Hiraoka, T. Hayashi, T. Sugimoto, H. Nakazumi, K. Yokogawa, M. Teramura, S. Yasuzuka, K. Murata, T. Mori, J. Am. Chem. Soc. 127 (2005) 14166;
(e) N. Hanasaki, M. Matsuda, H. Tajima, E. Ohmichi, T. Osada, T. Naito, T. Inabe, J. Phys. Soc. Jpn. 75 (2006) 033703.
[2] (a) R. Kumai, M.M. Matsushita, A. Izuoka, T. Sugawara, J. Am. Chem. Soc. 116 (1994) 4523;
(b) H. Sakurai, A. Izuoka, T. Sugawara, J. Am. Chem. Soc. 122 (2000) 9723.
[3] (a) J. Nakazaki, M.M. Matsushita, A. Izuoka, T. Sugawara, Tetrahedron Lett. 40 (1999) 5027;
(b) J. Nakazaki, I. Chung, M.M. Matsushita, T. Sugawara, R. Watanabe, A. Izuoka, Y. Kawada, J. Mater. Chem. 13 (2003) 1011.
[4] J. Nakazaki, Y. Ishikawa, A. Izuoka, T. Sugawara, Y. Kawada, Chem. Phys. 319 (2000) 385.
[5] (a) M.M. Matsushita, H. Kawakami, Y. Kawada, T. Sugawara, Chem. Lett. 36 (2007) 110;
(b) M.M. Matsushita, H. Kawakami, T. Sugawara, M. Ogata, Phys. Rev. B 77 (2008) 195208.
[6] P. Swoboda, R. Saf, K. Hummel, F. Hofer, R. Czaputa, Macromolecules 28 (1995) 4255.
[7] D.J. Sandman, G.W. Allen, L.A. Acampora, J.C. Stark, S. Jansen, M.T. Jones, G.J. Ashwell, B.M. Foxman, Inorg. Chem. 26 (1987) 1664.
[8] (a) P.E. Burrows, Z. Shen, V. Bulovic, D.M. McCarty, S.R. Forrest, J.A. Cronin, M.E. Thompson, J. Appl. Phys. 79 (1996) 7991;
(b) Ö. Mermer, G. Veeraraghavan, T.L. Francis, M. Wohlgenannt, Solid State Commun. 134 (2005) 631;
(c) J.S. Jiang, J.E. Pearson, S.D. Bader, Phys. Rev. B 77 (2008) 035303.
[9] (a) R. Kato, H. Kobayashi, Synth. Met. 41–43 (1991) 2093;
(b) T. Courcet, I. Malfant, K. Pokhodnia, P. Cassoux, New J. Chem. (1998) 585.